REVIEW / SYNTHÈSE

Électrons en excès dans les milieux polaires homogènes et hétérogènes

Annette Bernas, Christiane Ferradini et Jean-Paul Jay-Gerin

Résumé : Une synthèse des connaissances actuelles concernant la solvatation des électrons en excès ($e^-_{exc} \rightarrow e^-_{solv}$) produits par photoionisation ou par radiolyse dans les milieux polaires a été tentée. Sont successivement envisagées les diverses propriétés de l'espèce alors formée : les mécanismes proposés pour sa solvatation, sa structure, ses caractéristiques physico-chimiques. En dépit de certaines analogies entre les anions halogénure solvatés et e^-_{solv}, celui-ci ne paraît pas pouvoir en constituer le prototype. Le comportement de e^-_{exc} dans des systèmes hétérogènes modèles, tels que solutions micellaires et agrégats moléculaires, est également abordé et corrélé aux résultats relatifs aux solutions homogènes.

Mots clés : électrons en excès, milieux polaires homogènes et hétérogènes, photoionisation, radiolyse, solvatation, transfert de charge au solvant, propriétés de l'électron solvaté, solutions micellaires, agrégats moléculaires, comparaison avec la solvatation des anions.

Abstract: A review of our present knowledge concerning the solvation of excess electrons ($e^-_{exc} \rightarrow e^-_{solv}$) produced by photoionization or radiolysis in polar media has been attempted. Various properties of the solvated electron (proposed solvation mechanisms, structure, physicochemical characteristics) are considered. In spite of some similarities, e^-_{solv} does not seem to be a good prototype for solvated halide anions. The behavior of e^-_{exc} in heterogeneous model systems, such as micellar solutions and molecular clusters, is described and correlated with that observed in homogeneous media.

Key words: excess electrons, homogeneous and heterogeneous polar media, photoionization, radiolysis, solvation, charge transfer to solvent, properties of the solvated electron, micellar solutions, molecular clusters, comparison with the solvation of anions.

Table des matières

Reçu le 2 août 1994.[1]

A. Bernas. Laboratoire de photophysique moléculaire, Bât. 213 – Centre d'Orsay, Université de Paris–Sud, 91405 Orsay Cedex, France.
C. Ferradini. Laboratoire de chimie-physique (Unité de recherche associée n° 400 au Centre national de la recherche scientifique), Université René Descartes, 45, Rue des Saints-Pères, 75270 Paris Cedex 06, France.
J.-P. Jay-Gerin.[2] Groupe du Conseil de recherches médicales du Canada en Sciences des radiations et Département de médecine nucléaire et de radiobiologie, Faculté de médecine, Université de Sherbrooke, Sherbrooke, QC J1H 5N4, Canada.

1. Révision reçue le 1er novembre 1995.
2. Auteur à qui adresser toute correspondance à : Département de médecine nucléaire et de radiobiologie, Faculté de médecine, Université de Sherbrooke, Sherbrooke, QC J1H 5N4, Canada. Télephone : (819) 563-5555, poste : 4682. Fax: (819) 564-5442. Adresse électronique : JAYGERIN@COURRIER.USHERB.CA

I. Introduction

L'électron solvaté (e^-_{solv}), c'est-à-dire l'électron «en excès» (e^-_{exc}) stabilisé par interaction avec les dipôles de molécules solvant, présente les caractéristiques d'une véritable entité chimique; ses propriétés thermodynamiques et cinétiques peuvent être définies et déterminées.

La couleur bleue stable des solutions de métaux alcalins dans l'ammoniac liquide avait été observée dès la fin du siècle dernier (1), mais c'est Kraus (2) qui, le premier, a associé couleur et conductivité ionique de telles solutions à la présence d'*electrons surrounded with an envelope of ammonia.* C'est seulement en 1960 que l'avènement de la radiolyse pulsée a permis à Gilbert et al. (3) et à Keene (4) de mettre en évidence une forte absorption transitoire dans l'eau irradiée, absorption que Hart et Boag (5) ont confirmée et attribuée à l'électron hydraté (e^-_{aq}).

Depuis il a été bien établi que e^-_{solv} constitue un intermédiaire important, notamment en chimie sous rayonnement, photochimie et électrochimie. Le radical anion e^-_{aq} est apparu comme un réducteur efficace. Par ailleurs, e^-_{solv} et son précurseur non relaxé peuvent constituer des microsondes de la structure du milieu et de la dynamique de sa réorganisation.

Ces dernières années, un regain d'intérêt et d'activité s'est manifesté concernant l'électron solvaté (voir, par exemple, réfs. 6–11), et ceci grâce à de nouvelles approches tant expérimentales que théoriques. Entre autres, il faut citer, d'une part, l'utilisation de montages de spectroscopie laser femtoseconde et, d'autre part, l'avènement des techniques de simulation numérique. L'interaction entre expérience et théorie s'est avérée particulièrement bénéfique pour le développement de nos connaissances. Néanmoins, nous le verrons, beaucoup de problèmes subsistent.

Dans un tel contexte, nous avons tenté ici une mise au point sur l'ensemble de ces questions en prenant en compte les résultats les plus marquants obtenus, mais en tâchant autant que possible de rendre cet ensemble facilement accessible au non-spécialiste.

Ce travail, de nature surtout physico-chimique, est organisé de la façon suivante. Nous rappelons d'abord les données les plus significatives concernant la caractérisation, la dynamique et le mécanisme de solvatation de e^-_{exc} en solutions liquides homogènes. L'accent est mis sur les aspects de ce mécanisme qui restent controversés. La spécificité de e^-_{aq} est ensuite discutée. Enfin, à partir des propriétés de e^-_{solv} et plus particulièrement de e^-_{aq}, nous nous proposons de : (*i*) comparer les caractéristiques de la solvatation des électrons en excès à celles des ions halogénure X^-; (*ii*) confronter les informations relatives à e^-_{solv} en solutions homogènes, en solutions micellaires ou lié à des agrégats de molécules polaires.

II. Électrons en excès en solutions polaires homogènes

A. Techniques de production et d'analyse de e^-_{solv}

1. Techniques de production

L'énergie nécessaire à la formation de l'électron solvaté peut être apportée par différentes voies :

(*i*) *Chimique* : La formation de e^-_{solv} par dissolution de métaux alcalins dans l'ammoniac liquide ou dans l'eau présente surtout un intérêt historique (2). Notons néanmoins l'apparition de e^-_{aq} par réaction acido-basique des atomes H à pH élevé (pH > 11) (12).

(*ii*) *Électrochimique* : Des électrons solvatés peuvent être produits à la cathode pour des potentiels électriques suffisamment élevés ou être photoinjectés dans la solution électrolytique à partir d'électrodes métalliques ou semiconductrices. Les études photoélectrochimiques, largement développées depuis une trentaine d'années (13), ont permis en particulier d'estimer les distances de thermalisation de e^-_{exc} et l'énergie fondamentale de l'électron quasi-libre (e^-_{qf}) dans quelques liquides polaires (voir, par exemple, réf. 14).

(*iii*) *Photochimique* : Des processus d'ionisation peuvent aussi être engendrés par voie photochimique (photons d'énergie supérieure à quelques eV) (voir, par exemple, réf. 15). Ils concernent soit des molécules neutres, solvants purs ou solutés, soit des anions, tels que Cl^-, OH^-,... Suivant les conditions expérimentales, ces photoionisations peuvent être mono- ou multiphotoniques. Des avancées technologiques récentes ont permis d'obtenir des impulsions laser ultra-courtes (16). Les temps de résolution pouvant dorénavant atteindre couramment la centaine de femtosecondes ont ouvert la voie à de nombreux travaux permettant de suivre la dynamique de formation de e^-_{aq}.

(*iv*) *Radiolytique* : Les sources d'irradiation employées sont, soit des faisceaux d'électrons accélérés et le plus souvent pulsés (de 1 à 10 MeV), soit des rayons γ de l'ordre du MeV, soit plus rarement des ions lourds accélérés. Pour les impulsions d'électrons, les temps de résolution les plus courts restent supérieurs à environ 10 ps, soit de deux à trois ordres de grandeur plus élevés que ceux mentionnés plus haut. En revanche, la radiolyse pulsée s'est avérée particulièrement appropriée pour analyser quantitativement les mécanismes réactionnels des espèces transitoires, en particulier ceux impliquant des électrons solvatés (voir, par exemple, réf. 17).

Fig. 1. Spectres d'absorption du propanol-1 irradié à −121°C par des impulsions d'électrons de 5 ns : (*a*) à la fin de l'impulsion, (*b*) 200 ns après la fin de l'impulsion et (*c*) 1 μs après la fin de l'impulsion (d'après Baxendale et Wardman (19)).

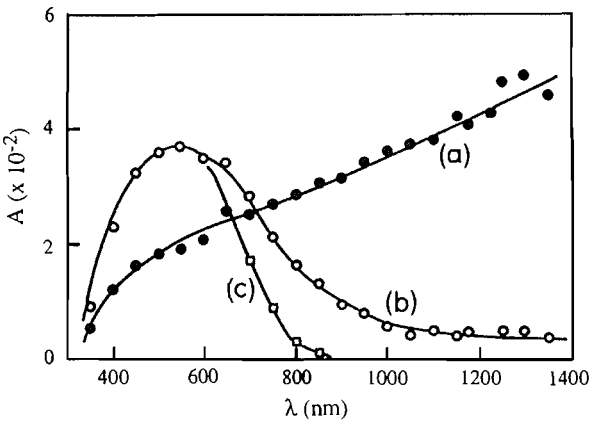

2. Méthodes analytiques

Une interception chimique de e^-_{solv} a été souvent utilisée dans le cas d'irradiations continues, les principaux capteurs préconisés étant N_2O, SF_6, Cd^{2+}, NO_3^-,...

Les techniques physiques les plus adaptées sont la conductimétrie, la résonance paramagnétique électronique (RPE) et surtout la spectroscopie d'absorption optique. La luminescence associée à la recombinaison des charges a également été analysée en intensité et en composition spectrale.

B. Dynamique et mécanisme(s) de solvatation

Tous les liquides polaires ne conduisent pas à la formation d'électrons solvatés. En effet, dans certains cas, la solvatation entre en compétition avec un processus d'attachement électronique. Ce dernier l'emporte, par exemple, pour l'acétonitrile, le formamide, la diméthylcétone (18).

Les premières études relatives à la solvatation de e^-_{exc} ont concerné divers alcools liquides à basses températures, ce qui permettait d'ajuster les temps de solvatation alors observés aux temps de résolution expérimentalement accessibles.

1. Dynamique de solvatation dans les alcools liquides

L'irradiation du propanol-1 à −121°C, c'est-à-dire à 6° au-dessus de son point de fusion, par des impulsions d'électrons de 5 ns (19) a conduit aux spectres reportés sur la figure 1. Une absorption dans l'infra-rouge, attribuée à une espèce transitoire e^-_{ir} et présente dès la fin de l'impulsion, disparaît en même temps que croît la bande centrée vers 550 nm correspondant à l'électron solvaté. À partir de la figure 1, les constatations suivantes ont été soulignées : (*i*) environ 50% de l'absorption correspondant à l'état relaxé e^-_{solv} sont déjà présents à la fin de l'impulsion (spectre *a*); (*ii*) le passage du spectre *b* au spectre *c* montre une diminution d'absorption dans le proche infra-rouge sans augmentation corrélative de la bande visible, ce qui suggère que le rappel de e^-_{ir} vers l'ion positif entre en compétition avec la solvatation.

Soulignons qu'une évolution similaire du spectre de e^-_{exc} a aussi été enregistrée dans le cas du propanol-1 vitreux à 77 (20) et 4 K (21) pour des échelles de temps évidemment beaucoup plus longues.

Des études dans le domaine picoseconde par radiolyse pulsée (22–24) et impulsions laser (24, 25) ont ensuite élargi le domaine de température et porté sur une série d'alcools aliphatiques de C_1 à C_{10}. Ces expériences ont pleinement confirmé l'existence de e^-_{ir} précurseur de e^-_{solv}. Kenney-Wallace et Jonah (23, 24) ont observé que l'évolution cinétique de l'absorbance à une longueur d'onde donnée (entre 450 et 750 nm) montre en effet un signal rapide qui apparaît dans le temps de résolution de l'appareil (<10 ps) et un signal lent (10–300 ps), indépendant de la longueur d'onde, décrit par une exponentielle (figure 2).

Les temps de solvatation de $e^-_{exc}(\tau_s)$, pris comme les inverses des constantes de vitesse exponentielles, augmentent régulièrement avec la longueur de la chaîne des alcools (voir tableau 1). Ceux-ci ont d'autre part été comparés aux différents temps de relaxation diélectrique τ_1, τ_2 et τ_3 qui correspondent respectivement (26, 27) : (*i*) au temps requis pour la rupture de liaisons hydrogène suivie de la réorientation moléculaire; (*ii*) au temps de rotation de molécules monomères et (ou) de petits multimères «libres» (c'est-à-dire, non liés par des liaisons hydrogène); (*iii*) au temps de réorientation des dipoles OH autour de la liaison C—O. Le tableau 1 met en évidence une bonne correspondance entre les valeurs τ_s et τ_2. Ceci suggère que la rotation moléculaire réglerait, pour une large part, la dynamique de solvatation de l'électron dans les alcools, laquelle procéderait en deux étapes successives, à savoir, localisation et solvatation.

La photoionisation de divers solutés en solutions alcooliques par impulsions laser de 6–10 ps a aussi été étudiée (28–30). Examinant à différentes longueurs d'onde l'évolution des spectres transitoires de e^-_{exc}, Hirata et al. (30) observent un déplacement continu vers le bleu de la bande d'absorption de l'électron et suggèrent que le processus global de solvatation impliquerait l'existence d'un état supplémentaire entre e^-_{ir} et e^-_{solv} (voir sect. II-B.3).

Les expériences de spectroscopie laser femtoseconde de Pépin et al. (32) utilisant des impulsions de ~300 fs très intenses à 620 nm (2 eV), ont par ailleurs mis en évidence une ionisation du méthanol liquide à la temperature ambiante par un processus d'absorption impliquant au moins trois photons. Ces auteurs observent dans le spectre de e^-_{exc} une transition discrète entre e^-_{ir} et une espèce transitoire apparaissant avec un temps caractéristique de 6,1 ± 0,6 ps. Simultanément, un déplacement spectral continu vers le bleu est observé pour l'une et l'autre de ces espèces. Pour l'espèce transitoire, ce déplacement est exponentiel avec un temps caractéristique de 13,6 ± 0,6 ps, en bon accord avec la valeur de 10,7 ± 1,7 ps déterminée par Hirata et al. (30). Des résultats analogues ont été obtenus récemment par Shi et al. (33) en utilisant des impulsions laser de ~150 fs à 312,5 nm (4 eV/photon), pour le méthanol, l'éthanol et le butanol-1 à 21°C (voir tableau 1). De plus, une évolution continue de l'espèce transitoire vers l'état relaxé e^-_{solv} a également été mise en évidence par Walhout et al. (34) pour les quatre alcools légers C_1 à C_4 à la température ambiante, lors d'expériences de spectroscopie d'absorption transitoire pompe-test de e^-_{solv} (vide infra), mettant en jeu trois impulsions laser consécutives.

Ces divers résultats montrent ainsi l'insuffisance d'un modèle de solvatation de l'électron n'impliquant que deux

Fig. 2. (*a*) Évolutions cinétiques de l'absorbance de e^-_{solv} à $\lambda = 514$ nm pour divers alcools aliphatiques de C_1 à C_{10} liquides à 295 K, normalisée à temps infini à l'absorbance maximale pour le méthanol. (*b*) Tracés semi-logarithmiques de l'absorbance en fonction du temps, à partir desquels les valeurs des temps de solvatation de e^-_{exc} (τ_s) sont calculées (voir texte). i-C_3 correspond à l'isopropanol ou propanol-2 (d'après Kenney-Wallace et Jonah (23)).

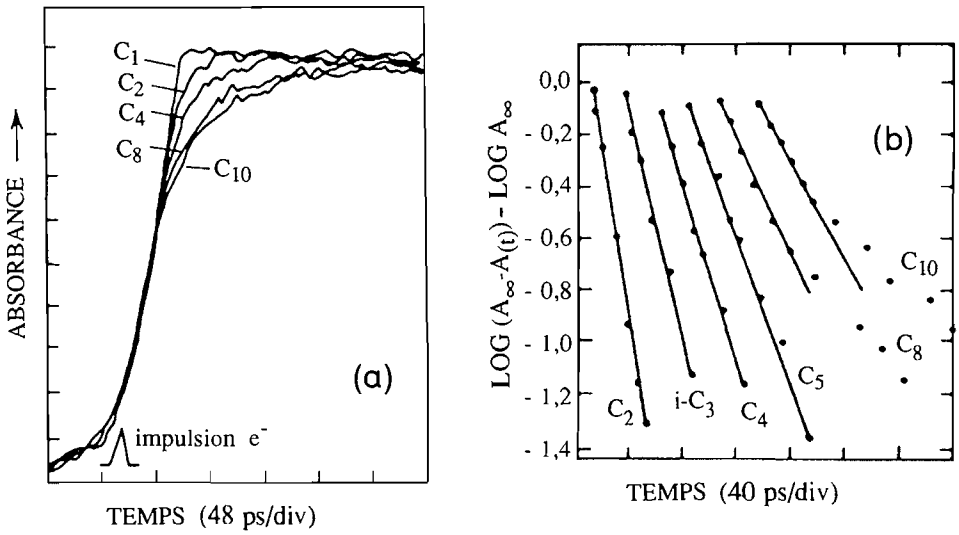

Tableau 1. Temps de solvatation τ_s de e^-_{exc} et temps de relaxation diélectrique τ_2 pour divers alcools à ~295 K.

Alcool	τ_s (ps)	τ_2 (ps)
Méthanol	10,7 ± 1 (22), 11 ± 1 (24), 17 ± 3 (28), < 10 (30), 9,5 ± 2 (31), 6,1 ± 0,6 (32), 7,1 ± 0,3 (33)	7,09,[a] 12,6[b]
Éthanol	23 ± 2 (22), 18 ± 2 (23, 24), 26 ± 5 (28), < 20 (29), 11 (30), ~21 (31), 15,2 ± 1 (33)	8,97,[a] 16,4[b]
Propanol-1	34 ± 3 (22), 25 ± 3 (23, 24), ~20 (29), 21 (30)	15,1,[a] 21,9[c]
Propanol-2	24 ± 3 (23, 24), 22 (30), ~20 (29)	14,5[a]
Butanol-1	39 ± 5 (22), 30 ± 3 (23, 24), ~30 (29), 26 (30), 45 ± 15 (31), 33 ± 3 (33)	27[c]
Pentanol-1	34 ± 3 (23, 24), 22 ± 6 (25), 41 ± 10 (31)	27,6[c]
Hexanol-1	~52 (31)	31[c]
Octanol-1	45 ± 5 (23, 24), ~45 (31)	38,7[c]
Décanol-1	51 ± 5 (23, 24), ~50 (29)	47,5[c]

[a]D'après Barthel et al. (27).
[b]Valeur extrapolée, d'après Chase et Hunt (22), à partir des données de Garg et Smyth (26) concernant les alcools de C_3 à C_{12}.
[c]D'après Garg et Smyth (26).

états. Soulignons qu'une telle conclusion n'est pas contredite par les données antérieures relatives à la dynamique de solvatation de l'électron dans les alcools liquides à basse température (19, 35, 36). En effet, celles-ci ne mettent pas clairement en évidence un point isobeste (voir, par exemple, réf. 37). Or, l'existence de celui-ci aurait témoigné de la seule participation de deux états électroniques distincts et de la relaxation exclusive du premier état vers le deuxième.

Fig. 3. Spectres d'absorption de e^-_{exc} mesurés à différents délais (entre 0 et 2 ps) après photoionisation selon un processus biphotonique (4 eV/photon) de l'eau liquide à 21°C (d'après Gauduel et al. (38)).

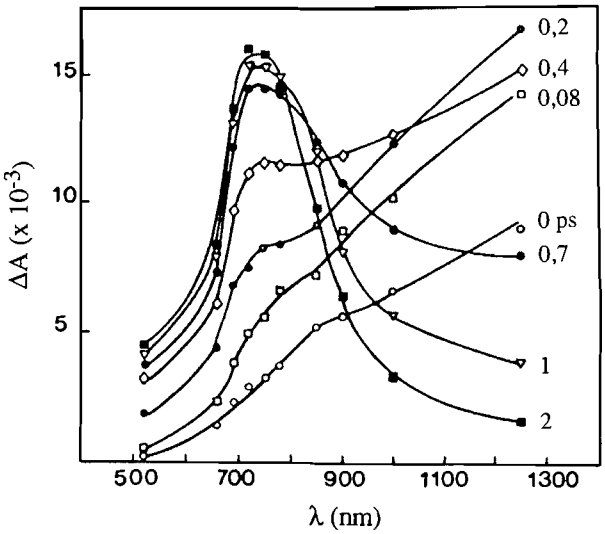

2. Dynamique de solvatation dans l'eau liquide pure

L'existence d'un précurseur de l'électron solvaté, déjà établie dans le cas des alcools, a été démontrée directement pour la première fois par Gauduel et al. (38) par photoionisation à deux photons de l'eau pure sous impulsions laser de ~100 fs à 310 nm (figure 3). Ces auteurs ont ainsi pu déterminer : un temps de montée de e^-_{ir}, $T_1 = 110 \pm 30$ fs, et un temps de relaxation $e^-_{ir} \rightarrow e^-_{aq}$, $T_2 = 240 \pm 40$ fs, cette relaxation suivant une loi cinétique du premier ordre. Le déclin de e^-_{ir} et la montée de e^-_{aq} apparaissent concomitants, mais on n'observe pas de transformation spectrale continue $e^-_{ir} \rightarrow e^-_{aq}$. La transition impliquerait donc, pour l'essentiel de la relaxation, deux états électroniques distincts.

Utilisant des techniques semblables de spectroscopie laser femtoseconde, Long et al. (39) ont conclu à l'existence d'un point isobeste à 820 nm. L'identification d'un tel point, qui corroborerait ainsi la conclusion que le passage $e^-_{ir} \rightarrow e^-_{aq}$ se fait selon une «vraie» transition entre deux états distincts, n'a cependant pas été retrouvée ni par Gauduel et al. (38, 40, 41) et ni, plus récemment, par Barbara et coll. (42). Il a d'autre part été noté que l'observation d'un point isobeste pourrait dépendre des conditions expérimentales, et en particulier de l'intensité du faisceau laser incident (38, 43).

Par ailleurs, Long et al. (39) ont noté une certaine similitude entre le spectre d'absorption trouvé pour e^-_{ir} et celui de e^-_{aq} (figure 4*a*), et considèrent que e^-_{ir} serait un état excité de l'état relaxé e^-_{aq} (voir sect. II-B.3). D'après ces auteurs, le temps de formation de e^-_{ir} serait de 180 ± 40 fs, alors que la relaxation $e^-_{ir} \rightarrow e^-_{aq}$ s'effectuerait en 540 ± 50 fs, durée comparable au temps de vie moyen des liaisons hydrogène dans l'eau liquide (44).

Plus récemment, les expériences de spectroscopie laser femtoseconde de Houde et collaborateurs (45, 46), utilisant des impulsions de ~150 fs à 620 nm (2 eV/photon), ont permis d'ioniser l'eau liquide via un processus d'absorption multiphotonique résonant mettant en jeu au moins quatre photons.

Fig. 4. (*a*) Spectres d'absorption de e^-_{ir} dans l'eau : d'après Long et al. (39) (□) et d'après Kimura et al. (42) (•). La courbe en tirets représente le spectre d'absorption de e^-_{aq} à titre de comparaison. (*b*) Coefficients d'extinction molaire, exprimés en M^{-1} cm^{-1}, de e^-_{aq} (courbe en tirets) et de e^-_{ir} (courbe en trait plein) calculés par Rossky et al. (81, 84; voir aussi réf. 10). À noter que le maximum théorique du spectre de e^-_{aq} est décalé de ~0,7 eV vers les hautes énergies par rapport au maximum expérimental.

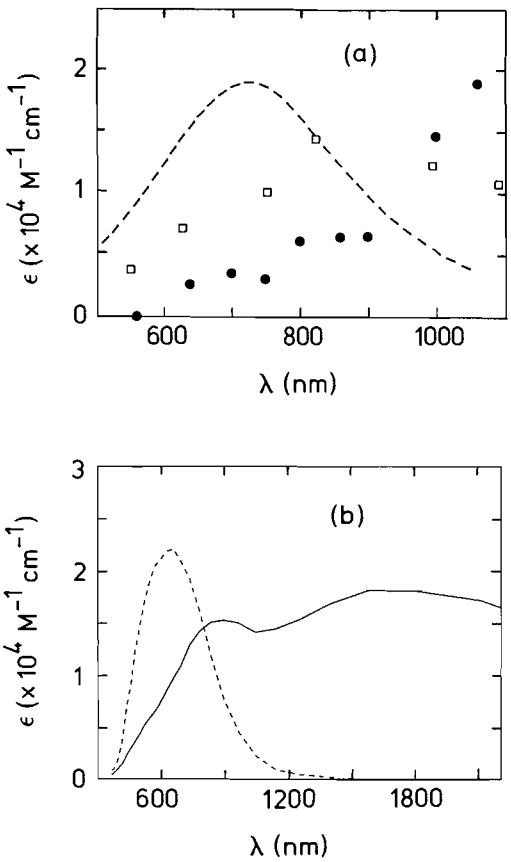

Les temps T_1 et T_2, estimés par ces auteurs, sont respectivement de 130 ± 40 et 620 ± 60 fs à 1100 nm (46).

Une autre méthode originale où e^-_{ir} est formé non pas à partir de l'électron quasi-libre mais à partir de l'électron déjà relaxé e^-_{aq}, utilise, ainsi qu'il a été cité précédemment, trois types d'impulsions laser consécutives (42). La première produit e^-_{aq}; après un retard de quelques nanosecondes, la deuxième, centrée à 780 nm (~1,6 eV) et d'une durée de 130 fs, blanchit e^-_{aq}; la troisième enfin sonde l'évolution temporelle de e^-_{ir} dans la gamme spectrale 540–1060 nm. Le temps de relaxation T_2 moyenné sur toutes les longueurs d'onde est trouvé égal à 310 ± 80 fs. Il faut néanmoins tenir compte du fait que la transition correspondant à T_2 n'implique pas ici l'état pleinement relaxé de l'électron. En effet, dans ces expériences, il a été mis en évidence, en apparente contradiction avec les résultats de Gauduel et al. (38), un déplacement continu du spectre intermédiaire vers le bleu avec un temps caractéristique relativement long (1,1 ± 0,2 ps). Comme nous le verrons plus loin, la dynamique complexe observée a amené

ces auteurs à compléter le modèle cinétique n'impliquant que deux états électroniques. Le spectre de e^-_{ir} obtenu en développant le modèle précédent est reporté sur la figure 4*a*.

Autres espèces formées parallèlement dans l'eau pure ou certaines solutions aqueuses : Il s'agit en particulier d'espèces formées par transfert de proton. C'est ainsi qu'en radiolyse, comme en photolyse de solvants associés, l'ionisation primaire conduisant au cation est accompagnée du transfert d'un proton quasi-instantané vers une molécule voisine, soit pour l'eau :

$$H_2O^+ + H_2O \rightarrow OH + H_3O^+ \ (\sim 10^{-14}\ s \text{ (voir, par exemple, réf. 47)})$$

Signalons toutefois que l'évolution de l'absorption due à l'hydratation de l'électron et mesurée par spectroscopie laser femtoseconde, soit à 625 nm (39), soit dans la gamme 410–460 nm (48), montre une composante à très courte durée de vie (~50–100 fs) qui pourrait être assignée au cation H_2O^+.

Par ailleurs, il a été avancé qu'un transfert de proton pouvait s'effectuer très rapidement à partir de H_2O neutre électroniquement excitée (49–52). En effet, en phase gazeuse, un tel transfert a été inféré de données de spectrométrie de masse (53). De plus, l'affinité protonique de H_2O est élevée : de 7,2 eV pour la molécule isolée, elle augmente de façon continue avec la taille des agrégats pour atteindre environ 10,5 eV pour des agrégats de 40 à 50 molécules (54).

Outre H, OH, H_2O^+ et H_3O^+, d'autres espèces intermédiaires peuvent apparaître très précocement : il s'agirait de paires hydratées $[H_3O^+{:}e^-{:}OH]_{nH_2O}$, de très faible durée de vie, formées par couplage transitoire de l'électron non relaxé avec la sphère d'hydratation du proton (40, 41). L'existence de ces paires de rencontre a été suggérée pour expliquer les résultats concernant la photoionisation de solutions aqueuses concentrées d'acide chlorhydrique (11 M en HCl) où toutes les molécules d'eau sont impliquées dans l'hydratation de H_3O^+ et de son contre-ion Cl^- (55). En effet, une bande d'absorption a été observée dans le proche infra-rouge, centrée à 920 nm, et un recours à D_2O permet, d'après les auteurs, de discriminer entre ces états électroniques hybrides et e^-_{ir}. À l'inverse de la formation et de la relaxation de e^-_{ir}, l'apparition et la durée de vie des paires mesurées dans la région infra-rouge sont influencées de façon importante par la substitution isotopique H/D. De plus, la relaxation des paires dans H_2O et D_2O est trouvée plus longue que la durée de vie de e^-_{ir} et la probabilité de former e^-_{aq} à partir de leur neutralisation apparaît très faible à température ambiante (41).

Dans le cas de solutions aqueuses de chlorure de sodium (1 ou 6 M), l'existence de paires de contact $[e^-{:}Cl]_{nH_2O}$ a également été postulée pour expliquer l'évolution de l'absorption dans le proche infra-rouge (820–1000 nm) (56). La disparition de ces paires se produirait, soit par reformation de Cl^-, soit par formation de e^-_{aq}, les temps caractéristiques correspondants étant respectivement de 330 et 750 fs. Toutefois, signalons que Long et al. (57) expliquent le destin du photoélectron dans des solutions aqueuses d'halogénures alcalins ou de NaOH sans invoquer la formation de paires de contact.

3. Mécanisme(s) de solvatation et définitions

Il est clair que, comme les ions solvatés, e^-_{solv} résulte d'un équilibre entre les puits de potentiel attractifs qui se développent quand les molécules solvant sont polarisées par l'électron en excès et l'énergie cinétique de ce dernier qui, à elle seule, conduirait à un état délocalisé.

On considère généralement que la solvatation procède en plusieurs étapes, selon la séquence suivante :

$$e^-_{qf} \rightarrow e^-_{th} \rightarrow e^-_{ir} \rightarrow e^-_{solv}$$

e^-_{qf} désigne un électron quasi-libre, tel que, par exemple, un électron de subexcitation (58, 59) dont l'énergie cinétique est typiquement de l'ordre de quelques électron-volts; e^-_{th} désigne un électron quasi-libre thermalisé, se trouvant donc, à l'énergie thermique près, au bas de la bande de conduction du liquide; la fonction d'onde associée à e^-_{th}, comme à e^-_{qf}, s'étend sur de nombreux diamètres moléculaires; e^-_{ir} désigne un électron localisé, incomplètement relaxé, dont la fonction d'onde ne s'étend que sur quelques diamètres moléculaires; e^-_{solv} désigne l'électron solvaté, c'est-à-dire un électron localisé, complètement relaxé, en équilibre avec le solvant; e^-_{exc} ou électron «en excès», recouvre l'ensemble des dénominations précédentes.

Les résultats de Hirata et al. (30) pour les alcools ont été mentionnés plus haut. Dans leur interprétation concernant la solvatation de e^-_{exc}, ces auteurs considèrent une espèce intermédiaire entre e^-_{ir} (dénoté e^-_{loc} ou e^-_t) et e^-_{solv} correspondant à un état «partiellement solvaté» (e^-_{ps}) :

$$e^-_{qf} \longrightarrow e^-_{th} \longrightarrow e^-_{loc}(e^-_t) \xrightarrow{[i]} e^-_{ps} \xrightarrow{[ii]} e^-_{solv}$$

L'étape [i], discrète, serait corrélée, nous l'avons vu, au temps de relaxation diélectrique τ_2 de l'alcool, en accord avec les interprétations de Chase et Hunt (22) et de Kenney-Wallace et Jonah (23, 24). La vitesse de l'étape [ii], plus lente et continue, serait, elle, assimilable à l'inverse du temps de relaxation diélectrique longitudinale $\tau_{L1} = (\varepsilon_\infty/\varepsilon_s)\tau_1$, où ε_s et ε_∞ sont les constantes diélectriques statique et à fréquence infinie du solvant. La solvatation de e^-_{exc} s'interpréterait donc, d'après Hirata et al. (30), par la réorientation initiale d'un petit nombre de molécules d'alcool «libres» dans la première couche de solvatation, suivie d'une stabilisation plus poussée due à la réorganisation de molécules de solvant plus éloignées, nécessitant la rupture de liaisons hydrogène. Il est intéressant de noter ici que cette succession temporelle est opposée à celle décrite par Onsager (dans réf. 60, voir Discussion p. 1819) dans l'approximation du continuum diélectrique, qui considère que la solvatation de e^-_{exc} procèderait d'abord des couches éloignées pour gagner ensuite les couches les plus proches de la charge (61).

Nous avons vu plus haut que, grâce à une résolution temporelle bien inférieure aux temps caractéristiques des phénomènes mis en jeu, des expériences de spectroscopie laser femtoseconde ont permis à Pépin et al. (32) d'étudier la solvatation de e^-_{exc} dans le méthanol liquide pur. Ces auteurs ont montré, en particulier, la coexistence de deux mécanismes de relaxation de l'espèce transitoire e^-_{ir}, l'un discret et l'autre continu. Le modèle hybride ainsi proposé implique deux états électroniques, l'un et l'autre relaxant via un déplacement continu vers le bleu et entre lesquels existe un mécanisme discret de transfert. Un tel modèle pourrait être en mesure de concilier certaines données apparemment contradictoires concernant la

solvatation de e^-_{exc}, non seulement dans les alcools mais également dans l'eau (32).

En ce qui concerne l'eau pure, nous avons évoqué précédemment que le recours à trois impulsions laser consécutives a permis à Barbara et coll. (42) d'apporter de nouvelles informations concernant la transition non radiative de l'état précurseur e^-_{ir}, considéré comme un état excité de e^-_{aq} (dénoté $e^-_{état\ p}$), vers l'état fondamental ($e^-_{état\ s}$). Ces auteurs ont ainsi été amenés à examiner la dynamique de solvatation d'un état intermédiaire $e^{-*}_{état\ s}$, dynamique qu'ils associent à une élévation locale de température. Cet état intermédiaire se relaxe de façon continue vers e^-_{aq}. Le schéma global peut être écrit :

$$e^-_{état\ p} \xrightarrow{310\ fs} e^{-*}_{état\ s} \xrightarrow[\text{déplacement continu}]{1,1\ ps} e^-_{état\ s}\ (e^-_{aq})$$

Remarquons qu'un tel schéma présente une grande ressemblance avec les mécanismes évoqués plus haut pour la solvatation de e^-_{exc} dans divers alcools (30, 32–34). Une telle analogie est toutefois restreinte par le fait que les échelles de temps mises en jeu pour décrire les phénomènes sont bien supérieures pour les alcools que pour l'eau.

Le mécanisme de solvatation de l'électron dans les alcools et l'eau apparaît ainsi plus complexe qu'il ne semblait *a priori*. Pour rendre son interprétation plus quantitative, bien des points restent à élucider; un certain nombre d'entre eux sont évoqués ci-dessous.

La formation de e^-_{qf} est-elle une étape obligée de la solvatation? Cette question concernerait en particulier le domaine d'énergie des photons proche du seuil d'ionisation du solvant et situé au-dessous du bas de la bande de conduction de celui-ci. Elle s'appliquerait notamment aux expériences de spectroscopie laser femtoseconde de l'eau liquide pour lesquelles l'énergie d'excitation est de 8 eV lors d'un processus biphotonique (λ_{exc} = 310 nm) (38, 39), les énergies du seuil d'ionisation et du bas de la bande de conduction, dans ce cas, étant respectivement de 6,5 ± 0,5 eV (62) et de ~8,9 (63) ou 10–12 eV (52).

Des données de photoélectrochimie avaient suggéré que les électrons en excès pouvaient être directement localisés dans des pièges préexistants de la solution électrolytique (64).

Nous avons récemment proposé une interprétation analogue pour la photoionisation de l'eau pure et des solutions aqueuses diluées (63). Il a ainsi été noté que les courbes exprimant la variation du rendement d'ionisation (ϕ_e) en fonction de l'énergie (E_{ph}) des photons incidents dans la région du seuil étaient exponentielles. De telles lois exponentielles sont également caractéristiques des bandes d'Urbach (65), traduisant l'existence d'états électroniques localisés dans la bande d'énergie interdite de divers solides amorphes ou désordonnés, ces états localisés étant corrélés au désordre du milieu.

Ces remarques suggèrent que lors de la photoionisation de l'eau liquide, pour E_{ph} voisin du seuil, les états électroniques finals pourraient se situer, non pas dans la bande de conduction, mais dans une bande d'états localisés s'étendant au-dessous de celle-ci; la variation de ϕ_e avec E_{ph} traduirait alors la distribution énergétique des états localisés dans la bande d'Urbach.

L'existence de telles bandes d'états localisés dans les liquides a été utilisée par Houée-Levin et Jay-Gerin (66) pour interpréter les spectres d'absorption optique des électrons e^-_{ir} dans l'eau à 21°C et dans certains alcools liquides à basse température, et a été confirmée pour l'eau (67–69) et le méthanol (70) liquides à température ambiante par des calculs de simulation de dynamique moléculaire.

Une localisation initiale des e^-_{exc} dans la bande d'Urbach a conduit également à envisager le dépiégeage possible de certains d'entre eux, faiblement liés, sous l'action du champ coulombien du cation parent (71). Les électrons ainsi libérés pourraient soit se recombiner avec l'ion positif géminé, soit se piéger à nouveau. Globalement, les pièges peu profonds se videraient au profit des pièges plus profonds, entraînant une diminution de la partie infra-rouge du spectre d'absorption de e^-_{ir}, spectre qui devrait donc présenter un maximum. Celui-ci n'a cependant pas encore été déterminé expérimentalement sans équivoque (pour le cas de l'eau, voir figure 4*a*).

Les pièges préexistants dans les liquides sont-ils nécessaires à la localisation de e^-_{exc}? Thermalisation et piégeage sont-ils concomitants? Les expériences de spectroscopie femtoseconde ne permettent pas de trancher le dilemme suivant : l'électron crée-t-il son propre puits de potentiel (autopiégeage ou *self-trapping*) ou se fixe-t-il dans des sites de piégeage préexistants, sites dus à des fluctuations de densité électronique ou d'orientation des molécules du solvant?

Les calculs de simulation de Schnitker et al. (67), mentionnés précédemment, ont conclu à l'existence, dans l'eau liquide, de sites préexistants favorables énergétiquement au piégeage de e^-_{exc}, de par leur dimension et leur profondeur. D'après ces auteurs, la distribution énergétique de ces sites s'étend jusqu'à environ 1,4 eV en-dessous du bas de la bande de conduction pour le site de localisation le plus favorable. On peut remarquer qu'une telle valeur est voisine de l'enthalpie libre d'hydratation de l'électron $\Delta G^0_{hyd} \sim -1{,}68$ eV/molécule (voir sect. II-D), indiquant ainsi l'existence de sites de piégeage préexistants de e^-_{exc} ayant une structure proche de celle correspondant à e^-_{aq}. Les calculs de simulation les plus récents de ces mêmes auteurs (69), également pour l'eau liquide, ont indiqué une concentration relativement élevée (~0,01 M) de l'ensemble des pièges préexistants, comparable aux valeurs minimales estimées par ailleurs par Mozumder (72).

Cependant, un modèle, pour lequel la paire «électron (d'énergie inférieure à ~1 eV) – ion positif» dans un milieu polaire est traitée comme un atome d'hydrogène plongé dans un continuum diélectrique qui se relaxe, conclut à la possibilité d'une localisation instantanée par auto-piégeage, localisation qui précéderait ainsi la thermalisation (73). Les pièges préexistants dans le liquide ne seraient alors pas nécessaires à la localisation de l'électron en excès.

Notons enfin que d'après le schéma précédemment décrit pour la photoionisation de l'eau pure et des solutions aqueuses diluées (63), les électrons photoéjectés ne seraient pas initialement dans un état quasi-libre, mais se localiseraient directement à partir d'états excitoniques, de type Mott–Wannier, du liquide (74) : thermalisation et piégeage seraient alors des processus quasi-synchrones.

La transition $e^-_{ir} \rightarrow e^-_{solv}$ est-elle ou non continue? En ce qui

concerne l'*eau liquide*, les premières études de spectroscopie laser femtoseconde ont abouti à la conclusion que le processus prédominant d'hydratation de e^-_{exc} n'était pas associé à la relaxation progressive des molécules de solvant entourant la charge, mais correspondait plutôt à un processus impliquant deux états électroniques distincts de e^-_{exc} (38, 39).

En revanche, divers calculs de simulation de dynamique «adiabatique»,[3] utilisant la méthode des intégrales de chemin et traitant le solvant–eau de manière classique (75, 76), ont indiqué un déplacement continu, allant de l'infra-rouge vers le visible, du maximum du spectre d'absorption de e^-_{exc}. De plus, selon ces mêmes calculs, la majeure partie du processus d'hydratation aurait lieu sur une échelle de temps de l'ordre de 80–100 fs. Ces désaccords avec l'expérience ont amené Rossky et Schnitker (75) à postuler que l'état responsable de l'absorption infra-rouge est un état «excité» de e^-_{aq} et que sa relaxation s'effectue de manière non adiabatique vers l'état fondamental. Selon ces auteurs (75, 77), le spectre de e^-_{aq} serait ainsi dominé par des transitions électroniques à partir d'un état fondamental (de type *s*) vers trois états excités, localisés (de type *p*), non dégénérés. À ceci s'ajouterait, à plus haute énergie, une composante spectrale moins intense comprenant des excitations vers un continuum d'états délocalisés. Dans un tel schéma, l'étape limitante dans la dynamique de solvatation de e^-_{exc} serait donc déterminée par la conversion interne de l'état excité de e^-_{aq}. Le spectre ainsi calculé par Rossky et al. (75, 77) a son maximum d'absorption situé à ~2,4 eV et une largeur à mi-hauteur de ~1,1 eV, alors que les valeurs expérimentales correspondantes sont respectivement de 1,73 et 0,85 eV (voir sect. II-C.2-a).

Un tel modèle, consistant à considérer e^-_{ir} comme un état excité de e^-_{aq}, a également été avancé par Long et al. (39) pour interpréter leurs résultats. Par ailleurs, soulignons que Messmer et Simon (78) n'ont pu reproduire qualitativement les données expérimentales de Gauduel et al. (38) qu'en prenant en compte une population d'électrons subissant une transition non adiabatique. Dans ce cas, l'analyse phénoménologique mènerait à la répartition suivante des électrons qui donnent lieu à la solvatation : 55% subiraient une transition non adiabatique, 20% conduiraient quasi-instantanément à e^-_{aq} et 25% s'hydrateraient de façon continue.

Des calculs de simulation de dynamique «non adiabatique» directe ou des simulations de dynamique moléculaire mettant en oeuvre diverses variantes de ces calculs, ont tenté d'explorer, dans une étape ultérieure, la validité du modèle d'hydratation en deux étapes (79–85), sans toutefois qu'une interprétation quantitative puisse être établie. Quelques remarques méritent, en particulier, d'être évoquées ici. Il est apparu, par exemple, que les vibrations des molécules d'eau jouaient un rôle substantiel dans la cinétique de disparition de l'intermédiaire mis en jeu. En effet, Webster et al. (79) ont trouvé une durée de vie de ~1 ps pour l'état e^-_{ir} en utilisant un modèle d'eau rigide. Si, au contraire, la flexibilité de la molécule d'eau est prise en compte, la valeur correspondante obtenue est ~160 fs (81), inférieure à celles données par l'expérience (240–620 fs, selon les auteurs; voir sect. II-B.2).

[3] Dans l'hypothèse d'une évolution «adiabatique», l'électron est astreint à rester dans l'état fondamental de la cavité où il s'est piégé, état déterminé par la configuration microscopique instantanée du solvant.

Par ailleurs, Neria et al. (80) ont mis en évidence un désaccord entre calcul et expérience concernant la durée de vie de e^-_{ir} dans H_2O et D_2O : le calcul à 300 K donne T_2 = 220 fs pour H_2O et 800 fs pour D_2O avec une marge d'erreur estimée à ~30%; cet effet isotopique est bien supérieur à celui trouvé expérimentalement ($(T_2)_{D_2O}/(T_2)_{H_2O}$ = 1,04 (86) ou ~1,35 (87)). Citons enfin un point abordé récemment par Rossky et coll. (81, 84) : des calculs du type de ceux évoqués ci-dessus font en effet apparaître un spectre d'absorption qui serait caractéristique de l'électron initialement «quasi-libre». Le maximum en serait situé vers 1400 nm avec un coefficient d'extinction molaire de $\sim 2{,}3 \times 10^4$ M^{-1} cm^{-1}. Cette dernière estimation traduit une interaction spectrale importante si l'on se réfère à la valeur correspondante pour e^-_{aq} ($1{,}9 \times 10^4$ M^{-1} cm^{-1} à ~300 K; voir réf. 88 et sect. II-C.2-a). L'origine d'une telle interaction demanderait à être examinée. Ces mêmes calculs (81, 84; voir aussi réf. 10) conduisent corrélativement pour e^-_{ir} au spectre donné figure 4*b* à titre de comparaison avec les valeurs expérimentales (figure 4*a*).

Les insuffisances des calculs actuels de simulation pour interpréter quantitativement l'hydratation de l'électron nous paraissent provenir de différentes causes, parfois déjà mentionnées. La première est l'emploi de pseudopotentiels très simplifiés pour décrire l'interaction électron–eau. Il nous paraîtrait souhaitable que ces pseudopotentiels soient préalablement validés, par exemple, en calculant à faible énergie les sections efficaces correspondantes en phase gazeuse et en comparant les résultats ainsi obtenus avec l'expérience. La deuxième cause concerne le fait que les pseudopotentiels utilisés sont construits afin de décrire l'état fondamental de l'électron, alors qu'ils sont également appliqués à la description des états «excités». Enfin, troisième cause, le traitement classique du solvant pose problème. Un traitement quantique est clairement souhaitable. Toutefois, la mise en oeuvre pratique des calculs palliant les insuffisances précédentes présente, pour le moment, de nombreux défis.

La situation a rebondi récemment, ainsi que nous l'avons déjà mentionné (voir sects. II-B.2 et II-B.3), par suite des expériences de Barbara et coll. (42) qui montrent que, pour l'eau liquide, l'état fondamental impliqué dans le processus d'hydratation se relaxe de façon continue vers e^-_{aq}, le temps caractéristique de ce déplacement spectral étant relativement long (1,1 ± 0,2 ps). Il faut souligner que l'existence, dans ce milieu, d'une telle relaxation continue n'avait pas jusqu'alors été mise en évidence.

Pour les *alcools liquides*, les premières études de dynamique de solvatation, exclusivement expérimentales, concluaient à un processus en deux étapes (localisation et solvatation), comme pour l'eau. Les travaux ultérieurs de Lewis et Jonah (89), concernant l'éthanol et le propanol-1, ont permis de mettre en évidence deux voies possibles de solvatation, l'une directe et rapide et l'autre, plus lente, impliquant l'électron piégé comme intermédiaire. D'après les études citées plus haut (30, 32–34), il semble actuellement qu'il faille envisager pour les alcools liquides, non seulement un déplacement continu vers le bleu de la bande visible du spectre, mais également la coexistence de deux mécanismes de relaxation de l'espèce transitoire e^-_{ir}, l'un discret et l'autre continu (32).

C. Propriétés physico-chimiques de e^-_{solv}

On considérera successivement structure, spectres d'absorp-

Fig. 5. Structure de e^-_{aq} obtenue par modulation d'écho de spin d'électrons piégés dans des matrices alcalines vitreuses irradiées par rayons γ à 77 K (d'après Kevan (94)).

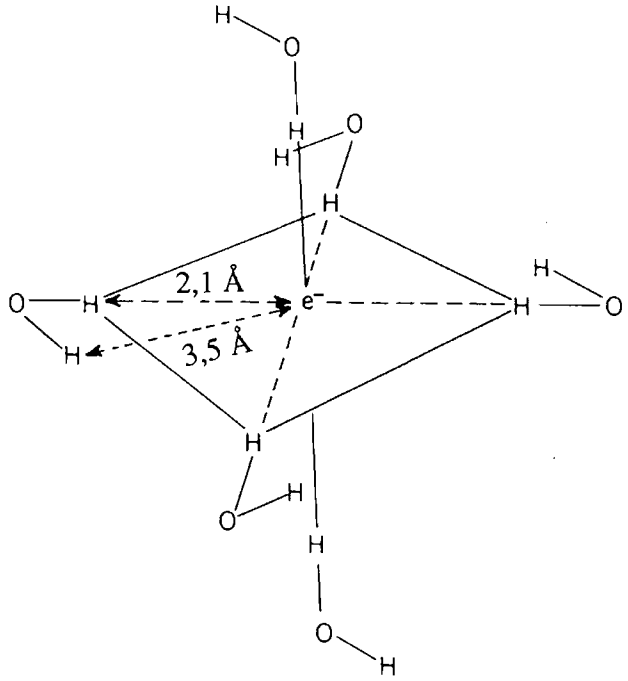

tion optique et de RPE, et mobilité de e^-_{solv}. Les propriétés de cette espèce, et surtout de e^-_{aq}, ont été abondamment étudiées durant les dernières décennies. En particulier, la structure de e^-_{aq} et les caractéristiques du spectre d'absorption optique ont permis la confrontation des modèles théoriques avec les données expérimentales.

Les récentes tentatives de modélisation physique d'un électron en excès dans un liquide ont utilisé deux approches principales : l'une est basée sur l'intégration numérique de l'équation de Schrödinger dépendante du temps pour une particule quantique se déplaçant dans un fluide classique (90), et l'autre sur la formulation de Feynman de la mécanique statistique quantique utilisant les intégrales de chemin (91, 92). En fait, la plupart des traitements théoriques proposés pour l'étude des propriétés de e^-_{solv} font usage de la seconde voie, associée aux techniques de simulation Monte Carlo ou de dynamique moléculaire. Ces traitements diffèrent cependant, soit dans le modèle choisi pour le solvant, soit dans le choix des potentiels qui décrivent l'interaction e^-_{exc}–solvant (voir, par exemple, réf. 93).

1. Structure de e^-_{solv}

Peu de données expérimentales sont disponibles au sujet de la structure de e^-_{solv}. En ce qui concerne les résultats se rapportant à e^-_{aq}, ceux-ci ont été principalement obtenus à 77 K par Kevan et coll. (94) en utilisant la technique de modulation d'écho de spin d'électrons piégés dans des matrices alcalines vitreuses irradiées par rayons γ. Ces résultats ont conduit à proposer la structure représentée figure 5 où l'électron est entouré de six molécules d'eau. Une liaison O—H de chacune de ces molécules d'eau étant orientée vers l'électron, l'ensemble présente une structure octaédrique. Il a été suggéré (95) qu'une telle géométrie pouvait constituer une représentation réaliste de e^-_{aq} dans l'eau liquide.

Les récents résultats de simulations paraissent en assez bon accord avec cette suggestion. Un nombre de coordination voisin de 6 est en effet obtenu à 300 K pour une distance électron–oxygène qui est statistiquement égale à 3,7 (96) ou 3,3 Å (75), à comparer à 3,1 Å, valeur déterminée expérimentalement par Kevan et coll. (94). Toutefois, un nombre de coordination de 4 (93, 97) ou entre 5 et 6 (98, 99) a aussi été proposé. En fait, les écarts trouvés pour ce nombre sont probablement liés aux très grandes fluctuations des dimensions de la cage de solvatation de e^-_{aq} (75, 77, 100). À titre de comparaison, on peut signaler que des calculs analogues conduisent à un nombre de coordination d'environ 7–8 pour les ions chlorure hydratés (Cl^-_{aq}) (101–103).

De plus, une étude de l'état fondamental de e^-_{aq} dans la gamme 77–300 K, basée sur un modèle de semi-continuum prenant en compte, non seulement la structure géométrique proposée par Kevan et coll. (94), mais également l'influence de la deuxième couche d'hydratation, a amené Pommeret et Gauduel (104) à conclure qu'il n'existe pas de différence structurale fondamentale entre l'électron piégé dans la glace ou hydraté dans l'eau liquide.

Notons, enfin, que la technique de modulation d'écho de spin a été également appliquée au cas de l'électron dans d'autres solides vitreux et en particulier dans le méthanol et l'éthanol (94). Les résultats obtenus pour ces deux alcools indiquent que la première couche de solvatation de e^-_{solv} se compose de quatre molécules approximativement équivalentes et disposées de façon tétraédrique. À l'inverse de l'eau, ce sont les dipoles moléculaires, et non pas les liaisons O—H, qui pointent vers l'électron. L'hydrogène le plus proche de l'électron (2,3 Å pour le méthanol) est celui du groupement hydroxyle. Pour l'éthanol, la valeur correspondante est 2,2 Å.

2. Propriétés spectroscopiques

(a) Spectres optiques

Caractéristiques générales : Le spectre d'absorption optique — pierre de touche du mécanisme de solvatation — est probablement la plus étudiée des propriétés de l'électron solvaté. Il permet à la fois d'identifier celui-ci et de tester la validité des traitements théoriques proposés.

Ce spectre est caractérisé essentiellement par une bande large (la largeur à mi-hauteur $W_{1/2}$ = 0,85 eV pour e^-_{aq} à 300 K, contre environ 0,3 eV pour l'électron piégé à 77 K dans la glace cristalline) sans structure, asymétrique avec une traîne vers le bleu (voir, par exemple, réfs. 7 et 105).

Tandis que la longueur d'onde correspondant au maximum d'absorption[4] (λ_{max}) est située dans le proche infra-rouge pour l'électron solvaté dans les solvants peu polaires tels que les éthers, les amines, etc., elle se situe dans le rouge pour l'électron hydraté ou solvaté dans les alcools à la température ambiante (pour e^-_{aq}, λ_{max} = 715 nm ou E_{max} = 1,73 eV; voir réf. 88 pour une compilation récente des propriétés spectrales de e^-_{solv} dans les liquides polaires).

[4] On sait que λ_{max} est reliée à l'énergie E_{max} associée au maximum d'absorption de e^-_{solv} par $E_{max} = 1240/\lambda_{max}$, où E_{max} est exprimée en eV et λ_{max} en nm.

Le coefficient d'extinction molaire au maximum d'absorption (ε_{max}) se révèle être une fonction linéaire de $1/W_{1/2}$; ceci découle du fait que la force d'oscillateur (f) correspondant au spectre d'absorption de e^-_{solv} varie peu d'un solvant à l'autre ($f \sim 0{,}6$) (106). Les valeurs de ε_{max} varient également de façon exponentielle avec E_{max}, relation qui permet, connaissant λ_{max} pour un solvant donné, de calculer ε_{max}, et donc de déduire du spectre de e^-_{solv} une estimation du rendement en électrons solvatés dans ce solvant (106; voir aussi réf. 7).

Notons enfin qu'une bande d'absorption de e^-_{solv} a été observée dans l'ultra-violet, avec un seuil situé vers 200 nm pour l'électron hydraté (107) et 240 nm pour l'électron ammonié (18, 108). D'après l'interprétation proposée, il s'agirait d'un déplacement vers le rouge de la première bande d'absorption du solvant, déplacement induit par la perturbation due à la présence de e^-_{solv} des transitions électroniques des molécules formant les premières couches de solvatation.

Effets de température et de pression : L'effet de température sur le spectre d'absorption de e^-_{aq} a été examiné par divers auteurs (109–113). Dans la gamme de −4 à 390°C, les travaux de Michael et al. (110) et de Christensen et Sehested (113) ont montré que l'allure générale de la bande d'absorption n'est pas sensiblement modifiée. En revanche, de −4 à 175°C, E_{max} se déplace de −0,003 eV/deg. Au-dessus de 175°C, le maximum d'absorption continue à se déplacer vers les énergies plus faibles, avec un coefficient de température moindre; cette variation se poursuit jusqu'à la température critique de l'eau (371°C pour D_2O), et même au-delà. Ce déplacement pourrait être attribué à la modification des pièges due à la rupture progressive des liaisons hydrogène et au changement de la structure associative de l'eau liquide. Miura et Hirata (114) ont développé, dans ce cadre, un modèle théorique de la stabilité de e^-_{aq} et ont pu prévoir le sens de cette influence. Notons, en revanche, qu'un tel déplacement n'a pas été retrouvé entre 300 et 373 K par l'application de méthodes de simulation Monte Carlo et d'intégrales de chemin (96). Le piégeage d'électrons à des températures supercritiques où l'eau serait à l'état monomérique à plus de 95% indiquerait, d'après Michael et al. (110), que la préexistence de pièges n'est pas une condition nécessaire à la solvatation.

Pour la glace cristalline, comme pour l'eau liquide, la valeur de E_{max} est décalée vers le bleu quand la température décroît et on n'observe pas de discontinuité à la température de fusion de la glace (115).

Par ailleurs, Elliot et Ouellette (116) rapportent, pour l'électron hydraté et pour des températures allant jusqu'à 200°C, une décroissance sensiblement linéaire de ε_{max} en fonction de la température, qui conduit à la valeur $\varepsilon_{max} \sim 1{,}6 \times 10^4$ M^{-1} cm^{-1} à 200°C.

L'influence de la pression, comme celle de la température, ne modifie que faiblement l'allure générale du spectre d'absorption de e^-_{aq}. Toutefois, quand la pression est augmentée, le maximum du spectre se déplace vers le bleu; pour des pressions allant jusqu'à 2 kbar et à 27°C, Jou et Freeman (117) ont ainsi observé pour e^-_{aq} une variation linéaire de E_{max} de +0,065 eV/kbar. Le sens d'un tel déplacement peut être attribué à la diminution des dimensions des cavités pièges pour l'électron.

Type de transition impliquée et largeur de bande : La nature

Fig. 6. (*a*) Comparaison des spectres d'absorption de l'électron hydraté expérimental et simulé (voir aussi figure 4). La ligne en tirets est obtenue par déplacement du spectre expérimental de ~0,7 eV vers les hautes énergies. (*b*) Sous-bandes *s–p* individuelles contribuant au spectre d'absorption simulé (d'après Rossky et Schnitker (75)).

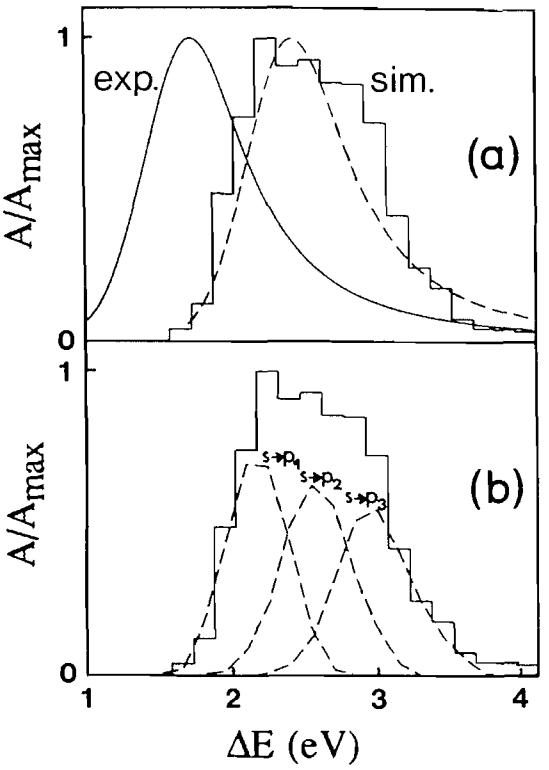

des transitions responsables du spectre d'absorption de e^-_{aq} a fait l'objet de nombreux travaux théoriques et expérimentaux qui relèvent principalement de deux interprétations (voir, par exemple, réfs. 118 et 119) : l'une d'entre d'elles considère que les transitions mises en jeu s'effectuent entre un état lié et le continuum, et l'autre envisage surtout des transitions entre états liés. C'est ainsi que Jortner et al. (120) ont proposé une interprétation basée sur une transition d'un état fondamental de type 1*s* vers un état excité lié de type 2*p* du solvant polarisé. Cependant, l'invariance de la forme de la bande d'absorption quand la température ou la pression varie a été considérée comme l'indice d'une prépondérance de transitions vers les états délocalisés de la bande de conduction du solvant (121), l'état fondamental e^-_{aq} n'étant pas de type *s* pur (et donc s'écartant d'une symétrie purement sphérique) (122). En revanche, les récents résultats de simulation de dynamique moléculaire ou Monte Carlo, utilisant les intégrales de chemin, semblent indiquer que la bande d'absorption de e^-_{aq} traduirait la transition fortement permise $1s \rightarrow 2p$ (75, 77, 85, 96, 100, 123). Ces derniers auteurs estiment ainsi que la bande peut être représentée par l'enveloppe de trois sous-bandes correspondant aux transitions de l'état 1*s* vers les trois états excités liés p_1, p_2, p_3 non dégénérés, et que la traîne d'absorption vers le bleu résulterait, elle, de transitions vers des états délocalisés (figure 6). La non-dégénérescence des trois états *p* serait due à l'anisotropie locale de l'interaction de e^-_{exc} avec le

solvant et leur séparation en énergie s'élèverait, selon les auteurs, à 0,8 (77, 83) ou 0,3 (85) eV. Notons qu'une résolution de la bande d'absorption expérimentale en plusieurs sous-bandes de forme gaussienne avait déjà conduit à une décomposition analogue (124).

La largeur inusitée de la bande d'absorption de e^-_{solv} est actuellement interprétée théoriquement comme étant due aux fluctuations en forme et en dimensions des cavités pièges (75, 77, 100; voir aussi sect. II-C.1). D'utiles informations à ce sujet peuvent être obtenues expérimentalement grâce à la méthode de dynamique de blanchiment (*spectral hole burning*) qui permet de sonder directement les caractéristiques spectrales différentielles de la bande d'absorption (voir, par exemple, réf. 125). En ce qui concerne e^-_{aq}, des résultats théoriques (76, 83, 125, 126) et expérimentaux (42, 127) ont été obtenus récemment par cette méthode (voir sects. II-B.2 et II-B.3). Soulignons, en particulier, les travaux réalisés par Schwartz et Rossky (126) et par Reid et al. (127) qui utilisent la lumière polarisée, l'électron hydraté étant alors une sonde de l'anisotropie locale de la cavité solvant. Selon ces derniers auteurs, une telle anisotropie s'établirait de manière simultanée avec l'excitation et décroîtrait en ~3 ps, montrant ainsi que des fluctuations anisotropes lentes du solvant pourraient intervenir dans la dynamique d'hydratation de e^-_{exc}.

Pour les alcools légers, soit vitreux à basse température, soit liquides à ~300 K, une autre méthode d'étude, basée sur le couplage entre e^-_{exc} et les modes vibrationnels intramoléculaires du solvant, a été proposée par Abramczyk et al. (128; voir aussi réf. 9) pour déterminer le profil des bandes d'absorption infra-rouge et visible de e^-_{exc}. Les résultats, obtenus dans le cadre d'une théorie de réponse linéaire, conduisent à la conclusion qu'il y aurait deux types d'électrons piégés : ceux absorbant dans le visible qui seraient associés aux groupements hydroxyle (couplage avec les modes d'élongation C–O ou de flexion O–H), et ceux absorbant dans l'infrarouge qui seraient piégés par les groupes alkyle (couplage avec les modes d'élongation C–H). La situation serait différente pour l'eau et les verres aqueux qui n'offriraient à e^-_{exc} qu'un seul type de piège. Selon les auteurs, une telle représentation pourrait rendre compte de la différence apparente des propriétés spectroscopiques de e^-_{exc} dans l'eau et les alcools. Toutefois, vu la valeur extrêmement élevée du champ électrique au voisinage de l'électron (jusqu'à 10^7 V/cm), on peut s'interroger sur la pertinence de l'emploi de la théorie de réponse linéaire utilisée par Abramczyk et collaborateurs, théorie qui suppose une perturbation faible du solvant par e^-_{exc}; il pourrait, en effet, être indispensable de prendre en compte l'intervention de phénomènes non linéaires (129).

(b) Spectres de RPE

Les spectres de RPE de l'électron piégé (e^-_p) sont généralement obtenus à partir de matrices vitreuses irradiées à basse température. Dans le cas de la glace (H_2O) cristalline aucun signal RPE de e^-_p n'est observé, le signal du radical OH masquant celui de l'électron. Toutefois, pour D_2O cristalline, un recuit préalable à la mesure facilite la disparition du radical OD et permet ainsi la mise en évidence d'un signal RPE de e^-_p (130). La raie unique caractéristique de e^-_p est en revanche directement observable dans des glaces vitreuses alcalines à 77 K, où le rendement en e^-_p peut atteindre des valeurs élevées (1,9 molécule/100 eV) pour des concentrations suffisantes en ions OH^- (131). Le facteur g ainsi mesuré est égal à 2,0008 (132) ou 2,0006 (133), valeurs proches de celle correspondant à un électron non lié (2,002 32).

Dans le cas des alcools vitreux, le blanchiment de e^-_p par la lumière visible substitue quantitativement le signal des radicaux $\dot{C}H_2OH$, $CH_3\dot{C}HOH$,..., dont la formation est initiée par la recombinaison des charges, à la raie unique relative à e^-_p (131).

Diverses expériences de RPE de e^-_{solv} ont été effectuées pour l'eau, le méthanol ou l'éthanol en phase liquide en utilisant soit la radiolyse pulsée (134–136), soit une photolyse continue (137). Cette dernière méthode donne pour e^-_{aq} une valeur du facteur g de 2,000 43 à 23,3°C (137), tandis que la radiolyse pulsée conduit respectivement à g = 2,002 05 et 2,001 97 pour e^-_{solv} dans le méthanol et l'éthanol à 22°C (136).

L'interprétation des résultats obtenus par RPE concernant e^-_{solv} reste encore difficile actuellement.

(c) Spectres d'absorption de e^-_{solv} et spectres CTTS des ions halogénure

De nombreux anions en solution, tout particulièrement les ions halogénure, présentent dans l'ultra-violet un spectre d'absorption intense immédiatement suivie par une production de e^-_{solv} dans le solvant. Franck et Scheibe (138) ont été les premiers à interpréter cette absorption comme l'indication d'un mécanisme de transfert de charge au solvant (*charge transfer to solvent* ou CTTS). La libération de l'électron, dans ce cas, n'est pas due à une photoionisation au sens classique, mais implique un état excité électronique intermédiaire de l'ion parent. L'électron concerné occupe une orbitale qui, quoique centrée sur l'atome d'halogène, recouvre la première couche de solvatation de l'anion. L'ensemble de la configuration de solvatation peut donc être considéré comme l'«accepteur» dans une transition de CTTS (139). L'énergie E_{max} au maximum d'absorption des bandes CTTS a été ensuite exprimée dans le cadre de divers formalismes (voir, par exemple, réfs. 15 et 140).

Le développement des techniques de spectroscopie femtoseconde a rendu accessibles les aspects dynamiques relatifs au CTTS. Divers résultats expérimentaux concernant principalement les ions iodure et chlorure (56, 57, 141) en solution aqueuse ont été publiés récemment.

Pour des solutions 1 M en NaI ou KI, Long et al. (57, 141) ont constaté l'existence d'un état lié CTTS dans lequel l'électron «piégé» serait un précurseur de l'espèce intermédiaire e^-_{ir}. Les temps caractéristiques de solvatation de l'électron dans ces conditions ont pu être mesurés. Dans le cas de I^-, Long et al. (141) ont obtenu $T_2 = 600 \pm 40$ fs; ce temps est peu différent de celui mesuré par photoionisation de l'eau pure (540 ± 40 fs; voir sect. II-B.2). En revanche, la formation de e^-_{ir} a été trouvée sensiblement plus lente ($T_1 = 400 \pm 40$ fs; voir réf. 141) que dans le cas de l'eau pure (180 ± 40 fs; voir sect. II-B.2). L'existence d'un point isobeste à 850 nm a été avancée pour le passage $e^-_{ir} \rightarrow e^-_{aq}$ et la transition correspondante serait discontinue (57, 141). Cependant, dans des travaux plus récents, Long et al. (141) ont suggéré que seule une faible fraction des électrons hydratés présents seraient produits selon le mécanisme CTTS précédemment décrit. D'après les auteurs, en effet, une fraction importante de ces e^-_{aq} seraient formés via un processus de photoionisation à trois photons (4 eV/photon), plutôt qu'à partir de l'excitation CTTS

à 8 eV. Ces auteurs (141) ont, de plus, indiqué que l'état CTTS initial évoluerait, pour une large part, vers l'état CTTS de plus basse énergie. Ce dernier état, dont le temps de formation serait inférieure à 50 fs (mesure limitée par le temps de résolution de l'appareil), se relaxerait ensuite en 80 ± 40 fs vers l'état fondamental de I^-.

Gauduel et al. (56), quant à eux, ont interprété leurs résultats concernant des solutions aqueuses de chlorure de sodium (1 ou 6 M) en supposant la formation non diffusionnelle de paires de contact électron–atome $[e^-{:}Cl]_{nH_2O}$, formation qui a été déjà évoquée plus haut (voir sect. II-B.2). D'après ces derniers auteurs, deux populations de paires électron–atome seraient formées, l'une se relaxant directement, en 330 fs, vers l'état fondamental de Cl^-, et l'autre conduisant en 750 fs à e^-_{aq}, via un processus de photodétachement électronique.

Afin de présenter une description moléculaire des états électroniques et des spectres CTTS précédemment cités, différents auteurs (84, 85, 142, 143) ont développé, parallèlement, des travaux de simulation. Les plus récents d'entre eux mettent en oeuvre des calculs de dynamique non adiabatique (84, 143; voir aussi réf. 10). Ceux-ci ont révélé l'existence de deux voies de relaxation électronique de l'état initialement créé par une photoexcitation de l'ion halogénure de 8 eV : l'une, mineure, conduirait au transfert direct, non adiabatique, de l'électron vers une des cavités pièges préexistantes du solvant, et l'autre, dominante, impliquerait, sur une échelle de temps inférieure à ~50 fs, une transition vers l'état le plus bas en énergie de la bande CTTS, suivie du détachement adiabatique de l'électron et d'une recombinaison géminée non diffusionnelle ultrarapide des paires électron – atome d'halogène alors formées. Ces résultats sont compatibles avec l'allure générale des phénomènes expérimentaux déjà décrits (56, 57, 141).

Par ailleurs, dès 1954, Platzman et Franck (144) ont suggéré une corrélation possible entre les valeurs de E_{max} correspondant aux maxima des spectres d'absorption de e^-_{solv} et des ions iodure solvatés. Une relation linéaire empirique a effectivement été établie dans ce cas par Fox et Hayon (145) pour toute une série de solvants. En dépit de l'analogie suggérée par une telle relation, un certain nombre de dissemblances ont été récemment soulignées (6), si bien que e^-_{solv} ne semble pas pouvoir être considéré comme le prototype d'un anion monoatomique X^- solvaté.

3. Mobilité de e^-_{solv}

La détermination de la mobilité (μ_e) de e^-_{solv} dans des solvants de diverses polarités et sa variation avec certains paramètres caractérisant soit e^-_{solv} lui-même, soit le solvant, permettent de mieux cerner le mécanisme de la migration d'un électron en excès dans ces milieux. Les valeurs de μ_e mesurées sont intermédiaires entre celles des anions solvatés et celles des conducteurs métalliques. Ceci résulte du fait que la mobilité électronique peut être de type ionique, c'est-à-dire, $\mu_e \sim 10^{-2}$–10^{-4} $cm^2\ V^{-1}\ s^{-1}$ (88, 146; voir aussi réf. 7), lorsque l'électron est solvaté et se déplace avec une cage de solvatation, ou voisine de celle de e^-_{qf}, c'est-à-dire, $\mu_e > 1$–10 $cm^2\ V^{-1}\ s^{-1}$ (voir, par exemple, réfs. 146 et 147), dans le cas où l'électron migre hors des sites de piégeage, ou encore une combinaison de ces deux mécanismes.

(a) Variation de μ_e avec E_{max}

Une relation simple ne peut être établie; cependant, si on porte E_{max} en fonction de μ_e pour différents solvants polaires, on peut distinguer deux régions : l'une pour $\mu_e < (2\text{–}3) \times 10^{-3}$ $cm^2\ V^{-1}\ s^{-1}$ où E_{max} augmente quand μ_e diminue, l'autre pour $\mu_e > 3 \times 10^{-3}$ $cm^2\ V^{-1}\ s^{-1}$ où E_{max} reste à peu près constante (~0,5 eV). On peut penser que le domaine des faibles valeurs de μ_e correspondrait à des liquides présentant des pièges profonds où l'électron serait en permanence stabilisé par les couches de molécules solvatantes. Au contraire, dans le domaine des valeurs de μ_e plus élevées, l'électron serait en interaction faible avec le solvant et sa migration facilitée (148–150; voir aussi réf. 7).

(b) Variation de μ_e avec la viscosité η du solvant

D'après les données de la littérature concernant les solvants polaires, la variation de μ_e en fonction de η peut être représentée, à la température ambiante, par une relation de la forme

$$\mu_e = C\eta^{-n}$$

où l'intervalle de confiance à 99% de l'exposant inclut la valeur $n = 1$. Une telle variation est en faveur d'un mécanisme de diffusion pour la migration de e^-_{solv} (151; voir aussi réf. 7), conclusion qui est d'ailleurs elle-même en accord avec les résultats de calculs de simulation obtenus pour e^-_{aq} (152–154) et pour l'électron ammonié (155).

4. Déclin de l'électron relaxé

Le déclin initial de e^-_{aq} a été mesuré pour des temps allant jusqu'à plusieurs centaines de picosecondes, ceci après photoionisation de l'eau pure et spectroscopie laser femtoseconde (31, 43, 45, 46, 48, 52, 57, 86, 87, 156–158). On observe des cinétiques de déclin analogues (50–60% des e^-_{aq} ayant disparu au bout d'environ 60–80 ps) dans les expériences de Lu et al. (156) et de Gauduel et al. (157), pour des photons de 4 eV et un processus supposé biphotonique (figure 7). Dans les conditions expérimentales de Houde et al. (45, 46), pour lesquelles l'excitation met en jeu au moins quatre photons de 2 eV, le déclin est plus lent (~20% pendant les 17 premières picosecondes). De même, la décroissance trouvée par Sander et al. (31, 52), pour un processus biphotonique impliquant des photons de 5 eV, est également lente (~30% à 180 ps). En revanche, McGowen et al. (158), se réclamant d'un processus à 3 photons (3,2 eV/photon), ne décèlent aucune évolution notable (≤5%) de l'absorption de e^-_{aq} pour des temps allant jusqu'à 700 ps.

Ces différentes vitesses de déclin ont été attribuées à une variation du nombre de photons absorbés simultanément selon les conditions expérimentales de chaque montage, entraînant donc une variation de la recombinaison géminée avec l'intensité de l'impulsion excitatrice (43). Suivant l'énergie absorbée, l'électron libéré se trouve plus ou moins éloigné de l'ion positif parent et son déclin serait d'autant plus lent qu'il serait plus éloigné. Malheureusement, il est difficile de comparer précisément, à ce point de vue, les techniques expérimentales, ce qui rend actuellement cette hypothèse difficilement vérifiable.

Nous avons vu plus haut (voir sect. II-B.2) que les espèces H_3O^+ et OH étaient formées avant l'hydratation de l'électron; ce sont elles qui, par les réactions géminées qu'elles entraînent, seraient responsables du déclin de e^-_{aq} à temps courts.

Fig. 7. Variation en fonction du temps de l'absorbance des électrons hydratés après photoionisation de l'eau pure à 21°C, pour des photons de 4 eV et un processus supposé biphotonique : (*a*) d'après Lu et al. (156), pour λ_{test} = 700 nm; (*b*) d'après Gauduel et al. (157), pour λ_{test} = 720 nm.

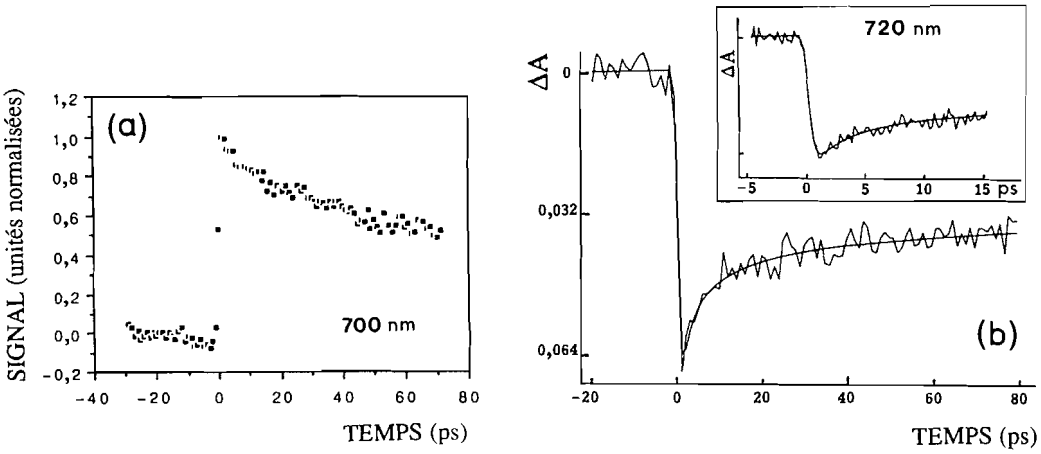

Tableau 2. Propriétés thermodynamiques de e^-_{aq} à 298 K.[a]

	Jortner et Noyes (162)	Hickel et Sehested (164 et 167)	Han et Bartels (165)	Schwarz (166)
ΔG^0_{hyd}	−157		−161 ± 14	
ΔH^0_{hyd}	−159	−142 ± 7	−126 ± 11	−142
ΔS^0_{hyd}	−7,9	49 ± 23	118 ± 20	67

[a]Valeurs exprimées en kilojoules par mole pour l'enthalpie libre et l'enthalpie, et en joules par mole et par degré pour l'entropie (1 kJ/mol = 1,0364 × 10^{-2} eV/molécule).

Ces réactions de recombinaison ont été récemment analysées par simulation; les résultats obtenus permettent de conclure (159, 160) que l'attraction par H_3O^+ limite la diffusion de e^-_{aq}, augmentant ainsi l'efficacité de la réaction de celui-ci avec OH : sur l'échelle de temps 0–80 ps, cette dernière serait ~7 fois plus probable que la recombinaison avec H_3O^+ (160).

Des expériences de déclin (8 eV, processus biphotonique) ont été également effectuées sur des solutions aqueuses 1 M en OH^- (57), Cl^- (56, 57) ou I^- (57). Selon Long et al. (57), la disparition de e^-_{aq} est plus lente que dans le cas de l'eau pure. Ainsi, après 70 ps, ces auteurs obtiennent respectivement pour les trois anions cités, 30, 20 et 11% d'électrons hydratés disparus. Les différences observées avec l'eau pure (50–60%) sont attribuées au fait que, dans ce dernier cas, e^-_{aq} se recombine avec un cation, alors qu'il se recombine avec une espèce neutre dans le cas des solutions anioniques. Par ailleurs, l'évolution cinétique complexe intervenant pour de telles solutions à des temps très courts (inférieurs à quelques picosecondes) a été étudiée, ainsi que son interprétation, par Long et al. (57, 141) et Gauduel et coll. (56); ces travaux ont été mentionnés ci-dessus, dans la section II-C.2-c.

Le déclin picoseconde de l'électron relaxé a, de plus, été mesuré dans D_2O par spectroscopie laser femtoseconde mettant en jeu un processus biphotonique (4 eV/photon). Un effet isotopique est constaté : 38% des électrons hydratés ont disparu au bout de 165 ps, contre 46% dans le cas de H_2O (87); d'autres auteurs (86; voir aussi réf. 11) rapportent les valeurs correspondantes suivantes, à ~100 ps : 49% pour D_2O et 55% pour H_2O. L'hypothèse avancée pour expliquer un tel effet repose sur le fait que D_2O est un liquide plus ordonné que H_2O, et que par conséquent la concentration des pièges d'électron y est plus faible (52). La distance moyenne séparant l'électron libéré de son cation parent est donc plus grande dans D_2O que dans H_2O; dans le premier cas, la recombinaison géminée de e^-_{aq} se trouve ainsi défavorisée.

D. Données thermodynamiques

Baxendale (161) le premier a considéré à la fois l'équilibre en solution aqueuse

$$e^-_{aq} + H_2O \rightleftarrows H_{aq} + OH^-_{aq}$$

et le cycle thermodynamique

$$e^-_{aq} + H^+_{aq} \rightarrow 1/2\ (H_2)_{aq}$$

$$e^-_g + H^+_g \rightarrow (H)_g \rightarrow 1/2\ (H_2)_g$$

ce qui conduit à la valeur de l'enthalpie libre d'hydratation de l'électron $\Delta G^0_{hyd} = -167$ kJ/mol.

À partir d'un cycle thermodynamique analogue et en supposant que les équations qui relient ΔG^0_{solv} et ΔS^0_{solv} au rayon d'un anion solvaté puissent être appliquées à e^-_{aq}, les termes enthalpique ΔH^0_{hyd} et entropique ΔS^0_{hyd} ont été évalués pour l'électron hydraté (162, 163).

Des études plus récentes et plus approfondies, s'appuyant soit sur l'équilibre $e^-_{aq} + H_2O \rightleftarrows H_{aq} + OH^-_{aq}$ (164, 165), soit sur l'équilibre $e^-_{aq} + (NH_4^+)_{aq} \rightleftarrows H_{aq} + (NH_3)_{aq}$ (166), ont conduit aux valeurs de ΔG^0_{hyd}, ΔH^0_{hyd} et ΔS^0_{hyd} rassemblées dans le tableau 2, valeurs exprimées en kilojoules par mole pour

l'enthalpie libre et l'enthalpie, et en joules par mole et par degré pour l'entropie. Ce tableau appelle un certain nombre de commentaires.

(*i*) Au vu des larges marges d'erreurs estimées par les différents auteurs, les valeurs précédentes montrent un accord raisonnable si l'on excepte celle de ΔS^0_{hyd} donnée par Jortner et Noyes (162).

(*ii*) La valeur absolue de ΔH^0_{hyd} est plus faible pour e^-_{aq} que pour les anions monoatomiques X^-_{aq}. Citons, par exemple : pour I^-, $\Delta H^0_{hyd} = -257$ kJ/mol et pour Cl^-, $\Delta H^0_{hyd} = -318$ kJ/mol (168). En d'autres termes, et comme on pouvait s'y attendre, e^-_{aq} est moins lié que les ions X^-_{aq}.

(*iii*) L'entropie d'hydratation relative à l'électron est positive, alors que tous les anions monoatomiques X^- sont caractérisés par une valeur de ΔS^0_{hyd} négative. Citons, par exemple : pour I^-, $\Delta S^0_{hyd} = -11{,}4$ J mol^{-1} deg^{-1} et pour Cl^-, $\Delta S^0_{hyd} = -49{,}4$ J mol^{-1} deg^{-1} (169). Les électrons hydratés apparaissent ainsi comme d'efficaces *structure breakers* dans l'eau (169, 170). Ce résultat serait explicable par le fait que la distribution radiale des molécules d'eau autour de l'électron est beaucoup plus diffuse qu'autour des anions classiques (voir, par exemple, réfs. 99 et 103).

Notons enfin que cette disparité entre les signes de ΔS^0_{hyd} pour e^-_{aq} d'une part et les ions X^-_{aq} d'autre part ne semble pas en faveur de l'interprétation de Robinson et coll. (171) qui assimilent l'électron hydraté à un complexe $(OH^-...H_3O)_{aq}$ en s'appuyant sur une certaine similitude entre les rôles joués par e^-_{aq} et les ions OH^-_{aq} ou H^+_{aq} vis-à-vis de l'organisation structurale des molécules d'eau voisines.

III. Électrons en excès en solutions micellaires

Les milieux microhétérogènes, dits «milieux organisés», qui sont des agrégats de molécules amphiphiles, naturelles ou synthétiques, neutres ou ioniques, ont fait l'objet de multiples études au cours des dernières décennies (voir, par exemple, réfs. 172–176). Nous ne considérerons ici que les *milieux organisés clos* (MOC), c'est-à-dire des globules lipidiques en solution aqueuse : micelles (Mi) directes et vésicules (Ve) ou des globules aqueux en solution hydrocarbonée (micelles inverses). Les caractéristiques spécifiques de ces systèmes dont on peut tirer profit sont principalement : (*i*) une aire interfaciale considérable si bien que les réactions en surface peuvent se substituer à des réactions en volume; (*ii*) l'existence fréquente d'un potentiel électrique interfacial qui peut être modulé expérimentalement et calculé de façon approximative; (*iii*) la compartimentation dans deux phases distinctes des réactifs et (ou) des espèces transitoires suivant leur caractère hydrophile ou hydrophobe, situation qui peut augmenter très notablement la durée de vie de ces dernières. Comme pour les solutions homogènes, les électrons en excès peuvent être produits soit par radiolyse, soit par photoionisation de chromophores appropriés. Dans le cas des Mi directes, les plus étudiées, les solutions micellaires sont généralement peu concentrées, de l'ordre de 10^{-4}–10^{-3} M. Les électrons produits par voie radiolytique sont ainsi formés dans la phase aqueuse, sans effet direct sur les agrégats micellaires. Dans ces conditions, l'objectif est essentiellement d'examiner le pouvoir catalytique des Mi ou Ve sur la réactivité des e^-_{aq} vis-à-vis des molécules de surfactant ou d'additifs micellisés. Les réactions obéissent à des lois complexes de cinétique non homogène (177). Cet aspect ne sera pas traité ici. En revanche, des expériences de photoionisation de composés micellisés peuvent apporter des informations intéressantes sur la dynamique et l'énergétique de la production de e^-_{exc} (176).

A. Dynamique de formation de e^-_{aq} en micelles directes ou inverses

La production de e^-_{aq} par ionisation biphotonique (4 eV/photon) de phénothiazine a été suivie, comme pour l'eau pure, sous excitation laser femtoseconde et spectroscopie d'absorption résolue dans le temps (178–180). Un état présolvaté absorbant dans l'infra-rouge, précurseur de e^-_{aq}, a été mis en évidence dans ce cas également. Le temps T_1 de montée de l'absorption infra-rouge est trouvé égal à 250 ± 20 fs pour les Mi directes (micelles cationiques Mi^+ ou anioniques Mi^-) et à 140 ± 10 fs pour les Mi inverses. Cette dernière valeur est proche de celle déterminée pour l'eau pure (110 ± 30 fs; voir sect. II-B.2); en revanche, la présence de micelles $Mi^\pm$ paraît retarder la formation de e^-_{ir}. Pour les Mi directes, la dynamique des étapes primaires de la photoionisation : séparation intramicellaire des charges et diffusion de e^-_{exc} vers la phase aqueuse, est trouvée la même pour Mi^+ et Mi^-.

Pour les systèmes micellaires cités ci-dessus, comme dans le cas de l'eau pure ($T_2 = 240 \pm 40$ fs; voir sect. II-B.2), e^-_{ir} relaxe vers l'état hydraté avec une seule constante de temps : $T_2 = 270 \pm 20$ fs (179, 180). Ceci suggère que la localisation initiale de e^-_{exc} et sa solvatation complète s'effectuent à une distance de l'interface micellaire pour laquelle la constante diélectrique et la force ionique sont celles relatives à l'eau en masse.

B. Énergies seuil d'ionisation et rendements en e^-_{aq} en micelles et vésicules

La photoionisation monophotonique du pérylène et de la tétraméthylbenzidine (TMB) incorporés dans des micelles directes anioniques, neutres (Mi^0) ou cationiques a été étudiée en fonction de la longueur d'onde d'excitation λ_{exc} et du potentiel électrique interfacial $\Delta\Psi$ (181, 182). Plusieurs conclusions peuvent être dégagées : (*i*) les courbes de rendement de photoionisation $\Phi_{e^-_{aq}}$ (λ_{exc}) sont décalées vers le rouge par rapport aux courbes de rendement relatives à des solutions organiques homogènes. Cette plus faible valeur de l'énergie seuil d'ionisation (E_i) répercute la variation de l'énergie fondamentale V_0 de l'électron quasi-libre avec le solvant considéré : eau liquide par comparaison avec un solvant organique. (*ii*) Pour un chromophore donné, la valeur de E_i n'est pas sensible à une variation du potentiel électrique interfacial. Ceci traduit le fait que $\Delta\Psi$ est au moins d'un ordre de grandeur inférieur aux autres facteurs qui contrôlent E_i, notamment V_0. (*iii*) les formes différentes des courbes $\Phi_{e^-_{aq}}$ (λ_{exc}) obtenues pour Mi^- d'une part, et pour Mi^0 et des solutions homogènes d'autre part, peuvent refléter une plus grande probabilité pour l'électron d'échapper à une recombinaison géminée dans le cas des micelles négatives.

L'effet du potentiel $\Delta\Psi$ sur le rendement de photoionisation a ensuite été précisé en modulant $\Delta\Psi$ par addition de différents sels à une solution micellaire de Mi^- (183, 184). On trouve ainsi par photoionisation du pérylène et de la TMB en Mi^- ou Ve^- que le rendement $\Phi_{e^-_{aq}}$ est une fonction linéaire de

Fig. 8. Rendements de photoionisation $\Phi_{e^-_{aq}}$ en Mi^- de SDS (*sodium dodecyl sulfate*) et en Ve^- de DHP (*dihexadecyl phosphate*) en fonction du potentiel électrique interfacial $\Delta\Psi$: (1) pérylène dans Mi^- SDS, (2) TMB dans Mi^- SDS et (3) TMB dans Ve^- DHP (d'après Bernas et al. (184)).

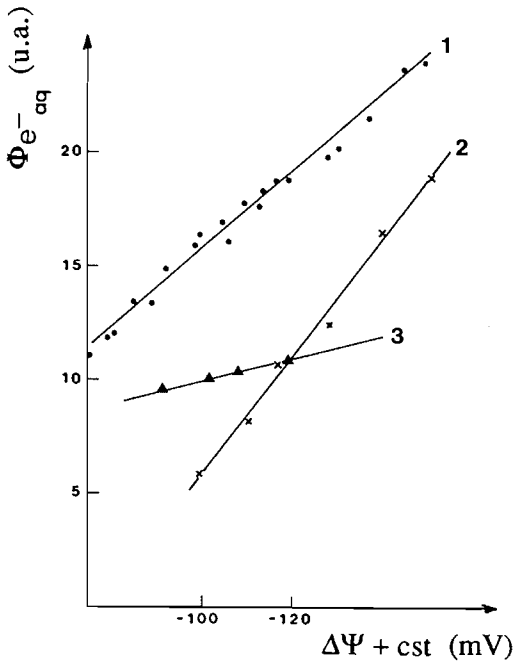

$\Delta\Psi$ (figure 8). Le potentiel négatif, répulsif pour e^-_{exc}, ou bien facilite l'éjection de l'électron à partir d'états de Rydberg s'étendant au-delà de l'interface micelle–eau, ou bien (et) oppose une barrière au retour de e^-_{aq} vers le cation qui reste micellisé.

C. Micelles inverses : Rendements en e^-_{aq} et organisation de l'eau

En micelles inverses, e^-_{aq} peut résulter de la photoionisation de chromophores hydrophiles ou hydrophobes, ou de la radiolyse du solvant hydrocarboné suivie de la localisation des e^-_{exc} dans le coeur aqueux des micelles. Des diverses études publiées, il est possible de dégager les conclusions suivantes.

(*i*) Dans les expériences de radiolyse picoseconde de Bakale et al. (185), l'efficacité de capture des électrons en excès par l'eau micellisée dans le système H_2O/AOT/isooctane[5] augmente avec le rapport des concentrations molaires $w_0 = [H_2O]/[AOT]$ qui caractérise le volume du coeur aqueux. Les microgouttes H_2O/AOT n'offriraient pas de pièges suffisamment profonds pour qu'il y ait attachement d'électron à chaque collision jusqu'à ce qu'au moins 30 molécules d'eau soient associées à chaque molécule de surfactant ($w_0 \geq 30$).

(*ii*) Excitation et spectroscopie laser femtoseconde ont de plus permis la caractérisation directe des étapes primaires du piégeage de e^-_{exc} dans l'eau micellisée. Ainsi, pour $w_0 = [H_2O]/[AOT] = 50$, Gauduel et al. (180) ont montré que la photoionisation d'un composé hydrophobe (phénothiazine) localisé à la périphérie micellaire donne naissance à deux

[5] AOT désigne le surfactant : di(2-éthylhexyl)sulfosuccinate de sodium.

Fig. 9. Spectre d'absorption transitoire de e^-_{aq} à 2 ps en micelles inverses de AOT pour trois valeurs du rapport des concentrations molaires $w_0 = [H_2O]/[AOT] = 50$, 5 et 0 (d'après Gauduel et al. (180)).

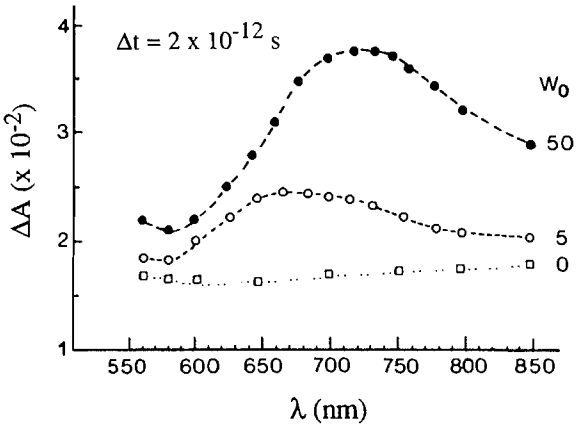

populations d'électrons. Les uns se piègent dans le solvant hydrocarboné (dans ce cas, le *n*-heptane) en 90 ± 10 fs, les autres s'hydratent en deux étapes : les e^-_{ir} apparaissant en 140 fs et relaxant vers l'état totalement hydraté en 270 fs. Comme mentionné plus haut, la similitude de ces temps caractéristiques avec ceux relatifs à l'eau pure suggère que localisation et solvatation s'effectuent alors au coeur de la poche aqueuse où aucune structure particulière n'est imposée par l'interface.

Pour $w_0 = 5$, où l'eau micellisée présente un temps de corrélation rotationnelle nettement plus élevé que l'eau en masse (186), la constante de temps T_2 correspondant à la formation de e^-_{aq} atteint 500 fs, alors que la composante rapide de piégeage de e^-_{exc} dans le *n*-heptane reste inchangée (90 fs) (180).

(*iii*) L'efficacité d'attachement de e^-_{exc} dans les micelles inverses H_2O/AOT dépend par ailleurs du solvant utilisé : elle est plus faible pour un solvant où la mobilité de e^-_{exc} est plus élevée (187). Ainsi, pour des micelles de taille comparable, la capture de e^-_{exc} a été trouvée, selon la valeur du rayon micellaire, de 5 à 20 fois plus efficace pour l'isooctane ($\mu_e = 6{,}5$ cm^2 V^{-1} s^{-1}) que pour le tétraméthylsilane ($\mu_e = 103$ cm^2 V^{-1} s^{-1}; voir, par exemple, réf. 147).

(*iv*) Pour $w_0 \geq 30$, le spectre d'absorption optique de e^-_{aq} est identique à celui obtenu dans l'eau pure. En abaissant w_0, on observe un déplacement vers le bleu du maximum d'absorption (figure 9), déplacement qui peut être associé à la forte concentration locale des contre-ions Na^+ à l'intérieur du coeur micellaire (180, 188–191); cette concentration atteindrait ~6 M pour $w_0 = 5$ et un degré de dissociation des molécules AOT de 0,5. L'existence d'une interface chargée se traduit donc par un gradient de concentration de e^-_{aq}, et de plus, les propriétés spectroscopiques de ce dernier dépendent de l'état d'organisation de l'eau dans la région interfaciale.

(*v*) La largeur de la bande d'absorption de e^-_{aq} diminue avec w_0 (188, 191, 192) et aussi avec la température. Ces observations ont été considérées comme l'indice d'un environnement plus ordonné, la bande d'absorption de e^-_{aq} présentant dans ces conditions une certaine analogie avec celle de l'électron piégé dans la glace à −194°C (192). Par ailleurs, Gębicki et al. (191) ont indiqué récemment que la forme de la bande

d'absorption de e^-_{aq} dépendrait, non seulement de w_0, mais également du type de solvant hydrocarboné utilisé.

(*vi*) e^-_{aq} n'est pas observé en-dessous d'une certaine taille critique de la poche d'eau correspondant à $w_0 \leq 5$ (180, 188, 189), ce qui pourrait signifier que toutes les molécules d'eau sont alors préférentiellement engagées dans les couches de solvatation des contre-ions Na^+. Une telle interprétation est confortée par de récents résultats de spectroscopies Raman et infra-rouge qui permettent de distinguer les contributions respectives de l'eau liée, dont la structure serait imposée par le surfactant, et de l'eau «libre», la contribution de cette dernière s'annulant justement pour $w_0 \sim 4$–6 (193, 194). En revanche, pour le système H_2O/AOT/isooctane, Jain et al. (195) distinguent trois types d'eau coexistant dans le volume du coeur micellaire : eau libre, eau liée et eau piégée à l'interface micellaire. Par spectroscopie infra-rouge et déconvolution en plusieurs gaussiennes du spectre dans la région d'élongation de O–H, ces auteurs estiment que, pour $w_0 = 5$, le nombre de molécules d'eau libres rapporté à une molécule de surfactant serait de 3. Pour un nombre d'agrégation moyen de 40 (196), correspondant à un rayon de coeur aqueux micellisé de ~12 Å, environ 120 molécules d'eau resteraient à l'état libre dans chaque micelle. La solvatation de e^-_{exc} pourrait cependant être trop lente pour entrer en compétition avec la diffusion de celui-ci. Soulignons enfin que la valeur seuil d'observabilité de e^-_{exc} peut dépendre de la mobilité de e^-_{exc}, c'est-à-dire de la nature du solvant hydrocarboné utilisé (187).

En résumé, l'ensemble des résultats présentés ci-dessus illustrent bien l'effet de l'état d'organisation des molécules d'eau dans les MOC. Ils soulignent également l'influence du potentiel électrique interfacial sur les rendements en électrons hydratés et sur leur distribution au voisinage de l'interface. Ces conclusions, valables pour des milieux organisés synthétiques, devraient pouvoir être étendues aux membranes naturelles qui impliquent une interface chargée stable, ainsi qu'aux poches aqueuses des bioagrégats.

IV. Agrégats négativement chargés

D'une façon générale, les expériences conduites depuis une à deux décennies sur les agrégats moléculaires ont évidemment tenté d'établir une transition entre la phase gazeuse et les phases condensées. Plus particulièrement, l'étude du processus d'attachement d'un électron en excès a été largement motivée par la possibilité d'assimiler les agrégats gazeux $(H_2O)_n^-$ et $(NH_3)_n^-$ à des modèles d'électrons solvatés dans le liquide correspondant.

Après la suggestion initiale (197) que des agrégats gazeux de dimensions suffisantes seraient susceptibles d'attacher un électron, on a été amené à examiner la formation, l'état et les propriétés de e^-_{exc} en fonction de n. Les résultats, tant expérimentaux que théoriques, ont alors permis de préciser la nature des forces de stabilisation de e^-_{exc} en milieu condensé.

A. Données expérimentales

1. Méthodes de production

Les premières évidences (198) d'agrégats négativement chargés $(H_2O)_n^-$ ont été obtenues à partir de jets supersoniques de vapeur d'eau (100–1000 Torr; 1 Torr = 133.3 Pa), à ~400 K, irradiée par les rayons β^- d'une source radioactive. Les

Fig. 10. Spectres de masse d'agrégats d'eau négativement chargés $(H_2O)_n^-$ et $(D_2O)_n^-$: (*a*) d'après Haberland et al. (199); (*b*) d'après Kondow et al. (202).

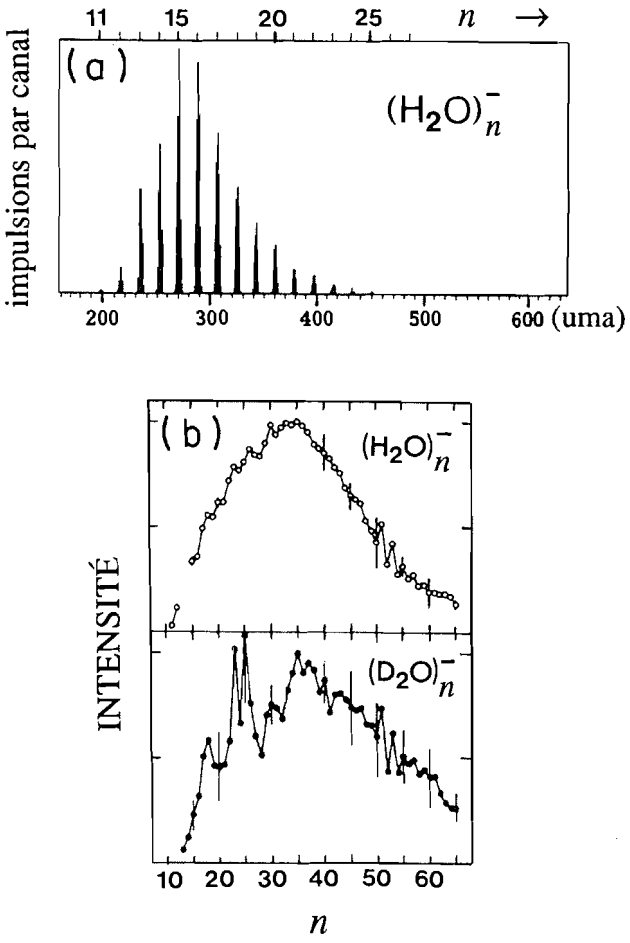

électrons émis sont rapidement thermalisés et une analyse par spectrométrie de masse à temps de vol montre un pic principal à la masse 198 ($n = 11$) avec un seuil à $n = 8$. Un montage amélioré (199, 200), où des photoélectrons d'énergie cinétique inférieure à 0,5–2 eV sont injectés dans un jet supersonique de vapeur d'eau en expansion, a permis de minimiser l'effet des impuretés, les seuls pics enregistrés étant alors ceux correspondant à $(H_2O)_n^-$ (figure 10*a*).

L'attachement d'électrons a également été réalisé sur des agrégats libres, préformés et froids, les électrons incidents ayant dans ce cas une énergie quasi-nulle (201). La formation d'anions $(H_2O)_n^-$ est observée pour $n \geq 11$ (ou $n \geq 12$ pour l'eau deutérée), en accord avec la distribution des valeurs de n trouvée par Haberland et coll. (198–200).

Les deux mécanismes suivants de déclin interviennent :

$$(H_2O)_n^- \rightarrow (H_2O)_m^- + (n - m)\, H_2O$$

$$(H_2O)_n^- \rightarrow (H_2O)_n + e^-$$

et c'est le deuxième qui apparaît comme le plus efficace. La probabilité de celui-ci décroît quand n augmente, ce qui atteste d'une augmentation parallèle de l'affinité électronique adiabatique d'un agrégat d'eau avec ses dimensions. Knapp et al.

(201) suggèrent qu'un piège peu profond pourrait être associé à un état de surface ne présentant pas de barrière de potentiel à l'électron. En revanche, ils notent qu'on ne peut trancher sur l'origine de la brusque montée de la section efficace de formation de $(H_2O)_n^-$ observée pour $n \geq 11$: s'agit-il d'une prélocalisation qui devient plus efficace ou d'une stabilité accrue de l'agrégat négatif relaxé?

Une toute autre approche a été mise en oeuvre par Kondow et coll. (202). Ces auteurs forment $(H_2O)_n^-$ et $(D_2O)_n^-$ par collision d'agrégats neutres avec des atomes de gaz rares excités dans des états de Rydberg élevés :

$$(H_2O)_n + Kr^{**} \rightarrow (H_2O)_n^- + Kr^+$$

l'électron transféré ayant alors une énergie de quelques dizaines de meV avec une distribution en énergie du même ordre. Dans ces conditions, il n'y aurait pas d'évaporation concomitante de molécule monomère après l'attachement de l'électron de Rydberg. Cette technique conduit, de nouveau, aux seuils d'attachement $n = 11$ pour H_2O et $n = 13$ pour D_2O (figure 10*b*). Si, de plus, les atomes de gaz rares sont excités par un laser accordable, l'énergie des électrons de Rydberg peut varier — entre environ 5 et 300 meV (203, 204). Ainsi, pour des valeurs élevées de cette énergie (≥50 meV) et en présence d'hélium comme gaz porteur des agrégats neutres, les anions $(H_2O)_2^-$, $(H_2O)_6^-$ et $(H_2O)_7^-$ ont pu être observés, conformément aux résultats antérieurs de Haberland et al. (200). Il a été montré aussi que l'énergie seuil d'observabilité de l'anion dimère dépend de la nature du gaz porteur utilisé (203). Enfin, sous des conditions expérimentales très spécifiques, cette même approche mettant en jeu des collisions d'atomes excités Xe** avec des agrégats mixtes eau–ammoniac a donné lieu à la formation d'anions $[(H_2O)_p(NH_3)_q]^-$ avec les nombres «magiques» $n = p + q = 2, 5, 6, 7, 9$ et au-dessus (205); les auteurs ont souligné que la production de l'anion dimère mixte $(H_2O...NH_3)^-$ constitue un test pour la théorie de l'attachement d'un électron à un dipôle.

2. Photodétachement et photofragmentation

Les spectres de photoélectrons (photodétachement) obtenus à partir d'agrégats $(H_2O)_n^-$ (n = 2–69) à l'aide de photons visibles consistent, pour $n \geq 11$, en des bandes uniques, larges et asymétriques (206). Les énergies correspondant aux maxima de ces spectres représentent les énergies verticales de détachement de l'électron; celles-ci augmentent régulièrement de 0,75 à 1,92 eV quand n passe de 11 à 69. Leur variation avec $n^{-1/3}$ est linéaire, avec une extrapolation à l'origine ($n \rightarrow \infty$) de 3,3 eV qui équivaudrait, d'après ces auteurs, au seuil photoélectrique (~3,2 eV) de e^-_{aq} dans la glace.

Parallèlement au photodétachement, on observe une photofragmentation; les rendements relatifs de ces deux processus compétitifs ont été déterminés pour $15 \leq n \leq 40$ en détectant simultanément les intensités des ions parents et fragments sous excitation par un faisceau laser pulsé d'énergie supérieure au seuil de photodétachement (0,8 eV) (207). Le rendement quantique de photofragmentation (ϕ_n) croît, à partir de zéro, pour n variant de 15 à 20, et atteint un palier égal à 0,56 ± 0,10 pour $n > 20$. Cette variation de ϕ_n avec la taille de l'agrégat est semblable à la distribution des ions parents $(H_2O)_n^-$ en fonction de n, les parents les plus abondants se fragmentant donc plus efficacement. Une telle corrélation indique que la dynamique de la réaction d'attachement de l'électron serait analogue à celle de son photodétachement au voisinage du seuil.

Fig. 11. Spectres de photodestruction d'agrégats d'eau $(H_2O)_n^-$, pour n = 18 (△) et 30 (■), et pour des photons variant entre 0,75 et 4,66 eV. La ligne en pointillés représente, à titre de comparaison, le spectre d'absorption de e^-_{aq} à 298 K (d'après Campagnola et al. (208)).

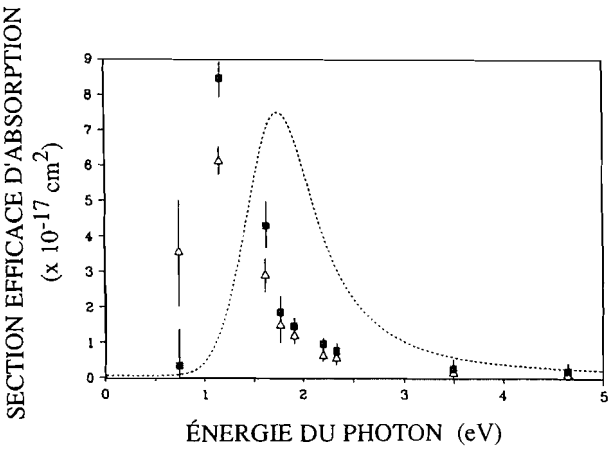

Compte tenu de ces deux processus compétitifs, c'est la photodestruction des ions parents, plutôt que le spectre d'action du photofragment, qui permet d'atteindre indirectement le spectre d'absorption de l'agrégat négatif. La figure 11 reproduit les résultats obtenus sur la photodestruction de $(H_2O)_n^-$ pour n = 18 et 30, et pour des photons variant entre 0,75 et 4,66 eV (208, 209). La section efficace de photodestruction pour $n = 30$, qui apparaît décalée vers le rouge (~0,5 eV) par rapport au spectre d'absorption de e^-_{aq} à 298 K, présente une certaine analogie avec ce dernier, en ce qui concerne notamment la force d'oscillateur et la traîne vers le bleu.

Ainsi, il apparaît que les paramètres qui contrôlent la forme du spectre de e^-_{aq} interviendraient aussi dans le cas des microagrégats chargés négativement. L'état «excité» de $(H_2O)_n^-$ peut être testé en examinant les conséquences de l'absorption : une transition état lié → continuum se traduirait par l'éjection de l'électron en excès (photodétachement), tandis qu'une transition état lié → état lié aboutirait, après conversion interne de l'énergie électronique vers des niveaux vibrationnellement excités de l'état fondamental, à une photofragmentation. Campagnola et coll. (209) ont ainsi pu déconvoluer le spectre d'absorption obtenu pour $(H_2O)_{30}^-$ en deux composantes distinctes représentant respectivement ces deux types de transitions, la traîne d'absorption vers les grandes énergies étant principalement due à la photoéjection.

3. Réactions de $(H_2O)_n^-$

L'étude des réactions de $(H_2O)_n^-$ avec différents capteurs d'électrons (O_2, CO_2, NO, N_2O, Br_2 et CH_3Br) a montré qu'il ne s'agissait pas de simples transferts de charge (210). La réaction globale observée serait du type suivant :

$$(H_2O)_n^- + X \rightarrow X^-(H_2O)_m + (n - m)\, H_2O$$

X désignant le capteur.

En effet, la perte de molécules d'eau neutres ($n - m$) impliquée dans de tels processus a été mise en évidence par un

déplacement de la courbe de distribution en masse de l'ion parent $(H_2O)_n^-$. Cette évaporation peut, d'autre part, être corrélée avec l'exothermicité évaluée pour le transfert de charge vers X de l'électron lié à l'agrégat, transfert suivi de l'hydratation de l'ion résultant.

On aurait ainsi provoqué dans un agrégat gazeux l'équivalent d'une «chimie en microsolution» (210).

B. Traitements théoriques

Des calculs de simulation employant la méthode Monte Carlo et les intégrales de chemin révèlent que deux molécules d'eau peuvent fixer un électron; il en est de même pour le trimère dans une configuration linéaire (93, 211). Cependant, les énergies de liaison de e^-_{exc} ainsi évaluées sont très faibles : 3–6 meV pour le dimère et 4–9 meV pour le trimère. Expérimentalement, $(H_2O)_2^-$ ou $(H_2O)_3^-$ ne sont observés qu'en présence d'un gaz rare (He, Ar ou Xe) porteur (199, 200, 203, 205).

Des agrégats plus volumineux $(H_2O)_n^-$ (n = 8–128) ont ensuite été étudiés, pour une large gamme de température (79–300 K), par Barnett et coll. (212–215), au moyen de simulations de dynamique moléculaire utilisant les intégrales de chemin. Ces auteurs ont ainsi trouvé que l'affinité électronique adiabatique[6] favorise la formation d'états de surface pour $8 \lesssim n < 32$. Pour des agrégats de plus grandes dimensions ($32 < n < 64$), une transition graduelle s'effectuerait vers un mode de localisation interne, mode qui prévaudrait ensuite pour $n \gtrsim 64$. Les calculs de Barnett et al. (123, 217) indiquent par ailleurs l'existence d'états excités liés pour l'un et l'autre mode de localisation de e^-_{exc}; les énergies d'excitation associées aux états de surface seraient, selon ces auteurs, environ moitié de celles relatives aux états internes stables pour des agrégats plus grands. De plus, d'après ces calculs, le spectre d'excitation correspondant au mode de localisation interne de e^-_{exc} ne dépendrait que très faiblement de la taille de l'agrégat, pour n compris entre 64 et 256 (217). Il est intéressant de souligner que cet état interne de e^-_{exc} pourrait être considéré comme un précurseur de e^-_{aq}. Les interactions attractives de polarisation à longue distance, dont l'importance a par ailleurs été soulignée récemment dans ce contexte (216), joueraient ainsi un rôle prédominant dans l'hydratation de l'électron dans l'eau liquide.

Notons toutefois que la zone de transition présumée (n = 32–64) entre états de surface et modes internes de localisation de e^-_{exc} n'apparaît pas dans les spectres mesurés de photoélectrons (photodétachement) de $(H_2O)_n^-$, où l'énergie verticale de détachement de l'électron varie de façon régulière dans la gamme $11 < n < 69$ (206).

Dans le cas de l'ammoniac, les calculs de simulation de Barnett et al. (214) et de Marchi et al. (218) ont indiqué que les agrégats chargés négativement $(NH_3)_n^-$ n'apparaissaient respectivement que pour $n \geq 32$ ou 36, en bon accord avec l'expérience (199, 200, 205, 219) et en contraste marqué avec les résultats trouvés pour $(H_2O)_n^-$ ($n \geq 11$). Cette dernière différence traduirait, selon les auteurs, une interaction électron–molécule plus faible pour l'ammoniac que pour l'eau. Signalons toutefois que ces calculs n'ont pas pu s'accorder sur le fait de savoir si la formation de $(NH_3)_n^-$ impliquait des états de surface ou des modes internes de localisation de e^-_{exc} (218).

Pour les agrégats d'eau $(H_2O)_n^-$, Barnett et coll. (212, 214, 215) ont de plus calculé les énergies de liaison, verticales (EVBE) ou adiabatiques (EABE), des états internes de e^-_{exc} et montré qu'elles variaient linéairement avec $n^{-1/3}$ (figure 12). D'autre part, une extrapolation vers $n \rightarrow \infty$ des EABE fournit une valeur (−1,7 eV) en bon accord avec l'enthalpie de solution ou d'hydratation (ΔH^0_{hyd}) de e^-_{aq} (voir sect. II-D et tableau 2). La variation avec n des EVBE et des EABE calculées pour les états internes de e^-_{exc} permet ainsi d'établir «une transition continue entre les effets microscopiques de solvatation dans des systèmes finis et dans des fluides polaires macroscopiques» (215).

Enfin, l'évolution de e^-_{exc} en interaction avec un agrégat d'eau a été analysée par simulation adiabatique de la transformation dynamique, en temps réel, du système électron–agrégat (220–222). Pour $(H_2O)_n^-$ où n = 256, à 300 K, les résultats indiquent que l'électron initialement dans un état de surface évolue en moins de 2 ps vers un état interne solvaté. La migration de e^-_{exc} accompagnant le passage de l'état de surface vers l'état interne serait caractérisée par un mécanisme de transfert de nature polaronique, sans «sauts» entre sites de localisation successifs, ni entraînement de molécules d'eau (221).

En résumé, les résultats tant théoriques qu'expérimentaux ont révélé la formation d'agrégats gazeux négativement chargés relativement stables pour $(H_2O)_n$ où $n \geq 11$. De plus, les calculs relatifs à $(H_2O)_n^-$ montrent que, pour n assez grand, un mode de localisation interne supplante la formation d'états de surface, si bien que ces agrégats chargés volumineux seraient assimilables à des précurseurs de l'électron hydraté en phase liquide.

Fig. 12. Énergies de liaison, verticale (EVBE) et adiabatique (EABE), de l'état de localisation interne d'un électron en excès dans des agrégats d'eau $(H_2O)_n^-$ à 79, 158 et 300 K, en fonction de $n^{-1/3}$ (d'après Barnett et al. (213, 215)).

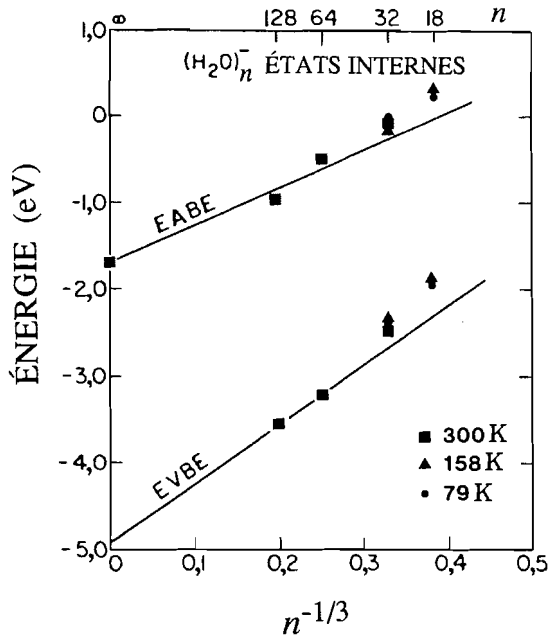

[6] Celle-ci, on le sait, prend en compte les énergies d'interaction de e^-_{exc} avec l'agrégat et de réorganisation moléculaire de ce dernier consécutive à la localisation de l'électron (voir, par exemple, réf. 216).

V. Conclusions

La solvatation des électrons en excès ($e^-_{exc} \rightarrow e^-_{solv}$) produits par radiolyse ou photoionisation a été étudiée principalement dans le cas de l'eau, des alcools liquides purs et de l'ammoniac.

En ce qui concerne les propriétés de e^-_{solv}, les nombres de coordination se sont avérés très voisins pour l'électron hydraté et l'anion Cl^-_{aq}, et le déplacement de la bande d'absorption de e^-_{solv} avec le solvant est trouvé analogue à celui observé pour les ions halogénure. En revanche, les données thermodynamiques et les traitements théoriques attestent d'une distribution de charge plus étalée pour e^-_{aq} que pour Cl^-_{aq}, ainsi que de grandes fluctuations dans la configuration de la cage de solvatation de l'électron hydraté.

Les avancées récentes réalisées dans la production d'impulsions laser ultracourtes et dans les calculs de simulation utilisant les méthodes de dynamique moléculaire et (ou) Monte Carlo associées aux intégrales de chemin, ont permis de mieux cerner le mécanisme séquentiel et la dynamique du processus de solvatation de e^-_{exc}. Pour l'eau liquide notamment, on a pu déterminer la cinétique d'apparition (temps caractéristique : $T_1 \sim$ 110–180 fs) et de relaxation (temps caractéristique : $T_2 \sim$ 240–620 fs) du précurseur de l'électron hydraté. La plupart des auteurs privilégient un modèle de solvatation, simple ou plus élaboré, mettant essentiellement en jeu deux états électroniques. Toutefois, la nature et le(s) mode(s) de déclin du précurseur de e^-_{aq} restent l'objet de controverses et l'existence d'un état intermédiaire entre e^-_{ir} et e^-_{aq} a été suggérée. La formation et le déclin ultra-rapides de paires hydratées $[H_3O^+:e^-:OH]_{nH_2O}$ (ou $[e^-:Cl]_{nH_2O}$ dans le cas de solutions aqueuses de chlorure de sodium) ont été analysés par spectroscopie femtoseconde. Une fraction des e^-_{exc} produits ne s'hydrate pas, mais disparaîtrait alors par un mécanisme de recombinaison non diffusionnel. Enfin, le caractère protique de l'eau et des alcools a été souligné, et l'intervention de transferts de protons, soit au stade de la formation de e^-_{exc}, soit au stade des recombinaisons géminées, a été invoquée.

Quant au méthanol, les expériences récentes de photoionisation multiphotonique du liquide pur ou de solutés en solution méthanolique montrent clairement l'insuffisance d'un modèle de solvatation n'impliquant que deux états.

Les conditions de formation de e^-_{solv} ont également été précisées par le recours à des systèmes modèles, tels que solutions micellaires et agrégats de molécules polaires. L'irradiation de solutions micellaires a clairement mis en évidence l'influence, sur les rendements et les propriétés spectroscopiques de e^-_{aq}, des interfaces ou interphases micellaires et de poches aqueuses modulables en taille. Pour les agrégats gazeux $(H_2O)_n^-$ ($n \sim$ 8–32), les calculs suggèrent que l'attachement de l'électron en excès se ferait dans un état de surface; en revanche, pour des agrégats suffisamment volumineux ($n \geq 64$), e^-_{exc}, initialement localisé en surface, évoluerait en quelques picosecondes vers un état interne, précurseur de l'électron hydraté dans l'eau liquide.

En conclusion, le caractère collectif, coopératif non seulement de la solvatation des électrons en excès, mais également des actes primaires d'excitation électronique et de séparation des charges, a été mis en relief, compliquant la description du mécanisme global de solvatation. En revanche, la coordination des résultats obtenus suivant les différentes approches évoquées, tant expérimentales que théoriques, devrait pouvoir conduire à une compréhension plus affinée de la formation de e^-_{solv}.

Enfin, il apparaîtrait souhaitable que les études de spectroscopie femtoseconde concernant l'électron solvaté soient étendues à une plus large gamme de solvants (alcools supérieurs, solvants polaires non protiques, par exemple) et étendues également vers l'infra-rouge plus lointain. L'observation simultanée à temps courts de l'évolution des électrons et des radicaux libres corrélés pourrait aussi apporter des informations précieuses et permettre une appréhension plus complète, et éventuellement plus générale, du processus de solvatation dans les milieux polaires.

Remerciements

Nos remerciements s'adressent à D. Grand et D. Solgadi qui ont bien voulu faire une lecture critique de certaines des pages de ce mémoire. C.F. et J.-P. J.-G. sont reconnaissants de l'aide financière que leur a apportée le Programme de coopération franco-québécoise en recherche médicale, le Programme de chercheurs invités du Fonds de la Recherche en Santé du Québec (FRSQ) et le Programme de subventions à la recherche en coopération de l'OTAN (Subvention n° 91/0996). J.-P. J.-G. remercie également le Conseil de Recherches Médicales du Canada pour son support financier, ainsi que le Programme d'échanges INSERM–FRSQ en recherche en santé pour lui avoir permis d'effectuer un stage de trois mois au Laboratoire de Chimie-Physique de l'Université Paris V.

Bibliographie

1. W. Weyl. Ann. Phys. Chem. (Leipzig), **121**, 601 (1864).
2. C.A. Kraus. J. Am. Chem. Soc. **30**, 1323 (1908).
3. C.W. Gilbert, J.P. Keene, P.F. Browne et T.J. Davy. *Dans* British Empire Cancer Campaign, 38th Annual Report, Part II. 1960. p. 498; J.P. Keene. Br. J. Radiol. **35**, 650 (1962).
4. J.P. Keene. Nature, **188**, 843 (1960); **197**, 47 (1963).
5. E.J. Hart et J.W. Boag. J. Am. Chem. Soc. **84**, 4090 (1962); J.W. Boag et E.J. Hart. Nature, **197**, 45 (1963).
6. T.R. Tuttle, Jr. et S. Golden, J. Phys. Chem. **95**, 5725 (1991).
7. J.-P. Jay-Gerin et C. Ferradini. *Dans* Excess electrons in dielectric media. *Éditeurs* : C. Ferradini et J.-P. Jay-Gerin. CRC Press, Boca Raton, Fla. 1991. p. 259.
8. Y. Hirata et N. Mataga. Prog. React. Kinet. **18**, 273 (1993).
9. H. Abramczyk et J. Kroh. Radiat. Phys. Chem. **43**, 291 (1994).
10. P.J. Rossky et J.D. Simon. Nature, **370**, 263 (1994).
11. Y. Gauduel. *Dans* Ultrafast dynamics of chemical systems. *Éditeur* : J.D. Simon. Kluwer Academic, Dordrecht. 1994. p. 81; J. Mol. Liquids, **63**, 1 (1995).
12. J. Jortner et J. Rabani. J. Phys. Chem. **66**, 2081 (1962).
13. G.C. Barker, A.W. Gardner et D.C. Sammon. J. Electrochem. Soc. **113**, 1182 (1966); A.M. Brodsky et Y.V. Pleskov. *Dans* Progress in surface science. Vol. 2. *Éditeur* : S.G. Davison. Pergamon, Oxford. 1972. p. 1.
14. A.M. Brodsky. *Dans* Excess electrons in dielectric media. *Éditeurs* : C. Ferradini et J.-P. Jay-Gerin. CRC Press, Boca Raton, Fla. 1991. p. 349.
15. J.-C. Mialocq. J. Chim. Phys. **85**, 31 (1988).
16. R.L. Fork, C.V. Shank et R.T. Yen. Appl. Phys. Lett. **41**, 223 (1982); A. Migus, A. Antonetti, J. Etchepare, D. Hulin et A. Orszag. J. Opt. Soc. Am. B: **2**, 584 (1985).
17. Y. Tabata (*Éditeur*). Pulse radiolysis. CRC Press, Boca Raton, Fla. 1991.

18. J. Belloni et J.L. Marignier. Radiat. Phys. Chem. **34**, 157 (1989).
19. J. H. Baxendale et P. Wardman. Nature, **230**, 449 (1971); J.H. Baxendale et P. Wardman. J. Chem. Soc. Faraday Trans. 1, **69**, 584 (1973).
20. J.H. Baxendale et P.H.G. Sharpe. Int. J. Radiat. Phys. Chem. **8**, 621 (1976).
21. M. Ogasawara, K. Shimizu et H. Yoshida. Radiat. Phys. Chem. **17**, 331 (1981).
22. W.J. Chase et J.W. Hunt. J. Phys. Chem. **79**, 2835 (1975); W.J. Chase. M.Sc. Thesis, University of Toronto (1976); J.W. Hunt. Adv. Radiat. Chem. **5**, 185 (1976).
23. G.A. Kenney-Wallace et C.D. Jonah. Chem. Phys. Lett. **39**, 596 (1976).
24. G.A. Kenney-Wallace et C.D. Jonah. J. Phys. Chem. **86**, 2572 (1982); G.A. Kenney-Wallace. Adv. Chem. Phys. **47**, 535 (1981).
25. H. Miyasaka, H. Masuhara et N. Mataga. Laser Chem. **7**, 119 (1987).
26. S.K. Garg et C.P. Smyth. J. Phys. Chem. **69**, 1294 (1965); L. Glasser, J. Crossley et C.P. Smyth. J. Chem. Phys. **57**, 3977 (1972).
27. J. Barthel, K. Bachhuber, R. Buchner et H. Hetzenauer. Chem. Phys. Lett. **165**, 369 (1990).
28. Y. Wang, M.K. Crawford, M.J. McAuliffe et K.B. Eisenthal. Chem. Phys. Lett. **74**, 160 (1980).
29. D. Huppert, G.A. Kenney-Wallace et P.M. Rentzepis. J. Chem. Phys. **75**, 2265 (1981).
30. Y. Hirata, N. Murata, Y. Tanioka et N. Mataga. J. Phys. Chem. **93**, 4527 (1989); Y. Hirata et N. Mataga. J. Phys. Chem. **94**, 8503 (1990); **95**, 9067 (1991).
31. M. Sander. Dissertation, Universität Göttingen (1992); M. Sander, U. Brummund, K. Luther et J. Troe. Ber. Bunsen-Ges. Phys. Chem. **96**, 1486 (1992).
32. C. Pépin, T. Goulet, D. Houde et J.-P. Jay-Gerin. J. Phys. Chem. **98**, 7009 (1994); J. Chim. Phys. Sous presse.
33. X. Shi, F.H. Long, H. Lu et K.B. Eisenthal. J. Phys. Chem. **99**, 6917 (1995).
34. P.K. Walhout, J.C. Alfano, Y. Kimura, C. Silva, P.J. Reid et P.F. Barbara. Chem. Phys. Lett. **232**, 135 (1995).
35. L. Gilles, M.R. Bono et M. Schmidt. Can. J. Chem. **55**, 2003 (1977).
36. K. Okazaki et G.R. Freeman. Can. J. Chem. **56**, 2305 (1978).
37. Y. Lin et C.D. Jonah. J. Phys. Chem. **97**, 295 (1993); *Dans* Ultrafast dynamics of chemical systems. *Éditeur* : J.D. Simon. Kluwer Academic, Dordrecht. 1994. p. 137.
38. Y. Gauduel, J.L. Martin, A. Migus, N. Yamada et A. Antonetti. *Dans* Ultrafast phenomena V. *Éditeurs* : G.R. Fleming et A.E. Siegman. Springer-Verlag, Berlin. 1986. p. 308; A. Migus, Y. Gauduel, J.L. Martin et A. Antonetti. Phys. Rev. Lett. **58**, 1559 (1987).
39. F.H. Long, H. Lu et K.B. Eisenthal. Phys. Rev. Lett. **64**, 1469 (1990).
40. S. Pommeret, A. Antonetti et Y. Gauduel. J. Am. Chem. Soc. **113**, 9105 (1991).
41. Y. Gauduel, S. Pommeret et A. Antonetti. J. Phys. Chem. **97**,134 (1993); Y. Gauduel. *Dans* Ultrafast reaction dynamics and solvent effects. AIP Conf. Proc. **298**, 191 (1994).
42. Y. Kimura, J.C. Alfano, P.K. Walhout et P.F. Barbara. J. Phys. Chem. **98**, 3450 (1994); J.C. Alfano, P.K. Walhout, Y. Kimura et P.F. Barbara. J. Chem. Phys. **98**, 5996 (1993).
43. F.H. Long, H. Lu, X. Shi et K.B. Eisenthal. Chem. Phys. Lett. **185**, 47 (1991).
44. O. Conde et J. Teixeira. J. Phys. (Paris), **44**, 525 (1983).
45. C. Pépin, D. Houde, H. Remita, T. Goulet et J.-P. Jay-Gerin. Phys. Rev. Lett. **69**, 3389 (1992); J. Chim. Phys. **90**, 745 (1993).
46. D. Houde, C. Pépin, T. Goulet et J.-P. Jay-Gerin. *Dans* Mode-locked and solid state lasers, amplifiers, and applications. *Éditeurs* : M. Piché et P. W. Pace. Proc. SPIE—Int. Soc. Opt. Eng. **2041**, 139 (1993).
47. A. Mozumder et J.L. Magee. Int. J. Radiat. Phys. Chem. **7**, 83 (1975).
48. Y. Gauduel, S. Pommeret, A. Migus et A. Antonetti. Chem. Phys. **149**, 1 (1990).
49. M. Anbar, G.A. St. John, H.R. Gloria et R.F. Reinisch. *Dans* Water structure at the water–polymer interface. *Éditeur* : H.H.G. Jellinek. Plenum, New York. 1972. p. 85.
50. P. Han et D.M. Bartels. J. Phys. Chem. **94**, 5824 (1990).
51. A. Bernas et D. Grand. J. Phys. Chem. **98**, 3440 (1994).
52. M.U. Sander, K. Luther et J. Troe. J. Phys. Chem. **97**, 11489 (1993); Ber. Bunsen-Ges. Phys. Chem. **97**, 953 (1993).
53. A.M. Peers et M. Cottin. J. Chim. Phys. **63**, 1346 (1966).
54. R. Knochenmuss, O. Cheshnovsky et S. Leutwyler. Chem. Phys. Lett. **144**, 317 (1988); R. Knochenmuss et S. Leutwyler. J. Chem. Phys. **91**, 1268 (1989).
55. Y. Gauduel, S. Pommeret, A. Migus, N. Yamada et A. Antonetti. J. Am. Chem. Soc. **112**, 2925 (1990).
56. Y. Gauduel, H. Gelabert et M. Ashokkumar. Chem. Phys. **197**, 167 (1995); M. Ashokkumar, H. Gelabert, A. Antonetti et Y. Gauduel. *Dans* Ultrafast reaction dynamics and solvent effects. AIP Conf. Proc. **298**, 107 (1994).
57. F.H. Long, H. Lu, X. Shi et K.B. Eisenthal. Chem. Phys. Lett. **169**, 165 (1990); F.H. Long, H. Lu et K.B. Eisenthal. J. Chem. Phys. **91**, 4413 (1989).
58. R.L. Platzman. Radiat. Res. **2**, 1 (1955).
59. V. Cobut, Y. Frongillo, J.-P. Jay-Gerin et J.P. Patau. Radiat. Phys. Chem. **40**, 589 (1992).
60. J. Jortner et A. Gaathon. Can. J. Chem. **55**, 1801 (1977).
61. I. Rips, J. Klafter et J. Jortner. J. Chem. Phys. **89**, 4288 (1988); M. Tachiya. Chem. Phys. Lett. **203**, 164 (1993).
62. D.N. Nikogosyan, A.A. Oraevsky et V.I. Rupasov. Chem. Phys. **77**, 131 (1983); A. Iwata, N. Nakashima, Y. Izawa et C. Yamanaka. Chem. Lett. 1939 (1993); J. W. Boyle, J.A. Ghormley, C.J. Hochanadel et J.F. Riley. J. Phys. Chem. **73**, 2886 (1969).
63. T. Goulet, A. Bernas, C. Ferradini et J.-P. Jay-Gerin. Chem. Phys. Lett. **170**, 492 (1990); A. Bernas, T. Goulet, J.-P. Jay-Gerin et C. Ferradini. *Dans* Proc. Tihany Symp. Radiat. Chem. 7th, 17 (1991).
64. C.E. Krohn, P.R. Antoniewicz et J.C. Thompson. Surf. Sci. **101**, 241 (1980); J.C. Thompson, P.R. Antoniewicz et C.E. Krohn. Comments Solid State Phys. **9**, 223 (1980); G.T. Bennett et J.C. Thompson. J. Chem. Phys. **84**, 1901 (1986).
65. F. Urbach. Phys. Rev. **92**, 1324 (1953); M.V. Kurik. Phys. Status Solidi, A **8**, 9 (1971).
66. C. Houée-Levin et J.-P. Jay-Gerin. J. Phys. Chem. **92**, 6454 (1988).
67. J. Schnitker, P.J. Rossky et G.A. Kenney-Wallace. J. Chem. Phys. **85**, 2986 (1986).
68. K.A. Motakabbir et P.J. Rossky. Chem. Phys. **129**, 253 (1989).
69. K.A. Motakabbir, J. Schnitker et P.J. Rossky. J. Chem. Phys. **97**, 2055 (1992).
70. M. Hilczer, W.M. Bartczak et M. Sopek. Radiat. Phys. Chem. **36**, 199 (1990); W.M. Bartczak, J. Kroh et M. Sopek. Radiat. Phys. Chem. **45**, 961 (1995).
71. J.-P. Jay-Gerin et C. Ferradini. Can. J. Chem. **70**, 1869 (1992).
72. A. Mozumder. Radiat. Phys. Chem. **32**, 287 (1988).
73. R. Schiller. Radiat. Phys. Chem. **34**, 61 (1989); J. Chem. Phys. **92**, 5527 (1990); *Dans* Excess electrons in dielectric media. *Éditeurs* : C. Ferradini et J.-P. Jay-Gerin. CRC Press, Boca Raton, Fla. 1991. p. 105.
74. E. Keszei et J.-P. Jay-Gerin. Can. J. Chem. **70**, 21 (1992).
75. P.J. Rossky et J. Schnitker. J. Phys. Chem. **92**, 4277 (1988).
76. R.N. Barnett, U. Landman et A. Nitzan. J. Chem. Phys. **90**, 4413 (1989).

77. J. Schnitker, K. Motakabbir, P.J. Rossky et R.A. Friesner. Phys. Rev. Lett. **60**, 456 (1988).
78. M.C. Messmer et J.D. Simon. J. Phys. Chem. **94**, 1220 (1990).
79. F.J. Webster, J. Schnitker, M.S. Friedrichs, R.A. Friesner et P.J. Rossky. Phys. Rev. Lett. **66**, 3172 (1991); F. Webster, P.J. Rossky et R.A. Friesner. Comput. Phys. Commun. **63**, 494 (1991).
80. E. Neria, A. Nitzan, R.N. Barnett et U. Landman. Phys. Rev. Lett. **67**, 1011 (1991); E. Neria et A. Nitzan. J. Chem. Phys. **99**, 1109 (1993).
81. T.H. Murphrey et P.J. Rossky. J. Chem. Phys. **99**, 515 (1993).
82. E. Keszei, S. Nagy, T.H. Murphrey et P.J. Rossky. J. Chem. Phys. **99**, 2004 (1993).
83. B.J. Schwartz et P.J. Rossky. J. Chem. Phys. **101**, 6902 (1994); **101**, 6917 (1994); J. Phys. Chem. **98**, 4489 (1994).
84. P.J. Rossky, T.H. Murphrey et W.-S. Sheu. *Dans* Ultrafast reaction dynamics and solvent effects. AIP Conf. Proc. **298**, 119 (1994).
85. A. Staib et D. Borgis. J. Chem. Phys. **103**, 2642 (1995); D. Borgis et A. Staib. Chem. Phys. Lett. **230**, 405 (1994).
86. Y. Gauduel, S. Pommeret, A. Migus et A. Antonetti. J. Phys. Chem. **95**, 533 (1991).
87. F.H. Long, H. Lu et K.B. Eisenthal. Chem. Phys. Lett. **160**, 464 (1989).
88. J.-P. Jay-Gerin et C. Ferradini. J. Chim. Phys. **91**, 173 (1994).
89. M.A. Lewis et C.D. Jonah. J. Phys. Chem. **90**, 5367 (1986).
90. A. Selloni, P. Carnevali, R. Car et M. Parrinello. Phys. Rev. Lett. **59**, 823 (1987).
91. R.P. Feynman et A.R. Hibbs. Quantum mechanics and path integrals. McGraw–Hill, New York. 1965.
92. D. Chandler et P.G. Wolynes. J. Chem. Phys. **74**, 4078 (1981).
93. D.F. Coker et B.J. Berne. *Dans* Excess electrons in dielectric media. *Éditeurs* : C. Ferradini et J.-P. Jay-Gerin. CRC Press, Boca Raton, Fla. 1991. p. 211.
94. D.-F. Feng et L. Kevan. Chem. Rev. **80**, 1 (1980); L. Kevan. Radiat. Phys. Chem. **17**, 413 (1981); J. Phys. Chem. **85**, 1628 (1981); Acc. Chem. Res. **14**, 138 (1981), et références citées.
95. D.P. Lin et L. Kevan. J. Phys. Chem. **81**, 1498 (1977).
96. A. Wallqvist, G. Martyna et B.J. Berne. J. Phys. Chem. **92**, 1721 (1988).
97. A. Wallqvist, D. Thirumalai et B.J. Berne. J. Chem. Phys. **86**, 6404 (1987).
98. M. Sprik, R.W. Impey et M.L. Klein. J. Stat. Phys. **43**, 967 (1986).
99. J. Schnitker et P.J. Rossky. J. Chem. Phys. **86**, 3471 (1987).
100. C. Romero et C.D. Jonah. J. Chem. Phys. **90**, 1877 (1989).
101. R.W. Impey, P.A. Madden et I.R. McDonald. J. Phys. Chem. **87**, 5071 (1983), et références citées.
102. J.D. Madura et B.M. Pettitt. Chem. Phys. Lett. **150**, 105 (1988).
103. C. Romero. J. Chim. Phys. **88**, 765 (1991).
104. S. Pommeret et Y. Gauduel. J. Phys. Chem. **95**, 4126 (1991).
105. E.J. Hart et M. Anbar. The hydrated electron. Wiley–Interscience, New York. 1970. p. 39.
106. J.-P. Jay-Gerin et C. Ferradini. Can. J. Chem. **68**, 553 (1990).
107. S.O. Nielsen, P. Pagsberg, E.J. Hart, H. Christensen et G. Nilsson. J. Phys. Chem. **73**, 3171 (1969); S.O. Nielsen, B.D. Michael et E.J. Hart. J. Phys. Chem. **80**, 2482 (1976).
108. J. Belloni, F. Billiau et E. Saito. Nouv. J. Chim. **3**, 157 (1979).
109. W.C. Gottschall et E.J. Hart. J. Phys. Chem. **71**, 2102 (1967).
110. B.D. Michael, E.J. Hart et K.H. Schmidt. J. Phys. Chem. **75**, 2798 (1971).
111. R.S. Dixon et V.J. Lopata. Radiat. Phys. Chem. **11**, 135 (1978).
112. F.-Y. Jou et G.R. Freeman. J. Phys. Chem. **83**, 2383 (1979).
113. H. Christensen et K. Sehested. J. Phys. Chem. **90**, 186 (1986).
114. S.-I. Miura et F. Hirata. J. Phys. Chem. **98**, 9649 (1994).
115. G. Nilsson, H. Christensen, P. Pagsberg et S.O. Nielsen. J. Phys. Chem. **76**, 1000 (1972), et références citées.
116. A.J. Elliot et D.C. Ouellette. J. Chem. Soc. Faraday Trans. **90**, 837 (1994).
117. F.-Y. Jou et G.R. Freeman. J. Phys. Chem. **81**, 909 (1977).
118. G.A. Kenney-Wallace et D.C. Walker. J. Chem. Phys. **55**, 447 (1971).
119. S. Golden et T.R. Tuttle, Jr. J. Chem. Soc. Faraday Trans. 2, **75**, 474 (1979).
120. J. Jortner. Radiat. Res. Suppl. **4**, 24 (1964); D.A. Copeland, N.R. Kestner et J. Jortner. J. Chem. Phys. **53**, 1189 (1970).
121. S. Golden et T.R. Tuttle, Jr. J. Chem. Soc. Faraday Trans. 2, **77**, 889 (1981).
122. T.R. Tuttle, Jr., S. Golden et G. Rosenfeld. Radiat. Phys. Chem. **32**, 525 (1988).
123. R.N. Barnett, U. Landman et A. Nitzan. J. Chem. Phys. **89**, 2242 (1988).
124. R. Lugo et P. Delahay. J. Chem. Phys. **57**, 2122 (1972).
125. K.A. Motakabbir, J. Schnitker et P.J. Rossky. J. Chem. Phys. **90**, 6916 (1989).
126. B.J. Schwartz et P.J. Rossky. Phys. Rev. Lett. **72**, 3282 (1994).
127. P.J. Reid, C. Silva, P.K. Walhout et P.F. Barbara. Chem. Phys. Lett. **228**, 658 (1994).
128. H. Abramczyk. J. Phys. Chem. **95**, 6149 (1991); H. Abramczyk et J. Kroh. J. Phys. Chem. **95**, 6155 (1991); Radiat. Phys. Chem. **39**, 99 (1992); J. Phys. Chem. **96**, 3653 (1992); H. Abramczyk, M. Barut et J. Kroh. Bull. Pol. Acad. Sci. Chem. **42**, 131 (1994).
129. I. Rips, J. Klafter et J. Jortner. J. Chem. Phys. **88**, 3246 (1988).
130. K. Kawabata. J. Chem. Phys. **65**, 2235 (1976), et références citées.
131. L. Kevan. *Dans* Actions chimiques et biologiques des radiations. 13ème Série. *Éditeur* : M. Haïssinsky. Masson, Paris. 1969. p. 57; J. Phys. Chem. **69**, 1081 (1965).
132. J.E. Bennett, B. Mile et A. Thomas. Nature, **201**, 919 (1964).
133. P.N. Moorthy et J.J. Weiss. Philos. Mag. **10**, 659 (1964).
134. E.C. Avery, J.R. Remko et B. Smaller. J. Chem. Phys. **49**, 951 (1968).
135. R.W. Fessenden et N.C. Verma. J. Am. Chem. Soc. **98**, 243 (1976); N.C. Verma et R.W. Fessenden. J. Chem. Phys. **65**, 2139 (1976).
136. H. Shiraishi, K. Ishigure et K. Morokuma. J. Chem. Phys. **88**, 4637 (1988), et références citées.
137. A.S. Jeevarajan et R.W. Fessenden. J. Phys. Chem. **93**, 3511 (1989).
138. J. Franck et G. Scheibe. Z. Phys. Chem. Abt. A: **139**, 22 (1928).
139. G. Stein. *Dans* Actions chimiques et biologiques des radiations. 13ème Série. *Éditeur* : M. Haïssinsky. Masson, Paris. 1969. p. 119.
140. M.J. Blandamer et M.F. Fox. Chem. Rev. **70**, 59 (1970).
141. F.H. Long, X. Shi, H. Lu et K.B. Eisenthal. J. Phys. Chem. **98**, 7252 (1994).
142. W.-S. Sheu et P.J. Rossky. J. Am. Chem. Soc. **115**, 7729 (1993); Chem. Phys. Lett. **202**, 186 (1993).
143. W.-S. Sheu et P.J. Rossky. Chem. Phys. Lett. **213**, 233 (1993).
144. R. Platzman et J. Franck. Z. Phys. **138**, 411 (1954).
145. M.F. Fox et E. Hayon. Chem. Phys. Lett. **25**, 511 (1974); J. Chem. Soc. Faraday Trans. 1, **72**, 1990 (1976), et références citées.
146. G.R. Freeman. *Dans* Kinetics of nonhomogeneous processes. *Éditeur* : G. R. Freeman. Wiley–Interscience, New York. 1987. p. 19.
147. J.-P. Jay-Gerin, T. Goulet et I. Billard. Can. J. Chem. **71**, 287 (1993).

148. J.-P. Dodelet et G.R. Freeman. Can. J. Chem. **53**, 1263 (1975); J.-P. Dodelet, F.-Y. Jou et G.R. Freeman. J. Phys. Chem. **79**, 2876 (1975).
149. J.A. Delaire, M.O. Delcourt et J. Belloni. J. Phys. Chem. **84**, 1186 (1980).
150. J.-P. Jay-Gerin et C. Ferradini. J. Chem. Phys. **91**, 3275 (1989).
151. J.-P. Jay-Gerin et C. Ferradini. Radiat. Phys. Chem. **38**, 83 (1991); E. Keszei, J.-P. Jay-Gerin et C. Ferradini. Radiat. Phys. Chem. **39**, 257 (1992).
152. J. Schnitker et P.J. Rossky. J. Phys. Chem. **93**, 6965 (1989).
153. R.N. Barnett, U. Landman et A. Nitzan. J. Chem. Phys. **93**, 8187 (1990).
154. G.S. Del Buono, P.J. Rossky et T.H. Murphrey. J. Phys. Chem. **96**, 7761 (1992).
155. M. Sprik et M.L. Klein. J. Chem. Phys. **91**, 5665 (1989).
156. H. Lu, F.H. Long, R.M. Bowman et K.B. Eisenthal. J. Phys. Chem. **93**, 27 (1989).
157. Y. Gauduel, S. Pommeret, A. Migus et A. Antonetti. J. Phys. Chem. **93**, 3880 (1989).
158. J.L. McGowen, H.M. Ajo, J.Z. Zhang et B.J. Schwartz. Chem. Phys. Lett. **231**, 504 (1994).
159. S.M. Pimblott. J. Phys. Chem. **95**, 6946 (1991).
160. T. Goulet et J.-P. Jay-Gerin. J. Chem. Phys. **96**, 5076 (1992); Proc. Tihany Symp. Radiat. Chem. 7th, 9 (1991).
161. J.H. Baxendale. Radiat. Res. Suppl. **4**, 139 (1964).
162. J. Jortner et R.M. Noyes. J. Phys. Chem. **70**, 770 (1966).
163. G. Lepoutre et J. Jortner. J. Phys. Chem. **76**, 683 (1972).
164. B. Hickel et K. Sehested. J. Phys. Chem. **89**, 5271 (1985).
165. P. Han et D.M. Bartels. J. Phys. Chem. **94**, 7294 (1990).
166. H.A. Schwarz. J. Phys. Chem. **95**, 6697 (1991).
167. B. Hickel. *Dans* Actions biologique et chimique des radiations ionisantes. Vol. II. *Éditeur* : B. Tilquin. Academia, Louvain-la-Neuve, Belgique. 1992. p. 79.
168. I. Rips et J. Jortner. J. Chem. Phys. **97**, 536 (1992), et références citées.
169. P. Han et D.M. Bartels. J. Phys. Chem. **95**, 5367 (1991).
170. K.N. Jha et G.R. Freeman. J. Chem. Phys. **48**, 5480 (1968).
171. G.W. Robinson, P.J. Thistlethwaite et J. Lee. J. Phys. Chem. **90**, 4224 (1986); H.F. Hameka, G.W. Robinson et C.J. Marsden. J. Phys. Chem. **91**, 3150 (1987).
172. K.L. Mittal et E.J. Fendler. Solution behaviour of surfactants. Theoretical and applied aspects. Plenum, New York. 1982.
173. V. Degorgio et M. Cozti (*Éditeurs*). Physics of amphiphiles. North-Holland, Amsterdam. 1985.
174. M. Grätzel. Heterogeneous photochemical electron transfer. CRC Press, Boca Raton, Fla. 1989.
175. M.P. Pileni (Éditeur). Structure and reactivity in reverse micelles. Elsevier, Amsterdam. 1989.
176. A. Bernas, D. Grand et S. Hautecloque. *Dans* Excess electrons in dielectric media. *Éditeurs* : C. Ferradini et J.-P. Jay-Gerin. CRC Press, Boca Raton, Fla. 1991. p. 367.
177. M. Tachiya. *Dans* Kinetics of nonhomogeneous processes. *Éditeur* : G.R. Freeman. Wiley–Interscience, New York. 1987. p. 575.
178. Y. Gauduel, A. Migus, J.L. Martin et A. Antonetti. Chem. Phys. Lett. **108**, 319 (1984).
179. Y. Gauduel, S. Berrod, A. Migus, N. Yamada et A. Antonetti. Biochemistry, **27**, 2509 (1988).
180. Y. Gauduel, S. Pommeret, N. Yamada, A. Migus et A. Antonetti. J. Am. Chem. Soc. **111**, 4974 (1989).
181. A. Bernas, D. Grand, S. Hautecloque et A. Chambaudet. J. Phys. Chem. **85**, 3684 (1981).
182. D. Grand, S. Hautecloque, A. Bernas et A. Petit. J. Phys. Chem. **87**, 5236 (1983).
183. S. Hautecloque, D. Grand et A. Bernas. J. Phys. Chem. **89**, 2705 (1985).
184. A. Bernas, D. Grand et S. Hautecloque. Radiat. Phys. Chem. **32**, 309 (1988).
185. G. Bakale, G. Beck et J.K. Thomas, J. Phys. Chem. **85**, 1062 (1981).
186. M. Wong, J.K. Thomas et T. Nowak. J. Am. Chem. Soc. **99**, 4730 (1977).
187. G. Bakale, G. Beck et J.K. Thomas. J. Phys. Chem. **96**, 2328 (1992).
188. M. Wong, M. Grätzel et J.K. Thomas. Chem. Phys. Lett. **30**, 329 (1975); M. Wong, J.K. Thomas et M. Grätzel. J. Am. Chem. Soc. **98**, 2391 (1976).
189. M.P. Pileni, B. Hickel, C. Ferradini et J. Pucheault. Chem. Phys. Lett. **92**, 308 (1982).
190. M.H. Abdel-Kader et P. Krebs. J. Chem. Soc. Faraday Trans. 1, **84**, 2241 (1988).
191. J.L. Gębicki, L. Gębicka et J. Kroh. J. Chem. Soc. Faraday Trans. **90**, 3411 (1994).
192. V. Calvo-Perez, G.S. Beddard et J.H. Fendler. J. Phys. Chem. **85**, 2316 (1981).
193. A. D'Aprano, A. Lizzio, V. Turco Liveri, F. Aliotta, C. Vasi et P. Migliardo. J. Phys. Chem. **92**, 4436 (1988).
194. G. Onori et A. Santucci. J. Phys. Chem. **97**, 5430 (1993).
195. T.K. Jain, M. Varshney et A. Maitra. J. Phys. Chem. **93**, 7409 (1989).
196. A. Maitra. J. Phys. Chem. **88**, 5122 (1984).
197. M.D. Newton. J. Phys. Chem. **79**, 2795 (1975).
198. M. Armbruster, H. Haberland et H.-G. Schindler. Phys. Rev. Lett. **47**, 323 (1981).
199. H. Haberland, H. Langosch, H.-G. Schindler et D.R. Worsnop. J. Phys. Chem. **88**, 3903 (1984); H. Haberland, H.-G. Schindler et D.R. Worsnop. Ber. Bunsen-Ges. Phys. Chem. **88**, 270 (1984).
200. H. Haberland, C. Ludewigt, H.-G. Schindler et D.R. Worsnop. J. Chem. Phys. **81**, 3742 (1984); Surf. Sci. **156**, 157 (1985).
201. M. Knapp, O. Echt, D. Kreisle et E. Recknagel. J. Chem. Phys. **85**, 636 (1986); J. Phys. Chem. **91**, 2601 (1987).
202. F. Misaizu, T. Kondow et K. Kuchitsu. Chem. Phys. Lett. **178**, 369 (1991); T. Kondow. J. Phys. Chem. **91**, 1307 (1987).
203. C. Desfrançois, N. Khelifa, A. Lisfi, J.P. Schermann, J.G. Eaton et K.H. Bowen. J. Chem. Phys. **95**, 7760 (1991); C. Desfrançois et J.P. Schermann. *Dans* Ultrafast reaction dynamics and solvent effects. AIP Conf. Proc. **298**, 528 (1994).
204. C. Desfrançois, H. Abdoul-Carime, N. Khelifa et J.P. Schermann. J. Chim. Phys. **92**, 409 (1995).
205. C. Desfrançois, B. Baillon, J.P. Schermann, S.T. Arnold, J.H. Hendricks et K.H. Bowen. Phys. Rev. Lett. **72**, 48 (1994).
206. J.V. Coe, G.H. Lee, J.G. Eaton, S.T. Arnold, H.W. Sarkas, K.H. Bowen, C. Ludewigt, H. Haberland et D.R. Worsnop. J. Chem. Phys. **92**, 3980 (1990).
207. L.A. Posey et M.A. Johnson. J. Chem. Phys. **89**, 4807 (1988); L.A. Posey, P.J. Campagnola, M.A. Johnson, G.H. Lee, J.G. Eaton et K.H. Bowen, J. Chem. Phys. **91**, 6536 (1989).
208. P.J. Campagnola, D.J. Lavrich, M.J. DeLuca et M.A. Johnson. J. Chem. Phys. **94**, 5240 (1991).
209. P.J. Campagnola, D.J. Lavrich et M.A. Johnson. J. Phys. IV (Paris), **1**, C5–93 (1991); D.J. Lavrich, P.J. Campagnola et M.A. Johnson. NATO ASI Ser. **B326**, 183 (1994).
210. L.A. Posey, M.J. DeLuca, P.J. Campagnola et M.A. Johnson. J. Phys. Chem. **93**, 1178 (1989).
211. A. Wallqvist, D. Thirumalai et B.J. Berne. J. Chem. Phys. **85**, 1583 (1986); D. Thirumalai, A. Wallqvist et B.J. Berne. J. Stat. Phys. **43**, 973 (1986).
212. R.N. Barnett, U. Landman, C.L. Cleveland et J. Jortner. J. Chem. Phys. **88**, 4429 (1988); Phys. Rev. Lett. **59**, 811 (1987); U. Landman, R.N. Barnett, C.L. Cleveland, D. Scharf et J. Jortner. J. Phys. Chem. **91**, 4890 (1987).

213. R.N. Barnett, U. Landman, C.L. Cleveland et J. Jortner. Chem. Phys. Lett. **145**, 382 (1988).
214. R.N. Barnett, U. Landman, C.L. Cleveland, N.R. Kestner et J. Jortner. J. Chem. Phys. **88**, 6670 (1988); Chem. Phys. Lett. **148**, 249 (1988).
215. R.N. Barnett, U. Landman, D. Scharf et J. Jortner. Acc. Chem. Res. **22**, 350 (1989).
216. P. Stampfli. J. Chem. Phys. **101**, 6024 (1994); P. Stampfli et K.H. Bennemann. Ber. Bunsen-Ges. Phys. Chem. **96**, 1220 (1992); Comput. Mater. Sci. **2**, 578 (1994).
217. R.N. Barnett, U. Landman, G. Makov et A. Nitzan. J. Chem. Phys. **93**, 6226 (1990).
218. M. Marchi, M. Sprik et M.L. Klein. J. Chem. Phys. **89**, 4918 (1988).
219. H. Haberland. *Dans* The chemical physics of atomic and molecular clusters. *Éditeur* : G. Scoles. North-Holland, Amsterdam. 1990. p. 619, et références citées.
220. R.N. Barnett, U. Landman et A. Nitzan. Phys. Rev. Lett. **62**, 106 (1989).
221. R.N. Barnett, U. Landman et A. Nitzan. J. Chem. Phys. **91**, 5567 (1989).
222. U. Landman, R.N. Barnett, J. Jortner et A. Nitzan. *Dans* Radiation research: a twentieth-century perspective. Vol. II. *Éditeurs* : W.C. Dewey, M. Edington, R.J.M. Fry, E.J. Hall et G.F. Whitmore. Academic, San Diego, Calif. 1992. p. 43.

Irreversible inhibition of 3-hydroxy-3-methylglutaryl-coenzyme A synthase from yeast by F-244 and (*RS*)-β-butyrolactone

Karen Bell, Endang Saepudin, and Paul Harrison

Abstract: The inhibition of 3-hydroxy-3-methylglutaryl coenzyme A (HMG-CoA) synthase from yeast was compared for both F-244 (**1**) and (*RS*)-β-butyrolactone (**5**). F-244 exhibits irreversible inhibition with an IC_{50} of 8 nM, similar to that reported for the rat liver enzyme, while the binding constant ($1/K_I$) and inactivation rate constant (k_{inact}) are similar to values reported for the human cytoplasmic enzyme. (*RS*)-β-Butyrolactone (**5**) also irreversibly inhibits the enzyme, but with much lower efficiency (IC_{50} 2 mM). The values for K_I (9 mM) and k_{inact} (0.0078 s^{-1}) for **5** were determined. The results show that k_{inact} for **5** and **1** differ by a factor of only 2.5, while K_I for **5** is higher by a factor of 1.8×10^5. Hence, the β-lactone ring is shown to be the sole essential structural feature in **1** for irreversible inactivation of HMG-CoA synthase; however, the remaining functionality enhances the binding of **1** to the enzyme relative to **5**.

Key words: HMG-CoA synthase, F-244, butyrolactone, irreversible, inhibitor.

Résumé : On a comparé l'inhibition de la synthase 3-hydroxy-3-méthylglutaryl coenzyme A (HMG-CoA) vis-à-vis le composé F-244 (**1**) anisi que de la (*RS*)-β-butyrolactone (**5**). Le composé F-244 présente une inhibition irréversible avec un IC_{50} de 8 nM, semblable à celle rapportée pour l'enzyme du foie de rat, alors que la constante de fixation ($1/K_I$) et la constante de la vitesse d'inactivation (k_{inact}) sont toutes les deux semblables aux valeurs rapportées pour l'enzyme cytoplasmique humain. La(*RS*)-β-butyrolactone (**5**) inhibe aussi l'enzyme d'une façon irréversible, mais son efficacité est beaucoup plus faible (IC_{50} de 2 nM). On a déterminé les valeurs de K_I (9 mM) et de k_{inact} (0,0078 s^{-1}) du composé **5**. Les résultats montrent que les valeurs de k_{inact} des composés **1** et **5** diffèrent par un facteur de 2,5 alors que la valeur de K_I du composé **5** est $1{,}8 \times 10^5$ fois plus élevée que celle du composé **1**. On montre donc que le noyau β-lactone est la seule caractéristique structurale essentielle du composé **1** pour l'inactivation irréversible de la synthase HMG-CoA; toutefois, par comparaison avec le composé **5**, les autres fonctions augmentent la fixation du composé **1** à l'enzyme.

Mots clés : synthase HMG-CoA, F-244, butyrolactone, irréversible, inhibiteur.

[Traduit par la rédaction]

Introduction

The antibiotic F-244 (**1**) (Fig. 1) is a member of a small but growing number of natural products containing the β-lactone moiety. F-244 was first isolated from *Cephalosporium* sp. ACC 1233 as antibiotic 1233A (1, 2), and subsequently from *Scopulariopsis* species as F-244 (3–5) and from *Fusarium* species as L-659,699 (3, 6). The biological activity of **1**, revealed through studies on both microorganisms (4) and plants (7), has been shown by experiments both in vivo (5, 6, 8–10) and in vitro (3–6, 11, 12) to arise from specific and potent inhibition of 3-hydroxy-3-methylglutaryl-coenzyme A (HMG-CoA) synthase, a key enzyme in the sterol biosynthetic pathway. Early reports by Greenspan et al. (6) describing reversible inhibition have since been corrected (8); it is now clear that F-244 is an irreversible inhibitor of the rat liver HMG-CoA synthase (12). Several syntheses of F-244 and related analogues have been reported (13–19), and a number of inhibition studies (17–21) have started to reveal structure–activity correlations.

Due to interest in developing F-244 and analogues as anti-hypercholesterolemic drugs, the structure–activity correlations have focused on compounds that are similar to F-244 in chemical structure: all have an extended hydrophobic chain at C-4, in most cases terminated with carboxylic acid or carboxymethyl groups, and all but one of the analogues reported to date have a substituent at C-3, usually either hydroxymethyl or alkoxymethyl. In the C-3 unsubstituted example of Mayer et al. (12), 3-(2′-(*ortho*-biphenyl)ethyl)oxetanone (**2**) was shown to be a reversible inhibitor of the rat liver enzyme; however, the analogue **3** is irreversible. Further, due to the high affinity of F-244 for HMG-CoA synthase, classical analysis of irreversible inhibition by F-244 using double-reciprocal plots shows that the enzyme does not saturate, so that only a lower limit could be placed on K_I (the equilibrium constant for enzyme–inhibitor dissociation) and k_{inact} (the inactivation rate constant for the second step) (12). Recently, K_I (53.7 nM) and k_{inact} (0.018 s^{-1}) for F-244 were determined using nonlinear regression to solve the substrate concentration vs. time profiles of mixtures of enzyme, substrates (acetyl- and ace-

Received October 5, 1994.[1]

K. Bell, E. Saepudin, and P. Harrison.[2] Department of Chemistry, McMaster University, 1280 Main Street West, Hamilton, ON L8S 4M1, Canada.

[1] Revision received October 5, 1995.

[2] Author to whom correspondence may be addressed. Telephone: (905) 525-9140, ext. 27290. Fax: (905) 525-9140. E-mail: PHARRISO@MCMAIL.CIS.MCMASTER.CA

Fig. 1.

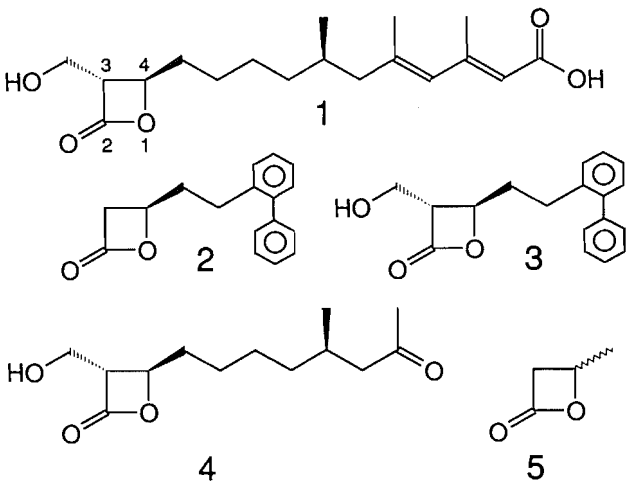

toacetyl-CoA), and inhibitor at various concentrations (22). For **4**, Mayer et al. (12) measured K_I (120 μM) and k_{inact} (0.14 s^{-1}). In other cases, the data have been presented as IC_{50} values, in order to draw comparisons between the efficacy of F-244 and analogues.

Our interest in the inhibition process led us to investigate simple β-lactones as inhibitors of HMG-CoA synthase and to evaluate K_I and k_{inact}. Herein, we describe the inhibition of HMG-CoA synthase by the simple inhibitor (*RS*)-β-butyrolactone (**5**), which forms the basis for further analysis of the influence of substituents on the fundamental inactivation parameters.

Experimental section

General

(*RS*)-β-Butyrolactone was purchased from Aldrich Chemical Co., and distilled prior to use. F-244 was prepared by incubation of *Fusarium* sp. ATCC 20788 by a modification of the procedure of Chabala et al. (23), and extracted and purified by column chromatography as described elsewhere (24). Yeast, coenzyme A esters, and all other biochemical reagents were purchased from Sigma and used as supplied.

Enzyme assay

The assay for HMG-CoA synthase was performed as described by Miller et al. (25).

3-Hydroxy-3-methylglutaryl-coenzyme A synthase

Freeze-dried yeast (*Saccharomyces cerevisiae*, cat. no. YSC-1, 100 g) was autolysed in 0.2 M Tris base/HCl buffer (pH 8.2, 400 mL) at 38°C for 4 h. Centrifugation gave a yellow supernatant preparation containing a total activity of 16 units of HMG-CoA synthase with a specific activity of 3–7 units/g. The enzyme was partially purified by a modification of the ethanol fractionation procedure of Middleton and Tubbs (26) (25–30% pellet, 5-fold purification), followed by an ammonium sulphate precipitation (35–55% pellet, 2-fold purification) and hydroxylapatite chromatography (potassium hydrogen phosphate/HCl buffer, 0.01 to 0.2 M, pH 6.8, 5-fold purification). The final preparation had a specific activity of 0.14 units/mg protein.

Fig. 2. Percentage inhibition of HMG-CoA synthase as a function of F-244 concentration. HMG-CoA synthase was incubated for 5 min with F-244, then assayed for activity relative to a control without F-244.

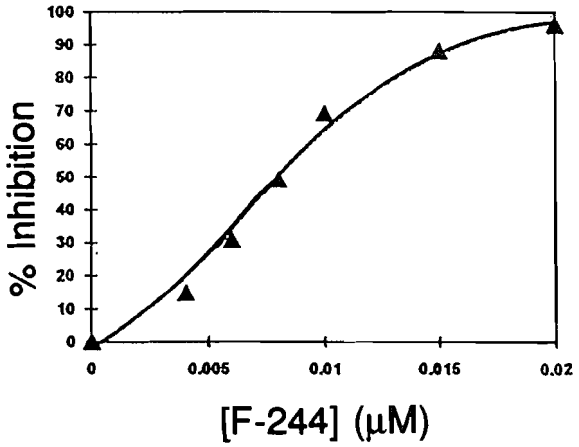

Inhibition with F-244

Method A

Volumes of a solution of F-244 in DMSO (150 μM) and DMSO to a total of 150 μL were added to 50 μL aliquots of the partially purified enzyme in 0.2 M Tris (pH 8.2, total volume 3 mL) to give final concentrations of 0, 4, 6, 8, 10, 15, and 20 nM in **1**. The mixtures were incubated 5 min at 30°C. Aliquots of the resulting solutions were withdrawn and assayed for activity. Dilutions of the enzyme–inhibitor complex to test for reversibility of inhibition were performed according to the method of Greenspan (6).

Method B

The partially purified enzyme was added to a mixture of F-244 (0, 0.1, 0.5, and 1 μM) and substrates acetoacetyl-CoA (7 μM) and acetyl-CoA (150 μM) in 0.1 M Tris (pH 8.0) containing $MgCl_2$ (20 mM) and EDTA (0.2 mM), according to the procedure of Rokosz et al. (22). The change in absorbance of acetoacetyl-CoA at 303 nm was monitored as a function of time. The data were solved for K_I and k_{inact} according to the equations derived by this group.

Inhibition with (*RS*)-β-butyrolactone

Volumes of a solution of **5** in DMSO (100 mM) and DMSO to a total of 120 μL were added to 30 μL aliquots of the partially purified enzyme in 0.2 M Tris (pH 8.2, total volume 3 mL) to give final concentrations of 0, 1, 2, 4, and 8 mM in **5**. Each of these mixtures was incubated at 30°C for 5 min. Aliquots of the resulting solutions were withdrawn after 0, 2, 4, 8, and 10 min, and assayed for enzyme activity.

Results and discussion

Antibiotic F-244 inhibits yeast HMG-CoA synthase in a concentration-dependent manner (Fig. 2) when the time of preincubation of **1** with the enzyme is kept constant at 5 min. The IC_{50} value is approximately 8 nM under these conditions, close to the value reported for the rat liver enzyme (9 nM) (12) for identical preincubation times. Time-dependent inhibition was established by comparing assays (method A) of enzyme–

Table 1. Time-dependent inhibition of yeast HMG-CoA synthase by F-244.

[F-244] (μM)	% Inhibition (no preincubation)	% Inhibition (5 min preincubation)
0.004	12	100
0.008	48	100
0.020	95	100
0.040	100	100

Note: HMG-CoA synthase and F-244 at the specified concentration were mixed. Aliquots were removed immediately, or after 5 min, added directly into the assay cell, and assayed immediately.

F-244 mixtures both immediately after, and 5 min after mixing (Table 1). The %inhibition observed increased with longer preincubation times. The method developed by Rokosz (method B) was used to determine K_I (50 nM) and k_{inact} (0.02 s^{-1}) for F-244 with yeast enzyme. The results obtained were similar to values reported for the human enzyme.

These observations show that the characteristics of inhibition by F-244 are very similar for yeast, rat liver, and human cytoplasmic enzymes. Indeed, a cysteine residue at the active site, which is involved in covalent thioester formation with the substrate acetyl-CoA in the first step of the catalytic cycle, has been strongly implicated in the yeast protein (26–28) and demonstrated to be present in the avian liver (29–31) and human cytoplasmic (22) enzymes. While these results are not surprising, it is interesting to note that cerulenin has been shown to inhibit the yeast enzyme (32), but not that of avian liver (5).

Inhibition of the same enzyme sample was studied with **5**, as a function of both concentration and time of preincubation (Fig. 3*a*). A double reciprocal plot of the data (Fig. 3*b*) gives a linear correlation ($R^2 = 0.9978$) and values of $K_I = 9$ mM and $k_{inact} = 0.0078$ s^{-1}. As is the case for **1**, dilution of inhibited enzyme under a variety of conditions failed to restore activity, while significant protection of the enzyme by the substrates occurred.

The data show that the mechanism of inhibition by **5** is qualitatively similar to that for **1**, i.e., time dependent and irreversible, demonstrating unambiguously that the β-lactone ring is the key component for irreversible inhibition. These results are in accord with previous studies, which show that hydrolysis of the β-lactone moiety results in inactive compounds (5, 6, 12). However, the results contrast with the observation that inhibition by **2** is reversible, but inactivation by **3** is irreversible, which had cast doubt on the hypothesis that the β-lactone is the only moiety responsible for irreversibility (12). It thus appears that the differences between **5** and **2** are attributable to structural differences in the enzyme–inhibitor complexes, as is also suggested by the 12 to 13-fold increase in k_{inact} for **2** relative to **1**. The value of k_{inact} for **5** is reduced relative to that for **1** by a factor of only 2.6, while K_I is increased for **5** by more than 10^5. Therefore, the substituents on the β-lactone ring play an important role in influencing the rate constant of the inactivation step.

It should be noted that the findings in the current study refer to racemic β-lactone **5**; in the absence of other effects, $K_I = 4.5$ mM if only one enantiomer is active. We are currently examining the individual enantiomers of **5**. The nature of the structural contributions to both K_I and k_{inact} is also being evaluated through systematic extension of the C-3 and C-4 substituents on the β-lactone ring. These results will be communicated in due course.

Fig. 3. (*a*) Plot of % activity remaining as a function of time during inhibition of HMG-CoA synthase by various concentrations of (*RS*)-β-butyrolactone; (*b*) double reciprocal re-plot of the data from (*a*). Concentrations: *, 1 mM; ■, 2 mM; ▲, 4 mM; X, 8 mM.

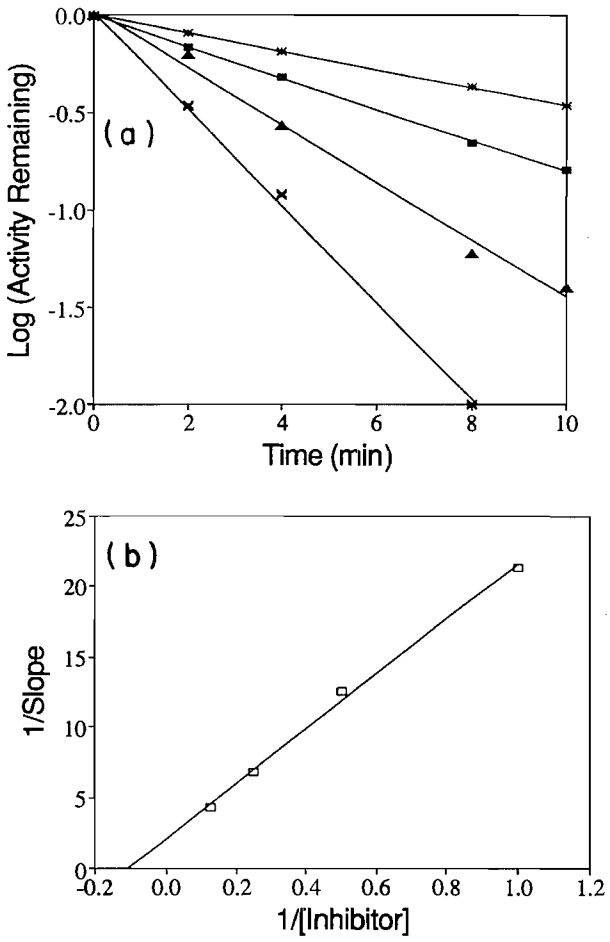

Conclusion

Examination of inhibition of yeast HMG-CoA synthase by F-244 (**1**) has shown that the characteristics of the irreversible inhibition are essentially the same as for the rat liver and human cytoplasmic enzymes. The simple analogue (*RS*)-β-butyrolactone (**5**) inhibits the yeast enzyme by an apparently identical mechanism. The results show that k_{inact} for **5** is only marginally lower than that for **1**, while K_I is much higher. Hence, the β-lactone ring is shown to be the essential structural feature in **1** for irreversible enzyme inactivation; however, the remaining functionality plays a role in enhancing the binding of **1** to the enzyme relative to **5**.

Acknowledgments

This work was financially supported by the Natural Sciences and Engineering Research Council of Canada. K.B. gratefully acknowledges the support provided by an Ontario Graduate

Studentship. E.S. is supported by a World Bank Studentship, administered through the World University Service of Canada.

References

1. D.C. Aldridge, D. Giles, and W.B. Turner. J. Chem. Soc. Chem. Commun. 639 (1970).
2. D.C. Aldridge, D. Giles, and W.B. Turner. J. Chem. Soc. C, 3888 (1971).
3. S. Omura, H. Tomoda, H. Kumagai, M.D. Greenspan, J.B. Yudkovitz, J.S. Chen, A.W. Alberts, I. Martin, S. Mochales, R.L. Monaghan, J.C. Chabala, R.E. Schwartz, and A.A. Patchett. J. Antibiot. **40**, 1356 (1987).
4. H. Tomoda, H. Kumagai, Y. Takahashi, Y. Tanaka, Y. Iwai, and S. Omura. J. Antibiot. **41**, 247 (1988).
5. H. Tomoda, H. Kumagai, H. Tanaka, and S. Omura. Biochim. Biophys. Acta, **922**, 351 (1987).
6. M.D. Greenspan, J.B. Yudkovitz, C.Y.L. Lo, J.S. Chen, A.W. Alberts, V.M. Hunt, M.N. Chang, S.S. Yang, K.L. Thompson, Y.C.P. Chiang, J.C. Chabala, R.L. Monaghan, and R.L. Schwartz. Proc. Natl. Acad. Sci. U.S.A. **84**, 7488 (1987).
7. J.M. Jacyno, H.G. Cutler, R.G. Roberts, and R.M. Waters. Agric. Biol. Chem. **55**, 3129 (1991).
8. M.D. Greenspan, H.G. Bull, J.B. Yudkovitz, D.P. Hanf, and A.W. Alberts. Biochem. J. **289**, 889 (1993).
9. H. Nagashima, H. Kumagai, H. Tomoda, and S. Omura. Life Sci. **52**, 1595 (1993).
10. H. Kumagai, H. Tomoda, and S. Omura. J. Antibiot. **43**, 397 (1990).
11. H. Tomoda, H. Kumagai, H. Tanaka, and S. Omura. J. Antibiot. **46**, 872 (1993).
12. R.J. Mayer, P. Louis-Flamberg, J.D. Elliott, M. Fisher, and J. Leber. Biochem. Biophys. Res. Commun. **169**, 610 (1990).
13. S. Wattanasin, H.D. Do, N. Bhongle, and F.G. Kathawala. J. Org. Chem. **58**, 1610 (1993).
14. P.M. Wovkulich, K. Shankaran, J. Kiegiel, and M.R. Uskokovic. J. Org. Chem. **58**, 832 (1993).
15. K. Mori and Y. Takahashi. Liebigs Ann. Chem. 1057 (1991).
16. Y.C.P. Chiang, S.S. Yang, J.V. Heck, J.C. Chabala, and M.N. Chang. J. Org. Chem. **54**, 5708 (1989).
17. H. Hashizume, H. Ito, K. Yamada, H. Nagashima, M. Kanao, H. Tomoda, T. Sunazuka, H. Kumagai, and S. Omura. Chem. Pharm. Bull. **42**, 512 (1994).
18. H. Hashizume, H. Ito, N. Kanaya, H. Nagashima, H. Usui, R. Oshima, M. Kanao, H. Tomoda, T. Sunazuka, T. Nagamitsu, H. Kumagai, and S. Omura. Heterocycles, **38**, 512 (1994).
19. H. Hashizume, H. Ito, T. Morikawa, N. Kanaya, H. Nagashima, H. Usui, H. Tomoda, T. Sunazuka, H. Kumagai, and S. Omura. Chem. Pharm. Bull. **42**, 2097 (1994).
20. T. Sunazuka, K. Tsuzuki, H. Kumagai, H. Tomoda, H. Tanaka, H. Nagashima, H. Hashizume, and S. Omura. J. Antibiot. **45**, 1139 (1992).
21. K.L. Thompson, M.N. Chang, Y.C.P. Chiang, S.S. Yang, J.C. Chabala, B.H. Arison, M.D. Greenspan, D.P. Hanf, and J. Yudkovitz. Tetrahedron Lett. 3337 (1991).
22. L.L. Rokosz, D.A. Boulton, E.A. Butkiewicz, G. Sanyal, M.A. Cueto, P.A. Lachance, and J.D. Hermes. Arch. Biochem. Biophys. **312**, 1, (1994).
23. J.C. Chabala, M.N. Chang, D.W. Graham, S.S. Yang, Y.C.P. Chiang and N.N. Girotra. Eur. Pat. Appl. no. 285 254 (1988); Chem. Abstr. **110**, 128659d (1989).
24. E. Saepudin and P. Harrison. Can. J. Chem. **73**, 1 (1995).
25. L.R. Miller, D.L. Raulston, and G.J. Schroepfer. Chem. Phys. Lipids, **47**, 177 (1988).
26. B. Middleton and P.K. Tubbs. Biochem. J. **126**, 27 (1972).
27. B. Middleton and P.K. Tubbs. Biochem. J. **137**, 15 (1974).
28. P.R. Stewart and H. Rudney. J. Biol. Chem. **241**, 1222 (1966).
29. I. Misra, C. Narasimhan, and H.M. Miziorko. J. Biol. Chem. **268**, 12 129 (1993).
30. H.M. Miziorko, C.E. Behnke, and H.H.L. Wang. Biochim. Biophys. Acta, **1041**, 273 (1990).
31. H.M. Miziorko, K.D. Clinkenbeard, W.D. Reed, and M.D. Lane. J. Biol. Chem. **250**, 5768 (1975).
32. T. Ohno, T. Kesado, J. Awaya, and S. Omura. Biochem. Biophys. Res. Commun. **57**, 1119 (1974).

Near-infrared and visible luminescence and absorption spectroscopy of low-coordinate organometallic rhenium compounds

Carole Savoie and Christian Reber

Abstract: Low-temperature absorption and luminescence spectra of four organorhenium compounds were measured in the visible and near-infrared spectral regions. Effects of the temperature, formal oxidation state, and the oxo-, bromo-, and organic ligands on the metal center are reported. The emission maxima of the four compounds show a large variation between 9000 and 14 200 cm^{-1}. Stokes shifts show a smaller variation from 3700 to 4200 cm^{-1}. Luminescence intensities are used to qualitatively characterize nonradiative relaxation processes.

Key words: luminescence spectra, absorption spectra, organorhenium compounds.

Résumé : Les spectres d'absorption et de luminescence à basse température de quatre complexes organométalliques du rhénium(III) et du rhénium(V) ont été mesurés dans les régions du visible et du proche infrarouge. Les effets apportés par la variation de la température, du degré d'oxydation et du nombre et caractère des ligands oxo, bromo et organiques sur le centre métallique ont été étudiés. Les énergies des maxima d'émission varient entre 9000 et 14 200 cm^{-1}. Les déplacements de Stokes montrent une variation plus faible de 3700 à 4200 cm^{-1}. Les résultats spectroscopiques nous renseignent sur les processus de relaxation impliqués lors des transitions.

Mots clés : spectroscopie de luminescence, spectroscopie d'absorption, composés organométalliques du rhénium.

1. Introduction

Rhenium shows a very rich organometallic chemistry with a wide variety of oxidation states and many different coordination geometries that have been explored over the past decade (1–3). The main emphasis of the work reported in the literature is on the synthesis, structure determination, and NMR spectroscopic properties of organorhenium compounds.

These systems offer a unique opportunity to examine a variety of coordination geometries, oxidation states, and ligand environments for the same transition metal center with electronic spectroscopic techniques. We present emission spectra of a series of organorhenium compounds with oxo and bromo ligands in the near-infrared and visible regions. The molecules studied are $ReBr_2(C_5(CH_3)_5)(CH_3C{\equiv}CCH_3)$ (A), $ReBr_2(C_5(CH_3)_5)(CH_2{=}CH\text{-}CH{=}CH_2)$ (B), $ReO(C_5(CH_3)_5)(C_6H_5C{\equiv}CC_6H_5)$ (C), and $ReO_2(CH_3)(CH_3C{\equiv}CCH_3)$ (D), presented in Scheme 1. They share low coordination numbers and an approximate C_s symmetry and were chosen for this study based on their varying ligand environments and metal oxidation states: compounds A–C in Scheme 1 have Re(III) metal centers ([Xe]$5d^4$ electron configuration), whereas compound D has a Re(V) metal center ([Xe]$5d^2$). The large spectroscopic differences between these molecules

Scheme 1.

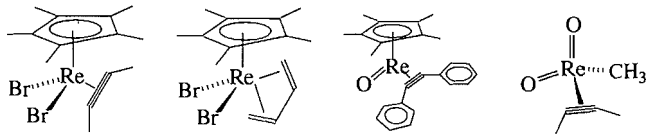

A B C D

indicate exceptionally large tuning ranges for properties such as the emitting state energy, an important quantity for selective photochemical and photocatalytical applications. Up to now, organometallic compounds of the heavy transition elements were only rarely studied from this perspective.

We present low-temperature absorption and luminescence spectra and establish a qualitative correlation between band energies and the nature of the ligands of compounds A–D. The near-infrared spectral region is of crucial importance for these studies, in contrast to traditional coordination compounds of the third-row transition metals, where the lowest energy excited states are often observed in the visible or ultraviolet regions, at significantly higher energies than for the organorhenium compounds studied in this work (4).

2. Experimental

The syntheses and crystal structures of compounds A–D are described in refs. 5–7. Compounds A (black), B (purple), and C (red-brown) were obtained in solid form from Dr. Roland A. Fischer. Compound D and its acetylene analogue (both yellow) were synthesized using the methods described in refs. 7 and 8, using trioxomethylrhenium(VII) as a starting material and mild, selective deoxidation with polymer-bound triphenylphosphine in order to obtain the Re(V) dioxo compound D.

Received June 23, 1995.

C. Savoie and C. Reber.[1] Département de chimie, Université de Montréal, C.P. 6128, Succursale Centre-ville, Montréal, QC H3C 3J7, Canada.

[1] Author to whom correspondence may be addressed. Telephone: (514) 343-7332. Fax: (514) 343-7586. E-mail: reber@ere.unmontreal.ca

The purity of our samples was checked by comparing ^{1}H NMR and IR spectra to the literature data (5–8). Thin crystalline samples suitable for spectroscopy were obtained either by slow evaporation of saturated solutions in dry methanol on quartz plates at room temperature or by cleaving thin samples from larger crystals. All solutions must be kept under an inert atmosphere to prevent decomposition of the molecules. The optical quality of the sample crystals was examined under a microscope between crossed polarizers, and extinction directions were determined. Only unpolarized spectra are reported in the following because the polarization direction had no significant effect on band intensities and positions, most likely due to the low crystal symmetries with multiple inequivalent sites for the chromophores in the crystal, leading to molecular units with different orientations relative to the polarization directions (5–8). The crystals, with typical areas of 0.5 mm^2, were mounted in a helium cryostat (Oxford Instruments CF 1204). All absorption spectra were measured with a Varian Cary 5E spectrophotometer. The instrumentation used for luminescence measurements is described in detail elsewhere (9). Both broadband UV light and the 514.5 nm line from an Ar^+ ion laser were used as excitation sources. Weak luminescence was found for compounds B–D; no luminescence was detectable for compound A. Emission at wavelengths longer than 1000 nm was detected with a Ge detector (ADC 403L, cooled to 77 K) and a lock-in amplifier. All spectra are corrected for system response (9, 10), but no smoothing or noise-removal routines were applied to experimental data.

3. Spectroscopic results

Emission was observed from three of the compounds in Scheme 1 between 600 and 1500 nm. The luminescence spectra of compounds B–D are shown in Fig. 1. The energy of the emission band maxima varies between 9000 and 14 200 cm^{-1}, an exceptionally large variation for a series of organometallic compounds of the same metal. The acetylene analogue of compound D shows a luminescence spectrum with a similar bandwidth and a higher energy band maximum (14 500 cm^{-1} at 20 K) than compound D. This comparison illustrates the small influence of the nature of the substituents on the alkyne ligands on the energy and properties of the emitting state. No emission was observed from compound A at wavelengths shorter than 2000 nm, most likely due to efficient nonradiative relaxation processes from its very low-energy first excited state. The luminescence intensities for all compounds decrease rapidly with increasing temperature, as illustrated in Fig. 1 with two selected temperatures. Figure 2 shows integrated band intensities as a function of temperature. Band maxima and bandwidths at low temperature are summarized in Table 1 for the compounds in Scheme 1.

The solid-state absorption spectra of all four molecules are shown in Fig. 3. The dibromo compounds A and B show onsets of their first absorption bands in the near-infrared region, in contrast to the oxo compounds C and D, where these onsets are in the visible. The energies of the first absorption bands show a variation similar to that of the luminescence band maxima. Transition energies were determined from the spectra in Figs. 2 and 3 and are summarized for all the compounds in Table 1. Absorption intensities and band positions show no large change with temperature, as expected for low-

Fig. 1. Low-temperature luminescence spectra of the organometallic rhenium compounds B (circle), C (square), and D (triangle) in Scheme 1.

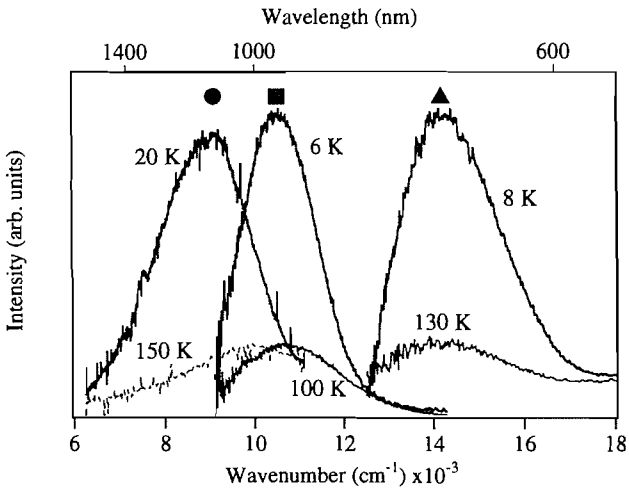

Fig. 2. Integrated luminescence intensities for compounds B, C, and D (Scheme 1) as a function of temperature. The symbols are defined in Fig. 1.

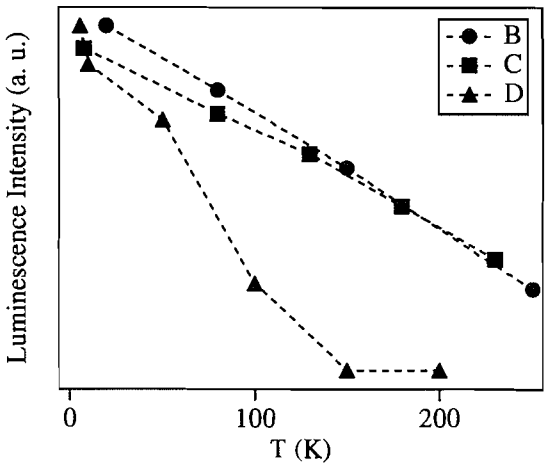

symmetry systems and similar to the experimental results for a series of organometallic mono-oxo rhenium compounds (11). The lowest energy absorption bands of compounds B–D in dichloromethane solution at room temperature are not as easily discernible as the corresponding bands in the low-temperature, solid-state spectra in Fig. 3. We determine extinction coefficients of 5, 33, and <1 M^{-1} cm^{-1} for the first absorption bands of compounds B–D, respectively. The higher energy visible bands in solution correspond well to the solid state spectra. Wavelengths (extinction coefficients) are as follows: A: 700 nm (365), 510 nm (1134), 340 nm (4713); B: 520 nm (62), 360 nm (124); C: 500 nm (200), 420 nm (450); D: 360 nm (193).

4. Discussion

The organorhenium compounds investigated in this work show a very large variation of their lowest excited state energies. This large tuning range is possible because of the unique,

Table 1. Absorption and luminescence band maxima and luminescence bandwidths.

Compound	Absorption max., cm^{-1}	Emission max., cm^{-1}	Bandwidth, cm^{-1}	Stokes shift, cm^{-1}
$ReBr_2(C_5(CH_3)_5)(CH_3C{\equiv}CCH_3)$ (A)	7 000[a]	—	—	—
$ReBr_2(C_5(CH_3)_5)(CH_2{=}CH\text{-}CH{=}CH_2)$ (B)	12 700[b]	9 000[c]	2 400[c]	3 700
$ReO(C_5(CH_3)_5)(C_6H_5C{\equiv}CC_6H_5)$ (C)	15 100[b]	10 900[c]	2 000[c]	4 200
$ReO_2(CH_3)(CH_3C{\equiv}CCH_3)$ (D)	18 000[b]	14 200[c]	2 450[c]	3 800

[a]Onset of band, T = 25 K.
[b]T = 80 K.
[c]T = 15 K.

Fig. 3. (*a*) Solid-state absorption spectra of compounds A at 80 K and B at 20 K. (*b*) Solid-state absorption spectra of compounds C at 6 K and D at 6 K.

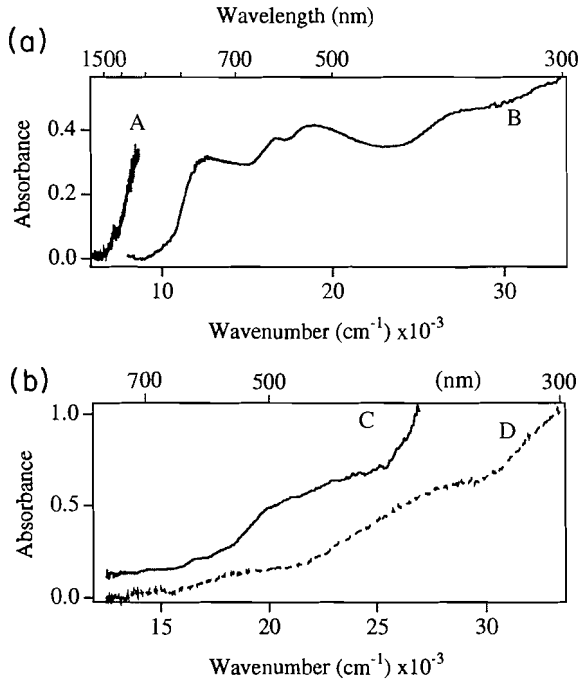

very rich organometallic chemistry of rhenium. We qualitatively examine some spectroscopic trends observed for compounds A–D and relate the emitting state energies to the nature of the ligands. The weak low-energy absorption bands for the luminescent compounds B–D are indicative of d-d transitions, an assignment supported by the low extinction coefficients observed in the solution spectra. This proposed assignment is further supported by the molecular orbital calculations for mono-oxo systems reported in ref 2. We notice that the absence of luminescence from compound A might not be caused exclusively by the low energy of its first excited state, but might be caused in part by a qualitatively different nature of this state. Large structural distortions are common to occur in charge-transfer excited states and would lead to more efficient nonradiative relaxation processes than for d-d emitting states with smaller distortions.

It was shown for an extended series of cyclopentadienyl compounds of nickel(II) that the d-d absorption band energies follow the standard spectrochemical series for common anionic ligands such as halides or the oxide ion (12). Based on these correlations, established for Ni(II), we expect the bromo compounds A and B to have lower energy excited states than the oxo systems C and D, corresponding to the observations in Figs. 1 and 3 and in qualitative agreement with our d-d assignment. Furthermore, the emitting state for compound C with only one oxo ligand is observed at lower energy than for compound D with two oxo ligands, again in agreement with the spectrochemical series. The rhenium–oxygen bond lengths are 1.709 Å for C and 1.74 Å for D, shorter than in *trans*-ReO_2 complexes, but longer than found for the majority of the known Re≡O organometallic compounds (13). The emitting state energy for the dioxo compound D varies by less than 1000 cm^{-1} from the band maxima obtained for Re≡O systems with a shorter rhenium–oxygen bond (11). This comparison illustrates the limited applicability of ligand-field concepts to our series of organometallic compounds. Transition energies appear to depend less strongly on metal–ligand bond length than expected from ligand-field theory. We note that the formal oxidation state of the metal center does not appear to be the main determinant of the emitting state energy, as illustrated by very similar emission band maxima for the Re(V) compound D and the Re(III) compounds in ref. 11. The energies of the first excited states obtained from the electronic spectra are summarized for compounds A–D in Fig. 4.

The higher energy absorption bands for compounds C and D in Fig. 3b are more intense than the first band, likely corresponding to the spin-allowed d-d transitions expected at higher energy than the spin-forbidden first bands (11). Compound B shows a series of bands with comparable intensities throughout the visible region, a different spectrum from those for compounds C and D, reflecting the different coordination geometries. A possible reason for the sequence of intense absorption bands of compound B throughout the visible spectral region could be low-energy intra- or intermolecular electron transfer transitions. Despite these large variations between the absorption spectra, the lowest energy excited state has some common characteristics for compounds B–D, illustrated by the similar luminescence bandwidths and the low extinction coefficients in the solution absorption spectra, qualitatively supporting our proposed d–d assignment.

The luminescence intensities decrease with increasing temperature, similar to those reported in ref. 11, where it was shown that luminescence lifetimes decrease in parallel with the intensities. The quantum yields of these luminescences are low and the lifetimes are expected to be much shorter than those expected for purely radiative transitions (11). Their use

Fig. 4. Energies of the lowest excited states for the series of organometallic rhenium compounds in Scheme 1. The energies are determined from the luminescence and absorption spectra in Figs. 1 and 3, respectively. Solid arrows denote observed luminescence transitions; the broken arrow for compound A indicates efficient nonradiative relaxation processes.

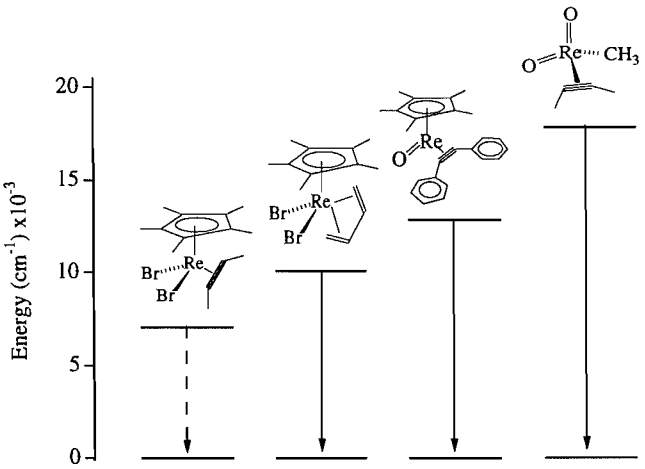

for the characterization of the emitting state is limited, and we made no attempt to measure them for compounds B–D. The decrease in luminescence intensity with temperature can be correlated with the number of oxo ligands: the most pronounced decrease is observed for compound D, which contains two high-frequency rhenium-oxo oscillators. A distinction between compounds B and C is not possible, illustrating that other high-frequency vibrations, most likely C-H oscillators, play an important role in the relaxation dynamics. This conclusion is in agreement with ref. 11, where a qualitative correlation between the decrease of both the luminescence intensity and lifetime with the number of C-H oscillators was established. Such qualitative arguments neglect the importance of intermolecular energy transfer processes to impurities, shown to be important in some organometallic solids (9, 10), and therefore a more quantitative analysis of the temperature dependence of the luminescence intensities is not possible from our data.

The Stokes shifts for compounds B–D are included in Table 1. Their large values indicate significant structural changes between the ground and lowest energy excited states. In contrast to the emitting state energies, there is no systematic variation of the Stokes shift for compounds B–D, and similar Stokes shifts between 3400 and 3700 cm^{-1} were obtained for the rhenium–oxo compounds in ref. 11. The lack of vibronic structure does not allow us to determine individual bond length changes, but the similar luminescence and absorption bandwidths of our compounds and those reported in ref. 11 indicate similar excited state distortions.

This work illustrates the large variation of the emitting state energy of organometallic rhenium compounds, establishing these molecules as new near-infrared chromophores with a very large tuning range. Excited-state energies and transition intensities reflect the nature of the ligands and the coordination geometry and indicate a potential for photochemical applications of these molecules.

Acknowledgments

We thank Dr. Roland A. Fischer (Technische Universität München, Germany) for the gift of some of the compounds used in this study. This work was made possible by research grants from the Natural Sciences and Engineering Research Council of Canada and Fonds pour la formation de chercheurs et l'aide à la recherche (Province of Quebec).

References

1. W.A. Herrmann. Angew. Chem. Int. Ed. Engl. **27**, 1297 (1988).
2. J.M. Mayer, D.L. Thorn, and T.H. Tulip. J. Am. Chem. Soc. **107**, 7454 (1985).
3. J.M. Mayer, T.H. Tulip, J.C. Calabrese, and E. Valencia. J. Am. Chem. Soc. **109**, 157 (1987).
4. A.J. Lees. Chem. Rev. **87**, 711 (1987).
5. W.A. Herrmann, R.A. Fischer, J.K. Felixberger, R.A. Paciello, P. Kiprof, and E. Herdtweck. Z. Naturforsch. B: Phys. Sci. **43**, 1391 (1988).
6. W.A. Herrmann, R.A. Fischer, W. Amslinger, and E. Herdtweck. J. Organomet. Chem. **362**, 333 (1989).
7. J.K. Felixberger, J.G. Kuchler, E. Herdtweck, R.A. Paciello, and W.A. Herrmann. Angew. Chem. Int. Ed. Engl. **27**, 946 (1988).
8. W.A. Herrmann, J.G. Kuchler, J.K. Felixberger, E. Herdtweck, and W. Wagner. Angew. Chem. Int. Ed. Engl. **27**, 394 (1988).
9. M.J. Davis and C. Reber. Inorg. Chem. **34**, 4585 (1995).
10. M.J. Davis and C. Reber. J. Lumin. **60/61**, 874 (1994).
11. C. Reber and J.I. Zink. Inorg. Chem. **30**, 2994 (1991).
12. J. Thomson and M.C. Baird. Can. J. Chem. **51**, 1179 (1973).
13. J.M. Mayer. Inorg. Chem. **27**, 3899 (1988).

Mechanistic variations in the formation of benzocyclooctatetraene from benzobicyclo[4.2.0]octa-2,4,7-triene

Christopher Owen Bender

Abstract: Benzocyclooctatetraene (i.e., COT, **2**) is the major product from the thermolysis and direct photolysis of 2,3-benzobicyclo[4.2.0]octa-2,4,7-triene (i.e., triene **1**). It is also a minor product from the sensitized irradiation of **1**. The mechanism of the reaction **1**→**2** was investigated using deuterium-labelled triene (i.e., **1***a/b*), which was prepared in a two-step procedure from a known triene mixture (**1***a*) containing deuterium at both C-4 (43%) and C-5 (97%): the thermolysis of **1***a* led to labelled COT **2***a*, which upon direct irradiation ($\lambda \geq 310$ nm) gave the deuterated triene mixture **1***a/b* in good chemical yield (61%) but in low quantum efficiency ($\Phi \approx 0.0001$). The COT produced from the direct irradiation (Corex filter) of **1***a/b* possessed different deuterium distributions than when generated thermally or from triplet sensitization (*p*-dimethylaminobenzophenone), as determined by ^{1}H NMR integration. The observed deuterium-labelling patterns are in accord with a Zimmerman di-π-methane rearrangement being involved in formation of the COT from S_1 of triene **1**, while a mechanism proceeding by initial cleavage of the cyclobutene C_1—C_6 bond appears to operate during the thermal or sensitized (T_1) generations of **2**.

Key words: mechanisms, rearrangements, photochemistry, di-π-methane.

Résumé : Le benzocyclooctatétraène (soit, le COT, **2**) est le principal produit soit lorsqu'on chauffe des solutions du composé 2,3-benzobicyclo[4.2.0]octa-2,4,7-triène (**1**), ou lorsqu'on le photolyse directement. Le composé COT **2** est aussi un produit mineur des irradiations sensibilisées du triène **1**. Le mécanisme pour la réaction **1**→**2** a été étudié à l'aide du triène marqué au deutérium (**1***a/b*). On a préparé le mélange **1***a/b* en deux étapes à partir du triène **1***a* contenant des atomes de deutérium à C-4 (43%) et à C-5 (97%) : la thermolyse du triène **1***a* conduit au COT **2***a* qui ensuite se transforme en **1***a/b* par irradiation directe, en bon rendement (61%) mais faible efficacité ($\Phi \approx 0{,}0001$). Les distributions de deutérium dans le COT obtenu par irradiation directe (filtre de Corex), par thermolyse ou par irradiation sensibilisée (*p*-diméthylaminobenzophénone), du **1***a/b* sont différentes. Des études de marquage suggèrent qu'une transposition di-π-méthane de Zimmerman est le mécanisme qui produit le COT à partir du S_1 du triène **1**, tandis que la voie suivie pendant la thermolyse ou l'irradiation sensibilisée (T_1) est une ouverture de la liaison C_1—C_6 du composé **1**.

Mots clés : mécanismes, transpositions, photochimie, di-π-méthane.

Introduction

There is current interest in the synthesis of benzocyclooctenes due to their demonstrated potential for conversion, via Birch reduction, to derivatives of the anti-cancer drug Taxol (1). Recently, we reported (2) that unsubstituted benzocyclooctatetraene (**2**) is the major product from both the thermolysis and the direct photolysis of 2,3-benzobicyclo[4.2.0]octa-2,4,7-triene (**1**). It is also a very minor product from sensitized irradiations of the triene. Details of the ground and excited-state products of triene **1** are summarized in Scheme 1. It was noted that a simple $2\sigma_s+2\pi_s$ electrocyclic opening (3) of the cyclobutene ring of triene **1** could account for the COT formation in each case, and experiments using deuterium-labelled starting material (**1**-d_2) gave results consistent with this mechanistic view, viz **1**-d_2→**2**-d_2 (Scheme 1). We now report further results based on a new labelling pattern that indicate that the pathways used in the formation of COT **2** from triene **1** involve different carbon reorganizations when formed from the singlet excited state than when generated from sensitization (T_1) or from thermolysis.

Scheme 1. Triene thermolysis and photolyses products.

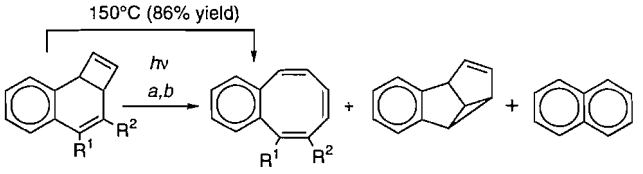

1, $R^1=R^2=H$	2		3
1-d_2, R^1=50%D, R^2=93%D	2-d_2		
Chemical yields			
a, Direct	39%	23%	8%
b, Sensitized	2%	54%	4%

Results

The deuterium-labelled triene used in the present study was

Received August 18, 1995.

C.O. Bender.[1] Department of Chemistry, University of Lethbridge, Lethbridge, AB T1K 3M4, Canada.

[1] Telephone: (403) 329-2307. Fax: (403) 329-2057.

Table 1. Hydrogen atom distributions of the nonaromatic positions in deuterated benzocyclooctatetraenes.

Entry no.	Origin	% Hydrogen atom distributions at: C-5,10 (s:d) δ 6.55	C-6,9 (s:d) δ 6.03	C-7,8[a] δ 5.88
1	Observed for thermolysis of **1***a*	1.56 (1:2.1)	1.04 (<0.05:1.0)	2.01
2	Calcd. for **1***a*→**2***a* or **1***a/b*→**2***a*	1.57 (1:1.9)	1.03 (0:1.0)	2.00
3	Observed for thermolysis of **1***a/b*	1.51 (1:1.9)	1.01 (<0.02:1.0)	2.01
4	Calcd. for **1***a/b*→**2***c*	1.57 (1:0.6)	1.03 (0.7:1.0)	2.00
5	Observed for sensit. hv of **1***a/b*	1.54 (1:1.9)	0.96 (<0.05:1.0)	1.96
6	Observed for direct hv of **1***a/b*	1.54 (1:3.2)	1.33 (0.1:1.0)	1.72
7	Calcd. for **1***a/b*→**2***a/b* or →**2***a/d*	1.57 (1:3.0)	1.30 (0.1:1.0)	1.73
8	Calcd. for **1***a/b*→**2***c/b*	1.57 (1:1.3)	1.30 (0.5:1.0)	1.73

[a]In each case the aromatic multiplet at δ 6.93–6.99 was set as the normalized integration standard of 2.00H; the other aromatic multiplet at δ 7.17–7.24 gave integral values within the range 2.00–2.04H.

Scheme 2. Preparation of deuterium-labeled triene mixture.

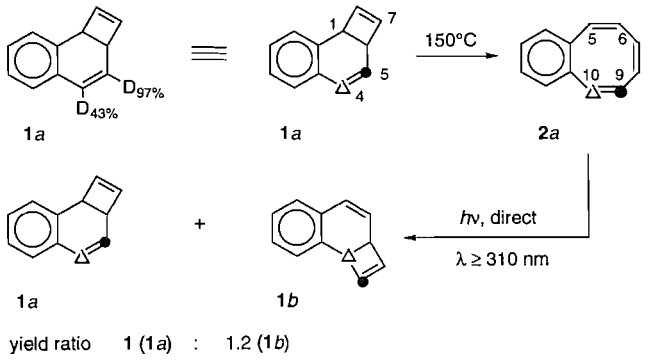

Scheme 3. Observed and possible label locations in COT product from triene thermolyses and photolyses.

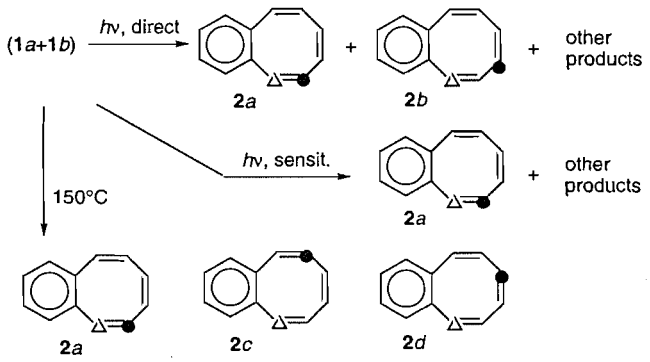

prepared in a two-step procedure from the known (2) triene mixture **1***a*, which contained deuterium at both C-4 (43%) and C-5 (97%) (Scheme 2). Thus, the thermolysis of **1***a* led to the labelled COT **2***a* (see Table 1, entry 1, for the ^{1}H NMR integrations of the aliphatic hydrogens), which upon direct irradiation (λ ≥ 310 nm) gave the deuterated triene mixture **1***a* and **1***b* in good chemical yield (61%, based on 35% conversion), but in low quantum efficiency (Φ ≈ 0.0001). The inefficiency of the rearrangement may provide an explanation for a previous report that found COT **2** to be unreactive (4). The label distributions in the isotopic triene mixture **1***a,b* were determined by proton NMR analysis (see Experimental); a small isotope effect ($k_{1b}/k_{1a} \leq 1.2$) in favour of the formation of **1***b* was observed in the 2π + 2π photoclosure step.

A solution of the mixture **1***a,b* in *n*-nonane, when heated to reflux (150°C) for 12 h, gave a 75% yield of COT product, which showed no deuterium attachment to C-7 and C-8 (i.e., the γ carbons) and corresponded uniquely to the presence of the mixture **2***a* (note Scheme 3). The observed and calculated ^{1}H NMR integration values are listed in Table 1 (see entries 3 and 2, respectively). Although in principle the isotopic mixture **2***c* (note structure in Scheme 3) would also lead to the same overall proton integrations as **2***a*, we were able to rule out the formation of **2***c* on the basis of the NMR peak ratios of the two types of signal (a singlet and a doublet)[2] observed for the COT α hydrogens (i.e., for H-5 and H-10), and also those found for the β hydrogens (i.e., H-6 and H-9). If **2***c* were present, the anticipated ratio of the singlet to doublet peaks would then be 1(s):0.6(d) for the α hydrogens, and 0.7(s):1.0(d) for the β hydrogens (see entry 4, Table 1). The observed ratios were 1(s):1.9(d) and <0.02(s):1.0(d), respectively, which agrees with the ratios required for **2***a* (see entry 2, Table 1).

In the case of the COT product isolated from the direct irradiation of the triene mixture **1***a,b*, the NMR hydrogen distributions were distinctly different from those found for the

[2] There are two types of signal observed for the α hydrogens: besides the doublet centred at δ6.55 ($J_{5(10),6(9)}$ = 12 Hz) there is a singlet at δ 6.55 that results from the absence of coupling when a β carbon is partially deuterated. The integration ratio of the singlet to doublet signals indicates the relative amount of deuterium at the β positions. The situation is similar for the β hydrogens, which occur as a doublet of triplets centred at δ 6.03 ($J_{6(9),5(10)}$ = 12 Hz, $J_{6(9),7(8)} = J_{6(9),8(7)}$ = 2 Hz), and which are accompanied by a broad singlet at δ6.03 when an α carbon is partially deuterated.

Scheme 4. Mechanisms that operate in semibullvalene photoformation.

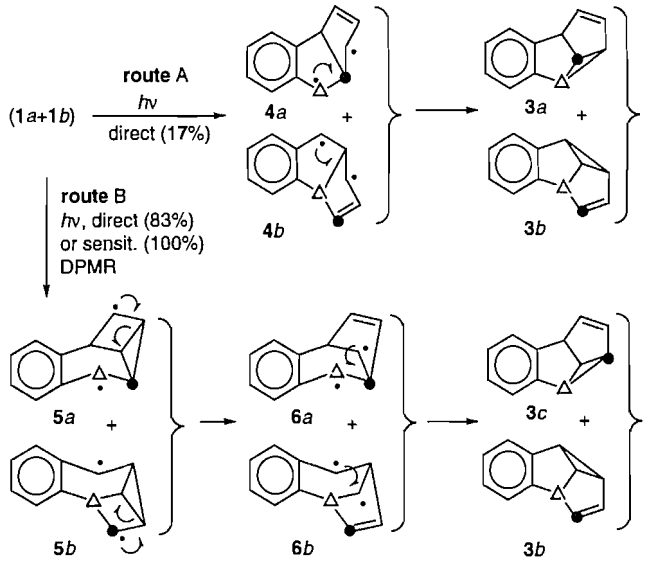

thermally generated COT.[3] Importantly, the integrations for the β hydrogens were heavy, while those for the γ hydrogens were light (note entry 6, Table 1), and accord well with a composite of 72.5% **2***a* and 27.5% **2***b* (note entry 7, Table 1). Although the formation of mixture **2***c* in place of **2***a* can be discounted, since this would have led to significantly different s:d ratios for the α and for the β hydrogen signals (see entry 8, Table 1), we are not able to eliminate the possibility that isotope mixture **2***d* (see structure in Scheme 3) forms part of the COT product in place of **2***b*: both **2***b* and **2***d* would give the same gross proton integrations and also the same s:d ratios for the α and for the β signal peaks (see entry 7, Table 1). Similar difficulties in interpretation of the proton distributions for related deuterated benzocyclooctatetraenes were encountered by Zimmerman, Givens, and Pagni (4), and arise from the C_{2v} symmetry of the benzo-COT system.

In contrast to the direct irradiation results, the COT material obtained from the sensitized irradiation of the triene mixture **1***a,b* showed NMR spectral details that were the same as those observed for the thermally generated COT **2***a* product (cf. Table 1, entries 5 and 3, respectively).[3]

The direct and sensitized photolyses of the deuterated triene also gave the labelled semibullvalenes (i.e., SB) **3***a–c*. The observed SB deuterium distributions (see Experimental) depend on the mode of excitation and fully confirm conclusions from a previous report (2) that the semibullvalene product from direct irradiation derives from two reaction pathways (note Scheme 4, route A (17%) and route B (83%)), whereas that from triplet senistization is provided uniquely by a Zimmerman di-π-methane (DPM) rearrangement (5) (Scheme 4, route B).

[3] To minimize complications due to possible kinetic isotope effects in the photolyses of triene mixture **1***a,b*, the runs were carried out to almost complete conversion of the starting material: ≥97% in the direct irradiation, and 96% in the case of sensitization.

Scheme 5. Mechanisms that account for COT formation from triene thermolysis and sensitized irradiation.

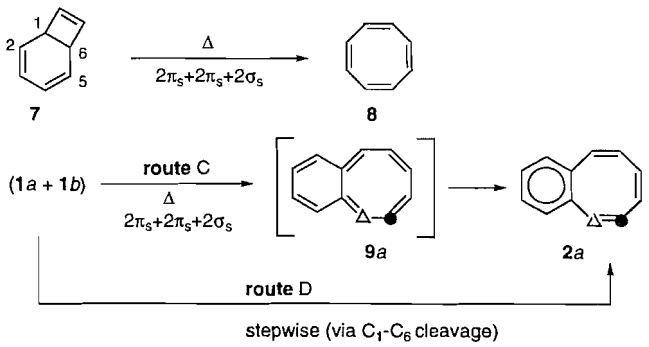

Discussion

The thermal rearrangement of the parent aliphatic triene **7** to COT **8** (Scheme 5) is a facile reaction (6) that is formally a $2\pi_s + 2\pi_s + 2\sigma_s$ electrocyclic opening of the six-membered ring (3). The concerted process, however, would be expected to be more demanding in the case of the benzo derivative **1** since the initial loss of aromaticity (note route C and structure **9***a*, Scheme 5) is required before bond reorganization can occur to give the boat structure of COT **2***a*. It is therefore not surprising that benzo-triene **1** has a half-life of ca. 1 h at 150°C whereas the parent triene **7** has a $t_{1/2}$ of 14 min at 0°C (6). An alternative explanation for the thermal rearrangement of triene **1** to COT **2** is that the reaction proceeds via a stepwise process (route D, Scheme 5) involving the initial cleavage of the strained C_1—C_6 bond of **1***a,b*. The observed deuterium labelling in **2***a* is in accord with operation of either route C or route D (Scheme 5).

The photochemical generation of COT from triene **1** is more complex. The previous study (2) of the excited-state reactivity of **1** showed that ≥98% of the COT produced from the direct irradiation originates from the S_1 state of the triene; the COT from sensitized runs is triplet derived (T_1). The present results now reveal that S_1 and T_1 engage different pathways when forming the COT. In the case of T_1, the observed COT deuterium-labelling pattern (entry 5, Table 1) is consistent with a process that proceeds with a simple opening of the cyclobutene ring of triene **1**, similar to the stepwise thermal pathway to COT **2***a* (cf. route D, Scheme 5).

The COT formed from S_1, on the other hand, must involve another mechanism, at least in part, since deuterium occurs also at the γ carbon(s) (note entry 6, Table 1). One possible rationale that does account for the observed label distribution involves the formation of the COT products **2***a* and **2***d*[4] via a 1:1 competition between the pathways depicted in Scheme 6 (routes E and F): **2***a* may derive in part (50%) from the $2\sigma_s + 2\pi_s$ electrocyclic process (route F) or stepwise, whereas **2***d* (27.5%) and additional **2***a* (22.5%) may arise from the initial C_5–C_8 diagonal bridging shown as route E. However, a point of concern with this rationale is that the latter mechanism has not been reported in derivatives of bicyclo[4.2.0]octatriene,

[4] We are unable to differentiate between isomer mixture **2***d* and **2***b* with the NMR data at hand, vide supra.

Scheme 6. Possible mechanism for COT formation from direct irradiation of triene.

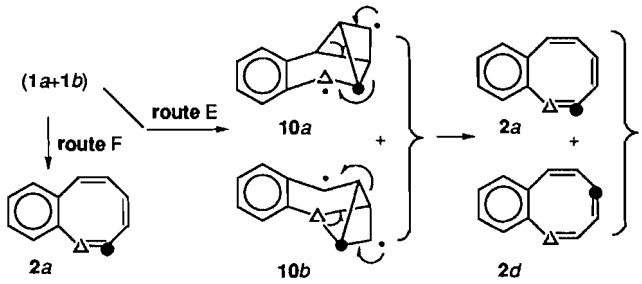

and diagonal bridging of this kind is unknown in other di-π-methane systems.[5]

A more simple explanation of the labelling results, and one that has literature precedence, involves the coformation of the COTs **2***a* and **2***b* from a single mechanistic pathway. This pathway proceeds by Zimmerman DPM rearrangement (5) of triene **1** and entails the initial formation and subsequent thermal reorganization of the symmetrical octavalene intermediate **12** (note Scheme 7). The final step is assumed to occur with equal facility via rupture of alternate pairs of allylic (*b* and *d*) and benzylic (*a* and *c*) bonds of **12**, i.e., 50% by cleavage of bonds *a* and *b*, and 50% by cleavage of bonds *c* and *d*. A similar mechanism was previously invoked by us (7) to account for the photochemical conversion of the 8-cyano triene **13** to equal amounts of the labelled cyano COTs **17** and **18** (see route G, Scheme 8). Interestingly, and as required by the present proposal for **1**, in the case of 8-cyano triene **13** the $2\sigma_s + 2\pi_s$ electrocyclic opening (route H, Scheme 8) was totally avoided, i.e., COT **19** was not detected. We have not obtained physical evidence for the formation of the octavalene **12** during the direct photolysis of **1**, but this may be due to the rate of rearrangement of **12**→**2** being much higher than the rate of formation of the octavalene at the photolysis temperature employed (ca. 20°C). The 1,4-diradical **5** is thus viewed to be a common species on the pathways to the major products observed in the photochemistry of triene **1**, and rearranges to give alternative vinylcyclopropanes, i.e., SB **3***b,c* (route B, Scheme 4) and the thermally unstable octavalene **12** (Scheme 7).

Scheme 7. Suggested mechanism for COT formation from direct irradiation of triene.

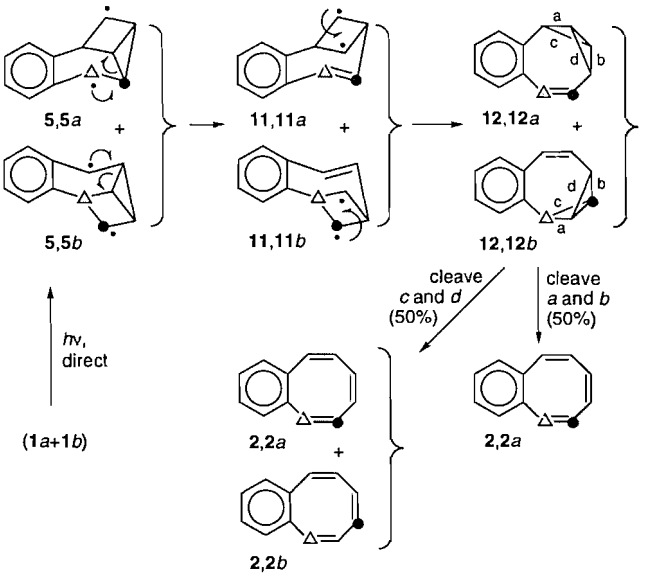

Structures denoted by "a" and "b" represent compounds labelled with deuterium at the positions marked by △ and ● . For structures denoted by a number only (e.g.,12) △ and ● = H.

Lastly, we note that the proposed pathway in Scheme 7 is attributed to S_1 of **1**. Although the occurrence of a DPM rearrangement from S_1 is uncommon in rigid molecules (5), it has precedent in other benzobicyclo[4.2.0]octa-2,4,7-trienes (8), e.g., **13** gives **17** and **18** (7).

Experimental

Instrumentation and materials

The ^1H spectra were recorded in $CDCl_3$ solvent at 250 MHz; the chemical shifts are in δ units and the coupling constants (*J*) in Hz. The abbreviations br, s, d, t, q, and m refer to broad, singlet, doublet, triplet, quartet, and multiplet, respectively. Cyclohexane solvent for photolyses was prepared by scrub-

[5] A referee has suggested an additional route that might account for the label distributions in the COT product obtained from the triene direct irradiation, viz. rearrangement of **1***a,b* to benzobarrelene (a photochemically allowed 1,3-shift), which then undergoes the well-known singlet-mediated transformation to COT (4). Evidence against this proposal exists from a previous study (2) based on the labelled triene **1**-d_2 (note structure in Scheme 1). If the benzobarrelene **20** (note Fig. 1 below) were formed from **1**-d_2 its subsequent photolysis would have led to the COT mixture **2***a,b*-d_2 through a pathway that involves initial 2π +2π bridging, mainly (94 ± 3%) between the benzo-vinyl portions of **20** (4). The NMR spectrum of the COT product therefore would have revealed a low hydrogen integration for the γ hydrogens. The reported (2) integration value was 1.97H, which indicates that within experimental error no deuterium was attached to the COT C-7 or C-8 positions. Hence the COT **2***a*-d_2 is not formed, and consequently (assuming reasonable isotope effects) the pathway depicted in Fig. 1 does not operate. Furthermore, careful monitoring of the photolysates of the direct irradiation of triene **1** revealed no trace of benzobarrelene (by NMR and GC analyses).

Fig. 1. Location of deuterium labels in COT product formed from benzobarrelene.

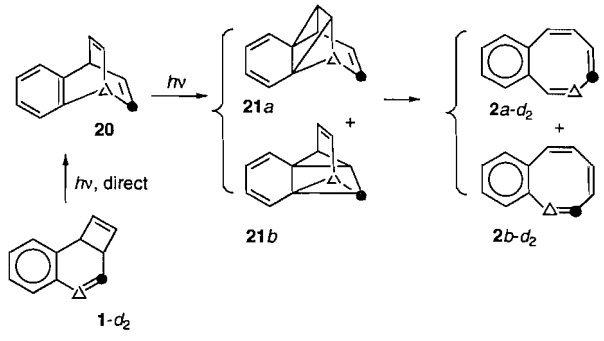

Scheme 8. Label locations in COT product from direct irradiation of 8-cyano triene.

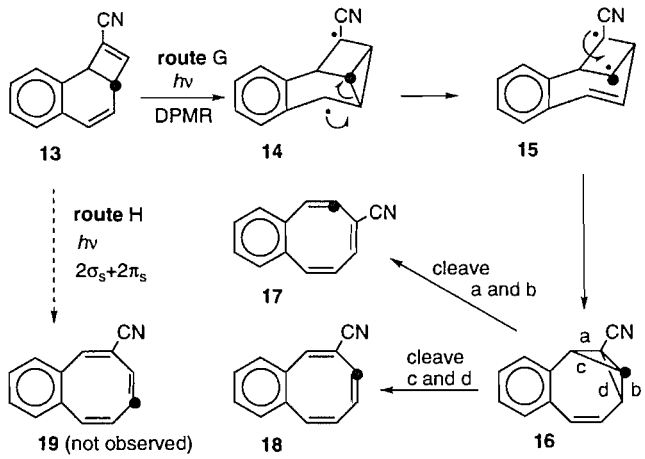

bing with 20% fuming sulfuric acid, followed by washing with 10% aqueous sodium hydroxide, drying ($MgSO_4$), and finally distilling from calcium hydride. Column chromatography was carried out on Silica Gel 60 (Merck; 230–400 mesh), or Lobar columns (Merck; size B, LiChroprep Si 60), or on Silica Gel 60/$AgNO_3$ columns (10:1, by weight). The GC analyses were determined by FID on a DB-23 fused silica capillary column (30 m × 0.25 mm; J&W Scientific).

General procedures for preparative photolyses

The apparatus consisted of a 450-W Hanovia medium-pressure mercury arc surrounded by a water-cooled quartz immersion well. Unless otherwise stated, the light was filtered through either a cylindrical sleeve of Pyrex, or Corex, or an aqueous lead nitrate solution (1 g of $Pb(NO_3)_2$ and 100 g of NaBr in 1 L of water; transmittance was 0% below 318 nm) contained in a concentric filter jacket (10 mm path length). Three types of sample cell were used. Cell A (200 mL sample volume) consisted of a cylindrical collar (Pyrex) that surrounded the aqueous filter jacket. Cell A was fitted with gas inlet and exit ports, and sample solutions were purged with argon prior to and during irradiations. Cell B (40 mL sample volume) and Cell C (3.5 mL) were a quartz test-tube-like vessel and a quartz cuvette, respectively; sample solutions contained therein were deoxygenated by flushing with argon and sealed under a positive pressure; the solutions were magnetically stirred throughout the course of the irradiations.

Deuterium-labelled triene **1**a

Deuterated triene **1***a* (97%-d_1 labelled at C-5 and 43%-d_1 labelled at C-4) was obtained as previously described (2); ^{1}H NMR: 7.00–7.17 (m, 4.35H, aromatics and residual $CHCl_3$), 6.26 (br s, 0.57H, H-4), 6.13 (d, 1.02H, H-7, $J_{8,7}$ = 2.7), 6.02 (dd, 0.98H, H-8, $J_{7,8}$ = 2.7, $J_{7,6}$ = 0.9), 5.88 (dd, 0.03H, H-5, $J_{5,4} = J_{5,6}$ = 4.5), 4.11 (d, 1.02H, H-1, $J_{1,6}$ = 4.5), and 3.64 (d, 1.00H, H-6, $J_{6,1}$ = 4.5).

Thermolysis of deuterium labelled triene **1**a

A solution of 186.6 mg (1.21 mmol) of triene **1***a* in 4 mL of *n*-nonane was refluxed (ca. 150°C) for 10 h. The thermolysis product was chromatographed on Silica Gel 60 (0.9 cm × 10 cm; hexane), to give 162.7 mg (87%) of COT **2***a*; mp 47–49°C (lit. (4) mp 48–50°C); ^{1}H NMR: 7.17–7.24 (m, 2.03H, aromatics), 6.93–6.99 (m, 2.00H, aromatics), 6.55 (d + br s, 1.56H, H-10 and H-5, $J_{10,9}$ = 11.8), 6.03 (dm, 1.04H, H-6 + H-9, $J_{9,10}$ = 11.5), and 5.88 (d, 2.01H, H-7 and H-8, J = 1.8); the ratio of the s:d at δ6.55 is given in entry 1, Table 1.

Formation of mixture **1**a,b *from direct irradiation of COT* **2**a

A solution of 162.0 mg (1.05 mmol) of **2***a* in 200 mL of cyclohexane was irradiated at >318 nm for 91 h in Cell A (ca. 35% conversion by GC). The photolysate was concentrated and chromatographed on a Silica Gel/$AgNO_3$ column (1 cm × 11 cm; 0.1% ethyl acetate – hexane). Two bands were observed. The first band contained 34.4 mg (21%) of the triene mixture **1***a,b*; ^{1}H NMR: 7.00–7.17 (m, 4.15H, aromatics and residual $CHCl_3$), 6.26 (d + br s, 0.81H, H-4), 6.13 (br s, 1.02H, H-7), 6.02 (br d, 0.46H, H-8, $J_{8,7}$ = 2.7), 5.88 (dd, 0.55H, H-5, $J_{5,4} = J_{5,6}$ = 4.5), 4.11 (d, 0.76H, H-1, $J_{1,6}$ = 4.5), and 3.64 (br d, 1.00H, H-6, $J_{6,1}$ = 4.5); the calculated integrations for a mixture of 55% **1***a* and 45% **1***b* are: 0.81 H-4, 1.00 H-7, 0.47 H-8, 0.56 H-5, 0.76 H-1, and 1.00 H-6. The second band off the column gave 105.8 mg (65%) of recovered COT **2***a*; ^{1}H NMR: 7.17–7.24 (m, 2.02H, aromatics), 6.93–6.99 (m, 2.00H, aromatics), 6.55 (d + br s, 1.60H, H-10 and H-5, $J_{10,9}$ = 11.8), 6.03 (dm, 1.01H, H-6 + H-9, $J_{9,10}$ = 11.5), and 5.88 (d, 1.98H, H-7 and H-8, J = 1.8).

Thermolysis of deuterium-labelled triene **1**a,b

A solution of 4.0 mg (0.026 mmol) of triene **1***a,b* in 1 mL of *n*-nonane was refluxed (ca. 150°C) for 12 h. The thermolysis product was chromatographed on Silica Gel 60 (0.9 cm × 10 cm; hexane), to give 3.0 mg (75%) of COT **2***a*; note Table 1, entry 3 for details of the ^{1}H NMR spectrum.

Direct irradiation of labelled triene mixture **1**a,b

A solution of 39.4 mg (0.26 mmol) of **1***a,b* and ca. 40 mg of dodecane (GC standard) in 40 mL of cyclohexane was irradiated (Corex filter) for 30 min in Cell B (97% conversion by GC). The photolysate was chromatographed, first on Silica Gel 60 (0.9 cm × 10 cm; 100 mL hexane) to remove polymeric materials, and then on a Lobar column with hexane solvent. The first band gave ca. 2 mg (5%) of naphthalene (identified by GC comparison with an authentic sample). The last band (i.e., third) gave 7.5 mg (19%) of deuterated 3,4-benzotricyclo[3.3.0.$0^{2,8}$]octa-3,6-diene (i.e., SB mixture **3***a-c*) as a colourless oil (GC purity >98%), which was identified by comparison of the chemical shifts and coupling constants of the ^{1}H NMR spectrum with that reported for authentic SB **3** (4); ^{1}H NMR: 7.31–7.35 (m, 1.00H, aromatic), 7.04–7.18 (m, 3.20H, aromatics), 5.60 (dd, 0.47H, H-6, $J_{6,7}$ = 5, $J_{6,5}$ = 2.3), 5.21 (m, 0.99H, H-7), 3.90 (dd, 0.77H, H-5, $J_{5,1}$ = 6.3, $J_{5,6}$ = 2), 3.29 (m, 0.94H, H-1), 3.04 (t, 0.81H, H-2, $J_{2,1} = J_{2,8}$ = 6.3), and 2.70–2.76 (m, 0.67H, H-8); the calculated integrations for a mixture of 7.7% **3***a*, 55% **3***b*, and 37.4% **3***c* (as required by 17% utilization of route A and 83% of route B, Scheme 4) are 0.47 H-6, 1.00 H-7, 0.76 H-5, 0.93 H-1, 0.81 H-2, and 0.64 H-8.

The contents of the second band from the Lobar chromatography were rechromatographed on a Silica Gel 60/$AgNO_3$ column (1 cm × 11 cm; 0.1% ethyl acetate – hexane). Two bands were observed. The first band contained 1.0 mg (2.5%) of recovered triene mixture **1***a/b*; ^{1}H NMR: 7.00–7.17 (m,

4.15H, aromatics and residual $CHCl_3$), 6.26 (d + br s, 0.84H, H-4), 6.13 (br s, 1.00H, H-7), 6.02 (br d, 0.38H, H-8, $J_{8,7}$ = 2.7), 5.88 (dd, 0.63H, H-5, $J_{5,4} = J_{5,6} = 4.5$), 4.11 (d, 0.71H, H-1, $J_{1,6} = 4.5$), and 3.64 (br d, 1.00H, H-6, $J_{6,1} = 4.5$). The second band off the column gave 11.8 mg (30%) of COT **2***a,b* (or perhaps **2***a,d*); note Table 1, entry 6 for details of the ^{1}H NMR spectrum.

Sensitized irradiation of labelled triene mixture ***1***a,b

A solution containing 12.9 mg (0.058 mmol) of *p*-dimethylaminobenzophenone, 43.5 mg (0.28 mmol) of **1***a,b*, and 29.3 mg of dodecane (GC standard) in 40 mL of cyclohexane was irradiated for 40 min in Cell B, with light filtered through a Pyrex and WG 345 glass (Schott) filter (95% conversion by GC). The photolysate was concentrated, chromatographed on Silica Gel 60 (0.9 cm × 10 cm; 100 mL hexane) to remove polymeric materials and sensitizer, and then rechromatographed on a Lobar column (hexane). The first band contained a trace of naphthalene (identified by GC comparison with an authentic sample). The second band gave 1.6 mg (4%) residual triene mixture **1***a/b*, ^{1}H NMR: 7.00–7.17 (m, 4.26H, aromatics and residual $CHCl_3$), 6.26 (d + br s, 0.81H, H-4), 6.13 (br s, 1.00H, H-7), 6.02 (br d, 0.43H, H-8, $J_{8,7}$ = 2.7), 5.88 (dd, 0.60H, H-5, $J_{5,4} = J_{5,6} = 4.5$), 4.11 (d, 0.74H, H-1, $J_{1,6} = 4.5$), and 3.64 (br d, 1.01H, H-6, $J_{6,1} = 4.5$). The third band gave ca. 1.0 mg (2%) of COT **2***a*: note Table 1, entry 5, for details of the ^{1}H NMR spectrum.

The final band gave 24.1 mg (55%) of SB mixture **3***b,c* (GC purity >98%); ^{1}H NMR: 7.31–7.35 (m, 1.00H, aromatic), 7.04–7.18 (m, 3.29H, aromatics), 5.60 (dd, 0.46H, H-6, $J_{6,7}$ = 5, $J_{6,5}$ = 2.3), 5.21 (m, 1.00H, H-7), 3.90 (dd, 0.76H, H-5, $J_{5,1}$ = 6.3, $J_{5,6}$ = 2), 3.29 (m, 1.01H, H-1), 3.04 (t, 0.80H, H-2, $J_{2,1} = J_{2,8}$ = 6.3), and 2.70–2.76 (m, 0.59H, H-8); the calculated integrations for a mixture of 55% **3***b*, and 45% **3***c* (as required by 100% utilization of route B Scheme 4) are 0.47 H-6, 1.00 H-7, 0.76 H-5, 1.00 H-1, 0.81 H-2, and 0.56 H-8.

Quantum efficiencies

The quantum yield for the conversion of COT **1**→**2** was performed on an apparatus previously described (9), which includes an optical bench arranged for beam splitting into a potassium ferrioxalate actinometer (10). Cyclohexane solutions (in Cell C, 3.5 mL) of COT **2** (8×10^{-3} M) were deoxygenated prior to irradiation by flushing with argon. A positive pressure of argon was maintained over the stirred solutions throughout the course of the irradiations carried out with light of wavelength 313 nm. The quantum yield of 0.0001 was obtained from two runs extrapolated to zero conversion. Product analyses were determined by GC (internal dodecane standard).

Acknowledgements

Financial support from the Natural Sciences and Engineering Research Council of Canada and technical assistance from C.L. Asplund is gratefully acknowledged.

References

1. (*a*) R.W. Jackson, R.G. Higby, J.W. Gilman, and K.J. Shea. Tetrahedron Lett. **33**, 4695 (1992); (*b*) R.W. Jackson, R.G. Higby, and K.J. Shea. Tetrahedron, **48**, 7013 (1992)
2. C.L. Asplund, C.O. Bender, and D. Dolman. Can. J. Chem. **72**, 1999(1994).
3. R.B. Woodward and R. Hoffmann. *In* The conservation of orbital symmetry. Verlag Chemie, Weinheim; Academic Press, New York. 1970.
4. H.E. Zimmerman, R.S. Givens, and R.M. Pagni. J. Am. Chem. Soc. **90**, 6096 (1968).
5. (*a*) H.E. Zimmerman. *In* Rearrangements in ground and excited states. Vol. 3. *Edited* by P. de Mayo. Academic Press, New York. 1980. Essay 16, pp. 131–166; (*b*) S.S. Hixson, P.S. Mariano, and H.E. Zimmerman. Chem. Rev. **73**, 531 (1973).
6. (*a*) E. Vogel, H. Keifer, and W.R. Roth. Angew. Chem. **76**, 432 (1964); (*b*) R. Huisgen and F. Mietzsch. Angew. Chem. Int. Ed. Engl. **3**, 83 (1964).
7. C.O. Bender, D. Dolman, and G.K. Murphy. Can. J. Chem. **66**, 1662 (1988).
8. (*a*) C.O. Bender, D.L. Bengtson, D. Dolman, and R.T. McKay. Can. J. Chem. **72**, 1556 (1994); (*b*) C.O. Bender, D.S. Clyne, and D. Dolman. Can. J. Chem. **69**, 70 (1991); (*c*) C.O. Bender, D. Dolman, and N. Tu. J. Org. Chem. **56**, 5015 (1991); (*d*) C.O. Bender, D. L. Bengtson, D. Dolman, and S.F. O'Shea. Can. J. Chem. **64**, 237 (1986);
9. C.O. Bender, D.L. Bengtson, D. Dolman, C.E.L. Herle, and S.F. O'Shea. Can. J. Chem. **60**, 1942 (1982).
10. C.G. Hatchard and C.A. Parker. Proc. R. Soc. London, Ser. A: **235**, 518 (1956).

Influence of vanadium(V) complexes on the catalytic activity of ribonuclease A. The role of vanadate complexes as transition state analogues to reactions at phosphate[1]

Chui Har Leon-Lai, Michael J. Gresser, and Alan S. Tracey

Abstract: The interactions of vanadate and its complexes of uridine, 5,6-dihydrouridine, and methyl β-D-ribofuranoside with bovine pancreatic ribonuclease A (RNase A) (EC 3.1.27.5) were studied by ^{51}V NMR spectroscopy and enzyme kinetics. From kinetic studies, it was found that neither inorganic vanadate nor the methyl β-D-ribofuranoside–vanadate complex significantly inhibited the RNase A catalyzed hydrolysis of uridine 2′,3′-cyclic monophosphate. The NMR binding studies were in full agreement with the kinetics studies and showed that neither inorganic vanadate nor the methyl β-D-ribofuranoside–vanadate complex was bound tightly by the enzyme. Approximate binding constants were $(5.0 \pm 1.0) \times 10^{-7}$ M and $(3.0 \pm 0.6) \times 10^{-6}$ M for the uridine– and 5,6-dihydrouridine–vanadate complexes, respectively. An induced-fit mechanism is suggested, in which the pyrimidine subsite of the active site of RNase A must be fully occupied for the enzyme to be able to tightly bind the transition state or transition state analog. Calculation of the binding energies of vanadate complexes in ribonuclease, phosphoglycerate mutase, and phosphoglucomutase revealed an excess of binding energy over the analogous phosphate derivative of about 25 kJ/mol for all enzymes, even though the binding constants themselves varied by about six orders of magnitude. This energy represents about 40% of that expected to be available for a trigonal-bipyramidal transition state and requires a reassessment of the role of vanadate as a transition state analogue for phosphate transfer.

Key words: vanadate, ribonuclease, transition state, binding constants, phosphate analogues, kinetics.

Résumé : Faisant appel à la spectrscopie RMN du ^{51}V et de la cinétique des enzymes, on a étudié les interactions entre le vanadate et ses complexes de l'uridine, de la 5,6-dihydrouridine et du β-D-ribofuranoside de méthyle avec la ribunucléase A du pancréas de boeuf (RNase A) (EC 3.1.27.5). Sur la base des études cinétiques, on a trouvé que, vis-à-vis de l'hydrolyse du monophosphate 2′,3′-cyclique de l'uridine de la RNase A, ni le vanadate inorganique ni le complexe du β-D-ribofuranoside de méthyle–vanadate n'inhibent cette réaction d'une façon significative. Les études par RMN ont montré qu'il ne se produit aucune fixation entre ces matériaux et elles étaient en parfait accord avec les études cinétiques; elles montrent aussi que ni le vanadate inorganique ni le complexe du β-D-ribofuranoside de méthyle–vanadate ne se complexent fortement avec l'enzyme. Les constantes apparentes de fixation ont respectivement de $(5{,}0 \pm 1{,}0) \times 10^{-7}$ M et $(3{,}0 \pm 0{,}6) \times 10^{-6}$ M pour les complexes de l'uridine et du 5,6-dihydrouridine avec le vanadate. On propose un mécanisme induit d'ajustement dans lequel il est important que tout le sous site de la pyrimidine du site actif de la RNase A soit occupé pour que l'enzyme soit capable de bien fixer l'état de transition ou son analogue. Des calculs d'énergie de fixation des complexes du vanadate dans la ribonucléase, la phosphoglycératemutase ou la phosphoglucomutase ont révélé que, pour chacun de ces enzymes, ces valeurs sont environs 25 kJ mol^{-1} supérieures à celle du dérivé analogue du phosphate, même si les constantes de fixation elles-mêmes varient par un facteur d'environ un million. Cette énergie représente environ 40% de toute l'énergie qui devrait être disponible pour un état de transition trigonal bipyramidal et elle nécessite une réévaluation du rôle du vanadate comme analogue de l'état de transition pour le transfert du phosphate.

Mots clés : vanadate, ribonucléase, état de transition, constante de fixation, analogue du phosphate, cinétique.

[Traduit par la rédaction]

Received June 27, 1995.

C.H. Leon-Lai, M.J. Gresser,[2] and A. S. Tracey.[3] Department of Chemistry, Simon Fraser University, Burnaby, BC V5A 1S6, Canada.

[1] This work was abstracted, in part, from the M.Sc. Thesis of C.H. Leon-Lai.

[2] Senior director, Biochemistry and Molecular Biology, Merck Frosst Centre for Therapeutic Research, C.P. 1005, Pointe Claire Dorval, QC H9R 4P8, Canada.

[3] Author to whom correspondence may be addressed. Telephone: (604) 291-4464. Fax: (604) 291-3765. E-mail: tracey@sfu.ca

Introduction

Ribonuclease A (RNase A) (EC 3.1.27.5) is a bovine pancreatic enzyme with a molecular weight of 13 700 (1).[4] It catalyzes the hydrolysis of ribonucleic acid (RNA), with the formation and decomposition of an intermediate cyclic 2′,3′-nucleotide (2). Inhibition exerted by a vanadate–uridine complex on the catalytic activity of RNase A was the first reported example of the influence of vanadium on an enzyme (3). An inhibition constant (K_i) value of 1.2×10^{-5} M was reported (3) from this early work.

Vanadate, in the presence of uridine or other nucleosides, gives rise to a number of complexes. The predominant products are dimeric in nature and their formation constants are large compared to those of the monomeric precursors. Recent work (4, 5) has evaluated the formation constant for the 2:2 complex and has also provided a value for the formation constant of the monomeric (1:1) complex. The nature of this equilibration process was not appreciated at the time of the original inhibition studies.

Questions concerning the mechanism of action of this enzyme have arisen over the past few years with the suggestion that the reaction proceeds via a triester intermediate instead of the generally accepted classical acid–base catalyzed mechanism (6, 7). The evidence seems to favour the classical mechanism for ribonuclease A (8). However, a steadily increasing number of ribonucleases have been discovered so it is important to fully understand the mechanism, or mechanisms, by which these enzymes operate. This problem has, to an extent, been recently addressed by extensive theoretical calculations (9–11) that have included interactions with the uracil base (10). Because of the affinity of ribonuclease A for vanadate-derived analogues to the cyclic phosphate substrate, additional possibilities for investigating the role of the uracil ring in the catalytic process have arisen.

A reevaluation of the binding of uridine–vanadate complex by ribonuclease is also of general interest since this provides information on the role that the vanadium centre in complexes of vanadate plays as an analogue to phosphate in this enzyme. It is also necessary if comparisons are to be drawn with other enzymic systems. Unfortunately, only a very few other systems have been studied in detail. However, a picture of the role of vanadate as a phosphate analogue begins to emerge from these studies that is inconsistent with the general picture of the role of vanadate as a transition state analogue to phosphate.

In this study, ^{51}V NMR spectroscopy has been utilized to study the binding of vanadate complexes of uridine, 5,6-dihydrouridine, and methyl β-D-ribofuranoside to ribonuclease. Enzyme kinetics studies have also been carried out in conjunction with these NMR studies. The results obtained here have been compared with those reported for phosphoglycerate mutase (12) and for phosphoglucomutase (13, 14).

Materials and methods

Bovine pancreatic ribonuclease A (lyophilized powder) was purchased from Boehringer Mannheim. All reagents used were of reagent grade. Both enzyme and reagents were used without any further purification. Vanadium(V) oxide, 99.99% (gold label) was purchased from Aldrich Chemical Co. Uridine 2′,3′-cyclic monophosphate (sodium salt), uridine, 5,6-dihydrouridine, and methyl β-D-ribofuranoside (crystalline) were purchased from Sigma Chemical Company. Tris buffer (tris(hydroxymethyl)aminomethane hydrochloride or tris(hydroxymethyl)aminomethane) was from either Boehringer Mannheim or Sigma Chemical Company. KCl and HCl (1 N) were from BDH Chemicals. NaOH (1 N) was from Anachemia Chemicals Inc. and Fisher Scientific. Reference buffer solutions (pH 4, 7, and 10) were from Canlab.

Solutions

Preparation of the vanadate stock solutions

For ^{51}V NMR studies: Stock solutions of sodium vanadate (NaH_2VO_4) were prepared by dissolving 0.5 mol equivalent of vanadium pentoxide (V_2O_5) in 1 equivalent of 1.0 M NaOH. The mixture was stirred until the orange color disappeared, generally overnight, to give a colourless solution. It was then combined with enough KCl and diluted with sufficient deionized distilled water to give a final concentration of 0.1 M NaH_2VO_4 and 0.35 M KCl.

For kinetics studies: Stock solutions of 1.0 mM sodium vanadate (0.35 M KCl) were prepared by dilution of the above 100 mM solution of vanadate. The dilution was made into 5.0 mM Tris/0.35 M KCl to near the desired final volume. The pH was adjusted to 7.0 with small aliquots of 0.1 N NaOH before diluting to the final volume.

Preparation of the ligand stock solutions

Stock solutions of uridine, 5,6-dihydrouridine, and methyl β-D-ribofuranoside were prepared by dissolving each of them in 0.35 M KCl/5.0 mM Tris buffer at a pH near 7.0. Subsequently, the pH was adjusted to 7.0 by the addition of appropriate quantities of 0.1 N HCl or 0.1 N NaOH. The concentration of the Tris buffer was low enough to avoid the formation of a significant amount of vanadate–Tris complexes (15) during the sample preparation. The concentration of uridine was determined by UV spectrophotometry (ε_{260} = 9.9 mM^{-1} cm^{-1}).

Preparation of the substrate

A solution of uridine-2′,3′-cyclic phosphate (U-2′,3′-P), in 0.35 M KCl/5.0 mM Tris buffer, pH 7.0, was prepared fresh on the day of use, prior to the kinetics experiments, and kept on ice. The concentration of substrate was determined spectrophotometrically (ε_{258} = 9.57 mM^{-1} cm^{-1}).

Preparation of the RNase A samples

For ^{51}V NMR spectroscopy: The enzyme samples were prepared by dissolving the lyophilized powder in a solution of 5.0 mM Tris buffer and 0.35 M KCl, the pH was adjusted to about 7 with small aliquots of 0.05 N NaOH, and vanadate was added to give a final concentration of 1.0 mM. The pH was adjusted again to 7.0 before bringing the solution to the final volume. It was done this way to avoid the formation of decavanadate which is an oligomer that hydrolyzes very slowly at neutral pH.

[4] List of abbreviations: U-2′;3′-P =uridine 2′:3′-cyclic monophosphate. U-3′-P =uridine 3′-monophosphate. RNase A = bovine pancreatic ribonuclease A. Tris = tris(hydroxymethyl)aminomethane.

Before the addition of vanadate to the enzyme sample, a small aliquot was withdrawn from the sample in order to determine the concentration of protein by reading the absorbance at 280 nm ($\varepsilon^{1\%}_{280}$ = 7.3, MW = 13 700 (1)). This procedure avoided the interference by vanadate, which also has a significant absorbance at this wavelength; 2.0 mL samples were used for the NMR spectroscopy.

For kinetics studies: Two enzyme stock solutions were prepared by dissolving the lyophilized powder in sufficient 5.0 mM Tris buffer solution to give a volume close to that desired. This was followed by adjustment of the pH to 7.0 using 0.05 N NaOH, then adding distilled water to give the desired final volume. The concentrations were 1.59 and 1.46 mg/mL.

The uridine–vanadate samples for the kinetics experiments were prepared by mixing the appropriate amounts of the ligand and vanadate stock solutions to obtain the desired final concentrations of reactants. These solutions were allowed to equilibrate approximately 1 h before combining with the ribonuclease. The assay conditions were 5.0 mM Tris, 0.35 M KCl, 14–16 μg/mL RNase A at pH 7.0, and 25°C.

NMR spectroscopy

^{51}V NMR spectra were obtained at 105 MHz on a Bruker WM-400 spectrometer. All spectra were obtained in the unlocked mode. Acquisition parameters were 0.05 s acquisition times, 50 kHz sweep widths, and 50° pulse widths. Each spectrum was obtained from 20 000 scans. All the spectra were zero filled from 4 K to 8 K and a line-broadening factor of 50 Hz was used before transformation to the frequency domain. The Fourier transform was done in the absolute intensity mode to allow signal intensities from different spectra to be compared. $VOCl_3$ was used as the external reference standard, and its signal was assigned as 0 ppm. When the Fourier transform was done in the relative intensity mode, the external/internal reference was a complex of V(V)–H_2O_2 contained in a concentric capillary tube within the standard NMR tube. The vanadium-51 signals from this solution occur at −765 and −625 ppm. This chemical shift reference was chosen because its signals do not interfere with the signals of the vanadate species of interest. Spectra were obtained at room temperature. A baseline correction was carried out before measurement of any signal intensities. The instrument manufacturer's software was used for all NMR measurements and manipulations.

UV–visible spectrophotometry

Reaction rates were obtained by monitoring the change in absorbance at 286 nm on a Hewlett Packard 8452A diode array spectrophotometer. UV cells (3 mL) with cylindrical stir bars were used for all experiments. The signal averaging time was 10 s, the scanning interval was 35 s, and the reaction rates were followed for 10 min. The rate of hydrolysis of uridine-2′,3′-cyclic phosphate was followed at 286 nm, using $\Delta\varepsilon_{286}$ = 600 M^{-1} cm^{-1} (1).

Equilibrium studies of vanadate plus ligands

Complex formation with uridine, 5,6-dihydrouridine, and methyl β-D-ribofuranoside was studied. The equilibrium constants for formation of the complexes were determined using standard techniques (5) under the conditions of 5.0 mM Tris buffer, 0.35 M ionic strength with added KCl and 1.0 mM vanadate, pH 7.0. The ligand concentration was varied from 0 to 21 mM for each of the various studies.

Binding of vanadate–ligand complexes to RNase A

Solutions were prepared by successive additions of small volumes of the stock ligand (uridine, 5,6-dihydrouridine, or β-methyl riboside) solution to 2.0 mL of a (1:1) enzyme–vanadate solution. The concentration of the ligand was varied from 0 to 60 mM and the binding of the vanadium–ligand complex to ribonuclease was monitored by ^{51}V NMR spectroscopy. The ribonuclease concentration for all studies was close to 1.0 mM.

Inhibition of RNase A by vanadate–uridine and vanadate–dihydrouridine complexes

Reaction solutions were prepared at 295 K by mixing the appropriate quantities of the ligand–vanadate stock solution with the uridine 2′,3′-cyclic phosphate solution. The reaction was then started by addition of 20 μL of enzyme solution to 2.0 mL of the reaction solutions. For uridine–vanadate the concentrations were 1.0 mM uridine or 1.0 mM uridine + 0.1 mM vanadate with 5.0 mM Tris buffer, 0.35 M KCl, pH 7.0, and 14–16 μg/mL of ribonuclease. The conditions were similar for the dihydrouridine experiments except that this nucleoside concentration was 39.6 mM. The rate measurements were made at 295 K and were started 1.5 min after the addition of ribonuclease and followed for 10 min. Except for the higher concentrations of substrate, the changes in the absorbance were linear with time throughout the entire 10 min, indicating that product inhibition was insignificant. The first 3 min of all runs were used for the determination of initial rates. In separate experiments it was confirmed that the initial rates were proportional to the enzyme concentration.

Results

Uridine, 5,6-dihydrouridine, and methyl β-D-ribofuranoside plus vanadate

The interactions of vanadate with nucleosides (4, 16–20) and β-methylriboside (5) have been studied by a number of workers. These studies have clearly shown that, under conditions of a few millimolar concentrations of vanadate with equivalent amounts of ligand at neutral pH, the major product of the reaction is a binuclear bisligand product. Early studies proposed that the coordination about the vanadium in this type of product was trigonal bipyramidal (21), although there has been some controversy over the details of the structure (5, 16, 18). A recent X-ray structure of an adenosine–vanadate dimer showed a slightly distorted square-pyramidal coordination about each of the vanadium nuclei of the dimer in the crystalline material (22). NMR studies strongly suggest that the square-pyramidal structure is retained in solution (22). It should, however, be noted that a trigonal-bipyramidal coordination has been proposed for similar compounds in aqueous solution (23).

The details of determining the formation constants for the products in solution have been discussed in detail elsewhere (4, 5) and that work has shown that the formation constant for the major product of the reaction of vanadate with nucleosides is about 5×10^7 M^{-3} (4). For the conditions of this study, the formation constants measured for the compounds of interest

here (uridine, (5.3 ± 0.2) × 10^7 M^{-3}; 5,6-dihydrouridine, (4.8 ± 0.4) × 10^7 M^{-3}; methyl β-D-ribofuranoside, (2.1 ± 0.1) × 10^7 M^{-3}) are close to the above value. Unfortunately, this formation constant for the dimer is not the one that is of most interest although the value is useful for comparative purposes. Signals corresponding to these products occur near −520 ppm, as can be seen in the relevant spectra of Fig. 1.

The formation constants of primary interest for this work is that of the tetrahedrally coordinated cyclic ester (VL) formed between the 2′ and 3′ hydroxyl groups of the ribose ring. Detailed investigation of a number of nucleosides has revealed the formation of a complex that is thought to correspond to such a product (4). From those studies, a formation constant of about 3 M^{-1} was obtained for each of the different nucleoside complexes. Such a detailed study has not been carried out here but, since the overall formation constants for the various dimers are not much different from the values obtained in the study mentioned above, a value of 3 M^{-1} has been assumed for this work. There is no reason to expect significant changes in formation constants since the reaction conditions for the two studies are similar.

NMR binding studies

Vanadium-51 is a quadrupolar nucleus and the linewidths of the V-51 NMR signal are determined by the efficiency of the quadrupole-induced nuclear relaxation. For vanadium attached to proteins of the size of ribonuclease, the quadrupolar induced relaxation is very efficient and the vanadium signal from bound vanadium is so broad that it is effectively lost in the baseline of the spectrum. As a consequence, the observed spectrum corresponds to the various species that are not bound. Because of this effect, the incorporation of vanadium into ribonuclease is readily quantitated.

Initial ^{51}V NMR experiments were carried out to determine the extent of the binding of vanadate itself to ribonuclease. Under the reaction conditions of this study, there was not enough vanadate being bound to be observable, that is, less than 10% of the vanadate in a 1.0 mM vanadate–1.0 mM ribonuclease solution. However, an X-ray study showing a single vanadate attached to ribonuclease T has been reported (24), so clearly vanadate can be bound.

Figure 1*a* shows the result of adding uridine, in a progressive manner, to a solution of 1.0 mM vanadate in the presence of 1.1 mM ribonuclease. There very clearly is a loss of observable vanadium signal intensity. The more rapid loss of signal intensity of the vanadate oligomers, compared to monovanadate itself, is expected for a system that is in equilibrium. Figure 1*b* shows similar behaviour for dihydrouridine. Tables 1 and 2 give the amounts of free and bound vanadium for the two studies. A similar procedure using methyl β-D-ribofuranoside provided no evidence for other than a possible weak binding of the ribofuranoside–vanadate complex.

To interpret the results of the binding studies it is necessary to account for all the equilibrations that vanadate undergoes while in the presence of the nucleoside, including self-condensation reactions. In addition, in the presence of ribonuclease there are additional equilibria that must be considered: the formation of the vanadate–nucleoside–ribonuclease (E·VL) complex and a nucleoside–ribonuclease (E·L) complex. It seems clear that any binding of vanadate itself or its oligomers to ribonuclease A is weak because no binding was observed in any of

Fig. 1. ^{51}V NMR spectra showing the loss of vanadium signal intensity as uridine (Fig. 1*a*) or 5,6-dihydrouridine (Fig. 1*b*) is added to a solution of vanadate (1 mM) in the presence of ribonuclease A (1.06 mM). The vanadium signals correspond to: −560 ppm, monovanadate; −572 ppm, divanadate; −572 ppm, tetravanadate; −583 ppm, pentavanadate. Conditions of the experiments: 5.0 mmol Tris buffer; pH 7.0; 0.35 M KCl and, for Fig. 1*a*, 0, 0.3, 1.0, 4.0, and 11.7 mM added uridine for traces e, d, c, b, and a, respectively; Fig. 1*b*, 0, 0.3, 1.1, 4.4, and 12.8 mM added dihydrouridine for traces e, d, c, b, and a, respectively.

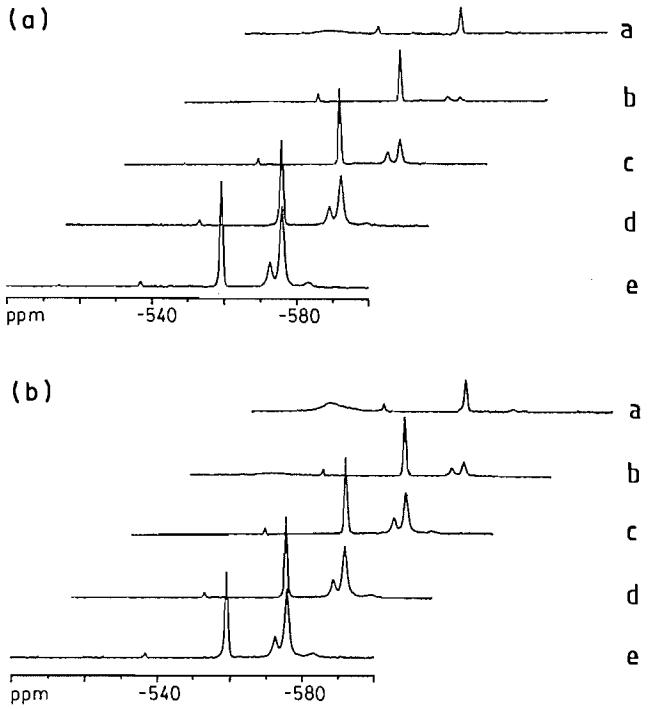

the studies carried out here. Assuming a minimum observable quantity of vanadate being bound as 10% of the total utilized in the binding study (vanadate to ribonuclease, 1:1), a lower limit of 0.01 M was estimated for a possible dissociation constant. The value would have to be much smaller than this before it would have a significant effect on the analysis of the binding studies. In agreement with the binding studies, kinetics studies showed no inhibition by vanadate. The kinetics result allowed a lower limit of 3.0 mM to be calculated for the inhibition constant of vanadate (3). This value is about a factor of 3 from the lower limit value estimated from the binding study.

Kinetics studies have clearly shown that free uridine is a reasonably efficient inhibitor of the function of ribonuclease A, its K_i being about 2 mM (see Table 3). This value is not much different from the lower limit value estimated for the dissociation of vanadate. However, nucleoside concentrations in this study range up to about two orders of magnitude larger than the free monomeric vanadate concentration, and the corresponding dissociation constant therefore influences the analysis of the results.

$$[1]\quad \frac{[V_b]}{[E_t]} = \frac{[V_i](K_7 + K_1K_6[L])}{1 + K_5[L] + [V_i](K_7 + K_1K_6[L])}$$

Equation [1] describes the proportion of bound vanadium as a function of the concentration of free uridine and free vana-

Table 1. Distribution of vanadium between free vanadate species and vanadate bound to ribonuclease A, determined in the presence of added uridine.[a,b]

[Uridine]	$[V_i]$	$[V_{vis}]$	$[V_b]$
0.0	0.36	1.00	0.00
0.2	0.35	0.90	0.10
0.3	0.31	0.76	0.24
0.4	0.32	0.74	0.26
0.6	0.29	0.63	0.37
1.0	0.27	0.51	0.49
2.0	0.23	0.37	0.63
4.0	0.17	0.26	0.74
6.9	0.14	0.24	0.76
7.9	0.12	0.20	0.80
12.0	0.09	0.22	0.78

[a]All concentrations are reported as mmol/L and, for vanadium, represent vanadium atom concentrations. V_i corresponds to monomeric vanadate while V_{vis} represents all vanadate species, including the monomer, oligomers, and uridine–vanadate complexes, that are observed in the NMR spectrum. V_b represents the enzyme-bound vanadium.

[b]Conditions for the experiments: total vanadate, 1.0 mM; RNase, 1.06 mM; Tris buffer, 5.0 mM; pH, 7.0; KCl, 0.35 M; total uridine, as indicated in table.

Table 2. Distribution of vanadium between vanadate bound to ribonuclease A and free vanadate species in the presence of 5,6-dihydrouridine.[a,b]

[Dihydrouridine]	$[V_i]$	$[V_{vis}]$	$[V_b]$
0.0	0.36	1.00	0.00
0.2	0.36	0.95	0.05
0.3	0.34	0.89	0.11
0.4	0.32	0.84	0.16
0.7	0.34	0.84	0.16
1.1	0.32	0.75	0.25
2.2	0.29	0.58	0.42
3.4	0.27	0.55	0.45
4.4	0.26	0.50	0.50
6.6	0.21	0.47	0.53
8.7	0.18	0.42	0.58
13.0	0.12	0.38	0.62

[a]All concentrations are reported as mmol/L and, for vanadium, represent vanadium atom concentrations. V_i corresponds to monomeric vanadate while V_{vis} represents all vanadate species, including the monomer, oligomers, and dihydrouridine–vanadate complexes, that are observed in the NMR spectrum. V_b represents the enzyme-bound vanadium.

[b]Conditions for the experiments: total vanadate, 1.0 mM; RNase A, 1.06 mM; Tris buffer, 5.0 mM; pH, 7.0; KCl, 0.35 M; total dihydrouridine, as indicated in table.

date in the equilibrated solution. The derivation of this equation is described in the Appendix. The binding curve, as described by eq. [1], contains terms for binding of the nucleoside, K_5, for binding of vanadate, K_7 ($1/K_7 = 0.01$ M), and for binding of the nucleoside–vanadate complex, K_6. In fact this latter value enters as the product K_1K_6, where K_1 is the formation constant for the nucleoside–vanadate complex. K_1 has a value close to 3 M^{-1} (4).

Fig. 2. A representation of the proportion of vanadate bound to ribonuclease A as a function of the amount of added uridine. The points present the experimental data while the curves were calculated as described in the Appendix. The best-fit curve was obtained using the parameters $K_1K_6 = 6 \times 10^6$ M^{-2}, $K_5 = 125$ M^{-1}, and $K_7 = 100$ M^{-1}, as required for eq. [1]. Conditions for the experiments: 1.06 mM RNase A, 1.0 mM vanadate, 5.0 mM Tris buffer, pH 7.0, 0.35 M KCl, and the indicated amounts of added uridine.

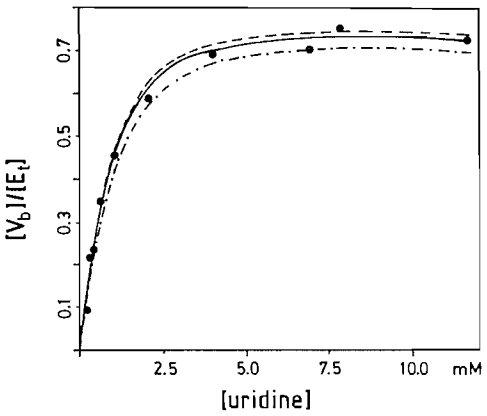

Fig. 3. The proportion of vanadate bound to ribonuclease A as a function of the amount of added 5,6-dihydrouridine is shown. The points present the experimental data while the curves were calculated as described in the Appendix. The best-fit curve was obtained using the parameters $K_1K_6 = 1 \times 10^6$ M^{-2}, $K_5 = 28$ M^{-1}, and $K_7 = 100$ M^{-1}, as required for eq. [1]. Conditions for the experiments: 1.06 mM RNase A, 1.0 mM vanadate, 5.0 mM Tris buffer, pH 7.0, 0.35 M KCl, and the indicated amounts of added dihydrouridine.

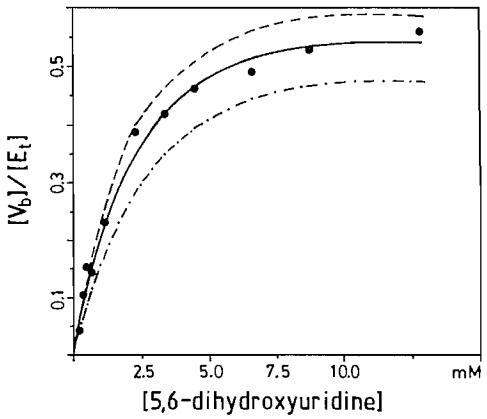

Figure 2 shows the proportion of vanadate bound by ribonuclease as a function of added uridine and also calculated curves that bracket the experimental values. The curve that best describes the experimental results has the values of $(6 \pm 1) \times 10^6$ M^{-2} for K_1K_6 with a value of 1.3×10^2 M^{-1} for K_5. If the inhibition constant for uridine is a true dissociation constant, then $1/K_5 = 8 \times 10^{-3}$ M should be equal to the inhibition constant reported for uridine from kinetics studies (3, 25). The two values are the same to within the errors of the experiments. The interaction constant, K_1K_6, gives a value of $(5 \pm 1) \times 10^{-7}$ M for the dissociation of VL from E·VL ($= 1/K_6$) when K_1 ($= 3$ M^{-1}) is factored out.

Table 3. Binding and inhibition of ribonuclease A by nucleosides and nucleoside/vanadate complexes.[a]

Inhibitor	Binding constant	Inhibition constant	Reference[b]
Uridine	7.7 mM	1.7 mM	A
		8.0 mM	B
		2.3 mM	C
Dihydrouridine	36 mM	41 mM	A
2′-Deoxyuridine		45 mM	B
Vanadate	>10 mM		A
		>0.3 mM	B
Uridine–vanadate	0.50 μM	0.45 μM	A
		0.49 μM	D
Dihydrouridine–vanadate	3.0 μM	1.1 μM	A
β-Methylriboside–vanadate	>0.2 mM		A

[a]Binding constants were determined from NMR studies; inhibition constants from kinetics experiments.
[b]References correspond to the following: A, this work; B, ref. 3; C, ref. 25; D, recalculated from Fig. 3 of ref. 3.

Dihydrouridine, in the presence of vanadate, also undergoes strong binding interactions with ribonuclease A. The results of the binding study and the corresponding calculated binding curves are shown in Fig. 3. The constants describing the best-fit curve are $K_1K_6 = (1.0 \pm 0.2) \times 10^6$ M^{-2} and $K_5 = 28 \pm 5$ M^{-1}. These values correspond to $(3.0 \pm 0.6) \times 10^{-6}$ M and $(3.6 \pm 0.7) \times 10^{-2}$ M for $1/K_6$ and $1/K_5$, respectively.

No binding of the methyl β-D-ribofuranoside–vanadate complex to the enzyme was found for any of the concentrations utilized. An apparent disappearance of less than 5% of the total vanadate signal intensities was observed when the concentration of the methyl riboside was increased from 15 to 60 mM. However, because of the uncertainty in the integration of the vanadium(V) signals, it is not clear that this can be ascribed to binding of the riboside–vanadate complex to the enzyme. However, a lower limit for the dissociation constant ($1/K_6 = 2 \times 10^{-4}$ M)) was estimated by assuming that no more than 5% of the enzyme was bound when the concentration of the ligand was 60 mM. This value is two to three orders of magnitude larger than those for the tightly bound complexes formed with uridine or 5,6-dihydrouridine (see above). From these results, it seems evident that a nonreacting portion of the substrate, the uracil group, is essential for the tight binding of the vanadate–nucleoside complex to ribonuclease A.

During the ligand titration experiments, it was found that after addition of uridine and 5,6-dihydrouridine, the pH of the enzyme-vanadate mixture increased. This observation is similar to that reported for phosphate-containing compounds (26) and it indicates that protons are required for the binding of these complexes to RNase A.

Kinetics studies

Independent kinetics experiments were also carried out for the two inhibitors. The procedure for analysis of the kinetics results was similar to that employed by Lindquist et al. (3) except that the inhibiting species was assumed to be only the uridine–vanadate monomeric complex, as supported by the crystal structure studies (27). It was necessary to use the formation constants K_1 and K_3 in eqs. [2] and [3] and the conservation equation, eq. [4], where cV_t corresponds to the total amount of vanadate in solution. For the analysis, it was not necessary to use the full eq. [4] because the concentrations of VUr and E·VUr together represent less than 1% of the total vanadate concentration. Therefore, using a simplified conservation equation and eq. [3], eq. [5] is obtained. Because of the low relative amount of vanadate used in these studies, at no time is the total amount of uridine, cUr_t, significantly different from the true concentration, [Ur], so the conservation equation for uridine is not required. Therefore, $[V_i]$ was calculated from eq. [5] using $[Ur] = cUr_t$. This value of $[V_i]$ was then used to calculate the concentrations of V_2Ur_2 and VUr. For the conditions used in this study (0.1 mM total vanadate and 1.0 mM total uridine) with $K_3 = 5.3 \times 10^7$ M^{-3}, [Ur] = 0.30 μM and $[V_2Ur_2] = 0.52$ μM. Similar calculations for dihydrouridine (0.1 mM total vanadate and 39.6 mM total dihydrouridine with $K_3 = 4.8 \times 10^7$ M^{-3}) gave the corresponding concentrations, $[V(H_2Ur)] = 2.7$ μM and $[V_2(H_2Ur)_2] = 37.5$ μM.

$$[2] \quad V_i + Ur \overset{K_1}{\rightleftharpoons} VUr, \qquad [V_i][Ur]K_1 = [VUr]$$

$$[3] \quad 2V_i + 2Ur \overset{K_3}{\rightleftharpoons} V_2Ur_2, \qquad [V_i]^2[Ur]^2K_3 = [V_2Ur_2]$$

$$[4] \quad cV_t = [V_i] + [VUr] + 2[V_2Ur_2] + [E{\cdot}VUr]$$

$$[5] \quad 2K_3[Ur]^2[V_i]^2 + [V_i] - cV_t = 0$$

Figure 4 shows the results of a kinetics study of the uridine–vanadate–ribonuclease A system. As can be seen from this figure and is well known for this system (3, 25), uridine is an inhibitor, and this is in keeping with the observation of uridine binding in the NMR study. The initial reaction velocity (v) of the kinetics equation then requires terms for inhibition by uridine and by the VUr complex as defined by eq. [6] where V_{max} is the maximum reaction velocity, [S] is the substrate concentration, K_m is the Michaelis constant, and the K_i are the inhibition constants.

$$[6] \quad \frac{1}{v} = \frac{K_m}{V_{max}}\left(1 + \frac{[Ur]}{K_{i;Ur}} + \frac{[VUr]}{K_{i;VUr}}\right)\frac{1}{[S]} + \frac{1}{V_{max}}$$

Fig. 4. The inverse rate of hydrolysis of cyclic 2′,3′-uridine monophosphate catalyzed by ribonuclease A is shown as a function of the inverse substrate concentration. Ribonuclease inhibitors: (●) no inhibitor added; (■) 1 mM uridine; (◆) 1 mM added uridine plus 0.1 mM vanadate. Conditions of the experiments: 14–16 μg/mL ribonuclease A; 5.0 mM Tris buffer; 0.35 M KCl; pH 7.0; 298 K. Each experimental point is the average of two independent determinations.

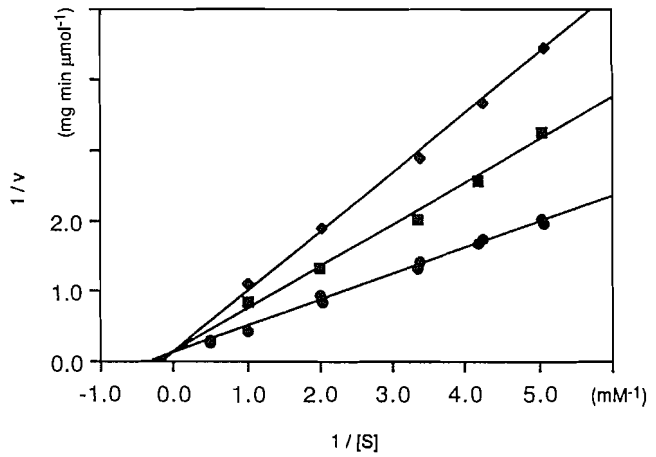

The bottom trace of Fig. 4 shows the results of the rate measurements in the absence of inhibitor so that the intercept gives $1/V_{max}$ and the slope K_m/V_{max}. The values, 0.09 ± 0.02 mg min μmol^{-1} and 380 ± 30 mg min for the intercept and slope, respectively, provided a value of 4.2 ± 1.5 mM for the K_m of 2′,3′-uridine monophosphate. This value of the Michaelis constant is close to that previously reported, about 9 mM (3, 28) and almost identical to the value determined here from the independent dihydrouridine study, $K_m = 3.7 \pm 1.6$ mM.

The centre trace of Fig. 4 was obtained when the reaction solution contained 1.0 mM uridine. The inhibition constant obtained was $K_{i;Ur} = 1.7 \pm 0.2$ mM, a value close to that previously reported, 2.3 mM (25). The corresponding value for dihydrouridine was 41 ± 6 mM.

The upper trace of Fig. 4 shows the influence of the uridine–vanadate complex on the rate measurements. The $K_{i;VUr}$ value determined for this complex was $(4.5 \pm 0.6) \times 10^{-7}$ M on the basis of the concentration of VUr obtained above. This value compares very favorably with the dissociation constant measured from the NMR binding experiments, $(5.0 \pm 0.4) \times 10^{-7}$ M. Reanalysis of the results of Lindquist et al. (Fig. 3 of ref. 3), with the correction for the occurrence of V_2Ur_2 in the reaction solution, yielded a value of 4.9×10^{-7} M for $K_{i;VUr}$. This value is in excellent agreement with that of the present study. The inhibition constant determined for dihydrouridine–vanadate was $(1.1 \pm 0.2) \times 10^{-6}$ M, a value quite close to that of the corresponding uridine complex. Table 3 summarizes the values for the binding constants obtained from the NMR measurements and the inhibition constants obtained from kinetics experiments.

Discussion

RNase A is potently inhibited by uridine 2′,3′-cyclic monovanadate and 5,6-dihydrouridine 2′,3′-cyclic monovanadate. The association constant for the binding of these complexes to the enzyme at pH 7.0 is 10^3 to 10^4 times larger than the estimated association constant for the uridine 2′,3′-cyclic monophosphate. There is little reason to suspect that tetrahedral vanadate will be bound much more strongly than tetrahedral phosphate in a ground state structure. In fact, tetrahedral vanadate esters are thought to be responsible for the activation of certain enzymes that normally require a phosphate ester for their function (29–31). The tight binding therefore suggests that, in the present case, the role of the vanadate complexes is that of transition state analogs. This is supported by the crystallographic structure for the complex between ribonuclease and uridine 2′,3′-cyclic monovanadate (27) that revealed that the amine group of Lys-41 and the imidazole rings of His-12 and His-119 are hydrogen bonded to the oxygens of a pentacoordinate vanadium(V). This coordination closely approximates the transition state structure originally proposed for the hydrolysis of pyrimidine 2′,3′-cyclic monophosphates catalyzed by RNase A (3). A recent crystallographic study of vanadate incorporated into rat acid phosphatase also revealed a similar coordination about the vanadium centre (32). However, recent NMR studies have suggested that there is a structural change in the ribonuclease on going from the crystalline material to its solution counterpart and that this change modifies the binding interactions of one of the histidines to the phosphate group (33).

From the binding studies and the kinetics results obtained here, it appears that there is a synergistic interaction involving the pyrimidine and the vanadate groups. The degree of this synergism was increased with the replacement of uridine by 5,6-dihydrouridine while replacement of the pyrimidyl group by a β-methoxy group caused a large loss in affinity of the enzyme for the riboside–vanadate complex. This suggests that, without the pyrimidine group, there can not be tight binding of the ribose–vanadate moiety to the enzyme and this emphasizes the importance of the amino acid residues, Thr-45, Phe-120, and Val-43, which interact with the base. The presence of strong interactions with the base is also supported by molecular dynamics simulations (10).

In the induced-fit mechanism of enzyme action (34), the catalytic groups at the active site of the free enzyme are not in optimal positions to exert effective catalytic activity. A substrate must have the minimal structural features to force a conformational change of the enzyme to the active form, so that a reaction can occur. The ^{51}V NMR binding studies and the kinetic inhibition studies of this work are consistent with this mechanism of action for RNase A but certainly do not require it. Other support for this possible mode of action is provided from alternate sources.

Evidence that a conformational change can occur in the active site of RNase A is available. X-ray data on the binding of cytidylic acid (2′-CMP) (35) and cytidine-N(3)-oxide 2′ phosphate (O(3)-2′-CMP) (35, 36) to RNase A have revealed different modes of binding and some significant displacements of side-chain atoms in the active site (Lys-41 and His-119). Also, it was found that Lys-7 and Lys-66 occupied different positions in the absence and presence of inhibitors at the active site (35, 36). Competitive inhibition studies using cytidine 2′-monophosphate and cytidine 3′-monophosphate have shown a conformational change due to the binding process (37). It was also concluded from temperature-dependence studies of ribonuclease-catalyzed opening of the cytidine cyclic 2′,3′-phosphate that conformational changes occur dur-

Scheme 1. E: ribonuclease in its receptive form. E*: ribonuclease in its activated state. R-V: vanadate component of the inhibitor complex. R-U: uracil component of the inhibitor complex. R-U,V: both components of the uridine–vanadate inhibitor.

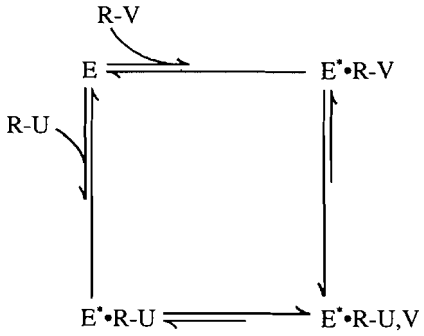

ing the catalytic cycle (38). Furthermore, X-ray analysis has shown that the free enzyme exists in two different conformations for which the imidazole ring of His-119 occupies two different sites (39) and evidence suporting this is available from NMR studies (33). Taken together, this evidence provides strong support for the existence of at least two different conformations available to RNase A.

The results obtained here can be explained by suggesting there are two interconvertible conformations of RNase A that differ in their affinity toward the various inhibitor complexes of vanadate. The low-affinity or inactive form of ribonuclease A (E) is complementary to the substrate, while the high-affinity or active form (E*) has a structure complementary to that of the transition state. In the absence of either the pyrimidyl group or the vanadate group, the low-affinity form of the enzyme predominates. The binding of either of these groups, in isolation, to their respective RNase subdomains is unfavorable. In the presence of both groups, the equilibrium between the two RNase A species is shifted towards the high-affinity form. Either subdomain, once it is occupied by its corresponding group, promotes a change in conformation of the RNase so that both groups of the ligand are fully accommodated. This leads to an overall energetically favorable interaction with the substrate. A reaction sequence that is consistent with the observed results is shown in Scheme 1.

When both the pyrimidyl and ribose-phosphate subsites of the active site are occupied, the reactive groups are brought together so that the full binding of the unstable five-coordinate phosphate can be achieved. The transition state energy required for forming the intermediate phosphate is high and some of the energy required is provided by binding of the pyrimidine group. Protein engineering studies on tyrosyl-tRNA synthetase (40) have provided direct evidence of transition state stabilization in enzyme catalysis. Taking at face value the fact that the β-methylriboside–vanadate complex is only weakly bound, it then appears that binding interactions to the ribose ring and the attached pentacoordinate vanadate are sufficient to approximately balance the energy requirements of ribonuclease for its active state. To the extent that the pentacoordinate vanadate in the enzyme complex is a good mimic of the phosphate transition state, this means that the additional energy required to achieve the transition state of phosphorus is matched by that available from the interactions of the uracil group of the nucleoside with the active-site threonine, valine, and phenylalanine that were identified in the X-ray work (35). Unfortunately, such considerations are complicated by entropic factors that must be taken into account when comparing the binding of the nucleoside–vanadate complex to the individual binding of riboside–vanadate and of the free nucleoside (41, 42). The energy of binding of the nucleoside–vanadate complex will be greater than the sum of the energies available from the binding of ribose–vanadate and the binding of the free nucleoside.

It is instructive to examine the role of vanadate and its complexes as transition state analogues a little more closely. If the K_m for 2′,3′-cyclic phosphouridine, as defined by eq. [6], is taken to approximately correspond to a true dissociation constant, then binding of this substrate occurs with an energy of about -14 kJ/mol (from $\Delta G = -RT \ln K$). This compares with −36 kJ/mol for the binding of the cyclic vanadiouridine complex. A similar comparison can be drawn for phosphoglycerate mutase. In this case, the specific cofactor, 2,3-bisphosphoglycerate, has a K_m of 3.3×10^{-7} M (43) while 2-vanadio-3-phosphoglycerate has a dissociation constant of 1×10^{-11} M (12). These two parameters correspond to −37 and −62 kJ/mol, respectively, for the association energy. Values close to this are also found for phosphoglucomutase where the K_m for 1,6-bisphosphoglucose is equal to 4.8×10^{-8} M while K_i for 6-vanadio-glucose-1-phosphate is 2×10^{-12} M (13). These constants correspond to $\Delta G = -41$ and −66 kJ/mol, respectively.

From these three examples it can be seen that the excess binding energy deriving from the replacement of a single phosphate by a vanadate in the enzyme complex falls within the range of 22 – 25 kJ/mol, this despite a range of about 10^6 in the values of the dissociation constants. This excess energy of binding might be considered to be dependent on two major factors: the energy required to generate the phosphate transition state and that required for the corresponding state with vanadate. To the extent that vanadate is a good substitute for phosphate, the excess energy of binding the enzyme complex is equal to the difference between these two binding energies.

It is possible to compare the transition and ground state energies by obtaining the values of the rate constant for catalyzed hydrolysis, k_{cat}, and the rate constant, k_{hyd}, for the noncatalyzed reaction. The ratio of these two values, k_{cat}/k_{hyd}, should roughly correspond to $K_m/K_{i;VUr}$ if the vanadate complex provides a good transition state analogue to the phosphate reaction. From the known hydrolysis rates of uridine cyclic phosphate, 4×10^{-9} s^{-1} at 298 K (44) and $k_{cat} = 4$ s^{-1}, the ratio obtained here for k_{cat}/k_{hyd} is 1×10^9, to be compared to $K_m/K_{i,VUr} = 1.6 \times 10^4$. (In ref. 44 the rate enhancement for the enzymic reaction is given as 7×10^9 for the analogous cytidine hydrolysis.) In energy terms, $RT \ln(K_m/K_{i,VUr}) = 22$ kJ/mol while $RT \ln(k_{cat}/k_{hyd}) = 54$ kJ/mol. These values are quite significantly different from each other and suggest that the reaction with pentacoordinate vanadate goes only about 40% of the way to a transition state structure in the ribonuclease reaction.

An approach to this problem that would provide valuable information would be to directly compare the activation energies for hydrolysis of the cyclic phosphate to the corresponding cyclic vanadate. Unfortunately, the rate of hydrolysis of the appropriate vanadate derivative is not known. However, if it is assumed that the transition state structure about phosphate

in the enzyme-catalyzed reaction is similar to that for ester hydrolysis, it is possible to estimate in an independent manner the excess energy available to vanadate. At 373 K, the energy of activation to hydrolysis, ΔE, for the methyl phosphate, glycerol-1-phosphate, and glucose-1-phosphate monoanions is close to 126 kJ/mol for all compounds with corresponding preexponential factors, A, (for $k = A \exp \Delta E/RT$), of 6.5×10^{12} s^{-1}, 4.3×10^{12} s^{-1}, and 5.0×10^{12} s^{-1} (45). For methyl phosphate the rate constant for hydrolysis is 8.2×10^{-6} s^{-1} compared to 6.1×10^{-6} s^{-1} for ethyl phosphate. Other closely related esters have similar rate constants. It can, therefore, reasonably be assumed that the preexponential factor for ethyl phosphate is close to 5×10^{12} s^{-1}. This, together with the rate of 6.1×10^{-6} s^{-1}, corresponds to a ΔE of 128 kJ/mol. This value is not exact but small errors are not significant. This calculated value for ethyl phosphate is the same as the value reported for methyl phosphate, 128 kJ/mol (45). Assuming these values of ΔE and A, a rate constant of 2.0×10^{-8} s^{-1} is calculated for the hydrolysis of ethyl phosphate at 328 K.

The rate constant for the hydrolysis of ethyl vanadate at 328 K is 1.2×10^{3} s^{-1} (46). If the preexponential factors for ethyl phosphate and ethyl vanadate are not exceedingly different, the difference in activation energies for hydrolysis between these two compounds can be estimated from the ratio of the two rate constants. On this basis, the energies required to obtain the pentacoordinate transition state structures are different by about 68 kJ/mol or ΔE_V = 60 kJ/mol and ΔE_P = 128 kJ/mol.

Since the excess binding energies of the vanadate complexes in the three enzyme–vanadate systems mentioned previously are about 25 kJ/mol, this analysis suggests there is a shortfall of about 40 kJ/mol in the excess binding energy available to these three enzymic reactions. Put another way, in all three enzymes, the enzyme–vanadate complex goes only about 40% of the way towards a transition state structure. This agrees with our analysis above for the studies carried out here with ribonuclease A. A different set of arguments has been advanced for phosphoglucomutase, suggesting that the reaction with vanadate proceeds about 45% of the way to the transition state in that particular system (14).

Some of this shortfall in energy may arise because the V—O bond lengths are slightly longer than P—O bond lengths, by about 0.15 Å, or about 10% of the bond length (47). It does not seem that this offers a reasonable explanation for other than a small proportion of the energy shortfall. However, there are some indications that the oxygens of pentacoordinate vanadate may not be as good hydrogen bond acceptors as those of the corresponding phosphate (47). It also does not seem likely that this will account for the large energy shortfall since, at least in ribonuclease, hydrogen bonding will still be present (47).

A plausible explanation for the observations of this work is that vanadate does not provide as good a transition state analogue as might be expected simply because the geometry about vanadium in the enzyme complex is not a good representation of the transition state actually utilized during the phosphate transfer step of either of these three enzymes. Indeed, the complexities inherent in phosphate ester hydrolysis have been examined and no clear answer is available (9, 11). Whatever the details of the structures of the transition states for phosphate, it seems that the incremental binding energies arising from the presence of the vanadium in these three different ligand–vanadium complexes in the different enyme systems are almost identical. This suggests that there is a structure associated with the phosphate reaction that is not mimicked well by vanadate and that costs about 40 kJ/mol of binding energy. Since it is reasonable to expect that pentacoordinate vanadate can assume a trigonal-bipyramidal structure with minimal costs in energy, this suggests that there are significant deviations from this structure in the phosphate reactions. Presumably, this structure will be similar for RNase A, phosphoglycerate mutase, phosphoglucomutase, and, possibly, other phosphate-transferring enzymes.

Acknowledgements

Thanks are gratefully extended to the Natural Sciences and Engineering Research Council of Canada for its financial support of this work and to the Merck Frosst Centre for Therapeutic Research for financial support to N.L.-L.

References

1. Worthington Biochemical Corporation. *In* Worthington Enzyme Manual. Freehold, N.J. 1972.
2. A. Fersht. *In* Enzyme structure and mechanism. Freeman, New York. 1985.
3. R.N. Lindquist, J.L. Lynn, Jr., and G.E. Lienhard. J. Am. Chem. Soc. **95**, 8762 (1973).
4. A.S. Tracey, J.S. Jaswal, M.J. Gresser, and D. Rehder. Inorg. Chem. **29**, 4283 (1990).
5. A.S. Tracey and C. H. Leon-Lai. Inorg. Chem. **30**, 3200 (1991).
6. R. Breslow and R. Xu. Proc. Natl. Acad. Sci. U.S.A. **90**, 1201 (1993).
7. R. Breslow and R. Xu. J. Am. Chem. Soc. **115**, 10705 (1993).
8. D. Herschlag. J. Am. Chem. Soc. **116**, 11631 (1994).
9. P. Tole and C. Lim. J. Am. Chem. Soc. **116**, 3922 (1994).
10. J.E. Straub, C. Lim, and M. Karplus. J. Am. Chem. Soc. **116**, 2591 (1994).
11. C. Lim and P. Tole. J. Am. Chem. Soc. **114**, 7245 (1992).
12. S. Liu, M.J. Gresser, and A.S. Tracey. Biochemistry, **31**, 2677 (1992).
13. M.D. Percival, K. Doherty, and M.J. Gresser. Biochemistry, **29**, 2764 (1990).
14. W.J. Ray, Jr. and J.M. Puvathingal. Biochemistry, **29**, 2790 (1990).
15. A.S. Tracey and M.J. Gresser. Inorg. Chem. **27**, 1269 (1988).
16. D.C. Crans, S.E. Harnung, E. Larsen, P.K. Shin, L.A. Theisen, and I. Trabjerg. Acta Chem. Scand. **45**, 456 (1991).
17. F.G.C. Geraldes and M.M.C.A. Castro. J. Inorg. Biochem. **35**, 79 (1989).
18. S.E. Harnung, E. Larsen, and E.J. Pedersen. Acta Chem. Scand. **47**, 674 (1993).
19. J. Richter and D. Rehder. Z. Naturforsch. B: Chem. Sci. **46**, 1613 (1991).
20. A.S. Tracey, M.J. Gresser, and S. Liu. J. Am. Chem. Soc. **110**, 5869 (1988).
21. M.J. Gresser and A.S. Tracey. J. Am. Chem. Soc. **108**, 1935 (1986).
22. S.J. Angus-Dunne, R.J. Batchelor, A.S. Tracey, and F.W.B. Einstein. J. Am. Chem. Soc. **117**, 5292 (1995).
23. W.J. Ray, Jr., D.C. Crans, J. Zheng, J.W. Burgner II, H. Deng, and M. Mahroof-Tahir. J. Am. Chem. Soc. **117**, 6015 (1995).
24. D. Kostrewa, H.-W. Choe, U. Heinemann, and W. Saenger. Biochemistry, **28**, 7592 (1989).
25. D.R. Pollard and J. Nagyvary. Biochemistry, **12**, 1063 (1973).

26. J.P. Hummel and H. Witzel. J. Biol. Chem. **241**, 1023 (1966).
27. B. Borah, C.-w. Chen, W. Egan, M. Miller, A. Wlodawer, and J.S. Cohen. Biochemistry, **24**, 2058 (1985).
28. E.J. del Rosario and G.G. Hammes. Biochemistry, **8**, 1884 (1969).
29. A.F. Nour-Eldeen, M.M. Craig, and M.J. Gresser. J. Biol. Chem. **260**, 6836 (1985).
30. D.G. Drueckhammer, J.R. Durrwachter, D.C. Pederson, D.C. Crans, L. Daniels, and C.-H. Wong. J. Org. Chem. **54**, 70 (1989).
31. P.J. Stankiewicz and A.S. Tracey. *In* Vanadium and its role for life. *Edited by* H. Sigel and A. Sigel. Marcel Dekker, Inc., New York. 1995.
32. Y. Lindqvist, G. Schneider, and P. Vihko. Eur. J. Biochem. **221**, 139 (1994).
33. T.D. Veenstra and L. Lee. Biophys. J. **67**, 331 (1994).
34. D.E. Koshland, Jr. Adv. Enzymol. **22**, 45 (1960).
35. B. Howlin, G.W. Harris, D.S. Moss, and R.A. Palmer. J. Mol. Biol. **196**, 159 (1987).
36. N. Borkakoti. Eur. J. Biochem. **132**, 89 (1983).
37. Y.P. Myer, E.A. Barnard, and K.P. Pranab. J. Biol. Chem. **254**, 137 (1979).
38. M.R. Eftink and R.L. Biltonen. Biochemistry, **22**, 5140 (1983).
39. N. Borkakoti, D.S. Moss, and R.A. Palmer. Acta Crystallogr. Sect. B: Struct. Crystallogr. Cryst. Chem. **B38**, 2210 (1982).
40. R.J. Leatherbarrow, A.R. Fersht, and G. Winter. Proc. Natl. Acad. Sci. U.S.A. **82**, 7840 (1985).
41. W.P. Jencks. Proc. Natl. Acad. Sci. U.S.A. **78**, 4046 (1981).
42. W.P. Jencks. Adv. Enzymol. **43**, 219 (1975).
43. P.J. Stankiewicz and L.F. Hass. J. Biol. Chem. **261**, 12715 (1986).
44. M.R. Eftink and R.L. Biltonen. Biochemistry, **22**, 5134 (1983).
45. J.R. Cox, Jr. and O.B. Ramsay. Chem. Rev. **64**, 317 (1964).
46. M.J. Gresser and A.S. Tracey. J. Am. Chem. Soc. **107**, 4215 (1985).
47. M. Krauss and H. Basch. J. Am. Chem. Soc. **114**, 3630 (1992).

Appendix

Calculation of the binding curve

The following conservation equations were taken into account:

[A.1] $[E_t] = [E] + [E{\cdot}L] + [E{\cdot}VL] + [E{\cdot}V_i]$

[A.2] $[V_t] = [V_i] + 2[V_2] + 4[V_4] + 2[V_2L_2] + [VL] + [E{\cdot}V_i] + [E{\cdot}VL]$

[A.3] $[L_t] = [L] + [VL] + 2[V_2L_2] + [E{\cdot}VL] + [E{\cdot}L]$

where $[E_t]$ = total RNase A concentration; $[E]$ = free RNase A concentration; $[E{\cdot}L]$ = RNase A–ligand complex concentration; $[E{\cdot}VL]$ = RNase A–vanadate–ligand complex concentration; $[E{\cdot}V_i]$ = RNase A–vanadate complex concentration, assuming that

[A.4] $[V_b] = [E{\cdot}VL] + [E{\cdot}V_i]$

and including the following equilibria

[A.5] $2\,V_i \overset{K_2}{\rightleftharpoons} V_2, \qquad K_2 = \dfrac{[V_2]}{[V_i]^2}$

[A.6] $4\,V_i \overset{K_4}{\rightleftharpoons} V_4, \qquad K_4 = \dfrac{[V_4]}{[V_i]^4}$

[A.7] $V_i + L \overset{K_1}{\rightleftharpoons} VL, \qquad K_1 = \dfrac{[VL]}{[V_i][L]}$

[A.8] $2\,V_i + 2L \overset{K_3}{\rightleftharpoons} V_2L_2, \quad K_3 = \dfrac{[V_2L_2]}{[V_i]^2[L]^2}$

[A.9] $E + L \overset{K_5}{\rightleftharpoons} E{\cdot}L, \qquad K_5 = \dfrac{[E{\cdot}L]}{[E][L]}$

[A.10] $E + VL \overset{K_6}{\rightleftharpoons} E{\cdot}VL, \quad K_6 = \dfrac{[E{\cdot}VL]}{[E][VL]}$

[A.11] $E + V_i \overset{K_7}{\rightleftharpoons} E{\cdot}V_i, \quad K_7 = \dfrac{[E{\cdot}V_i]}{[E][V_i]}$

The inhibition constant K_{iVL} is the dissociation constant of VL from E·VL and so is equal to $1/K_6$.

By making the appropriate rearrangements and substitutions into eqs. [A.3], [A.2], and [A.1], the following expressions are obtained:

[A.12] $[L]^2 2K_3 [V_i]^2 + [L] (1 + K_1[V_i] + K_5 [E] + K_1K_6 [E] [V_i]) - L_t = 0$

[A.13] $[V_i]^4 4K_4 + [V_i]^2 2(K_2 + K_3[L]^2) + [V_i](1 + K_1[L] + K_7[E] + K_1K_6[E][L]) - V_t - 0$

[A.14] $$[E] = \frac{[E_t]}{1 + K_5[L] + K_1K_6[L][V_i] + K_7[V_i]}$$

The fraction of total enzyme that is bound by vanadate (as a vanadate–ligand complex and (or) vanadate by itself) is

[A.15] $$\frac{[V_b]}{[E_t]} = \frac{[E{\cdot}VL] + [E{\cdot}V_i]}{[E_t]}$$

By making the appropriate substitutions into eq. [A.15], the final equation is obtained:

[A.16] $$\frac{[V_b]}{[E_t]} = \frac{[V_i](K_7 + K_1K_6[L])_t]}{1 + K_5[L] + [V_i](K_7 + K_1K_6[L])}$$

To obtain values of $[V_b]/[E_t]$ to construct a family of calculated curves, an iterative approach was used. Values for the equilibrium constants used for the iterative calculations were $K_2 = 470\ M^{-1}$, $K_4 = 6.3 \times 10^9\ M^{-3}$, and $K_7 = 0\ M^{-1}$. A value of 0 was assigned for K_7, since no binding of vanadate by RNase A was detected in any experiment. Values for K_1K_6 were assumed in order to calculate the ratio $[V_b]/[E_t]$ as a function of total ligand concentration and assumed K_5. The values assumed for K_1K_6 and K_5 were then varied until the values that best fit the experimental results were obtained. Since K_1 is known ($K_1 = 3.0\ M^{-1}$), K_6 is explicitly specified by this process and $1/K_6$ is the dissociation constant for the dissociation of uridine–vanadate from the enzyme complex. K_1K_6, in conjuncition with K_5, defines the shape of the binding curve.

The iterative procedure utilized is described as follows.

Step 1: Assume a value for K_1K_6 and for K_5. Use the closest experimental value for $[V_i]$ for the total ligand concentration and assume a reasonable value for [L], the free ligand concentration.

Step 2: Calculate [E] from eq. [A.14], then calculate [L] from eq. [A.12]. Use this new value of [L] to recalculate [E]. Repeat this procedure until [E] and [L] are constant.

Step 3: Use the values of [E] and [L] obtained above along with the assumed $[V_i]$ to calculate the left side of eq. [A.13]. If this value is not 0 to within 0.001 mM, adjust $[V_i]$ appropriately and repeat step 2.

Step 4: Repeat steps 2 and 3 until both the left sides of eq. [A.12] and [A.13] are satisfied to within 0.001 mM. Use these values of $[V_i]$ and [L] to calculate $[V_b]/[E_t]$ from eq. [A.16] for the assumed values of K_1K_6 and K_5.

A kinetic study on singlet molecular oxygen ($O_2(^1\Delta_g)$) generation and quenching by dihydroxynaphthalenes

Marta Luiz, Arnaldo T. Soltermann, Alicia Biasutti, and Norman A. Garcia

Abstract: A kinetic study on the aerobic ($O_2(^1\Delta_g)$-mediated) photooxidation of a series of dihydroxynaphthalenes was carried out. Members of this family of compounds include important environmental contaminants. The interaction with $O_2(^1\Delta_g)$, determined by both time-resolved phosphorescence and static methods, yields a quenching rate constant in the range of 10^5–10^9 M^{-1} s^{-1}, depending on the solvent polarity, pH, and substitution pattern of the dihydroxynaphthalene. According to experimental evidence, the mechanism of the interaction seems to be mediated by an encounter complex with a considerable charge transfer component. From a mechanistic point of view this characteristic of DHN indicates a behaviour very similar to that of simple substituted phenols and dihydroxybenzenes. Quantum yields for DHN photooxidation (Φ_r) indicate that these substrates are excellent candidates for $O_2(^1\Delta_g)$-mediated degradation under environment conditions. Furthermore, these compounds proved to be good self-sensitizers upon irradiation at 337 nm. Quantum yields (Φ_Δ) for the production of $O_2(^1\Delta_g)$ were determined to be on the order of 0.25 in benzene.

Key words: dihydroxynaphthalenes, photooxidation, quenching, sensitization.

Résumé : On a réalisé une étude cinétique de la photooxydation aérobique (avec médiation par le $O_2(^1\Delta_g)$) d'une série de dihydroxynaphtalènes. Les membres de cette famille sont des contaminants environnementaux importants. L'interaction avec le $O_2(^1\Delta_g)$ a été déterminée par des méthodes statiques ainsi que par phosphorescence résolue en fonction du temps et elle conduit à une constante de vitesse de désactivation de l'ordre de 10^5 à 10^9 M^{-1} s^{-1}, suivant la polarité du solvant, le pH et le patron de substitution du dihydroxynaphtalène. Sur la base des données expérimentales obtenues, il semble que le mécanisme de l'interaction soit l'objet d'une médiation de la part d'un complexe de rencontre qui implique une composante importante de transfert de charge. D'un point de vue mécanistique, cette caractéristique du DHN indique un comportement très semblable à celui des phénols et des dihydroxybenzènes simples, substitués. Les rendements quantiques pour la photooxydation du DHN (Φ_r) indiquent que ces substrats sont d'excellents candidats pour des dégradations avec médiation du $O_2(^1\Delta_g)$ dans des conditions environnementales naturelles. De plus, lorsqu'on les a irradiés à 337 nm, ces composés ont montré d'excellentes propriétés comme autosensibilisateurs. On a déterminé que les rendements quantiques (Φ_Δ) pour la production du $O_2(^1\Delta_g)$ sont de l'ordre de 0,25, dans le benzène.

Mots clés : dihydroxynaphtalènes, photoxydation, désactivation, sensibilisation.

[Traduit par la rédaction]

Introduction

Over the last few years we have focussed our investigation of the kinetic and mechanistic aspects of dye-sensitized photooxidations of different types of pollutants on those containing hydroxy-aromatic groups such as phenols (1–9), hydroxybiphenyls (10), and polyhydroxybenzenes (11). In the present contribution we examine this kind of photorreaction and, more specifically, singlet molecular oxygen [$O_2(^1\Delta_g)$]-mediated processes, in relation to dihydroxynaphthalenes (DHN). This family of polycyclic aromatic hydrocarbons constitutes a group of contaminants widespread in the environment. These compounds are released into natural aquatic media from diverse sources, industrial wastes and petroleum spills providing two massive contributions (12, 13).

A crucial objective of research in this area is to establish possible relationships between substrate and susceptibility to photooxidative degradation. The fraction of $O_2(^1\Delta_g)$-quenching events leading to effective photooxidation of the substrate, and the conditions favouring this process, are

Received March 6, 1995.

M. Luiz. Departamento de Química. Facultad de Ciencias Naturales. Universidad Nacional de La Patagonia, San Juan Bosco, 9000 Comodoro Rivadavia, Argentina.

A.T. Soltermann, A. Biasutti, and N.A. García.[1] Departamento de Química y Física, Universidad Nacional de Río Cuarto, 5800 Río Cuarto, Argentina.

[1] Author to whom correspondence may be addressed.

two important points to be elucidated. In this context, the characteristics of the reaction medium (solvent polarity and pH) frequently play decisive roles from a kinetic point of view. These aspects have been carefully examined in the present contribution, to establish the feasibility of environmental degradation of dihydroxynaphthalenes through an aerobic photosensitized process. As well, the potential role of DHN as $O_2(^1\Delta_g)$ generators, upon direct irradiation, was also explored by determination of their quantum yields (Φ_Δ) of $O_2(^1\Delta_g)$ production.

Experimental

Chemicals

Rubrene (Rub); Rose Bengal (RB); 1,3-dihydroxynaphthalene (1,3-DHN); 1,5-dihydroxynaphthalene (1,5-DHN); 2,3-dihydroxynaphthalene (2,3-DHN) and 2,7-dihydroxynaphthalene (2,7-DHN); 4,5-dihydroxynaphthalene 2,7-disulfonic acid (4,5-DHN-2,7 DS); 3,5-dihydroxynaphthalene 2,7-disulfonic acid (3,5-DHN-2,7 DS); 3,6-dihydroxynaphthalene 2,7-disulfonic acid (3,6-DHN-2,7 DS); 2-methoxynaphthalene; 9,10-dimethylanthracene (DMA), furfurylalcohol (FFA), 1,4-diazabicyclo[2.2.2]octane (DABCO), and sodium azide were purchased from Aldrich. The naphthalenes and DMA were purified by sublimation, except for the sulfonated derivatives, which were recrystallized from MeOH. The solvents benzene (Bz), toluene (Tol), and methanol (MeOH) were of the highest available purity. Water was triply distilled. All measurements were made on freshly prepared solutions. A Na_2HPO–NaOH buffer was employed to adjust aqueous solutions to pH 12. At this pH, only the ionized form of the substituted naphthalenes was spectrophotometrically detected.

Methods

Ground state absorption spectra were recorded employing a Hewlett Packard 8452A diode array spectrophotometer.

The irradiation setup, including the specific oxygen electrode (Orion 97-08) was described earlier (14). The temperature was kept at 22 ± 2°C throughout.

The kinetic laser spectrophotometer for time-resolved phosphorescence detection (TRPD) of $O_2(^1\Delta_g)$ was previously described (14). In the present case RB was the sensitizer. Typically, an absorbance of the dye of ca. 0.3 at 337 nm was employed. The decay kinetics were first order in all cases.

The $O_2(^1\Delta_g)$ lifetimes were evaluated in the absence (τ^0) and in the presence (τ) of the quencher, and their ratio plotted as a function of quencher concentration [DHN], according to a simple Stern–Volmer treatment (eq. [1]), as shown in Fig. 1 for 1,5-DHN.

$$[1] \qquad \tau^0/\tau = 1 + k_t\tau^0[\mathrm{DHN}]$$

In Bz–MeOH, k_t was mainly determined according to Carlsson et al. (15) on the basis of self-sensitized photooxidation of rubrene, provided that the results employing this simple methodology were coincident with those obtained by TRPD. The ratio of initial rates of rubrene photooxidation in the absence (V_0) and in the presence (V) of different concentrations of the DHN was plotted against the DHN concentration, and k_t was calculated from eq. [2]

$$[2] \qquad V_0/V = 1 + k_t[\mathrm{DHN}]/(k_d + k_{rRub}[\mathrm{Rub}])$$

In the present case $k_{rRub}[\mathrm{Rub}] \sim 370\ s^{-1}$ (assuming $k_{rRub} = 4.4 \times 10^7\ M^{-1}\ s^{-1}$, see ref. 16). Under these conditions the denominator of eq. [2] can be practically taken as equal to k_d. The value for $1/k_d$ employed in the calculations was 23 μs obtained from TRPD experiments.

For aqueous solutions, k_t was calculated from eq. [3] (graphical method) (16) by using RB as dye sensitizer and assuming reaction [9] to be the only source of oxygen uptake.

$$[3] \qquad \mathrm{rate}^{-1} = (I_a\Phi_\Delta)^{-1}\{(k_t/k_r) + k_d/k_r[\mathrm{DHN}]\}$$

where rate and I_a denote the velocity of substrate consumption and the intensity of light absorbed by the sensitizer, respectively. For experimental reasons we measured the rate of O_2 uptake (employing the selective oxygen electrode) instead of rate of substrate consumption (reaction [9]). This replacement is only valid for cases in which the stoichiometry of reaction [9] is 1:1 (see Results and discussion). A k_d value of $2.5 \times 10^5\ s^{-1}$ was employed in the calculations (17).

The k_r values obtained for DHN in both aqueous solutions and organic solvents were determined by the method of Foote and Ching (18), eq. [4],

$$[4] \qquad k_r = k_{rR}\ \mathrm{slope}_{DHN}/\mathrm{slope}_R$$

which compares the slopes of the first-order plots for substrate and reference uptake (slope_{DHN} and slope_R, respectively) against the irradiation time for the oxidizable substrate or a reference of known k_{rR}. The reference used were DMA (in organic media) and FFA (in water). The k_{rR} values employed for the hydrocarbon and the alcohol were $1.2 \times 10^7\ M^{-1}\ s^{-1}$ (16) and $1.2 \times 10^8\ M^{-1}\ s^{-1}$ (19), respectively.

The rate of DHN photooxidation in organic media was determined spectrophotometrically. In water, the oxygen uptake was measured instead of the DHN uptake. The accuracy of this methodology for substituted phenols has been discussed elsewhere (9).

The modus operandi for obtaining the Φ_Δ values by means of TRPD was as follows: the traces for individual luminiscence decay from DHN and the reference compound 2-methoxynaphthalene (for both sample and reference Abs_{337} = 0.1, 0.2, and 0.5) were fitted with monoexponential functions to yield the initial intensity I^0 at time $t = 0$. In all cases the linearity between laser pulse energy (typically 1 mJ per pulse) and I^0 was ensured. The respective I^0 values were plotted against the fraction of absorbed light, yielding linear plots. The slopes of these plots were compared with the slope of the reference 2-methoxynaphthalene ($\Phi_\Delta = 0.34$ in Bz (20)) to obtain the absolute values for DHN.

Results and discussion

The TRPD signal of $O_2(^1\Delta_g)$ generated by aerobic irradiation of the dye sensitizer (RB) was inhibited by the presence of DHN. The interaction can be kinetically depicted as follows:

$$[5] \qquad S + h\nu \longrightarrow {}^*S^1 \xrightarrow{k_{ISC}} {}^*S^3$$

$$[6] \qquad {}^*S^3 + O_2(^3\Sigma_g^-) \xrightarrow{k_{ET}} S + O_2(^1\Delta_g)$$

$$[7] \qquad O_2(^1\Delta_g) \xrightarrow{k_d} O_2(^3\Sigma_g^-)$$

$$[8] \qquad O_2(^1\Delta_g) + Q \xrightarrow{k_q} O_2(^3\Sigma_g^-) + Q$$

$$[9] \qquad O_2(^1\Delta_g) + Q \xrightarrow{k_r} \mathrm{Products}$$

Fig. 1. Stern–Volmer plots, according to eq. [2], for the quenching of $O_2(^1\Delta_g)$ by DHN in Tol–MeOH 4:1 (v/v). For 1,5-DHN the circles represent the τ^0/τ ratio, according to eq. [1], obtained through TRPD methodology.

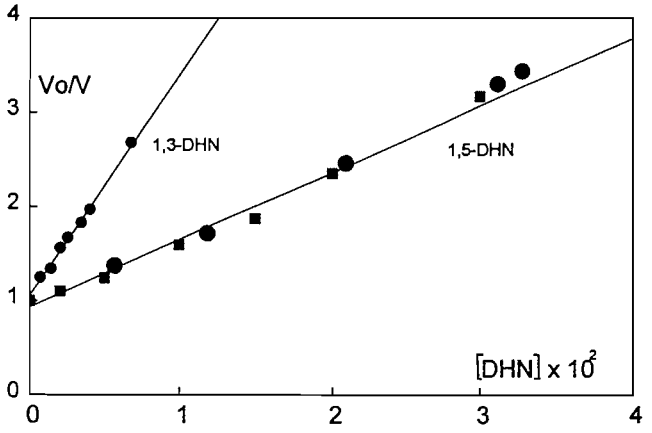

Fig. 2. Inverse plot, according to eq. [3], for the quenching of $O_2(^1\Delta_g)$ by 2,7-DHN in pure water and water of pH 12.

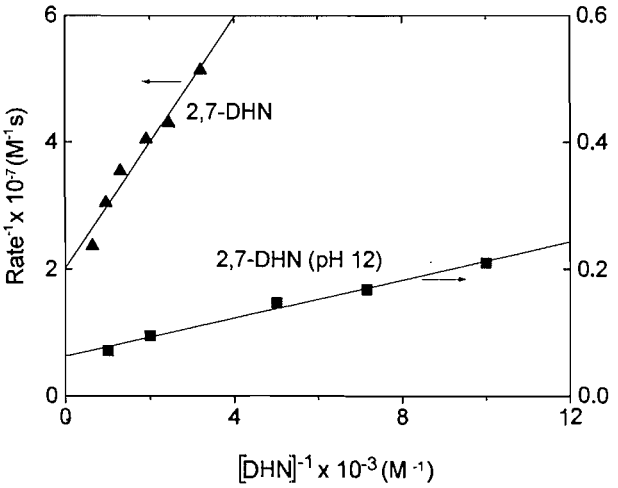

Table 1. Rate constants for the overall (k_t, M^{-1} s^{-1}) and chemical (k_r, M^{-1} s^{-1}) quenching of $O_2(^1\Delta_g)$ and upper limits for the photooxidation quantum yields (Φ_r) (see text) in several solvents and quantum yields for $O_2(^1\Delta_g)$ generation (Φ_Δ) in benzene, by a series of dihydroxynaphthalenes.

Compound	Solvent	$k_t \times 10^{-7}$	$k_r \times 10^{-7}$	Φ_r[a]	Φ_Δ
1,3-DHN	Water	287	14.5	0.046	
	Water, pH 12	140			
	Tol–MeOH (4:1)	1.0			
	Bz				0.21
1,5-DHN	Water	163	5.8	0.030	
	Water, pH 12[b]				
	MeOH[c]	0.61	0.015	0.009[d]	
	Tol–MeOH (4:1)	0.35			
	Bz				0.22
2,3-DHN	Water	415	5.2	0.011	
	Water, pH 12	150	150	0.86	
	Tol–MeOH (4:1)	0.011			
	Bz				0.24
2,7-DHN	Water	46.5	7.16	0.15	
	Water, pH 12	110	110	0.81	
	MeOH[c]	0.21			
	Tol–MeOH (4:1)	0.041			
	Bz				0.29
4,5-DHN-2,7 DS	Water	140	21.2	0.13	
	Water, pH 12	122	49.0	0.33	
	MeOH–Bz (10:1)	1.5			
3,5-DHN-2,7 DS	Water	4.0			
	Water, pH 12	53.3	50	0.63	
3,6-DHN-2,7 DS	Water	6.5	0.05	0.001	
	Water pH 12	52.5	44	0.56	

[a]Upper limit, calculated from eq. [10] employing [DHN] = 1 mM.
[b]Spontaneous dark oxidation.
[c]From ref. 22.
[d]Calculated in this work.

The sensitizer (S) absorbs convenient light and generates electronically excited singlet and triplet states (reaction [5]). From the excited triplet state an energy transfer reaction to ground-state triplet molecular oxygen [$O_2(^3\Sigma_g^-)$] can take place, producing the excited oxygen species $O_2(^1\Delta_g)$ (reaction [6]). It can decay by collision with surrounding molecules (typically the solvent, reaction [7]) or interact physically (reaction [8]) or chemically (reaction [9]) with an eventual quencher Q. Reactions [7] and (or) [8] are responsible for the already mentioned inhibition of the TRPD signal. In kinetic terms the addition k_q+k_r is known as k_t, the rate constant for the overall process of $O_2(^1\Delta_g)$ quenching.

Overall rate constants for $O_2(^1\Delta_g)$ quenching in Tol–MeOH were determined as described in the experimental section. Excellent agreement was found between the k_t values obtained using the time-resolved $O_2(^1\Delta_g)$ emission technique and the independent technique based on the autoperoxidation of rubrene (see Figs. 1 and 2 for typical cases of k_t determination in organic and aqueous solutions). The respective k_t values are listed in Table 1.

The absorption spectra of air-equilibrated solutions of DHN were strongly modified upon sensitized irradiation in both normal and alkalinized solvents, employing RB as a dye sensitizer. In Fig. 3 are shown, as typical examples, the results for 1,3-DHN and 4,5-DHN-2,7 DS in water. No spectral modifications were observed in the presence of quenchers frequently employed as $O_2(^1\Delta_g)$ testers (16) (either 1 mM sodium azide, in aqueous solution, or 60 mM DABCO, in Tol–MeOH). The same was true when Ar-saturated solutions of the DHN–RB mixtures were photolyzed.

Even when the TRPD experiments unambiguously demonstrate the existence of an important $O_2(^1\Delta_g)$ quenching by all the DHN assayed, the above-mentioned experiments indicate, according to currently accepted criteria (21), that the dye-sensitized *photooxidation* occurs via an $O_2(^1\Delta_g)$-mediated process.

The ability of DHN to act as $O_2(^1\Delta_g)$ quenchers, as determined by the experimental methods employed in this work, does not provide any information about the nature of the quenching mechanism. Distinction between the chemical and physical contributions to the overall rate constant was possible by employing an actinometric method, as described in the experimental section. The fourth column on Table 1 exhibits k_r values for DHN that were obtained employing FFA as a sacrificial reference compond (see Methods). This compound is a very convenient reference for $O_2(^1\Delta_g)$ reactions since its k_r value is independent of pH (19). An illustration of typical results is given in Fig. 4.

It should be stressed once more (8, 9) that for an $O_2(^1\Delta_g)$-mediated photooxidation process, neither the reactive rate constant nor the overall rate constant provide information in themselves about the efficiency of the real photodegradation for a given substrate. The knowledge of its actual significance, as extracted from the kinetic data, is only given by the photooxidation quantum yield (Φ_r) (eq. [10]).

$$[10] \qquad \Phi_r = \Phi_\Delta k_r[DHN]/(k_d + k_r[DHN])$$

Upper limits of Φ_r values for DHN at concentration 1 mM were calculated by means of eq. [10] (they are shown in Table 1). The value $\Phi_\Delta = 1$, corresponding to an ideal photosensitizer, was employed in the calculations. In these conditions

Fig. 3. Spectral evolution of DHN in water, upon sensitized irradiation. Sensitizer: RB, $Abs_{560} = 0.5$. Numbers on the spectra indicate irradiation time (min): (*a*) 1,3-DHN; (*b*) 4,5-DHN-2,7 DS.

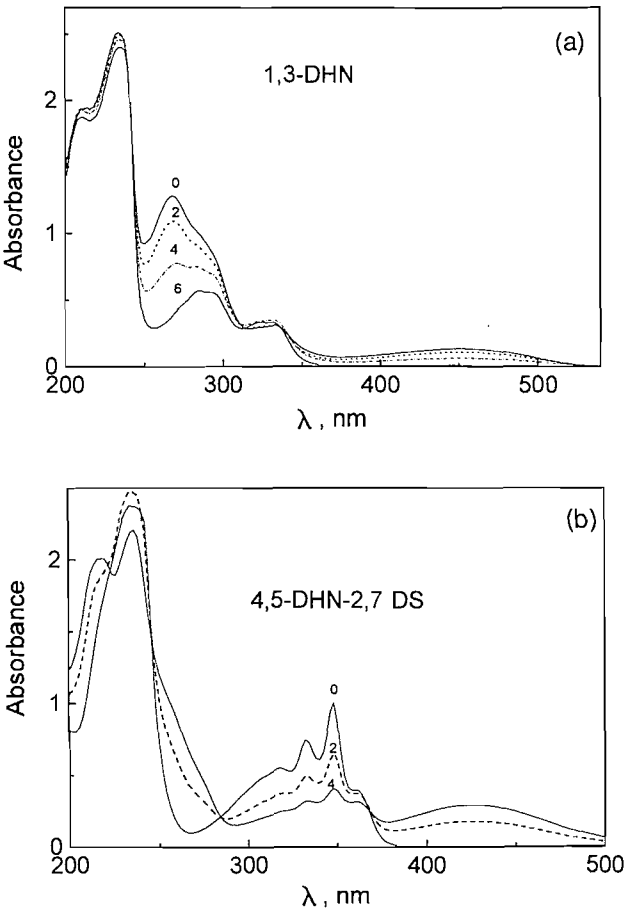

the Φ_r values indicate a moderate to high susceptibility of DHN to photosensitized degradation via an $O_2(^1\Delta_g)$-mediated process.

To evaluate the influence of the ionization of the -OH groups of DHN on the kinetics of the photooxidation process, both k_t and k_r were determined, where possible, at different pH values. Different solvent polarities were also explored. As follows from the data in Table 1, both pH and, expecially, solvent polarity affect the kinetics of the DHN–$O_2(^1\Delta_g)$ interaction. In extreme cases, differences higher than two orders of magnitude can be observed in k_t on going from water to a Tol–MeOH (4:1, *v*/*v*) mixture as solvent. Due to solubility problems in the 2,7-subsituted disulfonic acid derivatives, only the 4,5-DHN was assayed in the organic solvent mixture MeOH–Bz (10:1) (*v*/*v*). Also in this case a difference of two orders of magnitude between k_t in water and organic solvent was observed.

The ionization of the -OH groups in DHN (see Table 1) has a variable influence on the photooxidation process: depending on the particular substitution pattern the oscillations in k_t varied within a factor of ca. 8 (3,6-DHN-2,7 DS) to quasi insensitivity (4,5-DHN-2,7 DS) due to changes in the pH of the solution.

Fig. 4. First-order plots for oxygen uptake by 1,5-DHN, 2,7-DHN, and FFA (reference compound) in water. All substrates were 0.2 mM. Sensitizer: RB, Abs_{560} = 0.5.

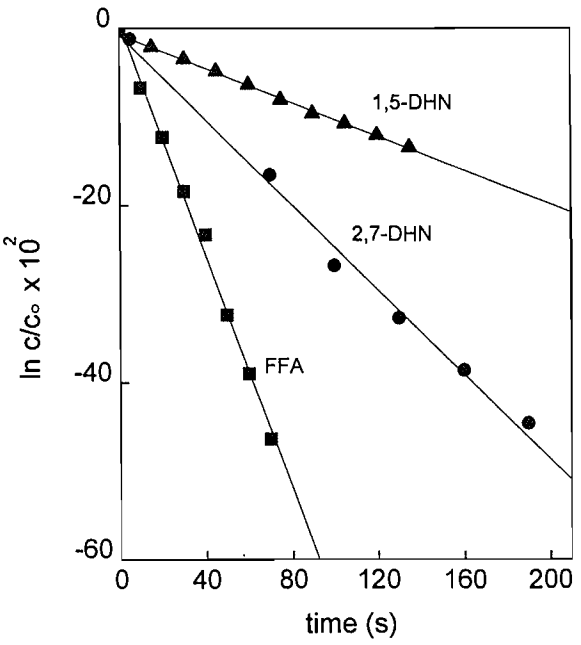

Finally, in Table 1 are listed the Φ_Δ values for the Bz-soluble DHN. This solvent was chosen in order to compare our results with the Φ_Δ values reported in the literature, for related substituted naphthalene derivatives (20).

The only published data on the $O_2(^1\Delta_g)$-mediated photooxidation of DHN belongs to Croux et al. (22). These authors reported kinetic information for a series of DHN substituted on both aromatic rings (the DHN derivatives in common with our work are 2,7 DHN and 1,5 DHN) employing methanol as a solvent. The reported k_t values varied between 53 and 2 $\times$ 10^6 M^{-1} s^{-1}, and the respective k_r values between 30 and 7 $\times$ 10^6 M^{-1} s^{-1}. The determination of photooxidation products indicates that DHN subsituted in position 1 yields a monohydroxy 1,4-naphthoquinone, whereas other DHN of the series (such as 2,6- and 2,7-DHN) react slowly with $O_2(^1\Delta_g)$ and do not give the quinone derivative (see Scheme 1).

The main conclusion is that the kinetic parameters of the reactivity of DHN with $O_2(^1\Delta_g)$ depend markedly on the substitution pattern given by the relative position of the two hydroxyl groups. Similar behaviour can be observed in our present results: 2,7-DHN and the disulfonated derivatives 3,5- and 3,6-DHN exhibit markedly lower values for the rate constants of both the overall and the reactive interactions with $O_2(^1\Delta_g)$.

Croux et al. (22) suggest that the photoreaction (Scheme 1), consisting of a concerted [2 + 4] cycloaddition reaction as an initial step, could be influenced by solvent polarity. This assumption is largely corroborated by our present results. Turning again to the data in Table 1, the strong solvent effect on k_t immediately suggests the intermediacy of a polar encounter complex $[O_2(^1\Delta_g)$–DHN]. The stabilization of the transition state by solvation could be explained by the contribution of an electron transfer component. The mechanism is schematically represented in eq. [12]:

Scheme 1.

[1] 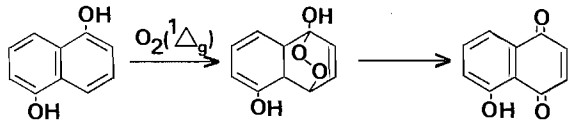

$$O_2(^1\Delta_g) + DHN \underset{k_{-D}}{\overset{k_D}{\rightleftharpoons}} [O_2(^1\Delta_g)\text{–DHN}] \xrightarrow{k_p} \text{Products}$$

[12] $\Big\downarrow k_{ISC}$

$$[O_2(^3\Sigma_g^-)\text{–DHN}] \longrightarrow O_2(^3\Sigma_g^-) + DHN$$

where k_D denotes the diffusion-dependent rate constant for the encounter pair formation. Events within the $[O_2(^1\Delta_g)$–DHN] encounter pair would subsequently result either in intersystem crossing to yield ground-state triplet oxygen or photooxidation products. This mechanism has been postulated to account for the bimolecular reactions of $O_2(^1\Delta_g)$ with indoles, amines, sulfides, phenols, and dihydroxybenzenes, among other families of compounds (4, 10, 23–26). On structural grounds, one can expect a certain similarity in the photooxidative kinetic behaviour of DHN to that of phenols and dihydroxybenzenes. For the last two families of compounds two neat characteristics for the rate constant for reaction with $O_2(^1\Delta_g)$ can be observed (9): (*a*) they are highly favoured by increasing the solvent polarity and (*b*) the k_t values for the ionized species (ionization of the -OH groups) exceed those of the non-ionized forms *at least* by one order of magnitude. As already pointed out, the first point is a common attribute for all DHN in Table 1. This fact constitutes a strong argument in favour of a charge transfer mechanism for the $O_2(^1\Delta_g)$-DHN interaction.

Regarding the ionization of the -OH groups in DHN, only for 3,5- and 3,6-DHN (disodium salts) does the pH effect on k_t parallel that reported for phenols. For the remaining DHN derivatives, k_t values are either similar or slightly lower than those for the non-ionized species. Nevertheless, the Φ_r values in aqueous alkaline solution are, without exception, much higher than those determined in any other solvent. In fact, even when in some cases the overall quenching process is more effective for the non-ionized DHN species, its low chemical reactivity largely prevails. This means that the fraction of product-yielding encounter complexes (irreversible electron transfer process) increases for the better electron-donor naphtholate species. Nevertheless, the characteristic parameter for the evaluation of the tendency to photooxidation of the DHN derivatives would be the oxidation potentials, unfortunately not available in the literature for any of these compounds.

Dihydroxynaphthalenes are excellent photosensitizers for the generation of $O_2(^1\Delta_g)$ by direct irradiation. The Φ_Δ values in Bz are in the range 0.21–0.29.

The quantum yield for singlet oxygen formation is given by the sum of contributions from oxygen quenching of the lowest singlet (S) and triplet (T) excited states of DHN.

[12] $\Phi_\Delta = \Phi_\Delta(S) + \Phi_\Delta(T)$

For air-saturated solutions (oxygen concentration in 1.91 mM Bz (27)) the contribution from the DHN excited singlet state can be neglected. Hence, the expression for the quantum yield of $O_2(^1\Delta_g)$ formation is reduced to:

[13] $$\Phi_\Delta = S_\Delta \Phi_T$$

where S_Δ represents the proportion of triplet DHN–$O_2(^3\Sigma_g^-)$ that leads to the formation of $O_2(^1\Delta_g)$ and Φ_T is the quantum yield for excited triplet state generation. On this basis, although no data have been reported on DHN excited triplet properties, our present determination of Φ_Δ constitutes an upper limit for Φ_T.

Recently McGarvey et al. (20) determined the Φ_Δ values for a series of monosubstituted naphthalenes. The efficiency of $O_2(^1\Delta_g)$ generation ranges from 0.83 for 1-nitronaphthalene to 0.34 for 1-methoxynaphthalene, Φ_Δ being 0.62 for the non-substituted hydrocarbon. These authors found an inverse correlation between the ionization potential of the sensitizer and the Φ_Δ value. Assuming that this dependency holds in the case of DHN, the lack of correlation between the estimated ionization potential and reactivity towards $O_2(^1\Delta_g)$ could be an indication, as above postulated, that the charge transfer interaction is not the only component in the photooxidative mechanism of DHN.

Concluding remarks

The strong solvent effect observed on the overall rate constant for the interaction of DHN with $O_2(^1\Delta_g)$ resembles the photooxidative kinetic behaviour of substituted phenols and dihydroxybenzenes. The interaction DHN–$O_2(^1\Delta_g)$ seems to be mainly driven by a charge transfer mediated mechanism, but in this case in conjunction with structural factors. Nevertheless, the rate constants for overall and reactive interactions do not depend on pH in the same manner as those of phenols. Even so, DHN are highly reactive towards $O_2(^1\Delta_g)$ when the -OH groups are ionized, as indicated by the Φ_r values.

Dihydroxynaphthalenes efficiently produce $O_2(^1\Delta_g)$ upon direct irradiation in Bz, with quantum yields near 0.25.

Both Φ_r and Φ_Δ values indicate that DHN-like contaminants are good candidates for an environmental $O_2(^1\Delta_g)$-mediated photooxidation. The photodegradative process is favoured in the alkaline range of pH and by solvents of high polarity.

Acknowledgements

Financial support from Consejo Nacional de Investigaciones Científicas y Técnicas (CONICET), Consejo de Investigaciones de la Provincia de Córdoba (CONICOR), and SECYT from Universidad Nacional de Río Cuarto and Universidad Nacional de La Patagonia SJB, all from Argentina, is gratefully acknowledged.

References

1. H.E. Gsponer, C.M. Previtali, and N.A. García. J. Photochem. **36**, 247 (1987).
2. H.E. Gsponer, C.M. Previtali, and N.A. García. Toxicol. Environ. Chem. **16**, 23 (1987).
3. M.C. Palumbo and N.A. García. Toxicol. Environ. Chem. **17**, 103 (1988).
4. S.G. Bertolotti, H.E. Gsponer, and N.A. García. Toxicol. Environ. Chem. **22**, 229 (1988).
5. S. Miskoski and N.A. García. Toxicol. Environ. Chem. **25**, 33 (1989).
6. M.C. Palumbo, N.A. García, M.I. Gutiérrez, and M. Luiz. Toxicol. Environ. Chem. **29**, 85 (1990).
7. M. Luiz, M.I. Gutiérrez, G. Bocco, S.G. Bertolotti, and N.A. García. Toxicol. Environ. Chem. **35**, 115 (1992).
8. N.A. García. J. Photochem. Photobiol. B: **14**, 381 (1992).
9. N.A. García. J. Photochem. Photobiol. B: **22**, 185 (1994).
10. D. Mártire, C. Evans, S. Bertolotti, S.E. Braslavsky, and N.A. García. Chemosphere, **26**, 1691 (1993).
11. D.O. Mártire, S.E. Braslavsky, and N.A. García. J. Photochem. Photobiol. A: **61**, 113 (1991).
12. V.A. Proskviriakov and A.E. Drabkin. Química del petróleo y del gas. Mir, Moscow. 1984.
13. S. Sporstol, N. Gjos, R.G. Lichtenthaler. K.O. Gustavsen, K. Urdal, and J.O.J. Skel. Environ. Sci. Technol. **17**, 282 (1983).
14. S. Miskoski and N.A. García. Photochem. Photoiol. **57**, 447 (1993).
15. D.J. Carlsson, T. Suprunchuk, and D.M. Wiles. Can. J. Chem. **52**, 3728 (1974).
16. F. Wilkinson and J.G. Brummer. J. Phys. Chem. Ref. Data, **10**, 809 (1981).
17. M.A.J. Rodgers. J. Am. Chem. Soc. **104**, 5542 (1982).
18. C.S. Foote and T.-Y. Ching. J. Am. Chem. Soc. **97**, 6209 (1975).
19. W.R. Hagg and J. Hoigné. Environ. Sci. Technol. **20**, 341 (1986).
20. D.J. McGarvey, P.G. Szekeres, and F. Wilkinson. Chem. Phys. Lett. **199**, 314 (1992).
21. C.S. Foote. Mechanisms of photooxydenation in porphyrin localization and treatment of tumors. Alan R. Liss, New York. 1984.
22. S. Croux, M.-T. Maurette, M. Hocquaux, A. Ananides, A.M. Braun, and E. Oliveros. New J. Chem. **14**, 161 (1990).
23. M.C. Palumbo, N.A. García, and G. Arguello. J. Photochem. Photobiol. B: **7**, 33 (1990).
24. C.S. Foote, R.W. Denny, L. Weaver, Y. Chang, and J. Peters. Ann. N.Y. Acad. Sci. **171**, 139 (1970).
25. H. Young, R.L. Martin, D. Feriozzi, D. Brewer, and R. Kayser. Photochem. Photobiol. **17**, 233 (1973).
26. A. Tine and J.J. Aaron. Can. J. Spectrosc. **29**, 121 (1984).
27. S.L. Murov. Handbook of photochemistry. M. Dekker, New York. 1973.

Electrochemically induced chain reactions: the addition of fluorene and indene to aromatic aldehydes initiated by electrochemical reduction

J.C. Gard, B. Hanquet, L. Roullier, Y. Mugnier, and J. Lessard

Abstract: The electrochemical reduction at −30°C of 2,6-dichlorobenzaldehyde (**1***a*), benzaldehyde (**1***b*), and terephthalaldehyde (**2**) in tetrahydrofuran with tetrabutylammonium perchlorate as supporting electrolyte, under an argon atmosphere and in the presence of fluorene or indene, gives carbinols resulting from the addition of fluorene or indene and requires only a catalytic amount of electricity. The chain reaction is initiated by proton abstraction from fluorene or indene by a base electrogenerated by reduction of the aldehyde and the propagation involves the addition of the carbanion to the aldehyde followed by regeneration of the nucleophile by proton transfer from the proton donor to the alkoxide anion (base-catalyzed addition). The voltammetric behavior of the aldehydes in the absence and in the presence of fluorene or indene is also presented.

Key words: electrochemical reduction, aromatic aldehydes, addition of fluorene (indene), base catalysis, chain reaction.

Résumé : La réduction électrochimique à −30°C des 2,6-dichlorobenzaldehyde (**1***a*), benzaldehyde (**1***b*) et terephtalaldehyde (**2**) dans le tetrahydrofurane contenant du perchlorate de tetrabutylammonium comme électrolyte support, sous atmosphère d'argon et en présence de fluorène ou d'indène, donne des carbinols provenant de l'addition basique du fluorène ou de l'indène et ne nécessite qu'une quantité catalytique d'électrons. La réaction en chaîne est initiée par l'arrachement d'un proton du fluorène ou de l'indène par une base électrogénérée par réduction de l'aldéhyde et les étapes de propagation sont l'addition du carbanion à l'aldéhyde suivie de la regénération du nucléophile par transfert de proton du donneur de proton à l'ion alkoxyde. Le comportement en voltamétrie des aldéhydes, en absence et en présence du fluorène ou d'indène, est également discuté.

Mots clés : réduction électrochimique, aldéhydes aromatiques, addition du fluorène (indene), catalyse basique, réaction en chaîne.

Introduction

Studies on electrochemically induced chain reactions have received considerable attention. Some representative examples are as follows: $S_{RN}1$ aromatic substitutions initiated by the electroreduction of an aryl halide (1), *cis–trans* isomerization of functionalized olefins (2), oxidation of alcoholates to aldehydes and ketones by aryl halides (3), electrooxidative initiation of triphenyltin hydride promoted radical reactions (4), ligand substitution of organometallic complexes (5), addition of chloroform to aldehydes (6), Michael reactions (7), and addition of fluorene and indene to nitrosobenzene (8). In the last two examples, the initiation step involves the generation of the nucleophile by hydrogen abstraction from a proton donor by a base generated by electroreduction of the electrophile or acceptor.

Received May 23, 1995.

J.C. Gard, B. Hanquet, L. Roullier and Y. Mugnier.[1] Laboratoire de synthèse et d'électrosynthèse organométalliques, associé au Centre national de la recherche scientifique (Unité de recherche associé n° 1685), Faculté des sciences, 6 Boulevard Gabriel, 2100 Dijon, France.
J. Lessard.[1] Laboratoire d'électrochimie et d'électrocatalyse, Département de chimie, Université de Sherbrooke, Sherbrooke, QC J1K 2R1, Canada.

[1] Authors to whom correspondence may be addressed. For J. Lessard, telephone: (819) 821-7091. Fax: (819) 821-8017.

In this paper, we present a new example of a chain process involving the addition of a nucleophile initiated by electrochemical reduction of the electrophile: the reaction between a proton donor such as fluorene (FlH_2) or indene (InH_2) and an aromatic aldehyde (ArCHO), induced by the electroreduction of the latter in tetrahydrofuran (THF) with n-Bu_4NClO_4 as the supporting electrolyte. We describe the results with 2,6-dichlorobenzaldehyde (**1***a*),[2] benzaldehyde (**1***b*), and terephthalaldehyde (**2**).

Results and discussion

Voltammetric reduction

The cyclic voltammogram of 2,6-dichlorobenzaldehyde (**1***a*) at −30°C in THF containing $(n\text{-Bu})_4NClO_4$ as supporting electrolyte and on a vitreous carbon electrode (Figs. 1a and 2a) shows two reduction peaks A_1 ($E_p = -1.55$ V vs. SCE) and A_2 ($E_p = -1.70$ V), and several oxidation peaks. In the presence of FlH_2 (Figs. 1b–1d) or InH_2 (Figs. 2b–2d), the voltammogram at the same sweep rate is modified: both peaks A_1 and A_2 decrease, and peak A_2 more so than peak A_1. With two to three equivalents of proton donor AH_2 (Figs. 1c and 2c), peak A_2 has disappeared. For peak A_1, the rapid drop of the current after the peak potential, resulting in a sharp, narrow, and symmetric peak (Figs. 1b–1d and Figs. 2b and 2c), is characteristic

[2] Preliminary results on the electroreduction of **1***a* in the presence of fluorene have been reported (9).

Fig. 1. Cyclic voltammogram of 2,6 dichlorobenzaldehyde (**1***a*) on a vitreous carbon electrode in THF–$(n\text{-Bu})_4NClO_4$ (0.2 M) at −30°C: (a) **1***a* alone; (b), (c), and (d), in the presence of 1, 2, and 10 equivalents of FlH_2 respectively. Starting potential: +0.3 V. Sweep rate: 0.02 V s^{-1}.

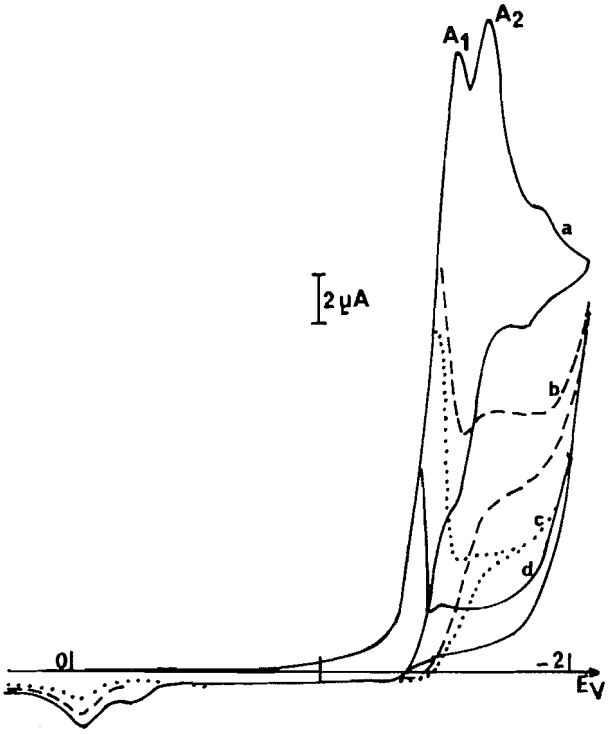

Fig. 2. Cyclic voltammogram of 2,6 dichlorobenzaldehyde (**1***a*) on a vitreous carbon electrode in THF–$(n\text{-Bu})_4NClO_4$ (0.2 M) at −30°C: (a) **1***a* alone; (b), (c), in the presence of 1, and 10 equivalents of InH_2, respectively. Starting potential: +1 V. Sweep rate: 0.02 V s^{-1}.

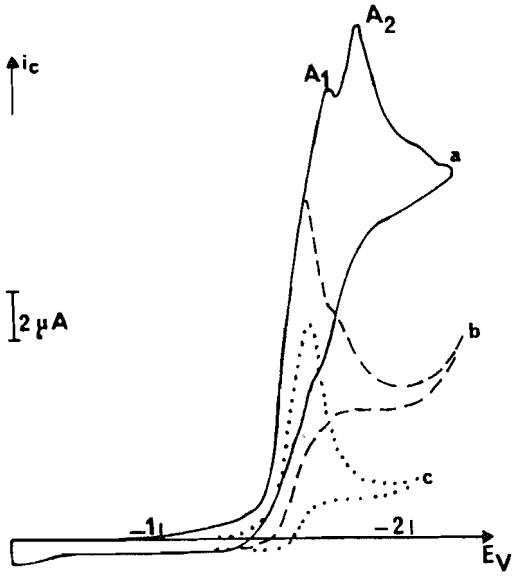

of a catalytic reaction occurring outside the diffusion layer (8, 10). This is further confirmed (*i*) by the fact that when the sweep rate is decreased, peak A_1 becomes smaller, and (*ii*) by the consumption of a catalytic amount of electrons in the controlled potential electrolysis performed on mercury, at −30°C,

Fig. 3. Cyclic voltammogram of benzaldehyde (**1***b*) on a vitreous carbon electrode in THF–$(n\text{-Bu})_4NClO_4$ (0.2 M) at −30°C: (a) **1***b* alone; (b) in the presence of 10 equivalents of FlH_2. Starting potential: −1 V. Sweep rate: 0.02 V s^{-1}.

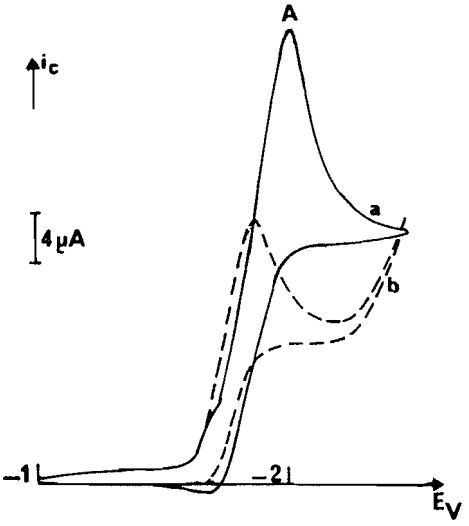

at the potential of peak A_1 and in the presence of 10 equivalents of AH_2 (ca. 0.03 and 0.02 mole of electrons per mole of **1***a* for FlH_2 and InH_2, respectively, see below). The voltammetric behavior of benzaldehyde (**1***b*) in the presence of proton donor AH_2 is similar to that of **1***a* as shown by the cyclic voltammograms of Fig. 3: a decrease of peak A (E_p = −2.0 V vs. SCE) and a change of its morphology in the presence of 10 equivalents of FlH_2 (Fig. 3b), characteristic of a catalytic process. And indeed, the electrolysis of **1***b* at −30°C, on mercury, in the presence of 20 equivalents of FlH_2 and at the potential of peak A, also consumed a catalytic amount of electron (ca. 0.25 and 0.2 mole of electrons per mole of **1***b* for FlH_2 and InH_2, respectively, see below). Peak A_1 in the cyclic voltammogram of 2,6-dichlorobenzaldehyde (**1***a*) (Figs. 1a and 2a) and peak A in the voltammogram of benzaldehyde (**1***b*) correspond to the reduction of the aromatic aldehyde to the radical anion (eq. [1]). This electrogenerated base, in the presence of proton donor AH_2, abstracts a proton from it to form the anion AH^- and a neutral radical (eq. [2]). The latter probably disappears in subsequent fast reactions. Reactions [1] and [2] constitute the initiation step of a chain reaction involving, as propagation steps, the nucleophilic addition of AH^- to the carbonyl (eq. [3]) followed by protonation of the resulting anions (bases) by AH_2 (eq. [4]) to regenerate the nucleophile AH^- and give a carbinol that has been isolated from the preparative electrolyses (see below). In the case of **1***a*, the radical anion can be converted to 2-chlorobenzaldehyde (see eqs. [5] and [6]), which is most probably responsible for peak A_2 (eq. [7]) in the voltammograms of **1***a* (Figs. 1 and 2). In the presence of AH_2, the elimination of chloride ion from **1***a* (eq. [5]) competes with its protonation (eq. [2]), leading to the chain process (eqs. [3] and [4]) outside the diffusion layer, and the formation of 2-chlorobenzaldehyde is completely suppressed with two (FlH_2) to three (InH_2) equivalents of proton donor (see Figs. 1c and 2c).

The voltammogram of terephthalaldehyde (**2**) (Fig. 4), recorded under the same conditions as those of **1***a* and **1***b*, differs from the latter in showing two redox systems, giving rise to peaks A/A′ and B/B′ that correspond to the formation of the

[1] $ArCHO + e^- \longrightarrow [ArCHO]^{\cdot -}$

peak A_1 (Figs. 1 and 2), peak A (Fig. 3)

[2] $[ArCHO]^{\cdot -} + AH_2 \longrightarrow [ArC\dot{H}OH] + AH^-$

[3] $ArCHO + AH^- \longrightarrow [ArCH(O^-)AH] \rightleftharpoons [ArCH(OH)A^-]$

[4] $[ArCH(OH)A^-] + AH_2 \longrightarrow ArCH(OH)AH + AH^-$

[5] 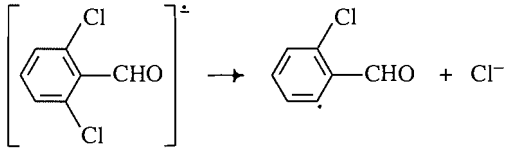

[6] 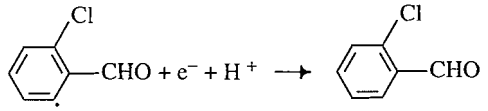

[7] 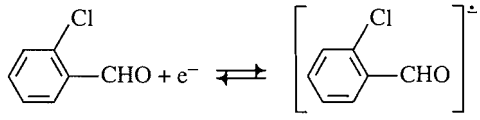

peak A_2 (Figs. 1a and 2a)

Fig. 4. Cyclic voltammogram of terephthaladehyde (**2**) on a vitreous carbon electrode in THF–$(n\text{-Bu})_4NClO_4$ (0.2 M) at −30°C: (a) **2** alone; (b) and (c) in the presence of 5 and 20 equivalents of InH_2, respectively. Starting potential: 0 V. Sweep rate: 0.02 V s^{-1}.

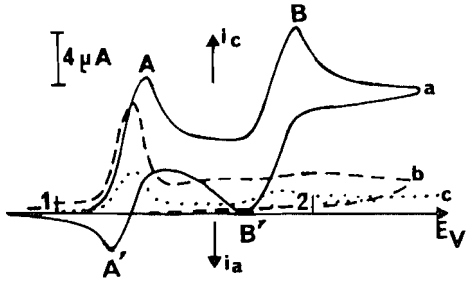

radical anion (eq. [8]) and the dianion (eq. [9]), respectively. In the presence of a proton donor (InH_2, Figs. 4b and 4f), the radical anion is protonated, the oxidation peak A′ and the system B/B′ disappear accordingly, and the reduction peak A behaves as peak A_1 in the voltammogram of **1***a* (see Figs. 1b–1d) and peak A in the voltammogram of **1***b* (see Figs. 1b and 2c): its height decreases with the concentration of AH_2 and its shape is characteristic of a catalytic reduction (see eqs. [1]–[4]). The same behavior was observed with FlH_2 as proton donor. And indeed, the controlled potential electrolysis of **2** at −30°C, on mercury, in the presence of 20 equivalents of FlH_2 and at the potential of peak A (−1.2 V) consumed 0.06–0.12 mole of electrons per mole of **2** and gave products resulting from the addition of FlH_2 to the carbonyl group (see below).

Controlled potential electroreductions

The controlled potential reductions of aldehydes **1***a*, **1***b*, and **2** were carried out at −30°C, on a mercury pool electrode, in

[8] 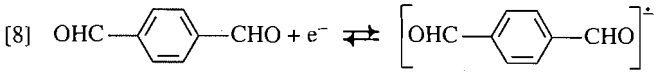

System A/A′

[9] 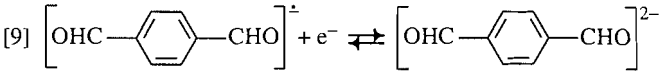

System B/B′

THF–$(n\text{-Bu})_4NClO_4$ (0.2 M), in the presence of an excess (10–20 equivalents) of proton donor (AH_2), under an atmosphere of argon and at a potential corresponding to the formation of the radical anion (peak A_1 in Figs. 1 and 2, peak A in Figs. 3 and 4). The solution became colored (see Table 1) and, after the current had dropped to zero, there was no reduction peak in the voltammogram of the electrolyzed solution from 0 to −1.8 V.[3] The electrolyzed solution was extracted after the current dropped to zero. The results are reported in Table 1. In the case of 2,6-dichlorobenzaldehyde (**1***a*) (Table 1, entries 1 and 2), the carbinols **3** (Scheme 1) were isolated in very good to excellent yields (74–93%). As already mentioned, the carbinols result from the nucleophilic addition of AH^- to the aldehyde (eq. [3]) followed by protonation of the resulting anion by AH_2 regenerating AH^- (eq. [4]), the chain process being initiated by the electrochemical generation of AH^- (eqs. [1] and [2]). In the case of benzaldehyde (**1***b*) (entries 3 and 4), the yields of isolated carbinols were much lower (14–28%) and the number of moles of electrons per mole of aldehyde consumed was larger (ca. 0.2 for **1***b* as compared to ca. 0.02 for **1***a*). The yields reflect the higher reactivity of **1***a* compared to that of **1***b* (fewer side products such as glycols and alcohols formed in the case of **1***a*), most probably due to the electron-withdrawing effect of the two chlorine atoms at the *ortho* positions of the carbonyl group in **1***a*.

With terephthalaldehyde (**2**) and fluorene (Table 1, entry 5), dehydration of the carbinol **4** occurred to a small extent during the electrolysis and (or) during the work-up to give the alkene **6** (1%) (Scheme 2). The total yield of isolated addition products was 33%. The controlled potential electrolysis in the presence of InH_2 was not performed because of the large number of isomeric carbinols possible.

It has long been known that FlH_2 can be added to aldehydes, mainly aromatic aldehydes, in the presence of a basic catalyst (e.g., potassium hydroxide) in refluxing ethanol to form dibenzofulvenes (11). By carrying out the reaction between FlH_2 and benzaldehyde (**1***b*), at room temperature and in sodium ethoxide – ethanol, the carbinol **3***b*$_1$ was isolated in a 23% yield (12). A dibenzofulvene was obtained in a 45% yield by reaction of benzaldehyde (**1***b*) with InH_2 in refluxing methanolic potassium hydroxide (13). Both FlH_2 and InH_2 were condensed with benzaldehyde (**1***b*) using $KF–Al_2O_3$ as the basic catalyst at room temperature (14). With FlH_2, a mixture of carbinol **3***b*$_1$ (32%) and a dibenzofulvene (63%) was obtained (14). With InH_2, a benzofulvene (66%) was isolated together with a product (14%) resulting from the addition of the 3-(α-hydroxyphenyl)-indene to another molecule of benzaldehyde followed by loss of one molecule of water (14). The complex $(InH)_2\,Ca{\cdot}NH_3{\cdot}THF$ was reported to react with ben-

[3] There was no reaction between FlH_2 and InH_2 and any of the aldehydes in the absence of an electron source (no potential applied).

Table 1. Controlled potential electroreduction of aromatic aldehydes (ArCHO) in the presence of fluorene (FlH_2) or indene (InH_2) as proton donor (AH_2) on a mercury electrode in THF–$(n\text{-}Bu)_4ClO_4$ (0.2 M) at –30°C followed by immediate extraction.[a]

Entry	ArCHO	E_w[b] (V)	AH_2	AH_2/ArCHO (molar ratio)	Mol of e^-/mol of ArCHO ($\times 10^3$)	Solution color	Carbinol(s)	Yield[c] (%)
1	**1***a*	–1.5	FlH_2	10	27	Pink	**3***a*$_1$	93
2	**1***a*	–1.6	InH_2	10	15	Orange-yellow	**3***a*$_2$	74[d]
3	**1***b*	–1.9	FlH_2	20	250	Red	**3***b*$_1$	28
4	**1***b*	–2.0	InH_2	20	200	Green	**3***b*$_2$	14[e]
5	**2**	–1.2	FlH_2	20	80	Orange-yellow	**4**	12[f]
							5	21

[a]The electrolyses were carried out under an argon atmosphere and the electrolyzed solution was extracted immediatedly after the current dropped to zero.
[b]Working potential vs. SCE.
[c]Yield of homogeneous compounds after chromatographic separation and extraction.
[d]The two diastereoisomers *RR* + *SS* and *RS* + *SR* were separated and isolated in 47% and 27% yield, respectively.
[e]Only the *RS* + *SR* diastereoisomer was isolated.
[f]Alkene **6** resulting from dehydration of **4** was isolated in small amounts (yield <1%).

Scheme 1.

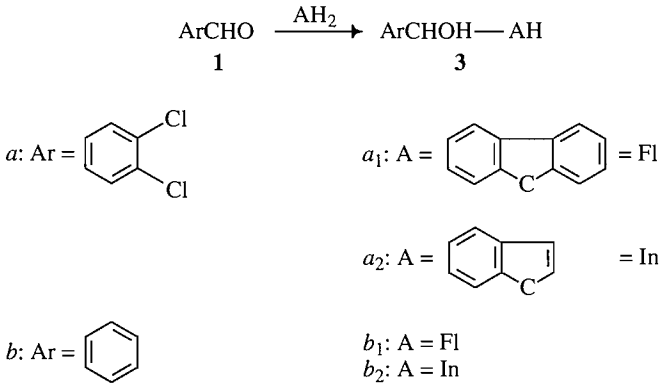

Scheme 2.

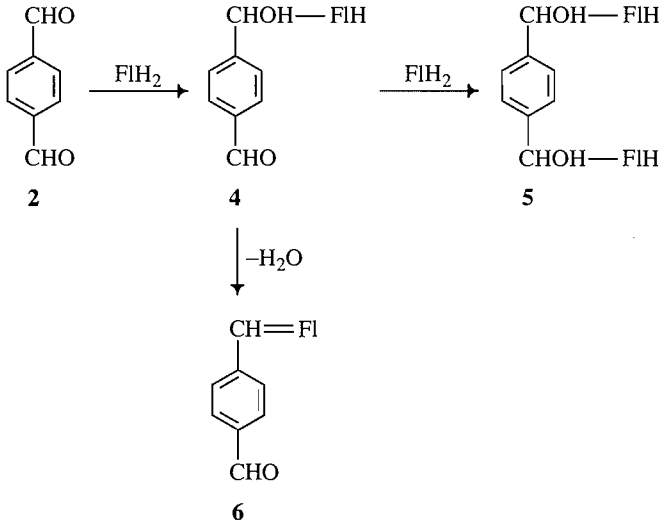

zaldehyde (15) in liquid ammonia to give the carbinol **3***b*$_2$ in a 50–55% yield (16). The reaction of terephthalaldehyde (**2**) with excess FlH_2 in ethanol, with sodium ethoxide as the base and at 60–70°C, was reported to afford a di-(dibenzofulvene) in an 11% yield (15). Finally, Ghera and Spinsak (11) observed that the condensation of FlH_2 and InH_2 with aliphatic aldehydes in pyridine at 0°C, using benzyltrimethylammonium hydroxide (Triton B) as base, gave the corresponding carbinols in substantial yields. At 25°C, in the same medium, the 9-(α-hydroxylalkyl)-fluorenes underwent dehydration to the corresponding bibenzofulvenes, which, in the presence of

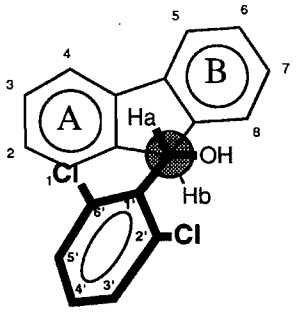

3*a*$_1$

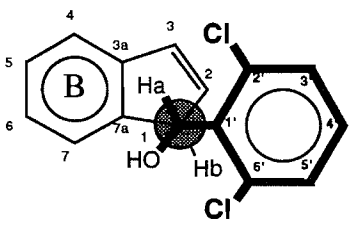

3*a*$_2$ (*RR* + *SS*)

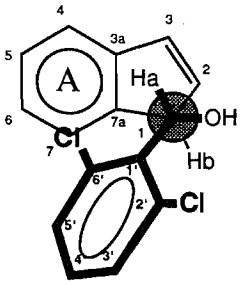

3*a*$_2$ (*RS* + *SR*)

Table 2. Mass spectral data.

Product	Molecular ion peak *m/z* (relative intensity, %)	Other peaks *m/z* (relative intensity, %)					
$3a_1$	340 (5.7)	322 (57) $-H_2O$	286 (10.7) –HCl	252 (15) –Cl	175 (65.7) $C_6H_3Cl_2CHOH$	165 (100) FlH	
$3a_2$ (*RR* + *SS*)	290 (25)	202 (29.3) –2Cl, $-H_2O$	175 (91.4) $C_6H_3Cl_2CHOH$	116 (100) InH_2			
$3a_2$ (*RS* + *SR*)	290 (34.3)	273 (35) –OH	238 (27.1) –Cl	202 (40) –HCl	175 (87.1) $C_6H_3C_{12}CHOH$	115 (100) InH	
$3b_1$	272 (1.3)	254 (12.8) $-H_{20}$	166 (100) FlH_2	107 (81.5) C_6H_5CHOH			
$3b_2$ (*RS* + *SR*)	222 (65.7)	204 (45.7) $-H_2O$	116 (92.1) InH_2	107 (100) C_6H_5CHOH	105 (98.6)?		
4	300 (31.4)	282 (7.8) $-H_2O$	253 (11.4) –CHO	165 (100) FlH	135 (65.7) $CHOC_6H_4CHOH$	105 (22.8) $CHOC_6H_4$	
5	466 (0.11)	448 (0.43) $-H_2O$	430 (20) $-H_2O$	301 (43.6) Fl(CHOH) $C_6H_4(CHOH)$	282 (45.7) Fl=C(OH) C_6H_4CH	252 (51.4) $FlC(C_6H_4)$	165 (100) FlH
6	282 (95.7)	253 (100) –CHO	126 (58.6) ?	113 (23.6) ?			

Table 3. Eluents for chromatographic separation, solvents for recrystallization, melting points, and microanalytical data.

Product	Chromatography eluent	Recrystallization solvent	Melting point (°C)	Molecular formula	Microanalytical data C (%) Calcd.	C (%) Found	H (%) Calcd.	H (%) Found	Cl (%) Calcd.	Cl (%) Found
$3a_1$	1: Ether, 4: hexane	Hexane	110	$C_{20}H_{14}Cl_2O$	70.40	70.42	4.14	4.20	20.78	21.26
$3a_2$ (*RR* + *SS*)	1: Ether, 4: hexane		Oil	$C_{16}H_{12}Cl_2O$						
$3a_2$ (*RS* + *SR*)	1: Ether, 4: hexane	Pentane	98	$C_{16}H_{12}Cl_2O$	66.00	65.44	4.15	4.71	24.35	22.63
$3b_1$	1: Ether 4: hexane	EtOH	119 (lit. (12) 121–122)	$C_{20}H_{16}O$						
$3b_2$ (*RS* + *SR*)	1: Ether, 4: hexane	Heptane	132 (lit. (16) 135)	$C_{16}H_{14}O$						
4	2: Ether, 3: pentane	2: Ether, 3: hexane	126	$C_{21}H_{16}O_2$	83.98	83.69	5.37	5.39		
5	3: Ether 7: hexane	$CHCl_3$	>266	$C_{34}H_{26}O_2$	87.52	84.71	5.62	5.50		
6	Hexane	Hexane	Oil	$C_{21}H_{14}O$	89.34	87.24	5.00	4.99		

an excess of FlH_2, afforded the corresponding 1,1-bis-(9-fluorenyl)-alkanes (11).

Structure of products

All compounds were characterized by mass spectrometry (Table 2). The crystalline compounds $3b_1$ and $3b_2$ are known and had melting points close to those reported in the literature (Table 3). Microanalytical data were obtained for all new crystalline compounds (Table 3). The structure of alcohol $3a_1$ was determined by ^1H and ^{13}C NMR spectroscopy and that of alcohols $3a_2$ by ^1H NMR spectroscopy. They are shown below.

The complete attribution of the protons of $3a_1$ was made

Fig. 5. (^{1}H–^{1}H) COSY spectrum of alcohol $3a_1$.

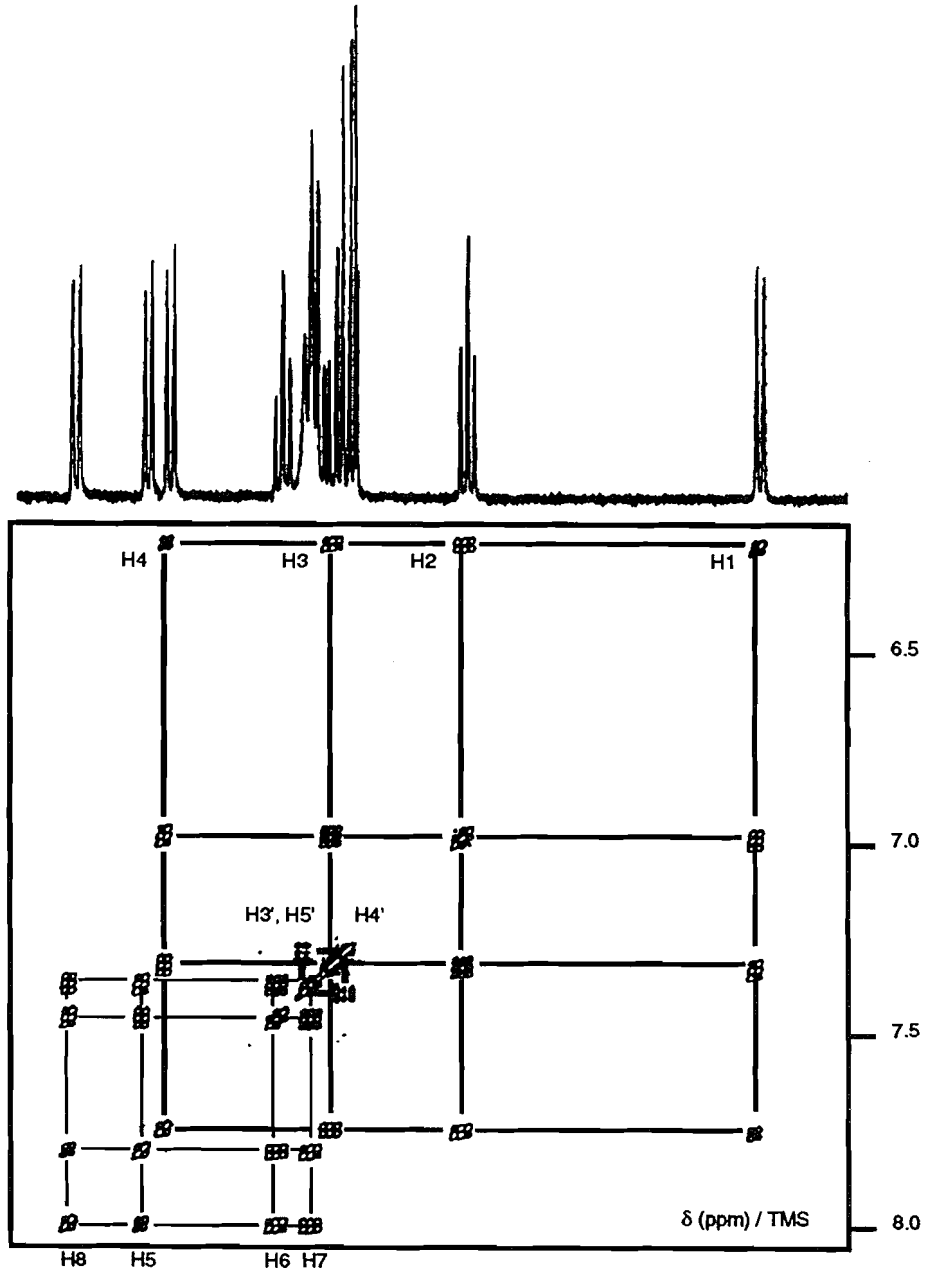

using COSY and NOE differential spectroscopy. Alcohol $3a_1$ exhibits a (^{1}H–^{1}H) COSY spectrum (Fig. 5) with three sets of protons. The first and the second set (four protons each) concern the fluorene backbone and the third set (three protons), the aryl group. Protons H3′ and H5′ and H4′ appear, respectively, as a broad doublet centered at 7.38 ppm and as a sharp triplet (7.27 ppm). This result indicates a restricted motion around the C1′—C4′ axis. Assignment of proton H8 is given by the NOE enhancement observed on this proton by presaturation of the OH. Consequently the set H8, H7, H6, and H5 (ring B) is easily deduced. It should be noticed that the chemical shifts observed for these protons are very similar whereas the important chemical shift difference for the second set of four protons (H1–H4) (ring A) indicates a preferred conformation of the dichlorophenyl ring almost perpendicular to the fluorene moiety, leaving H1 *inside* the shielding cone, hence the assignments of H1, H2, H3, and H4. The {^{1}H}–^{13}C NMR spectrum displays 18 individual resonances for the 20 carbon atoms (C2′, C6′ and C3′ and C5′ are broad resonances). The final attribution is made using the (^{1}H–^{13}C) COSY spectrum (see Fig. 6). The ^{1}H and ^{13}C NMR data parameters are given in the experimental part.

The stereochemistry of the two diastereoisomeric alcohols $3a_2$ (*RR* + *SS*) and $3a_2$ (*RS* + *SR*) was proven by NMR spectroscopy experiments, including homonuclear COSY and NOE differential spectroscopy. From comparison of the normal proton spectra of the two alcohols, it appears that the coupling constants between H_a and H_b are very similar (9.3 and 10.5 Hz), indicating an antiperiplanar orientation of the H_a-C-C-H_b system in both alcohols. The NMR spectra of Fig. 7

Fig. 6. (^{1}H–^{13}H) COSY spectrum of alcohol $3a_1$.

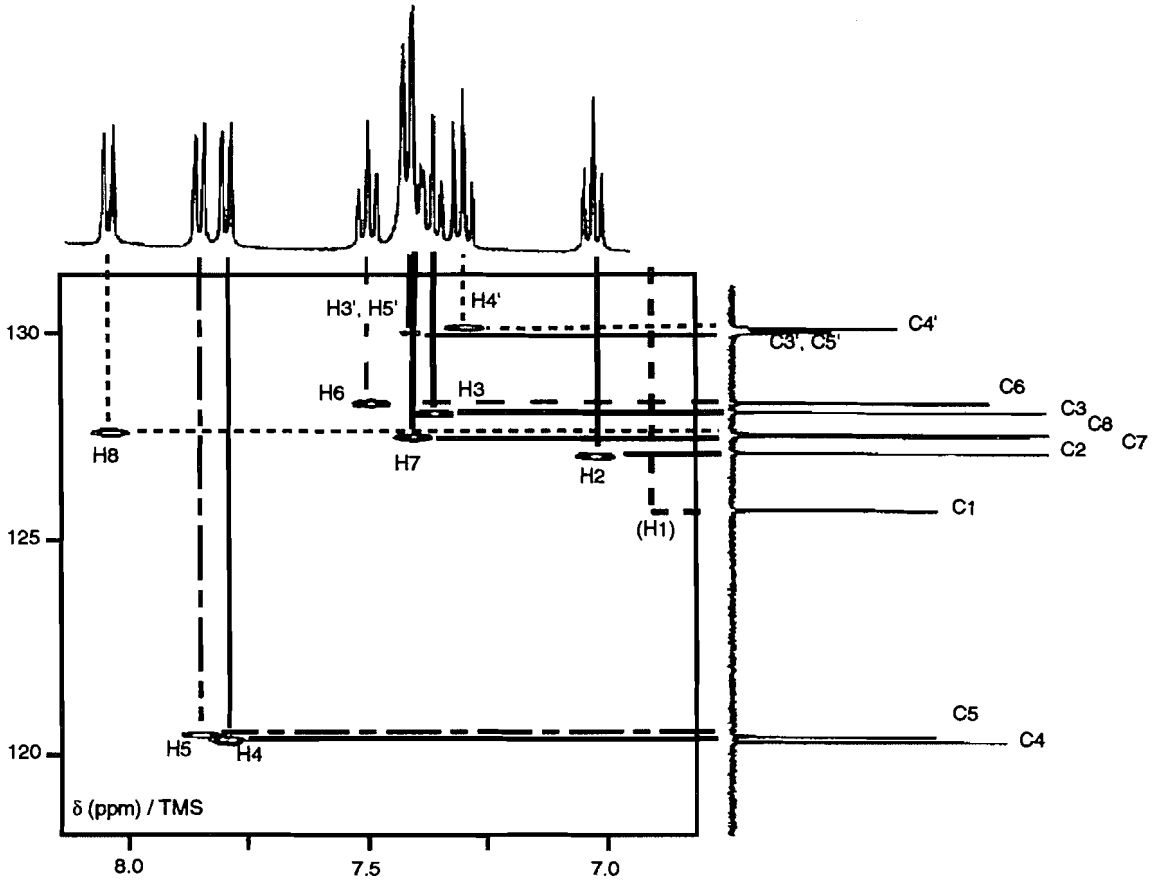

Fig. 7. ^{1}H NMR spectra of $3a_2$ (*RR* + *SS*) and $3a_2$ (*RS* + *SR*).

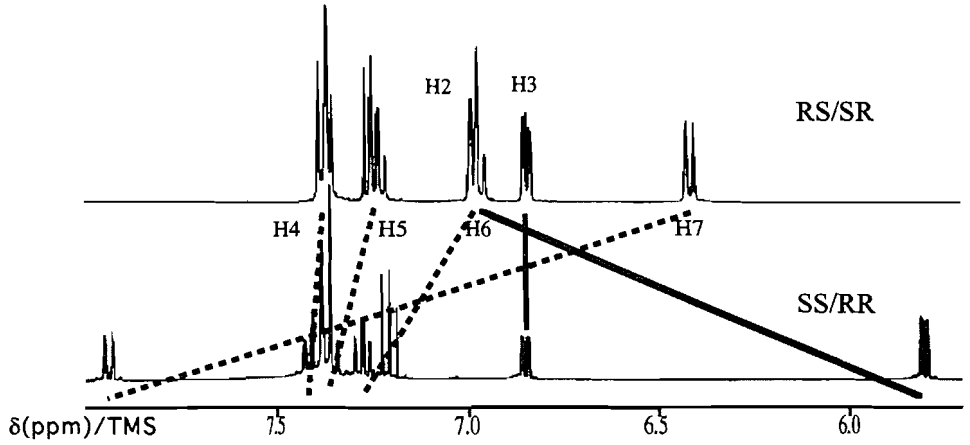

show clearly that the dichlorophenyl ring has a different position in the diastereoisomeric alcohols, as illustrated in the structures. The protons on the benzene ring B of the *RR* + *SS* diastereoisomer are in a location analogous to those of the protons of the ring B of alcohol $3a_1$ and the protons of ring A of the *RS* + *SR* diastereoisomer are in a similar location to those of ring A of alcohol $3a_1$. Indeed, proton H2 of the *RR* + *SS*, being in the shielding cone of the dichlorophenyl group, is strongly shielded with respect to proton H2 of the *RS* + *SR* isomer (Fig. 7). For the same reason, protons H7 and H6 of the *RS* + *SR* isomer are shielded with respect to these same protons of the *RR* + *SS* isomer (Fig. 7) but the shielding is smaller for proton H6 because it is further away from the dichlorophenyl group in the *RS* + *SR* isomer. Thus, the stereochemistry *RR* + *SS* and *RS* + *SR* was attributed respectively to the major (47%) and minor (27%) diastereoisomer of alcohol $3a_2$. The chemical shifts and coupling constants for alcohols $3a_2$ (*RR* + *SS*) and $3a_2$ (*RS* + *SR*) are given in the experimental part. Interest-

ingly, carbinol $3a_2$ exists as the α form. No sigmatropic rearrangement (17, 18) or base-catalyzed rearrangement (19) to the γ-form was observed (eq. [10]).

[10] 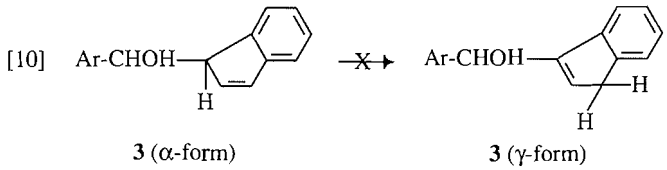

3 (α-form) 3 (γ-form)

Experimental part

Reagents

Tetrahydrofuran was purified by distillation under argon from sodium benzophenone ketyl. The supporting electrolyte was tetrabutylammonium perchlorate (0.2 M) in all cases. Fluorene, indene, 2,6 dichlorobenzaldehyde (**1***a*), benzaldehyde (**1***b*), and terephthalaldehyde (**2**) were all commercial products.

Apparatus and general procedures

All experiments were carried out under an argon atmosphere. In voltammetry, the working electrode was a vitreous carbon disc (diameter 1.2 mm) and, for the controlled potential electrolyses, a mercury electrode. In all cases, the reference electrode was a saturated calomel electrode (SCE) separated from the solution by a sintered glass disc. The auxiliary electrode was a platinum wire. All reagents in solution in THF were added, with a syringe previously purged with argon, to the THF–$(n\text{-Bu})_4NClO_4$ solution in the cell. The cyclic voltammetry experiments were conducted with a Tacussel PJT 24-1 potentiostat. The controlled potential electrolyses were carried out with an Amel 552 potentiostat equipped with a Tacussel IG5 integrator. For the experiments carried out at −30°C, the cell was placed in a cooling bath (acetone – liquid nitrogen). Melting points were determined on a Kofler apparatus and are uncorrected. The ^1H (400 MHz) and ^{13}C (100 MHz) NMR spectra were recorded from $CDCl_3$ solutions on a WM400 Bruker NMR spectrometer at the CSMUB (Centre de spectrométrie moléculaire de l'Université de Bourgogne). The chemical shifts (δ) are given in ppm (downfield from TMS) and the coupling constants (*J*) in hertz. The multiplicities are as follows: s, singlet; d, doublet; t, triplet. Mass spectra were taken on Kratos Concepts spectrometer. Silica gel Merck (280–400 mesh) was used for flash column chromatography and silica gel Merck BOF_{254} for thin-layer chromatography. Eluents for chromatographic separation, solvents for recrystallization, melting points, and microanalytical data are recorded in Table 3. The mass spectral and microanalytical data are given in Tables 2 and 3, respectively.

Typical electrolysis procedure

2,6-Dichlorobenzaldehyde (**1***a*) (152.7 mg, 0.87 mmol) was electrolyzed on a mercury electrode at −1.6 V vs. SCE with indene (1 mL, 10 mmol) at −30°C in THF (20 mL) containing $(n\text{-Bu})_4NClO_4$ (0.2 M). The electrolysis was stopped when the current dropped to zero (0.0015 electron per molecule of **1***a*). The orange-yellow solution was immediately poured into water and extracted with ether. Chromatography on silica gel with hexane–ether (4:1) as eluent gave two diastereoisomeric 3-[α-hydroxy-(2′,6′-dichloro-phenyl)]-indenes ($3a_2$). The less polar *RR* + *SS* isomer was isolated as an oil (119 mg, 47%). The more polar *RS* + *SR* isomer was recrystallized from pentane, mp 98°C (68 mg, 27%).

NMR spectral data

Carbinol $3a_1$: ^1H NMR δ ($CDCl_3$): 3.28 (s, 1H, *OH*), 4.87 (d, *J* = 9.8 Hz, 1H, *H9*), 5.08 (d, *J* = 9.8 Hz, 1H, H_a), 6.19 (ddd, *J* = 7.6, 1.8, and 0.8 Hz, 1H, *H1*), 6.96 (ddd, *J* = 7.6, 7.6, and 1.2 Hz, 1H, *H2*), 7.27 (t, *J* = 8.0 Hz, 1H, *H4′*), 7.30 (ddd, *J* = 1.8, 7.6, and 7.6 Hz, 1H, *H3*), 7.35 (ddd, *J* = 1.7, 7.5, and 7.5 Hz, 1H, *H7*), 7.37 (d, *J* = 8.0 Hz, 2H, *H3′*), 7.44 (ddd, *J* = 7.5, 7.5, and 1.2 Hz, 1H, *H6*), 7.74 (ddd, *J* = 0.8, 1.2, and 7.6 Hz, 1H, *H4*), 7.79 (ddd, *J* = 7.5, 1.7, and 0.8 Hz, 1H, *H5*), 7.98 (ddd, *J* = 0.8, 1.2, and 7.5 Hz, 1H, *H8*). ^{13}C NMR δ ($CDCl_3$): 52.14 (d, 1C, *C9*), 75.19 (d, 1C, C_a), 120.34 (d, 1C, *C4*), 120.45 (d, 1C, *C5*), 125.71 (d, 1C, *C1*), 127.12 (d, 1C, *C2*), 127.52 (d, 1C, *C7*), 127.59 (d, 1C, *C8*), 128.11 (d, 1C, *C3*), 128.33 (d, 1C, *C6*), 130.04 (d, 2C, *C3′* and *C5′*), 130.12 (d, 1C, *C4′*), 136.14 (s, 2C, *C2′* and *C6′*), 137.43 (s, 1C, *C1′*), 141.83 (s, 1C, *C5a*), 142.45 (s, 1C, *C9a*), 142.49 (s, 1C, *C4a*), 146.12 (s, 1C, *C8a*).
Carbinol $3a_2$ (RR + SS): ^1H NMR δ ($CDCl_3$): 3.41 (s, 1H, *OH*), 4.50 (d, *J* = 10.4 Hz, 1H, H_b), 5.02 (d, *J* = 10.4 Hz, 1H, H_a), 5.79 (dd, *J* = 2.0 and 5.6 Hz, 1H, *H2*), 6.85 (dd, *J* = 2.0 and 5.6 Hz, 1H, *H3*), 7.20 (t, *J* = 8.0 Hz, 1H, *H4′*), 7.25 (dt, *J* = 1.3 and 7.4 Hz, 1H, *H6*), 7.36 (dd, *J* = 8.0 and 8.0 Hz, 1H, *H5*), 7.36 (d, *J* = 8.0 Hz, 2H, *H3′* and *H5′*), 7.41 (d, *J* = 7.3 Hz, 1H, *H4*), 7.94 (d, *J* = 7.4 Hz, 1H, *H7*).
Carbinol $3a_2$ (RS + SR): ^1H NMR δ ($CDCl_3$): 3.25 (d, *J* = 9.3 Hz, 1H, *OH*), 4.41 (d, *J* = 9.3 Hz, 1H, H_b), 5.17 (dd, *J* = 9.3 and 9.3 Hz, 1H, H_a), 6.42 (d, *J* = 7.5 Hz, 1H, *H7*); 6.85 (dd, *J* = 5.6 and 1.8 Hz, 1H, *H2*), 6.97 (dd, *J* = 7.7 and 7.5 Hz, 1H, *H6*), 6.98 (d, *J* = 5.6 Hz, 1H, *H3*), 7.22 (dd, *J* = 7.5 and 7.5 Hz, 1H, *H5*), 7.25 (t, *J* = 7.8 Hz, 1H, *H4′*), 7.36 (dd, *J* = 7.5 and 1.8 Hz, 1H, *H4*), 7.38 (d, *J* = 7.8 Hz, 2H, *H3′* and *H5′*).

Acknowledgements

We are grateful to M.T. Compain for her technical assistance. We acknowledge financial support from the Ministère des Affaires Étrangères de France, l'Électricité de France (Novolect Bourgogne et Club d'Électrochimie organique), the Ministère des Relations Internationales du Québec, the Fonds pour la formation de chercheurs et d'aide à la recherche (FCAR) du Québec, and the Natural Sciences and Engineering Research Council of Canada. We thank Dr. J.C. Leblanc for helpful discussions.

References

1. (*a*) J.M. Savéant. Acc. Chem. Res. **13**, 323 (1980); (*b*) J. Simonet and N.J. Djeghidjech. J. Electroanal. Chem. **218**, 367 (1987); (*c*) J.M. Savéant. Bull. Soc. Chim. Fr. 225 (1988); (*d*) C. Amatore, C. Combellas, J. Pinson, J.M. Savéant, and A. Thiebault. J. Chem. Soc. Chem. Commun. 7 (1988); (*e*) M.A. Oturan, J. Pinson, J.M. Savéant, and A. Thiebault. Tetrahedron Lett. **30**, 1373 (1989); (*f*) J.M. Savéant. Adv. Phys. Org. Chem. **26**, 1 (1990); (*g*) N. Alan, C. Amatore, C. Combellas, A. Thiebault, and J.N. Verbeaux. J. Org. Chem. **55**, 6347 (1990); (*h*) P. Boy, C. Combellas, S. Fielding, and A. Thiebault. Tetrahedron Lett. **32**, 6705 (1991); (*i*) J.M. Savéant. Nouv. J. Chim. **16**, 131 (1992); (*j*) C. Thobie-Gautier, C. Degrand, M. Nour, and P.L. Compagnon. J. Electroanal. Chem. **344**, 383 (1993); (*k*) J.M. Savéant. Tetrahedron, **50**, 10117 (1994).

2. R.D. Rieke, H. Kojima, and K. Ofele. J. Am. Chem. Soc. **98**, 6735 (1976); L.S.R. Yeh and A.J. Bard. J. Electrochem. Soc. **124**, 189 (1977).
3. C. Amatore, J. Badoz-Lambling, C. Bonnel-Huyghes, J. Pinson, J.M. Savéant, and A. Thiebault. J. Am. Chem. Soc. **104**, 1979 (1982); C.P. Andrieux, J. Badoz-Lambling, C. Combellas, D. Lacombe, J.M. Savéant, A. Thiebault, and D. Zann. J. Am. Chem. Soc. **109**, 1518 (1987); P. Boy, C. Combellas, A. Thiebault, C. Amatore, and A. Jutand. Tetrahedron Lett. **33**, 491 (1992).
4. H. Tanaka, H. Suga, H. Ogawa, A.K.M. Abdul Hai, S. Torii, A. Jutand, and C. Amatore. Tetrahedron Lett. **33**, 6495 (1992).
5. S.W. Feldberg and L. Jeftif. J. Phys. Chem. **76**, 2439 (1972); J.W. Hershberger and J.K. Kochi. J. Chem. Soc. Chem. Commun. 212 (1982); A. Darchen, C. Mahé, and H. Patin. New J. Chem. **6**, 539 (1982); M. Guéguen, J.I. Guerchais, F.Y. Pétilloand, and J. Talarmin. J. Chem. Soc. Chem. Commun. 557 (1987); D. Astruc. Angew. Chem. Int. Ed. Engl. **27**, 643 (1988).
6. T. Shono, N. Kise, M. Matsuda, and T. Suzumoto. J. Org. Chem. **50**. 2527 (1985).
7. M.M. Baizer and J.L. Chruma. J. Org. Chem. **37**, 1951 (1972); M.M. Baizer, J.L. Chruma, and D.A. White. Tetrahedron Lett. 5209 (1973).
8. Y. Mugnier, J.C. Gard, Y. Huang, Y. Couture, A. Lasia, and J. Lessard. J. Org. Chem. **58**, 5329 (1993).
9. J.C. Gard, B. Hanquet, Y. Mugnier, and J. Lessard. J. Electroanal. Chem. **365**, 299 (1994).
10. C. Amatore, J. Pinson, J.M. Savéant. and A. Thiebault. J. Electroanal. Chem. **107**, 75 (1980).
11. E. Ghera and Y. Sprinsak. J. Am. Chem. Soc. **82**, 4945 (1960).
12. M. Avranoff and Y. Sprinsak. J. Am. Chem. Soc. **82**, 4953 (1960).
13. G. Kresze, H.G. Henkel, and H. Goetz. Ann. **18**, 674 (1964).
14. D. Villemin and M. Ricard. Tetrahedron Lett. **25**, 1059 (1984).
15. A. Sieglitz. Ber. Dtsch. Chem. Ges. B: **52**, 1513 (1919).
16. M. Kirilov, G. Petrov, and C. Angelo. J. Organomet. Chem. **113**, 225 (1976).
17. D.J. Field, D.W. Jones, and G. Kneen. J. Chem. Soc. Perkin Trans. 1, 1050 (1978).
18. D.J. Field, D.W. Jones, and G. Kneen. J. Chem. Soc. Chem. Commun. 754 (1975).
19. D.B. Taggart and E.C. Friedrich. J. Org. Chem. **40**, 720 (1975).

Novel experimental findings in the B–Z system employing mixed substrates

V. Jayalakshmi and R. Ramaswamy

Abstract: Certain novel features of the Belousov–Zhabotinsky (B–Z) system employing different mixed substrates and Mn(II) as the catalyst are presented. Malic acid is the common substrate together with one of malonic, citric, cyanoacetic, maleic, acetic, oxalic, or tartaric acid as the second substrate. The correlation of the oscillatory behaviour with values of exchange current density establishes the oscillatory control by the redox couple, namely, Mn(III)/Mn(II) and (or) Br_2/Br^-. Each substrate when used alone gives rise to an oscillatory behaviour with characteristic features that can be compared with the system containing mixed substrate. The combination of substrates provides different modes of oscillatory behaviour such as entrainment, independent, partial inhibition, or complete inhibition. These observations are rationalized in terms of relevant steps involved in the mechanism of the reaction.

Key words: mixed substrate, exchange current density, entrainment, independent, inhibition.

Résumé : On présente certaines caractéristiques nouvelles du système de Belousov–Zhabotinsky (B–Z) dans lesquelles on utilise des substrats mixtes et du Mn(II) comme catalyseur. L'acide malique est un substrat courant avec l'un ou l'autre des acides malonique, citrique, cyanoacétique, maléique, acétique, oxalique ou tartrique comme deuxième substrat. La corrélation du comportement oscillatoire avec les valeurs de la densité du courant d'échange permet d'établir que le contrôle oscillatoire dérive du couple redox, Mn(III)/Mn(II) et (ou) Br_2/Br^-. Lorsqu'on utilise les substrats seuls, ils donnent lieu à un comportement oscillatoire dont les caractéristiques particulières peuvent se comparer à celles d'un système contenant un substrat mixte. Les combinaisons de substrats conduisent à des modes différents de comportement tels qu'entraînement, indépendant, inhibition partielle ou inhibition complète. On peut rationaliser ces observations en fonction d'étapes appropriées impliquées dans le mécanisme de la réaction.

Mots clés : substrat mixte, densité du courant d'échange, entraînement, indépendant, inhibition.

[Traduit par la rédaction]

Introduction

Oscillatory reactions in the Belousov–Zhabotinsky (B–Z) and Briggs–Rauscher (B–R) systems have been investigated by employing a variety of organic substrates in aqueous as well as aqueous–organic mixed media (1–3). Oscillatory reactions with mixed organic substrates (4–6) have also received considerable attention. The present paper deals with certain novel experimental findings in the B–Z system employing mixed substrates with malic acid as the common substrate.

Experimental

The constituents of the experimental solution, with the exception of potassium bromate, were kept well stirred and thermostated in a polythene beaker. The addition of the last constituent ($KBrO_3$) triggered off the oscillations. The EMF oscillatory profile between a platinum indicator electrode and a saturated calomel (SCE) reference electrode was continously recorded. Different substrates were employed for the study, either individually or in combination with malic acid as the common substrate. The structures of the substrates employed have been tabulated for convenient reference.

Structures of different substrates employed.

S.No.	Substrate	Structure
1.	Malic acid	HOOC—CH_2—CH(OH)—COOH
2.	Citric acid	CH_2—COOH | C(OH)—COOH | CH_2—COOH
3.	Malonic acid	HOOC—CH_2—COOH
4.	Cyanoacetic acid	NC—CH_2—COOH
5.	Maleic acid	HOOC—CH=CH—COOH
6.	Acetic acid	CH_3—COOH
7.	Tartaric acid	CH(OH)—COOH | CH(OH)—COOH
8.	Oxalic acid	COOH | COOH

Results and discussion

(i) Malic acid and citric acid

The oscillatory profile of the malic acid – citric acid mixed substrate system under the concentration conditions indicated

Received March 29, 1995.

V. Jayalakshmi and R. Ramaswamy.[1] Department of Chemistry, Indian Institute of Technology, Madras – 600 036, India.

[1] Author to whom correspondence may be addressed. Fax: 044: 2350509.

Table 1. Oscillatory characteristics with malic acid and citric acid as substrates.[a]

Substrate	[S] M	Number of oscillations	Potential (V vs. SCE) Base value	Potential (V vs. SCE) Peak value	Amplitude (V)	Time per oscillation (min)	Duration (min)
Malic acid	0.05	40	0.775	1.050	0.275	1.00	40
Citric acid	0.05	30	0.600	0.825	0.225	0.50	15
	0.05	32	0.475	0.925	0.450	0.56	18
	+						
Malic acid	0.05						
+							
citric acid	0.025	1–30	0.590	0.820	0.230	0.50	15
	+						
	0.025	31–54				1.66	40

[a][$KBrO_3$] = 0.05 M; [H_2SO_4] = 2.0 M; [$MnSO_4$] = 0.005 M; temperature = 30 ± 0.1°C.

in Table 1 is presented in Fig. 1*b*. Each substrate when used alone in the B–Z reaction gives rise to characteristic features that permit identification of its oscillatory behaviour in the system with mixed substrates. The oscillatory reactions with the individual substrate under the concentration conditions indicated in Table 1 are presented in Figs. 1*a* and 2. The potential developed at the platinum indicator electrode is determined by the relative values of the exchange current density and (or) the relative concentrations of the redox couples involved. The values of the exchange current density for Pt/Mn(III), Mn(II), and that of Pt/Br_2, Br^- are comparable (10^{-5} A/cm^2). Therefore the potential range of oscillation can be decided by the relative concentration of Mn(III)/Mn(II) and Br_2/Br^-. The potential range of oscillation with malic acid as the substrate is 0.775–1.05 V (vs. SCE). The peak potential is as high as 1.05 V, indicative of the predominant potential control by the Mn(III)/Mn(II) redox couple. The standard potentials (vs. SHE) of the Mn(III)/Mn(II) and Br_2/Br^- redox systems are 1.488 and 1.066 V, respectively. However, the prevailing concentrations of the different species are much smaller. Thus the malic acid oscillatory profile is predominantly controlled by the Mn(III)/Mn(II) redox couple due to the nominal reactivity of the substrate towards bromination.

On the other hand, the potential range of oscillation in the citric acid system is 0.60–0.825 V (vs. SCE), which is indicative of mixed control of potential by both redox couples, namely, Mn(III)/Mn(II) and Br_2/Br^-. This is presumably due to the high reactivity of the substrate towards bromination, leading to considerable production and consumption of bromine.

This can be well understood in terms of the relevant steps involved in the FKN mechanism.

[1] $HOBr + Br^- + H^+ \rightleftharpoons Br_2 + H_2O$

[2] $BrO_2^{\bullet} + M^{n+} + H^+ \rightleftharpoons HBrO_2 + M^{(n+1)+}$

These steps lead to the formation of bromine and the oxidized form of metal ion. In addition, the reaction involving the substrate would lead to the consumption of bromine as well as the oxidized form of the metal ion according to the following steps:

[3] $S + Br_2 \rightleftharpoons Br{\cdot}S + Br^- + H^+$

[4] $S + M^{(n+1)+} \rightleftharpoons M^{n+} + \text{product}$

Steps [3] and [1] are more favoured in the citric acid system because of its high reactivity towards bromination. Enhancement in the production and consumption of bromine in the citric acid system is also reflected in the smaller time per oscillation (0.5 min) compared to that of malic acid (1.0 min) as indicated in Table 1. Thus the high reactivity of the substrate contributes considerably to the high frequency and mixed control of potential by both redox couples, namely, Mn(III)/Mn(II) and Br_2/Br^-.

The oscillatory profile observed in this mixed substrate system is almost identical to the oscillatory parameters with citric acid except for the increase in the amplitude of oscillations. The wave form, potential range, and the oscillatory period also clearly indicate that the oscillations are of the citric acid type and the role of malic acid is just to increase the amplitude of oscillations to the extent of 225 mV. Thus the system investigated here is an example of entrainment oscillations, in which citric acid is responsible for oscillations and the presence of malic acid increases the amplitude of oscillations.

The oscillatory behaviour of the system with 0.1 M of the individual substrate (malic acid or citric acid) leads to an increase in the frequency of oscillations due to an enhancement in the formation and consumption of bromine as well as of Mn(III). The solution containing a total concentration of 0.05 M of malic and citric acid (0.025 M each) gives an oscillatory behaviour that is identical with that of citric acid (0.05 M) for a duration of 15 min followed by an additional 24 oscillations in 40 min. Such an oscillatory behaviour can be termed as independent and persistent.

(ii) Malic acid and malonic acid

The oscillatory behaviour of this system under the concentration conditions indicated in Table 2 is presented in Fig. 3. The oscillatory profile observed with mixed substrate is identical to that of malonic acid in almost all aspects of the wave form, namely, potential range, frequency, and the alternation between a pink and a colourless solution. This clearly indi-

Fig. 1. Oscillatory behaviour of bromate–Mn(II) system at 30 ± 0.1°C. Concentration conditions: $[H_2SO_4]$ = 2.0 M; $[MnSO_4]$ = 0.005 M; $[KBrO_3]$ = 0.05 M. (*a*) Citric acid (0.05 M); (*b*) malic acid (0.05 M) + citric acid (0.05 M).

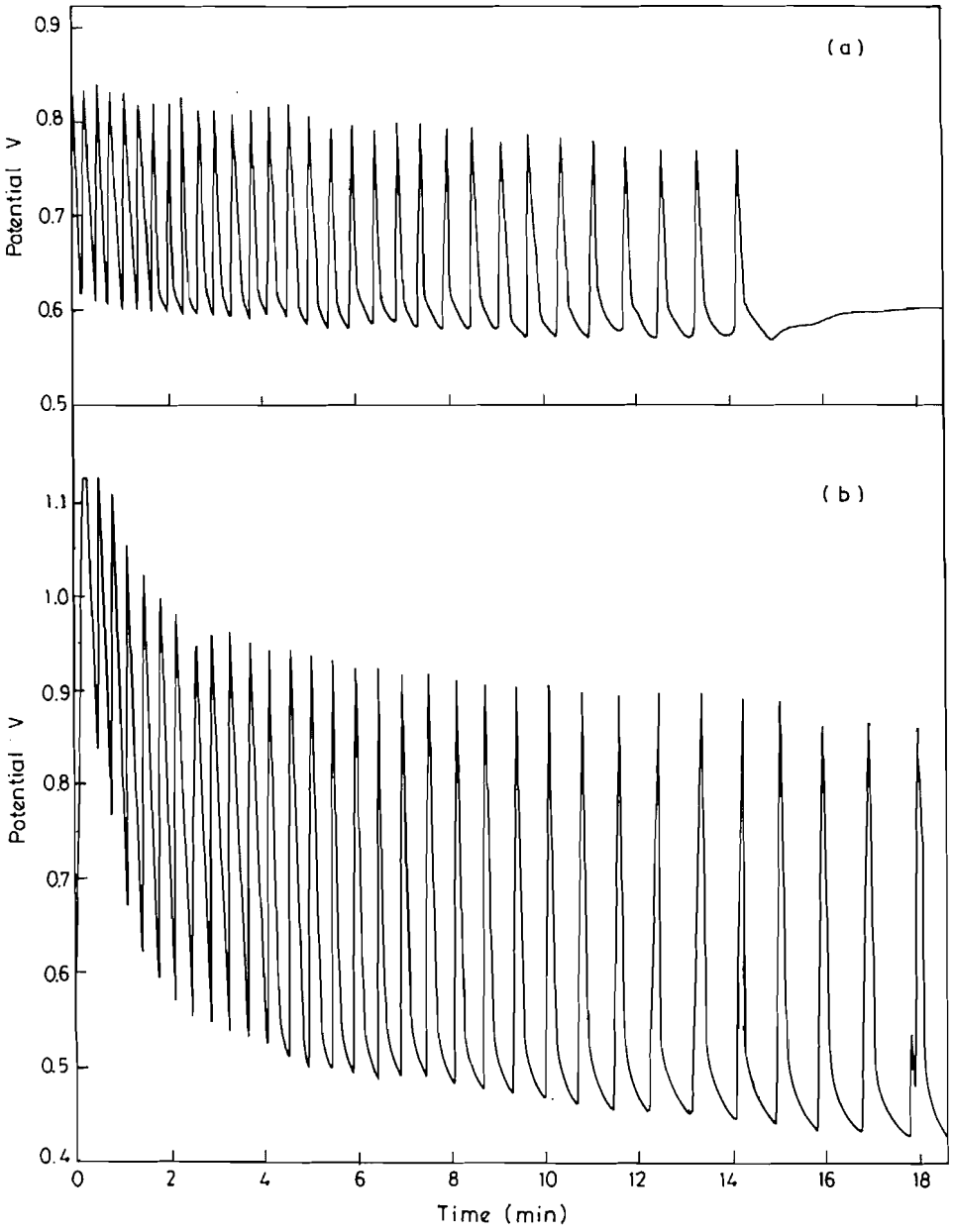

cates that the oscillations are of malonic acid type. The only difference between these two systems is in the number of oscillations. The presence of malic acid decreases the number of oscillations of the malonic acid system. Here, though the oscillations are controlled predominantly by malonic acid as the substrate, malic acid also participates in the reaction under the concentration conditions employed. This results in a decrease in the concentration of bromate, leading to an unfavourable concentration ratio of bromate to substrate at 9.5 min duration and a premature termination of oscillations. These observations can be substantiated on the basis of the relevant steps of the overall reaction involving the formation of Mn(III) and bromine (steps [1] and [2]) as well as their consumption (steps [3] and [4]). The unfavourable ratio of bromate to substrate disfavours steps [1] and [2], which would otherwise have resulted in the up reaction. This is further supported by the restart of oscillation by the addition of bromate at the 9.5 min mark. Thus this system represents an example of interrupted independent oscillations, where malonic acid mainly controls the nature of oscillations and the interruption is due to an effective decrease in the relative concentration of bromate.

The oscillatory behaviour of the system with 0.1 M malonic acid alone is characterized by a smaller time per oscillation due to an enhancement in the formation and consumption of bromine as well as of Mn(III). The solution containing 0.05 M

Table 2. Oscillatory characteristics with malic acid and malonic acid.[a]

Substrate	[S] M	Number of oscillations	Potential (V vs. SCE) Base value	Potential (V vs. SCE) Peak value	Amplitude (V)	Time per oscillation (min)	Duration (min)
Malic acid	0.05	40	0.775	1.050	0.275	1.00	40.0
Malonic acid	0.05	39	0.825	1.010	0.185	0.45	17.5
Malic acid + malonic acid	0.05 + 0.05	22	0.825	1.010	0.185	0.45	9.5
	0.025 + 0.025	39	0.825	1.020	0.195	0.45	17.5

[a][$KBrO_3$] = 0.05 M; [H_2SO_4] = 2 M; [$MnSO_4$] = 0.005 M; temperature = 30 ± 0.1°C.

Fig. 2. Oscillatory behaviour of bromate–Mn(II) system at 30 ± 0.1°C. Concentration conditions: [Malic acid] = 0.05 M; [$KBrO_3$] = 0.05 M; [$MnSO_4$] = 0.005 M; [H_2SO_4] = 2.0 M.

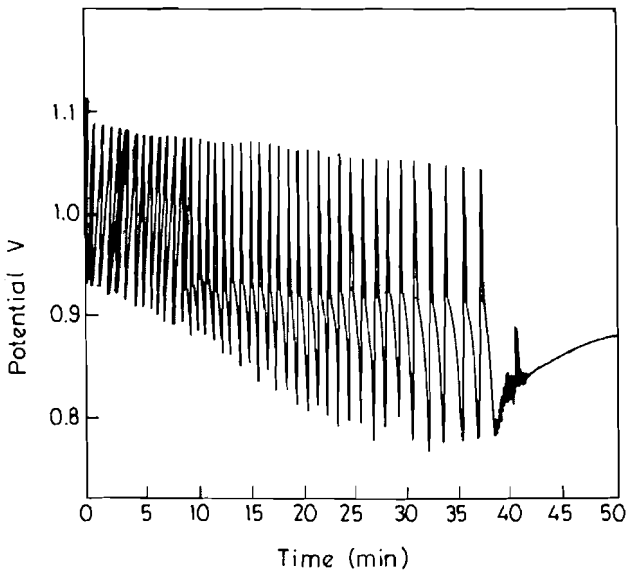

of the mixed substrate (0.025 M each) leads to an oscillatory behaviour identical with that of 0.05 M malonic acid alone. This behaviour can be termed as independent. The system behaves as if it contains only malonic acid.

(iii) Malic acid and cyanoacetic acid/maleic acid/acetic acid

In this set of experiments the second constituent, unlike malic acid, does not act as a substrate under the concentration conditions indicated in Table 3 and presented in Fig. 4. In all three systems the presence of the second substrate introduces an induction period, and decreases the duration and the number of oscillations. The second constituent is presumably involved in the following steps of the overall reaction.

[5] $BrO_3^- + HBrO_2 + H^+ \rightleftharpoons 2BrO_2^\bullet + H_2O$

[6] $BrO_2^\bullet + S \rightleftharpoons HBrO_2 + S_{ox}$

(S = substrate or added constituent; S_{ox} = oxidized product)

The course of the reaction involves steps [1]–[4] when malic acid is a single substrate. The inclusion of any one of the second constituents leads to a predominance of step [6] over steps [3] and [4]. This leads to a delay in the onset of oscillations and is manifest as an increase in the induction time as well as a decrease in the number of oscillations and in duration, resulting in partial inhibition. The reaction involving the second substrate in step [6] leads to a depletion in the bromate concentration in a non-oscillatory reaction as a result of which there is premature cessation of oscillations with smaller number and duration. This is confirmed by the restart of oscillation on addition of potassium bromate after the oscillations cease.

The system employing 0.1 M of the second substrate does not show oscillatory behaviour as with 0.05 M. Further, the system containing 0.05 M of the mixed substrate (0.025 M each) does not exhibit oscillatory behaviour. This is presumably due to high concentration of potassium bromate leading to consumption of substrate in a non-oscillatory reaction. This is substantiated by the fact that the system oscillates when the concentration of potassium bromate is reduced to 0.025 M.

(iv) Malic acid and tartaric acid/oxalic acid

The addition of either tartaric or oxalic acid to malic acid results in a total inhibition of oscillations. The potential remains constant at 1.01 V (vs. SCE) corresponding to the peak potential region. In these instances step [6], involving the consumption of substrate/added constituent, is totally overwhelming. The extent of reactions [3] and [4] is quite insignificant under these conditions, resulting in complete inhibition of oscillations.

It is interesting to note that the system exhibits oscillatory behaviour in a solution containing 0.05 M potassium bromate and 0.05 M mixed substrate (0.025 M each). The system changes from one of complete inhibition at 0.1 M mixed substrate to one of partial inhibition at a concentration of 0.05 M of mixed substrate resulting from a favourable concentration ratio of bromate to substrate.

Conclusion

A study of the B–Z reaction with mixed substrates provides valuable information regarding the key role of the substrate in the overall reaction. Different combinations of the substrates,

Fig. 3. Oscillatory behaviour of bromate–Mn(II) system at 30 ± 0.1°C. Concentration conditions: $[H_2SO_4] = 2.0$ M; $[MnSO_4] = 0.005$ M; $[KBrO_3] = 0.05$ M. (*a*) Malonic acid (0.05 M); (*b*) malic acid (0.05 M) + malonic acid (0.05 M).

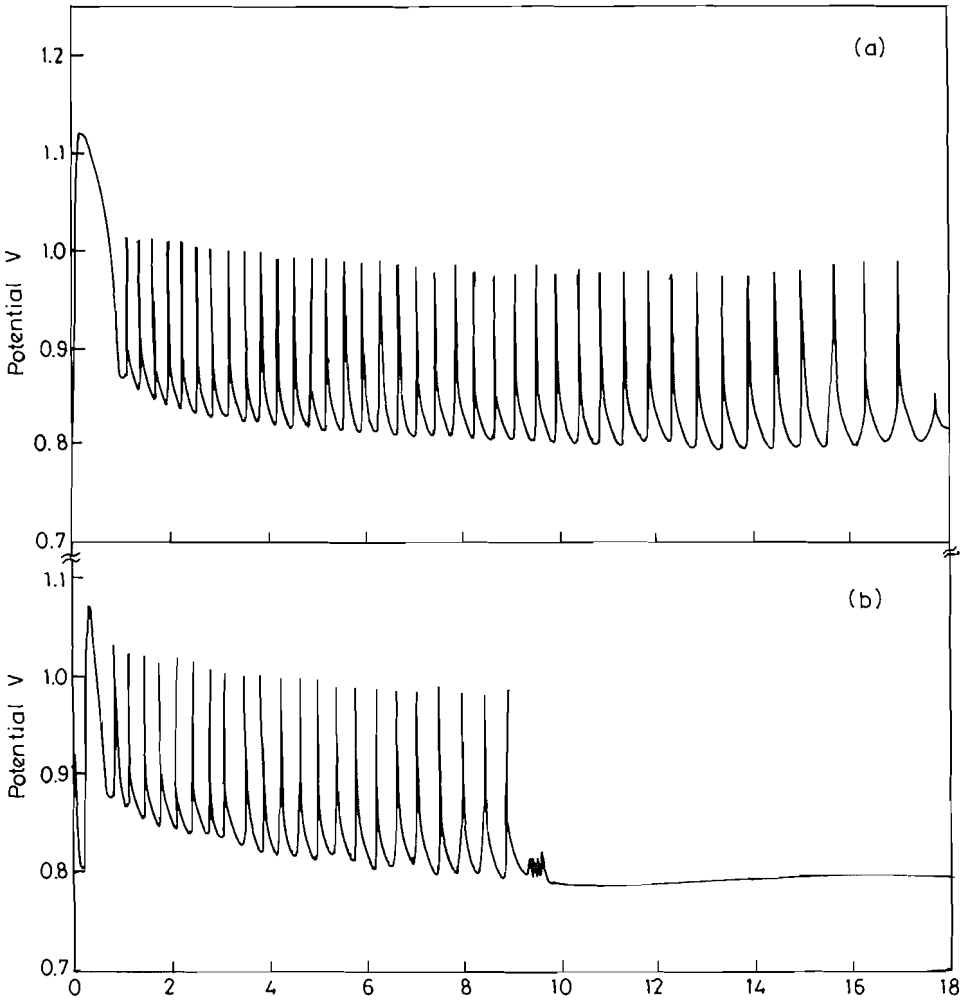

Table 3. Oscillatory characteristics with malic acid, cyanoacetic acid, maleic acid, and acetic acid.[a]

Substrate	[S] M	Number of oscillations	Potential (V vs. SCE) Base value	Potential (V vs. SCE) Peak value	Amplitude (V)	Time per oscillation (min)	Duration (min)	Induction period (min)
Malic acid	0.05	40	0.775	1.050	0.275	1.00	40	0
Cyanoacetic acid	0.05	—	—	—	—	—	—	—
Malic acid + cyanoacetic acid	0.05 + 0.05	18	0.850	1.025	0.175	0.88	24.6	8.6
Maleic acid	—	—	—	—	—	—	—	
Malic acid + maleic acid	0.05 + 0.05	10	0.840	1.050	0.210	1.40	26.5	12.5
Acetic acid	0.05	—	—	—	—	—	—	—
Malic acid + acetic acid	0.05 + 0.05	31	0.900	1.050	0.150	1.04	36.5	4.2

[a] $[KBrO_3] = 0.05$ M; $[H_2SO_4] = 2$ M; $[MnSO_4] = 0.005$ M; temperature = 30 ± 0.1°C.

Fig. 4. Oscillatory behaviour of bromate–Mn(II) system at 30 ± 0.1°C. Concentration conditions: $[H_2SO_4]$ = 2.0 M; $[MnSO_4]$ = 0.005 M; $[KBrO_3]$ = 0.05 M. (*a*) Malic acid (0.05 M) + cyano acetic acid (0.05 M); (*b*) malic acid (0.05 M) + maleic acid (0.05 M).

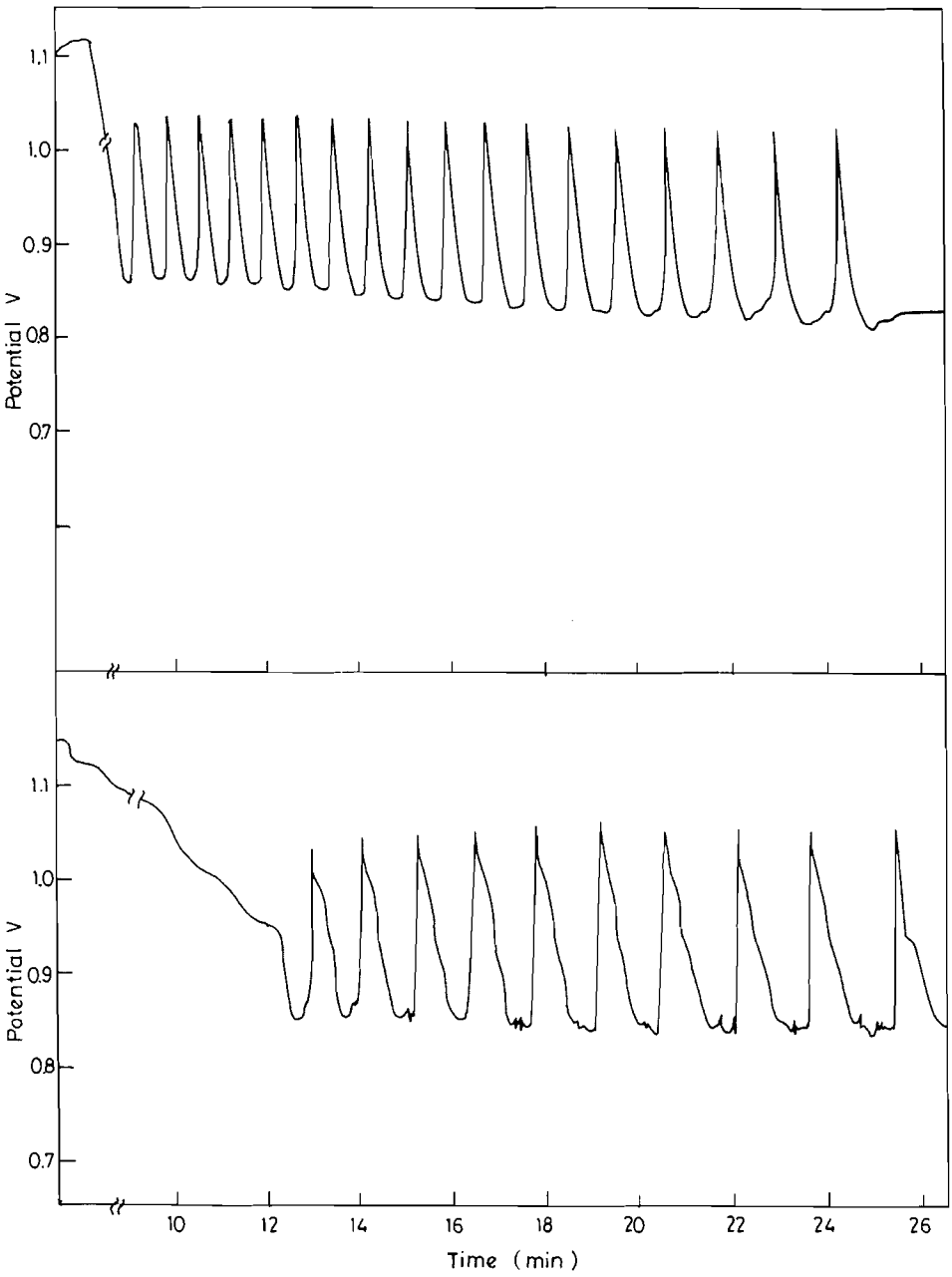

malic acid being common, provide different types of oscillatory behaviour of the system. The resultant pattern of behaviour is mainly governed by the reactivity of the second substrate in relation to malic acid. The behaviour of these systems can be well understood in the light of the relevant steps involved in the overall reaction.

References

1. R.J. Field and M. Burger (*Editors*). Oscillations and travelling waves in chemical systems. John Wiley and Sons, New York. 1987.
2. P.V. Lalitha and R. Ramaswamy. React. Kinet. Catal. Lett. **47**, 133 (1992).
3. V. Jayalakshmi and R. Ramaswamy. Int. J. Chem. Kinet. **27**, 197 (1995).
4. J. Heilweil, M.J. Henchman, and I.R. Epstein. J. Am. Chem. Soc. **98**, 3698 (1979).
5. R.P. Rastogi, R.D. Yadav, S. Singh, and A. Sharma. Indian J. Chem. **24A**, 43 (1985).
6. M.K. Ramreddy, K.C. Rajanna, and P.K. Saiprakash. Proc. Indian Acad. Sci. **98**, 333 (1987).

SCF-MO computational analysis of the geometric conformation and charge distribution in picric acid and alkali picrate salts

Zbigniew Zimpel, Barbara R. Nelson, and John A. Weil

Abstract: SCF-MO computations were employed in a study of picric acid, the −1 picrate ion, and Li, Na, and K picrates. Atomic coordinates from crystallographic structural analyses were used as initial parameters in the computation of the minimum-energy conformations of each free molecule at the 6-31G level. The Mulliken charge numbers for each atom in the optimized model molecules were calculated at the 6-31G** level. The induction and resonance effects of the OX group (X = H, Li, Na, K) on the trinitrophenyl ring are discussed. It is demonstrated that molecular (electron) isodensity surfaces (MIDCOs) describe charge-density results nicely compatible with the point Mulliken charge numbers.

Key words: picrates, SCF-MO, charge distribution.

Résumé : On a utilisé des calculs d'OM en champ auto-cohérent pour étudier l'acide picrique, l'ion picrate et les picrates de Li, Na et K. On a utilisé des coordonnées atomiques provenant d'analyses cristallographiques de structures comme paramètres initiaux dans les calculs des conformations d'énergies minimales de chacune des molécules libres au niveau 6-31G. Opérant au niveau 6-31G**, on a calculé les nombres de charge de Mulliken des molécules modèles optimisées. On discute des effets d'induction et de résonance des groupes OX (X = H, Li, Na, K) sur le noyau trinitrophényle. On a démontré que les surfaces d'isodensité électronique au niveau moléculaire décrivent bien l'adéquation entre les résultats de densité de charge et les nombres de charge de Mulliken.

Mots clés : picrates, OM en champ auto-cohérent, distribution de charge.

[Traduit par la rédaction]

Introduction

1-R substituted 2,4,6-trinitrobenzene derivatives (1-R-TNB) undergo nucleophilic aromatic substitution reactions that proceed via the two-step S_NAr addition–elimination mechanism shown in eqs. [1] and [2]. In the first step the nucleophile Nu^- attacks the electron-deficient ring and forms the σ-bonded species **1** (a σ adduct) in which $C_{(1)}$ is rehybridized from sp^2 to sp^3. The nucleophile can attack either at $C_{(1)}$ to produce a 1,1-bonded anion or at $C_{(3)}$ ($C_{(5)}$) to give a 1,3-bonded anion.[3] In the second step the aromatic ring is restored by expulsion either of R^- to yield the substitution product **2** (eq. [2]) or of Nu^- to regenerate the starting material (1).

The presence of the three electron-withdrawing nitro groups situated *meta* to each other on the phenyl ring is believed to promote the formation of **1** in two ways. First, replacement of hydrogen atoms by such groups enhances the rate of nucleophilic attack on the aromatic carbon ring of the molecule by withdrawing electron density from the originally electron-rich ring, via induction and resonance. Second, it increases the stability of **1** by delocalizing the −1 charge initially on the attacked aromatic ring into the three nitro groups. The increase in stability of **1** decreases the rate of decomposition of the σ adduct, back to the reactants or to product **2**. The stabilizing effect of the nitro groups, coupled with the use of 1-R-TNBs in which R^- is a poor leaving group, enables discrete and relatively stable σ adducts to form.

Figure 1 shows what are believed to be the most significant

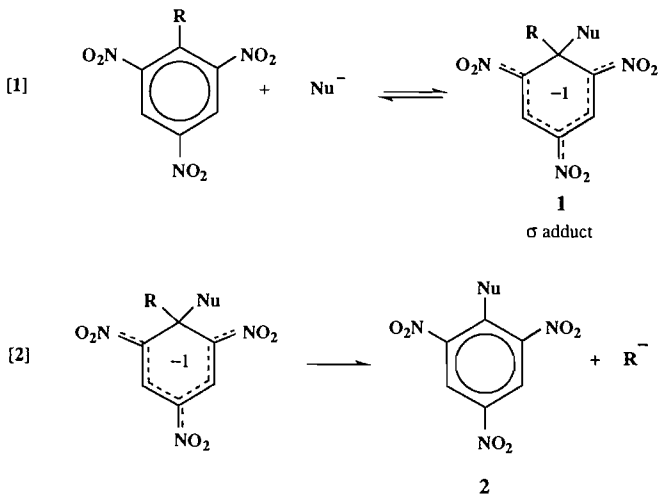

Received August 11, 1995.

Z. Zimpel,[1] B.R. Nelson, and J.A. Weil.[2] Department of Chemistry, University of Saskatchewan, 110 Science Place, Saskatoon, SK S7N 5C9, Canada.

[1] Also at the Institute of Molecular Physics, Polish Academy of Sciences, Smoluchowskiego 17/19, 60-179 Poznań, Poland.

[2] Author to whom correspondence may be addressed. Telephone: (306) 966-4658. Fax: (306) 966-4730. E-mail: john.weil@usask.ca

[3] The 1,1 anion is often referred to as a Meisenheimer complex. Both ions are called σ complexes or σ adducts.

Fig. 1. Some of the important resonance structures for the 1-*R*-2,4,6-trinitrobenzene molecule.

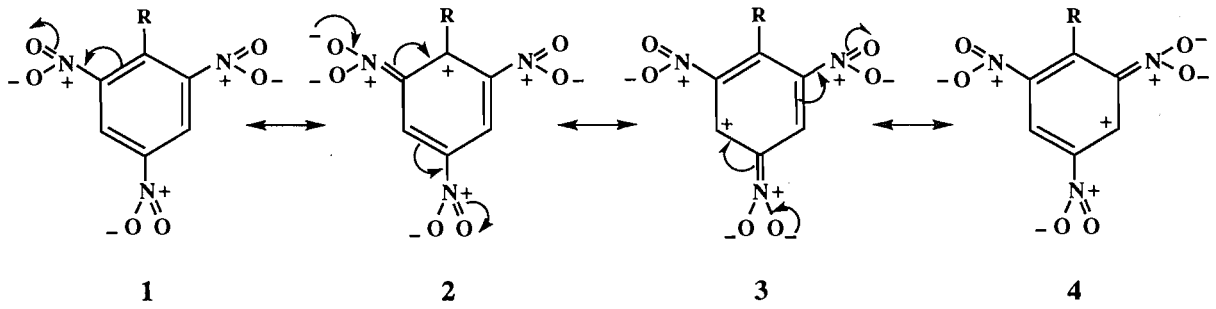

1 2 3 4

types of resonance structures in 1-R-TNB for activation of the ring toward nucleophilic substitution. Note that the shifted electron density is concentrated on the nitro oxygens and that electron density is withdrawn primarily from carbons at positions 1, 3, and 5. It is evident from resonance structure **2** that, if R is electron withdrawing, $C_{(1)}$ will be further activated to nucleophilic attack.

In our experimental research on the formation and reactions of σ adducts of 1-R-2,4,6-trinitrobenzenes,[4] we were curious about the quantitative extent to which the benzene ring is activated by the nitro groups and by R, and how the identity of R affects this activation. One 1-R-TNB compound in which we are specifically interested is picric acid. As is strongly indicated in both our experimental studies and in the literature (3, 4), it is the picrate –1 anion,[5] and not the picric acid molecule, that is attacked by the nucleophile to form the σ adduct. One commonly asked question regarding this reaction is: why does a negatively charged nucleophile attack the negatively charged picrate anion? The generally given qualitative answer is that the –1 charge on the picrate anion is withdrawn into the three nitro groups to such an extent that the ring remains activated (π-electron deficient), albeit somewhat less so than in the neutral picric acid molecule.

To obtain a more quantitative measure of ring activation in the picrate anion and to determine the charge distribution in the molecule, we performed self-consistent-field molecular orbital (SCF-MO) computations on picric acid, on the isolated picrate anion, and on three alkali picrates (Li, Na, and K). The three different picrate salts were studied to determine what effect(s) the identity of the cation has on the geometric conformation of and charge distribution in the anion.

As will be shown quantitatively, the presence of electron-withdrawing groups (such as NO_2 and OX (X = H, Li, Na, K)) results in considerable withdrawal of π-electron density from the phenyl ring in the molecules studied. Such withdrawal is expected to increase the susceptibility of the ring to nucleophilic attack, as is observed experimentally.

Fig. 2. The 1-*R*-2,4,6-trinitrobenzene molecule with atoms numbered.

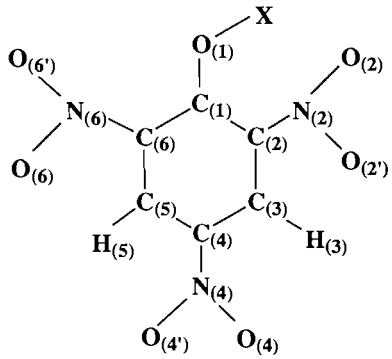

where:

X = H, Li, Na or **K**

Methods and results

SCF-MO computations using the Gaussian-92 package (6) were employed in the study of picric acid and its derivatives, namely the picrate anion and the alkali picrates, respectively, represented by $C_6H_2O(NO_2)_3^-$ and $C_6H_2O(NO_2)_3X$ with X = H, Li, Na, or K. The optimization of nuclear configuration (i.e., nuclear geometry defined in terms of internuclear distances, angles, and dihedral angles) was generally performed using the 6-31G split-valence basis set of atomic orbitals. In the geometry optimization of potassium picrate, the single-valence (SV) basis set of contracted AOs {63311/53680} of the ^2S ground state of potassium energy, described by Schäfer et al. (7), was employed. As was pointed out in ref. 7, the expansion of the SV basis set to a double-zeta (DZ) basis set does not result in a significant improvement of the atom energy. A triple-zeta-type basis (which leads to a slightly more accurate value of the ground-state potassium atom) is far too large for our computational capabilities.

The atom-numbering scheme for the substituted trinitrobenzene molecule is shown in Fig. 2. The crystallographic atomic coordinates were used as the initial parameters in calculating the minimum-energy conformations of model picric acid (8) and potassium picrate (9). The coordinates for potas-

[4] Our experimental research is primarily concerned with: (*i*) identifying the products (usually σ adducts but not necessarily so (2)) formed in the reaction between 1-R-TNBs and the acetone enolate and (*ii*) the reaction of these products with protons in acidic peroxide solution (B.R. Nelson and J.A. Weil, to be published). We found that the identity of the product(s) formed in these two reactions depends on the identity of R. Some of the properties of R that appear to determine the reaction path include size, electronegativity, hydrogen-bonding ability, and acidity.

[5] With a pK_a of 0.3 (5), picric acid is assumed to be 100% dissociated in the aqueous basic solutions necessary for the formation of the σ adduct. The picrate ion is the only trinitrophenyl species observed in the room-temperature ^1H NMR (300 MHz) spectrum of the initial reaction mixture.

Table 1. The definition of the symbols representing the structural parameters listed in Tables 2–5. The symbols r, r', and d are bond lengths, α and α' bond angles, and β, β', β_1, ..., $\beta_{6'}$ dihedral angles. Symbols $A_{(i)}$ (i = 1, 2, ...) represent the sequentially bonded atoms. The symbol X represents H, Li, Na, or K.

Atom	r	α	β	d	r'	α'	β'	β_2	$\beta_{2'}$	β_4	$\beta_{4'}$	β_6	$\beta_{6'}$
A_a	X	X	X	X	O	O	O	$O_{(2)}$	$O_{(2')}$	$O_{(4)}$	$O_{(4')}$	$O_{(6)}$	$O_{(6')}$
A_b	$O_{(1)}$	$O_{(1)}$	$O_{(1)}$	$O_{(2)}$	$C_{(1)}$	$C_{(1)}$	$C_{(1)}$	$N_{(2)}$	$N_{(2)}$	$N_{(4)}$	$N_{(4)}$	$N_{(6)}$	$N_{(6)}$
A_c	—	$C_{(1)}$	$C_{(1)}$	—	—	$C_{(2)}$	$C_{(2)}$	$C_{(2)}$	$C_{(2)}$	$C_{(4)}$	$C_{(4)}$	$C_{(6)}$	$C_{(6)}$
A_d	—	—	$C_{(2)}$	—	—	—	$C_{(3)}$	$C_{(1)}$	$C_{(1)}$	$C_{(3)}$	$C_{(3)}$	$C_{(5)}$	$C_{(5)}$

Table 2. Crystallographic structural parameters (defined in Table 1) for $C_6H_2O(NO_2)_3X$, where X = H or K (see Fig. 3). All distances are given in Å and all angles are given in degrees.

	Picric acid	Potassium picrate
Ref.	9	10
r	1.150	2.738
α	108	113
β	−16	−67
d	1.501	2.411
r'	1.312	1.243
α'	124	124
β'	180	−179
β_2	−7	29
$\beta_{2'}$	172	−152
β_4	−1	−5
$\beta_{4'}$	179	175
β_6	−18	24
$\beta_{6'}$	165	−155

sium picrate were used as the initial structural data in the optimization of both lithium and sodium picrate, for which no crystallographic diffraction data are reported in the literature.[6] The optimized geometry of the picrate anion was derived starting from the data for the potassium salt.

The relative position of each atom in the studied molecules is reported in standard internal molecular coordinates (bond lengths, bond angles, and dihedral angles[7]). These parameters are defined in Table 1 and include the definition of the position with respect to the rest of the molecule of X and $O_{(1)}$, as well as the rotation angles with respect to the carbon-ring plane of the three nitro groups. The relevant initial crystallographic structural parameters are given in Table 2. The calculated values for the 6-31G/6-31G** optimized structural parameters for picric acid, the picrate ion, and the alkali picrates are given in the upper part of Table 3. The calculated values for picric acid and lithium picrate from all three levels of optimization are given in Tables 4 and 5, respectively.

Whereas the geometry was optimized at the 6-31G level, polarization functions (p and d orbitals) were added to this basis to compute the Mulliken charges on individual atoms.

Table 3. The optimized 6-31G structural parameters (defined in Table 1) and the 6-31G/6-31G** charge numbers for picric acid, the picrate −1 ion, and the alkali picrates. All distances are given in Å and all angles are given in degrees.

	Picric acid	Picrate −1 ion	Lithium picrate	Sodium picrate	Potassium picrate
r	0.960	—	1.763	2.088	2.463
α	115.8	—	129.7	136.6	141.9
β	−2.9	—	−9.3	−19.1	−32.2
r'	1.324	1.231	1.266	1.258	1.251
α'	125.3	123.9	123.8	124.2	124.1
β'	−176.9	−169.1	−175.3	−173.8	−172.0
d	1.849	—	1.842	2.185	2.600
β_2	−0.6	29.3	3.7	10.4	16.6
$\beta_{2'}$	179.3	−152.9	−176.9	−170.6	−164.9
β_4	−0.7	−0.7	−0.8	−0.7	−0.9
$\beta_{4'}$	179.3	−179.3	179.2	179.3	179.1
β_6	−37.5	−25.5	−34.5	−33.1	−30.8
$\beta_{6'}$	139.7	152.3	143.0	144.4	146.8
X	0.427	—	0.802	0.833	0.931
$O_{(1)}$	−0.625	−0.599	−0.790	−0.771	−0.780
$C_{(1)}$	0.550	0.609	0.692	0.655	0.650
$C_{(2)}$	0.077	−0.028	−0.005	−0.002	−0.007
$C_{(3)}$	0.006	−0.010	0.008	0.006	0.010
$C_{(4)}$	0.084	0.015	0.061	0.056	0.048
$C_{(5)}$	0.015	−0.010	0.016	0.013	0.012
$C_{(6)}$	0.097	−0.028	0.039	0.033	0.016
$N_{(2)}$	0.510	0.512	0.533	0.516	0.496
$N_{(4)}$	0.492	0.514	0.488	0.487	0.484
$N_{(6)}$	0.469	0.512	0.476	0.478	0.479
$O_{(2)}$	−0.513	−0.445	−0.605	−0.587	−0.565
$O_{(2')}$	−0.423	−0.521	−0.410	−0.431	−0.452
$O_{(4)}$	−0.453	−0.521	−0.471	−0.477	−0.482
$O_{(4')}$	−0.449	−0.521	−0.462	−0.469	−0.475
$O_{(6)}$	−0.449	−0.521	−0.466	−0.470	−0.474
$O_{(6')}$	−0.402	−0.445	−0.419	−0.430	−0.444
$H_{(3)}$	0.298	0.244	0.286	0.282	0.277
$H_{(5)}$	0.292	0.244	0.283	0.278	0.274

[6] No references for lithium picrate or sodium picrate were found in the Cambridge Structural Database.

[7] The internuclear dihedral angle Δ for the atoms A_a, A_b, A_c, and A_d is defined as the angle between the planes defined by atoms A_a, A_b, A_c, and atoms A_b, A_c, A_d, with atoms A_b and A_c sharing the planes ($-180° \leq \Delta \leq 180°$). The sign is positive if the movement of the vector $A_b \rightarrow A_a$ towards the vector $A_c \rightarrow A_d$ is a right-handed screw motion. The various dihedral angles in the molecules discussed herein are designated β, β', β_1, β_2, $\beta_{2'}$,...., $\beta_{6'}$

Table 4. The optimized structural parameters (defined in Table 1) and the charge numbers for picric acid at the 6-31G**, 6-31G/6-31G**, 6-31G, and STO-3G levels. All distances are given in Å and all angles are given in degrees.

	6-31G**	6-31G/ 6-31G**	6-31G	STO-3G
r	0.954	0.960	0.960	1.024
α	110.8	115.8	115.8	103.3
β	−0.8	−2.9	−2.9	−0.3
r'	1.300	1.324	1.324	1.344
α'	124.8	125.3	125.3	122.0
β'	182.3	−176.9	−176.9	−179.5
d	1.782	1.849	1.849	1.451
β_2	−1.6	−0.6	−0.6	−0.3
$\beta_{2'}$	178.4	179.3	179.3	179.7
β_4	−0.4	−0.7	−0.7	−0.2
$\beta_{4'}$	179.6	179.3	179.3	179.8
β_6	−34.3	−37.5	−37.5	−9.1
$\beta_{6'}$	143.6	139.7	139.7	170.4
X	0.423	0.427	0.501	0.288
$O_{(1)}$	−0.601	−0.625	−0.729	−0.286
$C_{(1)}$	0.540	0.550	0.553	0.188
$C_{(2)}$	0.046	0.077	0.192	0.032
$C_{(3)}$	0.001	0.006	0.014	−0.013
$C_{(4)}$	0.065	0.084	0.151	0.063
$C_{(5)}$	0.008	0.015	0.031	−0.012
$C_{(6)}$	0.077	0.097	0.174	0.056
$N_{(2)}$	0.561	0.510	0.232	0.141
$N_{(4)}$	0.538	0.492	0.216	0.135
$N_{(6)}$	0.511	0.469	0.209	0.135
$O_{(2)}$	−0.528	−0.513	−0.447	−0.214
$O_{(2')}$	−0.431	−0.423	−0.350	−0.099
$O_{(4)}$	−0.463	−0.453	−0.385	−0.180
$O_{(4')}$	−0.458	−0.449	−0.381	−0.174
$O_{(6)}$	−0.456	−0.449	−0.385	−0.187
$O_{(6')}$	−0.415	−0.402	−0.327	−0.155
$H_{(3)}$	0.294	0.298	0.362	0.138
$H_{(5)}$	0.288	0.292	0.501	0.145

Table 5. The optimized structural parameters (defined in Table 1) and the charge numbers for lithium picrate at the 6-31G**, 6-31G/6-31G**, 6-31G, and STO-3G levels. All distances are given in Å and all angles are given in degrees.

	6-31G**	6-31G/ 6-31G**	6-31G	STO-3G
r	1.766	1.763	1.763	1.626
α	126.4	129.7	129.7	124.4
β	−12.0	−9.3	−9.3	−0.3
r'	1.240	1.266	1.266	1.280
α'	125.2	123.8	123.8	124.1
β'	−174.8	−175.3	−175.3	−179.6
d	1.843	1.842	1.842	1.685
β_2	6.6	3.7	3.7	−0.1
$\beta_{2'}$	−174.3	−176.9	−176.9	179.9
β_4	−0.4	−0.8	−0.8	−0.1
$\beta_{4'}$	179.6	179.2	179.2	180.0
β_6	−36.8	−34.5	−34.5	−5.9
$\beta_{6'}$	140.7	143.0	143.0	173.7
X	0.740	0.802	0.802	0.306
$O_{(1)}$	−0.779	−0.790	−0.822	−0.279
$C_{(1)}$	0.697	0.692	0.666	0.224
$C_{(2)}$	−0.032	−0.005	0.126	0.012
$C_{(3)}$	−0.001	0.008	0.005	−0.014
$C_{(4)}$	0.043	0.061	0.130	0.046
$C_{(5)}$	0.009	0.016	0.029	−0.012
$C_{(6)}$	0.018	0.039	0.138	0.038
$N_{(2)}$	0.579	0.533	0.237	0.160
$N_{(4)}$	0.533	0.488	0.211	0.132
$N_{(6)}$	0.517	0.476	0.211	0.132
$O_{(2)}$	−0.617	−0.605	−0.551	−0.191
$O_{(2')}$	−0.414	−0.410	−0.344	−0.090
$O_{(4)}$	−0.480	−0.471	−0.403	−0.189
$O_{(4')}$	−0.471	−0.462	−0.395	−0.182
$O_{(6)}$	−0.468	−0.466	−0.402	−0.194
$O_{(6')}$	−0.432	−0.419	−0.348	−0.167
$H_{(3)}$	0.281	0.286	0.356	0.131
$H_{(5)}$	0.275	0.283	0.353	0.139

Fig. 3. Chemical structures showing: (*a*) hydrogen bonding in picric acid, and (*b*) ionic bonding in potassium picrate.

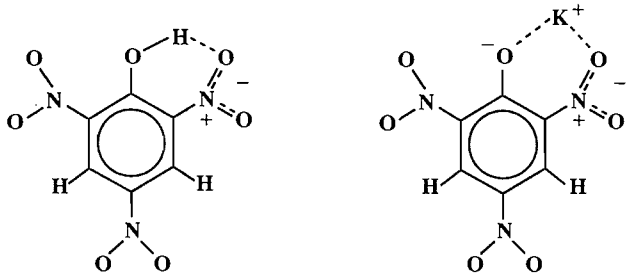

(a) (b)

This level of computation will be referred to as the 6-31G/6-31G** level. The 3*p* polarization function computed by Wachters (10) was also added to the SV set of AOs for potassium (7). It is widely agreed that while the molecular geometry is relatively less sensitive to the choice of an appropriate basis set of AOs, the calculated energy and charges are strongly dependent on this basis. This is demonstrated in Tables 4 and 5, where the structural data and charge numbers of the picric acid and lithium picrate molecules, obtained at the 6-31G**, 6-31G/6-31G**, 6-31G, and STO-3G levels, are shown. One can see that the structural parameters obtained at the 6-31G** and 6-31G levels are very similar. However, the atomic charges computed at the 6-31G** level are significantly different from those obtained at the 6-31G level. Because the computations performed at the 6-31G/6-31G** level for picric

acid and lithium picrate produce results very similar to those obtained at the pure 6-31G** level, and because full optimization of the geometry of sodium and potassium picrates at the 6-31G** level would be extremely time consuming, performing the computations at the 6-31G/6-31G** level is justified.

The electrical charge distribution[8] for each molecule in the optimized configuration is given in the lower part of Tables 3–5. Consideration both of structural parameters and of charge distribution allows address of such topics as the competition between the inductive effects of the nitro groups and of the oxygen atom at $C_{(1)}$, the relationship between the molecular conformation and the charge distribution on the molecule, the correlation between the charge on the carbon ring and the reactivity of the ring to nucleophilic attack, and the nature of the chemical bond between the alkali cation and the picrate anion.

To better understand how the presence and position of one or more nitro groups on the benzene ring affect the charge distribution in the molecule, model benzene, chlorobenzene, nitrobenzene, and TNB molecules were also optimized (6-31G/6-31G**) using typical bond lengths (11) rather than crystallographic data as initial input data. Optimization of these model molecules yielded planar conformations to within computational accuracy, with all bond angles close to 120°. Semi-empirical MO calculations on nitrobenzene by Matsunaga et al. (12) also indicate that the planar conformation is the most stable. The nitrobenzene model molecule with the nitro group arbitrarily fixed in an orientation perpendicular to the phenyl plane was also optimized to investigate the influence of the rotation of a nitro group on the relative magnitudes of the inductive and resonance effects. The charge distributions for benzene, the two nitrobenzene molecules, and TNB are depicted in Fig. 4.

Another type of analysis of the configuration of nuclei and the electron charge-density distribution can be carried out using charge-density maps. Such a display utilizes partially integrated electron probability densities derived from our SCF MO wave functions (13). The maps provide for visual techniques demonstrating the main features of the molecular geometry and its electron charge distribution. In the present contribution, we have produced molecular isodensity surfaces (MIDCOs) (14, 15) of the electron charge-density maps for picric acid (Fig. 5) and potassium picrate (Fig. 6). These maps were computed using the RHOCALC computer program (16).

Fig. 4. Charge numbers for benzene, nitrobenzene (with rotation angles $\beta_1 = 0$ and 90°), and 1,3,5-trinitrobenzene.

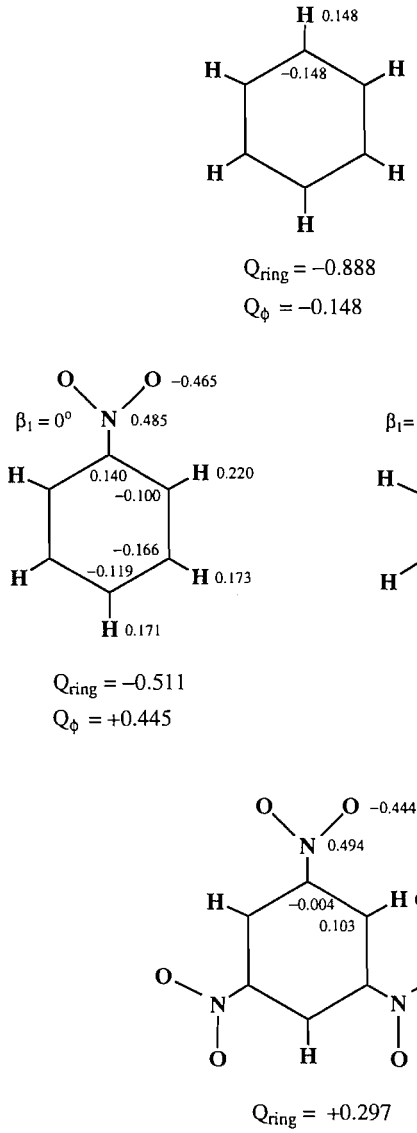

Discussion

Part A. Mulliken point charges

The following discussion of the optimized 1-R-TNB molecules is primarily concerned with the conformational geometry of, and the charge distribution in, each molecule. As will be shown, the two primary structural factors that influence both of these properties are: (*i*) the identity of the atom X, and (*ii*) the orientation and position of the nitro groups relative to X and to each other. There are three interrelated properties of X that are important: (*i*) its size, (*ii*) its ability to form intramolecular bonds, and (*iii*) its electron-withdrawing properties.

As noted above, the optimized configuration of the TNB molecule is planar, i.e., the ring is planar and the three nitro groups are coplanar with the ring. A functional group R substituted for one of the protons in TNB may interact with the two adjacent nitro groups, causing these adjacent nitro groups to rotate so that they are no longer coplanar with the ring. The degree to which rotation occurs is related to the size of R, the charge on R, and possibly other relevant factors such as intramolecular hydrogen bonding.

The presence at $C_{(1)}$ of groups such as OH that can hydrogen-bond with oxygens on the adjacent nitro groups tends to restrict rotation of the bonded nitro group. For example, even though one would expect rotation of both *ortho* nitro groups due to electrostatic repulsion between $O_{(1)}$ and the nitro oxy-

[8] The electrical charge on each atom is derived using Mulliken population analysis. The charge is presented as a "charge number," a unitless value calculated by dividing the electrostatic charge on the atom by the absolute value of the charge on an electron. Although the concept of a point atomic charge never exactly represents reality, it provides a quick and computationally inexpensive insight into molecular electronic charge-density distribution.

Fig. 5. Five top views and one side view of MIDCOs for picric acid at ρ_0 equal to (a) 0.01, (b) 0.03, (c) 0.05, (d) 0.1, (e) and (f) 0.2. The boundary density ρ_0 is expressed in $Å^{-3}$.

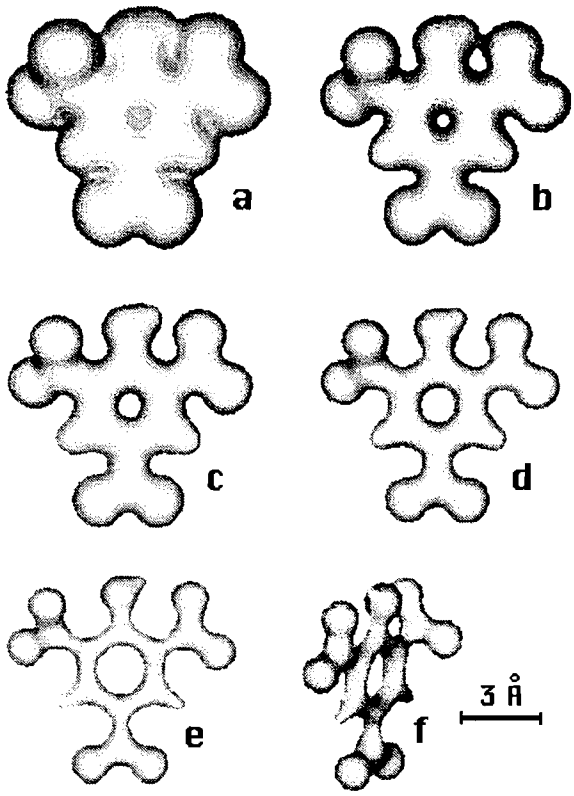

gens, the formation of the hydrogen bond between $H_{(1)}$ and $O_{(2)}$ in the picric acid molecule (Fig. 3*a*) forces the $N_{(2)}$ nitro group to be coplanar with the ring. Only the $N_{(6)}$ nitro group is rotated. Similarly, the picrate salts would be expected to form intramolecular ionic bonds between the cation X^+ and $O_{(1)}$ and $O_{(2)}$ (Fig. 3*b*), which would result in similar restricted rotation of the $N_{(2)}$ nitro group.

The charge distribution in 1-R-TNB compounds is significantly influenced by the inductive and resonance effects of the three nitro groups, by the electron-withdrawing (inductive) and (or) the electron-donating properties of R, and by the extent of nitro group rotation due to steric and electrostatic effects and intramolecular hydrogen bonding or ionic bonding. The effects on the molecular charge distribution of the number of nitro groups attached to the ring, their relative position on the ring, and their rotation angle with respect to the ring plane are illustrated by comparing the computed charge distributions in the benzene, nitrobenzene, and TNB molecules, shown in Fig. 4.

In benzene, which has D_{6h} ground-state symmetry, the charge number for each carbon atom is −0.148 and for each hydrogen atom +0.148. The ring charge number, Q_{ring},[9] is −0.888, as shown in Fig. 4. Replacing one ring hydrogen with a nitro group to form nitrobenzene results in the withdrawal of electron density from the phenyl ring to the nitro group via

[9] $Q_{ring} = \sum_{i=1}^{6} Q_{C_{(i)}}$ is the charge number of the carbon ring for the 1-R-2,4,6-trinitrobenzenes.

Fig. 6. Five top views and one side view of MIDCOs for potassium picrate at ρ_0 equal to (a) 0.01, (b) 0.03, (c) 0.05, (d) 0.1, (e) and (f) 0.2. The boundary density ρ_0 is expressed in $Å^{-3}$.

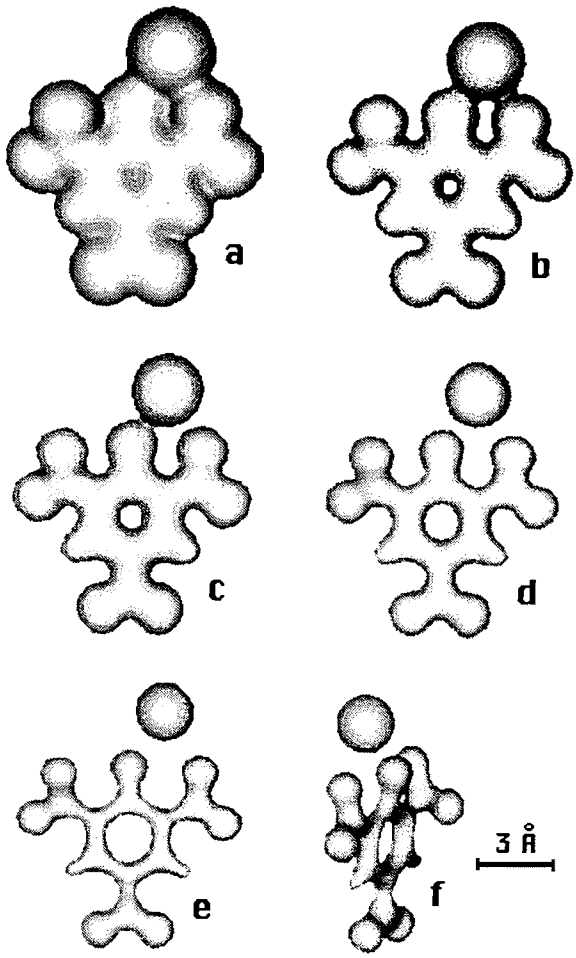

both induction and resonance. Maximum resonance withdrawal occurs when the nitrogen *p* orbital containing the lone pair of electrons is parallel with the π-*p* orbital of the attached ring carbon so that maximum overlap can occur. Resonance withdrawal of electron density in nitrobenzene occurs primarily at the *ortho* and *para* positions.

If the nitro group is coplanar with the ring (the angle β_1 of rotation of the nitro group equals 0°), charge can be visualized to be withdrawn by both induction and resonance. Comparison of the charge (Q_ϕ = +0.445)[10] on the C_6H_5 group in planar nitrobenzene (Fig. 4) with that (Q_ϕ = −0.148) on the phenyl group in benzene indicates the extent of electron withdrawal by the nitro group *via* both induction and resonance (Fig. 4). All the ring carbons experience a decrease in electron density, with $C_{(1)}$ showing the greatest change (from −0.148 to +0.140). The carbons *ortho* and *para* to the nitro group experience the next largest withdrawal.

If, however, the plane of the nitro group is perpendicular to the plane of the ring (β_1 = 90°), one expects electron withdrawal primarily via induction, since then there is no effective *p* orbital overlap. Figure 4 gives the charge distribution for the

[10] Q_ϕ is the sum of the charge numbers for the six carbons plus those of the five hydrogens.

Table 6. The charge number Q_{ring} for the carbon ring in picric acid, the picrate −1 ion, the picrate salts, and 2,4,6-trinitrobenzene.

	Picric acid	Picrate −1 ion	Li picrate	Na picrate	K picrate	Trinitrobenzene
Q_{ring}	+0.829	+0.548	+0.811	+0.761	+0.720	+0.297

nitrobenzene model molecule in which $\beta_1 = 90°$ and Q_ϕ = +0.431. The data show that electron withdrawal is primarily from $C_{(1)}$. Also the $C_{(4)}$ carbon atom "attracts" some electron density, increasing the electronic charge gradient on the phenyl ring. From the comparison of the charge distribution on the C_6H_5 portion of each nitrobenzene molecule, one can see that rotation of nitro group primarily modulates the inductive effect while the resonance effect varies relatively little.[11] Similar results were obtained by Hehre et al. (17) using the STO-3G basis set.

In TNB, where three nitro groups are *meta* to each other, resonance withdrawal of electron density is reinforced at $C_{(2)}$, $C_{(4)}$, and $C_{(6)}$, since each of these carbon atoms is *ortho* to two nitro groups and *para* to one. The charge number on each of these carbons is +0.103, as compared to −0.100 in nitrobenzene ($\beta_1 = 0°$) and −0.148 in benzene. The total charge number Q_{ring} on the carbon ring in TNB is +0.297, as compared to −0.511 in nitrobenzene and −0.888 in benzene. Thus the presence of three nitro groups on the phenyl ring activates the ring to nucleophilic substitution by withdrawing electron density from the carbon ring, giving it a positive charge.[12]

In picric acid the intramolecular hydrogen bond between $H_{(1)}$ and $O_{(2)}$ causes the $N_{(2)}$ nitro group to be coplanar with the phenyl ring. The $N_{(6)}$ nitro group is twisted ~38° out of plane.[13] The difference in the calculated charge numbers at $C_{(2)}$ (+0.077) and $C_{(6)}$ (+0.097) is the direct result of the difference in the rotation of the $N_{(2)}$ and $N_{(6)}$ nitro groups. As was shown in Fig. 4, rotation of the nitro group resulted in an increase in positive charge on the attached ring carbon. It is postulated that this increase is the result of the loss of back-bonding of the unshared electron pair on the nitro nitrogen when the nitro group is rotated.

Optimization of the model picrate −1 ion was performed for use as a reference structure for comparison with picric acid and the alkali picrates. It is recognized that the picrate anion without the presence of the counter-cation does not represent an "actual" species. It does, however, provide a starting point for discussions regarding the effects of the presence of the proton or cation on the conformation of, and the charge distribution in, the neutral molecule and the picrate salts.

In the picrate anion there are two interrelated effects that can cause rotation of the *ortho* nitro groups. These are the steric and electrostatic repulsion between $O_{(1)}$, which exhibits a negative charge number of −0.599, and $O_{(2)}$ and $O_{(6)}$, both of which are at −0.445 (Table 3). The fact that the magnitudes of the charges on $O_{(2)}$ and on $O_{(6)}$ are less than those on the other four nitro oxygens can be interpreted in terms of a stabilizing withdrawal of electron density to these other oxygens, to minimize the electrostatic repulsion. The combination of the steric and electrostatic repulsion results in a 30° twist[14] of the *ortho* nitro groups. Both the *ortho*-nitro groups are twisted to the same side of the planar ring (with $O_{(1)}$ and $O_{(6')}$ above the ring plane) and $O_{(1)}$ lies 10° out of the ring plane on the opposite side ("behind" the ring plane). Thus, the picrate anion has C_s symmetry, with $C_{(1)}$, $C_{(4)}$, and $O_{(1)}$ lying in the reflection plane situated perpendicular to the carbon ring. In picric acid and the picrate salts this symmetry is absent because the proton and alkali cations are not in the symmetry plane.

In the alkali picrates, intramolecular bonding between the cation X^+ and $O_{(1)}$ and $O_{(2)}$ influences the rotation angle of the $N_{(2)}$ nitro group, with the magnitude of this angle directly related to the size of the cation. The lithium ion, the smallest of the alkali cations, is the least distant (0.005 Å) from the $C_{(1)}$-$C_{(2)}$-$C_{(3)}$ plane and is approximately equidistant from $O_{(1)}$ and $O_{(2)}$. The interatomic distances r [Li···$O_{(1)}$] and d [Li···$O_{(2)}$] are 1.763 and 1.842 Å, respectively. These distances are less than the sum of the ionic radii of Li(+1) (0.68 Å (20)) and O(−2) (1.32 Å (20)), indicating an intramolecular bonding. With the larger Na^+ and K^+, the cations are positioned, respectively, 0.133 and 0.334 Å above the $C_{(1)}$-$C_{(2)}$-$C_{(3)}$ plane. To maintain the proper interatomic distances for ionic bonding of each cation to $O_{(1)}$ and $O_{(2)}$, the $N_{(2)}$ nitro group rotates ~10° for Na^+ and ~17° for K^+. As a consequence of this rotation, the dihedral angle β (Table 3) also increases, with the angle of rotation increasing with the size of the cation.

The deviations of the optimized molecular coordinates (particularly r, d, α, β, β_2, and $\beta_{6'}$) from those of the crystallographic data for picric acid and potassium picrate are primarily the result of intermolecular interactions that exist within the crystal but are absent in the free molecule. For example, in the potassium picrate crystal, the K^+ cation is coordinated with eight oxygen atoms (two $O_{(1)}$, four $O_{(2)}$ and two $O_{(4)}$) from four neighboring molecules (9). Similarly, intermolecular hydrogen bonding in picric acid results in a deviation of the optimized molecular configuration from the x-ray determined configuration. However, this interaction

[11] The optimized molecular conformation and the intramolecular rotational barrier of the nitro group in nitrobenzene have been calculated and compared with experimental data by Head-Gordon and Pople (18), who compared the results from 11 *ab initio* Hartree–Fock theoretical models, and also by Matsunaga et al. (12), who found that the semi-empirical (AM1) computations give good agreement.

[12] The π-electron charges for the atoms in TNB were calculated by Wennerström and Wennerström (19) using a modified SCF-MO-PPP (Pariser, Parr, Pople) method.

[13] The fact that the differences between dihedral angles β_2 and $\beta_{2'}$, β_4 and $\beta_{4'}$, and β_6 and $\beta_{6'}$ are not exactly 180° (Tables 3 and 4) is the result of the two oxygens in each nitro group being allowed to rotate independently about their respective C—N bonds during the conformational optimizations.

[14] The 2–4° differences between dihedral angles β_2 and β_6 and angles $\beta_{2'}$ and $\beta_{6'}$ are the result of the small deviations from planarity of the carbon ring.

does not influence the orientation of the nitro group at $C_{(2)}$, which proves that the intramolecular hydrogen bonding between the $H_{(19)}$ and $O_{(2)}$ is much stronger than any intermolecular interaction.

As shown by the data in Table 3, ~ -0.4 of the nominal -1 charge on $O_{(1)}$ of the model picrate anion has been drawn into and redistributed over the trinitrophenyl ring. Comparison of the charge numbers for picric acid and for the picrate ion show that the charge is redistributed primarily to the carbon atoms $C_{(2)}$ and $C_{(6)}$, and to the six nitro oxygens. Introduction of the lithium, sodium, or potassium cation to form the picrate salt shifts the electron density in the isolated picrate anion toward $O_{(1)}$ and $O_{(2)}$, due primarily to the electrostatic attraction of the cation. The electron densities on the other five nitro oxygens in the three picrate salts are less than those on the corresponding oxygens of the picrate anion. The magnitude of the positive charge on the cations confirms the presence of ionic bonding between the cation and $O_{(1)}$ and $O_{(2)}$, in agreement with the interpretation of the crystallographic data reported by Maartmann-Moe (9).

As shown in Table 6, withdrawal of electron density from the carbon ring is significantly greater for picric acid and the alkali picrates than for trinitrobenzene. This is due primarily to the presence of the electronegative oxygen atom $O_{(1)}$ in the former molecules. As expected, as the size of X increases, the magnitude of the positive charge on the carbon ring decreases, i.e., X withdraws less electron density from the ring. This is consistent with the corresponding increase in the magnitude of the charge numbers for X, as shown in Table 3.

Part B. Electron charge densities

In the second part of this paper we demonstrate that the electronic charge densities yield useful information about the character and strength of chemical bonds, and the configuration of atomic nuclei. Gratifyingly, this information can easily be graphically displayed, allowing conclusions to be derived from the pictorial representation of the electron charge distribution. Since the charge density is a function on a 3-dimensional space, it cannot be shown as a functional (4-dimensional) graph. The best way to plot a charge-density map is by using the molecular isodensity surfaces (MIDCOs). The topological features of these surfaces can then be interpreted in terms of the character and strength of chemical bonds. In general, there is a strong covalent bond between two atoms if they remain inside a connected isodensity surface, even at relatively high electron density thresholds. Otherwise, if an isodensity surface splits into two disconnected pieces each containing an atom, the covalent bond between these atoms is considered weak. The more electron charge is concentrated on a molecular group or individual atom, the larger are the connected components of isodensity surfaces surrounding this atom as compared to other groups or atoms. This powerful and very elegant method of analysis, based on the topological features of "Density Domains," was recently proposed and developed by Mezey (14, 15).

In Figs. 5 and 6, sets of six MIDCOs for the picric acid and potassium picrate molecule are presented. The electron charge-density function $\rho(\boldsymbol{r})$ is defined as the fractional number of electrons within a small volume element δV at $\boldsymbol{r}$ divided by δV (in $Å^3$). We are concerned with isodensity surfaces for given values ρ_0 of ρ. At low density ($\rho_0 = 0.01$) there is one connected surface with no holes for each molecule. However, even at this low density threshold one can see that the characters of the $O_{(1)}$—X and the $O_{(2)}$—X bonds are very different in picric acid while both bonds are more or less equivalent in potassium picrate. This can be observed in every picture in Figs. 5 and 6. In picric acid the first of these bonds is strongly covalent and the second bond is a hydrogen bond. In potassium picrate both bonds are much less covalent and the surface surrounding the potassium atom becomes disconnected below $\rho_0 = 0.1$. This fact and the spherical shape of the surface surrounding the potassium atom suggest that the bond type for both discussed bonds is ionic. The $O_{(1)}$—K bond is slightly more covalent than the $O_{(2)}$—K bond but the difference is only quantitative and not very significant. The size of the hydrogen atom and the intramolecular hydrogen bond explain why the nitro group at $C_{(2)}$ is coplanar with the phenyl ring. The much larger potassium ion repulses the two oxygen atoms $O_{(1)}$ and $O_{(2)}$ out of the phenyl ring plane. However, it appears quite likely that there is some interaction between the potassium atom and the oxygen atom $O_{(6)}$, resulting in a decrease of the angle by which the nitro group at $C_{(6)}$ is twisted about the $C_{(6)}$—$N_{(6)}$ bond.

Conclusions

It is evident from the data that the presence of electron-withdrawing groups such as NO_2 and OX (X = H, Li, Na, K) results in inductive and resonance withdrawal of the π-electron density from the phenyl ring into these electron-withdrawing groups. This shift in electron-charge distribution results in positive charge numbers Q_{ring} on the phenyl ring of TNB, picric acid, and the alkali picrate salts (Table 6). This means that the phenyl ring becomes more susceptible to nucleophilic attack.

The alkali-metal – picrate-group bonds are shown to be highly ionic with the picrate anion exhibiting a negative total charge number (< -0.8: Table 3). Therefore, as was suggested by the x-ray study of the potassium picrate crystal (9), one can treat the picrate group in alkali picrates as an independent species, the picrate anion. The computations carried out for a model free picrate anion give results that are reasonably close to those obtained for the alkali-metal salts. This fact additionally supports the conclusion about the ionic character of the alkali-metal – picrate-group bond.

Comparison of the charge numbers on the phenyl ring for the alkali picrates and for picric acid shows that the ionic character of the O—X bond in alkali picrates, resulting in more electron withdrawal onto the picrate group, does not significantly alter their Q_{ring} values as compared to that of picric acid. This is attributed to the stabilizing effect of the nitro groups, which have enough capacity to withdraw the excess electron charge from the phenyl ring. Similarly, the identity of the alkali–metal ion in the alkali picrates has only a moderate effect on the molecular configuration and charge distribution, which thus do not lead to any substantial redistribution of charges on the carbons of the phenyl ring (Table 3). Therefore, the identity of the atom X should not markedly influence the susceptibility of the phenyl rings to nucleophilic attack.

Acknowledgments

This work was supported by a research grant from the Natural Sciences and Engineering Research Council of Canada.

Z. Zimpel is the beneficiary of an International Fellowship grant from NSERC. We wish to extend our thanks to Dr. P.G. Mezey, for introducing us to the concept of Density Domains and for his friendly support.

References

1. F. Terrier. Nucleophilic aromatic displacement. VCH, New York. 1991.
2. D.L. Draper, R.J. Barton, B.E. Robertson, B.R. Nelson, and J.A. Weil. Can. J. Chem. **71**, 1057 (1993).
3. M.R. Crampton and M.A. El Ghariani. J. Chem. Soc. (B), 330 (1969).
4. B. Gibson and M.R. Crampton. J. Chem. Soc. Perkin Trans. 2, 648 (1979).
5. M.K. Chantooni, Jr. and I.M. Kolthoff. J. Phys. Chem. **80**, 1306 (1976).
6. M.J. Frisch, G.W. Trucks, M. Head-Gordon, P.M.W. Gill, M.W. Wong, J.B. Foresman, B.G. Johnson, H.B. Schlegel, M.A. Robb, E.S. Replogle, R. Gomperts, J.L. Andres, K. Raghavachari, J.S. Binkley, C. Gonzalez, R.L. Martin, D.J. Fox, D.J. DeFrees, J. Baker, J.J.P. Stewart, and J.A. Pople. Gaussian 92 (Revision A). Gaussian Inc., Pittsburgh, Pa. 1992.
7. A. Schäfer, H. Horn, and R. Ahlrichs. J. Chem. Phys. **97**, 2571 (1992).
8. E.N. Duesler, J.H. Engelman, D.Y. Curtin, and I.C. Poul. Cryst. Struct. Commun., **7**, 449 (1978).
9. K. Maartmann-Moe. Acta Crystallogr. Sect. B: Struct. Crystallogr. Cryst. Chem. **B25**, 1452 (1969).
10. A.J.H. Wachters. J. Chem. Phys. **52**, 1033 (1970).
11. F.H. Allen, O. Kennard, D. Watson, L. Brammer, A.G. Orpen, and R. Taylor. J. Chem. Soc. Perkin Trans. 2, S1 (1987).
12. T. Matsunaga, Y. Nakayama, M. Iida, S. Oinuma, N. Ishikawa, and T. Tanaka. Propellants, Explos. Pyrotech. **17**, 63 (1992).
13. A. Szabo and N. S. Ostlund. Modern quantum chemistry. McGraw–Hill, New York. 1989. Sect. 3.4.3.
14. P.G. Mezey. Shape in chemistry. VCH, New York. 1993. Chap. 2.
15. P.G. Mezey. Can. J. Chem. **72**, 928 (1994).
16. P.D. Walker and P.G. Mezey. Computer program library of the mathematical chemistry research unit. Department of Chemistry, University of Saskatchewan, Saskatoon. 1995.
17. W.J. Hehre, L. Radom, and J.A. Pople. J. Am. Chem. Soc. **94**, 1496 (1972).
18. M. Head-Gordon and J.A. Pople. Chem. Phys. Lett. **173**, 585 (1990).
19. H. Wennerström and O. Wennerström. Acta Chem. Scand. **26**, 2883 (1972).
20. R.C. Weast (*Editor*). Handbook of chemistry and physics. 70th ed. CRC Press, Boca Raton, Fla. 1989–1990, p. F-187.

In situ preparation of cyclopropanones with the bicyclo[3.1.0]hexan-6-one skeleton (substituted examples of the Loftfield intermediate). Confirmation of a very facile intramolecular alkyl cyclopropanone – dienol rearrangement

T. S. Sorensen and F. Sun

Abstract: Four substituted bicyclo[3.1.0]hexan-6-ones (cyclopropanones) were prepared *in situ*, starting from the corresponding 2,6-dibromocyclohexanone and reductively removing the bromine atoms with the organometallic salt $PPN^+Cr(CO)_4NO^-$. The reaction is essentially instantaneous at −78 or −100°C, and can be conveniently carried out in an NMR tube for easy characterization of the products by low-temperature ^1H and ^{13}C NMR spectroscopy. The 1,5-di-*tert*-butyl and 1-*tert*-butyl analogs were thermally stable to ca. 0°C, but the 1-*tert*-butyl-5-methyl and 1-*tert*-butyl-5-ethyl derivatives were extremely labile, rearranging at ca. −80°C into a cross-conjugated enol, where the methyl (or ethyl) substituent was converted into an exomethylene group. These enols were also characterized as *in situ* species using ^1H and ^{13}C NMR spectroscopy, and by allowing the enol → α,β-unsaturated ketone rearrangement to take place at about 25°C. The mechanism of the enol formation was investigated using a 1-*tert*-butyl-5-CD_3 analog, and the k_H/k_D ratio for enol formation was determined to be 6 ± 2. From this, the rate-determining step in the enol formation was postulated as a C-H → H-O transfer of a hydrogen atom in a cyclohexyl oxyallyl intermediate. The 1,5-di-*tert*-butylbicyclohexanone shows dynamic ^1H NMR line broadening, the origin of which is also proposed to involve a cyclohexyl oxyallyl intermediate.

Key words: cyclopropanone, oxyallyl, bicyclo[3.1.0]hexan-6-one, dienol, sigmatropic rearrangement.

Résumé : On a préparé quatre bicyclo[3.1.0]hexan-6-ones (cyclopropanones) substituées *in situ* à partir des 2,6-dibromocyclohexanones correspondantes, en procédant à l'élimination réductrice des atomes de brome par le sel organométallique $PPN^+Cr(CO)_4NO^-$. La réaction est essentiellement instantanée à −78 ou à −100°C et on peut facilement l'effectuer dans un tube à RMN pour une caractérisation facile des produits par spectroscopie RMN du ^1H et ^{13}C à basse température. Les analogues 1,5-di-*tert*-butyle et 1-*tert*-butyle sont thermiquement stables jusqu'à environ 0°C, mais les dérivés 1-*tert*-butyl-5-méthyle et 1-*tert*-butyl-5-éthyle sont extrêmement labiles qui se réarrangent à environ −80°C pour conduire aux énols à conjugaison croisée dans lesquels les groupes méthyle (ou éthyle) ont été transformés en groupes éxométhylène. On a aussi caractérisé ces énols sous la forme d'espèces *in situ* en faisant appel à la spectroscopie RMN du ^1H et du ^{13}C et en permettant au réarrangement énol → cétone α,β-insaturée de se produire à environ 25°C. On a étudié le mecanisme de formation de l'énol en utilisant un analogue 1-*tert*-butyl-5-CD_3: on a déterminé que la k_H/k_D pour le formation de l'énol est de 6 ± 2. Sur cette base, on en déduit que l'étape qui détermine la vitesse de formation de l'énol doit être un transfert C-H → H-O d'un atome d'hydrogène dans un intermédiaire cyclohexyl oxyallyle. Dans le spectre RMN du ^1H de la 1,5-di-*tert*-butylbicyclohexanone, on observe un élargissement dynamique de la raie dont l'origine implique probablement un intermédiaire cyclohexyl oxyallyle.

Mots clés : cyclopropanone, oxyallyle, bicyclo[3.1.0]hexan-6-one, diénol, réarrangement sigmatropique.

[Traduit par la rédaction]

Introduction

In a classic study involving the early use of a ^{14}C label in studying organic reaction mechanisms, Loftfield (1) discovered in 1950 that the Favorski rearrangement of 2-chlorocyclohexanone proceeded by way of a symmetrical intermediate, postulated to be the cyclopropanone **1** (R=H) (bicyclo-[3.1.0]hexan-6-one).

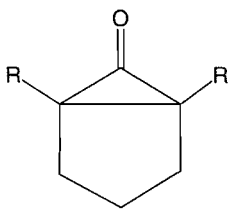

1 R=H
2 R=CH_3

To date there has been no direct observation of **1**. In a previous study (2), we attempted without success to prepare the 1,5-dimethyl analog **2** by the debromination of **3** at −78°C

Received August 4, 1995.

T. S. Sorensen[1] **and F. Sun.** The Department of Chemistry, University of Calgary, Calgary, AB T2N 1N4, Canada.

[1] Author to whom correspondence may be addressed. Telephone: (403) 220-5361. Fax: (403) 289-9488. E-mail: sorensen@acs.ucalgary.ca

with the reagent $PPN^+Cr(CO)_4NO^-$, a reaction type that worked well with larger rings and with various acyclic systems to produce near-quantitative *in situ* yields of the corresponding cyclopropanones.

In the case of the failed reaction **3** —X→ observable **2**, it was postulated that the cyclopropanone **2** was being formed, but that it was rearranging to a dienol **4** faster than it was being formed in the reaction of the organometallic anion with the dibromide **3**, as shown in eq. [1], where $k_2 > k_1$.

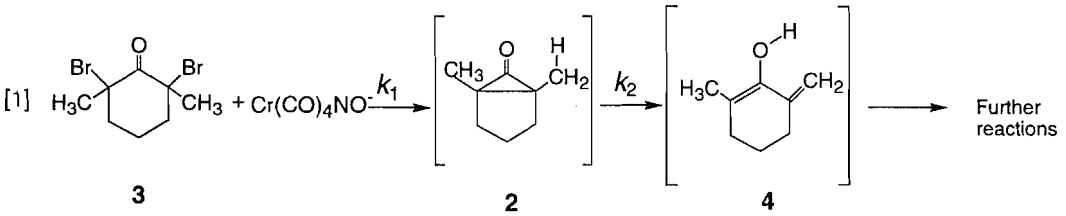

3 **2** **4**

Since **4** (acidic hydrogen) would also be expected to readily react with the $Cr(CO)_4NO^-$ reagent, the actual course and stoichiometry of the reaction was complex. The end result of all this, in terms of reaction products, has been published (2). However, it should be kept in mind that the evidence for **2** was circumstantial since this species was not directly observed.

In retrospect, and assuming that the fast rearrangement of **2** → **4** was taking place, it was apparent that the methyl groups in **2** vs. **1**, far from providing "steric protection" for the molecule, were in fact an Achilles heel allowing for the very facile rearrangement of **2** into the dienol **4** by the C → O shift of a methyl hydrogen. This same process has now been observed by us for a number of cyclopropanones and, although unexplored until recently, is one of the key reasons why cyclopropanones are such reactive molecules.

The obvious solution to the rearrangement problem is to use either tertiary substituents or hydrogen. In this paper, we show that this approach allows one to finally prepare and characterize *in situ* solutions of bicyclo[3.1.0]hexan-6-ones, but it should be emphasized that we have removed only the most urgent of the rearrangement routes available to these molecules and they remain too unstable to isolate in any conventional way.

Nevertheless, an analysis of the NMR spectra of these cyclopropanones does provide considerable structural information and, in addition, dynamic NMR observations with the 2,5-di-*tert*-butyl analog of **1** show that reversible ring opening to the presumed oxyallyl valence bond isomer is a very facile process.

As an added bonus, we have also been able to prepare and characterize *in situ* solutions of bicyclo[3.1.0]hexan-6-ones with one "reactive" substituent (CH_3 or CH_3CH_2) and one tertiary substituent. As expected, these are very labile, rearranging quite cleanly to the corresponding dienol, which can also be completely characterized by NMR spectroscopy as an *in situ* solution species. Using one of these examples (*t*Bu, CH_3) also allowed us to directly measure the large kinetic isotope effect associated with the rearrangement of the cyclopropanone to the dienol.

Results and discussion

In each case, the cyclopropanones **10–13** were generated *in situ* at low temperature in NMR tubes and characterized by both ^1H and ^{13}C NMR, using a procedure previously described (2, 3). The overall reaction is shown in eq. [2]. The starting dibromo ketones **5–9** were easily prepared by direct bromination, and the ketones themselves are either known or accessible by alkylation of 2-*tert*-Bu-cyclohexanone.

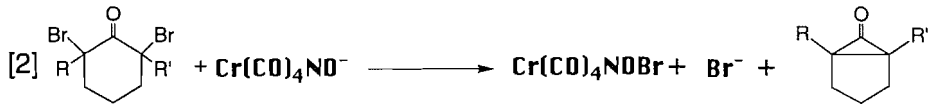

5 R=R'=tBu
6 R=tBu, R'=H
7 R=tBu, R'=CH_3
7a R=tBu, R'=CD_3
8 R=tBu, R'=CH_3CH_2
9

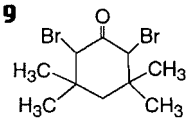

10 R=R'=tBu
11 R=tBu, R'=H
12 R=tBu, R'=CH_3
12a R=tBu, R'=CD_3
13 R=tBu,R'=CH_3CH_2

All attempts to convert dibromo ketone **9** into a characterizable cyclopropanone were unsuccessful. Some of the cyclopropanone may indeed be formed but, unless the product formation is clean, it is difficult to definitively interpret the experimental *in situ* NMR spectrum. Previously we had attempted[2] to prepare the parent bicyclo[3.1.0]hexan-6–one from 2,6-dibromocyclohexanone, again without success.

[2] A.P. Masters. Unpublished results.

Qualitative stability comparisons of the bicyclo[3.1.0]hexan-6-ones 10–13

Cyclopropanone **10** could be prepared at −78°C in methylene chloride (or CD_2Cl_2) solution. NMR spectra were obtained at intervals from −80 to −10°C, where a clean rearrangement to α, β-unsaturated ketone **14** (4) became rapid. Cyclopropanone **11** solutions were slightly more stable than those of **10**, but **11** rapidly decomposes at 20°C without forming a characterizable rearrangement product, i.e., no single dominant product was formed.

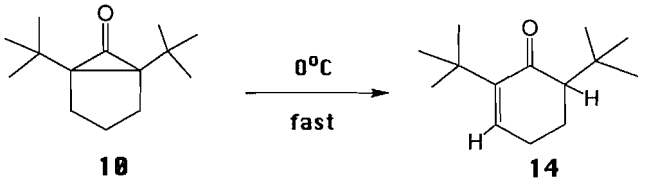

In contrast to **10** and **11**, and as mentioned in the Introduction, cyclopropanones **12** and **13** were very labile. Solutions of **12** in a $CDCl_2F$–CD_2Cl_2 mixture could be prepared at *ca.* −100 to −110°C, and NMR spectra were collected at −95°C. Even under these conditions there was a small amount of the rearrangement dienol formed during a 1 h ^{13}C NMR collection. Cyclopropanone **12** rearranges rapidly at −80°C to give a new species, identified by NMR spectroscopy as the aforementioned dienol **15** (a cross-conjugated enol). Cyclopropanone **13** is slightly more stable than **12**, but also cleanly rearranges to a dienol, in this case the stereoselective formation of **16**.

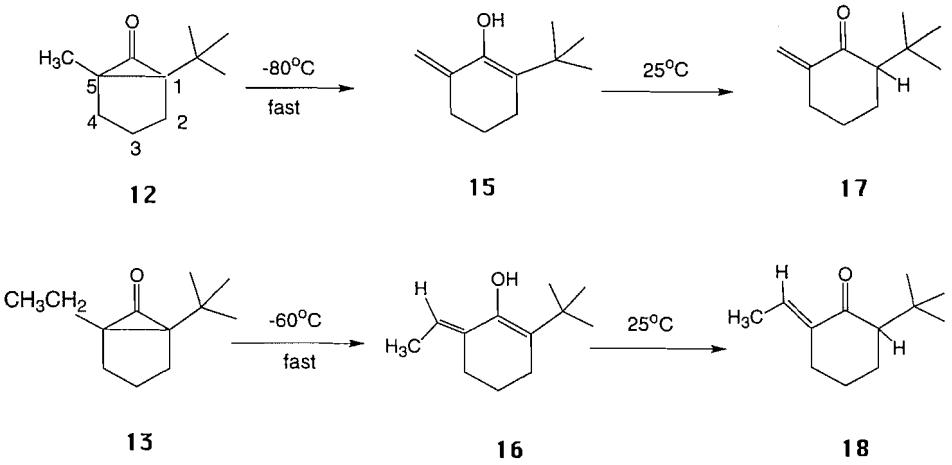

At about 25°C, dienols **15** and **16** are slowly rearranged to the α,β-unsaturated ketones **17** and **18**, respectively. These stable compounds can of course be isolated and characterized in the normal way. The key advantage of the systems **12** and **13** in probing the overall mechanism of the cyclopropanone rearrangement is that the intermediate dienols are formed at a much faster rate than that of their subsequent ketonization, so that definitive NMR characterization of a "clean" dienol product is possible.

NMR characterization of the cyclopropanones

In the *in situ* reactions corresponding to eq. [2], one first sees that the starting material (dibromo ketone) peaks have completely disappeared and are replaced by those we assign to the cyclopropanone. Since the latter are all alkyl-type hydrogens, the ^1H NMR spectra are not particularly distinctive, although in all cases the H-3 methylene hydrogens of the cyclopentane ring have distinctly different chemical shifts, one appearing at δ 1.78, and the other at 1.05 in **10** (δ 1.85 and 1.18 in **11**; 1.76 and 1.12 in **12**). The unusually high-field position of one of these signals (ranging from δ 1.05 to 1.18) is indicative of a shielding contribution from the carbonyl π bond, which in turn implies a boatlike conformation, as shown below:

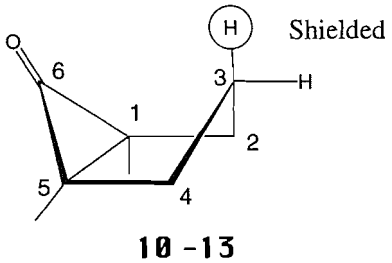

Simple bicyclo[3.1.0]hexanes also have a boat conformation (5). Further evidence for this boat conformation in **10–13** comes from a detailed analysis of the vicinal coupling constants in the cyclopentane ring (see Experimental).

The ^{13}C NMR results are more diagnostic in that the $^{13}C{=}O$ peak is quite deshielded, ca. δ 225–226 ppm in **11–13**. A similar result was previously observed with simple methyl-substituted cyclopropanones (2). Compound **10** is unusual in this series in having a more shielded ^{13}C carbonyl peak (δ 217.0).

Comparison of $Fe_2(CO)_9$ and $Cr(CO)_4NO^-$ for the debromination of α, α′-dibromo ketones

2,6-Dibromo-2,6-di-*tert*-butylcyclohexanone **5** reactions offer a direct comparison between the Noyori reaction (4) for the debromination of α,α′-dibromo ketones and that employed in our work. In benzene solvent, the major product of the $Fe_2(CO)_9$ reaction is compound **19** (80%), with smaller amounts of **20** (3%) and **14** (15%). With $Cr(CO)_4NO^-$, the bicyclohexanone **10** is formed, this rearranging below room temperature to **14**. The $Fe_2(CO)_9$ reaction clearly induces Wagner–Meerwein shifts, which Noyori has attributed to an oxyallyl-O-FeLn$^+$ intermediate (allyl cation character).

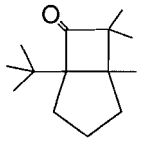

19

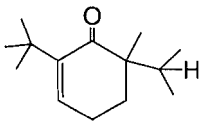

20

In contrast, we believe that the reactions using $Cr(CO)_4NO^-$ involve a very transitory "free" oxyallyl (see later discussion), which shows no tendency for Wagner–Meerwein rearrangements.

Rearrangement reaction of bicyclo[3.1.0]hexan-6-ones 12 and 13 into dienols 15 and 16

As briefly mentioned, bicyclo[3.1.0]hexan-6-ones **12** and **13** rearrange rapidly at low temperatures to give the dienols **15** and **16**, respectively. The characterization of these dienols involves: (*a*) *in situ* ^1H and ^{13}C NMR spectra that agree well with those expected for these structures. In particular, the exocyclic methylene hydrogens in the ^1H NMR and the alkene carbons, and absence of carbonyl carbon, in the ^{13}C NMR are diagnostic. The -OH is also located as a broad, temperature-dependent chemical-shift peak. These NMR data are given in the experimental section. (*b*) at 25°C, the *in situ* dienols are observed by NMR to rearrange to the corresponding α,β-unsaturated ketones **17** and **18**, respectively, which can be obtained on work-up.

Many simple enols and dienols have been previously characterized as *in situ* species (6, 7). In addition, NMR parameters for our dienols can be compared to those obtained from silyl enol ethers and related silyl dienol ethers (2).

An alkylcyclopropanone → dienol rearrangement, as far as we are aware, represents a previously unrecognized preparative method for obtaining cross-conjugated dienols.

Mechanism of the rearrangement reaction

The rearrangements **12** → **15** and of **13** → **16** formally involve a hydrogen transfer from the α-carbon of the alkyl substituent to the carbonyl oxygen. As sketched below, this hydrogen is not close in space to the carbonyl oxygen in **12** or **13**, and it would therefore seem unlikely that **12** or **13** is directly involved in the hydrogen transfer. One also observes that there are hydrogens on the ring carbons 2 and 4, which have a similar orientation to the carbonyl oxygen, but these ring hydrogens are *not observed* to be involved in dienol formation.

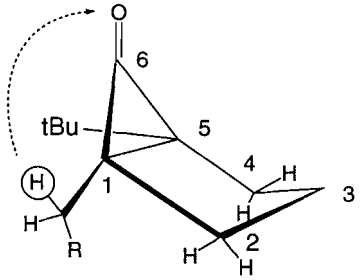

12 R=H

13 R=CH_3

There is considerable indirect evidence that cyclopropanones can interconvert with an oxyallyl by a disrotatory ring opening. In general, these oxyallyl valence-bond isomers are energetically less stable than cyclopropanones, but they can certainly serve as reactive intermediates. The rearrangement reaction, using solutions tenfold different in initial bicyclohexanone concentration, has the same rate within experimental error, showing that the reaction is not bimolecular in either the bicyclohexanone or an oxyallyl intermediate. If the latter is indeed present in very low concentrations, then a bimolecular reaction would be very unlikely. Accordingly, the overall reaction of **12** to **15** can be proposed to proceed as shown in eq. [3], where oxyallyl **19** is the intermediate in which the direct hydrogen transfer from C to O takes place. Note that in the disrotatory formation of the intermediate **19**, the alkyl substituent must end up *syn* to the oxyallyl oxygen atom since the opposite disrotatory mode is sterically impossible. This places the hydrogen on the α-carbon of the alkyl substituent in reasonably close proximity to the oxygen atom, compared to the situation in **12**. Conversely, the ring hydrogens are moved even further away.

[3] 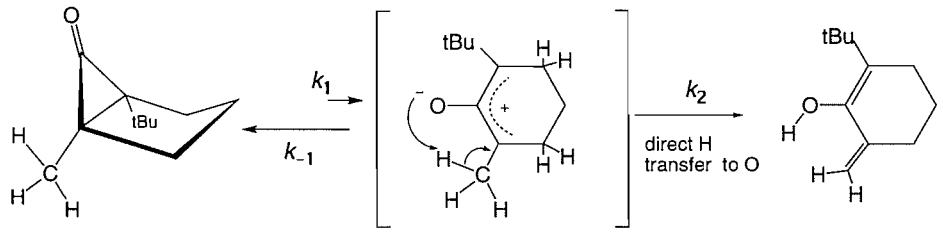

12 **19** **15**

In the eq. [3] mechanism, either the oxyallyl formation or the H transfer could be rate determining, although the latter possibility seemed much more likely since it was believed that the oxyallyl **19** was actually the first-formed species in the eq. [1] reaction (which "instantly" cyclizes to the cyclopropanone rather than rearranging to the dienol). In previous work (2), it had also been shown that H was preferred over D migration in a system where a competition between these two routes was set up. However, this observation would be expected regardless of whether k_1 or k_2 were rate-determining.

To clear up any doubts, we decided to carry out a k_H/k_D determination, and the rearrangement of **12** to **15** appeared to be ideally suited for this measurement, the rate comparison being between compounds **12** and **12a**. Since NMR spectroscopy was the tool being used to monitor the rearrangement, we prepared solutions in which both **12** and **12a** were present in the same NMR tube. These experiments involved allowing the rearrangement to proceed for a short time at −60 to −80°C and then quickly carrying out a reactant–product analysis at −95°C, where both reaction sets are essentially "quenched." Compounds **12** and **15** were monitored using ^{1}H NMR, and ^{2}H NMR was used for **12a** and **15a** (see Experimental for details). The data can be analyzed (8) to give k_H/k_D even though neither k_H or k_D is directly measured. In practice one obtains multiple values of k_H/k_D for each run by allowing the reaction to proceed and stop several times. The average of all these results gives a k_H/k_D ratio of 6 ± 2.

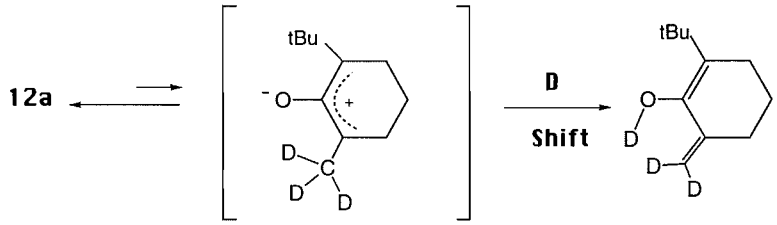

19a **15a**

The product analysis method being used here is actually better suited for determining smaller k_H/k_D ratios. For example, at the point where 50% of **12** has rearranged, only 11% of **12a** has reacted. Nevertheless, it would be even more difficult to attempt to accurately measure separate k_H and k_D rates, where the individual errors would be magnified in the k_H/k_D ratio.

Isotope effects of the size being observed here can only come from a primary isotope effect where the rate-determining step is the transfer of the hydrogen from carbon to oxygen, i.e., k_2 in eq. [3].

This rearrangement reaction can be considered, under the Woodward–Hoffmann rules (9), as an allowed, thermal, suprafacial sigmatropic rearrangement; i.e., in the Ψ_3 HOMO, both the original carbon terminus and the new oxygen site have in-phase coefficients, as shown in Fig. 1.

Approximate rearrangement kinetics were also determined for the first-order **12** → **15** reaction, k ca. 1×10^{-4} s^{-1}, $\Delta G^{\neq} = 13.5 \pm 1$ kcal/mol at −95°C.

We end this discussion with a minor caveat concerning our mechanism studies. The *in situ* solutions of the bicyclohexanones reported here also contain $Cr(CO)_4NOBr$ (a '"saturated" 18e$^-$ species) and the salt PPN^+Br^-, although some of the latter usually forms a precipitate at the bottom of the NMR tube at the low temperatures being used. It is not feasible to separate the very reactive bicyclohexanones (**12** and **13**) from the by-products, but with other more stable cyclopropanones we have done comparison studies between *in situ* samples containing by-products and solutions without these, and have noted no differences in the reaction rates, for example, the reversible ring-opening reaction of *cis*-di-*tert*-amylcyclopropanone to the corresponding oxyallyl has the same rate in both cases (10). In conclusion, we think it unlikely that either $Cr(CO)_4NOBr$ or PPN^+Br^- could somehow act as a catalyst in the dienol forming reaction.

Dynamic NMR observations involving bicyclo[3.1.0]hexan-6-one 10. Independent evidence for a cyclohexyl oxyallyl intermediate

In principle, a bicyclo[3.1.0]hexan-6-one → cyclohexyl oxyallyl equilibrium reaction could be probed by dynamic NMR techniques. The geminal hydrogen pairs in the cyclopentane ring of our bicyclohexanones are nonequivalent, and this is independent of whether the ring is a boat (preferred) or a chair conformer (in practice these nonequivalent hydrogens also mostly show separate ^{1}H NMR chemical shifts). However, if the bicyclic ring is opened to a cyclohexyl oxyallyl, then a ring conformer flip in this oxyallyl will interconvert geminal CH_2 pairs and result in a single averaged position for these, as illustrated in eq. [4]. for the C2 geminal pair.

[4] 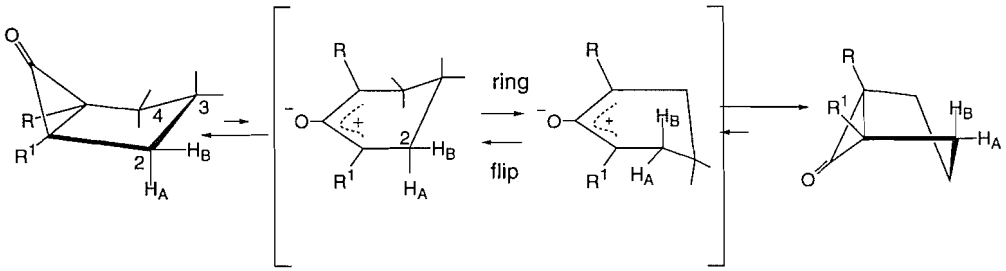

The reactive bicyclohexanones **12** and **13** do not show any dynamic NMR line-broadening, because they rearrange at quite low temperatures. Analogs **10** and **11** are better possibilities, and **10** does indeed show line-broadening coalescence of a type that agrees perfectly with that expected for the eq. [4] process. The actual line-broadening results, at temperatures −40 to −20°C, are somewhat ephemeral since **10** is irreversibly rearranging at −20°C (see earlier section).

The coalescence temperature for the averaging of the geminal C2–C4 methylene proton peaks in **10** (eq. [4], R = R^1 = *t*Bu) was ca. −20°C, giving $k = 250\ s^{-1}$, $\Delta G^{\neq} = 11.6$ kcal/mol.

To provide further verification of this degenerate exchange in **10**, spin-inversion transfer experiments were carried out, again using the C2–C4 geminal proton peaks (δ 2.50 (dt) and 2.25 (dd)). Experiments were conducted by inverting one or the other of these peaks and then measuring the response to this inversion using the modified Hoffman–Forsén procedure (11). Rate constants of 23 and 8 s^{-1} were obtained at temperatures of −54 and −64°C, $\Delta G^{\neq} = 11.4$ kcal/mol, in good agreement with the line-broadening data.

Cyclopropanone **11** does not show any ^{1}H NMR line broadening up to the decomposition temperature of +20°C ($\Delta G^{\neq}$ > ca. 15 kcal/mol). The large difference between **10** and **11** in the rate of the degenerate process shown in eq. [4] could arise from two factors: (*i*) nonbonded repulsions in **10** between the *tert*-butyl groups result in a destabilization of the cyclopropanone relative to the oxyallyl (at least compared to the situation in **11**) and (*ii*) oxyallyls appear to be stabilized by alkyl substituents (12), there being an extra *tert*-butyl substituent in the oxyallyl from **10**.

Other indirect evidence for a cyclohexyl oxyallyl intermediate

In a previous study (2) it was found that a bicyclo[4.1.0]heptan-7-one and a bicyclo[5.1.0]octan-8-one were considerably slower in undergoing the dienol rearrangement, compared to the (then unseen) bicyclo[3.1.0]hexan-6-one (see Introduction). These observations can be rationalized in terms of relative ring-strain effects. In each case, a strained cyclopropanone moiety is present, but the other ring is cyclopentyl, cyclohexyl, and cycloheptyl in this series. The corresponding oxyallyl (if indeed involved) would be, respectively, cyclohexyl, cycloheptyl, and cyclooctyl. In the bicyclo[3.1.0] case, a slightly strained cyclopentane ring opens to the optimal six-membered oxyallyl while, in comparison, in the bicyclo[4.1.0] situation a stable cyclohexane ring is being opened to a strained cycloheptyl oxyallyl. These opposing effects can rather nicely rationalize the observed behavior, and this provides yet further evidence for the oxyallyl intermediate as a key species in rationalizing the mechanism of the rearrangement.

To conclude this section, we have shown that an alkylcyclopropanone→cross-conjugated dienol rearrangement is a very facile process. The evidence indicates that an oxyallyl is the key reactive intermediate in this reaction and that the hydrogen transfer occurs only from a *syn*-substituent on this oxyallyl (obviously at least one hydrogen must be present on the α-carbon of this substituent). The rate-determining step is the hydrogen transfer itself and the kinetic data show that this is an extraordinarily facile shift, considering that a C—H bond is being broken. We hope in the future to model this reaction computationally.

Mechanism of the bicyclohexanone formation

The elegant ^{14}C labelling studies of Loftfield (1) established that the Favorski rearrangement of 2-chlorocyclohexanone proceeded by way of an unseen symmetrical intermediate, postulated by him to be bicyclo[3.1.0]hexan-6-one. However, Loftfield pictured this bicyclohexanone formation as a direct displacement of chloride by the enolate carbon. A few years later, Burr and Dewar (13) pointed out that the first symmetrical species must in fact be the corresponding zwitterionic structure (subsequently known as an oxyallyl) because the cyclohexanone enolate geometry did not permit an internal S_N2 displacement.

In our reactions, we assume that we produce the same initial halo-enolate as is postulated in the Favorski reaction (eq. [5])

[5] 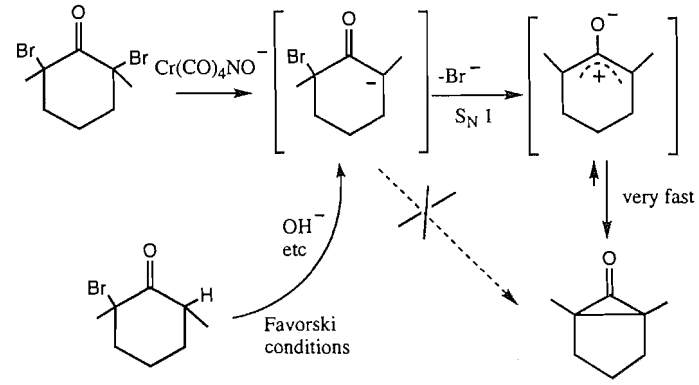

Fig. 1. Simple Hückel MOs for the 2-oxobuta-1,3-dienyl radical (occupied orbitals only). For the HOMO Ψ_3 orbital, the oxygen and C4 carbon have an in-phase relationship, a condition for an allowed suprafacial sigmatropic shift of the hydrogen atom from carbon to oxygen.

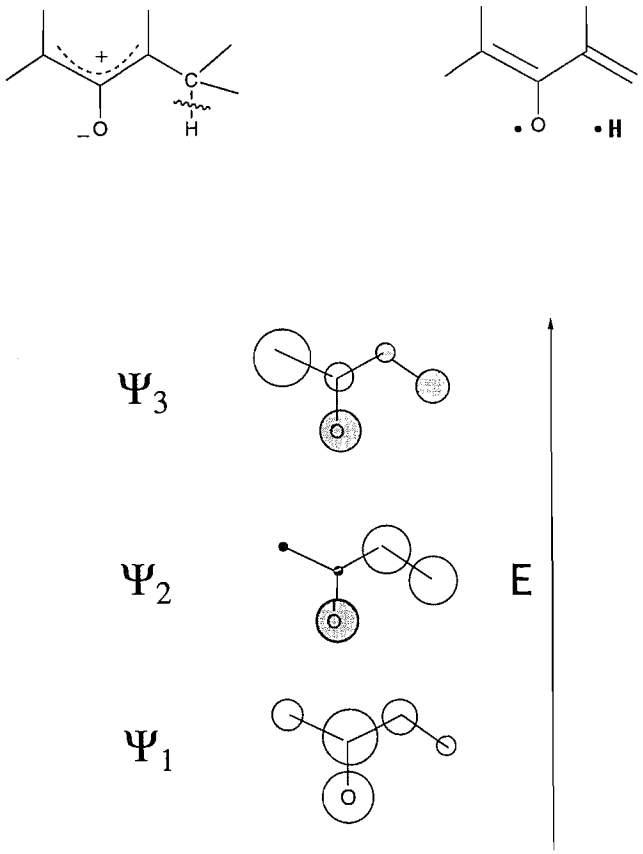

and that this intermediate follows the Dewar proposal to lose halide ion and first give the transient cyclohexyl oxyallyl, the bicyclohexanone forming from the latter by way of an extremely facile ring closure. Thus, in our case, the cyclohexyl oxyallyl is *both* the first-formed dehalogenated intermediate and, ultimately, the source of the bicyclohexanone instability because of a minute equilibrium concentration of this very reactive species.

Our success in preparing and characterizing observable bicyclo[3.1.0]hexan-6-ones stems from several factors:

(*i*) The methodology is very applicable to *in situ* low-temperature NMR determinations. Part of this success lies in the almost instantaneous reaction rate, even at quite low temperatures.

(*ii*) The $Cr(CO)_4NOBr$ by-product shows no interaction with the oxyallyl (or cyclopropanone) oxygen, in contrast to the by-products of some reducing metals (e.g., Zn (14)) or metal carbonyl (e.g., $Fe_2(CO)_9$ (4)) debrominations.

(*iii*) Favorski reaction deprotonation bases (or solvents) are generally nucleophilic towards either the carbonyl group of the cyclopropanone or a terminal carbon of an oxyallyl. In contrast, the anion $Cr(CO)_4NO^-$ appears to be unreactive.

However, we have not yet been successful in preparing the parent ketone **1** using this methodology.

Experimental

GC–MS measurements were performed on a Hewlett–Packard model 5890 gas chromatograph equipped with a 5971A mass selective detector. Split injection was used, employing a 12 m × 0.2 mm i.d. OV-101 column. High-resolution mass spectra were obtained on a Kratos MS-80. NMR spectroscopy was carried out on Bruker ACE-200, AMX-300, and AM-400 instruments (J in Hz, s = singlet, d = doublet, t = triplet, q = quartet, m = multiplet, b = broad. For $^{13}C\{^1H\}$ NMR, multiplicities were determined from DEPT 90 and 135 spectra. 2D NOESY and COSY spectra employed standard pulse sequences.

In situ NMR experiments

The operating procedure has been described in several earlier publications (2, 3). In the present work, cyclopropanones **12**, **12a**, and **13** required a preparation temperature of ca. −100 to −110°C (ethanol–N_2 slush bath at ca. −115°C with occasional short-duration removal of the NMR tube from the bath). After complete mixing the NMR tube was frozen in liquid N_2 prior to insertion into the precooled magnet. $CDFCl_2$ was used as the main solvent, with a few drops of CD_2Cl_2 being used to help dissolve the bromo ketone prior to addition to the organometallic salt.

Dibromo ketones

Ketones **5** (4), **6** (15), and **9** (16) were previously reported.

2,6-Dibromo-2-(1,1-dimethylethyl)-6-methylcyclohexanone 7

A solution of bromine (0.86 mL) and the ketone (1.28 g, 7.6 mmol) in 15 mL CCl_4 was sealed in a glass tube and heated for ca. 16 h at 80°C. The cooled reaction mixture was diluted with 20 mL CH_2Cl_2, washed successively with H_2O, 10% $NaHSO_3$, and brine, dried over anhydrous $MgSO_4$, and the solvent removed to give 2.3 g (93%) of the crude dibromo ketone (ca. 9:1 mixture of *cis* and *trans* isomers, by GLC or NMR). The major isomer could be crystallized from CH_3OH in a freezer, mp <30°C; ^1H NMR (major): 1.28 (s, 9H); 1.88–2.03 (m, 2H); 1.95 (s, 3H); 2.35–2.45(m, 2H); 2.60–2.88 (m, 2H). ^{13}C NMR: 16.6 (CH_3); 27.5 (CH_3); 29.8 (CH_2); 30.0 (CH_2); 35.7 (CH_2); 38.9 (Cq); 63.4 (Cq); 75.8 (Cq); 196.4 (Cq). MS: 326 (2), 270 (9) and 191, 189 (100); HRMS calcd. for $C_{11}H_{18}O^{79}Br^{81}Br$: 325.9705; found: 325.9710.

2,6-Dibromo-2-(1,1-dimethylethyl)-6-ethylcyclohexanone 8

2-(1,1-Dimethylethyl)cyclohexanone (0.77 g, 5.0 mmol) in 2 mL dry THF was added to an LDA solution (diisopropylamine, 0.85 mL, *n*-butyllithium, 2.2 mL of 2.5 M, in 10 mL of dry THF under nitrogen) at −25°C. After 20 min, the reaction mixture was cooled to −78°C and iodoethane (0.8 mL, 10 mmol) in THF (1 mL) was added. The solution was allowed to warm to room temperature and kept overnight. The reaction mixture was quenched with saturated NH_4Cl solution, and extracted with diethyl ether (3 × 25 mL). The organic solution was washed with water and brine, dried over anhydrous $MgSO_4$, and the solvent evaporated to give 0.77 g (93%) of crude product that is a mixture of *cis* and *trans* (ca. 40:60 by GLC and NMR). ^1H NMR (200 MHz): 0.88 (t, J = 7, 3H); 0.99, 1.00 (s, 9H) individual *t*Bu peaks; 1.10–2.30 (complex mult.). GC–MS (very similar for both isomers): 182 (M^+, 15), 167 (23), 126 (50), 98 (42), 41 (100). This crude compound in

CCl_4 (10 mL) and bromine (0.5 mL) was stirred overnight, diluted with 20 mL CH_2Cl_2, washed with water, 10% $NaHSO_3$, and brine, dried with anhydrous $MgSO_4$, and the solvent evaporated to give 1.40 g of an oily liquid, crude yield 98%. This material is a ca. 10:1 mixture of isomers by ^1H NMR. ^1H NMR (major): 1.00 (t, $J = 7$, 3H);1.29 (s, 9H); 1.80–2.90 (complex mult.). ^{13}C NMR: 9.8 (CH_3); 16.5 (CH_2); 27.5 (CH_3); 29.6 (CH_2); 31.5 (CH_2); 34.1 (CH_2); 39.0 (Cq); 69.4 (Cq); 76.4 (Cq); 195.1 (Cq). GC–MS: 340 (M^+, 1), 284 (5), 205, 203 (40), 57 (100); HRMS calcd. for $C_{12}H_{20}O^{79}Br^{81}Br$: 339.9862; found: 339.9828. The crude product was sufficiently pure to be used in the next step.

In situ *NMR characterization of bicyclo[3.1.0]hexan-6-ones* ***10–13***

1,5-Bis(1,1-dimethylethyl)bicyclo[3.1.0]hexan-6-one ***10:*** ^1H NMR (400 MHz): 2.48 (ddd, $J = 13$, 13, 6, 2H) H2 and H4 *anti* to cyclopropanone; 2.21(dd, $J = 13$, 6, 2H) H2 and H4 equatorial; 1.74 (dt, $J = 12.5$, 7, 1H) H3 equatorial; 1.04 (m, partly obscured by *t*Bu) H3 prow; 0.99 (s, 18H). ^{13}C NMR (100 MHz): 217.0 (C=O), 70.3 (C1-C5), 35.9 (C2-C4); 32.8 (C of tBu), 28.8 (CH_3 of *t*Bu); 21.2 (C3).

1-(1,1-Dimethylethyl)bicyclo[3.1.0]hexan-6-one ***11:*** ^1H NMR (400 MHz): 2.18–2.30 (m, 2H) H2 and H4 anti to cyclopropanone; 2.05 and 2.12 (both dd, J = 6.5, 12, 1H) H2 and H4 equatorial; 1.89 (d t, J = 12.5, 7, 1H) H3 equatorial; 1.85 (d, J = 5, 1H) H5; 1.24 (ttd, J = 12.5, 6.5, 12.5, 1H) H3 prow; 0.90 (s, 9H). ^{13}C NMR (100.MHz): 223.0 (C=O); 47.1 (C1); 31.4 (C2); 31.2 (C4); 29.9 (C of tBu); 29.8 (C5); 26.2 (CH_3 of tBu); 23.7 (C3).

1-(1,1-Dimethylethyl)-5-methylbicyclo[3.1.0]hexan-6-one ***12:*** ^1H NMR (400 MHz): 2.26 and 2.41 (both ddd, $J = 6$, 12, 12, 1H) H2 and H4 *anti* to cyclopropanone; 2.01–2.12 (m, 2H) H2 and H4 equatorial; 1.76 (dt, J = ca. 13 and 6) H3 equatorial; 1.23 (s, 3H); 1.12 (m, partly obscurred by impurity peak) H3 prow; 0.87 (s, 9H). ^{13}C NMR (100 MHz): 228.8 (C=O); 56.3 (C1); 47.1 (C5); 40.1 (C4); 34.4 (C2); 32.2 (C of *t*Bu); 27.3 (CH_3 of *t*Bu); 22.1 (C3); 13.1 (CH_3).

1-(1,1-Dimethylethyl)-5-ethylbicyclo[3.1.0]hexan-6-one ***13***: ^1H NMR (400 MHz): 2.27 and 2.43 (both ddd, $J = 6$, 10, 12, 1H) H2 and H4 *anti* to cyclopropanone; 2.08–2.18 (m, 2H) H2 and H4 equatorial; 1.70–1.90 (m, 2H) CH_2 of Et; 1.56 (dt, $J =$ 13, 6, 1H) H3 equatorial; 1.15 (partly obscured, 1H) H3 prow; 0.93 (t, $J = 7$, 3H); 0.90 (s, 9H). ^{13}C NMR (100 MHz): 226.4 (C=O); 56.1 (C1); 51.3 (C5); 36.1 (C2); 34.0 (C4); 31.7 (C of *t*Bu); 27.3 (CH_3 of *t*Bu); 21.8, 20.7 (C3, CH_2 of Et); 12.0 (CH_3 of Et).

Conformation of the bicyclo[3.1.0]hexan-6-one ring

In addition to the chemical shift discussion in the Results section, a boatlike conformation is also consistent with the detailed ^1H NMR data: (*a*) the H5 proton in **11** is a doublet of 5 Hz, indicating coupling to only one of the H4 hydrogens (one dihedral is ca. 90° in a boat structure). In a chair structure, two couplings would be expected; (*b*) in **10** (and in the others), the high-field hydrogen on C3 couples to both of the C2–C4 pairs of methylene hydrogens, with the largest coupling indicative of the expected vicinal diaxial interaction with the pair *anti* to the cyclopropanone ring.

In situ *NMR characterization of dienols* ***15*** *and* ***16***

2-(1,1-Dimethylethyl)-6-methylenecyclohex-1-en-1-ol ***15:*** (−50°C) ^1H NMR: 4.98 (bs); 4.66 (s); 4.53 (bs, temp. dep. δ) OH; 2.26, 2.17 (both t, $J = 6$, both 2H) C3 and C5 hydrogens; 1.56 (quin, $J = 6$, 2H) C4 hydrogens; 1.15 (s, 9H). ^{13}C NMR: 142.5, 142.3 (C1 and C6); 124.2 (C2), 104.0 (b, $=CH_2$); 34.0 (C of *t*Bu); 28.3 (CH_3 of *t*Bu); 31.6, 26.6, 23.2 (C3,4,5).

E-*2-(1,1-Dimethylethyl)-6-ethylidenecyclohex-1-en-1-ol* ***16***: The stereochemistry was assigned from the ketone **18** determination. (−40°C) ^1H NMR: 5.60 (bs, $\upsilon_{1/2} = 34$ Hz, 1H) =CH; 4.62 (bs, 1H) OH; 2.17, 2.10 (both poorly resolved triplets, 2H each) C3 and C5 hydrogens; 1.63 (bs, $\upsilon_{1/2} = 11$ Hz. 3H) CH_3; 1.51 (poorly resolved quint, 2H) C4 hydrogens; 1.12 (s, 9H). The alkene H and CH_3 show a coupling interaction (COSY). ^{13}C NMR: 142.8, 133.7 (C1 and C6); 121.5 (C2); 113.2 (b, =CH-); 33.8 (C of *t*Bu); 28.3 (CH_3 of *t*Bu); 25.8, 24.5, 22.6 (C3,4,5);12.8 (CH_3).

Kinetic isotope studies

A solution of ca. equal concentrations of **12** and **12a** was prepared as described for **12**. For **12**, the reactant–product ratios were obtained in several ways using ^1H NMR: (*a*) the *t*Bu peak of **12** and **15** differs by ca. 0.16 ppm and the peak height ratios of these can be used, although the H3 (prow) peak of **12** is also overlapping in this region; (*b*) the decrease of the peak at δ 2.41 in **12** can be compared to a fixed reference peak area (the CH_2 of diethyl ether at δ 3.4). For **12a**, ^2H NMR was used. The conversion of **12a** to **15a** is still relatively small in those cases where the **12**→**15** conversion is already substantial. The **12a** → **15a** conversion was monitored using the total ^2H area in the δ 4.25–5 ppm region (two peaks, $=C^2H_2$), relative to the area of the remaining $-C^2H_3$ peak at ca. 1.25. When the **12a** → **15a** reaction is allowed to proceed to completion there is a broad residual ^2H peak remaining in the δ 1–2 region, which we attribute to side reactions. Fortunately, at low conversions the error resulting from this is not a large factor. Based on the ^1H NMR results for $-O-^1H$ in **15** at low temperatures, the $-O-^2H$ peak is expected to be broadened into the baseline.

2-(1,1-Dimethylethyl)-6-methylenecyclohexanone ***17:*** ^1H NMR ($CDCl_3$): 5.64 and 5.03 (poorly resolved mult, 1H each) $=CH_2$; 2.35–2.75 (m, 2H) C5 hydrogens; 1.50–2.30 (mult); 1.02 (s, 9H). ^{13}C NMR (CD_2Cl_2): 213.6 (C=O), 148.8 (Cq); 117.7 ($=CH_2$), 58.5 (C6), 33.2 (C of *t*Bu); 28.0 (CH_3 of *t*Bu); 33.0, 26.4, 24.0 (C3,4,5). GC–MS: 166 (M^+), 110 (100), 95 (55), 82 (20), 81 (20). HRMS calcd. for $C_{11}H_{18}O$: 166.1358; found: 166.1343.

E-*2-(1,1-Dimethylethyl)-6-ethylidenecyclohexanone* ***18***: ^1H NMR ($CDCl_3$): 6.46 (qt, $J = 7$, 2, 1H)=CH-; 2.58 (bd, $J = 16$, 1H) H5; 2.33 (complex mult, 1H) H5; 2.15 (dd, $J = 11$, 7, 1H) H2; 2.05 (m, 1H) H3; 1.89 (m, 1H) H4; 1.45–1.65 (m, 2H) H3, H4); 1.69 (dt, $J = 7$, 2, 3H) CH_3; 0.99 (s, 9H). Stereochemical assignment: a NOESY spectrum shows a weak cross peak between the ethylidene CH_3 peak and the broad doublet at δ 2.58, which is assigned to the equatorial H5 hydrogen. In addi-

tion, comparisons with literature data on *cisoid* α,β-unsaturated ketones support the present assignment. ^{13}C NMR: 204.5 (C=O); 140.4 (C6); 131.6 (=CH); 57.2 (C2), 33.8 (C of *t*Bu); 28.1 (CH_3 of *t*Bu), 26.6, 25.7, 22.3 (C3, 4, 5); 14.1 (CH_3). GC–MS: 180 (M^+, 2), 165 (3), 109 (25), 95 (10). HRMS calcd. for $C_{12}H_{20}O$: 180.1514; found: 180.1485.

Acknowledgement

We thank the Natural Sciences and Engineering Research Council of Canada for generous financial support.

References

1. R.B. Loftfield. J. Am. Chem. Soc. **72**, 632 (1950); **73**, 4707 (1951).
2. C. Black, P. Lario, A.P. Masters, T.S. Sorensen, and F. Sun. Can. J. Chem. **71**, 1910 (1993).
3. A. Rauk, T.S. Sorensen, and F. Sun. J. Am. Chem. Soc. **117**, 4506 (1995).
4. R. Noyori, Y. Hayakawa, H. Takaya, S. Murai, R. Kobayashi, and N. Sonoda. J. Am. Chem. Soc. **100**, 1759 (1978).
5. R.L. Cook and T.B. Malloy, Jr. J. Am. Chem. Soc. **96**, 1703 (1974), and references therein.
6. (*a*) H.M.R. Hoffmann and E.A. Schmidt. J. Am. Chem. Soc. **94**, 1373 (1972); (*b*) E.A. Schmidt and H.M.R. Hoffmann. J. Am. Chem. Soc. **94**, 7832 (1972).
7. S.H. Bergens and B. Bosnich, J. Am. Chem. Soc. **113**, 958 (1991).
8. L. Melander. Isotope effects on reaction rates. The Ronald Press Co., New York. 1960. pp. 48–50.
9. R.B. Woodward and R. Hoffmann. The conservation of orbital symmetry. Verlag Chemie, Weinheim. 1970.
10. T.S. Sorensen and F. Sun. J. Am. Chem. Soc. **117**, 5592 (1995).
11. S. Forsén and R.A. Hoffman. J. Chem. Phys. **39**, 2892 (1963).
12. A.P. Masters, M. Parvez, T.S. Sorensen, and F. Sun. J. Am. Chem. Soc. **116**, 2804 (1994).
13. J.G. Burr, Jr. and M.J.S. Dewar. J. Chem. Soc. 1201 (1954).
14. H.M.R. Hoffmann. Angew. Chem. Int. Ed. Engl. **23**, 1 (1984).
15. H.M.R. Hoffmann, D. Wagner, and R. Wartchow. Chem. Ber. **123**, 2131 (1990).
16. B. Waegell and G. Ourisson. Bull. Soc. Chim. Fr. 496 (1963).

The asymmetric synthesis of aryltetralin lignans: (–)-isolariciresinol dimethyl ether and (–)-deoxysikkimotoxin

Don M. Coltart and James L. Charlton

Abstract: The total asymmetric syntheses of (−)-isolariciresinol dimethyl ether (**6**) and (−)-deoxysikkimotoxin (**7**) have been carried out, in an attempt to exploit a synthetic strategy recently developed for the synthesis of (−)-deoxypodophyllotoxin (**1**, R^1 = -CH_2-, Ar = 3,4,5-trimethoxyphenyl). In so doing, a generalized method for the synthesis of aryltetralin lignans has been developed that should be applicable to a variety of substitution patterns and stereochemistries. A one-pot, 100% regio-selective reduction–lactonization procedure has been developed for the conversion of the ester **18***b* to (−)-deoxysikkimotoxin, which gave 93% isolated yield in that step.

Key words: *ortho*-quinodimethanes, lignans, Diels–Alder, asymmetric, mandelate.

Résumé : Dans le but d'exploiter une stratégie de synthèse développée récemment pour la synthèse de la (−)-désoxypodophyllotoxine (**1**, R^1 = -CH_2-, Ar = 3,4,5-triméthoxyphényle), on a réalisé la synthèse totale asymétrique de l'éther diméthylique (**6**) de (−)-isolaricirésinol et de la (−)-désoxysikkimotoxine (**7**). On a ainsi développé une méthode généralisée de synthèse des lignanes aryltétralines que l'on devrait pouvoir appliquer à une variété de stéréochimies et de patrons de substitutions. On a développé une méthode unipot, 100% régiosélective, de réduction–lactonisation qui permet d'effectuer la conversion de l'ester **18***b* en (−)-désoxysikkimotoxine; pour cette étape, le rendement en produit isolé est de 93%.

Mots clés : *ortho*-quinodiméthanes, lignanes, Diels–Alder, asymétrique, mandélate.

[Traduit par la rédaction]

Introduction

The aryltetralin lignans make up a particular subclass of natural products collectively referred to as lignans. The occurrence of lignans in nature is widespread and they have been shown to possess considerable diversity in their biological activity (1). As such, there is a substantial interest in these compounds and their synthesis.

In a recent asymmetric synthesis of the aryltetralin lignan (−)-deoxypodophyllotoxin (**1**, R^1 = -CH_2-, Ar = 3,4,5-trimethoxyphenyl), a synthetic strategy was developed, shown retrosynthetically in Scheme 1, which gave the desired compound optically pure, in 6% isolated yield (2). As a key reaction, the synthesis relied on an asymmetric [4 + 2] cycloaddition occurring between the fumarate of methyl (*S*)-mandelate (**3**), and an appropriately substituted *ortho*-quinodimethane (**4**), to give the *endo* cycloadduct **2** (Scheme 1).

The *ortho*-quinodimethane in question was obtained via thermolysis of its corresponding α-hydroxy-α-aryl-benzocyclobutenol **5**. The synthetic route to the benzocyclobutenol, and the synthetic route by which the cycloadduct was elaborated to the target molecule, were sufficiently general that it was considered possible that variation of functional groups and stereochemistry of the resulting aryltetralin lignan might be achieved without adversely affecting the synthetic strategy. Hence, to broaden the scope of the synthetic strategy in question, and consequently develop a generalized method for the synthesis of aryltetralin lignans, an attempt was made to apply the method to the total asymmetric syntheses of (−)-isolariciresinol dimethyl ether (**6**) and (−)-deoxysikkimotoxin (**7**) (Scheme 2).

An asymmetric synthesis of deoxysikkimotoxin, the 6,7-dimethoxy analogue of deoxypodophyllotoxin, has not previously been reported in the literature. To date, only two total syntheses of optically pure isolariciresinol dimethyl ether have appeared in the literature (3, 4).

Results and discussion

Benzocyclobutenol **15***a* required for the synthesis of (−)-isolariciresinol dimethyl ether was obtained as outlined in Schemes 3 and 4, following, in part, earlier work carried out by Aidhen and Narasimhan (5). The monobromination of 3,4-dimethoxybenzaldehyde (**8***a*) was carried out using bromine and acetic acid, according to a modified literature procedure (6). Recrystallization of the crude product gave pure 2-bromo-4,5-dimethoxybenzaldehyde (**9**) in 86% yield. Aldehyde **9** was protected as its ethylene glycol acetal, and then subjected to halogen exchange by exposing it to *n*-butyllithium followed by iodine. Hydrolysis of the acetal protecting group gave, in 94% yield, 2-iodo-4,5-dimethoxybenzaldehyde (**10**) (7, 8). Conversion of **10** to benzyl alcohol **11** was carried out in 96%

Received August 17, 1995.

D.M. Coltart and J.L. Charlton.[1] Department of Chemistry, University of Manitoba, Winnipeg, MB R3T 2N2, Canada.

[1] Author to whom correspondence may be addressed. Telephone: (204) 474–9267; Fax: (204) 275–0905; E-mail: charltn@cc.umanitoba.ca

Scheme 1.

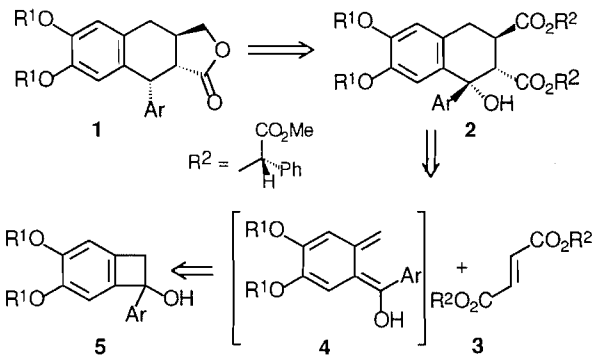

Scheme 2.

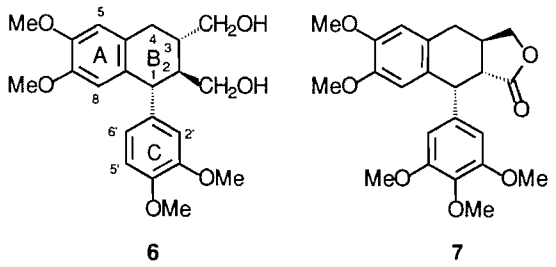

yield via sodium borohydride reduction. Exposure of **11** to hydrochloric acid afforded 2-iodo-4,5-dimethoxybenzyl chloride (**12**) in 76% overall yield from 3,4-dimethoxybenzaldehyde.

α-Aminonitrile **13***a* (Scheme 4), required for condensation with benzyl chloride **12**, was obtained using a modified Strecker synthesis (9). The reaction was originally carried out in methanol, but under these conditions it was found to give a mixture of the desired α-aminonitrile and a compound whose proton NMR spectrum corresponded to that of 3,4-dimethoxybenzaldehyde dimethyl acetal. The ratio of α-aminonitrile to acetal was 1.0 to 2.4. When carried out in ethanol, the analogous reaction gave a mixture of compound **13***a* and a compound that, based on its proton NMR spectrum, was assumed to be 3,4-dimethoxybenzaldehyde diethyl acetal, in a 2.0 to 1.1 ratio. The same reaction, using 2-propanol as the solvent, gave almost exclusive formation of the desired α-aminonitrile, with a very slight trace (less than 2%) of 3,4-dimethoxybenzaldehyde present. Presumably, the absence of acetal formation in the latter case was due to the use of a sterically hindered alcohol, a situation known to be unfavorable for acetal formation (10).

The coupling of benzyl chloride **12** and α-aminonitrile **13***a* was initiated by treating **13***a* with sodium hydride in *N*,*N*-dimethyl formamide, in order to generate its resonance-stabilized carbanion, followed by the addition of compound **12**. After acid-catalyzed hydrolysis, aryliodoketone **14***a* was obtained in 94% yield. Compound **14***a* was cyclized following the procedure of Aidhen and Narasimhan (5) by treating it with *n*-butyllithium, giving the desired benzocyclobutenol **15***a* in 74% isolated yield. It appears that metal halogen exchange with *n*-butyllithium is much faster than H abstraction or addition of *n*-butyllithium to the carbonyl group as has been noted

Scheme 3.

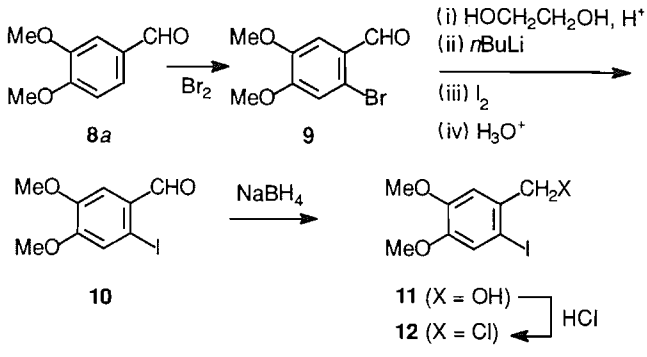

Scheme 4.

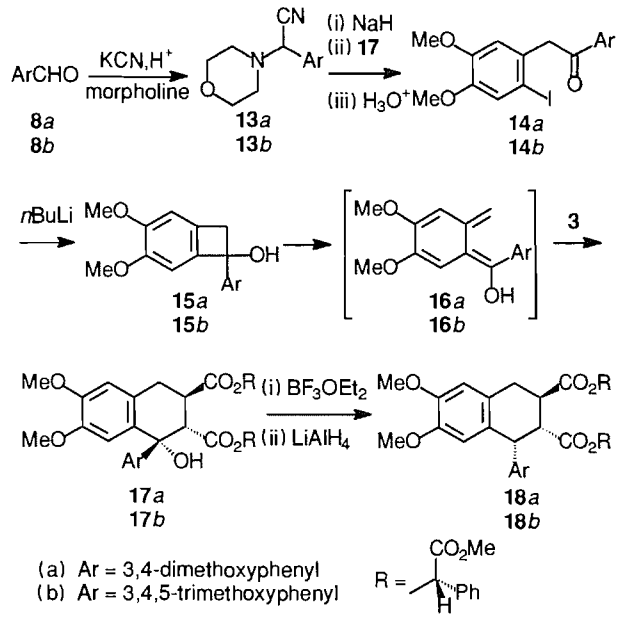

previously (refs. 5, 11, and references cited). The bromo compound analogous to **14***a* (I = Br) did not give the benzocyclobutenol **15***a* when treated with *n*-butyllithium, but gave instead material apparently derived from addition of *n*-butyllithium to the carbonyl group. This observation also parallels that of Aiden and Narasimhan (5).

Following a procedure used previously (12, 13), *ortho*-quinodimethane **16***a* was generated in refluxing toluene and trapped in situ with the fumarate of methyl (*S*)-mandelate, resulting in a 51% isolated yield of cycloadduct **17***a* after chromatography (Scheme 4). Justification for the geometry of the *ortho*-quinodimethane and the stereochemistry of the major cycloadduct has been given in an earlier publications (2, 13). Reductive removal of the C1 hydroxyl substituent from compound **17***a* was achieved according to the method of Bogucki and Charlton (2), and resulted in the formation of ester **18***a*. This gave the absolute stereochemistry at C1 required for (−)-isolariciresinol dimethyl ether. To establish the correct stereochemistry at C2 and C3, however, it was necessary to epimerize both centers. Concurrent epimerization and transesterification using sodium methoxide, followed by

Scheme 5.

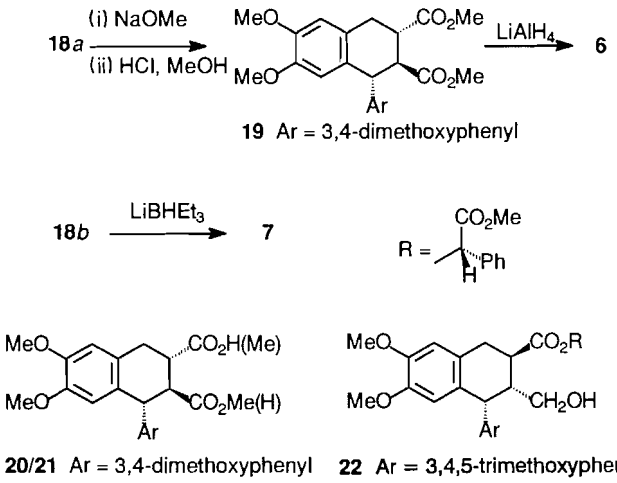

work-up with dilute acid, gave a compound presumed to be either the half ester **20** or **21** (Scheme 5), which, when treated with 3% hydrochloric acid in methanol, gave the all-*trans* dimethyl ester **19** in 83% isolated yield from **18***a*. (−)-Isolariciresinol dimethyl ether was obtained from compound **19** in 96% isolated yield by reduction with lithium aluminum hydride (3).

Given that the aromatic ring A of (−)-deoxysikkimotoxin possesses the same substitution pattern as that of (−)-isolariciresinol dimethyl ether, the benzyl chloride required for the α-aminonitrile coupling reaction of the (−)-deoxysikkimotoxin synthesis was the same as that for the synthesis of (−)-isolariciresinol dimethyl ether, namely compound **12** (Scheme 3). The aromatic ring C of (−)-deoxysikkimotoxin, however, bears methoxy substituents at the 3′, 4′, and 5′ positions and, as such, the α-aminonitrile **13***b* (Scheme 4) was required for its synthesis. Compound **13***b* was obtained according to a procedure previously reported (2). The coupling of benzyl chloride **12** and α-aminonitrile **13***b* was carried out in a manner analogous to that used for the coupling of compounds **12** and **13***a*. The product of this particular reaction, aryliodoketone **14***b*, was obtained in 91% isolated yield, and was readily cyclized to benzocyclobutenol **15***b* by treatment with *n*-butyllithium. Benzocyclobutenol **15***b* was thermolyzed to *ortho*-quinodimethane **16***b* in the presence of the fumarate of methyl (*S*)-mandelate. The proton NMR spectrum of the crude reaction product showed signals consistent with those expected for cycloadduct **17***b*, and did not indicate the presence of any other cycloadducts. The cycloadduct was obtained in 57% yield after chromatography. Reductive removal of the C1 hydroxyl substituent from this compound gave the ester **18***b* in a manner analogous to that used for the formation of compound **18***a*.

Given that compound **18***b* possessed the correct absolute stereochemistry required for (−)-deoxysikkimotoxin, **7**, the possibility of obtaining the target molecule directly, via the regioselective reduction of the ester substituent at C3 followed by lactonization, was explored. The conditions that were employed initially involved the use of three equivalents of lithium triethylborohydride at room temperature. This gave a mixture consisting of (−)-deoxysikkimotoxin and starting compound **18***b* in a ratio of approximately 1 to 1, as well as a trace amount of a compound presumed to be the γ-hydroxyester **22**. When the reaction conditions were altered such that six equivalents of lithium triethylborohydride were used, no starting material could be detected, but the reaction product was still a mixture consisting of (−)-deoxysikkimotoxin and the presumed γ-hydroxyester, in a ratio favoring (−)-deoxysikkimotoxin. In an attempt to increase the regioselectivity of the reduction reaction, the temperature of the reaction was lowered to 0°C. Proton NMR analysis of the crude product in this case indicated that all of the starting material had been consumed and showed the exclusive formation of (−)-deoxysikkimotoxin. Chromatography of the crude product afforded (−)-deoxysikkimotoxin in 93% isolated yield from compound **18***b*.

Conclusion

(−)-Isolariciresinol dimethyl ether and (−)-deoxysikkimotoxin were each synthesized in an asymmetric fashion with reasonable overall yields. The overall yield of (−)-isolariciresinol dimethyl ether was 9% from 3,4-dimethoxybenzaldehyde, and the overall yield of (−)-deoxysikkimotoxin was 11% from 3,4-dimethoxybenzaldehyde. This is the first total asymmetric synthesis of deoxysikkimotoxin that has been reported.

By achieving the aforementioned syntheses, the scope of the synthetic strategy developed by Bogucki and Charlton has been broadened to allow for different substitution patterns, functionality, and stereochemistry, thereby providing a generalized procedure for the synthesis of aryltetralin lignans. In particular, it was demonstrated that the methylenedioxy substituent of aromatic ring A can be replaced without adversely affecting the reaction sequence. It was also shown that removal of the 5′ methoxy substituent of aromatic ring C does not impede the synthetic strategy in any way. As well, it was established that the functionality and stereochemistry at carbons two and three of the aryltetralin lignan could be altered by epimerization during the final steps of the strategy.

The conversion of the reduction product **18***b* to (−)-deoxysikkimotoxin was achieved in one step with an overall yield of 93%, via a reduction–lactonization reaction that proceeded with unexpectedly high regioselectivity. This represents a substantial synthetic improvement in comparison to the synthesis of (−)-deoxypodophyllotoxin carried out by Bogucki and Charlton (2). Given the similarity of these compounds to one another, it seems reasonable to conclude that a corresponding improvement in the synthesis of (−)-deoxypodophyllotoxin could also be achieved.

Experimental

The analytical instruments employed have been described in a previous publication (14).

2-Bromo-3,4-dimethoxybenzaldehyde 9

Compound **9** was synthesized by adapting a literature procedure (6). To a round-bottom flask, equipped with a mechanical stirring apparatus, was added 3,4-dimethoxybenzaldehyde (20.09 g, 120.9 mmol) and glacial acetic acid (145 mL). The resulting suspension was stirred at room temperature and, once all of the 3,4-dimethoxybenzaldehyde

had dissolved, bromine (2 equivalents, 12.5 mL, 243 mmol) was added and stirring was continued for an additional 4 h. At that point, the mixture was diluted with ice-cold water (145 mL) and allowed to stand in a refrigerator at 5°C overnight. The mixture was then filtered and the resulting solid washed with ice-cold water (100 mL), and then refiltered. The solid was then recrystallized from 80/20 (v/v) methanol–water and dried in an oven overnight at 50°C. The process yielded a light beige crystalline compound (25.6 g, 104 mmol, 86%); mp 148–150°C; IR (CH_2Cl_2): 1682 (CO) cm^{-1}; ^1H NMR ($CDCl_3$) δ: 3.92 (s, 3H), 3.96 (s, 3H), 7.05 (s, 1H), 7.40 (s, 1H), 10.17 (s, 1H); ^{13}C NMR ($CDCl_3$) δ: 56.1 (CH_3), 56.4 (CH_3), 110.4 (CH), 115.4 (CH), 120.3 (C), 126.5 (C), 148.8 (C), 154.4 (C), 190.6 (CO); MS *m/e* (relative %): 246 (100), 245 (58), 244 (M^+, 99), 243 (53), 231 (17), 229 (16), 94 (45); HRMS calcd. for $C_9H_9{}^{79}BrO_3$: 243.9735; found: 243.9800.

2-Iodo-3,4-dimethoxybenzaldehyde 10

To a round-bottom flask was added 6-bromo-3,4-dimethoxybenzaldehyde (20.2 g, 82.3 mmol), benzene (300 mL), ethylene glycol (9.5 mL, 170.4 mmol), and *p*-toluenesulfonic acid hydrate (0.10 g, 0.53 mmol). The flask was attached to a Dean–Stark trap and refluxed for 5 h. The benzene was then evaporated to give a light yellow viscous liquid, which was filtered through silica gel (10 cm) with 50/50 (v/v) ethyl acetate/hexanes. The filtrate was evaporated to give a colorless crystalline compound. The crystals were dissolved in THF (150 mL) in a round bottom flask that was sealed with a rubber septum, flushed with nitrogen, and placed in a Dry Ice – acetone bath. At that point, *n*-butyllithium (44 mL of a 2.03 M solution in hexanes, 89 mmol) was added and the resulting solution was stirred for 15 min. Iodine (25.0 g, 98.5 mmol), dissolved in THF (80 mL), was then added and the mixture was stirred for 15 min, removed from the Dry Ice – acetone bath, and stirred for an additional 60 min. Saturated aqueous sodium bisulphite (10 mL) was added to dissipate the dark color caused by the iodine, leaving the solution light yellow. The THF portion was removed and the aqueous portion was extracted three times with ethyl acetate. The organic portions were combined and evaporated to give an oily residue. The residue was dissolved in methanol (50 mL) and to this was added 10% $HCl_{(aq)}$ (10 mL). The resulting solution was allowed to stir for 20 h at room temperature, by which time a colourless precipitate had formed. The product was extracted into CH_2Cl_2 and then evaporated to give a light colored oil. The oil was taken up in 50/50 (v/v) ethyl acetate/hexanes and filtered through silica gel (10 cm). Evaporation of the solvent gave colorless crystals (22.48 g, 77.0 mmol, 94%); mp 134–136°C; IR (CH_2Cl_2): 1695 (CO) cm^{-1}; ^1H NMR ($CDCl_3$) δ: 3.92 (s, 3H), 3.96 (s, 3H), 7.31 (s, 1H), 7.41 (s, 1H), 9.86 (s, 1H); ^{13}C NMR ($CDCl_3$) δ: 56.1 (CH_3), 56.5 (CH_3), 92.7 (C), 111.1 (CH), 121.8 (CH), 128.4 (C), 149.7 (C), 154.4 (C), 194.8 (CO); MS *m/e* (relative %): 292 (M^+, 100), 291 (31), 277 (5), 164 (10), 136 (10); HRMS calcd. for $C_9H_9IO_3$: 291.9596; found: 291.9629.

2-Iodo-4,5-dimethoxybenzyl alcohol 11

6-Iodo-3,4-dimethoxybenzaldehyde (1.52 g, 5.20 mmol) was dissolved in 2–propanol (40 mL). $NaBH_4$ (0.232 g, 6.14 mmol) was then added and the mixture was refluxed for 12 h. The resulting solution was made just acidic by the addition of 10% $HCl_{(aq)}$ and then evaporated to a minimum volume, after which it was taken up in dichloromethane and washed with water. The aqueous portion was saturated with NaCl and extracted three times with dichloromethane. The organic portions were combined, dried with $MgSO_4$, and evaporated to give off-white crystals (1.47 g, 5.00 mmol, 96%); mp 94–96°C; IR (CH_2Cl_2): 3605 (OH) cm^{-1}; ^1H NMR ($CDCl_3$) δ: 2.77 (bs, 1H), 3.84 (s, 6H), 4.56 (s, 2H), 6.98 (s, 1H), 7.19 (s, 1H); ^{13}C NMR ($CDCl_3$) δ: 55.8 (CH_3), 56.1 (CH_3), 68.7 (CH_2), 85.1 (C), 111.3 (CH), 121.3 (CH), 135.1 (C), 148.6 (C), 149.2 (C); MS *m/e* (relative %): 294 (M^+, 33), 166 (28), 71 (28), 69 (100), 57 (59); HRMS calcd. for $C_9H_{11}IO_3$: 293.9753; found: 293.9757.

2-Iodo-4,5-dimethoxybenzyl chloride 12

2-Iodo-4,5-dimethoxybenzyl alcohol (0.764 g, 2.60 mmol) was dissolved in dichloromethane (20 mL) and to that mixture was added glacial acetic acid (20 mL). HCl gas was passed through the resulting solution at a rate of approximately one bubble per second for 30 min. At that point, water (40 mL) was added to the solution and the organic portion was removed via a separatory funnel. The aqueous portion was then extracted twice with dichloromethane. The organic portions were combined and then washed with 10% $NaHCO_{3(aq)}$. The organic phase was removed, dried with $MgSO_4$, and evaporated to give off-white crystals (0.793 g, 2.55 mmol, 98%); mp 83–85°C; ^1H NMR ($CDCl_3$) δ: 3.85 (s, 3H), 3.86 (s, 3H), 4.63 (s, 2H), 6.96 (s, 1H), 7.22 (s, 1H); ^{13}C NMR ($CDCl_3$) δ: 51.2 (CH_2), 55.8 (CH_3), 56.1 (CH_3), 87.8 (C), 112.6 (CH), 121.5 (CH), 132.0 (C), 149.3 (C), 149.4 (C); MS *m/e* (relative %): 314 (M^+, 13) 312 (M^+, 36), 278 (23), 277 (100), 151 (15), 107 (18); HRMS calcd. for $C_9H_{10}{}^{35}ClIO_2$: 311.9414; found: 311.9426.

1-(3,4-Dimethoxyphenyl)-1-*N*-morpholinoacetonitrile 13*a*

3,4-Dimethoxybenzaldehyde (9.99 g, 60.1 mmol) was dissolved in 2-propanol (100 mL), in a round-bottom flask. In a separate flask KCN (3.93 g, 60.3 mmol) was dissolved in water (5 mL) and then morpholine (5.27 mL, 5.26 g, 60.4 mmol) was added with stirring, and the resulting mixture was cooled in an ice bath. At that point, concentrated HCl (4.96 mL, ca. 5.24 g, ca. 60 mmol) was added dropwise with stirring. The resulting suspension was then added all at once to the 3,4-dimethoxybenzaldehyde solution, and the final mixture was allowed to stir at room temperature for 7 days. The suspension that formed was filtered off and the filtrate was evaporated to a minimum volume, giving a viscous oil. The oil was taken up in ethyl acetate and washed with water, and the aqueous portion was subsequently extracted with ethyl acetate. The organic portions were combined, dried with $MgSO_4$, and evaporated to give a colorless crystalline compound (13.2 g, 50.3 mmol, 84%); mp 64–66°C; IR (CH_2Cl_2): 2305 (CN) cm^{-1}; ^1H NMR ($CDCl_3$) δ: 2.57 (m, 4H), 3.72 (m, 4H), 3.89 (s, 3H), 3.91 (s, 3H), 4.76 (s, 1H), 6.87 (d, 1H, J = 8.3), 7.01 (d, 1H, J = 2.0), 7.10 (dd, 1H, J = 2.0, 8.3); ^{13}C NMR ($CDCl_3$) δ: 49.9 (CH_2), 56.0_0 (CH_3), 56.0_2 (CH_3), 62.1 (CH), 66.6 (CH_2), 110.8 (CH), 110.9 (CH), 115.3 (C), 120.4 (CH), 124.8 (C), 149. 2 (C), 149.6 (C); MS *m/e* (relative %): 262 (M^+, 9), 177 (23), 176 (100), 151 (27), 111 (18), 97 (34), 83 (44), 69 (73), 57 (95); HRMS: calcd. for $C_{14}H_{18}N_2O_3$: 262.1317; found: 262.1361.

Aryliodoketone 14*a*

An NaH/oil mixture (50/50, w/w, 0.457 g, 9.53 mmol with respect to NaH) was combined with DMF (10 mL) in a round-bottom flask, which was subsequently sealed with a rubber septum and flushed with nitrogen. The α-aminonitrile **13*a*** (1.66 g, 6.33 mmol), dissolved in DMF (15 mL), was then added dropwise to the suspension over a period of 5 min. Once addition was complete, the benzyl chloride **12** (1.98 g, 6.33 mmol), dissolved in DMF (15 mL), was added dropwise to the suspension over a period of 5 min, and the resulting mixture was allowed to stir at room temperature for 1 h. At that point, 10% $HCl_{(aq)}$ (10 mL) was added to the suspension and the mixture was allowed to stir for 16 h at 65°C, causing the formation of a precipitate. The precipitate was isolated from the solution and washed with cold methanol, leaving a colorless crystalline compound (2.64 g, 5.96 mmol, 94%); mp 170–172°C; IR (CH_2Cl_2): 1682 (CO) cm^{-1}; ^1H NMR ($CDCl_3$) δ: 3.81 (s, 3H), 3.86 (s, 3H), 3.94 (s, 3H), 3.95 (s, 3H), 4.35 (s, 2H), 6.76 (s, 1H), 6.91 (d, 1H, J = 8.4), 7.26 (s, 1H), 7.57 (d, 1H, J = 2.0), 7.72 (dd, 1H, J = 2.0, 8.4); ^{13}C NMR ($CDCl_3$) δ: 49.6 (CH_2), 55.9 (CH_3), 56.0 (CH_3), 56.1_0 (CH_3), 56.1_5 (CH_3), 89.1 (C), 110.1 (CH), 110.6 (CH), 113.2 (CH), 121.6 (CH), 123.1 (CH), 129.8 (C), 131.0 (C), 148.5 (C), 149.0 (C), 149.4 (C), 153.4 (C), 195.4 (CO); MS *m/e* (relative %): 442 (M^+, 1), 315 (26), 165 (100); HRMS calcd. for $C_{18}H_{19}O_5$ (M − I): 315.1232; found: 315.1255.

Benzocyclobutenol 15*a*

The aryliodoketone (1.64 g, 3.71 mmol) was dissolved in THF (40 mL) under a nitrogen atmosphere, and cooled in a Dry Ice – acetone bath. *n*BuLi (2.5 M in hexanes, 3.0 mL, 7.5 mmol) was then added and the mixture was allowed to stir at low temperature for 30 min. At that point, 10% $NH_4Cl_{(aq)}$ (10 mL) was added and the mixture was allowed to stir while warming to room temperature. The THF portion was removed and the aqueous portion was extracted three times with dichloromethane. The organic portions were combined, dried with $MgSO_4$, and evaporated to give a yellow semisolid that, when chromatographed on silica gel using 60/40 (v/v) ethyl acetate/hexanes, gave a colorless crystalline compound (0.869 g, 2.75 mmol, 74%); mp 136–138°C; IR (CH_2Cl_2): 3583 (OH) cm^{-1}; ^1H NMR ($CDCl_3$) δ: 2.88 (bs, 1H), 3.44 (d, 1H, J = 13.4), 3.49 (d, 1H, J = 13.4), 3.84 (s, 3H), 3.85 (s, 3H), 3.86 (s, 3H), 3.88 (s, 3H), 6.78 (d, 1H, J = 8.3), 6.79 (s, 1H), 6.81 (s, 1H), 6.90 (dd, 1H, J = 2.0, 8.3), 7.06 (d, 1H, J = 2.0); ^{13}C NMR ($CDCl_3$) δ: 49.8 (CH_2), 55.9_0 (CH_3), 55.9_1 (CH_3), 56.2_0 (CH_3), 56.2_4 (CH_3), 80.5 (C), 105.3 (CH), 107.8 (CH), 109.1 (CH), 110.7 (CH), 117.8 (CH), 133.5 (C), 136.7 (C), 140.3 (C), 148.2 (C), 148.8 (C), 150.0 (C), 151.4 (C); MS *m/e* (relative %): 316 (M^+, 35), 315 (41), 301 (19), 286 (19), 285 (100), 179 (19), 165 (64), 69 (63), 55 (79); HRMS calcd. for $C_{18}H_{20}O_5$: 316.1311; found: 316.1283. Spectral data were identical to those reported for material prepared by an alternate route (12).

Cycloadduct 17*a*

This compound was prepared with slight modifications to a previously described method for the enantiomer (13). The fumarate of methyl (*S*)-mandelate (0.453 g, 1.10 mmol) was dissolved in toluene (5 mL) and heated to 98°C in an oil bath. The benzocyclobutenol **15*a*** (0.140 g, 0.44 mmol), dissolved in dichloromethane (4 mL), was then added and the mixture was allowed to boil, open to the atmosphere, until the dichloromethane had evaporated. At that point, a condenser was attached to the reaction flask and the mixture was refluxed for 48 h. The contents of the flask were then evaporated under reduced pressure, leaving a reddish-brown oil. Chromatography of the oil on silica gel with 40/60 (v/v) ethyl acetate/hexanes gave a colorless solid (0.164 g, 0.22 mmol, 51%); $[\alpha]_D^{20}$ 127.4 (*c* 0.31 g/100 mL in $CHCl_3$); IR (CH_2Cl_2): 3443 (OH), 1751 (CO) cm^{-1}; ^1H NMR ($CDCl_3$) δ: 3.17 (dd, 1H, J = 11.7, 16.5), 3.44 (dd, 1H, J = 4.6, 16.5), 3.61 (s, 3H), 3.63 (s, 3H), 3.73 (s, 3H), 3.82 (s, 3H), 3.87 (s, 3H), 3.92 (s, 3H), (H2 and H3 under the methoxyl signals), 5.74 (s, 1H), 5.90 (s, 1H), 6.45 (s, 1H), 6.66 (s, 1H), 6.87 (m, 2H), 6.99 (dd, 1H, J = 2.1, 8.4), 7.12 (d, 1H, J = 2.1), 7.17–7.27 (m, 3H), 7.36–7.42 (m, 3H), 7.44–7.47 (m, 2H); ^{13}C NMR ($CDCl_3$) δ: 32.4 (CH_2), 39.7 (CH), 52.6 (CH_3), 52.8 (CH_3), 54.9 (CH), 55.7 (CH_3), 55.8 (CH_3), 55.9 (CH_3), 56.0 (CH_3), 74.7 (CH), 74.9 (CH), 76.1 (C), 110.1 (2 × CH), 110.7 (CH), 112.1 (CH), 118.9 (CH), 125.7 (C), 127.1 (2 × CH), 127.6 (2 × CH), 128.4 (2 × CH), 128.7 (2 × CH), 129.0 (CH), 129.2 (CH), 132.4 (C), 132.8 (C), 133.2 (C), 139.2 (C), 147.9_0 (C), 147.9_3 (C), 148.5 (C), 148.7 (C), 169.3 (CO), 169.6 (CO), 171.5 (CO), 174.2 (CO); MS *m/e* (relative %): 710 (M^+ − H_2O, 29), 351 (64), 324 (40), 165 (21), 149 (64), 121 (100); HRMS calcd. for $C_{40}H_{38}O_{12}$ (M - H_2O): 710.2363; found: 710.2347. Spectral details were consistent with those reported for the enantiomer (13).

Ester 18*a*

The cycloadduct **17*a*** (0.0869 g, 0.12 mmol) was dissolved in dichloromethane (20 mL) under nitrogen, and cooled to −20°C. BF_3OEt_2 (0.10 mL, 0.80 mmol) was then added, causing the solution to turn dark blue. The mixture was cooled to −55°C and $LiAlH_4$ (0.37 M in diethyl ether, approximately 1.0 mL, approximately 0.37 mmol) was added dropwise until all of the blue had dissipated, followed by the dropwise addition of 50/50 (v/v) methanol/water (10 mL). The resulting solution was stirred for 20 min at −55°C and was then allowed to warm to room temperature. At that point, 10% $HCl_{(aq)}$ (1 mL) was added and the organic portion was separated from the aqueous portion. The aqueous portion was extracted three times with dichloromethane and the original organic portion was washed with 10% $HCl_{(aq)}$. The organic portions were combined, dried with $MgSO_4$, and evaporated to give an amorphous solid, which was chromatographed on silica gel with 30/70 (v/v) ethyl acetate/hexanes to give a colorless solid (0.0356 g, 0.05 mmol, 42%); $[\alpha]_D^{20}$ −54.3 (*c* 0.28 g/100 mL in $CHCl_3$); IR (CH_2Cl_2): 1746 (CO) cm^{-1}; ^1H NMR ($CDCl_3$) δ: 3.04 (m, 1H), 3.38 (m, 2H), 3.52 (m, 1H), 3.64 (s, 3H), 3.68 (s, 3H), 3.69 (s, 3H), 3.70 (s, 3H), 3.73 (s, 3H), 3.87 (s, 3H), 4.56 (d, 1H, J = 5.5, H1), 5.67 (s, 1H), 6.07 (s, 1H), 6.32 (dd, 1H, J = 1.9, 8.3), 6.39 (s, 1H), 6.43 (d, 1H, J = 8.3), 6.50 (d, 1H, J = 1.9), 6.69 (s, 1H), 6.99 (d, 2H, J = 7.3), 7.08 (t, 2H, J = 7.6), 7.16–7.36 (m, 4H), 7.44–7.47 (m, 2H); ^{13}C NMR ($CDCl_3$) δ: 31.8 (CH_2), 37.1 (CH), 45.7 (CH), 48.2 (CH), 52.4 (CH_3), 52.5 (CH_3), 55.4 (CH_3), 55.8 (3 × CH_3), 73.9 (CH), 74.6 (CH), 110.4 (2 × CH), 112.2 (CH), 112.8 (CH), 121.8 (CH), 125.6 (C), 127.0 (2 × CH), 127.9 (2 × CH), 128.2 (2 × CH), 128.6 (C), 128.7 (2 × CH), 129.2 (CH), 133.4 (C), 133.6 (C), 133.9 (C), 147.8 (C), 147.9 (C), 148.0 (C), 148.1 (C), 168.8 (CO), 169.5 (CO), 171.1 (CO), 174.2 (CO) ; MS *m/e* (relative %):

712 (M^+, 20), 563 (6), 518 (10), 485 (7), 398 (22), 397 (36), 351 (47), 325 (55), 149 (63), 121 (100); HRMS calcd. for $C_{40}H_{40}O_{12}$: 712.2520; found: 712.2502. Spectral data were consistent with those reported for the enantiomer prepared by another method (12).

Ester 19

Ester **18***a* (0.050 g, 7.02×10^{-2} mmol) was dissolved in dry methanol (10 mL) and sodium metal (0.240 g, 10.4 mmol) was added under nitrogen. The solution was stirred at reflux for 23 h. The mixture was acidified with 10% $HCl_{(aq)}$ and extracted three times with dichloromethane. The organic portions were combined, dried with $MgSO_4$, and evaporated to give a soft crystalline compound. The compound was dissolved in 3% HCl–methanol (10 mL) and stirred for 12 h. The resulting solution was extracted three times with dichloromethane and the organic portions were combined, dried with $MgSO_4$, and evaporated to give a soft crystalline compound. The compound was subsequently chromatographed on silica gel using 30/70 (v/v) ethyl acetate/hexanes to give a colourless solid (0.026 g, 5.85×10^{-2} mmol, 83%); mp 126–127°C; $[\alpha]_D^{20}$ −23.2 (*c* 0.21 g/100 mL in $CHCl_3$); ^{13}C NMR ($CDCl_3$) δ: 31.8 (CH_2), 43.3 (CH), 48.8 (CH), 51.6_7 (CH), 51.6_9 (CH_3), 52.1 (CH_3), 55.8 (CH_3), 55.9_0 ($2 \times CH_3$), 55.9_2 (CH_3), 110.7 (CH), 110.9 (CH), 111.7 (CH), 112.1 (CH), 121.5 (CH), 126.0 (C), 129.6 (C), 135.4 (C), 147.6 (C), 147.7 (C), 148.0 (C), 148.9 (C), 174.1 (CO), 174.5 (CO). Compound **19** had ^1H NMR, IR, and mass spectral properties identical to those previously reported (3).

Isolariciresinol dimethyl ether 6

The reduction of dimethyl ester **19** was carried out using the previously described procedure (3). The dimethyl ester **19** (0.0118 g, 0.027 mmol) was dissolved in dry THF (5 mL) under nitrogen and added dropwise to a suspension of $LiAlH_4$ (0.0012 g, 0.032 mmol) in THF (5 mL) under nitrogen. The mixture was allowed to reflux for 2 h. At that point, water (2 drops) and 10% $HCl_{(aq)}$ (0.5 mL) were added and then the mixture was dried with $MgSO_4$ and evaporated to give a solid. The solid was recrystallized from ethyl acetate – hexanes to give colorless crystals (0.0102 g, 0.026 mmol, 96%); mp 150–152°C; $[\alpha]_D^{20}$ −15.3 (*c* 0.49 g/100 mL in $CHCl_3$); ^{13}C NMR ($CDCl_3$), δ: 33.2 (CH_2), 39.9 (CH), 48.0 (CH), 48.2 (CH), 53.4 (CH_3), 55.8 ($2 \times CH_3$), 56.0 (CH_3), 62.8 (CH_2), 66.5 (CH_2), 110.8 (CH), 111.1 (CH), 112.0 (CH), 113.0 (CH), 121.9 (CH), 128.2 (C), 131.8 (C), 137.7 (C), 147.1 ($2 \times C$), 147.6 (C), 149.1 (C). Compound **6** had ^1H NMR, IR, and mass spectral properties identical to those previously reported (3).

Aryliodoketone 14*b*

An NaH/oil mixture (50/50, w/w, 0.367 g, 7.65 mmol with respect to NaH) was combined with DMF (10 mL) in a round-bottom flask, which was subsequently sealed with a rubber septum and flushed with nitrogen. The α-aminonitrile **13*b*** (1.04 g, 3.57 mmol), dissolved in DMF (15 mL), was then added dropwise to the suspension over a period of 5 min. Once addition was complete, the benzyl chloride **12** (1.13 g, 3.61 mmol), dissolved in DMF (15 mL), was added dropwise to the suspension over a period of 5 min, and the resulting mixture was allowed to stir at room temperature for 1 h. At that point, 10% $HCl_{(aq)}$ (10 mL) and water (10 mL) were added to the suspension and the mixture was allowed to stir for 16 h at 65°C, causing the formation of a precipitate. The precipitate was isolated from the solution and washed with cold methanol, leaving a colorless crystalline compound (1.53 g, 3.25 mmol, 91%); mp 147–150°C; IR (CH_2Cl_2): 1684 (CO) cm^{-1}; ^1H NMR ($CDCl_3$) δ: 3.81 (s, 3H), 3.86 (s, 3H), 3.92 (s, 3H), 3.93 (s, 6H), 4.35 (s, 2H), 6.76 (s, 1H), 7.26 (s, 1H), 7.29 (s, 2H); ^{13}C NMR ($CDCl_3$) δ: 49.8 (CH_2), 55.8 (CH_3), 56.1 (CH_3), 56.3 (CH_3), 60.8 (CH_3), 89.0 (C), 106.0 (CH), 112.8 (CH), 121.5 (CH), 130.7 (C), 131.5 (C), 142.6 (C), 148.5 (C), 149.4 (C), 152.9 (C), 195.6 (CO); MS *m/e* (relative %): 472 (M^+, 1), 344 (73), 329 (64), 195 (100); HRMS calcd. for $C_{19}H_{21}IO_6$: 472.0383; found: 472.0366.

Benzocyclobutenol 15*b*

The aryliodoketone **14*b*** (2.01 g, 4.25 mmol) was dissolved in THF (40 mL) under nitrogen, and cooled in a Dry Ice – acetone bath. *n*BuLi (2.5 M in hexanes, 3.6 mL, 9.00 mmol) was then added and the mixture was allowed to stir at low temperature for 30 min. At that point, 10% $NH_4Cl_{(aq)}$ (10 mL) was added and the mixture was allowed to stir while warming to room temperature. The THF portion was removed and the aqueous portion was extracted three times with dichloromethane. The organic portions were combined, dried with $MgSO_4$, and evaporated to give a yellow semisolid that, when chromatographed on silica gel using 50/50 (v/v) ethyl acetate/hexanes, gave a colorless crystalline compound (1.06 g, 3.05 mmol, 72%); mp 121–123°C; IR (CH_2Cl_2): 3588 (OH) cm^{-1}; ^1H NMR ($CDCl_3$) δ: 2.66 (s, 1H), 3.45 (d, 1H, J = 13.4), 3.52 (d, 1H, J = 13.4), 3.81 (s, 6H), 3.83 (s, 3H), 3.86 (s, 3H), 3.90 (s, 3H), 6.67 (s, 2H), 6.81 (s, 1H), 6.82 (s, 1H); ^{13}C NMR ($CDCl_3$) δ: 50.0 (CH_2), 56.1 (CH_3), 56.2 (CH_3), 56.3 (CH_3), 60.8 (CH_3), 80.8 (C), 102.8 (CH), 105.1 (CH), 107.8 (CH), 133.7 (C), 137.2 (C), 139.6 (C), 140.0 (C), 150.1 (C), 151.6 (C), 153.0 (C); MS *m/e* (relative %): 346 (M^+, 5), 315 (7), 195 (3), 88 (10), 86 (64), 84 (100); HRMS calcd. for $C_{19}H_{22}O_6$: 346.1416; found: 346.1431.

Cycloadduct 17*b*

The fumarate of methyl (*S*)-mandelate (1.94 g, 4.70 mmol) was dissolved in toluene (10 mL) and heated in an oil bath to 98°C. The benzocyclobutenol **15*b*** (0.623 g, 1.80 mmol), dissolved in dichloromethane (4 mL), was then added and the mixture was allowed to boil, open to the atmosphere, until the dichloromethane had evaporated. At that point, a condenser was attached to the reaction flask and the mixture was refluxed for 48 h. The contents of the flask were then evaporated under reduced pressure leaving a reddish-brown oil. Chromatography of the oil on silica gel with 40/60 (v/v) ethyl acetate/hexanes gave a colorless, crystalline compound (0.779 g, 1.03 mmol, 57%), mp 82–85°C; $[\alpha]_D^{20}$ +136 (*c* 0.30 g/100 mL in $CHCl_3$); IR (CH_2Cl_2): 3475 (OH), 1741 (CO) cm^{-1}; ^1H NMR ($CDCl_3$) δ: 3.17 (dd, 1H, J = 11.4, 16.4), 3.45 (dd, 1H, J = 4.3, 16.4), 3.59–3.92 (m, 2H), 3.63 (s, 6H), 3.73 (s, 3H), 3.79 (s, 6H), 3.87 (s, 3H), 3.90 (s, 3H), 5.75 (s, 1H), 5.90 (s, 1H), 6.46 (s, 1H), 6.66 (s, 1H), 6.73 (s, 2H), 6.95 (m, 2H), 7.20–7.28 (m, 2H), 7.36–7.40 (m, 4H), 7.44–7.48 (m, 2H); ^{13}C NMR ($CDCl_3$) δ: 32.3 (CH_2), 39.8 (CH), 52.6 (CH_3), 52.8 (CH_3), 54.8 (CH), 55.8 ($2 \times CH_3$; methoxy substituents on the 1,2,4,5 substituted aromatic ring), 56.2 ($2 \times CH_3$), 60.9 (CH_3), 74.7 (CH), 75.0 (CH), 76.3 (C), 104.1 ($2 \times CH$), 110.1 (CH), 112.1

(CH), 125.7 (C), 127.1 (CH), 127.6 (CH), 128.5 (CH), 128.7 (CH), 129.1 (CH), 129.3 (CH), 132.1 (C), 132.8 (C), 133.2 (C), 137.0 (C), 142.1 (C), 148.0 (C), 148.8 (C), 152.8 (C), 169.3 (CO), 169.5 (CO), 171.7 (CO), 174.1 (CO); MS *m/e* (relative %): 758 (M^+, 8), 740 (39), 548 (36), 381 (66), 355 (72), 107 (100); HRMS calcd. for $C_{41}H_{40}O_{13}$ (M − H_2O): 740.2469; found: 740.2457.

Ester 18*b*

The cycloadduct **17*b*** (0.0767 g, 0.10 mmol) was dissolved in dichloromethane (20 mL) under nitrogen, and cooled to −12°C. BF_3OEt_2 (0.10 mL, 0.81 mmol) was then added, causing the solution to turn dark blue. The mixture was cooled to −55°C and $LiAlH_4$ (0.37 M in diethyl ether, ca. 1.5 mL, ca. 0.56 mmol) was added dropwise until all of the blue had dissipated, followed by the addition of 50/50 (v/v) methanol/water (10 mL) dropwise. The resulting solution was stirred for 20 min at −55°C and was then allowed to warm to room temperature. At that point, 10% $HCl_{(aq)}$ (1 mL) was added and the organic portion was separated from the aqueous portion. The aqueous portion was extracted three times with dichloromethane and the original organic portion was washed with 10% $HCl_{(aq)}$. The organic portions were combined, dried with $MgSO_4$, and evaporated to give an off-white crystalline mass. Chromatography using silica gel and 30/70 (v/v) ethyl acetate/hexanes gave pure **18*b*** (0.0312 g, 0.043 mmol, 40%); $[\alpha]_D^{20}$ −43.0 (*c* 0.40 g/100 mL in $CHCl_3$); IR (CH_2Cl_2): 1744 (CO) cm^{-1}; ^1H NMR ($CDCl_3$) δ: 3.05 (m, 1H), 3.39 (5-line m, 2H), 3.52 (6 line m, 2H), 3.58 (s, 3H), 3.63 (s, 6H), 3.69 (s, 3H), 3.73 (s, 3H), 3.74 (s, 3H), 3.87 (s, 3H), 4.57 (d, 1H, J = 5.5), 5.70 (s, 1H), 6.04 (s, 1H), 6.12 (s, 2H), 6.42 (s, 1H), 6.70 (s, 1H), 7.10–7.45 (m, 10H); ^{13}C NMR ($CDCl_3$) δ: 31.8 (CH_2), 37.3 (CH), 46.2 (CH), 48.1 (CH), 52.5_0 (CH_3), 52.5_4 (CH_3), 55.8 (CH_3), 55.9 (CH_3), 56.2 (CH_3), 60.6 (CH_3), 74.1 (CH), 74.7 (CH), 107.2 (CH), 110.4 (CH), 112.2 (CH), 125.6 (C), 126.8, (CH), 127.9 (CH), 128.3 (C), 128.4 (CH), 128.7 (CH), 128.8 (CH), 129.2 (CH), 133.3 (C), 133.5 (C), 136.9 (C), 137.2 (C), 147.9 (C), 148.2 (C), 152.6 (C), 168.8 (CO), 169.4 (CO), 171.2 (CO), 174.1 (CO); MS *m/e* (relative %): 742 (M^+, 21), 578 (7), 548 (7), 515 (8), 427 (27), 381 (22), 355 (41), 149 (74), 121 (97), 107 (93), 91 (61), 77 (100); HRMS calcd. for $C_{41}H_{42}O_{13}$: 742.2625; found: 742.2575.

Deoxysikkimotoxin 7

Ester **18*b*** (0.0236 g, 3.17×10^{-5} mol) was dissolved in THF (5 mL), under nitrogen. Lithium triethylborohydride (191 μL of a 1 M solution in THF, 1.91×10^{-4} mol, 6 equivalents) was then added at 0°C, and the mixture was allowed to stir for 2 h. 10% $HCl_{(aq)}$ (5 mL) was added and the resulting solution was stirred overnight. The mixture was diluted with water and extracted three times with dichloromethane. The organic portions were combined, dried with $MgSO_4$, and evaporated to give a clear, amorphous solid that was chromatographed on silica gel using 40/60 (v/v) ethyl acetate/hexanes to give pure (−)-deoxysikkimotoxin (0.0122 g, 2.94×10^{-5} mol, 93%); $[\alpha]_D^{20}$ −85.8 (*c* 3.3 g/100 mL in $CHCl_3$); ^{13}C NMR ($CDCl_3$) δ: 32.8_0 (CH_2), 32.8_4 (CH), 43.4 (CH), 47.7 (CH), 55.9 (CH_3), 56.0 (CH_3), 56.2 (CH_3), 60.8 (CH_3), 72.1 (CH_2), 77.2 (C), 108.3 (CH), 111.4 (CH), 113.3 (CH), 127.1 (C), 129.4 (C), 136.4 (C), 148.0 (C), 148.2 (C), 152.5 (C), 175.0 (CO); MS *m/e* (relative %): 414 (M^+, 100), 246 (13), 181 (30); HRMS calcd. for $C_{23}H_{26}O_7$: 414.1679; found: 414.1649. Compound **7** had ^1H NMR and IR spectral properties identical to those previously reported (15).

Acknowledgment

We would like to acknowledge the financial assistance of the Natural Sciences and Engineering Research Council of Canada. We also acknowledge the technical assistance of Tad Foniok and Wayne Buchannon in recording NMR and mass spectra, respectively.

References

1. R.S. Ward. Chem. Soc. Rev. **11**, 75 (1982), and references cited.
2. D.E. Bogucki and J.L. Charlton. J. Org. Chem. **60**, 588 (1995).
3. J.L. Charlton and M.M. Alauddin. J. Org. Chem. **51**, 3490 (1986).
4. E. Brown and A. Daugan. Tetrahedron, **45**, 141 (1989).
5. I.S. Aidhen and N.S. Narasimhan. Tetrahedron Lett. **32**, 2171 (1991).
6. A.M.B. Orr, R. Robinson, and M.M. Williams. J. Chem. Soc. **111**, 946 (1917).
7. S. Kobayashi, M. Kihara, and Y. Yamahara. Chem. Pharm. Bull. **26**, 3113 (1978).
8. F.E. Ziegler and K.W. Fowler. J. Org. Chem. **41**, 1564 (1976).
9. A. Vogel. Textbook of practical organic chemistry. 4th ed. Longman, New York. 1978, pp. 755–756.
10. A.J. Meskens. Synthesis, 501 (1981).
11. M.P. Cooke. J. Org. Chem. **58**, 6833 (1993).
12. J.L. Charlton, S.P. Maddaford, K. Koh, S. Boulet, and M.H. Saunders. Tetrahedron: Asymmetry, **4**, 645 (1993).
13. S.P. Maddaford. Ph.D. Thesis, University of Manitoba, 1994.
14. J.L. Charlton, G.L. Plourde, K. Koh, and A.S. Secco. Can. J. Chem. **68**, 2022 (1990).
15. S. Takano, N. Sato, S. Otaki, and K. Ogasawara. Heterocycles, **25**, 69 (1987).

Electrochemical investigation of reduction of mercury complexes of 2-aminocyclopentene-1-dithiocarboxylic acid and some of its derivatives at mercury electrodes

A. Safavi and M.B. Gholivand

Abstract: Electrochemical techniques of polarography, cyclic voltammetry, and controlled potential electrolysis at mercury electrodes have permitted a detailed investigation of the reduction reactions associated with mercury 2-aminocyclopentene dithiocarboxylate complexes, $Hg(ACD)_2$, in dimethyl sulphoxide (DMSO). As a complementary study, the electrochemistry of the ligands themselves was investigated in DMSO solutions and at mercury electrodes. The lability of mercury(II) complexes and their rapid interaction with elemental mercury strongly influence the nature of the redox processes observed at mercury electrodes. Reduction of $Hg(ACD)_2$ at a mercury electrode occurs in an overall two-electron step as:

$$Hg(ACD)_2 + 2e^- \rightleftharpoons Hg + 2\ ACD^-$$

although mercury(I) is implicated as an intermediate.

Key words: reduction, electrochemical techniques, mercury complexes.

Résumé : Faisant appel à des techniques électrochimiques de polarographie, de voltampérométrie cyclique et d'électrolyse à potentiel contrôlé à des électrodes de mercure, on a réalisé une étude détaillée des réactions de réduction associées aux complexes du 2-aminocyclopentènedithiocarboxylate de mercure, $Hg(ACD)_2$, dans le diméthylsulfoxyde (DMSO). Comme étude complémentaire, on a aussi étudié l'électrochimie des coordinats eux-mêmes en solutions dans la DMSO et à des électrodes de mercure. La labilité des complexes du mercure(II) et leur interaction rapide avec le mercure élémentaire influencent fortement la nature des processus rédox observés aux électrodes de mercure. La réduction du $Hg(ACD)_2$ à l'électrode de mercure se produit par un processus global à deux électrons de la forme :

$$Hg(ACD)_2 + 2e^- \rightleftharpoons Hg + 2\ ACD^-$$

même si le mercure(I) est impliqué comme intermédiaire.

Mots clés : réduction, techniques électrochimiques, complexe du mercure.

[Traduit par la rédaction]

Introduction

Much interest in transition element – sulphur systems has been generated by organic, inorganic, and physical chemists over the past 10 years (1–3). The redox behaviour of dithiocarbamates and their metal complexes has been extensively studied (4–8) and is noteworthy for the stabilization of unusually high oxidation states of transition metals in metal dithiocarbamate complexes. In contrast, the electrochemistry of dithiocarboxylates has barely been investigated.

2-Aminocyclopentene-1-dithiocarboxylic acid, its derivatives, and their complexes have important applications, especially as fungicides (9, 10) and as models of sulphur–metal proteins (11). The electroanalytical behaviour of some of the above ligands at mercury electrodes and in aqueous media has recently been studied (12, 13). The anodic waves observed for these ligands in aqueous or aqueous–ethanolic media were attributed to mercury complex formation (12, 13). Detailed electroanalytical studies on the above ligands revealed an E_qC_i mechanism (quasi-revsersible electron transfer process followed by an irreversible chemical reaction), as follows, for oxidation of mercury in the presence of these ligands in aqueous or aqueous ethanolic solutions.

$$[1]\quad HG + ACD \rightleftharpoons Hg^{(I)}(ACD) + e^-$$

$$[2]\quad 2Hg^{(I)}(ACD) \rightarrow Hg^{(II)}(ACD)_2 + Hg^0$$

where ACD represents the 2-aminocyclopentene-1-dithiocarboxylate anion.

As part of a continuing study into the electrochemistry of

Received April 24, 1995.

A. Safavi[1] and M.B. Gholivand. Department of Chemistry, Faculty of Sciences, Shiraz University, Shiraz, Iran.

[1] Author to whom correspondence may be addressed. Fax: (071) 20027.

Fig. 1. Polarograms of ACDA at concentration (1) 5.22, (2) 6.67, (3) 8.00, and (4) 9.23 ($\times 10^{-4}$ M). Polarograms were recorded from −0.7 V vs. SCE towards more positive potentials.

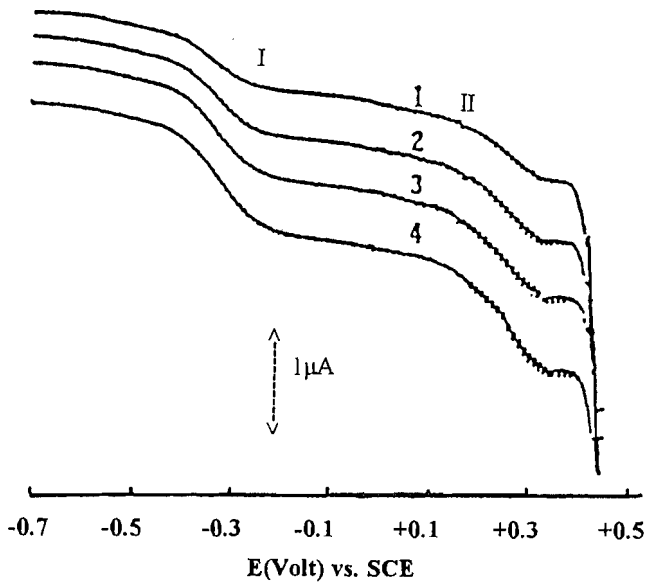

transition metal complexes of these ligands in nonaqueous solvents such as dimethyl sulphoxide (DMSO), it became necessary to first examine the electrochemical behaviour of the ligands in nonaqueous media, since a knowledge of the electrochemistry of the free ligand is a necessary prerequisite for understanding the redox behaviour of coordinated dithiochelates. DMSO was chosen as the most suitable solvent because the mercury complexes of ACD^- and its derivatives (e.g., $Hg(ACD)_2$) are completely insoluble in water and DMSO was found to be the best solvent for these complexes. Because the electrochemical behaviour of a redox couple can be changed dramatically when water is replaced by a nonaqueous solvent (14), and to aid in the interpretation of the electrochemical behaviour of the complexes, the ligands themselves as well as their complexes seemed to warrant an electrochemical investigation.

Experimental

Instrumentation

The electrochemical measurements were performed with a Princeton Applied Research (PAR) electrochemical system (Princeton, N.J.), model 170 polarographic analyzer. A dropping mercury working electrode (drop time = 2 s), an SCE reference electrode, and a platinum wire auxiliary electrode were used for all polarographic measurements. All measurements were made at 25 ± 0.2°C in DMSO containing 0.5 M $KClO_4$. Controlled potential electrolysis experiments were performed at a mercury pool electrode. The auxiliary and reference electrodes were identical with those used for polarographic measurements. Mercury used as dropping mercury electrode and mercury pool was supplied from Merck (Suprapur) and used without further purification.

Cyclic voltammograms were recorded with the PAR electrochemical system at a Metrohm hanging mercury drop electrode (HMDE). All solutions were thoroughly degassed with

Scheme 1

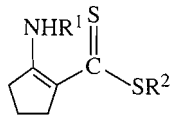

1, $R^1 = R^2 = H$
2, $R^1 = H$, $R^2 = NH_4^+$
3, $R^1 = CH_3$, $R^2 = H$
4, $R^1 = C_2H_5$, $R^2 = H$
5, $R^1 = H$, $R^2 = CH_3$
6, $R^1 = R^2 = CH_3$

pure argon and a continuous stream of argon was passed over the solutions while measurements were being performed.

Materials

ACDA, its ammonium salt, and its derivatives were prepared according to the procedure described by Takeshima and Yokoyama (15) and Bordas et al. (10). Stock solutions (4×10^{-3} M) of the above ligands were prepared in DMSO (Fluka).

The mercury(II) complexes of ACDA and its derivatives were prepared by the reaction of methanolic solutions of the appropriate ligand with mercury(II) nitrate in a 2:1 molar ratio, drying, and then recrystallizing (16).

Because of its hygroscopic nature and the expense of obtaining strictly anhydrous DMSO (17) and because it is well known that solution properties can change significantly when small amounts of water are added to nonaqueous solvents (14), experiments were conducted to determine the effect of traces of water in DMSO on our results. The experiments undertaken in the presence of alumina and deliberately added water (up to 1%) demonstrated that electrochemical measurements of ligands are insensitive to the presence of small amounts of water in DMSO.

Results and discussion

Electrochemistry of acid derivative ligands of ACDA

The ligands that were studied can be categorized into two groups: the acid derivatives of ACDA that differ from each other by the substitution on nitrogen (Scheme 1; **1**–**4**) and the ester derivatives of ACDA (Scheme 1; **5**, **6**) in which the hydrogen on the dithiocarboxylic acid group is substituted with an alkyl group. The electroanalytical behaviour of the acid derivatives is discussed first.

The polarogram of ACDA illustrated in Fig. 1 is typical of all the acid derivatives examined. The two oxidation waves are characteristic of ACDA and its acid derivatives. The second anodic wave occurred close to the anodic potential limit and is either due to oxidation of the Hg(I) complex or formation of mercury-rich cationic forms of the Hg(II) complex as is suggested for other Hg(II) dithiocarbamate complexes (7). Further work on this is in progress to characterize the oxidation wave II. However, most of the interest in relation to the anodic waves of the acid derivatives lies in the wave near −0.35 V (wave I), which we will consider in detail. Table 1 lists the half-wave potentials of wave I for various derivatives of ACDA at a concentration of 9×10^{-4} M in DMSO. The height of wave I is proportional to the square root of the column height ($h^{1/2}$) and concentration, showing the diffusion character of this wave. Voltammograms of ACDA at a rotat-

Table 1. The polarographic parameters of ACDA and its derivatives.

	Compound					
	1	**2**	**3**	**4**	**5**	**6**
$E_{1/2}$ (V)	−0.35[a]	−0.62[a]	−0.28[a]	−0.22[a]	+0.24	+0.23
Slope[b] (mV)	79	83	53	50	27[c]	24[c]
$E_{1/4} - E_{3/4}$	70	65	58	50	42	45
n[d]	1.18	1.02	0.90	0.88	0.97	0.94

[a]$E_{1/2}$ values are for the first oxidation process (process I).
[b]The slope of plot E vs. log $(i_d - i)/i$.
[c]The slope of the plot E vs. log $(i_d - i)/i^2$.
[d]Number of electrons transferred in the anodic process (coulometric analysis).

Fig. 2. Polarograms of the first oxidation wave of (1) 11.4×10^{-4} M ACDA; (2) solution (1) plus 6×10^{-4} M $Hg_2(NO_3)_2$; (3) solution (1) plus 10×10^{-4} M $Hg_2(NO_3)_2$. Polarograms were recorded from −0.6 V vs. SCE towards more positive potentials.

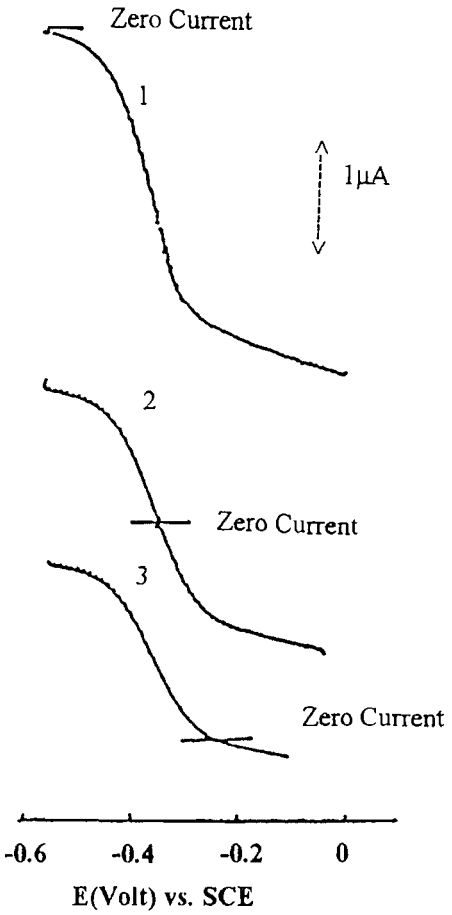

ing platinum working electrode showed no anodic wave at a potential range of −1 to zero. This indicates that wave I is due to the oxidation of mercury in the presence of the above ligands. With increasing concentration, half-wave potentials were essentially constant for the acid derivatives, which is an indication of a 1:1 (ligand:metal) mercury complex formation (18). Controlled potential coulometry at a potential on the plateau of wave I showed a one-electron oxidation process. Plots of E vs. log $(i_d - i)/i$ and $E_{1/4} - E_{3/4}$ data are also consistent with $n = 1$ (Table 1).

For further elucidation of the electrode mechanism associated with wave I, a solution of mercurous nitrate in DMSO was added to the polarographic cell containing ACDA, and its polarogram was recorded. A composite cathodic–anodic wave was obtained, as is illustrated in Fig. 2. By increasing the concentration of mercurous nitrate, the participation of the cathodic part was increased while the anodic current was decreased. By addition of a solution of mercuric nitrate in DMSO to a DMSO solution of ACDA, a cathodic wave was observed at wave I and a composite cathodic–anodic wave was observed at wave II. The height of the cathodic part of wave II was time dependent and decreased with time, while the height of the cathodic wave I increased. All these findings illustrate that wave I is due to Hg(I) compound formation and oxidation wave II is due either to the oxidation of the Hg(I) complex or to oxidation of the mercury electrode in the presence of the Hg(II) complex to form a mercury-rich compound. Later it was found that the oxidation wave II appears also as an anodic wave in the polarograms of synthetically prepared Hg(II) complexes and occurs at the same potential. The appearance of a composite cathodic–anodic wave upon addition of mercurous nitrate can normally be taken as evidence of the reversibility of the electrode process. However, other data obtained suggest that a quasi-reversible assignment is more appropriate.

Cyclic voltammetry was also used to study the mechanism of the electrode process on mercury. The diagnostic criteria used to interpret the cyclic voltammograms were those developed by Nicholson and Shain (19, 20) and Matsuda and Ayabe (21) as summarized by Bard and Faulkner (22) and Brown and Large (23). Directly measured parameters are (22, 23) the anodic and cathodic peak potentials, $E_{p,a}$ and $E_{p,c}$, peak currents $i_{p,a}$ and $i_{p,c}$, half peak potentials (i.e., the potentials at $i = 0.5i_p$), $E_{p,a/2}$, and $E_{p,c/2}$, and the scan rate, v. Derived terms are peak separation $E_{pp} = E_{p,a} - E_{p,c}$, the normalized peak currents $i_{p,c}/v^{1/2}$, $i_{p,a}/v^{1/2}$, the peak current ratio $i_{p,c}/i_{p,a}$, $E_{p,c/2} - E_{p,c}$, and $E_{p,a/2} - E_{p,a}$. Full experimental results are given elsewhere (13), but briefly, taking ACDA as an example, in a solution containing 1.5 mM of ACDA, an increase in scan rate from 0.01 to 0.20 V s^{-1} resulted in an increase in E_{pp} from 75 to 125 mV, with the cathodic and anodic peak potentials both shifting

Fig. 3. Cyclic voltammogram of 10^{-4} M ACDA Switching potential was held for (1) 0 s, (2) 15 s; scan rate, 0.2 V s^{-1}.

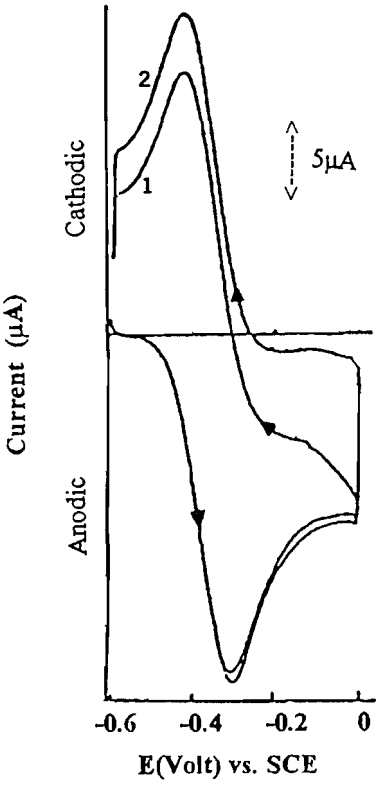

about 25 mV. $E_{p,c/2} - E_{p,c}$ increased by 20 mV, and also $E_{p,a/2} - E_{p,a}$ increased by 20 mV. The values of $i_{p,a}/v^{1/2}$ decreased from 47.5 to 43.5 and $i_{p,c}/v^{1/2}$ decreased from 46 to 43.5 with increase in scan rate. The ratio of $i_{p,c}/i_{p,a}$ was approximately constant at 0.97 ± 0.03. An experiment was conducted in which the switching potential was held for 15 s. No change in cyclic voltammetry parameters was observed by holding the switching potential for 15 s (Fig. 3). Although these results are consistent with a quasi-reversible electron transfer process without any coupled chemical reactions, the possibility of a fast disproportionation reaction such as

[3] $2Hg(ACDA) \quad Hg^0 + Hg(ACDA)_2$

cannot be ruled out.

Reduction of mercury(II) complexes of ACDA and its acid derivatives

Preliminary polarographic analysis indicated that each mercury complex of ACDA or its derivatives undergoes reduction in one step. The reduction wave appears at about −0.70 V for complexes of ACDA and its acid derivatives. In each case, the graphical plot of limiting current vs. the square root of the column height of mercury ($h^{1/2}$) was linear and passed through the origin. This is taken as evidence that the limiting currents are diffusion controlled. Figure 4 shows a dc polarogram, differential pulse polarogram, and cyclic voltammogram for reduction of $Hg^{II}(ACD)_2$ in a DMSO solution. Controlled-potential coulometry at the mercury pool electrode at a potential on the

Fig. 4. Reduction of $Hg(ACD)_2$ at the mercury electrode in DMSO (0.5 M $KClO_4$) at 25°C; (a) dc polarogram; (b) differential pulse polarogram; (c) cyclic voltammogram.

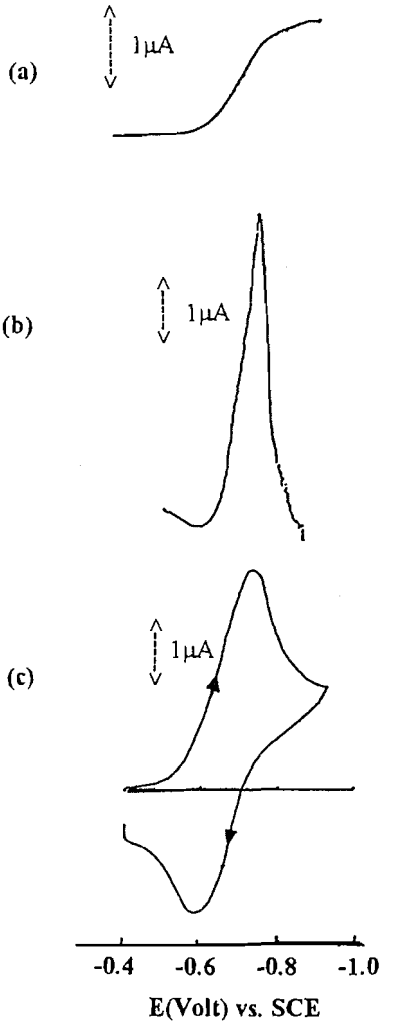

plateau of the reduction wave gave n values of 2 ± 0.1 for all the complexes. These data provide convincing evidence that, in DMSO, the overall electrode process is as follows.

[4] $HgL_2 + 2e^- \quad Hg + 2L^-$

If the above direct two-electron reduction step is accurate, the plot of E vs. log $(i_d - i)/i^2$ should be linear with a slope of 29 mV. Experimentally determined slopes are much greater than this for all the mercury complexes (Table 2). Table 2 also shows that $E_{1/4} - E_{3/4}$ values are close to that expected for a one-electron process. Therefore, while the overall electrode process was previously characterized by eq. [4], the reaction pathway in DMSO has yet to be considered.

The data in Table 2 suggest that a reversible one-electron transfer mechanism appears to be more accurate in describing the reduction process than a two-electron charge transfer step. Since coulometric data gave $n = 2$, it appears that the presence of a chemical reaction is prevalent in this reduction step. Thus, it is assumed that the reduction occurs via species other than the mercuric complex. The decomposition of mercuric com-

Table 2. Polarographic data for the reduction wave of mercury complexes.

Compound	$E_{1/2}$ (V vs. SCE)	Slope of plot E vs. log $[(i_d - i)/i]$	$E_{1/4} - E_{3/4}$ (mV)
Hg(ligand **2**)$_2$	−0.67[a]	85	75
Hg(ligand **3**)$_2$	−0.69[a]	83	60
Hg(ligand **4**)$_2$	−0.70[a]	65	55
Hg(ligand **5**)$_2$	−0.25	76	70
Hg(ligand **6**)$_2$	−0.21	65	60

[a] $E_{1/2}$ values are related to mercury complexes with the anion of each ligand and not its acidic form.

Fig. 5. Cyclic voltammograms of (1) 6.67×10^{-4} M $Hg^{(II)}(ACD)_2$; (2) solution (1) plus 0.5 mL of 10^{-4} M ACD^-; (3) solution (1) plus 1.5 mL of 10^{-4} M ACD^-. Scan rate, 0.05 V s^{-1}.

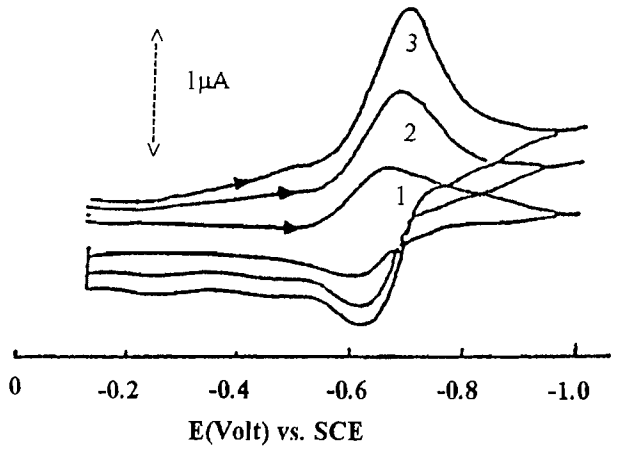

plexes seems feasible, as will be described later. This may take place via one of the following mechanisms.

[5] $Hg^{II}L_2 \ll Hg^0 + L_2$

[6] $2Hg^{II}L_2 \ll 2Hg^{I}L + L_2$

[7] $Hg^{II}L_2 + Hg^0 \ll 2Hg^{I}L$

If one of the above prechemical processes is taking place, the reduction wave may be due either to the reduction of the dimer (L_2) or of $Hg^{I}L$. If mechanism [5] applies, the product of the chemical reaction is the dimer (L_2) and thus the reduction wave is due to the reduction of this entity. The reduction of the dimer is a two-electron process with the slope of the plot of E vs. log $(i_d - i)/i$ nearly equal to 29 mV (13, 24). However, the slopes of the plots of E vs. log $(i_d - i)/i$ obtained for reduction waves in this study were much higher than this value (Table 2). Moreover, it was later proved (13, 24) that the dimer is converted to $Hg^{I}L$ in the presence of elemental mercury. Therefore, the reaction denoted by eq. [5] is ruled out.

Further investigation revealed that the polarogram of the ammonium salt of ACDA showed an oxidation wave with an $E_{1/2}$ value similar to that found for the reduction of the $Hg(ACD)_2$ complex. Also, when a DMSO solution of the ammonium salt of ACDA (denoted by ACD^-) was added to a solution of $Hg^{II}(ACD)_2$ in DMSO, a composite cathodic–anodic wave was obtained. In a similar manner the polarogram of each anion of the acid derivatives of ACDA showed an oxidation wave with $E_{1/2}$ value similar to that found for the reduction of the corresponding mercury complex in DMSO. Moreover, when the cyclic voltammogram of the ammonium salt of ACDA (ACD^-), in DMSO, was compared with that of $Hg(ACD)_2$ at HMDE, similar cyclic voltammograms were obtained (Fig. 5). It was discussed before that the anodic wave of ACDA and its acid derivatives in DMSO solutions is due to the formation of mercury(I) complex. Therefore, the reduction wave obtained in the case of these complexes is due to the reduction of $Hg^{I}L$. This means that the reduction of each mercuric complex occurs via a mercurous intermediate produced according to either eq. [6] or [7].

If eq. [6] is responsible for the prechemical step occurring before the reduction process, the coulometric analysis at the potential of the cathodic wave must yield $n = 1$, since each mole of Hg(II) complex yields only one mole of Hg(I) complex, which can undergo reduction at the electrode surface. The actual value of n obtained experimentally was equal to 2. Therefore, formation of $Hg^{I}L$ is most probably taking place via eq. [7]. If this reaction is correct, for each mole of $Hg^{II}L$ complex, two moles of $Hg^{I}L$ complex are produced that can then undergo reduction at the electrode surface. This is consistent with the coulometric data of $n = 2$ and also with the slopes of the linear plots of E vs. log $(i_d - i)/i$ and $E_{1/4} - E_{3/4}$ values, which show a one-electron cathodic process. Thus, the following mechanism is suggested for reduction of the mercuric complexes of ACDA and its acid derivatives on the mercury electrodes and in DMSO.

[7] $Hg^{II}L_2 + Hg^0 \ll 2Hg^{I}L$

[8] $2Hg^{I}L + 2e^- \quad 2Hg^0 + 2L^-$

The mercuric complexes of the ligands **3** and **4** all showed exactly the same electroanalytical behaviour and therefore the reduction mechanisms for these complexes all obey the above pattern. A similar mechanism has been suggested for mercury(II) dithiocarbamates (25–27).

For further elucidation of the electrode process, the cyclic voltammograms were analyzed. Full experimental data on individual complexes are given elsewhere (13) but, as an example, consider the cyclic voltammograms of 1.1 mM $Hg^{II}(ACD)$. As the scan rate increases from 0.02 to 0.2 V s^{-1}, the following observations in the cyclic voltammetry parame-

Fig. 6. (a) Polarograms of compound **5** at concentration (1) 0, (2) 1.67, (3) 2.86, and (4) 3.75 ($\times 10^{-4}$ M). Polarograms were recorded from −0.2 V vs. SCE towards more positive potentials. (b) The dependence of anodic wave current of compound **6** on its concentration.

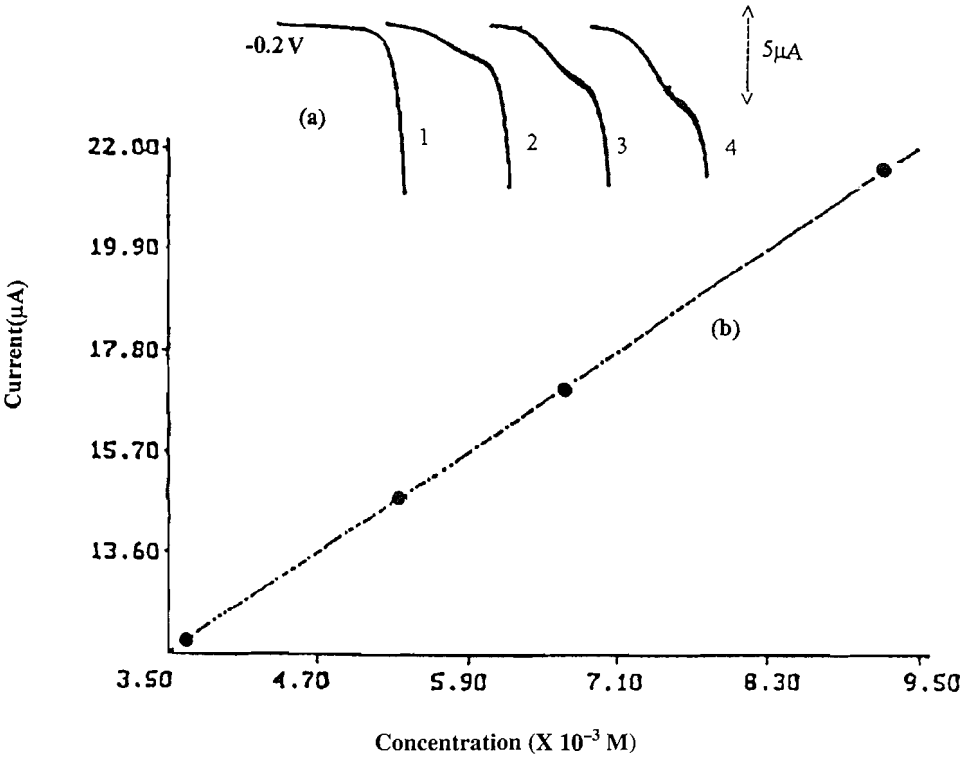

ters are obtained. The peak-to-peak separations E_{pp}, $E_{p,c/2} - E_{p,c}$, and $E_{p,a/2} - E_{p,a}$ were approximately constant at 80, 80, and 75 mV, respectively, and the ratio $i_{p,a}/i_{p,c}$ was constant at about 0.67. The values of $i_{p,c}/v^{1/2} = 0.41 \pm 0.02$ and $i_{p,a}/v^{1/2} = 0.62 \pm 0.03$ also remained effectively constant. An experiment was also conducted in which the switching potential was held for some time. No change in CV parameters was observed by holding the switching potential for 15 s. According to the diagnostic criteria (22, 23), these results are consistent with a quasi-reversible electron transfer process without any coupled chemical reaction. However, polarographic data show that the electrode reduction of the mercuric complex of ACDA and its acidic derivatives is accompanied by a prechemical reaction. It is reported (22) that the effect of the coupled prechemical reaction on the electrode reaction depends on the magnitudes of both the forward and backward rate constants, K_f and K_b (s^{-1}), and the equilibrium constant k. When k is large, the equilibrium lies so far to the right that most of the material is already in the form of the electroactive substance. The preceding reaction then has little effect on the electrochemical response, which appears as unperturbed Nernstian behaviour. This situation exists for mercuric complexes of ACDA and its acid derivatives.

Electrochemistry of ester derivative ligands of ACDA

The dc polarographic study of the esters of ACDA (compounds **5** and **6**) showed one anodic wave at about +0.24 V (Table 1 and Fig. 6*a*). The height of the wave was proportional to $h^{1/2}$ and concentration, showing the diffusion behaviour of this wave (Fig. 6*b*). The height of the polarographic wave of a solution at a given concentration of ester was about twice the height of the polarographic wave obtained in the case of the acid derivatives. The log plot analyses of the anodic wave of the esters together with $E_{1/4} - E_{3/4}$ data were consistent with $n = 2$ (Table 1), while coulometric analysis at a potential on the plateau of the anodic wave of each of the esters gave $n = 1$. Furthermore, no anodic wave was observed for esters in the potential range of −1 to +0.5 V on a rotating platinum electrode. It is therefore concluded that the anodic wave obtained for esters of ACDA arises from oxidation of mercury and formation of the mercury(II) complex. The fact that the half-wave potential of the anodic wave of esters is concentration dependent shows that the mercury complex is not 1:1 (ligand:metal) as in the case of the mercury(I) complex of the acid derivatives. For further illustration of the anodic wave of esters, to a solution of compound **6** in a polarographic cell was added a solution of mercurous nitrate in DMSO, and its polarogram was recorded; a new cathodic peak was observed at about −0.26 V. By increasing the concentration of mercurous nitrate the height of the cathodic wave at −0.26 V was increased, while addition of a DMSO solution of mercuric nitrate to a solution of one of the esters resulted in a cathodic wave at −0.26 V and a composite cathodic–anodic wave at about +0.24 V, as illustrated in Fig. 7. The height of the composite wave was time dependent. The participation of the cathodic part of the composite wave was decreased while the height of the cathodic part at −0.26 V was increased by time. These findings clearly indicate that the anodic wave obtained

Fig. 7. Polarograms of (1) 10^{-3} M of compound **6** plus 5.7×10^{-4} M $Hg(NO_3)_2$; (2) solution (1) after 10 min; (3) solution (1) after 20 min; (4) solution (1) after 30 min. Polarograms were recorded from −0.6 V vs. SCE towards more positive potentials.

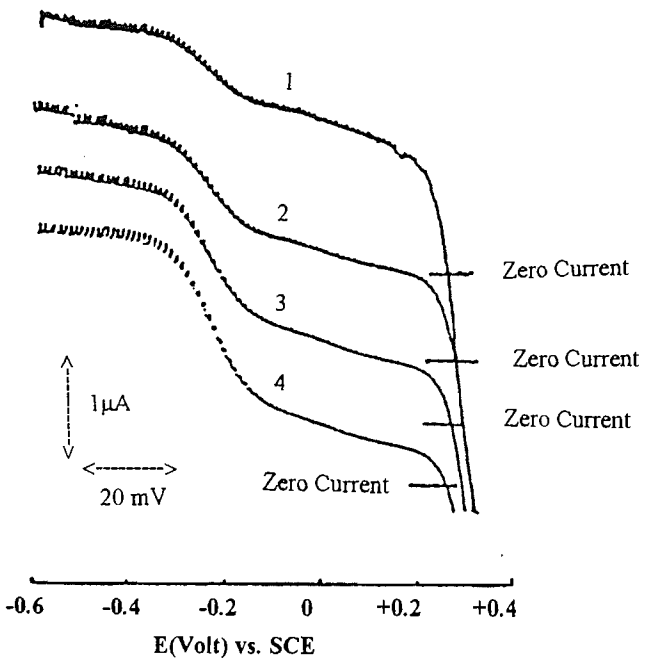

in the case of esters is due to Hg(II) rather than Hg(I) complex formation.

Cyclic voltammetry of solutions of esters individually at HMDE reflects the dc polarographic pattern of each ligand. One oxidation peak was obtained in each case and a cathodic peak was observed in the reverse scan. The diffusion behaviour of the anodic peak was also confirmed by its linear dependence on $v^{1/2}$ and on concentration.

In DMSO containing 5 mM of compound **5**, an increase in scan rate, v, from 0.02 to 0.2 V s^{-1} resulted in the following changes to the usual cyclic voltammetry parameters (22, 23): (*i*) an increase of the peak-to-peak separation, from 48 to 90 mV, with the cathodic potential, $E_{p,c}$, shifting more (27 mV) than the anodic peak potential, $E_{p,a}$ (15 mV); (*ii*) $E_{p,c/2} - E_{p,c}$ increased by 20 mV whereas $E_{p,a/2} - E_{p,a}$ increased by only 10 mV. Similarly, the values of $i_{p,c}/v^{1/2}$ and $i_{p,a}/v^{1/2}$ were about constant with scan rates at 1.57 ± 0.05 and 1.66 ± 0.06, respectively. The ratio $i_{p,c}/i_{p,a}$ increases slightly and approaches unity with increase in scan rate.

The above results are consistent with a quasi-reversible electron transfer process. The presence of a coupled chemical reaction can be deduced from the asymmetry of the cyclic voltammograms of esters, arising from the increasingly drawn-out nature of the cathodic branch with increasing scan rate, whereas changes in the anodic wave are smaller. However, changes in the cyclic voltammetry parameters with scan rate are not so distinct. The most likely reason is that the chemical reaction accompanying the electron transfer process is either too slow or too fast (22) with respect to the cyclic voltammetry time scale, so that its effect is not easily distinguished from cyclic voltammetry parameters. These results are in accordance with polarographic results that, as mentioned before, proved the presence of a chemical reaction coupled with the electron transfer process, i.e., conversion of Hg(II) complex to Hg(I) complex (the reverse of the disproportionation reaction). This conversion was relatively slow with respect to the cyclic voltammetry time scale. Thus, it is not surprising that the effect of the coupled reaction on the cyclic voltammograms is not so pronounced. The most probable mechanism associated with the oxidation of esters of ACDA on a mercury electrode is an EC process as follows.

[9] $Hg + 2L^- \rightleftharpoons Hg^{(II)}L_2 + 2e^-$

[10] $HgL_2 + Hg \rightleftharpoons 2Hg^{(I)}L$

This mechanism agrees well with the coulometric data for $n = 1$ and the slope of the plot of E vs. log $(i_d - i)/i^2$, together with $E_{1/4} - E_{3/4}$ data that showed a two-electron process.

Reduction of mercury complexes of the ester derivatives

Polarographic analysis of the mercuric complexes of the esters of ACDA (ligands **5** and **6**) indicated that these mercuric complexes undergo reduction in one step. The reduction wave that appears at about −0.25 V is diffusion controlled as its height is directly proportional to $h^{1/2}$ and concentration of the ligand. Cyclic voltammograms at mercury electrodes are those expected for a chemically reversible electrode process. Controlled potential coulometry of each of the complexes at a mercury pool electrode gave $n = 2$. A plot of E against log $(i_d - i)/i$ for each complex gave linear plots ($r = 0.998$) with slopes of 76 and 65 mV for mercury complexes of ligands **5** and **6**, respectively. $E_{1/4} - E_{3/4}$ values from dc polarograms are close to that expected for a one-electron charge-transfer step for the above complexes (Table 2).

It was proved before that, while in DMSO solutions ACDA and its acid derivatives undergo a one-electron anodic process at a mercury electrode, the ester derivatives of ACDA react at a mercury electrode via a two-electron oxidation process, giving the $Hg^{(II)}L_2$ complex. The wave due to the anodic oxidation of mercury in the presence of ester derivatives of ACDA occurred at about +0.24 V, which, as proved, is due to $Hg^{(II)}L_2$ formation. However, when a solution of synthetically prepared $Hg^{(II)}L_2$ is electrolyzed at a mercury electrode it is reduced to elemental mercury and L^- via a $Hg^{(I)}L$ intermediate. In fact, in this case the $Hg^{(I)}L$ complex undergoes reduction at about −0.25 V. That is why the half-wave potential of the reduction of the $Hg^{(II)}L_2$ complex (−0.25 V) is different (cf. Tables 1 and 2) from the half-wave potential of the anodic wave of the free ligand (+0.24 V). The $Hg^{(I)}L$ complex can then undergo reduction at about −0.25 V. All these findings show that although the overall electrode process is again

[11] $HgL_2 + 2e^- \rightleftharpoons Hg + 2L^-$

the data support the idea that, in DMSO solution, reduction of mercuric complexes of the ester derivatives occurs via a mercury(I) intermediate, as was suggested for mercuric complexes of the acid derivatives of ACDA.

It seems clear from the above discussion that, at mercury electrodes and in DMSO solutions and in the presence of the

above ligands, mercury(II) complexes reduce to elemental mercury via a mercury(I) intermediate.

Acknowledgment

The authors wish to express their gratitude to the Shiraz University Research Council for the support of this work.

References

1. D. Coucouvanis. Prog. Inorg. Chem. **11**, 294 (1970).
2. J.A. McCleverty. Prog. Inorg. Chem. **10**, 49 (1968).
3. R. Einsenberg. Prog. Inorg. Chem. **12**, 295 (1970).
4. D. Coucouvanis. Prog. Inorg. Chem. **26**, 301 (1979).
5. J. Willernse, J.A. Cras, J.J. Steggerda, and C.P. Keijzers. Struct. Bonding (Berlin), **28**, 83 (1976).
6. A.M. Bond and R.L. Martin. Coord. Chem. Rev. **54**, 23 (1984).
7. A.M. Bond, R. Colton, A.F. Hollenkamp, B.F. Hoskins, and K. McGregor. J. Am. Chem. Soc. **109**, 1969 (1987).
8. A.M. Bond, R. Colton, A.F. Hollenkamp, B.F. Hoskins, K. McGregor, and E.R.T. Tiekink. Inorg. Chem. **30**, 192 (1991).
9. G. Matolcsy, M. Hamran, and B. Bordas. Acta Phytopathol. **5**, 123 (1970).
10. B. Bordas, P. Sohar, G. Matolcsy, and P. Berencsi. J. Org. Chem. **37**, 1727 (1972).
11. D.M. Baird. J. Chem. Educ. **62**, 168 (1969).
12. A. Safavi and M.B. Gholivand. Anal. Lett. **25**, 1309 (1992).
13. M.B. Gholivand. Ph.D. Thesis. Shiraz University, Shiraz, Iran. 1991.
14. Y. Marcus. Ion solvation. Wiley, New York. 1985.
15. T. Takeshima and M. Yokoyama. J. Org. Chem. **34**, 730 (1969).
16. K. Nag and D.S. Joardar. Z. Naturforsch. Abt. B: **30**, 107 (1975).
17. D. Martin and H.G. Harthal. Dimethyl sulphoxide. Van Nostrand Reinhold, New York. 1975.
18. M. Esteban, E. Casassas, and L. Fernandez. Talanta, **33**, 843 (1986).
19. R.S. Nicholson and I. Shain. Anal. Chem. **36**, 706 (1964).
20. R.S. Nicholson. Anal. Chem. **37**, 1351 (1965).
21. H. Matsuda and Y. Ayabe. Z. Electrochem. **59**, 494 (1955).
22. A.J. Bard and L.R. Faulkner. Electrochemical methods, fundamentals and applications. Wiley, New York. 1980.
23. E.R. Brown and R.F. Large. *In* Physical methods of chemistry. Vol. 1, Pt. IIA. *Edited by* A. Weissberger and B.W. Rossiter. Wiley Interscience, New York. 1971.
24. A. Safavi and M.B. Gholivand. Electroanalysis. Submitted.
25. A.M. Bond, A.T. Casey, and J.R. Thackeray. Inorg. Chem. **12**, 887 (1973).
26. T.H. Randle, T.J. Cardwell, and R.J. Magee. Aust. J. Chem. **28**, 21 (1975).
27. A.M. Bond, R. Colton, M.L. Dillon, J.E. Moir, and D.R. Page. Inorg. Chem. **23**, 2883 (1984).

Radiation-induced dissolution of chromium oxide in aqueous solutions

Luis García Rodenas, Mauricio Chocrón, Pedro J. Morando, and Miguel A. Blesa

Abstract: Gamma irradiation of suspensions of a commercial sample of α-Cr_2O_3 in the presence of $KBrO_3$ in the concentration range $0.1 \leq [BrO_3^-] \leq 0.4$ mol dm^{-3}, at pH 4 and 25°C brings about oxidative dissolution. Release of Cr(VI) to the solution proceeds at a constant rate that increases with bromate concentration, even in conditions of quantitative e_{aq}^- scavenging. A mechanism of reactions is proposed in which OH and BrO_2 radicals oxidize surface Cr(III) to Cr(IV), and ionic release is achieved by oxidation of surface Cr(IV) by bromate. The corresponding set of equations was solved by a rigid method for the integration of ordinary differential equations, using these two heterogeneous rate constants as adjustable parameters. The calculated profiles are in close agreement with the experimental data.

Key words: chromium oxides, radiation-induced dissolution, oxidation dissolution.

Résumé : L'irradiation γ d'un échantillon commercial d'α-Cr_2O_3, en présence de $KBrO_3$, à des concentrations de BrO_3^- allant de 0,1 à 0,4 mol dm^{-3}, à un pH de 4 et à 25°C, provoque une dissolution oxydante. L'apparition de Cr(VI) dans la solution se produit à une vitesse constante qui augmente avec la concentration de bromate, même dans des conditions de piégeage quantitatif de e_{aq}^-. On propose un mécanisme des réactions dans lequel les radicaux OH et BrO_2 oxydent la surface du Cr(III) en Cr(IV) qui est par la suite oxydé par le bromate pour provoquer une apparition de chrome ionique. L'ensemble correspondant des équations a été résolu par une rude méthode pour l'intégration des équations différentielles ordinaires qui utilise ces deux constantes de vitesse hétérogènes comme paramètres ajustables. Les profils calculés sont en bon accord avec les données expérimentales.

Mots clés : oxydes de chrome, dissolution induite par les radiations, dissolution oxydante.

[Traduit par la rédaction]

Introduction

The interaction of chromium(III) oxides is governed by the chemical inertia of the d^3 Cr(III) ion. Substitution reactions on octahedral Cr(III) complexes in solution are slow, and can be accelerated only by severe distortions from the octahedral coordination (1) or by electron transfer to generate either Cr(II) or Cr(IV). Phase transfer of Cr(III) as involved in α-Cr_2O_3 can also be accelerated by oxidation (2, 3) or reduction,[2] as accomplished by heterogeneous electron transfer. Acid attack (4) is only effective in dissolving hydrous oxides.

Comparison of the behavior of the chromium(III) and iron(III) oxides is interesting for both fundamental and applied reasons. Iron(III) oxides are easily dissolved by reductive attack (5–9), whereas oxidation to Fe(VI) is only possible in strongly alkaline and (or) oxidative media (10). The reverse is true for chromium(III) oxides. As both oxides are present in the layers grown on stainless steel by corrosion, the sensitivity to aqueous attack is influenced by this contrasting behavior. In particular, whenever it is necessary to remove the oxide layers, a two-stage cleaning process is almost mandatory: an oxidative step to remove chromium oxides and a reductive stage to dissolve iron oxides (11). Cleaning of stainless steel surfaces is an important problem in nuclear technology, associated with the need to remove the radioactive oxides to decrease the radiation fields in the critical components of the heat transport circuit (chemical decontamination).

The dissolution of these oxides is influenced by radiation fields in two ways. First, the defect structure of the oxides is heavily influenced by the annealing effect of the radiation, and eventually by the creation of defects by neutron irradiation (for in-core components). Secondly, the radiolysis of the aqueous medium generates both oxidizing and reducing species, especially OH and e_{aq}^-.

The first effect has been explored in previous papers (12).[3] Concerning the influence of solvent radiolysis, Buxton et al. (13) have shown that colloidal haematite (α-Fe_2O_3) and magnetite (Fe_3O_4) dissolve following attack by one-electron reducing free radicals generated by the radiolysis aqueous solutions of propan-2-ol saturated with nitrous oxide. Also, Mulvaney et al. (14) reported the reductive dissolution of suspensions of manganese oxides (α-, δ-, and γ-MnO_2 and Mn_5O_8) under steady γ-irradiation of aqueous solutions of propan-2-ol saturated with nitrous oxide.

Received June 26, 1995.

L. García Rodenas, M. Chocrón, P.J. Morando, and M.A. Blesa.[1] Departamento Química de Reactores, Comisión Nacional de Energía Atómica, Avda. del Libertador 8250, 1429-Buenos Aires, Argentina.

[1] Author to whom correspondence may be addressed. Telephone: (54-1) 704-1365. Fax: (54-1) 704-1164. E-mail: blesa@cnea.edu.ar

[2] L. García Rodenas, A.M. Iglesias, P.J. Morando, and M.A. Blesa. Submitted.

[3] Also, M. dos Santos Afonso, M. Zysmilich, C.D. Di Risio, R.O. Marques, and M.A. Blesa. Submitted.

Whereas the reductive dissolution of Fe(III) oxides in media containing OH scavengers is well known, the possibility of oxidative dissolution of chromium(III) oxides in media containing e_{aq}^- scavengers has not been explored. In neutral aqueous solution, Patnaik et al. (15) reported the homogeneous radiolytic oxidation of chromium(III) sulfate in the presence of BrO_3^-.

In the present paper we report a kinetic study of the radiolytic dissolution of suspensions of α-Cr_2O_3 in the presence of $KBrO_3$ at pH 4 and 25°C.

Experimental

α-Cr_2O_3 was a commercial sample (Puratronic). It was characterized by chemical analysis: the assay of Cr was 68.40 wt.% measured by atomic absorption spectrometry (AAS) using a Varian AAR 5 spectrophotometer. The powder X-ray diffractogram obtained in a Philips X-ray PW 1130 demonstrated the product to be α-Cr_2O_3; its surface BET area was measured in a Micromeritics Accusorb 2100 E to be 1.73 $m^2\ g^{-1}$.

The dissolution experiments were performed in a cylindrical beaker, under continuous magnetic stirring. In a typical experiment 20 mg α-Cr_2O_3 was suspended in 50 cm^3 $KBrO_3$ solution of appropriate concentration at pH 4.0 and 25.0 ± 0.1°C. The reaction was started by placing the test tube in a standarized position in a ^{60}Co γ-irradiation facility (Ezeiza Atomic Center); the γ-dose rate in the tube position was 10.12 krad min^{-1}. Previous tests demonstrated that the thermally activated dissolution reaction was negligible during the whole time span of the irradiation experiments. The reaction progress was followed by periodically withdrawing samples with a syringe and filtering them through a 0.45-μm Nuclepore membrane; the concentration of Cr(VI) in the filtrate was determined spectrophotometrically using diphenylcarbazide (16). In some samples, total chromium was measured by AAS.

Results and discussion

Figure 1 shows the concentration of Cr(VI) dissolved from α-Cr_2O_3 as a function of time for different $KBrO_3$ concentrations. Thermal data (no irradiation) and total chromium concentration data are also shown. The oxide dissolves as Cr(VI) at a constant rate that is a function of the oxidant concentration.

The primary processes occurring during the radiolysis of water have been studied extensively (17). In particular, in aqueous $KBrO_3$ solutions, the hydrated electron reacts with BrO_3^- yielding BrO_2, which was postulated to readily oxidize dissolved Cr(III) (15). Therefore we propose the following mechanism for the radiation-induced dissolution of α-Cr_2O_3 in aqueous solutions of $KBrO_3$, reactions [1]–[9]:

[1] $H_2O \rightarrow e_{aq}^-, OH, H, H_2O_2, H_2$

[2] $BrO_3^- + e_{aq}^- + H_2O \rightarrow BrO_2 + 2\ OH^-$

[3] $\equiv Cr^{3+} + BrO_2 \rightarrow \equiv Cr^{4+} + \text{products}$

[4] $Cr_T + \equiv Cr^{4+} + BrO_3^- \rightarrow Cr(VI)_{aq} + \equiv Cr^{3+} + \text{products}$

[5] $\equiv Cr^{4+} + e_{aq}^- \rightarrow \equiv Cr^{3+}$

Fig. 1. Concentrations of Cr(VI) and total chromium (Cr_T) as a function of time from radiation-induced dissolution of Cr_2O_3 in aqueous solution of $KBrO_3$ at 25°C and pH 4.0. Experimental values: ⬟, 0.1; ▲, 0.3, and ○, 0.4 mol dm^{-3} $KBrO_3$ as [Cr(VI)] and ●, 0.4 mol dm^{-3} $KBrO_3$ as [Cr total]; ■, 0.4 mol dm^{-3} $KBrO_3$, no irradiation.
Calculated values: (_____).

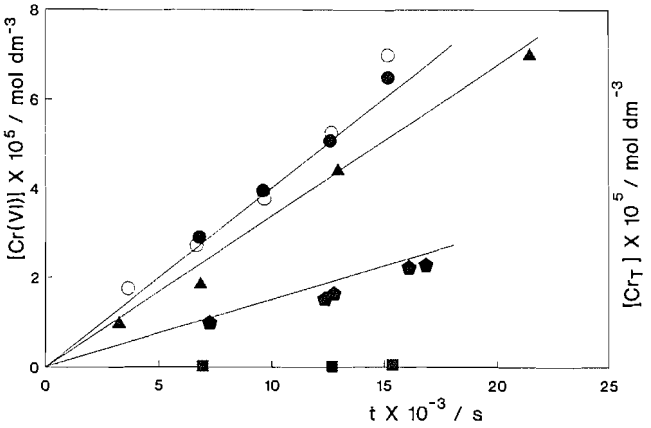

[6] $\equiv Cr^{3+} + OH \rightarrow \equiv Cr^{4+} + OH^-$

[7] $BrO_2 + BrO_2 \rightarrow Br_2O_4 + H_2O \rightarrow BrO_2^- + BrO_3^- + 2H^+$

[8] $OH + OH \rightarrow H_2O_2$

[9] $BrO_2^- + OH \rightarrow BrO_2 + OH^-$

In these equations, $\equiv Cr^{3+}$ and $\equiv Cr^{4+}$ represent surface chromium ions. To normalize the kinetic equations, the corresponding surface concentrations (in mol m^{-2}) were transformed into equivalent bulk concentrations (in mol dm^{-3}) using eq. [10]

[10] $[\equiv Cr^{3+}] = N_s S_e w / V$

where N_s = number of active sites per unit area, S_e = specific surface area, w = mass of oxide, and V = volume of solution. The N_s value was estimated to be 5 sites nm^{-2} (18). The value of instantaneous surface ($S = S_e w$) can be considered invariable throughout the experiment because the fraction of dissolved chromium is only about 2%. From eq. [10], the value $[\equiv Cr^{3+}] = 5.3 \times 10^{-6}$ mol dm^{-3} was obtained.

In eq. [4] $[Cr_T] = 1$ was introduced as a procedure to keep $[\equiv Cr^{3+}] + [\equiv Cr^{4+}]$ constant throughout the reaction. The rate is therefore given by

[11] $R = k_4\ [BrO_3^-]\ [\equiv Cr^{4+}]$

where k_4 is given in $mol^{-1}\ dm^3\ s^{-1}$.

Most of the rate constants involved in eqs. [2]–[9] are available from the literature. Equation [6] represents the heterogeneous attack of OH on ≡Cr(III). The equivalent homogeneous process has been studied, and the reported rate constant is $3.1 \times 10^8\ M^{-1}\ s^{-1}$ (19). In principle, it is possible to calculate the ratio of collisional frequencies of the heterogeneous to homogeneous reactions; see, for example, refs. 20 and 21. We

Table 1. Rate constants for reactions [2]–[9].

Reaction	Constant/M^{-1} s^{-1}	Reference
[2]	4.1×10^9	24
[3]	4.3×10^4	This work
[4]	3.8×10^{-3}	This work
[5]	1.3×10^{11}	Upper limit; see text
[6]	3.1×10^8	19
[7]	1.4×10^9	24
[8]	5.5×10^9	17
[9]	1.9×10^9	24

found, however, that the rate calculated using the homogeneous rate constant and the equivalent homogeneous concentration (eq. [10]) was similar to that calculated from the above-mentioned ratio. Furthermore, the values of k_3 and k_4 (our most important parameters, see below) are highly insensitive to large changes in k_6.

Using these literature data, only the heterogeneous rate constants for reactions, [3], [4], and [5] must be derived from our results. In fact, reaction [5] does not contribute to the dissolution behavior; even a diffusion-limited value cannot compete with the scavenging of e_{aq}^- by BrO_3^-, reaction [2], at the concentrations used in this work. A value $k_5 = 1.3 \times 10^{11}$ M^{-1} s^{-1} was nominally included in the calculations.

The set of reactions [1]–[9] implies that dissolution is achieved in two heterogeneous stages: (*a*) the oxidation of ≡Cr(III) to ≡Cr(IV) through the action of both BrO_2 and OH (reactions [3] and [6]); (*b*) the oxidation of ≡Cr(IV) to eventually yield dissolved Cr(VI) through the action of bromate (eq. [4]). Equations [7] and [8] represent the alternative pathways of BrO_2 and OH consumption through dimerization; the contribution of reaction [8] is negligible as compared to reaction [6] whereas, in the steady state, reaction [7] is the main pathway of BrO_2 disappearance. The buildup of BrO_2^- through eq. [7] in turn triggers the alternative OH consumption pathway, eq. [9].

The scheme of reactions leads to a limiting constant dissolution rate when $[\equiv Cr^{4+}]$ achieves a steady state value, given by:

$$[12] \quad R_{ss} = k_4 [BrO_3^-] [\equiv Cr^{4+}]_{ss}$$

The heterogeneous scheme, eqs. [1]–[9], bears resemblances to and dissimilarities with the scheme proposed by Patnaik et al. (15) for the homogeneous radiolytic oxidation of Cr(III) in bromate media. Patnaik et al. proposed homogeneous reactions equivalent to [3] and [6]; due to the higher [Cr(III)], the only fate for BrO_2 in his scheme is the reaction with Cr(III), at variance with the heterogeneous case. The second difference is the fate of Cr(IV); in homogeneous media, it disproportionates rapidly:

$$[13] \quad 3\ Cr(IV) \rightarrow 2\ Cr(III) + Cr(VI)$$

whereas on the surface of the solid, it survives long enough to accumulate. Its removal takes place as a rather slow chemical oxidation by bromate (eq. [4]).

The whole set of rate equations corresponding to the reaction scheme [1]–[9] was solved by a rigid method for the integration of ordinary differential equations (22), using standard G values for e_{aq}^- and OH of 2.8 molecules per 100 eV of absorbed energy. Table 1 shows the rate constants used in the optimized calculations. The results are in agreement with the qualitative analysis given above.

Fig. 2. Concentrations of ≡Cr(IV) as a function of time for different concentrations of $KBrO_3$.

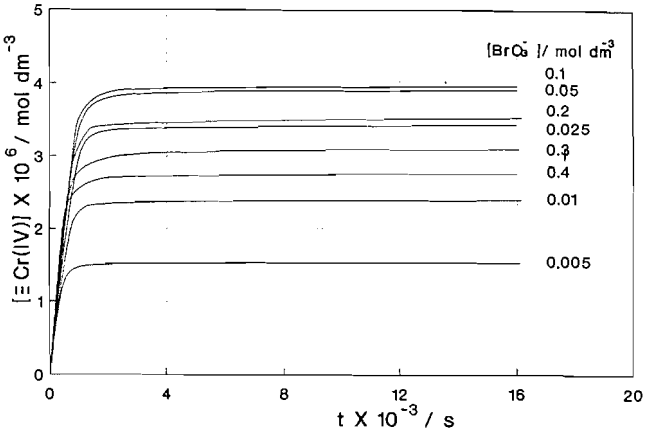

Fig. 3. Calculated steady state concentration of ≡Cr(IV) as a function of $KBrO_3$.

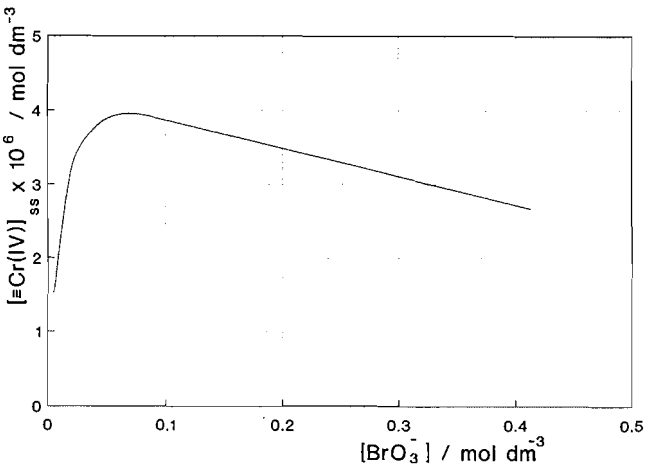

The calculated shapes of the dissolution profiles, expressed as Cr(VI) vs time, are in very good agreement with the experimental data, as shown in Fig. 1. The reaction scheme predicts that steady state concentrations of ≡Cr(IV) are reached at rather short times. These steady state values depend on the $KBrO_3$ concentration, as seen in Fig. 2. The data from Fig. 2 indicate a decrease in $[\equiv Cr^{4+}]_{ss}$ as the BrO_3^- concentration increases, within the explored range ($[BrO_3^-] \geq 0.1$ mol dm^{-3}). This effect is due to the increased rate of removal from the surface (eq. [12]). The rate of generation of $\equiv Cr^{4+}$ according to eq. [3] is insensitive to $[BrO_3^-]$ because the BrO_3^- ion is a very effective scavenger of e_{aq}^- (eq. [2]) and the rate of generation of BrO_2 radicals remains the same for the different bromate concentrations studied. Figure 3 shows the expected relationship between $[\equiv Cr^{4+}]_{ss}$ and $[BrO_3^-]$; the initial rise is completed for $[BrO_3^-] \cong 0.1$ mol dm^{-3}.

Radiation-induced dissolution is seen to be severely lim-

Fig. 4. Calculated effect of bromate concentration on the dissolution of α-Cr_2O_3. ●: experimental points.

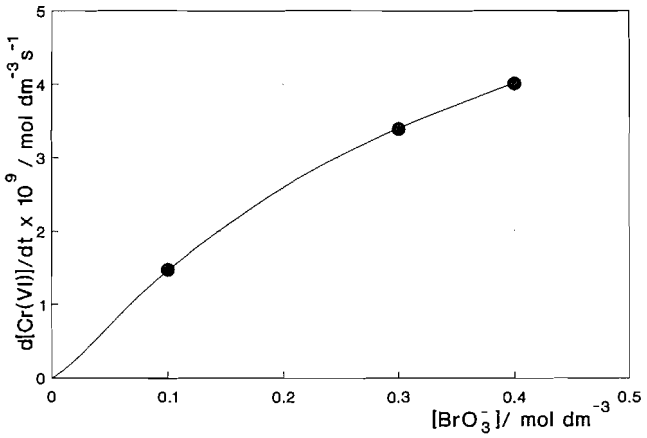

ited. In the absence of e_{aq}^- or OH scavengers, as in an operating reactor, recombination is much faster than any possible attack on iron or chromium oxides, and only the molecular products (H_2, H_2O_2) are of importance. Hydrogen influences the kinetics and increases the solubility of iron oxides in high temperature water, but it exerts little or no influence on chromium oxides, because of the low redox potential of the Cr(III)/Cr(II) couple. The influence of the other molecular product, hydrogen peroxide, is also negligible. Unless a very strongly alkaline medium is generated, dissolution does not take place. A kinetic study of the dissolution of Cr_2O_3 in hydrothermal media has shown that oxidation does not enhance the rate of basic dissolution that put $Cr(OH)_4^-$ into solution, although in this medium this species is readily oxidized in solution (23). Thus, water radiolysis per se is not efficient to bring about dissolution. Scavengers for e^- are required; in these conditions, reaction [6] in principle may lead to dissolution, but the sluggishness of the removal of $\equiv Cr^{4+}$ from the surface (reaction [4]) severely limits the dissolution rate. When BrO_3^- is the e^- scavenger, BrO_2 may also oxidize surface $\equiv$Cr(III), but in this case dimerization (eq. [7]) severely limits the dissolution rate. The rate is given by eq. [12]; from the data in Fig. 3, it is possible to calculate the rates at any given $[BrO_3^-]$. The maximum value, for $[BrO_3^-] = 0.4$ mol dm^{-3}, is $R \cong 4 \times 10^{-9}$ mol dm^{-3} s^{-1}, which is equivalent to 6×10^{-3} μmol m^{-2} s^{-1}.

The calculated rate vs. $[BrO_3^-]$ curve is shown in Fig. 4, together with experimental rate values. The model curve includes a sigmoidal behavior at low $[BrO_3^-]$ (< 0.05 mol dm^{-3}), outside the explored range, and a deviation from linearity, observed at high $[BrO_3^-]$, that is well accounted for as due to the decrease in $[\equiv Cr^{4+}]$ (see eq. [11]).

The sigmoidal trace at low $[BrO_3^-]$ is due to incomplete scavenging of e_{aq}^- by BrO_3^- (eq. [2]), and the operation of reaction [5]. In these conditions, other possible reactions, e.g., $e^-_{aq} + OH \rightarrow OH^-$, should also be included; the lack of experimental data does not warrant a detailed analysis of this region.

References

1. A.B. Zabin and H. Taube. Inorg. Chem. **3,** 963 (1964).
2. M.G. Segal and W.J. Williams. J. Chem. Soc. Faraday Trans. 1, **82,** 3245 (1986).
3. G.B. Reartes, P.J. Morando, M.A. Blesa, P. Hewlett, and E. Matijević. Chem. Mater. **3,** 1101 (1991).
4. G.B. Reartes, P.J. Morando, M.A. Blesa, P. Hewlett, and E. Matijević. Langmuir, **11,** 2277 (1995).
5. D. Bradbury, M. Segal, R.M. Sellers, T. Swan, and C.J. Wood. *In* Water chemistry of nuclear reactor systems 2. British Nuclear Energy Society, London. 1981. p. 403.
6. D. Bradbury, M. Segal, R.M. Sellers, T. Swan, and C.J. Wood. Report NP-3177, Electric Power Research Institute, Palo Alto, Calif. 1983.
7. E.C. Baumgartner, M.A. Blesa, H.A. Marinovich, and A.J.G. Maroto. Inorg. Chem. **22,** 2224 (1983).
8. B. Zinder and W. Stumm. Chimia, **39,** 280 (1985).
9. E.B. Borghi, P.J. Morando, and M.A. Blesa. Langmuir, **7,** 1652 (1991); E.B. Borghi, S.P. Alí, P.J. Morando, and M.A. Blesa. J. Nucl. Mater. In press.
10. F.A. Cotton and G. Wilkinson. *In* Advanced inorganic chemistry. Interscience Publishers, New York. 1966. p. 862.
11. M.A. Blesa, A.J.G. Maroto, and A.E. Regazzoni. Nihon Genshiryokee Gakkaishi, Proc. Int. Conf. Water Chemistry in Nuclear Power Plants, Fukui City, Japan. 1991.
12. M. dos Santos Afonso, C.D. Di Risio, A. Roitberg, R.O. Marques, and M.A. Blesa. Radiat. Phys. Chem. **36,** 457 (1990).
13. G.V. Buxton, T. Rhodes, and R.M. Sellers. J. Chem. Soc. Faraday Trans. 1, **79,** 2961 (1983).
14. P. Mulvaney, L. Denison, F. Grieser, R. Cooper, J. Sanders, and D. Meisel. J. Colloid Interface Sci. **121,** 1 (1988).
15. S.K. Patnaik, H.J. Arnikar, and D. Sarkhawas. Radiochem. Radioanal. Lett. **38,** 411 (1979).
16. A.I. Vogel. Química Analítica Cuantitativa. Vol. 2. Kapelusz, Buenos Aires.1961.
17. I.G. Draganić and Z.D. Draganić. *In* The radiation chemistry of water. Academic Press, New York.1971.
18. L. García Rodenas, P.J. Morando, M.A. Blesa, S. Duhalde, and C. Saragovi. Can. J. Chem. **71,** 771 (1993).
19. J.-C. Muller and C. Ferradini. J. Chim. Phys. **62,** 659 (1965).
20. R.J. Klingler and J.K. Kochi. J. Am. Chem. Soc. **102,** 4790 (1980).
21. R.J. Klingler and J.K. Kochi. J. Phys. Chem. **85,** 1733 (1981).
22. M.L. Michelsen. AIChE J. **22,** 594 (1976).
23. C.J. Farrow and A.R. Burkin. *In* Leaching and reduction in hydrometallurgy. A.R. Burkin, London. 1975. p.20.
24. G.V. Buxton and F.S. Dainton. Proc. R. Soc. London, Ser. A: **304,** 427 (1968).

The selective complexation of adamantane nitriles by tungsten pentacarbonyl

Valerie J. Jefford, Melbourne J. Schriver, and Michael J. Zaworotko

Abstract: Adamantyl-1,3,4-oxathiazol-2-one is usually prepared as a mixture with 1-adamantanecarbonitrile. To separate these two compounds the mixture is reacted with thf·$W(CO)_5$, which selectively forms a complex with the nitrile. The resulting mixture can then be readily separated into pure compounds by sublimation. Characterization data are presented, including the X-ray crystal structure of the nitrile complex, which can be prepared directly from the reaction of the adamantyl nitrile and thf·$W(CO)_5$. (Crystal data for $C_{16}H_{15}NO_5W$: orthorhombic, space group *Pmcn*, a = 10.5869(19) Å, b = 14.0622(22) Å, c = 23.342(4) Å, V = 3475.0(11) Å^3, Z = 8, R = 0.042.) The nitrile can be recovered from the complex by reaction with $P(C_6H_5)_3$ followed with separation by sublimation. The reaction of the related 1-cyano-3-(1,3,4-oxathiazol-2-on-5-yl)-adamantane with thf·$W(CO)_5$ yields a complex in which the site of coordination is shown spectroscopically to be the nitrile moiety. Semi-empirical calculations at the PM3 level indicate that the oxathiazolone heterocycle may be a poor ligand due to the influence of the exo- and endo-cyclic oxygen atoms.

Key words: oxathiazolone, nitrile, tungsten, complexation, selectivity, adamantane.

Résumé : L'adamantyl-1,3,4-oxathiazol-2-one est généralement préparée sous la forme d'un mélange avec l'adamantane-1-carbonitrile. Pour séparer ces deux composés, on fait réagir le mélange avec du thf·$W(CO)_5$ qui forme sélectivement un complexe avec le nitrile. Le mélange qui en résulte peut alors être séparé facilement en composés purs par sublimation. On présente des données de caractérisation, y compris la structure cristalline par diffraction des rayons X du complexe avec le nitrile qui peut être préparé directement par réaction de l'adamantylnitrile avec du thf·$W(CO)_5$. Les données cristallines pour $C_{16}H_{15}NO_5W$: orthorhombique, groupe d'espace *Pmcn*, a = 10,5869(19), b = 14,0622(22) et c = 23,342(4) Å, V = 3475,0(11) Å^3, Z = 8, R = 0,042. On peut récupérer le nitrile du complexe en faisant réagir ce dernier avec du $P(C_6H_5)_3$ et en procédant ensuite à une sublimation. La réaction du 1-cyano-3-(1,3,4-oxathiazol-2-on-5-yl)-adamantane apparenté avec du thf·$W(CO)_5$ fournit un complexe dans lequel il a été démontré par spectroscopie que le site de coordination est la portion nitrile. Des calculs semi-empiriques au niveau PM3 indiquent que l'hétérocycle oxathiazolone est probablement un mauvais coordinat à cause de l'influence des atomes d'oxygène exo- et endo-cycliques.

Mots clés : oxathiazolone, nitrile, tungstène, complexation, sélectivité, adamantane.

[Traduit par la rédaction)

Introduction

The 1,3-dipole cycloaddition reaction is an important synthetic route to a number of heterocyclic systems (1, 2). The nitrile sulphides **1** are a family of 1,3-dipoles that contain a sulphur–nitrogen π bond and have been the subject of several recent reviews (3, 4). They are typically generated in situ from precursor oxathiazolone heterocycles such as **2** in the presence of a dipolarophile to give five-membered ring heterocycles. We have reported the first systematic X-ray crystallographic analysis of the precursor ring and the cycloadducts from the reaction of adamantane – nitrile sulphide with the alkyne and thiazyl triple bonds and explored the chemistry of the first bis(nitrile sulfide) (5).

Received October 7, 1994.[1]

V.J. Jefford and M.J. Schriver.[2] Department of Chemistry, Memorial University, St. John's, NF A1B 3X7, Canada.
M.J. Zaworotko. Department of Chemistry, Saint Mary's University, Halifax, NS B3H 3C3, Canada.

[1] Revision received October 18, 1995.
[2] Author to whom correspondence may be addressed. Telephone: (709) 737-8744. Fax: (709) 737-3702. E-mail: mschriver@kean.ucs.mun.ca

The nitrile sulphides have been shown to readily decompose to the corresponding nitriles and elemental sulphur. In previous reports the preparation of the precursor oxathiazolone heterocycle has suffered from the premature generation of the 1,3-dipole, leading to significant loss of product and the generation of mixtures of heterocycles and nitriles. Indeed, we reported that the separation of adamantane oxathiazolone **2** from adamantane nitrile **3** was laborious and gave low yields of pure material (5).

In this work we report the separation of the nitrile **3** from an impure sample of **2** by selective complexation with tungsten pentacarbonyl. The preparation and the solid state structure of the nitrile complex **4** is described and compared with the structures of other nitrile·$W(CO)_5$ complexes. The selectivity of the complexation is confirmed by reaction with the bifunctional molecule 1-cyano-3-(1,3,4-oxathiazol-2-on-5-yl)-adamantane **5** and the site of complexation is shown spectroscopically to be the nitrile moiety, giving **6**.

Experimental

General procedures

Reagents used in synthesis ($W(CO)_6$ and $P(C_6H_5)_3$) were purchased from Aldrich and used as received. The pure com-

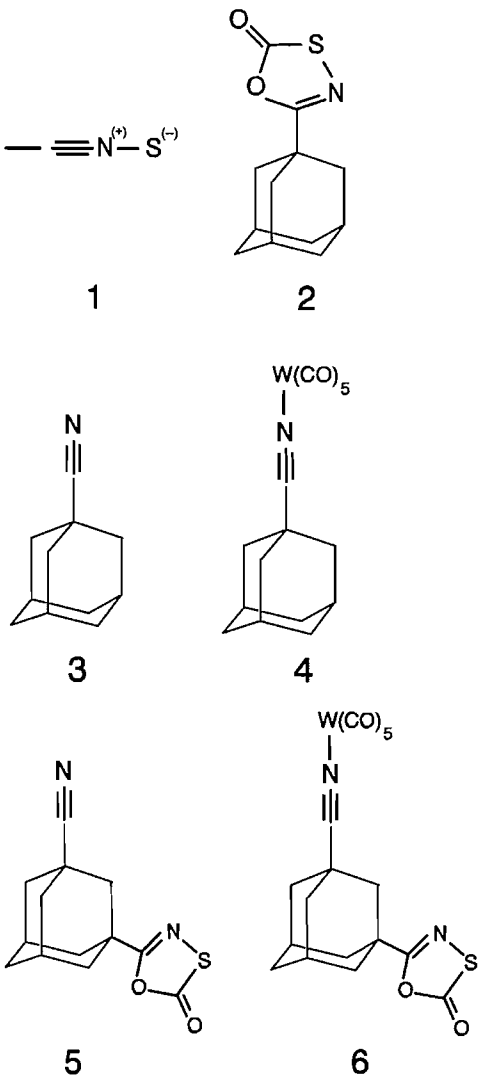

pounds and mixtures of $C_{10}H_{15}$-$\overline{COC(O)NS}$ and $C_{10}H_{15}$-CN were prepared from the literature procedures (5). The thf·$W(CO)_5$ was prepared as described in ref. 6 and was handled under a nitrogen atmosphere. Solvents were refluxed with the appropriate drying agent (C_6H_5Cl (CaH_2), C_4H_8O (Na), CH_2Cl_2 (CaH_2)) and distilled under nitrogen prior to use. Melting points were determined on a Mel-Temp II melting point apparatus and are uncorrected. Elemental analyses were carried out at Canadian Microanalytical Service Ltd., Delta, British Columbia, Canada. IR spectra were recorded from Nujol mulls on KBr plates using a Mattson Polaris FT-IR instrument or as solutions using a Perkin Elmer 283 instrument. NMR spectra were recorded on a General Electric 300 MHz instrument (^1H, ^{13}C). Chemical shifts are reported in ppm (high-frequency positive) relative to internal standards (^1H, ^{13}C: TMS). Mass spectra were recorded on a VG Micromass 7070HS double focusing spectrometer. Molecular orbital calculations were made using the HyperChem (version III) suite of semi-empirical programs from Autodesk operating on a 80486-based IBM compatible computer. Molecules were subjected to a full geometry optimization (Polak-Ribiere conjugate gradient) prior to single point calculation of the molecular orbitals.

Preparation and characterization data

$C_{10}H_{15}$-CN·$W(CO)_5$

Tungsten hexacarbonyl ($W(CO)_6$, 2.6 g, 7.4 mmol) was dissolved in approximately 250 mL of dry THF and irradiated (UV) under nitrogen for ~16 h. Adamantane nitrile (0.6 g, 3.7 mmol) was added, the reaction mixture was stirred for 48 h, and a yellow solution was obtained after filtration through Celite. A yellow solid (2.4 g) was recovered by the removal of solvent with a rotary evaporator and was transferred to a sublimation apparatus. The sublimation proceeded at room temperature (10^{-3} Torr; 1 Torr = 133.3 Pa) for 24 h and gave large, colourless crystals of excess $W(CO)_6$. The non-sublimed, yellow powder remaining was shown to be $C_{10}H_{15}C{\equiv}N{\cdot}W(CO)_5$ (1.1 g, 2.27 mmol, 60%). Crystals suitable for X-ray crystallographic analysis were grown from a hot hexanes solution. The relevant infrared and ^{13}C NMR data are given in Tables 1 and 2, respectively. Characterization data for $C_{10}H_{15}$-$C{\equiv}N{\cdot}W(CO)_5$: mp > 300°C. ^1H NMR, δ: 2.08 (9H), 1.76 (6H). Mass spectrum (IE, 70 eV) *m/z* (%, assign.): 483* (8, $C_{10}H_{15}$-CN-$W(CO)_5$, M^+), 455* (2, M^+-CO), 329 (56,M^+-2CO), 399 (11,M^+-3CO), 371 (10, M^+-4CO), 161 (80, $C_{10}H_{15}-CN^+$), 134 (100, $C_{10}H_{14}^+$) (* indicates that the peak is the strongest peak in an isotopic distribution pattern consistent with the presence of tungsten). Anal. calcd. (obsd.): C 39.61(39.39), H 3.12(3.19), N 2.89(2.76).

Reaction of $C_{10}H_{15}$-$\overline{COC(O)SN}$/$C_{10}H_{15}$-C≡N with thf·$W(CO)_5$

Tungsten hexacarbonyl ($W(CO)_6$, 11.9 g, 33.8 mmol) was dissolved in dry THF and irradiated (UV) under nitrogen for ~16 h. A mixture of adamantane nitrile and adamantane-oxathiazol-2-one (4.0 g) was added and the solution stirred for 48 h to give a brown solution from which a clear yellow solution was obtained after filtration through Celite. A yellow solid (9.2 g) was recovered by the removal of the solvent under vacuum. Sublimation of this solid at room temperature for 24 h (10^{-3} Torr) gave large, colourless crystals of excess $W(CO)_6$ (5.1 g). Pure adamantane-oxathiazol-2-one sublimed at 55°C over a period of 24 h (3.4 g, 13.1 mmol) . The non-sublimed, bright yellow residue was recrystallized from hot hexanes to give clear, yellow, needle-shaped crystals of $C_{10}H_{15}C{\equiv}N$-$W(CO)_5$ (0.7 g, 1.7 mmol).

Reaction of $\overline{NSC(O)OC}$-$C_{10}H_{14}$-C≡N with thf·$W(CO)_5$

Tungsten hexacarbonyl ($W(CO)_6$, 2.15 g, 6.10 mmol) was dissolved in approximately 250 mL of dry THF and irradiated (UV) under nitrogen for ~9 h. 1-Cyano-3-(1,3,4-oxathiazol-2-on-5-yl)-adamantane $\overline{NSC(O)OC}$-$C_{10}H_{14}$-C≡N (0.75 g, 3.05 mmol) was added and the reaction mixture was stirred for 48 h to give a yellow-brown solution from which a yellow solution was obtained after filtration through Celite. A sticky rust-brown solid was recovered by evaporation over several days and was washed with hot hexanes to give a dry khaki-coloured powder (1.46 g), which was transferred to a sublimation apparatus. The sublimation proceeded at 65°C (10^{-3} Torr) for 24 h and gave large, colourless crystals of $W(CO)_6$. The non-sublimed, khaki powder remaining was shown to be $\overline{NSC(O)OC}$-$C_{10}H_{14}$-C≡N·$W(CO)_5$ (0.54 g, 0.92 mmol, 30%). The relevant infrared and ^{13}C NMR data are given in

Table 1. Infrared spectra of free ligands and $W(CO)_5$ complexes.

$C_{10}H_{15}$-C≡N	$C_{10}H_{15}$-C≡N·W(CO)$_5$	NSC(O)OC-$C_{10}H_{14}$-C≡N	NSC(O)OC-$C_{10}H_{14}$-C≡N·W(CO)$_5$	Assignment
2230(w)		2230(w)		C≡N
	2076(m)		2072(m)	C≡O
	1915(s)		1908(s)	
		1765(m)	1769(m)	C≡O
		1741(m)	1746(m)	
	591(m)		596(m)	W–CO
1346,	1347, 1314, 1101,	1588, 1346, 1319,	1587, 1344, 1244, 1036,	(Adamantane
1316,	1090, 975, 934,	1266, 1123, 1099,	977, 924, 547	and ring
1100,	814, 699, 549	977, 921, 791		miscellaneous
1082,		729, 698, 572		vibrations
975, 938				(C–C, C–H,
813, 693,				C–O, C–N,
541				N–S))

Table 2. ^{13}C NMR spectral data of the free ligands and $W(CO)_5$ complexes.

$C_{10}H_{15}$-C≡N	$C_{10}H_{15}$-C≡N·W(CO)$_5$	NSC(O)OC-$C_{10}H_{14}$-C≡N	NSC(O)OC-$C_{10}H_{14}$-C≡N·W(CO)$_5$	Assignment
	200.0		199.7	W-C_1≡O
	196.5		196.3	W-C_2≡O
		173.7	173.7	C≡O
		164.7	164.3	C≡N
125.2	131.0	123.5	129.5	C≡N
39.8,	39.3,	40.3, 38.5,	39.9, 38.2,	$C_{adamantane}$
36.6,	35.4,	37.7, 37.3,	37.7, 37.3,	
30.1,	32.0,	34.1, 30.1,	34.0, 30.3,	
27.0	26.8	26.5	26.6	

[a]In some samples of this compound additional weak resonances were observed in the alkyl region (for example: 40.5, 39.7, 38.7, 38.3, 37.8, 32.2, 27.2 ppm).

Tables 1 and 2, respectively. Characterization data for NSC(O)OC-$C_{10}H_{14}$-C≡N·W(CO)$_5$: mp 115–123°C (dec.). ^1H NMR, δ: 2.33 (4H), 2.15–1.94 (8H), 1.78 (2H). Mass spectrum (IE, 70 eV) *m/z* (%, assign.): 350* (8, $W(CO)_6^+$ and expected peaks for sequential loss of CO), 262 (12, NSC(O)OC-$C_{10}H_{14}$-C≡N^+), 186 (20, $C_{10}H_{14}(CN)_2^+$), 159 (100, $C_{10}H_{14}CN^+$), 118 (15). Anal. calcd.(obsd.): C 36.88(35.06), H 2.41(2.77), N 4.78(4.45).

Reaction of $C_{10}H_{15}$-C≡N·W(CO)$_5$ with $P(C_6H_5)_3$

A mixture of $C_{10}H_{15}$-CN·W(CO)$_5$ (0.787 g, 1.62 mmol) and $P(C_6H_5)_3$ (0.426 g, 1.62 mmol) was dissolved in approximately 100 mL of thf. The reaction mixture was stirred while heating at 50°C for 19 h to give a green-yellow solution over a white solid. The solvent and volatile materials were removed by evacuation to give a khaki solid (1.26 g). The khaki solid was transferred to a sublimation apparatus and was heated to 50°C (10^{-3} Torr) for 24 h to give a sublimed white solid ($C_{10}H_{15}$-CN, 0.194 g, 1.20 mmol, 74%) and a non-sublimed khaki solid (($C_6H_5)_3$P-W(CO)$_5$, 0.96 g).

X-ray data collection, solution, and refinement for $C_{10}H_{15}$-C≡N·W(CO)$_5$

All pertinent crystallographic data are summarized in Table 3. Data were collected at room temperature (17 ± 1°C) on an Enraf–Nonius CAD-4 diffractometer (MoK_α, λ = 0.70930 Å, graphite monochromator) using the ω scan mode. Unit cell parameters were obtained from 24 reflections with 2θ angle in the range of 35.00°–41.00°. The choice of space group was based on systematically absent reflections. Data were corrected for Lorentz and polarization effects. Scattering factors were taken from the International tables for X-ray crystallography (7). An empirical absorption correction was made based on a series of ψ scans that resulted in minimum and maximum transmission factors of 0.712 and 0.998, respectively. The structure was solved via direct methods that revealed the presence of two independent molecules of **4**, both of which lie around crystallographic mirror planes. Hydrogen atoms were treated as follows: methylene hydrogen atoms were placed in calculated positions with D_{C-H} = 1.08 Å; methyne hydrogen atoms were located via difference Fourier map inspection. Hydrogen atoms were given temperature factors based on the

Fig. 1. ORTEP (16) views of the two independent molecules of $C_{10}H_{15}$-CN·W(CO)$_5$. (Selected bond distances (Å) and angles (deg): C111—C112 = 1.448(19), C211—C212 = 1.461(22), C111—N11 = 1.098 (18), C211—N11 = 1.132(20), N11—W1 = 2.227(12), N21—W2 = 2.204(12); C112-C111-N11 = 177.7(16), C212-C211-N21 = 178.6(16), C111-N11-W1 = 174.1(12), C211-N21-W2 = 174.9(12.)

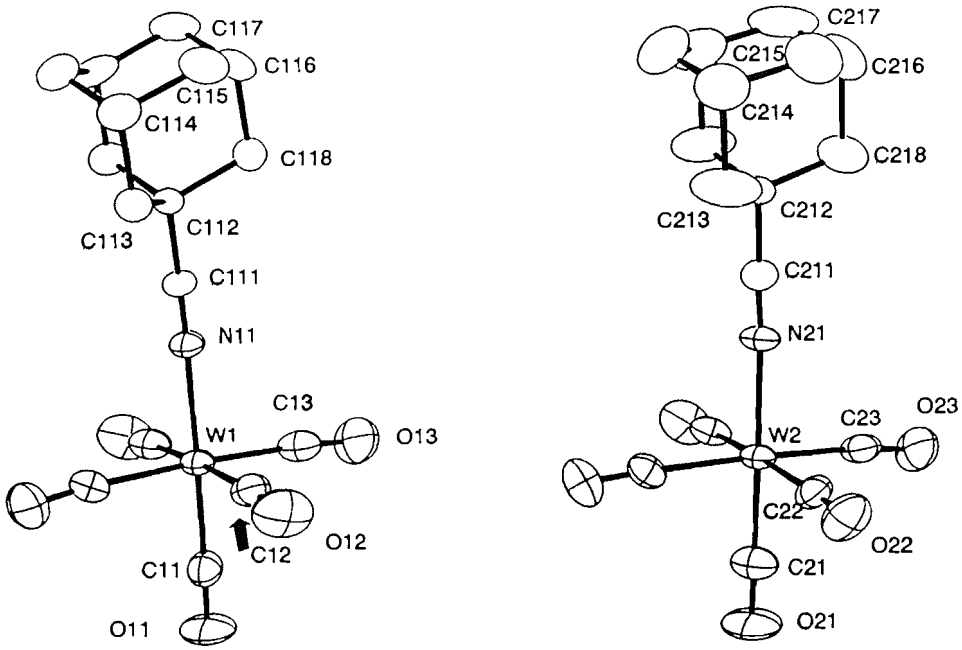

carbon atoms to which they are bonded and fixed during least-squares refinement. All crystallographic calculations were effected with the PC version of NRCVAX (8) implemented on a 80486-based IBM compatible computer. Fractional atomic coordinates and isotropic thermal parameters are given in Table 4 and selected bond distances and angles are given in the caption of Fig. 1. Supplementary material (anisotropic thermal parameters and structure factors) is available.[3]

Results and discussion

Preparation, characterization, and structure of adamantane-based nitrile tungsten pentacarbonyl complexes

Nitrile complexes of the Group VIA metal pentacarbonyls (M = Cr, Mo, W) are well known (6, 9, 10). In general, nitrile·metal pentacarbonyl complexes are useful intermediates in ligand substitution reactions due to the relative weakness of the metal–ligand bond. Complexes have been reported for a number of R-C≡N·W(CO)$_5$ compounds where the nitrile substituent can be alkyl, aromatic, or π-delocalized vinyl or acyl groups. However, such compounds have not been reported for any adamantane-based nitrile. Only one X-ray structure has been reported for R-C≡N·W(CO)$_5$ (R = CH_2COOH (10)). Metal carbonyl complexes with a higher order of nitrile substitution (M(CO)$_{6-n}$(RCN)$_n$ $n > 1$) have also been reported (11).

Table 3. Crystallographic data.

Formula	$C_{16}H_{15}NO_5W$
fw	485.14
Space group	*Pmcn* (no. 62, non-standard)
a, Å	10.5869(19)
b, Å	14.0622(22)
c, Å	23.342(4)
V, Å^3	3775.0(11)
Z	8
F(000)	1856
D_{calcd}, g cm^{-3}	1.855
Size, mm	0.20 × 0.40 × 0.50
μ, cm^{-1}	6.81
Max 2θ, deg	49.8
Reflections:	
Measured	3236
Unique	3236
Observed	1984[b]
Parameters	235
R^a	0.042
R_w	0.038
GoF	1.85

[a] $R = \Sigma\,||F_o| - |F_c||/\Sigma|F_o|$;
$R_w = [\Sigma(w(|F_o| - |F_c|)^2/\Sigma(w|F_o|)^2]^{1/2}$.
[b] $I_o > 3\sigma(I_o)$.

[3] The supplementary material can be purchased from: The Depository of Unpublished Data, Document Delivery, CISTI, National Research Council Canada, Ottawa, Canada K1A 0S2. Tables of atomic positional parameters, bond distances, and bond angles for $C_{16}H_{15}NO_5W$ have also been deposited with the Cambridge Crystallographic Data Centre, and can be obtained on request from The Director, Cambridge Crystallographic Data Centre, University Chemistry Laboratory, 12 Union Road, Cambridge, CB2 1EZ, U.K.

Table 4. Atomic parameters *x*, *y*, *z* and B_{iso} for (1-adamantylnitrile)$W(CO)_5$.

Atom	*x*	*y*	*z*	B_{iso}[a]
W1	1/4	0.76927(4)	0.13863(3)	3.99(3)
W2	3/4	0.57238(4)	0.14786(3)	4.24(4)
C11	1/4	0.9114 (13)	0.1339 (7)	5.5 (10)
O11	1/4	0.9909 (9)	0.1286 (7)	9.7 (10)
C12	0.3861(12)	0.7661 (8)	0.0777 (5)	5.3 (6)
O12	0.4614(10)	0.7719 (7)	0.0431 (4)	9.9 (6)
C13	0.3841(14)	0.7804 (9)	0.1984 (5)	6.5 (8)
O13	0.4609(11)	0.7917 (8)	0.2333 (4)	10.7 (7)
N11	1/4	0.6110 (8)	0.1411 (5)	4.1 (6)
C111	1/4	0.5331 (10)	0.1375 (7)	4.0 (8)
C112	1/4	0.4308 (9)	0.1302 (5)	3.0 (6)
C113	1/4	0.4098 (10)	0.0650 (6)	4.3 (8)
C114	1/4	0.2998 (11)	0.0554 (6)	4.9 (9)
C115	0.3671(12)	0.2590 (8)	0.0828 (5)	6.3 (7)
C116	0.3665(13)	0.2762 (7)	0.1467 (5)	5.7 (6)
C117	1/4	0.2344 (12)	0.1747 (7)	6.3 (11)
C118	0.3695(10)	0.3863 (7)	0.1568 (4)	4.7 (5)
C21	3/4	0.4302 (14)	0.1508 (8)	7.3 (13)
O21	3/4	0.3494 (9)	0.1510 (8)	11.7 (12)
C22	0.6105(12)	0.5658 (8)	0.0872 (5)	5.0 (6)
O22	0.5343(9)	0.5576 (7)	0.0538 (4)	7.9 (5)
C23	0.6153(13)	0.5716 (8)	0.2090 (5)	6.0 (7)
O23	0.5387(10)	0.5640 (7)	0.2432 (4)	9.5 (6)
N21	3/4	0.7286 (8)	0.1409 (5)	4.9 (7)
C211	3/4	0.8080 (11)	0.1330 (7)	4.6 (9)
C212	3/4	0.9101 (10)	0.1213 (7)	4.1 (8)
C213	3/4	0.9242 (14)	0.0567 (8)	9.9 (16)
C214	3/4	1.0366 (16)	0.0417 (8)	7.5 (13)
C215	0.6329(15)	1.0705 (10)	0.0697 (6)	8.7 (9)
C216	0.6337(17)	1.0672 (10)	0.1310 (6)	8.6 (10)
C217	3/4	1.1024 (14)	0.1592 (9)	10.0 (19)
C218	0.6345(16)	0.9541 (9)	0.1477 (6)	9.1 (9)

[a] B_{iso} is the mean of the principal axes of the thermal ellipsoid.

The preparation of R-C≡N·$W(CO)_5$ has been reported using a number of synthetic procedures. Photolytic generation of a thf·$W(CO)_5$ intermediate that reacts *in situ* with a nitrile has been successfully used to prepare a number of alkyl nitrile complexes (6). Thus the preparation of $C_{10}H_{15}$-C≡N·$W(CO)_5$ **4** and NSC(O)OC-$C_{10}H_{15}$-C≡N·$W(CO)_5$ **6** following this procedure gave reasonable yields as described in the literature. The elemental analyses for **6** revealed that the isolated compound was not analytically pure. The near absence of unassigned bands, resonances, or peaks in the spectra of **6** suggest that the impurities must be present in small amounts and (or) highly related to **6** in structure (i.e., $C_{10}H_{14}(CN)_2$·nW$(CO)_5$, n = 0, 1, 2).

The identity of **2** was established unequivocally by X-ray crystallography. The analysis of the spectroscopic data of **2** provides a framework for the determination of the mode of complexation in **6**. The infrared spectra of both compounds **2** and **6** are given in Table 1 and compared with the free ligands. Both compounds show bands assignable to the carbonyl and metal–carbon bonds expected in $W(CO)_5$ moieties (12). The infrared of **6** additionally indicates that the bands assignable to the heterocycle are essentially unaffected by complexation while the band assigned to the nitrile bond in the free ligand is not found in the spectrum of the complex. These observations are consistent with complexation of the free ligand **5** via the nitrile group. The mass spectra of **2** and **6** confirm the presence of tungsten carbonyls and the expected nitriles in the compounds.

The strongest evidence for the mode of complexation in the complex **6** is derived from the ^{13}C NMR spectral data. The ^{13}C NMR data for the free ligands and the complexes **4** and **6** are given in Table 2. The data clearly indicate the presence of $W(CO)_5$ in the compounds **4** and **6** with resonances assignable to the *trans* (**4**, 200.0 ppm; **6**, 199.7 ppm) and *cis* (**4**, 196.5 ppm, **6**, 196.3 ppm) carbonyl carbon atoms as described in the literature (9, 10). It has also been reported that the complexation of alkyl chalcogenonitriles (R-Ch-C≡N; Ch = S, Se (13)) and cyanoacetic acid (10) with $W(CO)_5$ results in a downfield shift of the nitrile carbon by 8.1 ± 0.9 ppm. Similar complexation with $Cr(CO)_5$ leads to a shift of +10.5 ± 0.3 ppm (10). In compounds **4** and **6** the nitrile carbon atoms resonate 5.8 and 6.0 ppm downfield from the corresponding carbon atoms in the free ligands. The smaller shift observed in the adamantane

nitriles may be a reflection of the nature of the substituent groups on the nitrile moiety. The resonances assigned to the carbon atoms in the adamantane moieties of **4** and **6** and the heterocycle in **6** are essentially unchanged by complexation, consistent with nitrile coordination in both compounds.

The crystallographic data relating to the structure of **4** are given in Tables 3 and 4 and Fig. 1. The structure of the adamantane moiety in **4** is not significantly ($\delta D > 3\sigma$, D is bond distance) different than the distances and angles observed in other mono-substituted adamantane compounds (5). The nitrile–metal bond gives an essentially linear W-N-C unit with bond angles at the carbon (177.7(16)°/178.6(16)°) and the nitrogen (174.1° (12)/174.9 (12)°) atoms not significantly different from the related angles in **7** (10). The W—N distance in **4** (2.227(12)/2.204(12) Å) is longer than that observed in **7** (2.178(7) Å) while the C—N distance is shorter (**4** 1.098(18)/1.132(20) Å; **7** 1.15(1)). This would indicate that the metal–

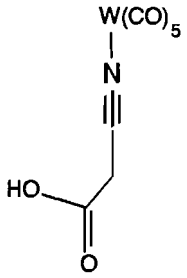

7

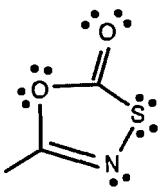

8

ligand interaction is weaker in **4** and the nitrile π bond is relatively stronger. The C—O bond distance in the *trans* carbonyl in **4** is shorter than in the *cis* carbonyls, as expected, but the difference is not as significant as that observed in other nitrile complexes (9, 10). The relative weakness of the metal–ligand bond in **4** that was indicated spectroscopically above is consistent with this observation and suggests that **3** has a relatively weak *trans* effect in metal carbonyl complexes.

Selective complexation of nitriles from nitrile–oxathiazolone mixtures

As stated above, we were interested in separating adamantyl oxathiazolone derivatives from the related nitriles by selectively changing the properties of one of the molecules. The protocols for the formation of metal pentacarbonyl complexes from the substitution reactions of thf·$M(CO)_5$ are well known so the mixture of **2** and **3** was reacted with thf·$W(CO)_5$ in thf at room temperature in the hope that a complex would form with only one of the molecules. This was indeed found to be true and subsequent work-up revealed that the reaction product was a mixture of a colourless white solid that sublimed readily at room temperature (shown to be excess $W(CO)_6$), a colourless white solid that sublimed at 60°C (shown to be pure **2**), and a non-sublimed yellow solid (shown to be pure **4**). Thus we have determined that we can purify samples of **2** that are contaminated with **3** by selective complexation of the nitrile with $W(CO)_5$. It is likely that this technique would be of general utility in the resolution of nitrile–oxathiazolone mixtures where the standard techniques of solubility, distillation or chromatography fail to give the desired separation. The nitrile

Fig. 2. View of the HOMO of H-COC (O) SN (ChemPlus / HyperChem).

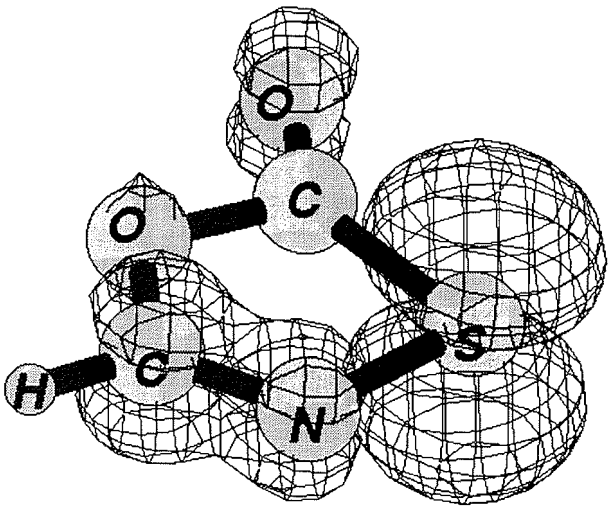

2 itself can be recovered as a pure compound by substitution in solution with triphenyl phosphine followed by sublimation.

If one considers a typical Lewis structure of an oxathiazolone heterocycle such as **8** it is observed that the ring bears multiple lone pairs that would be potential sites for coordination. On the other hand, the nitrile group is well known as a ligand that forms weak metal–ligand bonds and is easily displaced in substitution reactions (14). The reaction of thf·$W(CO)_5$ with a mixture of **2** and **3** gives a complex exclusively to the nitrile. There were no indications at any time that coordination to the heterocycle occurred. Reaction of thf·$W(CO)_5$ with pure **2** yielded only pure **2** and tungsten hexacarbonyl. The relative ligand ability of these moieties was dramatically demonstrated by the reaction of thf·$W(CO)_5$ with **5**, which was shown to form a complex exclusively via the nitrile moiety.

The simplest explanation of why coordination selectively occurs to the nitrile is that it must be a better ligand than the heterocycle for this metal system. The nitrile moiety, while recognised as giving weak metal–ligand bonds, is a π acid analogue of CO and is therefore a preferred ligand for $W(CO)_5$. The heterocycle, on the other hand, features lone pairs on both a π-bonded nitrogen and a sulfur atom, which should be reasonable sites for coordination by a medium soft Lewis acid such as $W(CO)_5$. It can be argued, however, by using simple electronegativity concepts, that the endocyclic and exocyclic oxygen atoms in the heterocycle must draw significant electron density away from the nitrogen and sulfur atoms. This process renders these atoms such poor Lewis bases that they do not form coordinate covalent bonds to the metal. These arguments are supported by semiempirical PM3 molecular orbital calculations on the parent oxathiazolone ring.[4] The calculated HOMO of this molecule is shown in Fig. 2 and the calculated atomic charges are given in **9**. A simple FMO (Frontier Molecular Orbital) analysis of the interaction

[4] A copy of the HyperChem PM3 logfile (matrix, eigenvalues, eigenvectors, and atomic charges) has been included with the supplementary material.

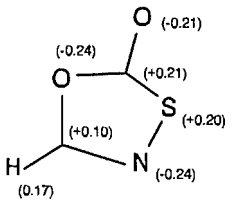

9

of Lewis acids and bases predicts that the atom that makes the greatest contribution to the acid LUMO should preferentially form a bond to the atom that makes the greatest contribution to the HOMO of the base (15). From Fig. 2 it is clear that the sulfur and nitrogen atoms do make significant contributions to the HOMO but the atom charges indicate that the atoms are electron deficient and are coulombically unsuited for coordination to the metal. The oxygen atoms are electron rich but are likely too hard to form a stable adduct to $W(CO)_5$. The complexation of this heterocycle could probably be accomplished with harder metal centers, such as the lighter, early transition metals. The formation of coordination complexes of oxathiazolone derivatives may provide information on the generation of the 1,3-dipoles from this heterocyclic family and will be the object of future investigations.

Acknowledgements

We thank the Natural Sciences and Engineering Research Council of Canada, Saint Mary's University, and Memorial University of Newfoundland for financial support. V.J.J. thanks the Natural Sciences and Engineering Research Council for an Undergraduate Student Research Award. M.J.S. thanks Dr. C.R. Lucas for many helpful discussions.

References

1. A. Padwa (*Editor*). 1,3-Dipolar cycloaddition chemistry. John Wiley and Sons, New York. 1984.
2. M. Regitz. Chem. Rev. **90**, 191 (1990).
3. R.M. Paton. Chem. Soc. Rev. **18**, 33 (1989).
4. C. Wentrup and P. Kambouris. Chem. Rev. **91**, 365 (1991).
5. J.N. Bridson, S.B. Copp, M.J. Schriver, S. Zhu, and M.J. Zaworotko. Can. J. Chem. **72**, 1143 (1994); J.N. Bridson, M.J. Schriver, and S. Zhu. Can. J. Chem. **73**, 212 (1995).
6. C. Dickson, A.W. McFarlane, and N.J. Coville. Inorg. Chem. Acta **158**, 205 (1989).
7. D.T. Cromer, and J.T. Waber. *In* International tables for X-ray crystallography. Vol. IV. Kynoch Press, Birmingham. 1974. Table 2.2B (Present Distributer: Kluwer Academic Publishers, Dordrecht and Boston.)
8. E.J. Gabe, Y. Le Page, J-P. Charland, F.L. Lee, and P.S. White. J. Appl. Crystallogr. **22**, 384, (1989).
9. W. Strohmeier and G. Schonäuer. Chem. Ber. **94**, 1346 (1961); J.M. Graham and M. Kilner. J. Organomet. Chem. **77**, 247 (1974); W. Buchner and W.A. Schenk. Inorg. Chem. **23**, 132 (1984); U. Kunze, H. Jawad, W. Conzelmann, and J. Strähle. Z. Anorg. Allg. Chem. **516**, 93 (1984); B. Denise, A. Massoud, A. Parlier, H. Rudler, J.C. Daran, J. Vaissermann, C. Alvarez, R. Patino, and R.A. Toscano. J. Organomet. Chem. **386**, 51 (1990).
10. D.J. Darensbourg, E.V. Atnip, and J.H. Reibenspies. Inorg. Chem. **31**, 4475 (1992).
11. R.H.T. Bleijerveld and K. Vrieze. Inorg. Chim. Acta, **19**, 195 (1976); D.J. Darensbourg, D.J. Zalewski, C. Plepys, and C. Campana. Inorg. Chem. **26**, 3727 (1987).
12. M.S. Davies, R.K. Pierens, and M.J. Aroney. J. Organomet. Chem. **458** 141 (1993).
13. M.H. Quick and R.J. Angelici. Inorg. Chem. **15**, 160 (1976).
14. R.B. King and A. Fronzaglia. Inorg. Chem. **5**, 1837 (1966).
15. I. Fleming. Frontier orbitals and organic chemical reactions. John Wiley and Sons, New York. 1976.
16. C.K. Johnson. ORTEPII, Report ORNL-5138, Oak Ridge National Laboratory, Oak Ridge, Tenn. 1976.

AM1 semiempirical study of benzopyrroles as dienes for Diels-Alder reaction

Branko S. Jursic

Abstract: A qualitative approach for quick evaluation of the reactivity of dienes such as cyclopentadiene, furan, pyrrole, indole, and isoindole for Diels–Alder reactions was applied. As qualitative methods, the frontier molecular orbital (FMO) energy gap and the Hammond postulate through bond orders and energy of the reaction were evaluated for such dienophiles as ethylene, 1,3-dioxa-4-cyclopentene, and maleic anhydride. It was demonstrated that pyrrole and benzopyrroles are poor dienes in comparison with cyclopentadiene and furan. Because the reaction is controlled by the HOMO of the diene there are special cases when isoindole can react as a diene, while the loss of indole aromaticity in the course of the reaction precludes the cycloaddition. Geometries of transition structures and the accompanying activation energies were calculated for pyrrole, indole, and isoindole as dienes. The stereoselectivity of the reaction is discussed and compared with experimental results.

Key words: benzopyrroles as dienes, Diels–Alder cycloaddition, Hammond postulate.

Résumé : On a appliqué une approche qualitative pour effectuer une évaluation rapide de la réactivité des dièenes, comme le cyclopentadiène, le furane, le pyrrole l'indole et l'isoindole dans des réactions de Diels–Alder. Les méthodes qualitative examinées pour des réactions avec des diénophiles comme l'éthylène, le 1,3-dioxacyclopent-4-ène et l'anhydride maléique comporte les méthodes qualitatives suivantes : la différence d'énergie des orbitales moléculaires frontières (OMF), le postulat de Hammond par le biais des ordres de liaison et l'énergie de la réaction. Il a été démontré que le pyrrole et les benzopyrroles sont de mauvais dièenes par comparaison avec le cyclopentadiène et le furane. Compte tenu du fait que la réaction est contrôlée par l'OM haute occupée du diène, il existe certains cas dans lesquels l'isoindole peut réagir comme un diène alors que la perte de l'aromaticité de l'indole au cours de la réaction empêche la cycloaddition de se produire. On a calculé les géométries des structures de transition et les énergies d'activation apparentées pour les cas du pyrrole, de l'indole et de l'isoindole comme dièenes. On discute de la stéréosélectivité de la réaction et on la compare avec les résultats expérimentaux.

Mots clés : benzopyrroles comme dièenes, cycloaddition Diels–Alder, postulat de Hammond.

[Traduit par la rédaction]

Introduction

Five-membered heterocyclic aromatic compounds are, from the theoretical standpoint, capable of acting like dienes in cycloaddition reactions. Nevertheless, there are not very many heterocycles that undergo cycloaddition reactions.[2] Usually, for these reactions to succeed, special activation of a heterocyclic compound or a very reactive dienophile is necessary. Most of the problems arise from the fact that, in the course of the reaction, the aromaticity of the heterocyclic ring is destroyed. If the reaction is accomplished, a Diels–Alder adduct can be one of the key intermediates on the long road to natural product synthesis (for selected publications, see ref. 2).

It is generally accepted that Diels–Alder reactions are concerted cycloadditions (3), although other mechanisms have also been proposed (4). For the all-carbon Diels–Alder reactions there is an enormous body of theoretical work (for a review see ref. 5); however, hetero Diels–Alder reactions are considerably under-investigated (6). From a synthetic point of view, it is probably the most important method for the preparation of heterocyclic and natural product compounds (7). This can be highlighted with five-membered heterocyclic compounds as dienes for Diels–Alder reactions (8).

We recently studied theoretically the suitability of pyrrole as diene for the Diels–Alder reaction for the cycloaddition reaction (9). The predicted activation energies are too high even for the Diels–Alder reaction in the case of pyrrole acting as diene. This is similar to an observation made for a cycloaddition reaction with cyclopentadiene as diene (10). The AM1 semiempirical method has proven to be very useful in determining the reactivity of benzothiophene and thiophenes in cycloaddition reactions with different dienophiles (11). Here we would like to present our theoretical results on dienophile addition to indole and isoindole.

Methodology

All calculations were performed on a DEC 7620 computer. Chem-3D Plus on a Macintosh IIfx was used as a graphical interface for drawing and visualizing all structures and for preparing input files for MOPAC (12). The transition states were located, optimized, and verified as explained in our previous

Received May 29, 1995.

B.S. Jursic.[1] Department of Chemistry, University of New Orleans, New Orleans, LA 70148, U.S.A.

[1] Telephone: (504) 286-6311. Fax: (504) 286-6860.
E-mail: bsjcm@uno.edu

[2] Oxazole systems are unusually efficient dienes for Diels–Alder reactions. For selected examples see refs. 1*a* and 1*b*. For selected publications with furan as diene see refs. 1*c*–1*e*.

Table 1. Frontier orbital energies (eV) for the diene and the dienophiles in the cycloaddition reaction.

Compound	HOMO	LUMO
Ethylene	−10.551 39	1.437 78
3,5-Dioxacyclopentene	−9.004 68	0.955 44
Maleic anhydride	−12.022 79	−1.618 99
Cyclopentadiene	−9.079 07	0.481 56
Furan	−9.316 84	0.722 86
Pyrrole	−8.656 99	1.378 40
Indole	−8.403 08	0.299 89
Isoindole	−7.796 00	0.141 74

A[a]		B		C	
I	II	I	II	I	II
Cyclopentadiene					
11.032 95	10.516 85	9.486 24	10.034 51	12.504 35	7.460 08
Furan					
11.274 25	10.754 62	9.727 54	10.272 28	12.022 79	7.697 85
Pyrrole					
11.929 79	10.094 77	10.383 08	9.612 43	13.401 19	7.038 00
Indole					
10.851 28	9.840 86	9.304 57	9.358 52	12.322 68	6.784 09
Isoindole					
10.693 13	9.233 78	9.146 42	8.751 44	12.164 53	6.177 01

[a]A: ethylene, B: 3,5-dioxa-4-cyclopentene, C: maleic anhydride.
I: $\Delta E = LUMO_{diene} - HOMO_{dienophile}$; II: $\Delta E = LUMO_{dienophile} - HOMO_{diene}$.

work.[3,4] Vibrational and thermal analyses were performed on all optimized structures.

Results and discussion

Qualitative evaluation of reactivity of cyclopentadiene, furan, pyrrole, indole, and isoindole

Three dienophiles: 1,3-dioxa-4-cyclopentene, ethylene, and maleic anhydride, were used for qualitative evaluation of the reactivity of pyrrole. Frontier molecular orbital (FMO) theory can be used to determine relative reactivity of reactants that are engaged in similar reactions (15). This involves the basis of the theory of maximal orbital overlap between frontier orbitals of reactants. Better molecular orbital overlap will be obtained between frontier orbitals that are similar in energies. The frontier orbital energy gaps (eV) between ethylene, 3,5-dioxa-4-cyclopentene, and maleic anhydride as dienophiles and cyclopentadiene, furan, pyrrole, indole, and isoindole as dienes are presented in Table 1. All of these compounds have been carefully chosen: ethylene as middle, maleic anhydride as electron-deficient, and 3,5-dioxa-4-cyclopentene as electron-rich dienophiles for Diels–Alder reactions. Two dienes, cyclopentadiene and furan, as aromatic dienes are used for determining the influence of aromaticity on the Diels–Alder reaction. Ethylene and maleic anhydride addition to cyclopentadiene is predicted to be a LUMO dienophile controlled reaction while, as expected, addition of electron-rich 3,5-dioxa-4-cyclopentene is HOMO dienophile controlled. A low energy gap is predicted for maleic anhydride and is in agreement with experimental observations (16). Furan as aromatic diene is predicted to have lower reactivity than cyclopentadiene, as is well documented in the literature (16, 17). Pyrrole is predicted to be more reactive then furan and the addition is LUMO dienophile controlled with electron-rich dienophiles such as 3,5-dioxa-4-cyclopentene. This finding is somewhat surprising because experimental results favor furan over pyrrole (18). Both benzopyrroles are predicted to be more reactive than cyclopentadiene, furan, and pyrrole as dienes. The most reactive is isoindole with a predicted FMO energy gap with maleic anhydride of only 6.18 eV.

One can argue that the frontier orbital approach to studying the reactivity is not reliable. There are many disadvantages; one major problem is that the energies of the frontier orbitals are computed separately. Consequently the steric and electronic interactions between reactants during the course of the

[3] For a detailed explanation of input files and key words for transition state computation by mopac see ref. 13.

[4] The transition state has to have only one imaginary frequency and that has become the major criterion for proving the transition state. For perspectives of transition state theory see refs. 14*a*–14*c*.

Table 2. Heats of formation for reactants and the cycloadduct products.[a]

Diene	Reactants	Cycloadduct	Difference
With 1,3-dioxa-4-cyclopentadiene as dienophile			
Cyclopentadiene	−18.06	−45.54	−27.48
Furan	−52.17	−70.12	−17.95
Pyrrole	−15.24	−21.20	−5.96
Indole	0.03	13.39	13.36
Isoindole	6.61	−12.80	−19.41
With ethylene as dienophile			
Cyclopentadiene	53.53	25.96	−27.57
Furan	19.42	1.40	−20.82
Pyrrole	56.35	52.24	−4.09
Indole	71.62	85.93	24.31
Isoindole	78.19	60.71	−17.48
With maleic anhydride as dienophile			
Cyclopentadiene	−38.29	−71.88	−33.59
Furan	−73.40	−94.46	−21.06
Pyrrole	−36.47	−45.47	−9.00
Indole	−21.20	−10.89	10.31
Isoindole	−14.63	−36.82	−22.19

[a]Heat of formations are −55.12 for 1,3-dioxa-4-cyclopentene, 16.47 kcal/mol for ethylene, and −76.35 kcal/mol for maleic anhydride.

reaction are totally neglected. Although indole is predicted to be more reactive than furan, for example, there is not a single literature report using indole as diene for a Diels–Alder reaction. There is an abundance of reports using furan in Diels–Alder reactions (17). To explore the energy change caused by the transformation of dienes into products, we have determined the heat of hydrogenation of two benzopyrroles. The hydrogen atoms are put in position where new CC bonds will be formed (structures **A** and **B**). According to AM1 calcula-

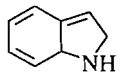

A

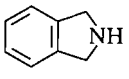

B

tions structure **A** is 9.53 kcal/mol above structure **B** in energy. These results are not surprising and can be explained by consideration of aromaticity. The heat of formation of isoindole is 6.57 kcal/mol above that of indole. All of this undoubtedly predicts that isoindole should be a much better diene than indole for Diels–Alder reactions.

If we consider only the energies of the reactants and products without performing time-consuming calculations of transition state structures, the qualitative reactivity can be estimated by applying Hammond's postulate (19). It seems reasonable that the reactants for an exothermic reaction will undergo a small change in geometry by reaching the transition state. The opposite is true for an endothermic reaction, which requires a quite considerable reorganization of geometry in the reactants. In other words, the more exothermic the reaction, the smaller the reaction barrier, contrary to the more endothermic reaction, where a higher reaction barrier results. Calculated exothermicity of the Diels–Alder reaction for ethylene and maleic anhydride is presented in Table 2. Although different values are obtained with different dienophiles, all calculations agree in general reactivity.

Table 3. Sum of bond orders of new forming CC bond of dienes with ethylene.

Cyclopentadiene	Furan	Pyrrole	Indole	Isoindole
0.821	0.874	0.956	0.933	0.874

The cycloaddition reaction with cyclopentadiene will be the most exothermic and, with indole, the most endothermic. If the Hammond principle is applied, indole should have the highest activation energy, followed by pyrrole and isoindole. The reactivity of isoindole is predicted to be somewhat similar to that of furan. This finding is different than that obtained with FMO, which predicts increasing reactivity in the following order: cyclopentadiene, furan, pyrrole, indole, and isoindole (Table 1). The qualitative order of reactivity for pyrrole and benzopyrrole agrees with experimental evidence (8).

The position of the transition structure with regard to reactants and products can be determined by the bond orders in its structure. The same results can be obtained by following any bond distance that undergoes change during the course of the reaction. For the sake of simplicity we will consider the sum of the bond orders for two CC bonds in formation between the dienes and dienophiles (Table 3). The lower bond order determines a transition structure closer to the reactants and consequently a lower activation barrier. The reactivity is predicted to be similar in general to that based on the Hammond postulate, except for indole. Again, this diene deviates from the other dienes. Further studies were carried out by estimation of activation energies for the cycloaddition reaction.

Transition state structures

Qualitative results presented here can be obtained in a short time period with modest computational power. We have demonstrated the shortcomings of these methods for reliable prediction of the reactivity. For example, pyrrole is predicted to be more reactive than both cyclopentadiene and furan, and isoindole is predicted, according to FMO, to be more reactive than all of the dienes studied. Nevertheless, this approach can sometimes be applied for very similar systems. To obtain a more accurate scale of reactivity of the benzopyrroles, the transition structures for ethylene, 1,3-dioxa-4-cyclopentene, and maleic acid anhydride addition to pyrrole, indole, and isoindole must be determined.

There are three transition state structures with ethylene as dienophile (Fig. 1). Transition state structures **1** and **3** have a bisecting plane of symmetry corresponding to a synchronous concerted mechanism for the cycloaddition reaction. Indole does not have a plane of symmetry separating the two CC double bonds that are considered in the Diels–Alder reaction. Consequently, all transition structures for a concerted Diels–Alder reaction with indole as dienophile must be asynchronous. Structure **2** demonstrates this effect.

For addition of both 1,3-dioxa-4-cyclopentene (Fig. 2) and maleic anhydride (Fig. 3) to pyrrole dienes, two stereoisomers

Fig. 1. Transition state structure for ethylene addition.

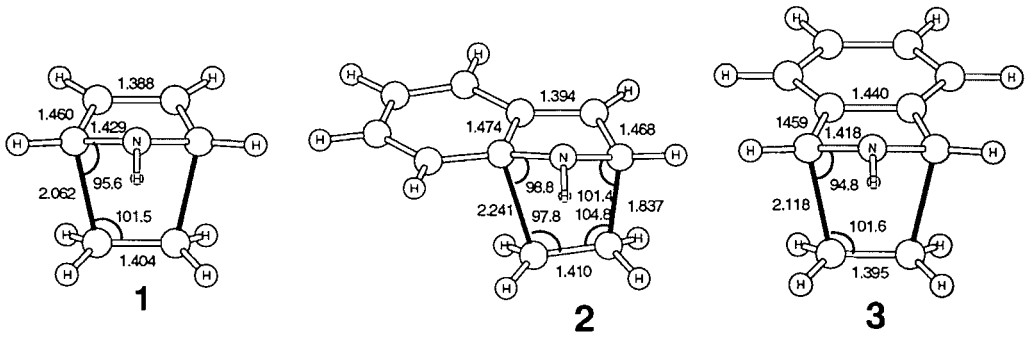

Fig. 2. Transition state structures for 1,3-dioxane-4-cyclopentene.

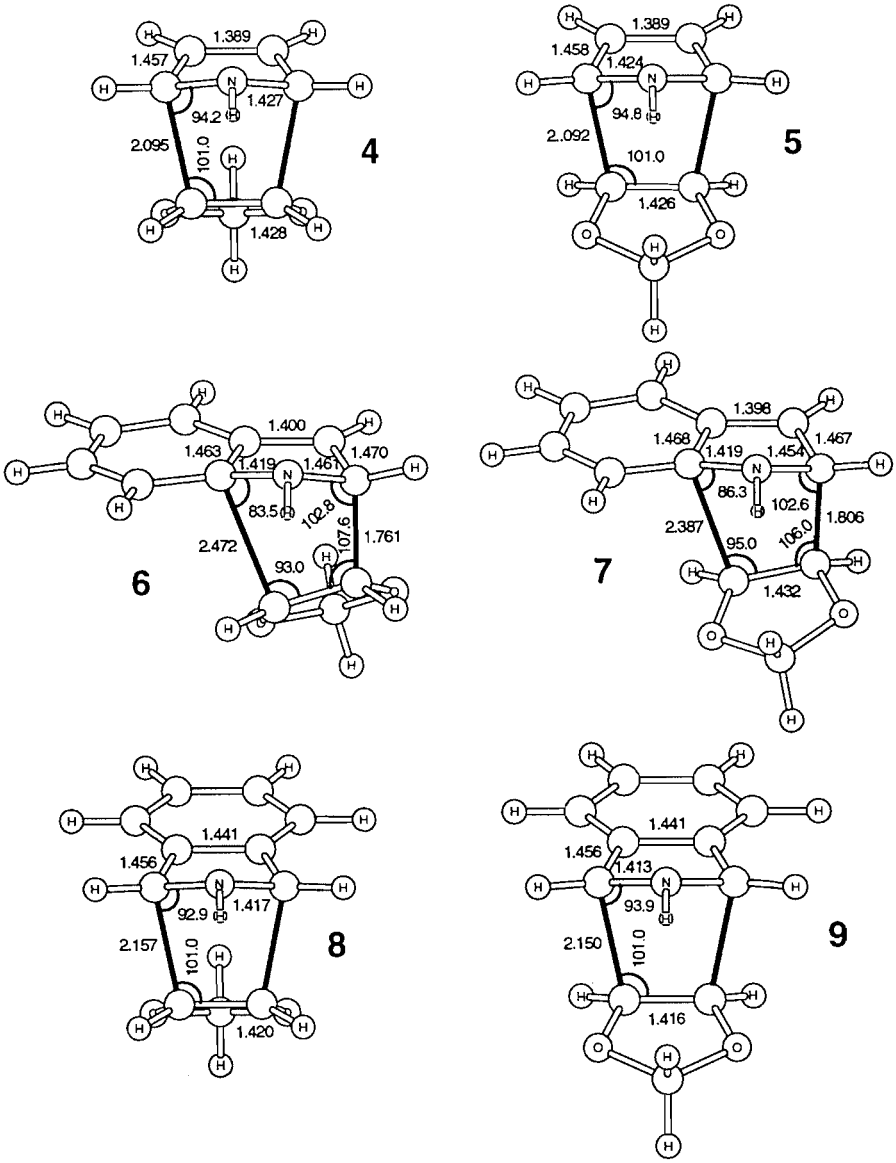

are possible. AM1 calculations of 1,3-dioxa-4-cyclopentene addition to pyrrole and isoindole produce transition structures (Fig. 2) that point to a synchronous concerted mechanism of Diels–Alder reactions. The transition state structures **6** and **7** for 1,3-dioxa-4-cyclopentene addition to indole indicate an asynchronous concerted cycloaddition. There should be considerable repulsion interaction between the oxygen lone pair of the dienophiles and the π orbitals of the indole benzene

Fig. 3. Transition state structures for maleic anhydride addition.

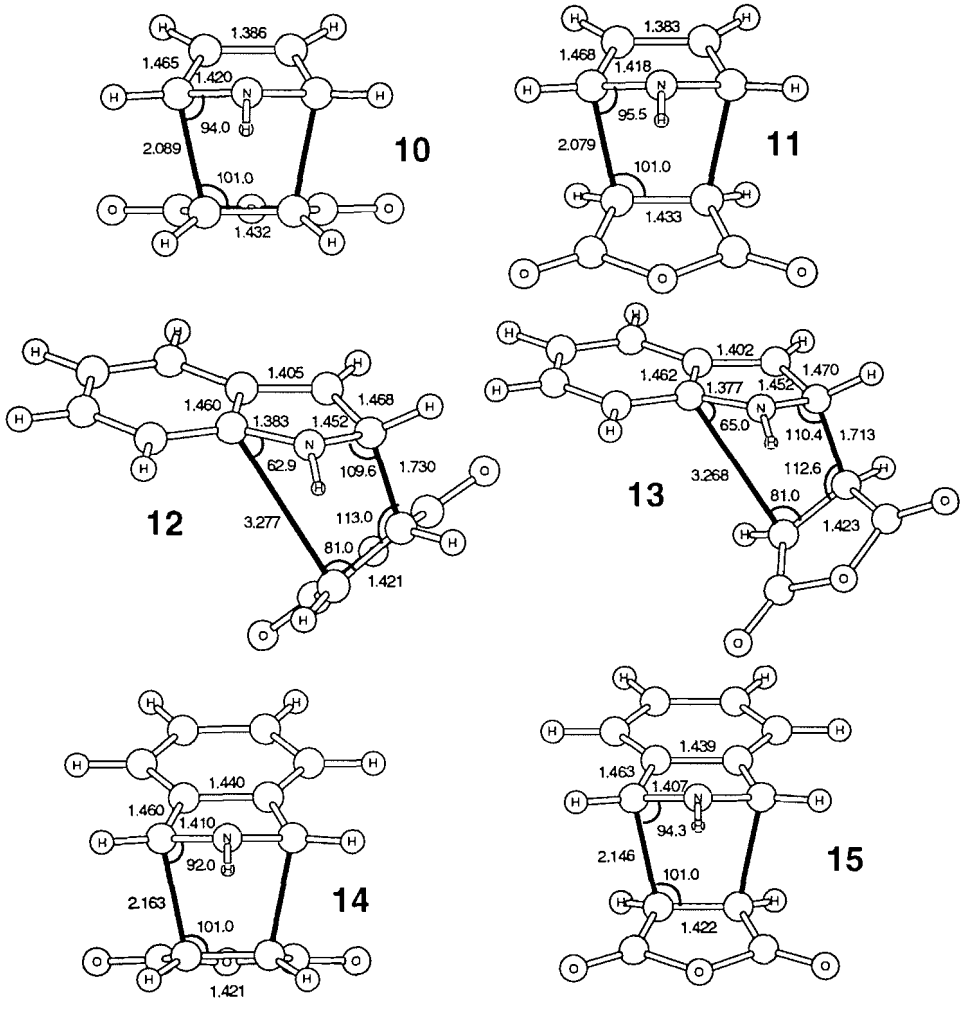

Table 4. AM1 estimated activation energies (kcal/mol).

Transition structure	ΔE	ΔE + ZPVE
1	33.54	34.70
2	43.66	45.00
3	26.22	27.51
4	37.74	37.75
5	32.24	32.07
6	47.01	47.19
7	41.69	41.86
8	32.24	32.07
9	25.38	25.10
10	30.44	30.40
11	26.28	26.31
12	37.41	37.31
13	34.89	34.92
14	25.22	25.10
15	18.81	18.62

ring. We assume that the electronic repulsion might be responsible for the high (0.581 Å) asynchronicity of transition structure **7**. For *endo* isomer **6** additional steric repulsions make this value even higher (0.761 Å).

Similar observations can be noted for the maleic anhydride addition (Fig. 3). Transition state structures with pyrrole and isoindole as diene were generated for a synchronous concerted Diels–Alder reaction. Here again, the longer new forming bond distance is in *endo* transition structures and again can be explained by repulsion interactions between diene and dienophile. There is considerable asynchronicity for transition structures **12** and **13** and, in fact, might represent the first transition structure in a two-step mechanism. Since one of the new forming bonds is longer than 3 Å, there should be reduced repulsion interaction with benzene π orbitals on oxygen n orbitals. Therefore, the asynchronicity of *endo* and *exo* isomers is almost identical (1.547 Å for **12** and 1.555 Å for **13**). The higher asynchronicity of these transition state structures can be explained by the fact that maleic anhydride is capable of stabilizing the negative charge while at the same time indole, bearing a partially positive charge, retains some aromaticity. Our results support this explanation.

Estimation of activation energies

The activation energies for these cycloaddition reactions are presented in Table 4. As expected on the basis of the Hammond postulate, indole showed a comparatively high activa-

tion barrier. For each dienophile, the order of reactivity is predicted to be isoindole, pyrrole, and indole.

The highest reactivity, as demonstrated by the FMO energy, is obtained for isoindole with maleic anhydride, demonstrating the HOMO character of indole for this reaction. Based on the values of predicted activation energies, with 18.62 kcal/mol for maleic anhydride addition to isoindole, the reaction should be experimentally feasible. The energy difference between the *exo* and *endo* isomers is 6.48 kcal/mol and favors exclusive formation of the *exo* isomer. On the other hand, for the same reaction with indole the predicted activation energy is 34.92 kcal/mol, too high to be experimentally achievable. Since the reaction is HOMO diene controlled, with electron-rich dienophiles the reaction will have a higher barrier. That was demonstrated by using 1,3-dioxa-4-cyclopentene as dienophile. Now the activation barriers for *exo* addition to indole and isoindole are 41.86 and 25.10 kcal/mol, respectively.

There are experimental results that fully support our AM1 calculations. Both indoles and pyrroles generally react with electron-deficient alkenes to give Michael addition product rather than the expected Diels–Alder cycloadducts (20). Isoindoles react with maleic anhydride to produce the Diels–Alder adduct. The reaction is reversible and, if formed, *endo* isomers can be converted readily into the *exo* isomers (21). Experimental evidence for indole as the diene for Diels–Alder reactions is not available.

Conclusions

It is demonstrated that the semiempirical AM1 method is useful for determining the reactivity of benzopyrroles as dienes for Diels–Alder reactions. The frontier molecular orbital (FMO) energy gap predicts higher reactivity of indole in comparison with pyrrole. This finding is contradictory to results obtained using both the Hammond postulate and the experimental data. The reaction is predicted to be HOMO diene controlled based on the frontier orbital correlation. It is suggested that the lower reactivity of indole is caused by loss of aromaticity in the course of the cycloaddition reaction, while with isoindole the aromaticity of the benzene ring is preserved. The predicted activation energy favors isoindole as diene in reactions with strong electron-deficient dienophiles. This finding is fully supported by the experimental data.

References

1. (*a*) D. Liotta, M. Saindane, and W. Ott. Tetrahedron Lett. **24**, 2473 (1983); (*b*) P.A. Jacobi, S.R. Kaczmarek, and U.E. Udodong. Tetrahedron Lett. **25**, 4859 (1984), (*c*) M.M. Campbell, A.D. Kaye, M. Sainsbury, and R. Yavarzadeh. Tetrahedron, **40**, 2461 (1984); (*d*) F. Brion. Tetrahedron Lett. **23**, 5299 (1982); (*e*) A.J. Guildford and R.W. Turner. J. Chem. Soc. Chem. Commun. 466 (1983).
2. (*a*) P.A. Jacobi, K.M. Touchette, and H.G. Selnick. J. Org. Chem. **57**, 6305 (1992); (*b*) P.A. Grieco, R.E. Zelk, R. Lis, and J. Finn. J. Am. Chem. Soc. **105**, 1403 (1983); (*c*) L.L. Klein. J. Am. Chem. Soc. **107**, 2573 (1985).
3. K.N. Houk and Y. Li. J. Am. Chem. Soc. **115**, 7478 (1993), and references therein.
4. (*a*) M.J.S. Dewar, S. Olivella, and J.J.P. Stewart. J. Am. Chem. Soc. **108**, 5771 (1986); (*b*) M.J.S. Dewar. Acc. Chem. Res. **25**, 537 (1992), and references therein.
5. (*a*) K.N. Houk, Y. Li, and J.D. Evanseck. Angew. Chem. Int. Ed. Engl. **31**, 682 (1992), and references therein; (*b*) K.N. Houk, R.J. Loncharich, J.F. Blake, and W.L. Jorgensen. J. Am. Chem. Soc. **111**, 9172 (1992); (*c*) W.L. Jorgensen, D. Lim, and J.F. Blake. J. Am. Chem. Soc. **115**, 2936 (1993); (*d*) Y. Li and K.N. Houk. J. Am. Chem. Soc. **115**, 7478 (1993); (e) R.A. Hancock and B.F. Wood. J. Chem. Soc. Chem. Commun. 351 (1988).
6. (*a*) L. Le Coz, C. Veyrat-Martin, L. Wartski, J. Seyden-Penne, C. Bois, and M. Philoche-Levisalles. J. Org. Chem. **55**, 4870 (1990); (*b*) T.N. Birkinshaw, A.B. Tabor, P. Kaye, P.M. Mayne, and P.R. Raithby. J. Chem. Soc. Chem. Commun. 1599 (1988); (*c*) B. Neder, T.R. Bailey, R.W. Franck, and S.M. Weinreb. J. Am. Chem. Soc. **103**, 7573 (1981); (*d*) E.L. Clennan, and A.D. Earlywine. J. Am. Chem. Soc. **109**, 7104 (1987); (*e*) F. Jensen and C.S. Foote. J. Am. Chem. Soc. **109**, 6376 (1987); (*f*) K. O'Shea and C.S. Foote. J. Am. Chem. Soc. **110**, 7167 (1988); (*g*) M.A. McCarrick, Y.-D. Wu, and K.N. Houk. J. Am. Chem. Soc. **114**, 1499 (1992); (*h*) J. Org. Chem. **58**, 3330 (1993).
7. (*a*) R.R. Schmidt. Acc. Chem. Res. **19**, 250 (1986); (*b*) S. Hanessian. Total synthesis of natural products. The chiron approach. Pergamon Press, Oxford. 1983; (*c*) J. Hamer (*Editor*). 1,4-Cycloaddition reactions. Academic Press, New York. 1967; (*d*) M.E. Jung, K. Shishido, L. Light, and L. Devis. Tetrahedron Lett. 4607 (1981); (*e*) F. Jensen and C.S. Foote. J. Am. Chem. Soc. **109**, 6376 (1987); (*f*) B. Nader, T. R. Bailey, R.W. Franck, and S.M. Weinreb. J. Am. Chem. Soc. **103**, 7573 (1981); (*g*) L. Le Coz, C. Veyrat-Martin, L. Wartski, J. Seyden-Penne, C. Bois, and M. Philoche-Levisalles. J. Org. Chem. **55**, 4870 (1990); (*h*) S.J. Danishefsky, E. Larson, D. Askin, and N. Kato. J. Am. Chem. Soc. **107**, 1246 (1985); (*i*) S.J. Danishefsky, H.G. Selznik, R.E. Zelle, and M.P. Deninno. J. Am. Chem. Soc. **110**, 4368 (1988); (*j*) S.J. Danishefsky, D.C. Myles, and D.F. Harrey. J. Am. Chem. Soc. **109**, 862 (1987); (*k*) M. Bednarsky and S.J. Danishefsky. J. Am. Chem. Soc. **108**, 7060 (1986); (*l*) K.F. McCule, J.W. Benbow, and S.J. Danishefsky. J. Am. Chem. Soc. **113**, 8185 (1991).
8. (*a*) B.S. Jursic and Z. Zdravkovski. J. Chem. Soc. Perkin Trans. 2, 1877 (1994); (*b*) J. Org. Chem. **59**, 3015 (1994); (*c*) J. Phys. Org. Chem. **7**, 634 (1994); (*d*) B.S. Jursic, Z. Zdravkovski, and S. Whittenburg. J. Phys. Org. Chem. **8**, 753 (1995).
9. B.S.Jursic and Z. Zdravkovski. J. Heterocycl. Chem. **31**, 1429 (1994).
10. B.S.Jursic and Z. Zdravkovski. J. Mol. Struct. (Theochem), **309**, 249 (1994).
11. (*a*) B.S. Jursic. J. Chem. Soc. Perkin Trans. **2**, 1217 (1995); (*b*) B.S. Jursic and D.T. Coupe. J. Heterocycl. Chem. **32**, 483 (1995); (*c*) B.S. Jursic. J. Heterocycl. Chem. **32**, 1445 (1995); (*d*) J. Heterocycl. Chem. **32**, 1499 (1995).
12. MOPAC version 6.0. Quantum Chemistry Program Exchange (QCPE), Program No. 455, 1990.
13. B.S. Jursic and Z. Zdravkovski. J. Mol. Struct. (Theochem), **303**, 177 (1994).
14. (*a*) W.J. Albery. Adv. Phys. Org. Chem. **28**, 139 (1993); (*b*) R.A. Marcus. Science, **256**, 1523 (1992); (*c*) I.W.M. Smith. Nature, **358**, 279 (1992).
15. (*a*) K. Fukui and H. Fujimoto. Bull. Chem. Soc. Jpn. **40**, 2018 (1967); (*b*) Bull. Chem. Soc. Jpn. **42**, 2018 (1969); (*c*) K. Fukui. Angew. Chem. Int. Ed. Engl. **21**, 801 (1982).
16. M.J.S. Dewar and A.B. Pierini. J. Am. Chem. Soc. **106**, 203 (1984), and references therein.
17. M.V. Sargent and F.M. Dean. *In* Comprehensive heterocyclic chemistry. Vol. 4. *Edited by* A.R. Katritzky and C.W. Rees. Pergamon Press, New York. 1984. p. 531.
18. R.A. Jones. *In* Comprehensive heterocyclic chemistry. Vol. 4. *Edited by* A.R. Katritzky and C.W. Rees. Pergamon Press, New York. 1984. p. 201.

19. (*a*) G.S. Hammond. J. Am. Chem. Soc. **77**, 334 (1955); (*b*) W.J. Le Noble, A.R. Miller, and S.D. Hamann. J. Org. Chem. **42**, 388 (1977); (*c*) A.R. Miller. J. Am. Chem. Soc. **100**, 1984 (1978).
20. (*a*) O. Diels, K. Alder, and H. Winkler. Liebigs Ann. Chem. **54**, 1446 (1931); (*b*) A. Gossauer. Die Chemie der Pyrrole. Springer Verlag, Berlin. 1974.
21. R. Bonnett and S.A. North. Adv. Heterocycl. Chem. **29**, 341 (1981).

Molar excess volumes of binary liquid mixtures: 2-pyrrolidinone with C_6–C_{10} *n*-alkanols

Begoña García, Francisco J. Hoyuelos, Rafael Alcalde, and José M. Leal

Abstract: The excess volumes V^E of the binary mixtures 2-pyrrolidinone – (C_6–C_{10}) *n*-alkanols have been calculated from density measurements over the whole composition range and the 298.15–318.15 K temperature range. The excess volumes were independent of temperature, but changed noticeably with the chain length of the alkanol. The V^E values were only positive starting from heptanol, with the maximum value, 0.239 cm^3 mol^{-1}, for equimolar decanol. The observed changeover V^E <0 to V^E >0 suggests that the steric effect is primarily responsible for the positive contributions to V^E. The thermal expansion coefficients α were evaluated from the variation of densities with temperature.

Key words: excess volumes, 2-pyrrolidinone, *n*-alkanols, liquid mixtures, hydrogen bonding.

Résumé : Utilisant des mesures de densités obtenues pour l'ensemble des compositions et à des températures allant de 298,15 à 318,15 K, on a calculé les volumes en excès, V^E, de 2-pyrrolidinone – (C_6–C_{10}) *n*-alcanols. Les volumes en excès sont indépendants de la température, mais ils varient d'une façon importante avec la longueur de l'alcanol. Les valeurs de V^E ne sont positives pour toutes les compositions qu'à partir de l'heptanol, avec la valeur maximale, 0,239 cm^3 mol^{-1}, pour le décanol équimolaire. La position du changement de V^E <0 à V^E >0 suggère que l'effet stérique est la cause principale des contributions positives au V^E. On a évalué les coefficients d'expansion thermique, α, à partir des variations des densités avec la température.

Mots clés : volumes en excès, 2-pyrrolidinone, *n*-alcanols, mélanges liquides, liaison hydrogène.

[Traduit par la rédaction]

Introduction

Despite the large number of studies on alcohol liquid mixtures, very few data are available for alcohol mixtures with 2-pyrrolidinone, a cyclic amide (lactam) with both basic (-CO) and acidic (-NH) groups of the peptide bond -NH-CO-. Owing to its high dipole moment (μ = 3.55 D), 2-pyrrolidinone is self-associated, forming dimers in dilute solutions and higher oligomers in concentrated solutions, as demonstrated by different techniques (1). This compound serves as a model for hydrogen bonding of bases of nucleic acids, and is useful in studying the interaction between alkanols and the carbonylamide group (2).

The state of aggregation of alkanols varies from the pure state to solution, and it depends on the nature of the other cosolvent. In the pure state *n*-alkanols are self-associated, forming both open and cyclic aggregates; the probability of the latter increases for smaller alkanols (3), but in nonpolar solvents is independent of the chain length (4). Based upon the excess volumes of pyridine–alkanol binary mixtures, Dewan et al. (5) reported that C_6–C_{10} alkanols in the pure state remain as 1:1 monomer – open dimer mixtures and C_1–C_5 alkanols as dimers, with ethanol as trimer.

Received May 9, 1995.

B. García, F.J. Hoyuelos, R. Alcalde, and J.M. Leal.[1]
Universidad de Burgos, Departamento de Química, Laboratorio de Química Física, 09001 Burgos, Spain.

[1] Author to whom correspondence may be addressed. Telephone: (3447) 258819. Fax: (3447) 258831.

In a previous paper on 2-pyrrolidinone – (C_1–C_5) alkanol mixtures (6), we reported negative V^E values over the whole composition range, and suggested a balance between dispersion forces and the specific interactions responsible for heteroassociations. We report here excess volumes and thermal expansion coefficients of 2-pyrrolidinone – (C_6–C_{10}) alkanol mixtures, calculated from density values measured at five different temperatures.

Experimental

The pure liquids, commercially available from Fluka and Aldrich (stated purity >99% GC), were used without further purification but, prior to measurements, they were degassed for several days with ultrasound and stored over freshly activated Fluka AG 3A molecular sieves. The binary mixtures were fully miscible over the entire composition range; the solutions were prepared by weighing the cosolvents with a Mettler AT 261 Delta Range balance (±0.01 mg) and syringing them into stoppered bottles. The error in the mole fraction of the samples was estimated at 10^{-5}. The purity of the chemicals was assessed by measuring their densities, with close agreement between the experimental and literature values (Table 1).

Densities were measured with an Anton Paar DMA 58 vibrating-tube digital densimeter (±10^{-5} g dm^{-3}), equipped with a Peltier element that ensures thermostatization and a resistance thermometer for electrical control of temperature (±0.01 K); the apparatus was calibrated at the working temperatures with *n*-nonane and doubly distilled and degassed

Table 1. Experimental physical properties of the pure liquids at different temperatures.

T	2-Pyrrolidinone		1-Hexanol		1-Heptanol		1-Octanol		1-Nonanol		1-Decanol	
(K)	Exp.	Lit. (ref.)	Exp.	Lit. (ref.)	Exp.	Lit. (ref.)	Exp.	Lit. (ref.)	Exp.	Lit. (ref.)	Exp.	Lit. (ref.)
(*a*) **Densities, ρ (g cm^{-3})**												
298.15	1.10712	1.10722 (2)	0.81501	0.8151 (7)	0.81869	0.8195 (7)	0.82164	0.8216 (7)	0.82412	0.8246 (7)	0.82615	0.8263 (7)
		1.10701 (2)		0.81501 (11)		0.81891 (11)		0.82148 (11)		0.82428 (11)		0.82671 (10)
		1.107 (6)		0.8150 (12)		0.81878 (13)		0.8223 (12)		0.82422 (13)		0.82615 (11)
				0.81505 (13)		0.81871 (7)		0.82161 (13)		0.82478 (7)		0.8270 (12)
				0.8160 (8, 15)		0.8197 (16)		0.8262 (8, 15)		0.82432 (19)		0.82642 (7)
				0.81526 (7)		0.8199 (17)		0.82167 (7)				
				0.8153 (16)		0.81891 (19)		0.82176 (19)				
				0.8156 (17)								
				0.81550 (19)								
303.15	1.10317	1.1020 (6)	0.81144	0.8114 (7)	0.81519	0.8157 (7)	0.81808	0.8182 (7)	0.82066	0.8216 (7)	0.82269	0.8230 (7)
				0.8114 (12)		0.81572 (14, 18)		0.82392 (8)				0.8237 (12)
				0.81205 (14, 18)		0.8160 (16)		0.8182 (12)				
				0.81353 (8, 15)				0.82188 (18)				
				0.8118 (16)								
308.15	1.09913	1.09896 (2)	0.80781	0.8078 (7)	0.81161	0.8121 (7)	0.81458	0.8146 (7)	0.81723	0.8181 (7)	0.81928	0.8194 (7)
		1.09915 (2)		0.8074 (12)		0.8125 (16)		0.8150 (12)				0.8201 (12)
				0.8081 (16)								
313.15	1.09518		0.80417	0.8041 (7)	0.80803	0.8112 (7)	0.81109	0.8112 (7)	0.81379	0.8147 (7)	0.81612	0.8161 (7)
				0.8040 (9)		0.8085 (9)		0.8112 (9)				0.8160 (9)
				0.8039 (12)				0.8113 (12)				0.8164 (12)
				0.81050 (8, 15)				0.81926 (8)				
318.15	1.09101	1.09105 (2)	0.80051	0.8006 (7)	0.80443	0.8048 (7)	0.80755	0.8076 (7)	0.81026	0.8110 (7)	0.81249	0.8126 (7)
				0.8002 (12)				0.8077 (12)				0.8129 (12)
(*b*) **Thermal expansion coefficients, α (10^4, K^{-1})**												
298.15	7.26		8.90	8.700 (20)	8.72	8.450 (20)	8.56	8.270 (20)	8.39	8.180 (20)	8.20	8.120 (20)
						8.2 (21)						
303.15	7.29		8.94		8.75		8.60		8.43		8.24	
308.15	7.32		8.98		8.79		8.63		8.46		8.27	
313.15	7.34		9.02	9.20 (9)	8.83	8.90 (9)	8.67	9.24 (9)	8.50		8.30	8.58 (9)
						9.2 (21)						
318.15	7.37		9.06		8.87		8.71		8.54		8.34	

Fig. 1. Experimental molar excess volumes V^E vs. X_1 at 298.15 K of (X_1) 2-pyrrolidinone + (1–X_1) *n*-alkanols: (◇) hexanol, (☆) heptanol, (★) octanol, (▲) nonanol, and (✱) decanol.

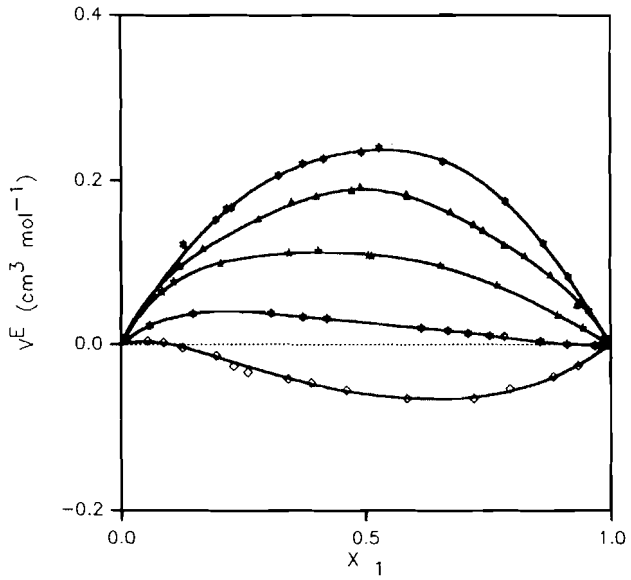

Fig. 2. Plot of molar excess volumes V^E of mixtures: (*a*) (0.5) 2-pyrrolidinone + (0.5) *n*-alkanol at 298.15 K (data for methanol to pentanol from ref. 6) and (*b*) pyridine + *n*-alkanol (data from ref. 5).

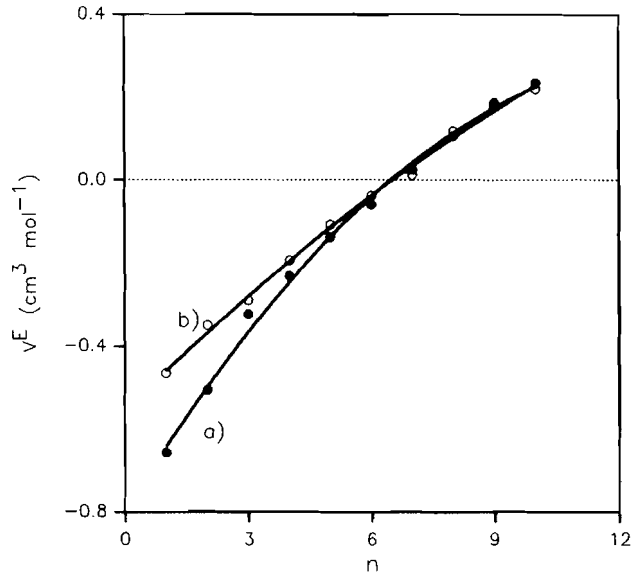

water as calibration standards. Only a small sample size is required for measurements (0.7 mL). To prevent the samples from preferential evaporation new solutions were made up at each temperature.

Results and discussion

Molar excess volumes V^E at different temperatures covering the whole composition range were calculated from the measured densities of the mixtures by means of the equation:

$$[1] \quad V^E = X_1M_1(\rho^{-1} - \rho_1^{-1}) + X_2M_2(\rho^{-1} - \rho_2^{-1})$$

where subscript 1 refers to 2-pyrrolidinone, M_i and ρ_i stand for the molar masses and densities of the pure components, and ρ is the density of the mixtures. The polynomial function [2] was fitted to the variation ρ vs. X_1:

$$[2] \quad \rho = \sum_{k=0}^{n} b_k X_1^k$$

the optimum number of coefficients b_k (Table 2)[2] was ascertained for each mixture with standard deviation σ and linear correlation coefficient r_{xy} as a criterion of goodness of fit. The Redlich–Kister equation [3] was fitted to the calculated V^E values as a function of X_1 (Table 3):

$$[3] \quad V^E = X_1X_2 \sum_{k=0}^{n} [a_k(2X_1 - 1)^k]$$

the a_k coefficients being ascertained with the standard deviation and χ^2 (Table 4).[2]

The excess volumes were independent of temperature, but changed with the alcohol size. Figure 1 shows the isothermal variation V^E vs. X_1 for all the five systems; the curves were sigmoid for hexanol (with positive values at lower X_1) and heptanol (with negative values at higher X_1) and positive for octanol to decanol. These results are consistent with those previously reported for 2-pyrrolidinone – (C_1–C_5) alkanol mixtures (6); the excess volumes were negative at all temperatures and compositions, and became smaller as the chain length of the alcohol increased. Figure 2 shows the equimolar excess volumes V^E vs. chain length of the alcohol. For comparison purposes the results reported by Dewan et al. (5) for (C_1–C_{10}) alkanol – pyridine (μ = 2.37 D) mixtures are also plotted; the two excess volume series differ noticeably for the smaller alkanols (V^E <0), but they gradually converge with increasing chain length and full agreement is reached in the hexanol to decanol (positive V^E) range.

Molar excess volumes of liquid mixtures reflect the result of different contributions arising from the structural changes undergone by the pure cosolvents. It is expected that positive contributions arise from the breakup interactions between like molecules, namely, the rupture of the hydrogen-bonded chains of alcohols and the loosening of the dipolar interactions between 2-pyrrolidinone (or pyridine) molecules (21, 22). The transition V^E <0 to V^E >0 from methanol to decanol suggests a steric effect that increases the mixture volume.

The most important source of negative contributions should be the different shape and size of the two components. Given that 2-pyrrolidinone is a poor proton acceptor and alkanols are relatively poor proton donors (23), it is reasonable to assume that heteroassociations (site–site interactions) do not contribute sufficiently to override the positive contributions. Steric effects and proton-accepting abilities increase as the alkanol chain length increases (24), with a net increase in the positive contributions to V^E. Figure 2 supports such an assumption.

[2] Table 2, containing coefficients for the least-squares fitting of eq. [2], and Table 4, containing the least-squares fitting of the results of eq. [3], have been deposited, and may be purchased from: The Depository of Unpublished Data, Document Delivery, CISTI, National Research Council Canada, Ottawa, Canada K1A 0R6.

Table 3. Molar excess volumes of (x_1) 2-pyrrolidinone + ($1-x_1$) (C_6–C_{10}) *n*-alkanol at different temperatures.

X_1	V^E (cm^3 mol^{-1})
2-Pyrrolidinone + 1-hexanol	
T = 298.15 K	
0.05449	0.003
0.08739	0.001
0.12549	–0.005
0.19414	–0.014
0.34125	–0.042
0.38956	–0.047
0.46179	–0.055
0.58553	–0.065
0.72280	–0.065
0.79591	–0.054
0.88367	–0.039
0.93378	–0.026
T = 303.15 K	
0.05610	0.014
0.13068	0.000
0.18398	–0.011
0.25021	–0.023
0.32228	–0.036
0.32545	–0.038
0.43486	–0.053
0.50582	–0.060
0.67997	–0.070
0.75471	–0.065
0.79422	–0.063
0.88385	–0.046
0.88634	–0.046
0.96531	–0.022
T = 308.15 K	
0.06526	0.009
0.09821	0.008
0.12271	0.005
0.27290	–0.027
0.32137	–0.038
0.41420	–0.055
0.54404	–0.067
0.64624	–0.069
0.69895	–0.071
0.78988	–0.066
0.83866	–0.063
0.89657	–0.049
0.94825	–0.033
T = 313.15 K	
0.02401	0.000
0.04852	0.003
0.08721	–0.001
0.14864	–0.009
0.26356	–0.026
0.27438	–0.028
0.35488	–0.042
0.35643	–0.043
0.36970	–0.044
0.39605	–0.049
0.45978	–0.055
0.47705	–0.059
0.54102	–0.065
0.69377	–0.073
0.78693	–0.068
0.90605	–0.039
0.93423	–0.030
T = 318.15 K	
0.05967	0.007
0.09386	0.010
0.21398	–0.004
0.34295	–0.034
0.36699	–0.041
0.48495	–0.061
0.49558	–0.062
0.59349	–0.074
0.64165	–0.072
0.67337	–0.070
0.75836	–0.066
0.83800	–0.061
0.91197	–0.041
0.96254	–0.022
2-Pyrrolidinone + 1-heptanol	
T = 298.15 K	
0.05893	0.022
0.14664	0.037
0.30728	0.037
0.37243	0.033
0.42159	0.031
0.61449	0.019
0.66930	0.016
0.71501	0.013
0.75478	0.010
0.78467	0.009
0.85749	0.003
0.85855	0.003
0.91099	0.000
0.96836	–0.002
T = 303.15 K	
0.08133	0.036
0.09957	0.044
0.19164	0.056
0.19578	0.056
0.22243	0.057
0.23073	0.057
0.27092	0.055
0.31731	0.054
0.36417	0.052
0.42043	0.044
0.46786	0.041
0.47158	0.041
0.54266	0.030
0.61650	0.023
0.66012	0.020
0.75163	0.008
0.79311	0.005
0.84865	0.001
0.89122	–0.005
0.97304	–0.004
T = 308.15 K	
0.02786	0.010
0.03390	0.015
0.06872	0.028
0.07762	0.031
0.29644	0.051
0.31653	0.049
0.35116	0.047
0.41034	0.042
0.45835	0.035
0.57904	0.021
0.62288	0.016
0.70589	0.005
0.76788	0.000
0.85616	–0.006
0.88763	–0.008
0.93834	–0.008
0.97264	–0.004
0.97859	–0.004
T = 313.15 K	
0.02974	0.017
0.05807	0.023
0.10323	0.040
0.18417	0.050
0.28303	0.053
0.41370	0.041
0.51144	0.028
0.58471	0.017
0.62836	0.012
0.66421	0.009
0.70424	0.004
0.80225	–0.002
0.90777	–0.004
T = 318.15 K	
0.07519	0.035
0.10455	0.040
0.18687	0.050
0.29864	0.047
0.36397	0.043
0.49414	0.029
0.57355	0.024
0.70379	0.011
0.78444	0.003
0.91148	–0.006
0.94203	–0.004
0.97751	–0.005
2-Pyrrolidinone + 1-octanol	
T = 298.15 K	
0.08465	0.063
0.10855	0.076
0.20387	0.098
0.34331	0.111
0.40378	0.114
0.50716	0.109
0.51418	0.108
0.65338	0.096
0.76903	0.071
0.89296	0.034
0.94385	0.019
0.98413	0.005
0.99409	0.004
T = 303.15 K	
0.03684	0.024
0.08286	0.047
0.12234	0.066
0.18303	0.087
0.21283	0.092
0.27314	0.105
0.31697	0.108
0.38106	0.114
0.40842	0.115
0.40909	0.115
0.41372	0.114
0.54950	0.110
0.60563	0.103
0.65062	0.097
0.69561	0.090
0.73295	0.082
0.77753	0.071
0.82588	0.056
0.82648	0.056
0.88845	0.038
0.94745	0.020
0.97419	0.007
T = 308.15 K	
0.07831	0.048
0.17934	0.085
0.18407	0.083
0.20978	0.092
0.26955	0.108
0.32956	0.114
0.41614	0.114
0.49078	0.109
0.56205	0.102
0.60188	0.096
0.73419	0.073
0.85935	0.040
0.86807	0.039
T = 313.15 K	
0.07339	0.046
0.08512	0.046
0.10002	0.061
0.22261	0.098
0.32794	0.116
0.44088	0.125
0.56178	0.112
0.60321	0.104
0.67943	0.089
0.73311	0.075
0.80928	0.058
0.85757	0.042
0.89543	0.031
0.95136	0.015
0.98332	0.004
T = 318.15 K	
0.07043	0.052
0.08871	0.059
0.10361	0.063
0.20116	0.095
0.29709	0.111
0.43226	0.110
0.44396	0.110
0.56222	0.103
0.64986	0.092
0.70304	0.079
0.74087	0.075
0.81318	0.053
0.91845	0.022
0.97357	0.007
2-Pyrrolidinone + 1-nonanol	
T = 298.15 K	
0.12064	0.094
0.16684	0.116
0.28152	0.153
0.34926	0.173

Table 3 (*concluded*).

X_1	V^E (cm^3 mol^{-1})	X_1	V^E (cm^3 mol^{-1})	X_1	V^E (cm^3 mol^{-1})	X_1	V^E (cm^3 mol^{-1})	X_1	V^E (cm^3 mol^{-1})
0.40064	0.180	0.08097	0.069	T = 318.15 K		T = 303.15 K		T = 313.15 K	
0.47267	0.187	0.19855	0.132	0.04237	0.034	0.09555	0.091	0.06363	0.066
0.49031	0.191	0.21925	0.140	0.12409	0.092	0.21673	0.164	0.12035	0.113
0.58500	0.183	0.30359	0.160	0.15733	0.115	0.27170	0.191	0.20580	0.168
0.58624	0.180	0.42381	0.179	0.24143	0.151	0.35308	0.218	0.23375	0.179
0.67522	0.162	0.53658	0.181	0.28467	0.167	0.43939	0.234	0.30867	0.210
0.72109	0.146	0.56341	0.177	0.34586	0.178	0.50110	0.237	0.39942	0.232
0.74033	0.139	0.74494	0.136	0.47644	0.180	0.55766	0.232	0.56326	0.235
0.78439	0.120	0.76772	0.126	0.51419	0.178	0.68955	0.206	0.65179	0.226
0.82608	0.107	0.82297	0.104	0.57759	0.176	0.72988	0.192	0.73406	0.204
0.87835	0.083	0.87460	0.078	0.71576	0.146	0.80555	0.157	0.80509	0.170
		0.90668	0.059	0.84601	0.091	0.83794	0.138	0.91619	0.087
T = 303.15 K				0.95065	0.031	0.88713	0.104	0.95748	0.048
0.07345	0.058	T = 313.15 K		0.95315	0.030	0.94379	0.054	0.98099	0.022
0.12134	0.089	0.03964	0.030			0.97839	0.023		
0.20211	0.129	0.08125	0.059	**2-Pyrrolidinone + 1-decanol**				T = 318.15 K	
0.22872	0.139	0.12359	0.083			T = 308.15 K		0.08341	0.073
0.28067	0.155	0.18653	0.124			0.04227	0.037	0.17904	0.150
0.42140	0.176	0.24242	0.143	T = 298.15 K		0.10593	0.097	0.20865	0.164
0.48105	0.178	0.26764	0.151	0.19332	0.153	0.16458	0.143	0.27814	0.199
0.50403	0.177	0.28443	0.162	0.21606	0.166	0.21359	0.171	0.28667	0.199
0.57208	0.173	0.32946	0.167	0.22563	0.167	0.28199	0.204	0.34153	0.220
0.66811	0.151	0.35136	0.177	0.32281	0.206	0.31373	0.213	0.48332	0.239
0.74797	0.128	0.49306	0.184	0.37137	0.220	0.49983	0.232	0.55389	0.237
0.78368	0.117	0.53892	0.179	0.41430	0.226	0.54312	0.233	0.60739	0.233
0.81897	0.103	0.61406	0.166	0.49271	0.234	0.60265	0.228	0.86590	0.144
0.83874	0.095	0.65973	0.162	0.52923	0.239	0.65341	0.217	0.91304	0.098
0.90287	0.060	0.75081	0.132	0.65961	0.223	0.73274	0.194	0.95607	0.056
		0.81789	0.108	0.78532	0.176	0.80799	0.158	0.98540	0.017
T = 308.15 K		0.88352	0.076	0.86340	0.123	0.90658	0.088		
0.04401	0.044	0.93290	0.040	0.91326	0.082	0.96084	0.039		
0.07822	0.067	0.98162	0.011	0.95623	0.040				

Fig. 3. Thermal expansion coefficients α of pure alkanols vs. *n*, number of carbon atoms, at 298.15 K, 303.15 K, and 313.15 K (data for methanol to pentanol from ref. 9).

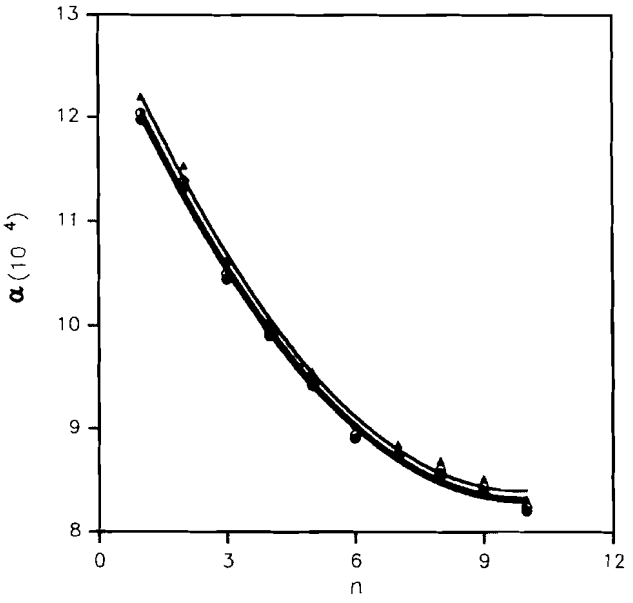

Fig. 4. Mean thermal expansion coefficients α for binary mixtures (X_1) 2-pyrrolidinone + (1–X_1) *n*-alkanols vs. *n*: (*a*) X_1 = 0, (*b*) X_1 = 0.3, (*c*) X_1 = 0.5, and (*d*) X_1 = 0.7.

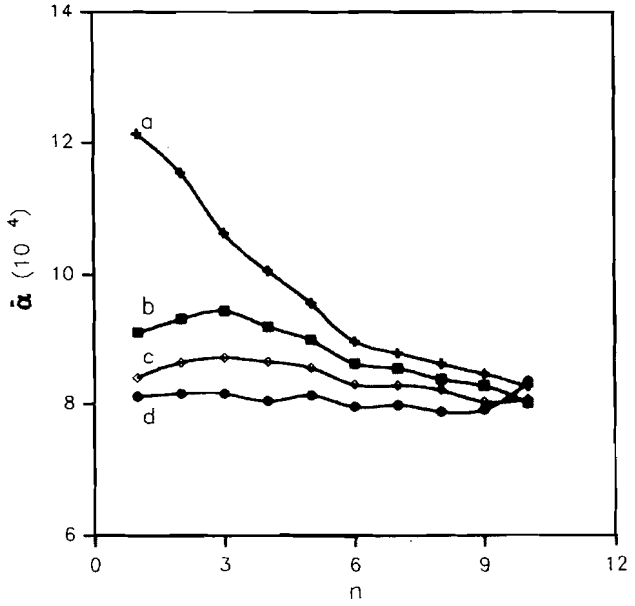

Table 5. Thermal expansion coefficients, α (K^{-1}).

	$10^4\ \alpha$				
X_1	298.15 K	303.15 K	308.15 K	313.15 K	318.15 K
2-Pyrrolidinone + 1-hexanol					
0.05	8.82	8.86	8.90	8.94	8.98
0.10	8.77	8.81	8.85	8.89	8.93
0.15	8.73	8.76	8.80	8.84	8.88
0.20	8.68	8.72	8.75	8.79	8.83
0.25	8.62	8.66	8.69	8.73	8.77
0.30	8.56	8.59	8.63	8.67	8.71
0.35	8.48	8.52	8.56	8.59	8.63
0.40	8.41	8.44	8.48	8.51	8.55
0.45	8.32	8.35	8.39	8.42	8.46
0.50	8.23	8.26	8.30	8.33	8.37
0.55	8.14	8.17	8.21	8.24	8.27
0.60	8.05	8.09	8.12	8.15	8.19
0.65	7.97	8.00	8.03	8.07	8.10
0.70	7.89	7.92	7.95	7.98	8.01
0.75	7.80	7.83	7.87	7.90	7.93
0.80	7.72	7.75	7.78	7.81	7.85
0.85	7.64	7.67	7.70	7.73	7.76
0.90	7.54	7.57	7.60	7.63	7.66
0.95	7.43	7.46	7.48	7.51	7.54
2-Pyrrolidinone + 1-heptanol					
0.05	8.67	8.71	8.75	8.79	8.82
0.10	8.62	8.66	8.69	8.73	8.77
0.15	8.58	8.62	8.66	8.70	8.73
0.20	8.56	8.59	8.63	8.67	8.71
0.25	8.52	8.56	8.59	8.63	8.67
0.30	8.48	8.51	8.55	8.58	8.62
0.35	8.41	8.45	8.48	8.52	8.56
0.40	8.35	8.39	8.43	8.46	8.50
0.45	8.29	8.32	8.36	8.39	8.43
0.50	8.22	8.25	8.28	8.32	8.35
0.55	8.14	8.17	8.21	8.24	8.28
0.60	8.07	8.11	8.14	8.17	8.21
0.65	8.00	8.03	8.06	8.10	8.13
0.70	7.92	7.95	7.98	8.01	8.04
0.75	7.83	7.86	7.89	7.92	7.96
0.80	7.73	7.76	7.79	7.82	7.85
0.85	7.62	7.65	7.68	7.71	7.94
0.90	7.50	7.53	7.56	7.59	7.62
0.95	7.83	7.41	7.44	7.47	7.50
2-Pyrrolidinone + 1-octanol					
0.05	8.54	8.58	8.61	8.65	8.69
0.10	8.50	8.54	8.58	8.61	8.65
0.15	8.45	8.49	8.53	8.56	8.60
0.20	8.40	8.44	8.47	8.51	8.55
0.25	8.36	8.39	8.43	8.46	8.50
0.30	8.32	8.36	8.39	8.43	8.46
0.35	8.29	8.33	8.36	8.40	8.43
0.40	8.26	8.29	8.32	8.36	8.40
0.45	8.21	8.25	8.28	8.31	8.35
0.50	8.16	8.19	8.22	8.26	8.29
0.55	8.08	8.12	8.15	8.18	8.22
0.60	8.01	8.04	8.07	8.11	8.14
0.65	7.92	7.95	7.98	8.01	8.05
0.70	7.82	7.85	7.88	7.91	7.95
0.75	7.74	7.77	7.80	7.83	7.86
0.80	7.66	7.69	7.72	7.65	7.78
0.85	7.59	7.62	7.65	7.68	7.71
0.90	7.53	7.56	7.59	7.62	7.65
0.95	7.46	7.49	7.52	7.55	7.58
2-Pyrrolidinone + 1-nonanol					
0.05	8.32	8.35	8.39	8.42	8.46
0.10	8.31	8.34	8.38	8.41	8.45
0.15	8.31	8.34	8.38	8.41	8.45
0.20	8.30	8.33	8.37	8.40	8.44
0.25	8.26	8.30	8.33	8.37	8.40
0.30	8.21	8.25	8.28	8.31	8.35
0.35	8.14	8.18	8.21	8.24	8.28
0.40	8.08	8.11	8.14	8.18	8.21
0.45	8.01	8.05	8.08	8.11	8.14
0.50	7.96	7.99	8.03	8.06	8.09
0.55	7.93	7.96	7.99	8.03	8.06
0.60	7.91	7.94	7.97	8.00	8.03
0.65	7.88	7.91	7.94	7.98	8.01
0.70	7.85	7.88	7.91	7.94	7.98
0.75	7.79	7.82	7.85	7.88	7.92
0.80	7.71	7.74	7.77	7.80	7.84
0.85	7.60	7.63	7.66	7.69	7.72
0.90	7.48	7.51	7.54	7.56	7.59
0.95	7.37	7.40	7.42	7.45	7.48
2-Pyrrolidinone + 1-decanol					
0.05	8.24	8.27	8.30	8.34	8.38
0.10	8.31	8.34	8.38	8.41	8.45
0.15	8.26	8.30	8.34	8.37	8.41
0.20	8.17	8.20	8.24	8.27	8.31
0.25	8.07	8.10	8.13	8.16	8.20
0.30	7.94	7.98	8.01	8.04	8.07
0.35	7.88	7.91	7.94	7.98	8.01
0.40	7.88	7.91	7.94	7.97	8.00
0.45	7.92	7.95	7.99	8.02	8.05
0.50	8.00	8.04	8.07	8.10	8.13
0.55	8.11	8.15	8.18	8.21	8.25
0.60	8.21	8.25	8.28	8.31	8.35
0.65	8.28	8.31	8.35	8.38	8.42
0.70	8.28	8.32	8.35	8.38	8.43
0.75	8.21	8.24	8.27	8.30	8.35
0.80	8.05	8.08	8.11	8.14	8.18
0.85	7.81	7.84	7.87	7.90	7.94
0.90	7.56	7.59	7.62	7.65	7.68
0.95	7.35	7.38	7.41	7.43	7.46

Thermal expansion coefficients, α, for each mixture were calculated from the experimental densities at different temperatures as:

$$[4] \quad \alpha = -\rho^{-1}(\Delta\rho/\Delta T)_P$$

Table 5 lists the α values of the mixtures calculated with eq. [4]. Figure 3 shows the plot α of the pure components vs. number of carbon atoms; as the variation with temperature is small, this permits calculation of an averaged $\bar{\alpha}$ value at each temperature. These averaged values are consistent with those reported using other types of functions (7). The fact that interactions between like molecules are stronger than between unlike molecules (25) explains why the positive contributions to excess volume depend on the alcohol chain length, but not on its dipole moment. Figure 4 shows the variation of α with the number of alkanol carbon atoms at different compositions of the mixtures. These values decrease with increasing X_1, and the difference in α at different concentrations decreases as the number of carbon atoms increases, which reveals that the role played by the chain length of the alcohol is even more important than the interactions between donor–acceptor groups of unlike molecules.

Acknowledgements

This work was supported by Junta de Castilla y León, Project VA74/93.

References

1. E. Dachwitz and M. Stockhausen. Ber. Bunsen-Ges. Phys. Chem. **89**, 959 (1985); J. Jadzyn, J. Malecki, and C. Jadzyn. J. Phys. Chem. **82**, 2128 (1978).
2. P.L. Pirilä-Honkanen and P.A. Ruostesuo. J. Chem. Eng. Data, **32**, 303 (1987); P.A. Ruostesuo, P.L. Pirilä-Honkanen, and L. Heikkinen. J. Phys. Org. Chem. **2**, 565 (1989).
3. A. D'Aprano, D. Donato, and E. Caponetti. J. Solution Chem. **8**, 135 (1979).
4. L. Wilson, R. Bicca de Alencastro, and C. Sandorf. Can. J. Chem. **63**, 40 (1985).
5. R.K. Dewan, S.K. Mehta, R. Parashar, and K. Bala. J. Chem. Soc. Faraday Trans. **87**, 1561 (1991).
6. B. García, C. Herrera, and J.M. Leal. J. Chem. Eng. Data, **36**, 269 (1991).
7. J. Ortega and J.D. García. Can. J. Chem. **66**, 1520 (1988).
8. R.P. Singh, C.P. Sinha, J.C. Das, and P. Ghosh. J. Chem. Eng. Data, **35**, 93 (1990).
9. R.K. Dewan, S.P. Gupta, and S.K. Mehta. J. Solution Chem. **18**, 13 (1989).
10. R. Bravo, M. Pintos, A. Amigo, and M. García. Phys. Chem. Liq. **22**, 245 (1991).
11. C. Yanes, A. Maestre, P. Pérez-Tejeda, and J.J. Calvente. J. Chem. Eng. Data, **38**, 512 (1993).
12. K.Y. Liew, C.E. Seng, and B.H. Ng. J. Solution Chem. **21**, 1177 (1992).
13. A. Amigo, R. Bravo, and M. Pintos. J. Chem. Eng. Data, **38**, 141 (1993).
14. K.S. Kumar and P.R. Naidu. J. Chem. Eng. Data, **38**, 156 (1993).
15. R.P. Singh, C.P. Sinha, J.C. Das, and P. Ghosh. J. Chem. Eng. Data, **34**, 335 (1989).
16. T.M. Aminabhavi, M.I. Aralaguppi, S.B. Harogoppad, and R.H. Balundgi. J. Chem. Eng. Data, **38**, 31 (1993).
17. T.M. Aminabhavi, S.K. Raikar, and R.H. Balundgi. Ind. Eng. Chem. Res. **32**, 931 (1993).
18. T.S. Vijayalakshmi and P.R. Naidu. J. Chem. Eng. Data, **37**, 368 (1992).
19. S.K. Garg, T.S. Banipal, and J.C. Ahluwalia. J. Chem. Eng. Data, **38**, 227 (1993).
20. I. Brown and F. Smith. Aust. J. Chem. **26**, 705 (1973).
21. M.G. Prolongo, R.M. Masegosa, I.M. Fuentes, and A. Horta. J. Phys. Chem. **88**, 2163 (1984).
22. R.J. Fort and T.E. Moore. Trans. Faraday Soc. **62**, 1112 (1962).
23. A.S.N. Murthy and C.N.R. Rao. Appl. Spectrosc. Rev. **2**, 69 (1968).
24. C. Pikkarainen. Finn. Chem. Lett. 109 (1980).
25. R. Riggio, H.E. Martínez, and N.Z. Salas. Can. J. Chem. **70**, 2859 (1992).

Transannular Diels–Alder cyclization of substituted 13-membered trienes. An approach to the B.C.D.[6.6.5] rings of the 14β-hydroxysteroids

Pascal Langlois, Pierre Soucy, Yves L. Dory, and Pierre Deslongchamps

Abstract: The transannular Diels–Alder strategy has been applied to three 13-membered macrocyclic trienes whose characteristics are: a *cis-trans* diene and a *cis* methoxymethyl enol ether as the dienophile. The successful trials led to three 6.6.5 tricyles having a *trans-syn-cis* geometry exactly as in the B.C.D. rings of the 14β-hydroxysteroids.

Key words: transannular, Diels–Alder, 14β-hydroxysteroids, 13-membered rings.

Résumé : La stratégie de Diels–Alder transannulaire a été appliquée sur trois trièmes macrocycliques à 15 membres dont les caractéristiques sont : un diène *cis-trans* et un éther d'énol méthoxyméthyle *cis* comme diénophile. Les essais positifs ont conduit à trois tricycles 6.6.5 ayant une géométrie *trans-syn-cis* exactement comme les cycles B.C.D. des 14β-hydroxystéroïdes.

Mots clés : transannulaire, Diels–Alder, 14β-hydroxystéroïdes, cycles à 13 membres.

Introduction

We have already demonstrated that 13-membered macrocyclic trienes can be nicely used in the synthesis of the A.B.C.[6.6.5] ring system of the Veratrum alkaloid family (1). We wish now to report on a similar approach towards the B.C.D.[6.6.5] ring skeleton of the 14β-hydroxysteroids. This class of compounds, the 14β-hydroxysteroids, may be divided into 2 subclasses: the 5α,14β-hydroxysteroids and the 5β,15β-hydroxysteroids, the latter groups being the more numerous as well as the most important with regards to therapeutic potency. The aglycones of the cardiac glycosides, digitoxin **1** (2), digoxin **2** (3), digitalin **3** (4), and diginatin **4** (5) (Scheme 1), belong to this family of compounds.

All the reported syntheses (6) of these compounds begin with already elaborated starting materials obtained by degradation of steroids. But the major common snag to the existing approaches is the tedious introduction of the 14β-hydroxyl group. As a consequence the different syntheses that have so far been designed lack versatility and do not allow the design of substituted analogues related to these important natural products.

Since we had recognized that the B.C.D.[6.6.5] ring system, common to all these compounds, could well be obtained via a transannular Diels–Alder reaction (Scheme 2), we carried out a preliminary model study aimed ultimately at the synthesis of 14β-hydroxysteroids. The B.C.D. framework possesses the

Scheme 1.

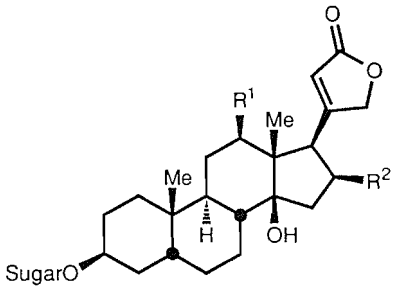

1 $R^1 = R^2 = H$ = digitoxin (aglycone: digitoxigenin)
2 $R^1 = OH$, $R^2 = H$ = digoxin (aglycone: digoxigenin)
3 $R^1 = H$, $R^2 = OH$ = digitalin (aglycone: gitoxigenin)
4 $R^1 = R^2 = OH$ = diginatin (aglycone: diginatigenin)

trans-syn-cis (TSC) geometry at the ring junctions; therefore the corresponding Diels–Alder adduct **6** requires the 13-membered TCC (*trans-cis-cis*) macrocyclic triene **7** as the precursor. Two models have been devised (Scheme 3) whose goals are, firstly, to check the feasibility of such an approach (model 1) and, secondly, to tackle the introduction of chirality in our systems (model 2). The latter concern, of particular importance, relies on the synthesis of chiral aldols (7) at the macrocyclic level, which could then transmit their chirality to the four stereogenic centres created during the transannular Diels–Alder reactions.

Results and discussion

Synthesis of the macrocycles

Model 1 (Schemes 4 and 6)
The monoprotected diol **8** (8) was oxidized using Swern's

Received August 16, 1995.

P. Langlois, P. Soucy, Y.L. Dory, and P. Deslongchamps.[1] Laboratoire de synthèse organique, Département de chimie, Faculté des sciences, Université de Sherbrooke, Sherbrooke, QC J1K 2R1, Canada.

[1] Author to whom correspondence may be addressed. Telephone: (819) 821-7002. Fax: (819) 821-7910.

Scheme 2.

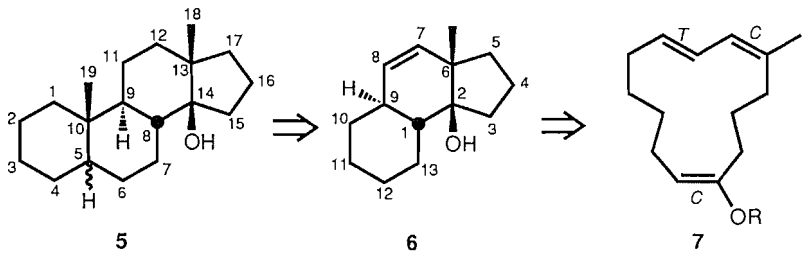

5 6 7

Scheme 3.

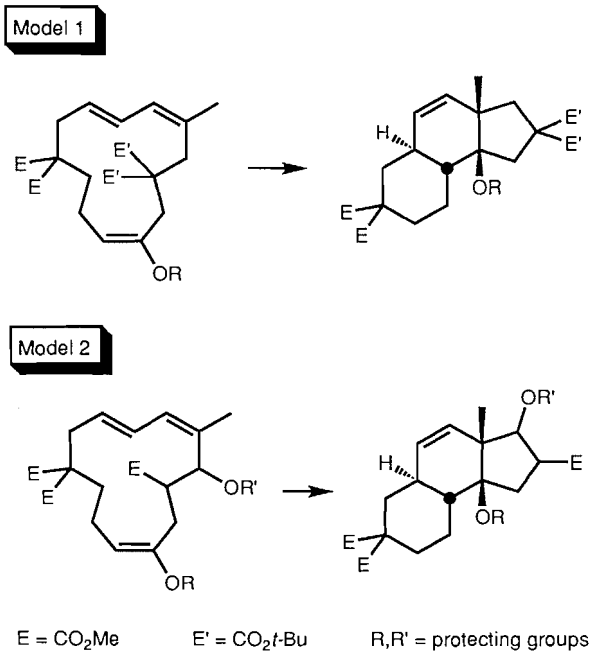

conditions (9) to the aldehyde **9**, which was then subsequently transformed into the enol ether **10** by the Horner–Emmons approach (10, 11) and in 54% yield from **8**; the unwanted geometrical isomer of **10** (11% of the mixture) was easily removed by flash chromatography. The alcohol **11** was obtained by diisobutyl aluminium hydride reduction (12) of the ester **10** in 69% yield. The allylic chloride **12** prepared from **11** using Meyer's conditions (13) (yield: 86%) was treated with di-*tert*-butyl sodiomalonate to give the monosubstituted malonate **13** in 72% yield. Deprotection of the silyl ether **13** by means of tetrabutylammonium fluoride afforded the alcohol **14** in 87% yield that was then protected as its benzoate ester **15** (14) in 79% yield.

The alcohol **16** (9) was oxidized to the aldehyde **17** by means of pyridinium chlorochromate (15) in 48% yield. The dienic ester **18** was then obtained by Horner–Emmons condensation (16) in 100% yield. The allylic chloride **20** was made from **18** by the same two-step procedure used to synthesize **12** from **10** (59% overall yield). The allylic chloride **20** was coupled with the malonate anion of **15** to yield the triene **21** in 88% yield. Mild basic hydrolysis of the benzoate **21** gave the corresponding alcohol **22** (83% yield), which was then converted to the mesylate **23** (100% yield) prior to coupling with dimethyl sodiomalonate to afford the tetraester **24** (79% yield). The silyl ether **24** was deprotected to the alcohol **25** (85% yield). Using Meyer's conditions (13) the alcohol **25** was subsequently transformed into the chloride **26** in 86% yield.

Several attempts to macrocyclize the allylic chloride **26** with cesium carbonate under high dilution conditions either in *N*,*N*-dimethylformamide or in acetonitrile proved unsuccessful, giving mostly the macrocyclic ketone **30** and very little cyclic enol **29** (Scheme 6). The alcohol **25** was then transformed into the corresponding acetate **27** (96% yield) and pivaloate **28** (80% yield). The macrocyclization step was carried out on both esters **27** and **28** via their π allyl palladium complexes (17) to yield the desired macrocycle **29** in 23 and 79% yields, respectively.

Model 2 (Schemes 5 and 6)

The allylic chloride **12** was transformed into the monosubstituted methyl malonate **31** by the same method used to prepare **13** from the same starting chloride **12** in 74% yield. The ester **32** was obtained by decarboxylation of **31** in 67% yield (18). Subsequent removal of the silyl protecting group (14) afforded the alcohol **33** (97% yield), which was transformed into the malonate **35** by the same two-step procedure that was followed to prepare **24** from **22** (75% overall yield). The alcohol **19** was oxidized under Swern's conditions (9) to the aldehyde **36** in 86% yield. Aldol condensation (19) between the dianion of the tetraester **35** and the aldehyde **36** produced the two aldols **37** and **38**, in 59% total yield (*erythro* isomer **37**: 42% of the mixture; *threo* isomer **38**: 58% of the mixture). The structures of the two aldols were assigned according to the NMR chemical shifts of the methoxy groups of the aldol ester moieties (3.53 ppm: *erythro* isomer; 3.69 ppm: *threo* isomer); it has long been observed in our laboratories (19) that similar aldol products displayed NMR spectra where the *erythro* methoxy signals were consistently upfield from their *threo* counterparts by 0.1–0.2 ppm. The silyl ether **37** was cleaved (8) to yield the diol **39** (80% yield), which was then selectively monoprotected as the primary benzoate ester **41** (15) in 72% yield. The remaining alcohol group of the *erythro* aldol **41** was protected as its silyl ether **43** (8) in 100% yield. The alcohol **45** obtained by hydrolysis of the benzoate **43** (76% yield) was transformed into the corresponding allylic chloride **47** (13) (96% yield), which was subsequently cyclized with cesium carbonate under high dilution conditions to give the macrocycle **49** in 59% yield. The same six-step procedure (**37** to **49**) was applied to the *threo* aldol **38** to synthesize the macrocycle **50** in 33% overall yield.

Diels–Alder reactions (Schemes 6, 7, and 8)

The Diels–Alder cycloaddition reactions were carried out on

Scheme 4.

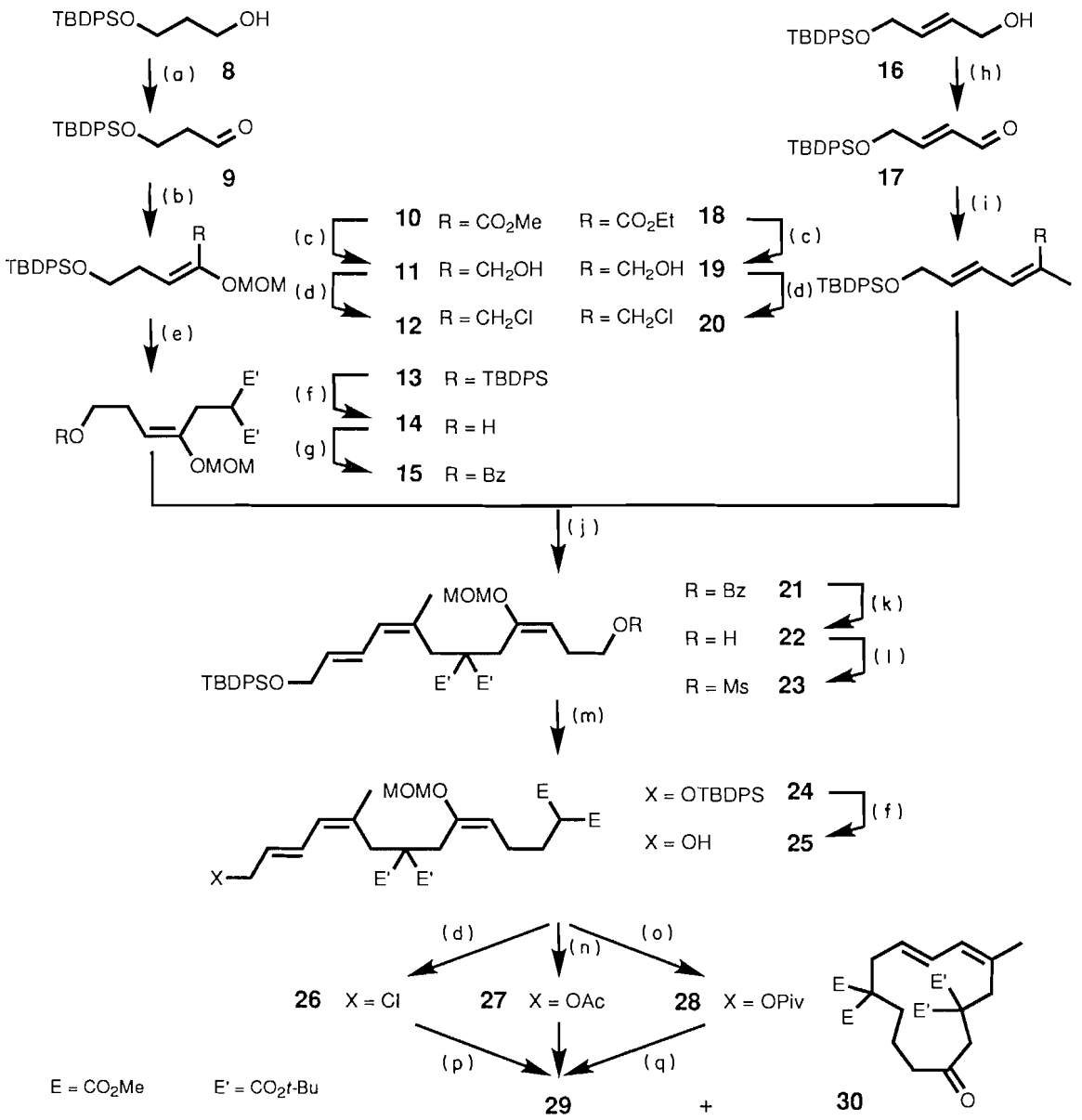

(a) $(COCl)_2$,DIPEA, DMSO, -60°C; (b) $(MeO)_2P(O)CH(OMOM)CO_2Me$, *n*-BuLi, THF, -78°C; (c) DIBAL, CH_2Cl_2, -78°C; (d) MsCl, LiCl, s-collidine, DMF, 0°C; (e) i: $CH_2E'_2$, NaH, DMF, THF, r.t.; ii:**12**, DMF, THF, r.t.; (f) TBAF, THF, r.t.; (g) PhCOCl, Pyr, r.t.; (h) PCC, NaOAc, CH_2Cl_2, 0°C; (i) $(CF_3CH_2O)_2P(O)CH(Me)CO_2Et$, 18-crown-6, KHMDS, THF, -78°C; (j) i: **15**, NaH, DMF, r.t.; ii: **20**, THF, r.t.; (k) K_2CO_3, MeOH, r.t.; (l) MsCl, NEt_3, CH_2Cl_2, 0°C; (m) i: CH_2E_2, NaH, DMF, THF, r.t.; ii: **23**, DMF, THF, r.t.; (n) Ac_2O, Pyr, 0°C; (o) *t*-BuCOCl, Pyr, CH_2Cl_2, r.t.; (p) $CsCO_3$; (q) $(Ph_3P)_4Pd$, $(Ph_2PCH_2)_2$, O-N,bistrimethyl silyl acetamide, THF, reflux.

the macrocyclic trienes **29**, **49**, and **50** in toluene at 180°C, 230°C, and 200°C, respectively (Scheme 6).

Model 1

The tetraester **29** led to the formation of three tricycles **51**, **52**, and **53** (78%, 11%, and 11% of the mixture, respectively; total yield: 66%). The triesters **52** and **53** were the result of the thermic decarboxylation of one *tert*-butyl ester either on the macrocycle **29** before Diels–Alder reaction or on the tricycle **51**. The structures of the adducts **51**, **52**, and **53** were assessed by the following chemical path (Scheme 7): the methoxymethyl ethers were cleaved by means of hydrochloric acid to give the corresponding alcohols **58**, **59**, and **60** (89%, 89%, and 80% yield). The alcohol **58** underwent *tert*-butyl ester hydrolysis and lactonization under acidic conditions; then treatment with diazomethane gave the lactone **61** (90% yield) whose structure was confirmed by X ray analysis (20). Acidic treatment of the alcohol **59** led to the lactone **62** in 81% yield. The alcohol **60** was treated in the same way as **58** to afford the unconjugated alkene-ester **63** (78% yield), thus proving the *anti* geometry of the *tert*-butyl ester with regard to the methoxymethyl ether in the Diels–Alder adduct **53**.

Scheme 5.

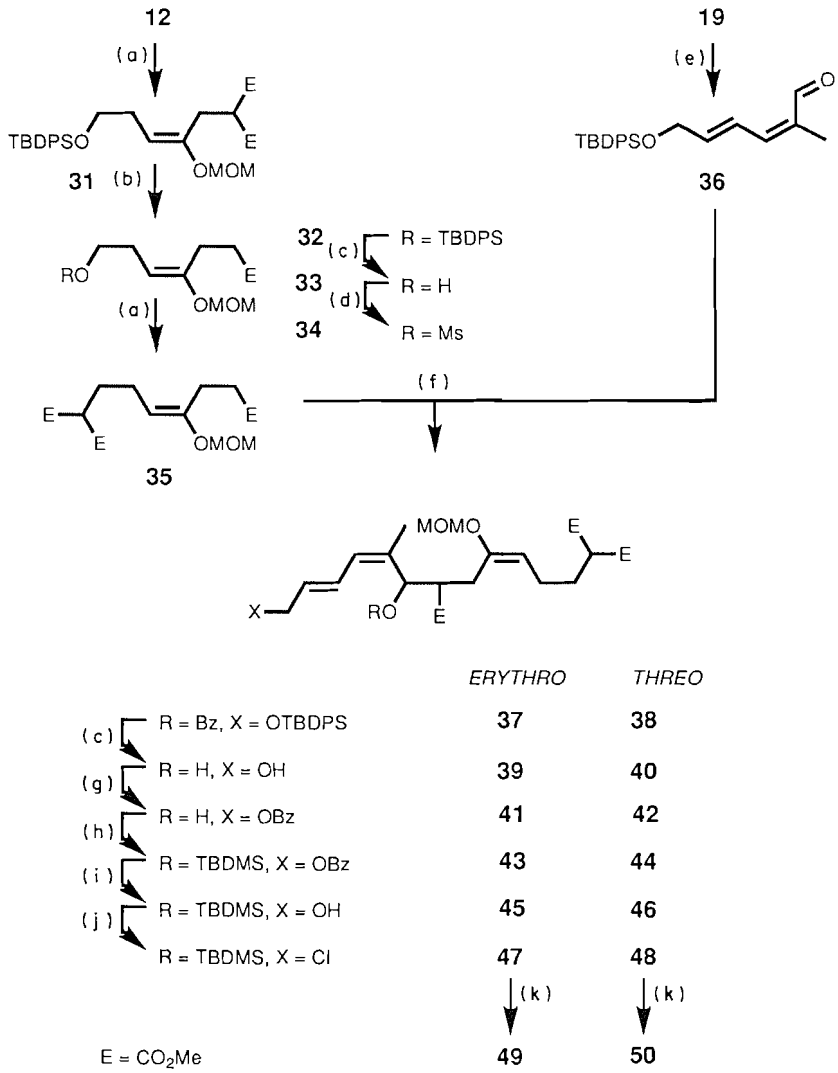

(a) i: CH_2E_2, NaH, DMF, THF, r.t.; ii: **12**, DMF, THF, r.t.; (b) NaCN, DMSO, H_2O, 90°C; (c) TBAF, THF, 0°C; (d) MsCl, NEt_3, CH_2Cl_2, 0°C; (e) MnO_2, pentane, CH_2Cl_2, r.t.; (f) i: **35**, LDA, THF, -78°C; ii: **36**, THF, -78°C; (g) BzCl, Pyr, CH_2Cl_2, 0°C; (h) TBDMSTF, NEt_3, THF, 0°C; (i) K_2CO_3, MeOH, r.t.; (j) MsCl, LiCl, s-collidine, DMF, 0°C; (k) Cs_2CO_3, MeCN, 95°C.

Model 2

The macrocycle *syn* **49** (*erythro* series) led to only one Diels–Alder adduct **54** (57% yield), the structure of which was proved chemically (Scheme 8). The methoxymethyl ether **54** was cleaved by means of dimethylboron bromide (21) to yield quantitatively the alcohol **64**, which then lactonized under acidic conditions to give the compound **66**. When treated under similar conditions the macrocycle *anti* **50** (*threo* series) also gave only one Diels–Alder adduct, **56** (94% yield), which did not afford a lactone as above, but rather the diol ester **67**, proving implicitly the *anti* geometry of the methoxymethyl ether and the ring D ester in the adduct **56**.

Geometry of the transition states (Scheme 9)

The transition state A en route from the macrocycle **29** to the adduct **51** is obviously in competition with no other transition state; therefore, no other adduct results from the Diels–Alder reaction of **29**. On the contrary, two transition states B and C may be considered to be issued from the tricycle **49**; C, however, displays a very severe steric interaction between the silyl ether and an external dienic proton (E side). As a consequence of this effect no corresponding adduct **55** is experimentally observed; the tricycle **54**, obtained through the steric-interaction-free transition state B, is the only reaction product. Regarding the Diels–Alder reaction from the macrocycle **50**, the outcome is the same: the only observed adduct **56** is issued from the transition state D displaying no major steric-disfavoring interaction, whereas the other possible isomeric adduct **57** is not obtained since it would arise from the hindered transition state E, which is sterically similar to C.

Scheme 6.

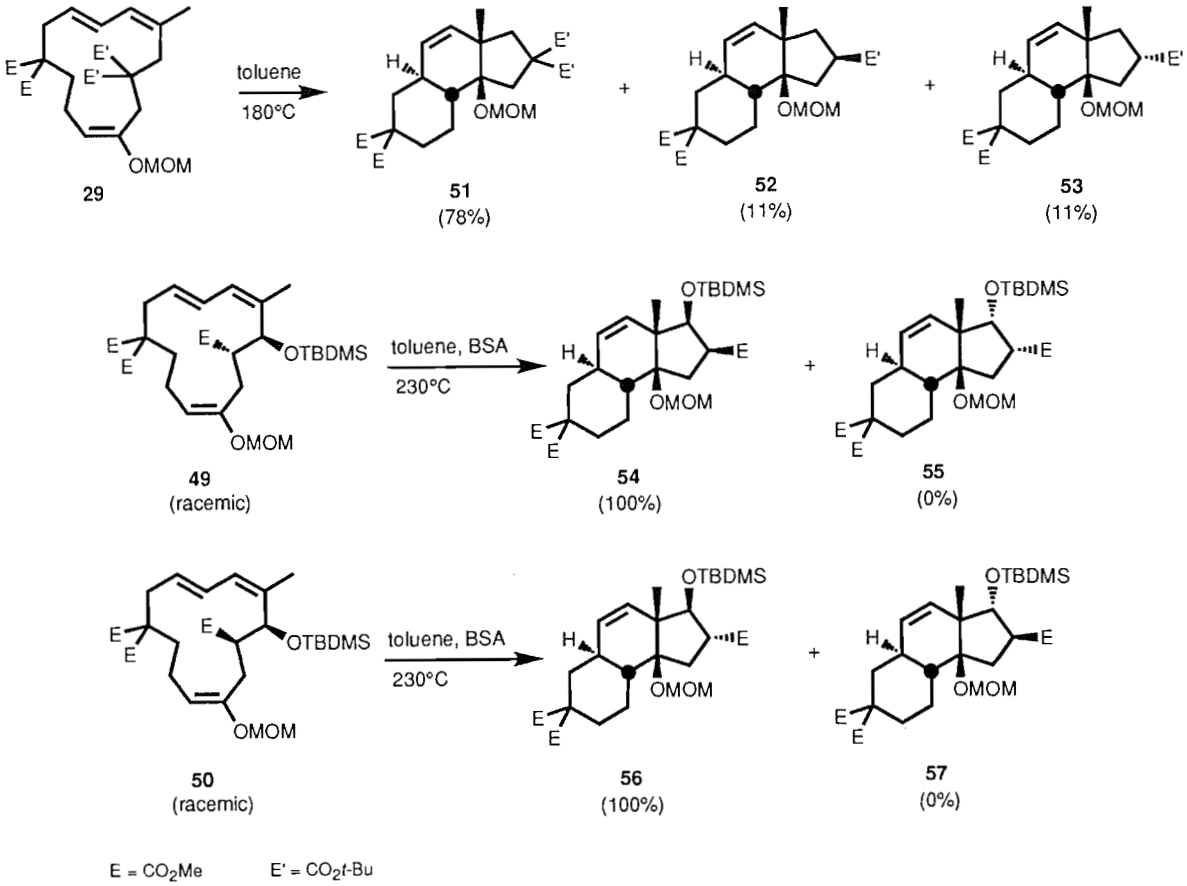

Scheme 7.

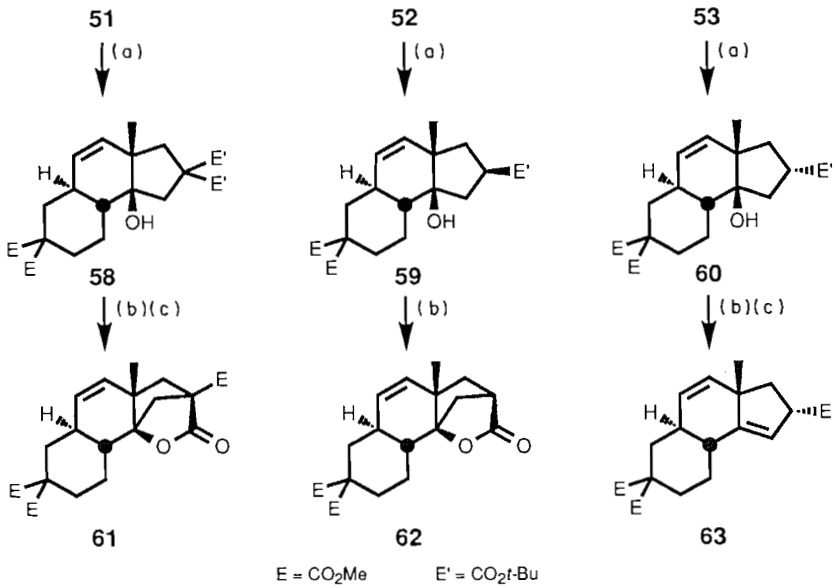

(a) 1.0 M HCl, MeOH, r.t.; (b) PTSA, C_6H_6, reflux; (c) CH_2N_2, ether, r.t.

Scheme 8.

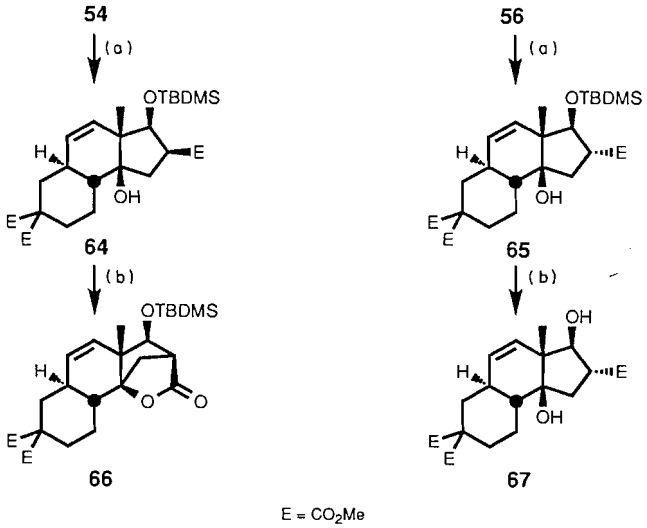

Scheme 9.

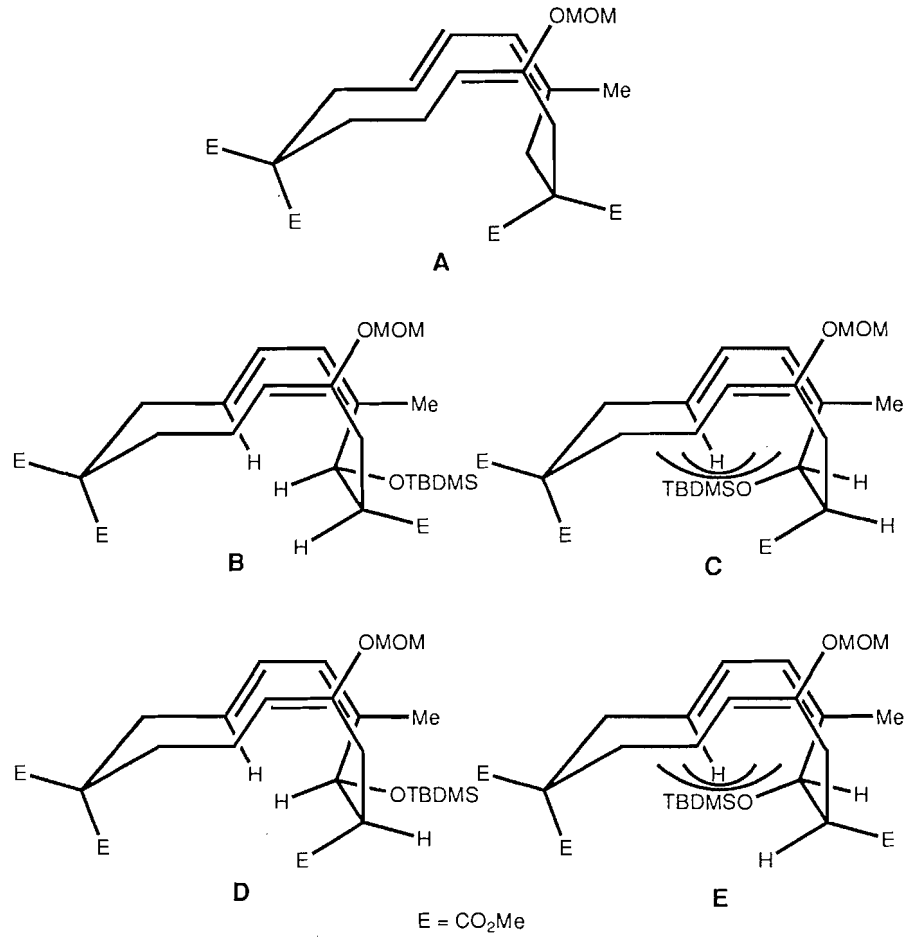

Conclusion

We have shown that the B.C.D. rings framework of the 14β-steroids could be obtained in a straightforward manner by means of the transannular Diels–Alder strategy from easily built macrocyclic trienes. Furthermore, the racemic Diels–Alder adducts with aldol moieties in the D ring have the same relative geometry at centres 8, 9, 13, 14, and 17 (steroid

nomenclature) thus proving that the silyl ether (position 17) is responsible on its own for the stereochemical fate of the Diels–Alder reactions, the aldol ester group stereochemistry having no effect. Therefore, stereochemical control of the alcohol group (position 17) should provide easy access to enantiomerically pure 14β-steroids.

We are currently investigating this route, together with the introduction of the A ring, which will end the synthesis.

Experimental section

Melting points were recorded on a Rinco M-50 apparatus and are uncorrected. MS data were determined at 70 eV on a VG Micromass ZAB-1F spectrometer. IR absorption spectra were measured on a Perkin Elmer 681. Proton (^{1}H) NMR spectra were recorded on a Bruker WM-250. Chemical shifts are reported relative to TMS (δ 0.00) with residual $CHCl_3$ as internal standard (δ 7.26) or residual C_6H_6 (δ 7.21).

All reactions were conducted in oven-dried (120°C) or flame-dried glassware under an atmosphere of dry argon, unless otherwise stated.

Aldehyde ***9***

To a solution of oxalyl chloride (4.46 mL, 51.1 mmol) in dichloromethane (112 mL) at −55°C was added a solution of dimethyl sulfoxide (7.59 mL, 106.9 mmol) in dichloromethane (23 mL). The mixture was added to a solution of the alcohol **8** (8) (14.0 g, 45.0 mmol) in dichloromethane (22 mL) over a 5 min period. The mixture was stirred for 45 min, then *N,N*-diisopropylethylamine (38.8 mL, 222.7 mmol) was added. The solution was allowed to warm up, then water was added at −10°C. The mixture was extracted with dichloromethane and washed with brine. Drying ($MgSO_4$) and removal of solvent afforded the title compound (14.0 g, 100%), which was used in the next step without further purification; ir (film): 3080–3005, 2960–2840, 1730, 1430, 1115 cm^{-1}; ^{1}H nmr ($CDCl_3$, δ ppm): 1.06 (9H, s, t-*Bu*), 2.62 (2H, td, *J* = 6 Hz, 2 Hz, CH_2CHO), 4.04 (2H, t, *J* = 6 Hz, CH_2OSi), 7.35–7.45 (6H, m, Ph), 7.65–7.75 (4H, m, Ph), 9.83 (1H, t, *J* = 2 Hz, *CH*O); ^{13}C nmr ($CDCl_3$, δ ppm): 19.10, 26.72, 46.33, 58.25, 127.74, 129.79, 133.21, 135.51, 201.89; ms *m/e*: 255 (M^+ − *t*-Bu).

Ester ***10***

A solution of 2-methoxymethyloxytrimethylphosphonoacetate (21.54 g, 89 mmol) (11) in tetrahydrofuran (30 mL) was treated at 0°C with *n*-butyllithium (1.65 M in hexane) (51.2 mL, 84 mmol) for 10 min. A solution of the aldehyde **9** (13.89 g, 45 mmol) in tetrahydrofuran (50 mL) was added at −78°C and the resulting mixture was stirred for 5 min at −78°C; then saturated aqueous ammonium chloride was added and the reaction mixture extracted with dichloromethane. Drying ($MgSO_4$) and removal of solvent afforded an oil that was purified by flash chromatography on silica gel (ethyl acetate – hexane, 5:95) to give the desire *E* olefin **10** (10.34 g, 54%) and its *Z* isomer (1.37 g, 7%).

Ester ***10*** *(*E *isomer)*: ir (film): 1725, 1640 cm^{-1}; ^{1}H nmr ($CDCl_3$, δ ppm): 1.05 (9H, s, t-*Bu*Si), 2.77 (2H, q, *J* = 6.5 Hz, $SiOCH_2CH_2$), 3.45 (3H, s, CH_2OMe), 3.74 (2H, t, *J* = 6.5 Hz, $SiOCH_2$), 3.78 (3H, s, CO_2Me), 4.96 (2H, s, OCH_2O), 5.92 (1H, t, *J* = 7.5 Hz, HC=C), 7.30–7.45 (6H, m, *Ph*), 7.65–7.70 (4H, m, *Ph*).

Z *isomer*: ir (film): 1720, 1640 cm^{-1}; ^{1}H nmr ($CDCl_3$, δ ppm): 1.05 (9H, s, t-*Bu*Si), 2.55 (2H, q, *J* = 6.5 Hz, $SiOCH_2CH_2$), 3.45 (3H, s, CH_2OMe), 3.76 (2H, t, *J* = 6.5 Hz, $SiOCH_2$), 3.78 (3H, s, CO_2Me), 4.99 (2H, s, OCH_2O), 6.41 (1H, t, *J* = 7.5 Hz, HC=C), 7.30–7.45 (6H, m, *Ph*), 7.65–7.70 (4H, m, *Ph*); ms *m/e*: 397 (M^+ − MeO), 371 (M^+ − t-*Bu*). HRMS (M^+ − t-*Bu*): 371.1315; found: 371.1304.

General procedure for the preparation of allylic alcohols

Alcohol ***11***

To a solution of the ester **10** (10.34 g, 24.0 mmol) in dichloromethane (300 mL) at −78°C was slowly added diisobutylaluminium hydride (1.5 M in toluene, 32.2 mL, 48.0 mmol). The mixture was stirred for 60 min at −78°C, then sodium sulfate decahydrate (28.0 g) was added and the resulting mixture was stirred at room temperature for 2 h. Acetone (210 mL) was added and the reaction mixture stirred for a further 15 h. The mixture was filtered, evaporated, and purified by flash chromatography (hexane – ethyl acetate, 6:4) to give the title compound (6.65 g, 69%); ir (film): 3600, 3440, 1670 cm^{-1}; ^{1}H nmr ($CDCl_3$, δ ppm): 1.05 (9H, s, t-*Bu*Si), 2.25–2.35 (3H, m, $SiOCH_2CH_2$ and O*H*), 3.43 (3H, s, CH_2OMe), 3.63 (2H, t, *J* = 6.5 Hz, $SiOCH_2$), 4.12 (2H, d, *J* = 6.0 Hz, CH_2OH), 4.90 (1H, t, *J* = 8.0 Hz, CH=C), 4.95 (2H, s, OCH_2O), 7.35–7.45 (6H, m, *Ph*), 7.65–7.70 (4H, m, *Ph*); ^{13}C nmr ($CDCl_3$, δ ppm): 19.10, 26.77, 29.68, 55.99, 59.33, 63.82, 93.99, 101.38, 127.64, 129.64, 133.51, 135.56, 154.04; ms *m/e*: 311 (M^+ − *t*-Bu + MeOH). HRMS (M^+ − *t*-Bu + MeOH): 311.1103; found: 311.1109.

Alcohol ***19***: Yield: 69%; ir (film): 3340 cm^{-1}; ^{1}H nmr ($CDCl_3$, δ ppm): 1.08 (9H, s, t-*Bu*Si), 1.33 (1H, br s, O*H*), 1.89 (3H, s, *Me*C=C), 4.24 (2H, s, CH_2OH), 4.27 (2H, d, *J* = 5.0 Hz, $SiOCH_2$), 5.73 (1H, dt, *J* = 15.0 Hz, 5.0 Hz, $SiOCH_2CH$=CH), 5.96 (1H, d, *J* = 11.0 Hz, *CH*=CMe), 6.56 (1H, ddt, *J* = 15.0 Hz, 11.5 Hz, 1.5 Hz, $SiOCH_2CH$=*CH*), 7.35–7.50 (6H, m, *Ph*), 7.65–7.75 (4H, m, *Ph*); ^{13}C nmr ($CDCl_3$, δ ppm): 19.17, 21.39, 26.77, 61.58, 64.18, 124.24, 127.61, 129.60, 131.74, 133.57, 135.48, 136.44; ms *m/e*: 309 (M^+ − *t*-Bu). HRMS (M^+ − *t*-Bu): 309.1311; found: 309.1306.

General procedure for the preparation of allylic chlorides

Chloride ***12***

To a solution of the alcohol **11** (900 mg, 22.5 mmol) in *N,N*-dimethylformamide (6 mL) at 0°C were added collidine (0.50 mL, 4.5 mmol), lithium chloride (381 mg, 9.0 mmol), and methane sulfonyl chloride (0.76 mL, 4.5 mmol). The mixture was stirred at room temperature for 1.5 h, poured over ice, and extracted with ether and hexane (1:4). Drying ($MgSO_4$) and removal of solvent gave an oil that was purified by column chromatography on Florisil (ethyl acetate – hexane, 1:49), to yield the title compound (813 mg, 86%); ir (film): 1670 cm^{-1}; ^{1}H nmr ($CDCl_3$, δ ppm): 1.06 (9H, s, t-*Bu*Si), 2.33 (2H, dt, *J* = 8.0 Hz, 7.0 Hz, $SiOCH_2CH_2$), 3.43 (3H, s, CH_2OMe), 3.67 (2H, t, *J* = 7.0 Hz, $SiOCH_2$), 4.03 (2H, s, CH_2Cl), 4.96 (2H, s, OCH_2O), 5.01 (1H, t, *J* = 8.0 Hz, *CH*=CMe), 7.35–7.50 (6H, m, *Ph*), 7.65–7.70 (4H, m, *Ph*); ^{13}C nmr ($CDCl_3$, δ ppm):

19.14, 26.75, 30.15, 40.46, 55.91, 63.52, 93.95, 103.66, 127.62, 129.60, 133.67, 135.53, 150.88; ms *m/e* 361 ($M^+ - t$-Bu). HRMS ($M^+ - t$-Bu): 361.1027; found: 361.1021.

Chloride ***20***: Crude yield: 86% (used in the next step without further purification).

Chloride ***26***: Crude yield: 86% (used in the next step without further purification).

Chloride ***47***: Yield: 96%; ir (film): 1735, 1665 cm^{-1}; ^1H nmr ($CDCl_3$ δ ppm): −0.02 (3H, s, Si*Me*), 0.08 (3H, s, Si*Me*) 0.89 (9H, s, t-*Bu*Si), 1.78 (3H, s, *Me*C═C), 1.97 (4H, m, $(CH_2)_2$CH═C), 2.43 (1H, dd, *J* = 13.5 Hz, 11.5 Hz, C═C(OMOM)C*H*H), 2.62 (1H, dd, *J* = 3.0 Hz, 13.5 Hz, C═C(OMOM)CH*H*), 2.85 (1H, ddd, *J* = 11.5 Hz, 9.5 Hz, 3.0 Hz, C*H*CO_2Me), 3.36 (1H, t, *J* = 7.0 Hz, C*H*$(CO_2Me)_2$), 3.36 (3H, s, CH_2O*Me*), 3.49 (3H, s, $CHCO_2$*Me*), 3.73 (6H, s, $CH(CO_2Me)_2$), 4.13 (2H, d, *J* = 7.0 Hz, CH_2Cl), 4.64 (1H, d, *J* = 9.5 Hz, C*H*OSi), 4.65 (1H, t, *J* = 6.4 Hz, C*H*═COMOM), 4.81 and 4.84 (2H, AB, *J* = 6.5 Hz, OCH_2O), 5.68 (1H, dt, *J* = 15.0 Hz, 7.0 Hz, C*H*═CHCH═CMe), 5.83 (1H, d, *J* = 11.0 Hz, C*H*═CMe), 6.52 (1H, dd, *J* = 14.5 Hz, 11.5 Hz, CH═C*H*CH═CMe).

Chloride ***48***: Yield: 99%; ir (film): 1735, 1665 cm^{-1}; ^1H nmr ($CDCl_3$, δ ppm): −0.06 (3H, s, Si*Me*), −0.01 (3H, s, Si*Me*), 0.81 (9H, s, t-*Bu*Si), 1.77 (3H, s, *Me*C═C), 1.8–2.0 (5H, m, $(CH_2)_2$CH═C and C═C(OMOM)C*H*H), 2.28 (1H, dd, *J* = 14.0 Hz, 12.0 Hz, C═C(OMOM)CH*H*), 2.87 (1H, ddd, *J* = 12.0 Hz, 10.0 Hz, 3.5 Hz, C*H*CO_2Me), 3.34 (1H, t, *J* = 7.0 Hz, C*H*$(CO_2Me)_2$), 3.36 (3H, s, CH_2O*Me*), 3.64 (3H, s, $CHCO_2$*Me*), 3.71 (3H, s, $CH(CO_2Me)_2$), 3.72 (3H, s, $CH(CO_2Me)_2$), 4.16 (2H, d, *J* = 7.5 Hz, CH_2Cl), 4.63 (1H, t, *J* = 7.5 Hz, C*H*═COMOM), 4.78 (1H, d, *J* = 10.0 Hz, C*H*OSi), 4.80 and 4.83 (2H, AB, *J* = 6.5 Hz, OCH_2O), 5.77 (1H, dt, *J* = 14.5 Hz, 7.5 Hz, C*H*═CHCH═CMe), 6.00 (1H, d, *J* = 11.0 Hz, C*H*═CMe), 6.62 (1H, dd, *J* = 15.0 Hz, 11.0 Hz, CH═C*H*CH═CMe).

General procedure for the preparation of malonates

Method A

Malonate ***13***

To a stirred suspension of sodium hydride (60% in oil, 0.89 g, 22.4 mmol) in tetrahydrofuran (31 mL) and *N,N*-dimethylformamide (31 mL) was added di-*tert*-butylmalonate (5.0 mL, 22.4 mmol). The resulting mixture was stirred for 15 min at room temperature, then added to a solution of the allylic chloride **12** (6.08 g, 14.99 mmol) in tetrahydrofuran (20 mL) and *N,N*-dimethylformamide (20 mL). The mixture was stirred at room temperature for 2 h, treated with saturated aqueous ammonium chloride, then extracted 3 times with ether and hexane (4:1). Drying ($MgSO_4$) and removal of solvent under reduced pressure gave an oil that was purified by flash chromatography (ethyl acetate – hexane, 1:40) to give the title compound (6.32 g, 72%); ir (CH_2Cl_2): 1730, 1670 cm^{-1}; ^1H nmr ($CDCl_3$, δ ppm): 1.03 (9H, s, t-*Bu*Si), 1.44 (18H, s, t-*Bu*CO_2), 2.29 (2H, q, *J* = 8.0 Hz, $SiOCH_2CH_2$), 2.66 (2H, d, *J* = 7.5 Hz, CH_2CH(t-*Bu*)$_2CO_2$), 3.38 (3H, s, CH_2O*Me*), 3.48 (1H, t, *J* = 6.0 Hz, C*H*(t-*Bu*)$_2CO_2$), 3.61 (2H, t, *J* = 6.5 Hz, $SiOCH_2$), 4.77 (1H, t, *J* = 7.5 Hz, CH═COMOM), 4.85 (2H, s, OCH_2O), 7.35–7.50 (6H, m, *Ph*), 7.65–7.70 (4H, m, *Ph*).

Malonate ***31***: Yield: 74%; ir (film): 1740 cm^{-1}; ^1H nmr ($CDCl_3$, δ ppm): 1.05 (9H, s, t-*Bu*), 2.28 (2H, q, *J* = 7.0 Hz, $SiOCH_2CH_2$), 2.76 (2H, d, *J* = 7.5 Hz, C═C(OMOM)CH_2), 3.38 (3H, s, CH_2O*Me*), 3.61 (2H, t, *J* = 7.0 Hz, $SiOCH_2$), 3.69 (1H, t, *J* = 7.5 Hz, C*H*$(CO_2Me)_2$), 3.70 (6H, s, CO_2*Me*), 4.80 (1H, t, *J* = 7.0 Hz, C*H*═COMOM), 4.84 (2H, s, OCH_2O), 7.35–7.50 (6H, m, *Ph*), 7.65–7.70 (4H, m, *Ph*); ^{13}C nmr ($CDCl_3$, δ ppm): 19.13, 26.74, 29.21, 29.97, 49.56, 52.44, 55.85, 64.00, 93.60, 99.82, 127.56, 129.48, 133.85, 135.53, 150.75, 169.34; ms *m/e*: 483 (M^+ − MeO), 469 (M^+ − MOM), 457 ($M^+ - t$-Bu). HRMS ($M^+ - t$-Bu): 457.1682; found: 457.1680.

Method B

Malonate ***24***

To a suspension of sodium hydride (60% in oil, 0.70 g, 17.7 mmol) in tetrahydrofuran (38.2 mL) and *N,N* dimethylformamide (38.2 mL) at 0°C was added dimethyl malonate (2.12 mL, 18.6 mmol). The mixture was stirred at room temperature for 15 min, then added to a solution of the mesylate **23** (2.78 g, 3.54 mmol) and potassium iodide (0.58 g, 3.54 mmol) in tetrahydrofuran (100 mL). The mixture was heated at 80°C for 17 h. The reaction mixture was poured over saturated aqueous ammonium chloride and extracted with ether and hexane (2:1). Drying ($MgSO_4$) and removal of solvent gave the crude product that was purified by flash chromatography on silica gel (ethyl acetate – hexane, 1:9) to give the title compound (2.44 g, 79%); ir (CH_2Cl_2): 1735, 1665 cm^{-1}; ^1H nmr ($CDCl_3$, δ ppm): 1.04 (9H, s, t-*Bu*Si), 1.43 (18H, s, t-*Bu*CO_2), 1.75 (3H, s, *Me*C═C), 1.80–2.18 (4H, m, $(CH_2)_2$), 2.78 (4H, d, *J* = 10.5 Hz, $CH_2C(CO_2t$-Bu$)CH_2$), 3.29 (3H, s, CH_2O*Me*), 3.34 (1H, t, *J* = 6.5 Hz, C*H*$(CO_2Me)_2$), 3.72 (6H, s, CO_2*Me*), 4.20 (2H, d, *J* = 5.5 Hz, CH_2OSi), 4.65 (1H, t, *J* = 6.5 Hz, C*H*═COMOM), 4.76 (2H, s, OCH_2O), 5.62 (1H, dt, *J* = 5.5 Hz, 15.5 Hz, C*H*═CMe), 5.85 (1H, d, *J* = 11.0 Hz, $SiOCH_2CH$═CH), 6.39 (1H, dd, *J* = 11.0 Hz, 1.0 Hz, $SiOCH_2CH$═C*H*), 7.35–7.50 (6H, m, *Ph*), 7.65–7.70 (4H, m, *Ph*).

Malonate ***35***: Yield: 76%; ir (CH_2Cl_2): 2948, 1731, 1438, 1222, 1158 cm^{-1}; ^1H nmr ($CDCl_3$, δ ppm): 1.85–2.10 (4H, m, $(CH_2)_2CH(CO_2Me)_2$), 2.35–2.50 (4H, m, $(CH_2)_2CO_2$Me), 3.36 (1H, *J* = 7.0 Hz, C*H*$(CO_2Me)_2$), 3.36 (3H, s, CH_2O*Me*), 3.65 (3H, s, $CHCO_2$*Me*), 3.72 (6H, s, $CH(CO_2Me)_2$), 4.61 (1H, td, *J* = 7.5 Hz, 1.5 Hz, C*H*═COMOM), 4.85 (2H, s, OCH_2O); ^{13}C nmr ($CDCl_3$, δ ppm): 24.17, 25.01, 29.40, 31.59, 50.65, 51.31, 52.24, 55.63, 93.24, 100.08, 152.92, 169.57, 173.15; ms *m/e*: 300 (M^+ − MeO), 2.87 (M^+ − MOM). HRMS: (M^+ − MeO): 300.1209; found: 300.1215.

General procedure for the cleavage of silyl ethers

Alcohol ***14***

To a solution of the diester **13** (4.82 g, 8.22 mmol) in tetrahydrofuran (160 mL) was added tetrabutylammonium fluoride (1 M in tetrahydrofuran 9.19 mL, 9.19 mmol). The mixture was stirred at room temperature for 2 h. The solvent was removed and the residue purified by flash chromatography (ethyl acetate – hexane, 2:3) to give the title compound (2.59 g, 87%); ir (CH_2Cl_2): 3600, 3500, 1730, 1670 cm^{-1}; ^1H nmr

(CD_3Cl_3, δ ppm): 1.44 (18H, s, t-*Bu*CO_2), 2.70 (2H, d, *J* = 7.5 Hz, C=C(OMOM)CH_2), 3.39 (3H, s, CH_2OMe), 3.55 (1H, t, *J* = 7.5 Hz, C*H*(CO_2t-Bu)$_2$), 4.75 (1H, t, *J* = 7.5 Hz, C*H*=COMOM), 4.90 (2H, s, OCH_2O).

Alcohol ***25***: Yield: 85%; ir (CH_2Cl_2): 3600, 3500, 1735, 1665 cm^{-1}; ^1H nmr ($CDCl_3$, δ ppm): 1.44 (18H, s, t-*Bu*CO_2), 1.74 (3H, s, *Me*C=C), 1.85–2.00 (4H, m, (CH_2)$_2$CH(CO_2Me)$_2$), 2.78 (4H, d, *J* = 17.5 Hz, CH_2C (CO_2t-Bu)$_2$CH_2-), 3.35 (1H, t, *J* = 7.5 Hz, C*H*(CO_2Me)$_2$), 3.44 (3H, s, CH_2OMe), 3.74 (6H, s, CO_2Me), 4.15 (2H, br t, *J* = 5.5 Hz, CH_2OH), 4.59 (1H, t, *J* = 7.5 Hz, C*H*=COMOM), 4.83 (2H, s, OCH_2O), 5.67 (1H, dt, *J* = 15.0 Hz, 5.0 Hz, C*H*=CMe), 5.86 (1H, d, *J* = 11.0 Hz, C*H*CHCH=CMe), 6.43 (1H, dd, *J* = 10 Hz, 15 Hz, CH=C*H*CH=CMe).

Alcohol ***33***: Yield: 97%; ir (CH_2Cl_2): 3615, 3510, 2950, 1730, 1665 cm^{-1}; ^1H nmr ($CDCl_3$, δ ppm): 2.24 (2H, dt, *J* = 7.5 Hz, 6.5 Hz, HOCH_2CH_2), 2.34 (1H, s, O*H*), 2.45–2.50 (4H, m, C=C(OMOM)(CH_2)$_2$), 3.35 (3H, s, CH_2OMe), 3.55 (2H, t, *J* = 6.5 Hz, CH_2OH), 3.62 (3H, s, CO_2Me), 4.63 (1H, t, *J* = 7.5 Hz, CH=COMOM), 4.86 (2H, s, OCH_2O); ^{13}C nmr ($CDCl_3$, δ ppm): 25.07, 30.12, 31.45, 51.52, 55.84, 62.58, 93.35, 97.92, 153.74, 173.58; ms *m/e*: 200 ($M^+ - H_2O$), 187 (M^+ − MeO). HRMS ($M^+ - H_2O$): 200.1049; found: 200.1047.

Diol ***39***: Yield: 80%; ir (CH_2Cl_2): 3470, 2950, 1735, 1665 cm^{-1}; ^1H nmr ($CDCl_3$, δ ppm): 1.79 (3H, s, *Me*C=C), 1.90–2.05 (4H, m, (CH_2)$_2$), 2.20 (1H, br, CHO*H*), 2.54 (1H, dd, *J* = 14.0 Hz, 10.5 Hz, C=C(OMOM)C*H*H), 2.68 (1H, dd, *J* = 14.0 Hz, 4.0 Hz, C=C(OMOM)CH*H*), 2.71 (1H, br, CH_2OH), 2.87 (1H, ddd, *J* = 10.5 Hz, 9.0 Hz, 4.0 Hz, C*H*CO_2Me), 3.35 (3H, s, CH_2OMe), 3.37 (1H, t, *J* = 7.0 Hz, C*H*(CO_2Me)$_2$), 3.52 (3H, s, CHCO_2Me), 3.72 (6H, s, CH(CO_2Me)$_2$), 4.16 (2H, d, *J* = 5.5 Hz, CH_2OH), 4.67 (1H, t, *J* = 7.0 Hz, C*H*=COMOM), 4.75 (1H, d, *J* = 9.0 Hz, C*H*OH), 4.82 and 4.84 (2H, AB, *J* = 6.5 Hz, OCH_2O), 5.72 (1H, dt, *J* = 15.0 Hz, 5.5 Hz, C*H*=CHCH=CMe), 5.90 (1H, d, *J* = 11.0 Hz, C*H*=CMe), 6.52 (1H, dd, *J* = 15.0 Hz, 11.0 Hz, CH=C*H*CH=CMe); ^{13}C nmr ($CDCl_3$, δ ppm): 17.73, 24.29, 29.40, 29.52, 49.13, 50.86, 51.43, 52.46, 55.75, 62.96, 70.26, 93.47, 101.09, 125.80, 127.69, 132.20, 136.92, 152.59, 169.85, 173.38; ms *m/e*: 440 ($M^+ - H_2O$). HRMS ($M^+ - H_2O$): 440.2046; found: 440.2043.

Diol ***40***: Yield 88%; ir (CH_2Cl_2): 3500, 2962–2852, 1734, 1666, 1435, 1260, 1093, 1019 cm^{-1}; ^1H nmr ($CDCl_3$, δ ppm): 1.60 (1H, br, CH_2OH), 1.78 (3H, s, *Me*C=C), 1.80–2.05 (4H, m, (CH_2)$_2$), 2.06 (1H, dd, *J* = 14.0 Hz, 4.5 Hz, C=C(OMOM)C*H*H), 2.28 (1H, br, CHO*H*), 2.36 (1H, dd, *J* = 14.0 Hz, 10.0 Hz, C=C(OMOM)CH*H*), 2.90 (1H, ddd, *J* = 10.0 Hz, 9.0 Hz, 4.5 Hz, C*H*CO_2Me), 3.34 (1H, t, *J* = 7.0 Hz, C*H*(CO_2Me)$_2$), 3,37 (3H, s, CH_2OMe), 3.68 (3H, s, CHCO_2Me), 3.71 (3H, s, C*H*(CO_2Me)$_2$), 3.72 (3H, s, CH(CO_2Me)$_2$), 4.19 (2H, d, *J* = 5.0 Hz, CH_2OH), 4.65 (1H, t, *J* = 7.5 Hz, C*H*=COMOM), 4.84 and 4.87 (2H, AB, *J* = 6.5 Hz, OCH_2O), 4.91 (1H, dd, *J* = 9.0 Hz, 4.0 Hz, C*H*OH), 5.82 (1H, dt, *J* = 15.0 Hz, 5.0 Hz, C*H*=CHCH=CMe), 6.04 (1H, d, *J* = 11.0 Hz, C*H*=CMe), 6.57 (1H, dd, *J* = 15.0 Hz, 11.0 Hz, CH=C*H*CH=CMe); ^{13}C nmr ($CDCl_3$, δ ppm): 17.53, 24.28, 29.34, 29.52, 47.70, 50.91, 51.79, 52.54, 55.87, 63.05, 70.45, 93.60, 101.26, 125.07, 129.02, 133.14, 136.34, 151.75, 169.84, 169.92, 175.16; ms *m/e*: 440 ($M^+ - H_2O$).

General procedure for the preparation of benzoates

Method A

Benzoate ***15***

To a solution of the alcohol **14** (2.46 g, 6.85 mmol) in anhydrous pyridine (12.0 mL) at 0°C was added benzoyl chloride (1.75 mL, 14.95 mmol). The mixture was stirred at room temperature for 3 h. The reaction mixture was extracted with dichloromethane and the organic layer was washed with saturated aqueous sodium bicarbonate. Drying ($MgSO_4$) and removal of the solvent gave an oily residue that was purified by flash chromatography (hexane – ethyl acetate, 4:1) to give the title compound (2.50 g, 79%); ir (CH_2Cl_2): 1725, 1670 cm^{-1}; ^1H nmr ($CDCl_3$δ ppm): 1.45 (18H, s, t-*Bu*CO_2), 2.51 (2H, q, *J* = 7.0 Hz, OCH_2CH_2), 2.73 (2H, d, *J* = 7.5 Hz, CH_2CH(CO_2t-Bu)$_2$), 3.39 (3H, s, CH_2OMe), 3.52 (1H, t, *J* = 7.5 Hz, C*H*(CO_2t-Bu)$_2$), 4.27 (2H, t, *J* = 7.0 Hz, BzOCH_2), 4.82 (1H, t, *J* = 7.5 Hz, C*H*=COMOM), 4.89 (2H, s, OCH_2O), 7.25–7.55 (3H, m, *Ph*), 8.03 (2H, m, *Ph*).

Method B

Benzoate ***41***

To a solution of the diol **39** (101 mg, 0.22 mmol) and pyridine (358 μL, 4.42 mmol) in dichloromethane (0.5 mL) at 0°C was added benzoyl chloride (27 μL, 0.23 mmol). The mixture was stirred at 0°C for 2 h, then treated with saturated aqueous sodium bicarbonate and extracted with dichloromethane. The organic extract was dried ($MgSO_4$) and the solvent was removed under reduced pressure. The crude product was purified by chromatography on silica gel (hexane – ethyl acetate, 4:1 to pure ethyl acetate) to afford the title compound (90 mg, 72%); ir (CH_2Cl_2): 1735, 1665, 1437 cm^{-1}; ^1H nmr ($CDCl_3$, δ ppm): 1.83 (3H, s, *Me*C=C), 1.90–2.10 (4H, m, (CH_2)$_2$), 2.38 (1H, d, *J* = 4.5 Hz, O*H*), 2.57 (1H, dd, *J* = 14.0 Hz, 10.5 Hz, C=C(OMOM)C*H*H), 2.70 (1H, dd, *J* = 14.0 Hz, 4.0 Hz, C=C(OMOM)CH*H*), 2.88 (1H, ddd, *J* = 10.0 Hz, 9.0 Hz, 4.0 Hz, C*H*CO_2Me), 3.37 (3H, s, CH_2OMe), 3.39 (1H, t, *J* = 7.0 Hz, C*H*(CO_2Me)$_2$), 3.54 (3H, s, CHCO_2Me), 3.74 (6H, s, CH(CO_2Me)$_2$), 4.70 (1H, t, *J* = 7.0 Hz, C*H*=COMOM), 4.79 (1H, dd, *J* = 9.5 Hz, 4.0 Hz, C*H*OH), 4.84 and 4.86 (2H, d, *J* = 6.5 Hz, OCH_2O), 4.85 (2H, d, 6.5 Hz, CH_2OBz), 5.79 (1H, dt, *J* = 15.0 Hz, 6.5 Hz, C*H*=CHCH=CMe), 5.95 (1H, d, *J* = 11.0 Hz, C*H*=CMe), 6.68 (1H, dd, *J* = 15.0 Hz, 11.0 Hz, CH=C*H*CH=CMe), 7.44 (2H, m, *Ph*), 7.56 (1H, m, *Ph*), 8.03 (2H, m, *Ph*); ^{13}C nmr ($CDCl_3$, δ ppm): 17.87, 24.28, 29.31, 29.50, 49.32, 50.82, 51.32, 52.38, 55.73, 65.24, 70.35, 93.48, 101.14, 126.36, 127.25, 128.22, 129.39, 132.84, 138.53, 152.54, 166.21, 169.74, 172.85; ms *m/e*: 530 (M^+ − MeOH). HRMS (M^+ − MeOH): 530.2152; found: 530.2135.

Benzoate ***42***: Yield: 69%; ir (CH_2Cl_2): 1735, 1665 cm^{-1}; ^1H nmr ($CDCl_3$, δ ppm): 1.81 (3H, s, *Me*C=C), 1.93 (4H, m, (CH_2)$_2$), 2.11 (1H, dd, *J* = 14.0 Hz, 4.5 Hz, C=C(OMOM)C*H*H), 2.36 (1H, br, O*H*), 2.40 (1H, dd, *J* = 14.0 Hz, 10.0 Hz, C=C(OMOM)CH*H*), 2.91 (1H, ddd, *J* = 10.0 Hz, 9.0 Hz, 4.5 Hz, C*H*CO_2Me), 3.34 (1H, t, *J* = 7.0 Hz, C*H*(CO_2Me)$_2$), 3.37 (3H, s, CH_2OMe), 3.70 (3H, s, CHCO_2Me), 3.71 (6H, s, CH(CO_2Me)$_2$), 4.67 (1H, t, *J* = 7.0

Hz, C*H*=COMOM), 4.83 and 4.86 (2H, AB, J = 7.0 Hz, OCH_2O), 4.85–4.95 (3H, m, CH_2OBz and C*H*OH), 5.86 (1H, dt, J = 15.0 Hz, 6.5 Hz, C*H*=CHCH=CMe), 6.06 (1H, d, J = 11.5 Hz, C*H*=CMe), 6.69 (1H, dd, J = 15.0 Hz, 11.5 Hz, CH=C*H*CH=CMe), 7.44 (2H, m, *Ph*), 7.56 (1H, m, *Ph*), 8.04 (2H, m, *Ph*); ^{13}C nmr ($CDCl_3$, δ ppm): 17.67, 24.27, 29.32, 29.45, 47.73, 50.81, 51.73, 52.36, 55.74, 65.24, 70.30, 93.54, 101.36, 127.15, 128.34, 128.52, 128.94, 129.50, 132.89, 136.16, 151.50, 166.22, 169.65, 174.95; ms *m/e*: 530 (M^+ − MeOH). HRMS (M^+ − MeOH): 530.2152; found: 530.2135.

Aldehyde 17

To a solution of the alcohol **16** (12.22 g, 37.46 mmol) in tetrahydrofuran at 0°C was added sodium acetate (9.21 g, 112.4 mmol) and pyridinium chlorochromate (12.11 g, 56.1 mmol). The mixture was stirred at 25°C for 2 h, diluted in ether, and filtered on Florisil. Flash chromatography (ethyl acetate – hexane, 1:4) of the residue after removal of solvent provided the title compound (5.80 g, 48%); ir (CH_2Cl_2): 1685 cm^{-1}; ^{1}H nmr ($CDCl_3$, δ ppm): 1.08 (9H, s, t-*Bu*Si), 4.45 (2H, m, SiOCH_2), 6.58 (1H, ddt, J = 15.0 Hz, 8.0 Hz, 3.0 Hz, CH=C*H*CH=O), 6.85 (1H, dt, J = 15.0 Hz, 3.0 Hz, C*H*=CHCH=O), 7.25–7.70 (10H, m, Ph), 9.61 (1H, d, J = 8.0 Hz, C*H*O).

Diene 18

To a solution of trifluoroethylphosphinate (6.2 g, 17.9 mmol) (11*b*) and 18-crown-6-ether (4.73 g, 17.9 mmol) in tetrahydrofuran (206 mL) at −78°C was added potassium bis-trimethylsilyl amide (0.5 M in toluene; 35.8 mL, 0.0179 mol). The mixture was stirred for 10 min at −78°C. A solution of the aldehyde **17** (5.80 g, 17.9 mmol) in tetrahydrofuran (10 mL) was slowly added over 30 min. The mixture was poured onto saturated aqueous ammonium chloride, then extracted with ether. Drying ($MgSO_4$) and removal of solvent under reduced pressure gave a crude product that was purified by flash chromatography (ethyl acetate – hexane, 1:9) to give the title compound (7.30 g, 100%); ir (film): 1710 cm^{-1}; ^{1}H nmr ($CDCl_3$, δ ppm): 1.07 (9H, s, t-*Bu*Si), 1.28 (3H, t, J = 7.0 Hz, OCH$_2$*Me*), 1.98 (3H, s, *Me*C=C), 4.22 (2H, q, J = 7.0 Hz, CO$_2$CH_2Me), 4.30 (2H, d, J = 4.5 Hz, CH_2OSi, C*H*=C(Me)CO$_2$Et), 5.96 (1H, dt, J = 15 Hz, 5.0 Hz, SiOCH$_2$C*H*=CH), 6.45 (1H, d, J = 11.5 Hz, C*H*=CMe), 7.25–7.50 (7H, m, SiOCH$_2$CH=C*H* and *Ph*), 7.65–7.75 (4H, m, *Ph*); ^{13}C nmr ($CDCl_3$, δ ppm): 14.29, 19.20, 20.81, 26.75, 60.27, 64.03, 126.59, 127.65, 129.64, 133.43, 134.76, 135.48, 135.77, 138.67, 167.72; ms *m/e*: 408 (M^+). HRMS (M^+): 408.2121; found: 408.2128.

Triene 21

To a suspension of sodium hydride (60% in oil, 0.20 g, 5.1 mmol) in *N,N*-dimethylformamide (9.5 mL) was added a solution of the benzoate **15** (2.40 g, 5.16 mmol) in tetrahydrofuran (18 mL). The mixture was stirred at room temperature for 30 min and a solution of the allylic chloride **20** (1.99 g, 5.10 mmol) in tetrahydrofuran (7 mL) was added. The reaction mixture was stirred at room temperature for 3 h, poured onto saturated aqueous ammonium chloride, and extracted 3 times with dichloromethane. Drying ($MgSO_4$) and removal of the solvent under reduced pressure afforded an oil that was purified by flash chromatography (ethyl acetate – hexane, 1:19) to give the title compound (3.68 g, 88%); ir (CH_2Cl_2): 1720, 1670 cm^{-1}; ^{1}H nmr ($CDCl_3$, δ ppm): 1.04 (9H, s, t-*Bu*Si), 1.44 (18H, s, t-*Bu*CO$_2$), 1.78 (3H, s, *Me*C=C), 2.38 (2H, q, J = 7.0 Hz, BzOCH$_2$CH_2), 2.85 (4H, d, J = 8.5 Hz, CH_2C(CO$_2$*t*-Bu)$_2$CH_2), 3.29 (3H, s, CH$_2$O*Me*), 4.15–4.30 (4H, m, BzOCH_2 and SiOCH_2), 4.78 (1H, t, J = 7.5 Hz, C*H*=COMOM), 4.78 (2H, s, OCH_2O), 5.63 (1H, dt, J = 15.0 Hz, 5.0 Hz, C*H*=CMe), 5.88 (1H, d, J = 10.0 Hz, C*H*=CHCH=CMe), 6.44 (1H, dd, J = 15.0 Hz, 10.0 Hz, CH=C*H*CH=CMe), 7.30–7.75 12H, m, *Ph*), 8.00–8.05 (3H, m, *Ph*).

General procedure for the cleavage of benzoates

Alcohol 22

To a solution of the diester **21** (3.68 g, 4.53 mmol) in methanol (20 mL) was added potassium carbonate (59 mg, 0.36 mmol). After stirring at room temperature for 24 h, the resulting mixture was poured over water and extracted 3 times with dichloromethane. Drying ($MgSO_4$) and removal of solvent under reduced pressure yielded an oil that was purified by flash chromatography (ethyl acetate – hexane, 1:9 to 3:7) to give the title compound (2.67 g, 83%); ir (CH_2Cl_2): 3600, 1730, 1660 cm^{-1}; ^{1}H nmr ($CDCl_3$, δ ppm): 1.05 (9H, s, (t-*Bu*Si), 1.44 (18H, s, t-*Bu*CO$_2$), 1.77 (3H, s, *Me*C=C), 2.18 (2H, q, J = 6.5 Hz, HOCH$_2$CH_2), 2.82 (2H, d, J = 3.0 Hz, CH_2C(CO$_2$*t*-Bu)$_2$CH_2), 3.31 (3H, s, CH$_2$O*Me*), 3.53 (2H, m, CH_2OH), 4.20 (2H, d, J = 5.5 Hz, CH_2OSi), 4.69 (1H, t, J = 7.5 Hz, C*H*=COMOM), 4.79 (2H, s, OCH_2O), 5.63 (1H, dt, J = 15.0 Hz, 5.0 Hz, C*H*=CMe), 5.87 (1H, d, J = 11.0 Hz, C*H*=CHCH=CMe), 6.43 (1H, dd, J = 15.0 Hz, 10.0 Hz, CH=C*H*CH=CMe), 7.35–7.45 (6H, m, *Ph*), 7.65–7.75 (4H, m, *Ph*).

Alcohol 45: Yield: 76%; ir (film): 3460, 2960–2860, 1735, 1665 cm^{-1}; ^{1}H nmr ($CDCl_3$, δ ppm): −0.02 (3H, s, Si*Me*), 0.09 (3H, s, Si*Me*), 0.89 (9H, s, t-*Bu*Si), 1.69 (1H, br, O*H*), 1.77 (3H, s, *Me*C=C), 1.99 (4H, m, (CH_2)$_2$), 2.45 (1H, dd, J = 14.0 Hz, 11.5 Hz, C=C(OMOM)C*H*H), 2.62 (1H, dd, J = 14.0 Hz, 3.5 Hz, C=C(OMOM)CH*H*), 2.85 (1H, ddd, J = 11.5 Hz, 9.5 Hz, 3.5 Hz, C*H*CO$_2$Me), 3.36 (3H, s, CH$_2$O*Me*), 3.38 (1H, t, J = 7.5 Hz, C*H*(CO$_2$Me)$_2$), 3.49 (3H, s, CHCO$_2$*Me*), 3.74 (6H, s, CH(CO$_2$*Me*)$_2$), 4.19 (2H, d, J = 5.5 Hz, CH_2OH), 4.65 (1H, t, J = 7.5 Hz, C*H*=COMOM), 4.67 (1H, d, J = 9.5 Hz, C*H*OSi), 4.82 and 4.85 (2H, AB, J = 6.5 Hz, OHC*H*O), 5.72 (1H, dt, J = 15.0 Hz, 6.0 Hz, C*H*=CHCH=CMe), 5.84 (1H, d, J = 11.0 Hz, C*H*=CMe), 6.48 (1H, dd, J = 15.0 Hz, 11.0 Hz, CH=C*H*CH=CMe); ^{13}C nmr ($CDCl_3$, δ ppm): −4.98, −4.76, 17.76, 17.99, 24.34, 25.66, 29.49, 29.85, 50.08, 51.00, 51.24, 52.39, 55.73, 63.34, 71.25, 93.48, 101.10, 126.21, 126.90, 131.94, 138.05, 152.60, 169.76, 172.92; ms *m/e*: 515 (M^+ − *t*-Bu). HRMS (M^+ − *t*-Bu): 515.2312; found: 515.2297.

Alcohol 46: Yield: 86%; ir (film): 2930–2850, 1735, 1665 cm^{-1}; ^{1}H nmr ($CDCl_3$, δ ppm): −0.05 (3H, s, Si*Me*), 0.04 (3H, s, Si*Me*), 0.82 (9H, s, t-*Bu*Si), 1.62 (1H, br, O*H*), 1.76 (3H, s, *Me*C=C), 1.80–2.15 (5H, m, (CH_2) and C=C(OMOM)C*H*H), 2.31 (1H, dd, J = 14.0 Hz, 12.0 Hz, C=C(OMOM)CH*H*), 2.90 (1H, ddd, J = 12.0 Hz, 10.0 Hz, 3.5 Hz, C*H*CO$_2$Me), 3.34 (1H, t, J = 6.5 Hz, C*H*(CO$_2$*Me*)$_2$), 3.37 (3H, s, CH$_2$O*Me*), 3.64 (3H, s, CHCO$_2$*Me*), 3.72 (3H, s, CH(CO$_2$*Me*)$_2$), 3.74 (3H, s, CH(CO$_2$*Me*)$_2$), 4.23 (2H, d, J = 5.5 Hz, CH_2OH), 4.64 (1H, t, J = 7.0 Hz, C*H*=COMOM), 4.80 and 4,83 (2H, AB, J = 6.5 Hz, OCH_2O), 4.84 (1H, d, J =

10.0 Hz, C*H*OSi, 5.83 (1H, dt, *J* = 15.0 Hz, 5.5 Hz, C*H*=CHCH=CMe), 6.01 (1H, d, *J* = 11.0 Hz, C*H*=CMe), 6.60 (1H, dd, *J* = 15.0 Hz, 11.5 Hz, CH=C*H*CH=CMe); ^{13}C nmr ($CDCl_3$, δ ppm): −5.48, −4.86, 17.89, 24.24, 25.51, 29.13, 29.56, 49.13, 50.90, 51.39, 52.55, 55.74, 63.25, 71.71, 93.65, 100.96, 125.59, 133.03, 137.06, 152.25, 169.88, 170.01, 174.69; ms *m/e*: 515 (M^+ − *t*-Bu). HRMS (M^+ − *t*-Bu): 515.2312; found: 515.2297.

General procedure for the preparation of mesylates

Mesylate 23

To a stirred solution of the alcohol **22** (2.51 g, 3.54 mmol) and pyridine (2.20 mL, 16.02 mmol) in dichloromethane (60 mL) at 0°C was added methanesulfonyl chloride (0.28 mL, 3.70 mmol). The mixture was stirred for 30 min, then quenched with ice and extracted with dichloromethane. Drying ($MgSO_4$) and removal of solvent afforded the crude product, which was filtered on Florisil (ethyl acetate – hexane, 3:7) to give the title compound (2.78 g, 100%), which was used in the next step without further purification; ir (CH_2Cl_2): 1725, 1660 cm^{-1}; ^{1}H nmr ($CDCl_3$, δ ppm): 1.05 (9H, s, t-*Bu*Si), 1.44 (18H, s, t-*Bu*CO_2), 1.76 (3H, s, *Me*C=C), 2.34 (2H, q, *J* = 7.5 Hz, MsOCH$_2$C*H*$_2$), 2.79 (4H, d, *J* = 6.5 Hz, C*H*$_2$C(CO$_2$*t*-Bu)$_2$C*H*$_2$), 2.94 (3H, s, *Ms*), 3.29 (3H, s, CH$_2$O*Me*), 4.09 (2H, t, *J* = 8.0 Hz, MsOC*H*$_2$), 4.20 (2H, d, *J* = 5.0 Hz, SiOC*H*$_2$), 4.65 (1H, t, *J* = 7.5 Hz, C*H*=COMOM), 4.77 (2H, s, OC*H*$_2$O), 5.63 (1H, dt, *J* = 15.0 Hz, 5.0 Hz, C*H*=CMe), 5.87 (1H, d, *J* = 11.0 Hz, C*H*=CHCH=CMe), 6.41 (1H, dd, *J* = 15.0 Hz, 10.0 Hz (CH=C*H*CH=CMe), 7.35–7.45 (6H, m, *Ph*), 7.65–7.75 (4H, m, *Ph*).

Mesylate 34: Yield 99%; ^{1}H nmr ($CDCl_3$, δ ppm): 2.48 (6H, m, C*H*$_2$CH=C(OMOM)(C*H*$_2$)$_2$), 2.99 (3H, s, *Ms*), 3.36 (3H, s, CH$_2$O*Me*), 3.66 (3H, s, CO$_2$*Me*), 4.16 (2H, t, *J* = 7.0 Hz, MsOC*H*$_2$), 4.65 (1H, t, *J* = 7.5 Hz, C*H*=COMOM), 4.88 (2H, s, OC*H*$_2$O).

Acetate 27

To a solution of the alcohol **25** (42 mg, 72 μmol) in pyridine (20 mL) was added acetic anhydride (1.0 mL). The mixture was stirred at 0°C for 24 h. The solvent was evaporated and the residue purified by flash chromatography (ethyl acetate – hexane, 3:17) to give the title compound (43 mg, 96%); ir (CH_2Cl_2): 1735, 1660 cm^{-1}; ^{1}H nmr ($CDCl_3$, δ ppm): 1.44 (18H, s, t-*Bu*CO_2), 1.75 (3H, s, *Me*C=C), 1.9–2.0 (4H, m, (C*H*$_2$)$_2$CH(CO$_2$Me)$_2$), 2.05 (3H, s, *Ac*), 2.78 (4H, d, *J* = 14.0 Hz, C*H*$_2$C(CO$_2$*t*-Bu)$_2$C*H*$_2$), 3.36 (1H, t, *J* = 7.5 Hz, C*H*(CO$_2$Me)$_2$), 3.40 (3H, s, CH$_2$O*Me*), 3.74 (6H, s, CO$_2$*Me*), 4.57 (2H, d, *J* = 7.0 Hz, AcOC*H*$_2$), 4.66 (1H, t, *J* = 7.5 Hz, C*H*=COMOM), 4.83 (2H, s, OC*H*$_2$O), 5.58 (1H, dt, *J* = 15.0 Hz, 7.0 Hz, C*H*=CMe), 5.85 (1H, d, *J* = 10.0 Hz, C*H*=CHCH=CMe), 6.51 (1H, dd, *J* = 15.0 Hz, 11.0 Hz, CH=C*H*CH=CMe).

Pivaloate 28

To a solution of the alcohol **25** (0.80 g, 1.40 mmol) in dichloromethane (5.5 mL) at 0°C were added pyridine (3.31 mL, 6.87 mmol) and trimethylacetylchloride (251 μL, 1.80 mmol). The mixture was stirred at room temperature for 3 h, then washed with satured aqueous ammonium chloride. Drying ($MgSO_4$) and removal of solvent under reduced pressure gave the crude product, which was purified by flash chromatography on silica gel (ethyl acetate – hexane, 3:7) to give the title compound (0.74 g, 80%); ir (CH_2Cl_2): 1735, 1660 cm^{-1}; ^{1}H nmr ($CDCl_3$, δ ppm): 1.19 (9H, s, *piv*), 1.43 (18H, s, t-*Bu*CO_2), 1.76 (3H, s, *Me*C=C), 1.85–2.00 (4H, m, (C*H*$_2$)$_2$ CH(CO$_2$Me)$_2$), 2.79 (4H, d, *J* = 14.0 Hz, C*H*$_2$C(CO$_2$*t*-Bu)$_2$C*H*$_2$), 3.37 (1H, t, *J* = 6.5 Hz, C*H*(CO$_2$Me)$_2$), 3.39 (3H, s, CH$_2$O*Me*), 3.74 (6H, s, CO$_2$*Me*), 4.56 (2H, d, *J* = 7.0 Hz, C*H*$_2$O piv), 4.68 (1H, t, *J* = 6.5 Hz, C*H*=COMOM), 4.82 (2H, s, OC*H*$_2$O), 5.59 (1H, dt, *J* = 15.0 Hz, 5.0 Hz, C*H*=CMe), 5.86 (1H, d, *J* = 11.0 Hz, C*H*=CHCH=CMe), 6.51 (1H, dd, *J* = 15.0 Hz, 10.0 Hz, CH=C*H*CH=CMe).

Ester 32

To a solution of the malonate **31** (2.8 g, 5.4 mmol) in dimethyl sulfoxide (55 mL) was added sodium cyanide (530 mg, 10.8 mmol). The mixture was stirred for 64 h at 90°C, then extracted with hexane and ether (1:1). The combined organic extract was dried ($MgSO_4$), solvent was removed under reduced pressure, and the residue was purified by flash column chromatography (hexane – ethyl acetate, 19:1) to yield the title compound (2.6 g, 67%); ir (film): 3055, 2950–2860, 1740, 1670 cm^{-1}; ^{1}H nmr ($CDCl_3$, δ ppm): 1.11 (9H, s, Si*t*-Bu), 2.30 (2H, dt, *J* = 7.5 Hz, 7.0 Hz, SiOCH$_2$C*H*$_2$), 2.48 (4H, m, *J* = 7.5 Hz, (C*H*$_2$)$_2$CO$_2$Me), 3.39 (3H, s, CH$_2$O*Me*), 3.65 (2H, t, *J* = 7.0 Hz, SiOC*H*$_2$), 3.67 (3H, s, CO$_2$*Me*), 4.72 (1H, t, *J* = 7.5 Hz, C*H*=COMOM), 4.87 (2H, s, OC*H*$_2$O), 7.35–7.50 (6H, m, *Ph*), 7.70–7.80 (4H, m, *Ph*); ^{13}C nmr ($CDCl_3$, δ ppm): 18.97, 25.34, 26.53, 30.11, 31.99, 51.52, 55.85, 64.16, 93.42, 98.13, 127.66, 129.59, 133.89, 135.56, 153.23, 173.54; ms *m/e*: 425 (M^+ − MeO), 411 (M^+ − MOM), 399 (M^+ − *t*-Bu). HRMS (M^+ − *t*-Bu): 399.1628; found: 399.1618.

Aldehyde 36

To a solution of the alcohol **19** (558 mg, 1.52 mmol) in dichloromethane (4 mL) and pentane (16 mL) at room temperature was added manganese dioxide (199 mg, 22.84 mmol). The resulting mixture was stirred for 2 h, then more manganese dioxide (662 mg, 76.13 mmol) was added. The mixture was stirred for another 2 h, then filtered on Celite. Solvent was removed under reduced pressure and the residue was purified by chromatography on silica gel (hexane – ethyl acetate, 24:1) to give the title compound (478 mg, 86%); ^{1}H nmr ($CDCl_3$, δ ppm): 1.09 (9H, s, t-*Bu*Si), 1.86 (3H, s, *Me*C=C), 4.36 (2H, d, *J* = 5.0 Hz, C*H*$_2$OSi), 6.06 (1H, dt, *J* = 15.0 Hz, 5.0 Hz, SiOCH$_2$C*H*=CH), 6.96 (1H, d, *J* = 11.0 Hz, C*H*=CMeCHO), 7.25–7.45 (7H, m, *Ph*, SiOCH$_2$CH=C*H*), 7.65–7.70 (4H, m, *Ph*), 10.28 (1H, s, C*H*O); ms *m/e*: 307 (M^+ − *t*-Bu).

Aldols 37 and 38

To a solution of diisopropylamine (0.25 mL, 1.80 mmol) in tetrahydrofuran (1.5 mL) at −78°C was added *n*-butyllithium (1.6 M in tetrahydrofuran, 1.1 mL, 1.74 mmol). The solution was stirred at 0°C for 20 min, then cooled to −78°C. The triester **35** (232 mg, 0.70 mmol) in tetrahydrofuran (0.5 mL) was added, and the reaction mixture stirred for 30 min at −78°C. The aldehyde **36** (509 mg, 1.40 mmol) in tetrahydrofuran was added and the reaction mixture stirred for another 30 min at −78°C. The reaction was quenched with saturated aqueous ammonium chloride, and extracted 3 times with dichlo-

romethane. The organic extract was dried ($MgSO_4$) and the solvent was removed under reduced pressure. The crude product was purified by chromatography on silica gel (hexane – ethyl acetate, 17:3 to 3:1) to afford the title compounds (overall yield: 286 mg, 59%; *erythro* isomer **37**: 42% of the mixture, *threo* isomer **38**: 58% of the mixture).

Aldol ***37***: ir (film): 3010, 2950–2850, 1735, 1665 cm^{-1}; ^1H nmr ($CDCl_3$, δ ppm): 1.07 (9H, s, t-*Bu*Si), 1.82 (3H, s, *Me*C=C), 1.85–2.05 (4H, m, $(CH_2)_2$), 2.29 (1H, d, J = 4.5 Hz, CHO*H*), 2.57 (1H, dd, J = 14.0 Hz, 10.5 Hz, C=C(OMOM)C*H*H), 2.69 (1H, dd, J = 14.0 Hz, 4.0 Hz, C=C(OMOM)CH*H*), 2.89 (1H, ddd, J = 10.5 Hz, 9.0 Hz, 4.0 Hz, C*H*CO_2Me), 3.37 (3H, s, CH_2O*Me*), 3.38 (1H, t, J = 7.0 Hz, C*H*$(CO_2Me)_2$), 3.53 (3H, s, $CHCO_2$*Me*), 3.72 (6H, s, C*H*$(CO_2Me)_2$), 4.25 (2H, d, J = 5.0 Hz, SiOCH_2), 4.69 (1H, t, J = 7.0 Hz, C*H*=COMOM), 4.77 (1H, dd, J = 9.0 Hz, 4.5 Hz, C*H*OH), 4.84 and 4.86 (2H, AB, J = 7.0 Hz, OCH_2-O), 5.69 (1H, dt, J = 15.0 Hz, 5.0 Hz, C*H*=CHCH=CMe), 5.93 (1H, d, J = 11.3 Hz, C*H*=CMe), 6.58 (1H, dd, J = 15.0 Hz, 11.5 Hz, CH=C*H*CH=CMe), 7.25–7.45 (6H, m, *Ph*), 7.65–7.70 (4H, m, *Ph*); ^{13}C nmr ($CDCl_3$, δ ppm): 17.93, 19.23, 24.42, 26.79, 29.35, 29.65, 49.56, 50.95, 51.41, 52.50, 55.88, 64.20, 70.64, 93.64, 101.22, 124.69, 127.66, 128.14, 129.63, 132.38, 133.64, 135.51, 136.01, 152.74, 169.86, 173.04; ms *m/e*: 696 (M^+), 639 (M^+ – *t*-Bu). HRMS (M^+ – *t*-Bu): 639.2625; found: 639.2635.

Aldol ***38***: ir (film): 3506, 3070, 2950–2850, 1755, 1670 cm^{-1}; ^1H nmr ($CDCl_3$, δ ppm): 1.08 (9H, s, t-*Bu*Si), 1.79 (3H, s, *Me*C=C), 1.80–2.05 (4H, m, $(CH_2)_2$), 2.06 (1H, dd, J = 14.0 Hz, 4.0 Hz, C=C(OMOM)C*H*H), 2.17 (1H, d, J = 4.5 Hz, CHO*H*), 2.39 (1H, dd, J = 14.0 Hz, 11.0 Hz, C=C(OMOM)CH*H*), 2.87 (1H, ddd, J = 11.0 Hz, 9.0 Hz, 4.0 Hz, C*H*CO_2Me), 3.31 (1H, t, J = 7.0 Hz, C*H*$(CO_2Me)_2$), 3.35 (3H, s, CH_2O*Me*), 3.69 (9H, s, CO_2Me), 4.26 (2H, d, J = 5.0 Hz, SiOCH_2), 4.66 (1H, t, J = 7.0 Hz, C*H*=COMOM), 4.81 and 4.84 (2H, AB, J = 7.0 Hz, OCH_2O), 4.86 (1H, dd, J = 9.0 Hz, 4.0 Hz, C*H*OH), 5.75 (1H, dt, J = 15.0 Hz, 5.0 Hz, C*H*=CHCH=CMe), 6.04 (1H, d, J = 11.3 Hz, C*H*=CMe), 6.58 (1H, dd, J = 15.0 Hz, 11.3 Hz, CH=C*H*CH=CMe), 7.25–7.45 (6H, m, *Ph*), 7.65–7.70 (4H, m, *Ph*); ^{13}C nmr ($CDCl_3$, δ ppm): 17.47, 19.16, 24.32, 26.75, 29.46, 29.53, 47.94, 50.88, 51.71, 52.37, 55.72, 64.15, 70.56, 93.56, 101.32, 124.21, 127.63, 129.35, 129.62, 133.02, 133.49, 135.44, 135.62, 151.65, 169.65, 174.90; ms *m/e*: 696 (M^+), 639 (M^+ – *t*-Bu). HRMS (M^+ – *t*-Bu): 639.2625; found: 639.2635.

General procedure for the preparation of silyl ether

Silyl ether ***43***

A solution of the alcohol **41** (9 mg, 16 μmol), triethylamine (6.9 μL, 48 μmol), and *tert*-butyldimethylsilyl triflate (8.8 mL, 38 μmol) was stirred at 0°C for 30 min, then treated with saturated aqueous ammonium chloride and extracted with dichloromethane. The organic extract was dried ($MgSO_4$) and the solvent was removed under reduced pressure. The residue was filtered on silica gel (ethyl acetate) to give the title compound (11 mg, 100%); ir (film): 1735, 1665 cm^{-1}; ^1H nmr ($CDCl_3$, δ ppm): −0.27 (3H, s, Si*Me*), 0.07 (3H, s, Si*Me*), 0.88 (9H, s, t-*Bu*Si), 1.77 (3H, s, *Me*C=C), 1.90–2.10 (4H, m, $(CH_2)_2$), 2.43 (1H, dd, J = 14.0 Hz, 11.5 Hz, C=C(OMOM)C*H*H), 2.62 (1H, dd, J = 13.5 Hz, 3.0 Hz, C=C(OMOM)CH*H*), 2.86 (1H, ddd, J = 11.5 Hz, 9.0 Hz, 3.0 Hz, C*H*CO_2Me), 3.35 (3H, s, CH_2OMe), 3.36 (1H, t, J = 8.0 Hz, C*H*$(CO_2Me)_2$), 3.48 (3H, s, $CHCO_2$*Me*), 3.72 (6H, s, $CH(CO_2Me)_2$), 4.65 (1H, t, J = 7.5 Hz, C*H*=COMOM), 4.68 (1H, d, J = 8.5 Hz, C*H*OSi), 4.80 and 4.83 (2H, AB, J = 6.5 Hz, OCH_2O), 4.86 (2H, d, J = 6.5 Hz, CH_2OBz), 5.77 (1H, dt, J = 15.0 Hz, 6.5 Hz, C*H*=CHCH=CMe), 5.87 (1H, d, J = 11.0 Hz, C*H*=CMe), 6.62 (1H, dd, J = 15.0 Hz, 11.5 Hz, CH=C*H*CH=CMe), 7.43 (2H, m, *Ph*), 7.55 (1H, m, *Ph*), 8.04 (2H, m, *Ph*); ^{13}C nmr ($CDCl_3$, δ ppm): −5.07, −4.84, 17.83, 18.05, 24.36, 25.70, 29.54, 29.88, 50.31, 50.98, 51.22, 52.40, 55.76, 65.19, 71.18, 93.52, 101.14, 126.26, 126.51, 128.30, 129.20, 129.53, 130.21, 132.90, 139.44, 152.58, 166.22, 169.72, 172.61; ms *m/e*: 619 (M^+ – *t*-Bu), 645 (M^+ – MeO), 676 (M^+). HRMS (M^+ – *t*-Bu): 619.2574; found: 619.2571.

Silyl ether ***44***: Yield: 100%; ir (film): 1735, 1665 cm^{-1}; ^1H nmr ($CDCl_3$, δ ppm): −0.06 (3H, s, Si*Me*), −0.02 (3H, s, Si*Me*), 0.80 (9H, s, t-*Bu*Si), 1.77 (3H, s, *Me*C=C), 1.85–1.95 (5H, m, $(CH_2)_2$ and C=C(OMOM)C*H*H), 2.40 (1H, dd, J = 14.0 Hz, 12.0 Hz, C=C(OMOM)CH*H*), 2.89 (1H, ddd, J = 12.0 Hz, 10.0 Hz, 3.0 Hz, C*H*CO_2Me), 3.33 (1H, t, J = 7.0 Hz, C*H*$(CO_2Me)_2$), 3.35 (3H, s, CH_2O*Me*), 3.64 (3H, s, $CHCO_2$*Me*), 3.71 (6H, s, $CH(CO_2Me)_2$), 4.64 (1H, t, J = 7.0 Hz, C*H*=COMOM), 4.80 and 4.83 (2H, AB, J = 6.5 Hz, OC_2O), 4.83 (1H, d, J = 10.0 Hz, C*H*OSi), 4.90 (2H, d, J = 7.0 Hz, CH_2-Bz), 5.87 (1H, dt, J = 15.0 Hz, 6.5 Hz, C*H*=CHCH=CMe), 6.04 (1H, d, J = 11.0 Hz, C*H*=CMe), 6.73 (1H, dd, J = 15.0 Hz, 11.5 Hz, CH=C*H*CH=CMe), 7.45 (2H, m, *Ph*), 7.57 (1H, m, *Ph*), 8.07 (2H, m, *Ph*); ^{13}C nmr ($CDCl_3$, δ ppm): −5.51, −4.91, 17.85, 20.97, 24.30, 25.39, 29.17, 29.54, 49.31, 50.87, 51.39, 52.38, 55.70, 65.14, 71.55, 93.64, 101.15, 127.13, 128.34, 128.52, 128.28, 128.31, 128.59, 129.56, 132.90, 136.55, 151.96, 166.20, 169.65, 169.72, 174.51; ms *m/e*: 619 (M^+ – *t*-Bu), 645 (M^+ – MeO), 676 (M^+). HRMS (M^+ – *t*-Bu): 619.2574; found: 619.2571.

General procedure for the macrocyclizations

Macrocyclic enol ether ***29*** *and macrocyclic ketone* ***30***

To a solution of sodium carbonate (303 mg, 0.61 mmol) in *N,N*-dimethylformamide (30 mL) was added a solution of the allylic chloride **26** (74 mg, 0.12 mmol) in *N,N*-dimethylformamide (10 mL) over a period of 15 h and at 65°C. The reaction mixture was stirred at 65°C for a further 18 h, left to cool down to room temperature, then filtered. The solvent was removed under reduced pressure and the residue was purified by chromatography on Florisil (ether – hexane, 3:7) to yield the macrocyclic ketone **30** (35 mg, 56%).

Another attempt run in acetonitrile yielded a mixture of the macrocycles **29** and **30** (68% and 32% of the mixture, respectively) in 28% overall yield.

Enol ether ***29***: ir (CH_2Cl_2): 1725, 1650 cm^{-1}; ^1H nmr ($CDCl_3$, δ ppm): 1.45 (18H, s, t-*Bu*), 1.74 (3H, s, *Me*C=CH), 2.75–2.90 (4H, m, $(CH_2)_2$), 2.75–2.90 (6H, m, $CH_2C(CO_2t\text{-}Bu)_2CH_2$ and CH_2CH=CH), 3.37 (3H, s, CH_2O*Me*), 3.72 (6H, s, CO_2*Me*), 4.80 (1H, m, C*H*=COMOM), 4.80 (2H, s, CH_2OMe), 5.22 (1H, dt, J = 15.0 Hz, 7.5 Hz, C*H*=CMe), 5.97 (1H, d, J = 11.0 Hz, CH_2CH=CH-), 6.40 (1H, dd, J = 11.0 Hz, 16.5 Hz, CH_2CH=C*H*); ms *m/e*: 566 (M^+).

Ketone ***30***: ir (CH_2Cl_2): 1730 cm^{-1}; ^1H nmr (CD_2Cl_2, −80°C, δ ppm): 1.10–1.80 (2H, m, CH_2), 1.28 (9H, s, t-*Bu*), 1.37 (9H, s, t-*Bu*), 1.61 (3H, s, CH=C*Me*), 1.90–2.10 (2H, m, CH_2), 2.30–2.85 (5H, m, CH_2), 3.15–3.35 (3H, m, CH_2), 3.62 (3H, s, CO_2Me), 3.64 (3H, s, CO_2Me), 5.15 (1H, m, CH=CMe), 5.75–6.00 (2H, m, CH_2CH=CH); ms *m/e*: 522 (M^+).

Macrocycle ***49***: Solvent: acetonitrile. Duration of addition: 15 h. Duration of additional stirring: 4 h. Temperature: reflux. Yield: 50%; ir (film): 1735, 1660, 1439, 1264, 1164, 1087 cm^{-1}; ^1H nmr ($CDCl_3$, δ ppm): 0.02 (3H, s, Si*Me*), 0.08 (3H, s, Si*Me*), 0.90 (9H, s, t-*Bu*), 1.59 (2H, m, CH_2CH_2CH=COMOM), 1.73 (3H, s, CH=C*Me*), 1.90–2.15 (3H, m, $CH_2CHC(OMOM)CHH$), 2.67 (1H, br, CH=C(OMOM)CH*H*), 2.82 (2H, m, CH_2CH=CH), 3.13 (1H, br, $CHCO_2Me$), 3.34 (3H, s, CH_2OMe), 3.64 (3H, s, $CHCO_2Me$), 3.73 (6H, s, $C(CO_2Me)_2$), 4.20 (1H, br, CHOSi), 4.65 (1H, m, CH=COMOM), 4.75 and 4.81 (2H, AB, J = 6.0 Hz, OCH_2O), 5.18 (1H, br, CH=CH), 5.90 (1H, br, CH=CMe), 7.08 (1H, br, CH_2CH=CH); ms *m/e*: 554 (M^+), 539 (M^+ − Me), 523 (M^+ − OMe), 509 (M^+ − MOM), 497 (M^+ − *t*-Bu). HRMS (M^+ − *t*-Bu): 497.2207; found: 497.2199.

Macrocycle ***50***: Solvent: acetonitrile. Duration of addition: 15 h. Duration of additional stirring: 4 h. Temperature: reflux. Yield: 64%; ir (film): 1735, 1660 cm^{-1}; ^1H nmr ($CDCl_3$, δ ppm): 0.00 (3H, s, Si*Me*), 0.04 (3H, s, Si*Me*), 0.86 (9H, s, t-*Bu*), 1.58 (2H, m, CH_2CH_2CH=COMOM), 1.74 (3H, s, C*Me*), 1.99 (2H, m, CH_2CH=COMOM), 2.18 (1H, m, CH=C(OMOM)CH*H*), 2.54 (1H, m, CH=C(OMOM)CH*H*), 2.76 (2H, m, CH_2CH=CH), 2.89 (1H, m, $CHCO_2Me$), 3.33 (3H, s, CH_2OMe), 3.63 (3H, s, $CHCO_2Me$), 3.72 (3H, s, $C(CO_2Me)_2$), 3.73 (3H, s, $C(CO_2Me)_2$), 4.69 (1H, m, CH=COMOM), 4.77 (2H, m, OCH_2O), 4.92 (1H, br, CHOSi), 5.32 (1H, br, CH_2CH=CH), 5.97 (1H, br, CH=CMe), 6.49 (1H, br, CH_2CH=CH); ^{13}C nmr ($CDCl_3$ δ ppm): −5.55, −5.19, 17.85, 20.40, 25.42, 29.41, 32.31, 35.59, 50.47, 51.03, 52.33, 52.43, 55.55, 56.50, 73.26, 93.35, 100.43, 124.75, 124.98, 130.85, 140.25, 153.56, 171.05, 171.59, 172.91; ms *m/e*: 554 (M^+), 539 (M^+ − CH_3), 523 (M^+ − OCH_3), 509 (M^+ − CH_2OCH_3), 497 (M^+ − *t*-Bu). HRMS (M^+ − *t*-Bu): 497.2207; found: 497.2199.

Alternative method used to prepare the macrocyclic enol ether ***29***

O,N-Bis(trimethylsilyl)acetamide (570 μL, 2.27 mmol) was added to a stirred solution of the pivaloate **28** (0.74 g, 1.10 mmol) in tetrahydrofuran (15 mL) at room temperature. The reaction mixture was refluxed for 5 h, cooled down to room temperature, then added over 14 h by means of a syringe pump to a refluxed solution of palladium(0) tetrakis(triphenylphosphine) (270 mg, 0.22 mmol) and 1,3 bis(diphenylphosphino) propane (97 mg, 0.23 mmol) in tetrahydrofuran (535 mL). The resulting mixture was refluxed for another 20 h. The solvent was removed under reduced pressure. The crude product was purified by flash chromatography (hexane – ethyl acetate, 24:1) to give the title compound (0.49 g, 79%).

The same method applied to the acetate **27** afforded the title compound in 23% yield.

General procedure for the Diels–Alder reactions

Tricycles ***51, 52, and 53***

A solution of the macrocycle **29** (351 mg, 0.62 mmol) in toluene (600 μL) was heated in a quartz tube (sealed under vacuum) at 185°C for 4 h. The resulting solution was concentrated under reduced pressure and the residue was purified by flash chromatography (hexane – acetone, 24:1) to give the pure tricycle **53** (25 mg) and a mixture of **51** and **52**. The mixture was purified by preparative thick-layer chromatography (hexane – ethyl acetate, 17:3; four elutions) to yield the tricycles **51** (171 mg) and **52** (26 mg). The overall yield of the reaction was 66% (**51**: 78% of the mixture, **52**: 11%, **53**: 11%).

Tricycle ***51***: mp 104–105°C; ir (CH_2Cl_2): 1730 cm^{-1}; ^1H nmr (C_6D_6, δ ppm): 0.90–1.30 (3H, m, *H*C1, H_{ax}C13, H_{ax}C12), 1.16 (3H, s, C*Me*), 1.36 (18H, s, t-*Bu*), 2.02 (1H, m, H_{eq}C13), 2.25–2.50 (2H, m, *H*C9, H_{ax}C5), 2.60–2.90 (5H, m, H_{ax}C3, H_2C10, H_{eq}C5, H_{eq}C12), 3.19 (1H, d, J = 15 Hz, H_{eq}C3), 3.22 (3H, s, O*Me*), 3.24 (3H, s, O*Me*), 3.30 (3H, s, O*Me*), 4.70 (2H, s, CH_2OMe), 5.14 (2H, dd, J = 10.5 Hz, 2.5 Hz, H_2C7), 5.24 (2H, dd, J = 10.5 Hz, and 0.5 Hz, *H*C8) (see Scheme 2 for atom numbers: **6**); ^{13}C nmr (C_6D_6, δ ppm): 22.8, 23.9, 27.7, 32.3, 33.7, 35.4, 37.1, 44.9, 45.3, 55.21, 55.2, 55.6, 80.4, 80.6, 89.0, 92.8, 129.1, 136.2, 170.7, 170.8, 171.3, 172.3; ms *m/e*: 505 (M^+ − OMOM). HRMS (M^+ − OMOM): 505.2861; found: 505.2791.

Tricycle ***52***: mp: 68–69°C; ir (CH_2Cl_2): 1730 cm^{-1}; ^1H nmr (C_6D_6, δ ppm): 1.14 (3H, s, C*Me*), 1.35 (9H, s, t-*Bu*), 1.30–1.85 (5H, m, *H*Cl, H_{ax}C10, H_{ax}C12, H_2C13), 1.95–2.45 (5H, m, H_2C3, *H*C9, H_2C5), 2.60–2.80 (3H, m, H_{eq}C10, H_{eq}C12), 3.08 (1H, m, *H*C4), 3.09 (3H, s, CH_2OMe), 3.25 (3H, s, CO_2Me), 3.32 (3H, s, CO_2Me), 4.34 and 4.63 (2H, AB, J = 7.5 Hz, OCH_2OMe), 5.17 (2H, dd, J = 10.5 Hz, 1.5 Hz, *H*C7), 5.29 (2H, dd, J = 10.5 Hz, 2.5 Hz, *H*C8) (see Scheme 2 for atom numbers: **6**); ^{13}C nmr (C_6D_6, δ ppm): 22.7, 24.2, 28.0, 30.5, 32.3, 37.6, 37.9, 41.0, 41.6, 44.8, 50.6, 52.06, 55.2, 55.5, 79.3, 89.5, 92.7, 127.3, 137.8, 171.3, 172.3, 174.8; ms *m/e*: 405 (M^+ − OMOM); HRMS (M^+ − OMOM): 405.2277; found: 405.2267.

Tricycle ***53***: mp: 89–90°C; ir (CH_2Cl_2): 1730 cm^{-1}; ^1H nmr (C_6D_6, δ ppm): 1.13 (3H, s, C*Me*), 1.40 (9H, s, t-*Bu*), 1.20–1.85 (4H, m, *H*C1, H_2C5, H_{ax}C13), 1.95–2.25 (5H, m, *H*C9, H_{ax}C10, H_{ax}C12, H_{ax}C3, H_{eq}C13), 2.40–2.80 (4H, m, *H*C4, H_{eq}C10, H_{eq}12, H_{eq}C3), 3.21 (3H, s, O*Me*), 3.25 (3H, s, O*Me*), 3.34 (3H, s, O*Me*), 4.71 and 4.73 (2H, AB, J = 7.0 Hz, OCH_2OMe), 4.99 (2H, dd, J = 10.0 Hz, 2.5 Hz, *H*C7), 5.16 (2H, dd, J = 10 Hz, 1.0 Hz, *H*C8) (see Scheme 2 for atom numbers: **6**); ^{13}C nmr (C_6D_6, δ ppm): 22.2, 23.7, 28.1, 31.0, 32.2, 37.0, 37.8, 41.7, 42.1, 45.0, 51.0, 52.06, 55.09, 79.4, 88.4, 92.8, 128.8, 136.8, 172.25, 174.3; ms *m/e*: 405 (M^+ − (OMOM). HRMS (M^+ −OMOM): 405.2277; found: 405.2267.

Tricycle ***54***: Solvent: acetonitrile, additive: *N,O*-bis(trimethylsilyl)acetamide (7.7 equiv.), reaction time: 3 h. Temperature: 230°C, yield: 57%; ir: 1735 cm^{-1}; ^1H nmr ($CDCl_3$, δ ppm): −0.01 (3H, s, Si*Me*), 0.07 (3H, s, Si*Me*), 0.89 (9H, s, t-*Bu*), 0.93 (3H, s, C*Me*), 1.10–2.60 (8H, m, $(CH_2)_2CHCHCH_2$), 1.91 (1H, dd, J = 15.5 Hz, 9.0 Hz, $CHHCHCO_2Me$), 2.67 (1H,

dd, J = 15.5 Hz, 12.5 Hz, CH*H*CHCO$_2$Me), 2.84 (1H, ddd, J = 12.5 Hz, 8.5 Hz, 4.0 Hz, C*H*CO$_2$Me), 3.39 (3H, s, CH$_2$O*Me*), 3.65 (3H, s, CO$_2$*Me*), 3.70 (3H, s, CO$_2$*Me*), 3.76 (3H, s, CO$_2$*Me*), 3.96 (1H, d, J = 4.0 Hz, C*H*OSi), 4.53 (1H, d, J = 7.5 Hz, OC*H*HO), 5.29 (1H, dd, J = 10.0 Hz, 2.5 Hz, C*H*=CH), 5.41 (2H, m, OCH*H*O, CH=C*H*); ^{13}C nmr (CDCl$_3$, δ ppm): −4.96, −3.75, 18.16, 19.02, 22.76, 25.99, 28.97, 29.70, 31.43, 33.87, 37.23, 46.26, 47.56, 51.54, 52.63, 52.71, 55.07, 55.49, 55.56, 81.26, 87.98, 92.75, 131.45, 135.00, 171.55, 172.14, 172.54; ms *m/e*: 554 (M$^+$), 539 (M$^+$ − Me), 523 (M$^+$ − OMe), 509 (M$^+$ − MOM), 497 (M$^+$ − *t*-Bu). HRMS (M$^+$ − *t*-Bu): 497.2207; found: 497.2204 ± 0.0014.

Tricycle ***56***: Solvent: acetonitrile, additive: *N,O*-bis(trimethylsilyl)acetamide (7.7 equiv.), reaction time: 3 h. Temperature: 200°C, yield: 94%; ir: 1735 cm^{-1}; ^{1}H nmr (CDCl$_3$, δ ppm): 0.03 (3H, s, Si*Me*), 0.06 (3H, s, Si*Me*), 0.88 (9H, s, t-*Bu*), 0.96 (3H, s, C*Me*), 1.10–2.60 (8H, m, (C*H*$_2$)$_2$C*H*C*H*CH$_2$), 1.92 (1H, dd, J = 15.0 Hz, 11.0 Hz, C*H*HCHCO$_2$Me), 2.28 (1H, dd, J = 15.0 Hz, 9.0 Hz, CH*H*CHCO$_2$Me), 3.03 (1H, ddd, J = 10.5 Hz, 9.0 Hz, 4.0 Hz, C*H*CO$_2$Me), 3.41 (3H, s, CH$_2$O*Me*), 3.65 (3H, s, CO$_2$*Me*), 3.69 (3H, s, CO$_2$*Me*), 3.76 (3H, s, CO$_2$*Me*), 4.14 (1H, d, J = 4.0 Hz, C*H*OSi), 4.73 (1H, d, J = 7.5 Hz, C*H*=CH), 4.98 (1H, d, J = 7.5 Hz, CH=C*H*), 5.24 (2H, s, OC*H*$_2$O); ^{13}C NMR (CDCl$_3$, δ ppm): −4.86, 18.06, 18.33, 23.35, 25.84, 29.68, 30.69, 31.82, 36.37, 37.03, 45.24, 51.65, 51.72, 52.69, 54.21, 55.08, 55.63, 82.65, 88.95, 92.70, 127.76, 136.06, 171.46, 172.48, 175.47; ms *m/e*: 554 (M$^+$), 539 (M$^+$ − Me), 523 (M$^+$ − OMe), 509 (M$^+$ − MOM), 497 (M$^+$ − *t*-Bu). HRMS (M$^+$ − *t*-Bu): 497.2207; found: 497.2204.

General procedure for the cleavage of methoxymethyl ethers

Method A

Alcohol ***58***

Hydrochloric acid (1 M, 0.35 mL, 0.35 mmol) was added to a solution of the ether **51** (0.15 g, 0.27 mmol) in methanol (5 mL). The mixture was stirred at room temperature for 5 h. Dichloromethane was added and the resulting solution was washed with saturated aqueous sodium bicarbonate. Drying (MgSO$_4$), removal of the solvent, and purification of the residue by flash chromatography (hexane – ethyl acetate, 4:1) gave the title compound (0.12 g, 89%); ir (CH$_2$Cl$_2$): 3600, 3500, 1725 cm^{-1}; ^{1}H nmr (C$_6$D$_6$, δ ppm): 1.11 (3H, s, C*Me*), 1.30 (9H, s, t-*Bu*), 1.32 (9H, s, t-*Bu*), 1.25–1.50 (2H, m, *H*C1, H_{ax}C13), 1.50–1.85 (2H, m, H_{ax}C12, H_{ax}C10), 2.10–2.25 (2H, m, *H*C9, H_{eq}C13), 2.35–2.90 (6H, m, H_{eq}C12, H_{eq}C10, H_2C3, H_2C5), 3.24 (3H, s, CO$_2$*Me*), 3.28 (3H, s, CO$_2$*Me*), 5.23 (2H, dd, J = 10.0 Hz, 1.5 Hz, *H*C7), 5.33 (2H, dd, J = 10.0 Hz, and 2.5 Hz, *H*C8) (see Scheme 2 for atom numbers: **6**); ^{13}C nmr (C$_6$D$_6$, δ ppm): 22.7, 23.3, 27.9, 32.3, 37.4, 37.7, 41.4, 43.7, 45.6, 52.4, 49.9, 55.6, 58.9, 81.9, 82.6, 127.6, 137.0, 171.0, 174.4; ms *m/e*: 466 (M$^+$ − t-*Bu*), 448 (M$^+$ − t-*Bu* – H$_2$O). HRMS (M$^+$ − t-*Bu* − H$_2$O): 448.2097; found: 448.2088.

Alcohol ***59***: Yield: 89%; ir (CH$_2$Cl$_2$): 3600, 3440, 1730 cm^{-1}; ^{1}H nmr (C$_6$D$_6$, δ ppm): 1.09 (3H, s, C*Me*), 1.33 (9H, s, t-*Bu*), 1.25 (1H, m, *H*C1), 1.90–2.25 (9H, m, *H*C9, H_{ax}C10, H_{ax}C12, H_2C3, H_2C5, H_2C13), 2.45 (1H, s, O*H*), 3.26 (3H, s, CO$_2$*Me*), 3.36 (3H, s, CO$_2$*Me*), 2.50–2.80 (3H, m, *H*C4, H_{eq}C10, H_{eq}C12), 5.06 (2H, dd, J = 10.0 Hz, 2.5 Hz, *H*C7), 5.13 (2H, dd, J = 10.0 Hz, 1.0 Hz, *H*C8) (see Scheme 2 for atom numbers: **6**).

Alcohol ***60***: Yield: 80%; ir (CH$_2$Cl$_2$): 3600, 3500, 1730 cm^{-1}; ^{1}H nmr (C$_6$D$_6$, δ ppm): 0.92 (3H, s, C*Me*), 1.34 (9H, s, t-*Bu*), 1.05–1.25 (1H, m, *H*C1), 1.55–2.40 (10H, m, *H*C9, H_{ax}C10, H_{ax}C12, H_2C5, H_2C3, H_2C13, OH), 2.60–2.85 (2H, m, H_{eq}C10, H_{eq}C12), 2.85–3.10 (1H, m, *H*C4), 3.26 (3H, s, CO$_2$*Me*), 3.29 (3H, s, CO$_2$*Me*), 5.11 (2H, dd, J = 10.0 Hz, 1.5 Hz, *H*C7), 5.27 (2H, dd, J = 10.0 Hz, 2.6 Hz, *H*C8) (see Scheme 2 for atom numbers: **6**).

Method B

Alcohol ***64***

Dimethylboron bromide (2 μL, 20 μmol) was added at −78°C to a stirred solution of the tricycle **54** (4 mg, 7 μmol) in dichloromethane (1 mL). The mixture was stirred for 1 h at −78°C, then added to saturated aqueous sodium bicarbonate (5 mL) and tetrahydrofuran (10 mL). The resulting mixture was vigorously stirred, then extracted several times with ether. The ether extract was washed with brine and aqueous sodium bisulfate (10%). Drying (MgSO$_4$) and removal of solvent under reduced pressure gave an oil that was purified by flash chromatography on silica gel (hexane – ethyl acetate, 9:1) to give the title compound (3.7 mg, 100%); ir: 3550, 1735, 1048 cm^{-1}; ^{1}H nmr (CDCl$_3$, δ ppm): −0.01 (3H, s, Si*Me*), 0.10 (3H, s, Si*Me*), 0.89 (9H, s, t-*Bu*), 1.07 (3H, s, C*Me*), 1.10–2.60 (10H, m, (C*H*$_2$)$_2$C*H*C*H*CH$_2$ and C*H*$_2$CHCO$_2$Me), 2.90 (1H, td, J = 10.0 Hz, 3.5 Hz, C*H*CO$_2$Me), 3.22 (1H, s, O*H*), 3.65 (3H, s, CO$_2$*Me*), 3.70 (3H, s, CO$_2$*Me*), 3.75 (3H, s, CO$_2$*Me*), 4.09 (1H, d, J = 3.5 Hz, C*H*OSi), 5.27 (1H, dd, J = 10.0 Hz, 2.5 Hz, C*H*=CH), 5.38 (1H, dd, J = 10.0 Hz, 1.5 Hz, CH=C*H*); ^{13}C nmr (CDCl$_3$, δ ppm)): −4.92, −3.97, 17.92, 18.17, 21.97, 25.91, 29.69, 31.50, 35.40, 35.81, 36.89, 42.97, 48.37, 51.62, 52.60, 53.50, 55.29, 81.36, 82.42, 130.91, 132.90, 171.60, 172.50; ms *m/e*: 510 (M$^+$), 495 (M$^+$ − Me), 494 (M$^+$ − H$_2$O), 453 (M$^+$ − *t*-Bu). HRMS (M$^+$ − *t*-Bu): 453.1945; found: 453.1936.

Alcohol ***65***: Yield: 75%; ir: 3550, 1735, 1049 cm^{-1}; ^{1}H nmr (CDCl$_3$, δ ppm): 0.12 (6H, s, Si*Me*$_2$), 0.90 (9H, s, t-*Bu*), 1.04 (3H, s, C*Me*), 1.10–3.00 (11H, m, (C*H*$_2$)$_2$C*H*C*H*CH$_2$ and C*H*$_2$C*H*CO$_2$Me), 3.26 (1H, s, O*H*), 3.63 (3H, s, CO$_2$*Me*), 3.70 (3H, s, CO$_2$*Me*), 3.78 (3H, s, CO$_2$*Me*), 4.28 (1H, d, J = 1.0 Hz, C*H*OSi), 5.15 (1H, dd, J = 10.0 Hz, 2.5 Hz, C*H*=CH), 5.27 (1H, dd, J = 10.0 Hz, 1.5 Hz, CH=C*H*); ^{13}C nmr (CDCl$_3$, δ ppm)): −5.11, −5.00, 17.79, 17.86, 22.30, 25.59, 25.72, 25.79, 31.82, 35.30, 36.78, 43.27, 50.73, 51.93, 52.43, 52.68, 55.34, 82.47, 83.33, 130.58, 132.43, 171.56, 172.55, 173.71; ms *m/e*: 510 (M$^+$), 495 (M$^+$ − Me), 494 (M$^+$ − H$_2$O), 453 (M$^+$ − *t*-Bu). HRMS (M$^+$ − *t*-Bu): 453.1945; found: 453.1936.

Procedure use for the lactonization attempts

Alcohol ***61***

A solution of the alcohol **58** (35 mg, 67 μmol) and paratoluenesulfonic acid monohydrate (1 mg) in benzene (1 mL) was refluxed for 4 h. The solvent was removed under reduced pressure, and the residue dissolved in either (2 mL). Diazomethane (ether solution, 1 mL) was added and the resulting mixture

was stirred for 1 h at room temperature. Removal of solvent under reduced pressure gave a solid residue that was crystallized from dichloromethane and ether to give the title compound (24 mg, 90%); mp 156–158°C; ir (CH_2Cl_2): 1790, 1740 cm^{-1}; ^1H nmr (C_6D_6, δ ppm): 0.87 (3H, s, CMe), 0.97 (1H, m, $H_{ax}C13$), 1.35–1.65 (4H, m, HC1, $H_{ax}C10$, $H_{ax}C5$, $H_{ax}C12$), 1.65–1.95 (4H, m, HC9), $H_{eq}C13$, H_2C3), 2.12 (1H, dd, $H_{eq}C5$), 2.40–2.62 (2H, m, $H_{eq}C12$, $H_{eq}C10$), 3.27 (3H, s, CO_2Me), 3.40 (3H, s, CO_2Me), 3.78 (3H, s, CO_2Me), 4.89 (2H, dd, J = 10.0 Hz, 1.5 Hz, HC7), 5.05 (2H, dd, J = 10.0 Hz, 2.5 Hz, HC8) (see Scheme 2 for atom numbers: **6**); ^{13}C nmr (C_6D_6, δ ppm): 22.9, 23.3, 30.9, 36.7, 37.3, 37.9, 40.8, 41.3, 52.1, 45.3, 52.2, 55.2, 57.3, 92.3, 126.6, 135.7, 171.1, 171.8, 172.7; ms m/e: 406 (M^+); HRMS (M^+): 406.1628; found: 406.1641.

Alcohol ***62***: The diazomethane treatment was omitted. Yield: 81%; mp 143–145°C; ir (CH_2Cl_2): 1780, 1730 cm^{-1}; ^1H nmr (C_6D_6, δ ppm): 0.93 (3H, s, C*Me*), 1.00–1.35 (4H, m, *H*C1, H_2C3, $H_{ax}C5$), 1.40 (1H, m, $H_{eq}C5$), 1.50–1.75 (3H, m, $H_{ax}C12$, $H_{ax}C13$), 1.80–2.00 (2H, m, $H_{eq}C13$, *H*C9), 2.34 (1H, m, *H*C4), 2.50–2.65 (2H, m, $H_{eq}C10$, $H_{eq}C12$), 3.25 (3H, s, CO_2Me), 3.33 (3H, s, CO_2Me), 4.90 (2H, dd, *J* = 10.0 Hz, 2.5 Hz, *H*C7), 5.07 (2H, dd, *J* = 10.0 Hz, 3.0 Hz, *H*C8) (see Scheme 2 for atom numbers: **6**); ms *m/e*: 348 (M^+); HRMS (M^+): 348.1573; found: 348.1570.

Ester ***63***: Yield: 78%; ir (CH_2Cl_2): 1735 cm^{-1}; ^1H nmr (C_6D_6, δ ppm): 0.93 (3H, s, C*Me*), 1.55–2.20 (8H, m, *H*C1, *H*C9, $H_{ax}C10$, $H_{ax}C12$, H_2C5, H_2C13), 2.75–2.60 (2H, m, $H_{eq}C10$, $H_{eq}C12$), 3.22 (3H, s, CO_2Me), 3.25 (3H, s, CO_2Me), 3.30 (3H, s, CO_2Me), 3.55 (1H, t, *H*C4), 5.21 (2H, dd, *J* = 10.0 Hz, 1.5 Hz, *H*C7), 5.37 (1H, br, *H*C3), 5.47 (2H, dd, *J* = 10.0 Hz, 2.5 Hz, *H*C8) (see Scheme 2 for atom numbers: **6**); ms *m/e*: 362 (M^+). HRMS (M^+): 362.1729; found: 362.1720.

Lactone ***66***: The diazomethane treatment was omitted. Yield: 76%; ir: 1770, 1730 cm^{-1}; ^1H nmr ($CDCl_3$, δ ppm): 0.07 (3H, s, Si*Me*), 0.11 (3H, s, Si*Me*), 0.90 (9H, s, t-*Bu*), 0.96 (3H, s, C*Me*), 1.10–2.90 (11H, m, $(CH_2)_2CHCHCH_2$ and CH_2CHCO_2), 3.72 (3H, s, CO_2Me), 3.76 (3H, s, CO_2Me), 4.07 (1H, d, *J* = 4.0 Hz, C*H*OSi), 5.27 (1H, d, *J* = 10.0 Hz, C*H*=CH), 5.55 (1H, dd, *J* = 10.0 Hz, 2.0 Hz, CH=C*H*); ^{13}C nmr ($CDCl_3$, δ (ppm): −5.03, −4.80, 17.36, 18.07, 22.06, 25.64, 30.75, 34.34, 36.38, 38.88, 47.76, 50.18, 52.70, 52.83, 55.10, 92.62, 127.12, 135.45, 171.45, 172.14, 174.68; ms *m/e*: 421 (M^+ − *t*-Bu). HRMS (M^+ − *t*-Bu): 421.1682; found: 421.1691.

Alcohol ***67***: The diazomethane treatment was omitted. Yield: 88%; ir: 1730 cm^{-1}; ^1H nmr ($CDCl_3$, δ ppm): 1.10 (3H, s, C*Me*), 0.8–2.8 (10H, m, $(CH_2)_2CHCHCH_2$ and CH_2CHCO_2Me), 3.00 (1H, ddd, *J* = 10.0 Hz, 7.5 Hz, 2.5 Hz, $CHCO_2Me$), 3.66 (3H, s, CO_2Me), 3.71 (3H, s, CO_2Me), 3.78 (3H, s, CO_2Me), 4.19 (1H, br, C*H*OH), 5.27 (2H, m, C*H*=C*H*); ^{13}C nmr ($CDCl_3$, δ ppm): 16.99, 22.26, 29.69, 31.72, 34.46, 36.76, 44.09, 50.64, 51.94, 52.01, 52.75, 55.23, 82.45, 83.12, 129.39, 133.76, 171.44, 172.43, 174.24; ms *m/e*: 378 (M^+ − H_2O). HRMS (M^+ − H_2O): 378.1678; found: 378.1674.

Acknowledgements

This work was supported financially by the Natural Sciences and Engineering Research Council of Canada (NSERCC), Bio-Mega/Boehringer Ingelheim Research Inc., and by the Fonds pour la Formation de Chercheurs et l'Aide à la Recherche (FCAR) du Québec.

References

1. M. Quimpère, L. Ruest, and P. Deslongchamps. Can. J. Chem. **70**, 2335 (1992).
2. W.A. Jacobs and R.C. Elderfield. J. Biol. Chem. **100**, 671 (1933).
3. R.B. Turner. Chem. Rev. **43**, 1 (1948).
4. W.A. Jacobs and A. Hoffmann. J. Biol. Chem. **67**, 333 (1926).
5. H. Linde, J.E. Murphy, and K. Meyer. Helv. Chim. Acta, **42**, 2040 (1959).
6. (*a*) W. Danieli, Y. Mazur, and F. Sondheimer. Tetrahedron, **22**, 3189 (1966); (*b*) S.F. Donovan, M.A. Avery, and J.E. McMurry. Tetrahedron Lett. **20**, 3287 (1979); (*c*) R. Marini-Bettolo, P. Flecker, T.Y.R. Tsai, and K. Wiesner. Can. J. Chem. **59**, 1403 (1981); (*d*) T. Milkova, H. Stein, A. Ponty, D. Böttger, and P. Welzel. Tetrahedron Lett. **23**, 413 (1982); (*e*) P. Welzel and H. Stein. Tetrahedron Lett. **22**, 3385 (1981).
7. (*a*) D.A. Evans and L.R. McGee. Tetrahedron Lett. **21**, 3975 (1980); (*b*) D. Boschelli, J.W. Ellingboe, and S. Masamune. Tetrahedron Lett. **25**, 3395 (1984); (*c*) H. Danda, M.M. Hansen, and C.H. Heathcock. J. Org. Chem. **55**, 173 (1990).
8. S. Hanessian and P. Lavallée. Can. J. Chem. **53**, 2975 (1975).
9. (*a*) A.J. Mancuso, S.-L. Huang, and D. Swern. J. Org. Chem. **34**, 2430 (1978); (*b*) K. Omura and D. Swern. Tetrahedron, **34**, 1651 (1978).
10. J. Boutagy and R. Thomas. Chem. Rev. **74**, 87 (1974).
11. E. Nakamura. Tetrahedron Lett. **22**, 663 (1981).
12. (*a*) E.G. Miller, J.W. Biss, and L.H. Schwartzman. J. Org. Chem. **24**, 627 (1959); (*b*) E. Winterfeldt. Synthesis, 617 (1975).
13. E.W. Collington and A.J. Meyers. J. Org. Chem. **36**, 3044 (1971).
14. (*a*) H.L. Goering and C.C. Tseng. J. Org. Chem. **46**, 5252 (1981); (*b*) A.P. Kozikowski, Y. Xia, and J.M. Rusnak. J. Chem. Soc. Chem. Commun. 1301 (1988).
15. (*a*) E.J. Corey and J.W. Suggs. Tetrahedron Lett. 2647 (1975); (*b*) G. Piancatelli, A. Scetti, and M. D'Auria. Synthesis, 245 (1982).
16. W.C. Still and C. Gennari. Tetrahedron Lett. **24**, 4405 (1983).
17. (*a*) B.M. Trost. Acc. Chem. Res. **13**, 385 (1980); (*b*) L.S. Hegedus. Tetrahedron, **40**, 2415 (1984).
18. (*a*) A.P. Krapcho, G.A. Dlynn, and B.J. Grenon. Tetrahedron Lett. 215 (1967); (*b*) A.P. Krapcho, J.F. Weinaster, J.M. Eidridge, E.G.E. Jahngen, Jr., A.J. Lovey, and W.P. Stephens. J. Org. Chem. **43**, 138 (1978); (*c*) A.P. Krapcho. Synthesis, 805 (1982).
19. (*a*) Y.L. Dory, C. Ouellet, S. Berthiaume, A. Favre, and P. Deslongchamps. Bull. Soc. Chim. Fr. **131**, 121 (1994); (*b*) Y.L. Dory, P. Soucy, and P. Deslongchamps. Bull. Soc. Chim. Fr. **131**, 121 (1994).
20. M. Drouin, P. Soucy, P. Deslongchamps, and A.G. Michel. Acta Crystallogr. Sect C: Cryst. Struct. Commun. **C46**, 2411 (1990).
21. Y. Guindon, H.E. Morton, and C. Yoakim. Tetrahedron Lett. **24**, 3969 (1983).

Synthesis and study of Pt(II)–nitrile complexes. Multinuclear NMR spectra and crystal structures of compounds of the types $[Pt(R\text{-}CN)Cl_3]^-$ and *cis* and *trans*-$Pt(R\text{-}CN)_2Cl_2$

Fernande D. Rochon, Robert Melanson, Eryk Thouin, André L. Beauchamp, and Corinne Bensimon

Abstract: Complexes of the type $[Pt(R\text{-}CN)Cl_3]^-$ were synthesized and studied by ^1H, ^{13}C, and ^{195}Pt NMR spectroscopies. The $^2J(^{195}Pt\text{-}^{13}C)$ coupling constants are about 240 Hz. The signals due to the cyano carbon atoms of the coordinated ligands were observed at higher fields than those of the free ligands. The shielding on the cyano carbon increases as the alkyl chain lengthens and also when the branching increases. The ^{195}Pt signals of all the complexes were observed around −2000 ppm. The crystal structures of $(NMe_4)[Pt(C_3H_7\text{-}CN)Cl_3]$ (**1**) and $(NMe_4)[Pt(p\text{-}HO\text{-}C_6H_4\text{-}CN)Cl_3]$ (**2**) were determined. Compound **1** is monoclinic, $P2_1/c$, $a = 8.384(5)$, $b = 15.336(19)$, $c = 11.759(9)$ Å, $\beta = 99.52(6)°$, $Z = 4$, $R = 0.054$, and $wR = 0.051$. Crystal **2** is tetragonal with $a = 16.222(6)$, $c = 12.052(5)$ Å, $Z = 8$, $R = 0.059$, and $wR = 0.044$. The Pt—Cl bond *trans* to the nitrile ligand is shorter than normal (2.276(3) Å for **1** and 2.264(7) Å for **2**) while the two other bonds are normal (2.293(4), 2.287(3) Å for **1** and 2.320(7), 2.275(8) Å for **2**). The Pt—N bonds are 1.97(1) Å (**1**) and 1.92(2) Å (**2**) and the segments Pt-N≡C-C are linear. Disubstituted compounds were also synthesized and studied by multinuclear NMR. The ^{195}Pt signals of the *cis* isomers were observed at lower fields than those of the *trans* isomers ($\Delta \approx 65$ ppm), while the ^{13}C signals of the cyano carbons of the *trans* isomers were observed at lower fields than those of the *cis* compounds ($\Delta \approx 0.6$ ppm). The *cis* complexes isomerize to the *trans* compounds upon heating. The crystal structures of *cis*-(**3**) and *trans*-$Pt(C_2H_5\text{-}CN)_2Cl_2$ (**4**) and also of *cis*-$Pt(p\text{-}HO\text{-}C_6H_4\text{-}CN)_2Cl_2$ (**5**) were determined. Crystal **3** is monoclinic, $P2_1/c$, $a = 7.506(5)$, $b = 9.539(5)$, $c = 14.823(7)$ Å, $\beta = 92.31(4)°$, $Z = 4$, $R = 0.050$, and $wR = 0.042$. The *trans* isomer **4** is monoclinic with the Pt atom on an inversion centre, $P2_1/c$, $a = 5.149(4)$, $b = 9.394(8)$, $c = 10.944(10)$ Å, $\beta = 97.84(7)°$, $Z = 4$, $R = 0.017$ and $wR = 0.020$. Finally, compound **5** is triclinic, $P\text{-}1$, $a = 7.464(3)$, $b = 10.712(6)$, $c = 12.291(5)$ Å, $\alpha = 75.63(4)°$, $\beta = 75.63(4)°$, $\gamma = 80.32(4)°$, $Z = 2$, $R = 0.045$, and $wR = 0.056$. The Pt—Cl bond distances for the *cis* isomers are 2.269(5), 2.270(4) Å for **3** and 2.274(2), 2.279(3) Å for **5** while they are 2.289(3) Å for the *trans* isomer (**4**). The Pt—N bonds are 1.962(14), 1.988(11) Å (**3**), 1.972(7), 1.976(7) Å (**5**) and 1.969(5) Å for **4**.

Key words: platinum, nitrile, NMR, isomerization, crystal structure.

Résumé : Des complexes de type $[Pt(R\text{-}CN)Cl_3]^-$ ont été synthétisés et étudiés par résonance magnétique nucléaire protonique, carbon-13 et platine-195. Les constantes de couplage $^2J(^{195}Pt\text{–}^{13}C)$ sont environ 240 Hz. La résonance des carbones cyano des ligands coordinés a été observée à un champ plus fort que celle des ligands libres. Ce blindage augmente lorsque la chaîne alkyle s'allonge et aussi lorsque le branchement augmente. Les signaux ^{195}Pt de tous les complexes ont été observés autour de −2000 ppm. Les structures cristallines des composés $(NMe_4)[Pt(C_3H_7\text{-}CN)Cl_3]$ (**1**) et $(NMe_4)[Pt(p\text{-}HO\text{-}C_6H_4\text{-}CN)Cl_3]$ (**2**) ont été déterminées. Le composé **1** est monoclinique, $P2_1/c$, $a = 8{,}384(5)$, $b = 15{,}336(19)$, $c = 11{,}759(9)$ Å, $\beta = 99{,}52(6)°$, $Z = 4$, $R = 0{,}054$ et $wR = 0{,}051$. Le cristal **2** est tétragonal avec $a = 16{,}222(6)$, $c = 12{,}052(5)$ Å. $Z = 8$, $R = 0{,}059$ et $wR = 0{,}044$. Le lien Pt—Cl en position *trans* du ligand nitrile est plus court qu'un lien normal (2,276(3) pour **1** et 2,264(7) Å pour **2**) tandis que les deux autres liens sont normaux (2,293(4), 2,287(3) Å pour **1** et 2,320(7), 2,275(8) Å pour **2**). Les liaisons Pt—N sont 1,97(1) Å (**1**) et 1.92(2) Å (**2**) et le segment Pt-N≡C-C est linéaire. Des complexes disubstitués ont également été synthétisés et étudiés par résonance magnétique multinucléaire. Les signaux ^{195}Pt des isomères *cis* ont été observés à des champs plus faibles que ceux des complexes *trans* ($\Delta \approx 65$ ppm), tandis que les résonances des carbones cyano des isomères *cis* ont été observées à des champs plus forts que celles des composés *trans* ($\Delta \approx 0.6$ ppm). Les complexes *cis* s'isomèrisent en isomères *trans* sous l'effet de la chaleur. Les structures cristallines de *cis*-(**3**) et *trans*-$Pt(C_2H_5\text{-}CN)_2Cl_2$ (**4**) et de *cis*-$Pt(p\text{-}HO\text{-}C_6H_4\text{-}CN)_2Cl_2$ (**5**) ont été déterminées. Le crystal **3** est monoclinique, $P2_1/c$, $a = 7{,}506(5)$, $b = 9{,}539(5)$, $c = 14{,}823(7)$ Å, $\beta = 92{,}31(4)°$, $Z = 4$, $R = 0{,}050$ et $wR = 0{,}042$. L'isomère *trans* (**4**) est monoclinique avec l'atome de Pt sur un centre d'inversion, $P2_1/c$, $a = 5{,}149(4)$, $b =$

Received July 17, 1995.

F.D. Rochon,[1] **R. Melanson, E. Thouin, and C. Bensimon.** Department of Chemistry, Université du Québec à Montréal, C.P. 8888, Montréal, QC H3C 3P8, Canada.
A.L. Beauchamp. Department of Chemistry, Université de Montréal, C.P. 6128, Montréal, QC H3C 3J7 Canada.

[1] Author to whom correspondence may be addressed.
Telephone: (514) 987-4896. Fax: (514) 987-4054. E-mail: rochon.fernande@uqam.ca

9,394(8), c = 10,944(10) Å, β = 97,84(7)°, Z = 4, R = 0,017 et wR = 0,020. Finalement, le composé **5** est triclinique, P-1, a = 7,464(3), b = 10,712(6), c = 12,291(5) Å, α = 75,63(4)°, β = 75,63(4)°, γ = 80,32(4)°, Z = 2, R = 0,045 et wR = 0,056. Les liens Pt—Cl des isomères *cis* sont 2,269(5), 2,270(4) Å (**3**) et 2,274(2), 2,279(3) Å (**5**), et 2,289(3) Å pour l'isomère *trans* (**4**). Les liaisons Pt—N sont 1,962(14), 1,988(11) Å (**3**), 1,972(7), 1,976(7) Å (**5**) et 1,969(5) Å (**4**).

Mots clés : platine, nitrile, RMN, isomérisation, structure cristalline.

Introduction

Although several disubstituted nitrile–Pt(II) complexes, mostly with acetonitrile and benzonitrile, have been reported (1–7), few mononitrile complexes have been studied (8–10). The synthesis of these compounds is important as starting material for the preparation of mixed-ligand complexes.

The nature of the Pt–nitrile bond is not very well known. IR data and X-ray diffraction of a few acetonitrile complexes have shown that CH_3CN is bonded through its lone pair of electrons on the nitrogen atom (2, 8, 10, 11) and the segment Pt-N≡C-C is linear. Acetonitrile is expected to accept electron density from the metal, much like CO, because of its empty π* orbitals. Therefore it was expected that its *trans* effect should be fairly large but this hypothesis has not been confirmed.

Disubstituted nitrile compounds are usually the *cis* isomers. It was expected that the *trans* isomers would be formed first and would then isomerize to the *cis* compounds, similarly to the sulfoxide complexes (12–15). In the latter compounds, the $(d–d)\pi$ bonding is much more efficient in the *cis* configuration than in the *trans* isomers. But recent studies on disubstituted complexes with acetonitrile, and dibenzonitrile seem to indicate that the *cis* compound is the first product formed, and isomerization then occurs (3, 16). The nature of the back-donation in Pt–nitrile compounds (d–π*) is quite different from that in Pt–sulfoxide (d–d) complexes. Bond lengths usually give information on the presence of multiple bonding but this is not always obvious. Multinuclear NMR spectroscopy can also give some indication on the strength of the Pt–ligand bond. The σ bond will cause a deshielding effect on the ligand and a shielding effect on the metal, while back-donation from the metal to the ligand should produce the opposite effect. We have measured the proton, carbon-13, and platinum-195 NMR spectra of several complexes of the types $[Pt(R\text{-}CN)Cl_3]^-$ and $Pt(R\text{-}CN)_2Cl_2$ in order to obtain information about the Pt–nitrile bond. To study disubstituted compounds, it is important to know exactly the nature of these compounds. A study was undertaken to determine the configuration of such compounds, which were also studied by IR spectroscopy and a few by X-ray diffraction. The potassium mononitrile complexes are not very stable and decompose quite readily. To stabilize the compounds, a larger cation was used. The tetramethylammonium salts proved much more stable and several complexes of the type $N(CH_3)_4[Pt(nitrile)Cl_3]$ were isolated and characterized. The compounds with butyronitrile and p-hydroxybenzonitrile gave crystals suitable for X-ray diffraction and their structures were determined. The crystal structures of the disubstituted complexes with propionitrile (*cis* and *trans*) and p-hydroxybenzonitrile were also studied. *trans*-$Pt(C_2H_5CN)_2Cl_2$ is the first example of this type of compound to be analyzed by X-ray diffraction methods. The results of these studies are described below.

Experimental

The ^{195}Pt NMR spectra were measured either on a Bruker WH-400 (85.83 MHz) or a Varian-300 (64.507 MHz) spectrometer. The proton and ^{13}C NMR spectra were obtained on the same instruments and occasionally (for ^1H) on a EM-360L (60 MHz) equipped with a signal averager (Varian V-2048) in order to measure the $J(^{195}Pt–^1H)$ couplings. The monosubstituted complexes were measured in D_2O, while the disubstituted complexes were measured in $CDCl_3$. The comparison with the free ligands is made with identical solvents, unless another solvent is specified. The external standard for the ^{195}Pt spectra was $[Pt(H_2O)_6]^{4+}$ (δ = 0 ppm). The IR spectra were measured on either a FTIR Bio-Rad 600 (resolution 1 cm^{-1}) or a P.E. 783. The decomposition points were measured on a Fisher–Johns instrument. The ligands were obtained from Aldrich and K_2PtCl_4 from Johnson Matthey and Co. The latter was recrystallized from water before use.

$(N(CH_3)_4)_2[PtCl_4]$ was prepared either by passing an aqueous solution of K_2PtCl_4 through a cation ($N(CH_3)_4^+$) exchange resin or by mixing directly an aqueous solution of K_2PtCl_4 with tetramethylammonium chloride. The yield is quantitative; mp 260–262°C (dec.); IR: ν(Pt–Cl): 318 and 303 cm^{-1}; ^1H NMR in D_2O, δ: 3.2 ppm.

$(N(CH_3)_4)[Pt(R\text{-}CN)Cl_3]$

The nitrile (1 mmol) was added to 5 mL of an aqueous solution containing 1 mmol of $(N(CH_3)_4)_2[PtCl_4]$. The solution was stirred until it became yellow (about 10 days). The mixture was filtered and the filtrate was evaporated to dryness. The residue was dissolved in a small quantity of acetone and the mixture was filtered to remove KCl and unreacted K_2PtCl_4. The filtrate was evaporated to dryness and dried under vacuum. $(N(CH_3)_4)[Pt(CH_3CN)Cl_3]$: Yield: quantitative; mp 150–158°C (dec.); IR (cm^{-1}): 2300 ν(C≡N), 2333 (δ(CH_3) + ν(C-C)), 345, 332, 310 (ν(Pt-Cl)); ^1H NMR, δ(ppm): 3.19 ($(CH_3)_4N^+$), 2.54s + d (CH_3), and $^4J(^{195}Pt–^1H)$ = 14.5 Hz. $(N(CH_3)_4)[Pt(C_2H_5CN)Cl_3]$: Yield: 40%; dec. mp 167-185°C (dec.); IR (cm^{-1}): 2295 ν(C≡N), 333, 323, 318 (ν(Pt-Cl)); ^1H NMR, δ(ppm): 3.19 ($(CH_3)_4N^+$), 1.41t(CH_3), 2.80q(CH_2), and $^4J(^{195}Pt–^1H)$ = 14 Hz. $(N(CH_3)_4)$ $[Pt(C_3H_7CN)Cl_3]$: Yield: 40%; mp 172–180°C (dec.); IR (cm^{-1}): 2290 ν(C≡N), 2342 (δ(CH_3) + ν(C-C)), 345, 333, 318 (ν(Pt-Cl)); ^1H NMR, δ(ppm): 3.20 ($(CH_3)_4N^+$), 1.03t(CH_3), 1.78m(CH_2), 2.97t(CH_2), and $^4J(^{195}Pt–^1H)$ = 15 Hz. $(N(CH_3)_4)[Pt(PhCN)Cl_3]$: Yield: 20%; mp 165–172°C (dec.); IR (cm^{-1}): 2285 ν(C≡N), 345, 339, 321 (ν(Pt-Cl)); ^1H NMR, δ(ppm): 3.19 ($(CH_3)_4N^+$), 7.75m (Ph).

$K[Pt(R\text{-}CN)Cl_3]$

The CH_3CN complex was prepared as already reported (8). The other complexes were synthesized in a similar way. The reaction time varied from 1 day to 1 week depending on the

ligand. The mixture was stirred on a cooling plate and evaporation was done below 30°C to avoid decomposition. $K[Pt(CH_3CN)Cl_3$: ^{13}C NMR, δ(ppm): 3.84, 117.39 (ligand: 1.72, 119.81). $K[Pt(C_2H_5CN)Cl_3$: IR (cm^{-1}): 2310 ν(C≡N) (ligand 2250), 342, 338, 333 ν(Pt-Cl). NMR, δ(ppm): ^1H, 1.27t, 2.90q (ligand: 1.22t, 2.44q); ^{13}C, 9.87, 12.99, 121.16 (ligand: 10.45, 11.10, 123.83). $K[Pt(C_3H_7CN)Cl_3$: IR (cm^{-1}): 2303 ν(C≡N) (ligand 2250), 328 (br) ν(Pt-Cl). NMR δ(ppm): ^1H, 1.02t, 1.72m, 2.90t (ligand: 1.01t, 1.66m, 2.44t); ^{13}C, 13.38, 19.05, 20.75, 120.21 (ligand: 13.38, 19.08, 19.27, 122.99). $K[Pt(C_4H_9CN)Cl_3$: IR (cm^{-1}): 2310 (ligand 2250) ν(C≡N), 345, 338, 325 ν(Pt-Cl). $K[Pt(CH_3)_2CHCN)Cl_3$: ^{13}C NMR, δ(ppm): 19.21, 22.11, 123.65 (ligand: 19.75, 20.29, 126.68). $K[Pt((CH_3)_3CCN)Cl_3$: IR (cm^{-1}): 2300 ν(C≡N) (ligand 2235), 343, 328, 310 ν(Pt-Cl). NMR δ(ppm): ^1H, 1.43s (ligand, neat: 1.39s); ^{13}C, 27.75, 30.77, 125.36 (ligand: 28.11, 28.84, 128.71). $K[Pt(PhCN)Cl_3$: IR (cm^{-1}): 2285 ν(C≡N) (ligand 2230), 355, 348, 335 ν(Pt-Cl). NMR δ(ppm): ^1H, 7.75m (ligand, 7.69d); ^{13}C, 117.24, 109.85, 134.68, 130.14, 135.99 (ligand: 119.26, 112.65, 132.48, 129.63, 133.27). $K[Pt(p\text{-}CH_3O\text{-}C_6H_4\text{-}CN)Cl_3$: IR ($cm^{-1}$): 2280 ν(C≡N), 352, 328, 310 ν(Pt-Cl). NMR δ(ppm): ^1H, 3.98s, 7.29d, 7.95d (ligand neat, 3.90s, 7.05d, 7.64d); ^{13}C, 56.73, 117.76, 101.12, 136.66, 116.02, 165.10 (ligand in $CDCl_3$: 55.5, 119.1, 103.9, 133.9, 114.9, 163.0). $K[Pt(p\text{-}HO\text{-}C_6H_4\text{-}CN)Cl_3$: IR ($cm^{-1}$): 2290 ν(C≡N), 340, 335, 320 ν(Pt-Cl). NMR δ(ppm): ^1H, 7.90, 7.48 (ligand neat, 7.60, 7.00); ^{13}C, 117.96, 100.35, 136.90, 117.33, 162.73 (ligand in $CDCl_3$: 119.6, 101.9, 134.0, 116.5, 161.4).

$Pt(R\text{-}CN)_2Cl_2$

These complexes can be prepared from the aqueous reaction of K_2PtCl_4 with an excess of the nitrile at room temperature as already reported for acetonitrile (1). $(N(CH_3)_4)_2[PtCl_4]$ can also be used as starting material and the yields are quantitative. $Pt(C_2H_5CN)_2Cl_2$: Yield: 85%; mp 155–163°C (dec.); IR (cm^{-1}): 2315 ν(C≡N), 351, 345 (ν(Pt-Cl)); ^1H NMR, δ(ppm): 1.42t (CH_3), 2.92q (CH_2), and $^4J(^{195}Pt\text{-}^1H)$ = 14 Hz. $Pt(C_3H_7CN)_2Cl_2$: Yield: 85%; mp 215–250°C (dec.); IR (cm^{-1}): 2304 ν(C≡N), 2343 δ(CH_3) + ν(C-C), 355, 348 (ν(Pt-Cl)); ^1H NMR, δ(ppm): 1.12t (CH_3), 2.95t (CH_2), 1.87m (CH_2), and $^4J(^{195}Pt\text{-}^1H)$ = 15 Hz. $Pt(C_4H_9CN)_2Cl_2$: Yield: 80%; IR (cm^{-1}): 2309 ν(C≡N), 359, 348 (ν(Pt-Cl)). $Pt(CH(CH_3)_2CN)_2Cl_2$: Yield: 80%; IR (cm^{-1}): 2303 ν(C≡N), 358, 352 (ν(Pt-Cl)). $Pt(C(CH_3)_3CN)_2Cl_2$: Yield: 80%; IR (cm^{-1}): 2301 ν(C≡N), 353(br) (ν(Pt-Cl)); ^1H NMR, δ(ppm): 1.43s. $Pt(PhCN)_2Cl_2$: Yield: 85%; mp 210–218°C (dec.); IR (cm^{-1}): 2290 ν(C≡N), 360, 345 (ν(Pt-Cl)); ^1H NMR, δ(ppm): 7.75m (Ph). $Pt(p\text{-}OH\text{-}C_6H_4\text{-}CN)_2Cl_2$: Yield: 75%; IR ($cm^{-1}$): 2290 ν(C≡N), 353, 340 (ν(Pt-Cl)). $Pt(p\text{-}CH_3O\text{-}C_6H_4\text{-}CN)_2Cl_2$: Yield: 75%; IR ($cm^{-1}$): 2280 ν(C≡N), 352 (br) (ν(Pt-Cl)); ^1H NMR, δ(ppm): 3.92s (CH_3), 7.65d, 7.06d.

The data collections (2θ/θ) were made at room temperature, either on a Syntex $P\bar{1}$ diffractometer (**1**, **5**) or a Siemens P4 (**2**, **3**, **4**), with graphite-monochromatized MoKα radiation (0.71069 Å). The cell parameters were calculated from the refined angles of 15–30 centered reflections. The experimental details of the crystallographic studies are shown in Table 1. The scan rate varied between 1° and 29° min^{-1}. An absorption correction based on the equations of the crystal faces was applied and the data were corrected for Lorenz and polarization effects. The calculations were done on a Siemens SHELXTL system, PC-plus version.

Results and discussion

$[Pt(R\text{-}CN)Cl_3]^-$ complexes

The complexes $K[Pt(R\text{-}CN)Cl_3]$ were synthesized from the aqueous reaction of K_2PtCl_4 with the nitrile in a mole to mole ratio of 1:1.5. In a 1:2 proportion, only the disubstituted compound is formed, while in a 1:1 ratio the reaction is slow and decomposition can occur. The monoacetonitrile compound is fairly stable and can be obtained overnight, but the complexes with other ligands are more slowly formed (1 day to 1 week) and are less stable. It is therefore important to cool the reaction medium during their synthesis. The crystals were too unstable in air for X-ray diffraction studies. Therefore the larger cation $N(CH_3)_4^+$ was used. The complexes were prepared from the aqueous reaction of $(N(CH_3)_4)_2[PtCl_4]$ with the nitrile (1:1 ratio) at room temperature. The reaction time was between 7 and 10 days. The compounds with butyronitrile and *p*-hydroxybenzonitrile were studied by X-ray diffraction.

The IR spectra of the $N(CH_3)_4^+$ complexes have shown that the ν(C≡N) vibration is observed at higher frequency in the coordinated ligand (Δ = 43–50 cm^{-1}), while Δ is slightly larger (55–65 cm^{-1}) for the K^+ compounds. This absorption at higher energy than in the free ligands is well known and has been discussed in detail for *cis*-$Pt(CH_3CN)_2Cl_2$ (11). The spectra showed three ν(Pt-Cl) ($2A_1$ and B_2) expected for a C_{2v} symmetry, between 345 and 310 cm^{-1}. The ^1H NMR spectra, measured on a low-field instrument, showed $^4J(^{195}Pt\text{-}^1H)$ coupling constants of 14–15 Hz.

The refined atomic parameters of the two complexes $N(CH_3)_4^+$ $[Pt(R\text{-}CN)Cl_3]$ where R = C_3H_7 and *p*-OH-C_6H_4, are listed in Table 2. Labelled diagrams of the molecules are shown in Figs. 1 and 2. As expected, the coordination around Pt(II) is square planar and the angles around Pt are close to 90 and 180°. The nitrile ligand is bonded through its lone pair of electrons on the N atom.

Some selected bond distances and angles are listed in Table 3. For each structure, the Pt—Cl bond in *trans* position to the nitrile ligand is shorter (2.276(3) Å for **1** and 2.264(7) Å for **2**) than the other two Pt—Cl bonds, which are normal (2.293(4), 2.287(3) Å for **1** and 2.320(7), 2.275(8) Å for **2**). Shorter Pt— Cl bonds located in *trans* position to CH_3CN (2.263(3)–2.277(5) Å) (11) and 2.266(2) Å (10)) have also been reported. The differences are not very large, but they are very consistent. The *trans* influence of nitriles seems therefore to be smaller than that of sulfoxides, halides, and amines. The short bond distances might also be due to the multiple nature of the Pt—N bonds located in *trans* position to the short Pt—Cl bonds. These results have shown that Pt—Cl bonds located in *trans* positions to nitrile ligands are definitely shorter than normal, and we suggest that the presence of multiple bonding in the *trans* bond is responsible for the bond shortening.

The Pt—N bonds are 1.97(1) Å for **1** and 1.92(2) Å for **2**. These values are similar to the reported values (10, 11), and are shorter than those observed for Pt–amine or Pt–pyridine bonds. The shortening might be ascribed to the presence of electron back-donation from the metal to the ligand. The segment Pt-N≡C-C is linear with angles Pt-N-C = 174(1)°, 171(2)° and N-C-C = 178(1)°, 176(3)° and

Table 1. Experimental details of the X-ray diffraction studies of the five crystals.

	1	2	3	4	5
Formula	$C_8H_{19}N_2Cl_3Pt$	$C_{11}H_{17}N_2OCl_3Pt$	$C_6H_{10}N_2Cl_2Pt$	$C_6H_{10}N_2Cl_2Pt$	$C_{14}H_{10}N_2O_2Cl_2Pt$
fw	404.24	494.72	376.15	376.15	504.24
Space group	$P2_1/c$	$P42bc$	$P2_1/c$	$P2_1/c$	P-1
a (Å)	8.384(5)	16.222(6)	7.506(5)	5.149(4)	7.464(3)
b (Å)	15.336(19)		9.539(5)	9.394(8)	10.712(6)
c (Å)	11.759(9)	12.052(5)	14.823(7)	10.944(10)	12.291(5)
α (°)	90.	90.	90.	90.	75.63(4)
β (°)	99.52(6)	90.	92.31(4)	97.84(6)	75.48(4)
γ (°)	90.	90.	90.	90.	80.32(4)
Volume (Å^3)	1491(2)	3172(3)	1061(1)	524.3(8)	915.7(8)
Z	4	8	4	2	2
F(000)	840	1872	688	344	472
ρ_{calcd} (Mg m^{-3})	1.854	2.072	2.356	2.382	1.828
μ(MoKα) (mm)	10.025	9.34	13.83	13.834	8.036
Crystal faces and distance from center (mm)	12 Faces with dimensions 0.18 × 0.35 × 0.71	(100) (-100) 0.048 (010) (0-10) 0.029 (001) (00-1) 0.120	(100) (-100) 0.22 (010) (0-10) 0.058 (001) (00-1) 0.011	(0-11) (01-1) 0.048 (011) (0-1-1) 0.067 (-114) (11-2)0.15	(010) (0-10) 0.063 (001) (00-1) 0.106 (110) (-1-10) 0.221
Transm. factor range	0.032–0.222	0.421–0.595	0.212–0.723	0.189–0.318	0.191–0.418
2θ max (°)	58	57	55	55	60
h, k, l	0→11, 0→20, −16→15	−1→21, −1→21, −1→16	0→9, 0→12, −19→19	0→6, 0→12, −14→14	0→9, −14→15, −16→17
Independent reflcns.	3975	2285	2754	1215	5149
Observed reflcns.	2246 ($F > 2.5\sigma(I)$)	1034 ($F > 4\sigma(F)$)	1447 ($F > 5.5\sigma(F)$)	863 ($F > 4.0\sigma(F)$)	3928 ($I > 2.5\sigma(I)$)
w^{-1}	$\sigma^2(F)$	$\sigma^2(F) + 0.0001(F^2)$	$\sigma^2(F) + 0.0001(F^2)$	$\sigma^2(F) + 0.0001(F^2)$	$\sigma^2(F)$
R	0.054	0.059	0.050	0.017	0.045
wR	0.051	0.044	0.042	0.020	0.056
S	1.63	1.14	1.88	1.3	1.58
$(\Delta/\sigma)_{max}$	0.08	0.06	0.08	0.000	0.07
$(\Delta^\rho)_{max}$ (e Å^3)	1.3 (close to Pt)	1.8 (close to Pt)	1.7 (close to Pt)	0.49 (close to Pt)	1.9

Fig. 1. Labelled diagram of $N(CH_3)_4[Pt(C_3H_7\text{-}CN)Cl_3]$ (**1**).

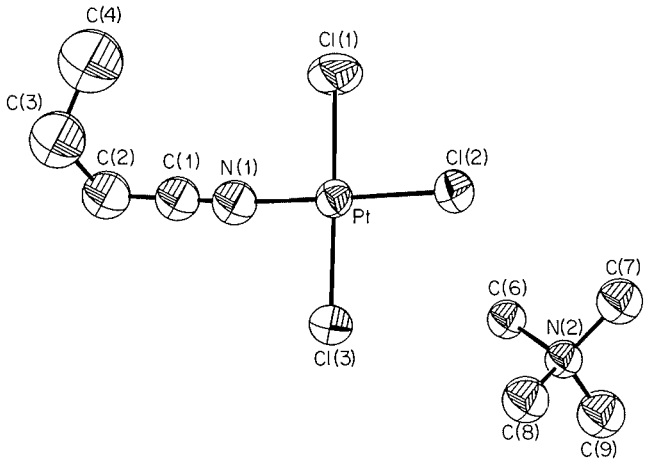

Fig. 2. Labelled diagram of the ion $[Pt(p\text{-}OH\text{-}C_6H_4\text{-}CN)Cl_3]^-$ (**2**).

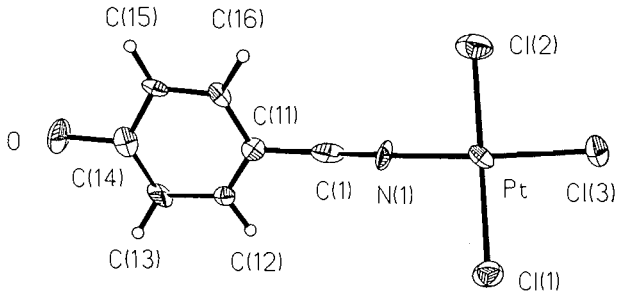

the N≡C bond distances are 1.13(2) and 1.13(4) Å for **1** and **2**, respectively.

The crystal $N(CH_3)_4[Pt(p\text{-}OH\text{-}C_6H_4\text{-}CN)Cl_3]$ is stabilized by intermolecular hydrogen bonding between the hydroxy group and Cl(3), located in *trans* position to the nitrile ligand. This hydrogen bond does not seem to affect the Pt—Cl(3) bond length. The distance O···Cl(3) is 3.271 Å. A packing diagram of the molecules has been prepared and is part of the supplementary material.[2]

[2] The following tables and figures have been deposited: anisotropic thermal factors (S1), H coordinates (S2), bond distances and angles (S3), weighted best planes (S4), and packing diagrams of crystal **2** (Fig. S1) and of crystal **5** (Fig. S2). This material may be purchased from: The Depository of Unpublished Data, Document Delivery, CISTI, National Research Council Canada, Ottawa, Canada K1A 0R6. With the exception of Tables S1 and S4, the above have also been deposited with the Cambridge Crystallographic Data Centre, and can be obtained on request from The Director, Cambridge Crystallographic Data Centre, University Chemical Laboratory, 12 Union Road, Cambridge, CB2 1EZ, U.K.

Table 2. Positional parameters ($\times 10^4$) with their e.s.d.'s and temperature factors (10^3). U_{eq} = 1/3 $\Sigma_i\Sigma_j U_{ij} a_i^* a_j^* a_i \cdot a_j$

Atom	x	y	z	U_{eq} (Å)
$N(CH_3)_4[Pt(C_3H_7\text{-}CN)Cl_3]$ (**1**)				
Pt	2265.2(5)	754.6(3)	−1968.1(3)	50.2
Cl(1)	3952(4)	126(3)	−3082(3)	90.3
Cl(2)	1490(4)	1775(2)	−3354(2)	69.6
Cl(3)	576(4)	1358(2)	−843(2)	83.5
N(1)	2880(12)	−176(7)	−827(7)	72
N(2)	1700(10)	4109(5)	−1684(6)	54
C(1)	3182(14)	−762(9)	−243(10)	71
C(2)	3545(17)	−1542(10)	475(11)	89
C(3)	3104(20)	−2342(11)	−234(14)	115
C(4)	3875(27)	−2532(14)	−1320(14)	172
C(5)	3090(12)	3522(8)	−1168(8)	59
C(6)	1744(17)	4247(9)	−2973(8)	83
C(7)	107(13)	3707(9)	−1530(9)	74
C(8)	1861(18)	5010(8)	−1095(10)	91
$N(CH_3)_4[Pt(p\text{-}OH\text{-}C_6H_4\text{-}CN)Cl_3]$ (**2**)				
Pt	7566(1)	1128(1)	3000	38(1)
Cl(1)	6275(4)	545(4)	3265(8)	56(2)
Cl(2)	8809(5)	1754(5)	2765(9)	75(3)
Cl(3)	7290(5)	1319(6)	1178(6)	59(2)
O	9024(15)	941(15)	9888(17)	69(4)
N(1)	7890(16)	922(16)	4506(17)	49(4)
N(2)	3693(16)	1240(18)	370(17)	39(4)
C(1)	8074(18)	916(16)	5408(25)	44(4)
C(2)	4414(19)	1189(19)	1405(28)	55(4)
C(3)	3622(22)	425(26)	−118(30)	71(4)
C(4)	3017(16)	1317(21)	1346(28)	56(4)
C(5)	3813(29)	2186(24)	−15(38)	109(4)
C(11)	8335(17)	848(14)	6596(23)	28(4)
C(12)	7787(18)	972(19)	7373(22)	29(4)
C(13)	7980(20)	933(21)	8469(22)	45(4)
C(14)	8757(20)	945(16)	8758(24)	46(4)
C(15)	9364(13)	879(12)	7926(30)	34(4)
C(16)	9100(17)	846(15)	6873(21)	29(4)
cis-$Pt(C_2H_5\text{-}CN)_2Cl_2$ (**3**)				
Pt	2117.2(8)	6185.3(6)	5033.9(4)	39.8(2)
Cl(1)	3148(7)	6689(5)	6457(3)	72(1)
Cl(2)	1182(6)	8431(4)	4831(3)	55(1)
N(1)	2823(15)	4191(12)	5202(8)	48(2)
N(2)	1255(15)	5789(11)	3793(9)	54(2)
C(1)	3331(15)	3134(16)	5294(11)	48(2)
C(2)	729(19)	5633(15)	3065(11)	57(2)
C(3)	3833(19)	1651(14)	5464(12)	63(2)
C(4)	12(19)	5451(16)	2160(11)	59(2)
C(5)	4431(20)	1326(17)	6394(12)	80(2)
C(6)	−1518(20)	6363(18)	1978(12)	82(2)

Table 2 (*concluded*).

Atom	x	y	z	U_{eq} (Å)
trans-$Pt(C_2H_5\text{-}CN)_2Cl_2$ (**4**)				
Pt	5000	0	5000	37(1)
Cl	4394(3)	2391(2)	5249(1)	61(1)
N	7345(8)	404(4)	3764(4)	44(1)
C(1)	8672(9)	647(5)	3057(4)	42(1)
C(2)	10370(10)	909(5)	2138(4)	47(1)
C(3)	11447(13)	−459(6)	1637(6)	56(2)
cis-$Pt(p\text{-}OH\text{-}C_6H_4\text{-}CN)_2Cl_2$ (**5**)				
Pt	1868.3(5)	955.4(3)	4261.5(3)	354
Cl(1)	538(3)	2918(2)	4652(2)	536
Cl(2)	1369(4)	1663(3)	2447(2)	631
O(1)	7043(11)	−6646(7)	3207(7)	705
O(2)	2847(11)	−799(8)	11359(5)	721
N(1)	2968(10)	−761(7)	3937(6)	439
N(2)	2262(10)	399(7)	5846(6)	460
C(1)	3570(12)	−1787(9)	3780(7)	439
C(2)	4451(12)	−3025(8)	3596(7)	440
C(3)	3622(14)	−3809(10)	3158(8)	518
C(4)	4527(15)	−5021(10)	3028(8)	567
C(5)	6247(14)	−5443(9)	3319(8)	518
C(6)	7039(14)	−4650(10)	3741(8)	584
C(7)	6130(13)	−3465(9)	3892(8)	508
C(8)	2425(13)	140(9)	6786(7)	450
C(9)	2573(12)	−109(9)	7946(6)	456
C(10)	3277(16)	−1279(10)	8472(8)	595
C(11)	3313(18)	−1523(10)	9660(9)	696
C(12)	2747(13)	−536(10)	10236(7)	529
C(13)	2072(15)	693(10)	9676(7)	550
C(14)	2003(14)	901(10)	8537(8)	558

The ^{195}Pt NMR spectra of the complexes were measured in D_2O and the results are shown in Table 4. The signals were observed between −1997 and −2020 ppm. The chemical shifts seem almost independent of the R substituent on the ligand. Pregosin (17) had observed a downfield shift when the ligand became sterically larger. Due to the linear nature of the Pt-N≡C-C segment, the binding site in nitriles is far from the R substituent, resulting in almost constant chemical shifts. The signals are observed at higher fields than those reported for $[Pt(amine)Cl_3]^-$ (−1822 to −1865 in DMF, −1855 to −1875 ppm in acetone (18)) and for $[Pt(pyridine)Cl_3]^-$ complexes (−1763 to −1897 ppm in D_2O (19)). The shielding observed for the mononitrile complexes (compared to amine complexes) might be attributed to the special nature of the Pt–nitrile bond. Nitrile ligands might be good π-donors in addition to their σ-donor ability.

The ^{13}C NMR spectra of the complexes were also measured in D_2O. The positions of the cyano carbons are listed in Table 4, along with Δ (complex–ligand) in order to evaluate the influence of the R substituents. The two ligands *p*-CH_3O-C_6H_4-CN and *p*-HO-C_6H_4-CN are not soluble in water, therefore their spectra were measured in $CDCl_3$. For comparison, Ph-CN was also measured in $CDCl_3$. The chemical shifts of the cyano carbon atoms are shifted towards higher field upon coordination. Most of the other C atoms are deshielded when compared to those of the ligands. The substituent effects on the ^{13}C chemical shifts in free nitriles were studied and it was found that the cyano carbon resonance shifts to higher field

Table 3. Selected bond distances (Å) and angles (°).

Bond	Distance	Bonds	Angle
$N(CH_3)_4[Pt(C_3H_7\text{-}CN)Cl_3]$ (**1**)			
Pt—Cl(1)	2.293(4)	Cl(1)-Pt-Cl(2)	90.6(1)
Pt—Cl(2)	2.276(3)	Cl(1)-Pt-Cl(3)	179.0(1)
Pt—Cl(3)	2.287(3)	Cl(1)-Pt-N(1)	88.2(3)
Pt—N(1)	1.97(1)	Cl(2)-Pt-Cl(3)	90.3(1)
N(1)-C(1)	1.13(2)	Cl(2)-Pt-N(1)	177.0(3)
C(1)-C(2)	1.47(2)	Cl(3)-Pt-N(1)	90.9(3)
		Pt-N(1)-C(1)	174(1)
		N(1)-C(1)-C(2)	178(1)
$N(CH_3)_4[Pt(p\text{-}OH\text{-}C_6H_4\text{-}CN)Cl_3]$ (**2**)			
Pt—Cl(1)	2.320(7)	Cl(1)-Pt-Cl(2)	177.5(3)
Pt—Cl(2)	2.275(8)	Cl(1)-Pt-Cl(3)	90.6(3)
Pt—Cl(3)	2.264(7)	Cl(1)-Pt-N(1)	92.6(8)
Pt—N(1)	1.92(2)	Cl(2)-Pt-Cl(3)	89.6(4)
N(1)-C(1)	1.13(4)	Cl(2)-Pt-N(1)	87.3(8)
		Cl(3)-Pt-N(1)	174.9(8)
		Pt-N(1)-C(1)	171(2)
		N(1)-C(1)-C(11)	176(3)
cis-$Pt(C_2H_5\text{-}CN)_2Cl_2$ (**3**)			
Pt—Cl(1)	2.269(5)	Cl(1)-Pt-Cl(2)	90.9(2)
Pt—Cl(2)	2.270(4)	Cl(1)-Pt-N(1)	90.4(4)
Pt—N(1)	1.988(11)	Cl(1)-Pt-N(2)	178.7(3)
Pt—N(2)	1.962(14)	Cl(2)-Pt-N(1)	177.4(4)
N(1)-C(1)	1.09(2)	Cl(2)-Pt-N(2)	88.2(3)
N(2)-C(2)	1.14(2)	N(1)-Pt-N(2)	90.5(5)
C(1)-C(3)	1.48(2)	Pt-N(1)-C(1)	175(1)
C(2)-C(4)	1.44(2)	Pt-N(2)-C(2)	176(1)
		N(1)-C(1)-C(3)	174(1)
		N(2)-C(2)-C(4)	178(1)
trans-$Pt(C_2H_5\text{-}CN)_2Cl_2$ (**4**)			
Pt—Cl(1)	2.289(3)	Cl(1)-Pt-N(1)	89.9(1)
Pt—N(1)	1.969(5)	Cl(1)-Pt-N(1a)	90.1(1)
N(1)-C(1)	1.124(7)	Pt-N(1)-C(1)	179.3(4)
		N(1)-C(1)-C(2)	178.1(5)
cis-$Pt(p\text{-}OH\text{-}C_6H_4\text{-}CN)_2Cl_2$ (**5**)			
Pt—Cl(1)	2.279(3)	Cl(1)-Pt-Cl(2)	89.2(1)
Pt—Cl(2)	2.274(2)	Cl(1)-Pt-N(1)	178.7(2)
Pt—N(1)	1.976(7)	Cl(1)-Pt-N(2)	88.9(2)
Pt—N(2)	1.972(7)	Cl(2)-Pt-N(1)	90.9(2)
O(1)-C(5)	1.35(1)	Cl(2)-Pt-N(2)	178.1(2)
O(2)-C(12)	1.36(1)	N(1)-Pt-N(2)	91.1(3)
N(1)-C(1)	1.16(1)	Pt-N(1)-C(1)	177.7(7)
N(2)-C(8)	1.15(1)	Pt-N(2)-C(8)	175.9(7)
C(1)-C(2)	1.42(1)	N(1)-C(1)-C(2)	175.3(9)
C(8)-C(9)	1.41(1)	N(2)-C(8)-C(9)	177(1)

with increasing electronegativity of the substituent R (20). The correlation was explained in terms of the π-bond polarization, which is caused by the electric field of the substituent. The chemical shifts are linearly dependent on the π-electron density on the nucleus and a change on the cyano carbon atom is caused by the variation of the π-bond polarization (20). The complexation of the nitrile ligand to platinum will increase the polarization of the bond. It can be observed from Table 4 that, upon complexation, the cyano carbon atoms become more shielded as the number of methyl groups increase (Δ(complex–ligand) = −2.4 for R = CH_3 to −3.4 ppm for R = $C(CH_3)_3$). There are at least three factors that could affect the electron density on the complexed ligand: the π-bond polarization effect as discussed above, which should increase the electron density on the cyano carbons as the number of methyl groups in the substituent R increases, the σ-bond, which should reduce the electron density on the nitrile ligand; and finally the π-back-donation, which should increase the electronic density of the ligand. Therefore, it is not easy to interpret the results of such studies. When the alkyl groups on the nitriles are replaced by phenyl groups, the shielding on the cyano carbon is slightly reduced (Table 4). The formation of complexes with these derivatives is favored by the mesomeric effect on the ligand, which increases the polarization of the C≡N π-bond.

The $^2J(^{195}Pt\text{–}^{13}C)$ were difficult to measure for several reasons: the low intensity of quaternary cyano carbon atoms, the high field of the instrument (a 400 MHz was used, since on lower field instruments, the compounds decomposed after several hours of accumulation) that causes low intensities for the satellites' couplings, and finally the close environment of a ^{14}N atom with a spin $I > ½$ that increases the relaxation time of the cyano carbon atom. The ^2J couplings vary from 223 to 257 Hz, but the values are not very precise. The couplings are quite high because of the large *s* character of the cyano carbon atoms.

$Pt(R\text{-}CN)_2Cl_2$ complexes

Some of these complexes are known in the literature, but their ^{195}Pt NMR spectra and their crystal structures (except for *cis*-$Pt(CH_3CN)_2Cl_2$) have not been reported. When the reactions were done at room temperature, only *cis*-$Pt(RCN)_2Cl_2$ was formed (or >95%), since only one peak was observed in ^{195}Pt NMR spectroscopy. These results are different from those published by Fraccarollo et al. (7), who reported that most of their products at room temperature were *cis–trans* mixtures containing between 7 and 15% of *trans* compounds, except for trimethylacetonitrile, which produced 80% of *trans* isomers after 4 days. But their experimental procedures were different. They used a much larger excess of nitrile ligands. The mixture was treated with dichloromethane and the isomers were separated by crystallization in organic solvents such as hot benzene, *n*-hexane, ether, and petroleum ether. We believe that the *trans* isomers were probably formed when dichloromethane was added to the mixture to extract the complexes. The *cis–trans* isomerization of these complexes in chloroform is discussed below.

The ^{195}Pt signals for all the *cis* complexes (Table 5) were observed at very similar fields (−2276 to −2288 ppm) except for *cis*-$Pt(p\text{-}CH_3O\text{-}C_6H_4\text{-}CN)_2Cl_2$, which was observed at slightly lower field (−2239 ppm). These values are at a

Fig. 3. Labelled diagram of *cis*-$Pt(C_2H_5\text{-}CN)_2Cl_2$ (**3**).

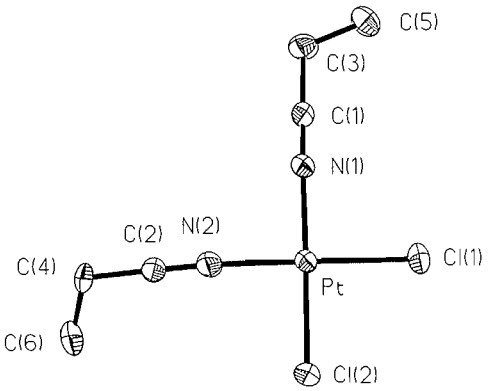

slightly higher field than those reported for the *cis* complexes of several primary amines (≈−2230 ppm), and the corresponding complexes with secondary amines (≈−2180 ppm) (18). These observations are in agreement with the results observed by Pregosin (17), who reported a ^{195}Pt downfield shift when the ligand became more sterically demanding close to the binding site. Nitriles are never bulky around the binding atom, resulting in slightly more shielded ^{195}Pt signals. As already mentioned for mononitrile complexes, nitriles might be good π-donors in addition to their σ-donor ability. The IR spectra of these complexes showed two ν(Pt-Cl) bands (or a large band) around 345 and 355 cm^{-1} as expected for C_{2v} symmetry and as already reported (2, 3, 7, 11).

The crystal structures of the *cis* complexes with C_2H_5-CN (**3**) and *p*-HO-C_6H_4-CN (**5**) were determined. The refined atomic parameters of the complexes are listed in Table 2. Labelled diagrams of the molecules are shown in Figs. 3 and 4. Some selected bond distances and angles are listed in Table 3. The Pt—Cl bonds are again shorter than normal (2.269(5), 2.270(4) Å for **3** and 2.274(2), 2.279(3) Å for **5**) as observed for the Pt(II)–mononitrile complexes discussed above and as reported for *cis*-$Pt(CH_3CN)_2Cl_2$ (11), confirming the small *trans* influence of nitriles. Again, we believe that the presence of multiple bonding in the *trans* bond is responsible for these bond shortenings.

The Pt—N bonds are 1.962(14), 1.988(11) Å for **3** and 1.976(7), 1.972(7) Å for **5**. These values are similar to those observed for *cis*-$Pt(CH_3CN)_2Cl_2$ (11), and are shorter than those usually reported for Pt–amine or Pt–pyridine bonds. The shortening might be due to the presence of electron back-donation from the metal to the ligand or (and) to the presence of π-donation from the ligand. The segments Pt-N≡C-C are linear with angles Pt-N-C = 175(1)°, 176(1)°; 177.7(7)°, 175.9(7)° and N-C-C = 174(1)°, 178(1)°; 175.3(9)°, 177(1)° for **3** and **5**, respectively. The nitrile bonds are 1.09(2), 1.14(2) Å for **3** and 1.15(1), 1.16(1) Å for **5**. The crystal *cis*-Pt(*p*-OH-C_6H_4-$CN)_2Cl_2$ is stabilized by intermolecular hydrogen bonds between the hydroxy groups and the chloro ligands. The distances O(1) ··· Cl(1) and O(2) ··· Cl(2) are 3.417(6) and 3.161(8) Å and the angles C-O ··· Cl are reasonable, 101.5(6)° and 111.3(6)°, respectively.

When the *cis* isomers were heated for a few hours at about 50°C in $CHCl_3$, they partly isomerized to the *trans* compounds. The ^{195}Pt NMR spectra showed a new signal at lower field than that of the *cis* isomers (Δ = 65 Hz). The isomerization was not complete. For the complex $Pt(C_2H_5CN)_2Cl_2$, the proportion of each isomer was about 50%. The mixture was

Fig. 4. Labelled diagram of *cis*-Pt(*p*-OH-C_6H_4-$CN)_2Cl_2$ (**5**).

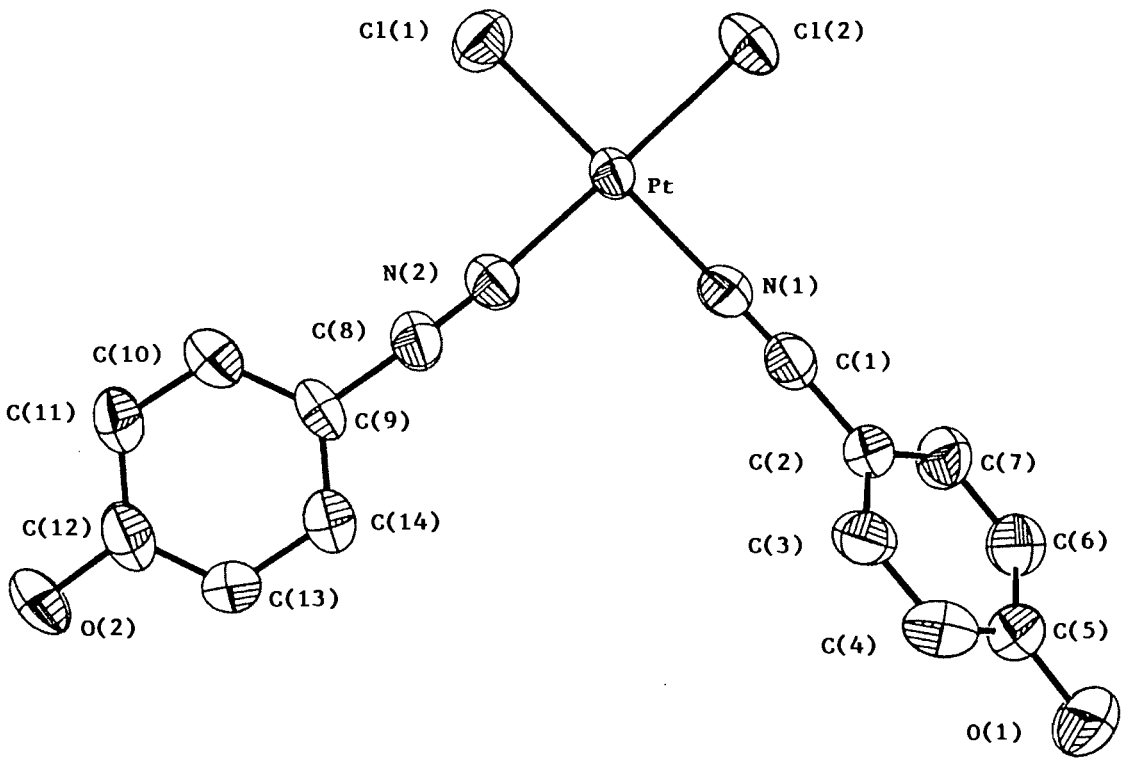

Table 4. ^{13}C (cyano carbon) and ^{195}Pt NMR spectra of $K[Pt(R\text{-}CN)Cl_3]$ in D_2O.

R	δ(*C*N), ppm	Δ(complex–ligand)	$^2J(^{195}Pt–^{13}C)$, Hz	δ(Pt), ppm
CH_3	117.4	−2.4	228	−2000
C_2H_5	121.2	−2.7	257	−2002
n-C_3H_7	120.2	−2.8	244	−1997
iso-C_3H_7	123.7	−3.0	223	
t-C_4H_9	125.4	−3.4	239	−2008
Ph	117.2	−2.0	244	−2020
		−1.6[a]		
CH_3O-Ph	117.8	−1.3[a]	n.o.	−2004
HO-C_6H_4	118.0	−1.6[a]	n.o.	−2003

[a]The ligands were measured in $CDCl_3$; n.o., not observed.

Table 5. ^{13}C (of the cyano C) and ^{195}Pt NMR signals of the $Pt(R\text{-}CN)_2Cl_2$ complexes (in $CDCl_3$).

	δ(^{13}C)		$^2J(^{195}Pt–^{13}C)$ (Hz)		δ(^{195}Pt) (ppm)	
R	*cis*	*trans*	*cis*	*trans*	*cis*	*trans*
C_2H_5	118.4	119.0	231	283	−2280	−2344
n-C_3H_7	117.4	118.2			−2277	
n-C_4H_9	117.4	118.4			−2276	
iso-C_3H_7	120.8	121.8	228		−2283	
t-C_4H_9	122.6	123.8			−2288	
Ph	115.3	116.8	234	289	−2284	−2350
p-CH_3O-C_6H_4					−2239	

Fig. 5. Labelled diagram of *trans*-$Pt(C_2H_5\text{-}CN)_2Cl_2$ (**4**).

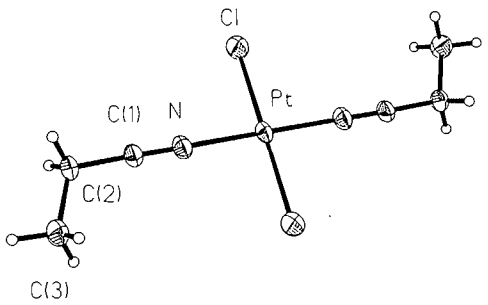

chromatographed on a silica gel column using CH_2Cl_2–CH_3OH as eluant. The separation was almost complete. The first compound to be eluted was the *trans* isomer, which was shown by ^{195}Pt NMR to contain about 5% of the *cis* isomer. The IR spectrum of the purified *trans* compound showed a single sharp ν(Pt-Cl) band at 347 cm^{-1}. These results are similar to those reported on *cis*-$Pt(R\text{-}CN)_2Cl_2$ (R = CH_3 and Ph), which were found to isomerize in the solid state, to the *trans* isomers with partial decomposition. In solution, a mixture of *cis* and *trans* isomers were obtained (4, 16).

These observations suggest that, at room temperature, the first compound formed in these reactions is the *cis* isomer, which then isomerizes to the *trans* compound upon heating. The *trans* effect of nitriles seems therefore to be smaller than that of chlorides. This result might appear surprising because of the presence of multiple bonding in the nitrile ligands. But the nature of the Pt–nitrile bond is very different from that with ligands having a high *trans* effect. Ligands which have a high *trans* effect can form π-bonds with the metal either through a $(d–d)\pi$ bond like sulfoxides or phosphines, or through the multiple bond of the ligand as observed for alkenes or alkynes, where the multiple bond of the ligand is perpendicular to the platinum plane. With nitriles, the segment Pt-N≡C-C is linear and therefore the triple bond of the nitrile is in the Pt square plane.

In ^{13}C NMR spectroscopy, the cyano carbon atoms of the *cis* isomers are more shielded (0.6–1.5 ppm) than those of the *trans* compounds (Table 5). The ^{195}Pt NMR spectra have shown that the *trans* isomers are more shielded (≈65 ppm), as expected from the results of ^{13}C NMR spectroscopy. The back-donation of electron density from the metal to the ligand is less effective in the *trans* isomer than in the *cis* isomer, which has very effective $\pi(d–\pi^*)$ bonding. The $^2J(^{195}Pt–^{13}C)$ coupling constants for the *trans* isomers (286 Hz) are larger than those for the *cis* compounds (231 Hz), as was observed by Fraccarollo et al. (7).

The crystal structure of *trans*-$Pt(C_2H_5CN)_2Cl_2$ (**4**) was determined. This is the first crystal structure report on a *trans* compound. The labelled diagram of the molecule is shown in Fig. 5. The Pt atom lies on an inversion centre. The Pt—Cl distances are 2.289(3) Å, very similar to the distances observed for the bonds located in *cis* positions to the nitrile in $[Pt(R\text{-}CN)Cl_3]^-$, in agreement with the hypotheses described above regarding short Pt—Cl bonds located in *trans* positions to nitrile ligands. The Pt—N bonds are 1.969(5) Å, identical to the values obtained in the crystals described above. The N-C

bond is 1.124(7) Å, and the Pt-N-C(1) and N-C(1)-C(2) angles are 179.3(4)° and 178.1(5)°, respectively.

Acknowledgment

The authors are grateful to the Natural Sciences and Engineering Research Council of Canada for financial support.

References

1. K.A. Hoffmann and G. Bugge. Ber. Dtsch. Chem. Ges. **40**, 1772 (1907).
2. A. Walton. Spectrochim. Acta, **21**, 1795 (1965); Can. J. Chem. **44**, 1480 (1966).
3. F.P. Fanizzi, F.P. Intini, L. Maresca, and G. Natile. J. Chem. Soc. Dalton Trans. 199 (1990).
4. T. Uchiyama, Y. Nakamura, T. Miwa, S. Kawaguchi, and S. Okeya. Chem. Lett. 337 (1980).
5. T. Uchiyama, Y. Toshiyasu, Y. Nakamura, T. Miwa, and S. Kawaguchi. Bull. Chem. Soc. Jpn. **54**, 181, (1981).
6. V. A. Golovnya and N. Tszya-Tszyan. Russ. J. Inorg. Chem. **7**, 715 (1960).
7. D. Fraccarollo, R. Bertani, M. Mozzon, U. Belluco, and R.A. Michelin. Inorg. Chim. Acta, **201**, 15 (1992).
8. T. Weil, L. Spauling, and M. Orchin. J. Coord. Chem. **1**, 25 (1971).
9. F.D. Rochon and L. Fleurent. Inorg. Chim. Acta, **143**, 81 (1988).
10. V.Y. Kukushkin, I.A. Krol, Z.A. Stazikova, and V.M. Tkachuk. Koord. Khim. **16**, 1406 (1990).
11. F.D. Rochon, R. Melanson, H.E. Howard-Lock, C.J.L. Lock, and G. Turner. Can. J. Chem. **62**, 860 (1984).
12. R. Melanson and F.D. Rochon. Acta Crystallogr. Sect. C: Cryst. Struct. Commun. **C44**, 1893 (1988).
13. R.H. Price, J.P. Birk, and B.B. Wayland. Inorg. Chem. **17**, 2245 (1978).
14. F.D. Rochon, P.C. Kong, and L. Girard. Can. J. Chem. **64**, 1897 (1986).
15. R.H. Price, R. Williamson, R.F. Schramm, and B.B. Wayland. Inorg. Chem. **11**, 1280 (1972).
16. V.Y. Kukushkin and V.M. Tkachuk. Z. Anorg. Allg. Chem. **613**, 123 (1992).
17. P.S. Pregosin. Coord. Chem. Rev. **44**, 247 (1982).
18. F.D. Rochon, M. Doyon, and I.S. Butler. Inorg. Chem. **32**, 2717 (1993).
19. C. Bensimon. Ph. D. Thesis. Université de Montréal. 1991.
20. T. Yonemoto. J. Magn. Reson. **12**, 93 (1973).

Some thermodynamic and transport properties of lithium salts in mixed aprotic solvents and the effect of water on such properties

Lorraine Couture, Jacques E. Desnoyers, and Gérald Perron

Abstract: In a continuing study on the optimization of the electrolyte medium for high-energy lithium batteries, volumes, heat capacities, and specific conductivities of $LiClO_4$ and LiBr were measured in mixtures of γ-butyrolactone (BUTY) and 1,2-dimethoxyethane (DME) and of propylene carbonate (PC) and BUTY. These results are compared with those of the electrolytes in the pure solvents. Phase diagrams are also reported when appropriate. The effect of addition of water to these binary and ternary systems was investigated with the same techniques. The mixtures DME–BUTY, PC–DME, DME–H_2O, and BUTY–H_2O are typical of mixtures of aprotic solvents and mixtures of aprotic solvents and water. The electrolytes at high concentrations in aprotic solvents of low dielectric constants are largely associated. The medium still conducts electrolytically since the ion pairs are in a state that resembles to a large extent that of a molten salt. With some systems at high concentration, stable solvates persist in the solution medium, as evidenced mostly by heat capacities, and are in equilibrium with either the excess solvent or unsolvated molten salts. In mixed solvents, the properties of electrolytes can largely be predicted from the binary systems and by the coexistence of these solvates. The properties of water in DME, BUTY, or mixtures of the two solvents are modified significantly in the presence of LiBr but only slightly with $LiClO_4$. These specific interactions, which affect the heat capacities much more than the volumes and which are especially large with the system LiBr–DME, could be responsible for the decrease in reactivity of water with lithium metal in an aprotic medium in the presence of certain electrolytes.

Key words: $LiClO_4$, LiBr, γ-butyrolactone, dimethoxyethane, propylene carbonate, lithium battery, aprotic solvent, water, association, solvates, solid–liquid phase diagrams, volumes, heat capacities, specific conductivities.

Résumé : Dans le cadre d'une étude sur l'optimisation du milieu électrolytique pour les piles au lithium à haute densité d'énergie, les volumes, capacités calorifiques et conductivités spécifiques du $LiClO_4$ et du LiBr ont été mesurés dans des mélanges de γ-butyrolactone (BUTY) et de 1,2-diméthoxyéthane (DME) et dans des mélanges de carbonate de propylene (PC) et de BUTY. Ces résultats ont été comparés aux propriétés équivalentes des électrolytes dans les solvants purs. Les diagrammes d'état sont aussi présentés pour plusieurs systèmes. L'effet d'addition d'eau à ces systèmes binaires et ternaires a aussi été étudié par les mêmes techniques. Les mélanges DME–BUTY, PC–DME, DME–H_2O et BUTY–H_2O sont typiques des mélanges de solvants aprotiques et de solvants aprotiques dans l'eau. Les électrolytes à forte concentration dans les solvants aprotiques de faible constante diélectrique sont fortement associés. Le milieu est quand même conducteur puisque les paires d'ions sont dans un état similaire à celui d'un sel fondu. Dans certains systèmes à forte concentration, des solvates stables existent en solution, tel que mis en évidence par les capacités calorifiques, et sont en équilibre avec soit un excès de solvant ou un excès de sel fondu non solvaté. Dans les solvants mixtes, les propriétés peuvent en grande partie être prédites par les systèmes binaires et par la coexistence de tels solvates. Les propriétés de l'eau dans le DME, le BUTY et le mélange des deux solvants sont modifiées de façon appréciable en présence de LiBr mais légèrement en présence de $LiClO_4$. Ces interactions spécifiques, qui affectent beaucoup plus les capacités calorifiques que les volumes, peuvent être responsables de la grande atténuation de la réactivité de l'eau au lithium en présence de LiBr.

Mots clés : $LiClO_4$, LiBr, γ-butyrolactone, diméthoxyéthane, carbonate de propylène, batterie au lithium, solvant aprotique, eau, association, solvates, diagrammes de phase solide–liquide, volumes, capacités calorifiques, conductivités spécifiques.

Introduction

Lithium batteries are often considered future leaders in the battery industry, mainly because of their high capacity for energy storage and low environmental impact. The relatively low solubility and conductivity of lithium salts in aprotic solvents and the reactivity of the solvents with lithium metal often limits the efficiency of such batteries. For these reasons, mixed aprotic solvents are often envisaged in optimization studies. For example, acetonitrile (AN) reacts slowly with lithium metal but mixtures of acetonitrile with propylene carbonate (PC) are quite stable (1). It is also interesting to note that the reactivity of the solvent with lithium is often altered significantly in the presence of an electrolyte (2). For example, while both SO_2 and AN react with lithium, the formation of a complex between LiBr and SO_2 decreases the reactivity with lithium (3, 4).

Received August 1, 1995.

L. Couture, J.E. Desnoyers, and G. Perron.[1] INRS – Énergie & matériaux, 1650, boul. Lionel-Boulet, P.O. Box 1020, Varennes, QC J3X 1S2, Canada.

[1] Author to whom correspondence may be addressed. Telephone: (514) 449-7951. Fax: (514) 449-7954.

Water is often one of the main impurities of the electrolyte medium since the solvents and the lithium salts are hygroscopic. The reaction of water with lithium metal forms a hydroxide or oxide that passivates the anode and generates hydrogen gas. This makes the battery unsafe for commercial use. To reduce the manufacturing cost of lithium batteries, it is desirable to reduce the need for highly dried solvents. This can be achieved by controlling the reactivity of water with lithium rather than trying to eliminate it completely from the electrolyte system. There are various ways of controlling this reactivity. Any physical process that hinders the adsorption of water should decrease the extent of reaction with lithium. This can be achieved by the formation of a protective film on the surface of lithium or by complexing or reacting water with additives or hygroscopic components in the aprotic solvent medium.

Most recent fundamental studies on the reactivity of water with lithium are concerned with the identification of the in situ film formed on the surface of the lithium metal exposed to various solutions and to the effect of water on the electrochemical rechargeability of the battery. Analytical techniques such as FTIR in external reflectance mode (5), XPS (6, 7), Raman spectroscopy (8), and electrochemical corrosion potential (9–11) have been used for this purpose. Indirect information on films can also be deduced from the investigation of chemical reactions involving lithium. In particular, Dey et al. (2) studied the reactivity of AN with lithium by differential scanning calorimetry and Holding and Fletcher (11) used the reaction of lithium with bromobenzene to study film formation on lithium foil. All these studies show that film formation is fast, even when experiments are performed in an argon dry box. A surface film will be formed with lithium in practically all batteries constructed with lithium foil and this will have some effect on the initial discharge curve or on the recycling.

The second approach in the control of the reactivity of water is to complex or react it with an additive in the solution. Investigations in our laboratory show that the presence of LiBr, and to a lesser extent $LiClO_4$, in γ-butyrolactone (BUTY) and 1,2-dimethoxyethane (DME) containing water significantly hinders the reactivity of the water with lithium metal. For example, the total time needed to completely consume a lithium pellet (0.014 mol) by reaction with 1 mol kg^{-1} of water is increased 150-fold in the presence of 1.5 mol kg^{-1} of LiBr in BUTY.

Relatively little is known about the properties of concentrated electrolytes in aprotic solvents. At very low concentration, the free ions are highly solvated and the concentration dependence will be governed by long-range Coulombic forces as predicted by the Debye–Hückel theory. As the concentration increases, association takes place and the ion pairs could also interact with the solvent. At still higher concentration, the properties of the electrolyte must approach those of a molten salt. The nature of the interactions becomes even more complex if mixed solvents or mixed electrolytes are used or if additives or contaminants such as water are present.

The present investigation is part of a continuing study on the characterization of the electrolyte medium for high-energy batteries through thermodynamic and transport properties. The volumes, heat capacities, and, to a lesser extent, compressibilities of electrolytes were measured in AN (12), PC (13, 14), and BUTY and DME (15). Transport properties were also measured with some systems (15). A simple association model has been proposed for the interpretation of the thermodynamic properties of electrolytes in acetonitrile (16) and work under way (17) shows that the Bjerrum association model can account quantitatively for the low concentration dependence of the partial molar volumes of electrolytes in aprotic solvents. It was also observed that stable solvates, which are identified in the solid–liquid phase diagrams, often persist in the solution above the melting point of the solvate and seem to affect the thermodynamic and transport properties of the solutions (18).

In this paper we report the properties of lithium salts in mixed aprotic solvents. The electrolytes chosen are $LiClO_4$ and LiBr and the mixed aprotic solvents are BUTY–DME and PC–DME. Only $LiClO_4$ was investigated in the mixture PC–DME. These solvents, which are used in commercial batteries, have many of the required characteristics for the electrolyte medium of lithium batteries (19) while having vastly different structures; BUTY and PC are cyclic molecules while DME is a linear one. DME is also an analog of polyethylene oxide, which is used in solid electrolyte lithium batteries (20).

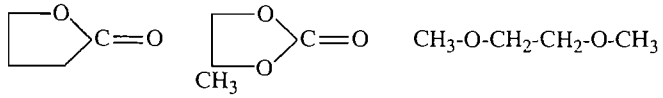

BUTY PC DME

In a second set of experiments, the effect of the presence of water on the thermodynamic and transport properties was investigated. The purpose of these investigations was to evaluate the importance of the interactions between water and the electrolytes and to understand the impact of such interactions on the reactivity of water with the lithium electrode. In particular, it is hoped that such investigations will explain the effectiveness of electrolytes such as LiBr in reducing the reactivity of traces of water in aprotic solvents with lithium metal.

The properties investigated are solid–liquid phase diagrams, volumes, heat capacities, and specific conductivities. In the case of the ternary system DME–H_2O–LiBr, the liquid–liquid phase diagram was also determined.

Experimental

The techniques for the determination of the thermal analyses, densities (d), heat capacities per unit volume (σ), and specific conductivities (k_{SP}) were the same as in previous studies (14). The ternary phase diagram LiBr–H_2O–DME was determined with the cloud point technique. The specific heat capacities were calculated from σ and d by the relation

$$[1] \quad c_p/c_{p_0} = [1 + (\sigma - \sigma_0)/\sigma_0](d_0/d)$$

where the subscript (0) refers to the pure solvent (binary systems) or reference mixed solvent (ternary system).

The origin and purity of the chemicals are the following. $LiClO_4$: Omega Chemical Products, dried at 205°C under vacuum. LiBr: Aldrich, dried under vacuum at 200°C. DME: American Chemicals, anhydrous, distilled in glass. BUTY: Omega Chemical Products, dried over molecular sieves, redistilled under vacuum. PC: Aldrich, 99.7% anhydrous, used as such.

Fig. 1. Solid–liquid phase diagrams of the systems $LiClO_4$–BUTY–DME, $LiClO_4$–PC–DME, and LiBr–BUTY–DME. Data are taken from Perron et al. (14).

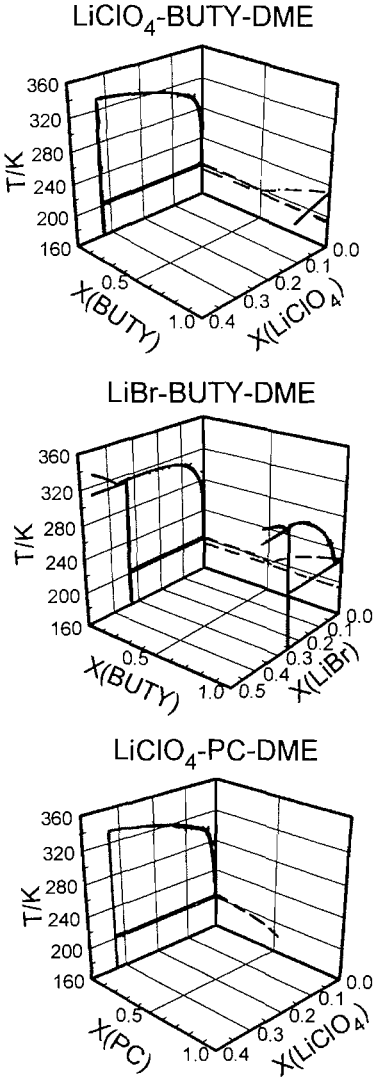

Results and discussion

The densities and heat capacities were used to calculate apparent molar quantities of components 1 or 2, $Y_{1,\varphi}$ and $Y_{2,\varphi}$, or excess thermodynamic quantities, V^{ex} or C^{ex}.

$$[2]\quad V_{2,\varphi} = (M_2/d) - 1000(d - d_0)/m_2 dd_0 = (M_2/d) - M_1(1 - X_2)(d - d_0)/X_{2d}dd_0$$

$$[3]\quad C_{p,2,\varphi} = (M_2c_p) + 1000(c_p - c_{p0})/m_2 = (M_2c_p) + M_1(1 - X_2)(c_p - c_{p0})/X_2$$

where M_1 and M_2 are the molecular mass of the solvent 1 and solute 2, respectively, m_2 is the molality (moles per kg of solvent or mixed solvent) of the solute, X_2 the mole fraction of the solute, and the subscript 0 refers to the reference system (pure solvent or mixed solvent).

$$[4]\quad Y^{ex} = Y - X_1Y_2^* - X_2Y_2^*$$

where Y is the overall property (volume or heat capacity) per total number of moles, the superscript (*) refers to the molar properties of the pure liquids, and X_i is the mole fraction of component i. The reduced excess properties are directly related to the apparent molar quantities (18),

$$[5]\quad Y^{ex}/X_1X_2 = (Y_{2,\varphi} - Y_2^*)/X_1 = (Y_{1,\varphi} - Y_1^*)/X_2$$

At infinite dilution (X_1 or $X_2 \rightarrow 0$), Y^{ex}/X_1X_2 will tend to $Y_2^\circ - Y_2^*$ and to $Y_1^\circ - Y_1^*$, where Y_2° and Y_1° are the standard infinite dilution partial molar quantities of the two components.

The original data on the mixtures of aprotic solvents and on the mixtures of aprotic solvents with water are given in Table 1. The parameters required to fit the reduced excess quantities of mixtures of aprotic solvents are given in Table 2. It is possible to measure $Y_2^\circ - Y_2^*$ more precisely than the absolute Y_2°, since it is not always easy to measure precisely Y_2° of the solvent. For example, with a flow instrument, a heat capacity cannot be measured to better than 0.5% and often the absolute error can be of the order of 1–2% (proper references, presence of impurities, etc). Also, as noted previously (15, 21), the calibration constants of some flow densimeters are slightly different for aqueous and nonaqueous systems. While this source of error hardly affects the reduced excess volumes of aqueous–organic mixtures, it affects systematically the absolute values of $V_{2,\varphi}$ by about 0.07 $cm^3\ mol^{-1}$ with the densimeter used. The Y_2° of the binary solvent systems are given in Table 3 along with the values of Y_2^* used for the calculations.

The original data for the ternary systems and for the phase diagrams are available as supplementary material[2] and only the trends will be shown graphically.

Since our aim is to compare the properties of the electrolytes in the solvents with those in the mixed solvents, we have chosen, when appropriate, to plot the data in three-dimensional graphs. Essentially, these graphs combine three two-dimensional graphs, e.g., the property of an electrolyte in solvent 1, in solvent 2, and in the mixed solvent at a fixed electrolyte concentration.

Solid–liquid phase diagrams

The solid–liquid phase diagrams for all the binary systems of the components DME, BUTY, PC, $LiClO_4$, and LiBr were taken from the literature or determined from thermal analysis and are shown in Fig. 1. The system DME–BUTY forms a simple eutectic and is close to being ideal since the phase diagram can be largely accounted for through the enthalpies of fusion assuming ideal solubilities. The mixture DME–PC forms a glass in the PC-rich zone and only a glass-transition temperature T_g is observed. No eutectic temperatures are observed. Still, in the DME-rich zone, the trends of the liquid–solid equilibria are those predicted from ideal solubilities. The phase diagram is possibly of the solid solution type. The solid–liquid phase diagram of $LiClO_4$–DME indicates that $LiClO_4$ forms a 1:2 complex with DME that melts at about 335 K. In BUTY, only the dilute region could be investigated since a T_g is present at higher concentrations. LiBr forms a 1:3 solvate in BUTY (mp 301 K) and a 1:2 solvate (mp 315 K) in

[2] A complete set of data may be purchased from: The Depository of Unpublished Data, Document Delivery, CISTI, National Research Council Canada, Ottawa, Canada K1A 0S2.

Table 1. Reduced excess volumes and heat capacities of solvent mixtures at 25°C.

DME-WATER					BUTY-WATER				
X DME	d-d_0 g cm^{-3}	$10^3\Delta\sigma/\sigma_0$	V^{ex}/X_1X_2 cm^3 mol^{-1}	C_p^{ex}/X_1X_2 JK^{-1} mol^{-1}	X BUTY	d-d_0 g cm^{-3}	$10^3\Delta\sigma/\sigma_0$	V^{ex}/X_1X_2 cm^3 mol^{-1}	C_p^{ex}/X_1X_2 JK^{-1} mol^{-1}
0.003 6670	−0.001 032	−0.93	−9.154	178.6	0.003 7041	0.002 534	−3.55	−2.886	85.4
0.007 2007	−0.001 952	−1.86	−9.303	178.0	0.007 2528	0.004 918	−7.18	−2.920	82.3
0.010 621	−0.002 689	−2.90	−9.607	176.1	0.010 797	0.007 247	−10.8	−2.936	80.9
0.014 267	−0.003 441	−4.22	−9.804	173.9	0.014 304	0.009 509	−15.1	−2.957	75.9
0.017 695	−0.004 058	−5.43	−10.009	172.5	0.017 742	0.011 711	−18.1	−3.005	78.0
0.026 310	−0.005 455	−9.31	−10.398	167.9	0.026 304	0.016 908	−27.3	−3.008	75.2
0.034 774	−0.006 604	−14.4	−10.727	162.1	0.034 808	0.021 749	−36.3	−2.979	73.5
0.043 157	−0.007 636	−19.9	−10.985	157.2	0.043 070	0.026 178	−45.7	−2.942	70.7
0.050 018	−0.008 516	−26.3	−11.122	150.9	0.049 985	0.029 188	−52.6	−2.694	71.3
0.099 184	−0.015 697	−76.5	−11.356	122.4	0.099 944	0.049 511	−108.8	−2.354	59.4
0.146 05	−0.025 370	−82.5	−10.753	99.0	0.150 05	0.064 178	−159.4	−2.056	52.8
0.200 02	−0.038 350	−200.3	−9.743	77.0	0.200 02	0.075 149	−201.6	−1.816	49.9
0.250 11	−0.050 293	−247.9	−8.830	67.2	0.249 97	0.083 668	−241.5	−1.624	45.8
0.299 92	−0.061 217	−290.9	−8.040	58.1	0.299 94	0.090 451	−275.2	−1.465	43.6
0.349 89	−0.070 959	−326.2	−7.387	52.1	0.346 82	0.095 685	−303.2	−1.342	42.1
0.385 31	−0.077 194	−347.5	−6.989	49.3	0.399 93	0.100 490	−331.1	−1.207	41.1
0.450 01	−0.087 275	−379.7	−6.384	46.6	0.449 96	0.104 286	−354.9	−1.098	40.4
0.493 35	−0.093 045	298.0[a]	−6.094	41.7	0.500 00	0.107 435	−380.8	−0.985	36.6
0.499 72	−0.093 975	−400.0	−6.021	46.2	0.500 01	0.107 459	−325.9	−0.989	37.9
0.549 99	−0.100 157	−420.1	−5.680	44.3	0.500 01	0.107 459	−328.1	−0.989	38.7
0.602 32	−0.105 793	210.3[a]	−5.420	38.4	0.500 44	0.107 476	−383.5	−0.987	34.6
0.602 64	−0.105 937	−438.5	−5.382	43.3	0.549 98	0.110 207	−401.1	−0.893	35.6
0.650 00	−0.110 671	−453.0	−5.143	43.4	0.599 95	0.112 555	−420.0	−0.792	34.6
0.700 11	−0.115 161	148.2[a]	−4.957	37.8	0.650 04	0.114 652	−438.0	−0.698	33.2
0.700 18	−0.115 293	−466.5	−4.904	44.9	0.699 99	0.116 483	175.9[a]	−0.595	38.0
0.739 26	−0.118 627	−474.9	−4.731	49.1	0.700 03	0.116 457	−454.0	−0.588	32.6
0.781 20	−0.121 891	97.9[a]	−4.600	32.6	0.752 07	0.118 16	−471.5	−0.467	29.4
0.798 38	−0.123 263	85.6[a]	−4.494	28.8	0.800 00	0.119 74	−486.5	−0.391	25.7
0.843 63	−0.126 625	−504.7	−4.247	42.9	0.800 01	0.119 722	103.5	−0.384	31.1
0.886 64	−0.129 531	−515.6	−4.055	39.3	0.850 01	0.121 227	−499.5	−0.280	23.7
0.900 01	−0.130 273	40.5[a]	−4.140	29.6	0.896 50	0.122 549	44.3[a]	−0.151	20.8
0.900 88	−0.130 407	38.0[a]	−4.039	25.4	0.899 97	0.122 642	49.2[a]	−0.137	30.7
0.949 99	−0.133 441	−527.1	−3.744	58.0	0.900 00	0.122 628	−511.8	−0.126	20.7
0.952 52	−0.133 561	18.0[a]	−3.800	26.5	0.949 93	0.124 111	−522.9	0.002	15.1
0.955 02	−0.133 642	16.9[a]	−3.962	25.7	0.953 36	0.124 221	18.5[a]	0.002	18.0
0.960 00	−0.133 917	15.1[a]	−3.997	26.2	0.960 00	0.124 424	14.8[a]	0.014	14.3
0.969 68	−0.134 547	11.1[a]	−3.703	24.8	0.962 08	0.124 474	15.2[a]	0.043	19.0
0.974 98	−0.134 745	9.27[a]	−4.153	25.0	0.970 00	0.124 73	10.9[a]	0.034	13.5
0.980 41	−0.135 143	7.38[a]	−3.653	27.4	0.974 07	0.124 856	9.86[a]	0.039	16.6
0.984 96	−0.135 291	5.46[a]	−4.448	23.3	0.980 00	0.125 03	7.28[a]	0.078	14.0
0.989 78	−0.135 660	3.63[a]	−3.521	23.7	0.980 00	0.125 03	−530.2	0.078	−16.5
0.994 53	−0.135 814	1.745[a]	−5.672	12.3	0.984 39	0.125 171	5.69[a]	0.067	14.2
1.000 00	−0.136 053	−549.3			0.990 00	0.125 339	3.53[a]	0.114	12.7
					0.994 75	0.125 49	1.76[a]	0.103	10.1
					1.000 00	0.125 654	−531.7		

[a]The aprotic solvent is the reference in these mixtures. The densities of the pure liquids are taken as: (H_2O) 0.997 047, (DME) 0.860 849, (BUTY) 1.122 701. The specific heat capacities are: (H_2O) 4.1796; (DME) 2.230; (BUTY) 1.738.

Table 1 (*concluded*).

BUTY–DME					PC–DME				
X DME	d-d_0 g cm^{-3}	$10^3\Delta\sigma/\sigma_0$	V^{ex}/X_1X_2 cm^3 mol^{-1}	C_p^{ex}/X_1X_2 JK^{-1} mol^{-1}	X BUTY	d-d_0 g cm^{-3}	$10^3\Delta\sigma/\sigma_0$	V^{ex}/X_1X_2 cm^3 mol^{-1}	C_p^{ex}/X_1X_2 JK^{-1} mol^{-1}
0.045 14	0.010 519	4.34	−4.799	9.88	0.100 20	0.032 053		−5.047	
0.087 788	0.020 464	8.42	−4.631	10.78	0.200 18	0.063 886		−4.537	
0.132 85	0.031 045	11.5	−4.508	9.73	0.300 18	0.095 972		−4.166	
0.176 71	0.041 448	15.0	−4.425	10.14	0.399 37	0.128 256		−3.888	
0.223 34	0.052 537	17.2	−4.298	9.39	0.476 88	0.153 793		−3.678	
0.280 10	0.066 244	20.6	−4.191	9.70	0.600 18	0.195 259		−3.411	
0.318 80	0.075 671	21.6	−4.113	9.09	0.699 54	0.229 519		−3.238	
0.399 24	0.095 662	24.2	−4.000	9.03	0.796 21	0.263 634		−3.099	
0.421 51	0.101 211	24.3	−3.946	8.79	0.899 98	0.301 153		−2.973	
0.454 28	0.109 521	24.8	−3.900	8.71	0.029 05	0.009 34	5.11	−5.527	14.54
0.504 13	0.122 314	25.6	−3.832	8.86	0.051 14	0.016 142	7.87	−4.715	11.85
0.599 92	0.147 494	23.9	−3.721	7.78	0.059 98	0.019 197	9.83	−5.222	13.18
0.641 14	0.158 568	23.2	−3.676	7.68	0.099 91	0.031 942	15.9	−5.025	13.15
0.700 03	0.174 655	21.8	−3.612	7.69	0.149 61	0.047 745	22.2	−4.748	12.14
0.749 46	0.188 406	19.7	−3.557	7.29	0.199 94	0.063 885	28.2	−4.589	11.65
0.800 60	0.202 938	17.7	−3.522	7.44	0.250 09	0.079 866	33.3	−4.345	11.19
0.849 79	0.217 111	15.2	−3.460	7.55	0.349 85	0.111 875	42.2	−3.931	10.44
0.900 06	0.231 913	12.3	−3.422	7.87	0.399 94	0.128 149	45.1	−3.767	9.88
0.949 89	0.246 878	8.32	−3.401	7.28	0.499 80	0.161 1	51.0	−3.506	9.15
					0.550 39	0.178 129	54.1	−3.419	8.78
					0.749 86	0.246 812	60.0	−3.006	6.71
					0.800 05	0.264 852	60.4	−3.019	6.35
					0.828 18	0.274 965	60.2	−2.989	5.21
					0.849 77	0.282 751	61.7	−2.954	6.98
					0.859 38	0.286 244	61.1	−2.947	5.32
					0.892 51	0.298 32	61.9	−2.903	5.45
					0.928 82	0.311 703	60.9	−2.886	1.30
					0.929 89	0.311 484	62.5	−2.192	6.29
					0.959 95	0.323 218	62.0	−2.796	1.14

The reference solvent in both cases is DME. The densities of the pure liquids are taken as: (DME) 0.861413; (BUTY) 1.123609; (PC) 1.199486. The specific heat capacities are: (DME) 2.183; (BUTY) 1.681; (PC) 1.669

Table 2. Parameters of the mixing function $Y^{ex}/X_1X_2 = A_Y + B_YX_2 + C_YX_2^2$ at 25°C.

System	Property	A_Y	B_Y	C_Y
BUTY(2)DME(1)	V/cm^3 mol^{-1}	−4.86	2.63	−1.18
	C_p/J K^{-1} mol^{-1}	10.392	−3.549	
PC(2)DME(1)	V/cm^3 mol^{-1}	−5.543	5.306	−2.685
	C_p/J K^{-1} mol^{-1}	13.585	−8.921	

DME. $LiClO_4$ forms a glass in PC and the phase diagram could not be determined.

Specific conductivities, volumes and heat capacities of binary and ternary systems

The reduced excess volumes and heat capacities for the binary systems BUTY–DME and PC–DME are shown in Fig. 2. This representation is more informative than the usual method of plotting excess thermodynamic functions, and the near linearity of these reduced functions shows that the nonideality of these mixtures of aprotic solvents can be defined nearly entirely by two functions, $Y_2° - Y_2^*$ and $Y_1° - Y_1^*$. These trends are typical of mixtures of aprotic solvents. The interactions are stronger for PC and BUTY surrounded by DME (more positive excess partial molar heat capacity and more negative excess partial molar volume) than for DME surrounded by the other aprotic solvent. The difference in the solvation of the two solvents is larger for the system PC–DME than for BUTY–DME. These values are comparable to those of PC in aromatic liquids (22).

At very low concentrations, electrolytes in aprotic solvents must be completely dissociated and the limiting trends in thermodynamic properties should be those expected from the Debye–Hückel theory. Similarly, the transport properties should be those of typical electrolytes The properties should thus vary with the square root of the molality or molarity. However, they behave as strongly associated electrolytes in aprotic solvents of low dielectric constant in the concentration range presently studied, which represents the working electrolyte concentrations of lithium batteries. At these concentrations, the systems resemble mixtures of polar liquids more

Table 3. Thermodynamic functions for mixtures at 25°C.

System	$V_2°$/cm^3 mol^{-1}	V_2^*/cm^3 mol^{-1}	$C°_{p,2}$/J K^{-1} mol^{-1}	$C^*_{p,2}$/J K^{-1} mol^{-1}
DME(BUTY)	101.24	104.65	207.1	196.7
BUTY(DME)	71.71	76.57	162.0	148.4
PC(DME)	79.56	85.10	185.6	172.0
DME(PC)	101.75	104.65	193.9	196.7
H_2O(BUTY)	18.20	18.07	88.0	75.3
BUTY(H_2O)	73.76	76.64	235.1	148.4
H_2O(DME)	14.48	18.07	102.1	75.3
DME(H_2O)	95.80	104.65	377.2	196.7

Fig. 2. Reduced excess volumes and heat capacities of the binary systems PC–DME and BUTY–DME at 25°C.

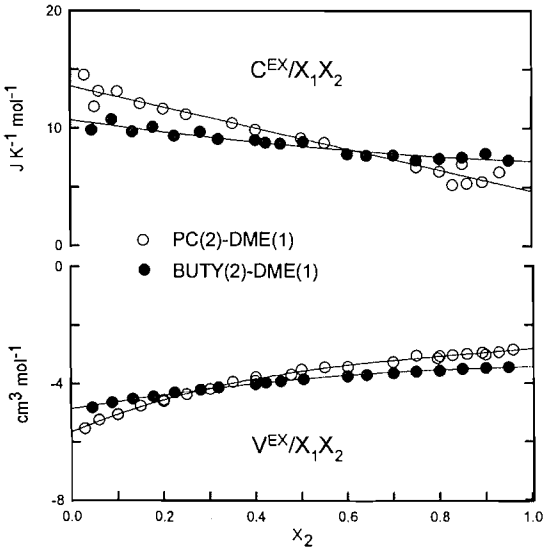

than electrolyte solutions. We therefore felt that it would be preferable to express all concentrations in terms of mole fractions to compare the trends in the properties.

The specific conductivities (k_{sp}) at 25°C are shown in Fig. 3. When the electrolytes are sufficiently soluble in the aprotic solvents, k_{sp} of the binary systems generally goes through a maximum; with the two present solvents the maximum is at about 0.7 mol kg^{-1}. For the ternary systems, the concentrations of the electrolyte were kept constant at 0.1 and 0.7 mol kg^{-1} and the mole fraction of the mixed solvent was changed from 0 to 1. The trends are the same for both electrolyte concentrations but are more pronounced at the higher concentration. Therefore, only the trends of $LiClO_4$ and LiBr at 0.7 mol kg^{-1}, corresponding to approximately 0.06 mole fraction, are shown in Fig. 3. As for the binary systems, k_{sp} of the ternary systems also goes through a maximum, as observed by many authors (1, 23). With both solvent mixtures, there is a gain in conductivity when a mixed solvent is used. This gain is particularly important with the system $LiClO_4$–PC–DME.

The trends in $V_{2,\varphi}$ and $C_{p,2,\varphi}$ of the two electrolytes in the mixed solvents are compared with the binary systems in Figs. 4 and 5. The results for LiBr in DME are for supercooled solutions. It has been shown (15), however, that these trends are quite similar to those at 45°C. For the ternary systems, the

Fig. 3. Specific conductivities $LiClO_4$–BUTY–DME, $LiClO_4$–PC–DME and LiBr–BUTY–DME. Data for the binary systems are from Perron et al. (14) and for the ternary system $LiClO_4$ in PC–DME are from Gores and Barthel (23). The open circles are for the electrolytes in each solvent and the closed circles are for the electrolyte in the mixed solvent.

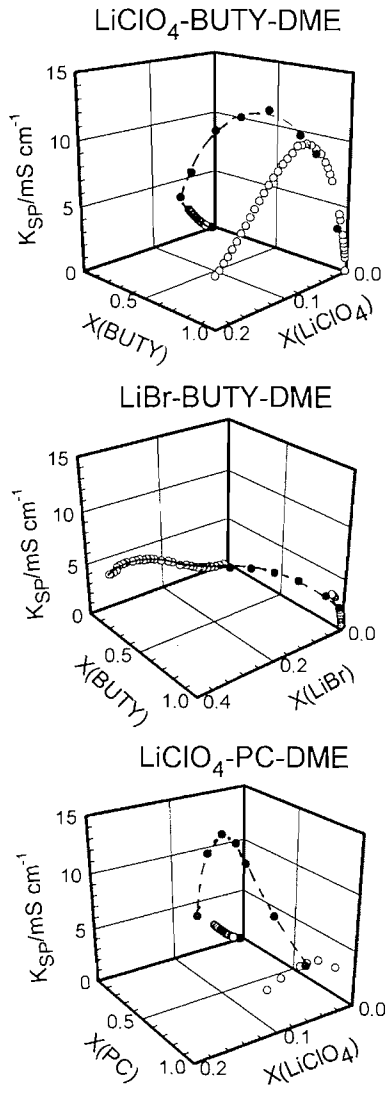

Fig. 4. Apparent molar volumes of the electrolytes in the systems $LiClO_4$–BUTY–DME, $LiClO_4$–PC–DME, and LiBr–BUTY–DME. Data for the binary systems are from Perron et al. (14). The open circles are for the electrolytes in each solvent and the closed circles are for the electrolyte in the mixed solvent.

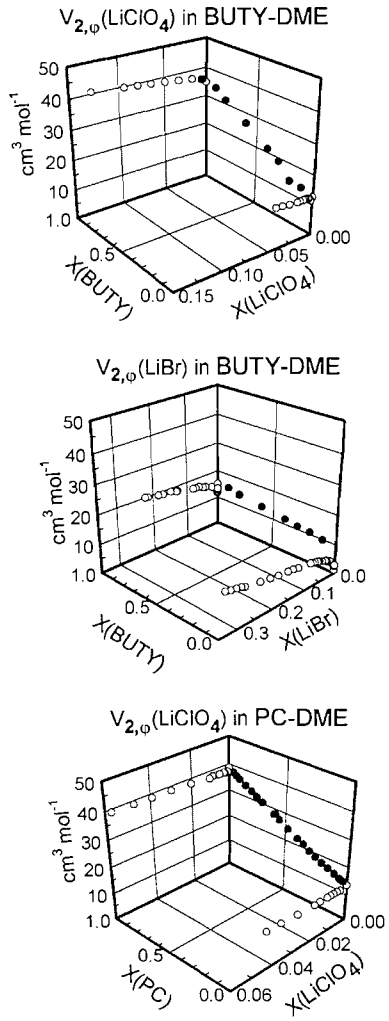

Fig. 5. Apparent molar heat capacities of the electrolytes in the systems $LiClO_4$–BUTY–DME, $LiClO_4$–PC–DME, and LiBr–BUTY–DME. Data for the binary systems are from Perron et al. (14). The open circles are for the electrolytes in each solvent and the closed circles are for the electrolyte in the mixed solvent.

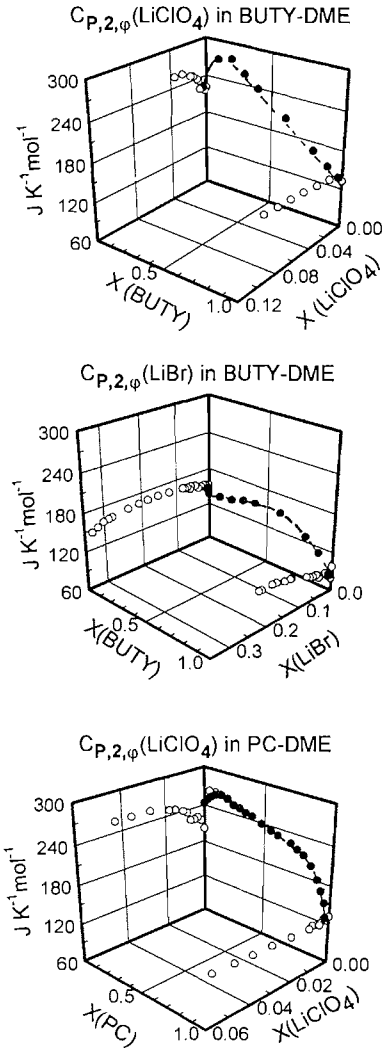

electrolyte concentrations were fixed at 0.1 mol kg^{-1}, which is less than 0.01 for the associated electrolyte on a mole fraction scale. It should be recognized that below 0.1 mol kg^{-1} the thermodynamic properties would undergo further changes due to the increasing presence of free ions. These trends at low concentration could be predicted if the association constant of the electrolyte and the variation of the dielectric constant with pressure and temperature are known (17).

The $V_{2,\varphi}$ of $LiClO_4$ in Fig. 4, in the concentration range investigated, are much larger in BUTY and PC than in DME and vary nearly linearly with the salt mole fraction in the binary systems and also vary linearly with the mole fraction of the mixed solvent. It is therefore expected that the $V_{2,\varphi}$ of $LiClO_4$ would also vary nearly linearly with the mole fraction of the mixed solvent at other salt concentrations. This of course would not be true if measurements could be made at very low concentrations where the electrolytes would be dissociated (15). $V_{2,\varphi}$ of LiBr varies nearly linearly in BUTY but decreases significantly at low concentration in DME. The trend in the mixed solvent BUTY–DME is also linear up to $X_{DME} = 0.9$ and then dips to a lower value as for the binary system.

As shown in Fig. 5, the $C_{p,2,\varphi}$ of the two electrolytes shows important nonlinear concentration dependences in DME. $LiClO_4$ varies nearly linearly with mole fraction in PC and shows only a small deviation from linearity at low concentration in BUTY. LiBr has a significant concentration dependence in BUTY and DME. $C_{p,2,\varphi}$ shows also a large deviation from linearity when the mole fraction of the mixed solvents is changed with all systems, expecially in the DME–rich region.

Electrolytes are largely associated at these concentrations. Association in these systems must be understood in the sense of Bjerrum; ion pairs are not necessarily in physical contact but are under the influence of strong Coulombic forces. This state resembles in many aspects that of a molten salt. For

example, it was shown (16) that when an associated electrolyte forms a nearly ideal solution with an aprotic solvent up to the molten salt (simple eutectic phase diagram), such as the system ethylammonium nitrate – acetonitrile, the thermodynamic properties of the associated electrolyte are approximately those of the molten salt. However, when stable complexes are formed in the solid state, as evidenced from the solid–liquid phase diagram, such solvates often persist in solution and the heat capacities of the associated electrolyte tend to those of the molten solvates (18). These heat capacities can be significantly different from those of the pure molten salt. Investigations under way in our laboratory on lithium bis-trifluoromethylsulfonylimide (LiTFSI) in DME definitely support the presence of stable solvates in solution.[3] In such cases, the association complex probably has a definite structure involving one or more solvent molecules. Therefore, at high mole fractions, the properties of such electrolytes are essentially those of solvated ion pairs in a molten salt.

The equivalent conductance Λ of unsolvated molten salts at 25°C, as in the case of ethylammonium nitrate (16), is quite low. However, in systems where stable solvates seem to exist in solution, Λ generally goes through a maximum at high concentrations. The conductance mechanism of such solutions is probably much closer to that of molten salts modified by the presence of a solvent than to the type of ionic conductance that is observed at very low concentrations. Unfortunately, thermodynamics and transport data do not give any insight into the structure of such species in solution. Still, the presence of solvated molten salts may offer an alternative avenue to triple ion formation (24, 25) to explain the high-concentration conductance. A model for such solvated ion pairs has been proposed by Blomgren (1).

It is important to note that the changes observed in heat capacities of electrolytes in aprotic solvents are often less evident with volumes. There are many examples of phenomena that are evident with heat capacities but not with volumes, e.g., post-micellar transitions and critical demixing. Being related to the second derivative of the chemical potential, properties such as heat capacities are more sensitive to second-order transitions than are volumes or enthalpies. This therefore suggests that the transitions that seem to be related to the formation of stable solvates in solution are probably second order in nature.

As shown in Fig. 1, LiBr forms stable solvates in both DME and BUTY while $LiClO_4$ can form such a complex only in DME. The solid–liquid phase diagrams of electrolytes in PC could not be measured. If the observed maxima in heat capacity can be attributed to the existence of similar complexes is solution, then the maximum in $C_{p,2,\varphi}$ for the electrolytes in BUTY–DME and two breaks for $LiClO_4$ in PC–DME (Fig. 5) could well be related to changes in the structure of such solvates. With volumes (Fig. 4), the changes in $V_{2,\varphi}$, when going from one solvent to another, are large and small changes in slopes are not evident.

There is a qualitative similarity between the trends in k_{sp} and $C_{p,2,\varphi}$ in mixed solvents. At 0.7 mol kg^{-1} in a low dielectric constant solvent like DME, the electrolytes are essentially fully associated. Yet, k_{sp} is larger in the mixed solvent than in pure PC, which has a high dielectic constant (Fig. 3).

[3] G. Perron, M. Pesant, D. Brouillette, and J. E. Desnoyers. Manuscript in preparation.

Effect of the presence of water

In the preceding section, it was suggested that the trends in the properties of electrolytes at high concentration in aprotic and mixed aprotic solvents were related to the presence of stable solvates in an excess of solvent or molten salt. Since $LiClO_4$ also forms stable 3:1 and 1:1 hydrates with water (26) and LiBr forms many unstable hydrates and one stable 1:1 hydrate (27), our hypothesis was that the presence of these hydrates may account for the large decrease in reactivity of traces of water with lithium metal in the presence of some electrolytes. To investigate this possibility, the addition of water to the binary and ternary systems of $LiClO_4$ or LiBr in BUTY and DME was investigated.

The phase diagrams of the mixtures BUTY–H_2O and DME–H_2O are shown in Fig. 6. With both systems, a simple eutectic is formed, but the melting points of BUTY and DME nearly coincide with the eutectic concentrations. There is therefore no evidence from phase diagrams of strong interactions in concentrated solutions.

The reduced excess volumes and heat capacities of the mixtures H_2O–BUTY and DME–H_2O are shown in Fig. 7. The volumes of the mixture H_2O–BUTY are in excellent agreement with those (not shown) of Abdullah et al. (28) except in the water-rich region. These authors expressed their data in the traditional way of excess quantities and missed the small changes at low BUTY concentrations. In the mixed solvent, the water concentration was kept at 1 mol kg^{-1}. Therefore the values of $Y_{2,\varphi} - Y_2^*$ are approximately equivalent to Y^{ex}/X_1X_2 at infinite dilution of H_2O and are shown in Fig. 7.

The trends of the binary systems are typical of most aprotic solvents with water. In the water-rich region, where the structural effects of water are important, the volumes go through a minimum (large with DME and small with BUTY) and the heat capacities decrease sharply. This is typical of all hydrophobic solutes in water, which show no tendency to autoassociate. The minimum in volume simply reflects the complexity of the effect of hydrophobic hydration on volumetric properties. In the transfer of a hydrophobic solute from the pure liquid state to infinite dilution in water, there is an increase in the "ice-likeness" of water (positive contribution to the volume) but at the same time a decrease in volume due to the occupation of free space by the solute in the water structure. At low concentration, the solute–solute interactions primarily reflect the decrease in hydrophobic hydration (negative second virial coefficient). At higher concentration, more and more contact pairs are formed between two hydrophobic solutes and there is a reappearance of free space (positive contribution to volume). With heat capacities, interactions between two hydrophobic solutes primarily reflect the reduction in hydrophobic hydration (negative second virial coefficient) whether or not the solutes come in contact.

The changes are much more important with DME than with BUTY since DME is more hydrophobic than BUTY (DME has four extra H atoms). On the other hand, in the organic-rich region that is of interest here, the reduced excess functions have the same sign as in the water-rich region but their magnitudes are much smaller. The changes for volumes are nearly linear with mole fraction. There is a small decrease in the reduced excess heat capacities as the mole fraction of the aprotic solvent tends to 1. The interactions are stronger for DME in the water-rich region and they are also stronger in the organic-

Fig. 6. Solid–liquid phase diagrams of the binary systems H_2O–BUTY and H_2O–DME; ○ are freezing points and × are eutectic points.

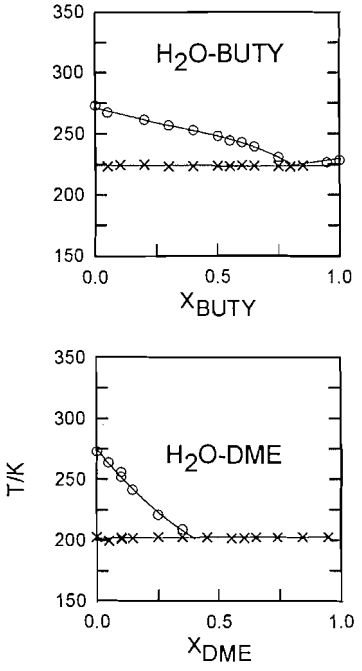

Fig. 7. Reduced excess volumes and heat capacities of H_2O in the systems H_2O–BUTY–DME at 25°C. The open circles are for the electrolytes in each solvent and the closed circles are for the electrolyte in the mixed solvent.

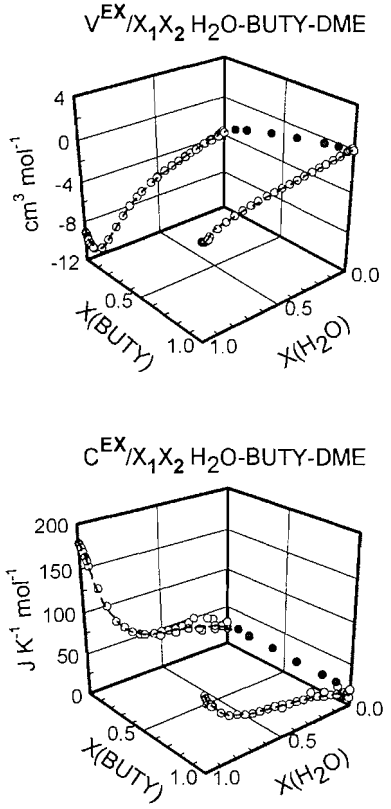

Fig. 8. Effect of the addition of LiBr and $LiClO_4$ on the apparent molar volume and heat capacity of H_2O in DME at 25°C.

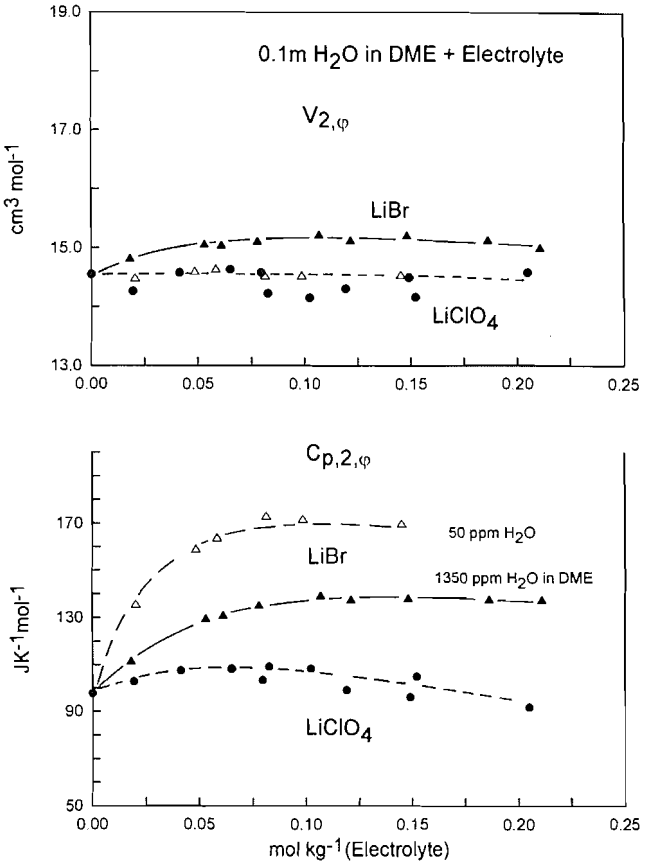

rich region. No anomalies are observed with the reduced excess volumes and heat capacities in the mixed solvent in the sense that they vary linearly from one solvent to the other.

Costas and Patterson (29) made a systematic study of the heat capacity of water in non-aqueous solvents and showed that the interactions in the organic-rich region of water–organic mixtures are related to the proton-acceptor nature of the solvent. The properties of water resemble to a large extent the properties of methanol in a proton acceptor. The high heat capacity is related to the formation of hydrogen-bonded complexes between water molecules and between water and the solvent molecules. The thermodynamic and spectroscopy studies of DeGrandpré et al. (30) confirm this.

The effect of addition of an electrolyte on the volume and heat capacity of water in DME is shown in Fig. 8. The concentration of water was kept at 0.1 mol kg^{-1} and the electrolyte concentration was varied up to about 0.2 mol kg^{-1}. In the presence of $LiClO_4$, both $V_{2,\varphi}$ and $C_{p,2,\varphi}$ of water are essentially constant in DME. In a previous study (12) it was observed that the effect of water was also negligible for $LiClO_4$ in AN.

It is difficult to eliminate water completely from DME. In the case of LiBr, experiments were therefore made with DME containing different initial quantities of water. The properties when H_2O is present increase with electrolyte concentration but seem to level off when the concentration of the electrolyte is equal to or larger than that of H_2O. Changes are more important with heat capacities than with volumes and the increase in properties is attenuated significantly when there is already

Fig. 9. Effect of H_2O on the apparent molar volume and heat capacity of LiBr in DME at 25°C.

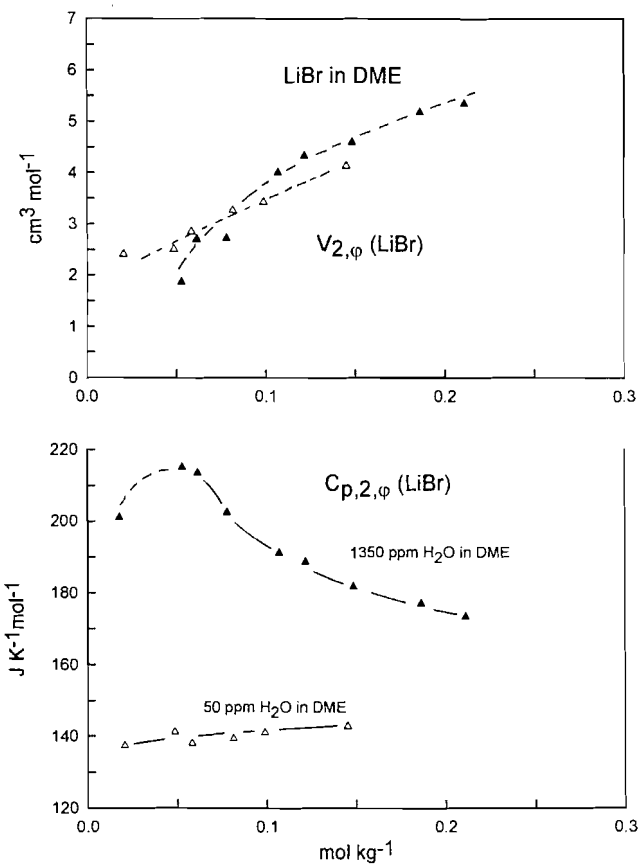

water in the solvent. It should be mentioned that work under way with LiTFSI[3] shows that this electrolyte *decreases* the heat capacity of water in DME. It is known that the NMR chemical shifts of Li^7 in aprotic solvents are largely affected by the presence of water and the effect is larger for LiBr than $LiClO_4$ (31, 32).

The strong interactions of LiBr with H_2O can also be illustrated from the effect of H_2O on the heat capacity of LiBr in DME. The above data were used to calculate $V_{2,\varphi}$ and $C_{p,2,\varphi}$ of LiBr in DME. The DME used for most of our studies contained less than 50 ppm of water while the addition of 0.0723 mol kg^{-1} of H_2O corresponds to the presence of 1300 ppm of water. New measurements were made with a sample containing less than 20 ppm. These data are compared in Fig. 9. While the presence of water does not have much effect on volumes, its effect on heat capacities is much more important; the heat capacities at low concentration can vary by a factor of 2 depending on the quantity of water present. Similar trends were observed for $C_{p,2,\varphi}$ of LiBr in acetonitrile containing small quantities of water (12) and seem to be present in all the aprotic solvents we studied.

The properties of LiBr in aprotic solvents are often anomalous when water is present. For example, dry LiBr is nearly insoluble in PC, while in the presence of a small quantity of water it is quite soluble. The reactivity towards lithium metal of traces of water in an aprotic solvent is largely decreased in the presence of LiBr. DME is completely miscible with water and LiBr is reasonably soluble in DME. However, the ternary

Fig. 10. Ternary phase diagram of the system LiBr–DME–H_2O at 25°C. The open circles are for the passage of the one-phase to the two-phase system and the filled circles are for the passage from the two-phase to the one-phase system.

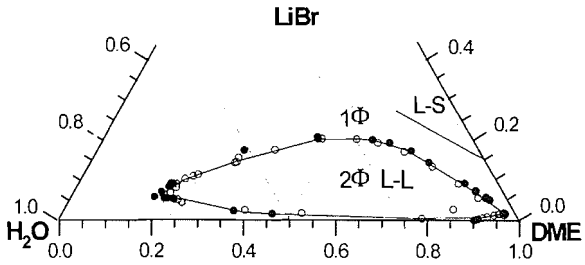

system H_2O–DME–LiBr separates into two liquid phases in the low-salt region. This phase diagram, determined with the cloud point technique, is shown in Fig. 10. The solid–liquid equilibrium was determined in the DME region only. The two-phase liquid region increases significantly with temperature (not shown). The binary solutions H_2O–DME and anhydrous LiBr–DME are colourless. However, when a small quantity of LiBr is added to DME containing water ($m(H_2O) > m(LiBr)$), the solution becomes yellowish and a small precipitate is formed after a few hours. When the LiBr concentration is equal to or larger than that of H_2O, the solution remains clear. This phenomenon occurs in the right-hand corner of the ternary phase diagram (Fig. 10).

There are therefore specific interactions between LiBr and H_2O in aprotic solvents that have major effects on the properties of these solutions. These specific interactions cannot be related simply to the hydration of Li^+ or to the presence of a stable hydrated ion pair since they depend significantly on the nature of the anion and all these lithium salts form stable hydrates. A clue to the role of LiBr may come throngh a comparison with the system LiBr–SO_2–AN. There is spectroscopic evidence to show that a complex is formed between halide anions and SO_2 (3) and these interactions lower the apparent association constant of LiBr in AN (4). There is possibly a similar interaction between H_2O and Br^- in some aprotic solvents and this influences the properties of H_2O.

The effect of adding an equimolar quantity of $LiClO_4$ or LiBr on the specific conductivities, apparent molar volumes, and heat capacities of water in the mixed solvent is shown in Fig. 11. In these new experiments, the concentrations of both H_2O and of the electrolytes were kept at 0.1 mol kg^{-1}. The addition of equimolar quantities of water has no effect on the specific conductivity of 0.1 mol kg^{-1} of electrolyte. The specific conductivity does not seem to be affected by the presence of water, presumably because we are not looking at a property of water in this case. The influence of electrolytes on the volumes and heat capacities of water in mixed solvents is consistent with Fig. 8. The presence of an electrolyte has only a small effect on the volumes of H_2O but a larger one on heat capacities and the changes are much larger with LiBr than with $LiClO_4$.

Conclusions

Electrolytes in mixed aprotic solvents and water in aprotic electrolyte solutions are complex systems. Still, some general

Fig. 11. Effect of the addition of an electrolyte on the specific conductivity, apparent molar volume, and apparent molar heat capacity of H_2O in the mixed solvent BUTY–DME at 25°C. For conductivities, ○ is for the electrolyte systems (0.1 mol kg^{-1}) without water in the mixed solvent and + and × are for the same systems with 0.1 mol kg^{-1} of water; for volumes and heat capacities, ○ is for the properties of 0.1 mol kg^{-1} of H_2O in the mixed solvent, + and × are for the same properties in the presence of 0.1 mol kg^{-1} $LiClO_4$ and LiBr.

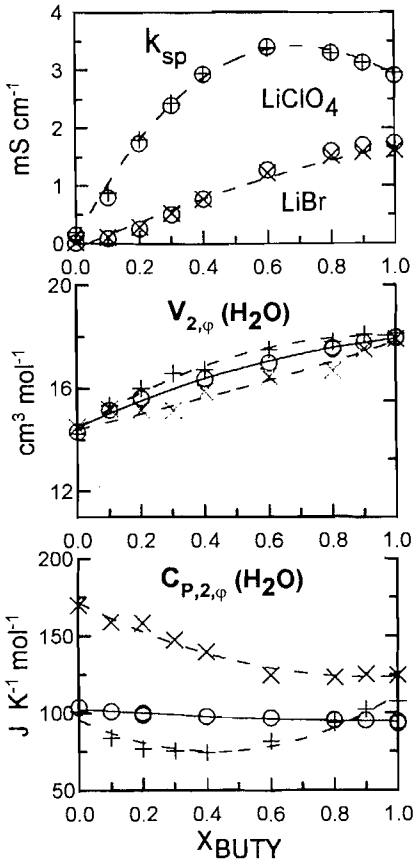

rules seem to apply to the interactions between the various components.

1. The phase diagrams and reduced excess thermodynamic properties of mixed aprotic solvents show no strong nonideality. There are no stable new species formed and the interactions change nearly linearly over the whole mole fraction range.

2. The phase diagrams of mixtures of water and aprotic solvents are also quite simple and the interactions of DME and BUTY with water are typical of those of other aprotic solvents. In the water-rich end, hydrophobic hydration predominates, while in the aprotic-rich end the interactions are typical of strong donor–acceptor molecules.

3. The ternary system DME–BUTY–H_2O is also quite simple in the organic end and can be predicted from the binary systems.

4. The electrolytes at high concentrations in aprotic solvents are largely associated in the Bjerrum sense and the heat capacity data suggest that these ion pairs exist as stable solvates in equilibrium with an excess of solvent or of unsolvated molten salt. In mixed solvents, the properties will be affected by the coexistence of these solvates.

5. The presence of water has only a small effect on the properties of $LiClO_4$ but a large effect on those of LiBr. In particular, the LiBr-DME–H_2O system demixes and, when H_2O is in excess of LiBr, the solution becomes yellowish. The strong interactions involving LiBr and H_2O in aprotic solvents are also evident in the quaternary system electrolyte–H_2O–DME–BUTY.

6. The specific conductivities, which generally go through a maximum when the electrolyte concentration increases and also when mixed solvents are used, are similar to those of molten salts at high concentration. The presence of traces of water, on the other hand, has little effect on this property.

7. The specific interactions between water and electrolytes in aprotic solvents are probably responsible for the large reduction in reactivity of water with lithium metal in aprotic solvents.

Acknowledgement

Grateful acknowledgement is given to the Department of the National Defence of Canada and to the Natural Sciences and Engineering Research Council of Canada for financial support. We would also like to thank Alain Hardy for his help with some of the measurements.

References

1. G. E. Blomgren. *In* Lithium batteries. *Edited by* J.P. Gabano. Academic Press, New York. 1983. Chap. 2.
2. A.N. Dey and R.W. Holmes. J. Electrochem. Soc. **126**, 1637 (1979); **127**, 775 (1980); **127**, 1000 (1980); **127**, 1886 (1980).
3. J. Woodhouse and T.H. Norris. Inorg. Chem. **10**, 614 (1971).
4. R.V. Moshtev and P. Zlatilova. Electrochem. Acta, **27**, 1107 (1982).
5. D. Aurbach, Y.E. In-Ely, and A. Zaban. J. Electrochem. Soc. **141**, L1 (1994).
6. K.R. Zavaldil and N.R. Armstrong. J. Electrochem. Soc. **137**, 2371 (1990).
7. Z.I. Takehara, Z. Ogumi, Ké Kanamura, and Y. Uchimoto. Proc. Symp. on Lithium Batteries. *Edited by* N. Doddapaneni and A.R. Landgrebe. The Electrochemical Society, Pennington, N.J. 1994. Vol. 94-4. p 13.
8. M. Odziemkowski, M. Krell, and D.E. Irish. J. Electrochem. Soc. **139**, 3052 (1992).
9. M. Odziemkowski and D.E. Irish. J. Electrochem. Soc. **139**, 3063 (1992), **140**, 1546 (1993).
10. D.E. Irish, Z. Deng, and M. Odziemkowski. J. Power Sources, **54**, 28 (1995).
11. A.D. Holding and D. Fletcher. Electrochem. Acta, **34**, 1529 (1989).
12. R. Zana, G. Perron, and J.E. Desnoyers. J. Solution Chem. **8**, 729 (1979).
13. R. Zana, J.E. Desnoyers, G. Perron, R.L. Kay, and K. Lee. J. Phys. Chem. **86**, 3996 (1982).
14. G. Perron, G. Trudeau, and J.E. Desnoyers. Can. J. Chem. **65**, 1402 (1987).
15. G. Perron, L. Couture, D. Lambert, and J.E. Desnoyers. J. Electroanal. Chem. **355**, 277 (1993).
16. G. Perron, A. Hardy, J.-C. Justice, and J.E. Desnoyers. J. Solution Chem. **22**, 1159 (1993).
17. J.-F. Côté, J.E. Desnoyers, and J.-C. Justice. J. Solution Chem. In press.
18. G. Perron, L. Couture, and J.E. Desnoyers. J. Solution Chem. **21**, 433 (1992).
19. J. Barthel, H.-J. Gores, G. Schmeer, and R. Wachter. *In* Topics in current chemistry. Vol 111. *Edited by* F.L. Boschke. Springer-Verlag, Heidelberg. 1983.

20. M. Armand, J.Y. Sanchez, M. Gauthier, and Y. Choquette. In The electrochemistry of novel materials. *Edited by* J. Lipkowski and P.N. Ross. VCH Publishers, New York. 1994.
21. R. DeLisi, S. Milioto, and R.E. Verrall. J. Solution Chem. **19**, 639 (1990).
22. E. Wilhelm, E. Jiminez, G. Roux-Desgranges, and J.-P. Grolier. J. Solution Chem. **20**, 17 (1991).
23. H.-J Gores and J. Barthel. J. Solution Chem. **9**, 939 (1980).
24. Y. Miyauchi, M. Hojo, N. Ide, and Y. Imai. J. Chem. Soc. Faraday Trans. **88**, 1425 (1992).
25. M. Hojo, T. Takegushi, M. Hagiwara, H. Nagai, and Y. Imai. J. Phys. Chem. **93**, 955 (1989).
26. A. Seidell. Solubilities of inorganic and metal compounds. 3rd ed. Vol. 1. Van Nostrand, New York. 1940. p. 920.
27. S. Iyoki, S. Ohmori, and T. Uemura. J. Chem. Eng. Data, **35**, 317 (1990).
28. M.O. Abdullah, S.H.F. At-Madaft, and A.M. Awwad. J. Chem. Eng. Data, **32**, 161 (1987).
29. M. Costas and D. Patterson. J. Chem. Soc. Faraday Trans. 1, **81**, 2381 (1985).
30. Y. DeGrandpré, J.B. Rosenholm, L.L. Lemelin, and C. Jolicoeur. *In* Solution behavior of surfactants. Vol. 1. *Edited by* K.L. Mital and E. Fendler. Plenum Press, New York. 1982. p. 431.
31. G.E. Maciel, J.K. Hancock, L.F. Lafferty, P.A. Mueller, and W.K. Musker. Inorg. Chem. **5**, 554 (1966).
32. Y.M. Cahen, P.R. Handy, E.T. Roach, and A.I. Popov. J. Phys. Chem. **79**, 80 (1975).

Peptaibol metabolites of *Tolypocladium geodes*

Youla S. Tsantrizos, Sotiria Pischos, Françoise Sauriol, and Paul Widden

Abstract: Three antibiotic peptides, LP237-F8 (**1**), F5 (**2**), and F7 (**3**), were isolated from the liquid culture of the fungus *Tolypocladium geodes*. Chemical shift assignments of the ^{1}H and ^{13}C NMR resonances and sequencing of these metabolites were achieved by extensive high-field 2D NMR spectroscopy. The N-terminal of peptides **1** and **2** is protected with an octanoyl (Oc) fatty acid unit, whereas that of peptide **3** is protected with a decanoyl (Dec) unit. The C-terminal of all three peptides is protected with the amino alcohol leucinol (Lol). All three metabolites contain the common amino acids Ala, Phe or Tyr, Pro, and Gln, as well as the unusual amino acid α-aminoisobutyric acid (Aib). In addition, peptides **1** and **2** contain the amino acid α-amino-α-ethyl-*n*-pentanoic acid (α-ethylnorvaline, EtNor), which has not been previously reported as a constituent of a natural product. Metabolites **1**, **2**, and **3** are new members of the class of natural products known as peptaibols.

Key words: *Tolypocladium geodes*, peptaibols, leucinol, α-amino-α-ethyl-*n*-pentanoic acid.

Résumé : On a isolé trois peptides antibiotiques, LP237-F8 (**1**), F5 (**2**) et F7 (**3**) à partir de milieux de culture liquides du champignon *Tolypocladium geodes*. On a attribué les déplacements chimiques des spectres RMN du ^{1}H et du ^{13}C ainsi que la séquence de ces métabolites en faisant un usage extensif de la spectroscopie RMN 2D à haut champ. Le groupe N-terminal des peptides **1** et **2** est protégé par une unité d'acide gras octanoyle (Oc) alors que celui du peptide **3** est protégé par une unité décanoyle (Dec.) Le groupe C-terminal de chacun de ces trois peptides est protégé par l'alcool aminé leucinol (Lol). Les trois métabolites contiennent les acides aminés usuels Ala, Phé ou Tyr, Pro et Gin ainsi que l'acide α-aminoisobutyrique (Aib), un acide aminé inhabituel. De plus, les peptides **1** et **2** contiennent l'acide aminé, α-amino-α-éthyl-*n*-pentanoïque (α-éthylnorvaline, EtNor), dont on n'a jamais rapporté la présence comme constituant d'un produit naturel. Les métabolites **1**, **2** et **3** sont de nouveaux membres de la classe des produits naturels connus comme des peptaïbols.

Most clés : *Tolypocladium geodes*, peptaïbols, leucinol, acide α-amino-α-éthyl-*n*-pentanoïque.

[Traduit par la rédaction]

Introduction

The *Tolypocladium geodes* isolate LP237 was originally found in soil samples collected at the Pennine mountains of England at an altitude of 600 meters.[2] Fungi of the *Tolypocladium* genus are commonly found in cold climates and include the well-known species *T. cylindrosporum* and *T. niveum*. *Tolypocladium geodes* is a much more rare organism and it is the species that is most sensitive to warm temperatures (2). In the past, the metabolites of several *Tolypocladium* fungi have been investigated (1, 3) and a number of biologically active peptides have been reported. These include the cyclosporins (for a review, see ref. 4), which are immunosuppressing cyclic undecapeptides of important pharmacological value, and two families of antibiotic peptides, the efrapeptins (5) and elvapeptins (6).

In the course of our screening program for novel fungal metabolites exhibiting potent antitumor activity, a mixture of cytotoxic peptides was isolated from the liquid cultures of *T. geodes* LP237. High levels of cytotoxicity were observed in assays using P388D1 murine leukemia cells (IC_{50} = ~0.5 μg/mL) and a number of human carcinoma cell lines (lung A549, ovarian OVCAR3, colon SW620, and breast MCF7, IC_{50} = 0.2–0.5 μg/mL). The structure of the main component in this mixture of peptides, antibiotic LP237-F8 (**1**), was recently reported (7). This paper describes the details on the isolation of several cytotoxic peptides from the liquid culture of *T. geodes* LP237 and the structure elucidation of two new metabolites, LP237-F5 (**2**) and F7 (**3**). The complete ^{1}H and ^{13}C chemical shift assignments were achieved by extensive high-field 1D and 2D NMR spectroscopy.

Metabolites **2** and **3** are structurally related to metabolite **1** (7). All three peptides (**1**, **2**, and **3**) have both the N- and C-terminals protected with a short fatty acid unit and the amino alcohol leucinol (Lol), respectively. They contain common amino acids such as Ala, Phe or Tyr, Pro, and Gln and the unusual amino acid α-aminoisobutyric acid (Aib), commonly found in peptaibols. Peptides **1** and **2** also contain the amino

Received October 5, 1995.

Y.S. Tsantrizos[1] and S. Pischos. Department of Chemistry and Biochemistry, Concordia University, 1455 de Maisonneuve Blvd West, Montréal, QC H3G 1M8, Canada.
F. Sauriol. Department of Chemistry, McGill University, 801 Sherbrooke Street West, Montréal, QC H3A 2K6, Canada.
P. Widden. Department of Biology, Concordia University, 1455 de Maisonneuve Blvd West, Montréal, QC H3G 1M8, Canada.

[1] Author to whom correspondence may be addressed. Telephone: (514) 848-3335. Fax: (514) 848-2868. E-mail: Youla@Vax2.Concordia.ca

[2] *Tolypocladium geodes* isolate LP237 was originally isolated by P. Widden in 1982. The taxomomic identity of this isolate was confirmed by J. Bissett (1) and the culture was deposited at the Biosystematics Research Institute, Ottawa, Canada.

Fig. 1. Peptaibol metabolites of *Tolypocladium geodes*.

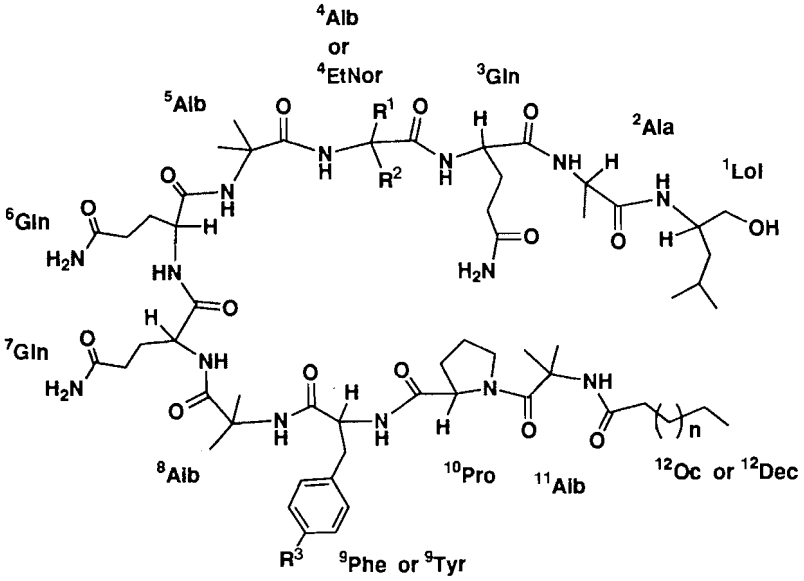

LP237-F8 (1), R^1 = Et, R^2 = *n*Pr (EtNor), R^3 = H (Phe), *n* = 4 (Oc)

LP237-F5 (2), R^1 = Et, R^2 = *n*Pr (EtNor), R^3 = OH (Tyr), *n* = 4 (Oc)

LP237-F7 (3), R^1 = R^2 = Me (Aib), R^3 = H (Phe), *n* = 6 (Dec)

acid α-amino-α-ethyl-*n*-pentanoic acid (α-ethylnorvaline, EtNor), which has not been previously reported as a constituent of a natural product. Metabolites LP237-F5 (**1**), F7 (**2**), and F8 (**3**) are novel linear peptides belonging to the family of natural products known as peptaibols.

Results and discussion

Isolation and purification of peptides

Liquid culture medium of 2% malt extract was inoculated with actively growing mycelium plugs of *T. geodes* and was incubated at 20°C on a rotary shaker for a period of 7 days. A bioassay-guided purification scheme was developed for the isolation of the extracellular cytotoxic metabolites of *T. geodes* produced under these fermentation conditions. The presence of active metabolites in fractions collected from each purification step was identified using the SOS Chromotest, a bacterial colorimetric assay that is widely used as a reliable test for the detection of genotoxic compounds (DNA-damaging compounds) (reviewed in ref. 8).

The fermentation broth was initially absorbed onto a column of Diaion HP 20 resin, which was eluted with a linear solvent gradient from H_2O to MeOH and then to acetone. The cytotoxic metabolites eluted from the column with aqueous MeOH (75–100%) and were further partitioned by size exclusion chromatography (Sephadex LH-20). Reverse-phase flash column chromatography (9) led to the isolation of a strongly cytotoxic and genotoxic mixture of peptides, exhibiting an IC_{50} value in the range of 5–10 ng/mL with P388D1 murine leukemia cells and a positive SOS Chromotest.

Mass spectral analysis of the cytotoxic mixture of peptides, by MALDI and ESI MS, indicated the presence of many different compounds ranging in molecular weight from *m/z* 1300 to 2000. Separation of these metabolites by C18 reverse-phase semi-preparative HPLC, using a solvent mixture of MeOH:H_2O:MeCN (70:20:10 with 0.1% TFA in all solvents) allowed the isolation of five peptides. At a flow rate of 4 mL/min, metabolites LP237-F5 (**2**), F6, F7 (**3**), F8 (**1**), and F9 eluted from the HPLC column with retention times of 16.4, 17.2, 20.7, 23.6, and 26.0 min, respectively. Each component was further purified by HPLC in order to obtain the pure peptides as white amorphous solids. At the present time, the structural assignments of the three main components, metabolites **1**, **2**, and **3**, have been completed (Fig. 1) and those of peptides LP237-F6 and F9 are in progress.

Structure determination of metabolite LP237-F5 (2)

Both MALDI and FAB MS of metabolite **2** suggested a molecular formula of $C_{65}H_{108}N_{14}O_{16}$ (MALDI MS (2,5-dihydroxy benzoic acid + NaCl or NaLi matrix) *m/z*: 1365.1 $(MCH_3+Na)^+$ and 1347.8 $(M+Li)^+$, FAB MS (NBA+NaCl matrix) *m/z*: 1363.5 $(M+Na)^+$; calculated mass for $C_{65}H_{108}N_{14}O_{16}Na$ = 1363.8).

The NMR spectral data of metabolite LP237-F5 (**2**) were very similar to those of the previously assigned peptaibol LP237-F8 (**1**) (7). However, metabolite **2** could easily be methylated with diazomethane (MALDI MS (2,5-dihydroxy benzoic acid + LiCl matrix) *m/z*: 1362.5 $(M+Li)^+$) whereas metabolite **1** was resistant to methylation under the same reaction conditions. Based on the NMR data, the difference in reactivity towards CH_2N_2 observed between **1** and **2** was attributed to the presence of a Tyr unit in **2** as opposed to a Phe unit in **1.** Complete acid hydrolysis of peptide **2** and amino acid analysis comfirmed the presence of the amino acid Tyr, in addition to Ala, Pro, and Glx in a ratio of 1:1:1:3 (10).

The ^{1}H NMR spectrum (500 MHz in DMSO-d_6) of **2** showed the presence of 21 resonances in the downfield region (Table 1, Fig. 2). The two doublets at δ 6.60 and 6.96 (J = 8.3 Hz, 2 × 2H) and the singlet at δ 9.18 (OH) were assigned to the Tyr unit. All of the remaining downfield protons could be exchanged in CD_3OD and they were assigned to 16 NH protons. The COSY NMR of **2** showed coupling between the NH resonances at δ 6.76, 6.80, 6.82 and those at 7.16, 7.27, 7.27, respectively (Fig. 2). Thus, these signals were assigned to three ε-NH_2 groups of Gln. From the combined ^{1}H and COSY NMR data (Table 1, Fig. 2), the α-H and the backbone NH protons could easily be assigned for the Tyr (δ 4.22, 7.73), Ala (δ 4.01, 7.52), ^{6}Gln (δ 3.92, 7.78), ^{7}Gln (δ 3.89, 7.73), ^{3}Gln (δ 3.81, 7.57), and Lol (δ 3.76, 6.65) units.

The remaining chemical shifts of each amino acid were assigned based on the combined ^{1}H, COSY, HMQC, HMBC, and NOESY NMR data (Tables 1 and 2). For example, coupling between the NH (δ 6.65) of Lol, the α-H resonance (δ 3.76), and the two non-equivalent -CH_2OH protons (δ 3.23 and 3.14) was clearly observed in the COSY NMR spectrum of metabolite **2**. The chemical shifts of the corresponding carbons were assigned from the HMQC spectrum at δ 48.77 (α-C) and 64.38 (-CH_2OH).[3] Furthermore, coupling between the α-H resonance and the two β-H (δ ~ 1.30), as well as between the two δ-CH_3 groups (δ ~ 0.78), the β-H (δ ~1.30), and the γ-H (δ ~1.58), was also observed in the COSY spectrum of **2**. The ^{13}C chemical shifts of the β-CH_2 (δ 40.15) and the γ-CH (δ ~ 25.4) were obtained from the HMQC data, whereas the ^{13}C shifts for the two δ-CH_3 groups (δ 23.6 and 21.9) were obtained from the HMBC spectrum.[3]

The order of the amino acid sequence of peptide **2** was based primarily on the NOESY NMR data. Strong NOE effects were observed between the backbone amide protons and the α-protons of neighboring residues and also between amide protons and the side chains of the neighboring amino acids. The most relevant NOE data for the sequence assignment (peptide backbone) are given in Table 2.

Fig. 2. Partial expansion of the COSY NMR spectrum (NH and αH regions) of LP237-F5 (500 MHz, DMSO).

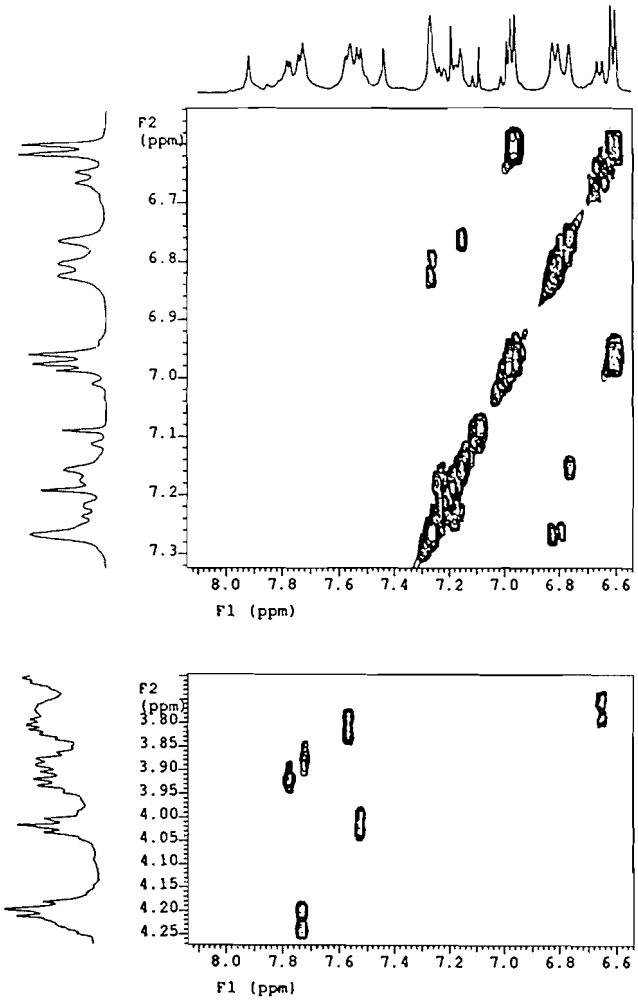

Structure determination of metabolite LP237-F7 (3)

FAB MS of metabolite **3** suggested a molecular formula of $C_{64}H_{106}N_{14}O_{15}$ ((NBA+NaCl matrix) *m/z*: 1333.8 $(M+Na)^+$; calculated mass for $C_{64}H_{106}N_{14}O_{15}Na$ = 1333.7859). Amino acid analysis of **3** indicated the presence of the same common amino acid units as in metabolite **1**, Phe, Ala, Pro, and Glx in a ratio of 1:1:1:3. Metabolite **3** was also resistant to methylation with diazomethane, suggesting the absence of free carboxyl or phenolic functionalities.

The ^{1}H NMR spectrum of LP237-F7 (**3**) was distinctly different from that of metabolite **1** in the upfield methyl region; a total of three methyl signals was observed at δ 0.7–0.9 in **3** as opposed to five in metabolite **1**. The two overlapping doublets observed (δ 0.887 and 0.893) were assigned to the two δCH_3 of Lol, and a triplet (δ 0.863) was assigned to the terminal methyl of the fatty acid unit. Thus, it was assumed that metabolite **3** did not contain the unusual amino acid EtNor, which was found in **1** and **2**. This assumption was further supported by the absence of the expected correlations in the COSY spectrum of **3** between the methyl region and the methylene region for the EtNor unit, as had been observed previously in the COSY spectum of metabolite **1**. Furthermore, a total of eight singlets due to methyls of Aib units (δ 2 × 1.409, 1.458, 1.470, 1.474, 1.535, 1.539, and 1.604) was observed in the ^{1}H spectrum of **3**. To account for (*a*) the similarities in the spectral data between **1** and **3**, (*b*) the difference in mass of 14 units, (*c*) the loss of the EtNor unit ($C_7H_{13}NO$, MW = 127), and (*d*) the addition of a fourth Aib unit (C_4H_7NO, MW = 85), it was proposed that peptide **3** contains a decanoyl (Dec) fatty acid instead of the Oc unit found in peptides **1** and **2**. The overlapping of many -CH_2- resonances in the ^{1}H NMR spectum of **3** did not permit exact chemical shift assignments for the Dec unit to be made; however, the presence of this unit was confirmed from the ^{13}C and HMQC NMR data of this metabolite. The remaining amino acid units of peptide **3** were identical to those of peptide **1**, and their chemical shift assignments (Table 3) were consistent with the NMR data; the combined NMR data from the ^{1}H, ^{13}C, COSY, HMQC, HMBC, TOCSY, ROESY, and NOESY spectra were used to confirm the proposed structural assignment (Fig. 1).

[3] Due to the very small amount of available material of metabolite **2** (~2 mg) a directly observed ^{13}C NMR spectrum was not obtained. However, the ^{1}H, COSY, HMQC, HMBC, and NOESY NMR data of **2** were similar to those of metabolite **1** and consistent with the proposed structure.

Table 1. ^{1}H (500 MHz) and ^{13}C (125 MHz) NMR data of **2** in DMSO-d_6.

Assignment		^{13}C [a](δ)	^{1}H (δ)	Intensity, mult., J (Hz)
^{1}Lol	α	48.77	3.760	1H, m
	β	40.00	1.309	2H, m
	γ	25.44	1.57[b]	1H, m
	δ	23.56, 21.92	0.77[b]	2 × 3H, d
	CH_2-OH	66.09	3.124, 3.244	2H, m
	NH		6.652	1H, d, J = 9.3 Hz
^{2}Ala	α	49.59	4.012	1H, m
	β	17.59	1.259	3H, d, J = 7.3
	NH		7.522	1H, d, J = 7.3
^{3}Gln, ^{6}Gln, ^{7}Gln				
	α	54.80	3.805	1H, m
		55.34	3.922	1H, m
		55.62	3.886	1H, m
	β	27.42–27.57	1.98–1.93[b]	2H, m
	γ	32.70	2.1–2.4[b]	2H, m
		32.99		
		33.14		
	NH		7.568	1H, d, J = 5.4
			7.730	
			7.775	
	εNH$_2$		6.763, 7.156	2H, br s
			6.802, 7.265	2H, br s
			6.823, 7.265	2H, br s
^{4}EtNor	α	60.27		
	β	30.35	1.29[b]	2H, m
	γ	32.99	1.29[b]	2H, m
	δ	13.97	0.81[b]	3H, t, J = 6.8
	NH		7.433	1H, s
	β′	26.54	2.19,[b] 1.61[b]	2H, m
	γ′	7.12	0.694	3H, t, J = 7.5
^{5}Aib, ^{8}Aib, ^{11}Aib				
	α	56.1–56.3		
	β	25.6, 26.6	1.30, 1.35	2 × 3H, s
		26.2, 26.0	1.35, 1.46	
		~24, 26.0	1.29, 1.39	
	NH		7.550	1H, s
			7.918	
			8.798	
^{9}Tyr	α	56.44	4.218	1H, m
	β	35.34	3.069, 2.778	2H, m
	1	—		
	2,6	129.8	6.966	2H, d, J = 8.3
	3,5	116.6	6.607	2H, d, J = 8.3
	4	—		
	NH		7.73[b]	1H
^{10}Pro	α	63.01	4.192	1H, t, J = 7.5
	β	29.62	2.027, 1.291	2H, m
	γ	26.83	1.68[b], 1.75[b]	2H, m
	δ	48.49	3.698, 3.302	2H, m
^{12}Oc	2′	35.07	2.25	2H, m
	3′	25.68	1.66	2H, m
	4′, 5′, 6′, 7′	29.0–31.5	1.17[b]–1.22[b]	8H, m
	8′	14.02	0.80[b]	3H, t

[a]Chemical shift assignment was based on the HMQC or HMBC NMR data; carbonyl and quaternary carbons could not be observed.

[b]Exact chemical shifts could not be determined due overlapping resonances in ^{1}H NMR spectrum.

Table 2. NOESY NMR data from the peptide backbone of **2** in DMSO-d_6.

	Assignment	^{1}H (δ)	NOEs observed[a]
^{1}Lol	α	3.760	βH (str), γH (med) NH (med), CH_2-O (med)
	NH	6.652	Ala-NH (str), Ala-βCH_3 (str), αH (med)
^{2}Ala	α	4.012	Lol-NH (str), NH (str), βCH_3 (str)
	NH	7.522	αH (med), βCH_3 (med), Lol-NH (v str), ^{3}Gln-αH (med), ^{3}Gln-βH (med)
^{3}Gln	α	3.805	NH (str), βH (med), γH (med), Ala-NH (w), Lol-NH (w)
	NH	7.568	αH (str), βH (v str), γH (med), EtNor-NH (str), EtNor-γH (med)
^{4}EtNor	NH	7.433	βH (med), β′H (med), γ′H (med), ^{5}Aib-NH (str), ^{5}Aib-CH_3 (v str), ^{3}Gln-NH (str)
^{5}Aib	NH	7.918	2CH_3 (v str), ^{4}α-EtNor-NH (str), ^{4}EtNor-β′H (med) ^{6}Gln-αH (str), ^{6}Gln-NH (str)
^{6}Gln	α	3.922	βH (v str), γH (med), ^{5}Aib-NH (str), ^{7}Gln-NH (str)
	NH	7.775	αH (med), βH (med), γH (med), ^{8}Aib-CH_3 (med)
^{7}Gln	α	3.886	βH (v str), γH (med), NH (str), ^{6}Gln-NH (v str)
	NH	7.73	^{8}Aib-2CH_3 (str), overlapping with Try-NH
^{8}Aib	NH	7.550	2CH_3 (v str), Try-NH (v str), Try-αH(med), Try-βH(med)
^{9}Tyr	α	4.218	βH (v str), NH (str), ^{8}Aib-NH (med), ^{6}Gln-βH (med)
	NH	7.73	αH (str), ^{8}Aib-2CH_3 (str), overlapping with Try-NH
^{10}Pro	α	4.192	βH (v str), Try-NH (str)
^{11}Aib		8.798	2CH_3 (v str), Oc-2′H (v str), Pro-δH (med)

[a]Quantification of the NOE's observed is presented as "very strong" (v str), "strong" (str), "medium" (med) or "weak" (w)

Conclusion

Linear peptides containing a C-terminal amino alcohol, Lol (11), Phol (phenylalaninol) (12), or Trpol (tryptophanol) (13), and a high proportion of the unusual amino acid Aib (14) belong to the class of natural products known as peptaibols. The *Trichoderma* metabolites trichorzianine A (13), trichosporin B (12*b*,*c*,*d*), tricholongin BI and BII (11*a*), trichogin A IV (11*b*), trichodecenins-I and -II (11*d*), and the alamethicins (12*f*) are among the best known peptaibols. The zervamicins (15), emerimicins (12*a*, 15), and hypelcin A (11*c*,*e*) represent examples of peptaibols produced by a few other fungi. The N-terminal amino acid of peptaibols is usually protected by an acetyl group; however, in trichogin A IV (11*b*) and the trichodecenins-I and -II (11*d*) it is protected with an octanoyl and a *cis*-4-decenoyl group, respectively. In peptides **1**, **2**, and **3**, the N-terminal amino acid is also protected with an octanoyl or decanoyl fatty acid unit, whereas the C-terminal is protected with a Lol unit. In addition to the common amino acids, Ala, Phe or Tyr, Pro, and Gln, these peptides contain several Aib units. Metabolites **1** and **2** also contain the novel amino acid α-amino-α-ethyl-*n*-pentanoic acid (α-ethylnorvaline, EtNor); to our knowledge, this amino acid has not been previously reported as a component of a natural product. However, EtNor has been found in extraterrestrial sediments such as the Murchison meteorite (16). EtNor has also been synthesized and shown to act as a competitive inhibitor of methionine (17).

The novel peptides LP237-F8 (**1**), LP237-F5 (**2**), and LP237-F7 (**3**) are the first peptaibols to be isolated from the *Tolypocladium* genus. Peptaibols are known to exhibit many unique biological activities, including the formation of voltage-gated ion channels in lipid bilayer membranes (18, 11*b*), induction of catecholamine secretion from adrenal chromaffin cells (19), uncoupling of oxidative phosphorylation in mitochondria (20), and the inhibition of cell multiplication in amoebae (21). The cytotoxicity of metabolites **1** (IC_{50} = ~30 μg/mL), **2** (IC_{50} = ~10 μg/mL), and **3** (IC_{50} = ~40 μg/mL) towards P388D1 murine leukemia cells was much lower than the mixture of peptides. Therefore, it is reasonable to assume that the most potent component of the mixture remains to be identified or that there is a synergistic effect associated with the antitumor activity of the mixture. The biological activities of the *T. geodes* metabolites are currently under further investigation.

Experimental

Spectral data

NMR spectra were obtained at 20–22°C using a Varian Unity-500 spectrometer (operating at 499.84 MHz for ^{1}H and 125.7 MHz for ^{13}C) or a Bruker AMX-600 spectrometer (operating at 600.13 MHz for ^{1}H and 150.9 MHz for ^{13}C). ^{1}H and ^{13}C- NMR chemical shifts are quoted in ppm and are referenced to the internal deuterated solvent downfield from tetramethylsilane (TMS). NOESY experiments performed on the Varian Unity-500 spectrometer (hypercomplex phase mode) were obtained using a mixing time of 400 ms with Varian's standard pulse program and 256 increments in *t*1.

Table 3. ^{1}H (600 MHz) and ^{13}C (150 MHz) NMR data of **3** in DMSO-d_6.

	Assignment	^{13}C (δ)	^{1}H (δ)	intensity mult., J (Hz)
[1]Lol	α	48.41	3.79	1H, br. m
	β	39.91	1.32[c]	2H, m
	γ	23.98[a]	1.65[c]	1H, m
	δ	21.55, 23.30	0.80[c]	2 × 3H, d
	CH_2-OH	64.06	3.171, 3.27[c]	2H, dd, J = 7.8, J = 10.8 and m
	NH		6.689	1H, d, J = 9.2 Hz
[2]Ala	α	49.26	4.039	1H, q, J = 7.3
	β	17.13	1.278	3H, d, J = 7.3
	CO	171.7[b]		
	NH		7.526	1H, d, J = 7.3
[3]Gln, [6]Gln, [7]Gln				
	α-6	55.01	3.935[c]	1H, m
	α-7	55.01	3.925[c]	1H, m
	α-3	54.45	3.826	1H, m
	β-6	25.9[b]	2.00[c]	2H, m
	β-7	25.9[b]	1.95[c]	2H, m
	β-3	25.9[b]	1.95[c], 2.00[c]	2H, m
	γ-6	31.71	2.10, 2.22	2H, m
	γ-7	31.35	2.15, 2.21	2H, m
	γ-3	31.35	2.20, 2.30	2H, m
	δ CO	~173–175[b]		
	εNH[2]		6.759, 7.163	2H, br s
	CO	~173–175[b]		
	NH-6		7.81	1H
	NH-7		7.732	1H, d, J = 5.5
	NH-3		7.580	1H, d, J = 4.4
	ε-NH_2		6.72, 6.76, 6.79	3H, 3s
			7.17, 7.25	1H and 2H, s
[4]Aib, [5]Aib, [8]Aib, [11]Aib				
	α	56.02		
		55.89		
		55.77		
		55.77		
	β	26.4–25.6[b]	1.307	3H, s
		23.5–22.59[b]	1.335	3H, s
			1.359	6H, s
			1.371	3H, s
			1.397	3H, s
			1.411	3H, s
			1.478	3H, s
	CO	~173-174[b]		
	NH-4		7.505	1H, s
	NH-5		7.859	1H, s
	NH-8		7.577	1H, s
	NH-11		8.771	1H, s
[9]Phe	α	55.28	4.346	1H, m
	β	35.86	3.220, 2.904	2H, dd, J = 13.8, 4.2
	1	137.60		
	2,6	128.80	7.22	2H, m
	3,5	127.97	7.22	2H, m
	4	126.28	7.28	1H, m
	CO	175.6[b]		
	NH		7.80[c]	1H

Table 3 (*concluded*).

	Assignment	^{13}C (δ)	^{1}H (δ)	intensity mult., J (Hz)
^{10}Pro	α	62.49	4.205	1H, t, J = 7.2
	β	28.04	2.02[c], 1.22[c]	2H, m
	γ	25.19[a]	1.65, 1.75	2H, m
	δ	48.39	3.70, 3.30	2H, m
	CO	171.7[b]		
^{12}Dec	CO-1′	~175.1[b]		
	2′	34.73[d]	2.26[d]	2H, m
	3′	~25.1[d]	1.64[d]	2H, m
	4′	28.51[d]	1.22[d]	
	5′	28.57[d]	1.22[d]	
	6′	28.57[d]	1.17[d]	
	7′	28.73[d]	1.17[d]	
	8′	31.11[d]	1.17[d]	
	9′	21.94[d]	1.18[d]	
	10′	13.79	0.81	3H, t, J = 7.1

[a]Chemical shift assignment could be interchanged.

[b]Although all of the expected carbonyl resonances (a total of 14 signals) were clearly observed in the ^{13}C NMR spectrum of metabolite **3**, the exact chemical shift of each amino acid unit could not be assigned due to extensive overlapping of the correlation signals in the HMBC spectrum.

[c]Exact chemical shifts could not be determined due overlapping resonances in ^{1}H NMR spectrum.

[d]Chemical shift assignment was based on the HMQC NMR spectrum.

Zero-filling in the evolution domain and linear prediction to lengthen the evolution domain were used to obtain the final data size of the 2048 × 2048 complex matrix. The HMQC experiments with a preceding BIRD nulling period were used with hypercomplex phase mode, and ^{13}C broadband waltz decoupling was applied during acquisition of the proton spectra. The HMBC experiment was acquired using similar conditions (without the null period and ^{13}C decoupling) and the τ delay was set to 100 ms for long-range coupling. NOESY experiments performed on the Bruker AMX-600 spectrometer were obtained using a mixing time of 300 ms and Bruker's standard pulse program, 256 increments in $t1$, and a 2048 × 2048 complex matrix. The HMQC and HMBC NMR spectra were acquired using Bruker's standard pulse programs for these experiments.

Mass spectra were obtained using a ZAB-E4F instrument for FAB MS, a Finnigan SSQ 700 instrument for the ESI MS, and a Kratos Kompact MALDI 3 V 4.0 instrument for MALDI MS. Ultraviolet spectra were recorded on a Hewlett Packard 8452A diode array spectrophotometer. Optical rotations were measured using a JASCO DIP-140 Digital polarimeter.

Chromatography

Reverse-phase flash column chromatography was carried out on silica gel (Silica Gel 60, 70–230 mesh) reacted with *n*-octadecyltrichlorosilane. C_{18} reverse-phase silica gel was prepared following literature procedures (9). All chromatographic solvents were fractionally distilled prior to use with the exception of HPLC grade solvents. Doubly distilled H_2O was filtered through a 0.45 mm filter membrane and HPLC grade MeOH and MeCN were filtered through a 0.5 mm filter membrane (Millipore Corp., Mississauga, Ont.) before they were used in HPLC. Analysis and purification were carried out on a semi-preparative reverse-phase C_{18} column: Waters NOVA-PAK (25 mm × 100 mm, 6 μm, 60 Å) using a Waters instrument (pump model W600EP), UV/VIS detector wavelength set to 210 nm (model M486P), Rheodyne injector. All retention times were automatically recorded from the time of injection.

General extraction of active metabolites

Stock cultures of *T. geodes* were maintained on 2% malt extract (Difco) plus 1.5% agar in slant tubes at 4°C. A small amount of mycelium was used to inoculate 2% malt extract agar plates, which were then incubated in the dark, at room temperature, for a period of 14 days. Plugs (~15 plugs/flask) of actively growing mycelium were used to inoculate 2% malt extract liquid medium (6 × 500 mL culture in 3 L flasks). The fermentation flasks were then incubated at 20°C on a rotary shaker at 120 rpm for 7 days. The mycelium was removed by filtration, and the resulting filtrate was absorbed onto a Diaion HP 20 column (60 mm × 25 cm), which was eluted with a linear gradient from 100% H_2O to 100% MeOH to 100% acetone, at a flow rate of 10 mL/min. The cytotoxic fractions that eluted from ~75% aqueous MeOH to 100% MeOH, were combined and evaporated to dryness to give ~1.5 g of a brown gum. The active crude (IC_{50} = 0.5 μg/mL on P388D1 murine leukemia cells) was subsequently dissolved in 2–5 mL of MeOH, loaded on a Sephadex LH-20 column (25 mm × 100 cm), and partitioned into 90 fractions (~8 mL each) by eluting with degassed MeOH at a flow rate of 0.7 mL/min.. Fractions 22–30 exhibited strong cytotoxic activity (IC_{50} = 52 ng/mL) and gave a strong positive SOS Chromotest. These fractions were combined, evaporated to dryness (~230 mg), and further purified by flash column chromatography on a C_{18} reverse-phase column (20 mm × 15 cm), using a linear solvent gradient from 100% H_2O to 100% MeOH to 100% CH_2Cl_2 at a flow rate of 2 mL/min. The cytotoxic metabolites eluted in the fractions collected from ~85% aqueous MeOH to ~95% aqueous MeOH; some of these fractions exhibited IC_{50} values in the 3–5 ng/mL range. However, each fraction contained a very small

amount of material that was still a mixture of several components. Therefore, the active fractions were combined and evaporated to dryness to obtain ~40 mg of cytotoxic crude, which was further analyzed by semi-preparative C_{18} reverse-phase HPLC. HPLC purification of the above cytotoxic crude, using a solvent mixture of MeOH:H_2O:MeCN (70:20:10, with 0.1% TFA in all solvents), allowed the isolation of five biologically active peptides; two of these metabolites, LP237-F6 and F9, are currently under investigation. At a flow rate of 4 mL/min, metabolites **1**, **2**, and **3** had a retention time of 23.6, 16.4, and 20.7 min respectively. All three peptides were purified by HPLC for a second time, using the same conditions, in order to isolate the pure compounds as amorphous white solids (~3.8 mg of **1**, ~1.2 mg of **2**, and ~6.2 mg of **3**). *Metabolite 2*: UV (MeOH, nm): max 226, min 276. $[\alpha]_D$ +9.50 (*c* 0.0027, MeOH). NMR data given in Table 1. *Metabolite 3*: UV (MeOH, nm): max 226, min 258. $[\alpha]_D$ +0.21 (c 0.0102, MeOH). NMR data given in Table 2. MS data for both metabolites reported in the discussion.

Acknowledgments

This work was supported by grants from the Natural Sciences and Engineering Research Council of Canada and le Fonds pour la Formation de Chercheurs et l'Aide à la Recherche du Québec. We are grateful to Dr. Theresa M. Allen's research group (Department of Pharmacology, University of Alberta) for performing the cytotoxicity bioassays on the P388D1 murine leukemia cells and Dr. Brian Leyland-Jones' group (Oncology Department, Faculty of Medicine, McGill University) for the bioassays on human carcinoma cell lines. We wish to thank Mr. Bernard Gibbs, Biotechnology Research Institute, National Research Council Canada, for the amino acid analysis of peptides **1**, **2**, and **3**. We also thank Dr. Orvil A. Mamer of the Biomedical Mass Spectrometry Unit for recording the FAB MS spectra, Mr. George Tsaprailis (Department of Chemistry and Biochemistry, Concordia University) for recording the ESI MS spectra, and Mr. Gerry Barbiero (Chemistry Department, McGill University) for recording the MALDI MS spectra. We also wish to thank Dr. M.T. Phan Viet, Laboratoire Régional de RMN, Université de Montréal, for recording all of the 600 MHz (^{1}H) NMR spectra.

References

1. J. Bissett. Can. J. Bot. **61**, 1311 (1983).
2. (*a*) P. Dowding and P. Widden. *In* Soil organisms and decomposition in tundra. *Edited by* A.J. Holding, O.W. Heal, S.F. MacLean, and P.W. Flanagan. Tundra Biome Steering Committee, Stockholm. 1974. pp. 123–150; (*b*) P. Widden. Mycologia, **79**, 298 (1987).
3. J. Weiser. Acta Entomol. Bohemoslov. **88**, 367 (1991).
4. Y.A. Ovchinnikov and V.T. Ivanov. *In* The proteins. Vol. V. *Edited by* H. Neurath and R.L. Hill. Academic Press, New York. 1982. pp. 547–555.
5. (*a*) C.G. Jackson, P.E. Linnett, R.B. Beechey, and P.J.F. Henderson. Biochem. Soc. Trans. **7**, 224 (1979); (*b*) D.A. Bullough, C.G. Jackson, P.J.F. Henderson, F.H. Cottee, R.B. Beechey, and P.E. Linnett. Biochem. Int. **4**, 543 (1982); (*c*) S. Gupta, S.B. Krasnoff, D.W. Roberts, and J.A.A. Renwick. J. Am. Chem. Soc. **113**, 707 (1991); (*d*) S.B. Krasnoff, S. Gupta, R.J. St. Leger, J.A.A. Renwick, and D.W. Roberts. J. Invertebr. Pathol. **58**, 180 (1991); (*e*) S. Gupta, S.B. Krasnoff, D.W. Roberts, J.A.A. Renwick, L.S. Brinen, and J. Clardy. J. Org. Chem. **57**, 2306 (1992).
6. D.A. Bullough, C.G. Jackson, P.J.F. Henderson, R.B. Beechey, and P.E. Linnett. FEBS Lett. **145**, 258 (1982).
7. Y.S. Tsantrizos, S. Pischos, and F. Sauriol. J. Org. Chem. On press.
8. P. Quillardet and M. Hofnung. Mutat. Res. **297**, 235 (1993).
9. (*a*) J.W. Blunt, V.L. Calder, G.D. Fenwick, R.J. Lake, J.D. McCombs, M.H.G. Munro, and N.B. Perry. J. Nat. Prod. **50**, 290 (1987); (*b*) Y.S. Tsantrizos, K.K. Ogilvie, and A.K. Watson. Can. J. Chem. **70**, 2276 (1992).
10. D.H. Spackman, W.H. Stein, and S. Moore. Anal. Chem. **30**, 1190 (1958).
11. (*a*) S. Rebuffat, Y. Prigent, C. Auvin-Guette, and B. Bodo. Eur. J. Biochem. **201**, 661 (1991); (*b*) C. Auvin-Guette, S. Rebuffat, Y. Prigent, and B. Bodo. J. Am. Chem. Soc. **114**, 2170 (1992); (*c*) K. Matsura, A. Yesilada, A. Iida, Y. Takaishi, M. Kanai, and T. Fujita. J. Chem. Soc. Perkin Trans. 1, 381 (1993); (*d*) T. Fujita, S. Wada, A. Iida, T. Nishimura, M. Kanai, and N. Toyama. Chem. Pharm. Bull. **42**, 489 (1994); (*e*) T. Fujita, Y. Takaishi, and T. Shiromoto. J. Chem. Soc. Chem. Commun. 413 (1979).
12. (*a*) R.C. Pandey, J.C. Cook, Jr., and K.L. Rinehart, Jr. J. Am. Chem. Soc. **99**, 5205 (1977); (*b*) T. Fujita, A. Iida, S. Uesato, Y. Takaishi, T. Shingu, M. Saito, and M. Morita. J. Antibiot. **41**, 814 (1988); (*c*) A. Iida, M. Okuda, S. Uesato, Y. Takaishi, T. Shingu, M. Morita, and T. Fujita. J. Chem. Soc. Perkin Trans. 1, 3249 (1990); (*d*) Y. Nagaoka, A. Iida, and T. Fujita. Chem. Pharm. Bull. **42**, 1258 (1994); (*e*) Q. Huang, Y. Tezuka, T. Kikuchi, A. Nishi, K. Tubaki, and K. Tanaka. Chem. Pharm. Bull. **43**, 223 (1995); (*f*) R.C. Pandey, J.C. Cook, Jr., K.L. Rinehart, Jr. J. Am. Chem. Soc. **99**, 8469 (1977).
13. B. Bodo, S. Rebuffat, M. El Hajji, and D. Davoust. J. Am. Chem. Soc. **107**, 6011 (1985).
14. I.M. Shaw and A. Taylor. Can. J. Chem. **64**, 164 (1986).
15. (*a*) A.D. Argoudelis, A. Dietz, and L.E. Johnson. J. Antibiot. **27**, 321 (1974); (*b*) K.L. Rinehart, Jr., L.A. Gaudioso, M.L. Moore, R.C. Pandey, and J.C. Cook, Jr. J. Am. Chem. Soc. **103**, 6517 (1981).
16. J.R. Cronin and S. Pizzarello. Geochim. Cosmochim. Acta, **50**, 2419 (1986).
17. C.J. Abshire and G. Planet. J. Med. Chem. **15**, 226 (1972).
18. (*a*) R.O. Fox, Jr. and F.M. Richards. Nature, **300**, 325 (1982); (*b*) G. Menestrina, K.P. Voges, G. Jung, and G. Boheim. J. Membrane Biol. **93**, 111 (1986); (*c*) S. Rebuffat, H. Duclohier, C. Auvin-Guette, G. Molle, G. Spach, and B. Bodo. FEMS Microbiol. Immunol. **105**, 151 (1992); (*d*) M.S.P. Sansom. Eur. Biophys. J. **22**, 105 (1993).
19. (*a*) A.R. Artalejo, C. Montiel, P. Sanchez-Garcia, G. Uceda, J.M. Guantes, and A.G. Garcia. Biochem. Biophys. Res. Commun. **169**, 1204 (1990); (*b*) E. Tachikawa, S. Takahashi, K. Furumachi, T. Kashimoto, A. Iida, Y. Nagaoka, T. Fujita, and Y. Takaishi. Mol. Pharmacol. **40**, 790 (1991); (*c*) R.I. Fonteriz, M.G. Lopez, J. Garcia-Sancho, and A.G.. Garcia. FEBS Lett. **283**, 89 (1991).
20. (*a*) Y. Takaishi, Y. Terada, and T. Fujita. Experientia, **36**, 550 (1980); (*b*) M.K. Mathew, R. Nagaraj, and P. Balaram. Biochem. Biophys. Res. Commun. **98**, 548 (1981); (*c*) M.K. Das, S. Raghothama, and P. Balaram. Biochemistry, **25**, 7110 (1986); (*d*) M. Okuda, A. Iida, S. Uesato, Y. Nagaoka, T. Fujita, Y. Takaishi, and H. Terada. Biol. Pharm. Bull. **17**, 482 (1994).
21. M.E. Hajji, S. Rebuffat, T.L. Doan, G. Klein, M. Satre, and B. Bodo. Biochim. Biophys. Acta, **978**, 97 (1989).

Conformational analysis and 2D NMR assignment strategies for lignin model compounds. The structure of acetoguaiacyl-dehydro-diisoeugenol methyl ether

Theodore M. Garver, Karen Joy Maa, and Kirk Marat

Abstract: The resolved ^{1}H and ^{13}C chemical shifts for the lignin model trimer acetoguaiacyl-dehydro-diisoeugenol methyl ether have been completely assigned using one- and two-dimensional NMR techniques. Identification of spin families and assignments within the spin families were made using routine one-dimensional experiments for chemical shifts and multiplicities, and COSY and heteronuclear correlation experiments to determine connectivities. NOESY, HOESY, and long-range heteronuclear correlation experiments were then used to determine the juxtaposition of the assigned groups and to provide a confirmation of assignments. Steady state NOE difference and time-dependent NOESY and HOESY experiments were then used to provide experimental measures of the trimer conformation. Semiempirical molecular orbital methods were used to calculate minimum energy structures and energy barriers for bond rotations within the molecule. We have found that for the trimer-size molecule the NOE experiments provide a less detailed picture of the molecular conformation than the molecular orbital results. A comparison of NOE and MO results with crystal structures from the literature indicates the extent to which side-chain and methoxyl torsion angles may be estimated using each method. The correlation between NOE and MO predictions for interatomic distances apparently is related to the narrow minima for β-O-4 torsion angles for which the different results confirm each other. Broad minima or low-energy barriers for torsion angle rotations may yield minimized structures by computational methods that are not experimentally justified.

Key words: semiempirical molecular orbital calculation, 2D NMR, conformation, lignin model, nuclear Overhauser effect.

Résumé : On a attribué tous les déplacements chimiques ^{1}H et ^{13}C du modèle de la lignine, le trimère acétoguaïacyl-déhydro-diisoeugénol-oxyde de méthyle, en faisant à des techniques de RMN mono- et bi-dimensionnelles. On a fait l'identification et les attributions des familles de spin en faisant appel à des expériences de routine en une dimension pour les déplacements chimiques et les multiplicités et des expériences COSY et de corrélation hétéronucléaires pour déterminer les connectivités. On a alors utilisé des expériences de corrélation NOESY, HOESY et de corrélation hétéronucléaire à longue distance pour déterminer la juxtaposition des groupes attribués et pour servir de confirmation aux attributions. On a alors utilisé des expériences de différences d'eOn à l'état stationnaire et de NOESY et d'HOESY en fonction du temps pour obtenir des mesures expérimentales de la conformation du trimère. On a utilisé des méthodes semiempiriques d'orbitales moléculaires pour calculer les structures d'énergie minimale et les barrières d'énergie aux rotations de liaison dans la molécule. On a trouvé que pour la molécule de la grosseur d'un trimère, les expériences d'eOn fournissent une représentation moins détaillée de la conformation de la molécule que les résultats d'orbitales moléculaires. Une comparaison des résultats des eOn et des calculs d'OM avec les structures cristallines obtenues à partir de la littérature indiquent que l'on peut évaluer les angles de torsion entre la chaîne latérale et le méthoxyle. La corrélation entre les prédictions faites sur la base des eOn et des calculs d'OM pour les distances interatomiques est apparemment reliée au fait que les minima pour les angles de torsion du β-O-4 pour lesquels les différents résultats se confirment mutuellement sont étroits. Des barrières aux rotations des angles de torsion qui seraient larges ou faibles peuvent conduire à des structures minimisées par des méthodes de calculs qui ne sont pas justifiées expérimentalement.

Mots clés : calculs semiempiriques d'orbitales moléculaires, RMN 2D, conformation, modèle pour la lignine, effet Overhauser nucléaire.

[Traduit par la rédaction]

Received August 25, 1995.

T.M. Garver[1] **and K.J. Maa.** Department of Chemistry, Lakehead University, Thunder Bay, ON P7B 5E1, Canada.
K. Marat. Department of Chemistry, University of Manitoba, Winnipeg, MB R3T 2N2, Canada.

[1] Author to whom correspondence may be addressed. Telephone: (807) 343-8619. Fax: (807) 343-8100. E-mail: tgarver@flash.lakeheadu.ca

Fig. 1. Structure of acetoguaiacyl-dehydro-diisoeugenol methyl ether or **1** with labels for ring and side-chain carbons and rotations about side-chain torsion angles.

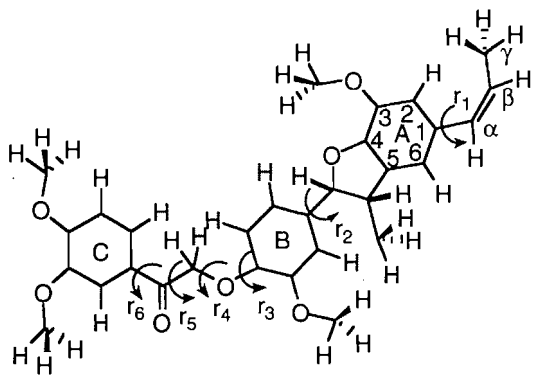

Introduction

Nuclear magnetic resonance analysis of the structure of lignin and lignin model compounds has focused on the identification of carbons and the side-chain protons (1). The assignment of aromatic protons and the further analysis of conformation normally have been excluded from the analysis. The application of 2D NMR to the study of macromolecular lignin has been limited (2–4) because lignin poses special problems related to short $T1$ and $T2$ relaxation times. Long correlation times found for the lignin macromolecule (5) lead to broad line widths (>10 Hz), which limit the resolution or detection of protons with small coupling constants. In NOE-type experiments, spin diffusion, resulting from long correlation times, will lead to a loss of the spatial dependence of the NOE peak intensity (6).

When all protons in a molecule have been assigned, NOE measurements between aromatic protons, side-chain protons, and methoxyl groups may assist in quantifying distances between protons and providing constraints for analyses of the three-dimensional structure. The difficulties in assigning aromatic proton resonances in lignin include the very small differences in chemical shift, the high spin multiplicities, and the relatively short relaxation times. Furthermore, the side chains, methoxyls, and aromatic groups constitute separated spin systems, which then must be linked together over three or four bonds and one or two quaternary carbons.

Acetoguaiacyl-dehydro-diisoeugenol methyl ether, or **1**, is a lignin model compound consisting of three guaiacyl-type units joined together by phenylcoumaran and β-O-4 type linkages as shown in Fig. 1. There is a vinylic side chain and a carbonyl group at the α carbon on the β-O-4 linked side chain. In addition there are three guaiacyl methoxyl groups at the aromatic 3 position. A fourth methoxyl exists as a methylated phenolic group. Overall, there are 19 different proton peaks and 30 different carbon peaks expected. Of these, seven protons and seven carbons are aliphatic, one carbon is carbonyl, four groups of 12 protons and four carbons are methoxyl, and eight protons and 18 carbons are aromatic.

Assignment strategies

The overall assignment scheme is to first identify different spin families or the directly coupled spins and then piece together the connectivities for the different spin groups. The

Fig. 2. COSY spectrum of **1** at 200 MHz with cross-peak connectivities drawn for two side-chain spin groups.

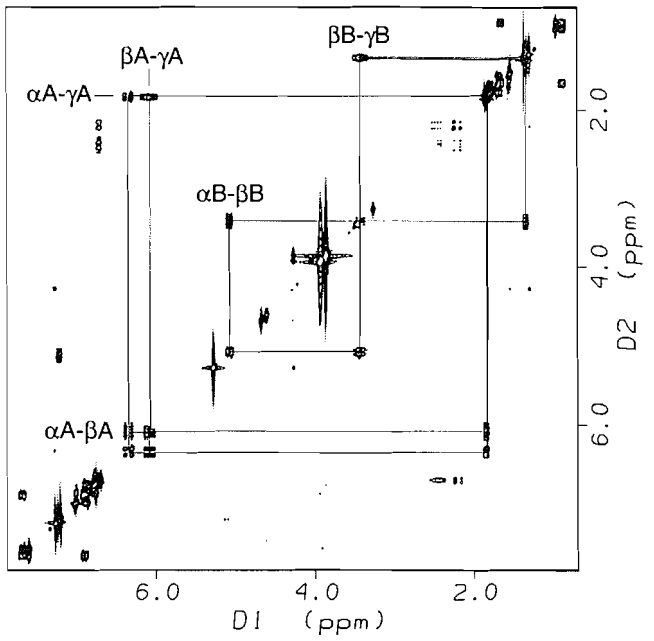

proton spin families may be identified using COSY (COrrelated SpectroscopY) spectra to group together aromatic protons and side-chain protons. The initial COSY spectra normally allow the assignment of the side-chain protons and will separate most of the aromatic protons into groups attached to the same rings. Single-bond carbon–proton connectivities are readily identified using standard single-quantum heteronuclear correlation type experiments. Heteronuclear correlation optimized for long-range couplings (7) provides an efficient method for connecting the side chains with the adjacent aromatic groups. NOESY (6, 8) HOESY (Heteronuclear Overhauser Enhancement SpectroscopY) (9, 10), HMQC (Heteronuclear correlation through Multiple Quantum Coherence) (8, 11), and HMBC (1H detected Multiple-Bond heteronuclear multiple-quantum Coherence) (8, 12) all provide complementary information, which may be used to knit the isolated spin groups into a coherent structure. Although some long-range couplings may be present in a COSY spectra, these normally may be used only for making preliminary assignments for aromatic side-chain connectivities. Methoxyl groups are assigned using a combination of HMBC, HOESY, and NOESY spectra, with confirmation of assignments with NOE difference spectra. Chemical shifts, spin multiplicities, and coupling patterns are required to make the assignments for the side-chain protons within the spin family. A comprehensive review of the carbon chemical shifts of lignin models by Kringstad and Mörck provides a reasonable starting point for assigning carbon chemical shifts (13, 14).

Identification of spin families

The three side-chain spin families can be readily identified from the COSY spectrum. These groups are illustrated by the lines connecting the protons within two side-chain spin families in the COSY spectrum as presented in Fig. 2. The third spin group is the singlet at 5.28 ppm. Integration and analysis

Table 1. Chemical shift assignments and coupling constants measured in $CDCl_3$ at 27°C on a 500 MHz (^1H) Bruker AMX spectrometer.

Position	Proton (ppm)	Carbon (ppm)	$^1J_{C-H}$ (Hz)	$^3J_{H-H}$ (Hz)	$^4J_{H-H}$ (Hz)
6A	6.75	113.3			
5A		133.1			
4A		146.5			
3A		144.1			
2A	6.78	109.3	151.4		
1A		132.2			
γA	1.86	18.3	125.7	6.6 βA	1.7 αA
βA	6.10	123.5	153.8	15.7 αA	
αA	6.35	130.9	148.9	15.7 βA	1.7 γA
6B	6.88	119.0	157.4	8.2 5B	2.0 2B
5B	6.79	114.1	158.7	8.2 6B	
4B		147.6			
3B		149.8			
2B	7.00	110.3	158.7	2.0 6B	
1B		134.2			
γB	1.37	17.7	127.0	6.8 βB	
βB	3.44	45.5	130.8	9.3 αB	
αB	5.10	93.4	150.1	9.3 βB	
6C	7.67	122.8	162.2	8.4 5C	2.0 2C
5C	6.90	110.2	161.1	8.5 6C	
4C		153.8			
3C		149.2			
2C	7.59	110.5	159.9	2.0 6C	
1C		127.8			
βC	5.28	72.0	143.8		
αC		193.1			
OMe4C	3.95				
OMe3C	3.93				
OMe3B	3.87				
OMe3A	3.89				

of the chemical shifts, multiplicities, and integrals readily lead to the assignments presented in Table 1. The coupling constants for α and β protons on the vinylic side chain are consistent with a *trans* configuration (15). The four methoxyl peaks at ~3.9 ppm are the only remaining unassigned proton resonances in the aliphatic region.

Resolution and assignment of aromatic ring protons

The eight aromatic protons present additional complications due to the difficulty of resolving multiplets from the overlapping peaks in the aromatic region. Furthermore, the observed position of the peaks changes with magnetic field strength because of the tight coupling between protons. The 500 MHz instrument used with resolution enhancement via a Lorentz to Gauss transformation significantly improves the resolution of these peaks (16). Peak integrals and a knowledge of the coupling patterns for substituted aromatic units (17) greatly assist in the identification of coupled aromatic protons (18). Protons on carbons 5 and 6 are normally AX doublets with about 8 Hz splitting. The proton on carbon 6 is normally split again with 2 Hz coupling to the *meta* proton at carbon 2; depending on chemical shift differences this coupling results in ABC, AMX, or ABX coupling. Examination of Fig. 3 clearly shows these coupling patterns in the distinct region between 7.5 and 8.0 ppm. The doublet at 7.59 and two doublets at 7.67 each belong to a single proton. The peaks between 6.75 and 6.95 ppm are much more difficult to resolve into the component peaks. As shown in Fig. 3*b*, this region consists of two groups with a total of five protons. Moreover, in this region the coupling constants (8.2–8.5 Hz) are sufficiently close to the differences in chemical shifts (0.9 ppm or 45 Hz at 500 MHz and 18 Hz at 200 ppm) that the AB character in the 200 MHz experiment becomes more an AX character in the 500 MHz experiment (19). Comparison of Figs. 3*a* and 3*b* shows how the field independence of the spin–spin coupling changes the observed chemical shift of these peaks. The single-quantum H/C correlation of this region, shown in Fig. 4, clearly resolves three doublets with couplings of about 8 Hz and two singlets. The H/C correlation also facilitated the assignment of the carbons adjacent to protons. These are reported with coupling constants in Table 1.

Protons were assigned to individual rings using a variety of long-range and nuclear Overhauser enhancement experiments. Consider the protons with chemical shifts centered at

Table 2. Carbon to proton crosspeaks (^{1}H ppm – ^{13}C ppm).

HMQC	HOESY	HMBC
7.67–122.8 6C	7.67–193.1 6C–αC	7.67–193.1 6C–αC
	7.67–127.8 6C–1C	7.67–153.8 6C–4C
	7.67–122.8 6C–6C	7.67–110.5 6C–2C
7.59–110.5 2C	7.59–193.1 2C–αC	7.59–193.1 2C–αC
	7.59–149.2 2C–3C	7.59–153.8 2C–4C
	7.59–127.8 2C–1C	7.59–149.2 2C–3C
	7.59–122.8 2C–6C	7.59–127.8 2C–1C
	7.59–110.5 2C–2C	7.59–122.8 2C–6C
7.00–110.3 2B	7.00–149.8 2B–3B	7.00–149.8 2B–3B
	7.00–134.2 2B–1B	7.00–147.6 2B–4B
	7.00–110.3 2B–2B	7.00–134.2 2B–1B
		7.00–119.0 2B–6B
		7.00–93.4 2B–αB
6.90–110.2 5C	6.90–110.2 5C–5C	6.90–153.8 5C–4C
		6.90–149.2 5C–3C
		6.90–127.8 5C–1C
6.88–119.0 6B	6.88–134.2 6B–1B	6.88–147.6 6B–4B
		6.88–110.3 6B–2B
		6.88–93.4 6B–αB
6.79–114.1 5B	6.79–147.6 5B–4B	6.79–149.8 5B–3B
	6.79–114.1 5B–5B	6.79–134.2 5B–1B
6.78–109.3 2A	6.78–144.1 2A–3A	6.78–146.5 2A–4A
	6.78–109.3 2A–2A	6.78–144.1 2A–3A
		6.78–130.9 2A–αA
		6.78–113.3 2A–6A
6.75–113.3 6A	6.75–133.1 6A–5A	6.75–146.5 6A–4A
	6.75–132.2 6A–1A	6.75–130.9 6A–αA
	6.75–123.5 6A–βA	6.75–109.3 6A–2A
	6.75–113.3 6A–6A	6.75–45.5 6A–βB
6.35–130.9 αA	6.35–130.9 αA–αA	6.35–113.3 αA–6A
		6.35–109.3 αA–2A
		6.35–18.3 αA–γA
6.10–123.5 βA	6.10–123.5 βA–βA	6.10–132.2 βA–1A
		6.10–18.3 βA–γA
5.28–72.0 βC	5.28–193.1 βC–αC	5.28–193.1 βC–αC
	5.28–72.0 βC–βC	
	5.28–147.6 βC–4B	
5.10–93.4 αB	5.10–134.2 αB–1B	5.10–134.2 αB–1B
	5.10–93.4 αB–αB	5.10–119.0 αB–6B
		5.10–110.3 αB–2B
	3.95–110.2 OMe4C–5C	3.95–153.8 OMe4C–4C
	3.93–110.5 OMe3C–2C	3.93–149.2 OMe3C–3C
	3.88–109.3 OMe3A–2A	3.88–144.1 OMe3A–3A
	3.87–110.3 OMe3B–2B	3.87–149.8 OMe3B–3B
3.44–45.5 βB	3.44–133.1 βB–5A	3.44–146.5 βB–4A
	3.44–45.5 βB–βB	3.44–133.1 βB–5A
		3.44–113.3 βB–6A
		3.44–93.4 βB–αB
		3.44–17.7 αB–γB
1.86–18.3 γA	1.86–18.3 γA–γA	1.86–130.9 γA–αA

Table 2 (*concluded*).

HMQC	HOESY	HMBC
		1.86–123.5 γA–βA
1.37–17.1 γB	1.37–17.7 γB–γB	1.37–133.1 γB–5A
		1.37–93.4 γB–αB
		1.37–45.5 γB–βB

Fig. 3. Proton NMR of the crowded portion of the aromatic region between 6.75 and 7.05 ppm at 200 MHz (*a*) and 500 MHz (*b*). In this area coupling, which may be described as AB in the 200 MHz spectrum, has more AX character in the 500 MHz spectra. Furthermore, the separation and relative positions of the peaks have changed.

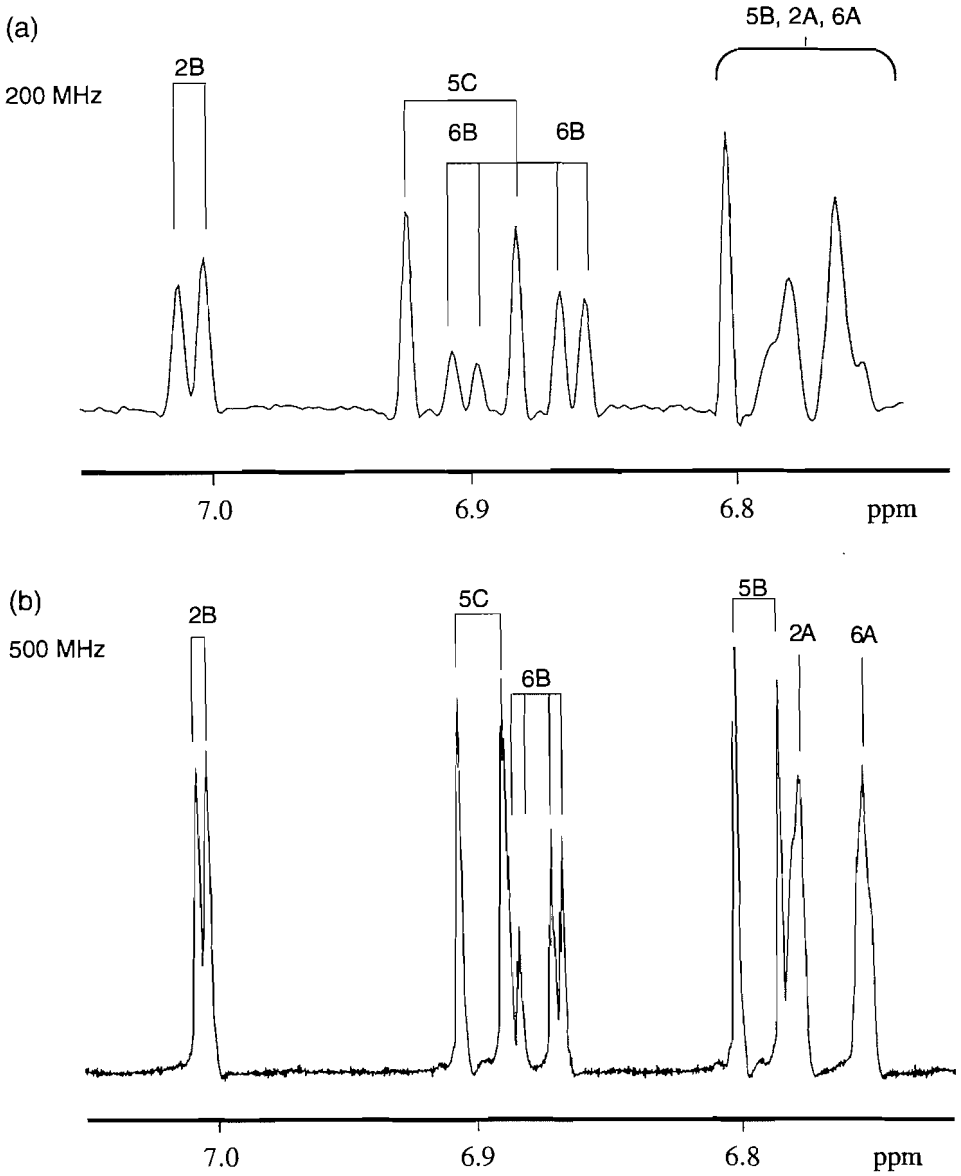

7.67, 7.59, and 6.90 ppm that have been identified as a group using COSY spectra and coupling constants. Long-range heteronuclear correlation data (Table 2) established connections from the α carbonyl carbon (193.1 ppm) to the protons at 7.67 and 7.59 ppm. NOESY spectra (Table 3) and NOE difference spectra (Table 3) have peaks between the side-chain proton $H_{\beta C}$ (5.28 ppm) and the protons 7.67 and 7.59 ppm. The carbonyl carbon is adjacent to ring C, therefore 7.67, 7.59, and 6.90 ppm are most likely on ring C. The positions of the ring protons were then deduced from coupling constants and con-

Fig. 4. Heteronuclear CH correlation (HMQC) experiment of the aromatic and vinylic regions of **1** at 500 MHz.

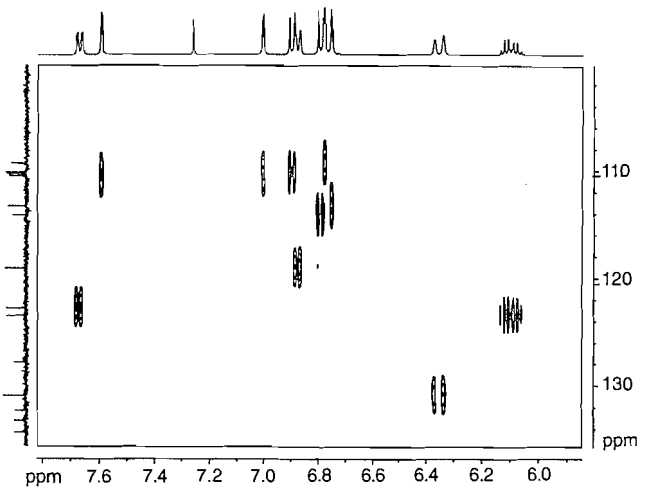

firmed by long-range experiments. In the ring C proton group there was ~8Hz coupling between the *ortho* protons at 7.67 and 6.90 ppm, ~2 Hz coupling between *meta* protons at 7.67 and 7.59 ppm, and the absence of coupling between *para* protons at 7.59 and 6.90 ppm. Hence the proton assignments for the ring protons are 7.67 for H_{6C}, 7.59 for H_{2C}, and 6.90 for H_{5C}. The long-range heteronuclear correlation between the carbonyl carbon at 193.1 ppm and the protons at 7.67 and 7.59 confirms that these are the protons on carbons 6 and 2. A similar analysis was used to establish the assignments given in Table 1 for the protons in the other rings. Carbon-13 chemical shifts were determined using 2D heteronuclear experiments (HOESY and HMBC) and articles by Kringstad and Mörck (13, 14).

Similarities in chemical shifts for the protons at certain ring positions were evident when our results were compared to other model compounds with similar side-chain structures and ring substitution (20–22). The protons at the 2 and 6 positions in rings with an adjacent carbonyl group were normally always shifted downfield to the region between 7.5 and 7.85 ppm. Given that all other aromatic protons are normally upfield from 7.05 ppm, the region between 7.5 and 7.85 may be used to obtain an estimate of the quantity of α carbonyl groups. This may potentially be applied to the analysis of the spectra of lignin derivative or lignin model compounds. The consistency of the reported chemical shifts in the literature also suggests that there is no significant change in the chemical shifts between monomer- and trimer-size lignin models.

Fig. 5. Spectra showing spin exchange with the methoxyl protons. Long-range heteronuclear correlation (HMBC) at 500 MHz (a) shows the spin–spin coupling to the methoxyl-substituted ring carbons. The heteronuclear NOE experiment (HOESY) for the same region (b) shows the incoherent spin exchange between the methoxyl protons and the carbons adjacent to the methoxyl-substituted carbon. NOESY spectra of the aromatic region (c) indicate spin exchange between the methoxyl protons and the protons attached to the carbons adjacent to the methoxyl-substituted ring carbon; these same peaks were also observed on COSY spectra.

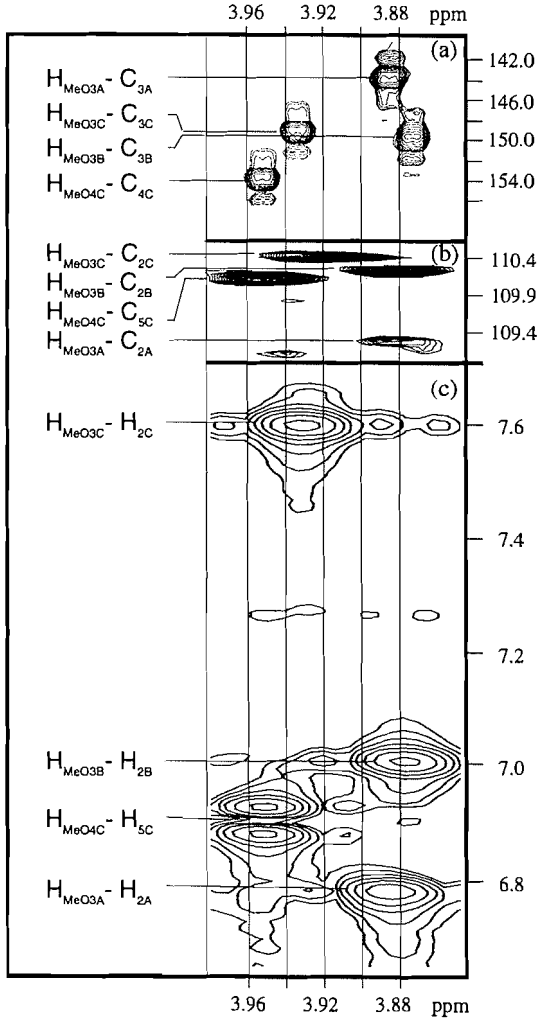

Assignment of methoxyl protons

Peaks on the proton spectrum corresponding to the methoxyl protons consisted of four peaks of equal height in a chemical shift range of 0.08 ppm. Both NOE and long-range spin–spin couplings were used to assign these difficult methoxyl protons. Cross peaks between the methoxyl protons and the methoxyl-substituted ring carbon as shown in Fig. 5*a* were observed in the long-range heteronuclear correlation experiment. Nuclear Overhauser effects observed using HOESY and NOESY spectra established dipolar spin exchange between the methoxyl protons and the proton and carbon adjacent to the methoxyl-substituted ring carbon (Fig. 5 and Table 2). The HOESY cross peaks for the methoxyl region shown in Fig. 5*b* indicate that the methoxyl protons are spatially closer to the carbons at position 2 than they are to any other ring carbon. NOESY spectra between C2 protons and methoxyl protons shown in Fig. 5*c* also confirm this spatial proximity. The proton NOE difference spectra also show cross relaxation between the methoxyl protons and the proton at C2.

NOE and molecular orbital analysis of conformation

We have compared semiempirical molecular orbital analysis with NOE analysis of the conformation of **1**. This molecule provides a reasonable model to study the limitations of these

Table 3. NOE steady state difference results.

Irradiate (ppm)	Observe (ppm)	Integral	Distance (Å) (MOPAC)
1.37 γB	3.44 βB	12.49	2.7
	5.10 αB	9.90	2.9
	6.75 6A	5.38	6A = 3.5
	6.78 2A		2A = 6.5
1.86 γA	6.10 βA	9.77	2.8
	6.35 αA	7.75	3.1
	6.75 6A	−0.99	5.4
3.44 βB	1.37 γB	4.64	2.7
	5.10 αB	1.96	3.0
	6.75 6A	1.96	3.0
	6.88 6B	2.64	3.3
	7.00 2B	4.33	3.5
3.87 OMe3B	6.78 2A	2.06	11.2
	7.00 2B	16.21	3.7
	7.59 2C	0.34	6.3
3.88 OMe3A	6.10 βA	−0.46	5.6
	6.35 αA	−0.50	6.9
	6.78 2A	12.41	3.9
	7.00 2B	2.56	7.2
	7.59 2C	0.19	11.1
3.93 OMe3C	6.90 5C	0.90	6.2
	7.00 2B	0.18	11.1
	7.59 2C	17.77	2.7
3.95 OMe4C	6.90 5C	14.31	2.7
	7.59 2C	1.13	6.2
	7.67 6C	−0.85	5.1
5.1 αB	1.37 γB	3.53	2.9
	3.44 βB	1.98	3.0
	6.88 6B	6.59	3.7
	7.00 2B	4.75	2.4
5.28 βC	6.79 5B	6.80	2.6
	6.88 6B	−0.66	5.1
	7.59 2C	2.29	4.4
	7.67 6C	6.37	2.5
6.10 βA	1.86 γA	6.48	2.8
	6.35 αA	3.03, −3.52	3.1
	6.75 6A	13.93	6A = 3.8
	6.78 2A		2A = 1.8
6.35 αA	1.86 γA	5.16	3.1
	6.10 βA	−0.55	3.1
	6.75 6A,	12.05	6A = 5.4
	6.78 2A		2A = 4.4

methods of conformational analysis for lignin oligomers. Among the significant conformational variables that have been addressed are the side-chain dihedral bond rotation and the methoxyl bond dihedral rotation. Different conformational energies for model compound **1** have been calculated by rotation of the side-chain dihedral angles r_1–r_6 as shown in Fig. 1.

Fig. 6. Heat of formation energies calculated using MNDO-PM3 semiempirical methods for torsion-angle bond rotations shown in Fig. 1 (r_1–r_6). Fisher projections shown on each graph correspond to minima or maxima for the conformational energies. For rotation 1, defined by $C_{\beta A}$-$C_{\alpha A}$-O_{1A}-C_{2A} (*a*), the projection at the local maximum at 90° is shown. The minimum at 90° for the rotation of $C_{\beta B}$-$C_{\alpha B}$-O_{1B}-C_{2A} (r_2) is shown in (*b*). Global minima at 200° and at 90° are shown for C_{3B}-C_{4C}-$O_{\beta C}$-$C_{\beta C}$ (*c*) and C_{4C}-$O_{\beta C}$-$C_{\beta C}$-$C_{\alpha C}$ (*d*). Local maxima at 90° are shown for $O_{\beta C}$-$C_{\beta C}$-$C_{\alpha C}$-C_{1C} (*e*) and $C_{\beta C}$-$C_{\alpha C}$-C_{1C}-C_{6C} (*f*).

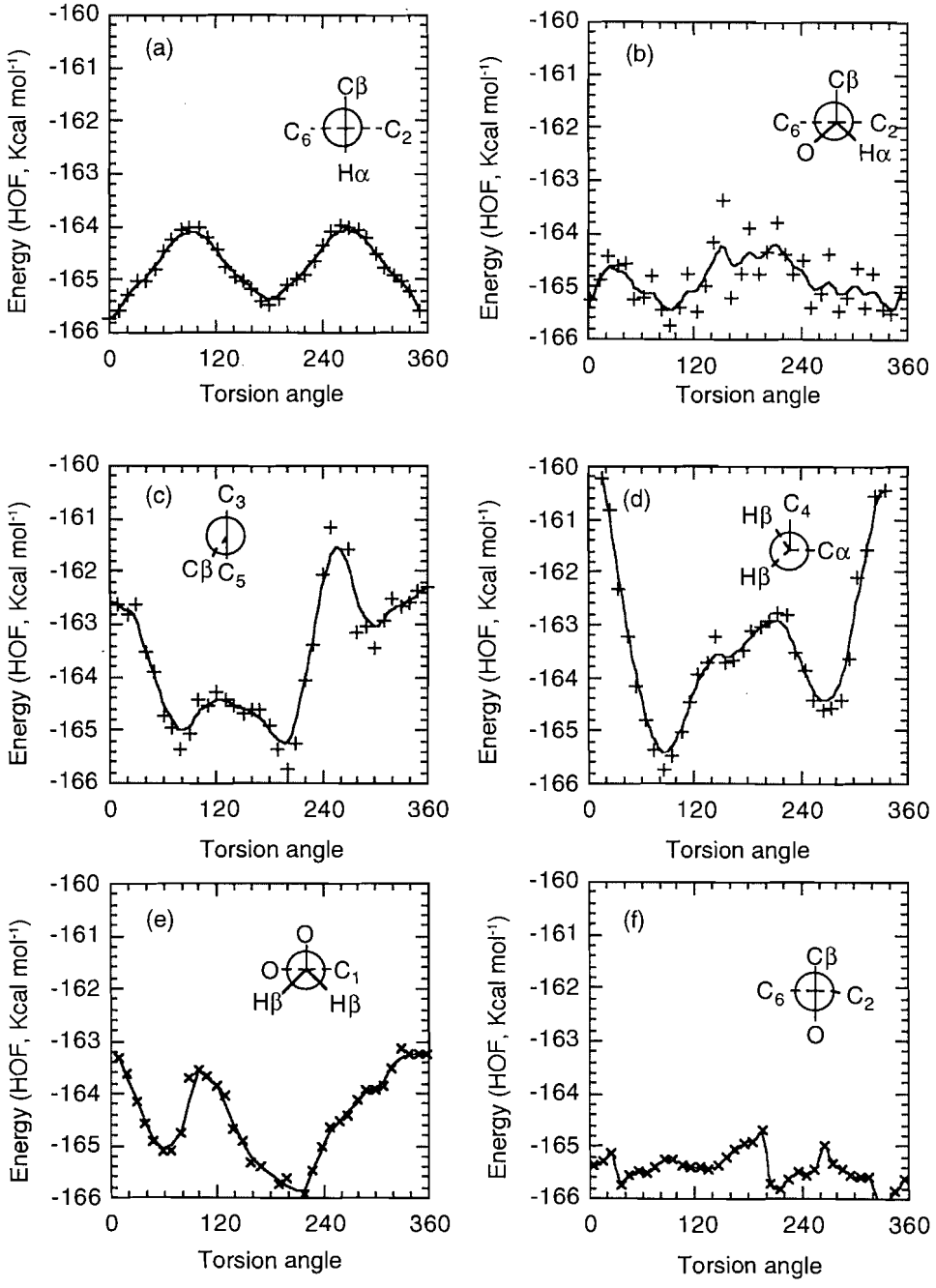

Our results may be compared to other NMR results (23), other molecular orbital or molecular mechanics results (24), and X-ray crystal structures (25–28).

We used the 1D NOE 1H difference and 2D NOESY and HOESY experiments for conformational analysis. Steady state NOE is obtained from the NOE difference experiment whereas NOEs from NOESY experiments are measured by transient effects (29). Internuclear distances obtained from the 1D experiment rely on the observation that NOE transfer rates are proportional to the inverse sixth power of the distance between dipolar nuclei (30). Distances from NOESY and HOESY experiments are estimated from the initial buildup rates of the NOE (29). Errors involved in estimating distances using NOE data include problems with measurement and accounting for competing relaxation pathways. In contrast, the errors for distance estimation with semiempirical calculations

Fig. 7. Steady state NOE difference intensities plotted against interatomic distances calculated from a structure (shown in Fig. 8) minimized using MNDO-PM3 semiempirical methods.

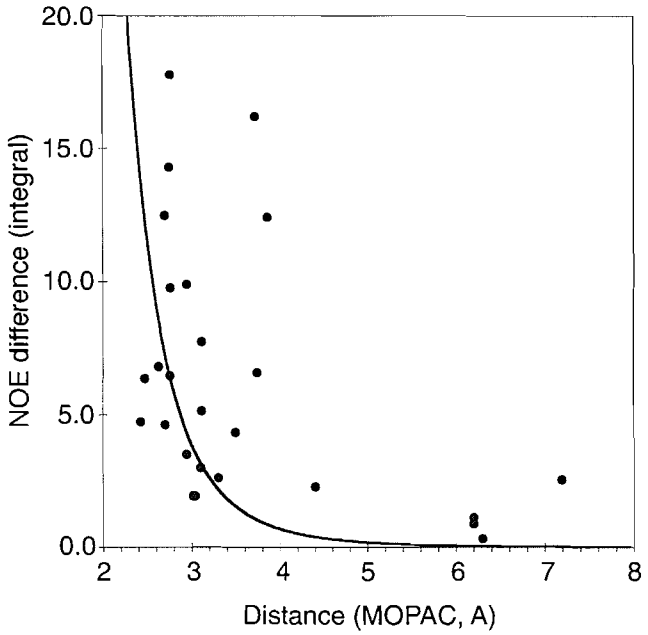

are due to the accuracy of the computational model, the differences between solution state and gas state geometries, and the possibility that the minimized structure is a local minima.

Conformations with the lowest overall energy and side-chain bond rotation energies were calculated using semiempirical molecular orbital methods on the MOPAC 93 program (31) installed on a SUN IPX computer. We have used the MNDO-PM3 method (Modified Neglect of Diatomic Overlap (32), Parametric Method 3 (33)), which neglects diatomic overlap in the secular equation. In this method the excessive repulsive energy arising from the MNDO method is empirically reduced using Gaussian attractive functions in calculating the nuclear energies (34). The full atomic parameter set has been optimized for calculating the heat of formation from the electron–electron and nuclear–nuclear interactions and the heats of formation of the constituent atoms (33). The SYMMETRY function was used for methyl proton bond lengths and angles, and all parameters except individual rotation bond angles were relaxed for these calculations. Bond rotation energies shown in Fig. 6 were obtained by calculating the energies of minimized structures for the rotamers at 10° torsion angle intervals. Optimization parameters SCFCRT and GNORM were set to 1.0×10^{-7} and 0.01, respectively. Given the computational power available on today's computers, this semiempirical MO approach provides a good compromise between computational economy and theoretical accuracy for conformational studies of molecules of this size. It should be noted that these semiempirical results correspond to gas phase heats of formation, which do not take into account the sometimes substantial effects of solvation.

Comparison of NOE results with molecular orbital minimized structures

NOE values that serve as experimental measures of the approximate distances between atoms may be compared to interatomic distances calculated using MO methods. In addition, the likelihood of a single conformation dominating the relationship between any two atoms may be addressed by examining bond torsion-angle rotation energy barriers. In the first approximation, when one considers dipole–dipole interaction between two nuclei, the rate of spin exchange by the nuclear Overhauser effect (cross relaxation) will be proportional to r^{-6} (35). In practice, our system with multiple spins that have both dipolar interactions and spin–spin coupling between many atoms is significantly more complicated (29). In Fig. 7 the steady state NOE values are plotted against the distances from the minimized structures. The fitted line in Fig. 7 shows the best fit of the steady state NOE intensity to a r^{-6} dependence.

Rotation at bonds conjugated to ring structures

At room temperature it appears that there is free rotation about the benzylic bond of the vinyl structure (Fig. 1, r_1). NOESY and NOE difference intensities between side-chain protons $H_{\alpha A}$ and $H_{\beta A}$ to the ring protons H_{2A} and H_{6A} are similar in magnitude. This indicates that similar populations of these two rotamers exist. Indeed, the NOE results conform to results from molecular orbital calculations for different rotamer conformations (Fig. 6*a*) that indicate that the energy difference is 0.22 kcal mol^{-1} between the two rotamers with the α–β conjugated double bond in plane with the aromatic ring. This energy difference corresponds to an equilibrium constant at room temperature of about 0.7. In addition, there is a 1.7 kcal mol^{-1} activation energy for rotation about the benzylic vinyl bond. The torsion-angle bond rotation about the benzylic bond at ring A is rapid compared to the chemical shift difference that may exist due to the chemical exchange ($\tau < 1/20$ Hz). It is also fast compared to the NOE buildup ($\tau << 1/1$ Hz). The NOE data corresponding to rotation at the benzylic bond on ring B (r_2 in Fig. 1, (b) in Fig. 6), however, clearly indicate a favored conformation in which the single benzylic proton is closer to the proton at the 2 ring position than the proton at the 6 ring position. This is difficult to see in the minimized structures shown in Fig. 8, but the calculated distances for the minimized structure are 2.82 Å and 3.45 Å for H_α to H_{C2} and H_{C6}. The steady state NOE (Table 3) and the NOESY buildup experiments (Table 4) both indicate that $H_{\alpha B}$—H_{6B} is farther apart than $H_{\alpha B}$—H_{2B}. The dominant conformation has $H_{\alpha B}$ and H_{2B} close together as shown in our calculated structure in Fig. 7. The calculation for the rotation about this bond showed some instabilities (Fig. 6*b*), but the favored conformation and a relatively low barrier to rotation are evident.

A priori one expects that conjugation of α carbonyl with ring C will restrict rotation about the benzylic bond defined by the torsion angle C_2-C_1-C_α-C_β. Our NOE results correspond well with this prediction, but the calculated results for this bond rotation showed some instabilities and an unexpectedly low-energy barrier for rotation. The relative intensities for the steady state NOE difference spectra between protons $H_{\beta C}$ and H_{6C} or H_{2C} are 6.37 and 2.29, respectively. This corresponds to distances of about 2.6 for the $H_{\beta C}$—H_{6C} interaction and 3.2 Å for the $H_{\beta C}$—H_{2C} interaction estimated from the empirical fit between all of the NOE difference data and the PM3 minimum structures as shown in Fig. 8.

Fig. 8. Perspective view of acetoguaiacyl-dehydro-diisoeugenol methyl ether minimized structure rotated to show the view with each aromatic ring in the plane.

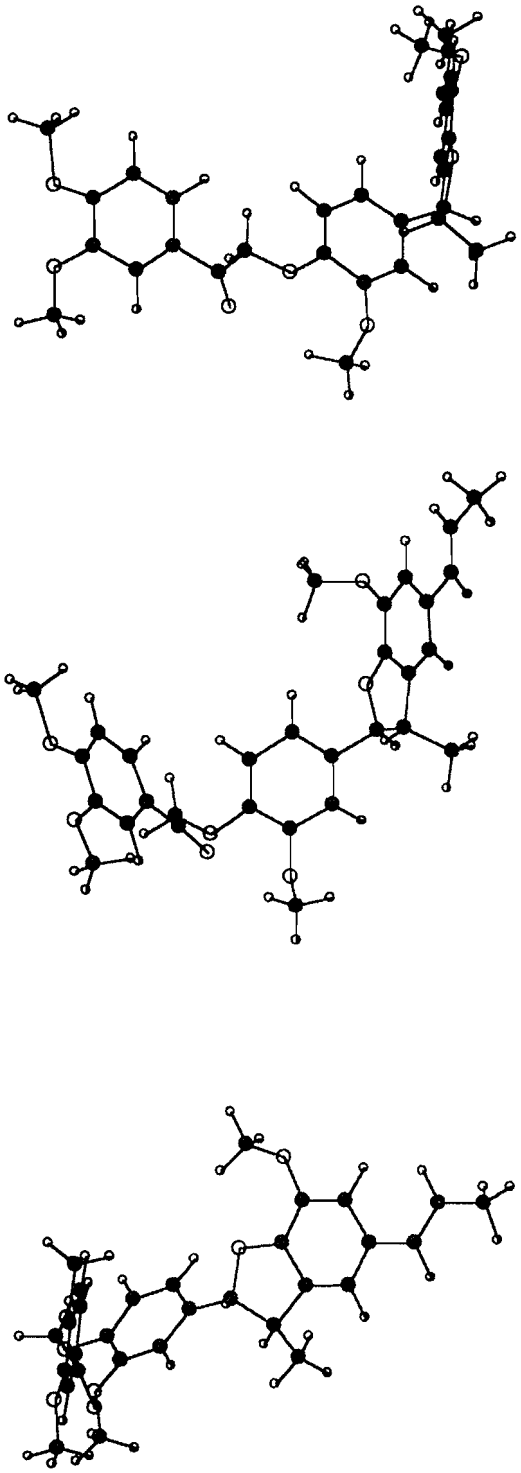

Rotation at the β-O-4 bond

The two torsion angles at the β-O-4 bond between rings B and C have the greatest rotation barriers as shown by the results presented in Figs. 6*c* and 6*d* for the rotamers calculated by the MNDO-PM3 method. For rotation about the torsion angle defined by C_{3B}-C_{4C}-$O_{\beta C}$-$C_{\beta C}$ (Fig. 6*c*) the principle constraints appear to be interaction of the β proton with the methoxyl and H_{5C} protons. The small rotation barrier at angles between 120° and 180° corresponds to interaction between the β protons and the C_5 hydrogen. The larger barriers between −120° (240°) and 90° correspond to interaction between the β protons and the methoxyl protons. The absence of NOE exchange between the β (ring C) protons and the methoxyl protons as well as the strong NOE between the β protons and the C5 proton indicates that the 200° torsion angle conformation is probably dominant in solution. Unfortunately, no HOESY peaks were observed between the 3 and 5 aromatic carbons and the β protons. The crystal structure for similar molecules with a γ CH_2OH substituent (26) showed a C_β-O-C_4-C_3 torsion angle of 172.3° corresponding to nearly the same conformation as we have found experimentally and by MNDO-PM3 calculations. The substantial energy barrier of about 5 kcal mol^{-1} for the rotation about the torsion angle C_4-O-C_β-C_α corresponds to the geometry in which the C_α and the carbonyl oxygen are in the plane of the aromatic ring B (a torsion angle of 0° as shown in Fig. 6*d*). The minimum for rotation about this axis is at ~82° and corresponds to the lowest steric interactions energy. This geometry is again similar to the 68.5° torsion angle found by Stomberg and Lundquist for a similar α-carbonyl β-O-4 structure (26).

Steric interactions between aromatic rings will restrict rotation about the α–β bond defined by $O_{\beta C}$-$C_{\beta C}$-$C_{\alpha C}$-C_{1C} as shown by the broad barrier to rotation between −120° and 40°. The minima for this bond rotation place the β-ether oxygen at a 60° angle to the aromatic plane of ring C as shown in Figs. 7 and 5*e*. Crystal structures for β-O-4 model compounds indicate that the minima at about −160° (−152.4°) is favored for α-carbonyl-containing compounds while the α-hydroxylated compounds crystallize with torsion angles in the minima between 50° and 65°.

Methoxyl rotation

In our experience the observed NOE values may not be used to distinguish the C_{MeO}-O_{MeO}-C_3-C_2 dihedral angles precisely with respect to the plane of the aromatic ring. However, NOESY and HOESY peaks and the NOE values were always consistent with a close proximity between the methoxyl protons and the aromatic C2 protons. Close examination of Tables 3 and 4 reveals that there is general agreement between the NOE and MO data with respect to determining the juxtaposition of the methoxyl protons relative to the ring protons. In Table 3 there are several steady state NOE peaks listed between methoxyl protons and protons on adjacent aromatic rings where the MOPAC calculated distance is over 10 Å. We did not see strong evidence of corresponding peaks in the NOESY spectra and we believe these peaks are artifacts of the steady state experiment. Also there are negative NOE peaks listed in Table 3 that we attribute to multi-spin effects. Crystal structures have shown that syringyl-type groups have methoxyl torsion angles of ±20° to the ring for one group and at about 85° for the second methoxyl group (27). Molecular mechanics (36) and molecular orbital studies (37) also have found similar dihedral angles for the methoxyl groups. For the three C3 methoxyls we have calculated minimum torsion angles (C_{MeO}-O_{MeO}-C_3-C_2) of 107° (ring A), 85° (ring B), and 167° (ring C). The methoxyl on the C4 position on ring C is in the ring plane

Table 4. Initial rates, selected NOESY peak intensities.

		Mixing Time (ms)		
		100	200	400
Peak (ppm)	Assignment	Intensity		
1.37–3.44	γB–βB	4.79	4.55	4.19
3.87–7.00	OMe3B–2B	1.98	3.58	6.39
3.89–6.78	OMe3A–2A	1.72	3.08	5.24
3.93–7.59	OMe3C–2C	1.84	3.19	5.70
3.95–6.90	OMe4C–5C	2.22	3.73	6.62
5.10–3.44	αB–βB	3.06	1.42	1.25
5.10–6.88	αB–6B	0.81	1.62	2.87
5.10–7.00	αB–2B	0.53	1.03	1.92
5.28–6.79	βC–5B	1.98	3.40	5.47
5.28–7.59	βC–2C	0.37	0.70	1.26
5.28–7.67	βC–6C	1.29	2.47	4.19
6.10–1.86	βA–γA	3.18	3.99	4.03
7.67–6.90	6C–5C	8.04	4.70	3.39

with a 0° angle to C5. Values for the energy barrier for methoxyl rotation have been estimated to be between 1.6 and 3.4 kcal mol^{-1} (37). We have calculated rotational energy barriers of between 1.3 and 2.0 kcal mol^{-1} for methoxyl rotation for this lignin model.

Experimental section

Acetoguaiacyl-dehydro-diisoeugenol methyl ether was kindly donated by Dr. Jerzy Arct at Lakehead University in Thunder Bay, Ontario. Spectra were obtained on a 200 MHz Bruker AC-E spectrometer at Lakehead University and a 500 MHz Bruker AMX spectrometer at the High-Field NMR facilities at the Prairie Regional NMR Centre, Winnipeg, Manitoba. Spectra were obtained at 300 K from samples dissolved in $CDCl_3$ (99.8%, Cambridge Isotope Laboratories) with TMS as internal standard. Carbon-13 spectra were obtained with two-level decoupling. The 200 MHz COSY pulse sequence was based on articles by Aue et al. (38) and Nagayama et al. (39). The COSY spectrum presented in Fig. 2 was obtained with 1K data points in *F*2, a sweep width of 1600 Hz, 256 *F*1 increments with 32 acquisitions each, and a relaxation delay between acquisitions of 5 s. Standard NOESY experiments (29) were performed at 200 MHz with 32 acquisitions for 256 increments in *F*1 and 1024 data points in *F*2 (Fig. 5*c*). The spectral width in both dimensions was 1602 Hz at 200.14 MHz. Phase-sensitive TPPI NOESY spectra were obtained at 500 MHz (D_1–90–D_0–90–D_9–90–FID) with mixing times of 0.1, 0.2, 0.4, 0.8, and 1.2 s, a 5 s relaxation delay, 16 acquisitions for 512 points with a spectral width of 7.631 ppm in *F*1, and 1024 points with a spectral width of 3816.79 Hz in *F*2 (Table 4). Heteronuclear Overhauser experiments using a standard carbon-detected HOESY pulse sequence were executed on the 200 and 500 MHz instruments (10, 40, 41). At 500 MHz the HOESY spectra (Fig. 5) were 4K in *F*2 with a sweep width of 23 809.52 Hz, 128 spectra with 64 acquisitions each in *F*1 at 500.14 MHz, and a mixing time of 2 s and the relaxation delay of 3.5 s. A 5.0 s saturation time was used for the steady state NOE difference method (42). Inverse-detected long-range H/C correlations via zero and double-quantum coherence (HMBC) (12) were optimized for long-range couplings of 5–10 Hz ($1/2J_{CH}$ delay = 0.070 s) with a low-pass *J* filter, *F*1 = 128 points, 198.776 ppm at 125.7699 MHz; *F*2 = 4096 points, 7.24 ppm at 500.136 MHz. Inverse-detected H/C correlations optimized for single bond couplings (HMQC) (11) (delay = 0.001 78 s for $(1/4)J$, $J_{CH} \sim 140$ Hz) were obtained at 500.1376 MHz with 128 points and a spectral width of 159.029 ppm in *F*1 (125.7699 MHz), and 4096 points over a 7.24 ppm (500.136 MHz) spectral width in *F*2.

Acknowledgments

We thank the Natural Sciences and Engineering Research Council of Canada and the Senate Research Committee of Lakehead University for financial support.

References

1. J. Ralph. Magn. Reson. Chem. **31**, 357 (1993).
2. R.M. Ede and G. Brunow. J. Org. Chem. **57**, 1477 (1992).
3. K. Lundquist and K. Stern. Nord. Pulp Pap. Res. J. 210 (1989).
4. N. Fukagawa, G. Meshitsuka, and A. Ishizu. J. Wood Chem. Technol. **11**, 373 (1991).
5. T.M. Garver. Polym. Prepr. (Am. Chem. Soc., Div. Polym. Chem.) **31**, 127 (1990).
6. R.R. Ernst, G. Bodenhausen, and W. Wokaun. Principles of nuclear magnetic resonance in one and two dimensions. Oxford University Press, Oxford. 1987.
7. L. Möller. J. Am. Chem. Soc. **101**, 4481 (1979).
8. K. Nakanishi. One-dimensional and two-dimensional NMR spectra by modern pulse techniques. University Science Books, Mill Valley, Calif. 1990.
9. G.C. Levy and C. Yu. J. Am. Chem. Soc. **105**, 6994 (1983).
10. P.L. Rinaldi. J. Am. Chem. Soc. **105**, 5167 (1983).
11. A. Bax and S. Subramanian. J. Magn. Reson. **67**, 565 (1986).
12. A. Bax and M.F. Summers. J. Am. Chem. Soc. **108**, 2093 (1986).

13. K. Kringstad and R. Mörck. Holzforschung, **37**, 237 (1983).
14. R. Mörck and K.P. Kringstad. Holzforschung, **39**, 109 (1985).
15. M. Karplus. J. Am. Chem. Soc. **85**, 2870 (1963).
16. J.K.M. Sanders and B.K. Hunter. Modern NMR spectroscopy, a guide for chemists. 2nd ed. Oxford University Press, Oxford. 1993.
17. M. Zanger. Org. Magn. Reson. **4**, 1 (1972).
18. H. Friebolin. Basic one- and two-dimensional NMR spectroscopy. VCH Publishers, New York. 1991.
19. F.A. Bovey, L. Jelinski, and P.A. Mirau. Nuclear magnetic resonance spectroscopy. 2nd ed. Academic Press, San Diego, Calif. 1988.
20. C.H. Ludwig. *In* Lignins: occurrence, structure, formation and reactions. *Edited by* K.V. Sarkanen and C.H. Ludwig. Wiley–Interscience, New York. 1971. pp. 299–344.
21. K. Lundquist. Nord. Pulp Pap. Res. J. **6**, 4 (1992).
22. X. Shen and A. van Heiningen. Can. J. Chem. **70**, 1754 (1992).
23. G. Cooley, R.D. Farrant, D.N. Kirk, S. Patel, S. Wynn, M.J. Buckingham, G.E. Hawkes, M.B. Hursthouse, A.M.R. Galas, et al. J. Chem. Soc. Perkin Trans. 2, 489 (1984).
24. J. Jakobsons and S.M. Shevchenko. Latv. PSR Zinat. Akad. Vestis, Kim. Ser. 186 (1990).
25. A. Estevez-Braun, R. Estevez-Reyes, and A.G. Gonzalez. Tetrahedron, **50**, 5203 (1994).
26. R. Stomberg and K. Lundquist. Nord. Pulp Pap. Res. J. **9**, 37 (1994).
27. R.F. Bryan and L. Fallon. J. Chem. Soc. Perkin Trans. 2, 341 (1976).
28. R.F. Bryan and M.S. Shen. Acta Crystallogr. Sect. B: Struct. Crystallogr. Cryst. Chem. **B34**, 327 (1978).
29. D. Neuhaus and M.P. Williamson. The nuclear Overhauser effect in structural and conformational analysis. VCH Publishers, New York. 1989.
30. R.A. Bell and J.K. Saunders. Can. J. Chem. **48**, 1114 (1970).
31. J.J.P. Stewart. MOPAC 93.00 Manual. Fujitsu Limited, Tokyo, Japan. 1993.
32. M.J.S. Dewar and W. Thiel. J. Am. Chem. Soc. **99**, 4899 (1977).
33. J.J.P. Stewart. J. Comput. Chem. **10**, 196 (1989).
34. M.J.S. Dewar, E.G. Zoebisch, E.F. Healy, and J.J.P. Stewart. J. Am. Chem. Soc. **107**, 3902 (1985).
35. M. Goldman. Quantum description of high-resolution NMR in liquids. Oxford Science Publications, Oxford. 1988.
36. T.J. Elder and S.D. Worley. Wood Sci. Technol. **18**, 307 (1984).
37. J. Jakobsons, J. Gravitis, and V.G. Dashevskii. Zh. Strukt. Khim. **22**, 43 (1981).
38. W.P. Aue, E. Bartholdi, and R.R. Ernst. J. Chem. Phys. **64**, 2229 (1976).
39. K. Nagayama, A. Kumar, K. Wüthrich, and R.R. Ernst. J. Magn. Reson. **40**, 321 (1980).
40. C. Yu and G.C. Levy. J. Am. Chem. Soc. **106**, 6533 (1984).
41. K. Köver and G. Batta. Prog. NMR Spectrosc. **19**, 223 (1987).
42. M. Kinns and J.K.M. Sanders. J. Magn. Reson. **56**, 518 (1984).

Properties of atoms in molecules: nuclear magnetic shielding

T.A. Keith and R.F.W. Bader

Abstract: This paper analyzes the nuclear magnetic shielding tensors underlying the chemical shift in NMR spectroscopy in terms of the field generated at the nucleus by the current $\boldsymbol{J}^{(1)}(\boldsymbol{r})$ induced by an external magnetic field. The magnetic field at nucleus $\mathcal{N}$ resulting from an element of the induced current density at a distance $r_{\mathcal{N}}$ is proportional to $\boldsymbol{r}_{\mathcal{N}} \times \boldsymbol{J}^{(1)}(\boldsymbol{r})/r_{\mathcal{N}}^3$, which defines the shielding density $\sigma_{\mathcal{N}}(\boldsymbol{r})$. The magnetic shielding of a nucleus is fundamentally an atomic property, a feature brought to the fore by using the theory of atoms in molecules, and the integration of $\sigma_{\mathcal{N}}(\boldsymbol{r})$ over the individual atomic basins relates the shielding tensor $\sigma_{\mathcal{N}}$ to a sum of atomic contributions. The shielding of nucleus $\mathcal{N}$ is primarily determined by the flow of current within the basin of atom $\mathcal{N}$, a contribution that varies from the approximate diamagnetic limit, given by the atomic Lamb value for the atom in the molecule, to values that are greatly reduced by the presence of paramagnetic current flows associated with particular bonding effects. Whether the contribution of a neighbouring atom is shielding or deshielding is readily understood by relating the form of the current flow within its basin to the magnetization density $\boldsymbol{r}_{\mathcal{N}} \times \boldsymbol{J}^{(1)}(\boldsymbol{r})$. A study of the currents induced in benzene shows that the extent to which a proton, bonded to a ring of atoms, is deshielded by the field exerted by its bonded neighbour provides a direct diagnostic test for a ring current and an accurate relative measure of its strength. The theory of atoms in molecules isolates transferable atomic properties, and because of this ability one finds, in addition to the anticipated result that a given functional group contributes identical amounts to the isotropic shielding $\bar{\sigma}_{\mathcal{N}}$ of a nucleus external to it through a series of molecules, the more remarkable result that the whole of the variation in $\bar{\sigma}_{\mathcal{N}}$ can have its origin in the basin of atom $\mathcal{N}$, the contribution from external groups remaining constant. For example, the external contribution to $\bar{\sigma}_{\mathcal{N}}$ for a carbon nucleus in a normal hydrocarbon is independent of chain length and position of $\mathcal{N}$ within the chain, the methyl group in ethane contributing the same shielding to a methyl carbon as does the butyl group in pentane. This constancy in external contributions to the shielding is also found for N, O, and F nuclei in substituted, saturated hydrocarbons.

Key words: NMR, magnetic shielding, current density, magnetic shielding density.

Résumé : Dans ce travail, on analyse les tenseurs du blindage magnétique nucléaire sous-jacents au déplacement chimique en spectroscopie RMN en fonction du champ généré au niveau du noyau par le courant $\boldsymbol{J}^{(1)}(\boldsymbol{r})$ induit par un champ magnétique externe. Le champ magnétique au niveau du noyau $\mathcal{N}$ qui résulte d'un élément de la densité du courant induit à une distance $r_{\mathcal{N}}$ est proportionnel à $\boldsymbol{r}_{\mathcal{N}} \times \boldsymbol{J}^{(1)}(\boldsymbol{r})/r_{\mathcal{N}}^3$ qui définit la densité de blindage $\sigma_{\mathcal{N}}(\boldsymbol{r})$. Le blindage magnétique d'un noyau est fondamentalement une propriété atomique, une caractéristique mise de l'avant par l'utilisation de la théorie des atomes dans les molécules, et l'intégration de $\sigma_{\mathcal{N}}(\boldsymbol{r})$ sur les basins atomiques individuels permet d'établir une relation entre le tenseur de blindage $\sigma_{\mathcal{N}}$ avec une somme de contributions atomiques. L'écoulement du courant dans le basin de l'atome $\mathcal{N}$, une contribution que diffère de la limite diamagnétique approximative donnée par la valeur atomique de Lamb pour l'atome de la molécule, limite le blindage du noyau $\mathcal{N}$ à des valeurs qui sont grandement réduites par la présence des écoulements de courant paramagnétique associés avec des effets de liaison particuliers. On peut facilement comprendre que la contribution d'un atome avoisinant est blindante ou déblindante en établissant une relation entre la forme de l'écoulement du courant dans son basin et la densité de magnétisation $\boldsymbol{r}_{\mathcal{N}} \times \boldsymbol{J}^{(1)}(\boldsymbol{r})$. Une étude des courants induits dans le benzène montre que, pour un proton par ailleurs lié à un cycle d'atomes, le degré de déblindage causé par le voisin qui lui est lié fournit une méthode directe de diagnostique pour un courant de cycle et une mesure relative correcte de sa force. La théorie des atomes dans les molécules permet d'isoler les propriétés atomiques transférables; à cause de cette caractéristique, il est possible d'observer, en plus du résultat anticipé selon lequel un groupe fonctionnel donné contribue des quantités égales au blindage isotrope, $\bar{\sigma}_{\mathcal{N}}$, d'un noyau qui lui est externe par une série de molécules, un résultat encore plus remarquable, à savoir que l'ensemble de la variation du $\bar{\sigma}_{\mathcal{N}}$ trouve son origine dans le basin de l'atome $\mathcal{N}$ et que la contribution des groupes externes reste constante. Par exemple, la contribution externe au $\bar{\sigma}_{\mathcal{N}}$ pour un noyau de carbone dans un hydrocarbure normal est indépendante de la longueur de la chaîne et de la position de l'atome $\mathcal{N}$ dans la chaîne; le groupe méthyle de l'éthane fait la même contribution à un atome de carbone que le groupe butyle du

Received September 18, 1995.

T.A. Keith. Department of Chemistry, Yale University, New Haven, CT 06511, U.S.A.

R.F.W. Bader.[1] Department of Chemistry, McMaster University, Hamilton, ON L8S 4M1, Canada.

[1] Author to whom correspondence may be addressed. Telephone: (905) 525-9140, ext. 23499. Fax: (905) 522-2509.

pentane. On a observé la même constance des contributions externes au blindage avec les noyaux de N, O et F dans les hydrocarbures saturés substitués.

Mots clés : RMN, blindage magnétique, densité de courant, densité de blindage magnétique.

[Traduit par la rédaction]

Atomic basis of the chemical shift

Nuclei of chemically inequivalent atoms of the same element give rise to distinct resonance signals in an NMR experiment, the chemical shift. The ability to distinguish between the atoms of a given element in a molecule makes the chemical shift the most important parameter to be derived from an NMR spectrum (1). The shift in signal relative to the bare nucleus is called the "nuclear magnetic shielding" and is the result of the external magnetic field inducing an electronic current within the molecule whose associated magnetic field at the nucleus partially shields or deshields it from the applied field. The nuclear magnetic shielding, like the magnetic susceptibility, is determined by the first-order current distribution induced by a uniform external magnetic field. The current density is the expectation value of the current operator (2), the product of the observables for the electron density and velocity, and for a field applied along the β Cartesian axis the first-order induced current density, $\boldsymbol{J}_\beta^{(1)}(\boldsymbol{r})$, is given by

$$\boldsymbol{J}_\beta^{(1)}(\boldsymbol{r}) = -(e/m)\sum_i \{\langle\psi^{(0)}|\hat{\delta}(\boldsymbol{r}_i - \boldsymbol{r})\hat{\boldsymbol{p}}_i|\psi_\beta^{(1)}\rangle + \langle\psi_\beta^{(1)}|\hat{\delta}(\boldsymbol{r}_i - \boldsymbol{r})\hat{\boldsymbol{p}}_i|\psi^{(0)}\rangle + (e/c)\langle\psi^{(0)}|\hat{\delta}(\boldsymbol{r}_i - \boldsymbol{r})\boldsymbol{A}_{\beta i}|\psi^{(0)}\rangle\} \quad [1]$$

where $\psi_\beta^{(1)}$ is the corresponding first-order correction to the wave function and $\boldsymbol{A}_{\beta i} = (1/2)\boldsymbol{B}_\beta \times (\boldsymbol{r}_i - \boldsymbol{r}_0)$ is the vector potential for an applied field $\boldsymbol{B}_\beta$ with gauge origin $\boldsymbol{r}_0$. The magnetic shielding of a given nucleus is basically an atomic property. Understanding the dependence of the shielding of a nucleus of a given atom on its chemical environment is predicated upon understanding the atomic contributions to the shielding in terms of the current density distribution, a step that is accomplished using the theory of atoms in molecules (3). This theory identifies an atom with a bounded region of real space whose properties, including those induced by an external field, are defined by the quantum action principle (4).

In the case of magnetic properties, the theory enables one to go beyond the definition of the atomic contributions, by leading to a method for their determination, one that takes advantage of the known result that the nucleus serves as the natural gauge origin for the calculation of the current in an isolated atom. The use of a separate nuclear-centred gauge origin for each atom in a molecule, termed the method of Individual Gauges for Atoms in Molecules (IGAIM) (5), enables one to calculate first-order magnetic response properties that are in relatively good agreement with experiment, using standard basis sets of moderate size. The properties are calculated directly from the wave functions obtained in conventional CPHF calculations. IGAIM, by assigning multiple gauge origins in real space, thus differs from GIAO (6) or IGLO (7, 8), which assign different gauges to individual atomic-centred basis functions or to localized molecular orbitals, respectively.

The theory also leads to a method for the relatively accurate and continuous determination of the first-order induced current density $\boldsymbol{J}^{(1)}(\boldsymbol{r})$, by extending the idea of the set of multiple real-space gauge origins used in IGAIM to the limit of a continuous set of gauge origins (9). In this method, the current is determined through the definition of a continuous set of gauge transformations (CSGT), a separate gauge origin to calculate the current $\boldsymbol{J}^{(1)}(\boldsymbol{r})$ at each point $\boldsymbol{r}$ in real space, yielding the following expression for the induced current distribution:

$$\boldsymbol{J}_\beta^{(1)'}(\boldsymbol{r}) = \boldsymbol{J}_\beta^{(1)}(\boldsymbol{r}) - (e/m)\sum_i \{\langle\psi^{(0)}|\hat{\delta}(\boldsymbol{r}_i - \boldsymbol{r})\hat{\boldsymbol{p}}_i|\psi_\beta^{(1)'}\rangle + \langle\psi_\beta^{(1)'}|\hat{\delta}(\boldsymbol{r}_i - \boldsymbol{r})\hat{\boldsymbol{p}}_i|\psi^{(0)}\rangle + (e/c)\langle\psi^{(0)}|\hat{\delta}(\boldsymbol{r}_i - \boldsymbol{r})\boldsymbol{A}'_{\beta i}|\psi^{(0)}\rangle\} \quad [2]$$

$\psi_\beta^{(1)'}$ is the additional first-order correction arising from the changed vector potential $\boldsymbol{A}'_{\beta i} = (1/2)\boldsymbol{B}_\beta \times \boldsymbol{d}(\boldsymbol{r})$, wherein $\boldsymbol{d}(\boldsymbol{r})$, the shift in gauge origin, is defined to be a continuous function of $\boldsymbol{r}$, the position vector in real space. The vector currents determined using the form of this method termed CSDGT (9) satisfy the local current conservation requirement that $\nabla\cdot\boldsymbol{J}^{(1)}(\boldsymbol{r}) = 0$ with relatively high numerical accuracy, enabling one to obtain faithful displays of the current and determine its topology for the first time (2, 9).

The atomic current theorem obtained from the theory of atoms in molcules enables one to define the atomic contributions to the magnetic susceptibility and relate them to the form of the current density (10). The resulting atomic contributions have been shown to recover Pascal's group increments for the magnetic susceptibilities of hydrocarbons, thus adding magnetic properties to the list of the measurable additive group contributions that are predicted by the theory, a list that includes heats of formation, populations, volumes, and electric polarizabilities.

The induced current that generates the field shielding a nucleus corresponds to a divergence-free flow of electron density. The electron density and the current are the expectation values of quantum observables that, according to Schrödinger (11), underlie the elucidation of the electric and magnetic properties of matter. The theory of atoms in molecules uses these two fields to obtain an atomic partitioning of the space of a molecule and of its magnetic properties, to obtain thereby a physical understanding of magnetic properties at the atomic level.

Computational methods

The nuclear magnetic shielding results reported here were calculated at the CPHF level using IGAIM (5). The CPHF

first-order wave functions were obtained from a locally modified version of CADPAC 4.0 (12), while the atomic integrations were done using AIMPAC.[2] The 6–311++G(2*d*,2*p*) Gaussian basis sets of Pople et al. (14) were used in all calculations. For consistency, all geometries were fully optimized at the HF level using the same basis set. All vector current maps were calculated using CSGT (9). Jameson (15) has reviewed the theoretical and physical aspects of nuclear shielding, including methods for its calculation and interpretation.

Magnetic shielding density and its relation to the induced current

Definition of atomic contribution to nuclear magnetic shielding

Jameson and Buckingham (16) have shown how properties induced by electric and magnetic fields can be expressed as integrals of corresponding property densities defined in real space in terms of the electronic charge and current distributions. In particular, the first-order magnetic dipole induced in a molecule by an external field $\boldsymbol{B}$ is related to the magnetization density in terms of the first-order induced current, as $(1/2c)\boldsymbol{r}\times\boldsymbol{J}^{(1)}(\boldsymbol{r})$. This is the density that determines the magnetic susceptibility of a molecule (10, 16). This same density, with origin located specifically at nucleus $\mathcal{N}$ and divided by $r_{\mathcal{N}}^3$, determines the local contribution that the induced current makes to the magnetic field at the position of nucleus $\mathcal{N}$. Specifically, the nuclear magnetic shielding tensor density for nucleus $\mathcal{N}$, $\sigma_{\mathcal{N}}(\boldsymbol{r})$, is defined in eq. [3] (16, 17):

$$[3]\qquad \sigma_{\mathcal{N}}(\boldsymbol{r})\cdot\boldsymbol{B} = (-1/c)\boldsymbol{r}_{\mathcal{N}}\times\boldsymbol{J}^{(1)}(\boldsymbol{r})/r_{\mathcal{N}}^3$$

The α,β component of the nuclear magnetic shielding tensor $\sigma_{\mathcal{N}}^{\alpha,\beta}$ is obtained by integration of the corresponding component of this density over the space of the molecule, an atom Ω at a time,

$$[4]\qquad \sigma_{\mathcal{N}}^{\alpha,\beta} = (-1/Bc)\sum_{\Omega}\int_{\Omega} d\boldsymbol{r}_{\mathcal{N}}\{\boldsymbol{r}_{\mathcal{N}}\times\boldsymbol{J}_{\beta}^{(1)}(\boldsymbol{r})/r_{\mathcal{N}}^3\}_{\alpha} = (-1/Bc)\sum_{\Omega}\sigma_{\mathcal{N}}^{\alpha,\beta}(\Omega)$$

The magnetic shielding, like all atomic properties, is additive. Because of the overall dependence of $\sigma_{\mathcal{N}}(\boldsymbol{r})$ on the inverse square of $r_{\mathcal{N}}$, the dominant contribution to $\sigma_{\mathcal{N}}$ is that arising from the basin of the atom containing nucleus $\mathcal{N}$, that is, $\sigma_{\mathcal{N}}(\mathcal{N})$. This quantity is referred to as the internal contribution, with the external contribution $\sigma_{\mathcal{N}}(\text{ext})$ equaling $\sigma_{\mathcal{N}} - \sigma_{\mathcal{N}}(\mathcal{N})$, that is, all atomic contributions other than that from atom $\mathcal{N}$. The nuclear magnetic shielding tensor is dimensionless and is generally reported in parts per million (ppm). The isotropic shielding, one-third of the trace of the tensor $\sigma_{\mathcal{N}}$, is labelled $\bar{\sigma}_{\mathcal{N}}$.

The expression for the first-order current calculated from perturbation theory, eq. [1], is expressed as a part depending on the first-order correction to the wave function, the "paramagnetic" part, and a part depending on the unperturbed electron density, the "diamagnetic" part (8, 10). Each can be considered to make a corresponding contribution to magnetic properties (1), as in Van Vleck's expression for magnetic susceptibility (18) or in Ramsey's corresponding expression for nuclear shielding (19), and references in the older literature (1) to such contributions generally refer to this breakdown of the current. While the total current is in principle independent of the gauge origin chosen for its calculation, this particular partitioning into para- and dia-magnetic contributions is not unique and is gauge origin dependent. Nonetheless, the total current exhibits regions in which the current flow is such as to generate a field internal to the region that is either opposed to the applied field or acts in concert with it, flows that are termed diamagnetic or paramagnetic, respectively. This characterization of the total current is both useful and valid, as is illustrated next.

Figure 1 displays the current density distribution for acetylene and its mono- and di-substituted fluoro compounds, for a field applied perpendicular to the molecular axis.[3] The regions of clockwise current flow enveloping the entire molecule and those confined within the basins of the fluorine atoms are termed diamagnetic because the interior magnetic field they generate is opposed to the applied field. It is these induced currents that are responsible for the diamagnetic nature of the susceptibility observed for most closed-shell molecules. However, within the basins of the carbon atoms one sees regions of current flow in the counterclockwise direction; the internal fields they generate reinforce the applied field and they are termed paramagnetic. The presence of paramagnetic currents reduces the value of the diamagnetic susceptibility and, in some molecules such as BH that possess a low-lying excited state of Π symmetry, can lead to a paramagnetic susceptibility for the molecule and to a net deshielding of a nucleus relative to the bare nucleus. The presence of both diamagnetic and paramagnetic current

[2] AIMPAC v is the most recent version of the program, described in ref. 13, and is available from R.F.W.B.

[3] Displays of the total induced current $\boldsymbol{J}^{(1)}(\boldsymbol{r})$ have been given previously for some diatomic (8) and polyatomic (20) molecules. In the former (8), trajectories representing the vector field are indicated by a succession of arrows. They are incapable of showing complex current patterns, for example (2), those in the vincities of linked spiral critical points found in ethylene and water and those in the immediate vicinity of nuclei. The reader may compare their current map for HF with the trajectory map given here (see Fig. 5). The polyatomic maps (20), obtained in single gauge origin calculations, have been demonstrated (2, 9) to seriously violate the criterion of current conservation, the condition that $\nabla\cdot\boldsymbol{J}^{(1)}(\boldsymbol{r}) = 0\forall\boldsymbol{r}$. Because of this, these maps (20) do not display behaviour consistent with that demanded of a divergenceless three-dimensional vector field (2, 21) and their topology is wrong. Only current maps obtained from the CSDGT method have been demonstrated to closely satisfy current conservation. The interested reader is invited to compare previous maps (8, 20) with those obtained using the CSDGT method presented here and elsewhere (2, 5, 9, 10). Specific failures in the prediction of the form of $\boldsymbol{J}^{(1)}(\boldsymbol{r})$ and in its critical points in previous maps (20) have been previously discussed (2, 22). Authors (23) of the single gauge origin approach (20) now advocate the CSGT method (9) for the determination of the current, since its use eliminates the unphysical features obtained in their previous maps, features that result from the failure to meet the demand of current conservation.

Fig. 1. Displays of the vector current density in HCCH, FCCH, and FCCF induced by an applied field directed out of and perpendicular to the indicated plane. The directions of the current flow are indicated by arrows. The maps in this and the remaining figures are overlaid with interatomic surfaces. Note the presence of paramagnetic (counterclockwise) flows in the basins of the carbon atoms.

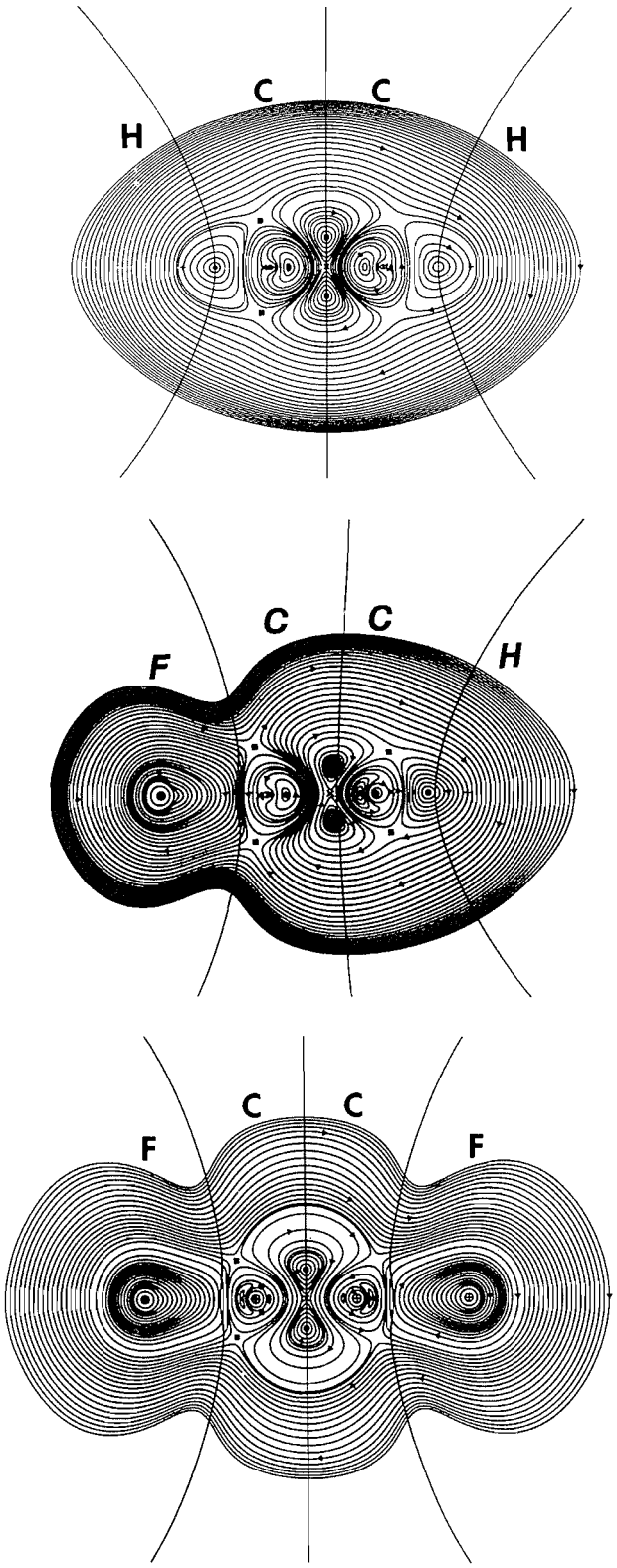

flows is real and is not an artifact of the calculation or dependent upon the choice of gauge origin (2, 9). While a special method using a continuous set of gauge transformations is required to obtain such maps in calculations employing a finite basis set (9), the obtained currents reflect the property of the true current as being an observable, independent of gauge origin.

While the overall effect of diamagnetic and paramagnetic currents is to make opposing contributions to the magnetic susceptibility of a molecule, the contribution from either type of current to the magnetic field exerted at the position of a particular nucleus within the molecule can be shielding or deshielding. The diamagnetic current flow about the position of a fluorine nucleus in both HCCF and FCCF, Fig. 1, generates a field at this nucleus strongly shielding it from the applied field. This same current flow can, however, as illustrated below, contribute to a relatively small shielding or deshielding of a neighbouring carbon nucleus. The presence of a paramagnetic current flow that is contained within the basin of a given atom will generally lead to a deshielding of its nucleus. Thus the carbon nuclei in these molecules will be relatively less shielded than the fluorine nuclei, because of the presence of the paramagnetic currents contained within their basins. The current distributions illustrated in Fig. 1 will be used to illustrate the contributions that the possible patterns of current flow make to the shielding of contained and distant nuclei.

A useful reference for determining the extent of shielding or deshielding of a nucleus in a molecule is given by the so-called Lamb shift (24) σ_L, which is the magnetic shielding density in eq. [3] integrated over the free atom. In this case, the shielding density is proportional to the atomic average of $1/r_{\mathcal{N}}$ as given in eq. [5]

$$[5] \qquad \bar{\sigma}_{L,\mathcal{N}} = (e^2/3mc^2) \int d\boldsymbol{r}\, \rho(\boldsymbol{r})/r_{\mathcal{N}}$$

This expression is exact for a free closed-shell atom where the current flow consists entirely of diamagnetic circular flows centred on the nucleus. Consequently, the Lamb shift represents an approximate upper limit to the diamagnetic shielding of a given nucleus arising from the flow of current within its own basin. In general, the shielding of a nucleus in a molecule is observed to be less than $\bar{\sigma}_{L,\mathcal{N}}$ because of the disruption of the atomic nature of the current flow and, in particular, because of the creation of paramagnetic currents that are frequently localized within the basin of a single atom, as seen in Fig. 1 for the carbon atoms. The average of $1/r_{\mathcal{N}}$ is readily determined for atom $\mathcal{N}$ in a molecule and the quantity

$$[6] \qquad \bar{\sigma}_L(\mathcal{N}) = (e^2/3mc^2) \int_{\mathcal{N}} d\boldsymbol{r}\, \rho(\boldsymbol{r})/r_{\mathcal{N}}$$

called the atomic Lamb shift, when compared with $\bar{\sigma}_{\mathcal{N}}(\mathcal{N})$, the internal contribution to $\bar{\sigma}_{\mathcal{N}}$, provides a useful measure of the effectiveness of the currents generated within the atomic basin of atom $\mathcal{N}$ in shielding its own nucleus. The value of the atomic Lamb shift for a fluorine atom in difluoroacetylene, for example, is 481 ppm, very similar to the value of 485 ppm obtained for $\bar{\sigma}_F(F)$, while for a carbon atom in the same molecule the two corresponding values are very different, equalling 256 and 132 ppm, respectively.

In the IGAIM method of calculating the atomic contribution to a magnetic property, the nucleus of the atom is chosen as the gauge origin for calculating the current within the atom. This choice uniquely determines the paramagnetic and diamagnetic contributions to the current in eq. [1]. Within this formalism, the atomic Lamb shift defined in eq. [6] is exactly the diamagnetic contrbution to $\bar{\sigma}_{\mathcal{N}}(\mathcal{N})$, the internal magnetic shielding of nucleus $\mathcal{N}$, while the difference $\bar{\sigma}_{\mathcal{N}}(\mathcal{N}) - \bar{\sigma}_{\mathrm{L}}(\mathcal{N})$ equals the paramagnetic contribution. For the examples given above, this difference equals 4 ppm for F and 124 ppm for C in FCCF. The atomic average of $1/r_{\mathcal{N}}$ for a bound atom is a physically measurable quantity and, thus, so is the diamagnetic contribution to the magnetic shielding of an atom in a molecule.

Essential topological characteristics of the induced current flows

The types of current flows induced in a molecule by an external magnetic field are described in terms of the seven possible critical points exhibited by the vector field $\boldsymbol{J}^{(1)}(\boldsymbol{r})$ (2). Only those topological features of $\boldsymbol{J}^{(1)}$ essential to the understanding of the diamagnetic and paramagnetic contributions to σ will be discussed here. The reader wishing a full account of the topology of $\boldsymbol{J}^{(1)}$ is referred to the earlier work (2, 22). The critical points are classified in terms of their rank and signature (r, s), as determined by the 3×3 coefficient matrix of $\nabla \boldsymbol{J}^{(1)}$. The current generated in a free closed-shell atom for any field direction or for a linear molecule in a field applied parallel to the molecular axis is planar and consists of a set of circular current loops centered on a $(2,0)$ critical point whose two roots are imaginary. This pattern of flow extends into the third dimension about an axis defined by the stagnation path, the line consisting of the continuous set of non-isolated $(2,0)$ critical points. Such a critical point is called a centre point and its associated set of flow lines is ubiquitous in the currents induced in molecules. Chemical bonding, however, frequently disrupts the centre point flows to give patterns associated with other critical points. The current distribution in acetylene (21) is described to illustrate the manner in which paramagnetic currents can be generated within a molecule.

The current distribution induced by a perpendicular field in acetylene, Fig. 1 (top), exhibits nine $(2,0)$ critical points lying along its internuclear axis and a central critical point that is a saddle point, a $(2,0)$ critical point with real eigenvalues. The name derives from its phase portrait being of the same form as for the gradient vector field derived from a scalar field that exhibits a saddle in two dimensions, as observed for a two-dimensional display of $\rho(\boldsymbol{r})$ in an internuclear region, for example. There is a $(2,0)$ centre point on each C—H bond path that coincides almost exactly with the position of the corresponding bond critical point. They serve as centres for diamagnetic current flows. There are two more centre points in each carbon basin, both of which lie relatively close to the carbon nucleus, one on either side. That on the hydrogen side serves as the locus for a small diamagnetic flow while the other serves as the centre of a much larger region of paramagnetic flow localized within the carbon basin. These two regions of flow are separated by trajectories originating and terminating at a saddle point that lies along the C—H bond path, close to the diamagnetic centre point. There are six off-axis critical points. The two lying along the C_2 axis serve as centre points for diamagnetic current flows, whose corresponding regions are separated by trajectories originating and terminating at the central saddle point. The remaining four off-axis critical points consist of two linked pairs of surface critical points, a pair of $(3, \pm 1)$ critical points, one pair for each C—H group. The surface each pair defines encompasses the C—H bonded current flow, as well as the flow about the two centre points within the carbon basin. The surfaces separate these regions from the diamagnetic flow about the entire molecule, as well as the diamagnetic flows about the C_2 symmetry axis.

Nuclear shielding in acetylenic molecules

The contributions to the shielding of the nuclei in the linear acetylenic molecules for a field applied parallel to the internuclear axis, $\sigma_{\|}$, arise from simple circular diamagnetic current flows about a $(2,0)$ stagnation path coincident with the molecular axis. One can compare the internal contributions $\sigma_{\|\mathcal{N}}(\mathcal{N})$ with the corresponding diamagnetic atomic Lamb shielding and, through a further comparison of the Lamb values with those obtained for perpendicular fields, $\sigma_{\perp}$, determine the deshielding resulting from the disruption of the atomic flows induced in the atomic basins by the bonding effects of neighbouring atoms.

The atomic contributions to the magnetic shielding of the nucleus indicated by a star are listed in Tables 1–3. Where known, experimental gas phase values or their shifts δ relative to a standard compound are indicated in the tables. The agreement between the calculated and experimental values is quite good for the C and H nuclei in the hydrocarbons. In all cases the trends predicted in the calculated values are in agreement with experiment, agreement that would improve if the calculations were carried out at the experimental rather than at the optimized geometries (8). In all cases, the remaining error is primarily in the internal contribution $\sigma_{\mathcal{N}}(\mathcal{N})$, the values listed under the starred atom.

The first observation concerns the basic atomic nature of $\bar{\sigma}_{\mathcal{N}}$, its dominant contribution arising from the current induced within the atomic basin containing nucleus $\mathcal{N}$, an observation true, but to a lesser extent, even for a proton. The principal internal contribution is from the atomic-like diamagnetic current induced by a field parallel to the molecular axis and this value differs, in general, from the atomic Lamb value by less than 1%. Atomic charges determined by the atomic populations are also listed in the tables. There is a small variation in the value of the atomic Lamb shielding, which, in general, parallels the population. Note that in HCCF, the largest positive charge is on the carbon once removed from F, the mobile electron density in the triple bond responding to the transfer of density to F from C_α by a shift of 0.17 au in the C|C interatomic surface towards C_β.

There are no paramagnetic currents induced in the basins of the fluorine atoms by a perpendicular field, the current maps in Fig. 1 showing diamagnetic flows about a single centre point situated at the position of the nucleus in the basin of each of the fluorine atoms in both the mono- and di-substituted molecules, the flow in the difluoro molecule being more regular than that in the monofluoro molecule.

Table 1. Atomic contributions to carbon shielding in acetylene molecules in ppm.[a]

Acetylene	$\bar{\sigma}_C = 118.1\,(117.2)^b$		$\bar{\sigma}_L(C) = 266.1$			
	H————	C*————	C————H		External $\sum$	Total
$q(\Omega)$	−0.136	+0.136	+0.136	−0.136		
$\sigma_\perp$	4.15	21.35	10.75	1.11	16.05	37.40
$\sigma_\parallel$	1.68	265.64	11.92	0.26	13.86	279.50
$\bar{\sigma}$	3.33	102.78	11.14	0.83	15.31	118.10
Fluoroacetylene	$\bar{\sigma}_C = 178.1\,(180 \pm 10)$		$\bar{\sigma}_L(C) = 257.7$			
	H————	C*————	C————F		External $\sum$	Total
$q(\Omega)$	+0.142	+0.566	+0.0438	−0.7522		
$\sigma_\perp$	4.73	107.82	13.58	0.19	18.50	126.32
$\sigma_\parallel$	1.64	260.10	17.88	2.17	21.69	281.79
$\bar{\sigma}$	3.70	158.58	15.01	0.85	19.56	178.14
	$\bar{\sigma}_C = 102.5\,(105 \pm 10)$		$\bar{\sigma}_L(C) = 262.7$			
	H————	C————	C*————F		External $\sum$	Total
$q(\Omega)$	+0.142	+0.566	+0.0438	−0.7522		
$\sigma_\perp$	1.25	6.76	3.10	−0.65	7.36	10.46
$\sigma_\parallel$	0.25	7.82	263.28	15.20	23.27	286.65
$\bar{\sigma}$	0.92	7.11	89.83	4.63	12.66	102.49
Difluoroacetylene	$\bar{\sigma}_C = 147.4$		$\bar{\sigma}_L(C) = 255.80$			
	F————	C*————	C————F		External $\sum$	Total
$q(\Omega)$	−0.743	+0.743	+0.743	−0.743		
$\sigma_\perp$	0.43	68.46	7.66	0.33	8.42	76.88
$\sigma_\parallel$	14.85	259.86	11.62	2.18	28.65	288.55
$\bar{\sigma}$	5.24	132.26	8.98	0.95	15.17	147.44

[a] $\sigma_\perp$ and $\sigma_\parallel$ denote the contributions to the shielding tensor from the indicated atom for a field applied parallel and perpendicular to the molecular axis, respectively. $\bar{\sigma}_L(C)$ is the atomic Lamb contribution, eq. [6].

[b] Numbers in parentheses are experimental values from ref. 27.

Table 2. Atomic contributions to fluorine shielding in acetylene molecules.

Fluoroacetylene	$\bar{\sigma}_F = 439.4$		$\bar{\sigma}_L(F) = 480.90$			
	H————	C————	C————F*		External $\sum$	Total
$q(\Omega)$	+0.142	+0.566	+0.044	−0.752		
$\sigma_\perp$	0.53	1.85	−1.28	412.91	1.10	414.01
$\sigma_\parallel$	0.08	1.43	6.52	482.14	8.03	490.17
$\bar{\sigma}$	0.38	1.71	1.32	435.99	3.41	439.40
Difluoroacetylene	$\bar{\sigma}_F = 488.8$		$\bar{\sigma}_L(F) = 480.75$			
	F————	C————	C————F*		External $\sum$	Total
$q(\Omega)$	−0.743	+0.743	+0.743	−0.743		
$\sigma_\perp$	0.89	1.81	−0.77	485.89	1.93	487.82
$\sigma_\parallel$	0.62	1.79	6.02	482.25	8.43	490.68
$\bar{\sigma}$	0.80	1.80	1.49	484.68	4.09	488.78

Correspondingly, the internal contributions to $\bar{\sigma}_F$ are very similar to the atomic Lamb values.

The presence of paramagnetic flows in the basins of the carbon atoms in all of the acetylene molecules greatly decreases the internal contributions to the magnetic shielding of the carbon nuclei for fields applied perpendicular to the axis, relative to their purely diamagnetic values found for the parallel field that are close to the limiting atomic Lamb values. This effect is most pronounced for the carbon adjacent to fluorine in HCCF where the internal contribution is reduced to 3 ppm. The value of this internal contribution to $\bar{\sigma}_C$ increases with the decreasing extent of the paramagnetic current flow in the basin of the carbon atom.

No paramagnetic flows are found with the basins of the hydrogen atoms, a general observation. The net charge on the hydrogen atom is relatively small in both HCCH and HCCF and the basin contributions are similar to the atomic Lamb values, being slightly greater for the atom with the larger population. The decrease in the perpendicular contribution is partly a result of the centre point for its diamagnetic flow

Table 3. Atomic contributions to hydrogen shielding in acetylene molecules.

Acetylene	$\bar{\sigma}_H = 30.2$	$\delta = 1.1\,(1.4)^a$	$\bar{\sigma}_L(H) = 20.62$			
	H*———	C———	C———	H	External $\sum$	Total
$q(\Omega)$	−0.136	+0.136	+0.136	−0.136		
$\sigma_\perp$	17.46	3.42	3.21	0.53	7.16	24.62
$\sigma_\parallel$	22.01	16.69	2.51	0.09	19.29	41.30
$\bar{\sigma}$	18.98	7.84	2.98	0.38	11.20	30.18
Fluoroacetylene	$\bar{\sigma}_H = 30.2$	$\bar{\sigma}_L(H) = 20.52$				
	H*———	C———	C———	F	External $\sum$	Total
$q(\Omega)$	+0.142	+0.566	+0.044	−0.752		
$\sigma_\perp$	17.27	3.25	3.66	0.15	7.06	24.33
$\sigma_\parallel$	21.77	16.09	3.28	0.74	20.09	41.81
$\bar{\sigma}$	18.77	7.53	3.53	0.35	11.41	30.16

[a] $\delta = \bar{\sigma}_H(CH_4) - \bar{\sigma}_H(C_2H_2)$ calculated; experimental value from ref. 8 in parentheses.

being displaced off the proton to the position of the bond critical point on the interatomic surface.

The total external contribution to the shielding is less than 1% for a fluorine nucleus, around 12% for a carbon nucleus, and around 40% for a proton. Contributions from atoms twice or thrice removed from the nucleus in question are nearly independent of their chemical nature, β hydrogens contributing essentially equal amounts to the shielding of a carbon nucleus as does a β fluorine. γ Hydrogen and fluorine atoms contribute nearly equal amounts to the shielding of a proton and $\bar{\sigma}_H$ is the same for both HCCH and HCCF. The external contributions for a parallel field, which are purely diamagnetic, decay rapidly in value with an increase in distance from $\mathcal{N}$. The same atom in different molecules, even when neighbouring the atom in question, contributes nearly the same shielding to a given $\mathcal{N}$. However, the contributions from neighbouring atoms for perpendicular fields are greatly reduced from the parallel field result, and are frequently smaller than those from the next nearest neighbour. In some cases their contribution is negative, corresponding to a deshielding of the nucleus. Their behaviour is best understood in terms of the properties of the shielding density, first displayed by Jameson and Buckingham for the hydrogen atom, the fluoride ion, and the hydrogen fluoride molecule (16).

Properties of the shielding density

Contour maps of the shielding density defined in eq. [3] and displayed in Fig. 2 provide a visual understanding of the local contribution made by $\boldsymbol{J}^{(1)}(\boldsymbol{r})$ to the magnetic shielding of a given nucleus. The shielding density for a nucleus $\mathcal{N}$ attains its maximum value in the region of the nucleus and decays rapidly away from this point. For a fluorine atom, the current induced by a perpendicular field consists of simple diamagnetic loops flowing about a single centre point located at the nucleus, Fig. 1. The shielding density displayed in Fig. 2a for F in FCCF is correspondingly simple and similar in form, resulting in positive contributions to the shielding from all points within the atomic basin. However, the same fluorine shielding density in Fig. 2a exhibits both positive and negative contributions over the basin of the neighbouring carbon atom and the net contribution from this atom to the shielding of the F nucleus is small and deshielding, Table 2.

To understand this behaviour, consider first the contribution to the shielding density of a carbon nucleus resulting from the simple diamagnetic flow around the nucleus of a neighbouring F atom in FCCF, whose contribution to $\bar{\sigma}_C$ is again vanishingly small and is actually negative in the molecule HCCF. The display of the shielding density for C in FCCF, Fig. 2b, shows that the shielding density within the basin of the fluorine atom makes both positive and negative contributions to the shielding of the C nucleus. This behaviour is easily understood in terms of the $\boldsymbol{r} \times \boldsymbol{J}^{(1)}$ component of the shielding density operator: the upwardly directed flow of the trajectories on the bonded side of the F nucleus makes negative contributions to $\sigma(\boldsymbol{r})$, while their downwardly directed flow in the nonbonded region makes positive contributions. The resulting near cancellation of the two contributions to the shielding is more pronounced the less distorted the current flow in the basin of the neighbouring atom. Thus the smallest shielding contributions to C are from neighbouring fluorines.

The shielding density for a perpendicular field arising from a neighbouring carbon is more complex because of the presence of paramagnetic current flows. Thus the shielding of a F nucleus from the density that lies within the basin of the neighbouring carbon atom, Fig. 2a, shows an inner pair of competing contributions arising from the innermost diamagnetic flow about the carbon nucleus (and similar to that noted above for the whole of a neighbouring F basin) that are encompassed by a pair of outer regions of opposite sign, arising from the paramagnetic current flow. The net result is once again a near cancellation, leading to a small negative contribution to the shielding of a F nucleus from a neighbouring carbon atom in both FCCF and HCCF. The same inner and outer counter polarizations of the shielding density are observed for the basin of the carbon neighbouring the C nucleus serving as origin in Fig. 2b. The map also makes clear the deshielding effect that the paramagnetic currents generated within the carbon basin has on its own nucleus. The shielding density for C in FCCF, Fig. 2b, shows a positive peak encompassing the nucleus surrounded by a region of deshielding density and thus the internal contribution to the shielding for a perpendicular field is much reduced from the parallel one.

All of these features of the shielding density are of a general nature as can be seen from the remaining displays of the

Fig. 2. Displays of the shielding density for acetylenic molecules. The quantity plotted is the diagonal element of the shielding tensor corresponding to the direction of the applied field for unit field strength and unit nuclear magnetic moment, the quantity $\{\boldsymbol{r}_{\supset\mathcal{N}} \times \boldsymbol{J}_{\alpha}^{(1)}(\boldsymbol{r})/r_{\supset\mathcal{N}}^{3}\}_{\alpha}$. Solid (dashed) contours denote positive (negative) values. The contour values range from 0.01 to 800 ppm, as generated by the set $\pm 1, \pm 2, \pm 4, \pm 8 \times 10^{n}$ with n beginning at -2 and increasing in steps of unity to 2. The shielding densities are for F and C in FCCF, (a) and (b), respectively, for C_{α} and C_{β} in FCCH, (c) and (d), respectively, for F and H in FCCH, (e) and (f), respectively and for C and H in HCCH, (g) and (h), respectively. Only the nucleus serving as origin for the shielding density is labelled. The density exhibits the highest contour value of 800 au in the immediate vicinity of each shielded nucleus.

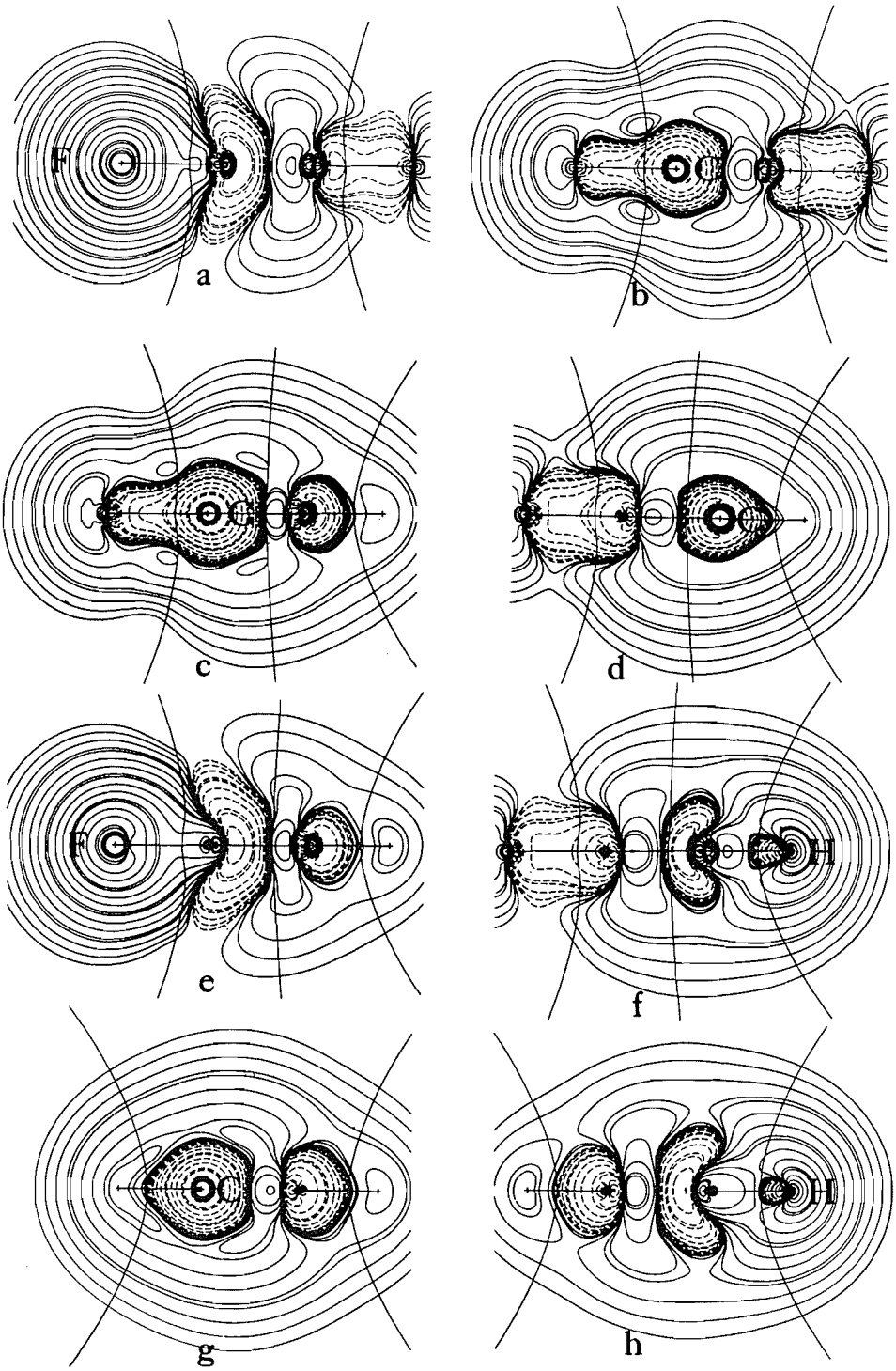

Table 4. Atomic contributions to proton shielding in hydrides in ppm.[a]

AH_n	q(H)	$\bar{\sigma}_L$(H)	$\bar{\sigma}_H$(H)	$\bar{\sigma}_H$(ex)[b]	$\sigma_{\parallel H}$	$\sigma_{\perp H}$	$\bar{\sigma}_H$	δ[c]
LiH	−0.92	27.2	26.4	0.0	28.1	25.6	26.4	5.1
BeH_2	−0.86	29.6	28.1	0.3(0.5)	31.2	26.8	28.4	3.1
BH_3	−0.70	30.5	25.4	−0.9(−0.9)	29.0	22.1	24.5	7.0
CH_4	−0.04	23.4	21.4	10.1(5.6)	31.5	31.5	31.5	0.0
H_2	0.00	21.7	20.6	5.9	27.9	25.9	26.5(26.2)[d]	5.0
NH_3	+0.35	17.2	17.3	14.2(11.8)	26.9	34.0	31.5	0.0(0.05)
OH_2	+0.63	11.5	14.0	16.4(15.5)	28.9	30.7	30.4	1.1(0.6)
FH	+0.78	7.8	11.2	16.7	45.6	18.9	27.6	3.9(2.5)

[a]The symbol $\parallel$ denotes a field applied parallel to the principal symmetry axis while the contributions labelled with $\perp$ denote the average value for the two perpendicular fields.
[b]The values in parentheses are the contributions from just the A atom.
[c]$\delta = \bar{\sigma}_H(CH_4) - \bar{\sigma}_H(AH_n)$ calculated; experimental gas phase value in parentheses from ref. 8.
[d]Experimental gas phase value from ref. 8.

shielding densities given in Fig. 2. The differing internal contributions to the shielding densities, $\sigma_\perp(\boldsymbol{r})$, for the C_α and C_β nuclei in FCCH, Figs. 2c and 2d, are noteworthy. While C_α has a larger electron population than does C_β, as reflected in its larger atomic Lamb value and its correspondingly larger value for $\sigma_\parallel$(C), its overall shielding is less. Figure 2 shows this to be the result of a relative increase in the positive over the negative contributions to the shielding density $\sigma_\perp(\boldsymbol{r})$ within the basin of C_β compared to that found in the basin of C_α, changes that are reflected in the decrease in the value of $\sigma_\perp$(C) from 108 for C_β to 3 ppm for C_α. The behaviour of the internal shielding density for carbon in acetylene, Fig. 2g, is intermediate between that for C_β and C_α, as is its value of $\bar{\sigma}_C$ and its internal contribution $\sigma_\perp$(C). The shielding maps for a proton, Figs. 2f and 2h, exhibit a small negative region on its bonded side, a feature that, as illustrated below, is characteristic of the proton shielding density in non-ionic bonds.

Proton shielding

In hydride molecules AH_n

The variation in the shielding of the proton and its atomic contributions through the series H_2 to HF are given in Table 4 and the current and shielding density plots for representative members shown in Figs. 3, 4, and 5. The shielding is a one-electron property and can be equated to a sum of orbital contributions, and the proton shielding in this set of molecules has been so discussed using localized molecular orbitals (8). The associated orbital current densities, which determine the orbital contributions to σ, are, however, not divergenceless and they do not meet the requirement of conservation of the current, as demanded of the real, physical current flow $\boldsymbol{J}^{(1)}(\boldsymbol{r})$ that is used here in the definition of the shielding density.

The currents in LiH, Fig. 3, and in BeH_2 given previously (2) are typical of ionic systems (see Table 4 for atomic charges). The currents for a $\perp$ field are, like the electron density, strongly localized within the individual atomic basins with circular diamagnetic currents flowing about a centre point in a hydride ion and a paramagnetic flow about a centre point localized within the cationic basin. The form of the

Fig. 3. Displays of the current and proton shielding densities in LiH for a field applied perpendicular to the internuclear axis. The shielding map is drawn to a slightly larger scale. Note the deshielding of the proton resulting from the paramagnetic current flow in the basin of the lithium atom.

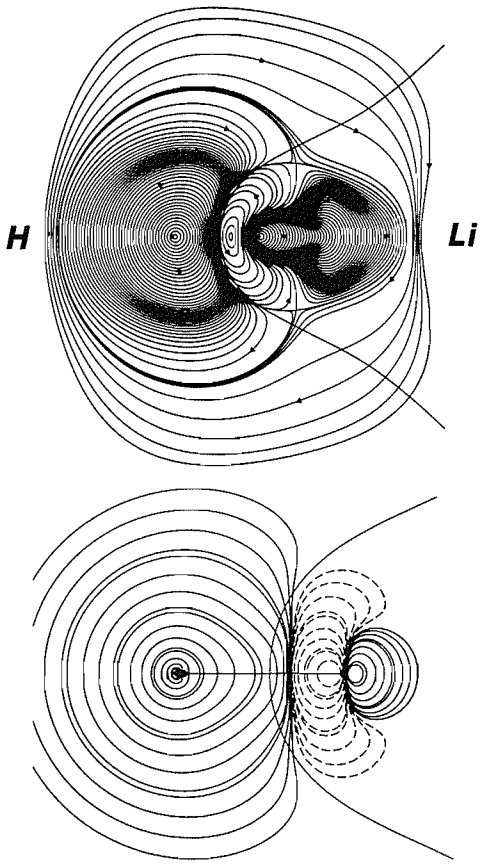

shielding density for the proton in LiH, for a perpendicular field, is similar to and readily related to the form of the induced current, Fig. 3. The simple diamagnetic current flow in the hydrogen basin gives rise to a corresponding pattern of positive contributions to $\sigma_\perp(\boldsymbol{r})$. Since the current for a parallel field is perforce diamagnetic, the two field directions

Fig. 4. Displays of the current, on LHS, and proton shielding densities for the BH_3 molecule for a field applied perpendicular to the plane of the nuclei in (a) and for one parallel to this plane in (b). The lower proton serves as origin in the shielding density in (a). Note the deshielding contribution arising from the paramagnetic current flow in the basin of the boron atom for the parallel field. The B–H interatomic surface is shown only for the current map in (b).

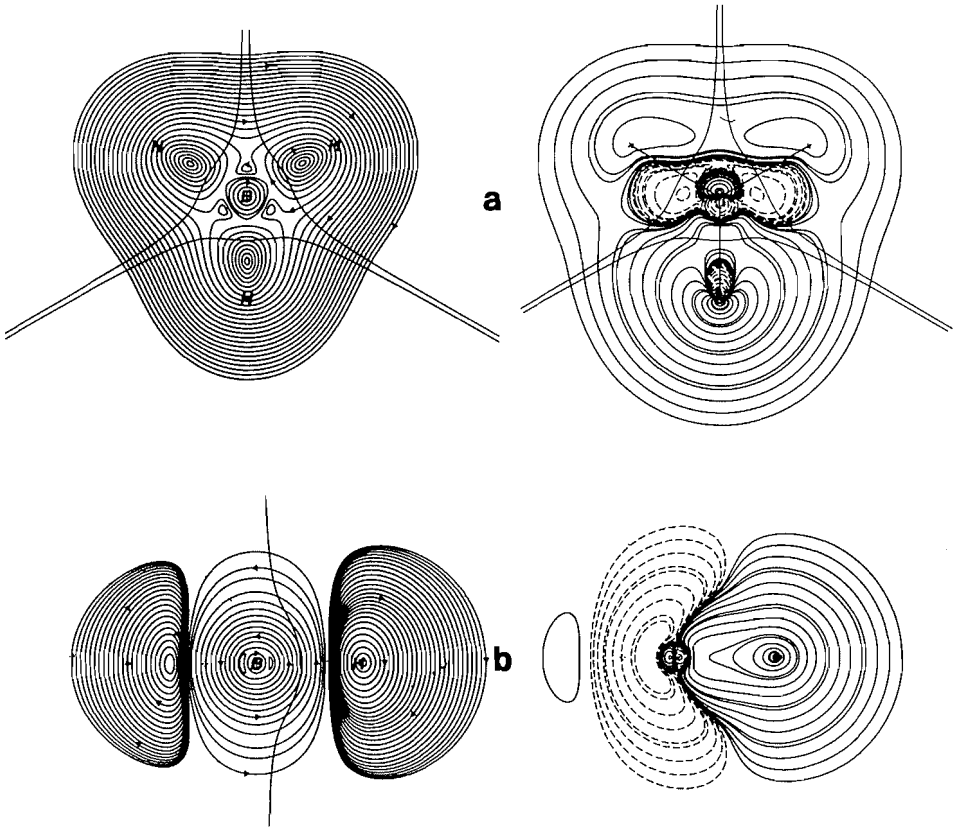

lead to nearly equal internal contributions and, because of their atomic nature, to values that closely bracket the atomic Lamb values. There is a one-to-one correspondence in the form of the paramagnetic and diamagnetic current regions with the deshielding and shielding regions of $\sigma_\perp(r)$ within the cationic basin, Fig. 3, and the resulting net deshielding contribution to $\sigma_\perp(r)$ effectively cancels the external contribution to $\bar{\sigma}_H$ resulting from the parallel field, a result that holds true for BeH_2 as well. Thus the $\bar{\sigma}_H$ values for the ionic systems LiH and BeH_2 are determined by the internal atomic contributions and are close to the corresponding atomic Lamb values.

A similar cancellation of the external contribution to $\bar{\sigma}_H$ occurs in BH_3, where a large paramagnetic flow for a field parallel to the plane of the nuclei and primarily confined to the basin of the boron atom, Fig. 4b, contributes to a net deshielding of the proton in the amount of −0.9 ppm. The reduced hydridic nature of BH_3, $q(H) = -0.7\ e$, is reflected in the movement of the centre point away from the position of the proton in the current induced by a field perpendicular to the molecular plane, leading to the formation of "bonded" current loops that are shared with the boron atom, Fig. 4a. Thus the internal shielding contributions are reduced by ≈5 ppm from the atomic Lamb value, as is the value of $\bar{\sigma}_H$. A considerable anisotropy in σ_H is predicted for this molecule, a result of the deshielding effect of the external contributions arising from the paramagnetic flow about the boron nucleus for a field applied parallel to the plane of the nuclei, as evidenced by the deshielding displayed in Fig. 4b.

The atomic contributions to the magnetic susceptibility $\bar{\chi}$ for LiH, BeH_2, and BH_3 mirror the same dominant properties of the current distributions. An atomic contribution to $\bar{\chi}$ is the sum of a basin contribution, determined by the atomic average of the magnetization density within the boundaries of the atom, and a surface contribution arising from the flux in the current through the interatomic surfaces bounding the atom (10). The atomic nature of the current in these ionic molecules results in near-vanishing contributions to $\bar{\chi}(\Omega)$ from the interatomic surface fluxes and the susceptibility is determined by the basin contributions $\bar{\chi}_b(\Omega)$. The value of $\bar{\chi}_b(A)$ is near zero for Li and *positive* for Be and B, a result of the magnetic dipole moment associated with the paramagnetic currents within the basins of these atoms being aligned parallel to the applied field, an effect that leads to large anisotropies in χ and to its relatively small values in these molecules.

In the remaining molecules, hydrogen is bonded to A in a covalent or polar manner and thus the external contribution to $\bar{\sigma}_H$ increases. The current for a perpendicular field in H_2 consists of a single set of elliptically shaped diamagnetic

Fig. 5. Displays of the current and proton shielding densities for the HF molecule for a field applied perpendicular to the internuclear axis.

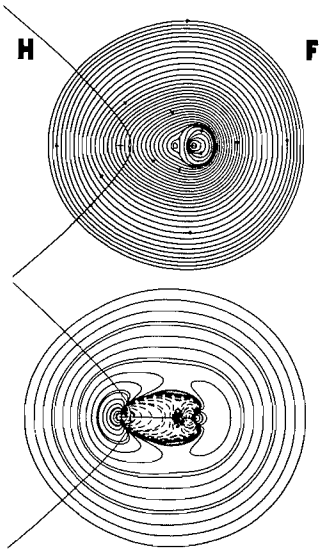

flow lines about a single centre point situated at the bond midpoint (22). This flow is not dissimilar to the diamagnetic flow induced by a field parallel to the internuclear axis and the anisotropy in σ_H is less than 10%. Thus the internal contributions $\bar{\sigma}_H(H)$ for both field directions bracket the atomic Lamb value and the external contributions, which contribute 22%, are nearly isotropic. The general form of the current distribution for the parallel field in BH_3, Fig. 4, is typical of those induced for corresponding fields applied along a threefold axis in CH_4 and NH_3 and for one applied perpendicular to the plane of the nuclei in H_2O (2). The bonded flows in BH_3 are replaced by spiral pairs that become increasingly contracted towards the A nucleus across the row, reaching a limiting form in HF where the whole of the current for a $\perp$ field is dominated by the flow about a centre point located at the fluorine nucleus, Fig. 5. The small oval-shaped region of negative shielding density found on the bonded side of the proton in BH_3, Fig. 4a, and in the acetylenic molecules, Fig. 2, is also found in H_2 and is characteristic of the remaining molecules in this series. In the hydrides of N, O, and F it is contiguous with a deshielding region in the core of the heavy nucleus, as found for the proton in HF, Fig. 5. The paramagnetic currents generated by any field direction become increasingly smaller in methane, ammonia, and water and are absent in hydrogen fluoride. Correspondingly, there is a decrease in the negative regions of the shielding density from methane through to HF, as illustrated in Fig. 5 for HF. The result is a sharp increase in the external contributions to $\bar{\sigma}_H$, one that arises primarily from the current flows in the basins of the A atoms. The particularly large shielding of the proton in HF for a parallel field, Table 4, is primarily a result of the shielding density within the basin of the fluorine atom generated by the circular diamagnetic current flow induced about the molecular axis, a neighbouring carbon in acetylene having a similar effect in increasing the shielding of a proton. Jameson and Buckingham (16) also comment on the sizable contributions to the proton shielding arising from the shielding density in the region around the F nucleus.

The decreasing hydrogen population across the row is accompanied by a decrease in the internal shielding contribution that, with the exception of HF, differs by no more than 2 ppm from the atomic Lamb value. This decrease in shielding is offset by the accompanying increase in the external shielding from A, two effects that are almost equally balanced in CH_4, NH_3, and H_2O, accounting thereby for the near equality in their $\bar{\sigma}_H$ values.

In hydrocarbon molecules

The relative degree of shielding of the proton in ethane, ethene, benzene, and ethyne was the subject of much early speculation in the attempts to relate observed chemical shifts to electronic structure (1). The values of $\bar{\sigma}_H$ and its separate contributions for the principal field directions for these molecules are given in Table 5, together with their atomic contributions. An argument based on changing hybridization would suggest a deshielding of the proton through the series corresponding to the transfer of charge from hydrogen to carbon that accompanies the change in hybridization on carbon from sp^3 to sp^2 to sp. These charge transfers are indeed borne out by the populations given in the table but the shielding does not follow the anticipated trend. The question arises as to why the proton in acetylene is nearly as shielded as it is in ethane and why it is more deshielded in benzene than it is in ethene. Pople et al. (1) have provided qualitative explanations of these apparent exceptions and the atomic contributions for the parallel and perpendicular fields given in Table 5 bear out their arguments and place them on a quantitative level.

The internal contributions to the isotropic shielding of the proton, $\bar{\sigma}_H(H)$, do parallel the atomic Lamb values $\sigma_L(H)$ and hence the trend predicted on the basis of the hybridization arguments, with the shielding of the proton being largest in methane and ethane, nearly identical in ethene and benzene, and least for acetylene where the hydrogen bears a net positive charge, and is, indeed, acidic. However, when the external contributions to $\bar{\sigma}_H$ are taken into account, this trend is lost — the external contribution is too small for benzene and too large for acetylene — and, as discussed below, this is primarily the result of the contributions from the neighbouring carbon atom for a field parallel to the principal symmetry axis.

The largest shielding contribution from a neighbouring carbon occurs in acetylene, and its value for a parallel field, equal to 16.8 ppm, is five times larger than for a perpendicular field. The large shielding contribution for a parallel field is, as discussed above, a result of the unhindered diamagnetic current flow induced about the internuclear axis in this case. In ethane and ethene, on the other hand, the contributions from C_α for the two field directions are nearly equal and both are smaller in magnitude than $\sigma_{\|H}(C_\alpha)$ by ~13 ppm.

The contributions of C_α to the shielding of the proton in ethene and benzene differ by only 0.7 ppm for a field parallel to the plane containing the nuclei. However, for the field perpendicular to this plane, the contribution from C_α in benzene, the *ipso* carbon, is deshielding, equal to −4.2 ppm, while in ethene its value is nearly isotropic, decreasing by only 0.2 ppm from its value of 2.8 ppm for a parallel field. As

Table 5. Atomic contributions to proton shielding in hydrocarbons in ppm.

C_nH_m	$\bar{\sigma}_H(H)$	$\bar{\sigma}_L(H)$	$q(H)$	$\bar{\sigma}_H(C_\alpha)$	$\bar{\sigma}_H(C_\beta)^a$	$\bar{\sigma}_H(H_\alpha)$	$\bar{\sigma}_H(C_\beta)^b$	$\bar{\sigma}_H$(ext)	$\bar{\sigma}_H$	δ^c
CH_4	21.4	23.4	−0.04	5.6		1.5		10.1	31.4	0.0
C_2H_6	21.6	23.8	−0.06	4.9	0.5	1.4	0.4	9.4	31.0	0.4(0.8)
C_2H_4	20.2	23.1	−0.02	2.8	1.5	1.1	0.4	6.1	26.3	5.1(5.1)
C_6H_6	20.1	23.2	−0.02	0.0	0.7 (or)	0.3 (or)	0.2 (me)	4.1	24.2	7.2(7.9)
C_2H_2	19.0	20.6	+0.14	8.0	2.9		0.4	11.3	30.3	1.1(1.4)

[a]The contributions for the *meta* and *para* carbons in benzene are 0.6 and 0.5 ppm, respectively.

[b]The values for ethane and ethene are averages, the individual values differing by no more than 0.1 ppm. The *meta* and *para* hydrogens give the same contributions in benzene.

[c]$\delta = \bar{\sigma}_H(CH_4) - \bar{\sigma}_H(C_nH_m)$ calculated; experimental gas phase value (other than bezene, which is for the liquid phase) in parentheses from ref. 8.

Fig. 6. Displays of shielding density for the proton indicated in each diagram in a σ_v symmetry plane containing the *ipso* and *para* carbon atoms. The *ipso* carbon is on the LHS and only a portion of the density over the basin of the *para* carbon is shown. (a) The applied field is perpendicular to the molecular plane. (b) The field is applied parallel to the molecular plane. The deshielding of the proton resulting from the density in the basin of the *ipso* carbon atom shown in (a) is generated by the ring current characteristic of an aromatic system. The bond path linking H to the *ipso* carbon is indicated along with the associated interactomic surface. The surface between the *ipso* and *para* carbons is planar and nearly coincident with the central positive and negative regions of the maps.

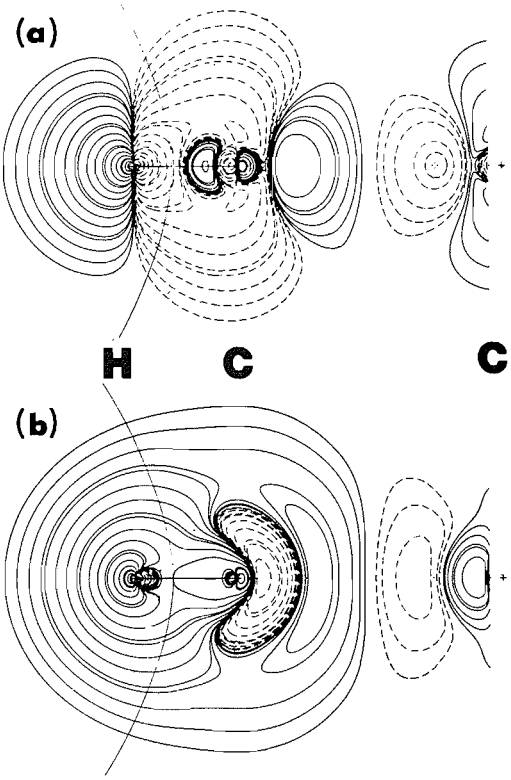

a result, the *ipso* carbon in benzene makes a zero contribution to the isotropic shielding of the proton compared to a value of 2.8 ppm from C_α in ethene.

This deshielding in benzene is a result of the substantial ring current induced on each side of the ring of carbon atoms by a perpendicular field, a current whose presence has been established by its accurate calculation and display (10), the most direct manner of demonstrating its existence. The negative contribution to the shielding density for the proton from within the basin of the *ipso* carbon atom in a perpendicular field, Fig. 6a, demonstrates that the magnetic field associated with the flow of the ring current through the basin of the *ipso* carbon atom reinforces the applied field over its basin, the effect responsible for the deshielding contribution of −4.2 ppm. Its form, with the large negative (deshielding) density in the basin of *ipso* carbon, is to be contrasted with that shown in Fig. 6b, the shielding density for a proton obtained for a field applied parallel to the plane of the ring. This latter density contributes +2.1 ppm to the shielding of the proton.

Waugh and Fesenden (25) modeled the effect of a ring current in terms of the field generated by a circular current of appropriate radius and obtained a value of −6.6 ppm for the deshielding, compared to the contribution of −4.2 ppm found here from the *ipso* carbon atom. The contributions to the shielding of a proton from the *ortho*, *meta*, and *para* carbons for an in-plane field exhibit a simple decay with increasing distance from the proton. However, for the perpendicular field, the contribution from the *ortho* carbon is zero, as opposed to *meta* and *para* contributions of 1.1 ppm. Thus there is a net deshielding of the proton resulting from the currents in the *ipso* carbon and a complete cancellation of the shielding and deshielding effects from those in the *ortho* carbon atoms.

Anisotropy in the proton shielding generally arises from the external contributions, as noted in the AH_n series, and in these molecules is predicted to be significant only in acetylene and benzene where $\Delta\bar{\sigma}_H = \sigma_{H\parallel} - \sigma_{H\perp} = 16.5$ and −5.6 ppm, respectively, the negative anisotropy in benzene being the result of the ring current. The ring current is also manifested in the nature of the atomic contributions to the magnetic susceptibility $\bar{\chi}$ for benzene, its large observed anisotropy being a result of the anisotropy in the C—C surface flux contributions, as opposed to an anisotropy in the basin contributions (10). Fleischer et al. (26), in studying LMO contributions to the proton shielding in benzene, find a π contribution of −3.2 ppm, which they ascribe to a ring current effect.

Shielding of nuclei in hydrocarbons and substituted hydrocarbons

Shielding of carbon nuclei

The atomic and group contributions to the isotropic carbon

Table 6. Atomic contributions to carbon shielding in normal alkanes in ppm.

C_nH_{2n+2}	$\bar{\sigma}_C(C)$	$\bar{\sigma}_C(H_\alpha)$	$\bar{\sigma}_C(G_\alpha)$	$\bar{\sigma}_C(G_\beta)$	$\bar{\sigma}_C(G_\gamma)$	$\bar{\sigma}_C(G_\delta)$	$\bar{\sigma}_C$(ext)	$\bar{\sigma}_C$[a]
CH_4	179.4	4.5					18.0	197.4(195.1)
C_2H_6	168.9	4.2	4.8(CH_3)				17.4	186.3(180.9)
C_3H_8 (C1)	161.2	4.2	3.8(CH_2)	1.1(CH_3)			17.5	178.8(170.8)
C_3H_8 (C2)	159.6	4.0	4.9(CH_3)				17.7	177.3(169.1)
C_4H_{10} (C1)	162.4	4.2	3.7(CH_2)	0.7(CH_2)	0.5(CH_3)		17.5	179.9(173.5)
C_4H_{10} (C2)	151.8	4.0	4.9(CH_3) 3.8(CH_2)	1.1(CH_3)			17.7	169.5(160.0)
C_5H_{12} (C1)	163.4	4.2	3.7(CH_2)	0.6(CH_2)	0.3(CH_2)	0.2(CH_3)	17.6	180.8
C_5H_{12} (C2)	154.5	4.0	4.9(CH_3) 3.7(CH_2)	0.7(CH_2)	0.5(CH_3)		17.8	172.3
C_5H_{12} (C3)	145.1	4.0	3.7(CH_2)	0.9(CH_3)			17.7	162.8

[a]The experimental gas phase value is in parentheses: from ref. 28.

Table 7. Atomic contributions to carbon shielding in normal alcohols in ppm.

Molecule	$\bar{\sigma}_C(C)$	$\bar{\sigma}_C(H_\alpha)$	$\bar{\sigma}_C(G_\alpha)$	$\bar{\sigma}_C(G_\beta)$	$\bar{\sigma}_C(G_\gamma)$	$\bar{\sigma}_C$(ext)	$\bar{\sigma}_C$[a]
CH_3OH	133.1	3.4	4.6(CH_3)			14.9	148.0(137.0)
$\underline{C}H_3CH_2OH$	160.9	4.2	3.7(CH_2)	0.8(OH)		17.0	177.9(168.5)
$CH_3\underline{C}H_2OH$	125.3	3.2	4.7(OH) 4.6(CH_3)			15.7	141.0(127.6)
$\underline{C}H_3CH_2CH_2OH$	166.9	4.3	3.9(CH_2)	0.8(CH_2)	0.3(OH)	17.8	184.6
$CH_3\underline{C}H_2CH_2OH$	153.1	3.9	3.6(CH_2) 4.9(CH_3)	0.8(OH)		17.2	170.3
$CH_3CH_2\underline{C}H_2OH$	119.4	3.2	4.6(OH) 3.4(CH_2)	1.1(CH_3)		15.5	134.9

[a]The experimental gas phase value is in parentheses: from ref. 28.

shielding constants $\bar{\sigma}_C$ for the first five members of the homologous series of normal hydrocarbons are presented in Table 6. The calculated shifts in shielding, relative to the value in methane, are in good agreement with experimental gas phase values. A comparison of the internal and external contributions to $\bar{\sigma}_C$ exhibits a remarkable feature: the whole of the variation in the shielding of a carbon nucleus arises from the basin contribution of the atom containing the nucleus in question, the external contribution to the shielding remaining essentially constant throughout the series, being independent of chain length and of the positioning of the nucleus within the chain.

The internal contribution is greatest for a primary carbon and increases with chain length. The external contributions are remarkably constant for equivalent atoms or functional groups, excluding methane. The contribution from a hydrogen bonded directly to the atom containing nucleus C, a contribution labelled $\bar{\sigma}_C(H_\alpha)$, exhibits characteristic values equal to 4.2 ppm when bonded to a methyl carbon and to 4.0 ppm when bonded to a methylene carbon. Similarly, contributions from methyl and methylene groups bonded directly to the carbon in question and denoted by $\bar{\sigma}_C(G_\alpha)$ both exhibit equally constant values as do the same groups once removed, contributions denoted by $\bar{\sigma}_C(G_\beta)$. Thus, replacing the neighbouring methyl group in ethane by a succession of three methylenes and a methyl group to obtain pentane, yields external contributions of 3.7, 0.6, and 0.3 from the methylene groups and 0.2 ppm from the terminal methyl. These values sum to yield 4.8 ppm, identical to the shielding contribution from the single methyl group in ethane.

This behaviour is not unique to the parent hydrocarbons but applies equally to their derivatives, as illustrated by the corresponding data for the normal alcohols given in Table 7. If one differentiates between the shielding of a carbon nucleus adjacent to the OH group and one once removed, one then recovers nearly constant external group contributions that sum to the same total value, with the exception of methanol. The OH group, for example, contributes 4.7 ppm to the shielding of an adjacent carbon nucleus, the same as the average shielding provided by a neighbouring methyl group. The methyl and methylene group contributions are the same, to within a few tenths of a part ppm, as those found in the parent hydrocarbons. These results indicate the possibility of assigning a set of group contributions to the shielding of a given nucleus in homologous series of molecules, the value depending upon the group's position relative to the nucleus in question. Equally useful is the knowledge that the external contribution is fixed for a carbon nucleus in a given homologous series of molecules, $\bar{\sigma}_C$(ext) equaling 17.7 ppm for a hydrocarbon and 17.4 ppm for a carbon in a normal alcohol not bearing the OH group and 15.6 ppm for the carbon that does.

The internal contribution to the shielding of the carbon nucleus in both series of alcohols is not constant and, as

Table 8. Group contributions to shielding of N, O, and F nuclei.

(*a*) Nitrogen

Molecule	Group contribution to $\bar{\sigma}_N$ in ppm				$\bar{\sigma}_L(N) = 339.5 \pm 0.1$ ppm				
	Y[a]	CH_2	CH_2	H_2	$\bar{\sigma}_N$(int)	$\bar{\sigma}_N$(ext)	$\bar{\sigma}_N$[b]	$-q$(N)	$-\bar{\chi}$(N)
CH_3NH_2	4.10			6.38	246.0	10.5	256.5	1.056	2.38
$CH_3CH_2NH_2$	1.05		3.08	6.37	238.0	10.5	248.5	1.079	2.45
$CH_3CH_2CH_2NH_2$	0.49	0.60	3.08	6.44	226.9	10.6	237.5	1.068	2.41
$NH_2CH_2CH_2NH_2$	0.44	0.70	3.10	6.38	243.3	10.6	253.9	1.096	2.48
$OHCH_2CH_2NH_2$	0.38	0.74	3.19	6.32	246.4	10.6	257.0	1.082	2.49
$FCH_2CH_2NH_2$	0.27	0.81	3.27	6.33	251.2	10.7	261.8	1.090	2.50

(*b*) Oxygen

Molecule	Group contribution to $\bar{\sigma}_0$ in ppm				$\bar{\sigma}_L(0) = 410.8$ ppm				
	Y	CH_2	CH_2	H	$\bar{\sigma}_0$(int)	$\bar{\sigma}_0$(ext)	$\bar{\sigma}_0$	$-q(0)$	$-\bar{\chi}(0)$
CH_3OH	3.39			2.03	341.4	5.3	341.4	1.259	2.29
CH_3CH_2OH	1.18		2.26	2.02	314.6	5.5	320.6	1.265	2.31
$CH_3CH_2CH_2OH$	0.38	0.65	2.17	2.03	316.3	5.2	321.6	1.267	2.30
$NH_2CH_2CH_2OH$	0.46	0.74	2.34	2.06	324.2	5.6	340.4	1.272	2.35
$OHCH_2CH_2OH$	0.38	0.77	2.34	2.02	329.2	5.5	334.8	1.272	2.34
FCH_2CH_2OH	0.29	0.82	2.42	1.99	333.3	5.5	338.9	1.270	2.33

(*c*) Fluorine

Molecule	Group contribution to $\bar{\sigma}_F$ in ppm			$\bar{\sigma}_L(F) = 480.3$ ppm				
	Y	CH_2	CH_2	$\bar{\sigma}_F$(int)	$\bar{\sigma}_F$(ext)	$\bar{\sigma}_F$[b]	$-q$(F)	$-\bar{\chi}$(F)
CH_3F	3.29			483.4	3.3	486.7	0.736	2.27
CH_3CH_2F	1.17		2.09	437.6	3.3	440.8	0.741	1.91
$CH_3CH_2CH_2F$	0.56	0.64	2.02	437.6	3.2	440.9	0.743	1.91
$NH_2CH_2CH_2F$	0.49	0.70	2.15	442.4	3.3	445.8	0.745	1.92
$OHCH_2CH_2F$	0.38	0.74	2.19	456.4	3.3	459.7	0.741	1.93
FCH_2CH_2F	0.29	0.79	2.28	461.6	3.4	465.0	0.736	1.92

[a]Y = CH_3, NH_2, OH, or F.

[b]Experimental values from ref. 27 are CH_3NH_2, 237 ± 10; CH_3F, 468 ± 15; CH_3CH_2F, 401 ± 10.

found for the hydrocarbons, it is the change in the internal contribution that is responsible for the substituent effect on the shielding $\bar{\sigma}_C$.

Shielding of nitrogen, oxygen, and fluorine nuclei

The behaviour found for the internal shielding of carbon nuclei is general. Table 8 lists the isotropic shielding tensors for nitrogen in the amino group, oxygen in the hydroxyl group, and fluorine nuclei in their methyl, ethyl, and propyl derivatives and in the series obtained by linking these same groups to the fragment YCH_2CH_2- with Y = CH_3, NH_2, OH, or F. We have previously illustrated how the contributions from a X = OH or F group to the population energy, volume, and magnetic susceptibility in the homologous series $CH_3(CH_2)_n$-X, assume essentially constant values when $n = 1$ or more. With the exception of methyl amine, the net charges on N, O, and F, $q(\Omega)$, and their contributions to the magnetic susceptibility, $\bar{\chi}(\Omega)$, are remarkably constant throughout both sets of molecules for the N, O, and F atoms. The same is not true of the shielding of their nuclei, however, and nearly the whole of the variation has its origin in the current flow within the basin of the atom containing the nucleus in question, the quantity $\bar{\sigma}_{\mathcal{N}}(\mathcal{N}) = \bar{\sigma}_{\mathcal{N}}(\text{int})$, as found above for the carbon nucleus. The external contributions throughout the series of molecules for all three nuclei exhibit only small variations. The individual contributions from chemically equivalent atoms, such as the hydrogens bonded to N and O or a methylene group bonded to N, O, or F or once removed, also exhibit only small variations. An NH_2, OH, or F group, bonded to a β carbon, makes a nearly constant contribution to the shielding of all three nuclei throughout all three series of molecules.

Thus substituent effects on the shielding of C, N, O, and F nuclei in these saturated systems are the result of small perturbations in the shielding density transmitted to the basin of the atom containing nucleus $\mathcal{N}$. What is remarkable is that these same substitutions and their accompanying perturbations leave the shielding contribution from the remainder of

the molecule unchanged. Clearly, the division of the magnetization density $\boldsymbol{r}_{\mathcal{N}} \times \boldsymbol{J}^{(1)}(\boldsymbol{r})$ by $r_{\mathcal{N}}^{-3}$, as found in the shielding density, causes the result that any perturbation of the current is most pronounced in the basin of nucleus $\mathcal{N}$ and, in the examples of saturated systems presented here, the effect is restricted to just this single contribution to within ±0.1 ppm. Even for unsaturated systems such as the acetylenes, the external contributions to the variations in nuclear shielding are small relatively and absolutely, contributing 2 or 3% to $\bar{\sigma}_C$ and less than 1% to $\bar{\sigma}_F$. While LMO contributions to σ predict essentially constant isotropic contributions from atomic core orbitals (8), this does not imply that the substituent-related perturbations of the shielding density do not occur close to nucleus $\mathcal{N}$, the opposite being evident for the carbons in Fig. 2. The result implies only that core orbitals are not appreciably mixed in by the angular momentum perturbation operator. In general, even LMO's removed from atom $\mathcal{N}$ will have tails that contribute to the shielding density in the basin of atom $\mathcal{N}$.

Conclusions

This paper provides a theoretical basis for the atomic nature of the magnetic shielding of nuclei. It does so by relating the shielding to the magnetic field exerted at a nucleus generated by the induced current, the primary contribution arising from the flow of current within its own atomic basin. An electronegative atom such as fluorine in a polar bond, or hydrogen in a hydridic molecule, exhibits an atomic-like diamagnetic current flow within its basin for all field directions and the internal contribution to $\bar{\sigma}_{\mathcal{N}}$ approaches the atomic Lamb value, $\bar{\sigma}_L(\mathcal{N})$. There is a correlation of the internal contribution to the shielding of a proton with the electron population of H that can, in some instances, carry over to $\bar{\sigma}_{\mathcal{N}}$ itself. However, in general, the effect of bonding on other atoms is to generate paramagnetic current flows of increasing extent within their basins and the internal contribution to the shielding is correspondingly reduced relative to $\bar{\sigma}_L(\mathcal{N})$. Because of this effect, there is, in general, no correlation of $\bar{\sigma}_{\mathcal{N}}$ with the electron population of atom $\mathcal{N}$.

A neighbouring atom X shields nucleus $\mathcal{N}$ from a field applied parallel to the X—$\mathcal{N}$ bond, but its shielding for a field perpendicular to the X—$\mathcal{N}$ bond is greatly reduced and may be deshielding, a direct consequence of the dependence of the shielding density on the appropriate components of $\boldsymbol{r}_{\mathcal{N}} \times \boldsymbol{J}^{(1)}(\boldsymbol{r})$. The most important observation concerning the contribution of neighbouring groups to the shielding of a nucleus, however, is its near constancy in many systems. As shown here, essentially all of the variations in the shielding of C, N, O, and F nuclei in different series of saturated molecules originate within the basin of the atom containing $\mathcal{N}$, the nucleus in question, the contribution from the groups making up the remainder of the molecule being independent of their number and, if sufficiently removed from $\mathcal{N}$, even of their chemical nature. This constancy in the external shielding contribution is obtained whether $\mathcal{N}$ is a terminal or an interior atom. Thus the external contribution to the shielding of a carbon nucleus at any position within a hydrocarbon containing two or more carbons is 17.6 ± 0.1 ppm.

The essential observation to be made is that the difference in chemical shifts observed for nucleus $\mathcal{N}$ in different environments is primarily determined by changes to the shielding density occurring within the basin of the atom $\mathcal{N}$. For example, the external contribution to the shielding of a carbon nucleus in a wide variety of bonding situations is found to vary by less than 10 ppm for $\bar{\sigma}_C$ values that range from 63 to 217 ppm, a value that is reduced to 6 ppm if one excludes molecules with two or more fluorines bonded to carbon. The averaging of the shielding density over the region of the molecule external to atom $\mathcal{N}$ exhibits a remarkable insensitivity to the size of the system and even to the chemical nature of groups twice removed from the atom in question. In addition, chemically equivalent groups are found to contribute characteristic, identical amounts to the external shielding. It appears that the external contribution to $\bar{\sigma}_{\mathcal{N}}$ increases with a decrease in the electronegativity of $\mathcal{N}$, as evidenced by the external contributions to the shielding of the C, N, O, and F nuclei decreasing in the order 17.6, 10.6, 5.5, and 3.3 ppm, respectively, found here. All of these observations, which bring to the fore the essential atomic nature of the magnetic shielding of a nucleus in a molecule, are obtained as a consequence of averaging the shielding density over the individual atomic basins defined by the zero-flux surface condition of a proper open system (3).

References

1. J.A. Pople, W.G. Schneider, and H.J. Bernstein. High resolution nuclear magnetic resonance. McGraw–Hill, New York. 1959.
2. T.A. Keith and R.F.W. Bader. J. Chem. Phys. **99**, 3669 (1993).
3. R.F.W. Bader. Atoms in molecules — a quantum theory. Oxford University Press, Oxford. 1990.
4. R.F.W. Bader. Phys. Rev. B, **49**, 13348 (1994).
5. T.A. Keith and R.F.W. Bader. Chem. Phys. Lett. **194**, 1 (1992).
6. R. Ditchfield. Mol. Phys. **27**, 789 (1974).
7. W. Kutzelnigg. Isr. J. Chem. **19**, 193 (1980).
8. W. Kutzelnigg, U. Fleischer, and M. Schindler. NMR, **23**, 165 (1990).
9. T.A. Keith and R.F.W. Bader. Chem. Phys. Lett. **210**, 223 (1993).
10. R.F.W. Bader and T.A. Keith. J. Chem. Phys. **99**, 3683 (1993).
11. E. Schrödinger. Ann. Phys. **81**, 109 (1926).
12. R.D. Amos and J.E. Rice. CADPAC: The Cambridge analytic derivatives package, Cambridge, U.K.
13. F.W. Biegler-König, R.F.W. Bader, and T.-H. Tang. J. Comput. Chem. **3**, 317 (1982).
14. R. Krishan, J.S. Binkley, R. Seeger, and J.A. Pople. J. Chem. Phys. **72**, 650 (1980); T. Clark, J. Chandreshakar, G.W. Spitznagel, and P. von Schleyer. J. Comput. Chem. **4**, 294 (1983); M.J. Frisch, J.A. Pople, and J.S. Binkley. J. Chem. Phys. **80**, 3265 (1984).
15. C.J. Jameson. Nucl. Magn. Reson. **24**, 44 (1995).
16. C.J. Jameson and A.D. Buckingham. J. Chem. Phys. **73**, 5684 (1980).
17. R. McWeeny and B.T. Sutcliffe. Methods of molecular quantum mechanics. Academic Press, New York. 1969. pp. 224–226; R. McWeeny. Proc. Indian Acad. Sci. **96**, 263 (1986).
18. J.H. Van Vleck. Electric and magnetic susceptibilities. Oxford University Press, New York. 1932.
19. N.F. Ramsey. Phys. Rev. **78**, 699 (1950).
20. P. Lazzeretti and R. Zanasi. Chem. Phys. Lett. **80**, 533 (1981); P. Lazzeretti, E. Rossi, and R. Zanasi. J. Chem. Phys. **77**, 3129 (1982); J. Am. Chem. Soc. **105**, 12 (1983); Int. J. Quantum Chem. **25**, 929 (1984); **25**, 1123 (1984); P. Lazzeretti, M. Malagoli, and R. Zanasi. NATO ASI Ser. **386**, 163 (1993).
21. J.W. Reyn. Z. Angew. Math. Phys. **15**, 540 (1964).
22. T.A. Keith. Ph. D. Thesis, McMaster University, March 1993.

23. R. Zanasi and P.W. Fowley. Chem. Phys. Lett. **238**, 270 (1995).
24. W.E. Lamb. Phys. Rev. **60**, 817 (1941).
25. J.S. Waugh and R.W. Fessenden. J. Am. Chem. Soc. **79**, 846 (1957).
26. U. Fleischer, W. Kutzelnigg, P. Lazzeretti, and V. Mühlenkamp. J. Am. Chem. Soc. **116**, 5298 (1994).
27. B.R. Appleman and B.P. Dailey. *In* Advances in magnetic research. Vol. 7. *Edited by* J.S. Waugh. Academic Press, New York. 1974. p. 231.
28. A.K. Jameson and C.J. Jameson. Chem. Phys Lett. **134**, 461 (1987).

Crystal chemistry of tetraradial species. Part 8. Mix and match: cation geometry, ion packing, hydrogen bonding, and π–π interactions in *cis*-2,2′-bipyridinium(1+) and 1,10-phenanthrolinium(1+) tetraphenylborates — and what about proton sponges?[1]

Pradip K. Bakshi, T. Stanley Cameron, and Osvald Knop

Abstract: The crystal structures at −20°C of *cis*-2,2′-bipyridinium(1+) (BPTB, $P2_1/n$, $a = 9.249(3)$, $b = 14.093(7)$, $c = 20.285(3)$ Å, $\beta = 92.86(2)°$, $Z = 4$) and 1,10-phenanthrolinium(1+) (PTB, $P2_1/c$, $a = 11.194(2)$, $b = 13.837(3)$, $c = 18.303(3)$ Å, $\beta = 107.82(1)°$, $Z = 4$) tetraphenylborates have been determined. Inasmuch as 1,10-phenanthroline is an aromatically bridged *cis*-2,2′-bipyridine, monoprotonation results, in both systems, in the formation of an intra-cation N—H...N′ hydrogen bond, the geometric and spectroscopic properties of which we have investigated. The cation skeleton in PTB is planar to 0.03(2) Å; in BPTB the dihedral angle between the two cation ring planes is 5.2°. In the pale yellow PTB there are significant π–π stacking interactions that persist into solution. The effect of protonation on the geometry of the 2,2′-bipyridine and 1,10-phenanthroline systems is examined in considerable detail and compared with the corresponding effects in the paraquat(2+) and similar cations. On both geometric and spectroscopic (infrared spectra between 10 and 295 K) evidence, the N—H...N′ hydrogen-bonding interaction is stronger in BPTB; in PTB this interaction is among the weakest reported in crystals, the ν(NH) stretching frequency at 10 K being as high as 3279 cm^{-1}. A detailed comparison of the geometries of the intra-cation N—H...N′ bonds in BPTB and PTB with those in classical and modified proton-sponge cations has led to the formulation of criteria useful in predicting the occurrence of proton-sponge-like properties.

Key words: bipyridinium ions, hydrogen bonding, phenanthrolinium ions, proton sponges, tetraphenylborates.

Résumé : Opérant à −20°C, on a déterminé les structures cristallines des tétraphénylborates du *cis*-2,2′-bipyridinium(1+) (BPTB, $P2_1/n$, $a = 9,249(3)$, $b = 14,093(7)$ et $c = 20,285(3)$ Å, $\beta = 92,86°$, $Z = 4$) et du 1,10-phénanthrolinium(1+), (PTB, $P2_1/c$, $a = 11,194(2)$, $b = 13,837(3)$ et $c = 18,303(3)$ Å, $\beta = 107,82°$, $Z = 4$). Comme la 1,10-phénanthroline est une *cis*-2,2′-bipyridine aromatiquement pontée, la monoprotonation de ces deux systèmes conduit à la formation d'une liaison hydrogène intramoléculaire N—H...N′ intra-cation dont on a étudié les propriétés géométriques et spectroscopiques. Le squelette du cation du PTB est plan à 0,03(2) Å près; dans le BPTB, l'angle dièdre entre les plans des deux cycles du cation est de 5,2°. Dans le PTB qui est jaune pâle, il existe des interactions d'empilement π–π importantes qui persistent même en solution. On a étudié en détail l'effet de la protonation sur la géométrie des systèmes de la 2,2′-bipyridine et de la 1,10-phénanthroline et on le compare avec les effets correspondants dans le paraquat(2+) et dans des cations similaires. Sur la base des données tant géométriques que spectroscopiques (spectres IR entre 10 et 295 K), l'interaction de la liaison hydrogène N—H...N′ est plus forte dans le BPTB; dans le PTB, cette interaction est l'une des plus faibles rapportés dans les cristaux, la fréquence d'élongation ν(NH) à 10 K ayant une valeur aussi élevée que 3279 cm^{-1}. Une comparaison détaillée des géométries des liaisons N—H...N′ intra-cation dans le BPTB et le PTB avec celles observées dans des cations classiques ou modifiés comme éponges à proton a conduit à la formulation de critères utiles pour prédire l'apparition de propriétés ressemblant à celles des éponges à proton.

Mots clés : ions bipyridinium, liaison hydrogène, ions phénanthrolinium, éponges à proton, tétraphénylborates.

[Traduit par la rédaction]

Received March 7, 1995.[2]

P.K. Bakshi,[3] T. Stanley Cameron, and Osvald Knop.[4] Department of Chemistry, Dalhousie University, Halifax NS, B3H 4J3, Canada.

[1] For Part 7 see ref. 1.

[2] Revision received November 16, 1995.

[3] Holder of a graduate scholarship, Canadian Commonwealth Scholarship and Fellowship Plan, and a Killam Graduate Scholarship.

[4] Author to whom correspondence may be addressed. Telephone: (902) 494-3317 or (902) 494-3305. Fax: (902) 494-1310.

Fig. 1. Correlated numbering scheme for cation skeletons.

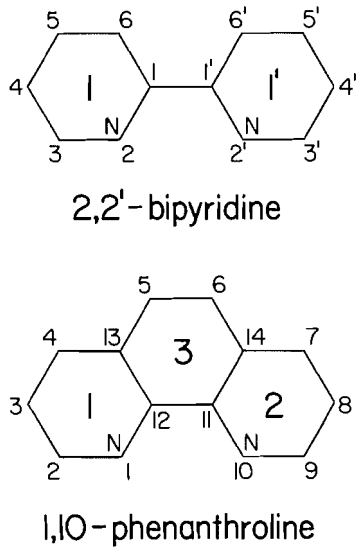

As part of our exploration of hydrogen bonding to aromatic π systems in crystals (2–5) we set out to investigate the nature of secondary bonding interactions in 2,2′-bipyridinium (BP) tetraphenylborate. Unaware at the time of the results of a preparative and ir study of BP salts of other anions (cf. below, refs. 6–8), we were not sure what stoichiometry and BP cation conformation to expect in a tetraphenylborate crystal, although the ionization constant of 2,2′-bipyridine (9) and the necessity of using strong acids to stabilize the BP^{2+} cation (10) pointed to the likelihood of a 1:1 rather than 1:2 stoichiometry. The 1:1 ratio eventually turned out to be the correct one, giving a product of the composition $(C_{10}H_9N_2)BPh_4$ (= BPTB), with the BP^+ cation in a very nearly planar *cis* conformation.[5] Since the near-planarity of the *cis* rotamer imparts aromatic character to the BP system, the BP^+ ion may be regarded as a subsystem of the aromatic, intrinsically planar 1,10-phenanthrolinium(1+) (= $phenH^+$) cation (Fig. 1). It therefore seemed of interest to see how differences between the two cations manifest themselves in the crystal structures of their tetraphenylborates, in which cation distortions resulting from cation–anion interaction could be expected to be small. Secondly, to the best of our knowledge no systematic investigation had previously been published of the effect of the dihedral angle ψ between the two phenyl ring planes on the C(1)—C(1′) and other bond lengths and angles in BP^+. While in BPTB ψ is only ~5°, angles of up to 19° have been reported in other BP^+ salts (cf. below). The present investigation thus seemed to offer an opportunity for assessing the effect of ψ from a statistical analysis of the observed variations in BP^+ geometry in crystals.

Table 1. Crystal data of 2,2′-bipyridinium(1+) (BPTB) and 1,10-phenanthrolinium(1+) (PTB) tetraphenylborates at −20°C.[a]

Parameter	BPTB	PTB
Formula	$BC_{34}H_{29}N_2$	$BC_{36}H_{29}N_2$
fw	476.4	500.5
Colour	Colourless	Pale yellow
Crystal size, mm^3	0.55 × 0.35 × 0.3	0.1 × 0.35 × 0.5
θ-range, deg[b]	2–23/23	2–23/20
a, Å	9.249(3)	11.194(2)
b, Å	14.093(7)	13.837(3)
c, Å	20.285(3)	18.303(3)
β, deg	92.86(2)	107.82(1)
V, $Å^3$	2640(3)	2699(2)
ρ_c, g/cm^3	1.196(1)	1.229(1)
Space group	$P2_1/n$ (no. 14)	$P2_1/c$ (no. 14)
F(000), e	1008	1056
Reflections:		
total measured	4136	5534
unique total	3861	3954
unique used ($I > 3\sigma(I)$)	1788	1703
$100R_{merg}$	5.7	2.8
d/p	5.4	4.8
$100R$; $100R_w$	4.1; 4.1	3.8; 4.0
G.O.F.	0.71	0.70
Residual e.d.[c]	−0.17/0.11	−0.15/0.11

[a]Rigaku AFC5 single-crystal diffractometer, λ = 0.71069 Å (graphite monochromator); μ_{Mo} = 0.65 cm^{-1}; *Z* = 4; unit weights.

[b]$\theta_{min} < \theta < \theta_{max}/n$. The lattice parameters and orientation matrices were obtained by least squares from the setting angles θ of *n* suitable reflections.

[c]Minimum and maximum residual electron density ($e/Å^3$) in final difference map.

Crystals of $phenH^+$ tetraphenylborate (PTB) were, in contrast to the colourless BPTB, pale yellow. The appearance of colour was suggestive of charge-transfer interactions arising from π–π stacking, possibly of the kind observed in *N*,*N*′-Me_2-4,4′-bipyridinium(2+) (= paraquat, PQ^{2+}) tetraphenylborate (PQTB, ref. 11), and prompted an ^1H nmr investigation of PTB in solution. Furthermore, the comparison of the intra-cation hydrogen bonding in BPTB and PTB and other relevant structures, which was supplemented by a study of the ir spectra of the two solids at temperatures between 10 K and ambient, has led to an extensive comparison of these cations with proton sponges (an important class of proton-sequestering agents in which a captured proton is strongly held between two closely spaced N atoms of a rigid planar cation system, cf. below), and to formulation of geometric criteria useful in predicting the occurrence of proton-sponge-like properties.

The crystal data of BPTB and PTB at −20°C appear in Table 1. The positional parameters of the nonhydrogen (Table A) and hydrogen (Table B) atoms, the anisotropic thermal parameters of the nonhydrogen atoms (Table C), interatomic distances and bond angles (Table D), deviations from the best planes through the ring skeletons (Table E), correlated mean bond lengths and angles in *cis*-BP^+ and in phen systems (Table

[5] *Housekeeping note:* (*1*) All the 2,2′-bipyridinium(1+) cations discussed in this paper are *cisoid* rather than *cis* (i.e., of C_s symmetry). However, to avoid clumsiness, they will be referred to as *cis* throughout, with the dihedral angle ψ clearly specified. A similar practice will be followed for *trans* and *transoid* conformations. (*2*) Crystallographic esd's are quoted in parentheses. Standard deviations of means of bond lengths and angles etc. are quoted in square brackets. The means were computed with unit weights and their standard deviations do not take account of the esd's of the individual component values. (*3*) *Literature structures:* Atom numbering schemes other than those in Fig. 1 have been converted to match. Bond lengths and angles not quoted in the original papers have been calculated from the available information.

Fig. 2. Projection of the unit cell of BPTB on (100). Large circles, N atoms; small circles, H(N2′) atoms.

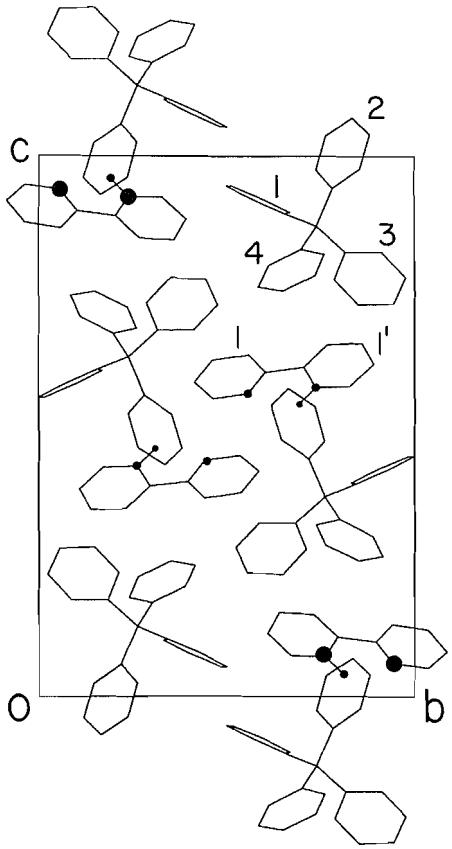

F), and summaries of bond lengths and angles in *cis*-BP^+ (Table G), $phenH^+$ (Table H), BP^{2+} (Table J), and 4,4′-BP^{2+} and PQ^{2+} Table K) salts have been deposited.[6]

Results and discussion

Crystal structures

Although the BPTB and PTB structures (Figs. 2 and 3) have the same space-group symmetry, they are not similar. However, the ion packing in the two must be of comparable efficacy, as the difference between the volume per formula unit is 24.1 Å^3, in agreement with the volume increment expected for the insertion of two aromatic ring carbons into BP^+, 25.4 Å^3 (12). Both structures are completely ordered.

The BP^+ cation has a *cis* conformation. Ring skeleton 1 is planar to 0.003[1] Å, ring skeleton 1′ to 0.002[1] Å, and ψ is only 5.2° (Table E). If the cation is treated as planar, the mean deviation of the nonhydrogen atoms from the best plane is 0.041[16] Å and the angles of the ring planes R1 and R1′ with the cation plane are ~2.6°. The bond lengths and angles in the cation are listed in Table 2. The thermal motion of the cation is satisfactorily described on the rigid-body-motion model (see Experimental).

The bond lengths and angles in the $phenH^+$ cation of PTB are listed in Table 2. The cation skeleton is planar to 0.029[17] Å; the individual rings R1, R2, and R3 are planar to 0.010[4], 0.011[5], and 0.007[4] Å, respectively, with the dihedral angles R2/R1 = 3.7°, R3/R1 = 1.2°, and R3/R2 = 2.6° (Table E), which indicates a slight departure from the ideal C_s conformation. The cations are confined to slabs ∥(100) which are cleanly separated by regions formed entirely by anion C—H bonds (Fig. 3, *left*). The PTB structure is unusual in that it consists of a bc packing of centrosymmetric (anion–cation–cation–anion) units arranged in such a way that the phenyl-2

Table 2. Correlated bond lengths (Å) and angles (deg) in BPTB and PTB.[a]

Atoms	BPTB	Atoms	PTB
N(2)—C(3)	1.336(6)	N(1)—C(2)	1.322(6)
C(3)—C(4)	1.378(7)	C(2)—C(3)	1.411(7)
C(4)—C(5)	1.377(7)	C(3)—C(4)	1.358(8)
C(5)—C(6)	1.388(7)	C(4)—C(13)	1.406(7)
	—	C(13)—C(5)	1.440(7)
	—	C(5)—C(6)	1.346(8)
	—	C(6)—C(14)	1.435(8)
C(6′)—C(5′)	1.378(7)	C(14)—C(7)	1.407(8)
C(5′)—C(4′)	1.392(7)	C(7)—C(8)	1.374(8)
C(4′)—C(3′)	1.375(7)	C(8)—C(9)	1.384(8)
C(3′)—N(2′)	1.346(6)	C(9)—N(10)	1.342(6)
N(2′)—C(1′)	1.358(5)	N(10)—C(11)	1.367(6)
C(1′)—C(1)	1.487(6)	C(11)—C(12)	1.435(7)
C(1)—N(2)	1.349(5)	C(12)—N(1)	1.357(6)
C(1)—C(6)	1.388(6)	C(12)—C(13)	1.412(6)
C(1′)—C(6′)	1.380(6)	C(11)—C(14)	1.413(6)
N(2) ... N(2′)	2.610(5)	N(1) ... N(10)	2.709(6)
C(6) ... C(6′)	3.078(7)	C(13) ... C(14)	2.861(9)
C(1)-N(2)-C(3)	117.7(4)	C(12)-N(1)-C(2)	116.8(4)
N(2)-C(3)-C(4)	122.7(5)	N(1)-C(2)-C(3)	123.2(5)
C(3)-C(4)-C(5)	119.6(5)	C(2)-C(3)-C(4)	119.6(5)
C(4)-C(5)-C(6)	118.9(5)	C(3)-C(4)-C(13)	119.7(5)
C(5)-C(6)-C(1)	118.1(4)	C(4)-C(13)-C(12)	116.4(5)
C(6)-C(1)-N(2)	123.1(4)	C(13)-C(12)-N(1)	124.3(5)
	—	C(4)-C(13)-C(5)	125.3(6)
	—	C(13)-C(5)-C(6)	122.2(6)
	—	C(5)-C(6)-C(14)	121.4(5)
	—	C(6)-C(14)-C(11)	117.4(6)
C(6′)-C(1′)-C(1)	126.8(4)	C(14)-C(11)-C(12)	121.7(5)
C(1′)-C(1)-C(6)	123.3(4)	C(11)-C(12)-C(13)	118.9(5)
	—	C(12)-C(13)-C(5)	118.3(6)
N(2)-C(1)-C(1′)	113.6(4)	N(1)-C(12)-C(11)	116.7(5)
C(1)-C(1′)-N(2′)	115.4(4)	C(12)-C(11)-N(10)	118.9(4)
C(1′)-N(2′)-C(3′)	124.4(4)	C(11)-N(10)-C(9)	123.1(5)
N(2′)-C(3′)-C(4′)	118.5(5)	N(10)-C(9)-C(8)	119.4(5)
C(3′)-C(4′)-C(5′)	118.9(5)	C(9)-C(8)-C(7)	119.6(6)
C(4′)-C(5′)-C(6′)	120.9(4)	C(8)-C(7)-C(14)	121.5(6)
C(5′)-C(6′)-C(1′)	119.5(4)	C(7)-C(14)-C(11)	117.0(5)
C(6′)-C(1′)-N(2′)	117.7(4)	C(14)-C(11)-N(10)	119.3(5)
	—	C(7)-C(14)-C(6)	125.6(6)

[a]Not corrected for thermal motion. Estimated RBM model corrections did not exceed +0.01 Å and 0.3° (cf. Experimental).

[6] This material can be purchased from: The Depository of Unpublished Data, Document Delivery, CISTI, National Research Council Canada, Ottawa, Canada K1A 0S2. Tables A, B, D, and G–K have also been deposited with the Cambridge Crystallographic Data Centre and can be obtained on request from The Director, CCDC, University Chemical Laboratory, 12 Union Road, Cambridge CB2 1EZ, U.K.

Fig. 3. Projections of portions of the PTB structure on (010) (*left*) and (100) (*right*).

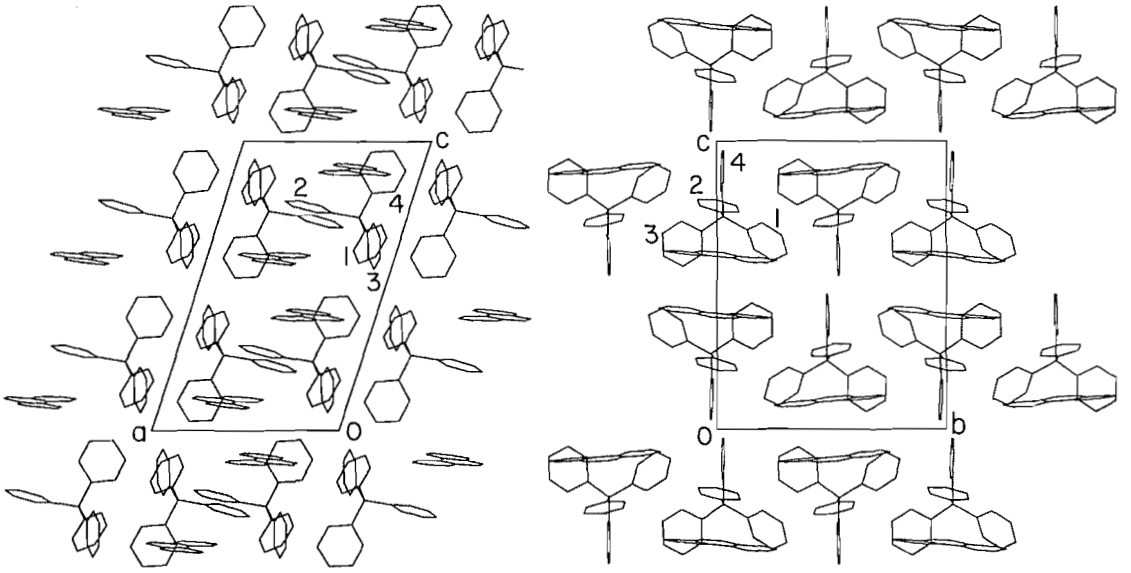

Fig. 4. π–π stacking in PTB. (*A*) Projection of the four-stack perpendicular to its pair of cation planes to display ring overlap. (*B*) Projection of the four-stack parallel to its cation planes to display spacing between ring planes. The features drawn in broken lines are related by inversion to those in solid lines. H(N10) atoms are indicated by black dots. Anion ring numbering as in Table A.

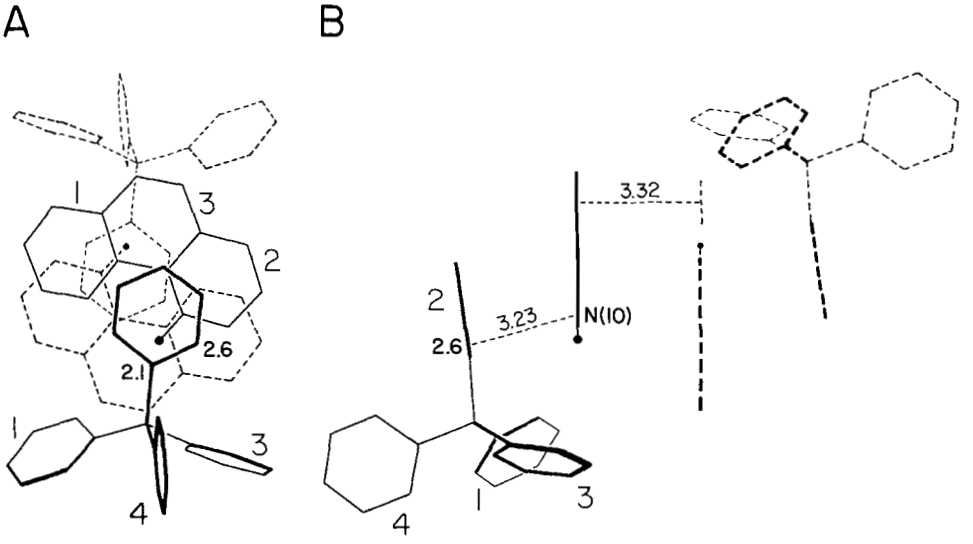

rings of the two anions are roughly parallel to the cation planes; the angle between the phenyl-2 and the cation planes is 9.8°. These four-stacks are clearly identifiable in Fig. 3 (*right*). Viewed perpendicular to the cation planes (Fig. 4*A*), adjacent phenyl-2 and phenH^+ rings are seen to overlap, as are the rings of the cation pairs. The perpendicular spacing between the cation ring planes is 3.32 Å (Fig. 4*B*). The shortest distances, in the region of overlap, between the carbons of phenyl-2- and the skeleton atoms of cation ring 2 are shown in Fig. 5. The perpendicular distances of N(10), C(11), and C(12) from the phenyl-2 plane are 3.15, 3.38, and 3.33 Å, respectively, i.e., ~3.3 Å on the average. As another interesting feature of the structure, the cation planes are nearly perpendicular (85°) to phenyl-4 rings in adjacent four-stacks, at ring-centre separations π_c(cat 1)...π_c(phenyl-4) and π_c(cat 2)...π_c(phenyl 4′) of 5.35 and 5.32 Å, respectively, and at the shortest C(cat)...C(an) distances illustrated in Fig. 5. These T-shaped edge-to-face orientations of cat–an pairs are thought to contribute to lowering of the crystal energy (cf. ref. 11 and below).

The arrangement of phenyl and cation rings in the four-stacks is indeed reminiscent of the π–π stacking in the red (deep yellow in acetone solution) PQTB, in which the centrosymmetric planar cation is sandwiched between two phenyl rings, one from each anion, at ψ(phenyl/cat) = 10°, and which also contains edge-to-face ring contacts (11). The PQTB structure is compared to PTB in more detail further on.

The H(N) atoms in BPTB and PTB were clearly visible in the respective difference maps (Fig. 6), at 1.10 Å from N(2′) in BPTB and 1.11 Å from N(10) in PTB. The protonation is associated with an increase in the CNC angle, in consequence of the strong σ-electron-withdrawing effect of the proton (1), and in

Fig. 5. π(cat)–π(an) stacking and edge-to-face inter-ion relations in PTB. (*Bottom*) Projection of two cat–an pairs in neighbouring four-stacks approximately on (100). A 2_1 axis relating the two pairs is roughly horizontal in the page. Only the relevant phenyl-2 and phenyl-4 rings are shown. Filled circles, B atoms; circles with dots, N atoms. Hydrogen atoms are not shown. (*Top*) Corresponding space-filling representation, slightly rotated for better visibility and with the H atoms included. Cations are drawn in heavier lines. Shortest cat–an distances in Å (broken lines): N(10)...C(2.5), 3.43; N(10)...C(2.6), 3.23; C(11)...C(2.4), 3.44; C(3)...C(4.5), 3.97; C(3)...C(4.6), 3.85; C(7)...C(4.6), 3.67; C(8)...C(4.6), 3.60.

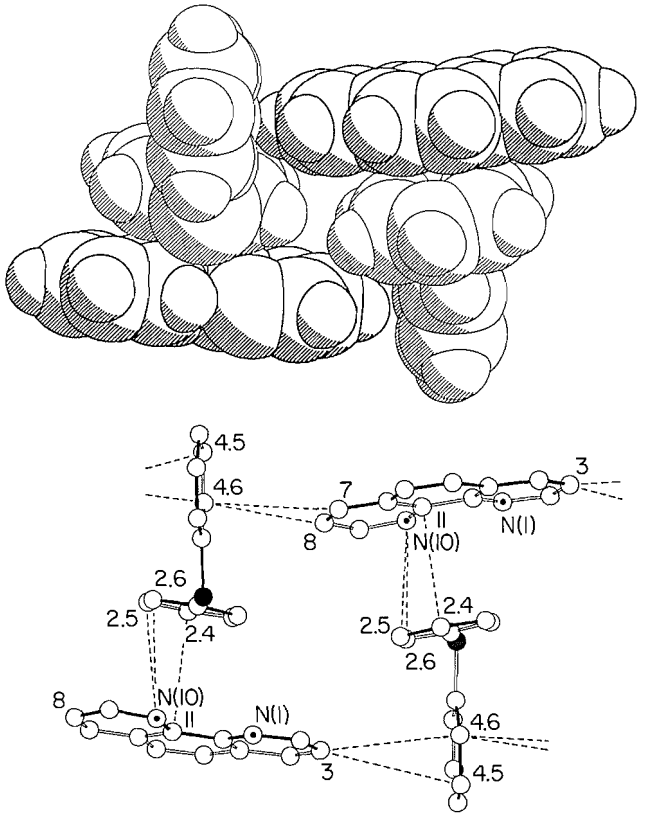

complete agreement with the analogous angle expansion in other BP^+ and $phenH^+$ salts (Tables 3 and G–K). The CNC angle at the protonated N atom, ~124°, can be compared with the 123.0° angle in the fully protonated BP^{2+}, and that at the unprotonated N with the 117.7° angle in 1,10-phenanthroline (= $phen^0$) (10, 19, 28; Table F). The H(N10)...N(1) distances and N(10)-H(N10)-N(1) angles in PTB are similar to those in the $phenH^+$ salts of the oxyacids (Table 3), in all of which there is a well-defined, strongly bent H-bond to an anion acceptor.[7]

The anion geometry in BPTB and PTB (Tables D and E) closely approximates the mean tetraphenylborate geometry described in ref. 3, except that in BPTB the symmetry of the $BC(\alpha)_4$ tetrahedron, though low, is recognizably related to S_4, whereas that of the distorted tetrahedral $BC(\alpha)_4$ core in PTB is not.

[7] Recently (21) a similar situation has been reported in the structure of **14** where the N-H-N angle corresponding to N(10)-H(10)-N(1) is only 97° and the H(N)...N distance is 2.56 Å (Table 3); cf. also ref. 23 and **ak** in Table 4).

Fig. 6. Difference Fourier maps revealing the positions of the H(N) atoms in the N(2)-C(1)-C(1′) cation plane of BPTB and the N(1)-N(10)-C(5) cation plane of PTB. Contour interval, 0.05 e/Å^3.

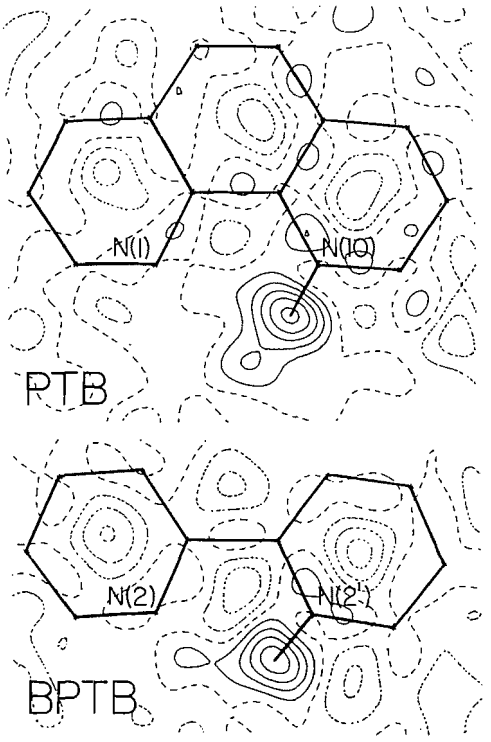

Cation geometry in BPTB and PTB

Among the correlated interatomic distances and bond angles in Table 2 the only ones that differ by more than 3σ are those affected by the relationship of ring 1 to ring 1′ in BP^+ and of ring 1 to ring 2 in $phenH^+$, viz. the bond pairs C(1)—C(1′)|C(11)—C(12), N(2)...N(2′)|N(1)...N(10), and C(6)—C(6′)|C(13)—C(14), and the bond-angle pairs C(1)-C(1′)-C(6′)|C(12)-C(11)-C(14), C(1′)-C(1)-C(6)|C(11)-C(12)-C(13), and C(1′)-C(1)-N(2)|C(11)-C(12)-N(1) (in BP^+ the angles involved are all exocyclic). The 3σ intervals in all the other bond-length and bond-angle pairs overlap. This indicates that the main difference between BP^+ and $phenH^+$ is in the extent of the in-plane inclination of the essentially rigid C_5N rings to the central C—C bond. This in-plane bending is almost certainly a consequence of the formation of an intra-cation N—H...N′ bond, the latter of course being the reason for the existence of the *cis* conformation to begin with: no *trans*-BP^+ cation has been reported to date. In BP^+ the bending takes place in such a way that the N atoms come closer together, while at the same time the C(6)...C(6′) separation increases, with attendant changes in the exocyclic C-C-C angles at C(1) and C(1′) but not in the endocyclic angles. In $phenH^+$ the bending is restrained by the presence of ring 3: the normalized ratio of the separation (N(1)...N(10)):(C(11)—C(12)):(C(13)...C(14)) is 1.89(1):1:1.99(2) compared to the corresponding ratio (N(2)...N(2′)):(C(1)—C(1′)):(C(6)...C(6′)) of 1.76(1):1:2.07(1) in BP^+.

Interestingly, a paired *t* statistic (t_p) for matching pairs of bond lengths in the C_5N rings of BPTB and PTB shows (two-tailed *t* test at the 0.01 and 0.05 significance levels) that the bond lengths in the two cations come from the same population: $t_p = -1.62$, $t_{11,0.01} = 3.11$, $t_{11,0.05} = 2.20$. A corresponding test shows this even more strongly for the matching endocy-

Table 3. Interatomic distances (Å) and bond angles in crystals containing N-H...(N*, X) bonds.[a]

Compound (ref.)	ψ[b]	Intra-ion bond[c]		Inter-ion bond[c]		
		H...N*	N-H-N*	N...X	H...X	N-H-X
1 (phenH)NO_3[d] (13)		2.36	102°	2.833	1.91	158°
2 (phenH)HSO_4 (14)		2.39	103°	2.714	1.92	153°
3 (phenH)ClO_4 (15)		2.40	104°	2.934	2.25	138°
4 (phenH)Cl[e] (16)		2.41	101°	2.74	1.91	147°
(phenH)BPh_4 = PTB		2.33	98°	[f]	[f]	[f]
BPTB[g]	5.2°	2.11	105°	3.278	2.55	123°
				3.312	2.37	142°
$[(BP^+)_3(NO_3^-)]$[h] (17):						
5 cation A	4.3°	2.26	105°	2.84	1.94	158°
6 cation B	6.6°	2.26	104°	2.78	1.88	158°
7 cation C	7.8°	2.27	104°	2.81	1.90	160°
8 BP^+[i] (18)	18.4°	2.27	105°	3.145	2.27	156°
$(BP^+)_2[B_{10}H_{10}^{2-}]$ (19):				[j]	[j]	[j]
9 cation 1	1.3°	2.09	114°			
10 cation 2	16.4°	2.15	109°			
11 $(BP^+)_2[ReCl_6^{2-}]$[k] (20)	19.0°	2.33	99°	3.310	2.52	147°
12 $(BP^+)I_7^-$[l]	1.5°					
13 $(BP^+)ClO_4$ (51)	16.6°			2.97		
14 [A] monopicrate[m] (21)		2.56	97°		1.82	155°

[a]Typical uncertainty in H...N* and H...X, 0.03 Å; in the angles, 3°.
[b]Angle between the two ring skeleton planes in BP^+.
[c]In $phenH^+$, N = N(10), H = H(N10), N* = N(1), X = O.
[d](phenH) $(NO)_3 \cdot HNO_3$.
[e](phenH)Cl·H_2O, X = O. The ir spectrum in ref. 22 is reported as that of the hemihydrate.
[f]See text.
[g]In BP^+, N = N(2′), H = H(N2′), N* = N(2); N...X and H...X, shortest N(2′)...C(phenyl-2) and H(N2′)...C(phenyl-2) distances; first line, X = C(2.5A); second line, X = C(2.6A) (Table D).
[h]In $[(BP^+)_3(NO_3^-)][Th(NO_3)_6]$.
[i]In $(BP^+)[Fe(BP)_3](ClO_4)_4$, X = O.
[j]Distances to H atoms of the anion.
[k]X = Cl.
[l]S.V. Sereda and O. Knop, to be published.
[m]A = *cis*-1-(*N*-Me_2N)-2-(*N*-Me_2NH)cyclopentane (1+).

clic angles: $t_p = 0.02$ for the same number of degrees of freedom. There is thus no fundamental difference in the geometric properties of the respective C_5N rings in BPTB and PTB. A similar comparison for pairs of bond lengths (but not angles) in the left-hand and the right-hand halves of each cation leads to the conclusion that in this respect rings 1 and 1′ in BP^+ are statistically equivalent, as are rings 1 and 2 in $phenH^+$.

Cation geometry: statistical treatment

It may be validly argued that the conclusions for BPTB and PTB alone are of limited significance. We have therefore compiled the geometric parameters of BP^+ and $phenH^+$ in a number of structures of acceptable quality (Tables 3, G, and H): eight sets for BP^+ (BPTB, **5–11**), four sets for $phenH^+$ (PTB, **1–3**);[8] both are of a reasonable size for statistical scrutiny. The results of the statistical comparisons are as follows.

(a) Bond lengths and angles in BP^+ compared to those in $phenH^+$ (Fig. 7)

The central C—C bond is significantly longer in BP^+ than in $phenH^+$, 1.476[9] as against 1.431[3] Å, and the angles flanking this bond (exocyclic in BP^+) are significantly different in the two cations. The C(5)-C(6)-C(1)|C(4)-C(13)-C(12) and C(5′)-C(6′)-C(1′)|C(7)-C(14)-C(6) angles (endocyclic in BP^+) also are significantly affected by the in-plane bending, as is the endocyclic N(2′)-C(1′)-C(6′) angle. The angles in the right half of the cation are affected more than those in the left, unprotonated half.

(b) Right half vs. left half (Figs. 7A, C)

The matching bond lengths in the two halves of $phenH^+$ are statistically equivalent at both the 0.01 and 0.05 significance levels; in BP^+ the lengths in the C(1)—N(2)|C(1′)—N(2′) and C(4)—C(5)|C(4′)—C(5′) bond pairs are weakly differentiated. Protonation thus introduces little left/right asymmetry

[8] The mean (uncorrected) bond lengths and angles in these two sets as well as in $phen^0$ (24), $(phen_2H^+)ClO_4^-$ (25), and $(phenH_2^{2+})(ClO_4)_2 \cdot H_2O$ (26) are listed in Table F. The bond lengths and angles in BPTB and PTB at −20°C and room temperature differ only within their stated esd's (results not presented here). The cation geometries in **4** and **12** are not sufficiently accurate to be combined with the others.

Fig. 7. Statistical comparison of matching experimental bond lengths and angles in the *cis*-BP^+ and $phenH^+$ systems. (*A*) Left half of the BP^+ cation compared to the right half. (*B*) BP^+ compared to $phenH^+$. (*C*) Left half of the $phenH^+$ cation compared to the right half. Orientations as in Fig. 1. Thin lines and unfilled angles: sample means of the matched pairs *not* different at the 0.01 (1%) or 0.05 (5%) significance levels. Heavy lines and filled angles: sample means different at the 0.01 or 0.05 significance levels.

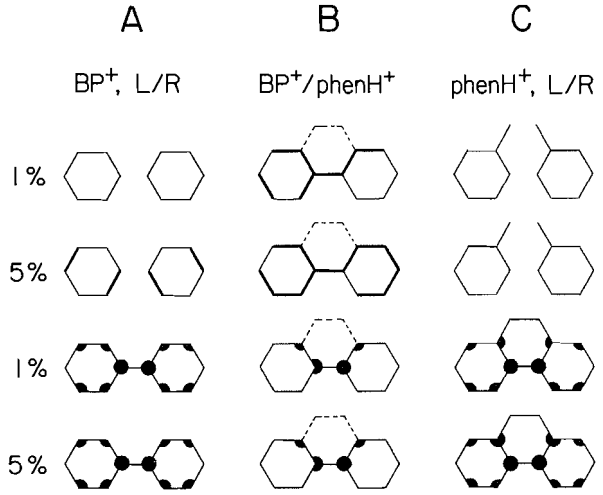

Fig. 8. Effect of protonation on experimental bond lengths and angles in the phen system (cf. caption of Fig. 7). (*A*) $phen^0$ compared with $phenH^+$. (*B*) $phenH^+$ compared with $phenH_2^{2+}$. (*C*) $phen^0$ compared with $phenH_2^{2+}$. Dotted lines: sample means of N(1)...N(10) distances, and of C(13)...C(14) distances, different at the 0.01 or 0.05 significance levels (large dots), or not different (small dots).

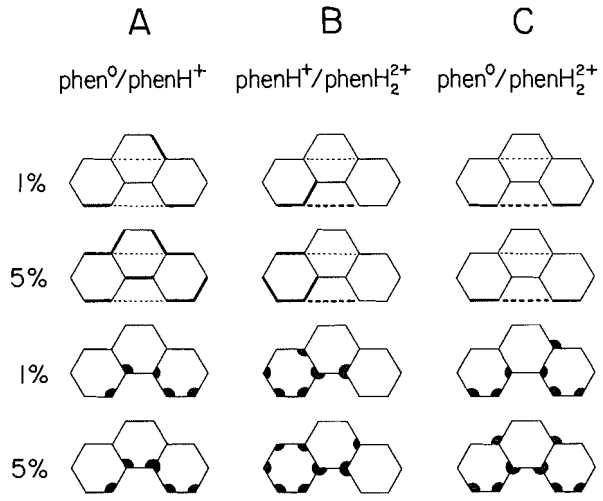

into the bond lengths of the BP^+ and $phenH^+$ ring systems (C(1)—C(1′), C(5)...C(6), and C(11)—C(12) are not testable). However, with the exception of C(3)-C(4)-C(5)IC(3′)-C(4′)-C(5′), *all* the *angles* in the two halves of BP^+ are statistically nonequivalent. A similar situation exists in $phenH^+$ (the peripheral angles in ring 3 are affected only weakly by protonation). The compensation for the increase in the endocyclic *ipso* angle on protonation is thus much more pervasive than for any change in the bond lengths.

Fig. 9. Effect of protonation on the geometry of the BP system (cf. caption of Fig. 7). (*A*) *trans*-BP^0 compared with *trans*-BP^{2+}. (*B*) Protonated ring 1′ of *cis*-BP^+ compared with one half of the *trans*-BP^{2+} cation.

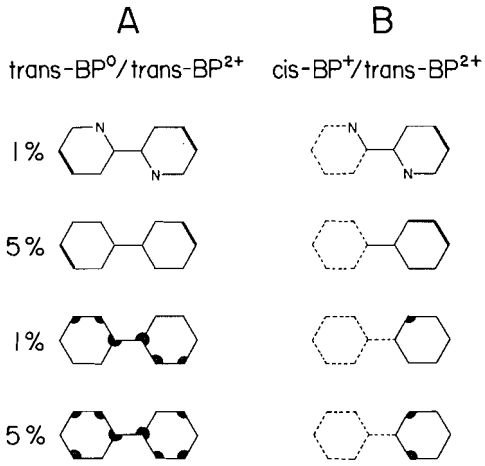

(c) Effect of successive protonation on the geometry of the phen and BP systems (Figs. 8A–C, Table F)

The changes for phen are most simply described by comparing the [N(1)...N(10)]:[C(11)—C(12)]:[C(13)...C(14)] ratios normalized to C(11)—C(12): $phen^0$, 1.87(1):1:1.95(2); $phenH^+$, 1.90(1):1:1.99(2); $phenH_2^{2+}$, 2.02(1):1:1.98(1). On second protonation the repulsion between the two N-hydrogens considerably lengthens the N(1)...N(10) distance, by ~8% from 2.722[9] to 2.873[4] Å, and that in spite of the increased positive charge on the ion and the engagement of the two H(N) atoms in inter-ion H-bonds to the same anion oxygen (26).

Although protonation of BP^+ converts the cation conformation from *cisoid* to *transoid*,[9] one can still trace its effect on the ring geometry by comparing the lengths and angles in the protonated ring 1′ with those in the BP^{2+} rings (Fig. 9*B*). From the Cl^- (28), SO_3F^- (10), and $B_{10}H_{10}^{2-}$ (19) salts, for which the cation geometry is adequately defined (Table J), one finds that the effect of the protonation on the ring bond lengths and endocyclic angles in BP^+ is quite limited and that the lengths of the central C—C bond in BP^+ and BP^{2+} are statistically equivalent ($t_9 = 1.03$, $t_{9,0.01} = 3.25$, $t_{9,0.05} = 2.26$).

(d) The effect of ψ on BP geometry

The effect of the loss of aromatic character attendant on loss of cation planarity is difficult to establish. On the one hand, the central C—C bond would be expected to lengthen; on the other hand, the effect of *ortho* repulsions will be reduced. From the present data there is no evidence of it in *cis*-BP^+, where the reported ψ_{cis} angles range from 1.3° to 19.0° (Table G), nor is there any indication of a ψ-dependent trend in *trans*-

[9] The range of ψ (in a planar *trans* conformation, $\psi_{trans} = 0°$) in the BP^{2+} cation is considerable: $(BP^{2+})Cl_2$ (28), 18.9°; $(BP^{2+})Br_2$ (29), 21.2°; $(BP^{2+})(SO_3F)_2$ (10), 31.5°; $(BP^{2+})(SeOCl_4)$ (52), 35.1° and 35.9°; $(BP^{2+})(B_{10}H_{10})$ (19), 44.4°; $(BP^{2+})I_6$ (30), 48.9°. No BP^{2+} planar by symmetry appears to have been reported to date. The distortion of these *transoid* BP^{2+} cations from planarity has been attributed (10) to the presence of N—H(N)...X bonds, X = O, Cl, etc., but see the next section.

BP^{2+}, as shown by analysis of variance for the available three sets of bond length and angles ($18.9° \leq \psi_{trans} \leq 44.4°$, Table J). This is consistent with a similar finding for the two forms of 4,4′-bipyridinium(2+) nitrate (31, 32), in one of which ψ_{trans} = 0° and in the other, ψ_{trans} = 39.0°; the mean length of the central C—C bond is 1.484[4] Å (Table K).

(e) Length of the central C—C bond

This length is in fact codetermined by a number of factors, the separate effects of which may be difficult or impossible to evaluate from experiment. Examination of the means for this bond length (uncorrected, in Å; Table F), with the PQ systems included,[10]

$phen^0$	1.454[6]	$phenH^+$	1.431[3]	$phenH_2^{2+}$	1.421[7]
BP^0	1.490[3]	BP^+	1.476[9]	BP^{2+}	1.469[9]
PQ^0	1.367[4]	$phen_2H^+$	1.434[7]	4,4-BP^{2+}	1.484[4]
		$PQ^{\cdot+}$	1.422[22]	PQ^{2+}	1.477[21][11]

shows that unless obvious chemistry is at work (loss of ring aromaticity in PQ^0 and formation of a C=C bond, cf. ref. 36), statistically supportable conclusions about differences in this bond length in the above biphenyl-like systems cannot be made on the crystallographic evidence available at present. The overall mean of these means is 1.456[25] Å.

Cation geometry: calculation vs. crystallography

No ab initio calculations on the uncomplexed phen systems appear to be available, but a number of semiempirical and ab initio (STO-3G) calculations on the uncomplexed bipyridines and their cations have been reported (37–47). The main conclusions are as follows:

1. The energy minimum found in a semiempirical calculation for BP^+ (37, 38, 48) was at ψ_{cis} = 0°, with an indication of a small H(N2′)...N(2) interaction.
2. The ground-state conformation of BP^{2+} is *transoid*, ψ_{trans} = 41.9°, with a higher-energy *cisoid* conformation, ψ_{cis} = 54.3° (41, 43).
3. The ground-state conformation of BP^0 is planar *trans*, with a subsidiary energy minimum at $\psi_{cis} \sim 50°$ (38–40, 44–49). The C(1)—C(1′) bond length varies between only 1.512 and 1.518 Å from planar *trans* to planar *cis* and at equilibrium is close to the uncorrected experimental value of 1.490(3) Å (27).
4. The ground-state conformation of $phen^0$ is not C_{2v} but C_2; the barrier for interconversion is only 4.7 kcal/mol (47, 49). The CNDO/2 calculation for $phenH^+$ (50) points to a situation similar to that found for BP^+ (37).

These limited results (*i*) confirm that the effect of ψ on the C(1)—C(1′) bond length in BP^+ can be expected to be small and that on the ring bond lengths even smaller and thus likely to be masked by fortuitous effects in a crystal. (*ii*) The conversion of *trans*-BP^0 to *cis*-BP^+ on protonation is coincident with the formation of an intra-cation N(2′)—H(N2′)...N(2) bond, as observed (cf. below). (*iii*) The optimized ψ_{trans} of free BP^{2+} being ~42°, the observed substantial deviations of the cation from *trans* planarity (ψ_{trans} = 19–49°, Table J) cannot be claimed (10) as arising from inter-ion H-bonding interactions with the anion, though the latter probably are at least in part responsible for the observed departures of ψ_{trans} from the optimized value.

[10] The cation bond lengths and angles in $(PQ^{2+})Cl_2$ (33), $(PQ^{2+})Cl_2 \cdot 2H_2O$ (34), $(PQ^{2+})Br_2$ (33), $(PQ^{2+})I_2$ (33), $(PQ^{2+})[CuCl_4]$ (35), and $(PQ^{2+})(BPh_4)_2$ (11) are compared in Table K. This table also contains relevant details for PQ^0 and $(PQ^{\cdot+})PF_6$ (36).

[11] 1.468[9] Å if the 1.521[7] Å value for $(PQ^{2+})(BPh_4)_2$ (11) is not included.

Fig. 10. Cation geometry and hydrogen bonding in BPTB. Projection on cation planes; distances in Å. Putative H-bonds are indicated by broken lines. Filled circle, H(N2′). Ring carbons are identified by appropriate numbers (Table A).

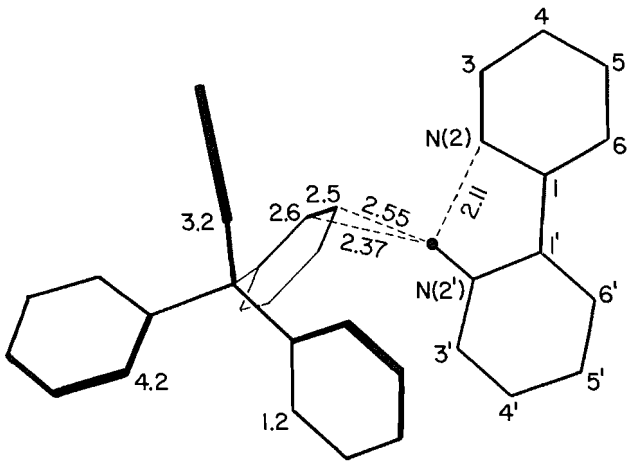

Hydrogen bonding: geometry

In BPTB only three interatomic distances qualify for possible H(N2′)...acc bonds: H(N2′)...N(2) = 2.11 Å, H(N2′)...C(2.6) = 2.37 Å, and H(N2′)...C(2.5) = 2.55 Å (Fig. 10). All the other H(N2′)...C(an) distances are at least 3.27 Å (Table D) and thus unlikely to give rise to effective H-bonding interactions (3). Although the N(2′)-H(N2′)-N(2) angle of 105° looks unfavourable even for a branched H-bond, the intra-cation H(N2′)...N(2) interaction must be significant: not only has the cation been forced into a *cis* conformation, but the N(2′)...N(2) separation, 2.610(5) Å, is 4% shorter than the corresponding mean N(1)...N(10) distance in $phenH^+$, 2.722[9] Å, and the C(6)...C(6′) separation, 3.078(8) Å, is 8% longer than the corresponding mean C(13)...C(14) distance in $phenH^+$, 2.846[24] Å (Table F). The H(N2′)...N(2) interaction must thus be strong enough to bend the *cis*-BP^+ ion in its plane and thus reduce the N(2′)...N(2) distance.

The N(2′)-H(N2′)-C(2.6) and N(2′)-H(N2′)-C(2.5) angles are 142° and 123°, respectively (Table 3). The distances of H(N2′) and N(2′) from the centre $\pi_c(2)$ of phenyl-2 of the nearest anion, 3.07 and 3.71 Å, respectively, and the corresponding mean distances $\bar{d}$[H(N2′)...C] and $\bar{d}$[N(2′)...C], 3.31[67] and 3.93[51] Å, respectively, are entirely consistent with the statistics of the branched H(N)...phenyl bonds in tetraphenylborates (Fig. 12 of ref. 3). Similarly, points for the differences Δ[H(N2′)...C] = $[H(N2')...C]_{max} - [H(N2')...C]_{min}$ and Δ[N(2′)...C] = $[N(2')...C]_{max} - [N(2')...C]_{min}$ for the C atoms of phenyl-2 fall within the distributions in Fig. 13 of ref. 3, where the Δ for a large number of N—H(N)...phenyl bonds are plotted against d[H(N)...π_c] and d[N...π_c], respectively, even though the Δ[H(N2′)...C] point is at the margin of the reference population. The N(2′)—H(N2′)...acc bond in Fig. 10 may thus be regarded as bifurcated, with an intra-cation com-

Fig. 11. Potential H-bonding acceptors X in PTB.
(*A*) N(10)—H(N10) bond and the cation plane are in the page.
(*B*) N(10)—H(N10) bond and the cation plane are perpendicular to the page, with H(N10) on top of N(10). Black dot, H(N10); 1.2 stands for C(1.2) in phenyl-1, etc. H(N10)...X distances are indicated by broken lines; NHX = N(10)-H(N10)-X. The fourth phenyl ring of the anion has been omitted.

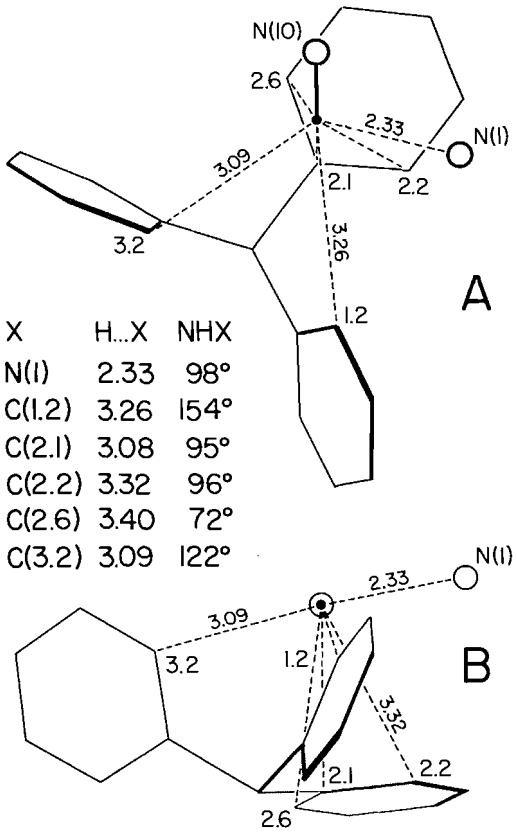

ponent engaging the lone pair on N(2) and an inter-ion component pointing at phenyl-2 of the nearest anion at an angle of 93° between N(2′)—H(N2′) and the ring plane.

Support for this interpretation comes from the existence of similar bifurcated N(2′)—H(N2′)...acc bonds in other BP^+ cations (Table 3). For example, in **11** H(N2′)...Cl(1A) = 2.52(3) Å, N(2′)...Cl(1A) = 3.310 Å, and N(2′)-H(N2′)-Cl(1A) = 147°.[12] This clearly corresponds to an N—H(N)...Cl branch of a bifurcated N—H(N)...Cl, X bond, with characteristics very similar to those observed for the stronger component of the bifurcated N—H(N)...2Cl bond in, for example, $(Et_3NH)_2SnCl_6$ (53) and $(Et_2NH_2)_2\ SnCl_6$ (54).

We now turn to PTB, in which the potential H-bond acceptor environment is represented in Fig. 11. The shortest interatomic H(N10)...acc approach is H(N10)...N(1) = 2.33 Å, N(10)-H(N10)-N(1) = 98°. This situation looks even less favourable for an effective H-bonding interaction than that in BPTB. Furthermore, because the N(1)...N(10) distances in $phen^0$ and $phenH^+$ are statistically indistinguishable, and ditto for C(13)...C(14) (cf. above and Tables 2 and F), it cannot be argued that the $phenH^+$ ion in PTB is significantly distorted by in-plane bending as a result of an H(N10)...N(1) interaction, in contrast to the *cis*-BP^+ cation.

[12] [*x*, *y*, *z*] of Cl(1A) = [−*x*, −*y*, −*z*] of Cl(1) in ref. 20.

The shortest H(N10)...C(an) distances in reasonable directions are H(N10)...C(3.2) = 3.09 Å (N(10)-H(N10)-C(3.2) = 122°) and H(N10)...C(1.2) = 3.26 Å (N(10)-H(N10)-C(1.2) = 154°), the corresponding H(N10)—C vectors being more or less in the extended cation plane (Fig. 11). These distances are substantially longer than similar distances in BPTB. While for phenyl-3 the N(10)...π_c(3) = 4.35 Å, H(N10)...π_c(3) = 3.94 Å, $\bar{d}$[N(10)...C] = 4.54 Å, $\bar{d}$[H(N10)...C] = 4.12 Å, Δ[N(10)...C] = 1.44 Å, and Δ[H(N10)...C] = 1.95 Å distances, though long, still fall within the respective plots for the bifurcated N—H(N)...π bonds of ref. 3, the corresponding distances for phenyl-1 are all well outside the populations of these plots.[13] It is therefore reasonable to view the geometry at H(N10) as corresponding to a very weak bifurcated N(10)—H(N10)...N(1),phenyl-3 bond with the H(N10)...N(1) branch as the stronger component. However, if the H(N10)...C(3.2) distance of 3.09 Å is admitted as a component of a bifurcated H-bond at an N(10)-H(N10)-C(3.2) angle of 122°, then the H(N10)...C(2.1) and H(N10)...C(2.2) distances of 3.08 and 3.32 Å, respectively, cannot be ignored, even though the corresponding N-H(N)-C angles are only ~95°, i.e., with the N(10)—H(N10) bond close to parallel to the phenyl-2 plane (Figs. 4*B* and 11*B*). So little is known about such H-bonding interactions that judgment must be reserved, for the present, as to the significance and importance of the participation of phenyl-2 in the H-bonding, but if the latter *is* claimed to be involved, then H(N10) will be described as bonded to N(1), phenyl-3, and phenyl-2, i.e., forming a branched H-bond of a type not provided for in the classification of ref. 3.

Hydrogen bonding: infrared spectra

As a supplement to crystallography we examined FT-ir spectra of fluorocarbon mulls of BPTB and PTB in the 3700–2700 cm^{-1} region between 10 and 295 K. In the 10 K spectrum of PTB a single sharp, unsplit ν(NH) peak was observed at 3278.7 cm^{-1}, well resolved from the ν(CH) absorptions, and of a height comparable to that of the strongest ν(CH) peak (Fig. 12). With increasing temperature this peak shifted progressively and smoothly to slightly lower frequencies (Fig. 13). The frequency lowering between 10 and 295 K amounted to 6.5 cm^{-1} (8.2 cm^{-1} when ν(NH) is referred to the strongest ν(CH) absorption, the frequency of which increased somewhat with temperature). There was no indication of a thermally induced phase transition in this spectral region.

The ν(NH) absorption in the 10 K spectrum of BPTB (Fig. 12) consisted of a prominent peak at 3147.2 cm^{-1}, of approximately twice the height of the strongest ν(CH) absorption. The peak showed incipient splitting, and there was no clean separation between it and the ν(CH) absorptions. In addition, it was flanked on the high-frequency side by small, well-resolved satellite peaks at 3199.3, 3183.2, and 3170.3 cm^{-1}, and on the low-frequency side by a subsidiary peak at 3125.1 cm^{-1}. The main peak and the subsidiary peak were replicated, on weak deuteration, at 2358.0 and 2344 cm^{-1}, respectively, confirming the correctness of the ν(NH) assignment (ν(NH)/

[13] The distance H(N10)...C(1.2) = 3.26 Å would correspond to an edge-on H-bond, i.e., almost an H(N10)...H(1.2) bond, unlikely to qualify for a π interaction, cf. Fig. 10 of ref. 3.

Fig. 12. The ν(NH) and ν(CH) region of the FT-ir spectra of BPTB and PTB in fluorocarbon mulls at 10 K. The principal ν(NH) stretching absorptions are indicated by blacks dots (see text).

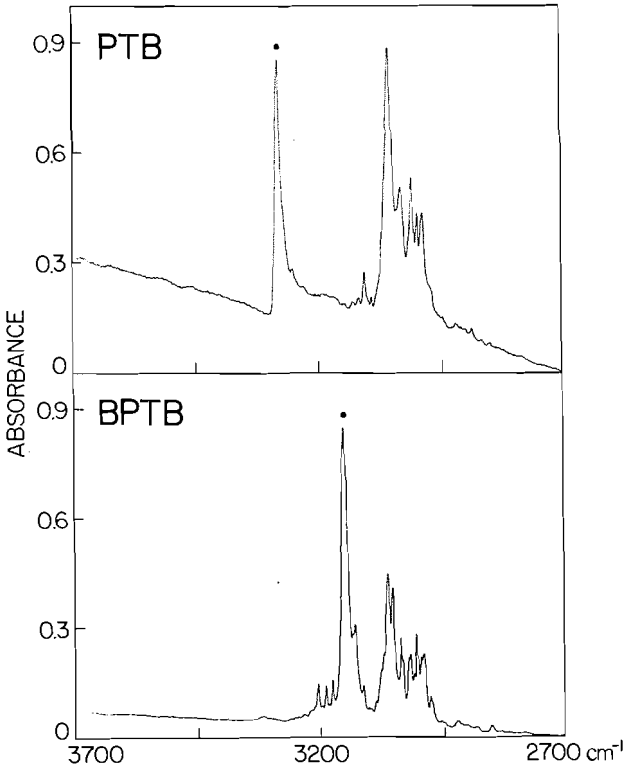

Fig. 13. Variation of the ν(NH) stretching frequency in BPTB and PTB with temperature. The quadratic regression of ν(NH) on T is represented by the solid line. Open circles: ν(NH) lowering referred to the frequency of the highest ν(CH) peak (see text). The broken line is to guide the eye only.

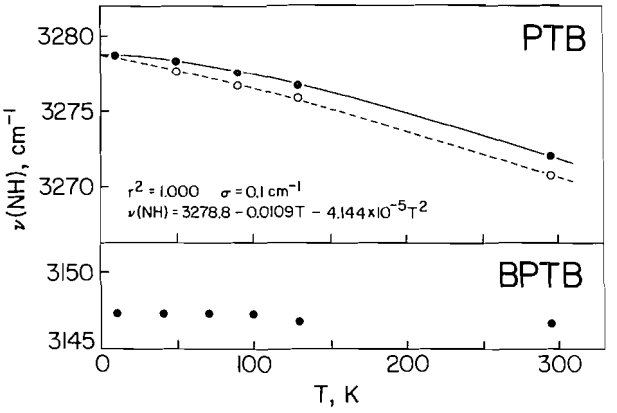

ν(ND) = 1.333). It was not possible to say with certainty whether or not the satellites were present also in the ν(ND) region; their origin and the origin of the splitting of the main peak were not investigated further.[14] The frequency of the ν(NH) absorption remained practically unchanged with temperature (Fig. 13).

The high frequency of the ν(NH) peak in the PTB spectrum is indicative of very weak H-bonding,[15] while the negative $d\nu/dT$ coefficient is consistent with the strengthening of a branched or highly bent N—H...acc bond with increasing temperature (58). To understand the nature of the H-bonding in PTB let us consider the following. The room-temperature ν(NH) frequencies reported in ref. 22 are in the range 3300–3100 cm^{-1} for the anhydrous ClO_4, BF_4, and I salts of $phenH^+$, but between 2950 and 2600 cm^{-1} for the hydrated Cl and Br salts, as confirmed by deuteration and having assigned the ν(OH) absorptions between 3430 and 3250 cm^{-1}. The crystal structure of $(phenH^+)ClO_4$ contains an H(N10)...$OClO_3$ = 2.25 Å bond; the H(N10)...OH_2 distance in the hydrated chloride is 1.91 Å, as are the H(N10)...O(an) distances in the anhydrous NO_3 and HSO_4 salts (Table 3). It thus seems that in those $phenH^+$ salts in which H(N10) is bonded to the oxygen of a water molecule or of a strongly H-bonding anion the ν(NH) frequency is in the 2950–2600 cm^{-1} range, whereas in the salts containing the weakly H-bonding ClO_4^-, BF_4^-, and I^- anions it is in the 3300–3100 cm^{-1} range. On this premise, and keeping in mind that on geometric evidence the H-bond involving H(N10) is bifurcated, we suggest that ν(NH) frequencies in the 3300–3100 cm^{-1} range result from N(10)–H(N10)...N(1) dominated H-bonds, whereas the 2950–2600 cm^{-1} frequencies correspond to bonds dominated by inter-ion N(10)—H(N10)...X interactions. Consequently the 3279 cm^{-1} absorption observed in the 10 K spectrum of PTB originates in a bifurcated H-bond dominated by the N(10)—H(10)...N(1) intra-cation interaction and, being well defined and "isolated," its frequency can be adopted as a standard for this type of H-bond. The effect of the increasing amplitude of thermal motion on the H(N10) atom will then be to bring this atom, dynamically, closer to the N(1) acceptor, increase the N(10)-H(N10)-N(1) angle, and thus strengthen the H-bonding interaction, as manifested in the observed lowering of the ν(NH) with increasing temperature.

In BPTB the frequency of the principal ν(NH) absorption at 10 K, 3147 cm^{-1}, is about 130 cm^{-1} lower than that in PTB, pointing to a stronger H-bonding interaction. The increased strength of the bifurcated N(1′)—H(N2′)...N(2),phenyl-2 bond in BPTB is consistent with the shorter intra-cation H(N2′)...N(2) distance and with the shortest H(N2′)...C(an) distances, H(N2′)...C(2.6) = 2.37 Å and H(N2′)...C(2.5) = 2.55 Å, both much shorter than similar distances in PTB (Fig. 10). The almost zero temperature dependence of ν(NH) in BPTB can arise from several conceivable causes and no definite scenario can be offered at present. For comparison, the frequency

[14] The room-temperature ν(NH) absorptions reported in ref. 6 for anhydrous BP^+BF_4, BP^+ClO_4, and BP^+SbCl_6 were also composite. Since the cation conformation in those salts is almost certainly similar to that in BPTB regardless of the nature of the *purely inorganic* counter-anion, the complexity of the ν(NH) absorption appears to arise either from vibrational interactions within the cation or from the existence of multiple potential energy minima associated with alternative orientations of the N—H bond. A detailed spectroscopic study seems indicated.

[15] The ν(NH) frequency of the solitary, bifurcated N—H...2 Cl bond in $(Et_3NH)_2SnCl_6$ (53) is 3117.8 cm^{-1} at 10 K and 3109.7 cm^{-1} at 293 K; in $(Me_3NH)_2SnCl_6$ (55) at 10 K it is 3187 cm^{-1} (mean). In contrast to these weak N—H...Cl bonds the ν(NH) frequencies in the strongly H-bonded Et_3NHX (56) at 10 K are 2740, 2685, and 2611 cm^{-1} (centroids) for X = I, Br, and Cl, respectively. The mean frequency of the ir-active $\nu_3(NH_4^+)$ fundamental in the very weakly H-bonded NH_4BPh_4 (57) at 10 K is 3236[30] cm^{-1}, the highest-frequency component being at 3284.5(5) cm^{-1} and thus comparable to ν(NH) in PTB.

Fig. 14. Schematic representation of 5- to 8-membered rings closed by the formation of an N—H...N′ bond (cf. Table 4). PS, cations **a–hh**; PS′, cations **pp–ww**; PS″, cations **jj–nn**; 1,2-bzH$^+$, cations **ac–ah**. Large circles, N atoms; small circles, H(N) atoms.

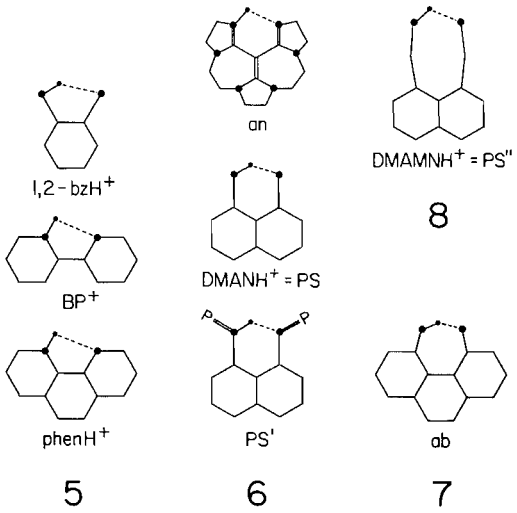

of the principal ν(NH) absorption in anhydrous BP^+BF_4 has been reported (6) as 3185 cm^{-1} (2390 cm^{-1} on deuteration), and those in anhydrous BP^+ClO_4 and BP^+SbCl_6 can be estimated from Fig. 3 of ref. 6 as 3190 and 3165 cm^{-1}, respectively.[16]

Proton sponges: essential geometry

In classical $DMANH^+$ and modified proton-sponge cations (Table 4, Fig. 14; refs. 59–99) the local geometry involving the N—H...N′ group is constrained by the rigidity of the naphthalene skeleton in much the same way as that in $phenH^+$ is constrained by the rigidity of the phen skeleton, and that in BP^+ by the *cisoid* conformation of the BP system. It is thus of interest to see what differences there are in the consequences of the N—H...N′ bond formation in these and similar systems.

The $d_1 = d$(N −H) and $d_2 = d$(H...N′) distances ($d_2 \geq d_1$) in the $DMANH^+$ proton sponges are related by

$$[1] \quad d_2 = d_1 \cos\alpha + [d_1^2(\cos^2\alpha - 1) + d_0^2]^{1/2}$$

where $d_0 = d$(N...N′) and α = NHN′ (Fig. 15). Inspection of Table 4 reveals that d_0 and α are relatively constant: the means for **a–hh** are $\bar{d}_0 = 2.583[21]$ Å and $\bar{\alpha} = 154.2[72]°$, i.e., $\sigma(\alpha)$ is of the order of the stated experimental esd of α and $\sigma(\bar{d}_0)$ is about four times the average experimental esd of d_0. Most of the 32 $DMANH^+$ points in the d_2 vs. d_1 plot of Fig. 15 fall within the limits calculated from eq. [1] for the two combinations that produce the largest effects in d_1,d_2, viz. $d_0 = \bar{d}_0 \pm \sigma(\bar{d}_0)$, $\alpha = \bar{\alpha} \mp \sigma(\bar{\alpha})$. With four exceptions, *all* the points are accommodated inside the $2\sigma(\bar{d}_0)$,$2\sigma(\bar{\alpha})$ band.

[16] References 6–8 and 22, which came to our attention only when the present investigation was well under way, contain ir spectra of a number of BP^+ and $phenH^+$ salts (*not* BPTB or PTB). Like the present paper, these references aim explicitly at interpreting the spectra in terms of the intra-cation bond. However, owing to the lack of crystallographic information at the time, their conclusions, while generally similar to ours, are supported by spectroscopic evidence alone.

Fig. 15. Variation of $d_2 = d$(H...N′) with $d_1 = d$(N—H) in proton-sponge, *cis*-BP^+, and $phenH^+$ cations (cf, Tables 3 and 4). Heavy line, regression of d_2 on d_1. Thin lines, $\pm1\sigma(\bar{d}_0)$, $\mp1\sigma(\bar{\alpha})$ limits; thin broken lines, $\pm2\sigma(\bar{d}_0)$, $\mp2\sigma(\bar{\alpha})$ limits (see text). Proton sponges: full circles, $DMANH^+$ cations; open circles, other cations of Table 4; **w**, **gg**, [N—H...N′]$^-$ bonds; **at**, ab initio value for $[N_2H_7]^+$.

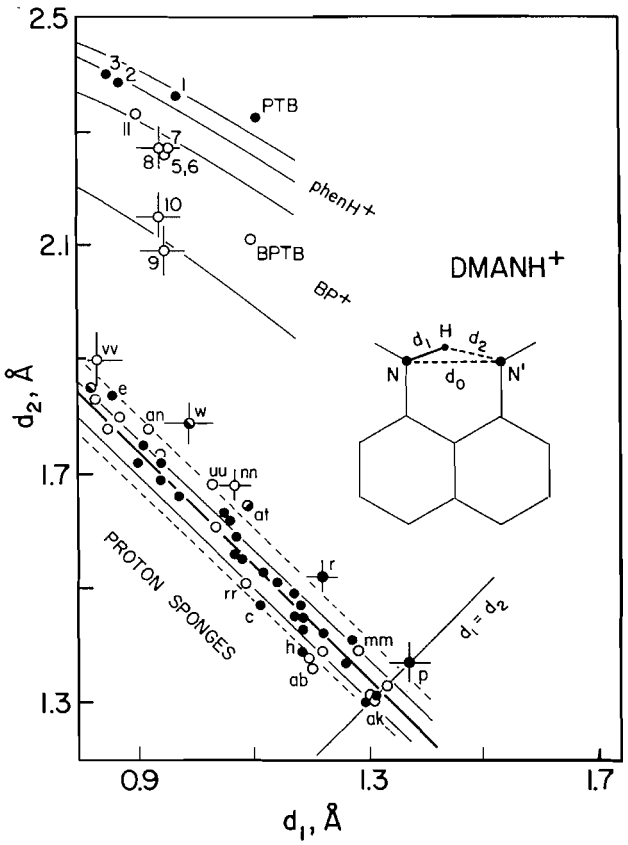

With the above values of $\bar{d}_0$ and $\bar{\alpha}$, eq. [1] closely approximates linear variation. Using the above 32 experimental points to regress d_2 on d_1 yields $d_2 = 2.656(55) - 1.017(49)d_1$, $r^2 = 0.97$, $\sigma = 0.03$ Å, i.e., statistically the slope is not different from −1. Thus within the experimental accuracy of the present sample, $d_1 + d_2 = 2.66$ Å, which in turn implies that the approximate locus of the H(N) position is a segment of an ellipse with N and N′ as the foci and a major axis of 1.33 Å, d_1 and d_2 being the focal radius vectors of the proton.

If Fig. 15 is a reasonable approximation to the actual gross behaviour of d_1 and d_2 in $DMANH^+$, with d_2/d_1 ranging from 1 to ~2, what is responsible for the wide variation in the asymmetry of the N-H-N′ in the first place? The ab initio calculation for free $[H_3N\text{-}H\text{-}NH_3]^+$ (**at**, $d_2/d_1 \sim 1.5$) indicates that, for N...N′ separations that are not extremely short, an *asymmetric* N-H-N′ bond is the ground-state norm.[17] The effect, in crystals, of a *second* acceptor X, which would generate a bifurcated N—H...N′,X bond, is not clear. In general, a short H...X separation would be expected to correspond to a lengthened N—H bond and probably to an increased $d_1 + d_2$, and possibly to an increased N-H-N′ bond symmetry. However, this is not

[17] For a recent account of ab initio studies of N-H-N′ interactions see ref. 99.

Table 4. Hydrogen-bonding geometry in proton sponges and their analogs.[a]

Compound	N...N′	N-H	H...N′	NHN′	Ref.
DMANH⁺ salts					
a BPh_4^-·MeCN·H_2O	2.522(1)	1.27	1.41	141	[b]
b Br^-·$2H_2O$	2.554(4)	1.31(1)	1.31(1)	153(3)	63
c $[C_6Cl_5O]^-[C_6Cl_5OH]_2$, 100 K	2.555(3)	1.11(2)	1.47(3)	162(2)	64
d BF_4^-	2.562(3)	1.30(3)	1.31(3)	159(2)	65
e $[C_6F_5O]^-[C_6F_5OH]_2$, 100 K[c]	2.565(3)	0.86(7)	1.84(7)	141(6)	87
f		1.07(6)	1.56(6)	154(6)	
g X^-[d]	2.570(3)	1.18(4)	1.47(4)	152(4)	86[e]
h X^-[d]	2.570(5)	1.19(7)	1.39(7)	170(6)	86[e]
i $[CHN_4]^-$·H_2O (C_s)[f]	2.573(2)	1.31(5)	1.31(5)	157(3)	88
j X^-, 150 K[d]	2.573(4)	1.19(7)	1.43(6)	158(5)	86[e]
k [squarate]$^{2-}$·$4H_2O$, 100 K[c]	2.574(3)	0.94(6)	1.69(6)	156(5)	68
m	2.594(3)	0.97(6)	1.66(6)	162(5)	
n $[TeOF_5]^-$ ($P\bar{1}$), 167 K	2.574(3)	1.17(5)	1.45(5)	158(4)	66
p $[TeOF_5]^-$ (*Cmcm*), 140 K (C_s)	2.577(4)	1.37(4)	1.37(4)	140(8)	67
q $[AlF_4]^-$	2.580(3)	1.26(4)	1.37(4)	158(3)	85
r $[O(Ph)C_2B_{10}H_{10}]^-$	2.577(3)	1.22(3)	1.52(3)	140(2)	69
s Hydrogen squarate, 150 K	2.583(2)	1.08(2)	1.55(2)	157(2)	70
t X^-, 150 K[d]	2.583(3)	1.12(4)	1.53(4)	155(3)	86[e]
u X^-[d]	2.588(7)	1.19(11)	1.45(11)	157(7)	86[e]
v TFANH⁻,[g] cation	2.588(4)	1.22(3)	1.42(3)	'56(3)	71
w anion	2.608(4)	0.99(4)	1.79(3)	138(3)	
x [chloranilate]$^{2-}$·$2H_2O$, 150 K	2.588(2)	1.07(3)	1.59(2)	152(2)	72
y 295 K	2.589(2)	1.14(3)	1.51(3)	155(2)	
z [hemimellitate H_2]$^-$·$\frac{1}{2}H_2O$[e]	2.604(2)	0.90(6)	1.72(7)	164(5)	73
aa		0.94(3)	1.72(2)	155(2)	
bb Hydrogen maleate	2.606(3)	1.17(3)	1.49(3)	157(3)	74
cc [2,4-$(NO_2)_2$-imidazolate]$^-$	2.606(3)	1.18(3)	1.47(1)	160(3)	75
dd [D-hydrogen tartrate]$^-$·$3H_2O$[c]	2.610(3)	0.83(14)	1.86(14)	149(13)	76
ee		0.91(5)	1.75(3)	157(5)	
ff an⁻,[g,h] cation	2.610(5)	1.05(5)	1.63(5)	152(5)	90
gg anion	2,600(5)	0.82(5)	1.85(5)	153(5)	
hh [3,4-furandicarboxylate]$^-$·H_2O	2,621(5)	1.06(2)	1.62(2)	155(2)	89
Other naphthalene-type cations					
ii $AH_2^{2+}Br_2$·$5H_2O$[i]	2.567(5)	1.22(1)	1.39(1)	158(5)	91
jj $DMAMNH^+NO_3^-$, 100 K[c]	2.629(2)	0.83(6)	1.83(5)	161(5)	92
kk		1.04(3)	1.61(3)	165(3)	
mm RT	2.642(3)	1.28(3)	1.39(3)	164(2)	81
nn $DMAMNH^+$ $[picrate]^-$	2.716(3)	1.07(3)	1.68(3)	162(3)	93
pp AH^+Br^-[j]	2.519(3)	1.20(7)	1.38(7)	154(6)	94
rr $AH^+BF_4^-$[j]	2.543(4)	1.09(6)	1.51(6)	155(6)	94
ss $AH^+PF_6^-$[j]	2.571(6)	0.87(6)	1.80(6)	147(6)	94
tt AH^+Br^-[k]	2.533(6)	0.94(6)	1.73(6)	141(6)	95
uu	2.534(6)	1.03(9)	1.68(9)	138(8)	
vv $AH^+PF_6^-$[m]	2.606(4)	0.83(5)	1.90(5)	143(5)	95
ww $AH^{2+}Br_2$·$2H_2O$[m]	2.584(4)	0.85(8)	1.78(8)	159(9)	95
Other condensed-ring systems					
xx $AH^+ClO_4^-$ (C_2)[n]	2.626(2)	1.31(3)	1.31(3)	177(7)	62, 77
yy $AH^+BF_4^-$[p]	2.587(3)	1.30(1)	1.30(1)	173(1)	77, 79
zz $AH^+BF_4^-$[q]	2.573(3)	1.29(1)	1.29(1)	175(2)	77, 79
ab $AH^+ClO_4^-$[r]	2.545(4)	1.20(2)	1.36(2)	167(1)	77, 78

Table 4. (*Concluded*)

Compound	N...N′	N-H	H...N′	NHN′	Ref.
Benzene and biphenyl-type cations					
ac AH^+X^- [d,t]	2.655(8)	1.11(7)	1.95(7)	118(5)	86[s]
ad AH^+X^- [d,t]	2.675(8)	0.94(11)	2.03(9)	125(7)	86[s]
ae AH^+X^- [d,t]	2.677(6)	0.87(6)	2.13(6)	121(5)	86[s]
af AH^+X^- [d,t]	2.719(5)	0.83(3)	2.25(3)	116(3)	86[s]
ag AH^+X^- [d,u]	2.627(5)	0.88(5)	2.10(4)	120(3)	86[s]
ah AH^+X^- [d,v]	2.584(3)	0.80(2)	2.05(3)	118(3)	86[s]
ai $AH_2^{2+}Br_2 \cdot H_2O$[w]	2.716			119	77, 83
aj AH^+Br^-[x]	2.650(6)	1.33(2)	1.33(2)	175(2)	77, 82
Other cations					
ak AH^+I^-[y]	2.600(3)	1.30(5)	1.30(5)	169(2)	80
am AH^+Cl^-[z]	2.526(3)				96
an $[C_{14}H_{20}N_6H]^+BPh_4^-$[aa]	2.541(5)	0.92(3)	1.78(1)	138	97
ap $AH^+ClO_4^-$, n.d., 120 K (C_i)[bb]	2.635(2)	1.317(1)	1.317(1)	180	98
ar $[(4\text{-Me-py})H]^+BPh_4^-$ (C_i)	2.610(5)	1.31(1)	1.31(1)	180	61
as $[N_2H_7]^+I^-$[cc]	2.69(5)				84
at $[N_2H_7]^+$ (C_{3v})[dd]	2.731	1.087	1.644	180	60

[a]Interatomic distances in Å, bond angles in deg. DMAN = 1,8-$(Me_2N)_2$-naphthalene; DMAMN = 1,8-$(Me_2NCH_2)_2$-naphthalene; TFAN = 1,8-$[CF_3C(O)NH]_2$-naphthalene.

[b]$P\bar{1}$, a = 11.226(2) Å, b = 18.837(4) Å, c = 8.365(2) Å, α = 92.64(2)°, β = 97.99(2)°, γ = 97.74(2)°, Z = 2, V = 1732(1) Å^3 (P.K. Bakshi, T.S. Cameron, and O. Knop, unpublished results).

[c]Resolved twofold positional disorder of H(N).

[d]Anion not specified in ref. 86.

[e]Reference 58 in our ref. 86.

[f]Tetrazole.

[g]Conjugated [N-H-N]$^+$, [N-H-N]$^-$ system.

[h]an = 1,8-bis(4-toluenesulfonamido)-2,4,5,7-$(NO_2)_4$-naphthalene.

[i]A = 1,4,5,8-$(Me_2N)_4$-naphthalene.

[j]A = 1-(Me_2N)-8-$(Ph_3P{=}N\text{-})$-naphthalene.

[k]A = 1,8-$(Ph_2MeP{=}N\text{-})$-naphthalene.

[m]A = 1,8-$(Ph_3P{=}N\text{-})$-naphthalene.

[n]A = 4,5-$(Me_2N)_2$-fluorene.

[p]A = 1,9-$(Me_2N)_2$-dibenzothiophene.

[q]A = 1,9-$(Me_2N)_2$-dibenzoselenophene.

[r]A = 4,5-$(Me_2N)_2$-phenanthrene.

[s]Reference 37 in our ref. 86.

[t]A = 1,2-$(Me_2N)_2$-benzene.

[u]A = 1-Me_2N-2-$(Ph_3P{=}N\text{-})$-benzene.

[v]A = 1,2-$(Ph_3P{=}N\text{-})_2$-benzene.

[w]A = 1,2,4,5-$(Me_2N)_4$-benzene.

[x]A = 2,2′-$(Me_2N)_2$-biphenyl, ψ_{cis} = 52°.

[y]A = 1,6-Me_2-1,6-diazacyclodecane; intra-annular N—H—N bond.

[z]A = 1,6-diazabicyclo[4.4.4]tetradecane; intra-annular N—H—N bond.

[aa]Vinamidinium type (Fig. 14); H-bond-containing ring planar to 0.073 Å.

[bb]AH^+ = $(\text{quinuclidinone})_2H^+$; neutron diffraction. Positional disorder cannot be excluded, but thermal parameters of central proton are not unusual.

[cc]In the $NH_4I \cdot NH_3$ adduct.

[dd]Ab initio optimization of the equilibrium geometry of $[H_3N{-}H{-}NH_3]^+$.

borne out unambiguously, if at all, by the present sample. Thus in **cc**, **ee**, and **hh** there appears to be no eligible second acceptor, yet d_1 in these cations ranges from 0.91(5) to 1.18(3) Å. In **x** and **aa** the resolved d_1 distances are 0.90(6) and 0.94(3) Å, with H...O = 2.58 and 2.50 Å, respectively; in **r**, d_1 = 1.22(3) Å, but H...O = 2.60(6) Å (all N—H...O bonds strongly bent). It would therefore seem imprudent to make definitive statements on the probable causes of the observed N—H...N′ asymmetry in crystals at this time. It is worth noting (Fig. 16) that in the five cations in Table 4 for which resolved twofold disorder of the H(N) atom has been reported, the alternative H(N) positions in each case conform closely (and certainly within their stated individual esd's) to the $DMANH^+$ regression line of Fig. 15.

Fig. 16. Relationship between the positions of the H(N) atoms in resolved positional disorder in proton-sponge crystals (full circles; **e–f, k–m, z–aa, dd–ee, jj–kk**, cf. Table 4), and the effect of temperature on the position of H(N) (open circles, **x–y**). Heavy line: d_2 on d_1 regression for proton sponges in Fig. 15.

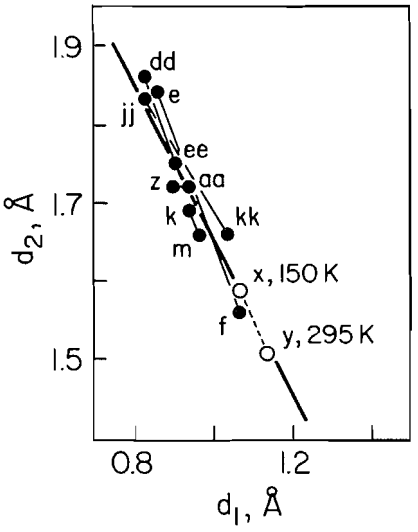

The $2\sigma(\bar{d}_0)$,$2\sigma\bar{\alpha}$) band also accommodates the d_1,d_2 points for cations other than $DMANH^+$, even though the local stereochemistries at their N—H...N′ bonds differ from that in $DMANH^+$ (the exceptions are **nn, pp, uu, vv, ab**).[18] Thus **xx, yy**, and **zz** are fused-ring variations on $DMANH^+$ with probably pseudosymmetric N-H-N′ bonds, and **jj** is a CH_2-expanded version of $DMANH^+$, with the two N atoms brought into a *syn* relationship by the H-bond. The cations in **ab** and **ar** are of particular interest in that in **ar** the centrosymmetric N-H-N′ group forms spontaneously on crystallization, without apparent constraint and yet with a d_0 value within 1σ of the above d_0 value for $DMANH^+$. In **ak**, even more interestingly, the monoprotonated saturated 1,6-Me_2-1,6-diazacyclodecane ring in the crystal spontaneously assumes a conformation that contains an intra-annular N-H-N′ bond with $d_0 = 2.60$ Å.

Proton sponges: comparison with BPTB and PTB

What distinguishes, geometrically, BP^+ and $phen^+$ from the proton sponges and their analogs, and where is the dividing line between the former and the cations that exhibit proton-sponge properties?[19]

The parameters considered here are d_0, d_1, d_2, and α, any one of which can be expressed in terms of the other three. Using only d_1 and d_2 (Figs. 15 and 17*A*), we see immediately that the points for the planar, non-proton-sponge BP^+, $phenH^+$, and 1,2-bzH^+ systems fall in a region of the plot with much larger d_2 distances. They also conform reasonably closely to the lines calculated from eq. [1] using the appropriate $\bar{d}_0$ and $\bar{\alpha}$

Fig. 17. (*A*) Correlation of d_1 and d_2 (cf. Fig. 14). Full circles, cations **ac–ah** of Table 4. The lines refer to $\bar{d}_0$ and $\bar{\alpha}$ in each group (see text); the line for PS is the d_2 on d_1 regression line of Fig. 14. (*B*) Variation of NHN′ = $\bar{\alpha}$ with N...N′ = $\bar{d}_0$ in the rings of Fig. 14; for **ab** and **an** only one d_0,α pair each is available. The broken line passes through the points corresponding to (essentially) planar, rigid ring systems.

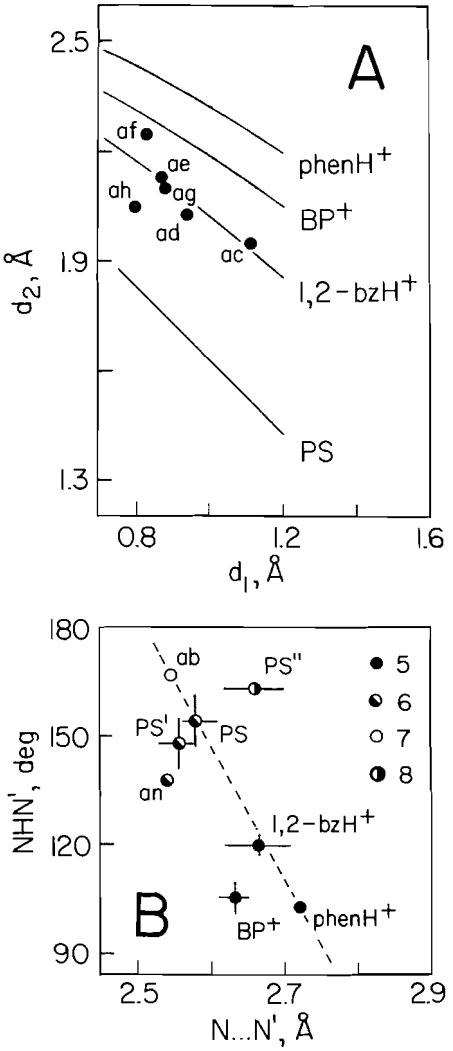

means for each cation class from Table 5.[20] These lines are well separated from the regression line for the proton sponges. This separation and the importance of the size of the ring closed by the N—H...N′ bond are evident in Fig. 17*B*, in which $\bar{\alpha}$ is plotted against $\bar{d}_0$ for several classes of cations. While this may be fortuitous, the points for the planar, rigid $phenH^+$, 1,2-bzH^+, and $DMANH^+$ systems are seen to lie on a straight line. This line accommodates even the point for **ab**, in which cation the steric crowding at the N atom is so severe as to produce a helical twist of 23° between the outer rings about the central C—C bond of the phenanthrene system (77, 78). The Me groups on the nitrogens apparently are so locked in place that they make the system rigid in spite of its nonplanarity.

[18] In the (N-H-N)-containing $TFAN^-$ *anion* (**w** in Table 4) the d_0 distance, 2.608(4) Å, is close to the above $\bar{d}_0$ mean but the NHN′ angle, 138(3)°, is significantly smaller than $\bar{\alpha}$.

[19] Normally as judged by the basicity of the cation, but for our present purposes by the ν(NH) stretching frequency in the crystal (see above), which in true proton sponges is depressed to values below 1000 cm^{-1}.

[20] The scatter of the points for BP^+ may in part be attributed to the *cisoid* rather than *cis* conformation of the cation (see above), and that of the 1,2-bzH^+ points may be due to the bulk of the Ph_3P group(s) on the N atom(s).

Table 5. Means of N...N′ distances and NHN′ angles (Fig. 17*B*).[a]

Cation	$\bar{d}_0$, Å	$\bar{\alpha}$, deg	Ring size	d_2/d_1 range	$\langle d_2/d_1 \rangle$
ab[b]	2.545(4)	167(1)	7	1.13(4)	1.13(4)
PS″	2.662[38]	163.7[13]	8	1.09(5)–2.20(22)	1.40[22][d]
PS[c]	2.583[21]	154.2[72]	6	1–2.14(26)	1.43[26][e]
PS′	2.557[29]	148.1[74]	6	1.15(13)–2.29(20)	1.60[39]
an[b]	2.541(5)	138	5	1.93(7)	1.93(7)
1,2-bzH$^+$	2.665[45]	119.6[27]	5	1.76(17)–2.39(18)	2.34[31]
BP$^+$	2.635[22]	105.6[41]	5	1.92(1)–2.59(12)	2.32[18]
phenH$^+$	2.722[9]	102.5[11]	5	2.10(1)–2.82	2.52[29]

[a]See Table 4 and Fig. 16. Ring size, number of atoms in the ring; $\langle d_2/d_1 \rangle$, mean d_2/d_1 value. The 7-membered rings in **zz**, **yy**, **xx**, and **aj** (d_0 = 2.573(3), 2.587(3), 2.626(2), 2.650(6) Å, respectively; α = 175(2)°, 173(1)°, 177(7)°, 185(2)°, respectively, the last-named value corresponding to a re-entrant angle) are not included in the table and Fig. 17*B*. Their N—H...N′ bond lengths are reported as symmetric, but the H(N) position may be disordered.

[b]Single values.

[c]N—H—N′ bonds reported as symmetric are not included in the means.

[d]Not including **jj**.

[e]Not including **e** and **dd**.

Fig. 18. (*A*) Correlation of the mean d_2/d_1 ratio with the mean NHN′ angle $\bar{\alpha}$. Full circles, proton-sponge cations; open circles, non-proton-sponge cations (cf. caption of Fig. 14). (*B*) Correlation of the mean NHN′ angle $\bar{\alpha}$ with the angle λ between the N...N′ vector and the idealized direction of the axis of the lone electron pair on N. Half-filled circle, estimate (from the correlation) of α for 1,8-naphthyridinium(1+) cation.

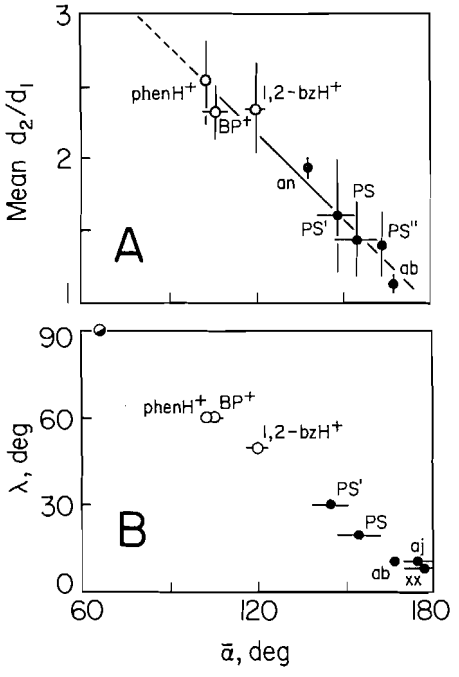

A comparison that includes the eight cations of Fig. 14 and takes account of three of the four parameters is presented in Fig. 18*A*. The unmistakable visual correlation of the mean d_2/d_1 values and $\bar{\alpha}$ (Table 5) can be approximated by a linear regression of $\langle d_2/d_1 \rangle$ on $\bar{\alpha}$: $\langle d_2/d_1 \rangle = 4.582 - 0.0200\bar{\alpha}$ ($r^2 = 0.96$, $\sigma = 0.09$ ~6% of range). The proton-sponge character is lost when simultaneously (*i*) $\langle d_2/d_1 \rangle$ is large, i.e., when the N—H...N′ bond is highly asymmetric and H(N) is close to N′; (*ii*) $\bar{\alpha}$ decreases, i.e., the N—H...N′ bond is highly bent. The dividing line between the proton-sponge and non-proton-sponge regimes appears to be at $\langle d_2/d_1 \rangle \sim 2$ and $\bar{\alpha} \sim 130°$. For $\langle d_2/d_1 \rangle > 2$ and $\bar{\alpha} < 130°$ the N—H...N′ configuration ceases to function as an effective two-centre force field.

To introduce the N...N′ separation explicitly, eq. [1] can be recast as

$$[2] \quad d_2/d_1 = \cos\alpha + [\cos^2\alpha + (d_0/d_1)^2 - 1]^{1/2}$$

for use with the individual cations. For the class parameters of Table 5,

$$[3] \quad \langle d_2/d_1 \rangle = 2.667 - 0.0190(\bar{\alpha} - 90) + 0.577(\bar{d}_0 - 2.5)$$

($r^2 = 0.96$, $\sigma = 0.07$). In this form the empirical correlation reveals the relative importances of changes in $\bar{\alpha}$ and $\bar{d}_0$: the range of $\bar{\alpha}$ being ~80° and that of $\bar{d}_0$, ~0.2 Å, it is clear that changes in $\bar{d}_0$ produce only a minor effect on $\langle d_2/d_1 \rangle$ and that $\bar{\alpha}$ is the major factor responsible for the proton-sponge properties. This is consistent with the smallness of the improvement that results when $\bar{d}_0$ is included in the regression.

The $\bar{\alpha}$ values are strongly correlated with the angle λ formed by the idealized direction of the axis of the lone pair on the N atom and the N...N′ vector (Fig. 18*B*). This correlation may proved helpful in estimating α in cations the structures of which have not yet been determined or in which H(N) is difficult to locate. Thus, for example, on monoprotonating 1,8-naphthyridine (100), quino[7,8-*h*]quinoline (101), and 1,14-diaza[5]helicene (102), the idealized λ angles in the cations are expected to be 90°, 30°, and perhaps ~0° respectively. From Fig. 18 the corresponding NHN′ angles would be estimated as ~66°, ~140°, and ~180°, i.e., the 1,8-naphthyridinium(1+) ion would not have proton-sponge characteristics.[21]

[21] Contrary to ref. 103, where a symmetric N-H-N′ bond has been proposed (cf. also ref. 100). The unprotonated quino[7,8-*h*]quinoline molecule is planar (101) and likely to remain so on protonation. The helical twist in the 1,14-diaza[5]-helicene molecule (102) renders estimation of λ uncertain.

π–π stacking in PTB: geometry

As pointed out earlier, some of the features of the PTB structure (face-to-face cat/an ring stacking, edge-to-face cat/an orientations) parallel similar features in the structure of PQTB, where they have been attributed to π–π interactions (11). Accounting for these features in these terms does not seem to contradict the set of rules announced in a position paper on the nature of π–π interactions (104), to the extent to which the rules are applicable to cat/an systems as complex as PQTB (cf. also ref. 105). A similar rationalization can therefore be adopted in describing the PTB structure.[22] However, PTB contains additional features, the quasi-discrete four-stacks (cf. above), which to our knowledge have not been reported previously but which, too, it is tempting to associate with π–π interactions, even though explicit support from current theory may be lacking.[23]

Each four-stack consists of a centrosymmetric pair of planar phenH$^+$ cations. Their perpendicular separation, 3.32 Å (Fig. 4*B*), is small enough to suggest attractive interaction, the like charges on the cations notwithstanding. Each cation in turn is flanked by the phenyl-2 ring of an anion, at a plane-to-plane angle of ~9°, i.e., about the same as the corresponding cat/phenyl angle in PQTB.[22] The shortest C(an)...N(an) distance, *d*[C(2.4)...N(10)], is 3.23 Å. The two cations in a pair thus constitute a cofacial $[cat_2]^{2+}$ dimer. Because of the inversion centre their relative orientation is such that the protonated N(10) atom of one cation is roughly above the unprotonated N(1) atom of the other, and the N(10) atom of the second cation is roughly below the N(1) cation of the first (Fig. 4*A*). The phenyl-2-ring and the cation in a pair are offset, roughly parallel to the cation plane. The overlap (Fig. 4*A*) between the cation ring 2 and the phenyl-2 ring is not substantial, but it brings the N(10)—H(N10) bond under (or above) the phenyl-2 ring. Thus, while the ion charges on the cations have the same sign, the atom charges and the electron densities at the vertically related N(1) and N(10)′ atoms are not the same. This difference may well generate an attractive interaction and thus reinforce the cofacial π–π interaction between the cation and the phenyl-2 ring in the four-stack. Each four-stack would then contain three cofacial interactions (phenyl-2/cat, cat/cat′, cat′/phenyl-2′) plus four edge-to-face cat/phenyl-4 interactions. The phenyl-4 groups involved in the T-geometry interactions mediate between adjacent four-stacks by organizing them into slabs parallel to (001) (Fig. 3).

[22] Consistent with the 1:2 stoichiometry of PQTB, the centrosymmetric PQ^{2+} cation is sandwiched between two anions to form discrete [an-cat-an] aggregates (11). Each cation ring is engaged by an anion in a simultaneous face-to-face and edge-to-face interaction, whereas in PTB the face-to-face and the edge-to-face anion ring partners of a cation are from different anions. In PQTB the cat/phenyl angle is 10° (9° in PTB), and the shortest edge-to-face $\pi_c...\pi_c$ distance between the cation and anion rings is 5.0 Å (5.32 and 5.35 Å in PTB). The shortest distances, in the region of face-to-face overlap, are C(cat)...phenyl plane = 3.27 Å and C(phenyl)...cation plane = 3.28 Å.

[23] On this point we paraphrase the apt comment made in ref. 104: where ab initio treatments are available, they reproduce experimental results well (106), but they do not explain the basic mechanisms of π–π interactions in a way that is helpful or predictive for the practical chemist (cf. also ref. 107). Besides, in situations believed to be governed by π–π interactions, there may be other determining factors at work.

π–π interactions: PTB in solution

The presence of charge-transfer interactions in the PTB crystal is betrayed by the pale yellow colour. The colour persists in solution but only in some solvents. Fresh solutions in acetone, MeCN, and DMSO appear colourless, at high concentrations slightly yellowish, but solutions in CH_2Cl_2, THF, and pyridine (less so in $CHCl_3$ and $MeNO_2$) are yellow. The uv–visible spectra of 6 mM solutions of PTB in CH_2Cl_2 and acetone are quite different. The spectrum of the CH_2Cl_2 solution contains a broad double absorption ($\Delta\lambda_{1/2}$ ~ 160 nm) extending from below 190 to about 480 nm (hence the yellow colour), with the maxima at 260 and 330 nm (ε ~ 300). On a hundredfold dilution this broad absorption resolves into a narrower band ($\Delta\lambda_{1/2}$ ~ 60 nm), with a maximum at 270 nm, and a small shoulder on the long-wavelength side. In contrast, the spectrum of the acetone solution has a single narrow absorption ($\Delta\lambda_{1/2}$ ~ 40 nm) between 280 and 460 nm, with a maximum at 340 nm (ε ~ 550). The BPh_4^- anion ($NaBPh_4$ in acetone) shows no significant absorption between 190 and 800 nm, while phen^0 in acetone has a sharp band at 330 nm (ε ~ 240); a sharp maximum at the same wavelength is observed also in the spectrum of a saturated solution of phenH$^+$Cl$^-$ in acetone.

Room-temperature ^{1}H nmr spectra of PTB solutions depend markedly on the solvent. To find out why the CH_2Cl_2 solutions are yellow but those in acetone and MeCN at comparable concentrations almost colourless, we obtained spectra of PTB, phen^0, and (*n*-Bu_4N)BPh_4 (= 4BTB) in the three deuterated solvents. The PTB solution in CD_2Cl_2 was examined at two concentrations, 0.01 and 0.04 M. For comparison, spectra were also obtained of $NaBPh_4$ (= NaTB) and phenH$^+BF_4^-$ in $(CD_3)_2CO$ and CD_3CN; unfortunately, these two salts are not sufficiently soluble in CD_2Cl_2, and phenH$^+BF_4^-$ is insoluble also in THF, hence the corresponding spectra are not available. The results are summarized in Fig. 19 (phen proton assignments as in ref. 108).

The phen^0 frequencies in the three solvents are quite similar. In the colourless PTB solutions in acetone and MeCN these frequencies are shifted downfield by more or less similar amounts, ranging from $\Delta\delta_{2,9}$ ~ 0.14 to $\Delta\delta_{4,7}$ ~ 0.55 ppm in acetone, and from $\Delta\delta_{2,9}$ ~ 0 to $\Delta\delta_{4,7}$ ~ 0.55 ppm in MeCN, i.e., in the direction expected for cation formation. The anion proton frequencies in the PTB solutions in acetone and MeCN show only very minor shifts relative to NaTB and 4BTB. In the yellow PTB solutions in CD_2Cl_2, however, the spectral changes are strikingly different. The H(3,8), H(4, 7), and H(5,6) frequencies in the 0.01 M solution again are shifted downfield relative to phen^0, $\Delta\delta$ ~ 0.06–0.31 ppm, but the H(2,9) frequency is shifted *upfield* by ~0.50 ppm. On increasing the concentration to 0.04 M all the cation H(C) frequencies shift upfield by amounts not exceeding 0.1 ppm, making the total upfield shift $\Delta\delta_{2,9}$ ~ −0.56 ppm relative to phen^0. At the same time, the *ortho* frequency of the anion undergoes a *downfield* shift of ~0.2 ppm relative to 4BTB, while the *meta* and *para* proton frequencies are shifted upfield by ca. −0.08 and ca. −0.15 ppm, respectively; these anion proton shifts are practically independent of the concentration.

The direction and magnitude of the shifts in the PTB solution spectra relative to the phen^0 and BPh_4^- reference spectra demonstrate the persistence of a vestigial, dynamic, short-range cation–anion structure in the CD_2Cl_2 solution (and probably also in the other coloured solutions) and its absence in the

Fig. 19. The ^{1}H nmr spectra of PTB and reference compounds in different solvents (*A–C*; centroid frequencies, TMS as reference). The spectra of PQTB and $PQ(PF_6)_2$ in $(CD_3)_2CO$ (ref. 11; $(CHD_2)_2CO$ in $(CD_3)_2CO$ as reference) are shown in *D*; note that, relative to the N position, H(3) and H(2), respectively, in the PQ system correspond to H(2) and H(3) in the phen system.

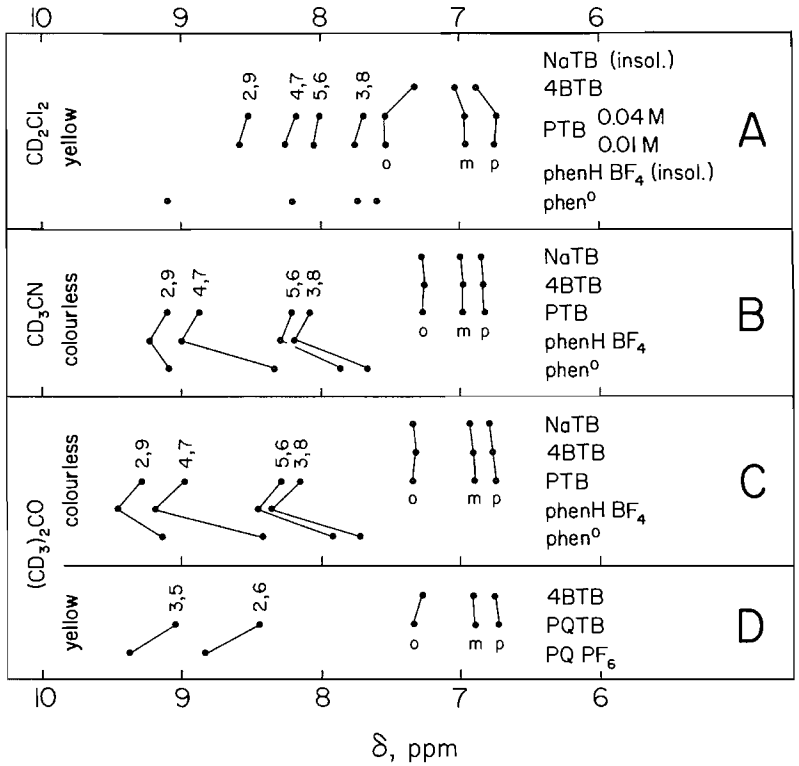

colourless acetone and MeCN solutions. The large upfield shift of proton H(2,9) on the carbon adjacent to the N atom and the downfield shift of the anion *ortho* protons both support the simultaneous existence of cofacial and T-shape interactions in the CD_2Cl_2 solutions. In this respect PTB in CD_2Cl_2 resembles PQTB in the deep-yellow acetone solution (Fig. 19*D*), for which similar but somewhat smaller shifts have been observed (11). The additional upfield shifts of all four PTB cation protons with increased concentration may arise from an overall reduction of dilution and thus from a higher probability of ion–ion encounter, but they would not be inconsistent with incipient formation of four-stack-like aggregates in the solution, especially since the anion proton shifts do not appear to vary with concentration. A detailed study of the concentration dependence of the shifts (also in the other yellow PTB solutions) would not be amiss.

Conclusions

Monoprotonation of BP^0 and phen^0 results in the formation of an intra-cation N—H...N′ H-bond that is strong enough to convert *trans*-BP^0 to a *cisoid* BP^+ and bend this cation in its plane so as to decrease the N...N′ separation. In BPTB the dihedral angle ψ between the two cation rings is 5.2°, but angles up to 19° are on record for other BP^+ salts. In $phenH^+$ an in-plane distortion is prevented by the rigidity of the fused ring system: N...N′ is 2.61 Å in BPTB but 2.71 Å in PTB. More generally, the N...N′ mean is 2.635[22] Å in a sample of eight BP^+ salts and 2.722[9] Å in a sample of four $phenH^+$ salts. The difference of ~0.09 Å is statistically significant, the observed variation in ψ notwithstanding.

The H-bond in BPTB and PTB is a bifurcated N—H...N′,phenyl bond in which the intra-cation H...N′ component dominates the inter-ion H...phenyl component. However, in PTB even the former is very weak: ν(NH) = 3299 cm^{-1} at 10 K, H...N′ = 2.33 Å. In BPTB, H...N′ = 2.11 Å and ν(NH) at 10 K is about 130 cm^{-1} lower than in PTB, i.e., the H-bond in BPTB is stronger, consistent also with the significantly shorter H...C(an) distances.

The crystal structure of PTB contains features characteristic of π–π interactions, the presence of which is manifested in the pale yellow colour of the solid and the well-developed yellow colour of its solutions in some nonaqueous solvents, e.g., CH_2Cl_2, $CHCl_3$, THF. The structure contains partially offset, nearly parallel (~9°) cofacial arrangements of phenyl(an)–cat–cat–phenyl(an) aggregates, with approximate vertical plane separations of 3.2–3.4 Å. In addition, it contains T-shaped, edge-to-face, cat/phenyl(an) pairs, with the two planes almost at right angles. In containing parallel as well as perpendicular π–π system arrangements, the PTB structure is reminiscent of the structure of paraquat(2+) tetraphenylborate (11), but the cofacial π–π four-stacks appear to be a novel feature.

Cation geometry

The correlated cation bond lengths and angles in a number of BP^+ and $phenH^+$ salts have been examined in detail, statistically, for geometric equivalence of rings 1 and 1′ in BP^+ and of rings 1 and 2 in $phenH^+$, for equivalence of the BP^+ and

phenH$^+$ ring systems, and for differential effects of protonation on the ring geometry of the phen system (Figs. 7–9). The results are highly informative and provide insight into the limits of usefulness of crystallographic evidence for detecting the consequences of N-protonation, the twist angle ψ, and the BP $\rightarrow$ phen ring closure for the geometries of the BP and phen ring systems. Among the more conspicuous results the following merit mention.

1. The mean CNC angle at the unprotonated N atom in *trans*-BP^0, *cis*-BP$^+$, phen^0, and phenH$^+$ is 117.1[5]°. On N-protonation the mean *ipso* angle in *cis*-BP$^+$, *trans*-BP^{2+}, phenH$^+$, and phenH$_2^{2+}$ is 123.2[3]°, i.e., protonation increases the angle consistently by ~6°, regardless of the degree of rigidity of the ring system.
2. The central C—C bond length and the ring geometry in the BP systems do not appear to correlate with the twist angle ψ.
3. With the exception of the phenH$^+$|phenH$_2^{2+}$ pair (Fig. 8*B*), the endocyclic C-C-C angles at carbons 4|4′ in the BP and carbons 3|8 in the phen systems (i.e., *para* to the central C—C bond) remain undifferentiated on *N*-protonation or BP $\rightarrow$ phen ring closure or both.
4. The correlated bond lengths in rings 1 and 2 of phenH$^+$, statistically, are not differentiated but all the endocyclic angles *are*, with the exception of those at carbons 3|8 (see point 3) and the peripheral carbons 5|6 (Fig. 7*C*). Similarly, the bond angles in ring 1 of BP$^+$, statistically, are all differentiated from the corresponding angles in ring 1′, with the exception of the angles at carbons 4|4′ (Fig. 7*A*).
5. The endocyclic angles at the peripheral carbons 5|6 and the C(5)—C(6) bond length in the phen system are insensitive to N-protonation (Figs. 8*A*, *C*).
6. The left/right ring symmetry in BP$^+$ and phenH$^+$, statistically, is much more pronounced in the bond angles than in the bond lengths (Figs. 7*A*, *C*), while the opposite is true of the BP$^+$|phenH$^+$ pair (Fig. 7*B*), where the endocyclic angles affected are those at carbons 13|14 (involved in the BP $\rightarrow$ phen ring closure) and the endocyclic angle at C(11).
7. The effect of protonating *trans*-BP^0 to *trans*-BP^{2+} on the ring bond lengths is remarkably selective, affecting only the bond length between the carbons *meta* and *para* to the N atom (Fig. 8*A*).
8. *N*-Protonation in one ring leads to a readjustment and differentiation of the bond angles in *both* rings except as under point 3 (Figs. 7*A*, *C*).

Although the available ab initio calculations on the BP and phen systems are not sufficiently detailed, where they exist they confirm the BP^0, BP$^+$, and BP^{2+} conformations observed in crystals. They also indicate that variations in the ring geometry on protonation may be too small to be established with confidence by crystallography, and the same may be true of the effect of the twist angle ψ on ring bond lengths and angles.

Proton sponges

A detailed survey of relevant crystal structures (Table 4) shows that the difference between the intra-cation N—H...N′ bond geometry in the BP$^+$ and phenH$^+$ cations and that in the proton sponges (typically 1,8-(Me$_2$N)$_2$-naphthalene-H(1+) = DMANH$^+$) is one of degree, not of kind. In planar or approximately planar cations containing intra-ion N—H...N′ bonds the parameters $d_0 = d$(N...N′), $d_1 = d$(N—H), $d_2 = d$(H...N′), and α = NHN′ are related by eq. [1]. When such cations are grouped by type (Table 5) and the group means $\bar{d}_0$ and $\bar{\alpha}$ are computed, the range of the $\bar{d}_0$ values is found to be relatively narrow, ~0.2 Å or ~7% of the overall $\bar{d}$(N...N′) mean, while the $\bar{\alpha}$ range is very substantial, ~65°. The mean ratio $\langle d_2/d_1 \rangle$ for each cation group can be taken as a geometric indicator of proton-sponge behaviour. If $\bar{d}_0$ is taken as essentially constant, the ratio can be approximated by $\langle d_2/d_1 \rangle = 4.582 - 0.0200\bar{\alpha}$ ($r^2 = 0.96$, $\sigma = 0.09$ Å ~6% of range) for BP^{2+}, phenH$^+$, and the cations of Table 5. The boundary between cations that have proton-sponge properties (high pK_a, low ν(NH) stretching frequency) and those that do not appears to fall at $\langle d_2/d_1 \rangle \sim 2$ and $\bar{\alpha} \sim 130°$ (Fig. 18*A*). For $\langle d_2/d_1 \rangle > 2$ and $\bar{\alpha} < 130°$ the N—H...N′ configuration ceases to function as an effective two-centre force field and loses its proton-sponge character. When $\bar{d}_0$ is introduced explicitly, the ratio can be approximated as $\langle d_2/d_1 \rangle = 2.667 - 0.0190(\bar{\alpha} - 90) + 0.577(\bar{d}_0 - 2.5)$ ($r^2 = 0.96$, $\sigma = 0.07$), i.e., changes in the N...N′ distances are relatively much less important in determining the proton-sponge character than changes in the NHN′ angle. The angle λ between the N...N′ vector and the axis of the lone electron pair on the protonated N atom is another important diagnostic parameter (Fig. 18*B*). To the best of our knowledge no clear evidence for the existence of statically symmetric ordered (i.e., single-well potential) N-H-N bonds has been provided by crystallography to date, in agreement with expectation from theoretical treatments.

Experimental

The free base was dissolved in dilute HCl and the resulting solution was added to an aqueous solution of NaBPh$_4$. The precipitate, which formed immediately, was washed with water and air-dried. Crystals suitable for X-ray work were obtained by recrystallizing the products from aqueous acetone by slow evaporation at room temperature.

Crystallography

The crystallographic information is summarized in Table 1. We wish to reiterate that, in general, organoammonium tetraphenylborate crystals are weak and fickle scatterers. As pointed out previously (3), significant reflections are seldom observed above a (sin θ)/λ limit of 0.48 Å^{-1} ($\theta = 20°$ for Mo radiation). Since in this laboratory X-ray data collection routinely extends to a limit of 0.55 Å^{-1} ($\theta = 23°$), the ratio of observed reflections to total measured unique reflections never exceeds 50%, as in the present case.

The TEXSAN package (109) was used in the data reduction, structure solution by direct methods, and structure refinement, with PLUTO (110) for special graphics. The anisotropic temperature factor is defined as $\exp[-2\pi^2(U_{11}h^2a^{*2} + ... + 2U_{23}klb^*c^* + ...)]$. The H(C) atoms, though seen in the difference maps, were placed geometrically (C—H, 1.08 Å, U_{iso}(H) = $1.2U_{eq}$(C) of the attached C atom) and not refined. The positions of the H(N) atoms were obtained from the difference maps and kept fixed during the final refinement (U_{iso}(H) = $1.2U_{eq}$(N) of the attached N).

A test of the cation in BPTB for conformity to rigid-body-motion behaviour (TLS analysis) resulted in $R(U_{ij}) = 6.1\%$ and rms(U_{ij}) = 0.0030 Å^2 compared to rms[esd(U_{ij})] = 0.0030 Å^2, i.e., the U_{ij} (Table C) are satisfactorily accounted for on the rigid-body-motion model. The largest mean librational ampli-

tude, 6.8°, is about a principal axis roughly parallel to the long cation axis, the mean amplitudes about the other two principal axes being 2.9° and 3.3°, respectively. The corresponding screw pitches do not exceed 0.02 Å/deg. The thermal corrections to the lengths of the bonds parallel to the long cation axis are ~0.004 Å; those to the lengths of the bonds inclined to the long cation axis are ~0.010 Å. Corrections to the bond angles are all less than |0.3|°.

Infrared spectra

The FT-ir spectra, at 2 cm^{-1} resolution, of fluorocarbon mulls supported on CaF_2 plates were obtained with a Boumem DA3.02 spectrometer fitted with a closed-cycle He refrigerator.

The ^1H nmr spectra

The room-temperature ^1H spectra of PTB solutions were obtained with a Bruker AC250F spectrometer operating at 251 MHz.

Acknowledgments

We thank Dr. S.V. Sereda for assistance with some of the X-ray diffraction work, Dr. M. Falk and Mr. Ping Seto for obtaining the FT-ir spectra, and Professor D.L. Hooper for obtaining the nmr spectra. This investigation was supported by grants from the Natural Sciences and Engineering Research Council of Canada to O.K. and T.S.C.

References

1. O. Knop and P.K. Bakshi. Can. J. Chem. **73**, 151 (1995).
2. O. Knop, T.S. Cameron, P.K. Bakshi, W. Kwiatkowski, S.C. Choi, and D. Adhikesavalu. Can. J. Chem. **71**, 1495 (1993).
3. P.K. Bakshi, A. Linden, B.R. Vincent, S.P. Roe, D. Adhikesavalu, and O. Knop. Can. J. Chem. **72**, 1273 (1994).
4. O. Knop, T.S. Cameron, P.K. Bakshi, A. Linden, and S.P. Roe. Can. J. Chem. **72**, 1870 (1994).
5. P.K. Bakshi, S.V. Sereda, O. Knop, and M. Falk. Can. J. Chem. **72**, 2144 (1994).
6. Z. Dega-Szafran. Bull. Acad. Pol. Sci. Ser. Sci. Chim. **15**, 393 (1967).
7. Z. Dega-Szafran. Bull. Acad. Pol. Sci. Ser. Sci. Chim. **16**, 107 (1968).
8. Z. Dega-Szafran. Bull. Acad. Pol. Sci. Ser. Sci. Chim. **16**, 115 (1968).
9. F.H. Westheimer and C.T. Benfey. J. Am. Chem. Soc. **78**, 5309 (1956).
10. C. Belin, J. Rozière, and J. Potier. Acta Crystallogr. Sect. B: Struct. Crystallogr. Cryst. Chem. **B37**, 1306 (1981).
11. G.J. Moody, R.K. Owusu, A.M.Z. Slawin, N. Spencer, J. Fraser Stoddart, J.D.R. Thomas, and D.J. Williams. Angew. Chem. Int. Ed. Engl. **26**, 890 (1987).
12. A.I. Kitaigorodsky. Molecular crystals and molecules. Academic Press, New York and London. 1973.
13. G. Thevenet and N. Rodier. Acta Crystallogr. Sect. B: Struct. Crystallogr. Cryst. Chem. **B34**, 880 (1978).
14. G. Thevenet and N. Rodier. Acta Crystallogr. Sect. B: Struct. Crystallogr. Cryst. Chem. **B34**, 1280 (1978).
15. G. Thevenet, P. Toffoli, and N. Rodier. Acta Crystallogr. Sect. B: Struct. Crystallogr. Cryst. Chem. **B34**, 2599 (1978).
16. G. Thevenet, P. Toffoli, N. Rodier, and R. Céolin. Acta Crystallogr. Sect. B: Struct. Crystallogr. Cryst. Chem. **B33**, 2526 (1977).
17. M.A. Khan, N. Kumar, and D.G. Tuck. Can. J. Chem. **62**, 850 (1984).
18. B.N. Figgis, B.W. Skelton, and A.H. White. Aust. J. Chem. **31**, 57 (1978).
19. D.J. Fuller, D.L. Kepert, B.W. Skelton, and A.H. White. Aust. J. Chem. **40**, 2097 (1987).
20. U. Englert, U. Koelle, and R.N. Nageswara. Z. Kristallogr. **209**, 780 (1994).
21. G. Fraenkel, V. Balasubramanian, H.L. Chang, and J. Gallucci. J. Am. Chem. Soc. **115**, 6795 (1993).
22. Z. Dega-Szafran. Rocz. Chem. **43**, 823 (1969).
23. M.D. Morse and J.P. Chesick. Acta Crystallogr. Sect. B: Struct. Crystallogr. Cryst. Chem. **B32**, 954 (1976).
24. S. Nishigaki, H. Yoshioka, and K. Nakatsu. Acta Crystallogr. Sect. B: Struct. Crystallogr. Cryst. Chem. **B34**, 875 (1978).
25. L. Maresca, G. Natile, and F.P. Fanizzi. J. Am. Chem. Soc. **111**, 1492 (1989).
26. G. Thevenet, N. Rodier, and P. Khodadad. Acta Crystallogr. Sect. B: Struct. Crystallogr. Cryst. Chem. **B34**, 2594 (1978).
27. M.H. Chisholm, J.C. Huffman, I.P. Rothwell, P.G. Bradley, N. Kress, and W.H. Woodruff. J. Am. Chem. Soc. **103**, 4945 (1981).
28. S.I. Troyanov, V.B. Rybakov, G.N. Mazo, and A.L. Il'inskii. Zh. Strukt. Khim. **30**, 193 (1989).
29. K. Nakatsu, H. Yoshioka, M. Matsui, S. Koda, and S. Ooi. Acta Crystallogr. Sect. A: Cryst. Phys. Diffr. Theor. Gen. Crystallogr. **A28**, S24 (1972).
30. S. Pohl. Z. Naturforsch. B: Anorg. Chem. Org. Chem. **38B**, 1535 (1983).
31. T.J.R. Weakley. Acta Crystallogr. Sect. C: Cryst. Struct. Commun. **C43**, 2144 (1987).
32. D.J. Barker, J.S. Buckleton, G.R. Clark, R.P. Cooney, and C.E.F. Rickard. J. Mol. Struct. **239**, 249 (1990).
33. J.H. Russell and S.C. Wallwork. Acta Crystallogr. Sect. B: Struct. Crystallogr. Cryst. Chem. **B28**, 1527 (1972).
34. A. Cousson, B. Bachet, B. Kokel, and M. Hubert-Habart. Acta Crystallogr. Sect. C: Cryst. Struct. Commun. **C49**, 942 (1993).
35. J.H. Russell and S.C. Wallwork. Acta Crystallogr. Sect. B: Struct. Crystallogr. Cryst. Chem. **B25**, 1691 (1969).
36. T.M. Bockman and J.K. Kochi. J. Org. Chem. **55**, 4127 (1990).
37. R. Benedix, P. Birner, and H. Hennig. J. Mol. Struct. **90**, 65 (1982).
38. V. Barone, F. Lelj, C. Cauletti, M.N. Piancastelli, and N. Russo. Mol. Phys. **49**, 599 (1983).
39. M. Yagi, K. Makiguchi, A. Ohnuki, K. Suzuki, J. Higuchi, and S. Nagase. Bull. Chem. Soc. Jpn. **58**, 252 (1985).
40. V. Barone, F. Lelj, L. Commissso, N. Russo, C. Cauletti, and M.N. Piancastelli. Chem. Phys. **96**, 435 (1985).
41. H.-J. Hofmann, R. Cimiraglia, and J. Tomasi. J. Mol. Struct. **139**, 213 (1986).
42. V. Barone, F. Lelj, and N. Russo. Int. J. Quantum Chem. **29**, 541 (1986).
43. E.I. von Nagy-Felsobuki. J. Heterocycl. Chem. **25**, 23 (1988).
44. J. Kao. J. Comput. Chem. **9**, 905 (1988).
45. V. Barone, C. Minichino, S. Fliszár, and N. Russo. Can. J. Chem. **66**, 1313 (1988).
46. C. Jaime and J. Font. J. Mol. Struct. **195**, 103 (1989).
47. C. Jaime and J. Font. J. Org. Chem. **55**, 2637 (1990).
48. R. Benedix, P. Birner, F. Birnstock, H. Hennig, and H.-J. Hofmann. J. Mol. Struct. **81**, 99 (1979).
49 R.P. Thummel, F. Lefoulon, and R. Mahadevan. J. Org. Chem. **50**, 3824 (1985).
50. T. Bluhm, H.H. Perkampus, and J.K. Knop. Ber. Bunsen-Ges. Phys. Chem. **77**, 116 (1973).
51. J. Lipkowski, P. Sgarabotto, and G.D. Andreetti. Cryst. Struct. Commun. **5**, 931 (1976).
52. B.-C. Wang and A.W. Cordes. Inorg. Chem. **9**, 1643 (1970).

53. O. Knop, T.S. Cameron, M.A. James, and M. Falk. Can. J. Chem. **59**, 2550 (1981).
54. T.S. Cameron, M.A. James, O. Knop, and M. Falk. Can. J. Chem. **61**, 2192 (1983).
55. O. Knop, T.S. Cameron, M.A. James, and M. Falk. Can. J. Chem. **61**, 1620 (1983).
56. M.A. James, T.S. Cameron, O. Knop, M. Neuman, and M. Falk. Can. J. Chem. **63**, 1750 (1985).
57. W.J. Westerhaus, O. Knop, and M. Falk. Can. J. Chem. **58**, 1355 (1980).
58. O. Knop, W.J. Westerhaus, and M. Falk. Can. J. Chem. **58**, 867 (1980).
59. M.R. Truter and B.L. Vickery. J. Chem. Soc. Dalton Trans. 395 (1972).
60. S. Scheiner and L.B. Harding. J. Am. Chem. Soc. **103**, 2169 (1981).
61. C. Glidewell and H.D. Holden. Acta Crystallogr. Sect. B: Struct. Crystallogr. Cryst. Chem. **B38**, 667 (1982).
62. H.A. Staab, T. Saupe, and C. Krieger. Angew. Chem. Int. Ed. Engl. **22**, 731 (1983).
63. D. Pyżalska, R. Pyżalski, and T. Borowiak. J. Cryst. Spectr. Res. **13**, 211 (1983).
64. J.A. Kanters, E.H. ter Horst, J. Kroon, and E. Grech. Acta Crystallogr. Sect. C: Cryst. Struct. Commun. **C48**, 328 (1992).
65. K. Woźniak, T.M. Krygowski, B. Kariuki, R.W. Jones, and E. Grech. J. Mol. Struct. **240**, 111 (1990).
66. P.K. Miller, K.D. Abney, A.K. Rappé, O.P. Anderson, and S.H. Strauss. Inorg. Chem. **27**, 2255 (1988).
67. P.J. Kellet, O.P. Anderson, S.H. Strauss, and K.D. Abney. Can. J. Chem. **67**, 2023 (1989).
68. J.A. Kanters, A. Schouten, J. Kroon, and E. Grech. Acta Crystallogr. Sect. C. Cryst. Chem. Struct. Commun. **C48**, 1254 (1992).
69. D.A. Brown, W. Clegg, H.M. Colquhoun, J.A. Daniels, I.R. Stephenson, and K. Wade. J. Chem. Soc. Chem. Commun. 889 (1987).
70. J.A. Kanters, A. Schouten, J. Kroon, and E. Grech. Acta Crystallogr. Sect. C: Cryst. Struct. Commun. **C47**, 807 (1991).
71. B. Brzeziński, E. Grech, J. Nowicka-Scheibe, T. Głowiak, Z. Malarski, and L. Sobczyk. J. Mol. Struct. **327**, 71 (1994).
72. J.A. Kanters, A. Schouten, A.J.M. Duisenberg, T. Głowiak, Z. Malarski, L. Sobczyk, and E. Grech. Acta Crystallogr. Sect. C: Cryst. Struct. Commun. **C47**, 2148 (1991).
73. M.L. Raves, J.A. Kanters, and E. Grech. J. Mol. Struct. **271**, 109 (1992).
74. E. Bartoszak, Z. Dega-Szafran, M. Grundwald-Wyspiańska, M. Jaskólski, and M. Szafran. J. Chem. Soc. Faraday Trans. **89**, 2085 (1993).
75. T. Głowiak, Z. Malarski, L. Sobczyk, and E. Grech. J. Mol. Struct. **157**, 329 (1987).
76. O.R. Israël, J.A. Kanters, and E. Grech. J. Mol. Struct. **274**, 151 (1992).
77. H.A. Staab and T. Saupe. Angew. Chem. Int. Ed. Engl. **27**, 865 (1988).
78. T. Saupe, C. Krieger, and H.A. Staab. Angew. Chem. Int. Ed. Engl. **25**, 451 (1986).
79. H.A. Staab, M. Höne, and C. Krieger. Tetrahedron Lett. **29**, 1905 (1988).
80. R.W. Alder, P. Eastment, N.M. Hext, R.E. Moss, A.G. Orpen, and J.M. White. J. Chem. Soc. Chem. Commun. 1528 (1988).
81. B. Brzeziński, T. Głowiak, E. Grech, Z. Malarski, and L. Sobczyk. J. Chem. Soc. Perkin Trans. 2, 1643 (1991).
82. H.A. Staab, C. Krieger, and M. Höne. Tetrahedron Lett. **29**, 5629 (1988).
83. H.A. Staab, K. Elbl, and C. Krieger. Tetrahedron Lett. **27**, 5719 (1986).
84. H.J. Berthold, W. Preibsch, and E. Vonholdt. Angew. Chem. Int. Engl. **27**, 1524 (1988).
85. N. Herron, D.L. Thorn, R.L. Harlow, and F. Davidson. J. Am. Chem. Soc. **115**, 3028 (1993).
86. A.L. Llamas-Saiz, C. Foces-Foces, and J. Elguero. J. Mol. Struct. **328**, 297 (1994).
87. N. Odiaga, J.A. Kanters, B.T.G. Lutz, and E. Grech. J. Mol. Struct. **273**, 183 (1992).
88. T. Głowiak, Z. Malarski, L. Sobczyk, and E. Grech. J. Mol. Struct. **270**, 441 (1992).
89. T. Głowiak, E. Grech, Z. Malarski, and L. Sobczyk. J. Mol. Struct. **295**, 105 (1993).
90. Z. Malarski, T. Lis, E. Grech, J. Nowicka-Scheibe, and K. Majewska. J. Mol. Struct. **221**, 227 (1990).
91. T. Barth, C. Krieger, F.A. Neugebauer, and H.A. Staab. Angew. Chem. Int. Ed. Engl. **30**, 1028 (1991).
92. O. Salas, J.A. Kanters, and E. Grech. J. Mol. Struct. **271**, 197 (1993).
93. B. Brzeziński, T. Głowiak, E. Grech, Z. Malarski, W. Sawka-Dobrowolska, and L. Sobczyk. J. Mol. Struct. **299**, 1 (1993).
94. A.L. Llamas-Saiz, C. Foces-Foces, J. Elguero, P. Molina, M. Alajarín, and A. Vidal. J. Chem. Soc. Perkin Trans. 2, 2033 (1991).
95. A.L. Llamas-Saiz, C. Foces-Foces, J. Elguero, P. Molina, M. Alajarín, and A. Vidal. J. Chem. Soc. Perkin Trans. 2, 1667 (1991).
96. R.W. Alder, A.G. Orpen, and R.B. Sessions. J. Chem. Soc. Chem. Commun. 999 (1983).
97. R. Schwesinger, M. Missfeldt, K. Peters, and H.G. von Schnering. Angew. Chem. Int. Ed. Engl. **26**, 1165 (1987).
98. J. Rozière, C. Belin, and M.S. Lehman. J. Chem. Soc. Chem. Commun. 388 (1982).
99. S. Scheiner. Acc. Chem. Res. **27**, 402 (1994).
100. P. Barbaro, C. Bianchini, M. Fochi, D. Masi, and C. Mealli. Acta Crystallogr. Sect. C: Cryst. Struct. Commun. **C48**, 625 (1992).
101. C. Krieger, I. Newsom, M.A. Zirnstein, and H.A. Staab. Angew. Chem. Int. Ed. Engl. **28**, 84 (1989).
102. H.A. Staab, M.A. Zirnstein, and C. Krieger. Angew. Chem. Int. Ed. Engl. **28**, 86 (1989).
103. M. Bacci, A. Dei, and R. Morassi. Inorg. Chim. Acta, **7**, 209 (1973).
104. C.A. Hunter and J.K.M. Sanders. J. Am. Chem. Soc. **112**, 5525 (1990).
105. J.-Y. Ortholand, A.M.Z. Slawin, N. Spencer, J.F. Stoddart, and D.J. Williams. Angew. Chem. Int. Ed. Engl. **28**, 1394 (1989).
106. S.L. Price and A.J. Stone. J. Chem. Phys. **86**, 2859 (1987).
107. C.J. Bender. Chem. Soc. Rev. **15**, 475 (1986).
108. R.M. Carman and J.R. Hall. Aust. J. Chem. **17**, 1354 (1964).
109. TEXSAN single crystal structure analysis software. Version 1.6 (1993). Molecular Structure Corporation. The Woodlands, Tex.
110. S. Motherwell and W. Clegg. PLUTO. Program for plotting molecular and crystal structures. University of Cambridge, Cambridge, U.K. 1978.

Acyl cyanides as carbonyl heterodienophiles: application to the synthesis of naphthols, isoquinolones, and isocoumarins

Richard Connors, Elisabeth Tran, and Tony Durst

Abstract: Irradiation of 2-methylbenzoyl cyanide (**3***a*) in acetonitrile solution results in the formation of its dimer, which upon loss of HCN gives rise to the cycloadduct **7***a*. The dimerization also proceeds efficiently with derivatives of **3***a* giving adducts **7***b* and **7***c*. When 2-methylaroyl cyanides are photolyzed in the presence of a more reactive acyl cyanide the mixed adducts **8***a–e* are obtained in excellent yields. The cycloadducts **7***a–c* and **8***a–e* react with carbon and nitrogen nucleophiles by a tandem addition–cyclization sequence furnishing substituted naphthols (**10***a* and **10***b*) and isoquinolones (**11***a–d*), respectively. Isocoumarins **12***a* and **12***b* were prepared from the adducts **8***a* and **8***e* by treatment with potassium *tert*-butoxide in THF.

Key words: naphthols, isoquinolones, isocoumarins, synthesis of; acyl cyanides; hetero Diels–Alder.

Résumé : L'irradiation du cyanure de 2-méthylbenzoyle (**3***a*) en solution dans l'acétonitrile conduit à la formation de son dimère qui, par perte de HCN, fournit le cycloadduit **7***a*. La dimérisation se produit aussi d'une façon efficace avec les dérivés du composé **3***a*; elle conduit alors aux composés **7***b* et **7***c*. Lorsqu'on effectue la photolyse des cyanures de 2-méthylaroyle en présence d'un cyanure d'acyle plus réactif, on obtient alors les produits mixtes **8***a–e* avec d'excellents rendements. Les cycloadduits **7***a–c* et **8***a–e* réagissent avec les nucléophiles carbonés et azotés par une séquence de réactions d'addition–cyclisation en tandem qui fournissent respectivement des naphtols (**10***a* et **10***b*) et des isoquinoléines (**11***a–d*) substitués. Par réaction des adduits **8***a* et **8***e* avec du *tert*-butylate de potassium dans le THF, on a préparé les isocoumarines **12***a* et **12***b*.

Mots clés : naphtols, isoquinoléines, isocoumarines, synthèse; cyanures d'acyle; hétéro Diels–Alder.

[Traduit par la rédaction]

Introduction

o-Quinodimethanes (OQDM) have seen extensive application in the synthesis of natural products (1). Diels–Alder reactions of these intermediates have been studied with both alkene- and heterodienophiles. Oppolzer (2) and Kametani et al. (3) have demonstrated that imines, nitriles, and aldehydes can serve as both inter- and intramolecular dienophiles with *o*-quinodimethanes generated via ring openings of benzocyclobutenes. Sammes and co-workers (4) reported that the dienol generated photochemically from 2-methylbenzaldehyde reacted efficiently with ground state aldehydes in a cycloaddition reaction. Other carbonyl-containing functional groups have not been observed as dienophiles in Diels–Alder reactions with *o*-quinodimethanes. Highly reactive ketones, such as ketomalonates, have received limited attention as dienophiles (5); there is only one report of the carbonyl group of an ester participating in a Diels–Alder reaction (6).

Our report (7) of the cycloaddition of both thermally and photochemically generated *o*-quinodimethanes with benzoyl and acetyl cyanide (see Scheme 2), represents the first example in which an acyl cyanide acts in such a capacity. The recent publication by Kessar et al. which describes the synthesis of various 3-aryl-3,4-dihydroisocoumarins and protoberberines involving fluorodesilylation of 2-((trimethylsilyl)-methyl) benzoyl chlorides, **1**, in the presence of aromatic aldehydes and 3,4-dihydroisoquinolium salts (8), is closely related to our work. This group also describes a "dimerization" of the chloride **1** to the isocoumarin **2** when the fluoride treatment was carried out in the absence of other trapping agents (Scheme 1).

In this paper we present a more detailed account of our earlier report including additional reactions involving several new dienes and dienophiles. In addition, considerable synthetic utility of the cycloadducts has also been demonstrated by their use as intermediates in the synthesis of highly functionalized naphthols, isoquinolones, and isocoumarins.

Discussion and results

At the outset of this study, we postulated that photoenolization of 2-methylbenzoyl cyanide (**3***a*) and, especially, some of the more crowded analogs such as 2-methoxy-6-methylbenzoyl cyanide **3***b* might lead to a benzocyclobutenone such as **6**, by electrocyclization of the intermediate dienol **4** to **5** followed by HCN loss (Scheme 3). Sammes and co-workers demon-

Received February 7, 1994.[1]

R. Connors,[2] E. Tran,[3] and T. Durst.[4] Ottawa-Carleton Chemistry Institute, Department of Chemistry, University of Ottawa, Ottawa, ON K1N 6N5, Canada.

[1] Revision received October 18, 1995.
[2] NSERCC post-graduate scholarship recipient, 1990–1992.
[3] NSERCC summer student, 1992.
[4] Author to whom correspondence may be addressed at: Department of Chemistry, University of Ottawa, Ottawa, Canada. Telephone: (613) 562-5800, ext. 6072. Fax: (613) 562-5170.

Scheme 1.

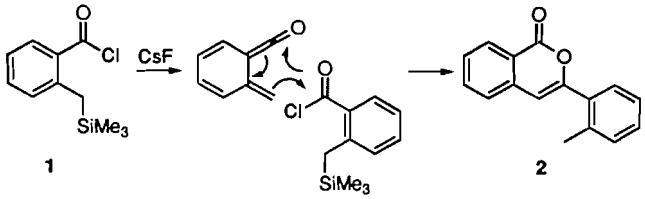

Scheme 2.

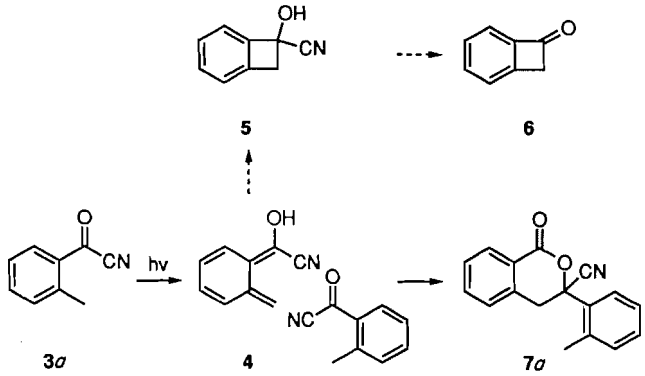

strated that photoenolization of **3***a*, in the presence of maleic anhydride, yields the expected cycloaddition product, confirming the intermediacy of **4** (9). Wagner (10) showed that substitution of the aldehydic hydrogen of 2-methylbenzaldehyde with either an alkyl or aryl group enhances benzocyclobutenol formation, presumably because of a greater propensity for cyclization by the sterically more crowded photoenol. Based on the possibility of a similar effect, we decided to reinvestigate the photochemsitry of **3***a*.

As was described in our preliminary communication (8), irradiation of 0.1–1.0 M acetonitrile solutions of **3***a* furnished an 80% yield of purified **7***a* (Scheme 2). Attempts to isolate the cyanohydrin **5** or the ketone **6** were unsuccessful, suggesting that **4** was not sterically crowded enough to facilitate benzocyclobutenol formation. The formation of **7***a* was interpreted as having resulted from the cycloaddition of **3***a* to photochemically generated **4**, followed by HCN loss.

The presence of the methoxy group in 2-methoxy-6-methylbenzaldehyde, while increasing steric crowding, is known to stabilize its photoenol by intramolecular hydrogen bonding, thus inhibiting benzocyclobutenol formation (11). Irradiation of compounds **3***b* and **3***c* in acetonitrile solution afforded the cycloadducts **7***b* and **7***c*, respectively, in excellent yields (Scheme 3). Photolysis of the *p*-methoxy analog **3***d* produced an intractable mixture. This was not altogether surprising since the similarly substituted aldehyde exhibits little useful photoactivity (12).

Compounds **3***b*–**3***d* were prepared from the appropriately substituted aldehydes (13) via a two-step sequence involving conversion to the TMS cyanohydrins (trimethylsilyl cyanide, ZnI_2), followed by oxidation (pyridinium dichromate) to the aroyl cyanides. The sequence was amenable to a one-pot procedure and afforded the desired compounds in approximately 60% overall yields from the requisite aldehydes.

The reaction between mixed aroyl cyanide pairs was also investigated. It was anticipated that benzoyl cyanide, being less sterically congested, should compete well with **3***a* as a

Scheme 3.

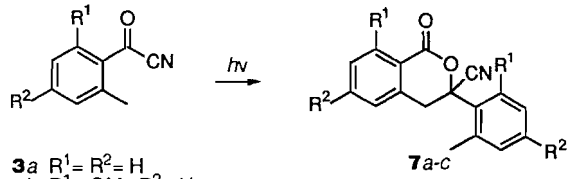

3*a* $R^1 = R^2 = H$
b R^1 = OMe R^2 = H
c R^1 = OMe R^2 = Me
d R^1 = H R^2 = OMe

Scheme 4.

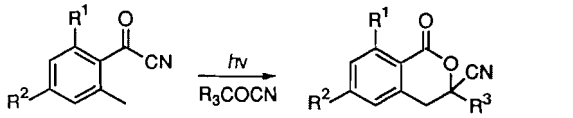

3*a* $R^1 = R^2 = H$
b R^1 = OMe R^2 = H
c R^1 = OMe R^2 = Me

8*a* $R^1 = R^2 = H$ R^3 = Ph
b R^1 = OMe R^2 = H R^3 = Ph
c R^1 = OMe R^2 = Me R^3 = Ph
d R^1 = OMe R^2 = H
R^3 = 2-MeO-4-MePh
e $R^1 = R^2 = H$ $R^3 = CH_3$

dienophile. Indeed, irradiation of an acetonitrile solution of **3***a*, in the presence of two equivalents of benzoyl cyanide, gave the cycloadduct **8***a* in 83% yield (Scheme 4); no trace of **7***a* was detected, even when only one equivalent of benzoyl cyanide was used. The aroyl cyanides **3***b* and **3***c* exhibited similar behavior when irradiated in the presence of benzoyl cyanide, furnishing the adducts **8***b* and **8***c* in excellent yield. Finally, the highly substituted cycloadduct **8***d* was prepared in 95% yield by irradiation of an acetonitrile solution of the 2,6-disubstituted benzoyl cyanide **3***b* in the presence of one equivalent of 2-methoxy-4-methylbenzoyl cyanide.

Cycloaddition between the cyanohydrin OQDMs and alkanoyl-substituted acylcyanides was also found to be highly efficient. For example, irradiation of 2-methylbenzoyl cyanide in the presence of 2 equivalents of acetyl cyanide afforded 50% of adduct **8***e*.

The cycloadducts **7** and **8** contain an interesting combination of functional groups, with the internally acylated cyanohydrin representing a masked carbonyl function that would be revealed by loss of HCN following ester cleavage (Scheme 5). Such a process would generate the intermediate **9**, which, depending on the nature of the nucleophile, would be able to undergo cyclization to a fused ring system. This process has been realized with nucleophiles such as methyllithium and various amines and resulted in the synthesis of highly functionalized 3-arylnaphthols and 3-substituted isoquinolones, respectively. Finally, treatment of the adducts **7** and **8** with strong bases afforded isocoumarins.

Preparation of 3-aryl-1-naphthols

Treatment of a THF solution of **7***a* with 2 equivalents of methyllithium at −78°C and slowly warming the reaction mixture to room temperature gave the naphthol **10***a* in 60% yield (Scheme 6). Compound **7***b* was similarly converted, in 78% yield, into the naphthol **10***b*, which was readily characterized by its ^1H NMR spectrum showing the methyl group at δ = 2.30, singlets at δ = 6.78 and 7.36 ppm due to the C2 and C4 hydrogens on the naphthol ring, seven additional aromatic

Scheme 5.

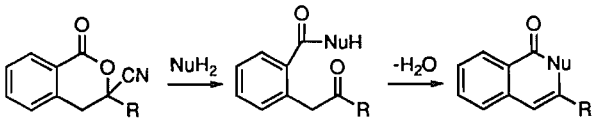

7,8 9

Scheme 6.

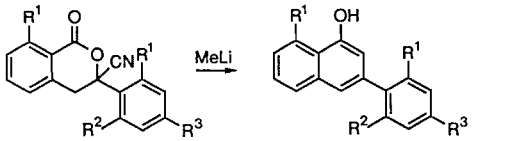

7*a* $R^1 = R^3 = H$ $R^2 = Me$
8*d* $R^1 = OMe$ $R^2 = H$ $R^3 = Me$

10*a* $R^1 = R^3 = H$ $R^2 = Me$
b $R^1 = OMe$ $R^2 = R^2 = H$ $R^3 = Me$

hydrogens, and a broad exchangeable singlet at 5.53 ppm corresponding to the phenolic hydrogen. Analysis of the ^1H NMR spectrum of the crude product indicated that complex mixtures consisting of a methyl ketone (compound **9**, NuH=CH_3, Scheme 5) and permethylated by-products were obtained when the same methodology was attempted with **7***c* and **7***d*. Presumably, the steric crowding in the 2,6-disubstituted biaryl adducts is sufficient to inhibit facile cyclization to the naphthols from the intermediate methyl ketones.

Isoquinolones and isocoumarins

In addition to the naphthols, the cycloadducts provided a facile route to various isoquinolones. The isoquinolone (1-oxo-1,2-dihydroisoquinoline) ring system is of interest owing to its presence in numerous alkaloids, in addition to its utility as a synthetic intermediate (14).

Compound **8***a* (Scheme 7), when refluxed with 1.5 equivalents of benzylamine in dry cyclohexane, yielded a viscous yellow oil that gave a complex proton NMR spectrum and exhibited a strong infrared absorbance at 1650 cm^{-1}. This material was readily converted to **11***a* (86%) upon further refluxing in 50% aqueous acetic acid. Compound **11***a* exhibited a strong infrared absorbance at 1652 cm^{-1}, confirming the presence of the amide functionality, as well as characteristic signals in the proton NMR spectrum at 5.23 and 6.43 ppm due to the benzyl and alkene hydrogens, respectively. The same methodology was applied to the synthesis of compounds **11***b–d* from **8***a* or **8***e* with yields ranging from 60 to 80%.

Finally, the potential for an isocoumarin synthesis was briefly investigated. The cycloadducts **8***a–e* are essentially masked isocoumarins that, it may be envisioned, have undergone addition of HCN across the 3,4 double bond. It follows that the isocoumarins should be accessible by base-catalyzed elimination of HCN. Initial attempts employing DBU or DBN, known to catalyze efficient dehydrohalogenation (15), gave unsatisfactory results with **8***a–e*. Potassium *tert*-butoxide proved to be the reagent of choice as treatment of an ice-cooled THF solution of compound **8***a* (Scheme 8) with 1.5 equivalents of the base yielded the known isocoumarin **12***a* (16) in 50% yield. Similarly, isocoumarin **12***b* (17) was prepared from **8***e* in 66% yield.

Scheme 7.

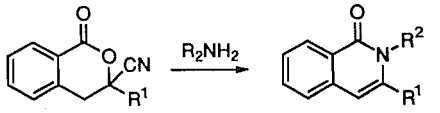

8*a* $R^1 = Ph$
e $R^1 = Me$

11*a* $R^1 = Ph$ $R^2 = Bn$
b $R^1 = Ph$ $R^2 = n$Bu
c $R^1 = Me$ $R^2 = Bn$
d $R^1 = Me$ $R^2 = n$Bu

Scheme 8.

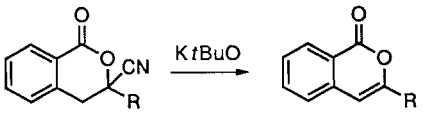

8*a* R= Ph
e R= Me

12*a,b*

Experimental section

General

Melting points were determined by use of a Gallenkamp digital melting point apparatus and are uncorrected. IR spectra were recorded as chloroform solutions on a Bomem–Michelson MB-100 spectrophotometer. ^1H and ^{13}C NMR spectra were obtained as $CHCl_3$ solutions on either a Varian XL-300 or a Gemini-200 spectrometer with the chemical shifts reported in ppm relative to TMS. Solvents for the extractions and chromatographic purifications (ethyl acetate = EA, and hexane = H) were routinely distilled prior to use. Reagent grade acetonitrile was used as received. Silica gel, 230–400 mesh, was used for flash chromatography.

2-Methylbenzoyl cyanide (*3a*) (**9**)

A mixture of 20 g (0.13 mol) of 2-methylbenzoyl chloride, 6.3 g (0.13 mol) sodium cyanide, and 0.1 g (0.36 mmol) of tetrabutylammonium chloride in 140 mL of 5:1 CH_2Cl_2–water was vigorously stirred at room temperature for 12 h, after which time IR analysis indicated complete reaction. After filtration of the solids the organic phase was separated, dried over magnesium sulfate, and concentrated in vacuo, giving 19.6 g of a yellow oil. Vacuum distillation furnished 11.3 g (60%) of a colorless liquid (bp 75–80°C/10 Torr; 1 Torr = 133.3 Pa) that solidified on standing. IR: 2222, 1680 cm^{-1}; ^1H NMR δ: 2.61 (s, 3H), 7.35 (d, 1H, J=7.5 Hz), 7.44 (dd, 1H, J = 7.5, 7.8 Hz), 7.60 (t, 1H, J = 7.5 Hz), 8.20 (d, 1H, J = 7.8 Hz); MS (EI) *m/z*: 145 (M^+), 118, 90.

2-Methoxy-6-methylbenzoyl cyanide (*3b*)

To an ice-cooled stirred solution of 5.0 g (33.3 mmol) of 2-methoxy-6-methylbenzaldehyde and 100 mg of zinc iodide (0.3 mmol) in 75 mL CH_2Cl_2 was added 3.6 g (4.9 mL, 36.7 mmol) of trimethylsilyl cyanide via syringe under nitrogen atmosphere. The mixture was allowed to warm to room temperature and TLC analysis (H/EA, 3:1) indicated complete conversion after 1 h after warming. The solvent was removed on a rotovap at 40°C and the concentrate passed through 20 g of 70–230 mesh silica gel with 150 mL of CH_2Cl_2. The CH_2Cl_2 solution of the TMS cyanohydrin was transferred to a

250 mL round-bottomed flask, cooled to 0°C under nitrogen atmosphere, and 18.8 g (50.0 mmol) of pyridinium dichromate was introduced, with efficient stirring, over 5 min. The mixture was stirred at room temperature for 12 h after which time the solvent was removed on a rotovap at 20°C. The residue was triturated with ether and the solution was filtered through 20 g 70–230 mesh silica gel. Concentration of the ether solution produced 4.2 g of crude **3***b*, which furnished 3.5 g (60%) of purified **3***b* as yellow needles after flash chromatography (3:1 H/EA); mp 55.3–56.1°C (CH_2Cl_2–hexane); IR: 2220, 1670 cm^{-1}; ^1H NMR δ: 2.39 (s, 3H), 3.96 (s, 3H), 6.86 (d, 1H, J = 7.5 Hz), 6.87 (d, 1H, J = 8.3 Hz), 7.43 (t, 1H, J = 8.4 Hz); ^{13}C NMR δ: 20.7, 56.1, 109.7, 114.8, 123.2, 124.2, 135.5, 142.2, 161.1, 167.6; MS (EI) *m/z*: 175 (M^+), 160, 148; HRMS calcd. for $C_{10}H_9NO_2$: 175.0633; found: 175.0635.

2-Methoxy-4,6-dimethylbenzoyl cyanide (3*c*)

A solution of 5.0 g (33.3 mmol) of 2-methoxy-4,6-dimethylbenzaldehyde in 75 mL of CH_2Cl_2 was treated as described for **3***b*. Concentration of the product mixture followed by trituration with ether and filtration of the solution through a silica gel plug gave 5.6 g of a tan-brown solid. The crude aroyl cyanide was readily crystallized from CH_2Cl_2–hexane, furnishing 4.6 g (79%) of pure **3***c* as yellow crystals, mp 71.8–72.5°C. IR: 2219, 1608 cm^{-1}; ^1H NMR δ: 2.34 (s, 3H), 2.35 (s, 3H), 3.93 (s, 3H), 6.65 (s, 1H), 6.66 (s, 1H); ^{13}C NMR δ: 21.0, 22.2 55.9, 110.4, 115.0, 120.6, 125.4, 142.6, 147.5, 161.5, 166.8; MS (EI) *m/z*: 189 (M^+), 174, 162; HRMS calcd. for $C_{11}H_{11}NO_2$: 189.0790; found: 189.0802.

2-Methyl-4-methoxybenzoyl cyanide (3*d*)

A solution of 5.0 g (33.3 mmol) of 2-methyl-4-methoxybenzaldehyde in 75 mL of CH_2Cl_2 was treated as described for **3***b*. Concentration of the product mixture followed by trituration with ether and filtration of the solution through a silica gel plug gave 5.1 g of a yellow solid. The crude aroyl cyanide crystallized from ether–hexane, furnishing 4.5 g (78%) of pure **3***d* as colorless needles, mp 62.0–62.8°C. IR: 2219, 1667 cm^{-1}; ^1H NMR δ: 2.59 (s, 3H), 3.90 (s, 3H), 6.79 (d, 1H, J = 2.0 Hz), 6.88 (dd, 1H, J = 2.0, 8.8 Hz), 8.15 (d, 1H, J = 8.8 Hz) ^{13}C NMR δ: 22.4, 55.7, 111.7, 113.6, 118.5, 124.9, 138.15, 146.0, 165.2, 166.6; MS (EI) *m/z*: 175 (M^+), 163, 148; HRMS calcd. for $C_{10}H_9NO_2$: 175.0633; found: 175.0648.

2-Methoxy-4-methylbenzoyl cyanide (3*e*)

A solution of 5.0 g (33.3 mmol) of 2-methoxy-4-methylbenzaldehyde in 75 mL of CH_2Cl_2 was treated as described for **3***b*. Flash chromatography (5:1 H/EA) gave 3.8 g (65%) **3***e* as a yellow oil, which solidified on storage at 0°C (mp 68.2–69.0°C). IR: 2221, 1608 cm^{-1}; ^1H NMR δ: 2.42 (s, 3H), 3.96 (s, 3H), 6.81 (s, 1H), 6.87 (d, 1H, J = 8.1 Hz), 7.84 (d, 1H, J = 8.1 Hz); ^{13}C NMR δ: 22.5, 55.9, 112.9, 114.3, 120.2, 122.1, 132.9, 150.5, 161.3, 164.7; MS (EI) *m/z*: 175 (M^+), 158, 149; HRMS calcd. for $C_{10}H_9NO_2$: 175.0633; found: 175.0646.

3,4-Dihydro-3-cyano-3-(2-methylphenyl)-1*H*-2-benzopyran-1-one (7*a*)

A solution of 300 mg (2.1 mmol) of 2-methylbenzoyl cyanide in 2.0 mL of acetonitrile (1.0 M), contained in a quartz test tube, was suspended 10 cm from a Hanovia medium-pressure mercury lamp and irradiated until TLC analysis indicated complete conversion of the starting material (5–6 h). Concentration of the solvent on a rotovap at 40°C followed by flash chromatography (5:1 H/EA) of the crude adduct gave 220 mg (81%) of **7***a* as white needles, mp 126.5–127.5°C (CH_2Cl_2–hexane); IR: 1747 cm^{-1}; ^1H NMR δ: 2.68 (s, 3H), 3.64 (d, 1H, J = 16.5 Hz), 3.75 (d, 1H, J = 16.5 Hz), 7.23–7.40 (m, 4H), 7.46–7.70 (m, 3H), 8.16 (d, 1H, J = 7.7 Hz); ^{13}C NMR δ: 20.9, 37.4, 77.4, 117.5, 123.7, 125.6, 126.4, 127.9, 129.0, 130.8, 130.8, 132.4, 133.1, 135.0, 135.6, 136.8, 162.0; MS (EI) *m/z*: 262 $(M-1)^+$, 245, 218; HRMS calcd. for $C_{17}H_{13}NO_2$: 263.0946; found: 263.0935.

3,4-Dihydro-3-cyano-8-methoxy-3-(2-methoxy-6-methylphenyl)-1*H*-2-benzopyran-1-one (7*b*)

A solution of 300 mg (1.7 mmol) of 2-methoxy-6-methylbenzoyl cyanide in 2.0 mL of acetonitrile, contained in a quartz test tube, was irradiated as described for **7***a* until TLC analysis (H/EA acetate 2:1) indicated complete conversion of the starting material (12 h). Concentration of the solvent on a rotvap at 40°C followed by flash chromatography (CH_2Cl_2) of the crude adduct gave 249 mg (90%) of **7***b* as a white solid. Recrystallization from CH_2Cl_2-hexane afforded colorless crystals, mp 145.3–146.0°C. IR: 1744 cm^{-1}; ^1H NMR δ: 2.61 (s, 3H), 3.46 (d, 1H, J = 16.9 Hz), 3.66 (d, 1H, J = 16.9 Hz), 3.87 (s, 3H), 3.94 (s, 3H), 6.85 (m, 3H), 6.98 (d, 1H, J = 8.3 Hz), 7.22 (dd, 1H, J = 7.8, 5.36 Hz), 7.53 (dd, 1H, J = 7.8, 8.3 Hz); ^{13}C NMR δ: 23.2, 38.2, 56.1, 56.2, 77.0 110.5, 111.9, 112.2, 118.2, 119.6, 122.4, 126.4, 130.0, 135.6, 138.2, 138.6, 156.4, 158.6, 161.4; MS (EI) *m/z*: 322 $(M-1)^+$, 278, 263; HRMS calcd. for $C_{19}H_{17}NO_4$: 323.1158; found: 323.1160.

3,4-Dihydro-3-cyano-8-methoxy-6-methyl-3-(2-methoxy-4,6-dimethylphenyl)-1*H*-2-benzopyran-1-one (7*c*)

A solution of 300 mg (1.6 mmol) of 2-methoxy-4,6-dimethylbenzoyl cyanide in 2.0 mL of acetonitrile was irradiated as above until TLC analysis indicated complete conversion of the starting material (16 h). Concentration of the solvent at 40°C followed by flash chromatography (2:1 H/EA) gave 140 mg (50%) of **7***c* (colorless crystals from CH_2Cl_2–hexane), mp 202.5–203.0°C. IR: 1741 cm^{-1}; ^1H NMR δ: 2.28 (s, 3H), 2.38 (s, 3H), 2.56 (s, 3H), 3.40 (d, 1H, J = 16.6 Hz), 3.58 (d, 1H, J = 16.6 Hz), 3.85 (s, 3H), 3.93 (s, 3H), 6.65 (s, 2H), 6.67 (s, 1H), 6.76 (s, 1H); ^{13}C NMR δ: 21.2, 22.2, 23.0, 38.4, 56.1, 56.1, 77.4, 109.7, 111.3, 112.6, 118.4, 119.7, 120.5, 127.2, 137.9, 138.6, 140.1, 147.0, 156.4, 158.9, 161.4; MS (EI) *m/z*: 351 (M^+), 350, 306; HRMS calcd. for $C_{21}H_{21}NO_4$: 351.1471; found 351.1466.

3,4-dihydro-3-cyano-3-phenyl-1*H*-2-benzopyran-1-one (8*a*)

A solution of 300 mg (2.1 mmol) of 2-methylbenzoyl cyanide and 550 mg (4.1 mmol) of benzoyl cyanide in 2.0 mL of acetonitrile was irradiated as described above for 6 h. Concentration of the solvent on a rotovap at 40°C followed by flash chromatography (5:1 H/EA) of the crude adduct gave 385 mg (75%) of **8***a*, colorless plates, mp 144.6–146.1°C, from ether–hexane. IR: 1748 cm^{-1}; ^1H NMR δ: 3.48 (d, 1H, J = 16.7 Hz), 3.60 d, 1H, J = 16.7 Hz), 7.34 (d, 1H, J = 7.5 Hz), 7.45–7.55 (m, 4H), 7.61–7.71 (m, 3H), 8.19 (d, 1H, J = s7.7 Hz); ^{13}C NMR δ: 40.8, 78.2, 117.8, 123.6, 125.1, 127.7, 129.0, 129.2,

130.1, 130.9, 135.0, 135.5, 135.7, 162.2; MS (EI) *m/z*: 249 (M^+), 203, 190; HRMS calcd. for $C_{16}H_{11}NO_2$: 249.07900; found: 249.0809.

3,4-Dihydro-3-cyano-8-methoxy-3-phenyl-1*H*-2-benzopyran-1-one (8*b*)

A solution of 300 mg (1.7 mmol) of 2-methoxy-6-methylbenzoyl cyanide and 450 mg (3.4 mmol) of benzoyl cyanide in 2.0 mL of acetonitrile was irradiated as above for 6 h. Concentration of the solvent followed by flash chromatography (3:1 H/EA) of the crude adduct gave 420 mg (88%) of **8*b*** as a white solid, mp 146.0–147.0°C. IR: 1748 cm^{-1}; ^1H NMR δ: 3.40 (d, 1H, J = 16.4 Hz), 3.46 (d, 1H, J = 16.4 Hz), 3.98 (s, 3H), 6.87 (d, 1H, J = 7.6 Hz), 7.02 (d, 1H, J = 8.6 Hz), 7.40–7.50 (m, 3H), 7.57 (t, 1H, J = 7.6 Hz), 7.65–7.75 (m, 2H); ^{13}C NMR δ: 41.2, 56.3, 77.5, 112.0, 112.3, 117.8, 119.6, 125.1, 129.1, 130.0, 135.7, 135.9, 138.0, 158.8, 161.6; MS (EI) *m/z*: 279 (M^+), 249, 220; HRMS calcd. for $C_{17}H_{13}NO_3$: 279.0895; found: 279.0888.

3,4-Dihydro-3-cyano-8-methoxy-6-methyl-3-phenyl-1*H*-2-benzopyran-1-one (8*c*)

A solution of 300 mg (1.6 mmol) of 2-methoxy-4,6-dimethylbenzoyl cyanide and 420 mg (3.2 mmol) of benzoyl cyanide in 2.0 mL of acetonitrile was irradiated as above for 6 h. Concentration of the solvent followed by flash chromatography (5:1 H/EA) gave 363 mg (78%) of **8*c***, white solid, mp 166.0–167.0°C. IR: 1746 cm^{-1}; ^1H NMR δ: 2.41 (s, 3H), 3.33 (d, 1H, J = 16.1 Hz), 3.47 (d, 1H, J = 16.1 Hz), 3.97 (s, 3H), 6.69 (s, 1H), 6.82 (s, 1H), 7.50 (m, 3H), 7.70 (m, 2H); ^{13}C NMR δ: 22.3, 41.2, 56.2, 77.4, 109.4, 112.9, 117.9, 120.4, 125.1 129.0, 129.9, 135.8 137.8, 147.6 159.0, 161.8; MS (EI) *m/z*: 293 (M^+), 263, 247; HRMS calcd. for $C_{18}H_{15}NO_3$: 293.1052; found: 293.1055.

3,4-Dihydro-3-cyano-8-methoxy-3-(2-methoxy-4-methylphenyl)-1*H*-2-benzopyran-1-one (8*d*)

A solution of 300 mg (1.7 mmol) of 2-methoxy-6-methylbenzoyl cyanide and 300 mg (1.7 mmol) of 2-methoxy-4-methylbenzoyl cyanide in 2.0 mL of acetonitrile contained in a quartz test tube was irradiated for 6 h after which time TLC analysis indicated complete conversion of the starting materials. Concentration of the solvent at 40°C followed by flash chromatography (2:1 H/EA acetate) of the crude adduct gave 526 mg (95 %) of **8*d*** as a yellow solid, mp 176.5–177.5°C. IR: 1745 cm^{-1}; ^1H NMR δ: 2.36 (s, 3H), 3.34 (d, 1H, J = 16.3 Hz), 3.78 (d, 1H, J = 16.3 Hz), 3.91 (s, 3H), 3.96 (s, 3H), 6.84 (m, 3H), 6.98 (d, 1H, J = 8.5 Hz), 7.53 (dd, 1H, J = 7.8, 7.6), 7.60 (d, 1H, J = 7.9 Hz); ^{13}C NMR δ: 21.5, 38.2, 55.9, 56.2, 77.4, 111.9, 112.3, 112.9, 117.6, 119.7, 121.0, 121.7, 126.1, 135.7, 138.6, 141.5, 155.8, 159.1, 161.4; MS (EI) *m/z*: 323 (M^+), 293, 278; HRMS calcd. for $C_{19}H_{17}NO_4$: 323.1158; found: 323.1161.

3,4-Dihydro-3-cyano-3-methyl-1*H*-2-benzopyran-1-one (8*e*)

A solution of 300 mg (2.1 mmol) of 2-methylbenzoyl cyanide and 285 mg (4.1 mmol) of acetyl cyanide in 2.0 mL of acetonitrile was irradiated as described above until TLC analysis indicated complete conversion of the starting material (12 h). Concentration of the solvent followed by flash chromatography (3:1 H/EA) gave 192 mg (50%) of **8*e*** as a white solid, mp 98.0–100.0°C. IR: 1746 cm^{-1}; ^1H NMR δ: 1.94 (s, 3H), 3.26 (d, 1H, J = 16.6 Hz), 3.32 (d, 1H, J = 16.6 Hz) 7.29 (d, 1H, J = 6.8 Hz), 7.48 (t, 1H, J = 6.4 Hz), 7.63 (dt, 1H, J = 1.4, 7.5 Hz), 8.12 (dd, 1H, J = 14, 7.5 Hz); ^{13}C NMR δ: 26.6, 38.26 (t), 77.4, 118.8, 123.34 (s), 127.6, 128.9, 130.89, 134.89, 135.4, 162.3; MS (EI) *m/z*: 187 (M^+), 172, 144; HRMS calcd. for $C_{11}H_9NO_2$: 187.0633; found: 187.0646

3-(2-Methylphenyl)-1-naphthol (10*a*)

To a stirred THF solution of 600 mg (2.3 mmol) of 3,4-dihydro-3-cyano-3-(2-methylphenyl)-1*H*-2-benzopyran-1-one (**8*a***), cooled to −78°C under nitrogen atmosphere, was added via syringe 1.8 mL (2.5 mmol) of MeLi (1.4 M in ether). The mixture was maintained at −78°C for 30 min before a second 1.8 mL aliquot of MeLi was administered. The reaction mixture was then warmed to room temperature over 30 min and left stirring overnight (15 h). The yellow solution was quenched by dropwise addition of 10% aqueous HCl and the resulting phases were separated. The aqueous layer was extracted with ether and the combined organic phases were washed with brine. The resulting ether solution was dried over $MgSO_4$ and concentrated on a rotvap, giving 412 mg of a brown oil. Flash chromatography (1:2 H/CH_2Cl_2) furnished 320 mg (60%) of **10*a*** as a brown oil. IR: 3577 cm^{-1}; ^1H NMR δ: 2.30 (s, 3H), 5.53 (s, 1H), 6.78 (s, 1H), 7.28 (s, 4H), 7.36 (s, 1H), 7.50 (m, 2H), 7.82 (m, 1H), 8.20 (m, 1H); ^{13}C NMR δ: 20.6, 110.9, 120.6, 121.5, 123.3, 125.1, 125.7, 126.7, 127.3, 127.7, 129.77 (d), 130.3, 134.5, 135.5, 139.7, 141.7, 151.0; MS (EI) *m/z*: 234 (M^+), 215, 202; HRMS calcd. for $C_{17}H_{14}O$: 234.1045; found: 234.1043.

8-Methoxy-3-(2-methoxy-4-methylphenyl)-naphthol (10*b*)

3,4-Dihydro-3-cyano-8-methoxy-3-(2-methoxy-4-methylphenyl)-1*H*-2-benzopyran-1-one (**8*d***) (100 mg; 0.3 mmol) was treated as described above for **10*a***, giving 108 mg of a brown oil. Flash chromatography (3:1 H/EA) furnished 78 mg (86%) of **10*b*** as a yellow oil. IR: 3404 cm^{-1}; ^1H NMR δ: 2.40 (s, 3H), 3.80 (s, 3H), 4.04 (s, 3H), 6.73 (d, 1H, J = 7.7 Hz), 6.81 (s, 1H), 6.85 (d, 1H, J = 8.4 Hz), 7.10 (d, 1H, J = 1.5 Hz), 7.27 (t, 2H, J = 7.6 Hz), 7.40 (d, 1H, J = 6.2 Hz), 7.42 (d, 1H, J = 1.6 Hz), 9.27 (s, 1H); ^{13}C NMR δ: 21.5, 55.5, 56.1, 103.7, 112.2, 112.4, 113.9, 119.3, 121.4, 122.1, 125.5, 127.4, 130.7, 136.6, 138.2, 138.9, 153.6, 156.0, 156.4; MS (EI) *m/z*: 294 (M^+), 267, 234; HRMS calcd. for $C_{19}H_{18}O_3$: 294.1256; found: 294.1264.

1-Oxo-3-phenyl-2-phenylmethyl-1,2-dihydroisoquinoline (11*a*)

A solution of 200 mg (0.8 mmol) of 3,4-dihydro-3-cyano-3-phenyl-1*H*-2-benzopyran-1-one (**8*a***) and 130 mg (1.2 mmol) benzylamine in 10 mL cyclohexane was heated to reflux for 15 h after which time TLC analysis indicated complete conversion of the starting materials. The solvent was removed on a rotovap, the concentrate dissolved in 10 mL 50% aqueous acetic acid, and the mixture heated to reflux for an additional 3 h. After cooling to room temperature, the product mixture was diluted with 20 mL water and extracted with three 15 mL portions of CH_2C1_2. The combined organic phases were dried over $MgSO_4$, filtered, and concentrated, giving a yellow oil that after flash chromatography (3:1 H/EA) furnished 217 mg (86%) of **11*a***. IR: 1652 cm^{-1}; ^1H NMR δ: 5.23 (s, 2H), 6.43 (s, 1H), 6.88 (m, 2H), 7.14–7.70 (m, 11H), 8.48 (d, 1H, J = 8.0

Hz); ^{13}C NMR δ: 48.5, 108.0, 125.2, 125.8, 126.7, 126.8, 126.9, 128.2, 128.2, 128.3, 128.8, 129.1, 132.5, 135.8, 136.4, 137.6, 143.8, 163.1; MS (EI) *m/z*: 310 $(M-1)^+$, 232, 205; HRMS calcd. for $C_{22}H_{17}NO$: 311.1310; found: 311.1287.

2-Butyl-1-oxo-3-phenyl-1,2-dihydroisoquinoline (11*b*)
A solution of 275 mg (1.1 mmol) of 3,4-dihydro-3-cyano-3-phenyl-1*H*-2-benzopyran-1-one (**8***a*) and 120 mg (1.7 mmol) of *n*-butylamine in 15 mL cyclohexane was treated as described for **11***a*. Flash chromatography (3:1 H/EA) gave 236 mg (77%) of **11***b* IR: 1648 cm^{-1}; ^1H NMR δ: 0.70 (t, 3H, $J = 7.4$ Hz), 1.11 (m, 2H), 1.52 (m, 2H), 3.92 (t, 2H, $J = 7.7$ Hz), 6.37 (s, 1H), 7.40 (m, 7H), 7.60 (t, 1H, $J = 7.4$ Hz); ^{13}C NMR δ: 13.4, 19.9, 30.7, 45.3, 107.7, 125.2, 125.6, 126.5, 127.9, 128.3, 128.8, 129.0, 132.2, 136.2, 136.2, 143.6, 162.7; MS (EI) *m/z*: 277 (M^+), 260, 234, 221; HRMS calcd. for $C_{19}H_{19}NO$: 277.1426; found: 277.1446.

1-Oxo-3-methyl-2-phenylmethyl-1,2-dihydroisoquinoline (11*c*)
A solution of 217 mg (1.2 mmol) of 3,4-dihydro-3-cyano-3-methyl-1*H*-2-benzopyran-1-one (**8***e*) and 200 mg (1.8 mmol) benzylamine in 15 mL cyclohexane was treated as described for **11***a*. Flash chromatography (4:1 H/EA) gave 165 mg (57%) of **11***c*: IR: 1657 cm^{-1}; ^1H NMR δ: 2.30 (s, 3H), 5.40 (s, 2H), 6.34 (s, 1H), 7.13 (d, 2H, $J = 7.6$ Hz), 7.23 (m, 3H), 7.41 (m, 2H), 7.59 (t, 1H, $J = 7.5$ Hz), 8.41 (d, 1H, $J = 8.1$ Hz); ^{13}C NMR δ: 20.6, 47.0, 106.1, 124.4, 125.0, 125.9, 126.3, 127.1, 128.2, 128.7, 132.3, 136.8, 137.6, 139.5, 163.4; MS (EI) *m/z*: 249 (M^+), 232, 172, 158; HRMS calcd. for $C_{17}H_{15}NO$: 249.1154; found: 249.1161.

2-Butyl-1-oxo-3-methyl-1,2-dihydroisoquinoline (11*d*)
A solution of 289 mg (1.5 mmol) of 3,4-dihydro-3-cyano-3-methyl-1*H*-2-benzopyran-1-one (**8***e*) and 210 mg (2.3 mmol) of *n*-butylamine in 15 mL cyclohexane was treated as described for **11***a*. Flash chromatography (4:1 H/EA) gave 281 mg (85%) of **11***d*: IR: 1651 cm^{-1}; ^1H NMR δ: 0.92 (t, 3H, $J = 7.2$ Hz), 1.41 (m, 2H), 1.64 (m, 2H), 2.35 (s, 3H), 2.35 (s, 3H), 4.01 (t, 2H, $J = 7.7$ Hz), 6.25 (s, 1H), 7.33 (m, 2H), 7.50 (t, 1H, $J = 8.3$ Hz), 8.31 (d, 1H, $J = 8.1$ Hz); ^{13}C NMR δ: 13.7, 20.3, 20.4, 30.9, 44.1, 105.9, 124.5, 124.8, 125.7, 127.8, 132.0., 136.6, 138.9, 162; MS (EI) *m/z*: 215 (M^+), 198, 186, 173; HRMS calcd. for $C_{14}H_{17}NO$: 215.1310; found: 215.1298.

3-Phenyl-1*H*-2-benzopyran-1-one (12*a*)
To a stirred solution of 100 mg (0.4 mmol) of 3,4-dihydro-3-cyano-3-phenyl-1*H*-2-benzopyran-1-one (**8***a*) in 15 mL of dry THF, cooled to 0°C, was added 70 mg (0.6 mmol) of potassium *tert*-butoxide under nitrogen atmosphere. The mixture was warmed to room temperature and stirred for 15 h after which time TLC analysis indicated complete conversion of the starting material. The reaction was quenched by dropwise addition of 6.0 mL 10% aqueous HCL followed by extraction with three 15 mL aliquots of CH_2C1_2. After drying over $MgSO_4$ and concentrating the solvent, the crude isocoumarin was purified by flash cohromatography (4:1 H/EA) to give 45 mg (50%) of **12***a*, mp 89–90°C. The spectral properties agreed with the literature values (16).

3-Methyl-1*H*-2-benzopyran-1-one (12*b*)
A stirred solution of 100 mg (0.5 mmol) of 3,4-dihydro-3-cyano-3-methyl-1*H*-2-benzopyran-1-one (**8***e*) in 15 mL dry THF was treated as described above and gave 57 mg (66%) of purified **12***b*, mp 74°C, after flash chromatography (CH_2Cl_2). The melting point and spectral characteristics agreed with the literature values (17).

Acknowledgements

Financial support in the form of a Natural Sciences and Engineering Research Council of Canada (NSERCC) post-graduate scholarship (R.C.), an NSERCC summer research fellowship (E.T.), and an NSERCC operating grant (T.D.) is gratefully acknowledged.

References

1. J.L. Charlton and M.M. Alauddin. Tetrahedron, **43**, 2873 (1987).
2. W. Oppolzer. Angew. Chem. Int. Ed. Engl. **11**, 1031 (1971).
3. T. Kametani, M. Kajiwara, T. Takahashi, and K. Fukumoto. J. Chem. Soc. Perkin Trans. 1, 737 (1975).
4. B.J. Arnold, P.G. Sammes, and T.W. Wallace. J. Chem. Soc. Perkin Trans. 1, 409 (1974).
5. M. Koreeda and M.A. Ciufilini. J. Am. Chem. Soc. **104**, 2308 (1982).
6. K.T. Tagmazyan, R.S. Mkrtchyan, and A.T. Babayan. Zh. Org. Khim. **10**, 1657 (1974).
7. R. Connors and T. Durst. Tetrahedron Lett. **33**, 7277 (1992).
8. S.V. Kessar, P. Singh, R. Vohra, N.P. Kaur, and D. Venugopal. J. Org. Chem. **57**, 6716 (1992).
9. B.J. Arnold, S.M. Mellows, P.G. Sammes, and T.W. Wallace. J. Chem. Soc. Perkin Trans. 1, 401 (1974).
10. P.J. Wagner. J. Am. Chem. Soc. **113**, 709 (1991).
11. Y. Kitaura and T. Matsuura. Tetrahedron Lett. 3309 (1967).
12. J.L. Charlton and K. Koh. Tetrahedron Lett. **29**, 5595 (1988).
13. F.M. Hauser and S.R. Ellenberger. Synthesis, 723 (1987).
14. M. Shamma and J.L. Moniot. Isoquinoline alkaloid research. Plenum Press, New York. 1978. p. 57.
15. H. Oediger, F. Muller, and K. Eiter. Synthesis, 591 (1972).
16. T.L. Gray, A. Peter, and R.S. Ward. Tetrahedron, **35**, 2539 (1979).
17. T. Sakamoto. Chem. Pharm. Bull. **34**, 2754 (1986).

Decomposition of tosylhydrazones of benzoin, benzoin acetate, and benzoin benzoate with alkali and metal complex hydrides

Tsukasa Iwadare, Yoshiyuki Ichinohe, and Kazuhiko Orito

Abstract: Treatment of tosylhydrazones of benzoin, benzoin acetate, and benzoin benzoate with alkali under protic and aprotic conditions yielded diphenyl acetylene together with desoxybenzoin. An increase in leaving aptitude of the adjacent group enhanced the formation of diphenyl acetylene. By treatment with $LiAlH_4$ and with $NaBH_4$, the tosylhydrazones gave stilbenes in good yields. Selective formation of *cis*- or *trans*-stilbene was observed in some cases.

Key words: tosylhydrazone, benzoin derivatives, decomposition, metal complex hydrides.

Résumé : Le traitement des tosylhydrazones de la benzoïne, de l'acétate de benzoïne et du benzoate de benzoïne par des alcalis dans des conditions tant protiques qu'aprotiques fournit du diphénylacétylène et de la désoxybenzoïne. Une augmentation du pouvoir migratoire du groupe adjacent tend à provoquer une formation accrue de diphénylacétylène. Par traitement avec du $LiAlH_4$ et du $NaBH_4$, les tosylhydrazones conduisent aux stilbènes avec de bons rendements. Dans certains cas, des formation sélectives de *cis*- ou *trans*- stilbène ont été observées.

Mots clés : tosylhydrazone, dérivés de la benzoïne, décomposition, hydrures métalliques complexes.

[Traduit par la rédaction]

Introduction

Since the report of Bamford and Stevens (1), a number of papers have been published (2, 3) on the decomposition of tosylhydrazones. The reaction developed by Shapiro and Heath (4) was particularly significant for progress in the synthesis of substituted alkenes. In recent years, there have been many studies on photolysis (5–7) and pyrolysis (8–13) of metal salts of tosylhydrazones via a carbene intermediate. Reductive decomposition of tosylhydrazones with $LiAlH_4$ and with $NaBH_4$ to alkane or alkene was reported by Caglioti and Magi (14–16). The reaction has been modified by using $NaBH_3CN$ (17) to give reduction products in excellent yields. However, there have been only a few reports (18–20) on the reaction of tosylhydrazones containing a leaving group on the adjacent carbon. In this paper, we report the reactions of such a tosylhydrazone.

Bamford and Stevens (1) reported that the tosylhydrazone (**1**) of benzoin gave desoxybenzoin (**2**) in 65% yield by decomposition in a protic solvent (Na, $HOCH_2CH_2OH$). Although they did not refer to the formation of diphenylacetylene (**3**), the reaction is expected to give **3** according to the reaction sequence shown (Scheme 1). The study by Hassner and Reuss (21) on the reaction of nitrooxazolidines with NaOMe, providing **3** through the same intermediate, gives supportive evidence for the reaction pathway to **3** assumed in Scheme 1.

Scheme 1.

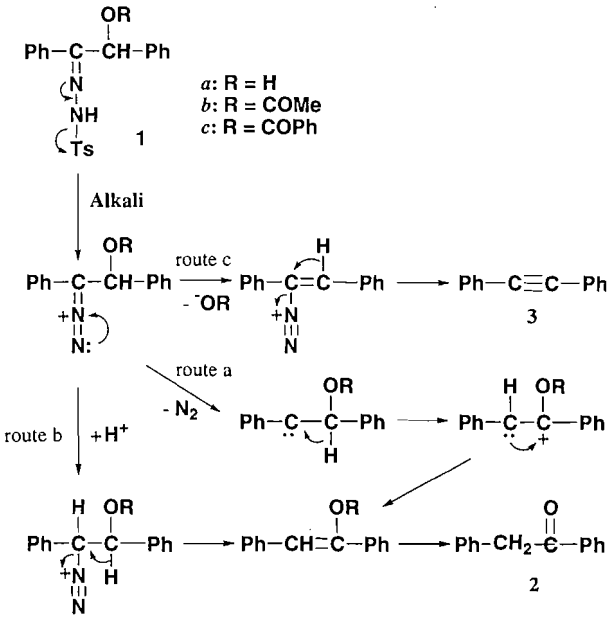

Results and discussion

Benzoin, benzoin acetate, and benzoin benzoate were con-

Received March 15, 1995.[1]

T. Iwadare.[1,2,3] Department of Chemistry, Yokohama City University, Kanazawaku, Yokohama 236, Japan.
Y. Ichinohe. Department of Chemistry, Faculty of Science and Engineering, Nihon University, Narashinodai, Funabashi, Chiba 274, Japan.
K. Orito. Laboratory of Organic Synthesis, Division of Molecular Chemistry, Graduate School of Engineering, Hokkaido University, Sapporo 060, Japan.

[1] Revision received November 20, 1995.
[2] Author to whom correspondence may be addressed.
[3] Present address: Software Research Laboratory, Nishinopporo 45, Ebetsu, Hokkaido 069, Japan. Telephone: 011-382-1155. Fax: 011-382-7788. E-mail: aizu@em.srl.co.jp

Table 1. Decomposition of tosylhydrazones (**1***a*,*b*,*c*) with alkali.

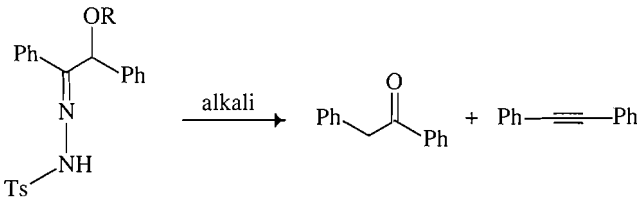

1*a*,*b*,*c* **2** **3**

a: R = H, *b*: R = COMe, *c*: R = COPh

Entry	Tosylhydrazone	Reaction conditions	Yield (%)[a] 2	3
1	**1***a*	$NaOCH_2CH_2OH$ in $(CH_2OH)_2$ reflux, 40 min	55.9	10.1
2	**1***b*	$NaOCH_2CH_2OH$ in $(CH_2OH)_2$ reflux, 40 min	42.7	52.6
3	**1***c*	$NaOCH_2CH_2OH$ in $(CH_2OH)_2$ reflux, 40 min	41.5	42.2
4	**1***a*	CH_3ONa in $(EtOCH_2CH_2)_2O$ reflux, 40 min	71.8	13.3
5	**1***b*	CH_3ONa in $(EtOCH_2CH_2)_2O$ reflux, 40 min	3.3	94.4
6	**1***c*	CH_3ON a in $(EtOCH_2CH_2)_2O$ reflux, 40 min	0	98.4

[a]GLC yields.

verted into the respective tosylhydrazones (**1***a*,*b*,*c*) by the usual method, and treated with alkali under protic and aprotic conditions. The product mixtures were separated by preparative TLC and analyzed by GLC. As shown in Table 1, the anticipated triple bond formation took place under both protic and aprotic conditions. Also, it was revealed that an increase in the leaving aptitude of the OR group (R = H, COMe, COPh) results in facile formation of **3**. Freedman and Schechter (22) have proven that decomposition of tosylhydrazones proceeds via a carbene intermediate under aprotic conditions. If elimination of the adjacent group does not take place a carbene intermediate (route a) is formed, and gives **2** via the enolate. However, an alternative pathway via protonation (route b) must also be considered for entries 1, 2, 3, and 4. The results revealed that the elimination (route c) of the acetoxyl and benzoyloxyl groups of **1***b* and **1***c* under aprotic conditions strongly predominates over the formation of **2**.

Djerassi and co-workers (23) showed that the reductive decomposition of tosylhydrazones with $LiAlH_4$ proceeds via a carbanion intermediate, which incorporates proton in the course of work-up leading to products. However, it seems reasonable to assume that alkene formation would be strongly favored in the presence of a suitable leaving group on the carbon adjacent to the incipient carbanion. Thus **1***a*, **1***b*, and **1***c* would be expected to give stilbenes (*cis*: **4**, *trans*: **5**) by decomposition with $LiAlH_4$ via the sequence shown in Scheme 2. Accordingly, **1***a*, **1***b*, and **1***c* were treated with $LiAlH_4$ in ethyl ether, THF, and dioxane, and the products were analyzed by GLC. While **4** and **5** were obtained in good yields in each case, stereoselectivity in the formation of stilbene isomers was observed only when ethyl ether was employed as a solvent

Scheme 2.

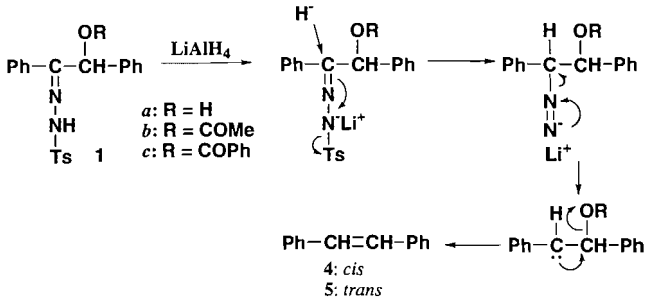

(entries 1, 2, 3), as shown in Table 2. Desoxybenzoin (**2**) and 1,2-diphenylethanol, which may form through protonation of the carbanion intermediate, were not detected at all.

Djerassi and co-workers demonstrated (23) that tosylhydrazones are decomposed to alkane or alkene by treatment with $NaBH_4$ through an alkyl diimide intermediate. In our experiments, if a similar carbanion intermediate is formed via the diimide by treatment of tosylhydrazones (**1***a*,*b*,*c*) with $NaBH_4$, stilbene must be produced. Thus **1***a*, **1***b*, and **1***c* were treated with $NaBH_4$ in dioxane, and the products were analyzed by GLC. As shown in Table 3, stilbenes (**4**, **5**) were formed in good yields. The results support the above assumption. Formation of **5** was selective only when **1***b* was the substrate (entry 2), and **1***c* afforded predominantly **4** (entry 3). However, a reasonable explanation of these differences in stereoselectivity cannot be given at the present point.

On the basis of the results, we conclude that (*i*) decomposition with alkali of tosylhydrazones containing a leaving group on the adjacent carbon gives rise to triple bond formation

Table 2. Decomposition of tosylhydrazones (**1***a*,*b*,*c*) with $LiAlH_4$.

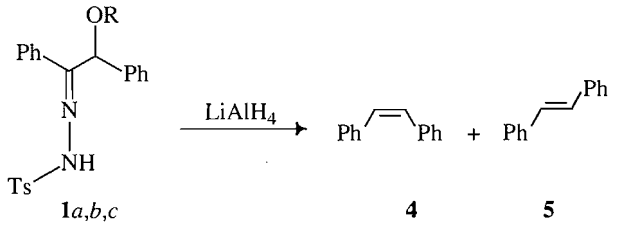

1*a*,*b*,*c* **4** **5**

a: R = H, *b*: R = COMe, *c*: R = COPh

Entry	Tosylhydrazone	Solvent and reaction conditions	Yield (%)[a] 4	5
1	**1***a*	Et_2O r.t. 1 h, reflux 1h	0	99.9
2	**1***b*	Et_2O r.t. 1 h, reflux 1h	5.7	82.9
3	**1***c*	Et_2O r.t. 1 h, reflux 1h	11.6	88.4
4	**1***a*	THF r.t. 1 h, reflux 1h	41.6	53.9
5	**1***b*	THF r.t. 1 h, reflux 1h	67.5	32.5
6	**1***c*	THF r.t. 1 h, reflux 1h	57.8	42.2
7	**1***a*	Dioxane r.t. 1 h, reflux 1h	42.6	57.1
8	**1***b*	Dioxane r.t. 1 h, reflux 1h	55.6	32.8
9	**1***c*	Dioxane r.t. 1 h, reflux 1h	32.6	61.6

[a]GLC yields.

Table 3. Decomposition of tosylhydrazones (**1***a*,*b*,*c*) with $NaBH_4$.

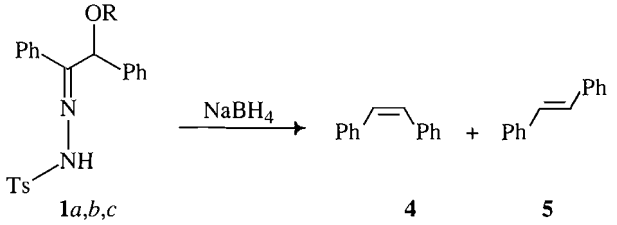

1*a*,*b*,*c* **4** **5**

a: R = H, *b*: R = COMe, *c*: R = COPh

Entry	Tosylhydrazone	Solvent and reaction conditions	Yield (%)[a] 4	5
1	**1***a*	Dioxane r.t. 1 h, reflux 1h	49.5	38.8
2	**1***b*	Dioxane r.t. 1 h, reflux 1h	3.6	96.4
3	**1***c*	Dioxane r.t. 1 h, reflux 1h	72.4	20.0

[a]GLC yields.

Scheme 3.

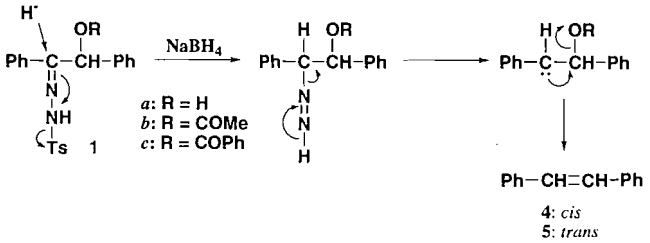

through the sequential pathway, as shown in Scheme 1 (route c), and (*ii*) treatment with metal complex hydrides yields alkenes resulting form 1,2-elimination between the incipient carbanion and the leaving group (Schemes and 2 and 3).

Experimental

Melting points were uncorrected. GLC analysis was carried out using a Hitachi 263-50 gas chromatograph and D-7500 integrator (Quadrex bonded fused silica capillary column methyl silicone (0.53 mm i.d. × 10 m × 3.0 mm) at 205°C; injector temperature, 180°C; detector temperature, 220°C; carrier gas, N_2; flow rate, 13.0 mL/min) for *cis*-stilbene (**4**) (retention time, 2.54 min), diphenylacetylene (**3**) (retention time, 3.78 min), *trans*-stilbene (**5**) (retention time, 4.34 min), desoxybenzoin (**2**) (retention time 4.51 min), and benzoin (retention time 5.63 min). Preparative TLC was performed on Merck silica gel 60 PF_{254}, being developed with a 1:1 mixture of benzene and hexane for **2** (R_f 0.33) and **3** (R_f 0.92), and also with hexane for **4** (R_f 0.53) and **5** (R_f 0.42). The products were identified by direct comparison with authentic samples prepared by the usual methods.

Preparation of tosylhydrazones (1*a*,*b*,*c*)

A solution of benzoin (2.5 g, 11.80 mmol) and tosylhydrazine (2.2 g, 11.81 mmol) in EtOH (30 mL) was refluxed for 4 h. EtOH was evaporated under reduced pressure, and the residue crystallized after standing overnight. Recrystallization from MeOH gave colorless needles of **1***a*, mp 145–145.5°C. Tosylhydrazones of benzoin acetate (**1***b*, mp 127–129°C) and benzoin benzoate (**1***c*, mp 153–154.5°C) were prepared in the same manner.

Decomposition of tosylhydrazones (1*a*,*b*,*c*) with sodium ethylene glycolate in ethylene glycol

Tosylhydrazone (**1***a*, **1***b*, or **1***c*, 2.6 mmol) was added to a solution of Na metal (60 mg, 2.61 mmol) in ethylene glycol (10 mL), and the solution was refluxed for 40 min. The cooled reaction mixture was diluted with water (50 mL), extracted with ether (50 mL), and the ethereal layer was washed successively with saturated brine (10 mL), water (10 mL), and then dried over anhydrous Na_2SO_4. After evaporation of the solvent, the residue was subjected to GLC analysis and to preparative TLC for isolation and identification of the products.

Decomposition of tosylhydrazones with NaOMe in diethyleneglycol diethyl ether

A solution of NaOMe (141 mg, 2.51 mmol) and tosylhydrazone (**1***a*, **1***b*, or **1***c*, 2.61 mmol) in diethyleneglycol diethyl ether (10 mL) was refluxed for 40 min. The reaction mixture was cooled, diluted with water (50 mL), and extracted with ether (50 mL). The extract was washed with water (5 × 10 mL), dried over anhydrous Na_2SO_4, and the solvent was evaporated. The residue was subjected to GLC analysis and to preparative TLC for isolation and identification of the products.

Decomposition of tosylhydrazones with $LiAlH_4$

A suspension of tosylhydrazone (**1***a*, **1***b*, or **1***c*, 2.61 mmol) and $LiAlH_4$ (100 mg, 2.64 mmol) in an appropriate solvent (30 mL) was stirred at room temperature for 1 h and then refluxed for 1 h. The excess $LiAlH_4$ was decomposed (24) by the successive addition of water (1 mL), 15% NaOH solution (1 mL), and water (3 mL). The precipitate that formed was filtered off, and the filtrate was extracted with ether (50 mL). The ethereal extract was washed with water (10 mL), dried over anhydrous Na_2SO_4, and the ether was evaporated. The residue was subjected to GLC analysis and to preparative TLC for isolation and identification of the products.

Samples of **4** and **5** were recovered unchanged after being subjected to the above reaction conditions.

Decomposition of tosylhydrazones with $NaBH_4$

A solution of tosylhydrazone (**1***a*, **1***b*, or **1***c*, 2.61 mmol) and $NaBH_4$ (100 mg, 2.65 mmol) in dioxane (30 mL) was stirred at room temperature for 1 h and then refluxed for an additional 2 h. The excess reagent was decomposed with acetic acid. The reaction mixture was made alkaline with 5% Na_2CO_3 solution, and then extracted with ether (50 mL). The ethereal layer was washed with water (10 mL), and then dried over anhydrous Na_2SO_4. The solvent was evaporated and the residue was subjected to GLC analysis and to preparative TLC.

Samples of **4** and **5** were recovered unchanged after being subjected to the above experimental conditions.

Acknowledgement

We thank Professor Shoji Eguchi of Nagoya University for helpful discussion.

References

1. W.R. Bamford and T.R. Stevens. J. Chem. Soc. 4735 (1952).
2. R.H. Shapiro. Org. React. (NY), **23**, 405 (1975), and literature cited therein.
3. R.M. Adlington and G.M. Barrett. Acc. Chem. Res. **16**, 55 (1983), and literature cited therein.
4. R.H. Shapiro and M.H. Heath. J. Am. Chem. Soc. **89**, 5734 (1967).
5. T. Ogata, K. Kawata, T. Oshikawa, H. Yoshida, and S. Inokawa. Nippon Kagaku Kaishi, 1370 (1988).
6. W. Kirmse and U. Mrotzeck. Chem. Ber. **121**, 485 (1988).
7. A.A. Frimer, J. Weiss, and Z. Rosental. J. Org. Chem. **59**, 2518 (1994).
8. P.K. Freeman, A.M. Tafesh, and B.E. Clapp. J. Org. Chem. **54**, 782 (1989).
9. H. Tomioka, Y. Ohtawa, and S. Murata. J. Chem. Soc. Perkin Trans. 1, 1864 (1989).
10. P.K. Freeman, J.C. Danino, B.K. Stevenson, K. Brian, and G.E. Clapp. J. Org. Chem. **55**, 3887 (1990).
11. M.E. Jung and A. Hagiwara. Tetrahedron Lett. **32**, 3025 (1991).
12. B. Miller, X. Shi, G. Grosu, and R. Zhou. J. Org. Chem. **58**, 2320 (1993).
13. C.O. Kappe, C.T. Pedersen, J. Catel, and Y. Mollior. J. Chem. Soc. Perkin Trans. 2, 351 (1994).
14. L. Caglioti and M. Magi. Tetrahedron Lett. 1261 (1982).
15. L. Caglioti and M. Magi. Tetrahedron, **19**, 1127 (1963).

16. L. Caglioti. Tetrahedron, **22**, 487 (1966).
17. R.O. Hutchins. C.A. Milewski, and B.E. Marynoff. J. Am. Chem. Soc. **95**, 3662 (1973).
18. S.J. Cristol and J.K. Harrington. J. Org. Chem. **28**, 1413 (1983).
19. T. Iwadare, I. Adachi, M. Hayashi, A. Matsunaga, and T. Kitai. Tetrahedron Lett. 4447 (1969).
20. P. Wieland. Helv. Chim. Acta, **53**, 171 (1970).
21. A. Hassner and R.H. Reuss. J. Org. Chem. **39**, 171 (1959).
22. L. Freedman and H. Schechter. J. Am. Chem. Soc. **81**, 5512 (1959).
23. M. Fischer, Z. Pelah, D.H. Williams, and C. Djerassi. Chem. Ber. **98**, 3236 (1985).
24. V.M. Micozic and M.L. Mihailovic. J. Org. Chem. **18**, 1190 (1953).

Kraft pulp bleaching using dimethyldioxirane: stability of the oxidants

J. Bouchard, C. Maine, R.M. Berry, and D.S. Argyropoulos

Abstract: Dimethyldioxirane (DMD) is a cyclic peroxide made by oxidizing acetone with peroxymonosulfate (PMS) in water buffered at pH 7.5 using sodium bicarbonate. It has been shown that DMD generation can be achieved in situ within a pulp suspension allowing very selective TCF bleaching of kraft pulp. This process involves simultaneous generation of DMD, reaction of PMS and DMD with residual lignin, and spontaneous decomposition of both oxidants. The first part of this work is a kinetics study of the decomposition of PMS and DMD as a function of pH under conditions similar to those for in situ bleaching. The effect of chelation as well as the effect of transition metal ions on decomposition rate was also investigated. DMD is very sensitive to pH and its half-life is very short under alkaline conditions. The presence of any transition metal ion that can be involved in a one-electron transfer is detrimental to DMD stability. However, fast reaction of DMD with pulp almost counteracts the effect of metal ions.

Key words: bleaching, peroxymonosulphate, dimethyldioxirane, metal ions, kinetics, decomposition, kraft pulp.

Résumé : Le diméthyldioxirane (DMD) est un peroxyde cyclique obtenu par oxydation de l'acétone avec le peroxymonosulfate (PMS) en milieu aqueux tamponné à pH 7,5 à l'aide du bicarbonate de sodium. La synthèse du DMD, lorsque réalisée in situ dans une suspension de pâte kraft, représente un procédé de blanchiment sans chlore très sélectif. Au cours de ce procédé, la synthèse du DMD, l'attaque de la lignine résiduelle par le DMD et le PMS ainsi que la décomposition naturelle de ces deux oxydants se produisent simultanément. Le première partie de ce travail consiste en une étude cinétique de la décomposition du DMD et du PMS en fonction du pH dans des conditions similaires à celle du procédé de blanchiment in situ. L'effet de la chelation ainsi que la présence d'ions métalliques ont également été étudiés. La décomposition du DMD est très sensible au pH et des demi-vies très courtes sont observées en milieu basique. La présence de métaux de transition pouvant échanger un électron s'avère néfaste à la stabilité du DMD mais la vitesse de réaction du DMD diminue grandement cet effet négatif.

Mots clés : blanchiment, peroxymonosulfate, diméthyldioxirane, ions métalliques, cinétique, décomposition, pâte kraft.

Introduction

The development of a totally chlorine-free (TCF) sequence for kraft pulp bleaching has focused on using molecular oxygen, hydrogen peroxide, and ozone. Recently, Lee, Hunt, and Murray have shown that dimethyldioxirane (DMD), a member of the cyclic peroxide family, can be used as a novel and selective non-chlorine bleaching agent (1–4). Effective bleaching of kraft pulp using DMD in either an isolated (1) or an in situ generated form (2) has been demonstrated.

Dimethyldioxirane is a stereospecific electrophilic oxygen transfer agent that allows epoxidation of unsaturated centres at room temperature. It is formed during the acetone-catalyzed decomposition of peroxymonosulfuric acid (H_2SO_5) as shown by Edwards et al. (5) and can be isolated as an azeotrope with acetone (6). Reviews on DMD chemistry have been published (7, 8), and new applications of this chemical routinely appear in the literature.

The specific reactions of DMD with lignin model compounds have been studied by Argyropoulos et al. (9) who have shown that DMD oxidizes the aromatic ring of both etherified and non-etherified (phenolic) lignin model compounds. DMD appears to be more reactive toward etherified structures than ClO_2, O_2, and H_2O_2. This higher reactivity partially explains the superiority of DMD because the etherified aromatic units are the majority in almost all residual lignins.

It has been assumed in these initial evaluations that DMD and the oxidant used in its preparation are relatively stable and that any decomposition has limited consequences on the progress of the required oxidation reactions. It is this assumption that is being more fully evaluated in this report.

Bleaching of kraft pulp by in situ generation of DMD

To generate DMD in situ, a method was demonstrated by Lee et al. (3, 4), whereby pulp is mixed with acetone, peroxymonosulphuric acid (PMS), and bicarbonate. This system is complex in that it involves the simultaneous in situ generation of DMD, the decomposition of oxidants, and the delignification of the pulp (Fig. 1).

Both DMD and PMS react with lignin but both oxidants are relatively unstable and undergo spontaneous decomposition that generates oxygen. As well, DMD is decomposed by reacting with PMS (5). To add to this complexity is the possible effect of interaction with water. While the decomposition of isolated DMD in nonaqueous media has been discussed previously (6), the stability of DMD as a function of the pH in aqueous solutions has not.

Received August 18, 1995.

J. Bouchard,[1] C. Maine, R.M. Berry, and D.S. Argyropoulos.[2] Pulp and Paper Research Institute of Canada, 570 Boul. St-Jean, Pointe Claire, QC H9R 3J9, Canada.

[1] Author to whom correspondence may be addressed. Telephone: (514) 630-4100. Fax: (514) 630-4134.

[2] Chemistry Department and Pulp and Paper Centre, McGill University, 3420 University, Montreal.

Fig. 1. Schematic of the reactions of delignification and chemical decomposition during in situ dimethyldioxirane bleaching.

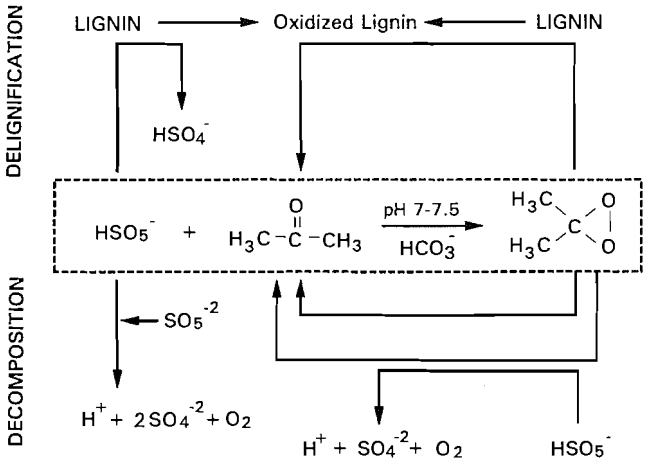

DMD stability (in a nonaqueous medium)

Isolated solutions of DMD can be kept for months at −20°C (10); however, at room temperature they decompose comparatively quickly with reported lifetimes ranging from a few hours (11) to 24 h (12). While it has been reported that DMD decomposition follows a complex rate law (11, 12), Singh and Murray (10) have shown that first-order kinetics can be obtained at low DMD concentrations (0.03 M). They also showed that autodecomposition of DMD at room temperature leads almost stoichiometrically to methyl acetate. No evidence was found for the formation of acetone diperoxide, acetol, or acetolacetate.

As previously mentioned, the effects of water and pH on DMD stability in aqueous solutions have not yet been addressed. Since the in situ DMD bleaching of kraft pulp requires a buffered aqueous solution, the effects of water and pH are particularly relevant and are addresed in this study.

Peroxymonosulfuric acid (PMS) stability

This inorganic peracid ($HOSO_2OOH$) has two ionization constants. The acidic proton has a $pK_{a_1} < 0$ while the peroxide proton is weakly acidic ($pK_{a_2} \approx 9.4$) (13). Ball and Edwards (14) studied the kinetics of spontaneous PMS decomposition as a function of pH and found that spontaneous decomposition is the sole mechanism when trace-metal catalysis is suppressed by chelation.

$$2\ HSO_5^- \rightarrow 2\ H^+ + 2\ SO_4^{-2} + O_2$$

In the pH range from 6 to 8 where HSO_5^- is the major species, Ball and Edwards proposed a rate law (eq. [1]) based on second-order kinetics.

$$[1] \quad -\frac{d\,[HSO_5^-]}{dt} = k_a \frac{[HSO_5^-]^2}{[H^+]}$$

They also reported that the log of the rate of decomposition, as a function of the pH, shows a typical bell-shaped profile with the maximum located at pK_{a2}. The slopes of the straight lines from both sides of the bell-shaped curve indicate first-order kinetics in both the peracid and its anion.

It should be remembered that in the Ball and Edwards study solutions of PMS have an active oxygen (AO) concentration of the order of 0.02 M. However, the AO concentration Lee et al. (3) found necessary for pulp bleaching was about one order of magnitude higher. Since commercial preparations of PMS have only recently become available in a solid state salt form, Ball and Edwards used a solution they prepared themselves that was roughly composed of half PMS and half sulphuric acid and also contained hydrogen peroxide. In recent work, hydrogen peroxide-free commercial preparations of PMS (2 $KHSO_5 \cdot KHSO_4 \cdot K_2SO_4$) have been used to generate DMD in situ. For this reason and due to differences between the earlier work of Ball and Edwards and the more recent work of Lee et al. (3), it was considered appropriate to determine whether the commercially produced PMS was comparable in terms of stability with the preparations tested by Ball and Edwards.

Stability of oxidants in presence of metal ions

Recently, Francis et al. (15) have shown that PMS is quite insensitive to the presence of transition metal ions (Mn, Fe, Cu, Ni, V, Co) except in the case of copper under alkaline conditions and cobalt at concentrations much higher than normally found in pulps. However, no work has been published on determining the effect of metal ions on DMD stability. The present study evaluates this significant parameter.

Experimental

DMD synthesis

Pure dimethyldioxirane was prepared according to general literature procedures (11, 16). Solutions in acetone were assayed for dioxirane content by iodometric titration, and only those solutions with molarity 0.06 M or higher were used. These solutions were stored over 5 Å molecular sieves at −20°C until required.

Peroxymonosulfate stability experiments

A series of experiments was done to show the relationship between the stability of commercially prepared PMS (Oxone, Dupont) and pH. Oxone was dissolved in buffered aqueous solution in order to give an active oxygen (AO) concentration of 0.139 mol/L, which corresponds to an AO charge of 2% on oven dried (o.d.) pulp at 10% consistency (1 g of oxone contains 0.045 g of active oxygen). The PMS solutions were buffered using phosphate (pH 5.0 through 8.8), bicarbonate (pH 7.1), or carbonate (pH 9.2) buffers (0.18–0.5 M). In some experiments, metal ions were chelated with EDTA (0.1%). At fixed intervals, 5 mL samples were analyzed iodometrically for residual AO concentration. The formation of HSO_4^- from HSO_5^- caused the pH to fluctuate slightly. As a result, the pH was periodically checked and, if necessary, readjusted to its target value.

A second series of experiments dealing with the effect of PMS concentration on its stability was done using PMS concentrations of 0.296, 0.198, and 0.088 mol/L. These values correspond to AO charges of 3.0, 2.0, and 0.9%, respectively, on o.d. pulp at 13.6% consistency. This work was carried out at pH 7.1 using bicarbonate buffer.

Effect of water or buffered aqueous solutions on DMD stability

Solutions of isolated DMD (0.066 M in acetone) or isolated DMD diluted in water (0.048 M DMD containing 28% water)

Fig. 2. Second-order kinetics of peroxymonosulfate decomposition at different pH. (Q) indicates chelating agent addition, $[PMS]_0$ is the concentration at zero reaction time.

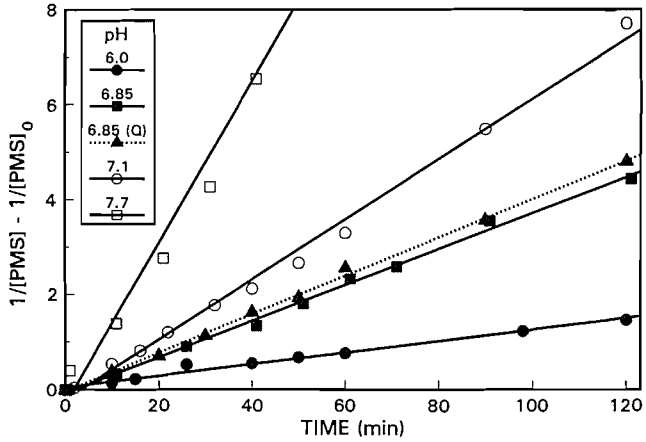

Fig. 3. Log of the PMS decomposition rate constant as a function of the pH in the presence of different buffering agents.

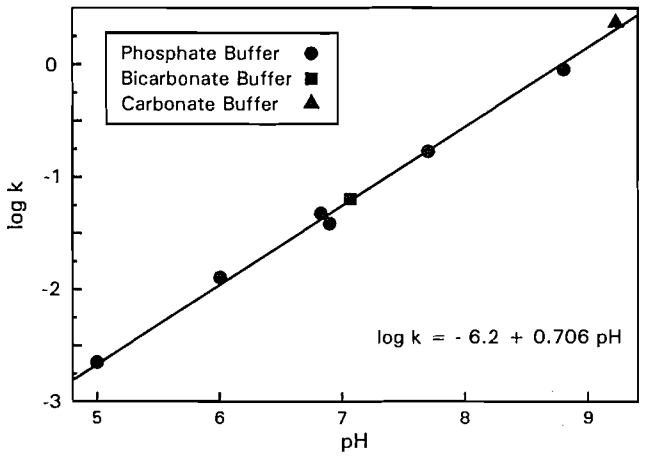

were used in these experiments. Decreases in DMD concentration as a function of time at room temperature were followed using iodometric titration. The solutions were monitored for at least three half-lives.

For monitoring the effect of pH on DMD stability, the procedure was the same as that described in the previous paragraph, except that 20 mL of a phosphate buffer (0.18 or 0.50 M) or bicarbonate buffer (0.1 M) was added to 30 mL of isolated DMD. The pH of the buffers ranged from 5 to 9.

Effect of metal ions on DMD stability

DMD–acetone solution (20 mL; 0.03 M) was added to 10 mL of 0.18 M phosphate buffer containing different metal ions at pH 7.0. The final metal ion concentration was 100 ppm in each case. The metal ions used were Mg^{+2} ($MgSO_4$), Mn^{+2} ($MnCl_2$), Fe^{+2} ($FeCl_2$), and Mn^{+4} (MnO_2). The solutions were monitored for at least three half-lives.

Results and Discussion

Effect of pH on decomposition rate constants of PMS

Figure 2 shows that at a fixed pH and temperature, PMS decomposition follows second-order kinetics and also that the decomposition is accelerated as the pH is varied from 6.0 to 7.7. Adding a chelant to the solution appears to have no effect. This conclusion is made because the two curves at pH 6.85, obtained with and without EDTA, gave very similar rate constants of 0.041 and 0.038 $(mol/L)^{-1}$ min^{-1} respectively. This result indicates that decomposition resulting from trace metal ions present in the buffer or in the commercial preparation of PMS itself is not a concern. Only the mechanism responsible for spontaneous decomposition is significant.

Fig. 4. Second-order kinetics of peroxymonosulfate decomposition at various PMS concentrations.

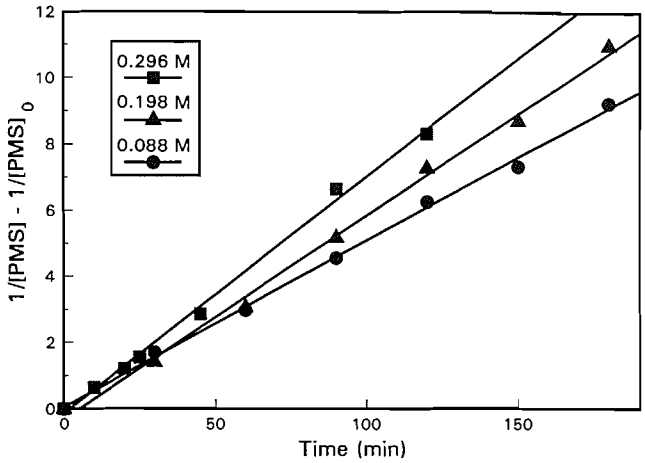

In Fig. 3, log k is plotted as a function of the pH as was done by Ball and Edwards (14). The slope of the linear relationship indicates that the dependence on the concentration of hydrogen ion is on the order of 0.7 as opposed to the first order measured by Ball and Edwards (14). Goodman and Robson (17) and, more recently, Francis et al. (15) have also used the solid triple potassium salt of PMS to study decomposition. Using their data, we calculated a 0.73 (Goodman and Robson) and 0.62 (Francis et al.) order of reaction with respect to hydrogen ion concentration. Goodman and Robson did not mention the PMS concentration used in their experiments while Francis et al. used 0.033 M. When our results were combined with theirs, the rate law of peroxymonosulphate decomposition becomes:

$$[2] \quad -\frac{d\,[HSO_5^-]}{dt} = k_a \frac{[HSO_5^-]^2}{[H^+]^{0.7}}$$

The reason why the triple potassium salt of PMS has a lower order of dependence on the hydrogen ion concentration remains unknown. The effect of PMS concentration on decomposition is shown in Fig. 4. This second-order plot illustrates the degradation at three concentrations of PMS at pH 7.1. These concentrations correspond to the range used for in situ DMD bleaching of pulp. The rate constant of decomposition increases slightly as the PMS concentration is increased. The linear relationship between the rate constants of decomposition and PMS concentration is shown in Fig. 5 and can be described by eq. [3].

$$[3] \quad k_a = 0.045 + 0.088\,[PMS]$$

Greater rates of decomposition of PMS have been reported when the ionic strength of the PMS solution is increased with

Fig. 5. Relationship between the rate constants of decomposition and PMS concentration.

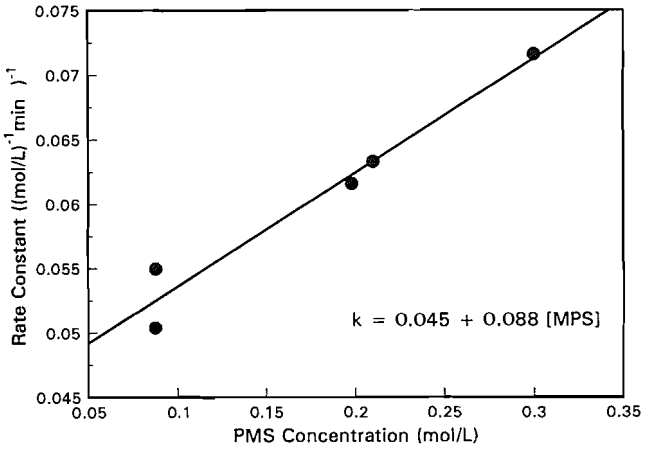

either potassium sulphate (14) or sodium sulphate (17). Since oxone carries a dead load of about 57% potassium sulphate salts, it is not surprising that we also observed higher rates of decomposition when we increased the PMS concentration at the same pH.

Effect of PMS decomposition on pulp bleaching

At present, kraft pulps bleached with PMS and acetone are initially buffered to pH 7.4 with sodium bicarbonate. According to our kinetic results, the half-life of PMS is 22.5 min at pH 7.4 while it is 10 times higher at pH 6.0. This suggests that PMS bleaching of kraft pulp should be done under acidic conditions where PMS has a greater stability. However, preliminary work has shown that the rate of pulp bleaching increases as the pH of the pulp suspension increases. Consequently pulp bleaches faster under alkaline conditions while, at the same time, PMS decomposes more quickly.

Another advantage of higher pH has been indicated by Francis et al. (15) who demonstrated a detrimental effect on pulp viscosity when pulp is bleached at pH below 4. The effect of pH on the kinetics of PMS bleaching will be elaborated in a future publication.

Effect of water and buffered aqueous solution on DMD stability

Decomposition of isolated DMD or DMD in an acetone–water mixture obeys first-order kinetics. Table I gives the observed decomposition rate constants and the half-life of DMD under different conditions. These data indicate that DMD decomposes about three to four times faster in the presence of water than in pure acetone. The natural pH of the water–acetone–DMD solution was 3.8. Bringing this pH close to neutrality (6.8) increases the degradation rate by a factor of about 30. Consequently, the half-life of the DMD, which is approximately 77 h as an acetone solution, drops to 27 h for acetone–water solution, and to 50 min when the pH of the acetone–water solution is brought to neutrality.

Pure DMD solutions were diluted using aqueous buffers to give an acetone/water ratio of 60:40. The decrease of DMD concentration as a function of time is shown in Fig. 6 over the pH range 5–9. The main conclusion from Fig. 6 is that DMD is much more stable in acidic conditions than in neutral or alkaline conditions. All these curves can be described by first-order kinetics. The rate constants as well as the half-life of DMD are presented in Table 2.

Fig. 6. First-order kinetics of dimethyldioxirane decomposition at different pHs.

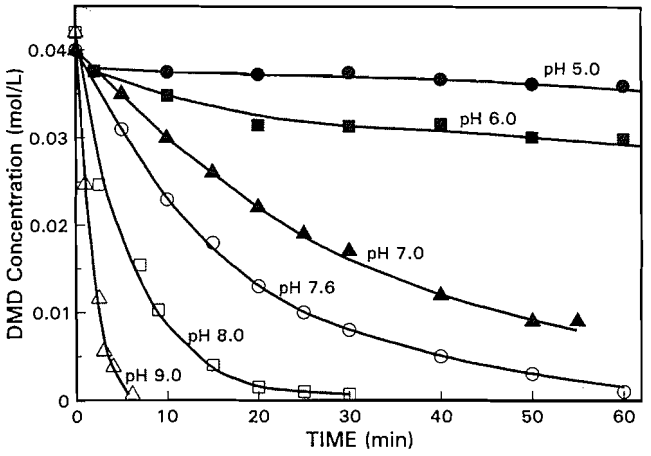

Table 1. First-order rate constants for DMD decomposition in acetone and an acetone–water mixture (70:30).

DMD solvent	DMD conc. (mol/L)	pH	k (min^{-1})	Half-life (min)
Acetone	0.044 – 0.066	—	1.2×10^{-4}	5800
Acetone–H_2O	0.048	3.8	4.2×10^{-4}	1650
Acetone–H_2O	0.040	6.8	1.4×10^{-2}	50

Table 2. First-order rate constants for degradation of DMD in buffered acetone–water solutions at different pHs (PO_4: phosphate buffer).

Buffer	pH	k_{obs} (min^{-1})	Half-life (min)	log k_{obs}
Water	3.8	4.2×10^{-4}	1650	−3.40
PO_4	5.0	1.0×10^{-3}	690	−3.00
PO_4	6.05	5.0×10^{-3}	140	−2.30
Water	6.8	1.4×10^{-2}	50	−1.90
PO_4	7.0	2.9×10^{-2}	24	−1.50
PO_4	7.2	4.2×10^{-2}	17	−1.40
Bicarb	7.6	5.4×10^{-2}	13	−1.30
PO_4	8.0	1.6×10^{-1}	4.3	−0.80
PO_4	9.0	6.2×10^{-1}	1.1	−0.20

DMD is relatively stable at room temperature under acidic conditions. However, under neutral conditions, the half-life of DMD is less than 30 min. Under the conditions used for kraft pulp bleaching (bicarbonate buffer, pH 7–7.5), the half-life of DMD is about 15 min.The last column of Table 2 gives the logarithmic values of k_{obs}.

The plot of log k_{obs} as a function of pH is shown in Fig. 7. The linear relationship between log k_{obs} and pH indicates the sensitivity of DMD to hydroxyl anion (or the stabilizing effect of the hydrogen ion) and is expressed by the following rate law:

Fig. 7. Log of the DMD decomposition rate constant as a function of the pH.

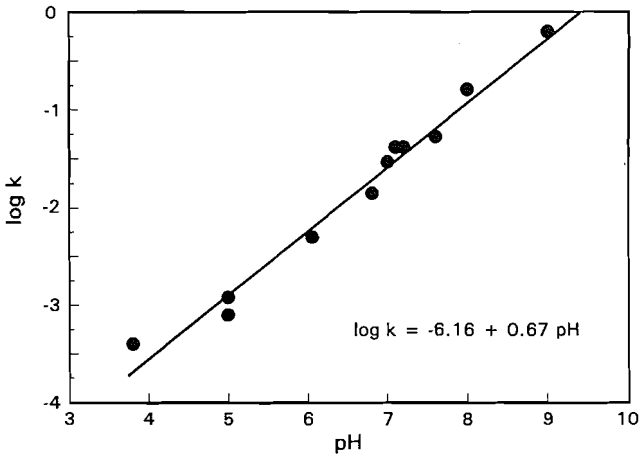

$$[4] \quad -\frac{d\,[DMD]}{dt} = k_{obs}\frac{[DMD]}{[H^+]^{0.7}}$$

Unlike PMS, DMD is not sensitive to the ionic strength or nature of the species used for buffering. For example, pure water, or buffers with concentrations of phosphate or bicarbonate ranging from 0 to 0.5 M, had no effect on the rate of decomposition of DMD.

Effect of transition metals on DMD decomposition

The relative rates of decomposition of DMD in buffered aqueous solutions spiked with 100 ppm of metal ions are shown in Fig. 8. The control experiment was given a value of 1 and the others were normalized accordingly. When the metal ions can not be further oxidized by one-electron transfer, e.g., Mg^{+2}, Mn^{+4}, they do not increase the decomposition rate of DMD. Moreover, Mg^{+2} seems to stabilize the cyclic peroxide. When this transfer of one electron is possible, e.g., Fe^{+2}, Mn^{+2}, the rate of decomposition of DMD increases by a factor of 10. This acceleration of decomposition, however, does not have a large impact because of the fast reaction of DMD with pulp. The need for a metal management strategy is therefore less critical. Lee et al. (2) have shown only a slight improvement in selectivity by doing a chelation stage prior to in situ DMD bleaching. If necessary, the removal of metal ions can be done by an acid treatment (18) or a chelation stage (19) followed by a wash step. Further work needs to be done regarding the positive role played by magnesium ion.

Effect of oxidant decomposition on in situ DMD bleaching

Lee et al. (2) have shown that all the oxidants (PMS and DMD) are consumed within 45 min during in situ bleaching of kraft pulp. However, they also observed, when mixing pure DMD solution with kraft pulp at room temperature, that all the DMD is consumed in a very short period of time. They concluded that the reaction rate of DMD with lignin is much faster than the reaction rate of PMS and acetone to yield DMD. Consequently, generation of DMD appears to be the rate determining step of in situ bleaching and therefore decomposition of PMS is likely the main oxidant-loss mechanism. As PMS is insensitive to metal ions, the omission of the chelation stage prior to in situ DMD bleaching has less impact than for a hydrogen peroxide bleaching stage.

Fig. 8. Relative rate of decomposition of DMD in the presence of different metal ions.

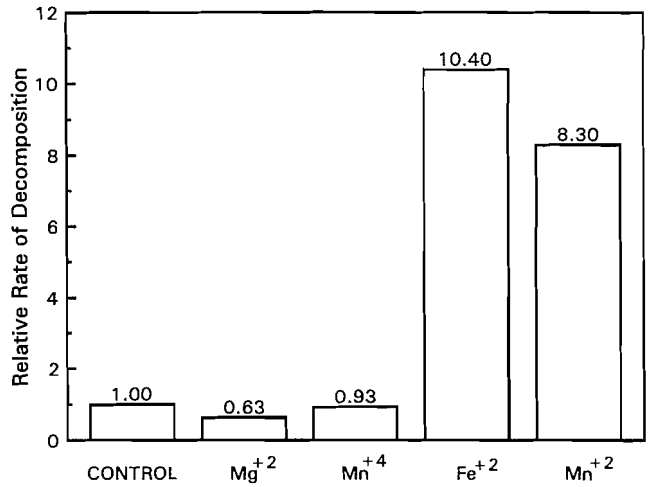

Under the conditions used for kraft pulp bleaching (bicarbonate buffer, pH 7–7.5), the half-life of PMS is 22 min and this would significantly affect the overall oxidant concentration. As a result the effective charge of DMD will not be equivalent to the applied charge on pulp.

Conclusions

1. As previously shown, the decomposition of peroxymonosulphate is second order in PMS and the rate of decomposition increases as the pH is increased from 5 to 9. The dependence of the reaction on hydrogen ion concentration was found to be a lower order (0.7) than that previously published in the literature.
2. There is a small dependence of the rate constant of decomposition on the concentration of PMS. The dependence causes an acceleration of decomposition as the PMS concentration is increased.
3. Dimethyldioxirane is quite stable (half-life>25 h) at room temperature in acetone or acetone–water solution as long as the pH is kept below 4.
4. The decomposition of DMD is first order in DMD and is unaffected by the ionic strength of the solution. The dependence of the reaction on hydrogen ion concentration is the same order as that observed in the decomposition of PMS.
5. Under kraft pulp bleaching conditions where the pH is buffered between 7 and 8, the half-life of DMD varies between 24 and 4 minutes while the half-life of PMS varies between 43 and 8.5 min.
6. The decomposition of DMD is accelerated by the presence of transition metal ions such as Fe^{+2} and Mn^{+2} but seems to be protected by the presence of Mg^{+2}. The impact of this acceleration is counteracted by the fast reaction of DMD with lignin in pulp.

Acknowledgments

To E. Morelli and J. Falle for technical assistance. Thanks also to Dr. C.-L. Lee and J. Wearing for helpful discussions and to

Dr. Chen for reviewing the manuscript. The financial contribution of Industry Canada is also acknowledged.

References

1. C.-L. Lee. PCT patent application, Intern. Publication Number WO91/12369. 1991.
2. C.-L. Lee, R.W. Murray, and K. Hunt. PCT patent application, Intern. Publication Number WO92/13993. 1992.
3. C.-L. Lee, K. Hunt, and R.W. Murray. Can. Pulp Paper Assoc. Tech. Sect. Proc. Annu. Meet. 79th, Montreal, January 1993. pp. B1–B8.
4. C.-L. Lee, K. Hunt, and R.W. Murray. Tappi J. **76** (11), 137 (1993).
5. J.O. Edwards, R.H. Pater, R. Curci, and F. Di Furia. Photochem. Photobiol. **30**, 63 (1979).
6. R.W. Murray and R. Jeyaraman. J. Org. Chem. **50**, 2847 (1985).
7. R.W. Murray. Chem. Rev. **89**, 1187 (1989).
8. R. Curci. Adv. Oxygenated Processes, **2**, 1 (1990).
9. D.S. Argyropoulos, Y. Sun, R.M. Berry, and J. Bouchard. Proc. Int. Pulp Bleaching Conf., Vancouver, B.C. June 1994. *Edited by* Tech. Sect., Can. Pulp Paper Assoc., Montreal. 1994. Poster Volume pp. 83–91.
10. M. Singh and R.W. Murray. J. Org. Chem. **57**, 4263 (1992).
11. W. Adam, Y.Y. Chan, D. Cremer, J. Gauss, D. Scheutzow, and M. Schindler. J. Org. Chem. **52**, 2800 (1987).
12. A.L. Baumstark, M. Beeson, and P.C. Vasquez. Tetrahedron Lett. **30**, 5567 (1989).
13. R. Curci and J.O. Edwards. *In* Organic peroxides. Vol. I. *Edited by* D. Swern. Wiley–Interscience, New York. 1970. p. 199.
14. D.L. Ball and J.O. Edwards. J. Am. Chem. Soc. **78**, 1125 (1956).
15. R.C. Francis, X.-Z. Zhang, P.M. Froass, and O. Tamer. Tappi J. **77**, (6), 133 (1994).
16. W. Adam, J. Bialas, and L. Hadjiarapoglou. Chem. Ber. **124**, 2377 (1991).
17. J.F. Goodman and P. Robson. J. Chem. Soc. 2871 (1963).
18. J. Bouchard, H.M. Nugent, and R.M. Berry. Proceedings of the International Pulp Bleaching Conference, Vancouver, B.C. June 1994. *Edited by* Technical Section, CPPA, Montreal. 1994. pp. 33–39.
19. J. Basta, L. Holtinger, and J. Hook. Proc. Int. Symp. Wood Pulping Chem. 6th, 237 (1991).

Preparation and analysis of some acetosugar esters of abscisic acid and derivatives[1]

J. Balsevich, G. Bishop, S.L. Jacques, L.R. Hogge, D.J.H. Olson, and N. Laganière

Abstract: Racemic abscisic acid (ABA), the *cis* and *trans* 1′, 4′-diols (ABA diols) derived from ABA by reduction of the 4′ ketone, and the corresponding 4′-O-acetates were converted into various acetosugar esters by reaction of their cesium salts with the 1-chloroacetosugars derived from glucose, galactose, lactose, and maltose. Analytical separations of the acetosugar esters using high-performance liquid chromatography (LC) on reverse-phase columns were developed. Continuous flow secondary ion mass spectra (CFSIMS) of the various acetosugar esters were obtained and an LC/CFSIMS protocol employing multiple reaction monitoring was used to detect ABA acetoglucose ester in an acetylated extract obtained from plant cells that had been treated with ABA.

Key words: abscisic acid, acetosugar esters, synthesis, chromatography, mass spectrometry.

Résumé : La réaction des sels de césium de l'acide abscissique (AAB) racémique, des diols-1′, 4′ *cis* et *trans* (diols de l'AAB) obtenus par réduction de la 4′-cétone ainsi que des 4′-O-acétates correspondants avec les 1-chloroacéto sucres dérivés de glucose, galactose, lactose et maltose, a permis de les transformer en esters d'acétosucres. On a développé une méthode analytique qui permet de séparer les esters d'acétosucres par chromatographie liquide (CL) à haute performance sur des colonnes en phase inversées. Pour chacun des esters d'acétosucres, on a obtenu les spectres de masse des ions secondaires en écoulement continue (SMISÉC) et un protocole de CL/SMISÉC faisant appel à un monitoring de réactions multiples a été utilisé pour l'ester acétoglucose ABA dans le produit d'extraction acétylé obtenu à partir de cellules de plantes traitées par du ABA.

Mots clés : acide abscissique, esters d'acétosucres, synthèse, chromatographie, spectrométrie de masse.

[Traduit par la rédaction]

(+)-Abscisic acid (ABA, Fig. 1) is a plant growth regulator that has also been implicated in a variety of stress-related responses (1). Several metabolites of endogenous and exogenously added ABA have been isolated and identified, including the reduction products, *cis* and *trans* ABA 1′, 4′-diols (2–5); the oxidized derivative, phaseic acid (6–8); and the glucose esters (β-D-glucose, C-1-linked) of ABA and the aformentioned compounds (Fig. 1) (9–12). There has also been a report of the detection of a maltose ester of ABA (13).

We were interested in following ABA metabolism, and in developing analytical methods to facilitate our studies; in particular, we sought to extend the utility of liquid chromatography–continuous flow secondary ion mass spectrometry (LC/CFSIMS), which we had earlier used to detect ABA glucose ester in a plant extract (14), to other ABA-derived conjugates, which we felt were potential metabolites. To achieve these objectives, samples of potential metabolites or suitable derivatives thereof were required as standards.

Previously, ABA glucose ester (β anomer) had been prepared by reaction of ABA (cesium or triethyl ammonium salt) with α-bromoacetoglucose followed by deacetylation of the intermediate acetoglucose ester with an enzyme preparation derived from sunflower seeds (*Helianthus annus*) (15, 16). ABA diols had been prepared by sodium borohydride reduction of ABA methyl ester, which yielded a mixture rich in both the 1′, 4′-*cis* and -*trans* diols (17).

To further extend earlier synthetic efforts as well as the use of LC/CFSIMS in analysis of metabolite mixtures, we report here the preparation of various acetosugar derivatives of ABA (and deuterated ABA) and the diols, and acetylated diols of ABA, and the development of LC and LC/CFSIMS protocols using these derivatives. The acetosugar derivatives were easily prepared and possessed good stability. Some deuterated analogs were prepared as an aid in assigning fragments in the mass spectrum and for potential use as internal standards. As an example of the utility of the developed protocol, a sample plant extract was analyzed.

Received August 23, 1995.

J. Balsevich,[2] G. Bishop, S.L. Jacques, L.R. Hogge, D.J.H. Olson, and N. Laganière. Plant Biotechnology Institute, National Research Council of Canada, Saskatoon, SK S7N 0W9, Canada.

[1] NRCC No. 38932.

[2] Author to whom correspondence may be addressed. Telephone: (306) 975-5275. Fax: (306) 975-4839. E-mail: jbalsevc@pbi.nrc.ca

Results and discussion

Selective reduction of ABA

Previous preparations of ABA diols involved reduction of ABA methyl ester with sodium borohydride (2, 17). This method was not selective as the ratio of *cis/trans* 1′, 4′-diols was ca. 2:1 (2). Formation of the sodium salt of ABA in THF followed by reduction with L-Selectride®, however, rapidly led to a very clean product that consisted predominantly of the 1′, 4′-*cis*-diol (*cis/trans* 10:1). Alternatively, reduction of the

Fig. 1. Preparation and structures of various acetosugar esters of ABA, ABA diols, and the 4′-O-acetates. Only the diastereomers derived from (+)-ABA are pictured; however, in the actual preparations racemic ABA was used.

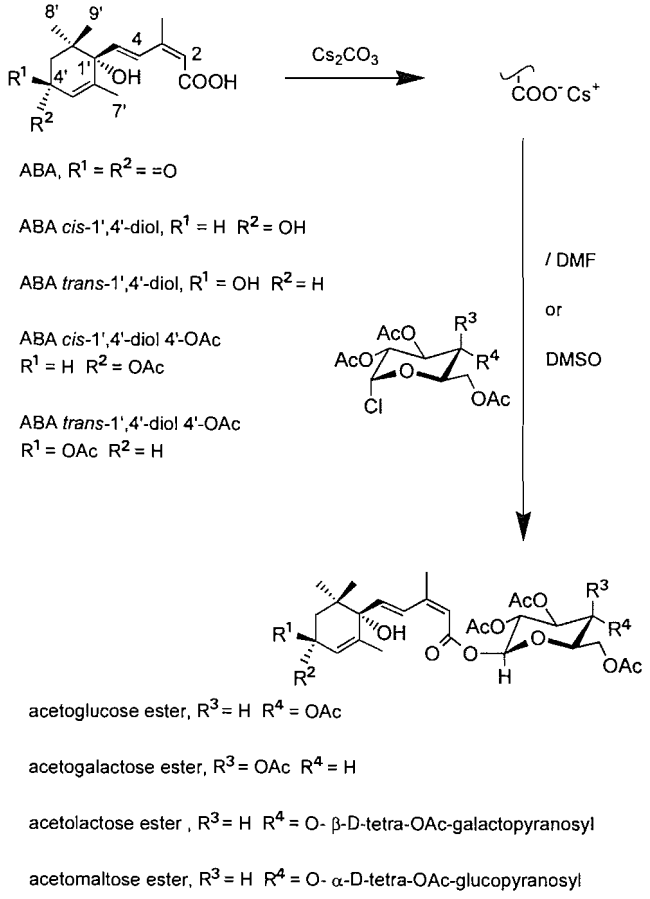

preformed sodium salt of ABA in THF with lithium aluminum hydride led to a product mixture containing predominantly the *trans* diol (*cis*/*trans* <1:20), contaminated with a small amount of conjugate reduction products (< 5%). The *trans* diol could be obtained in pure form via crystallization of either the acetate or methyl ester derivative. Similarly, the *cis* diol could be obtained in pure form via crystallization of the methyl ester.

Formation of acetosugar esters

The preparation of ABA acetoglucose ester was previously achieved by reaction of α-bromoacetoglucose with the cesium salt of ABA in DMF (16). This method had been used for the preparation of esters of amino acids by reaction of their cesium salts with alkyl halides (18). As an extension of these procedures, the cesium salts of ABA, hexadeutero ABA, ABA diols, and the C-4′ O-acetates of the ABA diols were prepared by treatment of the acids with Cs_2CO_3 and found to react effectively with α-chloroacetoglucose, -chloroacetogalactose, -chloroacetolactose, and -chloroacetomaltose in either DMF or DMSO (Fig. 1). β-Chloroacetoglucose did not react as well, providing ABA α-acetoglucose ester in only 21% yield. Attempted reactions with chloroacetomannose and chloroacetoglucosamine were unsuccessful. A summary of the acetosugar esters prepared is outlined in Table 1; the esters were obtained as diastereomeric mixtures, as racemic ABA and its

Table 1. Various acetosugar esters of ABA and derivatives prepared by reaction of acetochlorosugars with appropriate cesium salt.

Compound prepared	Reaction conditions	Isolated yield (%)
(±)-ABA β-D-acetoglucose ester	DMSO, 60°C, 5 h	53
d_6-(±)-ABA α-D-acetoglucose ester	DMF, RT, 4 d	21
(±)-ABA *cis* diol β-D-acetoglucose ester	DMSO, RT, 4 d	59
(±)-ABA *cis* diol C-4′-O-acetate β-D-acetoglucose ester	DMSO, RT, 4 d	52
(±)-ABA *trans* diol β-D-acetoglucose ester	DMF, RT, 4 d	53
(±)-ABA *trans* diol C-4′-O-acetate β-D-acetoglucose ester	DMF, RT, 4 d	55
(±)-ABA β-acetolactose ester	DMF, RT, 4 d	65
d_6-(±)-ABA β-D-aceto-galactose ester	DMF, RT, 4 d	49
(±)-ABA β-acetomaltose ester	DMF, 60°C, 5 h	61
(±)-ABA *cis* diol β-aceto-maltose ester	DMF, 60°C, 5 h	53
(±)-ABA *cis* diol C-4′-O-acetate β-acetomaltose ester	DMSO, RT, 4 d	48

diols were used in the preparations. Two sets of resonances were observed for some of the signals in the ^{1}H NMR spectra, but the chemical shifts differed only slightly.

Deacetylation of acetoglucose esters

Deacetylation of the acetoglucose esters of ABA and ABA *cis* diol using a crude enzyme preparation derived from sunflower seeds (15, 16) was successful in our hands; however, the deacetylation of acetolactose and acetomaltose derivatives was problematic, being complicated by solubility problems and incomplete deacetylation. This result led us to consider the use of the acetosugar ester derivatives rather than the sugar esters for development of a general analytical protocol.

LC of acetosugar esters

The LC trace in Fig. 2 shows the separation achieved on a reverse-phase ultrasphere ODS column employing CH_3CN/H_2O (52:48, isocratic) as solvent and 24 (12 pairs of diastereomers) acetosugar derivatives. The disaccharide derivatives, e.g., ABA acetomaltose and acetolactose esters, eluted later than the corresponding monosacharride derivatives and were well separated from each other. Separation of the α and β anomers of the acetoglucose esters of ABA was not achieved; however, separation of ABA β-acetogalactose ester from the acetoglucose esters was. The β-acetoglucose esters of the *cis* and *trans* ABA diols eluted slightly earlier than the ABA monosaccharide derivatives and were well separated from each other. The corresponding *cis* and *trans* acetate derivatives eluted much later, even later than the disaccharide esters of ABA and ABA diols; they were also well separated from

Fig. 2. HPLC separation of acetosugar esters of ABA, ABA diols, and the 4′-O-acetates, on a reverse-phase ultrasphere ODS column using isocratic acetonitrile–H_2O (52/48). Compounds: 1, ABA glucose ester; 2, ABA *trans*-1′, 4′-diol acetoglucose ester; 3, ABA *cis*-1′, 4′-diol acetoglucose ester; 4, ABA acetoglucose ester; 5, d_6-ABA α-acetoglucose ester; 6, d_6-ABA acetogalactose ester; 7, ABA acetolactose ester; 8, ABA *cis*-1′, 4′-diol acetomaltose ester; 9, ABA acetomaltose ester; 10, ABA *trans*-1′, 4′-diol 4′-OAc acetoglucose ester; 11, ABA *cis*-1′, 4′-diol 4′-OAc acetoglucose ester; 12, ABA *cis* 1′, 4′-diol 4′-OAc acetomaltose ester. All esters except 5 have β-D- configuration and are diastereomeric mixtures as racemic ABA was used in their preparation.

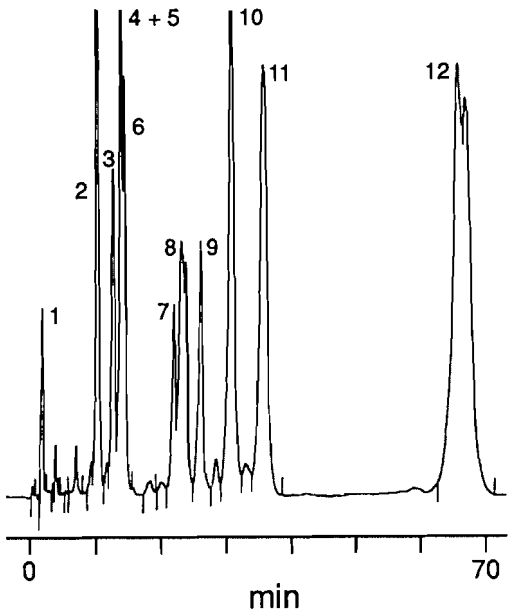

each other. The latest eluting compound was the C-4′-O-acetate of the *cis* diol of ABA acetomaltose ester. Diastereomeric pairs were not resolvable to any great extent on this column, although some separation of diastereomers was noted in the cases of the acetomaltose esters of ABA *cis* diol and the corresponding 4′-OAc.

To check on the separation of diastereomeric pairs, an LC analysis of some acetosugar esters was also performed on a Chiralcel OD column. This column, which contains a chiral stationary phase, had previously been used to resolve racemic ABA methyl ester (19). The results are summarized in Table 2. Overall, the best separation observed was between (+)- and (−) ABA-β-D-acetoglucose esters, which, under the conditions employed, were baseline resolved (R_t 11.3 and 16.9 min) with reasonable peak shapes; other ABA acetosugar esters generally eluted later, which resulted in broadened peaks and poorer resolution. The diastereomers of acetosugar esters derived from ABA diols and C-4′-O-acetates were not well separated. By comparison, (+)- and (−)-ABA methyl esters, under the same conditions, were also baseline resolved with retention times of 5.5 and 7.3 min, respectively.

MS of acetosugar esters

The continuous flow secondary ion mass spectra of the acetosugar esters contained strong ions due to the acetosugar fragments at *m/z* 331 for monosaccharides, and 619 and 331 for disaccharides (Table 3). ABA acetosugar esters exhibited weak but discernible M+1 ions as well as an ion at *m/z* 247 (253 for d_6-ABA) due to the loss of the O-acetosugar. Acetosugar esters of the *cis* and *trans* 1′, 4′-ABA-diols and their acetates unfortunately did not afford significant protonated parent (M+1) ions; a significant ion due to the ABA diol portion appeared at *m/z* 231, arising from loss of the O-sugar and either water (in the case of the diols) or acetic acid (in the case of the 4′-O-acetates).

Identification of d_6-ABA acetoglucose ester in an acetylated extract obtained from a maize cell suspension culture treated with d_6-ABA

To test the ability of LC/CFSIMS to detect an acetosugar ester in a plant extract, a maize cell suspension culture, which was known to metabolize ABA efficiently (20), was treated with d_6-ABA and the cells were isolated after 4 days and extracted with methanol. After acetylation, the extract was analyzed by LC/MS/MS. Figure 3 shows the reaction-monitoring chromatogram obtained for the transition *m/z* 601–331. The identity of the derivatized metabolite as the acetoglucose ester of ABA was established from its mass spectrum (Fig. 3) and cochromatography with an authentic sample. No other acetosugar esters were found in this extract.

In conclusion, various acetosugar esters of ABA and ABA derivatives were made readily available for use as reference and (or) internal standards in the analysis of plant extracts. The ability of LC/CFSIMS to detect these derivatives in acetylated extracts was shown, and should prove useful both quantitatively (via use of deuterated internal standards) and qualitatively in the study of ABA metabolism. Finally, the ready formation of various acetosugar derivatives by reaction of α-chloroacetosugars with the cesium salt of an acid would appear to be quite general and may represent a means for the resolution of some racemic acids.

Experimental

General

Solvents and reagents were of reagent grade and were used without further purification. Preparative layer chromatography was performed with 1 mm thick Merck Silica gel 60 F254 20 × 20 cm plates. Racemic abscisic acid was purchased from Aldrich Chemical Company. Deuterium-labeled abscisic acid was prepared by base-catalyzed exchange in D_2O/MeOD according to the procedure of Balsevich et al. (21). Infrared spectra (IR) were recorded using a Perkin–Elmer 257 grating infrared specrophotometer (films on NaCl). Ultraviolet spectra (UV)) were obtained (MeOH) with a Beckman DU-64 spectrophotometer. Proton nuclear magnetic resonance spectra (^{1}H NMR) were obtained with a Bruker AM 360 spectrometer with samples in deuterochloroform unless otherwise noted. An asterisk (*) beside a chemical shift listing denotes that two sets of signals were distinguishable for that resonance due to the two diastereomers. LC/CFSIMS and LC/MS/MS were peformed using a 0.32 × 150 mm Spherisorb 3 μm ODS-2 packed capillary column interfaced with a VG Analytical (Manchester, UK) 70-250 SEQ hybrid mass spectrometer equipped for continuous flow SIMS analysis according to Hogge et al. (14), except for gradient elution using a two-solvent system consisting of A: 2% glycerol and 0.1% trifluoro-

Table 2. Separation of some of the diastereomeric pairs of acetosugar esters of (±)-ABA and its diols by LC on a Chiralcel OD column. AcGE = acetoglucose ester, AcGalE = acetogalactose ester, AcME = acetomaltose ester, AcLE = acetolactose ester. With the exception of the second entry, all acetosugar esters were 1-O-β-D-linked.

Compounds	Retention times of diastereomers (min)	
(±)-ABA AcGE	11.3 [(+)-ABA AcGE][a]	16.9 [(−)-ABA AcGE][a]
(±)-ABA α-AcGE	16.3	20.3
(±)-ABA AcGalE	17.1	21.0
(±)-ABA AcME	20.2	26.3
(±)-ABA AcLE	17.7	21.7
(±)-*cis* Diol AcGE	10.8	10.8
(±)-*cis* Diol AcME	19.6	20.6
(±)-*trans* Diol 4′-OAc AcGE	9.5	9.5
(±)-*cis* Diol 4′-OAc AcGE	9.0	9.9
(±)-*cis* Diol 4′-OAc AcME	16.9	20.0

[a]The diastereomer due to (+)-ABA was found to be the faster eluting component in the case of the acetoglucose esters. This was determined by its isolation and saponification to (+)-ABA. Identification of other diastereomers was not done.

Table 3. CFSIMS data for some acetosugar derivatives of ABA and ABA diols. AcGE = acetoglucose ester, AcGalE=acetogalactose ester, AcME = acetomaltose ester, AcLE = acetolactose ester. With the exception of the fifth entry, all acetosugar esters were 1-O-β-D-linked.

	CFSIMS data: *m/z* (relative intensity)				
Compound	$[M+1]^+$	$[M+1-H_2O]^+$	$[M+1-HOAc]^+$	Non-sugar fragments	Sugar fragments
ABA AcGE	595(12)			247(7)	331(100)
ABA AcGalE	595(9)			247(5)	331(100)
d_6-ABA AcGE	601(8)			253(6)	331(100)
d_6-ABA AcGalE	601(7)			253(5)	331(100)
d_6-ABA α-AcGE	601(13)			253(5)	331(100)
ABA AcME	883(4)			247(6)	619(50), 331(100)
ABA AcLE	883(5)			247(7)	619(40), 331(100)
d_6-ABA AcLE	889(6)			253(6)	619(46), 331(100)
trans Diol AcGE	597(1)	579(2)		231(5)	331(100)
cis Ddiol AcGE	597(1)	579(3)		231(5)	331(100)
trans Diol-4′-OAc AcGE	639(1)	621(4)	579(3)	231(11)	331(100)
cis Diol 4′-OAc AcGE	—	621(2)	579(1)	231(7)	331(100)
cis Diol AcME	—	867(2)		231(6)	619(67), 331(100)
cis Diol-4′OAc AcME	927(1)	909(1)	867(1)	231(9)	619(45)), 331(62)

acetic acid in H_2O, and B: 80% CH_3CN, 2% glycerol, and 0.1% trifluoroacetic acid in H_2O. The gradient elution used was 50% A to 10% A in 10 min, which was held for a further 25 min. Analytical LC was performed on a Waters system equipped with a reverse-phase Ultrasphere 5 μm ODS 4.6 mm × 25 cm column using isocratic CH_3CN/H_2O (52:48) at a flow rate of 0.5 mL/min. UV detection at 262 nm was used. Chiral LC was performed with a Chiralcel OD 0.46 × 25 cm coated silica column (Daicel, Los Angeles, Calif.) using isocratic hexane/isopropanol (7:1) at a flow rate of 1 mL/min. Mass spectrometry (MS) was performed with a VG 70-250SEQ double focussing hybrid spectrometer. High-resolution mass spectrometry (HRMS) was performed using fast ion bombardment ionization with the sample in a glycerol matrix.

Reduction of ABA with L-Selectride® — (±)-ABA *cis*-1′, 4′-diol

A solution of ABA (264 mg, 1 mmol) in anhydrous THF (10

Fig. 3. Reaction monitoring chromatogram for the transition *m/z* 601–331 (insert), and the obtained CFSIMS spectrum from analysis of an acetylated plant extract.

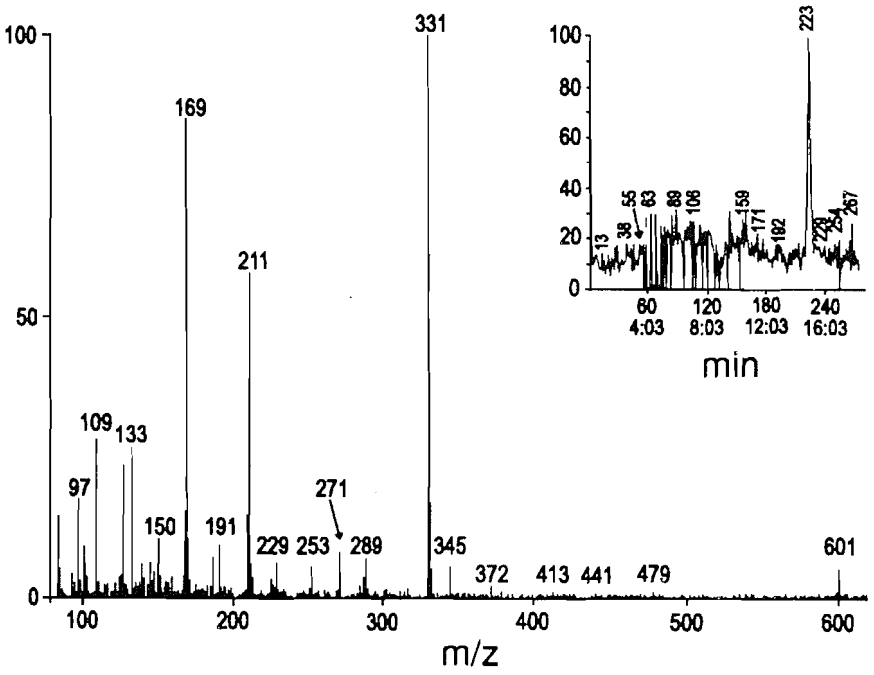

mL) was cooled to 0°C, treated with sodium hydride – mineral oil suspension (60%, 44 mg, 1.1 mmol), and stirred for 20 min. A 1 M solution of L-Selectride® (1.1 mL, 1.1 mmol) in THF was added at a dropwise rate over 10 min. The reaction was allowed to warm to ambient temperature and stirred for a further 3 h. Water (100 mL) was cautiously added and the aqueous solution washed with ethyl acetate (3 × 15 mL). The combined ethyl acetate washings were back-extracted with water (2 × 10 mL) and discarded. The aqueous portions were combined, made acidic by the addition of 1 N HCl (3 mL), and extracted with ethyl acetate (3 × 20 mL). The combined ethyl acetate extract was washed with water (2 × 5 mL), dried (Na_2SO_4), and concentrated in vacuo to afford a mixture consisting mainly of the *cis* diol plus ca. 9% of the *trans* diol as a white amorphous solid (260 mg, 0.98 mmol, 98%). The proportions of the two isomers were determined from the ^1H NMR spectrum of the reaction product. The diols were separated by preparative TLC on silica gel using EtOAc as solvent.

cis Diol: UV, λ_{max} (log ε): 262 (4.24); IR; ν_{max} (cm^{-1}): 3400, 2965, 1688, 1631, 1598, 1240; ^1H NMR; δ: 7.70 (1H, d, 16 Hz, C-5), 6.05 (1H, d, 16 Hz, C-4), 5.69 (1H, s, C-2), 5.64 (1H, bs, C-3′), 4.24 (1H, m, C-4′), 2.01 (3H, s, C-6), 1.79 (1H, ABX, 13 and 6 Hz, C-5′α or β), 1.71 (1H, ABX, 13 and 7 Hz, C-5′α or β), 1.65 (3H, s, C-7′), 1.00 (3H, s, C-8′ or 9′), 0.92 (3H, s, C-8′ or C-9′). MS (ammonia CI) *m/z*: 284 ($[M+18]^+$, 9%), 267 ($[M+1]^+$, 38%), 266 (M^+, 69%), 248 (35%), 231 (100%); HRMS, calcd. for $[M+glycerol]^+$ $C_{18}H_{31}O_7$: 359.2070; found: 359.2026.

trans Diol: mp 148–153°C; UV, λ_{max} (log ε): 262 (4.21); IR, ν_{max} (cm^{-1}): 3400, 2962, 1686, 1631, 1598, 1240; ^1H NMR, δ: 7.58 (1H, d, 16 Hz, C-5), 6.05 (1H, d, 16 Hz, C-4), 5.69 (1H, s, C-2), 5.67 (1H, bs, C-3′), 4.22 (1H, m, C-4′), 2.02 (3H, s, C-6), 1.78 (1H, ABX, 13 and 6.5 Hz, C-5′α), 1.64 (3H, s, C-7′), 1.61 (1H, ABX, 13 and 9.5 Hz, C-5′β), 1.02 (3H, s, C-8′ or 9′), 0.89 (3H, s, C-8′ or C-9′). ^1H NMR (D_2O); δ: 7.25 (1H, d, 16 Hz, C-5), 6.11 (1H, d, 16 Hz, C-4), 5.71 (1H, s, C-2), 5.54 (1H, bs, C-3′), 4.22 (1H, m, C-4′), 1.94 (3H, s, C-6), 1.66 (1H, ABX, 13 and 6 Hz, C-5′α), 1.54 (3H, s, C-7′), 1.46 (1H, ABX, 13 and 10 Hz, C-5′β), 0.91 (3H, s, C-8′ or 9′), 0.82 (3H, s, C-8′ or C-9′). MS (ammonia CI) *m/z*: 284 ($[M+18]^+$, 16%), 267 ($[M+1]^+$, 10%), 266 (M^+, 100%), 248 (30%), 231 (61%); HRMS, calcd. for $[M+glycerol]^+$ $C_{18}H_{31}O_7$: 359.2070; found: 359.2108.

The *cis* and *trans* diols were also converted to their methyl esters by treatment with ethereal diazomethane and afforded ^1H NMR spectra comparable to published data [2].

Reduction of ABA with lithium aluminum hydride — (±)-ABA *trans*-1′, 4′-diol

A solution of ABA (264 mg, 1 mmol) in anhydrous THF (10 mL) was cooled to 0°C, treated with sodium hydride–mineral oil suspension (60%, 40 mg, 1 mmol), and stirred for 20 min. $LiAlH_4$ (30 mg, 0.75 mmol) was added in several portions over 10 min. The reaction was allowed to warm to ambient temperature and stirred for a further 4 h. The reaction was poured into cold water (100 mL), washed with hexane (3 × 25 mL), acidified with 1 N HCl (3.5 mL), and extracted with EtOAc (3 × 30 mL). The EtOAc extract was dried (Na_2SO_4), filtered, and concentrated in vacuo to afford a mixture of the *trans* diol contaminated with ca. 5% overreduced products as a white amorphous solid (260 mg). The presence of overreduced products was determined from the ^1H NMR spectrum from signals at δ 3.6–3.9 attributable to saturated alcohols. The main product was the *trans* diol (C-4′ β-OH) identical to the minor product from above; virtually no *cis* diol was observable by NMR.

(±)-ABA *trans*-1′, 4′-diol C-4′-O-acetate

trans ABA diol (260 mg, ca. 0.9 mmol), obtained directly from the $LiAlH_4$ reduction of ABA without further purifica-

tion, was dissolved in a 1:2 (v/v) mixture of acetic anhydride and pyridine (1 mL), and let stand at ambient temperature for 17 h. The mixture was concentrated in vacuo, and the residue was dissolved in EtOAc (ca. 50 mL), washed with 1 N HCl (2×), water (3×), and concentrated in vacuo. The residue was treated with ethyl acetate (ca 1 mL) and stored at 0°C overnight. The resultant crystalline solid was isolated by filtration and the crystals dried in vacuo to afford the acetate as a white crystalline solid (170 mg), mp 185–188°C; UV, λ_{max} (log ε): 258 (4.18); IR, ν_{max} (cm^{-1}): 3400, 2960, 1720sh, 1710, 1680 sh, 1632, 1598, 1245; ^1H NMR ($CDCl_3$/DMSO-d_6, 3:1), δ: 7.61 (1H, d, 16 Hz, C-5), 6.02 (1H, d, 16 Hz, C-4), 5.55 (1H, s, C-2), 5.3 3 (1H, s, C-3′), 5.20 (1H, m, C-4′), 1.94 (3H, s, OAc), 1.91 (3H, s, C-6), 1.71 (1H, *A*BX, 6 and 13 Hz, C-5′β), 1.56 (3H, s, C-7), 0.94 (3H, s, C-8′), 0.81 (3H, s, C-9′). HRMS, calcd. for $[(M-H_2O)+H]^+$ $C_{15}H_{21}O_3$: 249.1491; found: 249.1457.

(±)-ABA *cis*-1′, 4′-diol C-4′-O-acetate

The *cis* diol (130 mg, 0.5 mmol) was treated as above except the crude product was purified by TLC on Silica gel using EtOAc to afford a colorless film (80 mg, 52%); UV, λ_{max} (log ε): 258 (4.20); ^1H NMR, δ: 7.68 (1H, d, 16 Hz, C-5), 5.93 (1H, d, 16 Hz, C-4), 5.68 (1H, s, C- 3′), 5.51 (1H, s, C-2) 5.26 (1H, m, C-4′), 2.01 (3H, s, OAc), 1.93 (3H, s, C-6), 1.80 (1H, ABX, 6 and 14 Hz, C-5′β), 1.72 (1H, ABX, 6 and 14 Hz, C-5′α), 1.62 (3H, s, C-7), 0.97 (3H, s, C-8′), 0.90 (3H, s, C-9′). HRMS, calcd. for $[(M-H_2O)+H]^+$ $C_{15}H_{21}O_3$: 249.1491; found: 249.1507.

Preparation of cesium salts of ABA, ABA diols, and diol acetates

Cesium salts were prepared by treating a solution of racemic ABA, or the ABA diols, or the acetates (1 mmol) in 50% aqueous methanol (10 mL) with cesium carbonate (0.5 mmol) and concentrating the resultant solution in vacuo. The residues were treated with benzene and concentrated in vacuo (2×), and then stored in a vacuum desiccator for 24 h. The cesium salts were obtained as colorless to pale yellow glasses and were used without further purification.

Preparation of α-chloroacetosugars and β-chloroacetoglucose

The α-chloroacetosugars were prepared by reaction of the peracetylated sugars with titanium tetrachloride in refluxing chloroform as outlined in refs. 22 and 23. β-Chloroacetoglucose was prepared by reaction of glucose pentaacetate with aluminum chloride in dichloromethane as outined in ref. 24.

General protocol for preparation of acetosugar esters

A solution of the appropriate cesium salt (1 mmol) in either DMF or DMSO (5 mL) was treated with the appropriate chloroacetosugar (1.1 mmol). After 4 days at ambient temperature or 5 h at 60°C, the reaction was treated with H_2O (30 mL) and extracted with EtOAc (3 × 20 mL). The combined organic extract was washed with 0.1 N NaOH (2 × 10 mL), H_2O (2 ×10 mL), brine (2 × 10 mL), and dried over anhydrous sodium sulfate. Evaporation of the solvent in vacuo afforded an amber oil, which was subjected to TLC on silica, gel using hexane/EtOAc (7:3) as solvent to afford the appropriate acetosugar ester as a colorless glass, generally in about 50% yield (see Table 1). ABA acetosugar esters gave UV spectra having λ_{max} (log ε): 272 (4.29), 240sh (4.07), while the acetosugar esters of ABA diols and C-4′-O-acetates gave λ_{max} (log ε): 272 (4.18). ABA acetosugar esters gave IR spectra having ν_{max} (cm^{-1}): 3500, 2962, 1748, 1663, 1630sh, 1598, 1224, 1070, 1040; acetosugar esters of ABA diols gave ν_{max}: 3515, 2964, 1750, 1633, 1598, 1228, 1070, 1038; acetosugar esters of the C-4′-O-acetates gave ν_{max}: 3510, 2954, 1755, 1735sh, 1633, 1598, 1225, 1070, 1040.

(±)-ABA β-D-*acetoglucose ester:* ^1H NMR (ref. 17), δ: 7.78 (1H, d, 16 Hz, C-5), 6.21, 6.20* (1H, d, 16 Hz, C-4), 5.92 (1H, bs, C-3′), 5.74 (1H, d, 8.6 Hz, sugar C-1), 5.72 (1H, s, C-2), 5.27 (1H, t, 9 Hz, sugar C-3 or 4), 5.20 (1H, t, 8.5 Hz, sugar C-2), 5.13 (1H, t, 9.5 Hz, sugar C-3 or C-4), 4.29 (1H, ABX, 12.5 and 3.4 Hz, sugar C-6), 4.11 (1H, ABX, 12.5 and 2 Hz, sugar C-6), 3.84 (1H, m, sugar C-5), 2.46, 2.44* (1H, AB, 17 Hz, C-5′α or β), 2.30 (1H, AB, 17 Hz, C-5′α or β), 2.06 (3H, s, OAc), 2.02 (3H, s, OAc), 2.01 (3H, bs, C-6), 2.00 (3H, s, OAc), 1.99 (3H, s, OAc), 1.91, 1.90* (3H, s, C-7′), 1.10 (3H, s, C-8′ or 9′), 0.99* (3H, s, C-8′ or 9′). HRMS, calcd. for $[M+H]^+$ $C_{29}H_{39}O_{13}$: 595.2391; found: 595.2361.

d_6-*(±)-ABA* β-D-*acetoglucose ester*: ^1H NMR: as above except lacking resonances at δ 5.92, 2.5–2.2, and 1.9. HRMS, calcd. for $[M+H]^+$ $C_{29}H_{33}D_6O_{13}$: 601.2767; found: 601.2787.

d_6-*(±)-ABA* α-D-*acetoglucose ester*: ^1H NMR, δ: 7.83, 7.82* (1H, d, 16 Hz, C-5), 6.39 (1H, d, 3.7 Hz, sugar C-1), 6.20, 6.19* (1H, d, 16 Hz, C-4), 5.80 (1H, s, C-2), 5.53 (1H, t, 10 Hz, sugar C-3 or 4), 5.13 (1H, t, 10 Hz, sugar C-3 or C-4), 5.10 (1H, dd, 10 and 3.7 Hz, sugar C-2), 4.2 (1H, ABX, 12.5 and 3.4 Hz, sugar C-6), 4.12 (1H, m, sugar C-5), 4.07 (1H, ABX, 12.5 and 2 Hz, sugar C-6), 2.1–1.97* (5 × 3H, 7s, 4 OAc and C-7′), 1.09, 1.08* (3H, s, C-8′ or 9′), 0.99 (3H, s, C-8′ or 9′). HRMS, calcd. for $[M+H]^+$ $C_{29}H_{33}D_6O_{13}$: 601.2767; found: 601.2776.

(±)-ABA β-D-*acetogalactose ester*: ^1H NMR, δ: 7.78, 7.77* (1H, 2 d, 16 Hz, C-5), 6.21, 6.19* (1H, 2 d, 16 Hz, C-4), 5.92 (1H, bs, C-3′), 5.73 (1H, s, C-2), 5.72 (1H, d, 8.4 Hz, sugar C-1), 5.41 (1H, t, 1.6 Hz, sugar C-4), 5.36, 5.35* (1H, 2 dd, 8 and 10 Hz, sugar C-2), 5.08 (1H, dd, 10 and 3.4 Hz, sugar C-3), 4.2–4.0 (3H, overlapping peaks, sugar C-5 and C-6), 2.45, 2.43* (1H, AB, 17 Hz, C-5′α or β), 2.29 (1H, AB, 17 Hz, C-5′α or β), 2.14, 2.10 (2 × 3H, 2s, 2 × OAc), 2.00 (6H, s, 2 × OAc), 1.97 (3H, s, C-6), 1.91, 1.89* (3H, s, C-7′), 1.09 (3H, s, C-8′ or 9′), 0.99 (3H, s, C-8′ or 9′). HRMS, calcd. for $C_{29}H_{39}O_{13}$: 595.2391; found: 595.2427.

d_6-*(±)-ABA* β-D-*acetogalactose ester*: ^1H NMR: as above except lacking resonances at δ 5.92, 2.5–2.2, and 1.9. HRMS, calcd. for $[M+H]^+$ $C_{29}H_{33}D_6O_{13}$: 601.2767; found: 601.2795.

(±)-ABA cis-*1′, 4′-diol* β-D-*acetoglucose ester*: ^1H NMR, δ: 7.73 (1H, d, 16 Hz, C-5), 6.12 (1H, d, 16 Hz, C-4), 5.76 (1H, d, 8.5 Hz, sugar C-1), 5.67 (1H, s, C-2), 5.62 (1H, bs, C-3′), 5.26 (1H, t, 9 Hz, sugar C-3 or 4), 5.18 (1H, t, 9 Hz, sugar C-3 or 4), 5.13 (1H, t, 9 Hz, sugar C-2), 4.39 (1H, ABX, 12 and 5 Hz, sugar C-6), 4.24 (1H, m, C-4′), 4.00 (1H, ABX, 12 and 2 Hz, sugar C-6), 3.85 (1H, m, sugar C-5), 2.08 (3H, s, OAc), 2.04

(3H, s, OAc), 2.02 (6H, s, OAc and C-6), 2.01 (3H, s, OAc), 1.80 (1H, ABX, 14 and 6, C-5′α or β), 1.71 (1H, ABX, 14 and 6, C-5′α or β), 1.66 (3H, s, C-7′), 1.00 (3H, s, C-8′ or 9′), 0.92 (3H, s, C-8′ or 9′).

(±)-ABA cis-*1′, 4′-diol C-4′-O-acetate* β-D-*acetoglucose ester*: ^{1}H NMR, δ: 7.71 (1H, d, 16 Hz, C-5), 6.09 (1H, d, 16 Hz, C-4), 5.74 (1H, d, 8.2 Hz, sugar C-1), 5.67 (1H, s, C-2), 5.57 (1H, bs, C-3′), 5.29 (1H, m, C-4′), 5.25 (1H, t, 9.5 Hz, sugar C-3 or 4), 5.17 (1H, t, 9 Hz, sugar C-2), 5.12 (1H, t, 9 Hz, sugar C-3 or C-4), 4.28 (1H, ABX, 12 and 5 Hz, sugar C-6), 4.10 (1H, m, sugar C-6), 3.83 (1H, m, sugar C-5), 2.05, 2.03, 2.01, 2.00, 1.99, 1.98 (6 × 3H, 6s, 5 × OAc and C-6), 1.83 (1H, m, C-5′α or β), 1.71 (1H, m, C-5′α or β), 1.66 (3H, s, C-7′), 1.01 (3H, s, C-8′ or 9′), 0.93 (3H, s, C-8′ or 9′). HRMS, calcd. for $[(M+H)-H_2O]^+$ $C_{31}H_{41}O_{13}$: 621.2547; found: 621.2562.

(±)-ABA trans-*1′, 4′-diol* β-D-*acetoglucose ester*: ^{1}H NMR, δ: 7.58, 7.57* (1H, 2d, 16 Hz, C-5), 6.18, 6.17* (1H, 2d, 16 Hz, C-4), 5.72, 5.71* (1H, 2d, 8.5 Hz, sugar C-1), 5.65 (1H, s, C-2), 5.63, 5.61* (1H, 2bs, C-3′), 5.22 (1H, t, 9.5 Hz, sugar C-3 or 4), 5.14 (1H, t, 9 Hz, sugar C-2), 5.10 (1H, t, 9.5 Hz, sugar C-3 or 4), 4.28–4.16 (2H, overlapping peaks, C-4′ and sugar C-6), 4.07 (1H, m, sugar C-6), 3.82 (1H, m, sugar C-5), 2.04*, 2.00, 1.99, 1.98, 1.97 (5 × 3H, 5s, 4 × OAc and C-6) 1.79 (1H, m, C-5′α or β), 1.62 (3H, s, C-7′), 1.53 (1H, m, C-5′α or β), 1.01 (3H, s, C-8′ or 9′), 0.87, 0.86* (3H, 2s, C-8′ or 9′). HRMS, calcd. for $[M+H]^+$ $C_{29}H_{41}O_{13}$: 597.2547; found: 597.2527

(±)-ABA trans-*1′, 4′-diol C-4′-O-acetate* β-D-*acetoglucose ester*: ^{1}H NMR, δ: 7.70* (1H, d, 16 Hz, C-5), 6.21* (1H, d, 16 Hz, C-4), 5.74* (1H, d, 8.5 Hz, sugar C-1), 5.67 (1H7, s, C-2), 5.50 (1H, bs, C-3′), 5.36 (1H, m, C-4′), 5.25 (1H, t, 9.4 Hz, sugar C-3 or 4), 5.18 (1H, t, 8.2 Hz, sugar C-2), 5.12 (1H, t, 9.4 Hz, sugar C-3 or 4), 4.27 (1H, ABX, 12.5 and 4.3 Hz, sugar C-6), 4.09 (1H, ABX, 12.5 and 2 Hz, sugar C-6), 3.82 (1H, m, sugar C-5), 2.05, 2.04, 2.01, 2.00, 1.99, 1.98 (6 × 3H, 6s, 5 × OAc and C-6), 1.87 (1H, m, C-5′α or -b), 1.68 (1H, m, C-5′α or -β), 1.65 (3H, s, C-7′), 1.06 (3H, s, C-8′ or 9′), 0.89, 0.88* (3H, 2s, C-8′ or 9). HRMS, calcd. for $[M+H]^+$ $C_{31}H_{43}O_{14}$: 639.2696; found: 639.2653.

(±)-ABA β-D-*acetolactose ester*: ^{1}H NMR, δ: 7.76 (1H, d, 16 Hz, C-5), 6.20, 6.19* (1H, d, 16 Hz, C-4), 5.91 (1H, s, C-3′), 5.70 (1H, d, 8 Hz, C-1 of glucose portion), 5.70 (1H, s, C-2), 5.34 (1H, m, C-4 of galactose portion), 5.26 (1H, t, 9 Hz), 5.1 (2H, overlapping peaks), 4.93 (1H, dd, 10 and 3 Hz, C-3 of galactose portion), 4.5–3.6 (8H, overlapping peaks, sugar H's), 2.45, 2.44* (1H, AB, 16 Hz, C-5′α or b), 2.29 (1H, AB, 16 Hz, C-5′α or β), 2.14, 2.09, 2.05, 2.04, 2.03, 2.02, 2.00 (7 × 3H, 7s, 7 × OAc), 2.07 (3H, s, C-6), 1.89 (3H, s, C-7′), 1.10 (3H, s, C-8′ or -9′), 0.99 (3H, s, C-8′ or 9′). HRMS, calcd. for $[M+H]^+$ $C_{41}H_{55}O_{21}$: 883.3236; found: 883.3285

d_6-*(±)-ABA* β-D-*acetolactose ester*. *^{1}H NMR*: as above, except lacking peaks at δ 5.91, 2.5–2.2, and 1.89. HRMS, calcd. for $[M+H]^+$ $C_{41}H_{49}D_6O$: 889.3613; found: 889.3642.

(±)-ABA β-D-*acetomaltose ester*: ^{1}H NMR, δ: 7.76* (1H, d, 16, C-5), 6.18* (1H, d, 16, C-4), 5.89 (1H, s, C-3′), 5.74 (1H, d, 8 Hz, sugar A C-1), 5.67 (1H, s, C-2), 5.37 (1H, d, 4 Hz, sugar B C-1), 5.35–5.25 (2H, overlapping sugar peaks), 5.04–4.94 (2H, overlapping sugar peaks), 4.82 (1H, dd, 10.5 and 4 Hz, sugar B C-2), 4.5–3.8 (6H, sugar A and B C-5's and C-6's), 2.08, 2.05, 2.01 (3 x 3H, 3s, 3 × OAc), 2.00 (3H, s, C-6), 1.98 (6H, s, 2 × OAc), 1.96, 1.95 (2 × 3H, 2s, 2 × OAc), 1.87 (3H, bs, C-7′), 1.07 (3H, s, C-8′ or -9′), 0.97 (3H, s, C-8′ or 9′). HRMS, calcd. for $[M+H]^+$ $C_{41}H_{55}O_{21}$: 883.3236; found: 883.3227.

(±)-ABA cis-*1′, 4′-diol* β-D-*acetomaltose ester*: ^{1}H NMR, δ: 7.71* (1H, d, 16 Hz, C-5), 6.10, 6.09* (1H, d, 16 Hz, C-4), 5.76 (1H, d, 8 Hz, sugar A C-1), 5.63 (2H, 2 × s, C-2, C-3′), 5.38 (1H, d, 4 Hz, sugar B C-1), 5.33 (1H, t, 10 Hz), 5.28 (1H, t, 10 Hz) 5.03 (1H, t, 10 Hz) 5.00 (1H, t, 9 Hz), 4.84 (1H, dd, 10 and 4 Hz, sugar B C-2), 4.43 (1H, m), 4.25–4.18 (3H, overlapping peaks, C-4′ and sugar C-6's), 4.03 (2H, overlapping peaks), 3.92 (1H, m), 3.82 (1H, m), 1.97, 2.10, 2.07, 2.02, 2.00 (4 × 3H, 4s, 4 × OAc), 1.99 (6H, 2s, C-6 and OAc), 1.96 (2 × 3H, s, 2 × OAc), 1.64 (3H, bs, C-7′), 1.00 (3H, s, C-8′ or -9′), 0.91 (3H, s, C-8′ or 9′). HRMS, calcd. for $[M+H]^+$ $C_{41}H_{57}O_{21}$: 885.3392; found: 885.3443

(±)-ABA cis-*1′, 4′-diol C-4′-O-acetate* β-D-*acetomaltose ester*: ^{1}H NMR, δ: 7.71 (1H, d, 16 Hz, C-5), 6.09* (1H, d, 16 Hz, C-4), 5.77 (1H, d, 8 Hz, sugar A C-1), 5.64 (1H, s, C-3′), 5.57 (1H, s, C-2), 5.38 (1H, d, 4 Hz, sugar B C-1), 5.34 (1H, t, 10 Hz), 5.29 (1H, t, 9 Hz), 5.28 (1H, m, C-4′) 5.03 (1H, t, 10 Hz) 5.01 (1H, t, 9 Hz), 4.84 (1H, dd, 10 and 4 Hz, sugar B C-2), 4.43 (1H, m), 4.22 (2H, overlapping peaks), 4.03 (2H, overlapping peaks), 3.93 (1H, m), 3.82 (1H, m), 2.10, 2.08, 2.04, 2.03, 2.00 (5 × 3H, 4s, 4 × OAc), 1.99 (6H, 2s, C-6 and OAc), 1.98, 1.97 (2 × 3H, 2s, 2 × Oac), 1.66 (3H, bs, C-7′), 1.01 (3H, s, C-8′ or -9′), 0.93 (3H, s, C-8′ or -9′). HRMS, calcd. for $[M+H]^+$: $C_{43}H_{59}O_{22}$: 927.3498; found: 927.3491.

Enzymatic deacetylation of ABA *cis* diol- and ABA acetoglucose esters

The acetoglucose esters of ABA and ABA *cis*-1′, 4′-diol were deacetylated using a modification of the procedure of Lehmann et al. (15) as follows. Enzyme preparation: dehusked sunflower seeds (9 g, Super Store) were added to cold (<10°C) pH 7.0 100 mM phosphate buffer (75 mL) and homogenized with an Ultra Turrax homogenizer for 2–3 min. The resulting suspension was centrifuged at 25 000*g* for 30 min. The middle aqueous layer was removed and re-centrifuged. The resulting clear aqueous portion, free of oil droplets, was used for deacetylations.

(±)-ABA cis-*1′, 4′-diol glucose ester*

A solution of the *cis* diol β-acetoglucose ester (230 mg, 0.39 mmol) in EtOH (15 mL) was added to a vigorously stirred solution of 100 mM pH 7.0 phoshate buffer (35 mL), and the sunflower seed enzyme preparation from above (60 mL). A further portion of EtOH (3 mL) was added dropwise over a period of 20 min and the resulting mixture stirred at ambient temperature for 20 h. Isopropanol (100 mL) was added and and the resulting mixture centrifuged at 10 000*g* for 30 min. The supernatant was concentrated in vacuo and the residue was triturated with a further portion of isopropanol (50 mL) and centrifuged again. The supernatant was concentrated in

vacuo and the residue (200 mg) subjected to thin-layer chromatography (silica gel), using CH_3CN/H_2O (93:7) as the solvent system, to yield the *cis* diol glucose ester as a white amorphous solid (75 mg, 0.18 mmol, 46%). ^1H NMR (D_2O), δ: 7.46 (1H, d, 16 Hz, C-5), 6.21 (1H, d, 16 Hz, C-4), 5.76 (1H, s, C-2), 5.59 (1H, bs, C-3), 5.50 (1H, d, 8 Hz, sugar C-1), 4.20 (1H, m, C-4′), 3.9–3.3 (6H, overlapping peaks, sugar C-2 C-6), 2.01 (3H, s, C-6), 1.70 (1H, ABX, 13 and 6 Hz, C-5′α or b), 1.57 (3H, s, C-7′), 1.53 (1H, ABX, 13 and 7 Hz, C-5′α or β), 0.89 (3H, s, C-8′ or 9′), 0.84 (3H, s, C-8′ or C-9′); CFSIMS, *m/z*: 429 (2%, M^++1), 411 (50%, M^++1−H_2O), 393 (28%, M^++1−2H_2O), 249 (44%), 231 (100%). HRMS, calcd. for $[M+H]^+ C_{21}H_{33}O_9$: 429.2125; found: 429.2177.

(±)-ABA glucose ester

A solution of ABA β-acetoglucose ester (230 mg, 0.39 mmol) was treated as above to yield ABA glucose ester as a colorless film (84 mg, 0.2 mmol, 51%) having an ^1H NMR spectrum similar to that reported in the literature (17). ^1H NMR (D_2O), δ: 7.50 (1H, d, 16 Hz, C-5), 6.26 (1H, d, 16 Hz, C-4), 5.97 (1H, bs, C-3′), 5.78 (1H, s, C-2), 5.49 (1H, d, 8 Hz, sugar C-1), 3.9–3.2 (6H, overlapping peaks, sugar C-2–C-6), 2.50 (1H, AB, 17 Hz, C-5′α or β), 2.16 (1H, AB, 17 Hz, C-5′α or β), 1.99 (3H, s, C-6), 1.85 (3H, s, C-7′), 0.9 6 (3H, s, C-8′ or 9′), 0.93 (3H, s, C-8′ or C-9′); CFSIMS, *m/z*: 427 (27%, M^++1), 409 (8%, M^++1−H_2O), 265 (base peak), 247 (77%). HRMS, calcd. for $[M+H]^+ C_{21}H_{31}O_9$: 427.1968; found: 427.1992.

Feeding of d_6-ABA to a maize cell suspension

Suspension cultures of corn (*Zea mays L.* cv Black Mexican Sweet) were maintained on modified Murashige–Skoog medium as described previously (20, 25). d_6-(±)-ABA (0.4 mg) in EtOH (30 μL) was added to the cell suspension (60 mL, ca. 2 g fresh wt. of cells) 24 h after being subcultured. After 4 d cells were separated from medium by filtration and extracted with methanol (100 mL). Cell material was removed by filtration and the methanol extract concentrated in vacuo. The residue was washed with hexane, redissolved in cold methanol/acetonitrile (1:1, 20 mL), filtered, and concentrated in vacuo. The residue was treated with Ac_2O/pyridine (1 mL of a 1:2 mixture, v/v). After 4 h, volatiles were removed in vacuo and the residue dissolved in 50% acetonitrile (aq) and used for the LC/CFSIMS analysis described earlier.

Acknowledgements

We thank Dr Adrian Cutler for supplying the maize cell suspension culture and Dr Suzanne Abrams for helpful discussions.

References

1. Progress in plant growth regulation. Plant Growth Subst. Proc. 14th Int. Conf. Amsterdam, 21–26 July, 1991. *Edited by* C.M Karssen, L.C. Van Loon, and D. Vreugdenhil. Kluwer Academic Publishers, Dordrecht. 1992.
2. N. Hirai, M. Okamoto, and K. Koshimizu. Phytochemistry, **25**, 1865 (1986).
3. W. Dathe and G. Sembdner. Phytochemistry, **21**, 1798 (1982).
4. G.T. Vaughn and B.V. Milborrow. Aust. J. Plant Physiol. **14**, 593 (1987).
5. B.V. Milborrow. J. Exp. Bot. **34**, 303 (1983).
6. W.V. Dashek, B.N. Singh, and D.C. Walton. Plant Physiol. **64**, 43 (1979).
7. L.A. Davis, J.L. Lyon, and F.T. Addicott. Planta, **102**, 294 (1972).
8. B.V. Milborrow. Chem. Commun. 966 (1969).
9. K. Koshimizu, M. Inui, H. Fukui, and T. Mitsui. Agric. Biol. Chem. **32**, 789 (1968).
10. J.A.D. Zeevart. Plant Physiol. **66**, 672 (1980).
11. G.C. Martin, I.M. Scott, S.J. Neill, and R.Horgan. Phytochemistry, **21**, 1079 (1982).
12. G.T. Vaughn and B.V. Milborrow. Phytochemistry, **27**, 2441 (1988).
13. N. Hirai and K. Koshimizu. Agric. Biol. Chem. **47**, 365 (1983).
14. L.R. Hogge, J.J. Balsevich, D.J.H. Olson, G.D. Abrams, and S.L. Jacques. Rapid Commun. Mass Spectrom. **7**, 6 (1993).
15. H. Lehmann, O. Miersch, and H.R. Schutte. Z. Chem. **15**, 443 (1975).
16. S.M. Southwick, A.Chung, T.L. Davenport, and J.W. Ryan. Plant Physiol. **81**, 323 (1986).
17. B.V. Milborrow and R.C. Noddle. Biochem. J. **119**, 727 (1970).
18. W. Su-Sun, B.F. Gisin, D.P. winter, R. Makofske, I.D.Kulesha, C. Tzougraki, and D. Meienhofer. J. Org. Chem. **42**, 1286 (1977).
19. D.I. Dunstan, C.A. Bock, G.D. Abrams, and S.R. Abrams. Phytochemistry, **31**, 1451 (1992).
20. J.J. Balsevich, A.J. Cutler, N. Lamb, L.J. Friesen, E.U. Kurz, M.R. Perras, and S.R. Abrams. Plant Physiol. **106**, 135 (1994).
21. J.J. Balsevich, S.R. Abrams, N. Lamb, and W.A. Konig. Phytochemistry, **36**, 647 (1994).
22. R.U. Lemieux. *In* Methods in carbohydrate chemistry. Vol. II, *Edited by* R.L. Whistler, M.L. Wolfrom, and J.N. BeMiller. Academic Press, New York. 1963. pp 223–224.
23. E. Pacsu. Ber. Dtsch. Chem. Ges. **61**, 1508 (1928).
24. R.U. Lemieux. *In* Methods in carbohydrate chemistry. Vol. II, *Edited by* R.L. Whistler, M.L. Wolfrom, and J.N. BeMiller. Academic Press, New York. 1963. pp. 224–225.
25. S.R. Ludwig, D.A. Somers, W.L. Peterson, B.F. Pohlmann, M.A. Zarovitz, B.G. Gengenbach, and J. Messing. Theor. Appl. Genet. **71**, 344 (1985).

Single-crystal polarized spectra in the near-infrared region: a local-mode analysis of the spectra of $M_2MnCl_4 \cdot 2X_2O$ (M = Cs, Rb; X = H, D)

Ian M. Walker and Paul J. McCarthy

Abstract: The polarized crystal spectra of $M_2MnCl_4 \cdot 2X_2O$ (M = Cs, Rb; X = H, D) have been measured at 10 K in the near-infrared region. The data have been analyzed using a local-mode model that includes the bending mode. The resulting parameters are related to hydrogen bonding in the crystals. The spectra of partially deuterated species show a large number of bands due to HOD vibrations. The parameters from these spectra are compared to those from the H_2O and D_2O spectra. Arguments as to the importance of Fermi resonance in these spectra are presented.

Key words: near-infrared, single crystal, hydrogen bond, Fermi resonance.

Résumé : Opérant à 10 K, dans la région du proche infrarouge, on a mesuré les spectres cristallins polarisés du $M_2MnCl_4 \cdot 2X_2O$ (M = Cs, Rb; X = H, D). On a analysé les données en utilisant un modèle de mode local qui incorpore le mode de déformation. Les paramètres qui en résultent peuvent être reliés à une liaison hydrogène dans les cristaux. Les spectres des espèces partiellement deutérées présentent un grand nombre de bandes dues à des vibrations HOD. On a comparé les paramètres dérivés de ces spectres avec ceux obtenus à partir des spectres du H_2O et du D_2O. On présente des arguments relatifs à l'importance de la résonance de Fermi dans ces spectres.

Mots clés : proche infrarouge, cristal unique, liaisons hydrogène, résonance de Fermi.

[Traduit par la rédaction]

Introduction

In several recent articles we have studied in detail the near-infrared (nir), low-temperature, polarized spectra of crystals containing H_2O (1–4) or the NH_2 group as found in a series of guanidinium salts (5). The absorptions that appear in this region between about 4000 and 10 000 cm^{-1} are due almost entirely to overtones and combinations of OH or NH stretching vibrations and to combinations of various quanta of stretching vibrations with bending and (or) librational modes. In all cases we used local-mode theory to calculate the energies of the vibrational bands. From the best fit between calculated and observed energies we have obtained a set of local-mode parameters that give the harmonic oscillator frequencies and anharmonicities of the OH or NH stretching vibrations, as well as the extent of coupling between nearby oscillators. Our purpose has been to estimate hydrogen-bond strength from the local-mode parameters obtained from an analysis of the spectra. From this we hope to see if there is any relationship between the estimated hydrogen-bond strength and the interatomic distances and bond angles reported for the crystal. In the long run this requires a large selection of data for OH and NH oscillators lying in diverse crystals on sites of varied symmetry.

Received July 14, 1995.

I.M. Walker.[1] Department of Chemistry, York University, Downsview, ON M3J 1P3, Canada.
P.J. McCarthy. Department of Chemistry, Canisius College, Buffalo, NY 14208, U.S.A.

[1] Author to whom correspondence may be addressed. Telephone: (905) 877-9162. E-mail: FS300075@SOL.YORKU.CA

Most recently we studied the spectra of $CsMnCl_3 \cdot 2H_2O$ (4). Here we report a study of the related compounds, $Cs_2MnCl_4 \cdot 2H_2O$, $Rb_2MnCl_4 \cdot 2H_2O$, and their deutero analogues. These salts crystallize in space group $P\bar{1}$ (C_i^1, no. 2) with $Z = 1$. A stereoscopic view of the unit cell is shown in Fig. 1, and the unit cell parameters (6) and selected interatomic distances and angles (6–8) are listed in Table 1. The structures consist of discrete *trans*-$\{MnCl_4(H_2O)_2\}$–anions interleaved with alkali cations. All atoms lie on general positions save manganese, which lies on the inversion centre. The water molecules thus occur in symmetry-related pairs, as do the two crystallographically distinct chloride ions (Table 1). Each OH group makes a nearly linear hydrogen bond to a chloride from a neighboring complex ion. As can be seen from Table 1, the two OH oscillators that make up the water molecule experience significantly different environments in the crystals. This is most noticeable in the Rb salt.

The IR spectra of these compounds have been reported by Stefov et al. (9, 10), who measured the spectra at room temperature and at liquid nitrogen temperature. Adams and Lock (11) had earlier reported the room temperature IR spectra of all these compounds as well as the liquid nitrogen IR and room temperature Raman spectra of some of them.

The crystals to be discussed are notable for the clear resolution of many of the nir bands. This feature has enabled us to give a rather detailed account of the stretch–bend combinations, and also of the energies of many vibrations of the HOD molecule in both lattices.

Local-mode theory

This approach has been found to be well suited to the study of the fundamental and overtone spectra of molecules containing

Fig. 1. Stereoscopic view of the unit cell of $Cs_2MnCl_4 \cdot 2H_2O$, looking down the *c*-axis. Only one hydrogen bond is shown; the other terminates on a chlorine atom in the adjacent unit cell. Hydrogen positions are from ref. 7, the rest are from ref. 6. The circles decrease in size in the order Cs, Cl, Mn, O. The H and O atoms are shown the same size.

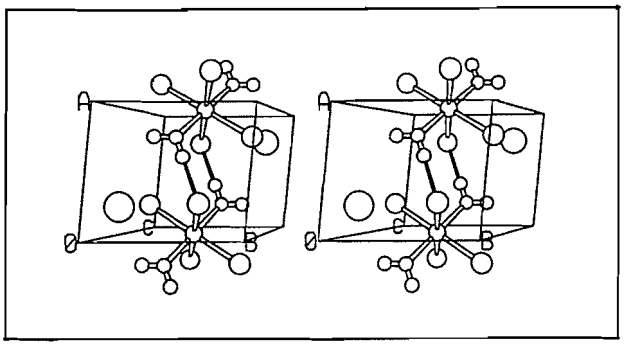

the OH, NH, and CH groups. Several reviews of the subject have appeared (12, 13), as well as a number of treatments of the theory for water and other small molecules (14–20). We have outlined elsewhere (2, 3) its application to water on general sites.

The energy level expressions that we chose for the present work are based on the Harmonically Coupled Anharmonic Oscillator (HCAO) model (14, 15) and are an adaptation of the work of Duncan et al. (18) to the case of water on a general site. The simplicity of this formulation is compatible with the small data sets common to crystal systems. The vibrational wave functions are written as products of harmonic oscillator basis functions in the three local coordinates. The two stretches are described by quantum numbers v_1 and v_2 and the bend by quantum number b. Thus for a water molecule the basis ket would be written $|v_1 v_2 b\rangle$. It is often desirable to adjust the energy of the lowest $|000\rangle$ state to zero. The resulting complete expression for the diagonal elements of the secular determinant, in units of cm^{-1}, is:

$$[1]\quad \langle v_1 v_2 b|H/hc|v_1 v_2 b\rangle = \omega_1 v_1 + \omega_2 v_2 + \omega_b b + X_1 v_1(v_1 + 1) + X_2 v_2(v_2 + 1) + X_b b(b + 1) + X_{s1b} v_1 b + X_{s2b} v_2 b$$

The first six terms on the right in eq. [1] are the traditional local-mode terms and are the largest ones energetically. Here, ω_1, ω_2, and ω_b are the harmonic frequencies of the two stretches and the bend, respectively, while X_1, X_2, and X_b represent the corresponding local-mode anharmonicities. Since the X terms are usually negative, states such as $|110\rangle$, which represents a stretch–stretch combination, occur at higher energy than the stretch overtones, $|020\rangle$ and $|200\rangle$. Because of the inequivalence of the O—H bonds in the compounds, the matrices contain a harmonic oscillator frequency and an anharmonicity for each OH oscillator.

The last two terms in eq. [1] represent the diagonal stretch–bend couplings for water on general sites. We find that X_{s1b} and X_{s2b} are small and nearly equal in these crystals, so that little error is introduced into the fitting procedure by combining these into one parameter, X_{sb}.

Allowance for coupling between stretching local modes is made by including off-diagonal elements of the form:

Table 1. Structural data for $M_2MnCl_4 \cdot 2H_2O$ (M = Rb, Cs).[a]

Unit cell parameters	Rb	Cs
a (Å)	5.66	5.74
b (Å)	6.48	6.66
c (Å)	7.01	7.27
α (deg)	66.7	67.0
β (deg)	87.7	87.8
γ (deg)	84.8	84.3
Bond distances and angles		
$H_A \cdots Cl_I$ (Å)	2.20[b]	2.31[b]
$H_B \cdots Cl_{II}$ (Å)	2.32[b]	2.29[b]
$O \cdots Cl_I$ (Å)	3.17	3.28
$O \cdots Cl_{II}$ (Å)	3.29	3.25
$O\text{-}H_A \cdots Cl_I$ (deg)	177[b]	176[b]
$O\text{-}H_B \cdots Cl_{II}$ (deg)	175[b]	174[b]
$Cl_I \cdots O \cdots Cl_{II}$ (deg)	105	108

[a]Space group $P\bar{1}$, with $Z = 1$. Unit cell parameters taken from ref 6.

[b]Calculated using hydrogen coordinates from ref. 7. These were computed by the method of Baur (8).

$$[2]\quad \langle v_i + 1, v_j - 1, b|H/hc|v_i v_j b\rangle = \lambda[(v_i + 1)v_j]^{1/2}$$

where λ is a measure of the coupling between the two oscillators.

The λ-coupling term causes the stretch local-mode functions to combine into sum and difference combinations; in the gas phase, these are written $|v00\rangle_+$ and $|v00\rangle_-$, respectively. When the diagonal energies are discernibly different and the λ-term is small, one term in the sum is predominant. Except in those cases where the functions in the sum are present to a nearly equal extent, the final eigenstates are labelled in the tables with the identity of the dominant term.

A vibrational manifold is defined as a collection of vibrational states of like energy. Each product of the form $|v_1 v_2 b\rangle$ can be described (18) by means of a manifold quantum number $V = v_1 + v_2 + b/2$. We make the usual approximation that only coupling within each manifold need be considered. For the sake of clarity, we also use the older notation, e.g., ν, 2ν, $\nu + \delta$, in the body of the text to refer to, for example, the stretch fundamental, overtone, and stretch–bend combinations, respectively.

Experimental

Well-formed crystals suitable for spectroscopy were grown from water by slow evaporation of a solution containing a 2:1 molar ratio of CsCl (or RbCl) and $MnCl_2 \cdot 4H_2O$. Moderately deuterated crystals were obtained from the same starting materials by slow evaporation of a D_2O solution over concentrated H_2SO_4 in a desiccator. More highly deuterated crystals were obtained by using anhydrous $MnCl_2$; water of hydration is removed by heating at about 120°C for a few hours. The materials grow as thin well-formed plates with one extinction direction nearly coincident with one of the edges. While the

Table 2. Calculated and observed energies and local-mode parameters for $M_2MnCl_4 \cdot 2H_2O$ (M = Cs, Rb).

M = Cs		M = Rb		
Obsd.[a]	Calcd.	Obsd.[a]	Calcd.	Assignment[b]
1620	1621	1622	1622	|001⟩
3210	3216	3211	3216	|002⟩
3326	3327	3328	3334	|010⟩
3430	3435	3388	3391	|100⟩
4787	4785	4785	4783	|003⟩
4924	4917	4934	4928	|011⟩
5030	5024	4989	4986	|101⟩
6307	6315	6328	6325	|020⟩
6555	6561	6469	6467	|200⟩
6758	6762	6727	6727	|110⟩
7869	7873	7890	7893	|021⟩
8116	8119	8033	8035	|201⟩
8320	8320	—	8294	|111⟩
—	8964	—		|030⟩
—	9378	—		|300⟩
9759	9750	—		|120⟩
—	9888	—		|210⟩
RMS	5.19		3.37	

Local-mode parameters[c]	M = Cs	M = Rb
ω_b	1647(9)	1649(8)
X_b	−13(3)	−14(2)
ω_1	3744(7)	3697(42)
X_1	−154(2)	−154(15)
ω_2	3667(7)	3684(23)
X_2	−170(2)	−174(7)
λ	0	−12(21)
X_{sb}	−32(3)	−27(3)

[a]All data in cm^{-1}. Data below 4000 cm^{-1} from ref. 9.

[b]The three digits in the ket give the number of quanta of OH_1, OH_2 stretches and HOH bend, respectively.

[c]All parameters in cm^{-1}. Standard deviations in parentheses.

indices of this principal face are not known, a pair of angles on opposite corners of the crystals are about 114°. This corresponds nicely to 180° − α as reported by Jensen (6). So it is quite likely that this crystal face represents the *bc* crystal plane. From the crystal data (6) and the calculated parameters of El Saffar (7) one finds that one of the O—H bonds of water lies nearly along the *b*-axis of the crystal. This oscillator should then be excited most strongly by light with *E*||*b*. This may help explain the difference in intensity of the |020⟩, |200⟩, and |110⟩ bands in the different polarizations noted below.

The crystals were mounted in a Displex cryogenic refrigerator and the nir spectra were recorded at 10 K using a Varian-2300 spectrophotometer. Polarized light was obtained by a pair of Glan–Thompson prisms. Spectra were taken with the electric vector of the light parallel to the extinction axes of the crystals.

For all the spectra recorded, the gain was set as low as possible (25.5) in order to maximize the signal-to-noise ratio. The instrument then automatically set the spectral bandwidth at a value that depended on the size and quality of the crystal. When a band appeared to be multiple, other scans were made with higher gain to see if the multiplet could be resolved. In all cases, we chose the largest and clearest crystal available. Without special optics, however, it is difficult to record the spectrum of a crystal smaller than about 1 mm × 0.25 mm. Even if it is of excellent optical quality, such a crystal will yield spectra with a rather low signal-to-noise ratio.

The band positions given in this report are the peak maxima. In the case of unresolved shoulders, no deconvolution was attempted, but the position of the underlying peak was estimated as well as possible.

Our room temperature IR spectra (CsCl pellets) recorded on a Nicolet 5DX FTIR spectrophotometer do not differ significantly from those of Stefov et al. (9, 10). It is their low-temperature data, however, that we use in the discussion below.

Results and discussion

Crystal spectra

The observed spectra in the region 4600–5200 cm^{-1} are shown in Figs. 2 and 3, while the spectra in the region 5700–6900 cm^{-1} are shown in Fig. 4. Figure 5 shows one polarization of the 3ν region of $Cs_2MnCl_4 \cdot 2H_2O$. Since the Cs and Rb salts are isomorphous, it is not surprising that their spectra are quite similar. One polarized spectrum recorded with light incident on the plate-like crystal shows only very weak bands and is much like the *E*||*b* spectrum of $CsMnCl_3 \cdot 2H_2O$ (4). Since in this latter crystal the *b*-axis is nearly perpendicular to the plane of the water molecules, it is quite likely that the weak polarization is largely perpendicular to the H_2O plane in the spectra of the present compounds. The orthogonal polarization contains more detail and has bands of considerably greater intensity. We were able to grow thick crystals of $Cs_2MnCl_4 \cdot 2H_2O$ only, and we recorded spectra on other faces of these crystals also. Most of these spectra appear to be various mixtures of the spectra orthogonal to the weak polarization. A notable feature is the extreme variability of the relative intensities of the |020⟩, |200⟩, and |110⟩ bands in the various orientations. While the band intensities differ in the various orientations, no new bands appear. For this reason we consider that we have recorded all the essential details in the spectra of both substances.

Spectra of HOH in crystals

The principal spectral bands used in the subsequent discussion are found in Table 2.

The two stretch plus bend combination (ν + δ) bands are found at 4924 and 5030 cm^{-1} (Cs) and at 4934 and 4989 cm^{-1} (Rb) (trace (*a*) in Figs. 2 and 3). As expected, the separation between the two bands (106 cm^{-1} (Cs) and 55 cm^{-1} (Rb)) closely matches the separations observed between the two fundamental stretches (104 cm^{-1} (Cs) and 60 cm^{-1} (Rb)).

The first stretch overtone (2ν) absorptions lie at 6307, 6555 cm^{-1} (Cs) and 6328, 6469 cm^{-1} (Rb). The band at 6555 cm^{-1} (Cs) shows weak satellite peaks lying about 46, 82, and 104 cm^{-1} to higher energy. Similar, but less well-defined, satellites are found above the 6469 cm^{-1} (Rb) band. These have been assigned (4) to lattice or hydrogen-bonding modes (see Fig. 4). The high-energy |110⟩ combination at 6758 cm^{-1} (Cs) and 6727 cm^{-1} (Rb) is broad and appears to be multiple. The extra features may be due to excitations of single stretch quanta on neighboring water molecules.

Fig. 2. Crystal spectra (4600–5200 cm^{-1}) of the orthogonal polarizations of $Rb_2MnCl_4 \cdot 2X_2O$ (X = H, D) at 10 K; (*a*) contains no D_2O; deuteration increases from (*b*) to the highly deuterated (*d*).

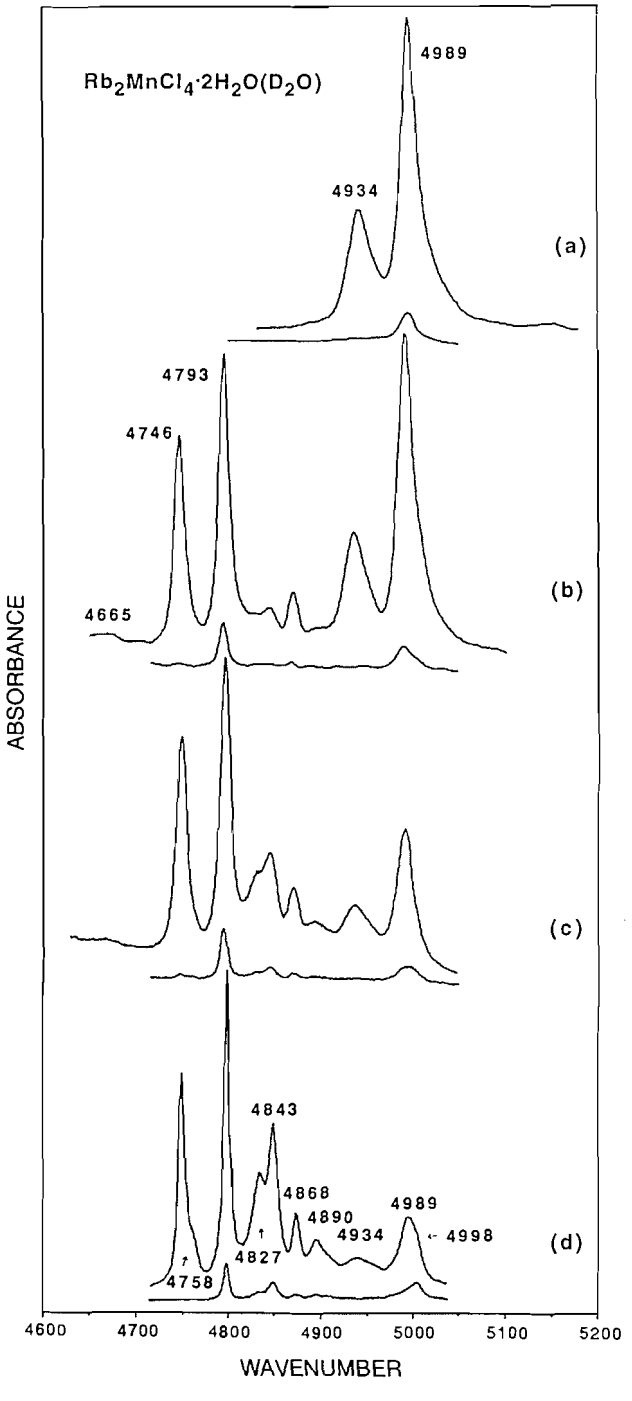

Each compound shows a set of very weak bands (not shown in the figures) in the 7460–8475 cm^{-1} region due mainly to $2\nu + \delta$. Three principal peaks of the Cs spectrum (7869, 8116, and 8320 cm^{-1}) and two of the Rb spectrum (7890 and 8033 cm^{-1}) have been used in the local-mode calculations discussed below. The separation between the principal bands within this manifold closely mirrors the separation between the bands in the stretch overtone manifold.

Fig. 3. Crystal spectra (4600–5200 cm^{-1}) of the orthogonal polarizations of $Cs_2MnCl_4 \cdot 2X_2O$ (X = H, D) at 10 K; (*a*) contains no D_2O, (*c*) is highly deuterated, and (*b*) is intermediate.

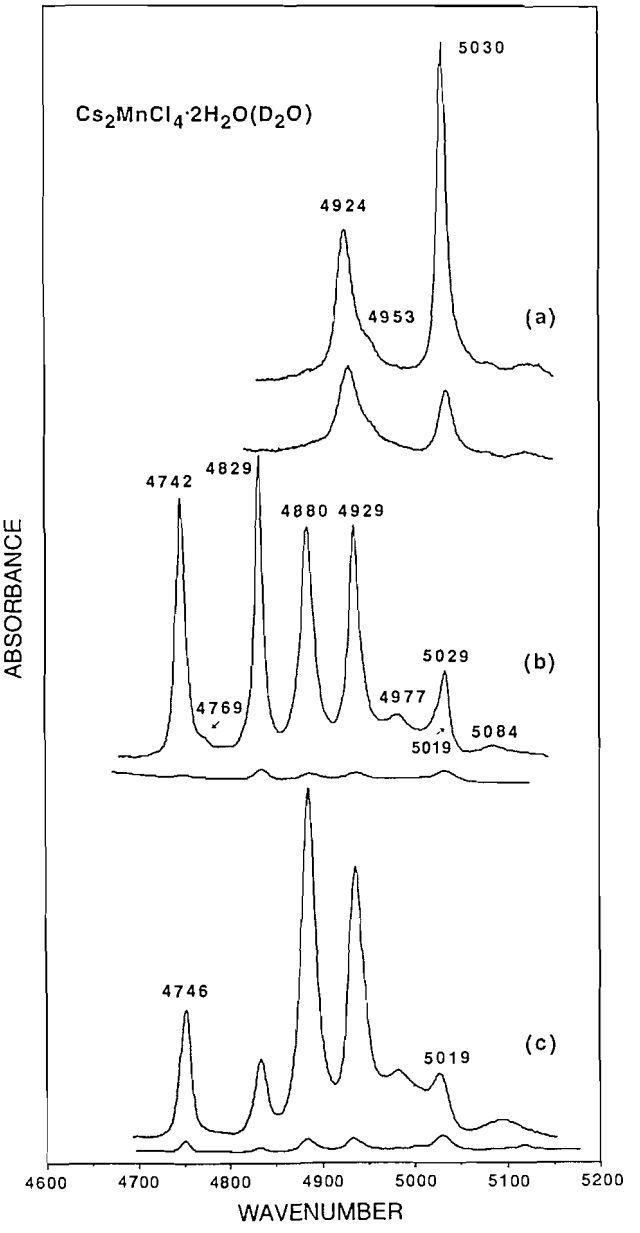

We were able to observe resolved second overtone (3ν) absorptions only in a 2 mm thick crystal of $Cs_2MnCl_4 \cdot 2H_2O$ (Fig. 5). The spectrum is at most 0.004 as strong as the strongest bands in the 2ν region. One maximum, representing a stretch combination band, corresponds rather well to expectation (see Table 2). The nature of the other two peaks is not clear; one may be the other combination band. The local modes $|300\rangle$ and $|030\rangle$, however, appear to be unobservably weak.

In gas-phase water, within a given manifold, stretch combinations are generally weaker than the stretch overtones. In several crystals that we have examined, the stretch combinations are of comparable intensity to the overtones in certain polarizations (2, 3), and in one case (4) they are more intense

Fig. 4. Crystal spectra (5700–6900 cm^{-1}) of the orthogonal polarizations of $M_2MnCl_4{\cdot}2HOD$ and $M_2MnCl_4{\cdot}2H_2O$ (M = Cs, Rb) at 10 K. The HOD spectra represent an intermediate degree of deuteration. The bands marked **p** are due to the polarizers.

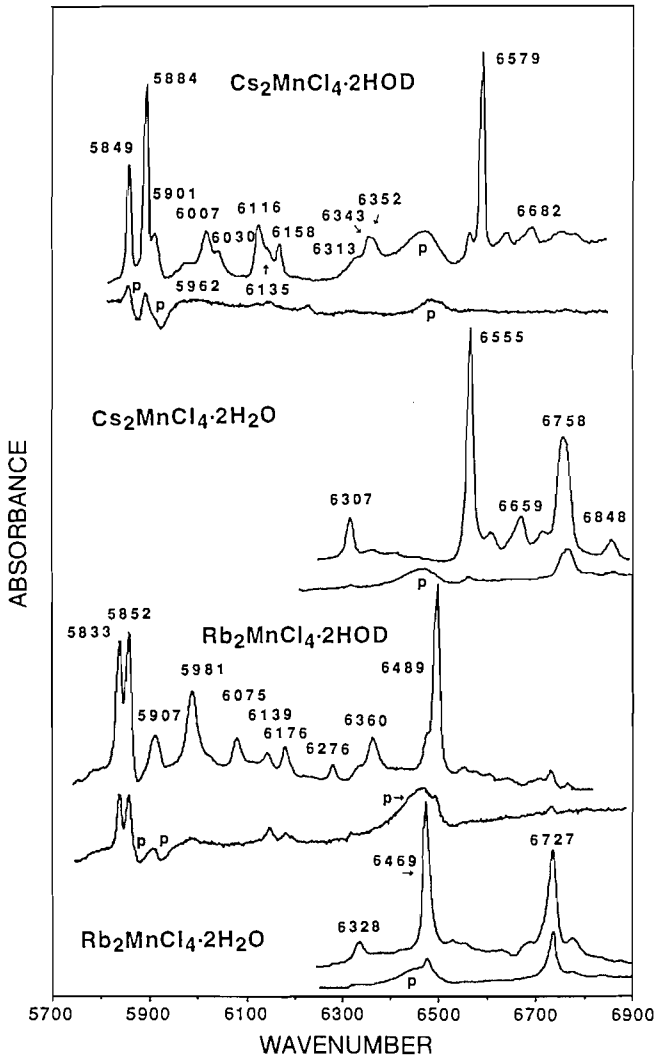

than the overtones. This effect may be attributable to modifications in the dipole moment operator due to hydrogen bonding.

Spectra of HOD and DOD in crystals

The principal maxima of the D_2O molecule are listed in Table 3, while those due to HOD may be found in Table 4. The spectra of the deuterated compounds are quite complex, since the crystals contain some H_2O and HOD in addition to D_2O. Although each of these has a distinct spectrum, bands from different species often lie in the same region and even overlap. In spite of this, however, rather secure assignment of many features is possible. Each assignment has been made on the basis of (*i*) the energy of the band, (*ii*) its change in intensity with increased deuteration, and (*iii*) the relative intensity of the band in the two polarizations.

For water on general sites, replacement of a proton by a deuteron can occur in two physically distinct ways; the two resulting isotopomers, i.e., H_1OD_2 and D_1OH_2, have distinctly

Fig. 5. Crystal spectrum (9600–10100 cm^{-1}) of the strong polarization of $Cs_2MnCl_4{\cdot}2H_2O$ at 10 K.

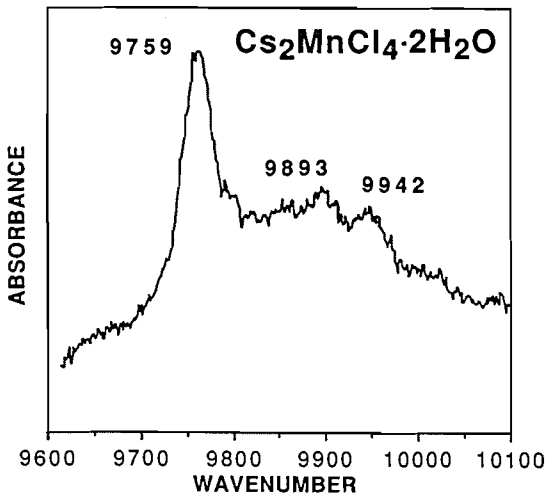

Table 3. Calculated and observed energies and local-mode parameters for $M_2MnCl_4{\cdot}2D_2O$ (M = Cs, Rb).

M = Cs		M = Rb		
Obsd.[a]	Calcd.	Obsd.[a]	Calcd.	Assignment[b]
1191	1191	1191	1191	$\|001\rangle$
2364	2364	2364	2364	$\|002\rangle$
2447	2447	2449	2449	$\|100\rangle_+$
2542	2542	2523	2523	$\|100\rangle_-$
4746	4757	4758	4761	$\|200\rangle_+$
4880	4877	4843	4841	$\|200\rangle_-$
5019	5011	4998	4997	$\|110\rangle$
5901	5890	5907	5904	$\|201\rangle_+$
6007	6010	5981	5983	$\|201\rangle_-$
6135	6143	6139	6140	$\|111\rangle$
RMS	6.36		1.80	

Local-mode parameters[c]	M = Cs	M = Rb
ω_b	1208(13)	1208(4)
X_b	−9(4)	−9(1)
ω_1	2704(41)	2653(20)
X_1	−86(15)	−75(7)
ω_2	2607(21)	2636(12)
X_2	−75(7)	−83(4)
λ	−30(8)	−33(2)
X_{sb}	−29(5)	−24(1)

[a]All data in cm^{-1}. Data below 4000 cm^{-1} from ref. 9.

[b]The three digits in the ket represent the number of quanta of OD_1, OD_2 stretches and DOD bend, respectively.

[c]All parameters in cm^{-1}. Standard deviations in parentheses.

different bending frequencies and stretch combination frequencies (Table 4). The spectra show a pair of bands at 3880, 3925 cm^{-1} (Rb) and 3864, 3953 cm^{-1} (Cs), which grow on the addition of H_2O. They can be assigned to the $\nu_{OD} + \delta_{HOD}$ combinations in the two HOD isotopomers. Other bands in the region that are sensitive to the D/H ratio are probably various

Table 4. Calculated and observed energies and local-mode parameters for $M_2MnCl_4 \cdot 2HOD$ (M = Cs, Rb).

M = Cs		M = Rb		Assignment[b]	
Obsd.[a]	Calcd.	Obsd.[a]	Calcd.	H_1OD_2	D_1OH_2
1421	1418	1426	1423	|001⟩	
1437	1434	1433	1429		|001⟩
2461	2460	2465	2467	|010⟩	
2527	2528	2501	2504		|100⟩
2822	2822	2833	2834	|002⟩	
2853	2853	2847	2846		|002⟩
3316	3317	3322	3325		|010⟩
3412	3418	3375	3378	|100⟩	
3864	3871	3880	3885	|011⟩	
3953	3955	3925	3927		|101⟩
4742	4744	4746	4748		|011⟩
4742	4747	4746	4754	|020⟩	
4829	4829	4793	4797	|101⟩	
4929	4926	4868	4863		|200⟩
5849	5845	5833	5828		|110⟩
5884	5878	5852	5845	|110⟩	
6158	6153	6176	6168	|021⟩	
6343	6346	6276	6281		|201⟩
6352	6357	6360	6364		|020⟩
6579	6578	6489	6489	|200⟩	
7783	7778	7786	7782		|021⟩
7982	7983	7903	7903	|201⟩	
RMS	3.78		4.27		

	M = Cs		M = Rb	
Local-mode parameters[c]	H_1OD_2	D_1OH_2	H_1OD_2	D_1OH_2
ω_b	1448(11)	1432(11)	1441(13)	1436(13)
X_b	−7(4)		−6(5)	
ω_H	3676(11)	3594(11)	3646(13)	3610(13)
X_H	−129(4)	−139(4)	−134(5)	−143(5)
ω_D	2632(11)	2659(11)	2646(13)	2648(13)
X_D	−86(4)	−65(4)	−90(5)	−72(5)
X_{sb}	−6(3)		−5(3)	

[a]All data in cm^{-1}. Data below 4000 cm^{-1} from ref. 9.

[b]For H_1OD_2, the three digits in the ket give the number of quanta of OH_1, OD_2 stretches and H_1OD_2 bend, respectively. For D_1OH_2, the three digits in the ket give the number of quanta of OD_1, OH_2 stretches and D_1OH_2 bend, respectively.

[c]All parameters in cm^{-1}. Standard deviations in parentheses.

combinations of the type $\nu_{OH} + \rho_{HOD}$. None of these is shown in the figures.

Figure 2 shows the spectra of four crystals of the Rb complex with different D/H ratios. The assignment of most of the bands is given in Tables 3 and 4. The significant band at 4827 cm^{-1} is probably one of the $\nu + 2\delta$ bands of D_2O. We can make no assignment for the features at 4665 and 4890 cm^{-1}.

In Fig. 3 are the spectra of three crystals of the Cs complex with different D/H ratios. Since these spectra contain fewer bands than the analogous Rb spectra, there appears to be more overlapping of bands with resulting multiple assignments. The assignments are given in Tables 3 and 4. While we have assigned the 4929 cm^{-1} band to |200⟩ of D_1OH_2, its intensity appears anomalous, and it may contain $\nu + \delta$ of H_2O. Since it remains very strong in the most deuterated crystal, it probably contains other absorptions as well. We can make no assignments for features at 4953 cm^{-1} (trace (*a*)), 4769 cm^{-1} (trace (*b*)), and 4977 and 5084 cm^{-1} (traces (*b*) and (*c*)).

In the partly deuterated crystals the doublet at 5833, 5852 cm^{-1} (Rb) and 5849, 5884 cm^{-1} (Cs) is due to $\nu_{OH} + \nu_{OD}$ in HOD molecules (see Fig. 4). The spectra do not appear to show any extra bands due to excitations on adjacent HOD units.

In both of the compounds, as H is replaced by D, the |020⟩ and |200⟩ bands of H_2O weaken and are replaced by the corresponding bands in HOD. These uncoupled modes are seen in Fig. 4 at 6352 and 6579 cm^{-1} (Cs) and 6360 and 6489 cm^{-1} (Rb); they lie about 20–45 cm^{-1} higher in energy than the cor-

responding bands in H_2O. The bands at 6579 cm^{-1} (Cs) and 6489 cm^{-1} (Rb) show weak satellites similar to those associated with the coupled modes.

In the 5900–6320 cm^{-1} region most of the remaining bands are assigned to $2\nu + \delta$ of D_2O and $2\nu_{OD} + \delta$ of HOD, as can be seen in Tables 3 and 4. In the Rb spectrum only the band at 6075 cm^{-1} cannot be assigned. In the more complex Cs spectrum, bands at 5962, 6030, 6116, and 6343 cm^{-1} remain unassigned.

Local-mode parameters

The procedures used to obtain the local-mode parameters are well documented (4); the parameter sets for HOH and DOD may be found at the bottom of Tables 2 and 3, respectively. Those for DOD are in general less certain than those for HOH or for HOD (Table 4) due to the much smaller data sets available in these crystals.

A total of 18 parameters is needed in order to describe the spectra of HOD at the level of theory used for H_2O. Questions of physical significance arise when attempting to analyze crystal spectra using such large parameter sets. Some simplification is possible by replacing the small X_{sb} and X_b parameters for each isotopomer by single global fitting parameters. In addition, since the λ-coupling has almost no effect on the computed stretch frequencies in HOD, this parameter was dropped from the treatment entirely. The resulting 12-parameter model gives a good fit to the many observed HOD features (Table 4).

Fermi resonance

Since local-mode parameters are properties of individual chemical bonds, they should not change when oscillators such as OH are transferred from an H_2O to a HOD environment. As a consequence, the average energy (barycentre) of the observed OH stretch fundamentals in H_2O and HOD should be the same. This is very nearly true for water in the gas phase (17, 21), and in crystals such as $K_2SnCl_4{\cdot}H_2O$, where the effects of hydrogen bonding are small (22). Comparison of the IR spectra of the more strongly hydrogen-bonded $BaCl_2{\cdot}2H_2O$ with its HOD analogue indicates, however, that the OH barycentres are on the average 5 cm^{-1} different (2, 3). In $Cs_2MnCl_4{\cdot}2H_2O$ this effect is especially clear; the barycentre of the H_2O stretch fundamentals (3378 cm^{-1}) is considerably increased relative to the HOD barycentre (3364 cm^{-1}).

In addition, the energies of the first overtone bands in $BaCl_2{\cdot}2H_2O$ and $CsMnCl_3{\cdot}2H_2O$ are markedly lower in energy than those of the HOD analogues (2–4). The crystals in this report show similar behaviour. These spectral variations cannot be accounted for by λ-coupling.

By contrast, the OD barycentres in DOD and HOD are usually the same within experimental error in most hydrogen-bonded crystals. This observation is by no means restricted to H_2O. In a study of a series of isotopically substituted ethylenes, substantial Fermi resonance was found in the CH spectra, but none was detectable in the CD spectra (18). An explanation for these phenomena has not been provided, but may lie in the interplay between kinetic and potential energy contributions to the Fermi resonance term.

Preliminary fitting of the HOH spectrum using a single Fermi resonance parameter has been undertaken, using the HOH and HOD data sets for the crystals in this study. Values close to 70 cm^{-1} for this parameter give a very good fit to the observable bands in the stretch fundamental and overtone (V = 1, 2) manifolds. The fit to the V = 3/2 (e.g., $\nu + \delta$), and V = 5/2 (e.g., $2\nu + \delta$) manifolds is, however, not as good.

The issue of Fermi resonance in these and other hydrogen-bonded crystals will be taken up in a future article.

Conclusions

Due to the low symmetry of the space group, we could not correlate the spectral properties of the OH_1 and OH_2 oscillators with the two distinct oscillators from Table 1 on the basis of polarization of the bands. Correlations of local-mode parameters with hydrogen-bond distances may not be meaningful for many crystals, since the O—H···Cl grouping is often not isolated from its neighbours. For example, from our study of $CsMnCl_3{\cdot}2H_2O$, the local-mode parameters are found to be very similar (4), but they do not reflect the very disparate hydrogen-bond distances reported for this compound (7, 23). And in the present instance, the rather large difference in O···Cl distances for $Rb_2MnCl_4{\cdot}2H_2O$ as compared with the relatively small difference in the Cs analogue is not reflected in the "best-fit" local-mode parameters. This is doubtless due in part to the fact that there are 12 distinct configurations of the O··Cl··O group with an angle between 98° and 121° and with the two O··Cl distances less than 4 Å. Any or all of these interactions might influence the spectroscopic parameters to some extent.

A perusal of the local-mode parameters for $M_2MnCl_4{\cdot}2XOY$ (M = Cs, Rb; X, Y = H, D) listed in Tables 2–4 reveals the following relations and trends:

1. In general, the values of the OH stretch anharmonicities show little variation between Cs and Rb salts. The difference between X_1 and X_2 appears to be real. The values reported in Table 2 for the H_2O data set are somewhat more negative than those for HOD in Table 4. All are much larger in absolute size than those computed for gas-phase water (ca. −80 cm^{-1}) (19, 20); this appears to be a consequence of hydrogen bonding. Some modification of the Morse oscillator model, perhaps the inclusion of an attractive potential term that reflects the presence of the negatively charged acceptor ion, could explain these deviations.

2. The value of ω_1 for the OH oscillator in the Cs compound is significantly larger than for ω_2, indicating the presence of a weaker hydrogen bond than is found in the Rb compound. The remaining harmonic stretch frequencies are comparable.

3. The ω values in HOH are larger than those in HOD. The same trends are observed in $BaCl_2{\cdot}2X_2O$(X = H, D) for three of the four distinct OH oscillators (3) as well as in $CsMnCl_3{\cdot}2X_2O$(X = H, D) (4). In this latter case all the values are not given explicitly in the reference but can be calculated from the data presented there.

4. For the HOD species the difference between the two ω_b parameters for the Cs complex is greater than between the two values for the Rb complex. This correlates with the values observed for the bending vibrations for the two complexes.

5. The λ-coupling in the D_2O complexes is smaller than the value calculated for D_2O in the gas phase (ca. −60 cm^{-1}) (19). This was also found for $BaCl_2{\cdot}2X_2O$ (2, 3), and is a consequence of hydrogen bonding.

The value of zero calculated for the λ-coupling in $Cs_2MnCl_4{\cdot}2H_2O$ is a direct consequence of the energy of the

observed |110⟩ state being less than the sum of the |100⟩ and |010⟩ energies. This is in turn a direct consequence of the interaction of the two stretch fundamentals with the first bend overtone (2δ) via Fermi resonance. A similar problem occurs in the Rb salt; the value of λ is artificially low as a result. Obtaining accurate values of λ will be the subject of a future article.

6. The average of the ratios for ω_D/ω_H and X_D/X_H in the complexes of both metals are, respectively, 0.722 ± 0.013 and 0.530 ± 0.058. These are very close to the theoretical values for a Morse oscillator, namely, 0.728 and 0.529.

7. The parameter X_{sb} for the H_2O and D_2O complexes is significantly larger in absolute size (-28 ± 3 cm^{-1}) than is observed in gas-phase water (-17 cm^{-1}) (21). On the other hand, X_{sb} is barely significant (-5 cm^{-1}) in the HOD spectra of $M_2MnCl_4 \cdot 2H_2O$. The physical significance of these trends is not known at present; the effect may be related to hydrogen bonding.

8. Finally, it is worth noting that the detailed study of the combination bands can permit each observed HOD bend mode to be assigned to a specific HOD isotopomer. This requires that the two bend frequencies be quite different in energy, as they are in the Cs salt. Such assignments cannot be made based on fundamental data in the bend region alone.

Spectra in the overtone region seem to be especially sensitive to small changes in the environment of the OH oscillators, even in isomorphous salts. Some possible reasons for the differences in the spectra of the Cs and Rb salts in the fundamental region have already been outlined (9). We note that on replacing Rb with Cs, there is a detectable increase in the unit cell volume. A closer look shows that the *b* and *c* cell edges increases more than the *a* edge, making the lattice expansion effect distinctly anisotropic (Table 1). There is undoubtedly a subtle shift in the relative dispositions of the complex anions to accommodate the larger alkali cation. The spectra indicate that one hydrogen bond, that formed by oscillator no. 1, is weakened as a result of this readjustment. OH_A is almost exactly parallel to the crystal *b*-axis, which joins together the two complex units in adjacent cells. It would be the more sensitive to the forcing apart of these complex ions. An accurate neutron diffraction study of the title compounds would be invaluable in pinning down these subtle changes in hydrogen-bond distances. Quantitative correlations of local-mode parameters with hydrogen-bond geometry, even in isostructural systems, must await the development of a more complete theory for the O—H···Cl hydrogen bond.

Acknowledgments

We are grateful to Dr. Robert Blessing of the Hauptman-Woodward Medical Research Institute for preparing Fig. 1. I.M.W. thanks the Natural Sciences and Engineering Research Council of Canada for financial assistance. P.J.M. thanks the Research Corporation for a grant to purchase the cryogenic refrigerator.

References

1. I.M. Walker and P.J. McCarthy. J. Phys. Chem. **93**, 2230 (1989).
2. P.J. McCarthy and I.M. Walker. Inorg. Chem. **29**, 820 (1990).
3. P.J. McCarthy and I.M. Walker. Inorg. Chem. **30**, 2772 (1991).
4. I.M. Walker and P.J. McCarthy. Can. J. Chem. **72**, 1211 (1994).
5. I.M. Walker and P.J. McCarthy. Inorg. Chem. **31**, 4122 (1992).
6. S.J. Jensen. Acta Chem. Scand. **18**, 2085 (1964).
7. Z.M. El Saffar. J. Chem. Phys. **52**, 4097 (1970).
8. W.H. Baur. Acta Crystallogr. **19**, 909 (1965).
9. V. Stefov, B. Soptrajanov, and V. Petrusevski. Croat. Chem. Acta, **65**, 151 (1992).
10. V. Stefov, B. Soptrajanov, and V. Petrusevski. J. Mol. Struct. **266**, 211 (1992).
11. D.M. Adams and P.J. Lock. J. Chem. Soc. (A), 2801 (1971).
12. B.R. Henry. J. Phys. Chem. **80**, 2160 (1976).
13. M.S. Child. Acc. Chem. Res. **18**, 45 (1985).
14. M.S. Child and L. Halonen. Adv. Chem. Phys. **57**, 1 (1984).
15. I.M. Mills and A.G. Robiette. Mol. Phys. **56**, 743 (1985).
16. P.R. Stannard, M.L. Elert, and W.M. Gelbart. J. Chem. Phys. **74**, 6050 (1981).
17. H.G. Kjaergaard, B.R. Henry, H. Wei, S. Lefebvre, T. Carrington, O.S. Mortensen, and M.L. Sage. J. Chem. Phys. **100**, 6228 (1994).
18. J.L. Duncan, A.M. Ferguson, and S.T. Goodlad. Spectrochim. Acta, **49A**, 149 (1993).
19. J.E. Baggott. Mol. Phys. **65**, 739 (1988).
20. J.E. Baggott. Mol. Phys. **62**, 1019 (1987).
21. W.S. Benedict, N. Gailar, and E.K. Plyler. J. Chem. Phys. **24**, 1139 (1956).
22. I.M. Walker and P.J. McCarthy. Can. J. Chem. **64**, 1012 (1986).
23. S.J. Jensen, P. Andersen, and S.E. Rasmussen. Acta Chem. Scand. **16**, 1890 (1962).

The effect of *ortho* and *para* substituents on the formation of the *E* and *Z* isomers of the arylhydrazones obtained from diazonium coupling with methyl 3-aminocrotonate and 3-aminocrotononitrile

Jason V. Jollimore, Marc Vacheresse, Keith Vaughan, and Donald L. Hooper

Abstract: Reaction of arene diazonium salts with 3-aminocrotononitrile or methyl 3-aminocrotonate affords the 2-arylhydrazono-3-oxobutanenitrile (**1** or **3** and **3'**) or the methyl 2-arylhydrazono-3-oxobutanoate (**2** and **2'** or **4** and **4'**). A series of these hydrazones has been prepared with a range of electron-withdrawing and -donating substituents in the *ortho* or *para* position of the aryl moiety. The hydrazones have been characterized by spectroscopic methods, with emphasis on the ^{1}H NMR spectra, which have been used to determine the configuration of the hydrazones as *E* or *Z* or a mixture of the two. The *para*-substituted hydrazononitriles (**1**) are formed as a single species, namely the *Z* isomer, whereas the *ortho* isomers are formed as a mixture of *E* and *Z* configurations (**3** and **3'**). The hydrazonobutanoates (**2** and **2'** or **4** and **4'**) are formed as *E/Z* mixtures regardless of the position of the substituent in the aryl moiety. Complete assignments of all signals in the ^{1}H NMR spectra have been made on the basis of the ability of the various substituents to participate in intramolecular hydrogen bonding and a mechanism is proposed to account for the variations in the proportions of *E* and *Z* isomers and the effect of the nature of the substituent on this ratio. ^{13}C NMR spectra of selected hydrazones have been recorded as an aid to structure assignment.

Key words: hydrazone, diazonium, NMR spectroscopy, *E/Z* isomers, crotonic acid derivatives.

Résumé : La réaction des sels d'arène diazonium avec le 3-aminocrotonitrile ou le 3-aminocrotonate de méthyle conduit au 2-arylhydrazono-3-oxobutanenitrile (**1** ou **3** et **3'**) ou le 2-arylhydrazono-3-oxobutanoate de méthyle (**2** et **2'** ou **4** et **4'**). On a préparé une série de ces hydrazones portant, en positions *ortho* ou *para* de la portion aryle, une variété de substituants ayant des caractères plus ou moins électroattracteurs ou électrodonneurs. On a caractérisé les hydrazones par des méthodes spectroscopiques, en particulier à l'aide de la RMN du ^{1}H qui a été utilisée pour déterminer que la configuration est *E* ou *Z* ou un mélange des deux. Les hydrazononitriles substitués en *para* (**1**) existent principalement sous la forme d'une seule espèce, l'isomère *Z*, alors que les isomères *ortho* forment un mélange des configurations *E* et *Z* (**3** et **3'**). Les hydrazonobutanoates (**2** et **2'** ou **4** et **4'**) conduisent à des mélanges *E/Z* quelle que soit la position du substituant dans la portion aryle. On a pu attribuer tous les signaux des spectres RMN du ^{1}H se basant sur la capacité des divers substituants à participer à des liaisons hydrogènes intramoléculaires et on propose un mécanisme pour expliquer les variations dans les proportions des isomères *E* et *Z* ainsi que l'effet de la nature des substituants sur ces rapports. Afin de faciliter l'attribution des structures, on a aussi enregistré les spectres RMN du ^{13}C d'hydrazones choisies.

Mots clés : hydrazone, diazonium, spectroscopie RMN, isomères *E/Z*, dérivés de l'acide crontonique.

[Traduit par la rédaction]

Introduction

In a previous report (1), the reaction of arene diazonium ions with 3-aminocrotononitrile (**8***a*) or methyl 3-aminocrotonate (**8***b*) was found to afford either the 2-arylhydrazono-3-oxobutanenitriles (**1**) or the methyl 2-arylhydrazono-3-oxobutanoates (**2**), respectively. The hydrazones were produced by diazonium coupling at the C2-vinylic carbon of the αβ-unsaturated ester or nitrile, followed by hydrolysis of the 3-amino substituent to the 3-oxo derivative. All of the examples in the previous study used arenediazonium ions with an electron-withdrawing substituent (NO_2, CN, CO_2R, $CONH_2$, or Br) in the *para* position of the aryl moiety. In the present work, we have extended this study to include electron-donating groups in the aryl moiety and we have also prepared the *ortho* isomers of all the hydrazones in this series. This paper reports the synthesis and characterization of an extended series of *ortho*- and *para*-substituted arylhydrazones, with an analysis of the ^{1}H NMR spectra with respect to the effect of the substituent on

Received September 27, 1995.

J.V. Jollimore, M. Vacheresse, and K. Vaughan.[1] Department of Chemistry, Saint Mary's University, Halifax, NS B3H 3C3, Canada.
D.L. Hooper. Department of Chemistry, Dalhousie University, Halifax, NS B3H 4J3, Canada.

[1] Author to whom correspondence may be addressed. Telephone: (902) 420–5650. Fax: (902) 496–8104. E-mail: kvaughan@husky1.stmarys.ca

Table 1. Physical data and yields of the 2-arylhydrazono-3-oxobutane nitriles (**1** and **3**) and the methyl 2-arylhydrazono-3-oxo butanoates (**2** and **4**).

Compound	X	Yield (%)	Melting point (°C)	Solvent	IR (cm^{-1})
1*e*	$CONH_2$	94	255–257	EtOH	3440, 3330, 3120, 2185, 1655, 1645
1*f*	COMe	89	203–205	EtOAc	3190, 2180, 1710, 1660
1*h*	Me	91	171–174	EtOAc	3200, 2170, 1640
1*i*	OMe	92	123–124	EtOAc	3180, 2170, 1650
1*j*	H	89	161–162	CCl_4	3180, 2170, 1645
3*a*	NO_2	73	197–198	EtOAc	3200, 2170, 1665, 1565, 1355
3*b*	CN	89	148–150	EtOH	3150, 2180, 1660
3*c*	CO_2Me	90	154–155	EtOAc	3110, 2180, 1680, 1660
3*d*	CO_2Et	63	141–142	CCl_4	3090, 2160, 1670, 1655
3*e*	$CONH_2$	67	252–254	EtOH	3520, 3440, 3390, 3300, 3140, 2170, 1660, 1640
3*f*	COMe	93	197–198	EtOAc	3040, 2170, 1660, 1630
3*g*	Br	99	123–125	Hexanes	3220, 2170, 1630
3*h*	Me	83	106	Hexanes	3300–3100(br), 2165, 1630
3*i*	OMe	97	151–153	Hexanes	3220, 2160, 1650
2*c*	CO_2Me	93	158–160	EtOAc	3130, 1697, 1680, 1655
2*f*	COMe	85	118–120	EtOAc	3142, 1675, 1660, 1639
2*h*	Me	91	78–80	Hexanes	3120, 1700, 1670
2*i*	OMe	65	65–69	Hexanes	3100, 1665, 1635
2*j*	H	64	49–55	Hexanes	3100(br), 1690, 1660
4*a*	NO_2	93	147–153	EtOAc	3110(br), 1680, 1650, 1550, 1350
4*b*	CN	99	126–130	EtOH	3115, 2190, 1695, 1670
4*c*	CO_2Me	99	102–104	Hexanes	3100, 1690, 1675, 1660
4*d*	CO_2Et	81	70–71	Hexanes	3400–3200(br), 3100(w), 1680, 1665, 1650
4*e*	COMe	71	160–162	EtOAc	3040(br), 1680, 1660(sh), 1630
4*f*	Br	85	118	Hexanes	3100(w), 1685, 1660
4*g*	Me	63	89–91	Hexanes	3080(br), 1680, 1650, 1630
4*h*	OMe	40	148–150	EtOAc	3100(br), 1685, 1660(sh)
5	3-Pyridyl	59	186–188	EtOH	3520, 3300, 3180, 2180, 1650, 1630

the relative amounts of the *E* and *Z* isomers of the hydrazones produced in the coupling reaction.

Experimental

All reagents were reagent grade materials purchased from the Aldrich Chemical Co. Ltd., and were used without further purification. Melting points were determined on a Reichert hot-stage microscope and are uncorrected. Infrared spectra were obtained using Nujol mulls, unless otherwise indicated, on a Perkin Elmer 299 spectrophotometer. ^1H and ^{13}C NMR spectra were obtained on the Bruker 250 and AMX400 MHz spectrophotometers of the Atlantic Region Magnetic Resonance Centre at Dalhousie University. Chemical shifts are relative to TMS (1%) internal standard.

2-Arylhydrazono-3-oxobutanenitriles (1 and 3) and Methyl 2-arylhydrazono-3-oxobutanoates (2 and 4)

General procedure

These compounds were prepared by the general procedure described previously (1). This procedure was successful in the preparation of the 2-(3′-pyridyl)-hydrazono-3-oxobutanenitrile (**5**) when 3-aminopyridine was used as the arylamine.

Table 1 shows the yields and physical data of the new hydrazones prepared for this study. The yields reported in Table 1 are those of the crude products; the melting points in Table 1 are those measured after recrystallization to constant melting point. Tables 2-6 list the complete spectroscopic data for all the hydrazones in these series, including those reported previously (1) for comparison. The percentages of *E* and *Z* isomers reported in Tables 3 and 4 represent the composition of the crude product as calculated from the relative integrations in the ^1H NMR spectra. In most cases of *E*- and *Z*-hydrazone mixtures, the isomers did not separate on TLC plates and the isomers cocrystallize when recrystallized, as indicated by the essentially unchanged ^1H NMR spectra of the recrystallized materials. The only cases where two spots were evident on TLC plates were the crude products of compounds **4***d*, **4***e*, **4***f*, and **4***g*, but even in those cases recrystallization did not effect a separation of the isomers.

2-(*ortho*-Carbamoylphenylhydrazono)-3-oxobutanenitrile (3*e*)

Modified procedure

Anthranilamide (0.01 mol) was dissolved in 10 M hydrochloric acid (40 mL) and the solution cooled to 0°C. The cold solu-

tion was diazotized with sodium nitrite (0.011 mol) in water and the resulting mixture stirred for 0.5 h. The diazonium salt solution was filtered and treated with a cold solution of 3-aminocrotononitrile (0.011 mol) dissolved in 2 M hydrochloric acid (1 equiv.) After stirring for 1 h in the cold, the solution was made alkaline with aqueous sodium bicarbonate solution, whereupon the yellow product precipitated immediately. The precipitate was filtered, dried, and recrystallized from a mixture of ethyl acetate and ethanol to afford the hydrazone (**3***e*), mp 252-254°C.

Results and discussion

Reaction of the diazonium ion (**7**) with 3-aminocrotononitrile (**8***a*) or methyl 3-aminocrotonate (**8***b*) affords excellent yields of the 2-arylhydrazono-3-oxobutanenitriles (**1** or **3** and **3′**) or the methyl 2-arylhydrazono-3-oxobutanoates (**2** and **2′** or **4** and **4′**). The reaction works equally well with *ortho*- or *para*-substituted arenediazonium ions; slightly lower yields are observed for compounds **2**/**2′***i*, **2′***j*, **4**/**4′***g*, and **4′***h*, which have electron-releasing groups in the aryl moiety. A modified pro-

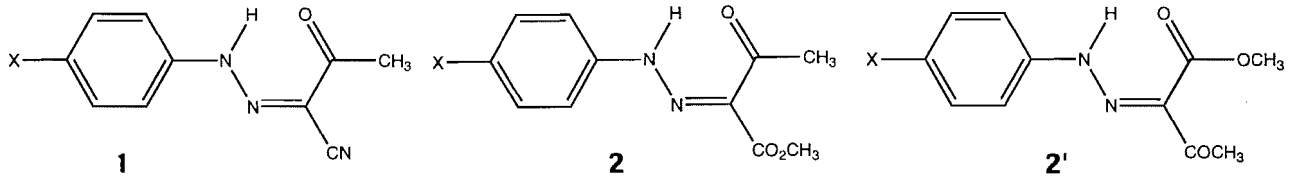

1 **2** **2′**

X: *a* = NO_2 *f* = COMe
b = CN *g* = Br
c = CO_2Me *h* = Me
d = CO_2Et *i* = OMe
e = $CONH_2$ *j* = H

cedure, derived from the work of Siddiqui and Stevens (2), was used for the preparation of the *ortho*-carbamoylphenyl diazonium ion en route to the 2-(*ortho*-carbamoylphenylhydrazono)-3-oxobutanenitrile (**3**/**3′**e); strongly acid conditions are required to prevent cyclization of the intermediate diazonium ion. The nitrile series was extended to include the 3-pyridylhydrazone (**5**).

Table 1 shows the frequency of the principal bands in the IR spectra of these hydrazones. The *para*-substituted 2-arylhydrazono-3-oxobutane-nitriles (**1**) have a single NH absorption in the range 3180–3220 cm^{-1}, nitrile absorption at 2170–2190 cm^{-1}, and ketone carbonyl at 1640–1660 cm^{-1}. In the *ortho*-substituted isomers (**3** and **3′**) the NH absorption band is shifted slightly to lower frequency; the nitrile and carbonyl absorption bands are largely unchanged. The methyl 2-arylhydrazono-3-oxo-butanoates (**2** and **2′** or **4** and **4′**) have a lower frequency NH absorption and an ester carbonyl band at higher frequency than the ketone carbonyl band. All compounds show the appropriate bands for the functional group present in the aryl substituent (X).

Table 2 shows the ^1H NMR chemical shifts of the *para*-substituted 2-arylhydrazono-3-oxobutanenitriles (**1***a–i*), including data previously reported (1) for comparison. It is immediately obvious that these hydrazones are formed in a single stereochemical form, namely, as the intramolecularly hydrogen-bonded *Z* isomer shown in structure **1**. The evidence for assignment of the *Z* configuration to these products is unequivocal: (*i*) firstly, the intramolecular hydrogen bond provides stabilization compared to the *E* isomer (not shown), which cannot form an intramolecular hydrogen bond; (*ii*) the chemical shift of the NH proton, 12.20–12.55 ppm, is consistent with hydrogen bonding to a ketone-carbonyl oxygen atom (3). In geometric isomers of hydrazones that preclude

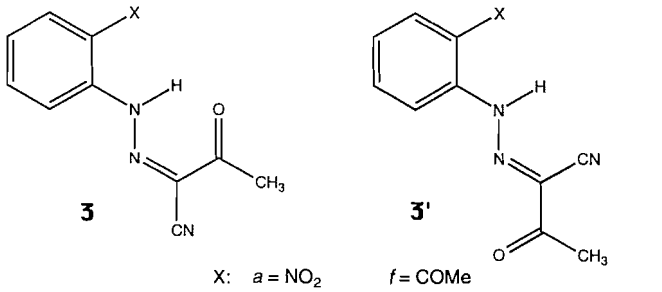

3 **3′**

X: *a* = NO_2 *f* = COMe
b = CN *g* = Br
c = CO_2Me *h* = Me
d = CO_2Et *i* = OMe
e = $CONH_2$ *j* = H

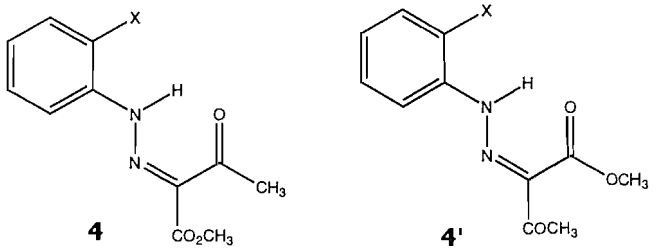

4 **4′**

X: *a* = NO_2 *e* = COMe
b = CN *f* = Br
c = CO_2Me *g* = Me
d = CO_2Et *h* = OMe

N-H···O=C hydrogen bonding, the NH chemical shift is around 9 ppm (4). The NH chemical shift in this series of hydrazones shows a progressive shift to lower frequency as the substituent is changed from strongly electron withdrawing

Table 2. ^{1}H NMR chemical shifts of the *para*-substituted *Z*-2-arylhydrazono-3-oxobutanenitriles (**1**).

Compound	X	Solvent[a]	NH	Aromatic (AA'BB')	CH_3 ketone	X
1*a*	NO_2	(c)	12.55	8.28, 8.24, 7.73, 7.69	2.55	—
1*b*	CN	(c)	12.41	7.89, 7.80, 7.68, 7.60	2.52	—
1*c*	CO_2Me	(c)	12.43	8.05, 7.99, 7.64, 7.58	2.58	3.89
1*d*	CO_2Et	(c)	12.39	8.10, 8.06, 7.70, 7.66	2.43	1.13(t) 4.29(q)
1*e*	$CONH_2$	(d)	12.35	7.96, 7.93, 7.60, 7.57	2.45	7.39 8.0(br)
1*f*	COMe	(d)	12.40	8.03, 8.00, 7.67, 7.60	2.47	2.58
1*g*	Br	(c)	12.26	7.60, 7.56, 7.49, 7.45	2.39	—
1*h*	Me	(d)	12.20	7.46, 7.42, 7.23, 7.20	2.39	2.29
1*i*	OMe	(d)	12.20	7.51, 7.48, 7.01, 6.98	2.39	3.77

[a]Solvent: (c) chloroform-*d*; (d) DMSO-d_6.

Table 3. ^{1}H NMR chemical shifts of the *ortho*-substituted 2-arylhydrazono-3-oxobutanenitriles (**3**).

			3 (*Z*)					**3'** (*E*)				
Compound	Solvent[a]	X	%	NH	Aromatic multiplet	CH_3 ketone	X	%	NH	Aromatic multiplet	CH_3 ketone	X
3*a*	(c)	NO_2	35	15.70	7.31–8.34	2.60	—	65	12.18	7.28–8.27	2.56	—
3*b*	(a)	CN	33	14.79	7.32–7.42	2.60	—	67	10.83	7.74–7.88	2.58	—
3*c*	(a)	CO_2Me	5	15.52	7.24–8.05	2.51	3.97	95	12.65	7.24–8.05	2.48	3.97
3*d*	(c)	CO_2Et	10	15.37	7.23–8.03	2.54	1.44(t) 4.47(q)	90	12.91	7.18–8.10	2.52	1.44(t) 4.47(q)
3*e*	(d)	$CONH_2$	7	15.69	7.31–8.32	2.43	8.01 8.55	93	14.04	7.23–7.98	2.43	8.01 8.55
3*f*	(c)	COMe	15	15.69	7.30–8.01	2.55	2.71	85	13.52	7.22–7.98	2.52	2.73
3*g*	(c)	Br	70	14.87	7.07–7.81	2.55	—	30	9.68	7.05–7.64	2.52	—
3*h*	(c)	Me	75	14.98	7.15–7.76	2.52	2.38	25	9.19	7.10–7.57	2.51	2.41
3*i*	(c)	OMe	55	14.82	6.93–7.72	2.49	3.95	45	9.73	6.93–7.72	2.49	3.95
3*j*	(c)	H	50	14.76	7.20–7.48	2.51	—	50	9.35	7.20–7.48	2.51	—
5	(c)	3-Pyridyl	100	14.66	7.36–8.71	2.55	—					

[a]Solvent: (a) acetone-d_6; (c) chloroform-*d*; (d) DMSO-d_6.

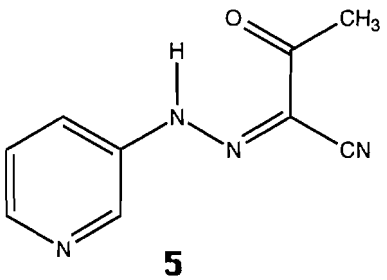

5

(NO_2 in **1***a*) to electron releasing (OMe in **1***i*), accompanied by a shift to lower frequency in the chemical shift of the protons in the methyl ketone moiety.

The *ortho*-substituted 2-arylhydrazono-3-oxobutanenitriles (**3***a–i*) are formed as mixtures of *E* and *Z* isomers (**3** and **3'**). The principal evidence for this is the ^{1}H NMR spectrum, which clearly shows the signals from both isomers. Table 3 shows the chemical shift assignments for the *E* and *Z* isomers of hydrazones **3***a–i*. All ^{1}H NMR spectra show two NH signals, the high-frequency NH resonance being assigned to the intramolecularly hydrogen-bonded *Z* isomer (**3**). In most cases, the signals from the acetyl methyl protons are resolved, and most of the aromatic multiplets of the two isomers can be discerned. The chemical shift of the NH proton in the *E* isomer (**3'**) correlates well with the nature of the X substituent, i.e., with its ability to hydrogen bond. When X is not able to form a strong hydrogen bond with the hydrazone NH, i.e., when X = H, Br, Me, or OMe, the chemical shift of the NH proton is at low frequency in the range 9.2–9.7 ppm as expected (3). In contrast, when the X substituent can form a strong intramolecular hydrogen bond, i.e., when X = NO_2, CO_2R, $CONH_2$, or COMe, the chemical shift of the hydrazone NH shifts back to the range 12–13 ppm, which is similar to the observed chemical shift of the NH in the *para*-substituted *Z* isomers (**1***a–i*). An intermediate effect is seen when X is a cyano group, which would not be expected to hydrogen bond, but which might cause a shift of ca. 1 ppm by a field effect.

The high-frequency NH signal in the NMR spectra of **3** is assigned to the *Z* isomer, and this chemical shift is similarly

dependent on the hydrogen-bonding ability of the substituent X. When X can form a strong intramolecular hydrogen bond, e.g., X = NO_2, CO_2R, $CONH_2$, or COMe, the NH chemical shift is found at ca. 15.70 ppm, which is to be expected for the chemical shift of a hydrazone NH proton hydrogen bonded to two potential hydrogen-bonding groups (3) as shown, for example, in structure **6**.[2] In the hydrazones with non-hydrogen

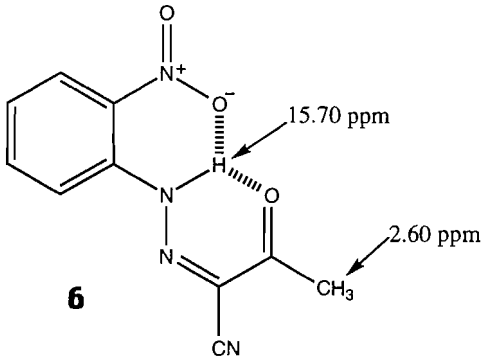

6

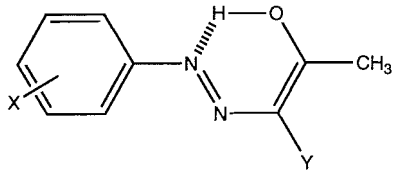

15 Y = CN or CO_2Me

bonding *ortho* substituents (X = CN, Br, Me, OMe), the chemical shift of the *Z*-hydrazone NH proton is shifted to higher frequency, ca. 14.8 ppm, which is still at a higher frequency than the chemical shift of the NH proton in the *Z* isomer of the *para*-substituted hydrazones (**1**). Thus, the *ortho* substituent (X) in the *Z*-hydrazone (**3**) may be exerting a steric effect on the alignment of the N-H··O=C hydrogen-bonding groups that brings the hydrogen and oxygen atoms closer together, strengthening the hydrogen bond and causing a shift of the NH proton signal to higher frequency.

Table 3 also shows the percentage of each diastereomer in the crude hydrazone mixtures; the composition has been determined from the relative integration of the signals in the ^1H NMR spectrum, and the percentages averaged from the NH and ketone methyl proton signals, which were in close agreement. In general, the presence of an electron-withdrawing X substituent favours formation of the *E* isomer (**3′**) and electron-releasing groups favour the *Z* isomer (**3**), which might be explained by a substituent effect on the mechanism of hydrazone formation. However, an acceptable mechanism must also be able to account for the change from 100% preference for the *Z* isomer with *para* substituents to the *E/Z* mixtures observed with *ortho* substituents.

A proposed mechanism, which may account for these observations, is shown in Scheme 1. Coupling of the diazonium ion (**7**) with the enamine (**8**) affords the arylazo-iminium ion (**9**), which deprotonates from the α-carbon to give the crucial intermediate arylazo-enamine (**10**). This rotamer (**10**) is ideally set up for an intramolecular proton shift, path (a), to give the 2-arylazo-3-imino derivative (**11**), which undergoes hydrolysis in the reaction mixture to give one isomer of the 2-arlhydrazono-3-oxo derivative (**12**). The alternative pathway leads from the rotamer (**10′**); when Y = CN, this rotamer (**10′**) cannot proceed via intramolecular proton transfer and proceeds by intermolecular proton transfer, path (b), to give the isomeric 2-arylazo-3-imino derivative (**13**), which hydrolyzes to give the other isomer of the 2-arylhydrazono-3-oxo derivative (**14**). The assignment of *E* or *Z* configuration to the products **12** and **14** depends on the nature and position of the substituent Y.

This mechanism seems to explain the observed product distribution. Reaction of the *para*-substituted arenediazonium ion (**7**) with 3-aminocrotononitrile (**8** , Y = CN) proceeds directly through the pathway → **9** → **10** → **11** → **12** to give a single product, the *Z*-2-arylhydrazono-3-oxobutanenitrile (**1**). The formation of a single product is determined by two factors: (i) the favourable entropy factor of the intramolecular process, path (a), over the intermolecular reaction, path (b); and (ii) the stability of the hydrogen-bonded product (**12** ≡ **1**) over the non-hydrogen-bonded product **14**. The presence of the substituent (X) in the *ortho* position of the intermediate **10** interferes sterically with the electron lone pair on the adjacent nitrogen atom, which in turn prevents the efficient abstraction of the N-H proton in the intramolecular process, path (a). This allows time for the conformational change to the rotamer (**10′**), resulting in formation of the isomer **14** in addition to **12**. Thus reaction of the *ortho*-substituted arenediazonium ion (**7**) with 3-aminocrotononitrile affords a mixture of the *E* isomer (**14** ≡ **3′**) and the *Z* isomer (**12** ≡ **3**).

The mechanism in Scheme 1 also explains the substituent effect on the preference for the *E* or *Z* isomer, **3** or **3′**. An electron-withdrawing substituent in the *ortho* position of the intermediate **10** reduces the electron density at the adjacent nitrogen atom and thus slows down path (a), allowing path (b) to become predominant. Thus it appears that a combination of steric and electronic effects determines the relative proportion of products obtained from paths (a) and (b) in Scheme 1.

Diazonium coupling with methyl 3-aminocrotonate (**8**, Y = CO_2Me) affords a mixture of the *E* and *Z* isomers of the methyl 2-arylhydrazono-3-oxobutanoates (**2** and **2′** or **4** and **4′**). The formation of mixtures is evident in almost all cases, whether the substituent is in the *ortho* or *para* position as shown by the data in Table 4, which shows all chemical shift assignments for the protons in these hydrazones. Only two examples, **2′***j* and **4′***h*, show complete preference for one species, which is the *Z* isomer in each case. In general, the product distribution shows similar dependence on the nature of the X substituent as in the nitrile series. In the *para*- substituted series (**2/2′***a–i*), the preferred form is the ketone-carbonyl hydrogen-bonded isomer (**2**, the *E* isomer), but in the *ortho*-

[2] There is an alternative explanation for the extremely high frequency of the NH signals (ca. 15.70 ppm) in many of these hydrazones, one which does not appear to have been expressed in the literature before. Chemical shifts in the range 15–16 ppm have been associated with an enolic proton of such species as acetylacetone and other β-diketones (*5b*), and this suggests that some of these hydrazones may be present as the enolic tautomer such as that shown in structure **15**. Of course, structure **15** is also the azo-tautomer of the hydrazone, and, although it may not be wise to resurrect the old hydrazone vs. azo compound vs. enehydrazine question (6), it seems that we might be negligent in not pointing out the potential of a tautomeric species like **15** as a possible explanation for some of our observations.

Scheme 1.

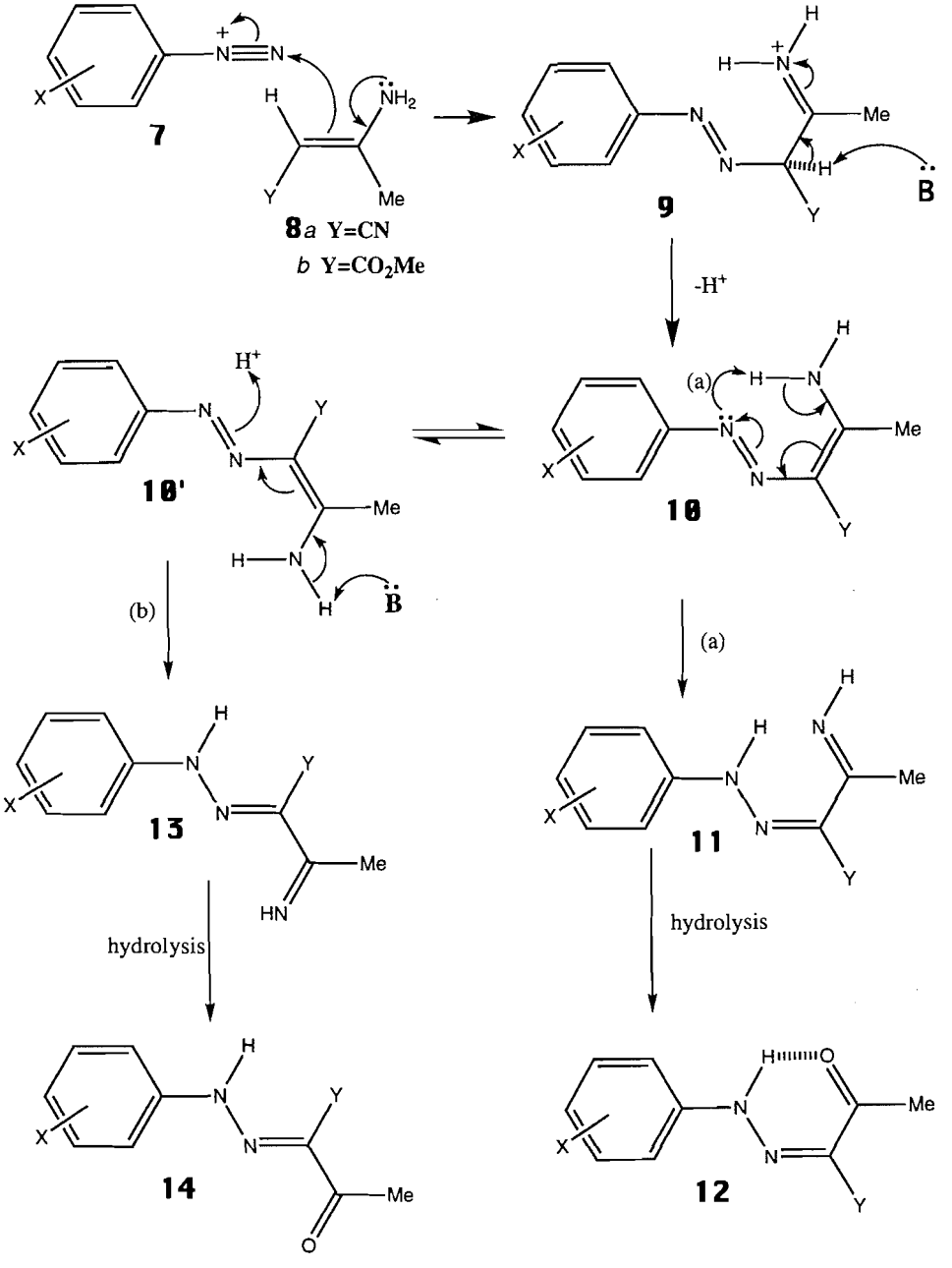

substituted series (**4**/**4**′*a–h*) there is a switch in the order of preference with electron-releasing groups, which favour the *Z* isomer (**4**′*f*, **4**′*g*, and **4**′*h*); this substituent effect is opposite to that observed in the *ortho*-substituted arylhydrazonocrotononitrile series (**3**/**3**′*a–i*).

Table 4 reveals a similar correlation of the chemical shift of the NH proton with the proximity of potential hydrogen-bonding groups. The *E* isomers of the *para*-substituted series (**2***a–i*) show NH signals at 11.50–12.80 ppm, consistent with hydrogen bonding to the neighbouring ketonic carbonyl function. The *Z* isomers of the same series (**2**′*a–i*) show NH signals shifted to higher frequency, ca. 14.7 ppm, which must reflect the stronger hydrogen bond between the hydrazone NH and the ester carbonyl oxygen. In the *ortho*-substituted series, the *E* isomers (**4***a–g*) display the NH chemical shift at 14.0–14.5 ppm in the presence of an electron-withdrawing group as compared to 13.1 ppm for other *ortho* substituents. The *Z* isomers (**4**′*a–h*) have the NH signal shifted to higher frequency due to the stronger hydrogen-bonding effect of the ester carbonyl oxygen atom.

The formation of both *E* and *Z* isomers (**2** and **2**′ or **4** and **4**′) is consistent with the mechanism in Scheme 1, when Y = CO_2Me. The driving force would appear to be the presence of the intramolecular hydrogen bond in both products (**14** and **13**, Y = CO_2Me), as a stabilizing influence that seems to override the entropy factor of the intramolecular process in path (a).

Table 4. ^{1}H NMR chemical shifts of the *ortho*- and *para*-substituted methyl 2-arylhydrazono-3-oxobutanoates (**2** and **4**).

			E Isomer (**2** or **4**)						*Z* Isomer (**2′** or **4′**)					
Compound	Solvent[a]	X	%	NH	Aromatic	CH_3 ketone	OCH_3 ester	X	%	NH	Aromatic	CH_3 ketone	OCH_3 ester	X
2*a*	(c)	NO_2	72	12.76	8.28, 8.31, 7.41, 7.54	2.41	3.94	—	28	14.59	8.26, 8.29, 7.49, 7.53	2.63	3.92	—
2*b*	(c)	CN	85	12.71	7.70, 7.67, 7.43, 7.39	2.52	3.92	—	15	14.57	7.69, 7.66, 7.51, 7.47	2.62	3.90	—
2*c*	(d)	CO_2Me	88	11.50(br)	7.99, 7.95, 7.53, 7.49	2.52	3.82	3.37	12	11.50(br)	7.99, 7.95, 7.60, 7.55	2.42	3.85	3.39
2*d*	(c)	CO_2Et	80	12.76	8.10, 8.07, 7.39, 7.35	2.52	3.92	1.40(t) 4.39(q)	20	14.68	8.08, 8.05, 7.46, 7.3	2.61	3.89	1.40(t) 4.39(q)
2*e*	(c)	$CONH_2$	60	12.80	7.89, 7.85, 7.42, 7.38	2.53	3.93	5.89 (br)	40	14.71	7.89, 7.85, 7.42, 7.38	2.62	3.90	5.71 (br)
2*f*	(d)	COMe	67	11.61	7.98, 7.94, 7.50, 7.46	2.52	3.83	2.39	33	14.0	7.98, 7.94, 7.59, 7.55	2.49	3.79	2.39
2*g*	(c)	Br	70	12.77	7.51, 7.48, 7.23, 7.21	2.49	3.90	—	30	14.77	7.50, 7.47, 7.30, 7.27	2.60	3.87	—
2*h*	(a)	Me	56	12.25	7.39, 7.36, 7.24, 7.21	2.39	3.81	2.31	44	14.70	7.42, 7.39, 7.24, 7.21	2.50	3.79	2.31
2*i*	(d)	OMe	68	11.85	7.43, 7.40, 6.99, 6.96	2.36	3.75	3.81	32	14.60	7.50, 7.48, 7.04, 7.02	2.49	3.77	3.81
2*j*	(c)	H	0						100	14.87	7.15–7.45(m)	2.60	3.87	—
4*a*	(c)	NO_2	95	14.04	7.17–8.28(m)	2.56	3.99	—	5	15.51	7.23–8.26(m)	2.64	3.93	—
4*b*	(d)	CN	73	13.10	7.21–7.92(m)	2.54	3.96	—	27	15.10	7.16–7.75(m)	2.64	3.91	—
4*c*	(c)	CO_2Me	75	14.23	7.113–8.100(m)	2.54	3.90	3.99	25	15.65	7.108–8.068(m)	2.63	3.97	4.01
4*d*	(c)	CO_2Et	90	14.24	7.11–8.09(m)	2.54	3.97	1.43(t) 4.47(q)	10	15.67	7.11–8.09(m)	2.63	3.90	1.43(t) 4.47(q)
4*e*	(c)	COMe	75	14.48	7.14–7.97(m)	2.53	3.99	2.70	25	15.77	7.17–8.14(m)	2.62	3.90	2.69
4*f*	(c)	Br	5	13.09	7.01–7.88(m)	2.52	3.95	—	95	14.94	7.01–7.88(m)	2.63	3.89	—
4*g*	(c)	Me	10	13.09	7.06–7.68(m)	2.51	3.92	2.38	90	15.09	7.09–7.82(m)	2.62	3.88	2.38
4*h*	(c)	OMe	0						100	14.93	6.90–7.17, 7.77–7.81 (m)	2.61	3.95	3.87

[a]Solvent: (a) acetone-d_6; (c) chloroform-*d*; (d) DMSO-d_6.

Table 5. ^{13}C NMR chemical shifts of selected 2-arylhydrazono-3-oxo butanenitriles (**1** and **3**) in DMSO-d_6.

Compound	X	Aromatic	C=O	C=N	CN	CH_3	X
1*b*	*p*-CN	145.4(C1) 116.8(C2,6) 118.9(C3,5) 133.8(C4)	192.6	110.45	116.7	24.7	106.3
1*e*	*p*-$CONH_2$	144.1 115.6 129.0 130.3	192.8	110.4	114.8	24.7	167.2
1*f*	*p*-COMe	145.5 115.8 130.0 132.9	192.7	110.6	115.4	24.7	26.6 Me 196.5 C=O
1*h*	*p*-Me	139.65 116.2 129.9 134.4	192.6	111.1	115.4	24.6	20.5
1*i*	*p*-OMe	157.0 114.7 117.7 135.5	192.6	111.3	112.4	24.5	55.4
3*b*	*o*-CN (in acetone)	143.7 135.5 135.1 126.0 119.1 101.1	192.9	110.1	116.5	25.2	117.3
3*c*	*o*-CO_2Me (in acetone)	144.0 136.0 131.9 124.7 118.9 116.4	192.5	110.6	115.1	24.6	53.2 OMe 168.8 C=O

A selected number of these hydrazones were analysed by ^{13}C NMR spectroscopy to provide additional corroboration of structure. Tables 5 and 6 record the ^{13}C NMR data obtained for these compounds. The pairing of signals seen in the ^1H NMR spectra is not routinely observed in the ^{13}C NMR spectra under standard procedures. The chemical shifts observed in cases where a major species is predominant are those of the major species, which makes unequivocal peak assignment using additivity rules (*5a*) possible. Compounds **2/2′***c* and **2/2′***f* contain two carbonyl groups that cannot be unambiguously assigned by simple inspection of the ^{13}C NMR spectrum. This problem was overcome using the 2-D NMR technique, Heteronuclear Multiple Bond Correlation (HMBC) spectroscopy, which shows the presence of coupling between the substituent carbonyl carbon and the aromatic protons *ortho* to it in the form of a crosspeak.

In the HMBC spectrum of **2/2′***c*, the signal at 165.8 ppm shows long-range coupling to aromatic protons in the form of a cross peak; thus the 165.8 ppm signal is assigned to the ester carbonyl group attached to the aromatic ring and by inference the signal at 162.7 ppm is assigned to the ester carbonyl carbon of the butanoate moiety. Having made these assignments for compound **2/2′***c*, the analogous assignments for compound **4/4′***c* (the *ortho* isomer of **2/2′***c*) followed logically without the necessity for a separate HMBC experiment. In the HMBC spectrum of **2/2′***f*, the signal at 196.4 ppm shows long-range coupling to aromatic protons in the form of a cross peak, thus enabling the assignment of this signal to the carbonyl carbon of the *para*-acetyl substituent and, hence, the assignment of the signal at 193.9 ppm to the carbonyl carbon of the 3-oxo substituent.

Acknowledgements

Financial assistance for this project was provided by the Saint Mary's University Senate Research Committee and by the Summer Employment/Experience Development (SEED) programme of Employment and Immigration Canada under a Federal/Provincial cost-sharing agreement. The residual funds from the 1994–1995 Natural Sciences and Engineering Research Council of Canada (NSERC) Operating Grant (to K.V.) were used to supplement the salaries of research assis-

Table 6. ^{13}C NMR chemical shifts of selected methyl 2-arylhydrazono-3-oxobutanoates (**2** and **4**) in DMSO-d_6.

Compound	X	Aromatic	C=O ester	C=O ketone	C=N	O-CH_3	C-CH_3	X
2*c*	*p*-CO_2Me	146.4 (C1) 114.7(C2,6) 130.9 (C3,5) 124.0	162.7	193.9	133.4	51.9	25.2	52.4 OCH_3 165.8 C=O
2*f*	*p*-COMe	146.3 114.5 130.2 131.2	162.8	193.9	133.3	52.4 (52.0)	25.3	26.5 OMe 196.4 C=O
2*h*	*p*-Me	140.8 116.3 130.8 128.3	164.5	193.5 (197.1)	135.0	52.0	26.5	20.8
2*i*	*p*-OMe	156.2 117.9 116.8 114.8	162.0	193.3	135.2	51.9	25.7	55.4
4*b*	*o*-CN	144.2 (C1) 134.4 (C3) 132.8 (C5) 124.2 (C4) 115.3 (C2) 100.9 (C6)	163.5	194.3 (197.4)	132.6	52.8 (52.4)	27.0 (30.8)	116.1
4*c*	*o*-CO_2Me	143.3 (C1) 134.9 (C3) 130.8 (C5) 123.1 (C4) 115.0 (C2) 115.4 (C6)	161.8 (166.0)	193.6 (195.0)	134.7	52.0	26.4 (30.4)	52.4 OMe 166.6 C=O

tants and to purchase essential supplies and chemicals, some of which were also provided by the Department of Chemistry at Saint Mary's University. We gratefully acknowledge the contribution of the Atlantic Regional Magnetic Resonance Centre at Dalhousie University in providing the NMR spectra.

References

1. D.S. Brown, J.V. Jollimore, M.P. Merrin, K. Vaughan, and D.L. Hooper. Can. J. Chem. **73**, 169 (1995).
2. M.S.S. Siddiqui and M.F.G. Stevens. J. Chem. Soc. Perkin Trans. 1, 2482 (1974)
3. D. Prasad, N. Prasad, R.M. Prasad, R.J. Ferrier, and S.M. Milgate. J. Chem. Soc. Perkin Trans. 1, 1397 (1984).
4. M.H. Elnagdi, K.U. Sadek, N.M. Taha, and Y.M. Yassin. Collect. Czech. Chem. Commun. **55**, 734 (1990).
5. R.M. Silverstein, G.C Bassler, and T.C. Morrill. Spectroscopic identification of organic compounds. 5th. ed. John Wiley & Sons, Inc., New York. 1991. (a) Table 5.9, p. 240; (b) p. 196.
6. A.J. Bellamy and R.D. Guthrie. J. Chem Soc. 2788 (1965); 3528 (1965).

The photochemistry of 3,3′,4,4′-tetramethoxy- and 4-hydroxy-3,3′,4′-trimethoxystilbene — models for stilbene chromophores in peroxide-bleached, high-yield wood pulps

William J. Leigh, T. Johnathan Lewis, Vincent Lin, and J. Alberto Postigo

Abstract: The photochemistry of the title compounds has been investigated in ethanol and tetrahydrofuran solution under aerobic and anaerobic conditions. Direct irradiation of *trans*-3,3′,4,4′-tetramethoxystilbene (*trans*-**1**) in deoxygenated ethanol leads to the rapid establishment of a photostationary state with the *cis* isomer, and the slower formation of the ethyl ether corresponding to addition of ethanol across the olefinic C=C bond and cyclobutane dimers. The same products are formed upon photolysis in the presence of oxygen under the same conditions but, in addition, two isomeric tetramethoxyphenanthrenes and 3,4-dimethoxybenzaldehyde are formed. Photolysis of *trans*-**1** in oxygenated tetrahydrofuran leads to the same products in different relative yields. Quantum yields for *cis,trans* photoisomerization, phenanthrene formation, and addition of ethanol have been determined by ferrioxalate actinometry. Direct irradiation of *trans*-4-hydroxy-3,3′,4′-trimethoxystilbene (*trans*-**2**) in ethanol solution also results in rapid *cis–trans* isomerization and the formation of (three) isomeric phenanthrene derivatives in photolyses carried out in the presence of oxygen, although the material balance is low. The various products of photolysis of *trans*-**2** have been independently synthesized by desilylation of the products isolated from photolysis of *trans*-4-*tert*-butyldimethylsiloxy-3,3′,4′-trimethoxystilbene (*trans*-**3**) under similar conditions. Fluorescence-quenching experiments have been carried out to determine the relative rates of quenching of the excited singlet states of *trans*-**1** and *trans*-**2** by alcohols and oxygen. The formation of aldehydes is proposed to arise via reaction of superoxide ion with stilbene radical cations, which are formed by electron-transfer quenching of the stilbene excited singlet state by oxygen.

Key words: stilbenes, lignin, photochemistry, photooxidation.

Résumé : On a étudié la photochimie des composés mentionnés dans le titre en solutions dans l'éthanol et le tétrahydrofurane, dans des conditions tant aérobiques qu'anaérobiques. L'irradiation direct du *trans*-3,3′,4,4′-tétraméthoxystilbène (*trans*-**1**) dans de l'éthanol désoxygéné conduit à la création rapide d'un état photostationnaire avec l'isomère *cis* et à une formation plus lente de l'éther éthylique correspondant à l'addition de l'éthanol sur la double liaison C=C oléfinique ainsi que des dimères cyclobutanes. Les mêmes produits se forment lors de la photolyse dans les mêmes conditions, en présence d'oxygène; toutefois, il se forme de plus deux tétraméthoxyphénanthrènes isomères ainsi que du 3,4-diméthoxybenzaldéhyde. La photolyse du *trans*-**1** dans du tétrahydrofurane oxygéné conduit à la formation des même produits avec des rendements relatifs différents. On a déterminé les rendements quantiques de la photoisomérisation *cis*, *trans*, de la formation du phénanthrène et de l'addition de l'éthanol par actinométrie ferrioxalate. L'irradiation directe du *trans*-4-hydroxy-3,3′,4′-triméthoxystilbène (*trans*-**2**) en solution dans l'éthanol effectuée en présence d'oxygène conduit aussi à une isomérisation *cis–trans* rapide et à la formation de (trois) dérivés phénanthrènes isomères, même si la balance des produits est faible. Les divers produits de photolyse du *trans*-**2** ont été synthétisés par des voies indépendantes par désilylation des produits isolés de la photolyse du *trans*-4-*tert*-butyldiméthylsiloxy-3,3′,4′-triméthoxystilbène (*trans*-**3**) dans des conditions semblables. On a effectué des expériences de désactivation de la fluorescence pour déterminer les vitesses relatives de désactivation des états singulets excités des composés *trans*-**1** et *trans*-**2** par les alcools et l'oxygène. On suggère que la formation des aldéhydes résulte de la réaction de l'ion superoxyde avec les cations radicaux du stilbène qui se forment par une désactivation du transfert d'électron de l'état singulet excité du stilbène par l'oxygène.

Mots clés : stilbènes, lignine, photochimie, photooxydation.

[Traduit par la rédaction]

Received October 6, 1995.

W.J. Leigh,[1] T.J. Lewis, V. Lin, and J.A. Postigo. Department of Chemistry, McMaster University, 1280 Main Street West, Hamilton, ON L8S 4M1, Canada.

[1] Author to whom correspondence may be addressed. Telephone: (905) 525-9140, ext. 23715. Fax: (905) 522-2509.

Introduction

The development of an understanding of the mechanisms of the various chemical processes responsible for the photochemical yellowing of lignin-rich pulp and paper products, and discovering ways of inhibiting these processes, is a matter of considerable commercial importance and intense current interest (1). It is generally agreed that oxidative processes involving the conversion of phenoxy radicals to quinonoid species represent the main contributor to photoyellowing, and various mechanisms for the formation of phenoxy radicals from photolysis of the more abundant chromophore types present in lignin, such as α-phenoxycarbonyl and -benzyl alcohol moieties, have been proposed (2–7).

Relatively little attention has yet been paid to the less-abundant chromophores that are present in lignin-rich papers as a result of condensation reactions that take place during alkaline bleaching processes. Castellan et al. have described qualitative results from the irradiation of several model compounds of this general type, stilbenes, benzofurans, biphenyls, diarylmethanes, and alkenylphenols, adsorbed on filter paper and in solution (8). This study was confined to measurements of the rates of photoinduced discolouration of the paper as a function of adsorbate and photolysis time. Interestingly, two of the compounds that proved to be most active under these conditions were *trans*-3,3′,4,4′-tetramethoxystilbene (*trans*-**1**) and *trans*-4-hydroxy-3,3′,4′-trimethoxystilbene (*trans*-**2**).

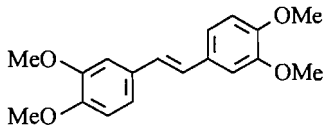

trans-**1**

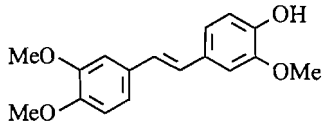

trans-**2**

Zhang and Gellerstedt have reported the results of a more detailed investigation of the photochemistry of *trans*-**2** on filter paper (9, 10). Using natural sunlight as an excitation source, they verified the substantial photoreactivity of this compound under these conditions, and isolated several dimers and a highly coloured *ortho*-quinonoid compound from the photolysis mixture. Interestingly, no evidence for the formation of the *cis* isomer or phenanthrene derivatives — the normal products expected from irradiation of stilbene derivatives (11–13) — was reported. While other explanations are possible, the "unusual" photoreactivity of **2** under these conditions may be due to the reaction medium being microcrystalline; the [2+2] photodimerization of stilbene and other phenylalkene derivatives in the crystalline solid phase is well documented (14). It remains to be determined whether these results are relevant to the photochemistry of stilbene chromophores in the amorphous molecular environment provided by natural lignin.

As part of a study designed to evaluate the importance of phenolic polyalkoxystilbenes and their photoproducts in contributing to the photoyellowing of lignin-rich materials, we report the results of the direct irradiation of **1**, **2**, and *trans*-4-*tert*-butyldimethylsiloxy-3,3′4′-trimethoxystilbene (*trans*-**3**) in ethanol and tetrahydrofuran solutions in the presence and absence of oxygen. The latter compound was prepared primarily as a synthon to aid in the preparation and isolation of the various phenanthrene derivatives expected from photooxidation of *trans*-**2**. We also report fluorescence-quenching studies

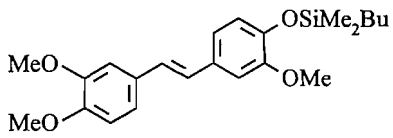

trans-**3**

of *trans*-**1**, *trans*-**2**, and a tetramethoxyphenanthrene derivative derived from the photooxidation of *trans*-**1**, which allows an assessment of the effects of oxygen and proton donors on the photochemistry of these compounds.

Results

Compounds *trans*-**1** and *trans*-**2** were synthesized according to the published procedures, while *trans*-**3** was synthesized by silylation of *trans*-**2** with *tert*-butyldimethylsilyl chloride. The latter compound exhibited spectroscopic and analytical data consistent with its proposed structure (see Experimental section). The ultraviolet absorption spectra of *trans*-**1** and *trans*-**2** exhibit maxima at ~335 nm in tetrahydrofuran (THF) solution. No changes in the spectra could be detected upon saturating the solutions with oxygen.

The three compounds were irradiated as solutions (0.002–0.015 M) in 95% ethanol and dry tetrahydrofuran (THF), under both nitrogen and oxygen atmospheres, with the progress of the reactions monitored by capillary GC, GC–MS, and ^{1}H NMR spectroscopy. Photoproducts were isolated by thick-layer chromatography, after both short and long irradiation times, and identified on the basis of spectroscopic data (vide infra). As expected, establishment of a photostationary state with the corresponding *cis* isomer is substantially more rapid than the formation of other products and, with broadband irradiation through a Pyrex filter, the photostationary states are rich in the *cis* isomer in all cases. Quantitative detection of *cis*-**2** was carried out by ^{1}H NMR spectroscopy in deuterated solvents, as the compound was found to undergo facile thermal isomerization to *trans*-**2** in the GC injector port at the temperatures required for GC analysis of the mixtures.

In nitrogen-saturated ethanol solution, prolonged irradiation of *trans*-**1** and *trans*-**3** led to isolable yields of solvent-addition products, which were identified as **4** and **5**, respectively; the latter consisted of a mixture of two regioisomers, which were not further separated. GC analysis of the photolysates during the very early stages of photolysis verified that the formation of these products accompanies photoisomerization to the *cis* isomers. Cyclobutane dimers **6**–**8** were also isolated; their yields were generally higher in irradiations carried out using the higher stilbene concentrations, but the concentration dependence was not examined in detail. These products could not be detected by GC analysis under the conditions employed, but were readily detectable in the ^{1}H NMR spectra of the crude reaction mixtures. Irradiation of oxygen-saturated ethanol solutions led to the additional formation of phenan-

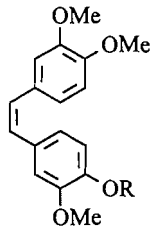

cis-**1** (R = Me)
cis-**2** (R = H)
cis-**3** (R = Si^tBuMe_2)

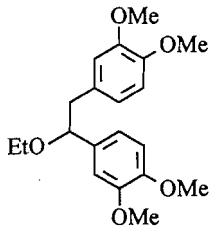

4

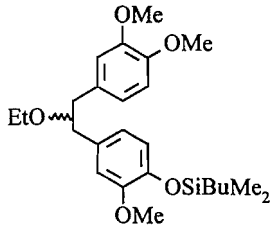

5

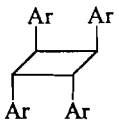

6

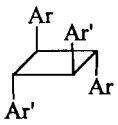

7*a*

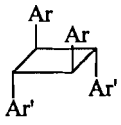

8*a,b*

Ar = 3,4-dimethoxyphenyl

a Ar' = 4-($Me_2{}^tBuSiO$)-3-methoxyphenyl
b Ar' = 4-hydroxy-3-methoxyphenyl

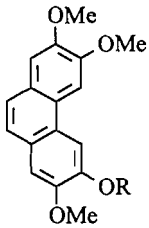

9

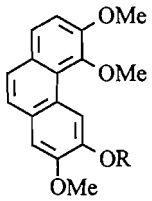

10

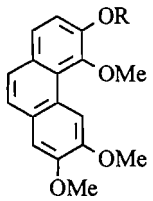

11

a R = Me
b R = H
c R = Si^tBuMe_2

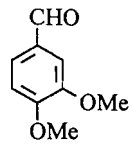

12

threne derivatives **9–11**, which were isolated by thick-layer chromatography, and 3,4-dimethoxybenzaldehyde (**12**). Minor yields of **9–11** were also obtained in the nitrogen-atmosphere experiments, but this was shown to be due to diffusion of air into the irradiation cells during the course of the experiment. Irradiation in THF solution under similar sets of conditions afforded the same products, with the exception of **4** and **5**. Prolonged irradiation of both *trans*-**1** and *trans*-**3** resulted in the development of a yellow colour and the formation of several minor products in each case. These could be detected by GC and GC–MS, but could not be isolated owing to their small yields; GC–MS data for some of these compounds are included in the Experimental section. Small amounts of highly coloured fractions containing mixtures of relatively polar minor products were generally obtained from the thick-layer plates, but the amounts were too low to warrant further attempts at separation. The infrared spectra of these mixtures showed them to be rich in carbonyl absorptions.

Prolonged irradiation of oxygen-saturated ethanol or THF solutions of *trans*-**2** led to the development of a deep yellow-brown colour, complex product mixtures, and poor material balances. Phenanthrenes **9***b*–**11***b* were identified as photoproducts on the basis of GC coinjections of authentic samples, which were synthesized by desilylation of **9***c*–**11***c* with tetrabutylammonium fluoride. In addition, a cyclobutane dimer (**8***b*) was isolated in low yield from irradiation in THF solution.

Table 1 summarizes the products obtained from irradiation of the three compounds under the various conditions employed, along with their chemical yields and material balances, as estimated by a combination of GC and ^1H NMR analysis of crude reaction mixtures.

The phenanthrenes **9–11** were identified on the basis of their ^1H and ^{13}C NMR, mass, and UV absorption spectra; NMR was particularly useful for the regiochemical assignments of individual sets of regioisomers. Compound **9***a* could be easily distinguished from **10***a* by NMR, owing to σ_v molecular symmetry. Phenanthrene **9***c* could be readily distinguished from **10***c* and **11***c* from the aromatic proton region in the ^1H NMR spectra, and by comparison to the spectra of **9***a* and **10***a*. Two of the compounds (which, coincidentally, elute together under our GC conditions) show singlets at $\delta \sim 9.2$ (due to the C4 ring proton) and must therefore possess alkoxy substitution at the 5-position of the phenanthrene ring system; by default, the compound without a singlet at $\delta \sim 9.2$ can be assigned to **9***c*. The aromatic region of the ^1H NMR spectrum of this compound compares quite favourably with that in the spectrum of the symmetrical tetramethoxyphenanthrene derivative **9***a*; the spectrum shows single-proton singlets at 7.76 and 7.88 ppm, a two-proton singlet at 7.53 ppm, and single-proton singlets at 7.19 and 7.20 ppm. This should be compared with the spectrum of **9***a*, which shows two-proton singlets at 7.79, 7.55, and 7.21 ppm. ^1H nOe experiments were employed to distinguish between **10***c* and **11***c*. The C7/C8 protons give rise to an AX splitting pattern, with doublets at ca. 7.2 and 7.6 ppm. Irradiation of the *tert*-butyl methyl singlets at ~1.08 ppm results in nOe enhancement of the singlet at 9.2 ppm for the compound assigned as **10***c*, and enhancement of the doublet at δ7.15 for the compound assigned as **11***c*. Irradi-

Table 1. Product yields from irradiation of stilbenes **1–3** in 95% ethanol and THF under various conditions.[a]

Compound	Conditions: Solvent	Conc/M	Conversion (%)	Products: Phenanthrenes	Others	Material balance (%)
trans-**1**	EtOH–N_2	0.002	30[c]	**9***a* (6%); **10***a* (5%)	**4** (19%)	n.d.
	THF–N_2	0.001	1	[d]	[d]	100
	EtOH–O_2	0.002	90[c]	**9***a* (26%); **10***a* (24%)	**4** (8%); **12** (32%)	51[e]
	THF–O_2	0.013	58[c]	**9***a* (21%); **10***a* (26%)	**12** (8%) + unident. (3%)	92[e,f]
trans-**2**	EtOH–O_2	0.003	5[c]	—	**12** (5%)	n.d.
	THF–N_2	0.001	1[g]	[d]	[d]	100
	THF–O_2	0.006	75[c]	**9***b* (19%); **10***b* (12%); **11***b* (22%)	**12** (14%) + unident. (8%)	80[e,f]
trans-**3**	EtOH–O_2	0.005	75[c]	**9***c* (15%); **10***c* (9%); **11***c* (21%)	**5** (15%); **12** (15%)	76[e,f]
	THF–O_2	0.0166	25[c]	**9***c* (5%); **10***c* (4%); **11***c* (11%)	**12** (5%) + unident. (0.25%)	95[e,f]

[a]Determined by GC–MS analysis of crude photolysis mixtures relative to internal standard, with no correction for detector response.
[b]Only those products observed by gas chromatography are reported (dimers **6–8** are undetectable by GC).
[c]The % conversion was determined by GC–MS, and calculated as $100\% \times (100\% - \%(trans\text{-}\mathbf{1} + cis\text{-}\mathbf{1})_{final})/(trans\text{-}\mathbf{1})_{initial}$.
[d]*cis,trans* Isomerization is the only photoprocess observed at the given conversion.
[e]Calculated as $100 \times (\%trans\text{-}\mathbf{1} + cis\text{-}\mathbf{1})_{NMR}/(\%trans\text{-}\mathbf{1} + cis\text{-}\mathbf{1})_{GC\text{-}MS}$.
[f]Most of the deficiency in the material balance was due to formation of cyclobutane dimers.
[g]Calculated as $100\% \times (\%(trans\text{-}\mathbf{1} + cis\text{-}\mathbf{1})_{final})/(trans\text{-}\mathbf{1})_{initial}$.

ation of two of the methoxy singlets in the spectrum of the latter compound results in enhancement of the singlet at 9.2 ppm, thus verifying the assignment. Unfortunately, the methoxy singlets are too closely spaced in the 500 MHz spectrum of **10***c* to allow meaningful information to be gleaned from analogous experiments in this case.

Identification of the cyclobutane dimers **6–8** was made on the basis of their ^{1}H NMR and mass spectra (15, 16). The ^{1}H NMR spectrum of the *trans-syn-trans* dimer **6** shows a multiplet at $\delta \sim 4.4$ ppm, which is characteristic of *trans-syn-trans* stereochemistry in stilbene photodimers (15). The spectra of the all-*trans* dimers **7***a* and **8***a,b* show characteristic resonances at $\delta \sim 3.7$ ppm (16, 17). The identities of the isomers **7***a* and **8***a* were established on the basis of their mass spectral fragmentation patterns (18); that of **8***b* was analogous to that of **8***a*. In most cases, the presence of other regio- and (or) stereoisomeric dimers was evident in the crude irradiation mixtures or in chromatographic fractions, but they could not be characterized owing to either the small amounts obtained or to the fact that they were obtained as mixtures with other minor products. The presence of these products is not evident by GC or GC–MS analyses of the crude irradiation mixtures under the conditions employed.

Prolonged photolysis of **1–3** produced several additional minor products that were detectable by GC–MS, and strongly coloured solutions (particularly in the case of **2**). While all attempts to isolate these products have so far proved unsuccessful, their GC retention times and mass spectra suggest them to be demethylation products of the phenanthrenes; i.e., dimethoxyphenanthrenedione and phenanthrenetetrone derivatives. Our efforts to rigorously identify these products are continuing.

Quantum yields for direct *cis,trans* photoisomerization of *cis*- and *trans*-**1** were determined using 300 nm excitation in deoxygenated ethanol and tetrahydrofuran (THF) solution by electronic actinometry using 0.001 M solutions. In ethanol, $\phi_{t\rightarrow c} = 0.35 \pm 0.04$ and $\phi_{c\rightarrow t} = 0.41 \pm 0.04$ while in THF, $\phi_{t\rightarrow c} = 0.40 \pm 0.04$ and $\phi_{c\rightarrow t} = 0.51 \pm 0.06$. The photostationary state is *cis*-**1** / *trans*-**1** = 1.38 ± 0.05 in ethanol solution for 300 nm excitation. The quantum yields for *cis,trans* isomerization matched the quantum yields for disappearance of the starting isomers in both solvents.

Quantum yields for formation of **4**, **9***a*, **10***a*, and **12** in oxygen-saturated ethanol were estimated relative to $\phi_{t\rightarrow c}$ and $\phi_{c\rightarrow t}$ from the slopes of concentration vs. time plots. The values obtained are $\phi_4 = 0.007 \pm 0.003$, $\phi_{9a} = 0.008 \pm 0.003$, $\phi_{10a} = 0.005 \pm 0.002$, and $\phi_{12} = 0.009 \pm 0.004$.

Irradiation of *trans*-**1** was also carried out in the presence of 2,6-di-*tert*-butylphenol as a free radical scavenger. Thus, a solution of *trans*-**1** (0.0054 M), *n*-hexadecane as internal standard, and 2,6-di-*tert*-butylphenol (0.006 M) in dry tetrahydrofuran was oxygenated with a stream of dry oxygen for 10 min, irradiated for 6 h with 300 nm light, and monitored by GC–MS and TLC at 1 h intervals. The formation of aldehyde **12** was evident in the earliest stages of photolysis, but reached a maximum yield that fell off at long (>8 h) photolysis times. Compounds *cis*-**1**, **9***a*, and **10***a* were isolated and identified by comparison with authentic samples obtained from previous photolysis experiments. The mixture contained enhanced amounts (~5% total) of two of the minor products whose mass spectra are consistent with dimethoxyphenanthrenedione structures (see Experimental section). Significantly, no evidence was obtained for the formation of products of more extensive demethylation, under these conditions.

Direct irradiation (300 nm) of an oxygenated, 0.014 M solution of tetramethoxyphenanthrene **10***a* in THF yielded minute amounts of a single unidentifiable product after several hours of photolysis. Irradiation (254 nm) of an oxygenated THF solution containing **10***a* (0.07 M), *trans*-**1** (0.013 M), and *n*-hexadecane as internal standard (under conditions where **10***a* absorbs >99% of the light) yielded a qualitatively similar product distribution to that obtained from photolysis of

trans-**1** under similar conditions: none of the products was formed in significantly enhanced or reduced yields under these conditions.

Samples of *cis*- and *trans*-**1** adsorbed on filter paper (ca. 0.5% by weight) were irradiated with 300 nm light (in a Rayonet reactor operating at half intensity) under an air atmosphere, extracted into dichloromethane, and analysed by gas chromatography. Photolysis of *trans*-**1** for 1 h under these conditions caused mild yellowing of the paper. GC analysis indicated that ca. 30% of the starting material had been consumed, but only a small amount of *cis*-**1** had formed (~2% of the amount of *trans*-**1** present) and there was no evidence for the formation of phenanthrenes **9***a* and **10***a*. Irradiation of *cis*-**1** under these conditions results in initially rapid conversion to the *trans* isomer, followed by behaviour similar to that observed upon irradiation of the sample of *trans*-**1** as described above.

Fluorescence emission spectra of *trans*-**1**, *trans*-**2**, and 2,3,6,7-tetramethoxyphenanthrene (**9***a*) were recorded in ethanol and THF solution. The spectra were unexceptional; those of *trans*-**1** and *trans*-**2** were indistinguishable from each other and from the spectrum of *trans*-**2** in toluene reported by Zhu and Gray (19), while that of **9***a* is similar to that of phenanthrene itself (20). Attempts were made to determine fluorescence lifetimes for the two stilbene derivatives using the time-correlated single-photon counting technique. In the case of *trans*-**1** in deoxygenated ethanol, fluorescence decay was too fast to be determined accurately with our system. This affixes an upper limit of ca. 0.5 ns for the singlet lifetime of *trans*-**1** in this solvent. In deoxygenated THF solution, fluorescence decay followed single exponential kinetics and exhibited an apparent lifetime of $\tau = 1.2 \pm 0.3$ ns. The lifetime was shortened to 0.9 ns in oxygen-saturated solution. Both values are very close to the limits of reliability of our system, and we do not consider them reliable. Similar results were obtained for *trans*-**2** in deoxygenated THF solution. The fluorescence lifetime of **9***a* was determined to be $\tau = 16.6 \pm 1.8$ ns in nitrogen-saturated THF, and $\tau = 3.5 \pm 0.4$ ns in oxygen-saturated solution under the same conditions.

The steady state fluorescence spectra of *trans*-**1** and *trans*-**2** in THF are quenched upon addition of ethanol, 2,2,2-trifluoroethanol (TFE), 1,1,1,3,3,3-hexafluoroisopropanol (HFIP), or oxygen to the deoxygenated solution. Stern–Volmer quenching experiments led to the $k_q\tau$ values listed in Table 2.

Table 2. Stern–Volmer constants ($k_q\tau/M^{-1}$) for fluorescence quenching of *trans*-**1** and *trans*-**2** by ethanol (EtOH), 2,2,2-trifluoroethanol (TFE), and 1,1,1,3,3,3-hexafluoroisopropanol (HFIP) in deoxygenated THF solution at 23°C.[a]

Alcohol	EtOH	TFE	HFIP	O_2
trans-**1**	0.13 ± 0.02	0.18 ± 0.03	0.27 ± 0.03	29 ± 9
trans-**2**	0.26 ± 0.04	0.36 ± 0.04	0.46 ± 0.03	47 ± 12

[a]Errors in the $k_q\tau$ values are given as twice the standard deviation from least-squares analysis of the Stern–Volmer plot.

Discussion

The general features of the photochemistry of *trans*-**1** and *trans*-**3** in solution are typical of the photochemistry of stilbene derivatives (11–13). *cis,trans* Photoisomerization occurs with relatively high efficiency, leading to a photostationary state that is rich in the *cis* isomer for 300 nm excitation; in rigorously deoxygenated, non-protic solvents, *cis,trans* isomerization is the only productive photoprocess detectable at short irradiation times. In the presence of oxygen, *cis,trans* isomerization is accompanied by the formation of 3,4-dimethoxybenzaldehyde (**12**) and phenanthrene derivatives (**9–11**), with efficiencies some two orders of magnitude lower than that of *cis,trans* isomerization. Phenanthrene derivatives are well known to be formed by a mechanism involving oxidation of 4a,4b-dihydrophenanthrene intermediates formed by photoelectrocyclic ring-closure of the *cis* isomer of the stilbene (11, 21). In the absence of oxidizing agents, these intermediates undergo thermal or photochemical cycloreversion to the *cis*-stilbene derivative from which they were formed. Thermal cycloreversion is relatively rapid; at room temperature in fluid solution, their lifetimes range from seconds to a few hours depending on substituent (21). Thus, the direct detection of these compounds in the present cases is not expected to be straightforward with the analytical methods employed in this work. The relevant chemistry is illustrated for *trans*-**1** in Scheme 1.

While compounds identifiable as 3,4,5,6-tetrasubstituted phenanthrene derivatives could not be detected in the irradiation mixtures from **1–3**, there appears to be little regioselectivity in the formation of the 2,3,6,7-tetrasubstituted regioisomer over the 2,3,5,6-isomer(s), at least according to GC analysis. Evidently, this lack of regioselectivity in the photocyclization of *meta*-substituted stilbene derivatives is common (11, 21).

The formation of ethyl ethers **4** (from **1**) and **5** (from **3**) in ethanol is presumably the result of excited singlet state quenching by protonation of the electron-rich stilbene double bond, followed by trapping of the resulting carbenium ion by the solvent. Photoprotonation of phenylalkenes is well documented (22–28), and is known to be enhanced by the presence of electron-donating aromatic substituents. The process occurs with relatively low efficiency (compared to *cis,trans* isomerization) in **1** and **3**, but competes effectively with phenanthrene formation and oxidative cleavage in the presence of oxygen. An upper limit for the rate constant for photoprotonation of *trans*-**1** by ethanol in THF solution is on the order of 5×10^8 M^{-1} s^{-1} (assuming a singlet lifetime of 1 ns), which seems reasonable considering the structure of the molecule compared to those of other phenylalkenes for which quantitative data exist in the literature (22–24, 28). It is interesting to note that the rate constant for this process varies by less than a factor of two for EtOH, TFE, and HFIP for both *trans*-**1** and -**2**, in spite of the fact that the pK_a's of the three alcohols vary substantially. To our knowledge, there are, unfortunately, no data available in the literature with which to compare these results.

The irradiations of *trans*-**1–3** in oxygenated ethanol solutions lead to lower yields of phenanthrenes than those obtained in oxygenated THF solutions at similar concentrations. As discussed above, the formation of ethyl ethers, corresponding to addition of ethanol across the olefinic C=C bond, provides a productive deactivation pathway for the excited states of *trans*-**1–3** that is not available in THF, but this accounts for only a fraction of the differences in the phenan-

Scheme 1.

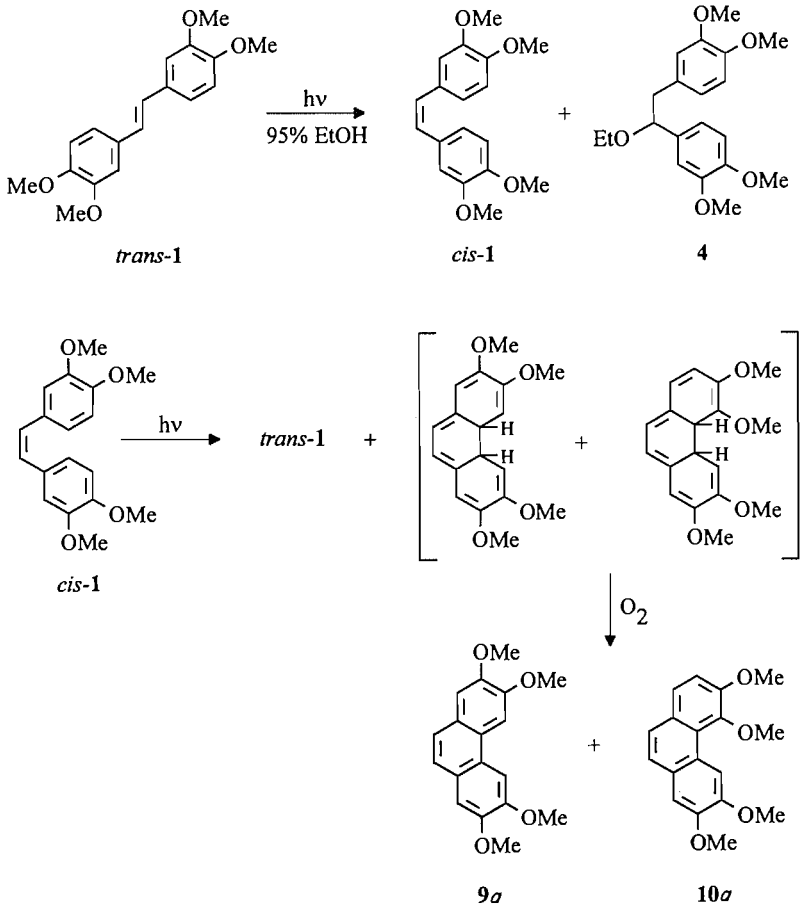

threne yields in the two solvents. The main contributor appears to be a higher propensity for dimer formation in the protic solvent. Similar solvent effects on stilbene photodimerization have been documented previously (18).

The formation of 3,4-dimethoxybenzaldehyde (**12**) as a primary product of photolysis of **1** in oxygen-saturated solution most likely results from the reaction of the olefin radical cation with superoxide ion, formed as a result of electron transfer quenching of the excited singlet state of the stilbene by molecular oxygen. There is a considerable body of evidence that supports this conclusion. First, the sensitized photooxygenation of stilbene derivatives with cyanoaromatics and *some* dye sensitizers (e.g., methylene blue) has been shown to proceed by an electron transfer mechanism (29–31), in which electron transfer quenching of the excited sensitizer by the olefin, followed by reduction of molecular oxygen by the sensitizer radical anion, results in the ultimate formation of oxidative cleavage products through reaction of the olefin radical cation and superoxide ion. The initial product of this reaction is thought to be the corresponding 1,2-dioxetane (29–32), although evidence that an ozonide may be involved in these reactions has also been reported (33). In the present cases, we believe that the mechanism for formation of superoxide and stilbene radical cation is direct electron transfer quenching of the excited singlet state of the stilbene by molecular oxygen. This is supported by fluorescence-quenching experiments (Table 2), which indicate that oxygen quenching of *trans*-**1** and -**2** proceeds at the diffusion-controlled rate (note that the Stern–Volmer constants reported in Table 2 indicate a quenching rate constant of $(2–5) \times 10^{10}$ M^{-1} s^{-1}, assuming singlet lifetimes of 1 ns for the two stilbene derivatives). The oxidation potential of **1** ($E_{1/2}^{ox} = 0.82$ V vs. SCE in acetonitrile;[2] a similar value can be expected for **2**) is clearly low enough that photoinduced electron transfer to molecular oxygen will be strongly exothermic. Once formed, $\mathbf{1}^{\cdot+}$ and $O_2^{\cdot-}$ can react to yield dioxetane **13** directly. This mechanism is related to that proposed for the photooxygenation of electron-rich styrenes and other arenes, which has been shown in some cases to proceed via direct excitation of a charge transfer complex between the arene and molecular oxygen (34, 35). However, no evidence for the formation of analogous charge transfer complexes could be obtained from the UV absorption spectra of *trans*-**1** and -**2** in oxygen-saturated THF or acetonitrile solution.

Another possible mechanism for the formation of **13** might involve generation of singlet oxygen ($^1O_2$) by back-electron-transfer of the initially produced radical ion pair (this should also produce the excited triplet state of **1**), followed by reaction of $^1O_2$ with ground state **1** (9). We believe that this mechanism can be discounted, on the basis that the relative yield of **12** (the product of decomposition of the presumed intermediate **13**) does not appear to be enhanced when the photolysis of

[2] We thank Professor M.S. Workentin for the oxidation potential measurement.

Scheme 2.

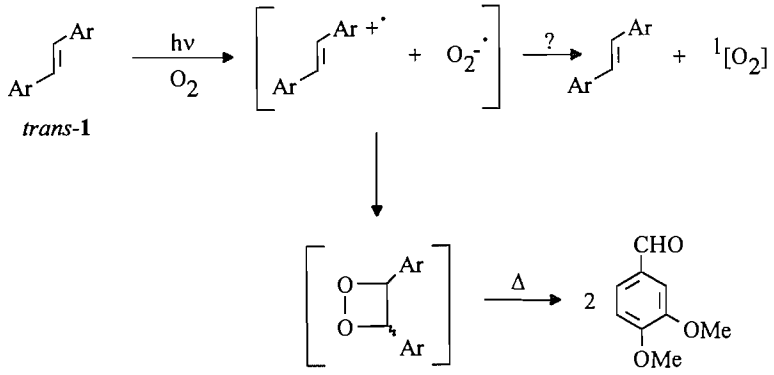

12

1 is sensitized by phenanthrene **9***a*. The phenanthrene can be expected to be a much more efficient sensitizer for the formation of superoxide ion (and thus $^1O_2$, by this mechanism) because of its longer singlet lifetime and lower oxidation potential compared to *trans*-**1** (36); fluorescence quenching experiments indicate that the excited singlet state of **9***a* is quenched just as rapidly by molecular oxygen as those of *trans*-**1** and -**2**. Phenanthrene **9***a* also has the potential of producing $^1O_2$ directly by triplet–singlet energy transfer, because intersystem crossing is expected to be efficient (37). In fact, the product distribution obtained in this experiment is similar to that produced in the direct irradiation of *trans*-**1**, suggesting that the dominant mechanism for reaction involves singlet energy transfer from **9***a* to **1**.

Thus, we suggest the tentative mechanism shown in Scheme 2 for the formation of **12** from photolysis of *trans*-**1** in oxygen-saturated solution. Further work is clearly required in order to conclusively identify the reactive oxygen species involved in the reaction, and to fully understand the mechanism(s) by which it is formed.

Of the three lignin-model stilbenes whose photochemistry has been investigated in the present work, **2** is the most relevant to the stilbene chromophores present in lignin-rich materials (10). It is also the most difficult to study because of the large number of minor, unisolable products produced upon its irradiation. Nevertheless, it is clear that UV irradiation of this compound in solution *does* result in the formation of products analogous to those produced from **1** under similar conditions: phenanthrenes derived from photocyclization/oxidation of the *cis* isomer, and products derived from oxidative cleavage of the olefinic double bond. Highly coloured (presumably) quinonoid materials are also formed, but in significantly higher yields than those obtained from photolysis of **1** or **3**.

The irradiation of **2** in solution bears only marginal resemblance to that obtained when the compound is adsorbed on filter paper (9). In the latter case, the main products are cyclobutane dimers and dimethoxybenzaldehyde **12**; minor products are reported to include a dimeric ether from addition of the phenolic OH in **2** across the double bond in a second molecule (which is related to the ethanol-addition products observed in the present work), and a stilbenequinone. In contrast to the solution phase results described here, no phenanthrene derivatives were reported. Furthermore, we observe the formation of only very minor amounts of compounds, tentatively identifiable as stilbenequinones, in the photolysis of **2** in oxygen-saturated solution. On the basis of our results for *trans*-**1**, it seems likely that the absence of phenanthrenes as photoproducts in the irradiation of *trans*-**2** on filter paper is due to the fact that the photostationary state consists of <5% of the *cis* isomer under these conditions. We believe that the extremely low *cis*-**1** content in the photostationary state for the filter paper irradiations is probably due to the reactant existing in a microcrystalline environment in which the *trans* isomer is thermodynamically favoured. The same is likely to be true for **2** under these conditions.

Summary and conclusions

Irradiation of polyalkoxystilbene derivatives in solution in the presence of oxygen leads to *cis,trans* isomerization, polyalkoxyphenanthrene formation, oxidative cleavage of the olefinic double bond, dimerization, and the formation of small amounts of highly coloured, carbonyl-containing compounds. The formation of phenanthrene derivatives is the result of photoelectrocyclization of the corresponding *cis*-stilbene isomer, followed by oxidation, and is a well-known reaction in stilbene photochemistry. For monochromatic 300 nm excitation in solution, the *cis/trans* photostationary state is rich in the *cis* isomer, so that cyclization to yield phenanthrene derivatives occurs with significant efficiency. The photostationary state obtainable with broadband irradiation with >300 nm light is undoubtedly lower in *cis* content, since the UV absorption spectra of the *cis* isomers extend slightly further to the red. However, our experiments show that phenanthrene formation still proceeds readily under these conditions.

Both the stilbenes and their phenanthrene photoproducts are powerful photoreductants, and are potentially capable of initiating oxidative processes involving reaction of superoxide ion and (or) singlet oxygen with *other components* in the natural lignin matrix. Defining the extent to which this might contribute to lignin photoyellowing is the subject of continuing investigation in our laboratory.

Experimental section

^1H NMR spectra were recorded on Bruker AC200, AC300, or AM500 spectrometers in deuteriochloroform solution, while ^{13}C NMR spectra were recorded on the Bruker AC200 or AM500 spectrometers. Spectra reported for new compounds

were recorded on the AM500 spectrometer unless otherwise noted, and are reported in parts per million relative to tetramethylsilane. Infrared spectra were recorded in carbon tetrachloride solution on a Biorad FTS-40 FTIR spectrometer or as the neat samples in the case of liquids. Ultraviolet absorption spectra were recorded on a Perkin Elmer Lambda 9 spectrometer interfaced to an IBM PS/2-286 microcomputer, or on a Hewlett–Packard HP8451 UV spectrometer. Fluorescence emission and excitation spectra and fluorescence lifetimes were recorded on a Photon Technologies Inc. LS-100 spectrofluorometer/single-photon counting system, which is controlled by a 486-33 PC using software provided by the manufacturer. Single-photon counting experiments employed a hydrogen flashlamp.

Gas chromatographic analyses were carried out using a Hewlett–Packard 5890 gas chromatograph equipped with a flame ionization detector, a Hewlett–Packard 3396 integrator, and a DB-1 megabore capillary column (5 m × 0.53 mm; Chromatographic Specialties, Inc.). GC–MS analyses were carried out using a Hewlett–Packard 5890 gas chromatograph equipped with a HP-5971A mass selective detector and a DB-5 microbore capillary column (30 m × 0.2 mm; Chromatographic Specialties, Inc.). Exact Masses were determined on a VGH ZABE mass spectrometer and employed a mass of 12.000 000 for carbon. Thick-layer chromatographic separations employed a Chromatotron (Harrison Research, Inc.) and 2 or 4 mm silica gel 60 (E. Merck) thick-layer plates.

Preparative photolyses were performed using a Hanovia 450 W medium-pressure mercury lamp and a Pyrex immersion well (at 20°C), or a Rayonet reactor equipped with 14 RPR-3000 Å lamps and a 120 mL capacity Pyrex container (at 27°C). Analytical-scale photolyses employed the latter in conjunction with a merry-go-round; samples (ca. 0.5 mL) were contained in 5 × 80 mm Pyrex tubes that were sealed with rubber septa. Experiments carried out using 254 or 419 nm radiation employed the Rayonet reactor equipped with 6 RPR-2537 or 10 RPR-4190 lamps, respectively.

Tetrahydrofuran (Caledon Reagent grade) was dried over sodium metal and distilled prior to use. Benzene (Fisher Reagent) was purified by several extractions with concentrated sulfuric acid, rinsed with dilute sodium bicarbonate solution, predried over sodium sulfate, and distilled from sodium metal. Methanol (Fisher Reagent) was distilled from magnesium. Ethanol (95%) was purchased from Caledon Chemical Co. and distilled prior to use. Absolute ethanol was purchased from BDH and distilled from magnesium. Pentane (BDH Omnisolv) was used as received from the supplier. *N,N*-Dimethylformamide (Caledon) was dried over potassium hydroxide and distilled prior to use. Neutral alumina, dichloromethane, diethyl ether, ethyl acetate, hexanes, potassium carbonate, potassium bicarbonate, anhydrous sodium sulfate, and HPLC-grade water were all used as received from Fisher Chemical Co. Benzophenone, *n*-butyllithium, *tert*-butyldimethylsilyl chloride, 3,4-dimethoxybenzylalcohol, *n*-hexadecane, imidazole, methylene blue, thionyl chloride, triphenylphosphine, and vanillin acetate were all used as received from Aldrich Chemical Co.

trans-3,3′,4,4′-Tetramethoxystilbene (*trans*-**1**) and *trans*-4-hydroxy-3,3′,4′-trimethoxystilbene (*trans*-**2**) were synthesized according to the method of Castellan et al. (8). They exhibited melting points (*trans*-**1**; mp 154.6–155.0°C; *trans*-**2**; mp 129.6–130.1°C) and spectroscopic data that were similar to the reported data in both cases.

trans-4-*tert*-Butyldimethylsiloxy-3,3′,4′-trimethoxystilbene (*trans*-3)

In a 100 mL round-bottom flask equipped with a condenser and magnetic stirrer were placed *trans*-**2** (1.0 g, 0.001 mol), *tert*-butyldimethylsilyl chloride (0.63 g, 0.0042 mol), imidazole (0.60 g, 0.0083 mol), and dry dimethylformamide (7 mL). The mixture was stirred at room temperature for 24 h, with periodic monitoring by thin-layer chromatography on neutral alumina using 15% ethyl acetate in hexane as the eluant. The product mixture was diluted with ether (15 mL), washed with water (2 × 5 mL), dried with anhydrous sodium sulfate, and filtered. Evaporation of the solvent yielded a slightly yellow solid, which was recrystallized from hexane–ethanol to yield colourless crystals of the desired product (1.18 g, 84%; mp 70.0–71.3°C); UV (ethanol) $\lambda_{max}(\varepsilon)$: 203 nm (36 800), 332 nm (39 400); IR: 3030 (s), 2960 (w), 2840 (w), 1601 (w), 1514 (s), 1465 (m), 1251 (s), 1027 (w), 902 (w) 815 (w); ^{1}H NMR, δ: 0.15 (s, 6H), 0.99 (s, 9H), 3.84 (s, 3H), 3.88 (s, 3H), 3.96 (s, 3H), 6.89 (d, 2H), 6.91 (m, 6H); ^{13}C NMR, δ: –4.6, 18.6, 25.7, 55.5, 55.9, 55.9, 108.7, 109.7, 111.3, 119.5(2), 121.0, 126.6, 126.9, 130.8, 131.5, 144.8, 148.7, 149.1, 151.1; MS, *m/e* (*I*): 400 (44), 343 (24), 328 (100), 286 (90), 271 (13), 73 (9). Exact Mass, calcd. for $C_{23}H_{32}SiO_4$: 400.207; found: 400.2076.

Preparation and isolation of photoproducts

(i) From irradiation of trans-***1***

(a) Irradiation of trans-***1*** *in 95% ethanol*

A continuously oxygenated solution of *trans*-**1** (0.30 g, 1.0 mmol) in 95% ethanol (500 mL) was placed in a Pyrex immersion well system and irradiated for 0.5 h with a 450 W medium-pressure mercury lamp. GC analysis of the mixture indicated the presence of five compounds, which were subsequently identified (in order of increasing retention time) as *cis*-**1**, **4**, **10***a*, *trans*-**1**, and **9***a*. The solvent was distilled in vacuo to yield a yellow solid residue, which was placed on the Chromatotron and eluted with a 0–7.5% ethyl acetate – hexane gradient. The five compounds eluted in the order **10***a* < *cis*-**1** < *trans*-**1** < **4** < **9***a* under these conditions. Compounds *cis*-**1**, **9***a*, and **10***a* were isolated in >90% purity as solids, and recrystallized several times from ethyl acetate – hexane mixtures. Compound **4** was isolated in ca. 80% purity after several repeated elutions, and finally isolated as a colourless oil by cyclic medium-pressure column chromatography on a 1 in. × 10 in. Merck Lobar silica gel column using 9% ethyl acetate in dichloromethane as the eluant. The purified yields of the five compounds were: *cis*-**1** (0.045 g), *trans*-**1** (0.055 g), **4** (0.061 g), **9***a* (0.065 g), **10***a* (0.020 g). They were identified on the basis of the following spectroscopic data.

cis-*3,3′4,4′-Tetramethoxystilbene (*cis-***1***)*: 0.045 g, 0.15 mmol, 15%, mp 119.3–120.2°C); UV (ethanol) $\lambda_{max}(\varepsilon)$: 200 nm (33 200), 296 nm (12 700); IR: 3030 (s), 2961 (w), 2839 (w), 1582 (w), 1513 (s), 1464 (m), 1421 (w), 1267 (s), 1140 (m), 1027 (m); ^{1}H NMR (300 MHz), δ: 3.71 (s, 6H), 3.90 (s, 6H), 6.40 (s, 2H), 6.77 (m, 2H), 6.90 (m, 4H); ^{13}C NMR, δ: 55.6, 55.8, 55.9, 108.6, 110.9, 111.3, 111.8, 119.5, 121.8, 126.7,

128.7, 130.2, 130.7, 148.1, 148.4, 148.7, 149.1; MS, *m/e* (*I*): 300 (100), 285 (20), 225 (10), 181 (8), 152 (9), 128 (11). Exact Mass, calcd. for $C_{18}H_{20}O_4$: 300.1374; found: 300.1377.

1-Ethoxy-1,2-bis(3,4-dimethoxyphenyl)ethane (**4**): 0.061 g, 18%. UV (ethanol), $\lambda_{max}(\varepsilon)$: = 202 nm (79 560), 229 nm (19 750), 279 nm (6760); IR: 3059 (w), 2968 (s), 2968 (s), 2836 (s), 1591 (w), 1516 (w), 1262 (w), 1155 (w); ^{1}H NMR (300 MHz), δ: 1.2 (t, 3H), 2.8 (dd, 1H), 3.05 (dd, 1H), 3.75 (s, 3H), 3.80 (s, 6H), 3.85 (s, 3H), 4.3 (t, 1H), 6.5–6.8 (m, 6H); ^{13}C NMR, δ: 14.2, 15.3, 22.5, 44.5, 55.7, 55.8, 61.0, 64.1, 83.2, 109.5, 110.6, 110.8, 133.0, 119.3, 121.4, 131.2, 135.0, 147.4, 148.3, 149.0; MS (NH_3 CI), *m/e* (*I*): 364 (5), 301 (100), 195 (95), 151 (8).

2,3,6,7-Tetramethoxyphenanthrene (**9***a*): 0.065 g, 22%, mp 178.9–179.4°C; UV (ethanol), $\lambda_{max}(\varepsilon)$: 218 nm (26 960), 254 nm (52 430), 285 nm (32 460), 299 nm (20 240); IR: 3011 (s), 2960 (w), 2836 (w), 1512 (s), 1481 (s), 1255 (s), 1197 (s), 1160 (s), 1112 (m), 1041 (w); ^{1}H NMR, δ: 4.02 (s, 6H), 4.12 (s, 6H), 7.21 (s, 2H), 7.55 (s, 2H), 7.79 (s, 2H); ^{13}C NMR, δ: 55.9, 56.1, 102.8, 108.4, 124.3, 126.4, 128.3, 148.8, 149.3; MS, *m/e* (*I*): 298 (100), 283 (5), 255 (10), 240 (12), 225 (10), 212 (7), 169 (8), 139 (5), 126 (6). Exact Mass, calcd. for $C_{18}H_{18}O_4$: 298.1205; found: 298.1225.

2,3,5,6-Tetramethoxyphenanthrene (**10**a): 0.020 g, 7%, mp 98–100°C; UV (ethanol), $\lambda_{max}(\varepsilon)$: 261 nm (65 600), 312 nm (12 590); IR: 3010 (s), 2960 (w), 2839 (w), 1514 (s), 1472 (s), 1422 (w), 1268 (s), 1241 (s), 1137 (w), 1103 (s), 1050 (w); ^{1}H NMR, δ: 3.96 (s, 3H), 4.03 (s, 3H), 4.04 (s, 3H), 4.08 (s, 3H), 7.22 (s, 1H), 7.28 (d, 1H), 7.49 (d, 1H), 7.55 (d, 1H), 7.63 (d, ^{1}H), 9.22 (s, 1H); ^{13}C NMR, δ: 55.5, 56.3, 59.8, 107.8, 108.5, 112.2, 123.6, 124.0, 124.4, 124.7, 125.0, 127.6, 128.2, 145.9, 148.2, 148.5, 150.7; MS, *m/e* (*I*): 298 (100), 283 (25), 255 (20), 240 (30), 225 (15), 197 (20), 169 (10), 139 (13), 126 (18), 87 (8), 63 (8). Exact Mass, calcd. for $C_{18}H_{18}O_4$: 298.1205; found: 298.1225.

(b) Irradiation of trans-**1** *in THF*

A solution of *trans*-**1** (0.19 g, 0.63 mmol) and *n*-hexadecane (5.65 mg, 0.025 mmol) in dry tetrahydrofuran (5 mL) was placed in a Pyrex tube sealed with a rubber septum, oxygenated with a stream of dry oxygen for 10 min, and then irradiated for 4.5 h with 300 nm light (Rayonet reactor, 14 lamps, 27°C), with periodic bubbling of oxygen through the solution. GC analysis of the photolysis mixture indicated that the conversion of the starting material to products was ca. 80%. The photolysate consisted of a mixture of 3,4-dimethoxybenzaldehyde (**12**) (8%), *cis*-**1** (41%), **9***a* (11%), **10***a* (22%), and *trans*-**1** (17%), in order of increasing retention times. *cis*- and *trans*-**1** were found to be thermally stable under the gas chromatographic conditions employed. The identity of **12** was established by GC–MS and after chromatographic isolation from the mixture (vide infra).

After a total of 7.5 h of irradiation (resulting in a deep yellow solution), there was a further enrichment of the product mixture in **9***a*, **10***a*, and **12**, and a concomitant decrease in the concentration of **1**. At this point the material balance accounted for (by GC and GC–MS analyses) was only ca. 80%.

Two minor products were detected by GC–MS analysis after 4.5 h of irradiation; they were also present after 7.5 h of irradiation in higher concentrations (~3% of the total). Their GC retention times were similar to those of **9***a* and **10***a*. The two products exhibit the following GC–MS data, consistent with their having 1,2,6,7- and 2,3,6,7-phenanthrenetetrone structures: *m/e* (*I*): 238 (12), 221 (2), 167 (100), 151 (4), 139 (78), 124 (21), 108 (12), 95 (6), 77 (8), 71 (21), 65 (3), 51 (2); *m/e* (*I*): 238 (13), 220 (0.5), 167 (100), 151 (1), 139 (77), 124 (17), 108 (10), 95 (7), 77 (7), 71 (10), 65 (2), 51 (5).

The ^{1}H NMR spectrum of the crude photolysis mixture (7.5 h irradiation) revealed the presence of unaccounted-for resonances in the δ3.5–4.5 range; with the assumption that these are due to the cyclobutane ring protons of photodimers, integration indicated that they accounted for ca. 15% of the total material.

The solvent was distilled under vacuum, and the yellow oil that remained was chromatographed on the Chromatatron using a 2 mm silica gel plate. Elution with 10% ethyl acetate – hexane afforded **10***a* (0.063 g, 33%), *cis*-**1** (0.013 g, 7%), *trans*-**1** (0.007 g, 4%), **9***a* (0.038 g, 20%). Further elution with 35% ethyl acetate – hexane afforded two additional compounds. 3,4-Dimethoxybenzaldehyde (**12**, 0.004 g, 2%) was identified by comparison to an authentic sample, while cyclobutane dimer **6** was identified on the basis of the following.

cis,trans,trans-*1,2,3,4-Tetra(3,4-dimethoxyphenyl)cyclobutane* (**6**): 0.057 g, 30%. ^{1}H NMR, δ: 3.63 (s, 6H), 3.78 (s, 6H), 4.27 (s, 2H), 6.49 (s, 1H), 6.50 (s, 1H), 6.65–6.90 (cplx m, 4H); ^{13}C NMR, δ: 47.54, 55.81, 55.97, 110.82, 112.09, 118.88, 120.04, 133.64, 147.36; MS, *m/z* (*I*): 601 (1), 300 (100), 285 (9), 151 (5); MS (NH_3 CI), *m/z* (*I*): 618 (100), 301 (45), 300 (54).

(c) Irradiation of trans-**1** *in the presence of 2,6-di*-tert-*butylphenol*

A solution of *trans*-**1** (0.243 g, 0.81 mmol), *n*-hexadecane (16.9 mg, 0.0747 mmol), and 2,6-di-*tert*-butylphenol (0.186 mg, 0.901 mmol) in dry tetrahydrofuran (15.0 mL) was placed in a 20.0 mL Pyrex container, sealed with a rubber septum, oxygenated with a stream of dry oxygen for 10 min, and then irradiated for 6 h with 300 nm light (Rayonet reactor, 12 lamps, 27°C). The reaction was monitored by GC–MS and TLC at 1 h intervals. Compounds *cis*-**1**, **9***a*, **10***a*, and **12** were formed in similar relative yields to those in irradiations in the absence of the phenol at irradiation times of less than 6 h. The yield of **12** was reduced substantially, however, at long irradiation times. Two new minor products, of GC retention times similar to those of **9***a* and **10***a*, were detected in the mixture after short irradiation times. These were tentatively identified on the basis of GC–MS as 5,6-dimethoxyphenanthrene-2,3-dione (*m/z* (*I*): 268 (100), 253 (81), 238 (3), 225 (31), 210 (90), 195 (11), 182 (1), 167 (47), 152 (8), 151 (9), 139 (33), 113 (5), 63 (5)) and 6,7-dimethoxyphenanthrene-2,3-dione (*m/z* (*I*): 268 (100), 253 (21), 225 (33), 210 (41), 195 (7), 182 (36), 167 (6), 152 (14), 139 (38), 75 (2), 63 (1)).

After 5 h of continuous irradiation the mixture showed an intense yellow color. The solvent was distilled under vacuum, and the yellow oil that remained was chromatographed on the Chromatotron using a 2 mm silica gel plate. Elution with 10% ethyl acetate – hexane allowed isolation of **10***a* (0.048 g,

20%), *cis*-**1** (0.041 g, 17%), *trans*-**1** (0.036 g, 15%), and **9***a* (0.029 g, 12%). Continued gradient elution to 30% ethyl acetate afforded **12** (0.024 g, 10%) and two new compounds (0.024 g, 5% each). The FT-IR spectrum of these compounds (CCl_4) showed the presence of carbonyl absorptions in the 1650–1710 cm^{-1} range, but their GC retention times did not match those of the two minor products observed in the crude reaction mixture (vide supra). Continued gradient elution to 50% ethyl acetate afforded **6** (0.007 g, 3%) and a third minor component (0.007 g, 3%) that is presumably an isomer of **6**.

(ii) From irradiation of trans-***3***

(a) Irradiation of trans-***3*** *in 95% ethanol*

A continuously oxygenated solution of *trans*-**3** (1.0 g, 2.5 mmol) in 95% ethanol (500 mL) was irradiated under similar conditions to those described above for *trans*-**1**. A single product, subsequently identified as *cis*-**3** (vide infra), was observed by GC analysis during the first 30 min of photolysis. Continued irradiation resulted in the slower formation of four other compounds that eluted between *cis*- and *trans*-**3** under the GC conditions employed (order of elution: *cis*-**3** < **5** < **11***c* = **10***c* < **9***c* < *trans*-**3**), and the development of a dark yellow colour. The irradiation was stopped after 1 h (ca. 75% conversion of *trans*-**3**), and the solvent was removed on the rotary evaporator to yield a brown oil. The mixture was chromatographed on the Chromatotron using a 4 mm silica gel thick-layer plate that was first deactivated with triethylamine, using an ethyl acetate – hexane gradient (1–8% ethyl acetate). The products eluted in the order **10***c* < *cis*-**3** < **11***c* < **9***c* < **5** < *trans*-**3**. Compounds *cis*-**3** and **10***c* were isolated in pure forms as a colourless oil and a crystalline solid, respectively. Compounds **9***c* and **11***c* initially eluted together, but could be separated with subsequent passes through the plate. Compound **9***c* was obtained as a colourless solid after recrystallization from ethyl acetate – hexane. Compound **11***c* was obtained as a pale yellow, low-melting solid that resisted further attempts at purification by either chromatography or recrystallization. Compound **5** was obtained as a colourless solid after two recrystallizations from hexane. Isolated chemical yields and spectroscopic properties of these materials are listed below. The material balance was typically less than 50% from photolyses in ethanol solution.

cis-*4*–tert-*Butyldimethylsiloxy-3,3′,4′-trimethoxystilbene (*cis-***3***)*: 0.112 g, 0.28 mmol, 11%; mp 53–55°C. UV (ethanol), $\lambda_{max}(\varepsilon)$: 201 nm (52 400), 281 nm (13 900); IR: 3001 (m), 2954 (s), 2932 (s), 2857 (s), 1509 (s), 1465 (s), 1289 (s), 1128 (s), 1031 (s), 899 (s), 839 (s); ^{1}H NMR, δ: 0.11 (s, 6H), 0.97 (s, 9H), 3.60 (s, 3H), 3.63 (s, 3H), 3.84 (s, 3H), 6.43 (s, 2H), 6.75 (m, 6H); ^{13}C NMR, δ: −4.7, 18.5, 25.7, 55.3, 55.5, 55.8, 110.8, 111.7, 112.6, 120.6, 121.8, 128.6, 128.9, 130.2, 131.1, 144.2, 148.1, 148.3, 150.5; MS, *m/e* (*I*): 400 (40), 343 (25), 328 (100), 253 (4), 209 (7),149 (7), 73 (8). Exact Mass, calcd. for $C_{23}H_{32}SiO_4$: 400.2070; found: 400.2069.

*1(2)-Ethoxy-1-(3-(*tert-*butyldimethylsiloxy)-4-methoxyphenyl)-2-(3,4-dimethoxyphenyl)ethane (***5***)*: 0.070 g, 0.16 mmol, 6%, mixture of regioisomers. *Major isomer* (67%): ^{1}H NMR, δ: 0.10 (s, 6H), 0.96 (s, 9H), 1.13 (t, 3H), 2.76 (quint, 1H), 3.04 (dd, 1H), 3.34 (m, 2H), 3.76 (s, 3H), 3.82 (s, 3H), 3.84 (s, 3H), 4.27 (m, 1H), 6.65 (cplx m, 6H); ^{13}C NMR, δ: −4.57, 15.34, 18.47, 25.72, 44.57, 55.35, 55.85, 55.94, 64.11, 83.32, 109.45, 110.61, 113.73, 119.27, 120.34, 121.66, 132.07, 134.97, 143.22, 148.26, 148.93, 150.30. *Minor isomer* (33%): ^{1}H NMR, δ: 0.13 (s, 6H), 0.97 (s, 9H), 1.13 (t, 3H), 2.76 (quint, 1H), 3.04 (dd, 1H), 3.34 (m, 2H), 3.66 (s, 6H), 3.73 (s, 3H), 4.27 (m, 1H), 6.65 (m, 6H). *Mixture*: UV (ethanol) $\lambda_{max}(\varepsilon$: 202 nm (50 900), 286 nm (11 100), 332 nm (19 260); IR (mixture): 3001 (m), 2954 (s), 2932 (s), 2857 (s), 1509 (s), 1465 (s), 1289 (s), 1128 (s), 1031 (s), 899 (s), 839 (s); MS, *m/e* (*I*): 446 (3), 400 (45), 389 (15), 343 (26), 328 (100), 313 (7), 295 (57).

*6-(*tert-*Butyldimethylsiloxy)-2,3,5-trimethoxyphenanthrene (***11***c)*: 0.057 g, 0.14 mmol, 6%; mp 51–53°C; UV (ethanol), $\lambda_{max}(\varepsilon)$: 201 nm (62 800), 260 nm (72 560); IR: 3030 (s), 2959 (m), 2933 (m), 1514 (s), 1470 (s), 1423 (m), 1265 (s), 1239 (s), 1085 (s), 838 (s); ^{1}H NMR (300 MHz), δ: 0.27 (s, 6H), 1.09 (s, 9H), 3.92 (s, 3H), 4.02 (s, 3H), 4.10 (s, 3H), 7.16 (m, 2H), 7.52 (m, 3H), 9.20 (s, 1H); ^{13}C NMR, δ: −4.4, −0.3, 18.3, 25.8, 55.7, 55.8, 59.3, 107.9, 108.7, 120.5, 124.0, 124.6, 124.8, 125.3, 128.3, 128.4, 128.7, 147.3, 148.2, 148.4, 148.6; MS, *m/e* (*I*): 398 (20), 326 (100), 163 (10), 73 (12), 57 (6). Exact Mass, calcd. for $C_{23}H_{30}SiO_4$: 398.1914; found: 398.1910.

*3-(*tert-*Butyldimethylsiloxy)-2,5,6-trimethoxyphenanthrene (***10***c)*: 0.11 g, 0.28 mmol, 11%; mp 95–97°C; UV (ethanol), $\lambda_{max}(\varepsilon)$: 202 nm (17 900), 261 nm (38 400); IR: 3030 (s), 2959 (m), 2934 (m), 1599 (m), 1512 (s), 1469 (s), 1275 (s), 1247 (s), 1103 (s), 1049 (m); ^{1}H NMR (300 MHz), δ: 0.25 (s, 6H), 1.07 (s, 9H), 3.94 (s, 6H), 4.0 (s, 3H), 7.21 (m, 2H), 7.50 (m, 3H), 9.15 (s, 1H); ^{13}C NMR, δ: −4.6, −0.5, 18.5, 25.8, 55.3, 56.4, 59.8, 108.6, 112.2, 118.8, 123.9, 124.3, 124.8, 125.3, 127.7, 129.2, 144.7, 146.3, 150.9, 151.0; MS, *m/e* (*I*): 398 (25), 341 (22), 326 (100), 311 (15), 268 (15), 163 (8), 134 (7), 89 (7), 73 (12), 57 (10). Exact Mass, calcd. for $C_{23}H_{30}SiO_4$: 398.1914; found: 398.1910.

*3-(*tert-*Butyldimethylsiloxy)-2,6,7-trimethoxyphenanthrene (***9***c)*: 0.083 g, 0.21 mmol, 8%; mp 95.0–96.8°C; UV (ethanol), $\lambda_{max}(\varepsilon)$: 255 nm (90 600), 286 nm (38 700); IR: 3030 (s), 2958 (m), 2934 (m), 1509 (s), 1478 (s), 1434 (m), 1272 (s), 1197 (s), 903 (s), 866 (m), 811 (m); ^{1}H NMR (300 MHz), δ: 0.23 (s, 6H), 1.06 (s, 9H), 3.94 (s, 3H), 4.02 (s, 3H), 4.09 (s, 3H), 7.18 (s, 2H), 7.52 (s, 2H), 7.76 (s, 1H), 7.88 (s, 1H); ^{13}C NMR, δ: −4.5, −4.4, −0.01, 0.30, 18.6, 25.8, 55.3, 55.8, 55.9, 103.0, 108.3, 108.7, 112.8, 124.2, 124.6, 126.2, 127.2, 145.3, 148.7, 149.2; MS, *m/e* (*I*): 398 (23), 341 (20), 326 (100), 240 (4), 163 (12), 73 (5). Exact Mass, calcd. for $C_{23}H_{30}SiO_4$: 398.1914; found: 398.1915.

GC analysis of exhaustively irradiated solutions of **3** in oxygenated THF indicate the primary relative phenanthrene yields to be similar to those obtained in ethanol solution. However, irradiation in THF allows isolation of **9***c*–**11***c* in significantly higher chemical yields than are obtained from irradiations in ethanol.

(b) Irradiation of trans-***3*** *in THF*

A solution of *trans*-**3** (1 g, 2.5 mmol) in dry tetrahydrofuran (15.0 mL) was oxygenated with a stream of dry oxygen for 10 min and then irradiated with 300 nm light (Rayonet reactor, 12 lamps, 27°C). The reaction was not monitored, but instead was stopped after 12 h of continuous irradiation. A deep orange

solution was obtained. The solvent from the reaction mixture was evaporated and the remaining dark orange oil was chromatographed using a 2-mm-thick Chromatotron plate that had previously been treated with triethylamine (5 drops in 600 mL of eluent). The less polar fractions (that eluted with 10:90 ethyl acetate:hexanes, containing **9***c*-**11***c*, *cis*-**3** and *trans*-**3**) represented 50% of the photolyzed material.

Continued gradient elution to 35% ethyl acetate afforded four additional fractions, the first and fourth of which consisted of single components. They were identified as the following on the basis of spectral data.

trans-*1,2-Bis(3,4-dimethoxyphenyl)*-cis,trans-*3,4-bis(4*-tert-*butyldimethylsiloxy-3-methoxyphenyl)-cyclobutane (***7***a)*: first fraction (oil), 0.201 g, 20%; ^{1}H NMR, δ: 0.055 (s, 6H), 0.93 (s, 9H), 3.54 (s, 3H), 3.64 (s, 3H), 3.76 (s, 3H), 4.25 (br s, 2H), 6.45 (d, 1H, *J* = 1.83 Hz), 6.52 (d, 1H, *J* = 1.97 Hz), 6.62 (dd, 1H, *J* = 1.87 Hz, *J* = 8.15 Hz), 6.65 (d, 2H, *J* = 8.10 Hz), 6.68 (dd, 1H, *J* = 2.0 Hz, *J* = 8.28 Hz); ^{13}C NMR (125.8 MHz), δ: −4.80, 18.31, 25.62, 47.31, 47.39, 55.34, 55.45, 55.63, 110.31, 112.00, 112.76, 119.92, 120.13, 120.18, 133.67, 134.45, 143.11, 147.16, 148.37, 150.23; MS, *m/z* (*I*): 550 (12), 501 (10), 400 (100), 354 (10), 328 (71), 300 (7), 284 (7), 151 (7); MS (NH_3 CI), *m/z* (*I*): 818 (38), 568 (20), 502 (11), 401 (100), 301 (21), 151 (15).

cis-*1,3-Bis(3,4-dimethoxyphenyl)*-trans,trans-*2,4-bis(4*-tert-*butyldimethylsiloxy-3-methoxyphenyl)-cyclobutane (***8***a)*: 4th fraction (oil), 0.191 g, 19%; ^{1}H NMR, δ: 0.073 (s, 6H), 0.96 (s, 9H), 3.55 (s, 3H), 3.63 (s, 3H), 3.78 (s, 3H), 4.23 (s, 1H), 4.24 (s, 1H), 6.46 (d, 1H, J = 1.99 Hz), 6.50 (d, 1H, *J* = 1.91 Hz), 6.59 (dd, 1H, *J* = 1.99 Hz, *J* = 8.13 Hz), 6.63 (d, 1H, *J* = 8.08 Hz), 6.67 (d, 1H, *J* = 8.28 Hz), 6.71 (dd, 1H, *J* = 1.99 Hz, *J* = 8.25 Hz); ^{13}C NMR, δ: −4.73, 18.36, 25.68, 47.38, 47.58, 55.39, 55.71, 55.76, 110.71, 112.79, 112.03,, 120.14, 120.10, 133.76, 134.44, 143.16, 147.23, 148.45, 150.35; MS, *m/z* (*I*): 501 (3), 400 (100), 343 (22), 328 (57), 310 (3), 286 (12), 195 (10), 73 (8); MS (NH3 CI), *m/z* (*I*): 818 (100), 569 (8), 464 (5), 402 (76), 328 (20).

The second fraction consisted of a mixture of two carbonylic compounds, which were tentatively identified as stilbenequinones on the basis of ^{1}H and ^{13}C NMR spectroscopy of the mixture, but they could not be rigorously identified. The third fraction consisted of a mixture of **12** and dimer **8***a*.

(iii) From irradiation of trans-*2*

(a) Irradiation of trans-*2 in 95% ethanol*

An oxygenated solution of *trans*-**2** (0.50 g, 1.7 mmol) in 95% ethanol (500 mL) was irradiated under similar conditions to those described above. GC and GC–MS analysis of the crude mixture after 15 min irradiation revealed the presence of a single product that was identified as *cis*-**2** (vide infra). Continued irradiation (30 min total) resulted in the solution turning yellow, and GC analysis indicated there to be substantial loss of volatile material with only a slight apparent increase in the yield of *cis*-**2** relative to the amount of *trans*-**2** present. The solvent was distilled from the reaction mixture under vacuum, yielding a dark yellow oily solid (0.49 g). ^{1}H NMR analysis of the crude photolysate indicated a *cis*-**2**/*trans*-**2** ratio of ca. 3:1.

The reaction mixture was chromatographed on a 4 mm silica gel thick-layer plate and eluted with dichloromethane. This allowed recovery of 0.013 g of *trans*-**2**, the first compound to elute. The second fraction consisted of *cis*-**2** (0.018 g) contaminated with a small amount of the *trans* isomer, as determined by ^{1}H NMR spectroscopy. GC analysis of this mixture indicated it to consist of *cis*-**2** and *trans*-**2** in a ~1:1 ratio, but lowering the injector temperature resulted in correspondingly higher amounts of the *cis* isomer in the mixture. ^{1}H NMR analysis of the mixture after storage for 24 h in the dark at room temperature indicated complete thermal isomerization to the *cis* isomer. The remaining material consisted of two dimeric products and **12**; these were isolated from the photolysis of *trans*-**2** in THF (vide infra).

cis-*4-Hydroxy-3,3′,4′-trimethoxystilbene (*cis-***2***)*: mp 131.9–132.3°C; UV (ethanol), $\lambda_{max}(\varepsilon)$: 200 nm (26 150), 303 nm (9780); GC/FTIR: 3564 (br m), 2983 (s), 2939 (m), 1724 (s), 1384 (s), 1325 (m), 1186 (s), 1143 (m), 957 (w), 919 (w); ^{1}H NMR (300 MHz), δ: 3.68 (s, 3H), 3.69 (s, 3H), 3.87 (s, 3H), 5.57 (s, 1H), 6.45 (s, 2H), 6.80 (m, 6H); ^{13}C NMR (AM500), δ: 55.80, 55.82, 55.89, 108.01, 108.56, 111.24, 114.48, 119.43, 120.11, 126.27, 149.08; MS, *m/e* (*I*): 286 (100), 271 (13), 211 (6), 168 (5), 165 (4), 143 (8), 77 (7), 45 (38). Exact Mass, calcd. for $C_{17}H_{18}O_4$: 286.1205; found: 286.1208.

Extended photolysis of **2** in oxygenated ethanol solution resulted in substantial loss of volatile material, the appearance of small amounts of three new products, and the development of a deep orange-brown colour. Attempts to isolate the three new products by thick-layer chromatography were unsuccessful.

Phenanthrenes **9***b*–**11***b* were prepared by desilylation of the corresponding *tert*-butyldimethylsiloxy compound **9***c*–**11***c*. For example, **9***c* (0.05 g, 0.18 mmol), tetra-*n*-butylammonium fluoride (0.066 g, 0.25 mmol), and tetrahydrofuran (0.25 mL) were placed in a 5 mL round-bottom flask and stirred at room temperature for 30 min, with periodic monitoring of the progress of reaction by thin-layer chromatography (silica gel, 15% ethyl acetate in hexane). The solvent was removed under vacuum, saturated aqueous ammonium chloride (5 mL) was added, and the mixture was extracted with anhydrous ether. The combined ether extracts were dried over anhydrous magnesium sulfate, filtered, and stripped of solvent on the rotary evaporator. The resulting yellow oil was chromatographed on a silica gel column, eluting with hexane (~100 mL) to remove unreacted starting material and other silicon-containing compounds, and then a 25% ethyl acetate – hexane mixture. Compound **9***b* was obtained as a colourless solid (0.033 g, 0.16 mmol, 93%) and recrystallized from ethyl acetate – hexanes and ethyl acetate. GC coinjection with crude mixtures from photolysis of **2** verified its presence in the photolysate. A similar procedure was employed for the synthesis of **10***b* and **11***b* from **10***c* and **11***c*, respectively.

*6-Hydroxy-2,3,7-trimethoxyphenanthrene (***9***b)*: mp 155–158°C; UV (ethanol), $\lambda_{max}(\varepsilon)$: 254 (65 800), 286 nm (29 470); IR: 3542 (m), 3030 (s), 1512 (s), 1480 (s), 1436 (m), 1266 (m), 1197 (s), 1159 (s), 1111 (m), 1041 (m), 864 (m); ^{1}H NMR, δ: 4.01 (s, 3H), 4.03 (s, 3H), 4.08 (s, 3H), 5.90 (s, 1H), 7.19 (s, 2H), 7.51 (s, 2H), 7.79 (s, 1H), 7.96 (s, 1H); ^{13}C NMR, δ: 55.90, 55.96, 103.10, 105.99, 107.65, 108.17, 123.96, 124.32,

124.36, 125.14, 126.10, 126.35, 145.60, 146.39, 148.81, 149.18; MS, *m/e* (*I*): 284 (100), 269 (13), 241 (14), 198 (8), 142 (12). Exact Mass, calcd. for $C_{17}H_{16}O_4$: 284.1048; found: 284.1047.

6-Hydroxy-2,3,5-trimethoxyphenanthrene (***11***b): mp 157.3–159.1°C; UV (THF) $\lambda_{max}(\varepsilon)$: 274 nm (20 180), 260 (25 600); IR (KBr): 3363 (br), 1601 (s), 1513 (s), 1474 (s), 1423 (s), 1370 (m), 1254 (s), 1154 (s), 1076 (s), 1042 (s), 860 (s), 779 (s); ^{1}H NMR, δ: 3.81 (s, 3H), 3.96 (s, 3H), 4.00 (s, 3H), 6.05 (br s, 1H), 7.14 (s, 1H), 7.18 (d, 2H, J = 3.8 Hz), 7.20 (s, 1H), 7.46 (m, 2H), 8.82 (s, 1H); ^{13}C NMR, δ: 55.76, 55.83, 60.29, 107.79, 108.06, 115.44, 122.12, 122.87, 124.08, 125.58, 125.94, 127.56, 128.49, 143.01, 147.69, 148.64, 148.94. MS, *m/z* (*I*): 284 (100), 269 (22), 241 (19), 226 (16), 198 (10), 181 (7), 142 (20), 121 (5), 71 (13), 57 (16). Exact Mass, calcd. for $C_{17}H_{16}O_4$: 284.1048; found: 284.1052.

3-Hydroxy-2,5,6-trimethoxyphenanthrene (***10***b): mp 147.4–149.6°C; UV (THF), $\lambda_{max}(\varepsilon)$: 255 nm (88 000), 287 nm (37 500), 301 (21 000); IR (KBr): 3416 (br), 1516 (s), 1474 (s), 1456 (m), 1427 (m), 1370 (m), 1270 (s), 1101 (s), 1053 (m), 818 (m); ^{1}H NMR, δ: 3.90 (s, 3H), 3.95 (s, 3H), 3.98 (s, 3H), 5.74 (br s, 1H), 7.13 (s, 1H), 7.20 (d, 1H, J = 8.7 Hz), 7.39 (d, 1H, J = 8.8 Hz), 7.43 (d, 1H, J = 8.7 Hz), 7.52 (d, 1H, J = 8.7 Hz), 9.09 (s, 1H); ^{13}C NMR, δ: 55.82, 56.68, 59.79, 107.63, 112.27, 112.78, 124.38, 124.54, 124.68, 124.81, 125.03, 127.99, 128.21, 145.07, 146.54, 146.71, 151.16; MS, *m/z* (*I*): 284 (100), 269 (59), 241 (11), 226 (8), 181 (9), 155 (10), 139 (9), 126 (7), 84 (14). Exact Mass, calcd. for $C_{17}H_{16}O_4$: 284.1048; found: 284.1049.

(b) Irradiation in THF

A solution of *trans*-**2** (0.261 g, 0.91 mmol) and *n*-hexadecane (0.169 g, 0.075 mmol) in dry tetrahydrofuran (15.0 mL) was oxygenated with a stream of dry oxygen for 10 min and then irradiated with 300 nm light (Rayonet reactor, 12 lamps, 27°C). The reaction was monitored by GC–MS analysis for 8 h at 1 h intervals. The formation of **9***b*, **10***b*, **11***b*, and **12** was observed to proceed linearly as a function of irradiation time.

After 5 h of irradiation, the solution had turned light yellow; GC analysis of the product mixture indicated it to consist of **12** (14%), **9***b* (19%), *trans*-**2** (12%), and **10***b*+**11***b* (12%). After 8 h of irradiation, the presence of other volatile minor products in the photolysate accounted for 8% of the mixture, as determined by GC–MS analysis. The retention times and mass spectral data of two of these products (ca. 4% each) coincide with those found for the two phenanthrenetetrones detected in the photolysis of *trans*-**1** (vide supra).

The solvent was distilled from the photolysate under vacuum, and the dark orange oil that remained was chromatographed on the Chromatotron using a 2 mm silica gel plate and gradient elution with ethyl acetate – hexane. Compounds *cis*-**2** and *trans*-**2**, **9***b*–**11***b*, and **12** were isolated, as well as one other fraction that contained a mixture of two dimeric compounds. This was followed by a fraction containing a single component, which was tentatively identified as cyclobutane dimer **8***b* on the basis of ^{1}H NMR and MS evidence.

cis-*1,3-Bis(3,4-dimethoxyphenyl)*-trans,trans-*2,4-bis(4-hydroxy-3-methoxyphenyl)-cyclobutane* (***8***a): 4th fraction (oil), 0.191 g, 19%; ^{1}H NMR, δ: 3.64 (s, 6H), 3.74 (s, 3H), 4.69 (s, 2H), 6.36 (s, 1H), 6.37 (s, 1H), 6.71 (cplx m, 4H); MS, *m/e* (*I*): 571 (1), 501 (1), 400 (51), 328 (60), 288 (39), 286 (51), 195 (100), 152 (31), 73 (29).

Irradiation of phenanthrene 10*a* under various conditions

A solution of **10***a* (2.1 mg, 0.007 mmol) in THF (0.5 mL) was placed in a Pyrex tube, sealed with a rubber septum, oxygenated with a stream of dry oxygen for 10 min, and then irradiated for 7 h with 300 nm light (Rayonet reactor, 12 lamps, 25°C), with monitoring of the photolysate at 1 h intervals by GC–MS. After 7 h of irradiation, only a single minor photoproduct could be detected (0.5 %, shorter retention time than **10***a*, M^+ = 330), in addition to remaining **10***a*.

A solution of **10***a* (10.1 mg, 0.034 mmol), *trans*-**1** (2 mg, 0.0066 mmol), and *n*-hexadecane (0.068 mg, 0.0003 mmol) in dry THF (0.5 mL) was placed in a quartz NMR tube, sealed with a rubber septum, and oxygenated with a stream of dry oxygen for 10 min. The solution was irradiated with 254 nm light ($[\varepsilon_6/\varepsilon_{trans\text{-}1}]_{254\ nm}$ = 55), and monitored at 20 min intervals by GC–MS. Compounds *cis*-**1**, **9***a*, and **12** were observed to form in similar relative yields to those produced upon irradiation of *trans*-**1** under similar conditions (vide infra). No new products could be detected in significant yields after photolysis to 50% (total) conversion of **1**.

Photostationary state and quantum yield determinations

Quantum yields were determined using an electronic actinometry system similar to that reported by Leigh and Arnold (38), using 300 nm light from a 100 W xenon lamp attached to a high-intensity monochromator. A Corning CS 7-54 glass filter was employed to remove the higher order spectral lines. The system was calibrated prior to each experiment by ferrioxalate actinometry. Solutions were contained in round Suprasil UV cells (1.0 × 2.54 cm) that were sealed with rubber septa. The samples were deoxygenated with a stream of nitrogen or oxygen for 15 min prior to photolysis, and stirred throughout using a 6 mm Teflon-coated magnetic stirrer. Product formation was followed by GC relative to *n*-eicosane as an internal standard. Relative FID response factors were determined for both *trans*- and *cis*-**1** by construction of working curves. Product yields were determined from plots of product concentration vs. accumulated photon counts. Quantum yields for the formation of **4** (in ethanol) and phenanthrenes **9***a* and **10***a* (in O_2-saturated solution) were estimated from runs ca. 10 times longer than those employed for the determination of quantum yields for *cis,trans* isomerization. The linearity of the system over these longer time scales was not, however, verified.

For photostationary state determinations, 10^{-3} M solutions of *cis*- and *trans*-**1** were purged for 15 min with a stream of nitrogen, and irradiated alternately in the system described above, with periodic monitoring of the course of reaction by GC. The irradiation was continued until the ratios of *cis*-**1**/*trans*-**1** in the two solutions achieved a common value (*cis*-**1**/*trans*-**1** = 1.38 ± 0.07).

Steady state fluorescence quenching experiments

Fluorescence spectra were recorded using ~5×10^{-6} M solutions of the stilbenes or phenanthrenes in dry THF containing various amounts of absolute ethanol, TFE, or HFIP, in 1 × 1

cm Suprasil quartz cuvettes that were sealed with rubber septums. The solutions were deoxygenated prior to recording the spectra by bubbling with a stream of dry nitrogen for a constant period of time. A fresh solution was employed for each spectrum recorded, and fluorescence intensities were estimated from the integrated emission spectra. For oxygen-quenching experiments, aliquots of standard solutions of *trans*-**1** and *trans*-**2** were placed in 10 mL volumetric flasks, and then premixed nitrogen–oxygen mixtures were bubbled through the solutions, topping the flasks up to the mark with fresh solvent when evaporation resulted in some loss. The compositions of the gas mixtures were controlled with a Matheson 73510-600 gas proportioner. Oxygen concentrations were calculated using a value of 0.0101 M for the concentration of oxygen in oxygen-saturated THF at 25°C (39).

Acknowledgments

We wish to thank Dr. D. Hughes for assistance with high-field NMR spectra, the McMaster Regional Centre for Mass Spectrometry for high-resolution mass spectra and Exact Mass determinations, and P. Palermo for technical assistance. The financial support of the Natural Sciences and Engineering Research Council (NSERC) National Centres of Excellence in Mechanical and Chemimechanical Wood Pulps is also gratefully acknowledged.

References

1. C. Heitner. *In* Photochemistry of lignocellulosic materials. ACS Symp. Ser. 531. *Edited by* C. Heitner and J.C. Scaiano. American Chemical Society, Washington. 1993. p. 1.
2. J.A. Schmidt, A.B. Berinstain, F. De Rege, C. Heitner, L.J. Johnston, and J.C. Scaiano. Can. J. Chem. **69**, 104 (1991).
3. N. Fukagawa and A. Ishizu. J. Wood Chem. Technol. **11**, 263 (1991).
4. J.A. Schmidt and C. Heitner. J. Wood Chem. Technol. **11**, 397 (1991).
5. J.C. Scaiano, J.C. Netto-Ferreira, and V. Wintgens. J. Photochem. Photobiol. A: **59**, 265 (1991).
6. J.K.S. Wan, M.Y. Tse, and M.C. Depew. Res. Chem. Intermed. **17**, 59 (1992).
7. B.J. Zhao, M.C. Depew, N.A. Weir, and J.K.S. Wan. Res. Chem. Intermed. **19**, 449 (1993).
8. A. Castellan, N. Colombo, A. Nourmamode, J.H. Zhu, D. Lachenal, R.S. Davidson, and L. Dunn. J. Wood Chem. Technol. **10**, 461 (1990).
9. L. Zhang and G. Gellerstedt. Proc. 7th Int. Symp. Wood and Pulping Chem. Beijing, 759 (1993).
10. G. Gellerstedt and L. Zhang. *In* Photochemistry of lignocellulosic materials. ACS Symp. Ser. 531. *Edited by* C. Heitner and J.C. Scaiano. American Chemical Society, Washington. 1993. p. 129.
11. F.B. Mallory and C.W. Mallory. Org. React. **30**, 1 (1984).
12. W.H. Laarhoven. Org. Photochem. **10**, 163 (1989).
13. H. Gorner and H.J. Kuhn. Adv. Photochem. **19**, 1 (1995).
14. G. Kaupp. *In* CRC handbook of organic photochemistry and photobiology. *Edited by* W.M. Horspool and P.-S. Song. CRC Press, Inc., Boca Raton, Fla. 1995. p. 50.
15. H. Shechter, W.J. Link, and G.V.D. Tiers. J. Am. Chem. Soc. **85**, 1601 (1963).
16. T. Wolff, F. Schmidt, and P. Volz. J. Org. Chem. **57**, 4255 (1992).
17. R.L. Graham and K.F. Freed. J. Chem. Phys. **96**, 1304 (1992).
18. Y. Ito, T. Kajita, K. Kunimoto, and T. Matsuura. J. Org. Chem. **54**, 587 (1989).
19. J.H. Zhu and D.G. Gray. J. Photochem. Photobiol. A: **87**, 267 (1995).
20. I.B. Berlman. Handbook of fluorescence spectra of aromatic molecules. Academic Press, London. 1965.
21. K.A. Muszkat. Top. Curr. Chem. **88**, 89 (1980).
22. P. Wan, S. Culshaw, and K. Yates. J. Am. Chem. Soc. **104**, 2509 (1982).
23. J. McEwen and K. Yates. J. Phys. Org. Chem. **4**, 193 (1991).
24. S.S. Hixson. Tetrahedron Lett. 277 (1973).
25. R.A. McClelland, V.M. Kanagasabapathy, and S. Steenken. J. Am. Chem. Soc. **110**, 6913 (1988).
26. R.A. McClelland, F. Cozens, and S. Steenken. Tetrahedron Lett. 31, 2821 (1990).
27. R.A. McClelland, C. Chan, F. Cozens, A. Modro, and S. Steenken. Angew. Chem. Int. Ed. Engl. **30**, 1337 (1991).
28. W.J. Leigh and J.A. Postigo. Can. J. Chem. **73**, 191 (1995).
29. J. Eriksen, C.S. Foote, and T.L. Parker. J. Am. Chem. Soc. **99**, 6455 (1977).
30. L.T. Spada and C.S. Foote. J. Am. Chem. Soc. **102**, 391 (1980).
31. K. Gollnick and A. Schnatterer. Photochem. Photobiol. **43**, 365 (1986).
32. J. Koo and G.B. Schuster. J. Am. Chem. Soc. **99**, 5403 (1977).
33. G.P. Kirschenheuter and G.W. Griffin. J. Chem. Soc. Chem. Commun. 596 (1983).
34. M. Kojima, H. Sakuragi, and K. Tokumaru. Tetrahedron Lett. **22**, 2889 (1981).
35. K. Onodera, G.-I. Furusawa, M. Kojima, M. Tsuchiya, S. Aihara, R. Akaba, H. Sakuragi, and K. Tokumaru. Tetrahedron, **41**, 2215 (1985).
36. C.K. Mann and K.K. Barnes. Electrochemical reactions in nonaqueous systems. Marcel Dekker, Inc., New York. 1970. p. 201.
37. V. Wintgens. *In* CRC handbook of organic photochemistry. Vol. 1. *Edited by* J.C. Scaiano. CRC Press, Boca Raton, Fla. 1989. p. 405.
38. W.J. Leigh and D.R. Arnold. Can. J. Chem. **59**, 3061 (1981).
39. R. Battino, T.R. Rettich, and T. Tominaga. J. Phys. Chem. Ref. Data, **12**, 163 (1983).

Chromatographie à contre courant et micelles inverses pour la séparation et l'extraction de cations métalliques[1]

Alain Berthod, Jun Xiang, Serge Alex et Colette Gonnet-Collet

Résumé : La chromatographie à contre courant (CCC) est une technique de séparation dans laquelle la phase stationnaire est un liquide. L'acide diéthylhexyl phosphorique (DEHPA) est capable de former des micelles inverses dans l'heptane. Des cations métalliques localisés dans une phase aqueuse peuvent passer dans la phase heptane par complexation–extraction dans le centre des micelles inverses de DEHPA. Un appareil CCC peut être considéré comme un puissant mélangeur et extracteur avec une efficacité de plusieurs centaines de plateaux. L'association de la technique CCC avec l'extraction par micelles inverses à permis de séparer les ions métalliques La^{3+}, Ce^{3+}, Pr^{3+} et Nd^{3+}. L'utilisation de phases mobiles à différents pH a permis de déterminer les constantes d'extraction et les coefficients de séparation de chaque ion. Les conditions de surcharge sont soulignées. Avec des solutions d'ions Co^{2+} et Ni^{2+}, l'utilisation de l'appareil CCC en mode dit chromatographie frontale a permis de concentrer une quantité maximale d'ion Co^{2+} dans la phase stationnaire heptane + DEHPA. Une partie de la solution a été désionisée, une autre partie ne contenait plus que des ions Ni^{2+}. La méthode permet également de déterminer les constantes d'extraction et les coefficients de séparation. L'utilisation de la technique CCC avec une phase stationnaire extractrice peut être généralisée en tant que filtre à ions pour extraire, concentrer des cations dans un faible volume de phase organique ou pour désioniser des phases aqueuses.

Mots clés : chromatographie à contre courant, CCC; filtration d'ions, extraction d'ions, désionisation, lanthanides, métaux de transition.

Abstract: Countercurrent chromatography (CCC) is a separation technique in which the stationary phase is a liquid. Diethylhexyl phosphoric acid (DEHPA) forms reverse micelles in heptane. Metallic ions, located in an aqueous phase, can be extracted into the aqueous core of the reverse micelles in the heptane phase. A CCC apparatus can be considered as a powerful mixing and extracting machine with efficiency above several hundreds of theoretical plates. La^{3+}, Ce^{3+}, Pr^{3+}, and Nd^{3+} lanthanide cations were separated using CCC with a DEHPA-containing heptane stationary phase. Studying the retention variations with aqueous mobile phase pH, it was possible to determine the lanthanide extraction constants and separation coefficients. Overloading conditions are described. Frontal chromatography was performed using a Co^{2+} and Ni^{2+} solution. The Co^{2+} ions were concentrated in the heptane + DEHPA stationary phase, a part of the solution was deionized, and another part was enriched in only Ni^{2+} ions. This method also produced the extraction constants and separation coefficients. The use of CCC with a complexing stationary phase can be applied to any cation for ion filtering and concentration, or for deionization of aqueous phases.

Key words: countercurrent chromatography, CCC; ion extraction, ion filtering, deionization, lanthanides, transition metals.

Introduction

La chromatographie à contre courant (CCC) est une technique de séparation avec une phase stationnaire et une phase mobile. À la différence des autres techniques de chromatographie, en CCC, la phase stationnaire est un *liquide* sans aucun support solide. La phase mobile, elle aussi liquide, demeure la seule à se déplacer dans la colonne. Il n'y a pas de circulation de liquides à contre courant dans la technique CCC comme son nom semble le laisser croire. L'inventeur de la technique, Yoishiro Ito (1), a publié plus d'une centaine d'articles scientifiques en utilisant le sigle CCC (2–4). Le nom, chromatographie à contre courant, et le sigle, CCC, se sont imposés.[3] Plusieurs dénominations plus adaptées ont été proposées : chromatographie de partage centrifuge ou chromatographie liquide–liquide centrifuge (6).

Les avantages d'une phase stationnaire liquide sont :

(*i*) une grande capacité : les solutés à séparer ont accès au volume de la phase stationnaire et non pas seulement à l'interface solide – phase mobile comme dans les autres techniques chromatographiques. C'est l'avantage principal de la CCC qui

Reçu le 22 juin 1995.

A. Berthod[2] et J. Xiang. Unité associée au Centre national de la recherche scientifique n° 435, Université de Lyon 1, Bat. 308, 69622 Villeurbanne cedex, France.
S. Alex. Institut de chimie et de pétrochimie, 6220 Sherbrooke Est, Montréal, QC H1N 1C1, Canada.
C. Gonnet-Collet. Institut Universitaire de technologie, mesures physiques, 28 avenue Léon Jouhaux, 42000 Saint-Etienne, France.

1. Communication présentée au 63ème congrès de l'ACFAS à Chicoutimi, Québec, Canada, du 22 au 26 mai 1995.
2. Auteur à qui adresser toute correspondance. Téléphone : 011 33 7243 1434. Fax : 011 33 7243 1078. E-mail : 100535.246@compuserve.com ou berthod@univ-lyon1.fr
3. Tant que l' International Union for Pure and Applied Chemistry (IUPAC) n'aura pas recommandé une autre dénomination que celle proposée par l'inventeur de la technique, Yoishiro Ito, les termes chromatographie à contre courant et le sigle CCC seront utilisés.

est plutôt utilisée dans la prépurification d'extraits chargés ou la séparation préparative;

(*ii*) un très grand choix de systèmes : les mélanges de solvants qui produisent un système biphasique liquide sont innombrables (7), certains systèmes liquides permettent de faire des gradients de composition (8);

(*iii*) une gamme de sélectivité originale comparée aux sélectivités obtenues en chromatographie liquide classique à phases stationnaires solides (silice nue ou silice greffée alkyle) (9);

(*iv*) l'inversion possible du rôle des phases : la phase mobile peut devenir la phase stationnaire et vice versa. En conséquence, aucun soluté injecté ne peut rester irréversiblement adsorbé dans la colonne CCC. S'il n'est pas élué, dû à sa forte affinité pour la phase stationnaire, on inverse le rôle des phases et le soluté est poussé hors de la colonne (9). Ainsi il y a toujours récupération totale des solutés injectés;

(*v*) la mesure des coefficients de partage liquide–liquide (10).

Un dernier avantage est que la technique CCC utilise tous les éléments périphériques classiques de la chromatographie liquide : pompes, détecteurs, vannes, collecteurs de fractions, intégrateurs. Seule la colonne est différente.

La technique a des inconvénients. Le principal est évident : il faut maintenir la phase stationnaire liquide en place pendant que l'on fait circuler la phase mobile. Une « colonne » CCC ne sera donc pas un simple tube rempli de phase stationnaire comme en chromatographie liquide classique. Des forces centrifuges seront nécessaires pour retenir la phase stationnaire liquide. Tous les appareils CCC modernes, qui ne sont en fait que la colonne CCC, comportent des rotors. Deux types d'appareils CCC sont commercialisés, les appareils à tubes enroulés, dits hydrodynamiques, et les appareils à tubes et canaux, dits hydrostatiques. Ils sont décrits dans de nombreux articles de revue (3, 4, 11).

La technique CCC peut être utilisée pour séparer des cations métalliques par extraction par solvant avec échange d'ions (12–16). Les lanthanides trivalents sont très difficiles à séparer en une seule extraction. Des procédés d'extraction multiples doivent être mis en oeuvre (17). La technique CCC est idéale, elle permet en un processus continu d'effectuer un nombre d'extractions très important. Ce nombre d'extractions correspond au nombre de plateaux théoriques de la colonne CCC. Il peut atteindre plusieurs centaines de plateaux voire plusieurs milliers (13, 15). La grande capacité de charge de la phase stationnaire liquide prend tout son intérêt. Le fait que l'échantillon introduit dans la colonne soit toujours totalement récupéré est également un énorme avantage lorsque des actinides ou autres ions radioactifs sont séparés.

Nous nous proposons dans ce travail de présenter rapidement les paramètres théoriques de la technique CCC. Une seconde étape montre que l'utilisation comme phase stationnaire en CCC d'une solution de micelles inverses dans l'heptane permet de séparer les premiers éléments de la famille des lanthanides. Une micelle inverse est une association de plusieures molécules de tensio-actif de telle sorte que les têtes polaires soient tournées vers l'intérieur de la micelle et les chaînes hydrophobes vers l'exterieur. Le centre polaire de la micelle inverse peut emprisonner des molécules d'eau et des cations métalliques. On montrera qu'on peut ainsi concentrer des métaux dans la phase organique micellaire en utilisant l'appareil CCC non pas en mode séparatif mais comme un filtre à ions. Les métaux de transition seront utilisés comme exemple.

La chromatographie à contre courant (CCC)

Comme il l'a été indiqué dans l'introduction, la CCC est une technique chromatographique dans laquelle la phase stationnaire est un liquide. Les solutés sont retenus par ordre de coefficient de partage croissant. Ils sont séparés par la colonne CCC et sortent sous forme de pics symétriques ou gaussiens. À la différence des autres types de chromatographie, le mécanisme de rétention des solutés est très simple : c'est uniquement le partage entre les deux phases liquides qui discrimine les solutés. Le volume de rétention, V_R, d'un soluté s'exprime par :

$$[1] \quad V_R = V_M + PV_S$$

V_M et V_S sont, respectivement, les volumes de phase mobile et de phase stationnaire dans la colonne. P est le coefficient de partage du soluté exprimé par :

$$[2] \quad P = \frac{[\text{soluté}]_{\text{phase stationnaire}}}{[\text{soluté}]_{\text{phase mobile}}} = \frac{V_R - V_M}{V_S}$$

La somme des volumes des phases, $V_M + V_S$, est égale au volume interne de la colonne, V_C. Le facteur Sf,

$$[3] \quad Sf = V_S / V_C$$

mesure le pourcentage de rétention de phase stationnaire par rapport au volume interne de la colonne CCC utilisé. Il permet de comparer d'un appareil à l'autre la quantité de phase stationnaire retenue.

Le facteur de capacité ou facteur de rétention, k', est très utilisé en chromatographie car il est indépendant du volume de la colonne chromatographique. Il s'exprime par :

$$[4] \quad k' = (V_R - V_M)/V_M$$

En utilisant l'équation [1], on obtient :

$$[5] \quad k' = P\,V_S/V_M$$

L'équation [5] montre qu'il y a une relation directe entre le facteur de rétention d'un soluté et son coefficient de partage dans le système liquide utilisé dans le chromatographe CCC. Si le coefficient de partage est connu ou s'il peut être mesuré, il pourra être utilisé pour prédire exactement le comportement chromatographique du soluté (4, 9, 11). Au contraire, la technique CCC pourra être utilisée pour déterminer avec précision les coefficients de partage dans les systèmes biphasiques liquides (9, 10, 19).

Le domaine utile de coefficient de partage s'étale de 0,05 à 100 (18). Un soluté ayant un coefficient de partage plus faible que 0,05 sera si peu retenu par la phase stationnaire qu'on ne pourra pas le différencier du volume mort V_M. Un soluté avec un coefficient P de 100 aura un volume de rétention supérieure à 100 fois le volume de phase stationnaire (eq. [1]) ce qui peut être prohibitif. D'autre part, un soluté très retenu va être élué de la colonne CCC en un pic étalé qui pourra être interprété comme une dérive de ligne de base.

Les paramètres principaux en CCC sont les volumes de rétention (V_R) des solutés. Ils ne dépendent que de leur coefficient de partage et des volumes de phases mobile (V_M) et stationnaire (V_S) retenus dans l'appareil. On pourra toujours transposer d'un appareil CCC à l'autre un résultat obtenu. Par exemple, l'appareil A, de volume V_C^A = 80 mL est capable de retenir 80% de phase stationnaire soit 64 mL. Le volume de phase mobile est donc de 16 mL (20%). Deux solutés 1 et 2 ont des volumes de rétention V_R^{A1} = 56 mL et V_R^{A2} = 80 mL. On calcule leur coefficient de partage P_1 = 0,5 et P_2 = 1. On veut séparer les deux solutés sur un appareil CCC B de volume V_C^B = 250 mL. Il retient moins bien la phase stationnaire du même système liquide : V_S = 150 mL (Sf = 60%) et V_M = 100 mL. Les volumes de rétention des solutés 1 et 2 sont calculés avec leur coefficient de partage qui ne dépend que du système liquide et non de l'appareil : V_R^{B1} = 100 + (0,5 × 150) = 175 mL et V_R^{B2} = 100 + (1 × 150) = 250 mL. Les chromatogrammes peuvent avoir une allure différente car l'efficacité de l'appareil A peut être différente de celle de l'appareil B. Par contre les volumes de rétention sont prévisibles.

L'efficacité, N, d'un appareil CCC peut atteindre plusieurs centaines de plateaux théoriques. Elle se mesure par la largeur des pics à mi-hauteur, $W_{0,5H}$, ou à 60% de leur hauteur, $W_{0,6H}$:

$$[6] \quad N = 4\left(\frac{V_R^2}{W_{0,6H}}\right) = 5{,}54\left(\frac{V_R^2}{W_{0,5H}}\right)$$

Elle est liée à la cinétique des échanges du soluté entre la phase stationnaire et la phase mobile.

Partie experimentale

Chromatographie à contre courant

Le modèle CPHV 2000 de la Société Française de Chromato-Colonne (Life Sciences-Shandon, Eragny, France) est un appareil de type hydrodynamique avec trois bobines de tubes enroulés connectées en série et portées par un rotor. Son prototype a été décrit par Ito (3). Chaque bobine contient 133 tours de tube Téflon (diamètre interne 1,6 mm) soit 29 m embobinés en 7 couches de 19 tours. Le volume d'une bobine est d'environ 54 mL. Plus d'informations sur l'appareil CCC seront trouvées dans un travail récent (19). Autour de l'appareil CCC ont été utilisés : une pompe Shimadzu LC6–A (Touzart & Matignon, Paris, France) pour pousser les phases, un détecteur évaporatif à diffusion de lumière (DEDL), connu également sous les termes anglais « evaporative light scattering detector » (ELSD), modèle DDL21 (Cunow, Eurosep, Cergy-Pontoise, France); un intégrateur Shimadzu CRC5-A (Touzart & Matignon) et une vanne d'injection Rhéodyne 4125. Le détecteur DEDL nébulise la phase liquide sortant de l'appareil CCC, l'aérosol est chauffé à 100°C, la phase liquide est évaporée, les sels dissous cristallisent et diffusent la lumière de la lampe du détecteur. Le détecteur DEDL permet d'observer sans problème les ions métalliques difficilement détectables par spectrophotométrie UV–visible.

Pour faire une analyse CCC, il faut préparer la « colonne » qui n'existe que lorsque le champ de forces centrifuges est présent, c'est à dire tant que le rotor de l'appareil tourne. L'appareil CCC est d'abord rempli par la phase stationnaire (heptane + complexant) à fort débit (8 mL/min) et sans rotation. Le rotor est mis en mouvement à 800 rotations par minute (rpm) et on commence à pousser la phase mobile (eau + tampon) à 2 mL/min dans le sens tête vers queue (2–4, 11, 14). La phase heptane qui sort de l'appareil CCC, déplacée par la phase aqueuse, est collectée dans une éprouvette graduée. Lorsque la phase aqueuse apparaît à la sortie de l'appareil CCC, deux phases sont observées dans l'éprouvette; la « colonne » est prête. Le volume de phase heptane déplacée est mesuré; il correspond à V_M, le volume de phase mobile dans l'appareil. V_S est calculé par $V_C - V_M$. Les volumes V_M et V_S permettent de calculer les coefficients P des ions ou solutés élués dans l'appareil CCC (eq. [1]).

Réactifs et solutés

L'acide di(2-éthyl hexyl) phosphorique ($C_{16}H_{35}PO_4$, M = 322 g/mol, d = 0,975 (20°C), pK_A = 1,4) est l'extractant utilisé, il sera représenté par le sigle DEHPA. Obtenu de Merck (Schuchardt, Allemagne), il a été utilisé tel que reçu. Le DEHPA est très utilisé en hydrométallurgie parce qu'il est très sélectif, résiste bien à l'hydrolyse et il est presque insoluble dans l'eau (20). En solution dans l'heptane, il forme des micelles dites « inverses » car le coeur de la micelle est polaire avec des molécules d'eau et les têtes phosphates anioniques. Les nitrates de lanthane, cérium, praséodyme et néodyme sont des produits Prolabo (Paris, France) ainsi que les acétates de cobalt, de nickel et de cuivre. L'heptane provient de SDS (Peypin, France).

Spectrométrie d'émission atomique à source plasma

Un spectromètre d'émission à source plasma (ICP-AES) Perkin–Elmer Optima 3000 a été utilisé pour déterminer les concentrations ioniques en métaux de transition (Co, Ni, Cu) lorsqu'ils n'étaient pas complètement séparés par la « colonne » CCC. Cet appareil est équipé d'un détecteur CCD (Charge Coupled Device). Il peut mesurer simultanément l'émission produite par plusieurs éléments. Nous l'avons réglé pour mesurer les trois éléments Co, Ni et Cu, à deux longueurs d'onde différentes pour chaque élément. Le tableau 1 donne les longueurs d'onde utilisées pour suivre les concentrations des trois métaux de transitions étudiés. La sensibilité indiquée est celle de Wohlers (21). Elle a été obtenue expérimentalement comme le rapport signal/fond pour des solutions de concentration 100 mg/L sur un appareil dont les conditions de travail ont été fixées (21). Les raies choisies sont les plus sensibles, libres d'interférence spectrale. L'énergie de la torche était de 1100 W. Le débit de la pompe péristaltique était de 1 mL/min. Les débits d'argon étaient de 1 L/min dans le nébuliseur de type « cross-flow », 1 L/min en circulation auxiliaire et 15 L/min dans la torche elle-même.

Résultats et discussion

Séparation des quatre premiers éléments lanthanides

Il a été montré que les solutions de DEHPA dans l'heptane étaient au moins sous forme de dimères. En présence d'eau, des micelles inverses se forment. Les chaînes diéthylhexyl sont en contact avec les molécules d'heptane, les têtes polaires phosphates anioniques s'assemblent au coeur de la micelle où elles emprisonnent de l'eau. Les protons assurent la neutralité électrique. C'est dans le coeur des micelles que les cations métalliques vont se localiser en remplaçant des protons du DEHPA (12–17, 20). La structure physico-chimique des

Tableau 1. Longueurs d'onde d'émission pour l'analyse par ICP-AES

	Co		Ni		Cu	
	λ (nm)	sensibilité[a]	λ (nm)	sensibilité[a]	λ (nm)	sensibilité[a]
Mesure 1	228,616	1000	221,647	630	224,700	1000
Mesure 2	238,892	2000	232,003	250	324,754	5012

[a]Sensibilité expérimentale selon Wohlers (21).

Tableau 2. Paramètres chromatographiques obtenus par CCC pour les lanthanides.

			La		Ce		Pr		Nd	
DEHPA (M)	pH	V_S (mL)	V_R (mL)	N (plat.)	V_R (mL)	N (plat.)	V_R (mL)	N (plat.)	V_R (mL)	N (plat.)
0,02	1,22	32	21,5	35	22	40	22,5	35	23	30
0,02	1,30	34	19	100	20,5	70	21,5	45	22,5	35
0,02	1,40	36	18	—	20	70	22	50	24,5	35
0,03	1,22	32	22	70	23,5	50	25,5	40	27,5	30
0,04	1,22	37	17,5	100	23,5	70	28	50	34,5	30
0,04	1,26	37	18	60	25,5	50	32	40	40	30
0,04	1,30	37	19	40	28,5	60	37	30	48	20
0,04	1,35	37	20	50	34	50	45,5	30	61	25
0,04	1,40	37	22	40	41,5	25	57,5	25	80	15
0,04	1,46	37	25,5	30	54,5	25	79	20	113	15
0,04	1,52	37	30,5	25	74,5	30	111	15	162	15
0,05	1,22	32	23,5	50	33,5	40	41	30	52	30

Volume de l'appareil CCC 53 mL; volume de phase mobile, $V_M = 53 - V_S$; vitesse de rotation 800 rpm; erreur relative 3% (volumes), 15% (plateaux théoriques); débit de phase aqueuse 2 mL/min; pH ajusté par HCl; volume injecté 200 µL, concentration 0,01M en chacun des cations, détection DEDL.

micelles inverses et de leurs associations avec les cations métalliques ne sera pas abordée dans ce travail.

Principe

Les composés organométalliques sont d'excellents complexants des ions métalliques qu'ils sont capables d'extraire de la phase aqueuse dans une phase organique selon :

$$[7] \quad M^{n+}_{aq} + n\,HA_{org} \rightleftarrows M(A)_{n,\,org} + n\,H^{+}_{aq}$$

La constante d'équilibre d'une telle réaction s'écrit :

$$[8] \quad K_{ex} = \frac{[MA_n]_{org}[H^+]^n_{aq}}{[M^{n+}]_{aq}[HA]^n_{org}}$$

Cette constante peut être reliée au coefficient de partage ou de distribution, P, obtenue par CCC (eq. [1]) :

$$[9] \quad P = K_{ex}\left(\frac{[HA]^+}{[HA^+]}\right)^n$$

Si deux cations métalliques n'ont pas la même constante d'extraction K_{ex}, ils n'auront pas le même coefficient P. Ils pourront donc être séparés par l'appareil CCC puisqu'ils sont nécessairement confrontés à la même concentration de complexant (même phase stationnaire) et au même pH (même phase mobile). Les rétentions relatives dépendront cependant du pH de la phase mobile et de la concentration en complexant dans la phase organique.

En prenant le logarithme de l'expression [9], on forme :

$$[10] \quad \log P = \log K_{ex} + n \log [HA] + n\,pH$$

L'équation (10) montre que le logarithme du coefficient P obtenu par CCC est linéairement relié à la fois au pH et au logarithme de la concentration en complexant. La pente correspond au nombre de molécules de complexant par ion métallique et l'ordonnée à l'origine permet d'estimer log K_{ex}.

Volume de rétention et pH

La figure 1 présente trois chromatogrammes CCC obtenus avec des conditions expérimentales différentes. Le premier chromatogramme montre que seul l'ion La^{3+} est séparé des trois autres, Ce^{3+}, Pr^{3+} et Nd^{3+}, avec une phase mobile acide à pH 1,40 et une concentration en DEHPA 0,04 M dans l'heptane. Chacun des ions lanthanides a été injecté séparément dans la même « colonne » CCC. Les tracés obtenus ont été indiqués sur le chromatogramme. Le deuxième chromatogramme montre l'accroissement des volumes de rétention dû au pH. Une augmentation de 0,12 unité du pH de la phase mobile double les volumes de rétention. Le tableau 2 rassem-

Fig. 1. Séparation des ions lanthanides par CCC. Volume de la colonne : V_C = 53 mL (1 bobine), V_S = 37 mL, rotation 800 rpm, débit de phase mobile aqueuse 2 mL/min, sens tête vers queue, détecteur à diffusion lumineuse, photomultiplicateur : 600 V, unité mV (arbitraire); gaz nébuliseur : air comprimé 1,5 kg/cm^2, température de séchage : 100°C. *A* : pH de la phase mobile = 1,4, chaque espèce cationnique a été injectée séparément et la courbe enveloppe est montrée. *B* : pH = 1,52, l'ion Pr^{3+} a été supprimé pour obtenir une résolution satisfaisante. *C* : pH = 1,52, effet de surcharge.

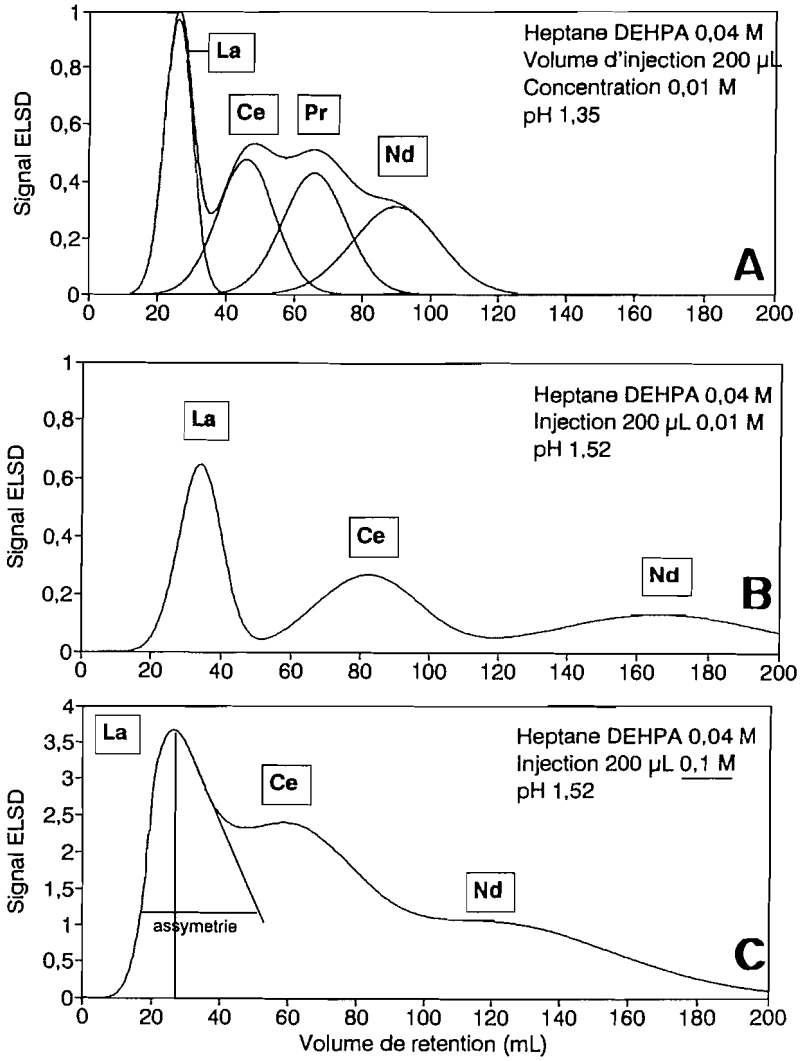

ble les résultats pour chaque ion qu'il ait été injecté seul ou en mélange avec les autres. Il donne également le nombre de plateaux correspondant à chaque pic. Ce nombre est lié à la cinétique de l'échange entre les phases (22). On note qu'il a tendance à diminuer lorsque le volume de rétention augmente. La cinétique de l'échange semble plus lente lorsque le cation est plus fortement retenu dans la phase organique.

Le troisième chromatogramme (figure 1*C*) montre l'effet d'un accroissement de la masse injectée. Les pics se déforment et deviennent asymétriques et les volumes de rétention diminuent. On a toutes les caractéristiques d'une surcharge de la phase stationnaire. La solution injectée contenait une concentration de 0,1 mol/L pour chacun des cations. Cette concentration est très supérieure à la concentration en complexant DEHPA dans la phase stationnaire (0,04 mol/L). Une partie des cations n'est pas complexée et avance dans la colonne jusqu'à ce qu'elle trouve de la phase stationnaire libre. L'ensemble des cations voit une colonne plus courte. Cela explique les diminutions de temps de rétention et les déformations de pic.

La figure 2 présente graphiquement les valeurs de coefficient *P* obtenues pour les lanthanides à différentes valeurs de pH. On note la forte augmentation de *P* avec le pH, comme l'exprime l'équation [9]. Les valeurs de log *P* ont été portées en fonction du pH selon l'équation [10]. Le tableau 3 donne les valeurs de pente, ordonnée à l'origine et coefficients de régression des droites obtenues. Les constantes K_{ex} sont également indiquées.

La facilité de la séparation de deux cations par extraction liquide–liquide est mesurée par le coefficient α_D, le facteur de

Tableau 3. Paramètres des droites log $P = f(\text{pH})$.

	La	Ce	Pr	Nd
Pente	3,18	3,13	2,91	2,90
Ordonnée à l'origine	−5,25	−4,55	−4,03	−3,83
Coefficient de régression	0,994	0,992	0,985	0,99
K_{ex}	0,16	0,68	1,11	1,70
log K_{ex}	−0,80	−0,168	0,044	0,23
α_D	4,2	1,6	1,5	

Erreur relative : 10%.

Fig. 2. Variation du coefficient de distribution P des ions lanthanides 57 à 60 en fonction du pH de la phase mobile. Conditions opératoires de la figure 1.

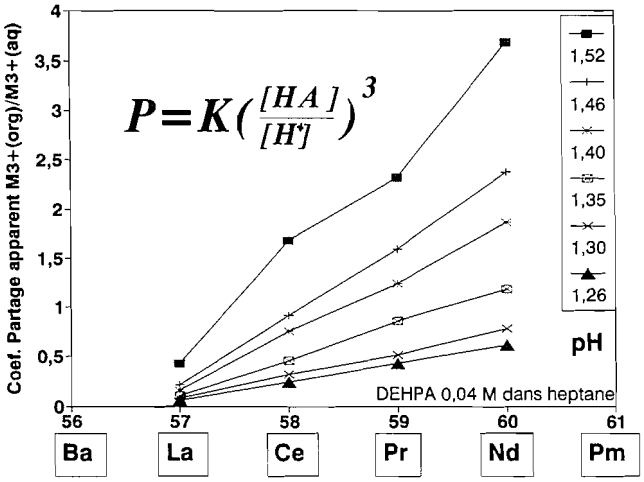

Fig. 3. Evolution du volume de rétention (mL) des ions néodyme Nd^{3+} en fonction de la concentration injectée; tous les autres paramètres sont inchangés.

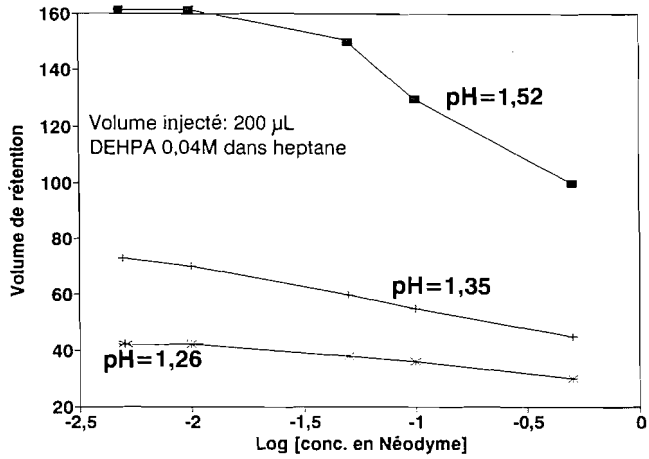

séparation, rapport des constantes d'extraction, K_{ex}, des deux cations considérés. α_D mesure le déplacement d'un cation par un autre. Les valeurs obtenues confirment les observations expérimentales : l'ion lanthane est facile à séparer des autres lanthanides avec un facteur de séparation de 4,2 avec le cérium, 7,9 avec le praséodyme et 11 avec le néodyme. Les autres ions lanthanides ont des facteurs de séparation plus faibles (tableau 3); leur séparation mutuelle sera difficile, mais pourtant possible par CCC (16).

Charge de la colonne

La figure 1*C* montre un effet de surcharge de la colonne CCC lorsqu'une plus grande masse d'ions lanthanides a été injectée. Les pics s'élargissent et les volumes de rétention diminuent. 200 µL de solution 0,1 M en chacun des ions, soit environ 2,8 mg de chaque ion ou 8,4 mg de cations (20 mg de sels nitrates), ont été injectés. La concentration des ions lanthanides en tête de colonne est 9 fois plus élevée que la concentration en complexant DEHPA. La plus grande partie des cations ne peut pas interagir avec la phase stationnaire saturée. Ils sont poussés par la phase mobile jusqu'à ce qu'ils trouvent de la phase stationnaire libre. Les cations sont en contact avec une partie seulement de la phase stationnaire. Ils semblent voir une colonne plus courte, d'où les volumes de rétention réduits, et avec moins de plateaux, d'où l'élargissement des pics.

La figure 3 montre que la surcharge de la phase stationnaire commence dès que la concentration en néodyme, injecté seul, dépasse 0,01 M. La concentration en complexant DEHPA est 0,04 M, la concentration maximale en cation dans la phase mobile est 0,04/3 = 0,013 M (eq. [5]). Lorsque plusieurs cations sont injectés ensemble (figure 1*C*), la concentration maximale peut être dépassée en tête de colonne. Les cations se déplaçant à des vitesses différentes dans la colonne et une dilution se produisant (élargissement de bande), la surcharge peut cesser en cours de séparation. Cette surcharge se produit pour les différentes valeurs du pH de la phase mobile. L'efficacité de la colonne CCC diminue rapidement avec la surcharge. Pour le néodyme (figure 3), elle passe de 20 plateaux pour une concentration injectée de 0,005 M à environ 6 plateaux pour la concentration 0,1 M.

Comme il l'a été décrit pour des séparations préparatives (3–5), pour pouvoir séparer de grandes quantités de cations lanthanides sans surcharge de colonne, il faut augmenter la teneur de la phase stationnaire en complexant. Il faudra également travailler à des pH faibles, avec des phases mobiles très acides, pour compenser l'augmentation de volume de rétention qui découle de l'augmentation de la concentration en complexant (eq. [10]). Une autre voie pour séparer de grandes quantités de solutés est la chromatographie frontale ou chromatographie de déplacement (23).

Séparation de métaux de transition

La technique de chromatographie frontale et de déplacement à été mise en oeuvre pour montrer qu'un appareil CCC peut être utilisé comme un filtre à ions pour séparer de grandes quantités d'ions ou pour concentrer dans un très petit volume de

Fig. 4. Chromatogramme frontal obtenu avec une colonne CCC chargée de 20 mL de phase stationnaire heptane + DEHPA 0,2 M. La phase mobile est une solution d'ions cobalt Co^{2+} 0,01 M et nickel Ni^{2+} 0,01 M. Mêmes conditions expérimentales que pour la figure 1. *A* : tracé brut obtenu sur l'enregistreur. Les variations de pH et de coloration sont indiquées. *B* : profil de concentration en ions Co^{2+} et Ni^{2+} reconstruit avec les analyses par ICP-AES faites sur les prélevements de *A*.

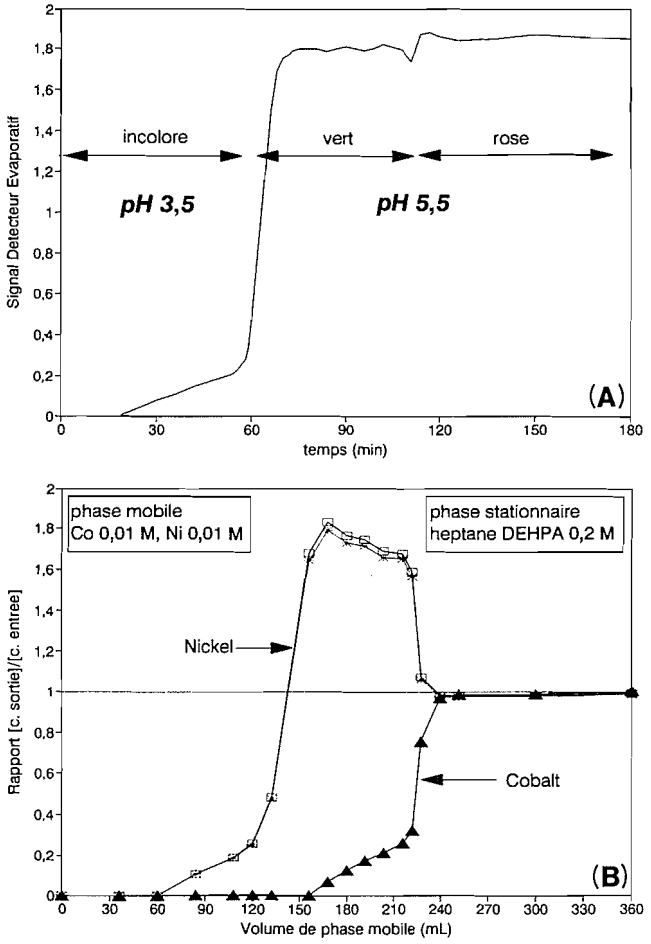

phase organique les ions contenus dans un grand volume de solution aqueuse.

Principe

L'appareil CCC est équilibré comme indiqué dans la partie expérimentale avec une phase stationnaire organique et une phase mobile aqueuse ne contenant aucun ion. Un grand volume (1 L) de solution aqueuse d'acétate de nickel, de cobalt ou de cuivre et leur mélange est préparé. Cette solution est poussée dans la colonne CCC en guise de phase mobile. La concentration totale en ions est mesurée en continu à la sortie d'appareil CCC par le détecteur évaporatif à diffusion de la lumière (DEDL).

Résultats

La figure 4*A* montre le tracé obtenu avec le DEDL lorsqu'une solution d'acétate de nickel (0,01 M ou 590 ppm) et de cobalt (0,01 M ou 590 ppm) est utilisée comme phase mobile avec un appareil CCC hydrodynamique de 53 mL de volume de colonne (une seule bobine). Le volume de la phase stationnaire, heptane + 0,2 M DEHPA, a été limité à 20 mL. En début de mesure, des variations de pH ont été notées. Le pH de la phase éluée était initialement de 6. Il descend jusqu'à 3,5 pour remonter à 5,5 lorsque le signal DEDL indique la présence d'ions (figure 4*A*). Puis, lors du développement du chromatogramme frontal, des variations de colorations ont été observées comme indiqué sur la figure 4*A*, sans que le signal DEDL ne change notablement. Des fractions de 5 mL ont été collectées toutes les 6 min. Ces fractions ont été analysées par ICP-AES selon la procédure décrite dans la partie expérimentale. Les teneurs en nickel et cobalt dans la phase éluée sont rapportées aux teneurs de la phase mobile entrant dans la colonne.

La figure 4*B* présente graphiquement les résultats des analyses ICP-AES. En début de chromatogramme, on mesure une très faible teneur en ions Co^{2+} et Ni^{2+}. Correspondant à la montée du signal DEDL, on mesure une concentration en nickel presque double de la concentration d'entrée. Le cobalt est absent. Puis le cobalt apparaît à la sortie de colonne et la concentration en nickel devient égale à la concentration d'entrée. On vide la colonne CCC, la phase stationnaire heptane à une couleur bleu foncé. Mise en présence d'une solution aqueuse très acide, elle se décolore. La solution acide réextrait les ions. Cette solution est également dosée par ICP-AES. Elle contient du cobalt pratiquement pur.

Interprétation

Des résultats similaires à ceux présentés par la figure 4 ont été obtenus avec des mélanges d'ions cuivre, cobalt et nickel. La figure 5 schématise le phénomène observé. À l'état initial, la colonne CCC est équilibrée avec de l'eau permutée comme phase mobile et une solution de DEHPA dans l'heptane comme phase stationnaire.

Lorsque la solution de cobalt et de nickel est introduite dans la colonne, il y a interaction des ions avec l'extractant de la phase stationnaire selon l'équation [7]. Les ions sont remplacés par des protons. Ces protons sont partiellement absorbés par les anions acétates. On mesure, à la sortie de colonne, une diminution du pH à une valeur de l'ordre de 3. Les ions nickel et cobalt sont absents. C'est l'étape de *désionisation*. Les ions cobalt et nickel sont capables de déplacer le proton du complexant DEHPA. Le cobalt a plus d'affinité pour l'extractant que le nickel. Il est capable de déplacer le nickel qui, repassant dans la phase mobile va se fixer plus loin dans la colonne. On observe une bande de phase stationnaire riche en nickel poussée par une bande de phase stationnaire riche en cobalt (figure 5). Cette étape de désionisation dure tant qu'il reste de la phase stationnaire propre (DEHPA) dans la colonne.

Lorsque le nickel atteint la fin de la phase stationnaire, il ne peut plus s'y adsorber, il reste donc dans la phase mobile et sort de la colonne. La concentration en protons n'est plus modifiée. Le pH devient celui de la phase mobile à l'entrée. La concentration en ions nickel est celle de la phase mobile à l'entrée augmentée du nickel déplacé par les ions cobalt. On mesure à la sortie une concentration en nickel supérieure à celle à l'entrée. Le cobalt est absent. Cette étape dure tant que les ions cobalt trouvent de la phase stationnaire contenant des ions nickel à déplacer.

Le processus se termine lorsque la phase stationnaire est

Fig. 5. Principe de la chromatographie frontale. La phase stationnaire comporte des bandes de concentration en une seule espèce ionique. Voir le texte.

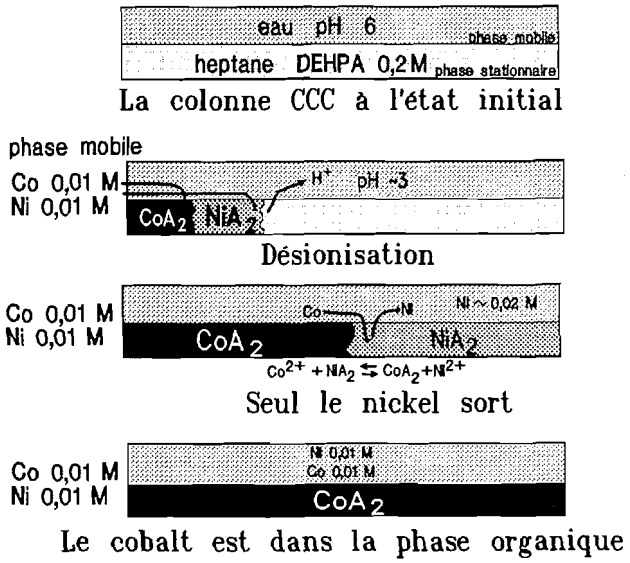

saturée en ions cobalt (figure 5). Les concentrations d'ions à l'entrée se retrouvent à la sortie. La phase stationnaire est riche en cobalt. La technique CCC permet (*i*) d'extraire les ions d'une phase aqueuse, (*ii*) de séparer ces ions par concentration d'une espèce dans une partie de la phase aqueuse et de l'autre espèce dans la phase stationnaire.

Volumes filtrés

La figure 6 présente les concentrations en ions et les volumes obtenus au cours des étapes décrites par la figure 5. La colonne CCC de 53 mL contenait 20 mL de phase stationnaire heptane + 0,5 M DEHPA. Les 33 premiers mL sont de l'eau (pH ~6), ils correspondent au volume V_M. Puis le pH diminue jusqu'à ~3,5. Pendant l'élution de 330 mL, la phase aqueuse sortant de la colonne CCC ne contient que des traces (moins de 1 ppm) d'ions nickel et cobalt. Le volume de phase aqueuse qui peut être désionisé par la colonne CCC, V_D, dépend du volume de la phase stationnaire, V_S, de la concentration en extractant, C_E, et de la charge, n_I, et des concentrations en ions, C_I, dans la phase mobile :

$$[11] \quad V_D = \frac{V_S C_E}{\Sigma(n_I C_I)}$$

Une solution enrichie en ions nickel et très appauvrie en ions cobalt sort ensuite. La concentration en nickel est de l'ordre de la concentration totale en ions dans la phase entrant dans la colonne CCC. Le volume de solution enrichie en nickel, V_{Ni}, correspond à :

$$[12] \quad V_{Ni} = \left[\frac{V_S C_E}{n_{Co} C_{Co}}\right] - V_D$$

équation dans laquelle n_{Co} et C_{Co} correspondent respectivement à la charge électrique et à la concentration en ions cobalt. Le volume V_{Ni} est la différence entre le volume de phase aqueuse nécessaire pour saturer la phase stationnaire en cobalt diminué du volume de phase aqueuse désionisée. Dans l'expérience de la figure 6, on a obtenu 165 mL de solution contenant 97,4% d'ions nickel (Ni^{2+} 0,0133 M ou 780 ppm; Co^{2+} 0,00035 M ou 20 ppm). Le rotor a alors été arrêté et la colonne CCC vidée. On a récupéré 20 mL de phase stationnaire heptane fortement colorée en bleu par les ions cobalt. Leur concentration s'élève à 0,285 M (17000 ppm) avec seulement 60 ppm d'ions nickel. La masse d'ions cobalt extraite avec une pureté de 99,3% est de 336 mg. La précision des analyses est de l'ordre de 5%. La précision des analyses par ICP est de l'ordre de 1%. La principale source d'erreur est l'échantillonnage : une partie de la phase stationnaire peut rester dans la machine.

Facteurs de séparation ou constantes de déplacement

Les valeurs de volume données par les équations [11] et [12] correspondent à un déplacement total des ions nickel par les ions cobalt. Ce n'est le cas que tant que les concentrations sont du même ordre de grandeur (figures 4 et 6). Lorsque la concentration en ions nickel est très supérieure à la concentration en ions cobalt, ces derniers ne peuvent pas déplacer complètement les premiers. Les équations [11] et [12] ne peuvent plus être utilisées. La figure 7 présente les résultats obtenus avec une phase contenant à l'entrée de la colonne 10 fois plus d'ions nickel que d'ions cobalt. L'équation [11] donne une valeur de volume désionisé de V_D = 454 mL. Il faut ajouter le volume V_M (33 mL). Les premiers ions nickel ne devraient se présenter qu'après 487 mL. Le signal DEDL change dès que 390 mL ont été élués hors de la colonne. L'équation [12] permet d'estimer le volume de phase ne contenant que du nickel à la concentration théorique de 0,011 M V_{Ni} = 4550 mL. L'expérience montre une montée régulière de la concentration en cobalt dès l'élution de 450 mL (figure 7). Lorsque les concentrations d'entrée sont égales aux concentrations à la sortie, la phase stationnaire est récupérée et analysée. Elle contient les deux espèces d'ions, nickel à la concentration 0,168 M (10 000 ppm) soit un enrichissement de 17 fois par rapport à la phase aqueuse, et cobalt 0,066 M (3900 ppm) correspondant à un enrichissement de 66 fois.

Ces résultats permettent d'estimer le facteur de séparation, α_D, ou la constante de déplacement du nickel par le cobalt, $K_{Co/Ni}$, exprimé par :

$$[13] \quad \alpha_D = K_{Co/Ni} = \frac{[CoA_2]_{org}[Ni^{2+}]_{aq}}{[NiA_2]_{org}[Co^{2+}]_{aq}} = \frac{K_{exCo}}{K_{exNi}}$$

$K_{Co/Ni}$ est voisin de 4. On note que les constantes de déplacement ou les facteurs de séparation ne dépendent pas du pH. Pourtant si la valeur du pH est faible, les ions Co^{2+} ou Ni^{2+} seront faiblement extraits par la phase organique.

Généralisation du procédé

La figure 8 montre la composition à la sortie de colonne CCC obtenue lorsqu'une solution des trois ions Co^{2+}, Ni^{2+} et Cu^{2+} à la même concentration, 0,1 M, entrait continûment dans l'appareil. Le mouvement des bandes de concentration décrit par la figure 5 peut être généralisé. Dans ce cas, c'est l'ion cuivre qui a la plus forte affinité pour la phase stationnaire, il déplace l'ion cobalt qui déplace lui-même l'ion nickel. Au pH de la phase entrante (5,6) et avec les concentrations de 0,1 M, les équations [11] et [12] sont utilisables. On calcule un

Fig. 6. Profil de concentration en ions Co^{2+} et Ni^{2+} reconstruit avec les analyses par ICP-AES. V_S = 20 mL, phase mobile pauvre en nickel. Conditions expérimentales de la figure 1.

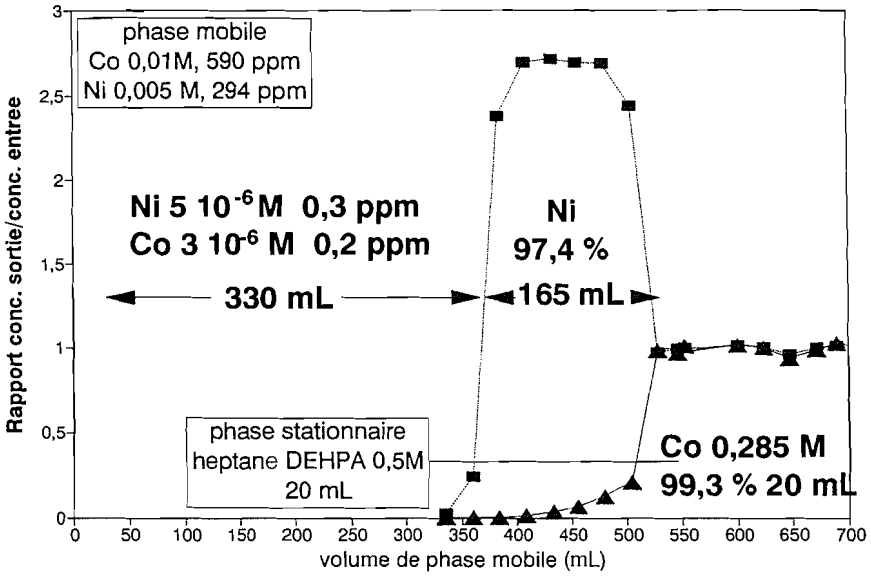

Fig. 7. Profil de concentration en ions Co^{2+} et Ni^{2+} reconstruit avec les analyses par ICP-AES. Phase mobile pauvre en cobalt qui ne peut plus saturer la phase stationnaire. Conditions expérimentales de la figure 1.

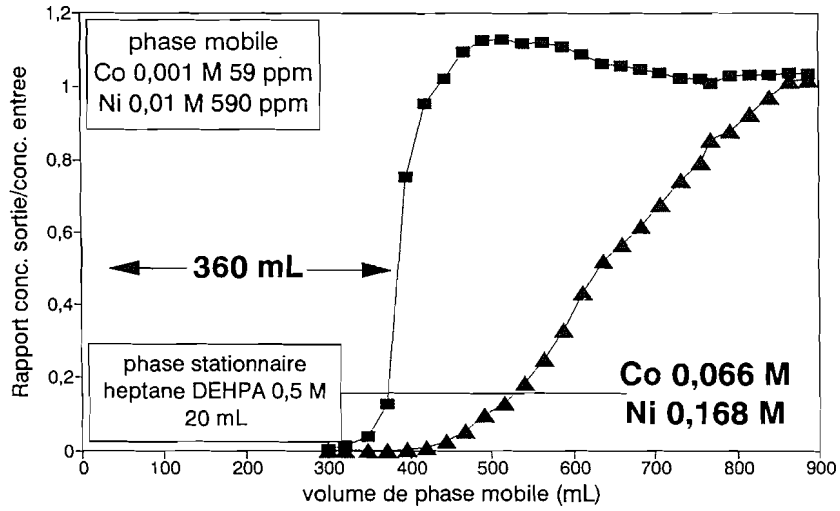

volume de phase désionisée, V_D, de $20 \times 0{,}2/(2 \times 3 \times 0{,}01)$ = 67 mL. Le saut de concentration en nickel est effectivement observé vers 100 mL ($V_D + V_M = 67 + 33$). L'équation [12] permet de calculer le volume de phase ne contenant que du nickel, V_{Ni} = 33 mL. On mesure expérimentalement $V_{Ni} \approx 40$ mL (figure 8).

Le cobalt sort ensuite de la colonne CCC à une concentration supérieure à celle entrante. L'excès est produit par le cobalt déplacé de la phase stationnaire par le cuivre. Mais le nickel est également présent (figure 8). Lorsque l'ion cuivre sort également de la colonne, c'est que la phase stationnaire est saturée. On a alors arrêté le rotor, vidé la colonne et mesuré les concentrations en chacun des ions dans la phase stationnaire. Elle contient majoritairement du cuivre (96,9%) avec des traces de nickel (0,7%) et de cobalt (2,4%).

On peut généraliser le procédé à l'extraction d'ions à faibles concentrations dans de grandes quantités de phase aqueuse. Une colonne CCC est un excellent extracteur et concentrateur qui pourra fonctionner avec une grande variété de phases extractrices. L'importance du pH est illustrée par le tableau 4 qui rassemble les valeurs K_{ex} et les constantes de déplacement des ions Co^{2+}, Ni^{2+} et Cu^{2+} avec les coefficients de distribution P calculés pour deux valeurs de pH.

Le tableau 4 montre que le cuivre déplace facilement le cobalt et le nickel jusqu'à des valeurs de pH aussi faibles que 2. Au-dessous de pH 3, les ions cobalt et nickel n'ont plus une affinité suffisante pour la phase stationnaire pour être extraits en totalité. Dès pH 4, les trois espèces ioniques ont des valeurs de $P > 200$. Elles sont extraites à plus de 99% par la phase stationnaire. Les valeurs de K_{ex} obtenues pour les ions lanthanides (tableau 3) montrent que ces ions pourraient être extraits complètement dès que le pH atteint 1,1.

On terminera en soulignant qu'il n'y a pas d'objection théorique pour que la méthode proposée dans cette étude soit

Fig. 8. Chromatographie frontale avec une solution de trois cations, Co^{2+}, Ni^{2+}, et Cu^{2+}. Les bandes successives de concentration sont : Ni^{2+} puis Co^{2+} et Cu^{2+} qui sature la phase stationnaire. Conditions expérimentales de la figure 1.

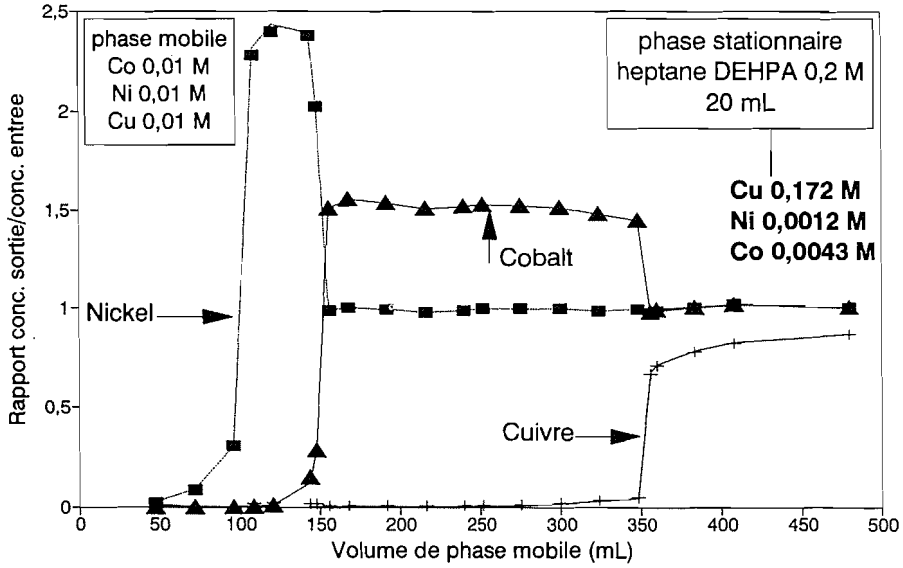

Tableau 4. Constantes des métaux de transition et importance du pH.

	Co	Ni	Cu
K_{ex}	$3{,}3 \times 10^{-5}$	$7{,}8 \times 10^{-6}$	$1{,}3 \times 10^{-3}$
log K_{ex}	−4,5	−5,1	−2,9
α_D	Co/Ni 4,2	Cu/Ni 170	Cu/Co 40
DEHPA = 0,5 M			
P pH = 1,0	$8{,}2 \times 10^{-4}$	$1{,}9 \times 10^{-4}$	0,032
P pH = 2,2	0,207	0,049	8,16
P pH = 4,0	825	195	32 500
P pH = 5,4	520 000	123 000	2×10^{7}

Erreur relative : 10%.

utilisée avec des effluents réels contenant de nombreuses espèces ioniques. Un classement des cations par ordre de constantes d'extraction croissantes doit être obtenu dans la phase stationnaire heptane. Le problème important est que la technique CCC est au stade du développement. Il n'y a pas encore, en 1995, de compagnies industrielles d'instrumentation qui produisent des appareils CCC en série. L'appareil utilisé pour faire cette étude fait partie d'une présérie de sept exemplaires. La société qui a produit ces appareils a été rachetée par une plus grande compagnie qui ne poursuivra pas les études en CCC. Des prototypes étant à l'étude dans plusieurs pays, il devrait être possible de se procurer une machine CCC fiable et facile d'emploi dans peu de temps.

Bibliographie

1. Y. Ito, I. Aoki et E. Kimura. Anal. Chem. **41**, 1579 (1969).
2. Y. Ito. CRC Crit. Rev. Anal. Chem. **17**, 65 (1986).
3. N.B. Mandava et Y. Ito. Chromatogr. Sci. Ser. Vol. **44**, (1989).
4. W.D. Conway. Countercurrent chromatography, theory and applications. VCH Publishers, Weinheim. 1990.
5. A.P. Foucault. Chromatogr. Sci. Ser. Vol. **68**, (1995).
6. J.M. Menet. Thèse de Doctorat, Université de Paris VII, mars 1995.
7. J.M. Sørenson et W. Arlt. Liquid–liquid equilibrium data collection. Chemistry Data Series, Dechema, Francfort. 1979.
8. A. Foucault et K. Nakanishi. J. Liq. Chromatogr. **12**, 2587 (1989).
9. A. Berthod, C.D. Chang et D.W. Armstrong. Chromatogr. Sci. Ser. **68**, 1 (1995).
10. A. Berthod et V. Dalaine. Analusis, **20**, 325 (1992).
11. A. Berthod. Instrum. Sci. Technol. **23**, 75 (1995).
12. V.M. Pukhovskaya, T.A. Maryutina, O.N. Grebneva, N.M. Kuz'min et B. Ya. Spivakov. Spectochim. Acta, **48B**, 1365 (1993); **50B**, 5 (1995).
13. E. Kitazume, M. Bhatnagar et Y. Ito. J. Chromatogr. **538**, 133 (1991).
14. K. Inaba, S. Muralidaran et H. Freiser. Anal. Chem. **65**, 1510 (1993).
15. T. Araki, T. Okazawa, Y. Kubo, H. Asai et H. Ando. J. Liq. Chromatogr. **11**, 2473 (1988).
16. K. Akiba, S. Sawai, S. Nakamura et W. Murayama. J. Liq. Chromatogr. **11**, 2517 (1988).
17. J.A. Marinsky et Y. Marcus. Ion exchange and solvent extraction. Vol. 12. M. Dekker, New York. 1995.
18. A. Berthod et D.W. Armstrong. J. Liq. Chromatogr. **11**, 567 (1988).
19. A. Berthod et M. Bully. Anal. Chem. **63**, 2508 (1991).
20. D.F. Peppard, G.W. Mason, J.L. Maier et W.J. Driscoll. J. Inorg. Nucl. Chem. **4**, 334 (1957).
21. C.C. Wohlers. ICP Inf. Newsl. **10**, 593 (1985).
22. S. Muralidaran et H. Freiser. Chromatogr. Sci. Ser. **68**, 317 (1995).
23. J.A. Jönsson. Chromatogr. Sci. Ser. **38**, (1987).

2-Azabuta-1,3-diene-4-carbonitriles: stereoselective synthesis and nucleophilic substitution at the carbon–nitrogen double bond

Antonio Lorente, Marta Casillas, Pilar Gomez-Sal, and Antonio Manzanero

Abstract: The synthesis of (*E*)-1-methoxy-2-azabuta-1,3-diene-4-carbonitriles was performed by methylation of N-alkenylamides **9** and **11**. The *Z* isomers were obtained by treatment of (*E*)-1-methylthio-2-azabuta-1,3-diene-4,4-dicarbonitriles with sodium methoxide in methanol. We also describe the reactions of (*E*)-1-methylthio-2-azabuta-1,3-diene-4,4-dicarbonitriles with pyrrolidine, which afforded 1-(1-pyrrolidinyl) derivatives **20**, **21**, and **23**. X-ray crystallographic analyses of **21** and **23** established the *E* stereochemistry of the C—N double bond.

Key words: 2-azabuta-1,3-diene-4-carbonitriles: stereoselective synthesis, nucleophilic substitution and X-ray diffraction; N-alkenylamides: methylation.

Résumé : On a effectué la synthèse des (*E*)-1-méthoxy-2-azabuta-1,3-diène-4-carbonitriles en effectuant la méthylation des N-alkénylamides **9** et **11**. On a obtenu les isomères *Z* en traitant les (*E*)-1-méthylthio-2-azabuta-1,3-diène-4,4-dicarbonitriles avec du méthylate de sodium dans le méthanol. On décrit aussi les réactions des (*E*)-1-méthylthio-2-azabuta-1,3-diène-4,4-dicarbonitriles avec la pyrrolidine qui conduisent aux dérivés 1-(1-pyrrolidinyle) **20**, **21** et **23**. On a déterminé la stéréochimie *E* de la double liaison C—N par une analyse cristallographique par diffusion des rayons X.

Mots clés : 2-azabuta-1,3-diène-4-carbonitriles : synthèse stéréosélective, substitution nucléophile, diffraction des rayons X; méthylation de N-alkénylamides.

[Traduit par la rédaction]

Introduction

The synthesis of imidates (1–3) or thioimidates (3–5) by alkylation of amides or thioamides is a process that is well documented. In a previous paper (6) we described a stereoselective synthesis of (*E*)-1-methylthio-2-azabuta-1,3-diene-4-carbonitriles (N-alkenyl thioimidates) **5** and **6** by methylation of adducts **3** and **4**, which were formed from addition of thioamides to methoxymethylene compounds **1** or ketene dithioacetals **2**. Treatment of **5***a* and **6***a* with sodium methanethiolate affords *Z* isomers **7** and **8**, respectively.

To gain further insight into the stereoselectivity of these alkylation processes we examined the methylation of adducts **9–11** to afford the 1-methoxy-1-phenyl-2-azabuta-1,3-dienes **12–14**. There are several studies (7–17) on nucleophilic substitutions at the C—N double bond. A nucleophilic addition–elimination mechanism or a pathway involving a nitrilium ion intermediate has been suggested. Herein we describe the reactions of 2-azabuta-1,3-dienes with sodium methoxide or pyrrolidine and their stereochemical results.

Scheme 1.

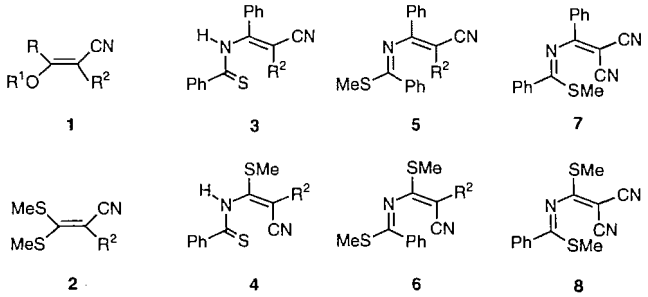

Results and discussion

The adducts **9–11** were obtained from benzamide and the unsaturated compounds **1** or **2** using NaH as the base. Methylation of adducts **9–11** with diazomethane occurs stereoselectively, affording (*E*)-1-methoxy-1-phenyl-2-azabuta-1,3-dienes **12–14**.

Stereoselective formation of 2-azabuta-1,3-dienes **5** and **6** and **12–14** cannot be explained by assuming an *E* conformation for the adducts because a radiocrystallographic study (18) of **3***b* showed it to have a *Z* conformation. The stereochemical

Received May 29, 1995.

A. Lorente[1] **and M. Casillas.** Departamento de Química Orgánica, Universidad de Alcalá, 28871, Alcalá de Henares, Madrid, Spain.
P. Gomez-Sal and A. Manzanero. Departamento de Química Inorgánica, Universidad de Alcalá, 28871, Alcalá de Henares, Madrid, Spain.

[1] Author to whom correspondence may be addressed. Telephone: 341-8854691. Fax: 341-8854686.

Scheme 2.

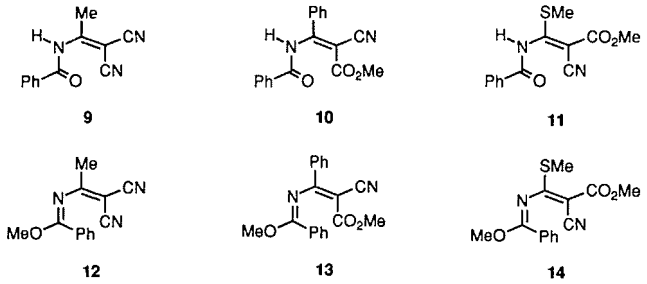

9 **10** **11**

12 **13** **14**

results obtained in the synthesis of these 2-azabuta-1,3-dienes can be accounted for by the lower steric hindrance in the transition state for the formation of the *E* isomers.

Scheme 3.

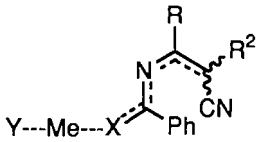

It is well established (19) that the *E* form of imidate or thioimidate esters is more stable than the *Z* form and *E*–*Z* interconvention can proceed by nitrogen inversion or by tautomerization and rotation about the C—N single bond. As we described in a previous paper (6), the 2-azabuta-1,3-dienes **5** and **6** retain their stereochemistry in solution but isomerization of the C—N double bond was achieved by treatment of **5***a* and **6***a* with sodium methanethiolate to afford the *Z* isomers **7** and **8**, respectively. We now report the conversion of (*E*)-1-methylthio-2-azabuta-1,3-diene-4,4-dicarbonitriles **5***a* and **6***a* to (*Z*)-1-methoxyderivatives **15** and **16** by treatment with sodium methoxide in methanol.

Scheme 4.

15 **16**

These results can be rationalized on the basis of the principle of stereoelectronic control. If we assume that an addition–elimination mechanism is followed, the reaction of methoxide ion on **5***a* and **6***a* gives the intermediate **17**, which can rotate to give other conformations with two lone pairs antiperiplanar to SMe, one of which (**18**) gives the *E* product and the other one (**19**) the *Z* product. The fact that only *Z* isomers were obtained can be explained by the greater unfavourable steric hindrance of intermediates **17** and **18**.

Scheme 5.

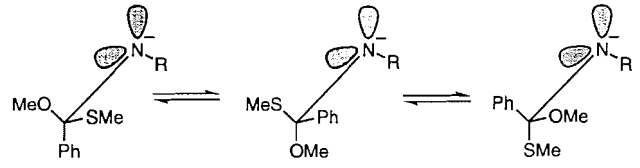

18 **17** **19**

The stereochemistry and mechanisms of amine substitution reactions at the C—N double bond have been studied (7–11, 16, 17). In a previous paper (20) were reported the reactions of **5***a* and **6***a* with nitrogen nucleophiles to afford different heterocyclic systems. We describe here the reactions of (*E*)-1-methylthio-2-azabuta-1,3-dienes **5***a* and **6***a* with pyrrolidine in propan-2-ol at room temperature to give (*E*)-1-(1-pyrrolidinyl)-2-azabuta-1,3-dienes **20** and **21**. In a similar manner the reaction of (*E*)-2-azabuta-1,3-diene **22** with pyrrolidine affords (*E*)-1-(1-pyrrolidinyl)-2-azabuta-1,3-diene **23**.

Scheme 6.

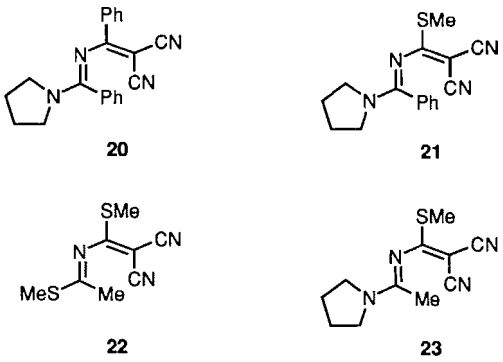

20 **21**

22 **23**

The stereochemical results of these reactions cannot be satisfactorily explained by an addition–elimination pathway because addition of pyrrolidine to **5***a* and **6***a* produces intermediate **24**, which can stereomutate to intermediates **25** and **26**. Both of these have one antiperiplanar electron pair set up for stereoelectronically controlled elimination of methanethiolate ion to afford (*E*)- or (*Z*)-1-(1-pyrrolidinyl)-2-azabuta-1,3-diene, respectively. However, the steric requirements of these intermediates could not account for the stereoselectivity of the reaction.

Scheme 7.

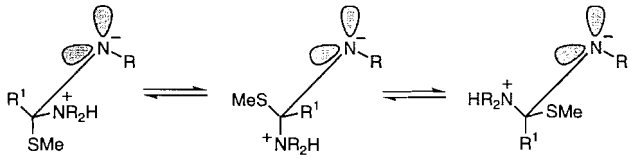

26 **24** **25**

It is possible that the reactions of 1-methylthio-2-azabuta-1,3-dienes with pyrrolidine proceed by an S_N2 or ion-pair (IP) mechanism (21). Additions of nucleophiles to nitrilium ions are known to occur so that the nucleophile and the electron pair on nitrogen are *anti* to each other (22–24), which could account for the observed stereochemical results. Another possibility is the synchronous displacement of the methanethiolate ion without formation of a tetrahedral intermediate (9, 25–27).

Structural study

In previous papers (6, 28) radiocrystallographic studies of 1-methylthio-2-azabuta-1,3-dienes were reported. We describe here the structure of 3-methylthio-1-(1-pyrrolidinyl)-2-azabuta-1,3-diene-4,4-dicarbonitriles **21** and **23**.

Description of the structure of compound ***21***

Positional parameters for non hydrogen atoms are given in Table 1. Figure 1 displays the structural formula with the labelling scheme and Tables 2 and 3 show selected geometric parameters. The azadiene framework deviates from coplanarity (C(1)-N(2)-C(3)-C(4)) but to a lesser extent than that found

Table 1. Atomic coordinates ($\times 10^4$) and equivalent isotropic displacement parameters ($Å^2 \times 10^3$) for **21**. U_{eq} is defined as one third of the trace of the orthogonalized U_{ij} tensor.

	x	*y*	*z*	U_{eq}
S(11)	1699(1)	5208(1)	843(1)	68(1)
C(1)	1731(2)	6429(2)	−1004(2)	40(1)
N(2)	1237(2)	6034(2)	−431(1)	48(1)
C(3)	1565(2)	5281(2)	−135(2)	43(1)
C(4)	1718(2)	4516(2)	−540(2)	45(1)
N(11)	1143(2)	7040(1)	−1359(1)	45(1)
N(6)	1282(3)	4441(2)	−1954(2)	71(1)
N(7)	2387(3)	3102(2)	86(2)	74(1)
C(6)	1482(2)	4479(2)	−1322(2)	49(1)
C(7)	2081(3)	3727(2)	−191(2)	52(1)
C(8)	1507(4)	6311(3)	1127(2)	84(1)
C(11)	2942(2)	6250(2)	−1226(2)	42(1)
C(12)	3777(3)	6243(2)	−673(2)	60(1)
C(13)	4905(3)	6040(4)	−859(2)	80(1)
C(14)	5188(3)	5841(3)	−1594(3)	77(1)
C(15)	4364(3)	5850(2)	−2142(2)	65(1)
C(16)	3244(3)	6060(2)	−1963(2)	54(1)
C(21)	1608(3)	7700(2)	−1879(2)	56(1)
C(22)	813(3)	8466(2)	−1746(2)	68(1)
C(23)	−333(3)	8052(3)	−1596(2)	76(1)
C(24)	−33(3)	7261(2)	−1120(2)	60(1)

Table 2. Selected bond lengths (Å) and angles (°) for **21**.

S(11)—C(3)	1.749(3)	S(11)—C(8)	1.779(4)
C(1)—N(2)	1.318(3)	C(1)—N(11)	1.321(3)
C(1)—C(11)	1.492(4)	N(2)—C(3)	1.325(4)
C(3)—C(4)	1.388(4)	C(4)—C(6)	1.418(4)
C(4)—C(7)	1.426(4)	N(11)—C(21)	1.475(4)
N(11)—C(24)	1.476(4)	N(6)—C(6)	1.148(4)
N(7)—C(7)	1.134(4)	C(11)—C(12)	1.383(4)
C(11)—C(16)	1.387(4)	C(12)—C(13)	1.392(5)
C(13)—C(14)	1.382(6)	C(14)—C(15)	1.369(6)
C(15)—C(16)	1.383(5)	C(21)—C(22)	1.515(5)
C(22)—C(23)	1.504(6)	C(23)—C(24)	1.519(5)
C(3)-S(11)-C(8)	102.1(2)	N(2)-C(1)-N(11)	117.9(2)
N(2)-C(1)-C(11)	122.3(2)	N(11)-C(1)-C(11)	119.7(2)
C(1)-N(2)-C(3)	125.5(2)	N(2)-C(3)-C(4)	124.5(3)
N(2)-C(3)-S(11)	118.5(2)	C(4)-C(3)-S(11)	116.8(2)
C(3)-C(4)-C(6)	121.2(3)	C(3)-C(4)-C(7)	122.0(3)
C(6)-C(4)-C(7)	116.8(3)	C(1)-N(11)-C(21)	126.5(2)
C(1)-N(11)-C(24)	120.6(2)	C(21)-N(11)-C(24)	111.3(2)
N(6)-C(6)-C(4)	179.2(3)	N(7)-C(7)-C(4)	179.0(3)
C(12)-C(11)-C(16)	119.3(3)	C(12)-C(11)-C(1)	118.7(3)
C(16)-C(11)-C(1)	121.9(3)	C(13)-C(12)-C(11)	119.9(3)
C(14)-C(13)-C(12)	120.0(3)	C(15)-C(14)-C(13)	120.1(3)
C(14)-C(15)-C(16)	120.2(3)	C(15)-C(16)-C(11)	120.4(3)
N(11)-C(21)-C(22)	102.1(2)	C(23)-C(22)-C(21)	104.2(3)
C(24)-C(23)-C(22)	103.3(3)	N(11)-C(24)-C(23)	103.8(3)

Fig. 1. ORTEP view of compound **21** showing the crystallographic numbering.

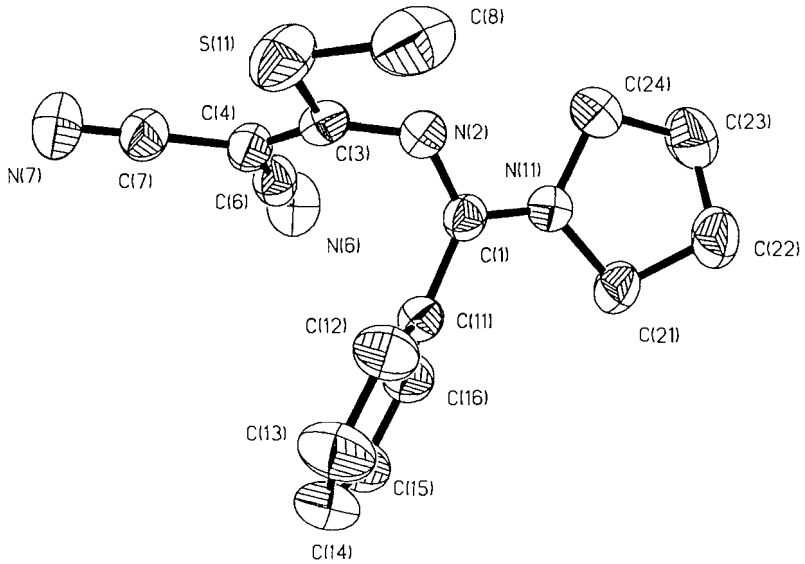

in 1-methylthio-2-azabuta-1,3-dienes (6). This allows better conjugation between the pyrrolidine nitrogen and the azadiene framework that produces a shortening of the N(11)—C(1) and N(2)—C(3) bonds and a lengthening of the C(1)—N(2) and C(3)—C(4) double bonds. The phenyl ring is twisted with respect to the plane defined by C(1), N(11), C(11), and N(2) atoms (torsion angle C(12)-C(11)-C(1)-N(2)), which restrains the conjugation. The N(2)-C(3)-C(4) bond angle is expanded whereas S(11)-C(3)-C(4) and S(11)-C(3)-N(2) are correspondingly contracted. These deviations can be considered a consequence of steric effects between the phenyl and dicyanomethylene groups. The stereochemistry of the C(1)—N(2) double bond is *E*. The methylthio group is almost coplanar with the C(3)—C(4) double bond and adopts a *syn* conformation.

Description of the structure of compound ***23***

Positional parameters are given in Table 4 and Fig. 2 displays the structural formula. Tables **5** and **6** show selected geometric parameters, which are similar to those found for compound **21**. The azadiene framework deviates from coplanarity and the stereochemistry of the C(1)—N(2) double bond is *E*. The methylthio group adopts a *syn* conformation.

Table 3. Selected torsion angles (°) for **21**.

C(1)-N(2)-C(3)-C(4)	−53.5(4)	C(24)-N(11)-C(1)-N(2)	−0.6(4)
C(21)-N(11)-C(1)-N(2)	163.9(3)	C(21)-N(11)-C(1)-C(11)	−11.9(4)
C(8)-S(11)-C(3)-N(2)	−7.8(3)	C(4)-C(3)-S(11)-C(8)	177.6(2)
C(7)-C(4)-C(3)-N(2)	179.5(3)	C(6)-C(4)-C(3)-S(11)	171.7(2)
C(6)-C(4)-C(3)-N(2)	−2.5(4)	C(7)-C(4)-C(3)-S(11)	−6.3(4)
C(3)-N(2)-C(1)-N(11)	162.3(3)	C(12)-C(11)-C(1)-N(11)	128.2(3)
C(12)-C(11)-C(1)-N(2)	−47.5(4)		

Table 4. Atomic coordinates ($\times 10^4$) and equivalent isotropic displacement parameters ($Å^2 \times 10^3$) for **23**. U_{eq} is defined as one third of the trace of the orthogonalized U_{ij} tensor.

	x	y	z	U_{eq}
S(11)	228(1)	2146(1)	651(1)	65(1)
C(1)	1790(2)	2546(2)	−1597(2)	46(1)
N(2)	1014(2)	2212(1)	−1077(2)	54(1)
C(3)	429(2)	2677(2)	−457(2)	47(1)
C(4)	−125(2)	3510(2)	−635(2)	49(1)
N(11)	2126(2)	2016(1)	−2302(2)	50(1)
N(6)	−87(2)	4232(2)	−2295(2)	74(1)
N(7)	−1367(2)	4232(2)	598(2)	89(1)
C(6)	−98(2)	3922(2)	−1545(2)	53(1)
C(7)	−808(2)	3913(2)	51(2)	60(1)
C(8)	1019(3)	1104(3)	559(3)	102(1)
C(11)	2353(2)	3451(2)	−1385(2)	65(1)
C(21)	1638(2)	1102(2)	−2529(2)	61(1)
C(22)	2274(3)	745(3)	−3354(4)	96(1)
C(23)	3206(3)	1293(3)	−3406(3)	120(2)
C(24)	3076(2)	2185(2)	−2870(2)	68(1)

Table 5. Selected bond lengths (Å) and angles (°) for **23**.

S(11)—C(3)	1.756(3)	S(11)—C(8)	1.786(3)
C(1)—N(2)	1.315(3)	C(1)—N(11)	1.318(3)
C(1)—C(11)	1.495(3)	N(2)—C(3)	1.323(3)
C(3)—C(4)	1.393(3)	C(4)—C(6)	1.413(4)
C(4)—C(7)	1.420(4)	N(11)—C(21)	1.467(3)
N(11)—C(24)	1.467(3)	N(6)—C(6)	1.147(4)
N(7)—C(7)	1.141(3)	C(21)—C(22)	1.505(4)
C(22)—C(23)	1.413(5)	C(23)—C(24)	1.480(4)
C(3)-S(11)-C(8)	101.8(1)	N(2)-C(1)-N(11)	117.5(2)
N(2)-C(1)-C(11)	123.5(2)	N(11)-C(1)-C(11)	118.9(2)
C(1)-N(2)-C(3)	127.7(2)	N(2)-C(3)-C(4)	125.6(2)
N(2)-C(3)-S(11)	117.5(2)	C(4)-C(3)-S(11)	116.7(2)
C(3)-C(4)-C(6)	120.0(2)	C(3)-C(4)-C(7)	121.5(2)
C(6)-C(4)-C(7)	118.2(2)	C(1)-N(11)-C(21)	122.0(2)
C(1)-N(11)-C(24)	126.0(2)	C(21)-N(11)-C(24)	111.6(2)
N(6)-C(6)-C(4)	178.0(3)	N(7)-C(7)-C(4)	179.2(3)
N(11)-C(21)-C(22)	103.8(2)	C(23)-C(22)-C(21)	107.7(3)
C(24)-C(23)-C(22)	110.3(3)	N(11)-C(24)-C(23)	103.5(2)

Structure and stereochemistry of 2-azabuta-1,3-dienes and their precursors

The configuration of the C—C double bond of adduct **10** was established by comparison with the ^1H NMR spectrum of dimethyl 1-benzamido-1-phenylmethylenemalonate (18) taking into account the shielding effect exerted by the phenyl group on the methoxycarbonyl. This configuration can be stabilized by the N-H.....O=C hydrogen bond as in the adduct **3***b* (18). The *Z* geometry of the C—C double bond in compound **11** was deduced from NOE experiments and can be explained by an attractive nonbonded CH_3S.....O=C interaction similar to that found in compound **6***b* (6).

The geometry of the C—N double bond of 2-azabuta-1,3-dienes was established on the basis of chemical shifts (Table 7) of the aromatic hydrogens on C1. The deshielding of the *ortho* hydrogens in compounds **15** and **16** indicates a coplanar arrangement of the phenyl and C—N double bond. This fact is similar to that found in (*Z*)-1-methylthio-2-azabuta-1,3-dienes **7** and **8**. On the contrary, the chemical shifts of the *ortho* aromatic hydrogens of compounds **12–14**, **20**, and **21** are similar to those of the corresponding hydrogens in (*E*)-1-methylthio-2-azabuta-1,3-dienes **5** and **6**. This fact allows us to assign an *E* configuration to the carbon–nitrogen double bond and a twisted conformation for the phenyl ring in solution, as found in the solid state for compound **21**.

Experimental

General

Melting points were determined with a Büchi SMP-20 apparatus and are uncorrected. IR were recorded on a Perkin Elmer 883 spectrophotometer. NMR spectra were obtained on a Varian Unity 300 instrument and mass spectra on a Hewlett Packard HP-5988 at 70 eV. Microanalyses were performed on a Heraeus CHN microanalyser. Flash column chromatography was carried out on silica gel SDS (230–400 mesh). Methoxymethylene compounds (**1**) were prepared using previously reported procedures (29, 30). Ketene dithioacetals (**2**) were prepared according to the procedure described by R. Gompper and W. Töpfl (31). The synthesis of methyl (*Z*)-3-benzamido-2-cyano-3-phenylpropenoate (**10**) was described in a previous paper (18) and methyl (*Z*)-3-benzamido-2-cyano-3-methylthiopropenoate (**11**) was prepared according to the reported procedure (32).

X-Ray diffraction

The crystals were mounted in an Enraf–Nonius CAD-4 automatic four-circle diffractometer, with bisecting geometry and graphite-oriented monochromator, using Mo K_α radiation (λ = 0.7107 Å). Unit cell parameters were calculated by least-squares refinement on diffractometer angles for 25 automatically centered reflections. Crystallographic and experimental details are summarized in Table 8.

Fig. 2. ORTEP view of compound **23** showing the crystallographic numbering.

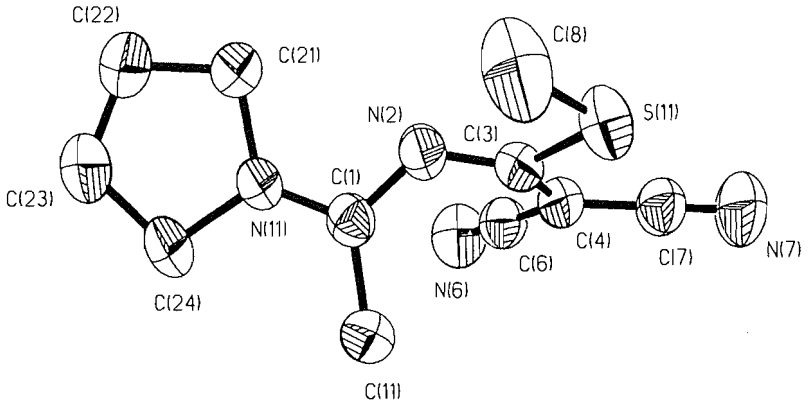

Table 6. Selected torsion angles (°) for **23**.

C(1)-N(2)-C(3)-C(4)	53.4(4)	C(21)-N(11)-C(1)-C(11)	177.6(2)
C(8)-S(11)-C(3)-N(2)	3.4(3)	C(4)-C(3)-S(11)-C(8)	177.6(2)
C(24)-N(11)-C(1)-C(11)	5.5(4)	C(11)-C(1)-N(2)-C(3)	18.2(4)

Table 7. ^{1}H and NMR[a] chemical shifts for 2-azabuta-1,3-dienes at 300 MHz.

	12	**13**	**14**	**15**	**16**	**20**	**21**	**23**
CH_3S			2.36				2.48	2.30
CH_3O	3.99	4.33	4.01	4.22	4.16 (s, 6H)			
CO_2CH_3		3.75	3.63					
Aromatics	7.44–7.60 (m)	7.55–7.93 (m)	7.54–7.63 (m)	7.55–7.65 (m, 6H)	7.54–7.63 (m, 2H)	6.97–7.0 (m, 3H)	7.41–7.44 (m, 2H)	
				8.02–8.07 (m, 2H)	8.42–8.45 (m, 3H)	7.05–7.24 (m, 3H)	7.50–7.57 (m, 3H)	
				8.47–8.53 (m, 2H)		7.27–7.33 (m, 2H)		
						7.42–7.62 (m, 2H)		
Others	2.32 (s, 3H, CH_3)					3.79 (t, J = 6.96, 2H, N-CH_2)	3.61 (t, J = 6.96, 2H, N-CH_2)	3.58 (t, J = 6.59, 2H, N-CH_2)
						3.39 (t, J = 6.77, 2H, N-CH_2)	3.44 (t, J = 6.77, 2H, N-CH_2)	3.43 (t, J = 6.59, 2H, N-CH_2)
						1.98–2.07 (m, 2H, CH_2)	1.95–2.04 (m, 2H, CH_2)	2.15 (s, 3H, CH_3)
						1.82–1.91 (m, 2H, CH_2)	1.82–1.91 (m, 2H, CH_2)	1.86–1.96 m, 4H, 2 CH_2)

[a]All spectra were registered in DMSO-d_6 with the exception of compound **13** ($CDCl_3$).

Data were collected at room temperature, using the $\omega/2\theta$ scan mode. Two check reflections measured every 90 min showed no significant variation. Intensities were corrected for Lorentz and polarization effects in the usual manner. No absorption or extinction corrections were made. The structures were solved by a combination of direct methods and Fourier synthesis and refined by least squares against F^2. All non hydrogen atoms were refined anisotropically. In **21**, the hydrogen atoms were found in the difference Fourier synthesis map and included in further refinement with fixed isotropic temperature factors. In **23** the hydrogen atoms were included from geometrical calculations with thermal parameters equivalent to the carbon to which they were attached. Final R_1 = 0.0664 and wR_2 = 0.1920 were obtained for **21** with a weighting scheme $w = 1/[\sigma^2(F_o^2) + (0.1301P)^2 + 0.6739P]$ and R_1 = 0.0515 and wR_2 = 0.1405 for **23** with a

Table 8. Crystal data and structure refinement for **21** and **23**.

	21	**23**
Empirical formula	$C_{16}H_{16}N_4S$	$C_{11}H_{14}N_4S$
Crystal size	0.25 × 0.3 × 0.2 mm	0.5 × 0.35 × 0.3 mm
Colour	Pale yellow	Pale yellow
Crystal habit	Rhombohedral	Hexagonal
Formula weight	296.39	234.32
Temperature	293(2) K	293(2) K
Wavelength	0.71069 Å	0.71069 Å
Crystal system	Orthorhombic	Orthorhombic
Space group	*Pbca*	*Pbca*
Unit cell dimensions	a = 11.669(1) Å	a = 12.669(1) Å
	b = 15.332(2) Å	b = 14.122(2) Å
	c = 17.770(3) Å	c = 14.150(2) Å
Volume	3179.2(7) Å^3	2531:6(5) Å^3
Z	8	8
Density (calculated)	1.238 g/cm^3	1.230 g/cm^3
Absorption coefficient	2.02 cm^{-1}	2.36 cm^{-1}
F(000)	1248	992
θ range for data collection	2.29–27.02	2.15–28.22
Index ranges	$0 < h < 14$, $0 < k < 19$, $0 < l < 22$	$0 < h < 16$, $0 < k$ 18, $0 < l < 18$
Reflections collected	3530	3179
Independent reflections	3466 (R_{int} = 0.0174)	3119 (R_{int} = 0.0099)
Refl. observed with $I > 2\sigma(I)$	2296	1936
Absorption correction	N/A	N/A
Refinement method	Full-matrix least squares on F^2	
Data/restraints/parameter	3446/0/190	3116/0/145
Goodness of fit on F^2	1.200	1.111
Final R indices ($I > 2\sigma(I)$)	R_1 = 0.0664, wR_2 = 0.1920	R_1 = 0.0515, wR_2 = 0.1405
Largest diff. peak and hole	0.458 and −0.440 e Å^{-3}	0.263 and −0.342 e Å^{-3}
Weighting scheme calcd.	$w = 1/[\sigma^2(F_o^2) + (0.1301P)^2 + 0.6739P]$	$w = 1/[\sigma^2(F_o^2) + (0.0761P)^2 + 1.0989P]$
	In both cases $P = (F_o^2 + 2F_o^2)/3$	

weighting scheme $w = 1/[\sigma^2(F_o)^2 + (0.0761P)^2 + 1.0989P]$ where $P = (F_o^2 + 2F_c^2)/3$ and $R_1 = \Sigma||F_o| - |F_o||/\Sigma|F_o|$ and $wR_2 = [|\Sigma(F_o^2 - F_c^2)^2|/|\Sigma w(F_o^2)^2|]^{1/2}$.

Calculations were performed with SHELXS-90 (33) and SHELXL-93 (34) programs on an Alpha AXP digital workstation.[2]

3-Benzamido-2-cyano-3-methylpropenenitrile 9

To a suspension of 80% NaH (142 mg, 7.3 mmol) in a mixture of dry benzene (15 mL) and dry *N,N*-dimethylacetamide (15 mL), 2-cyano-3-ethoxy-3-methylpropenenitrile (500 mg, 3.6 mmol) and benzamide (445 mg, 3.6 mmol) were added. The mixture was stirred at room temperature for 42 h and then poured into ice-water (50 mL). The aqueous layer was acidified with 10% hydrochloric acid and the precipitate formed was collected and recrystallized from hexane–benzene; 40% yield, mp 120–122°C; ν_{max} (KBr)/cm^{-1}: 3343, 2222, 1713, 1586 and 1476; δ_H (DMSO-d_6) 3.15 (s, 3H, CH_3), 7.54–7.90 (m, 5H, ArH), and 11.16 (s, 1H, NH); *m/z*: 211 (M$^+$, 15%), 106 (58), 105 (100), 77 (97), and 51 (84). Anal. calcd. for $C_{12}H_9N_3O$: C 68.22, H 4.30, N 19.9; found: C 68.05, H 4.41, N 20.01.

(*E*)-1-Methoxy-3-methyl-1-phenyl-2-azabuta-1,3-diene-4,4-dicarbonitrile 12

A solution of **9** (211 mg, 1 mmol) in dry ethyl acetate (20 mL) was methylated at 0°C with diazomethane (generated from Diazald® (750 mg, 3.5 mmol)). The solvent was removed at reduced pressure to afford the crude product, which was purified by flash column chromatography using hexane – ethyl acetate (5:1) as eluent; yield: 7%, mp 34–35°C (from hexane–benzene); ν_{max} (KBr)/cm^{-1}: 2256, 2226, 1658, and 1494; *m/z*: 225 (M$^+$, 44%), 210 (43), 193 (19), 153 (34), 105 (56), and 77 (100). Anal. calcd. for $C_{13}H_{11}N_3O$: C 69.31, H 4.93, N 18.66; found: C 69.10, H 4.89, N 18.91.

(1*E*, 3*Z*)-Methyl 4-cyano-1,3-diphenyl-2-azabuta-1,3-diene-4-carboxylate 13

A solution of **10** (153 mg, 0.5 mmol) in dry ethyl acetate (25 mL) was methylated at 0°C with diazomethane (generated from diazald (375 mg, 1.75 mmol)). The solvent was evapo-

[2] Tables of hydrogen coordinates and of isotropic and anisotropic displacement parameters for **21** and **23** have been deposited and can be purchased from: The Depository of Unpublished Data, Document Delivery, CISTI, National Research Council Canada, Ottawa, Canada K1A 0S2. The tables of hydrogen coordinates have also been deposited with the Cambridge Crystallographic Data Centre, and can be obtained on request from The Director, Cambridge Crystallographic Data Centre, University Chemical Laboratory, 12 Union Road, Cambridge, CB2 1EZ, U.K.

rated at reduced pressure and the crude product thus obtained was purified by flash column chromatography using hexane – ethyl acetate (6:1) as eluent; yield: 15%, mp 153–154°C (from propan-2-ol); ν_{max} (Nujol)/cm^{-1}: 2221, 1714, 1687, 1605, 1593, and 1462; *m/z*: 320 (M^+, 4%), 261 (4), 247 (10), 106 (8), 105 (100), 77 (32), and 51 (6). Anal. calcd. for $C_{19}H_{16}N_2O_3$: C 71.24, H 5.03, N 8.74; found: C 71.01, H 5.15, N 8.92.

(1*E*, 3*Z*)-Methyl 4-cyano-1-methoxy-3-methylthio-1-phenyl-2-azabuta-1,3-diene-4-carboxylate 14

A solution of **11** (200 mg, 0.725 mmol) in dry ether (70 mL) was methylated at 0°C with diazomethane (generated from diazald (550 mg, 2.56 mmol)). The solvent was removed at reduced pressure to afford the crude product, which was purified by flash column chromatography using hexane – ethyl acetate, 5:1 and then 3:1, as eluent; yield: 75%, mp 141–142°C (from propan-2-ol); ν_{max} (Nujol)/cm^{-1}: 2216, 1696, and 1644; *m/z*: 290 (M^+, 10%), 249 (15), 118 (5), 105 (100), and 77 (34). Anal. calcd. for $C_{14}H_{14}N_2O_3S$: C 57.92, H 4.86, N 9.65; found: C 57.81, H 4.9, N 9.71.

(*Z*)-1-Methoxy-1,3-diphenyl-2-azabuta-1,3-diene-4,4-dicarbonitrile 15

To a solution of sodium (23 mg, 1 mmol) in dry methanol (40 mL) was added **5***a* (151 mg, 0.5 mmol). The reaction mixture was heated at reflux for 2 h and then the solvent was removed at reduced pressure. The crude product thus obtained was purified by flash column chromatography using hexane – ethyl acetate (7:1) as eluent, affording 48 mg (31% yield) of **7**. With the same eluent 1-methoxy-2-azabuta-1,3-diene (**15**) was obtained; 68% yield, mp 151–152°C (from methanol); ν_{max} (KBr)/cm^{-1}: 2216, 1583, 1554, 1529, 1494, 1468, and 1449; δ_H ($CDCl_3$): 4.29 (s, 3H, OCH_3), 7.50–7.60 (m, 6H, ArH), 8.16–8.19 (m, 2H, ArH), and 8.57–8.60 (m, 2H, ArH); *m/z*: 287 (M^+, 100%), 257 (21), 256 (26), 184 (52), 156 (22), 155 (33), 129 (25), 128 (13), 127 (40), 104 (46), 103 (38) and 77 (39). Anal. calcd. for $C_{18}H_{13}N_3O$: C 75.23, H 4.56, N 14.63; found: C 75.41, H 4.51, N 14.22.

(*Z*)-1,3-Dimethoxy-1-phenyl-2-azabuta-1,3-diene-4,4-dicarbonitrile 16

To a solution of sodium (92 mg, 4 mmol) in dry methanol (25 mL), was added. **6***a* (110 mg, 0.4 mmol). The mixture was stirred at room temperature for 6 h. The solvent was removed at reduced pressure to afford the crude product, which was purified by flash column chromatography using hexane – ethyl acetate (3:1) as eluent; 27% yield, mp 164–165°C (from hexane–methanol); ν_{max} (KBr)/cm^{-1}: 2224, 1583, 1548, and 1461; *m/z*: 241 (M^+, 75%), 214 (27), 196 (26), 186 (27), 170 (18), 118 (53), 104 (100), 92 (69), and 77 (73). Anal. calcd. for $C_{13}H_{11}N_3O_2$: C 64.72, H 4.6, N 17.42; found: C 64.95, H 4.51, N 17.64.

(*E*)-1,3-Diphenyl-1-(1-pyrrolidinyl)-2-azabuta-1,3-diene-4,4-dicarbonitrile 20

To a solution of **5***a* (180 mg, 0.59 mmol) in dry propan-2-ol (20 mL) was added pyrrolidine (74 μL, 0.89 mmol). The mixture was stirred at room temperature for 23 h. The solvent was removed at reduced pressure to afford the crude product, which was washed with hexane and recrystallized from propan-2-ol; 95% yield, mp 170–171°C; ν_{max} (KBr)/cm^{-1}: 2212, 2201, 1581, 1546, 1512, 1486, and 1458; *m/z*: 326 (M^+, 26%), 272 (6), 257 (10), 192 (2), 153 (35), 104 (40), 77 (53), and 70 (100). Anal. calcd. for $C_{21}H_{18}N_4$: C 77.28, H 5.56, N 17.17; found: C 77.41, H 5.62, N 17.11.

(*E*)-3-Methylthio-1-phenyl-1-(1-pyrrolidinyl)-2-azabuta-1,3-diene-4,4-dicarbonitrile 21

To a solution of **6***a* (160 mg, 0.59 mmol) in dry propan-2-ol (20 mL) was added pyrrolidine (74 μL, 0.89 mmol). The mixture was stirred at room temperature for 23 h. The solvent was removed at reduced pressure to afford the crude product, which was washed with hexane and recrystallized from ethyl acetate; 83% yield, mp 138–139°C; ν_{max} (KBr)/cm^{-1}: 2205, 1579, 1453, and 1441; *m/z*: 296 (M^+, 27%), 249 (36), 207 (10), 180 (44), 153 (26), 146 (26), 123 (15), 104 (87), 91 (31), 77 (87), and 70 (100). Anal. calcd. for $C_{16}H_{16}N_4S$: C 64.84, H 5.44, N 18.9; found: C 64.99, H 5.33, N 19.02.

(*E*)-1-Methyl-3-methylthio-1-(1-pyrrolidinyl)-2-azabuta-1,3-diene-4,4-dicarbonitrile 23

To a solution of **22** (32 mg, 0.15 mmol) in dry propan-2-ol (20 mL) was added pyrrolidine (74 μL, 0.89 mmol). The mixture was stirred at room temperature for 22 h. The solvent was removed at reduced pressure to afford the crude product, which was recrystallized from ethyl acetate – hexane; 83% yield, mp 123–124°C; ν_{max} (KBr)/cm^{-1}: 2203, 1567, and 1424; *m/z*: 234 (M^+, 42%), 219 (14), 187 (25), 146 (19), 123 (20), 118 (46), 91 (12), and 70 (100). Anal. calcd. for $C_{11}H_{14}N_4S$: C 56.39, H 6.02, N, 23.91; found: C 56.11, H 6.12, N 24.07.

Acknowledgments

We thank the Consejería de Educación de la Comunidad Autónoma de Madrid (Grant C061/91) and the Universidad de Alcalá (Grant 001/95) for financial support.

References

1. W. Kantlehner. Adv. Org. Chem. **9**, 181 (1979).
2. W. Kantlehner. *In* Comprehensive organic synthesis. Vol. 6. *Edited by* B.M. Trost and I. Fleming. Pergamon Press, Oxford. 1991. pp. 501–503.
3. D.G. Neilson. *In* The chemistry of amidines and imidates. *Edited by* S. Patai. Interscience, New York. 1975. pp. 399–402.
4. W. Kantlehner. *In* Comprehensive organic synthesis. Vol. 6. *Edited by* B.M. Trost and I. Fleming. Pergamon Press, Oxford. 1991. pp. 508–509.
5. D.G. Neilson. *In* chemistry of amidines and imidates. Vol. 2. *Edited by* S. Patai and Z. Rappoport. J. Wiley and Sons, New York. 1991. pp. 429–431.
6. A. Lorente, J.L. Balcázar, and F. Florencio. J. Chem. Soc. Perkin Trans. 1, 3377 (1992).
7. R. Ta-Shma and Z. Rappoport. Tetrahedron Lett. 3813 (1971).
8. R. Ta-Shma and Z. Rappoport. J. Am. Chem. Soc. **98**, 8460 (1976).
9. R. Ta-Shma and Z. Rappoport. J. Am. Chem. Soc. **99**, 1845 (1977).
10. R. Ta-Shma and Z. Rappoport. J. Chem. Soc. Perkin Trans. 2, 659 (1977).
11. J.E. Johnson, E.A. Nalley, and C. Weidig. J. Am. Chem. Soc. **95**, 2051 (1973).
12. J.E. Johnson, E.A. Nalley, C. Weidig, and M. Arfan. J. Org. Chem. **46**, 3623 (1981).

13. M.T. McCormack and A.F. Hegarty. Tetrahedron Lett. 395 (1976).
14. A.F. Hegarty, M.T. McCormack, B.J. Hathaway, and L.J. Hulett. J. Chem. Soc. Perkin Trans. 2, 1136 (1977).
15. J.E. Rowe and A.F. Hegarty. J. Org. Chem. **49**, 3083 (1984).
16. J.E. Johnson, A. Ghafouripour, M. Arfan, S.L. Todd, and D.A. Sitz. J. Org. Chem. **50**, 3348 (1985).
17. J.E. Johnson, S.L. Todd, S.M. Dutson, A. Ghafouripour, R.M. Alderman, and M.R. Hotema. J. Org. Chem. **57**, 4648 (1992).
18. A. Lorente, L. Vaquerizo, A. Martín, and P. Gómez-Sal. Heterocycles, **41**, 71 (1995).
19. C.L. Perrin. *In* The chemistry of amidines and imidates. Vol. 2. *Edited by* S. Patai and Z. Rappoport. J. Wiley and Sons, New York. 1991. pp. 147–229.
20. A. Lorente, P. Gámez, and M.M. Contreras. Heterocycles, **38**, 113 (1994).
21. R.A. Sneen. Acc. Chem. Res. **6**, 46 (1973).
22. J.E. Johnson and S.C. Cornell. J. Org. Chem. **45**, 4144 (1980).
23. M.T. McCormack and A.F. Hegarty. J. Chem. Soc. Perkin Trans. 2, 1701 (1976).
24. A.F. Hegarty. Acc. Chem. Res. **13**, 448 (1980).
25. M.I. Page and W.P. Jencks. J. Am. Chem. Soc. **94**, 8828 (1972).
26. S.I. Miller. Tetrahedron, **33**, 1211 (1977).
27. D.N. Kevill, P.H. Daum, and R. Sapre. J. Chem. Soc. Perkin Trans. 2, 963 (1975).
28. J.L. Balcázar, F. Florencio, and S. Garcia-Blanco. Acta Crystallogr. Sect. C: Cryst. Struct. Commun. (*a*) **C41**, 1795 (1985); (*b*) **C43**, 1438 (1987); (*c*) **C44**, 1500 (1988); (*d*) **C43**, 1432 (1987).
29. A. Dornow and E. Schleese. Chem. Ber. **91**, 1830 (1958).
30. T. Hayashi. J. Org. Chem. **31**, 3253 (1966).
31. R. Gompper and W. Töpfl. Chem. Ber. **95**, 2861 (1962).
32. S. Kohra, Y. Tominaga, and A. Hosomi. J. Heterocycl. Chem. **25**, 959 (1988).
33. G.M. Sheldrick. Acta Crystallogr. Sect. A. Found. Crystallogr. **A46**, 467 (1990).
34. G.M. Sheldrick. SHELXL-93, University of Göttingen. 1993.

Effect of concentration, pH, and ionic strength on the viscosity of solutions of a soil fulvic acid

F. Rey, M.A. Ferreira, P. Facal, and A.A.S.C. Machado

Abstract: The influence of pH (3.0–8.0), ionic strength (0.005–0.10 M), and concentration (ca. 50–300 mg L^{-1}) on the viscosimetric behaviour of solutions of a soil fulvic acid has been determined. The results show a complex influence of the concentration on the specific viscosity with maxima at about 80–100 mg L^{-1} and a minimum at 140–160 mg L^{-1}. The viscosity is minimum at pH ca. 6 and decreases when the ionic strength increases. The results are interpreted by a rod-type model from which the dimensions of fulvic acid molecules are calculated.

Key words: soil fulvic acids, viscosity, configurational changes.

Résumé : On a déterminé l'influence du pH (3,0–8,0), de la force ionique (0,005–0,10 M) et de la concentration (environ 30–300 mg L^{-1}) sur le comportement viscosimétrique de solutions d'un acide fulvique de sol. Les résultats démontrent l'existence d'une influence complexe de la concentration sur la viscosité spécifique qui présente un maximum à environ 80–100 mg L^{-1} et un minimum à 140–160 mg L^{-1}. La viscosité est minimale à un pH d'environ 6 et elle diminue avec une augmentation de la force ionique. On interprète les résultats en fonction d'un modèle en forme de bâtonnets à partir duquel on a calculé les dimensions des molécules de l'acide fulvique.

Mots clés : acides fulviques du sol, viscosité, changements configurationnels.

[Traduit par la rédaction]

Introduction

The size and shape of humic substances play an important role in their effects in the environment, for instance in their interaction with the soil particles, their involvement in the binding of trace metals, their biological effects on plants and microorganisms, and their function in surface and groundwater quality. Important information about the size and shape of fulvic acid molecules in solution can be obtained by viscosimetric measurements. Therefore, different authors (1–6) have investigated the behaviour of humic substances by this technique. Although the calculation procedures are well established, the reported data are incomplete and results of most of them are not intercomparable because of differences in extraction and purification techniques (7).

Moreover, the aggregation of humic substances depends on their nature and the solution conditions under which they exist, for example, on the presence of electrolytes and the value of pH. The effect of these configurational changes may have to be considered in transport phenomena involving organic matter and associated metals, in particular for river humic substances. A theoretical explanation of these phenomena based on potentiometric and conductimetric data has recently been reported (8).

Considering these facts, it was decided to include viscosimetric measurements in a collaborative project in progress in our departments to study the behaviour of fulvic acids (FA) in solution (9–12). This work presents the results obtained in a systematic study of the influence of FA concentration (in the range 50–280 mg L^{-1}, which includes lower values than other studies reported in the literature (1–3)), pH (3.0–8.0), and inert electrolyte concentration (0.005–0.10 M) on the viscosimetric properties (at 298 K constant temperature) of low concentration solutions of a soil FA. From the results, the dimensions of FA particles were calculated assuming a rod-type model and their changes with the solution properties are discussed.

Received May 4, 1995.

F. Rey,[1] **M.A. Ferreira, and P. Facal.** Area de Química Física, Universidad de Vigo, Torrecedeira 86, Vigo, Spain.
A.A.S.C. Machado. LAQUIPAI, Departamento de Química, Faculdade de Ciencias, P-4050, Porto, Portugal.

[1] Author to whom correspondence may be addressed. Telephone: 34-8681-3688. Fax: 34-8681-3663. E-mail: FREY@SETEI.UVIGO.ES

Experimental

Reagents and materials

All reagents were p.a. or similar and were used without further purification. Deionized water with resistivity ≥20 MΩ cm was used.

KNO_3 was employed as background electrolyte to adjust the total ionic strength. For pH adjustments, 0.1 M HCl and 0.1 M NaOH were used.

The sample of FA used in the present work (described before (13)) was isolated from a Portuguese forest soil collected at Famalicao (near Oporto, 30 km to the northeast) by the IHSS standard procedure (14, 15). For that a sample of air-dried soil was acidified to pH 2 with 1 M hydrochloric acid solutions and kept for 15 days with occasional agitation. The solid and liquid phases were separated by filtration and the latter was concentrated through an Amberlite XAD-8 resin column. The nonadsorbed fraction was discarded, the column was washed with water until chloride ions (which interfere in the next stages of the process) were absent, and, finally, the column was eluted with 0.1 M NaOH. The liquid extracts recovered (that contain the fulvic acid "molecules") were

transformed to their acidic form by using a cation exchange resin (Merck) and were freeze-dried to get a powder sample. The yield of the process was about 0.5% (W/W).

Equipment

H^+ concentrations (as pH values) were measured with a Crison micro-pH 2002 pH-meter (±0.1 mV) and an Ingold electrode, calibrated at each ionic strength by standard HCl–NaOH titrations (16). Viscosity measurements were done with an Ostwald-type viscometer, having a flow time with distilled water of 345.4 ± 0.2 s at 298.0 K. A flow bath (Tectron 4373200) was used as thermostat (±0.1 K).

Procedure

Each individual sample was prepared by dissolving aliquots of a FA stock solution (about 1000 mg L^{-1}) in water, and the pH and (or) the neutral salt concentration (total ionic strength) were adjusted to the required values. Experiments were made at FA concentrations of 47.0, 62.0, 71.0, 82.0, 94.0 107.0, 118.0, 131.0, 163.0, 189.0, 236.0, and 289.0 mg L^{-1}, total ionic strengths of 0.005, 0.010, 0.030, 0.050, 0.070, and 0.10 M, and pH at 3.0, 4.0, 5.0, 6.0, 7.0, and 8.0. All experiments were repeated at least 20 times with different solutions and the mean values of flow time, obtained after outlier values were rejected using standard statistical tests (17), were used to calculate the viscosity values.

Calculations

Values of relative (η_r), specific (η_{sp}), and reduced (η_z) viscosity were obtained from the experimental absolute viscosity values using their respective definitions (3)

$$\eta_r = \frac{\eta}{\eta_0}$$

$$\eta_{sp} = \frac{\eta - \eta_0}{\eta_0}$$

$$\eta_z = \frac{\eta_{sp}}{c}$$

where η_0 is the absolute viscosity of water and c the concentration of the solutions.

Intrinsic viscosities ([η]) were calculated by extrapolation to zero concentration of the linear part of the reduced viscosity vs. concentration plots.

The viscosity-average molecular weight (M) was calculated using the Staudinger equation, which relates [η] to M

$$[1] \quad [\eta] = KM^{\alpha}$$

where α has a value of 0.67 (3). The value of K (298 K) was calculated using this value and the value of M obtained for the present sample of FA at $I = 0.1$ M by potentiometric measurements (908 g mol^{-1}). Particle (molecular) volumes were calculated by the approach of Chen and Schnitzer (3), using

$$[2] \quad V = \frac{M}{dN_A}$$

where d is the density of FA solutions and N_A is Avogadro's number.

To calculate the dimensions of FA particles, a model of their structure is required, and several different approaches (namely spheres, disks, and rods) have been proposed. Of these, spherical structures can be excluded in the present case because the [η] values obtained are greater than 0.025 (18). On the other hand, if a disk shape is assumed, the calculated thickness values are about 1 Å, not compatible with the postulated general structures of FA molecules (3). Because FA can be considered as a flexible linear colloid (19) a rod model can be used, and the length (a) and thickness (b) of the particles can be related to a $k([\eta])$ dependent factor by

$$[3] \quad k = \frac{(a/b)^2}{15\,(\ln 2a/b - 3/2)} + \frac{3\,(a/b)^2}{15\,(\ln 2a/b - 1/2)} + \frac{14}{15}$$

This equation can be solved by numerical iteration to calculate the a to b ratio. Individual values of a and b can be estimated from this ratio and the expression for the particle volume given as

$$[4] \quad V = \frac{\pi b^2 a}{4}$$

Results and discussion

The results obtained for the viscosimetric parameters of the FA studied are presented in Table 1. As values of the absolute viscosity for 0.1 M ionic strength show no significant differences from pure water viscosities, the values calculated for this ionic strength are not included.

Influence of the concentration of the fulvic acid

Figure 1 shows the variation of the specific viscosity of FA solutions when their concentration changes. For concentrations below of 80–100 mg L^{-1} (depending on pH and ionic strength), a rise in the specific viscosity occurs when the fulvic acid concentration increases. Then, the specific viscosity decreases with increase in the FA concentration up to about 160 mg L^{-1} (also dependent on pH and ionic strength) and after this value a linear increase is obtained. These results are in agreement with those obtained by Reuter (20), who indicated that a concentration of about 100 mg L^{-1} is a "special value" for the behaviour of humic materials. Besides, according to Ghosh and Schnitzer (1), FA presents important conformational changes in the 100–160 mg L^{-1} range when the concentration varies: at concentrations below 100 mg L^{-1} linear colloids prevail, but above 160 mg L^{-1} only spherocolloids exist; conformational changes occur in the range between these values, where both types of structure are present.

Influence of the ionic strength

In Figure 2 the reduced viscosity is plotted versus the FA concentration for different values of ionic strength but constant pH. The plots show a marked decrease in viscosity when the ionic strength increases, suggesting a coiling of fulvic acid molecules (which has been cited in the literature) due to repulsions by the counterions or neutralization by the added salt of the charges on the backbone of the macromolecule (21),

Table 1. Variation of the viscosity (and related parameters) of fulvic acid with ionic strength and pH.

I	pH	[η]	M (g/mol)	V (Å^3)	k	a/b	a (Å)	b (Å)
0.005	3.0	264	91 561	94 422	425	82.8	938	11.3
	4.0	194	57 810	59 616	312	69.4	715	10.3
	5.0	157	42 154	43 471	253	61.6	594	9.7
	6.0	136	34 022	35 085	219	56.7	524	9.2
	7.0	144	37 052	38 210	232	58.6	551	9.4
	8.0	156	41 754	43 059	251	61.3	591	9.6
0.010	3.0	254	86 433	89 133	409	81.0	907	11.2
	4.0	172	48 304	49 813	277	64.9	644	9.9
	5.0	136	34 022	35 085	219	56.7	524	9.2
	6.0	111	25 125	25 910	179	50.4	438	8.7
	7.0	132	32 540	33 557	213	55.7	510	9.2
	8.0	148	38 599	39 805	238	59.4	564	9.5
0.030	3.0	186	54 289	55 985	299	67.8	689	10.2
	4.0	121	28 577	29 470	195	53.0	472	8.9
	5.0	103	22 470	23 172	166	48.3	410	8.5
	6.0	85	16 870	17 397	137	43.2	346	8.0
	7.0	94	19 604	20 216	151	45.7	377	8.3
	8.0	102	22 146	22 838	164	47.9	406	8.5
0.050	3.0	109	24 452	25 216	175	49.8	430	8.6
	4.0	100	21 501	22 173	161	47.4	399	8.4
	5.0	76	14 275	14 721	122	40.3	312	7.7
	6.0	33	4 110	4 238	53	24.5	148	6.0
	7.0	68	12 091	12 469	109	37.7	283	7.5
	8.0	79	15 124	15 597	127	41.3	323	7.8
0.070	3.0	67	11 827	12 192	108	37.5	280	7.5
	4.0	65	11 304	11 657	105	36.9	272	7.4
	5.0	38	5 073	5 231	61	26.7	168	6.3
	6.0	13	1 023	1 055	21	23.6	63	4.6
	7.0	39	5 274	5 439	63	27.2	172	6.3
	8.0	50	7 641	7 880	81	31.6	216	6.8

Fig. 1. Variation of the specific viscosity with FA concentration for different experimental conditions: ■ pH = 4.00, I = 0.005; ▲ pH = 5.00, I = 0.01; + pH = 6.00, I = 0.03; * pH = 7.00, I = 0.05; □ pH = 8.00, I = 0.07; × pH = 3.00, I = 0.03.

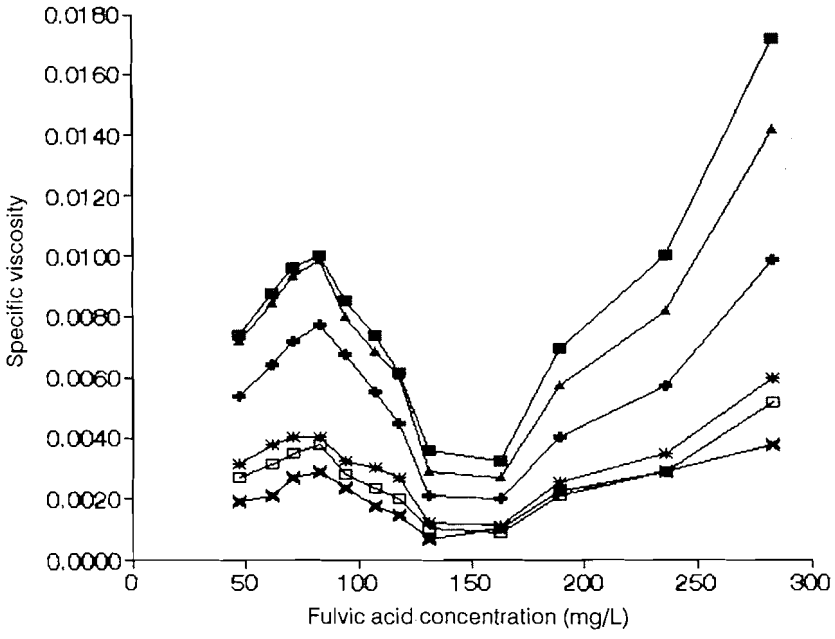

Fig. 2. Variation of the reduced viscosity with FA concentration at pH = 4.00 and different ionic strength: ■ $I = 0.005$; + $I = 0.01$; * $I = 0.03$; □ $I = 0.05$; × $I = 0.07$.

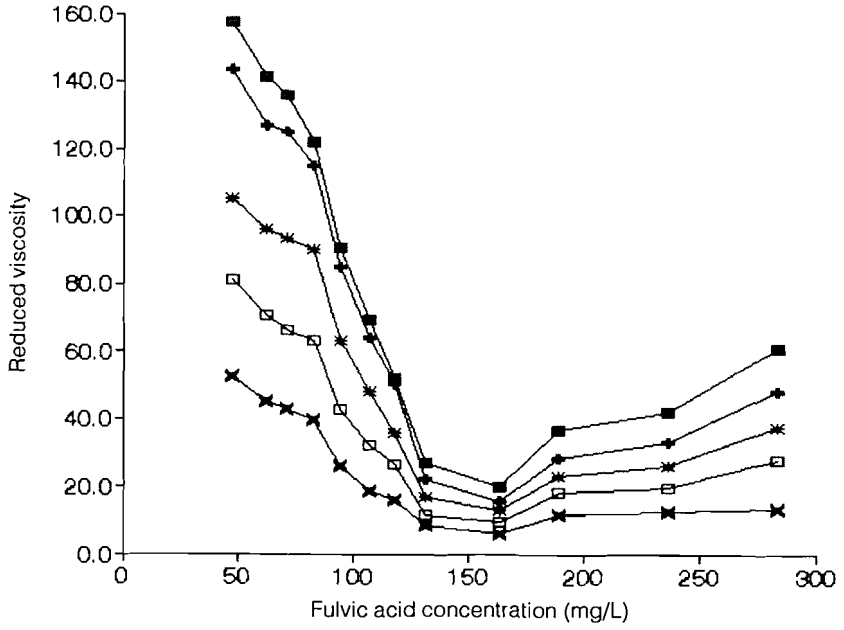

Fig. 3. Variation of the intrinsic viscosity with pH for different ionic strengths: ■ $I = 0.005$; + $I = 0.01$; * $I = 0.03$; □ $I = 0.05$; × $I = 0.07$.

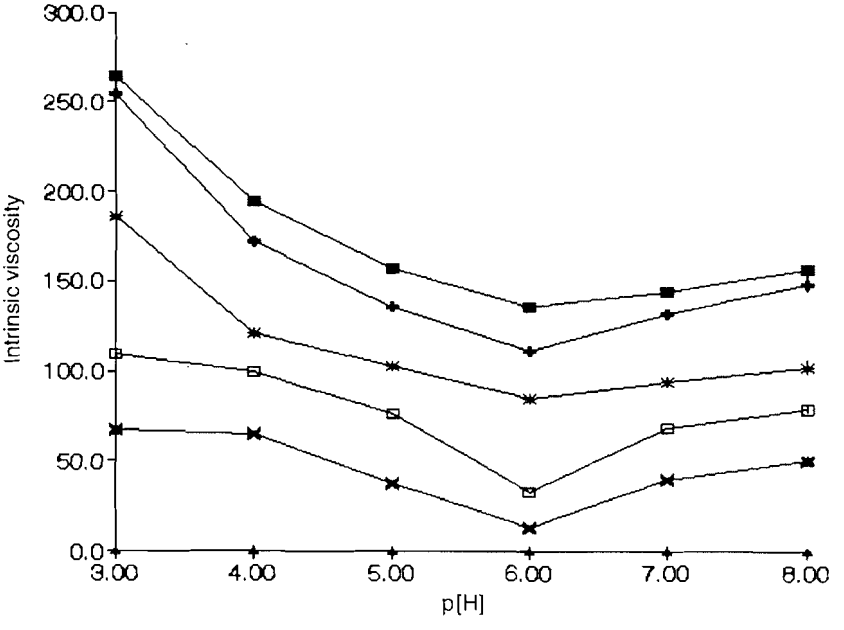

buildup of charges on the macromolecules of the fulvic acid (22), or polidispersity (23). According to Eagland (24), this variation is associated with suppression of the charge atmosphere of the polyelectrolyte molecules, which become less rodlike and hence more flexible.

From these plots, it can be seen that although the viscosity decreases in the presence of the salt, the pattern of the variation with FA concentration is maintained, with a minimum at about 160 mg L^{-1}. Ghosh and Schnitzer (1) concluded that at higher concentrations these polyelectrolytes behaved like uncharged spherocolloids, but the viscosity values suggest that the macromolecules should be considered as tightly coiled and flexible. These results are supported by the behaviour of FA solutions at high ionic strengths described here.

Influence of pH

In addition to polyelectrolyte concentrations and ionic strength, the viscosity of FA solutions varies with pH. Kumada and Kawamura (2) reported a diminution in the reduced viscosity of humic materials when the pH is increased

as the pH approaches 5.0, followed by an increase in the neutral and alkaline pH ranges. Other authors have reported a similar trend but with a minimum at a more acid value of pH (1).

Figure 3 presents the variation of the intrinsic viscosity with pH (for different constant values of ionic strength) for the FA solutions studied in the present work, and shows a minimum in $[\eta]$ between pH 6 and 7. At the lowest pH values, the FA particles remain uncharged, electrostatic repulsions are weak, and the particles present a higher association due to the possible formation of hydrogen bonds, van der Waals forces, and other weak forces (21) (see values of the average molecular weight in Table 1). When the pH increases, the association of the particles is destroyed due to the increase in electrostatic repulsions that are greater than the weak forces, and the aggregates break up because any sort of rearrangement disperses the fully ionized molecules to form small, discrete particles. The viscosity of the fulvic acid decreases until a minimum is reached at pH about 6. At still higher pH values, the intrinsic viscosity increases again, showing a new aggregation due to mineral bridges and intermolecular interactions (25). This behaviour is a common feature for polyelectrolytes of the weak acid type such as FA (26).

The dimensions of the FA aggregates (considered as rod-shaped) are strongly dependent on pH and ionic strength (see *a* and *b* values in Table 1) and present a ×15 variation for *a* values in the range analysed. The values obtained for *a* and *b* are larger than others reported in the literature obtained by viscosimetric measurements at higher FA concentrations (3), perhaps due to the low concentration range analysed in this work in which the molecules are more elongated, but the thickness of the particles is of the same order of magnitude (11.3–4.6 Å) and the values depend strongly on ionic strength but only slightly on pH. The *a* and *b* values suggest that the FA particles are elongated cylinders that change their aggregation states with the external characteristics of solution (namely pH and the presence of counterions).

Conclusions

As can be seen from the results of the present work, viscosimetric measurements of fulvic acids in solution can provide information about the dimensions and modification of the structure of fulvic acid molecules. However, on the other hand, pH plays an important role in the change of these structures, so it is very important to adjust the H^+ concentration when this type of experiment is done. Moreover, the presence of different concentrations of added salt can modify the arrangements of fulvic acid molecules in solution due to the existence of electrostatic interactions between the fulvic acids and the counterions. Because of this it is very important to state clearly the experimental conditions when the results of different experiments are to be compared.

Acknowledgments

The authors acknowledge an Acción Integrada Hispano Portguesa E35/95 from Conselho de Reitores das Universidades Portuguesas (Portugal) and B13/95 from Ministerio de Educación y Ciencia (Spain).

References

1. K. Ghosh and M. Schnitzer. Soil Sci. **129**, 266 (1980).
2. K. Kumada and Y. Kawamura. Soil Sci. Plant Nutr. **14**, 190 (1968).
3. Y. Chen and M. Schnitzer. Soil Sci. Soc. Am. J. **40**, 866 (1976).
4. C. Datta and S.K. Mukherjee. J. Indian Chem. Soc. **47**, 1105 (1970).
5. S.A. Visser. Plant Soil, **87**, 209 (1985).
6. C.E. Clapp, W.W. Emerson, and A.E. Olness. *In* Humic substances II: In search of structure. *Edited by* M.H.B. Hayes, P. MacCarthy, R.C. Malcolm, and R.S. Swift. Wiley, New York. 1989. p. 497.
7. M.H.B. Hayes and R.S. Swift. *In* The chemistry of soil constituents. *Edited by* D.J. Greenland and M.H.B. Hayes. Wiley, New York. 1978. p. 179.
8. E. Tombacz and E. Meleg. Org. Geochem. **15**, 375 (1990).
9. M.T.S.D. Vasconcelos, A.A.S.C. Machado, and F. Rey. Port. Electrochim. Acta, **9**, 221 (1991).
10. M.T.S.D. Vasconcelos, A.A.S.C. Machado, and F. Rey. Stud. Chem. **16**, 79 (1991).
11. C.S.P.C.O. Silva, J.C.G. Esteves da Silva, and A.A.S.C. Machado. Appl. Spectrosc. **48**, 363 (1994).
12. A.A.S.C. Machado, J.C.G. Esteves da Silva, and J.A.C. Maia. Anal. Chim. Acta, **292**, 121 (1994).
13. M.T.S.D. Vasconcelos, A.A.S.C. Machado, and A.P.L.M.G. Santos. Sci. Total Environ. **81/82**, 489 (1989).
14. International Humic Substances Society (IHSS), Outline of extraction procedures, distributed to the members of the IHSS (1981).
15. S. Kuwatsuka, A. Watanabe, K. Itoh, and S. Arai. Soil Sci. Plant Nutr. **38**, 23 (1992).
16. P.W. Linder, R.G. Torrington, and D.R. Williams. Analysis using glass electrodes. Open University Press, Mylton Keynes, England. 1984. pp. 44–47.
17. J.C. Miller and J.N. Miller. Statistics for analytical chemistry. Ellis Horwood, Chichester. 1988. pp. 62–64.
18. W. Flaig, H. Beutelspacher, and E. Rietz. *In* Soil components. *Edited by* J.E. Gieseking. Springer-Verlag, New York. 1975.
19. G.S. Manning. J. Phys. Chem. **79**, 262 (1975).
20. J.H. Reuter. Abstr. 1977 Annual Meeting of the Geological Society of America. 1977. pp. 1140–1141.
21. M. Adhikari, B. Mandal, and P. Sen. Proc. Indian Natl. Sci. Acad. **46A**, 387 (1980).
22. E. Tipping, M.M. Reddy, and M.M. Hurley. Environ. Sci. Technol. **24**, 1700 (1990).
23. J.H. Ephraim, C. Pettersson, M. Norden, and A.B. Allard. Environ. Sci. Technol. **29**, 622 (1995).
24. D. Eagland. *In* Water science review. Vol. 4. *Edited by* F. Franks. Cambridge University Press, Cambridge. 1989. p. 40.
25. D. Orlov. Humus acid of soils. A.A. Balkema, Rotterdam. 1985. p. 119.
26. Y. Kagawa. Kagaku (Kyoto), **26**, 243 (1956).

Solvent effects on the reactivity of solvated electrons with organic solutes in 1-butylamine–water mixtures

Yixing Zhao and Gordon R. Freeman

Abstract: The values of the rate constants of the reactions of e_s^- with the efficient scavengers nitrobenzene and acetone are $\geq 2 \times 10^6$ m^3 mol^{-1} s^{-1} in the whole range of 1-butylamine–water mixtures at 298 K; the reaction rates in the mixed solvents vary approximately as the solvent fluidity. In pure butylamine at 298 K, $k_2(e_s^- + \text{nitrobenzene}) = 84 \times 10^6$ m^3 mol^{-1} s^{-1} and $k_2(e_s^- + \text{acetone}) = 7.3 \times 10^6$ m^3 mol^{-1} s^{-1}. The values of the rate constants of the reactions of e_s^- with the inefficient scavengers phenol and toluene are $< 2 \times 10^5$ m^3 mol^{-1} s^{-1} in the whole range of 1-butylamine–water mixtures at 298 K and have a maximum at 50 mol% water and a minimum at 99 mol% water. In pure 1-butylamine at 298 K, $k_2(e_s^- + \text{phenol}) = 1.0 \times 10^4$ m^3 mol^{-1} s^{-1} and $k_2(e_s^- + \text{toluene}) = 0.28 \times 10^4$ m^3 mol^{-1} s^{-1}. The reaction rates with inefficient scavengers show strong dependence on the solvent composition and selective solvation of electron and scavenger. In the amine-rich region (0–30 mol% water), the rate constants increase with the *increase* of viscosity, indicating the chemical participation of solvent molecules in the reaction. In the water-rich region from 50 to 99 mol% water, the decrease of the rate constants indicates the nonhomogeneous solvation of the electrons by water and of the organic solutes by 1-butylamine. From 99 mol% to pure water the rate constant increases rapidly, which we attribute to insufficient 1-butylamine to coat the phenol or toluene molecules. The variation of the activation energies E_2 for the efficient scavengers, 14–27 kJ mol^{-1}, are similar to the variation of E_η in the mixed solvents. The values of E_2 for the inefficient scavengers are from 15 to 38 kJ mol^{-1} for phenol and from 6 to 21 kJ mol^{-1} for toluene. Both k_2 and E_2 for the inefficient scavenger reactions show a correlation with the temperature coefficient $-dE_{Amax}/dT$ of the optical absorption of e_s^- in the mixed solvents, but the reason is obscure.

Key words: 1-butylamine–water solvent, solvated electron, organic solutes, reactivity, solvent effects.

Résumé : Les constantes de vitesse pour les réactions des e_s^- avec les capteurs efficaces que sont le nitrobenzène et l'acétone sont $\geq 2 \times 10^6$ m^3 mol^{-1} s^{-1} pour l'ensemble des concentrations de la 1-butylamine–eau, à 298 K; la variation des vitesses de réaction dans les solvants mixtes suit approximativement celle de la fluidité du solvant. Dans la butylamine pure, à 298 K, $k_2(e_s^- + \text{nitrobenzène}) = 84 \times 10^6$ m^3 mol^{-1} s^{-1} et $k_2(e_s^- + \text{acétone}) = 7{,}3 \times 10^6$ m^3 mol^{-1} s^{-1}. Les valeurs des constantes de vitesse des réactions des e_s^- avec les capteurs inefficaces que sont le phénol et le toluène sont $< 2 \times 10^5$ m^3 mol^{-1} s^{-1} pour l'ensemble des concentrations de la 1-butylamine–eau à 298 K et elles présentent un maximum à 50 mol% d'eau et un minumum à 99 mol% d'eau. Dans la 1-butylamine pure, à 298 K, $k_2(e_s^- + \text{phénol}) = 1{,}0 \times 10^4$ m^3 mol^{-1} s^{-1} et $k_2(e_s^- + \text{toluène}) = 0{,}28 \times 10^4$ m^3 mol^{-1} s^{-1}. Les vitesses de réaction avec les capteurs inefficaces présentent une forte dépendance sur le composition et une solvation sélective de l'électron et des capteurs. Dans la région riche en amine (0–30 mol% d'eau), les constantes de vitesse augmentent avec une *augmentation* de la viscosité; ce résultat indique qu'il se produit une participation chimique des molécules de solvant dans la réaction. Dans la région riche en eau, de 50 à 90 mol%, la diminution des constantes de vitesse indique qu'il se produit une solvatation non homogène des électrons par l'eau et des solutés organiques par la 1-butylamine. Dans la région de 99–100 mol% d'eau, la constante de vitesse augmente rapidement; on attribue ce résultat au fait qu'il n'y a pas assez de 1-butylamine pour recouvrir les molécules de phénol ou de toluène. Dans les solvants mixtes, les énergies d'activation, E_2, des capteurs efficaces, 14–27 kJ mol^{-1}, ont des variations similaires aux E_η. Les valeurs E_2 des capteurs inefficaces varient de 15 à 38 kJ mol^{-1} pour le phénol et de 6 à 21 kJ mol^{-1} pour le toluène. Les valeurs tant de k_2 que de E_2 des réactions des capteurs inefficaces présentent toutes les deux une corrélation avec le coefficient de température, $-dE_{Amax}/dT$, l'absorption optique des e_s^- dans les solvants mixtes; les raisons sont toutefois obscures.

Mots clés : solvants mixtes 1-butylamine–eau, électrons solvatés, solutés organiques, effets de solvant.

[Traduit par la rédaction]

Received June 5, 1995.

Y. Zhao and G.R. Freeman.[1] Chemistry Department, University of Alberta, Edmonton, AB T6G 2G2, Canada.

[1] Author to whom correspondence may be addressed. Telephone: (403) 492-3468. Fax: (403) 492-8231. E-mail: knp@dept.chem.ualberta.ca

Introduction

The study of solvated electron (e_s^-) reactivity in mixed alcohol–water solvents has been fruitful in elucidating electron behavior in nonhomogeneous fluids (1–10). The reactivity of e_s^- depends on the nature of the coreactant and the structure of the solvent. Some reactions of e_s^- with solutes such as nitrobenzene (1, 4), Ag_s^+ (7), and H_s^+ (7) are diffusion controlled, and some are much slower, as in the case of toluene and phenol (3, 5). Solvent structure implies two aspects. One is the molecular structure, which in some cases affects the chemical participation of solvent molecules in a reaction (11, 12). The other is the solvent molecular packing, such as two- and three-dimensional structures in alcohol–water mixtures (8, 13).

Alcohol, water, and their mixtures are all strongly hydrogen-bonded liquids. It is now of interest to study e_s^- reactivity in mixtures containing a less strongly hydrogen-bonded component. We have chosen 1-butylamine–water, for practical reasons (ease of handling). The optical absorption spectra of e_s^- in these mixed solvents have recently been reported (14). There appears to be less selective solvation of electrons by water in these mixtures than was expected.

Experimental

The method of purification of 1-butylamine was reported in ref. 14. Nitrobenzene (A.C.S. reagent, >99%) and phenol (redistilled, >99%, mp 40–42°C) were obtained from Aldrich. Acetone (HPLC grade, >99.9%) and toluene (HPLC grade, >99.8%) were obtained from Sigma–Aldrich. Nitrobenzene, acetone, and phenol were used without further purification. Toluene was fractionally distilled from sodium under UHP argon (99.999%, Liquid Carbonic Canada) and the middle part was collected and stored in a flask under argon positive pressure.

For the measurement of the rate constant of phenol in pure water, phenol was melted in the bottle by placing the bottle in warm water, and then was pipetted into a volumetric flask and nanopure water was added. For the rest of the measurements of phenol reaction rate, phenol crystals were taken out of the bottle and placed in a watch glass, and then crystals of phenol without any color were scooped into a beaker to weigh. Then solvent was added, and the solution was transferred to a volumetric flask for final dilution.

Techniques of sample solution preparation, irradiation, and optical measurements were the same as described in ref. 9.

Results and discussion

Rate constants

Since the reaction of e_s^- with the solvent amine and water is negligible under our conditions (15), we only consider the following reactions:

[1] $e_s^- + I_S \rightarrow$ Products k_1

[2] $e_s^- + S_S \rightarrow$ Products k_2

where I_S represents residual impurities in the solvent and those produced by the radiation pulse, and S_S is an added solute. The observed first-order decay rate constant $k_{obs} = k_1[I] + k_2[S]$ was measured for the pure solvent and six concentrations of solute S. The value of the second-order rate constant k_2 was obtained from the slope of a plot of k_{obs} against solute concentration.

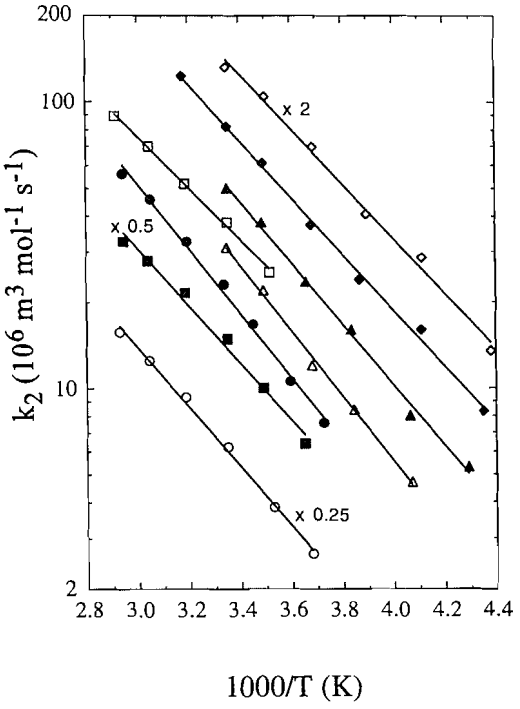

Fig. 1. Arrhenius plots of $k_2(e_s^- + \text{nitrobenzene})$ in 1-butylamine–water mixed solvents. Refer to Table 1 for symbols.

1-Butylamine is completely miscible with water. The rate constants of e_s^- for all solutes were measured in the following compositions in mol% water: 0.0, 10.0, 30.0, 50.0, 70.0, 90.0, 95.0, 97.0, and 100.0. In addition, the rate constants of e_s^- with phenol in 99.0, 99.5, and 99.8 mol% water were measured. The normal freezing point of 1-butylamine is 224 K, and the normal boiling point is 351 K. The values of k_2 for each solvent were measured from about 230 K to 344 K, depending on the freezing and boiling points of each composition.

Arrhenius plots of k_2 for the four organic solutes nitrobenzene, acetone, phenol, and toluene are given in Figs. 1–4; Table 1 contains the symbols for these figures. The rate constants k_2 (10^6 m^3 mol^{-1} s^{-1}) of nitrobenzene, acetone, phenol, and toluene in water at 298 K are 37, 7.2, 0.024, 0.011, which are consistent within experimental uncertainty with values reported by Maham and Freeman (16): 38, 7.7, 0.027, 0.013, and Lai and Freeman (3): 38, 7.7, 0.030, 0.011. Other results reported (15) are 30, 5.9, 0.018, 0.012.

In water, the rate constant $k_2(e_s^- + \text{phenol})$ at 298 K was 2.4×10^4 m^3 mol^{-1} s^{-1}. However, phenol will dissociate somewhat in water:

[3] 

Since the rate constant $k_{H^+}(e_s^- + H_3^+O)$ at 298 K is 2.9×10^7 m^3 mol^{-1} s^{-1} in water at very low ionic strengths

Fig. 2. Arrhenius plots of $k_2(e_s^- + \text{acetone})$ in 1-butylamine–water mixed solvents. Refer to Table 1 for symbols.

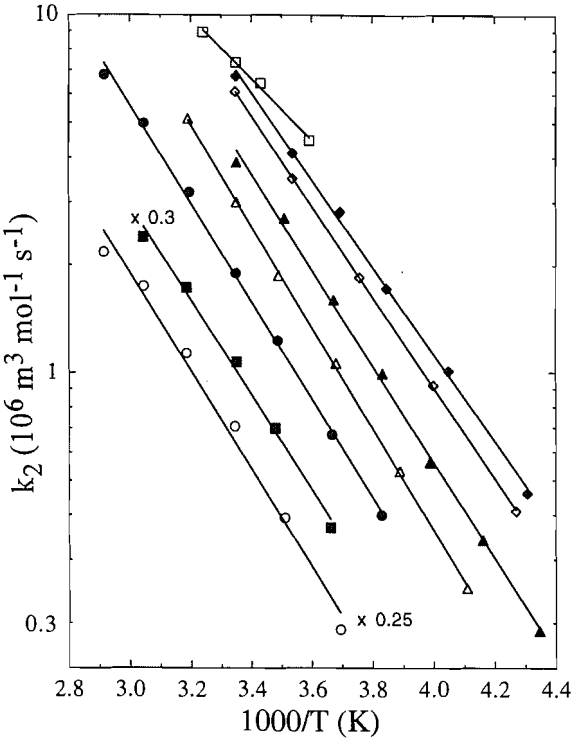

Fig. 3. Arrhenius plots of $k_2(e_s^- + \text{phenol})$ in 1-butylamine–water mixed solvents. Refer to Table 1 for symbols.

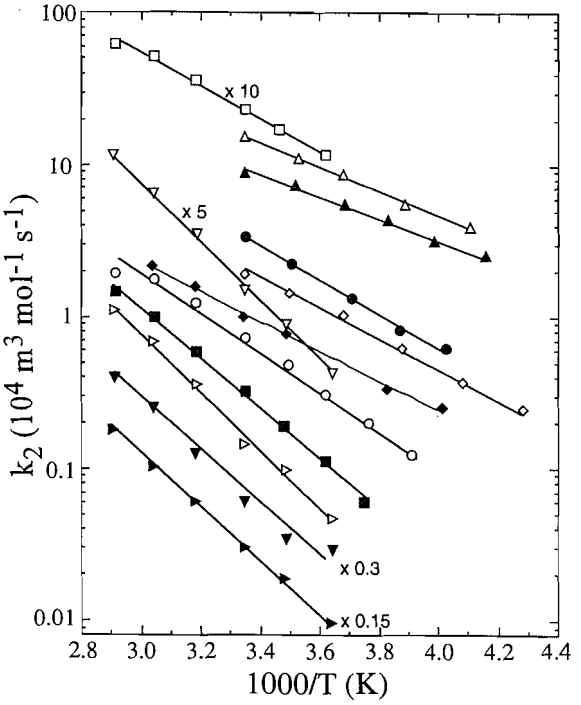

(10), it contributes to k_{obs} in the measurement of $k_2(e_s^- + \text{phenol})$. We used the method in ref. 8 to correct k_2 for phenol alone. That is, $[H_3^+O] = (K_a[\text{phenol}])^{1/2}$ is calculated over the range of [phenol] = 5–30 mol m^{-3} where K_a is the dissociation constant, and at 298 K it is 1.3×10^{-7} mol m^{-3}

Fig. 4. Arrhenius plots of $k2(e_s^- + \text{toluene})$ in 1-butylamine–water mixed solvents. Refer to Table 1 for symbols.

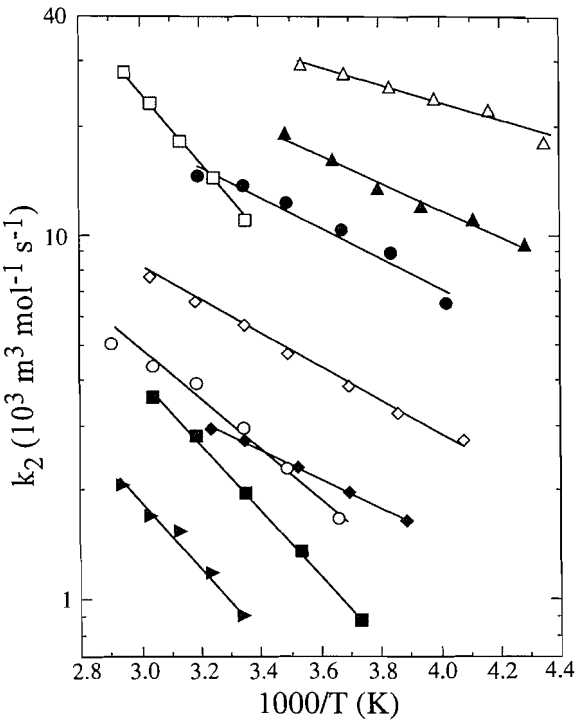

Table 1. Symbols for Figs. 1–4.

mol%	water	mol%	water
◆	0	■	95
◇	10	▶	97
▲	30	▷	99
△	50	▼	99.5
●	70	▽	99.8
○	90	□	100

(17). Then the actual value of $k_2(e_s^- + \text{phenol})$ was calculated from the slope of the $(k_{obs} - k_{H^+}[H_3^+])$ against [phenol] plot, and it is 2.1×10^4 m^3 mol^{-1} s^{-1}, which is 13% less than the uncorrected value. Since the values of K_a at other temperatures in water, and in all the other solvents, are not known, we could not make this correction for the other values. For this reason the values in Fig. 3 and Table 2 are uncorrected. Modern studies of the chemical–physical properties of the amine–water mixed solvents and of the phenol solutions would be valuable.

Composition dependence of k_2 at 298 K

Figure 5 shows the solvent composition dependences of $k_2(e_s^- + \text{organic solute})$ in 1-butylamine–water mixed solvents at 298 K. Reaction parameters are listed in Tables 2 and 3. From Fig. 5 we see that the reactions are divided into two groups: (*i*) nitrobenzene and acetone, which have k_2 10^6 m^3 mol^{-1} s^{-1}, and (*ii*) phenol and toluene, most of which have $k_2 < 10^5$ m^3 mol^{-1} s^{-1}. Both the order of magnitude and the patterns of the change of k_2 in the mixtures indicate that these two groups of reactions follow different

Table 2. Reaction rate parameters of e_s^- with phenol in 1-butylamine–water mixed solvents at 298 K.

H_2O mol%	k_2 (10^4 m^3 mol^{-1} s^{-1})	E_2 (kJ mol^{-1})	η^a (mPa s)	$E_\eta{}^b$ (kJ mol^{-1})	E_{Amax} (zJ)[c]	$k_1[I_S]^d$ (10^4 s^{-1})	$-dE_{Amax}/dT^c$ (zJ K^{-1})
Phenol (1–60 mol m^{-3} for k_2)							
0	1.0	19	0.47	9	115	17	0.43
10	2.0	17	0.59	12	143	17	0.36
30	9.6	15	0.88	15	189	70	0.30
50	15.0	16	1.45	19	214	140	0.27
70	3.4	22	2.21	21	248	35	0.30
90	0.74	27	2.14	21	273	14	0.41
95	0.31	31	~ 1.8		275	9	0.44
97	0.21	33	~ 1.5			5	
99	0.17	35	~ 1.3		277	4	0.46
99.5	0.20	38	~ 1.1			2	
99.8	0.33	36	~ 1.0			3	
100.0	2.4	20	0.89	17	278	7	0.47

[a]Reference 18, except for the pure 1-butylamine from ref. 19.
[b]Calculated from the data in ref. 18.
[c]Reference 14.
[d]In solvent without added solute.

Fig. 5. Solvent composition dependence of k_2 in 1-butylamine–water mixed solvents at 298 K. ○, nitrobenzene; ●, acetone; □, phenol; ■, toluene. Physical parameter reference lines are: ×, viscosity (18, 19); +, E_{Amax} (14).

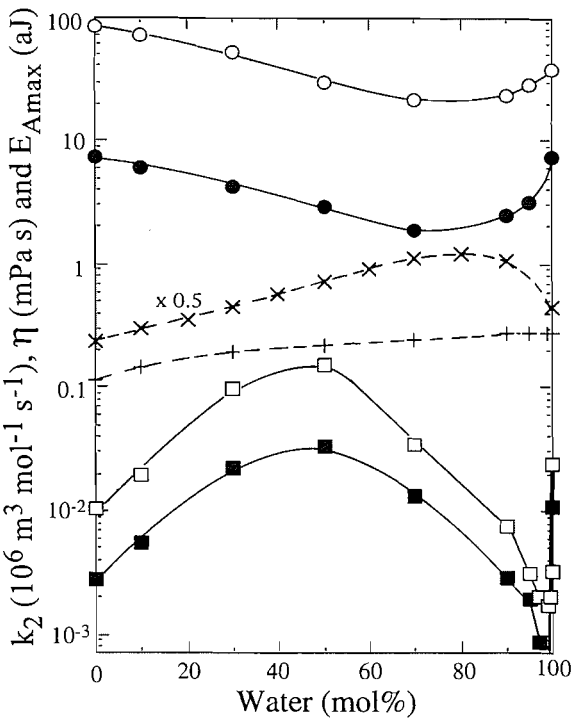

reaction mechanisms. While all the reactions involve electron transfer from a potential well in the solvent to a solute molecule, the transfer to toluene and phenol must be secured by a subsequent reaction, which is probably protonation by the solvent (3).

Nitrobenzene and acetone are efficient electron scavengers. The magnitudes of $k_2(e_s^-$ + nitrobenzene) and $k_2(e_s^-$ + ace-

Table 3. Reaction rate parameters of e_s^- with toluene, nitrobenzene, and acetone in 1-butylamine–water mixed solvents at 298 K.

H_2O mol%	k_2 (10^4 m^3 mol^{-1} s^{-1})	E_2 (kJ mol^{-1})
Toluene (0.7–150 mol m^{-3} for k_2)		
0	0.28	10
10	0.54	8
30	2.2	7
50	3.4	6
70	1.3	8
90	0.29	16
95	0.19	18
97	0.086	21
100	1.1	19
Nitrobenzene ((0.1–4.5) × 10^{-2} mol m^{-3} for k_2)		
0	8400	17
10	7100	20
30	5100	21
50	3000	22
70	2100	22
90	2400	21
95	2800	20
100	3700	17
Acetone ((1.7–50) × 10^{-2} mol m^{-3} for k_2)		
0	730	24
10	600	25
30	420	26
50	300	27
70	200	27
90	250	27
95	320	25
100	720	14

tone) in 1-butylamine–water mixtures are similar to those in methanol–water and ethanol–water mixtures (3), 1-propanol–water mixtures (4), and all isomeric butanol–water mixtures (18). However, the values of $k_2(e_s^- + \text{nitrobenzene})$ and $(e_s^- + \text{acetone})$ in the alcohol-rich region of all alcohol–water mixtures are nearly independent of water content whereas the $k_2(e_s^- + \text{nitrobenzene})$ and $k_2(e_s^- + \text{acetone})$ in the amine-rich region of 1-butylamine–water mixtures decrease as the water content is increased to 70 mol%. These rate constants in 1-butylamine–water mixtures decrease as the viscosity increases (19, 20). The reaction with nitrobenzene is diffusion controlled. The reaction with acetone is an order of magnitude slower and has an approximately 5 kJ mol^{-1} larger activation energy (Table 3), but the rates in the mixed solvents still correlate with solvent fluidity (Fig. 5).

Phenol and toluene are less efficient scavengers. Although the orders of magnitude of $k_2(e_s^- + \text{phenol})$ and $k_2(e_s^- + \text{toluene})$ in 1-butylamine–water mixtures at 298 K are in the same range as in alcohol–water mixtures (3, 4, 17, 21), the pattern of the change in the mixed solvents is quite different from that in alcohol–water mixtures. Instead of having a minimum at 60–70 mol% water as in alcohol–water mixtures, $k_2(e_s^- + \text{phenol})$ and $k_2(e_s^- + \text{toluene})$ have a maximum at 50 mol% water in 1-butylamine, and a sharp minimum at ~99 mol% water (Fig. 5). The values of $k_2(e_s^- + \text{toluene})$ could not be measured in 99.0–99.8 mol% water due to very low rate constants and low solubility of toluene in the solvents. The values of k_2 increase as the values of viscosty and E_{Amax} *increase* in the amine-rich region.

The increase of $k_2(e_s^- + RC_6H_5)$, R = CH_3 or OH, with increasing viscosity η (Fig. 5) is reminiscent of the behavior of $k(e_s^- + NO_{3,s}^-)$ in pure alcohols on increasing the length of the alkyl chain (12, 22). In both cases a transient intermediate reacts with the solvent (3, 12, 16, 21, 22), and the probability of this reaction increases superlinearly with increasing duration τ of the $[e_s^-, S_S]$ encounter pair. For toluene and phenol:

$$[4] \qquad e_s^- + RC_6H_5 \rightleftharpoons [e_s^-, RC_6H_5] \rightleftharpoons [RC_6H_5^-]$$

$$[5] \qquad [RC_6H_5^-] + HNHC_4H_9 \text{ or } HOH \rightarrow R\dot{C}_6H_6 + {}^-NHC_4H_9 \text{ or } {}^-OH$$

In the $(e_s^- + NO_{3,s}^-)$ reaction k_2 increased approximately linearly with η, which means $k_2 \propto \tau^2$, whereas in the RC_6H_5 reaction between zero and 30 mol% water in 1-butylamine k_2 increases approximately as η^3, which means $k_2 \propto \tau^4$. There seems to be an additional effect in the latter reaction, and we suggest it is that water, being a stronger acid than is the amine (17), is a better protonating agent for the phenylide ion in reaction [5].

At water contents >30 mol% the values of $k_2(e_s^- + RC_6H_5)$ increase less rapidly, and from 50 to 99 mol% water they decrease (Fig. 5). The decrease is attributed to nonhomogeneous solvation of the reacting entities: in the water-rich solvents e_s^- is preferentially solvated by the water, while phenol and toluene are selectively solvated by the butylamine. It becomes progressively more difficult for the e_s^- and RC_6H_5 to come within the reaction radius of each other.

The increase of $k_2(e_s^- + RC_6H_5)$ on going from 99.0 to 99.5, 99.8, and 100 mol% water is attributed to the RC_6H_5 being progressively less "coated" by amine molecules, thereby facilitating reactions [4] and [5]. The compressibility of solutions of butylamine in water has a minimum at 98.3 mol% water, which implies optimal packing of the molecules (23). This might be related to the minimum reaction rate, which we observed at our composition closest to 98.3%, namely, 99.0%. The partial molar volume of 1-butylamine has a minimum at 99.1 mol% water (23).

The first-order decay rates in the solvents without added solute showed a solvent composition dependence similar to those of the reactions with phenol and toluene (see $k_1[I_S]$ in Table 2). It therefore appears that the impurities react inefficiently with e_s^-, and are probably olefinic.

Smoluchowski–Stokes–Debye model

In the study of the reactions of e_s^- with organic solutes, the Smoluchowski–Stokes–Debye model has been used (3, 18, 24). The diffusion-controlled rate constant $k_2(e_s^- + S)$ for reaction of e_s^- with a polar solute S is approximately related to the solvent viscosity η by the Smoluchowski–Stokes–Debye equation (3, 8, 10, 25):

$$[6] \qquad k_2 = \frac{N_A k_B T}{1.5\eta}\left(\frac{1}{r_e} + \frac{1}{r_s}\right)(R_e + R_S)\kappa f = \frac{N_A k_B T}{1.5\eta} \cdot \frac{1}{r_d} \cdot f\kappa R_r$$

where N_A is Avogrado's constant, k_B is Boltzmann's constant, T is temperature, r_x and R_x are the effective radii for diffusion and reaction, respectively, κ is the probability that reaction occurs during one encounter, r_d is the effective radius for mutual diffusion of e_s^- and solute, R_r is the average center-to-center reactant separation when reaction occurs, κR_r is considered as an effective reaction radius, and the Debye factor f is given by:

$$[7] \qquad f = \frac{x}{(e^x - 1)}$$

$$[8] \qquad x = -\frac{\mu\xi^2}{4\pi\varepsilon_0\varepsilon R_r k_B T}$$

where x is the ratio of the Coulombic interaction energy of the reactants at R_r to thermal agitation energy $k_B T$, ε is the relative permittivity (26) of the medium between the reactants at separation R_r, and μ is the dipole moment of the solute reactant.

Equation [6] suggests that for diffusion-controlled reactions,

$$[9] \qquad \eta k_2 \approx \text{constant}$$

The solvent composition dependences of ηk_2 are shown in Fig. 6. The relatively efficient reactants nitrobenzene and acetone approximately follow relation [9]. However, the inefficient reactants phenol and toluene do not, as might be expected from the preceding discussion.

Correlation of small values of k_2 with $-dE_{\text{Amax}}/dT$

The temperature coefficient of the optical obsorption energy of e_s^- in these solvents, $-dE_{\text{Amax}}/dT$, has a minimum at 50

Fig. 6. Solvent composition dependence of ηk_2 in 1-butylamine–water mixtures at 298 K. The symbols are as in Fig. 5. ×, relative permittivity ε (26).

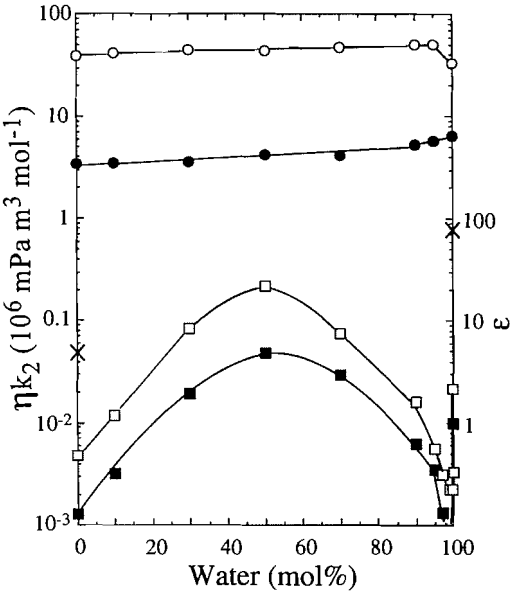

Fig. 7. Correlations of k_2 (phenol and toluene) with $-dE_{Amax}/dT$ (14) in 1-butylamine–water mixtures at 298 K. □, phenol; ■, toluene.

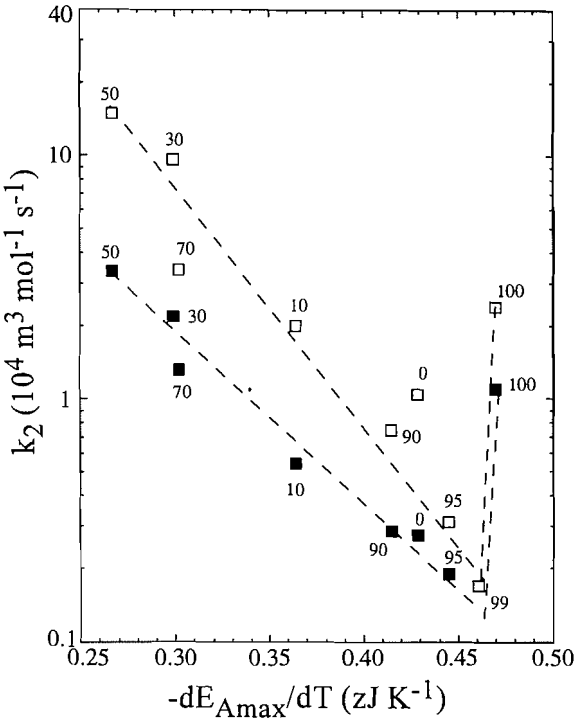

mol% water (14), where $k_2(e_s^- + \text{phenol or toluene})$ has a maximum (Fig. 5). A plot of log k_2 against $-dE_{Amax}/dT$ is roughly linear, with the exception of the 99–100% water zone (Fig. 7). We attributed the two sides of the hump in Fig. 5 to different effects, and we cannot interpret the approximate correlation shown in Fig. 7. We display it as a clue to future interpretation.

Fig. 8. Solvent composition dependence of E_2. Symbols are as in Fig. 5, plus E_η(×) and $-dE_{Amax}/dT$(+) in 1-butylamine–water mixtures.

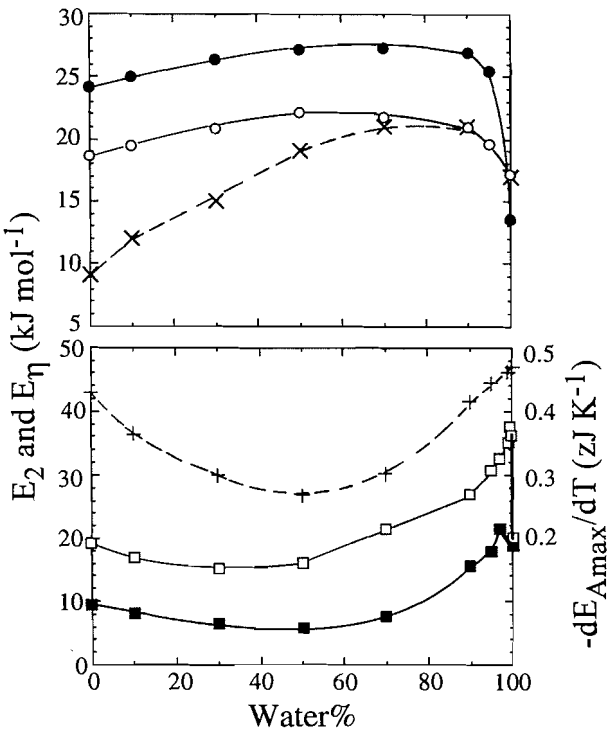

Activation energies

The solvent dependences of the activation energies of reaction, E_2, are compared with those of viscosity, E_η, and the temperature coefficient $-dE_{Amax}/dT$ (Fig. 8). The variation of E_2 for the efficient reactions of e_s^- with nitrobenzene and acetone is qualitatively similar to that of E_η. The larger values of E_2 compared to E_η in the amine-rich solutions might be attributed to a larger mobility μ and activation energy of mobility E_η of electrons than of molecules in the amine. A similar situation was noted in *tert*-butanol solvent (10).

The variations of E_2 for the inefficient reactions of e_s^- with phenol and toluene are in the opposite direction of those for the efficient reactions, and are in the same direction as those in $-dE_{Amax}/dT$ (Fig. 8). The zone 99–100% water remains an exception. The decrease of E_2 upon adding water to 1-butylamine is attributed to the increased ease of reaction [5]. The increase of E_2 at water contents >50 mol% is attributed to the increased segregation of the reactants by selective solvation in the different components of the solvent, which makes it more difficult for the reactants to encounter each other. The decrease of $E_2(e_s^- + \text{phenol})$ on going from 99.8 to 100.0 mol% water is due to the decrease of that segregation.

The values of both k_2 and E_2 for $(e_s^- + \text{toluene})$ are much smaller than those for $(e_s^- + \text{phenol})$ in all the solvents that contain 1-butylamine (Figs. 5 and 8). Thus the overall entropy of activation of the multi-step reactions is much more negative for the toluene than for the phenol reaction. Phenol is hydrogen bonded to the solvent, whereas toluene is not. In the amine-containing solvents, the ratio of concentrations of amine/toluene was always ≥10, and of amine/phenol was ≥2.

We think the toluene and phenol were always clustered by 1-butylamine. It is possible that the lack of hydrogen bonding of toluene to the solvent, and the presence of it for phenol, affects the relative orientations of the e_s^- and toluene or phenol as they diffuse together in reaction [4], and affects rotatability of the solvent molecules as the protonation reaction [5] occurs.

The reason for the minimum in $-dE_{Amax}/dT$ remains unknown.

Acknowledgements

We thank the Natural Sciences and Engineering Research Council of Canada for financial assistance, and the personnel of the Radiation Research Center for maintaining the accelerator and the electronic equipment.

References

1. O.I. Mićić and B. Čerček. J. Phys. Chem. **81**, 833 (1977).
2. B.H. Milosavljević and O.I. Mićić. J. Phys. Chem. **82**, 1359 (1978).
3. C.C. Lai and G.R. Freeman. J. Phys. Chem. **94**, 302 (1990).
4. Y. Maham and G.R. Freeman. J. Phys. Chem. **89**, 4347 (1985).
5. Y. Maham and G.R. Freeman. Can. J. Chem. **66**, 1706 (1988).
6. S.A. Peiris and G.R. Freeman. Can. J. Phys. **68**, 940 (1990).
7. S.A. Peiris and G.R. Freeman. Can. J. Chem. **69**, 157 (1991).
8. R. Chen and G.R. Freeman. Can. J. Chem. **71**, 1303 (1993).
9. R. Chen, Y. Avotinsh, and G.R. Freeman. Can. J. Chem. **72**, 1083 (1994).
10. Y. Zhao and G.R. Freeman. Can. J. Chem. **73**, 392 (1995); **73**, 389 (1995).
11. T.B. Kang and G.R. Freeman. Can. J. Chem. **71**, 1297 (1993).
12. Y. Zhao and G.R. Freeman. Can. J. Chem. **73**, 284 (1995).
13. A.D. Leu, K.N. Jha, and G.R. Freeman. Can. J. Chem. **60**, 2342 (1982).
14. Y. Zhao and G.R. Freeman. Can. J. Chem. **73**, 2126 (1995).
15. M. Anbar, M. Bambenek, and A.B. Ross. Selected specific rates of reactions of transients from water in aqueous solution. I. Hydrated electron. NSRDS-NBS **43**, U.S. Dept. of Commerce, Washington, D.C. 1973.
16. Y. Maham and G.R. Freeman. J. Phys. Chem. **91**, 1561 (1987).
17. P.W. Atkins. Physical chemistry. 4th ed. Freeman, New York. 1990. pp. 765, 951.
18. P.C. Senanayake and G.R. Freeman. J. Chem. Phys. **87**, 7007 (1987).
19. M.-J. Lee, S.-M. Hwang, and Y.-C. Kuo. J. Chem. Eng. Data, **38**, 577 (1993).
20. K.Y. Liew, C.E. Seng, and C.G. Lee. J. Solution Chem. **23**, 1293 (1994).
21. P.C. Senanayake and G.R. Freeman. J. Phys. Chem. **91**, 2123 (1987).
22. R. Chen and G.R. Freeman. J. Phys. Chem. **99**, 4970 (1995).
23. T. Moriyoshi, T. Tsubota, and K. Hamaguchi. J. Chem. Thermodyn. **23**, 155 (1991).
24. Y. Maham and G.R. Freeman. J. Phys. Chem. **92**, 1506 (1988).
25. P. Debye. Trans. Electrochem. Soc. **82**, 265 (1942).
26. Y.Y. Akhadov. Dielectric properties of binary solutions. Pergamon Press, Oxford. 1980. p. 144.

The use of bisphthalonitriles in the synthesis of side-strapped 1,11,15,25-tetrasubstituted phthalocyanines

Clifford C. Leznoff and David M. Drew

Abstract: Nucleophilic aromatic substitution reactions of 3-nitrophthalonitrile yield 3-hydroxyphthalonitrile and 3-neopentoxyphthalonitrile, the latter of which condensed to 1,8,15,22-tetraneopentoxyphthalocyanine as a mixture of isomers. Bisphthalonitriles such as 1,3-bis(2′,3′-dicyanophenoxy)-2,2-dipentylpropane, 1,3-bis(2′,3′-dicyanophenoxy)-2,2-diethylpropane, 1,3-bis(2′,3′-dicyanophenoxy)-2,2-dioctylpropane, and 1,3-bis(2′,3′-dicyanophenoxy)-2-methyl-2-trityloxymethylpropane all gave bis-crown-like 1,11,15,25-tetrasubstituted phthalocyanines as pure compounds when treated with lithium octoxide in 1-octanol at 196°C. A host of nine other bisphthalonitriles including 1,5-bis(2′,3′-dicyanophenoxy)-3-oxapentane, 1,1-bis(2′,3′-dicyanophenoxymethyl)cyclohexane, 1,2-bis(2′,3′-dicyanophenoxymethyl)benzene, and 2,5-bis(2′,3′-dicyanophenoxymethyl)furan did not dimerize to mononuclear phthalocynaines. The "*gem* dimethyl" effect was suggested as a reason for the successful macrocyclizations.

Key words: nucleophilic aromatic substitution, phthalonitriles, bisphthalonitriles, 1,11,15,25-tetrasubstituted phthalocyanines.

Résumé : Les réactions de substitutions aromatiques nucléophiles du 3-nitrophtalonitrile conduisent au 3-hydroxyphtalonitrile et au 3-néopentoxyphtalonitrile; ce dernier se condense pour conduire à la 1,8,15,22-tétranéopentoxyphtalocyanine sous la forme d'un mélange d'isomères. Lorsqu'on soumet les bisphtalonitriles, tels que les 1,3-bis(2′,3′-dicyanophénoxy)-2,2-dipentylpropane, 1,3-bis(2′,3′-dicyanophénoxy)-2,2-diéthylpropane, 1,3-bis(2′,3′-dicyanophénoxy)-2,2-dioctylpropane et 1,3-bis(2′,3′-dicyanophénoxy)-2-méthyl-2-trityloxyméthylpropane, à un traitement par de l'octylate de lithium en présence d'octan-1-ol à 196°C on obtient toujours des phtalocyanines 1,11,15,25-tétrasubstituées à l'état pur qui ressemblent à des couronnes doubles. Neuf autres bisnaphtonitriles, y compris les 1,5-bis(2′,3′-dicyanophénoxy)-3-oxapentane, 1,1-bis(2′,3′-dicyanophénoxyméthyl)cyclohexane, 1,2-bis(2′,3′-dicyanophénoxyméthyl)benzène et 2,5-bis(2′,3′-dicyanophénoxyméthyl)-furane, ne se dimérisent pas en phtalocyanines mononucléaires. L'effet «*gem*-diméthyle» a été suggéré pour expliquer le succès des macrocyclisations qui ont réussi.

Mots clés : substitution aromatique nucléophile, phtalonitriles, bisphtalonitriles, phtalocyanines 1,11,15,15-tétrasubstituées.

[Traduit par la rédaction]

Introduction

The synthesis of pure isomers of tetrasubstituted phthalocyanines (Pc) having one substituent in each of the benzene rings remains a difficult problem (1). Single isomers of 2,9,16,23- (2), 2,9,17,24- (3), and 1,8,15,22-tetrasubstituted phthalocyanines (4), and a 1,2-naphthalocyanine (5) have been prepared capitalizing on reactive substrates (2) or electronic (3) or steric constraints (4, 5) but methods towards the synthesis of pure 1,11,15,25-tetrasubstituted phthalocyanines have been only briefly reported by us in a preliminary communication (6). Recently, some specific pure Pc isomers have been separated by chromatography (7). We decided upon a "constrained" approach towards the synthesis of phthalocyanines having substituents in the 1,11,15,25 positions. If we could dimerize bisphthalonitriles with appropriate bridging groups, then 1,11,15,25-tetrasubstituted phthalocyanines containing bridging substituents (side straps) in the 1,25 and 11,15 positions would be obtained. The difficulty in this approach is the fact that polymerization would compete with dimerization. After exploring many different conditions we found that that condensation of bisphthalonitriles under high dilution at high temperatures for short reaction times led in some cases to the desired phthalocyanines as shown below.

Received August 31, 1995.

C. C. Leznoff[1] **and D. M. Drew**. Department of Chemistry, York University, North York (Toronto), ON M3J 1P3, Canada.

[1] Author to whom correspondence may be addressed. Telephone: (416) 736-2100, ext. 33838. Fax: (416) 736-5936. E-mail: FS300067@SOL.YORKU.CA

Results and discussion

Nucleophilic aromatic substitution reactions on 3-nitrophthalonitrile (**1**) (9) are not all that common (4, 8, 9) and hence we decided to examine some simple reactions of **1**. Thus treatment of **1** with K_2CO_3 and $NaNO_2$ in DMSO at reflux for 0.5 h, as for the preparation of 4-hydroxyphthalonitrile (10), led to 3-hydroxyphthalonitrile (**2**) in 43% yield. Similarly, treatment of **1** with neopentanol (2,2-dimethyl-1-propanol) and K_2CO_3 in DMSO at room temperature for *6 days* gave 3-neopentoxyphthalonitrile in 63% yield. The long reaction times were necessary to drive the reaction to completion probably due to steric hindrance of the substitution at the 3-position (4, 8) and the bulky alcohol used. Conversion of **3** to its diiminoisoindoline **4** proceeded normally (11, 12). Condensation of **4** at 150°C in 2-*N*,*N*-dimethylaminoethanol (DMAE) (11, 12)

Scheme 1.

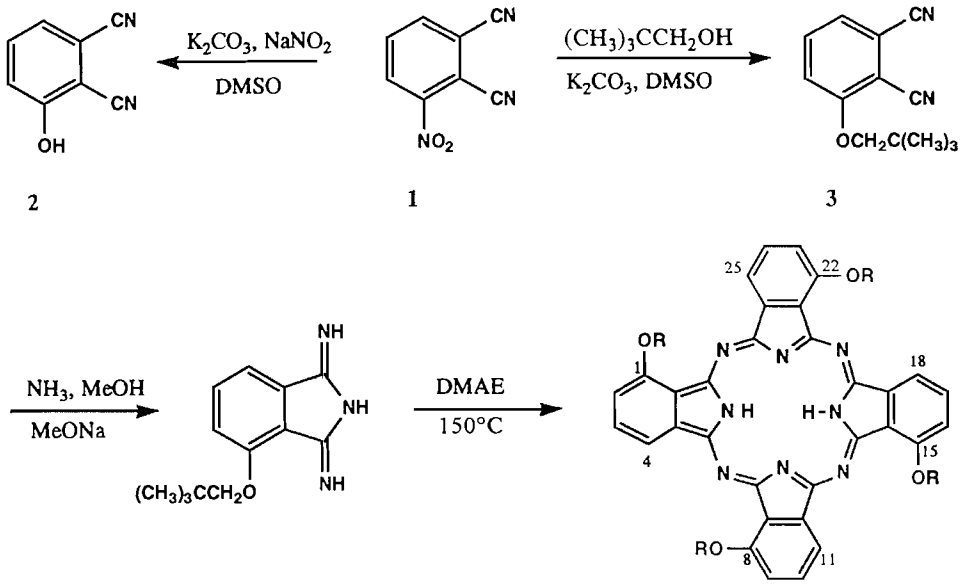

gave 1,8,15,22-tetraneopentoxyphthalocyanine (**5**) in 16% yield as a mixture with its 1,8,15,25, 1,8,18,25, and 1,11,15,25 isomers (Scheme 1).

Having established that phthalocyanines containing bulky substituents at positions adjacent to the macrocyclic core are readily prepared, we directed our attention towards the preparation of bisphthalonitriles bridged at the 3-position, for eventual dimerization to 1,11,15,25-tetrasubstituted phthalocyanines. Earlier, we had suggested (12) that β-hydrogens on substituents could lead to β-elimination reactions under the basic conditions of Pc formation and hence we concentrated our attention on bridging groups containing no hydrogens at the β-position, particularly β,β-dialkyl groups. Thus, treatment of **1** with a series of β,β-disubstituted-1,3-propanediols, such as the known 2-methyl-2-trityloxymethyl-1,3-propanediols (**6**) (12), the commercially available 2,2-diethyl-1,3-propanediol (**7**), 2,2-dipentyl-1,3-propanediol (**8**), and 2,2-dioctyl-1,3-propanediol (**9**), and K_2CO_3 in dimethyl sulfoxide (DMSO) at 20°C[2] while evacuated (4, 6) gave the bisphthalonitriles **10–13** in 43–94% yields. Diols **8** and **9** were prepared by lithium aluminum hydride reduction of diethyl 2,2-dipentylmalonate (13) and diethyl 2,2-dioctylmalonate (14), respectively. Dimerization of **10–13** under high-dilution conditions with lithium octoxide in 1-octanol at 196°C for 10 min gave the 1,25:11,15-bis(side-strapped) phthalocyanines **14–17** in 7–21% yields. Pcs **14**, **16**, and **17** were readily metallated to their phthalocyaninato zinc(II) compounds **18–20** in 90% yield by heating with zinc acetate in a 1:1 mixture of pyridine and *N,N*-dimethylformamide for 20 h at reflux conditions (Scheme 2). Attempts at cleavage of the side-strapped Pcs **14**[3] and **19** as examples, using BBr_3 (15, 16) as previously described for 2,9,16,23-tetraneopentoxyphthalocyanine (17), simply gave recovered starting materials, while cleavage with AlI_3 (18) gave decomposition of the phthalocyanine macrocycle.

Phthalocyanines **14** and **18** existed as an unequal mixture of *cis* and *trans* isomers as shown by NMR spectroscopy while Pc **15** was too insoluble for useful studies. Indeed, the insolubility of **15** and the attendant difficulties of purification meant that satisfactory analysis could not be obtained for this compound, although we feel that confirmation of structure is on firm ground with a good HRMS (see Experimental). The problems of working with **15** in fact led to the design of Pcs **16** and **17** having larger alkyl chains generating soluble, more readily characterized Pcs. Pcs **16**, **17**, **18**, and **19** were all sufficiently soluble for easy separation and study. In an attempt to obtain symmetrical hydroxymethyl substituents at the β-position and also to tie back the β-substituents into a ring system so that subsequent cleavage might proceed more readily, 5,5-dihydroxymethyl-2-phenyl-1,3-dioxane (**21**) (19) and 1,1-dihydroxymethylcyclohexane (**22**) (20) were treated as above, but over a 12–16 day period, to give 5,5-bis(2′,3′-dicyanophenoxymethyl)-2-phenyl-1,3-dioxane (**23**) and 1,1-bis(2′,3′-(dicyanophenoxymethyl)cyclohexane (**24**) in 73 and 65% yields, respectively (Scheme 3). Neither **23** nor **24** could be induced to undergo formation of mononuclear phthalocyanines and it appeared that only polymeric pigments were formed.

In attempts to make a larger variety of side-strapped phthalocyanines, including those of crown ethers and benzylic ethers that could be more readily cleaved (4), we treated a host

[2] Side-products at higher temperatures and shorter reaction times included **2**, etherols such as 3-(2′,3′-dicyanophenoxy-2,2-diethylpropan-1-ol, and bis(2,3-dicyanophenyl)ether (BDPE), mp 223–226°C; FT-IR(cm^{-1}): 3087, 3035, 2238 (C≡N), 1565, 1461, 1270, 813; ^1H NMR (acetone-d_6) δ: 702 (m, 4H), 6.78 (d, 2H, J = 8 Hz); ^{13}C NMR (acetone-d_6) δ: 158.29, 136.95, 131.18, 124.76, 118.24, 115.81, 113.02, 108.87; EI-MS for $C_{16}H_6N_4O$, *m/z* (relative intensity): 270 (M^+, 100) 242 (13) 127 (10).

[3] The trityl groups in **14** were removed by BBr_3 to give a mixture in 31% yield of the appropriate *cis* and *trans* diols, as a light blue solid; EI-MS for $C_{42}H_{34}N_8O_6$, *m/z* (relative intensity): 746 (M^+, 100), 716 (20), 355 (18), 281 (22), 207 (37), 119 (39), 73 (42).

Scheme 2.

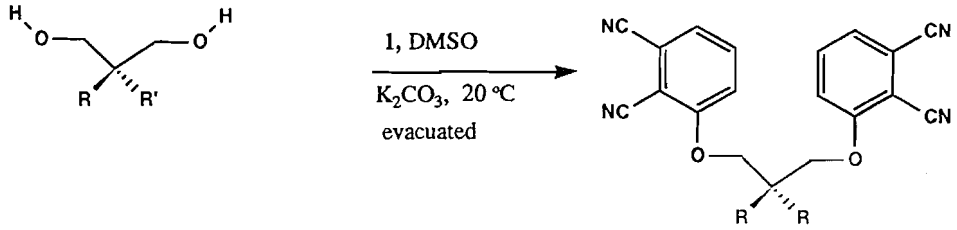

6 R = CH_3, R' = CH_2OTr

7 R = R' = C_2H_5

8 R = R' = C_5H_{11}

9 R = R' = C_8H_{17}

10 R = CH_3, R' = CH_2OTr

11 R = R' = C_2H_5

12 R = R' = C_5H_{11}

13 R = R' = C_8H_{17}

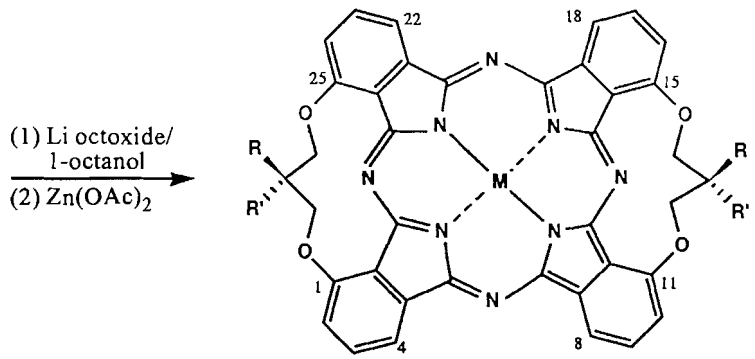

14 R = CH_3, R' = CH_2OTr, M = H_2, + *trans*

15 R = R' = C_2H_5, M = H_2

16 R = R' = C_5H_{11}, M = H_2

17 R = R' = C_8H_{17}, M = H_2

18 R = CH_3, R' = CH_2OTr, M = Zn, + *trans*

19 R = R' = C_5H_{11}, M= Zn

20 R = R' = C_8H_{17}, M = Zn

Scheme 3.

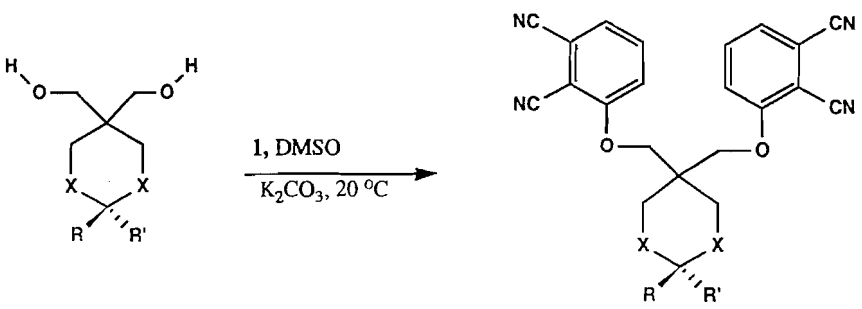

21 R = R' = H, X = O

22 R = R' = H, X = CH_2

23 R = R' = H, X = O

24 R = Ph, R' = H, X = CH_2

Scheme 4.

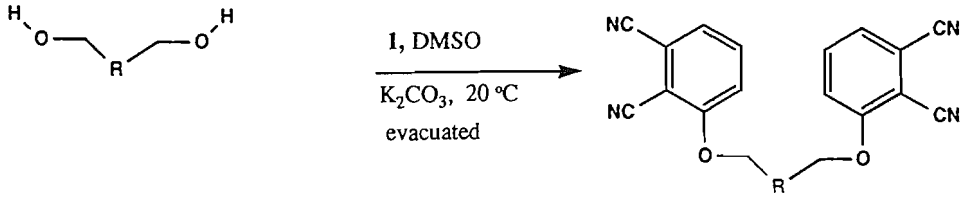

25 R = $-CH_2OCH_2-$

26 R =

27 R =

28 R =

29 R =

30 R =

31 R = $-CH_2OCH_2-$

32 R = R in **26**

33 R = R in **27**

34 R = R in **28**

35 R = R in **29**

36 R = R in **30**

of known symmetrical diols such as diethylene glycol (**25**), 1,2-dihydroxymethylbenzene (**26**), 2,2′-bis(hydroxymethyl)biphenyl (**27**) (21), 5-*tert*-butyl-1,3-dihydroxymethylbenzene (**28**) (22), 2,5-dihydroxymethylfuran (**29**), and *cis*-2,5-bis(hydroxymethyl)tetrahydrofuran (**30**) (23) as before to give the new bisphthalonitriles **31–37** in 19–56% yields. Unfortunately, none of **31–37** cyclized to bis side-strapped phthalocyanines under our standard conditions described above.

It is curious that among the 13 symmetrical bisphthalonitriles prepared for this study, only **10–13** underwent dimerization to mononuclear phthalocyanines. With hindsight it is possible to see that perhaps the "*gem* dimethyl (Thorpe–Ingold) effect "(24–26) is operating here as only **10–13** have noncyclic β,β-dialkyl substituents. The *gem* dimethyl effect was originally promulgated to explain favoured cyclization reactions in five- to seven-membered rings containing β,β-dimethyl substituents, but was later expanded to macrocyclic ring systems (27).

Spectroscopic and physical properties

It is well known that electron-donating substituents at the 1, 4, 8, 11, 15, 18, 22, and 25 positions of the phthalocyanine nucleus (cf. **5**) result in an enhanced bathochromic shift of the Q-band in their UV–VIS spectra (1, 7, 28, 29), when compared to similar substitution at the 2, 3, 9, 10, 16, 17, 23, and 24 positions of the Pc nucleus. Thus, **5** shows a typical λ_{max} at 726 nm. Surprisingly, **14–17** exhibit λ_{max} values at 708–711 nm (Fig. 1) rather than the values at ~730 nm exhibited in related pure 1,8,15,22-alkoxy-substituted Pcs (4, 7) and another pure 1,11,15,25-alkoxy-substituted Pc (7). We believe that the nature of the alkoxy substituent constrained in a ring system may cause the lone pair of electrons to lie partially out of conjugation with the benzo groups. Cook et al. (29) noticed that in one of their octaalkoxyphthalocyanines containing additional chloro substituents at the 2, 3, 9, 10, 16, 17, 23, and 24 positions, the λ_{max} is shifted hypsochromically by about 20 nm relative to other octaalkoxyphthalocyanines, and this latter example could be regarded as a partially constrained phthalocyanine. As usual, the Pc zinc(II) derivatives **18–20** (Table 2, Fig. 2) exhibit λ_{max} values of the Q-band having a hypsochromic shift of 20–25 nm compared to their metal-free counterparts.

The UV–VIS spectrum of **19** (Fig. 2) showed a spectral profile consistent with a PcM of D_{4h} symmetry in which a single intense Q-band absorption is found. The single Q-band absorption in the UV–VIS spectrum (suggesting a PcM with D_{4h} symmetry) conflicts somewhat with the actual geometry of **19** in which the 1,25:11,15-bis(side-strapped) PcZn **18** is, on a macromolecular scale, of D_{2h} symmetry. This observation strongly suggests that the peripheral sidestrap substituents do not affect, or only very weakly affect, the Pc macrocycle molecular orbitals involved in the Q-band HOMO–LUMO electron transition. These results are markedly different from other D_{2h} "opposite" Pcs in which Q-band splitting for metallophthalocyanines is observed (30, 31).

The ^1H NMR of ZnPc **18** taken in THF-d_8 clearly showed the ABX splitting pattern generated by the aromatic hydrogens of the Pc macrocycle (doublet–triplet–doublet at 9.02, 7.99, and 7.68 ppm, respectively). As for metal-free **14**, the presence of two possible side strap isomers generated two multiplets at 5.38 and 5.17 ppm for the methylene CH_2 hydro-

Fig. 1. The electronic spectrum for metal-free bis side-strapped Pc (**16**).

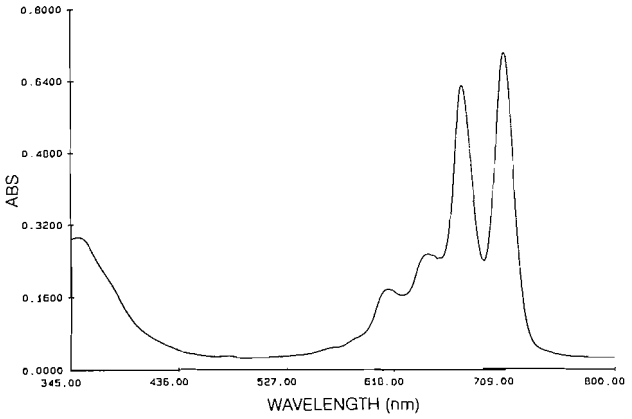

Fig. 2. The electronic spectrum of bis side-strapped zinc (II) Pc (**19**).

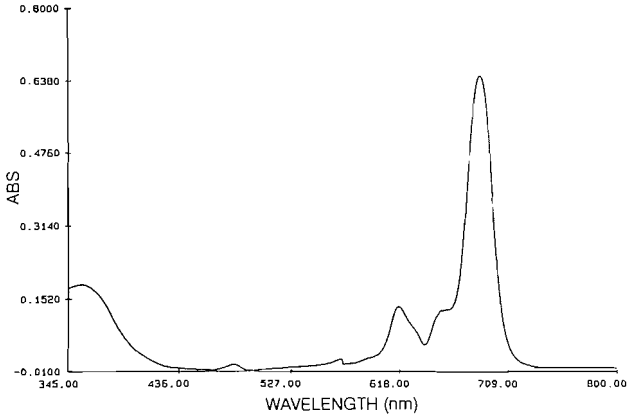

gens of the side-straps in addition to two pairs of singlets that arise from the 2'-methylene CH_2-OTr and 2'-methyl CH_3 hydrogens at 3.66,3.64 and 1.65,1.62 ppm, respectively.

The NMR spectrum of **17** was examined in the most detail as it was the most soluble of the bis side-strapped Pcs. The ^{1}H NMR spectrum of **17** in benzene-d_6 clearly showed the doublet–triplet–doublet signals arising from the ABX-spin-type aromatic hydrogens, and a singlet signal corresponding to the CH_2 hydrogens of the side straps. The internal N-H protons were evident as a broad proton signal shifted upfield to −6 ppm (6). Such a large upfield ^{1}H NMR chemical shift of the N-H hydrogens is typical for Pcs at high concentration or for cofacial binuclear Pcs (12, 32). This upfield chemical shift is a reflection of the strong cone of aromaticity generated by the ring current of the Pc macrocycle (32). At high Pc concentrations, or for Pcs that have a tendency toward cofacial π–π interaction (i.e., Pc aggregates, cofacial binuclear Pcs), the shielding imparted by the Pc macrocycle has profound effects upon the chemical shifts of hydrogens of proximal Pc neighbours.

These shielding effects experienced by the aromatic, side-strap, and internal hydrogens were explored by the acquisition of ^{1}H NMR spectra at varying concentrations of **17** in THF-d_8 (Table 1, Fig. 3 and 4). These data indicate that as the Pc solution concentration increases, Pc aggregation (or π–π stacking)

Table 1. ^{1}H NMR dilution shifts (ppm) of aromatic, side-strap, and internal hydrogens for Pc **17**.

17 (mol/L)	−log **17**	Aryl H-a	Aryl H-b	Aryl H-c	Strap CH_2	N-H
0.0050	2.301	7.75	7.27	6.83	4.32	−5.79
0.0025	2.602	7.91	7.39	6.96	4.45	−5.44
0.0005	3.301	8.32	7.67	7.25	4.74	−4.34

occurs, and results in shifts of Pc macrocycle (and side-strap) hydrogen signals to higher field. The shielding effects imparted by the Pc macrocycle affect the internal N-H hydrogens, the aromatic hydrogens, and the side-strap methylene (CH_2) hydrogens to varying degrees. For instance, the internal N-H hydrogens show the largest changes in chemical shift ($\Delta\delta$ = 1.45 ppm), whereas the change in chemical shift of the side-strap hydrogens is smaller ($\Delta\delta$ = 0.41 ppm). It appears that, in general, the hydrogen atoms closest to the core of the phthalocyanine macrocycle are most strongly influenced by the cone of aromaticity and π–π stacking shielding effects. This information can be used in assigning the signals observed in the ^{1}H NMR spectrum to the three types of Pc ring hydrogens. It would seem plausible that the aromatic hydrogen experiencing the greatest change in chemical shift as a result of changing the Pc concentration would be the aromatic hydrogen closest to the Pc core. In Pc isomers such as **17**, these would be the hydrogens at the 4, 8, 18, and 22 positions of the macrocycle and would be represented by one of the two doublet signals observed in the aromatic region of the ^{1}H NMR spectrum. The furthest downfield doublet signal (i.e., that closest to 8 ppm) exhibited the largest change of chemical shift ($\Delta\delta$ = 0.56 ppm) relative to the doublet found near 7 ppm ($\Delta\delta$ = 0.42 ppm). Even though there was only a one order of magnitude change in the concentration of Pc **17**, the data obtained from this experiment suggest that the 4-, 8-, 18-, and 22-position hydrogens can be assigned to this most downfield doublet signal (H-a in Fig. 3). This allowed an assignment of the highest field aromatic doublet signal (ca. 7 ppm) to the hydrogens at the 2, 10, 16, and 24 positions (H-c, i.e., adjacent to the side strap) and, intuitively, the triplet signal (ca. 7.5 ppm) to the hydrogens at the 2, 9, 16, and 23 positions of the Pc macrocycle. These hydrogen assignments were confirmed upon acquisition of a NOESY-NMR spectrum of **17**. Through-space NOE effects were observed between the side-strap CH_2 and macrocycle H-c hydrogens (i.e., the hydrogens in the position *ortho* to the side-strap), further validating the Pc ring hydrogen assignments determined from the ^{1}H NMR dilution shift experiment.

All new phthalocyanines and phthalonitriles exhibited parent ions in their FAB or EI mass spectra. IR data and good elemental analysis were consistent with the assigned structures. The directed syntheses of phthalocyanines having the unique substitution pattern at the 1,11,15,25 positions have been demonstrated by constraining the substitution pattern with bridges at the 1,25 and 1,11 positions.

Experimental

All organic solvents were dried by appropriate methods and distilled before use. All reagents were freshly distilled, or

Fig. 3. ^{1}H NMR dilution shifts of aromatic, side-strap, and internal hydrogens for Pc **17** taken in THF-d_8.

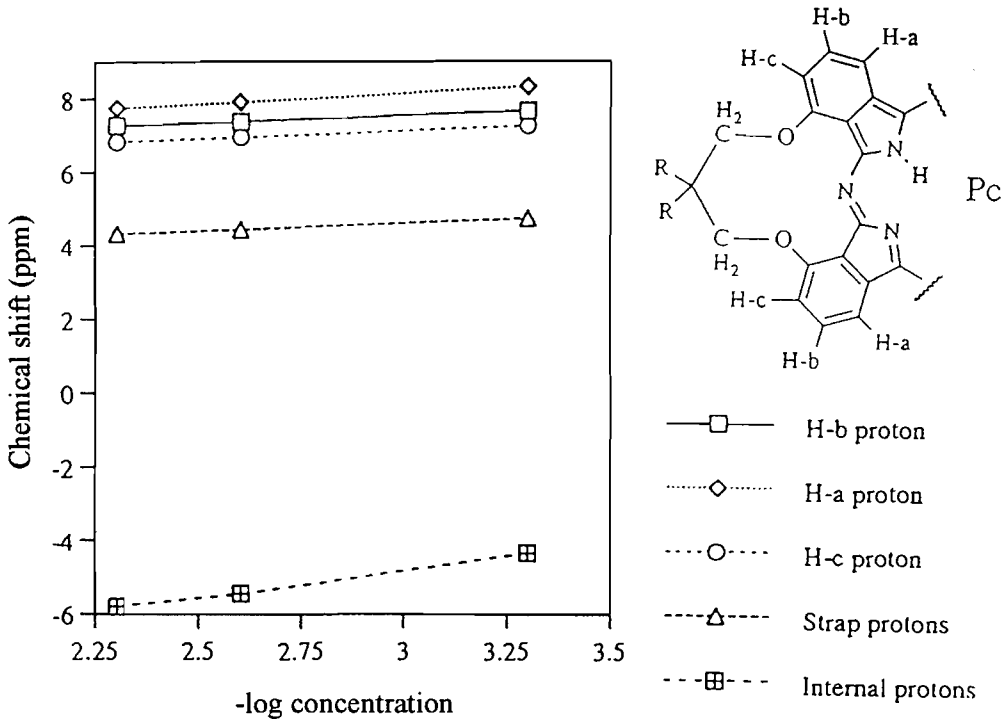

Fig. 4. The ^{1}H NMR spectrum of the downfield region of Pc **17** at 2.5×10^{-4} M in THF.

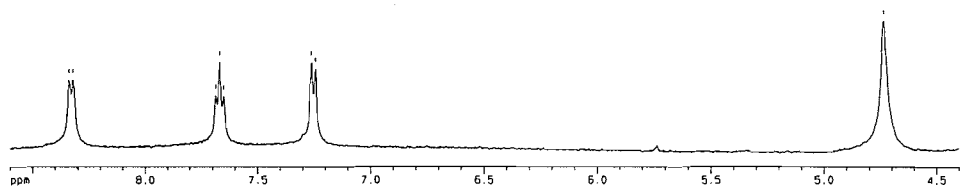

were recrystallized and then dried under reduced pressure, before use. Anhydrous potassium carbonate (K_2CO_3) was finely ground, oven dried at 250°C for 36 h, and then stored in sealed vials. Unless otherwise noted, magnetic stirring methods under an inert atmosphere (Matheson High Purity argon) were utilized during distillation or reaction processes, and round-bottom glass vessels chosen such that the quantity of reagents and solvent did not exceed half of the available volume. Water-cooled condensers were used if reaction processes were held near, or at, reflux conditions. Melting points were determined using a Kofler hot-stage melting point apparatus and are reported uncorrected. Infrared spectroscopy was performed on either a Pye Unicam SP3-200 or a Perkin Elmer 1310 infrared spectrophotometer and FTIR spectroscopy was performed on a Unicam Mattson 3000 FTIR spectrometer using samples prepared as KBr discs unless otherwise noted. Mass spectral analyses were performed by Dr. B. Khouw (York University, North York, Ontario, Canada), Dr. R. Smith (McMaster University, Hamilton, Ontario, Canada), and Dr. R. N. Cerny (Midwest Center for Mass Spectrometry, University of Nebraska–Lincoln, Lincoln, Nebraska, U.S.A.). HRMS were performed by Dr. R. Smith (McMaster University, Hamilton, Ontario, Canada). Nuclear magnetic resonance (NMR) spectroscopy was performed at 295–300 K unless otherwise noted, using either a Bruker Aspect AM3000 or a Bruker ARX 400 high-field Fourier Transform instrument. Chemical shifts are reported in parts per million relative to a tetramethylsilane (TMS) internal standard. Splitting patterns of proton resonances are described as singlets (s), doublets (d), triplets (t), quartets (q), doublets of doublets (dd), multiplets (m), or as broad signals (br). Coupling constants for signals other than singlets and multiplets are reported in hertz. ^{13}C NMR resonances are reported as the proton-decoupled chemical shifts. In addition to one-dimensional (1D) ^{1}H NMR and ^{13}C NMR, compounds requiring absolute structure determination were elucidated using combinations of 2D ^{1}H NMR (COSY and NOESY) and 2D carbon–proton (XH) correlations.

3-Hydroxyphthalonitrile (2)

In a manner similar to that previously described in the preparation of 4-hydroxyphthalonitrile (10), 865 mg (5.00 mmol) of 3-nitrophthalonitrile (**1**) (8, 9) was dissolved in 5 mL of DMSO. K_2CO_3 (760 mg, 5.51 mmol) and $NaNO_2$ (345 mg,

5.00 mmol) were added and the mixture heated at reflux for 30 min. After cooling, the reaction mixture was diluted with 20 mL of H_2O, and the mixture acidified to pH 3 with HCl and then centrifuged. The pellet was collected, resuspended in distilled water, homogenized by sonication, and again centrifuged. The supernatant liquid was discarded and the residue washed with methanol. The highly insoluble orange crude product was purified by column chromatography, using silica gel as the adsorbent and acetone as the eluting solvent. Evaporation of the solvent under reduced pressure gave a yellow solid that was recrystallized from glacial acetic acid to give 312 mg (43%) of **2** as an amorphous pale yellow solid (TLC: 10% CH_3CN–Bz, R_f = 0.03), mp 233–235°C; FT-IR (cm^{-1}): 3228br (O-H), 3072, 2255 (C≡N), 2230 (C≡N), 1584, 1467, 1316, 975, 807; ^1H NMR (DMSO-d_6) δ: 7.62 (t, 1H, J = 8 Hz), 7.39 (d, 1H, J = 8 Hz), 7.29 (d, 1H, J = 8 Hz); ^{13}C NMR (DMSO-d_6) δ: 162.42, 135.09, 123.75, 122.08, 116.16, 114.75, 114.50, 100.68; EI-MS m/z (%): 144 (M^+, 100), 116 (85), 89 (12). Anal. Calcd. for $C_8H_4N_2O$: C 66.67, H 2.78, N 19.44; found: C 66.77, H 2.95, N 18.76.

3-Neopentoxyphthalonitrile (3)

Compound **3** was prepared in similar fashion to 4-neopentoxyphthalonitrile (12) from 2.60 g (15 mmol) of 3-nitrophthalonitrile (**1**), 2.65 g (30 mmol) of neopentanol (3,3-dimethyl-1-propanol), and 5.0 g (36 mmol) of K_2CO_3 in 14 mL of DMF. A drying tube was used to maintain anhydrous conditions over the course of the 6 day reaction period required for complete consumption of **1**. The reaction mixture was poured into 100 mL of ice-cooled water and the organic products extracted with 3 x 30 mL of EtOAc. The EtOAc extracts were combined, washed once with 70 mL of cold water, once with 10 mL of brine, and then dried over $MgSO_4$. The drying agent was removed by filtration and the filtrate evaporated under reduced pressure to give 2.88 g of a crude product. The crude product was purified by column chromatography using 20% EtOAc – petroleum ether as the eluting solvent and then by recrystallization from EtOAc–hexane to give 1.77 g of white crystalline **3** (mp 120–121.5°C). A second crop of **3** was obtained from the mother liquor by addition of hexane followed by cooling to 5°C (0.24 g, mp 119–120.5°C). The combined yield of **3** was 2.01 g (62.6%) (TLC: 20% EtOAc – petroleum ether, R_f = 0.30); IR (cm^{-1}): 3080, 2950, 2220 (C≡N), 1580, 1470, 1300, 1055 (C-O), 790; ^1H NMR ($CDCl_3$) δ: 7.61 (t, 1H, J = 8 Hz), 7.33 (d, 1H, J = 8 Hz), 7.20 (d, 1H, J = 8 Hz), 3.74 (s, 2H), 1.10 (s, 9H); ^{13}C NMR ($CDCl_3$) δ: 161.72, 134.49, 124.84, 116.87, 116.81, 115.34, 112.87, 104.94, 79.51, 32.05, 26.33; EI-MS m/z (%): 214 (M^+, 5.6), 199 (12.5), 116 (5.3), 71 (100), 43 (84). Anal. calcd. for $C_{13}H_{14}N_2O$: C 72.87, H 6.59, N 13.07; found: C 73.20, H 6.60, N 13.23.

4-Neopentoxy-1,3-diiminoisoindoline (4)

Sodium methoxide was prepared from methanol (25 mL) and cleaned sodium metal (35 mg, 1.5 mmol). When methoxide formation was complete, 374.5 mg (1.750 mmol) of **3** was added, the mixture heated to reflux, and gaseous NH_3 bubbled through the solution. After 4.5 h of NH_3 addition the solution colour changed from colourless to light yellow. A small aliquot of the solution was removed and the solvent evaporated under reduced pressure. The absence of a C≡N stretch in the IR spectrum of this sample indicated that the reaction was complete. The reaction mixture was cooled to room temperature (RT) and concentrated to dryness under reduced pressure to give 467.1 mg of crude **4** (TLC: 20% EtOAc – petroleum ether, R_f = 0.01). The yellowish crude product was not further purified and was used immediately in the preparation of PcH_2 **5**; IR (cm^{-1}): 3460–3150br, 3320, 2980, 1605, 1480, 1260, 1055.

1,8,15,22-Tetraneopentoxyphthalocyanine (5)

A solution of 467 mg (1.75 mmol) of diiminoisoindoline **4** in 3 mL of 2-*N,N*-dimethylaminoethanol (DMAE) was heated at 150°C (silicon oil bath) for 36 h. The mixture was cooled to RT and the dark green-black slurry poured into 15 mL of cold water. Cold methanol (30 mL) was added, the mixture homogenized, and the fine precipitate centrifuged and collected in six fractions. The supernatant liquid from each fraction was discarded, and the pellets were resuspended in 5 mL of methanol and centrifuged. This centrifugation procedure was repeated until the supernatant liquid was almost colourless (four cycles). The pellets were combined to give 148 mg of crude material that was purified by flash chromatography using toluene as the eluting solvent. The first product eluted was concentrated under reduced pressure to give 58.6 mg (16%) of PcH_2 **5** as a dark blue, shining solid (TLC: 2% 2-methoxyethanol–toluene, R_f = 0.70), mp > 325°C; UV–VIS (THF) λ_{max} (nm): 318, 354, 630, 664, 696, 726; IR (cm^{-1}): 3280 (N-H), 2950, 1580, 1490, 1330, 1250 (Ar-O-C), 1055, 1035, 1000, 740s; ^1H NMR (THF-d_8) δ: 9.30–7.54 (m, 12H), 4.74–4.23 (m, 8H), 1.64–1.19 (m, 36H), −0.18 (m, 2H); EI-MS m/z (%): 858 (M^+, 100), 578 (17), 205 (30), 71 (18), 28 (29). Anal. calcd. for $C_{52}H_{58}N_8O_4$: C 72.73, H 6.76, N 13.05; found: C 72.56, H 6.60, N 12.87.

General methods of bisphthalonitrile syntheses

Method I (refs. 4, 33)

The distilled or recrystallized diol was placed in a 50 mL round-bottom flask equipped with a magnetic stirrer and distilled DMSO or DMF was added (5 mL/mmol diol) and heated to 50°C. Anhydrous K_2CO_3 (3–4 molar equiv.) and 2.2–2.5 equivalents of 3-nitrophthalonitrile (**1**) (8, 9) were added, the joint was well greased, fitted with a $MgSO_4$ drying tube, and the slurry stirred at rt, producing a pink-red coloured heterogeneous mixture. Two additional 0.25 equivalents of K_2CO_3 were then added at 24 h intervals and the mixture stirred for an additional 3 days or until all of **1** had been consumed. At each 24 h interval, the reaction slurry was briefly homogenized by sonication and the component profile monitored by TLC (10% CH_3CN–Bz).

At the end of the reaction period the mixture was poured into ice-water, the flask rinsed with water, and the rinsings were added to the ice-water. The orange-brown precipitate was collected by centrifugation, washed with 40 mL of 10% $NaHCO_3$ (aq.) (removing red-coloured products and yellow-coloured 3-hydroxyphthalonitrile (**2**)), and then with water. The residue was then washed with methanol, removing yellow coloured materials (mono-reacted diol and any excess **1**). The crude off-white coloured product was analyzed by TLC and recrystallized from either hot ethyl acetate, methanol, acetone, benzene, or acetonitrile. If TLC analysis indicated the presence of impurities (in particular, BDPE[2]) in excess of approx-

imately 15%, the crude product was first purified by column chromatography using silica gel adsorbant and 10% CH_3CN–Bz as the eluting solvent and then recrystallized. The white bisphthalonitrile was dried overnight at 70°C at 10^{-3} Torr (1 Torr = 133.3 Pa).

Method II

The distilled or recrystallized diol was placed in a 50 mL round-bottom flask equipped with a magnetic stirrer and distilled DMSO was added (5 mL/mmol diol). Anhydrous K_2CO_3 (0.54 equiv.) and 0.50 equivalent of **1** were added; the joint was well greased and then fitted with a Quick-Fit stopcock valve. The flask was evacuated to an internal pressure of approximately 20 Torr, the valve closed, and the mixture stirred rapidly at rt, immediately producing a pale pink heterogeneous mixture.

At 24 h intervals, the reaction slurry was briefly homogenized by brief sonication (with swirling) and the component profile monitored by TLC (10% CH_3CN–Bz). The flask was reevacuated and the slurry stirred. If all of **1** had been consumed, additional aliquots of carbonate (0.54 equiv.) and of **1** (0.50 equiv.) were added prior to evacuation and stirring. After the addition of 2.20–2.50 equivalents of **1**, the mixture was stirred for an additional 24 h and then monitored by TLC. Additional K_2CO_3 (0.5–1.5 equiv.) was added if unreacted **1** was present and the mixture then stirred for a further 24 – 96 h. The reaction mixture was then worked up as for Method I.

2,2-Dipentylpropan-1,3-diol (8)

In a manner similar to that previously described (19), a solution of 3.00 g (10.0 mmol) of diethyl 2,2-dipentylmalonate (13) in 4 mL of Et_2O was added dropwise to a stirred 5–10°C suspension of 1.15 g (30.3 mmol) of lithium aluminum hydride ($LiAlH_4$) in 25 mL of Et_2O. After addition of the diester, the mixture was heated at reflux for 2 h and then stirred at RT overnight. Active $LiAlH_4$ was quenched by addition of 2 mL of EtOAc and then 2 mL of 95% EtOH. The inorganic salts were removed by filtration through Celite, washed with Et_2O, and the filtrate was concentrated to dryness under reduced pressure. The oily residue was dissolved in 30 mL of Et_2O and extracted successively with 20 mL portions of 6 M NaOH, 4 M HCl, twice with 40 mL of H_2O, and finally with one 10 mL portion of brine. The organic phase was dried over $MgSO_4$ and then filtered. The filtrate was evaporated under reduced pressure to give 903 mg of a pale yellow oil. Distillation of this oil under reduced pressure gave 800 mg (37%) of diol **8** as a clear, colourless oil, bp 114–117°C/5 × 10^{-3} Torr; ^{1}H NMR ($CDCl_3$) : 3.92 (s, 2H, O*H*), 3.52 (s, 4H, CH_2OH), 1.37–1.24 (m, 16H, 4 × CH_2), 0.90 (t, 6H, J = 7 Hz, CH_3); ^{13}C NMR ($CDCl_3$) δ: 69.45, 41.03, 32.77, 30.80, 22.58, 22.52, 14.04; CI-MS (NH_3) *m/z* (%): 234 ($M^+ + 1 + NH_3$, 100). Hygroscopic **8** was analyzed as its product **12**.

2,2-Dioctylpropan-1,3-diol (9)

In a manner similar to the preparation of diol **8**, a solution of 7.75 g (20.0 mmol) of diethyl 2,2-dioctylmalonate (14) in 30 mL of Et_2O was added dropwise to a stirred 5–10°C suspension of 3.00 g (80.0 mmol) of $LiAlH_4$ in 50 mL of Et_2O. After addition of the diester, the mixture was heated to reflux for 2 h and then stirred at RT overnight. Active $LiAlH_4$ was quenched by addition of 5 mL of EtOAc and then 5 mL of 95% EtOH (aq.). The inorganic salts were removed by filtration through Celite, washed with Et_2O, and the filtrate was concentrated to dryness under reduced pressure. The sticky white residue was dissolved in 60 mL of Et_2O and extracted successively with 40 mL portions of 6 M NaOH, 4 M HCl, twice with 40 mL of H_2O, and finally with one 10 mL portion of brine. The organic phase was dried over $MgSO_4$ and evaporated under reduced pressure to give a yellowish oil. Distillation of the residue under reduced pressure gave 4.13 g (69%) of diol **9** as a colourless viscous oil that slowly solidified to a white wax at RT (23°C), bp 159–162°C/5 × 10^{-3} Torr; IR (cm^{-1}): 3500–3200br (OH), 2950, 2860, 1470, 1380w, 1030, 720; ^{1}H NMR ($CDCl_3$) δ: 3.56 (s, 4H), 1.27–1.22 (br m, 30H), 0.88 (t, 6H, J = 7 Hz); ^{13}C NMR ($CDCl_3$) δ: 69.47 (CH_2OH), 41.00 (4°*C*), 31.88, 30.79, 30.58, 29.55, 29.32, 22.85, 22.66, 14.08 (CH_2CH_3); EI-MS *m/z* (%): 282 (2), 269 (22), 252 (19), 154 (22), 139 (27), 111 (33), 97 (60), 83 (79), 69 (100). Anal. calcd. for $C_{19}H_{40}O_2$: C 76.00, H 13.42; found: C 76.43, H 13.96.

1,3-Bis(2′,3′-dicyanophenoxy)-2-methyl-2-trityloxymethylpropane (10)

Bisphthalonitrile **10** was prepared by Method II from 0.900 g (2.49 mmol) of diol **6** (12), 1.159 g (6.70 mmol) of 3-nitrophthalonitrile (**1**), and 1.460 g (10.6 mmol) of K_2CO_3 in 20 mL of DMSO at RT over a 6 day period. Aqueous work-up and EtOH washing of the crude product gave a pink coloured crude product. Recrystallization of this crude product from EtOAc–hexanes gave 1.44 g (94%) of white crystalline **10** (TLC: 10% CH_3CN–Bz, R_f = 0.85), mp 233–235°C; IR (cm^{-1}): 3090, 2920, 2220 (C≡N), 1580, 1450, 1290, 1060, 790, 700; ^{1}H NMR (CD_3CN) δ: 7.72 (t, 2H, J = 8 Hz), 7.5–7.2 (m, 19H), 4.22 (s, 4H), 3.30 (s, 2H), 1.27 (s, 3H); ^{13}C NMR (acetone-d_6) δ: 162.02, 144.71, 136.30, 129.42, 128.63, 127.84, 126.46, 118.73, 117.00, 116.25, 113.76, 105.07, 87.43, 72.02, 64.50, 41.83, 17.58; EI-MS *m/z* (%): 614 (M^+, 6), 537 (9), 243 (100), 165 (35), 105 (29). Anal. calcd. for $C_{40}H_{30}N_4O_3$: C 78.19, H 4.88, N 9.12; found: C 77.66, H 4.75, N 9.30.

1,3-Bis(2′,3′-dicyanophenoxy)-2,2-diethylpropane (11)

Bisphthalonitrile **11** was prepared by Method II from 692 mg (5.23 mmol) of commercially available 2,2-diethylpropan-1,3-diol (**7**), 2.00 g (11.56 mmol) of **1**, and 3.05 g (22.1 mmol) of K_2CO_3 in 10 mL of DMSO over a 7 day period. The yield of off-white solid **11**, after purification by column chromatography using 10% acetonitrile–benzene as eluting solvent and recrystallization from acetonitrile, was 870 mg (43%) (TLC: 10% CH_3CN–Bz, R_f = 0.79), mp 216–218°C; IR (cm^{-1}): 3080, 2960, 2220 (C≡N), 1580s, 1470, 1450, 1290, 1050 (C-O), 795s; ^{1}H NMR (CD_3CN) δ: 7.67 (t, 2H, J = 8 Hz), 7.35 (d, 2H, J = 8 Hz), 7.34 (d, 2H, J = 8 Hz), 4.11 (s, 4H), 1.63 (q, 4H, J = 15, 7.5 Hz), 0.94 (t, 6H, J = 7.5 Hz); ^{13}C NMR (acetone-d_6) δ: 162.25, 136.34, 126.46, 119.03, 116.96, 116.23, 113.94, 104.99, 71.98, 42.14, 23.69, 7.42; EI-MS *m/z* (%): 384 (M^+, 3), 259 (4), 241 (50), 145 (38), 97 (80), 55 (100). Anal. calcd. for $C_{23}H_{20}O_2N_4$: C 71.88, H 5.21, N 14.58; found: C 72.24, H 4.78, N 14.99.

1,3-Bis(2′,3′-dicyanophenoxy)-2,2-dipentylpropane (12)

Bisphthalonitrile **12** was prepared by Method II from 0.72 g

(3.3 mmol) of 2,2-dipentylpropan-1,3-diol (**8**), 1.40 g (8.1 mmol) of **1**, and 2.1 g (15.2 mmol) of K_2CO_3 in 7 mL of DMSO at RT over a 9 day period. Aqueous work-up and methanol washing of the solid reaction products gave a yellowish crude solid. Recrystallization of the crude product from acetonitrile gave 0.81 g (52%) of white crystalline **12** (TLC: 10% CH_3CN–Bz, R_f = 0.78), mp 173–174°C; IR (cm^{-1}): 3080, 2960, 2210 (C≡N), 1585, 1475, 1285, 1055, 795. ^1H NMR (CD_3CN) δ: 7.71 (t, 2H, J = 8 Hz), 7.45 (m, 4H), 4.13 (s, 4H), 1.54 (m, 4H), 1.3 (m, 12H), 0.86 (t, 6H, J = 7 Hz); ^{13}C NMR (acetone-d_6) δ: 162.27, 136.34, 126.48, 119.08, 116.94, 116.23, 113.95, 104.97, 72.56, 42.05, 33.25, 31.80, 23.05, 22.92, 14.22; EI-MS *m/z* (%): 469 (M^+ + 1, 50), 453 (10), 439 (18), 397 (21), 368 (30), 325 (72), 144 (100). Anal. calcd. for $C_{29}H_{32}N_4O_2$: C 74.36, H 6.84, N 11.97; found: C 74.20, H 6.93, N 12.00.

1,3-Bis(2′,3′-dicyanophenoxy)-2,2-dioctylpropane (13)

Bisphthalonitrile **13** was prepared by Method II from 3.05 g (10.2 mmol) of 2,2-dioctylpropan-1,3-diol (**9**), 3.9 g (22.5 mmol) of **1**, and 7.4 g (54 mmol) of K_2CO_3 in 25 mL of DMSO at RT over an 8 day period. Aqueous work-up and methanol washing of the solid reaction products gave a crude yellowish solid that was recrystallized from acetonitrile. A second recrystallization from ethyl acetate gave 3.17 g (57%) of white crystalline **13** (TLC: 10% CH_3CN–Bz, R_f = 0.80), mp 163–165°C; FT-IR (cm^{-1}): 3083, 2927, 2862, 2225 (C'N), 1518s, 1463, 1294, 1045, 798. ^1H NMR (acetone-d_6) δ: 7.86 (t, 2H, J = 8 Hz), 7.71 (d, 2H, J = 8 Hz), 7.55 (d, 2H, J = 8 Hz), 4.31 (s, 4H), 1.64 (m, 4H), 1.32 (m, 24H), 0.84 (t, 6H, J = 7 Hz); ^{13}C NMR (acetone-d_6) δ: 162.26, 136.35, 126.46, 119.06, 116.95, 116.22, 113.94, 104.99, 72.48, 42.06, 32.54, 31.66, 30.94, 29.88, 23.26, 23.11, 14.30; EI-MS *m/z* (%): 552 (M^+, 4.7), 523 (4.6), 509 (2.8), 495 (2.4), 469 (3.4), 409 (55), 145 (22), 43 (100). Anal. calcd. for $C_{35}H_{44}N_4O_2$: C 76.09, H 7.97, N 10.14; found: C 75.92, H 8.52, N 10.27.

General method of bis side-strapped phthalocyanine synthesis

A solution of the bisphthalonitrile was made using 1-octanol, tetrahydrofuran (THF), or mixtures of 1-octanol and THF. A syringe pump was used to add the bisphthalonitrile dropwise (ca. 0.02 mmol/min) to lithium octoxide in 1-octanol heated at reflux (ca. 196°C) in a modified air-cooled distillation apparatus that allowed rapid removal of cosolvent. In general, 10 mL of 1-octanol containing excess lithium metal was used for every 100 mg of bisphthalonitrile added. Pc formation was usually evident after 20 s of bisphthalonitrile addition. Upon addition of the bisphthalonitrile, the mixture was heated at reflux for an additional 2–10 min and then allowed to cool to RT. Water was then added and the mixture neutralized by addition of HCl (aq.) (ca. pH 7), giving a suspension that was homogenized by ultrasound. The mixture was then concentrated to near dryness under reduced pressure and the crude Pc product purified by centrifugation and chromatographic and recrystallization techniques.

1,25:11,15-Bis(2′-methyl-2′-trityloxymethylpropan-1′,3′-dioxy)phthalocyanine (14)

PcH_2 **14** was prepared, using the general method, by an 18 min dropwise addition of a solution of 300 mg (0.49 mmol) bisphthalonitrile **6** in 7 mL of THF to 30 mL of 1-octanol containing 50 mg (2.2 mmol) of cleaned lithium metal at 200°C. After addition of **6**, the mixture was heated at reflux for an additional 5 min and then cooled to RT. A general method work-up (similar to that of **17**) gave 200 mg of a blue-green crude solid. The solid was dissolved in THF, adsorbed on normal grade silica gel, then purified by flash chromatography (benzene as eluant) to yield a first fraction of almost pure **14** (determined by TLC). PcH_2 **14** was rechromatographed under the same conditions to yield 48 mg (16%) of **14** as a dark blue solid, mp >350°C; IR (cm^{-1}): 3280 (N-H), 3050, 2910, 2860, 1580, 1480, 1250 (Ar-O-C), 1030, 745, 700; UV–VIS (THF) λ_{max} nm log ε: 330 (4.75), 618 (4.45), 656 (4.64), 680 (5.11), 712 (5.13); ^1H NMR (380 K)(pyridine-d_5) δ: 9.07 (m, 4H), 8.06 (m, 16H), 7.84 (d, 4H, J = 6 Hz), 7.57 (m, 14H), 7.40 (t, 4H, J = 7 Hz), 5.41 (m, 4H), 5.21 (m, 4H), 4.00 and 3.99 (2s, 4H), 1.93 and 1.92 (2s, 6H), −1.70 (br s, 2H); +FAB-MS *m/z*: 1231 (M^+ + 1). Anal. calcd. for $C_{80}H_{62}N_8O_6$: C 78.05, H 5.04, N 9.11; found: C 77.93, H 5.21, N 8.88.

1,25:11,15-Bis(2′,2′-diethylpropan-1′,3′-dioxy)phthalocyanine (15)

Cleaned lithium metal (50 mg, 7.1 mmol) and 1-octanol (50 mL) were placed in a 100 mL three-neck flask and the mixture heated to 195–200°C until lithium 1-octoxide formation was complete. The flask was fitted for the modified distillation and a solution of 500 mg (1.3 mmol) of bisphthalonitrile **11** in 30 mL of THF was prepared. A syringe pump was used to add the solution of **11** to the well-stirred alkoxide at 195–200°C over a 20 min period and the evaporated THF was collected. The mixture was then heated for an additional 5 min and then cooled to RT. Water (5 mL) was added and the mixture was concentrated to near dryness under reduced pressure and then neutralized by the addition of dilute HCl (aq.). The solid material was suspended in 15 mL of MeOH and homogenized by ultrasound. The grey-green solid was collected and washed by repeated centrifugation and resuspension in MeOH. Finally, the pellet was dissolved in 5 mL of 50% THF–Bz and purified by silica-gel flash chromatography using benzene as the eluting solvent. A first fraction consisting of a diffuse band of blue pigment was collected. Immobile green and brown materials were not eluted from the column. The solvent of the collected fraction (ca. 300 mL) was removed under reduced pressure to yield 35 mg (7%) of PcH_2 **15** as a blue solid, mp >350°C; IR (cm^{-1}): 3280 (N-H), 2930, 2840, 1590, 1450, 1250 (Ar-O-C), 1040, 810, 750s. UV–VIS (benzene) λ_{max} nm (log ε): 352 (4.75), 614 (4.52), 646 (4.70), 672 (5.11), 708 (5.14). ^1H NMR (CF_3COOD) δ: 9.05 (d, 4H, J = 8 Hz), 8.49 (t, 4H, J = 8 Hz), 8.03 (d, 4H, J = 8 Hz), 5.10 (s, 8H), 2.13 (q, 8H, J = 7 Hz), 1.25 (t, 12H, J = 7 Hz); EI-MS *m/z* (%): 770 (M^+, 35), 211 (10), 145 (31), 55 (100); HRMS required for $C_{46}H_{42}N_8O_4$: 770.33290; found: 770.33220.

1,25:11,15-Bis(2′,2′-dipentylpropan-1′,3′-dioxy)phthalocyanine (16)

PcH_2 **16** was prepared as above from a 3 mL THF/1-octanol (2:1) solution of 150 mg (3.21×10^{-2} mmol) of bisphthalonitrile **12** added over a 5 min period to 15 mL of 1-octanol containing 15 mg (2.2 mmol) of lithium metal at 195–200°C. The mixture was heated for an additional 2 min, cooled to RT and worked up as previously described. PcH_2 **16** was separated

from dimeric and oligomeric Pc products by flash column chromatography (3% Bz–toluene as eluting solvent) as a fast moving blue pigment F1. A slower moving blue-green component was eluted after changing the eluting solvent to 1% THF–toluene. The desired fast moving mononuclear Pc pigment **16** was then treated twice by flash column chromatography (3% Bz–toluene as eluting solvent). This pigment was recrystallized from pyridine to yield 31.5 mg (21%) of PcH_2 **16** as a bright blue solid, mp >350°C; IR (cm^{-1}): 3300 (N-H), 2940, 2850, 1585w, 1460, 1250 (Ar-O-C), 1035, 800w, 745s; UV–VIS (THF) λ_{max} nm (log ϵ): 352.5 (4.76), 614 (4.53), 645 (4.70), 674 (5.10), 709 (5.14); ^{1}H NMR (benzene-d_6) δ: 8.87 (d, 4H, J = 8 Hz), 8.28 (t, 4H, J = 8 Hz), 7.75 (d, 4H, J = 8 Hz), 4.83 (s, 8H), 1.90 (m, 8H), 1.54 (m, 8*h*), 1.32 (m, 16H), 0.80 (m, 12H), −4.5 (s, 2H); +FAB-MS *m/z* (%): 940 (M^+, 2), 869 (1.2), 772 (1), 759 (1), 687 (0.5), 614 (1.5), 460 (5), 307 (34), 154 (100). Anal. calcd. for $C_{58}H_{66}N_8O_4$: C 76.05, H 8.02, N 10.14; found: C 75.92, H 8.52, N 10.27.

1,25:11,15-Bis(2′,2′-dioctylpropan-1′,3′-dioxy)phthalocyanine (17)

PcH_2 **17** was prepared as for **15** from a **20** mL THF/1-octanol (2:1) solution of 1.11 g (2.02 mmol) of bisphthalonitrile **13** added over a 7 min period to 75 mL of 1-octanol containing 85 mg (12.1 mmol) of lithium metal at 195–200°C. The mixture was heated for an additional 5 min, cooled to RT and worked up as previously described. The desired PcH_2 **17** was separated from oligomeric Pc pigments by flash chromatography (benzene as eluting solvent). Flash chromatography of this nearly pure pigment (benzene as eluting solvent) gave 207 mg (19%) of **17** as a dark blue, shining solid, mp >350°C; IR (cm^{-1}): 3290 (N-H), 2930, 2850, 1590w, 1460w, 1255 (Ar-O-C), 1030, 805w, 740s; UV–VIS (THF) λ_{max} nm (log ϵ): 352.5 (4.79), 613 (4.58), 646 (4.73), 675 (5.12), 709 (5.17); ^{1}H NMR (benzene-d_6) δ: 7.92 (d, 4H, J = 7 Hz), 7.25 (t, 4H, J = 7 Hz), 6.88 (d, 4H, J = 7 Hz), 4.44 (s, 8H), 1.58–1.88 (m, 56H), 1.15 (t, 12H, J = 6.8 Hz), −5.99 (s, 2H) (see Table 3); EI-MS *m/z* (%): 1107 (M^+ + 1, 32), 1077 (5), 806 (8), 660 (18), 556 (100). Anal. calcd. for $C_{70}H_{90}N_8O_4$: C 75.91, H 8.19, N 10.12; found: C 75.58, H 8.52, N 9.88.

1,25:11,15-Bis(2′-methyl-2′-trityloxymethylpropan-1′,3′-dioxy)phthalocyaninatozinc(II) (18)

PcZn **18** was prepared from 23 mg (1.87×10^{-2} mmol) of PcH_2 **14** and 50 mg (0.27 mmol) of $Zn(OAc)_2$ in a mixture of 2.5 mL of Py and 2.5 mL of DMF heated at reflux for 20 h. After cooling to RT, the solvents were removed under reduced pressure and the crude product purified by column chromatography using 20% THF–Bz as the eluting solvent. The solvents were removed under reduced pressure to give 22 mg (91%) of PcZn **18**, mp >330°C; UV–VIS (THF) λ_{max} nm (log ϵ): 336 (4.71), 617 (3.92), 654 (4.40), 686 (5.33); ^{1}H NMR (THF-d_8) δ: 9.02 (d, 4H, J = 7.5 Hz), 7.99 (t, 4H, J = 7.5 Hz), 7.77 (m, 12H), 7.68 (d, 4H, J = 7.5 Hz), 7.38 (m, 12H), 7.26 (m, 6H), 5.38 (m, 4H), 5.17 (m, 4H), 3.66 and 3.64 (2s, 4H), 1.65 and 1.62 (2s, 6H); +FAB-MS *m/z*: cluster at 1295 (M+2). Anal. calcd. for $C_{80}H_{60}N_8O_6Zn$: C 74.24, H 4.64, N 8.66; found: C 74.39, H 4.46, N 8.23.

1,25:11,15-Bis(2′,2′-dipentylpropan-1′,3′-dioxy)phthalocyaninato zinc(II) (19)

PcH_2 **16** (50 mg, 5.3×10^{-2} mmol) was dissolved in a mixture of 10 mL of pyridine and 8 mL of DMF. Zinc acetate (0.5 mg, 2.72 mmol) was added and the mixture heated to reflux for 14 h. The mixture was allowed to cool, the solvents were removed under reduced pressure, and the crude product was purified by flash chromatography using THF as eluting solvent. The THF was removed under reduced pressure and the product recrystallized from pyridine to give 47 mg (89%) of PcZn **19** as fine light-blue needles, mp >350°C; UV–VIS (THF) λ_{max} nm (log ϵ): 356 (4.74), 617 (4.62), 655 (4.56), 686 (5.42); ^{1}H NMR (benzene-d_6) δ: 8.87 (d, 4H, J = 8 Hz), 8.28 (t, 4H, J = 8 Hz), 7.74 (d, 4H, J = 8 Hz), 4.83 (s, 8H), 1.91 (m, 8H), 1.54 (m, 8H), 1.27 (m, 16H), 0.80 (t, 12H, J = 6.7); +FAB-MS *m/z* (%): 1002 (M^++1, 100), 932 (10), 821 (18), 640 (29), 634 (27), 610 (23). Anal. calcd. for $C_{58}H_{64}N_8O_4Zn$: C 69.48, H 6.43, N 11.18; found: C 69.51, H 6.50, N 10.92.

1,25:11,15-Bis(2′,2′-dioctylpropan-1′,3′-dioxy)phthalocyaninato zinc(II) (20)

PcH_2 **17** (67.7 mg, 6.12×10^{-2} mmol) was added to a mixture of 20 mL of pyridine and 20 mL of DMF containing 112 mg (0.61 mmol) of $Zn(OAc)_2$. The mixture was heated at reflux overnight and then cooled to RT. The solvents were removed under reduced pressure and the pigment purified by column chromatography (Et_2O as the eluting solvent). After evaporation of the solvent under reduced pressure, 62 mg (87%) of PcZn **20** was obtained, mp >330°C; UV–VIS (THF) λ_{max} nm (log ϵ): 356 (4.63), 480 (3.11), 617 (4.49), 655 (4.46), 685.5 (5.17); ^{1}H NMR (THF-d_8) δ: 8.94 (d, 4H, J = 7 Hz), 7.96 (t, 4H, J = 7 Hz), 7.56 (d, 4H, J = 7 Hz), 5.16 (br s, 8H), 1.96 (m, 8H), 1.89 (m, 8H), 1.60 (m, 40H), 1.00 (t, 12H, J = 7 Hz); +FAB-MS *m/z* (%): 1171 (M^+ + 1, 100), 905 (34), 791 (36), 641 (85), 626 (23), 612 (66). Anal. calcd. for $C_{70}H_{88}N_8O_4Zn$: C 71.81, H 7.58, N 9.57; found: C 71.53, H 7.11, N 9.93.

5,5-Bis(2′,3′-dicyanophenoxymethyl)-2-phenyl-1,3-dioxane (23)

Bisphthalonitrile **23** was prepared by Method II from 1.11 g (5 mmol) of 5,5-dihydroxymethyl-2-phenyl-1,3-dioxane (**21**) (19), 1.75 g (10.1 mmol) of **1**, and 3.1 g (22.5 mmol) of K_2CO_3 in 25 mL of DMSO at RT over a 16 day period. Aqueous work-up and methanol washing of the reaction products gave a pink-coloured solid. Double recrystallization of the pink solid from EtOAc gave 1.83 g (77%) of white crystalline **23** (TLC: 5% CH_3CN–Bz, R_f = 0.43), mp 180–182.5°C; IR (cm^{-1}): 3180, 3100s, 2990, 2880, 2245 (C≡N), 1585s, 1470br, 1395, 1300br, 1115, 1060br, 800s, 740, 700s; ^{1}H NMR (CD_3CN) δ: 7.74 (t, 2H, J = 8 Hz), 7.60 (d, 2H, J = 8 Hz), 7.50–7.36 (m, 7H), 5.59 (s, 1H), 4.70 (s, 2H), 4.55 (d, 2H, J = 12 Hz), 4.19 (s, 2H), 4.12 (d, 2H, J = 12 Hz); ^{13}C NMR (DMSO-d_6)δ: 160.74 and 160.53, 137.95, 136.09 and 136.02, 129.07, 128.19, 126.31, 126.20, 118.94 and 118.69, 115.73 and 115.70, 115.29 and 115.27, 113.48 and 113.39, 103.45 and 113.38, 101.40, 68.85, 68.42, 67.82, 38.36; EI-MS *m/z* (%): 476 (M^+, 63), 475 (23), 399 (5), 197 (60), 157 (25), 105 (100), 77 (22). Anal. calcd. for $C_{28}H_{20}N_4O_4$: C 70.58, H 4.23, N 11.76; found: C 70.25, H 4.66, N 12.00.

1,1-Bis(2′,3′-dicyanophenoxymethyl)cyclohexane (24)

Bisphthalonitrile **24** was prepared by Method II from 0.72 g (5 mmol) of 1,1-dihydroxymethylcyclohexane (**22**) (20), 2.25 g (13 mmol) of **1**, and 2.65 g (19 mmol) of K_2CO_3 in 20 mL of

DMSO over a 12 day period at RT. Aqueous work-up and methanol washing gave a pink coloured crude product. Double recrystallization of the crude product from acetone gave 1.28 g (65%) of bisphthalonitrile **24** as colourless crystals (TLC: 10% CH_3CN–Bz, R_f = 0.63), mp 246–247°C; IR (cm^{-1}): 3080s, 2910, 2850, 2220 (C≡N), 1775s, 1450br, 1290br, 1050, 930, 790s, 730; ^1H NMR (CD_3CN) δ: 7.72 (t, 2H, J = 8 Hz), 7.48 (d, 2H, J = 8 Hz), 7.42 (d, 2H, J = 8 Hz), 4.22 (s, 4H), 1.69–1.53 (m, 10H); ^{13}C NMR (DMSO-d_6) (330 K) δ: 160.84, 135.40, 125.21, 118.60, 115.17, 114.94, 112.90, 103.06, 72.24, 38.02, 28.87, 25.16, 20.32; EI-MS *m/z* (%): 396 (M^+, 32), 252 (100), 157 (77), 144 (87), 127 (93). Anal. calcd. for $C_{24}H_{20}N_4O_2$: C 72.73, H 5.05, N 14.14; found: C 73.03, H 4.77, N 13.78.

1,5-Bis(2′,3′-dicyanophenoxy)-3-oxapentane (31)

Bisphthalonitrile **31** was prepared by Method II from 0.795 g (7.50 mmol) of diethylene glycol (**25**), 2.17 g (18.3 mmol) of **1**, and 3.04 g (22.1 mmol) of K_2CO_3 in 10 mL of DMSO at 50°C over a 6 day period. After work-up by Method I, bisphthalonitrile **31** was obtained from the crude product by column chromatography (15% CH_3CN–Bz as the eluting solvent) as the first fraction collected. After recrystallization from acetonitrile, 509 mg (19%) of **31** was obtained as white needles (TLC: 15% CH_3CN–Bz, R_f = 0.50), mp 223–224°C; IR (cm^{-1}): 3090, 2925, 2220 (C≡N), 1580, 1470, 1300, 1140, 1065, 795; ^1H NMR (CD_3CN) δ: 7.70 (t, 2H, J = 8 Hz), 7.45 (d, 2H, J = 8 Hz), 7.44 (d, 2H, J = 8 Hz), 4.34 (t, 4H, J = 4 Hz), 3.94 (t, 4H, J = 4 Hz); ^{13}C NMR (DMSO-d_6) (330 K) δ: 160.73, 135.21, 125.49, 118.64, 115.25, 115.14, 113.03, 69.35, 68.57; EI-MS *m/z* (%): 358 (M^+, 4.5), 215 (17), 171 (100), 145 (25), 116 (14). Anal. calcd. for $C_{20}H_{14}N_4O_3$: C 67.04, H 3.91, N 15.64; found: C 66.73, H 3.87, N 15.42.

A second fraction eluted from the column consisted of a mixture (by TLC) of BDPE[2] and a monosubstitution product (etherol).

1,2-Bis(2′,3′-dicyanophenoxymethyl)benzene (32)

Bisphthalonitrile **32** was prepared by Method II from 1.068 g (7.5 mmol) of 1,2-dihydroxymethylbenzene (**26**) (Aldrich), 3.0 g (17.3 mmol) of **1**, and 3.0 g (21.7 mmol) of K_2CO_3 in 10 mL of DMSO at RT over a 6 day period. After aqueous work-up and washing with MeOH an off-white crude product was recovered. Recrystallization of the crude product from acetonitrile gave 760 mg (26%) of white **32** as an amorphous solid (TLC: 5% CH_3CN–Bz, R_f = 0.24), mp 254–256°C; FT-IR (cm^{-1}): 3167, 3085, 2924, 2235 (C≡N), 1583s, 1469, 1453, 1272, 1037, 802, 767, 734; ^1H NMR ($CDCl_3$) δ: 7.83 (t, 2H, J = 8 Hz), 7.73 (d, 2H, J = 8 Hz), 7.61 (m, 4H), 7.46 (m, 2H), 5.54 (s, 4H); ^{13}C NMR ($CDCl_3$) δ: 169.24, 135.28, 133.34, 128.66, 128.52, 125.69, 118.64, 115.24, 115.20, 113.09, 103.24, 68.88; EI-MS *m/z* (%): ion signals not observed. Anal. calcd. for $C_{24}H_{14}N_4O_2$: C 73.85, H 3.59, N 14.36; found: C 73.64, H 3.57, N 14.45.

2,2′-Bis(2″,3″-dicyanophenoxymethyl)biphenyl (33)

Bisphthalonitrile **33** was prepared by Method II from 400 mg (1.9 mmol) of 2,2′-dihydroxymethylbiphenyl (**27**) (21), 750 mg (4.34 mmol) of **1**, and 900 mg (6.52 mmol) of K_2CO_3 in 10 mL of DMSO over 4 days at RT. After aqueous work-up and methanol washing, the yellowish crude product was recrystallized twice from benzene to give 370 mg (42%) of bisphthalonitrile **33** as an off-white solid (TLC: 15% CH_3CN–Bz, R_f = 0.80), mp 193–194°C; FT-IR (cm^{-1}): 3085, 3030, 2892, 2229 (C≡N), 1581s, 1470s, 1301, 1286, 1034, 801, 789, 692; ^1H NMR ($CDCl_3$) δ: 7.57 (m, 4H), 7.42 (m, 4H), 7.36 (m, 2H), 7.31 (d, 2H, J = 8 Hz), 7.17 (d, 2H, J = 8 Hz), 4.92 (m, 4H); ^{13}C NMR ($CDCl_3$) δ: 160.77, 139.94, 134.83, 132.19, 130.21, 130.04, 129.06, 128.54, 125.22, 116.98, 116.88, 115.19, 113.14, 104.44, 70.04; EI-MS *m/z* (%): 466 (M^+, 8), 463 (10), 437 (9), 324 (42), 283 (38), 179 (100). Anal. calcd. for $C_{30}H_{18}N_4O_2$: C 77.25, H 3.86, N 12.02; found: C 76.85, H 3.78, N 11.88.

1,3-Bis(2′,3′-dicyanophenoxymethyl)-5-*tert*-butylbenzene (34)

Bisphthalonitrile **34** was prepared by Method II from 388 mg (2.00 mmol) of 3,5-dihydroxymethyl-*tert*-butylbenzene (**28**) (22), 850 mg (4.91 mmol) of **1**, and 1.06 g (7.68 mmol) of K_2CO_3 in 10 mL of DMSO at RT over a 5 day period. Aqueous work-up and methanol washing gave a greyish crude product. Recrystallization of this solid from acetonitrile gave 413 mg (46%) of white crystalline **34** (TLC: 15% CH_3CN–Bz, R_f = 0.76), mp 180-181°C; FT-IR (cm^{-1}): 3089, 2954, 2869, 2234 (C≡N), 1583s, 1471, 1295s, 1083, 795; ^1H NMR (acetone-d_6) δ: 7.86 (t, 2H, J = 8 Hz), 7.73 (d, 2H, J = 8 Hz), 7.67 (s, 2H), 7.59 (d, 2H, J = 8 Hz), 7.48 (s, 1H), 5.47 (s, 4H), 1.36 (s, 9H); ^{13}C NMR (acetone-d_6) δ: 162.03, 153.12, 136.72, 136.16, 126.61, 125.63, 124.77, 119.42, 117.30, 116.32, 114.05, 105.43, 72.23, 35.46, 31.54; EI-MS *m/z* (%): 446 (M^+, 15), 304 (46), 288 (38), 273 (12), 247 (100). Anal. calcd. for $C_{28}H_{22}N_4O_2$: C 75.34, H 4.93, N 12.56; found: C 75.39, H 4.96, N 12.55.

2,5-Bis(2′,3′-dicyanophenoxymethyl)furan (35)

Bisphthalonitrile **35** was prepared by a modification of Method II (using less than 2 equiv. of **1**) from 1.28 g (10.0 mmol) of 2,5-dihydroxymethylfuran **29** (Aldrich), 3.15 g (18.2 mmol) of **1** and 3.4 g (24.6 mmol) of K_2CO_3 in 25 mL of DMSO over a 6 day reaction period at RT. Aqueous work-up and MeOH washing of the reaction product gave a brown solid. Recrystallization of the highly insoluble crude product from 140 mL of acetone gave 1.94 g (56%, **1**) of white crystalline **35** (TLC: 15% CH_3CN–Bz, R_f = 0.57), mp >330°C; FT-IR (cm^{-1}): 3370, 3090, 2920, 2232 (C≡N), 1585s, 1474s, 1275s, 1030s, 809; ^1H NMR (CD_3CN) δ: 7.78 (t, 2H, J = 8 Hz), 7.60 (d, 2H, J = 8 Hz), 7.52 (d, 2H, J = 8 Hz), 6.66 (s, 2H), 5.29 (s, 4H); ^{13}C NMR (DMSO-d_6) (330 K) δ: 159.92, 149.45, 135.17, 125.94, 118.96, 115.35, 115.20, 112.94, 112.11, 103.44, 63.33; EI-MS *m/z* (%): 382 (M^+ + 2, 1.1), 237 (85), 144 (75), 116 (100), 94 (97). Anal. calcd. for $C_{22}H_{12}N_4O_3$: C 69.47, H 3.16, N 14.74; found: C 69.21, H 3.03, N 14.53.

***cis*-2,5-Bis(2′,3′-dicyanophenoxymethyl)tetrahydrofuran (36)**

Bisphthalonitrile **36** was prepared by Method II from 0.66 g (5 mmol) of *cis*-2,5-bis(hydroxymethyl)tetrahydrofuran (**30**) (23), 2.10 g (12.1 mmol) of **1**, and 2.40 g (17.4 mmol) of K_2CO_3 in 10 mL of DMSO at RT over a 10 day period. Work-up and recrystallization from methanol gave 820 mg (43%) of greyish-yellow crystalline **36** (TLC: 15% CH_3CN–Bz, R_f = 0.55), mp 186-188°C; FT-IR (cm^{-1}): 3085, 2977, 2879, 2226 (C≡N), 1563s, 1465s, 1260, 1100, 789; ^1H NMR (acetone-d_6)

δ: 7.81 (t, 2H, J = 8 Hz), 7.62 (d, 2H, J = 8 Hz), 7.53 (d, 2H, J = 8 Hz), 4.39 (m, 2H), 4.34 (m, 2H, J = 4.2 Hz), 4.29 (m, 2H, J = 4.2 Hz), 2.15 (m, 4H); ^{13}C NMR (acetone-d_6) δ: 162.44, 135.12, 126.36, 119.09, 117.11, 116.31, 114.20, 104.90, 78.69, 72.72, 28.30; +FAB-MS *m/z* (%): 385 (M^+ + 1, 100). Anal. calcd. for $C_{22}H_{16}N_4O_3$: C 68.75, H 4.17, N 14.58; found: C 68.65, H 4.16, N 14.24.

Acknowledgement

We are grateful to the Natural Sciences and Engineering Research Council of Canada for financial support of this research.

References

1. C.C. Leznoff. *In* Phthalocyanines; properties and applications. Vol. 1. *Edited by* C.C. Leznoff and A.B.P. Lever. VCH, New York. 1989.
2. S. Greenberg, A.B.P. Lever, and C.C. Leznoff. Can. J. Chem. **66**, 1059 (1988).
3. S. Gaspard and Ph. Maillard. Tetrahedron, **43**, 1083 (1987).
4. C.C. Leznoff, M. Hu, C.R. McArthur, Y. Qin, and J.E. van Lier. Can. J. Chem. **72**, 1990 (1994).
5. M. Hanack, G. Renz, J. Strähle, and S. Schmid. J. Org. Chem. **66**, 3501 (1991).
6. D.M. Drew and C.C. Leznoff. Synlett, 623 (1994).
7. M. Hanack, G. Schmid, and M. Sommerauer. Angew Chem. Int. Ed. Engl. **32**, 1422 (1993).
8. V.M. Derkacheva, S.S. Iodko, O.L. Kaliya, and E.A. Luk'yanets. Zh. Obshch. Khim. **51**, 2319 (1981).
9. C.C. Leznoff, D.S. Terekhov, C.R. McArthur, S. Vigh, and J. Li. Can. J. Chem. **73**, 435 (1995); R.D. George and A.W. Snow. J. Heterocycl. Chem. **32**, 495 (1995); D.M. Drew. Ph.D. Thesis, York University, 1995. pp. 50–52.
10. V.A. Ustinov, V.V. Plakhtinskii, G.X. Mironov, and N.S. Ryabukhina. Zh. Org. Khim. **15**, 1775 (1979).
11. P.J. Brach, S.J. Grammatica, O.A. Ossanna, and L. Weinberger. J. Heterocycl. Chem. **7**, 1403 (1970); G. Pawlowski and M. Hanack. Synthesis, 287 (1980).
12. C.C. Leznoff, S.M. Marcuccio, S. Greenberg, A.B.P. Lever, and K.B. Tomer. Can. J. Chem. **63**, 623 (1985).
13. A.W. Dox and E.G. Jones. J. Am. Chem. Soc. **50**, 2033 (1928).
14. W.M. Stanley. M.S. Jay, and R. Adams. J. Am. Chem. Soc. **51**, 1261 (1929).
15. J.F.W. McOmie and W.L. Watts. Chem. Ind. 1658 (1963).
16. J.F.W. McOmie, M.L. Watts, and D.E. West. Tetrahedron, **24**, 2289 (1968).
17. I. Rosenthal, E. Ben-Hur, S. Greenberg. A. Concepcion-Lam, D.M. Drew, and C.C. Leznoff. Photochem. Photobiol. **46**, 959 (1987).
18. M.V . Bhatt and J.R. Babu. Tetrahedron Lett. **25**, 3497 (1984); S. Anderson. Synthesis, 3497 (1984).
19. L.F. Fieser and M. Fieser. Reagents for organic synthesis. Vol. 1. J. Wiley and Sons, Inc., New York. 1967. p. 581.
20. G. Hummel and K. Ruhl. German Pat. 922,648 (1955); Chem. Abstr. **52**, 1219e (1958).
21. R. Kreher and W. Gerhardt. Liebigs Ann. Chem. 240 (1981).
22. M.A. McCall, J.R. Caldwell, H.G. Moore, and H.M. Beard. J. Macromol. Sci. Chem. **5**, 911 (1969).
23. J.M. Timki, S.S. Moore, D.M. Walba, P.C. Hiberty, and D.J. Cram. J. Am. Chem. Soc. **99**, 4207 (1977).
24. R.M. Beesley, C.K. Ingold, and J.F. Thorpe. J. Chem. Soc. **107**, 1080 (1915).
25. C.K. Ingold, J. Chem. Soc. **119**, 305 (1921); C.K. Ingold. J. Chem. Soc. **119**, 951 (1921).
26. N.L. Allinger and V. Zalkow. J. Org. Chem. **25**, 701 (1960).
27. B.L. Shaw. J. Am. Chem. Soc. **97**, 3856 (1975).
28. P.J. Duggan and P.F. Gordon. Eur. Pat. Appl. Ep. 155 780 (1985); Chem. Abstr. **105**, 72642 (1987).
29. M.J. Cook, A.J. Dunn, S.D. Howe, A.J. Thomson, and K.J. Harrison, J. Chem. Soc. Perkin Trans. 1, 2453 (1988).
30. N. Kobayashi, T. Ashida, and T. Osa. Chem. Lett. 2031 (1992).
31. N. Kobayashi, Y. Kobayashi, and T. Osa. J. Am. Chem. Soc. **115**, 10994 (1993).
32. T.R. Janson and J.J. Katz. *In* The porphyrins: physical chemistry, Part B. *Edited by* D. Dolphin. Academic Press, New York. 1979. p. 1.
33. W.O. Siegl. J. Heterocycl. Chem. **18**, 1613 (1981).

Chemical mapping of the active site of the glucoamylase of *Aspergillus niger*

Raymond U. Lemieux, Ulrike Spohr, Mimi Bach, Dale R. Cameron, Torben P. Frandsen, Bjarne B. Stoffer, Birte Svensson, and Monica M. Palcic

Abstract: A recently developed technique for the probing of the combining sites of lectins and antibodies, to establish the structure of the epitope that is involved in the binding of an oligosaccharide, is used to study the binding of methyl α-isomaltoside by the enzyme glucoamylase. The procedure involved the determination of the effects on the kinetics of hydrolysis of both monodeoxygenation and mono-*O*-methylation at each of the seven hydroxyl groups in order to gain an estimate of the differential changes in the free energies of activation, $\Delta\Delta G^{\ddagger}$. As expected, from previous publications, both deoxygenation and *O*-methylation of OH-4 (reducing unit), OH-4′, or OH-6′ strongly hindered hydrolysis, whereas the kinetics were virtually unaffected by either the substitutions at OH-2 or structural changes at C-1. The substitutions at OH-3 caused increases of 2.1 and 1.9 kcal/mol in the $\Delta\Delta G^{\ddagger}$. In contrast, whereas deoxygenation of either OH-2′ or OH-3′ caused much smaller (0.96 and 0.52 kcal/mol) increases in $\Delta\Delta G^{\ddagger}$, the mono-*O*-methylations resulted in severe steric hindrance to the formation of the activated complex. The relatively weak effects of deoxygenation suggest that the hydroxyl groups are replaced by water molecules and thereby participate in the binding by contributing effective complementarity. Methyl α-isomaltoside was docked into the combining site of the X-ray crystal structure at 2.4 Å resolution of the complex with the inhibitor acarbose. A fit free of steric interactions with the protein was found that has the methyl α-glucopyranoside unit in the normal $^4C_1$ conformation and the other glucose unit approaching a half-chair conformation with the interunit fragment defined by the torsion angles $\phi/\psi/\omega$ = 74°/134°/166° (O-5′—C-1′$\overset{\phi}{—}$O-6$\overset{\psi}{—}$C-6$\overset{\omega}{—}$C-5—O-5). The model provides a network of hydrogen bonds that appears to well represent the activated complex formed by the glucoamylase with both maltose and isomaltose since the structures appear to provide a sound rationale for both the specificity and catalysis provided by the enzyme.

Key words: monodeoxy and mono-*O*-methyl derivatives of methyl α-isomaltoside, enzyme binding domain, functioning of glucoamylase, differential changes in free energy of activation, characteristics of hydrogen bonding networks.

Résumé : Dans le but d'étudier la fixation de l'α-isomaltoside de méthyle par l'enzyme glucoamylase, on a fait appel à une technique, développée récemment pour l'examen des sites de fixation des lectines et des anticorps, pour établir la structure de l'épitope impliqué dans la fixation d'un oligosaccharide. La procédure implique la détermination des effets, provoqués sur la cinétique d'hydrolyse, par la monodésoxygénation ainsi que la mono-*O*-méthylation de chacun des sept groupes hydroxyles; on espère ainsi obtenir une évaluation des changements différentiels dans les énergies libres d'activation, $\Delta\Delta G^{\ddagger}$. Tel qu'on peut s'y attendre sur la base des publications antérieures, tant la désoxygénation que la *O*-méthylation des groupes OH-4 (unité réductrice), OH-4′ ou OH-6′ empêchent fortement l'hydrolyse alors que la cinétique n'est virtuellement pas affectée par des substitutions au niveau du OH-2 ou par des changements structuraux en C-1. Les substitutions en OH-3 provoquent des augmentations respectives de 2,1 et de 1,9 kcal mol^{-1} dans le $\Delta\Delta G^{\ddagger}$. Par opposition, alors que la désoxygénation du OH-2′ ou du OH-3′ provoque des augmentations beaucoup plus faibles (0,96 et 0,52 kcal mol^{-1}) du $\Delta\Delta G^{\ddagger}$, les mono-*O*-méthylations provoquent un fort encombrement stérique à la formation du complexe activé. Les effets relativement mineurs de la désoxygénation suggèrent que les groupes hydroxyles sont remplacés par des molécules d'eau et qu'ils participent ainsi à la fixation en apportant une contribution effective à la complémentarité. L'α-isomaltoside de méthyle a été inséré dans le site de combinaison de la structure cristalline de la diffraction des rayons X, à une résolution de 2,4 Å, du complexe avec l'inhibiteur acarbose. On a trouvé un ajustement sans interactions stériques avec la protéine qui possède une unité α-glucopyranoside dans la conformation $^4C_1$ normale et l'autre unité de glucose dont la conformation approche celle d'une demi-chaise pour laquelle le fragment interunitaire est défini par les angles de torsion $\phi/\Psi/\omega$ = 74°/134°/166° (O-5′—C-1′$\overset{\phi}{—}$O-6$\overset{\psi}{—}$C-6$\overset{\omega}{—}$C-5—O-5). Le modèle fournit un réseau de liaisons hydrogènes qui semble bien représenter le complexe activé formé par la glucoamylase avec

Received August 8, 1995.

R.U. Lemieux,[1] **U. Spohr, M. Bach, D.R. Cameron, and M.M. Palcic.** Department of Chemistry, University of Alberta, Edmonton, AB T6G 2G2, Canada.
T.P. Frandsen, B.B. Stoffer, and B. Svensson. Department of Chemistry, Carlsberg Laboratory, Gamle Calsberg Vej 10, DK-2500 Copenhagen Valby, Denmark.

[1] Author to whom correspondence may be addressed. Telephone: (403) 492-3599. Fax: (403) 492-8231. E-mail: ray.lemieux@ualberta.ca

tant le maltose que l'isomaltose puisque les structures semblent fournir une explication rationnelle tant pour la spécificité que pour la catalyse fournie par l'enzyme.

Mots clés : dérivés monodésoxy- et mono-*O*-méthylés de l'α-isomaltoside de méthyle, domaine de fixation d'un enzyme, fonctionnement de la glucoamylase, changements différentiels dans l'énergie libre d'activation, caractéristiques des réseaux de liaisons hydrogènes.

[Traduit par la rédaction]

Introduction

It is now well established that the specific binding of oligosaccharides by lectins and antibodies invariably involves the association of complementary polyamphiphilic surfaces (1, 2). The protein combining site is normally a shallow cavity (3, 4) within which several attractive polar interactions are established (5). It was reasonable to expect that the acceptance of an oligosaccharide into the active site of an enzyme is a similar event and that our recently established method (6–8) based on the differential effects on the extent of binding that result from monodeoxygenation and mono-*O*-methylation would shed light on the epitope that is presented to the enzyme for the recognition and binding that provides the catalysis.

The long known (9) industrially highly important amyloglucosidase (EC 3.2.1.3, AMG), referred to herein as glycoamylase, was chosen for this inquiry because the X-ray crystal structures are known for both the native protein (10, 11) and its complexes with inhibitors, namely, 1′-deoxynojirimycin (12) acarbose (13), and D-*gluco*-dihydroacarbose (13, 14). The structures of the complexes with their natural substrates, maltose and isomaltose, remain unknown.

The wild-type glucoamylase used in this study hydrolyzes maltose 30–50 times more rapidly than it does isomaltose (15). In view of the strong demand for the complementarity of the interacting surfaces, the epitopes of the activated complexes are expected to be very similar. Therefore, information gained as to the structure of the complex with isomaltose should apply to that with maltose. Methyl α-isomaltoside (**29**) was chosen as the reference compound for this study because of the much greater ease of the syntheses of all of the monodeoxy and mono-*O*-methyl derivatives. It was anticipated that the results would not only provide useful ancillary information on the mode of action of glucoamylase but also help to assess the use of this chemical probing technique to study the mode of enzyme catalysis when the X-ray crystal structure is not known.

Discussion of results

Synthesis

The procedures used to synthesize the target compounds (**29**–**35** and **56**–**62**) listed in Table 1 are outlined in Schemes 1, 2, and 3. These are now conventional and require little discussion. The various intermediates were well characterized by their ^{1}H NMR spectra, which indicated in all cases a high state of purity. The ^{13}C chemical shift data presented in Table 1 are obviously in accord with expectation based on the position of the chemical alteration of the reference methyl α-isomaltoside (**29**). Although some of the assignments are tentative, the conclusions reached as to structure are surely unequivocal.

Although not without precedent (8), the use of fluoride ion to open the stannylene ring formed on reactions of **1** with di-*n*-butyltin oxide is noteworthy. Except for the preparation of **47**, bromide-ion catalyzed glycosylations (16, 17) were used to establish the interunit α-D linkages of the various congeners of methyl α-isomaltoside (**29**). The yields of α-disaccharide were invariably high (>90%) but accompanied by a 5–10% formation of the β isomer. The separation of these isomers was accomplished by column chromatography. In several cases, the overall yields were very low because, in order to achieve high purity, the chromatograms had to be repeated two to three times. Because of the instability of 2-deoxyglycosyl bromides, the blocked 2′-deoxy disaccharide **47** was prepared using the 2-deoxyglucosyl chloride (**39**) and catalyzed by chloride ion. We are not convinced that, for the present purposes, the use of any of the more recently developed and highly vaunted procedures for α-glycosylation (18) are superior in convenience, yield, or cost to that employed herein.

Kinetics

The effects of the various structural changes presented in Table 1 on the kinetics of the hydrolysis of the interunit glycosidic bond of **29** at 318 K are presented in Table 2. The rationalization of these data is reserved for a separate communication (Frandsen et al., in preparation). At this time, attention is restricted to the effects of the structural changes on the free energy of activation ($\Delta\Delta G^{\ddagger}$) (19) using methyl α-isomaltoside (**29**) as the reference substrate. As seen in Table 2 and presented schematically in Fig. 1, the changes in $\Delta\Delta G^{\ddagger}$ spread over 6 kcal/mol. These changes in the energetics of reaction are readily appreciated with reference to the X-ray crystal structure at 2.4 Å resolution recently reported by Aleshin et al. (13) for the complex of the glycoamylase with the inhibitor of the enzyme's activity known as acarbose.

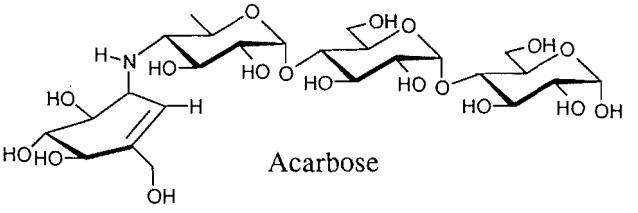

First of all, it is noteworthy that the three-dimensional structure of the native glucoamylase (10) (2.2 Å resolution) and that of its complex with acarbose (13) (2.4 Å resolution) are virtually superimposable and certainly do not differ within experimental certainly (12). The acceptance of methyl α-isomaltoside into the active site must be similar to that for the inhibitor. On this basis, the procedure used to dock methyl α-isomaltoside was to first bring the three key hydroxyl groups (OH-4, OH-4′ and OH-6′) within acceptable hydrogen bonding distances with the same proton-accepting groups for these hydroxyls present in the complex with the inhibitor (13). Since the intent was to model the transition state for the cleavage of the interglucosidic bond, it was decided to flatten the ring of the nonreducing unit to a half-chair conformation in line with

Table 1. The ^{13}C NMR chemical shifts[a] (ppm) for methyl α-isomaltoside (**29**) (δ) and congeners (δ_c).

		$\delta_c - \delta$													
	δ **29**	2-Deoxy **30**	3-Deoxy **31**	4-Deoxy **32**	2-OMe **33**	3-OMe **34**	4-OMe **35**	2′-Deoxy **55**	3′-Deoxy **56**	4′-Deoxy **57**	6′-Deoxy **58**	2′-OMe **59**	3′-OMe **60**	4′-OMe **61**	6′-OMe **62**
αDGlc(1′ → 6)															
C-1′	98.69	0.01	0.01	0.02	0.01	0.01	0.56	−0.91	−1.12	0.67	−0.1	−2.67	0.03	−0.16	0.01
C-2′	72.30	0.04	0.02	−0.04	−0.01	0.00	0.00	**−34.89**	−4.90	1.84	0.24	**8.96**	−0.46	0.00	−0.07
C-3′	73.90	0.02	0.02	−0.03	0.00	−0.03	−0.05	−4.81	**−38.69**	−5.85	−0.27	−0.90	**9.93**	−0.29	−0.11
C-4′	70.35	0.00	−0.03	0.05	−0.01	−0.01	−0.01	1.39	−5.40	**−35.42**	5.55	−0.01	−0.59	**9.67**	−0.09
C-5′	72.65	−0.01	−0.03	0.12	0.01	0.01	0.25	0.43	0.73	−2.95	−4.02	−0.24	0.06	−1.06	−1.54
C-6′	61.30	0.00	−0.03	0.05	0.00	0.00	−0.03	0.14	0.06	3.13	**−43.92**	−0.05	−0.14	−0.26	**10.43**
(1′ → 6)αDGlcOMe															
C-1	100.19	−0.95	−1.00	0.64	−2.74	0.01	−0.21	0.00	0.00	0.00	0.02	−0.02	0.02	−0.02	0.00
C-2	71.99	**−34.58**	−4.95	1.72	**9.08**	−0.41	0.03	−0.02	0.01	0.01	0.00	0.00	0.01	0.00	0.01
C-3	74.20	−4.88	**−38.65**	−6.10	−0.78	**9.98**	−0.52	−0.03	0.00	−0.06	0.04	−0.05	0.00	0.00	0.00
C-4	70.25	1.44	−5.49	**−35.20**	0.04	−0.53	**9.56**	−0.01	0.06	0.03	0.04	0.14	0.02	0.03	0.23
C-5	70.88	0.48	0.82	−3.07	−0.18	0.07	−1.05	−0.20	0.15	0.09	0.00	0.15	0.02	−0.01	−0.03
C-6	66.33	0.13	0.04	3.37	−0.04	−0.17	0.63	−0.56	−0.19	−0.02	0.04	0.00	0.05	0.03	0.14
CH_3O	56.01	−0.64	−0.23	−0.08	−0.24	0.01	−0.01	−0.07	−0.02	−0.01	0.00	−0.03	0.01	−0.02	−0.02
CH_3O	—	—	—	—	58.70	61.07	60.57	—	—	—	—	58.73	60.92	60.79	59.29

[a]0.05 M solutions in D_2O with dioxane as internal reference at 67.4 ppm (35) were measured at 75 MHz and 295 K. The assignments were made by inspection and are tentative.

Table 2. Effects of monodeoxygenation and mono-*O*-methylation of methyl α-isomaltoside as a substrate for the glucoamylase of *Aspergillus niger*.

Structural change	k_{cat} (s^{-1})	K_m (mM)	k_{cat}/K_m (s^{-1} mM^{-1})	$\Delta\Delta G^{\ddagger}$ (kcal/mol)[a]
None (**29**)	8.8×10^{-1}	22.4	3.9×10^{-2}	0
2-Deoxy (**30**)	5.0×10^{-1}	19.1	2.6×10^{-2}	0.26
2-*O*-Me (**33**)	5.6×10^{-1}	13.3	4.2×10^{-2}	−0.047
3-Deoxy (**31**)	3.6×10^{-2}	24.1	1.5×10^{-3}	2.1
3-*O*-Me (**34**)	2.3×10^{-2}	11.7	2.0×10^{-3}	1.9
4-Deoxy (**32**)	6.7×10^{-4}	8.8	7.6×10^{-5}	3.9
4-*O*-Me (**35**)	5.4×10^{-4}	33.0	1.7×10^{-5}	4.9
2′-Deoxy (**55**)	1.8×10^{-1}	21.2	8.5×10^{-3}	0.96
2′-*O*-Me (**59**)	—	—	6.7×10^{-5}	4.0
3′-Deoxy (**56**)	9.5×10^{-1}	56.9	1.7×10^{-2}	0.52
3′-*O*-Me (**60**)	—	—	3.3×10^{-5}	4.5
4′-Deoxy (**57**)	1.3×10^{-4}	21.2	6.0×10^{-6}	5.5
4′-*O*-Me (**61**)	4.7×10^{-5}	21.0	2.2×10^{-6}	6.2
6′-Deoxy (**58**)	1.5×10^{-4}	39.0	3.9×10^{-6}	5.8
6′-*O*-Me (**62**)	—	—	1.6×10^{-5}	4.9

[a] $\Delta\Delta G^{\ddagger} = -RT \ln [(k_{cat}/K_m)_{congener}/(k_{cat}/K_m)_{reference}]$ at $T = 318$ K (19).

Fig. 1. Effects of monodeoxygenations compared to those caused by mono-*O*-methylation presented as $\Delta\Delta G^{\ddagger}$ deoxy/$\Delta\Delta G^{\ddagger}$ O-Me at 318 K (see Table 2).

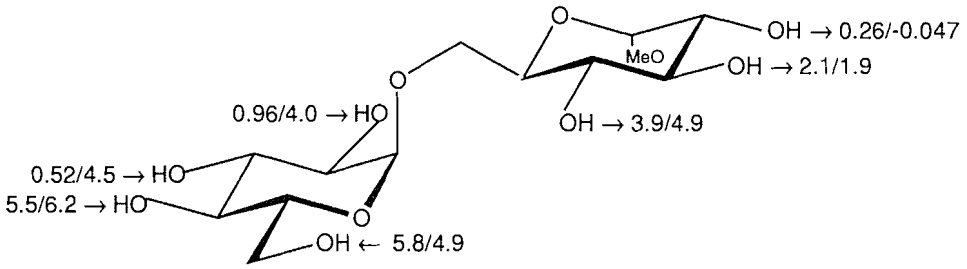

the expectation that the cleavage of the glycosidic bond occurs with participation of the ring oxygen, leading to double bond character for the C-1′—O-5′ bond. Since the cyclohexene ring of the acarbose in its complex with the glucoamylase has such a distortion, the procedure was simply to superimpose the pyranose ring of the nonreducing unit of the isomaltoside and the cyclohexene ring. GEGOP calculations (20) suggest that the distortion results in about 2.8 kcal/mol of strain. Rotations about the three bonds that join the two glucose units were then systematically made to find conformers that would maintain acceptable hydrogen bonding distances of OH-4 with Trp 178 and Arg 305, as depicted in Fig. 2, but which avoided all steric nonbonding interactions with the protein. The conformation that is defined by the ϕ/ψ/ω torsion angles of 74°/134°/166° (O-5′—C-1′$\overset{\phi}{}$O-6$\overset{\psi}{}$C-6$\overset{\omega}{}$C-5—O-5) and schematically depicted in Fig. 2 was found to uniquely meet these criteria. The internuclear distances between O-4, O-4′, and O-6′ of our docked model and O-3, O-4′, and O-6′ of the acarbose in the X-ray structure (13) are 0.21, 0.24, and 0.43 Å, respectively.

The model for the transition state (Fig. 2) provides a remarkable overall network of hydrogen bonding interactions. Clearly, some of the internuclear O-to-O distances are very short and the three O-to-N distances are very long. Nevertheless, the network appears acceptable in view of the 2.4 Å resolution of the crystal structure for the protein which provides the positions of the heavy nuclei to only ± 0.3 Å and that the system is subject to the dynamics of thermal agitation. This conclusion is strongly supported both by the kinds of hydrogen bonds that are formed and by the results of the kinetic investigation. Furthermore, the proposed hydrogen-bond network is also suitable for the formation of the transition state when methyl α-maltoside is the substrate (Fig. 3). This latter partial structure for the transition state is the same as that recently proposed by Coutinho and Reilly (21) except for the participation of Arg 54 as discussed below. The torsion angles for the interunit bonds proposed for the activated methyl α-maltoside of Fig. 3 are ϕ/ψ = 69°/98°, in contrast to the ϕ/ψ = 95°/105° values recently suggested (21) for binding in the ground-state conformation. GEGOP calculation indicates ϕ/ψ = 83°/91° values for the most favorable ground-state conformer. Svensson and co-workers (22–24) have recently reviewed relevant literature.

The differential effects of monodeoxygenation and mono-*O*-methylation listed in Table 2 and presented in Fig. 1 appear to be in agreement with the transition-state complex for methyl α-isomaltoside presented in Fig. 2. The small changes

Fig. 2. Schematic presentation of hydrogen bonding interactions in the transition state for the hydrolysis of methyl α-isomaltoside catalyzed by glucoamylase. The lengths (Å) of the proposed hydrogen bonds are: **1**, 2.60; **2**, 2.65; **3**, 3.44; **4**, 2.76; **5**, 3.39; **6**, 2.75; **7**, 3.27; **8**, 2.56; **9**, 2.62; **10**, 3.16; **11**, 2.65; **12**, 2.46; **13**, 3.04.

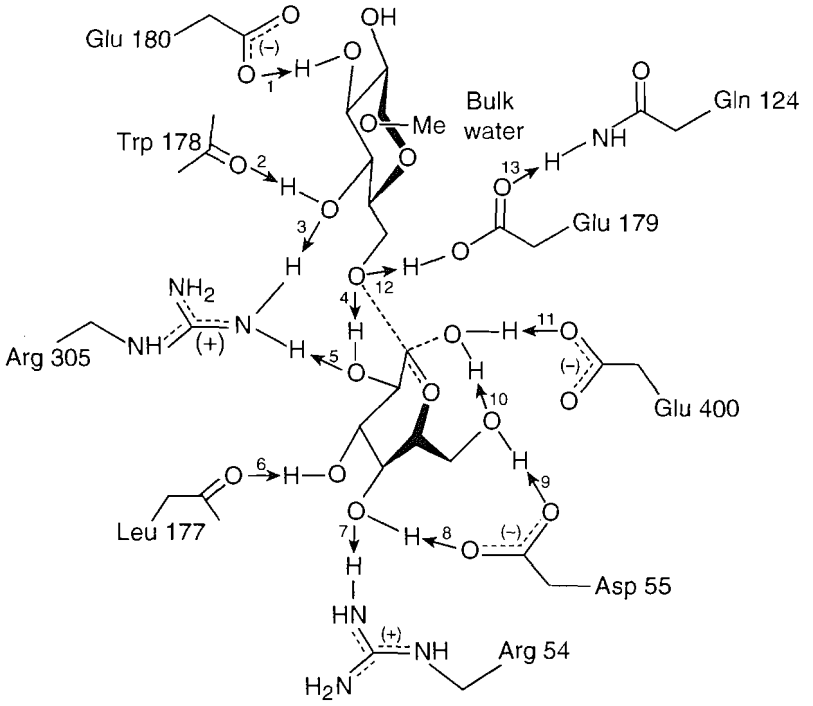

in $\Delta\Delta G^{\ddagger}$ that resulted from the substitutions at OH-2 suggest that this hydroxyl group resides in the complex at the periphery of the active site in contact with bulk water. The kinetic data for the hydrolyses of the interglycosidic bond of maltose, isomaltose, and related methyl glycosides are reviewed in Table 3 (25). The slight changes in $\Delta\Delta G^{\ddagger}$ within each group indicate that the substituents at C-1 are also exposed to bulk water, a conclusion in accord with the X-ray structure of the glucoamylase–acarbose complex (12). The small effects caused by the structural changes can be attributed to a change in the water structure about the C-1 substituents (26).

The nearly equal (about 2 kcal/mol) decreases in $\Delta\Delta G^{\ddagger}$ (Table 2) that resulted from the substitutions at OH-3 require that this hydroxyl group become involved in an interaction with the protein. The postulation that this ring interacts with Glu 180 is firmly established (27). That the effect of deoxygenation at position 3 of the isomaltoside is only about one third of that resulting from the same substitutional change for a maltoside (22, 27) is not necessarily surprising because OH-3 of the isomaltoside is in a much different environment near the aqueous phase than is OH-3 of the maltoside. The complex depicted in Fig. 2 has OH-3 well separated from Tyr 311 (not shown) and room appears to exist for an easy insertion of a methyl group on O-3 without rendering the compound essentially inactive as occurs on *O*-methylation of OH-4, OH-4′, or OH-6′. The maintenance of a hydrogen bond with Glu 180 would require the methoxy group to serve as the proton acceptor. In view of the close proximity of OH-3 to water, it is possible that a water molecule fills the space left vacant by the replacement of OH-3 by hydrogen. The filling of such voids by water was first firmly established by Quiocho et al. (28).

As seen from the strong deactivating effects of both kinds of substitutions at positions OH-4 and OH-4′ of the isomaltoside, as previously recognized (29), the interactions of these hydroxyl groups with the protein are highly important to the catalysis. It is to be noted in this regard that the roles played by these hydroxyl groups in achieving the transition state appear reinforced by their functioning cooperatively both as proton donors and proton acceptors. The strong charge delocalization thus provided to the activated complex would surely be of major importance to achievement of the distortion necessary for activation of the anomeric centre.

Since OH-2′ is in *syn*-clinal orientation to O-6, the two oxygen atoms can and may be hydrogen bonded in the transition state. This interaction, reinforced by the simultaneous acceptance of a proton from Arg 305 by O-2′, could well assist the hydrogen bonding of O-6 with Glu 179 to stretch the C-1′ to O-6 glycosidic bond.

As long recognized (13, 14), a water molecule is well positioned in the complex to make a nucleophilic attack at the incipient carbonium ionic centre. As indicated in both Figs. 2 and 3, the water molecule is held in place by hydrogen bonding with both the carboxylate group of Glu 400 and O-6′. The strength of this bond must be reinforced (30) by the hydrogen bonding bond of OH-6′ with the carboxylate group of Asp 55. The increased electron density at the oxygen atom of the water molecule, as the result of the hydrogen bonding of both of its hydrogen atoms, would importantly increase its nucleophilicity (13). Presumably the hydrogen-bond network involving Glu 400, Asp 55, and Arg 54 best accepts the distorted pyranose ring. These charge delocalizations together with the pull of electron charge from the aglyconic O-6 are, in all likeli-

Fig. 3. Schematic presentation of hydrogen bonding interactions in the transition state for the hydrolysis of methyl α-maltoside catalyzed by glucoamylase. The lengths (Å) of the proposed hydrogen bonds are: **1**, 2.99; **2**, 3.07; **3**, 3.00 with the remainder (**4**–**13**) the same as those proposed for the complex with methyl α-isomaltoside as substrate (Fig. 2).

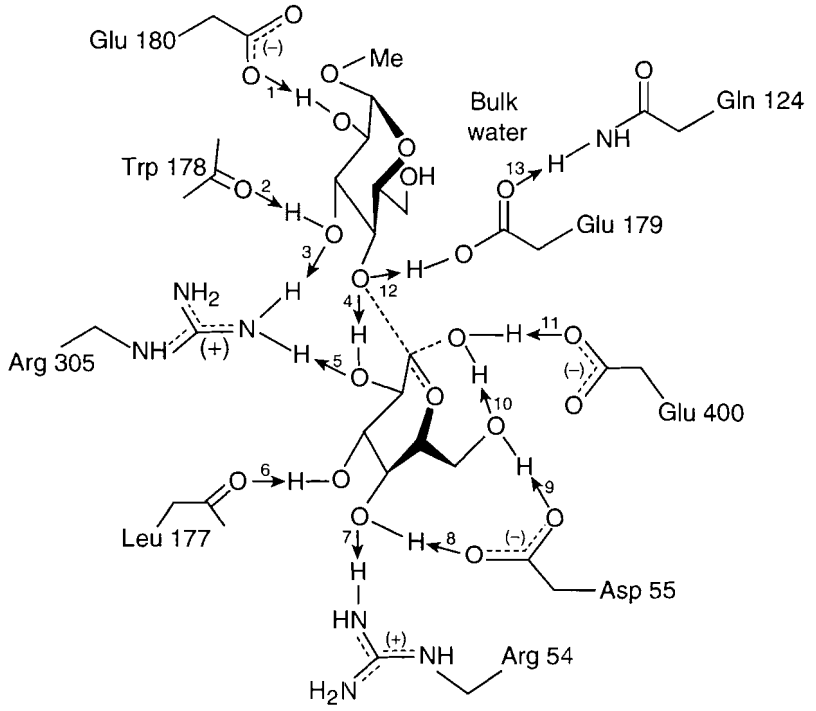

Table 3. Effects of structural changes at C-1 and C-2 on the kinetics of hydrolyses catalyzed by glucoamylase.

	k_{cat}/K_m (s^{-1} mm^{-1})	$\Delta\Delta G^{\ddagger}$ (kcal/mol)
1. **Hydrolyses of the C-1′—OC-4 bond** (25)		
Maltose (reference)	7.3	—
Methyl β-maltoside	7.0	0.026
Methyl 2-deoxy-β-maltoside	6.8	0.045
2. **Hydrolyses of the C-1′—OC-6 bond**		
Isomaltose (reference)	0.011	—
Methyl α-isomaltoside	0.039	−0.8
Methyl 2-deoxy-α-isomaltoside	0.026	−0.54

hood, at the source of the catalysis provided by glucoamylase for the hydrolysis of both isomaltose and maltose.

The hydrogen bonds formed by OH-2′ and OH-3′ with the protein must surely contribute importantly to the specificity of the catalysis. However, as seen in Table 2, deoxygenation at either one of these positions had relatively modest effects on the rates of hydrolysis. In contrast, the mono-*O*-methylations provided severe hindrance to complex formation. Attempts to place a water molecule into the cavity left by replacement of the hydroxyl groups by hydrogen met with unfavorable non-bonded interactions with the side chain of Arg 305 in the case of the 2′-position and Trp 417 in the case of the 3′-position. Low-energy movements of these side chains could provide sufficient free space to accommodate a water molecule. However, the water molecules could not be involved in attractive hydrogen bonds involving both their hydrogen atoms without movement of the protein-backbone structure. Molecular modelling was not attempted. Perhaps the formation of both hydrogen bonds is not mandatory. Presumably, a decision in this regard could be reached by examining the X-ray crystal structure of acarbose monodeoxygenated at either the 2- or 3-positions of the terminal cyclohexene-derived unit.

Experimental

General methods

The ^1H NMR spectra were measured at 300 MHz and 360 MHz (Bruker AM 300 and WM 360) with tetramethylsilane as internal standard for $CDCl_3$ solutions. The internal reference for D_2O solutions was acetone (2.225 ppm). The ^{13}C NMR

spectra were recorded at 75 MHz with dioxane (67.4 ppm) as reference for D_2O solutions and the $CDCl_3$ signal (77.06 ppm) as reference in $CDCl_3$ solutions. Optical rotations were measured at room temperature (23 ± 1°C) in a 1 dm cell on a Perkin–Elmer 241 polarimeter. Thin-layer chromatography was performed on precoated plates of silica gel (60-F254, E. Merck, Darmstadt) and visualized by spraying with the 5% sulfuric acid in ethanol followed by heating. For column chromatography silica gel 60 (230–400 mesh, E. Merck, Darmstadt) and distilled solvents were used. Solvents and reagents were purified and dried according to standard procedures. Melting points are uncorrected.

Kinetics

Glucoamylase GI was isolated from *Aspergillus niger* by affinity chromatography on an acarbose–Sepharose column (31); glucose diagnostic kits and glucose oxidase were from the Sigma Chemical Co.

Kinetic studies were carried out as previously described by measuring the amount of glucose released from substrates by coupling to glucose oxidase and horseradish peroxidase reactions (32). Incubations were carried out at 45°C in 500 μL microfuge tubes containing substrate and enzyme in 100–150 μL of 50 mM sodium acetate buffer, pH 4.5. Reactions were initiated by the addition of enzyme (8 μg–1.6 mg). At various time intervals ranging from 5 min for good substrates up to 1 h for the slow substrates, 15 μL aliquots were removed from the reaction mixtures and added to 300 μL of quench solution in microtiter plates. The quench solution contained 1.5 units of glucose oxidase, 0.3 units of horseradish peroxidase, and 24 μg of *o*-dianisidine in 1 M Tris·HCl buffer, pH 7.6. For substrates that yielded substituted glucose as a reaction product (compounds **55–62**), the glucose oxidase in the coupling system was increased to 13.5 units. The quenched solutions were covered with foil and color development was allowed to continue at ambient temperature for 1 h or until there was no further increase in absorbance. Standard curves with glucose or substituted glucose were set up in parallel in the microtiter plates. Absorbances were read at 450 nm in a microplate reader and the initial rates of reaction were estimated by linear regression analysis of the glucose released in the enzyme reactions as a function of time. Six to eight substrate concentrations were employed, ranging from 0.2 to 6 times K_m. The kinetic parameters k_{cat} and K_m were obtained by fitting the initial rate data to the Michaelis–Menten equation using the Enzfitter program.

Synthesis

*Methyl 2-*O*-benzyl-(**2**) and methyl 3-*O*-benzyl-4,6-*O*-(p-methoxybenzylidene)-α-*D*-glucopyranoside (**3**)*

A mixture of diol **1** (15 g, 48.0 mmol) (33) and di-*n*-butyltin oxide (12.8 g, 51.4 mmol) in benzene (450 mL) was refluxed with azeotropic removal of water. After 4 h, it was concentrated to 180 mL followed by the addition of tetra-*n*-butylammonium fluoride (18 g, 68.8 mmol), benzyl bromide (33 mL, 277.4 mmol), and 4 Å molecular sieves (45 g). After stirring at room temperature overnight, the solids were removed by filtration and the solvent was evaporated. Column chromatography on silica gel (hexane – ethyl acetate, 4:1, 3:1, 0.1% triethylamine) provided, in the first main fraction, compound **2** as a solid (7.0 g, 36%). $[\alpha]_D$ +29 (*c* 0.5, chloroform). ^{1}H NMR ($CDCl_3$) δ: 7.45–7.25 (m, 7H, Ph, *Ph*OMe), 6.88 (d, 2H, *Ph*OMe), 5.47 (s, 1H, C*H*PhOMe), 4.79 and 4.70 (ABq, 2H, $J_{A,B}$ 12.0 Hz, CH_2Ph), 4.60 (d, 1H, $J_{1,2}$ 3.5 Hz, H-1), 4.24 (dd, 1H, $J_{6,6'}$ 9.5 Hz, $J_{5,6}$ 4.5 Hz, H-6), 4.14 (t, 1H, $J_{2,3} \sim J_{3,4}$ 9.2 Hz, H-3), 3.80 (m, 1H, H-5), 3.79 (s, 3H, CH_3OPh), 3.68 (t, 1H, $J_{6',5}$ 10.0 Hz, H-6'), 3.47 (t, 1H, $J_{4,5}$ 9.5 Hz, H-4), 3.46 (dd, 1H, H-2), 3.37 (s, 3H, CH_3O), 2.45 (bs, 1H, OH). Anal. calcd. for $C_{22}H_{26}O_7$: C 65.66, H 6.51; found: C 65.83, H 6.53. Continued development of the column provided **3** (5.8 g, 30%) as a solid. $[\alpha]_D$ + 71.2 (*c* 0.5, chloroform). ^{1}H NMR ($CDCl_3$) δ: 7.45–7.25 (m, 7H, Ph, *Ph*OMe), 6.88 (d, 2H, *Ph*OMe), 5.53 (s, 1H, C*H*Ph), 4.95 and 4.78 (ABq, 2H, $J_{A,B}$ 11.5 Hz, CH_2Ph), 4.28 (dd, 1H, $J_{6,6'}$ 9.5 Hz, $J_{5,6}$ 4.5 Hz, H-6), 3.82 (m, s, 1H, 3H, CH_3OPh, H-5), 3.72 (dd, 1H, $J_{2,3}$ 8.5 Hz, H-2), 3.41 (s, 3H, CH_3O). Anal. calcd. for $C_{22}H_{26}O_7$: C 65.66, H 6.51; found: C 65.62, H 6.56.

*Methyl 3-*O*-benzyl-2-deoxy-4,6-*O*-(p-methoxybenzylidene)-α-*D*-arabino-hexopyranoside (**5**)*

Sodium hydride (~80% suspension, 0.42 g, 14 mmol) was added to a solution of **3** (2.79 g, 6.93 mmol) and imidazole (9 mg) in tetrahydrofuran (23 mL). After stirring for 30 min, carbon disulfide (3.3 mL, 55.9 mmol) was added and, after another 30 min, methyl iodide (0.9 mL, 14.5 mmol). The mixture, kept stirring for 30 min, was diluted with dichloromethane, followed by washing of the organic solution with aqueous saturated sodium hydrogen carbonate and water, prior to drying and evaporation. The residue, crude **4** (6.93 mmol), was taken up in toluene (41 mL) and reduced with tributyltin hydride (4.2 mL, 15.6 mmol) at reflux temperature overnight. The title compound **5** was obtained (1.20 g, 67%) by evaporation and chromatography on a column of silica gel (hexane – ethyl acetate, 3:1, 0.1% triethylamine). ^{1}H NMR ($CDCl_3$) δ: 7.48–7.25 (m, 7H, Ph, *Ph*OMe), 7.89 (d, 2H, *Ph*OMe), 5.58 (s, 1H, C*H*PhOMe), 4.82 and 4.67 (ABq, 1H, $J_{A,B}$ 12.0 Hz, CH_2Ph), 4.80 (bd, 1H, $J_{1,2}$ 3.5 Hz, H-1), 4.24 (m, 1H, $J_{6,6'}$ 9.5 Hz, $J_{5,6}$ 3.5 Hz, H-6), 4.00 (m, 1H, $J_{2ax,3}$ 11.0 Hz, $J_{2eq,3}$ 5.0 Hz, $J_{3,4}$ 8.5 Hz, H-3), 3.81 (s, 3H, CH_3OPh), ~3.78 (m, H-5, H-6'), 3.67 (t, 1H, $J_{4,5}$ 9.0 Hz, H-4), 3.32 (s, 3H, CH_3OPh), 2.26 (ddd, 1H, $J_{2ax,2eq}$ 13.5 Hz, $J_{1,2eq}$ 1.0 Hz, H-2eq), 1.79 (ddd, 1H, H-2ax). Anal. calcd. for $C_{22}H_{26}O_6$: C 68.38, H 6.78; found: C 68.40, H 6.81.

*Methyl 3-*O*-benzyl-4,6-*O*-(p-methoxybenzylidene)-2-*O*-[(methylthio)thiocarbonyl]-α-*D*-glucopyranoside (**4**)*

An analytical sample was obtained by column chromatography of the above crude preparation on silica gel (hexane – ethyl acetate, 3:1) and characterized by ^{1}H NMR spectroscopy. ^{1}H nmr ($CDCl_3$) δ: 7.45–7.25 (m, 7H, Ph, *Ph*OMe), 6.90 (d, 2H, *Ph*OMe), 5.72 (dd, 1H, $J_{1,2}$ 3.5 Hz, $J_{2,3}$ 9.5 Hz, H-2), 5.55 (s, 1H, C*H*Ph), 5.12 (d, 1H, H-1), 4.82 and 4.74 (ABq, 2H, $J_{A,B}$ 11.5 Hz, CH_2Ph), 4.30 (dd, 1H, $J_{6,6'}$ 9.5 Hz, $J_{5,6}$ 4.5 Hz, H-6), 4.20 (t, 1H, $J_{3,4}$ 9.5 Hz, H-3), 3.84 (m, 1H, H-5), 3.82 (s, 3H, CH_3OPh), 3.40 (s, 3H, CH_3O), 2.58 (s, 3H, CH_3S).

*Methyl 3-*O*-benzyl-2-deoxy-4-*O*-(p-methoxybenzyl)-α-*D*-arabino-hexopyranoside (**6**) and methyl 3-*O*-benzyl-2-deoxy-6-*O*-(p-methoxybenzyl)-α-*D*-arabino-hexopyranoside (**8**)*

Trimethylsilyl chloride (3 mL, 23.6 mmol) was added drop-

Scheme 1.

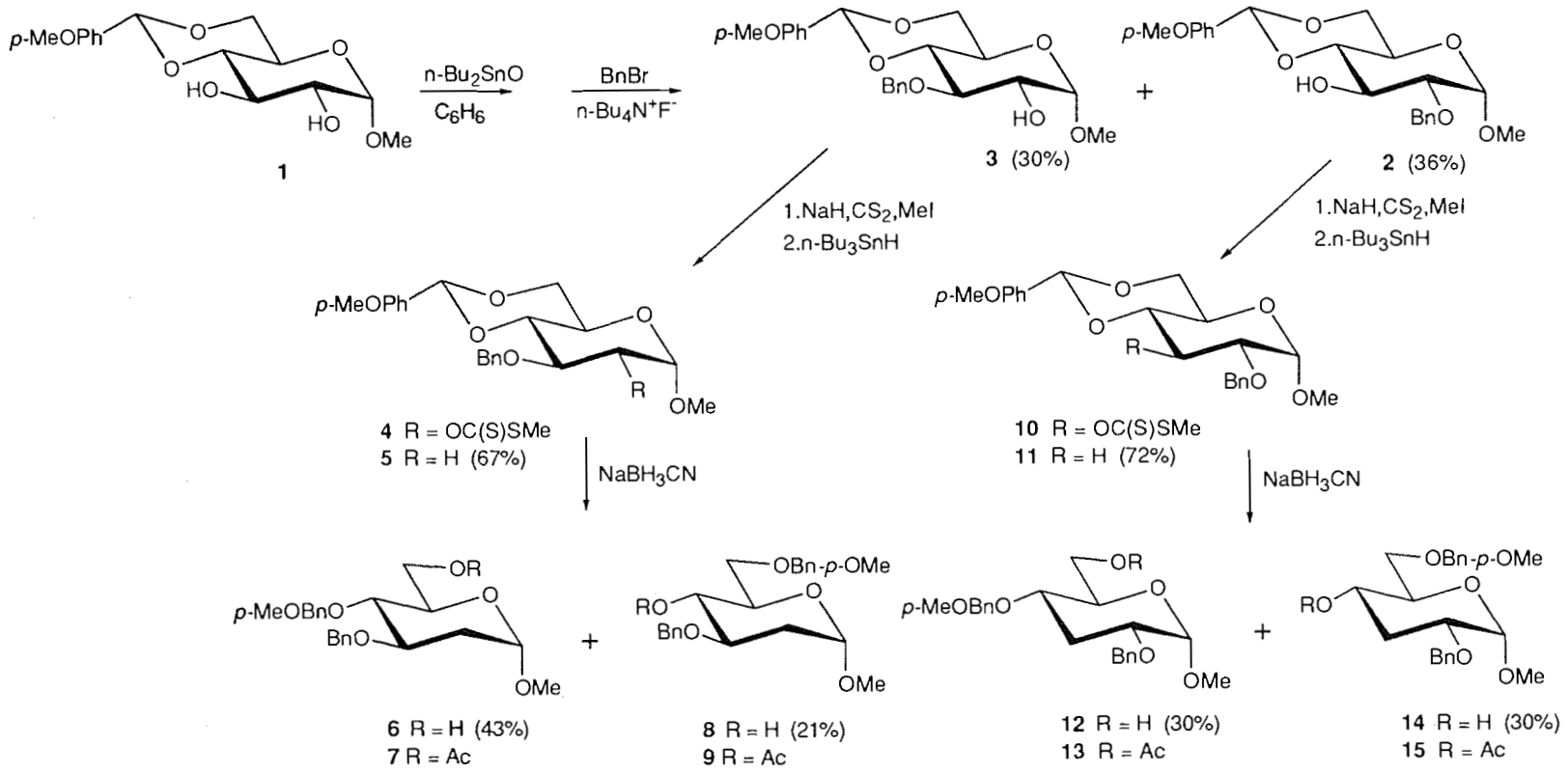

wise to a stirred mixture of **5** (1.53 g, 3.96 mmol), sodium cyanoborohydride (1.5 g, 23.9 mmol), and 4 Å molecular sieves (1.5 g) in acetonitrile (78 mL) at ice-bath temperature. After stirring for 6 h at room temperature (TLC check), it was poured into aqueous saturated sodium hydrogen carbonate and extracted with dichloromethane. The organic solution was washed with water, dried, and evaporated. Subsequent column chromatography (hexane – ethyl acetate, 2:1) provided, in the first main fraction, **8** as a syrup (328 mg, 21%). ^{1}H NMR ($CDCl_3$) δ: 7.40–7.25 (m, 7H, Ph, *Ph*OMe), 6.88 (d, 2H, *Ph*OMe), 4.84 (bd, 1H, $J_{1,2ax}$ 2.8 Hz, H-1), 4.67 and 4.54, 4.56 and 4.51 (2ABq, each 2H, $J_{A,B}$ 11.5 Hz, CH_2Ph, CH_2PhOMe), 3.80 (s, 3H, CH_3OPh), 3.78 (ddd, 1H, $J_{2eq,3}$ 5.0 Hz, $J_{2ax,3}$ 11.5 Hz, $J_{3,4}$ 8.5 Hz, H-3), 3.69 (m, 3H, H_2-6, H-5), 3.63 (m, 1H, H-4), 3.30 (s, 3H, CH_3O), 2.59 (bs, 1H, OH), 2.24 (ddd, 1H, $J_{2eq,2ax}$ 12.5 Hz, $J_{1,2eq}$ ~1 Hz, H-2eq), 1.64 (ddd, 1H, H-2ax). Anal. calcd. for $C_{22}H_{28}O_6$: C 68.02, H 7.26; found: C 67.49, H 7.09. Continued elution of the column provided syrupy **6** (657 mg, 43%). ^{1}H NMR ($CDCl_3$) δ: 7.4–7.2 (m, 7H, Ph, *Ph*OMe), 6.85 (d, 2H, *Ph*OMe), 4.85 and 4.60, 4.67 and 4.63 (2ABq, each 2H, $J_{A,B}$ 10.5, 11.5 Hz, CH_2Ph, CH_2PhOMe), 4.77 (bd, 1H, $J_{1,2ax}$ 3.5 Hz, H-1), 3.96 (ddd, 1H, $J_{2ax,3}$ 11.5 Hz, $J_{2eq,3}$ 4.5 Hz, $J_{3,4}$ 8.5 Hz, H-3), 3.78 and 3.73 (ABX, 2H, $J_{5,6}$ 3.0 Hz, $J_{6,6'}$ 11.5 Hz, $J_{5,6'}$ 5.0 Hz, H-6, H-6′), 3.76 (s, 3H, CH_3OPh), 3.61 (dt, 1H, $J_{4,5}$ 9.5 Hz, H-5), 3.48 (t, 1H, H-4), 3.27 (s, 3H, CH_3O), 2.27 (bdd, 1H, $J_{2ax,2eq}$ 13.0 Hz, $J_{1,2eq}$ ~1 Hz, H-2eq), 2.19 (bs, 1H, OH), 1.63 (ddd, 1H, H-2ax). Anal. calcd. for $C_{22}H_{28}O_6$: C 68.02, H 7.26; found: 68.05, H 7.35.

*Methyl 6-*O*-acetyl-3-*O*-benzyl-2-deoxy-4-*O*-(p-methoxybenzyl)-α-D-*arabino*-hexopyranoside (7)*

The 6-*O*-acetyl derivative of **6** was prepared in the usual manner using acetic anhydride and pyridine, 1:1. ^{1}H NMR ($CDCl_3$) δ: 7.40–7.20 (m, 7H, Ph, *Ph*OMe), 6.85 (d, 2H, *Ph*OMe), 4.85 and 4.54, 4.68 and 4.61 (2ABq, each 2H, $J_{A,B}$ 10.5, 11.5 Hz, CH_2Ph, CH_2PhOMe), 4.80 (bd, 1H, $J_{1,2ax}$ 2.5 Hz, H-1), 4.33 and 4.25 (ABX, 2H, $J_{5,6}$ 4.5 Hz, $J_{6,6'}$ 12.0 Hz, $J_{5,6'}$ 2.5 Hz, H-6, H-6′), 3.99 (ddd, $J_{2eq,3}$ 5.0 Hz, $J_{2ax,3}$ 11.5 Hz, $J_{3,4}$ 8.5 Hz, H-3), 3.78 (ddd, 1H, $J_{4,5}$ 9.0 Hz, H-5), 3.78 (s, 3H, CH_3OPh), 3.43 (t, 1H, H-4), 3.29 (s, 3H, CH_3O), 2.30 (bdd, 1H, $J_{2eq,2ax}$ 13.0 Hz, $J_{1,2eq}$ ~ 1 Hz, H-2eq), 2.06 (s, 3H, CH_3CO), 1.68 (ddd, 1H, H-2ax).

*Methyl 4-*O*-acetyl-3-*O*-benzyl-2-deoxy-6-*O*-(p-methoxybenzyl)-α-D-*arabino*-hexopyranoside (9)*

As for **6**, compound **8** was characterized by acetylation to the title compound. ^{1}H NMR ($CDCl_3$) δ: 7.40–7.20 (m, 7H, Ph, *Ph*OMe), 6.85 (d, 2H, *Ph*OMe), 5.02 (t, 1H, $J_{3,4}$ ~$J_{4,5}$ 9.5 Hz, H-4), 4.83 (bd, 1H, $J_{1,2}$ 2.5 Hz, H-1), 4.61 and 4.45, 4.49 and 4.43 (2ABq, each 2H, $J_{A,B}$ 11.5 Hz, CH_2Ph, CH_2PhOMe), 3.88 (ddd, 1H, $J_{2eq,3}$ 5.0 Hz, $J_{2ax,3}$ 11.5 Hz, $J_{3,4}$ 8.8 Hz, H-3), 3.79 (ddd, 1H, $J_{5,6}$ 3.5 Hz, $J_{5,6'}$ 5.5 Hz, H-5), 3.77 (s, 3H, CH_3OPh), 3.51 and 3.47 (ABX, 2H, $J_{6,6'}$ 10.0 Hz, H-6, H-6′), 3.32 (s, 3H, CH_3O), 2.26 (ddd, 1H, $J_{2eq,2ax}$ 13.0 Hz, $J_{1,2eq}$ ~ 1 Hz, H-2eq), 1.92 (s, 3H, CH_3CO), 1.75 (ddd, 1H, H-2ax).

*Methyl 2-*O*-benzyl-4,6-*O*-(p-methoxybenzylidene)-3-*O*-[(methylthio)thiocarbonyl]-α-D-glucopyranoside (10)*

Alcohol **2** (1.0 g, 2.49 mmol) was converted to the xanthate **10** as described for the preparation of **5**. ^{1}H NMR ($CDCl_3$) δ: 7.4–7.25 (m, 7H, Ph, *Ph*OMe), 6.88 (d, 2H, *Ph*OMe), 6.53 (t, 1H, $J_{2,3}$ ~ $J_{3,4}$ 9.5 Hz, H-3), 5.44 (s, 1H, C*H*Ph), 4.71 and 4.60 (ABq, 2H, $J_{A,B}$ 12.5 Hz, CH_2Ph), 4.69 (overlapped, H-1), 4.26 (dd, 1H, $J_{5,6}$ 4.5 Hz, $J_{6,6'}$ 10.0 Hz, H-6), 3.79, 3.41 (2s, each 3H, 2CH_3O), 2.59 (s, 3H, CH_3S).

*Methyl 2-*O*-benzyl-3-deoxy-4,6-*O*-(p-methoxybenzylidene)-α-D-*ribo*-hexopyranoside (11)*

Reduction of **10** as described above for **4** yielded the title compound (690 mg, 72%) after chromatography on a column of silica gel (hexane – ethyl acetate, 3:1, 0.1% triethylamine). ^{1}H NMR ($CDCl_3$) δ: 7.4–7.25 (m, 7H, Ph, *Ph*OMe), 6.88 (d, 1H, *Ph*OMe), 5.45 (s, 1H, C*H*Ph), 4.68 (d, 1H, $J_{1,2}$ 3.5 Hz, H-1), 4.66 and 4.58 (ABq, 2H, $J_{A,B}$ 12.5 Hz, CH_2Ph), 4.22 (dd, 1H, $J_{6,6'}$ 9.5 Hz, $J_{5,6}$ 4.5 Hz, H-6), 3.79 (s, 3H, CH_3OPh), 3.75 (ddd, 1H, $J_{5,6'}$ ~ $J_{4,5}$ 9.5 Hz, H-5), 3.64 (t, 1H, H-6′), 3.60 (dt, 1H, $J_{2,3ax}$ 11.5 Hz, $J_{2,3eq}$ 4.0 Hz, H-2), 3.47 (m, overlapped, H-4), 3.45 (s, 3H, CH_3O), 2.26 (td, 1H, $J_{3eq,4}$ 4.5 Hz, $J_{3eq,3ax}$ 11.5 Hz, H-3eq), 2.04 (q, 1H, $J_{3ax,4}$ 11.5 Hz, H-3ax). Anal. calcd. for $C_{22}H_{26}O_6$: C 68.38, H 6.78; found: C 67.91, H 6.81.

*Methyl 2-*O*-benzyl-3-deoxy-4-*O*-(p-methoxybenzyl)-α-D-ribo-hexopyranoside (12) and methyl 2-*O*-benzyl-3-deoxy-6-*O*-(p-methoxybenzyl)-α-D-*ribo*-hexopyranoside (14)*

Reductive cleavage of **11** (1.12 g, 2.90 mmol) with sodium cyanoborohydride (1.1 g, 17.5 mmol) in the presence of trimethylsilyl chloride (2.2 mL, 17.3 mmol) was performed as described for the preparation of **6**. Column chromatography on silica gel (hexane – ethyl acetate, 3:1) provided an approximately 1:1 mixture of the regio isomers **12** and **14** in 60% yield (672 mg). Repeated column chromatography in the same solvent provided the pure isomers **12** and **14** as syrups. Compound **12**: ^{1}H NMR ($CDCl_3$) δ: 7.40–7.20 (m, 7H, Ph, *Ph*OMe), 6.87 (d, 2H, *Ph*OMe), 4.64 (d, 1H, $J_{1,2}$ 3.5 Hz, H-1), 4.62 and 4.56, 4.56 and 4.38 (2ABq, each 2H, $J_{A,B}$ 11.0 Hz, CH_2Ph, CH_2PhOMe), 3.80 (s, 3H, CH_3OPh), 3.78 and 3.70 (ABX, 2H, $J_{5,6}$ 3.0 Hz, $J_{6,6'}$ 11.5 Hz, $J_{5,6'}$ 4.5 Hz, H-6, H-6′), 3.60 (m, 1H, H-5), 3.44 (ddd, 1H, $J_{2,3eq}$ 4.5 Hz, $J_{2,3ax}$ 11.5 Hz, H-2), 3.40 (s, 3H, CH_3O), 3.40 (overlapped, H-4), 2.32 (td, 1H, $J_{3eq,3ax}$ 11.5 Hz, $J_{3eq,4}$ 4.5 Hz, H-3eq), 1.90 (bs, 1H, OH), 1.86 (q, 1H, $J_{3ax,4}$ 11.5 Hz, H-3ax). Anal. calcd. for $C_{22}H_{28}O_6$: C 68.02, H 7.26; found: C 67.98, 7.28. Compound **14**: ^{1}H NMR ($CDCl_3$) δ: 7.40–7.20 (m, 7H, Ph, *Ph*OMe), 6.88 (d, 2H, *Ph*OMe), 4.63 (d, 1H, $J_{1,2}$ 3.3 Hz, H-1), 4.63 and 4.55, 4.52 and 4.47 (2ABq, each 2H, $J_{A,B}$ 12.0, 11.5 Hz, CH_2Ph, CH_2PhOMe), 3.80 (3, 3H, CH_3OPh), 3.71–3.53 (m, 4H, H-4, H-5, H_2-6), 3.50 (td, 1H, $J_{2,3eq}$ 4.5 Hz, $J_{2,3ax}$ 11.5 Hz, H-2), 3.40 (s, 3H, CH_3O), 2.19 (td, 1H, $J_{3eq,3ax}$ 11.5 Hz, H-3eq), 1.84 (m, 1H, H-3ax).

*Methyl 6-*O*-acetyl-2-*O*-benzyl-3-deoxy-4-*O*-(p-methoxybenzyl)-α-D-ribo-hexopyranoside (13)*

Compound **12** was further characterized by acetylation to **13**. ^{1}H NMR ($CDCl_3$) δ: 7.40–7.20 (m, 7H, *Ph*OMe), 6.88 (d, 2H, *Ph*OMe), 4.67 (d, 1H, $J_{1,2}$ 3.0 Hz, H-1), 4.63 and 4.57, 4.54 and 4.33 (2ABq, each 2H, $J_{A,B}$ 12.0, 11.0 Hz, CH_2Ph, CH_2PhOMe), 4.24 (d, 2H, $J_{5,6}$ 4.0 Hz, H_2-6), 3.81 (s, 3H, CH_3OPh), 3.77 (dt, 1H, $J_{4,5}$ 9.5 Hz, H-5), 3.48 (ddd, 1H, $J_{2,3ax}$ 11.5 Hz, $J_{2,3eq}$ 4.5 Hz, H-2), 3.41 (s, 3H, CH_3O), 3.34 (dt, 1H, $J_{3ax,4}$ 11.5 Hz, $J_{3eq,4}$ 4.5 Hz, H-4), 2.35 (td, 1H, $J_{3eq,3ax}$ 11.5 Hz, H-3eq), 2.01 (s, 3H, CH_3CO), 1.85 (q, 1H, H-3ax).

*Methyl 4-O-acetyl-2-O-benzyl-3-deoxy-6-O-(p-methoxybenzyl)-α-D-ribo-hexopyranoside (**15**)*

Compound **14** was characterized by acetylation to **15**. ^{1}H NMR ($CDCl_3$) δ: 7.40–7.20 (m, 7H, Ph, *Ph*OMe), 6.88 (d, 2H, *Ph*OMe), 4.81 (dt, 1H, $J_{3ax,4}$ 11.5 Hz, $J_{3eq,4}$ 4.5 Hz, $J_{4,5}$ 10.0 Hz, H-4), 4.68 (d, 1H, $J_{1,2}$ 3.3 Hz, H-1), 4.64 and 4.51, 4.55 and 4.37 (2ABq, each 2H, $J_{A,B}$ 11.5 Hz, CH_2Ph, CH_2PhOMe), 3.81 (s, 3H, CH_3OPh), 3.78 (ddd, 1H, $J_{5,6}$ 2.5 Hz, $J_{5,6'}$ 4.5 Hz, H-5), 3.58 (ddd, 1H, $J_{2,3ax}$ 11.5 Hz, $J_{2,3eq}$ 4.5 Hz, H-2), 3.50 and 3.44 (ABX, 2H, $J_{6,6'}$ 10.0 Hz, H-6, H-6'), 3.43 (s, 3H, CH_3O), 2.33 (dt, 1H, $J_{3eq,3ax}$ 11.5 Hz, H-3eq), 1.91 (s, 3H, CH_3CO) 1.84 (q, 1H, H-3ax).

General procedure for the preparation of substituted α-D-hexopyranosyl bromides

A solution of oxalyl bromide (250 μL, ~2.30 mmol) in dichloromethane (1 mL) was added dropwise to a stirred solution of the substituted hexopyranose (1.6 mmol) in dichloromethane (10 mL) and *N,N*-dimethylformamide (0.6 mL, 8.4 mmol). After 20 min, the mixture was poured into ice-water and the organic solution was washed twice with ice-cold water, dried, and evaporated. These products, which must have contained small equilibrium concentrations of the β anomer, were prepared just prior to use.

General procedure for bromide-ion catalyzed glycosidations

A solution of the substituted hexopyranosyl bromide (2.4 mmol) in dichloromethane (2.5 mL) was added to a stirred mixture of the alcohol (0.8 mmol), tetraethylammonium bromide (2.4 mmol), *N,N*-dimethylformamide (0.53 mL), and 4 Å molecular sieves (powdered, 1 g) in dichloromethane (1 mL). The mixture was stirred under nitrogen for 3 days and then quenched by the addition of methanol (0.3 mL). After stirring for another 30 min, it was diluted with dichloromethane, filtered through a pad of Celite, and the solution washed with saturated aqueous sodium hydrogen carbonate and water, followed by drying and evaporation. The crude product was applied to a silica gel column for purification.

Except for **6** and **12**, the 2,3,4-trisubstituted derivatives of methyl α-D-glucopyranosides (**17–21**), reported in Scheme 2, were prepared as previously reported (8). All of the bromides reported in Scheme 3 were prepared from literature compounds. In all cases, α-glucosylation predominated (~9α:1β); the yields of these mixtures were variable but acceptable for the present purposes. The chief difficulty was to obtain pure α isomers. Often, two or three successive chromatographic separations had to be conducted, normally using mixtures of hexane–dichloromethane – ethyl acetate.

*Methyl 2,3,4-tri-O-benzyl-6-O-(2,3,4,6-tetra-O-benzyl-α-D-glucopyranosyl)-α-D-glucopyranoside (**22**) (34)*

Obtained as a syrup. ^{1}H NMR ($CDCl_3$) δ: 7.40–7.10 (m, 35H, 7Ph), 4.98 (d, 1H, $J_{1',2'}$ 3.5 Hz, H-1'), 4.98–4.39 (m, 14H, 7CH_2Ph), 4.54 (d, overlapped, 1H, $J_{1,2}$ 3.5 Hz, H-1), 3.99 (t, 1H, $J_{2,3} \sim J_{3,4}$ 9.5 Hz, H-3), 3.96 (t, 1H, $J_{2',3'} \sim J_{3',4'}$ 9.5 Hz, H-3'), 3.54 (dd, 1H, overlapped, H-2'), 3.44 (dd, 1H, H-2), 3.35 (s, 3H, CH_3O).

*Methyl 3-O-benzyl-2-deoxy-4-O-(p-methoxybenzyl)-6-O-(2,3,4,6-tetra-O-benzyl-α-D-glucopyranosyl)-α-D-arabino-hexopyranoside (**23**)*

The α-glucosylation was conducted following the general procedure except for addition of 1 mol-equiv. of Hünig's base (diisopropylethylamine); mp 92–93°C (ether, hexane); $[\alpha]_D$ +77.6 (*c* 0.5, chloroform). ^{1}H NMR ($CDCl_3$) δ: 7.38–7.20 (m, 27H, 5Ph, *Ph*OMe), 6.80 (d, 2H, *Ph*OMe), 5.05 (d, 1H, $J_{1',2'}$ 3.5 Hz, H-1'), 4.97–4.40 (m, 12H, 5CH_2Ph, CH_2PhOMe), 4.74 (d, 1H, $J_{1,2ax}$ 3.5 Hz, H-1), 4.00 (t, 1H, $J_{3',4'} \sim J_{2',3'}$ 9.5 Hz, H-3'), 3.95 (m, overlapped, 1H, H-3), 3.74 (s, 3H, CH_3OPh), 3.57 (dd, overlapped, H-2'), 2.22 (ddd, 1H, $J_{2ax,2eq}$ 12.5 Hz, $J_{1,2eq} \sim 1$ Hz, $J_{2eq,3}$ 5.2 Hz, H-2eq), 1.57 (ddd, 1H, $J_{2ax,3}$ 11.5 Hz, H-2ax); ^{13}C NMR ($CDCl_3$) δ: 98.30 (C-1), 97.24 (C-1'), 81.81, 80.20 (C-2', C-3'), 78.14 (C-3), 77.76, 77.69 (C-4, C-4'), 75.52, 74.94, 74.58, 73.46, 72.43, 71.73 (5CH_2Ph, CH_2PhOMe), 70.99, 70.27 (C-5, C-5'), 68.65 (C-6'), 66.41 (C-6), 55.28 (CH_3O-1), 54.58 (CH_3OPh), 35.50 (C-2). Anal. calcd. for $C_{56}H_{62}O_{11}$: C73.82, H 6.86; found: C 73.82, H 6.80.

*Methyl 2-O-benzyl-3-deoxy-4-O-(p-methoxybenzyl)-6-O-(2,3,4,6-tetra-O-benzyl-α-D-glucopyranosyl)-α-D-ribo-hexopyranoside (**24**)*

Hünig's base was added as reported for the preparation of **23**. Repeated column chromatography only afforded 12% of pure syrup; $[\alpha]_D$ +80.6 (*c* 0.7, chloroform). ^{1}H NMR ($CDCl_3$) δ: 7.35–7.10 (m, 27H, 5Ph, *Ph*OMe), 6.80 (d, 2H, *Ph*OMe), 4.98 (d, 1H, $J_{1',2'}$ 3.5 Hz, H-1'), 4.98–4.33 (m, 12H, 5CH_2Ph, CH_2PhOMe), 4.61 (d, overlapped, 1H, $J_{1,2}$ 3.5 Hz, H-1), 3.99 (t, 1H, $J_{2',3'} \sim J_{3',4'}$ 9.5 Hz, H-3'), 3.74 (s, 3H, CH_3OPh), 3.65 (overlapped, H-4'), 3.55 (dd, overlapped, H-2'), 3.51 (overlapped, H-4), 3.38 (s, 3H, CH_3O), 3.33 (td, 1H, $J_{2,3eq}$ 4.5 Hz, $J_{2,3ax}$ 12.0 Hz, H-2), 2.25 (td, 1H, $J_{3ax,3eq}$ 12.0 Hz, $J_{3eq,4}$ 4.5 Hz, H-3eq), 1.82 (q, 1H, $J_{3ax,4}$ 11.5 Hz, H-3ax). ^{13}C NMR ($CDCl_3$) δ: 97.07 (C-1'), 97.00 (C-1), 81.88, 80.19 (C-2', C-3'), 77.78 (C-4'), 75.52, 75.00, 73.45, 72.34, 71.11, 70.32 (5CH_2Ph, CH_2PhOMe), 74.11 (C-2), 71.48 (C-4), 70.81, 70.16 (C-5, C-5'), 68.59 (C-6'), 66.06 (C-6), 54.88 (CH_3OPh), 55.28 (CH_3O-1), 30.20 (C-3). Anal. calcd. for $C_{56}H_{62}O_{11}$: C 73.82, H 6.86; found: C 73.60, H 6.90.

*Methyl 2,3-di-O-benzyl-4-deoxy-6-O-(2,3,4,6-tetra-O-benzyl-α-D-glucopyranosyl)-α-D-xylo-hexopyranoside (**25**)*

Obtained as a syrup (53%), $[\alpha]_D$ +50 (*c* 0.53, chloroform). ^{1}H NMR ($CDCl_3$) δ: 7.37–7.10 (m, 30H, 6Ph), 4.98–4.42 (m, 12H, 6CH_2Ph), 4.80 (d, 1H, $J_{1',2'}$ 3.5 Hz, H-1'), 4.63 (d, 1H, $J_{1,2}$ 3.5 Hz, H-1), 3.96 (t, 1H, $J_{2',3'} \sim J_{3',4'}$ 9.5 Hz, H-3'), ~3.92 (m, 2H, H-3, H-5), 3.82 (ddd, 1H, $J_{4',5'}$ 9.5 Hz, $J_{5',6'a}$ 3.0 Hz, $J_{5',6'b}$ 1.8 Hz, H-5'), 3.70 (dd, 1H, $J_{6'a,6'b}$ 10.5 Hz, H-6'a), 3.55 (dd, 1H, H-2'), 3.43 (dd, 1H, $J_{2,3}$ 9.5 Hz, H-2), 3.41 (dd, 1H, $J_{5,6a}$ 4.5 Hz, $J_{6a,6b}$ 10.5 Hz, H-6a), 3.34 (s, 3H, CH_3O), 2.11 (ddd, 1H, $J_{4ax,4eq}$ 13.0 Hz, $J_{3,4eq}$ 5.0 Hz, $J_{4eq,5}$ 2.0 Hz, H-4eq), 1.47 (q, 1H, $J_{3,4ax} \sim J_{4ax,5}$ 12.0 Hz, H-4ax). ^{13}C NMR ($CDCl_3$) δ: 98.92 (C-1), 97.28 (C-1'), 81.94, 80.61 (C-2', C-3'), 80.05 (C-2), 77.72 (C-4'), 75.36 (C-3), 75.61, 74.97, 73.47, 73.30, 72.99, 72.56 (6CH_2Ph), 70.32 (C-5'), 70.14 (C-6), 68.55 (C-6'), 66.52 (C-5), 55.19 (CH_3O), 34.15 (C-4). Anal. calcd. for $C_{55}H_{60}O_{10}$: C 74.98, H 6.86; found: C 74.68, H 6.84.

Scheme 2.

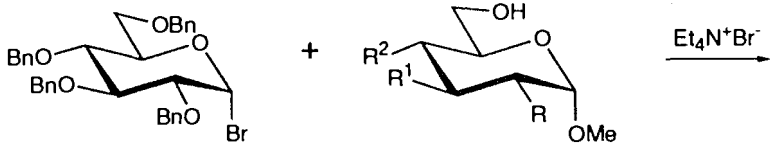

16

	R	R¹	R²
17	OBn	OBn	OBn
6	H	OBn	OBnOMe
12	OBn	H	OBnOMe
18	OBn	OBn	H
19	OMe	OBn	OBn
20	OBn	OMe	OBn
21	OBn	OBn	OMe

$Et_4N^+Br^-$

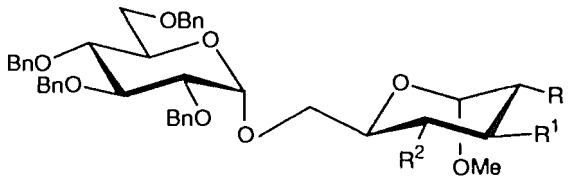

	R	R¹	R²
22	OBn	OBn	OBn
23	H	OBn	OBnOMe
24	OBn	H	OBnOMe
25	OBn	OBn	H
26	OMe	OBn	OBn
27	OBn	OMe	OBn
28	OBn	OBn	OMe

H_2/Pd(C)

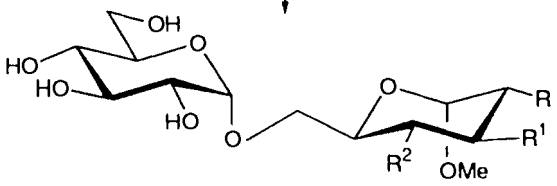

	R	R¹	R²
29	OH	OH	OH
30	H	OH	OH
31	OH	H	OH
32	OH	OH	H
33	OMe	OH	OH
34	OH	OMe	OH
35	OH	OH	OMe

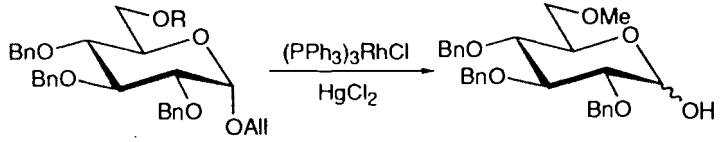

36 R = H
37 R = Me

38

*Methyl 3,4-di-*O*-benzyl-2-*O*-methyl-6-*O*-(2,3,4,6-tetra-*O*-benzyl-α-D-glucopyranosyl)-α-D-glucopyranoside (**26**)*
Obtained as a syrup (68%), $[\alpha]_D$ +78.4 (*c* 0.5, chloroform). ^{1}H NMR ($CDCl_3$) δ: 7.40–7.10 (m, 30H, 6Ph), 5.04 (d, 1H, $J_{1',2'}$ 3.5 Hz, H-1′) 5.00–4.42 (m, 12H, 6CH_2Ph), 4.82 (d, 1H, $J_{1,2}$ 3.5 Hz, H-1), 4.00 (t, 1H, $J_{2',3'} \sim J_{3',4'}$ 9.5 Hz, H-3′), 3.93 (t, 1H, $J_{2,3} \sim J_{3,4}$ 9.5 Hz, H-3), 3.61 (dd, 1H, H-2′), 3.48 and 3.42 (2s, each 3H, 2CH_3O), 3.23 (dd, 1H, H-2). ^{13}C NMR ($CDCl_3$) δ: 97.38 (C-1, C-1′), 82.35, 82.17 (C-2, C-3), 81.74, 80.24 (C-2′, C-3′), 77.65 (C-4, C-4′), 75.52, 75.52, 74.99, 74.91, 73.44, 72.44 (6CH_2Ph), 70.40, 70.32 (C-5, C-5′), 68.55 (C-6′), 66.18 (C-6), 59.19 (CH_3O-2), 55.12 (CH_3O-1). Anal. calcd. for $C_{56}H_{62}O_{11}$: C 73.82, H 6.86; found: C 73.93, H 6.94.

*Methyl 2,4-di-*O*-benzyl-3-*O*-methyl-6-*O*-(2,3,4,6-tetra-*O*-benzyl-α-D-glucopyranosyl)-α-D-glucopyranoside (**27**)*
Obtained pure as a syrup (35%), $[\alpha]_D$ +68 (*c* 0.5, chloroform). ^{1}H NMR ($CDCl_3$) δ: 7.40–7.10 (m, 30H, 6Ph), 4.98–4.37 (m, 12H, 6CH_2Ph), 4.94 (d, 1H, $J_{1',2'}$ 3.5 Hz, H-1′), 4.52 (d, 1H, $J_{1,2}$ 3.5 Hz, H-1), 3.96 (t, 1H, $J_{2',3'} \sim J_{3',4'}$ ~9.5 Hz, H-3′), 3.67 (s, 3H, CH_3O), 3.53 (dd, overlapped, H-2′), 3.35 (dd, overlapped, H-2), 3.33 (s, 3H, CH_3O). ^{13}C NMR ($CDCl_3$) δ: 97.97 (C-1), 97.24 (C-1′), 83.92, 79.95 (C-2, C-3), 81.74, 79.95 (C-2′, C-3′), 77.84, 77.63 (C-4, C-4′), 75.46, 74.86, 74.78, 73.39, 73.28, 72.56 (6CH_2Ph), 70.23, 70.16 (C-5, C-5′), 68.49 (C-6′), 66.19 (C-6), 61.12 (CH_3O-3), 55.08 (CH_3O-1). Anal. calcd. for $C_{56}H_{62}O_{11}$: C 73.82, H 6.86; found: C 73.57, H 6.74.

*Methyl 2,3-di-*O*-benzyl-4-*O*-methyl-6-*O*-(2,3,4,6-tetra-*O*-benzyl-α-D-glucopyranosyl)-α-D-glucopyranoside (**28**)*
Obtained pure as a solid (45%), mp 78–79.5°C (ether, hexane); $[\alpha]_D$ +55.4 (*c* 0.5, chloroform). ^{1}H NMR ($CDCl_3$) δ: 7.40–7.10 (m, 30H, 6Ph), 4.98 (d, 1H, $J_{1',2'}$ 3.5 Hz, H-1′), 4.95–4.44 (m, 12H, 6CH_2Ph), 4.53 (d, 1H, $J_{1,2}$ 3.5 Hz, H-1), 3.95 (t, 1H, $J_{2',3'} \sim J_{3',4'}$ 9.5 Hz, H-3′), 3.86 (t, 1H, $J_{2,3} \sim J_{3,4}$ 9.5 Hz, H-3), 3.85 (ddd, overlapped, H-5), 3.62 (dd, overlapped, H-4′), 3.55 (s, 3H, CH_3O), 3.54 (dd, overlapped, H-2′) 3.38 (dd, 1H, H-2), 3.34 (s, 3H, CH_3O), 3.32 (dd, 1H, $J_{4,5}$ 10.0 Hz, H-4). ^{13}C NMR ($CDCl_3$) δ: 98.00 (C-1), 97.32 (C-1′), 82.09, 80.01 (C-2, C-3), 81.75, 80.07 (C-2′, C-3′), 79.69 (C-4), 77.72 (C-4′), 75.63, 75.51, 74.97, 73.46, 73.39, 72.34 (6CH_2Ph), 70.43, 70.32 (C-5, C-5′), 68.65 (C-6′), 66.22 (C-6), 60.85 (CH_3O-4), 55.19 (CH_3O-1). Anal. calcd. for $C_{56}H_{62}O_{11}$: C 73.82, H 6.86; found: C 73.61, H 6.53.

General procedure for deblocking by hydrogenolysis
The blocked disaccharide (ca. 0.4 g) and 5% palladium-on-carbon (0.4 g) in methanol (22 mL) were hydrogenated in the hydrogen stream for 2–3 h. The catalyst was removed by filtration and the solvent evaporated. Gel filtration on a column of Sephadex LH 20 (ethanol–water, 1:1) provided the disaccharide as a white solid after lyophilization of an aqueous solution. The ^{13}C NMR data are reported in Table 1.

*Methyl 6-*O*-(α-D-glucopyranosyl)-α-D-glucopyranoside (**29**)*
The hydrogenolysis of **22** produced **29** in 96% yield. $[\alpha]_D$ +150.6 (*c* 0.5, water) (lit. (34) $[\alpha]_D^{22}$ +166 (water)). ^{1}H NMR (D_2O) δ: 4.96 (d, 1H, $J_{1',2'}$ 3.5 Hz, H-1′), 4.82 (d, 1H, $J_{1,2}$ 3.5 Hz, H-1), 3.99 (dd, 1H, $J_{6a,6b}$ 11.0 Hz, $J_{6a,5}$ 4.5 Hz, H-6a), 3.57 (H-2), 3.56 (H-2′), 3.42 (s, 3H, CH_3O).

*Methyl 2-deoxy-6-*O*-(α-D-glucopyranosyl)-α-D-*arabino*-hexopyranoside (**30**)*
The hydrogenolysis of **23** produced **30** in 90% yield. $[\alpha]_D$ +149.6 (*c* 0.5, water). ^{1}H NMR (D_2O) δ: 4.96 (d, 1H, $J_{1',2'}$ 3.5 Hz, H-1′), 4.92 (bd, 1H, $J_{1,2ax}$ 3.5 Hz, H-1), 4.03 (dd, 1H, $J_{6a,6b}$ 11.0 Hz, $J_{5,6a}$ 4.0 Hz, H-6a), 3.56 (dd, 1H, $J_{2',3'}$ 10.0 Hz, H-2′), 3.48, 3.44 (2t, 2H, H-4, H-4′), 3.38 (s, 3H, CH_3O), 2.16 (ddd, 1H, $J_{2eq,2ax}$ 13.5 Hz, $J_{1,2eq}$ 1Hz, $J_{2eq,3}$ 5.5 Hz, H-2eq), 1.74 (ddd, 1H, $J_{2ax,3}$ 11.5 Hz, H-2ax).

*Methyl 3-deoxy-6-*O*-(α-D-glucopyranosyl)-α-D-*ribo*-hexopyranoside (**31**)*
The hydrogenolysis of **24** produced **31** in quantitative yield. $[\alpha]_D$ +150.2 (*c* 0.5, water). ^{1}H NMR (D_2O) δ: 4.93 (d, 1H, $J_{1',2'}$ 3.7 Hz, H-1′), 4.71 (d, 1H, $J_{1,2}$ 3.7 Hz, H-1), 3.97 (dd, 1H, $J_{6a,6b}$ 11.0 Hz, $J_{6a,5}$ 4.0 Hz, H-6a), 3.83 (H-2), 3.54 (dd, 1H, $J_{2',3'}$ 9.8 Hz, H-2′), 3.45 (s, 3H, CH_3O), 3.43 (t, 1H, $J_{3',4'} \sim J_{4',5'}$ 9.5 Hz, H-4′), 2.17 (td, 1H, $J_{3ax,3eq}$ 12.0 Hz, $J_{2,3eq} \sim J_{3eq,4}$ 4.5 Hz, H-3eq), 1.72 (q, 1H, $J_{2,3ax} \sim J_{3ax,4}$ 11.0 Hz, H-3ax).

*Methyl 4-deoxy-6-*O*-(α-D-glucopyranosyl)-α-D-*xylo*-hexopyranoside (**32**) (29)*
The hydrogenolysis of **25** produced **32** in 95% yield. $[\alpha]_D$ +154 (*c* 0.5 water). ^{1}H NMR (D_2O) δ: 4.91 (d, 1H, $J_{1',2'}$ 3.8 Hz, H-1′), 4.82 (d, 1H, $J_{1,2}$ 4.0 Hz, H-1), 4.09 (m, 1H, $J_{4ax,5}$ 12.0 Hz, H-5), 3.90 (ddd, 1H, $J_{2,3}$ 10.0 Hz, $J_{3,4ax}$ 12.0 Hz, $J_{3,4eq}$ 5.0 Hz, H-3), 3.83 (dd, 1H, $J_{6'a,6'b}$ 12.0 Hz, $J_{5',6'a}$ 2.0 Hz, H-6′a), 3.62 (dd, 1H, $J_{6a,6b}$ 11.0 Hz, $J_{5,6b}$ 3.0 Hz, H-6b), 3.53 (dd, 1H, $J_{2',3'}$ 10.0 Hz, H-2′), 3.47 (dd, 1H, H-2), 3.39 (s, 3H, CH_3O), 3.39 (t, overlapped, $J_{4',5'} \sim J_{3',4'}$ 9.5 Hz, H-4′), 2.00 (ddd, 1H, $J_{4eq,4ax}$ 12.8 Hz, $J_{4eq,5}$ 1.8 Hz, H-4eq), 1.57 (q, 1H, H-4ax).

*Methyl 6-*O*-(α-D-glucopyranosyl)-2-*O*-methyl-α-D-glucopyranoside (**33**)*
The hydrogenolysis of **26** produced **33** in quantitative yield. $[\alpha]_D$ +155.2 (*c* 0.5, water). ^{1}H NMR (D_2O) δ: 5.07 (d, 1H, $J_{1,2}$ 3.6 Hz, H-1), 4.96 (d, 1H, $J_{1',2'}$ 3.7 Hz, H-1′), 4.00 (dd, 1H, $J_{6a,6b}$ 11.0 Hz, $J_{5,6a}$ 4.0 Hz, H-6a), 3.68 (t, $J_{3,4} \sim J_{2,3}$ 9.5 Hz, H-3), 3.56 (dd, 1H, $J_{2',3'}$ 9.8 Hz, H-2′), 3.54 (t, 1H, $J_{4,5}$ 9.5 Hz, H-4), 3.49 and 3.44 (2s, each 3H, 2CH_3O), 3.44 (t, overlapped, $J_{4',5'} \sim J_{3',4'}$ 9.5 Hz, H-4′), 3.32 (dd, 1H, H-2).

*Methyl 6-*O*-(α-D-glucopyranosyl)-3-*O*-methyl-α-D-glucopyranoside (**34**)*
The hydrogenolysis of **27** produced **34** in quantitative yield $[\alpha]_D$ +169.8 (*c* 0.5, water). ^{1}H NMR (D_2O) δ: 4.94 (d, 1H, $J_{1',2'}$ 3.8 Hz, H-1′), 4.79 (H-1), 3.99 (dd, 1H, $J_{6a,6b}$ 11.0 Hz, $J_{5,6a}$ 4.0 Hz, H-6a), 3.85 (ddd, overlapped, H-5), 3.84 (dd, 1H, $J_{6'a,6'b}$ 11.0 Hz, $J_{5',6'a}$ 1.8 Hz, H-6′a), 3.62 (dd, overlapped, $J_{2',3'}$ 9.5 Hz, H-2′), 3.60 (s, 3H, CH_3O), 3.58 (t, overlapped, $J_{4,5} \sim J_{3,4}$ 9.5 Hz, H-4), 3.54 (dd, 1H, H-2), 3.42 (5H, s, 2t, CH_3O, H-3, H-4′).

*Methyl 6-*O*-(α-D-glucopyranosyl)-4-*O*-methyl-α-D-glucopyranoside (**35**)*
The hydrogenolysis of **28** produced **35** in 97% yield. $[\alpha]_D$ +174.4 (*c* 0.5, water). ^{1}H NMR (D_2O) δ: 4.96 (d, 1H, $J_{1',2'}$ 3.7 Hz, H-1′), 4.78 (d, 1H, $J_{1,2}$ 3.6 Hz, H-1), 3.97 (dd, 1H, $J_{6a,6b}$ 11.5 Hz, $J_{5,6a}$ 4.5 Hz, H-6a), 3.86 (dd, 1H, $J_{5',6'a}$ 2.0 Hz, $J_{6'a,6'b}$ 11.0 Hz, H-6′a), 3.59 (dd, 1H, $J_{2,3}$ 9.2 Hz, H-2), 3.56 (s, 3H, CH_3O), 3.55 (dd, 1H, H-2′), 3.43 (t, 1H, $J_{3',4'} \sim J_{4',5'}$ 9.0 Hz,

H-4′), 3.40 (s, 3H, CH_3O), 3.31 (dd, 1H, $J_{3,4}$ 9.0 Hz, $J_{4,5}$ 10.0 Hz, H-4).

*Allyl 2,3,4-tri-*O*-benzyl-6-*O*-methyl-α-*D*-glucopyranoside (**37**)*

Sodium hydride (80% suspension, 1.7 g, 56.7 mmol) was added to a stirring solution of allyl 2,3,4-tri-*O*-benzyl-α-D-glucopyranoside (**36**) (9.2 g, 18.8 mmol) (36) in *N,N*-dimethylformamide (90 mL) at ice-bath temperature. After 30 min, methyl iodide (3.5 mL, 56.2 mmol) was added and stirring continued at room temperature for 4 h. The excess of hydride was destroyed by the addition of methanol and the product isolated in the usual manner. Chromatography using hexane – ethyl acetate (4:1) provided a pure syrup, $[\alpha]_D$ +29 (*c* 0.5, chloroform). ^{1}H NMR ($CDCl_3$) δ: 7.43–7.22 (m, 15H, 3Ph), 5.96 (m, 1H, CH_2=C*H*), 5.34 and 5.24 (2m, 2H, CH_2=CH), 5.06–4.60 (3ABq, each 2H, 3CH_2Ph), 4.82 (d, 1H, $J_{1,2}$ 3.5 Hz, H-1), 4.18 and 4.04 (2m, 2H, CH_2=CH-CH_2), 4.04 (t, 1H, $J_{2,3} \sim J_{3,4} \sim$ 9.5 Hz, H-3), 3.80 (ddd, 1H, $J_{5,6}$ 2.5 Hz, $J_{5,6'}$ 4.0 Hz, $J_{4,5}$ 10.0 Hz, H-5), 3.65 (t, overlapped, H-4), 3.64 and 3.55 (ABX, overlapped, 2H, $J_{6,6'}$ 11.0 Hz, H-6, H-6′), 3.58 (overlapped, H-2), 3.33 (s, 3H, CH_3O). Anal. calcd. for $C_{31}H_{36}O_6$: C 73.79, H 7.19; found: C 73.67, H 7.34.

*2,3,4-Tri-*O*-benzyl-6-*O*-methyl-α-*D*-glucopyranose (**38**)*

A mixture of **37** (8.7 g, 17.2 mmol), tris(triphenylphosphine)rhodium(I) chloride (1.2 g, 1.3 mmol), and 1,4-diazabicyclo[2.2.2]octane (0.53 g, 4.7 mmol) in 95% ethanol – toluene–water (7:3:1, 400 mL) was boiled under reflux with stirring for 20 h. The solvent was evaporated and the remainder was taken up in acetone (350 mL) containing mercuric oxide (0.24 g). A solution of mercuric chloride (25 g) in acetone–water (9:1, 175 mL) was added and the mixture stirred for 30 min. After solvent removal, the residue was taken up in dichloromethane, the solution was washed with aqueous saturated potassium bromide and water, and the organic solution concentrated. Purification on a column of silica gel (hexane – ethyl acetate, 3:1) provided an amorphous solid **38** (6.1 g, 76%). ^{1}H NMR ($CDCl_3$) δ: 7.40–7.20 (m, 15H, 3Ph), 5.22 (d, 1H, $J_{1,2}$ 3.5 Hz, H-1), 4.95 and 4.87, 4.88 and 4.62, 4.78 and 4.69 (3ABq, each 2H, $J_{A,B}$ 11.0, 11.5 Hz, 3CH_2Ph), 4.00 (m, 1H, $J_{4,5}$ 10.0 Hz, $J_{5,6}$ 3.5 Hz, $J_{5,6'}$ 2.0 Hz, H-5), 3.96 (t, 1H, $J_{2,3} \sim J_{3,4}$ 9.0 Hz, H-3), 3.61 (dd, overlapped, $J_{6,6'}$ 10.0 Hz, H-6), 3.60 (t, 1H, H-4), 3.57 (dd, overlapped, H-2), 3.54 (dd, 1H, H-6′), 3.34 (s, 3H, CH_3O), 2.83 (bs, 1H, OH).

*3,4,6-Tri-*O*-benzyl-2-deoxy-α-*D*-arabino-hexopyranosyl chloride (**39**)*

This reagent (37) was prepared just prior to use. ^{1}H NMR parameters were as previously reported (38).

*2,4,6-Tri-*O*-benzyl-3-deoxy-α-*D*-ribo-hexopyranosyl bromide (**40**)*

Prepared from 2,4,6-tri-*O*-benzyl-3-deoxy-D-*ribo*-hexopyranose (39). ^{1}H NMR ($CDCl_3$) δ: 7.45–7.15 (m, 15H, 3Ph), 6.59 (bd, 1H, $J_{1,2}$ 3.0 Hz, $J_{1,3eq} \sim$ 1 Hz, H-1), 4.65–4.38 (3ABq, 6H, 3CH_2Ph), 3.94 (ddd, 1H, $J_{4,5}$ 9.5 Hz, $J_{5,6}$ 3.0 Hz, $J_{5,6'}$ 2.0 Hz, H-5), 3.79 (dd, 1H, $J_{6,6'}$ 10.5 Hz, H-6), 3.69 (ddd, 1H, $J_{3ax,4}$ 11.0 Hz, $J_{3eq,4}$ 4.5 Hz, H-4), 3.66 (dd, 1H, H-6′), 3.44 (td, 1H, $J_{2,3eq}$ 4.5 Hz, $J_{2,3ax}$ 11.5 Hz, H-2), 2.33 (m, 1H, $J_{3eq,3ax}$ 11.5 Hz, H-3eq), 1.97 (q, 1H, H-3ax).

*2,3,6-Tri-*O*-benzyl-4-deoxy-α-*D*-xylo-hexopyranosyl bromide (**41**)*

Prepared from 2,3,6-tri-*O*-benzyl-4-deoxy-D-*xylo*-hexopyranose (40). ^{1}H NMR ($CDCl_3$) δ: 7.44–7.20 (m, 15H, 3Ph), 6.49 (d, 1H, $J_{1,2}$ 3.5 Hz), 4.77 and 4.68, 4.76 and 4.74, 4.55 and 4.53 (3ABq, each 2H, $J_{A,B}$ 12.0 Hz, 3CH_2Ph), 4.24 (m, 1H, H-5), 4.00 (ddd, 1H, $J_{2,3}$ 9.0 Hz, $J_{3,4ax}$ 12.0 Hz, $J_{3,4eq}$ 5.0 Hz, H-3), 3.52 (d, 2H, $J_{5,6}$ 4.5 Hz, H_2-6), 3.44 (dd, 1H, H-2), 2.13 (ddd, 1H, $J_{4ax,4eq}$ 13.0 Hz, $J_{4eq,5}$ 2.0 Hz, H-4eq), 1.70 (q, 1H, $J_{4ax,5}$ 12.0 Hz, H-4ax).

*2,3,4-Tri-*O*-benzyl-6-deoxy-α-*D*-glucopyranosyl bromide (**42**)*

Prepared from 2,3,4-tri-*O*-benzyl-6-deoxy-D-glucopyranose (41). ^{1}H NMR ($CDCl_3$) δ: 7.45–7.20 (m, 15H, 3Ph), 6.37 (d, 1H, $J_{1,2}$ 3.5 Hz, H-1), 5.00 and 4.84, 4.93 and 4.66, 4.75 and 4.72 (3ABq, each 2H, $J_{A,B}$ 11.0, 11.5 Hz, 3CH_2Ph), 4.07 (m, 1H, $J_{4,5}$ 9.5 Hz, $J_{5,6}$ 6.5 Hz, H-5), 4.03 (t, 1H, $J_{2,3} \sim J_{3,4} \sim$ 9.5 Hz, H-3), 3.48 (dd, 1H, H-2), 3.21 (t, 1H, H-4), 1.32 (d, 3H, H_3-6).

*3,4,6-Tri-*O*-benzyl-2-*O*-methyl-α-*D*-glucopyranosyl bromide (**43**)*

Prepared from 3,4,6-tri-*O*-benzyl-2-*O*-methyl-D-glucopyranose (42). ^{1}H NMR ($CDCl_3$) δ: 7.40–7.10 (m, 15H, 3Ph), 6.62 (d, 1H, $J_{1,2}$ 3.5 Hz, H-1), 4.94 and 4.79, 4.84 and 4.53, 4.58 and 4.47 (3ABq, each 2H, $J_{A,B}$ 11.0 Hz, 3CH_2Ph), 4.06 (m, 1H, $J_{4,5}$ 9.5 Hz, $J_{5,6}$ 2.5 Hz, $J_{5,6'}$ 2.0 Hz, H-5), 3.96 (t, 1H, $J_{2,3} \sim J_{3,4}$ 9.5 Hz, H-3), 3.80 (dd, overlapped, H-6), 3.78 (t, overlapped, H-4), 3.67 (dd, 1H, $J_{6,6'}$ 11.5 Hz, H-6′), 3.50 (s, 3H, CH_3O), 3.33 (dd, 1H, H-2).

*2,4,6-Tri-*O*-benzyl-3-*O*-methyl-α-*D*-glucopyranosyl bromide (**44**)*

Prepared from 2,4,6-tri-*O*-benzyl-3-*O*-methyl-D-glucopyranose (39). ^{1}H NMR ($CDCl_3$) δ: 7.45–7.20 (m, 15H, 3Ph), 6.38 (d, 1H, $J_{1,2}$ 3.8 Hz, H-1), 4.81 and 4.51, 4.72 and 4.68, 4.57 and 4.46 (3ABq, each 2H, $J_{A,B}$ 11.0, 12.0 Hz, 3CH_2Ph), 4.01 (ddd, 1H, $J_{4,5}$ 9.5 Hz, $J_{5,6}$ 3.0 Hz, $J_{5,6'}$ 2.0 Hz, H-5), 3.76 (dd, 1H, $J_{6,6'}$ 11.0 Hz, H-6), 3.72 (t, overlapped, $J_{2,3} \sim J_{3,4}$ 9.5 Hz, H-3), 3.68 (s, 3H, CH_3O), 3.65 (t, overlapped, H-4), 3.63 (dd, 1H, H-6′), 3.42 (dd, 1H, H-2).

*2,3,6-Tri-*O*-benzyl-4-*O*-methyl-α-*D*-glucopyranosyl bromide (**45**)*

Prepared from 2,3,6-tri-*O*-benzyl-4-*O*-methyl-D-glucopyranose (38). ^{1}H NMR ($CDCl_3$) δ: 7.40–7.25 (m, 15H, 3Ph), 6.39 (d, 1H, $J_{1,2}$ 3.8 Hz, H-1), 4.94 and 4.80, 4.60 and 4.50 (2ABq, each 2H, $J_{A,B}$ 11.0, 12.0 Hz, 2CH_2Ph), 4.69 (s, 2H, CH_2Ph), 3.95 (ddd, 1H, $J_{4,5}$ 10.0 Hz, $J_{5,6}$ 3.2 Hz, $J_{5,6'}$ 2.0 Hz, H-5), 3.91 (t, 1H, $J_{2,3} \sim J_{3,4}$ 9.0 Hz, H-3), 3.75 (dd, 1H, $J_{6,6'}$ 11.0 Hz, H-6), 3.65 (dd, 1H, H-6′), 3.49 (s, 3H, CH_3O), 3.48 (overlapped, H-4), 3.48 (dd, overlapped, H-2).

*2,3,4-Tri-*O*-benzyl-6-*O*-methyl-α-*D*-glucopyranosyl bromide (**46**)*

Prepared from **38**. ^{1}H NMR ($CDCl_3$) δ: 7.40–7.20 (m, 15H, 3Ph), 6.39 (d, 1H, $J_{1,2}$ 3.8 Hz, H-1), 4.98 and 4.83, 4.88 and 4.61 (2ABq, each 2H, $J_{A,B}$ 10.5 Hz, 2CH_2Ph), 4.70 (s, 2H, CH_2Ph), 4.03 (t, 1H, $J_{2,3} \sim J_{3,4}$ 9.5 Hz, H-3), 4.02 (overlapped, H-5), 3.72 (t, $J_{4,5}$ 9.5 Hz, H-4), 3.66 (dd, 1H, $J_{6,6'}$ 11.0 Hz, $J_{5,6}$

Scheme 3.

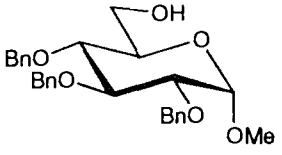

17

+

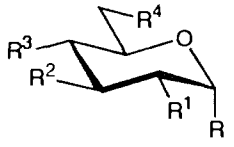

	R	R1	R2	R3	R4
38	OH	OBn	OBn	OBn	**OMe**
39	Cl	**H**	OBn	OBn	OBn
40	Br	OBn	**H**	OBn	OBn
41	Br	OBn	OBn	**H**	OBn
42	Br	OBn	OBn	OBn	**H**
43	Br	**OMe**	OBn	OBn	OBn
44	Br	OBn	**OMe**	OBn	OBn
45	Br	OBn	OBn	**OMe**	OBn
46	Br	OBn	OBn	OBn	**OMe**

$Et_4N^+Br^-$

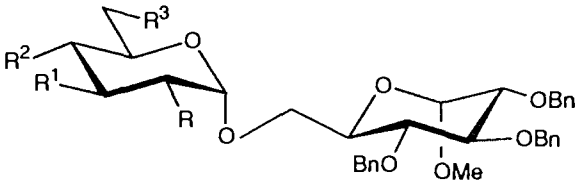

	R	R1	R2	R3
47	**H**	OBn	OBn	OBn
48	OBn	**H**	OBn	OBn
49	OBn	OBn	**H**	OBn
50	OBn	OBn	OBn	**H**
51	**OMe**	OBn	OBn	OBn
52	OBn	**OMe**	OBn	OBn
53	OBn	OBn	**OMe**	OBn
54	OBn	OBn	OBn	**OMe**

H_2 / Pd(C)

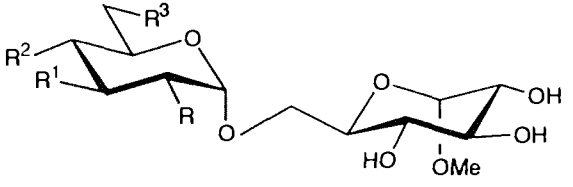

	R	R1	R2	R3
55	**H**	OH	OH	OH
56	OH	**H**	OH	OH
57	OH	OH	**H**	OH
58	OH	OH	OH	**H**
59	**OMe**	OH	OH	OH
60	OH	**OMe**	OH	OH
61	OH	OH	**OMe**	OH
62	OH	OH	OH	***OMe***

3.5 Hz, H-6), 3.54 (dd, 1H, $J_{5,6'}$ 2.0 Hz, H-6′), 3.51 (dd, 1H, H-2), 3.32 (s, 3H, CH_3O).

Methyl 2,3,4-tri-O-*benzyl-6*-O-*(3,4,6-tri*-O-*benzyl-2-deoxy*-α-D-arabino-*hexopyranosyl)*-α-D-*glucopyranoside (**47**)*

Freshly prepared chloride **39** (2.19 mmol) (37) was reacted with alcohol **17** (0.85 mmol) in the presence of Hünig's base (2.13 mmol) and tetraethylammonium chloride (5.3 mmol). Subsequent column chromatography (hexane–dichloromethane – ethyl acetate, 4:4:0.5, hexane – ethyl acetate, 3.5:1, 0.1% triethylamine) of the crude product provided **47** in 53% yield; mp 82–83°C (ether, hexane); $[\alpha]_D$ +61.2 (*c* 0.5, dichloromethane). ^{1}H NMR ($CDCl_3$) δ: 7.40–7.12 (m, 30, 6Ph), 5.03 (bd, 1H, $J_{1',2'ax}$ 3.5 Hz, $J_{1',2'eq}$ 1 Hz, H-1′), 5.40–4.00 (m, 12H, 6CH_2Ph), 4.63 (d, 1H, $J_{1,2}$ 3.7 Hz, H-1), 4.02 (t, 1H, $J_{2,3} \sim J_{3,4}$ 9.5 Hz, H-3), 3.97 (ddd, 1H, $J_{2'ax,3'}$ 11.0 Hz, $J_{2'eq,3'}$ 5.0 Hz, $J_{3',4'}$ 8.5 Hz, H-3′), 3.54 (dd, overlapped, H-2), 3.37 (s, 3H, CH_3O), 2.33 (ddd, 1H, $J_{2'eq,2'ax}$ 13.0 Hz, H-2′eq), 1.72 (ddd, 1H, H-2′ax). ^{13}C NMR ($CDCl_3$) δ: 97.96 (C-1), 97.84 (C-1′), 82.26, 80.05 (C-2, C-3), 78.19 (C-3′), 77.81, 77.26 (C-4, C-4′), 75.81, 74.91, 74.85, 73.43, 73.30, 71.73 (6CH_2Ph), 70.93, 69.80 (C-5, C-5′), 68.75 (C-6′), 65.71 (C-6), 55.13 (CH_3O), 35.31 (C-2). Anal. calcd. for $C_{55}H_{60}O_{10}$: C 74.98, H 6.86; found: C 75.07, H 6.88.

Methyl 2,3,4-tri-O-*benzyl-6*-O-*(2,4,6-tri*-O-*benzyl-3-deoxy*-α-D-ribo-*hexopyranosyl)*-α-D-*glucopyranoside (**48**)*

The bromide **40** (1.53 mmol) was reacted with **17** (0.81 mmol) under the conditions for bromide-ion catalyzed glycosylation. The product was purified by column chromatography (hexane–dichloromethane – ethyl acetate, 4:4:0.5) to provide an anomeric mixture in 64%. Further purification by column chromatography (hexane–chloroform – ethyl acetate, 6:10:0.5) provided pure **48** (14%) as a syrup. $[\alpha]_D$ +79.6 (*c* 0.5). ^{1}H NMR ($CDCl_3$) δ: 7.40–7.23 (m, 30H, 6Ph), 5.05 (d, 1H, $J_{1',2'}$ 3.2 Hz, H-1′), 5.04–4.37 (m, 12H, 6CH_2Ph), 4.60 (d, 1H, $J_{1,2}$ 3.5 Hz, H-1), 4.04 (t, 1H, $J_{2,3} \sim J_{3,4}$ 9.5 Hz, H-3), 3.70 (overlapped, H-4), 3.56 (td, 1H, $J_{2',3'ax}$ 12.0 Hz, $J_{2',3'eq}$ 4.5 Hz, H-2′), 3.49 (dd, 1H, H-2), 3.40 (s, 3H, CH_3O), 2.36 (td, 1H, $J_{3'eq,3'ax}$ 12.0 Hz, $J_{3'eq,4'}$ 4.5 Hz, H-3′eq), 1.95 (q, 1H, $J_{3'ax,4'}$ 11.0 Hz, H-3′ax). ^{13}C NMR ($CDCl_3$) δ: 97.97 (C-1), 96.22 (C-1′), 82.18, 80.16 (C-2, C-3), 77.96 (C-4), 75.63, 75.05, 73.43, 73.38, 70.79, 70.49 (6CH_2Ph), 73.77 (C-2′), 71.86 (C-4′), 70.71, 70.39 (C-5, C-5′), 68.69 (C-6′), 65.87 (C-6), 55.11 (CH_3O), 30.34 (C-3′). Anal. calcd. for $C_{55}H_{60}O_{10}$: C 74.98, H 6.86; found: 74.61, H 7.01.

Methyl 2,3,4-tri-O-*benzyl-6*-O-*(2,3,6-tri*-O-*benzyl-4-deoxy*-α-D-xylo-*hexopyranosyl)*-α-D-*glucopyranoside (**49**)*

The bromide **41** (2.30 mmol) was reacted with **17** (0.85 mmol) under the conditions for bromide-ion catalyzed glycosylation. The product was purified by column chromatography (hexane – ethyl acetate, 5.5:1) to provide an anomeric mixture of α:β = 9:1 in 90% yield. Further chromatography (hexane–chloroform – ethyl acetate, 6:12:1) afforded pure **49** (42% yield) as a crystalline solid, mp 74–75°C (ether, hexane); $[\alpha]_D$ +54 (*c* 0.5, chloroform). ^{1}H NMR ($CDCl_3$) δ: 7.37–7.16 (m, 30H, 6Ph), 5.00 (d, 1H, $J_{1',2'}$ 3.5 Hz, H-1′), 4.94–4.46 (m, 12H, 6CH_2Ph), 4.54 (d, 1H, $J_{1,2}$ 3.5 Hz, H-1), 3.97 (t, 1H, $J_{2,3} \sim J_{3,4}$ 9.0 Hz, H-3), ~3.89 (m, H-5′, H-3′), 3.81 (dd, overlapped, $J_{6a,6b}$ 11.0 Hz, $J_{5,6a}$ 4.5 Hz, H-6a), 3.76 (m, H-5), 3.72 (dd, 1H, $J_{5,6b}$ 1 Hz, H-6b), 3.62 (t, 1H, $J_{4,5}$ 9.0 Hz, H-4), 3.46 (dd, 1H, $J_{2',3'}$ 9.5 Hz, H-2′), 3.43 (dd, overlapped, H-2), 3.41 (m, 2H, H_2-6′), 3.30 (s, 3H, CH_3O), 2.02 (ddd, 1H, $J_{4'eq,4'ax}$ 12.5 Hz, $J_{4'eq,5'}$ 2.0 Hz, $J_{4'eq,3'}$ 5.0 Hz, H-4′eq), 1.50 (q, 1H, $J_{4'ax,3'} \sim J_{4'ax,5'} \sim$ 12.0 Hz, H-4′ax). ^{13}C NMR ($CDCl_3$) δ: 98.14 (C-1′), 97.97 (C-1), 82.17, 80.23 (C-2, C-3), 80.74 (C-2′), 78.03 (C-4), 75.70, 74.99, 73.39, 73.34, 72.44, 72.31 (6CH_2Ph), 74.54 (C-3′), 72.20 (C-6′), 70.41 (C-5), 66.92 (C-5′), 66.12 (C-6), 55.06 (CH_3O), 33.93 (C-4′). Anal. calcd. for $C_{55}H_{60}O_{10}$: C 74.98, H 6.86; found: C 74.94, H 6.91.

Methyl 2,3,4-tri-O-*benzyl-6*-O-*(2,3,4-tri*-O-*benzyl-6-deoxy*-α-D-*glucopyranosyl)*-α-D-*glucopyranoside (**50**)*

The bromide **42** (1.53 mmol) was reacted with **17** (0.51 mmol) under the conditions for bromide-ion catalyzed glycosylation. Column chromatography (hexane – ethyl acetate, 5:1) provided an anomeric α:β = 9:1 mixture in 92% yield that was purified by recrystallization from ethanol, mp 124–125°C; $[\alpha]_D$ +50.6 (*c* 0.5, chloroform). ^{1}H NMR ($CDCl_3$) δ: 7.40–7.20 (m, 30H, 6Ph), 4.99–4.55 (m, 12H, 6CH_2Ph), 4.89 (overlapped, $J_{1',2'}$ 3.5 Hz, H-1′), 4.56 (d, 1H, $J_{1,2}$ 3.8 Hz, H-1), 3.99 (t, 1H, $J_{2,3} \sim J_{3,4}$ 9.5 Hz, H-3), 3.93 (t, 1H, $J_{2',3'} \sim J_{3',4'}$ 9.5 Hz, H-3′), 3.77 (overlapped, H-5′), 3.67 (t, 1H, $J_{4,5}$ 9.5 Hz, H-4), 3.50 (dd, 1H, H-2′), 3.44 (dd, 1H, H-2), 3.35 (s, 3H, CH_3O), 3.10 (t, 1H, $J_{4',5'}$ 9.5 Hz, H-4′), 1.19 (d, 3H, $J_{5',6'}$ 6.5 Hz, H_3-6′). ^{13}C NMR ($CDCl_3$) δ: 98.04 (C-1), 97.00 (C-1′), 83.85 (C-4′), 82.16, 80.20 (C-2, C-3), 81.43, 80.44 (C-2′, C-3′), 75.70, 75.47, 75.15, 75.03, 73.39, 72.29 (6CH_2Ph), 70.49 (C-5), 66.80 (C-5′), 65.93 (C-6), 55.14 (CH_3O), 17.96 (C-6′). Anal. calcd. for $C_{55}H_{60}O_{10}$: C 74.98, H 6.86; found: C74.54, H 6.82.

Methyl 2,3,4-tri-O-*benzyl-6*-O-*(3,4,6-tri*-O-*benzyl-2*-O-*methyl*-α-D-*glucopyranosyl)*-α-D-*glucopyranoside (**51**)*

Bromide **43** (3.82 mmol) was reacted with **17** (0.64 mmol) under the conditions for bromide-ion catalyzed glycosylation. Column chromatography (hexane – ethyl acetate, 5:1) provided **51** in 73% yield as a solid; mp 96.5–97.5°C (ethanol); $[\alpha]_D$ +56.6 (*c* 0.5, chloroform). ^{1}H NMR ($CDCl_3$) δ: 7.40–7.10 (m, 30H, 6Ph), 5.06 (d, 1H, $J_{1',2'}$ 3.5 Hz, H-1′), 5.00–4.40 (m, 12H, 6CH_2Ph), 4.55 (d, 1H, $J_{1,2}$ 3.8 Hz, H-1), 3.99 (t, 1H, $J_{2,3} \sim J_{3,4}$ 9.5 Hz, H-3), 3.86 (t, 1H, $J_{2',3'} \sim J_{3',4'}$ 9.5 Hz, H-3′), 3.50 (dd, 1H, H-2), 3.41, 3.36 (2s, each 3H, 2CH_3O), 3.31 (dd, 1H, H-2′). ^{13}C NMR ($CDCl_3$) δ: 97.94 (C-1), 96.64 (C-1′), 82.38, 81.62 (C-2′, C-3′), 82.19, 79.88 (C-2, C-3), 77.89, 77.59 (C-4, C-4′), 75.81, 75.32, 74.90, 74.90, 73.41, 73.33 (6CH_2Ph), 70.30 (C-5, C-5′), 68.58 (C-6′), 66.07 (C-6), 58.41 (CH_3O-2′), 55.14 (CH_3O-1). Anal. calcd. for $C_{56}H_{62}O_{11}$: C 73.82, H. 6.86; found: C 73.64, H 6.86.

Methyl 2,3,4-tri-O-*benzyl-6*-O-*(2,4,6-tri*-O-*benzyl-3*-O-*methyl*-α-D-*glucopyranosyl)*-α-D-*glucopyranoside (**52**)*

Bromide **44** (1.28 mmol) was reacted with **17** (0.51 mmol) under the conditions for bromide-ion catalyzed glycosylation. Column chromatography (hexane–chloroform – ethyl acetate, 6:10:0.5) of the crude product (89% yield) provided pure **52** in 48% yield. $[\alpha]_D$ +71 (*c* 0.5, chloroform). ^{1}H NMR ($CDCl_3$) δ: 7.40–7.15 (m, 30H, 6Ph), 4.99–4.39 (m, 12H, 6CH_2Ph), 4.95 (d, 1H, $J_{1',2'}$ 3.6 Hz, H-1′), 4.53 (d, 1H, $J_{1,2}$ 3.7 Hz, H-1), 3.98 (t, 1H, $J_{2,3} \sim J_{3,4}$ 9.5 Hz, H-3), 3.65 (s, 3H, CH_3O), 3.44 (dd, 1H, $J_{2',3'}$ 9.5 Hz, H-2′), 3.42 (dd, 1H, H-2), 3.34 (s, 3H, CH_3O). ^{13}C NMR ($CDCl_3$) δ: 97.90 (C-1), 97.24 (C-1′), 83.68,

79.73 (C-2′, C-3′), 82.08, 80.14 (C-2, C-3), 77.72, 77.61 (C-4, C-4′), 75.63, 74.87, 74.70, 73.34, 73.29, 72.22 (6*C*H_2Ph), 70.31, 70.06 (C-5, C-5′), 68.43 (C-6′), 66.01 (C-6), 61.02 (CH_3O-3′), 55.06 (CH_3O-1). Anal. calcd. for $C_{56}H_{62}O_{11}$: C 73.82, H 6.86; found: C 73.64, H 6.86.

Methyl 2,3,4-tri-O-*benzyl-6*-O-*(2,3,6-tri*-O-*benzyl-4*-O-*methyl-α-D-glucopyranosyl)-α-D-glucopyranoside (**53**)*

Bromide **45** (2.46 mmol) was reacted with **17** (0.81 mmol) under the conditions for bromide-ion catalyzed glycosylation. Column chromatography (hexane – ethyl acetate, 5:1) provided an anomeric mixture of α:β = 9:1 in 92% yield, from which pure **53** was isolated by further chromatography (hexane–dichloromethane–acetone, 10:1:0.8) in 62% yield. $[\alpha]_D$ +80.4 (*c* 0.1, chloroform). ^{1}H NMR ($CDCl_3$) δ: 7.40–7.18 (m, 30H, 6Ph), 4.99–4.42 (m, 12H, 6CH_2Ph), 4.93 (d, 1H, $J_{1',2'}$ 3.8 Hz, H-1′), 4.54 (d, 1H, $J_{1,2}$ 3.5 Hz, H-1), 3.98 (t, 1H, $J_{2,3} \sim J_{3,4}$ 9.5 Hz, H-3), 3.84 (t, $J_{3',4'} \sim J_{2',3'}$ 9.5 Hz, H-3′), 3.70 (overlapped, H-5′), 3.62 (overlapped, H-4), 3.48 (dd, 1H, H-2′), 3.44 (s, 3H, CH_3O), 3.42 (dd, 1H, H-2), 3.35 (s, 3H, CH_3O), 3.33 (t, 1H, $J_{4',5'}$ 9.5 Hz, H-4′). ^{13}C NMR ($CDCl_3$) δ: 97.97 (C-1), 97.26 (C-1′), 82.15, 80.20 (C-2, C-3), 81.59, 79.85, 79.44 (C-2′, C-3′, C-4′), 77.90 (C-4), 75.70, 75.35, 74.99, 73.42, 73.37, 72.42 (6*C*H_2Ph), 70.39, 70.31 (C-5, C-5′), 68.65 (C-6′), 66.12 (C-6), 60.62 (CH_3O-4′), 55.13 (CH_3O-1). Anal. calcd. for $C_{56}H_{62}O_{11}$: C 73.82, H 6.86; found: 73.89, H 6.82.

Methyl 2,3,4-tri-O-*benzyl-6*-O-*(2,3,4-tri*-O-*benzyl-6*-O-*methyl-α-D-glucopyranosyl)-α-D-glucopyranoside (**54**)*

Bromide **46** (2.30 mmol) was reacted with alcohol **17** (0.81 mmol) under the conditions for bromide-ion catalyzed glycosylation. Column chromatography (hexane – ethyl acetate, 4:1) provided an anomeric mixture (α:β = 95:5) in quantitative yield. Further chromatography (hexane–chloroform – ethyl acetate, 6:10:1) afforded pure crystalline **54** (52% yield), mp 105–106°C (ether, hexane); $[\alpha]_D$ +51 (*c* 0.5, chloroform). ^{1}H NMR ($CDCl_3$) δ: 7.40–7.20 (m, 30H, 6Ph), 5.00–4.55 (m, 12H, 6CH_2Ph), 4.95 (d, 1H, $J_{1',2'}$ 3.5 Hz, H-1′), 4.55 (d, 1H, $J_{1,2}$ 3.5 Hz, H-1), 3.98, 3.95 (2t, 2H, H-3, H-3′), 3.52 (dd, overlapped, $J_{2',3'}$ 9.5 Hz, H-2′), 3.44 (dd, 1H, $J_{2,3}$ 9.5 Hz, H-2), 3.35, 3.29 (2s, each 3H, 2CH_3O). ^{13}C NMR ($CDCl_3$) δ: 97.98 (C-1), 97.36 (C-1), 82.14, 80.18 (C-2, C-3), 81.57, 79.96 (C-2′, C-3′), 77.80, 77.75 (C-4, C-4′), 75.69, 75.40, 74.97, 74.92, 73.36, 72.33 (6*C*H_2Ph), 70.96 (C-6′), 70.38, 70.09 (C-5, C-5′), 66.09 (C-6), 59.09 (CH_3O-6′), 55.13 (CH_3O-1). Anal. calcd. for $C_{56}H_{62}O_{11}$: C 73.82, H 6.86; found: C 74.02, H 6.76.

Methyl 6-O-*(2-deoxy-α-D-*arabino-*hexopyranosyl)-α-D-glucopyranoside (**55**)*

The hydrogenolysis of **47** produced **55** in 95% yield. $[\alpha]_D$ +150 (*c* 0.5, water). ^{1}H NMR (D_2O) δ: 5.04 (bd, 1H, $J_{1',2'ax}$ 2.8 Hz, $J_{1',2'eq}$ 1Hz, H-1′), ~4.8 (d, 1H, H-1), 3.94 (dd, 1H, $J_{6a,6b}$ 11.0 Hz, $J_{5,6a}$ 4.5 Hz, H-6a), 3.93 (dt, overlapped, $J_{2'eq,3'}$ 5.0 Hz, $J_{2'ax,3'}$ 11.5 Hz, H-3′), 3.87 (dd, 1H, $J_{6'a,6'b}$ 11.5 Hz, $J_{5',6'a}$ 2.5 Hz, H-6′a), 3.80 (dd and m, 2H, $J_{6'b,5'}$ 5.0 Hz, H-6′b, H-5), 3.70 (dd and m, 2H, $J_{6b,5}$ 1.8 Hz, H-6b, H-5′), 3.66 (t, 1H, $J_{2,3} \sim J_{3,4}$ 9.5 Hz, H-3), 3.58 (dd, 1H, $J_{1,2}$ 3.8 Hz, H-2), 3.48 (t, 1H, $J_{4,5}$ 9.5 Hz, H-4), 3.42 (s, 3H, CH_3O), 3.37 (t, 1H, $J_{3',4'} \sim J_{4',5'}$ 9.0 Hz, H-4′), 2.18 (ddd, 1H, $J_{2'ax}$, $J_{2'eq}$ 13.5 Hz, H-2′eq), 1.72 (ddd, 1H, H-2′ax).

Methyl 6-O-*(3-deoxy-α-D-*ribo-*hexopyranosyl)-α-D-glucopyranoside (**56**)*

The hydrogenolysis of **48** produced **56** in quantitative yield. $[\alpha]_D$ +163 (*c* 0.5, water). ^{1}H NMR (D_2O) δ: 4.85 (d, 1H, $J_{1',2'}$ 3.6 Hz, H-1′), 4.82 (d, 1H, $J_{1,2}$ 3.8 Hz, H-1), 4.01 (dd, 1H, $J_{6a,6b}$ 11.5 Hz, $J_{5,6a}$ 4.0 Hz, H-6a), 3.58 (dd, 1H, $J_{2,3}$ 9.5 Hz, H-2), 3.55 (t, 1H, $J_{3,4} \sim J_{4,5}$ 9.5 Hz, H-4), 3.44 (s, 3H, CH_3O), 2.18 (td, 1H, $J_{3'eq,3'ax}$ 12.0 Hz, $J_{2',3'eq} \sim J_{3'eq,4'}$ 4.5 Hz, H-3′eq), 1.79 (q, 1H, $J_{2',3'ax} \sim J_{3'ax,4'}$ 11.0 Hz, H-3′ax).

Methyl 6-O-*(4-deoxy-α-D-*xylo-*hexopyranosyl)-α-D-glucopyranoside (**57**)*

The hydrogenolysis of **49** produced **57** in quantitative yield. $[\alpha]_D$ +166.4 (*c* 0.5, water), ^{1}H NMR (D_2O) δ: 4.98 (d, 1H, $J_{1',2'}$ 3.8 Hz, H-1′), 4.82 (d, 1H, H-1), 4.00 (m, 3H, H-5′, H-6a, H-3′), 3.83 (ddd, 1H, $J_{4,5}$ 9.5 Hz, $J_{5,6a}$ 4.5 Hz, $J_{5,6b}$ 2.0 Hz, H-5), 3.73 (dd, 1H, $J_{6a,6b}$ 11.5 Hz, H-6b), 3.58 (dd, 1H, $J_{1,2}$ 3.8 Hz, $J_{2,3}$ 9.5 Hz, H-2), 3.52 (t, 1H, $J_{3,4}$ 9.5 Hz, H-4), 3.48 (dd, 1H, $J_{2',3'}$ 9.5 Hz, H-2′), 3.44 (s, 3H, CH_3O), 2.00 (ddd, 1H, $J_{4'eq,4'ax}$ 12.5 Hz, $J_{4'eq,3'}$ 5.2 Hz, $J_{4'eq,5'}$ 1.8 Hz, H-4′eq), 1.46 (q, 1H, $J_{4'ax,5'} \sim J_{3',4'ax}$ 12.0 Hz, H-4′ax).

Methyl 6-O-*(6-deoxy-α-D-glucopyranosyl)-α-D-glucopyranoside (**58**)*

The hydrogenolysis of **50** produced **58** in quantitative yield. $[\alpha]_D$ +152 (*c* 0.5, water). ^{1}H NMR ($CDCl_3$) δ: 4.88 (d, 1H, $J_{1',2'}$ 3.8 Hz, H-1′), 4.80 (d, 1H, H-1), 3.95 (dd, 1H, $J_{6a,6b}$ 11.0 Hz, $J_{6a,5}$ 4.5 Hz, H-6a), 3.80 (m, 2H, H-5, H-5′), 3.72 (dd, 1H, $J_{5,6b}$ 2.0 Hz, H-6b), 3.65 (2t, 2H, H-3, H-3′), 3.56 (2dd, 2H, $J_{2,3} = J_{2',3'}$ 9.5 Hz, $J_{1,2} = J_{1',2'}$ 3.8 Hz, H-2, H-2′), 3.50 (dd, 1H, $J_{3,4}$ 9.0 Hz, $J_{4,5}$ 10.0 Hz, H-4), 3.41 (s, 3H, CH_3O), 3.15 (t, 1H, $J_{3',4'}$ 9.0 Hz, $J_{4',5'}$ 10.0 Hz, H-4′), 1.26 (d, 3H, $J_{5',6'}$ 6.2 Hz, H_3-6′).

Methyl 6-O-*(2*-O-*methyl-α-D-glucopyranosyl)-α-D-glucopyranoside (**59**)*

The hydrogenolysis of **51** produced **59** in quantitative yield. $[\alpha]_D$ +163 (*c* 0.5, water), ^{1}H NMR (D_2O) δ: 5.20 (d, 1H, $J_{1',2'}$ 3.6 Hz, H-1′), 4.81 (d, 1H, H-1), 3.96 (dd, 1H, $J_{6a,6b}$ 11.0 Hz, $J_{5,6a}$ 4.5 Hz, H-6a), 3.86 (dd, 1H, $J_{6'a,6'b}$ 11.0 Hz, $J_{5',6'a}$ 2.0 Hz, H-6′a), 3.66 (t, 1H, $J_{2,3} \sim J_{3,4}$ 9.5 Hz, H-3), 3.57 (dd, 1H, $J_{1,2}$ 3.8 Hz, H-2), 3.50, 3.43 (2s, each 3H, 2CH_3O), 3.50, 3.44 (2t, each 1H, H-4, H-4′), 3.31 (dd, 1H, $J_{2',3'}$ 10.0 Hz, H-2′).

Methyl 6-O-*(3*-O-*methyl-α-D-glucopyranosyl)-α-D-glucopyranoside (**60**)*

The hydrogenolysis of **52** produced **60** in quantitative yield. $[\alpha]_D$ +150.8 (*c* 0.5, water). ^{1}H NMR (D_2O) δ: 4.92 (d, 1H, $J_{1',2'}$ 3.6 Hz, H-1′), 4.82 (d, 1H, $J_{1,2}$ 3.6 Hz, H-1), 3.99 (dd, 1H, $J_{6a,6b}$ 11.0 Hz, $J_{5,6a}$ 4.5 Hz, H-6a), 3.83 (dd, m, 2H, H-6′a, H-5), 3.61, 3.43 (2s, each 3H, 2CH_3O).

Methyl 6-C-*(4*-O-*methyl-α-D-glucopyranosyl)-α-D-glucopyranoside (**61**)*

The hydrogenolysis of **53** produced **61** in 89% yield. $[\alpha]_D$ +167 (*c* 0.5, water), ^{1}H NMR (D_2O) δ: 4.94 (d, 1H, $J_{1',2'}$ 3.6 Hz, H-1′), 4.80 (d, 1H, H-1), 3.96 (dd, 1H, $J_{6a,6b}$ 11.0 Hz, $J_{5,6a}$ 4.5 Hz, H-6a), 3.65 (t, 1H, $J_{2,3} \sim J_{3,4}$ 9.0 Hz, H-3), 3.56 (s, 2dd, 5H, H-2, H-2′, CH_3O), 3.49 (dd, 1H, $J_{4,5}$ 10.0 Hz, H-4), 3.42 (s, 3H, CH_3O), 3.23 (t, 1H, $J_{3',4'} \sim J_{4',5'}$ 9.5 Hz, H-4′).

*Methyl 6-O-(6-O-methyl-α-D-glucopyranosyl)-α-D-glucopyranoside (**62**)*

The hydrogenolysis of **54** produced **62** in quantitative yield. $[\alpha]_D$ +150 (*c* 0.5, water). ^{1}H NMR (D_2O) δ: 4.93 (d, 1H, $J_{1',2'}$ 3.8 Hz, H-1′), 4.81 (d, 1H, H-1), 3.97 (dd, 1H, $J_{6a,6b}$ 11.0 Hz, $J_{5,6a}$ 4.5 Hz, H-6a), 3.83 (m, 2H, H-5, H-5′), 3.56 (dd, overlapped, $J_{1,2}$ 3.8 Hz, $J_{2,3}$ 10.0 Hz, H-2), 3.54 (dd, overlapped, $J_{2',3'}$ 9.5 Hz, H-2′), 3.51, 3.41 (2t, overlapped, H-4, H-4′), 3.42, 3.39 (2s, each 3H, $2CH_3O$).

Acknowledgement

The syntheses were supported by a Natural Sciences and Engineering Research Council of Canada (NSERC) operational grant to R.U.L. (A170). The kinetic studies were supported by an NSERC grant to M.M.P. (OGP 3045) and Grants No. 3007 and 09-117 from the Danish National Agency of Industry and Trade to B.S.

References

1. U. Spohr, E. Paszkiewicz-Hnatiw, N. Morishima, and R.U. Lemieux. Can. J. Chem. **70**, 254 (1992).
2. L.T.J. Delbaere, M. Vandonselaar, L. Prasad, J.W. Quail, P.V. Nikrad, J.R. Pearlstone, M.R. Carpenter, L.B. Smillie, U. Spohr, and R.U. Lemieux. Can. J. Chem. **68**, 1116 (1990).
3. M. Cygler, D.R. Rose, and D.R. Bundle. Science, **253**, 442 (1991).
4. R.U. Lemieux. ACS Symp. Ser. **519**, 5 (1993).
5. H. Beierbeck, L.T.J. Delbaere, M. Vandonselaar, and R.U. Lemieux. Can. J. Chem. **72**, 463 (1994).
6. P.V. Nikrad, H. Beierbeck, and R.U. Lemieux. Can. J. Chem. **70**, 241 (1992).
7. R.U. Lemieux. Alfred Benzon Symp. **36**, Complex Carbohydrates in Drug Research. Munskgaard, Copenhagen. 1994. p. 188.
8. M.-H. Du, U. Spohr, and R.U. Lemieux. Glycoconjugate J. **11**, 443 (1994).
9. R.U. Lemieux and U. Spohr. Adv. Carbohydr. Chem. Biochem. **50**, 1 (1994).
10. A. Aleshin, A. Golubev, L.M. Firsov, and R.B. Honzatko. J. Biol. Chem. **267**, 19210 (1992).
11. A.E. Aleshin, C. Hoffman, L.M. Firsov, and R.B. Honzatko. J. Mol. Biol. **238**, 575 (1994).
12. E.M.S. Harris, A.E. Aleshin, L.M. Firsov, and R.B. Honzatko. Biochemistry, **32**, 1618 (1993).
13. A.E. Aleshin, L.M. Firsov, and R.B. Honzatko. J. Biol. Chem. **269**, 15631 (1994).
14. B. Stoffer, A.E. Aleshin, L.M. Firsov, B. Svensson, and R.B. Honzatko. FEBS Lett. **358**, 57 (1995).
15. J.H. Pazur and T. Ando. J. Biol. Chem. **237**, 297 (1962).
16. R.U. Lemieux, K.B. Hendriks, R.V. Stick, and K. James. J. Am. Chem. Soc. **97**, 4056 (1975).
17. U. Spohr and R.U. Lemieux. Carbohydr. Res. **174**, 211 (1988).
18. S.H. Kahn and R.A. O'Neill (*Editors*). Modern methods in carbohydrate synthesis. Harwood Academic Publishers, Amsterdam. 1996.
19. A.J. Wilkinson, A.R. Fersht, D.M. Blow, and G. Winter. Biochemistry, **22**, 3581 (1983).
20. R. Stulke-Prill and B. Meyer. Eur. J. Biochem. **194**, 903 (1991).
21. P.M. Coutinho and P.J. Reilly. Protein Eng. **7**, 393 (1994).
22. M.R. Sierks and B. Svensson. Protein Eng. **5**, 185 (1992).
23. B. Svensson, B. Stoffer, T.P. Frandsen, M. Søgaard, M.R. Sierks, K.W. Rodenburg, B.W. Sigurskjold, and C. Dupont. Alfred Benzon Symp. **36**, Complex Carbohydrates in Drug Research. Munksgaard, Copenhagen. 1994. p. 202.
24. B. Svensson. Plant Mol. Biol. **25**, 144 (1994).
25. M.R. Sierks, K. Bock, S. Refn, and B. Svensson. Biochemistry, **31**, 8972 (1992).
26. R.U. Lemieux, M.-H. Du, and U. Spohr. J. Am. Chem. Soc. **116**, 9803 (1994).
27. M.R. Sierks, C. Ford, P.J. Reilly, and B. Svensson. Protein Eng. **3**, 193 (1990).
28. F.A. Quiocho, D.K. Wilson, and N.K. Vyas. Nature, **340**, 404 (1989).
29. K. Bock, T. Skydstrup, and S. Refn. J. Carbohydr. Chem. **10**, 969 (1991).
30. R.U. Lemieux and A.A. Pavia. Can. J. Chem. **47**, 4441 (1969).
31. A.J. Clarke and B. Svensson. Carlsberg Res. Commun. **49**, 111 (1984).
32. M.M. Palcic, T. Skrydstrup, K. Bock, N. Le, and R.U. Lemieux. Carbohydr. Res. **250**, 87 (1993).
33. R. Johansson and B. Samuelson. J. Chem. Soc. Perkin Trans. 1, 2371 (1984).
34. J.-R. Pougny, J.-C. Jacquinet, M. Nassr, D. Duchet, M.-L. Milat, and P. Sinaÿ. J. Am. Chem. Soc. **99**, 6762 (1977).
35. M. Forsgren, P.-E. Jansson, and L. Kenne. J. Chem. Soc. Perkin Trans. 1, 2383 (1985).
36. P.A. Gent and R. Gigg. J. Chem. Soc. Perkin Trans. 1, 1835 (1974).
37. J.-M. Lancelin, L. Morin-Allory, and P. Sinaÿ. J. Chem. Soc. Chem. Commun. 335 (1984).
38. U. Spohr and M. Bach. Can. J. Chem. **71**, 1943 (1993).
39. K. Yoshimoto and Y. Tsuda. Chem. Pharm. Bull. **31**, 4335 (1983).
40. J. Kjihlberg, T. Frejd, K. Jansson, S. Kitzing, and G. Magnusson. Carbohydr. Res. **185**, 171 (1989).
41. S. Koto, N. Morishima, Y. Mori, H. Tanaka, S. Hayashi, Y. Iwai, and S. Zen. Bull. Chem. Soc. Jpn. **60**, 2301 (1987).
42. V.K. Srivastava and C. Schuerch. Tetrahedron Lett. **35**, 3269 (1979).

Quantum yield of singlet dioxygen and elucidation of the quenching mechanism for the reaction between the doublet excited states of tris(bipyridine)chromium(III) and triplet dioxygen

Acharee Tiyabhorn and K. Omar Zahir

Abstract: The formation of singlet dioxygen ($^1O_2$) in the reaction between the doublet excited states of tris(bipyridine)chromium(III) and triplet dioxygen in deuterium oxide was detected using near-infrared luminescence corresponding to singlet dioxygen decay. In addition, luminescence intensity measurements were used to determine the quantum yield of singlet dioxygen produced. A value of 0.86 ± 0.08 was obtained for the yield of $^1O_2$. Based on these quantum yield measurements, it is proposed that the major quenching mode is energy transfer quenching. However, considering that the $^1O_2$ yield is less than unity and electron transfer quenching is not a viable pathway, it is proposed that, in addition to the energy transfer quenching, physical quenching involving spin-catalyzed deactivation of $Cr(bpy)_3^{3+}$ may also be operative as a minor quenching pathway.

Key words: $Cr(bpy)_3^{3+}$, singlet dioxygen, quenching, quantum yield.

Résumé : Utilisant la luminescence infrarouge correspondant à la désactivation du dioxygène singulet, on a détecté la formation de dioxygène singulet ($^1O_2$) au cours de la réaction des états doublement excités du tris(bipyridine)chrome(III) et du dioxygène triplet dans l'oxyde de deutérium. De plus, on a utilisé des mesures d'intensité de la luminescence pour déterminer le rendement quantique du dioxygène singulet produit. On a obtenu une valeur de 0,86 ± 0,08 pour le rendement de $^1O_2$. Sur la base de ces mesures de rendements quantiques, il est proposé que le mode majeur de désactivation soit un transfert d'énergie. Toutefois, si l'on considère que le rendement en $^1O_2$ est plus petit que un et que la désactivation par un transfert d'électron n'est pas une voie réactionelle viable, il est suggéré que, en plus de la désactivation par transfert d'énergie, la désactivation physique impliquant une désactivation du $Cr(bpy)_3^{3+}$ catalysée par le spin puisse aussi agir comme voie mineure de désactivation.

Mots clés : $Cr(bpy)_3^{3+}$, dioxygène singulet, désactivation, rendement quantique.

[Traduit par la rédaction]

Introduction

The quenching of the luminescent excited states of polypyridyl complexes of transition metals, particularly those of Ru(II) and Cr(III), by triplet dioxygen ($^3O_2$) has been a subject of considerable interest for quite some time (1, 2). Such studies have provided useful fundamental information about the nature and reactivity of these excited states (3, 4). Furthermore, such studies also provide a simple method of evaluating new luminescent inorganic photosensitizers and their role in mechanistic inorganic photochemistry (5).

In the case of $^3O_2$ quenching of the $^*RuL_3^{2+}$ excited states, both direct energy transfer (6) and electron transfer (7) processes were initially proposed as the quenching mechanisms. Several reports on the yields of $^1O_2$ production have appeared, and quantum yield values ranging from 0.54 to 1.0 have been reported for a variety of RuL_3^{2+} complexes in various solvents (6, 8–10).

In the case of $(^2E)CrL_3^{3+}$, hereinafter referred to as $^*CrL_3^{3+}$, it has been suggested that the quenching of $^*CrL_3^{3+}$ by $^3O_2$ proceeds by an energy transfer pathway leading to singlet dioxygen formation (3, 4). However, until now, no direct experimental evidence has been presented in support of the proposed mechanism and, to the best our knowledge, no measurements of the $^1O_2$ quantum yields have been made. The only report presenting direct experimental evidence for the production of singlet dioxygen for Cr(III) complexes involves the quenching of the phosphorescent excited state of the complex $Cr(taca)(NCS)_3$ by triplet dioxygen (11). In that study, the detection and yield of singlet dioxygen was determined using chemical means. It should be noted here that the detection of $^1O_2$ and measurement of its quantum yields is a tricky business, and applicability of chemical methods for such studies has recently been questioned (10, 12). Emission intensity measurements are now considered to be the method of choice (10, 12) and should therefore be used for the detection as well as for the determination of the yields of singlet dioxygen (10, 12, 13). In this report, we provide direct spectroscopic evidence for the formation of $^1O_2$ as a result of the quenching of

Received June 26, 1995.

A. Tiyabhorn and K.O. Zahir.[1] Department of Chemistry, California State University at Northridge, Northridge, CA 91330-8262, U.S.A.

[1] Author to whom correspondence may be addressed. Telephone: (818) 885–2089. Fax: (818) 885–2912. E-mail: omar.zahir@huey.csun.edu

$^*Cr(bpy)_3^{3+}$, where bpy = 2,2′-bipyridine, by $^3O_2$. In addition, we have used luminescence intensity measurements to determine the quantum yields of $^1O_2$ produced. Such studies on the yields of singlet dioxygen are necessary in order to advance our understanding of the quenching mechanism, and to provide useful fundamental information about the nature of these donor excited states.

Experimental

Materials

Tris(bipyridine)chromium(III) perchlorate was prepared according to the published procedure (3) and the purity was checked by comparison with the reported UV–vis spectra (14). Deuterium oxide (99.9 atom % D) was obtained from Aldrich and was used as received. In all cases, the ionic strength of the solutions was adjusted to 0.1 M using sodium chloride. All solutions, unless specifically mentioned, were prepared using D_2O as the solvent. The desired solution concentrations of dioxygen were obtained by saturation of the solutions with pure dioxygen or air. All measurements were made at ambient temperature.

General instrumentation:

UV–visible absorption measurements were made using a Perkin–Elmer λ14 spectrophotometer. In a few instances when the lifetime of $^*Cr(bpy)_3^{3+}$ was measured, a home-built laser flash photolysis system similar to the one described elsewhere (15, 16) was used. In such studies, the excitation of 52–60 μM $Cr(bpy)_3^{3+}$ solution was carried out using the broadband output of Coumarin 420 dye. The emission decay of $^*Cr(bpy)_3^{3+}$ was monitored at 727 nm.

Near-infrared emission studies:

The detection of singlet dioxygen ($^1O_2$,$^1\Delta_g$) was carried out by observing the infrared luminescence at 1270 nm arising from the first-order decay of $^1O_2$. Our singlet dioxygen detection system was based on the one reported earlier (17–19). Some preliminary studies on $^1O_2$ detection were conducted at the Department of Chemistry, University of California, Los Angeles. All samples used in the luminescence studies were prepared using 420–440 μM $Cr(bpy)_3^{3+}$ in D_2O and were saturated with triplet dioxygen. The solutions were contained in a 1 cm^2 cuvette. The excitation of the samples was carried out using a 200 ns pulse arising from a modified Phase-R model DL-1100 flash lamp pumped dye laser using the appropriate coumarin dye solution. The 1270 nm radiation emerging from the solution was detected at a right angle to the laser beam using a Judson J-16TE2 (5 mm) germanium photodiode. The only element between the cuvette face and diode cover plate was a (2.5 × 2.5 cm) Corning 7–56 infrared long-pass filter that minimized any radiation below 1100 nm. The photodiode output current was amplified with a Judson preamplifier, operating at −20°C to reduce thermal noise. The output from the amplifier was then fed into a Nicolet model 430 digital oscilloscope interfaced to an IBM personal computer. As a control experiment, both Rose Bengal (RB) and tetraphenyl porphrin (TPP), which are known singlet dioxygen sensitizers, were used to produce $^1O_2$ luminescence, which was detected using the instrumentation described above. For quantum yield measurements, the decay kinetics for $^1O_2$ was obtained by the computer average of 20 laser shots. Within a particular set of experiments, the laser intensity was found to be very reproducible. Rose Bengal was used as a reference standard to quantitatively determine the yield of $^1O_2$ for the $Cr(bpy)_3^{3+}$–$^3O_2$ reaction. Both sets of experiments were performed on solutions under identical excitation conditions.

Results and discussion

Irradiation of a $Cr(bpy)_3^{3+}$ solution with visible light will lead to the formation of $^*Cr(bpy)_3^{3+}$. In the absence of triplet dioxygen, the $^*Cr(bpy)_3^{3+}$ will undergo unimolecular decay to the ground state as described in eq. [1].

$$[1]\quad {}^*Cr(bpy)_3^{3+} \xrightarrow{k_1} Cr(bpy)_3^{3+} + h\nu + \Delta$$

Under our experimental conditions, the lifetime of $^*Cr(bpy)_3^{3+}$ was measured in D_2O and was found to be 65 μs. This value is in excellent agreement with the value of 61 μs reported earlier (1) under slightly different conditions. In the presence of triplet dioxygen (aerated or pure dioxygen saturated solutions), the lifetime measurements gave an average value of (2.5 ± 0.4) × 10^7 M^{-1} s^{-1} for k_2, the second order rate constant for the quenching of $^*Cr(bpy)_3^{3+}$ by triplet dioxygen (eq. [2]). Again

$$[2]\quad {}^*Cr(bpy)_3^{3+} + {}^3O_2 \xrightarrow{k_2} Cr(bpy)_3^{3+} + {}^?O_2$$

the value of k_2 obtained in the present study is in very good agreement with the value of 2.9×10^7 M^{-1} s^{-1} in D_2O reported earlier (3) by Brunschwig and Sutin. A good knowledge of k_1 and k_2 is necessary for our subsequent studies involving quantum yield measurements.

Detection of near-infrared luminescence

In the presence of triplet dioxygen, the most commonly proposed quenching pathways for the deactivation of the excited states $^*Cr(bpy)_3^{3+}$ in solution are depicted in Scheme 1. The electron transfer pathways (**B**) (both reductive and (or) oxida-

Scheme 1.

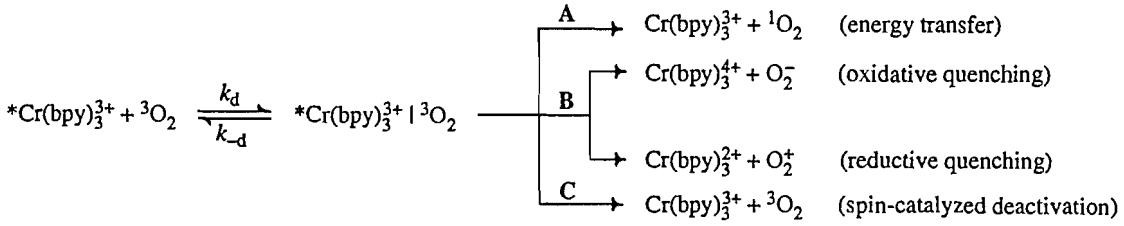

Fig. 1. Decay of near-infrared luminescence of singlet dioxygen obtained from the laser flash photolysis of $^3O_2$-saturated D_2O solution containing Rose Bengal as a sensitizer. (Thin line represents the decay curve extrapolated to zero time.)

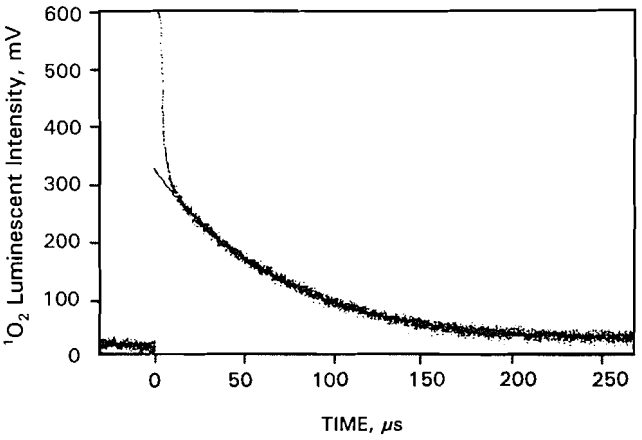

Fig. 2. Decay of near-infrared luminescence of singlet dioxygen obtained from the laser flash photolysis of $^3O_2$-saturated D_2O solution containing $Cr(bpy)_3^{3+}$ as a sensitizer. (Thin line represents the decay curve extrapolated to zero time.)

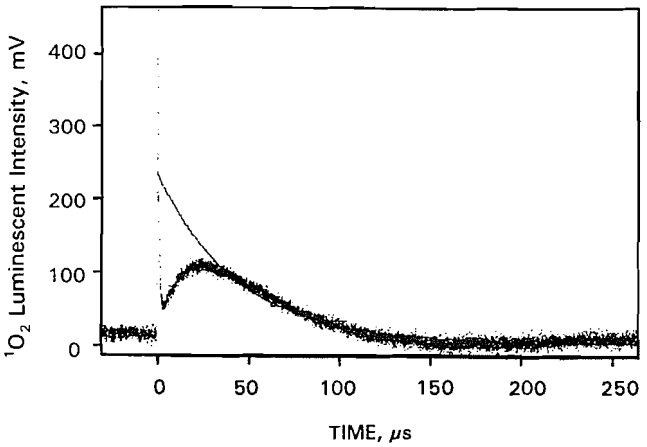

tive quenching) are considered to be endoergonic and have been ruled out (3, 4). If the energy transfer quenching pathway (**A**) is indeed operative, it will lead to the formation of singlet dioxygen. Energy transfer from $^*Cr(bpy)_3^{3+}$ to $^3O_2$ is energetically possible and spin allowed. The $^*Cr(bpy)_3^{3+}$ energy is 40.1 kcal/mol (1), which is enough to allow exothermic energy transfer to triplet dioxygen to give $^1O_2$ ($^1\Delta_g$ = 23 kcal/mol). The singlet dioxygen formed in reaction [2] can then decay to the ground state via eq. [3] and can be detected by observing

$$[3] \quad {}^1O_2 \xrightarrow{k_3} {}^3O_2 + h\nu' + \Delta$$

its near-infrared luminescence at 1270 nm. To validate the detection of singlet dioxygen in these studies, singlet dioxygen was initially generated using Rose Bengal, which is a well-documented sensitizer for singlet dioxygen. Formation and decay of $^1O_2$ produced in a D_2O solution containing Rose Bengal is shown in Fig. 1. The early intense component decayed rapidly and had a time constant of ~10 μs. The slow component is attributed to the 1270 luminescence of $^1O_2$ as it disappeared when triplet dioxygen in the solution was replaced with He gas. With Rose Bengal as a sensitizer, the lifetime of the singlet dioxygen was measured in D_2O and d_6–acetone and was found to be 62 and 710 μs, respectively. These values are in very good agreement with the singlet dioxygen lifetime reported for these two solvents (17–19).

Similarly, if $^1O_2$ luminescence is observed when Rose Bengal is replaced with $Cr(bpy)_3^{3+}$, it will provide direct evidence for the production of $^1O_2$ in reaction [2]. Indeed, when a solution containing 440 μM $Cr(bpy)_3^{3+}$ in D_2O saturated with triplet dioxygen was irradiated with a 420 nm laser pulse, infrared luminescence corresponding to $^1O_2$ production was observed as well. Again, in a control experiment, where all other components were present in the solution but triplet dioxygen was replaced with He gas, no infrared luminescence signal was observed. A profile of $^1O_2$ luminescence intensity vs. time for reaction [2] is shown in Fig. 2. An examination of Fig. 2 shows that, due to slow quenching of the $^*Cr(bpy)_3^{3+}$ by $^3O_2$ ($k_2 = 2.5 \times 10^7$ M^{-1} s^{-1} for $^*Cr(bpy)_3^{3+}$ as compared to 2.7×10^9 M^{-1} s^{-1} for $^*Ru(bpy)_3^{2+}$ and 1.6×10^9 M^{-1} s^{-1} for $^*RB$) (9), the formation of $^1O_2$ is not instantaneous but a rather prolonged process.

A computer program (KINSIM)[2] was used to simulate the formation and decay of $^1O_2$ using $[^*Cr(bpy)_3^{3+}] = 10$ μM, $k_1 = 1.5 \times 10^4$ s^{-1}, three different values of the quenching rate constant, k_2, as 2.5×10^6, 2.5×10^7, and 2.5×10^8 M^{-1} s^{-1}, and k_3 for the decay of $^1O_2$ as 1.6×10^4 s^{-1}. The profile for the formation and decay of $^1O_2$, obtained from these kinetic simulations, is depicted in Fig. 3. A comparison of the experimental (Fig. 2) and simulated (Fig. 3) plots show that for the k_2 value of 2.5×10^7 M^{-1} s^{-1}, which is the same as the experimentally determined value of the quenching rate constant, the profiles for $^1O_2$ formation and decay are quite similar. Therefore, based on our experimental results and computer simulations, we conclude that $^1O_2$ is indeed produced as a result of quenching of $^*Cr(bpy)_3^{3+}$ by $^3O_2$.

Quantum yield measurements

The magnitude of the infrared luminescence intensity has been used for quantitative determination of the yields of $^1O_2$ produced for a variety of reactions (10, 12, 13). Considering the problems associated with studies involving chemical trapping of $^1O_2$ reported earlier (12), the near-infrared luminescence emission method, which is clean and straightforward, has now become a method of choice. In these studies, the luminescence intensity of $^1O_2$ for a standard, usually Rose Bengal, acridine, or tetraphenyl porphyrin, is determined by extrapolation to zero time and then compared, under identical excitation conditions (i.e., absorbance, laser intensity), with the $^1O_2$ luminescence intensity arising from the reaction of interest. In the present study, the near-infrared luminescent intensity measurements were used to determine the quantum yield of $^1O_2$ formation for reaction [2] in D_2O as described below.

[2] The mechanism used for kinetic simulations was based on reactions [1]–[3]. The concentration of the $^*Cr(bpy)_3^{3+}$ used in the simulations was 8 μM, which was similar to the concentration usually produced under our experimental conditions. The concentration of the excited state can be varied either by changing the initial concentration of $Cr(bpy)_3^{3+}$ or by changing the laser intensity. The kinetic program used for simulation was KINSIM, which was a gift from Professor James Espenson, Iowa State University.

Fig. 3. Profile of singlet dioxygen formation and decay obtained for reactions [1]–[3] using the kinetic simulation program kinsim. The parameters used for simulations are $[^*Cr(bpy)_3^{3+}] = 8\ \mu M$, $k_1 = 1.5 \times 10^4\ s^{-1}$, $k_2 = 2.5 \times 10^6\ M^{-1}\ s^{-1}$ (triangle), $2.5 \times 10^7\ M^{-1}\ s^{-1}$ (circle) $2.5 \times 10^8\ M^{-1}\ s^{-1}$ (diamond), and $k_3 = 1.6 \times 10^4\ s^{-1}$.

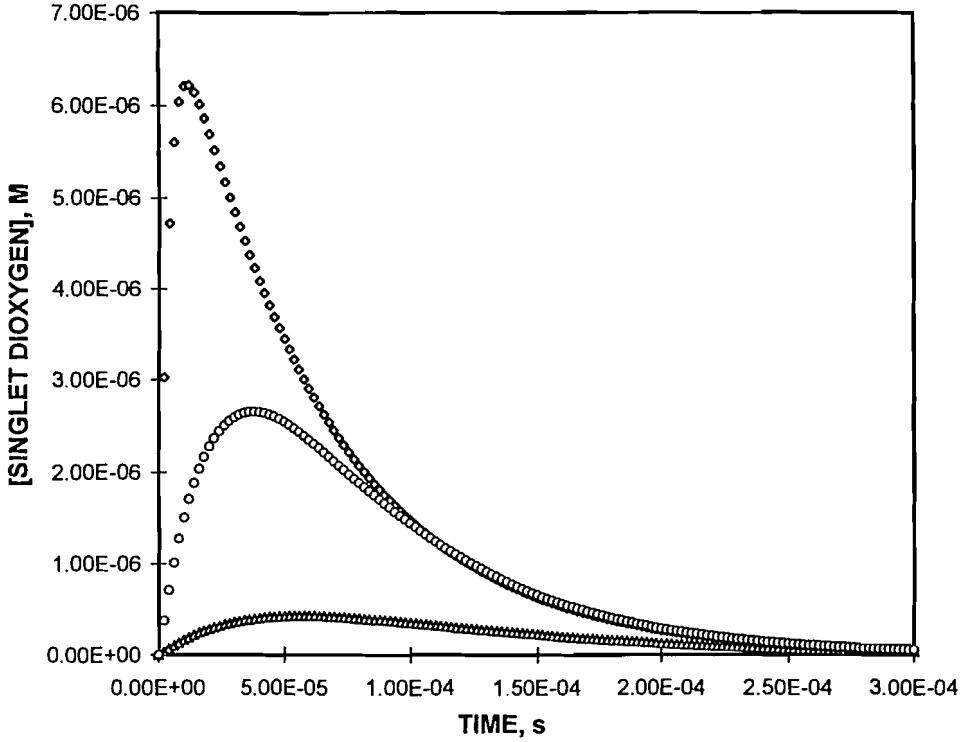

The exponentially decaying slow component corresponding to $^1O_2$ luminescence (Fig. 1 for Rose Bengal and Fig. 2 for $Cr(bpy)_3^{3+}$) was extrapolated to zero time. Referring to Figs. 1 and 2, this is the point defined by the intersection between the extrapolated part of the curve and the vertical rise of the luminescence signal. Considering the fact that the instrument response time was approximately 10 μs, and the $^3O_2$ quenching of the $^*Cr(bpy)_3^{3+}$ was rather slow, the decay curve between 40 and 200 μs was used for extrapolation to zero time. Within the same solvent under identical excitation conditions for Rose Bengal and $Cr(bpy)_3^{3+}$, the quantum yield of $^1O_2$ for reaction [2], hereafter referred to as $\Phi_\Delta(CR)$, can be calculated using eq. [4] (10):

$$[4]\quad \frac{I_0(CR)}{I_0(RB)} = \frac{\Phi(^*CR)\Phi_\Delta(CR)f(CR)}{\Phi_\Delta(RB)f(RB)}$$

Here $I_0(CR)$ and $I_0(RB)$ are the luminescence intensities at zero time for $Cr(bpy)_3^{3+}$ and Rose Bengal, respectively. $\Phi(^*CR)$ is the quantum yield for the formation of doublet excited state $^*CrL_3^{3+}$ and is equal to unity (1). $\Phi_\Delta(RB)$ is the quantum yield of $^1O_2$ for the Rose Bengal–$^3O_2$ system and has been determined by others (6, 8, 9, 13) as 0.80. The $f(CR)$ and $f(RB)$ are the fractions of the $Cr(bpy)_3^{3+}$ and Rose Bengal excited states, respectively, that are quenched by triplet dioxygen. The values of $f(CR)$ and $f(RB)$ were calculated using the expression $f = k_q[^3O_2]/k_d + k_q[^3O_2]$. Here k_d is the rate constant for the decay of the sensitizer excited state, and k_q is the second-order rate constant for the quenching of the excited states by triplet dioxygen. The lifetime of the Rose Bengal excited state was determined in the laboratory and was found to be 200 μs. Therefore, using $k_d = 5.0 \times 10^3\ s^{-1}$ and $[^3O_2] = 2.5 \times 10^{-4}$ M, a value of 0.98 was calculated for $f(RB)$. Similarly, using $[^3O_2]$ as 1.2×10^{-3} M, and the experimentally determined values of k_1 and k_2, a value of 0.66 was obtained for $f(CR)$. Using all the necessary data and applying eq. [4], a value of $\Phi_\Delta(CR) = 0.86 \pm 0.08$ was obtained for reaction [2] in D_2O.

Quenching mechanism

This value of 0.86 for the quantum yield of $^1O_2$ suggests that the energy transfer quenching (pathway **A** in Scheme 1) is the major quenching pathway for reaction [2] to occur. However, as the value of $\Phi_\Delta(CR)$ is less than unity, we suspect that, in addition to energy transfer quenching, another pathway, although minor, may also be operative. The electron transfer quenching mode (pathway **B**, reductive or oxidative) is considered to be endoergonic (3, 4). In addition, very little or opposite variation of quenching rate constant with $\Delta^\circ E$ of the reaction was observed (3). Based on these observations and other theoretical considerations, electron transfer quenching has been ruled out (3, 4). To account for the less than unity yield for $^1O_2$ production in reaction [2], we propose that, parallel to the energy transfer quenching, the physical quenching (pathway **C**) may be also operative. It is proposed that once the encounter complex $^*Cr(bpy)_3^{3+}|^3O_2$ is formed, the spin-catalyzed deactivation of the encounter complex will lead to the formation of $Cr(bpy)_3^{3+}|^3O_2$ which then dissociates to give ground state $Cr(bpy)_3^{3+}$ and $^3O_2$. This spin-catalyzed deactiva-

tion of the encounter complex can occur in parallel with the energy transfer mode that initially produces $Cr(bpy)_3^{3+}{}^1O_2$, which upon dissociation gives $Cr(bpy)_3^{3+}$ and $^1O_2$. Nevertheless, any contribution from the spin-catalyzed deactivation pathway (**C**) is expected to be minor.

In the case of $^*RuL_3^{2+}$ complexes, the excited state is a metal to ligand charge transfer excited state and is predominantly triplet in nature (2). Therefore, a triplet–triplet energy transfer process can be operative and was indeed observed for the majority of RuL_3^{2+} complexes with high yields of $^1O_2$ (10). In the case of $^*Cr(bpy)_3^{3+}$–$^3O_2$, however, the excited state $(^2E)Cr(bpy)_3^{3+}$ is metal centered and its deactivation leads to the formation of ground state $(^4A)Cr(bpy)_3^{3+}$. Energy transfer in this case is spin allowed as well, and can be considered similar to the singlet–triplet energy transfer process. The quenching of $^*CrL_3^{3+}$ by $^3O_2$ is observed to be approximately two orders of magnitude slower than the quenching of $^*RuL_3^{2+}$ by $^3O_2$. We propose that, in the case of chromium complexes, slower quenching by triplet dioxygen, is due to the poor overlapping of the donor–accepter orbitals.

Conclusion

Use of the infrared luminescence technique in the present studies clearly establishes that $^1O_2$ is produced as a result of $^3O_2$ quenching of $^*Cr(bpy)_3^{3+}$. From our quantum yield studies, we conclude that the quenching of $^*Cr(bpy)_3^{3+}$ by $^3O_2$ occurs via an energy transfer pathway and that $^1O_2$ can be produced in a high quantum yield. To account for the less than unity value of the $^1O_2$ quantum yield obtained in these studies, we suggest that, in addition to the energy transfer quenching that is the principle mode of quenching, physical quenching may also be operative as a minor quenching mode. We also propose that while elucidating the quenching mechanism for the luminescence excited states of transition metal complexes, in addition to the energy and electron transfer pathways, physical quenching should also be considered when assigning the quenching mechanism.

Acknowledgment

Some preliminary work on $^1O_2$ emission measurements was done at the Department of Chemistry, University of California at Los Angeles. One of the authors (K.O.Z.) is grateful to Professor Chris Foote and Dr. Jim Arbogast for their help with infrared emission studies, and many valuable suggestions. This work was sponsored by the Office of Research and Sponsored Projects, California State University, Northridge.

References

1. M.A. Jamesian, N. Serpon, and M.Z. Hoffman. Coord. Chem. Rev. **39**, 121 (1981).
2. K. Kalyanasundaram. Coord. Chem. Rev. **46**, 161 (1982).
3. B. Brunschwig and N. Sutin. J. Am. Chem. Soc. **100**, 7568 (1978).
4. N. Serpone, M.A. Jamieson, M.S. Henry, M.Z. Hoffman, F. Bolletta, and M.J Maestri. J. Am. Chem. Soc. **101**, 2907, (1979).
5. K. Kalyanasundaram. Photochemistry of polypyridine and porphyrin complexes. Academic Press, London. 1992.
6. J.N. Demas, E.W. Harris, and R.P. McBride. J. Am. Chem. Soc. **99**, 3547 (1977).
7. (*a*) C.T. Ling and N. Sutin. J. Phys. Chem **80**, 97 (1976); (*b*) Y. Kurimura, H. Yokota, and Y. Muraki. Bull. Chem. Soc. Jpn. **54**, 2450 (1981).
8. F. Wilkinson, W.P. Helman, and A.B. Ross. J. Phys. Chem. Ref. Data, **22**, 113 (1993).
9. K.O. Zahir and A. Haim. Photochem. Photobiol. **63**,167 (1992).
10. Q.G. Mulazzani, H. Sun, M.Z. Hoffman, W.E. Ford, and M.A.J. Rodger. J. Phys. Chem. **98**, 1145 (1994).
11. A.D. Kirk, C. Namasivayam, W. Risky, and D. Ristic-Petrovic. Inorg. Chem. **28**, 972 (1989).
12. Q.G. Mulazzani, M. Ciano, M.D. Angelantonio, M. Venturi, and M.A. J. Rodger. J. Am. Chem. Soc. **110**, 2451 (1988).
13. J.W. Arbogast and C.S. Foote. J. Am. Chem. Soc. **113**, 8886 (1991); R.C. Kanner and C.S. Foote. J. Am. Chem. Soc. **114**, 678 (1992).
14. E. Konig and S. Herzog. Inorg. Nucl. Chem. **32**, 585 (1970).
15. M.A. Hoselton, C.T. Lin, H. Schwartz, and N. Sutin. J. Am. Chem. Soc. **100**, 2383 (1978).
16. J.D. Melton, J.H. Espenson, and A. Bakac. Inorg. Chem. **25**, 4104 (1986).
17. (*a*) J.R. Hurst, J.D. McDonald, and G.B. Shuster. J. Am. Chem. Soc. **104**, 2065 (1982); (*b*) M.A.J. Rodger. J. Am. Chem. Soc. **105**, 6201 (1983).
18. J.G. Parker and W.D. Stanboro. J. Am. Chem. Soc, **104**, 2067 (1982).
19. P.R. Ogilby and C.S. Foote. J. Am. Chem. Soc. **104**, 2069 (1982).

Modified method of synthesis of N-substituted dithioesters of amino acids and peptides in the Pinner reaction[1]

Witold Neugebauer, Eric Pinet, Munsok Kim, and Paul R. Carey

Abstract: An improved method for the synthesis of dithioesters of amino acids and peptides has been developed. The syntheses have been carried out from the nitriles. The addition of thiol to the nitrile derivative in the Pinner step of dithioester synthesis was activated with hydrogen fluoride. A few examples of dithioester synthesis using liquid HF are described. Some novel dithioesters, which are model compounds for resonance Raman spectroscopic studies of dithioacylpapain intermediates, are described.

Key words: dithioesters, amino acids, Pinner reaction, HF, isotopes.

Résumé : Une méthode améliorée de synthèse de dithioesters d'acides amines et de peptides a été développée. Les synthèses ont été accomplies à partir des nitriles correspondants. L'addition du thiol au dérivé nitrile lors de la synthèse du dithioester, pendant la reaction de Pinner, a été activée par le fluorure d'hydrogène. Nous décrivons plusieurs exemples de synthèse de dithioesters employant du HF liquide, ainsi que plusieurs nouveaux dithioesters,composé-modéles employés dans les études des formes passagères de la dithioacylpapaine par la spectrométrie de résonance de Raman.

Mots clés : dithioesters, acides aminés, réaction de Pinner, HF, isotopes.

Introduction

Dithiocarboxylic acids and esters have recently attracted attention because of their structural and spectroscopic properties (1–5), and their application in organic synthesis (6). Since we have had difficulty in using available procedures for synthesis of dithioesters of N-substituted amino acids or small peptides, modification of the most general procedure seemed to be the best choice. Several methods of synthesis of this class of organo-sulphur compounds have been published (1, 7, 8) and reviewed (9). The most common route for dithioester synthesis is the procedure based on the Pinner reaction (10, 11). Thiols react with nitriles in the presence of hydrogen chloride to give imidothioesters and these are the key intermediates in the synthesis of dithioesters. In the modification reported here, the first step of the synthesis is dissolution of the nitrile in an excess of liquid hydrogen fluoride at a temperature below 0°C to most likely form the $[RCNH]^+HF_2^-$ adduct (eq. [1]) (12). In the presence of the third reaction component, mercaptan, thioimidate hydrofluoride is produced, $[RC(=NH_2)SR']^+HF_2^-$ (eq. [2]). Unlike the classic Pinner reaction with HCl saturated methylene chloride, all nitrile derivatives are completely soluble in the reaction mixture. Excess of hydrogen fluoride and mercaptan are removed under vacuum and the thioimidate hydrofluoride precipitated. It is then used under anhydrous conditions to react with H_2S in dry pyridine, forming the dithioester, eq. [3] (8).

Received September 6, 1995.

Witold Neugebauer,[2] Eric Pinet, Munsok Kim, and Paul R. Carey. Institute for Biological Sciences, National Research Council of Canada, Ottawa, ON, K1A 0R6, Canada.

[1] NRCC No. 39511.

[2] Author to whom correspondence may be addressed. Present address: Département de Pharmacologie, Faculté de Médecine, Université de Sherbrooke, Sherbrooke, QC, J1H 5N4, Canada. Telephone: (819) 820-6820. Fax: (819) 564 5400. E-mail: wneugeba@courrier.usherb.ca.

Experimental section

Materials

All solvents used (acetone, chloroform, toluene, diethyl ether, methanol) were of ACS purity and were purchased from BDH. Pyridine was purchased from BDH and distilled over KOH pellets. Ammonium chloride, *p*-halogen benzoyl chlorides, *p*-anisoyl chloride, and ethane thiol were purchased from Aldrich. Sodium cyanide, formaldehyde solution, and acetic acid were purchased from Anachemia Chemicals. Gaseous HF and H_2S were purchased from Matheson Gas, Canada. Anhydrous gas HF operations were undertaken in an HF apparatus (Biosearch). All final products were purified by crystallization and column chromatography on silica gel 60 (E. Merck) with toluene–chloroform—methanol as an eluent on medium pressure glass columns (Michel-Miller) 300 mm, Aldrich. Chromatographic purity of products was checked on TLC (silica gel, aluminium plates, E. Merck) in solvent systems A, chloroform–methanol 4:1, or B, chloroform. The final identity of the synthesized compounds was checked by FAB-MS spectrometry on Jeol, JMS-AX505H with dithiothreitol–dithioerythiol (DTT–DTE) or nitrobenzyl aldehyde (NBA) matrix, and in some cases by NMR spectroscopy.

Synthesis

General procedure of the Pinner reaction (2, 3, 3a, 3b, 3c, 3d, 3e, 3a1, 3a2, 3a3, 3a4, 3a5)

HF gas was liquified at the temperature of liquid nitrogen. N-substituted amino nitrile (10 mmol) and ethanethiol (13 mmol)

[1] $RCN + 2\,HF \longrightarrow [RCNH]^+ HF_2^-$

[2] $[RCNH]^+HF_2^- + R'SH \longrightarrow RC(=NH_2^+)-SR'\ HF_2^-$

[3] $RC(=NH_2^+)-SR'\ HF_2^- + H_2S + \bigcirc N \longrightarrow RC(=S)-SR' + \bigcirc N\cdot HF + NH_4F$

[4] $NH_4Cl + HC(=O)H + NaCN \longrightarrow CH_2{=}NCH_2CN + NaCl + H_2O$

[5] $CH_2{=}NCH_2CN + 2\,C_2H_5OH + H_2SO_4 \longrightarrow H_2NCH_2CN\cdot H_2SO_4 + CH_2(OC_2H_5)_2$

[6] $H_2NCH_2CN\cdot H_2SO_4 + X\text{-}\bigcirc\text{-}C(=O)Cl + 2\,NaOH \longrightarrow$

$X\text{-}\bigcirc\text{-}C(=O)NHCH_2CN + Na_2SO_4 + H_2O$

X= H, F, Cl, Br, I, OCH_3

were placed in a polyethylene reactor with a stirrer, at liquid nitrogen temperature, while HF (3 mL) was added. The reaction vessel was placed in the Biosearch HF apparatus and the reaction was held at 0°C and stirred for 1 h. The excess HF and ethanethiol were then evaporated at room temperature under a water aspirator and finally with an oil pump. The thioimidoester salts produced were precipitated (or solidified) by the addition of anhydrous diethyl ether. They were then decanted from ether, washed, decanted again, and used in the next synthetic step.

Dithiomethyl esters **4** and **6** require the use of liquified CH_3SH (instead of ethanethiol) prepared the same way as liquid HF. Similarly, thiomethyl ester (**1**) requires dry methanol. Dithioesters of dipeptides **5**, **6**, and **7** were formed after coupling of *N*-acetyl or *N*-methoxy phenylalanine to amino acetonitrile with DCC–pentafluorophenol in the standard manner (13).

Dithioesters

Pyridine , dried over KOH pellets, was saturated with dry H_2S at 0°C and thioimido esters were added while stirring and passing dry H_2S for 45 min. $H_2{}^{34}S$ generated from heating ^{34}S in paraffin was used for the isotopically substituted derivative (*3a*5). The coloured solutions (from light yellow to deep orange) were then poured into sufficient amounts of ice-cold 4 N HCl to neutralize the pyridine. The dithioesters were crystallized or precipitated and were collected by filtration and washed with cold water. The precipitates (crystals) were precipitated with water from acetone solution, then dissolved in chloroform and chloroform solution that was dried by rotary evaporation. The crude dithioesters were dissolved in a minimum volume of chloroform (1–3 mL) and purified on a silica gel column that was washed with toluene and solvent exchange under medium pressure from 10% chloroform in toluene (30 min) to 50% and 100% chloroform (65 min each). Finally the column was washed with methanol and toluene for the next purification. TLC identifications in solvent systems A and B were made, and the dithioesters were collected. Their identity was verified by FAB/MS spectrometry using NBA or DTT–DTE as a matrix.

General procedure for Strecker reaction (3a1, 3a2, 3a3, 3a4)

Isotopic substitutions were made using labelled substrates in a Strecker type synthesis; $Na^{13}CN$ (*3a*1), $H^{13}C(=O)H$ (*3a*2), $^{15}NH_4Cl$ (*3a*3), $DC(=O)D$ in D_2O (*3a*4).

NH_4Cl (2.16 g, 0.04) mol was dissolved in 6 mL (0.04 mol) formaldehyde at the ice-bath temperature and, while stirring, 2 g (0.04 mol) NaCN in 6 mL water was added dropwise over 2.5 h. Stirring continued for another 1.5 h and 1.33 mL of acetic acid was added dropwise over 1 h. After 2.5 h, the white precipitate was filtered, washed with cold water, and dried under high vacuum overnight. Yield 1.49 g (59.7%), mp 124–126°C, Schiff base derivative reaction [4].

CH_2NCH_2CN powder (1.49 g, 0.02 mol) was added to 1.3

Table 1. Products obtained in the Pinner reaction with liquid HF.

	Product	M + 1 (FAB/MS)	Yield (%)	Melting point (°C)
1	$CH_3C(=O)NHCH_2C(=S)OCH_3$	148	30	Oil
2	$CH_3C(=O)NHCH_2C(=S)SCH_2CH_3$	178	42	71
3	$C_6H_5C(=O)NHCH_2C(=S)SCH_2CH_3$	240	87	98
3*a*	*p*-$ClC_6H_4C(=O)NHCH_2C(=S)SCH_2CH_3$	274	67.8	94
3*b*	*p*-$BrC_6H_4C(=O)NHCH_2C(=S)SCH_2CH_3$	319	47.8	117
3*c*	*p*-$FC_6H_4C(=O)NHCH_2C(=S)SCH_2CH_3$	258	67.7	104
3*d*	*p*-$IC_6H_4C(=O)NHCH_2C(=S)SCH_2CH_3$	365	48.4	113
3*e*	*p*-$CH_3OC_6H_4C(=O)NHCH_2C(=S)SCH_2CH_3$	270	51.2	116
3*a*1	*p*-$ClC_6H_4C(=O)NHCH_2{}^{13}C(=S)SCH_2CH_3$	275	65.5	95
3*a*2	*p*-$ClC_6H_4C(=O)NH{}^{13}CH_2C(=S)SCH_2CH_3$	275	66.7	94
3*a*3	*p*-$ClC_6H_4C(=O){}^{15}NHCH_2C(=S)SCH_2CH_3$	275	40.2	95
3*a*4	*p*-$ClC_6H_4C(=O)NHCD_2C(=S)SCH_2CH_3$	276	61	99
3*a*5	*p*-$ClC_6H_4C(=O)NHCH_2C(={}^{34}S)SCH_2CH_3$	276	67	100
4	$C_6H_5C(=O)NHCH_2C(=S)SCH_3$	226	27	86
5	$CH_3C(=O)NHCH(CH_2C_6H_5)C(=O)NHCH_2C(=S)SCH_2CH_3$	325	37.4	132
6	$CH_3O)NHCH(CH_2C_6H_5)C(=O)NHCH_2C(=S)SCH_3$	299	27	130

mL H_2SO_4 in 5.85 mL ethanol and dissolved at room temperature. The solution was then placed in the ice-bath for 2–4 h. The precipitate was filtered, washed with cold ethanol, and dried under high vacuum overnight. The yield of amino acetonitrile sulphate, mp 152–153°C, was 89.7% (reaction [5]).

Amino acetonitrile salt (1.557 g, 0.01 mol) was dissolved in 13 mL of well-stirred 10% NaOH at the ice-bath temperature and, while stirring, 1.5 mL (0.0118 mol) *p*-chloro benzoylchloride in 3.5 mL THF was added over 20 min. The pH of the reaction was maintained at 14 by adding NaOH solution. After 3 h a quantitative amount of amido acetonitrile derivative was filtered and recrystallized from CCl_4. Further purification required dissolution in hot acetone, addition of charcoal, filtration through Celite 454, and precipitation of the final product with water (mp 145°C).

Results and discussion

The Pinner method of dithioester synthesis cannot be considered general for the preparation of this class of compounds, even though many attempts have been made. Using this approach, we tried to synthesize several dithioesters and the resulting yield was unsatisfactory (1), especially for the isotopic derivatives we wanted to make. Low yields in the classic Pinner procedure are a result of the poor solubility of N-substituted amino nitrile substrates in HCl saturated dichloromethane. Some of the N substitutions are not stable under these conditions especially in the presence of a trace amount of water. Use of liquid HF at low temperature gives full and immediate solubility of the N-substituted derivatives in the reaction mixture. This raises the reaction yield to the 70% range, which is a dramatic improvement over the old procedure (1). The final products synthesized by this improved method are summarized in Table 1. As an alternative, simple apparatus can be used: the reaction with HF could be performed in a polyethylene vessel, linked to the HF bottle on one side and a water aspirator on the other. This reactor must be capable of being cooled by liquid nitrogen and of being magnetically stirred. Such a simple arrangement for the reaction vessel could be considered as a general method for the synthesis of dithioesters of N-substituted amino acids and some peptides.

References

1. A.C. Storer, Y. Ozaki, and P.R. Carey. Can. J. Chem. **60**, 199 (1982).
2. K.I. Varughese, A.C. Storer, and P.R. Carey. J. Am. Chem. Soc. **106**, 8252 (1984).
3. P.R. Carey, H. Lee, Y. Ozaki, and A.C. Storer. J. Am. Chem. Soc. **106**, 8258 (1984).
4. H. Lee, A.C. Storer, and P.R. Carey. Biochemistry, **22**, 4781 (1983).
5. A.C. Storer, H. Lee, and P.R. Carey. Biochemistry, **22**, 4789 (1983).
6. K.M. Doyle and F. Kurzer. Chem. Ind. (London), 803 (1974).
7. D. Paquer. Bull. Soc. Chim. Fr. **5–6**, 1439 (1975).
8. C.S. Marvel, P. de Radzitzky, and J.J. Brader. J. Am. Chem. Soc. **77**, 5997 (1955).
9. S.R. Ramadas, P.S. Srinvasan, J. Ramachandran, and V.V.S.K. Sastry. Synthesis, 605 (1983).
10. A. Pinner and F. Klein. Ber. Dtsch. Chem. Ges. **11**, 1825 (1879).
11. J. Poupaert, A. Bruylants, and P. Crooy. Synthesis, 622 (1972).
12. R. West. J. Am. Chem. Soc. **79**, 4568 (1957); T.C. Waddington and F. Klanberg. J. Chem. Soc. 2329 (1960); D.W.A. Sharp. J. Chem. Soc. 2558 (1958).
13. W. König and R. Geiger. Chem. Ber. **103**, 788 (1970).

Rheological and interfacial properties of nucleic acid films studied by thickness – shear mode sensor and network analysis

Hongbo Su and Michael Thompson

Abstract: Complete characterization of the thickness – shear mode (TSM) acoustic wave sensor coated with films of nucleic acid and subjected to conductive solution loading is achieved through network analysis of impedance measurements. The responses of coated sensors with respect to series resonant frequency can be separated into two regions. When $0 < \sigma < 0.5\ \Omega^{-1}\ m^{-1}$ the frequencies for sensors with films of single strand (ss) DNA or polycytidylic (5′) (Poly C) in place rise significantly with increasing conductivity. The motional resistances for sensors coated with both species peak at the same value of conductivity where the frequency has the most rapid shift. In the second region ($0.5 < \sigma < 12\ \Omega^{-1}\ m^{-1}$), the frequency response for the ss DNA system exhibits a bell-shaped curve, with a minimum at $\sigma = 4\ \Omega^{-1}\ m^{-1}$. The motional resistances for both nucleic acid layers show reversible behaviour, whereas TSM sensors with bare PdO and Au electrodes yield little change. Models that consider only the bulk properties of solutions fail to explain the observed changes in frequency. On the other hand, an equivalent circuit model incorporating the rheological properties of nucleic acid layers on the sensor surface is successful in explaining the various responses.

Key words: DNA sensor, network analysis, thickness – shear mode sensor, DNA interfacial properties.

Résumé : Faisant appel à une analyse de réseau des mesures d'impédance, on a réalisé une caractérisation complète de senseurs enduits de films d'acide nucléique, opérant en mode de cisaillement de l'épaisseur et soumis à un chargement de solution conductrice. Les réponses des senseurs enduits par rapport à la fréquence de résonance en série ont pu être séparée en deux régions. Lorsque $0 < \sigma < 0{,}5\ \Omega^{-1}\ m^{-1}$, les fréquences des senseurs avec des films d'ADN à simples brins (sb) ou polycytidyliques (5′) (Poly C) en place augmentent beaucoup avec une augmentation de la conductivité. Les résistances au mouvement des senseurs enduits avec les deux espèces atteignent un sommet pour la même valeur de la conductivité alors que la fréquence présente le déplacement le plus rapide. Dans la deuxième région ($0{,}5 < \sigma < 12\ \Omega^{-1}\ m^{-1}$), la fréquence de réponse du système ADN sb présente une courbe en forme de cloche avec un minimum à $\sigma = 4\ \Omega^{-1}\ m^{-1}$. Les résistances au mouvement pour les deux couches d'acides nucléiques présentent dans les deux cas un comportement réversible alors que le senseur MCE avec des électrodes de PdO ou de Au nues ne présentent pratiquement pas de changements. Les modèles qui ne considèrent que les propriétés globales des solutions n'arrivent pas à expliquer les changements observés dans les fréquences. Par ailleurs, un modèle par circuit équivalent incorporant les propriétés rhéologiques des couches d'acide nucléique sur la surface du senseur permet d'expliquer les diverses réponses.

Mots clés : senseur à l'ADN, analyse de réseau, senseur en mode de cisaillement de l'épaisseur, propriétés interfaciales de l'ADN.

[Traduit par la rédaction]

Introduction

Technology associated with DNA hybridization has played a major role in the rapid progress of biological research since Watson and Crick deduced the three-dimensional structure of B DNA in 1953 (1, 2). However, the ^{32}P DNA labelling hybridization procedures that are currently employed have the following disadvantages: the effort required for labelling, the requirement for radiochemical facilities, and the laborious nature of studies of hybridization kinetics. There has been recent strong interest in the direct, real-time detection of hybridization in a biosensor format (3, 4). In the DNA biosensor strategy, a single strand nucleic acid attached to the surface of a transducer device can complex the complementary strand in the solution phase to generate a direct signal. Optical (5, 6), electrochemical (7–10), and acoustic wave (11–22) technologies have been dominant in attempts to develop a so-called DNA biosensor based on DNA hybridization.

With respect to acoustic wave sensors, the first report on the direct detection of nucleic acid interactions was provided by Fawcett et al. (11). A polyadenylic acid (5′) (Poly A) probe was covalently linked to a polymer via the pendent carboxylic acid groups. The resonant frequency for a 9-MHz crystal exhibited a 500 Hz decrease upon hybridization of polyuridylic acid (5′) (Poly U) with complementary Poly A. Since this early work, a number of articles have appeared employing similar procedures, resulting in microgravimetric measurements of nucleic acid based on gas-phase responses (12–14). Gold surfaces of a 9-MHz piezoelectric quartz crystal were

Received January 2, 1996.

H. Su and M. Thompson.[1] Department of Chemistry, University of Toronto, 80 St. George Street, Toronto, ON M5S 1A1, Canada.

[1] Author to whom correspondence may be addressed. Telephone: (416) 978-3575. Fax: (416) 978-8775. E-mail: bgranozi@alchemy.chem.utoronto.ca

pretreated by anodic oxidation followed by activation with γ-aminopropyltriethoxysilane. Sheared single stranded (ss) salmon sperm DNA probe was then electro-blotted onto the silanized surface of crystal electrodes and further immobilized on the surface by UV cross-linking. About 0.8 μg ss DNA was immobilized and hybridized to 0.57 μg cDNA, corresponding to 232 and 165 Hz decreases in resonant frequency for gas-phase measurement, respectively (12). Richards and Bach (13) performed an ingenious DNA hybridization experiment in which amplification of mass was obtained using iron oxide microparticles. These entities, bearing one of the reacting pairs, are attracted to the sensor surface by a magnetic field. Recently, Oyama and co-workers (14) reported that λ-phage DNA can be covalently immobilized onto the gold surface of a TSM sensor and that dissociation and hybridization of immobilized DNA can be monitored by impedance analysis in the gas phase. The occurrence of immobilization and hybridization of DNA were then said to be confirmed by a small decrease of f_{Gmax} (the frequency giving the maximum conductance) and increases of motional resistance. It should be emphasized that these various gas-phase microgravimetric measurements suffer from problems with nonspecific adsorption and highly variable hydration of nucleic acid.

The first in situ liquid-phase measurements involved an acoustic plate mode device, which was developed by Lade and co-workers (15). These authors employed the same carbodiimide activation immobilization procedure as described above. The hybridization of short oligomer dA with surface-bound dT was monitored by the frequency and relative phase changes. However, application-oriented DNA samples were not tested with respect to potential interferences in this work. Secondly, avidin was immobilized onto the surfaces of the gold electrode of a TSM sensor by irreversible absorption and the detection of herpes simplex virus nucleic acid through avidin–biotin interaction was demonstrated (16). A gold electrode was also employed to attach a single strand of DNA to a self-assembled monolayer of 11-mercaptoundecanoic acid (17). Calf thymus DNA was bound to the -COOH functional groups of the self-assembled 11-mercaptoundecanoic acid directed outward to the solution side by the carbodiimide activation reaction. A subsequent experiment also demonstrated direct detection of DNA hybridization (involving a conventional mass-based response). Ten-mer deoxynucleotide having a mercaptopropyl group at the 5′-phosphate end was prepared by the phosphoramidite method and then immobilized onto a gold surface via the SH group (18). However, no evidence was presented to confirm the occurrence of hybridization at the sensor–liquid interface.

We have reported in previous papers the in situ detection of polynucleotide (19) and pPT-2 DNA hybridization (20) at the surface of palladium electrodes sputtered onto underlying gold electrodes of TSM sensors. Hybridization of complementary strands of nucleic acid at the device–liquid interface results in series resonant frequency signals that are significantly higher than expected from the conventional Sauerbrey mass response. This effect was attributed to the perturbation of interfacial viscosity associated with the hybridization process.

A particularly important consideration in the development of an acoustic wave biosensor for DNA hybridization is the nature of TSM behaviour and transduction mechanism in liquid (a summary of theoretical approaches employed previously is given in Table 1; symbols are explained in Table 2). A

Table 1. Liquid phase theories of TSM acousitc wave sensors.[a]

Mathematical model	Authors (Ref.)
[1] $\Delta f_s = \frac{-2f_0^2}{\sqrt{\mu_Q \rho_Q}} \frac{\Delta m}{A}$	Sauerbrey (23)
[2] $\Delta f = -2.26 \times 10^{-6} f_0^{3/2} (\eta_L \rho_L)^{1/2}$	Bruckenstein and Shay (24)
[3] $\Delta f = -f_0^{3/2} \left(\frac{\eta_L \rho_L}{\mu_Q \rho_Q} \right)^{1/2}$	Kanazawa and Gordon (25)
[4] $\frac{\Delta f_s}{f_0} = \frac{\kappa^2}{\pi^2} \frac{\varepsilon_{22}}{\varepsilon_{22} + \varepsilon_L} \frac{\sigma^2}{\sigma^2 + \omega^2 (\varepsilon_{22} + \varepsilon_L)^2}$	Shana and Josse (26)
[5] $\dot{\eta} = \eta_0 \frac{1}{(1 + j\omega\tau)^v}$	Reed et al. (27)
[6] $Z_f = \frac{N\pi}{4\kappa^2 \omega_s C_0} \left(\frac{G\rho_f}{C''_{66} \rho_Q} \right)^{1/2} \times \tanh\left(j\omega T_f \sqrt{\frac{\rho_f}{G}} \right)^{1/2}$	Martin and Frye (28)
[7] $Z(\rho_q, c, e, \eta, \varepsilon, \rho_L, \nu, \alpha, h, A) = \frac{2\psi_0}{j\omega\varepsilon A A_3}$	Kipling and co-workers (29)
[8] $R_m = \frac{A}{\kappa^2} (2\pi f_0 \eta_L \rho_L)^{1/2}$	Muramatsu et al. (30)
[9] $R_m = \frac{\eta_Q}{\mu_Q C_1} \left(\frac{\omega}{\omega_s} \right)^2 + \omega_s \frac{L_1}{N\pi} \left(\frac{2\omega\rho_L \eta_L}{\mu_Q \rho_Q} \right)^{1/2}$	Martin and co-workers (31)

[a]A glossary of the symbols used is given in Table 2.

large number of studies have invoked the well-known Sauerbrey equation where changes in resonant frequency are considered to be proportional to added mass on the device surface (eq. [1], Table 1). However, the acoustic wave sensor is also affected by a number of other interfacial properties when it is being operated in the liquid phase. Recent research has centred on the role played by surface free energy, molecular slip, surface roughness, acoustoelectric coupling, and viscoelasticity. The latter property is expected to be crucial if a film of a macromolecular entity is imposed at the sensor–liquid interface. In this respect, correlation of changes in rheological properties of a polymer with the response of theTSM sensor in liquid has recently been examined (27, 28). It has been proposed that a thin film with viscoelastic properties can be regarded as rigid if $T_f << 1/\delta$, where $1/\delta$ is a constant for acoustic waves propagating through a film of thickness T_f, which is in the range of tens of hundreds of nanometers (32). Moreover, it has been demonstrated that the Langmuir–Blodgett multilayer system, as well as polymer films, with a thickness up to 300 nm can be regarded as rigid (33). However, examples of viscoelastic effects in TSM investigations have also been found. Orata and Buttry (34) showed that polyacrylamide films impregnated with hexokinase give much larger changes in frequency values

Table 2. Glossary of symbols used.

A	piezoelectrically active area of a TSM device
μ_Q	elastic constant of quartz (piezoelectrically stiffened)
C_{66}	stiffened elastic constant of the quartz crystal
C_{66}''	effective complex shear modulus of an AT-cut piezoelectric quartz crystal
C_m	motional capacitance
C_m'	motional capacitance for a uncoated TSM device
C_0	electrostatic capacitance
θ	phase angle of impedance
θ_{max}	maximum phase angle
σ	solution conductivity
σ_d	dissipation coefficient of the quartz crystal
τ	viscous relaxation time characteristic of the fluid
ν	parameter related to the distribution of viscous relaxation time
e	thickness of a quartz plate
ε	piezoelectric stress constant
ε_0	permittivity of free space
ε_l	permittivity of liquid
ε_s	permittivity of quartz
ε_{22}	dielectric constants for a quartz crystal
ε_L	dielectric constants for liquid
f_A	anti-resonant frequency
f_R	resonant frequency when the energy dissipation Rm equals zero
f_s	series resonant frequency
f_p	parallel resonant frequency
f_n	frequency at minimum impedance
f_m	frequency at maximum impedance
$f_{\theta max}$	frequency at maximum phase angle
Δf	series resonant frequency change
f_0	fundamental series resonant frequency of a quartz crystal
G	complex modulus of a polymer film
G'	shear storage modulus of a polymer film
G''	shear loss modulus of a polymer film
κ^2	acoustoelectric coupling constant
L_m	motional inductance
L_m'	motional inductance of an uncoated TSM device
Δm	mass change
n	number of faces of a crystal in contact with a liquid
N	harmonic number ($N = 1$ for fundamental mode)
η_L	bulk viscostiy of the liquid
$\dot{\eta}$	dynamic viscosity
ρ_L	bulk density of a liquid
ρ_Q	density of a quartz crystal
ρ_f	polymer density
Q	quality factor, defined as $\omega L_m/R_m$
r	equal to C_0/C_m
R_m	motional resistance
R_m'	motional resistance of an uncoated TSM device
T_α	DNA primary relaxation temperature, which is associated with motions of DNA chain segments. This relaxation is accompanied by large changes in the modulus and viscosity of a polymer
T_β	relaxation associated with the motions of groups attached to the DNA polymer backbone
T_f	thickness of a polymer immobilized on a TSM sensor surface
ω	angular frequency
$\|Z\|$	magnitude of impedance
R	resistance, the real part of Z
X	reactance, the imaginary part of Z
$\|Z\|_{min}$	minimum magnitude of impedance
$\|Z\|_{max}$	maximum magnitude of imedance
δ	loss tangent of a polymer film
δ_L	decay length of acoustic wave propagation, which is in the range of about 1 μm

than expected when glucose binds to the enzyme in the film. This was attributed to changes in the mechanical properties of the polymer film with a corresponding change in the product of the viscosity and density. The viscoelastic effect was also found in the investigation of polymer-coated acoustic wave devices in the gas phase. Grate et al. (35) demonstrated that the polymer-phase swelling can make a significant contribution to the response of polymer-coated surface acoustic wave vapour sensors. The response to this volume increase operates in the same direction as the gravimetric response, effectively multiplying the sensitivity of the sensor. More recently, Martin and Frye (28) characterized the relatively thick polymer-coated TSM sensor in the gas phase by impedance analysis. An equivalent circuit model was derived that relates the near-resonant electrical characteristics of a polymer-coated TSM sensor to the film properties. A different physical model was also proposed by Reed et al. (27) to describe the viscoelasticity of a TSM sensor in viscous liquid.

The ionic environment of an immobilized polynucleotide chain influences its behaviour. Long-range electrostatic repulsions will extend a DNA/RNA polymer beyond the average dimensions expected for an uncharged macromolecule; this effect will be more prominent at lower ionic strength. This expansion will, in turn, influence other properties of a DNA/RNA polymer, such as viscosity and moduli, at the solid–solution interface. Accordingly, the work described in the present paper is concerned with exposure of bare and nucleic acid coated sensors to solutions of varying conductivity and to different temperatures in order to examine such effects. The responses of the sensor, which are characterized by the acoustic wave network analysis technique, are considered in terms of models that invoke added mass effects, bulk solution properties, acoustoelectric coupling, and rheological parameters.

Experimental

Materials

Double strand calf thymus DNA solution (10 mg mL^{-1}) and polycytidylic acid(5′) (Poly C) were purchased from Sigma (St. Louis, Mo.) and used without further purification. All other reagents were analytical grade, and Millipore water (18.2 MΩ m^{-1}) was used. AT-cut quartz piezoelectric crystals (9 MHz) with gold electrodes were supplied by International Crystal Manufacturing, Co. Oklahoma City, Okla. Palladium was sputtered on the gold electrodes using a Perkin–Elmer Ultek 2400-8SA rf sputtering system. Presputtering was performed for 15 min, then about 50 nm of palladium was deposited on the surface. The formation of a surface PdO layer in an $Ar–O_2$ environment was confirmed by X-ray photoelectron

Fig. 1. Typical plots of the magnitude (|Z|) and phase angle (θ) of impedance of a 9-MHz TSM sensor upon water loading (*a*) and an equivalent electrical circuit (*b*). a: measured phase angle of the impedance; b: simulated phase angle from the equivalent circuit; c: measured magnitude of the impedance; d: simulated impedance from the equivalent circuit.

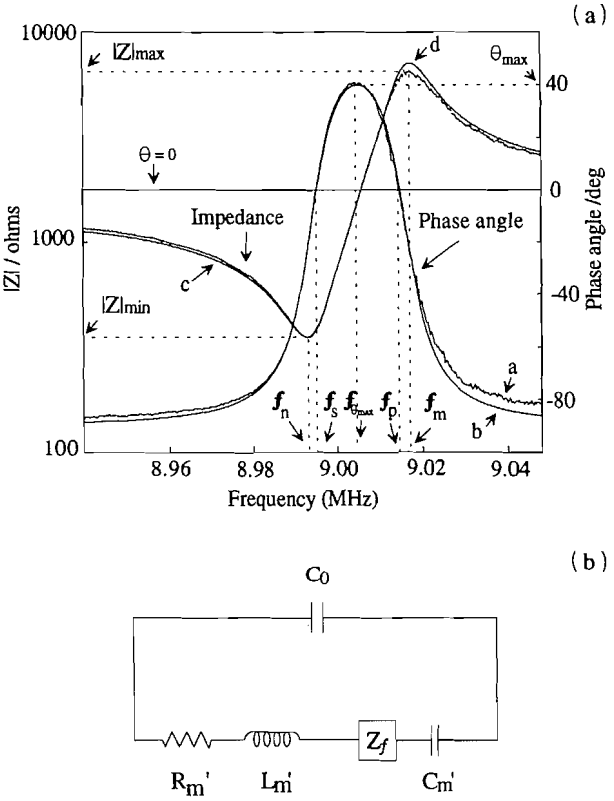

spectroscopy (XPS). The palladium target was obtained from Pure Tech, Inc. of New York.

Apparatus

The instrument used to characterize the TSM devices was an HP4195A Network/Spectrum Analyzer (Hewlett–Packard). An HP4195A impedance kit was used to make direct measurements of impedance as described previously (20). The values of the equivalent circuit elements of the quartz crystal are calculated internally by the HP 4195A from the measured data. All the data were transferred to an IBM compatible computer through an IEEE-488 bus.

Procedures

Denaturation of double strand DNA into single strand calf thymus DNA (ss CT DNA)

A 40 μL sample of double strand DNA solution was denatured by heating for 5 min at boiling water temperature, followed by rapid chilling in ice-water for at least 5 min. The denatured DNA solution was kept in an ice-water bath before using.

Surface immobilization of nucleic acids on TSMs

A 40 μL sample of a single strand calf thymus DNA solution (1 mg mL^{-1}) was placed on the palladium electrodes of the TSM device. The sensor was rinsed copiously with water and immersed in water at 70°C for 320 min, followed by drying with nitrogen gas. Poly C (1 mg mL^{-1}) was immobilized by the same procedure. The immobilization of nucleic acids was confirmed by XPS and the frequency changes before and after treatment. The sensor surfaces coated with nucleic acids exhibited very low advancing water angles (<10°), indicating a very hydrophilic surface.

Acoustic network analysis

Prior to the network analysis measurements, one face of a TSM sensor was exposured to Millipore water while the other was kept under nitrogen gas. The water was then drained off after stabilization and a 0.005 mM KCl sample solution was injected. The steady-state parameters were measured again after incubating for specific periods of time. Similar procedures were employed for higher concentrations of KCl solution. The measurements were also performed at various temperatures. The impedance responses of uncoated TSM devices agree with published results (36). To ensure reproducibility of the DNA/RNA-immobilized TSM performance, the experiments were repeated at least three times, using a new TSM device for each concentration. The conductivities of the various solutions were calculated from the corresponding solution concentrations.

Data fitting

Fits were performed by a program written in MathCad 4.0. This program uses a modified Neadler–Mead Simplex algorithm to minimize the sum of the squares of the differences between the measured and computed magnitudes of the impedance data.

Results and discussion

Acoustic network analysis

Before discussion of the responses of the nucleic acid coated TSM sensors it is necessary to review briefly the parameters yielded by network analysis of equivalent circuit data. The network analysis method is a passive technique that provides direct measurement of a large number of parameters, in addition to the series resonant frequency. The values of the magnitude and phase of the impedance of the quartz crystal can be determined at each frequency from the voltage and current, and electrical quantities can be found from the magnitude of the impedance–frequency curves (Fig. 1). Definitions of the various terms employed in the network analysis method are collected in Table 3.

Motional resistance R_m represents the dissipation of electrical energy in the quartz crystal. The energy is converted to thermal energy, which flows into the liquid environment in contact with the device in the form of an acoustic wave, including internal dissipation, air damping, surface friction, coating viscoelasticity, and mounting losses. The effects of the energy dissipation on the magnitude and phase angle of the impedance are demonstrated in Fig. 2 by assuming other parameters are constant. R_m is increased from 10 Ω to 1 kΩ and the magnitude of impedance and phase angle versus frequency curves is simulated. Increasing R_m causes the damping of both the |Z|–frequency and phase–frequency curves. The broadening and diminishing of the resonance peaks arises from power dissipation due to increasing R_m. An important

Table 3. Summary of the parameters employed in the network analysis method. (A glossary of the symbols used is given in Table 2.)

	Equations	Parameters
[10]	$\boldsymbol{Z} = \boldsymbol{R} + j\boldsymbol{X}$	Impedance, $\boldsymbol{Z}$ ($\boldsymbol{R}$ and $\boldsymbol{X}$ are resistance and reactance, respectively)
[11]	$\|\boldsymbol{Z}\| = \sqrt{(\boldsymbol{R}^2 + \boldsymbol{X}^2)}$	Magnitude of impedance of quartz, $\|\boldsymbol{Z}\|$
[12]	$\theta = \tan^{-1}(\boldsymbol{X}/\boldsymbol{R})$	Phase angle of impedance, θ
[13]	$f_S = f_S[1 + r/(2Q^2)]$	Series resonanct frequency, f_s
[14]	$f_P = f_R[1 + 1/(2r) - r/(2Q^2)]$	Parallel resonant frequency, f_p
[15]	$f_R = 1/[2\pi\sqrt{L_m C_m}]$	Resonant frequency, f_R
[16]	$f_A = \sqrt{1/(L_m C_m) + 1/(L_m C_0)}/(2\pi)$	Antiresonant frequency, f_A
[17]	$f_n = f_R[1 - r/(2Q^2)]$	Frequency at minimum $\|Z\|$, f_n
[18]	$f_m = f_R[1 + 1/(2r) + r/(2Q^2)]$	Frequency at maximum $\|Z\|$, f_m
[19]	$R_m = e^3\sigma_d/(8A\varepsilon^2)$	Motional resistance R_m for an unperturbed quartz crystal
[20]	$C_m = 8A\varepsilon^2/(\pi^2 e\mu_Q)$	Motional capacitance C_m for an unperturbed quartz crystal
[21]	$C_0 = k\varepsilon_0 A/e$	Electrostatic capacitance C_0

Fig. 2. Effect of the motional resistance R_m on the magnitude and phase of the impedance of a TSM sensor. 1: 10 Ω; 2: 100 Ω; 3: 300 Ω; 4: 600 Ω; 5: 800 Ω; 6: 1000 Ω.

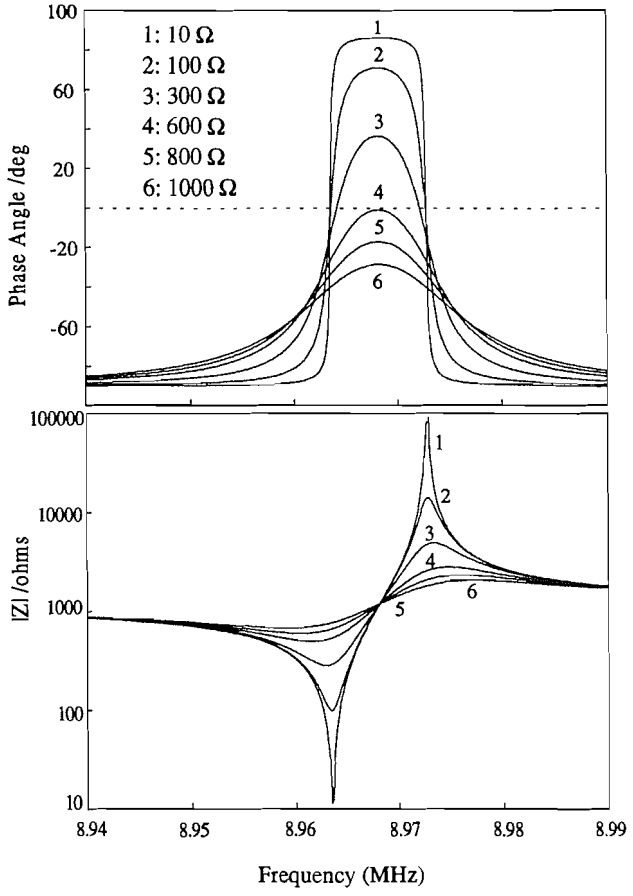

Fig. 3. Effect of the motional resistance R_m on the characteristic frequencies of a TSM sensor. The series and parallel resonant frequencies cease to exist when the maximum phase angle is below zero.

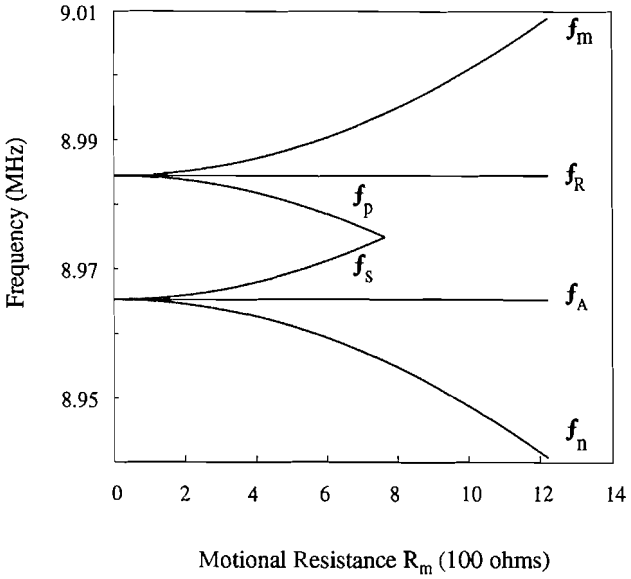

phenomenon is that when R_m reaches a certain value, as in the case where R_m = 800 Ω, the maximum phase angle becomes negative. The consequence is that the frequencies at zero phase angle, f_s and f_p, no longer exist. However, several other quantities can still be measured from the network analysis to describe the behaviour of the quartz resonator under these extreme conditions, including other characteristic frequencies. The effect of the motional resistance on the characteristic frequencies is shown in Fig. 3. With increasing R_m, the series res-

Fig. 4. Effect of the motional inductance L_m on the phase and magnitude of the impedance of a TSM sensor.

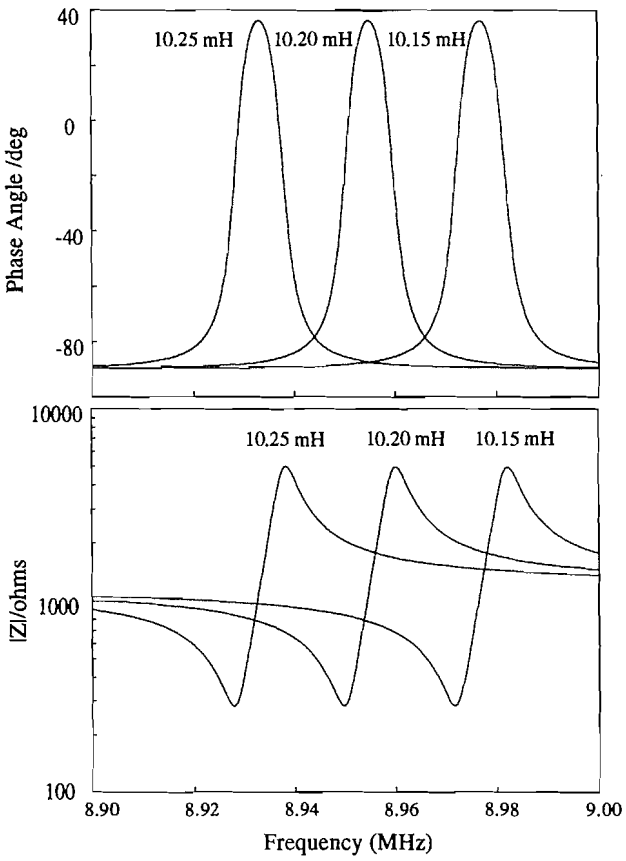

Fig. 5. Effect of the motional capacitance C_m on the phase and magnitude of the impedance of a TSM sensor.

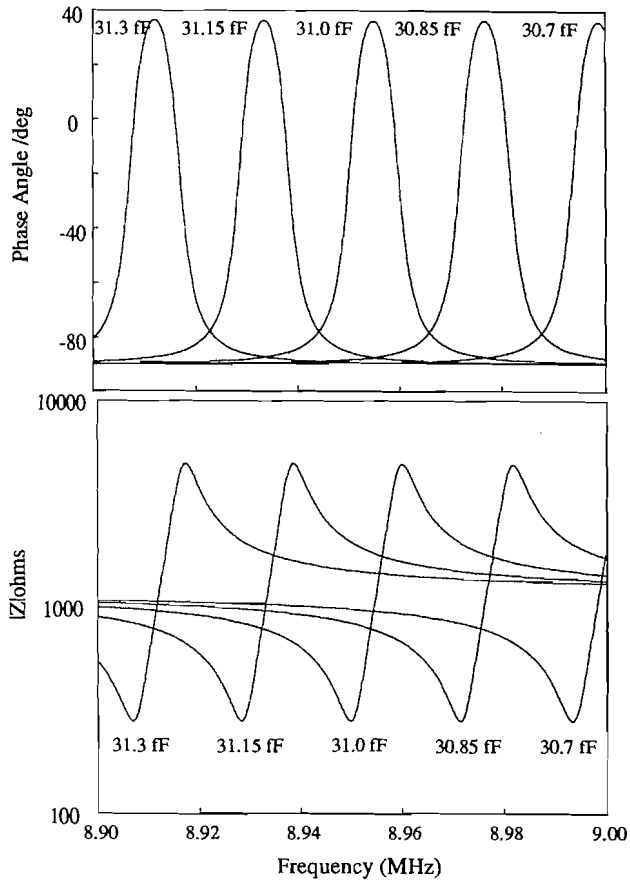

onant frequency and the parallel resonant frequency converge and eventually coincide. On the other hand, with increasing R_m the difference between f_m and f_n increases, reflecting the broadening of the resonance peak. Both f_m and f_n are strongly influenced by R_m and they always exist regardless of the value of R_m. Figure 3 indicates that the series resonant frequency f_s should increase almost linearly 10 kHz as R_m increases from 10 to 800 Ω. However, theoretical and experimental results have shown that f_s should decrease and R_m should increase with $(\rho_L\eta_L)^{1/2}$, as described by eqs. [3] and [9] (Table 1). This kind of discrepancy shows that further theoretical work should be undertaken to relate both series resonant frequency and motional resistance changes to liquid phase properties.

In the solution phase the motional inductance L_m represents the kinetic energy transfer between the TSM resonator and the conducting solution. The efficiency of the interaction depends on the coupling between the shear plane and the solution layer adjacent to the solid. Figure 4 shows the theoretical calculation of the magnitude of the impedance (bottom) and phase (top) as functions of frequency at various L_m. Although it has little effect on the shapes of |Z|–frequency and θ–frequency curves, L_m shifts them down to low frequency. C_m represents the elasticity of the quartz crystal, which corresponds to lattice-restoring forces. The effect of the motional capacitance on the magnitude of impedance and phase vs. frequency curves is illustrated in Fig. 5. Increasing C_m causes the upward movement of both |Z|–frequency and θ–frequency curves, without changing their pattern. In theory, both L_m and C_m have dramatic influences on a uncoated TSM sensor vibrating in a liquid. It would be expected that C_m would become more important when the TSM sensor is in contact with a viscoelastic fluid or a polymer film.

At frequencies far from the resonant frequency, the quartz plate is equivalent to a simple plate capacitor having a capacitance C_0. Figure 6 depicts the calculated results of |Z|–frequency and θ–frequency curves at five different electrostatic capacitances. C_0 is decreased from 25.0 to 10.0 pF and this causes the asymmetric damping of both curves. Furthermore, C_0 dominates the impedance near the condition of parallel resonance and diminishes it near series resonance. Accordingly, the measurement of f_p can be very useful in determining specific properties of the media surrounding the quartz crystal, especially in the case of electrolytes (26). From an equivalent circuit point of view, the formation of an electrical double layer at the TSM electrode – liquid interface can be regarded as an added shunt capacitance in parallel to the sensor. Thus, the measurement of C_0 under conductive solution loading consists of contributions from the quartz substrate as well as from the electrified interface.

Responses of nucleic acid coated sensors in contact with electrolyte

Series resonant frequency (f_s) changes for uncoated and nucleic acid coated resonators in contact with various KCl solutions are shown in Fig. 7(*a*). The changes relative to water are plotted against the solution ion conductivity, σ. The den-

Fig. 6. Effect of the electrostatic capacitance C_0 on the phase and magnitude of the impedance of a TSM sensor.

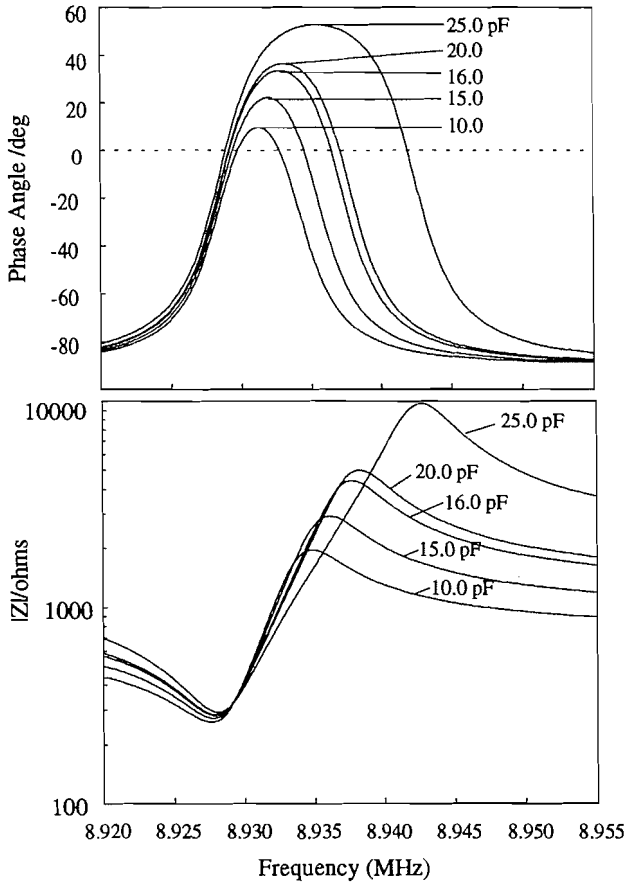

Fig. 7. Responses of the series resonant frequency f_s change (*a*) and the motional resistance R_m (*b*) of TSM sensors with one side in contact with KCl solution.

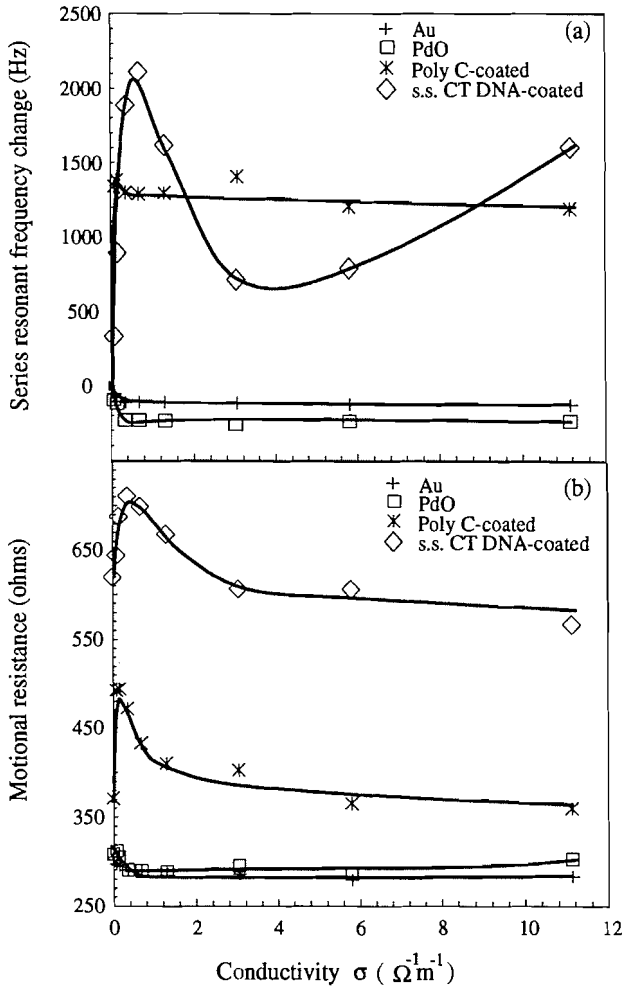

sity and viscosity of the solution are very similar to those of water. Therefore, an increase in ionic concentration does not change the trapped mass component, and thus the series resonant frequency, according to eq. [1] (Table 1). However, the series resonant frequencies of nucleic acid coated TSM sensors did change upon solution loading. Figure 7(*a*) clearly shows that the series resonant frequency responses of nucleic acid coated sensors can be separated into two regions. When $0 < \sigma < 0.5\ \Omega^{-1}\ m^{-1}$ (region I), the series resonant frequencies of ss calf thymus DNA and RNA homopolymer Poly C-coated resonators increase significantly with conductivity by 1400–2100 Hz. In the absence of any nucleic acid coating, however, a decrease of 100–300 Hz was observed, which is attributed to the acoustoelectric coupling effect (36). In region II ($0.5 < \sigma < 12\ \Omega^{-1}\ m^{-1}$), little change in f_s was observed with Poly C coated, bare PdO and Au sensors. However, the frequency response of the ss DNA coated sensor shows a bell-shaped curve with a minimum at $\sigma = 4\ \Omega^{-1}\ m^{-1}$. As mentioned above, motional resistance (R_m) changes will be governed by energy losses arising from propagation of the acoustic wave into the liquid. For solvents not containing electrolyte, it appears that the behaviour of R_m is dominated by the bulk properties of the liquid, expressed as the square root of the density–viscosity product (eq. [9], Table 1). When an electrolyte is involved, acoustoelectric coupling becomes very significant for uncoated TSM sensors. The motional resistance changes obtained for resonators (uncoated and nucleic acid coated) in contact with a series of KCl solutions are plotted against the solution ion conductivity (σ) in Fig. 7(*b*). This clearly shows that the change in R_m for nucleic acid coated sensors can be separated into two regions, in the same way as the changes in series resonant frequency. When $0 < \sigma < 0.5\ \Omega^{-1}\ m^{-1}$ (region I), the R_m of both ss calf thymus DNA and Poly C coated resonators shows significant variation, with a maximum at the same value of conductivity where f_s has the most rapid shift. However, the PdO- and Au-deposited TSM sensors without nucleic acid coatings show a small 20 Ω decrease, which may be caused by energy storage in the electrical double layer (36). In region II ($0.5 < \sigma < 12\ \Omega^{-1}\ m^{-1}$), the motional resistances of both Poly C and ss DNA coated TSM sensors decrease and then return to almost the original points, while the bare PdO and Au TSM sensors show little change.

Figure 8(*a*) shows the responses of the motional inductance of nucleic acid coated and uncoated TSM sensors upon solution loading. L_m decreases up to 15–20% for Au, PdO, and Poly C and 36% for the ss DNA coated sensors. This indicates a change in the decay length of the propagating wave in terms of coupling between the solid and solution. The decay length for a travelling shear wave in a liquid can be written as

Fig. 8. Responses of the motional inductance L_m change (*a*) and motional capacitance C_m (*b*) change of TSM sensors with one side immersed in KCl solutions. $L_m{}^w$ and $C_m{}^w$ are the motional inductance and capacitance upon water loading, respectively.

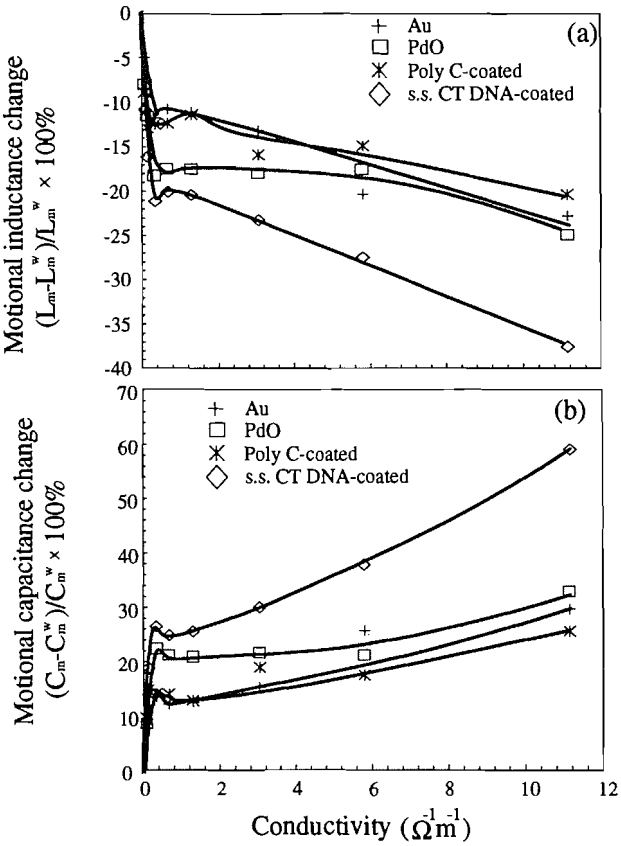

$$[22] \quad \delta_L = \left(\frac{2\eta_L}{\omega\rho_L}\right)^{1/2}$$

For the solution used here, the decay length is ca. 1.0 μm, which is comparable to the length of ss DNA or Poly C molecules. Accordingly, the molecular structure at the solid–solution interface will be critical in determining the coupling of the nucleic acid coated film.

It has been assumed that C_m can be considered a constant under solution loading because a Newtonian liquid does not exhibit any elasticity (37). However, Fig. 8(*b*) shows that C_m does have a 20% increase when the ionic conductivity reaches 10 Ω^{-1} m^{-1} with bare Au and PdO surfaces. This indicates that the KCl solution cannot be treated as a pure Newtonian liquid and the formation of an interfacial liquid structure may change its elastic properties. At the same time, C_m for an ss DNA coated TSM sensor increases 60% and this demonstrates that C_m becomes more important when the TSM sensor is coated with a thin DNA film. Clearly, theoretical (Figs. 4 and 5) and experimental (Fig. 8) results show that the responses of a nucleic acid coated TSM sensor will be significantly altered if C_m and L_m are changed significantly with little mass gain or loss. Accordingly, as mentioned previously, the device not only respond to mass changes at the liquid–solid interface, but to other factors.

The changes in C_0 for solutions of different conductivities

Fig. 9. Responses of the electrostatic capacitance change C_0 (*a*) and parallel resonant frequency f_P change (*b*) of TSM sensors with one side immersed in KCl solutions. $C_0{}^w$ is the electrostatic capacitance upon water loading.

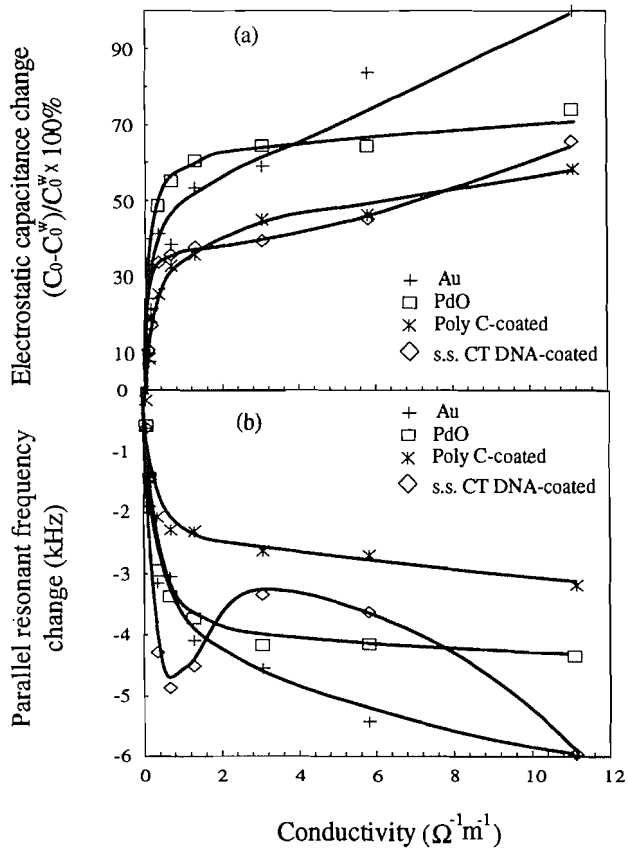

relative to the value for water, $C_0{}^w$, are shown in Fig. 9(*a*). The two distinct regions of C_0 change correspond to the respective Helmholtz–Perrin and Gouy–Chapman capacities of the double layer (37). It is clear that changes in double-layer capacitance result directly in a change in C_0 upon electrolyte solution loading. As shown in Fig. 9(*a*), the responses of C_0 with and without nucleic acid coatings show little difference in their patterns. Accordingly, the shift in electrostatic capacitance is primarily determined by the solution conductivity associated with changes in electrical double layer capacitance.

The shift of the parallel resonant frequency (Δf_p) with the ionic conductivity of the KCl solution is depicted in Fig. 9(*b*). The behaviour of f_p is drastically different from that of f_s: f_p shows a much greater sensitivity towards the conductive properties of the solution with bare PdO and Au TSM sensors. The parallel resonant frequency depends not only on the quartz crystal but also on the associated circuit and all capacitances in parallel with the device (eq. [14], Table 3). The measurement of f_p can be very useful in determining specific properties of the surrounding media such as in the case of electrolytes (26). However, the parallel resonant frequency response of an ss DNA coated TSM sensor shows different behaviour than the uncoated resonator. A dip, which is apparently associated with the changes of motional inductance and capacitance, is observed at a conductivity of 0.5 Ω^{-1} m^{-1} (Fig. 9(*b*)).

Fig. 10. Responses of the series resonant frequency f_s (*a*) and the motional resistance R_m (*b*) changes of TSM sensors as a function of temperature. A: theoretical calculations; B: uncoated TSM sensors; C: ss CT DNA-coated TSM sensors.

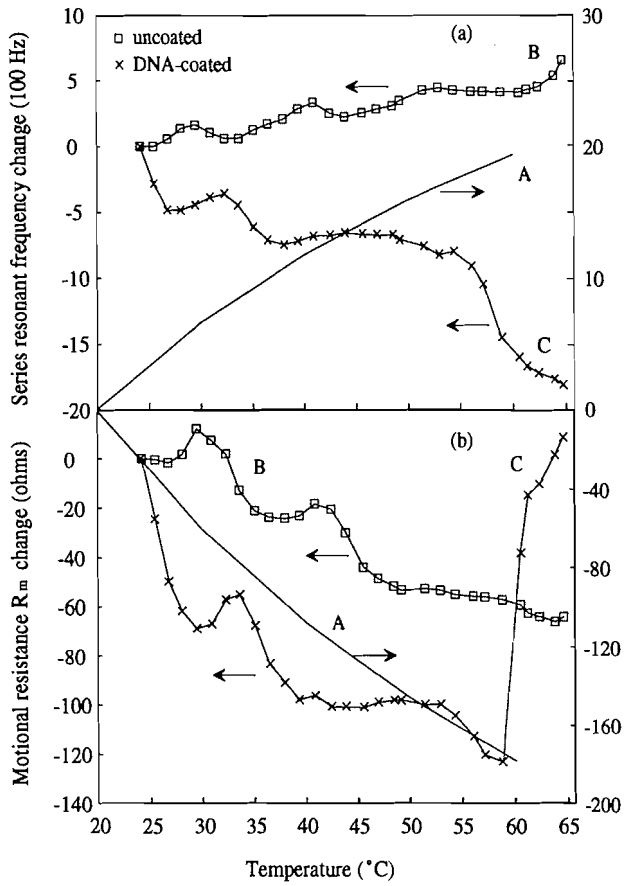

Fig. 11. Derivative of the series resonant frequency f_s (*a*) and the motional resistance R_m (*b*) changes of TSM sensors as a function of temperature. (*c*) The measured motional capacitance C_m of TSM sensors as a function of temperature. □: uncoated TSM sensors; ×: ss CT DNA-coated TSM sensors.

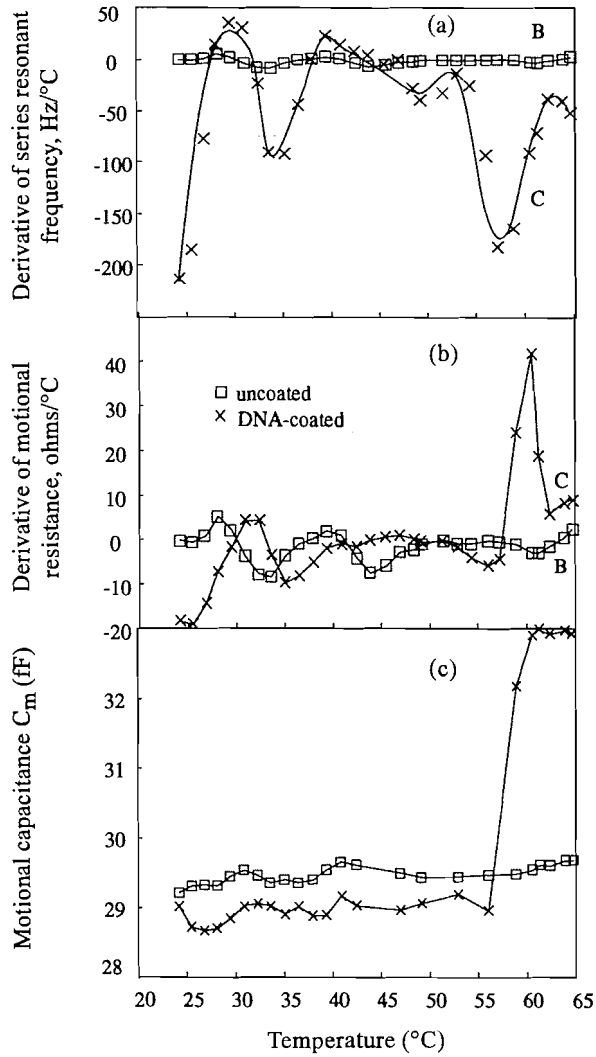

Effect of temperature on the responses of nucleic acid coated sensors

Since the series resonant frequency change of a resonator in liquid depends on ρ, μ, η_L, and ρ_L according to eq. [3] and each of these change with temperature, the frequency must also be temperature dependent. For AT-cut quartz crystals, the dependence of $T_c(-nf_o^{2/3}(1/\mu_Q\rho_Q)^{1/2})$ on temperature, from eq. [3], is (25)

$$[23] \quad T_c = -\frac{T_\rho + T_\mu}{2}$$

where $T_\rho = 36.4 \times 10^{-6}$/°C and $T_\mu = 17.8 \times 10^{-6}$/°C. Thus $T_c = 9.8 \times 10^{-6}$/°C, which is relatively small; therefore T_c (20°C) ≈ T_c (60°C) and the temperature factor in eq. [3] can be considered a constant for quartz crystals oscillating in solution over the temperature range studied. Accordingly, the frequency shift observed as the temperature increases is due to changes in the viscosity and density of water in the surface region.

Figure 10(*a*), curve B, shows that the series resonant frequency change (Δf_s) for an uncoated TSM sensor exhibits about a 700 Hz increase and three unusual peaks at 27°C, 38°C, and 52°C, respectively. The frequency remains constant when the solution is kept at a fixed temperature. The rate of temperature increase was very low and did not have a large effect on the frequency change curves. Shifts of only about several hertz were observed and the peak positions were the same. This means that the effect causing these three peaks does not constitute a dynamic process. The surface viscosity (16) and density and compressional wave generation (38) have been attributed to these observed frequency changes. Similar phenomena have also been observed by other researchers. Normura, Watanabe, and West (39) measured a peak near 23°C as the temperature was varied between 15 and 30°C. Muramatsu et al. (40) also found the Δf value at 25°C for water to be larger than that at 30°C; they explained this as due to the water molecules being more closely associated owing to reduced Brownian motion at 25°C.

It is interesting to note in Fig. 10(*a*), curve C, that the f_s of the DNA-coated TSM resonator *decreases* as the temperature increases, which is in the opposite direction to that of an uncoated TSM sensor (curve B). The results again show that the responses of a DNA-coated TSM sensor are not only a function of the properties of the solution contacting the quartz plate, but also of the DNA film. The derivatives of the series resonant frequency as a function of temperature are shown in Fig. 11(*a*). Two large peaks are observed and the correspond-

ing peak temperatures are assigned to the relaxation temperatures. Accordingly, as the temperature increases, the DNA polymer passes through the relaxation temperatures, T_β = 36°C and T_α = 58°C, respectively. α-Relaxation may be referred to as the primary relaxation associated with the motion of DNA chain segments. Relaxation associated with the motions of groups attached to the DNA polymer backbone may occur at temperatures below T_α and is referred to as β-relaxation. The α-relaxation is accompanied by large changes in the modulus and viscosity of a polymer.

The motional resistance R_m can be also calculated from eq. [9]. Figure 10(*b*) (curve A) shows that the theoretically calculated R_m decreases almost linearly with temperature from 580 to 382 Ω as the temperature is varied between 20 and 60°C. This does not follow the results obtained experimentally, as shown in Fig. 10(*b*), curve B. Curve B also shows three peaks corresponding to those for the series resonant frequency. This is reasonable since both R_m and Δf_s are related to the viscosity and density of the solution. For the uncoated TSM sensor, the motional resistance (R_m) change follows the same trend as that predicted but with different magnitude, in comparison with curves A and B in Fig. 10(*b*). The motional resistance (R_m) curves and their derivatives for DNA-coated TSM sensors are shown in Figs. 10(*b*) and 11(*b*) (curve C), respectively. The motional resistance of a DNA-coated TSM device increases rapidly as the temperature reaches T_α, and its derivative (Fig. 11(*b*), curve C) has two peaks near the α- and β-relaxation temperatures.

As demonstrated above (Fig. 5), the motional capacitance C_m, upon loading with electrolyte, becomes more important when the TSM sensor is treated with a thin DNA film. Figure 11(*c*) depicts motional capacitance changes as a function of temperature for the uncoated and DNA-coated TSM sensors. As the temperature rises, there is a small increase in C_m for the uncoated TSM device. For the DNA-coated device, C_m increases rapidly toward T_α and reaches a maximum as the DNA polymer undergoes primary relaxation, indicating a large change of elasticity in the DNA-coated film.

Analysis of sensor responses employing theoretical treatments of TSM behaviour in liquids

Equation [3] (Table 1), developed by Kanazawa, fails to explain the observed TSM signal change in f_s upon conductive solution loading (Fig. 7(*a*)). At 20°C, the viscosity and density values for 0.05 M KCl (ρ = 0.9984, η = 1.0017 cp) and 0.1 M KCl (ρ = 1.0029, η = 0.9996 cp) are very similar to those for water (ρ = 0.9982, η = 1.0020 cp). The series resonant frequency f_s will decrease by only 0.2 and 5 Hz for 0.005 and 0.1 M KCl, respectively. Therefore, the frequency change due to viscosity and density is considered to be negligible in the KCl concentration range employed in this work. Equation [3] also fails to explain the observed change in f_s with temperature (Fig. 10(*a*)). Figure 10(*a*), curve A, shows the series resonant frequency change as a function of temperature, as predicted by eq. [3], without considering the effects of surface viscosity or density, i.e., both of them are the same as the bulk where values of ρ_w and η_w are taken from the literature (41). The frequency shift should increase linearly over about 2000 Hz when the temperature is increased from 20 to 60°C, according to this equation.

The acoustoelectric coupling factor, κ^2, can be obtained by fitting the experimental data (Fig. 7(*a*)) to eq. [4] (Table 1) for sensors with gold and PdO surfaces. The values of κ^2 are 5.4×10^{-3} and 5.2×10^{-3} for gold and PdO surfaces, respectively, indicating that the acoustoelectric interactions are very similar for these two surfaces. Obviously, acoustoelectric coupling (eq. [4]) also fails to explain the responses of nucleic acid coated TSM sensors upon electrolyte solution loading.

The shear vibration of the quartz crystal results in mechanical interactions between the crystal and the nucleic acid film on its surface. The mechanical properties of the DNA/RNA films therefore influence the mechanical properties of the resonator, which results in corresponding changes in the electrical properties of the TSM sensor. When a periodic stress at a particular frequency range is applied to a polymer, periodic strains are induced. If the DNA polymer is above its glass transition temperature, T_g, the strains relax by thermal motion at a rate that is characteristic of the polymer and the temperature. If the characteristic relaxation time is much shorter than the period between stresses, the measured modulus is that of a soft material. If the periodic stresses occur faster than the material can relax, then the measured modulus will be that of a stiff glass.

It is well known that DNA macromolecules undergo viscoelastic changes in solution with increase in ionic conductivity (42). If a single DNA molecule is placed in a "thermodynamically good" solvent, such as water, the DNA segments and water molecules are attracted to one another and the average coil dimensions tend to increase in order to maximize the number of interactions between DNA polymer segments and water molecules. DNA also contains charged groups along the backbone, so additional effects may come into play as well. In pure water, a DNA polymer containing charged groups will tend to extend in order to minimize the repulsion between them. If a simple electrolyte such as KCl is dissolved in the water, the ions of opposite charge to those carried by the DNA polymer can neutralize its charge. Thus, as the ionic strength is increased, the polymer returns to its coiled shape. Accordingly, DNA films will swell greatly in pure water or in electrolyte solutions of low ionic strength; at high electrolyte concentrations, they will shrink. In summary, the structure of DNA is highly dependent on its hydration sheath, and the secondary and tertiary structures are, in part, dependent on the presence of cations in solution to screen the negative charge of the phosphate groups.

The series resonant frequency responses (Fig. 7(*a*)) can therefore be correlated with changes in DNA viscoelasticity upon KCl solution loading. When the ionic conductivity is less than 0.5 Ω^{-1} m^{-1} (region I), the Debye–Hückel screening length is greater than the effective contour distance between charges. Therefore, the charges begin to interact with each other and a stiffening of the chain is expected as σ increases. The series resonant frequency will therefore increase upon the expansion and stiffening of the DNA molecules. At ionic strength greater than 0.5 Ω^{-1} m^{-1} (region II), the Debye–Hückel screening length is less than the effective contour distance between charges on the DNA phosphate backbone after counterion condensation. The charges are therefore effectively screened from one another and so the DNA molecules shrink, resulting in a gradual decrease in f_s. The reason for f_s increasing again at very high ionic conductivity is not clear at the present time, but could be due to motional capacitance and

inductance changes. Furthermore, since the measurements extend only to 1 M KCl solution, the possibility exists that some structural changes may occur in DNA at higher salt concentrations.

The analysis described above provides only a qualitative explanation for the series resonant frequency change for the DNA-coated TSM sensor reported in Fig. 7(*a*). A quantitative analysis, as described below, can be obtained using the equivalent circuit model developed by Martin and Frye (28).

When a TSM sensor is in contact with a viscoelastic fluid or polymer film, the corresponding equivalent circuit can be modified as shown in Fig. 1, where Z_f represents the impedance of the viscoelastic film (eq. [6], Table 1). By fitting the impedance **Z** using eq. [24], the unique storage and loss moduli, G' and G'', can be extracted.

$$[24] \quad \mathbf{Z} = R'_m + j\omega L'_m + \frac{1}{j\omega C'_m} + Z_f$$

The corresponding dynamic viscosity can then be obtained from the following equation:

$$[25] \quad \dot{\eta} = \eta' + j\eta'' \equiv \frac{G''}{\omega} + \frac{jG'}{\omega}$$

As a specific model for this frequency dependence, a three-parameter model recently studied by DeKee et al. (43) is used. The dynamic viscosity $\dot{\eta}$ can be written according to eq. [26].

$$[26] \quad \dot{\eta} = \frac{\eta_0}{(1 + j\omega\tau)^{\nu}}$$

This three-parameter model has the advantage that values for two of these three parameters (τ and ν) can be obtained by fitting the data to eq. [26], while the third (η_0) can be obtained from published data for the liquids used here (27).

Very important information on the mechanical properties and nature of polymeric systems in a fluid state can be extracted by this dynamic method of investigation, in which polymers are subjected to cyclic deformation. In dynamic measurements, the energy stored in a polymer is determined. A measure of this energy is the storage modulus of elastic deformation G'. At the same time, the resistance of a polymer to deformation is determined from the dissipation of energy, i.e., conversion of a part of the work of deformation into heat in every cycle. This resistance of a body to deformation is characterized by the loss modulus G''. The ratio G''/G' is known as the mechanical loss tangent, δ, since it is the dissipative losses in each cycle that result in a phase shift of the deformation to the applied stress: as δ increases, the losses become greater.

The total impedance **Z** of a nucleic acid viscoelastic film on a TSM sensor is a function of nucleic acid film thickness, shear modulus and density, and the properties of the liquid contacting the quartz plate. Impedance vs. frequency measurements made for three solution conductivities on the DNA-coated TSM device are shown in Fig. 12. The points are measured directly from the network analyzer and solid lines are calculated from the equivalent circuit model using the best-fit values of G' and G'' from eq. [24] to determine **Z**, along with the

Fig. 12. Magnitude (*a*) and phase (*b*) of impedances measured (points) and calculated from the equivalent circuit model (lines) for a ss CT DNA-coated TSM sensor at three solution conductivities. A: 0; B: 0.14 Ω^{-1} m^{-1}; C: 5.8 Ω^{-1} m^{-1}.

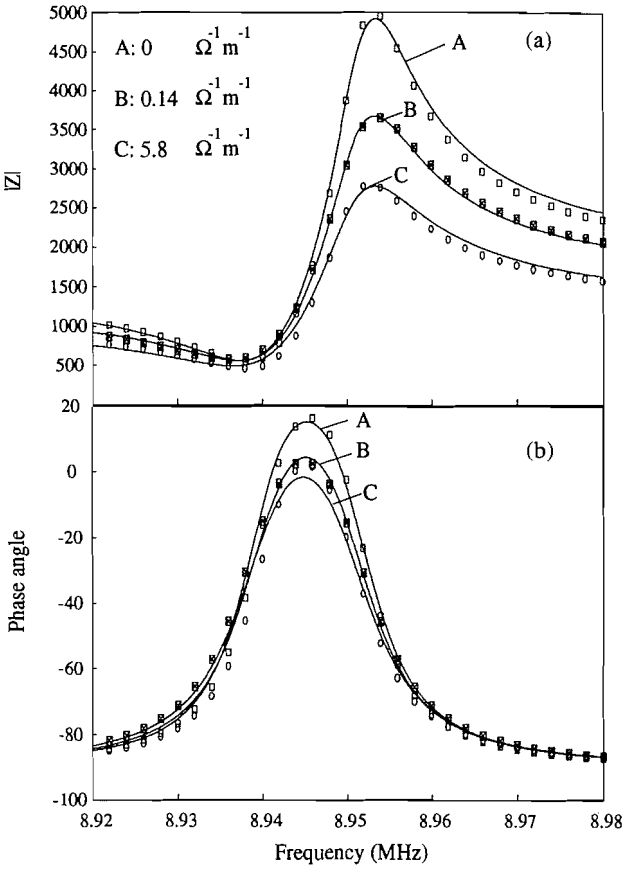

circuit elements determined from the measurements of the uncoated TSM devices. Figure 12 also shows that eq. [24] provides a good fit to each data set (lines), determining a unique combination of G' and G'' for each. It can be noted from Fig. 12 that as solution conductivity increases, the maximum phase angle and $|\mathbf{Z}|$ diminishes, i.e., the resonance is increasingly damped. However, the series resonance frequency does not change monotonically with the solution conductivity.

Figure 13 shows the impedance vs. characteristic frequency measured at three different temperatures (points) with the best-fit data calculated according to eq. [24] (solid lines). A good fit is defined for each data set. Note that increasing temperature causes less damping of both the magnitude–frequency and phase–frequency curves. This results in a decrease in the magnitude of the maximum impedance $|\mathbf{Z}|_{max}$ and the maximum phase angle, θ_{max}. The broadening and diminishing of the parallel resonance peaks arises from power dissipation as modelled by increasing R_m values.

This model can be used to interpret the experimental results obtained for conductive solution loading and temperature change (Figs. 7 and 10). According to eq. [6] (Table 1), the impedance Z_f of a DNA/RNA viscoelastic film on a TSM sensor is a function of device frequency, film thickness, polymer shear modulus, and density. The series resonant frequency response of DNA/RNA-coated TSM devices upon electrolyte solution loading is a complex function affected by all acoustic

Fig. 13. Magnitude (*a*) and phase (*b*) of the impedance measured (points) and calculated from the equivalent circuit mode (lines) for a ss CT DNA-coated TSM sensor at a number of temperatures.

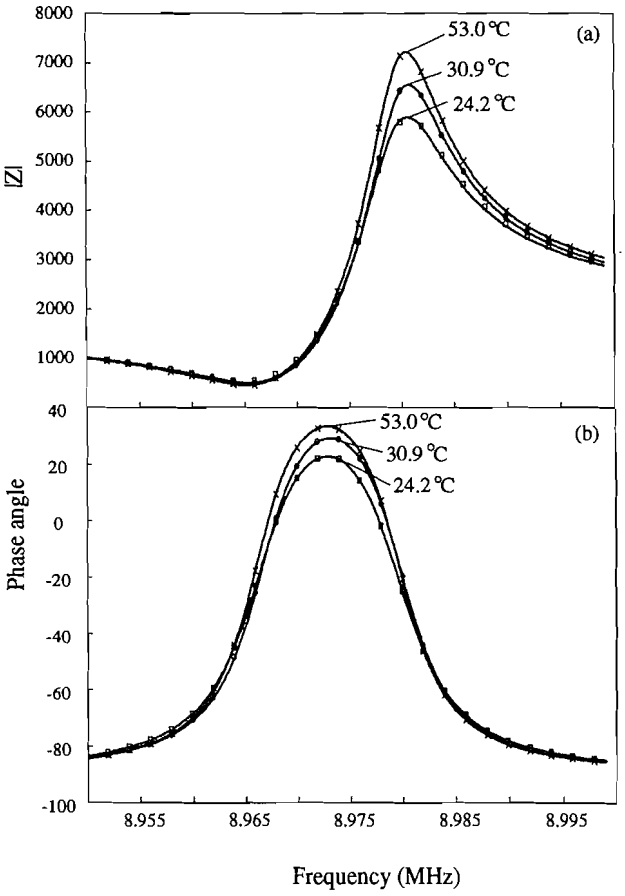

energy transfer and dissipation processes. In water, where the nucleic acid modulus is relatively high and the coil shape of the DNA molecules can be considered as relatively rigid, the entire thickness of the film moves almost synchronously with the device surface in the electrolyte solution. As the ionic conductivity increases, the charges begin to interact with each other, resulting in the expansion and stiffening of the chain. Thus, an increase in f_s is predicted as observed (Fig. 7(*a*)). Continuing decreases in modulus with increasing ionic conductivity increase the phase lag and the strain in the DNA film. When the DNA film's upper surface lags behind the motion at the nucleic acid – solution interface by $\pi/2$, a condition of dynamic DNA resonance is reached. This effect is observed in Fig. 7(*a*) for both ss DNA and Poly C coated TSM sensors. This dynamic resonance phenomena was first observed by Martin and Frye (28) in a study of relatively thick polymer-coated TSM sensors in the gas phase with changing temperature. At temperatures below that of film resonance, the TSM device frequency decreases with increasing temperature as the polymer expands and the modulus decreases. As film resonance is approached, the frequency drops more steeply. But at film resonance, the frequency suddenly increases to values exceeding the initial frequency.

As the ionic conductivity increases further, DNA molecules begin to shrink and the phase lag cannot be $\pi/2$. Accordingly, the series resonant frequency of the ss DNA coated TSM sensor decreases again. The R_m of a nucleic acid coated TSM sensor in pure water is significantly greater than that of the uncoated device, indicating the existence of energy losses other than those due to acoustoelectric coupling (Fig. 7(*b*), when $\sigma = 0$). The DNA film in the solid state is an insulator and exhibits piezoelectricity (44). However, the extent of hydration (water or relative humidity), coupled with the ionic strength, determines the polymorphic character of a DNA duplex. The first hydration shell of duplex DNA is not very permeable to ions. It consists of about 20 water molecules per nucleotide, on average, and does not form an "icelike" structure. The number of water molecules in the secondary hydration shell is not well defined structurally. It is permeable to ions and has some characteristics of bulk water. DNA molecules try to accommodate the varying activity of surrounding water molecules by conformational change, in order to optimize the balance between water–water, water–DNA, and intra-DNA interactions. DNA carries a cloud of counter- and co-ions with it and hydrated samples are ionic conductors, similar to a polyelectrolyte.

In low-ionic-strength electrolyte solutions or pure water, a DNA film will swell enormously. Thus, the corresponding motional resistance R_m increases (Fig. 7(*b*)), indicating more acoustic energy dissipation into the swollen DNA chain as it moves with the quartz plate. At high electrolyte concentrations, DNA molecules will shrink and the corresponding motional resistance decreases, returning close to the original point. This results in DNA molecules moving more easily with the quartz crystal, involving less dissipation of acoustic energy. Another important consideration will be the conductivity over acoustic wave decay length. The reduction in dissipation of acoustic energy with an increase of conductivity associated with mobile positive counterions has also been observed (45).

Equation [6] (Table 1) shows that the effective DNA film thickness T_f plays an important role in determining the magnitude and phase of the impedance of a TSM device. This model is based on the propagation of the acoustic shear wave at the film–air interface, destructive interference being interpreted as giving rise to greater impedance values. It is not strictly applicable to TSM liquid studies and some researchers believe that the presence of a liquid should only modify the absolute values of |**Z**|, the acoustic wave being only partially propagated at the DNA film–solution interface (46). Figure 14 depicts the changes of the real and imaginary parts (Re(**Z**) and Im(**Z**) of the impedance vs. the effective DNA film thickness for different loss tangents. When $T_f \approx 1700$ Å, the changes of Re(**Z**) and Im(**Z**) are much greater than for other thicknesses at various values of the loss tangent. This thickness corresponds to the establishment of destructive interference of the wave in the film when the phase shift is $\pi/2$, the interference attenuation being the greatest for thinner and less lossy films. The Re(**Z**) and Im(**Z**) peaks from Fig. 14 also broaden and diminish as δ increases when the DNA film thickness is ca. 1700 Å.

The effective thickness of a DNA-coated film at a solid–solution interface cannot be determined directly. Some researchers have used the Sauerbrey equation to estimate this, i.e., measurement of the series resonant frequency in the gas phase before and after DNA immobilization followed by calculation of the thickness based on eq. [1] (Table 1). However,

Fig. 14. The calculated real and imaginary parts of the impedance **Z** vs. DNA effective film thickness for a 9-MHz TSM device. δ is the loss tangent.

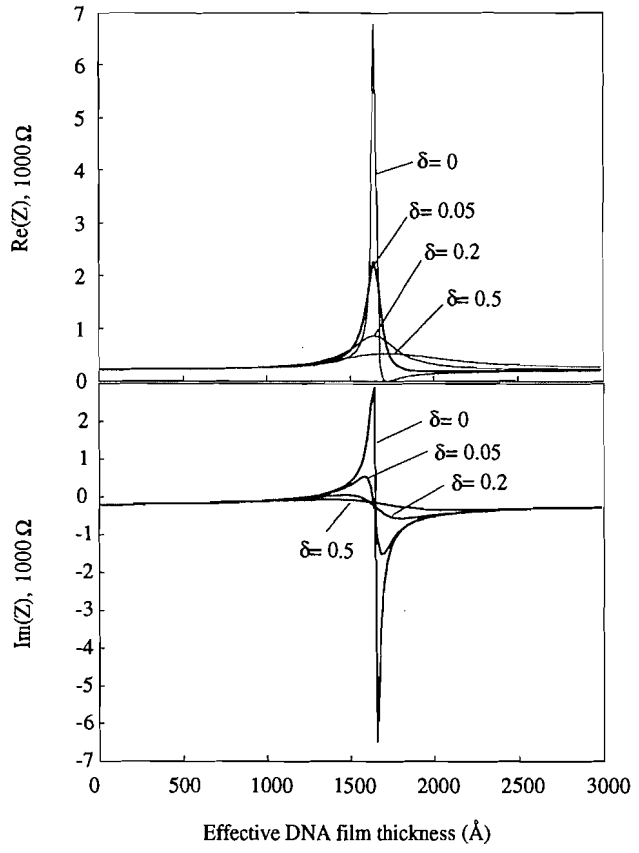

this results in large errors because the coating is assumed to possess the same acoustic properties as that of quartz. As well, the Sauerbrey relationship requires that the deposited film have a uniform thickness across the entire active region of a resonator, whereas the mass sensitivity of the resonator is actually a Gaussian-like distribution (47). Furthermore, the unremoved hydration of DNA will also lead to overestimation of the DNA film thickness. Finally, the DNA film thickness will be changed when the polymer swells upon solution loading.

The coverage of DNA on the surface will also affect the effective film thickness and thus the TSM sensor response. When a surface with low DNA coverage contacts a solution, strong DNA polymer–polymer interactions are replaced by weaker polymer–solvent interactions, and the DNA molecule acts as an isolated chain. The effect of the DNA coating on solvent flow can be predicted on the basis of a simple addition and is the result of inelastic collisions between the Brownian thermal continuum and a polymer chain that obeys Guassian statistics. The connection between the shear viscosity and molecular motion can be described by "normal mode" theories (48). In high-molecular-weight DNA polymers, interactions between elements within the same chain lead to the so-called "excluded-volume" effects. Increasing the DNA surface coverage allows DNA–DNA intermolecular interactions to influence the motion of the DNA polymer. These interactions can be envisaged to be of two types; firstly, because of the relatively close proximity of neighbouring chains, the perturbation of the lamellae flow caused by the polymer has not died down before the next polymer molecule is encountered; and, secondly, the occurrence of intermolecular interactions, which have a similar effect to the intramolecular interactions associated with excluded-volume effects observed for low-surface-coverage regimes. Both effects can be treated theoretically by the interaction of a "hydrodynamic screening" interaction. The moderately covered surface region would be expected to extend from the point where hydrodynamic flow ceases to be lamellar to a point where the DNA polymer completely fills the solution. But this does not lead to a point where the polymer completely fills the surface and effects significant interpenetration of the volume occupied by a neighbouring polymer molecule. At higher concentrations, DNA intercoil contact has been exchanged for dynamic contact as a consequence of coil–coil interpenetration and a pseudo-matrix gel is formed. Gel formation will occur when the time-averaged number of entanglements per chain exceeds a certain value. The probability of chain–chain contacts occurring depends upon the size of the coil and hence on the end-to-end distance for the DNA polymer. Accordingly, the effective DNA film thickness at various solution conductivities employed in the calculation are persistence lengths of DNA macromolecules obtained from the literature (42).

Other important parameters in describing the contribution of a DNA film to the impedance are the storage modulus of elastic deformation, G', and the loss modulus, G'' (or G' and loss tangent δ). The loss tangent has little contribution to the real and imaginary parts of the corresponding impedances for low DNA film thicknesses, and δ becomes dominant as T_f increases. By fitting the **Z** vs. frequency data measured with the DNA-coated TSM device at a number of conductivities, the values of G' and G'' (or δ) were extracted. The typical calculated values of G' and δ were 2×10^5 dyne/cm^2 and 0.02, respectively. Both values are relatively low compared to the DNA modulus in the dry gas phase ($G' = 10^{10}$ dyne/cm^2). The modulus of bulk DNA polymer is a function of the temperature, polymer film properties, and solution components. With DNA biopolymers, a significant change in G' can be obtained by varying the solution composition. G' typically decreases from 10^{10} to 10^7 dynes/cm^2 when the temperature increases from that of glass to rubbery states (44). Although little is known about the viscoelastic properties of a nucleic acid film immobilized on an oscillating TSM sensor surface with solution loading, or for that matter at any interface, it would seem likely that these properties are dynamic and change with the experimental conditions. Nevertheless, the experimental results here demonstrate that the TSM device is sensitive to intrinsic polymer properties. Using a network analyzer to measure admittance as a function of frequency and the equivalent circuit parameters, the DNA polymer elastic shear modulus G' and loss modulus G'' can be extracted.

The loss tangent δ is another important parameter that is dimensionless and conveys no physical magnitude but is a measure of the ratio of energy lost to energy stored in a cyclic deformation. It is a measure of the energy dissipated or lost as heat per cycle of sinusoidal deformation if G' is kept constant. Figure 15(*a*) depicts the loss tangent calculated from the equivalent circuit model vs. solution conductivity. This shows that δ decreases as conductivity increases and approaches a constant value at high conductivity. At low conductivity, the

Fig. 15. The calculated loss tangent δ (*a*) and viscous relaxation time τ (*b*) of TSM sensors with one side immersed in KCl solutions.

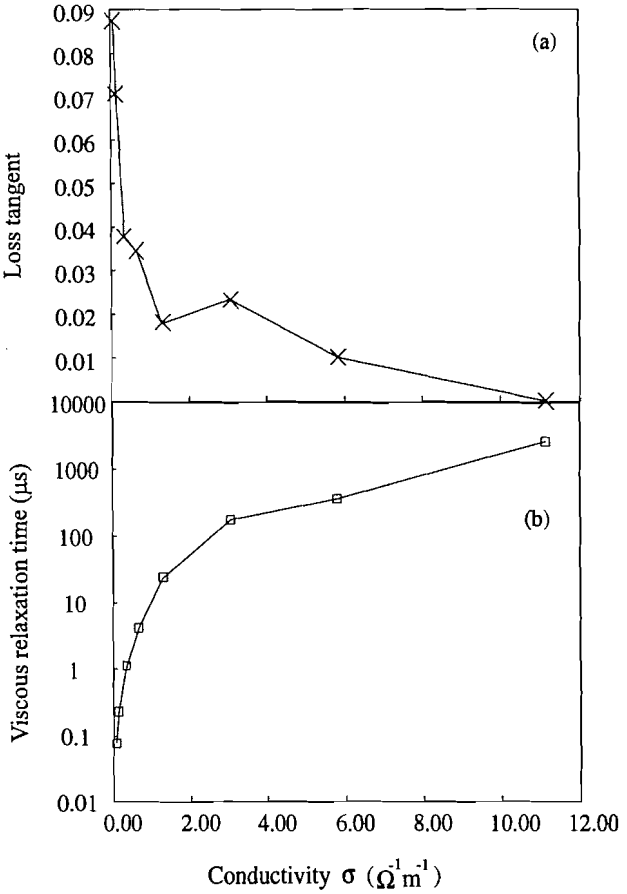

behaviour of DNA-immobilized molecules can be modelled by long thin rigid rods with dominant hydrodynamic interactions, giving rise to a high loss tangent. When the solution conductivity is raised, the DNA molecules can change to the flexible random coil structure with small loss tangent. At the same time, entanglement coupling occurs at high solution conductivity. On a molecular basis, this would correspond to the absence of larger molecular or atomic adjustments capable of dissipating energy within the period of deformation.

Figure 15(*b*) shows the calculated viscous relaxation time τ vs. solution conductivity, while the ν is in the range of 0.2–0.3 for all of the solutions studied. When the solution conductivity is not high enough (τ is large) or the period of application of the field is too short (high frequency), i.e., $\tau\omega >> 1$, the orientation moment will not have time to develop and the DNA polyions cannot redistribute fast enough to screen the field. When $\tau\omega << 1$, the orientation moment is fully established at each instant and reaches its maximum static value. On the other hand, for a DNA-coated TSM device upon conductive solution loading, the ionic species at the solid–solution interface can redistribute rapidly in response to an applied surface potential. The formation of an electrical double layer at the solid–solution interface may block the field from penetrating into the bulk solution.

Finally, it should be noted that eq. [24] does not take into account the surface morphology of the quartz crystal, the size of its pores compared to the acoustic wave length, etc. Also, when the "nonslip" condition, a basic assumption in all theories available, is not found to hold, one also expects changes in impedance **Z** to occur. The first detailed study of molecular slip at the solid–liquid interface of an AT-cut TSM sensor was recently reported by Kipling and co-workers (29). A new quantity, called the interfacial slip parameter, is introduced in one of the boundary conditions of the theory of a two-layer model of the TSM sensor in liquid. The interfacial slip parameter is a complex-valued quantity, defined as the displacement of a particle of liquid in contact with the sensor surface divided by the displacement of a particle on the surface of the sensor. The theoretical expression for the impedance of the TSM sensor is derived in terms of the interfacial slip parameter.

The water-advancing contact angles of both ss DNA and Poly C immobilized on TSM sensor surfaces are less than 10°, thus both surfaces are very hydrophilic and are completely wetted by the solutions. Therefore, the propagation of the shear wave into the solution is considered to be continuous. Accordingly, the interfacial free energy change and slippage between the solid–solution molecules have minimal effect on TSM sensor response under these conditions.

Acknowledgements

We are grateful to the Natural Sciences and Engineering Research Council of Canada and the Department of National Defence of Canada for support of this work.

References

1. J.D. Watson and F.H.C. Crick. Nature, **171**, 737 (1953).
2. E.J. Richards. *In* Current protocols in molecular biology. Vol. 1. *Edited* by F.M. Ausubel, R. Brent, R.E. Kingston, D.D. Moore, G.G. Sedman, J.A. Smith, and K.S. Struhl. Green Publishing Co. and John Wiley and Sons, Inc., New York. 1994. pp. 2.0.1–2.13.3.
3. M.E.A. Downs, S. Kobayashi, and I. Karube. Anal. Lett. **20**, 1897 (1987).
4. M.E.A. Downs. Biochem. Soc. Trans. **19**, 39 (1991).
5. (*a*) C.F. Mandenius, A. Chollet, M.M. Lenburg, and I. Lundström. Anal. Lett. **22**, 2961 (1989); (*b*) D. Pollard-Knight, D. Hawkins, D. Yenng, and D.P. Pashby. Ann. Biol. Clin. **1**, 692 (1990).
6. (*a*) P.A.E. Piunno. M.Sc. Thesis, University of Toronto, 1994; (*b*) P.A.E. Piunno, U.J. Krull, R.H.E. Hudson, M.J. Damha, and H. Cohen. Anal. Chim. Acta, **288**, 205 (1994).
7. K.M. Millan and S.R. Mikkelsen. Anal. Chem. **65**, 2317 (1993).
8. K.M. Millan, A. Saraullo, and S.R. Mikkelsen. Anal. Chem. **66**, 2943 (1994).
9. (*a*) K. Hashimoto, K. Ito, and Y. Ishimori. Anal. Chim. Acta, **286**, 219 (1994); (*b*) Anal. Chem. **66**, 3830 (1994).
10. X.H. Xu and A.J. Bard. J. Am. Chem. Soc. **117**, 2627 (1995).
11. N.C. Fawcett, J.A. Evans, L-C. Chen, and N. Flowers. Anal. Lett. **21**, 1099 (1988).
12. T.-Z Wu, H-H. Wang, and L.-C. Au. Chin. J. Microbiol. Immunol. (Taipei), **23**, 147 (1990).
13. J.C. Richards and D.T. Bach. Eur. Pat. 0295 965 (1988).
14. S. Yamaguchi, T. Shimomura, T. Tatsuma, and N. Oyama. Anal. Chem. **65**, 1925 (1993).
15. J.C. Andle, J.F. Vetelino, M.W. Lade, and D.J. McAllister. Sens. Actuators, B: **8**, 191 (1992).
16. R.C. Ebersole, J.A. Miller, J.R. Moran, and M.D. Ward. J. Am. Chem. Soc. **112**, 3239 (1990).
17. H. Su. M.Sc. Thesis, University of Toronto, 1991.
18. Y. Okahata, Y. Matsunobu, I. Kunihara, M. Masayuki, A. Murukami, and K. Makino. J. Am. Chem. Soc. **114**, 8299 (1992).

19. H. Su, M. Yang, K.M.R. Kallury, and M. Thompson. Analyst. **118**, 309 (1993).
20. H. Su, K.M.R. Kallury, M. Thompson, and A. Roach. Anal. Chem. **66**, 769 (1994).
21. H. Su and M. Thompson. Biosens. Bioelectron. **10**, 329 (1995).
22. H. Su. Ph.D. Thesis, University of Toronto, 1995.
23. G.Z. Sauerbrey. Z. Phys. **155**, 206 (1959).
24. S. Bruckenstein and M. Shay. Electrochim. Acta, **30**, 1295 (1985).
25. K.K. Kanazawa and J. Gordon. Anal. Chim. Acta, **175**, 99 (1985).
26. Z.A. Shana and F. Josse. Anal. Chem. **66**, 1955 (1994).
27. C.E. Reed, K.K. Kanazawa, and J.H. Kaufman. J. Appl. Phys. **68**, 1993 (1990).
28. (*a*) S.J. Martin and G.C. Frye. Proc. IEEE Ultrason. Symp. 393 (1991); (*b*) IEEE Proc. 1992 Solid State Sensor and Actuator Workshop, New York. 1992. p. 27.
29. F. Ferrante, A.L. Kipling, and M. Thompson. J. Appl. Phys. **76**, 3448 (1994).
30. H. Muramatsu, E. Tamiya, and I. Karube. Anal. Chem. **60**, 2141 (1988).
31. J.W. Grate, S.J. Martin, and R.M. White. Anal. Chem. **65**, 987A (1993).
32. W. Hingsberg, C. Wilson, and K.K. Kanazawa. J. Electrochem. Soc. **133**, 1448 (1986).
33. R.R. McCaffrey, S. Bruchenstein, and P.N. Prassad. Langmuir, **2**, 228 (1986).
34. O. Orata and D. Buttry. J. Am. Chem. Soc. **109**, 3584 (1987)
35. J.W. Grate, M. Klusty, R.A. McGill, M.H. Abraham, G. Whiting, and J. Andonian-Haftvan. Anal. Chem. **64**, 610 (1992)
36. M. Yang and M. Thompson. Anal. Chem. **65**, 3591 (1993)
37. M. Yang. Ph.D. Thesis, University of Toronto, 1993.
38. L. Tessier, F. Patat, N. Schmitt, G. Feuillard, and M. Thompson. Anal. Chem. **66**, 3569 (1994)
39. T. Nomura, M. Watanabe, and T.S. West. Anal. Chim. Acta, **175**, 107 (1985).
40. H. Muramatsu, E. Tamiya, and I. Karube. Anal. Chem. **60**, 2141 (1988).
41. D.R. Lide (*Editor*). Handbook of chemistry and physics. 73rd ed., CRC Press, Inc., Boca Raton, Fla. 1992.
42. G.S. Manning. Q. Rev. Biophys. **11**, 179 (1978).
43. D. Dekee, J. Stastna, and M.B. Powley. J. Non-Newtonian Fluid Mech. **26**, 149 (1987).
44. Z. Yi and Z. Shuhui, Ferroelectrics. **101**, 129 (1990).
45. H. Su, P. Williams, and M. Thompson. Anal. Chem. **67**, 1010 (1995).
46. M.A.M. Noël and P.A. Topart. Anal. Chem. **66**, 484 (1994).
47. M.D. Ward and E.J. Delawski. Anal. Chem. **63**, 886 (1991).
48. J.D. Ferry. Viscoelastic properties of polymers. John Wiley & Sons, New York. 1980.

Cd(II) complexes with phthalic acid: solution study and crystal structure of cadmium(II) phthalate hydrate

José Luis Lucas Vaz, Gérard Duc, Michelle Petit-Ramel, René Faure, and Olivier Vittori

Abstract: The acid–base properties of phthalic acid (H_2L) have been determined by simultaneous spectroscopic, potentiometric, and polarographic measurements. Stability constants of the complexes $CdHL^+$, CdL, CdL_2^{2-}, CdL_3^{4-}, $CdH_{-2}L_2^{4-}$ and their distribution versus pH were determined at 25°C and ionic strength in 0.1 M $NaNO_3$. The advantages of each method are pointed out in such a way as to describe more precisely the interactions between cadmium and phthalic acid over a wide range of ligand and metal concentrations. The crystal structure of the [CdL] complex has been established by single-crystal X-ray diffraction. $Cd(C_8H_4O_4)\cdot H_2O$ is orthorhombic, space group *Pbca*, $a = 23.463(5)$, $b = 9.293(2)$, $c = 7.730(1)$ Å, $Z = 8$, and $\rho = 2.323$ g cm^{-3}. The structure was refined to a final R value of 0.054 for 3231 unique reflections with $I > 3\sigma(I)$. The crystal is a three-dimensional polymeric network in which the Cd atom is seven-coordinated. The first ligand coordinates in a bidentate carboxylate (O,O′) mode (Cd—O = 2.372(5) and 2.445(5) Å); a second ligand is part of a seven-membered ring formed with its two carboxylate groups (Cd—O = 2.317(5) and 2.341(5) Å); two other phthalic ligands make one coordination bond (Cd—O = 2.255(5) and 2.449(5) Å) while the seventh bond is a water molecule (Cd—O = 2.333(6) Å).

Key words: crystal structure, cadmium complexes, phthalic acid complexes.

Résumé : Les propriétés acido-basiques de l'acide phtalique (H_2L) ont été déterminées par des mesures conjointes de spectrométrie, potentiométrie et de polarographie. Elles donnent accès aux constantes de stabilité des complexes $CdHL^+$, CdL, CdL_2^{2-}, CdL_3^{4-}, $CdH_{-2}L_2^{4-}$, ainsi qu'à leur distribution en fonction du pH à 25°C et pour une force ionique de 0,1 M $NaNO_3$. Les avantages de chaque méthode sont discutés pour cerner les interactions entre le cadmium et l'acide phtalique dans une large gamme de concentrations de ligand et de métal. La structure du complexe [CdL] a été établie par diffraction X. Le composé isolé, de formule $Cd(C_8H_4O_4),H_2O$, cristallise dans le système orthorhombique, groupe *Pbca*, avec $a = 23,463(5)$, $b = 9,293(2)$, $c = 7,730(1)$ Å, $Z = 8$ et $\rho = 2,323$ g.cm^{-3}. L'indice R final vaut 0,054 pour 3231 mesures indépendantes. Le cristal est un enchaînement polymérique tridimensionnel dans lequel l'atome de cadmium est heptacoordiné. Un premier groupe phtalato assure simultanément deux liaisons au moyen d'un groupe carboxylato bidentate (Cd—O = 2,372(5) et 2,445(5) Å); un deuxième coordinat forme un cycle de chélation à sept chaînons au moyen de ses deux groupes carboxylato (Cd—O = 2,317(5) et 2,341(5) Å); deux autres coordinats assurent chacun une seule liaison (Cd—O = 2,255(5) et 2,449(5) Å); le polyèdre de coordination est complété par une molécule d'eau (Cd—O = 2,333(6) Å).

Mots clés : structure cristalline, complexes du cadmium, complexes de l'acide phtalique.

Introduction

The toxic effects of Cd(II) are well established and documented (1). This ion has been found to induce various pathological effects, such as cardiovascular diseases (2, 3) and cancer. Most of the cadmium ion in eco-biological systems is complexed with biological ligands (4, 5). It has been reported that a large number of phthalate derivatives of cadmium demonstrate diverse pathological effects (6).

Received September 29, 1995.

J.L. Lucas Vaz, G. Duc, M. Petit-Ramel, and R. Faure.[1] Chimie analytique II, LICAS, Université Claude Bernard Lyon I, 43 boulevard du 11 novembre 1918, 69622 Villeurbanne cedex, France.

O. Vittori. Electrochimie analytique, LICAS, Université Claude Bernard Lyon I, 43 boulevard du 11 novembre 1918, 69622 Villeurbanne cedex, France.

[1] Author to whom correspondence may be addressed. Telephone: (33) 72 43 11 53. Fax: (33) 72 44 82 27.

The aim of this work is to evaluate the composition and stability constants using Differential Pulse Polarography (D.P.P) as a complementary method for potentiometric titrations. As an example of the interactions between cadmium and phthalic acid in the solid state, we report here the X-ray crystal analysis of a cadmium phthalate complex.

Experimental

Reagents

Phthalic acid (99.5%) and Cd(II) nitrate were obtained from Merck and used without further purification. In the potentiometric and polarographic measurements CO_2-free deionized water was used as the solvent. All the potentiometric and polarographic measurements were carried out in 0.1 M $NaNO_3$ as background electrolyte. Potentiometric titrations were performed with a 0.2 M NaOH (Prolabo) solution.

Potentiometric and spectrometric determinations

Equilibrium potentiometric determinations of the ligand pro-

tonation constants and the metal binding constants, in molar ligand to metal ratios of 2/1 and 5/1, were carried out by the glass electrode method at 25.0°C, in 0.1 M $NaNO_3$ solution. The potentiometric assembly consists of a double-walled titration cell under continuous flow of nitrogen, a temperature bath at 25.0°C, a glass electrode (Tacussel C18), a reference electrode (calomel), and a 5 mL capacity Tacussel autoburette monitored by a computer.

The pH-meter was calibrated and the electrode assembly standardized with buffer solutions of 0.05 M potassium hydrogen phthalate (pH = 4.005) and disodium tetraborate (pH = 9.196). The electrodes were calibrated (7) in a thermostated cell and the ionic product of the medium ($K_w = 1.649 \times 10^{-14}$) was calculated from an acid–base titration of HNO_3 by NaOH.

Spectrometric measurements for the protonation constants were made with a Varian 634S UV–VIS spectrometer equipped with 1 mm quartz cells at 25.0°C ($I = 0.1$ M $NaNO_3$). On addition of concentrated NaOH in H_2L solutions in the pH range 2–11, three successive forms appear, leading to three bands corresponding to the species H_2L (278 nm), HL^- (280 nm), and L^{2-} (272 nm).

The log K_{011} and log K_{021} values for the equilibria:

$$[1] \quad H^+ + L^{2-} \rightleftharpoons HL^- \qquad (K_{011})$$

$$[2] \quad H^+ + HL^- \rightleftharpoons H_2L \qquad (K_{021})$$

were calculated from the analytical concentration of the ligand and the log[H^+] values using a BASIC program that determines the equilibrium constants and the molar absorption coefficient necessary to calculate the absorbance values that would best fit the experimental absorbance values for a given spectrometric titration.

According to Beer–Lambert law, the absorbance and concentrations of absorbing species are calculated and then log K_{011} and log K_{021} are determined with the previously described procedure (8).

The complex formation between the metal ion M and the ligand L is described by the general equilibrium :

$$[3] \quad pM + qH + rL \rightleftharpoons M_pH_qL_r$$

The stability of the species $M_pH_qL_r$, labelled by the (pqr) parameters that define the number of metal ions, protons, and deprotonated ligands, respectively, is measured by the stoichiometric stability constant :

$$[4] \quad \beta_{pqr} = \frac{[M_pH_qL_r]}{m^p h^q l^r}$$

where m, h, l, are the free concentrations of Cd(II), proton, and phthalato ligand, respectively.

The state of the system is described by the following set of equations :

$$[5] \quad C_L = l + \Sigma r \times \beta_{pqr} \times m^p \times h^q \times l^r$$

$$[6] \quad C_M = m + \Sigma p \times \beta_{pqr} \times m^p \times h^q \times l^r$$

$$[7] \quad C_H = h - oh + \Sigma q \times \beta_{pqr} \times m^p \times h^q \times l^r$$

where C_L, C_M, C_H are the total concentrations of ligand, metal, and proton, respectively, and oh is the free concentration of OH^-. The experimental data: C_H, E (measured glass electrode potentials in mV) were transformed into standardized variables: $\bar{q}$, log h, $\bar{n}$, log l. where $\bar{q}$ is the number of hydrogen ions bound to a ligand anion and $\bar{n}$ the average number of ligand bound per metal ion.

The graphically estimated stability constants from the Bjerrum method (9) are refined with in-house NEWPRO and NEWSI BASIC programs. These programs are based on minimization of the function U related to the difference between calculated and experimental $\bar{q}$ values:

$$[8] \quad U = \Sigma(\bar{q}_{calc} - \bar{q}_{exp})^2$$

The standard deviation of $\bar{q}$ is given by :

$$[9] \quad \sigma^2(\bar{q}) = U_{min}/(n - m)$$

where n is the number of experimental points and m is the number of calculated constants. These calculations are repeated for several complex compositions, and the set of complexes that is really present will give the lowest values of U_{min} and $\sigma^2(\bar{q})$. The potentiometric method has been widely described elsewhere and more details can be found in ref. 10.

Differential pulse polarography

Pulse polarograms were obtained using a Tacussel PRG5 polarograph. The cell was equipped with a dropping mercury electrode a platinum auxiliary electrode, and a saturated calomel reference electrode. All electrochemical experiments were carried out in a thermostated cell under nitrogen atmosphere, at 25°C, pH 7; an ionic strength of 0.1 M was maintained using $NaNO_3$. Reagent-grade chemicals, deionized water, and hexa-distilled mercury were employed in all cases.

The polarographic half-wave potential was determined in a series of solutions containing a constant amount (4×10^{-5} M) of Cd(II) with phthalic acid concentrations ranging from 0 to 4.4×10^{-2} M.

The computation was performed by the conventional Donald–Deford–Hume method (11) using successive extrapolations, modified by Heath and Hefter for the D.P.P. measurements (12).

Because phthalic acid was in large excess with respect to Cd(II) ions, it was assumed that the presence of the metallic ions did not appreciably affect the free ligand concentration.

Preparation of CdL in solid state

To a stirred solution (50 mL) of 5×10^{-3} M phthalic acid (H_2L) and 5×10^{-3} M $Cd(NO_3)_2 \cdot 4H_2O$, concentrated NaOH was added progressively. At pH 7 some H_2L precipitated and was eliminated. The clear solution was evaporated very slowly at room temperature for 2 weeks. Colorless crystals of CdL appeared and were removed carefully from the bulk. Anal. calcd. for Cd $(C_8O_4H_4) \cdot H_2O$: Cd 38.18, C 32.61, O 27.17, H 2.04%; found: Cd 37.40, C 32.75, H 2.08%.

X-ray structure analysis of $Cd(C_8H_4O_2) \cdot H_2O$

The crystallographic data are given in Table 1. A single crystal ($0.40 \times 0.40 \times 0.15$ mm) was mounted on an Enraf–Nonius CAD4 diffractometer using graphite monochromated MoKα

Table 1. Crystallographic data for $CdL \cdot H_2O$.

Formula	$C_8H_6O_5Cd$
Formula weight	294.5
Space group	*Pbca*
a (Å)	23.463(5)
b (Å)	9.293(2)
c (Å)	7.730(2)
V (Å^3)	1685(1)
Z	8
ρ_{calc} (g/cm^3)	2.323
F(000)	1136
μ (cm^{-1})	25.8
Scan type	θ–2θ
Scan range	1.0 + 0.35 tg θ
Max 2θ	70°
Unique reflections	3699
Reflections $I > 3\sigma(I)$	3231
Parameters	127
R	0.054
Rw	0.087
Max Δ/σ final	0.09

radiation. Cell constants were obtained from a least-squares refinement using the setting angles of 25 reflections, in the range $12.7 < \theta < 21.3°$. The intensities of three standard reflections, which were measured after every 60 min of X-ray exposure time, drifted by 1.8%. A total of 3699 unique reflections was collected using the θ–2θ scan technique to a maximum 2θ value of 70°. The data were corrected for Lorentz and polarization effects and an empirical absorption correction was made.

The structure was solved by the Patterson method and subsequent Fourier syntheses. The final cycle of the full-matrix least-squares refinement was based on 3231 observed reflections ($I > 3\sigma(I)$) and 127 parameters and converged with R = 0.054, Rw = 0.087. The hydrogen atoms were constrained to idealized positions (C—H = 0.95 Å). Final atomic coordinates and equivalent thermal parameters for the non-hydrogen atoms are given in Table 2.

Selected bond distances and angles are given in Table 3. All computations were performed using the SDP program (13).

Results and discussion

Protonation equilibria

The protonation equilibria H_2L were studied potentiometrically by titrating acidified aqueous solutions (HNO_3) of the ligand (C_L from 10^{-3} to 4×10^{-3} M and ionic strength 0.1 M $NaNO_3$) with 0.2 M NaOH. Protonation constants were obtained from three sets of 20 experimental points in the pH range 2–11. The refined protonation constants are gathered in Table 4.

The protonation constants and molar absorbance were also determined by spectrometric treatment of the protonation equilibria. While protonated and deprotonated forms of phthalic acid absorb at close wavelengths, spectrometric and potentiometric treatments are in good agreement.

Cd(II) complexation equilibria

Acidified solutions of Cd(II) and H_2L, in molar ligand/metal

Table 2. Final positional coordinates and equivalent thermal parameters for the non-hydrogen atoms in $CdL \cdot H_2O$.

Atom	*x*	*y*	*z*	B_{eq}[a]
Cd	0.04377(2)	0.34235(5)	0.56992(6)	1.067(6)
O1	0.0621(3)	0.3415(6)	0.8645(7)	1.52(8)
O2	0.1204(3)	0.3356(7)	1.0852(7)	2.2(1)
O3	0.0221(2)	0.5775(6)	0.6561(7)	1.35(8)
O4	0.0414(3)	0.7585(7)	0.8427(8)	2.01(9)
C1	0.1421(3)	0.4997(7)	0.8569(9)	1.2(1)
C2	0.2004(4)	0.4868(9)	0.876(1)	1.9(1)
C3	0.2370(4)	0.586(1)	0.799(1)	2.3(1)
C4	0.2145(4)	0.700(1)	0.705(1)	2.2(1)
C5	0.1563(4)	0.7155(8)	0.690(1)	1.6(1)
C6	0.1182(3)	0.6149(7)	0.7643(8)	1.07(9)
C7	0.1054(3)	0.3871(7)	0.9413(9)	1.2(1)
C8	0.0568(3)	0.6490(7)	0.7525(8)	1.18(9)
Ow	0.1074(3)	0.4729(6)	0.3993(7)	1.80(9)

[a] $B_{eq} = 4/3\ \Sigma_i\Sigma_j\beta_{ij}a_ia_j$

Table 3. Selected bond distances (Å) and angles (°) for $CdL \cdot H_2O$.

Bonds			
Cd—O1	2.317(5)	C2—C3	1.39(1)
Cd—O3	2.341(5)	C3—C4	1.39(1)
Cd—Ow	2.333(6)	C4—C5	1.38(1)
Cd—O4^{i}	2.255(5)	C5—C6	1.42(1)
Cd—O3^{ii}	2.449(5)	C6—C8	1.48(1)
Cd—O1^{iii}	2.372(5)	O3—C8	1.287(9)
Cd—O2^{iii}	2.445(5)	O4—C8	1.271(9)
O1—C7	1.250(9)	C1—C2	1.38(1)
O2—C7	1.261(9)	C1—C6	1.405(9)
		C1—C7	1.50(1)
Angles			
O4^{i}-Cd-O1	82.5(2)	C2-C1-C6	121.0(7)
O4^{i}-Cd-O2^{iii}	113.4(2)	C2-C1-C7	117.5(6)
O4^{i}-Cd-O$_w$	157.0(2)	C6-C1-C7	121.5(6)
O4^{i}-Cd-O3	93.0(2)	C1-C2-C3	120.7(8)
O4^{i}-Cd-O1^{iii}	96.1(2)	C2-C3-C4	119.6(8)
O4^{i}-Cd-O3^{ii}	76.2(2)	C3-C4-C5	119.8(8)
O1-Cd-Ow	116.0(2)	C4-C5-C6	121.6(7)
O1-Cd-O3	76.3(2)	C1-C6-C5	117.2(7)
O1-Cd-O1^{iii}	128.4(2)	C1-C6-C8	125.8(6)
O1-Cd-O2^{iii}	79.2(2)	C5-C6-C8	116.8(6)
O1-Cd-O3^{ii}	145.0(2)	O1-C7-O2	121.1(7)
Ow-Cd-O3	79.3(2)	O1-C7-C1	119.7(6)
Ow-Cd-O1^{iii}	83.1(2)	O2-C7-C1	119.1(7)
Ow-Cd-O2^{iii}	84.8(2)	O3-C8-O4	122.9(7)
Ow-Cd-O3^{ii}	81.0(2)	O3-C8-C6	122.8(6)
O3-Cd-O1^{iii}	154.5(2)	O4-C8-C6	114.3(6)
O3-Cd-O2^{iii}	141.0(2)		
O3-Cd-O3 ^{ii}	77.4(2)		
O1^{iii}-Cd-O2^{iii}	54.0(2)		
O1^{iii}-Cd-O3^{ii}	81.7(2)		
O2^{iii}-Cd-O3^{ii}	134.8(2)		

Table 4. Phthalic acid protonation constants and molar absorbances (I = 0.1 M $NaNO_3$, t = 25°C).

Species		Potentiometry		Spectrometry	
pqr	Range	log K_{pqr}	Ref. 14	log K_{pqr}	ε (M^{-1} cm^{-1}) (λ *nm*)
021	pH < 3	2.78(2)[a]	2.76	2.87	1183(*272*) 1321(*277*) 1281(*280*)
011	3 < pH < 5	4.97(3)[a]	4.92	4.94	1084(*272*) 1310(*277*) 1437(*280*)
001	pH > 5				786(*272*) 721(*277*) 654(*280*)

[a]Values in parentheses are the standard deviation corresponding to the last significant digits (2 σ).

Fig. 1. Distribution of the successive cadmium complexes as a function of pH for the ligand/metal ratios (*a*) 2 and (*b*) 100.

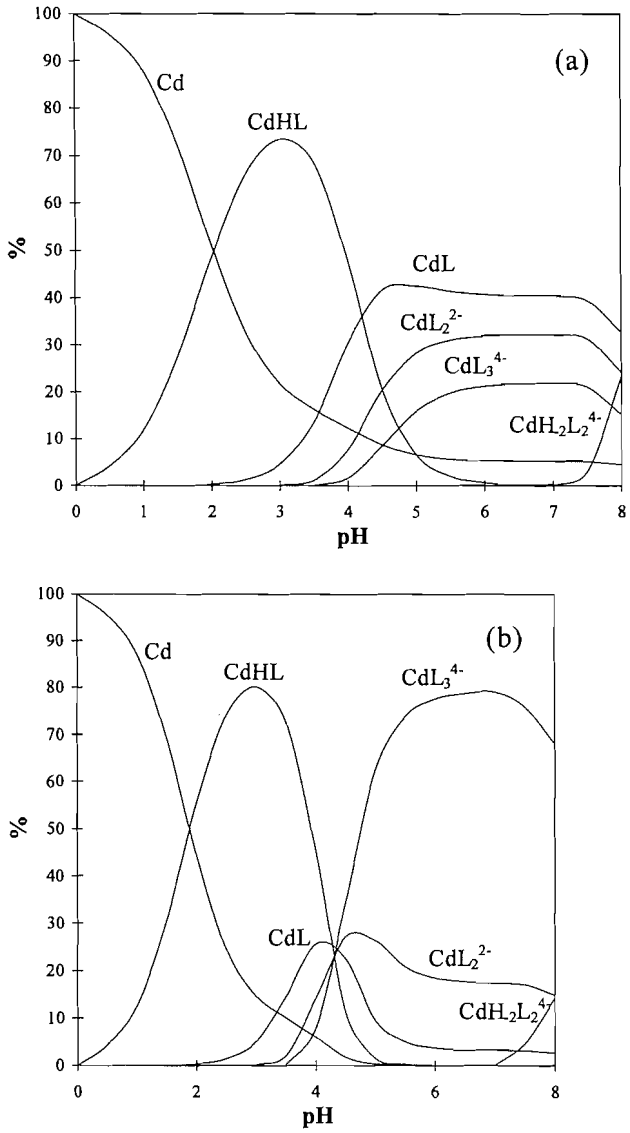

ratios of 2/1 to 5/1 (with $C_L = 4 \times 10^{-3}$ M), were titrated with 0.2 M NaOH at ionic strength 0.1 M $NaNO_3$ for studying the formation of the complexes. The titrations were extended to pH 8 before the beginning of precipitation. To avoid any error, all calculations were made only with data recorded before any precipitation (pH < 8).

Besides the two successive complexes CdL and CdL_2^{2-}, the formation of the protonated species $CdHL^+$ and $CdH_{-2}L_2^{4-}$ was determined. The stability constants were fitted by the least squares method from about 120 experimental data according to the pit-mapping procedure previously described (10). The constants that minimized the sums $U = \Sigma(\bar{q}_{cal} - \bar{q}_{exp})^2$ are reported in Table 5.

Polarography

Attention is paid to the fact that the classic potentiometric method for studying complexation in solution uses ligand/metal mole ratios of less than 10, therefore a high degree of coordination is never reached. In the case of a large excess of ligand (ligand/metal ratios of 1 to 1100), the D.P.P. method of complex determination, which allows easy differentiation of free cadmium ion from complexed cadmium at low metallic ion concentration (4×10^{-5} M), is used. In addition, the excess of ligand favors the formation of CdL_2^{2-} and CdL_3^{4-}.

The polarogram of a solution containing Cd(II) (4×10^{-5} M) and $NaNO_3$ (0.1 M) at pH 7 was characterized by an $E_{1/2}$ of –0.568 V/SCE corresponding to the reversible reduction of Cd(II). Addition of phthalic acid was found to shift the $E_{1/2}$ to a more negative value, and to decrease the intensity of the unique peak obtained. This observation is characteristic of the formation of the complexes.

As described previously (11, 12), analysis of the data in the 2×10^{-2} to 4.4×10^{-2} M concentration range of ligand revealed the formation of CdL, CdL_2^{2-}, and CdL_3^{4-} complexes under our experimental conditions. As we can estimate 1 mV as the experimental error in the $\Delta E_{1/2}$ measurements, the constants are then calculated with their error limits (Table 5).

It has to be noted that the graphical method employed here concerns only consecutive complexes of general formula $(CdL_n)^{2-2n}$, whereas other species such as hydroxylated and protonated complexes are omitted. In this way, it is not surprising that D.P.P. and potentiometry are not in accordance for either complex species or stability constants.

The results listed in Table 5 show that potentiometry gives equilibrium constants for CdL, CdL_2^{2-}, and $CdHL^+$. By introducing the CdL_3^{4-} stability constant in the potentiometric refinement, five constants can be refined simultaneously by the pit-mapping method, leading to more accurate values for the constants. These final values, with lower error limits, are listed in Table 5. The goodness of the results is then improved.

Figure 1 shows the distribution of all the species versus pH, in two different molar ligand/metal ratios. We can see that above pH 4 ca. 80% of the Cd(II) is complexed. At pH above 10, further addition of OH^- gave gradual precipitation of cad-

Fig. 2. ORTEP drawing, showing the cadmium environment and atom labelling in the crystal $CdL \cdot H_2O$.

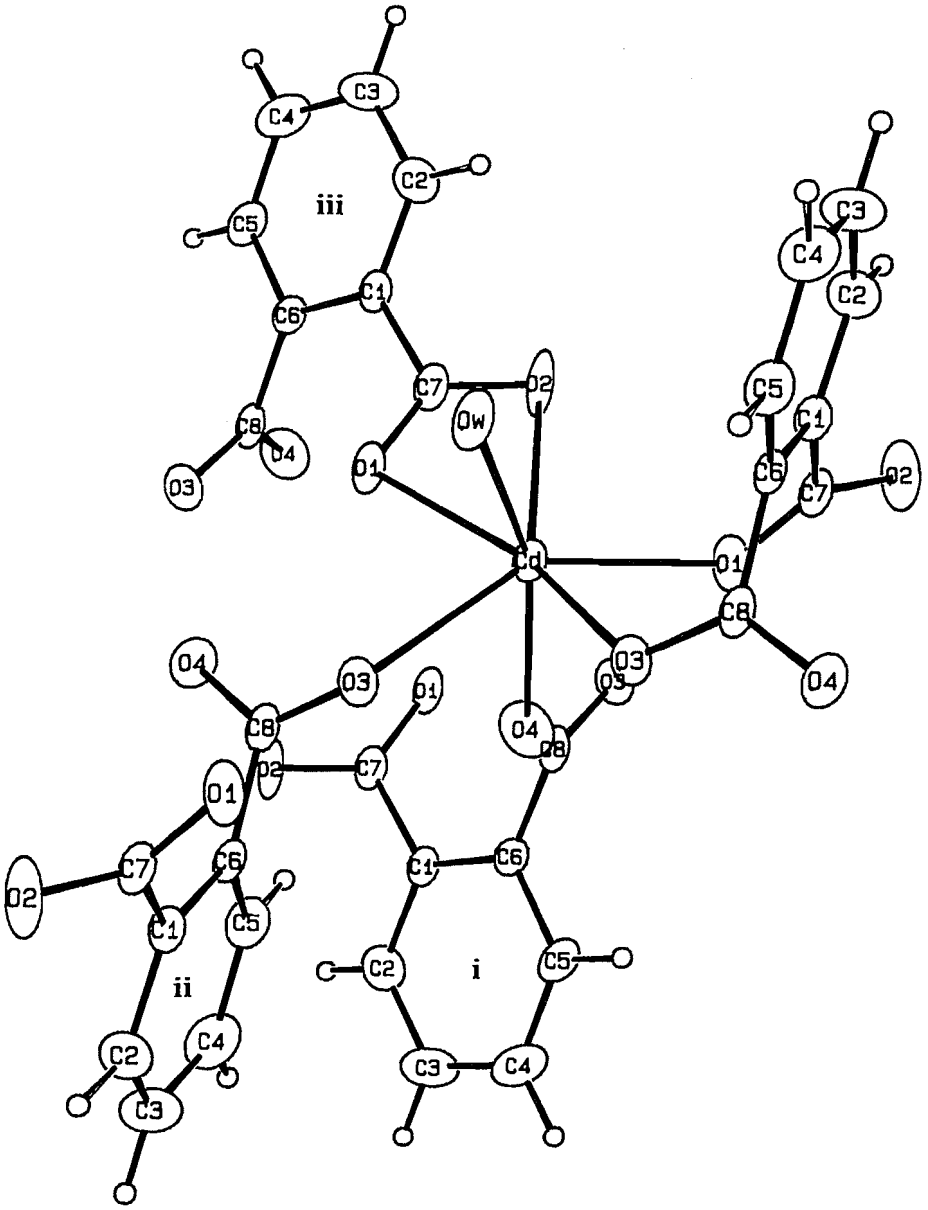

Table 5. Logarithms of the stability constants of the complexes $Cd_pH_qL_r$ (I = 0.1 M $NaNO_3$, t = 25°C).

		log β_{pqr}				
Species	Range	Potentiometry	D.P.P.	Final values	Ref. 14	Ref. 15
101	3 < pH < 7	2.78(2)[a]	1.81(6)[b]	2.82(2)[a]	2.50[c]	1.75[b]
102	5 < pH < 7	4.76(5)[a]	5.02(9)[b]	4.67(4)[a]		4.08[b]
103	5 < pH < 7		9.3(2)[b]	6.4(2)[a]		7.33[b]
111	2 < pH < 5	6.90(5)[a]		7.02(3)[a]		
1-22	pH > 7	−11.3(2)[a]		−7.8(2)[a]		

[a]Values in parentheses are the standard deviation corresponding to the last significant digits (2 σ).
[b]Values from potentiometric treatments.
[c]Values from polarographic treatments.

mium phthalate hydroxides. The predominant complexes are $CdHL^+$ and CdL when the ratio ligand/metal is 2 and CdL_3^{4-} for the ratio 100.

In conclusion, the use of potentiometry and D.P.P. permit the investigation of complex formation over a wide range of ligand and metal concentrations, so as to reveal all the complexes.

Crystal structure of $CdL \cdot H_2O$

Figure 2 shows the cadmium environment as a seven-coordinated polyhedron involving four phthalato ligands and one water molecule. A first ligand coordinates the Cd atom in a bidentate carboxylate (O,O′) mode (Cd—$O1^{iii}$ = 2.372(5) Å, Cd—$O2^{iii}$ = 2.445(5) Å). A second ligand is part of a seven-membered ring formed with its two carboxylate groups (Cd—O1 = 2.317(5) Å, Cd — O3 = 2.341(5) Å). Two other phthalic ligands make one coordination bond (Cd—$O4^{i}$ = 2.255(5) Å and Cd—$O3^{ii}$ = 2.449(5) Å). The seventh coordination bond is made through the water molecule (Cd—Ow = 2.333(6) Å).

This structure shows that all the carboxylate oxygen atoms of the deprotonated phthalic ligand are able to form coordination bonds. Thus, in CdL, O1 and O3 form two bonds each, while O2 and O4 form only one bond each. This hexadentate coordination fashion may be due to the conformation of the ligand, showing the two carboxylate groups clearly outside of the phenyl ring plane. The planes of the carboxylate groups make angles of 38.4(4)° and 72.1(2)° with that of the phenyl ring and the angle between them is 89.0(3)°.

The rotation of the carboxylate or carboxylic groups around their C—C bonds is generally found to be similar in most phthalate and hydrogenophthalate compounds, such as the following examples: 32° and 71° in $(NH_4)_2Pht$ (16), 27° and 67° in $Na(HPht) \cdot 1/2\ H_2O$ (17), 28.6° and 63.7° in $Cu(Pht)_2 \cdot 2\ H_2O$ (18), 28° and 71° in $Sr(HPht)_2 2\ H_2O$ (19), 34° and 78° in $Ca(Pht)_2 \cdot H_2O$ (20). However, some compounds show surprising rotation angle values: 88° and 5° in $Mn(HPht)_2 \cdot 2H_2O$ (21), 34.0° and 34.0° in H_2Pht (22). The most unexpected conformation has been found in $Li(HPht)2H_2O$ where the carboxylic and the carboxylate groups lie in the phenyl ring plane (23).

Supplementary material

Tables of anisotropic temperature factors, calculated hydrogen positions, and structure factors are available from R.F. on request.

References

1. D.F. Flick, H.F. Kraylill, and J.M. Dimitroff. Environ. Res. **4**, 71 (1971).
2. P.E. Carrol. J. Am. Med. Assoc. **198**, 267 (1966).
3. S.A. Gunn, T.C. Gould, and W.A.D. Anderson. Bull. Pathol. **8**, 42 (1967).
4. S.A. Dressing, R.P. Mass, and C.M. Weiss. Bull. Environ. Contam. Toxicol. 28, 172 (1982).
5. Y.-W. Hung. Bull. Environ. Contam. Toxicol. **28**, 546 (1982).
6. J. Nielsen, H. Welinder, and S. Skerfving. Br. J. Ind. Med. **42**, 769 (1992).
7. G. Gran. Analyst, **77**, 661 (1952).
8. M. Aliskandarani, E. Vernus, C. Comel, J. Jose, and M. Petit-Ramel. Analusis, **23**, 17 (1994).
9. N. Bjerrum. Metal ammine formation in aqueous solution. P. Haase and Son, Copenhagen. 1941.
10. A. Albourine, M. Petit-Ramel, G. Thomas-David, and J.J. Vallon. Can. J. Chem. **67**, 959 (1989).
11. D. Donald, D. Deford, and D.N. Hume. J. Am. Chem. Soc. **73**, 5321 (1951).
12. G.A. Heath and G.H. Hefter. J. Electroanal. Chem. **84**, 295 (1977).
13. B.A. Frenz and Associates Inc., SPD Structure Determination Package. College Station, Tex. 1982.
14. M. Yasuda, K. Suzuki, and K. Yamasaki. J. Phys. Chem. Soc. Jpn. **33**, (1960).
15. H.M. Killa. Transition Met. Chem. **17**, 55 (1992).
16. R.A. Smith. Acta Crystallogr. Sect. B: Struct. Crystallogr. Cryst. Chem. **B31**, 1773 (1975).
17. R.A. Smith. Acta Crystallogr. Sect. B: Struct. Crystallogr. Cryst. Chem. **B31**, 2345 (1975).
18. M.B. Cingi, A.N. Lanfredi, and M. Tiripicchio Camellini. Acta Crystallogr. Sect. B: Struct. Crystallogr. Cryst. Chem. **B34**, 134 (1978).
19. J.W. Bats, W. Schuckmann, and H. Fuess. Acta Crystallogr. Sect. B: Struct. Crystallogr. Cryst. Chem. **B34**, 2627 (1978).
20. W. Schuckman, H. Fuess, and J.W. Bats. Acta Crystallogr. Sect. B: Struct. Crystallogr. Cryst. Chem. **B34**, 3754 (1978).
21. J.W. Bats, A. Kallel, and H. Fuess. Acta Crystallogr. Sect. B: Struct. Crystallogr. Cryst. Chem. **B34**, 1705 (1978).
22. V.W. Nowacki and H. Jaggi. Z. Kristallogr. **109**, 272 (1957).
23. W. Gonscorek and H. Kuppers. Acta Crystallogr. Sect. B: Struct. Crystallogr. Cryst. Chem. **B31**, 1068 (1975).

Kinetics and mechanism of covalent addition of S(IV) species to the acridinium cation

Maria P. Ros, Jesus Thomas, Guillermo Crovetto, and Juan Llor

Abstract: The reaction of acridine with S(IV) species ($SO_2 \cdot H_2O$, HSO_3^-, and SO_3^{2-}) to form the adduct acridine–S (IV) has been studied spectrophotometrically throughout the pH range 2.6–8 in aqueous solutions. The observed pseudo-first-order rate constants, k_{obs}, were determined at 25°C and ionic strength $I = 0.11$ M, and the pH profile of the rate reached a maximum at pH $\approx$ 6.1. At constant pH the k_{obs} values were a linear function of the total S(IV) concentration with slopes that increased significantly with pH. These data are consistent with the rate-determining attack of SO_3H^- and SO_3^{2-} upon the C-9 of the acridinium cation. A nonlinear least-squares fitting of the experimental values to the model equation, within the overall pH region studied, yields the pH-independent rate constants $k_1 = 3.7 \pm 0.1$ and $k_2 = (6.24 \pm 0.04) \times 10^4$ M^{-1} s^{-1} for the attack of these two species, respectively. The experimental results agree very well with the kinetic model. Due to the experimental conditions used we did not detect any possible pseudobase formation in the pH range studied. The reactivity of the S(IV) species with acridine follows the order: $SO_3^{2-} \gg HSO_3^- \gg SO_2 \cdot H_2O$. The value obtained for the ratio k_1/k_2 is similar to the results given for other addition reactions of S(IV) species to the double bond of carbonyl compounds such as benzaldehyde and formaldehyde.

Key words: covalent addition, acridine, acridine – S(IV) adducts, kinetics and mechanism.

Résumé : L'acridine réagit avec le S(IV) sous la forme de $SO_2 \cdot H_2O$, HSO_3^- et SO_3^{2-} pour conduire à des adduits que l'on a étudié d'une façon spectrophotométrique à tous les pH allant de 2,6 à 8, en solutions aqueuses. On a déterminé les constantes de vitesse du pseudopremier ordre, k_{obs}, à 25°C et à une force ionique $I = 0,11$ M; les profiles des vitesses en fonction du pH atteignent un maximum à pH $\approx$ 6,1. À des pH constants, les valeurs de k_{obs} sont des fonctions linéaires de la concentration totale en S(IV) avec des pentes qui augmentent d'une façon importante avec le pH. Ces données sont en accord avec une attaque qui déterminerait la vitesse de la réaction du HSO_3^- et du SO_3^{2-} en position C-9 du cation acridinium. Un ajustement non linéaire par la méthode des moindres carrés des valeurs expérimentales obtenues dans la région globale de pH étudiés avec l'équation modèle permet de tirer des constantes de vitesses indépendantes du pH, $k_1 = 3,7 \pm 0,1$ et $k_2 = (6,24 \pm 0,04) \times 10^4$ M^{-1} s^{-1} pour les attaques respectives de ces deux espèces. Les résultats expérimentaux sont en bon accord avec le modèle cinétique. À cause des conditions expérimentales utilisées, on n'a pas pu détecter la formation de pseudobases dans la plage de pH étudiés. La réactivité des espèces S(IV) avec l'acridine est dans l'ordre suivant : $SO_3^{2-} \gg HSO_3^- \gg SO_2 \cdot H_2O$. La valeur obtenue pour le rapport k_1/k_2 est semblable à celle tirée de résultats rapportés pour d'autres réactions d'addition d'espèces S(IV) à des doubles liaisons de composés carbonylés, tels que le benzaldéhyde et le formaldéhyde.

Mots clés : addition covalente, acridine, adduits acridine – S(IV), cinétique et mécanisme.

[Traduit par la rédaction]

Introduction

The study of the covalent addition of nucleophilic reagents to N-heteroaromatic molecules is important as this type of reaction may occur in numerous biological process (1).

Acridine is a polynuclear nitrogen heterocycle and as such it belongs to this group of compounds, the derivatives of which are of pharmaceutical use (2) as labels in biological assays (3) and DNA-probe-based assays (4). Thus, equilibrium, kinetic, and thermodynamic data for the addition of several nucleophiles, such as the enolate ion of acetone (5) and the hydroxide ion (6), to the acridine *N*-methyl derivatives have been reported. Very few quantitative data, however, are available concerning the covalent additions of bisulfite and sulfite ions to acridine and its derivatives, although the addition of S(IV) species ($SO_2 \cdot H_2O$, HSO_3^-, and SO_3^{2-}) to derivatives of cytosine (7), uracil (8), pyrimidinium (9), and quinazolinium cations (10) etc. has been extensively studied. Pitmann and Sternson (11) estimated the equilibrium constant of the addition of the sulfite ion to the acridinium cation at 25°C and ionic strength $I = 1.0$ M and Hammond et al. (12) studied the addition of bisulfite to the 9-phenylcarboxylate-10-methylacridinium cation from the equilibrium point of view and describe some aspects of the macroscopic rate of the process. In any case, there is no information about the kinetics, mechanism, or any other factors that might affect the formation of adduct acridine–S(IV).

We have studied the kinetics of the covalent addition of the different S(IV) species to the N-heteroaromatic molecule acridine in water solution at 25°C at different pH values. We propose a mechanism for this reaction and we discuss the relative reactivity of different S(IV) species ($SO_2 \cdot H_2O$, HSO_3^-, and SO_3^{2-}) with acridine.

Experimental

Acridine (Aldrich) was crystallized by sublimation before

Received June 26, 1995.

M.P. Ros[1], J. Thomas, G. Crovetto, and J. Llor. Departamento de Química-Física, Universidad de Granada, Campus Universitario de Cartuja, 18071, Granada, Spain.

[1] Author to whom correspondence should be addressed. Fax: +34 58 272879.

being used. Solutions of pH 2 or below were obtained by using hydrochloric acid and for pH 11 or above by using sodium hydroxide. Other pH values were maintained by mixtures of sodium hydroxide and monochloroacetic acid, acetic acid and sodium acetate, citric acid and dibasic sodium phosphate, sodium carbonate and bicarbonate. All the solutions used were prepared with high-purity (18 MΩ cm) deionized water obtained from a Millipore MilliRO-4 MilliQ system, through which oxygen-free argon had been bubbled for 1 h. Ionic strength was held constant at $I = 0.11$ M with KCl. The sodium sulfite (Merck) was used without further purification, and its solutions were freshly prepared and were maintained under an Ar atmosphere. To stabilize the sodium sulfite solution against oxidation we added 1 mL of methanol per 100 mL (13). These S(IV) solutions were standardized by iodometric titration every half hour (14). UV–visible spectra of the mixture of acridine plus S(IV) species at equilibrium were always recorded before the first 15 min of the reaction (see Results) on a Perkin–Elmer spectrophotometer. When the buffered acridine solutions were prepared, a certain time (>10 min) was allowed for the equilibrium of the pseudobase formation to be reached. Ionization equilibrium constants of acridine, K_a^{Acr}, were determined by the general method of Albert and Serjeant (15). pH measurements were made using a PHM64 pH meter equipped with a GK2401C pH electrode.

Kinetic measurements were made with a Hi-Tech scientific SF-4 stopped-flow spectrophotometer by mixing the buffered acridine solutions in aqueous media with S(IV) species. The reactions were carried out under anaerobic conditions at different temperatures. The extent of the reaction was followed by monitoring the disappearance of acridine at 354 nm. The pH value of the initial reagent and the resulting solutions (effluents from the stopped-flow aparatus) were measured to confirm that they were constant. Each rate constant value thus obtained was determined as an average of at least three kinetic runs.

Results

We have obtained the UV–visible absorption spectra of buffered solutions ($1 < pH < 12$) of mixtures of acridine with increasing amounts of S(IV). The addition of S(IV) to solutions of acridine produces an adduct that absorbs at 278 nm (see for example Fig. 1, obtained at pH 3.26) and the intensity of this band is a function of the total S(IV) concentration ($[S(IV)]_T$) and pH (Fig. 1).

The addition of increasing concentrations of S(IV) produces a concomitant increase in absorbance in the region of 278 nm, which is accompanied by a decrease in the bands situated in the 320–360 nm range. The increasing absorbance in the 278 nm region is due to two factors: the adduct formation and the absorption band of the $SO_2{\cdot}H_2O$ species. For this reason, at acid pH values we see a significant increase in the absorbance at 278 nm although there is practically no adduct formation, and as a consequence we monitored the reaction at the wavelength of the acridine. The presence of the clear isosbestic point at 327 nm indicates an equilibrium between the acridine and a single acridine–S(IV) adduct as shown in Scheme 1. The structure obtained by the attack of bisulfite (**4**) is identical to that of the sulfite (**5**), due to the low acid pK values for sulfonic acids.

Fig. 1. UV-visible absorption spectra of buffered solutions of acridine ($[Acr]_T = 5 \times 10^{-5}$ M) balanced with different S(IV) concentrations at pH 3.26 and 25°C. $[S(IV)]_T \times 10^3$ M: 1, 0; 2, 0.13; 3, 0.33; 4, 0.67; 5, 1.33; 6, 3.76.

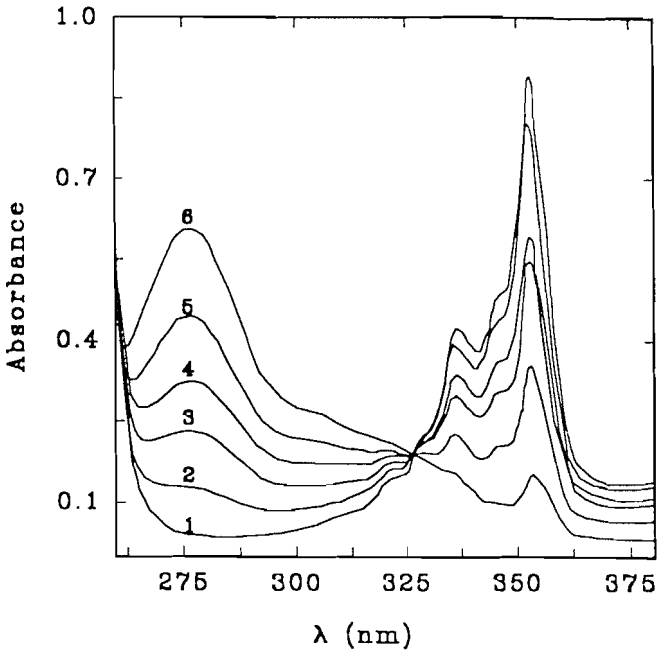

In general, 9,10-dihydroacridines (16) show an intense absorption band with a maximum in the 280 nm region similar to that which we obtained. Pitman and Sternson (11) proposed this structure for the acridine–S(IV) adduct and other authors have proposed similar structures for adducts formed with other acridine derivatives (5, 6, 17).

The percentage of adduct fraction formed as a function of pH has been calculated from the decrease in the absorbance of acridine at 354 nm using eq. [1]:

$$[1] \quad ([ADD]_f/[Acr]_0) = (A_0 - A)/A_0 \times 100$$

where A_0 and A are the absorbance of the pure acridine and that at equilibrium, respectively (Fig. 2).

As can be seen in Fig. 2 there is adduct formation in the pH range 2.5–8 and thus we measured rate constants in this pH range. On the other hand, we detected no reaction for $pH < 1$ and $pH > 11$ because there is no change to the acridine band at 354 nm at these pH values. In addition, we observed that the percentage of adduct formation decreases as the ionic strength increases (for example at pH 3.65, from 82.5 to 69% for ionic strength ranging from 6×10^{-3} to 0.6 M) and so this parameter has been carefully adjusted in this study.

The addition of S(IV) to acridine is a fast reaction in the presence of a considerable excess of sulfite species. Thus, pseudo-first-order conditions $[S(IV)]_T \gg [Acr]_T$, the total acridine concentration, were maintained throughout the study with a minimum 70-fold excess of S(IV). We determined the observed pseudo-first-order rate constants (k_{obs}) at 25°C as a function of pH and total S(IV) concentration, from the slope of the plots $\ln(A - A_0)$ vs. time, which were always linear ($r^2 > 0.99$). At constant pH, k_{obs} was a linear function of the total S(IV) concentration:

Scheme 1.

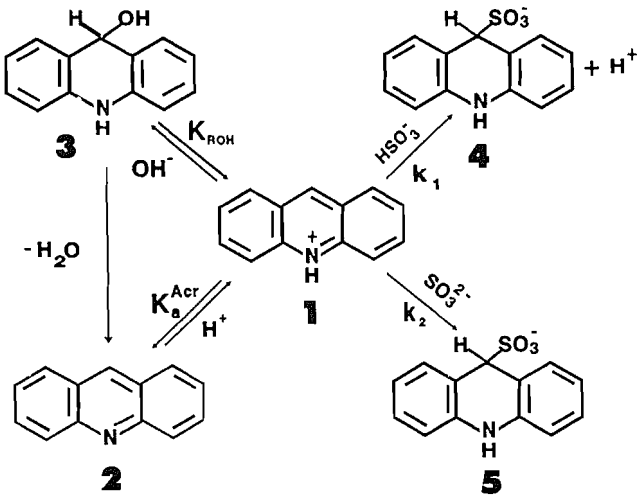

$k_{obs} = k_f [S(IV)]_T + k_d$

where the formation second-order rate constant, k_f, increases significantly with pH and the reverse rate constant, k_d, is very small.

We did not measure rate constants at pH <2.5 because the adduct formation was very small and there was practically no change in the absorbance signal. At 2.5 < pH < 8.0, at 25°C and $I = 0.11$ M, k_{obs} increases with pH; it reaches a maximum at pH 6.1 and then decreases (Table 1). We also studied the temperature effect (10–50°C) on the reaction rate at pH 4.00 and I = 0.15 M (Table 2).

On observing the absorption spectra of the acridine–S(IV) mixture some time after equilibrium has been reached we can see a progressive decrease in the peak corresponding to the adduct (278 nm), and an increase in the peak of acridine (354 nm) vs. time until it finally again reaches the initial spectrum of pure acridine. This behaviour is due to the reaction of O_2 with the S(IV) species. Thus, when the equilibrium for adduct formation is reached, if the S(IV) species concentration is not very high a displacement of the equilibrium towards the left occurs, obtaining acridine again. The pH of the solution always decreases during these processes due to the production of ion sulfate as a result of the oxidation of the S(IV) species (18).

This effect was observed at all the pH values, acridine and S(IV) concentrations, and ionic strengths studied. The stability of the acridine–S(IV) adduct is dependent on ionic strength and it begins to break down depending upon this parameter (from 15 min for $I = 10^{-3}$ M to 120 min for $I = 1$ M). For this reason, and as a precaution, all the measurements for this paper were recorded in time periods of less than 15 min, although we used an ionic strength of 0.11 M.

Discussion

Reagent considerations

Acridine can exist as three different species (Scheme 1) in aqueous solutions (16): acridinium cation (**1**: $AcrH^+$), anhydrous acridine (**2**: Acr), and pseudobase (**3**) depending upon the pH of three medium. In Scheme 1 we suggest the possibility of the formation of an acridine pseudobase (**3**) by adding OH^-.

Fig. 2. pH dependence of the percentage of adduct formation between acridine and S(IV) species at 25°C and $I = 0.11$ M, $[Acr]_T = 2 \times 10^{-4}$ M, $[S(IV)]_T = 4.86 \times 10^{-3}$ M. The broken lines indicate the fractions of S(IV) and acridine species calculated using the ionization equilibrium constant values given in the text.

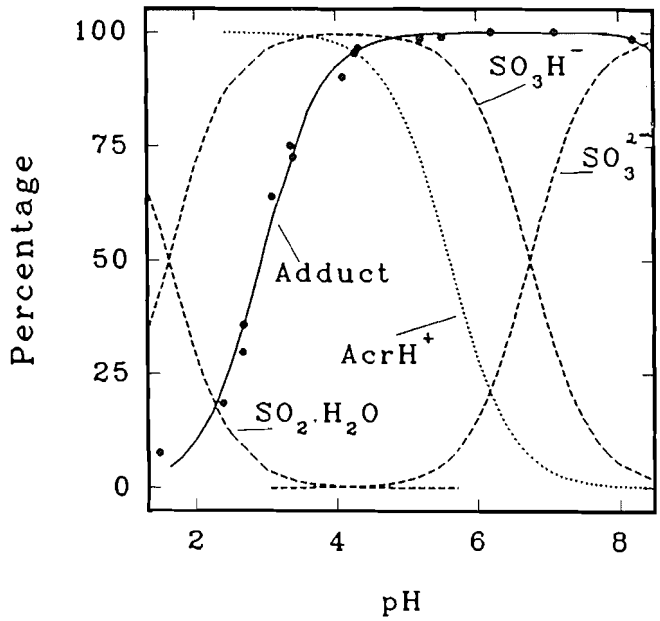

It is known that many reactions of heteroaromatic molecules in aqueous solutions are initiated by the covalent addition of water, a hydroxide ion, or other nucleophilic reagents across a double bond in the molecule (19–22). For example, Bunting and Meathrel studied the addition of OH^-/H_2O to 2-methyl-4-isoquinolinium, 10-methylacridinium, 10-methyl-9-phenylacridinium (6), and 1-methylquinolinium cations from both the kinetic and equilibrium points of view (23) and reported on the kinetic and activation parameters and the equilibrium constant. On the other hand, there is practically no information about the addition of a hydroxide ion to acridinium cation **1** (Scheme 1). Nevertheless, we detected evidence for the existence of this species in the form of a white precipitate in solutions with high OH^- concentrations (pH > 8) and the presence of a spectral band at 280 nm. The pseudobase is formed very quickly by reaction with the acridinium cation (**1**) but this association cannot be maintained stable in very basic solution. Due to the OH^- ions in the media the pseudobase decomposes to give anhydrous acridine (**2**), until we obtain the characteristic spectrum of the acridine molecule in a basic medium. Due to the presence of pseudobase **3** in our case, some necessary precautions were taken (see experimental procedure).

The S(IV) species in water solution may appear in three different forms: sulfur dioxide, bisulfite, and sulfite. There is some disagreement (24–27) over the values of the ionization equilibrium constants of these forms, K_{a1} and K_{a2}. The values of the equilibrium constants measured by Deveez and Rumpf (27) and Hayon et al. (18) were chosen for the calculations performed in the current study, considering the suggestion put forward by Maahs (28) about the different species of sulfur dioxide in water.

To account for the influence of ionic strength upon the equilibrium of the S(IV) species, and following the recommenda-

Table 1. Pseudo-first-order rate constants (k_{obs}) for the addition reaction of S(IV) species to acridine as a function of pH, in aqueous solutions at 25°C and I = 0.11 M. $[Acr]_T = 7.5 \times 10^{-5}$ M. The indicated errors are standard errors.

pH	$[S(IV)]_T \times 10^3$ M	k_{obs} (s^{-1})	pH	$[S(IV)]_T \times 10^3$ M	k_{obs} (s^{-1})
2.67	10.92	0.089 ± 0.002	4.28	10.87	2.27 ± 0.02
2.86	10.90	0.121 ± 0.001	4.41	11.17	3.06 ± 0.04
2.90	10.78	0.131 ± 0.002	4.67	11.15	4.9 ± 0.1
3.00	10.78	0.155 ± 0.002	4.92	11.14	8.0 ± 0.3
3.05	10.41	0.162 ± 0.001	5.20	11.04	15 ± 1
3.33	10.36	0.282 ± 0.005	5.27	11.04	16 ± 1
3.43	10.99	0.37 ± 0.03	5.44	11.04	18 ± 3
3.72	10.30	0.65 ± 0.02	5.96	11.04	30 ± 6
3.92	11.29	1.09 ± 0.01	6.68	10.71	23 ± 4
4.12	11.28	1.69 ± 0.01	7.47	10.69	8.4 ± 0.5
4.17	11.29	1.85 ± 0.02	7.99	10.35	2.5 ± 0.1

Table 2. Temperature dependence of (k_{obs}) values at pH 4.0 and I = 0.15 M. The indicated errors are standard errors. $[Acr]_T = 7.7 \times 10^{-5}$ M, $[S(IV)]_T = 1.082 \times 10^{-2}$ M.

T (°C)	k_{obs} (s^{-1})
10	0.562 ± 0.005
15	0.686 ± 0.006
20	0.85 ± 0.01
25	1.03 ± 0.01
30	1.26 ± 0.01
35	1.58 ± 0.02
40	1.85 ± 0.02
45	2.15 ± 0.06
50	2.39 ± 0.05

tions made by Clarke (29), the thermodynamic equilibrium constants K_{a1} and K_{a2} were corrected using Davies' approximation (30), eq. [2]:

$$[2] \quad \log \gamma = -Az^2 \left(\frac{I^{1/2}}{1 + I^{1/2}} - 0.2I \right)$$

where z is the ionic charge, I the ionic strength, and $A = 1.82 \times 10^6 (\varepsilon T)^{-3/2}$ (ε is the dielectric constant of water).

It is known that if the ion concentration is very high a new S(IV) species, pyrosulfite, may appear (18, 31). We have not considered the presence of $S_2O_5^{2-}$ in the reaction mechanism due to the fact that the total concentrations of S(IV) did not surpass 10^{-3} M.

Mechanism and kinetic analysis

According to all the observations described above, the following reaction mechanism for the adduct formation is proposed (Scheme 1) within the pH range of 2.5–8.0 and at 25°C.

This mechanism involves the nucleophilic addition of bisulfite and sulfite to the C-9 atom of the acridinium cation (**1**). Of the three acridine species, only the acridinium cation **1** reacts and the quaternary ring nitrogen was found to be essential for adduct formation (12), with the resulting loss of ring aromaticity. We did not obtain any kinetic information in basic solutions (pH > 8) due to pseudobase formation and the small value of k_{obs}. Sulphur dioxide is the principal constituent of acid solutions (pH < 2) and therefore no reaction is obtained under these conditions (Fig. 2).

The results obtained for k_{obs} as a function of pH can be explained by two rate-determining steps in the adduct formation, and, taking into account the low value of k_d, the rate law for this reaction scheme would be:

$$[3] \quad v = -\frac{d[Acr]_T}{dt} = k_1[AcrH^+]\,[HSO_3^-] + k_2[AcrH^+]\,[SO_3^{2-}]$$

where

$$[S(IV)]_T = [SO_2{\cdot}H_2O] + [SO_3H^-] + [SO_3^{2-}]$$

$$[Acr]_T = [Acr] + [AcrH^+]$$

and k_1 and k_2 are the pH-independent rate constants of the addition of SO_3H^- and SO_3^{2-} to the acridinium cation, respectively.

k_{obs} for the reaction was obtained under pseudo-first-order conditions in S(IV) and can be related to the k_1 and k_2 values by the equation:

$$[4] \quad k_{obs} = \left(\frac{k_1K_{a1}[H^+] + k_2K_{a1}K_{a2}}{D} \right) \beta[S(IV)]_T$$

where β and D are defined as:

$$\beta = 1/[(K_a^{Acr}/[H^+]) + 1]$$

$$D = [H^+]^2 + K_{a1}\,[H^+] + K_{a1}\,K_{a2}$$

The k_1 and k_2 values can initially be estimated by taking into account that, in the pH range 2.5–4.9, $K_{a1}[H^+] \gg [H^+]^2 + K_{a1}K_{a2}$, and thus eq. [5] can be obtained:

$$[5] \quad k_{obs} = \left(k_1 + \frac{k_2K_{a2}}{[H^+]} \right) \beta[S(IV)]_T$$

A plot of $k_{obs}/\beta[S(IV)]_T$ vs. $[H^+]^{-1}$ over this pH range was linear ($r^2 > 0.999$) and values of $k_1 = 9.07$ and $k_2 = 5.82 \times 10^4$ M^{-1} s^{-1} were obtained. With these initial values and using eq. [4], nonlinear regressions for the experimental values of $(k_{obs}D/[S(IV)]_T)$ vs. β (Fig. 3*A*) in the overall pH region studied yield $k_1 = (3.7 \pm 0.1)$ and $k_2 = (6.24 \pm 0.04) \times 10^4$ M^{-1} s^{-1}. Due to the influence of ionic strength, we used the following values for these calculations: $K_{a1} = 2.44 \times 10^{-2}$ M and $K_{a2} = 1.80 \times 10^{-7}$ M, which were obtained from the thermodynamic values (27, 18) and Davies equation (eq. [2]) and $K_a^{Acr} = 2.5 \times 10^{-6}$ M obtained by us.

For this fitting we used all the experimental data obtained at the different pH values and S(IV) concentrations (74 points). As can be seen in Fig. 3*A*, we obtained a very good fitting of the experimental data to eq. [4], where the standard error for the parameters k_1 (2%) and k_2 (0.6%) was very small. At pH values slightly higher than 4.2 ($\beta < 0.95$) Fig. 3*A* was linear with a slope (eq. [4]) given by $k_2K_{a1}K_{a2}$, due to the fact that $k_1K_{a1}[H^+] \ll k_2K_{a1}K_{a2}$, but at pH < 4.2 ($\beta > 0.95$) the situation changes and the first term is predominant.

In the plot log $(k_{obs}/[S(IV)]_T\beta)$ vs. pH (Fig. 3*B*), within the pH range 3.2–5.9 we obtained a straight line but outside this range the plot was not linear (eq. [4]). The straight line drawn in this figure was calculated with a slope of unity and an intercept of log $(k_2 \cdot K_{a2})$ using the k_2 value obtained above. At pH >6 the term $K_{a1}K_{a2}$ begins to become significant and we must expect k_{obs} values lower than the theoretical straight line, and at pH <3 the term $[H^+]^2$ is significant and the obtained k_{obs} values must be higher than the theoretical ones, as can be seen in Fig. 3*B*.

In Fig. 4 we can see that the theoretical curve fits the experimental points very well. We obtained a dependence with a maximum value of k_{obs} at pH 6.1, which is practically the average of the pK_{a2} and pK_a^{Acr} values. k_{obs} increases in the pH range where the concentration of SO_3^{2-} strongly increases (Fig. 2) and decreases at high pH values where the concentration of the acridinium cation decreases. This plot also confirms agreement of the experimental data with the proposed model and that the values used for the different equilibrium ionization constants of the reagents were correct.

In other kinetic and equilibrium studies (5,6) of related compounds pseudobase formation has sometimes been detected. To obtain information about this point we included the term $(1 + K_{ROH}/[H^+])$ on the right side of eq. [4], where K_{ROH} is the adduct formation equilibrium constant, and we repeated the nonlinear least-squares fitting of $(k_{obs}D/[S(IV)]T)$ vs. β, in the same way as shown in Fig. 3, with K_{ROH} as an additional parameter. We obtained the same value and accuracy for k_2, and an extremely small value for K_{ROH}, indicating that there is no pseudobase formation in the pH range and under the experimental conditions studied. In any case, and as indicated in the experimental section, the precautions taken during the experimental work to avoid interference caused by the formation of a pseudobase in the kinetic results were adequate.

The k_1 and k_2 values obtained in this study reveal the great difference in reactivity with the acridinium ion between HSO_3^- and SO_3^{2-}, with a k_2/k_1 ratio of 1.7×10^4. A similar value for this ratio (3×10^4) has been obtained with benzaldehyde–S(IV) (32) and formaldehyde–S(IV) (33) adducts. If the rate-limiting step of the reaction involves a bimolecular process, then $SO_2 \cdot H_2O$, HSO_3^- and SO_3^{2-} react with $AcrH^+$ at different rates. We obtained results showing that the reactivity of the S(IV) species with acridine follows the order: $SO_3^{2-} \gg HSO_3^- \gg SO_2 \cdot H_2O$. It is well known that the sulfite ion is a much stronger nucleophile than HSO_3^- in reactions with a wide variety of organic and inorganic substrates (34), and the same order of increasing reactivity has been obtained in the reaction of formaldehyde with sulfur dioxide to form hydroxymethanesulfonic acid (33).

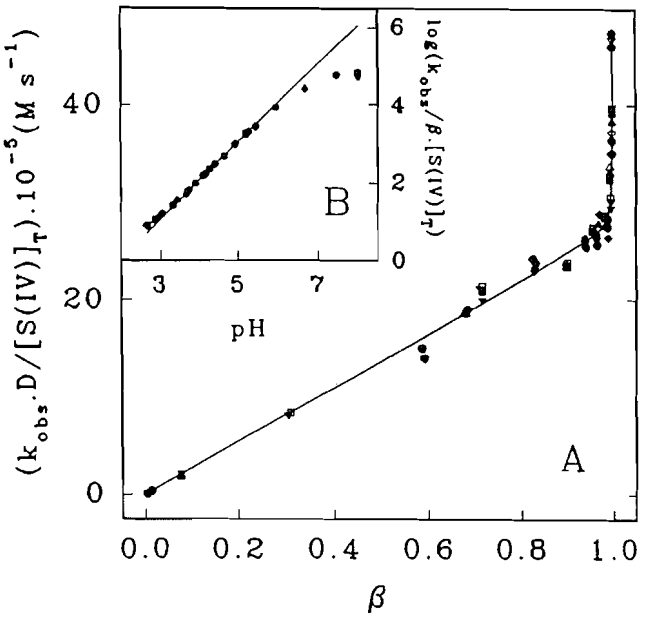

Fig. 3. *A*. Plot of $k_{obs}D/[S(IV)]_T$ vs. β over the pH range studied. The solid line is the theoretical line calculated using eq. [4] and the parameters k_1 and k_2 obtained from a nonlinear least-squares fitting. *B*. Dependence of log $(k_{obs}/\beta[S(IV)]_T)$ vs. pH. The solid line has been drawn with a slope of unity as indicated in the text.

The present mechanism assumes that the formation rates of the reagent species HSO_3^-, SO_3^{2-}, and $AcrH^+$ are very fast in comparison to the other step in the mechanism. Although there is some disagreement about the values of the formation rates of HSO_3^- (25, 35) from $SO_2 \cdot H_2O$, all of these are very high.

The temperature dependence of k_{obs} over the range from 10 to 50°C (at pH 4.0 and ionic strength 0.15 M) is given in Table 2 and Eyring's equation gives the values $\Delta H^{\ddagger} = 27.2$ kJ mol^{-1} and $\Delta S^{\ddagger} = -153.1$ J K^{-1} mol^{-1} for the enthalpy and entropy of activation. The value of the entropy of activation is more negative than we might generally expect for addition reactions of monopositive and mononegative ions. Similar values have been obtained for the addition of bisulfite to formaldehyde ($\Delta S^{\ddagger} = -108.0$ J K^{-1} mol^{-1} (33)), benzaldehyde ($\Delta S^{\ddagger} = -142.35$ J K^{-1} mol^{-1}), and other related compounds (32), and for methylglyoxal ($\Delta S^{\ddagger} = -77.7$ J K^{-1} mol^{-1} (36)). Bunting and Meathrel (6) obtained $\Delta S^{\ddagger} = -71.0$ J K^{-1} mol^{-1} for the reaction between 10-methylacridinium cation and OH^-. Olson et al. (32) have proposed that the transition complex for the addition of bisulfite to benzaldehyde is a cyclic structure formed between the carbonyl and bisulfite groups. In our case it is difficult to establish a possible structure for the transition complex, which would have a high charge separation that would contribute to the low value of $\Delta S^{\ddagger}$.

Fig. 4. Observed pseudo-first-order rate constant (k_{obs}) as a function of pH. The theoretical line has been drawn with the parameters given in the text.

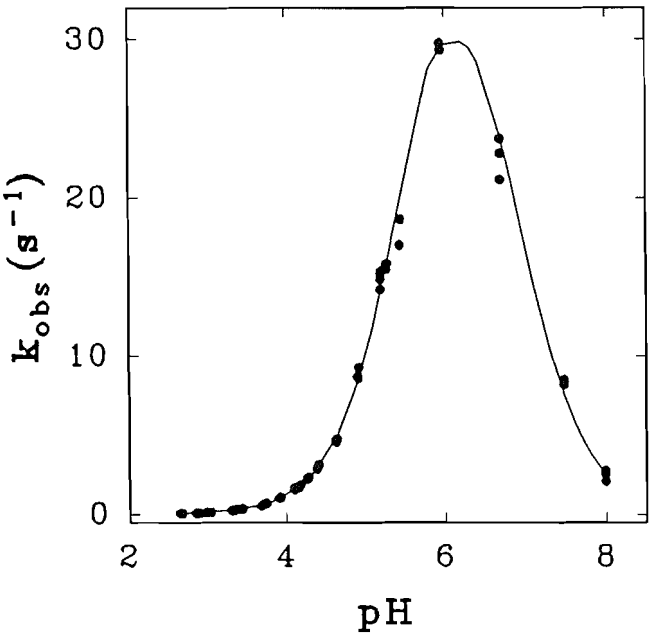

Acknowledgements

We thank Boehringer Ingelheim for partial financial support and our colleague Dr. J. Trout for revising the English text.

References

1. R.S. Sodum and F.L. Chung. Cancer Res. **51**, 137 (1991).
2. (*a*) H. Nakamura, A. Hase, and K. Funatsuki. Mem. Konan Univ. Sci. Ser. **37**, 177 (1990); (*b*) F. Dietlin and D. Fredj. Chem. Abstr. **114**, 75182s (1991); (*c*) G. Mathe. Chem. Abstr. **114**, 136064d (1991).
3. (*a*) I. Weeks, M.L. Sturgess, R.C. Brown, and J.S. Woodhead. Methods Enzymol. **133**, 366 (1986); (*b*) L.J. Kricka. Clin. Chem. **37**, 1472 (1991).
4. L.A. Arnold, P.W. Hammond, W.A. Wiese, and C.N. Nelson. Clin. Chem. **35**, 1588 (1989).
5. J.W. Bunting, C. Fu, and J.W. Tam. Can. J. Chem. **68**, 1972 (1990).
6. J.W. Bunting and W.G. Meathrel. Can. J. Chem. **51**, 1965 (1973).
7. (*a*) R. Shapiro, R.E. Servis, and M. Welcher. J. Am. Chem. Soc. **92**, 422 (1970); (*b*) R. Shapiro, V. DiFate, and M. Welcher. J. Am. Chem. Soc. **96**, 906 (1974).
8. (*a*) R.W. Erickson and E.G. Sander. J. Am. Chem. Soc. **94**, 2086 (1972); (*b*) G.S. Rork and I.H. Pitman. J. Am. Chem. Soc. **96**, 4654 (1974); (*c*) A.F. Sedor, D.G. Jacobson, and E.G. Sander. J. Am. Chem. Soc. **97**, 5572 (1975); (*d*) G.S. Rork and I.H. Pitman. J. Pharm. Sci. **64**, 216 (1975).
9. (*a*) I.H. Pitman and M.A. Ziser. J. Pharm. Sci. **59**, 1295 (1970); (*b*) F. Rise and K. Undheim. Acta Chem. Scand. **43**, 489 (1989).
10. M.J. Cho and I.H. Pitman. J. Am. Chem. Soc. **96**, 1843 (1974).
11. I.H. Pitman and L.A. Sternson. J. Am. Chem. Soc. **98**, 5234 (1976).
12. P.W. Hammond, W.A. Wiese, A.A. Waldrop III, N.C. Nelson, and L.J. Arnold, Jr. J. Biolumin. Chemilumin. **6**, 35 (1991).
13. I.M. Kolthoff and R. Belcher. Volumetric analysis. Vol. III. Interscience, New York, London. 1957.
14. D.A. Skoog and D.M. West. Fundamentals of analytical chemistry. 2nd ed. Holt, Rinehart and Winston, New York. 1969.
15. A. Albert and E.P. Serjeant. The determination of ionization constants. 3th ed. T. & A. Constable Ltd., Cambridge. 1984.
16. A. Albert. The acridines. 2nd ed. Edward Arnold Ltd., London. 1966.
17. J.W. Bunting and N.P. Fiztgerald. Can. J. Chem. **62**, 1301 (1984).
18. E. Hayon, A. Treinin, and J. Wilf. J. Am. Chem. Soc. **94**, 47 (1972).
19. M.J. Cho and I.A. Pitman. J. Am. Chem. Soc. **96**, 1843 (1973).
20. D. Beke. Adv. Heterocycl. Chem. **1**, 167 (1963).
21. C.J. Vosanger and J.J. Vosanger. Bull. Soc. Chim. Fr. 589 (1970).
22. C.J. Cooksey and M.D. Johnson. J. Chem. Soc. B, 1191 (1968).
23. J.W. Bunting and W.G. Meathrel. Can. J. Chem. **50**, 917 (1972).
24. A. Huss and C.A. Eckert. J. Phys. Chem. **81**, 2268 (1977).
25. S. Belike and D. Lamb. AIChE, **21**, 402 (1975).
26. H.V. Tartar and H.H. Garretson. J. Am. Chem. Soc. **63**, 808 (1941).
27. D. Deveze and M.P. Rumpf. C.R. Acad. Sci. **258**, 6135 (1964).
28. H.G. Maahs. Heterogeneous atmospheric chemistry. D.R. Schryer, Washington. 1982.
29. A.G. Clarke. Atmos. Environ. **15**, 1591 (1981).
30. I.N. Levine. Physical chemistry. McGraw–Hill, New York. 1978.
31. D.W.A. Bourne, T. Higuchi, and I.H. Pitman. J. Pharm. Sci. **63**, 862 (1974).
32. T.M. Olson, S.D. Boyce, and M.R. Hoffmann. J. Phys. Chem. **90**, 2482 (1986).
33. S. Boyce and M.R. Hoffmann. J. Phys. Chem. **88**, 4740 (1984).
34. L.C. Schroeter. Sulfur dioxide, applications in foods, beverages, and pharmaceuticals. Pergamon, New York. 1966.
35. (*a*) R.H. Betts and R.H. Voss. Can. J. Chem. **48**, 2035 (1970); (*b*) J.V. McArdle and M.R. Hoffmann. J. Phys. Chem. **87**, 5425 (1983); (*c*) D.L. Roberts. AIChe J. **26**, 593 (1980).
36. E.A. Betterton and M.R. Hoffmann. J. Phys. Chem. **91**, 3011 (1987).

The metabolites of *Trichoderma longibrachiatum*. Part II. The structures of trichodermolide and sorbiquinol

Romano Andrade, William A. Ayer, and Latchezar S. Trifonov

Abstract: *Trichoderma longibrachiatum* Rifai aggr. is a fungus reported to be antagonistic to the fungus *Mycena citricolor*, the causative agent of the American leaf spot disease of coffee. We have investigated the metabolites produced when *T. longibrachiatum* is grown in liquid culture and have isolated several new compounds. The structures of trichodermolide (**2**) and sorbiquinol (**3**) were determined by a combination of spectroscopic techniques, including ^{1}H and ^{13}C NMR, IR, UV, CD, ORD, and mass spectrometry, and by preparation of derivatives.

Key words: *Trichoderma longibrachiatum*, leaf spot disease, coffee, fungal metabolites.

Résumé : Le *Trichoderma longibrachiatum* Rifai aggr. est un champignon qui serait l'antagoniste du champignon *Mycena citricolor*, l'agent qui serait la cause de la maladie des taches sur les feuilles du café américain. On a étudié les métabolites produits lorsqu'on fait une culture liquide du *T. longibrachiatum* et on a isolé plusieurs nouveaux composés. On a déterminé les structures du trichodermolide (**2**) et du sorbiquinol (**3**) par une combinaison de techniques spectroscopiques, y compris la RMN du ^{1}H et du ^{13}C, l'IR, l'UV, le DC, la DRO et la spectrométrie de masse, ainsi qui par la préparation de dérivés.

Mots clés : *Trichoderma longibrachiatum*, maladie des taches sur les feuilles, café, métabolites de champignons.

[Traduit par la rédaction]

Introduction

In part 1 of this series (1), we described the isolation of several metabolites from liquid cultures of *Trichoderma longibrachiatum*, Rifai aggr. The studies leading to the assignment of structure **1** to trichodimerol, an intrinsically interesting natural product that possesses an axis of symmetry, were described. In this article we present evidence for the structural assignment of two other interesting new natural products produced by the fungus, the pale yellow compounds trichodermolide (**2**) and sorbiquinol (**3**).

Results and discussion

Trichodermolide (**2**) is a pale yellow, optically active glass showing maximum ultraviolet (UV) absorption at 280 nm. The molecular formula $C_{24}H_{28}O_5$ was determined by high-resolution mass spectrometry (HREIMS) and the molecular weight was confirmed by chemical ionization mass spectrometry (CIMS). The base peak in the electron impact mass spectrum (*m/z* 95) arises from fragmentation of the sorbyl chains ($H_7C_5CO^+$). The spectrum also shows a $M^+ - 95$ peak and a peak at *m/z* 352 corresponding to the loss of CO_2 (lactone carbon and oxygens). The infrared spectrum (IR) shows absorption at 1781 cm^{-1} (γ-lactone) and at 1687 and 1637 cm^{-1} (α,β-unsaturated ketone).

Received November 14, 1995.

R. Andrade, W.A. Ayer,[1] and L.S. Trifonov. Department of Chemistry, University of Alberta, Edmonton, AB T6G 2G2, Canada.

[1] Author to whom correspondence may be addressed. Telephone: (403) 492-5476. Fax: (403) 492-8231. E-mail: bill.ayer@ualberta.ca

The ^{1}H NMR spectrum of trichodermolide (**2**) in $CDCl_3$ shows three methyl singlets (δ 1.78, 1.45, and 1.24), and an AB quartet at δ 3.66 (J = 19 Hz) arising from the C-7 methylene group, an isolated three-hydrogen spin system at δ 2.45 (dd, 18.5 and 4 Hz), 3.26 (dd, 18.5 and 6 Hz), and 3.34 (dd, 4 and 6 Hz) for the C-14 methylene hydrogens and the C-5 methine hydrogen, respectively. Signals for the two *E,E*-sorbyl chains are readily apparent. When the spectrum is recorded in benzene the C-7 methylene signals split into clear doublets at δ 3.02 and 3.19 (J = 17 Hz). The large *geminal* coupling constants observed for the C-7 and C-14 methylene hydrogens are consistent with their location α to carbonyl groups (2).

The ^{13}C NMR spectrum of trichodermolide (**2**) (Table 1) shows 24 carbons: 5 methyl carbons, 2 methylene carbons, 1 sp^3 methine carbon (C-5, δ 56.0), 1 sp^3 quaternary carbon (C-4, δ 51.8), a tertiary carbon bearing oxygen (C-6, δ 87.2), 8 sp^2 carbons as doublets, 2 olefinic carbons as singlets, and 4 carbonyl carbons (δ 176.1 (lactone), 191.2, 195.5, and 196.6).

The molecular formula for trichodermolide indicates 11 unsaturations. Two sorbyl chains account for six, the lactone for two, the unsaturated ketone for two, and thus there is only one carbocyclic ring. The functionality described accounts for all five oxygens. A series of NOE experiments (in $CDCl_3$) served to further define structure **2**. The methine hydrogen at C-5 (δ 3.34) shows strong NOE enhancement with the methylene hydrogen at δ 2.45 (one H-14) and the methyls at δ 1.45 and 1.24. The methyl hydrogens at δ 1.24 (H-22) also show NOE enhancement with the methylene hydrogen at δ 3.26 (an H-14) and the methylene at δ 3.66 (H-7). The methylene at δ 3.66 in turn gives reciprocal enhancement with the alkenic methyl (H-21) at δ 1.76 as well as with two hydrogens (δ 6.15 and 7.24) of one of the sorbyl chains. The C-14 methylene

hydrogens (δ 3.26 and 2.45) give strong mutual enhancement as well as enhancement of hydrogens of the other sorbyl chain (δ 6.10 and 7.20).

These data define the constitution of trichodermolide as shown in structure **4** where the starred carbon atoms indicate the points of attachment of the lactone ring. It was now necessary to determine the orientation of the lactone ring, i.e., whether the lactone carbonyl carbon is attached to C-4 or to C-6. The selective INEPT technique (3) was used to locate the carbonyl carbon. The NOE results above indicate that the methyl group at C-4 resonates at δ 1.24, that at C-6 at δ 1.45. Selective Irradiation of the δ 1.24 hydrogens (CH_3 at C-4) gives rise to signals for the carbons at δ 51.8 (C-4), 148.6 (C-3), and the lactone carbonyl carbon (δ 176.1). Irradiation of the methyl hydrogens at δ 1.45 (CH_3 at C-6) gives signals for the carbons at δ 87.2 (C-6) and δ 191.2 (C-1). The carbon at δ 56.0 (C-5) was not enhanced in either experiment although it should be coupled ($^3J_{CH}$) to both methyls. The absence of enhancement may be due to the passive modulation of the carbon by the one-bond C—H coupling (4). Final confirmation of the ring substructure of trichodermolide was obtained from the HMBC spectrum, which showed the correlations (C/H's): 1/21, 23; 2/7, 21; 3/7, 21, 22; 4/7, 14, 22; 5/14, 22, 23; 6/5, 14, 23. The HMBC correlations 8/7, and 15/5, 14 assigned the carbonyl signals at 195.5 and 196.6 to C-8 and C-15, respectively. These results establish structure **2** (other than the stereochemistry at C-5) for trichodermolide.

Additional information on the stereochemistry of trichodermolide was obtained by the preparation of several derivatives. Hydrogenation over palladium on carbon produced an octahydro derivative (**5**), as confirmed by the HREIMS and CIMS. The IR (1782, 1715, and 1688 cm^{-1}) and UV (272 nm) spectra of octahydrotrichodermolide (**5**) indicated that the enone had resisted reduction.

Octahydrotrichodermolide (**5**) was selectively reduced with excess sodium borohydride in methanol for a short time to produce a mixture of epimeric alcohols, **6***a* and **6***b*. These could be separated through careful column chromatography. Neither epimer shows strong absorption in their UV spectra, indicating the enone was reduced. The IR spectra of both epimers show absorption for an alcohol (3460 and 3450 cm^{-1}) while their ^1H NMR spectra show the presence of two hexanoyl side chains.

α-Decahydrotrichodermolide (**6***a*) was acetylated by treatment with acetic anhydride to give the corresponding *O*-acetyl-α-decahydrotrichodermolide (**7***a*). The introduction of an acetyl group in **7***a* caused the expected shifts in its ^1H NMR spectrum when compared to the ^1H NMR spectrum of **6***a*. Comparison of the ^1H NMR chemical shifts reveals that H-1 is shifted downfield from δ 3.71 in **6***a* to δ 5.55 in **7***a*, which is expected for a secondary alcohol (5), and that Me-23 and Me-21 are shifted upfield from δ 1.46 and 1.69 in **6***a* to δ 1.35 and 1.53 in **7***a* (0.11 and 0.16 ppm, respectively). Similarly, β-decahydrotrichodermolide (**6***b*) was acetylated with acetic

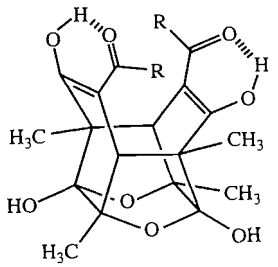

1

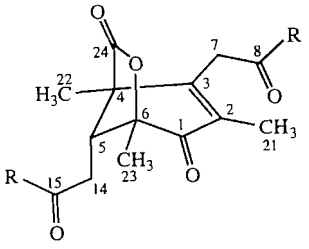

2 R = C_5H_7

5 R = *n*-C_5H_{11}

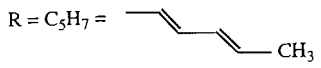

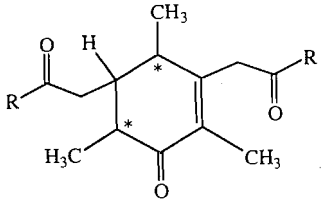

4

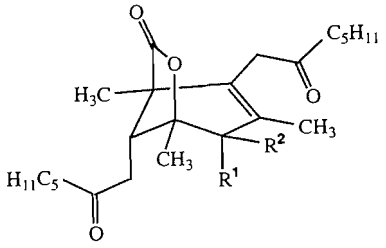

6*a* R^1 = OH, R^2 = H

6*b* R^1 = H, R^2 = OH

7*a* R^1 = OAc, R^2 = H

7*b* R^1 = H, R^2 = OAc

Table 1. ^{13}C NMR data of trichodermolide (**2**), octahydrotrichodermolide (**5**), α-decahydrotrichodermolide (**6***a*), *O*-acetyl-α-decahydrotrichodermolide (**7***a*), anhydrodecahydrotrichodermolide (**9**), and compound **10** ($CDCl_3$, 75.5 MHz).

	Chemical shift in δ (ppm[a,b])					
Carbon	**2**[c]	**5**[c]	**6***a*[c]	**7***a*[c]	**9**[c]	**10**
1	191.2	191.1	73.7	72.5	130.2a	
2	134.2	134.1	132.2	132.0	132.0	131.0a
3	148.6	149.6	128.0	129.6	130.5	135.4a
4	51.8	51.5	48.8	48.5	52.9	135.8a
5	56.0	55.6	46.6	46.6	49.6	—
6	87.2	86.9	84.3	83.4	77.1	—
7	35.1	37.1	37.2	37.1	33.1	44.9
8	195.5	206.9[a]	208.2[a]	208.2[a]	206.9	208.9
9	129.9[a]	43.0[b]	42.4[b]	42.4[b]	42.1	42.0
10	144.1[b]	23.6[c]	23.4	23.3[c]	23.4	23.4
11	124.4[c]	29.7[d]	31.4	31.3	31.3[a]	31.4
12	141.5[b]	22.4[e]	22.5	22.4	22.5	22.4
13	18.9	13.9	14.0	13.9	13.9[b]	13.9
14	42.0	44.3	43.2	43.2	92.9	—
15	196.6	207.5[a]	209.7[a]	209.9[a]	153.8	—
16	130.2[a]	43.2[b]	42.7[b]	42.7[b]	49.6	—
17	144.8[b]	23.4[c]	23.4	23.6[c]	26.8	—
18	126.9[c]	31.3[d]	31.4	31.4	31.4[a]	—
19	142.4[b]	22.4[e]	22.5	22.5	22.5	—
20	18.9	13.9	13.9	13.9	14.1[b]	—
21	11.6	11.5	20.4	20.8[d]	20.2	20.6
22	16.2	16.1[f]	16.2[c]	15.7	17.2[c]	16.7
23	16.2	16.3[f]	15.7[c]	15.6	15.6[c]	—
24	176.1	176.0	177.7	177.0	178.5	—
CO	—	—	—	169.6	—	—
Me	—	—	—	19.7[d]	—	—

[a]The assignments of the signals with the same superscript in the same column are interchangeable.
[b]Relative to the carbon of the solvent (77.0 for $CDCl_3$).
[c]Multiplicity from APT.
[f]Not observed.

anhydride to give *O*-acetyl-β-decahydrotrichodermolide (**7***b*). The introduction of the acetyl group causes shifts similar to the shifts in the ^1H NMR spectrum of **6***a* discussed above. These results are consistent with these methyls being α to the alcohol (for a similar example in aromatic systems, see ref. 6) in **6***a* and **6***b* and show that the enone is reduced selectively.

To determine the relative stereochemistry of the two isomers formed we attempted acid-catalyzed formation of the cyclic acetal **8**.

Compound **8** was not produced upon treatment with *p*-toluenesulphonic acid in methanol; instead this resulted in dehydration of the major epimer **6***a*, and simplified the isolation of the minor isomer *6b*, which did not undergo reaction. The dehydration product **9** was easily separated from *6b* by column chromatography. Mass spectrometry (HREIMS and CIMS) confirmed the molecular formula of **9** as $C_{24}H_{36}O_4$. The IR spectrum of **9** shows absorptions corresponding to lactone (1779 cm^{-1}) and ketone (1715 cm^{-1}) but no OH absorption. Comparison of the ^{13}C NMR spectra of anhydro derivative **9** with that of alcohol **6***a* indicates the presence of an additional double bond the alkenic carbons of which form part of an enol ether double bond (Table 1). Further comparison of the ^1H NMR spectra of the compounds shows that the three-hydrogen spin system in **6***a* is absent in **9** and has been replaced by two mutually coupled hydrogens at δ 4.56 and 2.19 ($J = 6$ Hz). The COSY spectrum of anhydrodecahydrotrichodermolide shows the expected correlations Me-21/H-1, H-7; H-5/H-1, H-14; and H-7/H-1, thus confirming the structure as shown in **9**.

The formation of anhydrodecahydrotrichodermolide (**9**) from the major reduction product, α-decahydrotrichodermolide (**6***a*), confirmed the stereochemistry shown and established the relative stereochemistry at C-5 in trichodermolide.

Prolonged exposure of compound **9** or **6***a* to strongly acidic conditions resulted in the formation of the aromatic compound **10**. Mass spectrometry of compound **10** shows a molecular formula $C_{23}H_{36}O_2$. Its IR spectrum shows the presence of a ketone (1704 cm^{-1}) and an aromatic ring (1450, 1418 cm^{-1}). The UV spectrum of compound **10** confirmed the presence of the aromatic group with low-intensity maxima at 205, 210, and 269 nm, indicating that the aromatic ring is unconjugated (7). Compound **10** displays a very simple ^1H NMR spectrum. It shows absorptions for one aromatic hydrogen (δ 6.92), four

Scheme 1.

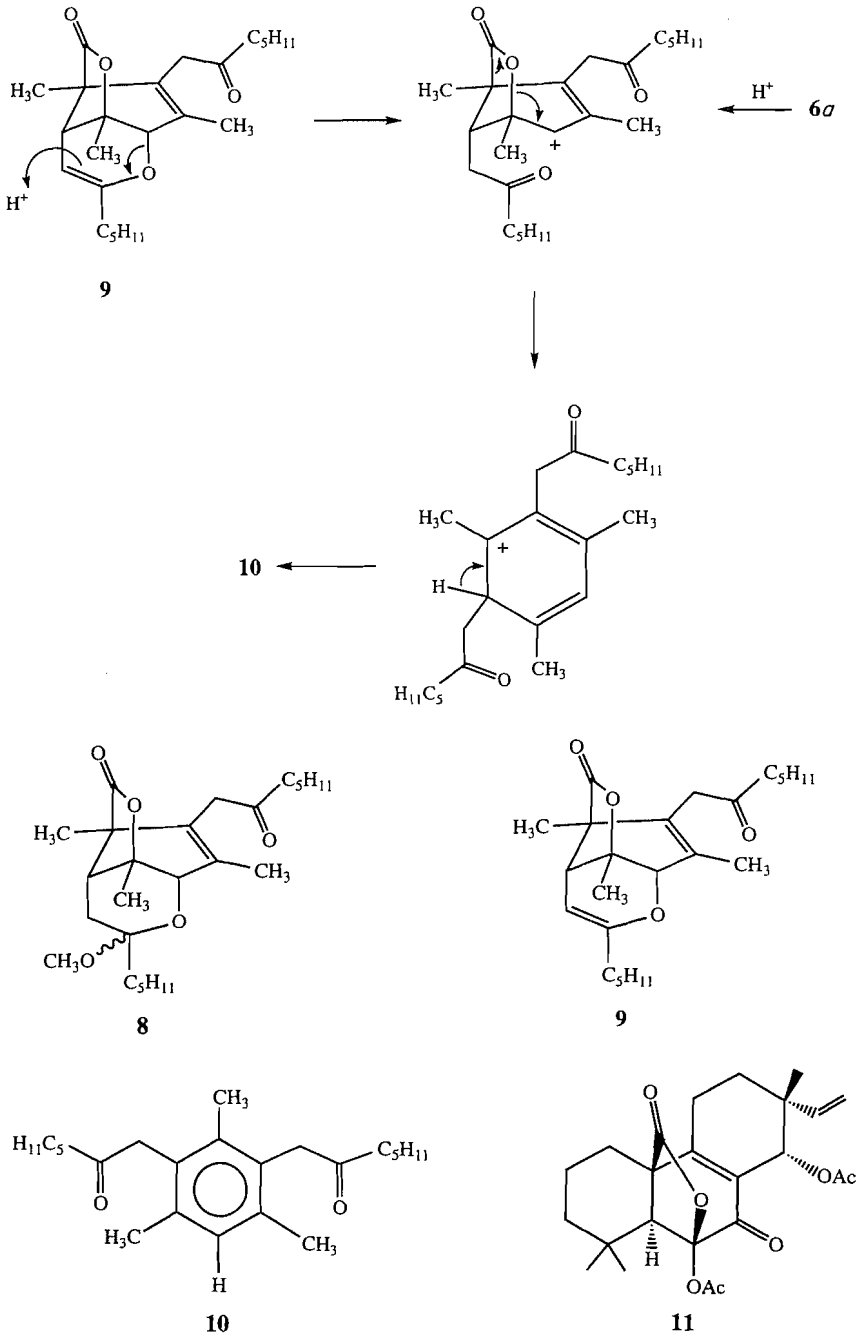

methylene benzylic hydrogens (δ 3.76), three aromatic methyls as singlets at δ 2.20 (6H) and δ 2.04 (3H), and two equivalent hexanoyl side chains. The simplicity of the ^{1}H NMR spectrum indicates that **10** possesses an element of symmetry.

To establish the relative distribution of the aromatic substituents a series of NOE experiments was performed on **10**. The methyl at δ 2.04 ppm gives NOE enhancement to the methylene hydrogens at δ 3.76, while the latter give enhancement to both aromatic methyls.

The aromatization of anhydrodecahydrotrichlodermolide (**9**) is not surprising since compounds containing similar functional groups are known to aromatize. For example, the acid-catalyzed decarboxylation of gibberellic acid (8) and the aromatization of 2β-hydroxy-19-oxo-4-androstene-3,17-dione to estrone (9) are known to occur in the presence of acid. A possible mechanistic pathway for the formation of **10** is shown in Scheme 1.

The determination of the absolute stereochemistry of trichodermolide (**2**) by analysis of its CD spectrum is complicated since it shows a series of Cotton effects. However the CD spectrum of octahydrotrichodermolide (**5**) is simpler. It displays a split Cotton effect with extrema of opposite sign at 270 and 222 nm (A = +28, positive chirality) due to the inherently dissymmetric α,β-unsaturated ketone chromophore, which shows homoconjugation to the lactone carbonyl (10). Examination of molecular models reveals that the π bond of

the lactone carbonyl of octahydrotrichodimerol is in a favourable position to homoconjugate with the double bond of the α,β-unsaturated ketone.

The UV spectrum of octahydrotrichodermolide displays characteristics in accordance with this assumption. These are: longer absorption wavelength and lower intensity than expected for the charge transfer band (ε = 5600 vs. 10 000, 272 vs. 237 nm) and a stronger n-π^* absorption (ε = 1200 vs. 100). These shifts and intensity changes confirm the homoconjugative effect (11).

Homoconjugation of lactone carbonyls with enones has been documented. Ellestad et al. (12) reported the UV and CD spectra of compound **11**. The UV spectrum of compound **11** shows maxima at longer wavelengths (260-265 nm) than other abietane derivatives with similar structure and a C-10 methyl (13). The CD spectrum of compound **11** shows a split Cotton effect, with extrema at 262 and 230 nm (A = +74.4, positive chirality) and its absolute stereochemistry is known (14). Since octahydrotrichodermolide (**5**) and compound **11** possess virtually the same chromophore and the same chirality in their CD spectra, we assign the absolute stereochemistry of trichodermolide as shown in **2**.

Sorbiquinol was obtained as a pale yellow amorphous solid, $[\alpha]_D$ +234 (MeOH). The molecular formula $C_{28}H_{32}O_7$ is based on HREIMS and CIMS data. The EIMS spectrum of sorbiquinol shows fragment ions at m/z 95 corresponding to a sorbyl side chain and a base peak at m/z 165 corresponding to the substituted benzoyl ion derived from sorbicillin (**12**), also isolated from this fungus (1). The CIMS shows fragment ions at m/z 233 (protonated sorbicillin) and at m/z 249, which could be derived from a sorbicillin o-quinol (**13**). Diels–Alder reaction between **12** and **13** gives rise to the bicyclo[2.2.2] adduct **3**. This structure nicely explains all the properties of sorbiquinol (**3**).

The UV spectrum shows base-induced shifts consistent with the enolic-phenol chromophores (see Experimental). The IR spectrum shows absorption for hydroxyl groups (3450 cm^{-1}), saturated ketone (1730 cm^{-1}), strongly chelated carbonyl (1627 cm^{-1}), and aromatic ring(s) (1606 cm^{-1}).

The ^1H NMR spectrum of sorbiquinol shows methyl singlets (δ 1.20, 1.16), two aromatic methyls (δ 2.26, 2.12), an aromatic methine (δ 7.59), two chelated hydroxyl groups (δ 13.98, 12.58), one E,E-sorbyl chain (δ 5.53, 7.17, 5.93, 6.08, and 1.82), a three-hydrogen spin system (δ 4.28 (dd, 6.5, 1.5), 3.26 (dd, 10, 6.5 Hz), and 3.32 (d, 1.5 Hz)), and an E-1-propenyl (δ 5.45 (dq, 15, 6.5 Hz, 1H), 5.02 (ddq, 15, 10, 1.5 Hz, 1H), and 1.60 (dd, 6.5, 1.5 Hz, 3H)) group. Decoupling experiments carried out in acetone allow us to connect the latter two fragments and build up the fragment H_3C-CH=CH-CH-CH-CH present between C-4 and C-17. The hydrogen at δ 5.02 (H-15) shows *trans* coupling (15 Hz) to the hydrogen at δ 5.45 (H-16) and is also coupled to the hydrogen at δ 3.26 (10 Hz, H-7), which in turn is coupled to the hydrogen at δ 4.28 (6.5 Hz, H-8). The latter hydrogen is also coupled to the methine hydrogen at δ 3.32 (1.5 Hz, H-4).

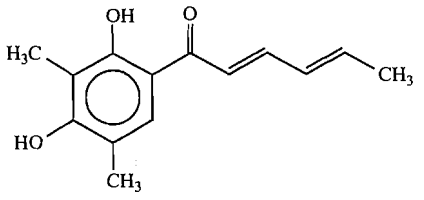

12

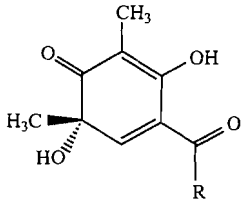

13 R = C_5H_7

16 R = C_5H_{11}

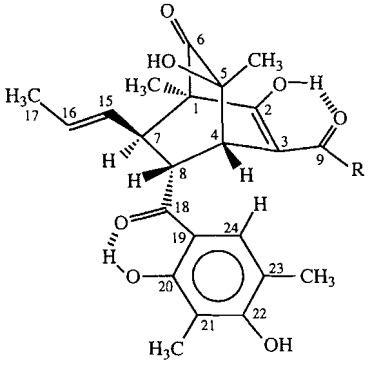

3 R = C_5H_7

14 R = C_5H_{11}

15 R = C_5H_{11}, 15,16-dihydro

The ^{13}C NMR spectrum of sorbiquinol (Table 2) shows 28 carbons. Six signals are assigned to methyl groups, three to aliphatic methines, six to sp^2 methines, one to a tertiary carbon bearing oxygen (δ 75.7), three to carbonyl groups (δ 211.5, 202.1, 198.0), three to oxygen-bearing sp^2 carbons (δ 168.8, 161.9, 159.0) that are not carbonyls, and four to non-hydrogen-bearing sp^2 carbons. A comparison of the ^1H and ^{13}C NMR spectra of sorbiquinol and sorbicillin (**12**) revealed that both compounds have the fragment $(HO)_2(H_3C)_2C_6HCO$. The presence of this fragment is also supported by the mass spectra of sorbiquinol (vide supra). An NOE experiment shows strong enhancement (26%) of the methine hydrogen at δ 4.48 (H-8) and an enhancement of the aromatic methyl at δ 2.24 upon irradiation of the aromatic hydrogen at δ 7.69 (H-24). This information locates the aromatic ring relative to C-8 and is in

Table 2. ^{13}C NMR data of sorbiquinol (**3**), tetrahydrosorbiquinol (**14**), and hexahydrosorbiquinol (**15**).

	Chemical shifts in δ (ppm[a,b])		
Carbon	**3**[c]	**14**[c,d]	**15**[c,d]
1	63.2	62.6	63.1
2	168.8	180.7	180.4
3	106.8	106.3	106.4
4	47.0[b]	47.0[b]	46.9[b]
5	75.7	75.4	75.4
6	211.5	211.4	211.6
7	46.5[b]	46.5[b]	42.7[b]
8	46.7[b]	47.0[b]	46.4[b]
9	198.0	196.9	197.5
10	117.2	31.7	32.7
11	142.4	26.1	26.1
12	130.8	31.5	31.6
13	139.4	22.1	21.1
14	18.9	13.9	13.8
15	128.6	127.2	33.3
16	130.6	130.5	20.7
17	17.8	17.8	14.0
18	202.1	202.2	202.9
19	112.0[a]	111.9[a]	111.3[a]
20	161.9	162.0	162.3
21	110.7	110.6	110.8[a]
22	159.0	159.0	159.0
23	115.0[a]	115.0[a]	115.2[a]
24	129.0	129.0	128.7
CH_3-C-1	10.0	9.7	9.7
CH_3-C-5	24.3	24.3	24.4
CH_3-C-21	7.5	7.5	7.5
CH_3-C-23	16.0	15.7	16.0

[a]Signals with the same superscript in the same column are interchangeable.
[b]Relative to the carbon of the solvent (77.0 for $CDCl_3$).
[c]Multiplicity from APT.
[d]Also obtained from [1-^{13}C]acetate-incorporated sorbiquinol.

agreement with the Diels–Alder hypothesis and the resulting structure **3**.

This structure is supported by further NOE experiments, carried out in acetone. The methine hydrogen at C-4 shows NOE with the methyl group on C-5 (δ 1.20). Similarly, the methyl at C-1 (δ 1.07) shows an NOE enhancement to the methine at δ 3.19 (H-7). In addition, the hydrogen at C-4 shows a strong NOE enhancement (25%) with the α-hydrogen of the sorbyl chain (δ 5.82). The NOE experiments proved very useful in determining the relative stereochemistry of sorbiquinol. The hydrogen at C-8 (δ 4.48) shows strong NOE enhancement (14%) with H-15 (δ 5.16), thus establishing that the 1-propenyl group is *cis* to H-8. The absence of enhancement between the methyl at C-5 (δ 1.20) and H-8 suggests that these two groups are in an *anti* arrangement. Conclusive results, however, were obtained from the ^{1}H NMR pyridine solvent shift study. Addition of ca. 20% of pyridine-d_5 to the $CDCl_3$ solution of sorbiquinol results in the signals for H-8 and H-15 being shifted downfield by 0.37 and 0.24 ppm, respectively, indicating that the C-5 hydroxyl group is *syn* to H-8 and H-15. Additional support of this assignment is provided by the relatively high-field signals of the C-5 methyl group (δ 1.20; usually ca. 1.50 ppm), which may be attributed to the shielding effect of the adjacent sorbyl enol system.

Catalytic hydrogenation of sorbiquinol over Pd/C for 1 h afforded the tetrahydro derivative **14** while reduction for 2 days gave the hexahydro derivative **15**. Compound **14** has the molecular formula $C_{28}H_{36}O_7$ as determined by HREIMS. The EIMS shows a hexanoyl chain (*m/z* 99) and a base peak at *m/z* 165, corresponding to $(HO)_2(H_3C)_2C_6HCO^+$. The ^{1}H and ^{13}C NMR spectra confirm that the sorbyl chain is replaced by a hexanoyl chain (Table 2). Under these conditions the C-15, C-16 double bond is not hydrogenated.

Hexahydrosorbiquinol (**15**) has molecular formula $C_{28}H_{38}O_7$ obtained from the HREIMS and confirmed by CIMS. All ^{1}H and ^{13}C NMR signals of compound **15** are similar to those of compound **14**, except those of the *E*-1-propenyl chain, which are replaced by the signals of an *n*-propyl group (Table 2). Similar to the parent compound sorbiquinol, the chemical ionization spectra of the hydrogenated derivatives **14** and **15** show retro-Diels–Alder fragment ions corresponding to sorbicillin (for **14**, at *m/z* 233) or dihydrosorbicillin (for **15**, at *m/z* 235) and tetrahydrosorbicillin-*o*-quinol **16** (for **14** and **15**).

The CD spectra of sorbiquinol, tetrahydrosorbiquinol, and hexahydrosorbiquinol all display a split Cotton effect with positive chirality. The absolute configuration of these compounds, however, cannot be unambiguously deduced from the CD spectra since the direction of the electric transition dipole moment vector of the aromatic chromophore cannot be readily determined. The similarity between the oxygenated sorbicillin subunits present in sorbiquinol, trichodimerol, and the very closely related metabolites of *Verticilliam intertextum* (15) suggests that they all may have the (*S*) configuration of the oxygen-bearing tertiary carbon atom (C-5 in sorbiquinol), present also in the key intermediate **13**.

Both trichodermolide (**2**) and sorbiquinol (**3**) proved to be inactive against *Mycena citricolor*, but they do represent new structural types of natural products.

Experimental

The general experimental section and the isolation and purification of trichodermolide and sorbiquinol are described in the first part of this series (1). The nuclear Overhauser enhancement determinations (NOE) are from difference spectra and are reported as enhanced area over the irradiated signal area in the difference spectrum. Trichodermolide and sorbiquinol showed the following characteristics:

Trichodermolide (2): $[\alpha]_D$ +97 (*c* 0.98, EtOH); FTIR ν_{max} (cm^{-1}): 3015, 2920, 1781, 1687, 1637, 1595, 1375, 1320, 1188, 997; UV (MeOH) λ_{max} nm (log ε): 280 (4.72), 217 (4.15); no change upon addition of NaOH or HCl; CD (EtOH) $\lambda_{extremum}$ nm (Δε): 224 (−15.4), 260 (+5.4), 273 (+2.9), 289 (+9); ORD (EtOH) $\lambda_{extremum}$ nm ([φ]): 240 (−49 000), 278 (−30 000), 300 (+15 000); ^{1}H NMR ($CDCl_3$) δ: 1.24 (s, 3H, H-22), 1.45 (s, 3H, H-23), 1.78 (s, 3H, H-21), 1.87 (d, 6 Hz, 3H, H-13), 1.89 (d, 6 Hz, 3H, H-20), 2.45 (dd, 18.5, 4 Hz, 1H, H-14), 3.26 (dd, 18.5, 6 Hz, 1H, H-14), 3.34 (dd, 6, 4 Hz, 1H, H-5), 3.66 (AB, 19 Hz, 2H, H-7), 6.10 (d, 15.5 Hz, 1H, H-9), 6.15 (d, 15.5 Hz, 1H, H-16), 6.20–6.25 (m, 4H, H-11, 12, 18, 19), 7.20 (dd, 15.5, 9.5 Hz, 1H,

H-17), 7.24 (dd, 15.5, 9.5 Hz, 1H, H-10); NOE δ: [1.24] (H-22): 3.66 (H-7) (4%), 3.34 (H-5) (10%), 3.26 (H-14) (3%); [1.45] (H-23): 2.45 (H-14) (6%), 3.34 (H-5) (9%); [1.78] (H-21): 3.66 (H-7) (7%); [2.45] (H-14): 3.34 (H-5) (8%), 3.26 (H-14) (20%), 6.15 (H-16) (3%), 7.20 (H-17) (3.5%); [3.34] (H-5): 1.24 (H-22) (2%), 1.45 (H-23) (3%), 2.45 (H-14) (10%); [3.66] (H-7): 1.78 (H-21) (11%), 1.24 (H-22) (3%), 6.10 (H-9) (15%), 7.24 (H-10) (19%); [3.26] (H-14): 2.45 (H-14) (27%), 6.15 (H-16) (6%), 7.20 (H-17) (7%); HMBC (C/H's): 1/21, 23; 2/7, 21; 3/7, 21, 22; 4/7, 14, 22; 5/14, 22, 23; 6/5, 14, 23; 8/7; 15/5, 14; ^{13}C NMR spectrum: see Table 1; HREIMS: 396.1936 (calcd. for $C_{24}H_{28}O_5$: 396.1937, 0.7%), 352 ($C_{23}H_{28}O_3$, 0.2%), 340 (0.2), 301 (0.2), 258 (0.3), 257 (0.7), 248 (1), 191 (2.8), 95 (100); CIMS (NH_3): 414 (M + 18, 15%), 397 (M + 1, 100%); TLC: R_f 0.45 (petroleum ether / EtOAc 5:2).

*Sorbiquinol (**3**)*: $[\alpha]_D$ +234 (*c* 0.36, MeOH); FTIR ν_{max} (cm^{-1}): 3450, 3020, 2960, 2920, 2850, 1730, 1627, 1606, 1562, 1380, 1166, 995; UV (MeOH) λ_{max} nm (ε): 292 (23 000), 359 (22 500), 374 (19 500); NaOH: 252 (18 200), 283 (18 300), 352 (27 000); HCl regenerated the original spectrum; CD(MeOH) $\lambda_{extremum}$ nm (Δε): 343 (+25), 296 (−28); *A* = +53; ORD (MeOH) $\lambda_{extremum}$ nm ([φ]): 362 (+38 000), 323 (−85 000), 272 (+73 000), 252 (+85 000); ^{1}H NMR ($CDCl_3$) δ: 1.16 (s, 3H, CH_3-C-1), 1.20 (s, 3H, CH_3-C-5), 1.60 (dd, 6.5, 1.5 Hz, 3H, H-17), 1.82 (dd, 7, 1.5 Hz, 1H, H-14), 2.12 (s, 3H, CH_3-C-21), 2.26 (s, 3H, CH_3-C-23), 3.26 (dd, 10, 6.5 Hz, 1H, H-7), 3.32 (d, 1.5 Hz, 1H, H-4), 4.28 (dd, 6.5, 1.5 Hz, 1H, H-8), 5.02 (ddq, 15, 10, 1.5 Hz, 1H, H-15), 5.45 (dq, 15, 6.5 Hz, 1H, H-16), 5.53 (d, 15 Hz, 1H, H-10), 5.93 (ddq, 15, 10, 1.5 Hz, 1H, H-12), 6.08 (dq, 15, 7 Hz, 1H, H-13), 7.17 (dd, 15, 10.5 Hz, 1H, H-11), 7.59 (s, 1H, H-24), 12.58 (s, 1H, OH-20), 13.98 (s, 1H, OH-2); (acetone-d_6) δ: 1.07 (s, 3H, CH_3-C-1), 1.20 (s, 3H, CH_3-C-5), 1.58 (dd, 7, 1.5 Hz, 3H, H-17), 2.24 (s, 3H, CH_3-C-23), 3.19 (dd, 10, 6.5 Hz, 1H, H-7), 3.50 (d, 1.5 Hz, 1H, H-4), 3.79 (br s, 1H, OH-5), 4.48 (dd, 6.5, 1.5 Hz, 1H, H-8), 5.16 (ddq, 15, 10, 1.5 Hz, 1H, H-15), 5.45 (dq, 15, 7 Hz, 1H, H-16), 5.82 (d, 15 Hz, 1H, H-10), 5.95 (ddq, 15, 10, 1.5 Hz, 1H, H-12), 6.13 (dq, 15, 7 Hz, 1H, H-13), 7.12 (dd, 10, 15 Hz, 1H, H-11), 7.69 (s, 1H, H-24), and 8.05 (br s, 1H, HO-22); NOE (acetone-d_6) δ: [1.07] (CH_3-C-1): 3.19 (H-7) (4%), 5.16 (H-15) (2%); [1.20] (H-27): 3.50 (H-4) (2%), 3.79 (OH-5) (0.7%); [1.58] (H-17): 5.16 (H-15) (2.5%), 5.45 (H-16) (4%); [3.19] (H-7): 4.48 (H-8) (2%), 5.16 (H-15) (2%); [3.50] (H-4): 1.20 (CH_3-C-5) (4%), 4.48 (H-8) (5%), 5.82 (H-10) (25%), 5.95 (H-12) (–2%), 7.69 (H-24) (16%); [4.48] (H-8): 3.19 (H-7) (4%), 3.50 (H-4) (5%), 5.16 (H-15) (14%), 5.45 (H-16) (−2%), 7.69 (H-24) (26%); [5.16] (H-15): 4.48 (H-8) (7%), 3.19 (H-7) (4%), 1.58 (H-17) (6%); [5.45] (H-16): 3.19 (H-7) (9%); [5.82] (H-10): 3.50 (H-4) (19%); [7.12] (H-11): 5.82 (H-10) (2%), 5.95 (H-12) (5%), 6.13 (H-13) (16%); [7.69] (H-24): 2.24 (CH_3-C-23) (9%), 4.48 (H-8) (24%), 3.50 (H-4) (5%), 5.82 (H-10) (-1%), 5.16 (H-15) (−2%), 5.45 (H-16) (−2%); ^{13}C spectrum: see Table 2; HREIMS: 480.2132 (calcd. for $C_{28}H_{32}O_7$: 480.2149, 17%), 452 (2), 434 (1), 248 (2), 233 (18), 232 (32), 217 (22), 191 (8), 165 (100), 95 (31); CIMS: 481 (M + 1, 12%), 249 (24), 233 (100); TLC: R_f 0.28 (2% EtOH – $CHCl_3$), 0.50 (6%).

Preparation of derivatives

Hydrogenation of trichodermolide

Trichodermolide (**2**) (58 mg) in ethyl acetate (10 mL) was hydrogenated over excess 5% palladium on carbon for 1 h at room temperature. The reaction mixture was filtered, concentrated, and purified by column chromatography (silica gel, C_6H_6:Et_2O 3:1, R_f 0.74) to give pure octahydrotrichodermolide (**5**) (30.1 mg, 51% yield): $[\alpha]_D$ +119 (*c* 0.55, $CHCl_3$); FTIR ν_{max} (cm^{-1}): 2956, 2923, 2872, 2850, 1782, 1715, 1688, 1618, 1463, 1379, 1304, 1184, 1052, 920; UV (MeOH) λ_{max} nm (ε): 219 (5600), 272 (5700), 325 (1200), 329 (1200); CD (MeOH) $\lambda_{extremum}$ nm (Δε): 270 (+13), 222 (−15); ORD (MeOH) $\lambda_{extremum}$ nm ([φ]): 288 (+24 000), 242 (−58 000); ^{1}H NMR ($CDCl_3$) δ: 0.89 (t, 7 Hz, 3H, H-13), 0.91 (t, 7 Hz, 3H, H-20), 1.22 (s, 3H, H-22), 1.30 (m, 8H, H-11,12,18,19), 1.46 (s, 3H, H-23), 1.60 (m, 4H, H-10,17), 1.75 (s, 3H, H-21), 2.30 (dd, 19, 3.5 Hz, 1H, H-14), 2.45 (m,[2] 2H, H-16), 2.52 (t, 7 Hz, 2H, H-9), 3.12 (dd, 19, 7.5 Hz, 1H, H-14), 3.24 (dd, 7.5, 3.5 Hz, 1H, H-5), 3.48 (AB, 17.5 Hz, 2H, H-7); NOE ($CDCl_3$) δ: [1.22] (H-22): 3.24 (H-5) (13%), 3.48 (H-7) (8%); [1.46] (H-23): 2.30 (H-14) (8%), 3.24 (H-5) (10%); [1.75] (H-21): 3.48 (H-7) (6%); [3.24] (H-5): 1.22 (H-22) (1%), 1.46 (H-23) (1%), 2.30 (H-14) (3.5%); ^{13}C NMR spectrum: see Table 1; HREIMS: 404.2552 (calcd. for $C_{24}H_{36}O_5$: 404.2564, 0.8%), 262 (33), 163 (19), 99 (100), 85 (20), 71 (79); CIMS: 405 (M + 1, 100%).

*Reduction of octahydrotrichodermolide (**5**)*

Octahydrotrichodermolide (**5**) (22 mg) was dissolved in benzene–ethanol (2 mL), cooled to 0°C, and excess sodium borohydride in ethanol was added. The reaction was quenched after 1.5 min by addition of saturated aqueous ammonium chloride (0.5 mL). The reaction mixture was diluted with water (8 mL), and extracted with ethyl acetate (3 × 15 mL). The ethyl acetate extract was concentrated and purified by column chromatography (silica gel, 2% EtOH – $CHCl_3$ R_f 0.24) to give α-decahydrotrichodermolide (**6***a*) (10.0 mg, 45% yield): FTIR ν_{max} (cm^{-1}): 3460, 2956, 2932, 2872, 2860, 1773, 1756, 1713, 1379, 1043, 925; ^{1}H NMR ($CDCl_3$) δ: 0.87 (t, 7 Hz, 3H, H-20), 0.88 (t, 7 Hz, 3H, H-13), 1.06 (s, 3H, H-22), 1.30 (m, 8H, H-11,12,18,19), 1.46 (s, 3H, H-23), 1.55 (m, 4H, H-10,17), 1.68 (s, 3H, H-21), 2.22 (br, 1H, OH-1), 2.44 (t, 7 Hz, 2H, H-9), 2.50 (m,[3] 2H, H-16), 2.71 (dd, 6.5, 5 Hz, 1H, H-5), 2.83 (dd, 18.5, 5 Hz, 1H, H-14), 2.99 (dd, 18.5, 6.5 Hz, 1H, H-14), 3.27 (s, 2H, H-7), 3.71 (d, 6 Hz, 1H, H-1); NOE ($CDCl_3$) δ: [1.06] (H-22): 2.71 (H-5) (2.3%), 3.27 (H-7) (3.8%); [1.46] (H-23): 2.71 (H-5) (3.1%), 2.83 (H-14) (1%), 3.71 (H-1) (2.7%); [1.68] (H-21): 3.27 (H-7) (1.5%), 3.71 (H-1) (1.5%); [3.27] (H-7): 2.44 (H-9) (5%), 1.68 (H-21) (7%), 1.06 (H-22) (4%); [3.71] (H-1): 2.22 (OH-1) (6%), 1.68 (H-21) (4%), 1.46 (H-23) (4%), 1.06 (H-22) (4%); ^{13}C NMR spectrum: see Table 1; HREIMS: 406.2730 (calcd. for $C_{24}H_{38}O_5$: 406.2720, 0.8%), 150 (19), 149 (22), 147 (37), 133 (28), 121 (50), 99 (100), 71 (70), and traces of starting material.

*Formation of anhydrodecahydrotrichodermolide (**9**)*

Octahydrotrichodermolide (**5**) (21.5 mg) was dissolved in benzene–ethanol (1 mL), and sodium borohydride (14.1 mg) in ethanol (1 mL) was added at 0°C. After 2 min the reaction was quenched by addition of saturated aqueous ammonium

[2] This signal is present as a multiplet, indicating that these hydrogens are diastereotopic and magnetically similar, forming an AA′BB′-like system.

[3] This signal is present as a multiplet, indicating that these hydrogens are diastereotopic (vide supra).

chloride (0.5 mL), diluted with water (5 mL), and extracted with chloroform (3 × 5 mL). The chloroform extract was evaporated, and the crude mixture was treated with *p*-toluenesulphonic acid (10 mg) in methanol (4 mL) for 2 weeks at room temperature. The methanol was removed under reduced pressure and the mixture purified by column chromatography (silica gel, 2% EtOH – $CHCl_3$) to afford β-decahydrotrichodermolide (**6***b*) (2.8 mg): FTIR ν_{max} (cm^{-1}): 3450, 2956, 2929, 2872, 2858, 1770, 1714, 1457, 1379, 1049; UV (MeOH): no absorptions detected; ^1H NMR ($CDCl_3$) δ: 0.89 (t, 7 Hz, 3H, H-20), 0.90 (t, 7 Hz, 3H, H-13), 1.03 (s, 3H, H-22), 1.30 (m, 8H, H-11,12,18,19), 1.49 (s, 3H, H-23), 1.56 (m, 4H, H-10,17), 1.68 (s, 3H, H-21), 2.32 (dd, 18, 3 Hz, 1H, H-14), 2.43 (t, 7 Hz, 2H, H-9), 2.53 (m,[3] 2H, H-16), 2.89 (dd, 7, 3 Hz, 1H, H-5), 3.19 (dd, 18, 7 Hz, 1H, H-14), 3.25 (AB, 18 Hz, 2H, H-7), 3.70 (br s, 1H, H-1); NOE ($CDCl_3$) δ: [1.03] (H-22): 3.25 (H-7) (1%), 2.89 (H-5) (5%); [1.49] (H-23): 3.70 (H-1) (3%), 2.89 (H-5) (3%); [1.68] (H-21): 3.70 (H-1) (2%), 3.25 (H-7) (0.8%); HREIMS: 406.2737 (calcd. for $C_{24}H_{38}O_5$: 406.2720, 0.8%), 361 (29), 248 (19), 245 (22), 149 (54), 147 (26), 133 (20), 121 (38), 99 (100), 71 (66); CIMS: 424 (M + 18, 100%), 407 (M + 1, 12%). Further chromatography with 3% Et_2O – C_6H_6 as eluant afforded aromatic compound **10** (2.6 mg): FTIR ν_{max} (cm^{-1}): 2958, 2928, 2871, 2858, 1704, 1450, 1418; UV (MeOH) λ_{max} nm (ε): 205 (13 000), 210 (15 000), 269 (400); no change upon addition of NaOH or HCl; ^1H NMR ($CDCl_3$) δ: 0.87 (t, 7 Hz, 6H), 1.26 (m, 8H), 1.56 (m, 4H), 2.04 (s, 3H, CH_3Ar), 2.20 (s, 6H, 2 × CH_3Ar), 2.40 (t, 7 Hz, 4H, $COCH_2$), 3.76 (s, 4H, 2 × CH_2Ar), 6.92 (s, 1H, ArH); ^{13}C NMR spectrum: see Table 1; HREIMS: 344.2714 (calcd. for $C_{23}H_{36}O_2$: 344.2715, 5%), 326 (21), 245 ($C_{17}H_{25}O$, 100%), 227 (24), 147 (23), 99 (44); CIMS: 362 (M + 18, 100%), 345 (M + 1, 1%), 245 (7); NOE δ: [2.04] (CH_3Ar): 3.76 (CH_2Ar) (4.3%), 2.20 (CH_3Ar) (−3.2%); [2.20] (CH_3Ar): 3.76 (CH_2Ar) (1.5%), 6.92 (ArH) (3.6%); [3.76] (CH_2Ar): 2.20 (CH_3Ar) (5%), 2.40 ($COCH_2$) (4%), 2.04 (CH_3Ar) (7.3%); [6.92] (ArH): 2.20 (CH_3Ar) (13.5%); and anhydrodecahydrotrichodermolide (**9**) (2.4 mg): FTIR ν_{max} (cm^{-1}): 2955, 2930, 2872, 2859, 1779, 1715, 1687, 1381, 1180, 1070; UV (MeOH) λ_{max} nm (ε): 202 (6000), 232 (2000); no change upon addition of NaOH or HCl; ^1H NMR ($CDCl_3$): 0.86 (t, 7 Hz, 6H, H-13,20), 1.04 (m, 4H, H-18,19), 1.17 (s, 3H, H-22), 1.20 (m, 4H, H-11,12), 1.43 (s, 3H, H-23), 1.43 (m, 2H, H-17), 1.53 (m, 2H, H-10), 1.68 (s, 3H, H-21), 2.04 (m,[3] 2H, H-16), 2.19 (d, 6 Hz, 1H, H-5), 2.37 (m, 2H, H-9), 3.21 (s, 2H, H-7), 4.08 (br s, 1H, H-1), 4.56 (d, 6 Hz, 1H, H-14); COSY ($CDCl_3$): Me-21 (δ 1.68)/H-1 (δ 4.08), H-7 (δ 3.21); H-5 (δ 2.19)/H-1 (δ 4.08), H-14 (δ 4.56); H-7 (δ 3.21)/H-1 (δ 4.08); NOE ($CDCl_3$) δ: [1.17] (H-22): 2.19 (H-5) (3.3%), 3.21 (H-7) (2%), 4.56 (H-14) (1%); [1.43] (H-23): 2.04 (H-16) (1%), 2.19 (H-5) (2.5%), 4.08 (H-1) (3.3%); [1.68] (H-21): 3.21 (H-7) (2%), 4.08 (H-1) (3.5%); [2.19] (H-5): 1.17 (H-22) (6%), 1.43 (H-23) (8%), 4.56 (H-14) (10%); [3.21] (H-7): 1.17 (H-22) (4%), 1.68 (H-21) (5.4%), 2.37 (H-9) (1%); [4.08] (H-1): 1.43 (H-23) (7%), 1.68 (H-21) (5.4%); [4.56] (H-14): 2.04 (H-16) (5%), 2.19 (H-5) (11%), 2.37 (H-9) (1%); ^{13}C NMR spectrum: see Table 1; HREIMS: 388.2611 (calcd. for $C_{24}H_{36}O_4$: 388.2615, 0.6%), 277 ($C_{18}H_{29}O_2$, 100%), 245 (21), 99 (55); CIMS: 406 (M + 18, 100%), 390 (M + 2, 36%).

α-Decahydrotrichodermolide (**6***a*) (4.5 mg) was treated with 1% methanolic *p*-toluenesulphonic acid (2 mL), at room temperature for 2 h. The reaction mixture was concentrated and purified by column chromatography (silica gel, 2% EtOH – $CHCl_3$), to give the enol ether anhydrodecahydrotrichodermolide (**9**) (3.5 mg, R_f 0.71).

α-Decahydrotrichodermolide (**6***a*) (3 mg) was acetylated by overnight reaction with acetic anhydride (1 mL) and pyridine (0.5 mL) at room temperature. The excess pyridine and acetic anhydride were removed azeotropically with toluene to give pure *O*-acetyl-α-decahydrotrichodermolide (**7***a*) (2.5 mg): FTIR ν_{max} (cm^{-1}): 2956, 2928, 2872, 2857, 1780, 1748, 1715, 1457, 1417, 1380, 1371, 1258, 1022, 931, 804; UV (MeOH): no UV absorptions detected; ^1H NMR ($CDCl_3$) δ: 0.89 (t, 7 Hz, 3H, H-20), 0.90 (t, 7 Hz, 3H, H-13), 1.10 (s, 3H, H-22), 1.30 (m, 8H, H-11, 12, 18, 19), 1.35 (s, 3H, H-23), 1.53 (s, 3H, H-21), 1.58 (m, 4H, H-10,17), 2.46 (t, 7 Hz, 2H, H-9), 2.54 (m,[3] 2H, H-16), 2.71 (m, 1H, H-14), 2.73 (1H, H-5), 3.09 (m, 1H, H-14), 3.31 (s, 2H, H-7), 5.29 (br s, 1H, H-1); NOE ($CDCl_3$) δ: [1.10] (H-22): 3.31 (H-7) (3%), 2.73 (H-5) (3%); [1.35] (H-23): 5.29 (H-1) (2.5%), 2.73 (H-5) (1%); [1.53] (H-21): 5.29 (H-1) (2.5%), 3.31 (H-7) (2%); [3.31] (H-7): 1.53 (H-21) (7%), 2.46 (H-9) (4%), 1.10 (H-22) (1%); ^{13}C NMR spectrum: see Table 1; HREIMS: 448.2831 (calcd. for $C_{26}H_{40}O_6$: 448.2826, 0.1%), 404 (M − CO_2, 0.2), 246 (41), 147 (47), 135 (6), 133 (42), 121 (16), 99 (100), 71 (72). Acetylation of β-decahydrotrichodermolide (**6***b*) in a similar way gave *O*-acetyl-β-decahydrotrichodermolide (**7***b*) (1.5 mg): FTIR ν_{max} (cm^{-1}): 2956, 2927, 2873, 2858, 1772, 1742, 1716, 1374, 1231, 1093, 1056, 1028; UV (MeOH): no absorption detected; ^1H NMR ($CDCl_3$) δ: 0.89 (t, 7 Hz, 6H, H-13, 20), 1.04 (s, 3H, H-22), 1.30 (m, 8H, H-11,12,18,19), 1.32 (s, 3H, H-23), 1.49 (s, 3H, H-21), 1.58 (m, 4H, H-10, 17), 2.43 (dd, 18, 3 Hz, 1H, H-14), 2.44 (t, 7 Hz, 2H, H-9), 2.55 (m, 2H, H-16), 2.92 (dd, 8.5, 3 Hz, 1H, H-5), 3.28 (dd, 18, 8.5 Hz, 1H, H-14), 3.29 (AB, 18 Hz, 2H, H-7), 5.40 (br s, 1H, H-1); HREIMS: 448.2817 (calcd. for $C_{26}H_{40}O_6$: 448.2826, 0.1%), 403 (M − CO_2, 8%), 248 (30), 245 (42), 133 (44), 121 (22), 99 (100), 71 (71); CIMS: 466 (M + 18, 100%), 449 (M + 1, 3%).

Aromatization of anhydrodecahydrotrichodermolide (9)

Anhydrodecahydrotrichodermolide (**9**) (8 mg) was refluxed overnight in 1% methanolic *p*-toluenesulphonic acid (2 mL). The reaction mixture was evaporated and purified by column chromatography (3% Et_2O – C_6H_6) to give the aromatic compound **10** (4 mg) and unreacted starting material.

Hydrogenation of sorbiquinol (3)

A mixture (58 mg) containing sorbiquinol and trichodimerol, obtained from the mycelial extract of *T. longibrachiatum* (UAMH 5068), was hydrogenated with excess 5% palladium on carbon in ethyl acetate (4 mL) at room temperature and pressure for 1 h. The reaction mixture was filtered through celite, evaporated, and purified by column chromatography (silica gel, 3% EtOH – $CHCl_3$) to give tetrahyrdosorbiquinol (**14**) (15 mg, 95% pure): $[\alpha]_D$ +86 (*c* 0.23, MeOH); FTIR ν_{max} (cm^{-1}): 3450, 2960, 2870, 2850, 1730, 1625, 1490, 1380, 1292, 1165, 1145; UV (MeOH) ν_{max} nm (ε): 217 (13 800), 232 sh, 290 (19 000); NaOH: 258 (12 400), 309 sh, 344 (29 000);

[4] The chemical shift and multiplicity was obtained from NOE difference spectra since these signals overlap in the reguar ^1H NMR spectrum.

HCl regenerated the original spectrum; ^{1}H NMR ($CDCl_3$) δ: 0.78 (t, 7.5 Hz, 3H, H-14), 1.00 (m, 4H, H-12, 13), 1.16 (s, 3H, CH_3-C-1), 1.23 (s, 3H, CH_3-C-5), 1.45 (m, 2H, H-11), 1.60 (dd, 7, 1.5 Hz, 3H, H-17), 1.96 (t, 8 Hz, 2H, H-10), 2.13 (s, 3H, CH_3-C-21), 2.26 (s, 3H, CH_3-C-23), 2.87 (s, 1H, OH-5), 3.245 (dd,[4] 10, 6.5 Hz, 1H, H-7), 3.247 (d,[4] 1.5 Hz, 1H, H-4), 4.27 (dd, 7, 1.5 Hz, 1H, H-8), 4.99 (ddq, 15, 10, 1.5 Hz, 1H, H-15), 5.44 (dq, 15, 7 Hz, 1 H, H-16), 7.60 (s, 1H, H-24), 12.79 (s, 1H, OH-20), 14.37 (s, 1H, OH-2); NOE ($CDCl_3$) δ: [1.16] (CH_3-C-1): 3.245 (H-7) (2.3%), 4.99 (H-15) (1.1%), 5.44 (H-16) (0.4%); [1.23] (CH_3-C-5): 3.247 (H-4) (2%); [1.96] (H-10): 3.247 (H-4) (7%); [2.26] (CH_3-C-23): 7.60 (H-24) (2%); [4.27] (H-8): 3.245 (H-4, H-7) (7%), 4.99 (H-15) (13%), 7.60 (H-24) (23%); [5.44] (H-16): 3.245 (H-7) (10%), 4.99 (H-15) (2%); [7.60] (H-24): 2.26 (CH_3-C-23) (7%), 3.247 (H-4) (6%), 4.27 (H-8) (22%), 4.99 (H-15) (–2.4%); ^{13}C NMR spectrum: see Table 2; CD (MeOH) $\lambda_{extremum}$ nm (Δε): 318 (+37), 284 (−41); A = +78; HREIMS: 484.2460 (calcd. for $C_{28}H_{36}O_7$: 484.2462, 3.3%), 252 (2), 232 (25), 165 (100), 99 (10), 95 (3); CIMS: 502 (M + 18, 3%), 485 (M + 1, 41%), 253 (32), 233 (100), 106 (82); tlc: R_f 0.26 (2% EtOH – $CHCl_3$), 0.52 (6%); and octahydrotrichodimerol (20 mg).

When the hydrogenation is allowed to proceed for 2 days, work-up of the reaction mixture in a similar way gave hexahydrosorbiquinol (**15**) (6 mg). $[\alpha]_D$ +117 (*c* 0.23, MeOH); FTIR ν_{max} (cm^{-1}): 3480, 2955, 2865, 1732, 1627, 1482, 1450, 1382, 1188, 757; UV (MeOH) λ_{max} nm (ε): 215 (15 900), 230 sh, 290 (19 000); NaOH: 257 (6900), 315 sh, 344 (23 000); HCl regenerated the original spectrum; ^{1}H NMR ($CDCl_3$) δ: 0.79 (m, 6H, H-14,17), 1.1 (m, 8H, H-12, 13, 15, 16), 1.21 (s, 3H, CH_3-C-5), 1.29 (s, 3H, CH_3-C-1), 1.47 (m, 2H, H-11), 1.94 (t, 7 Hz, 2H, H-10), 2.14 (s, 3H, CH_3-C-21), 2.27 (s, 3H, CH_3-C-23), 2.72 (m, 1H, H-7), 2.81 (s, 1H, OH-5), 3.22 (d, 1.5 Hz, 1H, H-4), 4.18 (dd, 7, 1.5 Hz, 1H, H-8), 5.36 (s, 1H, OH-22), 7.64 (s, 1H, H-24), 12.84 (s, 1H, OH-20), 14.38 (s, 1H, OH-2); NOE ($CDCl_3$) δ: [1.21] (CH_3-C-5): 1.47 (H-11) (3%), 2.81 (OH-5) (1%), 3.22 (H-4) (15%); [1.29] (CH_3-C-1): 2.72 (H-7) (2%); [1.94] (H-10): 1.47 (H-11) (10%), 3.22 (H-4) (7%); [3.22] (H-4): 1.21 (CH_3-C-5) (3%), 4.18 (H-8) (4%), 7.64 (H-24) (5%); [7.64] (H-24): 3.22 (H-4) (6%), 4.18 (H-8) (19%); ^{13}C NMR spectrum: see Table 2; CD (MeOH) $\lambda_{extremum}$ nm (Δε): 316 (+29), 285 (−34); *A* = +63; HREIMS: 486.2616 (calcd. for $C_{28}H_{38}O_7$: 486.2618, 17%), 253 (1.4), 235 (28), 191 (28), 165 (100), 99 (5); CIMS: 504 (M + 18, 34), 487 (M + 1, 100), 253 (78), 233 (79), 165 (54); TLC: R_f 0.25 (2% EtOH – $CHCl_3$), 0.56 (6%).

Acknowledgements

We acknowledge with thanks the financial support provided by the Natural Sciences and Engineering Research Council of Canada, the International Development Research Centre, and the Alberta Heritage Foundation for Medical Research. We also thank Lynne Sigler, University of Alberta Microfungus Herbarium, for cultures and valuable discussion.

References

1. R. Andrade, W.A. Ayer, and P.P. Mebe. Can. J. Chem. **70**, 2526 (1992).
2. L.M. Jackman and S. Sternhell. Applications of nuclear magnetic resonance spectroscopy in organic chemistry. 2nd ed. Pergamon, Great Britain. 1969. p. 273.
3. A. Bax. J. Magn. Reson. **57**, 314 (1984).
4. (*a*) M. Salazar and A.S. Zektzer. Magn. Reson. Chem. **26**, 24 (1988); (*b*) G.E. Martin and A.S. Zektzer. Magn. Reson. Chem. **26**, 631 (1988).
5. L.M. Jackman and S. Sternhell. Applications of nuclear magnetic resonance spectroscopy in organic chemistry. 2nd ed. Pergamon, Great Britain. 1969. p. 179.
6. J. Frei, C. Ganter, D. Kagi, K. Kocsis, M. Mijkovic, A. Siewinski, R. Wenger, K. Schaffner, and O. Jeger. Helv. Chim. Acta, **49**, 1049 (1966).
7. R.M. Silverstein, G.C. Bassler, and T.C. Morrill. Spectrometric identification of organic compounds. John Wiley and Sons, New York. 1981. p. 321.
8. R.J. Pryce. J. Chem. Soc. Perkin Trans. 1, 1179 (1984).
9. H. Hosoda and J. Fishman. J. Am. Chem. Soc. **96**, 7325 (1974).
10. P. Crabbé. An introduction to chiroptical methods in chemistry. Impresos Offsali-G.S.A., Mexico. 1971. p. 18.
11. A.I. Scott. Interpretation of the ultraviolet spectra of natural products. Pergamon, New York. 1964. p. 69.
12. G.A. Ellestad, M.P. Kunstmann, and G.O. Morton. J. Chem. Soc. Chem. Commun. 312 (1973).
13. W. Hewz and J.J. Schmid. J. Org. Chem. **34**, 3464 (1969).
14. G.A. Ellestad, M.P. Kunstmann, P. Mirando, and G.O. Morton. J. Am. Chem. Soc. **94**, 6206 (1972).
15. L.S. Trifonov, H. Hilpert, P. Floersheim, A.S. Dreiding, D.M. Rast, R. Skrivanova, and L. Hoesch. Tetrahedron, **42**, 3157 (1986).

Hydrogen evolution reaction at nickel boride electrodes in aqueous and in aqueous methanolic and ethanolic solutions

Behzad Mahdavi, Danielle Miousse, Joël Fournier, Hugues Ménard, and Jean Lessard

Abstract: The hydrogen evolution reaction (HER) was investigated at nickel boride pressed powder electrodes in aqueous and in aqueous methanolic (ethanolic) alkaline (1 M NaOH) solutions in the presence and the absence of NaCl (0.1 M) and H_3BO_3 (0.1 M) at 25°C by the steady-state polarization and ac impedance techniques. The ac impedance data were analyzed using the constant-phase element (CPE) model. It was found that the electrocatalytic behaviour of a nickel boride electrode for the HER was the same in all the above media and that the HER proceeds via the Volmer–Heyrovsky mechanism. The kinetic parameters of the HER were determined.

Key words: hydrogen evolution reaction, nickel boride electrodes, Tafel curves, ac impedance, kinetic parameters.

Résumé : La réaction de dégagement d'hydrogène (RDH) sur électrodes de borure de nickel faites de poudre pressée a été étudiée en milieu aqueux et aqueux méthanolique (éthanolique) alcalin (1 M NaOH) en présence et en absence de NaCl (0.1 M) et H_3BO_3 (0.1 M) à 25°C par les techniques de polarisation stationnaire et d'impédance ac. Le modèle d'élément de phase constant (EPC) a été utilisé pour l'analyse des données de l'impédance ac. Le comportement électrocatalytique d'une électrode de borure de nickel s'est avéré le même dans les différents milieux étudiés et la RDH fait intervenir un mécanisme Volmer–Heyrovsky. Les paramètres cinétiques de la RDH ont été déterminés.

Mots clés : réaction de dégagement d'hydrogène, électrodes de borure de nickel, courbes de Tafel, impédance ac, paramètres cinétiques.

Introduction

The hydrogen evolution reaction (HER) is of prime importance in the whole range of electrocatalytic processes and has therefore been one of the most studied cathodic reactions (1–5). In the recent past, due to its economic and environmental impact, an increased interest in the practical industrial application of low-overvoltage cathode electrolyses has been noted. Hydrogen has also played a major role in synthetic organic chemistry in the well-known catalytic hydrogenation process by which an unsaturated compound R, adsorbed at the surface of a catalyst M, (M(R)), is reduced by the adsorbed hydrogen M(H) (reactions [1]–[4]) (6).

[1] $H_2 + M = 2\ M(H)$

[2] $R + M = M(R)$

[3] $M(R) + 2\ M(H) = M(RH_2) + M$

[4] $M(RH_2) = RH_2 + M$

Such reactions generally require high temperatures and pressures. Another method of hydrogenation of these compounds under much milder conditions is electrocatalytic hydrogenation (**ECH**), in which the adsorbed hydrogen is formed in situ by electrolysis of water (reaction [5]). In this process, the hydrogenation reaction (eqs. [2]–[4]) is in competition with hydrogen evolution (reactions [6] and (or) [7] representing the electrochemical and chemical desorption of hydrogen respectively (Scheme 1)) and the efficiency of the ECH is determined by this competition.

Scheme 1.

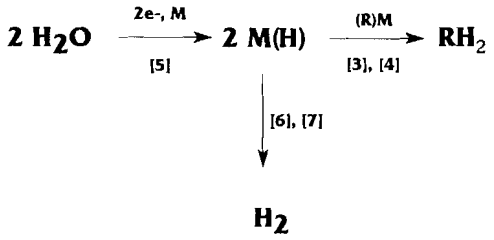

[5] $H_2O + e^- + M = (H)M + OH^-$ (Volmer)

[6] $(H)M + H_2O + e^- = H_2 + M + OH^-$ (Heyrovsky)

[7] $(H)M + (H)M = H_2 + M$ (Tafel)

In view of the conjunction of the HER and the ECH reactions, the kinetic and roughness factor parameters obtained from HER studies can clarify the understanding of the ECH process (7). However, the HER is often studied in aqueous alkaline solutions (1 M NaOH) (because the nickel-based electrodes, which are widely used in industrial processes, are stable in this medium) while the electrocatalytic hydrogenation of organic

Received September 15, 1995.

B. Mahdavi, D. Miousse, J. Fournier, H. Ménard, and J. Lessard.[1] Département de chimie, Université de Sherbrooke, QC J1K 2R1, Canada.

[1] Author to whom correspondence may be addressed. Telephone: (819) 821-7091. Fax: (819) 821-8017.

Scheme 2.

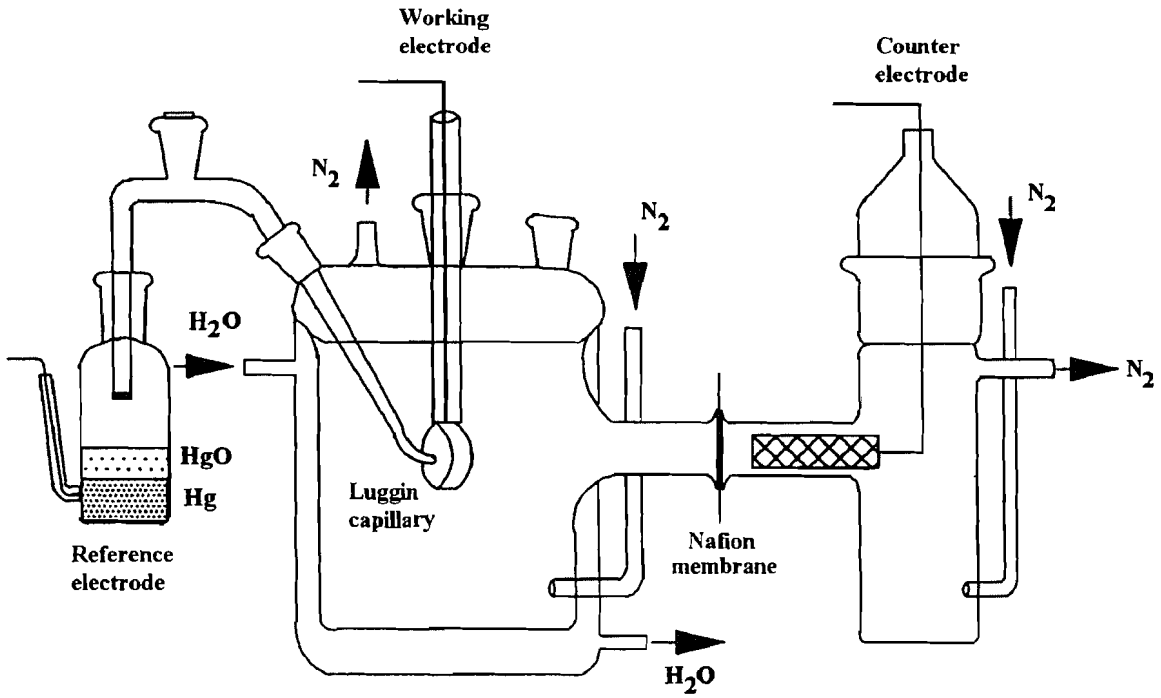

compounds is often carried out in methanolic or ethanolic solutions containing NaCl (0.1 M) and H_3BO_3 (0.1 M), an acid (8, 9). In fact, the organic solvent permits the dissolution of the organic products, NaCl is used as supporting electrolyte, and H_3BO_3 is used as a buffer to prevent rapid increase of the pH during the electrolysis (reaction [5]). To see if the results obtained in HER studies in aqueous alkaline solutions can be extrapolated to the ECH studies in alcoholic solutions containing NaCl and H_3BO_3, we have investigated HER at nickel boride pressed powder electrodes in aqueous alkaline (1 M NaOH) and in aqueous methanolic (ethanolic) solutions in the presence and in the absence of NaCl (0.1 M) and H_3BO_3 (0.1 M) at 25°C by the steady-state polarization and ac impedance techniques. The results are reported in this paper.

Experimental

Electrodes

Nickel boride (Ni_2B) was obtained as a powder (average particle size of 0.5 μm and specific surface area of 9 $m^2 g^{-1}$) (7) by reduction of nickel acetate with $NaBH_4$ in aqueous NaOH (9). The electrodes were obtained by pressing the particles at $p = 120$ MPa at room temperature. Silver epoxy (EPO-TEK H2OE, Epoxy Tech., Inc) was used to ensure a good electrical contact. One face and the sides of electrodes were coated with Epofix resin (Struers), known for its stability (i.e., no leaching) in alkaline solution (10–12), in order to obtain a projected geometric surface area of 1.1 cm^2 and avoid the effect of the edge plane defects.

Data acquisition

The Tafel plots were measured using an EG&G PAR 273. The potentiostat and an EG&G Lock-in Analyzer (model 5208) connected and controlled by an IBM-compatible microcomputer (by means of a GPIB PC2A interface) were used for the ac impedance measurements.

Electrolyses

The electrochemical cell (Scheme 2) consisted of two compartments made of Pyrex, separated by a reinforced Nafion cationic membrane (du Pont M-901CATH/MD). A cylindrical platinum grid (length 5.5 cm and diameter 2.5 cm) was used as anode. A Hg/HgO/1 M NaOH reference electrode was connected by a Luggin capillary. Solutions were made with spectrograde NaOH (Aldrich, 99.99%), deionized water ($R = 17.5$ MΩ cm) (Barnstead Nanopure), and commercial methanol(ethanol) (ACP) distilled before use. The equilibrium potential was measured in each solution at a platinized platinum electrode. In all media the value was identical within the experimental error (−920 mV). The electrochemical experiments were performed at 25°C in 1 M NaOH solutions. A reduction current of 100 mA cm^{-2} was applied to the cathode for 12 h prior to the measurements. Tafel curves were recorded galvanostatically in the current range of 300 mA cm^{-2} to 0.1 μA cm^{-2} after a galvanostatic activation of 15 min under a current of 100 mA cm^{-2}. The Tafel parameters were calculated after correction for the ohmic drop. The resistance of the solution was determined by ac impedance spectroscopy. Ten frequencies per decade were thus scanned from 10 kHz to 5 Hz at different dc overpotentials. In the frequency range of 5 – 0.05 Hz, the fast Fourier transform technique was used. The sinusoidal potential superimposed was 10 mV peak to peak.

Theory

The hydrogen evolution reaction involves the formation of adsorbed hydrogen (reaction [5], Volmer step) and its desorption (reaction [6], Heyrovsky step and (or) reaction [7], Tafel step). The rates of these reactions are given, in units of flux (mol cm^{-2} s^{-1}), by the following expressions (13, 14):

$$[8] \quad v_1 = k_1(1-\theta)\exp(-\beta_1 f\eta) - k_{-1}\theta\exp[(1-\beta_1)f\eta]$$

Fig. 1. Tafel plots obtained at 25°C on a nickel boride electrode in: (●) S_1: 1 M NaOH, (■)S_2: 1 M NaOH/MeOH (50/50)(v/v); (▲)S_3: 1 M NaOH/MeOH (50/50) (v/v) + 0.1 M NaCl; (◆) S_4: 1 M NaOH/MeOH (50/50) (v/v) + 0.1 M NaCl +0.1 M H_3BO_3. The points are experimental and lines were calculated from the rate constants shown in Table 3 using the CPE model.

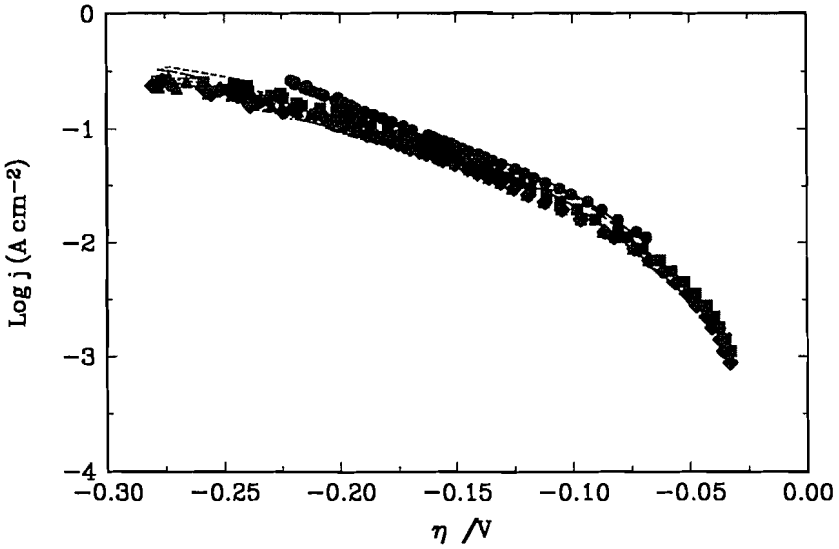

Scheme 3.

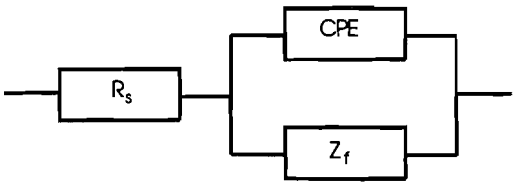

[9] $v_2 = k_2\theta \exp(-\beta_2 f\eta) - k_{-2}(1 - \theta) \exp[(1 - \beta_2)f\eta]$

[10] $v_3 = k_3\theta^2 - k_{-3}(1-\theta)^2$

where k_i is the reaction rate constant, which includes the concentrations of OH^- and H_2O, β_1 and β_2 are the symmetry coefficients for the Volmer and Heyrovsky steps, respectively, η is the overpotential, θ is the surface coverage by adsorbed hydrogen, and $f = F/RT$. The electrical equivalent model describing the HER on an ideally smooth electrode consists of the solution resistance, R_s, in series with the parallel connection of the double layer capacitance, C_{dl}, and faradaic impedance, Z_f (Scheme 3). The faradaic impedance, in the case when the mass transport can be neglected, is given by eq. [11]:

[11] $$Y_f = \frac{1}{Z_f} = A + \frac{B}{j\omega + C}$$

where

[12] $$A = -F\left(\frac{\delta r_0}{\delta \eta}\right)_\theta$$

[13] $$B = \frac{-F^2}{\sigma_1}\left(\frac{\delta r_1}{\delta \eta}\right)_\theta\left(\frac{\delta r_0}{\delta \theta}\right)_\eta$$

[14] $$C = -\frac{F}{\sigma_1}\left(\frac{\delta r_1}{\delta \theta}\right)_\eta$$

where $r_0 = v_1 + v_2$, $r_1 = v_1 - v_2 - 2v_3$, and σ_1 is the charge necessary for a monolayer coverage by adsorbed hydrogen. However, on solid electrodes, this model cannot describe adequately the observed impedance data because the nonhomogeneous surface of solid electrodes causes deformation of the complex plane plots. The CPE model was therefore proposed for cases where a depressed semicircle is observed on complex plane plots. In this case, the double layer capacity is substituted by the CPE and its impedance equals (15):

[15] $Z_{CPE} = 1/T(j\omega)^\Phi$

[16] $T = C_{dl}^{\Phi}(R_s^{-1} + A)^{(1-\Phi)}$

where ω is the angular frequency of the ac signal, T is a constant, ϕ is the phase angle related to the surface roughness, and parameter A is equal to $1/R_{ct}$ where R_{ct} is the charge transfer resistance (7, 16–23). For an ideally flat electrode, ϕ is equal to 1 and, thus, T is equal to C_{dl}.

Results and discussion

Nickel boride is a non-magnetic and non-pyrophoric black powder whose catalytic activity in catalytic hydrogenation (24, 25) and in electrocatalytic hydrogenation (7) reactions is similar to that of Raney nickel. Nickel boride electrodes obtained by pressing the powder have a very reproducible surface area (7) since there is no need of an activation method that can modify the surface irregularly as in the case of RaNi electrodes, which are obtained by leaching the pressed Raney alloy (26). However, to ensure that the observations made were due to changes in the solution composition and not to changes on the electrode itself, the same electrode was used during the entire experiment for each solvent.

Fig. 2. Tafel plots obtained at 25°C on a nickel boride electrodes in: (●) S_1: 1 M NaOH; (■)S_5: 1 M NaOH/EtOH (50/50) (v/v). The points are experimental and lines were obtained from the rate constants shown in Table 3 using the CPE model.

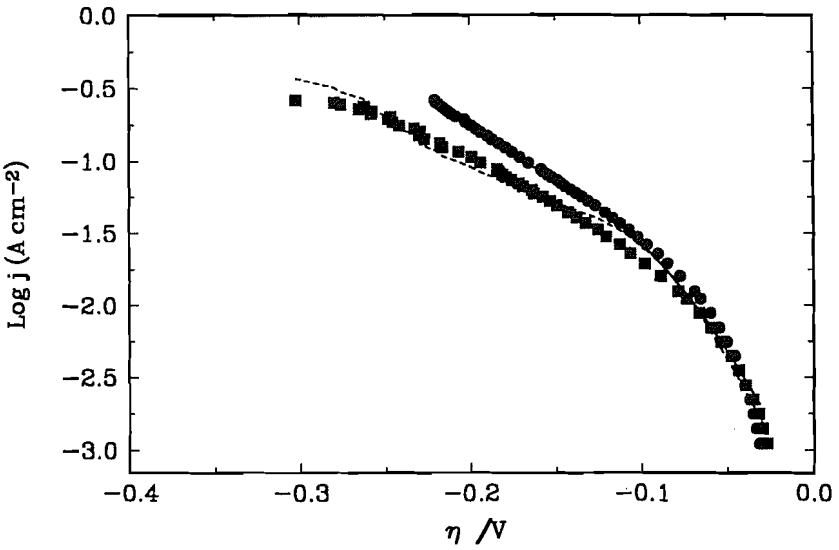

Table 1. Kinetic parameters obtained from the analysis of Tafel curves of nickel boride electrodes[a] at 25°C in aqueous 1 M NaOH: effect of MeOH, NaCl, boric acid, and EtOH.

Entry	Solution	j_0[b] (mA cm^{-2})	b[b] (mV)	r^2	$-\eta_{250}$[c] (mV)
1	S_1: NaOH (1 M)	2.6–3.2[d]	101–107[d]	0.998[d]	200–203[d]
2	S_2: NaOH (1 M) / MeOH (50/50) (v/v)	2.2	100	0.994	204
3	S_3: S_2 + 0.1 M NaCl	1.9	103	0.992	218
4	S_4: S_3 + 0.1 M H_3BO_3	2.4	111	0.994	223
5	S_5: NaOH (1 M) / EtOH (50/50) (v/v)	2.8	112	0.998	219

[a]The nickel boride electrodes were prepared by pressing the Ni_2B powder at p = 120 MPa.
[b]From the Tafel plots.
[c]Experimental value.
[d]Range obtained from two different experiments.

The electrochemical activity was studied by measuring Tafel curves. At potentials more negative than −0.10 V vs. Hg/HgO/1 M NaOH, the Tafel curves became linear (Figs.1 and 2). The linearization was studied by the least-squares method: r^2 values were calculated for the whole polarization curve starting from the most negative potentials and the part of the curve for which the determination coefficient reached a maximum value was considered as linear. The IR-corrected Tafel curves recorded in the different media (S_1: 1 M aqueous NaOH; S_2: 1 M NaOH/MeOH (50/50) (v/v); S_3: 1 M NaOH/MeOH (50/50) (v/v) + 0.1 M NaCl; S_4: 1 M NaOH/MeOH (50/50) (v/v) + 0.1 M NaCl +0.1 M H_3BO_3; and S_5: 1 M NaOH/EtOH (50/50) (v/v)) are shown in Figs. 1 and 2 and the corresponding parameters are recorded in Table 1. The values of parameters b, the Tafel slope, j_0, and the exchange current density are practically the same in all media. There is no change of $-\eta_{250}$ (the overpotential at the current density of 250 mA cm^{-2}) upon adding CH_3OH (compare entries 1 and 2) but a slight increase (≃15 mV) upon adding EtOH (entry 5). There is also a slight increase of $-\eta_{250}$ upon adding NaCl to the aqueous methanolic solution (≃15 mV, entry 3). The addition of H_3BO_3 to the aqueous methanolic NaCl solutions has almost no influence (entry 4).These results indicate that the nickel boride electrode is very active for the HER in these media (ECH conditions) and that the electrocatalytic activity is hardly affected by the presence of MeOH, NaCl, boric acid, and EtOH. Kam Cheong et al. (27) have already observed the same behaviour for composite-coated Raney nickel in solutions of methanol and 1 M KOH (%MeOH: 0–100).

The ac impedance technique led to depressed semicircles on the Nyquist complex plane plots over the whole range of overpotentials studied, for all measurements (Fig. 3). The real and the imaginary components were analyzed (18, 28–30) using the complex nonlinear least-squares fitting program (CNLS)

Fig. 3. Complex plane ac impedance spectra obtained on a nickel boride pressed powder electrode at 25°C in (*a*) S_1: 1 M NaOH; (*b*) S_2: 1 M NaOH/MeOH (50/50)(v/v); (*c*) S_3: 1 M NaOH/MeOH (50/50) (v/v) + 0.1 M NaCl; (*d*) S_4: 1 M NaOH/MeOH (50/50) (v/v) + 0.1 M NaCl +0.1 M H_3BO_3; (*e*) S_5: 1 M NaOH/EtOH (50/50) (v/v) for various overpotentials: η = 20 mV (●), η = 55 mV (■), and η = 85 mV (▲). The points correspond to experimental values and the lines were calculated by the CPE model.

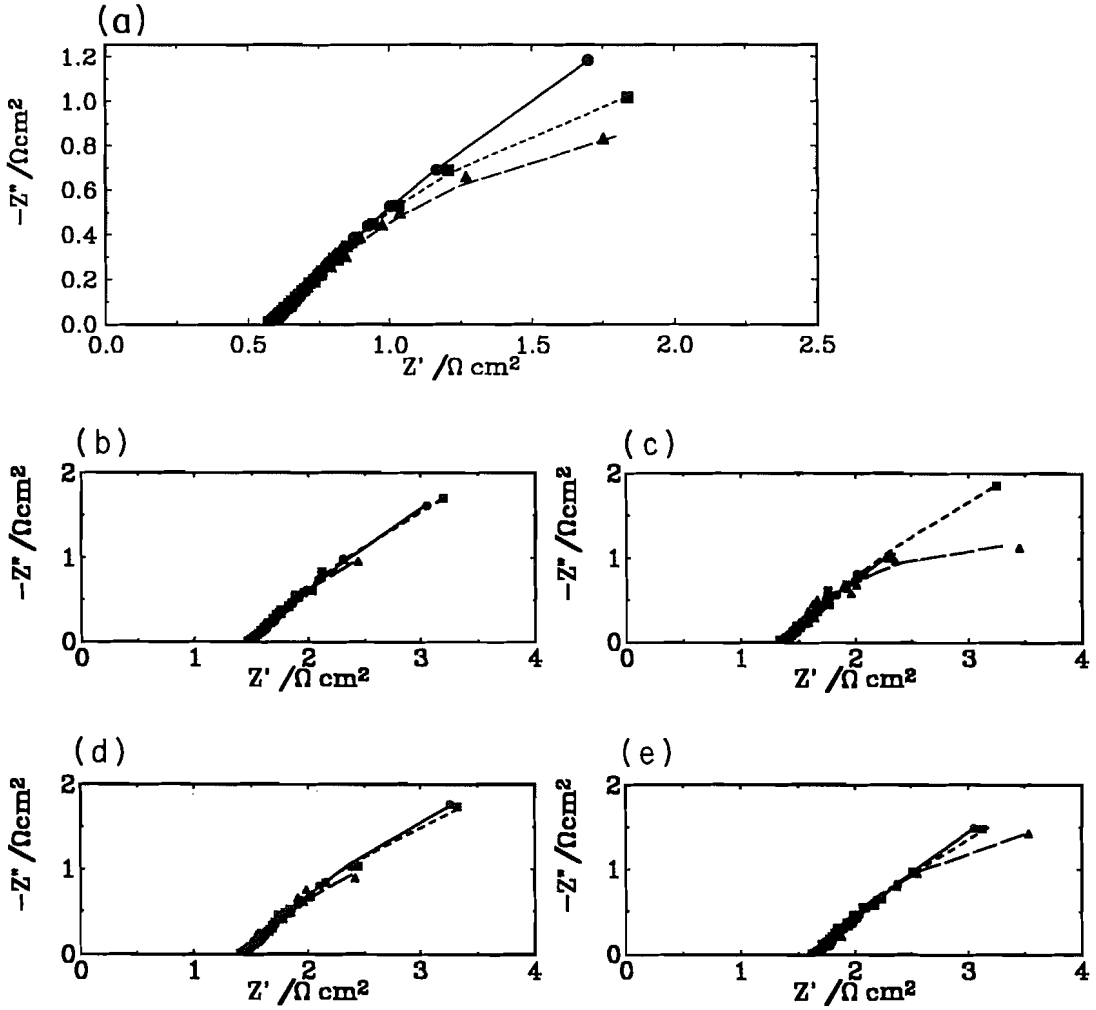

written by MacDonald et al. (31) and modified by Rami and Lasia (32). It was previously established (7, 33) that the experimental data of the HER at nickel boride electrodes could be represented by the CPE model (See Experimental). Figures 4 and 5 show the dependence of the double layer capacity, C_{dl}, on the overpotential for nickel boride electrodes in solutions S_1–S_5. A decrease of C_{dl} with η was observed in all media (Figs. 4 and 5). This decrease is due to hydrogen bubbles formed on the surface (7, 32) that block the pores and diminish the active surface area. The roughness factors R, estimated from the mean value of the experimental C_{dl} values measured at different overpotentials (see Figs. 4 and 5) divided by 27.9 μF/cm² (the capacity of a platinum smooth surface (32)), are presented in Table 2. The results of entries 1 and 2 show that the roughness factor is not affected by the presence of methanol, contrary to a report by Kam Cheong et al. (27) of an increase of the roughness factor of composite-coated RaNi electrodes (Raney nickel particles embedded in a nickel matrix) in aqueous methanol compared to water. They attributed this increase of R to a diminution of the surface tension of the methanolic solution (methanol has a lower surface tension than water) and, as a consequence, to a deeper penetration of the methanolic solution into the pores of the electrode surface and (or) to a better access to the smaller pores (then the surface appears to be larger). However, the pores at the surface of the nickel boride electrodes measured by mercury porosimetry (radius = 0.006 μm) are appreciably smaller than those at the surface of the composite RaNi electrodes (radius = 2.3 μm) and it is conceivable that, for much smaller pores, the penetration of methanol in the pores would be the same as that of water. A slight decrease of the roughness factor was observed when NaCl was added to the aqueous solution (from 11 000 in entry 2 to 9 000 in entry 3). This decrease could reflect the adsorption, on the nickel boride surface, of anions that would poison the catalyst. Chloride ions have been reported to poison Raney nickel in the catalytic hydrogenation of styrene (34). However, the decrease of the roughness factor in the presence of NaCl might not be significant since a similar R value of 10 000 was obtained after adding H_3BO_3 (solution S_4, entry 4). Similarly, the small increase of R upon adding ethanol (from 10 000 – 11 000 in

Fig. 4. Dependence of the double layer capacity, C_{dl}, on the overpotential for a nickel boride electrode in: (●) S_1: 1 M NaOH, (■)S_2: 1 M NaOH/MeOH (50/50)(v/v); (▲)S_3: 1 M NaOH/MeOH (50/50) (v/v) + 0.1 M NaCl; (◆) S_4: 1 M NaOH/MeOH (50/50) (v/v) + 0.1 M NaCl + 0.1 M H_3BO_3.

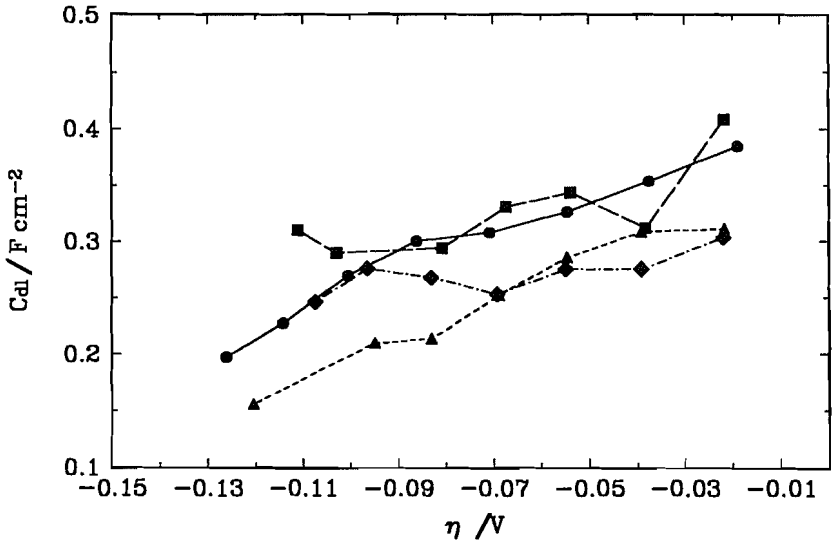

Fig. 5. Dependence of double layer capacity on the overpotential for a nickel boride electrode in: (●) S_1: 1 M NaOH; (■)S_5: 1 M NaOH/EtOH (50/50) (v/v).

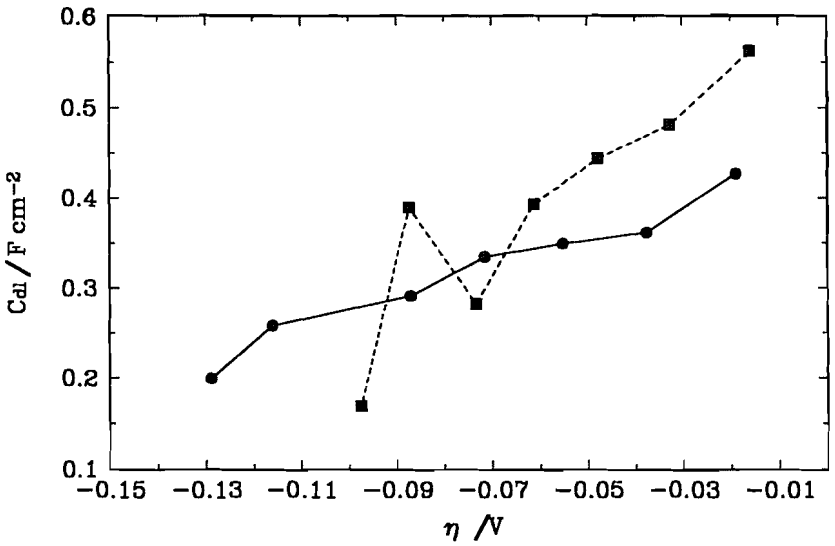

entry 1 to 14 000 in entry 5) is probably not significant. In fact, both the active surface area of Ni_2B electrodes and their intrinsic activity for the HER (as measured by the ratio of the exchange current density over the the roughness factor (j_0/R): ($(2.0–2.8) \times 10^{-7}$)) are not affected by the presence of CH_3OH, NaCl, H_3BO_3, and EtOH. If we assume that the active surface area for the ECH process is also not affected by the presence of MeOH or EtOH plus NaCl and H_3BO_3 in water, then the active surface for the HER in aqueous alkali should be proportional to the active surface for ECH, and the active surface for the HER obtained from ac impedance should constitute a good estimate of the active surface for ECH under the conditions used for ECH. It is only an approximate estimation because the hydrogenation step of the ECH process involves the reaction between the adsorbed organic substrate and chemisorbed hydrogen and, thus, the accessibility of the sites is not necessarily the same for the organic substrate and for chemisorbed hydrogen. However, the surface area for the HER obtained from ac impedance measurements in aqueous alkali (roughness factor of 10 000) should be a better estimate of the surface area active in ECH than the surface area measured by BET (specific surface area of 10.7 $m^2\ g^{-1}$) (7). Indeed, BET measurements involve a gas–solid interface whereas ac impedance measurements refer to a solid–solution interface as in the ECH process.

The dependency of $A(=1/R_{ct})$ (Figs. 6 and 7) and current

Table 2. Roughness factors and real current densities for the HER on nickel boride electrodes[a] at 25°C in aqueous 1 M NaOH: effect of MeOH, NaCl, boric acid, and EtOH.

Entry	Solution	C_{dl}[b] (F cm^{-2})	R	j_0/R[c] (A cm^{-2})
1[d]	S_1: NaOH (1 M)	0.30–0.32	10 000–11 000	(2.4–2.8) × 10^{-7}
2	S_2: NaOH (1 M) / MeOH (50/50) (v/v)	0.31	11 000	2.0 × 10^{-7}
3	S_3: S_2 + 0.1 M NaCl	0.25	9 000	2.1 × 10^{-7}
4	S_4: S_3 + 0.1 M H_3BO_3	0.27	10 000	2.5 × 10^{-7}
5	S_5: NaOH (1 M) / EtOH (50/50) (v/v)	0.39	14 000	2.0 × 10^{-7}

[a]See footnote *a* of Table 1.
[b]Mean values obtained from the experimental C_{dl} values measured at different overpotentials.
[c]Real current densities.
[d]See footnote *d* of Table 1.

Fig. 6. Variation of the logarithm of parameter $A(=1/R_{ct})$ with the overpotential for a nickel boride electrode: (●) S_1: 1 M NaOH; (■)S_2: 1 M NaOH/MeOH (50/50)(v/v); (▲)S_3: 1 M NaOH/MeOH (50/50) (v/v) + 0.1 M NaCl; (◆) S_4: 1 M NaOH/MeOH (50/50) (v/v) + 0.1 M NaCl + 0.1 M H_3BO_3. The points were obtained by the use of the CPE model and lines were calculated using the rate constants shown in Table 3.

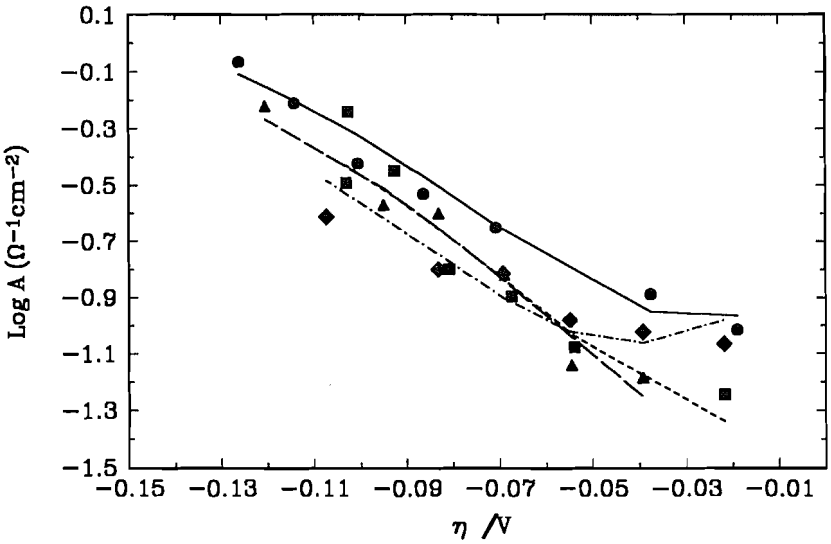

density j (Figs. 1 and 2) on the overpotential η was used to determine the rate constants k_i of the HER by applying the nonlinear least-squares (NLS) method (18, 28–30) assuming a Volmer–Heyrovsky mechanism. The kinetic results are presented in Table 3. The values of k_i are approximately identical in all media (entries 1 – 5). It means that HER under ECH conditions proceeds via the same mechanism as in an aqueous 1 M NaOH solution. It should be noted that in the case of the Volmer–Heyrovsky mechanism, two equivalent solutions are obtained when the values of k_1 and k_2, k_{-1} and k_{-2}, and α_1 and α_2, are interchanged. This permutation gives the same value for all experimentally accessible parameters (29). Therefore, the rate-determining step could not be determined.

Conclusion

The hydrogen evolution reaction (HER) at nickel boride pressed powder electrodes has been studied under conditions used in the electrocatalytic hydrogenation (ECH) of organic compounds (aqueous methanolic (ethanolic) solution containing 0.1 M NaCl and 0.1 M H_3BO_3). It was shown by steady-state polarization and ac impedance measurements that the electrodes have about the same activity, the same large surface area (roughness factor), and the same intrinsic activity under these conditions as in an aqueous 1 M NaOH solution. The ac impedance results were well approximated by the CPE model, and the parameters obtained were similar and the HER

Table 3. Kinetic parameters of the HER on nickel boride electrodes,[a] obtained from ac impedance and steady-state polarization measurements at 25°C in aqueous 1 M NaOH: effect of MeOH, NaCl, boric acid, and EtOH.

Entry	Solution	$k_1 \times 10^9$ (mol cm^{-2} s^{-1})	$k_{-1} \times 10^9$ (mol cm^{-2} s^{-1})	$k_2 \times 10^8$ (mol cm^{-2} s^{-1})	α_1[b]	α_2
1[c]	S_1: NaOH (1 M)	4.5 ± 0.2	(6.1–8.4) ± 1.3	(9.4–9.6) ± 0.6	1	(0.190–0.201) ± 0.008
2	S_2: NaOH (1 M) / MeOH (50/50) (v/v)	2.9 ± 0.2	27.2 ± 9.2	11.5 ± 0.8	1	0.106 ± 0.005
3	S_3: S_2 + 0.1 M NaCl	2.9 ± 0.2	46.1 ± 14.0	10.6 ± 0.6	1	0.113 ± 0.004
4	S_4: S_3 + 0.1 M H_3BO_3	2.3 ± 0.1	3.8 ± 0.7	10.4 ± 0.6	1	0.119 ± 0.004
5	S_5: NaOH (1 M) / EtOH (50/50) (v/v)	3.14 ± 0.04	1.7 ± 0.5	10.9 ± 0.7	1	0.099 ± 0.004

[a]See footnote *a* of Table 1.
[b]Assumed value.
[c]See footnote *d* of Table 1.

Fig. 7. Variation of the logarithm of parameter $A(=1/R_{ct})$ with the overpotential for a nickel boride electrode: (●) S_1: 1 M NaOH; (■)S_5: 1 M NaOH/EtOH (50/50) (v/v). The points were obtained by the use of the CPE model and lines were calculated using the rate constants shown in Table 3.

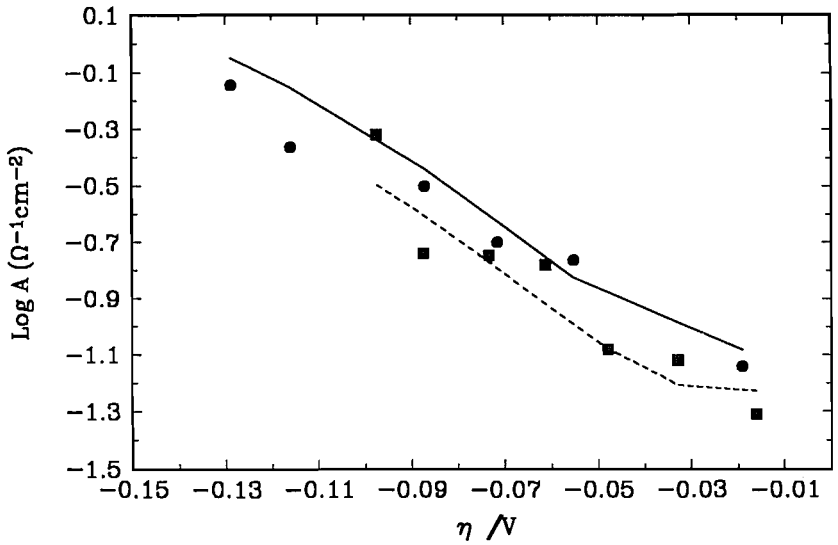

occurred according to the Volmer–Heyrovsky mechanism in all the media studied. In summary, we have shown that it is possible to extrapolate the results obtained from the HER in aqueous alkali to the media used for the ECH studies.

References

1. M. Enyo. *In* Comprehensive treatise of electrochemistry. Vol. 7. *Edited by* B.E. Conway, J.O'M. Bockris, E.B. Yeager, S.U.M. Kahn, and R.E. White. Plenum Press, New York. 1983. p. 241.
2. S. Trasatti. *In* Advances in electrochemical science and engineering. Vol. 2. *Edited by* H. Gerischer and C.W. Tobias. VCH, New York. 1992. p. 1.
3. J. O'M. Bockris. *In* Comprehensive treatise of electrochemistry. Vol. 7. *Edited by* B.E. Conway, E. Yeager, and R.E. White. Plenum Press, New York. 1981. p. 1505.
4. B.E. Conway. J. Electrochem. Soc. **124**, 410C (1977).
5. B.E. Conway, H. Angerstein-Kozlowska, M.A. Sattar, and B.V. Tilak. J. Electrochem. Soc. **130**, 1825 (1983).
6. R.L. Augustine. *In* Catalytic hydrogenation. Marcel Dekker, Inc., New York. 1985. p. 26.
7. B. Mahdavi, P. Los, M.-J. Lessard, and J. Lessard. Can. J. Chem. **72**, 2268 (1994).
8. B. Mahdavi, J.-M. Chapuzet, and J. Lessard. Electrochim. Acta, **38**, 1377 (1993).
9. B. Mahdavi, P. Chambrion, J. Binette, E. Martel, and J. Lessard. Can. J. Chem **73**, 846 (1995).
10. P. Los, A. Lasia, J. Fournier, L. Brossard, and H. Ménard. J. Electrochem. Soc. **141**, 2716 (1994).
11. J. Fournier, P.K. Wrona, A. Lasia, R. Lacasse, J.-M. Lalancette, L. Brossard, and H. Ménard. J. Electrochem. Soc. **139**, 2372 (1992).
12. P.K. Wrona, A. Lasia, M. Lessard, and H. Ménard. Electrochim. Acta, **37**, 1283 (1992).
13. A. Lasia. J. Electroanal. Chem. **266**, 69 (1969).

14. D.A. Harrington and B.E. Conway. J. Electroanal. Chem. **221**, 1 (1987).
15. G.J. Brug, A.L.G. van den Eeden, M. Sluyters-Rehbach, and J.H. Sluyters. J. Electroanal. Chem. **176**, 275 (1984).
16. J.-P. Candy, P. Fouilloux, M. Keddam, and H. Takenouti. Electrochim. Acta, **27**, 1585 (1982).
17. E. Potvin, A. Lasia, H. Menard, and L. Brossard. J. Electrochem. Soc. **138**, 900 (1991).
18. L. Chen and A. Lasia. J. Electrochem. Soc. **138**, 3321 (1991).
19. Y. Choquette, L. Brossard, A. Lasia, and H. Menard. Electrochim. Acta, **35**, 1251 (1990).
20. P. Los, A. Rami, and A. Lasia. J. Appl. Electrochem. **23**, 135 (1993).
21. P. Los, A. Lasia, L. Brossard, and H. Menard. J. Electroanal. Chem. **360**, 101 (1993).
22. P. Los, L. Brossard, H. Dumont, A. Lasia, J. Lessard, and H. Menard. Proc. 5th Canadian Hydrogen Workshop, Ottawa, February 1992. p. 39.
23. D.A. Harrington and B.E. Conway. Electrochim. Acta, **32**, 1703 (1987).
24. C.A. Brown. J. Org. Chem. **35**, 1900 (1970).
25. R. Paul, P. Buisson, and N. Joseph. Ind. and Eng. Chem. **44**, 1006 (1952).
26. D. Robin, M. Comtois, A. Martel, R. Lemieux, A. Kam Cheong, G. Belot, and J. Lessard. Can. J. Chem. **68**, 1218 (1990).
27. A. Kam Cheong, A. Lasia, and J. Lessard. J. Electrochem. Soc. **140**, 2721 (1993).
28. Y. Choquette, L. Brossard, A. Lasia, and H. Ménard. J. Electrochem. Soc. **137**, 1723 (1990).
29. A. Lasia and A. Rami. J. Electroanal. Chem. **294**, 123 (1990).
30. Y. Choquette, L. Brossard, A. Lasia, and H. Ménard. Electrochim. Acta **35**, 1251 (1990).
31. J.R. Macdonald, J. Schoonman, and A.P. Lehner. J. Electroanal. Chem. **131,** 77 (1982).
32. A. Rami and A. Lasia. J. Appl. Electrochem. **22**, 376 (1992).
33. P. Los and A. Lasia. J. Electroanal. Chem. **333**, 115 (1992).
34. J.N. Pattison and E.F. Degering. J. Am. Chem. Soc. **73**, 611 (1951).

Evidence for the role of the α-helix in the xylosylation reactions involving the glycosaminoglycan-bearing serine of decorin/DS-PGII as shown by ^{1}H NMR, CD, and molecular modeling studies

Yunjun Wang, Paul G. Scott, Jan Sejbal, and George Kotovych

Abstract: The conformation of four peptides (N-terminal acetylated and unacetylated 14-mers DEASGIGPEEHFPENH$_2$ and 24-mers AcQKGLFDFMLEDEASGIGPEEHFPENH$_2$ with a normal and an oxidized methionine residue) containing the sequence Asp-Glu-Ala-Ser-Gly-Ile-Gly (DEASGIG), which is known to play an important role in the xylosylation reactions involving the glycosaminoglycan-bearing serine of decorin/DS-PGII, were studied by two-dimensional proton NMR techniques, circular dichroism spectroscopy, and molecular dynamics in a methanol–water mixture. The 14-residue peptide comprises the first (i.e., N-terminal) 14 amino acids of the mature decorin protein and the 24-residue peptide incorporates an additional (N-terminal) sequence of 10 amino acids derived from the procore of decorin. The resonance heterogeneity induced by the isomerization of the two prolines (Pro^8, Pro^{13} in the 14-mer, and Pro^{18}, Pro^{23} in the 24-mer) in the peptides studied was evaluated from TOCSY and NOESY NMR spectra. The *trans-trans*, *trans-cis*, and *cis-trans* isomers exist in approximate 68:25:7 proportions in the methanol–water mixture. The NOE distance constraints were used as input parameters for molecular dynamics and restrained energy minimization calculations. It was demonstrated that the conformation of the DEASGIG fragment was affected by the presence of the 10 amino acids at the N-terminal end of the 24-mer, and that the serine is part of an α-helix. The results indicate that an α-helix is present in the 24-mer beginning at the N-terminal end with Lys^2 and ending at Gly^{15}, and suggest that this could be the signal for the xylosylation of serine Ser^{14}. A type VIb β turn was observed, involving the C-terminal *cis*-proline in the sequence His-Phe-Pro-Glu.

Key words: xylosylation, nascent helix, α-helix, *cis*-proline, type VIb β-turn, molecular dynamics.

Résumé : Faisant appel à des techniques de RMN du proton bidimensionnelles, à la spectroscopie du dichroïsme circulaire et à de la dynamique moléculaire dans un mélange méthanol–eau, on a étudié la conformation de quatre peptides (les 14-mères DEASGIGPEEHFPENH$_2$ non acétylé et acétylé sur le N-terminal et les 24-mères AcQKGLFDFMLEDEASGIGPEEHFPENH$_2$ portant une méthionine normale et une oxydée) qui comportent la séquence Asp-Glu-Ala-Ser-Gly-Ile-Gly (DEASGIG) qui est connue pour jouer un rôle important dans les réactions de xylosylation impliquant la sérine de la décorine/DS PGII portant un glycosaminoglycane. Le peptide à 14 résidus comporte les 14 premiers (c'est-à-dire, N-terminal) acides aminés de la protéine décorine mature et le peptide à 24 résidus incorpore une séquence additionnelle (N-terminale) de 10 acides aminés dérivée du procore de la décorine. L'hétérogénéité de la résonance induite par l'isomérisation des deux prolines (Pro^8, Pro^{13} dans le 14-mère et Pro^{18}, Pro^{23} dans le 24-mère) des peptides étudiés a été évaluée par des spectres RMN TOCSY et NEOSY. Les isomères *trans-trans*, *trans-cis* et *cis-trans* existent dans les proportions approximatives de 68 : 25 : 7 dans le mélange méthanol–eau. Les contraintes de distance des EON ont été utilisés comme paramètres connus pour les calculs de dynamique moléculaire et de minimisation de l'énergie restreinte. Il a été démontré que la conformation du fragment DEASGIG est affectée par la présence des 10 acides aminés de l'extrémité N-terminale du 24-mère et que la sérine fait partie d'une hélice α. Les résultats indiquent qu'il existe une hélice α dans le 24-mère, qu'elle commence à l'extrémité N-terminale avec la Lys^2, qu'elle se termine avec le Gly^{15} et ils suggèrent que ceci pourrait être le signal pour la xylosylation de la sérine, Ser^{14}. On a observé un virage de type VIb β impliquant la *cis*-proline C-terminale dans la séquence His-Phé-Pro-Glu.

Mots clés : xylosylation, hélice naissante, hélice α, *cis*-proline, virage de type VIb β, dynamique moléculaire.

[Traduit par la rédaction]

Received September 29, 1995.

Y. Wang, J. Sejbal, and G. Kotovych.[1] Department of Chemistry, University of Alberta, Edmonton, AB T6G 2G2, Canada.
P.G. Scott. Department of Biochemistry, University of Alberta, Edmonton, AB T6G 2G2, Canada.

[1] Author to whom correspondence may be addressed. Telephone: (403) 492-5477. Fax: (403) 492-8231. E-mail: George.Kotovych@Ualberta.ca

Introduction

Proteoglycans (PGs) are extracellular macromolecules that are present in, and profoundly influence physical properties (e.g., resilience and distensibility) of, connective tissues. In non-cartilaginous soft connective tissues such as skin, tendon, ligament, etc., the predominant PGs are decorin and biglycan, which consist of highly homologous protein cores of about 35 kDa (1) to which are attached glycosaminoglycan (GAG) chains of dermatan (DS) or chondroitin sulphate: one in decorin (2) and two in biglycan (3), close to the amino terminus. The GAGs are polyanionic and dominate the properties of the PGs carrying them. The small PGs may affect collagen fibril morphology and (or) the organization of collagen fibrils into fibres and fibre bundles (4). Failure to efficiently synthesize GAG chains on the skin decorin protein core has been linked to the connective tissue derangements seen in progeroid syndrome (5).

Biosynthesis of GAG chains is initiated, probably in the rough endoplasmic reticulum, by the enzyme xylosyltransferase, which transfers xylose from uridine diphosphate (UDP) to certain serines in the protein cores (6). The specificity of xylosyltransferase is incompletely defined, but it is known that a xylosylated serine is immediately N-terminal to glycine (most often) or to alanine (occasionally). Additional recognition factors must be important, however, because the sequences of both decorin and biglycan include several non-glycosylated Ser-Gly and Ser-Ala sequences. Similar uncertainty surrounds the control of O-glycosylation in glycoproteins (7). It has been suggested, on the basis of predictions of secondary structure rather than on direct physical evidence, that serine should be in a β turn in order to be a candidate for glycosylation (8). The earliest sequence information on decorin was used to predict that residues 2–5 (Glu-Ala-Ser-Gly) would adopt a β turn (9). It was subsequently shown (2) that the single dermatan sulfate chain of skin decorin (then called "proteodermatan sulfate") was located on Ser^4. A preliminary circular dichroism study did not detect a β turn in a peptide comprising the amino-terminal 21 residues of bovine skin decorin (10) but, in view of the evidence for proteolytic processing of the protein core subsequent to translation (11), this negative finding cannot be considered a valid test of the hypothesis. This is because the procore of decorin, the probable substrate for xylosyltransferase (11), carries an additional 14 amino acids between the suggested scissile bond for signal peptidase (12) and the N-terminus, and could adopt a distinct secondary structure in this sequence.

In this paper we report a study by NMR and circular dichroism spectroscopy of four peptides. The first peptide comprises the N-terminal 14 amino acids of the mature decorin protein. The second has this same sequence extended in the N-terminal direction by the incorporation of an additional 10 amino acids derived from the procore of decorin. An additional 24-mer in which the methionine was oxidized to the sulfoxide was also studied. The fourth peptide was the 14-mer with an acetyl group at the N-terminal end. This was included in an attempt to differentiate the effect of blocking the N-terminus from the effect of the additional N-terminal sequence in the 24-mer. The results indicate that an α-helix is present and suggest that this could be a signal for xylosylation of serine in this small PG.

Experimental

Sample preparation

The 24 amino acid peptide $CH_3COQKGLFDFMLEDEASGIGPEEHFPENH_2$ was synthesized by the Alberta Peptide Institute. The 14-mer $DEASGIGPEEHFPENH_2$, the acetylated 14-mer $CH_3CODEASGIGPEEHFPENH_2$, and the oxidized 24-mer $CH_3COQKGLFDFM(O)LEDEASGIGPEEHFPENH_2$ were synthesized on a Biolynx™ 4175 manual peptide synthesizer using FMOC amino acid derivatives (Pharmacia Canada Inc., Baie d'Urfe, Quebec). The peptides were purified by reverse-phase high-performance liquid chromatography on a Beckman model 200 HPLC using a Vydac TP218 column (The Separations Group, Hesperia, Calif.). The purification was carried out using a linear gradient of 0–50% acetonitrile in 0.1% (v/v) trifluoroacetic acid. Purity was assessed by amino acid analysis and mass spectrometry. There were no impurity peaks seen in the NMR. These four samples, 24-mer and oxidized 24-mer, 14-mer, and acetylated 14-mer, are abbreviated as NQ24, OQ24, D14, and AD14, respectively, in the following discussion.

Samples for CD experiments were prepared by dissolving purified peptides in water, and the pH was adjusted to 5.5 or 7.0 by adding 50 mM sodium phosphate buffer at that pH. The required volume of methanol was then added.

The samples used for ^1H NMR experiments were prepared by dissolving peptides in H_2O. The pH was then adjusted to 5.5 by adding diluted NaOH or HCl, followed by CD_3OH to make the solvent at 60/40 methanol/water mixture. Before the NMR experiments, the sample was degassed with argon. After 2D experiments, an aliquot of the OQ24 and AD14 samples was diluted tenfold with 60/40 CD_3OH/H_2O for 1D experiments. These dilution experiments indicated that there was no aggregation.

Circular dichroism spectroscopy

The CD spectra were recorded at room temperature on a Jasco JA20 spectropolarimeter with a thermostated cell holder. Mean residue ellipticities, $[\theta]_{mrw}$ (deg cm^2 $dmol^{-1}$), were calculated in the usual fashion using a mean residue weight of 108.1 for the 14-mer and 110.6 for the 24-mer, calculated from the composition of the peptides. Each spectrum is the average of 16 or 32 scans.

NMR spectroscopy

All experiments were carried out on the Varian Unity 500 NMR spectrometer using a proton-selective 5 mm probe with a 90° proton pulse length of about 9.0 μs at normal power levels. During the experiments the temperature was always controlled to ±0.1°C. For data collection and processing, VNMR software (versions 3.2 and 4.1) was used on the Sun Sparc 4/330 and Sparc 4/470 workstations, respectively. 2D spectra were acquired non-spinning, whereas for one-dimensional experiments the spinner was turned on. All chemical shifts are measured relative to the undeuterated fraction of the methyl group of CD_3OH at 3.30 ppm. All two-dimensional NMR experiments (13) were carried out in the phase-sensitive mode by using the hypercomplex technique (States–Haberkorn–Ruben method) (14). The decoupler and transmitter offsets were always set equal, a sweep width of 5000 Hz was used in

both dimensions, and typically 2K (zero filling to 4K) data points in t_2 and 256 points (zero filling to 1K) experiments in t_1 were acquired. All two-dimensional experiments were preceded by 8 dummy scans but none were applied between individual t_1 increments. The preacquisition delay alfa[2] was carefully and individually adjusted for every 2D experiment. First point distortions caused by analog filters (15) were empirically determined values. No further correction routines were necessary.

The TOCSY (16) experiments were carried out using the basic pulse sequence proposed by Bax and Davies (17). Water suppression was achieved by solvent presaturation during the relaxation period. A 2 ms trim pulse preceded the 80 ms MLEV-17 spin-lock (field strength 7.0 kHz). The NOESY (18, 19) experiments were carried out with the 90°–$t1$–90°–t_m–90°–FID pulse sequence and 1.5 s solvent presaturation. For data processing, approximately 90° shifted squared sine bell weighting functions were used in both dimensions.

Distances were calculated from NOESY spectra with a mixing time of 250 ms for all non-trivial cross peaks by integration of their 3D volumes in the following way: (*a*) cross peaks were integrated and carefully checked for contribution from baseline distortions; whenever possible, the volume was measured in both cross peaks, above and below the diagonal, and the two values were averaged to minimize slight phase imperfections; (*b*) where applicable, the volume was normalized for the contributions of more than two protons to the cross peak by a factor $(2N_aN_b)/(N_a + N_b)$, where N_a and N_b are the number of protons responsible for the diagonal peaks a and b, respectively (20); (*c*) the ββ′ interaction of the His and Phe protons was used as reference at 1.8 Å; and (*d*) corrections for isomers arising from *cis*-proline were made. The internuclear distance r was then calculated since the NOESY cross-peak volume is proportional to $1/r^6$ (21).

Molecular modeling

The program BIOGRAF (Version 3.2.1, Molecular Simulations, Inc. Burlington, Mass., U.S.A.) on the Sun SPARC 470 Workstation (Sun OS 4.1.3 operating system) was used for all calculations. The program Hyperchem (Release 2, Autodesk, Inc.) was used for plotting the stereo structures. The Dreiding II force field was used for all calculations. For all energy minimizations, the conjugate-gradient method was used; 400–800 steps were typically needed for convergence (less than 0.1 kcal mol^{-1} RMS force). Distribution of charges was calculated by the Gasteiger method (22). All simulations were carried out for the molecule with all hydrogen atoms. The dielectric constant of a vacuum ($\epsilon = 1$) was used for all calculations. The molecular dynamic runs were performed with 1 fs steps at 300 K, unless another temperature is mentioned. The list of nonbonded interactions and hydrogen bonds was updated every 0.1 ps during the dynamic runs and every 50 steps during energy minimizations. Cutoff distance for this list was 9 Å. In the Monte Carlo searches, all dihedral angles were set to random values except angles in rings and ω dihedral angles in the backbone.

The acetylated 14-mer (AD14) and acetylated 24-mer with nonoxidized methionine residues (NQ24) were built and subjected to molecular modeling. Where applicable, the constraints used for the first structure were those listed in Table 1 for the *trans*(Pro[8])-*cis*(Pro[13]) (TC) isomer of AD14. For the second structure, constraints used are listed in Table 2 for the *trans*(Pro[18])-*trans*(Pro[23]) isomer (TT). These constraints were calculated from the NOESY spectra of OQ24 since these spectra were better resolved in comparison with that of NQ24, where heterogeneity caused by the *cis* prolines produced more overlap.

Both structures were subjected to the Monte Carlo search: 50 conformers were generated and minimized without solvent shell. All atoms were set movable and all NOESY restraints were applied with a maximum force of 1000 kcal $Å^{-1}$ mol^{-1}. For both structures, the coordinates of the areas of interest (residues 11–14 for the 14-mer and 3–11 for the 24-mer) in the three lowest energy conformers were matched. Resulting structures were averaged and minimized with constraints. Minimized structures were solvated with water (diamond grid, 2.8 Å distance between solvent molecules, 2.6 Å inner cutoff of shell from peptide, 6.6 Å outer cutoff) and the whole system was minimized again. The unsolvated 24-mer and solvated 14-mer and 24-mer were subjected to 100 ps dynamic runs. The first 80 ps were constrained, the last 20 ps were unconstrained. Every 1 ps the structure was written to the trajectory. Coordinates of 20 conformers from the last 20 ps were averaged (peptide only), resolvated where dynamic runs were performed with the solvent shell, and minimized. Backbone dihedral angles of the resulting structures are given in Table 3.

The structure of the nascent helix was also tested by the following procedure: The N-terminal part of the 14-mer (residues 1–10) was folded into an α-helix with backbone torsion angles $\phi = -57°$, $\psi = -47°$, and $\omega = 180°$ and the resulting structure was subjected to constrained minimization. Then a constrained dynamic run of overall length 20 ps was performed. Every 1 ps the structure was minimized without constraints and written to the trajectory file.

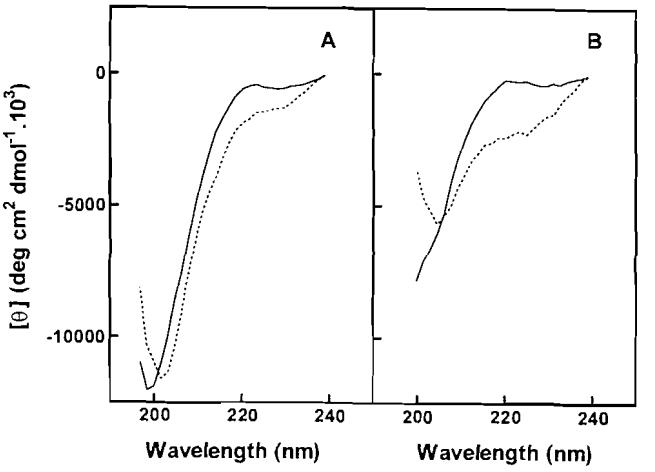

Fig. 1. Circular dichroism spectra of unacetylated 14-mer (*A*) and acetylated 24-mer (*B*) in 0.05 M sodium phosphate buffer (—) pH 5.5 or in 60% methanol/40% sodium phosphate buffer (----). See text for other details.

Results

Circular dichroism spectroscopy

The spectra in Fig. 1 show that both the unacetylated 14-mer

[2] Varian NMR Spectrometer Systems. System Operation Manual. VNMR. Version 5.1, Pub. No. 87-190100-00, Rev. A0295.

Table 1. Constraints for the TC isomer of AD14 used for molecular modeling.

Restrained atoms	Distance (Å)	Restrained atoms	Distance (Å)
CH_3CO-D1NH	2.6	A3αH-NH	2.5
D1αH-E2NH	2.4	I6αH-NH	2.5
E2αH-A3NH	2.3	P8αH-δ(3.70)	3.0
A3αH-S4NH	2.3	P8αH-δ(3.61)	3.2
S4αH-G5NH	2.3	E9αH-NH	2.3
G5ααH-I6NH	2.3	D1αH-A3NH	3.8
G7ααH-P8δδ	2.0	E2αH-S4NH	3.8
P8αH-E9NH	2.0	A3αH-G5NH	3.8
D1NH-E2NH	3.3	S4αH-I6NH	3.7
E2NH-A3NH	2.8	G7α(4.01)H-E9NH	3.7
A3NH-S4NH	2.5	P8αH-E10NH	3.1
S4NH-G5NH	2.5	E2NH-S4NH	4.6
G5NH-I6NH	2.4	E9NH-E10NH	2.5
G7NH-P8δ(3.70)	3.1	E10NH-H11NH	2.8
G7NH-P8δ(3.61)	3.3	P13δ(3.52)-E14NH	4.8
P8δ(3.70)-E9NH	2.8	E14NH-Term.NH(7.80)	3.5
P8δ(3.61)-E9NH	3.3	E10αH-H11NH	2.1
D1βH-E2NH	2.9	P13αH-F12β(3.06)	3.4
E2βH-A3NH	4.3	P13αH-F12β(2.92)	3.3
A3βH-S4NH	3.1	P13αH-E14NH	2.5
E10ββH-H11NH	3.5	E14αH-NH	2.8
E2γ(2.08)-A3NH	3.5	E14αH-Term.NH(7.80)	2.8
E2γ(1.96)-A3NH	3.2	F12αH-P13αH	2.0
D1αH-NH	2.8	F12αH-E14NH	2.8
E2αH-NH	2.7		

Table 2. Constraints for the TT isomer OQ24 used for molecular modeling.

Restrained atoms	Distance (Å)	Restrained atoms	Distance (Å)
dNN(*i*,*i* + 1)		E12-A13	2.3
Q1-K2	3.0	A13-S14	2.4
K2-G3	3.0	S14-G15	2.5
G3-L4	2.8	G15-I16	2.1
F5-D6	2.3	G17-P18	2.6
D6-F7	2.5	P18-E19	2.1
F7-M8	2.3	H21-F22	2.2
M8-L9	2.2	F22-P23	2.6
D11-E12	2.5	P23-E24	2.2
E12-A13	2.3	E24-Term.NH (7.56)	3.0
A13-S14	2.4	**dαβ(*i*,*i* + 3)**	
S14-G15	2.3	G3(4.10)-D6	3.4
G15-I16	2.3	G3(3.87)-D6	4.1
I16-G17	2.5	L4-F7(3.18)	2.9
G17-P18(3.72)	3.5	L4-F7(3.04)	2.9
G17-P18(3.62)	3.6	F5-M8	2.5
P18(3.72)-E19	2.9	D6-L9	2.7
P18(3.62)-E19	3.5	F7-E10	2.7
E19-E20	2.4	M8-D11	2.6
H21-F22	2.5	D11-S14	3.2
E24-Term.NH	3.4	**Others**	
dαN(*i*,*i* + 1)		K2α-D6β	2.9
Q1-K2	2.0	D6β-K2β	2.6
K2-G3	2.2	D6β-K2γ	2.9
G3(3.86)-L4	2.3	D6β-K2δ	3.0
F5-D6	2.4	G3NH-D6NH	3.8
M8-L9	2.3	L4α-F7NH	3.0
D11-E12	2.3	D11α-S14NH	3.2

Table 3. Backbone torsion angles based on the minimized averaged structures obtained from molecular dynamics

	AD14 solvated[a]		(A)	NQ24 in vacuum		(B)	NQ24 solvated		(C)
Residue	ϕ	ψ	ω	ϕ	ψ	ω	ϕ	ψ	ω
1 Gln				—	173.8	−177.3	—	170.8	−169.8
2 Lys				153.5	−119.6	171.8	143.5	−87.8	173.1
3 Gly				93.1	−5.5	178.9	−114.2	−0.7	−179.1
4 Leu				−144.2	−56.0	177.6	−74.5	−34.4	178.5
5 Phe				−67.5	−54.5	173.8	−59.6	−51.9	176.0
6 Asp				—63.4	−30.4	173.9	−65.7	−7.2	173.7
7 Phe				−67.3	−8.9	172.4	−79.2	−16.0	171.9
8 Met				−91.2	−15.2	172.3	−74.9	−41.8	169.9
9 Leu				−84.3	−44.0	169.7	−56.5	−53.1	175.0
10 Glu				−65.8	−4.6	175.0	−69.0	3.6	172.8
11 Asp	—	−5.6	+174.2	−87.4	−45.5	169.3	−99.3	−47.1	170.3
12 Glu	−99.6	−6.6	−175.7	−61.0	−7.6	173.0	−57.6	−36.5	170.7
13 Ala	−104.5	−67.0	174.8	−117.0	9.4	−175.2	−50.4	−19.6	175.8
14 Ser	−122.7	29.3	−174.3	−49.0	−33.2	177.9	−61.4	−18.8	172.6
15 Gly	−61.6	−9.4	173.2	−58.4	−13.7	170.4	−62.1	−13.4	171.0
16 Ile	−72.3	57.1	172.1	−131.5	12.7	−168.4	−130.6	11.0	−168.2
17 Gly	114.5	−74.1	−167.2	−82.8	−67.1	178.5	−81.8	−67.5	−179.3
18 Pro	−79.6	51.2	162.0	−87.7	−119.2	−175.8	−85.3	−119.9	−176.7
19 Glu	−121.6	−22.6	179.3	−156.4	−2.5	179.0	−155.2	−5.7	−179.8
20 Glu	−108.2	122.1	−177.3	−70.7	174.6	−167.9	68.0	174.0	−167.9
21 His	146.8	39.6	173.8	−62.5	−28.2	−172.8	−61.7	−28.9	−172.5
22 Phe	−142.7	78.6	−31.6	79.6	106.2	−169.7	79.9	107.4	−169.7
23 Pro	−67.9	−3.9	173.1	−74.8	−5.6	−177.2	−74.9	−5.4	−177.6
24 Glu	−132.7	—	—	−115.3	—	—	−113.6	—	—

[a]The residue numbers are from 1 to 14.

and the acetylated 24-mer possessed little, if any, regular secondary structure in a purely aqueous solvent. Including methanol at 60 or 70% (v/v), however, induced some secondary structure, more marked in the 24-mer than the 14-mer. Replacing the methanol with an equal volume of trifluoroethanol gave identical spectra, as did altering the pH from 5.5 to 7 (data not shown).

NMR spectroscopy

The resonance assignments (Table 4) of the peptides studied are based on TOCSY experiments and sequential NOEs of the type $\alpha(i)$-NH(i + 1), NH(i)-NH(i + 1) and $\beta(i)$-NH(i + 1) (21). The *trans* isomers of the two prolines predominate but assignment problems arose from the presence of the *cis* isomers. The *cis* form allows much closer contacts between αCH(i) and αCH(i + 1) and between NH(i) and αCH(i + 1), whereas the *trans* form favors short distances between αCH(i) and $\delta CH_2(i$ + 1) and between NH(i) and $\delta CH_2(i$ + 1). The presence of *cis* isomers for the two prolines was unequivocally shown by diagnostic NOESY cross peaks (see Fig. 2*a*). The strong cross peaks between αCH of Phe^{12} and δCH_2 of Pro^{13}, between αCH of Gly^7 and δCH_2 of Pro^8, between δCH_2 of Pro^{13} and NH of Glu^{14}, and between δCH_2 of Pro^8 and NH of Glu^9, show that these two prolines are mainly in the *trans* conformation. The two weaker sets of cross peaks between αCH of Phe^{12} and αCH of Pro^{13} and between αCH of Pro^{13} and NH of Glu^{14} show the presence of the *cis* form of the Pro^{13}. The small proportion of *cis* isomer to Pro^8 was demonstrated by the weak interactions between αCH_2 of Gly^7 and αCH of Pro^8 (see Fig. 2*a*). Weak intra-residue interactions between αCH_2 and NH of Gly^7 could also be observed (see Fig. 5); however, the low population precluded obtaining further NOE interaction patterns for this *cis* isomer. No further interactions of the α protons between Gly^7 and Pro^8 and between Phe^{12} and Pro^{13} were detected, so three isomers arising from *cis* proline were found. They were: *trans*(Pro^8)-*trans*(Pro^{13}) (TT); (TC); and *cis*(Pro^8)-*trans*(Pro^{13}) (CT). Resonance heterogeneity arising from *cis* Pro^8 and *cis* Pro^{13} can be found in the region of I^6-G^7-P^8-E^9-E^{10}-H^{11}-F^{12}-P^{13}-E^{14}-NH_2 and in the region of E^9-E^{10}-H^{11}-F^{12}-P^{13}-E^{14}-NH_2, respectively. Selected regions of the spectra are shown in Fig. 2*b* and Fig. 2*c*. The observed resonance heterogeneity, illustrating these effects, is summarized in Fig. 3.

By comparing the integration of the terminal NH in one-dimensional spectra, the TT, TC, and CT isomers were found at a ratio of about 68:25:7 for AD14. The observed NOEs for the TT and TC isomers are summarized schematically in Fig. 4. An observed medium-range NOE between αCH of Phe^{12} and NH of Glu^{14} (Fig. 5) suggests the presence of a turn, and molecular modeling shows a type VIb β turn, where Pro^{13} would be in the i = 2 position in the turn. No further medium- or long-distance NOEs were detected for the CT isomer due to its low abundance. The three isomers discussed above exist in the same proportion in all peptides studied.

Part of the NOESY spectrum of AD14 is shown in Fig. 5. Similar NOE patterns were observed for the peptides AD14

Table 4. ^{1}H NMR resonance assignments[a] and NH temperature coefficients[b] of the peptides studied: (*a*) AD14[c] and D14[d], (*b*) NQ24[e], and (*c*) OQ 24[f].

(*a*) AD14

Residue	NH	Hα	Hββ′	Hγγ′	Other H	NH temp. coeff. (−ppb/°C)
CH_3CO					CH_3CO: 2.01	
D1	8.31	4.59	2.69; 2.62			5.6
E2	8.86	4.18	2.08; 1.96	2.31; 2.31		5.0(3.7)
A3	8.41	4.30	1.41			4.3(2.6)
S4	8.08	4.34	3.89; 3.89			2.5(3.9)
G5	8.26	4.00; 3.86				2.7(2.0)
16	7.88	4.22	1.85	1.43; 1.11	γCH_3: 0.88; δCH_3: 0.82	3.3(3.0)
G7	8.45	4.18; 4.02				6.2(5.9)
P8		4.37	2.25; 2.25	1.97; 1.97	δ,δ′: 3.70; 3.61	
E9	8.74	4.17	1.92; 1.92	2.24; 2.24		3.7(3.5)
E10	8.14	4.16	1.86; 1.86	2.15; 2.15		2.9(3.0)
H11	8.26	4.60	3.10; 3.00		2H: 8.48; 4H: 7.18	5.6(5.4)
F12	8.46	4.82	3.17; 2.90		Ave. ring: 7.28	7.3(6.8)
P13		4.38	2.25; 2.25	1.97; 1.97	δδ′: 3.71; 3.54	
E14	8.55	4.23	2.07; 1.95	2.31; 2.31		6.3(5.4)
NH_2	7.62; 7.13					4.7; 6.0
G7 CT	8.27	4.04; 3.68				6.0
P8 CT		4.58				
E9 CT	8.72	4.25	1.92; 1.92	2.24; 2.24		4.2
H11 CT	8.47	4.62	3.11; 3.00			6.5
F12 CT	8.54	4.82	3.17; 2.89			7.8
NH_2 CT	7.66; 7.13					4.5; 5.7
E9 TC	8.77	4.23				4.2
E10 TC	8.17	4.23	1.88; 1.88	2.21; 2.21		3.0
H11 TC	8.36	4.65	3.21; 3.06		2H: 8.54; 4H: 7.27	5.0
F12 TC	8.36	4.63	3.06; 2.92		Ave. ring: 7.23	7.3
P13 TC		3.79	1.85; 1.38	1.67; 1.64	δ,δ′: 3.52; 3.30	
E14 TC	8.79	4.13	1.97; 1.97	2.27; 2.27		6.2
NH_2 TC	7.80; 7.10					5.9; 5.7

(*b*) NQ24

Residue	NH	Hα	Hββ′	Hγγ′	Other H	NH temp. coeff. (−ppb/°C)
CH_3CO					CH_3CO: 2.01	
Q1	8.33	4.28	2.04; 1.94	2.31; 2.31	δNH_2: 7.68; 6.85	4.7(5.2)
K2	8.47	4.30	1.72; 1.72	1.45; 1.38	δδ′: 1.57; 1.57 εε′: 2.83; 2.74	4.3(5.0)
G3	8.89	3.86; 4.18				7.1(7.6)
L4	8.35	4.10	1.45; 1.45	1.37	δCH_3: 0.88; 0.79	6.8(7.7)
F5	8.34	4.50	3.15; 2.97		Ave. ring: 7.23	8.9(9.3)
D6	7.77	4.38	2.65; 2.57			0.7(0.6)
F7	7.92	4.40	3.20; 3.08		Ave. ring: 7.24	1.9(3.0)
M8	8.09	4.23	2.57	2.44	εCH_3: 2.08	4.7(3.1)[g]
L9	7.97	4.20	1.73; 1.73	1.58	δCH_3: 0.87; 0.83	3.4(2.8)[g]
E10	8.11	4.10	2.08; 2.08	2.38; 2.22		0.6(0.2)[g]
D11	8.26	4.52	2.70; 2.70			5.0(5.4)
E12	8.50	4.12	2.10; 2.10	2.35; 2.27		1.6(1.6)
A13	8.27	4.26	1.45			2.0(2.4)
S14	7.93	4.34	3.95; 3.95			0.0(0.0)

Table 4 (*concluded*).

(*b*) NQ24

Residue	NH	Hα	Hββ′	Hγγ′	Other H	NH temp. coeff. (−ppb/°C)
G15	8.14	3.94; 3.94				0.8(0.6)
I16	7.91	4.23	1.85	1.46; 1.12	γCH_3: 0.88; δCH_3: 0.82	3.7(4.4)
G17	8.49	4.22; 4.01				5.3(5.8)
P18		4.38	2.25; 2.25	2.00; 2.00	δδ′: 3.74; 3.63	
E19	8.97	4.14	1.95; 1.95	2.26; 2.26		4.7(4.6)
E20	8.13	4.17	1.90	2.14		1.3(1.8)
H21	7.98	4.51	2.94; 2.90		2H: 7.86; 4H: 6.93	3.4(4.0)
F22	8.21	4.84	3.17; 2.91		Ave. ring: 7.27	5.6(6.0)
P23		4.38	2.23	1.95	δδ′: 3.63; 3.56	
E24	8.60	4.20	1.95; 1.95	2.27; 2.06		5.7(6.1)
NH_2	7.49; 7.03					

(*c*) OQ24

Residue	NH	Hα	Hββ′	Hγγ′	Other H	NH temp. coeff. (−ppb/°C)
M8(I)	8.32	4.36	2.25[h]	2.89[h]	εCH_3: 2.68	3.2
M8(II)	8.30	4.33	2.29[h]	2.96; 2.94[h]	εCH_3: 2.79	2.9
L9(I)	8.18	4.18	1.69; 1.69	1.54	δCH_3: 0.88; 0.85	2.8
L9(II)	8.16	4.18	1.69	1.54	δCH_3: 0.88; 0.85	2.7
E10(I)	8.37	4.12	2.05; 2.05	2.35; 2.35		0.3
E10(II)	8.32	4.11	2.05; 2.05	2.35; 2.35		0.1

[a]Chemical shifts are reported in ppm relative to the methyl group of CD_3OH at 3.30 ppm downfield from tetramethylsilane (TMS). Only parts of data are shown here.

[b]The temperature coefficients are the result of a linear regression analysis of the chemical shifts measured from TOCSY spectra at 5°C intervals from 5°C to 30°C.

[c]The data were recorded at 500 MHz in CD_3OH/H_2O (60/40 v/v%) at a concentration of 2.3 mM. The pH was 5.5 in water, and the temperature was 10 ± 0.1°C.

[d]The NH temperature coefficients of peptide D14 are shown in parentheses. The data were recorded at 500 MHz in CD_3OH/H_2O (60/40 v/v%) at a concentration of 1.6 mM, the pH was 5.5 in water.

[e]The data were recorded at 500 MHz in CD_3OH/H_2O (60/40 v/v%) at a concentration of 1.7 mM. The pH was 7.0 in 25 mM buffer, and the temperature was 15 ± 0.1°C. Only the data for the TT isomer are shown here. The NH temperature coefficients of peptide OQ24 are shown in parentheses. The data were recorded at 500 MHz in CD_3OH/H_2O (60/40 v/v%) at a concentration of 2.0 mM, the pH was 5.5 in water.

[f]A doubling of peaks is due to equal amounts of *R* and *S* sulfoxides.

[g]Average value of the data in Table 4*c*.

[h]Assignments may be interchanged and are ambiguous due to spectral overlap.

and D14: continuous dNN(i,i + 1) connectivities, consecutive weak dαN(i,i + 2) connectivities, and the lack of i,i + 3 medium-range NOEs show that these two peptides have a similar conformation, that is, a nascent helix (23), which is characterized by an ensemble of turnlike structures in the early stages of helix formation (24). There are close connections between chemical shifts and the local secondary structure (25, 26). The net structural shifts obtained by comparing the chemical shift with the random structure (22) for the peptides studied are shown schematically in Fig. 6. The closely similar net shift patterns indicate similar structures for D14 and AD14. The more negative value of D1 of peptide D14 is attributed to the effect of the positive charge at the N-terminus. The NH temperature coefficients (see Table 4) also confirm a similar structure for each pair of peptides. This agrees with the CD results, which were identical for D14 (Fig. 1) and AD14 (not shown).

The presence of the sulfoxide in the Met residue in peptide OQ24 splits the peaks of M^8 into two signals of equal intensity, indicating that equal amounts of sulfoxides with *R* and *S* configuration were formed (27). The NH peaks of Leu^9 and Glu^{10} were also doubled (Table 4*c*). However, the NMR studies show that the sulfoxide group has no effect on the OQ24 peptide conformation. The peptides NQ24 and OQ24 have the same conformation. The medium-range (i)–(i + 3) NOEs (part of data is presented in Fig. 7), low temperature coefficients (see Table 4), and the α-proton shifts (25, 26) (see Fig. 6) indicate that the peptides OQ24 and NQ24 adopt an α-helical

Fig. 2. The contour plots of the two-dimensional 500 MHz NMR spectra of peptide AD14. The concentration was 2.3 mM at pH 5.5 (measured in H_2O) in CD_3OH/H_2O (60/40 v/v%), temperature 10 ± 0.1°C. (*a*) The αH-βH region of the NOESY spectrum, mixing time 250 ms. (*b*) Part of αH-NH region of the TOCSY spectrum. (*c*) Part of NH-βH region of the TOCSY spectrum.

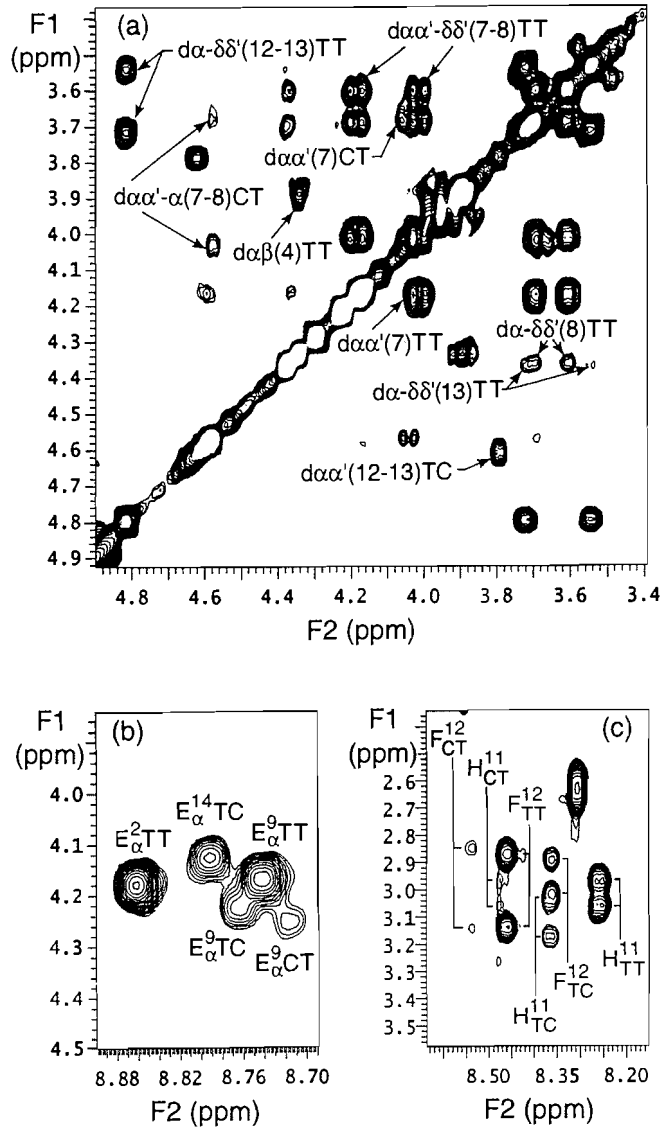

Fig. 3. The observed resonance heterogeneity caused by *cis–trans* isomerization of the prolines in AD14.

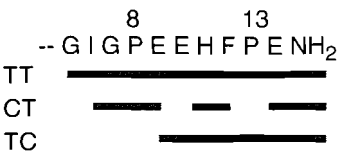

structure from the N-terminus to around Gly^{15}. The low temperature coefficients from Asp^6 to Gly^{15} indicate that the NH protons are protected from solvent and probably hydrogen-bonded.

All of the above data have been correlated with the molecular modeling. As was mentioned above, both 14-mers measured give the similar set of NOESY cross speaks useful for the calculation of distance constraints; in the case of the 24-mers, the situation is similar. Furthermore, the C-terminal part of all peptides shows the same NMR patterns (NOESY, chemical shifts, temperature dependencies, *cis–trans* isomerization); therefore, the proposal that the C-terminus of all peptides has the same conformation is reasonable. Two structures were built for evaluation by molecular modeling: (*i*) AD14 with a *cis* bond between Phe^{12} and Pro^{13} for the evaluation of the nascent helix in the N-terminal part of the peptide and the nature of the turn at the C-terminus: nascent helix is present in both 14-mers, and the C-terminal turn is present in all peptides with a *cis* proline in position 13 for the 14-mers or position 23 for the 24-mers; (*ii*) acetylated 24-mer (NQ24) with all peptide bonds *trans* for the determination of the structure of the α-helix at the N-terminus of both 24-mers.

Fig. 4. Survey of NOE effects recorded for the peptides studied: (*a*) AD14, (*b*) part of AD14 for TC conformation, (*c*) OQ24. For the proline, δ protons are used instead of the NH proton. Solid lines (■) indicate unambiguous NOEs, hatched lines (////) indicate NOEs that are ambiguous due to spectral overlap, and blank spaces ( ) indicate that an NOE was not observed because of overlapping chemical shifts. The thickness of the bars indicates the strength of the NOE.

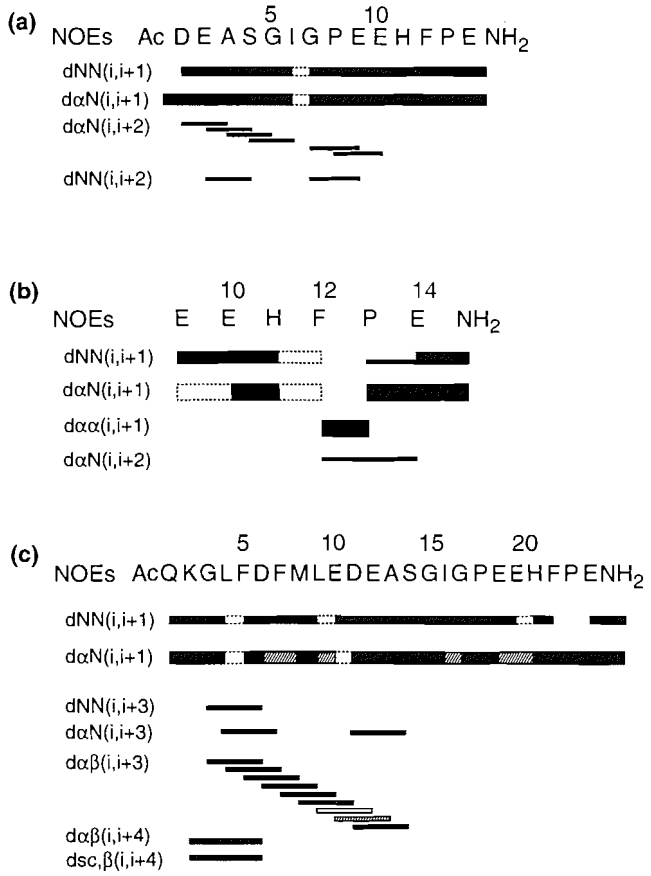

The NOESY spectra for the N-terminal part of AD14 show a series of $i,i+2$ connectivities. In this part of the peptide, low temperature dependencies for the NH protons are also observed. Similar sequences of $i,i+2$ NOE connectivities were observed by Dyson et al. for some short peptides (23, 24,

Fig. 5. The αH-NH region of the 500 MHz phase-sensitive NOESY spectra of AD14. The experimental conditions were the same as outlined in Fig. 2*a* and interesting NOEs are labelled.

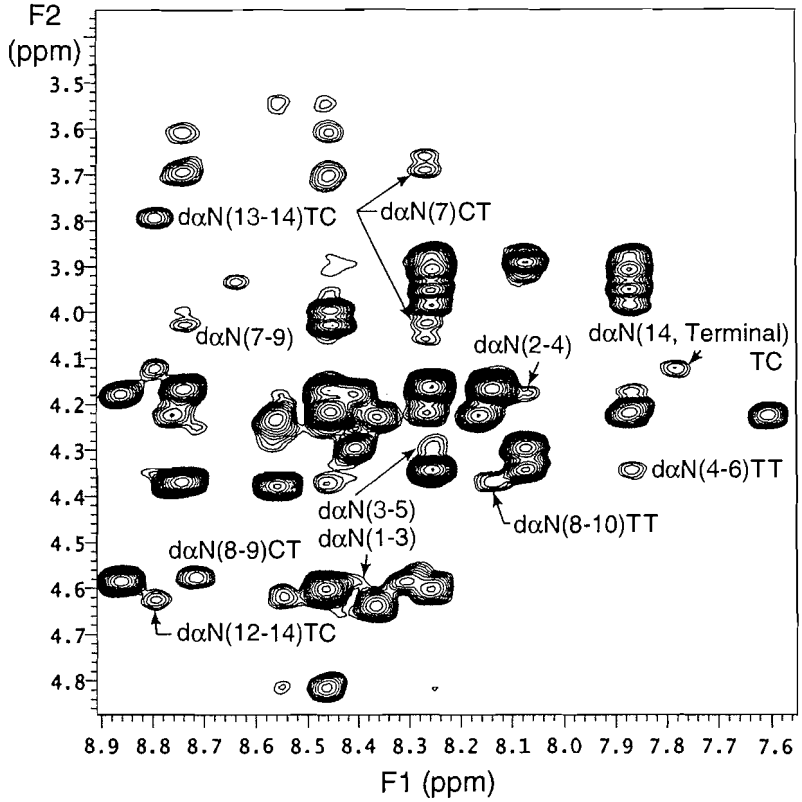

Fig. 6. Net structural shifts of the α proton (□) for peptides (*a*) AD14, (*b*) D14, (*c*) OQ24, and (*d*) NQ24. (■) α′ proton for Gly. For Gly[15] in OQ24 and NQ24, the chemical shifts of the αα′ protons are very similar, hence the average value is used.

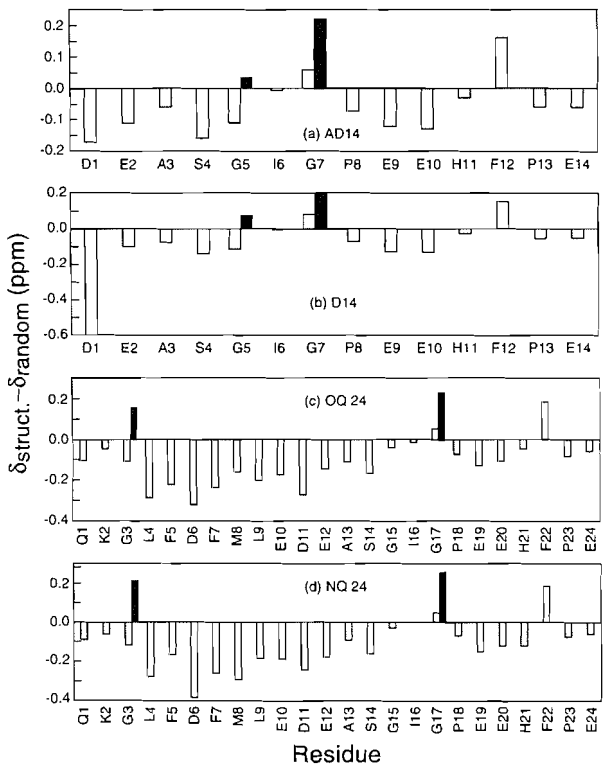

28). This structural element was named the "nascent helix" and it was assumed to consist of rapidly interconverting turns. Recently the term "nascent helix" was also used for small populations of the helical structure in solution (29). Our nascent helix in the 14-mer is a typical case of rapidly interconverting turns. No $i,i+3$ connectivities characteristic for an α-helix were found and the absence of helical fragments is also seen in the CD spectra. Our modeling study started with constrained minimization of randomly generated conformers. Some helical structures were obtained, but these structures quickly unfold when constraints are removed. Unfolding leads to structures with most $i,i+2$ distances observed in the NOESY spectra between 4 and 7 Å. Also, a dynamic run starting from the α-helix (see Experimental) shows an instability of the whole system. From 20 conformers, 11 relax after removing the constraints to the fragments of an α-helix, and 9 relax to structures containing one or two ideal or nonideal turns, mainly type II β-turns. These calculations are in agreement with Dyson et al. (23, 24, 28), namely, that no stable structure is characterized by consecutive $i,i+2$ NOE connectivities, and these connectivities arise from random structures containing some population of turn in various positions. Table 3, column A, gives the backbone dihedral angles for the averaged structure from the last 20 ps of the 100 ps dynamic run (see Experimental). It is seen that this structure relaxes to a random coil with a nonideal type I β-turn in positions Ser[4] to Gly[7].

The same modeling of the AD14 reveals the nature of the C-terminal turn in the conformations containing the *cis*-peptide

Fig. 7. Parts of the contour plot of the two-dimensional 500 MHz NMR NOESY spectrum of peptide OQ24, mixing time 250 ms. The concentration was 2.0 mM at pH 5.5 (measured in H_2O) in CD_3OH/H_2O (60/40 v/v%), temperature 15 ± 0.1°C.

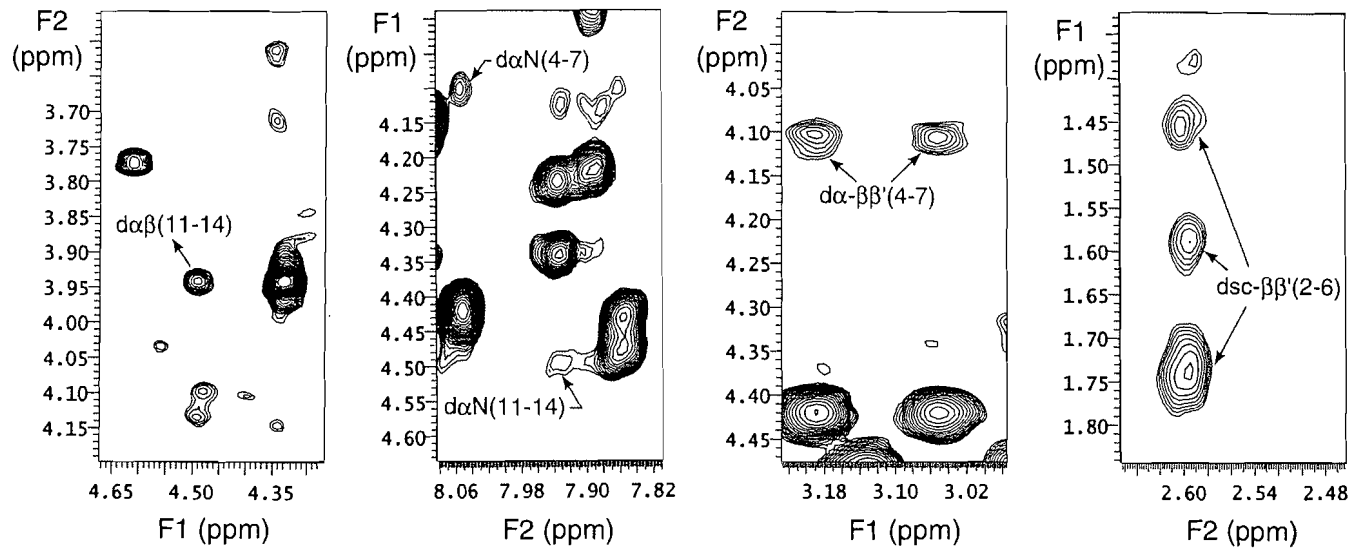

bond between Phe[12] and Pro[13]. Because of the low population of *cis* peptide, no additional constraints to the basic *i,i* + 2 were available, and the Monte Carlo search with constrained minimization led to various turns. The average of the dynamic run starting from the three best conformers led to the nonideal type VIb β-turn (30) (see Table 3, under (A)) as the most probable or most populated conformation for the C-terminus for our peptides containing *cis*-proline. Figure 8*A* shows the averaged minimized structure for the 14-mer with *cis*-proline in position 13; the stereo view of the same structure is in Fig. 9. Figure 8*B* represents the match of the last 20 conformers from the 100 ps dynamic run.

The average conformer from the Monte Carlo search of the 24-mer was subjected to dynamic runs without solvent as well as in the solvent (water) shell. Figure 8*C* shows the averaged minimized structure for the 24-mer with all bonds *trans* modeled without solvent; the backbone data for this structure are listed in Table 3, under (B). Figure 8*D* shows a match of the last 20 conformers from the dynamic run. Figure 10 represents the stereo view of the average minimized structure of the peptide after modeling with the shell of solvent. Backbone data for this structure are in Table 3, under (C). Both structures exhibit a helical structure from Lys[2] to Gly[15]. Analysis of the chemical shifts of the α protons and NOE connectivities shows a continuous helical structure; the temperature dependencies of the NH protons suggest possible disruptions of helix at residues 8 and 11. The structure modeled without solvent shell exhibited disruption of the helical structure at residue 13. This is probably caused by an over-estimation of repulsion between charges in the preceding residues during the calculation "in vacuo." When the dynamic run is performed with peptide in the water shell, the structure of the helix is improved (see data in Table 3, compare data under (B) and (C)). Finally, dihedral angles at the C terminal end of the helix (involving residues 14–17) are similar to those for a type I β-turn.

Discussion

A comparison of the data for the acetylated 14-mer (AD14) with the unacetylated 14-mer (D14) indicates a nascent helix in both peptides. This is consistent with the N-terminal capping preferences for amino acids (31) in α-helical peptides. For example, for the acetyl group the helix fraction is 0.578, whereas when the charged Asp is the N-terminal amino acid with a charged NH_3^+ N-terminus, the fraction of helix for the same control peptide is 0.527 (31).

At the C-terminal end of the peptides, the temperature coefficients and α-proton shifts show that the sequence Ile-Gly-Pro-Glu-Glu-His-Phe-Pro-Glu is of the same conformation in all four peptides studied. The overlap of the spectra and the resonance heterogeneity caused by the prolines prevent further conclusions. The unique ability of the proline to form *cis* peptide bonds and undergo *cis–trans* isomerization (32, 33) is well known. The significance of the study of the isomerization of the proline is twofold: first, the isomerization of proline induces resonance heterogeneity for amino acids adjacent to it; on the other hand, the *cis* and *trans* isomerization forms differ in their solution conformation and are of biological significance (33). In this paper, the peptides have two proline residues and, statistically, four possible isomers could be produced, but in fact three were found.

The addition of the N-terminal 10 amino acids in the 24-mers forms a complete helix ranging from the N-terminal end Lys[2] to Gly[15]. Consequently, the region of interest D^{11}-E^{12}-A^{13}-S^{14}-G^{15} is part of the α-helix, and the N-terminal 10 amino acids promote the α-helix character for this region of the peptide that contains the S that is xylosylated in decorin. Bourdon et al. (34) carried out a kinetic analysis of the xylose-acceptor efficiencies (V_{max}/K_m) of two peptides: FMLE-DEASGIGP and CDEASGIGPEVPDDRD related to human decorin and several variants of these. Both peptides were

Fig. 8. Top left (*A*): Average minimized structure for the 14-mer with *cis*-proline in position 13. Top right (*B*): The last 20 conformers from the 100 ps dynamic run for the 14-mer with *cis*-proline position 13. Bottom left (*C*): Average minimized structure for the 24-mer with all bonds *trans* modeled without solvent. Bottom right (*D*): The last 20 conformers of the 24-mer from the dynamic run.

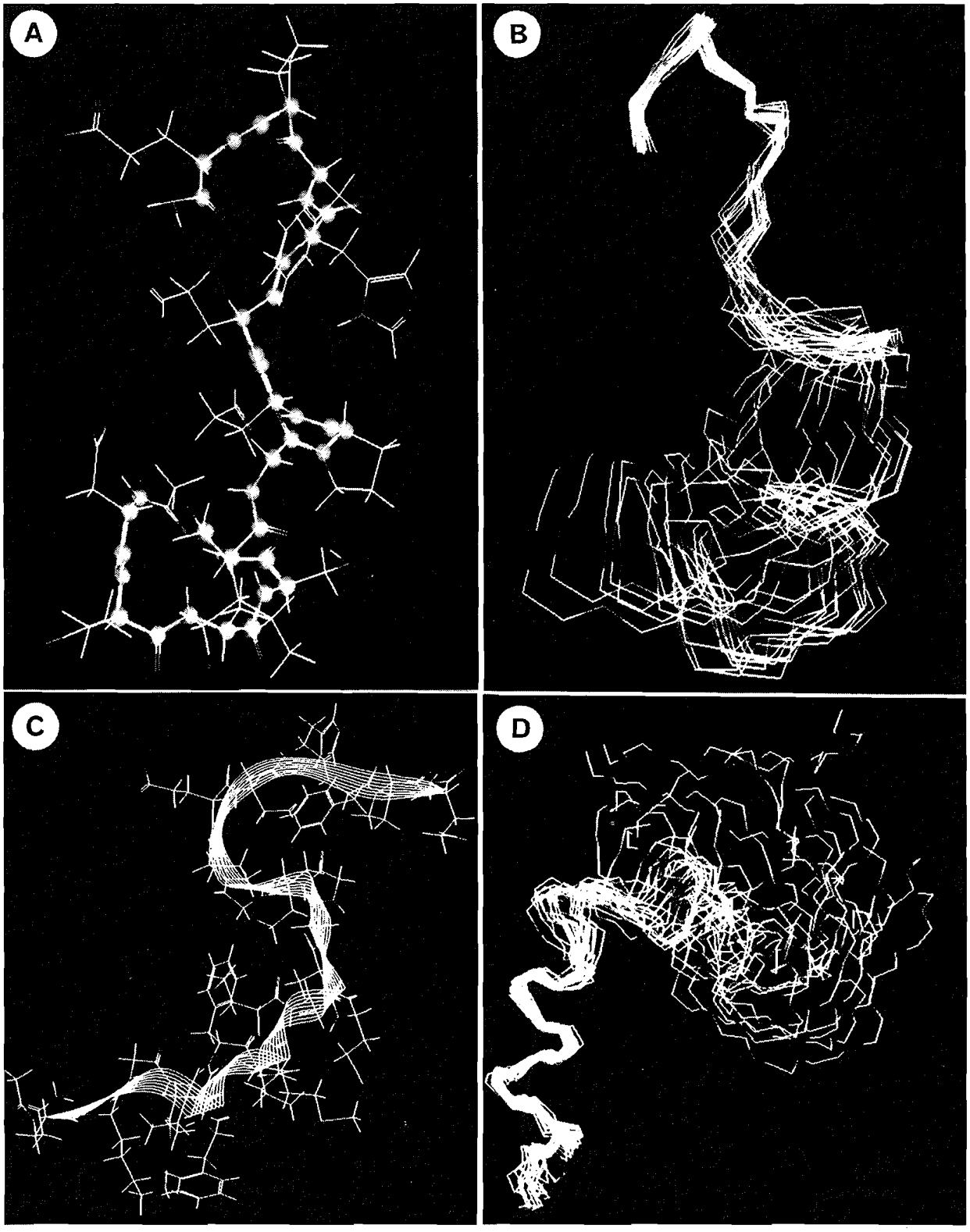

Fig. 9. Stereo view of the average minimized structure for the 14-mer with *cis*-proline in position 13.

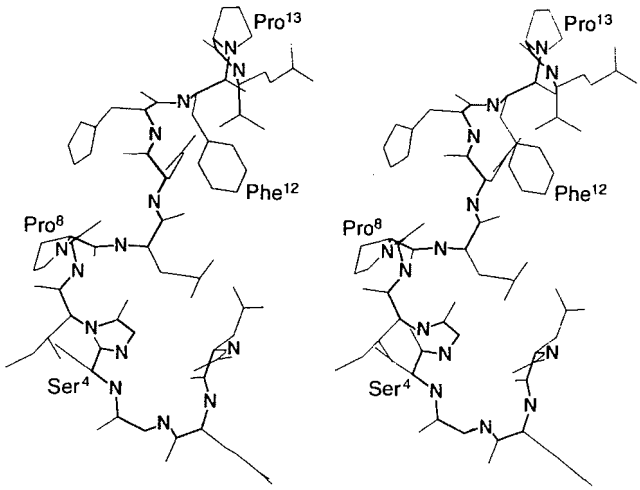

Fig. 10. The stereo view of the average minimized structure of the 24-mer after modeling with the shell of solvent.

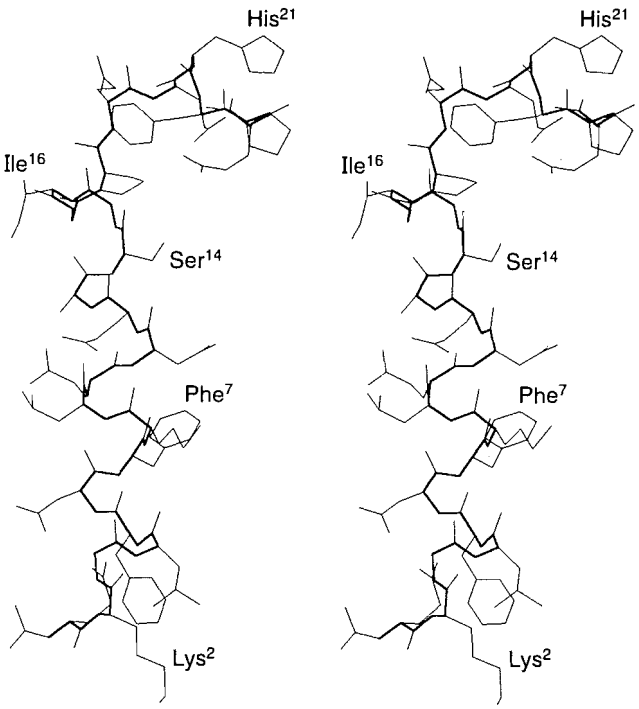

acceptors, indicating that they contain the minimum recognition sequence for xylosyltransferase activity, which may be SGXG (34). The N-terminal cysteine in CDEASGIGPEVPDDRD (which is not present in decorin) may be analogous to the N-acetyl group in the 14-mer studied here. It would be of interest to study the solution conformations of these peptides to determine whether they adopt the (nascent) helical structures described here.

While the adoption of an α-helical conformation by the N-terminal segment of the 24-mer could have been predicted from the amino acid sequence by the method of Chou and Fasman (35), the conclusion of the first 5 amino acids (DEASG) of the mature proteoglycan in this helix is somewhat unexpected because this segment was originally predicted to adopt a type I β-turn (9), and these are usually considered to disrupt helices (35). In either a β-turn or an α-helix, the serine (S^{14}), which in decorin becomes xylosylated, would be exposed on the outside of a turn. This may be one structural factor controlling glycosylation enzyme activity (8).

The N-terminal portion of the helix in the 24-mer shows a peak of hydrophobicity and amphipathicity, detected by the sequence helical hydrophobic moment method of Eisenberg (36; data not shown), centered around F^5. Amphipathic helices are found on the surfaces of globular proteins and are common in α/β proteins, the structural class to which decorin and the other small proteoglycans almost certainly belong (10). This helix could thus serve to position the consensus xylosylation sequence for accessibility to xylosyltransferase.

Conclusions

Asp^1-Glu^2-Ala^3-Ser^4-Gly^5 (DEASG) at the N-terminal end of the 14-mer peptide forms a nascent helical structure. Acetylation of the N-terminus has no effect on the structure. The addition of a further 10 amino acids to the N-terminus forms a helical structure that begins at the N-terminus Lys^2 and ends at Gly^{15}. A type VIb β-turn has been observed, involving the C-terminal *cis*-proline in the sequence His^{11}-Phe^{12}-Pro^{13}-Glu^{14} based on the observed NOE spectra and the modeling of the AD14.

Acknowledgments

The authors gratefully acknowledge the financial assistance of the University of Alberta, the Natural Sciences and Engineering Research Council of Canada (NSERC), and the Medical Research Council (MRC) and thank Elena Edwards for the peptide synthesis and amino acid analysis.

References

1. L.W. Fisher, J.D. Termine, and M.F. Young. J. Biol. Chem. **264**, 4571 (1989).
2. R.K. Chopra, C.H. Pearson, G.A. Pringle, D.S. Fackre, and P.G. Scott. Biochem. J. **232**, 277 (1985).
3. P.J. Neame, H.U. Choi, and L.C. Rosenberg. J. Biol. Chem. **264**, 8653 (1989).
4. J.E. Scott, C.R. Orford, and E.W. Hughes. Biochem. J. **195**, 573 (1981).
5. E. Quentin, A. Gladen, L. Roden, and H. Kresse. Proc. Natl. Acad. Sci. U.S.A. **87**, 1324 (1990).
6. H.P. Hoffman, N.B. Schwartz, L. Rodén, and D.J. Prockop. Connect. Tissue Res. **12**, 151 (1984).
7. I.B. Wilson, Y. Gavel, and G. von Heijne. Biochem. J. **275**, 529 (1991).
8. J.-P. Aubert, G. Biserte, and M.H. Loucheux-Lefevre. Arch. Biochem. Biophys. **175**, 410 (1976).
9. C.H. Pearson, N. Winterbottom, P.G. Scott, and D.S. Fackre. Biochem. Soc. Trans. **11**, 747 (1983).
10. P.G. Scott. *In* Dermatan sulphate proteoglycans: chemistry, biology, chemical pathology. *Edited by* J.E. Scott. Portland Press, London. 1993. p. 81.
11. R.S. Sawhney, T.M. Hering, and L.J. Sandell. J. Biol. Chem. **266**, 9231 (1991).
12. T. Krusius and E. Ruoslahti. Proc. Natl. Acad. Sci. U.S.A. **83**, 7683 (1986).

13. R.R. Ernst, G. Bodenhausen, and A. Wokaun. *In* Principles of nuclear magnetic resonance in one and two dimensions. Clarendon Press, Oxford. 1987.
14. D.J. States, R.A. Haberkorn, and D.J. Ruben. J. Magn. Reson. **53**, 528 (1983).
15. G. Otting, H. Widmer, G. Wagner, and K. Wuthrich. J. Magn. Reson. **66**, 187 (1986).
16. L. Braunschweiler and R.R. Ernst. J. Magn. Reson. **53**, 521 (1983).
17. A. Bax and D.G. Davis. J. Magn. Reson. **65**, 355 (1985).
18. J. Jeener, R. Meier, P. Bachmann, and R.R. Ernst. J. Chem. Phys. **71**, 4546 (1979).
19. A. Kumar, R.R. Ernst, and K. Wuthrich. Biochem. Biophys. Res. Commun. **95**, 1 (1980).
20. M.P. Williamson and D. Neuhaus. J. Magn. Reson. **72**, 369 (1987).
21. K. Wüthrich. NMR of proteins and nucleic acids. Wiley–Interscience, New York. 1986.
22. J. Gasteiger and M. Marsili. Tetradhedron, **36**, 3219 (1980).
23. H.J. Dyson, M. Rance, R.A. Houghten, P.E. Wright, and R.A. Lerner. J. Mol. Biol. **201**, 201 (1988).
24. H.J. Dyson and P.E. Wright. Annu. Rev. Biophys. Biophys. Chem. **20**, 519 (1991).
25. D.S. Wishart, B.D. Sykes, and F.M. Richards. J. Mol. Biol. **222**, 311 (1991).
26. K. Ösapay and D.A. Case. J. Biomol. NMR, **4**, 215 (1994).
27. J.L. Markley and M. Kainosho. *In* NMR of macromolecules. A practical approach. *Edited by* G.C.K. Roberts. Oxford University Press, Oxford. 1993. pp. 101–152.
28. H.J. Dyson, G. Merutka, J.P. Waltho, R.A. Lerner, and P.E. Wright. J. Mol. Biol. **226**, 795 (1992).
29. G.W. Buchko, A. Rozek, Q. Zhong, and R.J. Cushley. Pept. Res. **8**, 86 (1995).
30. H.J. Dyson, M. Rance, R.A. Houghten, P.E. Wright, and R.A. Lerner. J. Mol. Biol. **201**, 161 (1988).
31. A.J. Doig and R.L. Baldwin. Protein Sci. **4**, 1325 (1995).
32. P. Amodeo, M. Antonietta, C. Morelli, and A. Motta. Biochemistry, **33**, 10754 (1994).
33. C. McInnes, C.M. Kay, R.S. Hodges, and B.D. Sykes. Biopolymers, **34**, 1221 (1994).
34. M.A. Bourdon, T. Krusius, S. Campbell, N.B. Schwartz, and E. Ruoslahti. Proc. Natl. Acad. Sci. U.S.A. **84**, 3194 (1987).
35. P.Y. Chou. *In* Prediction of protein structure and principles of protein conformation. *Edited by* G.D. Fasman. Plenum Press, New York. 1989. p. 549.
36. D. Eisenbert, R.M. Weiss, and T.C. Terwilliger. Nature, **299**, 371 (1982).

Calculation of phase diagrams and thermodynamic properties of 18 binary common-ion systems of Na,K,Ba//F,MoO_4,WO_4

James Malcolm Sangster

Abstract: Phase diagram and thermodynamic data of 18 binary common-ion molten salt systems in Na,K,Ba//F,MoO_4,WO_4 were optimized by computer algorithm. The phase diagram data as well as single-salt data were retrieved from an extensive critical literature search. Expressions for the excess properties of solution phases and thermodynamic properties of intermediate compounds were thereby obtained. These data were used to generate a "best" phase diagram for each binary system considered.

Key words: molten salts, phase diagrams, thermodynamic properties.

Résumé : On a fait un lissage par ordinateur des données thermodynamiques et des diagrammes de phases de 18 systèmes de sels fondus d'ions communs représentés par Na,K,Ba//F,MoO_4,WO_4. Les données de diagramme de phases et des sels purs ont été obtenues à moyen d'une recherche critique bibliographique assez complète. On a donc obtenu des expressions analytiques pour les propriétés en excès des solutions ainsi que les propriétés thermodynamiques des composés intermédiaires. Ces expressions ont été utilisées dans le calcul du diagramme de phases de chaque système.

Mots clés : sels fondus, diagrammes de phases, propriétés thermodynamiques.

[Traduit par la rédaction]

Introduction

The thermodynamic basis for the calculation and interpretation of phase diagrams is well known (1). Once the thermodynamic properties of simple and solution phases are known, a computer can be used to carry out the iterative process involved in calculating the phase boundaries at equilibrium (2). This is a general approach, which can and has been adapted successfully to the calculation of binary and ternary phase diagrams of alloy systems (3, 4), common-ion and reciprocal ternary molten salt systems (5–8), and organic systems (9–11). In this article, this type of calculation is applied to binary molten salt systems containing cations Na,K,Ba and anions F,MoO_4,WO_4.

Critical analysis of thermodynamic/phase diagram data for binary common-ion molten salt systems

A critical analysis of the phase diagram and thermodynamic data of 18 binary common-ion molten salt systems was accomplished with the use of a computer-assisted technique already used for 70 binary alkali halide systems (12). The method is described in some detail in the previous work (12) and is summarized here. An exhaustive literature search was made for phase diagram and thermodynamic data for each system; all references are included here. These data were optimized simultaneously with the use of the computer algorithm to yield analytical expressions that best represent the thermodynamic properties of the solution and intermediate phases. These expressions were then used to generate the phase diagrams (13). The interactive computer programs used (13) are available on-line, as well as in personal computer version on diskette, available from the author. Such phase diagrams automatically incorporate necessary thermodynamic constraints, such as the Gibbs–Duhem relation, the phase rule, the correct limiting liquidus slopes, etc. As in the previous work (12), data not tabulated in original publications were read off published phase diagrams.

Properties of the pure components

The calculational procedure outlined above requires expressions for the Gibbs energy of transition and fusion of the solid components involved. These thermodynamic properties, which were used in the calculation of the final phase diagrams, are summarized in Table 1. These data were based on information from standard sources (14–18). For some salts involved in the present work, these sources differed significantly among themselves, and some necessary data were missing and hence had to be estimated. The choice of data finally adopted for each salt is discussed in the Appendix.

Common anion systems

KF (A) – NaF (B)

This system was examined in a previous publication (12) and no new data have since appeared to necessitate a revision. It is a simple eutectic system with a limited solid solution based on KF. The results (12) are summarized here. The excess enthalpy of the liquid

Received July 7, 1995.[1]

J.M. Sangster.[2] Sangster Research Laboratories, Suite 402, 3475 de la Montagne, Montreal, QC H3G 2A4, Canada.

[1] Revision received January 15, 1996.

[2] Telephone: (514) 340-4304. Fax: (514) 340-5840. E-mail: j704αmusic.mus.polymtl.ca

Table 1. Gibbs energies of transition and fusion of the pure salts.[a]

$\Delta_{trs}G^0 = a + bT + cT^2 + dT \ln T + e/T$ (J mol^{-1})

Salt	Transition	T (°C)	a	b	$c \times 10^3$	d	$e \times 10^{-6}$
Fluorides							
Na	s → l	996	10 847.2	156.584	4.9495	−23.978	−1.065
KF	s → l	857	13 762.7	127.037	7.2110	−20.962	0
BaF_2	α → β	1207	−23 021.9	165.214	1.8828	−20.836	−0.7531
	β → l	1368	45 536.0	−127.795	0	13.514	0
Molybdates							
Na_2MoO_4	α → β	461	−7 703.1	451.825	39.288	−71.253	0
	β → γ	592	−7 763.4	85.3722	0	−11.297	0
	γ → δ	640	5 301.1	22.7149	0	−4.1840	0
	δ → l	690	14 371.9	42.5687	0	−8.3680	0
K_2MoO_4	α → β	338	47 392.9	−98.3401	34.0000	0	0
	β → γ	450	5 000.0	−6.91563	0	0	0
	γ → δ	471	14 380.0	−19.3280	0	0	0
	δ → l	926	−62 658.8	627.906	0	−81.200	0
$BaMoO_4$	s → l	1457	7 489.3	338.714	14.518	−49.325	−1.185
Tungstates							
Na_2WO_2	α → β	588	−5 733.0	542.610	47.960	−85.303	0.5640
	β → γ	590	4 113.0	−4.76600	0	0	0
	γ → l	694	23 799.0	−24.6112	0	0	0
K_2WO_4	α → β	370	35 140.0	−54.650	0	0	0
	β → γ	455	5 000.0	−6.86813	0	0	0
	γ → δ	585	14 380.0	−16.7600	0	0	0
	δ → l	926	−8 876.6	494.718	31.100	−74.000	0
$BaWO_4$	s → l	1510	−4 747.0	424.927	17.364	−60.542	0

[a]Sufficient significant figures are given to enable accurate reproduction of phase diagrams.

[1] $H^E(l) = -355x_Ax_B$ J mol^{-1}

was measured calorimetrically and the excess entropy was

[2] $S^E(l) = -2.541$ J mol^{-1} K^{-1}

The solid solution was represented by a Henrian activity coefficient

[3] $RT \ln \gamma_B = 24\,770$ J mol^{-1}

which was assumed to be temperature independent. The calculated eutectic was 719°C, $x_B = 0.400$ and there was 5 mol% solubility of NaF in KF at the eutectic temperature. An uncertainty of ±5°C was assigned to this calculated phase diagram (12).

BaF_2 (A) – KF (B)

Phase diagram data were obtained by the visual-polythermal method (19) and thermal analysis (20). Neither work mentions the BaF_2 transition at 1207°C. A eutectic summary is given in Table 2. The excess enthalpy of the liquid was determined at 1081°C by solid–liquid mixing calorimetry (21), and the result is

[4] $H^E(l) = x_Ax_B(-14\,700 - 1580x_A - 1240x_A^2)$ J mol^{-1}

The liquidus data of Pushin and Bashov (20) are obviously faulty near $x_B = 0$. For the optimization, only liquidus data at $x_B > 0.4$ were used, together with eq. [4], to deduce one excess entropy coefficient:

Table 2. Reported eutectic data for BaF_2 (A) – KF (B).

T (°C)	x_B	Ref.
750	0.70	20
729	0.73	19
729	0.74	22

[5] $S^E(l) = -15.224x_Ax_B$ J mol^{-1} K^{-1}

The phase diagram, Fig. 1, was calculated with the use of eqs. [4] and [5] and shows a calculated eutectic at 745°C, $x_B = 0.711$. A much more strongly composition-dependent excess entropy would allow the calculated liquidus to better approximate the liquidus data of ref. 19, but it would then show a marked inflection on the LHS; the behaviour shown in Fig. 1 was judged to be more probable. The BaF_2 transition appears on the calculated liquidus at $x_B = 0.184$. An uncertainty of ±20°C may be assigned to the calculated diagram.

BaF_2 (A) – NaF (B)

Phase diagram data were obtained by thermal analysis (23) and by the visual-polythermal method (24). A eutectic summary is given in Table 3. The excess enthalpy of the liquid was determined at 1081°C by solid–liquid mixing colorimetry (21) and the result is

Fig. 1. The system BaF_2 (A) – KF (B). ×: ref. 19; ●: ref. 20.

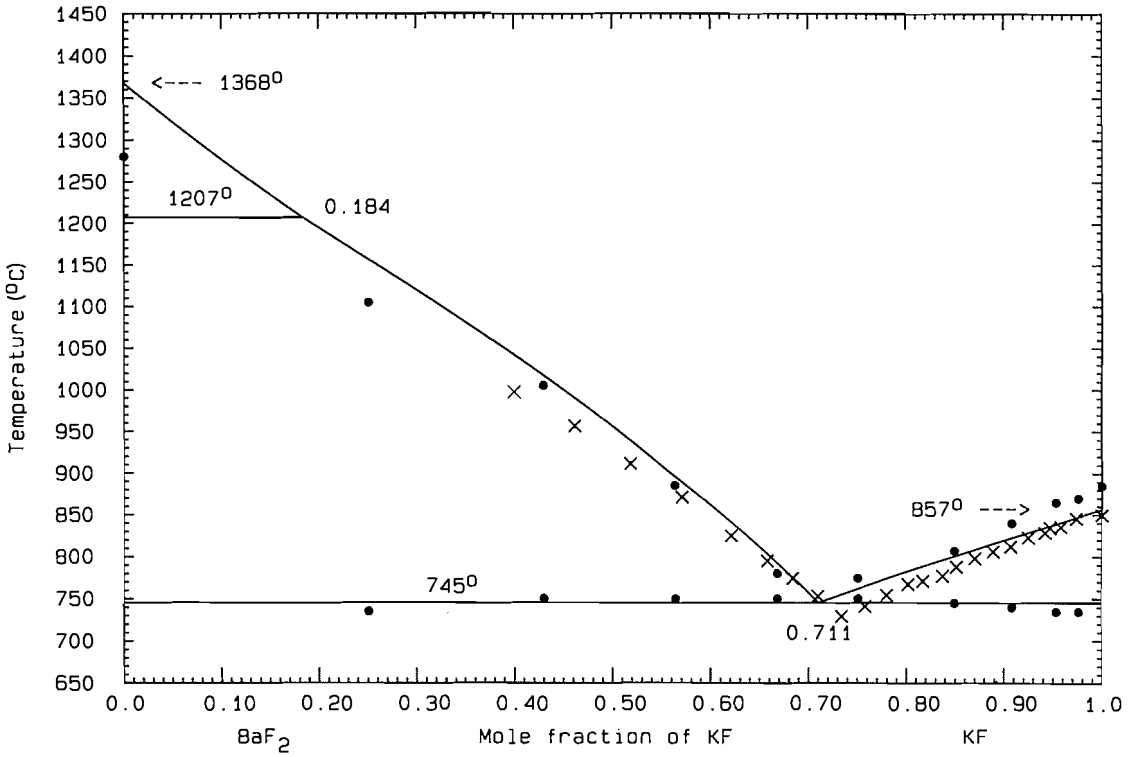

Table 3. Reported eutectic data for BaF_2 (A) – NaF (B).

T (°C)	x_B	Ref.
812	0.63	24
823	0.56	23
820	0.63	25

Table 4. Reported invariant points for $BaMoO_4$ (A) – K_2MoO_4 (B) from ref. 26.

	T (°C)	x_B
Eutectic	924	0.91
Peritectic	1067	0.51
Maximum	936	0.97
Eutectoid	455	0.95

[6] $H^E(l) = x_A x_B(-2670 - 105x_A - 1160x_A^2)$ J mol^{-1}

The BaF_2 transition at 1207°C is not mentioned in either investigation (23, 24) and the liquidus data of Grube (23) on the LHS are clearly in error. In the optimization, the excess enthalpy, eq. [6], was used together with the liquidus data of Grube (23) at $x_B > 0.6$ and all the data of the other report (24), to give one excess entropy coefficient

[7] $S^E(l) = -1.7211x_A x_B$ J mol^{-1} K^{-1}

The phase diagram was calculated with the use of eqs. [6] and [7] and is shown in Fig. 2. The calculated eutectic is 821°C, $x_B = 0.614$ and the calculated liquidus agrees well with the selected liquidus data. The BaF_2 transition appears on the calculated liquidus at $x_B = 0.172$. An uncertainty of ±10°C may be assigned to the calculated diagram.

$BaMoO_4$ (A) – K_2MoO_4 (B)

The phase diagram was investigated by the visual-polythermal method, thermal analysis, and X-ray diffraction (26). The reported invariant points are summarized in Table 4. The X-ray diffraction data of the compound were indexed according to trigonal symmetry for the 1:1 stoichiometry $K_2Ba(MoO_4)_2$ (a = 0.606 nm, c = 2.134 nm, Z = 3, space group $R3m$), isostructural with $K_2Pb(SO_4)_2$ (palmerite). The local maximum at $x_B = 0.97$, apparently well established by thermal analysis (26), is an unusual feature not often observed in molten salt systems. Similar maxima apparently occur in the systems Na,Ca//CO_3 (27), Na,Ba//SO_4 (28), an Na,Ca//SO_4 (29). Such a maximum, very close to the pure salt composition, has puzzled investigators; it is apparently not due to the presence of a compound. It has been suggested (30) that in these cases the multiply charged cation enters the sublattice of the singly charged cation, thereby creating vacancies and stabilizing the structure (30). Whatever the explanation, this effect is very difficult, if not impossible, to reproduce with the use of simple thermodynamic models. For present purposes, the maximum was ignored and a solid solution was included to reproduce the observed eutectic. The limited number of liquidus data (none above 1109°C) could be well accounted for by an excess Gibbs energy of the liquid

[8] $G^E(l) = -10\,000x_A x_B$ J mol^{-1}

Fig. 2. The system BaF_2 (A) – NaF (B). ●: ref. 23; ×: ref. 24.

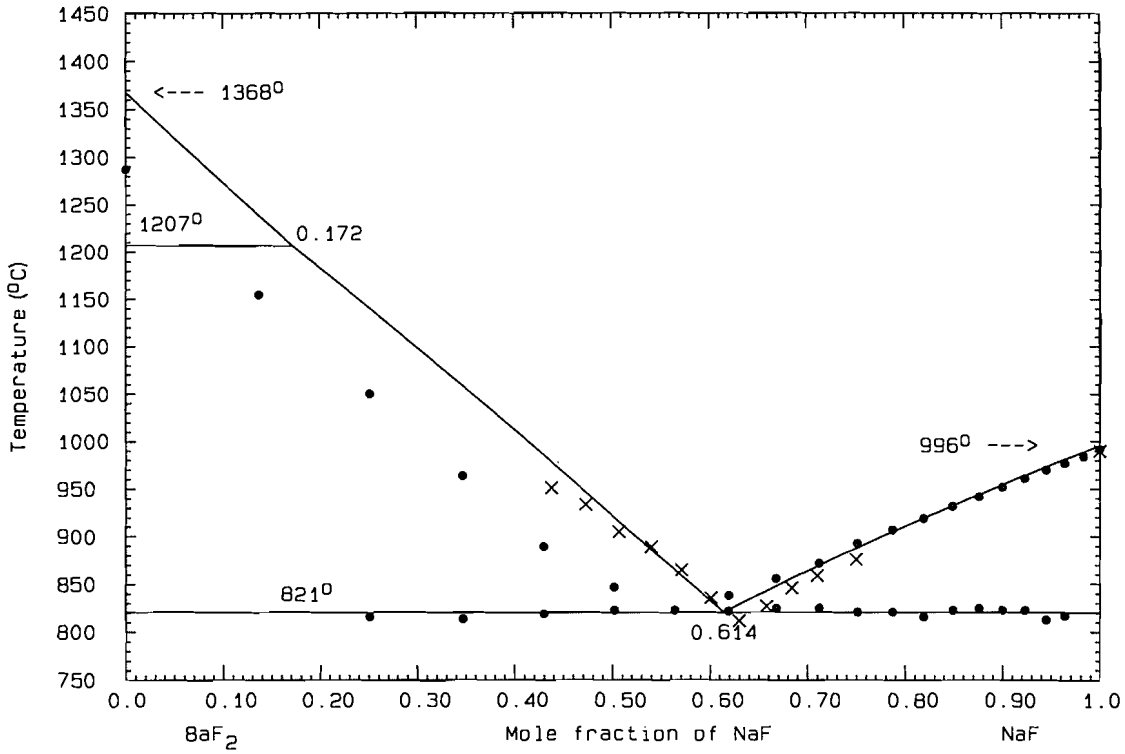

and properties for the 1:1 compound, $(K_2MoO_4 \cdot BaMoO_4)/2$, as follows:

[9] $\Delta_{fus}G^0 = 61\,333 - 45.7628T$ J mol^{-1}

[10] $\Delta_fG^0 = -63\,833 + 40.0000T$ J mol^{-1}

The solid solution was represented by a Henrian activity coefficient

[11] $RT \ln \gamma_A = 7000$ J mol^{-1}

assumed to be temperature independent. The phase diagram, Fig. 3, was calculated with the use of eqs. [8], [10], and [11]. The calculated eutectic is 922°C, $x_B = 0.900$, and the calculated peritectic is 1067°C, $x_B = 0.513$. The solid solution extends practically to the eutectic composition. The calculated eutectoid is 470°C, $x_B = 0.966$. The reported eutectoid (26) is not thermodynamically consistent with the limited extent of solid solution observed (26). An uncertainty of ±20°C may be assigned to the calculated phase diagram.

$BaMoO_4$ (A) – Na_2MoO_4 (B)

Data for this system were obtained by thermal analysis (31, 32) and the visual-polythermal method (32). The reported eutectic (32) was 685°C, $x_B = 0.92$ or (31) 678°C, $x_B = 0.90$. The existence of a solid solution based on Na_2MoO_4 was claimed (31), together with a local maximum at 694°C, $x_B = 0.96$. No such solid solution was mentioned in the other report (32), although the liquidus data near $x_B = 1$ of these authors (32) could be interpreted as evidence for a maximum. As explained in the analysis for the analogous $BaMoO_4$–K_2MoO_4 above, such a maximum might exist. Again, as in the analogous system, this possible maximum was ignored and a limited solid solution was included in the calculated phase diagram since the experimental limiting liquidus slope (32) definitely indicates the presence of such a solid solution.

The liquidus data of Petrosyan et al. (32) show an inflection point, unusual curvature, and abrupt descent to the eutectic; such behaviour is rather unlikely for a simple eutectic system. The liquidus data of Posypaiko et al. (31) were therefore optimized, with the result

[12] $G^E(l) = x_Ax_B(-16\,300 + 24\,212x_B - 7723x_B^2)$ J mol^{-1}

The solid solution was represented by a Henrian activity coefficient

[13] $RT \ln \gamma_A = 20\,000$ J mol^{-1}

assumed to be independent of temperature. The phase diagram Fig. 4, was calculated with the use of eqs. [12] and [13] and shows a calculated eutectic of 686°C, $x_B = 0.900$, with 8.1 mol% solid solubility of $BaMoO_4$ in Na_2MoO_4 at the eutectic temperature. There is a calculated eutectoid at 593°C, $x_B = 0.938$. An uncertainty of ±10°C may be assigned to Fig. 4.

$BaWO_4$ (A) – K_2WO_4 (B)

Scanty liquidus data were obtained by the visual-polythermal method (31); these data were read off the limiting binary edge of a ternary phase diagram. These authors reported a eutectic at 924°C, $x_B = 0.62$, together with "restricted solid solutions." No subsolidus data are available. The stoichiometry of the intermediate compound was established (31) by X-ray analysis (data not reported) to be 1:1. The compound $K_2Ba(WO_4)_2$ is apparently isostructural with $K_2Ba(MoO_4)_2$ and hence with

Fig. 3. The system $BaMoO_4$ (A) – K_2MoO_4 (B). ●: ref. 26.

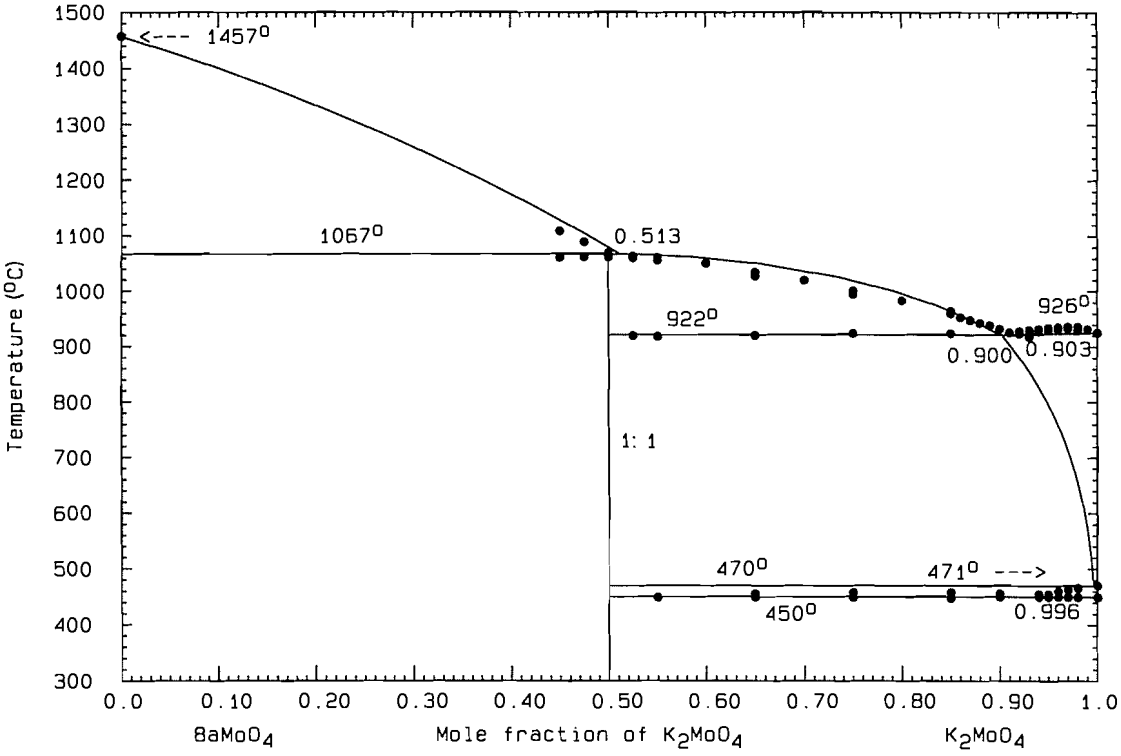

Fig. 4. The system $BaMoO_4$ (A) – Na_2MoO_4 (B). ●: ref. 46; ×: ref. 32.

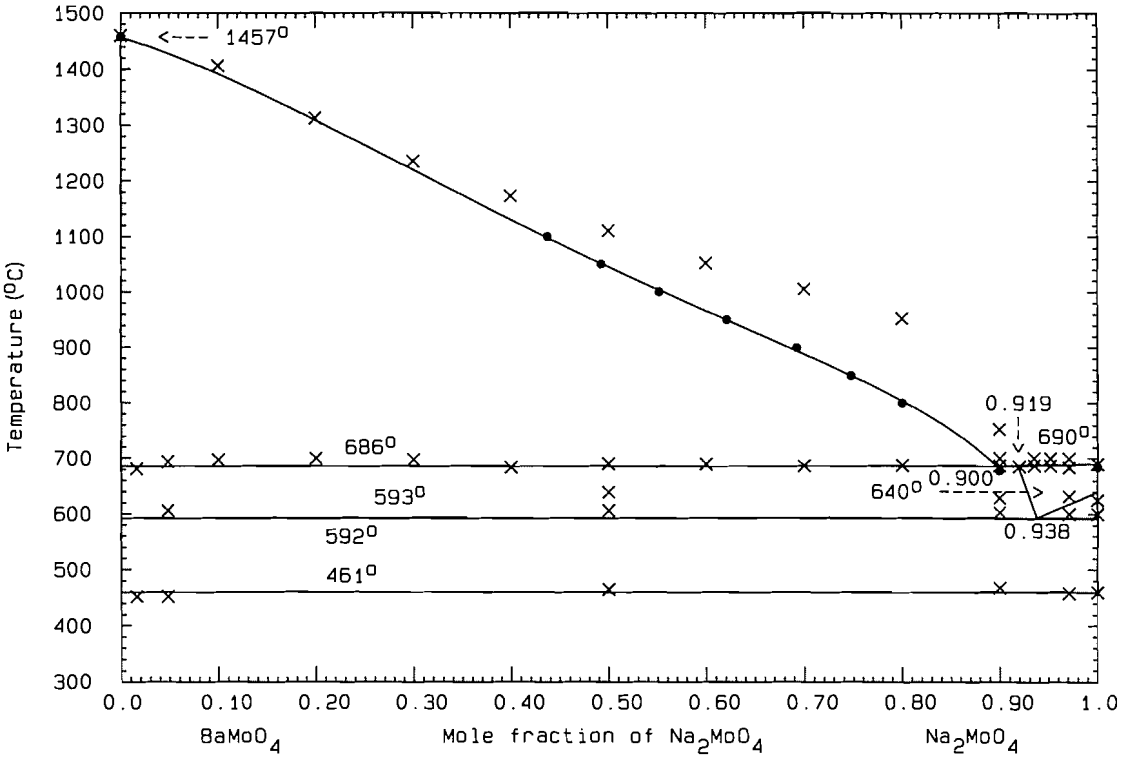

$K_2Pb(SO_4)_2$ (26, 31). The authors (31) also reported a "maximum" temperature in the liquidus near $x_B = 1$, but gave no further information. The limiting liquidus slope (31) at $x_B = 1$ clearly indicates the presence of solid solution based on K_2WO_4. Since the liquidus data are so sparse, no computer optimization was possible; instead, the phase diagram was constructed by trial and error, starting with reasonable estimates of the required thermodynamic data. The phase diagram, Fig. 5, was calculated with the use of eq. [14] for the liquid

Fig. 5. The system $BaWO_4$ (A) – K_2WO_4 (B). ●: ref. 31.

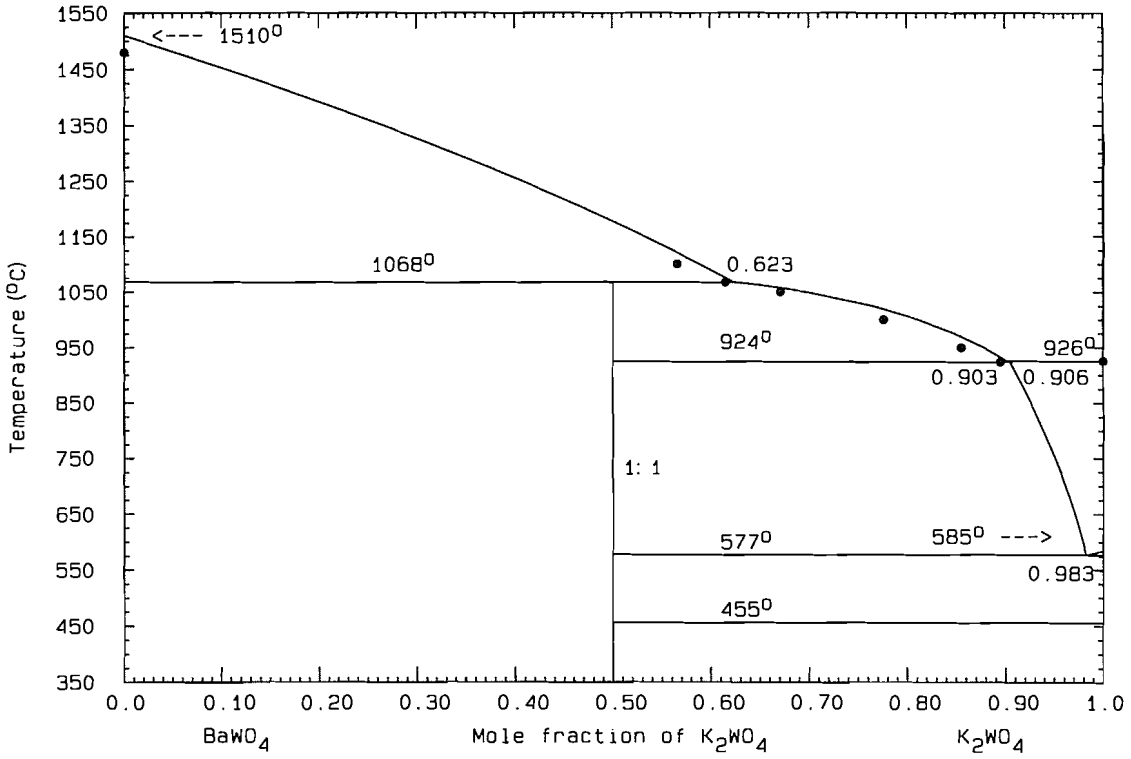

[14] $G^E(l) = -2000x_Ax_B$ J mol^{-1}

and for the 1:1 compound, as $(BaWO_4{\cdot}K_2WO_4)/2$,

[15] $\Delta_{fus}G^0 = 48\,338 - 35.7628T$ J mol^{-1}

[16] $\Delta_fG^0 = -48\,838 + 30.0000T$ J mol^{-1}

where the quantities in eqs. [15] and [16] are, respectively, the Gibbs energy of fusion and formation (from the pure liquids). The solid solution was represented by a Henrian activity coefficient

[17] $RT \ln \gamma_A = 13\,750$ J mol^{-1}

assumed to be temperature independent. The phase diagram, Fig. 5, was calculated with the use of eqs. [14], [16], and [17] and the calculated eutectic is 924°C, $x_B = 0.903$, agreeing with experiment (32). The calculated peritectic is 1068°C, x_B = 0.623, also agreeing with experiment. There is a calculated eutectoid at 577°C, $x_B = 0.983$. The solid solution extends to a maximum of 9.4 mol% at the eutectic temperature. Since the experimental liquidus data are so sparse, no uncertainty can be reliably assigned to the calculated phase diagram.

$BaWO_4$ (A) – Na_2WO_4 (B)

The phase diagram was investigated by thermal analysis, the visual-polythermal method, and X-ray analysis (33). These authors reported a eutectic of 680°C, $x_B = 0.96$; another report (25) gave 678°C, $x_B = 0.94$. The liquidus data (33) were optimized to give an excess Gibbs energy of the liquid

[18] $G^E(l) = x_Ax_B(-2153 + 8285x_B)$ J mol^{-1}

and the phase diagram calculated with the use of this expression is shown in Fig. 6. The calculated eutectic is 681°C, x_B = 0.958. A maximum uncertainty of ±20°C may be assigned to the calculated phase diagram.

K_2MoO_4 (A) – Na_2MoO_4(B)

The phase diagram was investigated by thermal analysis (34) and by the visual-polythermal method (35–37). There is disagreement concerning the subsolidus behaviour in this system. A continuous solid solution across the whole composition range was claimed (34, 38), whereas other investigators (35–37) postulate the existence of two incongruently melting compounds. A summary of invariant points is given in Table 5. Amadori (34) does not state a minimum liquidus temperature, but from his tabulated data it is approximately 661°C, $x_B = 0.8$. The situation is extraordinarily confused, as the existence of compounds is postulated only on the basis of breaks in the liquidus curve (35, 36, 39, 40). From the limiting liquidus slopes at both ends of the phase diagram, it is evident that extensive solid solutions exist at both locations. In preliminary calculations, it was found that, if complete solid solution were assumed at the liquidus temperature, the separation between liquidus and solidus on the LHS would be as much as 60°C at a given composition; on the RHS the separation is only a few degrees. The only investigator to use thermal analysis (34) did not report separate liquidus and solidus thermal arrests, and it is implicit that the liquidus and solidus are very close together over the whole composition range. For present purposes, it was decided to construct a phase diagram with terminal solid solutions and with two compounds (35–37). The liquid was assumed to be ideal

[19] $G^E(l) = 0$

Fig. 6. The system $BaWO_4$ (A) – Na_2WO_4 (B). ●: ref. 33.

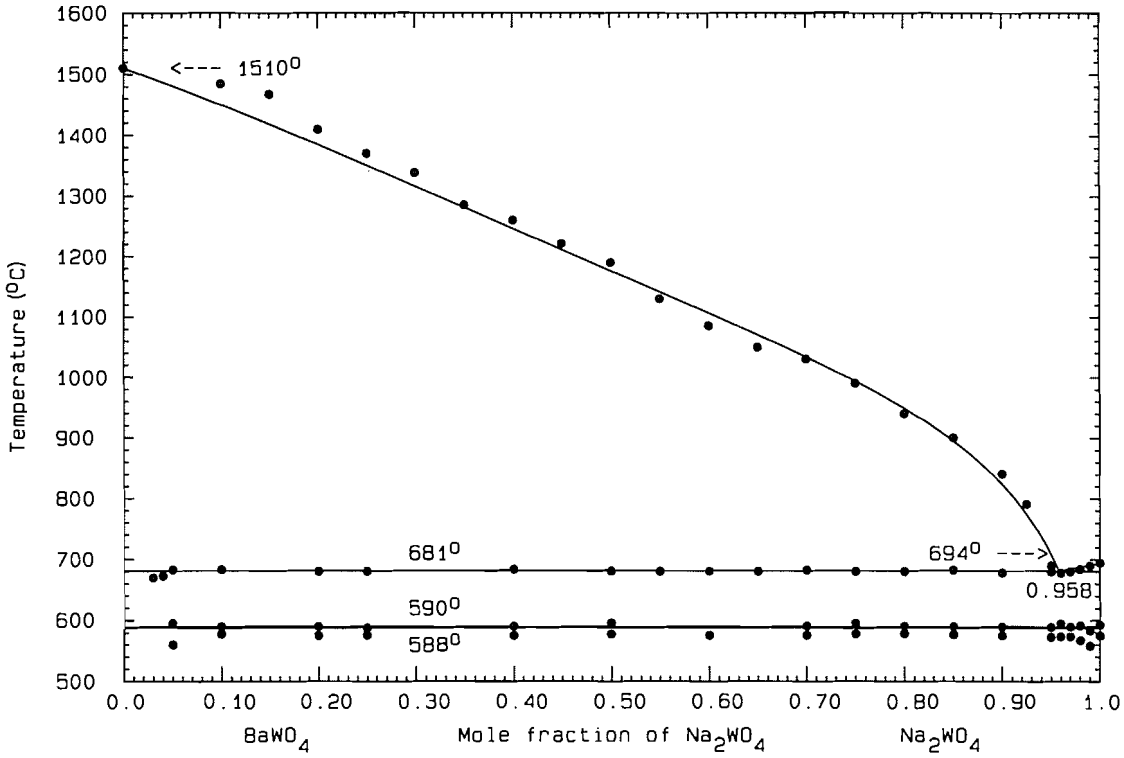

Table 5. Reported invariant points for K_2MoO_4 (A) – Na_2MoO_4 (B).

	T (°C)	x_B	Refs.
Peritectic	736	0.46	36, 39
	743	0.50	41
	737	0.54	35
Peritectic	683	0.63	36, 39
	682	0.64	41
	686	0.63	35
Eutectic	667	0.81	35
	660	0.84	36, 39
	663	0.81	41
Minimum	656	≈0.8	38

and thermodynamic properties of other phases chosen in order to reproduce the observed liquidus (34–36) as closely as possible. Thus, the two end solid solutions were represented by two Henrian activity coefficients

[20] $RT \ln \gamma_B = 9000$ J per mole of Na_2MoO_4

[21] $RT \ln \gamma_A = 9600$ J per mole of K_2MoO_4

For the compound $(K_2MoO_4 \cdot Na_2MoO_4)/2$,

[22] $\Delta_{fus}G^0 = 78\,900 - 81.5256T$ J mol^{-1}

[23] $\Delta_f G^0 = -78\,900 + 70.0000T$ J mol^{-1}

and for $(Na_2MoO_4 \cdot 2K_2MoO_4)/3$,

[24] $\Delta_{fus}G^0 = 61\,710 - 60.5840T$ J mol^{-1}

[25] $\Delta_f G^0 = -61\,710 + 70.0000T$ J mol^{-1}

The phase diagram, Fig. 7, calculated from eqs. [19]–[21], [23], and [25], shows a calculated eutectic of 664°C, $x_B = 0.760$ and calculated peritectics 682°C, $x_B = 0.673$ and 736°C, $x_B = 0.462$. The solid solutions extend to 25.3 and 21.1 mol% at the peritectic and eutectic temperatures, respectively. There are two calculated eutectoids, at 461°C, $x_B = 0.015$ and 552°C, $x_B = 0.932$. The calculated fusion properties of the compounds, eqs. [22] and [24], are very different from the fusion properties of the pure salts and hence the quantities of eqs. [23] and [25] are to be considered as fitting parameters only and are not to be interpreted as actual suggested properties of these compounds. The entire subsolidus is conjectural. An uncertainty of ±20°C may be assigned to the calculated liquidus.

K_2WO_4 (A) – Na_2WO_4 (B)

The phase diagram was investigated by thermal analysis (34, 44, 42) and by the visual-polythermal method (42–44). The data of Amadori (34) are reproduced exactly by later authors (42). Like the previous system, this system is not well characterized. A summary of invariant points is given in Table 6. As in the previous analogous system, Amadori (34) postulated complete solid solubility with a 1:1 compound decomposing in the subsolidus, whereas other investigators proposed the existence of two compounds (42–44). The two systems K,Na//MoO_4 and K,Na//WO_4 are almost identical with respect to the liquidus, and the same approach to the calculation of the phase diagram was adopted here. For the liquid, again

Fig. 7. The system K_2MoO_4 (A) – Na_2MoO_4 (B). ○: ref. 34; ●: ref. 36; ×: refs. 35, 37. The subsolidus is conjectural.

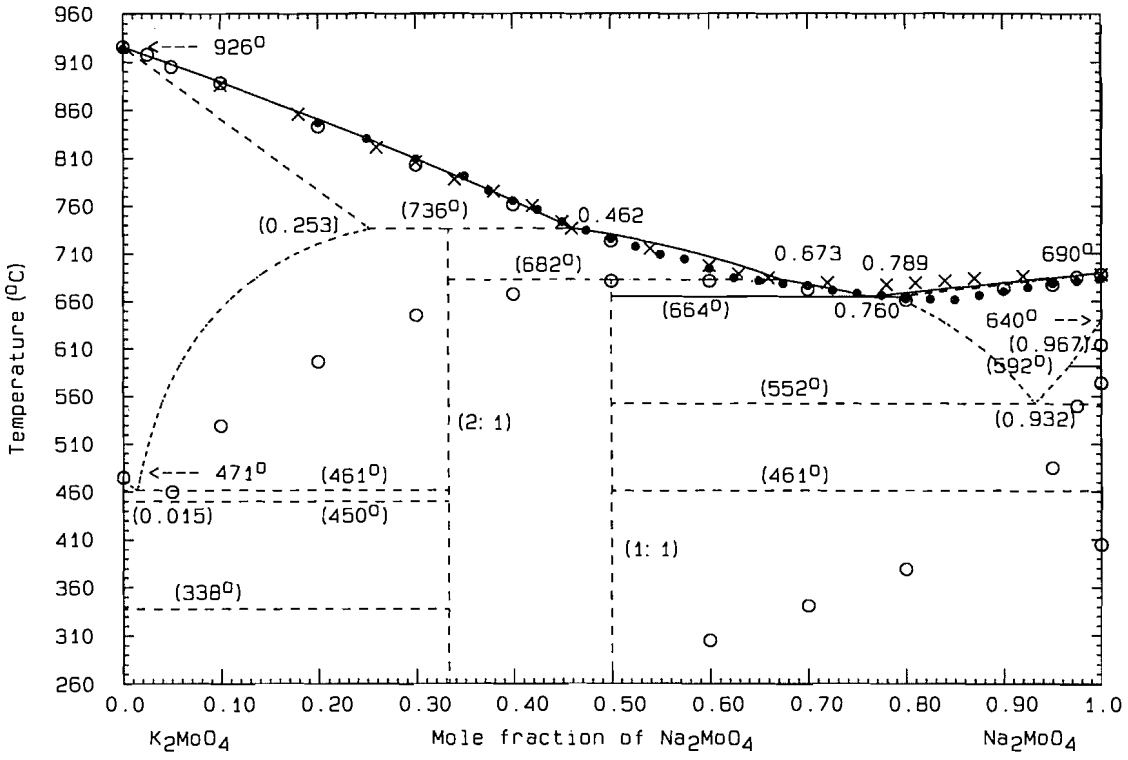

Table 6. Reported invariant points for K_2WO_4 (A) – Na_2WO_4 (B).

	T (°C)	X_B	Refs.
Minimum	636	0.81	34, 42
	≈646	≈0.82	41
Peritectic	678	0.60	43
	689	0.55	44
Peritectic	646	0.76	43
Eutectic	642	0.84	43
	≈645	≈0.86	44
Eutectoid	327	≈0.97	42

[26] $G^E(l) = 0$

and for the two end solid solutions

[27] $RT \ln \gamma_A = 12\,000$ J per mole of K_2WO_4

[28] $RT \ln \gamma_B = 12\,000$ J per mole of Na_2WO_4

being two Henrian activity coefficients assumed to be independent of temperature. For the compound $(Na_2WO_4 \cdot K_2WO_4)/2$ the expressions

[29] $\Delta_{fus}G^0 = 43\,146 - 45.7628T$ J mol^{-1}

[30] $\Delta_f G^0 = -43\,146 + 40.0000T$ J mol^{-1}

were deduced, and for $(Na_2WO_4 \cdot 2K_2WO_4)/3$,

[31] $\Delta_{fus}G^0 = 44\,200 - 45.2920T$ J mol^{-1}

[32] $\Delta_f G^0 = -44\,200 + 40.0000T$ J mol^{-1}

As in the analogous molybdate system, eqs. [29] and [31] represent thermodynamic properties very different from those of the pure salts and hence are to be regarded only as fitting parameters. The phase diagram, Fig. 8, was calculated with the use of eqs. [26], [27], [28], [30], and [32]. The calculated eutectic is 644°C, $x_B = 0.759$ and the calculated eutectoids are 565°C, $x_B = 0.023$ and 561°C, $x_B = 0.924$. The calculated peritectics are 690°C, $x_B = 0.524$ and 656°C, $x_B = 0.694$. The two solid solutions extend to 26.7 and 17.7 mol% at the peritectic and eutectic temperatures, respectively. An uncertainty of ±25°C may be assigned to the calculated liquidus. The entire calculated subsolidus is conjectural.

Common cation systems

BaF_2 (A) – $BaMoO_4$ (B)

A few liquidus data were reported (45) from visual-polythermal measurements. The reported eutectic (45) is 958°C, x_B = 0.37. The same eutectic temperature is mentioned in a later report (46). The experimental (45) melting point of BaF_2 is grossly erroneous, and hence the LHS liquidus data are also probably more or less in error. For calculation of the phase diagram, however, a eutectic temperature of 958°C was taken as guide, and a eutectic composition $0.3 < x_B < 0.4$ was assumed. The phase diagram was calculated with the use of eq. [33]

[33] $G^E(l) = x_A x_B(-8300 - 3000x_B)$ J mol^{-1}

Fig. 8. The system K_2WO_4 (A) – Na_2WO_4 (B). ×: ref. 41; ●: ref. 42; △: ref. 43; ○: ref. 44. The subsolidus is conjectural.

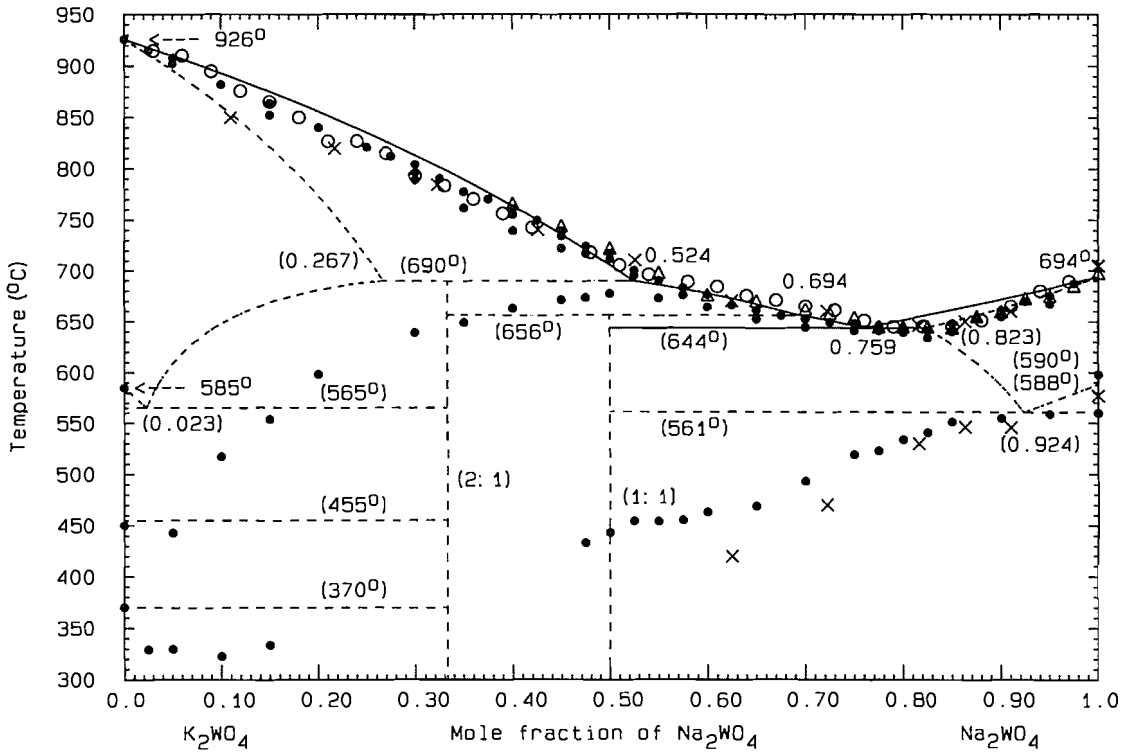

and is shown in Fig. 9. The calculated eutectic is 960°C, x_B = 0.380 and the BaF_2 transition appears on the calculated liquidus at x_B = 0.155. Since the experimental liquidus data (45) are so sparse and suspect, there is a large uncertainty (±20°C) in Fig. 9.

BaF_2 (A) – $BaWO_4$ (B)

Only one datum is available for this system, a eutectic report (25) of 988°C, x_B = 0.33. Since there are no liquidus data for optimization, an approximate excess Gibbs energy of the liquid

[34] $G^E(l) = x_A x_B(-10\,000 + 1600x_B)$ J mol^{-1}

was used to calculate the phase diagram, Fig. 10. The calculated eutectic is 988°C, x_B = 0.377 and the BaF_2 transition appears on the calculated liquidus at x_B = 0.159.

$BaMoO_4$ (A) – $BaWO_4$ (B)

There are no phase diagram data available for this system, as the liquidus lies at very high temperatures. From limited thermal analysis, X-ray diffraction, and electrical conductivity data at lower temperatures (47), it is reasonable to assume that there is complete solid solubility at the liquidus temperature and that both solid and liquid solutions are close to ideal (31). The phase diagram, Fig. 11, was calculated with the use of the quantities

[35] $G^E(l) = 0$

[36] $G^E(s) = 0$

and the calculated phase diagram shows no minimum. The phase diagram is necessarily conjectural.

KF (A) – K_2MoO_4 (B)

The phase diagram was investigated by thermal analysis (48, 49) and the visual-polythermal method (37). A summary of invariant points is given in Table 7. The reported melting point of the compound is (37, 48–50) 752, 752, 754, and 752°C, respectively. The compound was characterized by X-ray diffraction (48) and its heat of fusion, measured calorimetrically (50), is 58 kJ per mole of KF·K_2MoO_4. There is good agreement (±5°C) concerning the liquidus on the LHS, but some scatter on the RHS. The excess enthalpy of the liquid was measured by direct calorimetry at 1000°C, and the result (49) is used here:

[37] $H^E(l) = x_A x_B(894 + 9x_A)$ J mol^{-1}

All the liquidus data (37, 48, 49) were optimized together with eq. [37] to give two excess entropy coefficients

[38] $S^E(l) = x_A x_B(4.2765 - 5.9481x_B)$ J mol^{-1} K^{-1}

and the calculated properties of the compound (KF·K_2MoO_4)/2 are

[39] $\Delta_{fus}G^0 = 27\,502 - 26.8262T$ J mol^{-1}

[40] $\Delta_f G^0 = -27\,611 + 21.0634T$ J mol^{-1}

The phase diagram was calculated with the use of eqs. [37], [38], and [40] and is shown in Fig. 12. The calculated eutectics are 720°C, x_B = 0.295 and 748°C, x_B = 0.579. The compound melts congruently at 752°C. An uncertainty of ±5°C may be assigned to the calculated LHS liquidus.

Fig. 9. The system BaF_2 (A) – $BaMoO_4$ (B). ●: ref. 45.

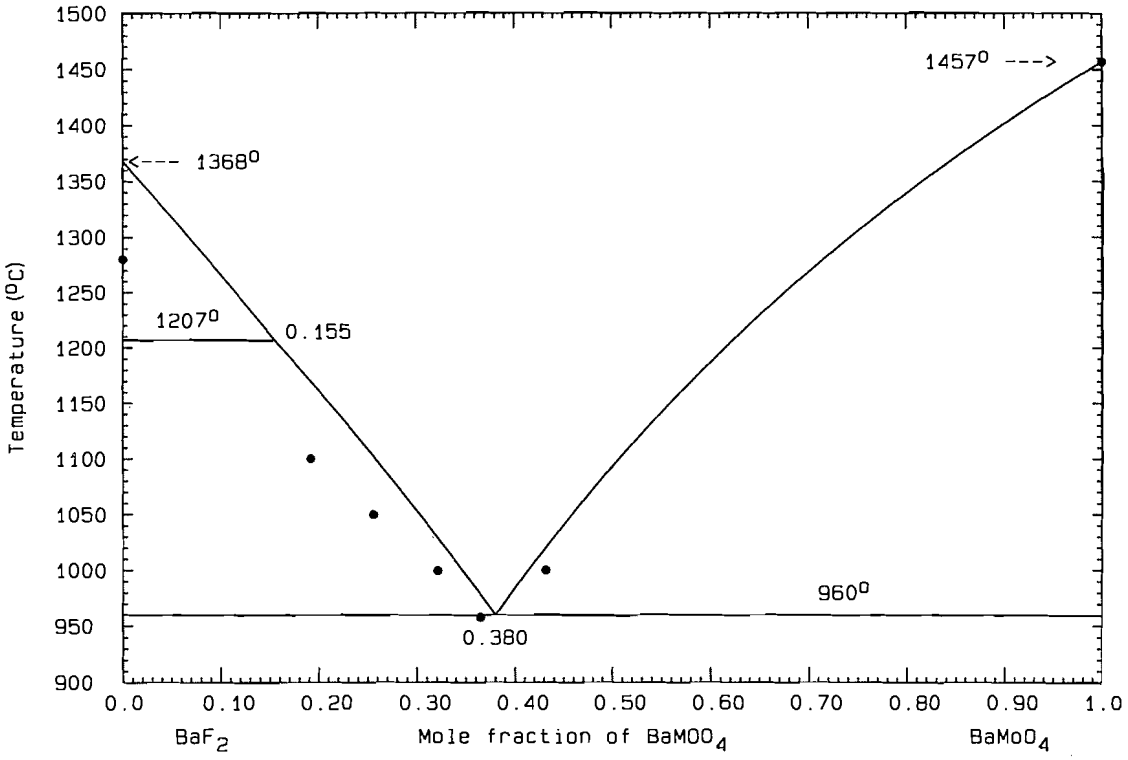

Fig. 10. The system BaF_2 (A) – $BaWO_4$ (B). ●: ref. 25. The diagram is conjectural.

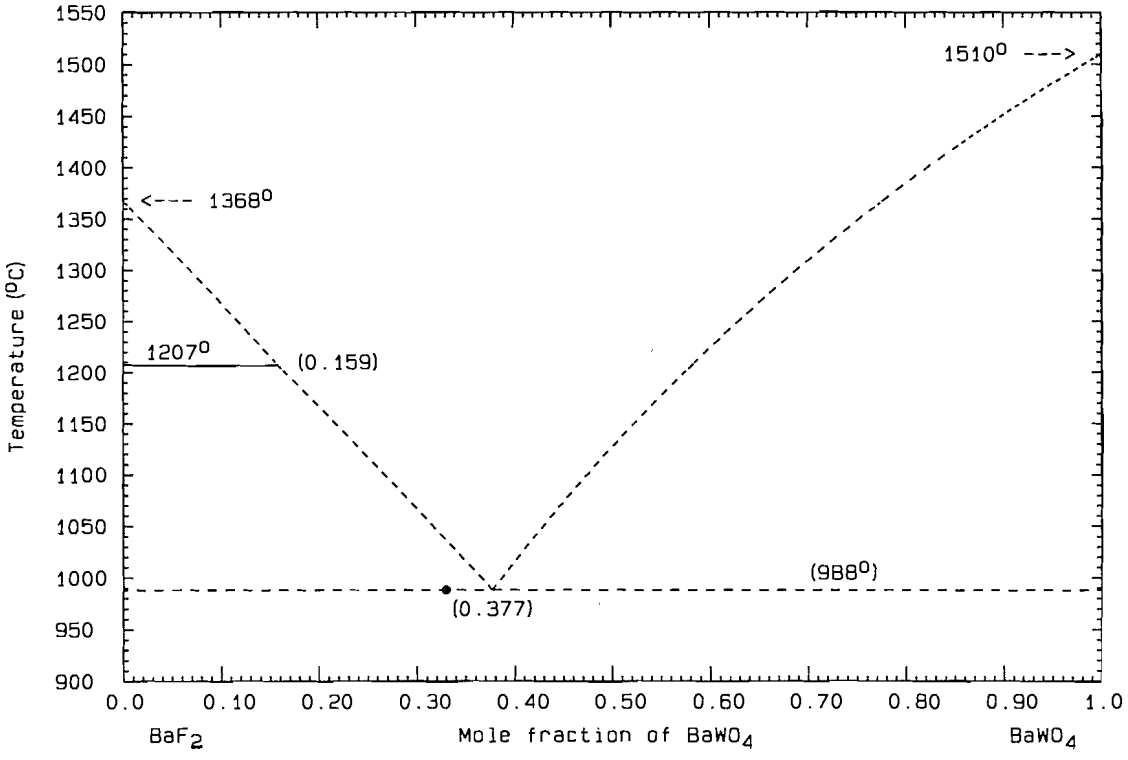

KF (A) – K_2WO_4 (B)

The phase diagram was investigated by thermal analysis (48, 49) and by the visual-polythermal method (51, 52). An invariant point summary is given in Table 8. All investigators (44, 45, 48, 49, 51–53) report the presence of a congruently melting 1:1 compound at temperatures 761, 759, and 764°C, respectively. The excess enthalpy of the liquid was measured at 1000°C by direct calorimetry (49) and the result is used here:

[41] $H^E(l) = x_A x_B(660 + 25x_A)$ J mol^{-1}

Fig. 11. The system $BaMoO_4$ (A) – $BaWO_4$ (B). The diagram is conjectural.

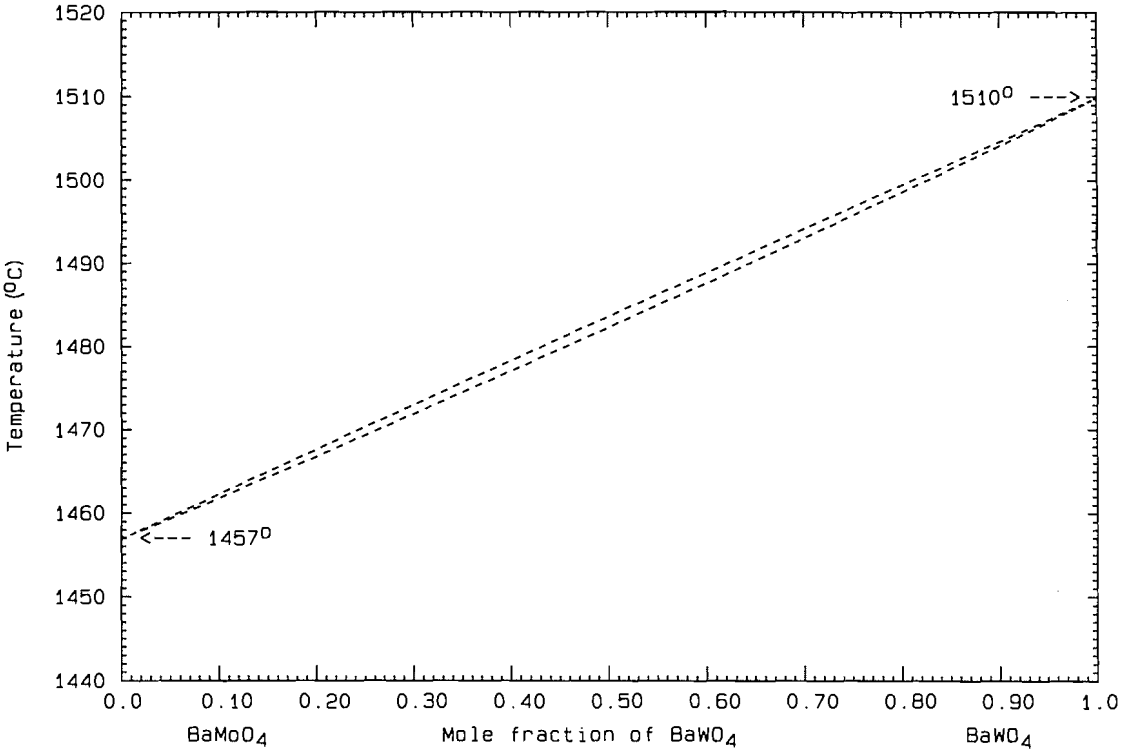

Fig. 12. The system KF (A) – K_2MoO_4 (B). ●: ref. 48; ○: ref. 49; ×: ref. 37.

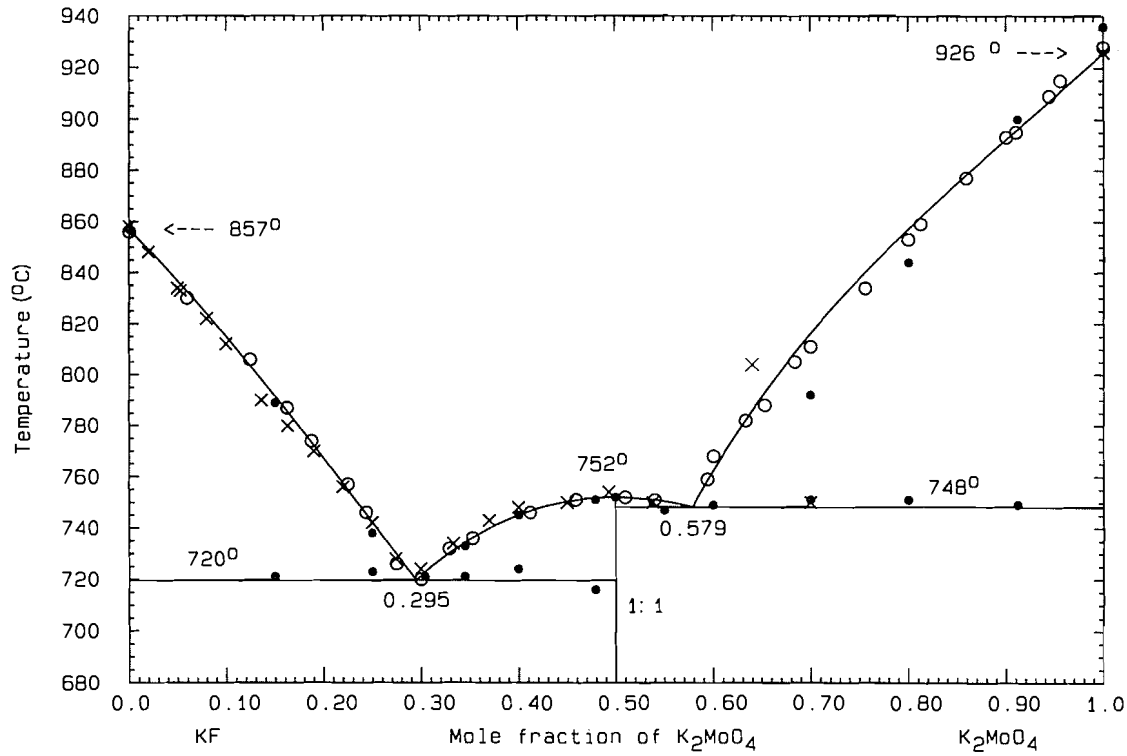

Reported liquidus data (48, 49, 51, 52) agree better in the central region of the phase diagram than elsewhere, where there is up to 30°C difference at a given composition. All liquidus data were optimized together with eq. [41] to give two excess entropy coefficients

$$[42] \quad S^{E}(l) = x_A x_B(8.6300 - 4.2726x_B) \quad \text{J mol}^{-1}\ \text{K}^{-1}$$

The phase diagram, Fig. 13, was calculated with the use of eqs. [41] and [42] and shows calculated eutectics of 724°C, x_B =

Fig. 13. The system KF (A) – K_2WO_4 (B). ●: ref. 48; ×: ref. 49; ○: ref. 51; △: ref. 52.

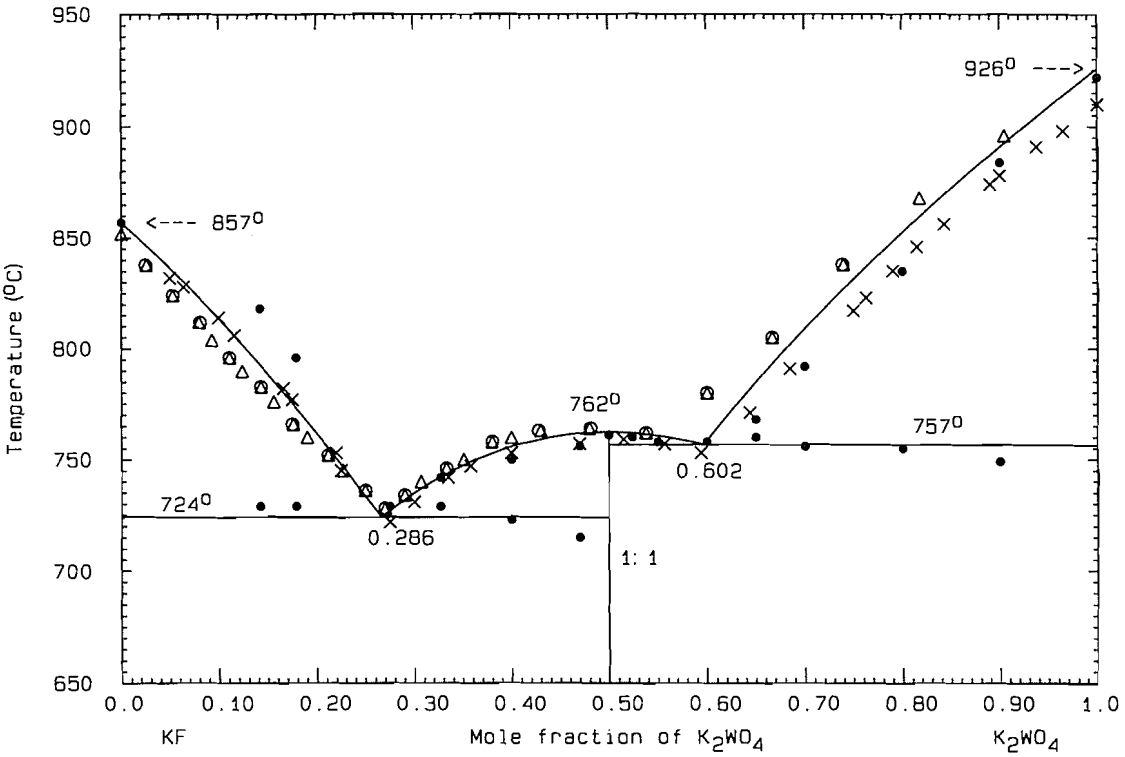

Table 7. Reported invariant points for KF (A) – K_2MoO_4 (B).

	T (°C)	x_B	Refs.
Eutectic	722	0.30	48
	722	0.29	37
	720	0.29	49
Eutectic	749	0.60	48
	748	0.57	37
	748	0.56	49
1:1	752		48
	754		37
	752		49

Table 8. Reported invariant points for KF (A) – K_2WO_4 (B).

	T (°C)	x_B	Refs.
Eutectic	757	0.60	48
	752	0.60	49
	760	0.56	51–53
Eutectic	729	0.28	48
	724	0.27	49
	728	0.27	51–53

0.286 and 757°C, $x_B = 0.602$. The compound $(KF{\cdot}K_2WO_4)/2$ is represented by the properties

[43] $\Delta_{fus}G^0 = 38\,932 - 37.5982T$ J mol^{-1}

[44] $\Delta_fG^0 = -38\,736 + 30.2136T$ J mol^{-1}

and its calculated melting point is 762°C. An uncertainty of ±20°C may be assigned to the calculated phase diagram.

K_2MoO_4 (A) – K_2WO_4 (B)

This system was studied by thermal analysis (cooling mode, ref. 54) and by the visual-polythermal method (43, 55). Amadori (54) does not report a minimum in the liquidus, since his melting point for K_2WO_4 is 32°C lower than the accepted value. According to Mateiko and Bukhalova (43), the liquidus is flat at 920°C over most of the composition range. Like the previous analogous system with Na as cation, the solution phases are almost ideal (43, 55). For the calculation of the phase diagram, the following quantities were used:

[45] $G^E(l) = 0$

[46] $G^E(s, \delta) = 650x_Ax_B$ J mol^{-1}

[47] $G^E(s, \gamma) = 100x_Ax_B$ J mol^{-1}

[48] $G^E(s, \beta) = 100x_Ax_B$ J mol^{-1}

[49] $G^E(s, \alpha) = 100x_Ax_B$ J mol^{-1}

The calculated phase diagram, Fig. 14, was constructed with the use of eqs. [45]–[49]. The calculated minimum is 920°C,

Fig. 14. The system K_2MoO_4 (A) – K_2WO_4 (B). ●: ref. 54; ×: refs. 43, 55. The subsolidus is conjectural.

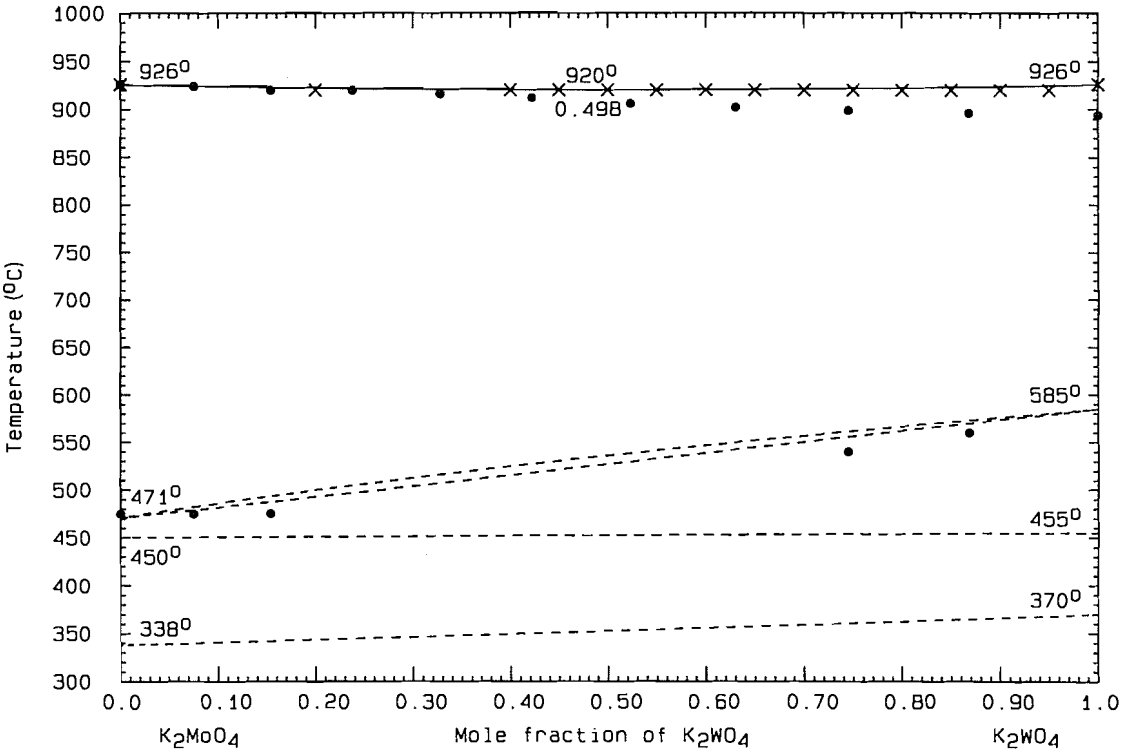

x_B = 0.498. The two-phase regions are all very narrow and there are no minima or maxima in the subsolidus. The calculated subsolidus is conjectural. The uncertainty in the calculated liquidus may be assigned at ±3°C.

NaF (A) – Na_2MoO_4 (B)

The phase diagram was investigated by thermal analysis (37, 48, 49) and the visual-polythermal method (45). There is fairly good agreement on the liquidus among these reports (about ±10°C). A summary of invariant points is given in Table 9. The compound was identified by X-ray diffraction (45, 48), the stoichiometry being 1:1 or 2:1, respectively. The 1:1 stoichiometry was chosen as the more probable, in view of the identity of compounds in analogous systems reviewed in the present work. The excess enthalpy of the liquid was measured by direct calorimetry at 1000°C, and the result (49) is used here:

[50] $H^E(l) = x_A x_B(3067 - 1601x_A + 6801x_A^2)$ J mol^{-1}

It was found that one excess entropy coefficient

[51] $S^E(l) = 8.0000x_A x_B$ J mol^{-1} K^{-1}

permitted a good fit to the liquidus to be made; the properties of the compound (NaF·Na_2MoO_4)/2 were

[52] $\Delta_{fus}G^0 = 36\,792 - 39.3519T$ J mol^{-1}

[53] $\Delta_f G^0 = -35\,800 + 31.5907T$ J mol^{-1}

The phase diagram was calculated with the use of eqs. [50], [51], and [53] and is shown in Fig. 15. The calculated eutectic is 618°C, x_B = 0.805 and the calculated peritectic is 664°C, x_B = 0.633. An uncertainty of ±10°C may be assigned to the calculated phase diagram.

Table 9. Reported invariant points for NaF (A) – Na_2MoO_4 (B).

	T (°C)	x_B	Refs.
Eutectic	627	0.85	48
	611	0.80	37
	611	0.80	45
	620	0.81	49
Peritectic	673	0.63	48
	660	0.65	37
	660	0.65	45
	665	0.65	49

NaF (A) – Na_2WO_4 (B)

The phase diagram was investigated by thermal analysis (25, 48, 49) and the visual-polythermal method (25, 51). A summary of invariant points is given in Table 10. The liquidus data of Mateiko and Bukhalova (51) are evidently erroneous, while those of the other investigators (25, 48, 49) agree to within 20°C. The stoichiometry of the compound was given as 1:1 by Schmitz-Dumont and Weeg (48), based on X-ray diffraction. This stoichiometry was assumed by later workers (51). The other authors (25) assumed a 2:1 stoichiometry. The excess enthalpy of the liquid was measured at 1000°C by direct calorimetry and the result (49)

Fig. 15. The system NaF (A) – Na_2MoO_4 (B). ●: ref. 48; △: ref. 49; ×: ref. 37; ○: ref. 45.

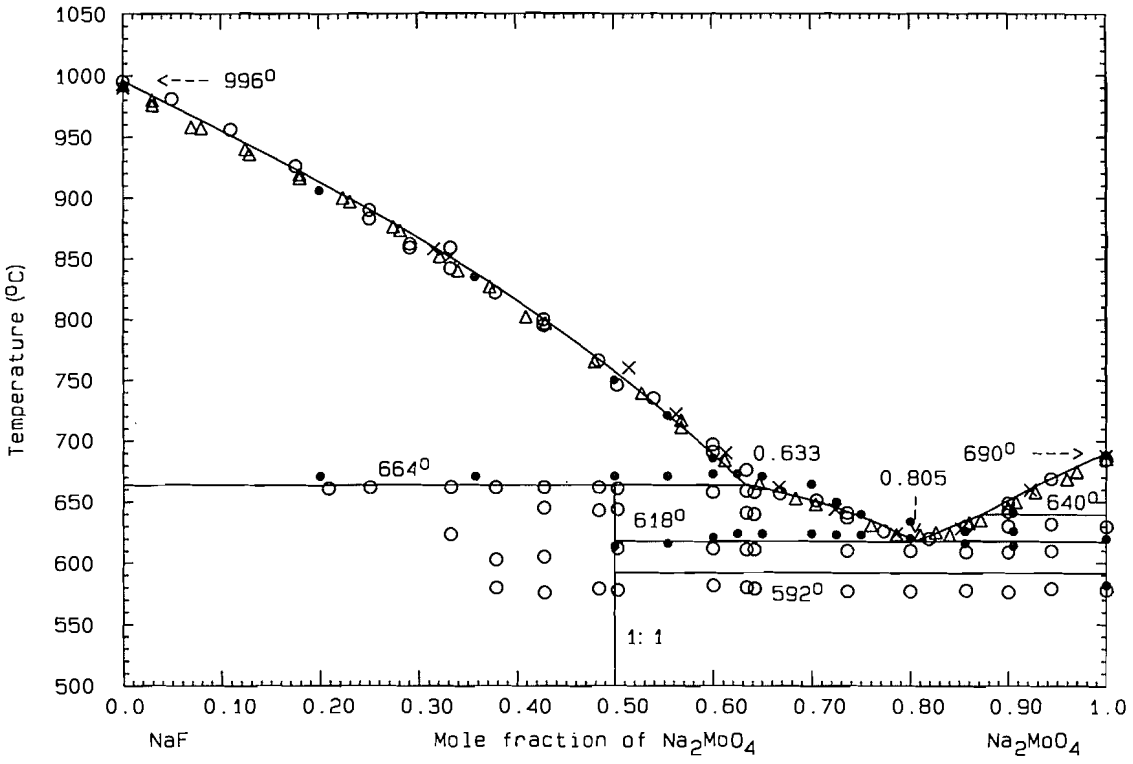

Table 10. Reported invariant points for NaF (A) – Na_2WO_4 (B).

	T (°C)	x_B	Refs.
Eutectic	635	0.80	48
	638	0.82	49
	650	0.88	51
	632	0.81	25
Peritectic	693	≈0.63	48
	691	0.60	49
	716	0.67	51
	690	0.57	25

[54] $H^E(l) = x_A x_B(2483 - 121x_A + 5554x_A^2)$ J mol^{-1}

was used here. The liquidus data (25, 48, 49) were optimized together with eq. [54] to give two excess entropy coefficients

[55] $S^E(l) = x_A x_B(8.1390 - 7.0541x_B)$ J mol^{-1} K^{-1}

and the calculated properties of the compound $(KF{\cdot}K_2WO_4)/2$ are

[56] $\Delta_{fus}G^0 = 25\,513 - 26.2550T$ J mol^{-1}

[57] $\Delta_f G^0 = -24\,560 + 19.3409T$ J mol^{-1}

The phase diagram, Fig. 16, was calculated with the use of eqs. [54], [55], and [57] and has a calculated eutectic of 633°C, x_B = 0.804. The calculated peritectic for the 1:1 compound is 693°C, x_B = 0.587. If the liquidus data of Mateiko and Bukhalova (51) are disregarded, an uncertainty of ±10°C may be assigned to the calculated phase diagram.

Na_2MoO_4 (A) – Na_2WO_4 (B)

The phase diagram was investigated by thermal analysis (cooling mode, ref. 56 (heating mode, ref. 57) and by the visual-polythermal method (43). A minimum liquidus temperature at 676°C, x_B = 0.60 was reported (43). The phase diagram had been calculated previously by a method similar to the present one (58), but the authors were apparently unaware of the work of Bottelberghs and van Buren (57), which is by far the most complete and reliable study of this system to date. These authors (57) also used X-ray diffraction and electrical conductivity measurements to establish the subsolidus. The calculations in the present work were based on the results of these workers (57). The liquid was assumed to be ideal

[58] $G^E(l) = 0$

and all the solid solutions were taken to be regular, as previously suggested (57). For the highest-temperature solid solution (δ), the hypothetical Gibbs energy of fusion of Na_2WO_4(δ) was set at $2000 - 2.058T$ J mol^{-1} (the exact value of this quantity is not crucial for the reproduction of the phase boundaries in the final phase diagram). The excess Gibbs energy of this solid solution turned out to be

[59] $G^E(s, \delta) = 350x_A x_B$ J mol^{-1}

In the earlier calculation (58), this quantity was $120x_A x_B$ J mol^{-1}. For the other solid solutions

[60] $G^E(s, \gamma) = -300x_A x_B$ J mol^{-1}

Fig. 16. The system NaF (A) – Na_2WO_4 (B). △: ref. 25; ●: ref. 48; ×: ref. 49; ○: ref. 51.

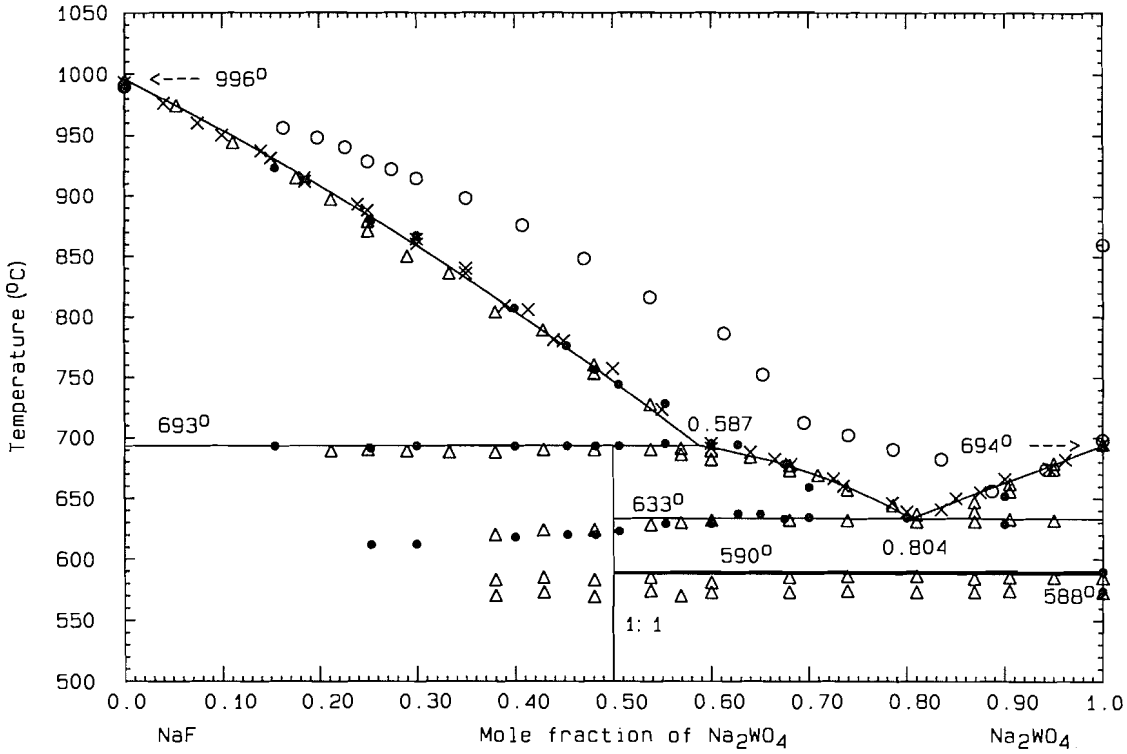

Fig. 17. The system Na_2MoO_4 (A) – Na_2WO_4 (B). ○: ref. 43; ×: ref. 56; ●: ref. 57.

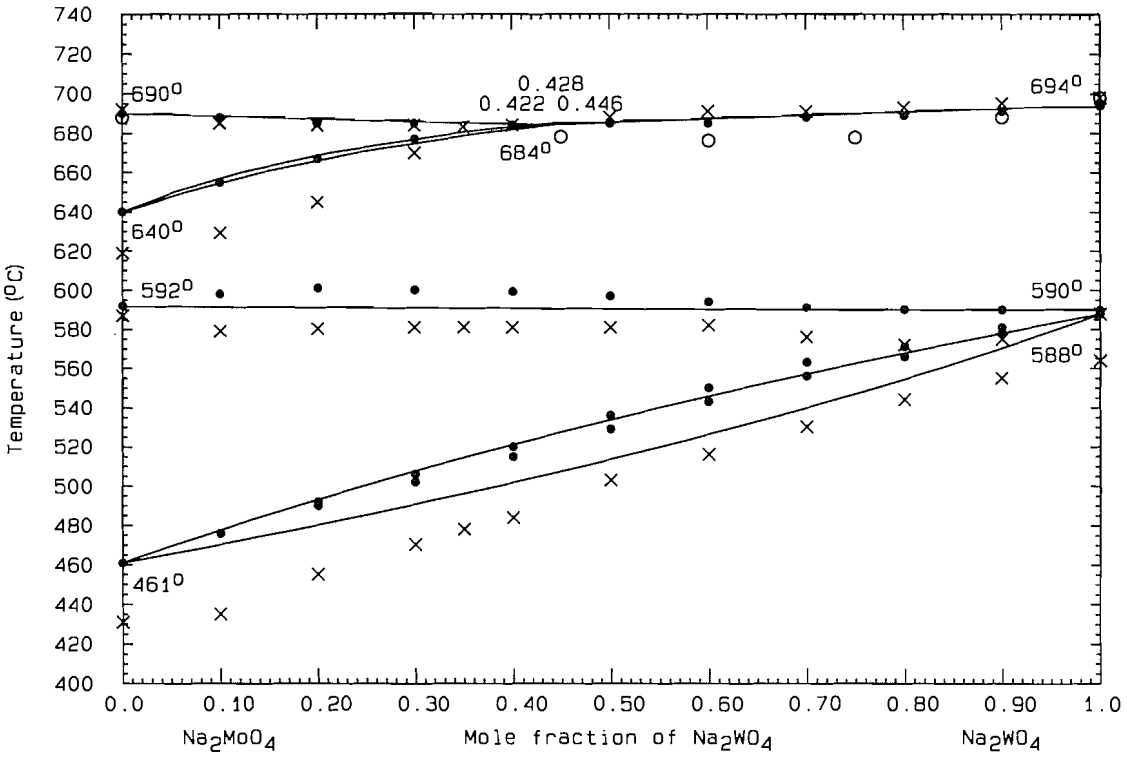

[61] $G^E(s, \beta) = -295.5x_Ax_B$ J mol^{-1}

[62] $G^E(s, \alpha) = 200x_Ax_B$ J mol^{-1}

For purposes of comparison, the previous calculation (58) used the expression $x_Ax_B(-683 - 227x_B)$ J mol^{-1} for $G^E(s, \delta)$, and $G^E(s, \beta)$ was approximately $-113x_Ax_B$ J mol^{-1}, according to Bottelberghs and van Buren (57). The calculated phase diagram, Fig. 17, was calculated with the use of eqs. [58]–[62], and the calculated eutectic is 684°C, $x_B = 0.423$. There are no

maxima or minima in the subsolidus. The two-phase regions are all quite narrow, except for the $\alpha \rightarrow \beta$ transition, where the enthalpies of transition are relatively large. An uncertainty of $\pm 5°C$ may be assigned to the calculated liquidus.

Acknowledgment

Thanks are due to Professors C.W. Bale and A.D. Pelton, Center for Research in Computational Thermochemistry, École Polytechnique, Montreal, for use of computing facilities.

References

1. A.D. Pelton. *In* Physical metallurgy. 3rd ed. *Edited by* R.W. Cahn and P. Haasen. North-Holland, Amsterdam. 1983.
2. A.D. Pelton and C.W. Bale. CALPHAD: Comput. Coupling Phase Diagrams Thermochem. **1**, 253 (1977).
3. M.T. Clavaguera-Mora, C. Comas, and N. Clavaguera. CALPHAD: Comput. Coupling Phase Diagrams Thermochem. **18**, 141 (1994).
4. W. Zakulski, Z. Moser, K. Rzyman, H.L. Lukas, S.G. Fries, M. Sikiernik, R. Koczmarczyk, and R. Castanet. J. Phase Equilib. **14**, 184 (1993).
5. C.W. Bale and A.D. Pelton. CALPHAD: Comput. Coupling Phase Diagrams Thermochem. **6**, 255 (1982).
6. J. Sangster and A.D. Pelton. J. Phase Equilib. **12**, 511 (1991).
7. M.-L. Saboungi and M. Blander. J. Am. Ceram. Soc. **58**, 1 (1974).
8. A.D. Pelton, C.W. Bale, and P.L. Lin. Can. J. Chem. **62**, 457 (1984).
9. N. Klipp, P.R. van der Linde, and H.A.J. Oonk. CALPHAD: Comput. Coupling Phase Diagrams Thermochem. **15**, 235 (1991).
10. J. Sangster. J. Phys. Chem. Ref. Data, **23**, 295 (1987).
11. J. Sangster. J. Phase Equilib. **14**, 340 (1993).
12. J. Sangster and A.D. Pelton. J. Phys. Chem. Ref. Data, **16**, 509 (1987).
13. W.T. Thompson, C.W. Bale, and A.D. Pelton. "F*A*C*T (Facility for the Analysis of Chemical Thermodynamics), Programs FITBIN and POTCOMP". École Polytechnique/McGill University, Montreal. 1985.
14. D.R. Stull and H. Prophet. JANAF Thermochemical Tables, 2nd ed. NSRDS-NBS 37. U.S. Department of Commerce, Washington, D.C. 1971.
15. M.W. Chase, C.A. Davies, J.R. Downey, D.J. Farris, R.A. McDonald, and A.N. Syverud. J. Phys. Chem. Ref. Data, **14**, Suppl. No. 1 (1985).
16. I. Barin, O. Knacke, and O. Kubaschewski. Thermochemical properties of inorganic subtances (and Supplement). Springer-Verlag, Berlin. 1973, 1976.
17. I. Barin. Thermochemical data of pure substances. VCH Verlagsgesellschaft, Weinheim. 1989.
18. D.D. Wagman, W.H. Evans, V.B. Parker, R.H. Schumm, I. Harlow, S.M. Bailey, K.L. Churney, and R.L. Nuttall. J. Phys. Chem. Ref. Data, **11**, Suppl. No. 2 (1982).
19. E.I. Banashek and A.G. Bergman. Dokl. Akad. Nauk SSSR, **57**, 905 (1947).
20. N.A. Pushin and A.V. Baskov. Z. Anorg. Chem. **81**, 347 (1913).
21. K.C. Hong and O.J. Kleppa. J. Phys. Chem. **82**, 1596 (1978).
22. V.T. Berezhnaya and G.A. Bukhalova. Russ. J. Inorg. Chem. (Engl. Transl.), **12**, 1148 (1967).
23. G. Grube. Z. Elektrochem. Angew. Phys. Chem. **33**, 481 (1927).
24. A.G. Bergman and E.I. Banashek. Izv. Sekt. Fiz.-Khim. Anal., Inst. Obshch. Neorg. Khim., Akad. Nauk SSSR, **22**, 196 (1953).
25. A.S. Trunin, G.E. Shter, and A.S. Kosmynin. Izv. Vyssh. Uchebn. Zaved., Khim. Khim. Tekhnol. **18**, 1347 (1975).
26. A.S. Trunin, G.E. Shter, and V.N. Serezhkin. Russ. J. Inorg. Chem. (Engl. Trans.), **20**, 1227 (1975).
27. R. Niggli. Z. Anorg. Allg. Chem. **98**, 241 (1916).
28. G. Calcagni. Gazz. Chim. Ital. **42**, 652 (1912).
29. H. Müller. Neues Jahrb. Mineral. Geol. **30**, 1 (1910).
30. H.W. Billhardt. Glastech. Ber. **42**, 272 (1969).
31. V.I. Posypaiko, A.S. Trunin, and G.E. Shter. Russ. J. Inorg. Chem. (Engl. Transl.), **20**, 932 (1975).
32. Yu.G. Petosyan, E.V. Tkachenko, and V.M. Zhukovskii. Izv. Akad. Nauk SSSR, Neorg. Mater. **11**, 1618 (1975).
33. I.N. Smirnova and I.P. Kislyakov. Izv. Akad. Nauk SSR, Neorg. Mater. **1**, 1162 (1965).
34. M. Amadori. Atti Ist. Veneto Sci. Lett. Arti, **72**, 903 (1913).
35. G.A. Bukhalova and Z.A. Mateiko. Zh. Obsch. Khim. **25**, 887 (1955).
36. A.G. Bergman and E.I. Korobka. Russ. J. Inorg. Chem. (Engl. Transl.), **4**, 853 (1959).
37. Z.A. Mateiko and G.A. Bukhalova. Zh. Obsch. Khim. **25**, 1673 (1955).
38. I.N. Belyaev and M.L. Sholokhovich. Zh. Obsch. Khim. **23**, 1265 (1953).
39. A.G. Bergman and E.I. Bogatova. Russ. J. Inorg. Chem. (Engl. Trans.), **9**, 1178 (1964).
40. A.M. Gasanaliev, N.N. Vediev, M.A. Dibirov, and Yu. I. Volovik. Russ. J. Inorg. Chem. (Engl. Transl.), **29**, 1515 (1984).
41. J.A.M. van Liempt. Z. Anorg. Allg. Chem. **122**, 175 (1922).
42. T.I. Drobasheva, I.N. Belyaev, and I.A. Tokman. Russ. J. Phys. Chem. (Engl. Transl.), **47**, 755 (1973).
43. Z.A. Mateiko and G.A. Bukhalova. Russ. J. Inorg. Chem. (Engl. Transl.), **2**, 308 (1957).
44. M.L. Sholokhovich and A.G. Bergman. Zh. Obsch. Khim. **24**, 936 (1954).
45. A.S. Trunin, G.E. Shter, and A.S. Kosmynin. Russ. J. Inorg. Chem. (Engl. Transl.), **20**, 921 (1975).
46. N.V. Verdiev and A.M. Gasanaliev. Izv. Vyssh. Urchebn. Zaved., Tsvet. Metall. 65 (1986).
47. E.I. Getman, T.A. Ugnivenko, and T.G. Sukhoterina. Deposited Document VINITI 346-76 (1976).
48. O. Schmitz-Dumont and A. Weeg. Z. Anorg. Allg. Chem. **265**, 139 (1951).
49. S. Julsrud and O.J. Kleppa. Acta Chem. Scand. Ser. A: **35**, 669 (1981).
50. L. Kosa, I. Nerad, O. Patrick I. Proks, J. Strecko, and K. Adamkovicova. Thermochim. Acta, **244**, 69 (1994).
51. Z.A. Mateiko and G.A. Bukhalova. Russ. J. Inorg. Chem. (Engl. Transl.), **2**, 274 (1957).
52. A.I. Kislova, V.I. Posypaiko, and A.G. Bergman. Russ. J. Inorg. Chem. (Eng. Transl.), **29**, 359 (1955).
53. A.I. Kislova and A.G. Bergman. Russ. J. Inorg. Chem. (Engl. Transl.), **4**, 857 (1959).
54. M. Amadori. Atti Accad. Naz. Lincei. Cl. Sci. Fis. Mat. Nat. Rend. **22**, 609 (1913).
55. A.S. Trunin, I.K. Garkushin, and S.A. Datsyuk. Russ. J. Inorg. Chem. (Engl. Transl.), **21**, 1526 (1976).
56. H.E. Boeke. Z. Anorg. Chem. **50**, 355 (1906).
57. P.H. Bottelbergs and F.R. van Buren. J. Solid State Chem. **13**, 182 (1975).
58. W.W. Liang, P.L. Lin and A.D. Pelton. High Temp. Sci. **12**, 41 (1980).
59. L. Denielou, Y. Fournier, J.-P. Petitet, and C. Tequi. C.R. Seances Acad. Sci. Ser. C: **272**, 1855 (1971).
60. G. Petit and C. Bourlange. C.R. Hebd. Seances Acad. Sci. **246**, 2865 (1958).
61. P. Caillet. Bull. Soc. Chim. Fr. 4750 (1967).
62. A.S. Koster, F.X.N.M. Kools, and G.D. Rieck. Acta Crystallogr. Sect. B: Struct. Crytallogr. Cryst. Chem. **B25**, 1704 (1969).

63. J. Thoret and P. Silvestre. C.R. Seances Acad. Sci. Ser. C: **279**, 103 (1974).
64. E.S. Zolotova and K.E. Mironov. Russ. J. Inorg. Chem. (Engl. Transl.), **34**, 109 (1988).
65. C. Dion and A. Noel. Bull. Soc. Chim. Fr. 257 (1983).
66. B.M. Gatehouse and P. Leverett. J. Chem. Soc. A: 899 (1969).
67. T.M. Yanushkevich and V.M. Zhukhovskii. Inorg. Mater. **8**, 1794 (1972).
68. L.L.Y. Chang, M.G. Scroger, and B. Phillips. J. Am. Ceram. Soc. **49**, 388 (1966).
69. O.I. Tokunov and I.P. Kislyakov. Izv. Vyssh. Uchebn. Zaved., Khim. Khim. Tekhnol. **15**, 1609 (1972).
70. E.R. Kreidler. J. Am. Ceram. Soc. **55**, 514 (1972).

Appendix

Thermodynamic properties of the pure salts

NaF, KF

The C_p and fusion data were taken from a standard source (16). These data are almost identical to those in later compilations (14, 15, 17).

BaF_2

Previous reports on the melting point (16, 20, 23, 45, 46) indicated 1287 or 1290°C; a higher value of 1368°C (15, 17) was adopted here. The heat of fusion is 28 450 J mol^{-1} (16) or 23 359 J mol^{-1} (15, 17); the latter value is used here. There is a transition at 967°C, apparently second order (zero enthalpy change) (15, 17); this was ignored in favour of the transition at 1207°C, $\Delta_{trs}H = 2674$ J mol^{-1} (15, 17). The C_p data were taken from the older compilation (16).

Na_2WO_4

The melting point is given as 694–696°C (15–17, 49, 57, 59) and the heat of fusion 23 800–30 380 J mol^{-1} (15–17, 57, 59). The data of Bottelberghs and van Buren (57) have been adopted here. The α-solid is cubic *Fd3m*, while the β-solid is orthorhombic $Pbn2_1$. This is distinguished from another (γ-solid) orthorhombic variety *Fddd* (57). The enthalpies of fusion and transition were taken from ref. 15. The C_p of the α-solid was taken from ref. 15, while those of the other solids and liquid were assigned a constant value of 209.2 J mol^{-1} K^{-1} (15, 17).

Na_2MoO_4

The melting point is 686–690°C (16, 17, 32, 49, 57, 59, 60) and the heat of fusion 19 240–22 426 J mol^{-1} (16, 17, 57, 59, 60). Three transitions have been reported (16, 17, 32, 49, 57, 59) at temperatures between 445 and 461°C (21 760– 24 230 J mol^{-1}), between 585 and 600°C (1880–2090 J mol^{-1}), and between 625 and 642°C (7680–9121 J mol^{-1}). The chosen data were from refs. 17 and 57. The α, β, γ, and δ solids are, respectively, cubic *Fd3m*, orthorhombic $Pbn2_1$, orthorhombic *Fddd*, and hexagonal $P6_3/mmc$ (57). The C_p of solids and liquid were taken from ref. 17.

K_2WO_4

This salt is not very well characterized. The compilations (14–17) contain no information on fusion or transition. Phase diagram and other reports (31, 43, 44, 48, 49, 59, 60) indicate a melting point in the range 910–926°C. The heat of fusion, according to calorimetric measurements, is (60) 44 350 or (59) 35 140 J mol^{-1}. There are transitions at 370°C (42, 48), 450 or 455°C (61), and at 575 or 585°C (34, 42). It was decided to include all three transitions, making K_2WO_4 and K_2MoO_4 similar to Na_2MoO_4. The form at room temperature (α), is monoclinic *C2/m* (62). Since experimental transition enthalpies could not be found, these were given nominal values (α → β, 35 140 J mol^{-1}; β → γ, 5000 J mol^{-1}; γ → δ, 14 380 J mol^{-1}). K_2MoO_4 was used as a guide for the assignment of the relative magnitudes of these enthalpies. The exact values of these transition enthalpies do not critically affect the calculation of the phase diagrams reported in the present work. The C_p of all solids were set at $136 + 0.0622T$ J mol^{-1} K^{-1}, which is a simple additive result from $K_2O + WO_3$ (17). The C_p of the liquid was set at 211 J mol^{-1} K^{-1}, i.e., the value of the solid at the melting point.

K_2MoO_4

There is no information on fusion or transition properties (14–17). Its melting behaviour is very similar to that of K_2WO_4; phase diagram and other sources give a melting point in the range 891–938°C (26, 43, 48, 49, 60, 63, 64) and 926°C was chosen as the best value. The heat of fusion, from calorimetry, is (60) 45 190 or (49) 34 700 J mol^{-1}. At least three transitions have been reported. The lowest is 315–338°C (26, 48, 61, 63–65). The other two chosen here are 435–465°C (26, 48, 61, 63, 64) and 471–480°C (26, 34, 48, 61, 65). The γ → δ transition enthalpy (14 380 J mol^{-1}) was estimated from the subsolidus part of a phase diagram (26). The other two transition enthalpies were nominally assigned in the same manner as K_2WO_4. Again, the exact value of these enthalpies is not crucial for calculating phase diagrams. The α-solid is monoclinic *C2/m*, and it is suggested (66) that the β-solid is orthorhombic, and the γ-solid, simple hexagonal. The C_p of all solids was set at $133.8 + 0.068T$ J mol^{-1} K^{-1}, a simple additive result from $K_2O + MoO_3$ (17). The C_p of the liquid was set at 215 J mol^{-1} K^{-1}, i.e., the value for the solid at the melting point.

$BaMoO_4$

No fusion properties are found in the compilations (14–17). From phase diagram reports (26, 45, 46, 67), a temperature of 1457°C was adopted. The heat of fusion was estimated from the limiting liquidus slope of a phase diagram at pure $BaMoO_4$ (67); a similar type of estimation (32) yielded the value 53.6 kJ mol^{-1}. A transition at 1259°C (32) is not found in any compilation (14–17) and hence was disregarded. The C_p of the solid was taken from Barin's compilations (16, 17). The C_p of the liquid was taken to be 182 J mol^{-} K^{-1}, i.e., that of the solid at the melting point.

$BaWO_4$

No fusion properties are found in the compilations (14–17). The melting point, from phase diagram and other reports, is in the range 1475–1510°C (31, 33, 45 68–70). The heat of fusion was estimated from the limiting liquidus slope at pure $BaWO_4$ of a phase diagram (33). The C_p of the solid was taken from Barin's compilations (16, 17) and the C_p of the liquid was put equal to that of the solid at the melting point.

Expedient synthesis of unsaturated amide alkaloids from *Piper* spp: Exploring the scope of recent methodology

George M. Strunz and Heather J. Finlay

Abstract: The Sakai aryl aldehyde – cyclic ketone aldol – Grob fragmentation sequence was extended to cinnamaldehyde and cyclohexanone, and the product was elaborated to analogues of the alkaloid piperstachine. The effects of substituents on the reaction involving cinnamaldehyde were studied. The aldol-fragmentation sequence failed with benzaldehyde when cyclooctanone or cyclobutanone was substituted for cyclohexanone or cyclopentanone, and the reasons for this failure were examined. Four-carbon Wittig homologation of the piperonal–cyclobutanone aldol-fragmentation product, a hypothetical route to alkaloids such as retrofractamide A, was thus not viable. Instead, three-carbon homologation of the readily available piperonal–cyclopentanone product, using alkyne chemistry recently disclosed by Lu and Trost, afforded these alkaloids in excellent overall yield. The alkyne isomerization was also used to effect efficient syntheses of pellitorine and several other non-aromatic 2*E*,4*E*-dienoic *Piper* amide alkaloids.

Key words: *Piper*, amides, alkaloids, insecticides, aldol, fragmentation, cinnamaldehydes, alkyne, redox, isomerization.

Résumé : La séquence de Sakai, qui peut consister en une réaction d'aldol entre un aldéhyde et une cétone cyclique suivie d'une fragmentation de Grob, fut utilisée pour préparer des analogues de l'alcaloïde piperstachine à partir du cinnamaldéhyde et de la cyclohexanone. L'influence des substituants sur la réaction du cinnamaldéhyde furent également étudiées. La séquence aldol fragmentation entre le benzaldéhyde et la cyclooctanone ou la cyclobutanone ne fonctionne pas malgré que la cyclopentanone et la cyclohexanone produisent le résultat anticipé. Ce résultat fut étudié en détail. Le produit obtenu à paritr de la cyclobutanone, suite à une homologation de Wittig de quatre carbones, aurait ainsi donné accès aux alcaloïdes tels la réfractamide A. Cependant, une homologation de trois carbones sur le produit de la séquence de Sakai entre le pipéronal et la cyclopentanone fournit ces alcaloïdes en d'excellents rendements en utilisant la chimie acétylenique développé récemment par Lu et Trost. L'isomérisation acétylenique fut aussi employée pour la synthèse de la péllitorine et plusieurs autres alcaloïds amidiques non-aromatiques 2*E*,4*E*-dienoiques des espèces *Piper*.

Mots clés : *Piper*, amides, alcaloïdes, insecticides, aldol, fragmentation, cinnamaldéhydes, alkyne, redox, isomérization.

Introduction

Problems associated with the continued widespread use of synthetic broad-spectrum pesticides, including development of resistance and impact on non-target organisms, have provided impetus for the development of alternative control agents and measures. In this context, plant-derived substances, used as botanical pesticides from antiquity, have increasingly been revisited as being more likely to meet present-day needs for environmental compatibility. The insecticidal and other biological properties of some unsaturated amides, e.g., pipercide **1**, isolated from *Piper* spp. have generated renewed interest in the study of these compounds (1, 2).

A semisystematic nomenclature for *Piper* amides has been advocated by Tsuda and co-workers (3) that, although not in general use, offers some advantages in terms of clarity and brevity and will be adopted in this paper. In Tsuda's system, compounds possessing an aromatic ring and an amide group are assigned the general name "piperamide." Where the aromatic nucleus bears a methylenedioxy group, the alkaloids are designated piperamide A, B, or C *m*:*n* with A, B, and C representing piperidine, *N*-isobutyl, or pyrrolidine amide, respectively, *m* indicating the number of carbons between the nitrogen and the aromatic nucleus, and *n* the number of double bonds in the chain. The position and geometry of the double bonds are indicated in parentheses.

We recently developed efficient methodology for the concise stereoselective synthesis of some *Piper* amides, including pipercide, **1** (piperamide-B11:3(2*E*,4*E*,10*E*)), piperolein A, **2** (piperamide A7:1(6*E*)), and **3**, (piperamide-C7:2(2*E*,6*E*))[2] (6, 7). This approach (Scheme 1) was based on an aldol condensation – Grob-type fragmentation sequence, originally disclosed by Sakai and co-workers (8). Thus, cyclohexanone was first condensed with piperonal under catalysis by boron triflu-

Received November 15, 1995.

This paper is dedicated to Professor John A. Findlay, a long-time friend and colleague, on the occasion of his (formal) retirement.

G.M. Strunz[1] **and H.J. Finlay.** Canadian Forest Service – Maritimes Region, P.O. Box 4000, Fredericton, NB E3B 5P7, Canada.

[1] Author to whom correspondence may be addressed. Telephone: (506) 452-3531. Fax: (506) 452-3525.

[2] The name sarmentosine assigned to this compound (4) should be reserved for a nitrile glucoside isolated earlier from *Sedum sarmentosum* (5). We wish to thank Professor A. Nahrstedt for bringing this to our attention.

oride. Addition of a glycol (preferably 1,3-propane diol (6)) then produced an acetal **II** ($x = 4$), which underwent fragmentation affording the glycol ester intermediate **III** ($x = 4$), with exclusively *E* geometry about the double bond. The methodology has proved to be eminently suitable for the synthesis of *Piper* amides such as **2** and **3** ($m = 7$), which were prepared via direct amidation of the versatile intermediate **III** ($x = 4$). Alternatively, the latter was readily reducible to an aldehyde, **IV** ($x = 4$, R′ = H), which could be homologated by 4C Wadsworth–Emmons (phosphonocrotonate) reaction affording entry to pipercide, **1** ($m = 11$).

The corresponding nor-piperamides ($m = 6$ or 10) are accessible, if cyclopentanone is substituted for the six-membered ketone (6). The susceptibility of the processes occurring in the course of the aldol condensation – fragmentation sequence to subtle steric and stereoelectronic effects raises interesting questions about the scope of the methodology, e.g., when other sized cyclic ketones (cylobutanone, cycloheptanone etc.) are used.

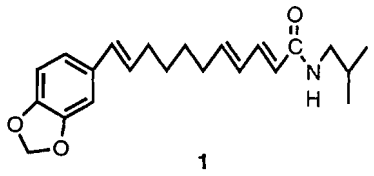

1

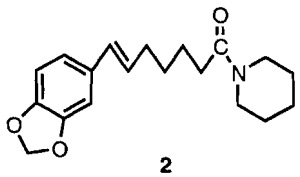

2

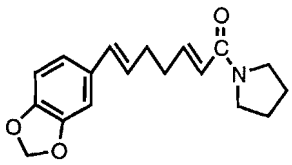

3

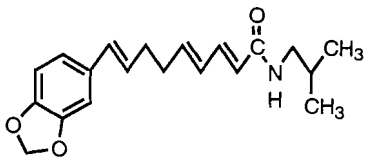

4

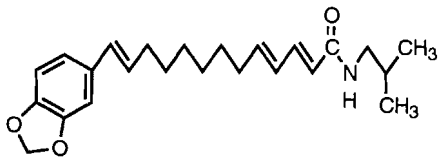

5

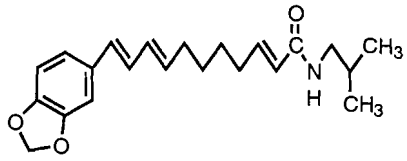

6

7

8

9

10

An aldol condensation – fragmentation sequence involving cyclobutanone and piperonal (if feasible) could, for instance, with subsequent 4C homologation, lead to facile syntheses of compounds like retrofractamide A, **4** (piperamide-B9:3(2*E*,4*E*,8*E*) from *Piper refractum* (9), piperamide-A9:3(2*E*,4*E*,8*E*) from *P. longum* (10) and piperamide-C9:3(2*E*,4*E*,8*E*) from *P. nigrum* (3) (Scheme 1). On the other hand, synthesis of guineensine **5** (piperamide-B13:3(2*E*,4*E*,12*E*)) from *P. guineense* (11) or piperolein B (piperamide-A9:1(8*E*)) from *P. nigrum* (12) dictates an aldol condensation – fragmentation involving cyclooctanone and piperonal.

If the aldol condensation – fragmentation sequence could be conducted with a homologue of piperonal, 3′,4′-methylenedioxycinnamaldehyde, and cyclohexanone, then reduction, Wadsworth–Emmons (2C) homologation, and amidation would constitute a facile synthesis of piperstachine **6** (piperamide-B11:3(2*E*, 8*E*, 10*E*), an alkaloid from *P. trichostachyon* (13) (Scheme 2).

This paper discloses our observation that the Sakai aldol

Scheme 1.

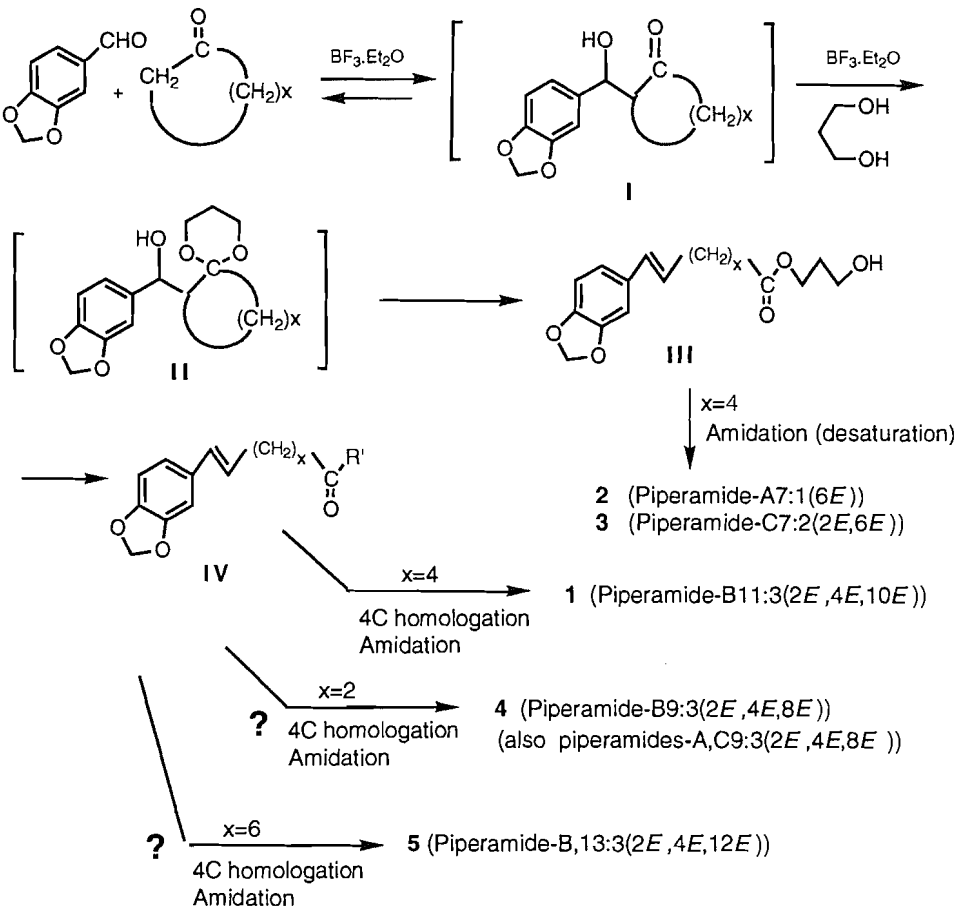

condensation – fragmentation sequence can be satisfactorily extended to *cinnamaldehyde* (but not so readily to 3′,4′-methylenedioxycinnamaldehyde) and cyclohexanone, opening the way to a short synthesis of a "demethylenedioxy" analogue of piperstachine **6**, and related compounds. We report also on our unsuccessful attempts to effect the condensation–fragmentation process using cyclobutanone or cyclooctanone with piperonal to give **III** (and **IV**) (x = 2 and x = 6, respectively). Alternative, efficient methodology to gain access to **4** and the other 9:3(2*E*,4*E*,8*E*) amide alkaloids is described, in which 3C homologation of the readily available **IV** (x = 3) (6), exploiting recently disclosed alkyne chemistry (14, 15), replaces 4C homologation of the elusive **IV** (x = 2).

Results

(a) Condensation–fragmentation with cyclohexanone and cinnamaldehydes: synthesis of piperstachine (11:3(2*E*,8*E*,10*E*)) analogue and related compounds

The condensation–fragmentation process proceeded readily with cyclohexanone when cinnamaldehyde was substituted for benzaldehyde or piperonal, and the ester **VI** (R,R′ = H), was obtained in 59% yield. Four-carbon (phosphonocrotonate) Wadsworth–Emmons homologation of the aldehyde from **VI** (R,R′ = H) and subsequent amidation by appropriate methodology allowed the synthesis of the model compounds **7** and **8** in overall yields of 22 and 36%, respectively. Similarly, the aldehyde from **VI** (R,R′ = H) was converted, via 2C (phosphonoacetate) Wadsworth–Emmons homologation and amidation to "desmethylenedioxypiperstachine" **9**, (overall yield from cinnamaldehyde ~33%) (Scheme 2). (The corresponding piperidyl amide **10** was also prepared in similar yield.) Exploitation of this concise strategy for the synthesis of piperstachine requires 3′,4′-methylenedioxycinnamaldehyde as starting material but, perhaps not surprisingly, the presence of the ether functionality in the aromatic ring had a detrimental effect on the condensation–fragmentation process, and **VI** (R = 3′,4′-methylenedioxy) was obtained in only ~14% yield (Table 1), deemed insufficient to make this route competitive with the previous synthesis (13).

In view of the effect of the methylenedioxy aromatic substituent on the yield of the condensation–fragmentation process, the effects of other substituents were briefly examined using readily available substituted cinnamaldehydes. The influences of substituents R and R′ on the course of the reaction (Table 1) are in general as expected based on their electron-donating or withdrawing properties (and steric effects of R′), and are consistent with Sakai's observations for substituted benzaldehydes (8).

(b) Attempted piperonal–cyclooctanone condensation–fragmentation

As mentioned in the Introduction and indicated in Scheme 1, the product **III** (x = 6), *if it could be prepared from piperonal and cyclooctanone*, would be readily transformed to the *P. guineense* alkaloid guineensine **5** (piperamide-B13:3(2*E*,4*E*,12*E*) via 4C-(crotonate) Wadsworth–Emmons

Scheme 2.

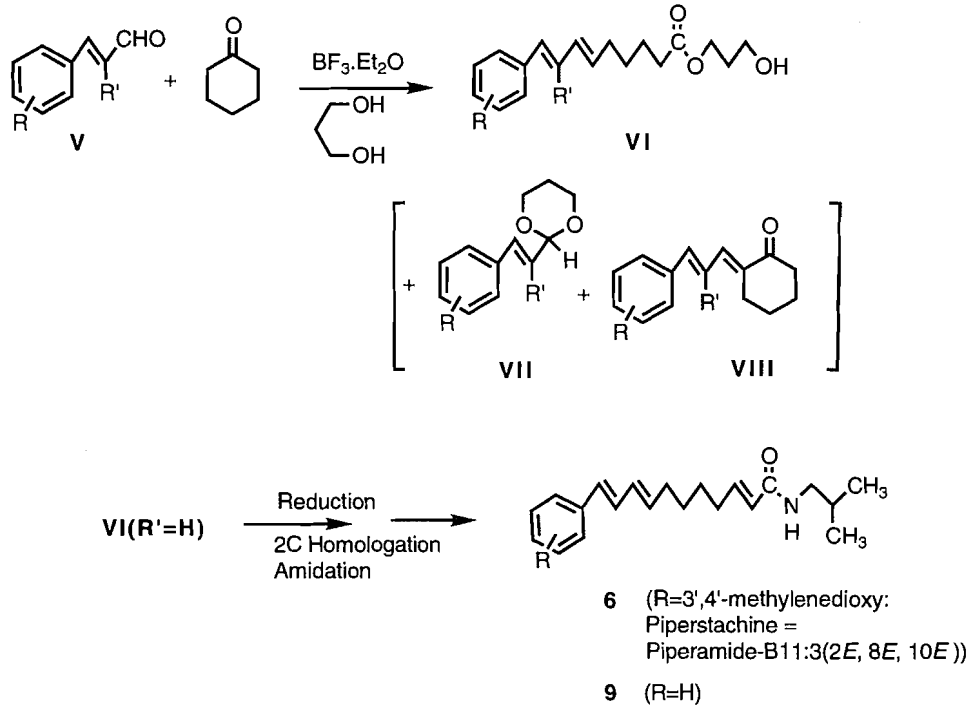

6 (R=3',4'-methylenedioxy: Piperstachine = Piperamide-B11:3(2*E*, 8*E*, 10*E*))

9 (R=H)

Table 1. Products of BF_3-catalyzed reaction of substituted cinnamaldehydes with cyclohexanone and 1,3-propanediol.

Entry	R	R′	Fragmentation product **VI**, %	Aldehyde acetal **VII**, %
1	H	H	59	—[a]
2	3′,4′-OCH_2O	H	14	—[a]
3	H	Cl	0	61[b]
4	2′-NO_2	H	0	17[b]
5	4′-NO_2	H	0	27[b]
6	H	CH_3	26	—[a]
7	2′-OCH_3	H	20	—[a]

[a]Acetals formed, but not readily separable from **VIII**, product of aldol dehydration.

[b]Isolated yields substantially lower than total acetal **VII** formed because of coelution with starting aldehyde and cyclohexanone.

homologation of **IV** (x = 6) and amidation) as well as piperolein B (piperamide-A9:1(8*E*)) from *P. nigrum* (by direct amidation). Attempts to effect the condensation–fragmentation under a variety of conditions were, however, to no avail and resulted in a complex mixture of products that appeared to contain some aldol **I** (x = 6), but no glycol ester **III** (x = 6). To investigate factors contributing to this different behaviour exhibited by the larger ring homologue, models **11** and **12** of the putative intermediates **I** and **II** (x = 6; Scheme 1), were independently prepared by alternative routes, and their behavior under "fragmentation conditions" was observed. Aldol **11**

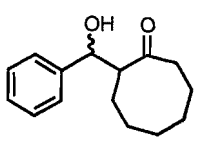

11

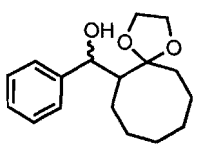

12

was made using Mukaiyama methodology (16), as a mixture of epimers (*anti*:syn~ 65:35). The purified *anti* epimer was immediately treated with propylene glycol and BF_3-etherate. Chromatography afforded the dehydrated product 2-benzylidinecyclooctanone in 40% yield and ~46% of an inseparable (1:1) mixture of cyclooctanone and the propylene glycol acetal of benzaldehyde: no cyclooctanone acetal was observed.

Preparation of **12** was accomplished in low yield by acetalization (slow!) of 2-ethoxycarbonyl cyclooctanone with ethylene glycol, reduction/oxidation (LAH/Swern) to the 2-formyl derivative of the acetal, and, finally, reaction of this (very unstable) material with phenyllithium. Treatment of **12**, in THF solution with BF_3-etherate under anhydrous conditions, resulted in the isolation, after bicarbonate quench and work-up, only of benzaldehyde and cyclooctanone.

It seems clear that the major factor militating against the fragmentation process in the cyclooctanone–piperonal case is the slow rate of acetalization of the initially formed aldol intermediate, which allows alternative pathways to take precedence. (The extensively enolized carbonyl group of cyclooctanone itself is known to be very unreactive towards nucleophilic attack (17).) The observation that **12** (*even if it were* formed from **11** in a Lewis acid – glycol mixture) fails to undergo Grob-type fragmentation, yielding instead products of a retroaldol-type cleavage, could possibly be due to stereoelectronic effects (cf. ref. 6) or to the Lewis acid complexing with an acetal oxygen rather than the hydroxyl group.

(c) 9:3(2*E*,4*E*,8*E*) (or 5:1(4*E*)) Amides formally accessible via piperonal–cyclobutanone condensation–fragmentation

Attempts to effect the condensation–fragmentation sequence using cyclobutanone, piperonal, and 1,3-dihydroxypropane under BF_3 catalysis led to almost quantitative recovery of the

Scheme 3.

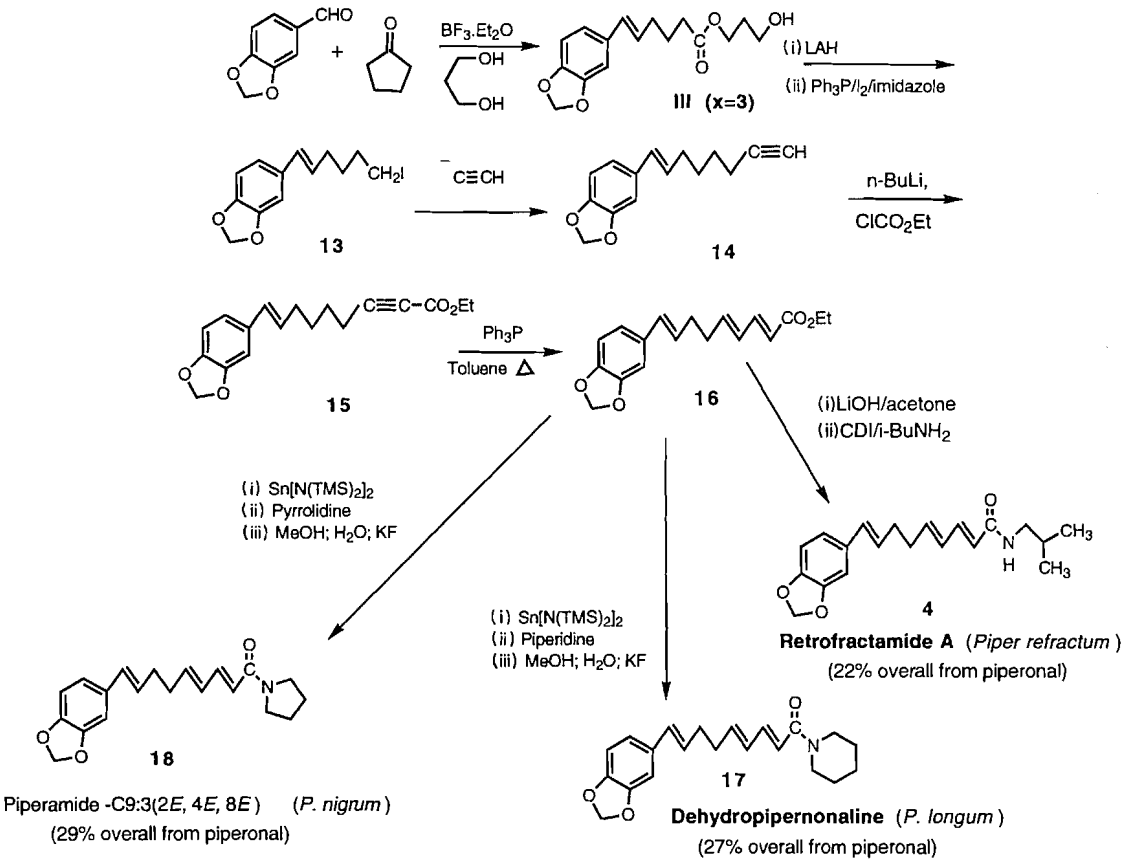

piperonal – propylene glycol acetal, suggesting that the essential initial aldol condensation is an unfavorable process.

In lieu of *four-carbon* (crotonate) Wadsworth – Emmons homologation of the elusive **IV** (x = 2, R′ = H), followed by amidation, the 9:3(2*E*,4*E*,8*E*) amides (3, 9, 10) could be prepared via a suitable *three-carbon* homologation of **III** (x = 3), readily available from cyclopentanone and piperonal as described above. Methodology recently developed by Ma and Lu (14) and Trost and Kazmaier (15), involving transition metal or triphenylphosphine-catalyzed isomerization of an activated alkyne, proved to be ideally suited to effect the desired 3C homologation at the appropriate oxidation level. Thus the alkaloids retrofractamide A, **4** (piperamide-B9:3(2*E*,4*E*,8*E*)) (9), dehydropipernonaline **17** (piperamide-A9:3(2*E*,4*E*,8*E*)) (10), and **18** (piperamide-C9:3(2*E*,4*E*,8*E*) (3) were readily synthesized in good yield as follows, by a short stereoselective route exploiting the two recently developed methodologies aldol condensation – fragmentation (8) and alkyne isomerization (14, 15)) (Scheme 3): Lithium acetylide – ethylene diamine complex was alkylated with iodide **13**, simply prepared in two steps from glycol ester **III** (x = 3). The anion of the resulting alkyne, **14**, reacted with ethyl chloroformate affording alkyne ester **15**. As alkynoic amides are less reactive substrates for the internal redox process than the corresponding esters (14, 15), amidation was postponed until after the isomerization. Accordingly, **15** was heated under reflux with Ph_3P in toluene (15), giving the 2*E*,4*E*,8*E* ester **16** in excellent yield. Amidation was effected in one pot by the Roskamp procedure (18) for the piperidine and pyrrolidine amides, and by hydrolysis and carbonyldiimidazole-induced coupling for the isobutylamide. Retrofractamide A (**4**) from *P. refractum* (9) was obtained in an overall yield of 22% from piperonal, dehydropipernonaline (**17**) from *P. longum* (10) in 27% overall yield, and piperamide-C9:3(2*E*,4*E*,8*E*) (**18**) (3) in 29% overall yield.

(d) General route to non-aromatic 2*E*,4*E* dienoic amide alkaloids

The efficacy of our route to retrofractamide A and the other 9:3(2*E*,4*E*,8*E*) piperamides prompted us to turn our attention to the simpler non-aromatic 2*E*,4*E*, dienoic *Piper* amides, some of which, including **19** and **21**, were synthesized earlier by Ma and Lu (14). The key reaction in Lu's route to the dienoic amides was rearrangement of the corresponding 2-ynoic amides under catalysis by ruthenium or iridium complexes of Ph_3P. The alkynoic amide precursors were prepared by classical methodology via carboxylation of the appropriate terminal alkynes (19) and suitable elaboration of the resulting carboxylic acids. We have developed a simple, efficient general stereoselective synthesis of these alkaloids that, while running essentially parallel to Lu's sequence, differs in some important details that, we suggest, may confer on it some advantages in terms of convenience and yield. The new route is exemplified by the synthesis of pellitorine (**19**) (2, 4) in five steps from propiolic acid with overall yield 52% (Scheme 4). Application of this general synthetic route afforded **20** (from *P. nigrum* (3)) in 61% overall yield from propiolic acid; **21**, achillia amide (20) in 66% yield; **22** and **23** (from *P. guineense* (11)) in 39% and 50% yield, respectively; and **24** (from *P. trichostachyon* (21)) in 50% overall yield.

Scheme 4.

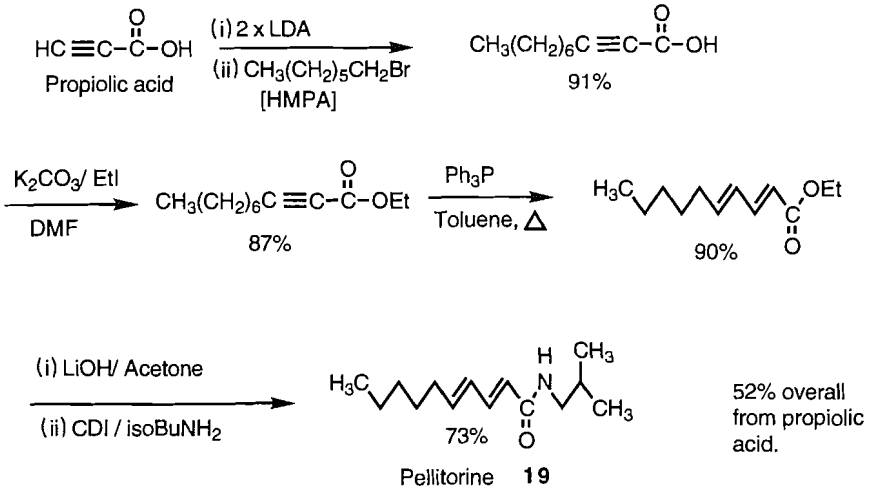

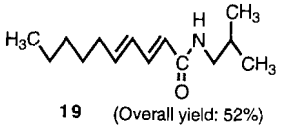

19 (Overall yield: 52%)

P. nigrum
(Also Compositae & Rutaceae)

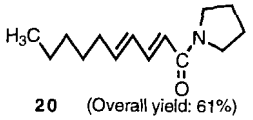

20 (Overall yield: 61%)

P. nigrum
Tsuda *et al.* 1988

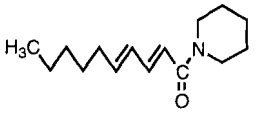

21 (Overall yield: 66%)

Achillia amide
Bohlmann *et al.* 1973

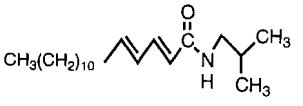

22 (Overall yield: 39%)

P. guineense
Okogun and Ekong 1974

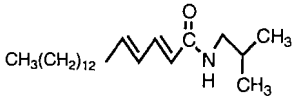

23 (Overall yield: 50%)

P. guineense
Okogun and Ekong 1974

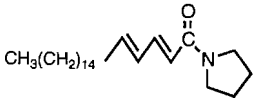

24 (Overall yield: 50%)

P. trichostachyon
Singh *et al.* 1971

As a result of the present study and previous work (6, 7), more than a dozen unsaturated amides, mostly alkaloids from various *Piper* spp., are readily accessible and several are presently being assayed for insecticidal activity against such economically important insect pests as spruce budworm (*Choristoneura fumiferana*), gypsy moth (*Lymantria dispar*), and forest tent caterpillar (*Malacosoma disstria*).

Experimental

Details concerning instrumentation may be found in ref. 6.

9-Phenyl-6*E*,8*E*-nonadienoic acid propylene glycol ester, VI (R = R′ = H)

Boron trifluoride etherate (5.3 mL, 42 mmol) was added dropwise under argon to a solution of cinnamaldehyde (0.75 mL, 5.9 mmol) in dry freshly distilled THF (15 mL) at 0°C. The solution was stirred for 10 min, after which cyclohexanone (0.61 mL, 5.9 mmol) dissolved in dry THF (10 mL) was added dropwise with stirring over a 20 min period. The ice bath was removed and the mixture allowed to attain ambient temperature during 70 min. To the resulting dark green mixture was added propane-1,3-diol (2.2 g, 31 mmol) and the stirred (now purple) reaction mixture was set aside at ambient temperature for 14 h. The product was worked up by addition of the mixture to a saturated aqueous solution of $NaHCO_3$ (ca. 200 mL) and extraction with ether (3 × 50 mL). The combined organic extracts were washed successively with saturated $NaHCO_3$ (2 × 20 mL) and saturated brine (2 × 20 mL) and, after being dried over $MgSO_4$, were evaporated to dryness under reduced pressure. The resulting crude red oil was subjected to chromatography on a column of silica gel with hexane – EtOAc (3:2) as eluent, to furnish 1.016 g (59%) of ester **VI** (R = R′ = H) as a relatively polar pale yellow oil. This product was rather unstable and, in order to avoid decomposition, was either reduced directly or stored frozen in benzene. It displayed the following spectroscopic characteristics: IR ($CHCl_3$): 3600, 3440, 1720, 1640, 1595, 1460, 1040, 985, and 880 cm^{-1}; ^1H NMR ($CDCl_3$, 200 MHz) δ: 1.35–1.55 (2H, m), 1.55–1.75 (2H, m), 1.86 (2H, pent, J = 6.0 Hz), 2.16 (2H, q, J = 7.2 Hz), 2.34 (2H, t, J = 7.2 Hz), 3.68 (2H, t, J = 6.0 Hz), 4.23 (2H, t, J = 6.0 Hz), 5.79 (1H, dt, J = 7.0 and 15.2 Hz), 6.21 (1H, dd, J = 10.2 and 15.4 Hz), 6.44 (1H, d, J = 15.8 Hz), 6.74 (1H, dd, J = 10.2 and 15.8 Hz), 7.20–7.45 (5H, m); HREIMS, *m/z* (relative intensity) (ion): 288.1723 (33) (M^+) (calcd. for $C_{18}H_{24}O_3$: 288.1725), 212 (36) ($M^+ - C_3H_6(OH)_2$), 169 (13) ($C_{13}H_{13}$), 156 (72) ($C_{12}H_{12}$), 143 (65) ($C_{11}H_{11}$), 131 (86) (C_9H_7O), 128 (100) ($C_{10}H_8$), 115 (52) (C_9H_7), 113 (28) ($C_6H_9O_2$), 103 (53) (C_8H_7) 91 (80) (C_7H_7) 84 (26) (C_5H_8O), 77 (57) (C_6H_5).

9-(3′,4′-Methylenedioxyphenyl)-6*E*,8*E*-nonadienoic acid propylene glycol ester, VI (R = 3′,4′-methylenedioxy, R′ = H)

Boron trifluoride etherate (2.5 mL, 20 mmol) was added dropwise under argon to a solution of 3′,4′-methylenedioxycinnamaldehyde[3] (0.491 g, 2.79 mmol) in dry freshly distilled THF (15 mL) at 0°C. The solution was stirred for 10 min, after which cyclohexanone (0.28 mL, 2.7 mmol) dissolved in dry THF was added slowly dropwise with stirring. The ice bath was removed and the mixture was set aside with stirring for 7.5 h, after which propane-1,3-diol (1.1 g, 14 mmol) was added and stirring resumed at ambient temperature for 14 h. The product was worked up as above and purified by flash chromatography on silica gel with hexane–EtOAc (3:2) as eluent. The chromatographically pure ester **VI** (R = 3′,4′-methylenedioxy, R′ = H) (131 mg, 14%) was a yellow oil: IR ($CHCl_3$): 3675, 3600, 3500, 2945, 2900, 1720, 1600, 1485, 1440, 1040, 990, and 930 cm^{-1}; ^1H NMR ($CDCl_3$, 200 MHz) δ: 1.40–1.55 (2H, m), 1.55–1.75 (2H, m), 1.85 (2H, pent, J = 6.0 Hz), 2.13 (2H, q, J = 7.0 Hz), 2.32 (2H, t, J = 7.2 Hz), 3.67 (2H, q, J = 5.4 Hz), 4.22 (2H, t, J = 6.2 Hz), 5.72 (1H, dt, J = 7.2 and 14.8 Hz), 5.92 (2H, s), 6.15 (1H, dd, J = 10.0 and 15.0 Hz), 6.33 (1H, d, J = 15.6 Hz), 6.56 (1H, dd, J = 10.0 and 15.6 Hz), 6.73 (1H, s), 6.76 (1H, d, J = 1.4 Hz), 6.90 (1H, d, J = 1.4 Hz), HREIMS, *m/z* (relative intensity) (ion): 332.1624 (73) (M^+) (calcd. for $C_{19}H_{24}O_5$: 332.1624), 257 (11) (M − $O(CH_2)_3OH$), 228 (11) M^+ − $CO_2(CH_2)_3OH$), 187 (64) ($C_{12}H_{11}O_2$), 176 (64) ($C_{10}H_8O_3$), 173 (100) ($C_{11}H_9O_2$), 167 (19) ($C_8H_7O_4$), 159 (31) ($C_{10}H_7O_2$), 157 (40) ($C_{11}H_9O$), 149 (76) ($C_8H_5O_3$), 147 (29) ($C_9H_7O_2$), 143 (18) ($C_{10}H_7O$), 135 (54) ($C_8H_7O_2$), 128 (32) ($C_{10}H_8$), 122 (17) ($C_7H_6O_2$), 113 (30) ($C_6H_9O_2$), 95 (18) (C_7H_{11}), 89 (26) (C_5H_7), 87 (16) ($C_4H_7O_2$).

Substituted 9-phenylnona-6*E*,8*E*-dienoic acid propylene glycol esters, VI

The procedure for the preparation of **VI** (R = H, R′ = CH_3) and **VI** (R = 2′-OCH_3) (Entries 6 and 7, Table 1), was essentially as for **VI** (R = R′ = H), using the appropriate substituted (commercially available) cinnamaldehydes. The former displayed IR ($CHCl_3$): 3600, 3500, 2940, 2870, 1725, 1600, 1490, 1460, 1440, 1390, 1380, 1150, 1080, 1050, 970, 920, and 870 cm^{-1}; ^1H NMR ($CDCl_3$, 200 MHz) δ: 1.50 (2H, m), 1.69 (2H, m), 1.88 (2H, sept, J = 6.2 Hz), 1.99 (3H, d, J = 1.2 Hz), 2.20 (2H, dt, J = 7.0 and 6.4 Hz), 2.36 (2H, t, J = 7.2 Hz), 3.70 (2H, br t, J = 4.6 Hz), 4.26 (2H, t, J = 6.0 Hz), 5.77 (1H dt, J = 15.4 and 7.0 Hz), 6.26 (1H, dd, J = 15.8 and 0.8 Hz), 6.44 (1H, br s) 7.25–7.40 (5H, m). HREIMS, *m/z* (relative intensity) (ion): 302.1888 (19) (M^+) (calcd. for $C_{19}H_{26}O_3$: 302.1882), 226 (9) (M^+ − $(CH_2)_3(OH)_2$), 183 (13) ($C_{14}H_{15}$), 155 (25) ($C_{12}H_{11}$), 143 (100) ($C_{11}H_{11}$), 129 (44) ($C_{10}H_9$), 115 (18) (C_9H_7), 91 (30) (C_7H_7).

The latter showed IR ($CHCl_3$): 3600, 3500, 2940, 2850, 1720, 1595, 1485, 1460, 1440, 1395, 1050, 1035, 995, and 915 cm^{-1}; ^1H NMR ($CDCl_3$, 200 MHz) δ: 1.40–1.55 (2H, m), 1.50–1.75 (2H, m), 1.85 (2H, sept, J = 6.4 Hz), 2.14 (2H, dt, J = 7.4 and 7.0 Hz), 2.32 (2H, t, J = 7.2 Hz), 3.67 (2H, m), 3.83 (3H, s), 4.22 (2H, t, J = 6.2 Hz), 5.75 (1H, dt, J = 15.2 and 7.0 Hz), 6.21 (1H, m), 6.74 (1H, d, J = 1.4 Hz), 6.75–6.95 (3H, m), 7.18 (1H, dd, J = 15.2 and 7.4 Hz), 7.42 (1H, d, J = 7.6 Hz); HREIMS, *m/z* (relative intensity) (ion): 318.1822 (86) (M^+) (calcd. for $C_{19}H_{26}O_4$: 318.1831), 242 (21) (M^+ − $(CH_2)_3(OH)_2$), 214 (14) (M^+ − $HCO_2(CH_2)_3OH$), 200 (14) ($C_{14}H_{16}O$), 186 (62) ($C_{13}H_{14}O$), 173 (59) ($C_{12}H_{13}O$), 159 (52) ($C_{11}H_{11}O$), 145 (40) ($C_{10}H_9O$), 131 (73) (C_9H_7O), 128 (24) ($C_{10}H_8$), 121 (100) (C_8H_9O), 119 (18) (C_8H_7O), 115 (35) (C_9H_7), 91 (65) (C_7H_7), 79 (15) (C_6H_7).

9-Phenylnona-6*E*,8*E*-dienal

A solution of glycol ester **VI** (R = R′ = H) (0.901 g, 3.13 mmol) in dry THF (10 mL) was added dropwise at 0°C to a slurry of LAH (0.179 g, 4.84 mmol) in dry THF (40 mL). After the initial evolution of hydrogen, the stirred mixture was allowed to attain ambient temperature during 3.5 h, when TLC analysis showed the reaction to be complete. After cautious sequential addition of water (0.1 equiv.), NaOH (15% aqueous) (0.1 equiv.), and water (0.3 equiv.), the mixture was stirred for 20 min. Magnesium sulfate was then added, the slurry was filtered through Celite and evaporated to dryness under reduced pressure. The resulting alcohol, 9-phenyl-6*E*,8*E*-nonadien-1-ol (642 mg, 95%) was sufficiently pure to be subjected directly to Swern oxidation. It displayed the following spectroscopic characteristics: IR ($CHCl_3$): 3600, 3425, 2930, 2850, 1640, 1595, and 990 cm^{-1}; ^1H NMR ($CDCl_3$, 200 MHz) δ: 1.35–1.50 (4H, m), 1.50–1.65 (2H, m), 2.10–2.25 (2H, m), 3.65 (2H, t, J = 6.4 Hz), 5.82 (1H, dt, J = 7.0 and 15.2 Hz), 6.21 (1H, dd, J = 10.3 and 15.2 Hz), 6.44 (1H, d, J = 15.4 Hz), 6.75 (1H, dd, J = 10.2 and 15.6 Hz), 7.20–7.45 (5H, m); HREIMS, *m/z* (relative intensity) (ion): 216.1517 (84) (M^+) (calcd. for $C_{15}H_{20}O$: 216.1512), 155 (24) ($C_{12}H_{11}$), 143 (97) ($C_{11}H_{11}$), 130 (90) ($C_{10}H_{10}$), 115 (77) (C_9H_7), 111 (8) ($C_7H_{11}O$), 104 (48) (C_8H_8), 91 (100) (C_7H_7), 77 (23) (C_6H_5).

Swern oxidation (22) of the alcohol (642 mg, 2.97 mmol) yielded the desired aldehyde, 9-phenyl-6*E*,8*E*-nonadienal (611 mg, 96%) as a pale yellow oil. This product was sufficiently pure to be used directly in the subsequent Horner–Emmons reaction. A sample after preparative thin-layer chromatography displayed the following spectroscopic characteristics: IR ($CHCl_3$): 2940, 2860, 2740, 1720, 1640, 1595, 1490, 1450, and 990 cm^{-1}; ^1H NMR ($CDCl_3$, 200 MHz) δ: 1.40–1.60 (2H, m), 1.60–1.75 (2H, m), 2.17 (2H, q, J = 6.6 Hz), 2.45 (2H, dt, J = 1.8 and 7.0 Hz), 5.79 (1H, dt, J = 7.0 and 15.0 Hz), 6.21 (1H, ddt, J = 10.0, 15.4, and 1.0 Hz), 6.44 (1H, d, J = 15.8 Hz), 6.74 (1H, dd, J = 10.0 and 15.4 Hz), 7.20–7.40 (5H, m), 9.77 (1H, t, J = 1.8 Hz); HREIMS, *m/z* (relative intensity) (ion): 214.1356 (67) (M^+) (calcd. for $C_{15}H_{18}O$: 214.1357), 155 (13) ($C_{12}H_{11}$), 143 (80) ($C_{11}H_{11}$), 128 (100) ($C_{10}H_8$), 115 (52) (C_9H_7), 104 (72) (C_8H_8), 91 (67) (C_7H_7), 77 (20) (C_6H_5).

Ethyl 13-phenyltrideca-2*E*,4*E*,10*E*,12*E*-tetraenoate

n-Butyllithium (0.78 mL of 2.5 M solution in hexane, 1.95 mmol) was added dropwise by syringe to a stirred solution of triethyl 4-phosphonocrotonate (486 mg, 1.95 mmol) in dry THF (15 mL) at –78°C under argon. Stirring was continued for 20 min, and a solution of the aldehyde prepared above (378 mg, 1.77 mmol) in dry THF (5 mL) was then added dropwise. The pale yellow mixture was stirred at –78°C for a further 10 min, and was then allowed to attain ambient temperature during 1.5 h before the reaction was quenched by cautious addi-

[3] Prepared by reduction of the methyl ester of commercially available 3′,4′-methylenedioxycinnamic acid with sodium bis(2-methoxyethoxy)aluminium hydride, and Swern oxidation of the resulting alcohol.

tion of 1% NH_4Cl (ca. 10 mL). The mixture was extracted with ether (3 × 20 mL) and the extracts were washed with water (2 × 10 mL), dried over $MgSO_4$, and evaporated to dryness under reduced pressure. The crude ester product was passed through a short column of silica gel with hexane–EtOAc (6:1) as eluent, affording chromatographically pure ethyl 13-phenyltrideca-2*E*,4*E*,10*E*,12*E*-tetraenoate (406 mg, 74%) as a colorless oil: IR ($CHCl_3$): 2995, 2940, 2860, 1700, 1640, 1620, 1600, 1450, 1375, 1300, 1140, 1040, 1000, and 990 cm^{-1}; ^1H NMR ($CDCl_3$, 200 MHz) δ: 1.23 (3H, t, J = 7.0 Hz), 1.40 (4H, pent, J = 3.4 Hz), 2.12 (4H, m) 4.14 (2H, q, J = 7.2 Hz), 5.73 (1H, d, J = 15.2 Hz), 5.75 (1H, dt, J = 7.0 and 15.2 Hz), 6.04–6.24 (3H, m), 6.39 (1H, d, J = 15.5 Hz), 6.70 (1H, dd, J = 10.2 and 15.6 Hz), 7.15–7.40 (6H, m); HREIMS *m/z* (relative intensity) (ion): 310.1929 (11) (M^+) (calcd. for $C_{21}H_{26}O_2$; 310.1933), 237 (22) ($M^+ - CO_2C_2H_5$), 219 (10) ($C_{14}H_{19}O_2$), 206 (15) ($C_{13}H_{18}O_2$), 197 (12) ($C_{15}H_{17}$), 169 (14) ($C_{13}H_{13}$), 158 (39) ($C_{12}H_{14}$), 143 (50) ($C_{11}H_{11}$), 128 (77) ($C_{10}H_8$), 117 (78) (C_9H_9), 91 (100) (C_7H_7), 79 (23) (C_6H_7).

13-Phenyltrideca-2*E*,4*E*,10*E*,12*E*-tetraenoic acid

The ethyl ester (406 mg, 1.31 mmol) was heated under reflux for 1.5 h in acetone containing LiOH (3 mL of 1.0 M aqueous solution). The mixture was evaporated to near dryness under reduced pressure, and was then made acidic by addition of 2 M HCl and extracted with EtOAc (3 × 50 mL). The carboxylic acid was extracted from the organic phase into saturated $NaHCO_3$ (4 × 50 mL). The aqueous phase was made acidic by addition of 2 M HCl and the organic acid was reextracted with EtOAc (3 × 50 mL). The extracts, after being dried over $MgSO_4$ and evaporated to dryness, afforded 305 mg (83%) of colorless crystalline 13-phenyl-2*E*,4*E*,10*E*,12*E*-tridecatetraenoic acid, sufficiently pure to be used directly in the subsequent amidation step. A pure specimen melted at 99.5–101°C, and displayed IR absorption ($CHCl_3$) at 3200–2500, 2950, 2930, 2860, 1680, 1640, 1615, 1300, 1110, 1000, 990, and 910 cm^{-1}; ^1H NMR ($CDCl_3$, 200 MHz) δ: 1.46 (4H, t, J = 3.4 Hz), 2.17 (4H, m), 5.79 (1H, d, J = 15.4 Hz), 5.79 (1H, dt, J = 10.0 and 15.4 Hz), 6.12–6.30 (3H, m), 6.44 (1H, d, J = 15.8 Hz), 6.75 (1H, dd, J = 10.2 and 15.6 Hz), 7.15–7.45 (6H, m); HREIMS, *m/z* (relative intensity) (ion): 282.1615 (20) (M^+) (calcd. for $C_{19}H_{22}O_2$: 282.1620), 191 (17) ($C_{12}H_{15}O_2$), 178 (19) ($C_{11}H_{14}O_2$), 169 (17) ($C_{13}H_{13}$), 158 (44) ($C_{12}H_{14}$), 128 (87) ($C_{10}H_8$), 120 (16) ($C_7H_4O_2$), 117 (66) (C_9H_9), 91 (100) (C_7H_7), 79 (24) (C_6H_7).

13-Phenyltrideca-2*E*,4*E*,10*E*,12*E*-tetraenoic acid isobutylamide, 7

The carboxylic acid prepared above (305 mg, 1.08 mmol) in CH_2Cl_2 was stirred with 1,1′-carbonyldiimidazole (210 mg, 1.30 mmol) at 0°C under argon. After 45 min, a solution of isobutylamine (119 mg, 1.62 mmol) in CH_2Cl_2 (1 mL) was added and the reaction mixture was set aside with stirring for 14 h. After addition of water (ca. 10 mL) the product was taken up in CH_2Cl_2 and the organic solution was washed successively with $NaHCO_3$ (2 × 20 mL) and water (2 × 20 mL). The organic solution was dried ($MgSO_4$) and the product obtained on removal of solvent was purified by chromatography on silica gel with hexane–EtOAc (3:2) as eluent, to give pure amide **7** as a colorless solid: mp 87.5–92°C, IR ($CHCl_3$): 3450, 2960, 2870, 1660, 1635, 1620, 1510, and 995 cm^{-1}; ^1H NMR ($CDCl_3$, 200 MHz) δ: 0.93 (6H, d, J = 6.6 Hz), 1.45 (4H, pent, J = 3.4 Hz), 1.78 (1H, sept, J = 6.8 Hz) 2.18 (4H, m), 3.16 (2H, t; J = 6.4 Hz), 5.45 (1H, br s), 5.75 (1H, d, J = 15.0 Hz), 5.80 (1H, dt, J = 7.0 and 15.2 Hz), 6.04–6.16 (1H, m), 6.21 (1H, dd, J = 10.8 and 15.2 Hz), 6.44 (1H, d, J = 15.6 Hz), 6.75 (1H, dd, J = 10.2 and 15.4 Hz), 7.15–7.45 (6H, m); HREIMS, *m/z* (relative intensity) (ion): 337.2387 (56) (M^+) (calcd. for $C_{23}H_{31}NO$: 337.2406), 246 (29) ($C_{16}H_{24}NO$), 217 (26) ($C_{14}H_{19}NO$), 180 (14) ($C_{11}H_{18}NO$), 155 (15) ($C_{12}H_{11}$), 152 (31) ($C_9H_{14}NO$), 147 (20) ($C_{11}H_{15}$), 137 (18) ($C_{10}H_{17}$), 128 (60) ($C_{10}H_8$), 117 (59) (C_9H_9), 105 (24) (C_8H_9), 91 (90) (C_7H_7), 79 (24) (C_6H_7), 69 (100) (C_5H_9).

13-Phenyltrideca-2*E*,4*E*,10*E*,12*E*-tetraenoic acid piperidylamide, 8

The ester ethyl 13-phenyltrideca-2*E*,4*E*,10*E*,12*E*-tetraenoate (65 mg, 0.23 mmol) was treated with the Roskamp (18) reagent $Sn[N(TMS)_2]_2$ (0.28 mmol) and piperidine (27 mg, 0.34 mmol) in hexane. The mixture was set aside with stirring at ambient temperature for 12 h. Chromatography on a preparative silica gel plate (hexane–EtOAc (2:1)) of the product obtained on work-up (18) furnished 27 mg of unreacted ethyl 13-phenyltrideca-2*E*,4*E*,10*E*,12*E*-tetraenoate and 50 mg of the amide **8**, as a colorless oil that solidified on storage in the refrigerator (92% based on consumed starting material). IR ($CHCl_3$): 3000, 2940, 2860, 1645, 1620, 1590, 1440, 1140, 1120, 990, and 850 cm^{-1}; ^1H NMR ($CDCl_3$, 200 MHz) δ: 1.43 (4H, pent, J = 3.6 Hz), 1.50–1.70 (6H, m), 2.15 (4H, m), 3.53 (4H, br s), 5.78 (1H, dt, J = 7.0 and 14.8 Hz), 6.02 (1H, dt, J = 6.4 and 15.0 Hz), 6.10–6.24 (2H, m), 6.24 (1H, d, J = 14.6 Hz), 6.42 (1H, d, J = 15.6 Hz), 6.73 (1H, dd, J = 10.2 and 15.6 Hz), 7.15–7.40 (6H, m); HREIMS, *m/z* (relative intensity) (ion): 349.2392 (63) (M^+) (calcd. for $C_{24}H_{31}NO$: 349.2405), 229 (28) ($C_{15}H_{19}NO$), 192 (20) ($C_{12}H_{18}NO$), 164 (52) ($C_{10}H_{14}NO$), 143 (24) ($C_{11}H_{11}$), 138 (12) ($C_8H_{12}NO$), 132 (12) (C_9H_8O), 128 (53) ($C_{10}H_8$), 127 (31) ($C_7H_{13}NO$), 117 (57) (C_9H_9), 112 (100) ($C_6H_{10}NO$), 91 (79) (C_7H_7), 84 (61) ($C_5H_{10}N$), 77 (28) (C_6H_5).

Ethyl 11-phenylundeca-2*E*,8*E*,10*E* trienoate

n-Butyllithium (1.0 mL of 2.5 M solution in hexane, 2.5 mmol) was added dropwise by syringe to a stirred solution of triethyl phosphonoacetate (572 mg, 2.46 mmol) in dry THF (15 mL) at –78°C under argon. Stirring was continued for 20 min, and a solution of the aldehyde prepared above (438 mg, 2.05 mmol) in dry THF (5 mL) was then added dropwise. The pale yellow mixture was stirred at –78°C for a further 10 min, and was then allowed to attain ambient temperature over 1.5 h before the reaction was quenched by cautious addition of 1% NH_4Cl (ca. 10 mL). The crude ester product obtained on conventional work-up was passed through a short column of silica gel with hexane–EtOAc (6:1) as eluent, affording chromatographically pure ethyl 11-phenyl-(2*E*,8*E*,10*E*) undecatrienoate (421 mg, 73%) as a colorless oil: IR ($CHCl_3$): 2995, 2940, 2860, 1705, 1660, 1600, 1450, 1370, 1040 and 990 cm^{-1}; ^1H NMR ($CDCl_3$, 200 MHz) : 1.28 (3H, t, J = 7.2 Hz), 1.47 (4H, pent, J = 3.4 Hz), 2.19 (4H, m) 4.18 (2H, q, J = 7.2 Hz), 5.79 (1H, dt, J = 7.0 and 15.2 Hz), 5.81 (1H, d, J = 15.8 Hz), 6.20 (1H, dd, J = 10.2 and 15.2 Hz), 6.43 (1H, d, J = 15.6 Hz), 6.74 (1H, dd, J = 10.2 and 15.6 Hz), 6.96 (1H, dt, J = 7.0 and 15.6 Hz), 7.20–7.45 (5H, m); HREIMS, *m/z* (relative intensity) (ion): 284.1792 (13) (M^+) (calcd. for $C_{19}H_{24}O_2$:

284.1776), 210 (38) ($C_{16}H_{18}$), 202 (17) ($C_{13}H_{14}O_2$), 193 (29) ($C_{12}H_{17}O_2$), 155 (19) ($C_{12}H_{11}$), 141 (38) ($C_{11}H_9$), 128 (100) ($C_{10}H_8$), 119 (51) (C_9H_{11}), 91 (77) (C_7H_7), 77 (13) (C_6H_5).

11-Phenylundeca-2*E*,8*E*,10*E*-trienoic acid

Hydrolysis of the above ethyl ester (294 mg, 1.04 mmol), accomplished using the same procedure as for its homologue, afforded 265 mg (96%) of colorless crystalline 1-phenyl-2*E*,8*E*,10*E* undecatrienoic acid, sufficiently pure to be used directly in the subsequent amidation step. A pure specimen melted at 105.5–107°C, and displayed IR absorption ($CHCl_3$) at 3200–2600, 2940, 2860, 1695, 1650, 1600, and 990 cm^{-1}; ^1H NMR ($CDCl_3$, 200 MHz) δ: 1.47 (4H, m), 2.10–2.35 (4H, m), 5.77 (1H, dt, J = 7.0 and 15.0 Hz), 5.82 (1H, d, J = 15.6 Hz), 6.19 (1H, dd, J = 10.2 and 14.8 Hz), 6.43 (1H, d, J = 15.8 Hz), 6.73 (1H, dd, J = 10.0 and 15.6 Hz), 7.06 (1H, dt, J = 7.0 and 15.6 Hz), 7.20–7.40 (5H, m); HREIMS, *m/z* (relative intensity) (ion): 256.1456 (41) (M^+) (calcd. for $C_{17}H_{20}O_2$: 256.1463), 211 (22) ($M^+ - CO_2H$), 165 (24) ($C_{10}H_{13}O_2$), 158 (15) ($C_{12}H_{14}$), 143 (78) ($C_{11}H_{11}$), 128 (100) ($C_{10}H_8$), 115 (44) (C_9H_7), 104 (29) (C_8H_8), 91 (65) (C_7H_7), 77 (15) (C_6H_5), 69 (61) (C_5H_9).

11-Phenylundeca-2*E*,8*E*,10*E*-trienoic acid isobutylamide, 9

The carboxylic acid (191 mg, 0.746 mmol) afforded the corresponding isobutylamide **9** (206 mg, 89%) using the 1,1′-carbonyldiimidazole coupling procedure described for the homologue **7**. Amide **9** was a colorless solid, mp 119–127°C, IR ($CHCl_3$): 3450, 2960, 2930, 2860, 1670, 1640, 1510, and 990 cm^{-1}; ^1H NMR ($CDCl_3$, 200 MHz) δ: 0.88 (6H, d, J = 6.4 Hz), 1.48 (4H, t, J = 3.2 Hz), 1.78 (1H, sept, J = 6.6 Hz) 2.18 (4H, m), 3.14 (2H, t, J = 6.8 Hz), 5.45 (1H, br s), 5.75 (1H, d, J = 15.4 Hz), 5.79 (1H, dt, J = 6.6 and 15.2 Hz), 6.19 (1H, dd, J = 10.2 and 15.0 Hz), 6.43 (1H, d, J = 15.8 Hz), 6.74 (1H, dd, J = 10.2 and 15.6 Hz), 6.82 (1H, dt, J = 6.8 and 15.4 Hz), 7.25–7.45 (5H, m); HREIMS, *m/z* (relative intensity) (ion): 311.2245 (62) (M^+) (calcd. for $C_{21}H_{29}NO$: 311.2249), 220 (53) ($C_{14}H_{22}NO$), 211 (48) ($C_{16}H_{19}$), 196 (20) ($C_{15}H_{16}$), 194 (22) ($C_{12}H_{20}NO$), 154 (62) ($C_9H_{16}NO$), 143 (50) ($C_{11}H_{11}$), 141 (43) (C_8H_5NO), 128 (84) ($C_{10}H_8$), 121 (73) (C_9H_{13}), 115 (44) (C_9H_7), 105 (14) (C_7H_5O), 91 (100) (C_7H_7), 81 (19) (C_6H_9), 77 (17) (C_6H_5), 74 (8) ($C_4H_{12}N$).

11-Phenylundeca-2*E*,8*E*,10*E*-trienoic acid piperidylamide, 10

The ester, ethyl 11-phenyl-2*E*,8*E*,10*E*-undecatrienoate, furnished the amide **10** directly in 86% yield via the Roskamp procedure (18). IR ($CHCl_3$): 3000, 2940, 2860, 1655, 1600, 1440, and 990 cm^{-1}; ^1H NMR ($CDCl_3$, 200 MHz) δ: 1.46 (4H, m), 1.54 (4H, m), 2.17 (4H, q, J = 6.0 Hz), 3.51 (4H, br s), 5.78 (1H, dt, J = 7.0 and 15.0 Hz), 6.10–6.25 (1H, m), 6.23 (1H, br d, J = 15.0 Hz), 6.42 (1H, d, J = 15.6 Hz), 6.73 (1H, dd, J = 10.8 and 15.8 Hz), 6.81 (1H, dt, J = 7.0 and 15.0 Hz), 7.15–7.40 (5H, m); HREIMS, *m/z* (relative intensity) (ion): 323.2237 (48) (M^+) (calcd. for $C_{22}H_{29}NO$: 323.2248), 232 (34) ($C_{15}H_{22}NO$), 206 (15) ($C_{13}H_{20}NO$), 166 (69) ($C_{10}H_{16}NO$), 153 (22) ($C_9H_{15}NO$), 138 (100) ($C_8H_{12}NO$), 131 (95) (C_9H_7O), 127 (32) ($C_7H_{13}NO$), 115 (21) (C_9H_7), 112 (61) ($C_6H_{10}NO$), 103 (42) (C_8H_7), 91 (40) (C_7H_7), 84 (77) ($C_5H_{10}N$), 77 (38) (C_6H_5).

syn- and *anti*- Cyclooctanone-benzaldehyde aldol products, 11 (cf. ref. 16)

n-Butyllithium (2.5 M in hexane, 4.0 mL, 10 mmol) was added dropwise under argon to a solution of diisopropylamine (1.40 mL, 10.0 mmol) in dry THF at –78°C. The solution was stirred at –78°C for 30 min, and a solution of cyclooctanone (1.260 g, 10.0 mmol) in dry THF (5 mL) was then added dropwise by syringe. Stirring was continued at –78°C for a further 30 min, when trimethylsilyl chloride (1.27 mL, 10.1 mmol) was slowly added. The stirred mixture was set aside at –78°C for 1 h. Dilution with ether (70 mL) resulted in precipitation of a white salt that was removed by filtration (2×) through a bed of Celite, and evaporation of solvents in vacuo then furnished a pale yellow oil. The product was chromatographed on a column of silica gel with hexane as eluent to give 1.527 g (77%) of cyclooctanone TMS enol ether. ^1H NMR ($CDCl_3$, 200 MHz) δ: 0.19 (9H, s), 1.50 (8H, br s), 2.01 (2H, br m), 2.18 (2H, br m), 4.74 (1H, t, J = 8.2 Hz).

$TiCl_4$ (0.32 mL, 2.75 mmol) was added dropwise with stirring to a solution of benzaldehyde (0.292 g, 2.75 mmol) in freshly distilled CH_2Cl_2 (20 mL) at –78°C under an atmosphere of argon. Addition of the cyclooctanone TMS enol ether in CH_2Cl_2 (10 mL) followed by stirring for 1 h afforded a dark orange-colored solution. Water (ca. 20 mL) was cautiously added, and the mixture was extracted with ether (3 × 20 mL). The extracts were dried over $MgSO_4$ and the solvent removed under reduced pressure to produce a colorless oil. The isomeric products were separated by flash chromatography on silica gel with hexane–EtOAc (7:1) as eluent. The overall yield was 51%, with *anti* and *syn* products in a ratio of 64:36.

anti *Isomer*: IR ($CHCl_3$): 3600, 3450, 2930, 2860, 1685, 1600, 1450, and 1260 cm^{-1}; ^1H NMR ($CDCl_3$, 200 MHz) δ: 1.55–1.85 (10H, m), 2.33 (2H, m), 3.14 (1H, m), 4.83 (1H, m), 7.30–7.40 (5H, m); HREIMS, *m/z* (relative intensity) (ion): 232.1453 (9) (M^+) (calcd. for $C_{15}H_{20}O_2$: 232.1463), 214 (32) ($M^+ - H_2O$), 175 (31) ($C_{11}H_{11}O_2$), 157 (11) ($C_{11}H_9O$), 147 (11) ($C_9H_7O_2$), 126 (83) ($C_8H_{14}O$) 117 (19) (C_9H_9), 112 (15) ($C_7H_{12}O$), 107 (76) (C_7H_7O), 98 (100) ($C_6H_{10}O$), 91 (25) (C_7H_7), 84 (51) (C_5H_8O), 77 (88) (C_6H_6).

syn *Isomer*: IR ($CHCl_3$): 3600, 3450, 2930, 2860, 1685, 1600, 1450, and 1260 cm^{-1}; ^1H NMR ($CDCl_3$, 200 MHz) δ: 1.15–2.05 (10H, m), 2.25 (2H, m), 3.03 (1H, dt, J = 4.8 and 11.6 Hz), 4.95 (1H, d, J = 4.8 Hz), 7.25–7.40 (5H, m); HREIMS, *m/z* (relative intensity) (ion): 232.1470 (3) (M^+) (calcd. for $C_{15}H_{20}O_2$: 232.1463), 214 (12) ($M^+ - H_2O$), 175 (11) ($C_{11}H_{11}O_2$), 126 (74) ($C_8H_{14}O$), 117 (16) (C_9H_9), 107 (42) (C_7H_7O), 98 (100) ($C_6H_{10}O$), 91 (13) (C_7H_7), 84 (25) (C_5H_8O), 77 (34) (C_6H_5).

Attempted fragmentation of *anti* aldol 11

Boron trifluoride etherate (0.24 mL, 2.0 mmol) was added dropwise by syringe under argon to a stirred solution of **11** (*anti* isomer) (64 mg, 0.27 mmol) in dry THF at 0°C. Propane-1,3-diol (100 mg, 1.32 mmol) was added immediately and the stirred solution allowed to attain ambient temperature during 14 h. The mixture was poured into saturated $NaHCO_3$ and the products were extracted with ether (3 × 50 mL). The extracts were washed successively with saturated brine (30 mL) and

water (30 mL), dried over $MgSO_4$, and evaporated under reduced pressure. The resulting pale yellow oil was subjected to flash chromatography on silica gel (hexane–EtOAc, 4:1) affording, in the early eluates, the styrene 2-benzylidinecyclooctanone (24 mg, 40%). IR ($CHCl_3$): 2925, 2860, 1670, 1595, 1490, 1445, 1345, 1320, 1280, 1160, 1120, 1080, 990, and 870 cm^{-1}; ^1H NMR ($CDCl_3$, 200 MHz) δ: 1.50–1.90 (8H, m), 2.72 (2H, t, J = 6.4 Hz), 2.82 (2H, t, J = 6.2 Hz), 7.30–7.40 (5H, m), 7.48 (1H, s); MS, *m/z* (relative intensity) (ion): 214 (100) (M^+, $C_{15}H_{18}O$), 159 (18) ($C_{11}H_{11}O$), 130 (37) (C_9H_6O), 115 (32) (C_9H_7), 104 (27) (C_8H_8), 91 (29) (C_7H_7).

Further elution produced an unresolved mixture of cyclooctanone and the acetal (1,3-dioxane) of benzaldehyde (37 mg, ratio 1:1 by NMR).

Putative hydroxy-acetal intermediate 12

To a refluxing slurry of KH (35% dispersion in mineral oil, 1.25 g, 11.0 mmol) in benzene (15 mL) was added rapidly a mixture of cyclooctanone (630 mg, 5.00 mmol) and diethyl carbonate (1.33 g, 7.50 mmol) under argon (24). The mixture was heated under reflux for 30 min. Standard work-up (24) yielded a pale yellow oily product, that, after passage through a short column of silica gel (hexane–EtOAc, 4:1), furnished *2-ethoxycarbonylcyclooctanone* (964 mg, 97%) as a colorless oil: IR ($CHCl_3$): 2925, 2860, 1740, 1700, 1640, 1470, 1400, 1380, 1320, and 1100 cm^{-1}; ^1H NMR ($CDCl_3$, 200 MHz) (keto form, 63%) δ: 1.19 (3H, t, J = 7.0 Hz), 1.35–1.95 (10H, m), 2.00–2.15 (2H, m), 3.53 (1H, dd, J = 6.0 and 9.0 Hz), 4.10 (2H, q, J = 7.0 Hz); (enol form, 37%) δ: 1.26 (3H, t, J = 7.0 Hz), 1.35–1.95 (8H, m) 2.30–2.55 (4H, m), 4.16 (2H, q, J = 7.0 Hz); HREIMS, *m/z* (relative intensity) (ion): 198.1266 (100) (M^+) (calcd. for $C_{11}H_{18}O_3$: 198.1256), 170 (45) ($M^+ - C_2H_4$), 152 (82) ($M^+ - C_2H_6O$), 143 (27) ($C_7H_{11}O_3$), 130 (25) ($C_6H_{10}O_3$), 124 (40) ($C_8H_{12}O$), 109 (35) ($C_6H_5O_2$), 96 (36) (C_6H_8O), 84 (14) (C_5H_8O).

A solution of 2-ethoxycarbonylcyclooctanone (964 mg, 4.87 mmol) in benzene (50 mL) containing ethylene glycol (3.0 mL) and pTSA (ca 5 mg) was heated under reflux with azeotropic removal of water using a Dean Stark apparatus. After 4 days, the reaction mixture was diluted with ether (50 mL) and the solution poured into 10% aqueous $NaHCO_3$. The organic phase was washed with saturated brine, dried over $MgSO_4$, and evaporated to dryness in vacuo. The resulting pale yellow oil (2.15 g) was subjected to flash chromatography on silica gel (hexane–EtOAc, 4:1) affording the pure *acetal (dioxolane) of 2-ethoxycarbonylcyclooctanone* (730 mg, 60%) as a colorless oil: IR ($CHCl_3$): 2930, 1720, 1460, 1440, 1380, 1160, 1040, 975, and 950 cm^{-1}; ^1H NMR ($CDCl_3$, 200 MHz) δ: 1.23 (3H, t, J = 7.2 Hz), 1.50–1.80 (8H, m), 1.80–2.00 (4H, m), 2.95 (1H, dd, J = 2.6 and 9.0 Hz), 3.90–4.00 (4H, m), 4.11 (2H, q, J = 7.2 Hz); HREIMS, *m/z* (relative intensity) (ion): 242.1525 (20) (M^+) (calcd. for $C_{13}H_{22}O_4$: 242.1518), 213 (22) ($M^+ - C_2H_5$), 197 (66) ($M^+ - C_2H_5O$), 171 (100) ($C_8H_{11}O_4$), 169 (23) ($M^+ - C_3H_5O_2$), 141 (16) ($C_8H_{13}O_2$), 127 (25) ($C_7H_{11}O_2$), 99 (75) ($C_5H_7O_2$), 86 (39) ($C_4H_6O_2$).

The ester-acetal (46 mg, 0.19 mmol) dissolved in dry THF (1.0 mL) was added under an inert atmosphere to a stirred slurry of LAH (11 mg, 0.30 mmol) in THF 0°C. The stirred mixture was allowed to attain ambient temperature over 1 h, and work-up as described for a previous LAH reduction (vide supra) furnished a quantitative yield (38 mg) of the *2-hydroxymethyl derivative of cyclooctanone dioxolane*, sufficiently pure to be used directly for the subsequent Swern oxidation. IR ($CHCl_3$): 3500, 2930, 1460, 1440, 1410, 1150, 1080, 1025, and 950 cm^{-1}; ^1H NMR ($CDCl_3$, 200 MHz) δ: 1.45–1.90 (12H, m), 2.12 (1H, sept, J = 3.4 Hz), 3.05 (1H, br s), 3.50–3.75 (2H, m), 3.85–4.00 (4H, m); HREIMS, *m/z* (relative intensity) (ion): 200.1410 (11) (M^+) (calcd. for $C_{11}H_{20}O_3$: 200.1412), 183 (29) ($M^+ - OH$), 169 (32) ($M^+ - CH_3O$), 141 (17) ($C_8H_{13}O_2$), 129 (100) ($C_6H_9O_3$), 116 (38) ($C_5H_8O_3$), 99 (88) ($C_5H_7O_2$), 86 (14) ($C_4H_6O_2$).

Swern oxidation (22) produced the *2-formyl derivative of cyclooctanone dioxolane*: IR ($CHCl_3$): 2925, 2875, 1720, 1465, 1440, 1160, 1080, and 950 cm^{-1}; ^1H NMR ($CDCl_3$, 200 MHz) δ: 1.50–1.95 (10H, m), 2.00–2.15 (2H, m), 2.75 (1H, dt, J = 1.8 and 8.2 Hz), 3.80–4.05 (4H, m), 9.72 (1H, d, J = 1.8 Hz). This very unstable product (22 mg, 0.11 mmol) was immediately dissolved in dry THF (1.0 mL) and, at –78°C with stirring under an argon atmosphere, was treated with phenyllithium (0.068 mL of 1.8 M solution in cyclohexane–ether, 0.13 mmol). The reaction mixture was stirred at –78°C for 1.5 h, and then aqueous NH_4Cl (1%, 1.0 mL) was added, and the mixture was extracted with ether (3 × 10 mL). Solvent was removed from the dried extracts in vacuo, and chromatography of the residue on a preparative silica gel plate afforded the desired *hydroxy-acetal* ***12*** (6.0 mg). ^1H NMR ($CDCl_3$, 200 MHz) δ: 1.40–1.95 (12H, m), 2.36 (1H, m), 4.00–4.15 (4H, m), 4.74 (1H, d, J = 9.4 Hz), 5.06 (1H, s), 7.25–7.45 (5H, m); HREIMS, *m/z* (relative intensity) (ion): 276.1762 (4) (M^+) (calcd. for ($C_{17}H_{24}O_3$: 276.1761), 259 (6) ($M^+ - H_2O$), 192 (12) ($C_{11}H_{12}O_3$), 175 (10) ($C_{11}H_{11}O_2$), 170 (41) ($C_{10}H_{18}O_2$), 149 (12) ($C_8H_5O_3$), 142 (22) ($C_8H_{14}O_2$), 127 (14) ($C_8H_{15}O$), 120 (13) (C_8H_8O), 115 (29) ($C_6H_{11}O_2$), 105 (34) (C_7H_5O), 99 (100) ($C_5H_7O_2$), 86 (32) ($C_4H_6O_2$), 77 (23) (C_6H_5).

Attempted fragmentation of 12

Boron trifluoride etherate (0.011 mL, 0.089 mmol) was added by syringe under argon to a stirred solution of the hydroxy-acetal **12** (6.0 mg, 0.022 mmol) in dry THF (3.5 mL) at 0°C. The mixture was allowed to attain ambient temperature and was stirred for 14 h, when it was poured into saturated $NaHCO_3$ (ca. 5 mL). The mixture was extracted with ether (3 × 10 mL) and the extracts were dried over $MgSO_4$ and evaporated under reduced pressure. Analysis of the crude product by TLC and NMR revealed that fragmentation had not occurred, and the only identifiable products were benzaldehyde and cyclooctanone.

1-Iodo-6-(3′,4′-methylenedioxyphenyl)-5*E*-hexene, 13

To a solution of triphenylphosphine (2.96 g, 11.3 mmol) in ether:acetonitrile (3:1) (20 mL) was added imidazole (840 mg, 12.4 mmol) and iodine (2.61 g, 10.2 mmol). The slurry was stirred at ambient temperature for 5 min and a solution of the alcohol (754 mg, 3.43 mmol) (6) derived from **III** (x = 3) in the same solvent mixture (15 mL) was then added. The resulting yellow slurry was set aside with stirring for 14 h, then diluted with hexane (ca. 100 mL) and filtered through a short column of silica gel. Chromatography on a column of silica gel (hexane–EtOAc, 20:1) afforded the pure iodide **13** (1.13 g, 91%) as a colorless oil that solidified on standing: IR ($CHCl_3$): 3000, 2940, 2900, 2860, 1605, 1485, 1440, 1360, 1125, 1100, 1040, 970, 940, 915, and 860 cm^{-1}; ^1H NMR ($CDCl_3$, 200 MHz) δ:

1.59 (2H, q, J = 7.0 Hz), 1.81–1.92 (2H, m), 2.22 (2H, dt, J = 7.0 and 7.2 Hz), 3.22 (2H, t, J = 6.8 Hz), 5.94 (2H, s), 6.02 (1H, dt, J = 6.8 and 15.8 Hz), 6.31 (1H, d, J = 15.8 Hz), 6.75 (2H, s), 6.90 (1H, s).

8-(3′,4′-Methylenedioxyphenyl)-oct-7*E*-en-1-yne, 14

A solution of iodide **13** (303 mg, 0.918 mmol) in dry DMSO (1.5 mL) was added slowly under argon during 1 h to a slurry of lithium acetylide – ethylenediamine complex (141 mg, 1.53 mmol) in DMSO (1.5 mL) at 8–10°C. Stirring was continued for a further 1 h, whereupon conventional work-up afforded the alkyne **14** (195 mg, 93%) as a colorless oil, sufficiently pure to be used directly in the subsequent step. IR ($CHCl_3$): 3300, 2930, 2860, 2125, 1605, 1485, 1440, 1360, 1130, 1100, 1040, 965, 940, and 865 cm^{-1}; ^1H NMR ($CDCl_3$, 200 MHz) δ: 1.56 (4H, pent, J = 3.4 Hz), 1.93 (1H, t, J = 2.6 Hz), 2.15–2.25 (4H, m), 5.91 (2H, s), 6.01 (1H, dt, J = 6.8 and 15.6 Hz), 6.28 (1H, d, J = 15.8 Hz), 6.72 (2H, s), 6.87 (1H, s).

Ethyl 9-(3′,4′-methylenedioxyphenyl)-non-8*E*-en-2-ynoate, 15

n-Butyllithium (2.5 M in hexane, 0.41 mL, 1.0 mmol) was added dropwise under argon to a stirred solution of **14** (195 mg, 0.855 mmol) in dry THF at 0°C. The mixture was stirred at 0°C for 30 min and ethyl chloroformate (11 mg, 1.03 mmol) was then added dropwise. Stirring was continued for a further 1 h at 0°C and the mixture then allowed to attain ambient temperature during an additional 1 h. Water (10 mL) was added and the product extracted with ether (3 × 30 mL). The oil obtained after washing and drying of the extracts and removal of solvent in vacuo was subjected to flash chromatography on silica gel. Elution with hexane–EtOAc afforded 42 mg of unreacted starting material and 160 mg of the alkyne ester, **15** (79% based on starting material consumed). IR ($CHCl_3$): 2995, 2950, 2910, 2225, 1700, 1600, 1490, 1445, 1370, 1250, 1080, 1040, 970, and 865 cm^{-1}; ^1H NMR ($CDCl_3$, 200 MHz) δ: 1.28 (3H, t, J = 7.0 Hz) 1.50–1.60 (4H, m), 2.17 (2H, dt, J = 6.6 Hz and 6.8 Hz), 2.33 (2H, t, J = 5.2 Hz), 4.19 (2H, q, J = 7.0 Hz), 5.91 (2H, s), 5.98 (1H, dt, J = 6.8 and 15.8 Hz), 6.27 (1H, d, J = 16.0 Hz), 6.71 (2H, s), 6.86 (1H, s).

Ethyl 9-(3′,4′-methylenedioxyphenyl)-nona-2*E*,4*E*,8*E*-trienoate, 16

Alkyne ester **15** (118 mg, 0.395 mmol) in dry toluene (3.0 mL) containing glacial acetic acid (3 drops) and triphenylphosphine (33 mg, 0.13 mmol) was heated under vigorous reflux for 48 h. The residue obtained on concentration of the mixture in vacuo was subjected to flash chromatography on silica gel. Elution with hexane–EtOAc (8:1) furnished trienoate **16** (99 mg, 84%) as a colorless oil: IR ($CHCl_3$): 2980, 2930, 2900, 2890, 1695, 1640, 1620, 1490, 1440, 1370, 1305, 1160, 1140, 1100, 1040, 1005, 965, 940, and 865 cm^{-1}; ^1H NMR ($CDCl_3$, 200 MHz) δ: 1.27 (3H, t, J = 7.0 Hz), 2.31 (4H, m), 4.18 (2H, q, J = 7.0 Hz), 5.78 (1H, d, J = 15.4 Hz), 5.91 (2H, s), 5.90–6.20 (3H, m), 6.30 (1H, d, J = 15.6 Hz), 6.72 (2H, s), 6.86 (1H, s), 7.24 (1H, dd, J = 10.2 and 15.4 Hz).

9-(3′,4′-Methylenedioxyphenyl)-nona-2*E*,4*E*,8*E*-trienoic acid isobutylamide: retrofractamide A, 4

9-(3′,4′-Methylenedioxyphenyl)-nona-2*E*,4*E*,8*E*-trienoic acid was obtained in quantitative yield by hydrolysis of the ester using aqueous LiOH in acetone as described above. The pure acid melted at 161–163°C; IR ($CHCl_3$): 3500–2400, 2995, 1690, 1640, 1620, 1490, 1445, 1045, 1005, 970, and 940 cm^{-1}; ^1H NMR ($CDCl_3$, 200 MHz) δ: 2.33 (4H, m), 5.78 (1H, d, J = 15.2 Hz), 5.92 (2H, s), 5.95–6.25 (3H, m), 6.31 (1H, d, J = 15.8 Hz), 6.73 (2H, s), 6.86 (1H, s), 7.33 (1H, br dd, J = 10.2 and 15.2 Hz).

Coupling of the carboxylic acid with isobutylamine through the agency of 1,1′-carbonyldiimidazole (vide supra) afforded, after preparative layer chromatography on a silica gel plate (hexane: EtOAc, 3:2), a 72% yield of retrofractamide A, **4**. A recrystallized sample melted at 130–132°C (lit. (9) mp 129°C). IR ($CHCl_3$): 3450, 2950, 2925, 2875, 1660, 1630, 1615, 1490, 1440, 1100, 1040, 1000, 970, and 870 cm^{-1}; ^1H NMR ($CDCl_3$, 200 MHz) δ: 0.90 (6H, d, J = 6.6 Hz), 1.78 (1H, sept, J = 6.8 Hz), 2.29 (4H, m), 3.14 (2H, t, J = 6.8 Hz), 5.51 (1H, br s), 5.75 (1H, d, J = 15.0 Hz), 5.91 (2H, s), 5.95–6.20 (3H, m), 6.29 (1H, d, J = 15.8 Hz), 6.72 (2H, s), 6.86 (1H, s), 7.17 (1H, dd, J = 10.0 and 15.0 Hz); HREIMS, *m/z* (relative intensity) (ion): 327.1837 (9) (M^+) (calcd. for $C_{20}H_{25}NO_3$: 327.1834), 161 (88) ($C_{10}H_9O_2$), 131 (100) (C_9H_7O), 103 (32) (C_8H_7), 77 (6) (C_6H_5).

9-(3′,4′-methylenedioxyphenyl)-nona-2*E*-4*E*,8*E*-trienoic acid piperidylamide: dehydropipernonaline, 17

Ethyl 9-(3′,4′-methylenedioxyphenyl)-nona-2*E*,4*E*,8*E*-trienoate, **16**, was transformed directly in 88% yield to the piperidyl amide, **17**, dehydropipernonaline, using the Roskamp procedure as described above (18). The synthetic alkaloid melted at 97–98°C (with softening at 86°C) (lit. (10) mp 98–99°C). IR ($CHCl_3$): 3400, 2990, 2945, 2860, 1645, 1620, 1590, 1490, 1440, 1360, 1140, 1120, 1100, 1040, 1020, 970, 930, 910, and 860 cm^{-1}; ^1H NMR ($CDCl_3$, 200 MHz) δ: 1.50–1.70 (6H, m), 2.30 (4H, m), 3.47 (2H, br s), 3.57 (2H, br s), 5.91 (2H, s), 5.95–6.20 (3H, m), 6.25 (1H, d, J = 15.0 Hz), 6.29 (1H, d, J = 15.0 Hz), 6.72 (2H, s), 6.86 (1H, s), 7.22 (1H, dd, J = 10.2 and 14.8 Hz); HREIMS, *m/z* (relative intensity) (ion): 339.1838 (13) (M^+) (calcd. for $C_{21}H_{25}NO_3$: 339.1834), 161 (100) ($C_{10}H_9O_2$), 131 (78) (C_9H_7O), 103 (21) (C_8H_7), 84 (4) ($C_5H_{10}N$).

9-(3′,4′-Methylenedioxyphenyl)-nona-2*E*,4*E*,8*E*-trienoic acid pyrrolidylamide

This alkaloid, **18**, was similarly prepared from ethyl 9-(3′,4′-methylenedioxyphenyl)-nona-2*E*,4*E*,8*E*-trienoate, **16**, in 94% yield by the Roskamp method (18). Melting point 99°C (with softening at 90°C) (lit. (3) mp 105–106°C); IR ($CHCl_3$): 3400, 2970, 2890, 1650, 1620, 1590, 1490, 1430, 1360, 1100, 1040, 1000, 970, 940, 920, and 865 cm^{-1}; ^1H NMR ($CDCl_3$, 200 MHz) δ: 1.80–2.00 (4H, m), 2.30 (2H, m), 3.51 (4H, q, J = 4.8 Hz), 5.91 (2H, s), 5.95–6.20 (4H, m), 6.29 (1H, d, J = 15.8 Hz), 6.72 (2H, s), 6.86 (1H, s), 7.25 (1H, dd, J = 10.0 and 15.6 Hz); HREIMS, *m/z* (relative intensity) (ion): 325.1665 (13) (M^+) (calcd. for $C_{20}H_{23}NO_3$: 325.1678), 161 (100) ($C_{10}H_9O_2$), 131 (99) (C_9H_7O), 103 (29) (C_8H_7), 98 (5) (C_5H_9NO),77 (10) (C_6H_5).

Ethyl 2*E*,4*E*-decadienoate

The dianion of propiolic acid (0.46 mL, 7.5 mmol), generated using the procedure of Danheiser and co-workers (23), was alkylated with iodoheptane (1.23 mL, 7.50 mmol) to furnish

1.15 g (91%) of *2-decynoic acid*. The latter, without purification, was converted directly (K_2CO_3/EtI) to the ethyl ester (22). The ester, *ethyl 2-decynoate*, (1.17 g, 87%), after filtration through a short column of silica gel required no further purification. Ethyl 2-decynoate (96.4 mg, 0.492 mmol) in dry toluene (1.0 mL) containing glacial acetic acid (2 drops) and triphenylphosphine (28 mg, 0.11 mmol) was heated under reflux for 3.5 h (17). The residue obtained after removal of solvent under reduced pressure was chromatographed on a preparative silica gel plate (hexane–EtOAc, 20:1) affording 87 mg (90%) of the desired ester, ethyl 2*E*,4*E*-decadienoate. These compounds were characterized on the basis of their spectra as follows:

Alkynoic acid: IR ($CHCl_3$): 3400–2400, 2925, 2860, 2225, 1700, 1690, 1460, 1275, and 1040 cm^{-1}; ^1H NMR ($CDCl_3$, 200 MHz) δ: 0.82 (3H, t, J = 6.5 Hz), 1.20–1.30 (8H, m), 1.57 (2H, pent, J = 7.2 Hz), 2.32 (2H, t, J = 7.0 Hz), 10.4 (1H, br s).

Alkynoic ester: IR ($CHCl_3$): 2930, 2860, 2225, 1700, 1460, 1370, 1260, and 1080 cm^{-1}; ^1H NMR ($CDCl_3$, 200 MHz) δ: 0.86 (3H, t, J = 6.5 Hz), 1.20–1.35 (8H, m), 1.28 (3H, t, J = 7.2 Hz), 1.56 (2H, m), 2.30 (2H, t, J = 7.0 Hz), 4.19 (2H, q, J = 7.2 Hz).

Dienoic ester: IR ($CHCl_3$): 2950, 2930, 2860, 1700, 1640, 1620, 1460, 1375, 1300, 1260, 1140, 1035, 1000, and 980 cm^{-1}; ^1H NMR ($CDCl_3$, 200 MHz) δ: 0.88 (3H, t, J = 6.8 Hz), 1.28 (3H, t, J = 7.2 Hz), 1.26–1.29 (4H, m), 1.42 (2H, m), 2.15 (2H, q, J = 5.6 Hz), 4.19 (2H, q, J = 7.0 Hz), 5.77 (1H, d, J = 15.4 Hz), 6.10–6.16 (2H, m), 7.25 (1H, m).

2*E*,4*E*-Decadienoic acid isobutyl amide: pellitorine, 19 (refs. 2, 4)

2*E*,4*E*-Decadienoic acid was obtained in 83% yield by hydrolysis of the ester using aqueous LiOH in acetone as described above. IR ($CHCl_3$): 3400–2400, 2960, 2940, 2860, 1700, 1640, 1620, 1420, 1280, and 1005 cm^{-1}; ^1H NMR ($CDCl_3$, 200 MHz) δ: 0.87 (3H, t, J = 6.4 Hz), 1.27 (4H, m), 1.42 (2H, m), 2.16 (2H, m), 5.63 (1H, d, J = 15.4 Hz), 6.15–6.20 (2H, m), 7.24–7.39 (1H, m).

Coupling of the carboxylic acid with isobutylamine through the agency of 1,1′-carbonyldiimidazole (vide supra) afforded, after preparative layer chromatography on a silica gel plate (hexane: EtOAc, 3:2), an 82% yield of pellitorine, **19**. A sample melted at 70°C (lit. (4) mp 66–68°C): IR ($CHCl_3$): 3450, 2965, 2935, 2880, 2865, 1665, 1635, 1620, 1510, 1470, 1160, and 1000 cm^{-1}; ^1H NMR ($CDCl_3$, 200 MHz) δ: 0.86 (3H, t, J = 6.8 Hz), 0.90 (6H, d, J = 6.6 Hz), 1.20–1.30 (4H, m), 1.35 (2H, pent, J = 7.2 Hz), 1.77 (1H, sept, J = 6.8 Hz), 2.13 (2H, q, J = 6.6 Hz), 3.14 (2H, t, J = 6.6 Hz), 5.74 (1H, d, J = 15.6 Hz), 5.76 (1H, m), 6.04 (1H, dt, J = 6.4 and 15.2 Hz), 6.11 (1H, dd, J = 9.9 and 15.6 Hz), 7.17 (1H, dd, J = 9.9 and 15.0 Hz); ^{13}C NMR (100 MHz, $CDCl_3$) δ: 14.0 20.1 22.5, 28.5, 28.6, 31.3, 32.9, 46.9, 121.7, 128.2, 141.2, 143.2, 166.4; HREIMS, *m/z* (relative intensity) (ion): 223.1943 (36) (M^+) (calcd. for $C_{14}H_{25}NO$: 223.1937), 208 (8) ($C_{13}H_{22}NO$), 152 (32) ($C_9H_{14}NO$), 151 (100) ($C_{10}H_{15}O$), 110 (10) (C_8H_8NO), 96 (32) (C_5H_6NO), 81 (22) (C_5H_5O).

2*E*,4*E*-Decadienoic acid pyrrolidyl amide, 20 (ref. 3)

Ethyl 2*E*,4*E*-decadienoate was transformed directly in 85% yield to the pyrrolidyl amide alkaloid **20**, using the Roskamp procedure as described above (18). IR ($CHCl_3$): 3400, 2955, 2935, 2875, 1645, 1620, 1590, 1430, 1340, and 1000 cm^{-1}; ^1H NMR ($CDCl_3$, 200 MHz) δ: 0.89 (3H, t, J = 6.8 Hz), 1.30 (4H, m), 1.43 (2H, m), 1.87 (2H, t, J = 6.6 Hz), 1.96 (2H, t, J = 6.6 Hz), 2.15 (2H, q, J = 6.8 Hz), 3.52 (2H, t, J = 6.6 Hz), 3.54 (2H, t, J = 6.4 Hz), 6.09 (1H, dt, J = 9.6 and 15.0 Hz), 6.09 (1H, d, 15.0 Hz), 6.19 (1H, dd, J = 9.6 and 15.2 Hz), 7.27 (1H, dd, J = 9.8 and 15.0 Hz); HREIMS, *m/z* (relative intensity) (ion): 221.1782 (39) (M^+) (calcd. for $C_{14}H_{23}NO$: 221.1779), 192 (38) ($C_{12}H_{18}NO$), 178 (31) ($C_{11}H_{16}NO$), 164 (41) ($C_{10}H_{14}NO$), 150 (100) ($C_9H_{12}NO$), 137 (15) ($C_8H_{11}NO$), 113 (16) ($C_6H_{11}NO$), 98 (35) (C_5H_8NO), 95 (16) (C_6H_7O), 81 (49) (C_5H_5O), 70 (52) (C_4H_8N).

2*E*,4*E*-Decadienoic acid piperidyl amide, Achillea amide, 21 (ref. 20)

Ethyl 2*E*,4*E*-decadienoate was similarly transformed directly in 93% yield to the piperidyl amide alkaloid **20**, using the Roskamp procedure as described above (18). IR ($CHCl_3$): 3400, 2995, 2930, 2860, 1645, 1620, 1585, 1440, 1260, 1140, 1020, 1000, and 860 cm^{-1}; ^1H NMR ($CDCl_3$, 200 MHz) δ: 0.86 (3H, t, J = 6.6 Hz), 1.27 (4H, m), 1.39 (2H, m), 1.50–1.70 (6H, m), 2.12 (2H, dt, J = 6.4 and 7.4 Hz), 3.47 (2H, br s), 3.58 (2H, br s), 6.02 (1H, dt, J = 6.4 and 15.0 Hz), 6.16 (1H, dd, J = 10.0 and 15.2 Hz), 6.23 (1H, d, J = 15.0 Hz), 7.21 (1H, dd, J = 10.0 and 14.8 Hz); HREIMS, *m/z* (relative intensity) (ion): 235.1945 (18) (M^+) (calcd. for $C_{15}H_{25}NO$): 235.1936), 192 (21) ($C_{12}H_{18}NO$), 164 (75) ($C_{10}H_{14}NO$), 138 (27) ($C_8H_{12}NO$), 112 (12) ($C_6H_{10}NO$), 95 (15) (C_6H_7O), 84 (100) ($C_5H_{10}N$), 69 (23) (C_5H_9).

2*E*,4*E*-Hexadecadienoic acid isobutyl amide, 22

The synthesis of this alkaloid (from *Piper guineense*) (11) was accomplished in overall yield 39%, via a route analogous to that employed for synthesis of pellitorine (vide supra) but with bromotridecane used in lieu of iodoheptane for alkylation of propiolic acid.

2-Hexadecynoic acid: IR ($CHCl_3$): 3400–2400, 2930, 2225, 1700, 1460, and 1270 cm^{-1}; ^1H NMR ($CDCl_3$, 200 MHz) δ: 0.86 (3H, t, J = 6.4 Hz), 1.24 (20 H, br s), 150–1.60 (2H, m), 2.33 (2H, t, J = 7.0 Hz).

Ethyl 2-hexadecynoate: IR ($CHCl_3$): 2925, 2850, 2220, 1700, 1460, 1370, 1255, and 1080 cm^{-1}; ^1H NMR ($CDCl_3$, 200 MHz) δ: 0.86 (3H, t, J = 6.2 Hz), 1.23 (20 H, br s), 1.28 (3H, t, J = 7.2 Hz), 1.56 (2H, m), 2.30 (2H, t, J = 7.0 Hz), 4.19 (2H, q, J = 7.2 Hz).

Ethyl 2E,4E-hexadecadienoate: IR ($CHCl_3$): 2930, 2860, 1700, 1640, 1620, 1460, 1375, 1305, 1270, 1140, 1040, 1000, and 975 cm^{-1}; ^1H NMR ($CDCl_3$, 200 MHz) δ: 0.88 (3H, t, J = 6.4 Hz), 1.26 (18 H, br s), 1.29 (3H, t, J = 7.2 Hz), 2.20 (2H, m), 4.19 (2H, q, J = 7.0 Hz), 5.78 (1H, d, J = 15.4 Hz), 6.11–6.17 (2H, m), 7.27 (1H, m).

2E,4E-Hexadecadienoic acid: IR ($CHCl_3$): 3600–2400, 2935, 2860, 1690, 1640, 1620, 1460, 1440, 1420, 1380, 1260, 1110, and 1005 cm^{-1}; ^1H NMR ($CDCl_3$, 200 MHz) δ: 0.88 (3H, t, J = 6.4 Hz), 1.21 (2H, m), 1.26 (16H, br s), 2.17 (2H, m), 4.60 (1H, br s), 5.79 (1H, d, J = 15.4 Hz) 6.17–6.22 (2H, m), 7.25–7.30 (1H, m).

2E,4E-Hexadecadienoic acid isobutylamide, ***22***: mp 78.5–84°C; IR ($CHCl_3$): 3450, 2965, 2935, 2860, 1660, 1635, 1620, 1510, 1465, and 1000 cm^{-1}; ^1H NMR ($CDCl_3$, 200 MHz) δ: 0.86 (3H, t, J = 6.6 Hz), 0.90 (6H, d, J = 6.8 Hz), 1.24 (16 H, br s), 1.39 (2H, m), 1.78 (1H, sept, J = 6.8 Hz), 2.11 (2H, q, J = 6.8 Hz), 3.14 (2H, t, J = 6.6 Hz), 5.52 (1H, br s), 5.73 (1H, d, J = 14.8 Hz), 6.04 (1H, dt, J = 6.4 and 15.0 Hz), 6.11 (1H, dd, J = 9.9 and 15.4 Hz), 7.17 (1H, dd, J = 9.9 and 15.0 Hz); HREIMS, *m/z* (relative intensity) (ion): 307.2875 (16) (M^+) (calcd. for $C_{20}H_{37}NO$: 307.2875), 235 (35) ($C_{16}H_{27}O$), 223 (32) ($C_{14}H_{25}NO$), 152 (43) ($C_9H_{14}NO$), 151 (100) ($C_{10}H_{15}O$), 110 (13) ($C_6H_{18}NO$), 96 (46) (C_5H_6NO), 81 (42) (C_5H_5O), 67 (22) (C_5H_7), 57 (19) (C_4H_9).

2*E*,4*E*-Octadecadienoic acid isobutyl amide, 23

The synthesis of this alkaloid (from *Piper guineense*) (11) was accomplished in overall yield 50%, via a route analogous to the above but with bromopentadecane used for alkylation of propiolic acid.

2-Octadecynoic acid: IR ($CHCl_3$): 3600–2400, 2925, 2860, 2225, 1700, 1460, and 1260 cm^{-1}; ^1H NMR ($CDCl_3$, 200 MHz) δ: 0.86 (3H, t, J = 6.4 Hz), 1.24 (24 H, br s), 1.55 (2H, m), 2.33 (2H, t, J = 7.0 Hz).

Ethyl 2-octadecynoate: IR ($CHCl_3$): 2930, 2860, 2225, 1700, 1465, 1375, 1260, and 1080 cm^{-1}; ^1H NMR ($CDCl_3$, 200 MHz) δ: 0.85 (3H, t, J = 6.2 Hz), 1.23 (24 H, br s), 1.28 (3H, t, J = 7.2 Hz), 1.45–1.60 (2H, m), 2.30 (2H, t, J = 7.0 Hz), 4.19 (2H, q, J = 7.2 Hz).

Ethyl 2E,4E-octadecadienoate: IR ($CHCl_3$): 2930, 2855, 1700, 1640, 1620, 1460, 1375, 1305, 1140, 1035, 1000, 910, and 875 cm^{-1}; ^1H NMR ($CDCl_3$, 200 MHz) δ: 0.80 (3H, t, J = 6.2 Hz), 1.18 (18 H, br s), 1.21 (3H, t, J = 7.2 Hz), 1.30–1.40 (2H, m), 2.05–2.15 (2H, m) 4.12 (2H, q, J = 7.2 Hz), 5.70 (1H, d, J = 15.6 Hz), 5.95–6.20 (2H, m), 7.10–7.30 (1H, m).

2E,4E-Hexadecadienoic acid: mp 59–61°C; IR ($CHCl_3$): 3400–2400, 2925, 2860, 1685, 1640, 1620, 1460, 1420, 1305, 1270, 1150, and 1005 cm^{-1}; ^1H NMR ($CDCl_3$, 200 MHz) δ: 0.88 (3H, t, J = 6.4 Hz), 1.26 (20H, br s), 1.38 (2H, m), 2.18 (2H, m), 5.78 (1H, d, J = 15.6 Hz), 6.10–6.30 (2H, m), 7.31 (1H, br dd, J = 10.0 and 14.8 Hz), 9.00 (1H, br s).

2E,4E-Octadecadienoic acid isobutylamide, ***23***: mp 92–94°C; IR ($CHCl_3$): 3450, 2960, 2930, 2860, 1660, 1635, 1615, 1510, 1465, and 1000 cm^{-1}; ^1H NMR ($CDCl_3$, 200 MHz) δ: 0.86 (3H, t, J = 6.6 Hz), 0.90 (6H, d, J = 6.6 Hz), 1.23 (20 H, br s), 1.30–1.40 (2H, m) 1.80 (1H, m), 2.12 (2H, q, J = 6.2 Hz), 3.14 (2H, t, J = 6.2 Hz), 5.44 (1H, m), 5.72 (1H, d, J = 15.0 Hz), 6.00–6.20 (2H, m), 7.28 (1H, ddd, J = 1.8, 9.2, and 15.0 Hz); HREIMS, *m/z* (relative intensity) (ion): 335.3181 (38) (M^+) (calcd. for $C_{22}H_{41}NO$: 335.3187), 263 (75) ($C_{18}H_{31}O$), 152 (50) ($C_9H_{14}NO$), 131 (100) (C_9H_7O), 119 (24) (C_8H_7O), 96 (31) (C_5H_6NO), 91 (41) (C_7H_7), 84 (28) (C_5H_8O), 81 (33) (C_5H_5O), 77 (30) (C_6H_5).

2*E*,4*E*-Eicosadienoic acid pyrrolidyl amide, 24

The synthesis of this alkaloid (from *Piper trichostachyon*) (21) was accomplished via a route analogous to the above but with bromoheptadecane used for alkylation of propiolic acid.

2-Eicosynoic acid: IR ($CHCl_3$): 3500–2400, 2925, 2855, 2225, 1700, 1460, and 1260 cm^{-1}; ^1H NMR ($CDCl_3$, 200 MHz) δ: 0.86 (3H, t, J = 6.5 Hz), 1.24 (26 H, br s), 1.37 (2H, m) 2.33 (2H, t, J = 7.2 Hz).

Ethyl 2-eicosynoate: IR ($CHCl_3$): 2925, 2855, 2225, 1700, 1600, 1465, 1375, 1260, and 1080 cm^{-1}; ^1H NMR ($CDCl_3$, 200 MHz) δ: 0.86 (3H, t, J = 6.4 Hz), 1.23 (28 H, br s), 1.28 (3H, t, J = 7.2 Hz), 1.56 (2H, m), 2.30 (2H, t, J = 7.0 Hz), 4.19 (2H, q, J = 7.2 Hz).

Ethyl 2E, 4E-eicosadienoate: IR ($CHCl_3$): 2930, 2860, 1700, 1640, 1620, 1460, 1375, 1305, 1260, 1145, 1005, and 915 cm^{-1}; ^1H NMR ($CDCl_3$, 200 MHz) δ: 0.87 (3H, t, J = 6.4 Hz), 1.25 (24H, br s), 1.36 (2H, m), 2.15 (2H, q, J = 5.8 Hz), 4.19 (2H, q, J = 7.2 Hz), 5.77 (1H, d, J = 15.2 Hz), 6.15–6.20 (2H, m), 7.25 (1H, dd, J = 9.4 and 15.2 Hz).

2E,4E-Eicosadienoic acid pyrrolidylamide, ***24***: mp 78–79°C (lit. (21) mp 65–67°C); IR ($CHCl_3$): 3400, 2930, 2860, 1650, 1620, 1590, 1430, 1345, 1005, 915, and 870 cm^{-1}; ^1H NMR ($CDCl_3$, 200 MHz) δ: 0.85 (3H, t, J = 6.4 Hz), 1.23 (24 H, br s), 1.36 (2H, m), 1.80–2.00 (4H, m), 2.12 (2H, q, J = 6.6 Hz), 3.50 (4H, q, J = 5.4 Hz), 6.00–6.25 (3H, m), 7.25 (1H, dd, J = 10.2 and 14.8 Hz); HREIMS, *m/z* (relative intensity (ion): 361.3326 (37) (M^+) (calcd. for $(C_{24}H_{43}NO)$: 361.3345), 318 (67) ($C_{22}H_{24}NO$), 186 (30) ($C_{13}H_{14}O$), 173 (30) ($C_{12}H_{13}O$), 159 (25) ($C_{11}H_{11}O$), 150 (63) ($C_9H_{12}NO$), 131 (100) (C_9H_7O), 121 (56) (C_8H_9O), 98 (14) (C_5H_8O), 91 (51) (C_7H_7), 84 (28) (C_5H_8O), 77 (23) (C_6H_5), 55 (32) (C_4H_7).

References

1. M. Miyakado and H. Yoshioka. Agric. Biol. Chem. **43**, 2413 (1979).
2. M. Miyakado, I. Nakayama and N. Ohno. *In* Insecticides of plant origin. *Edited by* J.T. Arnason, B.J.R. Philogene, and P. Morand. ACS Symp. Ser. **387**. Am. Chem. Soc. Washington, D.C. 1989.
3. F. Kiuchi, N. Nakamura, Y. Tsuda, K. Kondo, and H. Yoshimura. Chem. Pharm. Bull. **36**, 2452 (1988).
4. K. Likhitwitayawuid, N. Ruangrungsi, G.L. Lange, and C.P. Decicco. Tetrahedron, **43**, 3689 (1987).
5. J.F. Li, X.L. Huang, and C.Q. Ye. Yao Hsueh T'ung Pao, **16**, 12 (1981).
6. G.M. Strunz and H. Finlay. Tetrahedron, **50**, 11113 (1994).
7. G.M. Strunz and H. Finlay. Phytochemistry, **39**, 731 (1995).
8. S. Nagumo, A. Matsukuma, H. Suemune, and K. Sakai. Tetrahedron, **49**, 10501 (1993).
9. A. Banerji, D. Bandyopadhyay, M. Sarkar, A.K. Siddhanta, S.C. Pal, S. Ghosh, K. Abraham, and J.N. Shoolery. Phytochemistry, **24**, 279 (1985).
10. N. Shoji, A. Umeyama, N. Saito, T. Takemoto, A. Kajiwara, and Y. Ohizumi. J. Pharm. Sci. **75**, 12 (1986).
11. J.I. Okogun and D.E.U. Ekong. J. Chem. Soc. (C), 2195 (1974).
12. R. Grewe, W. Freist, H. Neumann, and S. Kersten, Chem. Ber. **103**, 3752 (1970).
13. N. Viswanathan, V. Balakrishnan, B.S. Joshi, and W. von Philipsborn. Helv. Chim Acta, **58**, 2026 (1975).
14. D. Ma and X. Lu Tetrahedron, **46**, 3189 (1990).
15. B.M. Trost and U. Kazmaier. J. Am. Chem. Soc. **114**, 7933 (1992).
16. T. Mukaiyama, K. Banno, and K. Narasaka. J. Am. Chem. Soc. **96**, 7503 (1974).

17. L.F. Fieser and M. Fieser. Topics in organic chemistry. Reinhold Publishing Corp., New York. 1963. p. 458.
18. W.B. Wang and E.J. Roskamp. J. Org. Chem. **57**, 6101 (1992); W.B. Wang, J.A. Restituyo, and E.J. Roskamp. Tetrahedron Lett. **34**, 7217 (1993).
19. R.A. Raphael and F. Sondheimer. J. Chem. Soc. 115 (1950).
20. F. Bohlmann and C. Zedro. Chem. Ber. **106**, 1328 (1973).
21. J. Singh, K.L. Dhar, and C.K. Atal. Tetrahedron Lett. 2119 (1971).
22. A.J. Mancuso and D. Swern. Synthesis, 165 (1981).
23. B.S. Bronk, S.J. Lippard, and R.L. Danheiser. Organometallics, **12**, 3189 (1993).
24. A.G. Fallis, J.F. Kingston, and J. Hellou. Synthesis, 1014 (1984).

2,3-Pyrazinedicarboxylates of cobalt(II), nickel(II), and copper(II); magnetic properties and crystal structures

Long Mao, Steven J. Rettig, Robert C. Thompson, James Trotter, and Shihua Xia

Abstract: Complexes of singly and doubly deprotonated 2,3-pyrazinedicarboxylic acid ($pyzdcH_2$) have been prepared and studied. Crystal data: $[Ni(pyzdcH)_2(H_2O)_2]$, **1**, monoclinic, $P2_1/n$, $a = 9.2897(8)$ Å, $b = 7.6931(8)$ Å, $c = 10.1044(9)$ Å, $\beta = 93.378(7)°$, $Z = 2$; $[Cu(pyzdcH)_2]_x \cdot 2xH_2O$, **2**, monoclinic, $P2_1/n$, $a = 6.598(1)$ Å, $b = 14.198(2)$ Å, $c = 8.586(2)$ Å, $\beta = 97.65(2)°$, $Z = 2$;. $[Co(pyzdc)(H_2O)_2]_x \cdot 2xH_2O$, **3**, monoclinic, $C2/c$, $a = 12.5777(9)$ Å, $b = 7.5191(9)$ Å, $c = 11.839(1)$ Å, $\beta = 110.754(4)°$, $Z = 4$; $[Ni(pyzdc)(H_2O)_2]_x \cdot 2xH_2O$, **4**, monoclinic, $C2/c$, $a = 12.4772(7)$ Å, $b = 7.452(1)$ Å, $c = 11.9166(5)$ Å, $\beta = 112.302(2)°$, $Z = 4$; $[Cu(pyzdc)(H_2O)_2]_x \cdot 2xH_2O$, **5**, monoclinic, $C2/c$, $a = 12.784(2)$ Å, $b = 7.527(2)$ Å, $c = 12.323(2)$ Å, $\beta = 116.150(2)°$, $Z = 4$. The structures were solved by Patterson (**1**), direct (**2**, **3**), or isomorphous replacement methods (**4** and **5** are isomorphous with **3**) and were refined by full-matrix least-squares procedures to $R = 0.028$, 0.030, 0.029, 0.030, and 0.030 ($R_w = 0.026$, 0.029, 0.027, 0.025, and 0.027) for 1894, 1694, 2476, 1867, and 1412 reflections with $I \geq 3\sigma(F^2)$, respectively. The structure of **1** consists of monometallic $[Ni(pyzdcH)_2(H_2O)_2]$ units linked by hydrogen-bonding interactions in a three-dimensional network. In **2** extended chains of copper ions are linked by double-bridging $pyzdcH^-$ groups while **3**, **4**, and **5** have structures in which $pyzdc^{2-}$ ligands bridge metal centers to form extended linear chains. Magnetic susceptibility studies reveal antiferromagnetic interactions in **1**, **2**, **3**, **4**, and **6** (**6** is Cu(pyzdc)). The magnitude of exchange ($-zJ = 0.033$ cm^{-1} for **1** and $-J = 0.11$, 0.74, 0.049, and 1.14 cm^{-1} for **2**, **3**, **4**, and **6**, respectively) is discussed in terms of the structures and d-electron configurations involved.

Key words: metal 2,3-pyrazinedicarboxylates, synthesis, X-ray structure, antiferromagnetism.

Résumé : On a préparé et étudié des complexes déprotonés et di-déprotonés de l'acide pyrazine-2,3-dicarboxylique ($pyzdcH_2$). Données cristallines : $[Ni(pyzdcH)_2(H_2O)_2$, **1**, monoclinique, $P2_1/n$, $a = 9,2897(8)$, $b = 7,6931(8)$ et $c = 10,1044(9)$ Å, $\beta = 93,378(7)°$, $Z = 2$; $[Cu(pyzdcH)_2]_x \cdot 2xH_2O$, **2**, monoclinique, $P2_1/n$, $a = 6,598(1)$, $b = 14,198(2)$ et $c = 8,586(2)$ Å, $\beta = 97,65(2)°$, $Z = 2$; $[Co(pyzdc)(H_2O)_2]_x \cdot 2xH_2O$, **3**, monoclinique, $C2/c$, $a = 12,5777(9)$, $b = 7,5191(9)$ et $c = 11,839(1)$ Å, $\beta = 110,754(4)°$, $Z = 4$; $[Ni(pyzdc)(H_2O)_2]_x \cdot 2xH_2O$, **4**, monoclinique, $C2/c$, $a = 12,4772(7)$, b, $= 7, 452(1)$ et $c = 11,9166(5)$ Å, $\beta = 112,302(2)°$, $Z = 4$; $[Cu(pyzdc)(H_2O)_2]_x \cdot 2xH_2O$, **5**, monoclinique, $C2/c$, $a = 12,784(2)$, $b = 7,527(2)$ et $c = 12,323(2)$ Å, $\beta = 116,150(2)°$, $Z = 4$. On a résolu les structures par les méthodes de Patterson (**1**), directe (**2**, **3**) et de remplacement isomorphe (**4** et **5** sont isomorphes par rapport à **3**) et on les a affinées par les méthodes des moindres carrés, matrice complète, jusqu'à des valeurs de $R = 0,028$, 0,030, 0,029, 0,030 et 0,030 ($R_w = 0,026$, 0,029, 0,027, 0,025 et 0,027) pour respectivement 1894, 1694, 2476, 1867 et 1412 réflexions avec $I \geq 3\sigma(F^2)$. La structure du composé **1** consiste d'unités monométalliques $[Ni(pyzdcH)_2(H_2O)_2]$ reliées par des interactions de liaisons hydrogènes dans un arrangement tridimensionnel. Dans le composé **2**, des chaînes allongées d'ions de cuivre sont reliées par des groupes $pyzdcH^-$ qui créent des doubles ponts alors que les composés **3**, **4** et **5** comportent des structures dans lesquelles des coordinats $pyzdc^{2-}$ servent de ponts entre des centres métalliques pour former de longues chaînes linéaires. Des études de susceptibilité magnétique révèlent l'existence d'interactions antiferromagnétiques dans les composés **1**, **2**, **3**, **4** et **6** (dans le **6** il s'agit du Cu(pyzdc)). On discute de l'amplitude de l'échange ($-J = 0,033$ cm^{-1} pour **1** et $-zJ = 0,11$, 0,74, 0,049 et 1,14 cm^{-1} pour respectivement les composés **2**, **3**, **4** et **6**) en termes des structures et des configurations des électrons d'impliquées.

Mots clés : pyrazine-2,3-dicarboxylates métalliques, synthèse, structure par diffraction des rayons X, antiferromagnétisme.

[Traduit par la rédaction]

Introduction

2,3-Pyrazinedicarboxylic acid ($pyzdcH_2$) has six donor atoms for coordination and, deprotonated, readily forms metal complexes (1–11). Our interest in these compounds stems from the variety of ways the $pyzdc^{2-}$ and $pyzdcH^-$ ligands can potentially bridge metal centers forming polymetallic compounds. The compound $Co(pyzdc) \cdot 2H_2O$, for example, has an extended chain structure in which the metals are bridged by 1,4-diazine links that are supported by chelate formation involving carboxylate substituents adjacent to the ring nitrogens (8). Numerous studies on complexes of pyrazine itself (12) have shown that, in many instances, the unsupported 1,4-

Received October 13, 1995.

L. Mao, S.J. Rettig, R.C. Thompson,[1] J. Trotter, and S. Xia. Department of Chemistry, University of British Columbia, 2036 Main Mall, Vancouver, BC V6T 1Z1, Canada.

[1] Author to whom correspondence may be addressed. Telephone: (604) 822-4979. Fax: (604) 822-2847. E-mail: robert.c.thompson@mtsg.ubc.ca

diazine link provides a relatively efficient pathway for magnetic exchange; comparisons of the magnetic properties of compounds such as $Co(pyzdc)\cdot 2H_2O$ with those of related pyrazine systems should permit an evaluation of the effects of the chelate support on the mediation of exchange.

Previous studies involving divalent Mn, Fe, Co, Ni, Cu, and Zn, and which focussed mainly on the synthesis of complexes and on their characterization by spectroscopic and thermochemical methods (1–7), identified so-called 2:1 and 1:1 complexes of composition $M(pyzdcH)_2\cdot xH_2O$ and $M(pyzdc)\cdot xH_2O$. Only limited crystallographic information is reported on these systems. X-ray studies have shown $Co(pyzdc)\cdot 2H_2O$ and $Zn(pyzdc)\cdot 3H_2O$ to have polymetallic chain structures (8, 9) and $Co(pyzdcH)_2\cdot 2H_2O$ to be monometallic (10). Magnetic susceptibility studies on this group of compounds have involved some room temperature measurements on the 1:1 complexes (5), variable temperature measurements in the high temperature range (300–80 K) on Cu(pyzdc), $Co(pyzdcH)_2\cdot 2H_2O$, and $Ni(pyzdcH)_2\cdot 2H_2O$ (2), and measurements to low temperatures on $Co(pyzdcH)_2\cdot 2H_2O$ (10) and $Cu(pyzdcH)_2\cdot 3H_2O$ (11).

In view of the limited studies available we decided to systematically investigate these systems with emphasis on X-ray determined structures and magnetic measurements to cryogenic temperatures. This paper describes work on the 2:1 complexes $[Ni(pyzdcH)_2(H_2O)_2]$ (**1**) (the cobalt analogue has been structurally and magnetically well characterized (10)) and $[Cu(pyzdcH)_2]_x\cdot 2xH_2O$ (**2**) and the 1:1 complexes $[M(pyzdc)(H_2O)_2]_x\cdot 2xH_2O$ (where M = Co, Ni, and Cu; compounds **3**, **4**, and **5**, respectively) and Cu(pyzdc), **6**. We report the crystal structures of **1** through **5** as well as magnetic susceptibility measurements to 4 K on all compounds except **5**.

Experimental

Syntheses

All chemicals were at least reagent grade quality and were used without further purification. All products, with the exception of **5**, are air stable.

*Diaquabis(hydrogen-2,3-pyrazinedicarboxylato(1⁻))-nickel(II), $[Ni(pyzdcH)_2(H_2O)_2]$, **1***

2,3-Pyrazinedicarboxylic acid (0.42 g, 2.5 mmol) was dissolved in 60 mL water and slowly added to a 60 mL aqueous solution of $Ni(NO_3)_2\cdot 6H_2O$ (0.36 g, 1.25 mmol). After standing for 2–3 weeks, the solution yielded green crystals. After selecting suitable crystals for X-ray analysis, the rest of the product was collected by filtration, washed with water, and dried in vacuo at room temperature for 24 h. Anal. calcd. for $C_{12}H_{10}N_4NiO_{10}$: C 33.60, H 2.35, N 13.06; found: C 33.86, H 2.46, N 13.02.

*Poly-bis-μ-(hydrogen-2,3-pyrazinedicarboxylato(1⁻))-copper(II) dihydrate, $[Cu(pyzdcH)_2]_x\cdot 2xH_2O$, **2***

Prepared as above employing 1.25 mmol of copper(II) acetate monohydrate in 60 mL water and 2.5 mmol $pyzdcH_2$ in 100 mL water. On standing overnight the solution produced a precipitate as a blue powder. This was collected by filtration, washed with water, and dried in vacuo at room temperature for 24 h. Analytical data showed this material to be a hemihydrate. The dihydrate, **2**, was obtained as crystalline material suitable for X-ray analysis by recrystallization from water followed by drying in air. The crystals are air stable and samples were ground to a powder for elemental analysis and subsequent studies. Anal. calcd. for $C_{12}H_{10}CuN_4O_{10}$: C 33.22, H 2.32, N 12.92; found: C 33.17, H 2.33, N 12.94.

*Poly-diaqua-μ-2,3-pyrazinedicarboxylatocobalt(II) dihydrate, $[Co(pyzdc)(H_2O)_2]_x\cdot 2xH_2O$, **3***

2,3-Pyrazinedicarboxylic acid (0.42 g, 2.5 mmol) was dissolved in 100 mL water and the solution was adjusted to pH 5 with 1.0 M aqueous NaOH. This solution was added slowly to a 60 mL aqueous solution of $Co(NO_3)_2\cdot 6H_2O$ (0.76 g, 2.5 mmol). Orange crystals deposited after the solution was left standing for about 2 d. Crystals suitable for X-ray diffraction studies were selected, then the remainder were separated by filtration, washed with water, and dried in vacuo at room temperature for 24 h. Anal. calcd. for $C_6H_{10}CoN_2O_8$: C 24.26, H 3.39, N 9.43; found: C 24.21, H 3.39, N 9.31.

*Poly-diaqua-μ-2,3-pyrazinedicarboxylatonickel(II) dihydrate, $[Ni(pyzdc)(H_2O)_2]_x\cdot 2xH_2O$, **4***

Prepared from $Ni(NO_3)_2\cdot 6H_2O$ by the procedure described above for **3**. In this case, however, it took several months before green crystals appeared. Anal. calcd. for $C_6H_{10}N_2NiO_8$: C 24.28, H 3.39, N 9.44; found: C 24.02, H 3.35, N 9.32.

*Poly-diaqua-μ-2,3-pyrazinedicarboxylatocopper(II) dihydrate, $[Cu(pyzdc)(H_2O)_2]_x\cdot 2xH_2O$, **5***

Crystals of **5** were obtained from $Cu(NO_3)_2\cdot 3H_2O$ by the procedure used to obtain crystalline **3**. Green crystals appeared in the solution after 2 d. X-ray analysis of a freshly isolated crystal, mounted wet in a capillary and then sealed, showed it to be **5**. The crystals of **5**, however, rapidly decompose in air with loss of water from the lattice, making it impossible to obtain microanalytical data or to carry out subsequent studies on the compound.

*2,3-Pyrazinedicarboxylatocopper(II), Cu(pyzdc), **6***

Crystals of **5** were removed by filtration from the solution described above, washed with water, and dried in vacuo at room temperature for 24 h. Anal. calcd. for $C_6H_2CuN_2O_4$: C 31.38, H 0.88, N 12.20; found: C 31.57, H 1.02, N 11.90.

X-ray crystallographic analyses of 1–5

Crystallographic data appear in Table 1. The final unit-cell parameters were obtained by least squares on the setting angles for 25 reflections with 2θ = 24.6°–45.9° for **1**, 29.9°–38.8° for **2**, 50.0°–66.0° for **3**, 26.0°–39.6° for **4**, and 33.2°–42.5° for **5**. The intensities of three standard reflections, measured every 200 reflections throughout the data collections, showed only small random fluctuations. The data were processed,[2] corrected for Lorentz and polarization effects, and for absorption (based on azimuthal scans for three reflections).

The structures were solved by Patterson (**1**) or direct (**2**, **3**) methods. The structure analysis of **3** was initiated in the centrosymmetric space group *C*2/*c* on the basis of the *E*-statistics, this choice being confirmed by the subsequent successful solution and refinement of the structure. Compounds **4** and **5**

[2] *teXsan*: Crystal structure analysis package. Molecular Structure Corporation, The Woodlands, Texas, U.S.A. (1985 and 1992).

Table 1. Crystallographic data.[a]

Compound	1	2	3	4	5
Formula	$C_{12}H_{10}N_4NiO_{10}$	$C_{12}H_{10}CuN_4O_{10}$	$C_6H_{10}CoN_2O_8$	$C_6H_{10}N_2NiO_8$	$C_6H_{10}CuN_2O_8$
fw	428.93	433.78	297.09	296.85	301.70
Crystal system	Monoclinic	Monoclinic	Monoclinic	Monoclinic	Monoclinic
Space group	$P2_1/n$	$P2_1/n$	$C2/c$	$C2/c$	$C2/c$
a, Å	9.2897(8)	6.598(1)	12.5777(9)	12.4772(7)	12.784(2)
b, Å	7.6931(8)	14.198(2)	7.5191(9)	7.452(1)	7.527(2)
c, Å	10.1044(9)	8.586(2)	11.839(1)	11.9166(5)	12.323(2)
β, °	93.378(5)	97.65(2)	110.754(4)	112.302(2)	116.150(7)
V, Å^3	720.9(1)	797.2(2)	1047.0(2)	1025.2(1)	1064.3(3)
Z	2	2	4	4	4
ρ_{calc}, g/cm^3	1.976	1.807	1.885	1.923	1.883
$F(000)$	436	438	604	608	612
μ(Mo K_α), cm^{-1}	14.20	14.37	16.75	19.29	20.88
Crystal size, mm	0.08 × 0.20 × 0.25	0.12 × 0.15 × 0.30	0.20 × 0.25 × 0.30	0.08 × 0.10 × 0.35	0.06 × 0.15 × 0.35
Transmission factors	0.88–1.00	0.89–1.00	0.87–1.00	0.98–1.00	0.76–1.00
Scan type	ω–2θ	ω–2θ	ω–2θ	ω–2θ	ω–2θ
Scan range, deg in ω	1.37 + 0.35 tan θ	1.25 + 0.35 tan θ	1.37 + 0.35 tan θ	1.47 + 0.35 tan θ	1.26 + 0.35 tan θ
Scan speed, deg/min	16 (up to 9 scans)	16 (up to 9 scans)	32 (up to 9 scans)	16 (up to 9 scans)	32 (up to 9 scans)
Data collected	$+h$, $+k$, $\pm l$	$+h$, $+k$, $\pm l$	$+h$, $+k$, $\pm l$	$+h$, $+k$, $\pm l$	$+h$, $+k$, $\pm l$
$2\theta_{max}$, deg	70	65	100	90	75
Crystal decay, %	Negligible	Negligible	Negligible	Negligible	Negligible
Total reflections	3514	3198	5887	4050	3067
Total unique reflections	3355	2987	5729	3921	2966
R_{merge}	0.021	0.023	0.024	0.032	0.032
Reflections with $I \geq 3\sigma(F^2)$	1894	1694	2476	1867	1412
No. of variables	144	144	100	99	99
R	0.028	0.030	0.029	0.030	0.030
R_w	0.026	0.029	0.027	0.025	0.027
gof	1.44	1.95	1.70	1.44	1.56
Max Δ/σ (final cycle)	0.0002	0.0003	0.0002	0.0001	0.00009
Residual density e/Å^3	−0.25 to 0.32	−0.30 to 0.31	−0.40 to 0.60	−0.18 to 0.16	−0.41 to 0.41

[a]Temperature 294 K, Rigaku AFC6S diffractometer, Mo K_α radiation (λ = 0.71069 Å), graphite monochromator, takeoff angle 6.0°, aperture 6.0 × 6.0 mm at a distance of 285 mm from the crystal, stationary background counts (scan/background time ratio 2:1), $\sigma^2(F^2) = [S^2(C + 4B)]/Lp^2$ (S = scan speed, C = scan count, B = normalized background count), function minimized $\Sigma w(|F_o| - |F_c|)^2$ where $w = 4F_o^2/\sigma^2(F_o^2)$, $R = \Sigma||F_o| - |F_c||/\Sigma|F_o|$, $R_w = (\Sigma w(|F_o| - |F_c|)^2/\Sigma w|F_o|^2)^{1/2}$, and gof = $[\Sigma w(|F_o| - |F_c|)^2/(m - n)]^{1/2}$. Values given for R, R_w, and gof are based on those reflections with $I \geq 3\sigma(F^2)$.

are isomorphous with **3**. Compounds **3** and **4** are also isostructural, but because of the longer M–OH_2 distances in **5** the hydrogen-bonding in this complex differs from that in **3** and **4** (see below). In all five complexes the asymmetric unit contains half the formula unit, the metal atoms all lying on crystallographic inversion centres. Non-hydrogen atoms were refined with anisotropic thermal parameters and hydrogen atoms were refined with isotropic thermal parameters. A correction for secondary extinction was applied for **3**, the final value of the extinction coefficient being 1.13(3) × 10^{-6} (Zachariasen isotropic type 2). Neutral atom scattering factors for all atoms (13) and anomalous dispersion corrections for the non-hydrogen atoms (14) were taken from the *International tables for X-ray crystallography*. Final atomic coordinates and equivalent isotropic thermal parameters, bond lengths, bond angles, and hydrogen-bonding parameters appear in Tables 2–7. Hydrogen atom parameters, anisotropic thermal parameters, and torsion angles have been deposited as supplementary material.[3]

Physical measurements

Thermal Gravimetric Analysis (TGA) was performed on powdered samples using a TA Instruments TGA 51 thermogravimetric analyzer. Samples of 5–20 mg were heated at 10°C/min in an atmosphere of dry nitrogen at a flow rate of 100 mL

[3] Supplementary material mentioned in the text may be purchased from: The Depository of Unpublished Data, Document Delivery, CISTI, National Research Council Canada, Ottawa, Canada K1A 0S2. Tables of bond lengths and angles involving hydrogen atoms have also been deposited with the Cambridge Crystallographic Data Centre and can be obtained on request from The Director, Cambridge Crystallographic Data Centre, University Chemical Laboratory, 12 Union Road, Cambridge CB2 1EZ, U.K.

Table 2. Final atomic coordinates (fractional) and B_{eq} (Å^2).[a]

Atom	x	y	z	B_{eq}
1				
Ni(1)	0	1/2	1/2	1.66(1)
O(1)	0.13299(12)	0.67358(15)	0.41978(11)	2.06(4)
O(2)	0.34160(13)	0.7100(2)	0.33080(12)	2.53(5)
O(3)	0.64197(13)	0.2875(2)	0.31109(13)	2.96(5)
O(4)	0.55101(15)	0.5469(2)	0.27554(15)	3.39(6)
O(5)	0.08303(15)	0.5584(2)	0.69165(13)	2.37(5)
N(1)	0.17340(14)	0.3441(2)	0.46838(12)	1.72(5)
N(2)	0.4159(2)	0.1584(2)	0.41396(14)	2.38(6)
C(1)	0.2834(2)	0.4242(2)	0.41030(15)	1.59(5)
C(2)	0.4063(2)	0.3282(2)	0.3827(2)	1.77(5)
C(3)	0.3065(2)	0.0838(2)	0.4710(2)	2.47(7)
C(4)	0.1838(2)	0.1764(2)	0.4978(2)	2.12(6)
C(5)	0.2509(2)	0.6168(2)	0.3850(2)	1.75(6)
C(6)	0.5428(2)	0.3900(2)	0.3189(2)	2.16(6)
H(1)	0.457(3)	0.632(4)	0.297(3)	8.0(8)
H(2)	0.155(2)	0.599(3)	0.695(2)	3.5(5)
H(3)	0.089(2)	0.478(3)	0.736(2)	2.8(5)
H(4)	0.317(2)	−0.028(3)	0.496(2)	3.9(5)
H(5)	0.110(2)	0.122(2)	0.544(2)	2.5(4)
2				
Cu(1)	1/2	1/2	1/2	2.29(1)
O(1)	0.3257(2)	0.61064(10)	0.4632(2)	2.58(6)
O(2)	0.0332(3)	0.65714(11)	0.3251(2)	4.22(8)
O(3)	−0.2393(3)	0.56273(12)	0.0387(2)	3.58(8)
O(4)	−0.3718(2)	0.54346(13)	0.2606(2)	3.72(8)
O(5)	−0.5243(3)	0.67833(14)	−0.0342(2)	3.76(9)
N(1)	0.2678(2)	0.43498(12)	0.3705(2)	2.05(6)
N(2)	−0.0879(3)	0.37517(12)	0.1931(2)	2.58(7)
C(1)	0.1181(3)	0.4967(2)	0.3213(2)	1.94(6)
C(2)	−0.0598(3)	0.46575(14)	0.2324(2)	2.01(7)
C(3)	0.0627(4)	0.3156(2)	0.2422(3)	2.9(1)
C(4)	0.2420(3)	0.3448(2)	0.3317(3)	2.48(8)
C(5)	0.1609(3)	0.59702(14)	0.3722(2)	2.33(8)
C(6)	−0.2395(3)	0.53027(15)	0.1803(2)	2.23(8)
H(1)	−0.354(6)	0.612(3)	0.024(5)	1.2(1)
H(2)	0.029(3)	0.251(2)	0.213(2)	2.5(5)
H(3)	0.347(3)	0.305(2)	0.362(2)	2.8(5)
H(4)	−0.504(4)	0.716(2)	−0.073(3)	2.7(7)
H(5)	−0.646(5)	0.659(2)	−0.092(4)	7.0(9)
3				
Co(1)	1/4	1/4	1/2	1.552(6)
O(1)	0.18125(7)	0.50126(12)	0.47054(7)	2.12(3)
O(2)	0.01962(8)	0.64578(12)	0.37735(9)	2.82(3)
O(3)	0.17910(9)	0.1999(2)	0.63240(10)	2.96(4)
O(4)	0.31745(12)	0.2719(2)	0.85753(10)	3.79(5)
N(1)	0.09008(8)	0.20265(13)	0.35791(8)	1.64(3)
C(1)	0.04235(8)	0.35667(14)	0.30733(9)	1.43(3)
C(2)	0.04758(10)	0.0506(2)	0.30276(11)	2.14(4)
C(3)	0.08304(9)	0.51754(15)	0.38909(9)	1.62(3)
H(1)	0.221(2)	0.230(2)	0.703(2)	5.5(6)
H(2)	0.119(2)	0.258(2)	0.621(2)	4.5(5)
H(3)	0.323(2)	0.196(3)	0.912(2)	5.7(5)
H(4)	0.305(2)	0.364(3)	0.885(2)	7.3(7)
H(5)	0.0812(11)	−0.055(2)	0.3381(12)	1.8(3)

Table 2 (*concluded*).

Atom	x	y	z	B_{eq}
4				
Ni(1)	1/4	1/4	1/2	1.327(7)
O(1)	0.18318(9)	0.50200(15)	0.47798(9)	1.79(3)
O(2)	0.02069(10)	0.6517(2)	0.37769(11)	2.46(4)
O(3)	0.17853(11)	0.1888(2)	0.62830(12)	2.28(4)
O(4)	0.3181(2)	0.2772(2)	0.85330(13)	3.36(6)
N(1)	0.09269(10)	0.2052(2)	0.35823(10)	1.40(3)
C(1)	0.04358(11)	0.3612(2)	0.30793(12)	1.30(4)
C(2)	0.04953(13)	0.0510(2)	0.30346(14)	1.78(4)
C(3)	0.08466(12)	0.5219(2)	0.39210(12)	1.47(4)
H(1)	0.221(2)	0.222(3)	0.694(2)	3.9(6)
H(2)	0.118(2)	0.238(3)	0.613(2)	3.6(5)
H(3)	0.331(2)	0.200(4)	0.910(2)	5.4(7)
H(4)	0.314(3)	0.371(4)	0.872(2)	6.4(8)
H(5)	0.0868(14)	−0.058(2)	0.3402(15)	1.7(3)
5				
Cu(1)	1/4	1/4	1/2	1.91(1)
O(1)	0.19653(12)	0.4945(2)	0.48083(12)	2.21(5)
O(2)	0.04042(13)	0.6597(2)	0.37861(15)	2.97(6)
O(3)	0.1684(2)	0.1820(3)	0.6437(2)	3.32(7)
O(4)	0.3376(2)	0.2972(3)	0.8605(2)	4.18(9)
N(1)	0.09685(13)	0.2117(2)	0.35680(13)	1.52(5)
C(1)	0.0467(2)	0.3668(2)	0.3072(2)	1.44(6)
C(2)	0.0519(2)	0.0588(3)	0.3031(2)	1.71(6)
C(3)	0.0971(2)	0.5239(3)	0.3928(2)	1.74(6)
H(1)	0.213(3)	0.213(5)	0.706(3)	6(1)
H(2)	0.110(3)	0.227(4)	0.636(3)	4.6(8)
H(3)	0.340(3)	0.250(4)	0.908(3)	4.1(8)
H(4)	0.332(4)	0.388(5)	0.873(4)	8(1)
H(5)	0.090(2)	−0.042(3)	0.343(2)	2.2(5)

[a] $B_{eq} = (8/3)\pi^2\Sigma\Sigma U_{ij} a_i^* a_j^* (\mathbf{a}_i \cdot \mathbf{a}_j)$

min^{-1}. Magnetic susceptibilities over the temperature range ~4 to ~82 K were measured at applied fields of 7 501 or 9 225 Oe using a P.A.R. model 155 vibrating sample magnetometer as previously described (15). Samples were held in Kel-F capsules and corrections were made for background signal over the entire temperature range studied. Magnetic susceptibilities were corrected for diamagnetism of all atoms (cobalt, −12; nickel, −11; copper, −11; $pyzdc^{2-}$ and $pyzdcH^-$, -68; H_2O, −12) and temperature independent paramagnetism of nickel and copper, 200 and 60, respectively. All corrections are in units of 10^{-6} cm^3 mol^{-1}. Complete magnetic data have been deposited as supplementary material. Carbon, hydrogen, and nitrogen analyses were performed by P. Borda of this department.

Results and discussion

Synthesis and thermoanalysis

2:1 complexes

$[Ni(pyzdcH)_2(H_2O)_2]$, **1**, was prepared under conditions similar to those described previously (2) with the main difference being that the solutions were some 20 times more dilute, result-

Table 3. Bond lengths (Å) with estimated standard deviations in parentheses for **1** and **2**.

	Length			Length	
Bond	M = Ni	M = Cu	Bond	M = Ni	M = Cu
M(1)—O(1)	2.021(1)	1.948(1)	N(1)—C(4)	1.326(2)	1.328(3)
M(1)—O[a]	2.091(1)	2.405(2)	N(2)—C(2)	1.346(2)	1.336(3)
M(1)—N(1)	2.048(1)	1.996(2)	N(2)—C(3)	1.328(2)	1.330(3)
O(1)—C(5)	1.248(2)	1.266(2)	C(1)—C(2)	1.401(2)	1.384(3)
O(2)—C(5)	1.256(2)	1.230(2)	C(1)—C(5)	1.531(2)	1.506(3)
O(3)—C(6)	1.218(2)	1.300(2)	C(2)—C(6)	1.532(2)	1.518(3)
O(4)—C(6)	1.288(2)	1.197(3)	C(3)—C(4)	1.385(2)	1.386(3)
N(1)—C(1)	1.356(2)	1.346(3)			

[a]**1**, M = Ni, O = O(5); **2**, M = Cu, O = O(4), symmetry operation: $-x$, $1-y$, $1-z$.

Table 4. Bond angles (deg) with estimated standard deviations in parentheses for **1** and **2**.

	Angle			Angle	
Atoms	M = Ni	M = Cu	Atoms	M = Ni	M = Cu
O(1)—M—O(1)*	180	180	N(1)—C(1)—C(2)	119.4(1)	120.0(2)
O(1)—M—O[a]	91.64(5)	94.49(6)	N(1)—C(1)—C(5)	111.4(1)	115.1(2)
O(1)—M—O*[a]	88.36(5)	85.51(6)	C(2)—C(1)—C(5)	129.2(1)	125.0(2)
O(1)—M—N(1)	79.59(5)	83.66(6)	N(2)—C(2)—C(1)	120.6(1)	121.6(2)
O(1)—M—N(1)*	100.41(5)	96.34(6)	N(2)—C(2)—C(6)	110.8(1)	115.4(2)
O[a]—M—O*[a]	180	180	C(1)—C(2)—C(6)	128.6(2)	122.9(2)
O[a]—M—N(1)	91.12(5)	91.50(6)	N(2)—C(3)—C(4)	121.5(2)	122.1(2)
O[a]—M—N(1)*	88.88(5)	88.50(6)	N(1)—C(4)—C(3)	120.4(2)	120.0(2)
N(1)—M—N(1)*	180	180	O(1)—C(5)—O(2)	123.1(2)	126.3(2)
M—O(1)—C(5)	116.7(1)	114.6(1)	O(1)—C(5)—C(1)	117.3(1)	115.9(2)
M[b]—O(4)—C(6)	—	145.0(2)	O(2)—C(5)—C(1)	119.6(1)	117.9(2)
M—N(1)—C(1)	114.9(1)	110.5(1)	O(3)—C(6)—O(4)	121.6(2)	125.1(2)
M—N(1)—C(4)	125.6(1)	130.5(1)	O(3)—C(6)—C(2)	118.3(2)	113.0(2)
C(1)—N(1)—C(4)	119.5(1)	119.0(2)	O(4)—C(6)—C(2)	120.1(1)	121.7(2)
C(2)—N(2)—C(3)	118.7(1)	117.3(2)			

*Denotes symmetry operation: $-x$, $1-y$, $1-z$ for **1**; $1-x$, $1-y$, $1-z$ for **2**.
[a]**1**, M = Ni, O = O(5); **2**, M = Cu, O = O(4), symmetry operation: $-x$, $1-y$, $1-z$, O(4)*, symmetry operation: $1+x,y,z$.
[b]Symmetry operation: $-1+x,y,z$.

Table 5. Bond lengths (Å) with estimated standard deviations in parentheses for **3**–**5**.[a]

	Length		
Atoms	M = Co, **3**	M = Ni, **4**	M = Cu, **5**
M—O(1)	2.0555(9)	2.031(1)	1.941(1)
M—O(3)	2.094(1)	2.092(1)	2.472(2)
M—N(1)	2.1458(9)	2.074(1)	1.996(2)
O(1)—C(3)	1.275(1)	1.275(2)	1.275(2)
O(2)—C(3)	1.228(1)	1.224(2)	1.220(2)
N(1)—C(1)	1.344(1)	1.344(2)	1.342(2)
N(1)—C(2)	1.331(2)	1.330(2)	1.326(2)
C(1)—C(1)'	1.397(2)	1.396(3)	1.389(3)
C(1)—C(3)	1.520(1)	1.521(2)	1.526(3)
C(2)—C(2)'	1.391(2)	1.399(3)	1.394(4)

[a]Symmetry operation: (') $-x$, y, $1/2-z$.

Table 6. Bond angles (deg) with estimated standard deviations in parentheses for **3–5**.[a]

Atoms	Angle		
	M = Co, **3**	M = Ni, **4**	M = Cu, **5**
O(1)—M—O(1)*	180	180	180
O(1)—M—O(3)	91.57(4)	91.62(5)	92.65(6)
O(1)—M—O(3)*	88.43(4)	88.38(5)	87.35(6)
O(1)—M—N(1)	78.37(3)	80.12(4)	82.74(5)
O(1)—M—N(1)*	101.63(3)	99.88(4)	97.26(5)
O(3)—M—O(3)*	180	180	180
O(3)—M—N(1)	91.57(4)	91.50(5)	92.53(7)
O(3)—M—N(1)*	88.43(4)	88.50(5)	87.47(7)
N(1)—M—N(1)*	180	180	180
M—O(1)—C(3)	116.94(7)	115.77(9)	115.7(1)
M—N(1)—C(1)	110.67(7)	110.76(9)	111.3(1)
M—N(1)—C(2)	128.98(8)	128.35(9)	127.4(1)
C(1)—N(1)—C(2)	118.90(9)	119.8(1)	120.8(2)
N(1)—C(1)—C(1)'	119.96(6)	119.55(8)	119.1(1)
N(1)—C(1)—C(3)	113.93(8)	113.8(1)	112.8(1)
C(1)'—C(1)—C(3)	125.97(6)	126.39(8)	127.9(1)
N(1)—C(2)—C(2)'	120.59(6)	120.02(8)	119.5(1)
O(1)—C(3)—O(2)	125.3(1)	125.7(1)	125.0(2)
O(1)—C(3)—C(1)	114.99(9)	114.8(1)	114.3(2)
O(2)—C(3)—C(1)	119.62(9)	119.4(1)	120.5(2)

[a]Symmetry operations: (*) 1/2 − *x*, 1/2 − *y*, 1 − *z* (') − *x*,*y*, 1/2 − *z*.

ing in the deposition of crystals suitable for X-ray studies. The presence of two molecules of water per metal was shown by microanalysis and TGA, which confirmed the earlier result (7) that the compound is thermally stable to about 150°C and decomposes with the loss of two moles of H_2O and two moles of CO_2 over the range 150–277°C. While the 2:1 complexes are generally reported as dihydrates (2), the one report of the copper derivative is as a trihydrate (11). We do not observe this formulation; however, compound **2**, like the 2:1 complexes of other metals, contains two water molecules. TGA studies show that **2** loses both molecules of water over the temperature range 50–160°C. The explanation for the relative ease of dehydration of **2** compared to the situation for **1** comes from structural studies which reveal that the water molecules are coordinated to the metal in **1** but are not coordinated in **2** (see below).

1:1 complexes

Previous work has revealed significant variations in the degree of hydration of the 1:1 complexes. Those of Mn, Fe, Co, and Ni have been reported both as tetrahydrates (5), and as dihydrates (7), that of Cu as anhydrous (2, 6), a hemihydrate (5), and a monohydrate (7) and that of Zn as a tetrahydrate (5), a dihydrate (7), and a trihydrate (9). This variation in degree of hydration was commented on earlier (5). Our synthetic method, which yields crystalline samples from dilute solutions, gave, for Co, Ni, and Cu (**3**, **4**, and **5**), complexes that have four water molecules per metal, two coordinated and two lattice, as shown by subsequent X-ray analysis. For **3** and **4** TGA showed the loss of four molecules of water over the ranges 40–300°C and 40–324°C, respectively, in agreement with earlier studies on the tetrahydrates (5). The copper compound, **5**, readily loses water under ambient conditions and

Fig. 1. The structure of $[Ni(pyzdcH)_2(H_2O)_2]$ (**1**), with atom numbering scheme; 33% probability thermal elipsoids are shown.

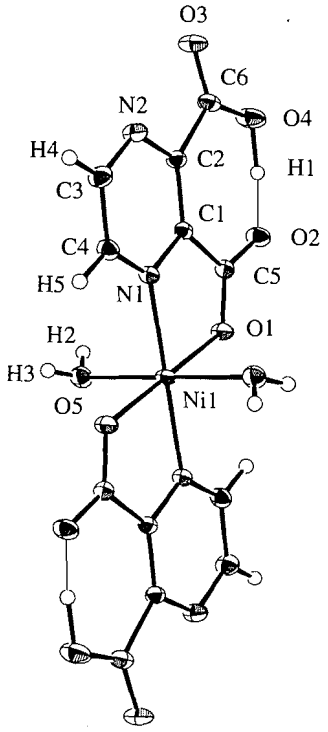

could not be characterized further. TGA studies of **6** confirmed the anhydrous nature of the compound and showed it to be thermally stable to 240°C.

Structural and magnetic studies

2:1 complexes

Crystals of $[Ni(pyzdcH)_2(H_2O)_2]$ (**1**) are isomorphous with those of the cobalt analogue (10). The structure of **1** with the atom numbering scheme is shown in Fig.1. In the monometallic $[Ni(pyzdcH)_2(H_2O)_2]$ unit the metal is *trans*-coordinated by two $pyzdcH^-$ ligands via chelate interactions involving nitrogen N(1) adjacent to the deprotonated carboxylate and oxygen O(1) of that group. The other nitrogen and the protonated carboxylate on each ligand are not coordinated to the metal. There is a strong intramolecular hydrogen bond involving the carboxylate hydrogen and oxygen O(2). Six coordination about the metal is completed by two axially coordinated water molecules. Hydrogen-bonding interactions involving the water hydrogens and the carboxylate noncoordinated oxygens O(3) on neighbouring molecules generates a three-dimensional network, a portion of which is shown in Fig. 2.

Although $[Co(pyzdcH)_2(H_2O)_2]$ (isostructural with **1**) is a monometallic complex, O'Connor and Sinn (10) pointed out that the hydrogen-bonding network provided by the water molecules can provide a pathway for magnetic exchange. By careful analysis of the low temperature magnetic data these authors were able to show the presence of weak antiferromagnetism in the cobalt complex. The magnetic moments measured for the nickel analogue **1** at the higher temperatures studied are relatively independent of temperature (Fig. 3) and of a magnitude expected for magnetically dilute nickel(II) complexes (16). The observed decrease in magnetic moment

Table 7. Hydrogen bond geometry (Å, deg).*

D—H···A		D—H	H···A	D···A	D—H···A
1					
O(4)—H(1)···O(2)		1.12(3)	1.29(3)	2.408(2)	171(3)
O(5)—H(2)···O(3)[a]		0.74(2)	2.08(2)	2.818(2)	175(2)
O(5)—H(3)···O(3)[b]		0.77(2)	2.22(2)	2.959(2)	162(2)
2					
O(3)—H(1)···O(5)		1.03(4)	1.50(4)	2.512(2)	167(4)
O(5)—H(4)···O(2)[c]		0.66(2)	2.03(2)	2.680(3)	172(3)
O(5)—H(5)···N(2)[d]		0.92(3)	1.92(3)	2.408(3)	174(3)
3–5					
O(3)—H(1)···O(4)	**3**	0.84(2)	1.83(2)	2.672(2)	174(2)
	4	0.80(2)	1.87(2)	2.667(2)	174(2)
	5	0.76(3)	1.97(3)	2.734(3)	174(3)
O(3)—H(2)···O(2)[e]	**3**	0.84(2)	1.89(2)	2.721(2)	167(2)
	4	0.80(2)	1.95(2)	2.732(2)	165(2)
	5	0.78(3)	2.04(3)	2.824(2)	178(3)
O(4)—H(3)···O(1)[f]	**3**	0.85(2)	2.03(2)	2.874(2)	173(2)
	4	0.85(3)	2.05(3)	2.876(2)	165(2)
	5	0.67(3)	2.52(3)	3.155(3)	158(3)
O(4)—H(3)···O(2)[f]	**5**	0.67(3)	2.49(3)	3.069(3)	146(3)
O(4)—H(4)···O(1)[g]	**3**	0.80(2)	2.37(2)	3.043(2)	142(2)
	4	0.74(3)	2.37(3)	3.106(2)	159(3)
O(4)—H(4)···O(3)[h]	**5**	0.71(4)	2.22(4)	2.898(3)	159(4)

*Superscripts refer to symmetry operations:
[a] $1 - x, 1 - y, 1 - z$.
[b] $-1/2 + x, 1/2 - y, 1/2 + z$.
[c] $-1/2 + x, 3/2 - y, -1/2 + z$.
[d] $-1 - x, 1 - y, -z$.
[e] $x, 1 + y, 1 + z$.
[f] $1/2 - x, -1/2 + y, 3/2 - z$.
[g] $x, 1 - y, 1/2 + z$.
[h] $1/2 - x, 1/2 + y, 3/2 - z$.

Fig. 2. Stereoscopic view showing part of the H-bonding network in $[Ni(pyzdcH)_2(H_2O_2]$ (**1**).

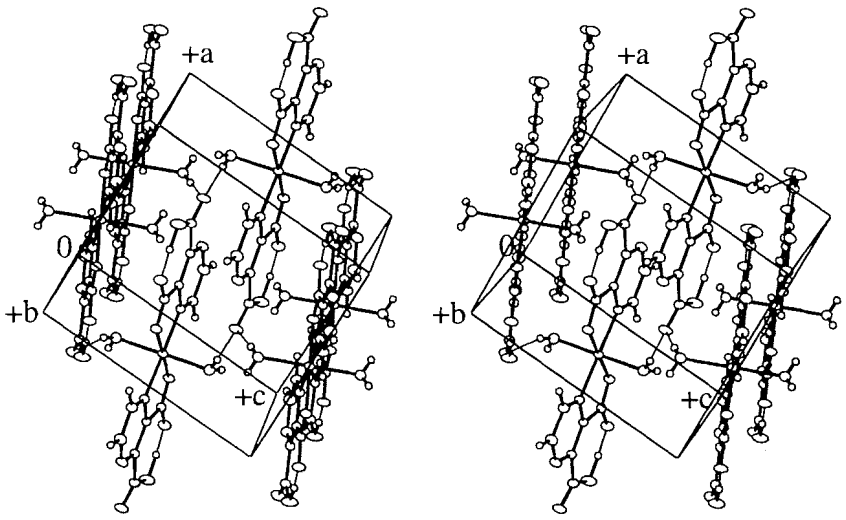

Fig. 3. Magnetic moment versus temperature plots.
Experimental data: circles at the top, middle, and bottom are for $[Co(pyzdc)(H_2O)_2]_x \cdot 2xH_2O$ (**3**), $[Ni(pyzdc)(H_2O)_2]_x \cdot 2xH_2O$ (**4**), and Cu(pyzdc) (**6**), respectively; triangles at middle and bottom are for $[Ni(pyzdcH)_2(H_2O)_2]$ (**1**) and $[Cu(pyzdcH)_2]_x \cdot 2xH_2O$ (**2**), respectively. Lines are calculated from theory as described in the text.

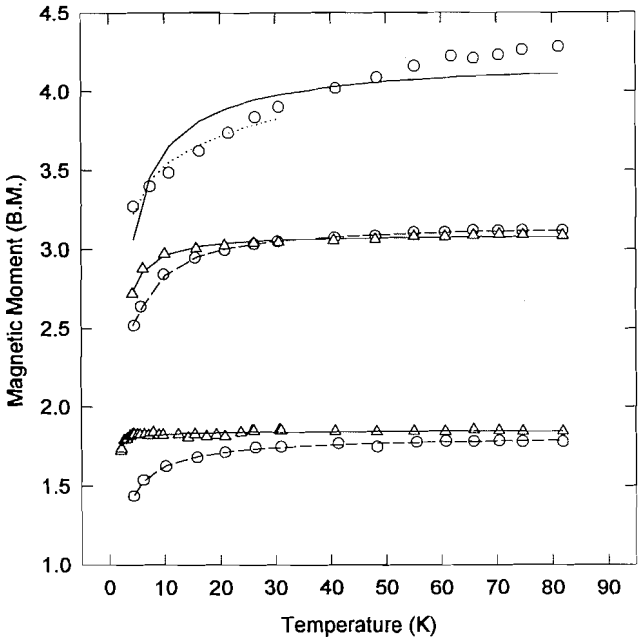

at low temperatures is caused by the effects of Zero Field Splitting, ZFS (17), accompanied possibly by very weak exchange effects. Accordingly, we examined fits of the magnetic susceptibility data over the temperature range ~80 to ~4 K employing the previously published equation for the susceptibility, χ_m, of an $S = 1$ system including ZFS (18), with χ_m modified by the molecular field approximation to include the effects of weak spin interactions (19). The equation employed for the exchange-corrected susceptibility, χ_m', is:

$$[1] \quad \chi_m' = (\chi_m/[1 - (2zJ/Ng^2\mu_B^2)\chi_m])$$

where J is the exchange coupling constant, z is the number of interacting nearest neighbours, and the remaining terms have their usual meaning. In the fitting procedure D (the zero-field splitting parameter), g, and zJ were employed as variable parameters. Fits of experimental data to the model were made using a nonlinear least-squares procedure with the following function minimized:

$$[2] \quad F = \left[\frac{1}{n}\sum_{i=1}^{n}\left(\frac{\chi^i_{calc} - \chi^i_{obs}}{\chi^i_{obs}}\right)^2\right]^{1/2}$$

where n is the number of data points. F provides a measure of the goodness of fit between theory and experiment. The parameter values giving the best agreement between experiment and theory are $D = 4.0$ cm^{-1}, $zJ = -0.033$ cm^{-1}, and $g = 2.19$ ($F = 0.0074$).[4] The experimental magnetic moments as well as the line calculated using the best fit parameters are shown in Fig. 3. The fit gives $|D| \gg |zJ|$, a necessary requirement for applying the molecular field approximation (17).

Ignoring intermolecular exchange (setting $J = 0$) in analysing the magnetic data of **1** gives poorer agreement between experiment and theory, indicating the presence of weak antiferromagnetic exchange, mediated by the H-bonding network. Of relevance here are previous studies on some monometallic tetrakis(pyridine) nickel(II) complexes (20) that showed very similar magnetic properties to those seen for **1**. In fact, the D, zJ, and g parameter values obtained for $Ni(py)_4Cl_2$ (20), a complex known to have a monometallic *trans*-octahedral structure (21), are, within experimental uncertainty, the same as those obtained in the present work for **1**. We conclude that the intermolecular H-bonding network, present in **1** but absent in the pyridine complex, provides a pathway for exchange that, however, is not measurably better than that provided by normal non-bonding contacts.

Crystals of $[Cu(pyzdcH)_2]_x \cdot 2xH_2O$ (**2**) have the same stoichiometry and belong to the same space group as **1**. Compound **2**, however, is not isostructural with **1**. The structure of **2** with the atom numbering scheme is shown in Fig. 4. In this structure, each copper is *trans*-coordinated by two chelating $pyzdcH^-$ ligands to form planar $Cu(pyzdcH)_2$ units as in **1**. In **2**, however, the axial positions are not occupied by water molecules but instead are occupied by the non-protonated oxygen atoms O(4) of protonated carboxylate substituents on neighbouring $Cu(pyzdcH)_2$ units. This results in extended chains of copper ions linked by double-bridging $pyzdcH^-$ groups. The lattice water molecules link chains in a three-dimensional H-bonded network, part of which is shown in Fig. 5.

Since the $Cu(pyzdcH)_2$ units in **2** are connected in chains by conventional coordinative interactions the potential for magnetic exchange is greater than in **1**. In spite of this, the magnetic moment of **2** is relatively constant down to about 4 K. For **2** we extended the measurements to 2 K and observed a decrease in moment at the low temperatures indicative of very weak antiferromagnetic exchange (Fig. 3). Anticipating that intrachain coupling would be significantly stronger than interchain coupling via the H-bonding network, we analysed the magnetic susceptibilities of **2** (over the full temperature range studied) according to the Weng linear chain model with the coefficients generated by Hiller *et al.* (22) for $S = 1/2$. The best fit to the data was obtained with the parameters $g = 2.14$ and $J = -0.11$ cm^{-1} ($F = 0.016$) and the line calculated with these parameter values is shown in Fig. 3. Although this analysis confirms antiferromagnetic exchange in **2**, it is clearly very weak. This is probably a consequence of the fact that the $Cu(pyzdcH)_2$ units in **2** are linked via long, axial, Cu—O bonds (2.405(2) Å) combined with the fact that the plane of the CO_2 group is almost orthogonal to the plane of the pyrazine ring, thus eliminating a delocalized π-electron pathway for exchange. Finally, it should be noted that in an earlier study (11) of a 2:1 copper complex of composition $Cu(pyzdcH)_2 \cdot 3H_2O$ the authors found no evidence for exchange in measurements to 6 K. It is possible that the compound studied in the earlier work has the same linear chain structure as **2** with an additional water of hydration.

1:1 complexes

$[Co(pyzdc)(H_2O)_2]_x \cdot 2xH_2O$ (**3**) and the nickel (**4**) and copper

[4] Here and elsewhere in this work the uncertainties in the magnetic parameters are estimated to be approximately 2% in g and 10% in the other parameters.

Fig. 4. Stereoscopic view of the structure of part of the chain in $[Cu(pyzdcH)_2]_x \cdot 2xH_2O$ (**2**) with atom numbering scheme; 33% probability thermal elipsoids are shown.

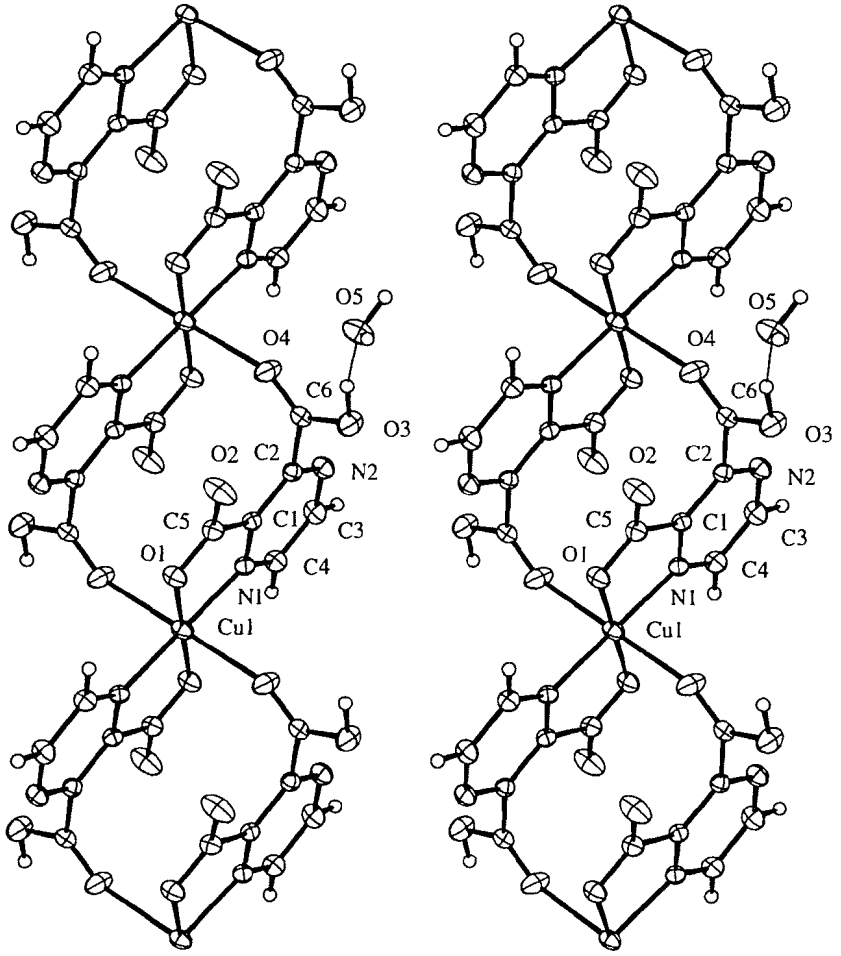

Fig. 5. Stereoscopic view showing part of the H-bonding network in $[Cu(pyzdcH)_2]_x \cdot 2xH_2O$ (**2**).

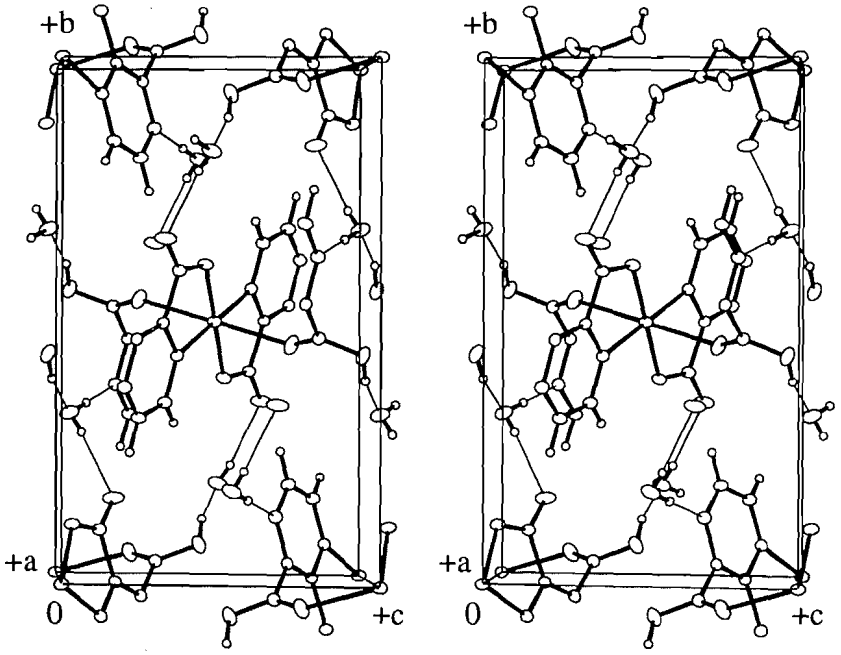

Fig. 6. The structure of part of the chain in $[Co(pyzdc)(H_2O)_2]_x \cdot 2xH_2O$ (**3**) with atom numbering scheme; 33% probability thermal elipsoids are shown.

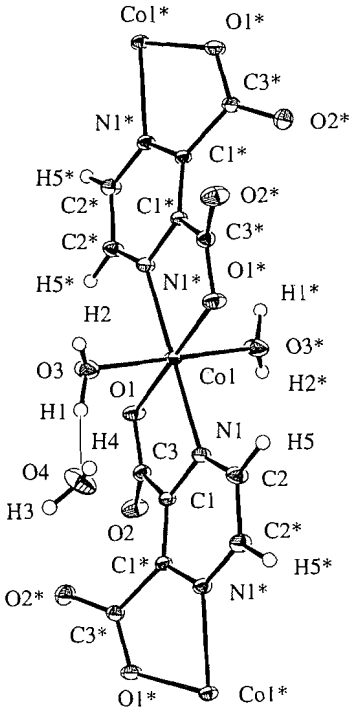

(**5**) analogues are isomorphous; they have structures in which $pyzdc^{2-}$ ligands bridge metal ions to form extended linear chains.The structure of **3** with the atom numbering scheme is shown in Fig. 6. In this structure the $pyzdc^{2-}$ ligand coordinates to two metal centers via chelate interactions involving each nitrogen N(1) and an oxygen O(1) from the adjacent carboxylate substituent. Six coordination on each metal is completed by oxygens O(3) of axially coordinated water molecules and two additional water molecules are present in the lattice. As shown in Fig. 7, the chains in **3** are linked in a three-dimensional array by H-bonding interactions involving all water molecules. The H-bonding network in **4** is the same as in **3** but it differs in **5**. In the latter, as shown in Fig. 8, the lattice water hydrogen H(3) H-bonds to O(1) as in **3** and **4** but forms an additional H bond to noncoordinating carboxylate oxygens O(2). The other lattice water hydrogen H(4) does not H-bond to O(1) as in **3** and **4** but, instead, H-bonds to the coordinated water oxygen O(3).

The crystal structure of a 1:1 complex of composition $Co(pyzdc)\cdot 2H_2O$ was previously reported (8). This compound, which belongs to the space group *Pcca*, has the same linear chain structure as **3**, with axially bonded waters but no lattice water. This lack of lattice waters and the associated H-bonding interactions has a measurable effect on the bond parameters in the immediate environment of the metal. In $Co(pyzdc)\cdot 2H_2O$ the CoN_2O_4 chromophore is non-centrosymmetric. The bond angles show greater deviation from regular octahedral angles than is observed here for **3**. The two Co—O (coordinated water) distances are shorter (2.069(4) and 2.033(4) Å) than the corresponding distance (2.094(1) Å) in **3**. The two Co—O(carboxylate) bond distances (2.069(4) and 2.037(4) Å) bracket the corresponding distance (2.0555(9) Å) in **3** but the average (2.053(4) Å) is the same within error. The Co—N distances (2.173(4) and 2.135(4) Å) also bracket the corresponding distance (2.1458(9) Å) in **3**; however, in this case the average distance (2.154(4) Å) is slightly greater. In view of these structural differences involving what is likely to be the dominant exchange pathways in **3** and $Co(pyzdc)\cdot 2H_2O$, the magnetic properties of the latter could be measurably different from those reported here for **3**.

Compounds **3**, **4**, and **5** all have the same extended chain structures involving chelate supported 1,4-diazine links between metal centers. Although the chains are connected via H-bonded networks, results obtained on compounds such as **1** indicate that interchain exchange via these pathways will likely be very weak. Magnetic studies on these compounds, then, should permit an evaluation of intrachain exchange via the supported diazine links and its dependence on d-electron configuration.

The analysis of magnetic data for cobalt(II) complexes in distorted octahedral environments as seen in $[Co(pyzdc)(H_2O)_2]_x \cdot 2xH_2O$ (**3**) is complicated by the fact that, in addition to possible magnetic exchange effects, single ion effects such as electron delocalization, spin-orbit coupling, distortions from regular stereochemistry, and crystal field mixing of excited states into the ground state affect the magnetic properties (23). The problem is simplified if it is assumed that the distortion from O_h symmetry is strong enough to leave a well-isolated orbital singlet as the ground state (24). Under this assumption the magnetic susceptibilities of **3** were analysed (over the full temperature range studied) according to the Weng model with the coefficients generated by Hiller et al. (22) for $S = 3/2$. The solid line in Fig. 3 shows the best fit ($g = 2.17$ and $J = -0.380$ cm^{-1}, $F = 0.072$) that could be obtained with this model and it is clearly poor. An alternative approach to the problem is to consider the fact that spin-orbit coupling leads to a Kramers doublet as the lowest level and, assuming that at low temperatures this is the only thermally occupied level, the magnetic susceptibilities in the low temperature region (31–4 K) were analysed using the Weng model for an effective spin $S = 1/2$. Attempts to fit the data employing g, J, and Temperature Independent Paramagnetism (TIP) as variable parameters gave good agreement with experiment but an unrealistically high value of TIP (0.017 cm^3 mol^{-1}). We decided instead to fix TIP at 0.006 cm^3 mol^{-1}, the value determined for the very weakly magnetically coupled $[Co(pyzdcH)_2(H_2O)_2]$ by high-precision magnetic measurements at low temperatures (10). Because of the similarities in the metal chromophores of **3** and $[Co(pyzdcH)_2(H_2O)_2]$, the TIP should be much the same in the two compounds. The dotted line in Fig. 3 covering the low temperature region was calculated from theory using the best fit parameters $g = 4.31$ and $J = -0.74$ cm^{-1} ($F = 0.027$). Considering the difficulties in analysing this system, not too much significance should be placed on the actual parameter values; nonetheless, the results do support the presence of measurable exchange in **3.** This should be contrasted with the earlier report that the pyrazine-bridged complexes, $Co(pyz)_2X_2$ (X = Cl or Br), give no evidence for magnetic exchange down to 1.8 K (25). This suggests that in this cobalt system the effect of supporting the diazine bridge through chelate formation is to enhance the exchange.

The magnetic data for $[Ni(pyzdc)(H_2O)_2]_x \cdot 2xH_2O$ (**4**) were

Fig. 7. Stereoscopic view showing part of the H-bonding network in $[Co(pyzdc)(H_2O)_2]_x \cdot 2xH_2O$ (**3**).

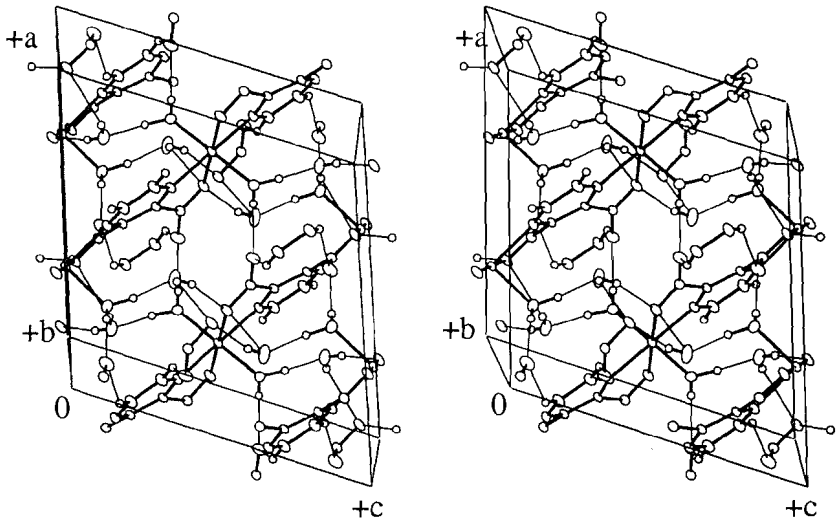

Fig. 8. Stereoscopic view showing part of the H-bonding network in $[Cu(pyzdc)(H_2O)_2]_x \cdot 2xH_2O$ (**5**).

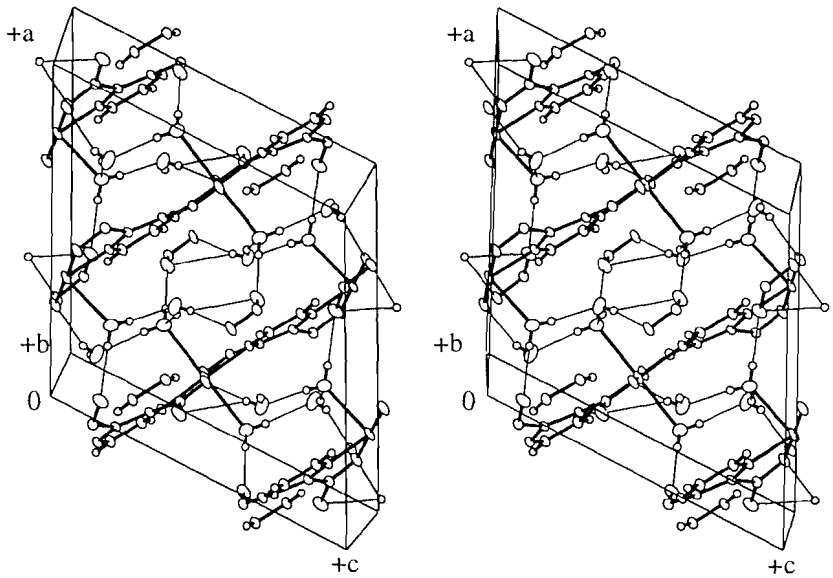

analysed as described above for **1**. Excellent agreement between experiment and theory (Fig. 3) was obtained with the parameters $g = 2.24$, $zJ = -0.098$ cm^{-1}, and $D = 3.3$ cm^{-1} ($F = 0.0029$). Significantly, the D values for **1** and **4** are very similar, consistent with similarities in the metal chromophores of the two compounds, while $-zJ$ is significantly greater for the pyzdc^{2-}-bridged **4**. Since **4** has a linear chain structure, $z = 2$ and therefore $J = -0.049$ cm^{-1}. This value is comparable to the J values determined in earlier work (20) for three complexes assumed to have monopyrazine-bridged structures ($-J$ in the range 0.018 to 0.047 cm^{-1}). The earlier work concluded that pyrazine is significantly poorer at mediating magnetic exchange between nickel centers than, for example, between copper or iron centers (20) and it appears that pyzdc^{2-} is not significantly better, in spite of the presence of the chelate-supported bridges. It was suggested previously (20) that a factor in accounting for weaker exchange in nickel versus copper pyrazine complexes is longer metal–N bond lengths in the Ni complexes, an effect not countered, as it is in Fe complexes, by the presence of additional pathways for exchange involving t_{2g} unpaired electron density. This relative order of bond lengths (Ni—N = 2.074(1), Cu—N = 1.996(2) Å; Table 5) is observed for **4** and **5**, supporting the notion that the relatively long metal–N bond distance is contributing to the weakness of the exchange in both pyz- and pyzdc^{2-}-bridged complexes of nickel.

Due to its instability in air, we were unable to study the magnetic properties of $[Cu(pyzdc)(H_2O)_2]_x \cdot 2xH_2O$ (**5**); however, the anhydrous derivative, Cu(pyzdc) (**6**), was investigated (Fig. 3). This compound was previously studied at high temperatures (2) and our low temperature results mesh very well with the earlier work. The magnetic susceptibilities (80 – 4 K) were analysed using the Weng model for $S = 1/2$ and excellent agreement between experiment and theory was

obtained with the parameters $g = 2.10$ and $J = -1.14$ cm^{-1} ($F = 0.0087$). It seems likely that the basic chain structure of **5** is retained in **6** with the axially coordinated water molecules replaced by weak coordinative interactions involving carboxylate oxygens from neighbouring chains. Magnetic exchange interactions via these long Cu—O bonds are likely to be very weak (as seen for **2**); considering this and the fact that the experimental susceptibilities show excellent agreement with values calculated from theory for linear chains, we conclude the exchange observed in **6** is mediated primarily by the pyzdc^{2-} ligands. The pathway provided by these ligands in **6** is clearly better at mediating exchange than that provided by the pyzdcH$^-$ ligands in **2** ($-J$ values of 1.14 and 0.11 cm^{-1}, respectively); however, considering that $-J$ values as large as 16.8 cm^{-1} have been observed in extended chain compounds of copper(II) in which the metals are bridged by pyrazine itself (25), the magnitude of the coupling in **6** is still rather weak. An explanation for this comes from a consideration of the probable structure of **6** as inferred from the X-ray determined structure of **5**. The pyrazine ligand is bound in the equatorial plane of the copper chromophore and, as a result of the chelate interaction, the plane of the pyrazine ring is forced to be nearly coplanar with the equatorial plane.[5] Earlier studies (26) have shown that under such structural conditions magnetic exchange interactions in copper pyrazine complexes is likely to be weak. This is because the magnitude of the exchange is determined from the overlap of the $d_{x^2-y^2}$ magnetic orbital and the pyrazine π-system, which becomes significant only when the pyrazine ring is canted out of the xy-plane. In $Cu(pyz)(NO_3)_2$, for example (27, 28), where the canting angle is about 50°, the exchange interaction ($-J = 3.7$ cm^{-1}) is significantly greater than that observed here for **6**.

Summary and conclusions

Of the six compounds studied in this work, all have extended chain structures with the exception of $[Ni(pyzdcH)_2(H_2O)_2]$ (**1**). The monometallic units in **1** are linked in a three-dimensional array by H-bonding interactions, which are shown to provide pathways for intermolecular exchange that are no better than would be expected for non-bonding contacts. In $[Cu(pyzdcH)_2]_x \cdot 2xH_2O$ (**2**) the pyzdcH$^-$ ligands exhibit a form of coordination not previously reported for this group. Although the metals are doubly bridged by these ligands, the links involve weak axial Cu—O bonds and a ligand geometry that prevents π-electron delocalization throughout the bridge. This leads to only very weak antiferromagnetic exchange in **2**.

The compounds $[M(pyzdc)(H_2O)_2]_x \cdot 2xH_2O$ (M = Co, Ni, and Cu ; **3**, **4**, and **5**, respectively) all have linear chain structures with pyzdc^{2-} ligands forming chelate-supported 1,4-diazine links between metal centers. Magnetic studies on **3**, **4**, and **6** (Cu(pyzdc), the anhydrous form of **5**) reveal intrachain antiferromagnetic interactions mediated by the bridging ligands. While the analysis of the magnetic data indicates that the magnitude of the exchange in the Ni and Cu compounds (**4** and **6**) is not greatly different from that observed in analogous systems involving unsupported pyrazine bridges, this appears not to be the case for the Co system (**3**). The presence of the chelate interactions in the pyzdc^{2-} bridge imposes a geometrical constraint on the bridge and in the case of copper(II), in particular, this limits the potential for exchange. Such geometrical constraints may not be so important in the case of metals with unpaired t_{2g} electron density, as in cobalt(II) compounds, and with this in mind we are attempting to prepare and study complexes of iron(II) and manganese(II) that are isostructural with **3**.

[5] The dihedral angle between these planes is approximately 13.3° in **5**.

Acknowledgements

Financial support from the Natural Sciences and Engineering Research Council of Canada is gratefully acknowledged.

References

1. H. Ley, C. Schwarte and O. Munnich. Ber. Dtsch. Chem. Ges. B: **57**, 349 (1924).
2. R.W. Mathews and R.A. Walton. Inorg. Chem. **10**, 1433 (1971).
3. J.P. Antinelli and M.R. Paris. C. R. Seances Acad. Sci. Ser. C: **274**, 51 (1972).
4. A. Tenhunen. Acta Chem. Scand. **26**, 1291 (1972).
5. R.L. Chapman, F.S. Stephens, and R.S. Vagg. Inorg. Chim. Acta, **26**, 247 (1977).
6. H. Kuramoto, M. Inoue, S. Emori, and S. Sugiyama. Inorg. Chim. Acta, **32**, 209 (1979).
7. A.L. Magri, A.D. Magri, F. Balestrieri, E. Cardarelli, G. D'Ascenzo, and A. Pazanelli. Thermochim. Acta, **48**, 253 (1981).
8. P. Richard, D. Tran Qui, and E.F. Bertaut. Acta Crystallogr. Sect. B: Struct. Crystallogr. Cryst. Chem. **B29**, 111 (1973).
9. P. Richard, D. Tran Qui, and E.F. Bertaut. Acta Crystallogr. Sect. B: Struct. Crystallogr. Cryst. Chem. **B30**, 628 (1974).
10. C.J. O'Connor and E. Sinn. Inorg. Chem. **20**, 545 (1981).
11. C.L. Klein, C.J. O'Connor, R.J. Majeste, and L.M. Trefonas. J. Chem. Soc. Dalton Trans. 2419 (1982).
12. P.J. Steel. Coord. Chem. Rev. **106**, 221 (1990).
13. International tables for X-ray crystallography. Vol. IV. Kynoch Press, Birmingham, U.K. (present distributor Kluwer Academic Publishers. Boston, Mass., U.S.A.). 1974. pp. 99–102.
14. International tables for crystallography. Vol. C. Kluwer Academic Publishers, Boston, Mass., U.S.A. 1992. pp. 200–206.
15. J.S. Haynes, K.W. Oliver, S.J. Rettig, R.C. Thompson, and J. Trotter. Can. J. Chem. **62**, 891 (1984).
16. L. Sacconi. *In* Transition metal chemistry, a series of advances. Vol. 4. *Edited by* R.L. Carlin. Marcel Dekker, New York. 1968. pp. 199–298.
17. C.J. O'Connor. *In* Progress in inorganic chemistry. Vol. 29. *Edited by* S.J. Lippard. Interscience, New York. 1982. p. 203.
18. R.L. Carlin. J. Chem. Educ. **43**, 521 (1966).
19. R.L. Carlin, C.J. O'Connor, and S.N. Bhatia. J. Am. Chem. Soc. **98**, 3523 (1976).
20. T. Otieno and R.C. Thompson. Can. J. Chem. **73**, 275 (1995).
21. G.J. Long and P.J. Clarke. Inorg. Chem. **17**, 1394 (1978).
22. W. Hiller, J. Strahle, A. Datz, M. Hanack, W.E. Hatfield, L.W. terHaar, and P. Gutlich. J. Am. Chem. Soc. **106**, 329 (1984).
23. B.N. Figgis, M. Gerloch, J. Lewis, F.E. Mabbs, and G.B. Webb. J. Chem. Soc. A, 2086 (1968).
24. V.T. Kalinnikov, Yu. V. Rakitin, and W.E. Hatfield. Inorg. Chim. Acta, **31**, 1 (1978).
25. S. Emori, M. Inoue, and M. Kubo. Coord. Chem. Rev. **21**, 1 (1976).
26. H.W. Richardson, J.R. Wasson, and W.E. Hatfield. Inorg. Chem. **16**, 484 (1977).
27. A. Santoro, A.D. Mighell, and C.W. Reimann. Acta Crystallogr. Sect. B: Struct. Crystallogr. Cryst. Chem. **B26**, 979 (1970).
28. H.W. Richardson, and W.E. Hatfield. J. Am. Chem. Soc. **98**, 835 (1976).

Structural studies of organoboron compounds LXIV.[1] Boron chelate formation with glycolohydroxamic acids, and the crystal and molecular structure of 5-(1-hydroxycyclohexyl)-2,2-diphenyl-1,3-dioxa-4-azonia-2-borata-4-cyclopentane

Wolfgang Kliegel, Ute Schumacher, Steven J. Rettig, and James Trotter

Abstract: The syntheses of representative diphenyl- and difluoroboron chelates of 2-hydroxycarbohydroxamic acids (glycolohydroxamic acids) are reported. Crystals of 5-(1-hydroxycyclohexyl)-2,2-diphenyl-1,3-dioxa-4-azonia-2-borata-4-cyclopentene, **2***a*, are triclinic, a = 11.5717(5), b = 11.7262(4), c = 14.3529(5) Å, α = 90.277(6)°, β = 110.497(5)°, γ = 96.814(5)°, Z = 4, space group $P\bar{1}$. The structure was solved by direct methods and refined by full-matrix least-squares procedures to R = 0.042 and R_w = 0.056 for 5318 reflections with $I \geq 3\sigma(F^2)$. Compound **2***a* is the first *N*-unsubstituted hydroxamatoborate derivative to be structurally characterized by an X-ray crystallographic analysis. The solid state structure of **2***a* consists of centrosymmetric, hydrogen-bonded tetrameric units that also feature intermolecular O—H···π(aromatic) interactions. Bond lengths include: B—O(N) = 1.557(2) and 1.553(2) Å, B—O(C) = 1.558(2) and 1.566(2) Å, B—C(phenyl) = 1.592(3)–1.601(3) Å.

Key words: hydroxamatoborate, organoboron compound, crystal structure.

Résumé : On a effectué la synthèse de chélates représentatifs diphényl- et difluorobore des acides 2-hydroxycarbohydroxamiques (acides glycolohydroxamiques). Les cristaux du 5-(1-hydroxycyclohexyl)-2,2-diphényl-1,3-dioxa-4-azonia-2-boratacyclopent-4-ène, **2***a*, sont tricliniques, groupe d'espace $P\bar{1}$, avec a = 11,5717(5), b = 11,7262(4) et c = 14,3529(5) Å, α = 90,277(6)°, β = 110,497(5)° et γ = 96,814(5)°, Z = 4. On a résolu la structure par des méthodes directes et on l'a affinée par la méthode des moindres carrés, matrice complète, jusqu'à des valeurs de R = 0,042 et R_w = 0,056 pour 5318 réflexions avec $I \geq 3\sigma(F^2)$. Le composé **2***a* est le premier dérivé hydroxamatoborate *N*-non-substitué à être caractérisé par diffraction des rayons X. La structure du composé **2***a* à l'état solide consiste en des unités tétramères centrosymétriques réunies par des liaisons hydrogènes qui comportent aussi des interactions O—H···π(aromatique). Les longueurs des liaisons incluent : B—O(N) = 1,557(2) et 1,553(2) Å, B—O(C) = 1,558(2) et 1,566(2) Å, B—C(phényle) = 1,592(3)–1,601(3) Å.

Mots clés : hydroxamatoborate, composés orbanoborés, structures cristallines.

[Traduit par la rédaction]

Introduction

2- and 3-Hydroxycarbohydroxamic acids and their chelating abilities are of interest in drug research on the anti-inflammatory and analgesic activities of hydroxamic acids (1). In the course of our investigations of hydroxamic acids as bi- or polydentate ligands in the formation of boron chelates (2–15) we chose two different 2-hydroxycarbohydroxamic acids (glycolohydroxamic acids), the 2,2-dialkyl derivative **1***a* and a 2,2-diaryl derivative, the benzilohydroxamic acid **1***b*, for the reaction with diphenylborenium (Ph_2B^+) and difluoroborenium (F_2B^+) ion-delivering reagents. Because of the presence of four different (nucleophilic) ligand functions within a compound of type **1**, various chelating modes could be expected. Furthermore, no in-depth structural descriptions of *N-un*substituted hydroxamato–borate complexes have yet been reported.

Received August 21, 1995.

W. Kliegel and U. Schumacher. Institut für Pharmazeutische Chemie der Technischen Universität Braunschweig, Beethovenstrasse 55, 38106 Braunschweig, Germany.
S.J. Rettig and J. Trotter.[2] Department of Chemistry, University of British Columbia, 2036 Main Mall, Vancouver, BC V6T 1Z1, Canada.

[1] Previous paper in this series: ref. 24.

[2] Author to whom correspondence may be addressed. Telephone: (604) 822–4865. Fax: (604) 822–2847. E-mail: james.trotter@mtsg.ubc.ca

Experimental

5-(1-Hydroxycyclohexyl)-2,2-diphenyl-1,3-dioxa-4-azonia-2-borata-4-cyclopentene, 2*a*

1-Hydroxy-1-cyclohexanecarbohydroxamic acid (16) (0.32 g, 2.0 mmol) and oxybis(diphenylborane) (0.35 g, 1.0 mmol) are refluxed in 50 mL of benzene for 10 min using a Dean–Stark

trap for continuous removal of water. The solution is evaporated in vacuo to a residue of 2–4 mL. After addition of petroleum ether and cooling, colorless crystals are obtained. Yield: 0.14 g (22%); mp 137–139°C (from ethanol – petroleum ether). Infrared (KBr): 3520, 3140 (O-H/N-H), 1600 (C=O/C=N) cm^{-1}; ^1H nmr (90 MHz, $CDCl_3$–TMS); δ (ppm): 0.80–2.10 (m, -$(CH_2)_5$-), 3.85 (s, v br, exchangeable, OH), 6.95–7.65 (m, 10 aromatic H), 11.8 (s, v br, exchangeable, NH). Anal. calcd. for $C_{19}H_{22}BNO_3$: C 70.61, H 6.86, N 4.33; found: C 70.52, H 6.93, N 4.34. The substance gives a deep blue color reaction with diphenylcarbazone in methanolic solution, indicating the presence of the diphenylboron moiety (17).

Crystals suitable for X-ray analysis were obtained by slow crystallization from absolute ethanol – petroleum ether: mp 136°C.

5-(1-Hydroxy-1,1-diphenylmethyl)-2,2-diphenyl-1,3-dioxa-4-azonia-2-borata-4-cyclopentene, 2*b*

2-Hydroxy-2,2-diphenylacetohydroxamic acid (benzilohydroxamic acid) (16) (0.73 g, 3.0 mmol) and oxybis(diphenylborane) (0.52 g, 1.5 mmol) are reacted as described for **2***a*. Yield: 0.72 g (59%) of colorless crystals; mp 106–108°C (from ethanol). Infrared (KBr): 3450, 3250 (O-H/N-H), 1600 (C=O/C=N) cm^{-1}; ^1H nmr (90 MHz, $CDCl_3$–TMS); δ (ppm): 3.7 (s, v br, exchangeable, OH), 6.93–7.70 (m, 20 aromatic H), 11.2 (s, v br, exchangeable, NH). Anal. calcd. for $C_{26}H_{22}BNO_3$: C 76.68, H 5.44, N 3.44; found: C 76.46, H 5.41, N 3.50. The substance gives a deep blue color reaction with diphenylcarbazone in methanolic solution, indicating the presence of the diphenylboron moiety (17).

2,2-Difluoro-5-(1-hydroxycyclohexyl)-1,3-dioxa-4-azonia-2-borata-4-cyclopentene, 3*a*

1-Hydroxy-1-cyclohexanecarbohydroxamic acid (16) (0.32 g, 2.0 mmol) is mixed with 30 mL of dried diethyl ether and 2.0 mmol of dimethyl ether – trifluoroboron complex. After the addition of freshly regenerated molecular sieve (4 Å, 1.5 g) the solution is stored at room temperature for 12 h. The molecular sieve is removed, and the solution evaporated in vacuo. Crystallization starts spontaneously or after the addition of petroleum ether. Yield: 0.13 g (31%) of a white powder; mp 121–124°C (from CH_2Cl_2 – petroleum ether). Infrared (KBr): 3470, 3230 (O-H/N-H), 1625 (C=O/C=N) cm^{-1}; ^1H nmr (90 MHz, $CDCl_3$–TMS); δ (ppm): 1.10–2.35 (m, -$(CH_2)_5$-), 5.8 (s, v br, exchangeable, OH and NH). Anal. calcd. for $C_7H_{12}BF_2NO_3$: C 40.62, H 5.84, N 6.77; found: C 40.78, H 5.96, N 6.57.

X-ray crystallographic analysis of 2*a*

Crystallographic data for **2***a* appear in Table 1. The final unit-cell parameters were obtained by least squares on 2 sin θ/λ values for 25 reflections with 2θ = 40.4°–48.0°. The intensities of three standard reflections, measured every hour of X-ray exposure time throughout the data collection showed only small random fluctuations. The data were processed[3], corrected for Lorentz and polarization effects, but not for absorption in view of the low value of μ.

The structure was solved by direct methods, the coordinates of the non-hydrogen atoms being determined from an *E*-map or from subsequent difference Fourier syntheses. The structure analysis was initiated in the centrosymmetric space group $P\bar{1}$ on the basis of the *E*-statistics, this choice being confirmed by the subsequent successful solution and refinement of the structure. The asymmetric unit contains two crystallographically independent molecules of **2***a*. Non-hydrogen atoms were refined with anisotropic thermal parameters and hydrogen atoms were refined with isotropic thermal parameters. A correction for secondary extinction was applied, the final value of the extinction coefficient being $1.20(10) \times 10^5$ (Hamilton isotropic type I). Neutral atom scattering factors for all atoms and anomalous dispersion corrections for the non-hydrogen atoms were taken from the *International tables for X-ray crystallography* (18). The largest peak on the final difference map (0.62

[3] Locally written software for data processing, locally modified versions of the Oak Ridge National Laboratory crystallographic programs (ORFLS, ORFEE, and ORTEP II) and MULTAN80.

Table 1. Crystallographic data.[a]

Compound	**2***a*
Formula	$C_{19}H_{22}BNO_3$
fw	323.20
Crystal system	Triclinic
Space group	$P\bar{1}$
a, Å	11.5717(5)
b, Å	11.7262(4)
c, Å	14.3529(5)
α, deg	90.277(6)
β, deg	110.497(5)
γ, deg	96.814(5)
V, Å^3	1809.1(2)
Z	4 (two independent molecules)
ρ_{calc}, g/cm^3	1.187
F(000)	688
Radiation (λ, Å)	Mo (0.7107̇3)
μ, cm^{-1}	0.74
Crystal size, mm	0.40 × 0.42 × 0.50
Transmission factors	No absorption correction
Scan type	ω–2θ
Scan range, deg in ω	0.70 + 0.35 tan θ
Scan speed, deg/min	1.8–20.1
Data collected	$+h, \pm k, \pm l$
$2\theta_{max}$, deg	55
Crystal decay, %	Negligible
Total reflections	8267
Total unique reflections	8267
Reflections with $I \geq 3\sigma(F^2)$	5318
No. of variables	610
R	0.042
R_w	0.056
gof	1.96
Max Δ/σ (final cycle)	0.29 (H atom parameter)
Residual density e/Å^3	−0.18 to 0.62

[a]Temperature 294 K, Enraf–Nonius CAD4-F diffractometer, graphite monochromator, takeoff angle 2.7°, aperture 2.0 + 1.0 tan θ mm at a distance of 173 mm from the crystal, scan extended by 25% on each side for background measurement (scan/background time ratio 2:1), $\sigma^2(F^2) = [S^2(C + 4B) + (0.04F^2)^2]/Lp^2$ (S = scan rate, C = scan count, B = normalized background count), function minimized $\Sigma w(|F_o| - |F_c|)^2$ where $w = 4F_o^2/\sigma^2(F_o^2)$, $R = \Sigma||F_o| - |F_c||/\Sigma|F_o|$, $R_w = (\Sigma w(|F_o| - |F_c|)^2/\Sigma w|F_o|^2)^{1/2}$, and gof = $[\Sigma w(|F_o| - |F_c|)^2/(m - n)]^{1/2}$. Values given for R, R_w, and gof are based on those reflections with $I \geq 3\sigma(F^2)$.

Table 2. Final atomic coordinates (fractional) and U_{eq} (10^3 Å^2).[a]

Atom	x	y	z	U_{eq}
O(1)	−0.2773(1)	0.4705(1)	0.7119(1)	50
O(2)	−0.0863(1)	0.5114(1)	0.8455(1)	47
O(3)	0.0313(1)	0.3702(2)	0.6817(1)	58
N	−0.1756(1)	0.4336(1)	0.6963(1)	44
C(1)	−0.0731(2)	0.4605(2)	0.7708(1)	41
C(2)	0.0515(2)	0.4368(2)	0.7704(1)	44
C(3)	0.1265(2)	0.5514(2)	0.7656(2)	54
C(4)	0.2615(2)	0.5379(3)	0.7808(2)	68
C(5)	0.3223(2)	0.4801(3)	0.8760(2)	73
C(6)	0.2513(2)	0.3632(2)	0.8765(2)	68
C(7)	0.1166(2)	0.3753(2)	0.8641(2)	55
C(8)	−0.2657(2)	0.3959(2)	0.8834(1)	45
C(9)	−0.3910(2)	0.3520(2)	0.8622(2)	56
C(10)	−0.4263(3)	0.2616(2)	0.9117(2)	68
C(11)	−0.3371(3)	0.2094(2)	0.9825(2)	75
C(12)	−0.2141(3)	0.2487(2)	1.0039(2)	74
C(13)	−0.1792(2)	0.3410(2)	0.9556(2)	59
C(14)	−0.2650(2)	0.6247(2)	0.8447(1)	48
C(15)	−0.1753(2)	0.7180(2)	0.8880(2)	62
C(16)	−0.2064(3)	0.8253(2)	0.9036(2)	80
C(17)	−0.3287(3)	0.8432(3)	0.8754(2)	85
C(18)	−0.4196(3)	0.7538(2)	0.8315(2)	82
C(19)	−0.3889(2)	0.6468(2)	0.8167(2)	66
B	−0.2284(2)	0.5023(2)	0.8257(2)	45
O(1′)	0.7153(1)	0.3201(1)	0.5075(1)	44
O(2′)	0.5536(1)	0.1770(1)	0.5074(1)	47
O(3′)	0.3770(1)	0.4146(1)	0.4547(1)	44
N′	0.5979(1)	0.3559(1)	0.4813(1)	40
C(1′)	0.5148(2)	0.2753(1)	0.4874(1)	38
C(2′)	0.3853(2)	0.2965(1)	0.4758(1)	38
C(3′)	0.2890(2)	0.2168(2)	0.3930(2)	49
C(4′)	0.1578(2)	0.2329(2)	0.3855(2)	74
C(5′)	0.1399(3)	0.2145(3)	0.4837(3)	94
C(6′)	0.2337(3)	0.2924(3)	0.5661(3)	82
C(7′)	0.3663(2)	0.2793(2)	0.5749(2)	56
C(8′)	0.7827(2)	0.1399(2)	0.6014(2)	48
C(9′)	0.8924(2)	0.1022(2)	0.6014(2)	60
C(10′)	0.9795(3)	0.0687(2)	0.6871(3)	81
C(11′)	0.9585(4)	0.0686(3)	0.7744(3)	96
C(12′)	0.8510(4)	0.1034(3)	0.7775(2)	94
C(13′)	0.7633(3)	0.1400(2)	0.6923(2)	69
C(14′)	0.6797(2)	0.1314(2)	0.3991(1)	46
C(15′)	0.5946(3)	0.0358(2)	0.3540(2)	63
C(16′)	0.5899(3)	−0.0158(2)	0.2666(2)	80
C(17′)	0.6707(3)	0.0276(3)	0.2205(2)	86
C(18′)	0.7556(3)	0.1223(3)	0.2625(2)	78
C(19′)	0.7596(2)	0.1738(2)	0.3505(2)	60
B′	0.6879(2)	0.1869(2)	0.5033(2)	43

[a] U_{eq} = 1/3 trace(diagonalized U).

e Å^{-3}) is located near the center of symmetry (0, 1/2, 1/2) that coincides with the center of the tetrameric hydrogen-bonded structural unit (see below). This peak is most likely an artifact of systematic errors in the data. All other residual peaks are less than 0.26 e Å^{-3}. Final atomic coordinates and equivalent isotropic thermal parameters, bond lengths, bond angles, and intra-annular torsion angles appear in Tables 2–5, respectively. The two independent molecules of **2***a* are shown in Fig. 1 and the packing arrangement is shown in Fig. 2. Hydrogen atom parameters, anisotropic thermal parameters, and torsion angles are included as supplementary material.[4]

Table 3. Bond lengths (Å) with estimated standard deviations in parentheses.

Bond	Length	Bond	Length
O(1)—N	1.388(2)	O(1′)—N′	1.393(2)
O(1)—B	1.557(2)	O(1′)—B′	1.553(2)
O(2)—C(1)	1.289(2)	O(2′)—C(1′)	1.284(2)
O(2)—B	1.558(2)	O(2′)—B′	1.566(2)
O(3)—C(2)	1.423(2)	O(3′)—C(2′)	1.425(2)
N-C(1)	1.292(2)	N′-C(1′)	1.293(2)
C(1)—C(2)	1.502(2)	C(1′)—C(2′)	1.500(2)
C(2)—C(3)	1.526(3)	C(2′)—C(3′)	1.531(3)
C(2)—C(7)	1.526(3)	C(2′)—C(7′)	1.524(3)
C(3)—C(4)	1.528(3)	C(3′)—C(4′)	1.519(3)
C(4)—C(5)	1.507(4)	C(4′)—C(5′)	1.508(5)
C(5)—C(6)	1.513(4)	C(5′)—C(6′)	1.505(5)
C(6)—C(7)	1.529(3)	C(6′)—C(7′)	1.521(4)
C(8)—C(9)	1.404(3)	C(8′)—C(9′)	1.393(3)
C(8)—C(13)	1.387(3)	C(8′)—C(13′)	1.398(3)
C(8)—B	1.601(3)	C(8′)—B′	1.600(3)
C(9)—C(10)	1.380(3)	C(9′)—C(10′)	1.384(4)
C(10)—C(11)	1.376(4)	C(10′)—C(11′)	1.357(5)
C(11)—C(12)	1.367(4)	C(11′)—C(12′)	1.369(5)
C(12)—C(13)	1.385(3)	C(12′)—C(13′)	1.397(4)
C(14)—C(15)	1.391(3)	C(14′)—C(15′)	1.389(3)
C(14)—C(19)	1.403(3)	C(14′)—C(19′)	1.391(3)
C(14)—B	1.592(3)	C(14′)—B′	1.596(3)
C(15)—C(16)	1.386(4)	C(15′)—C(16′)	1.371(4)
C(16)—C(17)	1.372(4)	C(16′)—C(17′)	1.378(4)
C(17)—C(18)	1.367(4)	C(17′)—C(18′)	1.371(4)
C(18)—C(19)	1.379(4)	C(18′)—C(19′)	1.382(4)

Results and discussion

The colorless crystalline products resulting from the reactions of **1** with the boron reagents show elemental analyses consistent with the expected 1:1 diphenyl- and difluoroboron chelates, in accordance with the infrared and ^{1}H nmr spectroscopic data. Furthermore, an intact chelated diphenylboron moiety is detected by the blue color reaction with diphenylcarbazone (17) in the case of the reaction of **1** with oxybis(diphenylborane). Unfortunately neither the infrared absorption in the region of N-H/O-H stretching frequencies between 3200 and 3500 cm^{-1}, the broad NH/OH proton signals in the ^{1}H nmr spectra, nor the other spectral features are sufficient to estab-

[4] Copies of material on deposit may be purchased from the Depository of Unpublished Data, Document Delivery, CISTI, National Research Council Canada, Ottawa, Canada K1A 0S2. Tables of hydrogen atom coordinates and bond lengths and angles involving hydrogen atoms have also been deposited with the Cambridge Crystallographic Data Centre and can be obtained on request from The Director, Cambridge Crystallographic Data Centre, University Chemical Laboratory, 12 Union Road, Cambridge CB2 1EZ, UK.

Table 4. Bond angles (deg) with estimated standard deviations in parentheses.

Bonds	Angle(deg)	Bonds	Angle(deg)
N-O(1)-B	103.6(1)	N′-O(1′)-B′	103.7(1)
C(1)-O(2)-B	107.4(1)	C(1′)-O(2′)-B′	107.5(1)
O(1)-N-C(1)	112.7(1)	O(1′)-N′-C(1′)	112.3(1)
O(2)-C(1)-N	114.2(2)	O(2′)-C(1′)-N′	114.5(2)
O(2)-C(1)-C(2)	122.5(2)	O(2′)-C(1′)-C(2′)	123.0(1)
N-C(1)-C(2)	123.3(2)	N′-C(1′)-C(2′)	122.5(2)
O(3)-C(2)-C(1)	107.8(1)	O(3′)-C(2′)-C(1′)	107.0(1)
O(3)-C(2)-C(3)	107.7(2)	O(3′)-C(2′)-C(3′)	111.7(2)
O(3)-C(2)-C(7)	112.5(2)	O(3′)-C(2′)-C(7′)	107.2(2)
C(1)-C(2)-C(3)	108.1(2)	C(1′)-C(2′)-C(3′)	110.7(1)
C(1)-C(2)-C(7)	109.1(1)	C(1′)-C(2′)-C(7′)	109.0(2)
C(3)-C(2)-C(7)	111.5(2)	C(3′)-C(2′)-C(7′)	111.1(2)
C(2)-C(3)-C(4)	111.8(2)	C(2′)-C(3′)-C(4′)	110.8(2)
C(3)-C(4)-C(5)	111.5(2)	C(3′)-C(4′)-C(5′)	111.2(2)
C(4)-C(5)-C(6)	110.8(2)	C(4′)-C(5′)-C(6′)	111.7(2)
C(5)-C(6)-C(7)	110.2(2)	C(5′)-C(6′)-C(7′)	111.7(2)
C(2)-C(7)-C(6)	112.2(2)	C(2′)-C(7′)-C(6′)	111.4(2)
C(9)-C(8)-C(13)	115.9(2)	C(9′)-C(8′)-C(13′)	116.7(2)
C(9)-C(8)-B	120.7(2)	C(9′)-C(8′)-B′	121.2(2)
C(13)-C(8)-B	123.3(2)	C(13′)-C(8′)-B′	122.1(2)
C(8)-C(9)-C(10)	122.2(2)	C(8′)-C(9′)-C(10′)	122.0(3)
C(9)-C(10)-C(11)	119.9(2)	C(9′)-C(10′)-C(11′)	120.4(3)
C(10)-C(11)-C(12)	119.5(2)	C(10′)-C(11′)-C(12′)	119.6(3)
C(11)-C(12)-C(13)	120.4(2)	C(11′)-C(12′)-C(13′)	120.8(3)
C(8)-C(13)-C(12)	122.1(2)	C(8′)-C(13′)-C(12′)	120.5(3)
C(15)-C(14)-C(19)	115.6(2)	C(15′)-C(14′)-C(19′)	116.7(2)
C(15)-C(14)-B	121.7(2)	C(15′)-C(14′)-B′	121.4(2)
C(19)-C(14)-B	122.7(2)	C(19′)-C(14′)-B′	121.8(2)
C(14)-C(15)-C(16)	122.1(2)	C(14′)-C(15′)-C(16′)	122.1(3)
C(15)-C(16)-C(17)	120.5(3)	C(15′)-C(16′)-C(17′)	119.9(3)
C(16)-C(17)-C(18)	119.1(3)	C(16′)-C(17′)-C(18′)	119.7(3)
C(17)-C(18)-C(19)	120.5(3)	C(17′)-C(18′)-C(19′)	120.0(3)
C(14)-C(19)-C(18)	122.2(3)	C(14′)-C(19′)-C(18′)	121.5(3)
O(1)-B-O(2)	98.5(1)	O(1′)-B′-O(2′)	98.3(1)
O(1)-B-C(8)	109.6(2)	O(1′)-B′-C(8′)	108.8(2)
O(1)-B-C(14)	109.8(2)	O(1′)-B′-C(14′)	111.7(2)
O(2)-B-C(8)	108.5(2)	O(2′)-B′-C(8′)	111.1(2)
O(2)-B-C(14)	110.2(2)	O(2′)-B′-C(14′)	108.6(2)
C(8)-B-C(14)	118.4(2)	C(8′)-B′-C(14′)	116.8(2)

Table 5. Intra-annular torsion angles (deg) with standard deviations in parentheses.

Atoms	Value(deg)	Atoms	Value(deg)
B-O(1)-N-C(1)	−14.1(2)	B′-O(1′)-N′-C(1′)	16.1(2)
O(1)-N-C(1)-O(2)	2.8(2)	O(1′)-N′-C(1′)-O(2′)	−5.9(2)
B-O(2)-C(1)-N	10.2(2)	B′-O(2′)-C(1′)-N′	−7.5(2)
C(1)-O(2)-B-O(1)	−16.9(2)	C(1′)-O(2′)-B′-O(1′)	15.7(2)
N-O(1)-B-O(2)	17.6(2)	N′-O(1′)-B′-O(2′)	−17.9(2)
C(7)-C(2)-C(3)-C(4)	51.4(3)	C(7′)-C(2′)-C(3′)-C(4′)	55.1(2)
C(2)-C(3)-C(4)-C(5)	−54.4(3)	C(2′)-C(3′)-C(4′)-C(5′)	−56.1(3)
C(3)-C(4)-C(5)-C(6)	58.0(3)	C(3′)-C(4′)-C(5′)-C(6′)	56.3(3)
C(4)-C(5)-C(6)-C(7)	−58.2(3)	C(4′)-C(5′)-C(6′)-C(7′)	−55.2(4)
C(5)-C(6)-C(7)-C(2)	55.9(3)	C(5′)-C(6′)-C(7′)-C(2′)	54.1(3)
C(3)-C(2)-C(7)-C(6)	−52.6(3)	C(3′)-C(2′)-C(7′)-C(6′)	−54.1(3)

Fig. 1. Stereoviews of the two independent molecules of **2***a*; 50% probability thermal ellipsoids are shown for the non-hydrogen atoms.

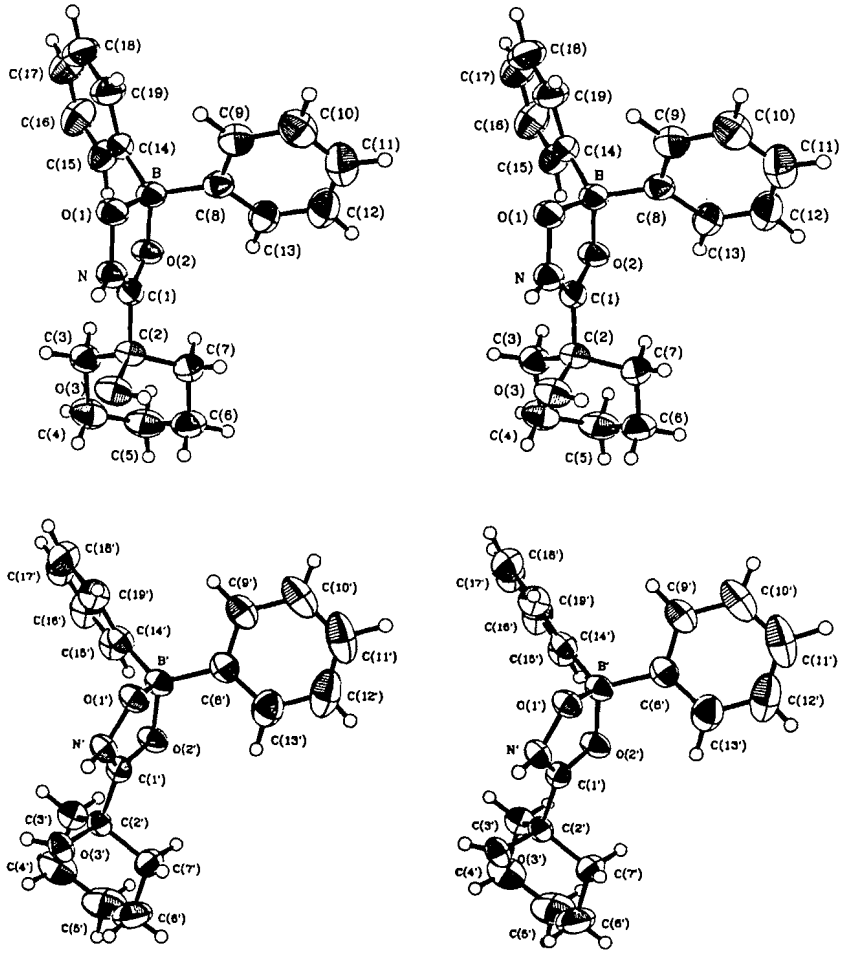

Fig. 2. Stereoview of the packing arrangement of **2***a*; 50% probability thermal ellipsoids are shown for the non-hydrogen atoms. Broken lines indicate hydrogen bonds.

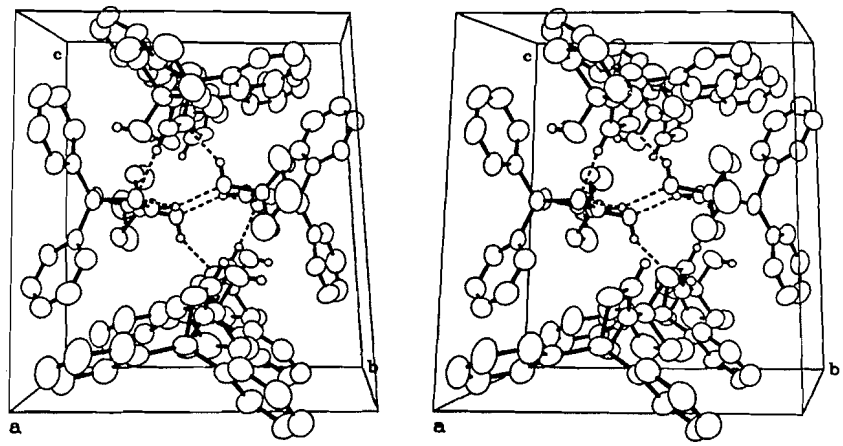

lish unambiguously the expected regular five-membered hydroxamatoborate ring structures **2** and **3** that correspond to the established ring systems of diphenyl- and difluoroboron chelates of various *N*-substituted hydroxamic acid derivatives (2, 3, 6, 9–11).

The observed spectroscopic data could also be assigned to

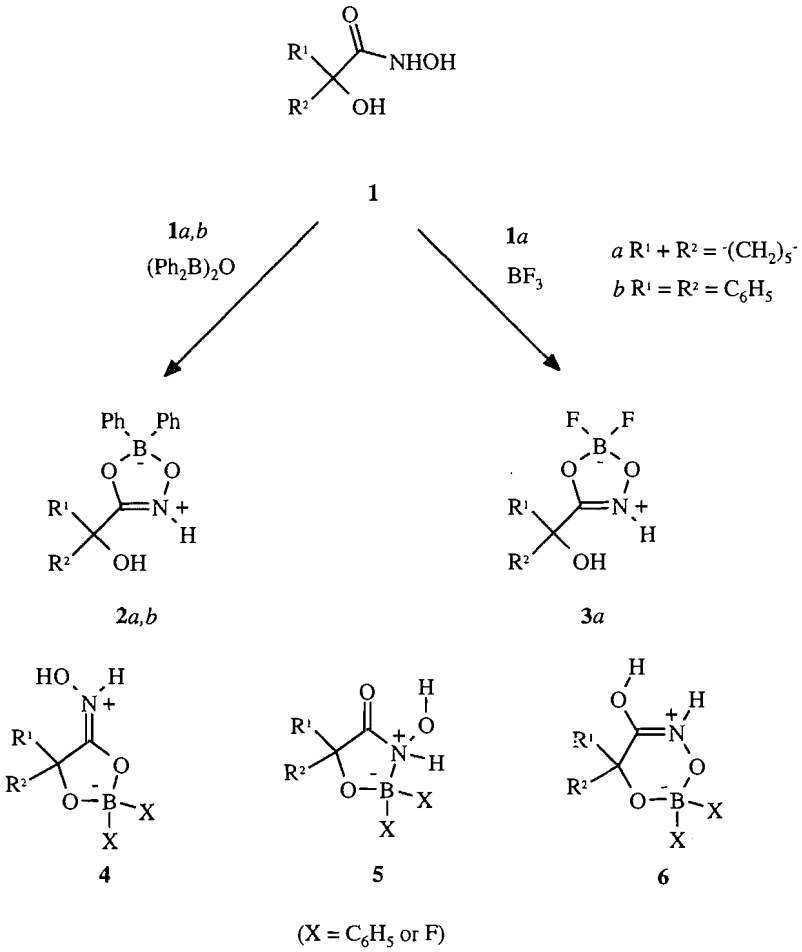

alternative five-membered chelate ring systems, **4** and **5**, or to the six-membered ring isomer **6**.[5] Structure **4** would involve the alkanol and the carbonyl groups as chelating ligands, as found in the five-membered difluoroboron chelate moiety of compound **7**, the molecular structure of which has been determined by an X-ray crystallographic analysis (14). The five-membered isomer **5**, which would have to be formed by a very weak N→B donor bond from the amide nitrogen atom to the boron atom, seems quite improbable. In the six-membered ring skeleton of the isomeric boron chelate **6**, however, the alkanol and the *N*-hydroxy groups would serve as coordinating ligands, as observed in the difluoroboron chelate ring portion

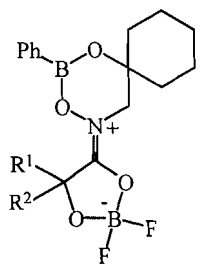

7

($R^1 = R^2 = 4\text{-}CH_3OC_6H_4$)

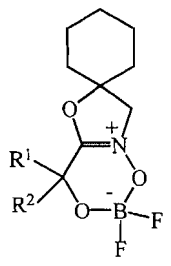

8

($R^1 = R^2 = C_6H_5$)

of the fully characterized compound **8** (12). To exclude the possible alternative chelate ring structures (**4** and **6** in particular) an X-ray crystallographic analysis of compound **2***a*, which gave the best crystals, was carried out.

The X-ray crystallographic analysis established the five-membered chelate ring structure (Fig. 1) analogous to those of the boron chelates of *N*-substituted hydroxamic acids (2, 3, 6, 9–11). In **2***a*, as in the *N*-substituted hydroxamatoborates, the hydroxamic acid serves as a "normal" *O,O*-bidentate ligand and forms the expected five-membered BONCO ring. This ring skeleton can also be ascribed, with a high degree of probability, to the other diphenylboron derivative (**2***b*) and to the difluoroboron derivative (**3***a*). To the best of our knowledge, **2***a* is the first structurally characterized example of an *N*-unsubstituted hydroxamatoborate complex in the literature. The crystallographic analysis is an especially important aspect of this work in view of the additional alternative modes of chelate formation offered by the α-hydroxy group neighboring the hydroxamic acid function.

In the crystal the chelate rings of **2***a* are further stabilized by intermolecular O—H···O and N—H···O hydrogen bonds that form centrosymmetric tetrameric units (**2***a*-tetramer, Fig. 2). Hydrogen bond geometry is as follows: O(3′)—H(O3′)···O(1)($-x$, $1-y$, $1-z$), O—H = 0.85(3) Å, O···H = 1.96(3) Å, O···O = 2.708(2) Å, O—H···O = 146(2)°; N—H(N)···O(1′)($-1+x$, y, z), N—H = 0.90(2) Å, N···H = 1.94(2) Å, N···O = 2.806(2) Å, N—H···O = 161(2)°; and N′-H(N′)···O(3′)(1–x, 1–y, 1–z), N—H = 0.97(2) Å, N···H =

[5] The formulae **2–6** depict only one important form out of the many possible resonance structures for each of the molecules.

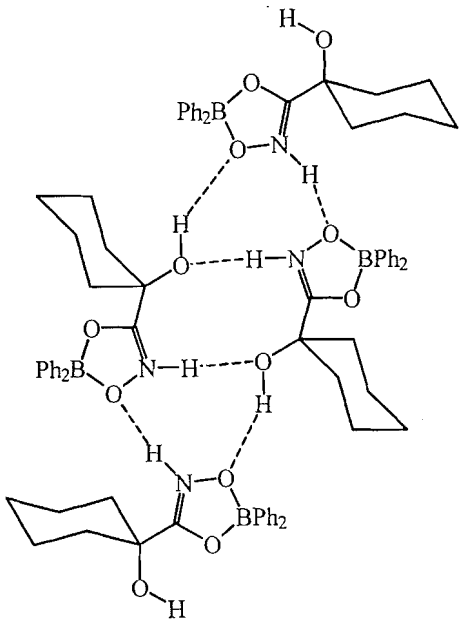

2*a* - tetramer

1.96(2) Å, N···O = 2.788(2) Å, N—H···O = 159(2)°. The tetrameric assembly can be described as a centrosymmetric dimer composed of "primed" molecules that features a central 10-membered ring containing two N—H···O bonds. The central ring is flanked by two "unprimed" molecules via one N—H···O and one O—H···O hydrogen bond each, forming eight-membered rings as shown in formula **2*a***-tetramer. The tetramers thus consist of two of each type of molecule (denoted by primed and unprimed atom labels) present in the solid state. Involved in the hydrogen bonding are the acidic hydroxamic acid N-H groups (the acidity of which is enhanced by the boron chelate formation) of all four molecules and the alcoholic O-H groups of the two primed molecules that function both as H-bond acceptors and donors as depicted in **2*a***-tetramer. All four hydroxamic N-O oxygen atoms act as H-bond acceptors, indicating higher electron density at these oxygen atoms than at the carbonyl oxygen atoms. The second pair of alcoholate O-H groups (unprimed molecules) are involved in intermolecular, intra-tetramer O—H···π(aromatic) interactions with the C(8′-13′) phenyl rings, further stabilizing the tetrameric unit (see Fig. 2). The H(O3)···C(phenyl) distances range from 2.65(3) Å for C(9′) to 3.33 Å for C(12′) (average 3.00 Å), and H(O3) is displaced 2.56(3) Å from the mean plane of the phenyl ring. All distances between the tetramers correspond to van der Waals interactions.

The short C=N distances (1.292(2) and 1.293(2) Å) show considerable double bond character, similar to that observed in the *N*-substituted hydroxamatoborates (2, 3, 6, 9–11). Plots of π-bond order vs. C—N bond length (19) and calculation (20) indicate that the C=N bonds have a π-bond order of about 0.85. The π-bond order of the C(1)—O(2) bonds (1.289(2) and 1.284(2) Å) is estimated to be about 0.56 from a plot of C—O distance vs. MO-π-bond order (21) and about 0.58 from calculation (20). These data fully support the *B,N*-betaine formulation of the chelates **2** and **3**, displaying the partial double bond character of the C—N bond and the weakened double bond character of the C=O bond of the hydroxamate ligands. This tendency is distinctly pronounced in the boron chelates compared to the average bond distances found in hydroxamic acids and their metal complexes (22). The average C-N, C—O, and N-O bond lengths for the boron chelate **2*a*** are 1.293, 1.287, and 1.391 Å, respectively. The corresponding values for metal chelates are 1.312, 1.269, and 1.376 Å (22); and those for hydroxamic acids are 1.325, 1.247, and 1.394 Å (22). The mean C-B/mean O-B bond length ratio of 1.025 is similar to those reported for other hydroxamato borates and is slightly less than the average value of 1.035 for "Ph_2BO_2" complexes having five-membered chelate rings (9, 10, 23), indicative of weak-to-intermediate binding strength of the *O,O*-chelating ligand to the "Ph_2B^+" moiety.

The hydroxamate group and the cyclohexane ring are oriented roughly perpendicular to one another, with the hydroxamate occupying an equatorial position, in both of the crystallographically independent molecules of **2*a***. Thus the N—H and C(2)—O(3) bonds are approximately coplanar, favoring the formation of the 10-membered hydrogen-bridged ring that is the central feature of the tetrameric associate of **2*a*** (see above). The five-membered BONCO chelate rings in both of the independent molecules have flattened and slightly distorted *B*-envelope conformations while the cyclohexane rings have nearly ideal chair conformations (see Table 5).

Acknowledgments

We thank the Natural Sciences and Engineering Research Council of Canada and the Fonds der Chemischen Industrie, Frankfurt am Main, for financial support.

References

1. K. Tanaka, K. Matsuo, A. Nakanishi, T. Hatano, H. Izeki, Y. Ishida, and W. Mori. Chem. Pharm. Bull. **31**, 2810 (1983).
2. S.J. Rettig, J. Trotter, W. Kliegel, and D. Nanninga. Can. J. Chem. **55**, 1 (1977).
3. S.J. Rettig, J. Trotter, W. Kliegel, and D. Nanninga. Can. J. Chem. **56**, 1676 (1978).
4. W. Kliegel and D. Nanninga. Pharmazie, **38**, 131 (1983).
5. W. Kliegel and D. Nanninga. Chem. Ber. **116**, 2616 (1983).
6. W. Kliegel, D. Nanninga, S.J. Rettig, and J. Trotter. Can. J. Chem. **61**, 2493 (1983).
7. W. Kliegel, M. Tajerbashi, S.J. Rettig, and J. Trotter. Can. J. Chem. **66**, 2621 (1988).
8. W. Kliegel, M. Tajerbashi, S.J. Rettig, and J. Trotter. Can. J. Chem. **67**, 1644 (1989).
9. W. Kliegel, M. Tajerbashi, S.J. Rettig, and J. Trotter. Can. J. Chem. **68**, 69 (1990).
10. W. Kliegel, U. Schumacher, M. Tajerbashi, S.J. Rettig, and J. Trotter. Can. J. Chem. **69**, 545 (1991).
11. W. Kliegel, M. Tajerbashi, S.J. Rettig, and J. Trotter. Can. J. Chem. **69**, 673 (1991).
12. W. Kliegel, U. Schumacher, S.J. Rettig, and J. Trotter. Can. J. Chem. **69**, 681 (1991).
13. W. Kliegel, U. Schumacher, S.J. Rettig, and J. Trotter. Can. J. Chem. **69**, 1212 (1991).
14. W. Kliegel, L. Preu, U. Schumacher, S.J. Rettig, and J. Trotter. Can. J. Chem. **70**, 1176 (1992).
15. W. Kliegel, U. Schumacher, S.J. Rettig, and J. Trotter. Can. J. Chem. **70**, 1188 (1992).
16. D. Geffken and H.-J. Kämpf. Chem.-Ztg. **103**, 19 (1979).

17. (*a*) R. Neu. Z. Anal. Chem. **176**, 334 (1960); (*b*) B. Friese and F. Umland. Anal. Chim. Acta, **96**, 303 (1978).
18. International tables for X-ray crystallography. Vol. IV. Kynoch Press, Birmingham, U.K. (present distributor Kluwer Academic Publishers, Boston, Mass.). 1974. pp. 99–102 and 249.
19. (*a*) L.M. Trefonas, R.L. Flurry, R. Majeste, E.A. Meyers, and R.F. Copeland. J. Am. Chem. Soc. **88**, 2145 (1966); (*b*) G. Häfelinger. Chem. Ber. **103**, 2902 (1970).
20. J.P. Paolini. J. Comput. Chem. **11**, 1160 (1990).
21. G. Häfelinger. Chem. Ber. **103**, 2922 (1970).
22. W.L. Smith and K.N. Raymond. J. Am. Chem. Soc. **103**, 3341 (1981).
23. W.O. Nelson, C. Orvig, S.J. Rettig, and J. Trotter. Can. J. Chem. **66**, 132 (1988).
24. W. Kliegel, U. Riebe, S.J. Rettig, and J. Trotter. Can. J. Chem. **73**, 835 (1995).

COMMUNICATION

Use of ^{19}F NMR as a direct probe of Δ^9 desaturase cryptoregiochemistry: a feasibility study

Peter Buist, Dale Marecak, Brian Dawson, and Bruce Black

Abstract: ^{19}F NMR can be used to monitor the relative efficiency with which various fluorinated aromatic sulfides are oxidized by the Δ9 desaturating system of *Saccharomyces cerevisiae*. Thus the sulfoxy acids produced from methyl *S*-(4-(trifluoromethyl)benzyl)-8-mercaptooctanoate (**3***d*), methyl *S*-(4-(trifluoromethyl)phenyl-2-ethyl))-8-mercaptooctanoate (**3***e*), and methyl *S*-(4-(trifluoromethyl)benzyl)-9-mercaptononanoate (**4***c*) were observed in the supernatant of *S. cerevisiae* cultures at concentrations of ~140, ~45, and ~10 μM, respectively. This paper lays the methodological basis for a novel, in vitro "thia test" of cryptoregiochemistry and provides further experimental evidence that the yeast Δ9 desaturase initiates oxidation of stearoyl CoA at C-9.

Key words: ^{19}F NMR, desaturase, chiral sulfoxidation, hydrocarbon activation.

Résumé : On a utilisé la RMN du ^{19}F pour évaluer l'efficacité relative de l'oxydation de divers sulfures aromatiques fluorés par le système désaturant Δ9 du *Saccharomyces cerevisiae*. On a ainsi observé les sulfoxyacides produit à partir du *S*-(4-(trifluorométhyl)benzyl)-8-mercaptooctanoate de méthyle (**3***d*), du *S*-(4-(trifluorométhyl)phényl-2-éthyl)-8-mercaptooctanoate de méthyle (**3***e*) et du *S*-(4-(trifluorométhyl)benzyl)-9-mercaptononanoate de méthyle (**4***c*) qui se retrouvaient dans le liquide surnageant les cultures de *S. cerevisiae* à des concentrations respectives d'environ 140, 45 et 10 μM. Cette publication décrit les bases méthodologiques d'un nouveau "thia test" in vitro de cryptorégiochimie et elle fournit des données expérimentales qui suggèrent que le levure Δ9 désaturase initie l'oxydation du stéaroylCoA en C-9.

Mots clés : RMN du ^{19}F, désaturase, sulfoxydation chirale, activation d'hydrocarbures.

[Traduit par la rédaction]

The biological *syn*-dehydrogenation (desaturation) of fatty acids as exemplified by the Δ9 desaturase-mediated transformation of stearoyl CoA (**1**) to give oleyl CoA (**2**) is a remarkable example of enzymic selectivity (1). A possible mechanism (2, 3) for this process involves regioselective hydrogen abstraction by an iron oxo species, followed by carbocation formation and subsequent proton elimination (Scheme 1). We have devised a simple "thia test" for determining the site of initial oxidation (cryptoregiochemistry) that consists of comparing the relative efficiency of oxo transfer to 9- vs. 10-thia substrate analogues (Scheme 1). Using a whole cell *Saccharomyces cerevisiae* Δ9 desaturating system, we have determined (4) that the yield of sulfoxide products obtained upon incubation of 9-thia fatty acids, such as **3***a–c*, is consistently higher than yields obtained with the corresponding 10-thia analogues (**4***a,b*) (Scheme 2). We have interpreted this data to mean that yeast Δ9 desaturation is initiated at C-9 of the parent stearoyl substrate. Renewed interest in the mechanism of fatty acid desaturation has arisen recently with the isolation and characterization of the soluble, plant Δ9 desaturases (5). Unlike the membrane-bound, non-heme monoiron Δ9 desaturases of which the *S. cerevisiae* and rat liver enzymes are prototypical examples (6), the plant enzymes are soluble and contain a carboxylate-bridged, non-heme diiron center. It would be of considerable interest to compare the mechanisms of these two classes of desaturases and thus there is an urgent need to modify our "thia test" so that it can be used with enzyme preparations and micromolar amounts of substrate. In this communication, we wish to report a possible solution to this problem.

It occurred to us that if our thia analogues were labelled with an appropriately situated fluorine substituent, the desaturase-mediated sulfoxidation could be monitored directly by ^{19}F NMR spectroscopy (7). Thus 4-(trifluoromethyl)phenyl substituted sulfides (**3***d,e*, **4***c*) were synthesized in good yield

Received October 26, 1995

P.H. Buist[1] **and D.M. Marecak.** Ottawa–Carleton Chemistry Institute, Department of Chemistry, Carleton University, 1125 Colonel By Drive, Ottawa, ON K1S 5B6, Canada.
B. Dawson and B. Black. Bureau of Drug Research, Health Protection Branch, Health Canada, Tunney's Pasture, Ottawa, ON K1A 0L2, Canada.

[1] Author to whom correspondence may be addressed. Telephone: (613) 788-2600, ext. 3643 or 3589. Fax: (613) 788-3749. E-mail: pbuist@ccs.carleton.ca

Scheme 1.

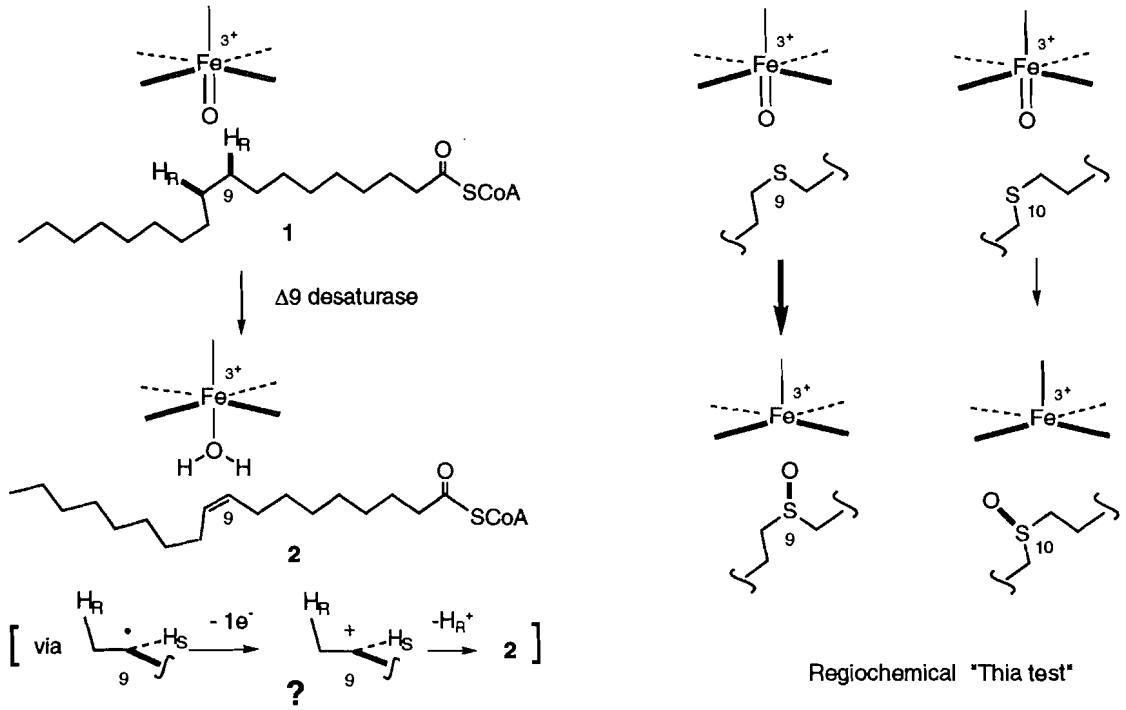

Scheme 2.

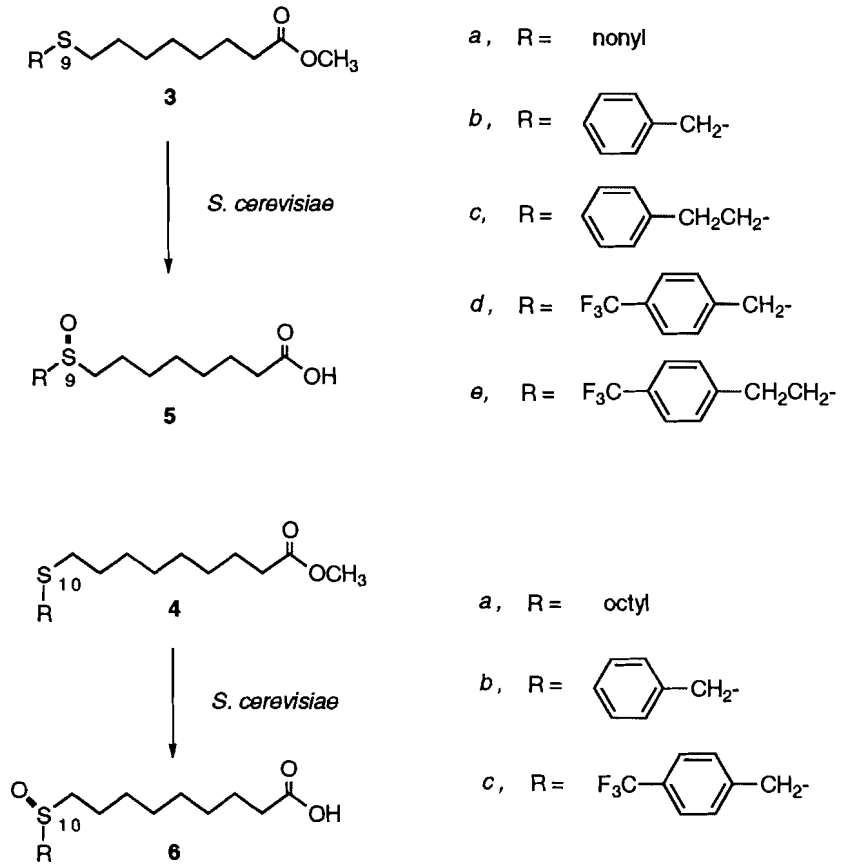

via selective S-alkylation of the appropriate ω-mercaptoalkanoic acids using previously published procedures (8). Commercially available 4-(trifluoromethyl)benzyl bromide was used as the alkylating agent in the synthesis of **3***d* and **4***c*. The preparation of **3***e* required the use of 4-(trifluoromethyl)phenyl-2-ethyl bromide (synthesized from 4-(trifluoromethyl)phenylacetic acid via a reduction ($LiAlH_4$) – bromination (PBr_3) sequence). Racemic sulfoxide reference standards (**5***d*,

Fig. 1. ^{1}H-decoupled ^{19}F NMR (376.5 MHz) spectra of cell-free supernatants containing micromolar amounts of sulfoxides (S-O) produced by oxidation of the corresponding sulfides (S) via the Δ9 desaturase of *S. cerevisiae*. (*A*): sulfoxide (**5***d*) produced from sulfide **3***d*: (*B*): sulfoxide **5***e* produced from sulfide **3***e*; and (*C*): trace sulfoxide **6***c* produced from sulfide **4***c*. An asterisk is used to designate an unknown trace impurity in the starting material.

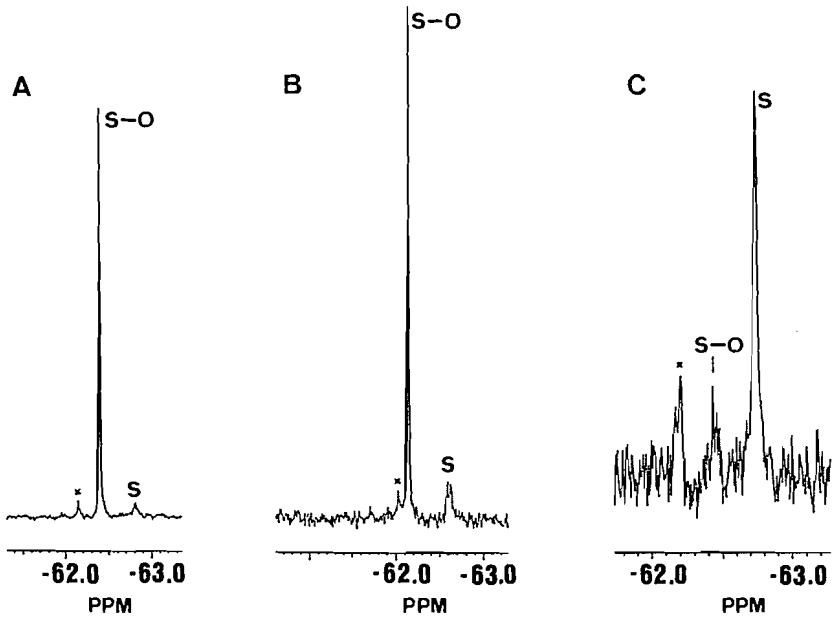

e, **6***c*) were prepared by oxidation of the corresponding sulfide methyl ester using one equivalent of *m*-chloroperoxybenzoic acid–CH_2Cl_2 (4) followed by hydrolysis using 2 N ethanolic KOH. All structural assignments were confirmed by ^{1}H NMR, MS, and elemental analyses.

Each fluorinated substrate methyl ester (160 μmol) was administered as 5% w/v ethanolic solutions to growing cultures (300 mL) of *S. cerevisiae* as previously described (4, 9). After growth, the yeast cells were allowed to settle and 500 μL aliquots of the resultant clear supernatants were examined by ^{1}H-decoupled ^{19}F NMR.[2] The partial NMR spectra obtained in each experiment are displayed in Fig. 1. We were gratified to see that the spectra were "clean" and exhibited two signals that we were able to assign to substrate and product with the help of synthetic standards. (We did not see any fragmentation products arising from oxidative cleavage α to sulfur in accordance with results of previous experiments (9)). In each spectrum, the ^{19}F resonance of the sulfoxy acid products[3] appeared at lower field (Δδ = 0.3 –0.5 ppm) than the signal due to the corresponding sulfide (Table 1).[4] By adding a known quantity of an internal standard (4-(trifluoromethyl)benzyl alcohol) after incubation, the concentration of sulfoxide produced in each experiment was determined as follows: **5***d*, ~140 μM (26%[5] conversion of sulfide); **5***e*, ~45 μM (8% conversion); **6***c*, ~10 μM (~ 2% conversion). These values for % conversion can be

[2] D_2O (50 μL) was added to each aliquot to provide a spectral lock. Use of ^{1}H decoupling eliminates unresolved, long-range coupling to neighbouring aromatic protons and results in a ca. twofold increase in sensitivity. All ^{19}F NMR spectra were obtained on a Bruker AM 400 (9.4 T) spectrometer operating at 376.50 MHz with a dedicated 5 mm ^{19}F/^{1}H probe and ^{19}F-specific preamplifier. A Bruker 400 MHz band-pass filter and a 376.5-MHz band-stop filter were used in the proton decoupler channel, and a 376.5 MHz band-pass filter and a 400 MHz band-stop channel were used in the fluorine observe channel for all acquisitions. Proton decoupling was achieved by using low power (composite phase decoupling). Chemical shifts are reported relative to external trichlorofluoromethane ($CFCl_3$) at 0.00 ppm. Spectra were acquired with 32 K data points and processed with ca. 2 Hz line broadening after zero-filling to 64 K. Other instrumental parameters include: T = 300 K, PW = 5.3 ms (90 deg), RD = 3.0 s. Acquisition time: 15 min.

[3] It should be noted that the sulfoxide product is produced in hydrolyzed form because the sulfide methyl ester must be converted to the corresponding CoA thioester in the yeast cell before attempted desaturation (= oxygenation) can take place. The sulfoxide CoA product is hydrolyzed to the free carboxylate form upon its excretion into the culture medium (pH 7). As would be expected, the difference in ^{19}F NMR chemical shifts for the free carboxylate and methyl ester forms of the sulfoxides is very small and ranges from 0.00 to ca. 0.03 ppm at pH 7.

[4] Only a small amount of sulfide is seen in the supernatants since these compounds associate with and are taken up by the yeast cells. Indeed, ^{19}F NMR spectra of the cell slurry in each experiment showed a broad ($w_{1/2}$ = 0.2 ppm) signal corresponding to that of the starting material.

[5] An independent check of the validity of this value was accomplished by extracting **5***d* from the acidified culture medium using CH_2Cl_2, followed by methylating the carboxylic acid group with diazomethane (4). A 26% yield of sulfoxide was obtained, in good agreement with the value estimated by ^{19}F NMR. The stereochemistry of this material was also assessed by ^{1}H NMR analysis using our newly developed (10) chiral shift reagent, (*S*)-(+)-α-methoxyphenylacetic acid. This allowed us to assign the "*S*" configuration to the major enantiomer (>96% ee), a result matching that obtained previously (4) for the corresponding nonfluorinated compound (**5***b*).

Table 1. ^{19}F NMR chemical shift data for trifluoromethyl aromatic fatty acid sulfides and the corresponding sulfoxides.

^{19}F Chemical Shift (ppm)[a]				
Substrates[c]		Products[c]		Δδ (ppm)[b]
3*d*	−62.81 ± 0.04	**5***d*	−62.40 ± 0.02	0.41 ± 0.05
3*e*	−62.64 ± 0.04	**5***e*	−62.14 ± 0.02	0.50 ± 0.05
4*c*	−62.74 ± 0.04	**6***c*	−62.43 ± 0.02	0.31 ± 0.05

[a]The uncertainty in the chemical shift values is based on data from at least five ^{19}F NMR spectra.

[b]Δδ = δ(sulfoxide)−δ(sulfide). It is somewhat surprising that the Δδ for **3***e*, **5***e* is greater than the Δδ for **3***d*, **5***d* despite the fact that the CF_3 group in **3***e*, **5***e* is one methylene group further removed from the sulfur atom. It is possible that premicellar aggregate formation is influencing the ^{19}F chemical shifts although we find that the chemical shifts of both sulfoxides and sulfides do not vary appreciably over a concentration range of 5–150 μM in biological media.

[c]Detection limits are typically 10 μM using 15 min acquisition times.

compared to the isolated yields obtained in previous experiments for the corresponding nortrifluoromethyl thiasubstrates: **5***b* (49%, ref. 4), **5***d* (17%, unpublished data), **6***b* (6%, ref. 4). Thus it is clear that each of the fluorinated sulfides is less efficiently oxidized, by a factor of ca. 2–3, than its nortrifluoromethyl analogue. This is an important result since it implies that the trifluoromethyl group is far enough away from the sulfur atom so that it would not dramatically bias the outcome of a "thia test" involving the two fluorinated sulfides with equivalent chain lengths: **3***e* and **4***c*. The cryptoregiochemistry of various Δ9 desaturases could be assessed in vitro by monitoring the appearance of ^{19}F NMR signals due to the corresponding sulfoxide products, **5***e* and **6***c*.[6] An additional advantage of this approach is that the ^{19}F chemicals shifts of the two sulfoxides are sufficiently different (0.29 ppm, see Table 1) to allow the "thia test" to be conveniently carried out as a direct competition experiment.

In summary, we have illustrated how some of the characteristics of ^{19}F NMR methodology (high sensitivity, lack of interferences, wide chemical shift range) can be used to develop a novel probe for the mechanistic study of a long-neglected biological reaction.

Acknowledgement

We wish to thank the Natural Sciences and Engineering Research Council of Canada (NSERC) for a postgraduate scholarship to D.M. and for financial support of this work. The technical assistance of Natalie Vo is greatly appreciated.

References

1. H. Cook. *In* Biochemistry of lipids and membranes. *Edited by* D.E. Vance and J.E. Vance. The Benjamin Cummings Publishing Co. Ltd., Menlo Park, Calif. 1985. pp. 191–203.
2. P.R. Ortiz de Montellano. Trends Pharmacol. Sci. **10**, 354 (1989).
3. J.R. Collins, D.L. Camper, and G.H. Loew. J. Am. Chem. Soc. **113**, 2736 (1991).
4. P.H. Buist and D.M. Marecak. J. Am. Chem. Soc. **114**, 5073 (1992).
5. B.G. Fox, J. Shanklin, J. Ai, T.M. Loehr, and J. Sanders-Loehr. Biochemistry, **33**, 12776 (1994).
6. J.E. Stukey, V.M. McDonough, and C.E. Martin. J. Biol. Chem. **265**, 20144 (1990).
7. C. Walsh. Adv. Enzymol. **55**, 197 (1982).
8. P.H. Buist, H.G. Dallmann, R.R. Rymerson, and P.M. Seigel. Tetrahedron Lett. **28**, 857 (1987).
9. P.H. Buist and D.M. Marecak. Can. J. Chem. **72**, 176 (1994).
10. P.H. Buist, D.M. Marecak, H.L. Holland, and F.M. Brown. Tetrahedron: Asymmetry, **6**, 7 (1995).

[6] It is reasonable to expect that the difference in ^{19}F NMR chemical shift of the CoA or ACP thioester derivatives of sulfoxides **5***e* and **6***c* would be similar to the observed chemical shift difference of the free carboxylate forms of **5***e* and **6***c* (See footnote 4).

1995 R.U. Lemieux Award Lecture
Ketenes and bisketenes: organic chemistry in microcosm[1]

Annette D. Allen, Jim D. Colomvakos, Ian Egle, Ronghua Liu, Jihai Ma, Romeo M. Marra, Michael A. McAllister, and Thomas T. Tidwell

Abstract: Silyl substituents stabilize ketenes, and permit the preparation of persistent bisketenes, which show characteristic ^{13}C, ^{17}O, and ^{29}Si NMR chemical shifts. The structures and conformations of bisketenes have been examined, as well as their interconversion with cyclobutenediones. A tetraketene has been prepared, and the hydration reactivity of carbon suboxide has been measured.

Key words: bisketenes, structures and conformations; cyclobutenedione interconversion.

Résumé : Les substituants silyle stabilisent les cétènes et ils rendent possible la préparation de biscétènes persistants qui présentent des déplacements chimiques caractéristiques en RMN du ^{13}C, du ^{17}O et du ^{29}Si. On a étudié les structures et les conformations des biscétènes ainsi que celles de leurs produits d'interconversion en cyclobutènediones. On a préparé un tétracétène et on a mesuré la réactivité d'hydratation du sous-oxyde de carbone.

Mots clés : biscétènes, structures et conformations; interconversion en cyclobutènediones.

[Traduit par la rédaction]

The preparation of the first bisketene, carbon suboxide (**1**), by the dehydration of malonic acid, was reported in 1906 by Diels and Wolf (*1a*) and it was soon found by Staudinger and Bereza (*1b*) that the same bisketene could be obtained by a bisdehalogenation (eq. [1]).

[1] $$HO_2CCH_2CO_2H \xrightarrow{P_2O_5} \underset{\mathbf{1}}{O{=}C{=}C{=}C{=}O} \xleftarrow{Zn} ClOCCBr_2COCl$$

Staudinger and Anthes (*2a*) attempted to prepare the simplest bisketene, carbon monoxide dimer **2**, by an analogous dehalogenation route, but this was unsuccessful, and gave only carbon monoxide (eq. [2]). Despite strenuous efforts **2** is still unknown (*2b–d*), although the most recent calculations predict that this molecule is an energy minimum (*2e*). Other investigations have succeeded in the preparation of some higher carbon oxides, including C_4O_2 (*2f,g*) and C_5O_2 (*2h,i*), under gas phase or matrix conditions.

Other bisketenes that Staudinger et al. attempted unsuccessfully to prepare include 1,2-bisketene (**3**) and 1,4-quinoketene (**4**) (*3a,b*). Ketene **3** and a number of derivatives have subsequently been prepared and observed under matrix isolation

[2] 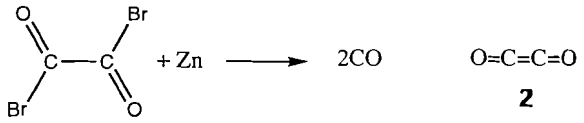

2

conditions, or in solution by fast UV or IR measurement techniques (*3c–h*) as reviewed elsewhere (4). The benzannulated analogue of **3**, namely, **5**, which is isomeric to **4**, has also been studied (*3i–k*). Evidence has been obtained for the formation and polymerization of **4** by the reductive dehalogenation of terephthalyl chloride (**4***a*) with alkali metals (*3n*), and this species has been directly observed, with an IR band at 2082 cm^{-1}, by photolysis of [2.2]paracyclophane-1,10-dione in an Ar matrix at 10 K (*3o*).

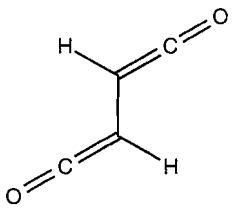

3

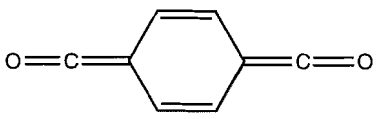

4

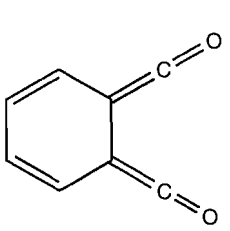

5

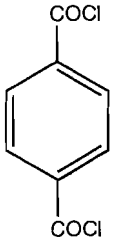

4a

Received October 10, 1995.

A.D. Allen, J.D. Colomvakos, I. Egle, R. Liu, J. Ma, R.M. Marra, M.A. McAllister, and T.T. Tidwell.[2] Department of Chemistry, University of Toronto, Toronto, ON M5S 1A1, Canada.

[1] This work was presented by Professor Tidwell as the Lemieux Award Lecture at the 78th Annual Conference of the Canadian Society for Chemistry, Guelph, Ontario, May 28, 1995.

[2] Author to whom correspondence may be addressed. Telephone: (416) 287–7217. Fax: (416) 287–7204.

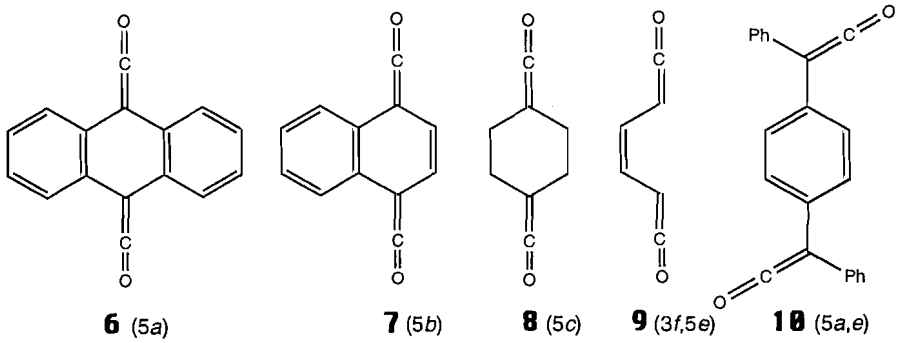

6 (5*a*) **7** (5*b*) **8** (5*c*) **9** (3*f*,5*e*) **10** (5*a*,*e*)

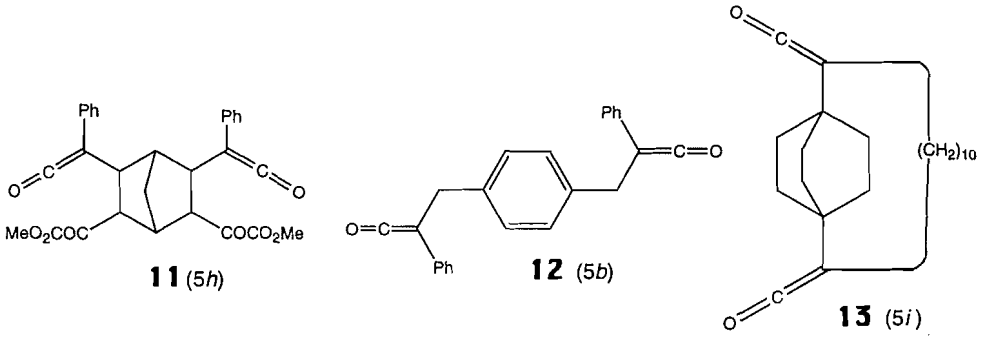

11 (5*h*) **12** (5*b*) **13** (5*i*)

[3] $SiH_3CH{=}C{=}O + CH_3CH{=}CH_2 \xrightarrow[11.5\ kcal/mol]{\Delta E \doteq} CH_3CH{=}C{=}O + SiH_3CH{=}CH_2$

[4] 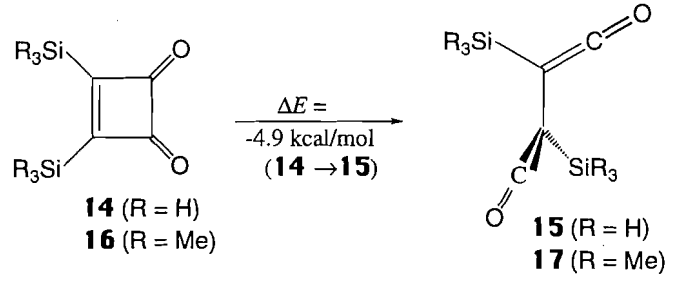

14 (R = H) **15** (R = H)
16 (R = Me) **17** (R = Me)

Several bisketenes in which the ketenyl groups are not directly bonded to one another have been prepared and directly observed, and examples **6–13** are shown (5*a–h*). These have been prepared by zinc dehalogenation of α-bromo acyl halides (**6, 7, 10, 12**), bis(dehydrohalogenation) (**8**), photochemical ring opening (**9**), and double Wolff rearrangement (**13**). Other reactions involving the conversion of two functional groups such as diazoketone (5*i*), dioxinone (5*j*), and isopropenyl ether (5*k*) to ketenyl groups in molecules may have occurred successively so that bisketenes were never present.

Investigations in our laboratory have focused on the influence of silyl substituents in the stabilization of ketenes and bisketenes (6, 7). Molecular orbital calculations at the MP2/6-31G*//MP2/6-31G* level for the isodesmic reaction of eq. [3] indicate that the SiH_3 substituent is 11.5 kcal/mol more stabilizing for ketene than is CH_3 compared to the effect on alkenes (6*d*,*e*). The ring opening of the cyclobutenedione **14** to the bisketene **15** is calculated (6*g*) to be exothermic by 4.9 kcal/mol (eq. [4]). These bisketenes are calculated to have the twisted conformation shown, as discussed in more detail below.

Experimentally, the ring opening of **16** to **17** proceeds quantitatively on heating, and there is good agreement between the calculated E_{act} for ring opening of **14** of 27.2 kcal/mol and the experimental $\Delta H^{\ddagger}$ of 29.4 kcal/mol for **16** (6*g*, 7*a*). This confirmation of the predictive power of ab initio molecular orbital calculations of the stabilities of ketenes and analogous molecules has encouraged us to extend these studies, and useful results have also been obtained for isocyanates (7*d*), diazo compounds, allenes, diazirines, and cyclopropenes, as well as for a variety of ketenes (6*d*,*e*), and the magnitude of the stabilization is related to the coefficient of the cumulene LUMO (7*d*).

The origin of the stabilization of ketenes by silyl substituents has been of interest since the first preparation of $Me_3SiCH{=}C{=}O$ (6*a*), when it was found that this ketene had no tendency to dimerize, in contrast to all other aldoketenes known at that time. Calculations predict that all of the cumulenes are stabilized by electropositive substituents (6*d*,*e*, 7*d*) but so far this effect has been most extensively investigated experimentally with ketenes. Two specific descriptive expla-

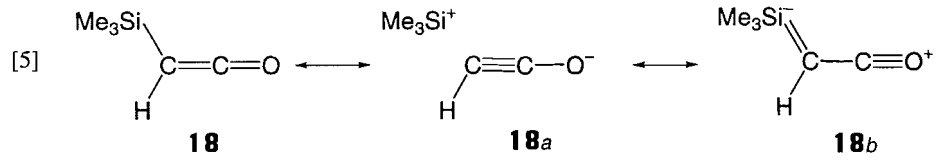

nations that have been advanced for this phenomenon are overlap of the C—Si σ bond with the in-plane π bond of the carbonyl as shown in eq. [5] (6*b*), and also p_π–d_π donation of electrons from the electron-rich β-carbon of the ketene to silicon as in **18***b* (6*c*). Molecular orbital calculations (6*d*,*e*) gave a quantitative measure of the stabilizing effect of silicon (eq. [3]), but the calculated structure of $SiH_3CH{=}C{=}O$ was inconclusive regarding any strong structural evidence for the type of overlap shown in eq. [5]. The alternative of p_π–d_π overlap is regarded as unimportant in other contexts (4*a*, 6*f*).

Study of the ^{13}C, ^{17}O, and ^{29}Si NMR spectra of silylketenes and bisketenes (8*a*) provides evidence for the type of "neutral hyperconjugation" shown in **18***a* (8*b*). Thus the ^{13}C and ^{17}O resonances of silylketenes are shifted upfield by 18.7–26.4 and 59–85 ppm, respectively, compared to other ketenes, while the ^{29}Si resonance is shifted downfield by 4–12 ppm in comparison to silylalkenes (Table 1). This is the effect expected if there is increased negative charge density on the carbonyl carbon and oxygen, and increased positive charge on the silicon, whereas just the opposite effects would be expected if there were charge donation to the silicon, as in **18***b*. Chemical shifts are affected by a variety of factors besides atomic charges, and so the use of such shifts to evaluate "neutral hyperconjugation" must be used with caution (8*b*), but nevertheless charges exert a major influence and the consistent results for three different nuclei and a variety of substrates are highly supportive of the phenomenon shown in **18***a*.

Calculations of the chemical shifts of $Me_3SiCH{=}C{=}O$ and $(CH_3)_2C{=}C{=}O$ using the IGLO method, basis set II, with MP2/6–31G* optimized geometries gave the results shown below, with experimental values in parentheses for comparison (8*a*).

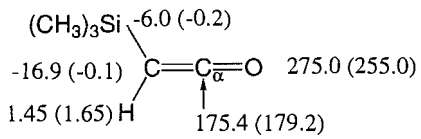

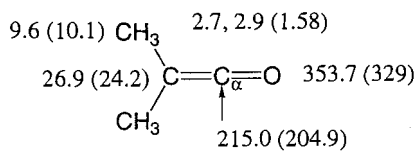

The calculated values are in reasonable but not exact agreement with the experimental values but, most importantly, the calculations reproduce the large effects of Si substitution on chemical shifts for $^{13}C_\alpha$ (Δδ calcd. 39.6, obsd. 25.7 ppm) and ^{17}O (Δδ calcd. 78.7, obsd. 74 ppm). Some of the differences between the calculated and experimental chemical shifts may arise from factors such as solvent effects, but for the analysis of trends these calculated values appear to be quite useful.

Other factors besides electronic charge distributions as shown in eq. [5] undoubtedly affect the chemical shifts, but nevertheless the fact that the observed shifts are consistent in all cases with the effects expected from electron donation from the C—Si bond to the carbonyl group, and opposite from the effects expected for electron donation toward Si, provide a powerful argument for the importance of the former effect as opposed to the latter.

Similar behavior is also observed in α-silylated ketones, in which downfield shifts in the ^{29}Si NMR of the silyl groups are observed relative to $(CH_3)_4Si$ and upfield shifts in the ^{17}O NMR are shown relative to non-silylated model compounds (8*a*).

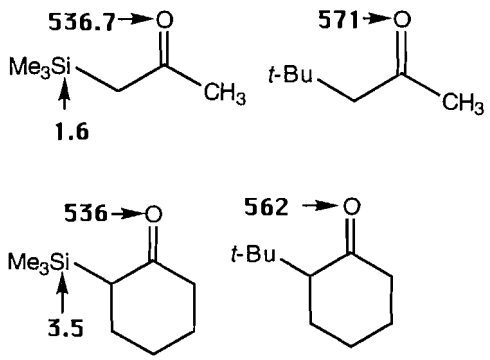

For the parent bisketene **3** the HF/6-31G*//HF/6-31G* calculated relative energies of the twisted, *anti*, and *syn* conformations are 0.0, 2.4, and 4.0 kcal/mol, respectively (6*g*). The difference of 1.6 kcal/mol between the *syn* and *anti* conformers may be due to a repulsion between the electron-deficient C_α carbons. For the $SiMe_3$ substituted bisketenes **17** the difference between the *syn* and *anti* conformers is 8.2 kcal/mol (6*h*) and the larger difference of 6.6 kcal/mol evidently reflects a steric effect.

The twisted conformation **17**, with a dihedral angle of 105° between the ketenyl units, is calculated to be 2.8 and 11.0 kcal/mol, respectively, more stable than the *anti* and *syn* conformations corresponding to **17***a* and **17***b* (6*h*). A major population of the *anti* conformation **17***a* is also ruled out by the measured dipole moment of 2.7 D for the bis(trimethylsilyl) analogue **17**, compared to a measured dipole moment of 1.7 D for $Me_3SiCH{=}C{=}O$ (6*h*). The *syn* rotamer **17***b* can be excluded from consideration because of the apparent large steric interactions and calculated low stability of this conformation.

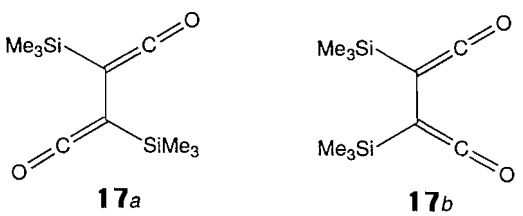

Table 1. NMR chemical shifts in $CDCl_3$ of ketenes and reference compounds (8*a*).

Ketene	$\delta^{13}C$ (C_α)	$\delta^{17}O$	$\delta^{29}Si$
$Me_2C{=}C{=}O$	204.9	329	
t-$Bu_2C{=}C{=}O$	203.4	330.6 (331.5)[a]	
$PhCMe{=}C{=}O$	205.6		
$Ph_2C{=}C{=}O$	201.3	340[a]	
$Me_3SiCH{=}C{=}O$	179.2	255.0	−0.2
$Me_3SiCPh{=}C{=}O$	182.5		−0.6
$(Me_3SiC{=}C{=}O)_2$	181.8	269.2 (269.0)[a]	3.2
$(t\text{-}BuMe_2SiC{=}C{=}O)_2$	182.2	270.5	10.6
$Me_3SiCH_2CO_2H$			3.8
$Me_3SiCH_2CO_2Et$			3.2
$Me_3SiCH_2COCH_3$	206.8	536.7	1.6
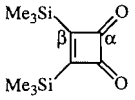	202.0	499.1	−8.4
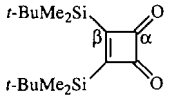	202.1		0.4
CH_3COCH_3	206.5	565.3 (571)[a]	
$Me_3SiCH{=}CH_2$			−6.6
$Me_3SiC_6H_5$			−4.5

[a] CH_3CN solvent

We have suggested that a major reason that the bisketenes **15** and **17** are not coplanar is because of the repulsion between the electrons in the *p* orbitals at C_β of the ketenes (6*g*,*h*). These carbons carry a high negative charge density, as evidenced by the remarkably high-field ^{13}C NMR chemical shift of C_β in **17** of δ 4.5, and, to avoid the π–π repulsion in a coplanar array as in **19**, the dienyl units twist out of planarity. The phenomenon of unfavorable π–π interactions with electron-rich groups at C_β of ketenes has also been found in the computed geometries of ketenes substituted with the lone pair containing substituents OH, SH, NH_2, and PH_2, which are predicted (6*d*,*e*) to have conformations in which the lone pairs are twisted out of conjugation with the C=C π bond, as illustrated for NH_2 (**20**). This behavior has been confirmed experimentally for the ketene $(CF_3S)_2C{=}C{=}O$, for which the twisted conformation **21** with the S—CF_3 bond almost perpendicular to the molecular plane was found to be favored, using electron diffraction (9).

The *ortho* isomer **5** of "quinoketene" **4** (3*i*–*k*) has been generated in CH_3CN solution at 23 ± 2°C by laser flash photolyis of benzocyclobutadienedione **22** (10*a*), and directly observed by time-resolved infrared spectroscopy (TRIR). The rate constant for ring closure was measured as 1.9×10^4 s^{-1} both from the disappearance of the ketene band at 2128 cm^{-1} of **5**, and from the reappearance of the ketone band at 1781 cm^{-1} of **22** (10*a*). This reclosure is calculated at the MP2/6-31G*//MP2//6-31G* level to be exothermic by 38.2 kcal/mol and, based on the observed rate constants and the assumption that $\Delta S^{\ddagger} = 0$ for this process, the barrier to ring closure is 6 kcal/mol (10*a*).

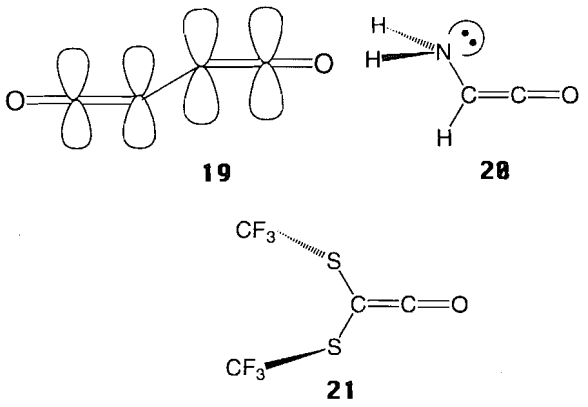

19 **20** **21**

[6] 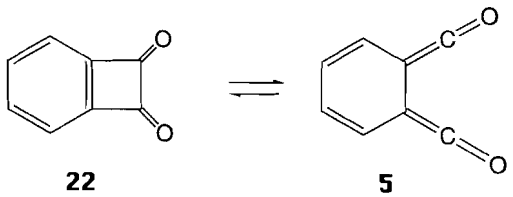

22 **5**

The 38.2 kcal/mol greater stability calculated for **22** relative to **5** is remarkably high, for, even though **22** possesses an aromatic benzene ring, this is fused to a strained cyclobutenedione ring. However, this latter ring system may possess some aromatic stability itself, and furthermore the 1,2-bisketene unit of **5** is destabilized relative to an ordinary diene, as shown by the isodesmic energy change of eq. [7] (6*d*). The ketenyl groups of **5** are calculated to be twisted out of planarity with a dihedral angle of 34.2°, and thus **5** resembles other bisketenes such as **15** and **17** in this respect. In the case of a coplanar conformation of **5** there would be not only π-electron repulsion at C_β, but also repulsion of the positively charged C_α carbonyl carbons. Antiaromaticity of **5** due to a high electron density at the two C_β ketenyl carbons giving 8π electron character similar to that proposed for heptafulvenone **23** (10*b*) may also contribute to the high preference for **22** relative to **5**.

A variety of long-lived 1,2-bisketenes **24** substituted with stabilizing silyl groups ($R_3{}^1Si$ = Me_3Si, *t*-$BuMe_2Si$, i-Pr_3Si) have been prepared from photolysis or thermolysis of the corresponding cyclobutenediones (**25**), as shown in eq. [8] (7). When these bisketenes have two silyl substituents they are thermodynamically stable relative to the cyclobutenedione precursors (7*a*), but in examples substituted with one Me_3Si group and either Ph (**26**) or Me (**27**) the bisketene is rather long lived at room temperature, but reverts to the more stable cyclobutenedione at measurable rates at higher temperatures (7*b*,*c*).

[7] $(CH{=}C{=}O)_2 + 2CH_2{=}CH_2 \xrightarrow[-11.9\ kcal/mol]{\Delta E =} (CH{=}CH_2)_2 + 2CH_2{=}C{=}O$

3

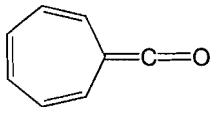

23

[8]

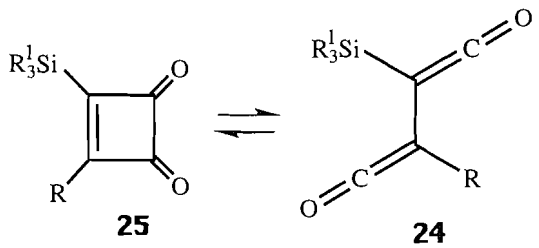

25 **24**

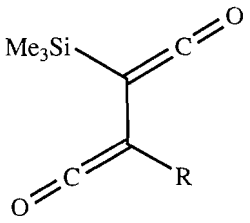

26 (R = Ph)
27 (R = Me)

Using flash photolysis and time-resolved infrared detection, a number of rather unstable 1,2-bisketenes have been generated and directly observed (10*a*). The examples **26** and **27** bearing a single Me_3Si are quite long lived at room temperature and their ring closure to the thermodynamically more stable cyclobutenediones was only observed at elevated temperatures. Surprisingly, for the long-known examples **28***a* (R^1 = Ph, R^2 = H) and **28***b* ($R^1 = R^2$ = Ph) conventional photolysis and UV detection were sufficient for observation of the bisketenes, which were found to have half-lives of 1 h and 18 s, respectively, at 25°C. Summarizing the examples that have been observed, the scale of reactivities is as shown. The observed difference between **26** and **5** is a factor of 10^{10} and, based on the measured rate of ring opening of **16** to **17** and the equilibrium constant for this process estimated by the calculated energy difference of the process for R = SiH_3 of 4.9 kcal/mol (eq. [4]), the rate of ring closure of **17** may be estimated as less than that of **26** by a factor of 10^5, giving a total span in reactivity of 10^{15}.

As noted above, bisketenes **4** and **6–13** where the ketenyl groups are non-adjacent have been prepared and directly observed (5). Poly(ketenes) have also been generated (11) by photolysis of poly(cyclobutenediones) in a matrix at 30 K, as in the conversion of **29** to form hexa(ketene) **30**, which displayed an IR band at 2115 cm^{-1} (eq. [10]). Further photolysis led to decarbonylation and possible formation of cyclooctadecanonyne (C_{18}).

[9]

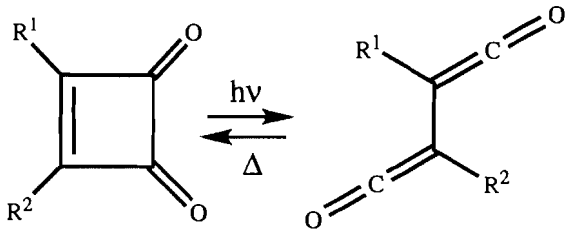

Relative rates of cyclobutenedione formation from bisketenes:

R^1,R^2	Me_3Si, Me_3Si **17**	Me_3Si, Ph **26**	Me_3Si, Me **27**	Ph, H **28***a*	Ph, Ph **28***b*	**5**
k_{rel}	~10^{-5}	1.0	2	84	2×10^4	10^{10}

[10]

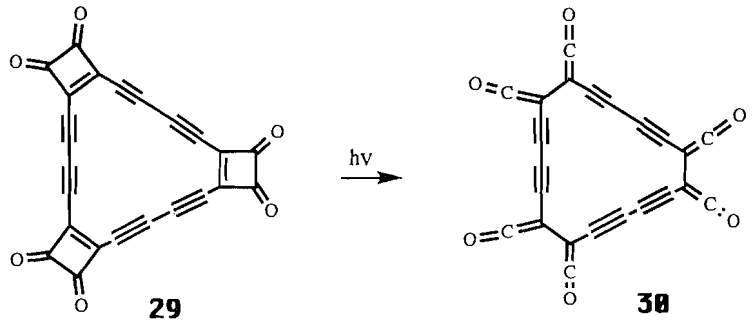

29 **30**

Using the route shown in Scheme 1 we have prepared the bis(cyclobutenedione) precursor **32** for a long-lived tetraketene **33** stabilized by Me_3Si groups, and studied its reactivity (12). Photolysis of **32** with 350 nm light led to the formation of a new species with λ_{max} 280 nm and an ^1H NMR spectrum ascribed to the tetraketene structure **33**, formed by photochemical ring opening of **32**, probably by a stepwise process via the bisketene **34** (eq. [11]). Evidence for the structure of **33** includes the ketenyl IR band observed at 2086 cm^{-1}, which is comparable to that at 2093 cm^{-1} for bis(ketene) **26** (7*b*,*c*), and the very distinctive signals in the ^{13}C NMR spectrum at δ 6.9 and 32.8 for the Me_3Si and aryl-substituted ketenyl carbons, as compared to the values for the corresponding carbons of **26** at δ 7.9 and 33.5, respectively. Upon heating of **33** with monitoring of the UV absorption the initial conversion of **33** to **34**, and then a slower conversion of **34** to **32** could be observed.

Scheme 1.

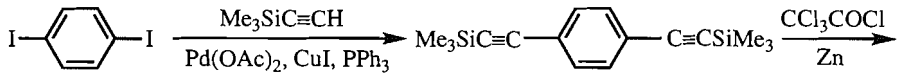

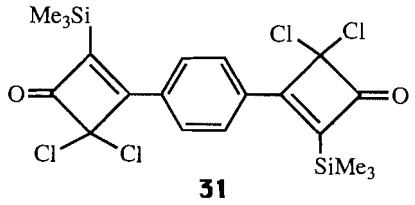

31

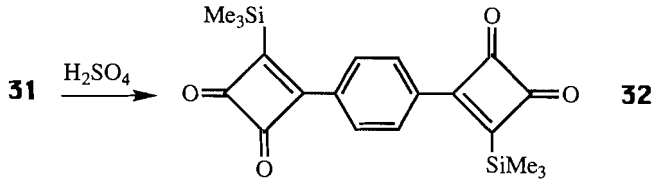

32

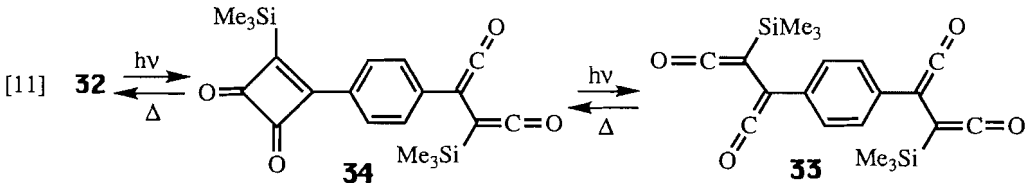

We have also been attracted (13) to the study of reactivity of carbon suboxide, the first bisketene (1), which despite its long history has seldom been the object of mechanistic examination (14, 15). In particular, the hydration reactivity of C_3O_2 was of interest both for comparison to other ketenes (16, 17), and also because of a recent proposal (14*a*) that C_3O_2 is present on comet Halley, which is largely composed of water ice (14*a*). Carbon suboxide is known to react with water to form $CH_2(CO_2H)_2$, with alcohols ROH to form esters $CH_2(CO_2R)_2$, and with HCl to form $CH_2(COCl)_2$ (15*c*). As shown in eq. [12] for alcohol addition, acylketenes **35** have been implicated as intermediates in these reactions (15*d*) but these have not been well characterized when formed from this source because their reactivity toward nucleophiles appears comparable to that of C_3O_2.

[12] $O{=}C{=}C{=}C{=}O \xrightarrow{ROH} RO_2CCH{=}C{=}O \xrightarrow{ROH} CH_2(CO_2R)_2$

1 **35**

Experimentally the hydration reactivity of C_3O_2 is less than that of $CH_2{=}C{=}O$ in both the acid-catalyzed and neutral reactions, by factors of 5.2×10^4 and 2.5×10^3, respectively, in water at 25°C. Only a single rate process was observed in each case, and this is assigned to the initial reaction of carbon suboxide.

As a guide to understanding this behavior and to test possible mechanistic proposals, the structures and energies (Table 2) of some of the species involved in these reactions were calculated by ab initio methods at the MP2/6-31G* + ZPVE// MP2/6-31G* level, as has been done previously for other ketenes (6*d*,*e*,*g*, 16).

The mechanism of ketene hydration has been interpreted (4*a*, 17) as involving an initial nucleophilic attack by H_2O at the carbonyl carbon to give a rather polar transition state resembling **36** that is also solvated by additional water molecules. This forms an intermediate enediol **37**, or the corresponding enolate, and then is rapidly converted to acetic acid (eq. [13]). This mechanism is favored even though the addition of water to the C=C bond to form acetic acid directly is more favorable, but the calculated barrier via **36** is lower than that for addition to the C=C bond, which involves rehybridization of both carbon atoms.

[13] $CH_2{=}C{=}O \xrightarrow{H_2O}$ 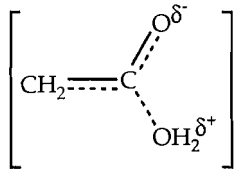 $\longrightarrow$ 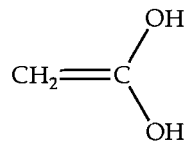

36

37

The analogous addition of H_2O to C_3O_2 could occur by 1,2-addition to the C=O bond to produce as the first intermediate the geminal diol **38**, which could then isomerize to the ketenyl carboxylic acid **39** (eq. [14]). Just as for $CH_2{=}C{=}O$ (16), the direct addition of H_2O to the C=C bond of C_3O_2 to form **39** is calculated to be of lower energy than is formation of **38** but,

although the barriers for the formation of **38** and **39** have not been calculated, formation of the geminal diol is relatively more favorable for C_3O_2 compared to $CH_2{=}C{=}O$, and so this route (eq. [14]) appears plausible for C_3O_2 as well.

[14] 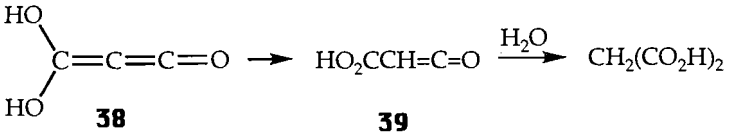

For the reaction of C_3O_2 in dilute HCl, the linear dependence on $[H^+]$ of the rate and the isotope effect ($k_H{}^+/k_D{}^+$ = 1.21), are both consistent with a mechanism involving rate-limiting proton transfer to C_β (eq. [15]), as has been proposed for other ketenes (4*a*, 6*f*, 17). Protonation at C_β in C_3O_2 would be favored by the high negative charge density at this carbon, as indicated by the ^{13}C NMR chemical shift of δ −14.6 (15*e*), and by the favorable bisacylium-type resonance expected for this species, as shown in **40**. Whether or not **40** would have a sufficient lifetime under the conditions to exist as a genuine intermediate is a question that cannot be answered at present.

[15] 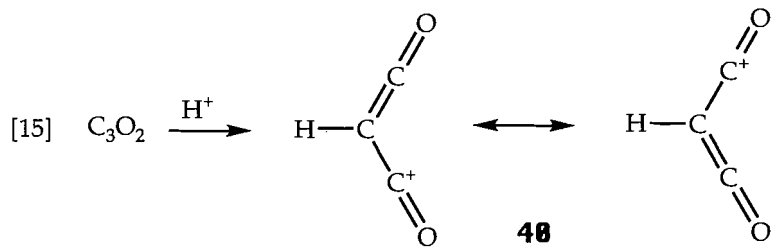

comet Halley is composed mainly of water ice, which is warmed significantly during the passages of the comet near the Sun, raises the question of whether any C_3O_2 ever present on comet Halley could survive during the long existence of this celestial body. Uncertainties as to the actual proximity of the putative C_3O_2 and the water ice, and the temperature, preclude a definitive judgment. Experiments to test the reactivity of C_3O_2 in an ice matrix may be informative in this regard.

Table 2. MP2/6-31G* + ZPVE//MP2/6-31G* calculated energies (kcal/mol) for reactions of carbon suboxide and ketene.

Reaction	ΔE (kcal/mol)
$O{=}C{=}C{=}C{=}O + H^+ \rightarrow O{=}C{=}CH{-}\overset{+}{C}{=}O$	−182.9
$CH_2{=}C{=}O + H^+ \rightarrow CH_3\overset{+}{C}{=}O$	−199.2
$O{=}C{=}C{=}C{=}O + H_2O \rightarrow (HO)_2C{=}C{=}C{=}O$	9.9
$O{=}C{=}C{=}C{=}O + H_2O \rightarrow HO{-}C{\equiv}C{-}CO_2H$	19.6
$O{=}C{=}C{=}C{=}O + H_2O \rightarrow HO_2CCH{=}C{=}O$	−23.5
$(HO)_2C{=}C{=}C{=}O \rightarrow HO_2CCH{=}C{=}O$	−33.4
$HO{-}C{\equiv}C{-}CO_2H \rightarrow HO_2CCH{=}C{=}O$	−43.0
$HO_2CCH{=}C{=}O + H_2O \rightarrow HO_2CCH{=}C(OH)_2$	−20.2
$CH_2{=}C{=}O + H_2O \rightarrow CH_2{=}C(OH)_2$	−6.0
$CH_2{=}C(OH)_2 \rightarrow CH_3CO_2H$	−35.4
$HO_2CCH{=}C(OH)_2 \rightarrow CH_2(CO_2H)_2$	−12.3
$O{=}C{=}C{=}C{=}O + OH^- \rightarrow {}^-O{-}C{\equiv}C{-}CO_2H$	−62.2
${}^-O{-}C{\equiv}C{-}CO_2H \rightarrow HO{-}C{\equiv}C{-}CO_2^-$	31.5
${}^-O{-}C{\equiv}C{-}CO_2H \rightarrow O{=}C{=}CH{-}CO_2^-$	−11.2
$CH_2{=}C{=}O + OH^- \rightarrow CH_2{=}C(OH)O^-$	−75.6
$CH_2{=}C(OH)O^- \rightarrow CH_3CO_2^-$	−30.7

The calculated results in Table 2 indicate that the gas phase protonations of both C_3O_2 and $CH_2{=}C{=}O$ are favored to occur at carbon rather than at oxygen, and that protonation is predicted to be more favorable for ketene than for C_3O_2, by 16.3 kcal/mol, in agreement with the experimental results.

As noted above there is a recent proposal (14*a*) that the source of atomic carbon in the coma and nucleus material of comet Halley could be C_3O_2. In particular it was envisaged (14*a*) that photolysis of C_3O_2 to produce atomic carbon (14*b*) could give rise to the carbon observed. However the appreciable reactivity of C_3O_2 with liquid water, and the fact that

In summary, our studies of bisketenes, which have been underway since 1992, and some of which are described here, have involved organic synthesis, kinetic and theoretical studies, flash photolysis, spectroscopy, stereochemistry, and photochemistry. Further studies in polymer and organometallic chemistry are underway. Thus ketenes provide a view in microcosm of much of the field of organic chemistry. Each new advance has revealed even more opportunities in this area, and we look forward to the new discoveries that will appear in the last decade of the first century of bisketene chemistry.

Acknowledgement

Financial support of the research described herein by the Natural Sciences and Engineering Research Council of Canada and the Ontario Centre for Materials Research is gratefully acknowledged.

References

1. (*a*) O. Diels and B. Wolf. Chem. Ber. **39**, 689 (1906); (*b*) H. Staudinger and S. Bereza. Chem. Ber. **41**, 4461 (1908).
2. (*a*) H. Staudinger and E. Anthes. Chem. Ber. **46**, 1426 (1913); (*b*) D.M. Birney and J.A. Berson. J. Am. Chem. Soc. **107**, 4553 (1985); (*c*) J.A. Berson, D.M. Birney, W.P. Dailey III, and J.F. Liebman. *In* Molecular structure and energetics. Vol. 6. VCH Publishers, New York. 1988. Chap. 9; (*d*) D. Sülze, D. Weiske, and H. Schwarz. Int. J. Mass Spectrom. Ion Processes, **125**, 75 (1993); (*e*) D.A. Dixon, A.J. Arduengo III, K.D. Dobbs, and D.V. Khasnis. Tetrahedron Lett. **36**, 645 (1995); (*f*) G. Maier, H.P. Reisenauer, H. Balli, W. Brandt, and R. Janoschek. Angew. Chem. Int. Ed. Engl. **29**, 905 (1990); (*g*) D. Sülze and H.

Schwarz. Angew Chem. Int. Ed. Engl. **29**, 908 (1990); (*h*) G. Maier, H.P. Reisenauer, U. Schäfer, and H. Balli. Angew Chem. Int. Ed. Engl. **27**, 566 (1988); (*i*) G. Maier, H.P. Reisenauer, and A. Ulrich. Tetrahedron Lett. **32**, 4469 (1991).

3. (*a*) H. Staudinger and W. Kreis. Helv. Chim. Acta, **6**, 321 (1923); (*b*) H. Staudinger and K. Clar. Chem. Ber. **44**, 1623 (1911); (*c*) G. Maier, H.P. Reisenauer, and T. Sayrac. Chem. Ber. **115**, 2192 (1982); (*d*) M. Kasai, M. Oda, and Y. Kitahara. Chem. Lett. 217 (1978); (*e*) R. Hochstrasser and J. Wirz. Angew. Chem. Int. Ed. Engl. **28**, 181 (1989). (*f*) H. Tomioka, H. Fukao, and Y. Izawa. Bull. Chem. Soc. Jpn. **51**, 540 (1978); (*g*) R.D. Miller and S. Kirchmeyer. J. Org. Chem. **58**, 90 (1993); (*h*) N. Obata and T. Takizawa. Bull. Chem. Soc. Jpn. **50**, 2017 (1977); (*i*) H.A. Staab and J. Ipaktschi. Chem. Ber. **101**, 1457 (1968); (*j*) D.R. Boate, L.J. Johnson, P.C. Kwong, E. Lee-Ruff, and J.C. Scaiano. J. Am. Chem. Soc. **112**, 8858 (1990); (*k*) T. Mosandl and C. Wentrup. J. Org. Chem. **58**, 747 (1993); (*l*) F. Toda and P. Garratt. Chem. Rev. **92**, 1688 (1992); (*m*) C.F. Jewell, Jr., L.S. Liebeskind, and M. Williamson. J. Am. Chem. Soc. **107**, 6715 (1985); (*n*) J.H.P. Utley, Y. Gao, and R. Lines. J. Chem. Soc. Chem. Commun. 1540 (1993); (*o*) R. Marquardt, W. Sander, T. Laue, and H. Hopf. Liebigs Ann. 1643 (1995).
4. (*a*) T.T. Tidwell. Ketenes, John Wiley, Inc., New York. 1995; (*b*) A.D. Allen, J. Ma, M.A. McAllister, T.T. Tidwell, and D.-c. Zhao. Acc. Chem. Res. **28**, 265 (1995); (*c*) A.D. Allen, R. Liu, J. Ma, M.A. McAllister, T.T. Tidwell, and D.-c. Zhao. Pure Appl. Chem. **67**, 777 (1995).
5. (*a*) A.T. Blomquist and Y.C. Meinwald. J. Am. Chem. Soc. **79**, 2021 (1957); (*b*) A.T. Blomquist. U.S. Patent 3,002,024; Chem. Abstr. **56**, 86576 (1962); (*c*) W.R. Hatchard and A.K. Schneider. J. Am. Chem. Soc. **79**, 6261 (1957); (*d*) G. Maier, L.H. Franz, H.G. Hartan, K. Lanz, and H.P. Reisenauer. Chem. Ber. **118**, 3196 (1985); (*e*) E. LeGoff. Ph.D. Thesis, Cornell University, 1960; (*f*) F.M. Beringer, R.E.K. Winter, and J.A. Castellano. Tetrahedron Lett. 6183 (1968); (*g*) M. Christl, U. Lanzendörfer, M.M. Grötsch, E. Ditterich, and J. Hegmann. Chem. Ber. **123**, 2031 (1990); (*h*) P.E. Eaton and B.D. Leipzig. J. Am. Chem. Soc. **105**, 1656 (1983); (*i*) M.B. Rubin, M. Bargurie, S. Kosti, and M. Kaftory. J. Chem. Soc. Perkin Trans. 1, 2670 (1980); (*j*) H.-D. Stachel. Angew. Chem. **69**, 507 (1957); (*k*) C.S. Rothman. J. Am. Oil Chem. Soc. **45**, 189 (1968).
6. (*a*) L.L. Shchukovskaya, R.I. Pal'chik, and A.N. Lazarev. Dokl. Akad. Nauk SSSR, **164**, 357 (1965); (*b*) W.T. Brady and T.C. Cheng. J. Org. Chem. **42**, 732 (1977); (*c*) W. Runge. Prog. Phys. Org. Chem. **13**, 315 (1981); (*d*) L. Gong, M.A. McAllister, and T.T. Tidwell. J. Am. Chem. Soc. **113**, 6021 (1991); (*e*) M.A. McAllister and T.T. Tidwell. J. Org. Chem. **59**, 4506 (1994); (*f*) A.D. Allen and T.T. Tidwell. Tetrahedron Lett. **32**, 847 (1991); (*g*) M.A. McAllister and T.T. Tidwell. J. Am. Chem. Soc. **116**, 7233 (1994); (*h*) N.H. Werstiuk, J. Ma, M.A. McAllister, T.T. Tidwell, and D.-c. Zhao. J. Chem. Soc. Faraday. Trans. **90**, 3383 (1994).
7. (*a*) D.-c. Zhao, A.D. Allen, and T.T. Tidwell. J. Am. Chem. Soc. **115**, 10097 (1993); (*b*) A.D. Allen, W.-Y. Lai, J. Ma, and T.T. Tidwell. J. Am. Chem. Soc. **116**, 2625 (1994); (*c*) A.D. Allen, R. Ji, W.-Y. Lai, J. Ma, and T.T. Tidwell. Heteroat. Chem. **5**, 235 (1994); (*d*) M.A. McAllister and T.T. Tidwell. J. Chem. Soc. Perkin Trans. 2, 2239 (1994).
8. (*a*) A.D. Allen, I. Egle, R. Janoschek, H.-W. Liu, J. Ma, R.M. Marra, and T.T. Tidwell. Chem. Lett. 45 (1996); (*b*) J.B. Lambert and R.A. Singer. J. Am. Chem. Soc. **114**, 10246 (1992).
9. M. Korn, H.-G. Mack, H.-W. Praas, C.O.D. Vedova, and H. Oberhammer. J. Mol. Struct. **352/353**, 145 (1995).
10. (*a*) A.D. Allen, J.D. Colomvakos, I. Egle, J. Lusztyk, M.A. McAllister, T.T. Tidwell, B. Wagner, and D.-c. Zhao. J. Am. Chem. Soc. **117**, 7552 (1995); (*b*) M.A. McAllister and T.T. Tidwell. J. Am. Chem. Soc. **114**, 5362 (1992).
11. (*a*) F. Diederich and Y. Rubin. Angew. Chem. Int. Ed. Engl. **31**, 1101 (1992); (*b*) F. Diederich, Y. Rubin, O.L. Chapman, and N.S. Goroff. Helv. Chim. Acta, **77**, 1441 (1994).
12. R. Liu and T.T. Tidwell. Can. J. Chem. **73**, 1818 (1995).
13. A.D. Allen, M.A. McAllister, and T.T. Tidwell. J. Chem. Soc. Chem. Commun. 2547 (1995).
14. (*a*) W.T. Huntress, Jr., M.N. Allen, and M. Delitsky, Nature, **352**, 316 (1991); (*b*) C.E.M. Strauss, S.H. Kable, G.K. Chawla, P.L. Houston, and I.R. Burak. J. Chem. Phys. **94**, 1837 (1991).
15. (*a*) L. Birkhofer and P. Sommer. Chem. Ber. **109**, 1701 (1976); (*b*) U. Schmidt and M. Schwochau. Monatsh. Chem. **98**, 1492 (1967); (*c*) G. Hagelloch and E. Feess. Chem. Ber. **84**, 730 (1951); (*d*) H. Binder and W. Lindner. J. Chromatogr. **77**, 323 (1973); (*e*) E.A. Williams, J.D. Cargioli, and A. Ewo. J. Chem. Soc. Chem. Commun. 366 (1975).
16. (*a*) M.T. Nguyen and A.F. Hegarty. J. Am. Chem Soc. **106**, 1552 (1984); (*b*) J. Andraos, A.J. Kresge, M.R. Peterson, and I.G. Csizmadia. J. Mol. Struct. (Theochem), **232**, 155 (1991); (*c*) P.N. Skancke. J. Phys. Chem. **96**, 8065 (1992); (*d*) X. Duan and M. Page. J. Am. Chem. Soc. **117**, 5114 (1995); (*e*) M.T. Nguyen, D. Sengupta, G. Raspoet, and L.G. Vanquickenborne. J. Phys. Chem. **99**, 11883 (1995); (*f*) N.I. Butkovskaya, G. Manke II, and D.W. Setser. J. Phys. Chem. **99**, 11115 (1995).
17. (*a*) T.T. Tidwell. Acc. Chem. Res. **23**, 273 (1990); (*b*) A.D. Allen and T.T. Tidwell. J. Am. Chem. Soc. **109**, 2774 (1987); (*c*) A.D. Allen, M.A. McAllister, and T.T. Tidwell. Tetrahedron Lett. **34**, 1095 (1993); (*d*) R. Leung-Toung, M.R. Peterson, T.T. Tidwell, and I.G. Csizmadia. J. Mol. Struct. (Theochem), **183**, 319 (1989); (*e*) J. Andraos, A.J. Kresge, and N.P. Schepp. Can. J. Chem. **73**, 549 (1995).

1995 Merck Frosst Award Lecture
Quinone methides: relevant intermediates in organic chemistry[1]

Peter Wan, Beverly Barker, Li Diao, Maike Fischer, Yijian Shi, and Cheng Yang

Abstract: *ortho* and *para*-Quinone methides (2-methylene-3,5-cyclohexadien-1-one and 4-methylene-2,5-cyclohexadien-1-one, respectively) are intermediates in a variety of important chemical systems. In particular, *o*-quinone methides are useful in synthesis for the construction of chroman ring systems. A brief account of the relevance of quinone methide chemistry will be provided. This is followed by a review of recent studies from our laboratory on efficient methods for the photogeneration of quinone methides, concentrating on the use of hydroxy-substituted benzyl alcohols in aqueous media. It is shown that this method is general since it provides access to *o*-, *m*-, and *p*-quinone methide isomers. When appropriately substituted, all of these quinone methide isomers have been spectroscopically characterized by laser flash photolysis, making this technique the one of choice for studying the dynamics of these reactive intermediates. The mechanism of photochemical generation from hydroxybenzyl alcohols and extensions of the reaction to photogeneration of fluorenyl and biphenyl quinone methides will also be presented.

Key words: quinone methide, biphenyl quinone methide, carbocation, photosolvolysis, photodehydroxylation, hetero-Diels–Alder reaction.

Résumé : Les méthides d'*o*- et *p*-quinones (respectivement 2-méthylènecyclohexa-3,5-dièn-1-one et 4-méthylènecyclohexa-2,5-dièn-1-one) sont des intermédiaires dans une variété de systèmes chimiques importants. En particulier, les méthides d'*o*-quinones sont utiles en synthèse pour la construction de systèmes incorporant le noyau chromane. On fournit un bref résumé de l'importance de la chimie des méthides de quinone. On présente ensuite une revue des études récentes réalisées dans notre laboratoire sur des méthodes efficaces de photogénération des méthides de quinone, en se concentrant sur l'utilisation, en milieux aqueux, d'alcools benzyliques substitués par des groupes hydroxyles. On montre que cette méthode est générale puisqu'elle permet d'obtenir facilement les isomères *ortho*, *méta* et *para* des méthides de quinone. Lorsqu'ils sont substitués d'une façon adéquate, tous ces isomères de méthides de quinone ont pu être caractérisés d'un façon spectroscopique par photolyse éclair au laser qui en fait une technique de choix pour l'étude dynamique de ces intermédiaires réactifs. On présente aussi le mécanisme de la génération photochimique à partir des alcools hydroxybenzyliques et des extensions de la réaction à la photogénération des méthides de quinones dérivés du fluorényle et du biphényle.

Mots clés : méthide de quinone, méthide de quinone du biphényle, carbocation, photosolvolyse, photodéshydroxylation, réaction d'hétéro-Diels–Alder.

[Traduit par la rédaction]

Introduction

Quinone methides (QMs) (1, 2) are structurally related to both benzoquinones (BQs) and quinone dimethides (QDMs, also known as *o*-xylylenes). As is the case for BQs and QDMs, two isomers of QMs are well known (*ortho* and *para* isomers **1** and **2**) with the *meta* isomer **3** being of theoretical interest (3). Unlike BQs and QDMs, QMs are highly polarized and hence are reactive under both nucleophilic and electrophilic condi-

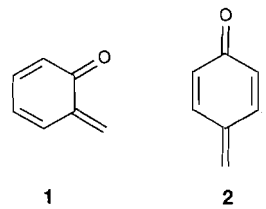

1 **2**

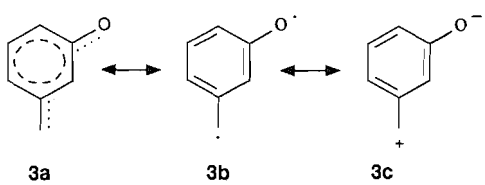

3a **3b** **3c**

Received December 22, 1995.

P. Wan,[2] B. Barker, L. Diao, M. Fischer, Y. Shi, and C. Yang. Department of Chemistry, Box 3055, University of Victoria, Victoria, BC V8W 3P6, Canada.

[1] This paper is based on the Merck Frosst Centre for Therapeutic Research Award Lecture presented by Professor Wan at the 78th Annual Conference of the Canadian Society for Chemistry, Guelph, Ontario, May 28 – June 1, 1995.

[2] Author to whom correspondence may be addressed. Telephone: (604) 721-7193. Fax: (604) 721-7147. E-mail: pwan@uvic.ca

Scheme 1.

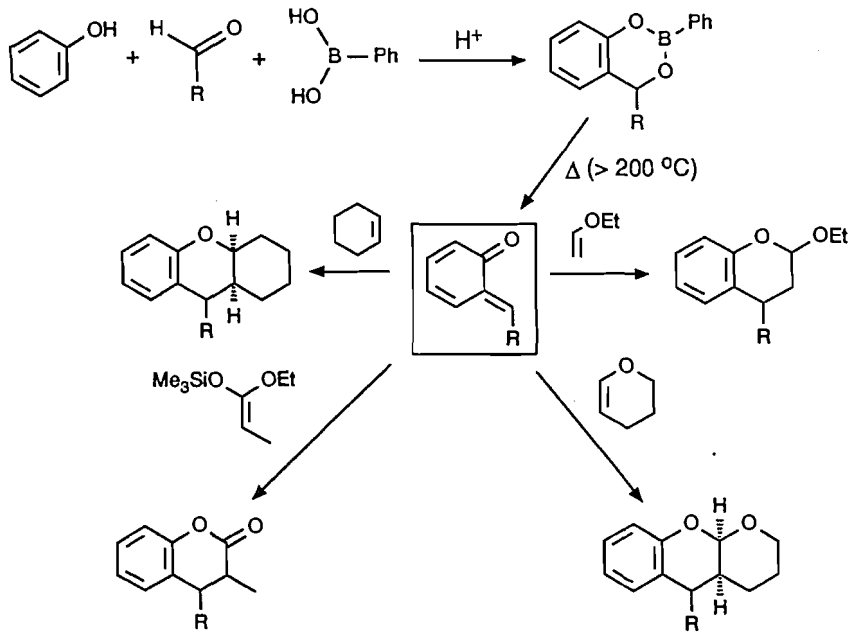

tions (1, 2). Since reaction generally gives an aromatic phenol ring, the driving force inherent in this transformation makes QMs highly reactive intermediates.

ortho-Quinone methides are widely used in organic synthesis for carrying out "reverse electron demand" Diels–Alder [4+2] cycloadditions with electron-rich alkenes, to give chroman derivatives (1, 2, 4). Because of this utility, various thermal methods for generating *o*-QMs have been developed during the last two decades, including methods involving Ag_2O oxidation of phenols (5), high-temperature dehydration of *o*-hydroxybenzyl alcohols (6), fluoride-induced desilylation of silyl ethers (7), and thermal extrusion of small molecules (8). Generation of *o*-QMs from the extrusion of phenyl boronic acid from 1,3,2-benzodioxaborins has been reported by Lau and Defresne and co-workers (9) as a simple and general method for making *o*-QMs for synthesis (Scheme 1). The required 1,3,2-benzodioxaborins are readily made by condensation of phenylboronic acid with phenol and the required aldehyde. The *o*-QMs obtained from this method were trapped using a variety of standard agents such as ethyl vinyl ether and a ketene acetal. The cycloaddition of an *o*-QM with an electron-rich alkene has been employed as a key step in total syntheses, some representative examples are carpanone (10), hexahydrocannabinol (7), and thielocin A1β (11).

para-Quinone methides have also been used in synthesis, notably by Angle et al. (12). In these systems, *p*-QMs were generated, via Ag_2O oxidation of the corresponding *p*-substituted phenol, that subsequently react via (*a*) formal [3+2] cycloaddition with an alkene, to give indanes or (*b*) undergo intramolecular cyclization to give a variety of *p*-hydroxyphenyl-substituted ring systems.

p-QMs are believed to be crucial intermediates in the biosynthesis and subsequent chemistry of lignin (13). The polymerization of coniferyl alcohol, the predominant *p*-coumaryl alcohol of softwood lignins, is believed to involve initial coupling of two coniferyl alcohol phenoxyl radicals, to give various *p*-QM structural isomers, which subsequently react further in the polymerization process to yield lignin. The aging of lignin can also involve formation of transient *p*-QMs in the chemistry.

p-QMs have been proposed to be the key intermediates in the known toxicity of common phenols found in spices, flavouring agents, and food preservatives such as BHT (butylated hydroxytoluene) (14). These phenols are oxidized during the metabolic process to their corresponding *p*-QMs, which are believed to be responsible for their toxicity, due to their ability to alkylate cellular macromolecules such as proteins and DNA. The highly electrophilic character of QMs also makes them useful as the critical intermediate of several antitumour/antibiotic drugs (14*a*). For example, the mode of action of mitomycin C (a clinically used anticancer drug) involves a bioreductive step (Scheme 2) followed by loss of CH_3OH and opening of the aziridine ring, to generate an *o*-QM, which alkylates DNA (14*a*, 15). Due to the relevance of DNA alkylation by QMs, studies have been directed at sequence-specific alkylation of DNA using both thermally and photochemically generated QMs (16).

In view of the widespread relevance of QMs in organic and biological chemistry, it would be desirable to devise a general photochemical method for forming QMs since this would allow one to study their reaction dynamics without the encumbrance associated with thermal methods. During our studies of photosolvolysis of benzyl alcohols, we were fortunate enough to recognize that a simple and general photochemical method is indeed available using readily available substrates. Moreover, the method is capable of generating *m*-QMs, in addition to the more common *ortho* and *para* isomers. The rest of this review summarizes our work on QM photogeneration carried out during the last decade.

Photosolvolysis of hydroxybenzyl alcohols: parent quinone methides

For many years, our interest was focused on photochemical reactions of aromatic substrates that could be thought to arise

Scheme 2.

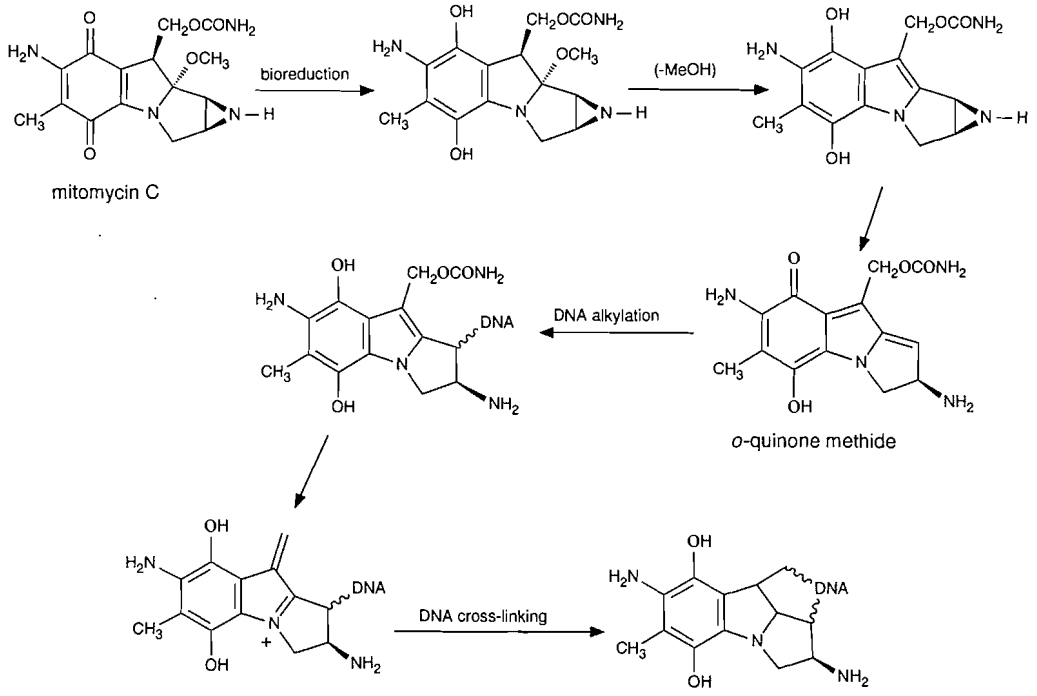

from a change in acidity or basicity of an attached functional group on excitation to the excited singlet state (S_1) (17). Much of the pioneering work in this area is attributable to Wan and Yates (18) who in the early 1980s first studied in mechanistic detail the photohydration of aromatic alkenes and alkynes via S_1, in neutral or moderately acid aqueous solution, conditions under which thermal hydration was nonexistent. The rationale for the more efficient *photo*hydration of these substrates was believed to be due to the enhanced basicity of the alkene or alkyne moiety in S_1 (17, 18), arising from significant charge delocalization from the benzene ring to the unsaturated moiety.

At about the same time, Wan, Yates, Turro, and co-workers (19, 20) showed that certain benzyl alcohols efficiently photosolvolyzed by formal loss of hydroxide ion (photodehydroxylations) to give the corresponding carbocation intermediates. These reactions could also be thought of as arising from a change in excited pK_a. That is, the benzyl alcohol becomes a stronger pseudo base in S_1 (or the corresponding benzyl cation becomes a weaker pseudo acid in S_1) (eq. [1]) (17). Using this

$$[1] \qquad ArCH_2OH^{*} \rightleftharpoons ArCH_2^{+\bullet} + {}^{-}OH$$

simple idea, we investigated the possible photodehydroxylation of a wide variety of benzyl alcohols (17, 20) and discovered several interesting systems that showed particularly efficient reaction, some of which are summarized in Chart 1. Two of the most reactive systems were 2,6-dimethoxybenzyl alcohol (**6**) and 9-fluorenol (**7**), both reacting via initial C—OH bond heterolysis to give the corresponding carbocation intermediate. When only one *o*-methoxy group was used (*o*-methoxybenzyl alcohol (**5**)), the quantum yield for methyl ether formation (Φ) was reduced significantly. However, *o*-hydroxybenzyl alcohol (**4**) reacted with a Φ value approaching that of **6** and we proposed at the time a mechanism involving assistance of the *o*-hydroxyl group and that, instead of a benzyl carbocation intermediate as required for **5**–**7**, **4** reacted via *o*-QM **1**.

Chart 1.

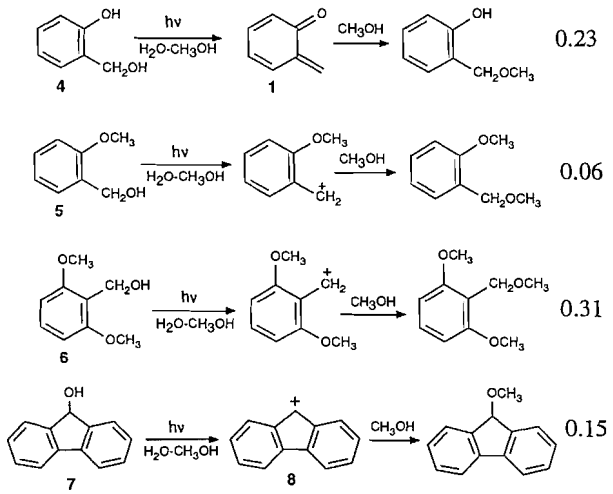

Phenols and hydroxyaromatics are known to be much stronger acids in S_1 (17, 21) with $pK_a(S_1)$ values generally in the 1–4 range, 6–9 orders of magnitude more acidic than in the ground state. The enhanced electron-donating power of the oxygen substituent in S_1 is responsible for the increased acidity of the phenolic hydroxyl group (eq. [2]). Yates and coworkers (22) have shown that use of an *o*-hydroxyl group results in more efficient photohydration of styrene and phenylacetylene. They proposed that a fast intramolecular proton transfer from the more acidic ArOH to the alkyne or alkene moiety is responsible for the enhanced reactivity. A similar

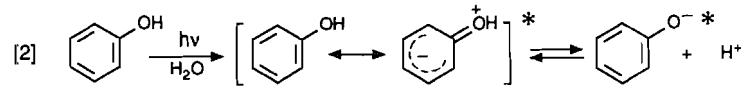

Scheme 3.

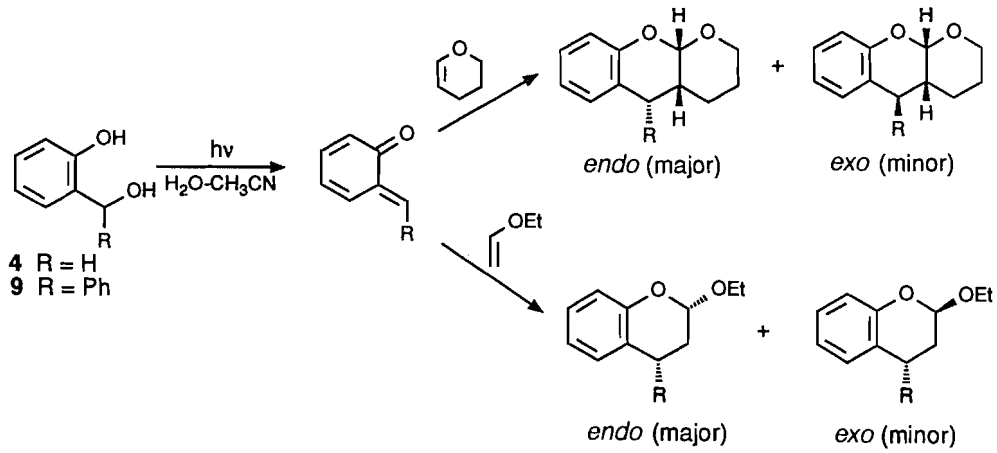

mechanism could be envisioned for the reaction of **4** in which loss of hydroxide ion is concerted with deprotonation of the phenolic proton, giving rise to *o*-QM **1**, resulting in a more efficient photosolvolysis reaction. Additional evidence for formation of **1** from **4** came from the discovery of a photocondensation reaction to form phenol-formaldehyde resins on photolysis of **4** in basic aqueous solution (23). In the initial step of this process, photochemically generated **1** is alkylated at the benzylic carbon by the substrate (via the *ortho* position of the phenol), which is sufficiently nucleophilic in the phenolate form. This step gives rise to a "dimer" of **4** that on subsequent photoreaction gives rise to phenol–formaldehyde oligomers.

Prior to our investigations of QM photogeneration, occasional reports of photochemical methods for their generation have appeared in the literature. Some of these methods have involved (*i*) decarbonylation of lactones (24); (*ii*) photolysis of *o*-hydroxybenzyl derivatives (25); (*iii*) photoisomerization of chromenes (26); and (*iv*) photolysis of benzoquinones and Vitamin K derivatives (27). None of these methods could be considered to be general since only selected *o*-QMs were photogenerated. We decided to investigate the full potential of using hydroxybenzyl alcohols as photochemical precursors of QMs since all three isomers (*ortho*, *meta*, and *para*) of the substrate were readily available and there was potential that all three isomers might react to give the corresponding QM. We discovered that this was indeed the case (28).

Product studies provided the initial evidence for a general method of QM photogeneration (28). For example, photolysis of *o*-hydroxybenzyl alcohols **4** and **9** in aqueous CH_3CN in the presence of ethyl vinyl ether or dihydropyran gave the corresponding [4+2] cycloaddition products (Scheme 3) in > 80% yield. Photolysis of **4**, **9**, and the corresponding *meta* and *para* isomers **10–13** in aqueous methanol gave the corresponding methyl ethers with quantum yields in the order $o > m \gg p$. The corresponding methoxy derivatives of these compounds, e.g., **15**, showed much less or no reaction, confirming the requirement of a hydroxy group and hence consistent with a mechanism involving a QM in the reaction of the hydroxy-substituted benzyl alcohols. Product studies of photosolvolysis of *o*-aminobenzyl alcohol in CH_3OH–H_2O are consistent with formation of an *o*-quinone methide imine intermediate

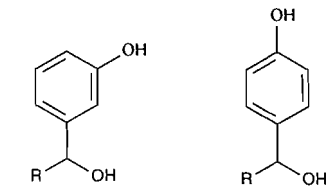

10 R = H
11 R = Ph

12 R = H
13 R = Ph

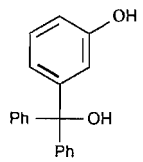

14

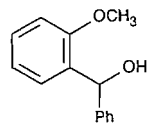

15

(29) although such intermediates are not readily trapped with dienophiles.

We have also shown that intramolecular trapping of a photogenerated *o*-QM can be readily accomplished using *o*-hydroxybenzyl alcohol **16** (Scheme 4).[3] Photolysis of **16** in aqueous CH_3CN resulted in high yields of the expected tetrahydrocannabinol derivative **18** via **17**. Interestingly, under the same conditions, *o*-hydroxybenzyl alcohol **19** gave no reaction. However, photolysis of **19** in 1:1 CH_3OH–H_2O resulted in high yields of methyl ether **22**, indicative of formation of *o*-QM **20**. The failure of *o*-QM **20** to undergo [4+2]

[3] B. Barker and P. Wan. Unpublished results.

Scheme 4.

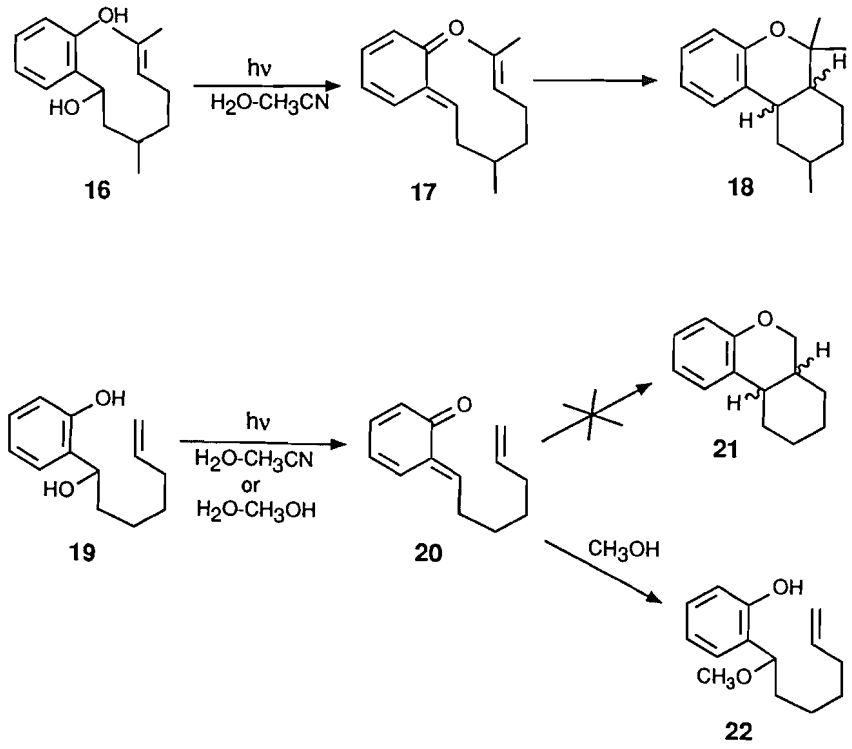

cycloaddition to give **21** is simply due to the fact that the terminal alkene used as the "dienophile" in this reaction is not sufficiently electron rich to compete with nucleophilic quenching of **20**, which gives back substrate when H_2O is the only nucleophile.

Direct evidence for QM photogeneration came from nanosecond laser flash photolysis (LFP) studies of α-phenyl-substituted hydroxybenzyl alcohols **9**, **11**, **13**, and **14** and some of their corresponding methoxy-substituted derivatives (28). LFP experiments were carried out at 20°C using a YAG laser at 266 nm of flowing solutions to avoid complications arising from product photolysis and long-lived species. LFP of each of **9**, **11**, **13**, and **14** gave strongly absorbing transients all of which were unaffected by oxygen and which could be quenched by adding ethanolamine as nucleophile. Shown in Fig. 1 are the spectra observed for **9** and **13**, which we have assigned to their corresponding QM. LFP of their methoxy-substituted derivatives (on the benzene ring) failed to give any signal consistent with QM formation from **9** and **13**. The transients in Fig. 1 showed no observable decay in neutral pH (up to 2 ms, the longest time window of the detection equipment used). Indeed, LFP is unnecessary for **9** and **13** since we found that when solutions were photolyzed in a cuvette and UV–vis spectra taken quickly, it was possible to observe the clean decay (to base line) of the same transients, with lifetimes in the order of 5–40 s depending on the proportion of water used.

Transients observed on LFP of **11** and **14** were also strong but much shorter lived (30 ns and 10 μs, respectively) (Fig. 2). The λ_{max} and bandshape of these spectra are essentially identical to the corresponding diaryl and triarylmethyl cations photogenerated by McClelland et al. (30) using photoheterolysis of appropriate arylmethyl substrates. Although McClelland et al. (30) did not photogenerate *m*-hydroxy-substituted arylmethyl cations, the lifetimes of those that were reported are informative. For example, diarylmethyl cations without strongly stabilizing substituents have lifetimes of less than 10 ns in aqueous solution and are not detectable by standard nanosecond LFP; τ was estimated to be 1 and 6 ns for the diphenylmethyl and the (*p*-methylphenyl)phenylmethyl cations, respectively. The lifetimes of the parent trityl (triphenylmethyl) cation and the (*m*-methoxyphenyl)diphenylmethyl cation were measured to be 7 and 6 μs, respectively. It is clear that the transients observed from **11** and **14** are arylmethyl carbocations, but their lifetimes are too long to be simply the corresponding *m*-hydroxy-substituted species. The rationale is as follows. The deprotonated hydroxy group (O^-) is an electron-donating group on the benzene ring, at either the *meta* or *para* position ($\sigma_m = -0.47$; $\sigma_p = -0.81$) (31), unlike the simple hydroxy group, which is actually electron withdrawing at the *meta* position ($\sigma_m = +0.12$) (31). If the transient from **11** were simply the (*m*-hydroxyphenyl)phenylmethyl carbocation, its expected lifetime in aqueous solution, using data from McClelland et al. (30), would be *less* than 1 ns and hence not observable using our LFP system. Its much longer observed lifetime (30 ns) is consistent with a deprotonated hydroxyl group. Additional evidence that the transients observed in Fig. 2 are not simple arylmethyl cations is the fact that the corresponding 3-methoxy derivative of **14** did not give any observable transient by LFP. Moreover, **11** and **14** (and not their corresponding 3-methoxy derivatives) gave high yields (>50%) of the corresponding methyl ether products on photolysis at 254 nm in 1:1 MeOH–H_2O. We thus assign the transients in Fig. 2 as *m*-QMs **25** and **26**, from **11** and **14**, respectively. *m*-QMs and *m*-xylyl systems in particular have

Fig. 1. Spectra observed on LFP of hydroxybenzyl alcohols **9** and **13** in aqueous CH_3CN. These transients showed no observable decay within the 2 ms time scale, the longest available using the detection system employed (reprinted with permission from the American Chemical Society).

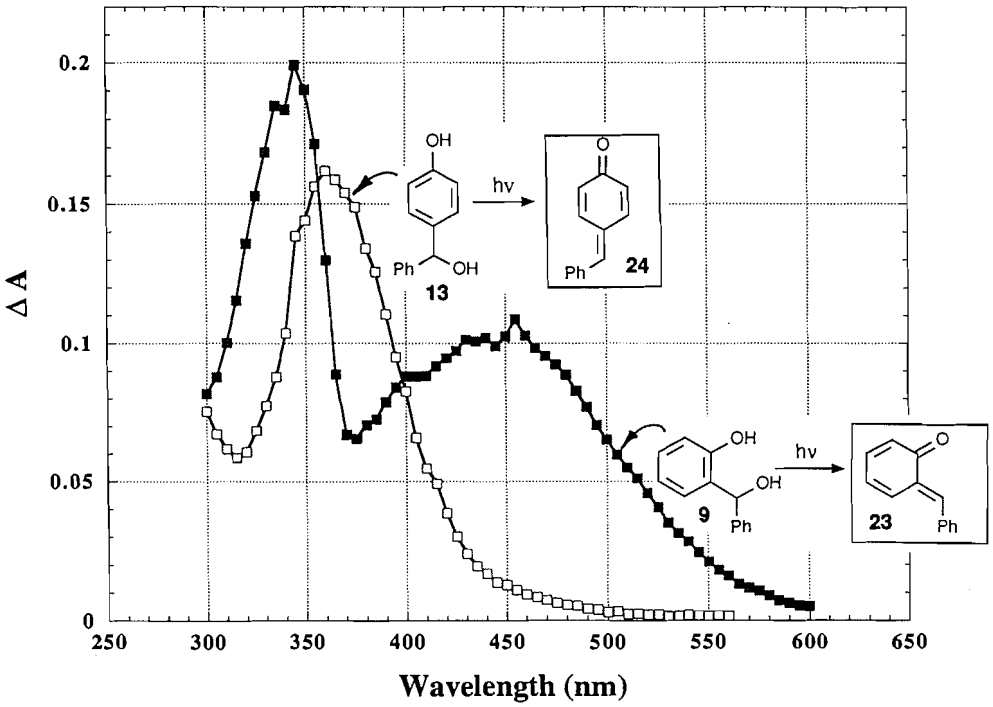

Fig. 2. Transient spectra observed on LFP of **11** and **14** in aqueous CH_3CN. Inset: clean first-order decay of **26** with a lifetime of 10 μs. The lifetime of **25** was 30 ns (reprinted with permission from the American Chemical Society).

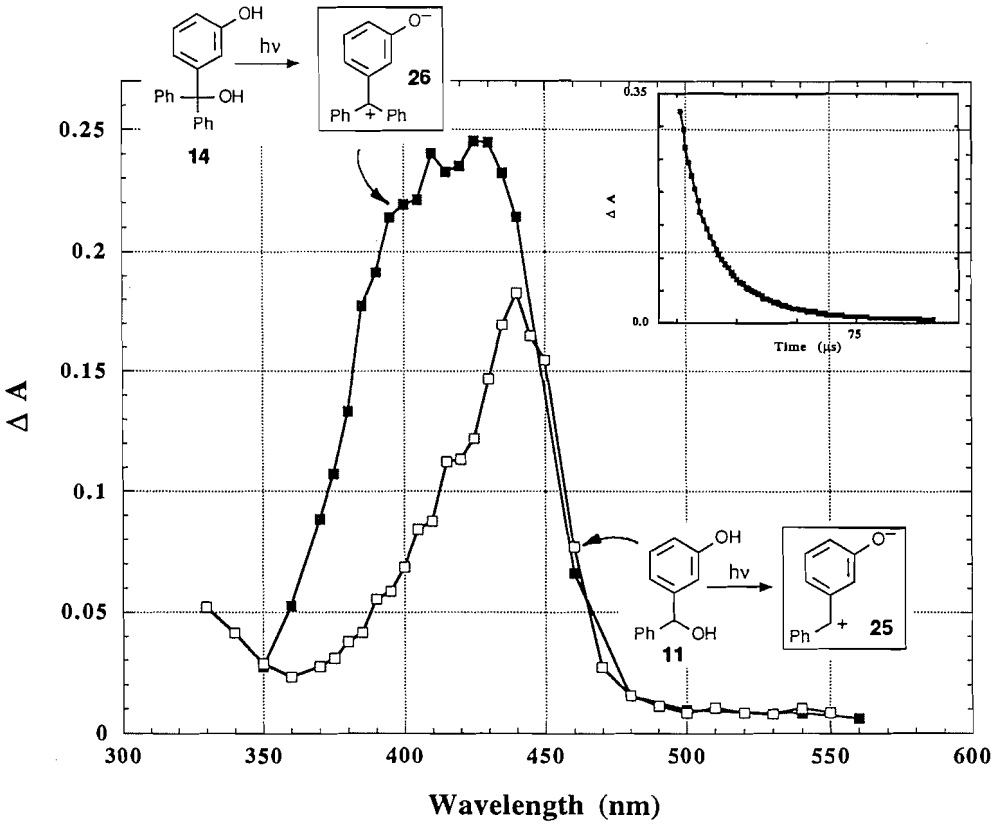

Fig. 3. Plot of relative quantum yield for formation of **23** from **9** vs. pH, as measured by ΔA at λ_{max} = 450 nm using LFP.

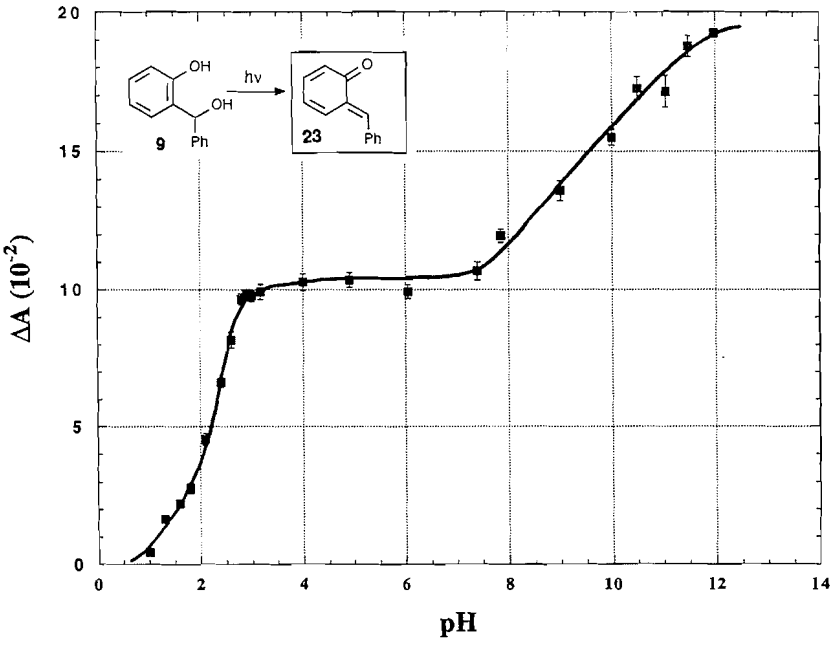

Scheme 5.

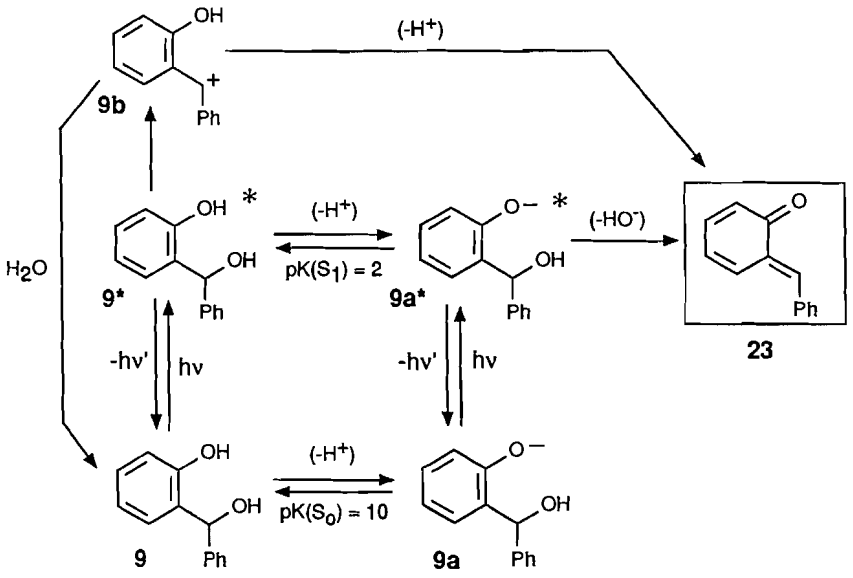

received considerable theoretical and experimental study (3). The present method offers a simple and efficient way for photogenerating *m*-QMs in their zwitterionic singlet states.

A particularly informative measurement available from LFP studies is the measurement of relative quantum yield for QM formation as a function of pH or in different solvents. Such relative quantum yields are readily measured by recording the absorbance change (ΔA) at the wavelength of interest (λ_{max} of transient) on photolysis at a particular pH (or solvent) and taking the average of several runs, keeping the absorbance at λ_{excit} (266 nm) constant. A plot of relative quantum yield for formation of **23** from **9** versus pH is shown in Fig. 3.[4] The sharp increase in the yield of **23** between pH 1 and 3 indicates that excited state dissociation to the electronically excited phenolate ion is a required step in the mechanism. This plot is essentially a titration curve with an estimated $pK_a(S_1) \approx 2.5$ for this compound. Direct excitation of the ground state phenolate ion also results in higher yields of **23**, as indicated by another titration curve with $pK_a(S_0) \approx 9.8$. These observations may be rationalized with a mechanism shown in Scheme 5. The prod-

[4] L. Diao and P. Wan. Unpublished results.

Scheme 6.

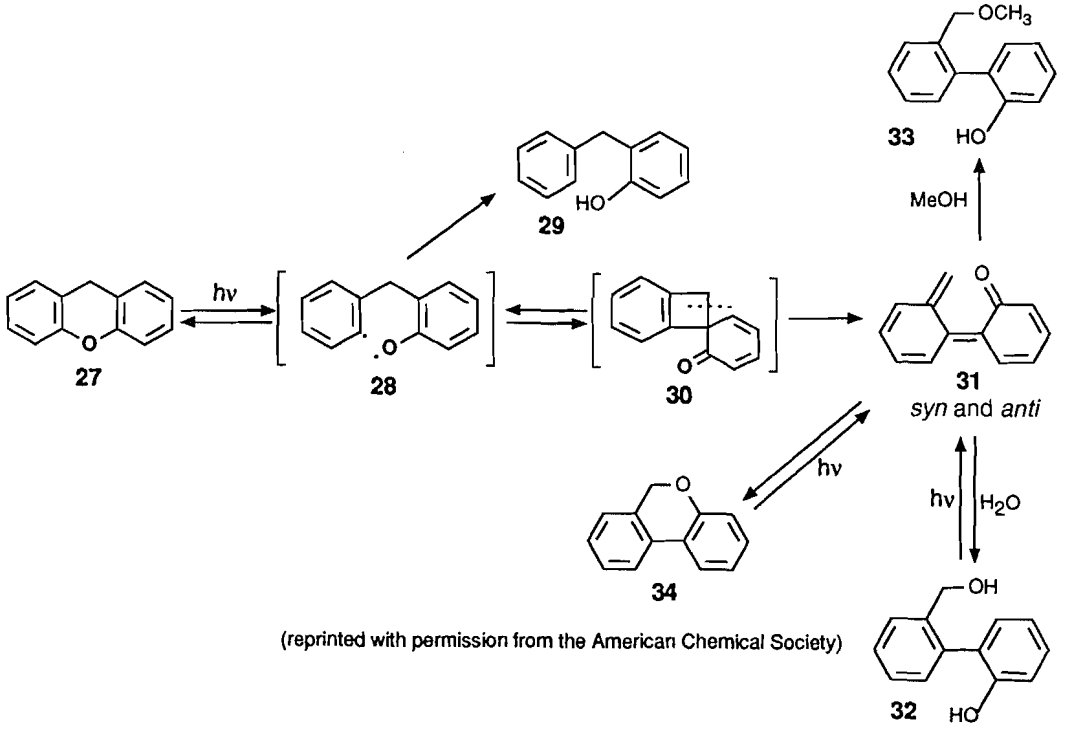

uct-forming step is loss of hydroxide ion of the excited state phenolate ion **9a***. Excitation of **9** at pH <8 results in **9***, which dissociates to **9a***. Since the yield of **23** is lower at these pHs, it implies that this equilibrium is not fully established, which is reasonable since fluorescence, intersystem crossing, and internal conversion are competing deactivational modes still available for **9*** (and **9a***). The possibility of a contributing pathway to **23** via carbocation **9b** cannot be excluded although the fraction reacting via this route is probably small since the corresponding methoxy derivative **15** is significantly less reactive in photosolvolysis than **9.**

Recent LFP studies of the parent *o*-hydroxybenzyl alcohol **4** and related compounds show that the parent *o*-QM chromophore (e.g., **1**, **17**, and **20**) absorbs with $\lambda_{max} \approx 390$ nm with lifetimes in aqueous solution that are considerably shorter than those of **23** and **24**.[4] LFP experiments of these simpler systems are complicated by observation of the corresponding radical cations, which absorb in the same region but have much shorter lifetimes. We have also extended the above method for QM photogeneration to a variety of other systems that formally have an *o*-hydroxybenzyl alcohol moiety. For example, photolysis of Vitamin B_6 in the presence of ethyl vinyl ether[4] gave the expected [4+2] adduct, implying that a variety of related *o*-QMs based on the pyridine ring system will be photogenerable. Additional examples are described individually in the sections that follow.

Biphenyl quinone methides

It was our venture into diaryl ether photochemistry that led to the discovery of a method for photogenerating biphenyl quinone methides. We observed that curious rearrangements were occurring on photolysis of xanthene (**27**) (32*a*) and *o*-phenoxybenzyl alcohol (32*b*) in aqueous solution. The mechanism for xanthene (**27**) to 5*H*-dibenzo[*b*,*d*]pyran (**34**) photoisomerization is shown in Scheme 6. Photolysis of **27** results in the expected homolysis of the aryl-O bond, to give biradical **28**, which can be trapped with 2-propanol to give **29**. In aqueous solution, however, *ipso* attack of the phenyl radical at the *ortho* position of the other ring results in the spiro ketone **30**, which subsequently gives *o*,*o*′-biphenyl quinone methide **31**. Electrocyclic ring closure gives the major product **34**. Nucleophilic trapping of **31** by water and by CH_3OH, if used as a cosolvent, gives **32** and **33**, respectively.

Scheme 6 posed the question of whether **31** could be photogenerated by photolysis of **32** or **34**. These questions have been addressed in a detailed mechanistic study of the photocyclization of 2-(2′hydroxyphenyl)benzyl alcohol (**32**) and related compounds (33), the mechanism of which is shown in Scheme 7. Evidence for reaction from an electronically excited phenolate ion **32a*** was obtained from a plot of quantum yield for formation of **34** as a function of pH, which showed two sigmoidal curves at pH $\approx$1 ($pK_a(S_1)$ and at pH $\approx$10 ($pK_a(S_0)$). Since ground state **32** is highly twisted (dihedral angle of 72° in the *syn* geometry by X-ray crystallography; its solution structure may differ to some extent due to solvation) whereas product **34** is essentially planar, the mechanism shown in Scheme 7 also involves twisting of the bond joining the two benzene rings on the S_1 surface. This twisting motion probably takes place before or concerted with deprotonation of S_1, either process of which is believed to be very fast. LFP experiments have been carried out in an attempt to detect **31** but have so far failed, which suggests that such QMs are very short lived (<5 ns). Although it was not possible to rule out formation of *anti*-**31**, the lack of any observable visible transient in LFP experiments would suggest it is not formed in

Scheme 7.

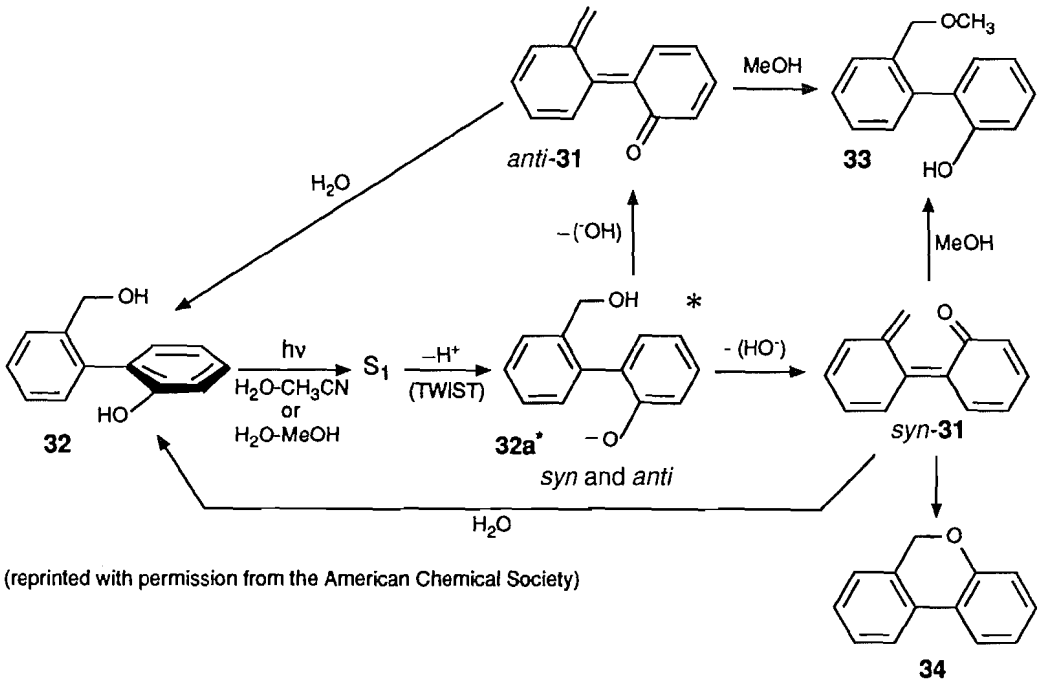

Chart 2.

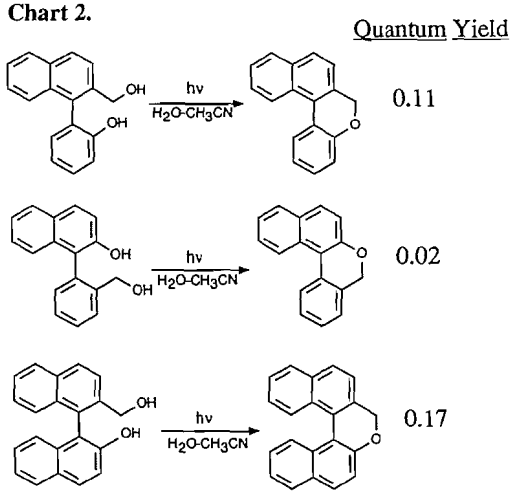

any significant amount. Such an intermediate cannot close to give **34** and hence should be sufficiently long lived to be detectable with nanosecond LFP. The fact that **32** exists only in the *syn* geometry in the X-ray structure might suggest that it is also the major conformation in aqueous solution, which would tend to give mostly *syn*-**31** on photolysis.

We have extended the photocyclization of **32** to a variety of other biaryls to test the generality of this reaction.[5] As shown in Chart 2, we have found that biaryls incorporating a naphthalene ring undergo the photocyclization and in most cases with high quantum efficiency. Indeed, the highly twisted binaphthyl system (dihedral angle ≈ 90°) reacts with the highest quantum efficiency, to yield a binaphthyl pyran that is much less twisted (dihedral angle ≈ 35°). These results are consistent with the well-known tendency of biaryls to twist to a more planar geometry on electronic excitation (33). With appropriately substituted *o,o'*-substituents, this inherent twisting motion results in net chemistry.

To obtain direct spectroscopic evidence for photogeneration of biphenyl quinone methides, we required biphenyl derivatives that on reaction (loss of water) would give biphenyl quinone methides that cannot cyclize, and hence extend their lifetime in aqueous solution. Such substrates are biphenyl alcohols **35** and **37** (34) (Fig. 4). LFP of these alcohols gave very long wavelength transients (λ_{max} = 570 and 530 nm, respectively) assigned to the corresponding biphenyl quinone methides **36** and **38**, with lifetimes of 0.47 and 67 μs, respectively (Fig. 4). Photolysis in CH_3OH–H_2O gave the expected methyl ether substitution products. Biphenyl quinone methides have much shorter lifetimes than to the *o*- and *p*-QMs discussed earlier. This is probably due to the fact that biphenyl quinone methides can gain two benzene rings on nucleophilic addition at the benzylic carbon, which is a very significant driving force.

Fluorenyl quinone methides

We first reported the facile photogeneration of the 9-fluorenyl cation (**8**) from 9-fluorenol (**7**) in aqueous solution (Chart 1) (35). This carbocation is unique amongst those we have photogenerated in that it is formally antiaromatic in the ground state. Indeed, it is one of the more elusive diarylmethyl carbocations in physical organic chemistry. Its facile photogeneration (35) has now opened up a method for studying the chemistry and dynamics of 9-fluorenyl cations in aqueous solution (17). We wondered whether it would be possible to photogenerate a fluorenyl quinone methide using the obvious substrate, 1-hydroxy-9-fluorenol (**39**). LFP of **39** in aqueous solution produced a long-lived ($\tau > 2$ ms) and strongly absorb-

[5] Y. Shi and P. Wan. Unpublished results.

Fig. 4. Transient spectra observed on LFP of **35** and **37** in aqueous CH_3CN, to give biphenyl quinone methides **36** and **38**, respectively. Inset: first-order decay of **36** in H_2O (τ = 0.47 μs) (reprinted with permission from the Journal of the Chemical Society, Chemical Communications).

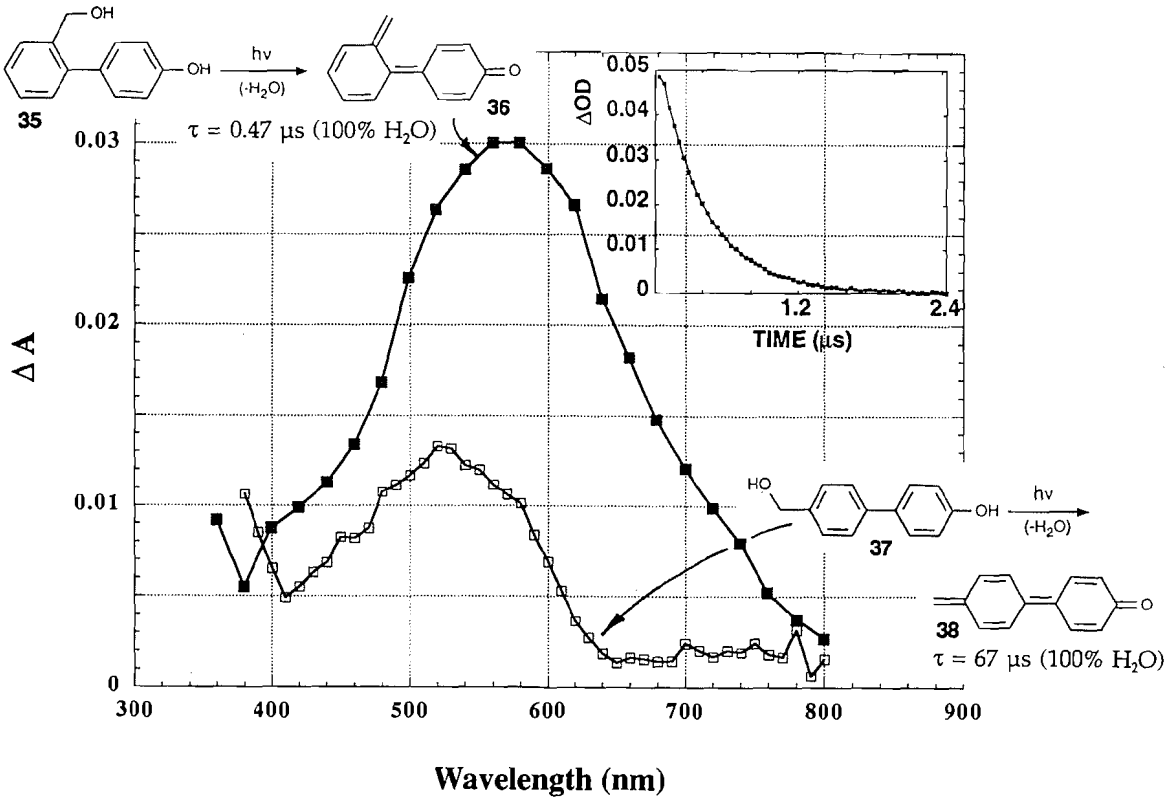

ing transient with λ_{max} = 450 nm, consistent with formation of fluorenyl quinone methide **40**[6] (eq. [3]). This was confirmed with trapping studies using CH_3OH and ethyl vinyl ether,

[3] 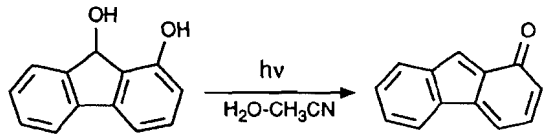

which gave high yields of the expected products. The long lifetime (>2 ms) of **40** (**8** itself has a lifetime in the ps range (17)) is consistent with a quinone methide structure that effectively removes much of the antiaromatic character of the 9-fluorenyl cation. We are currently investigating the photochemical behaviour of other isomers of this system.

Summary

We have shown that all the QM isomers can be photogenerated readily, with high efficiency for the *ortho* and *meta* isomers, by photolysis of the corresponding hydroxybenzyl alcohols in aqueous solution. The method appears sufficiently general for the photogeneration of a wide variety of these intermediates and this is shown by extension of the method to biphenyl, fluorenyl, and heteroaromatic systems. It is possible to characterize photogenerated QMs spectrophotometrically, and that *m*-QMs react as zwitterions in aqueous solution. The utility of the photochemical method of QM generation in preparative chemistry and detailed kinetic and mechanistic studies of QM chemistry are continuing in our laboratory.

[6] M. Fischer, Y. Shi, and P. Wan. Unpublished results.

Acknowledgements

I am grateful to all of my present and former students for their contributions in increasing our understanding of the mechanistic photochemistry of aromatic molecules. Without their hard work and dedication, none of the above work and our other contributions would have been made. Dr. Cornelia Bohne provided invaluable help in laser flash photolysis experiments. We thank Dr. Victor Snieckus for a sample of 1-hydroxy-9-fluorenone. The continuing support of the Natural Sciences and Engineering Research Council (NSERC) of Canada is gratefully acknowledged. Partial funding came from the University of Victoria, the Petroleum Research Fund, administered by the American Chemical Society, and a starter grant from the Research Corporation.

References

1. (*a*) A.B. Turner. Q. Rev. **28**, 347 (1964); (*b*) H.-U. Wagner and R. Gompper. *In* The chemistry of the quinonoid compounds. Vol. 1, Part 2. *Edited by* S. Patai. Wiley, New York. 1974; (*c*) P. Grünanger. *In* Houben–Weyl Methoden der Organischen Chemie. Vol. VII/3b. *Edited by* E. Müller and O. Bayer. G. Thieme Verlag, Stuttgart. 1979. pp. 395–521.

2. C.W.G. Fiswick and D.W. Jones. *In* The chemistry of the quinonoid compounds. Vol. 2, Part 1. *Edited by* S. Patai and Z. Rappoport. Wiley, Chichester. 1988. pp. 403–453.
3. J. Berson. *In* The chemistry of the quinonoid compounds. Vol. 2, Part 1. *Edited by* S. Patai and Z. Rappoport. Wiley, Chichester. 1988. pp. 455–536.
4. (*a*) G. Desimoni and G. Tacconi. Chem. Rev. **75**, 651 (1975); (*b*) D. Boger and S.N. Weinreb. Hetero Diels–Alder methodology in organic synthesis. Academic Press, New York. 1987; (*c*) F. Fringuelli and A. Taticchi. Dienes in the Diels–Alder reaction. Wiley, New York. 1990.
5. (*a*) D.A. Bolon. J. Org. Chem. **35**, 3666 (1970); (*b*) L. Jurd. Tetrahedron, **33**, 163 (1977).
6. A. Arduini, A. Bosi, A. Pochini, and R. Ungaro. Tetrahedron, **41**, 3095 (1985).
7. J.P. Marino and S.L. Dax. J. Org. Chem. **49**, 3671 (1984).
8. M. Yato, T. Ohwada, and K. Shudo. J. Am. Chem. Soc. **112**, 5341 (1990).
9. (*a*) J.D. Chambers, J. Crawford, H.W.R. Williams, C. Dufresne, J. Scheigetz, M.A. Bernstein, and C.K. Lau. Can. J. Chem. **70**, 1717 (1992); (*b*) S. Bissada, C.K. Lau, M.A. Bernstein, and C. Dufresne. Tetrahedron Lett. **35**, 3691 (1994).
10. O.L. Chapman, M.R. Engel, J.P. Springeer, and J.C. Clardy. J. Am. Chem. Soc. **93**, 6696 (1971).
11. (*a*) Y. Génisson, P.C. Tyler, and R.N. Young. J. Am. Chem. Soc. **116**, 759 (1994); (*b*) Y. Génisson and R.N. Young. Tetrahedron Lett. **35**, 7747 (1994).
12. (*a*) S.R. Angle, D.O. Arnaiz, J.P. Boyce, R.P. Frutos, M.S. Louie, H.L. Mattson-Arnaiz, J.D. Rainer, K.D. Turnbull, and W. Yang. J. Org. Chem. **59**, 6322 (1994); (*b*) S.R. Angle and D.O. Arnaiz. J. Org. Chem. **57**, 5937 (1992); (*c*) S.R. Angle and J.D. Rainier. J. Org. Chem. **57**, 6883 (1992).
13. (*a*) G.J. Leary. Wood Sci. Technol. **14**, 21 (1980); (*b*) S.M. Shevchenko and A.G. Apushkinskii. Russ. Chem. Rev. **61**, 1 (1992) .
14. (*a*) D.C. Thompson, J.A. Thompson, M. Sugumaran, and P. Moldeus. Chem.-Biol. Interact. **86**, 129 (1992); (*b*) J.L. Bolton, H. Sevestre, B.O. Ibe, and J.A. Thompson. Chem. Res. Toxicol. **3**, 65 (1990); (*c*) J.L. Bolton, L.G. Valerio, Jr., and J.A. Thompson. Chem. Res. Toxicol. **5**, 816 (1992); (*d*) J.L. Bolton, N.M. Acay, and V. Vukomanovic. Chem. Res. Toxicol. **7**, 443 (1994).
15. (*a*) M. Tomasz, A.K. Chawla, and R. Lipman. Biochemistry, **27**, 3182 (1988); (*b*) M. Egbertson and S.J. Danishefsky. J. Am. Chem. Soc. **109**, 2204 (1987).
16. (*a*) T. Li, Q. Zeng, and S.E. Rokita. Bioconjugate Chem. **5**, 497 (1994); (*b*) M. Chatterjee and S.E. Rokita. J. Am. Chem. Soc. **116**, 1690 (1994).
17. P. Wan and D. Shukla. Chem. Rev. **93**, 571 (1993).
18. P. Wan and K. Yates. Rev. Chem. Intermed. **5**, 157 (1984).
19. (*a*) N.J. Turro and P. Wan. J. Photochem. **28**, 93 (1985); (*b*) P. Wan, K. Yates, and M.K. Boyd. J. Org. Chem. **50**, 2881 (1985).
20. (*a*) P. Wan and B. Chak. J. Chem. Soc. Perkin Trans. 2, 1751 (1986); (*b*) P. Wan, B. Chak, and E. Krogh. J. Photochem. Photobiol. A: **46**, 49 (1989); (*c*) B. Hall and P. Wan. J. Photochem. Photobiol. A: **56**, 35 (1991); (*d*) D. Budac, D. Shukla, E. Krogh, and P. Wan. J. Photochem. Photobiol. A: **67**, 33 (1992); (*e*) D. Shukla and P. Wan. J. Photochem. Photobiol. A: **79**, 55 (1994).
21. J.F. Ireland and P.A.H. Wyatt. Adv. Phys. Org. Chem. **12**, 131 (1976).
22. (*a*) M. Isaks, K. Yates, and P. Kalanderopoulos. J. Am. Chem. Soc. **106**, 2728 (1984); (*b*) P. Kalanderopoulos and K. Yates. J. Am. Chem. Soc. **108**, 6290 (1986).
23. P. Wan and D. Hennig. J. Chem. Soc. Chem. Commun. 939 (1987).
24. (*a*) O.L. Chapman and C.L. McIntosh. J. Chem. Soc. Chem. Commun. 383 (1971); (*b*) C.L. McIntosh and O.L. Chapman. J. Chem. Soc. Chem. Commun. 771 (1971).
25. (*a*) S. Hamai and H. Kokubun. Bull. Chem. Soc. Jpn. **47**, 2085 (1974); (*b*) A. Padwa, D. Dehm, T. Oine, and G.A. Lee. J. Am. Chem. Soc. **97**, 1837 (1975).
26. (*a*) A. Padwa and G.A. Lee. J. Chem. Soc. Chem. Commun. 795 (1972); (*b*) C. Lenoble and R.S. Becker. J. Photochem. **33**, 187 (1986)
27. (*a*) D. Creed. J. Chem. Soc. Chem. Commun. 121 (1976); (*b*) D. Creed, B.J. Hales, and G. Porter. Proc. R. Soc. London, Ser. A: **334**, 505 (1973); (*c*) R.P. Gandhi, M.P.S. Ishar, R. Srivastava, and R. Sarin. J. Photochem. Photobiol. A: **78**, 153 (1994).
28. P. Wan, C. Yang, and L. Diao. J. Am. Chem. Soc. **117**, 5369 (1995).
29. C. Yang and P. Wan. J. Photochem. Photobiol. A: **80**, 227 (1994).
30. R.A. McClelland, V.M. Kanagasabapathy, N.S. Banait, and S. Steenken. J. Am. Chem. Soc. **111**, 3966 (1989).
31. S.L. Murov, I. Carmichael, and G.L. Hug. Handbook of photochemistry. 2nd ed. Marcel Dekker, New York. 1993. p. 345.
32. (*a*) C.-G. Huang, D. Shukla, and P. Wan. J. Org. Chem. **56**, 5437 (1991); (*b*) C.-G. Huang and P. Wan. J. Org. Chem. **56**, 4846 (1991).
33. C.-G. Huang, K.A. Beveridge, and P. Wan. J. Am. Chem. Soc. **113**, 7676 (1991).
34. Y. Shi and P. Wan. J. Chem. Soc. Chem. Commun. 1217 (1995).
35. (*a*) P. Wan and E. Krogh. J. Chem. Soc. Chem. Commun. 1207 (1985); (*b*) J. Am. Chem. Soc. **111**, 4887 (1989)

Wavelength dependence and solvent effects on the ligand field photochemistry: the ring closure process in the excited $[Fe(CN)_5(tn)]^{3-}$ complex

Jailson Farias de Lima and Neyde Yukie Murakami Iha

Abstract: The solvent composition and wavelength effects on the quantum yield of the photoinduced ring closure process of the $[Fe(CN)_5(tn)]^{3-}$ complex (tn = 1,3-diaminopropane) were investigated. The reactivity was shown to be controlled by the macroscopic properties of water–glycerol mixtures. A sharp decrease in quantum yields with increasing medium viscosity was observed for all the irradiation wavelengths employed (313, 334, 365, 404, and 434 nm). The observed quantum yields ranged from 0.24 (λ_{irr} = 313 nm, 66.48 wt.% of acetonitrile) to 0.010 (λ_{irr} = 404 or 434 nm, 61.85 wt.% of glycerol). The overall efficiency is a complex function of the dynamics of radical recombination and dissociation pathways. The proposed cage model for the deactivation dynamics of the excited states illustrates that the decrease in medium viscosity favors a diffusional escape of the cyanide from the solvent cage.

Key words: photochemistry, pentacyanoferrate(II) complexes, solvent effect, wavelength effect.

Résumé : L'effet de la composition du solvant et de la longueur d'onde de l'excitation dans le rendement quantique du processus photoinduit de fermeture d'anneau du complexe $[Fe(CN)_5(tn)]^{3-}$ (tn = 1,3-diamineпropane) a été etudié. La reactivité semble être controlée par les proprietés macroscopiques des mélanges de solvant eau–glycerol. Une décroissance abrupte dans le rendement quantique est observée avec la variation de la viscosité du milieu, pour tous les longueurs d'onde d'irradiation employées (313, 334, 365, 404 et 434 nm). Le rendement quantique observé varie de 0,24 (λ_{irr} = 313 nm; 66,48% poids acétonitrile) à 0,010 (λ_{irr} = 404 ou 434 nm; 61,85% poids glycerol). L'efficacité totale est une fonction complexe de la dynamique des étapes de dissociation et de recombinasion radicale. Le modéle cage proposé pour la dynamique de deactivation des états excités montre que la décroissance dans la viscosité du milieu favorise la sortie de la cyanide de la cage du solvant.

Mots clés : photochimie, complexes de pentacyanoferrate(II), effet du solvant, effet de la longueur d'onde de l'excitation.

Introduction

Wavelength dependence and solvent effects on photoinduced reactions have been reported for a large number of transition metal complexes (1–11). Most of the literature addresses the analysis of the influence of solvent on intra- and intermolecular electron transfer processes (11–17) in which the reaction rate is controlled by solvent movements. Solvent mixtures in different proportions have been employed in order to change those properties of the medium that can be quite easily adjusted.

Wavelength-dependent photolabilization reactions constitute another class in which the solvent plays an important role in determining quantum yields. Particular emphasis has been placed on complexes of d^6 transition metal ions, and among them Co(III) complexes have historically been used as attractive model systems for such studies (2–9). The classical approach to this phenomenon is concerned with the competition between geminate recombination and solvent cage escape. When this competition can be related to properties of the solvent, one has an indication that the species will react on time scales sufficiently long to reach an equilibrium with the solvent environment. Despite its simplicity, this model has been shown to be consistent with a significant number of the available experimental results, although the data from some particular systems do not fit within its conceptual framework (3, 10, 11, 17).

During the last few years we have been studying the photochemical behavior of pentacyanoferrate(II) complexes, $[Fe(CN)_5L]^{3-}$. The investigated photoreactions include the labilization of either L (18–20) or a cyanide ligand (19, 21–23). The cyanide photolabilization was found to be strongly wavelength dependent. For the 365 nm irradiations, it was also observed that quantum yields of the process decreased with increasing glycerol concentration in the aqueous solution of the complex (23). The previously reported results allowed us to postulate a solvent cage mechanism for the reactive deactivation of the excited states of these complexes.

Following these studies, we now report the effect of glycerol concentration on quantum yields for the 313, 334, 404, and 434 nm irradiations. To analyze the solvent effect in further detail, experiments were performed with water–acetonitrile mixtures, including the 365 nm irradiation. The latter system has quite different properties then the water–glycerol mixtures.

Received October 11, 1995.

J.F. Lima and N.Y. Murakami Iha.[1] Instituto de Química, Departamento de Química Fundamental, Universidade de São Paulo, Caixa Postal 26. 077, 05599-970, São Paulo, SP, Brazil.

[1] Author to whom correspondence may be addressed. Telephone: 55-11-818 79 51. Fax: 55-11-815 55 79. E-mail: neydeiha@quim.iq.usp.br.

Fig. 1. Quantum yield for the ring closure reaction vs. viscosity of the water–glycerol mixtures.

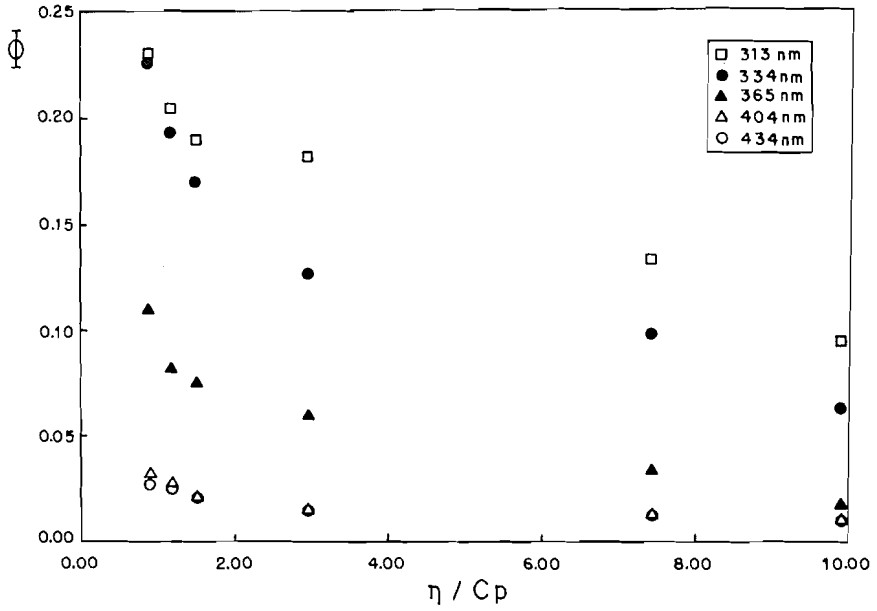

Experimental

Materials

The $Na_3[Fe(CN)_5NH_3]\cdot 3H_2O$ salt was synthesized according to slight modifications of a published procedure (24). The pentacyanoferrate(II) complex with 1,3-diaminopropane was always freshly prepared in the mixed aqueous solution by direct reaction of $Na_3[Fe(CN)_5NH_3]$ with a severalfold excess of the ligand. The ligand was purified by distillation under reduced pressure. Glycerol (Sigma Grade) and chromatographic grade acetonitrile (Merck) were used as supplied. The potassium tris(oxalate)ferrate(III) salt was prepared and purified according to literature procedure (25). *N*-Methylpyrazinium iodide was synthesized and recrystallized according to a procedure adapted from that described by Bahner and Norton (26).

Physical measurements and procedures

The continuous photolyses were performed using an Oriel 200 W Hg(Xe) arc lamp model 6291. Monochromatic irradiations were obtained by using Oriel interference filters to isolate the 313, 334, 365, 404, or 434 nm Hg line. The photolysis system is described in detail elsewhere (22, 23). The starting complex, $[Fe(CN)_5(tn)]^{3-}$, and the photoproduct, $[Fe(CN)_4(tn)]^{2-}$, absorb at the same wavelength with similar absorption coefficients. For this reason, direct spectrophotometric analysis is unsuitable for quantitative determinations. The analytical method involves the conversion of the starting complex, $[Fe(CN)_5(tn)]^{3-}$, to a highly absorbing species. The tetracyanoferrate(II) is inert toward substitution and can be isolated and further characterized. The light intensity at each wavelength was determined by tris(oxalate)ferrate(III) actinometry (25) carried out before and after each photolysis run. All absorption spectra were recorded on a Beckman DU 70 spectrophotometer at 25.0°C.

The concentration of the starting complex ranged from 3.2 to 6.0 mM depending on the irradiation wavelength employed.

Results and discussion

The $[Fe(CN)_5(tn)]^{3-}$ complex exhibits a low-intensity absorption band (λ_o = 395 nm, $\varepsilon_o = 4.5 \times 10^2$ M^{-1} cm^{-1}), which is assigned to the ligand field transition $^1A_1 \rightarrow {}^1E(1)$, under C_{4v} symmetry (27). An additional high-intensity band, with the maximum absorption located around 250 nm, is ascribed to a charge transfer transition from iron(II) to the cyanide ligands (27).

The continuous photolysis of aqueous or mixed aqueous solutions of $[Fe(CN)_5(tn)]^{3-}$ in the presence of a large excess of 1,3-diaminopropane yields the chelated tetracyanoferrate(II) complex as the only photoproduct (21–23) according to eq. [1].

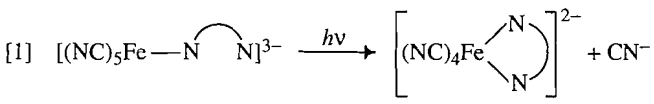

Quantum yields for the ring closure process at different excitation wavelengths and glycerol content in the mixed solvent are shown in Table 1. The observed pattern for the 313, 334, 404, and 434 nm irradiations aligns with that previously reported for the 365 nm excitation (23). Figure 1 shows the role of solvent viscosity, whose decrease clearly favors a diffusional escape of the cyanide ion from the solvent cage. For the 404 and 434 nm excitations, the quantum yield, 0.010, was the lowest value determined in this work. The reduction in photoconversion was less pronounced for the 313 nm irradiation (0.230 to 0.095), indicating a more efficient escape from the solvent cage.

An extrapolation of the data in Fig. 1 to zero viscosity indicates primary quantum yields of bond cleavage around 0.4 (313 or 334 nm), 0.2 (365 nm), and 0.06 (404 or 434 nm).

A good correlation between quantum yields and the reciprocal of the dielectric constant values can be seen from the data of Table 1 for different solvent compositions. This behav-

Table 1. Quantum yield for ring closure for different water–glycerol mixtures.[a]

Glycerol (wt.%)	η^b/Cp	ε^b	Φ_{313}	Φ_{334}	$\Phi_{365}{}^c$	Φ_{404}	Φ_{434}
00.00[c]	0.89	78.54	0.230	0.226	0.110	0.032	0.028
10.73	1.18	75.80	0.205	0.193	0.082	0.028	0.026
19.30	1.51	74.05	0.190	0.170	0.075	0.021	0.020
38.25	2.97	69.32	0.182	0.127	0.060	0.014	0.014
57.34	7.45	63.37	0.134	0.098	0.035	0.012	0.012
61.85	9.90	61.75	0.095	0.063	0.018	0.010	0.010

[a]$[[Fe(CN)_5(tn)]^{3-}] = 3.0 - 6.0$ mM; $T = (25.0 \pm 0.2)$°C.
[b]Reference 36.
[c]Reference 23.

Table 2. Quantum yield for ring closure for different water–acetonitrile mixtures.[a]

CH_3CN (wt.%)	η^b/Cp	ε^b	Φ_{313}	Φ_{334}	Φ_{365}	Φ_{404}	Φ_{434}
00.00	0.89	78.54	0.230	0.226	0.110	0.032	0.028
22.08	0.97	69.22	0.195	0.163	0.064	0.025	0.019
53.60	0.73	53.96	0.230	0.178	0.072	0.024	0.017
66.48	0.60	48.30	0.244	0.197	0.077	0.028	0.020

[a]$[[Fe(CN)_5(tn)]^{3-}] = 3.0 - 6.0$ mM; $T = (25.0 \pm 0.2)$°C.
[b]Reference 36.

ior is somehow unexpected since the parameters of the elementary electrostatic theory, such as dipole moment, polarizability, and dielectric constant, are usually found to be unsuitable for the description of solvent effects (28). Double reciprocal plots ($1/\Phi$ vs. $1/\eta$ and $1/\Phi$ vs. $1/\varepsilon$) do not present better correlations.

Water and glycerol are very much alike. They exhibit a strong tendency to form intermolecular hydrogen bonds (29, 30), and keep the solvent structure from changing due to preferential solvation. Specific interactions, such as hydrogen bonding, have been recognized for a long time to be more important than dispersion forces, depending on polarizabilities, in accounting for solvent effects (28, 30). The magnitude of the bulk solution properties for water–glycerol mixtures can be considered close to that for the coordination sphere. It is possible to correlate each set of variations of quantum yield with viscosity as an index of the microstructure, and dielectric constant as a measure of solvent polarity. A similar pattern for viscosity was reported by Scandola et al. for some isoelectronic cyanocobaltate(III) complexes (2, 4) and by Langford and Malkhasian (8) for amine complexes of Co(III).

Glycerol solutions are one of the best systems for analyzing the effect of viscosity on quantum yields without a great variation of dielectric constant. On the other hand, a remarkable change in dielectric constant values can be obtained using acetonitrile as the water cosolvent. Table 2 shows quantum yield values of the ring closure process for different excitation energies and water–acetonitrile compositions. One can see that the dielectric constant value decreases by roughly one third on going from aqueous solutions to 66.48 wt.% of acetonitrile. The quantum yield variation for the 313 or 334 nm irradiation presents a similar trend with viscosity as that observed for the water–glycerol system. The 365, 404, and 434 nm irradiation data do not align with the former ones.

As previously discussed (23), the 313 nm excitation populates exclusively the $Fe \rightarrow CN^-$ charge transfer state, namely ^1CT. According to one of our proposed mechanisms, in this condition, an excess of energy allows an efficient escape of the cyanide ion from the solvent cage. The quantum yield of aqueous solutions for this irradiation wavelength is around 0.23, while a higher value was obtained for 66.48 wt. % of acetonitrile. At this excitation energy the generation of the primary radical pair has the highest efficiency, and the difference in quantum yields reflects changes in the diffusional escape of the cyanide ion, which can be attributed to the 30% reduction in bulk solvent viscosity.

The reduction in viscosity, on going from aqueous solution to 66.48 wt.% acetonitrile, is expected to lead to higher efficiencies. This trend has not been observed for the 365 nm irradiations because the lowest limit to populating the ^1CT state with reasonable efficiency should be around this energy. The absence of the extra energy, which allows the cyanide to escape from the cage, makes the yields markedly lower when compared to those obtained for aqueous solutions.

For the 404 or 434 nm excitation, which populates exclusively the ^1LF state, little change was observed upon the increase of acetonitrile content in the medium. In this case the photoreactive channel is expected to be from the ^3LF state whereas an increasing participation of the ^1LF reactive channel is obtained at higher excitation energies.

According to the so-called mechanical cage effect, it is likely that the rate of vibrational energy transfer to the solvent medium can limit the rate of thermal equilibrium of the excited states. Their deactivations can be altered according to

the solvent composition. Since the cosolvents employed, water and acetonitrile, differ in their hydrogen bond properties (31), coupling differences between the metal complex and the solvent can lead to solvent-dependent rates of nonradiative deactivation to the ground state. Due to the lack of a systematic correlation such as those obtained for water–glycerol systems, the data can reflect the existence of preferential solvation by water. If the composition of the first solvation shell differs significantly from the bulk solution, solvation structures change considerably within small areas around the solute particles. Thus, in this case, macroscopic properties of the solvent are not good parameters for correlations.

The higher quantum yields obtained for the 313 nm excitation represent a pronounced break in the general trend for the water–acetonitrile series. They indicate the existence of an electronic perturbation caused by the solvent due to the higher nucleophilicity of acetonitrile in comparison to water (32–34). It is difficult to analyze the role of dielectric constant in the photochemical behavior of this complex since the quantum yield variation is dominated by the effect of viscosity.

The cage effect mechanism is a simple model to explain photochemical behavior that presents wavelength-dependent reactions. Recently, flash photolysis experiments showed that the solvent mixture not only changes the macroscopic properties of the solvent but also alters the efficiency of primary radical formation. Langford and co-workers (11) also pointed out the importance of the so-called thermal solvent cage, where the dynamics are controlled by the rate at which the energy is dissipated from the excited species to the solvent. For the $W(CO)_5py$ system (35), the quantum yields for pyridine substitution depend mainly on the "mechanical" cage effect at the highest excess excitation energy, while the thermal effect is pronounced at an intermediate excess excitation energy.

The solvent can also play a role in dictating the orbital population of the Frank–Condon excited state for charge transfer transitions (7). Considering that there are no noticeable changes in the position or shape of the absorption spectrum bands for water–glycerol mixtures, it can be concluded that, in this case, the quantum yield variation results not from the solvent-induced perturbation of electronic states but from variation in the kinetic parameters that govern excited state deactivation. This factor can be important to the water–acetonitrile system where the direct ^1CT population may be altered due to solvent composition in the coordination sphere. The absence of direct measurement of the intermediates in a fast time domain for such complexes precludes a determination of the mechanism. However, the two proposals are both consistent with the reported data but not mutually exclusive.

In fact, these two approaches are complementary in the sense that the medium property parameters are related to the dynamics of deactivation for formation of the final photoproduct. On the other hand, the wavelength dependence accounts for different efficiencies of primary radical formation in the very first step achieved before the deactivation process takes place. The overall quantum yield reflects the balance between solvent and irradiation wavelength effects. This work shows that for a determined excitation energy, the characteristics of the medium can shift the balance from one mode to another, tuning the efficiency of the photochemical process. The results point out that wavelength energy is as important as solvent properties in determining the overall quantum yield. For high energy excitations, the observed data reflect limitations imposed by the medium.

Acknowledgments

We thank the Conselho Nacional de Desenvolvimento Científico e Tecnológico (CNPq) and the Fundação de Amparo à Pesquisa do Estado de São Paulo (FAPESP) for financial support.

References

1. This work was presented in part at Photochem. Photophys. Coord. Compd. (Proc. Int. Symp.), 11th, Kraków, Poland, July 1995.
2. F. Scandola, C. Bartocci, and M.A. Scandola. J. Am. Chem. Soc. **95**, 7898 (1973).
3. J.F. Endicott, G.J. Ferraudi, and J.R. Baker. J. Am. Chem. Soc. **97**, 219 (1975).
4. F. Scandola, M.A. Scandola, and C. Bartocci. J. Am. Chem. Soc. **97**, 4757 (1975).
5. P.C. Ford, D. Wink, and J. Dibenedetto. Prog. Inorg. Chem. **30**, 213 (1983).
6. C.H. Langford. Acc. Chem. Res. **17**, 96 (1984).
7. J.F. Endicott, T. Ramasami, R. Tamilarasan, R.B. Lessard, C.K. Ryu, and G.R. Brubaker. Coord. Chem. Rev. **77**, 1 (1987).
8. C.H. Langford and A.Y.S. Malkhasian. J. Am. Chem. Soc. **109**, 2682 (1987).
9. C.H. Langford and E. Lindsey. Inorg. Chem. **29**, 1450 (1990).
10. C. Moralejo and C.H. Langford. Inorg. Chem. **30**, 567 (1991).
11. E. Lindsey, A.Y.S. Malkahasian, and C.H. Langford. Inorg. Chem. **33**, 944 (1994).
12. T. Kakitani and N. Mataga. J. Phys. Chem. **89**, 4752 (1985).
13. H. Rau and G. Greiner. Z. Phys. Chem. **170**, 73 (1991), and references therein.
14. M.J. Weaver. Chem. Rev. **92**, 463 (1992).
15. C.M. Previtalli, Pure Appl. Chem. **67**, 127 (1995).
16. H.J. Wolff, D. Bürbner, and U.E. Steiner. Pure Appl. Chem. **67**, 167 (1995).
17. C.H. Langford and C. Moralejo. *In* Photoinduced electron transfer. *Edited by* M.A. Fox and M. Chanon. Elsevier, Amsterdam. 1988. Part A, pp. 420–451.
18. H.E. Toma, N.M. Moroi, and N.Y. Murakami Iha. An. Acad. Brasil. Cienc. **54**, 315 (1982).
19. N.Y. Murakami Iha, J.F. Lima, and H.E. Toma. Proc. 34th Annu. Meet. Coord. Chem. Nagaoka, Japan, October 1984.
20. N.Y. Murakami Iha, H.E. Toma, and J.F. Lima. Polyhedron, **7**, 1687 (1988).
21. H.E. Toma and N.Y. Murakami Iha. Inorg. Chem. **21**, 3573 (1982).
22. N.Y. Murakami Iha and J.F. Lima. Inorg. Chem. **30**, 4576 (1991).
23. J.F. Lima, S.N. Motonaga, and N.Y. Murakami Iha. J. Photochem. Photobiol. A: **84**, 177 (1994).
24. G. Brauer. Handbook of preparative inorganic chemistry. Vol. 2. 2nd ed. Academic Press, New York. 1965. p. 1511.
25. C.G. Hatchard and C.A. Parker. Proc. R. Soc. London, **235**, 518 (1958).
26. C.T. Bahner and L.L. Norton. J. Am. Chem. Soc. **72**, 2881 (1950).
27. H.E. Toma, E. Giesbrecht, J.M. Malin, and E. Fluck. Inorg. Chim. Acta, **14**, 11 (1975).
28. V. Gutmann and G. Resch. Pure Appl. Chem. **53**, 1447 (1981).
29. S. Taniewska-Osinska. Chem. Soc. Rev. **22**, 205 (1993).
30. P.L. Huyskens, C.V. Pauwels, and K. Seghers. Bull. Soc. Chim. Belg. **101**, 449 (1992).

31. K. Nakanishi. Chem. Soc. Rev. **22**, 177 (1993).
32. H.E. Toma and M.S. Takasugi. J. Solution Chem. **12**, 547 (1983).
33. R.W. Soukup and R. Schmid. J. Chem. Educ. **62**, 459 (1985).
34. J.R. Winkler, C. Creutz, and N. Sutin. J. Am. Chem. Soc. **109**, 3470 (1987).
35. C.H. Langford and L.E. Shaw. Photochem. Photophys. Coord. Compd. (Proc. Int. Symp.), 11th, Kraków, Poland, July 1995.
36. G.J. Jans and R.P.T. Tomkins (*Editors*). Handbook of nonaqueous electrolytes. Vol. 1. Academic Press, New York. 1973. pp. 85 and 100.

Synthèse et analyse structurale de nouvelles *méso*-arylporphyrines glycosylées en vue de l'application en photothérapie des cancers

Olivier Gaud, Robert Granet, Mourad Kaouadji, Pierre Krausz, Jean Claude Blais et Gerard Bolbach

Résumé : Nous décrivons la synthèse de 13 nouvelles *méso*-glycosylarylporphyrines pour lesquelles la partie glucidique est séparée du substituant aryle par l'intermédiare d'un bras espaceur. Ces composés sont synthétisés par différentes méthodes : glycosylation des *ortho*- et *para*-hydroxyalkyloxyarylporphyrines, condensation d'aldéhydes glycosylés avec du pyrrole ou du *méso*-(*p*-tolyl)dipyrrométhane. Dans une seconde étape la partie glucidique est déprotégée en milieu basique. Dans tous les cas, les glucides *O*-liés présentent une configuration β. Ces composés sont caractérisés par différentes méthodes spectrales. Une étude détaillée de la RMN permet d'attribuer tant en ^{1}H qu'en ^{13}C les différents signaux aux noyaux tolyles, aryles, pyrroles, alkyles et glycosyles. Nous discutons de l'allure des spectres obtenus en spectrométrie UV–visible et enfin nous présentons les résultats de spectrométrie de masse obtenus par une nouvelle méthode de désorption laser adaptée à ces molécules de haut poids moléculaire. Par leur pouvoir sensibilisateur, ces molécules constituent de bons candidats pour la thérapie photodynamique.

Mots clés : porphyrines, glycosylations, photothérapie, cancer.

Abstract: The synthesis of 13 novel *meso*-glycosylarylporphyrins where the carbohydrate moiety is separated from the aryl substituent by a spacer arm is described. These compounds were synthesized by different methods, either by direct glycosylation of the *ortho*- or *para*-hydroxyalkoxyarylporphyrin or by condensation of glycosylated aldehyde with pyrrole or *meso*-(*p*-tolyl)dipyrromethane. In all cases, a β configuration was observed. Deprotection of the sugar then followed in a basic medium. The compounds were characterized by a variety of means. A detailed ^{1}H and ^{13}C NMR study allowed complete structural determination. The UV–visible and laser desorption mass spectra are presented. Due to their sensitizing abilities, these resultant compounds are of considerable interest for photodynamic therapy.

Key words: porphyrins, glycosylations, phototherapy, cancer.

Depuis la première publication de Mironov et al. (1), l'étude des porphyrines glycosylées (2) a pris une importance sans cesse croissante en raison de son impact, en particulier en thérapie photodynamique (PDT). Plusieurs travaux effectués ces dernières années ont montré que les porphyrines solubles dans l'eau tendent à se concentrer davantage dans les tumeurs que dans les tissus sains. Ainsi, une tumeur enrichie en porphyrines peut être sélectivement détruite par irradiation sans toucher aux tissus non atteints (3). Après un travail préliminaire (4), nous présentons la synthèse de 13 nouvelles porphyrines glycosylées (figure 1) du type *méso*-arylporphyrine, dont la partie saccharidique est séparée du macrocycle tétrapyrrolique par un bras espaceur. Nous avons, en particulier, fait varier la position du bras sur le groupement phényle (*ortho* ou *para*), la nature du glucide représenté par un monosaccharide (glucosyle ou ribosyle) ou un disaccharide (maltosyle ou lactosyle) ainsi que le nombre d'entités osidiques fixées sur le macrocycle tétrapyrrolique (une à quatre en série glucosyle). De telles structures nous semblent être de bons candidats pour la PDT. En effet, le bras espaceur devrait accroître le caractère amphiphile de ces composés en permettant de disposer de molécules à la fois solubles dans l'eau et capables de s'intégrer facilement aux membranes phospholipidiques. Par ailleurs, il est maintenant admis que la présence d'unités glucidiques peut améliorer le ciblage de ces substrats vis-à-vis de certaines tumeurs (5).

Reçu le 3 août 1995.

O. Gaud, R. Granet, M. Kaouadji et P. Krausz.[1] Université de Limoges, Laboratoire de chimie des substances naturelles, 123, Avenue Albert Thomas F-87060 Limoges Cedex, France.
J.C. Blais et G. Bolbach. Université Pierre et Marie Curie, Laboratoire de chimie organique structurale et biologique, Centre national de la recherche scientifique EP 103, 4, Place Jussieu F-75252 Paris Cedex, France.

1. Auteur à qui la correspondance doit être adressée. Téléphone : (33) 55 45 74 75. Fax : (33) 55 45 72 02.

Synthèse

Monoglycosylporphyrines 1a,b–4a,b

Deux méthodologies sont utilisées. La première (voie A, schéma 1) part des *ortho*- ou *para*-5-hydroxyphényl-10,15,20-tritolylporphyrines **10a,b** synthétisées selon la méthode de Little et al. (6). Ces porphyrines sont alkylées en milieu DMF-K_2CO_3 par le 3-bromopropan-1-ol pour mener, avec des rendements quasi-quantitatifs, aux 5-hydroxypropyloxyphényl-10,15,20-tritolylporphyrines **11a,b**, (7). Ces derniers composés sont ensuite glycosylés par des dérivés *per*acétylés du glucose, du maltose ou du lactose ou par le 1-*O*-acétyl 2,3,5-tribenzoate-β-D-ribose par le système $SnCl_4$–CH_2Cl_2 à température ambiante. En fin de réactions, l'analyse des pro-

Fig. 1.

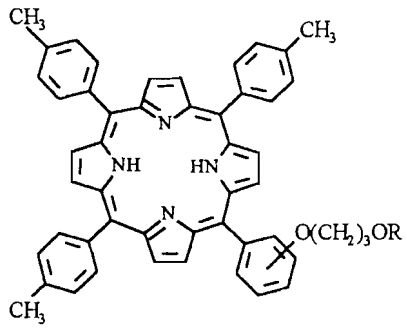

1a,b R = Glc
2a,b R =Rb
3a,b R = Mal
4a,b R = Lac

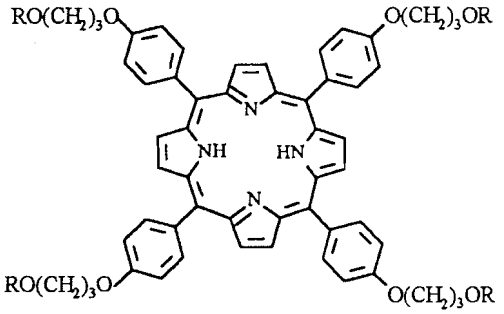

5 R = Glc
6 R = Mal

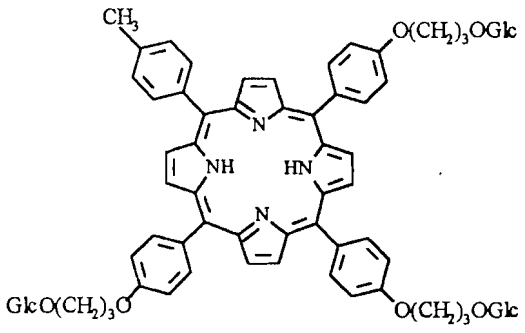

7

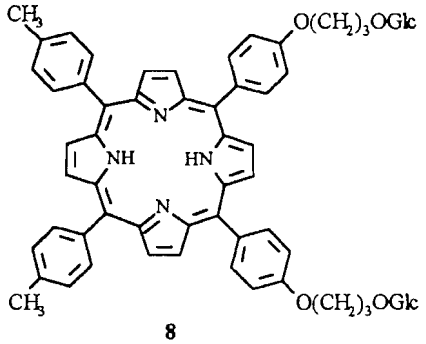

8

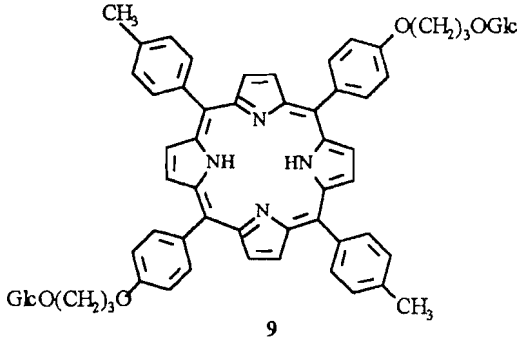

9

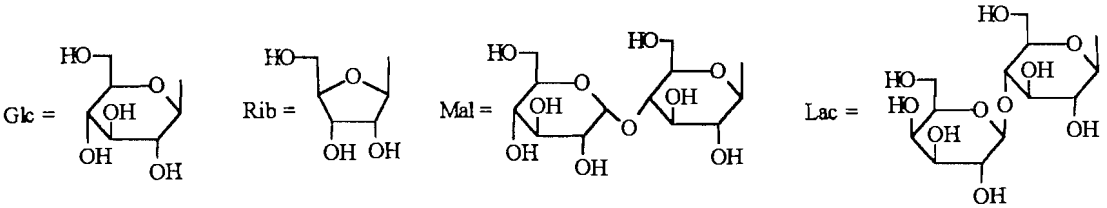

a et b réfèrent respectivement aux composés *ortho* et *para*.

duits formés montre, outre les produits attendus **12a,b–15a,b**, des glucides de départ, des produits de dégradation de ces derniers ainsi que des traces des porphyrines **11a** ou **11b** et de leur dérivé acétylé au niveau du groupement hydroxyle (*o*- et *p*-(acétyloxypropyloxy)phényltritolylporphyrine). Comme attendu dans ce type de glycosylation, on note l'absence de porphyrines α-glycosylées. Les produits obtenus, **12a,b–15a,b,** sont purifiés par chromatographie préparative sur couche mince de gel

Schéma 1.

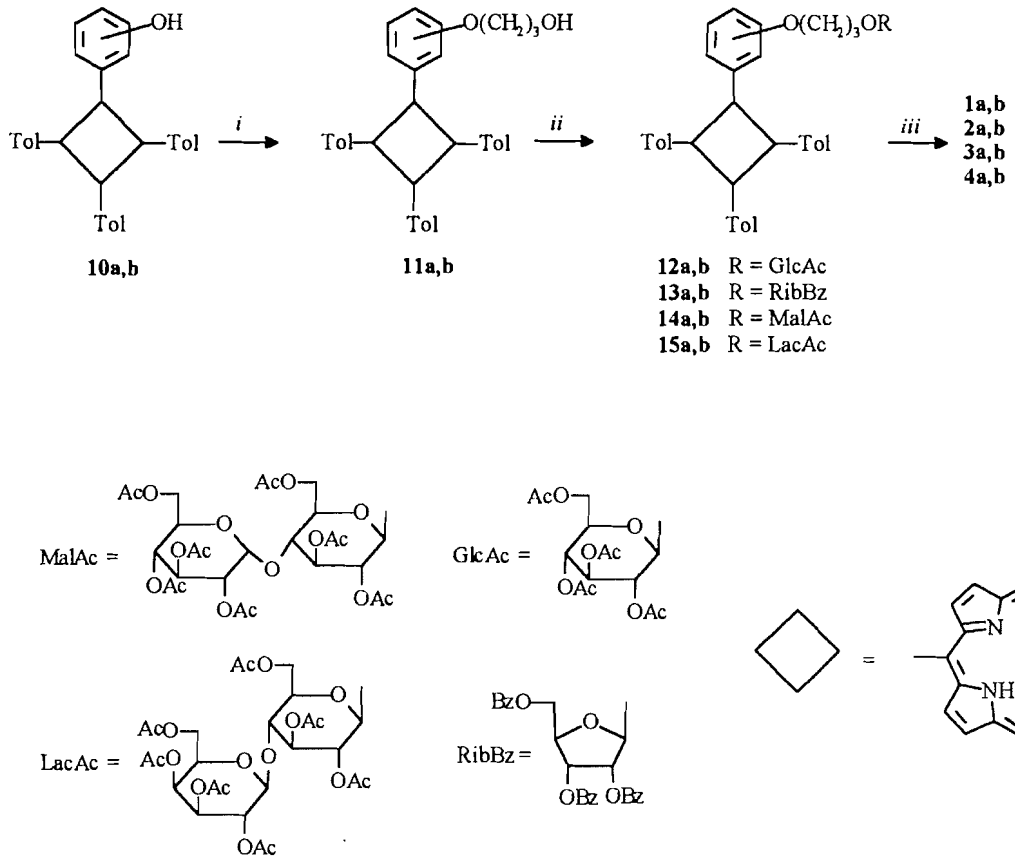

(*i*) $Br(CH_2)_3OH/K_2CO_3/DMF$, (*ii*) $SnCl_4/CH_2Cl_2$/glucide acétylé ou benzoylé, (*iii*) $MeONa/MeOH/CH_2Cl_2$.
a et **b** réfèrent respectivement aux composés *ortho* et *para*.

de silice. Tous présentent, comme le montrent les constantes de couplage des protons anomériques, une configuration β (tableau 2-3, réf. 8). Les rendements de réaction varient de 20 à 70%. Ils sont maximaux pour les dérivés monosaccharidiques *para*-substitués. Nous avons également obtenu les composés **12a,b** et **14b** par une deuxième méthode (voie B, schéma 2). Celle-ci nécessite la synthèse préalable, en deux étapes, des précurseurs aldéhydiques glycosylés **17a,b** et **18b**. La première consiste à faire réagir l'*ortho*- ou le *para*-hydroxybenzaldéhyde sur le 3-bromopropan-1-ol en milieu K_2CO_3–DMF. Elle conduit aux intermédiaires **16a,b** qui sont purifiés par chromatographie sur colonne de silice avec des rendements acceptables (Rdt 65–75%). Dans une deuxième étape, ces dérivés sont glycosylés par le glucose ou le maltose *per*acétylé avec le système $SnCl_4$–CH_2Cl_2. Les β glycosides obtenus, **17a,b** et **18b**, sont isolés par chromatographie et (ou) cristallisation avec des rendements de 20 à 35%. Ces précurseurs glycosylés sont alors condensés sous reflux dans l'acide propionique, sur des quantités stoechiométriques de *para*-tolualdéhyde (3 equiv.) et de pyrrole (4 équiv.). Ces conditions expérimentales mènent aux porphyrines **12a,b** et **14b** avec des rendements de l'ordre de 10%. Cette deuxième voie de synthèse permet d'accéder plus rapidement aux monoglycosylporphyrines avec des rendements comparables à ceux de la voie A. Elle implique par contre, la formation de quantités importantes de précurseurs glycosylés qui ne se prêtent pas toujours à des purifications aisées. Les porphyrines glycosylées synthétisées par les deux voies, sont ensuite déprotégées par le méthylate de sodium en milieu CH_2Cl_2–MeOH. Les réactions sont totales en 1 h et les porphyrines obtenues sont isolées après purification sur colonne de Sephadex LH20 avec des rendements de l'ordre de 80%. Elles sont toutes peu solubles dans l'eau, mais cette solubilité augmente lorsqu'on passe d'un mono à un disaccharide ou encore par passage d'une substitution *para* à une substitution *ortho*.

Tétraglycosylporphyrines 5,6

Ces deux composés sont synthétisés selon le schéma 2. Les condensations des précurseurs glycosylés **17b** et **18b** sur le pyrrole sont effectuées par la méthode de Lindsey et al. (9) en milieu CH_2Cl_2 et en présence d'acide trifluoroacétique (TFA). Les porphyrinogènes formés en 1 h pour le composé glucosylé et en 4 h pour le composé maltosylé sont ensuite oxydés par addition de *p*-chloranile. Les porphyrines **19** et **20** sont alors purifiées par chromatographie sur colonne de silice et isolées avec des rendements respectifs de 36 et 16%. Ces deux composés sont désacétylés par le méthylate de sodium dans des conditions similaires à celles précédemment employées. Les porphyrines déprotégées **5** et **6** présentent toutes les deux une bonne solubilité dans l'eau.

Di- et triglycosylporphyrines 7–9

Tout comme la monoglycosylporphyrine **12b**, les di- et triglycosylporphyrines **22**, **23**, **21**, sont synthétisées selon le schéma

Schéma 2.

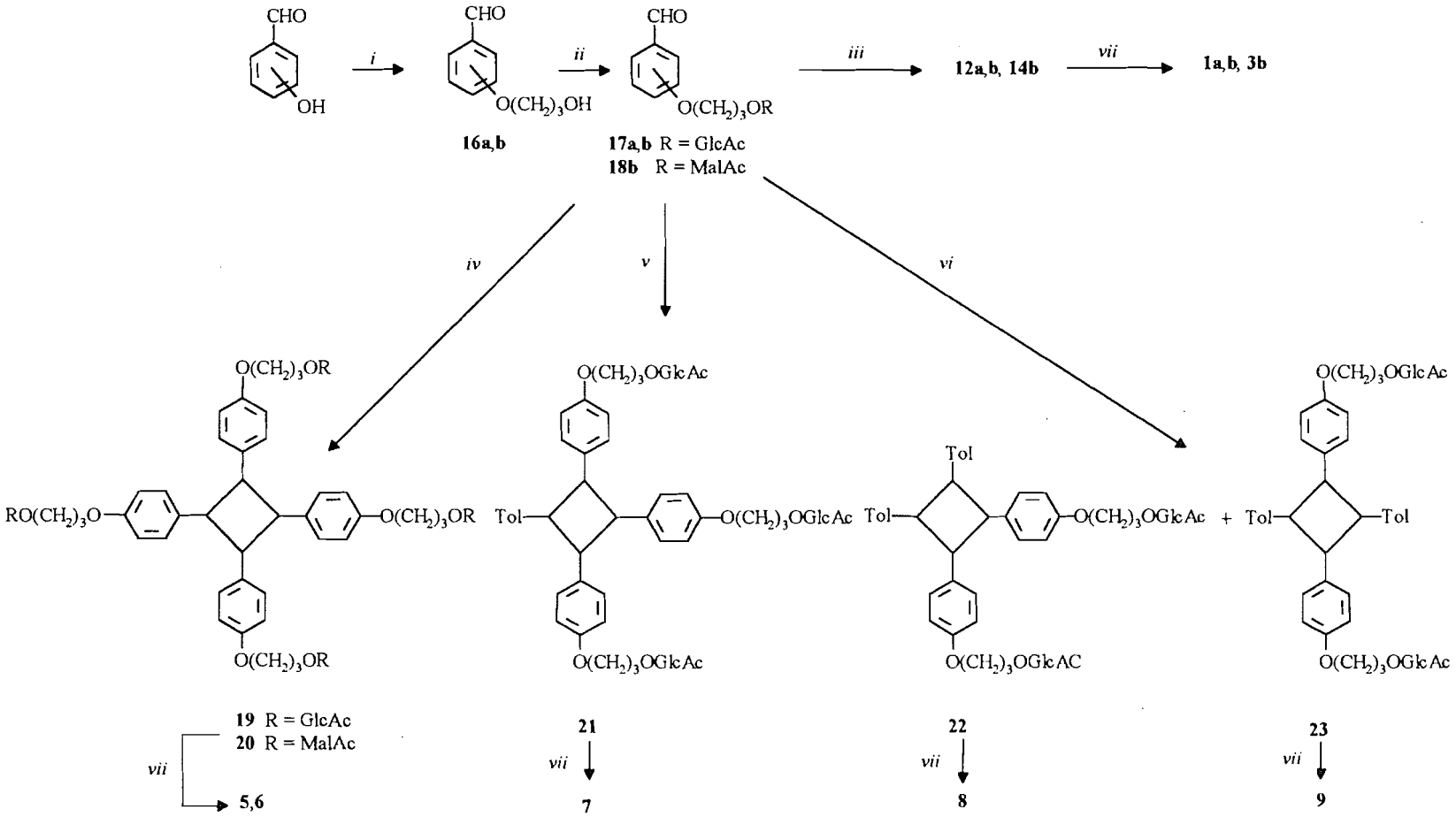

(*i*) $Br(CH_2)_3OH/K_2CO_3/DMF$, (*ii*) $SnCl_4/CH_2Cl_2$/glucide acétylé, (*iii*) *para* tolualdéhyde 3éq./ pyrrole 4 éq./EtCOOH, (*iv*) pyrrole 1 éq./CF3COOH puis *para* chloranile, (*v*) *para* tolualdéhyde 0,33 éq./pyrrole 1,33 éq./EtCOOH, (*vi*) *para* tolualdéhyde 1 éq./pyrrole 2 éq./EtCOOH, (*vii*) $McONa/McOH/CH_2Cl_2$.
a et **b** réfèrent respectivement aux composés *ortho* et *para*. Les abréviations retenues sont définies sur le Schéma 1.

Schéma 3.

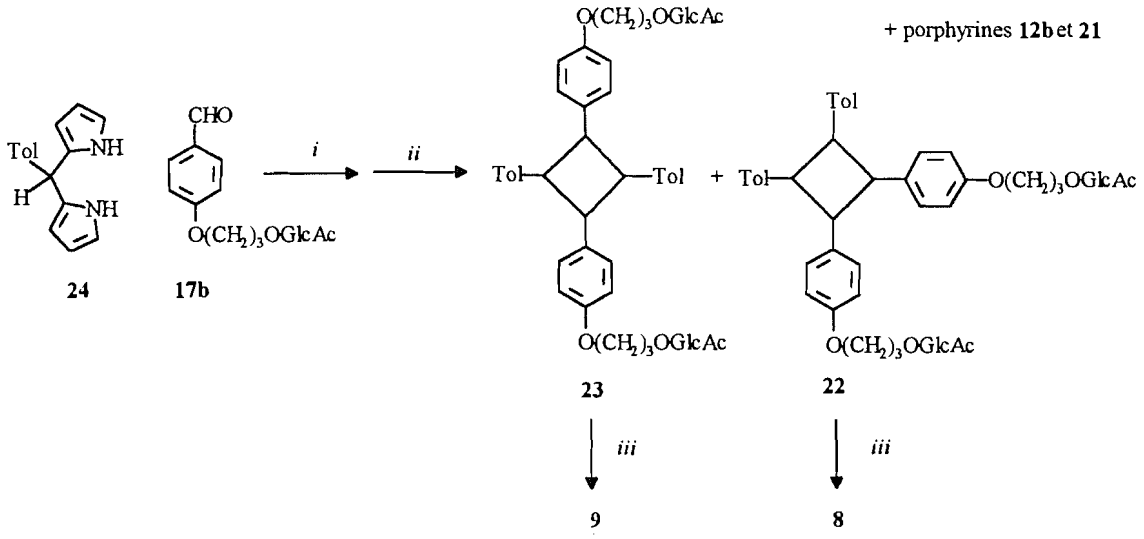

(*i*) CH_2Cl_2/BF_3Et_2O, (*ii*) *p*-chloranile, (*iii*) $MeONa/MeOH/CH_2Cl_2$.

Les abréviations retenues sont définies sur le Schéma 1.

Tableau 1. Spectres UV–visible des porphyrines.[a]

Composé	Soret	IV	III	II	I	$\varepsilon_{II}/\varepsilon_{I}$
1a	418 (255,3)	514 (10,7)	548 (5,0)	594 (2,8)	650 (2,7)	1,1
1b	418 (359,3)	516 (12,9)	552 (7,9)	594 (3,7)	650 (3,4)	1,1
2a	418 (332,0)	514 (15,3)	548 (7,5)	592 (4,4)	648 (3,6)	1,2
2b	417 (409,3)	516 (14,3)	550 (8,4)	592 (4,0)	650 (4,0)	1,0
3a	418 (330,1)	514 (13,5)	548 (7,2)	592 (4,1)	648 (3,4)	1,2
3b	418 (367,4)	516 (14,4)	552 (8,9)	594 (4,2)	650 (4,2)	1,0
4a	418 (279,9)	514 (13,4)	548 (6,6)	592 (3,9)	648 (3,2)	1,2
4b	418 (323,2)	516 (12,6)	550 (7,6)	594 (3,7)	650 (3,7)	1,0
5	420 (229,3)	518 (9,8)	554 (7,6)	596 (3,3)	650 (5,0)	0,7
6	422 (143,1)	518 (7,1)	554 (5,5)	596 (2,5)	652 (3,4)	0,7
7	420 (140,5)	518 (6,1)	554 (4,3)	596 (1,8)	650 (2,1)	0,9
8	420 (287,0)	516 (13,4)	552 (9,7)	594 (5,1)	650 (4,4)	1,1
9	420 (287,0)	516 (12,7)	552 (8,4)	594 (4,1)	650 (3,9)	1,1
11a	420 (691,8)	516 (28,8)	552 (16,2)	592 (9,5)	648 (6,8)	1,4
11b	420 (441,6)	516 (17,1)	552 (10,4)	592 (5,3)	648 (5,6)	0,9
12a	420 (454,1)	516 (15,8)	550 (8,3)	592 (5,4)	648 (4,8)	1,1
12b	420 (400,0)	516 (14,1)	552 (8,6)	592 (4,9)	648 (4,7)	1,0
13a	420 (371,5)	516 (15,1)	552 (7,4)	592 (4,7)	646 (3,8)	1,2
13b	420 (338,8)	516 (12,9)	552 (8,7)	592 (4,5)	648 (4,1)	1,1
14a	420 (326,6)	516 (14,8)	552 (7,4)	590 (4,6)	646 (3,6)	1,3
14b	420 (446,7)	516 (17,4)	552 (10,4)	592 (5,7)	648 (5,5)	1,0
15a	420 (410,7)	516 (15,2)	550 (7,5)	592 (4,6)	646 (3,7)	1,2
15b	420 (590,1)	516 (19,3)	552 (11,3)	592 (5,8)	648 (5,5)	1,0
19	422 (398,1)	518 (13,8)	556 (10,0)	594 (4,7)	650 (7,1)	0,7
20	422 (169,0)	518 (5,9)	556 (4,2)	594 (2,0)	650 (2,5)	0,8
21	422 (494,0)	518 (17,3)	554 (11,5)	594 (5,6)	650 (6,2)	0,9
22	422 (562,1)	516 (13,4)	552 (9,7)	594 (5,1)	650 (4,4)	1,1
23	420 (606,6)	516 (16,5)	552 (10,6)	594 (4,5)	650 (4,4)	1,0

[a] λ_{max} (nm) (coefficient d'absorption ($\varepsilon \times 10^{-3}$ mol^{-1} l cm^{-1})), ~20°C, Les composés amphiphiles **1a,b–9** sont en solution dans le mélange THF/H_2O (8/2). Les composés lipophiles **11a,b–23** sont en solution dans CH_2Cl_2.

Tableau 2. Spectre de RMN ^{1}H des composés **12a,b–15a,b** dans $CDCl_3$.

H	12a[a]	12b[a]	13a	13b	14a	14b[a]	15a[a]	15b[a]
Pyrroles								
2	8,82 d (4,8)[b]	8,83 d (4,9)[b]	8,81 d (4,8)[b]	8,84 d (5,1)[b]	8,78 d (4,8)[b]	8,87 d (4,5)[b]	8,80 d (4,8)[b]	8,84 d (4,9)[b]
3	8,90 d (4,8)[c]	8,87 d (4,9)[b]	8,87 d (4,8)[b]	8,88 d (5,1)[b]	8,88 d (4,8)[b]	8,90 d (4,5)[b]	8,92 d (4,8)[c]	8,87 d (4,9)[b]
7	8,78 d (4,8)[c]	8,87 d (4,9)[c]	8,87 d (4,8)[c]	8,88 d (5,1)[c]	8,88 d (4,8)[c]	8,90 d (4,5)[c]	8,90 d (4,8)[c]	8,87 d (4,9)[c]
8	8,86 d (4,8)[b]	8,83 d (4,9)[c]	8,81 d (4,8)[c]	8,84 d (5,1)[c]	8,78 d (4,8)[c]	8,87 d (4,5)[c]	8,77 d (4,8)[b]	8,84 d (4,9)[c]
13,17	8,91 s[d]	8,86 s	8,84 s[e]	8,86 s	8,89 s[e]	8,89 s	8,89 d (4,8)[d]	8,86 s
12,18	8,87 s[d]	8,86 s	8,83 s[e]	8,86 s	8,87 s[e]	8,89 s	8,86 d (4,8)[d]	8,86 s
NH	2,70 s él.	2,73 s él.	2,69 s él.	2,73 s él.	2,71 s él.	2,70 s él.	–2,70 s él.	–2,74 s él.
***p*-Tolyes**								
2,6	8,18 m	8,10 d (7,9)	8,06 d él. (8,2) 8,09 d él. (8,2) 8,04 d él. (8,2)	8,11 d (8,6)	8,16 d él. (7,4) 8,12 d él. (7,4) 8,09 d él. (7,4)	8,13 d (7,8)	8,11 él. (6,0)	8,10 d (7,9)
3,5	7,56 d él. (8,2)	7,56 d (7,9)	7,55 m	7,56 d él. (8,6)	7,60 d él. (7,4) (×1) 7,57 d él. (7,4) (×2)	7,57 d (7,8)	7,57 m	7,56 d (7,9)
Me	2,72 s	2,71 s	2,72 s 2,69 s 2,64 s	2,72 s	2,72 s	2,73 s	2,74 s (×1) 2,72 s (×2)	2,71 s
Aryle								
2		8,12 d (8,5)		8,11 m		8,14 d (8,6)		8,12 d (8,7)
3	7,31 d él. (8,2)	7,27 d (8,5)	7,40 m	7,27 d (8,7)	7,32 d él. (7,9)	7,28 d (8,6)	7,31 d él. (7,3)	7,28 d (8,7)
4	7,76 dt (8,01-1,7)		7,77 m		7,75 dt (7,9-1,7)		7,75 dt (7,3-1,7)	
5	7,36 t (7,3)	7,27 d (8,5)	7,40 m	7,27 d (8,7)	7,36 dt (7,9-1,2)	7,28 d (8,6)	7,36 t (7,3)	7,28 d (8,7)
6	8,08 m	8,12 d (8,5)	8,06 m	8,11 m	8,03 dd (7,2-1,7)	8,14 d (8,6)	8,03 dd (7,5-1,7)	8,12 d (8,7)
Bras								
α	3,98 dt (8,4-4,6) 3,86 dt (8,4-3,6)	4,32 t (5,6)	4,03 m 3,94 m	4,34 t él. (6,0)	3,93 m[e]	4,32 m[e]	3,94 m[e]	4,31 t (6,1)
β	1,24 m	2,27 m	1,20 m	2,34 quint. él. (6,1)	1,20 m[e]	2,27 m[e]	1,30 m[e]	2,25 m
γ_a	2,37 m	4,23 m	2,90 dt (9,3-3,5)	4,16 dt (9,7-5,9)	2,85 m[e]	4,22 dt (9,6-5,3)[e]	2,89 m[e]	4,20 m
γ_b	2,07 m	3,92 dt (9,5-6,6)	2,41 dt (9,3-6,0)	3,87 dt (9,7-6,3)	2,45 m[e]	3,94 dt (9,6-6,6)[e]	2,28 m[e]	3,88 m
***O*-Glycosyles**								
1	2,45 d (8,0)	4,65 d (7,7)	4,62 s	5,42 s él.	3,73 d (7,9)	4,71 d (7,9)	3,72 d (7,9)	4,63 d (8,0)
2	4,37 dd (9,6-8,0)	5,10 dd (9,6-7,6)	5,37 d (4,9)	5,81 d él. (4,8)	4,53 dd (9,4-7,9)	4,97 dd (9,4-7,9)	4,66 dd (9,5-7,9)	5,15 dd (10,7-7,7)
3	4,08 t (9,6)	5,28 t (9,6)	5,57 dd (6,6-5,0)	5,96 dd (6,4-4,9)	4,99 t (9,2)	5,37 t (9,1)	4,93 t (8,9)	5,28 t (9,0)
4	4,40 t (9,6)	5,15 t (9,5)	4,33 m	4,80 m	3,75 t (9,2)	4,01 t (9,4)	3,60 t él. (8,9)	3,86 t él. (9,0)
5	1,12 m	3,78 ddd (9,5-4,6-2,4)			3,00 m	3,81 ddd (9,5-3,8-3,0)	3,10 m[b]	3,70 m
5_a			4,21 dd (11,7-4,6)	4,81 m				
5_b			4,00 dd (11,7-5,7)	4,63 dd (12,7-6,7)				

Tableau 2 (*fin*).

H	**12a**[a]	**12b**[a]	**13a**	**13b**	**14a**	**14b**[a]	**15a**[a]	**15b**[a]
6_a	2,92 dd (12,5-4,0)	4,34 dd (12,0-4,6)			3,81 m	4,60 dd (12,1-2,6)	4,12 m[b]	4,57 d él. (11,5)
6_b	2,26 dd (12,5-2,0)	4,18 m			3,81 m	4,35 m	3,86 m[b]	4,15 m
1′					5,31 d (4,0)	5,49 d (4,0)	4,43 d (7,7)	4,54 d (7,7)
2′					4,86 dd (10,5-4,0)	4,92 dd (10,4-4,0)	5,18 dd (10,5-3,5)	5,00 dd (9,4-8,0)
3′					5,40 dd (10,4-9,4)	5,44 t (10,2)	4,96 dd (10,5-3,5)	4,98 dd (10,7-3,4)
4′					5,05 t (9,9)	5,11 d (9,8)	5,36 d él. (3,5)	5,38 d (2,6)
5′					3,85 m	3,96 m	3,86 m[b]	3,88 m
$6'_a$					4,25 dd (12,4-3,8)	4,35 m	4,12 m	4,15 m
$6'_b$					3,99 dd (12,4-2,0)	4,12 m	4,12 m	4,15 m
Acétyles								
	1,88 s (×2)	2,13 s			2,08 s	2,23 s	2,21 s	2,18 s (×2)
	1,75 s	2,08 s			2,06 s	2,15 s	2,05 s	2,09 s (×4)
	1,66 s	2,05 s			2,04 s (×2)	2,10 s	2,02 s (×2)	1,99 s
		2,04 s			1,94 s	2,09 s (×2)	2,00 s	
					1,88 s	2,07 s (×2)	1,75 s	
					1,65 s		1,63 s	

Les protons benzoïques du composé **13a** sont enregistrés à δ pm : ca. 7,90, ca. 7,83 et ca. 7,76, t él. (3 × 2H, J = 7,1 Hz, H-2,6), ca. 7,57, ca. 7,55 et ca. 7,53 t él. (3 × 1H, H-4), ca. 7,40, ca. 7,26 et ca. 7,12 t él. (3 × 2H, J = 7,7 Hz, H-3,5). Les protons benzoïques du composé **13b** sont enregistrés à δ ppm : 8,12, 8,06 et 7,92, dd (3 × 2H, J = 8,5-1,4 Hz, H-2,6), ca. 7,50 m (3H, H-4), ca. 7,45 m (2H, H-3,5), 7,33 et 7,20 t (2 × 2H, J = 8,5 Hz, H-3,5).

[a]Composé dont l'attribution des signaux est vérifiée par COSY.

[b–d]Les attribution affectées du même exposant dans une même colonne sont réversibles.

[e]Attribution déterminée par irraditions sélectives.

2 en adaptant la stoechiométrie des réactifs. Ces synthèses sont cependant peu sélectives et donnent lieu à la formation d'un mélange de porphyrines, de chlorines et de produits de polymérisation. Dans ces conditions, nous obtenons le composé **21** avec un rendement de 4%. Par contre la synthèse des diglycosylporphyrines substituées sur les positions 5,10 (composé *cis*) **22** ou 5,15 (composé *trans*) **23** du macrocycle donne des résultats moins satisfaisants (Rdt < 2%). Dans ce dernier cas, nous avons cherché à adapter une troisième voie de synthèse de façon à limiter la formation des composés parasites (voie c, Schéma 3). Parmi les différentes voies qui permettent d'accéder à un cycle porphyrinique, la condensation d'unités dipyrrométhane avec un aldéhyde représente une méthode importante. En imposant la géométrie d'une partie de la molécule, elle permet de limiter la formation d'isomères. Cette méthode a récemment été utilisée pour la synthèse de *méso*-arylporphyrines disubstituées (10–15) ou tétrasubstituées (16–19). Pour notre part nous avons réalisé cette synthèse selon la procédure développée par Lee et Lindsey (19). L'unité dipyrrométhane (**24**) est préparée en faisant réagir le *para*-tolualdéhyde sur un excès de pyrrole en absence de solvant. Après évaporation du pyrrole, le composé **24** est chromatographié sur silice par élution au toluène en présence de 1% de triéthylamine. Dans une deuxième étape, ce composé est mis à réagir en présence de $BF_3{\cdot}Et_2O$ sur le précurseur **17b** en milieu CH_2Cl_2 sous atmosphère inerte. Le porphyrinogène formé est ensuite oxydé par addition de *p*-chloranile. Dans les conditions décrites par Lindsey, cette réaction conduit par acidolyse du dipyrrométhane, puis par recombinaison des unités libérées à la formation d'un mélange de porphyrines. Dans une deuxième série d'essais nous avons réalisé ces condensations dans l'acide propionique, mais ce système ne s'est pas révélé efficace. En effet dans ces conditions, la complexité du mélange obtenu reste identique et les rendements de réaction diminuent. Pour améliorer les premiers résultats obtenus dans le système CH_2Cl_2–$BF_3{\cdot}Et_2O$, nous avons anticipé l'addition du *p*-chloranile et ramené la température d'oxydation à celle du milieu ambiant. Dans ces conditions nous avons sensiblement augmenté la proportion du composé **23** par rapport aux autres glycoporphyrines **12b**, **21**, et **22**. Par la voie C, nous avons donc isolé par chromatographie sur silice la monoglycosylporphyrine **12b** (Rdt 16%), les *cis* et *trans* diglycosylporphyrines **22** et **23** (Rdt 5%, Rdt 9%) et la triglycosylporphyrine **21** (Rdt 2%). Les isomères **22** et **23** de R_f très voisins, n'ont pu être séparés qu'à la suite d'une triple élution sur plaques de gel de silice. Comme attendu, le composé **22** est le plus polaire. Tout comme les mono- et tétraglycosylporphyrines les porphyrines **21**, **22**, **23** sont déprotégées par le méthylate de sodium et mènent après purification sur colonne de Sephadex LH20 aux composés **7**, **8**, **9** avec de bons rendements (Rdt > 80%). Ces composés présentent une solubilité dans l'eau, intermédiaire entre celles des monoglycosylporphyrines et celles des tétraglucosylporphyrines.

Analyses spectroscopiques

Spectrométrie UV–visible

Tous les spectres d'absorption UV–visible des porphyrines lipophiles **11**–**21** sont mesurés dans le dichlorométhane (tableau 1). L'analyse des résultats montre la bande de Soret vers 420 nm ainsi que les quatre bandes, I, II, III et IV de moindre intensité généralement attendues pour ce type de porphyrines (20). La plupart de ces spectres sont de type *étio* ($\epsilon_{IV} > \epsilon_{III} > \epsilon_{II} > \epsilon_I$). En passant cependant des spectres des composés *ortho*- à ceux des composés *para*-substitués on note une diminution relative de l'intensité de la bande II par rapport à celle de la bande I. Cette variation conduit pour les composés **20**, **21** et **22** à des spectres atypiques présentant un coefficient d'absorption ϵ_I supérieur à ϵ_{II}. Nous avons réalisé les spectres des composés amphiphiles **1**–**9** dans le mélange mixte tétrahydrofurane/eau 8:2 (tableau 1). Dans ce milieu, nous retrouvons des spectres d'allure similaire à ceux précédemment décrits. Tout comme leurs homologues acétylés ou benzoylés, ces composés présentent des variations des bandes I et II par passage d'une substitution *ortho* à une substitution *para* du *méso*-phényle. Par contre, lorsque ces spectres sont réalisés dans l'eau pure, ils présentent des variations importantes; ils montrent ainsi un élargissement ou un dédoublement de la bande de Soret avec une diminution du coefficient d'absorption. Ce phénomène est réversible après addition de THF. Par analogie aux résultats observés par Fuhrhop et al. (21) ces comportements spectraux peuvent être interprétés par la formation d'agrégats.

Spectrométrie de masse

En raison de la non volatilité des porphyrines, les méthodes classiques de spectrométrie de masse (IE, IC) se révélent inadaptées. Les spectres de massse sont par conséquent effectués avec les modes d'ionisation SIMS ou MALDI. Les monoglycosylporphyrines protégées 12a,b–15a,b sont analysées en mode SIMS. Comme nous l'avons déjà montré sur des composés de ce type (22), les spectres obtenus en mode positif présentent les pics moléculaires $(M+H)^+$. De plus, on observe dans tous les cas, un pic de fragmentation correspondant au départ du propyloxyglucosyle. Les autres porphyrines sont analysées en mode MALDI. Le pic moléculaire est toujours présent avec ce mode d'ionisation et on note en général l'absence d'ions fragments.

RMN ^{1}H

Les spectres de résonance magnétique nucléaire du proton des composés glycosylés sont enregistrés à 200 MHz dans $CDCl_3$. Les attributions détaillées des signaux sont rassemblées dans les tableaux 2 et 3. Elles reposent sur l'intégration, le découplage sélectif homonucléaire mais également sur les spectres 2D de corrélation homonucléaire ^{1}H–^{1}H (COSY). Les spectres de RMN ^{1}H des précurseurs ainsi que ceux des octaacétylmaltose et lactose sont utilisés comme références. La RMN du proton de ces composés présente sept groupes de signaux : (*i*) les protons β pyrroliques vers 9 ppm; (*ii*) les signaux des *méso*-substituants aromatiques entre 8,2 et 7,2 ppm; (*iii*) les protons osidiques entre 5 et 3 ppm dans le cas des composés substitués en position *para* et entre 5 et 2 ppm pour celui des composés *ortho*-substitués; (*iv*) les protons de la chaîne hydrocarbonée entre 4 et 1,5 ppm qui sont souvent confondus avec certains protons glucidiques; (*v*) les signaux CH_3 tolyles à 2,7 ppm; (*vi*) les protons des groupements acétyles vers 2 ppm; (*vii*) les protons NH pyrroliques vers –2,7 ppm. L'analyse fine de la zone β pyrrolique permet d'appréhender la symétrie de ces molécules (figure 2). Alors que les protons β pyrroliques des composés **19** et **20** (un seul type de substituant) résonnent sous la forme d'un singulet, ceux des composés mixtes (tolyle et aryloxypropyloxyglucosyle) se présentent sous la forme de figures plus com-

Tableau 3. RMN ^{1}H des composés **19–23** dans $CDCl_3$ (δ ppm (*J* Hz)).

H	19	20	21	22	23
Pyrroles					
2	8,85 s	8,83 s	8,83 d él. (5,3)[a]	8,83 d (4,6)[a]	8,84 d (4,8)
3	8,85 s	8,83 s	8,87 d él. (5,3)[a]	8,87 d (4,6)[a]	8,87 d (4,8)
7	8,85 s	8,83 s	8,85 s	8,85 s	8,87 d (4,8)
8	8,85 s	8,83 s	8,85 s	8,85 s	8,84 d (4,8)
12	8,85 s	8,83 s	8,85 s	8,87 d (4,6)[b]	8,84 d (4,8)
13	8,85 s	8,83 s	8,85 s	8,83 d (4,6)[b]	8,87 d (4,8)
17	8,85 s	8,83 s	8,87 d él. (5,3)[b]	8,85 s	8,87 d (4,8)
18	8,85 s	8,83 s	8,83 d él. (5,3)[b]	8,85 s	8,84 d (4,8)
NH	−2,74 s él.	−2,75 s él.	−2,74 s él.	−2,74 s él.	−2,74 s él.
***p*-Toyles**					
2,6			8,10 d (7,8)	8,10 d (7,8)	8,10 d (7,9)
3,5			7,56 d (7,9)	7,56 d (7,8)	7,56 d (7,9)
Me			2,71 s él.	2,71 s él.	2,71 s él.
Aryles					
2,6	8,12 d (8,5)	8,11 d (8,6)	8,11 d (8,5)	8,12 d (8,6)	8,12 d (8,6)
3,5	7,27 d (8,5)	7,27 d (8,6)	7,27 d (8,5)	7,26 d (8,6)	7,27 d (8,6)
Bras					
α	4,32 t él. (6,0)	4,31 m	4,32 m	4,32 t él. (6,2)	4,31 t él. (6,2)
β	2,26 quint. (6,0)	2,26 m	2,26 m	2,27 quint él. (6,1)	2,36 quint. él. (6,1)
γ_a	4,23 m	4,17 m	4,23 m	4,23 m	4,13 m
γ_b	3,92 dt (9,5-6,6)	3,94 m	3,92 dt (9,6-6,6)	3,92 dt (9,6-6,6)	3,92 dt (9,6-6,6)
***O*-Glycosyles**					
1	4,65 d (7,7)	4,68 d (7,9)	4,65 d (7,7)	4,65 d (7,7)	4,65 d (7,7)
2	5,09 dd (9,5-7,7)	4,93 dd (9,5-7,9)	5,10 dd (9,6-7,6)	5,10 dd (9,6-7,6)	5,10 dd (9,7-7,7)
3	5,28 t (9,3)	5,33 t (9,0)	5,28 t (9,3)	5,28 t (9,5)	5,28 t (9,6)
4	5,14 t (9,5)	4,06 m	5,15 t (9,6)	5,15 t (9,5)	5,15 t (9,5)
5	3,77 ddd (9,5-4,5-2,5)	3,77 ddd (9,5-4,0-3,0)	3,78 ddd (9,5-4,6-2,5)	3,78 ddd (9,6-4,6-2,5)	3,77 ddd (9,6-4,8-2,5)
6_a	4,34 dd (12,3-4,5)	4,56 dd (11,9-2,6)	4,34 dd (12,1-4,5)	4,34 dd (12,1-4,6)	4,34 dd (12,1-4,8)
6_b	4,20 dd (12,3-2,5)	4,27 m	4,20 dd (12,1-2,5)	4,20 dd (12,1-2,6)	4,20 dd (12,1-2,6)
1′		5,45 d (3,8)			
2′		4,87 dd (10,4-4,0)			
3′		5,39 t él. (9,4)			
4′		5,07 t (9,6)			
5′		4,01 m			
6_a′		4,27 m			
6_b′		4,06 m			
Acétyles					
	2,13 s	2,19 s	2,13 s	2,13 s	2,13 s
	2,08 s	2,11 s	2,08 s	2,08 s	2,08 s
	2,05 s	2,06 s (×2)	2,05 s	2,06 s	2,06 s
	2,04 s	2,03 s (×2)	2,04 s	2,04 s	2,04 s
		2,01 s			

[a,b]Les attributions affectées du même exposant dans une même colonne sont réversibles.

plexes. Bien que dans la plupart des cas il y ait chevauchement des signaux et donc dégénérescence des figures, on peut cependant différencier les figures des protons β pyrroliques de ces composés diversement substitués. Comme attendu, les signaux des protons β pyrroliques des composés **12**b et **21** s'apparentent à deux doublets et un singulet. Ceux du composé **22** s'apparentent à deux doublets et deux singulets. Par contre les signaux des protons β pyrroliques du composé **23** apparaissent nettement sous la forme de deux doublets; ils confirment la symétrie double de ce type de composé. Le passage des porphyrines substituées en position *para* du *méso*-phényle à celles substituées en position *ortho* entraîne des changements significatifs dans la résonance de l'ensemble des noyaux. La substitution d'un glycosyloxypropyloxy en position *ortho* induit une perte

Fig. 2. Comportement des protons β pyrroliques (δ 8,7–9,0) dans les composés **19**, **12b**, **21**, **22** et **23** dans $CDCl_3$ à 30°C.

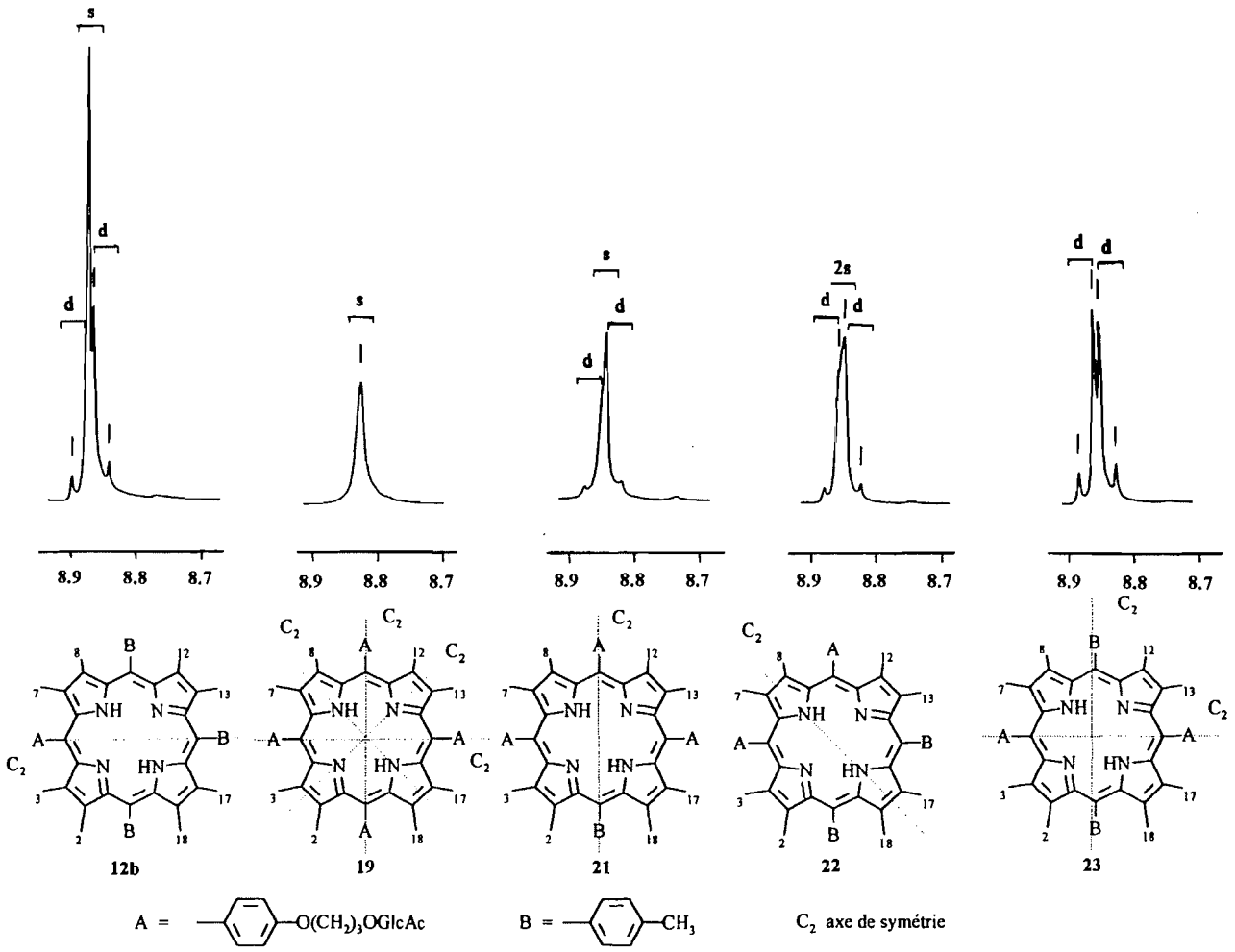

de symétrie et provoque du fait de la non équivalence des noyaux, un élargissement des signaux aromatiques des tolyles. Elle conduit également à la multiplication des signaux β pyrroliques. Comme le montrent les exemples de la figure 3, les protons β pyrroliques des monoglucosylporphyrines se présentent sous la forme de deux doublets et un singulet dans le cas du composé *para*-substitué **12b** et quatre doublets et deux singulets dans celui du composé *ortho* **12a**. Les protons alkyles (α–γ), également affectés par le changement de substitution, présentent un blindage significatif par rapport à la série *para* (tableau 2). Celui-ci augmente lorsque l'on s'éloigne du groupement *méso*-aryle ($\Delta\delta$ Hγ > $\Delta\delta$ Hβ > $\Delta\delta$ Hα). L'unité glycosyle en série *ortho* est également blindée par rapport à son analogue *para*. Si par exemple on compare les résultats des porphyrines glucosylées **12a** et **12b** on observe un blindage significatif de tous les protons osidiques et en particulier des protons H-1 ($\Delta\delta$ 2 ppm), H-5 ($\Delta\delta$ 2,66 ppm) et H-$6_{a,b}$ (1,32 < $\Delta\delta$ < 1,92 ppm). Les protons acétyles glycosidiques sont par contre moins affectés (0,1 < $\Delta\delta$ < 0,2). En série *ortho*, le remplacement du glucose acétylé par un autre glucide (ribose benzoylé, maltose ou lactose acétylé) transforme sensiblement certaines régions spectrales. Les figures des protons β pyrroliques et tolyles sont modifiées et, de plus, le blindage des protons glycosyloxypropyloxy est variable. En série *para*, de telles variations ne sont pas observées. Dans les dérivés *ortho*, la proximité de l'enchaînement propyloxyglycosyle du macrocycle porphyrinique engendre par compression stérique la déformation de celui-ci et l'inclusion de l'alkyloxyglycosyle dans la cavité qui en résulte. Cette situation permet d'expliquer le blindage des protons aliphatiques situés dans le cône d'anisotropie du macrocycle (23).

RMN ^{13}C

Pour confirmer les structures de ces nouvelles glycoporphyrines acétylées ou benzoylées nous avons également réalisé les spectres de RMN du ^{13}C. Les résultats sont rassemblés dans les tableaux 4 et 5. La discrimination entre certains carbones quaternaires éthyléniques et certains carbones tertiaires éthyléniques est basée sur l'utilisation de la séquence DEPT 135. Elles sont vérifiées dans le cas du composé **13b** par une expérience de couplage hétéronucléaire longue distance (COLOC). Les carbones primaires, secondaires et tertiaires sont confirmés grâce aux spectres 2D de corrélation hétéronucléaire directe ^{1}H–^{13}C (XHCORR). En série homologue polyglucosylées (composés **12b**, **19**, **21**, **22** et **23**) l'intégration relative des noyaux confirme les structures attendues. En série monoglycosylée, le changement de la nature de l'unité glucidique des composés *para*-substitués **12b**–**15b** ne modifie pas l'allure des spectres obtenus. Par contre par passage d'une substitution *para* à une substitution *ortho*, on retrouve les

Fig. 3. RMN ^{1}H des composés **12a** et **12b** dans $CDCl_3$: x = $CHCl_3$, y = HOD, z = hydrocarbures.

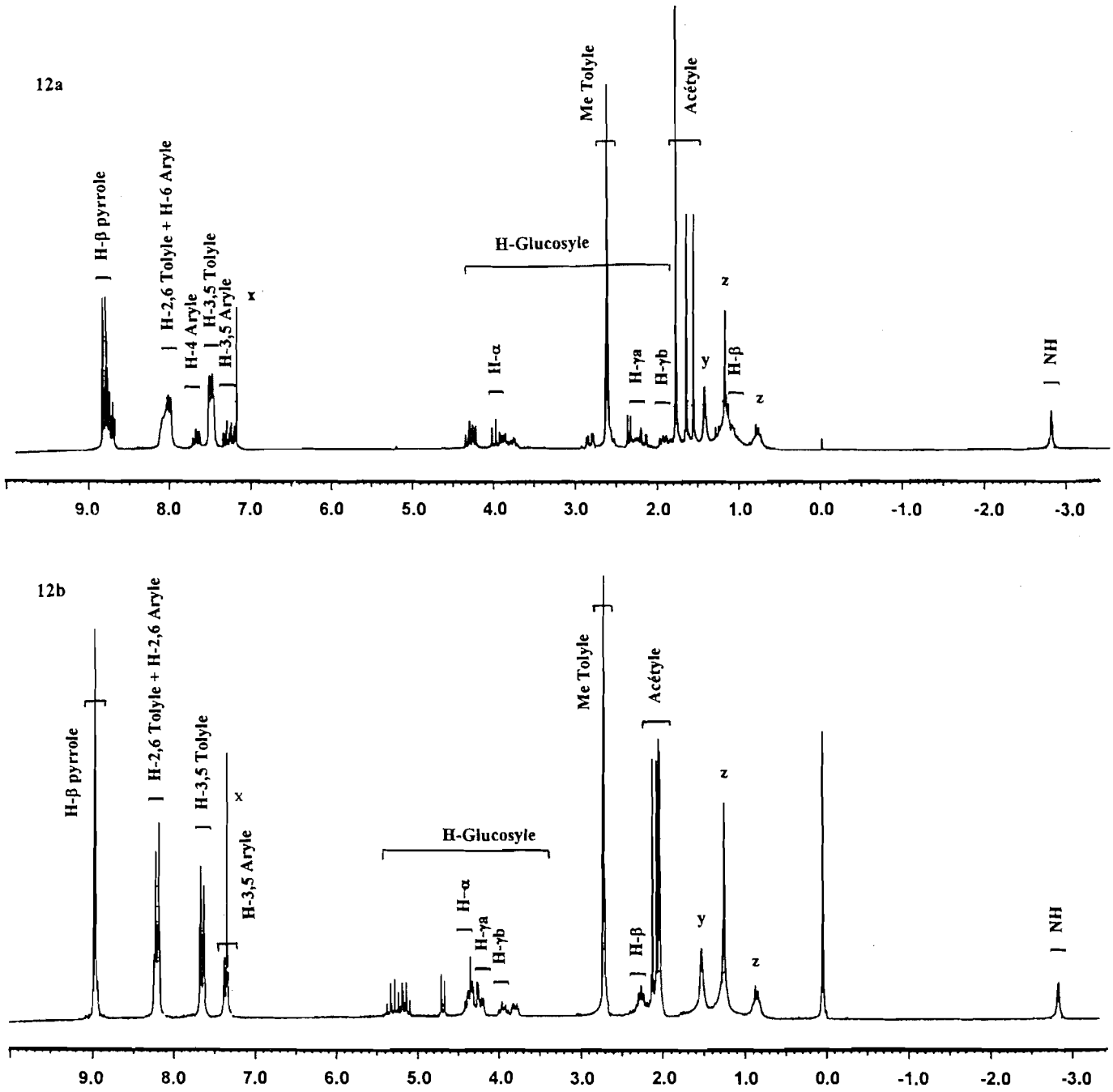

variations de déplacements chimiques observées en RMN ^{1}H. Les porphyrines **12a–15a** présentent toutes un blindage de l'unité glycosyloxypropyloxy qui augmente lorsqu'on s'éloigne des *méso*-substituants aryles. Ces variations s'accompagnent également de dédoublements des signaux C aryle et C tolyle, ce qui traduit une perte de symétrie de la molécule et donc une déformation du macrocycle porphyrinique.

Conclusion

Dans cet article, nous avons décrit la synthèse et la caractérisation d'une nouvelle classe de porphyrines glycosylées pour laquelle la ou les parties glucidiques sont séparées de la partie porphyrinique par l'intermédiaire d'un bras espaceur. Ces composés possèdent des propriétés amphiphiles différentes. Ils présentent sous leur forme déprotégées des solubilités dans l'eau qui varient avec le nombre et la taille des unités glucidiques fixées mais également avec l'orientation de la substitution. Une étude détaillée de spectroscopie RMN de ces composés sous leur forme protégée nous a permis de mettre en évidence, pour les dérivés *ortho*-substitués, l'existence d'un repliement de la partie osidique sur le macrocycle. Nous pensons qu'une telle conformation, si elle persiste après désacétylation, assure une protection du macrocycle et favorise sa

Tableau 4. Spectres de RMN ^{13}C des composés **12a,b–15a,b** dans $CDCl_3$.

C	12a	12b[a]	13a	13b	14a[a]	14b[a,b]	15a	15b[a]
Pyrroles								
α	146,6[c]	146,8[c]	146,5[c]	146,8[c]	146,5[c]	146,8[c]	146,4[c]	146,6[c]
β	131,1[c]	131,1[c]	130,9[c]	130,9[c]	131,0[c]	131,0[c]	131,0[c]	131,0[c]
Méso								
5	115,9	119,7	116,0	119,7	115,9	119,7	115,9	119,7
10,20	119,9	120,1	119,7	120,0	119,8	120,1	119,9	120,1
15	120,4	120,1	120,1	120,0	120,3	120,1	120,3	120,1
***p*-Tolyles**								
1	139,3	139,3	139,5	139,3	139,4	139,3	139,3	139,3
	139,2 (×2)		139,3 (×2)		139,3 (×2)		139,2	
							139,1	
2,6	134,6	134,5	134,5	135,6	134,5	134,5	134,5	134,5
3,5	127,4	127,4	127,3	127,4	127,4	127,4	127,6	127,4
							127,4 (×2)	
4	137,4	137,4	137,2	137,2	137,3	137,3	137,6	137,3
	137,3 (×2)		137,1 (×2)				137,3 (×2)	
Me	21,5	21,5	21,5	21,5	21,5	21,5	21,5	21,5
Aryle								
1	131,4	134,8	131,2	134,6	131,4	134,8	131,4	134,8
2	158,7	135,6	158,7	135,6	158,7	135,6	158,6	135,6
3	112,0	112,7	111,7	112,7	112,1	112,7	111,7	112,7
4	129,9	158,7	129,9	158,7	129,8	158,7	129,8	158,7
5	119,7	112,7	119,4	112,7	119,7	112,7	119,6	112,7
6	135,4	135,6	135,5	135,6	135,8	135,6	135,7	135,6
Bras								
α	64,3	64,4	64,4	64,7	64,8	64,4	64,3	64,4
β	28,8	29,6	28,7	29,6	28,8	29,6	28,7	29,6
γ	65,8	66,7	64,7	65,1	66,0	66,7	65,6	66,7
***O*-Glycosyles**								
1	99,9	101,1	105,1	105,7	99,8	100,6	100,0	100,9
2	67,1	71,4	75,4	75,7	72,0	72,3	71,6	71,6
3	72,3	72,8	72,4	72,7	75,1	75,5	72,7	72,6
4	70,0	68,4	78,5	79,1	72,8	72,9	76,5	76,4
5	70,9	71,9	64,4	65,1	71,6	72,3	72,7	72,6
6	60,0	62,0			62,3	62,9	61,6	62,1
1′					95,6	95,6	101,3	101,1
2′					69,9	70,1	69,2	69,2
3′					69,4	69,4	71,1	71,0
4′					68,1	68,1	66,7	66,8
5′					68,4	68,6	70,7	70,8
6′					61,4	61,6	60,8	60,7
Acétyles	20,5 (×3)	20,8 (×2)			20,8	20,9 (×2)	20,8 (×2)	20,9 (×2)
	20,3	20,6 (×2)			20,6 (×5)	20,7 (×2)	20,6 (×5)	20,7
					20,3	20,6 (×3)		20,6 (×3)
						170,6		20,5

Tableau 4 (*fin*).

C	12a	12b[a]	13a	13b	14a[a]	14b[a,b]	15a	15b[a]
	170,1	170,7			170,5	170,5 (×2)	170,3	170,3 (×2)
	169,7	170,3			170,1	170,2	170,1 (×3)	170,1 (×2)
	169,0 (×2)	169,4			170,0	170,0	169,5 (×2)	169,7
		169,3			169,8	169,7	169,0	169,6
					169,4 (×3)	169,4		169,1

Les carbones benzoiques de **13a** sont enregistrés à δ ppm : 165,8 165,2 et 165,0 (3 × 1C, C-7), 133,2 (2C, C-4), 132,8 (1C, C-4), 129,7 (4C, C-2,6), 129,5 (2C, C-2,6) 129,0 et 129,2 (3C, C-1), 128,4, 128,3 128,1 (3 × 2C, C-3,5).

Les carbones benzoïques de **13b** sont enregistrés à δ ppm : 166,2 165,4 et 165,3 (3 × 1C, C-7), 134,4 (2C, C-4), 133,1 (1C, C-4), 129,6 (6C, C-2,6), 129,0 (3C, C-1), 128,5 128,4 128,2 (3 × 2C, C-3,5).

[a]Composé dont l'attribution des signaux est vérifiée par XHCORR.

[b]Composé dont l'attribution des signaux est vérifiée par COLOC.

[c]Les signaux correspondant aux C pyrroliques α et β se présentent sous la forme de figures élargies du fait de la tautomérie.

solubilisation dans l'eau. Des essais biologiques sont actuellement en cours afin de déterminer l'incorporation, la rétention et la phototoxicité vis à vis de lignées de cellules cancéreuses.

Partie expérimentale

Méthodes générales

Les spectres UV–visible sont réalisés sur un spectrophotomètre UV–visible à barrette de diodes Hewlett Packard 8452 A. Tous les spectres sont effectués dans des cellules en quartz de 1 ou 0,1 cm de trajet optique à une concentration de l'ordre de 10^{-6} M. Les pouvoirs rotatoires $[\alpha]_D$ sont mesurés à 22°C au polarimètre Jasco DIP-370 pour la raie D du sodium, dans une cuve de 1 dm de longueur. Les températures de fusion sont mesurées sur un banc Kofler ou en tube capillaire sur un appareil de Thomas Hoover et ne sont pas corrigées. Les spectres de RMN du proton et du carbone 13 sont réalisés en solution dans $CDCl_3$ sur un appareil Bruker AC-200 (200 MHz pour ^1H et 50 MHz pour ^{13}C). Les déplacements chimiques (δ) sont donnés en ppm par rapport au tétraméthylsilane (TMS). Les constantes de couplage J sont mesurées en hertz (Hz). Les spectres de masse par impact électronique (IE) sont effectués au Laboratoire départemental d'analyse de Limoges sur un appareil Shimadzu QP 100. Les spectres de masse SIMS (Secondary Ion Mass Spectrometry) et MALDI-TOF MS (Matrice Assisted Laser Desorption Ionisation Time of Flight Mass Spectrometry) sont réalisés au Laboratoire de chimie structurale organique et biologique de l'Université Pierre et Marie Curie. L'analyse élémentaire est réalisée au Service régional de microanalyse à l'Université Pierre et Marie Curie de Paris.

Réactifs et solvants

Tous les solvants ou réactifs de qualité RP proviennent de chez Aldrich, Prolabo ou Janssen. Le pyrrole est distillé sur CaH_2 sous pression réduite juste avant son utilisation. Le dichlorométhane est distillé sur P_2O_5 puis sur CaH_2; le carbonate de potassium est stocké à 120°C.

Chromatographie

Les chromatographies analytiques sur couche mince (CCM) sont réalisées sur plaques de gel de silice ($60F_{254}$ Merck). Les composés non colorés sont révélés sous irradiation UV et (ou) pulvérisation d'une solution de H_2SO_4 2 N suivie d'un chauffage à 150°C durant 2 min; le dipyrrométhane est révélé par exposition aux vapeurs de brome. Les chromatographies sur colonne sont réalisées sur silice (60AAC, 15–40 μm, Merck), sur polyamide (Macherey–Nagel) ou sur Sephadex LH20 (Pharmacia). Les éluants utilisés sont les suivants : toluène/acétate d'ethyle 95:5 (A), toluène/acétate d'éthyle 60:40 (B), toluène/acétone 98:2 (C), toluène/acétone 85:15 (D), toluène/acétone 80:20 (E), toluène/acétone 70:30 (F), toluène/acétone/méthanol 70:15:15 (G), toluène/éther de pétrole 80:20 (H), toluène/triéthylamine 99:1 (I), méthanol/$CHCl_3$/acétone 6:2:2 (J), CH_2Cl_2/éthanol 90:10 (K), CH_2Cl_2/éthanol 85:15 (L), CH_2Cl_2-éthanol 80:20 (M), CH_2Cl_2/éthanol/H_2O 4:6:2 (N), THF/H_2O 80:20 (O).

Synthèses

*5-[2-(3-Hydroxypropyloxyphényl)]-10,15,20-tritolylporphyrine (**11a**)*

Dans un ballon surmonté d'un réfrigérant, coiffé par une garde à $CaCl_2$, on introduit a l'abri de la lumière, 50 mg d'*ortho*-hydroxyphényltritolylporphyrine (**10a**) (0,07 mmol, 1 équiv.), 200 mg de carbonate de potassium (1,50 mmol, 20 équiv.) et 4 mL de DMF fraîchement distillé. À ce milieu hétérogène porté 15 min à 60°C, on ajoute 0,067 mL de 3-bromopropan-1-ol (0,74 mmol, 10 équiv.). L'ensemble est porté à léger reflux et la réaction est suivie par CCM. Après 2 h de réaction, le DMF est évaporé sous pression réduite. Le solide obtenu est dissous dans 10 mL de CH_2Cl_2 et la phase organique est lavée à l'eau distillée (3 × 10 mL), séchée sur sulfate de magnésium, filtrée, puis évaporée. Le mélange obtenu est purifié par chromatographie préparative sur plaques de gel de silice (éluant D). On isole ainsi 42 mg du composé **11a** (Rdt 80%). R_f 0,35 (éluant D). RMN ^1H, δ : 8,9 (s él., 8H, H β pyr.), 8,1 (d él., 6H, J = 7,2 Hz, H-2,6 Tol), 7,9 (d él., 1H, H-6 Ar), 7,7 (m, 1H, H-4 Ar), 7,5 (d, 2H, J = 7,2 Hz, H-3,5 Tol), 7,3 (m, 2H, H-3,5 Ar), 4.2 (t él., 2H, J = 6,0 Hz, H-α), 3,8 (t él., 2H, J = 6,0 Hz, H-γ), 2,7 (s, 9H, CH_3 Tol), 2, 1 (quint él., 2H, J = 6,0 Hz, H-β), –2,7 (s él., 2H, NH), UV–visible (tableau 1). SM (MALDI); *m/z* : 730, 8 $(M+H)^+$.

*5-[4-(3-Hydroxypropyloxyphényl)]-10,15,20-tritolylporphyrine (**11b**)*

Ce composé est synthétisé à partir de la *para*-hydroxyphényl-

Tableau 5. Spectres de RMN ^{13}C des composés **19–23** dans $CDCl_3$.[a]

C	19	20	21	22	23
Pyrroles					
α	146,8[b]	147,0[b]	146,8[b]	146,8[b]	146,8[b]
β	131,2[b]	130,9[b]	130,9[b]	131,7[b]	131,0[b]
Méso					
5	119,6	119,7	119,7	119,6	119,6
10	119,6	119,7	119,7	120,1	119,6
15	119,6	119,7	119,7	119,6	120,1
20	119,6	119,7	120,1	120,1	120,1
***p*-Tolyles**					
1			139,3	139,3	139,3
2,6			134,5	134,5	134,5
3,5			127,4	127,4	127,4
4			137,3	137,3	137,3
Me			21,5	21,5	21,5
Aryles					
1	134,7	134,7	134,7	134,7	134,7
2,6	135,6	135,6	135,6	135,6	135,6
3,5	112,7	112,7	112,7	112,7	112,6
4	158,7	158,7	158,7	158,7	158,7
Bras					
α	64,4	64,5	64,4	64,4	64,4
β	29,6	29,6	29,6	29,6	29,6
γ	66,7	66,8	66,7	66,7	66,7
***O*-Glycosyles**					
1	101,1	100,6	101,1	101,1	101,1
2	71,4	72,3	71,4	71,4	71,4
3	72,7	75,4	72,9	72,9	72,9
4	68,5	72,9	68,5	68,5	68,5
5	71,9	72,3	71,9	71,9	71,7
6	62,0	62,9	62,0	62,0	62,0
1′		95,6			
2′		70,0			
3′		69,4			
4′		68,1			
5′		68,6			
6′		61,6			
Acétyles	20,7	20,9	20,7 (×2)	20,7 (×2)	20,8
	20,6 (×3)	20,7	20,6 (×2)	20,6 (×2)	20,7
		20,6 (×5)			20,6 (×2)
	170,6	170,5 (×3)	170,7	170,6	170,7
	170,3	170,2	170,3	170,3	170,3
	169,4	169,9	169,4	169,4	169,4
	169,3	169,6	169,3	169,3	169,3
		169,4			

[a]Les attributions des carbones osidiques des composés **19–23** sont réalisées par analogie avec celles des composés **12b** et **14b**. L'intégration relative de chacun des noyaux aryles par rapport aux tolyles confirme la structure attendue de ces composés.

[b]Les signaux correspondant aux C pyrroliques α et β se présentent sous la forme de figures élargies du fait de la tautomérie.

tritolylporphyrine selon la méthode décrite pour le composé **11a**. En partant des mêmes quantités, on isole après 1 h de réaction, traitement et purification 50 mg du composé **11b** (Rdt 95%). R_f 0,40 (éluant D). RMN ^{1}H, δ: 8,9 (s él., 8H, H β pyr.), 8,1 (d él., 6H, J = 7,2 Hz, H-2,6 Tol), 8,1 (d él., 2H, J = 7,2 Hz, H-2,6 Ar), 7,5 (d él., 6H, J = 7,2 Hz, H-3,5 Tol), 7,1 (d él., 2H, J = 7,2 Hz, H-3,5 Ar), 4.2 (t él., 2H, J = 6,0 Hz, H-α), 3,7 (t él., 2H, J = 6,0 Hz, H-γ), 2,7 (s, 9H, CH_3, Tol), 2,1 (quint. él., 2H, J = 6,0 Hz, H-β), –2,7 (s él., 2H, NH). UV–visible (tableau 1). SM (MALDI); m/z : 730, 8 $(M+H)^+$.

*2-(3-Hydroxypropyloxy)benzaldéhyde (**16a**)*

Dans un ballon surmonté d'un réfrigérant, et d'une garde à $CaCl_2$, on dissout 6,1 g d'*ortho*-hydroxybenzaldéhyde (50 mmol, 1 équiv.), en présence de 10,3 g de carbonate de potassium (1,5 équiv.) dans 30 mL de DMF. L'ensemble est porté 15 min à reflux puis 6 mL de 3-bromopropanol (1,5 équiv.) sont ajoutés au milieu. La réaction est poursuivie 8 h sous reflux. Le DMF est alors éliminé par évaporation sous vide et le résidu obtenu est dissous dans 50 mL de CH_2Cl_2, celui-ci est lavé par une solution de soude à 5% (3 × 100 mL), rincé par de l'eau distillée (2 × 100 mL) et séché sur sulfate de magnésium. Après filtration, le solvant est évaporé sous pression réduite et l'huile résultante est chromatographiée sur colonne de silice (éluant acétate d'éthyle/éther de pétrole 4:6 à 6:4). Après évaporation du solvant, on obtient 4,5 g du composé **16a** sous la forme d'une huile incolore (Rdt 50%). R_f 0,23 (éluant B). RMN ^{1}H, δ: 10,37 (s 1H, CHO), 7,79 (dd, 1H, J = 7,5; 1,8 Hz, H-6), 7,53 (ddd, 1H, J = 9,2; 7,5; 1,8 Hz, H-4), 7,03 (t él., 1H, J = 9,2 Hz, H-5), 7,00 (d, 1H, J = 8,4 Hz, H-3), 4.23 (t, 2H, J = 6,0 Hz, H-α), 3,89 (t, 1H, J = 5,8 Hz, H-γ), 2,11 (quint., 2H, J = 5,8 Hz, H-β). RMN ^{13}C; δ : 190,0 (CHO), 160,7 (C-2), 135,9 (C-6), 130,1 (C-4), 124,6 (C-1), 120,7 (C-5), 112,4 (C-3), 66,1 (C-α), 59,7 (C-γ), 31,6 (C-β). Analyse élémentaire calc. pour $C_{10}H_{12}O_3$ (180,20 g mol^{-1}): C 66,65; H 6,71; trouvée : C 66,37; H 6,63.

*4-(3-Hydroxypropyloxy)benzaldéhyde (**16b**)*

Les conditions opératoires sont les mêmes que celles décrite pour le composé **16a**. Après 4 h de reflux et purification on obtient 5,4 g du produit **16b** sous la forme d'une huile translucide (Rdt 60%). R_f 0,28 (éluant B). RMN ^{1}H; δ : 9,86 (s, 1H, CHO), 7,83 (d, 2H, J = 8,8 Hz, H-2,6), 7,00 (d, 2H, J = 8,8 Hz, H-3,5), 4.19 (t, 2H, J = 6,0 Hz, H-α), 3,86 (t, 2H, J = 5,8 Hz, H-γ), 2,07 (quint., 2H, J = 6,0 Hz, H-β). RMN ^{13}C; δ : 190,9 (CHO), 163,9 (C-4), 132,0 (C-2,6), 129,9 (C-1), 114,7 (C-3,5), 65,5 (C-α), 59,6 (C-γ), 31,6 (C-β). Analyse élémentaire calc. pour $C_{10}H_{12}O_3$ (180,20 g mol^{-1}) : C 66,65; H 6,71; trouvée : C 66,45; H 6,62.

Procédure générale de glycosylation des ortho- *et* para-*hydroxybenzaldéhydes*

Dans un bicol surmonté d'une garde à $CaCl_2$ contenant le glucide *per*acétylé (5,4 mmol, 1,2 équiv.) en solution dans 25 mL de dichlorométhane, on introduit sous courant d'argon et à 0°C, 0,7 mL de tétrachlorure d'étain (5,4 mmol, 1,2 équiv.). Après 15 min d'agitation, 0,8 g du composé **16a** ou **16b** (4,5 mmol, 1 équiv.) en solution dans 2 mL de CH_2Cl_2 sont ajoutés à ce mélange. La température du milieu est ramenée à température ambiante et la réaction est poursuivie durant 8 h. Le mélange réactionnel est alors neutralisé par addition d'une solution glacée, saturée en hydrogénocarbonate de sodium jusqu'à la neutralité. La phase organique est lavée par de l'eau distillée (3 × 20 mL), séchée sur sulfate de magnésium, filtrée puis évaporée sous vide.

*2-[3-(2,3,4,6-Tétra-*O*-acétyl-β-*D*-glucosyloxy)propyloxy)benzaldéhyde (**17a**)*

En partant de 2,1 g de 1,2,3,4,6-penta-*O*-acétyl β-D-glucopyranose on obtient après réaction et traitement, une huile qui est purifiée par chromatographie sur colonne de silice (éluant B). On isole ainsi 600 mg d'une huile incolore qui cristallise au bout de quelques jours à 4°C (Rdt 25%). F 40–45°C. R_f 0,41 (éluant B). $[\alpha]_D$ +7,40 (c 0,21, $CHCl_3$). RMN ^{1}H; δ : 9,50 (s, 1H, CHO), 7,82 (dd, 1H, J = 7,7; 1,8 Hz, H-6), 7,54 (ddd, 1H, J = 8,5; 7,5; 1,8 Hz, H-4), 7,02 (t él., 1H, J = 7,5 Hz, H-5), 6,97 (d él., 1H, J = 8,5 Hz, H-3), 5,19 (t, 1H, J = 9,3 Hz, H-3 Glc), 5,08 (t, 1H, J = 9,3 Hz, H-4 Glc), 4,98 (dd, 1H, J = 9,4; 7,8 Hz, H-2 Glc), 4,52 (d, 1H, J = 7,8 Hz, H-1 Glc), 4,24 (dd, 1H, J = 12,4; 4,8 Hz, H-6_a Glc), 4,15 (m, 1H, H-6_b Glc), 4.15 (m, 2H, H-α), 4,07 (m, 1H, H-γ_a), 3,76 (m, 1H, H-γ_b), 3,72 (m, 1H, H-5 Glc), 2, 10 (m, 2H, H-β); quatre singulets à 2,07 (3H), 2,02 (3H), 1,99 (3H), 1,89 (3H) (CH_3CO). RMN^{13} C; δ : 189,5 (CHO), 170,6, 170,2, 169,4, 169,2 (4, C, CH_3**CO**), 161,3 (C-2), 135,9 (C-4), 128,5 (C-6), 124,9 (C-1), 120,8 (C-5), 112,5 (C-3), 100,9 (C-1 Glc), 72,7 (C-5 Glc), 71,6 (C-3 Glc), 71,3 (C-2), 68,4 (C-4), 66,1 (C-γ), 64,5 (C-α), 61,7 (C-6 Glc), 29,3 (C-β); 20,5 (4C, **CH$_3$**CO). Analyse élémentaire calc. pour $C_{24}H_{30}O_{12}$ (510,49 g mol^{-1}) : C 56,46; H 5,92; trouvée : C 56,39; H 6,01.

*4-[3-(2,3,4,6-Tétra-*O*-acétyl-β-*D*-glucosyloxy)propyloxy)benzaldéhyde (**17b**)*

Ce composé est synthétisé à partir du dérivé **16b**. On isole après réaction et purification par recristallisation dans un mélange diéthyléther/éther de pétrole (4:1), 800 mg de cristaux blancs (Rdt 35%). F 120–122°C. R_f 0,42 (éluant B). $[\alpha]_D$ -6,87 (c 4,5; $CHCl_3$). RMN ^{1}H; δ : 9,87 (s, 1H, CHO), 7,83 (d, 2H, J = 8,8 Hz, H-2,6), 7,00 (d, 2H, J = 8,8 Hz, H-3,5), 5,11 (t, 1H, J = 9,3 Hz, H-3 Glc), 5,06 (t, 1H, J = 9,5 Hz, H-4 Glc), 4,88 (dd, 1H, J = 9,3; 7,8 Hz, H-2 Glc), 4,51 (d, 1H, J = 7,8 Hz, H-1 Glc), 4,22 (dd, 1H, J = 12,3; 4,7 Hz, H-6_a Glc), 4,15 (m, 1H, H-6_b Glc), 4.10 (t, 2H, J = 6,0 Hz, H-α), 4,05 (m, 1H, H-γ_a), 3,76 (m, 1H, H-γ_b), 3,69 (m, 1H, H-5 Glc), 2,20 (m, 2H, H-β); quatre singulets à 2,06 (3H), 2,01 (3H), 1,99 (3H), 1.89 (3H) (CH_3CO). RMN ^{13}C; δ : 190,0 (CHO), 170,5, 169,3, 169,2 (2C) (4 C, CH_3**CO**), 163,9 (C-4), 131,9 (C-2,6), 130,1 (C-1), 114,7 (C-3,5), 101,0 (C-1 Glc), 72,7 (C-5 Glc), 71,6 (C-3 Glc), 71,2 (C-2), 68,4 (C-4), 66,1 (C-γ), 64,5 (C-α), 61,9 (C-6 Glc), 29,2 (C-β), 20,5 (4C, **CH$_3$**CO). Analyse élémentaire calc. pour $C_{24}H_{30}O_{12}$ (510,49 g mol^{-1}) : C 56,46; H 5,92; trouvée : C 56,40; H 6,05.

*4-[3-(2,3,6,2′,3′,4′6′-Hepta-*O*-acétyl-β-*D*-maltosyloxy)propyloxy)]benzaldéhyde (**18b**)*

En partant de 4,4 g de β-D-maltose *per*acétate on obtient après réaction et traitement 5,6 g de produit brut. Celui-ci est fractionné par chromatographie flash sur colonne de silice (éluant éther de pétrole/acétate d'éthyle 6:4 à 4:6). Une seconde purification est réalisée sur plaques de silice (éluant H) et mène à 600 mg de produit pur (Rdt 20%). F 62–64°C. R_f 0,57 (éluant B). $[\alpha]_D$ +42,4 (c 1,0; $CHCl_3$). RMN ^{1}H, δ : 9,87 (s, 1H,

CHO), 7,82 (d él., 2H, J = 8,8 Hz, H-2,6), 6,98 (d él., 2H, J = 8,8 Hz, H-3,5), 5,40 (d, 1H, J = 7,3 Hz, H-1′ Glc), 5,35 (dd, 1H, J = 10,4; 9,7 Hz, H-3′ Glc), 5,24 (5, 1H, J = 9,0 Hz, H-3 Glc), 5,04 (t, 1H, J = 9,7 Hz, H-4′ Glc), 4,84 (dd, 1H, J = 10,5; 4,1 Hz, H-2′ Glc), 4,82 (dd, 1H, J = 9,5; 8,0 Hz, H-2 Glc), 4,54 (d, 1H, J = 7,9 Hz, H-1 Glc), 4,47 (dd, 1H, J = 12,1; 2,8 Hz, H-6_a Glc), 4,25 (dd, 1H, J = 12,7; 3,9 Hz, H-$6'_a$ Glc), 4,21 (dd, 1H, J = 12,1; 4,5 Hz, H-6_b Glc), 4,09 (t él., 2H, J = 6,2 Hz, H-α), 4.05 (m, 1H, H-γ_a), 4,04 (dd, 1H, J = 12,2; 2,6 Hz, H-$6'_b$ Glc), 3,99 (t él., 1H, J = 9,4 Hz, H-4 Glc), 3,95 (m, 1H, H-5′ Glc), 3,72 (dt, 1H, J = 9,3; 6,3 Hz, H-γ_b), 3,68 (m, 1H, H-5 Glc), 2,10 (m, 2H, H-β); sept singulets à 2.12 (3H), 2,09 (3H), 2,03 (3H), 1,99 (3H), 2,02 (3H), 1,99 (3H), 1,88 (3H) (CH_3CO). RMN ^{13}C; δ : 190,7 (CHO), 170,5 (2C), 170,4, 170,1, 169,9, 169,5, 169,4 (7 CH_3**CO**), 163,7 (C-4), 131,9 (C-2,6), 129,9 (C-4), 114,7 (C-3,5), 100,4 (C-1 Glc), 95,5 (C-1′ Glc), 75,3 (C-3 Glc), 72,7 (C-4 Glc), 72,2 (C-5 Glc), 72,1 (C-2 Glc), 70,0 (C-2′ Glc), 69,3 (C-3′ Glc), 68,5 (C-5′ Glc), 68,0 (C-4′ Glc), 66,2 (C-γ), 64,5 (C-α), 62,7 (C-6 Glc), 61,7 (C-6′ Glc), 29,2 (C-β), 20,8 (2C), 20,6, 20,5 (3C), 20,4 (**CH_3**CO). Analyse élémentaire calc. pour $C_{36}H_{46}O_{20}$ (798,74 g mol^{-1}) : C 54,13; H 5,80; trouvée : C 54,12; H 5,85.

Synthèse des porphyrines monoglycosylées

Voie A (schéma 1)

*Procédure générale de glycosylation des 5-(hydroxypropyl-oxyphényl)-10,15,20-tritolylporphyrines (**12a,b–15a,b**)*

En milieu rigoureusement anhydre, sous argon, dans un bicol surmonté d'un réfrigérant, le glucide acétylé ou benzoylé est mis en solution dans 10 mL de CH_2Cl_2. À cette solution refroidie à 0°C, on introduit le tétrachlorure d'étain. Après 15 min d'agitation, le composé **11a** ou **11b** en solution dans 2 mL de CH_2Cl_2 sec est ajouté au milieu. La réaction controlée par CCM est alors poursuivie à température ambiante. En fin de période de réaction, le milieu est neutralisé par addition d'une solution glacée saturée en hydrogénocarbonate de sodium. La phase organique est extraite par le dichlorométhane (2 × 15 mL), lavée à l'eau distillée (3 × 15 mL) puis séchée sur sulfate de magnésium. Après filtration, le solvant est évaporé et résidu est chromatographié.

*5-[2-[3-(2,3,4,6-Tétra-*O*-acétyl-β-D-glucosyloxy)propyl-oxy)]-10,15,20-tritolylporphyrine (**12a**)*

En partant de 40 mg de **11a** (0,054 mmol, 1 équiv.), 110 mg de 1,2,3,4,6-penta-*O*-acétyl β-D-glucopyranose (0,27 mmol, 5 équiv.) et 0,025 mL de tétrachlorure d'étain (0,27 mmol, 5 équiv.), on obtient après 18 h de réaction, traitement et purification sur plaques de gel de silice (éluant D) 20 mg du composé **12a** (Rdt 35%). R_f 0,67 (éluant D). RMN ^1H (tableau 2). RMN ^{13}C (tableau 4). UV–visible (tableau 1). SM (SIMS); m/z : 1063,1 $(M + H)^+$, 672,8 $[M - (CH_2)_3\text{-O-GlcAc}]^+$.

*5-[4-[3-(2,3,4,6-Tétra-*O*-acétyl-β-D-glucosyloxy)propyl-oxy)]phényl]-10,15,20-tritolylporphyrine (**12b**)*

En partant de 30 mg de **11b** (0,04 mmol, 1 équiv.), 80 mg de 1,2,3,4,6-penta-*O*-acétyl β-D-glucopyranose (0,20 mmol, 5 équiv.) et 0,023 mL de tétrachlorure d'étain (0,20 mmol, 5 équiv.), on obtient après 2 h de réaction, traitement et purification sur plaques de gel de silice (éluant D) 25 mg du composé **12b** (Rdt 60%). R_f 0,55 (éluant D). RMN ^1H (tableau 2). RMN ^{13}C (tableau 4). UV–visible (tableau 1). SM (SIMS); m/z : 1063,1 $(M + H)^+$, 672,8 $[M - (CH_2)_3\text{-O-GlcAc}]^+$.

*5-[2-[3-(2,3,5-Tri-*O*-benzoyl-β-D-ribosyloxy)propyl-oxy)]phényl]-10,15,20-tritolylporphyrine (**13a**)*

O-Acétyl-2,3,5 tribenzoate-β-D-ribofuranose (100 mg, 0,20 mmol, 5 équiv.) et 30 mg de composé **11a** (0,04 mmol, 1 équiv.) sont mis à réagir en présence de 0,025 mL de $SnCl_4$ (0,20 mmol, 5 équiv.). Après 16 h de réaction, on isole par traitement puis par chromatographie sur plaques de silice (éluant A) 27 mg du composé **13a** (Rdt 60%). R_f 0,75 (éluant A.). RMN ^1H (tableau 2). RMN ^{13}C (tableau 4). UV–visible (tableau 1). SM (SIMS); m/z : 1175,9 (M^+), 672,8 $[M - (CH_2)_3\text{-O-RbBz}]^+$.

*5-[4-[3-(2,3,5-Tri-*O*-benzoyl-β-D-ribosyloxy)propyl-oxy)]phényl]-10,15,20-tritolylporphyrine (**13b**)*

Le composé **13b** est synthétisé à partir de **11b**. En partant des mêmes quantités que celle utilisées pour **13a**, on isole après 2 h de réaction, traitement et purification sur plaques de gel de silice 35 mg du composé désiré (Rdt 75%). Ce composé se dégradant partiellement sur silice nous en avons repurifié 25 mg par chromatographie moyenne pression sur polyamide (éluant H) afin d'obtenir un échantillon analytique. R_f 0,60 (éluant A). RMN ^1H (tableau 2). RMN ^{13}C (tableau 4). UV–visible (tableau 1). SM (SIMS); m/z : 1176,2 $(M + H)^+$, 672,8 $[M - (CH_2)_3\text{-O-RbBz}]^+$.

*5-[2-[3-(2,3,6,2,3,4,5,6-Hepta-*O*-acétyl-β-D-maltosyl-oxy)propyloxy)]phényl]-10,15,20-tritolylporphyrine (**14a**)*

En partant de 50 mg de **11a** (0,06 mmol, 1 équiv.), 200 mg de β-D-maltose *per*acétate (0,30 mmol, 5 équiv.) en présence de 0,045 mL de tétrachlorure d'étain (0,30 mmol, 5 équiv.), on isole après 24 h de réaction, traitement et purification sur plaques de gel de silice (éluant E) 20 mg d'un mélange de deux porphyrines glucosylées difficilement séparables. Afin d'obtenir un échantillon analytique nous avons chromatographié ce mélange sur plaques de silice par cinq migrations successives (éluant C). On isole ainsi 10 mg de **14a** (Rdt 12%) et 5 mg d'impureté non identifiée. R_f 0,54 (éluant E). RMN ^1H (tableau 2). RMN ^{13}C (tableau 4). UV–visible (tableau 1). SM (SIMS); m/z : 1350,4 $(M+M)^+$, 672,8 $[M - (CH_2)_3\text{-O-MalAc}]^+$.

*5-[4-[3-(2,3,6,2,3,4,5,6-Hepta-*O*-acétyl-β-D-maltosyl-oxy)propyloxy)]phényl]-10,15,20-tritolylporphyrine (**14b**)*

Ce composé est synthétisé à partir de **11b**. En partant des mêmes quantités que celles utilisées pour **14a**, on obtient après 6 h de réaction, traitement et purification sur plaques de gel de silice (éluant E) 30 mg du composé **14b** (Rdt 38%). R_f 0,54 (éluant E). RMN ^1H (tableau 2). RMN ^{13}C (tableau 4). UV–visible (tableau 1). SM (SIMS); m/z : 1350,4 $(M+M)^+$, 672,8 $[M - (CH_2)_3\text{-O-MalAc}]^+$.

*5-[2-[3-(2,3,6,2,3,4,5,6-Hepta-*O*-acétyl-β-D-lactosyloxy)propyloxy)]phényl]-10,15,20-tritolylporphyrine (**15a**)*

β-D-Lactose *per*acétate (200 mg, 0,30 mmol, 5 équiv.) additionné à 50 mg de composé **11a** (0,06 mmol, 1 equiv.) en présence de 0,035 mL de $SnCl_4$ (0,30 mmol, 5 équiv.) donnent après 24 h de réaction, traitement puis purification sur plaques de gel silice (éluant E) 17 mg du composé **15a** (Rdt 21%). R_f

0,54 (éluant E). RMN ^{1}H (tableau 2). RMN ^{13}C (tableau 4). UV–visible (tableau 1). SM (SIMS); *m/z* : 1350,4 $(M+H)^+$, 672,8 $(M - (CH_2)_3\text{-O-LacAc})^+$.

*5-[4-[3-(2,3,6,2,3,4,5,6-Hepta-*O*-acétyl-*β*-D-lactosyloxy)propyloxy)]phényl]-10,15,20-tritolylporphyrine (**15b**)*

La synthèse du composé **15b** est réalisée à partir du composé **11b**. En partant des quantités utilisées pour **15a** on obtient après 6 h de réaction, traitement et purification sur plaques de gel de silice (éluant E) 34 mg du composé **15b** (Rdt 42%). R_f 0,50 (éluant E). RMN ^{1}C (tableau 2). RMN ^{13}C (tableau 4). UV–visible (tableau 1). SM (SIMS); *m/z* : 1350,4 $(M+H)^+$, 672,8 $(M - (CH_2)_3\text{-O-LacAc})^+$.

Voie B (schéma 2)

Méthode générale

Dans un bicol surmonté d'un réfrigérant et d'une garde à $CaCl_2$, le précurseur glycosylé **17a,b** ou **18b** et le *para*-tolualdéhyde sont dissous dans l'acide propionique. Le mélange est porté à léger reflux et le pyrrole est ajouté à l'aide d'une seringue. La réaction est alors poursuivie durant 45 min à reflux. Après refroidissement du milieu, l'acide propionique est éliminé par évaporation à la pompe à palette. Le solide noir obtenu est fractionné par passage sur colonne de silice (2.5 cm × 20 cm, éluant CH_2Cl_2/EtOH 100/0 à 97/3). Le premier produit élué, la tétratolylporphyrine, est suivie dans l'ordre par la porphyrine monoglycosylée, les diglycosylporphyrines, la triglucosylporphyrine puis finalement par le tétraglucosylporphyrine. Les deux dernières porphyrines sont mal séparées, elles sont accompagnées de goudrons. Les proportions de chacun des composés sont fonction des proportions des réactifs employés. Dans chaque cas, les porphyrines brutes sont soumises à une purification ultérieure.

*5-[2-[3-(2,3,4,6-Tétra-*O*-acétyl-*β*-D-glucosyloxy)propyloxy)]phényl]-10,15,20-tritolylporphyrine (**12a**)*

Par réaction de 115 mg de *para*-tolualdéhyde (1,2 mmol, 3 équiv.), 160 mg de précurseur glycosylé **17a** (0,4 mmol, 1 équiv.) et 0,090 mL de pyrrole (1.6 mmol, 4 équiv.) en solution dans 25 mL d'acide propionique, on isole après fractionnement puis purification sur plaques de gel de silice (éluant D) 32 mg du composé **12a** (Rdt 8%).

*5-[4-[3-(2,3,4,6-Tétra-*O*-acétyl-*β*-D-glucosyloxy)propyloxy)]phényl]-10,15,20-tritolylporphyrine (**12b**)*

Le composé **12b** est synthétisé à partir du précurseur **17b**. En partant des mêmes quantités que celles employées pour **12a**, on isole après fractionnement et chromatographie sur plaques de gel de silice 36 mg du composé désiré (Rdt 9%).

*Méthode générale de synthèse des tétraglycosylporphrines (**19**, **20**)*

À l'obscurité, dans un bicol muni d'un réfrigérant et d'une garde à $CaCl_2$, 0,035 mL de pyrrole (0,5 mmol, 1 équiv.) et 0,5 mmol de précurseur **17b** ou **18b** (1 equiv.) sont dissous sous courant d'argon dans 50 mL de CH_2Cl_2. Ce mélange est agité pendant 15 min à température ambiante puis 0,040 mL d'acide trifluoroacétique (0,5 mmol, 1 équiv.) sont ajoutés au milieu. La réaction est poursuivie sous agitation durant 1–4 h. Au terme de la réaction, 90 mg de *p*-chloranile (0,38 mmol) sont alors ajoutés au milieu et l'ensemble est porté à léger reflux durant 1 h. Le solvant est évaporé sous vide et le résidu obtenu est purifié par passage sur colonne de silice (12 cm × 2 cm, éluant CH_2Cl_2/éthanol 100:0 à 95:5) puis par chromatographie sur plaques de gel de silice (éluant G).

*5,10,15,20-Tétra[4-[3-(2,3,4,6-Tétra-*O*-acétyl-*β*-D-glucosyloxy)propyloxy)]phénylporphyrine (**19**)*

À partir de 250 mg de composé **17b** (0,5 mmol, 1 équiv.) et 0,035 mL de pyrrole (0,5 mmol, 1 équiv.) on isole après 1 h de réaction et oxydation, 100 mg du composé **19** (Rdt 36%). R_f 0,46 (éluant G). RMN ^{1}H (tableau 3). RMN ^{13}C (tableau 5). UV–visible (tableau 1). SM (MALDI); *m/z* : 2232 $(M + H)^+$.

*5,10,15,20-Tétra[4-[3-(2,3,4,6-Tétra-*O*-acétyl-*β*-D-maltosyloxy)propyloxy)]phényl]porphyrine (**20**)*

À partir de 400 mg de composé **18b** (0,5 mmol, 1 équiv.) et 0,035 mL de pyrrole (0,5 mmol, 1 équiv.) on isole après 4 h de réaction puis oxydation, 70 mg du composé **20** (Rdt 16%). R_f 0,55 (éluant G). RMN ^{1}H (tableau 3). RMN ^{13}C (tableau 5). UV–visible (tableau 1). MS (MALDI); *m/z* : 3386 $(M+H)^+$.

*Poly-[(2,3,4,6-tétra-*O*-acétyl)glycosyloxypropyloxy]tolylporphyrine (**21**, **22**, **23**)*

Par réaction de 1,0 g de précurseur glycosylé **17b** (2,0 mmol, 3 équiv.), 80 mg de para-tolualdéhyde (0,65 mmol, 1 équiv.) et 0,175 mL de pyrrole (2,65 mmol, 4 équiv.) en solution dans 25 mL d'acide propionique on obtient après fractionnement la mono (**12b**), les di- (**22**, **23**) et la triglucosylporphyrine (**21**). Chacune de ces porphyrines est alors purifiée par chromatographie. Les composés **22** et **23** sont séparées par une triple élution sur plaque de silice (éluant D). Le composé **21** est purifié par passages successifs sur colonne de polyamide (éluant H) puis sur colonne de Sephadex LH20 (éluant J) et **12b** est isolé comme précédemment. On récupère ainsi 20 mg de **12b** (Rdt 2,8%), 2 × 7 mg de **22** et **23** (Rdt 1,5%), 36 mg de **21** (Rdt 3,0%). **21**: R_f 0,36 (éluant F). RMN ^{1}H (tableau 3). RMN ^{13}C (tableau 5). UV–visible (tableau 1). MS (MALDI); m/z : 1841 $(M+H)^+$.

Voie C (schéma 3)

méso-*(p-Tolyl)dipyrrométhane (**24**)*

Dans un ballon, 0,5 mL de *para*-tolualdéhyde (4,1 mmol, 1 équiv.) sont mélangés à 11,2 mL de pyrrole (0,16 mol, 40 équiv.). À cette solution, dégazée par barbotage d'argon durant 10 min, on ajoute 0,032 mL d'acide trifluoroacétique (0,4 mmol, 0,1 équiv.). Le mélange est agité 15 min à température ambiante jusqu'à disparition totale de l'aldéhyde. Il est ensuite dilué par addition de 50 mL de dichlorométhane, neutralisé par une solution aqueuse d'hydroxyde de sodium 0,1 N, rincé à l'eau distillée puis séché sur sulfate de magnésium. Après évaporation du pyrrole à température ambiante, le produit est porté sous vide (1 Torr (133.3 Pa)) durant 1 h. On obtient ainsi un solide brunâtre qui est chromatographié sur colonne de silice (éluant I). Après évaporation du solvant on récupère 650 mg de solide verdâtre (Rdt 66%). *F* 114°C (litt. (19) *F* 111–112°C). R_f 0,24 (éluant I). IR (KBr) ν (cm^{-1}) : 3415 (N-H), 1690, 1640 (C—O). Analyse élémentaire calc. : pour $C_{16}H_{16}N_2$ (236,13 g mol) : C 81,38; H 6,83; N 11,86; trouvé : C 81, 53; H 6,82; N 12,17.

5,10-Bis[(2,3,4,6-tétra-O-*acétyl)glyosyloxypropyloxy]-15,20-ditolylporphyrine* (**22**, *et 5,15-bis[(2,3,4,6-tétra*-O-*acétyl)glyosyloxypropyloxy]-10,20-ditolylporphyrine* (**23**)

Dans un ballon 130 mg de précurseur glycosidique **17b** (0,25 mmol, 1 équiv.) et 60 mg de dipyrrométhane **24** (0,25 mmol, 1 équiv.) sont mis en solution dans 25 mL de CH_2Cl_2. À ce milieu protégé de la lumière et purgé 15 min par barbotage d'argon, on ajoute 0,033 mL d'une solution 2,5 M de $BF_3{\cdot}Et_2O$. Après 10 min d'agitation, 50 mg de *p*-chloranile (0,2 mmol) sont additionnés au milieu et la réaction est poursuivie à température ambiante durant 1 h 30. Le solvant est évaporé sous vide et la résidu obtenu est fractionné par chromatographie sur colonne de silice (éluant CH_2Cl_2/éthanol 100:0 à 98:2). Après évaporation des différentes fractions, on récupère 20 mg de monoglycosylporphyrine (16%), 30 mg du mélange des diglycosylporphyrines et 5 mg de la triglycosylporphyrine. Le mélange des deux isomères de la diglucosylporphyrine est séparé par chromatographie sur plaques de gel de silice par une triple élution (éluant C). Le composé **22** substitué sur les carbones *méso*-adjacents (*cis*) est le plus retenu. On isole ainsi 9 mg du composé **22** (Rdt 5%) et 16 mg du composé **23** (Rdt 9%). **22** : R_f 0,43 (éluant E). RMN ^1H (tableau 3). RMN ^{13}C (tableau 5). UV–visible (tableau 1). SM (MALDI); *m/z* : 1453 $(M+H)^+$. **23** : R_f 0,46 (éluant E). RMN ^1H (tableau 3). RMN ^{13}C (tableau 5). UV–visible (tableau 1). SM (MALDI); *m/z* : 1453 $(M+H)^+$.

Procédure générale de déprotection

À 25 mg de porphyrine en solution dans 1 mL de CH_2Cl_2/MeOH (80:20), on ajoute 1,5 équivalent de méthylate de sodium (solution 1 M dans le méthanol) par groupement protecteur acétylé ou benzoylé. Le milieu réactionnel est agité à température ambiante durant 1 h puis la porphyrine est précipitée par addition d'éther de pétrole. Après filtration, lavage à l'éther de pétrole, la porphyrine isolée est purifiée par chromatographie sur colonne de Sephadex LH20 (éluant O).

*5-[2-[3-(*β-D-Glucosyloxy)propyloxy]phényl]-10,15,20-tritolylporphyrine (**1a**) : 17 mg (Rdt 80%). R_f 0,65 (K). UV–visible (tableau 1). SM (MALDI); *m/z* : 895 $(M+H)^+$.

*5-[4-[3-(*β-D-Glucosyloxy)propyloxy]phényl]-10,15,20-tritolylporphyrine (**1b**) : 17 mg (Rdt 80%). R_f 0,48 (K). UV–visible (tableau 1). SM (MALDI); *m/z* : 895 $(M+H)^+$.

*5-[2-[3-(*β-D-Ribosyloxy)propyloxy]phényl]-10,15,20-tritolylporphyrine (**2a**) : 16 mg (Rdt 85%). R_f 0,90 (K). UV–visible (tableau 1). SM (MALDI); *m/z* : 864 $(M+H)^+$.

*5-[4-[3-(*β-D-Ribosyloxy)propyloxy]phényl]-10,15,20-tritolylporphyrine (**2b**) : 16 mg (Rdt 85%). R_f 0,77 (K). UV–visible (tableau 1). SM (MALDI); *m/z* : 864 $(M+H)^+$.

*5-[2-[3-(*β-D-Maltosyloxy)propyloxy]phényl]-10,15,20-tritolylporphyrine (**3a**) : 16 mg (Rdt 85%). R_f 0,40 (L). UV–visible (tableau 1). SM (MALDI); *m/z* : 1056 $(M+H)^+$.

*5-[4-[3-(*β-D-Maltosyloxy)propyloxy]phényl]-10,15,20-tritolyporphyrine (**3b**) : 17 mg (Rdt 90%). R_f 0,20 (L). UV–visible (tableau 1). SM (MALDI); *m/z* : 1056 $(M+H)^+$.

*5-[2-[3-(*β-D-Lactosyloxy)propyloxy]phényl]-10,15,20-tritolyporphyrine (**4a**) : 15 mg (Rdt 85%). R_f 0,41 (L). UV–visible (tableau 1). SM (MALDI); *m/z* : 1056 $(M+H)^+$.

*5-[4-[3-(*β-D-Lactosyloxy)propyloxy]phényl]-10,15,20-tritolyporphyrine (**4b**) : 15 mg (Rdt 85%). R_f 0,24 (L). UV–visible (tableau 1). SM (MALDI); *m/z* : 1056 $(M+H)^+$.

*5,10,15,20-Tétrakis[4-[3-(*β-D-glucosyloxy)propyloxy]phénylporphyrine (**5**) : 14 mg (Rdt 80%). R_f 0,65 (N). UV–visible (tableau 1). SM (MALDI); *m/z* : 1560 $(M+H)^+$.

*5,10,15,20-Tétrakis[4-[3-(*β-D-maltosyloxy)propyloxy]phénylporphyrine (**6**) : 16 mg (Rdt 80%). R_f 0,65 (N). UV–visible (tableau 1). SM (MALDI); *m/z* : 2209 $(M+H)^+$.

*5,10,15-Tris[4-[3-(*β-D-glucosyloxy)propyloxy]phényl]-20-tolylporphyrine (**7**) : 13 mg (Rdt 80%). R_f 0,65 (N). UV–visible (tableau 1). SM (MALDI); *m/z* : 1338 $(M+H)^+$.

*5,10-Bis[4-[3-(*β-D-glucosyloxy)propyloxy]phényl]-15,20-ditolylporphyrine (**8**) : 14 mg (Rdt 75%). R_f 0,10 (M). UV–visible (tableau 1). SM (MALDI); *m/z* : 1116 $(M+H)^+$.

*5,15-Bis[4-[3-(*β-D-glucosyloxy)propyloxy]phényl]-10,20-ditolylporphyrine (**9**) : 15 mg (Rdt 80%). R_f 0,28 (M). UV–visible (tableau 1). SM (MALDI); *m/z* : 1116 $(M+H)^+$.

Bibliographie

1. A.F. Mironov, G.M. Isaeva, V.I. Shvets, R.P. Evstigneeva, A.N. Stepanov, A. Perov et S.E. Kupriyanov. Inorganick Eiaya Khimia, **4**, 1410 (1987).
2. Y. Kuroda, T. Hiroshige, T. Sera, Y. Shiroiwa, H. Tanaka et H. Ogoshi. J. Am. Chem. Soc. **111**, 1912 (1989); Ph. Maillard, J.L. Guerquin-Kern, M. Momenteau et S. Gaspard. J. Am. Chem. Soc. **111**, 9125 (1989); Y. Kuroda, T. Hiroshige, T. Sera et H. Ogoshi. Carbohydr. Res. **192**, 347 (1989); R. Bonnet, A.N. Nizhnik et M. Berembaum. J. Chem. Soc. Chem. Commun. 1822 (1989); G. Fülling. D. Schröder et B.F. Franck. Angew. Chem. Int. Ed. Engl. **28**, 1519 (1990); P. Kuz, G. Knerr et L. Czuchajowski. Tetrahedron Lett. **31**, 5133 (1990); A. Bourhim, S. Czernercki, P. Krausz, A. Viari et P. Vigny. Carbohydr. Chem. **9**, 761 (1990); L. Czuchajowski, J. Habdas, H. Niedbala et V. Wandrekar. Tetrahedron Lett. **3**, 7511 (1991); L. Czuchajowski et H. Niedbala. Med. Chem. Lett. **2**, 1645 (1992); K. Kohata, Y. Yamaguchi, H. Higashio, T. Odashima et H. Hishii. Chem. Lett. 477 (1992); J. H. Fuhrhop, C. Demoulin, C. Boettcher, J. Köning et U. Siggel. J. Am. Chem. Soc. **114**, 4159 (1992); O. Nakajima, H. Mizoguchi, Y. Hashimoto et S. Iwasaki. J. Am. Chem. Soc. **114**, 9203 (1992); L. Czuchajowski, J. Habdas, H. Niedbala et V. Wandrekar. Heterocycl. Chem. **29**, 479 (1992); K.R. Adams, M. Berembaum, R. Bonnet, A. Nizhnik, A. Salgado et M.A. Vallés. J. Chem. Soc. Perkin Trans. 1, 1465 (1992); G. Casiraghi, M. Cornia, G. Rassu, C. Del Sante et P. Spanu. Nat. Prod. Lett. **1**, 45 (1992); Tetrahedron, **48**, 5619 (1992); N. Ono, M. Bougaushi et K. Maruyama. Tetrahedron Lett. **33**, 1629 (1992); Ph. Maillard, C. Heul et M. Momenteau. Tetrahedron Lett. **33**, 8081 (1992); T. Suzuki, K. Horie, T. Yamashita, M. Bitoh, S. Konishi et M. Kishimoto. Chem. Lett. 1265 (1993); K. Driaf, P. Krausz, B. Verneuil, M. Spiro, J.C. Blais et G. Bolbach. Tetrahedron Lett. **34**, 1027, 1993; Ph. Maillard, J.L. Guerquin-Kern, C. Huel

et M. Momenteau. J. Org. Chem. **58**, 2774 (1993); L. Czuchajowski et H. Li. Tetrahedron Lett. **35**, 1629 (1994); M. Cornia, G. Casiraghi, S. Binacchi, F. Zanardi et G. Rassu. J. Org. Chem. **59**, 1226 (1994); D. Oulmi, Ph. Maillard, J.L. Guerquin-Kern, C. Heul et M. Momenteau. J. Org. Chem. **60**, 1554 (1995).
3. T.J. Dougherty, G.B. Grindey, R. Fiel, K.R. Weishaupt et D.G. Boyle. J. Natl. Cancer Inst. **55**, 115 (1975); H. van den Bergh. Chem. Br. **22**, 430 (1986); S.B. Brown et T.G. Truscott. Chem. Br. **29**, 955 (1993).
4. A. Bourhim, O. Gaud, R. Granet, P. Krausz et M. Spiro. Synlett, 563 (1993).
5. C. Kieda et M. Monsigny. Invasion Metastasis, **6**, 347 (1986); M. Monsigny, A.C. Roche, P. Midoux, C. Kieda et R. Mayer. *Dans* Lectins and glycoconjugates in oncology: structure, function, clinical application. *éditeurs* : H.J. Gabius et G.A. Nagel. Springer-Verlag, Heidelberg. 1988. pp. 1–23.
6. R.G. Little, J.A. Anton, P.A. Loach et J.A. Ibers. J. Heterocycl. Chem. **12**, 345 (1975).
7. R.G. Little. J. Heterocycl. Chem. **15**, 203 (1978).
8. C. Altona et M. Sundaraligam. J.Am. Chem. Soc. **95**, 2333 (1973).
9. J.S. Lindsey, I.C. Schreiman, H.C. Hsu, P.C. Kearbey et A.M. Marguerettaz. J. Org. Chem. **52**, 827 (1987).
10. G.M. Sanders, M. van Dijk, A. van Veldhuizen et H.C. van der Plas. J. Org. Chem. **53**, 5272 (1988).
11. G.M. Sanders, M. van Dijk. A. van Veldhuizen et H.C. van der Plas. J. Chem. Soc. Chem. Commun. 1311 (1986).
12. H.K. Hombrecher et G. Horter. Liebigs Ann. Chem. 219 (1991).
13. A. Lecas-Nawrocka, B. Boitrel et E. Rose. Tetrahedron Lett. **33**, 481 (1992).
14. H.K. Hombrecher, G. Horter et C. Arp. Tetrahedron, **48**, 9451 (1992).
15. G. Shipps et J. Rebeck. Tetrahedron Lett. **35**, 6823 (1994).
16. D. Hammel, P. Erk, B. Schuler, J. Heinze et K. Müllen. Adv. Mater. **4**, 737 (1992).
17. D.M. Wallace, S.H. Leung. M.O. Senge et K.M. Smith. J. Org. Chem. **58**, 7245 (1993).
18. J. Setsune et M. Hashimoto. J. Chem. Soc. Chem. Commun. 657 (1994).
19. C.H. Lee et J.S. Lindsey. Tetrahedron, **50**, 11427 (1994).
20. J.E. Falk. Porphyrins and metalloporphyrins. Elsevier, Amsterdam. 1964.
21. J.H. Fuhrhop, C. Demoulin, C. Boettcher, J. Köning et U. Siggel. J. Am. Chem. Soc. **114**, 4159 (1992).
22. M. Spiro, J.C. Blais, G. Bolbach, F. Fournier, J.C. Tabet, K. Driaf, O. Gaud, R. Granet et P. Krausz. Int. J. Mass Spectrom. Ion Processes, **134**, 229 (1994).
23. R.J. Abraham. Mol. Phys. **4**, 165 (1961); T.J. Janson, A.R. Kane, J.F. Sullivan, K. Knox et M.E. Kenney. J. Am. Chem. Soc. **91**, 5210 (1969).

Energétique des liaisons inter et intramoléculaires dans les trois isomères de l'aminophénol

Raphaël Sabbah et Meriem Gouali

Résumé : Le présent travail porte sur l'étude thermodynamique des trois isomères de l'aminophénol de formule générale : C_6H_7NO. Il a été réalisé en utilisant quatre techniques : la calorimétrie de combustion de faibles quantités de substance (quelques milligrammes par essai), la calorimétrie de sublimation, l'analyse thermique différentielle et la mesure de capacités calorifiques. Cette étude nous a permis : de déterminer les enthalpies de combustion, de sublimation et de fusion de ces composés; de préciser la stabilité relative des trois isomères; de déterminer les énergies de conjugaison expérimentales et de les comparer aux valeurs théoriques; de déterminer qualitativement et quantitativement les interactions intermoléculaires; de déterminer les enthalpies d'atomisation des trois composés et de vérifier qu'elles sont compatibles aux valeurs calculées à partir des contributions énergétiques précédemment déterminées au laboratoire; de discuter de l'existence d'une liaison hydrogène intramoléculaire dans l'isomère *ortho*.

Mots clés : thermodynamique; thermochimie; calorimétrie; analyse thermique différentielle; 2-aminophénol ou *ortho*-aminophénol; 3-aminophénol ou *méta*-aminophénol; 4-aminophénol ou *para*-aminophénol; enthalpie de combustion, de sublimation, de fusion, d'atomisation, enthalpies des liaisons inter et intramoléculaires; liaison hydrogène; énergie de conjugaison; température du point triple.

Abstract: The present work is concerned with a thermodynamic study of the three aminophenol isomers (general formula: C_6H_7NO). It was achieved using four techniques: combustion calorimetry of small amounts of substance (a few milligrams), sublimation calorimetry, differential thermal analysis, and heat capacity measurements. From this study, it was possible: to determine the enthalpies of combustion, sublimation, and fusion of these compounds; to discuss the relative stability of the three molecules; to determine the intermolecular enthalpy bonds; to determine the experimental resonance energies and to compare them with the theoretical values; to determine the atomization enthalpies and to compare them with the values calculated from the energetical contributions previously determined in our laboratory; to consider the existence of an intramolecular hydrogen bond in the *ortho* isomer.

Key words: thermodynamics; thermochemistry; calorimetry; differential thermal analysis; 2-aminophenol or *ortho*-aminophenol; 3-aminophenol or *meta*-aminophenol; 4-aminophenol or *para*-aminophenol; enthalpy of combustion, of sublimation, of fusion, of atomization, enthalpy of inter and intramolecular bonds; hydrogen bond; resonance energy; triple point temperature.

I. Introduction

Les aminophénols possèdent de nombreuses applications industrielles. Ils servent à la coloration des fourrures et le 4-aminophénol est utilisé comme révélateur photographique et comme intermédiaire dans la synthèse du paracétamol. Le 2-aminophénol est utilisé dans la fabrication d'un insecticide : le phosalone (1).

Très peu d'études thermodynamiques ont été réalisées sur les aminophénols. La plus récente concerne les travaux de Nuñez et al; elle a constitué pratiquement la seule référence pour la plupart des résultats de notre étude (2).

Ce travail a pour but de mettre en évidence le lien existant entre les grandeurs énergétiques et la structure des aminophénols, d'interpréter et de discuter l'importance relative des forces de cohésion cristalline. Il trouve ses applications dans l'industrie mais également dans l'environnement avec les problèmes liés à l'élimination et au stockage des déchets.

Reçu le 31 octobre, 1995.

R. Sabbah[1] **et M. Gouali.** Centre de Thermodynamique et de Microcalorimétrie du Centre National de la Recherche Scientifique, 26, rue du 141ème RIA, 13331 - Marseille, Cedex 03, France.

1. Auteur à qui les demandes de tirés à partir devront être adressées.

II. Partie expérimentale

II.1. Produits utilisés

Les trois substances étudiées sont des produits Aldrich de pureté supérieure ou égale à 98%, repurifiées par trois sublimations successives sous une pression résiduelle de 1,3 Pa à 373 K pour le 3-aminophénol et le 4-aminophénol. Le 2-aminophénol a été préalablement recristallisé dans du méthanol absolu avant de subir le même traitement que les deux autres isomères (2).

À l'état pur, les aminophénols sont incolores. Exposés à l'air, ils s'oxydent en brunissant. Nous avons pu vérifier que la lumière est responsable de cette oxydation et que l'humidité est un facteur secondaire favorisant ce phénomène. Ce sont des substances instables qui se décomposent souvent à des températures inférieures à leur point de fusion. C'est pourquoi, après leur purification, nous les avons stockées dans des flacons en verre brun, maintenus sous vide dans un dessiccateur en présence de soude.

La réactivité des aminophénols avec l'oxygène a été étudiée en fonction de divers paramètres dans les références 3, 4, et 5. Dans sa thèse (6), Perrin étudie les phénols d'une façon plus générale et montre que ces composés, à l'état pur et maintenus dans l'obscurité, ne se colorent pas à l'air et n'absorbent pas d'oxygène. Nous avons pu vérifier cette propriété avec les aminophénols.

Ce sont également des substances nocives par inhalation, par contact avec la peau et par ingestion. Leur toxicité a fait l'objet de quelques études (7, 8). C'est pourquoi, nous avons travaillé sous hotte en nous munissant de masque et de gants toutes les fois qu'il s'agissait de manipuler d'importantes quantités de produits pendant des temps relativement longs.

II.2. Appareillages, techniques et modes opératoires

II.2.1. Analyse thermique différentielle

Nous avons utilisé la version moyenne température de l'analyseur thermique différentiel et les cellules expérimentales en verre décrites dans la référence 9.

Dans toutes nos expériences: (*i*) la vitesse de montée en température du four a été de 0,2 K min^{-1}; (*ii*) la masse de substance utilisée a été d'environ 100 mg, déterminée par double pesée à l'aide d'une balance Mettler, type M5, sensible au μg et dont l'inexactitude des pesées est de ±2 μg; (*iii*) la préparation des échantillons et leur mise en container ont été conduites de la façon décrite dans la référence 9.

La mesure des températures a été faite à l'aide de deux thermocouples (thermocoax, type 2ABI 15), l'un est solidaire de l'échantillon, l'autre de la référence (alumine-α). La différence entre les fem délivrées par ces deux thermocouples est amplifiée par un microvoltmètre AOIP, type EVA, sensibilité 300 μV pleine échelle. Le signal ainsi amplifié est envoyé simutanément à un enregistreur Sefram, type Gépérac, pour le visualiser, et à un multimètre Keithley, modèle 175, pour le digitaliser. Un autre multimètre Keithley modèle 196, sensibilité 300 μV (résolution 100 nV) est utilisé pour mesurer la fem correspondant à la température de l'échantillon. Les données issues de ces deux multimètres sont envoyées vers un ordinateur en vue de leur traitement à l'aide d'un programme écrit et mis au point au laboratoire. En appliquant l'équation de Clausius-Clapeyron à l'équilibre solide ⇔ liquide et la loi de Raoult, ce programme permet de déterminer la pureté de l'échantillon, son enthalpie de fusion ainsi que la température de son point triple.

Comme indiqué dans la référence 9, l'étalonnage (*i*) en température de notre analyseur thermique a été réalisé à partir d'échantillons rigoureusement purs de naphtalène, de fluorène, d'acides benzoïque, diphénylacétique et anisique, de carbazole et d'anthraquinone, dont la température de leur point triple est bien connue dans la littérature; celle-ci est comprise entre 353 et 558 K; (*ii*) en énergie a été réalisé à partir d'échantillons rigoureusement purs de naphtalène, de fluorène, d'acides benzoïque et diphénylacétique, dont l'enthalpie de fusion est bien connue dans la littérature.

II.2.2. Calorimétrie de combustion

Les enthalpies de combustion de nos composés ont été déterminées en utilisant un calorimètre monopile basculant CRMT (sensibilité : 0,0623 V W^{-1}) équipé d'une microbombe en acier inoxydable (Superimphy 625) de volume interne égal à 42 cm^3 à la température ambiante.

Le signal issu du calorimètre est amplifié par un microvoltmètre électronique AOIP, modèle EVA, sensibilité 30 mV pleine échelle, avant son envoi simultané sur un intégrateur éléctronique, conçu, réalisé et mis au point au laboratoire, qui détermine l'aire des thermogrammes $dQ/dt=f(t)$ et sur un enregistreur potentiométrique (Sefram, modèle Servotrace) qui le visualise.

La rotation du calorimètre suivant plusieurs plans permet à toutes les génératrices de la bombe d'être lavées par l'eau déminéralisée placée en son fond (1 cm^3).

Comme indiqué dans la référence 10, les substances à étudier sont mises sous forme de pastilles. À cet effet, nous avons utilisé un ensemble piston-moule façonné dans un acier trempé, ce qui a pour effet d'éviter l'entraînement dans les pastilles de traces de métal et d'augmenter ainsi la qualité des résultats.

Les pesées ont été effectuées sur une microbalance Mettler, modèle UM3, équipée d'un jeu de poids étalonnés par le N.I.S.T. Sa portée est de 3 g et sa sensibilité de 0,1 μg. L'erreur commise avec cette balance sur une pesée de quelques milligrammes est de l'ordre de ±0,2 μg. Dans toutes nos pesées, nous avons tenu compte des corrections de poussée de l'air pour calculer les masses réelles.

Une fois garnie, la bombe est remplie d'oxygène sous une pression de 3,04 MPa. L'oxygène utilisé à cet effet, provient de l'Air Liquide et son degré de pureté est supérieur à 99,995% (fraction molaire d'azote < 10^{-5}). La durée d'une expérience a toujours été de 120 min à partir du moment de la mise de feu.

Après chaque expérience, nous avons déterminé, dans la phase aqueuse, les concentrations d'acide nitrique par titrage acido-basique en présence de phénolphtaléine avec une solution de soude préalablement titrée à l'aide d'une solution d'acide oxalique de concentration connue; et vérifié, à l'aide des tubes de Dräger, l'absence d'oxyde de carbone et d'oxydes d'azote (NO, NO_2) dans la phase gazeuse.

Des tests préliminaires ont été effectués dans le but de déterminer les meilleures conditions expérimentales. Afin de mettre en évidence, dans ces conditions, l'oxydation éventuelle de nos substances sous 3,04 MPa d'oxygène, des pastilles de chacun des trois isomères ont été placées dans la bombe et abandonnées pendant 1,5 h (temps nécessaire pour atteindre l'équilibre thermique dans nos expériences). Nous avons ainsi pu vérifier que : (*i*) l'aspect de nos pastilles restait inchangé (pas de coloration jaune, violette ou brune caractéristique de l'oxydation à l'air de nos substances); (*ii*) la masse avant et après chaque expérience restait invariable.

Nous en avons conclu qu'il n'y avait pas d'oxydation de la substance restée à l'abri de la lumière ou de réaction détectable dans nos conditions expérimentales, ce qui confirme les conclusions de Perrin (6).

II.2.3. Calorimétrie de sublimation

Nous avons utilisé un calorimètre Tian-Calvet (sensibilité 0,0185 V W^{-1}) associé à un montage différentiel doté de cellules d'effusion de Knudsen pour déterminer les enthalpies de sublimation de nos composés. L'étalonnage de notre système calorimétrique a été réalisé par effet Joule avant et après chaque série d'expériences. Le mode opératoire a été décrit dans la référence 11. Précisons que :

le signal issu du calorimètre est amplifié par un nanovoltmètre Keithley modèle 147, sensibilité 30 μV pleine échelle,

Tableau 1. Grandeurs physiques à 298,15 K des substances étudiées.

Substance	Formule brute	M^a (mol g^{-1})	ρ (g cm^3)	$-(\delta U/\delta P)_T$ (J g^{-1} MPa^{-1})
Acide benzoïque	$C_7H_6O_2$	122,1234	1,32 (14)	0,12
Coton	$CH_{1,791}O_{0,850}$	27,4157	1,50 (14)	0,29
2-Aminophénol	C_6H_7NO	109,1277	1,328 (2)	0,1 (2)
3-Aminophénol	C_6H_7NO	109,1277	1,328 (2)	0,1 (2)
4-Aminophénol	C_6H_7NO	109,1277	1,328 (2)	0,1 (2)

[a]Calculées à partir du tableau des masses atomiques de 1993 (13).

Tableau 2. Degrés de pureté, températures du point triple et enthalpies de fusion des aminophénols.

	Pureté (mol%)	$T^a_{p.t.}$ (K)	$\Delta_{fus}H_m$ (kJ mol^{-1})
2-Aminophénol	99,96 ± 0,01	449,23 ± 0,02	25,4 ± 0,5
3-Aminophénol	99,95 ± 0,01	394,83 ± 0,02	19,6 ± 1,4
4-Aminophénol	99,81 ± 0,03	462,50 ± 0,12	26 ± 2

[a]Définies par rapport à l'échelle EIT-90 (15).

puis digitalisé par un multimètre numérique Keithley modèle 175 et enregistré sur un enregistreur potentiométrique, Sefram, modèle Servotrace;

le diamètre des trous d'effusion pratiqués dans des joints en Téflon de 0,2 mm d'épaisseur est de 0,7, 0,8 et 1,5 ou 2 mm, respectivement, dans le cas du 2-aminophénol, 3-aminophénol et 4-aminophénol;

l'ouverture et la fermeture de l'orifice d'effusion des cellules sont pilotées par l'ordinateur;

toutes les pesées ont été effectuées à l'aide d'une balance Mettler, type UM3.

L'acquisition et le traitement des données sont réalisés à l'aide d'un ordinateur et d'un programme conçu et mis au point au laboratoire. Il permet, entre autres, de déterminer l'aire des thermogrammes et, à partir du coefficient d'étalonnage, l'enthalpie de sublimation de nos composés à la température de l'expérience $\Delta_{sub}H_m(T)$.

Des tests préliminaires sont nécessaires pour la détermination des conditions expérimentales précisées ci-dessus et dans le tableau 6: diamètre du trou d'effusion, température du calorimètre, sensibilité de l'amplificateur Keithley, quantité de substance à utiliser.

La faible pression de vapeur saturante de nos composés à 298,15 K nous a obligés à travailler entre 332 et 337 K. De plus, nous avons admis l'identité :

$$\Delta_{sub}H_m(T) \equiv \Delta_{sub}H^\circ_m(T)$$

II.2.4. Mesure des capacités calorifiques

Pour calculer $\Delta_{sub}H^\circ_m$ (298,15 K) à partir de $\Delta_{sub}H^\circ_m$ (T), il est nécessaire de connaître :

le comportement thermique de nos substances entre 298,15 K et T. Nous nous sommes donc assurés que nos substances ne présentaient aucun changement de phase dans cet intervalle;

la capacité calorifique à pression constante des phases condensée et gazeuse des substances étudiées à 298,15 K et T de façon à pouvoir appliquer la relation suivante :

$$\Delta_{sub}H_m^\circ(298{,}15\ \text{K}) = \Delta_{sub}H^\circ_m(T) + \int_T^{298{,}15\ \text{K}} [C^\circ_{p,m}(g) - C^\circ_{p,m}(s)]\, dT$$

La différence enthalpique $H^\circ_m(T) - H^\circ_m(298{,}15\ \text{K})$ à l'état solide a été déterminée par la méthode de chute à l'aide d'un calorimètre Tian-Calvet et d'un four maintenus respectivement à 298,15 K et T. Le calorimètre a été préalablement étalonné en utilisant des échantillons d'alumine-α.

Quant aux valeurs des capacités calorifiques à l'état gazeux $C^\circ_{p,m}(g)$ aux températures 298,15 K et T, elles ont été déterminées à partir d'une méthode incrémentale en utilisant les capacités calorifiques à l'état gazeux des molécules de benzène, de phénol et d'aniline (12).

Les différents calorimètres et analyseur thermique, leurs périphériques ainsi que les balances sont placés dans des salles thermorégulées à (19,0 ± 0,2)°C.

III. Résultats

Les constantes physiques de nos composés sont résumées dans le tableau 1.

III.1. Analyse thermique différentielle

Cette étude nous a posé quelques difficultés dues essentiellement à la décomposition des aminophénols au moment de leur fusion. C'est la raison pour laquelle pour chaque échantillon, seuls ont été retenus les résultats issus de la première fusion minimisant ainsi les risques d'erreurs dus au phénomène de décomposition. Nous consignons dans le tableau 2 les principaux résultats obtenus. Les valeurs de la température du point triple sont compatibles avec celles de la littérature. Quant aux enthalpies de fusion, aucune comparaison n'est possible par manque, à notre connaissance, de valeurs publiées.

Tableau 3. Combustion du 2-aminophénol.

m(subst.) (mg)	m(coton) (mg)	S (V s)	$n(HNO_3) \times 10^6$ (mol)	$-\Delta U$ (J)	$-W_1$ (J)	W_2 (J)	$-\Delta_c U°_m$(s, 298,15 K) (kJ mol^{-1})
4,7440	0,3093	8,912694	9,63	143,102	5,073	0,703	3158,97
5,1211	0,2371	9,510954	10,90	152,708	3,889	0,787	3154,50
4,5046	0,2388	8,380425	7,33	134,556	3,917	0,560	3151,29
6,5776	0,2710	12,192474	10,26	195,763	4,445	0,792	3160,98
5,4966	0,2470	10,221309	8,01	164,114	4,051	0,629	3165,34
7,1962	0,2061	13,221681	9,38	212,288	3,380	0,758	3156,52
4,6604	0,1986	8,631219	7,81	138,583	3,257	0,592	3154,92
5,3703	0,1990	9,944016	7,05	159,661	3,264	0,568	3166,55
4,1799	0,2446	7,816842	6,58	125,507	4,012	0,507	3158,74
4,5635	0,2764	8,534910	7,40	137,037	4,533	0,567	3155,02

$\Delta_c U°_m$(s, 298,15 K) = −(3158,3 ± 1,5) kJ mol^{-1}
$\Delta_c H°_m$(s, 298,15 K) = −(3160,1 ± 1,5) kJ mol^{-1}
$\Delta_f H°_m$(s, 298,15 K) = −(201,3 ± 1,5) kJ mol^{-1}

Symboles : S = aire des thermogrammes; ΔU = variation de l'énergie interne de la bombe et de son contenu; W_1 = énergie de combustion du coton; W_2 = corrections pour passer à l'état standard.

III.2. Calorimétrie de combustion

L'équivalent énergétique du système calorimétrique (U_{calor}) a été déterminé à partir de six combustions d'acide benzoïque, échantillon 39i du N.I.S.T. pour lequel $\Delta u°_c$(s, 298,15 K) = (−26 414 ± 3) J g^{-1} (16). Dans chaque expérience, nous avons utilisé environ 5 mg d'acide et 0,2 mg de coton (dont l'énergie de combustion, préalablement déterminée au laboratoire, a pour valeur $\Delta u°_c$(s, 298,15 K) = (−16 399 ± 23) J g^{-1} (17)). Nous avons trouvé U_{calor} = (16,056 ± 0,007) J V^{-1} s^{-1}.

Les enthalpies standard de combustion de nos composés (tableaux 3–5) concernent la réaction suivante :

$$C_6H_7NO(s) + 29/4\ O_2(g) \rightarrow 6\ CO_2(g) + 7/2\ H_2O(l) + 1/2\ N_2(g)$$

et sont calculées à l'aide d'un ordinateur et d'un programme écrit et mis au point au laboratoire, à partir de nos valeurs expérimentales en tenant compte des corrections dites de Washburn.

Nos valeurs expérimentales sont inférieures aux valeurs de Nuñez *et al* (2) d'environ 0,3%, 0,2% et 0,1% respectivement, pour les isomères *ortho*, *méta* et *para*. N'ayant pas rencontré de difficultés particulières en calorimétrie de combustion des aminophénols qui seraient dues à leur volatilité, à leur hygroscopicité et (ou) à leur oxydation (à condition d'éviter l'exposition prolongée des pastilles à la lumière), nous pensons que la masse de substance brûlée, déterminée à partir de nos pesées initiales, est plus fiable que celle qui est calculée à partir de la quantité de CO_2 issue de la combustion comme l'ont fait Nuñez *et al*. Par ailleurs, signalons l'absence dans leur travail de toute indication relative à la pureté des substances étudiées.

III.3. Calorimétrie de sublimation et mesures des capacités calorifiques

Les enthalpies de sublimation de nos substances sont consignées dans le tableau 6. Comme on peut le constater (tableau 7), nos résultats à 298,15 K sont plus faibles que les valeurs de Nuñez et al. (2).

Si l'on se réfère à la méthode expérimentale, utilisée par ces auteurs pour la détermination des enthalpies de sublimation ou de vaporisation, décrite dans la référence 18, on se rend compte que le signal endothermique mesuré par le microcalorimètre correspond à une énergie de sublimation à une température T et non pas à une enthalpie puisque la pression n'est pas constante tout au long du changement d'état. Une correction relative à la différence $\Delta_{sub}H_m(T) - \Delta_{sub}U_m(T)$, égale à RT, avec T = 414 K (température à laquelle ont été réalisées les mesures), ne peut pas expliquer, à elle seule, l'écart observé entre nos valeurs et celles de ces auteurs. A noter que cette différence est aussi constatée si l'on compare les valeurs des enthalpies de sublimation des trois isomères de l'acide chlorobenzoïque obtenues au laboratoire (19) avec celles qui ont été mesurées par Adedeji et al. (18) en utilisant la même méthode.

Par ailleurs, signalons que Dunn (20) a déterminé l'enthalpie de sublimation du 4-aminophénol dans l'intervalle de température (403 < T/K < 430) et a trouvé 92 kJ mol^{-1}. Ramenée à 298,15 K, cette valeur, égale à 98,2 kJ mol^{-1}, s'écarte davantage de la valeur de Nuñez et al. (Δ = 10,9 kJ mol^{-1}) que de la nôtre (Δ = 5,5 kJ mol^{-1}).

En utilisant les résultats expérimentaux obtenus par calorimétrie de combustion et de sublimation, nous avons calculé l'enthalpie molaire standard de formation à l'état gazeux de chacun des trois isomères (tableau 7).

III.4. Enthalpie d'atomisation

À une température donnée, la réaction d'atomisation des aminophénols s'écrit :

$$C_6H_7NO\ (g) \rightarrow 6\ C(g) + 7\ H(g) + N(g) + O(g)$$

En conséquence, l'enthalpie liée à cette réaction est égale à :

$$\Delta_{a,exp}H°_m = 6\ \Delta_f H°_m\,[C(g)] + 7\ \Delta_f H°_m\,[H(g)] + \Delta_f H°_m\,[N(g)] + \Delta_f H°_m\,[O(g)] - \Delta_f H°_m\,[C_6H_7NO(g)]$$

Les valeurs de $\Delta_{a,exp}H°_m$ de nos substances (tableau 7) ont

Tableau 4. Combustion du 3-aminophénol.

m(subst.) (mg)	m(coton) (mg)	S (V s)	$n(HNO_3) \times 10^6$ (mol)	$-\Delta U$ (J)	$-W_1$ (J)	W_2 (J)	$-\Delta_c U°_m$(s, 298,15 K) (kJ mol^{-1})
6,2033	0,3018	11,544774	9,26	185,363	4,950	0,724	3161,08
5.7671	0,3051	10,742577	7,88	172,483	5,004	0,631	3157,19
7,1966	0,1696	13,208022	8,00	212,068	2,782	0,676	3163,33
5,0332	0,2988	9,395730	3,27	150,858	4,901	0,339	3157,23
5,2535	0,2484	9,770910	7,86	156,882	4,074	0,613	3161,45
6,8798	0,3148	12,762756	10,13	204,919	5,163	0,794	3155,94

$\Delta_c U°_m$(s, 298,15 K) = −(3159,4 ± 1,2) kJ mol^{-1}
$\Delta_c H°_m$(s, 298,15 K) = −(3161,2 ± 1,2) kJ mol^{-1}
$\Delta_f H°_m$(s, 298,15 K) = −(200,2 ± 1,2) kJ mol^{-1}

Symboles : S = aire des thermogrammes; ΔU = variation de l'énergie interne de la bombe et de son contenu; W_1 = énergie de combustion du coton; W_2 = corrections pour passer à l'état standard.

Tableau 5. Combustion du 4-aminophénol.

m(subst.) (mg)	m(coton) (mg)	S (V s)	$n(HNO_3) \times 10^6$ (mol)	$-\Delta U$ (J)	$-W_t$ (J)	W_2 (J)	$-\Delta_c U°_m$(s, 298,15 K) (kJ mol^{-1})
7,2004	0,3236	13,380483	8,49	214,837	5,307	0,708	3164,86
5,7881	0,2547	10,745574	6,51	172,531	4,177	0,550	3163,75
8,1542	0,2937	15,099174	9,90	242,433	4,817	0,818	3169,08
5,8586	0,2749	10,910880	7,11	175,185	4,509	0,588	3168,24
7,0711	0,2625	13,080783	8,73	210,025	4,305	0,717	3163,80
5,9348	0,3075	11,080341	8,61	177,906	5,043	0,678	3166,10
6,5196	0,2552	12,069702	7,95	193,791	4,186	0,655	3162,73

$\Delta_c U°_m$(s, 298,15 K) = −(3165,5 ± 0,9) kJ mol^{-1}
$\Delta_c H°_m$(s, 298,15 K) = −(3167,4 ± 0,9) kJ mol^{-1}
$\Delta_f H°_m$(s, 298,15 K) = −(194,1 ± 0,9) kJ mol^{-1}

Symboles : S = aire des thermogrammes; ΔU = variation de l'énergie interne de la bombe et de son contenu; W_1 = énergie de combustion du coton; W_2 = corrections pour passer à l'état standard.

été calculées en utilisant les valeurs de $\Delta_f H°_m$(g, 298,15 K) de C, H, N et O consignées dans la référence 22.

Dans le présent travail, l'incertitude qui accompagne les résultats expérimentaux représente l'écart moyen, $\sigma_m = \pm \{(x - x_0)^2/n(n-1)\}^{1/2}$, x étant chacune des n valeurs entrant dans le calcul de la moyenne x_0. Lorsque la valeur expérimentale est fonction de plusieurs variables, l'incertitude calculée tient compte de l'erreur sur chacune de ces variables.

IV. Discussion

IV.1. Énergie de conjugaison

L'énergie de conjugaison est la différence entre l'énergie réelle de la molécule et l'énergie qu'elle aurait si les divers systèmes insaturés qu'elle comporte étaient indépendants. Sur le plan pratique, pour la déterminer, il suffit d'utiliser les enthalpies standard de combustion à l'état gazeux de la molécule réelle et de la molécule fictive non conjuguée. La première de ces grandeurs s'obtient expérimentalement et la seconde nécessite le recours aux systématiques. En ce qui nous concerne, nous avons utilisé celle de Klages qui est consignée dans la référence 23.

Nous avons également calculé l'énergie de conjugaison théorique à l'aide de la méthode de calcul indiquée dans la référence 24 et ce, en utilisant les paramètres suivants : $\alpha_O = \alpha + 2{,}500\ \beta_0$; $\alpha_N = \alpha + 2{,}250\ \beta_0$; $\beta_{(C\text{-}O)} = 0{,}750\ \beta_0$; $\beta_{(C\text{-}N)} = 0{,}750\ \beta_0$ (β_0 est l'intégrale de recouvrement de la molécule de benzène; elle est égale à 131,7 kJ mol^{-1}).

Les valeurs de l'énergie de conjugaison expérimentale et théorique (tableau 8) ainsi obtenues sont compatibles. De plus et comme on peut le constater, l'énergie de conjugaison du 2-aminophénol étant la plus élevée laisse supposer que cet isomère serait le plus stable.

IV.2. Liaisons intramoléculaires dans les aminophénols

Par définition, l'enthalpie d'atomisation d'une molécule est égale à la somme des liaisons intramoléculaires compte tenu des facteurs de stabilisation et de déstabilisation. Pour retrouver, par le calcul, l'enthalpie d'atomisation de nos composés, nous avons tenu compte du principe de la transférabilité et avons utilisé les valeurs énergétiques des différentes liaisons intramoléculaires préalablement déterminées au laboratoire à partir d'autres molécules.

Pour ce qui est des liaisons C_b—C_b du cycle benzénique, nous avons utilisé le procédé de calcul consigné dans la référence 10. Celui-ci fait intervenir un paramètre lié à la géométrie de la molécule, l'indice de liaison l_{rs} entre deux atomes directement liés r et s, obtenu à partir du calcul

Tableau 6. Sublimation des aminophénols.

Substance	T (K)	m (mg)	$\Delta_{sub}H°_m(T)$ (kJ mol^{-1})	$\Delta_{sub}H°_m(T)$ (kJ mol^{-1})	$\int_{298,15\ K}^{T} C°_{p,m}(s)dT$ (kJ mol^{-1})	$\int_{298,15\ K}^{T} C°_{p,m}(g)dT$ (kJ mol^{-1})	$\Delta_{sub}H°_m(298,15\ K)$ (kJ mol^{-1})
2-Aminophénol	332	5,8164	91,72	93,48 ± 0,83	7,50 ± 0,03	4,65 ± 0,01	96,33 ± 0,83
		6,5243	94,58				
		5,7021	93,45				
		6,9587	91,70				96,90 ± 0,56
		5,8302	95,97				
	337	7,8777	93,36	95,28 ± 0,74	7,50 ± 0,03	5,32 ± 0,01	97,46 ± 0,74
		7,0490	95,28				
		8,2672	96,69				
		6,7137	96,36				
		6,0811	93,86				
		8,2697	93,83				
		5,3756	99,84				
		7,4670	98,20				
		6,8574	93,11				
		7,9379	91,45				
		6,2713	96,05				
3-Aminophénol	335	17,4442	98,25	98,81 ± 0,86	7,84 ± 0,02	5,07 ± 0,01	101,58 ± 0,86
		16,2064	101,43				
		14,1928	98,36				
		17,8025	99,77				
		15,2853	96,23				
4-Aminophénol	335	5,8374	96,54	101,14 ± 0,65	7,50 ± 0,02	5,01 ± 0,01	103,63 ± 0,65
		7,0356	102,94				
		7,3777	102,61				
		6,4776	99,83				
		6,8090	101,54				
		7,3536	103,59				
		6,2340	100,68				
		6,2213	101,99				
		8,7727	100,63				
		6,7850	102,39				
		6,0029	97,53				
		6,7102	103,43				

Tableau 7. Ensemble des grandeurs thermodynamiques relatives aux aminophénols et leur comparaison aux résultats de la littérature.

Grandeur (kJ mol^{-1})	2-Aminophénol		3-Aminophénol		4-Aminophénol	
	Ce travail	Littérature	Ce travail	Littérature	Ce travail	Littérature
$\Delta_{sub}H°_m(298,15\ K)$	96,90±0,56	103,8±0,9 (2)	101,58±0,86	104,7±1,2 (2)	103,63±0,65	109,1±1,4 (2) 92,0 (403–430 K) (20)
$-\Delta_cH°_m(s, 298,15\ K)$	3160,1±1,5	3170,5±0,5 (2)	3161,2±1,2	3167,4±0,6 (2)	3167,4±0,9	3170,9±0,5 (2)
$-\Delta_fH°_m(s, 298,15\ K)$	201,3±1,6		200,2±1,3		194,1±1,0	179,1 (21)
$-\Delta_cH°_m(g, 298,15\ K)$	3257,0±1,6		3262,8±1,5		3271,0±1,1	
$-\Delta_fH°_m(g, 298,15\ K)$	104,4±1,7		98,6±1,6		90,5±1,2	
$\Delta_{a,exp}H°_m$	6652,2±2,2		6646,4±2,1		6638,3±1,8	

théorique de l'énergie de conjugaison (fig.1). La relation reliant H_{rs} à l_{rs} s'écrit (H_{rs} / kJ mol^{-1}) = 246,0 l_{rs} + 342,6. Quant à $H(C_b—H)$, $H(C_b—OH)$ et $H(C_b—NH_2)$, nous avons respectivement utilisé les valeurs 415,88 (25); 841 (26) et 1102,37 kJ mol^{-1} (25).

Les valeurs ainsi calculées sont égales à 6633,2; 6631,7 et

Tableau 8. Energie de conjugaison des aminophénols.

	2-Aminophénol	3-Aminophénol	4-Aminophénol
$E_{conj\ exp}$ (kJ mol^{-1})	184,3	175,6	167,4
$E_{conj\ théor}$ (kJ mol^{-1})	177,3	176,7	177,2

Fig. 1. Indices de liaison dans les trois isomères de l'aminophénol.

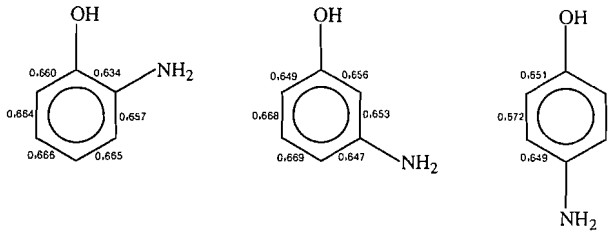

2-aminophénol 3-aminophénol 4-aminophénol

6632,7 kJ mol^{-1} respectivement, pour l'isomère *ortho*, *méta* et *para* et sont en parfait accord avec les résultats expérimentaux consignés dans le tableau 7.

IV.3. Liaisons intermoléculaires dans les aminophénols

L'enthalpie de sublimation d'une substance organique est liée aux interactions intermoléculaires. Dans le cas des aminophénols, ces interactions sont du type van der Waals et concernent les forces de dispersion et d'interactions dipolaires. À côté de ces interactions, il existe aussi des liaisons hydrogène intermoléculaires. Il nous a donc paru intéressant de déterminer la part énergétique de chacune d'elles. Pour ce faire, nous avons appliqué un procédé de calcul déjà utilisé au laboratoire (26–31). Il consiste, dans notre cas, à déterminer la contribution énergétique des forces de dispersion (London) en considérant qu'elle est égale à l'enthalpie de sublimation des diméthylbenzènes, composés isoélectroniques des aminophénols.

À une température donnée (ici 298,15 K), la différence D_1 des enthalpies de sublimation des aminophénols et des diméthylbenzènes correspondants représente la somme des énergies d'interaction dipolaire et des liaisons hydrogène intermoléculaires (tableau 9).

Afin de déterminer la contribution énergétique des interactions dipolaires D_2, nous avons comparé les enthalpies de sublimation des dichlorobenzènes, composés isoélectroniques des aminophénols et des diméthylbenzènes, qui présentent un moment dipolaire mais ne forment pas de liaisons hydrogène intermoléculaires, à celles des diméthylbenzènes correspondants. Comme on peut le constater, celle-ci est faible.

La différence $D_1 - D_2$, soit 38,5 kJ mol^{-1}, représente la part énergétique pouvant être attribuée à la somme des liaisons hydrogène intermoléculaires mises en évidence par des études cristallographiques (32–35). Celles-ci ont montré l'existence de deux types de liaisons hydrogène intermoléculaires dans les molécules d'aminophénols: N—H···O et O—H···N. Ces liaisons forment, dans le cas du 2-aminophénol (32, 33), des feuillets liés entre eux par de faibles forces de van der Waals.

La liaison O—H···N est plus forte que N—H···O. En effet, l'électronégativité de O étant plus importante que celle de N,

Tableau 9. Comparaison des enthalpies de sublimation des aminophénols, des diméthylbenzènes et des dichlorobenzènes.

	$\Delta_{sub}H°_m$(298,15 K) (kJ mol^{-1})		
	ortho	*méta*	*para*
OH, $NH_2 \rightarrow$ A	96,90	101,58	103,63
Cl, Cl $\rightarrow$ B	64,35	62,78	65,15
CH_3, $CH_3 \rightarrow$ C	59,82	58,26	60,18
D_1 = A − C	37,08	43,32	43,45
D_2 = B − C	4,53	4,52	4,97
$D_1 - D_2$	32,55	38,80	38,48

la liaison O—H est plus polarisée et la charge δ^+ portée par l'hydrogène est plus importante, induisant ainsi une liaison H···N plus forte. La longueur de la liaison O···N est d'ailleurs plus petite dans le cas de O—H···N (2,780 Å (33), 2,764 Å (32)) que dans celui de N—H···O (3,113 Å (33), 3,114 Å (32)).

On sait que la force d'une liaison est inversement proportionnelle à sa longueur. Afin de déterminer la contribution enthalpique de chacun de ces deux types de liaisons hydrogène intermoléculaires à partir de l'enthalpie attribuée à leur ensemble, soit 38,5 kJ mol^{-1}, nous avons, dans un premier temps, utilisé la relation donnée par Jaskólski (36) pour calculer le taux de raccourcissement de la distance interatomique entre deux atomes H et X liés par une liaison hydrogène intramoléculaire et admis que nous pouvions confondre liaison hydrogène intra et intermoléculaire.

Cette relation s'écrit :

$$\Delta(HX) = [W(H) + W(X) - R(H\cdots X)] / [W(H) + W(X)]$$

$\Delta(HX)$ représente le raccourcissement de la liaison H···X, $W(H)$ et $W(X)$ représentent respectivement les rayons de van der Waals des atomes H et X; $R(H\cdots X)$ représente la distance réelle entre les atomes H et X.

Appliquée dans notre cas avec X = N ou O, la relation précédente nous permet de calculer $\Delta(HN)$ et $\Delta(HO)$. Les valeurs de $W(H)$ = 1,00 Å; $W(O)$ = 1,52 Å et $W(N)$ = 1,55 Å ont été empruntées à la référence 37.

À défaut de trouver dans la référence 34 les distances interatomiques du 4-aminophénol qui présente l'avantage de ne pas contracter de liaisons hydrogène intramoléculaires, nous avons adopté pour les distances $R(H\cdots N)$ et $R(H\cdots O)$ respectivement les valeurs 1,77 et 2,22 Å données avec la structure cristalline du 2-aminophénol (33). Le rapport $\Delta(HN)/\Delta(HO)$ est égal à 2,6.

La seule étude cristallographique sur le 4-aminophénol a été réalisée par Brown (34). Cet auteur propose trois liaisons hydrogène intermoléculaires par molécule de 4-aminophénol. La troisième liaison nous paraît être contestable si l'on se réfère à la valeur de la distance (N—H···O = 3,18 Å) qui est relativement élevée comparée à celles des liaisons de même type. Toutes les autres études cristallographiques, réalisées sur l'isomère *ortho* ou *méta* (32, 33, 35), montrent l'existence de deux liaisons hydrogène par molécule d'aminophénol, l'une de type N—H···O et l'autre de type O—H···N. En conséquence, nous avons supposé qu'il en était de même pour le 4-aminophénol, ce qui nous a permis, à partir de la valeur du rapport $\Delta(HN)$ / $\Delta(HO)$, d'attribuer une énergie d'environ

10,7 kJ mol^{-1} pour la liaison N—H···O et 27,8 kJ mol^{-1} pour la liaison O—H···N. Dans son ouvrage (38), Julg propose une énergie variant de 8,4 à 12,6 kJ mol^{-1} pour la liaison N—H···O dans les oximes et de 16,7 à 29,3 kJ mol^{-1} pour la liaison O—H···N, ce qui est tout à fait compatible avec nos résultats.

IV.4. Liaison hydrogène intramoléculaire dans l'isomère *ortho*

À la suite de leurs études cristallographiques sur le 2-aminophénol, Ashfaquzzaman et Pant (32), d'une part, et Korp et al. (33), d'autre part, proposent une structure en feuillets formés par des molécules liées entre elles par des liaisons hydrogène intermoléculaires de type N—H···O et O—H···N.

Cette organisation engendre des cavités dans lesquelles peuvent s'infiltrer d'autres molécules permettant ainsi aux molécules du 2-aminophénol de jouer le rôle de composés d'insertion ou clathrates. L'existence d'un hydrogène libre de la fonction NH_2 pourrait partiellement expliquer le fait que des molécules comme l'eau et l'éthanol soient attirées préférentiellement à l'intérieur de ces cavités.

En conséquence, si l'on admet les conclusions tirées par Ashfaquzzaman et Pant et Korp et al., il n'y aurait pas de place pour une liaison hydrogène intramoléculaire dans l'isomère *ortho*. Pourtant, quelques observations faites sur les propriétés physico-chimiques des aminophénols tendraient à attribuer la différence entre les valeurs de l'enthalpie de sublimation des isomères *ortho* et *para*, soit 6,73 kJ mol^{-1}, à une liaison hydrogène intramoléculaire :

1. La pression de vapeur saturante à 335 K de l'isomère *ortho* (0,5 Pa) est plus forte que celle des deux autres isomères : *méta* (0,4 Pa) et *para* (0,06 Pa), évaluées à partir de nos résultats expérimentaux d'après la méthode de calcul indiquée dans la référence 25.

2. La température du point triple (ou de fusion), qui renseigne sur la force des liaisons intermoléculaires, est plus élevée dans le cas de l'isomère *para* que dans celui de l'isomère *ortho*. Il en est de même pour l'enthalpie de fusion (tableau 2).

Enfin précisons que, même si elle existe, cette liaison hydrogène intramoléculaire serait faible et du même ordre de grandeur que celle que l'on pourrait rencontrer dans le cas du 1,2-dihydroxybenzène (6,63 kJ mol^{-1}) (26), composé ayant, par ailleurs, une structure cristalline analogue à celle du 2-aminophénol (39). Toutefois, une autre explication peut être envisagée pour interpréter la différence entre les enthalpies de sublimation des isomères *ortho* et *para* aussi bien dans le cas de l'aminophénol que dans celui du dihydroxybenzène sans qu'elle ne soit en contradiction avec les structures cristallines respectives de ces composés. Elle consiste à supposer que les liaisons hydrogène intermoléculaires, qui associent les molécules par deux dans les isomères *ortho*, soient suffisamment fortes pour qu'un certain nombre de ces molécules passe de l'état solide à l'état gazeux sous forme de dimères. Dans ce cas, l'enthalpie de sublimation ne tiendrait pas compte de toutes les liaisons hydrogène intermoléculaires et serait inférieure à l'enthalpie de sublimation de l'isomère *para* pour lequel seules des molécules monomères existent en phase gazeuse.

Remerciements

L'un de nous (M.G.) remercie les gouvernements Algérien et Français pour l'octroi d'une bourse d'études lui ayant permis de préparer une thèse de doctorat dont ce travail constitue une partie.

Bibliographie

1. H.G. Franck et J.W. Stadelhofer. Industrial aromatic chemistry raw materials, processes, products. Springer, Berlin. 1988.
2. L. Nuñez, L. Barral, S. Gavilanes Largo et G. Pilcher. J. Chem. Thermodyn. **18**, 575 (1986).
3. L. Prati, M. Rossi et N. Ravasio. J. Mol. Catal. **75**, 347 (1992).
4. K. Jackowska, J. Bukowska et A. Kudelski. J. Electroanal. Chem. **350**, 177 (1993).
5. A. Kudelski et J. Bukowska. J. Mol. Struct. **275**, 145 (1992).
6. R. Perrin. Thèse, Faculté des Sciences de l'Université de Lyon, 1964.
7. N. Irving Sax. Dangerous properties of industrial materials. 4th ed. Van Nostrand Reinhold , New York. 1975.
8. C. Klos, M. Koob, C. Kramer et W. Dekant. Toxicol. Appl. Pharmacol. **115**, 98 (1992).
9. R. Sabbah et I. Antipine. J. Therm. Anal. **32**, 1929 (1987); R. Sabbah et L. El Watik., J. Therm. Anal. **36**, 2299 (1990).
10. R. Sabbah et I. Antipine. Bull. Soc. Chim. Fr. **3**, 392 (1987).
11. R. Sabbah, I. Antipine, M. Coten et L. Davy. Thermochim. Acta, **115**, 153 (1987).
12. D.R. Stull, E.F. Westrum, Jr. et G.C. Sinke. The chemical thermodynamics of organic compounds. Wiley, New York. 1969.
13. Atomic weights of the elements 1993. Pure Appl. Chem. **66**, 2423 (1994).
14. W.D. Good et N.K. Smith. J. Chem. Eng. Data, **14**, 102 (1969).
15. H. Preston-Thomas. Metrologia, **27**, 3 (1990).
16. J.D. Cox et G. Pilcher. Thermochemistry of organic and organometallic compounds. Academic Press, London. 1970.
17. R. Sabbah et M. Coten. Thermochim. Acta, **49**, 307 (1981).
18. F.A. Adedeji, D.L.S. Brown, J.A. Connor, M. Leung, M.I. Paz-Andrade et H.A. Skinner. J. Organomet. Chem. **97**, 221 (1975).
19. R. Sabbah et H. Hirtz. Bull. Soc. Chim. Fr. **127**, 26 (1991).
20. S.A. Dunn. J. Am. Chem. Soc. **76**, 6191 (1954).
21. M.S. Kharasch. J. Res. Natl. Bur. Stand. (U.S.), **2**, 359 (1929) citée dans la réf. 2.
22. Report of the codata task goup on key values for thermodynamics. J. Chem. Thermodyn. **10**, 903 (1978).
23. G.W. Wheland. Resonance in organic chemistry. Wiley, New York. 1955.
24. R. Sabbah, M. Gilbert et A. Julg. Thermochim. Acta, **10**, 345 (1974).
25. R. Sabbah et M. Laffitte. Thermochim. Acta, **25**, 376 (1978).
26. R. Sabbah et E.N.L.E. Buluku. Can. J. Chem. **69**, 481 (1991).
27. R. Sabbah et M. Gouali. Aust. J. Chem. **47**, 1651 (1994).
28. R. Sabbah et O. Pemenzi. C.R. Acad. Sci. Paris, **317**, 575 (1993).
29. P. Knauth et R. Sabbah. Can. J. Chem. **68**, 731 (1990).
30. P. Knauth et R. Sabbah. Bull. Soc. Chim. Fr. **5**, 834 (1988).
31. S. Skoulika et R. Sabbah. Thermochim. Acta, **61**, 203 (1983).
32. S. Ashfaquzzaman et A.K. Pant. Acta Crystallogr. Sect. B: Struct. Crystallogr. Cryst. Chem. **B35**, 1394 (1979).
33. J.D. Korp, I. Bernal, L. Aven et J.L. Mills. J. Cryst. Mol. Struct. **11**, 117 (1981).
34. C.J. Brown. Acta Crystallogr. **4**, 100 (1951).
35. C. Derango, S. Brunie, G. Tsoucaris, J.P. Declercq et G. Germans. Cryst. Struct. Commun. **3**, 485 (1974).
36. M. Jaskólski. Proc. IV Symp. Org. Cryst. Chem. 13 (1982), Poznan, Pologne, citée par T. Dziembowska. Pol. J. Chem. **68**, 1455 (1994).
37. S.N. Vinogradov. Molecular interactions, Vol. 2. *Édité par* H. Ratajczak et W.J. Orville-Thomas. Wiley, New York. 1980.
38. A. Julg. Chimie théorique. Dunod, Paris. 1964.
39. C.J. Brown. Acta Crystallogr. **21**, 170 (1966).

Substituted tetra-2,3-pyrazinoporphyrazines. Part I. Angular annelation of tetra-2,3-quinoxalinoporphyrazine

Svetlana V. Kudrevich, Maria G. Galpern, Evgeny A. Luk'yanets, and Johan E. van Lier

Abstract: Several derivatives of 2,3-dicyanopyrazine were prepared via the condensation of *o*-quinones with diaminomaleodinitrile. Benzo[*f*]quinoxaline-2,3-dinitrile was obtained from 1,2-naphthoquinone, and a series of isomeric, di-*tert*-butyl substituted 5,6-(9,10-phenanthro)-2,3-dicyanopyrazines were prepared from the corresponding di-*tert*-butyl-9,10-phenanthrenequinones. Complexation of benzo[*f*]quinoxaline-2,3-dinitrile, and unsubstituted 5,6-(9,10-phenanthro)-2,3-dicyanopyrazine, with an appropriate metal salt yielded metal complexes of tetra-2,3-(benzo[*f*]quinoxalino)porphyrazine and tetra-2,3-[5,6-(9,10-phenanthro)]porphyrazine, respectively. Metal-free tetra-2,3-[5,6-(9,10-phenanthro)porphyrazine was obtained from the dilithium derivative by demetallation in HCl. These compounds have limited solubility in organic solvents, such as quinoline, and are aggregated in solutions. To eliminate the aggregation phenomenon and to determine the spectral properties of angularly annelated naphthalocyanine aza analogs, we prepared several isomeric tetra-2,3-[5,6-(di-*tert*-butyl-9,10-phenanthro)pyrazino]porphyrazines. These octa(*tert*-butyl) substituted complexes were synthesized via complexation of di-*tert*-butyl substituted 5,6-(9,10-phenanthro)-2,3-dicyanopyrazines with metal salts in the presence of urea, quinoline, and tri(*n*-butyl)amine, and purified by silica gel chromatography. They are soluble in chloroform and substantially monomerized in solutions. A hypsochromic shift of the Q-band of octaaza naphthalocyanines versus their carbocyclic analogs was observed for all aza analogs, with the extent of the shift depending on the composition of the aromatic macrocycle. Thus, the first angularly annelated benzo ring addition causes a hypsochromic shift (~25 nm) of the Q-band of tetra-2,3-quinoxalinoporphyrazine, whereas addition of a second condensed benzo ring has little effect.

Key words: phthalocyanine, aza analog, tetra-2,3-quinoxalinoporphyrazine, angular annelation.

Résumé : Plusieurs dérivés de 2,3-dicyanopyrazine ont été préparés via la condensation de *o*-quinones avec le diaminomaleodinitrile. Le benzo[*f*]quinoxaline-2,3-dinitrile a été obtenu de la 1,2-naphthoquinone et plusieurs isomères de di-*tert*-butyl-5,6-(9,10-phenanthro)-2,3-dicyanopyrazines ont été préparés à partir des di-*tert*-butyl-9,10-phenanthrenequinones correspondants. La condensation de benzo[*f*]quinoxaline-2,3-dinitrile et de 5,6-(9,10-phenanthro)-2,3-dicyanopyrazine non substitué avec un sel du métal approprié a produit des complexes métalliques de tetra-2,3-(benzo[*f*]quinoxalino)porphyrazine et de tetra-2,3-[5,6-(9,10-phenanthro]porphyrazine, respectivement. La tetra-2,3-[5,6-(9,10-phenanthro)porphyrazine sans métal a été obtenu du dérivé de dilithium par la démétallisation dans HCl. Ces composés ont une solubilité limitée dans les solvants organiques tels que la quinoline et sont agrégés dans les solutions. Afin d'éliminer le phénomène d'agrégation et pour déterminer les propriétés spectrales des azaanalogues de naphthalocyanine avec d'anneaux angulaires condensés, nous avons préparé plusieurs isomères de tetra-2,3-[5,6-(di-*tert*-butyl-9,10-phenanthro)pyrazino]porphyrazines. Ces complexes substitués d'octa(*tert*-butyl) ont été synthétisés via la complexation de di-*tert*-butyl substitué 5,6-(9,10-phenanthro)-2,3-dicyanopyrazines avec des sels du métal en présence d'urée, de quinoline et d'amine tri-*n*-butylique, et purifiés par la chromatographie sur gel de silice. Ils sont solubles dans le chloroforme et sont monomérisés substantiellement en solutions. Un déplacement hypsochromique de la bande Q des octaaza naphthalocyanines versus leurs analogues carbocycliques a été observé pour tous les azaanalogues, avec la grandeur du déplacement relié à la composition du macrocycle aromatique. Par conséquent, l'addition d'un premier anneau benzo angulaire produit un déplacement hypsochromique (~25 nm) de la bande Q du tetra-2,3-quinoxalinoporphyrazine, alors que l'addition d'un deuxième anneau benzo condensé a peu d'effet.

Mots clés : phtalocyanine, azaanalogue, tetra-2,3-quinoxalinoporphyrazine, annélation angulaire.

Received November 3, 1995.

S.V. Kudrevich and J.E. van Lier.[1] MRC Group in the Radiation Sciences, Faculty of Medicine, Université de Sherbrooke, Sherbrooke, QC J1H 5N4, Canada.
M.G. Galpern and E.A. Luk'yanets. Organic Intermediates and Dyes Institute, 1/4 B. Sadovaya, Moscow 103787, Russia.

[1] Author to whom correspondence may be addressed. Telehone: (819) 563-5555, ext. 4603. Fax: (819) 564-5442. E-mail: jvanlier@courrier.usherb.ca

Introduction

The potential use of aza analogs of phthalocyanine (AzaPc) and naphthalocyanine (AzaNc) as electrocatalysts for oxygen reduction (1, 2), materials for electrochromic displays (3–5), media for optical data storage with a large-capacity memory (6–8), and photosensitizers for photodynamic therapy of cancer (9, 10) has been extensively investigated in the past decade. We previously reported on the synthesis and properties of an AzaPc series differing in the number and position of nitrogen atoms in the macrocycle, as well as in the number of attached linearly condensed benzo rings. The main changes in the UV–VIS spectra of Pc and Nc, resulting from linear annelation and aza substitution in the macrocycles, were readily explained by quantum chemical calculations (11–14). Subsequently we investigated the effect of aryl substitution on the UV–VIS spectra in a series of octaaza Pcs and tetraaza Ncs (15). As an extension of this work we studied the influence of *angular* annelation on the electronic spectra of AzaPc. We now report on the synthesis and spectral properties of angularly annelated derivatives of the tetra(2,3-quinoxalino)porphyrazine, i.e., metal complexes of tetra-2,3-(benzo[*f*]quinoxalino)porphyrazine, tetra-2,3-[5,6-(9,10-phenanthro)]porphyrazine, and the *tert*-butyl substituted analogs.

Results and discussion

Precursors

The dinitriles of heterocyclic *o*-dicarboxylic acids are the best precursors for the synthesis of AzaPcs. Unlike syntheses with other derivatives of *o*-dicarboxylic acids, the use of *o*-dinitriles affords pure AzaPcs in high yields. Several derivatives of 2,3-dicyanopyrazine (**1**) were prepared via the condensation of *o*-quinones with diaminomaleodinitrile (**2**) (16). Thus, 5,6-(9,10-phenanthro)-2,3-dicyanopyrazine (**5**) (16) was obtained by condensation of phenanthrenequinone and compound **2** with 80% yield.

In contrast to phenanthrenequinone, the condensation of 1,2-naphthoquinone (**3**) and compound **2** proceeds with low yield (10%), affording benzo[*f*]-quinoxaline-2,3-dinitrile (**4**) along with the oxidation products of **2** (Scheme 1). Varying reaction conditions, such as temperature, quantities of reagents, or the use of an inert atmosphere, did not improve the yield of the desired dinitrile.

Di-*tert*-butyl substituted (9,10-phenanthro)-2,3-dicyanopyrazines (**10***a–c*) were obtained from the reaction of **2** with the appropriate di-*tert*-butyl-9,10-phenanthrenequinones (**9***a–c*) (Scheme 2). The latter compounds were prepared using a modified oxidation procedure of the isomeric polyalkylated phenanthrenes (17). Chromatographic separation on silica gel using a mixture of chloroform–hexane as eluant gave three isomeric products. Based on ^{1}H NMR spectroscopy data, these isomers were assigned as 2,7- (**9***a*), 2,6- (**9***b*), and 3,6-di-*tert*-butyl-9,10-phenanthrenequinone (**9***c*), produced in a 1:2:1 ratio. This ratio is in accordance with substitution of H atoms in the phenanthrene molecule at the sterically accessible positions, assuming an equal reactivity for those positions. The main patterns of the ^{1}H NMR spectra of *o*-dinitriles **10***a–c* resemble those of the parent *o*-quinones, which allowed us to assign the isomers (Table 1).

Scheme 1.

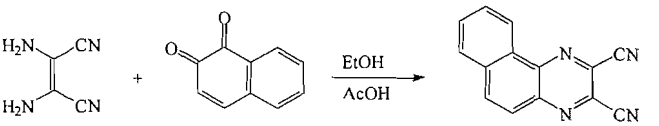

2 **3** **4**

Substituted Nc octaaza analogs: synthesis, purification, and spectral properties

The metal complexes of tetra-2,3-(benzo[*f*]quinoxalino)porphyrazine (**6***a,b*) and tetra-2,3-[5,6-(9,10-phenanthro)]porphyrazine (**7***b–g*) were obtained from the dinitriles **5** and **4** and the appropriate metal salts upon heating in the presence of urea and quinoline. We previously found these conditions optimal for the synthesis of Pc and Nc aza analogs (10, 14, 15). Metal-free tetra-2,3-[5,6-(9,10-phenanthro)]porphyrazine **7***a* was obtained by demetallation in HCl of the dilithium derivative, which in turn was prepared by treatment of compound **5** with metallic Li in amyl alcohol (Scheme 3) (18).

Compounds **6***a,b*, **7***a–g* were obtained as dark green solids. Unlike Pcs, they cannot be sublimated in high vacuum and they are only slightly soluble in organic solvents such as DMF, DMSO, and quinoline.

All Nc octaaza analogs were purified by extensive washing of the reaction mixtures with dilute HCl, hot water, and organic solvents followed by multiple reprecipitation from concentrated sulfuric acid, drying, and continuous extraction of impurities with hot methanol–acetone in a Soxlet apparatus until the intensity ratio between the absorption bands in the UV–VIS spectra remained constant. It is known that Pc hetero analogs are prone to form hydrates (14, 19). Accordingly, we dehydrated the analytical samples of complexes **6***a,b* and **7***a–g* by heating in acetic anhydride. The results of elemental analysis are compared to values calculated for anhydrous compounds (Table 2). The symmetry of the annelated AzaNc is evident from their structural drawings; complexes **7** retain the symmetry of tetra-(2,3-quinoxalino)porphyrazine whereas **6** may exist as a mixture of type isomers, one of which is shown in Scheme 3.

The metal complexes **6***a,b* and **7***b–g* are only slightly soluble in quinoline ($\sim 10^{-6}$ M) and at this concentration they are extensively aggregated. Nevertheless, we can draw some preliminary conclusions concerning the effects of aza substitution and angular annelation on the UV–VIS absorption maxima of Nc octaaza analogs. Thus, vanadyl tetra-4,5-(9,10-phenanthro)Pc (20) has an absorption maximum at 776 nm in quinoline (shoulder due to strong aggregation), whereas its octaaza analog **7***b* shows a peak at 700 nm. Comparison of the spectra of quinoline solutions of PcVO (21) vs. vanadyl tetra-2,3-pyrazinoporphyrazine (11) (λ_{max} 695 nm vs. 635 nm, shift of −60 nm), NcVO (22) vs. vanadyl tetra-2,3-quinoxalinoporphyrazine (11) (λ_{max} 819 nm vs. 725 nm (shift of −94 nm), and vanadyl anthracyanine (22) vs. vanadyl tetra-2,3-benzo[*g*]quinoxalinoporphyrazine (14) (λ_{max} 932 nm vs. 830 nm, shift of −102 nm) shows, in all cases, hypsochromic shifts of the Q-band of AzaPc and AzaNc as compared to their carbocyclic analogs, with the extent of the shift depending on the structure of the aromatic macrocycle.

The UV–VIS spectral properties of linearly annelated AzaPc have previously been reported (11–14). Thus, for octaaza Pcs each additional benzo ring causes a strong batho-

Table 1. ^{1}H NMR spectra of di-*tert*-butyl-9,10-phenanthrenequinones **9***a–c* and di-*tert*-butyl-(9,10-phenanthro)-2,3-dicyanopyrazines **10***a–c* in chloroform-*d*.

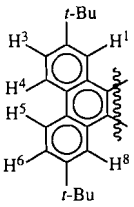

2,6-Di-*tert*-Bu isomers

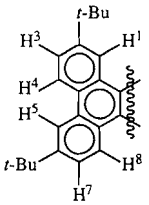

2,7-Di-*tert*-Bu isomers

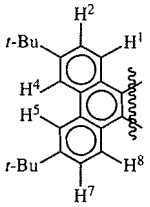

3,6-Di-*tert*-Bu isomers

	δ, ppm			δ, ppm			δ, ppm	
	9*a*	**10***a*		**9***b*	**10***b*		**9***c*	**10***c*
H1, H8	8.15d (2H) ($J_{1,3}$ 2 Hz)	9.13d (2H) ($J_{1,3}$ 2.2 Hz)	H1	8.14q (1H) ($J_{1,3}$ 2 Hz $J_{1,4}$ 0.4 Hz)	9.15d (1H) ($J_{1,3}$ 2.2 Hz)	H1, H8	8.10d (2H) ($J_{1,2}$ 9 Hz)	9.01d (2H) ($J_{1,2}$ 8.6 Hz)
			H8	8.07q (1H) ($J_{8,7}$ 9 Hz $J_{8,5}$ 0.4 Hz)	9.04d (1H) ($J_{8,7}$ 8.6 Hz)			
			H4	7.96d (1H) ($J_{4,3}$ 9 Hz)	8.58d(1H) ($J_{4,3}$ 8 Hz)			
H4, H5	7.9d (2H) ($J_{3,4}$ 9 Hz)	8.54 d (2H) ($J_{3,4}$ 8.6 Hz)	H5	7.98d (1H) ($J_{5,7}$ 2 Hz)	8.62s (1H)	H4, H5	8.00d (2H) ($J_{2,4}$ 2 Hz)	8.61d (2H) ($J_{2,4}$ 1.8 Hz)
H3, H6	7.7q (2H) ($J_{3,4}$ 9 Hz $J_{3,1}$ 2 Hz)	7.98q (2H) ($J_{3,4}$ 8.6 Hz $J_{3,1}$ 2.2 Hz)	H3	7.72q (1H) ($J_{3,4}$ 9 Hz $J_{3,1}$ 2 Hz)	8.20q (1H) ($J_{3,4}$ 8 Hz $J_{3,1}$ 2 Hz)	H2, H7	7.45d (2H) ($J_{2,1}$ 9 Hz $J_{2,4}$ 2 Hz)	7.85q (2H) ($J_{2,1}$ 0.08 Hz $J_{2,4}$ 0.02 Hz)
			H7	7.45q (1H) ($J_{7,8}$ 9 Hz $J_{7,5}$ 2 Hz)	8.02–8.09m (1H)			
CH_3 (*t*-Bu)	1.35s (18H)	1.52s (18H)	CH_3 (*t*-Bu)	1.38s (9H) 1.35s (9H)	1.524s (9H) 1.522s (9H)	CH_3 (*t*-Bu)	1.38s (18H)	1.55s (18H)

Scheme 2.

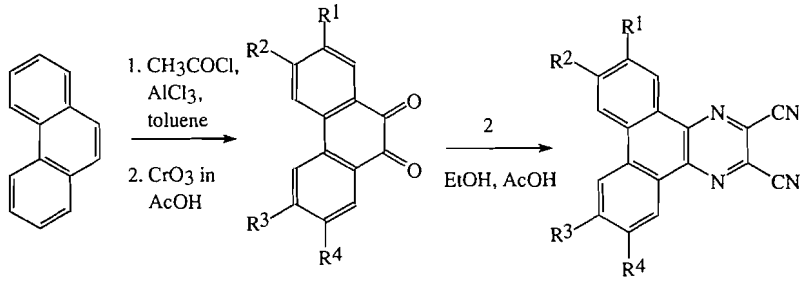

8 **9** **10**

9*a*, **10***a*: $R^1 = R^4 = t$-Bu, $R^2 = R^3 = H$

9*b*, **10***b*: $R^1 = R^3 = t$-Bu, $R^2 = R^4 = H$

9*c*, **10***c*: $R^2 = R^3 = t$-Bu, $R^1 = R^4 = H$

chromic shift of the Q-band (80–100 nm). This displacement of absorption maxima with sequential annelation, which does not change the symmetry of the molecule, is due to the extension of the aromatic system of the macrocycle. This correlation was first noticed in the series of Pc aza analogs; it was also observed in the sequence porphyrazine – Pc – 2,3–Nc (23) – anthracyanine (24) and recognized as a common feature of Pc related compounds.

How does the *angular* annelation affect the spectral properties of the aza analogs? The absorption maximum of the

Table 2. Tetra-2,3-(benzo[*f*]quinoxalino)porphyrazines **6***a,b* and tetra-2,3-[5,6-(9,10-phenanthro)porphyrazines **7***a–g*.

Compound	M	Starting salt	Yield, %	Molelcular formula	Found (calculated) % C	% H	% N	UV–VIS (quinoline), nm /relative intensity/
6*a*	VO	VCl_3	34	$C_{56}H_{24}N_{16}OV$	67.26 (68.09)	2.89 (2.45)	22.48 (22.69)	700, 460 /1.2:1/
6*b*	Cu	CuCl	42	$C_{56}H_{24}N_{16}Cu$	67.54 (68.32)	2.74 (2.46)	22.37 (22.76)	689, 460 /1.25:1/
7*a*	HH	—	22	$C_{72}H_{34}N_{16}$	76.83 (77.00)	3.02 (3.05)	19.90 (19.95)	Insoluble
7*b*	VO	VCl_3	71	$C_{72}H_{36}N_{16}OV$	72.10 (72.79)	2.66 (2.71)	18.80 (18.86)	706, 440 /1.2:1/
7*c*	GaOH	$Ga_2(SO_4)_3$	64	$C_{72}H_{33}GaN_{16}O$	71.48 (71.60)	2.68 (2.75)	18.52 (18.55)	694, 440 /1.34:1/
7*d*	AlOH	$AlCl_3$	42	$C_{72}H_{33}AlN_{16}O$	74.01 (74.22)	2.83 (2.85)	19.21 (19.23)	692, 438 /1.3:1/
7*e*	Cu	CuCl	57	$C_{72}H_{32}CuN_{16}$	72.85 (72.99)	2.65 (2.72)	18.88 (18.92)	684, 460 /1.4:1/
7*f*	Co	$CoCl_2$	42	$C_{72}H_{32}CoN_{16}$	73.04 (73.28)	2.58 (2.73)	18.87 (18.99)	680, 452 /1.2:1/
7*g*	Zn	$Zn(OAc)_2 \cdot 2H_2O$	55	$C_{72}H_{32}ZnN_{16}$	72.04 (72.88)	2.99 (2.77)	18.37 (18.89)	690, 440 /1.32:1/

Scheme 3.

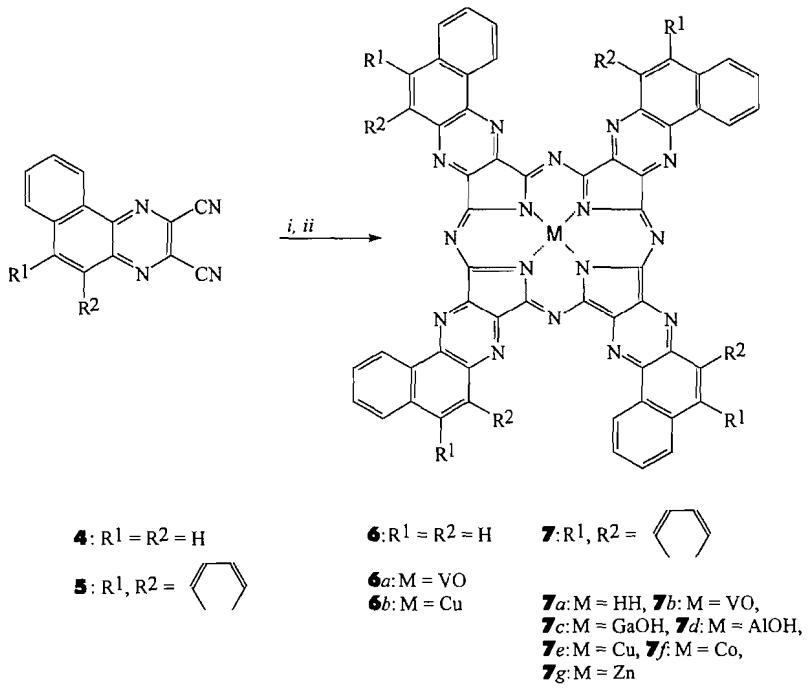

4: $R^1 = R^2 = H$

5: R^1, R^2 =

6: $R^1 = R^2 = H$

6*a*: M = VO
6*b*: M = Cu

7: R^1, R^2 =

7*a*: M = HH, **7***b*: M = VO,
7*c*: M = GaOH, **7***d*: M = AlOH,
7*e*: M = Cu, **7***f*: M = Co,
7*g*: M = Zn

i (for **7***a*): 1. $LiOC_5H_{11}$ in $C_5H_{11}OH$, 2. HCl;
ii: MX, urea, quinoline

vanadyl tetra-2,3-(benzo[*f*]quinoxalino)porphyrazine (**6***a*) is located at 700 nm, whereas the vanadyl tetra-2,3-[5,6-(9,10-phenanthro)]porphyrazine (**7***b*) shows a maximum at 706 nm, and vanadyl tetra-2,3-quinoxalinoporphyrazine at 725 nm (all spectra in quinoline). Therefore, the first angularly annelated benzo ring causes a *hypsochromic* shift of the Q-band, and the second annelated benzo ring hardly affects the absorption maximum. Furthermore, aggregation of Pc molecules in solutions affects the position of the long-wave absorption maxima and in general increases with the size of the molecule (25). Thus, to perform an accurate study of the spectral properties of the angularly annelated Nc aza analogs, we required a

Scheme 4.

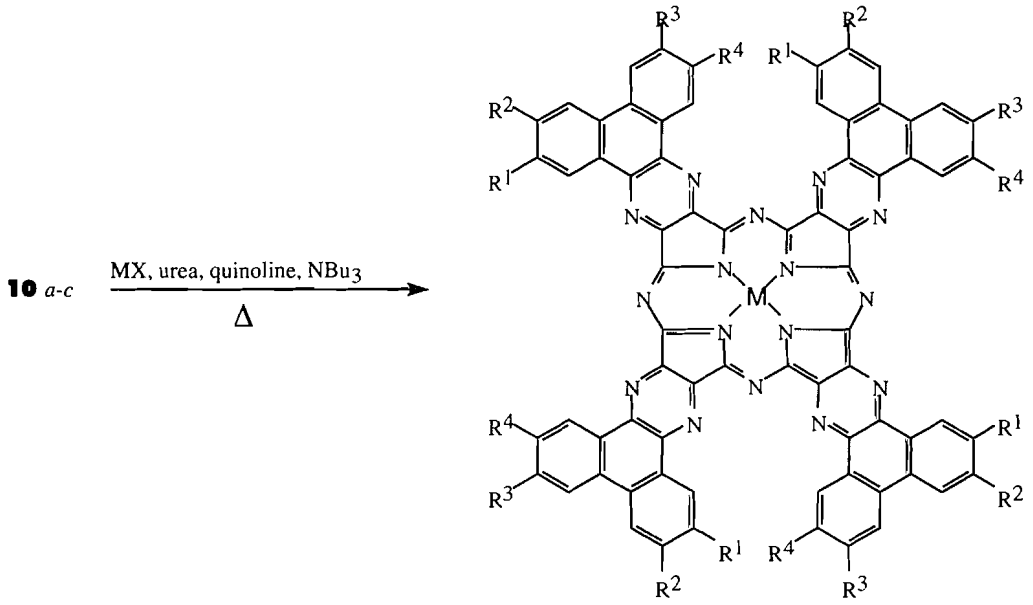

11*a*: M = Cu, $R^1 = R^4 = t$-Bu, $R^2 = R^3 = H$
11*b*: M = Cu, $R^1 = R^3 = t$-Bu, $R^2 = R^4 = H$
11*c*: M = Cu, $R^2 = R^3 = t$-Bu, $R^1 = R^4 = H$
11*d*: M =AlCl, $R^1 = R^3 = t$-Bu, $R^2 = R^4 = H$
11*e*: M = Zn, $R^1 = R^3 = t$-Bu, $R^2 = R^4 = H$
11*f*: M = VO, $R^1 = R^3 = t$-Bu, $R^2 = R^4 = H$

series of more soluble derivatives that were less prone to aggregation.

Alkyl substitution is known to increase solubility and several synthetic routes for the preparation of alkyl-substituted AzaPcs have been reported (12, 13, 15, 26, 27). Based on prior experience, we selected *tert*-butyl substitution onto the benzene rings of the macrocycle and synthesized the isomeric tetra-2,3-[5,6-(di-*tert*-butyl-9,10-phenanthro)pyrazino]porphyrazines (**11***a–f*) by complexation of the corresponding dinitriles **10***a–c* with the metal salts in the presence of urea (Scheme 4). Among all solvents (neutral and basic) tested for this reaction, a 1:1 (v/v) mixture of quinoline and tri(*n*-butyl)amine was found to be the most suitable. The isomeric precursors differ in reactivity: under comparable conditions the 2,6-substituted dinitrile is the most reactive, whereas the 3,6-substituted isomer is the least reactive. Compounds **11***a–f* were purified by chromatography on silica gel. Chloroaluminium complex **11***d* was eluted with acetone, whereas the hydroxyaluminium derivative, obtained by reprecipitation of **11***d* from concentrated H_2SO_4, remained absorbed to the silica and was impossible to eluate even with pyridine. Complexes **11***a–f* were characterized by MS, UV–VIS spectral data, and combustion analysis (Table 3). The symmetry of the isomeric octa(*tert*-butyl) substituted AzaNcs **11***b* and **11***c* does not change as compared to their unsubstituted analog **7***e*, whereas compounds **11***a,d–f* represent a mixture of type isomers. The UV–VIS spectrum of the compound **11***d* (in chloroform) is presented in Fig. 1. The intense peak at 690 nm is indicative of substantial monomerization, confirming the effect of *tert*-butyl substitution on the solubility of the dye. The Q-band is narrow with resolved vibrational structure, whereas the position of the main absorption maximum remains the same as observed for the complex **7***d* (in quinoline). This spectrum shows that double angular annelation of octaaza Ncs causes a hypsochromic shift of the Q-band of about 25 nm. It should be noted that low solubility and strong aggregation of the unsubstituted carbocyclic analogs did not permit measurement of their absorption maxima (21), whereas substituted or any other soluble derivatives of tetra(9,10-phenanthro)Pc are unknown.

Finally we prepared a series of angularly annelated derivatives of the tetra-2,3-quinoxalinoporphyrazine, both unsubstituted and featuring the *tert*-butyl moieties on the benzo rings of the macrocycle. The spectral properties of these novel compounds are described and the influence of octaaza substitution and angular annelation on the position of the long-wave absorption maxima is presented.

We are currently using these data to develop Pc-related structures with "tuned" absorption maxima and selected solubility. Such compounds, containing at least one benzo[*f*]-quinoxaline or 9,10-phenanthropyrazine ring per molecule, could find application as photosensitizers in medicine or as agents for the preparation of Langmuir–Blodgett films.

Experimental

Materials and methods

FAB-MS were obtained on an LG Autospec Q mass spectrometer from the Department of Chemistry, Université de Montréal. High-resolution Direct Inlet Probe (DIP) mass spectra (HR-MS) were obtained on a V9 Micro-mass model ZAB-1F apparatus at 70 eV ionization voltage. 1H NMR spectra were taken on a Bruker AC-300 (300 MHz) spectrometer. UV–VIS

Table 3. Metal complexes of isomeric tetra-5,6-[(di-*tert*-butyl-9,10-phenanthro)-pyrazino]porphyrazines.

Compound	M	Starting salt	Yield, %	Molelcular formula	Found (calculated) % C	% H	% N	FAB-MS *m/e*	λ_{max}, nm (log ε) (in chloroform)
11*a*	Cu	CuCl	44	$C_{104}H_{96}CuN_{16}$	76.44 (76.47)	5.88 (5.92)	13.73 (13.72)	1633 (18%, M^+), 1618 (100%, $M^+ - CH_3$), 1603 (100%, $M^+ - 2CH_3$)	680 (4.88), 628 (4.4), 380 (4.58)
11*b*	Cu	CuCl	52	$C_{104}H_{96}CuN_{16}$	76.40 (76.47)	5.81 (5.92)	13.65 (13.72)		680 (4.9), 628 (4.34), 378 (4.64)
11*c*	Cu	CuCl	28	$C_{104}H_{96}CuN_{16}$	76.38 (76.47)	5.90 (5.92)	13.68 (13.72)		680 (4.91), 628 (4.3), 380 (4.6)
11*d*	AlCl	$AlCl_3$	54	$C_{104}H_{96}AlClN_{16}$	76.44 (76.51)	5.95 (5.93)	13.13 (13.73)	1632 (30%, M^+), 1617 (100%, $M^+ - CH_3$)	690 (4.95), 630 (4.4), 389 (4.7)
11*e*	Zn	$Zn(OAc)_2 \cdot 2H_2O$	57	$C_{104}H_{96}ZnN_{16}$	76.37 (76.46)	5.78 (5.91)	13.63 (13.71)	1633 (23%, M^+, ^{63}Zn), 1618 (100%, $M^+ - CH_3$)	692 (5.01), 630 (4.44), 387 (4.6)
11*f*	VO	VCl_3	67	$C_{104}H_{96}N_{16}OV$	74.99 (76.30)	6.44 (5.91)	12.95 (13.70)	1636 (15%, M^+), 1621 (100%, $M^+ - CH_3$)	704 (5.15), 642 (4.42), 354 (4.5)

Fig. 1. UV–VIS spectrum of **11***d* in chloroform.

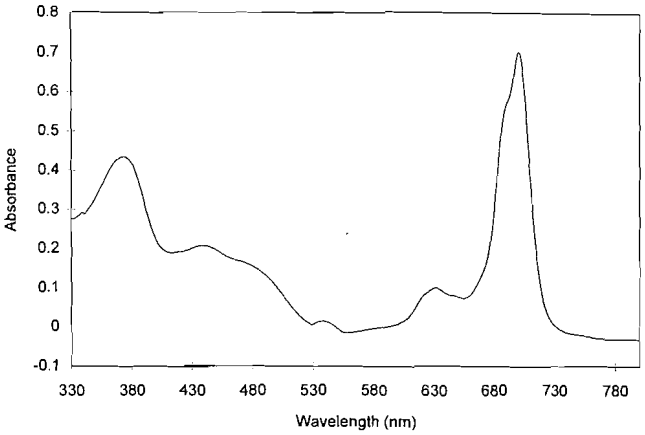

spectra were recorded with a Hitachi U-2000 spectrophotometer. Melting points were determined on a Fisher–Johns apparatus and are uncorrected. Preparative chromatography was conducted on 70–230 mesh silica gel (Aldrich, U.S.A.). TLC was performed on 0.25 mm thick Polygram SIL G/UV^{254} plates (Macherey–Nagel, Germany).

Diaminomaleodinitrile, 1,2-naphthoquinone, and phenanthrene were obtained from a commercial source (Aldrich). All solvents were HPLC grade and were used without further purification unless otherwise stated.

5,6-Phenanthro-2,3-dicyanopyrazine (**5**) was prepared by a published method (16).

*2,7-Di-*tert*-butyl-9,10-phenanthrenequinone (**9**a), 2,6-di-*tert*-butyl-9,10-phenanthrenequinone (**9**b), and 3,6-di-*tert*-butyl-9,10-phenanthrenequinone (**9**c) (Scheme 2)*

These compounds were prepared using a modified procedure of Petrova et al. (17). *tert*-Butyl chloride (25 mL) was added gradually to the stirred mixture of phenanthrene (10 g, 0.056 M) and anhydrous $AlCl_3$ (0.4 g) in dry CCl_4 (40 mL). After evolution of HCl had ceased, the dark blue mixture was heated to 60°C and maintained at this temperature for 5 h. Then 3 mL of water was added and the solvent was evaporated. The residue (brown slurry) was dissolved in 60 mL of glacial acetic acid. A solution of 16.8 g CrO_3 in 50 mL of 50% aqueous acetic acid was added gradually and the mixture was heated to 110°C, stirred at this temperature for 1 h, cooled to room temperature, and poured into 0.5 L of cold water. Chloroform (250 mL) was added to extract the precipitated orange slurry, phases were separated, and the aqueous phase was extracted repeatedly with chloroform. All extracts were combined, dried with anhydrous Na_2SO_4, chloroform was evaporated, and the residue was chromatographed on silica gel with chloroform–hexane (3:2) to yield **9***a* (2.06 g, 11.5% based on phenanthrene), **9***b* (4.3 g, 24%), and **9***c* (2.5 g, 14%).

2,3-Dicyano-benzo[f]*quinoxaline (**4**) (Scheme 1), 5,6-[2,7-di-*tert*-butyl-(9,10-phenanthro)]-2,3-dicyanopyrazine (**10***a*), 5,6-[2,6-di-*tert*-butyl-(9,10-phenanthro)]-2,3-dicyanopyrazine (**10**b), and 5,6-[3,6-di-*tert*-butyl-(9,10-phenanthro)]-2,3-dicyanopyrazine (**10**c) (Table 1, Scheme 2)*

These compounds were prepared by condensation of **2** with the appropriate *o*-quinones **3**, **9***a*, **9***b*, or **9***c* (16).

Compound **4** was purified on silica gel using CH_2Cl_2 as eluant (R_f 0.6). Slightly yellow crystals, 10%, mp 207°C. ^{1}H NMR, δ, ppm (in $CDCl_3$): 9.25–9.22 (m, 1H), 8.33 (d, 1H, J = 9.2 Hz), 8.08–7.92 (m, 4H). HR-MS *m/e*: calcd. 230.0592; found: 230.0602. Anal. calcd. for $C_{14}H_6N_4$: C 73.04, H 2.63, N 24.34; found: C 73.02, H 2.61, N 24.02.

Compounds **10***a*, **10***b*, and **10***c* were obtained as yellow powders after recrystallization from ethanol.

10*a*: Yield 62%, decomp. >340°C. HR-MS *m/e*: calcd. 392.2001; found: 392.1997. DIP-MS *m/e*: 392 (M^+, 31), 377 ($M^+ - CH_3$, 100). Anal. calcd. for $C_{26}H_{24}N_4$: C 79.56, H 6.16, N 14.27; found: C 79.67, H 6.16. N 14.20.

10*b*: Yield 70%, decomp. >300°C. HR-MS *m/e*: calcd. 392.2001; found: 392.2004. DIP-MS *m/e*: 392 (M^+, 20), 377 ($M^+ - CH_3$, 100). Anal. calcd. for $C_{26}H_{24}N_4$: C 79.56, H 6.16, N 14.27; found: C 79.51, H 6.08, N 14.07.

10*c*: Yield 78%, mp 275–276°C. HR-MS *m/e*: calcd: 392.2001; found: 392.1994. DIP-MS *m/e*: 392 (M^+, 30), 377 ($M^+ - CH_3$, 100) Anal. calcd. for $C_{26}H_{24}N_4$: C 79.56, H 6.16, N 14.27; found: C 79.24, H 6.20, N 14.09.

Metal complexes of tetra-2,3-(benzo[f]*quinoxalino)-porphyrazine* ***6***a *and* ***6***b *(Scheme 3, Table 2).*

A mixture of 0.230 g (1 mmol) of the dinitrile **4** and 1 mmol of salt (VCl_3 or CuCl) was heated at 250°C for 2 h. The dark green cake obtained was finely ground, washed with dilute HCl, hot water, methanol, and acetone, air dried, then reprecipitated from H_2SO_4 until the UV–VIS spectrum remained constant. The analytical samples were further extracted (Soxlet) with acetone for 24–72 h. Finally, the dark green solid remaining in the Soxlet thimble was dehydrated by refluxing with acetic anhydride for 2 h and drying at 100°C, 1 Torr (133.3 Pa) for 4 h.

*Tetra-2,3-[5,6-(9,10-phenanthro)pyrazino]porphyrazine (***7***a) (Scheme 3, Table 2)*

Metallic lithium (0.01 g, 1.43 mmol) was dissolved in freshly distilled isoamyl alcohol (1 mL) at 60°C, and the solution was allowed to cool to room temperature. The dinitrile **5** (0.14 g, 0.5 mmol) was added in small portions and the temperature of the stirred mixture was brought to 110°C over a 20–30 min period. Heating was discontinued after the mixture turned an intense dark green colour. The resulting solution was allowed to cool to room temperature, then diluted with 15 mL of ethanol. The precipitate was collected by centrifugation, then washed with 1 N HCl, water, ethanol, and acetone. An analytical sample of compound **7***a* was prepared as described for complexes **6***a,b*. Compound **7***a* is insoluble in organic solvents, including quinoline.

*Metal complexes of tetra-2,3-[5,6-(9,10-phenanthro)-pyrazino]-porphyrazine (***7***b–g) (Scheme 3, Table 2). General procedure*

A mixture of dinitrile **5**, metal salt (in molar ratio 1:1), urea (500 mg per 100 mg of dinitrile), and quinoline (1 mL per 100 mg of dinitrile) was heated to 300–320°C for 3–4 h. The solvent was removed by washing the mixture with methanol and acetone on a glass filter. Further purification was performed as described for compounds **6***a,b*.

*Metal complexes of isomeric tetra-2,3-[5,6-(di-*tert*-butyl-9,10–phenanthro)pyrazino]porphyrazines (***11***a–f) (Scheme 4, Table 3). General procedure*

A mixture of the dinitrile **10***a–c*, metal salt (in molar ratio 1:1), urea (500 mg per 100 mg of dinitrile), quinoline, and tri(*n*-butyl)amine (0.5 mL each per 100 mg of nitrile) was heated to 300°C for 1–2 h, then allowed to cool to room temperature and extracted with chloroform. The combined extracts were dried and concentrated, the complexes were precipitated upon addition of hexane, filtered, redissolved in chloroform, and chromatographed on silica gel (eluant: chloroform for compounds **11***a–c*, **11***e*, **11***f*, acetone for **11***d*). Precipitation from chloroform–hexane mixtures afforded compounds **11***a–f* as dark olive-green solids.

Acknowledgements

Financial support by the Medical Research Council of Canada and the "Ministère de l'Enseignement Supérieur et de la Science du Gouvernement du Québec (Programme d'Actions Structurantes)" is gratefully acknowledged.

References

1. A.A. Tanaka, C. Fierro, D.A. Sherson, and E. Yaeger. Mater. Chem. Phys. **22**, 431 (1989).
2. K.A. Radyushkina, M.V. Merenkova, M.R. Tarasevich, M.G. Galpern, S.V. Kudrevich, and I.G. Novozhilova. Elektrokhimiya, **28**, 1032 (1992).
3. M. Yamana, N. Kashiwazaki, M. Yamamoto, and T. Nakano. Jpn. J. Appl. Phys. Part 2, **26**, L1113 (1987).
4. D. Schlettwein, D. Woehrle, and N.I. Jaeger. J. Electrochem. Soc. **135**, 2882 (1989).
5. K. Kasuga, K. Nishikori, T. Mihara, M. Handa, K. Sogabe, and K. Isa. Inorg. Chim. Acta, **174**, 153 (1990).
6. H. Hagiwara, S. Tai, N. Hayashi, M. Katayose, T. Akimoto, and K. Vejima. Jpn. Kokai Tokkyo Koho JP 03 13 384 [91 13 384] (1991).
7. T. Sato and S. Miyazaki. Jpn. Kokai Tokkyo Koho JP 03 65 385 [91 65 385] (1991).
8. S. Tai, N. Hayashi, K. Kamijima, M. Katayose, T. Akimoto, and H. Hagiwara. Eur. Pat. Appl. EP 344 891 (1989).
9. K. Teuchner, A. Pfarrherr, H. Stiel, W. Freyer, and D. Leupold. Photochem. Photobiol. **57**, 465 (1993).
10. S. V. Kudrevich, M. G. Galpern, and J. E. van Lier. Synthesis, 779 (1994).
11. M.G. Galpern and E.A. Luk'yanets. Zh. Obsch. Khim. **39**, 2536 (1969).
12. E.G. Galpern, E.A. Luk'yanets, and M.G. Galpern. Izv. Akad. Nauk SSSR, Ser. Khim. 1976 (1973).
13. M.G. Galpern and E.A. Luk'yanets. Khim. Geterotsikl. Soedin. 858 (1972).
14. M.G. Galpern and E.A. Luk'yanets. Zh. Obsch. Khim. **41**, 2549 (1971).
15. M.G. Galpern, S.V. Kudrevich, and I.G. Novozhilova. Khim. Geterotsikl. Soedin. 58 (1992).
16. H.W. Rothkopff, D. Woehrle, R. Muller, and G. Koßmell. Chem. Ber. **108**, 875 (1975).
17. E.S. Petrova, S.P. Ivashchenko, D.B. Askerov, and E.A. Luk'yanets, Manuscript deposited at VNIITEKIM (Moscow), 17.12.87, N 1374–XP87. Russian Referative Journal of Chemistry, 7Zh 195 (1988).
18. P.A. Barrett, D.A. Frye, and R.P. Linstead. J. Chem. Soc. 1157 (1938).
19. R.P. Linstead, E.G. Noble, and J.M. Wright. J. Chem. Soc. 911 (1937).
20. S.A. Mikhalenko, L.A. Yagodina, and E.A. Luk'yanets. Zh. Obsch. Khim. **46**, 1598 (1976).
21. W. Freyer and L.Q. Minh. J. Prakt. Chem. **329**, 365 (1987).
22. W. Freyer. Z. Chem. **26**, 217 (1986).
23. S.A. Mikhalenko and E.A. Luk'yanets. Zh. Obsch. Khim. **39**, 2554 (1969).

24. V.N. Kopranenkov and E.A. Luk'yanets. Zh. Obsch. Khim. **41**, 2341 (1971).
25. B.D. Berezin. *In* Coordination compounds of porphyrins and phthalocyanines. John Wiley and Sons, New York. 1981. p. 230.
26. K. Ohta, T. Watanabe, T. Fujimoto, and I. Yamamoto. J. Chem. Soc. Chem. Commun. 1611 (1989).
27. S. Tokita, M. Kojima, N. Kai, K. Kurogi, H. Nishi, H. Tomoda, S. Saito, and S. Shiraishi. Nippon Kagaku Kaishi, **2**, 219 (1990).

The reactions of $O(^3P)$ with some carboxylic acids and esters

P. Caravan, Suzanne M. Budge, and John M. Roscoe

Abstract: The reactions of $O(^3P)$ with formic acid, acetic acid, methyl acetate, ethyl acetate, *n*-propyl acetate, and isopropyl acetate have been studied kinetically as a function of temperature. The rate constants were measured in a discharge-flow system under pseudo-first-order conditions with a large excess of the organic reagent. No reaction could be found between $O(^3P)$ and either formic acid or acetic acid in the temperature range 300–420 K. The acetate esters, on the other hand, reacted with $O(^3P)$ at readily measurable rates over the same temperature range. The temperature dependence of the rate constants for these reactions in the temperature range 300–580 K is given, in the units L mol^{-1} s^{-1}, by:

O + methyl acetate: $\ln k = (19.46 \pm 0.24) - (1740 \pm 170)/T$
O + ethyl acetate: $\ln k = (20.30 \pm 0.35) - (1750 \pm 310)/T$
O + *n*-propyl acetate: $\ln k = (21.80 \pm 0.41) - (1920 \pm 400)/T$
O + isopropyl acetate: $\ln k = (19.91 \pm 0.36) - (1430 \pm 250)/T$

The lack of measurable reaction with the carboxylic acids, the systematic increase in the preexponential factor with increasing size of the ester group, and the observation of a significant yield of acetic acid among the products of the reactions with the esters indicate that attack by $O(^3P)$ is predominantly at the ester function. Linear free energy correlations are used to compare the results for the esters with those for reactions of $O(^3P)$ with other organic compounds containing oxygen.

Key words: kinetics, mechanism, reactions of $O(^3P)$ with esters.

Résumé : On a étudié la cinétique, en fonction de la température, des réactions du $O(^3P)$ avec les acides formique et acétique, les acétates de méthyle, d'éthyle, de *n*-propyle et d'isopropyle. On a mesuré les constantes de vitesse dans un système d'écoulement à décharge sous des conditions de pseudo premier ordre, en présence d'un grand excès du réactif organique. On n'a pas pu détecter de réaction entre le $O(^3P)$ et les acides formique et acétique pour la plage de température allant de 300 à 420 K. Par ailleurs, pour les mêmes températures, les esters acétiques réagissent avec le $O(^3P)$ à des vitesses qui peuvent être mesurées. La relation entre les constantes de vitesse et la température pour ces réactions dans la plage de température allant de 300 à 580 K est donnée par les équations suivantes, en unités L mol^{-1} s^{-1} :

O + acétate de méthyle : $\ln k = (19{,}46 \pm 0{,}24) - (1740 \pm 170)/T$
O + acétate d'éthyle : $\ln k = (20{,}30 \pm 0{,}35) - (1750 \pm 310)/T$
O + acétate de *n*-propyle : $\ln k = (21{,}80 \pm 0{,}41) - (1920 \pm 400)/T$
O + acétate d'isopropyle : $\ln k = (19{,}91 \pm 0{,}36) - (1430 \pm 250)/T$

Le fait qu'il ne se produise pas de réactions à des vitesses mesurables avec les acides carboxyliques, qu'il y a une augmentation systématique dans le facteur préexponentiel avec l'augmentation du groupe ester et que l'on observe la formation d'acide acétique avec un rendement significatif parmi les produits des réactions avec les esters indique que l'attaque par $O(^3P)$ se fait surtout au niveau de la fonction ester. On a utilisé des corrélations linéaires d'énergie libre pour comparer les résultats pour les esters avec ceux pour des réactions de $O(^3P)$ avec d'autres composés organiques contenant de l'oxygène.

Mots clés : cinétique, mécanisme, réactions du $O(^3P)$ avec les esters.

Introduction

In earlier work from this laboratory, we compared the reactivity of a series of alcohols and a series of ketones with $O(^3P)$ (1). While the activation energies for the reactions of $O(^3P)$ with the ketones were comparable to those for the reactions with the alcohols and showed a similar trend with increasing chain length, the preexponential factors for the reactions with the ketones were some 5–10 times smaller than those for the reactions with the alcohols. The Taft reaction parameter was also significantly more negative for the reactions of $O(^3P)$ with the ketones than for the reactions with the alcohols. We report here the results of kinetic experiments on the reactions of $O(^3P)$ with formic acid, acetic acid, and a series of acetate esters. This extends the measurements made with the ketones to further examine the role of substituents, and the effect of accumulation of polarizable atoms such as oxygen, on the reactivity of organic compounds toward $O(^3P)$.

Examination of the literature failed to reveal any previous work on the reactions of $O(^3P)$ with carboxylic acids. How-

Received September 27, 1995.

P. Caravan, S.M. Budge, and J.M. Roscoe.[1] Department of Chemistry, Acadia University, Wolfville, N.S., B0P 1X0

[1] Author to whom correspondence may be addressed. Telephone: (902) 542-2200.

ever, the reactions of some acetate and formate esters have been studied from approximately 300 to 420 K by measuring the rate of loss of the organic reagent under conditions of excess $O(^3P)$ in a flow system (2). In that work, the Arrhenius preexponential factors were approximately an order of magnitude larger than those for the reactions with ketones and the activation energies were significantly larger than those for the reactions of $O(^3P)$ with either ketones or alcohols (e.g., refs. 1, 3–8). We report here experiments made under conditions of large excess of the esters that complement the earlier work by employing conditions in which secondary reactions of $O(^3P)$ are less likely to be important. Our measurements also cover a somewhat larger temperature range than the earlier work and the series of acetate esters has been expanded to include isopropyl acetate.

Experimental

The reactions were studied in a conventional discharge-flow system operated at a pressure of approximately 1 Torr (133.3 Pa) (1, 3, 5, 7). Gas flow velocities in the cylindrical reaction vessel ranged from approximately 700 to 1100 cm s^{-1}. The excess reactant entered the reaction vessel through a moveable inlet and the $O(^3P)$ concentration was monitored at a fixed point at the downstream end of the reaction vessel as the inlet was moved along the axis of the reaction vessel. The reaction vessel was heated electrically and the temperature was measured with a calibrated iron–constantan thermocouple located in the tip of the moveable reactant inlet. This made it possible to also determine the uniformity of the temperature within the heated part of the reaction vessel. At the highest temperatures used, the variation in temperature was no more than ±2°C over the part of the reaction vessel used for the kinetic measurements and this variation decreased at lower temperatures.

Atomic oxygen was prepared by titrating $N(^4S)$ atoms, formed in a microwave-powered discharge in N_2, with NO. This avoids possible interference from O_2, which has been found to alter the secondary reactions in some reactions of $O(^3P)$ (3). The concentration of $O(^3P)$ was controlled and kept small by allowing only a very small part of the total N_2 flow to pass through the discharge. The rest of the N_2 mixed with the discharge products before entering the reaction vessel. This arrangement made it possible to achieve as much as a 1000-fold excess of the organic reagent over $O(^3P)$, thereby minimizing the effects of secondary reactions of atomic oxygen with intermediates such as OH radicals. The concentration of $O(^3P)$ was monitored by observing the NO_2 chemiluminescence produced by adding a small (a few percent) excess of NO beyond the titration end point. The initial concentration of $O(^3P)$ was determined from the flow rate of NO at the titration end point in the absence of the organic reagent. The rate constants were independent of the excess amount of NO used.

The flow rate of N_2 was measured with a calibrated capillary flowmeter. Flow rates of the other stable species were measured by determining the rate of increase of pressure in an initially evacuated vessel of known volume. Flow rates of formic acid and acetic acid were calibrated periodically by trapping the material, at a flow rate measured as above, for a known period of time at the temperature of liquid nitrogen. The collected material was then titrated with standard NaOH solution.

Formic acid (MacArthur, 88% min.) was analysed by gas chromatography and found to contain no detectable organic impurities. The sample contained 92% formic acid and 8% water, which is necessary for stability. The formic acid was used without drying since it has been found that dry formic acid gives erratic kinetic results (9). Acetic acid (BDH 99.7%), acetone (Anachemia, toxigraphic, distilled in glass), methyl acetate (Aldrich, anhyd., 99%+), ethyl acetate (Aldrich, anhyd., 99.8%), *n*-propyl acetate (Aldrich, 99%), and isopropyl acetate (Aldrich, 99%) were analysed by gas chromatography and contained no detectable organic impurities. All these reagents were thoroughly degassed before use. A few kinetic measurements were made periodically on the reaction of $O(^3P)$ with acetone, which has been well characterized under conditions similar to those used in this work (1, 4), to verify that the entire apparatus was functioning reliably. Gas chromatographic analysis was done on an 8 ft × 1/4 in. column packed with Porapak Q. Both flame ionization and thermal conductivity detectors were used, the latter being required for water analyses. Product analysis was done by collecting the condensable material leaving the reaction vessel in two traps cooled with liquid nitrogen. The samples were then removed for chromatographic analysis. The organic reactant was always present in sufficient excess that it could be used as an internal standard in these analyses. The traps were located sufficiently far from the end of the reaction vessel to ensure that all reaction intermediates were consumed before the sample was collected for analysis.

The pseudo-first-order loss of $O(^3P)$ was analysed by the Guggenheim method (10). The advantages of this approach were described in a recent publication (11). Briefly, the data are divided into two sets with pairs of points in the sets separated by a constant time interval Δt. If the signals due to $O(^3P)$ in the two sets are S_1 and S_2 and the signal decays as a single exponential with a constant background, it may be shown that

$$\ln(S_1 - S_2) = -k_{obs}t_1 + \ln[S_0(1 - \exp(-k_{obs}\Delta t))]$$

where t_1 is the time corresponding to signal S_1. Since the signal at "zero time", S_0, and Δt are constants, a plot of $\ln(S_1 - S_2)$ against t_1 will be linear with slope $-k_{obs}$, the "observed" overall pseudo-first-order rate constant. Typical Guggenheim plots are found in Fig. 1. These plots typically had correlation coefficients of 0.99 or better and the pseudo-first-order rate constants calculated from them had standard deviations of less than ±5%.

It is often the case that the first-order heterogeneous loss of atomic species upstream from the tip of the moveable inlet differs appreciably from that downstream from the inlet tip where the surface/volume ratio is smaller and the adsorption of reactants and products can also alter the behaviour of the surface. We have adopted the practice of calculating second-order rate constants by obtaining the slope of a plot of the pseudo-first-order rate constants against the concentration of the excess reactant (1, 7, 11). Such plots have the form

$$k_{obs} = k_0 + k_R[\text{Reactant}]$$

where k_{obs} is the pseudo-first-order rate constant, k_R is the second-order rate constant, and k_0 is the intercept, which represents the difference in first-order atom loss, in the absence of

Fig. 1. Representative Guggenheim analysis plots for first-order rate constants; (○) methyl acetate, 584 K, [O] = 1.05×10^{-8} mol L^{-1}, [CH_3OAc] = 4.83×10^{-6} mol L^{-1}; (●) ethyl acetate, 488 K, [O] = 1.26×10^{-8} mol L^{-1}, [C_2H_5OAc] = 4.34×10^{-6} mol L^{-1}; (□) isopropyl acetate, 510 K, [O] = 1.38×10^{-8} mol L^{-1}, [C_3H_7OAc] = 9.36×10^{-7} mol L^{-1}; (■) *n*-propyl acetate, 335 K, [O] = 1.53×10^{-8} mol L^{-1}, [C_3H_7OAc] = 3.22×10^{-6} mol L^{-1}.

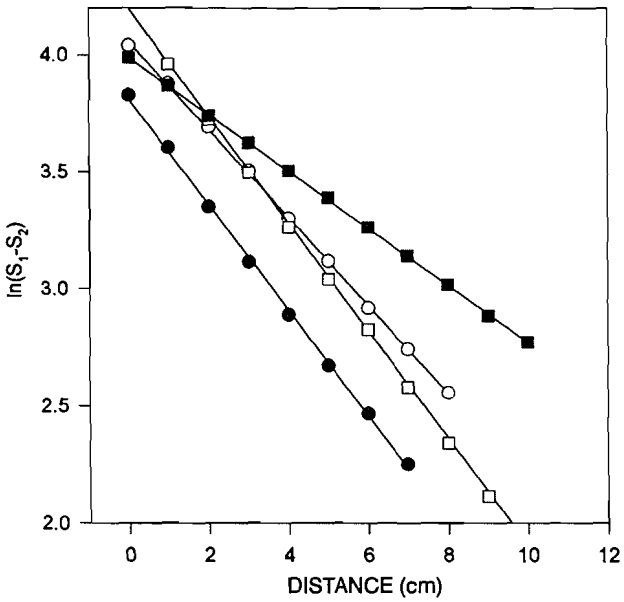

Fig. 2. Representative concentration dependence of pseudo-first-order rate constants; (○) methyl acetate, 506 K; (Δ) ethyl acetate, 488 K; (□) isopropyl acetate, 350 K; (▽) *n*-propyl acetate, 430 K.

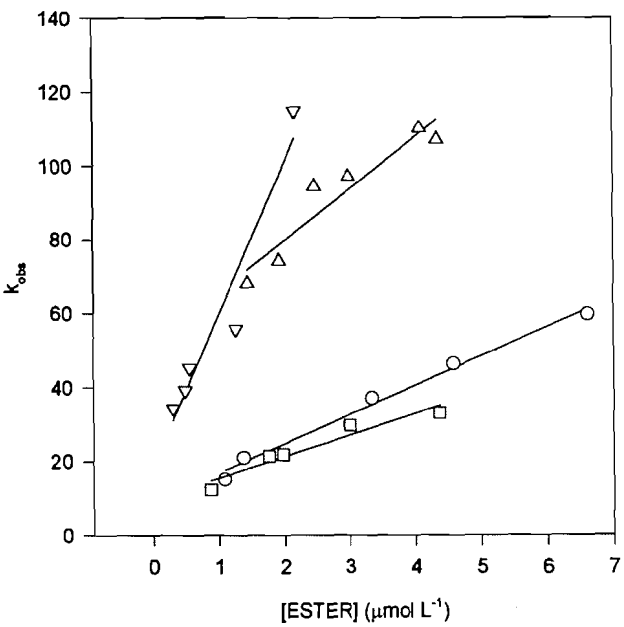

reactant, upstream and downstream from the tip of the moveable reactant inlet. Interpretation of the value of k_0 is difficult at best since it can be either positive or negative depending on the relative effectiveness of heterogeneous atom loss upstream and downstream from the tip of the moveable inlet. Some typical plots are found in Fig. 2. The quality of these plots was not as good as that of the Guggenheim plots, due in part to the smaller number of data points and to the larger number of variable parameters from one run to another. However, the correlation coefficients were better than 0.90 and in many cases better than 0.95.

Results and discussion

Reactions of $O(^3P)$ with carboxylic acids

Thirty kinetic experiments with formic acid and eleven with acetic acid at temperatures from 300 K to 420 K did not result in measurable consumption of $O(^3P)$. It has been found that (9, 12, 13), in the reactions of OH with formic acid and acetic acid, the monomeric form of the acid is much more reactive than the dimer. The possibility that the apparent lack of reactivity might be due to dimerization of the acid was tested by calculating the monomer/dimer concentration ratios for our experiments using the equilibrium data reported by Büttner and Maurer (14). In the experiments with formic acid, the monomer/dimer ratio ranged from 40 to 5.8×10^4 while in the experiments with acetic acid the ratio ranged from 20 to 1.3×10^4. It is clear that, in all our experiments, by far the dominant form of the carboxylic acid was the monomer.

Experiments to measure the rate constant for the reaction of $O(^3P)$ with acetone were used periodically to verify the correct functioning of the apparatus, as described in the experimental section. The reaction conditions used in these experiments were the same as those used to examine the behaviour of the carboxylic acids. In all cases, the results with acetone were in excellent agreement with those in the literature (1, 4). It is clear from these results that the lack of reaction of formic acid and acetic acid with $O(^3P)$ in our experiments was a real effect and not an experimental artifact.

The rate constants for reactions of $O(^3P)$ with organic compounds have been found to correlate well with those for the reactions of OH radicals with the same compounds (15, 16). Figure 3 shows such a correlation for the reactions of $O(^3P)$ and OH with a selection of aldehydes, ketones, ethers, and alcohols (9, 12, 13). The intersections of the vertical lines with the regression line indicate the rate constants to be expected for the reactions of $O(^3P)$ with formic acid and acetic acid if the mechanisms of their reactions were consistent with the rest of the correlation. On this basis, the rate constant at room temperature for the reaction of $O(^3P)$ with formic acid would be estimated to be approximately 1×10^6 L mol^{-1} s^{-1} while the rate constant for the reaction of $O(^3P)$ with acetic acid under the same conditions is estimated to be 2×10^6 L mol^{-1} s^{-1}. The lower limit of reliable measurement of second-order rate constants in our apparatus is approximately 1×10^5 L mol^{-1} s^{-1}, so the predicted magnitudes of the rate constants for the reactions of $O(^3P)$ with formic acid and acetic acid are well within the accessible range of our experiments. The other reactions in the correlation proceed by hydrogen abstraction, so we may conclude that, if $O(^3P)$ does react with formic acid and acetic acid at a rate that is too slow for us to measure, the reaction is unlikely to proceed by the same kind of hydrogen abstraction process as that followed by the other reactions in the correlation.

The reactions of $O(^3P)$ with acetate esters

Kinetic data

The four acetate esters examined all consumed $O(^3P)$ at

Fig. 3. Correlation of rate constants for reactions of $O(^3P)$ with aldehydes, ethers, ketones, alcohols, and esters with the rate constants for the corresponding reactions of OH; (○) aldehydes, ethers, ketones, and alcohols taken from refs. 9, 12, and 13; (□) methyl acetate, ethyl acetate, and *n*-propyl acetate taken from ref. 2; (Δ) the four acetate esters studied in this work.

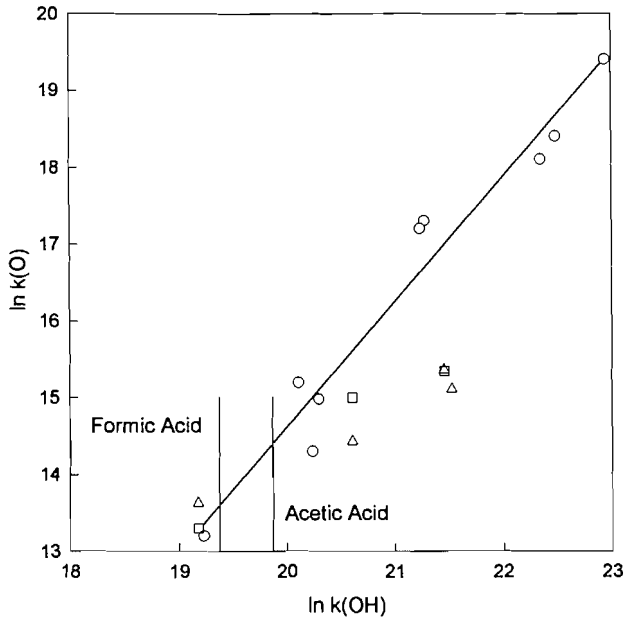

Table 1. Summary of kinetic data.

Temperature (K)	$k_R \times 10^{-6}$ (L mol^{-1} s^{-1})	Temperature (K)	$k_R \times 10^{-6}$ (L mol^{-1} s^{-1})
O + methyl acetate		**O + ethyl acetate**	
312	1.3 ± 0.3	367	7.8 ± 0.6
370	1.9 ± 0.4	389	11 ± 1
473	8.1 ± 0.4	391	8 ± 2
506	7.9 ± 0.5	397	5 ± 1
536	11 ± 1	414	10 ± 2
553	16 ± 3	433	13 ± 2
584	13 ± 6	458	10 ± 2
		460	9 ± 2
		482	13 ± 2
		486	15 ± 3
		488	14 ± 2
		531	40 ± 8
		556	40 ± 10
		574	32 ± 4
O + *n*-propyl acetate		**O + isopropyl acetate**	
303	4 ± 1	306	4.1 ± 0.6
335	10 ± 2	350	5.8 ± 0.9
353	90 ± 20	392	15 ± 3
373	22 ± 5	429	18 ± 4
376	35 ± 5	510	21 ± 6
409	25 ± 6	515	40 ± 10
430	41 ± 7	541	18 ± 2
482	33 ± 9	576	40 ± 10

readily measurable rates. The kinetic data are summarized in Table 1 and the temperature dependence is presented in Fig. 4. In general, the results obtained in this work were comparable to those reported by Mix et al. (2), which are also plotted in Fig. 4 for comparison. While the agreement is good for the reaction of $O(^3P)$ with *n*-propyl acetate, our results for methyl acetate and ethyl acetate are progressively lower than theirs as the temperature increases. The source of this disagreement is unclear. However, the earlier work measured the rate of loss of the organic reactant in the presence of a large (typically less than 100-fold at the higher temperatures) excess of atomic oxygen. It is possible that, at the higher temperatures, reactions of atomic hydrogen formed by the reaction of $O(^3P)$ with OH might have consumed enough of the organic reagent to lead to a larger rate constant than would be measured in our experiments. This effect would be least important for the reaction of $O(^3P)$ with *n*-propyl acetate since the rate constants for this reaction are the largest and competition from reactions of atomic hydrogen might be expected to be the least efficient.

Mechanisms and products

The reactions to be considered under our experimental conditions are

[1] $O + RHOAc \rightarrow OH + ROAc$

[2] $O + OH \rightarrow O_2 + H$

[3] $OH + RHOAc \rightarrow H_2O + ROAc$

[4] $O + ROAc \rightarrow$ Products

In writing reaction [1], we have assumed that the oxygen atom abstracts a hydrogen atom from the -OR part of the molecule. The lack of reactivity of acetic acid suggests that the CH_3CO_2 part of the molecule is unreactive. The observation that the Arrhenius preexponential factors increase systematically with increasing size of the -OR group also supports this assumption. The rate constants for reactions [2] and [3] are known from previous work (8, 17) and, with the results of our experiments, permit estimation of the relative importance of reactions [1]–[3]. In all our experiments, the rate of reaction [3] was at least a factor of four larger than the rate of reaction [2], so the dominant fate of OH was reaction with the ester rather than reaction with $O(^3P)$. This is borne out by measurements of the yields of water in the reaction of $O(^3P)$ with methyl acetate, presented in Table 2, in which the water yields were nearly equal to the amount of $O(^3P)$ consumed. The rate constant for reaction [4] is not known. However, the measured yields of water in Table 2 would be inconsistent with a large rate constant for reaction [4] and we conclude that this reaction does not play a major role in the reaction of $O(^3P)$ with methyl acetate. The rate constants for the reaction of $O(^3P)$ with methyl acetate were the smallest, at a given temperature, of any of the esters studied so it seems reasonable to generalize this conclusion to the other three reactions as well. This is supported by the limited analytical data in Table 2 for the reaction of $O(^3P)$ with ethyl acetate in which the yields of water were comparable to those in the reaction with methyl acetate.

Acetic acid was identified as a reaction product by spiking samples of the reaction products with known amounts of ace-

Fig. 4. Arrhenius plots for the reactions of $O(^3P)$ with acetate esters. (*a*) Methyl acetate: (○) this work, (●) ref. 2; (*b*) ethyl acetate: (Δ) this work, (▲) ref. 2; (*c*) *n*-propyl acetate: (∇) this work, (▼) ref. 2; (*d*) isopropyl acetate: (□) this work.

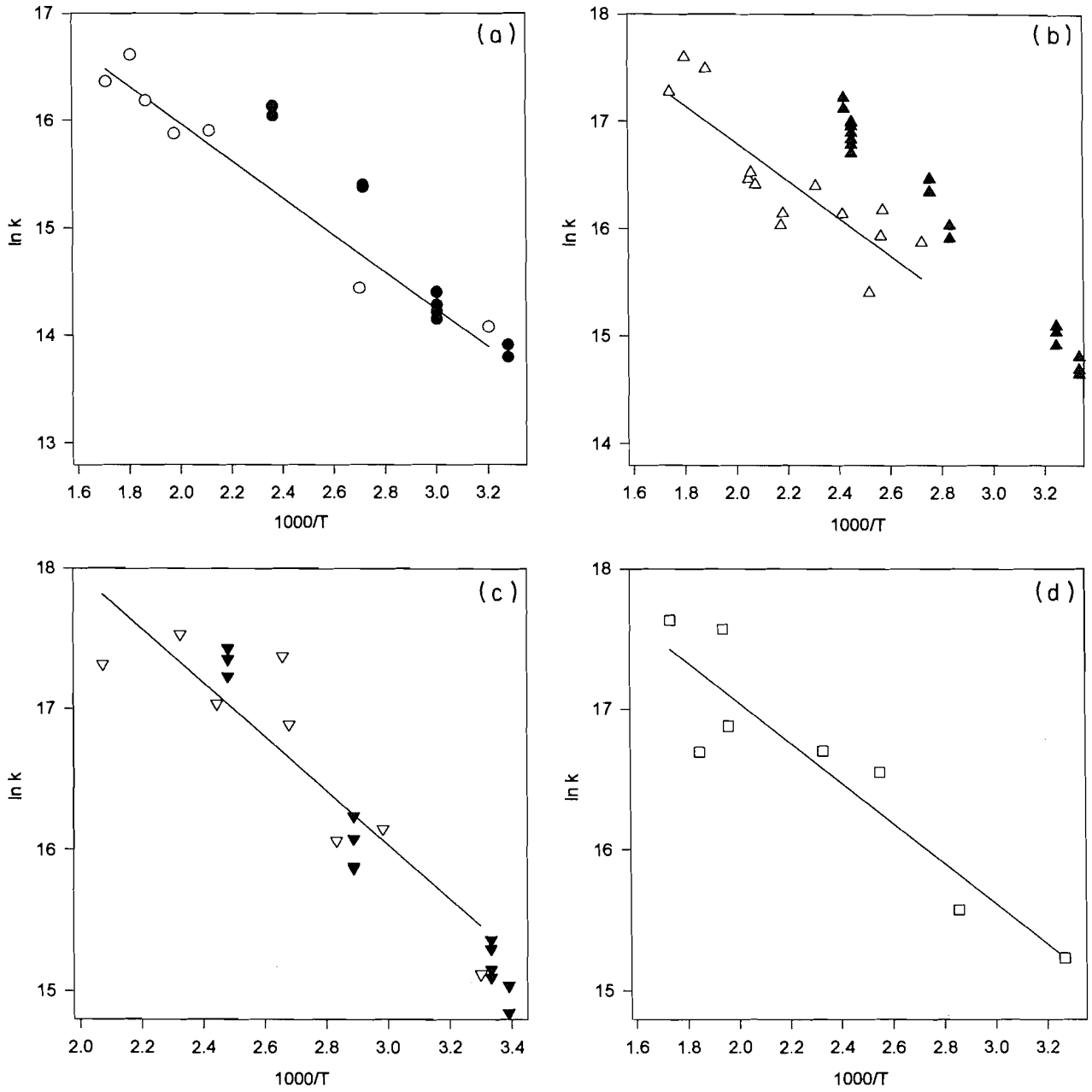

tic acid. The peak in the chromatograms of these samples, which increased in size in proportion to the amount of the spike, was attributed to acetic acid. Similar experiments in which samples of products from the reactions of $O(^3P)$ with methyl acetate and ethyl acetate were spiked with methanol and ethanol resulted in the appearance of new peaks in the gas chromatograms. This suggests that appreciable amounts of methanol and ethanol were not present in the reaction products. If the -OR group of the ester survived the reaction with $O(^3P)$ one might expect OR radicals to be present and to produce the parent alcohol by hydrogen abstraction from the ester. These chromatographic results support our postulate that the oxygen atom attacks the -OR part of the ester molecule and that the CH_3CO_2 unit survives unchanged. The observation of comparatively small yields of acetic acid may reflect a relatively facile decarboxylation of the CH_3CO_2 radical in competition with the reactions leading to formation of acetic acid.

Arrhenius parameters

The Arrhenius parameters for the reactions studied here are summarized in Table 3. Also shown for comparison are the results of ref. 2 and the parameters for the reactions of $O(^3P)$ with a series of ketones. The rate constants at 298 K for the reactions of the esters, calculated from the data of both sources, are also plotted in Fig. 3. The rate constants at 298 K required for Fig. 3 are found in Table 4, which summarizes the data used in the Taft analysis to be discussed later. While our Arrhenius preexponential factors and activation energies are

Table 2. Product yields in the reaction of $O(^3P)$ with methyl acetate and ethyl acetate.

$[Ester]/[O]_0$	$[H_2O]/[O]_0$	$[HOAc]/[O]_0$
CH_3OAc, 389 K		
79.4	1.06	0.27
42.0	0.86	0.20
20.6	0.83	—
11.9	0.88	0.23
CH_3OAc, 506 K		
37.0	—	0.27
24.6	—	0.29
15.2	0.92	—
C_2H_5OAc, 389 K		
49.0	0.85	0.29
5.17	0.99	0.31

Table 3. Summary of Arrhenius parameters.

Organic reactant	A (L mol^{-1} s^{-1})	E_a (kJ mol^{-1})	Reference
Methyl acetate	$1.2 \times 10^{10} \pm 25\%$	$22 \pm 6\%$	2
Methyl acetate	$2.8 \times 10^{8} \pm 24\%$	$14 \pm 10\%$	This work
Ethyl acetate	$1.4 \times 10^{10} \pm 36\%$	$20 \pm 7\%$	2
Ethyl acetate	$6.6 \times 10^{8} \pm 35\%$	$14 \pm 18\%$	This work
n-Propyl acetate	$1.6 \times 10^{10} \pm 38\%$	$20 \pm 12\%$	2
n-Propyl acetate	$2.9 \times 10^{9} \pm 41\%$	$16 \pm 20\%$	This work
Isopropyl acetate	$4.4 \times 10^{8} \pm 36\%$	$11 \pm 17\%$	This work
2-Propanone	$6.4 \times 10^{8} \pm 18\%$	$17 \pm 10\%$	1
2-Butanone	$5.0 \times 10^{8} \pm 19\%$	$10 \pm 23\%$	1
3-Pentanone	$2.9 \times 10^{8} \pm 32\%$	$8.6 \pm 50\%$	1

smaller than those in ref. 2, the rate constants calculated at 298 K from the Arrhenius parameters of the two studies are in reasonable agreement, presumably because the effect of the larger activation energies in ref. 2 tends to be qualitatively the same as that of the comparatively small preexponential factors calculated from our results. The difference in the Arrhenius parameters in the two studies may be partly due to the somewhat narrower temperature range used in ref. 2. The spread in their data would have resulted in a somewhat steeper Arrhenius plot and the somewhat longer extrapolation of this steeper plot to obtain the preexponential factor would have led to much larger values of the preexponential factors than those obtained with our data. The preexponential factors obtained in our experiments are comparable to those obtained for the reactions of $O(^3P)$ with ketones (1, 4) but are roughly an order of magnitude smaller than those found for the reactions of $O(^3P)$ with alcohols (7, 8). The activation energies obtained from our data are also comparable to those found for the reactions of $O(^3P)$ with ketones (1, 4) and with primary alcohols (7, 8).

Fig. 5. Taft plots for the reactions of $O(^3P)$ and OH with acetate esters. (○) $O(^3P)$ correlated with polar substituent parameters only ($\delta = 0$); (●) $O(^3P)$ correlated using both the polar substituent parameters and the steric substituent parameters; (□) OH correlated using both the polar substituent parameters and the steric substituent parameters.

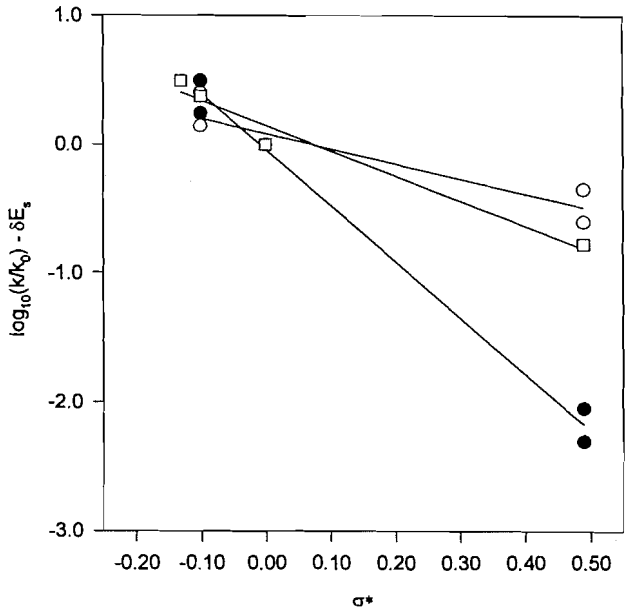

Linear free energy correlations

Figure 3 indicates that both the results of this work and those of ref. 2 are well correlated with the rate constants for the reactions of OH with the same esters. However, in both cases the rate constant for the reaction of $O(^3P)$ with methyl acetate falls on the correlation with the other organic compounds while the points for the remaining esters fall significantly below the main correlation. This implies a smaller reactivity of $O(^3P)$ toward the esters than toward the other compounds in the correlation. In ref. 2, this would be attributed to a comparatively large activation energy while in our work it is attributed to an abnormally small Arrhenius preexponential factor.

Table 4 provides data for a Taft linear free energy analysis (18) of the reactions of $O(^3P)$ and OH with acetate esters. The relevant plots are presented in Fig. 5. The data are fitted to the equation

$$\log_{10}(k/k_0) = \rho^*\sigma^* + \delta E_s$$

The value of ρ^* measures the sensitivity of the reaction to transmission of polar effects to the reaction centre while the value of δ reflects the sensitivity of the reaction to steric effects. Implicit in the use of this analysis in the present case is the assumption that the oxygen atom preferentially, but probably not exclusively, abstracts the hydrogen atom α to the ester oxygen. This is consistent with the behaviour found in the reactions of $O(^3P)$ with alcohols (7). The open circles in Fig. 5 present the data with δ set to zero. The filled circles in that figure represent the data fitted to allow for both polar and steric effects. The sum of squares of relative y-deviations for the results calculated with the inclusion of steric effects (2.8) is slightly smaller than that neglecting steric effects (3.2), suggesting that the data may be better correlated when both effects are included. The values of

Table 4. Summary of data for Taft correlations.[a]

Reaction	k_{298} (L mol^{-1} s^{-1})	σ*	E_s	Reference
O + methyl acetate	8.23×10^5	0.49	1.24	This work
O + methyl acetate	8.15×10^5	0.49	1.24	2
O + ethyl acetate	1.84×10^6	0.00	0.00	This work
O + ethyl acetate	3.29×10^6	0.00	0.00	2
O + *n*-propyl acetate	4.67×10^6	−0.10	−0.07	This work
O + *n*-propyl acetate	4.60×10^6	−0.10	−0.07	2
OH + methyl acetate	2.09×10^8	0.49	1.24	17
OH + ethyl acetate	8.96×10^8	0.00	0.00	17
OH + *n*-propyl acetate	2.08×10^9	−0.10	−0.07	17
OH + *n*-butyl acetate	2.50×10^9	−0.115	−0.36	17

[a]In all cases, the reference compound is the one for which σ* = E_s = 0.00 by definition. Values of σ* and E_s were taken from ref. 18.

Table 5. Summary of Taft parameters for reactions of $O(^3P)$.

Reaction	Taft ρ*	Taft δ	Standard deviation	Reference
O + acetate esters	−4.36	1.38	0.13	This work
OH + acetate esters	−1.96	0.12	0.13	17
O + alcohols	−2.37	0.01	0.17	7
OH + alcohols	−1.31	0.01	0.06	7
O + alkanes	−4.48	0.37	0.00	7
OH + alkanes	−4.55	0.55	0.00	7
O + aldehydes	−1.29	0.01	0.08	7
OH + aldehydes	−0.82	0.01	0.09	7

ρ* and δ obtained from the latter plot are −4.36 and +1.38, respectively. The comparatively large negative value of ρ* suggests that, as expected, $O(^3P)$ is an electrophile and the reaction is significantly facilitated by inductive transfer of electron density to the reaction centre.

Table 5 provides a summary of the Taft parameters determined for the reactions of $O(^3P)$ and OH with a variety of organic compounds. The reactions of $O(^3P)$ and OH consistently have negative values of ρ*, indicating that both are electrophilic, with $O(^3P)$ generally being the more electrophilic reagent. The difference between $O(^3P)$ and OH is much greater for the compounds containing oxygen than for the alkanes, where both reagents have approximately the same sensitivity to transmission of polar effects. Among the compounds containing oxygen, the order of sensitivity to polar effects for the reactions of both $O(^3P)$ and OH is acetate esters > alcohols > aldehydes. The effect of the electronegative ester oxygen may be moderated somewhat by the adjacent carbonyl, making the sensitivity greater to polar effects originating in the alkyl group than is the case in the alcohols. In the aldehydes, the carbonyl presumably dominates the polar effects to such an extent that residual polar effects originating in the alkyl group are much less significant, leading to a comparatively small value of ρ*. Of the compounds examined, only the alkanes and esters have appreciable sensitivity to steric effects. In the case of the esters, both OH and $O(^3P)$ show significant sensitivity to steric effects, with the $O(^3P)$ reactions being the more sensitive. This would be consistent with the picture of a reaction resulting from an addition complex formed between the oxygen atom and the ester, followed by rearrangement and formation of products in competition with simple decomposition back to reactants.

Acknowledgement

Financial support for this work was provided by the Natural Sciences and Engineering Research Council of Canada through award of a summer research assistantship to Peter Caravan and an operating grant.

References

1. J.M. Roscoe. Can. J. Chem. **64**, 1458 (1986).
2. K.-H. Mix, V. Schliephake, and H. Gg. Wagner. Z. Phys. Chem. Neue Folge, **150**, 17 (1986).
3. C.M. Owens and J.M. Roscoe. Can. J. Chem. **54**, 984 (1976).
4. J.H. Lee and R.B. Timmons. Int. J. Chem. Kinet. **9**, 133 (1977).
5. A.L. Ayub and J.M. Roscoe. Can. J. Chem. **57**, 1269 (1979).
6. R.L. Failes, D.L. Singleton, G. Paraskevopoulos, and R.S. Irwin. Int. J. Chem. Kinet. **14**, 371 (1982).
7. J.M. Roscoe. Can. J. Chem. **61**, 2716 (1983).
8. F. Westley, D.H. Frizzell, J.T. Herron, R.F. Hampson, and W. G. Maillard. NIST Standard Reference Database 17, Ver. 5.0, 1993.
9. G.S. Jolly, D.J. McKenney, D.L. Singleton, A.R. Bossard, and G. Paraskevopoulos. J. Phys. Chem. **90**, 6557 (1986).
10. D.P. Shoemaker, C.W. Garland, and J.W. Nibeler. Experiments in physical chemistry. 5th ed. McGraw–Hill, New York. 1989. pp. 289–290.
11. S. Budge and J.M. Roscoe. Can. J. Chem. **73**, 666 (1995).

12. D.L. Singleton, R.S. Irwin, G. Paraskevopoulos, G.S. Jolly, and D.J. McKenney. J. Am. Chem. Soc. **110**, 7786 (1988).
13. D.L. Singleton, G. Paraskevopoulos, and R.S. Irwin. J. Am. Chem. Soc. **111**, 5248 (1989).
14. R. Büttner and G. Maurer. Ber. Bunsen-Ges. Phys. Chem. **87**, 877 (1983).
15. J.S. Gaffney and S.Z. Levine. Int. J. Chem. Kinet. **11**, 1197 (1979).
16. R. Atkinson. Chem. Rev. **86**, 69 (1986).
17. T.J. Wallington, P. Dagaut, R. Liu, and M.J. Kurylo. Int. J. Chem. Kinet. **20**, 177 (1988).
18. N.B. Chapman and J. Shorter. Advances in linear free energy relationships. Plenum, London. 1972.

An AM1 calculational study of the protonation and reactions of 3,4-dihydro-2-oxo-1,4-ethanoquinoline, 3,4-dihydro-2-oxo-1,4-propanoquinoline, 3,3,4,5-tetrahydro-2-oxo-1,5-ethanobenzazepine, 3,3,4,5-tetrahydro-2-oxo-1,5-propanobenzazepine, and *N*-methyl-4-bromo-2-methylacetanilide

N.H. Werstiuk, R.S. Brown, and Q. Wang

Abstract: The gas phase N- and O-protonation of distorted amides 3,4-dihydro-2-oxo-1,4-ethanoquinoline (**1***a*), 3,4-dihydro-2-oxo-1,4-propanoquinoline (**1***b*), 3,3,4,5-tetrahydro-2-oxo-1,5-ethanobenzazepine (**1***c*), and 3,3,4,5-tetrahydro-2-oxo-1,5-propanobenzazepine (**1***d*) and normal amides 4-bromo-2,*N*-dimethylacetanilide (**5***a*) and 2,*N*-dimethylacetanilide (**5***b*), along with the N-protonation of benzoquinuclidine (**7**), has been studied calculationally at the semiempirical level of theory with AM1. Calculated enthalpies of N- and O-protonation (proton affinities) indicate that **1***a*, **1***b*, and **1***c* should protonate on nitrogen and **1***d*, **5***a*, and **5***b* on oxygen. A satisfactory straight-line relationship between the calculated proton affinities of **1***a*, **1***b*, **1***c*, and **7** with experimental solution pK_a's is used to estimate the solution pK_a of **1***d*. Results of a calculational study on the gas phase N- and O-methylation of **1***b*, **1***c*, and **1***d* are nicely in accord with the findings of an experimental solution phase study of the methylation–hydrolysis of **1***b* and **1***d*: while **1***b* methylates on nitrogen, **1***d* methylates on oxygen. A calculational study of possible pathways of hydrolysis of the N-protonated amides indicates that solvolysis of the hydrates of these species represents a viable route for their conversion to ring-opened products.

Key words: protonation, methylation, reactions, distorted amides, AM1 calculations.

Résumé : Faisant appel à des calculs AM1 au niveau semiempirique, on a étudié les N- et O-protonations d'amides déformés (3,4-dihydro-2-oxo-1,4-éthanoquinoléine (**1***a*), 3,4-dihydro-2-oxo-1,4-propanoquinoléine (**1***b*), 3,3,4,5-tétrahydro-2-oxo-1,5-éthanobenzazépine (**1***c*) et 3,3,4,5-tétrahydro-2-oxo-1,5-propanobenzazépine (**1***d*)) et d'amides normaux (4-bromo-2,*N*-diméthylacétanilide (**5***a*) et 2,*N*-diméthylacétanilide (**5***b*)) ainsi que la protonation de la benzoquinuclidine (**7**). Les enthalpies calculées pour les N- et O-protonations (affinités protoniques) indiquent que les composés **1***a*, **1***b* et **1***c* devraient se protoner sur l'azote alors que les composés **1***d*, **5***a* et **5***b* devraient se protoner sur l'oxygène. Une relation linéaire satisfaisante entre les affinités protoniques calculées des composés **1***a*, **1***b*, **1***c* et **7** avec les valeurs expérimentales des pK_a en solution a été utlisée pour évaluer le pK_a en solution du composé **1***d*. Les résultats des calculs sur les N- et O-méthylations en phase gazeuse des composés **1***b*, **1***c* et **1***d* sont en bon accord avec les observations d'une étude expérimentale en solution de la méthylation–hydrolyse des composés **1***b* et **1***d* : alors que le composé **1***b* se méthyle sur l'azote, le composé **1***d* se méthyle sur l'oxygène. Une étude par calculs des diverses voies possibles pour l'hydrolyse d'amides N-protonés indique que la solvolyse des hydrates de ces espèces représente une route viable pour leurs conversions en produits résultants d'ouvertures de cycles.

Mots cles : protonation, méthylation, réactions, amides déformés, calculus AM1.

[Traduit par la rédaction]

Introduction

By studying a group of benzo-substituted bicyclic amides Brown and co-workers showed that distorting the amide linkage away from planarity leads to a dramatic change in the basicity of the amides and their reactivities in H_2O (1, 2). The kinetics of hydrolysis of distorted amides 3,4-dihydro-2-oxo-1,4-ethanoquinoline (**1***a*), 3,4-dihydro-2-oxo-1,4-propanoquinoline (**1***b*), 3,3,4,5-tetrahydro-2-oxo-1,5-ethanobenzazepine (**1***c*), 3,3,4,5-tetrahydro-2-oxo-1,5-propanobenzazepine (**1***d*), and N-methyl-4-bromo-2-methylacetanilide (**5***a*) were studied as a function of pH and the general hydrolytic mechanism shown in Scheme 1 was used to account for the pH–rate profiles. It was suggested that in going from **1***d* to **1***a* the site of protonation changes from oxygen to nitrogen giving rise to N-

Received September 28, 1995.

N.H. Werstiuk.[1] Department of Chemistry, McMaster University, Hamilton, ON L8S 4M1, Canada.
R.S. Brown[1,2] **and Q. Wang.** Department of Chemistry, University of Alberta, Edmonton, AB T6G 2G2, Canada.

[1] Authors to whom correspondence may be addressed.
[2] Present address: Department of Chemistry, Queen's University, Kingston, ON K7L 3N6, Canada.

Scheme 1.

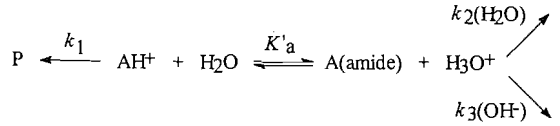

Table 1. Rate, dissociation constants, and enthalpies of activation for hydrolysis of amides.

Amide[a]	k_1 (s^{-1})	pK'_a	k_1/K'_a (M^{-1} s^{-1})	$\Delta H^{\neq}$[b]
1*a*	4.45	3.71	2.28×10^4	10.26[c]
1*b*	8.3	0.65	29.5	6.25[d]
1*c*	101	−2.8	56	6.60[d]
1*d*	—	—	1.21×10^{-4}	15.96[e]
5*a*	—	—	2.2×10^{-7}	19.70[e]

[a]Data taken from ref. 2.
[b]The values are in kcal/mol.
[c]At pH 3.2.
[d]At pH 2.0.
[e]At pH 1.5.

protonated amides as reactive intermediates in the case of **1***a*, **1***b*, and **1***c*. This change was reflected in the nature of the pH–rate profiles; plateaus are seen at progressively lower pH in going from **1***a* to **1***c*. Using the rate data fitted to the appropriate kinetic expression for Scheme 1, Brown and co-workers determined kinetic pK_a's for **1***a*, **1***b*, and **1***c*. Table 1 shows the observed rate constants and the kinetic pK_a's for **1***a*, **1***b*, and **1***c*. A kinetic pK_a could not be determined for **1***d*, the least reactive amide, because it does not exhibit a plateau between pH 0.0 and 3.0. The availability of the structural and kinetic data for these amides prompted us to undertake a computational study of **1***a*–**1***d*, **5***a*, and *N*-methyl-*o*-methylacetanilide (**5***b*), (*a*) to calculate the geometries and relative energies of the N- and O-protonated species, (*b*) to provide support for the postulated changes in basicity, and (*c*) to gain insight into possible mechanisms of ring opening of the protonated species in H_2O. This paper documents the results of our study.

Experimental

I. Calculational method

The geometrical structures of the amides and their N- and O-protonated analogues were generated and optimized with MMX of PCMODEL (3) or MM+ of HYPERCHEM (4) and used as input for AM1 calculations with AMPAC (5), MOPAC (6), or HYPERCHEM. In the case of the AM1 calculations, the keyword PRECISE was used to tighten the convergence criteria. For the HYPERCHEM calculations, the optimizations were terminated when the RMS of the gradient dropped below 0.1 kcal/mol. In the case of the additions of H_2O to the N-protonated amides, the geometrical structures of the solvated substrates and the hydrates were generated with PCMODEL, optimized, and then used as input for the semiempirical calculations. In some cases, the locations of the H_2O molecules were adjusted prior to the optimization calculations by making appropriate changes in the input Z-matrix. Transition structures were calculated by refining the geometries at the maxima of the potential energy surfaces obtained for stretching the amide N—C bonds or shortening the H_2O...C=O internuclear distances for nucleophilic addition of H_2O in 0.1 Å increments with SIGMA or NLLSQ calculations.[3]

II. Methylation of 3,4-dihydro-2-oxo-1,4-propanoquinoline (**1***b*) and 2,3,4,5-tetrahydro-2-oxo-1,5-propanobenzazepine (**1***d*)

(a) **1***b*

Amide **1***b* (15.16 mg, 0.081 mmol) was dissolved in 0.5 mL of CD_2Cl_2 in an NMR tube. In a dry box flushed with argon, methyl trifluoromethanesulfonate (9.17 μL, 0.081 mmol) was injected into the solution. The reaction mixture was monitored periodically by ^1H NMR over a period of 90 h. ^1H NMR of **1***b* (200 MHz, CD_2Cl_2); δ: 7.12–7.45 (4 H, m), 3.75–3.91 (1 H, m), 3.04–3.22 (2 H, m), 2.62 (2 H, d, $J = 2$ Hz), 1.12–2.12 (4 H, m); the CH_3 protons of methyl triflate appear as a singlet at δ 4.21 ppm. During the reaction, a new peak appears at δ 3.65.

The reaction was terminated at 90 h by the addition of 2 mL of H_2O and the mixture extracted with 3×20 mL of CH_2Cl_2. The combined organic extracts were dried ($MgSO_4$) and the volatiles removed to yield a residue that was directly analyzed by ^1H NMR and MS. ^1H NMR (200 MHz, $CDCl_3$), δ: 6.92–7.22 (4 H, m), 3.45–4.00 (2 H, m), 2.88 (3 H, m), 2.82 (3 H, s), 1.48–1.95 (4 H, m). *m/z* (relative intensity): 219 (M^+ 69%), 174 ($M^+ - CO_2$ 38%), 160 ($M^+ - CH_2CO_2H$ 38%), 146 (16%), 132 (31%). Exact Mass calcd. for $C_{13}H_{17}NO_2$: 219.1259; found: 219.1255.

(b) Authentic N*-methyl-5-(2-hydroxycarbonylmethyl)-2,3,4,5-tetrahydrobenzazepine (**8**)*

To a flask was added NaH (60% dispersion, 0.546 g, 13.6 mmol, washed with hexane 3 times), 5-(hydroxycarbonylmethyl)-2,3,4,5-tetrahydrobenzazepine (0.30 g, 1.46 mmol), and 20 mL of dry THF. To this was added CH_3I (0.23 mL, 3.7 mmol) after which the mixture was heated at reflux overnight. The reaction mixture was worked up by the addition of 20 mL of H_2O, and extracted with 3×25 mL of $CHCl_3$. The combined extracts were dried ($MgSO_4$) and the volatiles removed to yield a crude product that was purified by column chromatography (SiO_2, ethyl acetate). The final product was a light yellow oil. ^1H NMR (200 MHz, $CDCl_3$), δ: 6.84–7.20 (4 H, m), 3.45–3.82 (2 H, m), 2.90 (3 H, m), 2.82 (3 H, s), 1.52–1.90 (4 H, m). *m/z* (relative intensity): 219 (M^+ 66%), 174 ($M^+ - CO_2$ 32%), 160 ($M^+ - CH_2CO_2H$ 100%), 146 (20%), 132 (38%). Exact Mass calcd. for $C_{13}H_{17}NO_2$: 219.1259; found: 219.1257.

*(c) Methylation of 2,3,4,5-tetrahydro-2-oxo-1,5-propanobenzazepine (**1**d)*

In a dry box, 5.90 μL of methyl trifluoromethanesulfonate (0.052 mmol) was injected into a solution of amide **1***d* (10.46 mg, 0.052 mmol) in 0.5 mL of CD_2Cl_2. The reaction mixture was monitored by ^1H NMR over a period of 9 days. At time zero, ^1H NMR (200 MHz, CD_2Cl_2), δ: 7.25–7.38 (2 H, m), 7.12–7.24 (2 H, m), 4.36–4.52 (1 H, m), 3.08–3.21 (1 H, m), 2.81–2.94 (1 H, m), 2.02–2.32 (3 H, m), 1.20–1.68 (3 H, m).

[3] The keyword SIGMA invokes the McIver–Komornicki gradient norm minimization routines. The keyword NLLSQ invokes Bartel's nonlinear least-squares gradient norm minimization method.

Over the course of the reaction, the ratios of the CH_3OTf and the other generated CH_3 singlets at δ 4.45, δ 4.21, and δ 3.50 were 21:1:7.

The mixture was worked up as above for the methylation of **1***b* and the crude mixture directly analyzed by ^1H NMR and MS. ^1H NMR (200 MHz, $CDCl_3$), δ: 6.68–7.09 (4 H, m), 3.65 (3 H, s), 3.18–3.32 (1 H, m), 2.72–2.88 (2 H, m), 1.58–2.38 (8 H, m). *m/z* (relative intensity): 233 (M^+ 41%), 202 ($M^+ - OCH_3$ 12%), 174 ($M^+ - CO_2CH_3$ 5%), 160 ($M^+ - CH_2CO_2Me$ 76%), 146 ($M^+ - CH_2CH_2CO_2Me$ 100%), 132 (11%). Exact Mass calcd. for $C_{14}H_{19}NO_2$: 233.1416; found: 233.1414.

Since the new peak at δ 3.50 in the reaction mixture might be attributed to the N-methylated acid corresponding to **8**, the remaining aqueous layer was neutralized with dilute HCl to pH 4.0 and extracted with CH_2Cl_2. There was no material isolated so we speculate that the δ 3.50 peak was from CH_3OH formed from the reaction of CH_3OTf with adventitious H_2O.

*(d) Authentic 5-(2-methoxycarbonylethyl)-2,3,4,5-tetrahydrobenzazepine (**9**)*

HCl gas was bubbled through a solution of the corresponding amino acid (0.0734 g, 0.33 mmol) in 10 mL of CH_3OH for 30

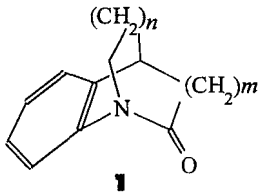

1

a, $n = m = 1$
b, $n = 2$; $m = 1$
c, $n = 1$; $m = 2$
d, $n = 2$; $m = 2$

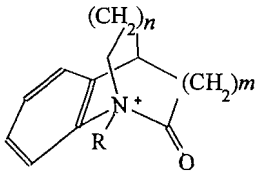

2

a, $n = m = 1$; R = H
b, $n = 2$; $m = 1$; R = H
c, $n = 1$; $m = 2$; R = H
d, $n = 2$; $m = 2$; R = H
e, $n = 2$; $m = 1$; R = CH_3
f, $n = 1$; $m = 2$; R = CH_3
g, $n = 2$; $m = 2$; R = CH_3

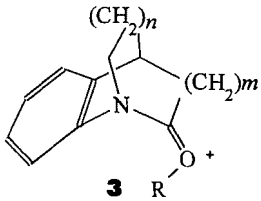

3

a, $n = m = 1$; R = H
b, $n = 2$; $m = 1$; R = H
c, $n = 1$; $m = 2$; R = H
d, $n = 2$; $m = 2$; R = H
e, $n = 2$; $m = 1$; R = CH_3
f, $n = 1$; $m = 2$; R = CH_3
g, $n = 2$; $m = 2$; R = CH_3

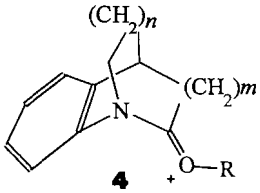

4

a, $n = m = 1$; R = H
b, $n = 2$; $m = 1$; R = H
c, $n = 1$; $m = 2$; R = H
d, $n = 2$; $m = 2$; R = H
e, $n = 2$; $m = 1$; R = CH_3
f, $n = 1$; $m = 2$; R = CH_3
g, $n = 2$; $m = 2$; R = CH_3

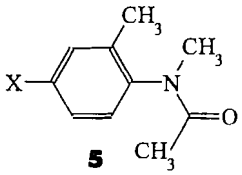

5

a, X = Br
b, X = H

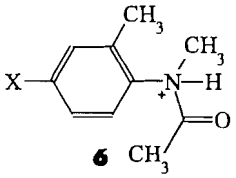

6

a, X = Br
b, X = H

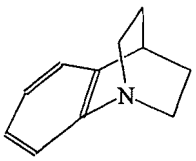

7

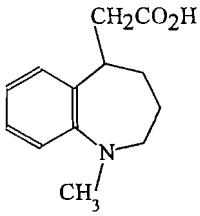

8

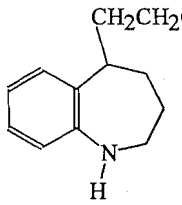

9

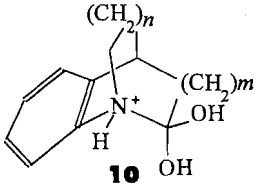

10

a, $n = 2$; $m = 1$
b, $n = 2$; $m = 2$

min. The solution was then heated to reflux overnight. The solvent was removed by rotary evaporation and 5 mL of H_2O was then added to the residue. The pH of the solution was adjusted to pH 10 (NaOH dropwise) and the mixture extracted with 3 × 10 mL of CH_2Cl_2). The organic layers were washed with H_2O and dried (Na_2SO_4). The crude product (~50 mg) was purified by chromatography (SiO_2, petroleum ether – ethyl acetate; 75:15). Further purification was effected by dissolving the product in ether and bubbling HCl through the solution. After refrigeration, the HCl salt of **9** formed as white crystals. These were dissolved in 10 mL of saturated Na_2CO_3 and the free amine was extracted with 3 × 20 mL of CH_2Cl_2. The combined organic layers were dried (Na_2SO_4) and evaporated to yield a solid that was analyzed by ^1H NMR and MS. ^1H NMR (200 MHz, $CDCl_3$), δ: 6.62–7.08 (4 H, m), 3.65 (3 H, s), 3.18 (1 H, m), 2.72–2.90 (2 H, m), 1.58–2.38 (8 H, m). *m/z* (relative intensity): 233 (M^+ 46%), 202 ($M^+ - OCH_3$ 12%), 174 ($M^+ - CO_2Me$ 2%), 160 ($M^+ - CH_2CO_2Me$ 75%), 146 ($M^+ - CH_2CH_2CO_2Me$ 100%), 132 (9%). Exact Mass calcd. for $C_{14}H_{19}NO_2$: 233.1416; found: 233.1410.

Results and Discussion

Calculated geometries and heats of formation of N- and O-protonated amides

The optimized equilibrium geometries of **1***b*–**1***d* and **5***a* (structural formulas not shown) calculated with AM1 correspond closely to the molecular structures of **1***b*–**1***d* and **5***a* obtained by X-ray diffraction (1, 7). Although the X-ray structure of **1***a* has not been reported, the AM1 computed geometry is probably accurate, based on the close similarity of the computed and experimental geometries for the other members of the series. The seven-membered ring of **1***c* adopts a chair conformation, while the eight-membered ring of **1***d* adopts a crown conformation. The torsional angle between the planar amide group and the plane of the phenyl ring of acetanilide **5***a* is 73.3°. Figure 1 shows the optimized geometrical structures of the N-protonated amides **2***a*–**2***d* and **6***a* labelled with selected geometrical parameters obtained with AM1. In the case of **6***a* and **6***b* (not shown), the most stable geometrical structure has the N—H bond *cis* to the methyl group at C2 of the phenyl ring. The values in brackets correspond to the values calculated for the unprotonated amides **1***a*–**1***d* and **5***a*; the values in parentheses are the bond lengths of the starting materials obtained by X-ray diffraction. There is a progressive decrease in the calculated N—C(O) bond lengths in going from **1***a* to **5***a*: **1***a* 1.480 Å, **1***b* 1.459 Å, **1***c* 1.459 Å, **1***d* 1.426 Å, and **5***a* 1.395 Å. These results are in accord with the expectation that the resonance interaction increases in going from **1***a* to **1***d*. While the anticipated shortening of the N—C(O) bonds through the series **1***a*–**1***d* seen in the X-ray diffraction data (parentheses) is reproduced with the AM1 calculations, the computed bond lengths (brackets) are around 0.05 Å longer than those obtained experimentally. That the N—C(O) bond of **1***d* is longer than the N—C(O) bond of **5***a* suggests that the interaction of the former's lone pair with the carbonyl group does not occur to the same extent as in **5***a* even though **1***d* has two 3-carbon bridges. As found experimentally with X-ray crystallography (7) and expected on the basis of ab initio calculations (8, 9), the C=O bond lengths calculated with AM1 increase only to a small degree through the series **1***a*–**1***d* and **5***a* (Fig. 1).

Fig. 1. Displays of the AM1 optimized geometrical structures of N-protonated amides ((*a*) **2***a*; (*b*) **2***b*; (*c*) **2***c*; (*d*) **2***d*; (*e*) **6***a*) and selected structural parameters of these species. The values shown in brackets are the AM1 calculated bond lengths of the corresponding amides; the experimental values are shown in parentheses.

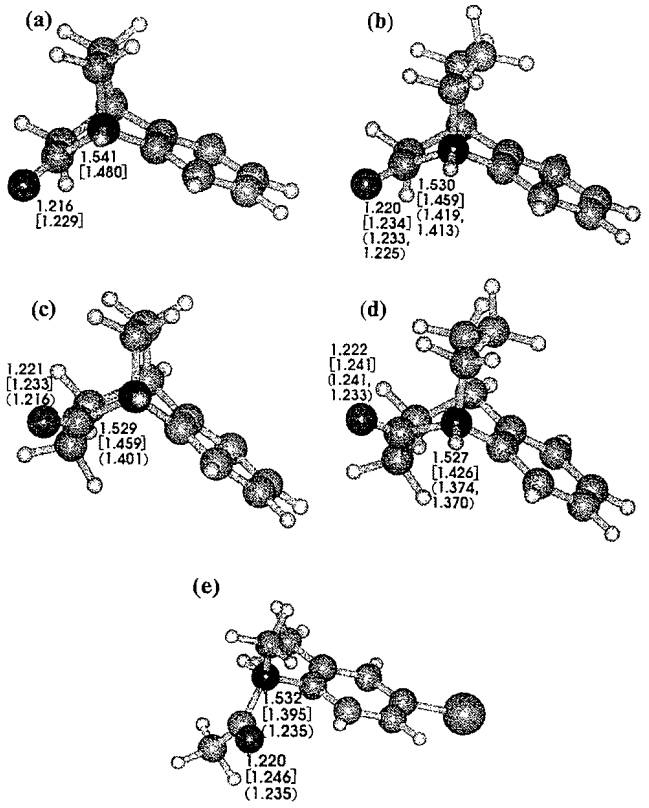

Protonation of the nitrogen results in a large increase in the N—C(O) bond lengths (see Fig. 1), 0.061 Å for **1***a*, 0.071 Å for **1***b*, 0.070 Å for **1***c*, 0.101 Å for **1***d*, and 0.137 Å for **5***a*, but the C=O bonds shorten only slightly: 0.013, 0.014, 0.012, 0.019, and 0.026 Å for **1***a*, **1***b*, **1***c*, and **5***a*, respectively. In the case of **1***b*, **1***c*, **1***d*, and **5***a*, these changes undoubtedly arise predominantly from a loss of the resonance interaction upon formation of the N—H bond. Because there is little interaction of the lone pair with the carbonyl group,[4] the source of the unusual lengthening of the N—C(O) bond of **1***a* in going to **2***a* is presently unknown. But, it is possible that our AIMPAC studies[4] will provide information on this point. The other bonds to nitrogen also lengthen upon protonation (Ar-N- by

[4] Using the theory of atoms in molecules, specifically the AIMPAC computational package (10), we have undertaken a study of the topology of the charge density of amides **1***a*–**1***d* and **5***b*, in large part to characterize the nonbonded charge concentrations (lone pairs) on nitrogen. The Laplacians of ρ at the (3, −3) critical points of benzoquinuclidine (**7**) and **1***a* are virtually identical. This finding and the fact that the torsional angle between the (3,−3) critical point of the nonbonded charge concentration and the C=O group of **1***a* is 4.5° indicate that there is no interaction between the nitrogen lone pair and the π system of the carbonyl group.

Fig. 2. Displays of the AM1 optimized geometrical structures of the *cis*-O-protonated amides ((*a*) **3***a*; (*b*) **3***b*; (*c*) **3***c*; (*d*) **3***d*; (*e*) O-protonated **5***a*) and selected structural parameters of these species; those of the *trans* diastereomers are shown in square brackets.

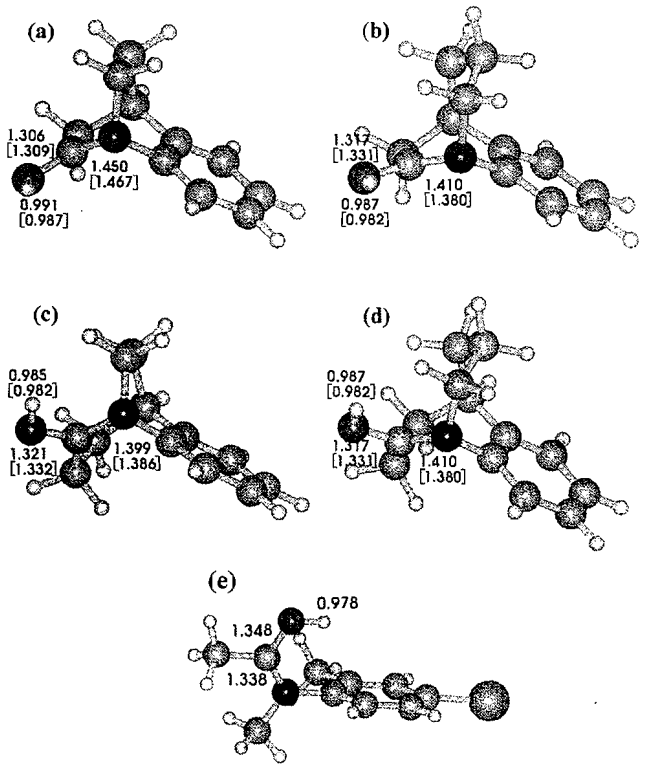

0.016 and -CH_2-N- by 0.036 Å, respectively), but not to the same degree. These increases in the N—C(O) bond lengths calculated with AM1 are in accord with the results of an ab initio calculational study we have undertaken on **1***a*–**1***d* and **2***a*–**2***d* (at the HF/6-31G** level of theory) and with data reported on N-protonation of 1-azabicyclo[2.2.2]octan-2-one (the N—C(O) bond length increased by 0.071 Å) and 1-azabicyclo[3.3.1]nonan-2-one (the bond lengthened by 0.137 Å) obtained at the 6-31G* level of theory (11). In going from **2***a* to **2***d*, there is a progressive increase in the O-C-N^+-H torsional angle (**2***a*, 1.4°; **2***b*, 16.5°; **2***c*, 22.5°; **2***d*, 53.9°). Up to the present time, there have been no reports of X-ray crystallographic structure determinations of N-protonated amides.

The geometrical structures of the *cis*-O-protonated amides **3***a*–**3***d* and the most stable conformer of the O-protonated **5***a* are shown in Fig. 2 along with selected geometrical parameters. Values for the *trans*-O-protonated isomers **4***a*–**4***d* are shown in square brackets. That there is an increase in the resonance interaction involving the nitrogen lone pair in going from **1***a* to **1***d* is seen in the elongation of the C=O bond that accompanies O-protonation (**3***a* 0.077 Å, **3***b* 0.083 Å, **3***c* 0.088 Å, **3***d* 0.096) and a shortening of the C—N bond (**3***a* 0.030 Å, **3***b* 0.049 Å, **3***c* 0.060 Å, **3***d* 0.167 Å) relative to neutral amides and the N-protonated analogues is seen from the data in Fig. 1. In the case of O-protonated **5***a*, where full interaction of the nitrogen lone pair and C=O is possible, the C=O bond length increases by 0.175 Å and the N—C(O) bond shortens by 0.057 Å relative to the neutral amide. The H-O-C-N torsional angles of the O-protonated amides **3***a*, **3***b*, **3***c*, and **3***d*, respectively, are 179.2°, 175.5°, 175.4°, 172.5°.

The calculated heats of formation of amides **1***a*–**1***d*, **5***a*, and **5***b*, and the N-protonated compounds **2***a*–**2***d*, **6***a* and **6***b*, along with the calculated proton affinities (PA's, the negatives of the enthalpies of N-protonation) are given in Table 2. Also included in Table 2 are the AM1 calculated heats of formation of the O-protonated species **3***a*–**3***d* (the =O^+-H bonds are *cis* to the bridgehead nitrogen) and **4***a*–**4***d* (the =O^+-H bonds are *trans* to the bridgehead nitrogen) along with the PA's. It is seen that the nitrogen PA's of **1***a*–**1***c* range from 216.8 to 214.9. The accuracy of these values is unknown at present because the gas phase PA's of distorted amides have not been measured. In this connection, the PA's for N-protonation of 1-azabicyclo[2.2.2]octan-2-one and 1-azabicyclo[3.3.1]nonan-2-one calculated with AM1 are 214.1 and 211.7 kcal/mol, respectively. These values are smaller than the values (238.8 and 228.8 kcal/mol) at the HF/6-31G*//6-31G* levels of theory (11). It is noteworthy that the AM1 calculated PA for O-protonation of formamide (198.4 kcal/mol) is identical to the experimental value of 198.41 kcal/mol (12). On the other hand, *ab initio* calculations at the MP2/6-31G*//4-31G level of theory provided a PA of 203.7 kcal/mol for O-protonation, 5.3 kcal/mol higher than the experimental value (13). On the basis of the calculated enthalpies of formation, **1***a*–**1***c* should undergo equilibrium protonation preferentially on nitrogen, **1***d* should protonate on both oxygen and nitrogen, and **5***a* and **5***b* should protonate preferentially on oxygen. The reason for the difference in the gas phase stabilities of the *cis*- and *trans*-O-protonated species (Table 2) is unknown, although intramolecular hydrogen bonding to the nitrogen and (or) hyperconjugation of the oxygen lone pair with the C—N bond may give rise to the difference in stability of the diastereomers. We also calculated the enthalpies of formation of 3,4-dihydro-2,5-ethanoquinoline (benzoquinuclidine) (**7**) and the corresponding N-protonated species, and those data, along with the calculated enthalpy of protonation (PA), and available experimental pK_a's (2, 14) are given in Table 2.

A plot of PA (N-protonated) vs. the observed solution pK_a gives the satisfactory straight-line relationship in eq. [1], r^2= 0.98. Some sort of relationship is anticipated although one must be mindful that the solution pK_a's depend heavily on

$$[1] \quad \text{PA (N-protonated)} = 0.50\ \text{p}K_a + 215.3$$

solvation, which may be reflected in differential ΔS values in the various solution equilibria, but cannot be accounted for in the gas phase enthalpy calculations. Nevertheless, if we extrapolate the line to estimate the solution pK_a for N-protonated **2***d*, a value of −11.7 is obtained. As far as we are aware, there are no directly measured solution pK_a's of N-protonated amides. Even though our estimated value falls outside the range of the pK_a's (−7.22 to −8.38) of five noncyclic N-protonated amides estimated from rates of acid-catalyzed N–H exchange by Williams (15), it is possible that the relief of angle strain as seen in the case of the solvolysis of 1-chlorobicyclo[3.3.3]undecane (16) is the source of the higher than expected acidity of **2***d*. The results of our study suggest that AM1 calculations might be useful for predicting the pK_a's of N-protonated amides.

Table 2. Calculated enthalpies of formation and proton affinities.

Amide or amine	ΔH_f[a]	ΔH_f N-protonated	ΔH_f *cis*-O-protonated	ΔH_f *trans*-O-protonated	PA[b] N-protonated	pK_a	PA *cis*-O-protonated	PA *trans*-O-protonated
1*a*	11.4	160.0	180.2	186.8	216.8	3.7	196.9	190.4
1*b*	−0.71	148.9	163.9	167.8	216.0	0.56	201.1	197.2
1*c*	−0.93	149.6	162.2	166.1	214.9	−0.28	202.6	198.7
1*d*	−9.6	146.4	146.5	147.6	209.4		209.6	208.5
5*a*	−8.3	156.4	145.0	146.5	201.1		210.6	212.4
5*b*	−13.7	148.3	136.8	141.0	203.7		215.2	211.0
7	34.5	180.6			219.3	7.8[c]		

[a]The values in kcal/mol.
[b]PA = $-\Delta H_{prot}$ = $-[\Delta H_f$(protonated substrate) − ΔH_f(substrate) − $\Delta H_f(H^+)$; $\Delta H_f(H^+)$ taken as 365.4 kcal/mol.
[c]See ref. 14.

Table 3. AM1 heats of formation of N- and O-methylated amides.

Methylated amide	**2***e*	**2***f*	**2***g*	**3***e*	**3***f*	**3***g*	**4***e*	**4***f*	**4***g*
ΔH_f[a]	158.8	165.7	170.6	159.0	164.6	169.5	156.4	151.1	151.5

[a]In kcal/mol.

Methylation of 3,4-dihydro-2-oxo-1,4-propanoquinoline (1*b*), 3,3,4,5-tetrahydro-2-oxo-1,5-ethanobenzazepine (1*c*), and 3,3,4,5-tetrahydro-2-oxo-1,5-propanobenzazepine (1*d*)

We also studied the methylation of **1***b*, **1***c* and **1***d* by calculating the enthalpies of formation of N- and O-methylated compounds **2***e*–**2***g*, **3***e*–**3***g*, and **4***e*–**4***g* (Table 3). The N-methylated compounds derived from **1***b* and **1***c* are more stable than the *cis*- and trans-*O*-methyl species. In the case of **1***d*, the O-methyl diastereomers are calculationally more stable (*cis* 5.3 kcal/mol and *trans* 4.9 kcal/mol) than the N-methyl compound. Yet the N-protonated species **2***d* and the *cis*-O-protonated isomer **3***d* are nearly identical in energy (Table 2). Why the methylation of **1**d differs from the protonation is not evident at this time. If the relative energies of the methylated amides are important in determining the rates of the methylation, then **1***b* and **1**c will kinetically methylate on nitrogen and **1***d* will yield the O-methylated *trans* isomer.

This question was experimentally addressed as follows (17). Methylation of each of **1***b* and **1***d* by $CH_3OSO_2CF_3$ in CD_2Cl_2 was monitored by ^1H NMR over a 96 h period. During this time, in the case of **1***b* the peak attributable to $CH_3OSO_2CF_3$ at δ 4.21 diminished in intensity concomitant with the growth of a new singlet at δ 3.65. In the case of **1***d* the loss of the $CH_3OSO_3CF_3$ singlet gave rise to one at δ 4.45. In each case, the reaction mixture was quenched by the addition of H_2O, and worked up to yield products that were immediately subjected to exact mass and ^1H NMR analysis. The spectra of the respective materials proved to be identical with authentic N-methylated ring-opened **8** (in the case of **1***b*) and authentic methyl ester **9** (in the case of **1***d*). Overall, the processes are depicted in eqs. [2] and [3]. The above kinetic methylation studies give results for the position of methylation that are in full accord with what is expected on the basis of AM1 calculations, which show that **1***b* should methylate on nitrogen and **1***d* should methylate on oxygen.

Hydrolysis of N-protonated amides

A series of calculations was also undertaken to provide information about the mechanism of hydrolysis of the N-protonated amides. In the first study, **2***a* and **2***c* were converted to the N-protonated hydrates, **10***a* and **10***b*, which are found to be

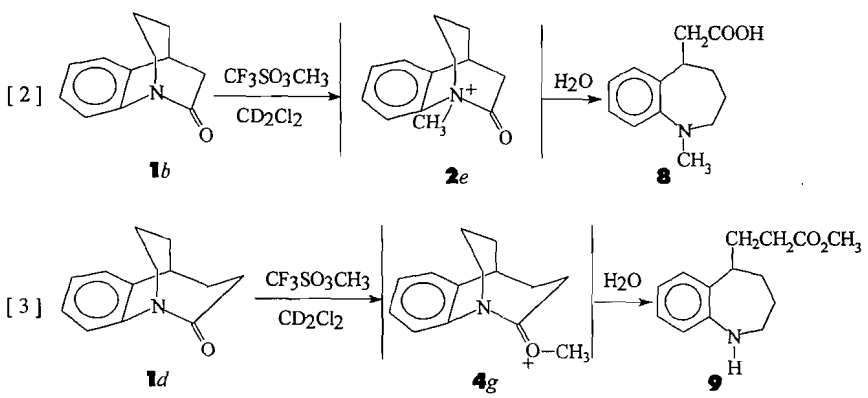

Table 4. AM1 enthalpies of formation of N-protonated amides plus one isolated water, and the corresponding N-protonated hydrates.

Protonated amide	$\Sigma\Delta H_f^a$ prot. amide and H_2O	ΔH_f hydrate
2*a*	101.1	85.4
2*c*	90.5	77.0

[a]In kcal/mol.

Table 5. AM1 enthalpies of formation and activation for N—$C(OH)_2$ bond cleavage of N-protonated hydrates with zero, one, and two associated H_2O molecules.

Hydrate	$\Sigma\ \Delta H_f^a$ hydrate and no H_2O	$\Sigma\ \Delta H_f^a$ hydrate and H_2O	$\Sigma\ \Delta H_f^a$ hydrate and $2H_2O$	ΔH_f TS hydrate	ΔH_f TS $1H_2O$	ΔH_f TS $2H_2O$	$\Delta H^{\neq}$ no H_2O	$\Delta H^{\neq}$ $1H_2O$	$\Delta H^{\neq}$ $2H_2O$
10*a*	85.4	13.9	−54.7	93.2	22.6	−46.7	7.8	8.7	8.0
10*c*	77.0	5.4	−62.8	86.2	15.4	−53.2	9.2	10.0	9.6

[a]In kcal/mol.

roughly 16 and 13 kcal/mol, respectively, more stable than their corresponding N-protonated amides and one isolated H_2O molecule (Table 4). We next looked at heterolysis of the N-protonated hydrates in the presence of zero, one, and two associated H_2O molecules to determine the effects of solvating the hydrates. The HN^+—$C(OH)_2$ bonds of **10***a* and **10***b* were stretched in 0.1 Å increments with full geometry optimization (including the associated H_2O molecules) to calculate the potential energy profiles and transition structures for the heterolysis of the unsolvated and solvated hydrates into the corresponding dihydroxy carbenium ions. The associated enthalpies of formation for the hydrates and transition structures are given in Table 5. The calculated $\Delta H^{\neq}$'s shown in Table 5 (8.0–10.0 kcal/mol) fall in the range of the experimental values (Table 1), but the magnitudes are reversed. While the rate-determining steps for the hydrolyses of **1***a*, **1***b*, and **1***c* are not known with certainty, the work of Guthrie et al. — the calculated $\Delta G^{\neq}$ for heterolysis of the HN^+—$C(OH)_2$ bond of the N-protonated hydrate of *N*-methylformanilide where relief of strain is not an important factor is 12.4 kcal/mol — provides support for the calculational results (18). The computed potential energy profile for heterolysis of **10***a*·$2H_2O$ is displayed in Fig. 3. Figures 4*a* and 4*b* show the transition structures for heterolysis of **10***a*·$2H_2O$ and **10***c*·$2H_2O$ labelled with the N—$C(OH)_2$ bond lengths and showing the location of the two solvating waters. The dihydroxy carbenium ion in reality is probably not the final product of the heterolysis, which should be the N-protonated carboxylic acid. In support of this, we have calculated the ΔH_f for the N-protonated amino acids resulting from N—C cleavage of **10***a* and **10***c* with one associated water, the values being 6.67 and 3.59 kcal/mol. With two associated waters, the ΔH_f values are −64.13 and −68.85 kcal/mol, respectively, for the N-protonated amino acids derived from **10***a*·$2H_2O$ and **10***c*·$2H_2O$. These values are substantially lower than the corresponding dihydroxy carbenium ions (carbenium ion derived from **10***a*·$1H_2O$, 19.37; **10***a*·$2H_2O$, −50.41 kcal/mol; **10***c*·$1H_2O$, −55.26 kcal/mol), but we have not explored theoretically the possible routes for the required $C^+(OH)_2 \rightarrow$ N proton transfer. The important result of the calculated enthalpies for heterolysis is the apparent insensitivity of the $\Delta H^{\neq}$ to the presence of the solvating waters. This result is in accord with heats of hydration of NH_4^+ in the presence of one, two, or three water molecules obtained experimentally in the gas phase and with AM1 calculations. The experimental gas phase heats of hydration of NH_4^+ in the presence of one, two, and three water molecules are −17.3, −14.7, and −13.4 kcal/mol, respectively (19); AM1 calculations give values of −15.3, −13.1, and −14.9 kcal/mol, respectively (20). Importantly, the low activation energy for cleavage suggests that the N-protonated hydrates, once formed, easily proceed to products through low-energy pathways involving simple N—$C(OH)_2$ cleavage, followed by rapid proton transfers to yield the N-protonated carboxylic acids as the final products.

In a second study, N-protonated amides **2***a* and **2***b* were solvated with two and three water molecules and subjected to HN^+—C(O) stretches of 0.1 Å to ring open to the corresponding acylium ion. The ΔH_f values for the processes are given in Table 6 while the transition structures are displayed in Figs. 4*c* and 4*d*. Two points are of note. First, the computed ΔH_f values for the geometry-optimized N-protonated amides with associated water molecules are higher than for the corresponding hydrates (e.g., ΔH_f (**2***a*·$2H_2O$) − ΔH_f (**10***a*·$1H_2O$) = 8.2 kcal/mol; ΔH_f (**2***a*·$3H_2O$) − ΔH_f (**10***a*·$2H_2O$) = 9.0 kcal/mol), confirming that solvation does not alter the relative stabilities of the N-protonated amides and corresponding hydrates. Second, the heterolysis of **2***a* → acylium ion in the presence of two or three H_2O molecules proceeds with a $\Delta H^{\neq}$ of 17.9 or 19.2 kcal/mol: the corresponding $\Delta H^{\neq}$ values for the similar heterolysis of **2***c* are 20.8 and 28.8 kcal/mol. These high barriers render N—C cleavage of **2***a,c* to the acylium ions far less likely than the pathways involving hydrate formation followed by N—$C(OH)_2$ cleavage.

Table 6. AM1 enthalpies of activation for heterolysis of solvated N-protonated amides to acylium ions.

Substrate	$\Sigma \Delta H_f^a$ subs. and $2H_2O$	$\Sigma \Delta H_f^a$ subs. and $3H_2O$	ΔH_f TS $2H_2O$	ΔH_f TS $3H_2O$	$\Delta H^{\neq}$ $2H_2O$	$\Delta H^{\neq}$ $3H_2O$
2*a*	22.1	−45.7	40.0	−26.5	17.9	19.2
2*c*	13.4	−58.8	34.2	−30.8	20.8	28.8

[a]In kcal/mol.

Table 7. AM1 enthalpies of activation for nucleophilic ring opening of solvated N-protonated amides.

Substrate	$\Sigma \Delta H_f^a$ subs. and $2H_2O$	$\Sigma \Delta H_f^a$ subs. and $3H_2O$	ΔH_f TS $2H_2O$	ΔH_f TS $3H_2O$	$\Delta H^{\neq}$ $2H_2O$	$\Delta H^{\neq}$ $3H_2O$
2*a*	22.1	−45.7	50.4	[b]	28.3	[b]
2*c*	13.4	−58.8	59.0	−2.9	44.6	55.9

[a]In kcal/mol.
[b]Attempts to refine the transition structure at the maximum of the potential energy surface with SIGMA or NLLSQ calculations failed.

Fig. 3. AM1 potential energy profile for the heterolysis of hydrate **10a** solvated with two water molecules.

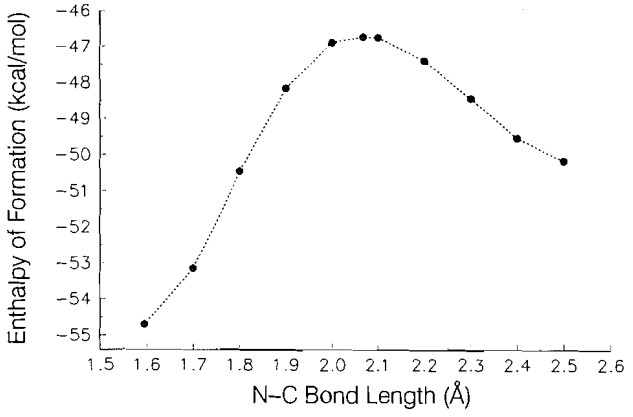

Fig. 4. Displays of the transition structures and the C—N bond lengths (Å) for the heterolysis of N-protonated hydrates and N-protonated amides solvated with two H_2O molecules: (*a*) **10***a*; (*b*) **10***c*; (*c*) **2***a*; (*d*) **2***c*.

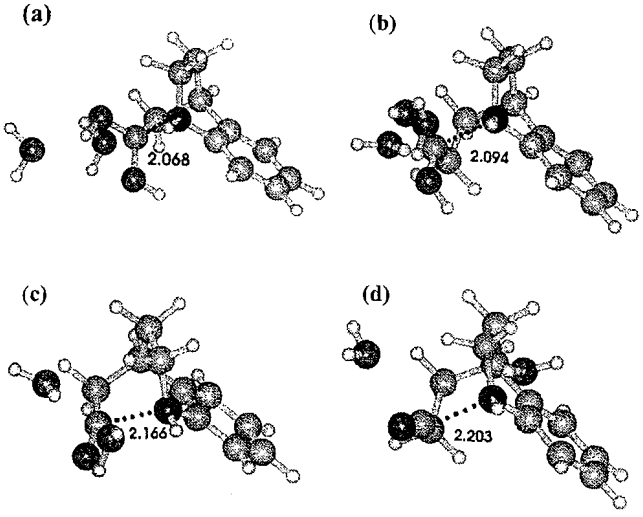

As a final check on the viability of other N—C bond cleavage pathways, a water molecule of the above solvated amides (**2***a*,*c*) was allowed to attack the C=O group. This was done by selecting the H_2O best aligned for nucleophilic attack, and decreasing the H_2O...C=O distance in 0.1 Å increments. The ΔH_f values of the solvated N-protonated amides, the transition structures, and the $\Delta H^{\neq}$'s are given in Table 7. It is seen that the $\Delta H^{\neq}$'s for the nucleophilic reaction of **2***a* and **2***c* with H_2O

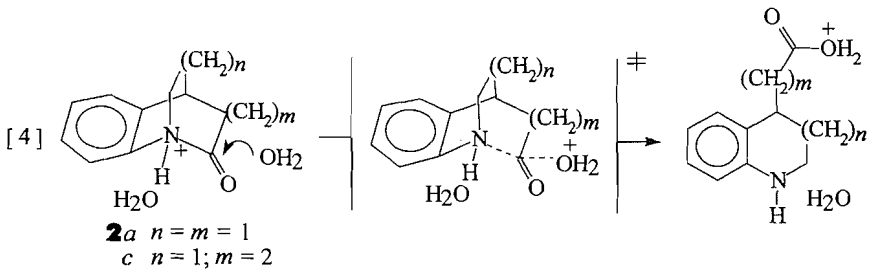

2*a* $n = m = 1$
c $n = 1; m = 2$

are very much larger than the $\Delta H^{\ddagger}$'s found calculationally for the solvolysis of the N-protonated hydrates and amides as well as the values found experimentally. The calculated process is depicted in eq. [4] and leads to the corresponding O-protonated carboxylic acids. Because the O-protonated carboxylic acid is a very strong acid, proton transfer, possibly occurring simultaneously with ring opening, to a solvating water molecule would be fast. The neutral amino acid with the hydronium ion bonded with the carbonyl group would, in a fast process in the solvent cage, transform into the N-protonated amino acid. We have not investigated possible routes for the proton transfers calculationally. Nevertheless, this study suggests that the N-protonated distorted amides do not hydrolyse via the nucleophilic ring-opening reaction depicted in eq. [4].

Acknowledgement

We thank the Natural Sciences and Engineering Research Council of Canada for financial support.

References

1. V. Somayaji and R.S. Brown. J. Org. Chem. **51**, 2676 (1986).
2. Q.-P. Wang, A.J. Bennet, R.S. Brown, and B.D. Santarsiero. J. Am. Chem. Soc. **113**, 5757 (1991).
3. PCMODEL, Version 4.0. Molecular modeling software. Available from Dr. K. Gilbert, Serena Software, Box 3076, Bloomington, IN 47402-0823.
4. HYPERCHEM. Release 2.0. A molecular modeling package. Autodesk Inc., 2320 Marinship Way, Sausalito, CA 94965.
5. Dewar Research Group and J.J.P. Stewart. Austin Model 1, Package 1.0. QCPE, 506 (1986).
6. J.J.P. Stewart. MOPAC, a semi-empirical molecular orbital program. QCPE, 455 (1983).
7. V. Somayaji, K.I. Skorey, R.S. Brown, and R.G. Ball. J. Org. Chem. **51**, 4866 (1986).
8. K.B. Wiberg and K.E. Laidig. J. Am. Chem. Soc. **109**, 5935 (1987).
9. K.B. Wiberg and R. Glaser. J. Am. Chem. Soc. **114**, 841 (1992).
10. R.F.W. Bader. Atoms in molecules — a quantum theory. Clarendon Press, Cambridge. 1990.
11. A. Greenberg and C.A. Venanzi. J. Am. Chem. Soc. **115**, 6951 (1993).
12. S.G. Lias, J.E. Bartmess, J.F. Liebman, J.L. Holmes, R.D. Levin, and W.G. Mallard. J. Phys. Chem. Ref. Data, **17**, Suppl. No. 1 (1988).
13. A.E. Howard and P.A. Kollman. J. Am. Chem. Soc. **110**, 7195 (1988).
14. B.M. Wepster. Recl. Trav. Chim. Pays-Bas, **71**, 1171 (1952).
15. A.J. Williams. J. Am. Chem. Soc. **98**, 5645 (1976).
16. W. Parker, R.L. Tranter, C.I.F. Watt, L.W. Chang, and P.v.R. Schleyer. J. Am. Chem. Soc. **96**, 7121 (1974).
17. Q.-P. Wang. Ph.D. Thesis, University of Alberta, 1991.
18. J.P. Guthrie, J. Barker, P.A. Cullimore, J. Lu, and D.C. Pike. Can. J. Chem. **71**, 2109 (1993).
19. P. Kebarle. *In* Environmental effects on structure and properties. *Edited by* B. Pullman. D. Reidel, Dordrecht, The Netherlands. 1976. p. 81.
20. J.P.P Stewart. J. Comput. Chem. **10**, 221 (1989).

Synthesis and characterization of polymer-bound selenium coronands: enhancing the stability of reactive dications by restricting intermolecular interactions

Ivan Cordova-Reyes, Hanbin Hu, Jian-Hua Gu, Elizabeth VandenHoven, Ali Mohammed, Steven Holdcroft, and B. Mario Pinto

Abstract: The stepwise synthesis of 1,5,9,13-tetraselenacyclohexadecan-3-ol **7** from the reaction of sodium propane-1,3-bisselenolate-2-ol with 4,8-diselenaundecan-1,11-di-*p*-toluenesulfonate **5** in THF and ethanol in 62% yield is described. Compound **5** is obtained from the corresponding diol **3**, which is obtained, in turn, from the reaction of sodium propane-1,3-bisselenolate with two equivalents of 3-chloropropanol. 1,5-Diselenacyclooctan-3-ol **9** and 1,5,9,13-tetraselenacyclohexadecan-3,11-diol **10** are obtained in yields of 43% and 11%, respectively, from the one-step reaction of sodium propane-1,3-bisselenolate-2-ol with 1,3-dibromopropane. Polymers with pendant selenium coronands, 1,5-diselenacyclooctane (8Se2) and 1,5,9,13-tetraselenacyclohexadecane (16Se4), have been prepared by free radical polymerization of the corresponding selenium coronands **9** and **7**, derivatized as their acryloyl esters **11** and **12**. Copolymers of methyl acrylate and 3,7-diselenacyclooctyl acrylate **11** have also been prepared in analogous fashion. The polymers have been characterized by ^{1}H and ^{13}C NMR, IR, and UV–visible spectroscopy. The redox chemistry of polymer-bound selenium coronands in solution, and in the form of thin films coated on electrodes, has been determined by electrochemical methods. Selenium coronands attached to the polymer chain exhibit enhanced oxidative stability compared to monomeric analogues, presumably because restrictive motion of polymer-bound moieties inhibits inter- and intra-molecular degradation reactions. Electroactivity of polymer-modified electrodes is restricted to a few monolayers close to the electrode surface. Spatial separation of coronands along the chain, achieved by copolymerization with electro-inert methyl acrylate, gave copolymer-modified electrodes that possessed even greater redox stability than their corresponding homopolymers. Furthermore, by blending electro-inert poly(methyl acrylate) with electroactive selenium coronand copolymers, polymer-modified electrodes that possessed superior electrochemical stability were obtained.

Key words: selenium coronands, polymers, electrochemistry, dications.

Résumé : On décrit la synthèse par étape (rendement de 62%) du 1,5,9,13-tétrasélénacyclohexadécan-3-ol, **7**, réalisée par réactions par étapes du propane-1,3-bissélénolate-2-ol de sodium avec le di-*p*-toluènesulfonate de 4,8-disélénundécan-1,11-diyle, **5**, dans le THF et l'éthanol. On obtient le composé **5** à partir du diol **3** correspondant qui est obtenu, à son tour, par la réaction du propane-1,3-bissélénolate de sodium avec deux équivalents de 3-chloropropanol. Les 1,5-disélénacyclooctan-3-ol, **9**, et 1,5,9,13-tétrasélénacyclohexadécan-3,11-diol, **10**, ont été obtenus avec des rendements respectifs de 43% et de 11% par des réactions en une étape du propane-1,3-bissélénolate-2-ol de sodium avec le 1,3-dibromopropane. On a préparé des polymères portant des pendants de coronands de sélénium, 1,5-disélénacyclooctane (8Se2) et 1,5,9,13-tétrasélénacyclohexadécane (16Se4), en procédant à la polymérisation des coronands séléniés correspondants, **9** et **7**, transformés en dérivés sous la forme de leurs esters acryloyles, **11** et **12**. Opérant d'une façon analogue, on a aussi préparé les copolymères de l'acrylate de méthyle et l'acrylate de 3,7-disélénacyclooctyle, **11**. On a caractérisé les polymères par leurs spectres RMN du ^{1}H et du ^{13}C ainsi que par leurs spectres IR et UV–visible. Faisant appel à des méthodes électrochimiques, on a déterminé la chimie rédox des coronands du sélénium liés à ces polymères, en solution ainsi que sous la forme de films minces sur des électrodes. Les coronands du sélénium attachés au polymère présentent une stabilité oxydative qui est augmentée par rapport aux analogues monomériques, probablement à cause des restrictions aux mouvements des portions attachées au polymère qui inhibent les réactions de dégradations inter- et intramoléculaires. L'électroactivité des électrodes modifiées par le polymère est restreinte à quelques monocouches proches de la surface de l'électrode. La séparation spatiale des coronands le long de la chaîne, qui est réalisée par une copolymérisation avec de l'acrylate de méthyle électro-inerte, fournit des électrodes modifiées par le copolymère qui possèdent une stabilité rédox encore plus grande que celle des homopolymères correspondants. De plus, en mélangeant du

Received November 29, 1995.

I. Cordova-Reyes, H. Hu, J.-H. Gu, E. VandenHoven, A. Mohammed, S. Holdcroft,[1] and B.M. Pinto.[1] Department of Chemistry, Simon Fraser University, Burnaby, BC V5A 1S6, Canada.

[1] Authors to whom correspondence may be addressed. Telephone: (604) 291-4327. Fax: (604) 291-3765.

poly(acrylate de méthyle) électro-inerte avec des copolymères électroactifs de coronands du sélénium, on a obtenu des électrodes modifiées par le polymère qui possèdent une stabilité électrochimique supérieure.

Mots clés : coronands du sélénium, polymères, électrochimie, dications.

[Traduit par la rédaction]

Introduction

We recently reported the synthesis of a novel class of compounds, the selenium coronands (1–3). Of interest to us was the comparison of properties between the selenium coronands and the lighter sulfur congeners, in particular, the preferential stabilization of transition metal ions by these macrocycles, the effect of ligand conformation on chelation, and the propensity for electron transfer reactions in the free ligands as well as in the metal-ion complexes. Towards this end, we have reported the conformational analysis of the free ligands (1, 2), their metal-ion complexation properties (4–6), and the unusual electron transfer reaction of a Cu(II)–selenium coronand complex (4). Although the metal-ion complementarity and structural features of the complexes are similar to those of the sulfur congeners (4–8), the observed differences in electron transfer chemistry (4) were not anticipated and were linked to the propensity for transannular stabilization in the ligands.

We now report the synthesis of functionalized selenium coronands for incorporation into polymers or for the ready attachment of aliphatic or functionalized chains. The latter compounds are of interest for the development of transition-metal ion-selective electrodes and membrane transport systems or for the generation of water soluble or micellar transition-metal ion transport systems. We also report the synthesis of the first polymer-bound selenium coronands for investigation as new materials together with their characterization by spectroscopic and electrochemical techniques. We describe the electrochemistry of polymers in solution and in the form of polymer-modified electrodes, and illustrate how spatial control of the coronands leads to stabilization of their oxidized state.

Results and discussion

Synthesis

The strategy for the synthesis of the polymeric selenium coronands involved the synthesis of a selenium coronand bearing a hydroxyl functional group, which could be used subsequently to tether the selenium coronands to a second functional group to form a reactive monomer. An acrylate ester was chosen as the latter functional group and radical-initiated vinyl polymerization as the method of polymerization. The route is general in that it can be adapted to yield different polymers by choice of the vinyl group attached to the coronand or the selenium coronand itself. The strategy is illustrated here for the case of two selenium coronands, as their acrylate esters. In addition, copolymers have been synthesized from the selenium coronand-containing monomers and other reactive monomers.

The monomers were synthesized as follows. Reaction of the bisselenolate anion, derived from propane-1,3-bisselenocyanate **1** (9) by sodium metal reduction in liquid ammonia, with 2 equivalents of 3-chloropropanol **2** afforded the acyclic diol containing two selenium atoms, namely 4,8-diselenaundecane-1,11-diol **3** in 89 % yield (Scheme 1). Tosylation of the diol **3** gave a mixture of the monotosylate **4** (21%) and the

Scheme 1.

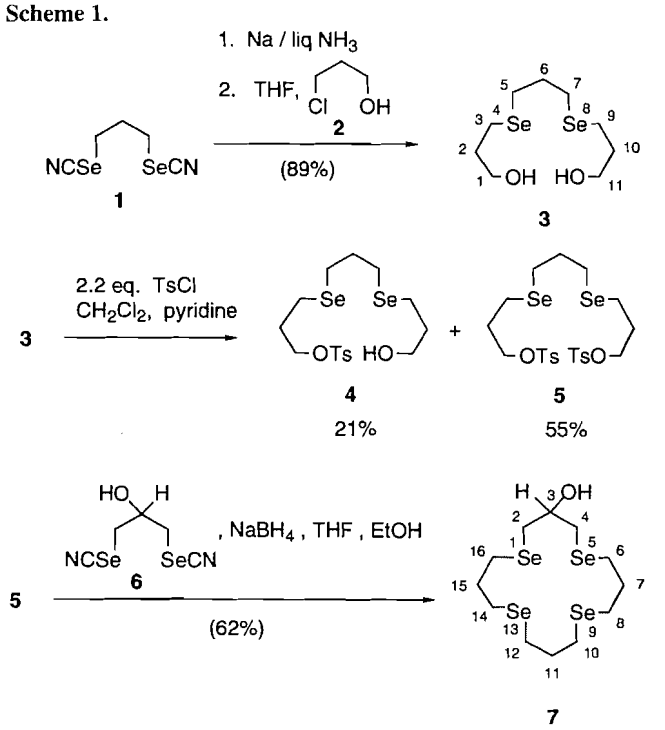

desired ditosylate **5** (55%). Conversion of the ditosylate to the functionalized coronand was effected by treatment with the bisselenolate anion derived from 1,3-bisselenocyanatopropan-2-ol **6**. Compound **6** was obtained, in turn, from the nucleophilic displacement of 1,3-diiodo-2-propanol with potassium selenocyanate in acetone. The optimum conditions for the cyclization reaction consisted of the simultaneous addition of the ditosylate **5** and the bisselenocyanate **6** to a suspension of sodium borohydride in a mixture of THF and ethanol over a period of 10 h. The target 16-membered selenium coronand containing four selenium atoms and a hydroxyl moiety **7** was obtained in a yield of 62%.

The synthesis of the mono-functionalized 8-membered coronand and the difunctionalized 16-membered coronand was a one-step synthesis that consisted of the reaction of the bisselenolate anion derived from **6** and 1,3-dibromopropane **8** (Scheme 2). 1,5-Diselenacyclooctan-3-ol **9** and 1,5,9,13-tetraselenacyclohexadecan-3,11-diol **10** were obtained in yields of 43% and 11%, respectively.

Reaction of 1,5-diselenacyclooctan-3-ol **9** with acryloyl chloride in THF and dichloromethane containing triethylamine afforded the acrylate ester **11** in 87% yield (Scheme 3). Similarly, 1,5,9,13-tetraselenacyclohexadecan-3-ol **7** was converted to its acrylate ester **12** in 75% yield. The monomer **11** was polymerized in oxygen-free benzene containing AIBN as a radical initiator to give poly(1,5-diselenacyclooctyl acrylate) (poly(8Se2)) **13** in 90% yield (Scheme 4). An analogous reaction of the monomer **12** afforded poly(1,5,9,13-tetraselenacyclohexadecyl acrylate) (poly(16Se4)) **14** in 95% yield.

Scheme 2.

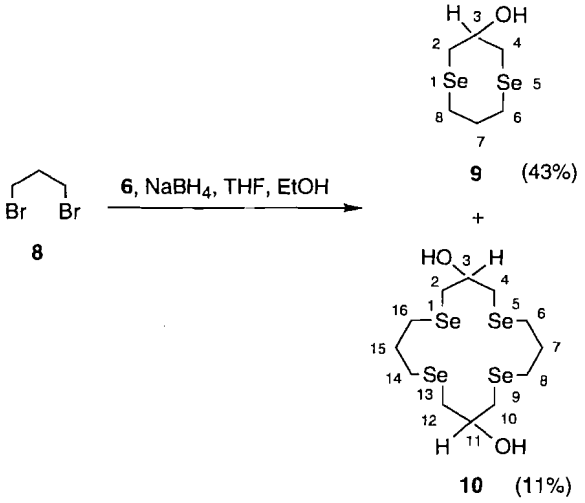

Scheme 3.

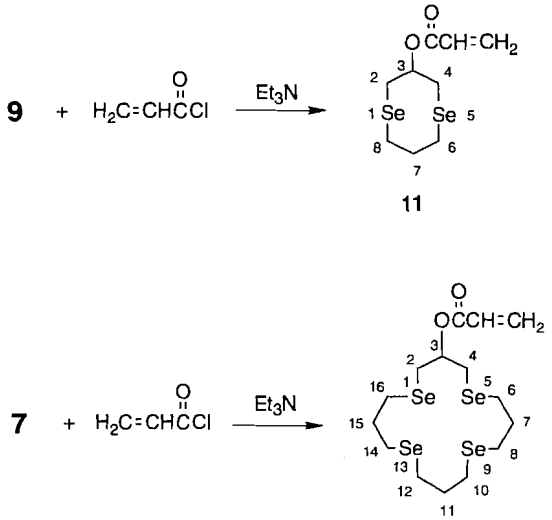

Copolymers consisting of 1,5-diselenacyclooctyl acrylate units and methyl acrylate units were prepared with mixtures of methyl acrylate **15** and 1,5-diselenacyclooctyl acrylate **11** in analogous fashion to that described above (Scheme 5). A starting ratio of **11**:**15** of 1:1 yielded a copolymer **16** with a ratio of diselenacyclooctyl acrylate:methyl acrylate units of 1.4:1, as determined by integration of the peaks for H_3 and OCH_3 in the ^{1}H NMR spectrum. A separate experiment with a starting ratio of **11**:**15** of 1:2 yielded a copolymer **16** with a ratio of diselenacyclooctyl acrylate:methyl acrylate units of 0.75:1.

The microanalysis for **13** was calculated based on a degree of polymerization of 8 and on the assumption that chain termination had occurred via disproportionation, to give one $(CH_3)_2CHC(CN)H$ unit per molecule. In the case of **14**, a molecular weight determination was not possible but a degree of polymerization of 8 was found to be consistent with the analytical data.

^{1}H NMR spectra

The ^{1}H NMR spectra of poly(8Se2) **13** and mono 8Se2 **11** (Fig. 1) clearly show that the vinyl hydrogens of mono 8Se2 (5.70 ppm to 6.50 ppm) disappear after the polymerization.

Scheme 4.

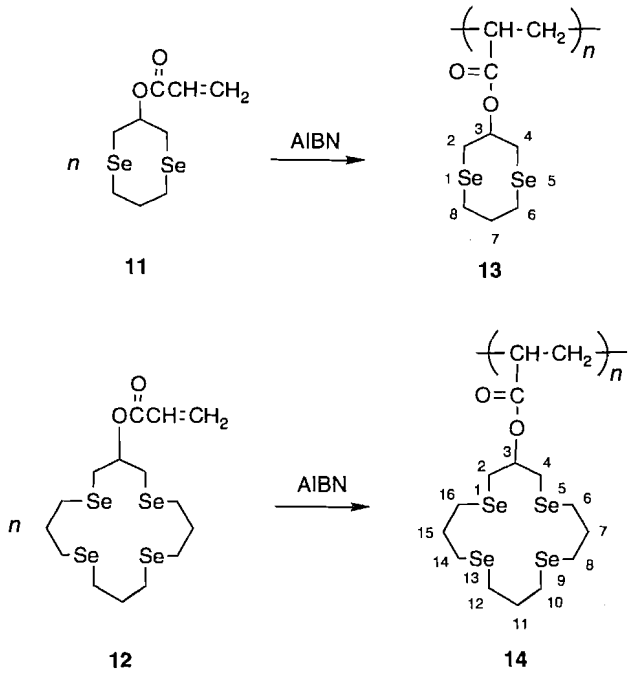

Scheme 5.

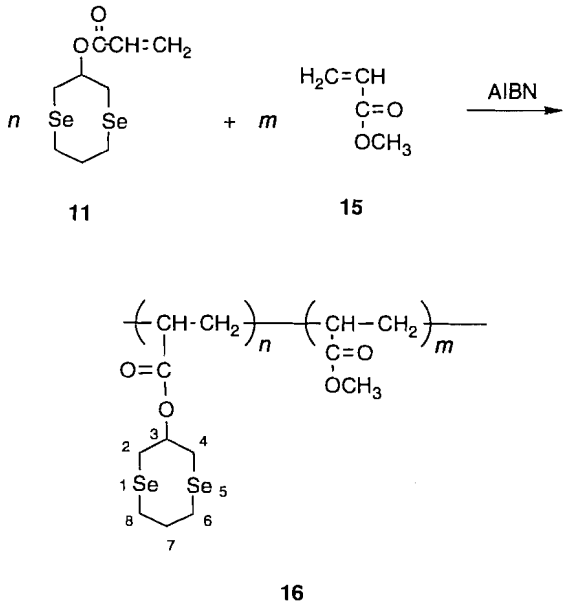

Several new signals, associated with backbone hydrogens of the polymer chain, appear in the region 1.40–2.30 ppm. For poly(8Se2), the peak at 2.27 ppm is assigned to -CO-C*H*-CH_2- of the polymer backbone and the peaks at 1.46, 1.64, and 1.88 ppm to the two diastereotopic methylene protons (-CO-CH-CH_2). The complexity of these signals indicates that the structure of the poly(8Se2) is an atactic polymer. Comparison of the spectra of mono 16Se4 **12** and poly(16Se4) **14** indicates similar features to those of the lower homologues, mono 8Se2 **11** and poly(8Se2) **13** (Fig. 2).

Electrochemistry of selenium coronands

Selenium coronands 8Se2 and 16Se4 were electrochemically

Fig. 1. ^{1}H NMR spectra of (*a*) mono 8Se2 **11** and (b) poly(8Se2) **13**.

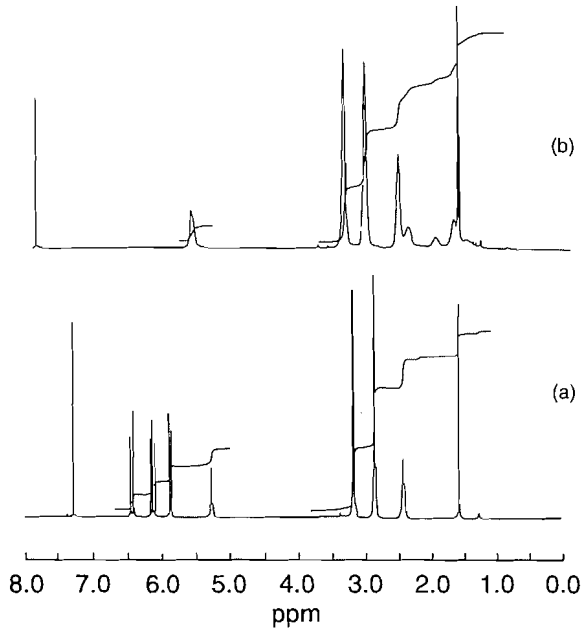

Fig. 2. ^{1}H NMR spectra of (*a*) mono 16Se4 **12** and (*b*) poly(16Se4) **14**.

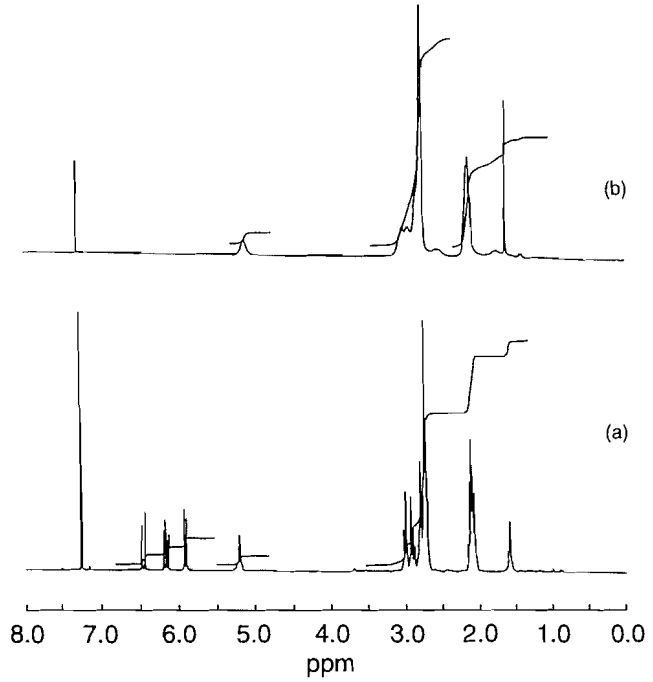

oxidized at carbon electrodes. The redox processes are complex due to subsequent chemical reactions following electron transfer. Previous studies on the electrochemistry of 16Se4 in dichloromethane–TEAP electrolyte revealed that radical cation and dication intermediates undergo rapid chemical rearrangement via one of two paths (6, 10). The first path is intermolecular in nature, in which oxidized species react with neutral ligands, as shown below; L represents the selenium coronand and subscripts refer to different selenium coronands. The second pathway occurs intramolecularly via transannular

Fig. 3. Scan rate dependence on cyclic voltammograms of 1×10^{-3} M 1,5-diselenacylcyclooctane (8Se2) in 0.1 M TEAP – CH_3CN. Reference electrode, Ag/AgCl.

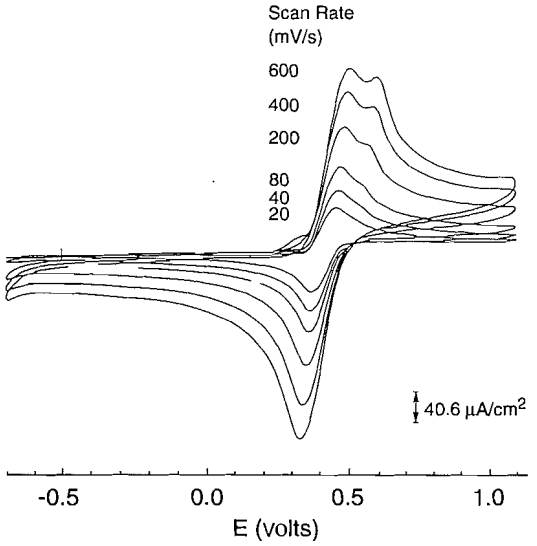

stabilization (4,6,10). The scheme is analogous to that proposed by Asmus and Musker for the oxidation of 1,5-dithiacyclooctane (11).

$$[1] \quad L_1 \xrightarrow{-e^-} L_1^{+\cdot} \xrightarrow{L_2} [L_1 - L]^{+\cdot}$$

In the present study, the electrochemistry of free and polymer-bound selenium coronands was investigated in acetonitrile and dichloromethane, respectively; polymer-modified electrodes were studied in acetonitrile. Cyclic voltammograms of 8Se2 in acetonitrile–TEAP were found to be quasi-reversible. Previous studies in CH_2Cl_2 established that the oxidation proceeded by a two-electron transfer process (6, 10, 12). In acetonitrile solvent, a single oxidation peak was observed at slow voltage sweep rates (<20 mV/s) whereas two oxidation peaks were observed at faster sweep rates (Fig. 3). These results are consistent with previous electrochemical studies of selenium coranands (6, 10, 12) and sulfur coronands (11). Thus, by drawing upon previous reports, the electrochemistry can be explained in the following manner (Scheme 6). Following oxidation of 8Se2 to form a radical cation, either a second electron is removed to form a diradical cation with subsequent formation of a transannular bond or, alternatively, the radical cation undergoes transannular stabilization prior to losing a second electron. Under the fast scan rate regime, two oxidation peaks are observed due to two one-electron transfer steps. We suggest the occurrence of a "slow" transannular reaction of the intermediates. The oxidation process is designated an EEC (electrochemical–electrochemical–chemical) process. At slow scan rate, e.g., <20 mV/s, transannular stabilization occurs on the time scale of the experiment so that only one two-electron oxidation peak is observed. This pathway represents an ECE process.

We and others have previously established that the opportunity exists for inter-coronand reactions between oxidized and neutral species during the electrochemical process (eq. [1]) (6, 10, 11). Thus, the concentration of the coronand is expected to play an important role. Indeed, as the concentration of the selenium coronand is increased from 10^{-3} M to 10^{-2} M, inter-

Scheme 6.

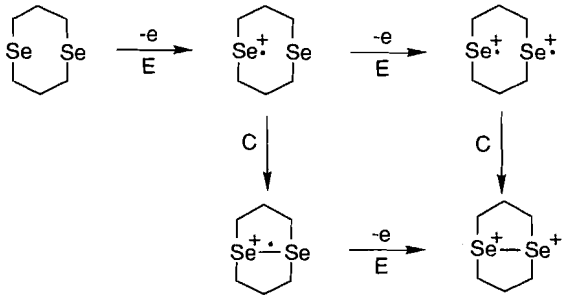

Fig. 4. Concentration dependence of cyclic voltammograms of 1,5-diselenacylcyclooctane (8Se2) in 0.1 M TEAP – CH_3CN: (*a*) 1×10^{-3} M, (*b*) 1×10^{-2} M. Reference electrode, Ag/AgCl; scan rate, 20 mV/s.

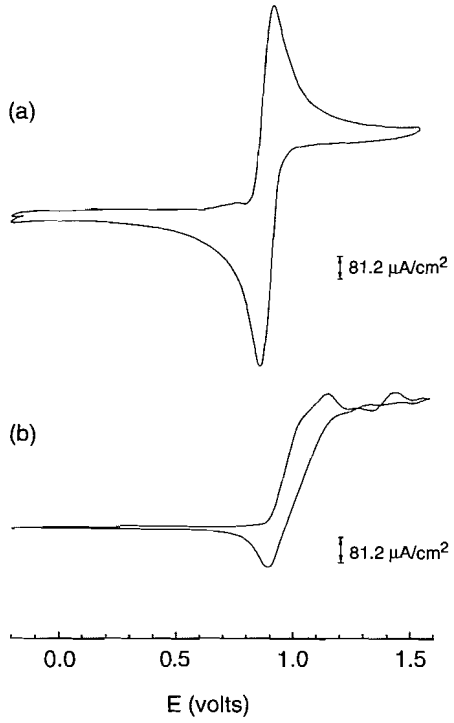

molecular reactions between oxidized products and neutral selenium coronand are more pronounced, and it becomes difficult to observe the corresponding re-reduction peak, as observed in Fig. 4. In addition, at higher concentrations, a red/brown precipitate (elemental selenium) is formed near the electrode surface upon oxidation.

A cyclic voltammetric study shows that the redox chemistry of 16Se4 in acetonitrile–TEAP (Fig. 5) is slightly different from that of 8Se2. Each oxidation peak corresponds to a one-electron transfer (6, 10). We propose that the radical cation formed, $[16Se4]^{+\cdot}$, rapidly undergoes transannular stabilization, and a new selenium–selenium bond is formed. The proposal is based on the observation of such transannular stabilization in the dication, $[16Se4]^{2+}$, and on the similarity of λ_{max} values (256 nm) for the dication and the radical cation observed in spectroelectrochemical experiments (10). Removal of a second electron prior to transannular stabilization, i.e., the EE process, is not competitive on the time scale of the experiment. Thus, it appears that oxidation of 16Se4 is

Scheme 7.

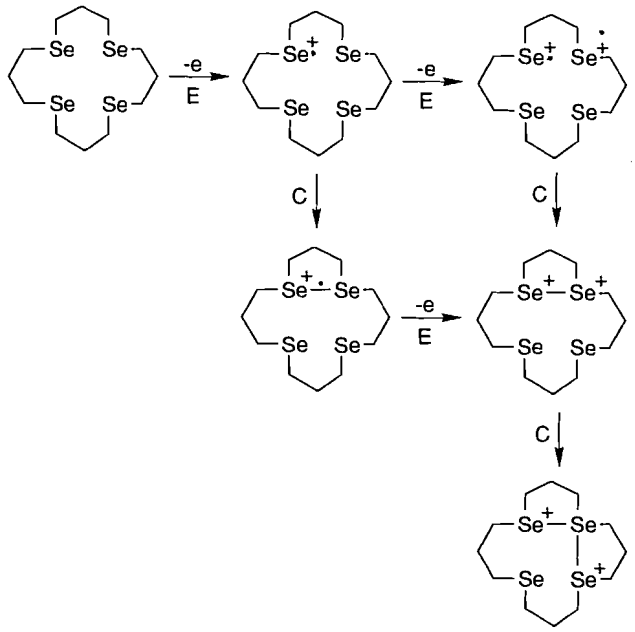

Fig. 5. Concentration dependence of cyclic voltammograms of 1,5,9,13-tetraselenacyclohexadecane (16Se4) in 0.1 M TEAP – CH_3CN: (*a*) 1×10^{-4} M, (*b*) 1×10^{-2} M. Reference electrode, Ag/AgCl; scan rate: 20 mV/s.

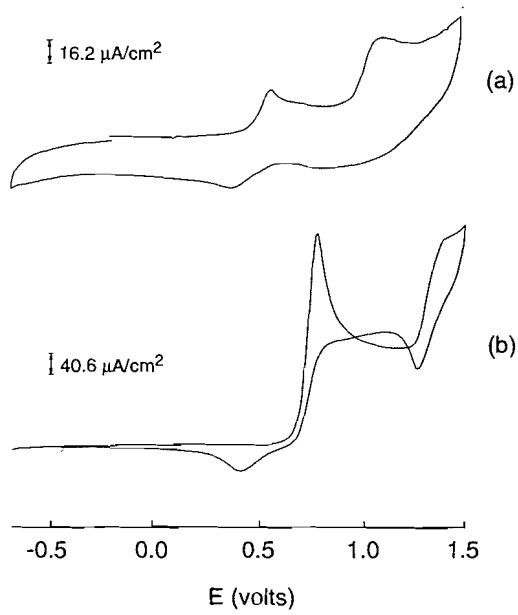

dominated by an ECEC process, as shown in Scheme 7. As a result of rapid transannular stabilization of the radical cation, changing the potential scan rate affects the shapes of cyclic voltammograms to a lesser degree than 8Se2 (not shown); if the redox process had gone through the EECC process as shown in Scheme 7, the ratio of anodic to cathodic peak currents would have exhibited considerable scan rate dependence. As was the case with 8Se2, increasing the concentration of the 16Se4 has a pronounced effect on the voltammograms, as shown in Fig. 5. Cyclic voltammetry obtained with the lowest concentration of 16Se4 shows two

Fig. 6. Cyclic voltammograms of poly(8Se2) **13** in 0.1 M TEAP – CH_3CN: (*a*) 1×10^{-4} M, (*b*) 1×10^{-3} M, (*c*) 1.3×10^{-2} M. Reference electrode, Ag/AgCl; scan rate: 20 mV/s. Concentrations are given with respect to pendant selenium coronands.

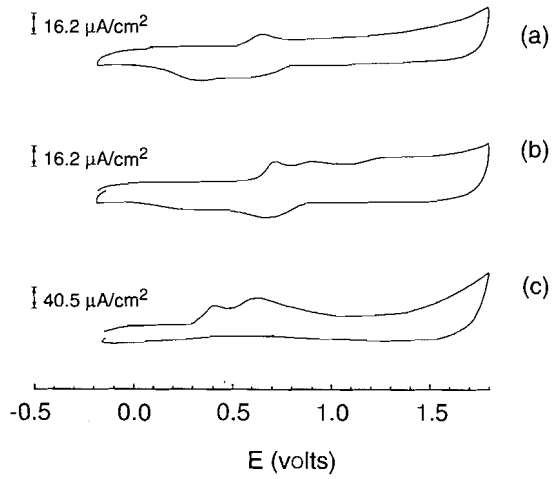

Fig. 7. Cyclic voltammograms of poly(16Se4) **14** in 0.1 M TEAP – CH_2Cl_2: (*a*) 1×10^{-4} M, (*b*) 5×10^{-3} M. Reference electrode, Ag/AgCl; scan rate, 80 mV/s. Concentrations are given with respect to pendant selenium coronands.

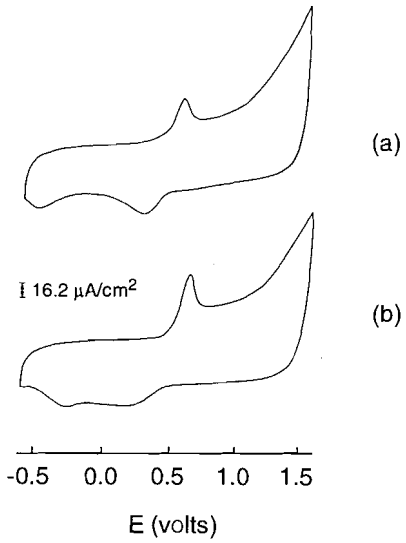

relatively reversible electrochemical oxidations, but as the concentration is increased the voltammetry deviates from Nernstian behaviour and gives rise to irregular voltammetric responses. We attribute this behaviour to the prevalence of intermolecular reactions of the oxidized intermediates with neutral ligand at high concentrations of the reactant. This effect is less pronounced for 16Se4 than for 8Se2, presumably because of the relative stability of $[16Se4]^{2+}$ over $[8Se2]^{2+}$. For both 8Se2 and 16Se4, the oxidation peak current varies linearly with the square root of scan rate, indicating that anodic oxidation is diffusion controlled.

Cyclic voltammetric studies of the monomers 1,5-diselenacyclooctylacrylate (mono8Se2) **11** and 1,5,9,13-tetraselenacyclohexadecyl acrylate (mono16Se4) **12** show that their redox behaviour is similar to that of the corresponding selenium coronands, indicating that the double bond associated with the monomer has no obvious effect on the redox properties of the coronand. We have also synthesized 1,5,9,13-tetraselenacyclohexadecyl propionate, in which the double bond in mono16Se4 **12** is saturated. The cyclic voltammograms of this compound are similar to that of mono16Se4, indicating that the functionality connecting the selenium coronands to the polymer chain has no electronic influence on the electrochemistry of the coronand. The relationship of i_{pa} versus $\upsilon^{1/2}$ for all small molecules evaluated in this study was linear, indicating diffusion-controlled electrochemistry.

Electrochemistry of poly(selenium coronands)

For the poly(selenium coronands), the electroactive pendant funtionalities are sterically crowded by virtue of their covalent attachment to the polymer backbone. As a result, the microscopic concentration of selenium coronands is relatively high both in solution and in the solid state, even though the macroscopic polymer concentration may be low. In principle, the high concentration of coronands might facilitate intermolecular reactions and, therefore, the redox properties of the polymer in the solution would be expected to be irreversible. Alternatively, the close juxtapositioning of electroactive functionality might facilitate electron hopping along, and between, polymer chains. Figures 6 and 7 show cyclic voltammograms of poly(8Se2) **13** and poly(16Se4) **14** in solution for various concentrations of polymer.

The voltammograms of low molar concentrations of the poly(8Se2) **13** ($[8Se2] < 10^{-3}$ M) show a relatively high degree of reversibility. This is surprising since the local concentration of the selenium coronand bound to a polymer chain in a polymer solution is estimated to be 0.1–1 M based on the root-mean-square volume of a polymer coil in a good solvent. Upon increasing the concentration of poly(8Se2), the reduction peaks gradually disappear into the baseline and, as with the oxidation of 8Se2 in solution, new oxidation peaks appear. This is believed to be due to a corresponding increase in intermolecular coupling reactions between oxidized and neutral selenium coronands on different polymer chains.

In contrast, no obvious changes in the shapes of voltammograms with increasing concentration are observed for poly(16Se4) **14** (Fig. 7). The anodic peak current remains constant with increasing concentration, which indicates electroprecipitation of the polymer to form a polymer-modified electrode. It will be shown in a following section that poly(selenium coronands) in the form of thin films on electrodes exhibit enhanced reversibility and stability compared to polymers oxidized in solution.

Copolymers of mono8Se2 and methylacrylate were prepared in which the diluting effect of the methylacrylate group was employed to partially separate 8Se2 selenium coronands on the polymer chains. Thus, electron transfer processes between adjacent selenium coronands should be interrupted and intermolecular reactions inhibited. Figure 8 shows the cyclic voltammograms of two copolymers. Cop8Se2-A possesses a molar 8Se2 to methylacrylate ratio of 1.4:1, and Cop8Se2-B possesses a ratio of 0.75:1. A direct comparison of the behaviour of poly(8Se2) **13**, (Fig. 6) with that of the copolymers at an equivalent coronand concentration of $\sim 10^{-3}$ M confirms that separation of the electroactive units along the chain leads to much greater reversibility upon anodic oxidation. When the concentration of the copolymer in solution is

Fig. 8. Cyclic voltammograms of copolymers in 0.1 M TEAP – CH_2Cl_2: (*a*) Cop8Se2-A **16** (1.0×10^{-3} M), (*b*) Cop8Se2-B **16**, (1.05×10^{-3} M). Reference electrode, Ag/AgCl; scan rate: 20 mV/s. Concentrations are given with respect to pendant selenium coronands.

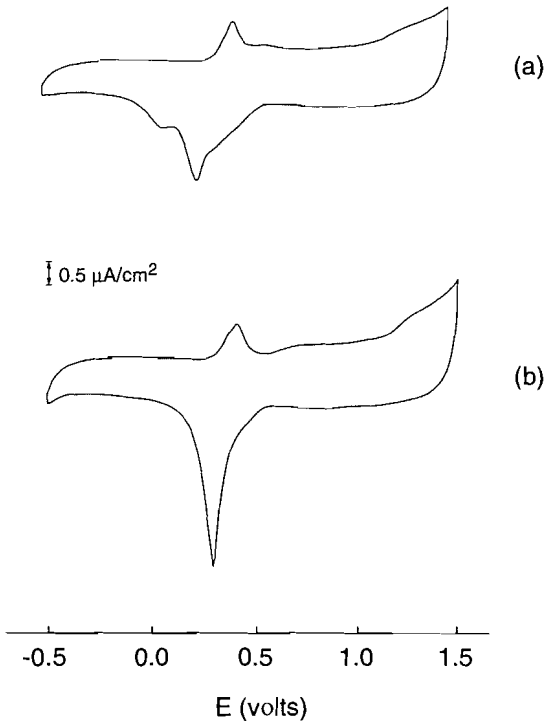

increased such that the coronand concentration increases from 10^{-4} to 10^{-2} M, a loss in reversibility similar to that observed for poly(8Se2) **13** is observed, indicating that interchain coupling reactions become increasingly important at high concentration.

Polymer modified electrodes

In the previous section, the cyclic voltammetry of polymers in solution has been described. However, for applications of ion-selective and ion-permeable membranes, and for electrocatalysis, it is necessary to understand redox processes occurring in swollen films (13). This was achieved by studying poly(8Se2) polymer-modified electrodes in acetonitrile–TEAP electrolyte. This electrolyte was chosen because acetonitrile swells the polymer, thus allowing electrolyte to access the polymer–electrode interface but not dissolve it. A cyclic voltammogram of polymer-modified electrodes based on poly(8Se2) **13** is shown in Fig. 9*a*. The reverse potential cycle indicates that the redox couple is partially reversible. This is remarkable given that the concentration of 8Se2 in the film is calculated to be ~3 M. We believe that this enhanced stability is due to the physical constraint of the selenium coronands in the film that serves to restrict intra-chain and inter-chain coupling reactions. Polymer-modified electrodes using poly(16Se4) **14** also exhibit quasi-reversible cyclic voltammograms (Fig. 9*b*). The electrochemistry of poly(8Se2) **13** and poly(16Se4) **14** was not completely reversible, and a loss of electroactivity was observed upon repetitive cycling. However, copolymers Cop8Se2-A and Cop8Se2-B were found to be much more stable to repetitive potential cycling than the corresponding

Fig. 9. Cyclic voltammograms of polymer modified electrodes in 0.1 M TEAP – CH_3CN: (*a*) poly(8Se2) **13**, (*b*) poly(16Se4) **14**. Scan rate: 160 mV/s.

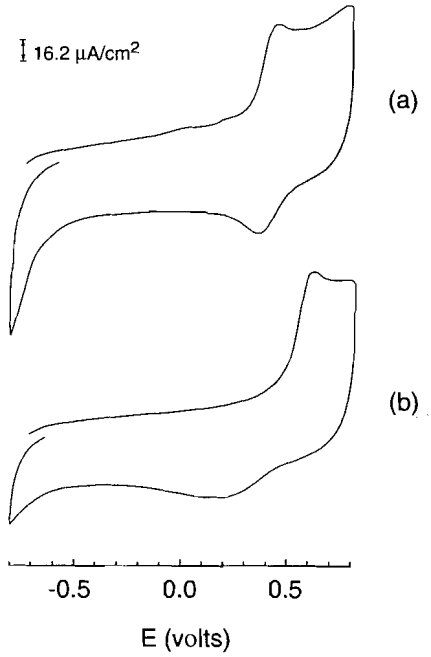

Fig. 10. Ratio of Q_c/Q_a against number of redox cycles for polymer-modified electrodes in 0.1 M TEAP – CH_3CN: (*a*) Cop8Se2-B **16**, (*b*) Cop8Se2-A **16**, (*c*) poly(8Se2) **13**.

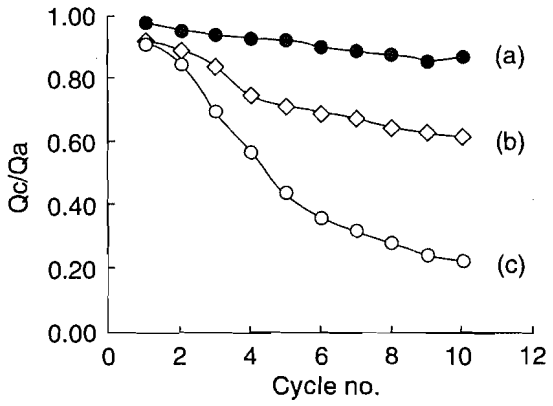

homopolymer. We attribute this behaviour to the spatial separation of coronands and lesser extent of intermolecular coupling reactions in the copolymer samples. A reasonable measure of the electroactive stability was obtained by plotting the cathodic to anodic charge ratio, i.e., charge under the re-reduction peak divided by the charge under the oxidation peak (Q_c/Q_a), against the number of potential cycles. A decreasing Q_c/Q_a ratio with the number of scans indicates instability of the oxidized form. Figure 10 indicates that electrochemical stability increases in the order poly(8Se2) < Cop8Se2-A < Cop8Se2-B, consistent with the decreasing concentration, and increasing spatial separation, of 8Se2 in the polymer films.

In addition to separating coronands along the polymer chain, we attempted to physically separate poly(8Se2) chains from one another by preparing polymer blends in which poly(8Se2) **13**, Cop8Se2-A **16**, and Cop8Se2-B **16** were

Table 1. Characteristics of electrodes modified with films of poly(selenium coronands).

	poly(8Se2) (**13**)	poly(16Se4) (**14**)
Q_a (C)[a]	4.8×10^{-6}	4.47×10^{-6}
Γ_{exp} (mol/cm^2)[b]	4.35×10^{-10}	4.05×10^{-10}
d (μm)[c]	0.1	1.0
Γ_{calc} (mol/cm^2)[d]	4.54×10^{-8}	2.60×10^{-7}

[a]Q_a, charge under anodic peak.
[b]Γ_{exp}, experimentally determined electroactive surface coverage.
[c]Film thickness.
[d]Γ_{calc}, calculated surface coverage of coronands.

Fig. 11. Ratio of Q_c/Q_a against number of redox cycles for polymer-modified electrodes in 0.1 M TEAP – CH_3CN: (*a*) 1:1 Cop8Se2-A **16**/poly(methylacrylate) blend; (*b*) 1:1 Cop8Se2-B **16**/poly(methylacrylate) blend; (*c*) 1:1 poly(8Se2) **13**/poly(methylacrylate) blend.

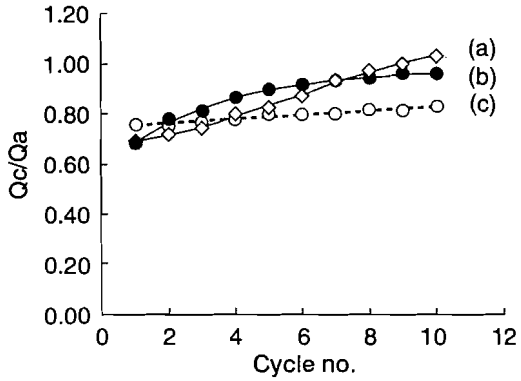

mixed, and solution-cast with an inert polymer, poly(methylacrylate) (PMA). Blends of poly(8Se2) with PMA represent polymer systems in which the coronands are juxtaposed to one another along the polymer chain but in which individual chains are diluted in the solid state by inert polymer chains. For blends of the copolymers, the coronands are separated along the chain, in addition to having the polymer chains physically separated from one another. Cyclic voltammograms of the polymer-blend-modified electrodes indicate superior electrochemical stability compared to pure poly(8Se2) **13** and its copolymers, as evidenced from the plot of Q_c/Q_a against the number of scans (Fig. 11). Many of the films showed an increase in Q_c/Q_a with increasing scan number, which can be explained in terms of a break-in period in which swelling of polymer chains is facilitated by oxidation–re-reduction cycles. This is a common phenomenon for polymer-modified electrodes in cases in which the electrolyte is a relatively poor solvent for the polymer.

To determine whether redox activity remained close to the electrode surface or was propagated throughout the films, the extent of oxidation of polymer-modified electrodes was investigated by comparing the charge under the anodic curve with the calculated surface coverage of 8Se2. The number of moles of coronands involved in oxidation processes was calculated from:

$$[2] \quad Q = nF\Gamma_{exp}$$

where Q is the amount of charge passed, n is the number of electrons involved in the redox process, F is Faraday's constant, and Γ_{exp} is the experimentally observed number of moles of coronand on the electrode surface. The results are summarized in Table 1. Γ_{exp} was found to be substantially less than the calculated number of moles in the film, Γ_{calc}. Values of Γ_{exp} are typical of monolayer coverages on electrode surfaces, indicating that oxidation of the polymer films was restricted to only several monolayers at most. Confinement of electroactivity to the electrode is similary attributed to poor electron-transfer kinetics between adjacent redox centres.

Conclusions

The syntheses of the first polymer-bound selenium coronands, poly(8Se2) and poly(16Se4), have been achieved. These poly(selenium coronands) are electroactive polymers. Their redox chemistry is rich, but complex, due to inter- and intramolecular reactions that occur following oxidation. The selenium coronands attached to the polymer chain are sterically crowded and, although the microscopic concentration of selenium coronands is relatively high, intermolecular reactions are reduced compared to analogous concentrations of free coronands in solution. The selenium coronand functionality is even less mobile when the polymers are in the form of thin films; the latter exhibit enhanced stability in their oxidized form compared to polymer-bound selenium coronands in solution. Further separation of the coronands was achieved by their copolymerization or by blending with inert polymers. In both cases, the stability of the oxidized state and redox reversibility of the selenium coronands are enhanced.

These results show that spatial separation of electroactive units along the chain by copolymerization, and dilution of electroactive polymer chains by polymer blending, is a useful strategy for obtaining electrochemically stable polymer-modified electrodes for cases in which intermolecular reaction between electroactive species is a major pathway leading to degradation and loss of electroactivity.

Experimental

Melting points were determined on a Fisher–Johns melting point apparatus and are uncorrected. ^{1}H NMR and ^{13}C NMR spectra were recorded on a Bruker AMX-400 NMR spectrometer at 400.13 and 100.6 MHz, for proton and carbon, respec-

tively. All spectra were recorded in deuterochloroform and chemical shifts are given in ppm downfield from TMS. Chemical shifts and coupling constants were obtained from a first-order analysis of the spectra. Infrared spectra were recorded on a Perkin–Elmer 599B infrared spectrophotometer. UV–visible absorption spectra were carried out on a Perkin–Elmer Lamda 3A UV–visible spectrophotometer. Electron impact mass spectra were measured on a Hewlett–Packard HP-5985 mass spectrometer at 70 eV. Chemical ionization mass spectra were measured on a Hewlett–Packard HP-5985 mass spectrometer with isobutane as the reacting gas. Average molecular weights of polymers were determined by GPC, which included size exclusion chromatography combined with a Spectra-Physics model SP8000 UV–vis spectrophotometer and a Waters model R400 refractive index detector. Electrochemical studies were performed on a Pine RDE4 bipotentiostat and a Hewlett–Packard HP 7046A X-Y recorder.

Analytical thin-layer chromatography (TLC) was performed on aluminum plates precoated with Merck silica gel 60F-254 as the adsorbent. The developed plates were air-dried, exposed to UV light and (or) sprayed with 5% sulfuric acid in ethanol, and heated at 150°C. All compounds were purified by flash chromatography, on Kieselgel 60 (230–400 mesh).

Solvents were distilled before use and were dried, as necessary, by literature procedures. Solvents were evaporated under reduced pressure and below 40°C. Reactions performed under nitrogen were effected by means of standard Schlenk-tube techniques. Microanalyses were performed by M.K. Yang of the Microanalytical Laboratory of Simon Fraser University.

4,8-Diselenaundecan-1,11-diol (3)

To propane-1,3-bisselenocyanate **1** (9) (10.0 g, 39.7 mmol) in liquid ammonia (300 mL) was added Na metal in small pieces until a colourless homogeneous solution was obtained. To the solution was added dry THF (60 mL). A solution of 3-chloro-1-propanol **2** (7.50 g, 79.4 mmol) in dry THF (15 mL + 2 × 5mL rinse) was then added dropwise. The ammonia was allowed to escape and the reaction mixture was diluted with THF (100 mL). The reaction mixture was filtered and evaporated in vacuo to yield a light yellow oil. Purification by silica gel chromatography (hexane:ethyl acetate (1:1)) gave **3** (11.29 g, 89%, R_f 0.34); ^{1}H NMR δ : 1.89 (2H, p, H_6),1.98 (4H, p, H_2, H_{10}), 2.30 (2H, s, OH), 2.64 (8H, t, J = 6.4 Hz, H_3, H_5, H_7, H_9), 3.70 (4H, t, J = 6.1 Hz, H_1, H_{11}); ^{13}C NMR δ : 20.2 (C_6, J_{Se-C} = 30 Hz), 23.6 (C_2, C_{10}, J_{Se-C} = 34 Hz), 30.9 (C_5, C_7), 32.9 (C_3, C_9), 62.1 (C_1, C_{11}); CI MS *m/e*: 321 (M^+ + 1 isotopic cluster). Anal. calcd. for $C_9H_{20}Se_2O_2$: C 33.97, H 6.34; found: C 33.97, H 6.42.

4,8-Diselenaundecan-1,11-bis-*p*-toluenesulfonate (5) and 4,8-diselenaundecan-1-ol-11-*p*-toluenesulfonate (4)

To a solution of **3** (0.50 g, 1.57 mmol) in CH_2Cl_2 (10 mL) was added dropwise a solution of *p*-toluenesulfonyl chloride (0.66 g, 3.46 mmol) in pyridine (0.9 mL, 11.25 mmol). The reaction mixture was stirred at room temperature for 19 h. The reaction mixture was diluted with CH_2Cl_2 (120 mL) and then washed with water (3 × 45 mL), 10% HCl (3 × 45 mL), saturated $NaHCO_3$ (3 × 45 mL), and water (3 × 45 mL). The organic layer was dried ($MgSO_4$), and evaporated in vacuo to give a light yellow oil. Purification by silica gel flash chromatography (hexane:ethyl acetate (3:1); R_f 0.27) gave **5** (0.55 g, 55%) and **4** (R_f 0.08) (0.16 g, 21%).

4: ^{1}H NMR δ: 1.88 (2H, p, H_6), 1.96 (4H, p, H_2, H_{10}), 2.43 (6H, s, Me), 2.52 8H, m, H_3, H_5, H_7, H_9), 4.1 (4H, t, J = 7.3 Hz, H_1, H_{11}), 7.34 (4H, d, J = 8.8 Hz, Ar), 7.77 (4H, d, J = 8.8 Hz, Ar); ^{13}C NMR δ : 19.1 (C_6), 21.6 (C_2, C_{10}), 23.7 (Me), 29.8 (C_5, C_7), 30.8 (C_3, C_9), 69.6 (C_1, C_{11}), 127.9 ($C_{4'}$), 129.9 ($C_{3'}$, $C_{5'}$), 133.1 ($C_{2'}$, $C_{6'}$), 144.8 ($C_{1'}$). Anal. calcd. for $C_{23}H_{32}O_6S_2Se_2$: C 44.09, H 5.15; found: C 43.96, H 5.01.

5: ^{1}H NMR δ : 1.85–1.99 (7H, m, H_2, H_6, H_{10}, OH-11), 2.43 (3H, s, Me), 2.52–2.65 (8H, m, H_3, H_5, H_7, H_9), 3.70 (2H, t, J = 6.6 Hz, H_{11}), 4.1 (2H, t, J = 6.9 Hz, H_1), 7.34 (2H, d, J = 8.7 Hz, Ar), 7.80 (2H, d, J = 8.7 Hz, Ar); ^{13}C NMR δ : 19.6 (C6), 20.3 (C_{10}), 21.6 (C_2), 23.6 (Me), 29.8 (C_5, C_7), 30.9 (C_3), 33.0 (C_9), 62.3 (C_{11}), 69.6 (C_1), 127.9 ($C_{4'}$), 129.9 ($C_{3'}$, $C_{5'}$), 133.1 ($C_{2'}$, $C_{6'}$), 144.8 ($C_{1'}$). Anal. calcd. for $C_{16}H_{26}O_4SSe_2$: C 40.68, H 5.55; found: C 40.64, H 5.42.

1,3-Bisselenocyanatopropan-2-ol (6)

Note: This procedure should be carried out in a well-ventilated fume hood. To a solution of 1,3-diiodo-2-propanol (10.1 g, 32.4 mmol) in reagent grade acetone (150 mL) was added potassium selenocyanate (9.03 g, 62.7 mmol). The reaction mixture was refluxed overnight, filtered, and evaporated in vacuo. Purification of the residue by silica gel flash chromatography (hexane:ethyl acetate (2:1) R_f 0.51) gave **6** as a solid (6.29 g, 75%); ^{1}H NMR δ : 3.20 (2H, dd, J_{gem} = 13.0 Hz, J_{vic} = 7.0 Hz, H_1 and H_3), 3.29 (1H, d, J = 5.0 Hz, OH), 3.39 (2H, dd, J_{gem} = 13.0 Hz, J_{vic} = 4.5 Hz, $H_{1'}$ and $H_{3'}$), 4.35 (1H, m, H_2); ^{13}C NMR δ : 34.6 (C_1, C_3), 69.3 (C_2), 101.5 (SeCN). **Note:** This compound has an extremely pungent odor and was used immediately without further characterization.

1,5,9,13-Tetraselenacyclohexadecan-3-ol (7)

Note: This procedure should be carried out in a well-ventilated fume hood. To a suspension of $NaBH_4$ (0.45 g) in THF (225 mL) and EtOH (25 mL) was added simultaneously, via two separate syringes connected to an automated syringe pump, 1,3-bisselenocyanatopropan-2-ol (**6**) (0.428 g, 1.60 mmol) in EtOH (60 mL) and **5** (0.80 g, 1.60 mmol) in THF (60 mL). The addition time was 10 h and the reaction mixture was allowed to stir at room temperature for 24 h. The reaction mixture was diluted with THF (100 mL) and then washed with water (300 mL). The water layer was then extracted with dichloromethane (5 × 95 mL). The CH_2Cl_2 layer was washed with water (2 × 100 mL), and dried over anhydrous $MgSO_4$. Evaporation of the solvent gave white crystals that required further purification. Flash chromatography (hexane:ethyl acetate (6:1)) gave white crystals **7** (0.400 g, 62%), which were recrystallized from ethyl acetate; mp 54–55°C. FTIR: 3428 cm^{-1} (OH str.); ^{1}H NMR δ : 2.00–2.10 (6H, m, H_7, H_{11}, H_{15}), 2.64–2.79 (12H, m, H_6, H_8, H_{10}, H_{12}, H_{14}, H_{16}), 2.71 (2H, dd, H_2, H_4, J_{gem} = 13.0 Hz, J_{vic} = 7.5 Hz), 2.87 (1H, br s, OH)), 2.90 (2H, dd, $H_{2'}$, $H_{4'}$, J_{gem} = 13.0 Hz, J_{vic} = 5.0 Hz), 3.88 (1H, m, CH(OH)); ^{13}C NMR δ : 23.8 (C_{11}), 24.1 (C_7, C_{15}), 31.2 (C_6, C_8, C_{14}, C_{16}), 31.8 (C_2, C_4), 69.9 (C_3). CI MS *m/e*: 502 (M^++1 isotopic cluster). Anal. calcd. for $C_{12}H_{24}OSe_4$: C 28.82, H 4.84; found: C 28.99, H 4.86.

1,5-Diselenacyclooctane-3-ol (8) and 1,5,9,13-tetraselenacyclohexadecan-3,11-diol (9)

1,3-Propanebisselenocyanate-2-ol (**6**) (2.50 g, 0.093 mol) was dissolved in dry THF (220 mL) and EtOH (25 mL) and put

into a three-necked round-bottom flask. Sodium borohydride (3.5 g, 0.093 mol) was added in small portions at room temperature until the solution became yellowish white. The mixture was stirred for a few minutes. 1,3-Dibromopropane (2.03 g, 0.010 mol) was dissolved in a mixture of THF and EtOH (1:1) (70 mL) and was added dropwise to the reaction flask over 2 h. The reaction mixture was stirred at room temperature for 20 h. All processes were carried out under N_2. The reaction mixture was filtered and the filtrate was placed on the rotary evaporator to remove most of the solvent. Water (100 mL) was added to the residue and extracted with CH_2Cl_2 (3 × 120 mL). The organic layers were combined, washed with water (3 × 100 mL), and dried over $MgSO_4$. Removal of the CH_2Cl_2 gave a crude yellow oil (2.90 g). The products were separated on a silica-gel column with ethyl acetate – hexane (1:3.5) as eluent. The fractions with R_f 0.43 were combined to yield **9** as an oil (1.04 g, 43%) and those with R_f 0.10 were combined to give **10** as a white solid (0.54 g, 11%).

9: ^{1}H NMR δ: 4.00 (1H, m, H_3), 3.16 (2H, dd, $J_{H2,H2'}$ = 13.2 Hz, $J_{H3,H4}$ = 3.2 Hz, H_2, H_4), 2.99 (2H, dd, $J_{H4,H4'}$ = 14 Hz, $J_{H3,H4'}$ = 6.8 Hz, $H_{2'}$, $H_{4'}$), 2.83 (2H, ddd, $J_{H6,H6'}$ = 11.6 Hz, $J_{H6,H7'}$ = 7.6 Hz, $J_{H6,H7}$ = 3.8 Hz, H_6, H_8), 2.71 (2H, ddd, $J_{H6,H6'}$ = 12.0 Hz, $J_{H6',H7}$ = 7.6 Hz, $J_{H6',H7'}$ = 4.2 Hz, $H_{6'}$, $H_{8'}$), 2.33–2.50 (2H, m, H_7, $H_{7'}$), 2.21 (1H, d, OH); ^{13}C NMR δ : 23.9 (C_6, C_8), 30.2 (C_2,C_4), 30.8 (C_7), 69.4 (C_3). Anal. calcd. for $C_6H_{12}OSe_2$: C 27.92, H 4.68; found: C 28.14, H 4.62.

10: mp 79–80°C; IR, cm^{-1}: 3400 (OH str.); ^{1}H NMR δ : 2.72 (4H, p, J = 6.4 Hz, H_7, H_{15}), 2.64–2.90 (18H, m, H_2, H_4, H_6, H_8, H_{10}, H_{12}, H_{14}, H_{16}, OH-3, OH-11), 3.88 (2H, m, H_3, H_{11}); ^{13}C NMR δ : 30.6 (C_3, C_{11}), 35.1 (C_7, C_{15}), 37.8 (C_2, C_4, C_{10}, C_{12}), 77.2 (C_6, C_8, C_{14}, C_{16}). EIMS: 498 (M^+-18). Anal. calcd. for $C_{12}H_{24}O_2Se_4$: C 27.91, H 4.65; found: C 28.07, H 4.56.

1,5-Diselenacyclooctyl acrylate (mono 8Se2) (11)

1,5-Diselenacyclooctan-3-ol (**9**) (0.64 g, 0.002 mol) was dissolved in dry THF (190 mL) and CH_2Cl_2 (10 mL). The solution was cooled in ice and triethylamine (1.52 g, 0.015 mol) was added. Acryloyl chloride (0.24 g, 0.0026 mol) was dissolved in THF (30 mL) and added dropwise with vigorous stirring over 17 min to the reaction mixture. The reaction mixture was stirred overnight at room temperature. The triethylammonium salts were removed by filtration, and the filtrate containing mono 8Se2 was evaporated until most of the solvent was removed. The residue was dissolved in dichloromethane (100 mL). The organic solution was first washed with a mixture of 1 M HCl (15 mL) and H_2O (45 mL), then with a mixture of saturated $NaHCO_3$ (5 mL) and H_2O (45 mL), and finally with H_2O (3 × 150 mL). The organic layer was dried over $MgSO_4$, and removal of the solvent afforded crude mono 8Se2 as a straw-colored oil. The product was chromatographed on a silica-gel column with ethyl acetate – hexane (1:20) as eluent. The fractions containing pure **11** (R_f 0.3) were combined, and the product was isolated as a thick oil (0.67 g, 87%). IR (KBr), cm^{-1}: 1710 (C=O), 1180 (C-O-C); UV, λ_{max} : 234 nm (ε 3.10 × 10^3 cm^{-1} M^{-1}); ^{1}H NMR (400 MHz, $CDCl_3$) δ : 2.40 (2H, m, H_7), 2.83 (4H, m, H_6, H_8), 3.15 (4H, m, H_2, H_4), 5.23 (1H, m, H_3), 5.83 (1H, dd, J_{H-H_Z} = 10.5 Hz, J_{gem} (H_Z,H_E) = 1.5 Hz, -HC=CH_Z), 6.09 (1H, dd, J_{H-H_E} = 17.5 Hz, J_{H-H_Z} = 10.5 Hz, -*H*C=CH_2), 6.39 (1H, dd, J_{gem}(H_Z,H_E) = 1.5 Hz, J_{H-H_E} = 17.5 Hz, -HC=CH_E); ^{13}C NMR (100 MHz, $CDCl_3$) δ : 24.2 (C_7), 26.6 (C_6, C_8), 30.9 (C_2, C_4), 73.8 (C_3), 128.5 (=*C*H$_2$), 130.9 (CO-*C*H=), 165.0 (-*C*=O); MS : 312 (M^+). Anal. calcd. for $C_9H_{14}O_2Se_2$: C 34.65, H 4.52; found: C 34.68, H 4.48.

1,5,9,13-Tetraselenacyclohexadecyl acrylate (mono 16Se4) (12)

1,5,9,13-Tetraselenacyclohexadecan-3-ol (**7**) (0.125g, 0.25 mmol) was dissolved in dry THF (20 mL) and CH_2Cl_2 (10 mL). The solution was cooled in ice and triethylamine (0.030 g, 0.3 mmol) was added. Acryloyl chloride (0.24 g, 0.026 mmol) was dissolved in THF (20 mL) and added dropwise with vigorous stirring over 10 min. The reaction mixture was stirred overnight at room temperature. The triethylammonium salts were removed by filtration, and the filtrate containing mono 16Se4 was evaporated until most of the solvent was removed. The residue was dissolved in dichloromethane (60 mL). The organic solution was first washed with a mixture of 1 M HCl (15 mL) and H_2O (30 mL), then with a mixture of saturated $NaHCO_3$ (5 mL) and H_2O (30 mL), and finally with H_2O (3 × 100 mL). The organic layer was dried with $MgSO_4$, and removal of the solvent afforded crude mono 16Se4 as a straw-colored oil. The product was chromatographed on a silica-gel column with a mixture of ethyl acetate and hexane (1:20). The fractions containing pure **12** (R_f 0.15) were combined, and the product was isolated as a thick oil (0.10 g, 75%). IR (KBr), cm^{-1} : 2925 (C-H), 1718 (C=O), 1180 (C-O-C), 1630 (C=C) ; UV, λ_{max} : 246 nm (ε 4.92 × 10^3 cm^{-1} M^{-1}); ^{1}H NMR (400 MHz, $CDCl_3$) δ : 2.00–2.30 (6H, m, H_7, H_{11}, H_{15}), 2.65–2.85 (12H, m, H_6, H_8, H_{10}, H_{12}, H_{14}, H_{16}), 2.85–3.05 (4H, m, H_2, H_4), 5.15 (1H, m, H_3), 5.86 (1H, dd, J_{H-H_Z} = 10 Hz, J_{gem} (H_Z,H_E) = 2 Hz, -HC=CH_Z), 6.13 (1H, dd, dd, J_{H-H_E} = 17 Hz, J_{H-H_Z} = 10 Hz, -*H*C=CH_E), 6.44 (1H, dd, J_{gem} (H_Z,H_E) = 2 Hz, J_{H-H_E} = 17 Hz, -HC =CH_E); ^{13}C NMR (100 MHz, $CDCl_3$) δ : 23.5 (C_{11}), 23.7 (C_7, C_{15}), 24.7 (C_{10}, C_{12}), 27.1 (C_6, C_8, C_{14}, C_{16}), 31.6 (C_2), 31.8 (C_4), 73.7 (C_3), 128.2 (=CH_2), 132.2 (CO-CH=), 165.4 (C=O); MS: 554 (M^+). Anal. calcd. for $C_{15}H_{28}O_2Se_4$: C 32.51, H 4.73; found: C 32.79, H 4.87.

Poly(1,5-diselenacyclooctyl acrylate) (13)

Mono 8Se2 (**11**) (0.20 g, 0.64 mmol) and AIBN (5% mole ratio to the monomer) were dissolved in benzene (0.80 g, 10.3 mmol). This solution was placed in a glass ampoule and degassed in three freeze–thaw cycles, sealed under vacuum, and heated for 110 h at 60°C. The solution was then poured into MeOH (7 mL) and the polymer was precipitated (0.20 g). The polymers were purified by repeated dissolution–precipitation steps from chloroform–methanol; yield: 0.18 g, 90%; IR (KBr), cm^{-1}: 1705 (C=O), 1155 (C-O-C); UV, λ_{max}: 244 nm (ε 9.00 × 10^3 cm^{-1} M^{-1}); ^{1}H NMR (400 MHz, $CDCl_3$) δ : 1.46, 1.64, 1.88 (2H, br, -CH_2-CH-CO), 2.27 (1H, br, -CH$_2$-C*H*-CO), 2.40 (2H, br, H_7), 2.85 (4H, br, 2 H_6's, 2 H_8's), 3.15 (4H, 2 H_2's, 2 H_4's), 5.16 (1H, br, H_3); ^{13}C NMR (100 MHz, $CDCl_3$) δ : 24.4 (C_4), 26.6, 26.8 (C_6, C_8, CO-CH-*C*H$_2$-), 31.0 (C_2, C_4), 41.5 (CO-*C*H-CH$_2$-), 74.5 (C_3), 173.4 (C=O). Gel permeation chromatography (GPC) gave the average molecular weight of the soluble fraction as 2500. Anal. calcd. for compound **13**: C 36.04, H 4.20; found: C 35.75, H 4.52.

Poly(1,5,9,13-tetraselenacyclohexadecyl acrylate) (14)

Mono16Se4 (**12**) (100 mg, 0.18 mmol) and AIBN (5% mole ratio to the monomer) were dissolved in benzene (0.40 g, 5.1

mmol). This solution was placed in a glass ampoule and degassed in three freeze–thaw cycles, sealed under vacuum, and heated for 110 h at 60°C. The solution was then poured into MeOH (7 mL) and the polymer was precipitated (0.20 g). The polymers were purified by repeated dissolution–precipitation steps from chloroform–methanol; yield: 94.8 mg, 95%; IR (KBr), cm^{-1}: 2923 (C-H), 1728 (C=O), 1156 (C-O-C); UV, λ_{max} : 246 nm (ε 3.90×10^3 cm^{-1} M^{-1}); ^1H NMR (400 MHz, $CDCl_3$) δ : 1.70–2.13 (2H, br, CH_2-CH-CO), 1.95–2.19 (6H, br, 2 H_7's, 2 H_{11}'s, 2 H_{15}'s), 2.50 (1H, br, -CH_2-CH-CO), 2.60–2.80 (12H, br, 2 H_6's, 2 H_8's, 2 H_{10}'s, 2 H_{12}'s, 2 H_{14}'s, 2 H_{16}'s), 2.80–3.20 (4H, br, 2 H_2's, 2 H_4's), 5.10 (1H, br, H_3); ^{13}C NMR (100 MHz, $CDCl_3$) δ : 23.8 (C_7, C_{11}, C_{15}), 24.8 (C_{10}, C_{12}), 27.0 (-CO-CH-CH_2), 27.1 (C_6, C_8, C_{14}, C_{16}), 31.4 (C_2), 31.8 (C_4), 41.5 (CO-CH-CH_2), 73.7 (C_3), 173.5 (C=O). A molecular weight determination was not possible owing to the insolubility of the sample. Anal. calcd. for compound **14**: C 33.14, H 5.14; found: C 32.81, H 4.85.

Copolymer of 1,5-diselenacyclooctyl acrylate and methyl acrylate (16)

Methyl acrylate **15** (25 g, 0.29 mmol) was washed with 1.0 M aqueous NaOH (3 × 20 mL) in order to remove inhibitors such as hydroquinone, and then with water (3 × 30 mL). It was then dried over $CaCl_2$ and fractionally distilled under reduced pressure. The product was stored under nitrogen in the dark until further use. A mixture of methyl acrylate **15** (25.8 mg, 0.3 mmol), 1,5-diselenacyclooctyl acrylate **11** (93.6 mg, 0.3 mmol), and AIBN (4.92 mg, 0.015 mmol) in benzene (0.478 g, 6.1 mmol) was degassed with three freeze–thaw cycles and sealed under vacuum. The mixture was heated at 60°C for 110 h. The mixture was poured into methanol (20 mL) and the polymer was precipitated. The polymer was purified by three dissolution–precipitation steps from chloroform–methanol; yield: 98 mg, 82%. IR (KBr), cm^{-1}: 1706 (C=O), 1165 (C-O-C); UV, λ_{max}: 240 nm (ε 4.50×10^3 cm^{-1} M^{-1}); ^1H NMR δ: 1.46, 1.66, 1.92 (2H, br, -CH_2-CH-CO), 2.28 (1H, br, -CH_2-CH-CO), 2.40 (2H, br, H_7), 2.84 (4H, br, 2 H_6's, 2 H_8's), 3.12 (4H, br, 2 H_2's, 2 H_4's), 3.67 (3H, br, OCH_3), 5.14 (1H, br, H_3). A ratio of diselenacyclooctyl acrylate:methyl acrylate units of 1.4:1 was determined by integration of the peaks for H_3 and OCH_3 in the ^1H NMR spectrum.

In a separate experiment, a mixture of methyl acrylate **15** (34 mg, 0.40 mmol), 1,5-diselenacyclooctyl acrylate **11** (62.4 mg, 0.2 mmol), and AIBN (4.92 mg, 0.015 mmol) in benzene (0.387 g, 5.0 mmol) was treated as described above; yield: 83 mg, 85%. IR (KBr), cm^{-1}: 1708 (C=O), 1167 (C-O-C); UV, λ_{max}: 239 nm (ε 5.00×10^3 cm^{-1} M^{-1}); ^1H NMR δ: 1.46, 1.64, 1.91 (2H, br, -CH_2-CH-CO-), 2.27 (1H, br, -CH_2-CH-CO-), 2.38 (2H, br, H_7), 2.82 (4H, br, 2 H_6's, 2 H_8's), 3.11 (4H, br, 2 H_2's, 2 H_4's), 3.65 (3H, br, OCH_3), 5.14 (1H, br, H_3). A ratio of diselenacyclooctyl acrylate:methyl acrylate units of 0.75:1 was determined by integration of the peaks for H_3 and OCH_3 in the ^1H NMR spectrum.

Chemical oxidation of polymers

Under an N_2 atmosphere, $NOBF_4$ (8 mg) was placed in a UV cell. The cell was sealed by a rubber stopper. Dry CH_2Cl_2 (1 mL) was syringed into the UV cell to dissolve the $NOBF_4$. Polymer solution (3 mL, 10 mg/1 mLCH_2Cl_2) was then added into the cell and a UV–visible measurement was made.

Cyclic voltammetric measurements

A three-electrode system was used for cyclic voltammetry. The working electrode (WE) was a glassy carbon disc electrode polished with 3 μm aluminum oxide powder (Micro Metallurgical Ltd.), and washed with distilled water and acetone prior to each experiment. The counter-electrode (CE) was a Pt wire and the reference electrode (RE) was KCl(saturated)–Ag/AgCl. The electrolyte was 0.1 M TEAP in acetonitrile. The solutions were flushed with N_2 for about 10 min prior to use and measurements were performed at 25°C using a Pine RDE4 bipotentiostat and a Hewlett–Packard HP 7046A X-Y recorder.

Acknowledgments

We are grateful to the Natural Sciences and Engineering Research Council of Canada for financial support.

References

1. B.M. Pinto, B.D. Johnston, R.J. Batchelor, F.W.B. Einstein, and I.D. Gay. Can. J. Chem. **66**, 2956 (1988); B.M. Pinto, R.J. Batchelor, B.D. Johnston, F.W.B. Einstein, and I.D. Gay. J. Am. Chem. Soc. **110**, 2990 (1988); B.M. Pinto, B.D. Johnston, R.J. Batchelor, and J.-H. Gu. J. Chem. Soc. Chem. Commun. 1087 (1988).
2. R.J. Batchelor, F.W.B. Einstein, I.D. Gay, J.-H. Gu, B.D. Johnston, and B.M. Pinto. J. Am. Chem. Soc. **111**, 6582 (1989).
3. I. Cordova-Reyes, E. VandenHoven, A. Mohammed, and B.M. Pinto. Can. J. Chem. **73**, 113 (1995).
4. R.J. Batchelor, F.W.B. Einstein, I.D. Gay, J.-H. Gu, B.M. Pinto, and X. M. Zhou. J. Am. Chem. Soc. **112**, 3706 (1990).
5. R.J. Batchelor, F.W.B. Einstein, I.D. Gay, J-H. Gu, and B.M. Pinto. J. Organomet. Chem. **411**, 147 (1991).
6. (*a*) B.M. Pinto, R.J. Batchelor, F.W.B. Einstein, I.D. Gay, J. Gu, and X. Zhou. 76th Canadian Society for Chemistry Conference, Sherbrooke, Quebec, Canada. June, 1993. Abstr. 683; (*b*) R.J. Batchelor, F.W.B. Einstein, I.D. Gay, J.-H. Gu, B. M. Pinto, and X. Zhou. Inorg. Chem. In press.
7. P.F. Kelly, W. Levason, G. Reid, and D.J. Williams. J. Chem. Soc. Chem. Commun. 1716 (1993).
8. N.R. Champness, P.F. Kelly, W. Levason, G. Reid, A.M.Z. Slawin, and D.J. Williams. Inorg. Chem. **34**, 651 (1995).
9. B.M. Pinto, B.D. Johnston, and R. Nagelkerke. Heterocycles, **28**, 389 (1989).
10. X.-M. Zhou. Ph.D. Thesis, Simon Fraser University, Burnaby, B.C., Canada, 1993.
11. (*a*) K.D. Asmus. Acc. Chem. Res. **12**, 436 (1979); (*b*) W.K. Musker. Acc. Chem. Res. **13**, 200 (1980).
12. (*a*) H. Fujihara, R. Akaishi, A. Nakamura, and N. Furukawa. Tetrahedron Lett. **31**, 6375 (1990); (*b*) F. Iwasaki, M. Morimoto, M. Yasui, R. Akaishi, H. Fujihara, and N. Furukawa. Acta Crystallogr. Sect. C: Cryst. Struct. Commun. **C47**, 1463 (1991); (*c*) H. Fujihara, R. Akaishi, and N. Furukawa. Tetrahedron Lett. **49**, 1605 (1993).
13. (*a*) R.W. Murray. Chemically modified electrodes. *In* Electroanal. Chem. **13**. *Edited by* A.J. Bard. Marcel Dekker, New York. 1984; (*b*) N. Oyama and F.C. Anson. Anal. Chem. **52**, 1192 (1980); (*c*) H. Mao and P.G. Pickup. J. Phys. Chem. **93**, 6480 (1989); (*d*) R.W. Murray and K.-N. Kuo. J. Electroanal. Chem. **131**, 37 (1982).

Intramolecular 1,2-alkyl shifts in unsymmetric dialkoxycarbenes studied by very low vapour pressure (VLVP) pyrolysis – mass spectrometry

Dennis Suh, David L. Pole, John Warkentin, and Johan K. Terlouw

Abstract: Methoxy-(2,2,2-trifluoroethoxy)carbene radical cations, CH_3O-C-$OCH_2CF_3^{\cdot+}$, $\mathbf{1}^{\cdot+}$, are cleanly generated by the dissociative electron ionization (EI) of 2-methoxy-5,5-dimethyl-2-(2,2,2-trifluoroethoxy)-Δ^3-1,3,4-oxadiazoline **I**. Neutralization–reionization (NR) mass spectrometry of the neutral carbene **1**, generated by one-electron reduction of $\mathbf{1}^{\cdot+}$, shows no recovery ion signal and thus **1** is not a viable species within the μs time scale of the experiment. Very low vapour pressure (VLVP) pyrolysis – mass spectrometry of **I** in conjunction with (multiple) collision experiments shows that **1** completely isomerizes, via a 1,2-trifluoroethyl shift, into methyl 3,3,3-trifluoropropionate, $CF_3CH_2C(=O)OCH_3$, **1a**. This technique was also used to study the related dialkoxycarbenes C_2H_5O-C-OCH_2CF_3, **2**, CH_3O-C-OC_2H_5, **3**, and CH_3O-C-$OCH(CH_3)_2$, **4**, generated from the corresponding 2,2-dialkoxy-5,5-dimethyl-Δ^3-1,3,4-oxadiazolines. The pyrolytically generated carbene **2** behaves analogously to **1** and completely isomerizes to ethyl 3,3,3-trifluoropropionate, **2a**. The neutral carbenes **3** and **4** undergo only a partial isomerization via 1,2-alkyl shifts in which the ethyl and isopropyl groups show a slightly greater migratory aptitude, respectively, than the methyl group. The differences in migratory aptitude are explained in terms of a transition state model similar to that of a 1,2-H shift in carbenes, with development of negative charge in the migrating group. The greater migratory aptitude of CF_3CH_2, as compared to CH_3 and CH_3CH_2, is attributed to the stabilization of negative charge in the transition state by strongly electron-withdrawing β-fluorines whereas the differences in migratory aptitude between the alkyl groups in **3** and **4** are largely due to the greater polarizability of isopropyl and ethyl groups, as compared to the methyl group.

Key words: dialkoxycarbenes, pyrolysis, tandem mass spectrometry.

Résumé : On peut générer proprement les cations radicaux méthoxy-(2,2,2-trifluoroéthoxy)carbènes, CH_3O-C-$OCH_2CF_3^{\cdot+}$, $\mathbf{1}^{\cdot+}$, en procédant à une ionisation électronique (IE) dissociative de la 2-méthoxy-5,5-diméthyl-2-(2,2,2-trifluoroéthoxy)-Δ^3-1,3,4-oxadiazoline, **I**. La spectroscopie par neutralisation–réionisation (NR) du carbène neutre, **1**, généré par une réduction à un électron du $\mathbf{1}^{\cdot+}$, ne présente pas de signal correspondant à de la récupération d'ion et le composé **1** n'est donc pas une espèce appropriée à l'échelle de temps, μs, de l'expérience. La spectrométrie de masse du composé **I** avec pyrolyse à très basse tension de vapeur (VLVP), réalisée de concert avec des expériences de (multiples) collisions ont montré que le composé **1** s'isomérise complètement, par le biais d'un déplacement-1,2 d'un groupe trifluoroéthyle, en un 3,3,3-trifluoropropionate de méthyle, $CF_3CH_2C(=O)OCH_3$, **1a**. On a aussi utilisé cette technique pour étudier des dialkoxycarbènes apparentés : C_2H_5O-C-OCH_2CF_3, **2**, CH_3O-C-OC_2H_5, **3**, et CH_3O-C-$OCH(CH_3)_2$, **4**, générés à parti des 2,2-dialkoxy-5,5-diméthyl-Δ^3-1,3,4-oxadiazolines correspondantes. Le carbène **2** préparé d'une façon pyrolytique se comporte d'une façon analogue à **1** et il s'isomérise complètement en 3,3,3-trifluoropropionate d'éthyle, **2a**. Les carbènes neutres, **3** et **4**, ne subissent que des isomérisations partielles, par les biais de déplacements 1,2 d'alkyles dans lesquels les groupes éthyle et isopropyle présentent respectivement des aptitudes migratoires plus grandes par rapport au groupe méthyle. Les différences dans les aptitudes migratoires peuvent être expliquées en fonction d'une modèle d'état de transition semblable à celui d'un déplacement 1,2 d'hydrogène dans les carbènes, avec le développement de la charge négative dans le groupe qui migre. La plus grande aptitude migratoire du CF_3CH_2 par comparaison avec le CH_3 et le CH_3CH_2 peut être attribué à la stabilisation de la charge négative dans l'état de transition par le caractère très électroaffinitaire des fluors en β alors que les differences dans les aptitudes migratoires entre les groupes dans les composés **3** et **4** sont largement dues à la plus grande polarisabilité des groupes isopropyle et éthyle par comparaison avec celle du groupe méthyle.

Mots clés : dialkyloxycarbènes, pyrolyse, spectrométrie de masse en tandem.

[Traduit par la rédaction]

Received November 7, 1995.

D. Suh, D.L. Pole, J. Warkentin,[1] and J.K. Terlouw.[1] Department of Chemistry, McMaster University, 1280 Main Street West, Hamilton, ON L8S 4M1, Canada.

[1] Authors to whom correspondence may be addressed. Telephone: (905) 525-9140. Fax: (905) 522-2509.

Introduction

The chemistry of carbenes in solution is well documented (1, 2) and methylene, the simplest carbene, is a well-understood compound (3). The electronic and molecular structures of singlet and triplet methylene and the energy difference between these states (ΔE_{ST}) has been determined both experimentally (4) and theoretically (5). Methylene has a triplet ground state whereas other carbenes bearing heteroatomic substituents, like alkoxy groups, have singlet ground states. This is explained by overlap of the lone pairs in heteroatoms with the vacant *p* orbital in the carbene (6).

Although many alkylcarbenes have been spectroscopically characterized under matrix isolation conditions (1, 2), their direct observation in solution is very difficult because they readily undergo 1,2-H migration. However, substituents directly attached to the carbenic carbon can have a dramatic influence on the activation barriers for the 1,2-H shift to this centre (7, 8). Thus, substitution of a methoxy group at the carbenic carbon of an alkylcarbene suppresses the characteristic 1,2-H migration (9) and the direct spectroscopic observation of methylmethoxycarbene in solution has been reported (10).

In view of the high reactivity of most carbenes in addition and insertion reactions, it is very difficult to generate carbenes as stable species in the condensed phase. However, many neutral carbenes have been generated and characterized in the gas phase (11–13) and their reactivity with respect to intramolecular reactions *vis-à-vis* their behaviour in solution can be studied in a collision-free environment. The mass spectrometer provides such an environment for the study of reactive intermediates like carbenes.

In this study, which follows earlier work on dimethoxycarbene (12), the unsymmetric dialkoxycarbene radical cations **1–4** were generated by dissociative electron ionization (EI) of the 2,2-disubstituted-Δ^3-1,3,4-oxadiazolines **I–IV** and the carbene ions were characterized on the basis of their collisional activation (CA) mass spectra (reviews: ref. 14). The advantages of using these precursors, for which an efficient synthetic method has recently been developed (15), are not only that they are stable at room temperature but also that they generate abundant carbene radical cations upon electron impact ionization and undergo thermal decomposition to yield carbenes under relatively mild conditions. These features make them promising precursors for the generation and characterization of these elusive carbenes by the techniques of Neutralization–Reionization (NR) mass spectrometry (reviews: ref. 16) and Very Low Vapour Pressure (VLVP) pyrolysis – mass spectrometry (17) in conjunction with (multiple) collision experiments (18). In particular, the reactivities of neutral dialkoxycarbenes, **1–4**, with respect to intramolecular isomerization via 1,2-alkyl shifts, were studied in detail by VLVP pyrolysis – mass spectrometry.

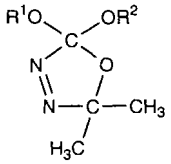

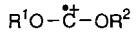

I $R^1 = CH_3$, $R^2 = CH_2CF_3$ ($m = 228$)
II $R^1 = C_2H_5$, $R^2 = CH_2CF_3$ ($m = 242$)
III $R^1 = CH_3$, $R^2 = CH_2CH_3$ ($m = 174$)
IV $R^1 = CH_3$, $R^2 = CH(CH_3)_2$ ($m = 188$)

1$^{\cdot+}$ $R^1 = CH_3$, $R^2 = CH_2CF_3$ (*m/z* 142)
2$^{\cdot+}$ $R^1 = C_2H_5$, $R^2 = CH_2CF_3$ (*m/z* 156)
3$^{\cdot+}$ $R^1 = CH_3$, $R^2 = CH_2CH_3$ (*m/z* 88)
4$^{\cdot+}$ $R^1 = CH_3$, $R^2 = CH(CH_3)_2$ (*m/z* 102)

Results and discussion

Methoxy-(2,2,2-trifluoroethoxy)carbene ions, 1$^{\cdot+}$: generation and characterization

In an earlier study (12), we reported that dimethoxycarbene (DMC) radical cations, $CH_3O\text{-}C\text{-}OCH_3^{\cdot+}$, are cleanly generated by the dissociative electron ionization (EI) of 2,2-dimethoxy-5,5-dimethyl-Δ^3-1,3,4-oxadiazoline. It was further shown, using NR mass spectrometry, that the one-electron reduction of the carbene ion yields the neutral carbene as a stable species in the rarefied gas phase. The neutral carbene was also generated by VLVP mass spectrometry, albeit only in a mixture with its isomer methyl acetate. The methyl acetate was proposed to be formed by intramolecular isomerization of the neutral carbene via a 1,2-CH_3 migration. The reactivity of oxacarbenes, however, can be varied by "tuning" or modifying the electronic properties of the carbenic alkoxy substituent (19). For example, the trifluoroethoxy group, CF_3CH_2O, (σ_R^+ −0,56) is a less effective electron donor than the methoxy group (σ_R^+ −0.66) because of the inductive effect of the CF_3 group. Thus, the methoxy-(2,2,2-trifluoroethoxy)carbene **1** is expected to be somewhat more reactive than DMC. This caused us to examine the stability and reactivity of **1** relative to DMC by both NR and VLVP pyrolysis experiments on **I**.

Neutral carbenes can conveniently be studied by NR and VLVP mass spectrometry if the corresponding cations can be distinguished from isomeric structures, particularly those resulting from intramolecular reactions. Therefore, we will first establish the structure of $C_4H_5F_3O_2^{\cdot+}$ radical cations generated by dissociative EI of **I**, on the basis of its collision-induced dissociation characteristics (14).

The 70 eV EI mass spectra of **I** and its deuterium labelled isotopomer **I-*d*$_3$** ($R^1 = CD_3$, $R^2 = CH_2CF_3$) are shown in Table 1. Due to the presence of the orthoester moiety in the precursor molecule, the mass spectra do not show the molecular ions at *m/z* 228 and 231, respectively.

The molecular ion **I**$^{\cdot+}$ undergoes three primary fragmentations to produce product ions at *m/z* 200, 197, and 129, which result from the losses of N_2, $CH_3O^{\cdot}$, and $CF_3CH_2O^{\cdot}$, respectively. The loss of N_2 also occurs under pyrolytic conditions (see below). However, the $[M - N_2]$**I**$^{\cdot+}$ peak observed in the EI mass spectrum is due to the dissociative ionization since the complementary pyrolysis product, ionized acetone (*m/z* 58 in **I** and **I-*d*$_3$**), is absent in the EI mass spectrum.

The major dissociation reactions of **I**$^{\cdot+}$ are shown in Scheme 1*a*. The rationalization is based on the metastable ion (MI) and the collisional activation (CA) mass spectra of the most important fragment ions arising from the fragmentation of **I** and **I-*d*$_3$**. The ion structures proposed in this scheme are based on a comparison of their CA mass spectra with those of reference ions of established structure.

Scheme 1*a*.

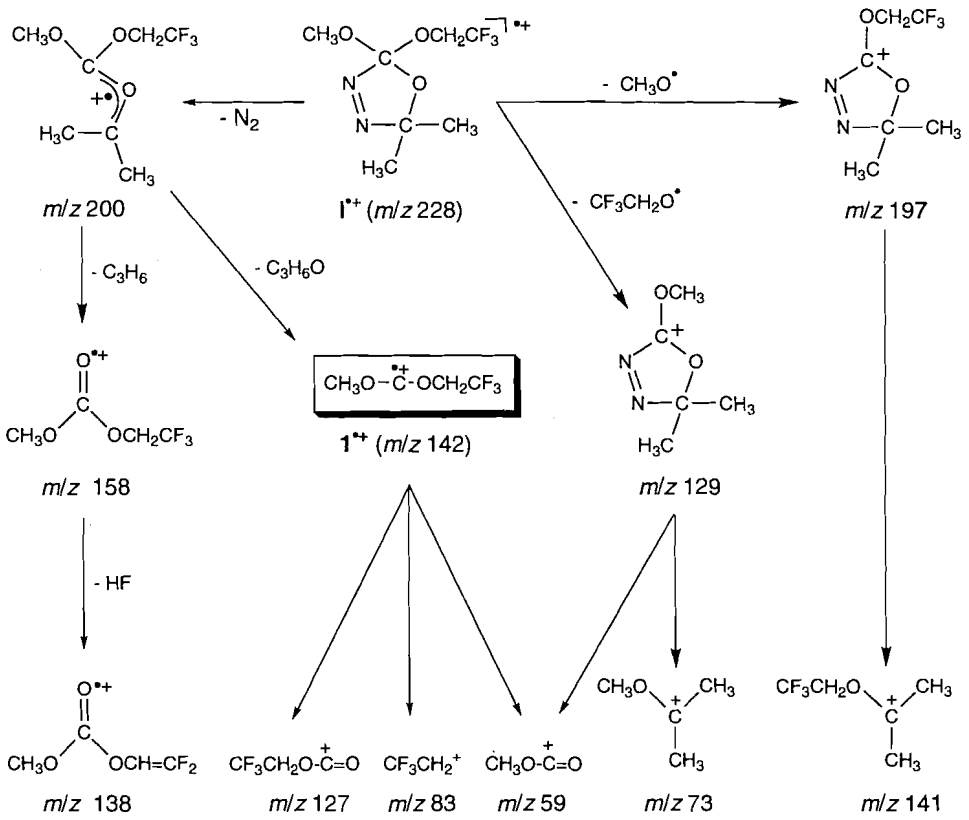

The carbene radical cations, *m/z* 142 in $\mathbf{1}^{\cdot+}$ and *m/z* 145 in $\mathbf{1}$-$d_3^{\cdot+}$, are formed via consecutive losses of N_2 and acetone molecules, see Scheme 1*a*.

The CA mass spectrum of $\mathbf{1}^{\cdot+}$, see Fig. 1*a*, is characterized by a peak at *m/z* 59 (CH_3O-C=O^+), which is shifted to *m/z* 62 (CD_3O-C=O^+) in the CA mass spectrum of $\mathbf{1}$-$d_3^{\cdot+}$, and by peaks at *m/z* 83 ($CF_3CH_2^+$) and *m/z* 127 (loss of $CH_3^{\cdot}$). The base peak shown at *m/z* 59 in the CA mass spectrum indicates that the structure of the *m/z* 142 ions is indeed that of $\mathbf{1}^{\cdot+}$ (18). The spectrum also contains weak peaks in the *m/z* 29–33 and 61–69 regions, but these are of limited diagnostic value.

The CA mass spectra of the isomers methyl 3,3,3-trifluoropropionate, $\mathbf{1a}^{\cdot+}$, and 2,2,2-trifluoroethyl acetate, $\mathbf{1b}^{\cdot+}$, are characteristically different from that of $\mathbf{1}^{\cdot+}$, see Figs. 1*c* and 1*d*. The spectra of $\mathbf{1a}^{\cdot+}$ and $\mathbf{1b}^{\cdot+}$ are both dominated by a peak at *m/z* 122 resulting from the unimolecular (metastable) loss of HF. However, the structures of the *m/z* 122 ions generated from $\mathbf{1a}^{\cdot+}$ and $\mathbf{1b}^{\cdot+}$ are not the same: the deuterium-labelled isotopomer $\mathbf{1a}$-$d_3^{\cdot+}$ ($CF_3CH_2C(=O)OCD_3$) shows a specific loss of DF in its CA mass spectrum whereas $\mathbf{1b}$-$d_3^{\cdot+}$ ($CD_3C(=O)OCH_2CF_3$) exclusively eliminate HF. This is corroborated by the different CA mass spectra of the *m/z* 122 $[M - HF]^{\cdot+}$ ions generated from metastable ions $\mathbf{1a}^{\cdot+}$ and $\mathbf{1b}^{\cdot+}$, see Fig. 2: the *m/z* 91 ions, which form the base peak in the spectrum of the former, are not present in the spectrum of the latter. Thus, the base peaks in the "pure" CA mass spectra of $\mathbf{1a}^{\cdot+}$ and $\mathbf{1b}^{\cdot+}$ are formed by the *m/z* 91 and *m/z* 43 ions, respectively. The CA mass spectrum of $\mathbf{1a}^{\cdot+}$ is entirely different from that of $\mathbf{1b}^{\cdot+}$ in that *m/z* 91, which forms the base peak in the spectrum of the former, is absent in the spectrum of the latter. Thus, the carbene ion $\mathbf{1}^{\cdot+}$ and its isomers $\mathbf{1a}^{\cdot+}$ and $\mathbf{1b}^{\cdot+}$ can easily be distinguished on the basis of their CA mass spectra.

Methoxy-(2,2,2-trifluoroethoxy)carbene ions, $\mathbf{1}^{\cdot+}$: NR experiments

The NR spectra of $\mathbf{1}^{\cdot+}$ and the isomeric esters $\mathbf{1a}^{\cdot+}$ and $\mathbf{1b}^{\cdot+}$ are shown in Fig. 3. Unfortunately a recovery signal is absent in these spectra. In the case of the ester ions, where the structure diagnostic *m/z* 91 and *m/z* 43 ions dominate the NR spectra, the absence of the recovery signal could be attributed to failure of the wholly vertical process of collision-induced ionization to regenerate stable ions $\mathbf{1a}^{\cdot+}$ and $\mathbf{1b}^{\cdot+}$ from stable molecules **1a** and **1b** (see ref. 16*e* for a similar case involving CH_3CH_2F). The spectrum of $\mathbf{1}^{\cdot+}$ on the other hand bears little or no resemblance to the CA mass spectrum and in particular the structure diagnostic *m/z* 59 ion $CH_3OC{=}O^+$ is completely absent.

This implies that neutralization leads to dissociation of the incipient neutrals, most likely via $\mathbf{1} \rightarrow CH_3^{\cdot} + CO_2 + CF_3CH_2^{\cdot}$, the dissociation of lowest energy requirement (cf. ref. 12 where the NR spectrum of dimethoxy carbene is discussed in detail). Indeed, the collision-induced dissociative ionization spectrum (CIDI) (16*d*) of the $CF_3CH_2^{\cdot}$ neutrals generated from metastable ions $\mathbf{1}^{\cdot+}$ is closely similar in appearance to the NR mass spectrum of $\mathbf{1}^{\cdot+}$, the only difference being an increased intensity of *m/z* 44 ($CO_2^{\cdot+}$) and *m/z* 15 ($CH_3^{\cdot+}$) in the latter.

Thus NR experiments on **1** using cyclopropane for neutralization do not show it to be a stable species on the μs time scale of the experiment: the incipient neutral carbene appears to completely dissociate and intramolecular isomerization into $\mathbf{1a}^{\cdot+}$ and (or) $\mathbf{1b}^{\cdot+}$ is not observed. The same appears to be true

Table 1. 70 eV EI mass spectra[a] of **I** and **I-d_3** and the VLVP pyrolysis mass spectrum of **I**.

m/z	**I**	**I-d_3**	**I** (pyr.)	*m/z*	**I**	**I-d_3**	**I** (pyr.)
203	—	8	—	91	9	—	7
				90	9		
200	11	—	—	83	34	60	14
197	51	40	—	80	—	11	—
169			4	78	—	—	29
162	—	54	—	77	—	—	24
161		20	—	76	—	40	—
159	84	—	—	73	49	—	—
158	42	—	—	70	12	10	—
146	—	11	—	69	3	9	12
145	—	19	—	64	3	8	—
144			2	63	—	5	18
143	14	—	37	62	—	100	—
142	35	34	17	61	23	15	11
141	32	18	5	60	13	6	7
139	37	—	—	59	100	16	22
138	2			58	—	—	73
132	—	40	—	56	15	—	—
131			7				
129	36	—	5	48	—	14	—
128			4	47	—	9	—
127	12	8	3	46	—	4	—
123			2	45	19	8	12
122	—	—	16	44	12	6	29
112	5	3	5	43	44	46	100
111	—	—	59	42	61	67	12
101	3		6	41	21	40	7
98	—	7	—	40	4	9	—
97	—	8	7				
95	5	—	3				
94	6	—	15				

[a]Spectra normalized to the base peak height = 100; ions below *m/z* 40 have not been considered.

for the other carbenes investigated in this study, and so these oxacarbenes seem not suitable to be studied by NR mass spectrometry. It is noteworthy, however, that dihydroxy-carbene, HO-C-OH (13*c*, 20), shows an intense recovery signal in its NR spectrum and it was studied in detail using the technique.

Methoxy-(2,2,2-trifluoroethoxy)carbene, 1: pyrolysis experiments

Table 1 shows the 70 eV EI/MS of **I** at a pyrolysis inlet temperature of 430°C, where the pyrolysis is 100% complete. In this spectrum ions at *m/z* 197 and 159, characteristic of the dissociative electron ionization of the intact precursor molecule, see Scheme 1*a*, could no longer be detected. Scheme 1*b* shows the major fragmentations of **I** upon VLVP pyrolysis.

The first step of the pyrolysis involves loss of N_2 to generate the intermediate ylide *m* = 200, which either dissociates into the carbene **1** by loss of an acetone molecule or rearranges via a 1,4-H shift into the orthoester. The orthoester *m* = 200, thus formed, is not expected to show molecular ions upon EI.

The CA mass spectrum of the pyrolytically generated *m/z* 142 ions from **I** appeared to be identical with the spectrum of the ester **1a** shown in Fig. 1*c*. Moreover the CA mass spectrum

Fig. 1. CA mass spectra of *m/z* 142 ions (*a*) $\mathbf{1}^{\cdot+}$ from EI of methoxy-2,2,2-trifluoroethoxycarbene; (*b*) generated after incomplete pyrolysis (350°C, 60–70% conversion, see text) of **I**; (*c*) $\mathbf{1a}^{\cdot+}$ from EI of methyl 3,3,3-trifluoropropionate; and (*d*) $\mathbf{1b}^{\cdot+}$ from EI of 2,2,2-trifluoroethyl acetate.

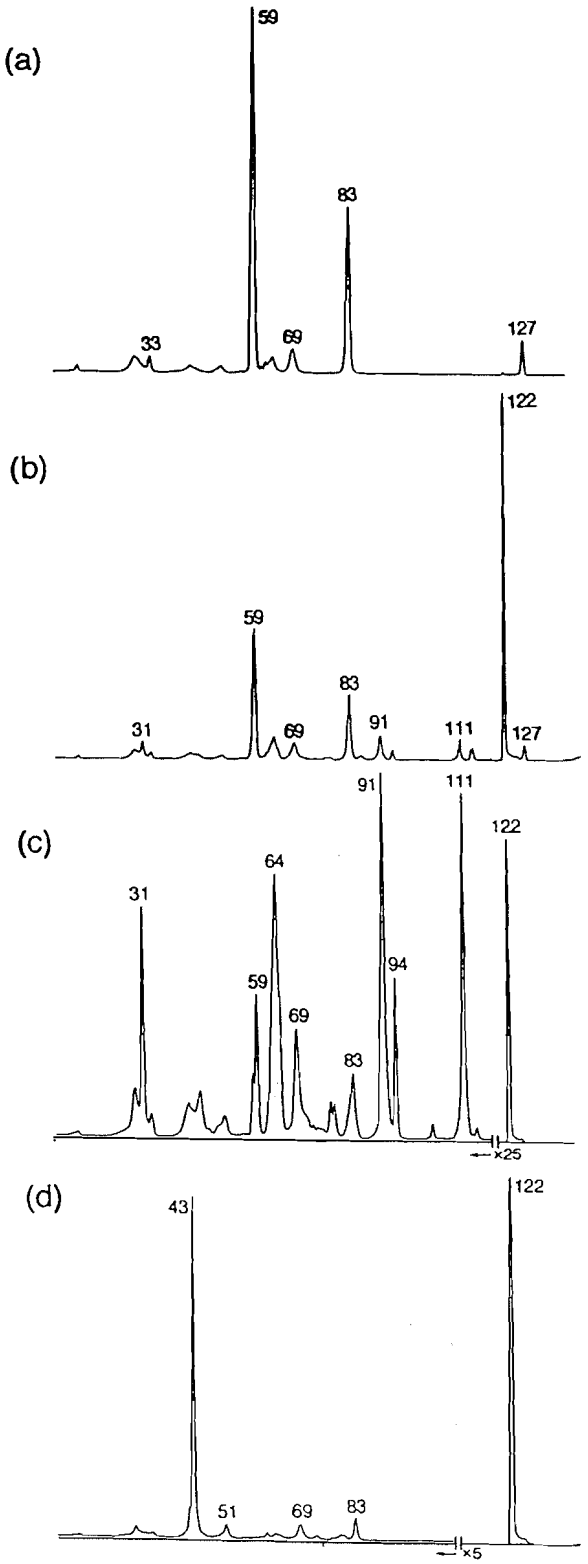

Fig. 2. CA mass spectra of *m/z* 122 ions generated from metastable (*a*) methyl 3,3,3-trifluoropropionate, $\mathbf{1a}^{\cdot+}$and (*b*) 2,2,2-trifluoroethyl acetate, $\mathbf{1b}^{\cdot+}$.

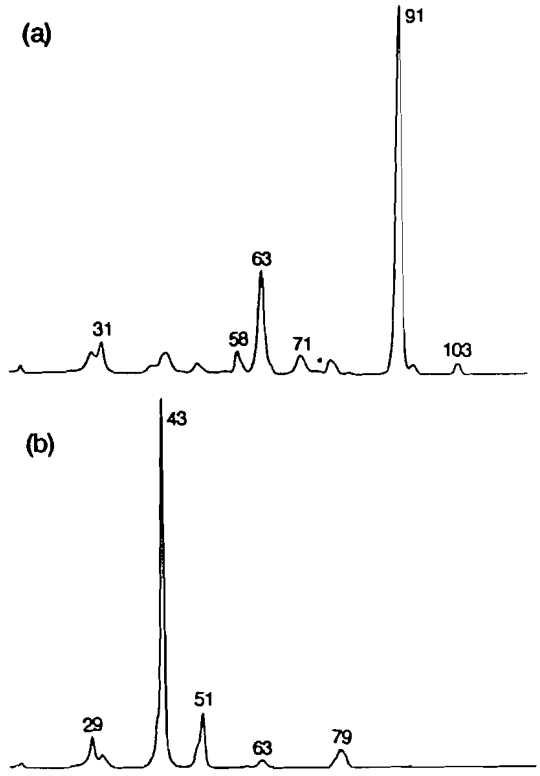

Fig. 3. NR mass spectra of *m/z* 142 ions (*a*) $\mathbf{1}^{\cdot+}$ from EI of methoxy-2,2,2-trifluoroethoxycarbene; (*b*) $\mathbf{1a}^{\cdot+}$ from EI of methyl 3,3,3-trifluoropropionate; and (*c*) $\mathbf{1b}^{\cdot+}$ from EI of 2,2,2-trifluoroethyl acetate.

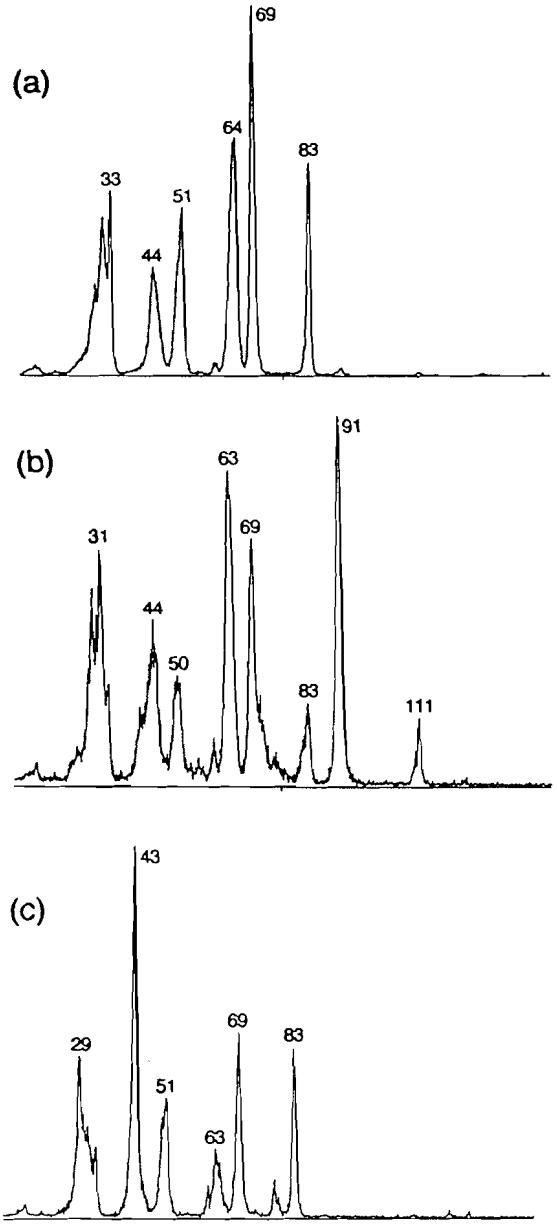

of the *m/z* 145 ions generated upon pyrolysis of the isotopomer **I-d_3** showed a specific loss of DF. These observations clearly indicate that, upon pyrolysis of **I**, the incipient neutral dialkoxycarbene **I** undergoes unimolecular isomerization into **1a**, not **1b**. Moreover, when the pyrolysis is complete, as monitored by the *m/z* 142 : *m/z* 197 peak intensity ratios, no intact carbene could be detected.

Pyrolysis starts at ca. 280°C (10%), reaches ca. 60–70% at 350°C, and is essentially complete at 410°C. At this temperature the CA mass spectrum is essentially that of the ester **1a** and analysis of the spectrum indicates that <5% of the ions $\mathbf{1}^{\cdot+}$ result from the pyrolytically generated neutral carbene. The CA mass spectrum of the *m/z* 142 ions recorded at a pyrolysis temperature of 350°C is shown in Fig. 1*b*. It represents a 1:1 mixture of ions $\mathbf{1}^{\cdot+}$ and $\mathbf{1a}^{\cdot+}$.

Ethoxy-(2,2,2-trifluoroethoxy)carbene, 2: pyrolysis experiments

The next precursor molecule studied was 2-ethoxy-5,5-dimethyl-2-(2,2,2-trifluoroethoxy)-Δ^3-1,3,4-oxadiazoline, **II**. Analogous to the methyl analogue **I**, carbene radical cations $\mathbf{2}^{\cdot+}$ are formed by dissociative EI of **II**. However, their intensity is much reduced relative to that of the methyl analogue. This is due to the fact that the molecular ion $\mathbf{II}^{\cdot+}$ undergoes two major primary fragmentations (ca. 97%) to form ions at *m/z* 197 and 143, which results from the losses of $CH_3CH_2O^{\cdot}$ and $CF_3CH_2O^{\cdot}$, respectively. The loss of N_2 also occurs, but to a small extent (ca. 3%).

The CA mass spectrum of $\mathbf{2}^{\cdot+}$ (see Fig. 4*a*) shows characteristic peaks at *m/z* 136 (loss of HF), *m/z* 129 (loss of $C_2H_3^{\cdot}$), *m/z* 83 ($CF_3CH_2^+$), and *m/z* 28 ($C_2H_4^{\cdot+}$) and it is diagnostically different from its isomers, ethyl 3,3,3-trifluoropropionate $\mathbf{2a}^{\cdot+}$ and 2,2,2-trifluoroethyl propionate $\mathbf{2b}^{\cdot+}$ (see Figs. 4*c* and 4*d*). This indicates that indeed the carbene radical cations $\mathbf{2}^{\cdot+}$ are generated by the dissociative EI of **II**.

Upon VLVP pyrolysis, ions at *m/z* 197 and 143, characteristic of the dissociative ionization of the intact precursor molecule, could no longer be detected. Analogous to the methyl analogue **I**, neutral carbenes **2** are generated by consecutive losses of N_2 and acetone molecules.

The CA mass spectrum of the *m/z* 156 ions generated after pyrolysis of **II** at ca. 430°C is shown in Fig. 4*b* and it is characteristically different from that obtained from ions generated by EI of **II**. The intensity of *m/z* 28, which forms the base peak

Scheme 1*b*.

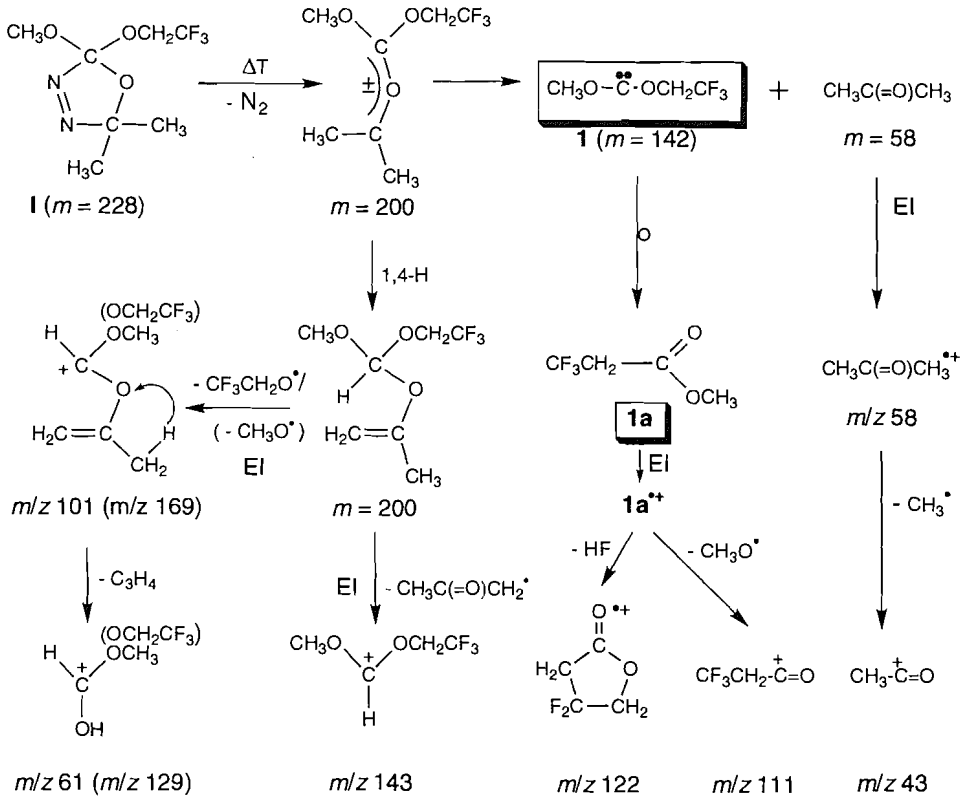

in the spectrum of the latter, is reduced considerably in the spectrum of the former. Moreover, the *m/z* 128 ions form the base peak and the *m/z* 136 ions are barely detectable in the spectrum of the former. This suggests that the neutral carbene **2** generated may have undergone unimolecular isomerization upon VLVP pyrolysis.

To verify this proposal, the CA spectrum of *m/z* 156 ions generated after pyrolysis of **II** at ca. 430°C is compared with that of its isomers **2a** and **2b**. It is seen that the CA mass spectrum of *m/z* 156 generated after pyrolysis of **II** is superimposable upon that of $\mathbf{2a}^{\cdot+}$ and characteristically different from that of $\mathbf{2b}^{\cdot+}$. The *m/z* 136 ions, which form the base peak in the spectrum of $\mathbf{2b}^{\cdot+}$, are hardly present in the spectrum of *m/z* 156 ions generated after pyrolysis of **II**.

These observations indicate that prior to ionization the carbene **2** generated after pyrolysis of **II** has undergone unimolecular isomerization into **2a**, not **2b**. This behaviour parallels that of the methoxy analogue **1** where it also is the trifluorethyl group that migrates. A mechanistic proposal for this intramolecular rearrangement will be discussed below.

Ethoxymethoxycarbene, 3: pyrolysis experiments

Similar to the behaviour of **I** and the dimethoxy analogue of **I**, dissociative EI of **III** yields abundant carbene radical cations $\mathbf{3}^{\cdot+}$ via consecutive losses of N_2 and acetone molecules, see Scheme 2*a*.

The CA mass spectrum of $\mathbf{3}^{\cdot+}$ is shown in Fig. 5*a*. The spectrum is dominated by peaks at *m/z* 61 and 57 and it is characteristically different from that of ionized methyl propionate $\mathbf{3a}^{\cdot+}$ and that of ionized ethyl acetate $\mathbf{3}^{\cdot+}$ (see Figs. 5*c* and 5*d*). Ions at *m/z* 70, which form the base peak in $\mathbf{3b}^{\cdot+}$, are barely detectable in the spectrum of $\mathbf{3}^{\cdot+}$ and *m/z* 61 ions, which are the base peak in $\mathbf{3}^{\cdot+}$, are not present in the CA mass spectrum of $\mathbf{3a}^{\cdot+}$. Thus, the CA mass spectrum of the carbene $\mathbf{3}^{\cdot+}$ is readily distinguishable from that of its isomers $\mathbf{3a}^{\cdot+}$ and $\mathbf{3b}^{\cdot+}$. The peak at *m/z* 57 (loss of $CH_3O^{\cdot}$) in the CA mass spectrum of $\mathbf{3}^{\cdot+}$, however, points to a partial conversion, prior to dissociation, of the carbene radical cations $\mathbf{3}^{\cdot+}$ into the more stable isomer $\mathbf{3a}^{\cdot+}$. This is because the *m/z* 57 ions do not have the structure of the high-energy $C_3H_5O^+$ isomer $CH_3CH_2OC^+$ (21) but rather are $CH_3CH_2C{=}O^{+\cdot}$. This follows from the observation that the CA mass spectrum of the collisionally generated $(M - CH_3O^{\cdot})^+$ ions from $\mathbf{3}^{\cdot+}$ is identical with that from $\mathbf{3}^{\cdot+}$ (spectra not shown), which is known to generate $CH_3CH_2C{=}O^+$.

The major unimolecular reactions of **III** upon VLVP pyrolysis are shown in Scheme 2*b*. The CA mass spectrum of the *m/z* 88 ions from the pyrolysis of **III** at ca. 430°C is characteristically different from that obtained in the EI experiments: compare Fig. 5*b* and 5*a*. The peak at *m/z* 70, which is absent in the CA mass spectrum of $\mathbf{3}^{\cdot+}$, has a significant intensity and the height of *m/z* 57 has increased considerably, such that it becomes the base peak in the CA mass spectrum. The peak at *m/z* 70 in Fig. 5*b* points to a partial isomerization of the neutral carbene **3** into **3b** prior to ionization. This proposal is substantiated by the observation that the CA mass spectrum of the collisionally generated *m/z* $(M - H_2O)^+$ ions in Fig. 5*b* is superimposable upon that from $\mathbf{3b}^{\cdot+}$, see Fig. 6.

In addition, the CA mass spectrum of the collisionally generated *m/z* 61 $(M - C_2H_3^{\cdot})^+$ ions in Fig. 5*b* shows a weak signal at *m/z* 43, see Fig. 7*b*, which forms the base peak in that from **3b**, see Fig. 7*c*. These results indicate that, upon pyroly-

Scheme 2*a*.

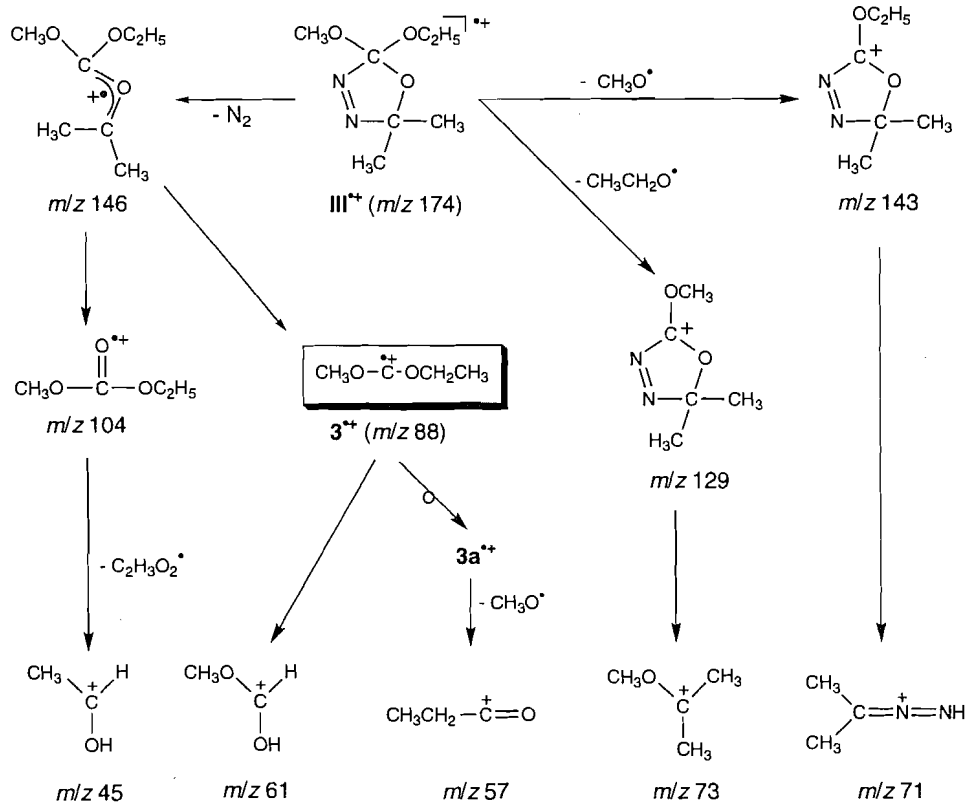

Scheme 2*b*.

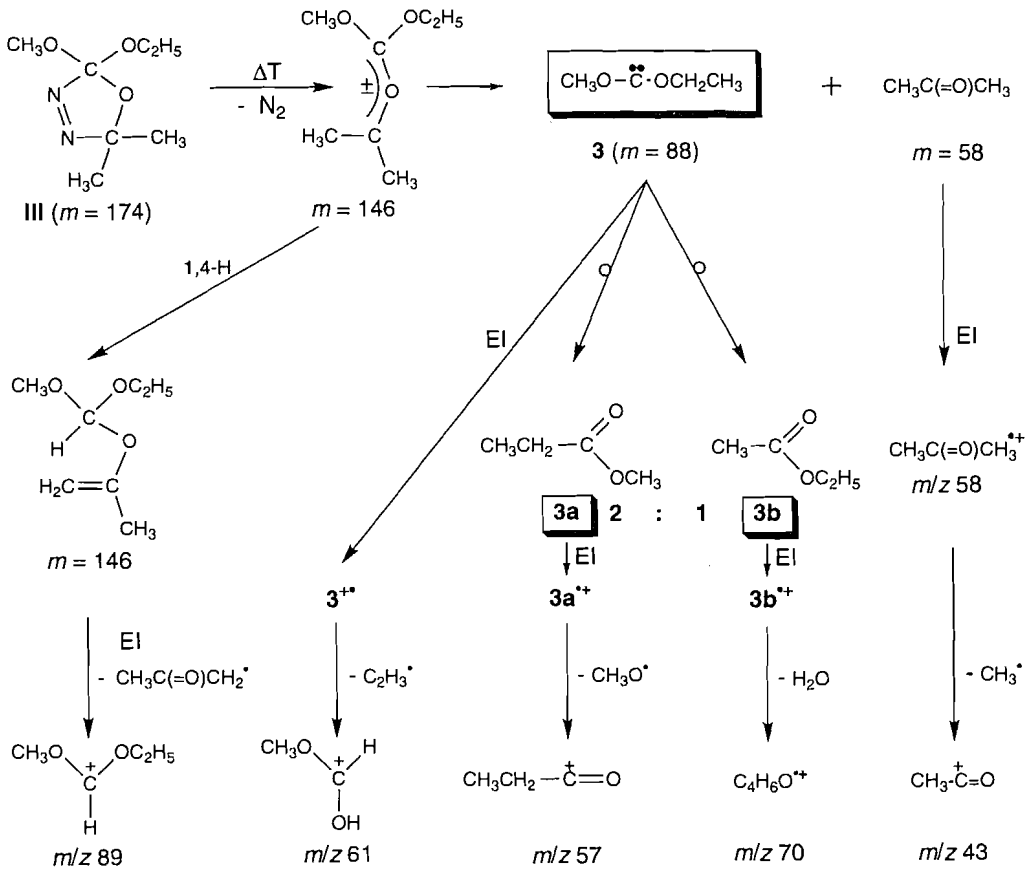

Fig. 4. CA mass spectra of *m/z* 156 ions (*a*) $\mathbf{2}^{\cdot+}$ from EI of ethoxy-2,2,2-trifluoroethoxycarbene; (*b*) generated after pyrolysis of **II**; (*c*) $\mathbf{2a}^{\cdot+}$ from EI of ethyl 3,3,3-trifluoropropionate; and (*d*) $\mathbf{2b}^{\cdot+}$ from EI of 2,2,2-trifluoroethyl propionate.

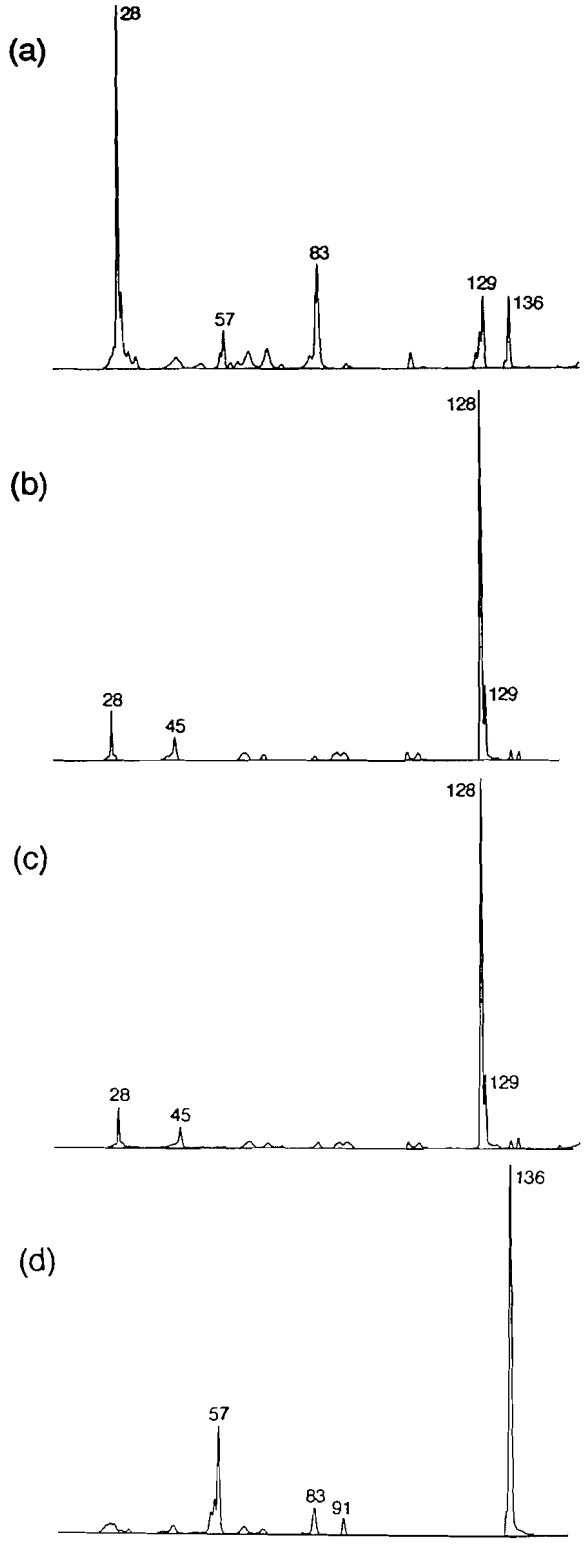

Fig. 5. CA mass spectra of *m/z* 88 ions (*a*) $\mathbf{3}^{\cdot+}$ from EI of ethoxymethoxycarbene; (*b*) generated after pyrolysis of **III**; (*c*) $\mathbf{3b}^{\cdot+}$ from EI of ethyl acetate; and (*d*) $\mathbf{3a}^{\cdot+}$ from EI of methyl propionate.

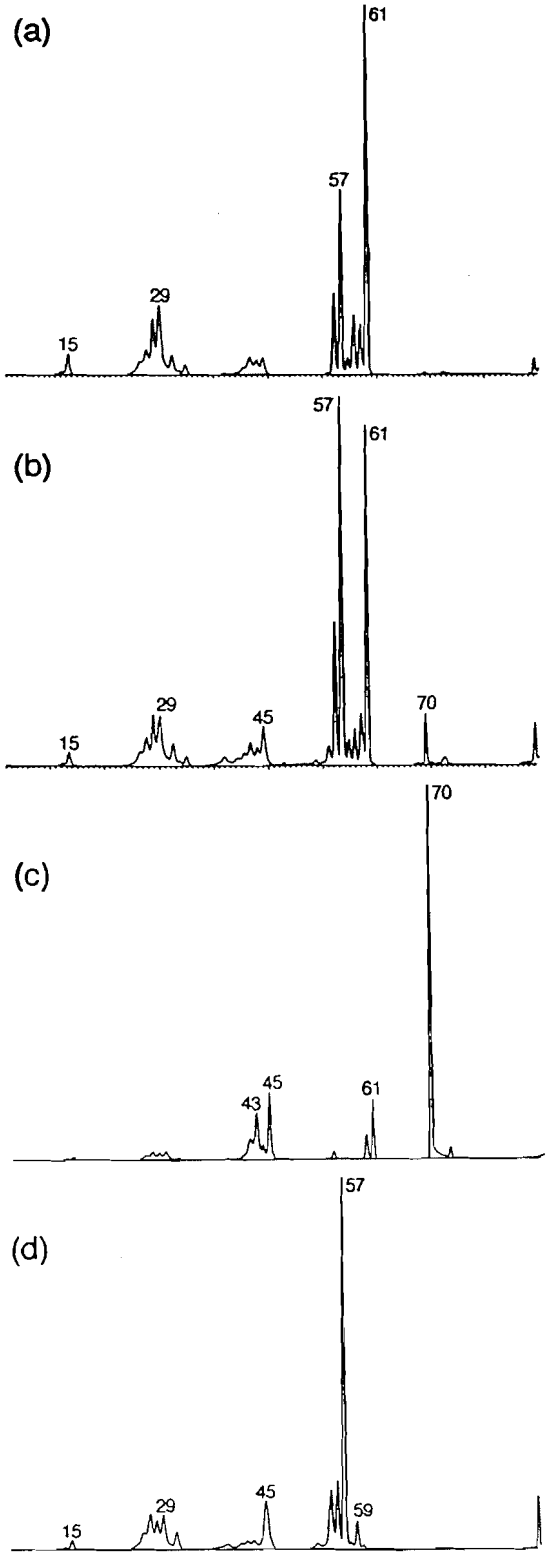

Fig. 6. CA mass spectra of collisionally generated $C_4H_6O^{\cdot+}$ ions from (*a*) *m/z* 88 ions after pyrolysis of **III** and (*b*) ionized ethyl acetate.

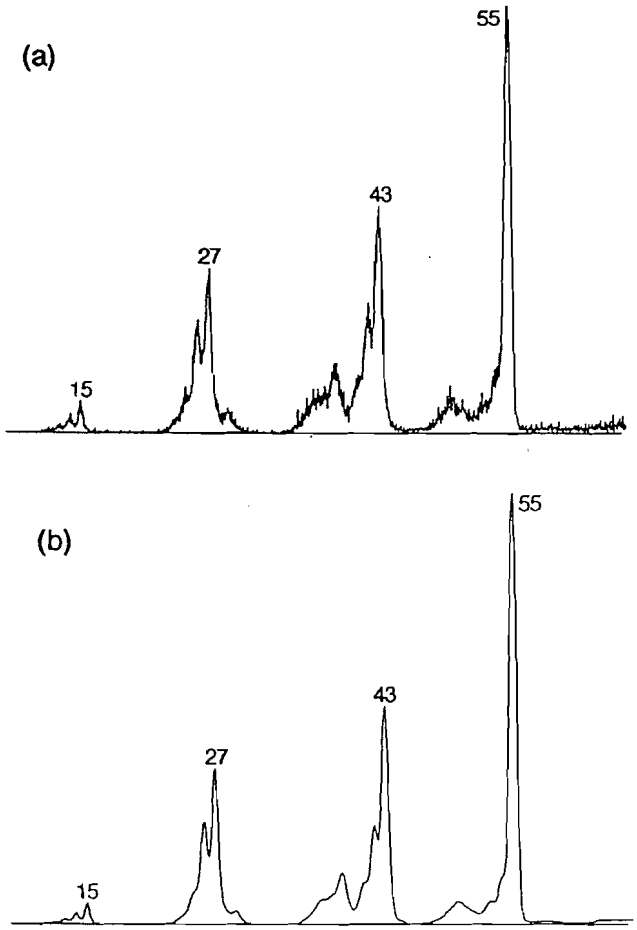

Fig. 7. CA mass spectra of collisionally generated $C_2H_5O_2^{\cdot+}$ ions from (*a*) ionized ethoxymethoxycarbene; (*b*) *m/z* 88 ions after pyrolysis of **III**; and (*c*) ionized ethyl acetate.

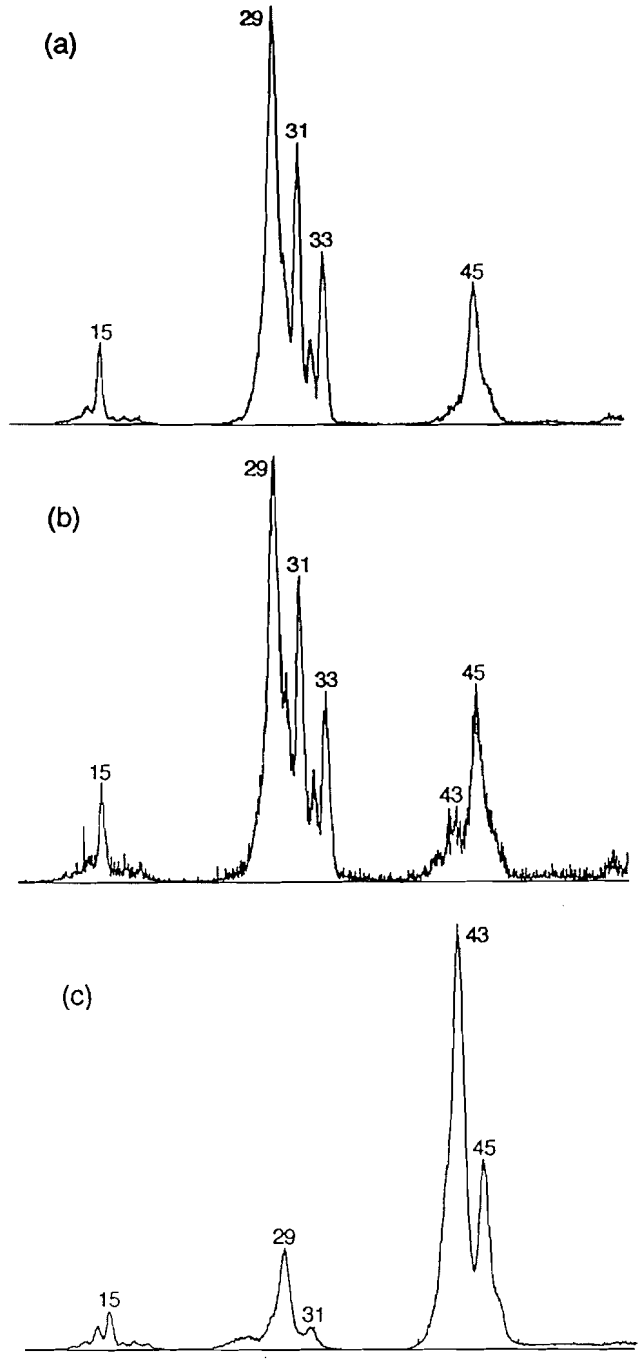

sis, the neutral carbene **3** undergoes a partial unimolecular rearrangement, via a 1,2-methyl shift, to **3b**.

From combined experimental and theoretical studies (22), it appears that the most stable *m/z* 61 $C_2H_5O_2^+$ ions in the gas phase are the conjugatively stabilized carbenium ions $CH_3C(OH)_2^+$, protonated acetic acid, and $HC(OH)(OCH_3)^+$, protonated methyl formate. These $C_2H_5O_2^+$ isomers can readily be distinguished on the basis of their collision-induced dissociation characteristics.

Through comparative collision experiments, the structures of the collisionally generated *m/z* 61 $C_2H_5O_2^+$ ions from $\mathbf{3}^{\cdot+}$ and that from $\mathbf{3b}^{\cdot+}$ were established to be protonated methyl formate and protonated acetic acid, respectively (see Figs. 7*a* and 7*c*). Note, however, from Figs. 7*a* and 7*b*, that the majority of the *m/z* 61 ions in the pyrolysis CA mass spectrum Fig. 5*b* represent protonated methyl formate ions (23) and not protonated acetic acid.

As shown in Fig. 5*b*, the *m/z* 57 ions form the base peak in the CA mass spectrum of *m/z* 88 ions generated by pyrolysis of **III**. The CA mass spectrum of the collisionally generated *m/z* 57 $(M - CH_3O^{\cdot})^+$ ions in Fig. 5*b* appears to be identical with that from **3a** (spectra not shown). This indicates that prior to ionization the neutral carbene **3** undergoes a second partial unimolecular rearrangement, into **3a** via a 1,2-ethyl shift. The above results indicate that the carbene **3** is generated by VLVP pyrolysis but only in admixture with **3a** and **3b**. Isomers **3a** and **3b** are formed from unimolecular rearrangement of the neutral dialkoxycarbene **3** via 1,2-ethyl and 1,2-methyl shifts, respectively.

Based upon analysis of the collision efficiencies of the isomeric ions and the mass spectral characteristics of the esters it follows that Fig. 5*b* represents a mixture of 10% $\mathbf{3}^{\cdot+}$, 80% $\mathbf{3a}^{\cdot+}$, and 10% $\mathbf{3b}^{\cdot+}$ and that the *neutral* esters **3a** and **3b** are formed from **3** in a ratio of 2:1. A mechanism for this intramolecular rearrangement will be discussed below.

Scheme 3*a*.

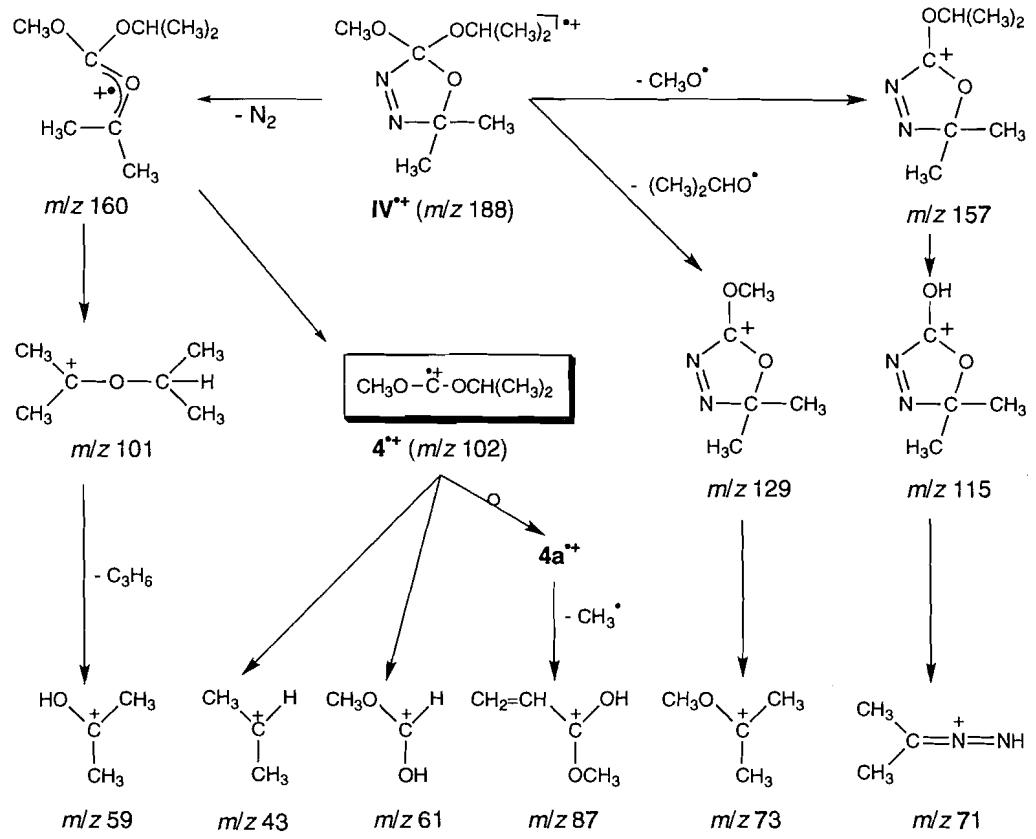

Isopropoxymethoxycarbene, 4: pyrolysis experiments

Unlike the oxadiazolines discussed above, the molecular ion $\mathbf{IV}^{\cdot+}$ undergoes one major (ca. 90%) primary fragmentation to form ions at *m/z* 129, which results from the loss of $(CH_3)_2CHO^{\cdot}$. Losses of N_2 and $CH_3O^{\cdot}$ also occur, but to a very small extent (ca. 6 and 4%, respectively). The major EI dissociations of **IV** are shown in Scheme 3*a*.

The ylide radical cation (*m/z* 160), formed via loss of N_2, readily dissociates to form ions at *m/z* 101. This process predominates over the formation of the carbene radical cations (*m/z* 102). Note that the intensities of $\mathbf{4}^{\cdot+}$ (*m/z* 102) and that of *m/z* 101 are 2 and 12% of the base peak at *m/z* 59, respectively. Thus, it is expected that a significant fraction of ions $\mathbf{4}^{\cdot+}$ results from the ^{13}C contribution from *m/z* 101.

The CA mass spectrum of $\mathbf{4}^{\cdot+}$ is characterized by peaks at *m/z* 87, 61, and 43 (see Fig. 8*a*) and it is structure-diagnostically different from that of methyl isobutyrate $\mathbf{4a}^{\cdot+}$ and that of isopropyl acetate $\mathbf{4b}^{\cdot+}$ (see Figs. 8*c* and 8*d*). The ions at *m/z* 87 and 61, which result from the dominant collision-induced dissociations in $\mathbf{4}^{\cdot+}$, are not present in the CA mass spectrum of $\mathbf{4b}^{\cdot+}$ and $\mathbf{4a}^{\cdot+}$, respectively. Thus, the carbene radical cation $\mathbf{4}^{\cdot+}$ can easily be distinguished from its isomers $\mathbf{4a}^{\cdot+}$ and $\mathbf{4}^{\cdot+}$ on the basis of its collision induced dissociation characteristics. The peaks at *m/z* 60 and 59 in the CA mass spectrum of $\mathbf{4}^{\cdot+}$ result (largely) from the ^{13}C contribution from *m/z* 101 ($C_5H_9O_2^{\cdot+}$) ions (The CA mass spectrum of *m/z* 101 ions (spectrum not shown) is dominated by a peak at *m/z* 59, i.e., *m/z* 101 $\rightarrow C_2H_3O_2^+ + C_3H_6$).

The peak at *m/z* 87 in the CA mass spectrum of $\mathbf{4}^{\cdot+}$ may originate from a direct bond cleavage in the carbene ion to yield the isopropoxycarbonyl cation, $(CH_3)_2CH\text{-}O\text{-}C{=}O^+$. This proposal was verified by comparing the CA mass spectrum of the collisionally generated $(M - CH_3^{\cdot})^+$ ions from $\mathbf{4}^{\cdot+}$ with that from $\mathbf{4a}^{\cdot+}$. The structure of $(M - CH_3^{\cdot})^+$ ions from $\mathbf{4a}^{\cdot+}$ is established as $CH_2{=}CHC(OH)(OCH_3)^+$ (24), a carbenium ion stabilized by three electron donating groups. Although they are not shown, the two CA mass spectra are superimposable, and thus the carbene radical cation $\mathbf{4}^{\cdot+}$ appears to isomerize partially into its isomer $\mathbf{4a}^{\cdot+}$ prior to dissociation. This is substantiated by the fact that the loss of $CH_3^{\cdot}$ from $\mathbf{4}^{\cdot+}$ is associated with a larger kinetic energy release value than that from $\mathbf{4a}^{\cdot+}$ 95 vs. 85 meV, respectively).

Through comparative collision experiments, the structures of the collisionally generated *m/z* 61 $C_2H_5O_2^+$ ions from $\mathbf{4}^{\cdot+}$ and that from $\mathbf{4b}^{\cdot+}$ were established as protonated methyl formate and protonated acetic acid, respectively. However, a weak signal at *m/z* 43, which forms the base peak in protonated acetic acid, in the CA mass spectrum of the collisionally generated $(M - C_3H_5^{\cdot})^+$ ions from $\mathbf{4}^{\cdot+}$ points to a unimolecular isomerization for a minor fraction of the carbene radical cations into its isomer $\mathbf{4n}^{\cdot+}$ prior to dissociation (see Fig. 7*a* for spectrum of pure protonated methyl formate).

The major fragmentations of **IV** upon VLVP pyrolysis are shown in Scheme 3*b*.

The first step of the pyrolysis involves loss of N_2 molecule to generate the intermediate ylide (*m* = 160). This ylide, in turn, either dissociates into the carbene **4** via loss of acetone molecule or rearranges via a 1,4-H shift into the orthoester. The orthoester *m* = 160, thus formed, is not expected to show molecular ions upon EI.

One of the major primary fragmentations from this orthoester forms ions at *m/z* 101, i.e., by loss of $(CH_3)_2CHO^{\cdot}$. Note

Scheme 3*b*.

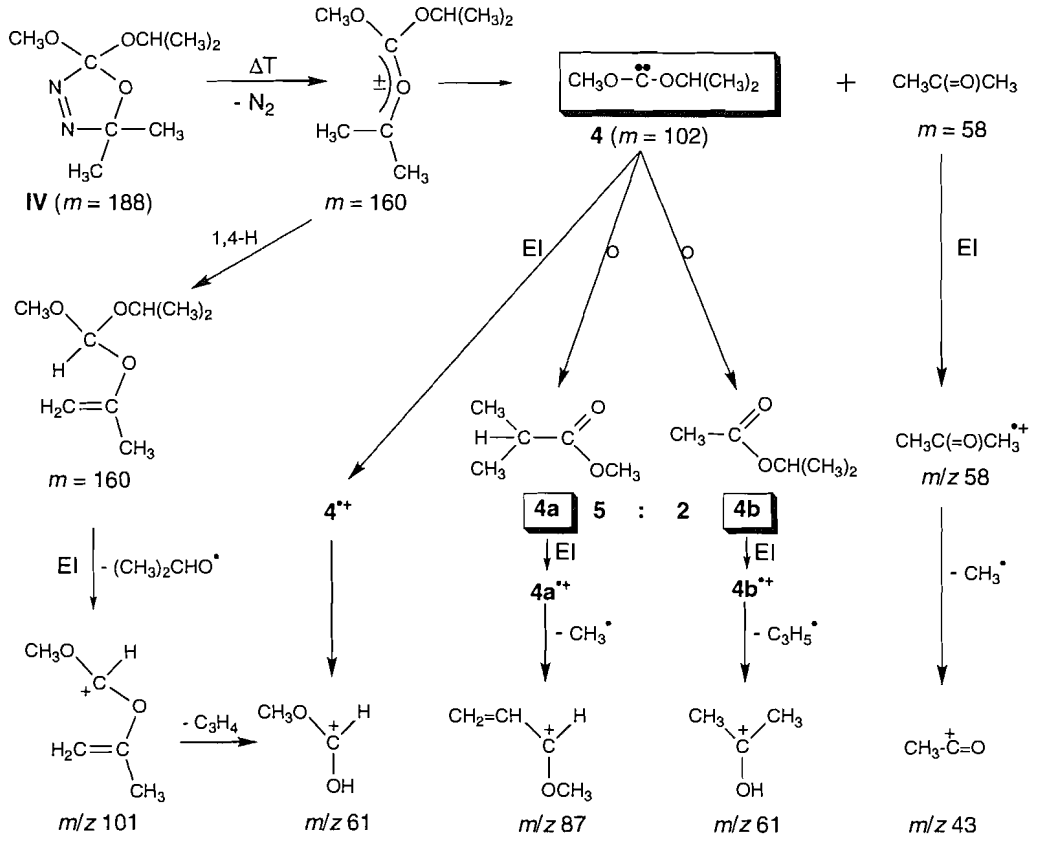

that the relative intensity ratio of *m/z* 101 to $\mathbf{4}^{\cdot+}$ (*m/z* 102) is ca. 5:1. Thus, it is expected that a significant amount of $\mathbf{4}^{\cdot+}$ ions results from the ^{13}C contribution from *m/z* ions.

The CA mass spectrum of the *m/z* 102 ions obtained during pyrolysis of **IV** at ca. 430°C, when the pyrolysis is complete, is characteristically different from that generated in the EI experiments (compare Figs. 8*a* and 8*b*). The pyrolysis CA mass spectrum is dominated by a peak at *m/z* 87 and the intensities of the *m/z* 61 and 43 ions are considerably reduced. The peaks at *m/z* 61 and 62 in the spectrum (largely) result form the ^{13}C contribution from *m/z* 101 ions (the CA mass spectrum of *m/z* 101 ions is dominated by a peak at *m/z* 61, i.e., *m/z* 101 → $C_2H_5O_2^+ + C_3H_4$). In addition, the *m/z* 61 ions are now largely $CH_3C(OH)_2^+$, characteristic of ethyl acetate, **4b**. These observations indicate that upon pyrolysis some of the neutral carbene molecules **4** have retained their original structure, as witnessed by the signal at *m/z* 43, but that the majority have isomerized into the isomers **4a** and **4b**, via 1,2-isopropyl and 1,2-methyl shifts, respectively.

Based upon analysis of the collision efficiencies of the isomeric ions and the mass spectral characteristics of the esters it follows that Fig. 8*b* represents a mixture of 30% $\mathbf{4}^{\cdot+}$, 60% $\mathbf{4a}^{\cdot+}$, and 10% $\mathbf{4b}^{\cdot+}$ and that the *neutral* esters **4a** and **4b** are formed from **4** in a ratio of 5:2. A mechanism for this intramolecular rearrangement will be discussed below.

Mechanistic proposal for the intramolecular 1,2-alkyl shifts from dialkoxy carbenes

From the VLVP pyrolysis – mass spectrometry on the various dialkoxy oxadiazolines, it follows that the corresponding neutral dialkoxycarbenes are generated, albeit not free, from the thermodynamically more stable isomers. It is noted that the neutral dialkoxycarbenes **1** and **2**, which have the trifluoroethyl functional group, have completely isomerized to the more stable isomers **1a** and **2a**, respectively, whereas partial isomerization is observed for the other dialkoxycarbenes **3** and **4**.

It has been proposed that the isomerization of dimethoxycarbene (DMC) into its isomer methyl acetate in the gas phase occurs via a reaction akin to a Wolff rearrangement, i.e., by a 1,2-CH_3 shift (25, 26). In the previous study (12), we suggested another possibility, i.e., the bimolecular reaction between CH_3 radicals produced by the thermal decomposition of the carbene and the intact carbene, yielding 1,1-dimethoxyethyl radicals that may subsequently decompose into methyl molecules (eq. [1]):

The mechanism below was tested in this study by the copyrolysis of the precursor molecule with its D-labelled analogue 2,2-bis[trideuteromethoxy]-5,5-dimethyl-Δ^3-1,3,4-oxadiazoline. An increase in the intensity of *m/z* 77, which could be either $CH_3C(=O)OCD_3^{\cdot+}$ and (or) $CD_3C(=O)OCH_3^{\cdot+}$, would

[1]

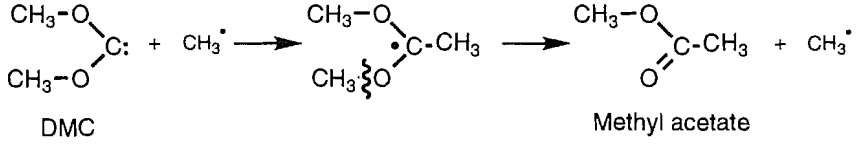

Fig. 8. CA mass spectra of *m/z* 102 ions (*a*) $\mathbf{4}^{\cdot+}$ from EI of isopropoxymethoxycarbene (* indicates the ^{13}C contribution from *m/z* 101 ions); (*b*) generated after pyrolysis of **IV**; (*c*) $\mathbf{4b}^{\cdot+}$ from EI of isopropyl acetate; and (*d*) $\mathbf{4a}^{\cdot+}$ from EI of methyl isobutyrate.

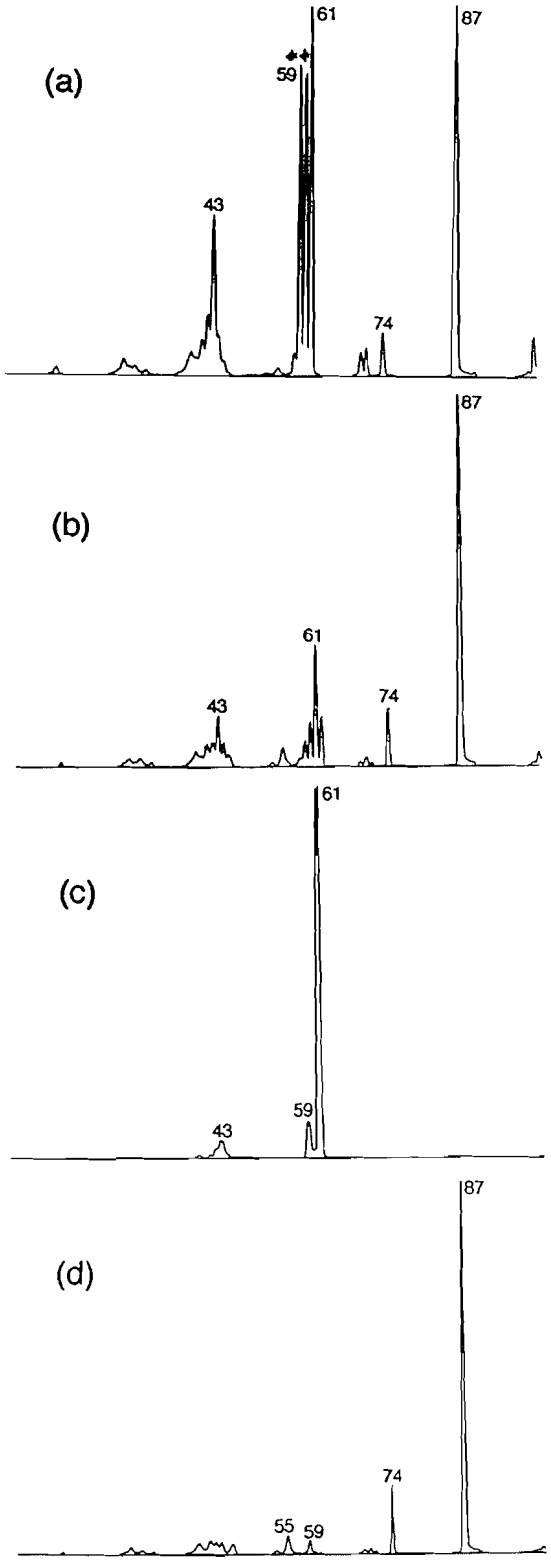

substantiate the proposal. However, the copyrolysis of the labelled and unlabelled precursor molecules in a 1:1 mixture at ca. 440°C does not increase the intensity of *m/z* 77 ions to a significant extent. Thus, the bimolecular mechanism does not add significantly to the unimolecular rearrangement of DMC and this probably also holds true for the carbenes reported in this study.

For DMC there is only one possible isomer, methyl acetate, whereas the ethoxymethoxycarbene **3** could undergo unimolecular isomerization to form two possible isomers, **3a** and **3b**. From the comparative collision experiments, it was concluded that isomer **3a** is formed in larger amount than isomer **3b** (see above). The same trend is found for the isopropoxymethoxycarbene **4**; **4a** is produced in larger amount than **4b**. It seems that the migration of the primary and secondary groups is more favourable than that of the methyl group.

In the case of methoxy- and ethoxy-(2,2,2-trifluoroethoxy)carbenes (**1** and **2**), only the 2,2,2-trifluoroethyl group migrates to form methyl and ethyl 3,3,3-trifluoropropionate **1a** and **2a**, respectively. There is no evidence for methyl and ethyl migration upon VLVP pyrolysis experiments. This indicates that the electron-withdrawing trifluoroethyl group plays a major role in the unimolecular rearrangement because both ethyl and methyl migrations have been observed for the ethoxymethoxycarbene **3**.

There is a body of evidence to suggest that carbene rearrangements progress through a transition state that features the development of negative charge on the migrating group (MG, eq. [2]) and hence these rearrangements are termed hydride shifts (1). For instance, an electron-donating substituent (R^1) at C-2 of a carbene (eq. [2]) greatly facilitates migration, since it stabilizes the development of positive charge at the migration origin (27). Furthermore, the geometries of the transition states calculated for a number of carbene migrations suggest hydride migration to the "vacant" *p*-orbital lying perpendicular to the plane of the carbenic substituents (9). Although these conclusions arise from results on 1,2-H migrations, extrapolations to 1,2-alkyl migrations is reasonable.

Our results indicate that trifluoroethyl has a large migratory aptitude compared to either methyl or ethyl. There is no doubt that β-fluorines are anion stabilizing; the computed stabilization energy of $CF_3CH_2^-$ relative to $CH_3Ch_2^-$ is 46.0 kcal/mol (28). It follows that trifluoroethyl migrates with development of negative charge in the migrating group as described above. The simplest assumption is that methyl, ethyl, and isopropyl groups migrate by the same mechanism, but with much less negative charge buildup on those migrating groups at the appropriate transition states.

The slightly greater migratory aptitude of ethyl and isopropyl groups, as compared to methyl, is not easy to explain. While there is no doubt that alkyl substituents appear to be electron donating (and base strengthening) in solution (29), there is a body of experimental evidence that shows them to be stabilizing to either cationic or anionic centres in the gas phase. The latter behaviour has been attributed largely to polarizability (30, 31). Combined computational and experimental (28) studies suggest that $CH_3CH_3^-$ and $(CH_3)_2CH^-$ are both somewhat less stable than CH_3^-, although the opposite trend could probably be accommodated without exceeding the error limits of the method.

If the migrating group moves with carbanion character, it

[2] 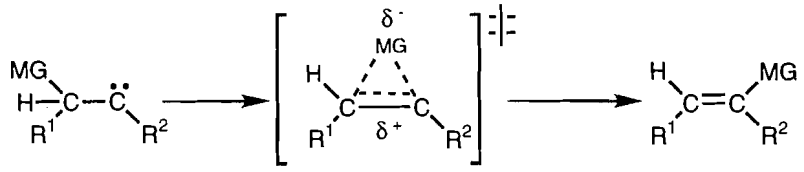

[3] 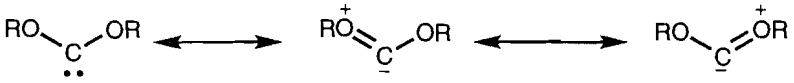

must be migrating to the electron-deficient site of the singlet carbene. Dialkoxycarbene singlets do not have a "vacant" *p*-orbital at carbon, because of conjugative localization of oxygen lone pairs to provide some π-bonding (eq. [3]). The partial double bond character between the carbene carbon and the oxygen substituents is reflected in the large barrier for rotation about the C—O bond of dihydroxycarbene (ca. 20 kcal/mol) (32).

Dialkoxycarbenes are different from carbenes such as singlet *tert*-butylmethylene, **5**. The computed energy minimum for **5** possesses a bridged structure, with one methyl group eclipsing the *p*-orbital at the carbene centre and populating it by hyperconjugation (33). The ground state is set up geometrically for methyl migration.

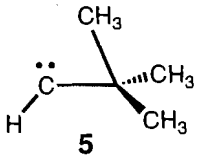

5

In contrast, both RO bonds of dioxycarbenes lie in the OCO plane (32, 34), but not necessarily in the sickle conformation drawn (eq. [4]). For migration to the π-system, a twist about a C—OR bond is presumably required, most likely in concert with transfer of R from oxygen to carbon. It is clear that such a rotation would be easier for the ROC—OCH_2CF_3 bond because it would have a lower bond order than the other carbenic C—O bond. Thus, the more facile transfer of CF_3CH_2, as compared to CH_3 or CH_3CH_2, is attributed to the higher ground state energies of **1** and **2** (less π-bonding and consequently easier rotation) and lower transition state energies because of the ability of CF_3CH_2 to migrate with more charge than can be accommodated by ethyl or methyl.

If the migrating group adopts some carbanion character, it is clear that the "stationary" fragment must be cation-like. Thus an extreme representation of the charge separation at the transition states for rearrangements reported here is in terms of an acylium ion – carbanion pair (eq. [5]).

Experimental

The CA and NR mass spectra were measured using the custom-built VG Analytical ZAB-R mass spectrometer (35). The NR mass spectra were obtained using cyclopropane $(Cp)^2$ for neutralization (main beam transmission $T = 80\%$) and oxygen for reionization ($T = 80\%$); oxygen was also used as the collision gas in the CA experiments.

The ZAB-R mass spectrometer is a three-sector BE_1E_2 (B = magnetic sector, E = electric sector) type instrument whose design is based on the standard, nonextended geometry of the ZAB-2F. The instrument is equipped with four collision gas chambers of which the two located in the second field-free region (in front of E_1) were used for the NR experiments. The double collision experiments (18, 22) involved mass (B) and energy (E_1) selected ions generated from collisions in the second field-free region that were analysed by obtaining CA mass spectra in the third field-free region using a scan of E_2. The pyrolysis experiments were also performed on this instrument. The VLVP pyrolysis unit has been described previously (37). Briefly, the pyrolysis oven is constructed of silica and has a high-temperature zone of c. 25 mm length. The exit of the oven into the ion source was situated ca. 10 mm from the ionizing electron beam. The samples were introduced into the pyrolysis unit by evaporation from a small glass bulb kept at room temperature.

Compounds **I**, **III**, and **IV** were synthesized using the method described in ref. 15, and the IE/MS of **III** and **IV** are reported below.

2-Acetoxy-2-ethoxy-5,5-dimethyl-Δ^3-1,3,4-oxadiazoline and ethyl 2,3-diaza-4-methylacetoxypent-2-enoate

Acetone (ethoxycarbonyl)hydrazone was prepared by dissolv-

[4] 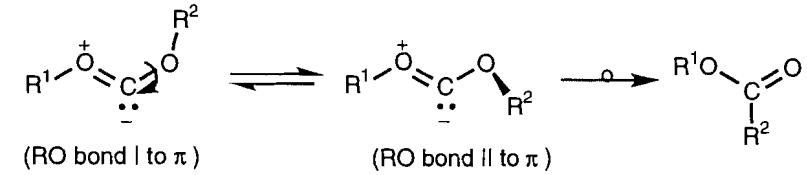

(RO bond I to π) (RO bond II to π)

[5] 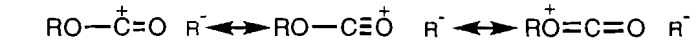

[2] For the use of organic neutralization agents, see ref. 36.

ing ethyl carbazate in acetone with $MgSO_4$ added as a desiccant and stirring overnight. Filtration and removal of solvent yielded hydrazone pure enough to use for the next step. Acetone carboethoxyhydrazone (10 g) was dissolved in 250 mL of dichloromethane and cooled with stirring in an ice bath near 0°C. Solid lead tetraacetate (32 g, 1.05 equiv.) was added to the cooled contents of the flask over 5 min. After stirring at ice temperature for 30 min, the bath was removed and the reaction mixture was allowed to warm to room temperature where it was left stirring for about 4 h or until the lead diacetate salts had precipitated as a free-flowing white solid. The mixture was then extracted with sodium bicarbonate solution to remove acetic acid and the lead salts. Drying with $MgSO_4$ and evaporation of the solvent gave product that was found to be a mixture of ca. 66% oxadiazoline and ca. 34% of the acyclic impurity (by NMR).

2-Acetoxy-2-ethoxy-5,5-dimethyl-Δ^3-1,3,4-oxadiazoline
^{1}H NMR (200 MHz, $CDCl_3$) δ: 1.24 (t, 3H, ^3J = 7.2 Hz), 1.62 (s, 6H, $C(CH_3)_2$), 2.06 (s, 3H, CH_3CO_2), 3.89 (m, 2H); ^{13}C NMR (50 MHz, $CDCl_3$) δ: 15.0, 22.4, 24.1, 24.4, 61.4, 100.4, 133.8, 166.4; EI/MS, *m/z* (%): 143 (5), 71 (4), 59 (29), 43 (100).

Ethyl 2,3-diaza-4-methyl-acetoxypent-2-enoate
^{1}H NMR (200 MHz, $CDCl_3$) δ: 1.37 (t, 3H, ^3J = 7.1 Hz), 1.48 (s, 6H), 2.06 (s, 3H, CH_3CO_2), 4.38 (q, 2H, ^3J = 7.1 Hz); EI/MS, *m/z* (%): 101 (40), 59 (35), 43 (100).

2-Ethoxy-2-(2,2,2-trifluoroethoxy)-5,5-dimethyl-Δ^3-1,3,4-oxadiazoline II

2-Acetoxy-2-ethoxy-5,5-dimethyl-Δ^3-1,3,4-oxadiazoline (15) (1 equiv., a mixture of oxadiazoline and acyclic impurity) was dissolved in dichloromethane with trifluoroethanol (5 equiv.). Acetic acid (5 mL) was added and the resulting solution was left at room temperature overnight.

Formation of **II** and consumption of acetoxy oxadiazoline can be followed easily by GC. When the exchange was complete, KOH pellets were added to the reaction mixture, which was then stirred at room temperature overnight. Water was added to the reaction mixture and the organic layer was collected and washed with sodium bicarbonate solution. Drying and evaporation of the solvent yielded **II**, which was used without further purification. ^{1}H NMR (200 MHz, $CDCl_3$) δ: 1.22 (t, 3H, ^3J = 7.0 Hz), 1.48 (s, 3H), 1.54 (s, 3H), 4.127 (q, 1H, $^3J_{HF}$ = 8.4 Hz, OCH_2CF_3), 4.136 (q, 1H, $^3J_{HF}$ = 8.4 Hz, OCH_2CF_3); ^{13}C NMR (50 MHz, $CDCl_3$) δ: 14.8, 23.7, 24.0, 60.9, 61.9 (q, $^2J_{CF}$ = 37 Hz, OCH_2CF_3), 120.4 (C5), 135.7(C2); ^{19}F NMR (471 MHz, $CDCl_3$) δ: −74.553 (t, 1H, $^3J_{HF}$ + 8.5 Hz); EI/MS, *m/z* (%): 214 (1), 197 (27), 173 (3), 172 (17), 156 (9), 145 (23), 143 (10), 141 (16), 136 (1), 135 (1), 129 (3), 128 (3), 127 (6), 125 (20), 113 (2), 87 (13), 83 (47), 71 (17), 70 (5), 69 (2), 64 (5), 63 (2), 61 (17), 60 (5), 59 (100), 58 (4), 57 (13), 56 (7), 45 (11), 44 (3), 43 (39), 42 (56), 41 (35), 40 (7).

2-(Trideuteromethoxy)-2-(2,2,2-trifluoroethoxy)-5,5-dimethyl-Δ^3-1,3,4-oxadiazoline I-d_3

2-Acetoxy-2-(trideuteromethoxy)-5,5-dimethyl-Δ^3-1,3,4-oxadiazoline was prepared as follows. Methyl carbazate-d_3 was prepared by adding CD_3OD (3 equiv. to 1,1′-carbonyldiimidazole (1 equiv.) in dichloromethane, letting stand for 2 h, and then adding hydrazine monohydrate (10 equiv.) and letting stand overnight. Evaporation of the solvent and removal of excess hydrazine under higher vacuum yielded methyl carbazate-d_3, which was used without further purification. Simply dissolving the carbazate in acetone in the presence of a desiccant ($MgSO_4$) and allowing to stand overnight yielded the labelled (methoxycarbonyl)-hydrazone of acetone. Oxidation and exchange were analogous to the published procedure (15) for the unlabelled molecule. The product was used without further purification. ^{1}H NMR (200 MHz, $CDCl_3$) δ: 1.49 (s, 3H), 1.55 (s, 3H), 4.13 (q, 1H, $^3J_{HF}$ = 8.4 Hz, OCH_2CF_3), 4.14 (q, 1H, $^3J_{HF}$ = 8.4 Hz, OCH_2CF_3); ^{13}C NMR (50 MHz, $CDCl_3$) δ: 23.7, 24.0, 61.9 (q, $^2J_{CF}$ = 36 Hz, OCH_2CF_3), 120.8, 132.2. (q, $^1J_{CF}$ = 277 Hz), 128; ^{19}F NMR (471 MHz, $CDCl_3$) δ: −74.558 (t, 1H, $^3J_{HF}$ = 8.4 Hz).

2,2-Bis(Trideuteromethoxy)-5,5-dimethyl-Δ^3-1,3,4-oxadiazoline

Preparation of 2-acetoxy-2-(trideuteromethoxy)-5,5-dimethyl-Δ^3-1,3,4-oxadiazoline was described above. Exchange of this product with methanol-d_4 yielded 2,2-bis(trideuteromethoxy)-5,5-dimethyl-Δ^3-1,3,4-oxadiazoline. Acyclic byproduct was hydrolyzed as usual with KOH pellets. Bicarbonate extraction and drying yielded product that was used without further purification.

2-Ethoxy-2-methoxy-5,5-dimethyl-Δ^3-1,3,4-oxadiazoline ***III***
EI/MS, *m/z* (%): 146 (5), 144 (3), 143 (24), 130 (5), 129 (45), 105 (7), 104 (24), 89 (5), 88 (41), 87 (14), 77 (39), 73 (34), 71 (28), 70 (7), 61 (20), 60 (23), 59 (100), 58 (9), 57 (25), 56 (23), 45 (22), 44 (14), 43 (51), 42 (43), 41 (33), 40 (9).

2-Ethoxy-2-isopropoxy-5,5-dimethyl-Δ^3-1,3,4-oxadiazoline ***IV***
EI/MS, *m/z* (%): 160 (3),157 (2), 131 (2), 130 (5), 129 (43), 119 (2), 118 (16), 117 (4), 115 (9), 113 (7), 104 (2), 103 (2), 102 (2), 101 (12), 88 (2), 87 (5), 77 (26), 74 (5), 73 (40), 71 (18), 61 (8), 60 (8), 59 (100), 58 (5), 57 (3), 56 (11), 45 (15), 44 (11), 43 (63), 42 (28), 41 (30), 40 (5).

2,2,2-Trifluoroethyl acetate was synthesized by estrerification of acetic anhydride with 2,2,2-trifluoroethanol. Methyl and ethyl 3,3,3-trifluoropropionate were synthesized according to the method described in ref. 38 with some modifications. The experimental details are as follows: A 40 mL autoclave containing 7.4 g (0.056 mol) of oxalacetic acid was cooled with liquid N_2. One third of the SF_4 required was added with liquid N_2 cooling. The autoclave was slowly warmed to ice temperature and then to room temperature. Then the autoclave was again cooled with liquid N_2 and noncondensabile residues were pumped off; this sequence was repeated 2 times. For the third time, the autoclave was slowly warmed to ice temperature and excess HF was removed through vacuum. Then, the mixture in the autoclave was shaken for 12 h using an automatic shaker. The contents were then poured into a Teflon bottle. To a small aliquot was added an excess of CH_3OH–CH_3CH_2OH and the mixture was left in the refrigerator for 1 day. The esters were then purified by preparative GLC.

Methyl 3,3,3-trifluoropropionate ***1a***
GC/MS, *m/z* (%): 142 (9), 123 (2), 122 (9), 112 (3), 111 (100),

110 (5), 91 (55), 84 (3), 83 (33), 82 (8), 81 (19), 71 (4), 69 (34), 64 (28), 63 (11), 59 (43), 51 (5), 50 (2), 49 (5), 47 (5), 45 (6), 43 (5), 42 (11), 41 (2).

Ethyl 3,3,3-trifluoropropionate **2**a
GC/MS, *m/z* (%): 156 (3), 141 (2), 129 (7), 128 (5), 111 (100), 91 (25), 89 (9), 83 (17), 69 (18), 64 (11), 63 (3), 51 (1), 49 (2), 47 (1), 45 (13), 44 (2), 43 (4), 42 (6).

Acknowledgements

The authors thank M. El-Saidi for providing samples **III** and **IV**. J.K.T. and J.W. thank the Natural Sciences and Engineering Research Council of Canada for financial support. D.S. is grateful to Professor G.J. Schrobilgen for his expert help in the synthesis of the trifluoropropionates and thanks Dr G.A. McGibbon for valuable comments.

References

1. W. Kirmse. *In* Carbene chemistry. 2nd ed. Academic Press, New York. 1971.
2. M. Jones, Jr. and R.A. Moss (Editors). *In* Carbenes. Wiley, New York. 1973.
3. I. Shavitt. Tetrahedron, **41**, 1531 (1985).
4. D.G. Leopold, K.K. Murray, A.S. Miller, and W.C. Lineberge. J. Chem. Phys. **83**, 4849 (1985).
5. R.D. Bach, M.-D. Su, E. Aldabbagh, J.L. Andres, and H.B. Schlegel. J. Am. Chem. Soc. **115**, 10237 (1993).
6. K.K. Irikura, W.A. Goddard III, and J.L. Beauchamp. J. Am. Chem. Soc. **114**, 48 (1992).
7. J.E. Jackson, N. Soundararajan, W. White, M.T.H. Liu, R. Bonneau, and M.S. Platz. J. Am. Chem. Soc. **111**, 6874 (1989).
8. G.-J. Ho, K. Krogh-Jespersen, R.A. Moss, S. Shen, R.S. Sheridan, and R. Subramanian. J. Am. Chem. Soc. **111**, 6875 (1989).
9. J.D. Evanseck and K.N. Houk. J. Phys. Chem. **94**, 5518 (1990).
10. R.S. Sheridan, R.A. Moss, B.K. Wilk, S. Shen, M. Wlostowski, M.A. Kesselmayer, R. Subramanian, G. Kmiecik-Kawrynowicz, and K. Krogh-Jespersen. J. Am. Chem. Soc. **110**, 7563 (1988).
11. (*a*) C. Wesdemiotis and F. W. McLafferty. J. Am. Chem. Soc. **109**, 4760 (1987); (*b*) R. Feng, C. Wesdemiotis, and F.W. McLafferty. J. Am. Chem. Soc. **109**, 6521 (1987); (*c*) D. Sülzle, T. Drewello, B.L.M. van Baar, and H. Schwarz. J. Am. Chem. Soc. **110**, 8330 (1988).
12. T. Wong, J. Warkentin, and J.K. Terlouw. Int. J. Mass Spectrom. Ion Processes, **115**, 33 (1992).
13. (*a*) G.A. McGibbon, C.A. Kingsmill, and J.K. Terlouw. Chem. Phys. Lett. **222**, 129 (1994); (*b*) G.A. McGibbon, P.C. Burgers, and J.K. Terlouw. Int. J. Mass Spectrom. Ion Processes, **136**, 191 (1994); (*c*) P.C. Burgers, G.A. McGibbon, and J.K. Terlouw. Chem. Phys. Lett. **224**, 539 (1994).
14. (*a*) K. Levsen and H. Schwarz. Angew. Chem. Int. Ed. Engl. **15**, 509 (1976); (*b*) Mass Spectrom. Rev. **2**, 77 (1983); (*c*) J.L. Holmes. Org. Mass Spectrom. **20**, 169 (1985); (*c*) R.G. Cooks. J. Mass Spectrom. **30**, 1215 (1995).
15. (*a*) M. El-Saidi, K. Kassam, D. Pole, T. Tadey, and J. Warkentin. J. Am. Chem. Soc. **114**, 8751 (1992); (*b*) K. Kassam, D.L. Pole, M. El-Saidi, and J. Warkentin. J. Am. Chem. Soc. **116**, 1161 (1994).
16. (*a*) C. Wesdemiotis and F.W. McLafferty. Chem. Rev. **87**, 485 (1987); (*b*) J. K. Terlouw and H. Schwarz. Angew. Chem. Int. Ed. Engl. **26**, 805 (1987); (*c*) H. Schwarz. Pure Appl. Chem. **61**, 685 (1989); (*d*) J.K. Terlouw. Adv. Mass Spectrom. **11**, 984 (1989); (*e*) J.L. Holmes. Mass Spectrom. Rev. **8**, 513 (1989); (*f*) F.W. McLafferty. Science (Washington D.C.), **247**, 925 (1990); (*g*) Int. J. Mass Spectrom. Ion Processes, **118/119**, 221 (1992); (*h*) N. Goldberg and H. Schwarz. Acc. Chem. Res. **27**, 347 (1994).
17. R.F. Brown. *In* Pyrolytic methods in organic chemistry. Academic Press, New York. 1980.
18. S. Villeneuve and P.C. Burgers. Org. Mass Spectrom. **21**, 733 (1986).
19. (*a*) R.A. Moss, W. Liu, and C.-S. Ge. J. Phys. Org. Chem. **6**, 376 (1993); (*b*) C.-S. Ge, E.A. Jefferson, and R.A. Moss. Tetrahedron Lett. **34**, 7549 (1993); (*c*) R.A. Moss, S. Xue, and W. Liu. J. Am. Chem. Soc. **116**, 1583 (1994).
20. F.A. Wiedmann, J. Cai, and C. Wesdemiotis. Rapid Commun. Mass Spectrom. **8**, 804 (1994).
21. B.L.M. van Baar, P.C. Burgers, J.K. Terlouw, and H. Schwarz. J. Chem. Soc. Chem. Commun. 1607 (1986).
22. (*a*) H. Halim. Ph.D. Thesis, Technische Universität Berlin, 1986; (*b*) B.L.M. van Baar, H. Halim, J.K. Terlouw, and H. Schwarz. J. Chem. Soc. Chem. Commun. 728 (1986).
23. D. Suh, C.A. Kingsmill, P.J.A. Ruttink, P.C. Burgers, and J.K. Terlouw. Int. J. Mass Spectrom. Ion Processes, **146/147**, 305 (1995).
24. P.C. Burgers, K.J. van den Berg, H. Visser, and J.K. Terlouw. Int. J. Mass Spectrom. Ion Processes, **101**, 83 (1990).
25. M. Jones, Jr. Acc. Chem. Res. **7**, 415 (1974).
26. R.W. Hoffmann. Angew. Chem. Int. Ed. Engl. **10**, 529 (1971).
27. A. Nickon. Acc. Chem. Res. **26**, 84 (1993).
28. J. March. *In* Advanced organic chemistry. 4th ed. Wiley–Interscience, New York. 1992. Chap. 8, and references therein.
29. J.E. Bartmess, J.A. Scott, and R.T. McIver, Jr. J. Am. Chem. Soc. **101**, 6056 (1979).
30. E.J. Aitken, J.K. Bahl, K.D. Bomben, J.K. Gimzewski, G.S. Nolan, and T.D. Thomas. J. Am. Chem. Soc. **102**, 4873 (1980).
31. G. LeRoy, C. Wilante, D. Peeters, and M.M. Uyewa. J. Mol. Struct. (Theochem), **124**, 107 (1985).
32. (*a*) M. Rasanen, T. Raaska, H. Kunttu, and J. Murto. J. Mol. Struct. (Theochem), **208**, 79 (1990); (*b*) D. Feller, W.T. Borden, and E.R. Davidson. J. Chem. Phys. **71**, 4987 (1979).
33. B.M. Armstrong, M.L. McKee, and P.B. Shevlin. J. Am. Chem. Soc. **117**, 3685 (1995).
34. (*a*) R.A. Moss, M. Wlostowski, S. Shen, K. Krogh-Jespersen, and A. Matro. J. Am. Chem. Soc. **110**, 4443 (1988); (*b*) R.A. Moss, M. Wlostowski, J. Terpinski, G. Kmiecik-Lawrynowicz, and K. Krogh-Jespersen. J. Am. Chem. Soc. **109**, 3811 (1987).
35. H.F. van Garderen, P.J.A. Ruttink, P.C. Burgers, G.A. McGibbon, and J.K. Terlouw. Int. J. Mass Spectrom. Ion Processes, **121**, 159 (1992).
36. (*a*) M-Y. Zhang and F.W. McLafferty. J. Am. Soc. Mass Spectrom. **3**, 108 (1992); (*b*) T. Wong, J.K. Terlouw, T. Weiske, and H. Schwarz. Int. J. Mass Spectrom. Ion Processes, **13**, R23 (1992).
37. J.K. Terlouw, J.L. Holmes, and F.P. Lossing. Can. J. Chem. **61**, 1722 (1983).
38. F.A. Bloshchitsa, A.I. Burmakov, B.V. Kunshenko, L.A. Alekseeva, and L.M. Yagupol'skii. Zh. Org. Khim. **21**, 1286 (1985).

Polyhalide anions in crystals. Part 1. Triiodides of the Me_4N^+, Me_4P^+, quinuclidinium, 1-azoniapropellane, and 1,4-diazoniabicyclo[2.2.2]octane ($DabcoH_2^{2+}$) cations, and 1,10-phenanthrolinium(1+) tribromide

Pradip K. Bakshi, Margaret A. James, T. Stanley Cameron, and Osvald Knop

Abstract: Crystal-structure determinations are reported for Me_4NI_3 (4MI3, *Pnnm*, a = 10.107(2), b = 14.141(2), c = 8.252(5) Å, Z = 2), quinuclidinium I_3 (QI3, *Pnnm*, a = 10.290(2), b = 14.011(2), c = 8.813(2) Å, Z = 2), Me_4PI_3 (4MPI3, $P4_2/m$, a = 15.098(4), c = 13.770(4) Å, Z = 10), 1-azoniapropellane I_3 (API3, $P2_1/c$, a = 15.131(7), b = 28.453(6), c = 22.848(8) Å, β = 108.53(3)°, Z = 24), 1,4-diazoniabicyclo[2.2.2]octane $(I_3)_2$ (Da2I3, $P2_1/m$, a = 9.671(6), b = 8.127(2), c = 11.144(3) Å, β = 96.60(3)°, Z = 2), and 1,10-phenanthrolinium(1+) Br_3 (phenBr3, $P\bar{1}$, a = 8.370(2), b = 10.410(4), c = 8.171(2) Å, α = 107.52(2)°, β = 97.35(1)°, γ = 94.84(2)°, Z = 2). The nearly isostructural 4MI3 and QI3 are of a distorted *anti*-NiAs type. The 4MPI3 and API3 structures can be regarded as consisting of distorted CsCl-type coordination cuboids; both are unexpectedly complex, 4MPI3 (not isostructural with 4MI3) containing cations of two and anions of three types, API3 containing cations of six and anions of seven types. API3 thus represents an extreme case of a frustrated CsCl structure. The ion packing in Da2I3 is related to that in CaF_2. The distortion of one of the two nonequivalent I_3^- anions in Da2I3 is one of the largest, if not *the* largest on record (I—I = 2.793(2) and 3.167(2) Å, I-I-I = 172.47(4)°), and attributable to the involvement of the anion in a strong N—H...I bond, H...I = 2.78 Å. The bifurcated H-bond in which the protonated cation nitrogen in phenBr3 is engaged has an intra-cation, N—H(N)...N, branch and an inter-ion branch, N—H(N)...Br.

Key words: crystal structure, hydrogen bond, polyhalide anions, tribromides, triiodides.

Résumé : On a déterminé les structures cristallines du Me_4NI_3 (4MI3, *Pnnm*, a = 10,107(2), b = 14,141(2) et c = 8,252(5) Å, Z = 2), du quinuclidinium I_3 (QI3, *Pnnm*, a = 10,290(2), b = 14,011(2) et c = 8,813(2) Å, Z = 2), du Me_4PI_3 (4MPI3, $P4_2/m$, a = 15,098(4) et c = 13,770(4) Å, Z = 10), du 1-azoniapropellane I_3 (API3, $P2_1/c$, a = 15,131(7), b = 28,453(6) et c = 22,848(8) Å, β = 108,53(3)°, Z = 24), du 1,4-diazoniabicyclo[2.2.2]octane $(I_3)_2$ (Da2I3, $P2_1/m$, a = 9,671(6), b = 8,127(2) et c = 11,144(3) Å, β = 96,60(3)°, Z = 2) et du 1,10-diphénanthrolinium(1+) Br_3 (phenBr3, $P\bar{1}$, a = 8,370(2), b = 10,410(4) et c = 8,171(2) Å, α = 107,52(2)°, β = 97,35(1)° et γ = 94,84(2)°, Z = 2). Les composés 4MI3 et QI3 qui sont pratiquement isostructuraux sont d'un type *anti*-NiAs déformé. Les structures 4MPI3 et API3 peuvent être considérées comme étant formées de cuboïdes de coordination du type CsCl déformé; les deux sont beaucoup plus complexes que prévus avec le 4MPI3 (qui n'est pas isostructural avec le 4MI3) contenant deux types de cations et trois types d'anions alors que l'API3 contient des cations de six types et des anions de sept types. L'API3 représente donc un cas extrême d'une structure de CsCl frustrée. L'empilement ionique dans de Da2I3 est lié à celui du CaF_2. La distortion de l'un des deux anions I_3^- non équivalents dans le Da2I3 est l'une des plus importantes, si non la plus importante, à avoir été rapportée (I—I = 2,793(2) et 3,167(2) Å, I-I-I = 172,47(4)° et on peut l'attribuer à une implication de l'anion dans une forte liaison N—H...I, H...I = 2,78 Å. La liaison hydrogène présentant une bifurcation, dans laquelle le cation protoné de l'azote du $phenBr_3$ est impliqué, présente une branche intracation, N—H(N)...H, et un branche interion, N—H(N)...Br.

Mots clés : structure cristalline, liaison hydrogène, anions polyhalogénés, tribromures; triiodures.

[Traduit par la rédaction]

Received November 6, 1995.

P.K. Bakshi,[1] M.A. James,[2] T.S. Cameron, and O. Knop.[3] Department of Chemistry, Dalhousie University, Halifax, NS B3H 4J3, Canada.

[1] Holder of a graduate scholarship, Canadian Commonwealth Scholarship and Fellowship Plan, and of a Killam Graduate Scholarship.
[2] Present address: Chemistry Department, Mount Saint Vincent University, Halifax, NS B3M 2J6, Canada.
[3] Author to whom correspondence may be addressed. Telephone: (902) 494-3317 or (902) 494-3305. Fax: (902) 494-1310.

Fig. 1. Projections of the 4MI3 (*A*) and QI3 (*B*) structures on (001). Stippled circles, I atoms at $z = 0$; large open circles, I atoms at $z = \frac{1}{2}$; filled circles, cations with centroids at $z = 0$; small open circles, cations with centroids at $z = \frac{1}{2}$. The cations are disordered (see text); only one orientation is shown in each projection. N—H(N)...I(21) bonds in QI3 are represented by broken lines.

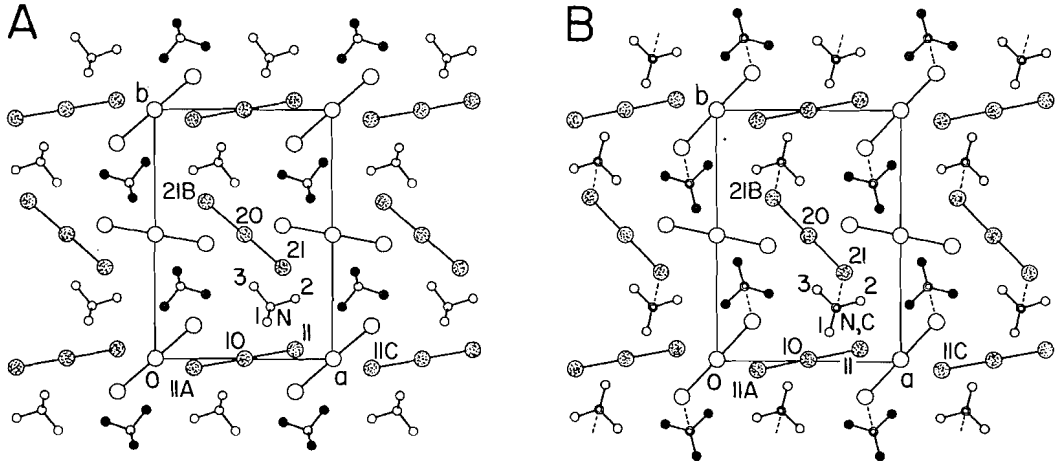

By far the largest number of the many (ideally) linear X_3^- (X = I, Br, Cl) anions in reported crystal structures are homoatomic and triiodides. Because of its size the I_3^- ion is often used as a counter anion of convenience, useful in stabilizing large cations, but its subservient role in preparative chemistry should not conceal certain aspects that make this anion (and Br_3^- and Cl_3^-) interesting.[4] (*i*) I_3^- is not often linear symmetric and, even if it is, by virtue of a crystallographic centre of symmetry at the centre atom, the possibility of a static or dynamic disorder about the inversion centre, resulting in an *averaged* centrosymmetric geometry, may not be ruled out.[5] (*ii*) Even for the centrosymmetric triiodide anions the reported distance between the two outer atoms has a range of ~0.4 Å. This is a dimensional variation of a magnitude not observed with other anions and one that cannot be dismissed, given the accuracy with which the positions of the I atoms in a structure can be determined both by X-ray and neutron diffraction. (*iii*) Last not least, the rodlike character of I_3^- combined with the tendency of a crystal to attain maximum density of packing gives rise to a variety of I_3^- orientations and ion coordinations and hence of space-group symmetries. Analysis of the dependence of the crystal symmetry and packing on the size and shape of the counter cation is a worthwhile and legitimate task for the crystal chemist. Although the nature and properties of the I_3^- anion have received frequent attention over the years, these and other aspects are not yet completely understood, in part because of lack of a systematic approach to the effect of the cation.

Preparatory to our own investigation now in progress we report in the following on our determinations of the crystal structures of five triiodides and a tribromide of the compact, asymmetric title cations. Crystal data of the title compounds are assembled in Table 1 and the positional parameters of anisotropically refined nonhydrogen atoms in Table 2. Details of the determinations are described in the Experimental. The following information has been deposited:[6] positional parameters and isotropic temperature factors of C and N atoms in API3 (Table A); positional parameters and isotropic temperature factors of H atoms (Table B); anisotropic thermal parameters of nonhydrogen atoms (Table C); and interatomic distances and bond angles other than those involving solely the halogen atoms (Table D).[7]

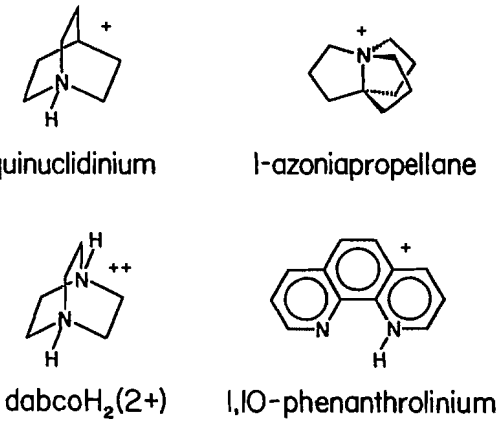

Results

Individual structures

4MI3 and QI3

Apart from differences in the cation structures these two

[4] Review of earlier literature and discussions placing the triiodide ion in the larger context of polyiodide-anion chemistry will be found, for example, in refs. 1–3.

[5] See for example the two nonequivalent I_3^- anions in 1,1′-Me_2-ferricenium (4) and 1-Me-hexamethylenetetrammonium(1+) (5) triiodides.

[6] This material may be purchased from: The Depository of Unpublished Data, Document Delivery, CISTI, National Research Council Canada, Ottawa, Canada K1A 0S2. Tables A, B, and D have also been deposited with the Cambridge Crystallographic Data Centre, and can be obtained on request from the Director, CCDC, University Chemical Laboratory, 12 Union Road, Cambridge CB2 1EZ, U.K.

[7] Throughout, estimated standard deviations resulting from crystal-structure refinements are cited in parentheses. The standard deviations of *means* (e.g., of bond lengths or angles) are cited in brackets. In calculating the means the component values were entered at unit weights, regardless of their individual esd's.

Table 1. Crystal data of the title compounds.[a]

Parameter	4MI3	QI3	4MPI3	API3	Da2I3	phenBr3
Formula	$C_4H_{12}I_3N$	$C_7H_{14}I_3N$	$C_3H_{12}I_3P$	$C_{10}H_{18}I_3N$	$C_6H_{14}I_6N_2$	$C_{12}H_9Br_3N_2$
fw	454.9	492.9	471.8	533.0	875.8	420.9
Crystal size, mm^3	0.3 × 0.25 × 0.06	0.1 × 0.2 × 0.4	0.55 × 0.3 × 0.35	0.18 × 0.22 × 0.41	0.25 × 0.28 × 0.36	0.25 × 0.3 × 0.5
θ-range, deg[b]	2.5–30/21	2.5–30/24	2–23/22	1.6–23/23	2–30/19	2–23/22
μ, cm^{-1}	78.9	73.3	75.4	60.1	105.8	90.7
Max/min[c]	1.00–0.44	1.00–0.56	1.00–0.75	1.00–0.75	1.00–0.56	1.00–0.41
a, Å	10.107(2)	10.290(2)	15.098(4)	15.131(7)	9.671(6)	8.370(2)
b, Å	14.141(2)	14.011(2)	15.098(4)	28.453(6)	8.127(2)	10.410(4)
c, Å	8.252(5)	8.813(2)	13.770(4)	22.848(8)	11.144(3)	8.171(2)
α, deg	90	90	90	90	90	107.52(2)
β, deg	90	90	90	108.53(3)	96.60(3)	97.35(1)
γ, deg	90	90	90	90	90	94.84(2)
V, $Å^3$	1179(1)	1271(1)	3139(3)	9327(10)	870(1)	667.7(3)
Z	4	4	10	24	2	2
ρ_c, g/cm^3	2.564(2)	2.577(2)	2.497(1)	2.278(3)	3.342(4)	2.093(1)
Space group	*Pnnm* (no. 58)	*Pnnm* (no. 58)	$P4_2/m$ (no. 84)	$P2_1/c$ (no. 14)	$P2_1/m$ (no. 11)	$P\bar{1}$ (no. 2)
F(000), e	808	888	2100	5856	764	400
Reflections:						
total measured	1834	1969	2509	13906	6069	1993
unique total	1834	1969	2310	13328	2718	1845
unique used	1680[d]	1018[e]	1198[e]	3522[d]	1940[e]	1061[e]
$100R_{merg}$	—	—	3.0	8.9	8.5	2.5
d/p	11.4	17.6	11.9	10.1	26.2	6.9
$100R$; $100R_w$	4.6[f]	5.4; 5.2	2.7; 2.5	5.7[g]	4.4; 4.8	2.7; 2.9
G.O.F.	1.10	2.08	1.52	0.98	1.78	1.13
Residual e.d.[h]	−0.92/1.26	−1.06/0.85	−0.51/0.66	−0.83/2.10	−1.39/1.53	−0.42/0.44

[a]4MI3, Me_3NI_3; QI3, quinuclidinium I_3; 4MPI3, Me_4PI_3; API3, 1-azoniapropellane I_3; Da2I3, 1,4-diazoniabicyclo[2.2.2]octane $(I_3)_2$, $DabcoH_2^{2+}(I_3^-)_2$; phenBr3, 1,10-phenanthrolinium(1+) Br_3. For additional details see Experimental.

[b]$\theta_{min} > \theta > \theta_{max}/n$. The lattice parameters and orientation matrices were obtained by least squares from the setting angles θ of suitable *n* reflections.

[c]Maximum/minimum transmission factors (empirical absorption corrections).

[d]Number of reflections used in the calculation of *R* on $2\sigma(I)$; *all* unique reflections were used in the SHELXL-93 refinement.

[e]$I > 3\sigma(I)$.

[f]$100R$ on $2\sigma(I)$; $100R_w$ = 17.2% (on F^2).

[g]$100R$ on $2\sigma(I)$; $100R_w$ = 26.1% (on F^2), C and N atoms refined isotropically.

[h]Minimum and maximum residual electron density ($e/Å^3$) in final difference map.

orthorhombic compounds are isostructural, with similar unit-cell dimensions (Fig. 1). There are two nonequivalent I_3^- ions in the structures, with their centre atoms I(10) and I(20) at sites of C_{2h} symmetry and with U_{ii} values not suggestive of disorder across the inversion centre. The anions are situated in layers ||(001), each layer also containing the centroids of the cations (cf. below). The *antiferro* arrangement of the anion orientations in each of the two anion systems is consistent with the anions being located on a dichromatic orthorhombic P_I Bravais lattice. The anions are discrete; the inter-anion I...I distances all exceed 4.35 Å (Table 3).

The ion packing is of a distorted *anti*-NiAs type. In an *idealized* hexagonal *anti*-NiAs cell *H* ($P6_3mc$) the anions would be at (0, 0, 0; 0, 0, ½) and the cations at ±(⅓, ⅔, ¼), i.e., forming a layer sequence *AbAc*...; the coordination polyhedron of a cation would be an octahedron of symmetry D_{3d} and that of an anion a trigonal prism of symmetry D_{3h}. This *H* cell can be transformed by

$$\begin{pmatrix} x_O \\ y_O \\ z_O \end{pmatrix} = \begin{pmatrix} -\frac{1}{2} & 0 & \frac{1}{2} \\ 0 & 1 & 0 \\ \frac{1}{2} & 0 & \frac{1}{2} \end{pmatrix} \begin{pmatrix} x_H \\ z_H \\ y_H \end{pmatrix} + \begin{pmatrix} \frac{1}{2} \\ 0 \\ 0 \end{pmatrix}$$

into an orthogonal cell *O* corresponding to the *Pnnm* cell, with an axial ratio $a_O/c_O = \sqrt{3}$. The coordinates of the atoms in the *O* cell would then be (½, 0, 0; ½, ½, 0) for the anions and ±(⅔, ¼, ½) for the cations. The actual fractional coordinates of atoms I(10) and I(20) in 4MI3 and QI3 are (½, 0, 0; ½, ½, 0); those of the N atoms in 4MI3 are ±(0.6434, 0.2105, ½), a_O/c_O = 1.225; and those of the cation centroids in QI3, ±(0.6502, 0.2075, ½), a_O/c_O = 1.168. The ratio $r = c_H/a_H = 2b_O(a_O^2 + c_O^2)^{-1/2}$ (which in a hexagonal close packing of equal spheres would be $(8/3)^{-1/2}$ = 1.633) is 2.19 in 4MI3 and 2.07 in QI3. The larger internal angle in the base of the pseudohexagonal cell corresponding to *Pnnm* is 101.6° in 4MI3 and 98.8° in QI3, both values well below the ideal angle of 120° but leaving no doubt about the packing type.

Table 2. Positional parameters ($\times 10^4$) of nonhydrogen atoms in the title compounds.[a]

Atom	x	y	z	Atom	x	y	z
4MI3							
I(10)	1/2	0	0	C(1)	6254(24)	1527(14)	3505(20)
I(11)	7844(1)	0379(1)	0	C(1*)	5776(31)	2472(17)	6501(26)
I(20)	1/2	1/2	0	C(2)	7835(12)	2441(14)	1/2
I(21)	7153(1)	3656(1)	0	C(3)	5514(21)	2923(14)	1/2
N	6434(10)	2105(7)	1/2	C(3*)	6188(38)	1060(10)	1/2
Q13							
I(10)	1/2	0	0	N,C	6502(9)	2075(6)	3575(10)
I(11)	7781(1)	0418(1)	0	C(1)	6145(12)	1078(7)	4110(12)
I(20)	1/2	1/2	0	C(2)	7831(9)	2363(7)	4118(13)
I(21)	6939(1)	3487(1)	0	C(3)	5483(9)	2805(7)	4097(12)
4MPI3							
I(10)	0	0	0	P(1)	2978(2)	0801(2)	2487(3)
I(11)	−1579(1)	1134(1)	0	C(1)	3655(8)	0431(8)	3479(1)
I(20)	2162(1)	4030(1)	0	C(2)	3511(8)	0537(8)	1365(9)
I(21)	1458(1)	2206(1)	0	C(3)	2823(9)	1959(8)	2600(10)
I(22)	2874(1)	5824(1)	0	C(4)	1937(9)	0243(9)	2530(10)
I(30)	5667(1)	1898(1)	0	P(2)	1/2	1/2	1/4
I(31)	5697(1)	1908(1)	−2125(1)	C(5)	4473(9)	4191(8)	1750(10)
API3							
I(1)	9900(1)	2485(1)	5061(1)	I(11)	11608(2)	2661(1)	6717(1)
I(2)	8622(1)	2447(1)	3788(1)	I(12)	13055(2)	2659(1)	6129(1)
I(3)	7443(2)	2421(1)	2497(1)	I(13)	11714(2)	6153(1)	6545(1)
I(4)	3273(1)	2486(1)	−1604(1)	I(14)	11692(1)	5126(1)	6629(1)
I(5)	4559(1)	2477(1)	−0327(1)	I(15)	11639(2)	4107(1)	6719(1)
I(6)	5751(2)	2458(1)	0959(1)	I(16)	1/2	0	1/2
I(7)	7499(2)	5068(1)	9150(1)	I(17)	4921(2)	1032(1)	5024(1)
I(8)	8463(2)	5021(1)	8225(1)	I(18)	1/2	1/2	1/2
I(9)	9526(2)	5000(1)	7368(1)	I(19)	5875(2)	5120(1)	4046(1)
I(10)	10150(2)	2659(1)	7303(1)				
Da2I3							
I(10)	7908(1)	1/4	7213(1)	I(22)	0028(1)	1/4	2930(1)
I(11)	8885(1)	1/4	9671(1)	N	2761(7)	0957(8)	7149(6)
I(12)	6404(1)	1/4	4535(1)	C(1)	2112(9)	1565(11)	8228(7)
I(20)	2771(1)	1/4	1885(1)	C(2)	1911(10)	1543(12)	6016(8)
I(21)	5389(1)	1/4	0870(1)	C(3)	4229(8)	1580(10)	7215(7)
phenBr3							
Br(1)	−0231(1)	0980(1)	2697(1)	C(7)	4729(10)	2791(9)	6618(11)
Br(2)	2527(1)	0363(1)	2376(1)	C(8)	4138(11)	1831(8)	7331(13)
Br(3)	−3106(1)	1732(1)	3142(1)	C(9)	4771(11)	1972(9)	9018(12)
N(1)	8116(9)	5078(7)	12113(9)	N(10)	5879(8)	2997(7)	9974(9)
C(2)	9245(11)	6098(9)	13092(11)	C(11)	6475(10)	3974(8)	9331(11)
C(3)	9921(11)	7117(9)	12519(12)	C(12)	7672(10)	5068(8)	10432(11)
C(4)	9470(10)	7097(8)	10838(12)	C(13)	8287(10)	6037(8)	9731(11)
C(5)	7746(11)	5931(8)	7947(11)	C(14)	5916(9)	3875(8)	7583(10)
C(6)	6615(11)	4902(9)	6939(11)				

[a]Parameter values of atoms in special positions are not multiplied by 10^4.

Stoichiometry and symmetry require that in *Pnnm* the cation in 4MI3 and QI3 be located on an element of symmetry, in these two structures on a mirror plane at $z = 0$ or $\frac{1}{2}$. This implies that the cation itself contains a mirror plane. The orientation of the Me_4N^+ cation (Fig. 1; N, C(2), and C(3) in *m*. C(1) duplicated by *m*) satisfies this requirement, i.e., the 4MI3 structure is correctly described in *Pnnm*. However, refinement on this model resulted in unreasonably high values of some of

Table 3. Interatomic distances (Å) and bond angles (deg) in the anions of the title compounds.

Atoms	Distance	Atoms	Angle
4MI3			
I(20)—I(21)	2.889(2)	I(11)-I(10)-I(11A)	180
I(20)—I(21B)	2.889(2)	I(21)-I(20)-I(21B)	180
I(10)—I(11)	2.924(2)		
I(10)—I(11A)	2.924(2)	A $1-x$ $-y$ z	
I(11)...I(21)	4.686(2)	B $1-x$ $1-y$ z	
I(11)...I(11C)	4.358(2)	C $2-x$ y z	
QI3			
I(20)—I(21)	2.910(1)	I(11)-I(10)-I(11A)	180
I(20)—I(21B)	2.910(1)	I(21)-I(20)-I(21B)	180
I(10)—I(11)	2.921(1)		
I(10)—I(11A)	2.921(1)	Symmetry code as for 4MI3	
I(11)...I(21)	4.386(2)		
I(11)...I(11C)	4.567(2)		
4MPI3			
I(20)—I(22)	2.914(2)	I(21)-I(20)-I(22)	179.48(6)
I(30)—I(31)	2.926(1)	I(11)-I(10)-I(11D)	180
I(30)—I(31F)	2.926(1)	I(31)-I(30)-I(31F)	178.15(6)
I(10)—I(11)	2.936(2)	I(11)-I(10)-I(21)	87.78(3)
I(10)—I(11D)	2.936(2)	I(11D)-I(10)-I(21)	92.22(3)
I(20)—I(21)	2.951(2)	I(21J)-I(20J)-I(30F)	93.54(2)
I(10)...I(21)	3.993(2)	I(21K)-I(20K)-I(30)	93.54(2)
I(20)...I(31C)	3.999(2)	I(10)-I(21)-I(20)	167.73(3)
I(22)...I(30A)	4.085(2)	I(20)-I(22)-I(30A)	168.97(6)
I(11)...I(30B)	4.315(2)	I(20J)-I(31F)-I(30)	172.71(4)
I(11D)...I(30E)	4.315(2)	I(20K)-I(31)-I(30)	172.71(4)
		I(22)-I(30A)-I(31G)	89.28(3)
A $1-x$ $1-y$ 0		I(22)-I(30A)-I(31H)	89.28(3)
B $x-1$ y 0		I(22J)-I(20J)-I(31F)	86.52(2)
C y $1-x$ $\frac{1}{2}+z$		I(22K)-I(20K)-I(31)	86.52(2)
D $-x$ $-y$ 0			
E $1-x$ $-y$ 0		H $1-x$ $1-y$ $-z$	
F x y $-z$		J $1-y$ x $\frac{1}{2}$	
G $1-x$ $1-y$ z		K $1-y$ x $-\frac{1}{2}$	
API3 (up to 4.3 Å)			
I(8)—I(9)	2.904(3)	I(1)-I(2)-I(3)	176.64(9)
I(18)—I(19)	2.908(3)	I(4)-I(5)-I(6)	177.08(10)
I(18)—I(19B)	2.908(3)	I(7)-I(8)-I(9)	176.22(10)
I(11)—I(12)	2.910(3)	I(10)-I(11)-I(12)	179.69(10)
I(14)—I(15)	2.910(3)	I(13)-I(14)-I(15)	178.93(11)
I(5)—I(6)	2.920(3)	I(17)-I(16)-I(17A)	180
I(10)—I(11)	2.922(3)	I(19)-I(18)-I(19B)	180
I(2)—I(3)	2.923(3)	I(1)-I(2)-I(13G)	98.8(1)
I(7)—I(8)	2.928(3)	I(1)-I(11)-I(10)	94.6(1)
I(13)—I(14)	2.930(3)	I(1)-I(11)-I(12)	85.2(1)
I(1)—I(2)	2.938(3)	I(2)-I(3)-I(6)	172.7(1)
I(16)—I(17)	2.940(3)	I(2)-I(13G)-I(14G)	171.3(1)
I(16)—I(17A)	2.940(3)	I(3)-I(2)-I(13G)	80.5(1)
I(4)—I(5)	2.947(3)	I(3)-I(6)-I(5)	173.9(1)
I(3)...I(6)	3.632(3)	I(4)-I(11E)-I(10E)	83.9(1)
I(1)...I(11)	3.877(3)	I(4)-I(11E)-I(12E)	96.2(1)
I(4)...I(11E)	3.895(3)	I(10)-I(11)-I(15)	90.7(1)
I(2)...I(13G)	4.057(3)	I(11)-I(15)-I(14)	175.5(1)
I(11)...I(15)	4.113(3)	I(12)-I(11)-I(15)	89.6(1)

Table 3 (*concluded*).

Atoms	Distance	Atoms	Angle
I(9)...I(14)	4.152(3)		
I(6)...I(12H)	4.232(3)	D x $\frac{1}{2}-y$ $\frac{1}{2}+z$	
I(3)...I(10J)	4.264(3)	E $x-1$ y $z-1$	
		F x y $1+z$	
A $1-x$ $-y$ $1-z$		G $2-x$ $1-y$ $1-z$	
B $1-x$ $1-y$ $1-z$		H $x-1$ $\frac{1}{2}-y$ $z-\frac{1}{2}$	
C x $\frac{1}{2}+y$ $\frac{1}{2}-z$		J x $\frac{1}{2}-y$ $z-\frac{1}{2}$	
Da2I3			
I(10)—I(11)	2.793(2)	I(11)-I(10)-I(12)	172.47(4)
I(20)—I(21)	2.890(2)	I(21)-I(20)-I(22)	179.64(4)
I(20)—I(22)	3.017(2)	I(10)-I(11)-I(21A)	97.57(4)
I(10)—I(12)	3.167(2)	I(10)-I(11)-I(22B)	177.97(4)
I(11)...I(22B)	3.673(2)	I(10)-I(12)-I(21)	166.57(4)
I(11)...I(21A)	3.775(2)	I(10)-I(12)-I(22C)	95.51(4)
I(12)...I(21)	4.089(2)		
I(12)...I(22C)	4.114(2)	B $1+x$ y $1+z$	
		C $1+x$ y z	
A x y $1+z$		D $1-x$ $-y$ $1-z$	
phenBr3			
Br(1)—Br(2)	2.473(2)	Br(2)-Br(1)-Br(3)	177.56(6)
Br(1)—Br(3)	2.628(2)		
Br(2)...Br(3B)	3.713(2)	B $1+x$ y z	
Br(1)...Br(2A)	4.105(2)	C $1+x$ y $1+z$	
Br(1)...Br(1A)	4.347(2)	D $-x$ $-y$ $1-x$	
		E $1-x$ $-y$ $1-z$	
A $-x$ $-y$ $-z$		F x y $1+z$	

Fig. 2. Hydrogen bonds in QI3 and Da2I3 viewed approximately perpendicular to the plane of the bond (top) and down the cation axis (bottom); 50% probability thermal ellipsoids on nonhydrogen atoms. In QI3 the probability of the I(21) atom participating in *two* H-bonds is 25% or less (see text), whereas in Da2I3 *both* H(N) atoms of the divalent cation are H-bonded and the cations form *uninterrupted* H-bonded chains ||*b*.

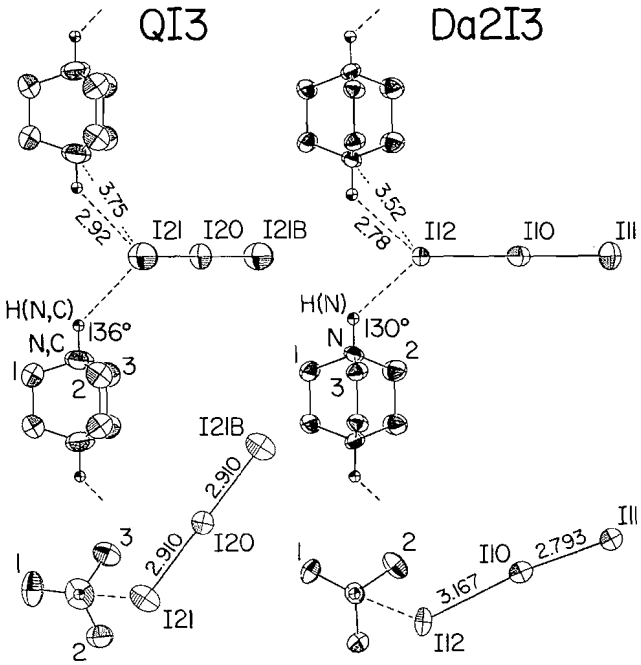

Fig. 3. Projection of the 4MPI3 structure on (001). Filled circles, I atoms at $z = 0$ (except I(31), which coincides with I(30)). All P(1) atoms are at $z \sim \pm \frac{1}{4}$, all P(2) atoms are at $z = \pm \frac{1}{4}$.

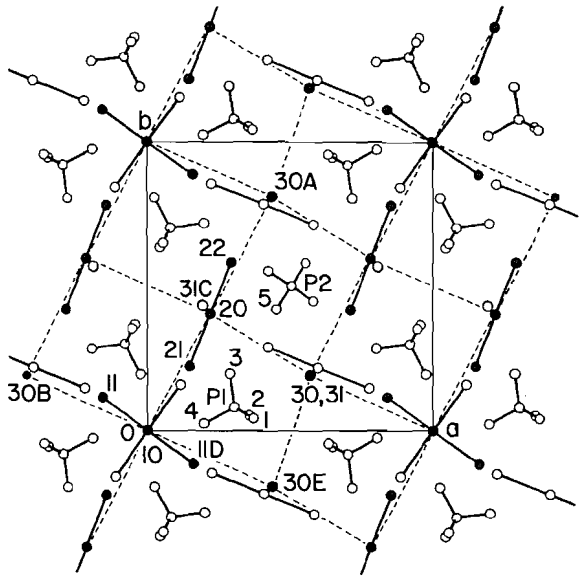

the U_{ii} of C(1) and C(3). An attempt to resolve this problem is described in the Experimental.

In QI3 the C–N axis of the cation is polar, hence placing the cation in a mirror plane averages the cation orientation ||*c*. The structure can thus be described as correctly assigned in *Pnnm* but with the cation in twofold orientational disorder about the

Fig. 4. (Top) The coordination cuboids of cations 1 and 2 in 4MPI3. Open circles, anion a1; stippled, a2; filled, a3. The top and bottom of the two subcells are in mirror planes ($z = \frac{1}{2}, 0$). (Bottom) The corresponding idealized Schlegel diagrams (down *c*). Large squares, $z = 0$; small squares, $z = \frac{1}{2}$. Anion numbers appear inside the circles. Orientations of the anions are indicated by the line segments attached to the circles. X identifies the face common to the two cuboids.

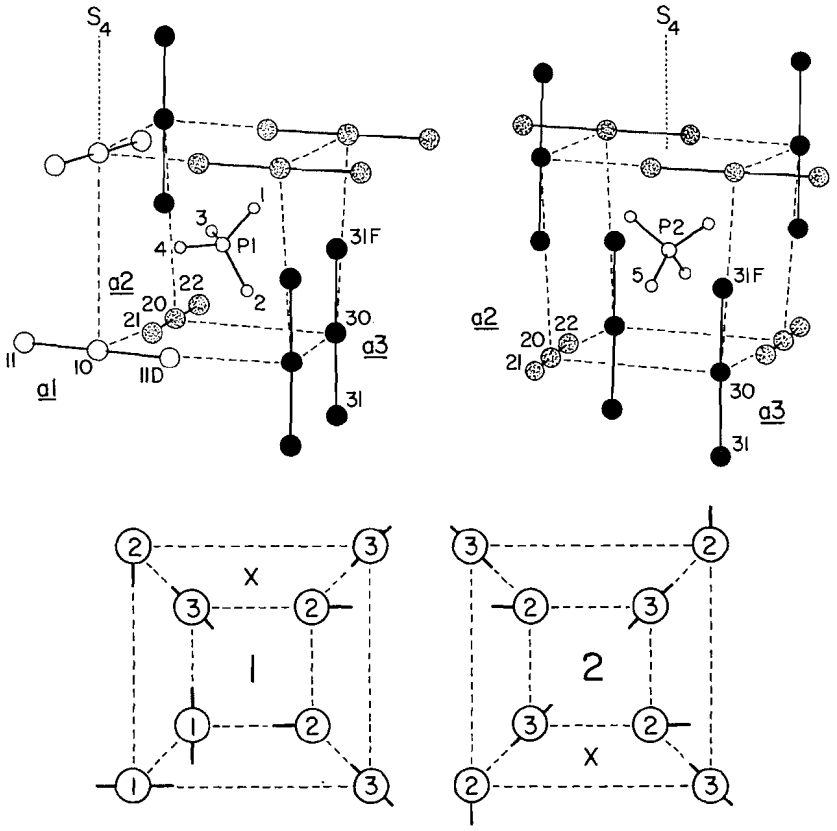

mirror plane. Alternatively, an attempt can be made to refine the structure as fully ordered in an orthorhombic subgroup of *Pnnm*. For reasons explained in the Experimental we have adopted the solution of the structure in the centrosymmetric group, i.e., the disordered *Pnnm* model.

The shortest (N, C)...I and H(N, C)...I distances in the disordered QI3 are to I(21), 3.75(1) and 2.92(2) Å, respectively, (N, C)-H(N, C)-I(21) = 136(3)°; and to I(11), 4.13(1) and 3.39(2) Å, respectively, (N, C)-H(N, C)-I(11) = 129(3)° (all values based on (N, C)—H(N, C) = 1.05 Å). Although these N-H-I angles seem unfavourable for hydrogen bonding, comparison with a similar situation in Da2I3 (Fig. 2, cf. below) supports the view that (N, C)—H(N, C)...I(21) at least must be considered as a legitimate though highly bent hydrogen bond. In the disordered structure the majority of the I(21) atoms would be, statistically, the recipients of one N—H...I(21) bond only, in contrast to the Da2I3 salt.

4MPI3

Surprisingly, this compound is not isostructural with 4MI3. It has a lower density than the latter: on replacing N by P the volume V_I per formula unit increases by ~6% while the corresponding increase in mass is only ~4%. The packing arrangement is thus less compact in 4MPI3 than in 4MI3.

For its simple chemistry 4MPI3 has an unexpectedly complex structure. The unit cell, of relatively high tetragonal symmetry, contains two I_3^- anions a1 = I(11)-I(10)-I(11D) ||(001) of symmetry C_{2h}, four anions a2 = I(21)-I(20)-I(22) ||(001) of symmetry C_s, and four anions a3 = I(31)-I(30)-I(31F)||*c*, also of symmetry C_s. Anion a2 is *in* a crystallographic mirror plane, whereas anion a3 is halved by it (Fig. 3). There are eight $Me_4P(1)^+$ cations c1 of symmetry C_1 and two $Me_4P(2)^+$ cations c2 of symmetry S_4 in the unit cell. Each cation is inside a cuboid cell of ~6.9 Å edge length, formed by the centre atoms of anions (Fig. 4), with the CH_3 groups oriented to avoid static interference with the anions. The anions defining a coordination cuboid are approximately located in horizontal (i.e., ||(001)) or vertical (i.e., ||*c*) edges of the cuboid. These cuboids thus tesselate the 4MPI3 structure in such a way that the overall packing can be described as of a distorted 8:8 CsCl type.

The anions are segregated in layers ||(001) at $z = 0, \frac{1}{2}$ and the cations in layers ||(001) at $z \sim \pm \frac{1}{4}$. However, while a1 and a2 are wholly in the $z = 0, \frac{1}{2}$ layers, a3 is perpendicular to them, with the result that the I(31) atoms of a3 are almost in the cation layers. The shortest inter-anion I...I distances below 4.5 Å are, within a layer ||(001), I(10)...I(21) = 3.993 Å, I(22)...I(30A) = 4.085 Å, and I(11)...I(30B) = 4.315 Å; between layers, I(20)...I(31C) = 3.999 Å (Table 3, Fig. 3). The I atoms involved form, within a layer, a quasi-linear I(10)...I(21)-I(20)-I(22)...I(30A) chain terminated perpendic-

Fig. 5. Projection of the API3 anion substructure on (100). Broken lines: shortest inter-anion I...I distances (Å) between anion layers, I(2)...I(13) and I(11)...I(15). The N atoms in cations 1–6 are black.

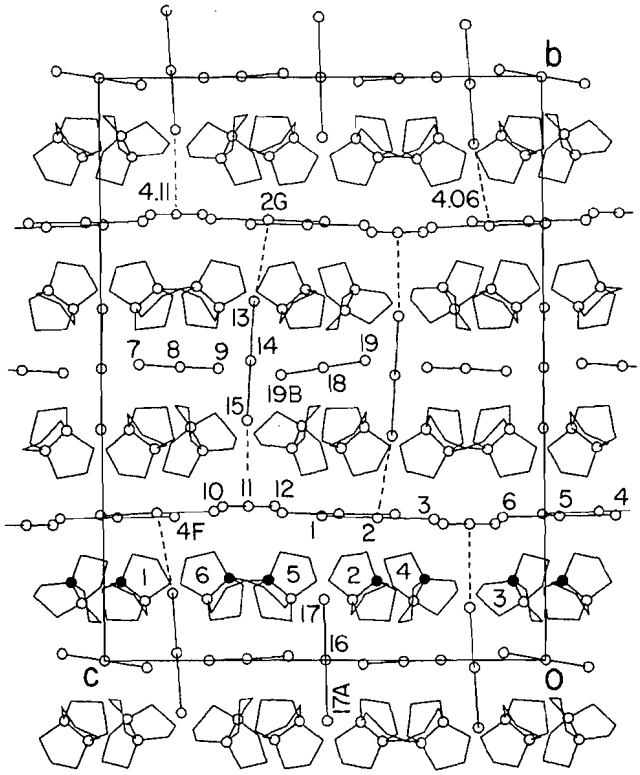

ularly at I(10) by a1 and at I(30A) by a3. Similarly, a3 forms a quasi-linear I(20K)...I(31)-I(30)-I(31F)...I(20J) chain perpendicularly terminated by a2 anions. These I...I ≥ 4 Å separations are too long for effective bonding interaction, hence the anions in 4MPI3 are regarded as discrete.

The cation geometry is unexceptional (Table D).

API3

Even more so than 4MPI3, this structure is surprisingly complex for a cation as compact as 1-azoniapropellane. Its large monoclinic cell contains 24 formula units: six sets of nonequivalent C_1 cations, two sets of centrosymmetric I_3^- anions a6 and a7, and five sets of nonequivalent slightly distorted anions a1–a5 (Tables 2 and 3).[8] The anions are arranged in layers ||(010), at approximate heights $y = 0, \pm \frac{1}{4}, \frac{1}{2}$. The atoms of a1, a2 and a4, in the $y \sim \pm \frac{1}{4}$ layers, are almost coplanar; anions a3 and a5, in the $y \sim 0, \frac{1}{2}$ layers, are almost parallel to (010), while anions a6 and a7 are perpendicular to (010). The layers of cations ||(010) are sandwiched between the anion layers, with the cation centroids roughly at $y = \pm \frac{1}{8}, \pm \frac{3}{8}$ (Fig. 5).

The ion packing in API3 is seen in the projection of the anions on (010) (Fig. 6). In addition to the anion layers ||(010) two other such systems are present: one ||($\bar{1}$01) and the other approximately ||(102). These three anion systems tesselate the structure into CsCl-type cuboids of approximate edge length of 7.3 Å, similar to those in 4MPI3 (Figs. 3 and 4). The vertices of these cuboids are formed by the centre atoms of the anions, with the

[8] Anion a1, I(1) to I(3); a2, I(4) to I(6); a3, I(7) to I(9); a4, I(10) to I(12); a5, I(13) to I(15); a6, I(17)-I(16)-I(17A); a7, I(19)-I(18)-I(19B).

Fig. 6. (Top) API3 anion substructure projected on (010). Numbers indicate cation positions (in parentheses, positions *equivalent* to those in Table 2). (Bottom) Schlegel diagrams (down *b*) of the corresponding idealized (cat)(an)$_8$ coordination cuboids in the approximate $0 \leq y \leq \frac{1}{4}$ slab of the API3 structure. Large squares, $y \sim 0$; small squares, $y \sim \frac{1}{4}$; cation centroids at $y \sim \frac{1}{8}$. The anions a1 to a4 and a7 are located in horizontal (i.e., ||(010)) and anions a5 and a6 in vertical (i.e., ||*b*) edges of the cuboids. See also Fig. 4.

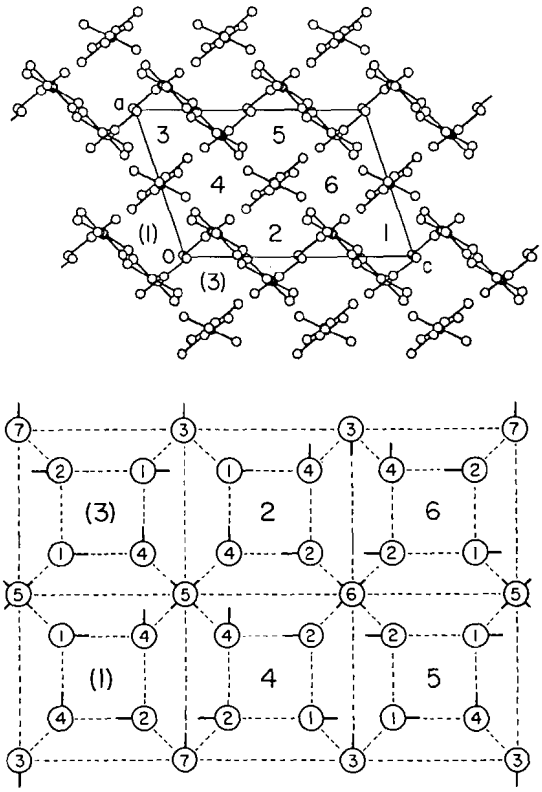

anions aligned in the edges of the cuboids in such a way that a1–a4 and a7 are in edges ||(010), and a5 and a6 in edges ||*b*. The orientations of the anions in a translation motif of adjacent cuboids are displayed in the Schlegel diagrams of Fig. 6.

The shortest inter-anion I...I distances below 4 Å are I(3)...I(6) = 3.632 Å, I(1)...I(11) = 3.877 Å, and I(4)...I(11B) = 3.895 Å (Table 3), all within an anion layer ||(010). The atoms involved form a quasi-linear I(11E)...I(4)-I(5)-I(6)...I(3)-I(2)-I(1)...I(11) chain, which is terminated at each end (at atoms I(11) and I(11E)) by an a4 anion perpendicular to the chain. The shortest I...I distances *between* neighbouring anion layers ||(010) are I(2G)...I(13) = 4.057 Å, i.e., between a1 and a5, and I(11)...I(15) = 4.113 Å, i.e., between a4 and a5. These distances involve the terminal atoms of anion a5, which thus provides a perpendicular link between the centre atoms of a1 and a4 in neighbouring anion layers: I(2G)...I(13)-I(14)-I(15)...I(11).

The positions and orientations adopted by the cations[9] inside their respective coordination cuboids are all different (Fig. 7). In spite of this the vertical (i.e., ||*b*) heights of the cation *centroids* in a cation layer ||(010) are remarkably constant: the mean *y*(centroid) in Figs. 5 and 7 is 0.1201(25) (ideally, $\frac{1}{8}$), corresponding to a standard deviation of only 0.07 Å verti-

[9] For comparison of cation geometry see 1-azoniapropellane tetraphenylborate (6).

Fig. 7. Cations in an approximate $0 \leq y \leq \frac{1}{4}$ slab of the API3 structure (see Fig. 6). The only symmetry operations relating these cations are unit-cell translations (cations in other slabs are of course related by $P2_1/c$ symmetry operations). Filled circles, N atoms; open circles, C(n0) (n = 1–6) atoms. Broken lines represent approximate boundaries of the coordination cuboids.

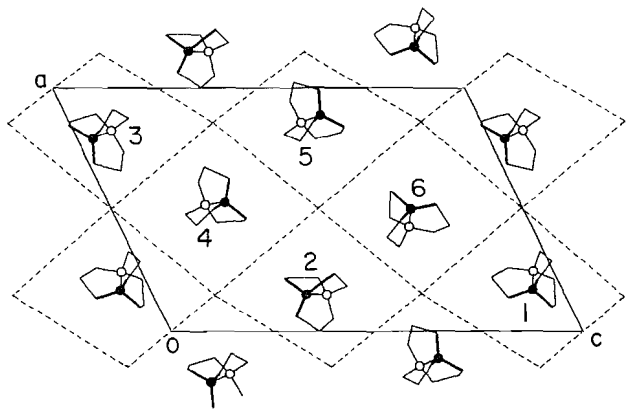

cally. None of the cation N–C axes is oriented ||b. This may be due to the presence, in each cuboid, of the terminal atoms I(13) and I(15) of a5 or I(17) of a6 or both, which protrude about 2.8 Å vertically into the space between the iodine layers, i.e., are roughly at the same vertical height as the cation centroids and thus sterically interfere with the cation hydrogens (Fig. 5). Regardless of the precise orientation of a cation, the N atoms in a cation layer are all ~0.5 Å in the same direction from the cation centroid, i.e., all the N atoms in the structure face the iodine layers at $y \sim \pm \frac{1}{2}$ rather than those at $y \sim 0$, $\frac{1}{2}$ (Fig. 5).

Da2I3

In this monoclinic layer structure (Fig. 8*A*) all the I atoms and the centroids of the 1,4-diazoniabicyclo[2.2.2]octane cations are located on mirror planes ||(001), at $y = \pm \frac{1}{4}$. The cations and the two nonequivalent I_3^- anions have therefore C_s symmetry. If the cation centroids were shifted from $y = \pm \frac{1}{4}$ to $y = 0$, $\frac{1}{2}$ (i.e., by about 2 Å ||b), the domain D outlined in Fig. 8B, which is related to a doubled B-centred cell (**a** + **c**, **b**, – **a** + **c**), would constitute a projection of a distorted CaF_2-type ion packing, somewhat reminiscent of the packing in the cubic $(N_2H_6)Cl_2$ (7). The alternating orientations of the ions are most simply described by regarding the ions as being located on distorted orthorhombic, dichromatic Bravais B_A lattices.

Anion a1 = I(11)-I(10)-I(12) is noticeably bent, whereas anion a2 = I(21)-I(20)-I(22) is almost linear (Table 3). The distortion of a1 from centrosymmetry (I(10)—I(11) = 2.793 Å, I(10)—I(12) = 3.167 Å, I-I-I = 172.5°) is even larger than in NH_4I_3 (2.797 Å, 3.113 Å, 178.6°; ref. 8) and (1-Me-cytosinium)I_3 (2.794 Å, 3.123 Å, 177.6°; ref. 9); significantly, both these structures contain inter-ion hydrogen bonds (cf. below). The I-I-I angle in a1 in fact appears to be the smallest on record in a triiodide anion.[10]

The shortest interanion I...I distances occur within the layers ||(001): I(11)...I(22B) = 3.673 Å, I(11)...I(21A) = 3.775 Å. Both are appreciably shorter than such distances in 4MI3 and QI3, >4.35 Å (Table 3), but they are comparable to similar distances in other triiodides, e.g., 3.651 Å in $[Pd(en)_2](I_3)_2$ (cited in ref. 8), 3.755 Å in (1-Me-cytosinium)I_3 (9), and 3.770 Å in TlI_3 (11).[11] If these two distances are regarded as corresponding to weak bonding interactions, then a2 anions in a layer are seen to be joined by I(11) atoms of a1 to form zigzag chains ||a, with pendant -I(10)-I(12) segments: ...I(22)-I(20)-I(21)...I(11)[-I(10)-I(12)]... (Fig. 8*B*). In these chains a1 and a2 are roughly orthogonal: I(10)-I(11)-I(21A) = 97.6°, I(21A)-I(11)-I(22B) = 80.2°, I(11)-I(22B)-I(20B) = 78.2°.

Although the crystallographic symmetry of the cation is only C_s, its refined geometry is close to D_{3h}. The three shortest N...I distances are 3.524(7) Å to I(12), 3.881(7) Å to I(21), and 3.884(7) Å to I(22C); the corresponding distances from the placed N(H) atom are 2.78, 3.21, and 3.24 Å, respectively (Table D). The smallest of the three, 3.524 and 2.78 Å, respectively, are each about 0.2 Å shorter than the corresponding N...I and H(N)...I distances in QI3 (Fig. 2), in which the cation has a similar local geometry, and also shorter than the smallest (freely refined) N...I and H(N)...I distances in NH_4I_3, 3.69(1) and 2.82(3) Å, respectively, N-H(N)-I = 168(2)° (8). The H(N) atom is thus clearly involved in a hydrogen bond to I(12),[12] in spite of the smallness of the N-H(N)-I(12) = 130° angle, with I(12) being the recipient of two such m-related bonds (Fig. 2). The N—H(N)...I(12) bonds link the cations into uninterrupted cat...I(12)...cat... chains ||b.

The simultaneous, symmetric engagement of I(12) in two H-bonds would be expected to affect the I(10)—I(12) bond length. Indeed, this bond is lengthened to 3.167 Å, which in turn produces an appreciable shortening (cf. ref. 13) of the conjugate I(10)—I(11) bond, 2.793 Å, and reduces the atom charge on I(11). The resulting induced polarity of a1 is probably responsible for the short I(11)...I(22B) = 3.673 Å contact and thus for a weak bonding interaction with a2 anions in the zigzag chain. This view is supported by the near orthogonality at I(11) of the a1 and a2 anions in a chain, which is consistent with the existence of 90° p–p interactions such as are commonly observed in higher polyiodide anions in crystals.[13] The participation of a1, with its I(12) atom H-bonded and its I(11) atom joining the a2 anions in the chain, is thus different from a2, but neither anion can be regarded as discrete. A similar situation is observed, for much the same reason, in NH_4I_3 (8), where atom I(1) of the anion is H-bonded to three cations and atom I(2′) of another anion is almost collinear with the first anion, I(3)...I(2′) = 3.881 Å.

The validity of the claim that H-bonding indeed causes sig-

[10] An I-I-I angle of 172.7(1)° has been reported for I_3^- in $[L_2Mn^{III}{}_2(\mu\text{-}O)(\mu\text{-}OAc)_2](I_3)I\cdot H_2O$, L = 1,4,7-triazacyclononane (10), but the bond-length disproportionation in this anion is smaller than that in a1 of Da2I3, 2.851 Å and 3.112 Å, respectively.

[11] The corresponding distances in NH_4I_3 (8), RbI_3 (11), and CsI_3 (12) (all three isostructural with TlI_3) are 3.881, 3.921, and 3.972 Å, respectively.

[12] There were indications, in the difference map, of the placed H(N) atom being broadly displaced in the direction of I(12). These are not presented here, as the closeness of I(12) to the presumed H(N) features may have distorted the map. It may also be noted (Fig. 8*B*) that it is the displacement of the cations toward the I(12) atoms that differentiates the shape of domain D (broken edges !) from that of a translated doubled B-cell referred to above, i.e., the distortion of the quasi-CaF_2 packing in Da2I3 is partially attributable to the hydrogen bonding.

[13] Orthogonal p–p bonding interactions in polyiodide structures will be discussed in detail in a sequel in this series.

Fig. 8. Projection of the Da2I3 structure on (010). Stippled circles, I atoms at $y = \frac{1}{2}$; large open circles, I atoms at $y = \frac{1}{2}$; filled circles, cations with centroids at $y = \frac{1}{4}$; small open circles, cations with centroids at $y = \frac{3}{4}$. (*A*) Principal axes of cation libration L_1 and L_2 are in the page, L_3 is perpendicular to the page and coincident with the N–N′ axis. H(N)...I(12) H-bonds are represented by broken lines. (*B*) Solid outline: domain *D* related to ion packing (see text). Dashed lines, anion zigzag chains in $y = \pm \frac{1}{4}$ layers. See Table 3 for I...I distances and I-I-I angles.

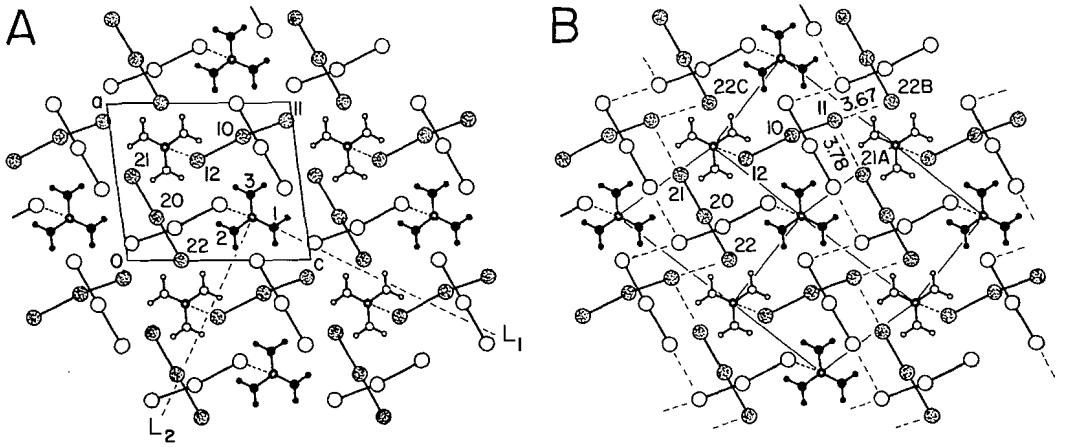

Fig. 9. The phenBr3 structure projected on (100) (left) and on (001) (right). Large circles, Br atoms; smallest circles, H(N10) atoms. The bifurcated N(10)—H(N10)...Br(3), N(1) bonds are represented by broken lines. The quasi-coplanar Br(1) atoms (left) define the pseudo-hexagonal channels ||*a* containing the cation stacks.

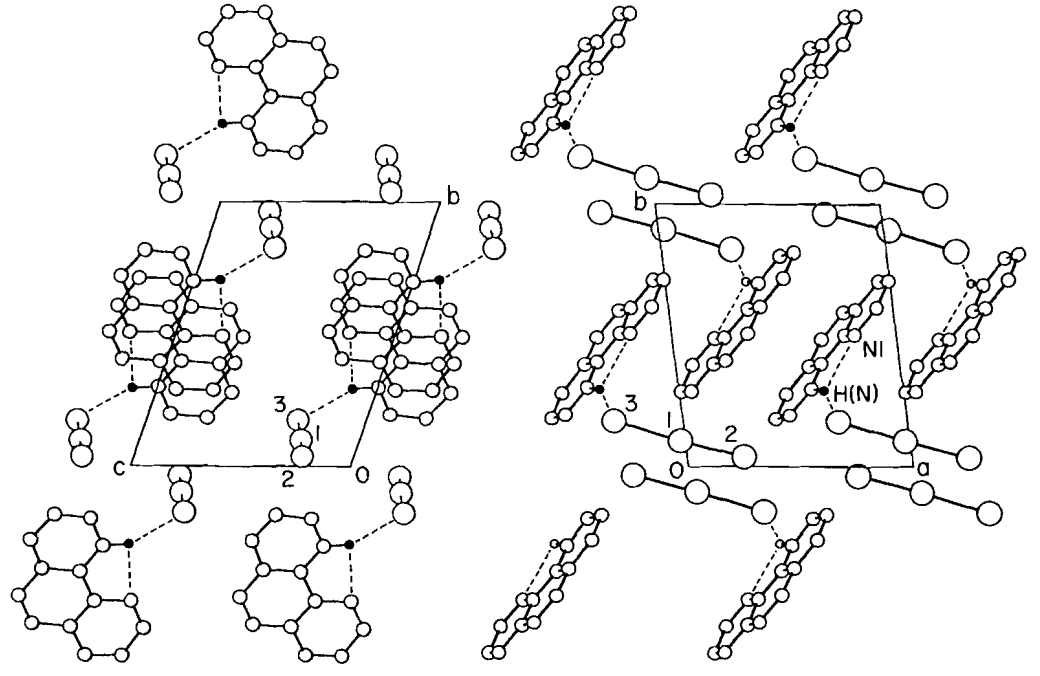

nificant asymmetry of the I_3^- anion and in turn a decrease in inter-anion I...I distances is discussed in more detail in Conclusions.

phenBr3

The phenH^+ cations are obliquely stacked inside pseudo-hexagonal channels ||*a* and defined by the Br(1) atoms (Fig. 9, left). The perpendicular spacing between the parallel neighbouring cation planes in the stacks is 3.46(2) Å, probably too long for an effective π–π stacking interaction. The Br_3^- anion is asymmetric, Br(2)-Br(1)-Br(3) = 177.6° (Table 3). The anion is discrete, although the shortest inter-anion Br...Br distance, 3.713 Å, appears to be at the van der Waals limit.

The cation (Fig. 10) is planar. The mean deviation of the non-hydrogen atoms from the best plane through these atoms is 0.005[2] Å in ring R1, 0.007[4] Å in R2, 0.004[2] Å in R3; and 0.012[9] Å in the cation as a whole. The angles between the best planes are R2/R1 = 1.2°, R3/R1 = 0.1°, R3/R2 = 1.4°, cation/R1 = 0.3°, cation/R2 = 1.0°, and cation/R3 = 0.4°. The protonated N atom was identified unambiguously as N(10), on clear evidence from both a difference Fourier map and the endocyclic C-N-C angle, which is 115.2(8)° for C(2)-N(1)-C(12) but

Fig. 10. Cation atom and ring numbering, and the bifurcated H-bond in phenBr3.

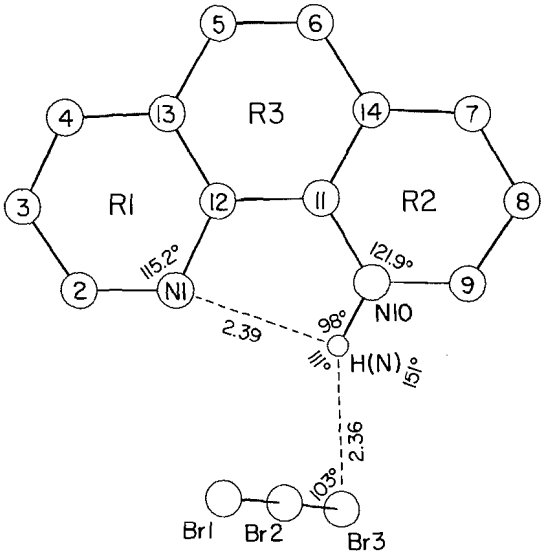

121.9(7)° for C(9)-N(10)-C(11), consistent with expectation (means in $phenH^+$ ions, 116.4[3]° at the unprotonated and 123.2[3]° at the protonated N atom, cf. ref. 14). The H(N) atom is engaged in a bifurcated H-bond, with an inter-ion branch to Br(3) and an intra-cation branch to N(1) (Fig. 10).

The geometry of the cation (Table D) matches closely that of other reported $phenH^+$ cations and is also essentially identical with that of the neutral $phen^0$ molecule (14):

Distance, Å	phenBr3	⟨$phenH^+$⟩	⟨$phen^0$⟩
N(1)...N(10)	2.731(10)	2.722[9]	2.724[2]
C(11)...C(12)	1.440(12)	1.431[3]	1.454[6]
C(13)...C(14)	2.840(12)	2.846[24]	2.841[11]
C(5)—C(6)	1.349(13)	1.339[6]	1.331[9]

The geometry of the intra-cation H-bond resembles the corresponding mean geometry in the $phenH^+$ cation: H(N)...N(1) = 2.39 Å, N(10)-H(N)-N(1) = 98°, (N(10)—H(N) taken as 1.02 Å), compared to the means 2.38[3] Å and 101.6[21]° respectively (14). The H(N)...Br separation is 2.36 Å and the N(10)-H(N)-Br(3) and H(N)-Br(3)-Br(2) angles are 151° and 103°, respectively.

Discussion

The structures of all five title triiodides are of the layer type; the phenBr3 structure can be described as consisting of parallel anion channels that contain oblique cation stacks.

Layer structures are frequently encountered in triiodides. The layer occupancy can be mixed, i.e., each layer contains cations *and* anions, or the cations and the anions can be segregated in separate layers.[14] Which arrangement will prevail depends on the ion-packing type. For 6:6 ion coordination the most common is the distorted (sometimes strongly) NaCl type, characteristic of mixed layers. This type is observed, for example, in the isostructural *Pnma* MI_3 (M = Tl, Rb, Cs, NH_4; layers ||(010) at $y = \pm \frac{1}{4}$; refs. 8, 11, 12) and also in a number of trihalides with heteroatomic anions. However, in 4MI3 and QI3 the alternative 6:6 *anti*-NiAs arrangement (*Pnnm*, layers ||(001), $z = 0, \frac{1}{2}$) is observed instead. Segregation of the cations and anions into separate layers is characteristic of the CsCl-type packing, e.g., in the Et_4NI_3 dimorphs (*Cmca*, layers ||(100), $x_{cat} = \pm \frac{1}{4}$, $x_{an} = 0, \frac{1}{2}$; *Pnma*, layers ||(010), $y_{cat} \sim 0, \frac{1}{2}$, $y_{an} = \pm \frac{1}{4}$, ref. 15) or in 1-Me-hexamethyleneammonium(1+) I_3 ($P2_1/c$, layers ||(100), $x_{cat} \sim \pm 0.21$, $x_{an} = 0, \frac{1}{2}$, ref. 5). Two of the title triiodides fall in this category: in 4MPI3 the layers are ||(001), $z_{cat} \sim \pm \frac{1}{4}$, $z_{an} = 0, \frac{1}{2}$; in API3 the layers are ||(010), $y_{cat} \sim \pm\frac{1}{8}, \pm\frac{3}{8}$, $y_{an} \sim 0, \pm\frac{1}{4}, \frac{1}{2}$ (Fig. 5). The monohydrate of KI_3 (*Pc*, ref. 16) also is of this type: layers ||(100), $x[K^+ + H_2O] \sim 0.86$, $x_{an} \sim 0.37$. Although the 1:2 compound Da2I3 is of a distorted 4:8 fluorite type, all the ions are in *mixed* layers ||(010), at $y = \pm\frac{1}{4}$.

Ion packing

The *anti*-NiAs-type packing found in 4MI3 and QI3 is relatively uncommon in organoammonium compounds. In $(Et_4N)[MX_4]$ (M = Ga, Fe, In, Tl; X = Hal)[15] it is undistorted *hexagonal* ($P6_3mc$), as in the aristotype. However, in $(Et_4N)[GaI_3Cl]$ (I and Cl disordered) and $(Et_4N)[FeI_4]$(*II*), which have the same *Pnnm* space-group symmetry as 4MI3 and QI3, the cation and anion positions are reversed, i.e., the packing is of the *NiAs* type. In these two structures a_O/c_O = 1.80 and 1.79, respectively; r = 1.255 and 1.254, respectively (cf. above). The volumes V_1 per formula unit of the 6:6 $(Et_4N)[FeI_4]$(*II*) and its NaCl-type $(Et_4N)[FeI_4]$(*I*) isomorphs are closely similar, 452 as against 458 Å^3.

In the simplest cases of the *CsCl-type* structures an I_3^- anion of one type only would be sufficient to generate the $[cat][an]_8$ coordination cuboid. This is seen in, for example, $[K(H_2O)]I_3$ (cf. above) and also in the two tetragonal ($P\bar{4}2_1m$) heteroatom trihalides $(PCl_4)[ICl_2]$ (18) and $(Me_4N)[ICl_2]$ (19). As the size of the cation and its complexity increase or its shape varies, I_3^- anions of a single type may not be able to coordinate the cation in a manner that would result in a 3-dimensional 8:8 crystal. Two or more types of anion may then be required to accomplish this. Thus in each of the *Cmca* and *Pnma* dimorphs of Et_4NI_3 (15) two types of I_3^- generate the coordination cuboid, while in the tetragonal 4MPI3 three and in the unusual case of API3 as many as seven types of I_3^- anions are required. The projections of the 4MPI3 and API3 structures in Figs. 3 and 6 show that, in spite of the increase in the number of nonequivalent anions, the 8:8 coordination geometry is closely satisfied: the edges and vertices of the cuboid cells defined by the projected anions are immediately recognized. It thus appears that the increase in the number of anion types and the adjustment of the space-group symmetry provide the compromise required to achieve and maintain the essentially spatially homogeneous CsCl-type packing in triiodide structures that qualify, by their (unspecified) cation/anion size ratio, for 8:8 coordination. The API3 structure thus represents an extreme variety of a frustrated CsCl-type packing.

Alternative descriptions

It should be noted that some of the reported triiodide structures can alternatively be described as, for example, channel structures. Thus the triclinic $(n\text{-}Bu_4N)I_3$ (20) has been described as

[14] In this context anion means the entire anion or its centre atom; cation refers to the cation centroid.

[15] For these and related structures see ref. 17.

consisting of cation channels ||*c* with the I_3^- ions approximately in the channel axes and with the interleaved, fully extended cations in planes approximately ||(001). This is a natural description of this structure and one that suited the authors' purposes. However, the structure can as well be described as a layer structure consisting of separate cation and anion layers ||(010) ($y_{cat} \sim \pm\frac{1}{4}$, $y_{an} \sim 0, \frac{1}{2}$) or as a distorted CsCl-type structure. Similarly, the 4MPI3 structure can be described as one consisting of channels ||*c* (Fig. 3), the API3 structure as one with channels ||*b*, and Da2I3 as one with channels ||*b*.

Hydrogen bonding

The distance from the placed H(N) atom to I(12) in Da2I3, 2.78 Å, is significantly shorter than the corresponding distance in QI3, 2.92 Å (Fig. 2). The H(N)...I(12) distance will be even shorter, and the N-H(N)-I(12) angle larger, if account is taken of the (undetermined) lengthening of the N—H(N) bond and of the displacement of the H(N) atom toward I(12), both expected consequence of H-bond formation.[12] Similar short H(N)...I distances (with located hydrogens) have been reported in 1-Me-cytosinium (MCI3, ref. 9) and ammonium (8) triiodides. Schematic comparison of the three structures leaves no doubt that the asymmetry of the anion, in particular the lengthening of the proximal I—I bond, is associated with the presence of the short H(N)...I bond (atom numbering as in original):

Da2I3

(1.02)	2.78	3.167(2)	2.793(2)	3.673(2)	
N—H(N).....	I(12)	—I(10)	—I(11)	.....	I(22B)
130°		178.6°	178°		

MCI3

[1.035]	*d*	3.123(1)	2.794(1)	3.755(1)	
2 N— 2 H(N).....	I(1)	—I(2)	—I(3)	.....	I(1')
α		177.6°	166.6°		83°

NH_4I_3

[0.88[4]]	*d*	3.114(2)	2.797(1)	3.881(2)	
4 N— 4 H(N).....	I(1)	—I(2)	—I(3)	.....	I(2')
α		178.6°	172.4°		

(MCI3, *d*, α: 2.67 Å, 152°; 2.66 Å, 149°. NH_4I_3, *d*, α: 2.81(4) Å, 158(4)°; 2.82(3) Å, 167(3)°; 2.87(2) Å, 168(2)°, 2×). Unlike in Da2I3, where there is only one H(N)-donor, in MCI3 the I(1) atom is the recipient of two H-bonds from one cation, and in NH_4I_3 I(1) is the recipient of four H-bonds from four cations. These examples illustrate extremes of deformability of the I_3^- anion under the influence of crystal environment, and of the particular efficacy of short H-bonds in this regard. The fact that the lengthening of the I—I bond is more substantial in Da2I3 than in the other two structures, despite the presence of multiple H-bond donors in the latter, is probably attributable to the double charge on the cation.

A short N—H(N)...I bond would be expected (cf. under Da2I3 above) to produce, apart from the lengthening of the I—I bond in the associated anion, a reduction in the shortest inter-anion I...I distances at the other end of the anion. The I(11)...I(22B) distance in Da2I3 and the I(3)...I(1′) distance in MCI3, both to terminal atoms of anions in the planar zigzag anion chains (Fig. 8; cf. Fig. 3 of ref. 9), are indeed quite short and suggestive of weak I...I bonding interactions; in NH_4I_3 the corresponding I(3)...I(2′) distance is ~0.2 Å longer than in Da2I3 and to the *centre* atom of an anion in the planar herringbone anion pattern (Fig. 1 of ref. 8). The large asymmetry of the H-bonded anion and the shortness of the I(11)...I(22B) distance in Da2I3 strongly suggest that both are the effects of the H-bonding in this structure, and similarly in MCI3, i.e., H-bonding is an active participant significantly co-responsible for the overall structural features of Da2I3 and MCI3. This does not appear to be the case in NH_4I_3. This triiodide is isostructural with TlI_3, RbI_3, and CsI_3. When the I(3)...I(2′) distances in these four compounds (8, 11, 12, 21) are plotted against $V^{1/3}$ (V = unit-cell volume; Fig. 11), the four points fall on a straight line ($r^2 = 0.990$), i.e., the I(3)...I(2′) distance in NH_4I_3 is consistent with those in the other compounds and depends on the gross variable V. However, while the I(1)—I(2) bond lengths in the other triiodides vary linearly with $V^{1/3}$, that in NH_4I_3 is a striking misfit. The short H-bonds to NH_4I_3 thus affect the anion asymmetry but their effect does not appear to extend beyond the other end of the anion and the I(3)...I(2′) distance is not shortened by the agency of the H-bond. The difference in the atom charges on the centre and terminal atoms of the I_3^- anions is of course also a factor.[16]

In contrast to the above structures the H-bonding in QI3 does not produce asymmetry in anion a2, with its centre atom I(20) at an inversion centre: the U_{ii}[I(20)], if anything, are somewhat smaller than those of the other I atoms in the Q3 structure (Table C). Then again, the H-bonds to the two terminal atoms of a2 are longer than the H-bonds in the above struc-

Fig. 11. Thick line, filled circles: variation of the shortest inter-anion distance I(3)...I(2′) in the isostructural MI_3 (M = Tl, Rb, Cs, NH_4; *Pnma*; Cs, LT, 113 K; Cs, RT, room temperature) with $V^{1/3}$ (see text). Broken lines, open circles: variation of the longer I—I bond length in the I_3^- anion with I(3)...I(2′) and $V^{1/3}$.

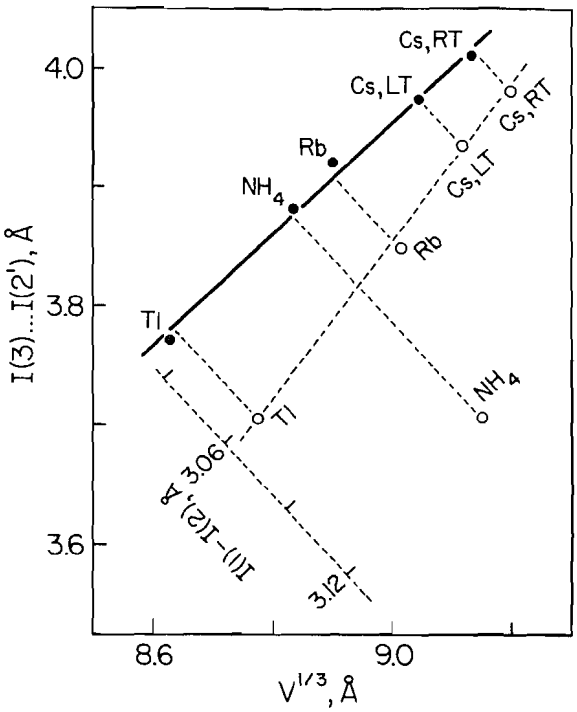

[16] The existence of a relationship between the lengthening of the proximal I—I bond and the shortening of the distal inter-anion I...I distance in H-bonded triiodides is being investigated, as is the variation of the H(X)-I-I angle in X-H(X)...I-I-I groupings, both in literature structures and in a number of newly determined structures (to be reported shortly).

tures and, by virtue of the crystallographic centrosymmetry of a2, (statistically) balanced about the inversion centre. Moreover, as crystallographically centrosymmetric I_3^- anions go, the I—I bond length in a2, 2.910(2) Å, and the total length of the anion, 5.820(2) Å, are at the low end of the range for such anions (cf. Table 2 of ref. 8).

Conclusions

The five title triiodides have structures of the layer type. The ion packing in 4MI3 and QI3 is of an orthorhombically distorted 6:6 *anti*-NiAs type; in 4MPI3 and API3 it is of the CsCl type; and in the 1:2 compound Da2I3 it is of a monoclinically distorted fluorite type, with the cations and anions in mixed layers. In the phenBr3 structure, obliquely stacked cations are accommodated inside parallel anion channels. The following features of the structures merit emphasis:

1. The asymmetry of one of the two I_3^- anions in Da2I3 appears to be the largest on record: I(11)—I(10) = 2.797 Å, I(10)—I(12) = 3.167 Å, I(11)-I(10)-I(12) = 172.5°. This asymmetry is associated with the short N—H(N)...I(12) bond (N...I(12) = 3.524 Å, H(N)...I(12) = 2.78 Å) and demonstrates clearly the extent to which H-bonding is able to distort the I_3^- anion in a crystal. The charge displacement the distortion produces in the anion has further repercussions in the structure, in that it shortens the inter-anion I...I distance at the non-H-bonded end of the anions and leads indirectly to formation of planar zigzag anion chains in the crystal.

2. The crystal structures of 4MPI3 and API3 are unexpectedly complex. 4MPI3, which is not isostructural with 4MI3, contains cations of two and anions of three types; API3, with its very large unit cell for its chemical simplicity, contains cations of six and anions of seven types. The complexity of these structures appears to be the result of a compromise between a tendency to maintain an 8:8 coordination and an unfavourable cation/anion ratio, which in these two cases possibly is at the boundaries separating different packing regimes:[17]

Compound	V_I, Å^3	Type	cat/an
TlI_3 (11)	160	[NaCl]	1/1
NH_4I_3 (8)	172	[NaCl]	1/1
RbI_3 (11)	176	[NaCl]	1/1
CsI_3 (12, 21)	190	[NaCl]	1/1
2MI3	232	NaCl	1/1
4MI3	295	*anti*-NiAs	1/2
4MPI3	314	CsCl	2/3
QI3	318	*anti*-NiAs	1/2
TrI_3	341	*anti*-NiAs	1/1
MHMTI3 (5)	354	CsCl	1/2
Et_4NI_3(*I*) (15)	380	CsCl	1/2
Et_4NI_3(*II*) (15)	383	CsCl	1/2
API3	389	CsCl	6/7
$MeEt_2PhNI_3$ (22)	410	CsCl	1/2

[17] V_I, volume per formula unit; cat/an, number of nonequivalent cations to number of nonequivalent anions. 2MI3 = $Me_2NH_2I_3$, TrI_3 = tropanium I_3 (K.N. Robertson, T.S. Cameron, and O. Knop, to be published). MHMTI3 = 1-Me-hexamethylenetetrammonium(1+) I_3, 1-Me-1,3,5,7-tetraazaadamantan-1-ium I_3. Brackets indicate strong departure from aristotype.

Unfortunately, because of present paucity of structural information on triiodides of compact, quasi-spherical cations with $V_I > 400$ Å^3 it is not clear what general packing arrangements to expect beyond API3. Below TlI_3 hydrated species appear to prevail, e.g., $KI_3 \cdot H_2O$ (16) and the structurally unexplored hydrates of LiI_3 and NaI_3.

Experimental

The title compounds were prepared by combining a solution of the appropriate halide in a suitable solvent (mostly MeOH) with a stoichiometric amount of an MeOH solution of iodine or bromine, and allowing the resulting solution to crystallize by controlled evaporation at room temperature. Deviations from this procedure are noted under the individual compounds below. The trihalides were recrystallized if required. However, controlling the size and quality of the crystals was not without problems, as large crystals had to be sectioned, not always with entirely gratifying results.

Diffraction intensities were measured at 20(2)°C using a Rigaku AFC5R system with either a sealed 2.4 kW Mo-anode tube (4MI3, QI3, API3, Da2I3, phenBr3) or a rotating-anode tube (4MPI3) (graphite monochromator, λ(Mo Kα) = 0.71069 Å). All intensities were corrected for Lorentz, polarization, absorption (ψ-scans), and secondary extinction as well as for time-decay effects where appropriate. The anisotropic temperature factor is defined as $\exp[-2\pi^2(U_{11}h^2a^{*2} + ... + 2U_{23}klb^*c^* + ...)]$. The structures were solved by direct methods (23) and refined using the TEXSAN-TEXRAY crystallographic software package (24) except for 4MI3 and API3, where the SHELXL-93 system (25) was used, for 4MI3 to model the disorder and for API3 because of the complexity of the structure. The function minimized was $\Sigma w(|F_o| - |F_c|)^2$, with unit weights except for 4MI3 and API3. Since the H atoms were placed geometrically (C—H, 1.08 Å, N—H, 1.02 Å) and not refined (U_{iso}(H) = 1.2U_{eq}(C, N) of the attached atom), no esd's are quoted on distances and angles involving H atoms. The residual electron-density maxima were all close to the halogen atom. Tables of structure factors are available from the authors.

4MI3

Straightforward refinement in *Pnnm* (I(10) in 2(*d*), I(20) in 2(*b*), I(11) and I(21) in 4(*g*), all other atoms in 8(*h*)) gave an acceptable structure but some of the U_{ii} of C(1) and C(3) were unreasonably high. Examination of the thermal ellipsoids of the cation atoms revealed that the cation undergoes large-amplitude librational motion essentially about its N–C(2) axis. Splitting the undifferentiated C(1) and C(3) positions (SHELXL-93, $w^{-1} = \sigma^2F_o^2 + (0.0506p)^2 + 5.35p$, $p = [(F_o^2)_{max} + 2F_c^2]/3$) significantly reduced the contentious U_{ii} values, although they still remained high (Table C). This twofold splitting is probably too simple to account for the observed U_{ii} values. Since no additional clues were available, no further attempts were made to improve the agreement.[18]

QI3

As stated above, this structure can be correctly refined in

[18] The existence of diffuse scattering in 4MI3 (as well as in $(Me_4N)IC1_2$ and $(Et_4N)I_3$(*I*)) attributed to orientational disorder of the anion in the unit cell has been reported in ref. 26.

Pnnm but with the cation in twofold orientational disorder across the mirror plane. A fully ordered structure would require refinement in an orthorhombic subgroup of *Pnnm*. Of the three possible subgroups of index 2, $P2_12_12$, *Pnn*2, and $Pmn2_1$ (in two settings, $Pn2_1m$ and $P2_1nm$), the last-named is not applicable because it does not remove the mirror plane perpendicular to the cation C–N axis. However, the difference between refining the disordered structure in *Pnnm* and the fully ordered structure in a noncentrosymmetric subgroup rests on the difference of the scattering powers of an averaged $\frac{1}{2}$(C + N) atom and a C or N atom, i.e., only 0.23% of $F(000)$, in a unit cell the scattering power in which is dominated by the iodine atoms at $z = 0, \frac{1}{2}$. Lacking confidence in the soundness of a subgroup refinement in these circumstances, we present the disordered structure as the one supportable by the data set.

TLS analysis of the anisotropic thermal parameters in the disordered structure showed that the U_{ij} values of the nonhydrogen cation atoms cannot be accounted for satisfactorily on a rigid-body-motion model: $R(U_{ij}) = 13.9\%$, $R_w(U_{ij}) = 14.0\%$, $\text{rms}(U_{ij}) = 0.0071$ Å^2, $\text{rms}[\text{esd}(U_{ij})] = 0.0062$ Å^2. However, the analysis indicated a mean amplitude of libration about a principal axis $\parallel c$ of ~6°.

API3

Because of the large number of nonequivalent cation atoms (60 C, 6 N, 108 H) in the presence of 19 nonequivalent iodine atoms in the unit cell, the N and C atoms were refined only isotropically, with constraint on the C—C and C—N bond lengths, using SHELXL-93. To judge by the large U_{ii} values of some of the I atoms (Table C), the structure at room temperature is quite mobile.[19]

Da2I3

The small black crystals that were deposited within a few hours on mixing stoichiometric amounts of Dabco iodide and iodine solutions in MeOH were not of a quality suitable for single-crystal X-ray diffraction. A sample of the crystals was therefore sealed in contact with dry MeCN, placed in a temperature-cycling recrystallization apparatus, and the temperature was cycled between 26 and 40°C (cycle time of about an hour) for 3 months. During this period a number of chunky crystals had grown on the sides of the container; these were of a size and quality suitable for data collection.

The thermal motion of the cation is consistent with the rigid-body-motion model: TLS analysis of the anisotropic thermal parameters of the C and N atoms gave an $\text{rms}(U_{ij})$ of 0.0029 Å^2 compared to $\text{rms}[\text{esd}(U_{ij})] = 0.0042$ Å^2. The mean amplitudes about the principal axes of libration L were 2.8° about L_1 (= line of intersection of the mirror plane halving the cation with the N-C(1)-C(1′)-N′ plane), 3.9° about L_2 (through the cation centroid and perpendicular to L_1), and 6.3° about $L_3 \parallel b$ (= the N-N′ axis). The geometry of these librational motions is consistent with the cation orientation relative to the I(12) atom, to which the cation is H-bonded (Fig. 8*A*). The mean components of the translational motion along the crystallographic axes were ~0.17, ~0.17, and ~0.14 Å, respectively.

phenBr3

TLS analysis of U_{ij}(C, N) gave $R(U_{ij}) = 10.2\%$, $R_w(U_{ij}) = 10.7\%$, $\text{rms}(U_{ij}) = 0.034$ Å^2 compared to $\text{rms}[\text{esd}(U_{ij})] = 0.0047$ Å^2, with the maximum mean amplitude about a principal libration axis of 4.4°. Librational corrections to bond lengths calculated on the rigid-body-motion model were between 0.002 and 0.006 Å, with a mean of 0.0043 Å. The largest differences between the calculated and observed U_{ii} values were for C(7) and C(8). They are probably attributable to the close proximity of H(7) and H(8) to the nearest Br(2) and Br(3) atoms: H(8)...Br(3D) = 2.92 Å, H(7)...Br(2) = 2.95 Å, H(7)...Br(3B) = 3.04 Å, all below or at the limit of the sum of Pauling's van der Waals radii, ~3.15 Å.

[19] As pointed out by a referee, the axes of the $P2_1/c$ cell (Table 1) can be transformed by (1,0,0/-1,0,-2/0,1,0) to yield a *C*-centred pseudo-orthorhombic cell, $a = 15.131$, $b = 43.330$, $c = 28.453$ Å, 90°, 90°, 89.2°. Examination of the diffraction intensities, however, leads to a clear rejection of a *C*-centred cell, i.e., there is no significance to the transformation.

Acknowledgments

This investigation was supported by research grants from the Natural Sciences and Engineering Research Council of Canada to T.S.C. and O.K., and from the Mount Saint Vincent University Research Fund to M.A.J.

References

1. H.A. Bent. Chem. Rev. **68**, 587 (1968).
2. K.-F. Tebbe. *In* Homoatomic rings, chains and macromolecules of main-group elements. *Edited by* A.L. Rheingold. Elsevier, Amsterdam. 1977. pp. 551–606.
3. T.J. Marks and D.W. Kalina. *In* Extended linear chain compounds. Vol. 1. *Edited by* J.S. Miller. Plenum Press, New York and London. 1982. pp. 197–331.
4. J.W. Bats, J.J. de Boer, and D. Bright. Inorg. Chim. Acta, **5**, 605 (1971).
5. P.K. Hon, T.C.W. Mak, and J. Trotter. Z. Kristallogr. **158**, 213 (1982).
6. O. Knop, T.S. Cameron, P.K. Bakshi, A. Linden, and S.P. Roe. Can. J. Chem. **72**, 1870 (1994).
7. J. Donohue and W.N. Lipscomb. J. Chem. Phys. **15**, 115 (1947).
8. K.-F. Tebbe, B. Freckmann, M. Hörner, W. Hiller, and J. Strähle. Acta Crystallogr. Sect. C: Cryst. Struct. Commun. C**41**, 660 (1985).
9. M. Rossi, L.G. Marzilli, and T. Kistenmacher. Acta Crystallogr. Sect. B: Struct. Crystallogr. Cryst. Chem. **B34**, 2030 (1978).
10. U. Bossek, K. Wieghardt, B. Nuber, and J. Weiss. Inorg. Chim. Acta, **165**, 123 (1989).
11. K.-F. Tebbe and U. Georgy. Acta Crystallogr. Sect. C: Cryst. Struct. Commun. C**42**, 1675 (1986).
12. J. Runsink, S. Swen-Walstra, and T. Migchelsen. Acta Crystallogr. Sect. B: Struct. Crystallogr. Cryst. Chem. **B28**, 1331 (1972).
13. O. Knop, S.C. Choi, and D.C. Hamilton. Can. J. Chem. **70**, 2574 (1992).
14. P.K. Bakshi, T.S. Cameron, and O. Knop. Can. J. Chem. **74**, 201 (1996).
15. T. Migchelsen and A. Vos. Acta Crystallogr. **23**, 796 (1967).
16. R. Thomas and F.H. Moore. Acta Crystallogr. Sect. B: Struct. Crystallogr. Cryst. Chem. **B36**, 2869 (1980).
17. O. Knop, T.S. Cameron, D. Adhikesavalu, B.R. Vincent, and J.A. Jenkins. Can. J. Chem. **65**, 1527 (1987).
18. W.F. Zelezny and N.C. Baenziger. J. Am. Chem. Soc. **74**, 6151 (1952).
19. G.J. Visser and A. Vos. Acta Crystallogr. **17**, 1336 (1964).
20. F.H. Herbstein, M. Kaftory, M. Kapon, and W. Saenger. Z. Kristallogr. **154**, 11 (1981).

21. M.C. Morris, H.F. McMurdie, E.H. Evans, B. Paretzkin, H.S. Parker, N.P. Pyrros, and C.R. Hubbard. Standard X-ray diffraction powder patterns. NBS Monograph 25, section **19**. Washington, D.C. 1982.
22. K.-F. Tebbe and W. Lindenthal. Z. Anorg. Allg. Chem. **619**, 1483 (1993).
23. G.M. Sheldrick. SHELXS-86. *In* Crystallographic computing. *Edited by* G.M. Sheldrick, C. Kruger, and R. Goddard. Oxford University Press, 1985.
24. TEXSAN-TEXRAY single-crystal structure analysis package. Molecular Structure Corporation, The Woodlands, Tex. 1993.
25. G.M. Sheldrick. SHELXL-93 crystal structure refinement program. Institute of Inorganic Chemistry, University of Göttingen. 1993.
26. H. Pritzkow and H. Hartl. Acta Crystallogr. Sect. B: Struct. Crystallogr. Cryst. Chem. **B29**, 1777 (1973).

*N*10-(2′-Mercaptoethanoyl)-2,2,5,5-tetramethyl-3,4-diathia-7,10-diazabicyclo[5.3.0]decane and its reaction with oxotrichlorobis(triphenylphosphine)-rhenium(V)

H. Alarabi, R.A. Bell, H.E. Howard-Lock, J. Kowanetz, and C.J.L. Lock

Abstract: The ligand molecule *N*10-(2′-mercaptoethanoyl)-2,2,5,5-tetramethyl-3,4-dithia-7,10-diazabicyclo[5.3.0]decane has been prepared and characterized by ^{1}H and ^{13}C NMR spectroscopy and by mass spectrometry. The protected analogue, *N*10-[(2′-triphenylmethylthio)ethanoyl]2,2,5,5-tetramethyl-3,4-dithia-7,10-diazabicyclo[5.3.0]decane dimethanol hemihydrate, was examined by the same techniques and also by X-ray crystallography. Crystals were triclinic, *P*-1, a = 11.125(2), b = 11.986(2), c = 13.562(3) Å, α = 103.54(3)°, β = 90.29(3)°, γ = 107.11(3)°, and Z = 2. The crystal was unstable in air at room temperature, so measurements were made on a crystal sealed in a tube that contained methanol vapour. Intensities were measured with a Rigaku AFC6R diffractometer and monochromated CuKα radiation (λ = 1.54178 Å). The structure was solved by direct methods and refined to R = 0.1497, wR = 0.0655 based on 5000 independent reflections. The high residuals were caused by solvent disorder. Bond lengths and angles were normal. The reaction of the ligand with oxotrichlorobis(triphenylphosphine) rhenium(V) yielded an unexpected asymmetric complex, oxo(1,1-dimethyl-1,8-dimercapto-3,6-diazaoctan-7-onato-N^3,N^6,S^1,S^8) rhenium(V). Crystals were monoclinic, $P2_1/n$, a = 10.633(2), b = 11.221(2), c = 11.678(1) Å, β = 116.10(1)°, Z = 4. Intensities were measured with a Siemens P4 diffractometer and monochromated MoKα radiation (λ = 0.71073 Å). The structure was solved by the heavy atom method and refined to R = 0.0471, wR = 0.0340 based on 2866 unique reflections. Most bond lengths and angles were normal. The Re≡O distance of 1.681(5) Å was longer than normal. It is postulated that this was caused by competitive π bonding between the deprotonated amidic nitrogen atom and the rhenium atom, as shown by the short Re—N distance (1.997(6) Å) compared to the equivalent distance for the amine nitrogen atom (Re—N, 2.151(4) Å).

Key words: N_2S_2 ligands, rhenium, crystal structure.

Résumé : On a préparé la molécule du coordinat *N*10-(2′-mercaptoéthanoyl)-2,2,5,5-(tétraméthyl-3,4-dithia-7,10-diazabicyclo[5.3.0]décane et on l'a caractérisée par spectroscopie RMN du ^{1}H et ^{13}C ainsi que par spectrométrie de masse. On a étudié l'analogue protégé, l'hémihydrate du *N*10-[(2′-triphénylméthylthio)éthanoyl]-2,2,5,5-tétraméthyl-3,4-diathia-7,10-diazabicyclo[5.3.0]décane diméthanol, par les mêmes techniques ainsi que par cristallographie aux rayons X. Les cristaux sont tricliniques, *P*-1, a = 11,125(2), b = 11,986(2) et c = 13,562(3) Å, α = 103,54(3)°, β = 90,29(3)° et γ = 107,11(3)° et Z = 2. Les cristaux sont instables à l'air à la température ambiante; les mesures ont donc dû être faites sur un cristal scellé dans un tube contenant des vapeurs de méthanol. Les intensités ont été mesurées sur un diffractomètre Rigaku AFC6R à l'aide d'un rayonnement monochromatique CuKα (λ = 1,54178 Å). On a résolu la structure par des méthodes directes et on l'a affinée jusqu'à des valeurs de R = 0,1497 et R_w = 0,0655 sur la base de 5000 réflexions indépendantes. Les hautes valeurs des résidus sont causées par un désordre du solvant. Les longueurs et les angles de liaison sont normaux. La réaction du coordinat avec l'oxotrichlorobis(triphénylphosphine)rhénium(V) conduit à la formation d'un complexe asymétrique inattendu, l'oxo(1,1-diméthyl-1,8-dimercapto-3,6-diazaoctan-7-onato-N^3,N^6,S^1,S^8)rhénium(V). Les cristaux sont monocliniques, $P2_1/n$, a = 10,633(2), b = 11,221(2) et c = 11,678(1) Å, β = 116,10(1)° et Z = 4. Les intensités ont été mesurées avec un diffractomètre Siemens P4 en utilisant un rayonnement monochromatique MoKα (λ = 0,71073 Å). La structure a été résolue par la méthode aux atomes lourds et affinée jusqu'à des valeurs de R = 0,0471 et R_w = 0,0340 pour 2866 réflexions uniques. La plupart des longueurs et des angles de liaisons sont normaux. La distance R≡O à 1,681(5) Å est plus longue que la normale. On suggère que ceci est causé par une liaison π compétitive entre l'atome d'azote amidique déprotoné et l'atome de rhénium, tel que montré par

Received November 4, 1995.

H. Alarabi, R.A. Bell, H.E. Howard-Lock, J. Kowanetz, and C.J.L. Lock.[1] Laboratories for Inorganic Medicine, Departments of Chemistry and Pathology, McMaster University, ABB266A, Hamilton, ON L8S 4M1, Canada.

[1] Author to whom correspondence may be addressed. Telephone: (905) 525-9140, ext. 24760. Fax: (905) 522-2509. E-mail: lack@mcmaster.ca.

la courte distance Re—N (1,997(6) Å) par comparaison avec la distance équivalente pour l'atome d'azote de l'amine (Re—N, 2,151(4) Å).

Mots clés : coordinat N_2S_2, rhénium, structure cristalline.

[Traduit par la rédaction]

Scheme 1. The reduction of 3,3,10,10-tetramethyl-1,2-dithia-5,8-diazacyclodeca-4,8-diene.

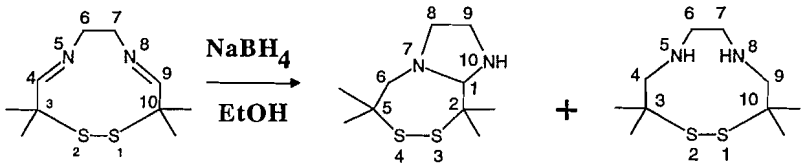

3 **4** **5**

Introduction

In a previous paper we reported that an attempt to prepare the ligand, *N*-(2′-mercaptoethyl)-*N*,*N*′-bis(2-methyl-2-mercaptopropyl)ethylenediamine), **1**, gave instead 2,2,5,5,-tetramethyl-3,4,13-trithia-7,10-diazabicyclo[8.3.0]-tridecane, **2** (1). This was because, as Joshua et al. (2) had shown, the major product of the reduction of 3,3,10,10-tetramethyl-1,2-dithia-5,8-diazacyclodeca-4,8-diene, **3**, was 2,2,5,5-tetramethyl-3,4-dithia-7,10-diazabicyclo[5.3.0]decane, **4**, rather than 3,3,10,10-tetramethyl-1,2-dithia-5,8-diazacyclodecane, **5**, as had been reported previously (3) (Scheme 1). The reaction of **4** with ethylene sulphide was extremely slow and led to the formation of **2**. This prevented the added 2-mercaptoethyl group from binding to the metal.

This paper describes further investigation of the addition of a 2-mercaptoethanoyl group to **4**. The interaction of the resultant ligand with a rhenium complex was studied subsequently.

Experiments

All commercially available chemicals were purchased and used without any further purification. Bulk organic solvents were obtained from Caledon Laboratories, Georgetown, Ont., specialist organic chemicals from Aldrich Chemical Co., Milwaukee, Wis., inorganic acids and solid chemicals from Fisher Scientific, Nepean, Ont. or BDH Chemicals, Toronto, Ont., and $CDCl_3$ from Cambridge Isotope Laboratories, Andover, Mass. Infrared spectra were recorded on Perkin Elmer 283 or Bio Rad FTS-40 spectrometers. Samples were ground with KBr (1–5% w/w) and pressed into pellets. Spectra were calibrated with a polystyrene standard. Raman spectra were recorded on a Jobin Yvon Mole S-3000 1 m spectrometer. It was equipped with 1800 grooves/mm holographic gratings, and Lexel 3500 krypton (λ = 647.1 nm) and Stabilite 2106 argon (λ = 514.5 nm) lasers were used to generate the exciting lines. The spectrometer was equipped with a 1-in. CCD detector. ^1H and ^{13}C NMR spectra were obtained on Bruker AC-200, AC-300, and AM-500 Fourier spectrometers equipped with 5 mm dual frequency ^1H–^{13}C probes. Samples were dissolved in appropriate deuterated solvents and sealed in 507-PP thin-wall 5 mm NMR tubes. Tetramethylsilane was used as an internal standard. Instruments were deuterium-locked to the deuterated solvent. The ^1H spectra were acquired at 200.13, 300.13, or 500.14 MHz in 8 scans in 16K data points. The free induction decays were processed with exponential multiplication (line broadening 0.3 Hz) and were zero-filled to 32K before Fourier transformation. The ^{13}C spectra were acquired at 50.324 MHz (AC-200) or 125.76 MHz (AM-500). Sweep widths were 2500.00 Hz for ^1H and 12 195.122 Hz for ^{13}C. Chemical ionization (CI) and electron impact (EI) mass spectra were recorded on a VG Analytical ZAB-E double focussing mass spectrometer. Low-resolution spectra were recorded for routine sample analysis. Typical experimental conditions were as follows: resolution = 1000, electron energy = 70 eV, source temperature 200°C, source pressure = 2×10^{-6} mbar for EI and 4×10^{-5} mbar for CI (1 bar = 100 kPa). Analytical thin-layer chromatography (TLC) was performed on DC-Alufolien Kieselgel $60F_{254}$ silica-coated aluminium sheets with a stationary phase layer thickness of 0.2 mm. Compounds were developed with iodine vapour. Preparative chromatographic separations were carried out with the use of columns (2 cm × 50 cm) packed with chromatographic silica gel (100–200 mesh).

2-(Triphenylmethylthio)ethanoic acid, 6

This compound was synthesized according to the published procedure (4). Glacial acetic acid (20.0 mL), mercaptoethanoic acid (2.09 g, 1.6 mL, 22.7 mmol), and triphenylmethanol (6.00 g, 23.0 mmol) were mixed and kept warm at 70°C until the reactants dissolved (≈ 5 min). Boron trifluoride etherate (5.0 mL) was added and the heat source was removed. The resulting yellow solution was stirred magnetically at room temperature until a white precipitate had formed (≈ 45 min). The reaction mixture was poured into 50.0 mL of ice-cold distilled water, and deposited a white solid that was removed by filtration and washed thoroughly with water. The product was then recrystallized from toluene; yield: 5.38 g (16.1 mmol, 71%); mp 159–161°C (lit. (4) mp 158.5–160.0°C); TLC; R_f = 0.33 (CH_2Cl_2–CH_3OH, 9:1); IR (KBr pellet), ν_{max} cm^{-1} (relative intensity): 3000 br (62, ν_{OH}), 1709 (82, $\nu_{C=O}$), 1595 (32), 1487 (54), 1445 (51), 1410 (43), 1385 (33), 1292 (67), 1227 (21), 1180 (21), 1152 (48), 1082 (30), 1030 (32), 995 (18), 905 br (34), 843 (20), 768 (44), 745 (95), 709 (74), 699 (100), 625 (19), 618 (50); ^1H NMR ($CDCl_3$), δ: 2.95 (s, 2H, S-CH_2), 7.30 (m, 15H, aryl), 10.20 (s, 1H, CO_2H); ^{13}C NMR ($CDCl_3$), δ: 34.68 (S-CH_2), 67.46 (C-Ph_3), 126.9 (*para* aryl), 128.10 (*meta*

aryl), 129.42 (*ortho* aryl), 144.11 (ipso aryl), 175.79 (CO_2H); MS (DEI), *m/z* (relative intensity): 243 (100, CPh_3^+), 215 (9), 165 (88, $CPh_3^+ - C_6H_6^{\cdot}$), 115 (7); MS (DCI): 352 (4, $M^{\cdot} + NH_4^+$), 243 (100, CPh_3^+), 165 (6, $CPh_3^+ - C_6H_6^{\cdot}$).[2]

N10-[(2-Triphenylmethylthio)ethanoyl]-2,2,5,5-tetramethyl-3,4-dithia-7,10-diazabicyclo[5.3.0]-decane dimethanol hemihydrate, 7

Two methods were used in the synthesis of **7**. Method A involved the use of *N,N'*-carbonyldiimidazole (CDIM) (5, 6) and method B involved the use of 1,3-dicyclohexylcarbodiimide (DCC).

Method A

Compound **6** (3.60 g, 10.8 mmol) was dissolved in tetrahydrofuran (THF) (15.0 mL). To this solution, *N,N'*-carbonyldiimidazole (1.77 g, 10.9 mmol) was added and the mixture was stirred for 3 h under a nitrogen atmosphere at room temperature. Compound **3** (2.50 g, 10.8 mmol) was then added to the solution and the mixture was stirred under nitrogen for another 24 h. The THF was evaporated under reduced pressure and the residue was partitioned between methylene chloride (25.0 mL) and 0.1 M HCl solution (25.0 mL). The aqueous layer was washed with methylene chloride (3 × 15.0 mL). The methylene chloride portions were combined, and washed successively with 0.1 M HCl solution (15.0 mL), 5% sodium bicarbonate solution (15.0 mL), and water (3 × 15.0 mL). The methylene chloride solution was dried over anhydrous sodium sulphate and the solvent removed by evaporation under reduced pressure. This resulted in the isolation of a colourless oil, which solidified to give a colourless solid, **7**, upon addition of methanol (10.0 mL). The solid was collected by vacuum filtration and washed with methanol (3 × 10.0 mL). Yield = 4.16 g (7.6 mmol, 70%).

Method B

Compound **6** (4.00 g, 12.0 mmol) was dissolved in methylene chloride (25.0 mL) and 1,3-dicyclohexylcarbodiimide (DCC) (2.52 g, 12.2 mmol) was added to the resulting solution. The mixture was stirred at room temperature for 1 h under a nitrogen atmosphere. Compound **4** (2.79 g, 12.0 mmol) was added, and the mixture was stirred for another 18 h. The colourless precipitate that formed, dicyclohexylurea (DCU), was removed by filtration and washed with methylene chloride (2 × 20.0 mL). The filtrate was extracted with 0.5 M HCl solution (20.0 mL), 5% sodium bicarbonate solution (20.0 mL), and water (3 × 20.0 mL). Additional precipitate that formed in the methylene chloride layer, DCU, was removed by filtration. The solution was dried with anhydrous sodium sulphate and the methylene chloride was removed by evaporation under reduced pressure. Methanol (10.0 mL) was added to the remaining oil. This resulted in the formation of a colourless precipitate, **7**, that was collected by filtration and washed with methanol (3 × 10.0 mL). Yield = 4.93 g (9.0 mmol, 75%).

Compound **7** showed the following: mp 166–168°C; TLC, $R_f = 0.68$ (chloroform); IR (KBr): 1661 cm^{-1}, $\nu_{C=O}$; ^1H NMR ($CDCl_3$), δ: 1.22 (s, 6H, 2 × CH_3), 1.24 (s, 3H, CH_3), 1.27 (s, 3H, CH_3), 2.51 (d, J = 14.7 Hz, 1H), 2.67 (m, 1H), 2.90 (d, J = 2.4 Hz, 2H), 2.97–3.32 (complex multiplet, 4H), 4.65 (s, 1H), 7.27 (m, 9H, aryl), 7.44 (m, 6H, aryl); ^{13}C NMR ($CDCl_3$), 16 signals were observed: δ 20.03 (CH_3), 25.00 (CH_3), 26.72 (CH_3), 28.14 (CH_3), 36.50 (SCH_2), 47.92 (CH_2N), 53.74 (2 × $C(CH_3)_2$), 54.75 (CH_2N), 66.05 ($CH_2C(CH_3)_2$), 67.21 (CPh_3), 86.23 (CHN), 126.90 (*para* aryl), 128.06 (*meta* aryl), 129.42 (*ortho* aryl), 143.91 (ipso aryl), 167.70 ($C{=}O$); MS (DCI) *m/z* (relative intensity): 549 (1, $M^{\cdot+} + 1$), 307 (47, $M^{\cdot+} - C(Ph)_3^{\cdot} + 2H$), 275 (9, $M^{\cdot+} - SC(Ph)_3 + 2H$), 243 (100, $C(Ph)_3^+$), 231 (14, $M^{\cdot+} - COCH_2SC(Ph)_3$), 199 (10, 231 − S), 157 (14, 231 − $SC(CH_3)_2$), 125(10, 231 − $SSC(CH_3)_2$); MS (DEI): 549 (1, $M^{\cdot+} + 1$), 474 (12, $M^{\cdot+} - SC(CH_3)_2$), 243 (78, $C(Ph)_3^+$), 231 (100, $M^{\cdot+} - C{\cdot}O{\cdot}CH_2SC(Ph)_3$), 165 (19, $C(Ph)_3^+ - C_6H_6^{\cdot}$).

N10-(2-Mercaptoethanoyl)-2,2,5,5-tetramethyl-3,4-dithia-7,10-diazabicyclo[5.3.0]decane, 8

The use of trifluoroacetic acid for the removal of trityl groups was reported by Brenner et al. (7). The trityl-protected compound **7** (1.00 g, 1.8 mmol) was dissolved in 5.0 mL of trifluoroacetic acid. Triethylsilane (0.31 mL, 2.0 mmol) was added to the orange solution. The solution turned colourless and a colourless precipitate formed immediately. The mixture was transferred into a separatory funnel and partitioned between hexanes (10 mL) and water (10 mL). The aqueous phase was filtered through Celite, washed with hexanes (3 × 10 mL), and the water was removed under reduced pressure. The product, **8**, was recovered from the aqueous phase as a colourless oil. Yield: 0.28 g (0.91 mmol, 51%); ^1H NMR ($CDCl_3$), δ: 1.24 (s, 6H, 2 × CH_3), 1.28 (s, 3H, CH_3), 1.35 (s, 3H, CH_3), 2.07 (t, 1H, exchangeable SH), 2.58 (d, J = 15.1, 1H), 3.00 (m, 1H), 3.31 (m, 5H), 3.69 (m, 1H), 4.72 (s, 1H); MS (DEI), *m/z* (relative intensity): 307 (15, $M^{\cdot+} + 1$), 232 (100, $M^{\cdot+} - COCH_2SH$), 217 (4, $M^{\cdot+} - HSCH_2C{\cdot}O{\cdot}N$), 199 (42, 231 − S), 157 (63, 231 − $SC(CH_3)_2$), 125 (14, 231 − $SSC(CH_3)_2$), 83 (6, $C_4H_7N_2^+$); MS (DCI): 307 (100, $M^{\cdot+} + 1$), 275 (6, $M^{\cdot+} + 1$ − S), 233 (25, $M^{\cdot+} + 1 - COCH_2SH$), 199 (6, 231 − S), 157 (7, 231 − $SC(CH_3)_2$).

Oxo(1,1-dimethyl-1,8-dimercapto-3,6-diazaoctan-7-onato-N^3,N^6,S^1,S^8)rhenium(V), 9

$ReO(P(Ph)_3)_2Cl_3$ (150.0 mg, 0.18 mmol) (8) was dissolved in chloroform (100 mL) to give a light green solution. Upon addition of **8** (80 mg, 0.26 mmol), the solution turned dark red. Triethylamine (0.5 mL) was added to the mixture and the solution was stirred for 24 h. The chloroform was removed under reduced pressure. The remaining residue was washed with diethyl ether (3 × 15 mL), dried, redissolved in chloroform (3.0 mL), and passed through a chromatography silica gel column. Elution with a chloroform–methanol mixture (80:20) led to the isolation of the product **9**. Yield: 27 mg (0.064 mmol,

[2] Tables of anisotropic displacement coefficients, bond lengths and angles for the phenyl groups in **7**, hydrogen atom coordinates and isotropic displacement coefficients, vibrational spectral data, and figures showing the cellular packing have been deposited and can be purchased from: The Depository of Unpublished Data, Document Delivery, CISTI, National Research Council Canada, Ottawa, Canada K1A 0S2. The tables of bond lengths and angles, hydrogen atom coordinates, and figures showing the cellular packing have also been deposited with the Cambridge Crystallographic Data Centre, and can be obtained on request from The Director, Cambridge Crystallographic Data Centre, University Chemical Laboratory, 12 Union Road, Cambridge, CB2 1EZ, U.K.

Table 1. Structure determination summary for **7** and **9**.

Crystal data		
Formula	$C_{31}H_{36}N_2O_3S_3 \cdot (CH_4O)_2 \cdot 0.5H_2O$, **7**	$C_8H_{15}N_2O_2ReS_2$, **9**
Colour; habit	Colourless plate	Red needle
Crystal size (mm)	0.2 × 0.4 × 0.3	0.2 × 0.2 × 0.4
Crystal system	Triclinic	Monoclinic
Space group	$P-1$	$P2_1/n$
a (Å)	11.125(2)	10.633(2)
b (Å)	11.986(2)	11.221(2)
c (Å)	13.562(3)	11.678(1)
α (deg)	103.54(3)	
β (deg)	90.29(3)	116.10(1)
γ (deg)	107.11(3)	
Volume (Å^3)	1675.1(8)	1251.3(4)
Z	2	4
Formula weight	649.9	421.5
Density (calc.) (Mg/m^3)	1.288	2.238
Density (meas.) (Mg/m^3)		2.21(2)
Absorption coefficient (mm^{-1})	1.15	10.0
F(000)	333	800
Data collection		
Index ranges	$0 \le h \le 13$	$-1 \le h \le 13$
	$-15 \le k \le 15$	$-1 \le k \le 14$
	$-12 \le l \le 12$	$-15 \le l \le 14$
No. of standards, variation	4, 0.40%	3, 3.85%
Reflections collected	5275	3660
Independent reflections	5000 (R_{int} = 0.0375)	2866 (R_{int} = 0.0 264)
Reflections used	5000	2866
Absorption correction, A^*	1.29–1.63	5.09–8.02
Solution and refinement		
Number of parameters refined	345	136
Final R Indices		
R	0.1497	0.0471
wR	0.0655	0.0340
Goodness-of-fit, S	1.88	1.13
Largest Δ/σ	0.002	0.002
Mean Δ/σ	0.000	0.001
Data:parameter ratio	14.5:1	21.1:1
Largest difference peak (e Å^{-3})	0.65	1.03
Largest difference hole (e Å^{-3})	−0.55	−0.98

7: diffractometer used, Rigaku AFC6R; radiation, CuKα (λ = 1.54178 Å); monochromator, highly oriented graphite crystal; 2θ range, 12.5°–152.1°; scan type, ω–2θ; scan speed, variable, 2.00°–29.30°/min in ω; standard reflections, 3 measured every 150 reflections.

9: diffractometer used, Siemens P4, rotating anode; radiation, MoKα (λ = 0.71073 Å), monochromator, highly oriented graphite crystal; 2θ range, 7.0°–45.0°; scan type, ω–2θ; scan speed, variable, 3.00°–60.00°/min in ω; standard reflections, 3 measured every 97 reflections.

Both: temperature, 296 K; scan range (ω), 0.8° plus Kα; background measurement, stationary crystal, and stationary counter at beginning and end of scan, each for 0.25 of total scan time; absorption correction, ψ-scan. Reflections with $-3\sigma < I < 0$ were treated by the method of French and Wilson (17) and included in the refinement. Software programs used, Siemens SHELXTL PC (Siemens Analytical Instruments Inc., Madison, Wis., 1990); solution, direct methods; refinement method, full-matrix least squares; quantity minimized, $\Sigma w(|F_o| - |F_c|)^2$, hydrogen atoms, riding model, fixed isotropic U; weighting scheme, $w^{-1} = \sigma^2(F)$.

Table 2. Atomic coordinates ($\times 10^4$) and equivalent isotropic displacement coefficients ($Å^2 \times 10^3$) for *N*10-[2′-(triphenylmethylthio)ethanoyl]-2,2,5,5-tetramethyl-3,4-dithia-7,10-diazabicyclo[5.3.0]decane dimethanol hemihydrate, **7**.

Atom	*x*	*y*	*z*	*U*(eq)[a]
C(1)	674 (5)	8219 (5)	11185 (4)	59 (3)
C(2)	1881 (6)	7955 (6)	11525 (5)	65 (3)
S(3)	1694 (2)	7657 (2)	12811 (1)	78 (1)
S(4)	419 (2)	6010 (2)	12612 (1)	83 (1)
C(5)	−1129 (6)	6274 (6)	12598 (5)	70 (3)
C(6)	−1109 (6)	7259 (5)	12046 (4)	64 (3)
N(7)	−432 (4)	7191 (4)	11136 (4)	56 (2)
C(8)	−1180 (6)	6960 (5)	10190 (4)	68 (3)
C(9)	−193 (6)	7296 (5)	9452 (4)	68 (3)
N(10)	724 (4)	8359 (4)	10126 (3)	54 (2)
C(21)	3053 (6)	9103 (6)	11737 (5)	89 (4)
C(22)	2134 (6)	6911 (6)	10786 (5)	89 (4)
C(51)	−1493 (7)	6674 (6)	13690 (5)	108 (5)
C(52)	−2027 (7)	5040 (6)	12018 (5)	102 (4)
C(11)	1205 (6)	9458 (6)	9934 (5)	56 (3)
O(1)	1682 (4)	10377 (4)	10607 (3)	67 (2)
C(12)	1195 (5)	9485 (5)	8819 (4)	59 (3)
S(13)	2222 (2)	8631 (2)	8214 (1)	60 (1)
C(14)	2105 (5)	8701 (5)	6858 (4)	53 (3)
C(15)	2994 (6)	9868 (6)	6663 (5)	60 (3)
C(16)	3244 (6)	9876 (6)	5648 (5)	75 (4)
C(17)	4024 (8)	10921 (8)	5441 (6)	95 (5)
C(18)	4566 (7)	11927 (8)	6206 (8)	108 (5)
C(19)	4299 (7)	11925 (7)	7206 (7)	101 (4)
C(20)	3519 (6)	10889 (6)	7435 (6)	78 (3)
C(23)	740 (6)	8531 (5)	6558 (4)	52 (3)
C(24)	−185 (6)	7505 (6)	6675 (5)	66 (3)
C(25)	−1455 (7)	7378 (6)	6506 (5)	82 (4)
C(26)	−1825 (6)	8277 (7)	6220 (5)	80 (4)
C(27)	−918 (6)	9280 (6)	6087 (5)	71 (3)
C(28)	363 (6)	9413 (5)	6266 (4)	60 (3)
C(29)	2581 (6)	7649 (5)	6288 (5)	59 (3)
C(30)	3739 (6)	7588 (6)	6622 (5)	69 (3)
C(31)	4202 (7)	6685 (7)	6127 (6)	85 (4)
C(32)	3549 (8)	5857 (7)	5255 (6)	87 (4)
C(33)	2437 (8)	5942 (6)	4896 (5)	89 (4)
C(34)	1941 (6)	6830 (6)	5426 (5)	72 (3)
C(50)	4860	1952	557	127 (3)
O(50)[b]	3879	2259	1110	114 (4)
O(51)[b]	3741	2194	346	111 (6)
O(52)[b]	3976	2163	1424	119 (9)
C(51)	3508	4894	2124	209 (5)
O(53)[b]	4132	4283	2358	255 (6)
O(54)[b]	4349	4638	1173	252 (11)
O(55)[b]	4683 (22)	4037 (17)	−110 (17)	347 (12)

[a]Equivalent isotropic *U* defined as one third of the trace of the orthogonalized U_{ij} tensor.

[b]These atoms were given partial occupancies: O(50), 0.46; O(51), 0.30; O(52), 0.24; O(53), 0.625; O(54), 0.375, O(55), 0.50.

36%). A dark green band remained at the top of the column and was not recovered. IR (KBr pellet): 3433 cm^{-1}, ν_{N-H}; 1607 cm^{-1}, $\nu_{C=O}$; 973 cm^{-1}, $\nu_{Re=O}$; Raman: 972 cm^{-1}, $\nu_{Re=O}$.

X-ray crystallography

Single crystals of **7** were obtained by the addition of methanol (2.0 mL) to a solution of the compound (100 mg) in chloroform (5.0 mL). Crystals separated when the solution was left to evaporate slowly at −15°C. The crystals were unstable and turned to powder when left dry for 3 h. Consequently, the crystal chosen for the data collection was sealed into a capillary tube that was saturated with methanol vapour. Single crystals of **9** were obtained by allowing a solution of the compound in dimethylformamide to evaporate at room temperature. The density was measured by suspending the crystals in a mixture of bromoform and carbon tetrachloride.

For **7**, automatic unit cell determination and data collection were performed on a Rigaku AFC6R diffractometer with the use of CuKα (λ = 1.54178 Å) radiation. Unit cell parameters were refined by least-squares fit of positional parameters for 21 reflections (50.83° ≤ 2θ ≤ 73.78°). Temperature factors for non-hydrogen atoms were refined anisotropically. Details of crystal data and solution refinement are listed in Table 1. Table 2 lists the atomic coordinates. The asymmetric unit contained half a water and two methanol molecules. The position of the methanol molecules could not be clearly defined. They were highly disordered. Attempts to refine the positional parameters were unsuccessful. Atoms moved away from the position in which they were first located and the temperature factors increased to $U > 0.6$ $Å^2$. At the same time peaks appeared in the difference map where the atom had been originally. Eventually the atoms in the methanol molecules were fixed at the points where they were first detected in the difference map. Occupancies were varied to make the temperature factors of atoms of a given type in a given molecule approximately the same. The carbon and oxygen atoms were chosen by considering atoms within 2.9 Å that might be involved in hydrogen bonding. Thus, the first methanol molecule was made up of three fractional oxygen atoms, O(50), O(51), O(52), and C(50) and the second was made up of two fractional oxygen atoms, O(53) and O(54), and C(51). The occupancy of the water molecule site, O(55), was arbitrarily set at 0.5. It could not be greater than 0.5 since two water molecule sites were only 1.8 Å apart. Other close interactions with oxygen atoms from the methanol molecules suggested a similar upper limit. The relatively high residuals ($R = 0.1497$, $R_w = 0.0655$, $S = 1.88$) are partly caused by this disorder and also by the large number of weak reflections with $F < \sigma_F$ (2582). For **9** the crystal was glued to the end of a glass fibre. Automatic unit cell determination and data collection were performed on a Siemens P4 diffractometer with the use of MoKα (λ = 0.71073 Å) radiation. Unit cell parameters were refined by least-squares fit of positional parameters for 23 reflections (7.28° ≤ 2θ ≤ 24.73°). Temperature factors of the non-hydrogen atoms were refined anisotropically. Details of crystal data and solution refinement are listed in Table 1 and Table 3 lists the atomic coordinates.

Results and discussion

Reaction Scheme 2 summarizes the syntheses described here. Unlike the reaction of **4** with ethylene sulphide, which required a period of 1 week and a large excess of ethylene sulphide before any appreciable product could be recovered, the coupling of 2-(triphenylmethylthio)ethanoic acid, **6**, with **4** in

Scheme 2. The preparation of **7** and **9**.

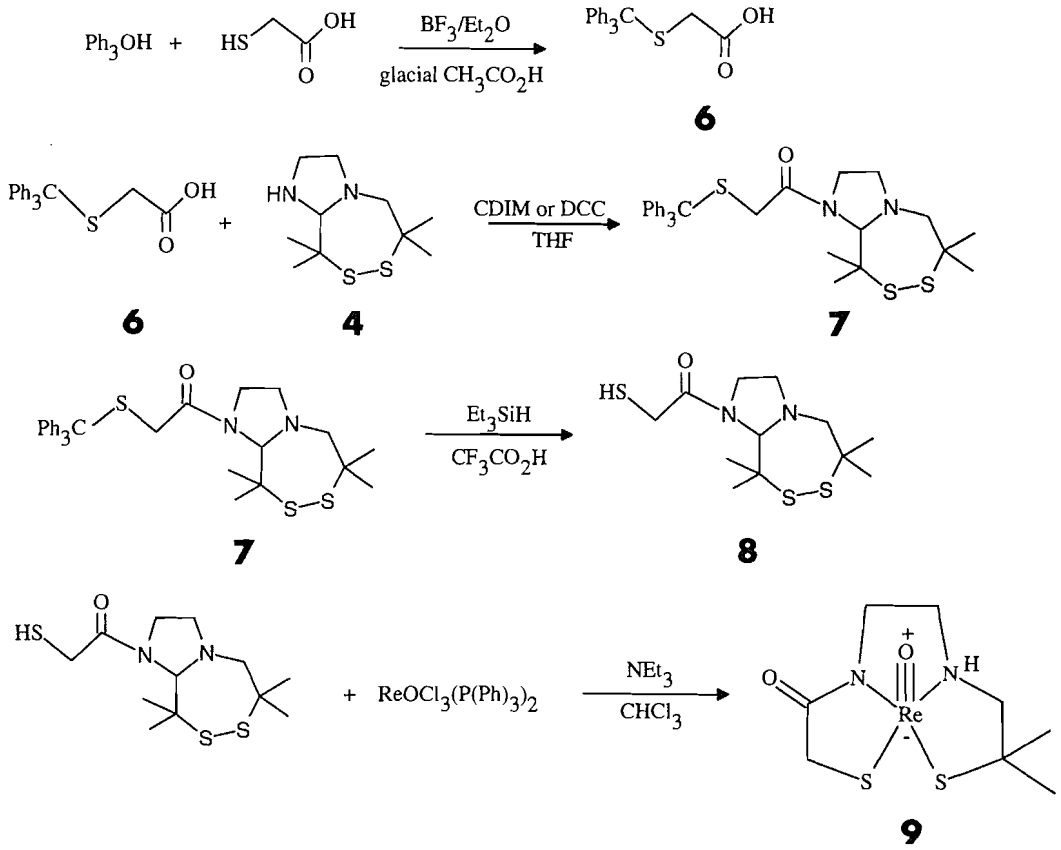

Table 3. Atomic coordinates ($\times 10^4$) and equivalent isotropic displacment coefficients ($Å^2 \times 10^3$) for $ReC_8H_{15}N_2O_2S_2$, **9**.

Atom	*x*	*y*	*z*	*U*(eq)[a]
Re(1)	53 (1)	701 (1)	2356 (1)	27 (1)
O(1)	−73 (5)	1580 (5)	1145 (4)	46 (2)
S(1)	−983 (2)	1578 (2)	3480 (2)	31 (1)
C(1)	453 (7)	2547 (5)	4569 (6)	31 (2)
C(2)	1751 (7)	1769 (6)	5092 (6)	35 (2)
N(1)	1929 (5)	1155 (5)	4031 (5)	30 (2)
C(3)	2897 (7)	103 (6)	4496 (7)	40 (3)
C(4)	2765 (6)	−611 (6)	3365 (7)	45 (3)
N(2)	1238 (6)	−736 (5)	2547 (5)	36 (2)
C(5)	734 (8)	−1791 (6)	1935 (7)	45 (3)
C(6)	−812 (8)	−1867 (6)	1194 (7)	46 (3)
S(2)	−1697 (2)	−657 (2)	1607 (2)	41 (1)
C(11)	142 (8)	2934 (7)	5670 (6)	46 (3)
C(12)	610 (9)	3632 (6)	3833 (7)	48 (3)
O(2)	1501 (6)	−2639 (4)	1987 (6)	59 (3)

[a]Equivalent isotropic *U* defined as one third of the trace of the orthogonalized U_{ij} tensor.

the presence of *N,N'*-carbonyldiimidazole (CDIM) or 1,3-dicyclohexylcarbodiimide (DCC) required only 24 h of stirring at room temperature and resulted in a high yielding reaction (75%). The product, **7**, was recovered in high purity as a colourless solid. It was characterized by electron impact and chemical ionization mass spectroscopy, ^1H and ^{13}C NMR spectroscopy, and X-ray crystallography. The NMR spectrum was assigned by comparison with the NMR spectra of **4**. Further confirmation of this assignment was achieved with the use of a $^{13}C/^1H$ correlation NMR spectrum.

The next step in the synthesis involved the deprotection of the sulphur atom in compound **7** by removal of the trityl group with trifluoroacetic acid and triethylsilane. This led to the isolation of **8** in 51% yield. Compound **8** was a colourless oil that was characterized by mass and ^1H NMR spectroscopy. The presence of a thiol group in **8** was confirmed by the appearance of a triplet at 2.07 ppm in the proton NMR spectrum, which was assigned to the SH proton. Upon addition of D_2O, this triplet disappeared and the splitting in the signal at 3.31 ppm, which was assigned to the CH_2 protons next to the SH group, was removed.

The reaction of the deprotected ligand **8** with $ReOCl_3(P(Ph)_3)_2$ led to the isolation of an unexpected rhenium complex **9**. This complex contained neither an N2S3 pentadentate ligand nor did it contain a thiazolidine ring-containing ligand. Instead, the X-ray structure showed that a 2-methyl-2-mercaptopropyl fragment had been lost from the ligand in the course of the reaction. The resultant rhenium complex contained the unusual asymmetric monoamine–monoamide–dithiol (MAMA) N2S2 ligand. The synthesis of asymmetric N2S2 ligands (9) and their reactions with technetium (10) have been reported previously, but the complex described here

Fig. 1. The molecule *N*10-[2′-(triphenylmethylthio)ethanoyl]-2,2,5,5-tetramethyl-3,4-dithia-7,10-diazabicyclo[5.3.0]decane, **7**, with the atom numbering. Hydrogen atoms have been omitted for clarity.

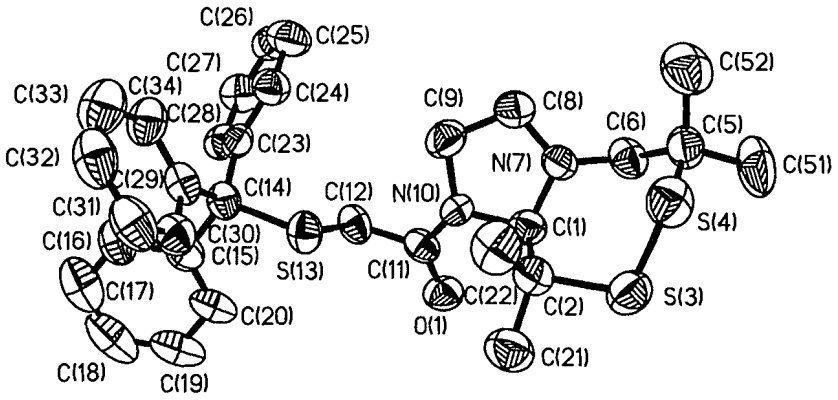

Table 4. Bond lengths (Å) and angles (°) for *N*10-[2′(triphenylmethylthio)-ethanoyl]-2,2,5,5-tetramethyl-3,4-dithia-7,10-diazabicyclo[5.3.0]decane dimethanol hemihydrate, **7**.

Lengths			
C(1)—C(2)	1.558 (10)	C(2)—S(3)	1.862 (7)
S(3)—S(4)	2.020 (2)	S(4)—C(5)	1.841 (8)
C(5)—C(6)	1.534 (10)	C(6)—N(7)	1.448 (8)
N(7)—C(8)	1.450 (8)	C(8)—C(9)	1.519 (8)
C(9)—N(10)	1.476 (6)	N(10)—C(1)	1.484 (8)
C(1)—N(7)	1.450 (7)	C(2)—C(21)	1.559 (8)
C(2)—C(22)	1.508 (9)	C(5)—C(51)	1.541 (9)
C(5)—C(52)	1.543 (8)	N(10)—C(11)	1.355 (9)
C(11)—C(12)	1.521 (9)	C(11)—O(1)	1.228 (7)
C(12)—S(13)	1.824 (7)	S(13)—C(14)	1.865 (6)
C(14)—C(15)	1.538 (8)	C(14)—C(23)	1.512 (9)
C(14)—C(29)	1.552 (9)	C(50)—O(50)	1.42
C(50)—O(51)	1.40	C(50)—O(52)	1.56
C(51)—O(53)	1.24	C(51)—O(54)	1.62
Angles			
N(10)-C(1)-C(2)	110.7 (5)	C(1)-C(2)-S(3)	108.4 (4)
C(2)-S(3)-S(4)	106.3 (2)	S(3)-S(4)-C(5)	105.0 (2)
S(4)-C(5)-C(6)	110.7 (4)	C(5)-C(6)-N(7)	114.3 (5)
C(6)-N(7)-C(8)	115.9 (5)	N(7)-C(8)-C(9)	103.3 (5)
C(8)-C(9)-N(10)	100.2 (4)	C(9)-N(10)-C(1)	109.0 (4)
C(2)-C(1)-N(7)	110.5 (5)	N(10)-C(1)-N(7)	103.9 (4)
C(1)-C(2)-C(21)	111.6 (6)	C(1)-C(2)-C(22)	112.5 (5)
S(3)-C(2)-C(21)	101.7 (4)	S(3)-C(2)-C(22)	110.5 (5)
C(21)-C(2)-C(22)	111.6 (5)	S(4)-C(5)-C(51)	110.8 (5)
S(4)-C(5)-C(52)	103.3 (5)	C(6)-C(5)-C(51)	108.3 (6)
C(6)-C(5)-C(52)	111.5 (5)	C(51)-C(5)-C(52)	112.1 (5)
C(1)-N(7)-C(6)	114.3 (4)	C(1)-N(7)-C(8)	108.5 (5)
C(1)-N(10)-C(11)	120.9 (4)	C(9)-N(10)-C(11)	126.3 (5)
N(10)-C(11)-C(12)	116.0 (5)	N(10)-C(11)-O(1)	122.9 (6)
O(1)-C(11)-C(12)	121.1 (6)	C(11)-C(12)-S(13)	107.5 (5)
C(12)-S(13)-C(14)	103.5 (3)	S(13)-C(14)-C(15)	113.0 (4)
S(13)-C(14)-C(23)	107.8 (4)	S(13)-C(14)-C(29)	103.2 (5)
C(15)-C(14)-C(23)	112.1 (6)	C(15)-C(14)-C(29)	107.2 (5)
C(23)-C(14)-C(29)	113.2 (4)	C(14)-C(15)-C(16)	117.3 (5)
C(14)-C(15)-C(20)	122.6 (6)	C(14)-C(23)-C(24)	119.2 (6)
C(14)-C(23)-C(28)	122.0 (5)	C(14)-C(29)-C(30)	118.7 (5)
C(14)-C(29)-C(34)	122.1 (6)		

Table 5. Bond lengths (Å) and bond angles (°) for $ReC_8H_{15}N_2O_2S_2$, **9**.

Lengths			
Re(1)—O(1)	1.681 (5)	Re(1)—S(1)	2.276 (2)
Re(1)—S(2)	2.262 (2)	Re(1)—N(1)	2.151 (4)
Re(1)—N(2)	1.997 (6)	S(1)—C(1)	1.850 (6)
C(1)—C(2)	1.516 (9)	C(2)—N(1)	1.502 (10)
N(1)—C(3)	1.502 (8)	C(3)—C(4)	1.498 (11)
C(4)—N(2)	1.485 (8)	N(2)—C(5)	1.364 (9)
C(5)—C(6)	1.486 (11)	C(6)—S(2)	1.833 (9)
C(1)—C(11)	1.526 (12)	C(1)—C(12)	1.540 (10)
C(5)—O(2)	1.237 (10)		
Angles			
O(1)-Re(1)-S(1)	110.6 (2)	O(1)-Re(1)-S(2)	108.8 (2)
O(1)-Re(1)-N(1)	108.9 (2)	O(1)-Re(1)-N(2)	112.4 (3)
S(1)-Re(1)-S(2)	89.4 (1)	S(1)-Re(1)-N(1)	82.2 (2)
S(1)-Re(1)-N(2)	136.6 (2)	S(2)-Re(1)-N(1)	141.9 (2)
S(2)-Re(1)-N(2)	82.6 (2)	N(1)-Re(1)-N(2)	78.6 (2)
Re(1)-S(1)-C(1)	100.8 (3)	Re(1)-S(2)-C(6)	99.8 (3)
Re(1)-N(1)-C(2)	117.1 (4)	Re(1)-N(1)-C(3)	110.9 (4)
Re(1)-N(2)-C(4)	117.0 (4)	Re(1)-N(2)-C(5)	124.0 (5)
S(1)-C(1)-C(2)	105.6 (4)	C(1)-C(2)-N(1)	110.8 (5)
C(2)-N(1)-C(3)	112.2 (5)	N(1)-C(3)-C(4)	108.5 (5)
C(3)-C(4)-N(2)	105.6 (6)	C(4)-N(2)-C(5)	119.0 (6)
N(2)-C(5)-C(6)	115.7 (7)	C(5)-C(6)-S(2)	111.6 (5)
S(1)-C(1)-C(11)	109.1 (5)	S(1)-C(1)-C(12)	109.9 (4)
C(2)-C(1)-C(11)	108.7 (5)	C(2)-C(1)-C(12)	112.2 (7)
C(11)-C(1)-C(12)	111.2 (6)	N(2)-C(5)-O(2)	122.9 (7)
C(6)-C(5)-O(2)	121.4 (6)		

Fig. 2. The structure of the rhenium complex oxo(1,1-dimethyl-1,8-dimercapto-3,6-diazaoctan-7-onato-N^3,N^6,S^1,S^8)rhenium(V), **9**, showing the atom numbering.

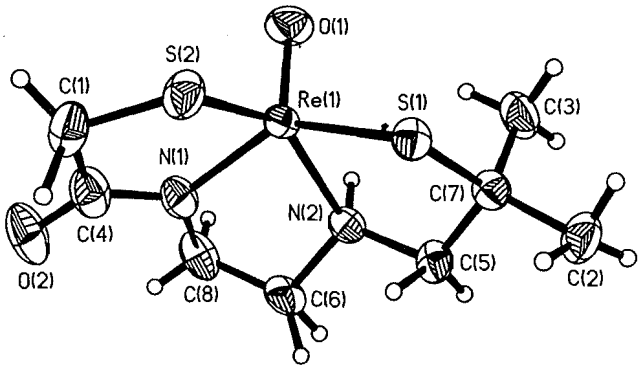

represents the first example of a rhenium asymmetric N2S2 complex that has been examined by X-ray crystallography. In addition to the X-ray structure determination, complex **9** was characterized by vibrational spectroscopy. The Re≡O stretching frequency dominated the Raman spectrum and occurred at 972 cm^{-1}. The IR spectrum showed a strong absorption ($\nu_{Re\equiv O}$) at 973 cm^{-1}. It also showed the amide C=O absorption at 1606. The Re≡O stretch was well within the range of several well-characterized Re(V) complexes that contain the $(Re\equiv O)^{3+}$ core (11).

The structure of **7** is shown in Fig. 1 and selected bond lengths and angles are given in Table 4. The molecule was bicyclic, comprising 5-membered and 7-membered rings fused together. All the bond distances and bond angles were within the expected range. The S(3)—S(4) disulphide bond was 2.006(4) Å, which is slightly shorter than the disulphide bond in 2,2,5,5-tetramethyl-3,4,13-trithia-7,10-diazabicyclo[8.3.0]tridecane 2.020(2) Å) (1). The C(2)-S(3)-S(4)-C(5) torsional angle was 84.3(2)°. The amido nitrogen atom, N(10), had a shorter bond to C(11), 1.355(9) Å, than those to C(1) and C(9), which were 1.484(8) and 1.476(6) Å, respectively. This was expected because of the considerable π character of the N(10)—C(11) bond. S(13)—C(14) was significantly longer than C(12)—S(13) (1.865(6) vs. 1.824(7) Å). For thiazolidine compounds, we noted previously that a C—S bond adjacent to a bulky group is longer than normal and the other C—S bond is shorter than normal. The same effect appears to be present here even though the sulphur atom is not part of a ring system.

The structure of **9** is shown in Fig. 2 and selected bond distances and bond angles are given in Table 5. The ligand atoms bound to the rhenium atom formed a rough square pyramid such that the rhenium atom lay 0.747(5) Å above the best S(1), N(1), N(2), S(2) plane. The Re=O bond (1.681 (5) Å) was longer than most distances observed for these five coordinate complexes. This was probably caused by the presence of multiple bond character in the bond from the rhenium atom to the deprotonated nitrogen atom. We have noted this effect before (13). Although Re—O_{oxo} bonds are typically written as double bonds, they are really triple bonds. The extra bonding is provided by donation of electron density from an oxygen atom *p* orbital to an empty *d* orbital on the rhenium atom. Chatt and Rowe noted that the resultant Re—O bond is essentially nonpolar (14), with the result that the

oxygen atom cannot be protonated and is susceptible to nucleophilic attack (15). In **9** the multiple bonding from the rhenium atom to the deprotonated nitrogen atom weakens the Re—O bond and makes it longer and more polar. The result is that the oxo atom can act as a hydrogen bond acceptor (e.g., oxo(1,1,8,8-tetraethyl-3,6-diazaoctane-1,8-dithiolato)-rhenium, N(H)...O_{oxo} distance, 2.877(4) Å, Re—O distance, 1.709(2) Å (16); oxo(1,9-dimercapto-1,1,9,9-tetramethyl-3,7-diazanonato-*S,S,N,N'*)rhenium(V), N(H)...O_{oxo} distance, 2.967(6) Å, Re—O distance 1.685(3) Å (13)). Compound **9** also showed hydrogen bonding, but in this case, the oxo ligand was not involved. The competitive hydrogen bonding between the amino nitrogen atom and the amido oxygen atom on the ligand backbone was, apparently, favoured. The two Re—N distances were significantly different. The Re(1)—N(2) distance was 1.997(6) Å compared to 2.151(4) Å for the Re(1)—N(1) distance. This was in accordance with the observation that N(2), the amido nitrogen atom, became deprotonated upon chelation to Re(1), whereas N(1), the amino nitrogen atom, couples to the rhenium atom only through its lone-pair electrons. All other bond lengths and angles were in the expected range.

For **7** all intermolecular interactions were van der Waals. Pairs of phenyl rings, related by inversion centres, were parallel but the overlap of the rings was minimal. Pairs of adjacent molecules of **7**, related by inversion centres, were connected by an extensive hydrogen bonding network that involved the methanol and water molecules and O(1). These interactions were isolated, however: there was no evidence of any hydrogen-bonded chain or network formation. For **9** all the intermolecular interactions were van der Waals except for the N(1)—H(1)...O(1)′ hydrogen bond between molecules related by the 2_1 axis. This resulted in hydrogen-bonded chains of molecules up and down the *b* direction.

Acknowledgements

We acknowledge, with thanks, financial support from the Natural Sciences and Engineering Research Council of Canada. We also thank the Libyan Secretariat for Scientific Research for the grant of a scholarship to H.A. We thank Dr. J.F. Britten and Dr. D.W. Hughes for help with the acquisition of the X-ray and NMR data, respectively.

References

1. H. Alarabi, R.A. Bell, R. Faggiani, H.E. Howard-Lock, C.J.L. Lock, and A.V. Kramer. Inorg. Chem. **34**, 1688 (1995).
2. A.V. Joshua, J.R. Scott, S.M. Smith, R.G. Ball, and W.J. Lown. J. Org. Chem. **52**, 2447 (1987).
3. H.F. Kung, M. Molar, J. Billings, R. Wicks, and M. Blau. J. Nucl. Med. **25**, 326 (1984).
4. T. Konno, J.R. Kirchhoff, M.J. Heeg, W.R. Heineman and E. Deutsch. J. Chem. Soc. Dalton Trans. 3069 (1992).
5. H.A. Staab. Angew. Chem. Int. Ed. Engl. **1**, 360 (1962).
6. L.M. Gustavson, T.N. Rao, D.S. Jones, A.R. Fritzberg, and A.R. Srinivasan. Tetrahedron Lett. **32**, 5485 (1991).
7. D. Brenner, A. Davison, J. Lister-James, and A.G. Jones. Inorg. Chem. **23**, 3793 (1984).
8. N.P. Johnson, C.J.L. Lock, and G. Wilkinson. J. Chem. Soc. 1054 (1964).
9. T.N. Rao, L.M. Gustavson, A. Srinivasan, S. Kasina, and A.R. Fritzberg. Nucl. Med. Biol. **19**, 889 (1992).
10. L.C. Francesconi, G. Graczyk, S. Wherli, S.N. Shaikh, D. McClinton, S. Liu, J. Zubieta, and H.F. Kung. Inorg. Chem. **32**, 3114 (1993).
11. T.W. Jackson, M. Kojima, and R.M. Lambrecht. Aust. J. Chem. **46**, 1093 (1993).
12. (*a*) R. Faggiani, H.E. Howard-Lock, C.J.L. Lock, and R. Orgias. Can. J. Chem. **69**, 1 (1991); (*b*) H.E. Howard-Lock, C.J.L. Lock, M.L. Martins, R. Faggiani, and M. Duarte. Can. J. Chem. **65**, 878 (1987); (*c*) H.E. Howard-Lock, C.J.L. Lock, and P.S. Smalley. Can. J. Chem. **63**, 2411 (1985).
13. C.J.L. Lock and Z. Wang. Acta Crystallogr. Sect. C. In press.
14. J. Chatt and G.A. Rowe. J. Chem. Soc. 4019 (1962).
15. W.D. Courier. Ph.D. Thesis, McMaster University, Hamilton, Canada (1971).
16. A. Najafi, M.M. Alauddin, A. Sosa, C.Q. Ma, D.C.P. Chen, A.L. Epstein, and M.E. Siegel. Nucl. Med. Biol. **19**, 205 (1991).
17. S. French and K. Wilson. Acta Crystallogr. Sect. A: Cryst. Phys. Diffr. Theor. Gen Crystallogr. **A34**, 517 (1978).

Estimation of the fines content of Athabasca oil sands using instrumental neutron activation analysis

Kingsley K. Donkor, Byron Kratochvil, and M. John M. Duke

Abstract: Knowledge of the "fines" or clay-rich mineral fraction is necessary for the efficient extraction of bitumen from bulk oil sands, and has environmental implications in tailings disposal. Current methods for estimating the fines in oil sand are laborious and of questionable accuracy. We propose here their estimation directly in bulk oil sand by instrumental neutron activation analysis (INAA) of the trace and major elements determinable. Correlations between fines content and individual elements fall in the range of 0.80 to 0.81 for dysprosium, samarium, and europium, and 0.75 to 0.77 for sodium, potassium, aluminum, and titanium. These results follow the expected geochemical relationships between major and trace elements and the mineral fraction of the oil sands. Principal component analysis (PCA) using a combination of elements gave correlations with fines content no better than those obtained from individual elements. However, the PCA approach can be considered more robust. Advantages of INAA over conventional methods to estimate the fines content of unprocessed oil sand include minimal sample preparation (including elimination of the use of organic solvents), rapid turnaround time, and the potential for automation.

Key words: instrumental neutron activation analysis, oil sand, elemental correlations, fines.

Résumé : Si l'on veut faire une extraction efficace du bitume à partir des sables bruts contenant de l'huile, il est important d'avoir une bonne connaissance des «fines» ou fraction minérale riche en argile; de plus, ces connaissances ont des implications dans la façon dont on dispose des résidus. Les méthodes courantes pour évaluer les fines sont très laborieuses et on peut se poser des questions sur leur précision. Dans ce travail, on propose de les évaluer directement dans les sables bruts contentant de l'huile en faisant appel à une analyse instrumentale par activation de neutrons (AIAN) des éléments que l'on peut déterminer comme éléments principaux ou à l'état de trace. Des corrélations entre les contenus des fines et les éléments individuels se situent entre 0,80 et 0,81 pour le dysprosium, le samarium et l'europium et 0,75 et 0,77 pour le sodium, le potassium, l'aluminium et le titane. Ces résultats sont en accord avec les relations géochimiques attendues entre les éléments principaux et ceux à l'état de trace et la fraction minérale des sables contenant de l'huile. L'analyse des composants principaux (ACP), utilisant une combinaison d'éléments, conduit à des corrélations entre le contenu des fines qui ne sont pas meilleures que celles obtenues pour des éléments individuels. Toutefois, l'approche ACP peut etre considérée comme plus sûre. Les avantages de l'AIAN par rapport aux méthodes conventionnelles pour l'évaluation des contenus en fines pour un sable non traité contenant de l'huile incluent la préparation minimale de l'échantillion (y compris l'élimination de l'utilisation de solvant organiques), le rapide temps de retour et le potentiel pour l'automation.

Mots clés : analyse instrumentale par activation de neutrons, sables contenant de l'huile, corrélations élémentaires, fines.

[Traduit par la rédaction]

Introduction

The oil sands of Alberta represent one of the world's largest known oil reserves. Total oil reserves are estimated to be over 800 billion barrels of crude oil of which approximately 80% occurs in the Athabasca region (1). The Athabasca oil sands are a mixture of solids, bitumen, and water. The bulk of the solids is composed of sand-sized particles (mostly quartz), variable amounts of fines, and traces of heavy minerals. Fines are defined as mineral matter passing through a 325 U.S. (<44 μm) mesh sieve, and may be further subdivided into silt-sized (<44 μm >2 μm) and clay-sized (<2 μm) particles. Mineralogically the silt-sized fines of the Athabasca oil sands consist primarily of quartz and minor feldspar. The clay-sized fraction comprises minerals including illite and kaolinite (1).

Fines are detrimental to the hot-water processing of the oil sand, and to the disposal of the tailings stream, in that they stay suspended in the water phase. In the hot-water process these suspensions can form a barrier that prevents separation of bitumen. Breaking this barrier requires additional water and greater agitation.[3] With prior knowledge of the bitumen and fines levels of the incoming feed, plant processes can be opti-

Received June 16, 1995.[1]

K.K. Donkor and B. Kratochvil.[2] Department of Chemistry, University of Alberta, Edmonton, AB T6G 2N8, Canada.
M.J.M. Duke. SLOWPOKE Nuclear Reactor Facility, University of Alberta, Edmonton, AB T6G 2N8, Canada.

[1] Revision received January 5, 1996.
[2] Author to whom correspondence may be addressed. Telephone: (403) 492-4665. Fax: (403) 492-8231. E-mail: Ron.Kratochvil@UAlberta.Ca

[3] G.R. Thompson. Personal communications.

mized and bitumen yields optimized. To determine processing requirements, oil sand companies carry out extensive coring programs in which cores are collected, sampled, and subsequently analyzed for bitumen and solids content. The analytical method most used for estimating the fines content has been particle size analysis with a Microtrac analyzer (2). This method involves prior removal of bitumen with organic solvents, is applicable over only a limited particle-size range, and cannot accurately measure nonspherical particles. The latter drawback may lead to a bias in the estimation of fines content.

Since the fines in the Alberta oil sands are predominantly clay minerals and silt-sized quartz we decided to investigate the possibility of developing an elemental "fingerprint" for their estimation. Quartz usually contains few impurities, therefore elements not present in the bitumen, pore water, or trace heavy minerals are likely to be associated with the clays. Of particular interest in this regard are the rare earth elements (REE). Numerous studies on the distribution and abundances of the REE in sedimentary rocks have been carried out and the salient conclusions summarized (3). Findings relevant to this study include the following: (*a*) the bulk of the REE in clastic sedimentary rocks are found in the clay (< 2 μm) and silt-sized fractions; (*b*) the silt-sized fraction of clastic sedimentary rocks tends to have lower total REE contents than the clay-sized fraction though the relative abundances between the two are similar; (*c*) the sand-sized fraction of clastic sedimentary rocks tends to have a lower total REE content than either the silt- or clay-sized fractions (on account of the extremely low REE levels in quartz, and fairly low REE levels in feldspars); (*d*) there is no correlation between REE content and clay mineralogy. These findings suggest that elemental analysis (especially one including the REE) might be developed as an indicator of the fines content of bulk oil sand.

For the elemental analyses, instrumental neutron activation analysis (INAA) (4–6) was chosen on account of its multielemental capability, speed, and ease of sample preparation. Using INAA, the concentrations of 11 elements could be readily determined following irradiation in a SLOWPOKE reactor via their short-lived radionuclides in samples of bulk oil sand.

Reported here is a study of the distribution of these elements over a 20 m length of oil sand core, along with an evaluation of the degree of correlation between their concentrations and the levels of fines present in the bulk oil sand.

Experimental

Samples and sample preparation

The oil sand core used in this study was provided by Syncrude Canada Ltd. from a region of the Athabasca oil sand deposit mined by Syncrude near Fort McMurray, Alberta. The core was approximately 20 m long and 7 cm in diameter, and was encased in 4 mm thick polyvinyl chloride. The section of the oil sands deposit transected by the core varied in grade from 1% to 15% bitumen by weight.

To obtain samples across a range of bitumen concentrations the core was visually stratified into regions defined as lean, medium, or rich in bitumen content. Eight test portions of oil sand, each weighing approximately 0.5 g, were selected from random locations in each of the three regions. The samples were placed directly into clean, 1.5 mL polyethylene irradiation vials that had been previously soaked in 10% nitric acid for several days, and rinsed thoroughly with deionized water and then with nanopure water to remove surface impurities. Each 1.5 mL vial was heat-sealed and inserted into a clean 7 mL polyethylene vial together with an additional empty 1.5 mL vial that served as a spacer. The 7 mL polyethylene vials were then heat-sealed and capped.

An additional 24 test portions, each weighing 2–3 g, were taken from locations immediately adjacent to the regions of the core from which the 0.5 g samples were obtained. These larger samples were subjected to Soxhlet extraction with 15–20 mL of toluene to separate the bitumen from the solids (7). The toluene extracts were centrifuged using a small bench-top centrifuge to remove most of the particulate material that passed through the filter thimble, then were quantitatively transferred to weighing dishes, and the toluene was evaporated overnight in a fumehood at room temperature. The dishes were reweighed and the amount of bitumen in the original samples calculated from the difference in the weights of the dishes before and after evaporation. Data processing was carried out on 23 samples, one from the bitumen-rich strata having been lost during the extraction process.

The solids remaining in the Soxhlet extraction thimbles were removed, weighed, and dry-sieved through a 325 mesh (44 μm) stainless steel sieve to separate the fines. Test portions of fines from each of the 23 sieved fractions were weighed into 1.5 mL nitric acid-washed polyethylene vials and prepared for analysis in the same manner as the 0.5 g bulk oil sand test portions.

Given that adjacent samples were collected for INAA and Soxhlet extraction, it became necessary to determine the local elemental variability of the oil sand. For this purpose nine transverse sections of core, representing a range of bitumen levels, were selected. Four subsamples of approximately 10 g each were collected with a scoop from each transverse section, weighed into acid-washed 7 mL irradiation vials, and sealed as described earlier for INAA. Following INAA, the portions were left for a week to decay, at which time they posed no radiation hazard. The decayed samples were then analyzed for their bitumen and solids content by Soxhlet extraction using 2.5–5.0 g portions as described earlier. Because of possible concerns about the representativeness of 0.5 g or even 10 g test portions, an additional experiment was done in which a 30 g test portion of oil sand was collected from a site adjacent to each of the nine locations sampled previously and also analyzed as above.

Three soil reference materials, SO-1, SO-2, and SO-3 (CANMET, Ottawa, Canada), were used as standards for quantification of all elements studied except chlorine. A fourth, SO-4, was run as a quality control sample. Three sediment reference materials, BCSS-1, MESS-1, and PACS-1 (National Research Council of Canada, Ottawa, Canada), were also analyzed, the former as a chlorine standard and the latter two for quality control purposes. Three sets of these standards were prepared, one weighed and sealed in 1.5 mL vials as for the 0.5 g samples, the second prepared in 7 mL irradiation vials as for the 10 g samples, and the third in 27 mL vials as for the 30 g samples.

INAA of elements that produce short-lived radionuclides

All irradiation and counting operations were performed at the

Table 1. Concentrations of elements (microgram per gram, unless otherwise stated) measured by INAA for 23 approximately 0.5 g portions of bulk oil sand.

Sample no.	Wt% bitumen	Wt.% fines	Al (%)	K (%)	V	Dy	Sm	Ti	Ba	Na	Cl	Mn	Eu
1	6.4	18.4	2.34	0.57	35	2.9	3.7	1990	183	870	321	52	0.68
2	4.4	32.2	3.73	0.73	49	4.9	5.3	4230	207	1180	306	71	0.99
3	4.0	20.2	2.85	0.54	37	3.1	4.3	3110	182	980	354	57	0.66
4	4.0	27.4	2.15	0.63	33	2.5	3.3	2580	185	1010	250	68	0.53
5	10.3	9.6	1.30	0.28	29	1.3	2.4	1740	121	420	295	36	0.31
6	9.6	13.7	1.54	0.38	28	1.4	1.6	1850	134	550	262	53	0.35
7	5.8	29.1	2.06	0.45	33	2.0	2.5	1680	139	740	382	102	0.50
8	7.7	21.7	1.99	0.50	36	2.0	2.8	2700	170	750	358	269	0.40
9	9.3	15.0	1.35	0.33	30	1.7	1.9	1970	125	370	125	39	0.35
10	7.7	19.4	2.05	0.45	35	1.9	2.4	2340	194	840	423	93	0.46
11	4.1	28.8	3.19	0.80	47	3.7	5.4	3980	199	1230	309	235	0.78
12	3.3	36.5	3.12	0.64	56	3.7	5.8	3700	219	1440	491	227	0.80
13	0.9	47.7	7.29	0.88	90	4.3	7.1	4620	233	1600	539	121	0.83
14	3.4	34.2	2.48	0.54	32	2.5	3.0	1800	168	780	132	59	0.53
15	6.5	30.7	1.55	0.52	41	3.1	3.2	2460	186	800	122	47	0.64
16	5.8	26.1	2.64	0.52	34	2.3	3.6	2550	170	820	135	68	0.55
17	5.8	29.7	2.93	0.61	41	3.1	3.0	2240	177	950	215	62	0.68
18	4.4	27.8	4.16	0.59	51	3.2	3.8	3380	191	1020	184	131	0.71
19	7.4	28.9	1.43	0.36	28	2.0	2.7	2200	136	390	523	36	0.45
20	8.0	25.4	0.85	0.26	27	1.9	2.7	2040	126	250	118	25	0.44
21	12.2	10.9	0.64	0.24	32	0.6	0.9	630	125	240	640	12	0.16
22	14.1	10.6	0.59	0.20	31	0.6	1.1	820	113	180	447	9	0.17
23	13.1	7.4	0.59	0.40	30	0.5	1.1	750	163	340	218	16	0.20

University of Alberta SLOWPOKE-II Nuclear Reactor Facility. For the 0.5 g analyses, standards and unknowns were individually irradiated for 5 min at a thermal neutron flux of 1×10^{12} n cm^{-2} s^{-1}. Following a variable but timed decay period (ca. 20 min) each test portion was counted for 5 min (live-time) at a sample-to-detector distance of 6 cm. The 10 g test portions used in the lateral heterogeneity study were irradiated for 3 min at a thermal neutron flux of 1×10^{10} n cm^{-2} s^{-1}, allowed to decay for 15 min, then counted for 5 min (live-time) at a sample-to-detector distance of 6 cm to obtain data for Mn, K, Na, Dy, Eu, V, Al, Ti, Sm, Cl, and Br. The 30 g samples were irradiated in the outer site of the reactor for 5 min at a reduced thermal neutron flux of 5×10^9 n cm^{-2} s^{-1}, allowed to decay for 15 min, then counted for 5 min (live-time) at a sample-to-detector distance of 10 cm to obtain data for V, Al, and Ti. All samples were recounted for 10 min (live-time) at a sample-to-detector distance of 6 cm after a total of 120 min to obtain data for the elements listed above, with the exceptions of Sm and Cl. For Sm the amounts were below detection for several samples and near the limit of detection for the others: for Cl a 30 g standard was not run because earlier measurements on smaller samples had shown that concentrations did not vary with the fines content.

The γ-spectroscopy counting system included an automatic sample-changer mechanism modified from a Nuclear Chicago γ-ray counter interfaced to a PC with an Aptec MCA card for data acquisition. A vertical, closed-end, hyperpure (p-type) coaxial Ge detector (model 18180, EG & G Ortec, Oak Ridge, Tennessee, U.S.A.) operated at +2500 V was utilized for all γ spectroscopy. Detector specifications included a relative efficiency of 19.7%, a measured full width half maximum of 1.91 keV, and a peak-to-Compton ratio of 58:1 for the 1332 keV full energy peak of ^{60}Co. Signals from the Ge detector were amplified using an Aptec 6300 spectroscopy amplifier and the signals digitized by a Nuclear Data (ND) 575 ADC.

Spectral peak searching was accomplished using the software program SPAN (8). Spectrometer dead times were maintained at less than 10% for each sample. Decay corrections, dead-time corrections (9), and quantification of elements were performed using in-house programs along with two spreadsheet programs: Quattro Pro (V4.0; Borland Inc., U.S.A.) and Excel (V4.0; Microsoft Corp., U.S.A.). Concentrations of all elements were determined via an adaptation of the comparator (semi-absolute) method of INAA (10). Reference standards SO-1, SO-2, SO-3, and BCSS-I were used to determine specific activities (counts/microgram) for each element. The accuracy of the procedure was checked by analyzing the reference materials SO-4, MESS-1, and PACS-1. Measured and certified values were in good agreement for all three reference materials (11).

Results and discussion

Correlations of elemental data in oil sand and fines content

Eleven elements (Al, K, Na, Ti, Mn, Cl, Dy, Sm, Eu, Ba, and V) were determined with reasonable precision in the 23 0.5 g oil sand test portions using the analysis scheme described above. Table 1 lists the results of the INAA determinations of these elements, along with the values found for bitumen and fines by Soxhlet extraction and sieving. Correlation coeffi-

Table 2. Correlation coefficients of elemental concentrations versus weight percent *fines* in oil sand for 23 0.5 g test portions ranging from 5 to 50 wt.% fines.

Element	*r*-Value (fines)
Dysprosium (Dy)	0.81
Europium (Eu)	0.80
Samarium (Sm)	0.80
Aluminium (Al)	0.77
Sodium (Na)	0.77
Potassium (K)	0.76
Titanium (Ti)	0.75
Vanadium (V)	0.72
Barium (Ba)	0.69
Manganese (Mn)	0.44
Chlorine (Cl)	0.00

cients between the elemental concentrations and the fines content in the oil sand are listed in Table 2. With the exception of chlorine, all elements correlate positively with fines content, yielding *r*-values ranging from 0.69 to 0.81. Chlorine concentrations showed little or no correlation with fines content. This random distribution may be due (at least in part) to the occurrence of variable amounts of dissolved chloride salts in pockets of water trapped within the interstices of the sand particles.[3] Also, the Cl concentrations in bitumen average about 200 μg/g (11) compared with about 300 μg/g in the bulk solids. The correlation scatter plots for four elements (Dy, Sm, Eu, and Cl) are shown in Fig. 1. The scatter plots for dysprosium, europium, and samarium yield good correlations (*r*-value = 0.80) and can be used as models for measuring the fines content in oil sand. Using the uncertainty in the slopes of the plots and propagation of errors, the relative uncertainty for fines estimation is of the order of 10%.

A major reason why correlation between the REE and the fines is not even greater is likely to be due to passage of small clay particles through the Soxhlet extraction thimbles into the bitumen and to losses during dry sieving of the solids. In addition, the fraction of the fines composed of clays varies from sample to sample. The remainder of the fines is composed largely of quartz, which will tend to dilute the elemental signature from the clay-sized fraction. Furthermore, the Athabasca oil sands contain variable trace amounts of over 20 heavy minerals (12), the majority of which are iron-rich and REE-poor. However, some of them, such as zircon, apatite, and epidote, may contain fairly high levels of REE that could introduce additional variability in correlation. INAA of the bitumen extracts also showed dysprosium, samarium, europium, aluminium, sodium, and potassium contents to be very low and in some cases below detection limits (11).

Principal Component Analysis (PCA) (VM SAS V.120.1091 statistical package) was used to calculate correlations involving combinations of the elements determined in the 0.5 g oil sand samples with the fines content for the various test portions. Figure 2 shows correlation plots of fines content against combinations of (*a*) all the elements analyzed, (*b*) dysprosium, samarium, and europium. The PCA combination of Dy, Sm, Eu, Al, K, and Na, elements commonly associated with clay minerals, gave an *r*-value of 0.80. The correlations obtained were comparable to those of the individual elements. A possible advantage of using the PCA method for combining elements is that it tends to be more robust than correlation based on a single element in the event of analytical error in the determination of a single element.

Cross correlation of element concentrations in the 0.5 g oil sand samples showed strong positive correlations among the lanthanides (Dy, Sm, and Eu) and between Na and K. This is illustrated in Fig. 3 for Dy vs. Eu and Na vs. K. The correlations seen here among the lanthanides are similar to those found in other geological materials such as shales (4, 13–15). Since these elements correlate strongly among themselves in a variety of sedimentary materials, it is not surprising that multiple correlations by PCA do not give improved fits.

Oil sand regions with high bitumen content tend to contain less of those elements commonly associated with clay minerals, as shown in the inverse correlation of the fines with bitumen content in Fig. 4. An inverse relationship between bitumen content and clays is expected because increased clay content would reduce sediment permeability, thereby impeding bitumen infiltration. The correlation of vanadium with bitumen content differs from the other elements in that it levels off above 8% bitumen (Fig. 5). INAA of extracted bitumen shows a vanadium content of about 200 μg/g, while the fines contain about 30 μg/g (11). Vanadium in bitumen, like nickel, has been shown to be chemically bound in heterocyclic ring structures (16).

Evaluation of lateral heterogeneity in the oil sand core

Figure 6 shows the relative standard deviations of the selected elements determined for a set of four subsamples within each of the nine transverse sections studied. It can be seen that for all test portions from the nine regions, the relative standard deviations (RSDs) of the values for vanadium are less than 10%, those for dysprosium, barium, titanium, and aluminum are less than 17%, and for potassium, samarium, and europium are less than 20%. Also, except for one value for manganese of 26% and one for sodium of 27%, the RSDs for these two elements are less than 20%. On the other hand, chlorine shows significant scatter, with RSDs ranging from 10% to 60%. Since the majority of the elements studied had RSDs less than 20%, the core section was considered sufficiently homogenous in terms of the measured elements for the purpose of this study.

Results of the Soxhlet extraction analyses for bitumen and solids yielded RSD values ranging from 1% to 6% for bitumen, and less than 2% for solids (Table 3). These values also showed little lateral variability across the core for the nine zones studied, and indicate that a single 5 g sample adequately represents the transverse section of the core in terms of bitumen and solids content.

Correlations between element concentrations and fines content for the 30 g samples were also calculated for eight elements. The results of the correlations were compared with similar calculations for the 0.5 and 10 g samples. The results, Table 4, show no significant differences among the correlations for the eight elements listed. Test portion size does not appear, therefore, to affect the correlation results over this sample size range, and the results indicate that 0.5 g test portions were adequately representative for this study.

Fig. 1. Correlation plots for (*a*) dysprosium, (*b*) samarium, (*c*) europium, (*d*) chlorine concentrations versus fines content for 0.5 g portions of bulk oil sand.

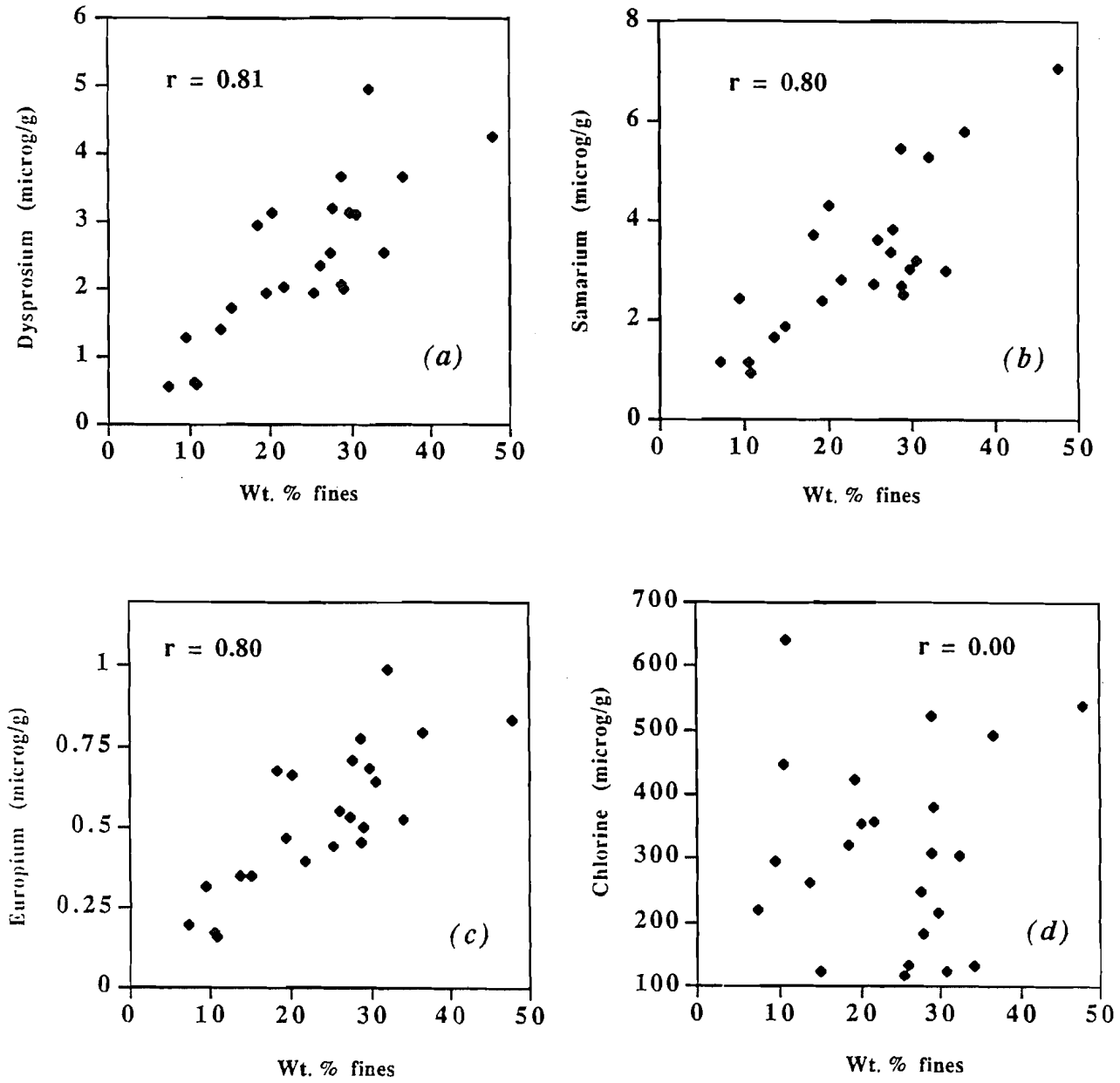

In summary, correlations between fines content, defined as oil sand solids passing a 44 μm sieve, and the concentrations of several elements in the solids are sufficiently strong to warrant further study of elemental analysis as a way of measuring fines in bulk oil sand. Such studies, including comparisons with alternative methods, are currently underway. INAA appears to provide a straightforward way of determining a number of elements for this purpose.

Conclusions

Several elements, determined via their short-lived radionuclides by INAA, correlate well with the fines content of Athabasca oil sand as determined by toluene extraction and sieving of the resulting solids. Multielement correlations by principal component analysis gave about the same values as those obtained for individual elements, but may be more robust. Elemental and bitumen analyses of test portions collected across a test core in sizes ranging from 0.5 to 30 g showed little lateral heterogeneity over the 7 cm width of the core. INAA was chosen as the analytical method because analyses could be done nondestructively on samples without pretreatment and with rapid turnaround times. Manpower requirements are small and could be reduced even further by automation of the counting and reporting operations. Correlation between fines content and elemental concentrations will likely be improved as better methods of fines measurements are developed.

Fig. 2. Combinations of element concentrations correlated by PCA with fines content: (*a*) combination of Dy, Al, Eu, Sm, Ti, K, Na, V, Ba, Cl, and Mn; (*b*) combination of Dy, Eu, and Sm.

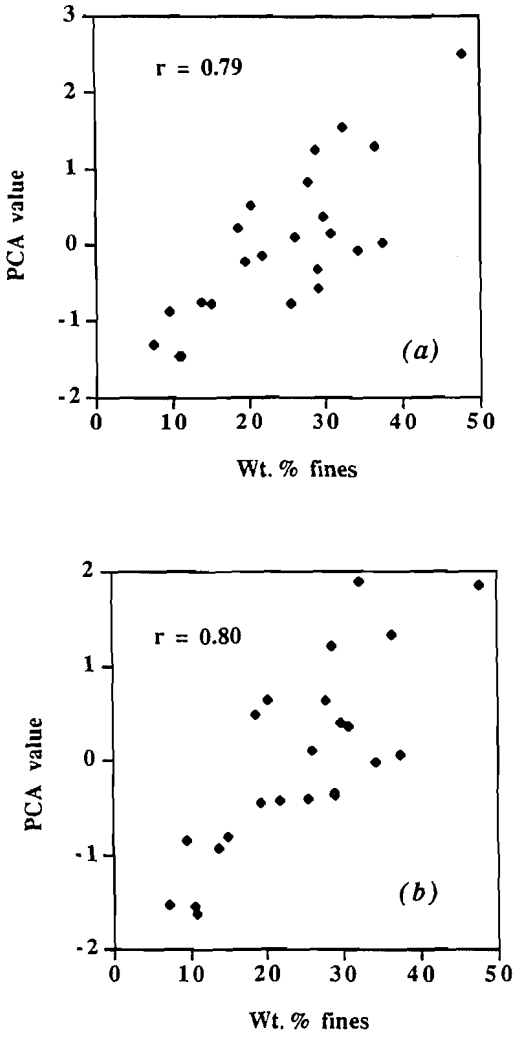

Fig. 3. Cross-correlation plots for (*a*) Eu versus Dy and (*b*) Na versus K concentrations for 0.5 g portions of bulk oil sand.

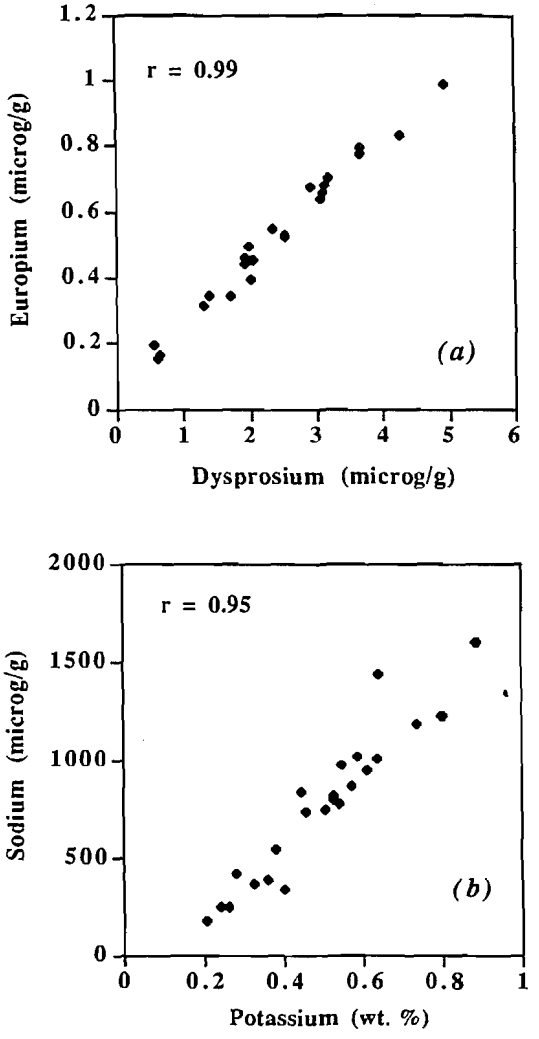

Table 3. Relative standard deviations of weight percent bitumen and solids for nine transverse sections of oil sand core, as determined by Soxhlet extraction. Each value is the % RSD of four samples within a transverse section.

Transverse section	% RSD for bitumen	% RSD for solids
1	4.6	0.3
2	5.3	0.3
3	5.8	1.2
4	5.0	0.4
5	3.5	0.5
6	1.5	0.2
7	2.9	0.3
8	3.1	1.8
9	1.7	0.4

Table 4. Correlations between concentrations of elements that produce short-lived radionuclides and weight percent *fines* for 0.5, 10, and 30 g test portions of bulk oil sand (n = 9).

Elements	r (0.5 g)	r (10 g)	r (30 g)
Aluminum	0.77	0.88	0.92
Barium	0.91	0.76	0.93
Dysprosium	0.89	0.89	0.89
Europium	0.91	0.84	0.88
Manganese	0.70	0.66	0.71
Potassium	0.86	0.90	0.91
Sodium	0.85	0.84	0.91
Titanium	0.87	0.87	0.73
Vanadium	0.79	0.68	0.81

Fig. 4. Relationship of fines to bitumen content for 23 0.5 g test portions of bulk oil sand.

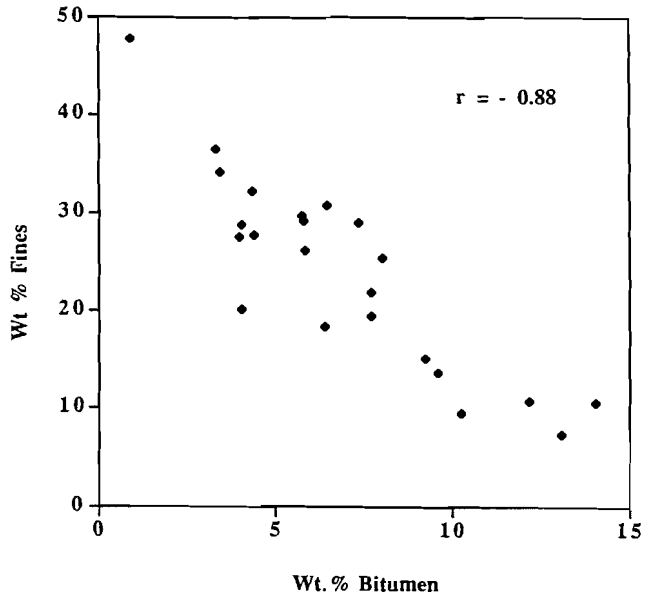

Fig. 5. Relationship between vanadium concentrations and bitumen content for 0.5, 10, and 30 g test portions of bulk oil sand (square: 0.5 g, diamond: 10 g, cross: 30 g).

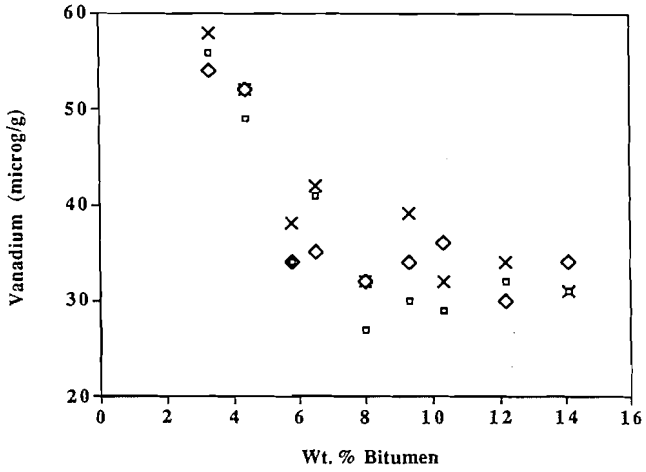

Fig. 6. Relative Standard Deviations (RSD) of concentrations of 11 elements over 9 transverse sections of oil sand core. (Each bar represents the percent RSD value for a set of four samples within a single transverse section.)

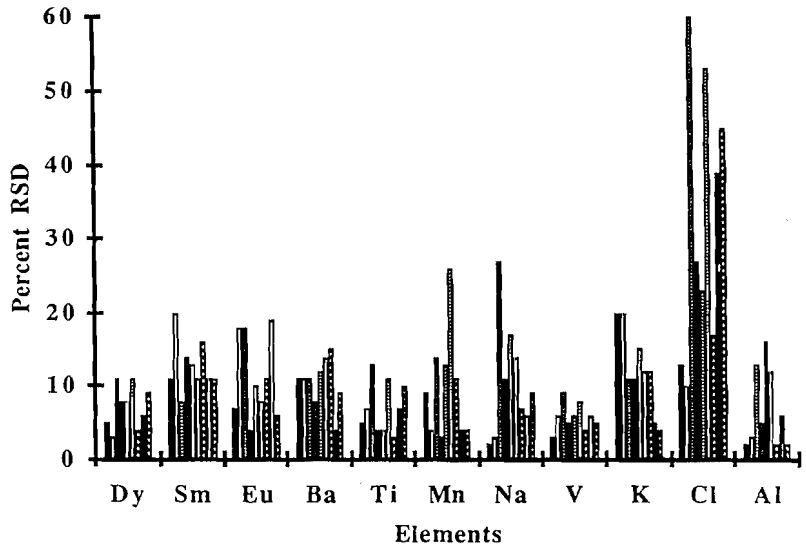

Acknowledgements

The authors thank Syncrude Canada Ltd. for providing the oil sand core used in this study, and Dr. Rob Schutte and Gordon R. Thompson, Syncrude Research Department, Edmonton, for numerous helpful discussions. Financial assistance was provided by the Department of Chemistry, University of Alberta, and the Natural Sciences and Engineering Research Council of Canada.

References

1. L.G. Hepler and C. Hsi (*Editors*). AOSTRA technical handbook on oil sands, bitumens and heavy oils, no. 6. AOSTRA, Edmonton, Canada. 1989.
2. J.T. Bulmer and J. Starr (*Editors*). Syncrude analytical methods for oil sand and bitumen processing. AOSTRA, Edmonton, Canada. 1979.
3. S.R. Taylor and S.M. McLennan, The continental crust: its composition and evolution. Blackwell, Oxford. 1985.

4. D. DeSoete, R. Gibjels, and J. Hoste. Neutron activation analysis. Wiley, London. 1972.
5. G. Erdtmann and H. Petri. Nuclear activation analysis: fundamentals and techniques. *In* Treatise on analytical chemistry. Pt. 1. Vol. 14. *Edited by* P.J. Elving. Wiley, New York. 1986.
6. S.J. Parry. Activation spectrometry in chemical analysis. Wiley, New York. 1991.
7. R.C. Shaw and B. Kratochvil. Anal. Chem. **62**, 167 (1990).
8. L. Wang. Nucl. Electron. Detect. Technol. (China) (He Dianzixue Yu Tance Jishu), **6**, 356 (1986).
9. T. Takeuchi, S. Uehara, and T. Hayashi. J. Radionanal. Chem. **56**, 25 (1980).
10. C. Bergerioux, G. Kennedy, and L. Zikovsky. J. Radionanal. Chem. **50**, 229 (1979).
11. K.K. Donkor, Ph.D. Thesis, Department of Chemistry, University of Alberta, Edmonton. 1995.
12. J.A. Bichard. Oil sands composition and behaviour research. AOSTRA, Edmonton, Canada. 1987.
13. P. Henderson. Developments in geochemistry, no. 2. Rare earth element geochemistry. Elsevier, New York. 1984.
14. L.A. Haskin, T.R. Wildeman, F.A. Frey, K.A. Collins, C.R. Keedy, and M.A. Haskin. J. of Geophys. Res. **71**, 6091 (1966).
15. W.B. Nance and S.R. Taylor. Geochim. Cosmochim. Acta, **40**, 1539 (1976).
16. R.H. Filby and D. Strong. Vanadyl porphyrin distribution in the Alberta oil-sand bitumens. *In* Metal complexes in fossil fuels. *Edited by* R.H. Filby and J.F. Branthaver. American Chemical Society, Washington D.C. 1987.

Structure and wavelength modification in retinylidene iminium salts

George R. Elia, Ronald F. Childs, James F. Britten, Daniel S.C. Yang, and Bernard D. Santarsiero

Abstract: The spectroscopic and structural properties of the perchlorate and triflate salts of *N*-*n*-butyl-retinylidene imine, **2** and **3**, have been examined in solution and solid phases. In solution these salts were found to exhibit very similar UV and NMR spectroscopic properties. However, in the solid state marked differences in their absorption spectra (**2**, λ_{max} = 504 nm; **3**, λ_{max} = 445 nm) and ^{13}C NMR spectra were found. The structures of the two salts were determined by X-ray crystallography. The cations in each of the salts were shown to have very similar conformations, detailed structures, and packing in their crystal lattices. The differences in the spectroscopic properties of the salts in the solid state could not be accounted for on the basis of any structural differences in the cations themselves. In terms of cation–anion interactions, a strong hydrogen bonding interaction was found in each case between the N-H proton and an oxygen atom of the counterion. However, there were significant differences between the two salts in terms of the N—H···O internuclear distances (**2**, N—H···O = 2.939(7) Å and in **3**, 2.85(1) Å). The results are strongly suggestive that the wavelength and positive charge delocalization in retinylidene iminium salts are controlled by variation of the distance between the anion and the proton bonded to the Schiff base nitrogen atom. The work reported here represents the first examples of secondary retinylidene iminium salts containing an N-alkyl substituent to be successfully analyzed by X-ray crystallography. The relationship of these observations in the solid state to the spectroscopic properties of the natural visual pigments is explored.

Key words: retinylidene iminium salts, iminium salts, cation–anion interactions.

Résumé : On a étudié les propriétés spectroscopiques et structurales des perchlorate et triflate de la *N*-*n*-butyl-rétinylidène imine, **2** et **3**, tant en solution qu'en phase solide. En solution, on a trouvé que ces sels présentent des propriétés spectroscopiques UV et RMN qui sont très semblables. Toutefois, à l'état solide, on a observé des différences marquées dans leurs spectres d'absorption (**2**, λ_{max} = 504 nm; **3**, λ_{max} = 445 nm) et dans leurs spectres RMN du ^{13}C. On a déterminé les structures des deux sels par diffraction des rayons X. Dans chacun de ces sels, les cations ont des conformations, des structures détaillées et des empilements très semblables. On ne peut pas expliquer les différences observées dans les propriétés spectroscopiques des sels à l'état solide sur la base de différences de structures dans les cations eux-mêmes. En termes d'interactions cation–anion, on a observé une forte interaction de liaison hydrogène entre le proton N-H et l'atome d'oxygène du contre-ion. Toutefois, il existe des différences importantes entre les deux sels en termes de distances internucléaires (**2**, N—H···O = 2,939(7) Å et dans **3**, 2,85(1) Å. Les résultats suggèrent fortement que la longueur d'onde et la délocalisation de la charge positive dans les sels rétinylidène iminium est contrôlée par une variation de la distance entre l'anion et le proton relié à l'atome d'azote de la base de Schiff. Le présent travail représente les premiers exemples des sels rétinylidène iminium secondaires contenant un substituant N-alkyle à avoir été examinés par diffraction des rayons X. On examine la relation de ces observations à l'état solide avec les propriétés spectroscopiques des pigments visuels naturels.

Mots clés : sels rétinylidène iminium, sels d'iminium, interactions cation–anion.

[Traduit par la rédaction]

Introduction

Over the past two decades there has been considerable interest in the natural pigments rhodopsin (1) and bacteriorhodopsin (2). The protein rhodopsin (R) consists of the 11-*cis* isomer of retinal covalently linked via a protonated Schiff base linkage to an apoprotein opsin consisting of 348 amino acids. In contrast, bacteriorhodopsin (bR) comprises all-*trans* retinal connected via a similar linkage to a lysine residue of a protein consisting of 248 amino acids (3).

Much attention has been given to seeking an understanding of the origin of the absorption spectra of these two pigments. A simple retinylidene Schiff base absorbs at 370 nm while its protonated counterpart exhibits a red-shifted absorption band at 440 nm (methanol) (4). In comparison, the natural pigments have absorption maxima at 506 nm for bovine rhodopsin and 570 nm for bacteriorhodopsin (5, 6). Thus, while protonation accounts for some of the bathochromic shift there are additional factors at play in the natural pigments.

There have been a number of studies addressing the mech-

Received November 7, 1995.

G.R. Elia, R.F. Childs,[1] and J.F. Britten. Department of Chemistry, McMaster University, Hamilton, ON L8S 4M1, Canada.
D.S.C. Yang. Department of Biochemistry, McMaster University, Hamilton, ON L8S 4M1, Canada.
B.D. Santarsiero. Molecular Structure Corporation, The Woodlands, TX 77381-4238, U.S.A.

[1] Author to whom correspondence may be addressed. Telephone: (905) 525-9140, ext. 27270. Fax: (905) 521-1993. E-mail: rchilds@mcmail.cis.mcmaster.ca

anism by which the apoprotein can regulate the electronic properties of the chromophore. Cation–anion interactions have been suggested to be an important determinant in wavelength regulation. Blatz et al. showed that there was a linear relationship between the reciprocal of the square of the anion radius and the energy difference between the ground and the first excited states of a retinylidene salt (4). This correlation was then used to calculate the position of the absorption maximum as a function of the internuclear distance between the protonated Schiff base nitrogen atom and the counterion. However, the center to center distances calculated by Blatz have been criticized as being far too large to be present in a stable pigment (7).

On the basis of theoretical calculations performed on a protonated Schiff base of 11-*cis* retinal, Honig et al. suggested that a favourable chromophore–protein interaction is not only one in which the protonated Schiff base nitrogen atom is closely associated with a counterion but where an additional negative charge or polar group is positioned at the cyclohexenyl end of retinal (7). In principle, a charge located near the β-ionone ring could stabilize the excited state, resulting in a spectroscopic red shift. Studies on the dihydroretinals reported by Nakanishi, Honig, and co-workers were used to show that a negative charge could be located in the vicinity of the C5,C6 bond (8–10) and a positive charge near C7 (11). Solid state ^{13}C NMR experiments by Harbison et al. confirmed these results (12).

The conformation adopted by the C6,C7 bond of the retinal chromophore is also an important factor in wavelength regulation of retinylidene iminium salts (13). Solid state ^{13}C NMR studies of bR have been used to suggest that bR has a 6-s-*trans* conformation (12,13). Previous work in this group using a combination of solid state UV and ^{13}C NMR spectroscopic techniques suggested that the 6-s-*trans* conformation about the C6,C7 bond in a retinylidene iminium salt is associated with a large red shift in its corresponding absorption maximum (14).

Recent solution work by Sheves and co-workers has shown that a red shift in the absorbance spectrum of retinylidene iminium salts is accompanied by downfield ^{13}C NMR chemical shifts of the odd-numbered polyene carbons of the unsaturated chain (15). It was suggested that weakening of the Schiff base – counterion interaction causes a significant enhancement in π-electron delocalization along the polyene chain, leading to the observed spectroscopic properties.

Despite the considerable amount of attention focused on the spectral properties of retinylidene iminium salts, considerable uncertainty still exists with respect to the structure of these chromophores, the relative placement of other charged groups, and the relationship of their structure with their charge delocalization and electronic properties. In this study, a series of retinylidene iminium salts **1–4** were synthesized and characterized both in solution and the solid state. A unique combination of X-ray crystallography, solid state ^{13}C NMR, FTIR, and UV spectroscopic techniques have been used in an integrated manner to address the mechanisms by which the electronic properties of the retinal chromophore can be modified by its environment and, particularly, by the placement of counterions.

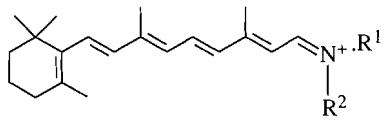

1, R^1 = *n*-Butyl, R^2 = H, X = $CF_3SO_3^-$
2, R^1 = *tert*-Butyl, R^2 = H, X = ClO_4^-
3, R^1 = *tert*-Butyl, R^2 = H, X = $CF_3SO_3^-$
4, R^1 = Phenyl, R^2 = Me, X = ClO_4^-

Table 1. Initial isomeric composition[a,b] of **1–4**.

	Isomer percentage		
Compound	All-*trans*	15-*cis*	13-*cis*
1	97.4	nd[c]	2.6
2	96.8	nd	3.2
3	98.8	nd	1.2
4[d]	95.5	4.5	nd

[a]Assayed by ^1H NMR, CH_2Cl_2, solvent, 22°C.
[b]Errors are ±5%.
[c]Not detected.
[d]Acquired at −60°C.

Results

The iminium salts **1–3** were synthesized using a modified procedure of Blatz et al. (4) while salt **4** was prepared by the method of Pankratz and Childs (16). Mixtures of the different isomers of **1–4** were obtained in these preparations, Table 1. The salts **1–3** were also found to be thermally unstable in CD_2Cl_2 solution, undergoing relatively slow isomerizations about various C=C bonds. In contrast, the isomerization of **4** was found to be fairly rapid at room temperature in CD_2Cl_2.

The ^1H NMR spectral data for **1–4** are summarized in Table 2. Assignments were based on first-order coupling constant information and comparison to previous work (14, 17, 18). In iminium salts **1–3** the aldiminium proton appears as a doublet of doublets. The largest of the coupling constants results from coupling across the C=N bond to the proton on the nitrogen (ca. 16 Hz). The presence and magnitude of these coupling constants are indicative of protonation on nitrogen and an *anti* C=N configuration (19).

Solution ^{13}C NMR data for **1–4** are given in Table 3. Assignment of the carbon atoms was accomplished by ^1H–^{13}C hetero shift correlations, J-modulated spin echo experiments, and comparison with literature data (14, 20). All spectra were acquired at ambient temperatures except for **4**, which was obtained at −60°C in order to minimize thermal isomerization. Comparison of the spectra with those of the corresponding imines shows that protonation of the imines produces a general downfield shift of the odd-numbered olefinic carbons and a slight upfield shift of the even-numbered carbons (20).

Solid state ^{13}C NMR spectra of the salts were obtained using cross polarization magic angle spinning (CPMAS) methods. The ^{13}C NMR chemical shifts of these compounds are listed in Table 3. Identification of the quaternary and methyl carbons was facilitated using a delay without coupling sequence that suppresses CH and CH_2 resonances (21). The remainder of the resonances were assigned by comparison with solution spectra and literature data (13,14).

Solution and solid state absorption spectra maxima of **1–4**

Table 2. (*a*) ^{1}H NMR chemical shift data (ppm) for retinylidene iminium salts.[a,b]

	Compound			
Position	1	2	3	4
C(2)H	1.49t	1.50t	1.49t	1.42t
C(3)H	1.63m	1.61m	1.62m	1.55m
C(4)H	2.06t	2.06t	2.06t	2.02t
C(7)H	6.54d	6.46d	6.53d	6.64d
C(8)H	6.26d	6.23d	6.26d	6.31d
C(10)H	6.32d	6.30d	6.33d	6.64d
C(11)H	7.47dd	7.44dd	7.46dd	7.67dd
C(12)H	6.54d	6.58d	6.56d	6.79d
C(14)H	6.78d	6.67d	6.89d	6.42d
C(15)H	8.21dd	8.19dd	8.19dd	8.43dd
C(16)H	1.05s	1.05s	1.05s	1.00s
C(17)H	1.05s	1.05s	1.05s	1.00s
C(18)H	1.74s	1.74s	1.74s	1.74s
C(19)H	2.10s	2.10s	2.10s	2.13s
C(20)H	2.31s	2.31s	2.31s	2.43s
NH	10.7bs	10.9bs	11.7bs	—
C(1′)H	3.66t	—	—	—
C(1″)H	—	—	—	3.88s
C(2′)H	1.78m	1.50s	1.50s	7.57d
C(3′)H	1.42m	—	—	7.46dd
C(4′)H	0.97t	—	—	7.53dd

[a]s = singlet, t = triplet, dd = doublet of doublets, bs = broad singlet, m = multiplet.

[b]Referenced to CD_2Cl_2 at 5.32 ppm. Measured at 22°C.

(*b*) ^{1}H,^{1}H coupling constant data (Hz) for retinylidene iminium salts.

	Compound			
	1	2	3	4
$J_{7,8}$	16.1	15.9	16.1	15.9
$J_{10,11}$	11.8	11.8	11.7	11.7
$J_{11,12}$	14.9	14.9	14.8	14.5
$J_{14,15}$	11.4	11.2	11.1	11.7
$J_{15,NH}$	15.4	15.4	15.8	—

are given in Table 4. Solid state samples were prepared by smearing micro-crystalline fragments onto a glass or quartz slide. The resulting absorption peaks were typically broader than those obtained from solution but still Gaussian in shape.

Single crystals of **2** and **3** suitable for X-ray crystallographic studies were generated by slow diffusion of diethyl ether into acetonitrile solutions of each compound. Crystals large enough for crystallographic analysis were exceedingly difficult to grow although, once obtained, the crystals were found to be stable to light and moisture at room temperature. The structures of **2** and **3** were determined by X-ray crystallography. Two different projections of the cation–anion pairs of **2** and **3** are shown in Figs. 1 and 2 and views of the unit cell packing are shown in Figs. 3 and 4, respectively.

Discussion

The two salts **2** and **3** have identical cations and only differ in their respective anions. Ideally, for the type of analyis undertaken here they should also have the same anion and only differ in the relative placement of the anion with respect to the cation. The alternative approach, used here, is to vary the anion. However, in doing this it is important to keep the changes as small as possible and to use a closely related series of anions. Unfortunately, retinylidene salts are difficult to obtain as single crystals. As such, the ideal has to be balanced by the realities of obtaining materials that not only are suitable for structure determination using single crystal X-ray techniques but that also differ in terms of their solid state spectroscopic properties. In this work salts **2** and **3** were found to both crystallize as well as exhibit different absorption spectra in the solid state. The two anions are different; however, they are similar in that they are each the salt of a strong acid and possess a single negative charge formally located on oxygen atoms bonded to the central atom (Cl or S).

In solution the properties of **2** and **3** are very similar. Thus the long-wavelength absorption maxima of CH_2Cl_2 solutions of **2** (472 nm) and **3** (465 nm) (Table 4) are essentially the same. Similarly, the ^{13}C NMR spectra of these two salts in solution are virtually identical, Table 3, Fig. 5. It is clear that in CH_2Cl_2 solution variation in the anion of the two salts has little effect on the conformation or charge distribution of the iminium cation.

Despite their similarity in solution it is also clear that there are major differences in these two salts when they are in the solid state. Thus the absorption maxima of **2** (504 nm) and **3** (445 nm) as crystalline solids differ by 59 nm, Table 4. Not only is there a substantial difference in the absorption spectra of the two salts in the solid state but **2** shows an uncharacteristic red shift in its absorption maximum in the solid as compared to the solution phase. In contrast, the chromophore of **3** (as well as those of **1** and **4**) exhibits the typical blue shift generally found with iminium salts (14,18). These results clearly suggest that the chromophores of **2** and **3** are different when in the solid state.

The dramatic differences in the solid state absorption spectra of **2** and **3** are accompanied by major and systematic differences in their solid state ^{13}C NMR spectra, Fig. 5. Examination of Fig. 5 reveals three significant differences. First, the solid state ^{13}C NMR spectra for these compounds differ significantly in the chemical shifts of the odd-numbered carbons, particularly C15, C13, C11, and C9. Second, the resonance positions of these carbons are further downfield in **2** than in **3**. Lastly, the magnitude of the differences between **2** and **3** tends to decrease with increasing distance from the nitrogen atom. The odd-numbered carbons of an iminium salt are particularly sensitive to π-electron distribution along the polyene chain. The systematic pattern in the differences in chemical shift for the odd-numbered carbons in the solid state spectra of **2** and **3** would indicate that less positive charge is delocalized over the polyene carbon atoms in **3** than in **2**.

The differences observed in the properties of **2** and **3** in the solid state stand in marked contrast to their similarity in solution. It is clear that the origin of these different properties of the chromophore in **2** and **3** in the solid state must be due to some specific interaction or conformational difference present

Table 3. ^{13}C NMR chemical shift data (ppm) for retinylidene iminium salts.[a]

	Compound							
	1		**2**		**3**		**4**	
Position	Soln.	Solid	Soln.	Solid	Soln.	Solid	Soln.[b]	Solid
C1	34.6	34.3	34.3	36.7	34.8	34.1	34.3	34.6
C2	40.1	39.3	40.1	45.2	39.9	44.2	39.4	44.0
C3	19.5	19.7	19.3	19.9	19.6	20.3	19.2	20.0
C4	33.7	34.3	33.4	34.8	33.8	36.8	33.6	36.1
C5	132.4	130.2	132.1	136.8	132.5	137.0	133.5	136.9
C6	137.9	138.9	137.6	140.1	138.1	138.0	136.7	140.2
C7	132.4	130.2	132.6	134.3	132.9	133.1	134.5	133.0
C8	137.1	138.6	137.1	136.8	137.5	136.9	136.7	139.3
C9	147.1	144.7	146.9	147.6	147.1	143.9	151.3	148.1
C10	129.9	130.4	129.8	129.7	129.9	128.8	134.1	130.3
C11	139.2	138.6	139.1	140.1	139.1	137.9	143.8	141.6
C12	133.6	130.2	133.4	133.4	133.7	133.1	135.0	133.0
C13	165.5	165.9	164.8	167.2	164.7	161.8	171.3	170.7
C14	119.6	119.3	119.6	120.3	119.8	121.5	118.1	121.4
C15	164.8	164.8	158.8	161.0	159.3	158.0	160.6	159.1
C16	29.1	29.6	28.6	29.9	29.0	27.5	28.8	29.5[c]
C17	29.1	29.6	28.6	29.9	29.0	27.5	28.8	31.3[c]
C18	21.9	23.3	21.7	22.3	21.9	20.3	22.1	21.7
C19	14.6	13.5	13.2	12.8	13.4	11.1	13.7	13.2
C20	14.8	13.5	14.4	15.5	14.7	14.2	13.7	13.2
C1′	52.6	52.2	59.5	60.3	59.6	61.2	145.0	143.0
C1″	—	—	—	—	—	—	41.8	41.6
C2′	31.4	29.6	28.4	32.2	28.6	30.4	130.5	133.3
C3′	19.9	19.7	—	—	—	—	122.6	133.3
C4′	13.5	13.5	—	—	—	—	130.5	133.3

[a]Solution spectra referenced to CD_2Cl_2 at 53.8 ppm. Solid state spectra referenced to adamantane at 29.5 ppm and 38.6 ppm. Measured at 22°C.
[b]Measured at −60°C.
[c]Assignment may be reversed.

only in the crystal lattices of these two salts. For this reason it is of interest to examine carefully the solid state structures of these two salts.

Comparison of the structures of the two salts

As is evident from an examination of Figs. 1 and 2, the two salts have remarkably similar structures and packing arrangements within the crystal lattice. As was found in our earlier work with an N-phenyl substituted retinylidene iminium salt (22), the cations in **2** and **3** are bowed in the plane defined by atoms N, C14, C15, and C21 and bent normal to this plane, Figs. 1 and 2. The angle of intersection of the plane defined by C1, C4, C5, C6 and N, C14, C15, C21 is 20° for both **2** and **3**. The C6-C7-C8 bond angles of 130.1(5)° for **2** and 132(1)° for **3** are similar in size, with both being large as a result of the steric interactions between the methyl groups at C1 and the hydrogen atom at C8. Other relatively large bond angles are found at C7-C8-C9, C9-C10-C11, C11-C12-C13, and C13-C14-C15.

In terms of conformation, as can readily be seen in Figs. 1 and 2, both cations have a *trans* configuration about each of the C—C single and double bonds of their unsaturated chains. In particular, it should also be stressed that **2** and **3** both have an s-*trans* configuration about the C6—C7 bond. The C5-C6-C7-C8 torsion angles (173.3(5)° and 174(1)°, respectively), are the same within the experimental error.

Table 4. Absorption spectral data (nm) for retinylidene iminium salts.[a]

Compound	λ_{max} (nm)	ε_{max} ($\times 10^{-4}$)	λ_{max}(solid) (nm)
1	476	4.36	444
2	472	4.18	504
3	465	4.51	445
4	564[b]	4.25	505

[a]In CH_2Cl_2 at 22°C.
[b]At −70°C.

With the exception of the C20—C13 bond lengths, all bond lengths of the cations are the same within experimental error. The significance of this difference in the C20—C13 internuclear distance will be discussed later.

In summary, from the examination of the cations themselves there are no obvious differences in their conformations or structures that could account for their different solid state

Fig. 1. The conformation of **2**.

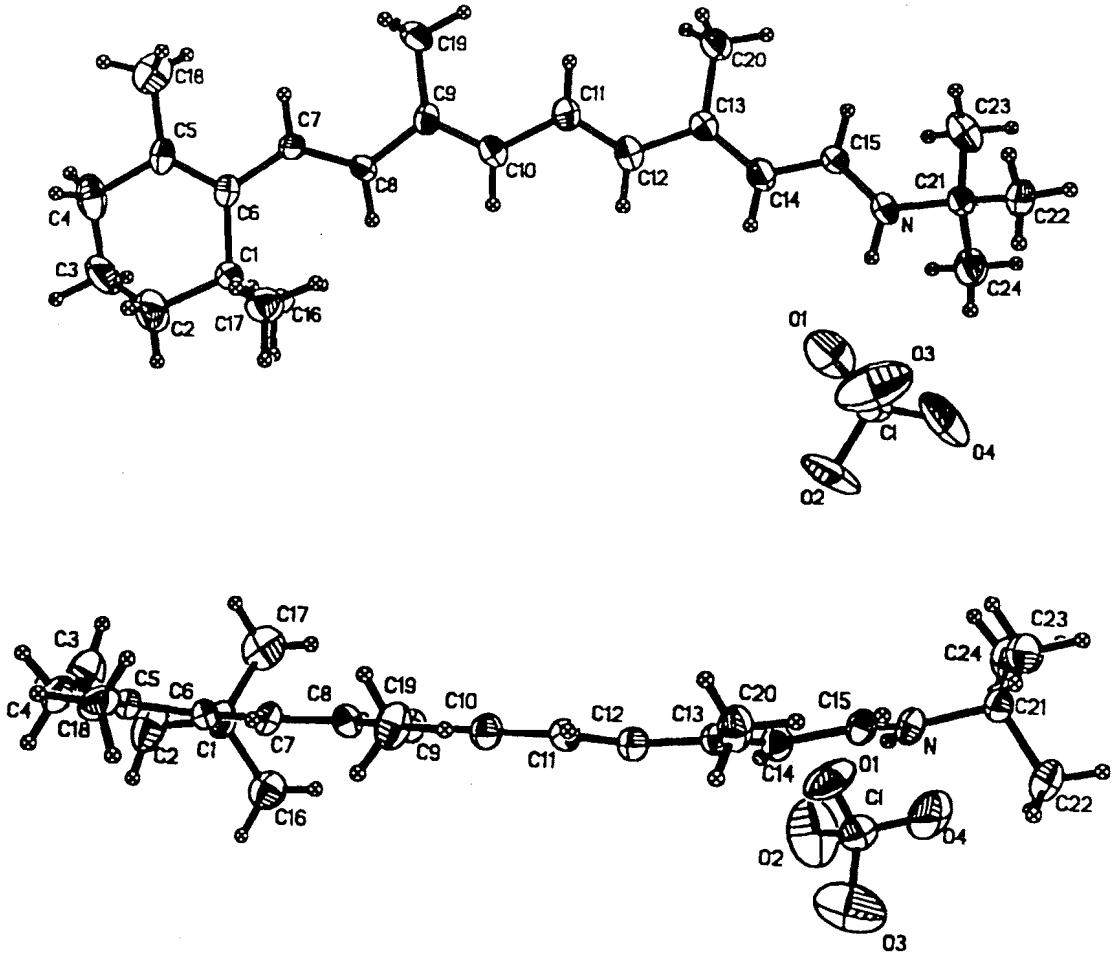

spectroscopic properties. The origin of the spectroscopic differences of the two salts must lie in the way the cations interact with other ions present within the crystal lattice.

Crystal packing and cation–anion interactions

The salts **2** and **3** were found to have different space groups and this impacts on the packing within the crystalline lattices. However, as can be seen from an examination of Figs. 3 and 4, in each case the cation–anion pairs are spatially arranged in a very similar manner with respect to each other. In each case the retinylidene cations lie on top of one another in a comparable π–π stacking fashion. The polar ends of the cations in **2** and **3** are all directed toward one another while the relatively nonpolar β-ionone rings are grouped together.

The closest cation–anion interactions in **2** and **3** are the hydrogen bonding interactions between the iminium proton of a cation and an oxygen atom of the perchlorate or triflate counterions. In general, it has been found from previous X-ray crystallographic determinations of salts that for organic cations with an OH or NH group bonded to a positively charged system there is always an anion located nearby such that a linear hydrogen bond exists between the anion and the hetero-atom bearing the proton. This has been found to be the case, for example, in every reported structure of protonated ketones (23). Similarly, in crystal structures of ammonium salts the anion is found to form a linear hydrogen bond with the acidic proton on the nitrogen (24).

Linear or near-linear hydrogen bonds exist between the proton on the nitrogen and an oxygen atom on the anion of both **2** and **3**. The N—H and H—O internuclear distances are imprecise owing to the uncertainty associated with crystallographically determined hydrogen atom positions. However, the corresponding N---O internuclear distances are determined with good precision. Examination of these cation–anion distances in the lattices of **2** and **3** shows that there is a very important difference. The shortest N---O distance in **2** (2.939(7) Å) is significantly longer than that in **3** (2.85(1) Å) (difference 7σ where $\sigma = (\sigma_1^2 + \sigma_2^2)^{1/2}$). The N---O contact in **3** is shorter than the sum of the van der Waals radii of the respective neutral atoms (2.90 Å).

The shorter N---O distance in **3** as compared to **2** would suggest a stronger hydrogen bonding interaction is present in the former salt. This is corroborated by the observation that the ^{1}H NMR chemical shift of the N(H) proton in **3** is 0.8 ppm further downfield from the analogous proton in **2**.

The observation of an abnormally short C13—C20 bond length of 1.47(1) Å in **3** versus 1.519(8) Å in **2** led to a detailed investigation of possible other significant cation–anion secondary interactions. Significant differences exist between the contacts observed in the two salts in terms of interactions involving C20—H---O and C20—H---F hydrogen bonds. In **3** two of the protons on C20 were found to be participating in hydrogen bonding with a fluorine or oxygen atom, respectively, of different anions, Fig. 6. The observed internuclear

Fig. 2. The conformation of **3**.

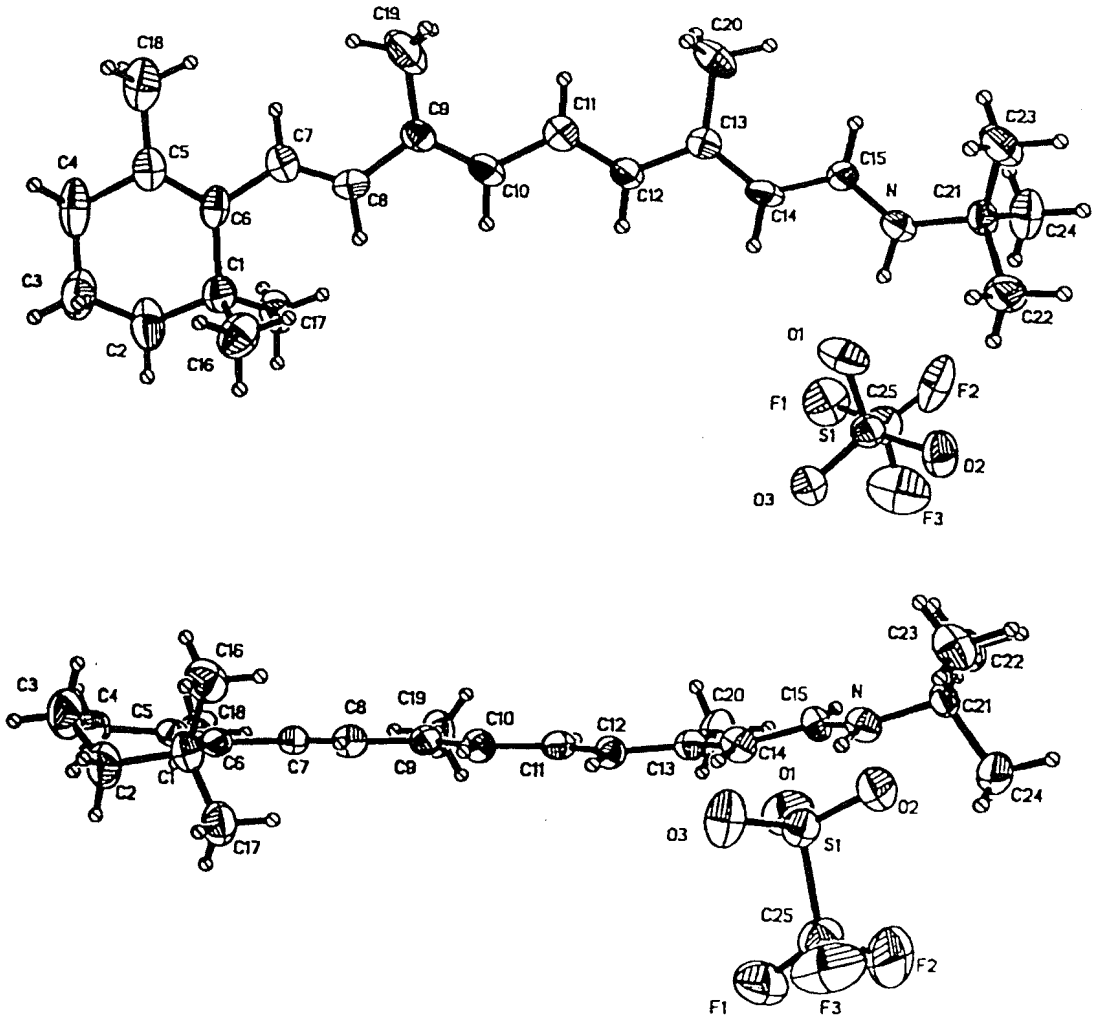

distances in **3** were F3---C20 (3.22(2) Å) and O3---C20 (3.34(1) Å). Although these distances are outside the sum of the van der Waals radii for fluorine and carbon (3.05 Å) and oxygen and carbon (3.10 Å), they are shorter by ca. 0.5 Å than the comparable interactions in **2**. (The closest C—H---O interaction in **2** is O2---C20 (3.800(8) Å).

Taylor and Kennard have shown in an extensive study of C—H hydrogen bonding interactions that C—H---O contacts are electrostatic and that they occur within certain distances (C---O, 3.0–4.0 Å) and angles (ϕ, ~90°–180°) (25). There are numerous examples of C–H---O bonds in the literature and it has been suggested that these interactions contribute significantly to the stability and tertiary structures of biomolecules such as nucleosides and amino acids (25–27). An activated C—H bond is polarized C(δ^-)—H(δ^+). As such, interaction of an anion with the C20 protons in combination with the partial positive charge on C13 would be expected to induce a shortening of the C13—C20 single bond.

The role of the anion in the ^{13}C NMR spectra

As was mentioned above, while the ^{13}C NMR spectra obtained for compounds **2** and **3** in solution are virtually identical there are significant differences in their chemical shifts in the solid state, Fig. 5. The resonance positions of the odd-numbered carbons of the polyenic chain of **3** are at higher field than the corresponding resonances of **2**, indicating that there is less positive charge induced on the carbon framework in **3**. As was established above, the only significant differences in the two structures in the solid state is in their hydrogen bonding interactions between the cations and anions. It must be concluded that the origin of the differences in the solid state ^{13}C NMR spectra are directly attributable to these hydrogen bonding interactions.

The regularity of the differences in chemical shifts of the unsaturated carbons in the solid state ^{13}C NMR spectra of the two salts suggests that the primary effect is due to the large variation in the N—H---O internuclear distances. The different N—H---O distances in **2** and **3** will result in a difference in the relative strengths of the hydrogen bonding interaction involving the nitrogen atom on the cations with an oxygen atom on the anion. The triflate counterion in **3** interacts more strongly with the N(H) proton than does perchlorate in **2**. As a result the N—H bond in **3** will be weaker through the stronger hydrogen bonding interaction with the triflate counterion. This will lead to a reduction in the fraction of positive charge induced on the carbon framework and the ^{13}C NMR chemical shifts of C15, C13, C11, and C9 in **3** will resonate at higher fields than those found in **2**. In the case of **2**, where the

Fig. 3. Unit cell packing in **2** with view along *y*-axis.

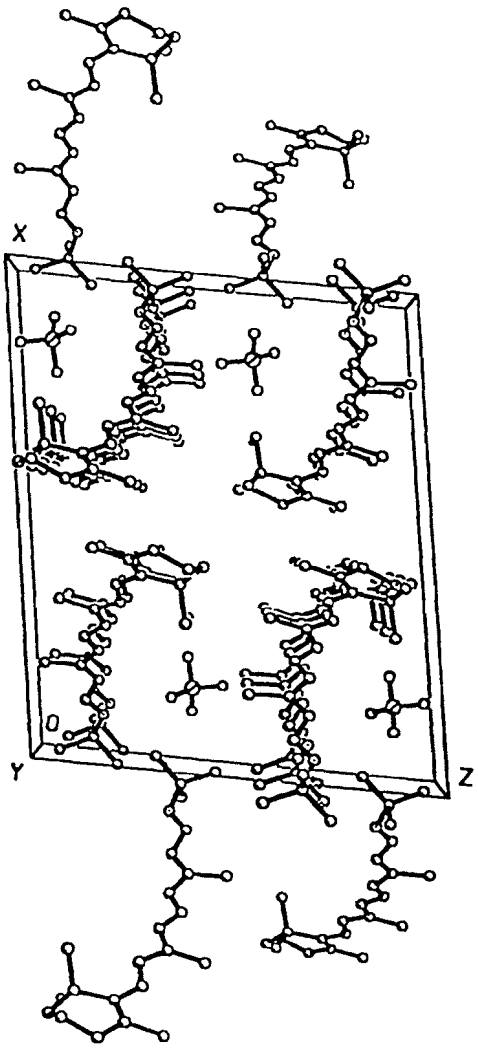

Fig. 4. Unit cell packing in **3** with view along *y*-axis.

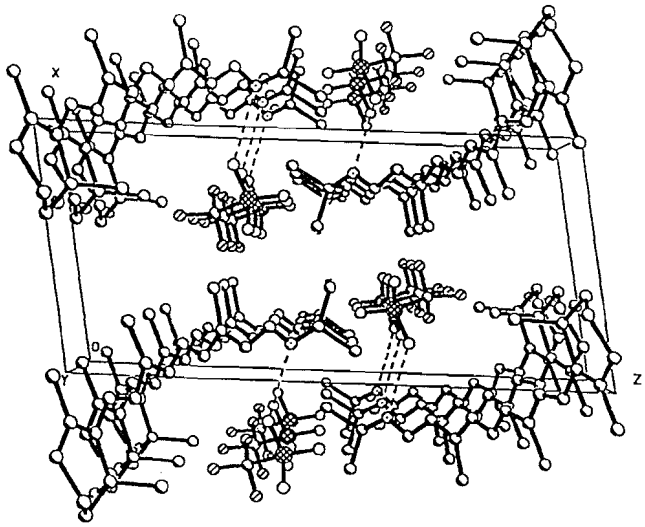

N—H---O1 interaction is much weaker than in **3**, more positive charge is borne by the odd-numbered carbons in the polyene chain. The secondary hydrogen-bonded interactions involving C20 in **3** could serve to assist delocalization of the positive charge through electron release to C13 along the polyenyl chain. However, we note that Bader has shown through theoretical calculations that if a hyperconjugative mechanism is operational at C20, then the C13—C20 bond should possess some π-character and, consequently, a downfield shift of the C20 resonance might be expected (28). No downfield shift was seen for C20 in **3** as compared to **2**.

One way of viewing the importance of these interactions of different anions with the N—H proton is to remember that a hydrogen atom in a molecule formally can only have a bond valence of 1. In the absence of any hydrogen bonding interaction, a full positive charge will formally reside on the nitrogen atom and carbon framework of a protonated imine. Hydrogen bonding of the N—H proton to a Lewis base will reduce the N—H bond valence in proportion to the bond valence associated with the hydrogen bond. This will result in a reduction of the fraction of positive charge induced on the nitrogen/carbon framework of the molecule. The importance of this hydrogen bonding on the degree of charge induction on a protonated imine can be seen by comparison of the properties of **2/3** with **4**. As can be seen from the data in Table 3, the solid state ^{13}C NMR chemical shifts of C13 and C11 in **4** are shifted further downfield by 3.5 and 1.5 ppm, respectively, relative to **2**. In compound **4** where the nitrogen atom is doubly substituted, the perchlorate counterion cannot participate in hydrogen bonding and so attenuates the fraction of positive charge to be delocalized on to the polyene carbons.

The solid state ^{13}C NMR chemical shifts for C15, C13, C11, and C9 in bR were reported by Harbison et al. to be 163.2, 169.0, 139.1, and 146.4 ppm, respectively (12). The ^{13}C NMR chemical shift differences between bR and **2/3** are illustrated in Fig. 7. The chemical shift values for C15 and C13 in bR are each shifted downfield by approximately 2 ppm compared to **2**, and by 5 ppm and 7 ppm compared to **3**, indicating that bR contains slightly more positive charge at C15 and C13 than do the comparable atoms in **2**.

The FTIR results corroborate the solid state ^{13}C NMR work described above in that the C=C stretching frequencies for bR, **2**, and **3** are 1530, 1539, and 1553 cm^{-1}, respectively (29). The lower stretching frequency exhibited by bR is suggestive of a decreased C=C bond strength caused by more extensive positive charge delocalization in its polyene chain.

Examination of the chemical shift differences of carbons C6–C8 in **2**, **3**, and bR (Fig. 7) reveals that these carbon atoms are substantially shifted to lower field in **2/3** than the corresponding carbon atoms in bR. This would indicate that there is a different type of specific interaction at the ring end of the retinylidene chromophore in bR than is observed in **2** and **3**. Harbison et al. (12) and Sheves and co-workers (15) have suggested that there is a nonconjugated positive charge present in the vicinity of C7–C9 in bR. However, in the recently reported structure of bR there are no obvious positive charges near these carbon atoms (30). The effect of the protein on ^{13}C NMR chemical shifts in bR may be due to the interaction of the polyene chain with four tryptophan residues (Trp86, Trp138, Trp182, and Trp189) that line the retinal pocket. It is possible that such an interaction with aromatic ring currents may be responsible for the observed effects.

Effect of cation/anion placement on absorption spectra

The absorption maxima of retinylidene iminium salts **2** (472

Fig. 5. Differences in ^{13}C chemical shift between **2** and **3**. Positive difference means that **3** is at higher field than **2**.

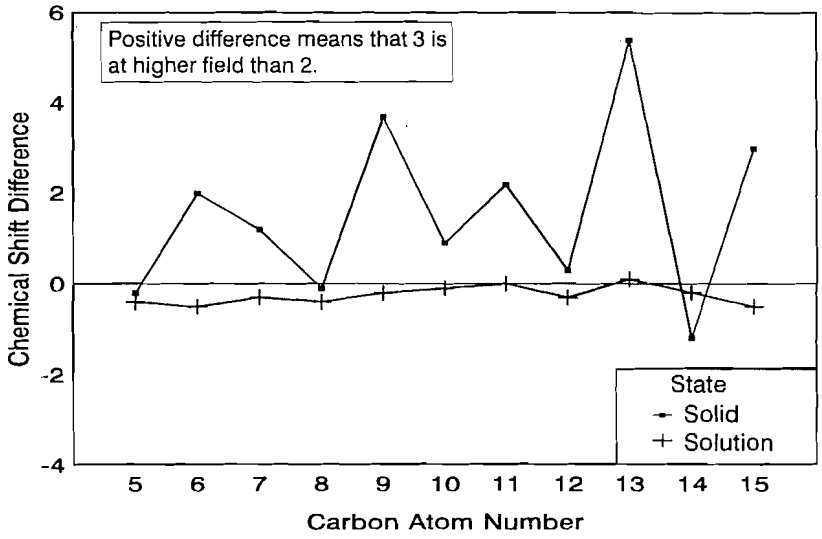

Fig. 6. Bottom view of hydrogen bonding interactions in **3**.

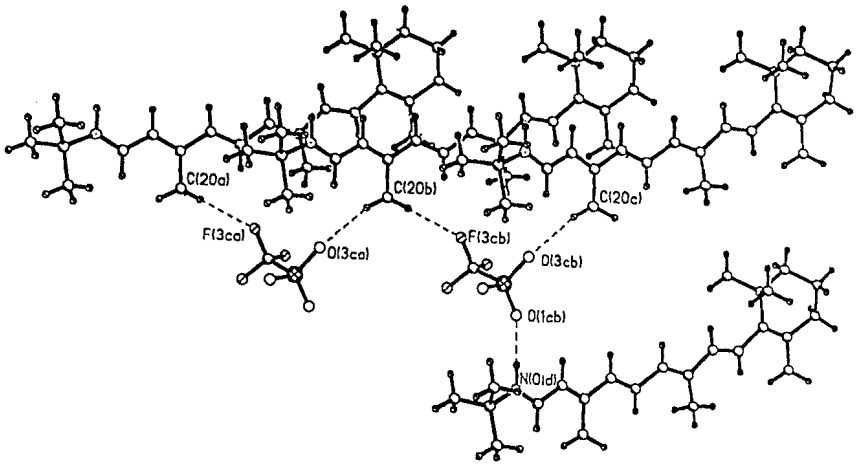

nm) and **3** (465 nm) are very similar in CH_2Cl_2 solution, Table 4. In contrast, their solid state absorption maxima differ by 59 nm (2631 cm^{-1}). As has been suggested earlier, this difference is consistent with a conformational change about the C6—C7 single bond (14) and indeed, Honig, Ebrey, and co-workers have indicated that twisting about the C6—C7 bond could alter the absorption maximum by about 50 nm (7).

The crystal structures of **2** and **3** show that both cations have 6-s-*trans* conformations in the solid state and, as such, the difference in their absorption spectra cannot be accounted for on the basis of conformational effects. Rather, the 2631 cm^{-1} (7.5 kcal/mol) difference in the absorption maxima of **2** and **3** in the solid state must primarily be the result of the variation in the differences in internuclear distance between N and O1. As was demonstrated above, the longer hydrogen-bonded interaction between O1 in ClO_4^- with the N-H proton in **2** results in more charge being induced on the carbon framework of this salt as compared to **3**. This will have the effect of destabilizing (raising) the ground state energy of **2** as compared to **3** and so causing a red shift in its absorption spectrum. *This result strongly supports the suggestion of Sheves (15) that the position of the absorption maximum of a retinylidene iminium salt can be simply regulated by change in the strength of the hydrogen bonding interaction between the N-H proton and the counterion.*

Conclusion

This work demonstrates the power of combining detailed structural and solid state packing information with solid state spectroscopic techniques to unravel the impact of cation–anion interactions in determining the properties of a system. Similar approaches could be used with other organic salts and lead to a better understanding of the importance of the placement of the counterion in determining the charge distribution, etc. of an organic ion.

Experimental section

CH_2Cl_2 was refluxed over P_2O_5 and distilled under a dry N_2 atmosphere prior to use. Similarly, diethyl ether was distilled from $LiAlH_4$, CH_3CN from P_2O_5 and then CaH_2. Dry solvents were stored over 4 Å molecular sieves in a glove bag that was

Fig. 7. Differences in ^{13}C chemical shift between bR and **2/3**. Positive difference means that carbon resonance of **2** or **3** is at higher field than bR.

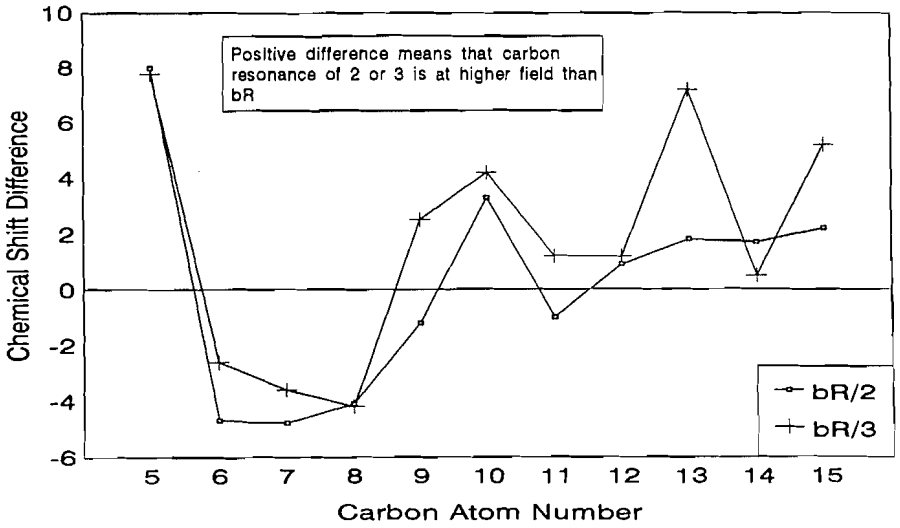

continuously purged with N_2 in the presence of solid P_2O_5. Tertiary butylamine, *n*-butylamine, and *N*-methyl aniline were distilled and kept over 4 Å molecular sieves. CD_2Cl_2 (purchased in sealed 1 g ampules) and $CDCl_3$ were used without further purification. All-*trans* retinal (Aldrich) was used without further purification. All work was carried out under a nitrogen atmosphere and in dim red light. Solution ^1H NMR spectra were acquired at 500 MHz on a Bruker AM500 spectrometer. Solution ^{13}C NMR spectra were acquired on either a Bruker AC200 (50 MHz) spectrometer or a Bruker AM500 (125.8 MHz) spectrometer.

Solid state ^{13}C NMR spectra

Room temperature solid state ^{13}C NMR spectra of crystalline samples were obtained by CPMAS techniques with the use of a Bruker MSL100 (25 MHz) spectrometer. Spinning rates were approximately 4000 Hz. Methyl and quaternary carbon resonances were assigned using a delay without decoupling pulse sequence (21). Samples (0.1 g) were mixed with NaCl, finely ground, and densely packed into alumina rotors under a dry N_2 atmosphere. Adamantane was used as an external reference, and displayed resonances at 29.5 ppm (CH) and 38.6 ppm (CH_2) relative to tetramethylsilane.

UV spectra

Absorption spectra were recorded on a Hewlett Packard 8451A spectrophotometer. Solutions of the various compounds (about 10^{-5} M) were placed in 1 cm quartz cells to record their absorption spectra. Solid state absorption spectra were obtained from crystalline samples smeared onto a glass or quartz slide. A similar slide was used as a reference.

Infrared spectra

Infrared spectra were recorded on a Biorad-Digilab FTS-40 FTIR spectrometer. The samples were prepared as thin KBr discs.

Synthesis

All imines were synthesized using a modified procedure of Blatz et al. (14). The corresponding iminium salts were prepared by addition of an ethereal solution of the desired acid to the imine dissolved in ether at room temperature under a N_2 atmosphere.

Preparation of salts 1–3

Tertiary butylamine or *n*-butylamine (10 mmol) was added to a solution of retinal (1 mmol) in dry ether under a N_2 atmosphere and in the absence of light. The reaction mixture was stirred for 24 h over 4 Å molecular sieves. The mixture was filtered and ether and excess amine were removed under vacuum. The imine was rinsed three times with dry ether (5 mL) and the flask evacuated to ensure complete removal of amine (excess amine would interfere in the subsequent protonation). The imine was not characterized and was used immediately in the following step. Protonation was accomplished at room temperature by slow dropwise addition of an ethereal solution of either CF_3SO_3H or ClO_4H to an ethereal solution of imine. The resulting salt was filtered, recrystallized from CH_3CN–ether mixtures at −20°C, and dried under vacuum.

Preparation of 4

Freshly distilled *N*-methyl aniline (75 mg, 0.7 mmol) in dry ether (5 mL) was cooled in an ice bath. A slight excess of perchloric acid (110 mg of 70% $HClO_4$, 0.8 mmol) was added dropwise. A solution of all-*trans* retinal (200 mg, 0.7 mmol) in dry ether (2 mL) was added and the mixture stirred and allowed to stand until the salt precipitated from solution within about 10 min. The product was filtered, washed with dry ether, recrystallized from CH_3CN–ether, and dried under vacuum (yield 250 mg, 75%).

Single crystal X-ray crystallography. Collection of data

Single crystals (flat red needles) of iminium salts **2** (0.01 × 0.10 × 0.30 mm) and **3** (0.10 × 0.001 × 1.00 mm) suitable for X-ray diffraction studies were obtained from distillation of diethyl ether into an acetonitrile solution of each salt at −20°C.

Compound **2**: $C_{24}H_{38}ClNO_4$ fw = 440.02
Monoclinic, $P2_1/c$, a = 20.179(3), b = 7.585(1), c =

Table 5. Atomic coordinates for **2**.

Atom	*x*	*y*	*z*	B_{iso}* or B_{eq}
Cl	0.15527(10)	−0.75906(24)	0.40008(10)	5.55(9)
O1[a]	0.1353(7)	−0.6184(12)	0.3469(6)	9.7(5)
O2[a]	0.1679(10)	−0.6950(26)	0.4785(8)	13.8(10)
O3[a]	0.2191(5)	−0.8273(21)	0.3936(7)	13.9(8)
O4[a]	0.1049(7)	−0.8854(15)	0.3945(6)	11.1(6)
O5[b]	0.0910(21)	−0.758(6)	0.371(3)	18.6(14)*
O6[b]	0.1536(17)	−0.743(5)	0.4785(17)	10.4(14)
O7[b]	0.1734(18)	−0.645(5)	0.350(3)	14.0(15)*
O8[b]	0.1662(18)	−0.9137(25)	0.3565(15)	10.9(14)
N	0.0837(2)	−0.6528(5)	0.1712(3)	4.4(2)
C1	0.3815(3)	0.6587(7)	0.3945(3)	4.3(3)
C2	0.4190(4)	0.7973(8)	0.4511(5)	7.9(4)
C3	0.4126(4)	0.9774(9)	0.4175(4)	7.8(4)
C4	0.4416(3)	0.9842(7)	0.3404(5)	6.1(3)
C5	0.4196(3)	0.8352(7)	0.2819(4)	4.0(3)
C6	0.3908(3)	0.6854(7)	0.3046(3)	3.7(3)
C7	0.3680(3)	0.5545(6)	0.2437(3)	3.4(2)
C8	0.3328(3)	0.4042(7)	0.2495(3)	3.5(2)
C9	0.3123(3)	0.2784(6)	0.1846(3)	3.7(2)
C10	0.2805(3)	0.1338(7)	0.2035(3)	4.3(3)
C11	0.2531(3)	−0.0099(7)	0.1500(3)	3.9(3)
C12	0.2253(3)	−0.1510(7)	0.1781(4)	4.4(3)
C13	0.1900(3)	−0.2906(6)	0.1311(3)	3.7(3)
C14	0.1594(3)	−0.4168(7)	0.1689(3)	4.3(3)
C15	0.1143(3)	−0.5446(7)	0.1320(3)	3.8(3)
C16	0.4104(3)	0.4817(8)	0.4278(4)	5.7(3)
C17	0.3064(4)	0.6672(9)	0.4014(4)	6.7(4)
C18	0.4350(3)	0.8686(7)	0.1978(5)	6.1(3)
C19	0.3277(3)	0.3133(7)	0.1007(3)	5.3(3)
C20	0.1870(3)	−0.2887(7)	0.0389(4)	5.6(3)
C21	0.0314(3)	−0.7884(6)	0.1396(3)	3.8(3)
C22	0.0664(3)	−0.9633(7)	0.1423(4)	5.5(3)
C23	−0.0005(3)	−0.7433(8)	0.0521(4)	6.4(3)
C24	−0.0199(3)	−0.7830(8)	0.1974(4)	6.5(4)

[a]O1, O2, O3, O4: occupancy 0.70.
[b]O5, O6, O7, O8: occupancy 0.30.

16.556(7)Å, β = 99.12(2)°, V = 2502(2)Å^3, Z = 4, ρ_c = 1.168 g/cm^3, μ = 15.68 cm^{-1} (23°C, CuKα, λ = 1.54178) Å.

Compound **3**: $C_{25}H_{38}F_3NO_3S$ fw = 489.64

Monoclinic, $P2_1$, a = 9.068(3), b = 7.919(3), c = 19.243(9)Å, β = 99.87(3)°, V = 1361.5(9)Å^3, Z = 2, ρ_c = 1.194 g/cm^3, μ = 14.11 cm^{-1} (23°C, CuKα, λ = 1.54178 Å).

Cell constants were obtained from least-squares refinements using the setting angles of 24 carefully centered reflections in the range 47.04° < 2θ < 81.43° for **2** and 17 centered reflections in the range 21.19° < 2θ < 26.07° for **3**. Reflection intensities were measured using θ/2θ scans on a Rigaku AFC5R diffractometer for **2** ($2\theta_{max}$ = 100° (+h, +k, ±l), 5609 measured, 3242 unique, R_{int} = 0.053) and a Rigaku AFC6R diffractometer for **3** ($2\theta_{max}$ = 120° (+h, +k, ±l), 2229 measured, 2078 unique, R_{int} = 0.065). Both instruments used a 12 kW rotating anode generator. The data for both compounds were corrected for Lorentz and polarization effects and absorption. For **2**, an empirical absorption correction, based on azimuthal scans or several reflections, was applied, which resulted in transmission factors ranging from 0.84 to 1.00. In the case of **3** an empirical absorption correction using the program DIFABS (31) was applied, resulting in a transmission factor range from 0.53 to 1.00, which appears to be an *under*estimate for such a thin needle.

Table 6. Atomic coordinates for **3**.

Atom	*x*	*y*	*z*	B_{iso} or B_{eq}
S1	−0.7135(3)	−1.4740(1)	0.6197(1)	5.0(1)
F1	−0.6403(8)	−1.550(1)	0.7531(3)	9.4(5)
F2	−0.747(1)	−1.744(1)	0.6880(4)	11.6(6)
F3	−0.5257(9)	−1.683(1)	0.6826(5)	13.0(6)
O1	−0.8460(7)	−1.407(1)	0.6382(4)	8.2(5)
O2	−0.7332(8)	−1.575(1)	0.5564(4)	7.0(4)
O3	−0.5950(8)	−1.357(1)	0.6266(4)	7.8(5)
N	−0.1557(8)	−1.401(1)	0.5785(4)	4.8(4)
C1	0.289(1)	−0.135(2)	0.8816(6)	6.0(6)
C2	0.392(1)	−0.003(2)	0.9206(7)	8.7(8)
C3	0.329(2)	0.167(2)	0.9113(8)	8.8(9)
C4	0.185(2)	0.179(2)	0.9438(6)	8.0(7)
C5	0.083(1)	0.032(2)	0.9231(5)	5.3(5)
C6	0.126(1)	−0.109(1)	0.8904(5)	5.0(5)
C7	0.014(1)	−0.237(1)	0.8704(5)	4.9(5)
C8	0.020(1)	−0.379(1)	0.8353(5)	4.9(5)
C9	−0.097(1)	−0.505(1)	0.8149(5)	4.5(5)
C10	−0.063(1)	−0.646(1)	0.7824(5)	4.9(5)
C11	−0.161(1)	−0.783(1)	0.7577(5)	4.7(5)
C12	−0.114(1)	−0.917(1)	0.7270(5)	4.3(5)
C13	−0.205(1)	−1.051(1)	0.6938(5)	4.3(5)
C14	−0.143(1)	−1.169(1)	0.6571(5)	4.8(5)
C15	−0.219(1)	−1.290(1)	0.6115(5)	4.1(5)
C16	0.298(1)	−0.132(2)	0.8018(6)	7.5(7)
C17	0.350(1)	−0.298(2)	0.9152(7)	7.5(7)
C18	−0.070(1)	0.060(2)	0.9398(5)	7.9(7)
C19	−0.245(1)	−0.465(2)	0.8325(6)	9.1(8)
C20	−0.366(1)	−1.048(2)	0.6968(6)	7.6(7)
C21	−0.219(1)	−1.527(1)	0.5269(5)	4.4(5)
C22	−0.129(1)	−1.515(2)	0.4659(5)	6.9(7)
C23	−0.378(1)	−1.488(2)	0.4956(5)	7.2(6)
C24	−0.203(1)	−1.694(2)	0.5628(6)	7.5(7)
C25	−0.656(1)	−1.619(2)	0.6896(7)	6.9(8)

Solution and refinement of structures

Both structures were solved by direct methods (32), and the space group of **3** was verified to be noncentrosymmetric. The oxygen atoms of the perchlorate ion in **2** were found to be disordered in a 0.7:0.3 ratio. All non-hydrogen atoms were, with the exception of two of the disordered oxygen atoms O5 and O7 in **2**, refined anisotropically. Neutral atom scattering factors were taken from Cromer and Waber (33). Anomalous dispersion corrections (34) were applied to all non-hydrogen atoms. Full-matrix least-squares refinements, minimizing $\Sigma w(|F_o| - |F_c|)^2$, where $w = 4F_o^2/\sigma^2(F_o^2)$, were used in both cases. Hydrogen atoms were fixed in calculated positions. All calculations were performed using the TEXSAN crystallographic software package of Molecular Structure Corporation (35).

The final refinement cycle for **2**, using 1854 reflections with $I > 2.0\sigma(I)$, resulted in R = 0.059, S = 2.20, and $R_w = (\Sigma w(|F_o| - |F_c|)^2/\Sigma w F_o^2)^{1/2}$ = 0.072, and gave a clean Fourier difference map (−0.20 to 0.30 e/Å^3). The final refinement cycle for **3**,

using 1330 reflections with $I > 3.0\sigma(I)$, resulted in $R = 0.057$, $S = 2.16$, and $R_w = 0.039$, and gave a clean Fourier difference map (-0.17 to 0.19 e/Å^3). Positional parameters and equivalent isotropic temperature factors for the non-hydrogen atoms of both structures are found in Tables 5 and 6, respectively.[2]

Acknowledgement

We would like to thank the Natural Sciences and Engineering Research Council of Canada for financial support, and Brian Sayer and Don Hughes (McMaster University) for their NMR assistance.

References

1. W. Stoeckenius and R. Rowen. J. Cell Biol. **34**, 65 (1962).
2. G. Wald. Science, **162**, 230 (1968).
3. D. Oesterhelt and W. Stoeckenius. Nature New Biol. **233**, 149 (1971).
4. P.E. Blatz, J.H. Mohler, and V. Navangul. Biochemistry, **11**, 848 (1972).
5. G. Wald and P.K. Brown. J. Gen. Physiol. **37**, 189 (1953).
6. B. Morig. Annu. Rev. Phys. Chem. **29**, 31 (1977).
7. B. Honig, A.D. Greenberg, H. Dinur, and T.G. Ebrey. Biochemistry, **15**, 4593 (1976).
8. K. Nakanishi, V. Balogh-Nair, M. Arnaboldi, K. Tsujimoto, and B. Honig. J. Am. Chem. Soc. **102**, 7945 (1980).
9. M.G. Motto, M. Sheves, K. Tsujimoto, V. Balogh-Nair, and K. Nakanishi. J. Am. Chem. Soc. **102**, 7947 (1980).
10. U. Dinur, B. Honig, and K. Schulten. Chem. Phys. Lett. **72**, 493 (1980).
11. J. Lugtenburg, M. Muradin-Szweykowska, C. Heeremans, J. A. Pardoen, G.S. Harbison, J. Hersfeld, R.G. Griffin, S.O. Smith, and R.A. Mathies. J. Am. Chem. Soc. **108**, 3104 (1986).
12. S. Harbison, S. Smith, J. Pardoen. J. Courtin, J. Lugtenburg, J. Herzfeld, R. Mathies, and R. Griffin. Biochemistry, **24**, 6955 (1985).
13. G.S. Harbison, P.P.J. Mulder, H. Pardoen, J. Lugtenburg, J. Herzfeld, and R.G. Griffin. J. Am. Chem. Soc. **107**, 4809 (1985).
14. R.F. Childs, G.S. Shaw, and R.E. Wasylishen. J. Am. Chem. Soc. **109**, 5362 (1987).
15. A. Albeck, N. Livnah, H. Gottlieb, and M. Sheves. J. Am. Chem. Soc. **114**, 2400 (1992).
16. M. Pankratz and R.F. Childs. J. Org. Chem. **30**, 4553 (1985).
17. P.E. Blatz and J.H. Mohler. Biochemistry, **14**, 2304 (1975).
18. G.S. Shaw. PhD. Thesis, McMaster University, 1988.
19. R.F. Childs and B.D. Dickie. J. Chem. Soc. Chem. Commun. 1268 (1981); R.F. Childs and G.S. Shaw. *In* The photochemistry of carbenium ions and related species. Marcel Dekker, Inc., New York. 1991. p. 111.
20. D. Cossette and D. Vocelle. Can. J. Chem. **65**, 1576 (1987).
21. S.J. Opella and M.H. Frey. J. Am. Chem. Soc. **101**, 5854 (1979).
22. B. Santarsiero, M. James, M. Mahendran, and R.F. Childs. J. Am. Chem. Soc. **112**, 9416 (1990).
23. R.F. Childs, M. Mahendran, S. D. Zweep, G.S. Shaw, S.K. Chadda, N.A.D. Burke, B.E. George, R. Faggiani, and C.J.L. Lock. Pure Appl. Chem. **58**, 111 (1986); R.F. Childs, R. Faggiani, C.J.L. Lock, M. Mahendran, and S.D. Zweep. J. Am. Chem. Soc. **108**, 1692 (1986); R.F. Childs, M.D. Kostyk, C.J.L. Lock, and M. Mahendran. J. Am. Chem. Soc. **112**, 8912 (1990).
24. J.-O. Lundgren. Acta. Crystallogr. Sect. B: Struct. Crystallogr. Cryst. Chem. **B35**, 1027 (1979); V.H. Hartl. Acta. Crystallogr. Sect. B: Struct. Crystallogr. Cryst. Chem. **B31**, 1781 (1975); A.J. Serewicz, B.K. Robertson, and E.A. Meyers. J. Phys. Chem. **69**, 1915 (1965).
25. R. Taylor and O. Kennard. J. Am. Chem. Soc. **104**, 5063 (1982).
26. G.R. Desiraju. Acc. Chem. Res. **24**, 290 (1991).
27. W. Suenger. Angew. Chem. Int. Ed. Engl. **12**, 591 (1973); G.A. Jeffrey and H. Maluszynska. Int. J. Biol. Macromol. **4**, 173 (1982).
28. R.F.W. Bader. Can. J. Chem. **64**, 1036 (1986).
29. K.J. Rothschild and H. Marrero. Proc. Natl. Acad. Sci. U.S.A. **79**, 4045 (1982).
30. R. Henderson, J.M. Baldwin, T.A. Ceska, F. Zemlin, E. Beckmann, and K.H. Downing. J. Mol. Biol. **213**, 899 (1990).
31. J. Walker and L. Stuart. Acta. Crystallogr. Sect. A: Found. Crystallogr. **A39**, 158P (1983).
32. C.J. Gilmore. MITHRIL: an integrated direct methods computer program. University of Glasgow, Scotland. J. Appl. Crystallogr. **47**, 42 (1984); P.T. Beurskens. DIRDIF: direct methods for difference structures — an automatic procedure for phase extension and refinement of difference structure factors. Technical Report 1984/1 Crystallography Laboratory, Toernooiveld, 6525 Ed Nijmegen, Netherlands.
33. D.T. Cromer and J.T. Waber. International tables for X-ray crystallography. Vol. IV. Kynoch Press, Birmingham, England. 1974. Table 2.2A.
33. D.T. Cromer. International tables for X-ray crystallography. Vol. IV. Kynoch Press, Birmingham, England. 1974. Table 2.3.1.
35. TEXSAN–TEXRAY Structure analysis package, Molecular Structure Corporation, The Woodlands, Texas. 1985.

[2] Tables of hydrogen atom positional parameters and isotropic temperature factors, anisotropic temperature factors for all non-hydrogen atoms, interatomic bonds and bond angles, torsion angles, least-squares planes, intermolecular contacts, and F_o F_c reflection intensities have been deposited. They may be purchased from: The Depository of Unpublished Data, Document Delivery, CISTI, National Research Council Canada, Ottawa, Canada, K1A 0S2. Tables of hydrogen atom parameters, bond lengths and angles for the anions, and packing diagrams for the cells have also been deposited with the Cambridge Crystallographic Data Centre and can be obtained on request from the the Director, Cambridge Crystallographic Data Centre, University Chemical Laboratory, 12 Union Road, Cambridge CB2 1EZ, U.K.

The photochemical nucleophile–olefin combination, aromatic substitution (photo-NOCAS) reaction. Part 11: Involving (*R*)-(+)-α-terpineol and (*R*)-(+)-limonene, substituting on 1,4-dicyanobenzene[1]

Donald R. Arnold, Dennis A. Connor, Kimberly A. McManus, Pradip K. Bakshi, and T. Stanley Cameron

Abstract: Irradiation of an acetonitrile–methanol (3:1) solution of 1,4-dicyanobenzene (**1**), biphenyl (**5**), and (*R*)-(+)-limonene (**21**) leads to formation of the 1:1:1 (methanol: **21**: **1**) photo-NOCAS adducts: 4-[(1*R*,2*S*,4*R*)-4-isopropenyl-2-methoxy-1-methylcyclohexyl]benzonitrile (**23**, 30%), 4-[(1*S*,2*R*,4*R*)-4-isopropenyl-2-methoxy-1-methylcyclohexyl]benzonitrile (**24**, 2%), 4-[(1*R*,2*R*,5*R*)-5-isopropenyl-2-methoxy-2-methylcyclohexyl]benzonitrile (**25**, 3%), and 4-[(1*S*,2*S*,5*R*)-5-isopropenyl-2-methoxy-2-methylcyclohexyl]benzonitrile (**26**, 1%). When an acetonitrile solution (no added methanol) of 1,4-dicyanobenzene (**1**), biphenyl (**5**), and (*R*)-(+)-α-terpineol (**22**) was irradiated under these conditions, the products were the cyclized 1:1 (**22**: **1**) photo-NOCAS adducts: (1*R*,2*S*,5*R*)-2-(4-cyanophenyl)-2,6,6-trimethyl-7-oxabicyclo[3.2.1]octane (**27**, 21%) and (1*S*,4*R*,6*R*)-6-(4-cyanophenyl)-1,3,3-trimethyl-2-oxabicyclo[2.2.2]octane (**28**, 2%). Structural assignments were based primarily upon detailed analysis of ^{1}H and ^{13}C nmr spectra and, for four of the products (**24**, **26**, **27**, and **28**), structures were firmly established by X-ray crystallography. The mechanism for the formation of these products is discussed, with emphasis on the intramolecular reactions of the intermediate alkene radical cations. Molecular mechanics (MM3) calculations gave information regarding the structure and energy of the conformers of **21** and **22** that was useful for predicting/explaining the observed reactivity on the basis of approach vector analysis; the transition state for cyclization incorporates the nucleophile and the alkene radical cation carbon atoms at the vertices of an obtuse triangle orthogonal to the plane of the π-system.

Key words: photoinduced electron transfer, radical cations, cyclization, terpenes.

Résumé : L'irradiation d'une solution de 1,4-dicyanobenzène (**1**), de biphényle (**5**) et de (*R*)-(+)-limonène (**21**) dans un mélange acétonitrile–méthanol (3 : 1) conduit à la formation d'adduits photo-NOCAS (substitution aromatique par combinaison photochimique de nucléophile et d'oléfine) 1 : 1 : 1 (méthanol : **21** : **1**) : 4-[(1*R*,2*S*,4*R*)-4-isopropényl-2-méthoxy-1-méthylcyclohexyl]benzonitrile (**23**, 40%, 4-[(1*S*,2*R*,4*R*)-4-isopropényl-2-méthoxy-1-méthylcyclohexyl]benzonitrile (**24**, 2%), 4-[(1*R*,2*R*,5*R*)-5-isopropényl-2-méthoxy-1-méthylcyclohexyl]benzonitrile (**25**, 3%) et 4-[(1*S*,2*S*,5*R*)-5-isopropényl-2-méthoxy-2-méthylcyclohexyl]benzonitrile (**26**, 1%). Quand on irradie dans les mêmes conditions un mélange de 1,4-dicyanobenzène (**1**), de biphényle (**5**) et de (*R*)-(+)-α-terpinéol (**22**) en solution dans de l'acétonitrile (sans y avoir ajouté de méthanol), les produits formés sont les adduits de photo-NOCAS cyclisés 1 : 1 (**22 : 1**) suivants : (1*R*,2*S*,5*R*)-2-(4-cyanophényl)-2,6,6-triméthyl-7-oxabicyclo[3.2.1]octane (**27**, 21%) et (1*S*,4*R*,6*R*)-6-(4-cyanophényl)-1,3,3-triméthyl-2-oxabicyclo[2.2.2]octane (**28**, 2%). Les attributions de structures ont été principalement faites sur la base d'études détaillées des spectres RMN du ^{1}H et du ^{13}C; de plus, pour quatre des produits (**24**, **26**, **27** et **28**), les structures ont été établies d'une façon ferme par diffraction des rayons X. On discute du mécanisme de formation de ces produits en insistant sur les réactions intramoléculaires des cations radicaux d'alcènes intermédiaires. Des calculs de mécanique moléculaire (MM3) fournissent de l'information relative à la structure et à l'énergie des conformères des composés **21** et **22** qui est utile pour prédire/expliquer la réactivité observée en se basant sur une approche d'analyse vectorielle; l'état de transition de la cyclisation incorpore le nucléophile et les atomes de carbones du cation radical de l'alcène aux sommets d'un triangle obtus orthogonal par rapport au plan du système π.

Mots clés : transferts photoinduits d'électrons, cations radicaux, cyclisation, terpènes.

[Traduit par la rédaction]

Received November 29, 1995.

D.R. Arnold,[2] D.A. Connor, K.A. McManus, P.K. Bakshi, and T.S. Cameron. Department of Chemistry, Dalhousie University, Halifax, NS B3H 4J3, Canada.

[1] This is also Part 38 of the series Radical ions in photochemistry; see refs. 1 and 2 for preceding parts of these series.

[2] Author to whom correspondence may be addressed. Telephone: (902) 494-3714. Fax: (902) 494-1310. E-mail: arnold@chem1.chem.dal.ca

Introduction

The first examples of the photochemical nucleophile–olefin combination aromatic substitution (photo-NOCAS) reaction involved methanol, serving as the nucleophile, simple olefins, e.g., 2-methylpropene (**2**), and 1,4-dicyanobenzene (**1**) (reaction [1]) (3*a*,*b*). The major product results from the nucleophile (methanol) combining with the olefin radical cation ($\mathbf{2}^{+\bullet}$), at the less substituted carbon, followed by substitution of the resulting β-alkoxyalkyl radical at the *ipso* position of the 1,4-dicyanobenzene radical anion ($\mathbf{1}^{-\bullet}$) to give the *anti*-Markovnikov adduct (**3**). Subsequent studies have confirmed that the *anti*-Markovnikov mode of addition is preferred, and a mechanism, consistent with all of the observations, has been proposed (1, 3).

The scope of this reaction has recently been extended to include conjugated dienes (1*b*), nonconjugated dienes (1*d*,*e*), and alkenols (1*a*). The reactions of the nonconjugated dienes and alkenols (reactions [2], [3], [4], and [5]) are particularly relevant to this work. The intermediates involved in these reactions, alkene radical cations and alkyl radicals, can (and do) undergo intramolecular cyclization. This additional bond-forming reaction, proceeding to a more complex difunctional product, greatly extends the synthetic utility of the photo-NOCAS reaction. Of course, before this process is even considered for inclusion in a retrosynthetic strategy, the scope and limitations of the reaction will have to be understood. Rules, analogous to Baldwin's rules (4), for the cyclization of ionic intermediates, and Beckwith's rules (5), for the cyclization of radical intermediates, will have to be defined for radical ions.

The nonconjugated dienes previously studied were 2,5-dimethyl-1,5-hexadiene (**6**) and 2,6-dimethyl-1,6-heptadiene (**9**). Both of these dienes lead to 1:1:1 adducts indicative of intramolecular cyclization, at the radical cation stage, forming the 1,4-distonic radical cations, followed by attack of the nucleophile (methanol) and coupling of the resulting alkyl radical at the *ipso* position of the 1,4-dicyanobenzene radical anion ($\mathbf{1}^{-\bullet}$). The products include six- and seven-membered saturated ring systems, resulting from 1,6-*endo*, *endo* and 1,7-*endo*, *endo* cyclization of the radical cations (reactions [2] and [3]) (1*d*,*e*).

Reaction [1] (3*a*,*b*)

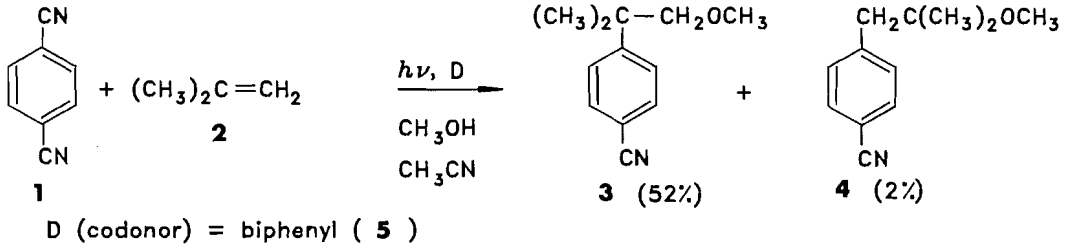

1 **3** (52%) **4** (2%)

D (codonor) = biphenyl (**5**)

Reaction [2] (1*d*)

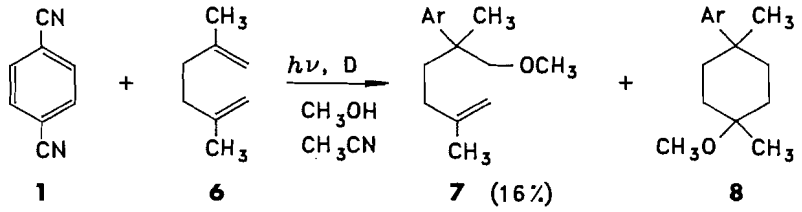

1 **6** **7** (16%) **8**

trans (4%) and *cis* (9%)

D = biphenyl (**5**)
Ar = 4-cyanophenyl

Reaction [3] (1*e*)

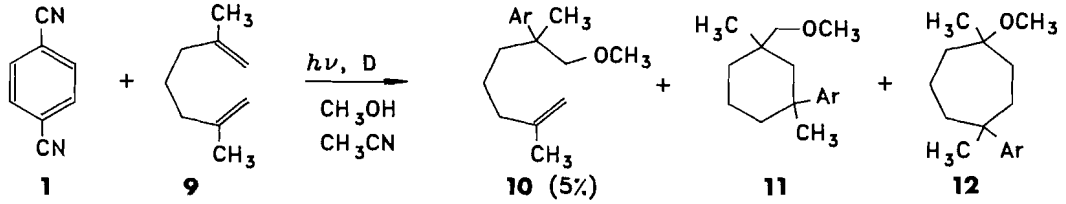

1 **9** **10** (5%) **11** **12**

cis (12%) *cis* (12%)
trans (11%) *trans* (10%)

D = biphenyl (**5**)
Ar = 4-cyanophenyl

Reaction [4] (1*a*)

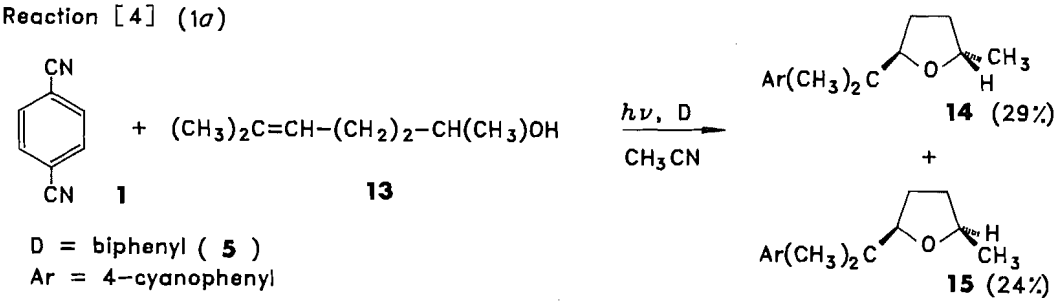

D = biphenyl (**5**)
Ar = 4-cyanophenyl

Reaction [5] (1*a*)

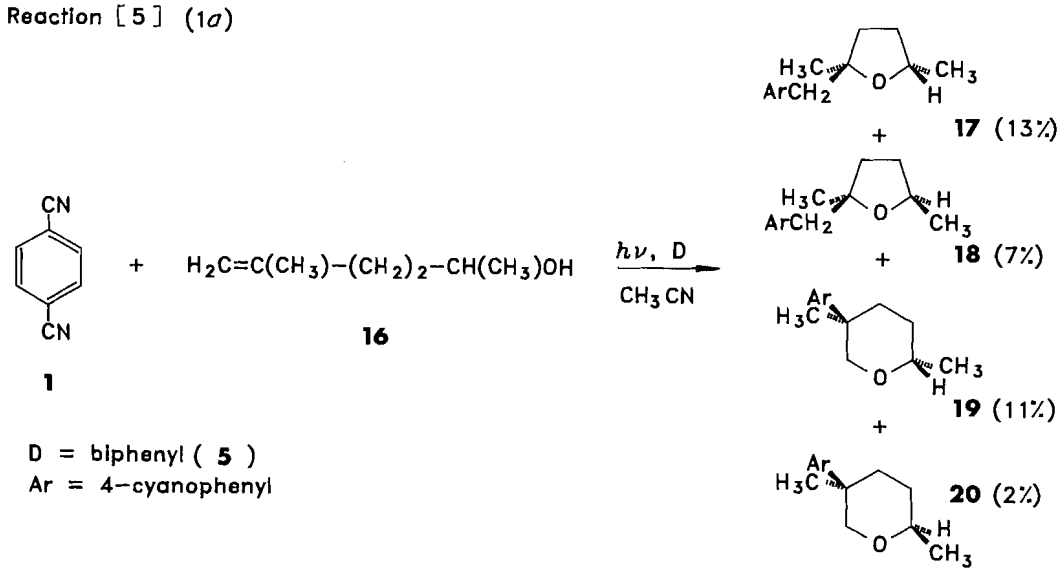

D = biphenyl (**5**)
Ar = 4-cyanophenyl

Additional examples of intramolecular cyclization were observed with the alk-4-enols: 6-methyl-5-hepten-2-ol (**13**) and 5-methyl-5-hexen-2-ol (**16**). Initial formation of the alkene radical cation was followed by intramolecular nucleophilic attack by the hydroxyl group; 1,5-*exo* and 1,6-*endo* cyclized products were formed (reactions [4] and [5]) (1*a*).

We have now extended this study to two interesting related alkenes: a 1,5-diene, (*R*)-(+)-limonene ((4*R*)-1-methyl-4-(1-isopropenyl)cyclohexene) (**21**), and a 1,4-alkenol, (*R*)-(+)-α-terpineol ((4*R*)-4-(1-hydroxy-1-methylethyl)-1-methyl-1-cyclohexene) (**22**). We recognized, at the outset, that there were additional steric constraints associated with these cyclic systems, relative to the acyclic analogues, that might hinder/inhibit cyclization of the radical cations. Furthermore, the original stereogenic carbon will not be epimerized under these mild reaction conditions and, if the radical cations and (or), in the case of limonene (**21**), the intermediate β-alkoxyalkyl radical do cyclize, this process would lead to interesting chiral bicyclic structures.

Results

The acetonitrile–methanol (3:1) solution of 1,4-dicyanobenzene (**1**), biphenyl (**5**), and the alkene was irradiated, using our typical reaction conditions, with a medium-pressure mercury vapour lamp through Pyrex. Progress of the reaction was monitored by capillary column gas chromatography with a flame ionization detector (gc/fid). The first indication of the structure of the products was obtained from a gas chromatograph equipped with a mass selective detector (gc/ms). The products were isolated by medium-pressure liquid chromatography (mplc). The yields generally were based upon the quantity of pure isolated products with 1,4-dicyanobenzene (**1**) as the limiting reagent. The alkene was present in excess. When the photo-NOCAS products were difficult to separate, the total weight of the mixture was obtained and the ratio(s) of the isomers was determined by gc/fid (integrated peak intensity). These ratios were similar to those observed on the crude reaction mixture. The ratio of products was not dependent on the extent of conversion: these ratios remained constant during the irradiation.

The products from (*R*)-(+)-limonene (**21**) (reaction [6]) were the 1:1:1 (methanol: **21**: **1**) photo-NOCAS adducts: 4-[(1*R*,2*S*,4*R*)-4-isopropenyl-2-methoxy-1-methylcyclohexyl]-benzonitrile (**23**, 30%), 4-[(1*S*,2*R*,4*R*)-4-isopropenyl-2-methoxy-1-methylcyclohexyl]benzonitrile (**24**, 2%), 4-[(1*R*,2*R*,5*R*)-5-isopropenyl-2-methoxy-2-methylcyclohexyl]benzonitrile (**25**, 3%), and 4-[(1*S*,2*S*,5*R*)-5-isopropenyl-2-methoxy-2-methylcyclohexyl]benzonitrile (**26**, 1%). Isomers **23** and **24** result from *anti*-Markovnikov addition to the cyclic alkene; their combined yields make this the major mode of addition. Isomers **25** and **26** result from Markovnikov addition to the cyclic alkene. Under these conditions (methanol, 6 M) we found no evidence for cyclization of either the initially formed alkene radical cation ($\mathbf{21}^{+\bullet}$) or the intermediate β-alkoxyalkyl radical. Lowering the concentration of methanol (1 M) led to

Reaction [6]

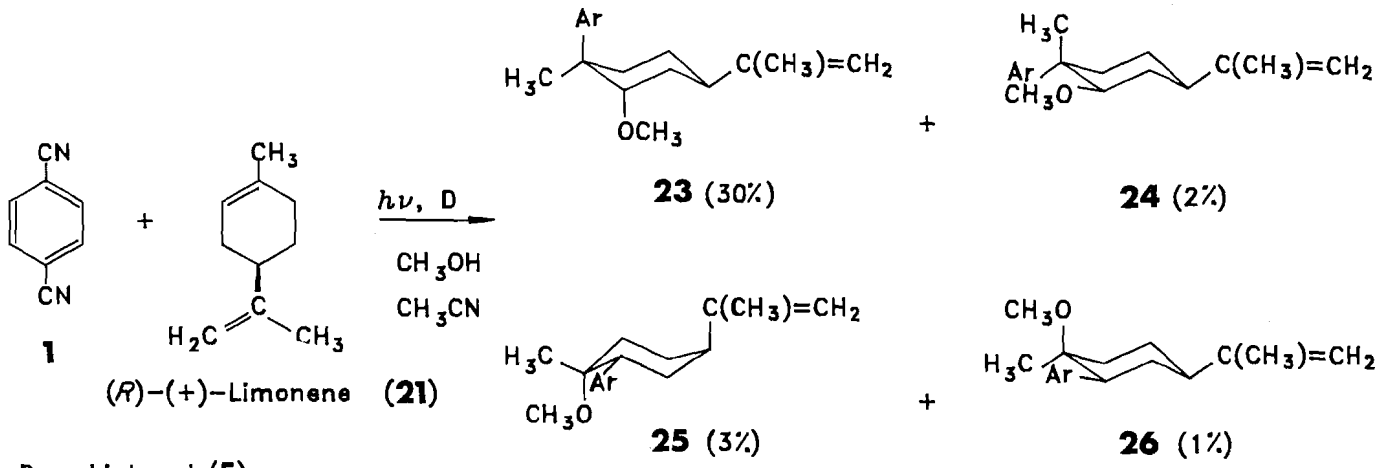

D = biphenyl (**5**)

Ar = 4-cyanophenyl

Reaction [7]

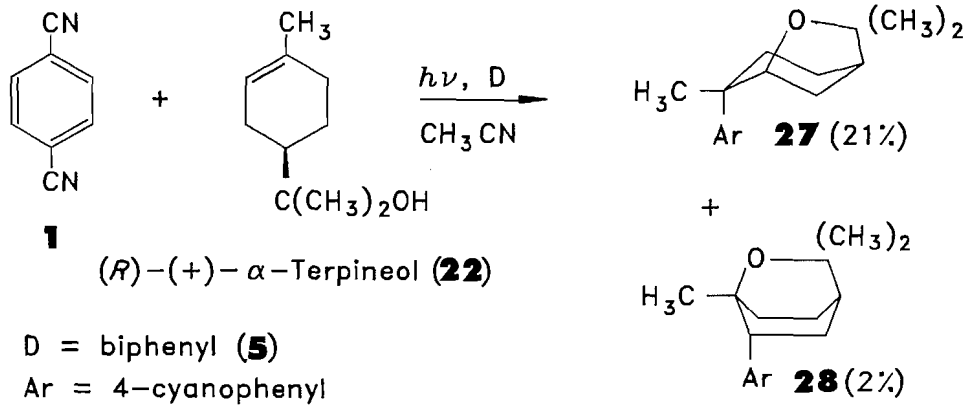

D = biphenyl (**5**)

Ar = 4-cyanophenyl

decreased yields of the 1:1:1 adducts, but no cyclized products were detected (gc/ms).

When an acetonitrile solution (no added methanol) of 1,4-dicyanobenzene (**1**), biphenyl (**5**), and (*R*)-(+)-α-terpineol (**22**) was irradiated under these conditions, the products were the cyclized 1:1 (**22** : **1**) photo-NOCAS adducts: (1*R*,2*S*,5*R*)-2-(4-cyanophenyl)-2,6,6-trimethyl-7-oxabicyclo[3.2.1]octane (**27**, 21%) and (1*S*,4*R*,6*R*)-6-(4-cyanophenyl)-1,3,3-trimethyl-2-oxabicyclo[2.2.2]octane (**28**, 2%) (reaction [7]). Compound **27**, the major product, results from intramolecular 1,5-*exo* cyclization of the radical cation **22**$^{+\bullet}$. The minor product (**28**) results from 1,6-*endo* cyclization. When this irradiation was carried out in the usual mixed solvent, acetonitrile–methanol (3:1), the yield of cyclized products was greatly reduced and 1:1:1 (methanol : **22** : **1**) adducts became major products. These 1:1:1 adducts were detected (gc/ms) but were not isolated.

Structural assignments

Structural assignments for the products were based primarily upon detailed analysis of ^{1}H and ^{13}C nmr spectra and, for four of the products (**24**, **26**, **27**, and **28**), structures were firmly established by X-ray crystallography.[3] All of the products resulting from (*R*)-(+)-limonene (**21**) exhibit ^{1}H nmr spectra having an AA′XX′ pattern at 7–8 ppm, clearly indicating the presence of a 1,4-disubstituted aryl group. Also observed was a singlet at 3.1–3.4 ppm, which is consistent with a methoxy methyl group. The evidence of the signals of two protons in the vinyl region of the ^{1}H nmr spectrum of these products suggests the addition has taken place across the endocyclic alkene. These common features support the assumption that these products are 1:1:1 adducts involving the more heavily substituted cyclic alkene, without intramolecular cyclization into the double bond of the isopropenyl side chain.

The ^{13}C nmr spectra show a pair of doublets and three sin-

[3] Data for **24**, **26**, **27**, and **28** may be purchased from: The Depository of Unpublished Data, Document Delivery, CISTI, National Research Council Canada, Ottawa, Canada K1A 0S2. Details of data collection, structural analysis and refinement, and tables of interatomic distances and bond angles have also been deposited with the Cambridge Crystallographic Data Centre and may be obtained on request from the Director, Cambridge Crystallographic Data Centre, University Chemical Laboratory, 12 Union Road, Cambridge, CB2 1EZ, U.K.

glets in the aromatic region, a singlet–triplet combination at low field, a mid-field quartet, and two high-field quartets, confirming the presence of the 4-cyanophenyl, the olefin, the methoxy methyl group, and two additional methyl groups, respectively.

The regiochemistry of the products from (*R*)-(+)-limonene (**21**) was determined from the shifts of the ^{13}C and ^{1}H nmr signals. In the ^{13}C nmr spectra, the signals of a carbon adjacent to an oxygen generally occur at lower field (72–94 ppm), relative to those adjacent to the 4-cyanophenyl group (37–55 ppm) (1, 3). The *anti*-Markovnikov adducts would have a quaternary carbon bearing methyl and aryl groups (37–55 ppm) and a methine carbon substituted by a methoxy group (72–94 ppm) (1, 3). Isomers **23** and **24** each have an off-resonance doublet at 81.56 and 84.42 ppm, respectively, and a singlet at 43.27 and 43.11 ppm, respectively; therefore, these are the *anti*-Markovnikov adducts. The Markovnikov adducts would have a quaternary carbon bearing methyl and methoxy groups (72–94 ppm) and a methine carbon substituted by an aryl group (37–55 ppm). Isomers **25** and **26** each show a singlet at 76.04 and 73.67 ppm, respectively, and an off-resonance doublet between 38 and 55 ppm.

In the ^{1}H nmr, the signals of a proton on a carbon adjacent to an oxygen generally occur at lower field (3.2–3.7 ppm) than those adjacent to the 4-cyanophenyl group (2.4–3.0 ppm) (1, 3). The ^{1}H nmr spectra of isomers **23** and **24** show a single proton signal at 3.84 and 3.45 ppm, respectively. These are assigned to protons geminal to the methoxy group and thus confirms that these are *anti*-Markovnikov adducts. Isomers **25** and **26** have single proton signals at 3.09 and 2.56 ppm, respectively. These are assigned to protons geminal to the 4-cyanophenyl group. No single proton signals were observed in the region 3.2–3.7 ppm. This evidence confirms that these isomers, **25** and **26**, are Markovnikov adducts.

The stereochemical assignments for these isomers were more difficult to establish. Each of these isomers has three stereogenic centres, including one that was the original juncture of the ring and the isopropenyl substituent. This centre is not expected to epimerize under these (mild) reaction conditions; thus, once the relative configuration of the substituents is established, the absolute configuration will also be known. The structures of isomers **24** and **26** were firmly established by X-ray crystallography. These results confirm the validity of the interpretation based upon the nmr spectra. The assignment of stereochemistry for the other isomers, **23** and **25**, rests entirely upon the interpretation of the nmr, aided by comparison of the nmr spectra with those of the isomers **24** and **26**.

Compound **24**, 4-[(1*S*,2*R*,4*R*)-4-isopropenyl-2-methoxy-1-methylcyclohexyl]benzonitrile, shows a doublet of doublets at 3.45 ppm in the ^{1}H nmr spectrum. The coupling constants are 11.2 Hz and 4.2 Hz. These must be the axial–axial and axial–equatorial couplings of an axial proton geminal to the methoxy group. This is consistent with the X-ray determined structure for this compound, which shows the methoxy group in the equatorial position (Fig. 1).

The overlap of the other signals in the ^{1}H nmr spectrum made a complete assignment of the ring protons difficult. However, with the aid of proton–proton decoupling experiments, a "quartet" was found in the three-proton multiplet at 1.38–1.57 ppm which collapsed to a "triplet" upon irradiation of the proton geminal to the methoxy group. This "quartet" has

Fig. 1. X-ray structure of 4-[(1*S*,2*R*,4*R*)-4-isopropenyl-2-methoxy-1-methylcyclohexyl]benzonitrile (**24**).

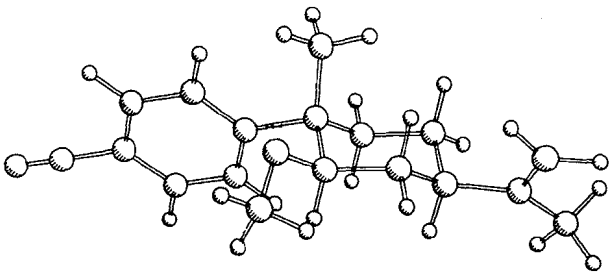

a coupling of ca. 12 Hz, as does the "triplet" resulting from decoupling. As the methoxy group has vicinal protons on only one side, this "quartet" (1.38–1.57 ppm) must be partially due to an axial proton on C-3, vicinal to both the methoxy and isopropenyl groups. The three observed coupling constants of ca. 12 Hz each indicate that there must be two axial–axial couplings and a geminal coupling, evidence that the isopropenyl group must be in the equatorial position, in agreement with the X-ray structure.

The ^{13}C nmr spectral support for the axial position of the cyclohexyl methyl was provided by the coupling between the methyl carbon and the vicinal protons. This coupling ($^{3}J_{C-H}$) follows a Karplus relationship similar to that pertaining to vicinal proton–proton coupling ($^{3}J_{H-H}$), dependent on the dihedral angle of the coupled nuclei (6). In general, the magnitude of $^{3}J_{C-H}$ is ca. 0.6 that of analogous $^{3}J_{H-H}$. In the ^{13}C nmr spectrum of **24**, the quartet at 16.69 ppm was assigned to the cyclohexyl methyl group (evidence for this is provided in the structural proof of compound **23**). This quartet has a 16 Hz width at half-height. This broad a peak indicates the methyl group is axial, producing two axial–axial and one axial–equatorial vicinal proton–carbon interactions. Assignment of an axial methyl group is consistent with the X-ray results.

The assignment of the two methyl quartets in the ^{13}C nmr was done rigorously for the major product (**23**; 4-[(1*R*,2*S*,4*R*)-4-isopropenyl-2-methoxy-1-methylcyclohexyl]benzonitrile) and by comparison with others. A two-dimensional heterocorrelation spectrum of **23** showed correlation of the lower field quartet (29.14 ppm) in the ^{13}C nmr spectrum with the higher field singlet (1.19 ppm) in the ^{1}H nmr spectrum, as well as the higher field quartet (21.03 ppm) in the ^{13}C nmr spectrum with the lower field singlet (1.61 ppm) in the ^{1}H nmr spectrum. (The assignment of the methyl signals in the proton spectra had been done by double irradiation of the vinyl protons.) The quartets in the ^{13}C nmr spectra of the other products were assigned on the basis of shifts. Each ^{13}C nmr spectrum had a quartet near 21 ppm with half-height width about 25 Hz. The other quartet was found either lower or higher (16–29 ppm) and with half-height widths ranging from 10 to 16 Hz. The quartet (near 21 ppm) with the more consistent shift from isomer to isomer and a wider half-height was assigned to the methyl on the vinyl side chain since it is in a more consistent environment from isomer to isomer and because coupling through a double bond is expected to be greater. The other quartet in each spectrum is the cyclohexyl methyl group. This was consistent with the assignment done by heterocorrelation for **23**.

The major product, **23**, is the *anti*-Markovnikov stereoiso-

Fig. 2. X-ray structure of 4-[(1*S*,2*S*,5*R*)-5-isopropenyl-2-methoxy-2-methylcyclohexyl]benzonitrile (**26**).

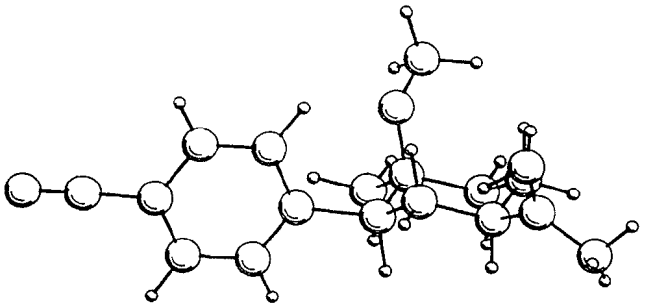

Fig. 3. X-ray structure of (1*R*,2*S*,5*R*)-2-(4-cyanophenyl)-2,6,6-trimethyl-7-oxabicyclo[3.2.1]octane (**27**).

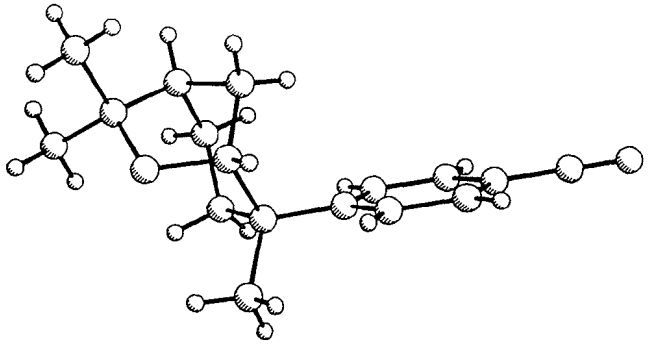

Fig. 4. X-ray structure of (1*S*,4*R*,6*R*)-6-(4-cyanophenyl)-1,3,3-trimethyl-2-oxabicyclo[2.2.2]octane (**28**).

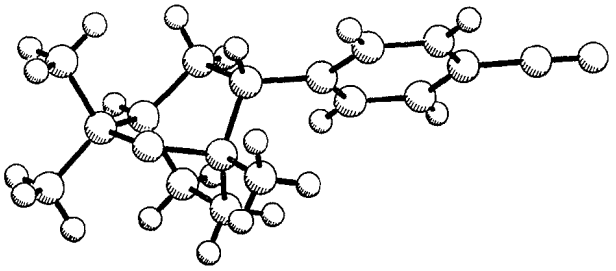

mer of the product, **24**, whose structure was determined by X-ray analysis. The ring protons of **23**, assigned using double irradiation experiments and COSY data, confirm the coupling relationships. There is a single proton resonance at 3.84 ppm which is the proton geminal to the methoxy group. The resonance exhibits a doublet of doublets having couplings of 4.0 Hz and 1.9 Hz . By comparison to the corresponding signal (3.45 ppm; 11.2 Hz and 4.2 Hz) in the other *anti*-Markovnikov product, **24**, the geminal proton must be equatorial and the methoxy group axial. The resonance at 2.32 ppm, a multiplet consisting of two 12.0 Hz couplings, was assigned as the proton geminal to the isopropenyl group. It must be coupled to both vicinal axial protons by 12.0 Hz. This indicates that the isopropenyl group must be in the equatorial position and the geminal proton is in the axial position.

The configuration at C-1, bearing a methyl and aryl ring, could not be simply determined by the carbon–proton coupling constant because the quartet at 29.14 ppm in the ^{13}C nmr spectrum showed no discernable fine structure and a half-height width of 15 Hz. Consequently, a two-dimensional NOESY spectrum was obtained as well. A nuclear Overhauser effect was observed between the cyclohexyl methyl group (1.19 ppm) and the vicinal axial methoxy proton (3.43 ppm) and the vicinal axial ring proton (1.95 ppm). Another nuclear Overhauser effect was observed between the aryl group protons (7.49 ppm) and the 1,3-diaxial protons (1.16 and 1.27 ppm). These results indicated that the methyl group was equatorial and the aryl group was axial.

The stereochemistry of product **26**, 4-[(1*S*,2*S*,5*R*)-5-isopropenyl-2-methoxy-2-methylcyclohexyl]benzonitrile, has been established by X-ray diffraction (Fig. 2) and the nmr data are in agreement. The single proton resonance at 2.56 ppm is the lowest field signal after the aromatic, vinyl, and methoxy proton signals and was assigned as the benzylic proton; a proton on a carbon adjacent to the 4-cyanophenyl group is in the range of 2.4–3.0 ppm (1, 3). The resonance at 2.56 ppm is a doublet of doublets having couplings of 12.1 Hz and 3.2 Hz. The benzylic proton was thus assigned to the axial position, putting the aryl ring in the equatorial position. This is in agreement with the structure and conformation established by X-ray diffraction. The cyclohexyl methyl group, geminal to the methoxy group, exhibits a quartet in its coupled ^{13}C nmr spectrum with a half-height width of 10 Hz. This supports the assignment that the methyl group is in the equatorial position.

The ^1H nmr spectrum of product **25**, 4-[(1*R*,2*R*,5*R*)-5-isopropenyl-2-methoxy-2-methylcyclohexyl]benzonitrile, includes a doublet of doublets (8.7 and 4.5 Hz) at 3.09 ppm. This signal was assigned to the benzylic proton. The couplings indicate that the benzylic proton is axial and the aryl group is in the equatorial position. Decoupling experiments indicate that the resonance at 2.41 ppm is due to the proton geminal to the isopropenyl group. A 500 MHz spectrum shows that the signal at 2.41 ppm is a quintet. If the proton is axial, it should not couple equally to the four vicinal protons as the experimental quintet indicates must be the case. The isopropenyl group is therefore axial. A NOESY correlation between one of the vinyl protons and the benzylic proton is further evidence of the 1,3-diaxial placement of the isopropenyl group and the benzylic proton. The cyclohexyl methyl group is assigned the equatorial position because the coupled ^{13}C nmr spectrum shows the width of the quartet (19.25 ppm) at half-height is ca. 10 Hz. This is too narrow for an axial methyl, which would have two axial–axial and one axial–equatorial proton couplings. This is consistent with the quartet (23.01 ppm) in product **26**, which is known to represent an equatorial methyl group as well.

The products resulting from (*R*)-(+)-α-terpineol (**22**) were identified as (1*R*,2*S*,5*R*)-2-(4-cyanophenyl)-2,6,6-trimethyl-7-oxabicyclo[3.2.1]octane (**27**) and (1*S*,4*R*,6*R*)-6-(4-cyanophenyl)-1,3,3-trimethyl-2-oxabicyclo[2.2.2]octane (**28**). The overall structures of **27** and **28** were firmly established by X-ray analysis of a single crystal (Figs. 3 and 4, respectively). The ^1H and ^{13}C nmr spectra are consistent with these structures. For **27**: the ^1H nmr spectrum exhibits three singlets in the aliphatic region, indicative of the three methyl groups: a benzylic methyl group and two methyl groups bonded to the same carbon, which is adjacent to a chiral centre; these two methyl groups are therefore nonequivalent. A broad doublet at low field (4.25 ppm) indicates a methine group at the bridgehead adjacent to an oxygen. An AA′XX′ pattern in the aromatic region of the ^1H nmr spectrum is indic-

ative of the 4-cyanophenyl group. The ^{13}C nmr spectrum of **27** indicates three methyl groups, two of which have very similar shifts (29.70 and 30.12 ppm). A singlet at 44.94 ppm indicates a benzylic quaternary carbon, and a singlet and doublet at 83.00 and 83.07 ppm, respectively, support the bridgehead methine group and quaternary carbon, both adjacent to oxygen. The signal of a carbon adjacent to an oxygen generally occurs at lower field (72–94 ppm) than those adjacent to the 4-cyanophenyl group (1, 3).

The ^1H and ^{13}C nmr spectra of **28** are also consistent with the structure determined by X-ray analysis of a single crystal (Fig. 4). The ^1H nmr spectrum exhibits three singlets in the aliphatic region, indicative of three methyl groups. The proposed structure has a methyl group at a bridgehead, as well as two methyl groups bonded to the same carbon, which is adjacent to a stereogenic centre; these two methyl groups are therefore nonequivalent. A triplet of triplets at lower field (2.50 ppm) indicates a methine group at the bridgehead not adjacent to an oxygen, unlike compound **27**, which indicates a much lower field signal (4.25 ppm) for the methine group at the bridgehead, thus supporting that the methine group is adjacent to an oxygen. An AA′XX′ pattern in the aromatic region of the ^1H nmr spectrum is indicative of the 4-cyanophenyl group. The ^{13}C nmr spectrum of **28** indicates three methyl groups, two of which have the same shift (28.94 ppm). A doublet at 49.39 ppm indicates a benzylic methine carbon, and two singlets at 72.90 and 73.78 ppm support the bridgehead quaternary carbon and the quaternary carbon, both adjacent to oxygen. The signal of a carbon adjacent to an oxygen generally occurs at lower field (72-94 ppm), than those adjacent to the 4-cyanophenyl group (1, 3). Another doublet at 33.59 ppm indicates the bridgehead methine group not adjacent to oxygen.

Discussion

The first steps of the photo-NOCAS reaction involve electron transfer from the donor (olefin) to the first excited singlet state of the acceptor (1,4-dicyanobenzene (**1**)) . The free energy for this process can be calculated using the Weller equation (eq. [8] (7)); electron transfer to the first excited singlet state of **1** from either (*R*)-(+)-limonene (**21**) or (*R*)-(+)-α-terpineol (**22**) is exergonic by at least 45 kJ mol^{-1} (Table 1). This process can be expected to occur at the diffusion-controlled rate (7).

[8] (7) $\Delta G_{et} = F\,(E_{1/2}{}^{ox}\,(D) - E_{1/2}{}^{red}\,(A) - e/\varepsilon\alpha) - E_{0,0}\,(A)$

Previous results have shown that the efficiency of the photo-NOCAS reaction can be increased by the addition of biphenyl (**5**), serving as a codonor. The explanation for this enhancement is based upon the relative efficiency of escape from the solvent cage of the initially formed alternative geminate radical ion pairs (1, 3). These reactions, [6] and [7], were also made more efficient upon the addition of the codonor, biphenyl (**5**).

Single electron transfer from (*R*)-(+)-limonene (**21**) can be expected to occur predominantly from the more substituted cyclic alkene, site of the more stable radical cation (**21**$^{+\bullet}$). The analogous acyclic diene radical cations, **6**$^{+\bullet}$ and **9**$^{+\bullet}$, cyclize 1,6-*endo*, *endo* and 1,7-*endo*, *endo* (reactions [2] and [3]) (1*d*,*e*). There is also evidence (esr spectroscopy) for the cyclization, and subsequent rearrangement, of the radical cation of 4-vinylcyclohexene (9). However, neither 4-vinylcyclohexene nor limonene (**21**) gave cyclized products upon anodic oxidation in methanol (10). Evidently, cyclization of the vinylcyclohexene and limonene (**21**$^{+\bullet}$) radical cations is slow in methanol solution relative to competing processes (nucleophilic attack, deprotonation, further anodic oxidation).

These results can be explained in terms of the alternative conformations available to limonene (**21**) and to the corresponding radical cation (**21**$^{+\bullet}$); there is good evidence that the structure of the alkene radical cation is similar to that of the neutral molecule (11). Molecular mechanics (MM3) calculations were used to determine the structure and relative energies of the conformers (Table 2*a*). Four conformers were identified; as expected, the global minimum conformer has the half-chair structure with the isopropenyl side chain equatorial.

Table 1. The oxidation potentials of (*R*)-(+)-limonene (**21**) and (*R*)-(+)-α-terpineol (**22**) and the calculated free energy change (ΔG_{et}) for the electron transfer process from the alkene to the electronic excited singlet state of the acceptor, 1,4-dicyanobenzene (**1**).

Alkene	$E_{1/2}{}^{ox}$(V)[a]	ΔG_{et}(kJ mol^{-1})[b]
(*R*)-(+)-Limonene (**21**)	2.15	−46.2
(*R*)-(+)-Terpineol (**22**)	1.97	−63.6

[a]Oxidation potentials were measured at a platinum electrode relative to the saturated calomel electrode (SCE), using tetraethylammonium perchlorate (0.1 m TEAP) as the electrolyte in acetonitrile. The anodic waves were irreversible; the half-wave potentials were estimated by subtracting 0.028 V from the peak potentials (8).

[b]Based upon the Weller equation (eq. [8]) (7); $E_{0,0}$ (**1**) 408.4 kJ mol^{-1}, $E_{1/2}{}^{red}$ (**1**) −1.66 V, the Coulombic attraction term was taken to be 5.4 kJ mol^{-1} (3*a*).

Table 2. (*a*) Conformations (MM3) of (*R*)-(+)-limonene (**21**). (*b*) Conformations (MM3) of (*R*)-(+)-α-terpineol (**22**).

(*a*)

	∠C2-C3-C4-C5[a]	∠C3-C4-C5-O6[a]	Δ*H*(kJ mol^{-1})[b]
Axial-*anti*	81.5	137.2	13.9
Axial-*syn*	76.3	−11.0	5.2
Equatorial	−173.7	108.3	−1.6
Equatorial	−174.3	−115.2	−2.1

(*b*)

	∠C2-C3-C4-C5[a]	∠C3-C4-C5-C6[a]	Δ*H*(kJ mol^{-1})[b]
Axial-*anti*	83.2	−170.3	−273.0
Axial-*gauche*	84.5	67.4	−274.7
Axial-*syn*	79.6	−60.4	−286.1
Equatorial	−174.2	−54.6	−288.5
Equatorial	−172.8	60.1	−290.8
Equatorial	−174.3	−177.2	−291.4

[a]Sign of dihedral angle A-B-C-D: when looking through B toward C, if D is counterclockwise from A, negative.

[b]Heat of formation.

Fig. 5. (*R*)-(+)-Limonene, **21** (*axial-syn*). C1—C6, 3.54 Å. C2—C6, 3.27 Å.

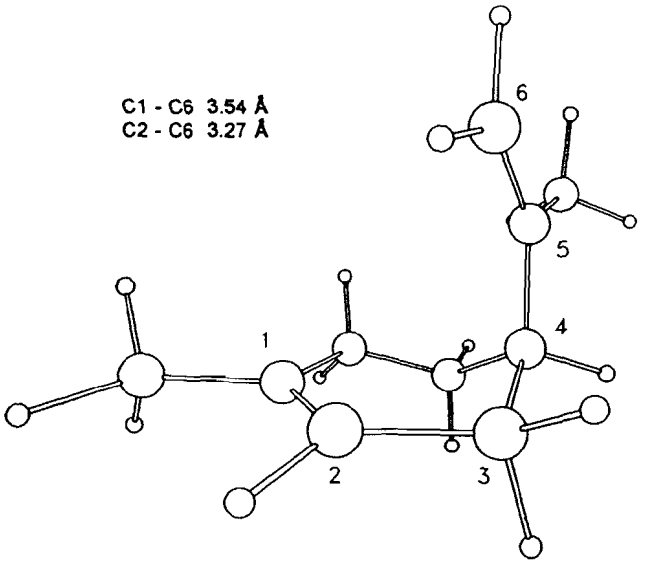

The conformer required for cyclization, axial-*syn* (Fig. 5), is 7.3 kJ mol^{-1} less stable than this global minimum and is a minor (2.4% at 10°C) component of the equilibrium mixture. Furthermore, the structure of this axial-*syn* conformer is not favourably orientated for cyclization; the C1—C6 (3.54 Å) and C2—C6 (3.27 Å) distances are long. In addition, the isopropenyl π-molecular orbital (C5—C6), which must serve as the nucleophile, is not directed toward the half-filled π-bond of the radical cation (C1—C2). In view of these structural considerations, formation of 1:1:1 photo-NOCAS adducts, resulting from intermolecular nucleophilic (methanol) attack at the more heavily substituted (easier to oxidize) endocyclic double bond, without prior cyclization, is reasonable (reaction [6]).

It is interesting to compare the regio- and stereochemistry of these 1:1:1 photo-NOCAS adducts with those obtained from 1-methylcyclohexene (**29**) under analogous conditions (reaction [9]); the products from these reactions are similar. The *anti*-Markovnikov mode of addition dominates (86 and 89%) in both reactions. Coupling of the resulting β-alkoxyalkyl radical, with the 1,4-dicyanobenzene radical anion ($\mathbf{1}^{-\bullet}$), occurs preferentially from the pseudo-axial position *trans* to the methoxy group; **23** and **30** are the major products. Pseudo-axial attack generally dominates during radical additions to substituted cyclohexenes (12). The initial attack of methanol on the limonene radical cation ($\mathbf{21}^{+\bullet}$) also occurs preferentially

Fig. 6. (*R*)-(+)-α-Terpineol, **22** (*axial-syn*). C1—O6, 3.09 Å. C2—O6, 3.12 Å.

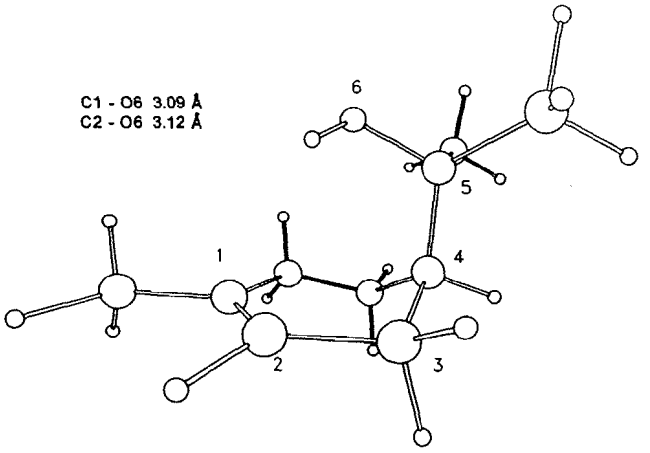

from the pseudo-axial position, of the half-chair conformer, *trans* to the equatorial isopropenyl side chain.

The radical cations of the acyclic analogues of terpineol (**22**), 6-methyl-5-hepten-2-ol ($\mathbf{13}^{+\bullet}$) and 5-methyl-5-hexen-2-ol ($\mathbf{16}^{+\bullet}$), undergo 1,5-*exo* and 1,6-*endo* cyclization under photo-NOCAS conditions (reactions [4] and [5]). The radical cation of terpineol ($\mathbf{22}^{+\bullet}$) also cyclizes both 1,5-*exo* and 1,6-*endo* (reaction [7]). Six conformers of terpineol (**22**) were identified by molecular mechanics (MM3). The conformer required for cyclization, axial-*syn* (Fig. 6), is 5.3 kJ mol^{-1} less stable than the global minimum and is a minor participant (4.9%, 10°C) at equilibrium. This conformer is nicely oriented for cyclization; the C1—O6 (3.09 Å) and C2—O6 (3.12 Å) distances are relatively short and a nonbonding pair of electrons on the oxygen (O6) is directed toward the radical cation (C1—C2). The thermal barrier for inverting the half-chair conformation of cyclohexenes is small; equilibration may occur during the lifetime of the radical cation. The preference for C2—O6 bonding, 1,5-*exo* cyclization, may be attributed to the relative stability of the intermediates. The major product (**27**) results from the *anti*-Markovnikov mode of addition, followed by coupling of the β-alkoxyalkyl radical, from the pseudo-axial position *trans* to the alkoxy group, with the dicyanobenzene radical anion ($\mathbf{1}^{-\bullet}$).

Conclusions

Knowledge of the scope and limitations of the photo-NOCAS reaction, involving methanol as the nucleophile, and of the

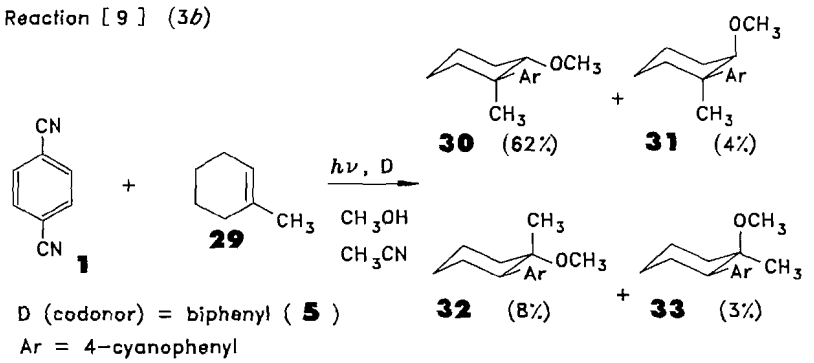

behaviour of alkene radical cations, continues to grow. The intramolecular reactivity of alkene radical cations, 1,5-*exo* and 1,6-*endo* cyclization, can be predicted using approach vector analysis; the favoured transition state incorporates the nucleophile and the alkene radical cation carbon atoms at the vertices of an obtuse triangle orthogonal to the plane of the π-system (4). The occurrence of cyclization can be explained/predicted on the basis of structural information obtained from molecular mechanics (MM3) calculations. These reactions have significant synthetic utility.

Experimental

General information

The ^1H and ^{13}C nmr spectra were obtained from a Bruker 250 MSL spectrometer or from a Nicolet 360 NB nmr spectrometer. Spectra were recorded in parts per million (ppm) and frequencies are reported relative to tetramethylsilane. Infrared spectra (ir) were recorded on a Nicolet 205 FTIR or on an air-purged Perkin–Elmer 180 grating spectrometer and are reported in wave numbers (cm^{-1}). Elemental analyses were performed by Canadian Microanalytical Service Ltd., B.C. Exact Mass determinations were obtained using a ZAB-E spectrometer. Measurements of optical rotation were carried out in ethanol solution on a Perkin–Elmer 141 polarimeter. Melting points were determined using a Cybron Corporation Thermolyne apparatus with a digital thermocouple and are corrected. Product yields and progress of the reactions were determined using a Hewlett–Packard (HP) 5890 gas chromatograph with a DB-1701 fused silica WCOT column (30 m × 0.25 mm, 0.25 μm film thickness) and a calibrated flame ionization detector (gc/fid) and are based upon 1,4-dicyanobenzene (**1**) as the limiting reagent. An HP 3392A integrator was interfaced with the gc/fid to obtain peak areas. An HP 5890 gas chromatograph with a 5% phenyl methyl silicone fused silica WCOT column (25 m × 0.20 mm, 0.33 μm film thickness) interfaced with an HP 5970 mass selective detector (gc/ms) was also used for product analyses. Mass spectra are reported as *m/z* (relative intensity). Separation of product mixtures was generally carried out using preparative medium-pressure liquid chromatography (mplc) (*3b*). The mplc consists of a 2.5 cm × 1 m column packed with thin-layer chromatography (tlc) grade silica gel (without binder) (cat. no. 7747 Merck) at a pressure of 15 psi using helium (1psi = 6.9 kPa). Connected to the mplc was a uv spectrophotometer – fraction collector that collects ca. 10 mL fractions. Dry column flash chromatography (dc/fc) was also used (13). This column was also packed with thin-layer chromatography grade silica gel (without binder) (cat. no. 7747 Merck). Fraction sizes were ca. 5 mL.

Materials

Acetonitrile (Fisher ACS grade) was distilled twice, first from sodium hydride and then from phosphorus pentoxide. It was then passed through a column of basic alumina, refluxed over calcium hydride for 24 h (under a nitrogen atmosphere), fractionally distilled (under nitrogen), and stored over molecular sieves (3 Å) (14). Methanol was distilled and then stored over molecular sieves (4 Å). Dicyanobenzene-1,4 (**1**) (Aldrich) was purified by treatment with Norite in methylene chloride, followed by recrystallization from 95% ethanol. Tetraethylammonium perchlorate (TEAP) (Aldrich) was recrystallized three times from water and then dried in a vacuum oven for 15 h, 70°C, 0.25 Torr (1 Torr = 133.3 Pa). The (*R*)-(+)-limonene (**21**) (97%) was obtained from the Aldrich Chemical Co. The rotation was measured to be $[\alpha]_D^{21.5}$ +97.0 (*c* 1.26, 95% ethanol). Aldrich reports the rotation to be $[\alpha]_D^{20}$ +123 (neat). The (*R*)-(+)-α-terpineol (**22**) (99%) was obtained from the Fluka Chemika-BioChemika Co. The rotation was measured to be $[\alpha]_D^{21}$ +87.9 (*c* 2.02, absolute ethanol). Fluka reports the rotation to be $[\alpha]_D^{20}$ +85 ± 2 (neat).

Irradiations

Irradiations involving (*R*)-(+)-limonene (**21**) were carried out on solutions of 1,4-dicyanobenzene (**1**), the diene, and biphenyl (**5**) in acetonitrile–methanol (3:1). Irradiations involving (*R*)-(+)-α-terpineol (**22**) were carried out on solutions of acetonitrile with 1,4-dicyanobenzene, the alk-4-enol, and biphenyl. Solutions were irradiated in either 2 cm i.d. Pyrex tubes or 5 mm Pyrex nmr tubes, which were degassed by nitrogen ebullition. These samples were irradiated at 10°C using a CGE 1 kW medium-pressure mercury vapour lamp contained in a water-cooled Pyrex immersion well.

Cyclic voltammetric measurements

Cyclic voltammetry was used to obtain the oxidation potential of the alkenes. The apparatus has been described (15). The working electrode was a platinum sphere (1 mm diameter) and the counter electrode was a platinum wire. The reference electrode was a saturated calomel electrode (sce), which was connected to the solution (TEAP 0.1 M, acetonitrile) through a Luggin capillary. The alkene concentration was ca. 0.005 M. Since the anodic wave was irreversible, the half-wave potential was taken as 0.028 V before the anodic peak potential (8).

Formation of the methanol, (*R*)-(+)-limonene (21), 1,4-dicyanobenzene (1) photo-NOCAS adducts 23, 24, 25 and 26: reaction [6]

A solution of (*R*)-(+)-limonene (**21**) (7.8 mL, 6.6 g, 0.048 mol), 1,4-dicyanobenzene (**1**) (3.1 g, 0.024 mol), and biphenyl (**5**) (3.7 g, 0.024 mol) in acetonitrile–methanol (3:1, 240 mL) was degassed by nitrogen ebullition and irradiated for 8–10 days using a 1 kW lamp at 10°C. The solvent was removed on a rotary evaporator and the crude photolysate was separated by chromatography (mplc) using a linear solvent gradient (hexanes–dichloromethane). Further purification was achieved via additional chromatography using mplc and dc/fc. Four 1:1:1 adducts were isolated: **23**, **24**, **25**, and **26**.

4-[(1R,2S,4R)-4-Isopropenyl-2-methoxy-1-methylcyclohexyl]benzonitrile (23)

The yield of **23** was 30%: $[\alpha]_D^{22}$ +48.5 (*c* 1.30, 95% ethanol); infrared (PE-180) ν: 3060(w), 2918(s), 2855(m), 2812(w), 2220(s), 1645(w), 1610(s), 1506(m), 1460(s), 1375(w), 1194(m), 1112(s), 1096(s), 1084(s), 1016(w), 874(m), 824(s); ^1H nmr (361.08 MHz, $CDCl_3$) δ_{TMS}: 1.16 (m, 1H, $^2J_{3ax-3eq}$ = 13.0 Hz, $^3J_{3ax-4ax}$ = 12.0 Hz, $^3J_{2eq-3ax}$ = 1.9 Hz, axial H of methylene group (3ax-H)), 1.19 (s, 3H, cyclohexyl CH_3), 1.27 (m, 1H, $^3J_{5ax-6ax}$ = 13.8 Hz, $^3J_{4ax-5ax}$ = 12.0 Hz, $^2J_{5ax-5eq}$ = 11.5 Hz, $^3J_{5ax-6eq}$ = 3.4 Hz, axial H of methylene group (5ax-H)), 1.61 (s, 3H, vinyl CH_3), 1.66 (m, 1H, $^2J_{5ax-5eq}$ = 11.5 Hz, $^3J_{5eq-6ax}$ = 3.8 Hz, $^3J_{5eq-6eq}$ = 3.8 Hz, $^3J_{4ax-5eq}$ = 3.4 Hz, equatorial H of methylene (5eq-H)), 1.92 (m, 1H, $^2J_{3ax-3eq}$ = 13.0 Hz, $^3J_{2eq-3eq}$ =

4.0 Hz, $^3J_{3eq-4ax}$ = 3.4 Hz, equatorial H of methylene (3eq-H)), 1.95 (m, 1H, $^2J_{6ax-6eq}$ = 13.8 Hz, $^3J_{5ax-6ax}$ = 13.8 Hz, $^3J_{5eq-6ax}$ = 3.8 Hz, axial H of methylene group (6ax-H)), 2.09 (m, 1H, $^2J_{6ax-6eq}$ = 13.8 Hz, $^3J_{5eq-6eq}$ = 3.8 Hz, $^3J_{5ax-6eq}$ = 3.4 Hz, equatorial H of methylene (6eq-H)), 2.32 (m, 1H, $^3J_{3ax-4ax}$ = 12.0 Hz, $^3J_{4ax-5ax}$ = 12.0 Hz, $^3J_{3eq-4ax}$ = 3.4 Hz, $^3J_{4ax-5eq}$ = 3.4 Hz, axial H of alkene-substituted carbon (4ax-H)), 3.43 (s, 3H, OCH_3), 3.84 (dd, 1H, $^3J_{2eq-3eq}$ = 4.0 Hz, $^3J_{2eq-3ax}$ = 1.9 Hz, H of methoxy-substituted carbon (2eq–H)), 4.56 (s, 1H, vinyl H), 4.62 (s, 1H, vinyl H), 7.49 (d, 2H, $^3J_{2'-3'}$ = 8.2 Hz, $^3J_{5'-6'}$ = 8.2 Hz, H's adjacent to alkyl-substituted aryl carbon (2'-H, 6'-H)), 7.61 (d, 2H, $^3J_{2'-3'}$ = 8.2 Hz, $^3J_{5'-6'}$ = 8.2 Hz, H's adjacent to cyano-substituted aryl carbon (3'-H, 5'-H)); ^{13}C nmr (90.80 MHz, $CDCl_3$) δ: 21.03 (q, 125.0 Hz, vinyl CH_3), 27.08 (t, 124.7 Hz), 29.14 (q, 126.3 Hz, cyclohexyl CH_3), 29.14 (t, 129.4 Hz), 30.83 (t, 129.8 Hz), 37.62 (d, 125.8 Hz, CH, alkene substituted), 43.27 (s, quaternary carbon, aryl substituted), 57.17 (q, 140.6 Hz, OCH_3), 81.56 (d, 139.6 Hz, CH, methoxy substituted), 108.51 (t, 154.6 Hz, alkene CH_2), 109.36 (s, quaternary aryl carbon, cyano substituted), 118.89 (s, CN), 126.98 (d, 160.0 Hz, aromatic CH adjacent to alkyl- substituted aryl carbon), 132.21 (d, 165.4 Hz, aromatic CH adjacent to cyano-substituted carbon), 149.36 (s), 152.92 (s); ms *m/z*: 53(25), 58(25), 67(36), 68(37), 79(56), 81(25), 94(75), 111(100), 116(29), 143(48), 269(4). Anal. calcd. for $C_{18}H_{23}NO$: C 80.26, H 8.61, N 5.20; found: C 80.09, H 8.54, N 5.24.

*4-[(1S,2R,4R)-4-Isopropenyl-2-methoxy-1-methylcyclohexyl]benzonitrile (**24**)*

The yield of **24** was 2%: $[\alpha]_D^{21}$ −16.2 (*c* 0.50, 95% ethanol); infrared (PE-180) *ν*: 3090(w), 2954(s), 2884(m), 2840(w), 2252(s), 1662(w), 1623(m), 1522(m), 1472(m), 1466(m), 1110(s), 1075(w), 1033(w), 886(m), 824(m); ^{1}H nmr (361.08 MHz, $CDCl_3$) δ_{TMS}: 1.35 (s, 3H, cyclohexyl CH_3), 1.38–1.57 (m, 3H), 1.64–1.75 (m, 2H), 1.78 (s, 3H, vinyl CH_3), 2.02–2.13 (m, 2H), 3.13 (s, 3H, OCH_3), 3.45 (dd, 1H, $^3J_{2ax-3ax}$ = 11.2 Hz, $^3J_{2ax-3eq}$ = 4.2 Hz, H of methoxy-substituted carbon (2ax-H)), 4.76 (s, 1H, vinyl H), 4.77 (s, 1H, vinyl H), 7.55 (d, 2H, $^3J_{2'-3'}$ = 8.5 Hz, $^3J_{5'-6'}$ = 8.5 Hz, H's adjacent to alkyl-substituted aryl carbon (2'-H, 6'-H)), 7.61 (d, 2H, $^3J_{2'-3'}$= 8.5 Hz, $^3J_{5'-6'}$ = 8.5 Hz, H's adjacent to cyano-substituted aryl carbon (3'-H, 5'-H)); ^{13}C nmr (90.80 MHz, $CDCl_3$) δ: 16.69 (q, 125.9 Hz, cyclohexyl CH_3), 20.81 (q, 125.1 Hz, vinyl CH_3), 26.85 (t, 126.7 Hz), 31.06 (t, 127.6 Hz), 38.96 (t, 126.1 Hz), 43.11 (s, quaternary carbon, aryl substituted), 43.90 (d, 130.2 Hz, CH, alkene substituted), 56.96 (q, 141.1 Hz, OCH_3), 84.42 (d, 139.7 Hz, CH, methoxy substituted), 109.09 (t, 155.2 Hz, alkene CH_2), 109.46 (s, quaternary aryl carbon, cyano substituted), 119.15 (s, CN), 127.00 (d, 161.7 Hz, aromatic CH adjacent to alkyl-substituted aryl carbon), 131.77 (d, 163.8 Hz, aromatic CH adjacent to cyano-substituted carbon), 148.91 (s), 155.12 (s); ms *m/z*: 53(15), 67(25), 68(23), 79(30), 81(16), 94(50), 107(14), 111(100), 115(13), 116(23), 126(13), 128(12), 130(12), 142(16), 143(50), 156(14), 222(14), 269(6). X-ray data: see footnote 3.

*4-[(1R,2R,5R)-5-Isopropenyl-2-methoxy-2-methylcyclohexyl]benzonitrile (**25**)*

The yield of **25** was 3%: $[\alpha]_D^{21}$ +25.9 (*c* 1.03, 95% ethanol); infrared (PE-180) *ν*: 3082(w), 2932(s), 2872(m), 2824(w), 2232(m), 1643(w), 1606(w), 1504(w), 1454(m), 1372(m), 1117(m), 1092(m), 1072(m), 867(m), 815(m); ^{1}H nmr (361.08 MHz, $CDCl_3$) δ_{TMS}: 0.95 (s, 3H, cyclohexyl CH_3), 1.67 (m, 1H), 1.72 (s, 3H, vinyl CH_3), 1.70–1.92 (m, 4H), 2.05–2.12 (m, 1H), 2.41 (m, 1H, $^3J_{4ax-5eq}$ = 5.6 Hz, $^3J_{4eq-5eq}$ = 5.6 Hz, $^3J_{5eq-6ax}$ = 5.6 Hz, $^3J_{5eq-6eq}$ = 5.6 Hz, equatorial hydrogen of alkene-substituted carbon (5eq-H)), 3.09 (dd, 1H, $^3J_{1ax-6ax}$ = 8.7 Hz, $^3J_{1ax-6eq}$ = 4.5 Hz, benzylic axial H (1ax-H)), 3.16 (s, 3H, OCH_3), 4.80 (s, 1H, vinyl H), 4.87 (s, 1H, vinyl H), 7.39 (d, 2H, $^3J_{2'-3'}$ = 8.2 Hz, $^3J_{5'-6'}$ = 8.2 Hz, H's adjacent to alkyl-substituted aryl carbon (2'-H, 6'-H)), 7.57 (d, 2H, $^3J_{2'-3'}$ = 8.2 Hz, $^3J_{5'-6'}$ = 8.2 Hz, H's adjacent to cyano-substituted aryl carbon (3'-H, 5'-H)); ^{13}C nmr (90.80 MHz, $CDCl_3$) δ: 19.25 (q, 124.6 Hz, cyclohexyl CH_3), 21.77 (q, 118.0 Hz, vinyl CH_3), 25.56 (t, 126.5 Hz), 31.63 (t, 123.2 Hz), 31.75 (t, 123.2 Hz), 38.41 (d, 125.8 Hz), 48.06 (d, 128.8 Hz), 48.35 (q, 140.7 Hz, OCH_3), 76.04 (s, quaternary carbon, methoxy substituted), 109.90 (s, quaternary aryl carbon, cyano substituted), 110.36 (t, 154.1 Hz, alkene CH_2), 119.08 (s, CN), 130.20 (d, 161.2 Hz, aromatic CH adjacent to alkyl-substituted aryl carbon), 131.48 (d, 165.7 Hz, aromatic CH adjacent to cyano-substituted carbon), 147.09 (s), 148.96 (s); ms *m/z*: 55(24), 72(50), 85(100), 108(37), 116(19), 154(19), 194(37). Exact Mass calcd. for $C_{18}H_{23}NO$: 269.1780; found: 269.1780.

*4-[(1S,2S,5R)-5-isopropenyl-2-methoxy-2-methylcyclohexyl]benzonitrile (**26**)*

The yield of **26** was 1%: $[\alpha]_D^{21}$ +63.8 (*c* 1.03, 95% ethanol); infrared (PE-180) *ν*: 3080(w), 2982(s), 2956(s), 2932(s), 2867(m), 2842(m), 2240(s), 1655(m), 1615(m), 1513(m), 1462(m), 1446(m), 1392(s), 1167(m), 1141(m), 1078(s), 884(m), 834(m); ^{1}H nmr (361.08 MHz, $CDCl_3$) δ_{TMS}: 0.89 (s, 3H, cyclohexyl CH_3), 1.24–1.35 (m, 1H), 1.52–1.64 (m, 3H), 1.74 (s, 3H, vinyl CH_3), 2.00–2.10 (m, 2H), 2.12–2.18 (m, 1H), 2.56 (dd, 1H, $^3J_{1ax-6ax}$ = 12.1 Hz, $^3J_{1ax-6eq}$ = 3.2 Hz, benzylic axial H (1ax-H)), 3.12 (s, 3H, OCH_3), 4.71 (s, 1H, vinyl H), 4.73 (s, 1H, vinyl H), 7.43 (d, 2H, $^3J_{2'-3'}$ = 8.3 Hz, $^3J_{5'-6'}$ = 8.3 Hz, H's adjacent to alkyl-substituted aryl carbon (2'-H, 6'-H)), 7.53 (d, 2H, $^3J_{2'-3'}$ = 8.3 Hz, $^3J_{5'-6'}$ = 8.3 Hz, H's adjacent to cyano-substituted aryl carbon (3'-H, 5'-H)); ^{13}C nmr (90.80 MHz, $CDCl_3$) δ: 20.98 (q, 124.9 Hz, vinyl CH_3), 23.01 (q, 125.6 Hz, cyclohexyl CH_3), 26.48 (t, 127.3 Hz), 33.81 (t, 126.4 Hz), 33.81 (t, 126.4 Hz), 45.33 (d, 118.2 Hz), 48.30 (q, 139.6 Hz, OCH_3), 55.10 (d, 123.4 Hz), 73.67 (s, quaternary carbon, methoxy substituted), 108.66 (t, 155.2 Hz, alkene CH_2), 109.75 (s, quaternary aryl carbon, cyano substituted), 119.34 (s, CN), 130.42 (d, 162.7 Hz, aromatic CH adjacent to alkyl-substituted aryl carbon), 131.33 (d, 165.1 Hz, aromatic CH adjacent to cyano-substituted carbon), 149.14 (s), 149.69 (s); ms *m/z*: 55(24), 72(56), 85(100), 93(11), 108(43), 116(12), 130(11), 269(1). X-ray data: see footnote 3.

Formation of the (*R*)-(+)-α-terpineol (22) and 1,4-dicyanobenzene (1) photo-NOCAS adducts 27 and 28: reaction [7]

A solution of (*R*)-(+)-α-terpineol (**22**) (3.6 g , 0.023 mol), 1,4-dicyanobenzene (**1**) (1.5 g, 0.012 mol), and biphenyl (**5**) (1.8 g, 0.012 mol) in acetonitrile (120 mL) was degassed by nitrogen ebullition and irradiated for 11 days using a 1 kW lamp at 10°C. The crude photolysate was separated by chromatography (mplc) using a linear solvent gradient (hexanes – diethyl ether (3%), hexanes (97%)). Two 1:1 adducts were isolated: **27** and **28**.

(1R,2S,5R)-2-(4-Cyanophenyl)-2,6,6-trimethyl-7-oxabicyclo[3.2.1]octane (27)

The yield of **27** was 21%: $[\alpha]_D^{21}$ −33.7 (*c* 0.54, absolute ethanol); the melting point was 89–90°C; infrared (Nicolet 205, KBr pellet) *ν*: 2978(s), 2965(s), 2929(s), 2223(s), 1607(s), 1469(m), 1460(m), 1382(m), 1365(m), 1133(m), 1069(s), 1015(s), 998(s), 891(s), 842(s); ^{1}H nmr (250.13 MHz, $CDCl_3$) δ_{TMS}: 1.22 (s, 3H, CH_3), 1.25 (s, 3H, CH_3), 1.45 (s, 3H, CH_3), 1.20–2.20 (m, 7H, H's on 6-membered ring), 4.25 (br d, 1H, ^3J = 6.6 Hz, H at bridgehead adjacent to oxygen), 7.41 (d, 2H, $^3J_{2'-3'}$ = 8.4 Hz, $^3J_{5'-6'}$ = 8.4 Hz, H's adjacent to alkyl-substituted aryl carbon (2′-H, 6′-H)), 7.62 (d, 2H, $^3J_{2'-3'}$ = 8.4 Hz, $^3J_{5'-6'}$ = 8.4 Hz, H's adjacent to cyano-substituted aryl carbon (3′-H, 5′-H)); ^{13}C nmr (62.90 MHz, $CDCl_3$) δ: 22.73 (q), 25.37 (t), 29.56 (t), 29.70 (q), 30.12 (q), 33.60 (t), 41.74 (d, CH at bridgehead not adjacent to oxygen), 44.94 (s, quaternary carbon, aryl substituted), 83.00 (s, quaternary carbon adjacent to oxygen), 83.07 (d, CH at bridgehead adjacent to oxygen), 109.48 (s, quaternary aryl carbon, cyano substituted), 119.00 (s, CN), 127.31 (d, aromatic CH adjacent to alkyl-substituted aryl carbon), 132.30 (d, aromatic CH adjacent to cyano-substituted aryl carbon), 153.32 (s, quaternary carbon, alkyl substituted); ms *m/z*: 55(14), 69(12), 83(13), 97(14), 112(13), 115(12), 116(22), 142(27), 143(100), 144(26), 156(12), 168(18), 211(21), 255(25). Exact Mass calcd. for $C_{17}H_{21}NO$: 255.1611; found: 255.1607. X-ray data: see footnote 3.

(1S,4R,6R)-6-(4-Cyanophenyl)-1,3,3-trimethyl-2-oxabicyclo[2.2.2]octane (28)

The yield of **28** was 2%: $[\alpha]_D^{21}$ +39.3 (*c* 0.50, absolute ethanol); the melting point was 169–170°C; infrared (Nicolet 205, KBr pellet) *ν*: 2979(s), 2954(s), 2918(s), 2887(s), 2219(s), 1604(m), 1497(m), 1465(m), 1411(m), 1371(m), 1357(m), 1286(w), 1225(m), 1180(m), 1152(m), 1120(m), 1090(m), 1047(m), 984(s), 924(w), 852(m), 838(m); ^{1}H nmr (250.13 MHz, $CDCl_3$) δ_{TMS}: 0.80 (s, 3H, CH_3), 1.32 (s, 3H, CH_3), 1.33 (s, 3H, CH_3), 1.49–1.78 (m, 5H, H's of methylene groups on 6-membered rings), 2.10–2.24 (m, 1H, H of methylene group), 2.50 (tt, 1H, H at bridgehead), 3.12 (m, 1H, benzylic H), 7.38 (d, 2H, $^3J_{2'-3'}$ = 8.6 Hz, $^3J_{5'-6'}$ = 8.6 Hz, H's adjacent to alkyl-substituted aryl carbon (2′-H, 6′-H)), 7.61 (d, 2H, $^3J_{2'-3'}$= 8.6 Hz, $^3J_{5'-6'}$= 8.6 Hz, H's adjacent to cyano-substituted aryl carbon (3′-H, 5′-H)); ^{13}C nmr (62.90 MHz, $CDCl_3$) δ: 23.06 (t), 25.93 (q, CH_3 at bridgehead), 26.67 (t), 28.94 (q, two CH_3's), 31.27 (t), 33.59 (d, CH at bridgehead), 49.39 (d, benzylic CH), 72.90 (s), 73.78 (s), 110.14 (s, quaternary aryl carbon, cyano substituted), 118.97 (s, CN), 129.81 (d, aromatic CH adjacent to alkyl-substituted aryl carbon), 132.04 (d, aromatic CH adjacent to cyano-substituted aryl carbon), 149.37 (s, quaternary carbon, alkyl substituted); ms *m/z*: 53(10), 55(21), 58(15), 67(11), 68(14), 69(32), 71(45), 77(10), 83(18), 89(7), 93(39), 108(100), 109(9), 111(36), 115(7), 116(18), 126(64), 127(13), 128(9), 129(14), 130(8), 140(9), 153(6), 154(12), 155(6), 156(11), 255(6). X-ray data: see footnote 3.

Acknowledgments

This work was supported by grants from the Natural Sciences and Engineering Research Council of Canada. We thank Dr. D.L. Hooper at the Atlantic Regional Magnetic Resonance Centre at Dalhousie University for the high-field nmr spectra and for help in the preparation of the manuscript. Exact mass determinations, 500 MHz ^{1}H nmr spectra, and the optical rotations were measured at the Institute for Marine Biosciences, Halifax.

References

1. (*a*) K.A. McManus and D.R. Arnold. Can. J. Chem. **73**, 2158 (1995); (*b*) Can. J. Chem. **72**, 2291 (1994); (*c*) D.R. Arnold, X. Du, and H.J.P. de Lijser. Can. J. Chem. **73**, 522 (1995); (*d*) D.R. Arnold, K.A. McManus, and X. Du. Can. J. Chem. **72**, 415 (1994); (*e*) D.A. Connor, D.R. Arnold, P.K. Bakshi, and T.S. Cameron. Can. J. Chem. **73**, 762 (1995).
2. (*a*) D.R. Arnold, X. Du, and J. Chen. Can. J. Chem. **73**, 307 (1995); (*b*) A.L. Perrott and D.R. Arnold. Can. J. Chem. **70**, 272 (1992); (*c*) R. Popielarz and D.R. Arnold. J. Am. Chem. Soc. **112**, 3068 (1990).
3. (*a*) R.M. Borg, D.R. Arnold, and T.S. Cameron. Can. J. Chem. **62**, 1785 (1984); (*b*) D.R. Arnold and M.S. Snow. Can. J. Chem. **66**, 3012 (1988); (*c*) D.R. Arnold and X. Du. Can. J. Chem. **72**, 403 (1994).
4. (*a*) J.E. Baldwin. J. Chem. Soc. Chem. Commun. 734 (1976); (*b*) J. Chem. Soc. Chem. Commun. 738 (1976).
5. (*a*) A.L.J. Beckwith. Tetrahedron, **37**, 3073 (1981); (*b*) A.L.J. Beckwith and C.H. Schiesser. Tetrahedron, **41**, 3925 (1985); (*c*) A.L.J. Beckwith, I.A. Blair, and G. Phillipou. Tetrahedron Lett. 2251 (1974); (*d*) A.L.J. Beckwith, C.J. Easton, and A.K. Serelis. J. Chem. Soc. Chem. Commun. 482 (1980); (*e*) A.L.J. Beckwith, T. Lawrence, and A.K. Serelis. J. Chem. Soc. Chem. Commun. 484 (1980); (*f*) A.L.J. Beckwith and T. Lawrence. J. Chem. Soc. Perkin Trans. 2, 1535 (1979); (*g*) A.L.J. Beckwith, G. Phillipou, and A.K. Serelis. Tetrahedron Lett. **22**, 2811 (1981); (*h*) A.L.J. Beckwith and G. Moad. J. Chem. Soc. Chem. Commun. 472 (1974).
6. J.L. Marshall. Carbon–carbon and carbon–proton NMR coupling: application to organic stereochemistry and conformational analysis. Verlag Chemie International, Deerfield Beach, Fla. 1983.
7. D. Rehm and A. Weller. Isr. J. Chem. **8**, 259 (1970).
8. (*a*) R.S. Nicholson and I. Shain. Anal. Chem. **36**, 706 (1964); (*b*) Anal. Chem. **37**, 178 (1965).
9. G-F. Chen and F. Williams. J. Am. Chem. Soc. **113**, 7792 (1991).
10. (*a*) T. Shono, A. Ikeda, J. Hayashi, and S. Hakozaki. J. Am. Chem. Soc. **97**, 4261 (1975); (*b*) V. Montiel, M. Lopez-Segura, A. Aldaz, M. Grande, and F. Barba. Electrochim. Acta, **29**, 1123 (1984).
11. (*a*) X. Du, D.R. Arnold, R.J. Boyd, and Z. Shi. Can. J. Chem. **69**, 1365 (1991); (*b*) H. Koppel, W. Domcke, L.S. Cederbaum, and W. Von Niessen. J. Chem. Phys. **69**, 4252 (1978); (*c*) T. Shida, Y. Egawa, H. Kubodera, and T. Kato. J. Chem. Phys. **73**, 5963 (1980).
12. (*a*) N.A. LeBel, R.F. Czaja, and A. DeBoer. J. Org. Chem. **34**, 3112 (1969); (*b*) S.E. Bottle, W.K. Busfield, and I.D. Jenkins. J. Chem. Soc. Perkin Trans. 2, 2145 (1992).
13. L.M. Harwood. Aldrichimica Acta, **18**, 25 (1985).
14. A. Okamoto, M.S. Snow, and D.R. Arnold. Tetrahedron, **42**, 6175 (1986).
15. D.R. Arnold and D.D.M. Wayner. Can. J. Chem. **64**, 100 (1986).

Solvent effect on preferred protonation sites in nicotinate and isonicotinate anions

Jean-Claude Hallé, Jacques Lelievre, and François Terrier

Abstract: Potentiometric determinations of the two successive acidities of nicotinic and isonicotinic acids (AH_2^+) have been carried out in aqueous dimethyl sulfoxide mixtures containing up to 95% Me_2SO by volume. In both systems, the results reveal that the addition of Me_2SO induces a proton transfer from the pyridinium ring to the carboxylate group, the tautomeric equilibrium between the neutral forms of the two acids being displaced toward the zwitterionic form ($AH^{\pm}$) in aqueous solution, but toward the molecular form (AH°) in Me_2SO. An analysis of the data by means of Hammett relationships previously established for benzoïc acids over the whole range of H_2O/Me_2SO mixtures allowed the four microscopic acidity constants as well as the tautomeric equilibrium constant K_T pertaining to the complete ionization scheme of the two acids to be determined. At 20°C, there are equal populations of the tautomeric AH° and $AH^{\pm}$ species in the mixtures containing 38 and 47% Me_2SO for the nicotinic and isonicotinic systems, respectively. Hammett relationships describing the ionization behaviour of a number of substituted pyridinium cations in H_2O/Me_2SO mixtures are also discussed. Possible reasons accounting for the peculiar effects exerted by the NH_2, $CONH_2$, and COOH substituents on the process are suggested.

Key words: nicotinic and isonicotinic acids, substituted pyridines, acidities, tautomeric equilibrium, protonation sites, water – dimethyl sulfoxide mixtures.

Résumé : Les deux acidités successives des acides nicotinique et isonicotinique (AH_2^+) ont été déterminées par potentiométrie dans des milieux eau–diméthylsulfoxyde contenant jusqu'à 95% de Me_2SO en volume. L'addition de Me_2SO provoque le transfert protonique du cycle pyridinium vers le groupement carboxylate, de sorte que la forme zwittérionique $AH^{\pm}$, très majoritaire dans l'eau, cède progressivement la place à la forme moléculaire AH° qui devient unique dans le diméthylsulfoxyde. Le traitement des résultats, à l'aide des relations de Hammett d'énergie libre préalablement établies pour les acides benzoïques dans les mélanges H_2O/Me_2SO, permet les déterminations des quatre constantes microscopiques et de la constante de tautomérie K_T décrivant le schéma des ionisations successives de ces deux diacides. À 20°C, on a égalité entre les populations des formes zwittérionique ($AH^{\pm}$) et moléculaire (AH°) dans les milieux contenant respectivement 38% (acide nicotinique) et 47% (acide isonicotinique) de Me_2SO en masse. Les relations de Hammett d'énergie libre, décrivant l'ionisation d'un grand nombre de pyridines substituées dans les mélanges H_2O/Me_2SO, sont discutées. Les effets particuliers observés pour les substituants NH_2, $CONH_2$ et COOH sont analysés.

Mots clés : acides nicotinique et isonicotinique, pyridines substituées, acidités, equilibre tautomère, sites de protonation, milieux eau–diméthylsulfoxyde.

Introduction

A previous ^1H and ^{13}C nmr study has revealed that the tautomeric equilibrium between the neutral forms $AH^{\pm}$ and AH° of nicotinic acid, i.e., pyridine-3-carboxylic acid, is strongly solvent dependent (1), being largely displaced toward the zwitterionic form ($AH^{\pm}$) in aqueous solution (2–5) but almost completely biased toward the molecular form (AH°) in a 20:80 (v/v) water/dimethyl sulfoxide (Me_2SO) mixture (1). (Scheme 1). Obviously, such a structural change is expected to affect the reactivity of nicotinic acid, especially with respect to its potential ambident reactivity toward alkylating agents (6) or its behaviour as a general acid–base catalyst. This makes it of interest to know how the populations of the two tautomers $AH^{\pm}$ and AH° are progressively reversed on adding increasing amounts of Me_2SO to aqueous solutions of nicotinic acid. Also of interest are the medical uses of Me_2SO (7–11).

Scheme 1.

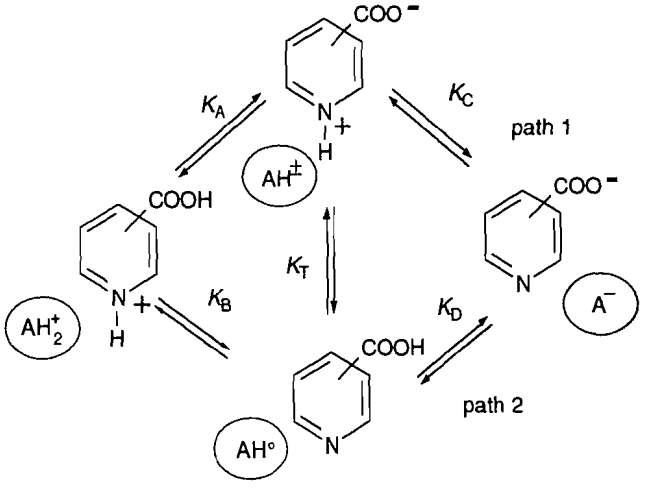

Received November 2, 1995.

J.-C. Hallé,[1] J. Lelievre, and F. Terrier. Université de Versailles-Saint Quentin en Yvelines Laboratoire, Synthèse, interactions et réactivité en chimie organique et bioorganique - EP J 102 du Centre national de la recherche scientifique, Bâtiment Lavoisier, 45 avenue des États-Unis, 78035 Versailles Cedex, France.

[1] Author to whom correspondence may be addressed. Telephone: 33 1 39 25 44 51. Fax: 33 1 39 25 44 52. E-mail: terrier@chimie.uvsq.fr

Table 1. Influence of solvent composition (H_2O/Me_2SO) on apparent and thermodynamic pK_a values (t = 20°C).

Compound		Percentage of Me_2SO (by weight)											
		0	10.8	21.3	31.7	41.4	51.2	61.2	70.5	80.4	86.4	91.0	95.5
Nicotinic acid	pK_{a_1}	2.03[a]	2.09	2.15	2.18	2.14	2.05	1.91	1.6	1.4	1.4	1.5	1.6
	pK_{a_2}	4.90[a]	4.72	4.56	4.44	4.37	4.50	4.74	5.30	6.12	6.89	7.53	8.14
	pK_D	3.63[a]	3.72	3.78	3.98	4.16	4.44	[b]	[b]	[b]	[b]	[b]	[b]
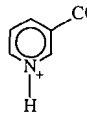	pK_C	4.88[a]	4.67	4.48	4.26	3.95	3.61						
	pK_A	2.05[a]	2.14	2.23	2.36	2.56	2.94						
	pK_B	3.30[a]	3.09	2.93	2.64	2.35	2.11	[c]	[c]	[c]	[c]	[c]	[c]
	K_T	0.05_6[a]	0.11_2	0.20_0	0.52_5	1.6_2	6.7_6						
	τ%	5.3[a]	10	17	34	62	87	100	100	100	100	100	100
Isonicotinic acid	pK_{a_1}	1.75[a]	1.74	1.82	1.92	1.95	1.96	1.87	1.7	1.5	1.5	1.6	1.7
	pK_{a_2}	4.96[a]	4.82	4.65	4.52	4.40	4.40	4.60	5.10	5.80	6.44	7.13	7.70
	pK_D	3.46[a]	3.55	3.59	3.78	3.94	4.21	4.53	[b]	[b]	[b]	[b]	[b]
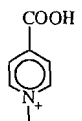	pK_C	4.95[a]	4.80	4.61	4.43	4.22	3.95	3.77					
	pK_A	1.76[a]	1.76	1.86	2.01	2.13	2.41	2.70					
	pK_B	3.25[a]	3.01	2.88	2.66	2.41	2.15	1.94	[c]	[c]	[c]	[c]	[c]
	K_T	0.03_2[a]	0.05_6	0.09_5	0.22_4	0.52_5	1.8_2	5.7_5					
	τ%	3.1[a]	5.3	8.7	18	34	65	85	100	100	100	100	100

[a]This work. For other aqueous values previously reported see, for example: ref. 3 (T = 22°C; nicotinic acid: pK_{a_1} = 2.07, pK_{a_2} = 4.81, pK_A = 2.11, pK_B = 3.13, pK_C = 4.77, pK_D = 3.75, τ = 9%; isonicotinic acid: pK_{a_1} = 1.84, pK_{a_2} = 4.86, pK_A = 1.86, pK_B = 3.26, pK_C = 4.84, pK_D = 3.44, τ = 4%), and ref. 4 (t = 25°C; nicotinic acid: pK_{a_1} = 1.98, pK_{a_2} = 4.82, pK_A = 2.07, pK_B = 2.72, pK_C = 4.76, pK_D = 4.08, τ = 18%); isonicotinic acid: pK_{a_1} = 1.68, pK_{a_2} = 4.91, pK_A = 1.70, pK_B = 2.94, pK_C = 4.89, pK_D = 3.65, τ = 5%).

[b]Identical to pK_{a_2}.

[c]Identical to pK_{a_1}.

In this paper, we report a complete potentiometric analysis of the two acidities of the nicotinic acid cation AH_2^+ and of the related isomeric species derived from isonicotinic acid, i.e., pyridine 4-carboxylic acid, over the whole range of H_2O/Me_2SO mixtures. The apparent acidity constants K_{a_1} and K_{a_2} associated with the two successive deprotonation steps of AH_2^+ (eq. [1]) were determined and compared with the acidity constants associated with deprotonation of a few related monoacids, i.e., pyridinium cations and benzoic acids. On this basis we were able to estimate the various individual equilibrium constants K_A, K_B, K_C, K_D and therefore the tautomeric equilibrium constant K_T associated with Scheme 1. Our study provides a comprehensive understanding of the solvent effect on the equilibrium $AH^{\pm} \rightleftarrows AH°$ for the two isomers.

$$[1] \quad AH_2^+ \overset{K_{a_1}}{\rightleftharpoons} \underbrace{AH^{\pm} + AH°}_{AH} \overset{K_{a_2}}{\rightleftharpoons} A^-$$

Results and discussion

Table 1 summarizes the pK_{a_1} and pK_{a_2} values potentiometrically determined (see experimental section) for the two acidities of nicotinic acid and isonicotinic acid in aqueous solution as well as in a large number of aqueous Me_2SO mixtures containing up to 95.5% Me_2SO by weight (95% by volume). Table 2 gives the pK_a values measured for the ionization of a large number of substituted pyridinium and related pyrimidinium and quinolinium cations in the same media. As can be seen, the acidity of these cations is enhanced on addition of Me_2SO to the aqueous solutions, the effect being maximum for a Me_2SO content of ca. 80–85% by volume. This situation is consistent both with the few data previously reported in the literature for pyridinium cations (25) and the behaviour observed for similar NH^+/N equilibria in the anilinium (26–28) and imidazolium (29) series. Measurements of solvent transfer activity coefficients for various NR_4^+-type ions have been made (30) that have emphasized a somewhat better solvation of these cations by Me_2SO than by water, accounting for the observed decrease in the pK_a values. In contrast, it is well known that the acidity of carboxylic acids markedly decreases on transfer from aqueous to Me_2SO solutions (30, 31) as a result of the inability of Me_2SO to stabilize carboxylate anions by hydrogen-bonding solvation (30, 32). On these grounds, the influence of the Me_2SO content on the two successive deprotonations of the two nicotinic acids may be readily understood, at least qualitatively, by looking at Figs. 1. These compare the variations in the corresponding pK_{a_1} and pK_{a_2} values to those in the pK_a values for the reference acid compounds, i.e., pyridinium cation and benzoic acid.

As can be seen, changes in pK_{a_1} and pK_{a_2} of the AH_2^+ species in water-rich media ($\leq$20% Me_2SO) parallel those observed in the pK_a values of benzoic acid and pyridinium cation, respectively. Obviously this behaviour is in accord with deprotonation of AH_2^+ occurring according to path 1 of Scheme 1 and therefore with formation of the zwitterion $AH^{\pm}$ as the major species resulting from the first deprotonation process in these very aqueous media. However, it is also clear that it is the reverse situation that prevails in Me_2SO-rich mixtures

Table 2. Influence of solvent composition (H_2O/Me_2SO) on pK_a values of susbstituted pyridinium cations and related heterocyclic cations (t = 20°C [a]).

Substituent	Percentage of Me_2SO (by weight)												
	0	10.8	21.3	31.7	41.4	51.2	61.2	70.5	80.4	86.4	91.0	95.5	100
4-NMe_2	9.70[b]	9.47	9.27	9.04	8.78	8.50	8.13	7.85	7.70	7.65	7.78	7.86	
4-NH_2	9.20[c]	9.07	8.90	8.74	8.51	8.24	8.02	7.84	7.81	7.84	8.01	8.23	
2-NH_2	6.80[d]	6.63	6.50	6.34	6.13	5.88	5.62	5.41	5.32	5.34	5.44	5.59	
4-Me	6.06[e]	5.85	5.64	5.43	5.13	4.78	4.50	4.13	3.92	3.89	3.94	3.97	
2-Me	5.95[f]	5.75	5.57	5.33	5.07	4.71	4.41	4.07	3.84	3.78	3.85	3.88	
3-Me	5.71[g]	5.52	5.31	5.09	4.78	4.41	4.11	3.78	3.52	3.50	3.57	3.62	
4-Ph	5.30[h]	5.13	4.93	4.69	4.44	4.08	3.75	3.44	3.15	3.19	3.26	3.34	
H	5.23[i]	5.06	4.88	4.65	4.38	4.03	3.71	3.40	3.12	3.15	3.21	3.29	3.53q
3-$CONH_2$	3.28[j]	3.09	2.94	2.71	2.45	2.27	2.00	1.8	1.7	1.7	1.8	1.90	
2-OMe	3.33[k]	3.11	2.94	2.70	2.42	2.02	1.7	1.4	1.2	1.2	1.3	1.4	
3-COOEt	3.23[l]	3.04	2.82	2.60	2.36	1.96	1.6	1.3	1.1	1.1	1.2	1.3	
3-Cl	2.84[m]	2.68	2.47	2.30	2.12	1.8	1.4	1.1	—	—	—	—	
Quinolinium cation	4.94[n]	4.64	4.37	4.13	3.76	3.48	3.15	2.86	2.52	2.53	2.61	2.68	
2-Amino pyrimidinium cation	3.56[o]	3.51	3.43	3.30	3.10	2.87	2.76	2.61	2.48	2.53	2.66	2.79	
4,6-Dimethyl pyrimidinium cation	2.70[p]	2.65	2.57	2.42	2.23	2.01	1.8	1.6	1.5	1.5	1.6	1.7	

[a]Except when indicated.
[b]Reference 12 reports 9.70.
[c]Reference 13 reports 9.17.
[d]Reference 13 reports 6.86; Reference 14 reports 6.82.
[e]Reference 15 reports 6.02.
[f]Reference 15 reports 5.97.
[g]Reference 15 reports 5.68.
[h]Reference 16 reports 5.35 at 25°C.
[i]Reference 13 reports 5.23; Reference 15 reports 5.17.
[j]Reference 17 reports 3.33; Reference 18 reports 3.35 at 25°C.
[k]Reference 19 reports 3.28; Reference 20 reports 3.28 at 25°C; Reference 15 reports 3.40.
[l]Reference 15 reports 3.35.
[m]Reference 15 reports 2.84.
[n]Reference 13 reports 4.94; Reference 20 reports 4.93; Reference 21 reports 4.96.
[o]Reference 13 reports 3.54; Reference 22 reports 3.71.
[p]Reference 23 reports 2.7.
[q]Calculated (van't Hoff equation) from pK_a at 25°C (3.45) and standard enthalpy of ionization (ΔH_i^0 = 27.7 kJ mol^{-1}): reference 24.

(≥50% for nicotinic acid and ≥60% for isonicotinic acid). Then, the variations in pK_{a_1} and pK_{a_2} become closely similar to those in the pK_a values of pyridinium ion and benzoic acid, respectively. These results indicate that deprotonation of AH_2^+ now occurs according to path 2 of Scheme 1, thus confirming previous nmr observations that AH° is the predominant neutral form of nicotinic and isonicotinic acids in media of high Me_2SO content (1).

In the intermediate mixtures with a Me_2SO concentration in the range 20–60% the first deprotonation of AH_2^+ occurs concomitantly via paths 1 and 2 to yield a mixture of both tautomers $AH^{\pm}$ and AH° whose relative concentrations are governed by the equilibrium constant K_T. In such media, the measured acidity constants K_{a_1} and K_{a_2} become apparent acidity constants which are related to the four individual equilibrium constants of Scheme 1 by the following three independent equations [2]–[4].

$$[2] \quad K_A + K_B = K_{a_1}$$

$$[3] \quad \frac{1}{K_C} + \frac{1}{K_D} = \frac{1}{K_{a_2}}$$

$$[4] \quad \frac{K_B}{K_A} = \frac{K_C}{K_D} = K_T$$

To analyze such a system, an additional relationship is needed that is usually provided by use of extrathermodynamic assumptions (33–35). However, another method has been shown to be applicable, when the acidity measurements are carried out in various aquo-organic mixtures (28, 29, 36). It is based on the experimental observation that the pK_a values determined in a given solvent S_1 for a series of structurally similar X-substituted acids (pK_X^{S1}) obeying the Hammett relationships [5] (37) are linearly related to the pK_a values measured for these acids in another solvent S_2 (pK_X^{S2}). Using eq. [5], where the influence of the solvent is included in

$$[5] \quad pK_H^S - pK_X^S = \rho^S \sigma^X$$

$$[6] \quad pK_X^{S_2} = \frac{\rho^{S_2}}{\rho^{S_1}} pK_X^{S_1} + pK_H^{S_2} - \frac{\rho^{S_2}}{\rho^{S_1}} pK_H^{S_1}$$

the reaction constant ρ^S, and eliminating the substituent constant σ_X between two solvents S_1 and S_2 affords eq. [6], which shows that plots of $pK_X^{S_2}$ vs. $pK_X^{S_1}$ must be linear with slopes

Fig. 1. Influence of solvent composition (H_2O/Me_2SO) on the measured acidity constants K_{a_1} and K_{a_2} (X—X) of the cationic forms of nicotinic and isonicotinic acids and on the microscopic constants K_A, K_B, K_C and K_D (● - - - - - ●); $t = 20°C$.

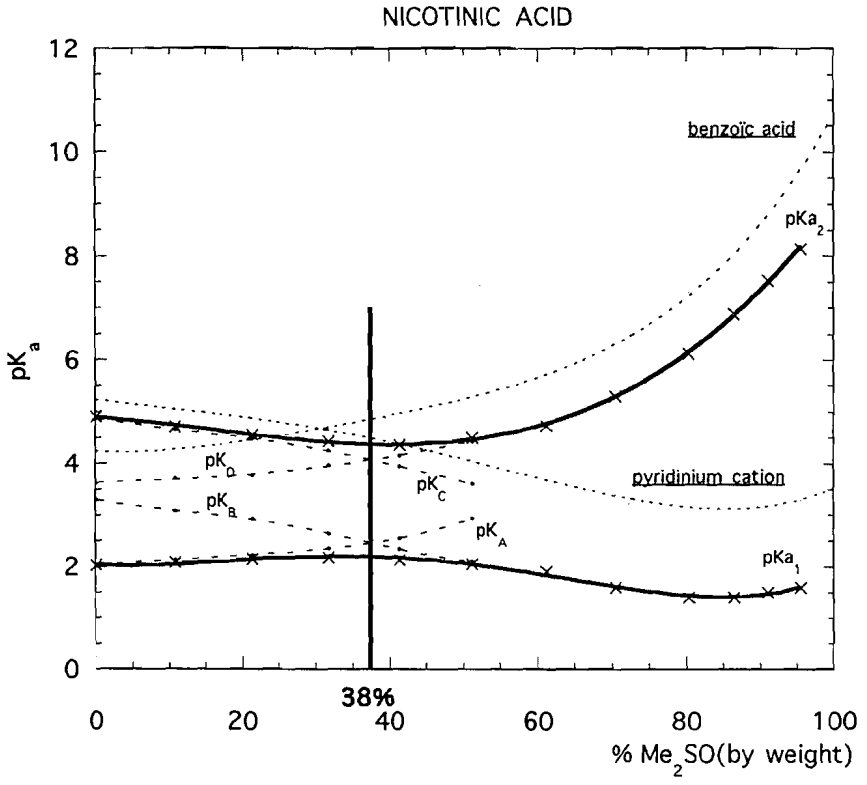

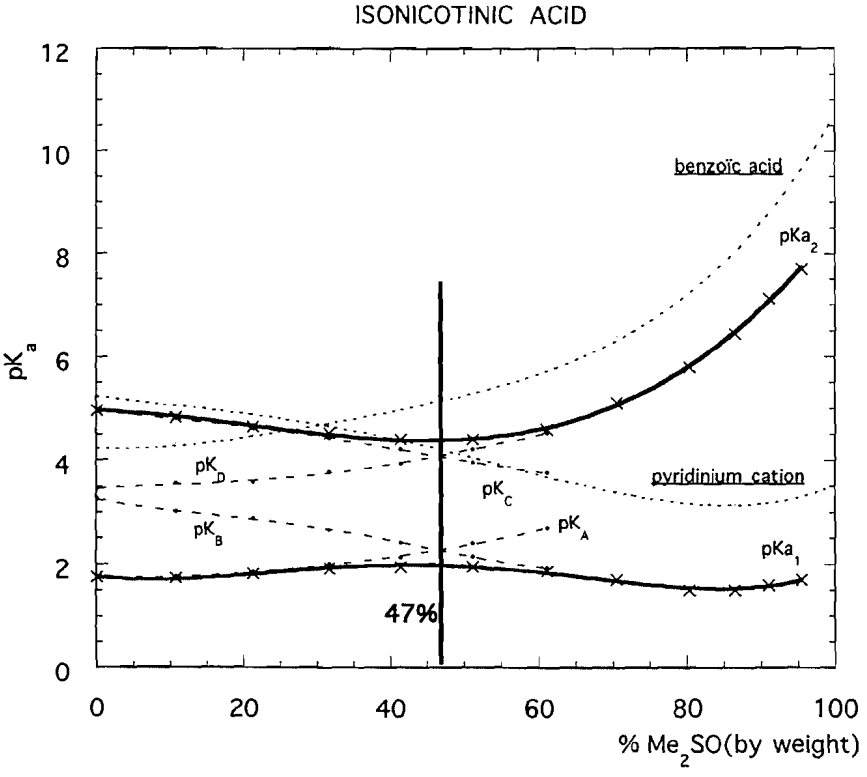

Table 3. Influence of solvent composition (H_2O/Me_2SO) on the slope and intercept values of the graph $pK_X^{H_2O/Me_2SO}$ versus $pK_X^{H_2O}$ (eq. [6]) for *meta* and *para* benzoic acids.[a]

	Percentage of Me_2SO (by weight)										
	10.8	21.3	31.7	41.4	51.2	61.2	70.5	80.4	86.4	91.0	95.5
Slopes	0.988	1.088	1.156	1.262	1.331	1.463	1.617	1.852	1.954	2.081	2.191
Intercepts	0.132	−0.170	−0.217	−0.426	−0.391	−0.514	−0.477	−0.590	−0.232	−0.120	+0.116
Calculated $pK_D^{H_2O}$ values for nicotinic acid	4.64	4.35	4.03	3.80	3.67	3.59	3.57	3.62	3.65	3.68	3.66
					$pK_D^{H_2O} = 3.63 \pm 0.06$						
Calculated $pK_D^{H_2O}$ values for isonicotinic acid	4.75	4.43	4.10	3.82	3.60	3.50	3.45	3.45	3.42	3.48	3.46
					$pK_D^{H_2O} = 3.46 \pm 0.04$						

[a]The slope and intercept values were calculated by linear regression analysis from previously published data (28, 29). The mean-square deviation analysis is always slower than 0.04 pK unit.

Fig. 2. Influence of solvent composition (H_2O/Me_2SO) on the percentage amount τ of molecular form AH° for nicotinic (●) and isonicotinic (X) acids; $t = 20°C$.

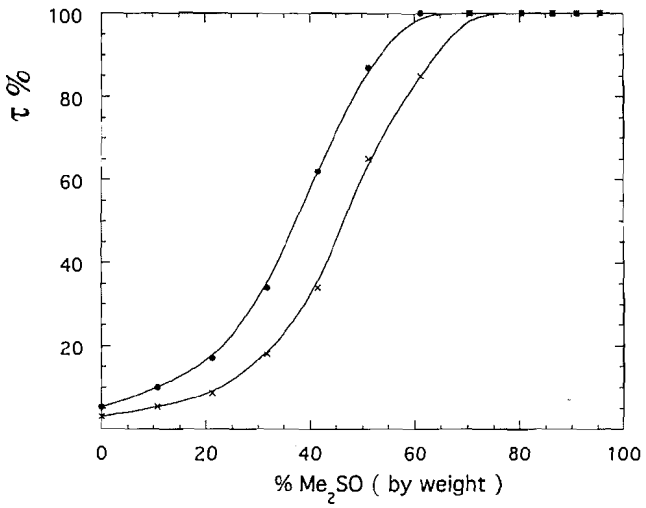

and intercepts being characteristic of the class of acids studied and depending only upon the solvents (28, 29, 36, 38, 39). In agreement with this expectation, the acid–base behaviour of oxygen acids like carboxylic acids and phenols (28, 38) and of nitrogen acids like anilinium (28) and imidazolium (29) cations was found to conform nicely to eq. [6] in H_2O/Me_2SO and H_2O/N-methylacetamide mixtures (39).

The similarity observed in the solvent dependence of the pK_{a_2} values for each of the two nicotinic acids studied and the pK_a value of benzoic acid at Me_2SO contents ≥50–60% suggests that the COOH functionality of AH° forms behaves, not only qualitatively but quantitatively, as that of other benzoic acids. Should this be true, the various relationships (eq. [6]) previously determined for *meta*- and *para*-substituted benzoic acids (28, 29) should hold nicely for pyridine carboxylic acids, allowing the pK_D values for ionization of the COOH groups of AH° to be calculated in water as well as in water-rich mixtures where they are not directly accessible. Such $pK_a^{H_2O} = pK_D^{H_2O}$ values estimated from eq. [6] with $pK_X^{S_2} = pK_a^{H_2O/Me_2SO}$, $pK_X^{S_1} = pK_a^{H_2O}$, are summarized in Table 3 for the two nicotinic acids (see Table 3 also for slopes and intercept values). As can be seen, the $pK_D^{H_2O}$ values obtained show remarkable consistency, affording the following average values: $pK_D^{H_2O} = 3.63 \pm 0.06$ for nicotinic acid and $pK_D^{H_2O} = 3.46 \pm 0.04$ for isonicotinic acid. Similar calculations of pK_D in all mixtures with ≤50 or 60% Me_2SO content also afforded satisfactory pK_a values for ionization of the COOH group of the AH° forms. The knowledge of pK_D in these systems is important since it makes possible to calculate the corresponding pK_A, pK_B, and pK_C values from eqs. [2]–[4]. The results are given in Table 1 and illustrated by the broken-line plots of Fig. 1. Plots of pK_A and pK_B, as well as those of pK_C and pK_D, versus the Me_2SO content, intersect in the mixtures containing 38 and 47% Me_2SO for nicotinic acid and isonicotinic acid, respectively. In these two mixtures, the tautomeric equilibrium constant, K_T, is equal to 1, with the differences between pK_{a_2} and pK_C as well as those between pK_A and pK_{a_1} fitting eq. [7] satisfactorily:

$$[7] \quad pK_{a_2} - pK_C = pK_A - pK_{a_1} = \log_{10} 2$$

$$[8] \quad \tau = \frac{100\,K_T}{1 + K_T}$$

From eq. [8], the percentages τ in the molecular forms AH° of nicotinic and isonicotinic acids have been calculated and are included in Table 1. The τ values calculated for aqueous solutions are equal to 5.3 and 3.1, respectively, at 20°C, in good agreement with those previously determined by Green and Tong at 22°C ($\tau = 9$ and 4, respectively) from a comparison of the acid–base behaviour of the two nicotinic acids with that of the related methyl esters (3). Figure 2 shows the rapid increase in the population of the molecular form with increasing Me_2SO content of the solutions. In mixtures with ≥80% Me_2SO, AH° becomes essentially the only neutral form of the two acids in the solutions, thus confirming our previous nmr observations.[1]

In principle, the determination of the various microscopic equilibrium constants K_A, K_B, K_C, and K_D in the intermediate range of Me_2SO concentrations could also derive from an estimation of the K_B values for the NH^+/N ionization of the pyri-

Fig. 3. Correlations $pK_X^{H_2O/Me_2SO}$ versus $pK_X^{H_2O}$ for substituted pyridines (see Table 2). Composition of H_2O/Me_2SO mixtures: (*a*) 10.8%, (*b*) 21.3%, (*c*) 31.7%, (*d*) 41.4%, (*e*) 51.2%, (*f*) 61.2%, (g) 70.5%, (*h*) 80.4%, (*i*) 86.4% Me_2SO (w/w). The slopes and intercepts values of the lines are available as supplementary material (Table 4); see footnote 2.

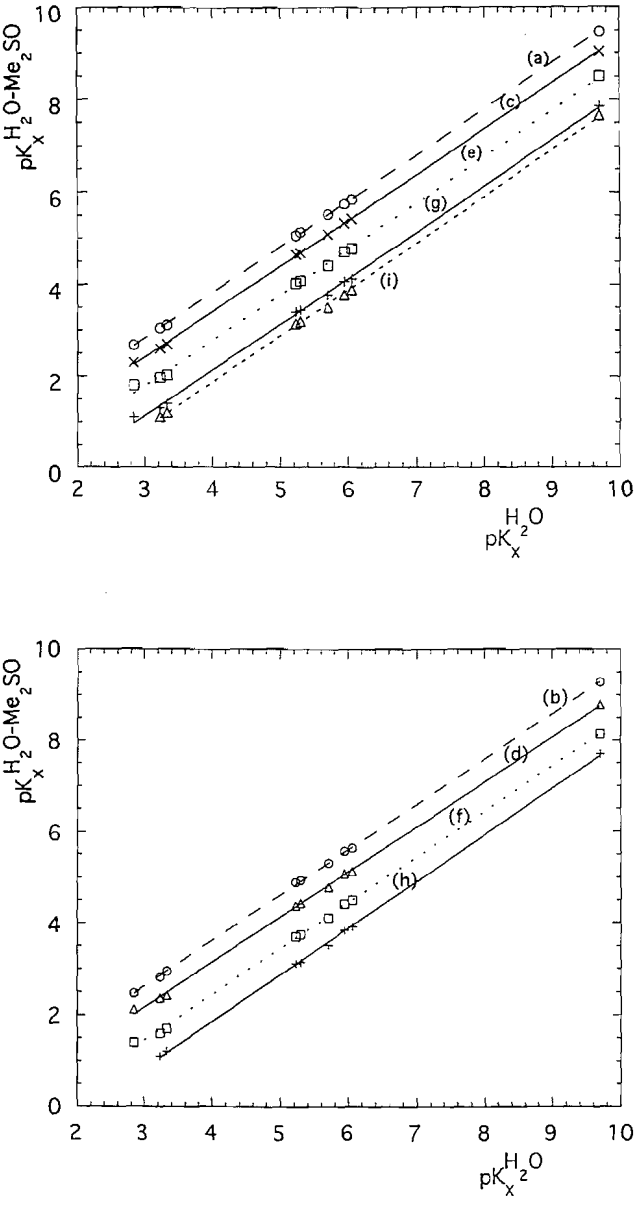

dinium ring of AH_2^+ through the use of appropriate Hammett relationships. We found, however, that a treatment of the data based on the correlation established for anilinium cations did not afford consistent results (28). This failure called for the construction of Hammett relationships pertaining directly to the behaviour of a homogeneous set of pyridinium cations and related heterocyclic cations in H_2O/Me_2SO mixtures (Table 2).

Prior to discussing the Hammett behaviour of these cations, some general features regarding the results summarized in Table 2 are worth mentioning. In a general way, our measured $pK_a^{H_2O}$ values are in excellent agreement with previous reports. Also, the pK_a values measured for the 2-aminopyridinium cation in H_2O/Me_2SO mixtures are fully consistent with previous determinations by Pawlak and Bates in these media (25). In contrast, our $pK_a^{H_2O/Me_2SO}$ values for the unsubstituted pyridinium cation differ notably from those reported by Gowland and Schmid in mixtures with $\leq$50% Me_2SO (40). Extrapolation of the pK_a values that we measured over the range 0–95% Me_2SO to pure Me_2SO (see Fig. 1) leads, however, to a $pK_a^{Me_2SO}$ value in good agreement with that directly determined by Benoit et al. in this solvent (24).

Another noteworthy result is that the acidity of all heterocyclic cations studied in this work increases continuously upon addition of Me_2SO up to 80–85% by weight, i.e., a mole fraction of $\approx$ 0.5. This behaviour is the same as that previously found for other NH^+/N acids such as anilinium (28) and imidazolium (29) cations. As shown by Fig. 3, the various $pK_X^{H_2O/Me_2SO}$ vs. $pK_X^{H_2O}$ plots are essentially parallel, with slopes being equal or very close to unity (see Table 4 in supplementary material[2]). Such a solvent independence of the reaction constant ρ^S is not surprising in itself – similar behaviour was previously observed for imidazolium cations (29) — but it implies that the difference in the acidity of two given compounds in the series remains the same over the whole range of Me_2SO concentrations. In this respect, it is interesting to note that the difference in the pK_a values for the NH^+/N ionization of nicotinium cation (pK_B, Table 1) and the related ethyl ester (Table 2) does not follow this behaviour well: the ΔpK value increases from $\leq$0.1 in water-rich media to $\approx$0.3 in Me_2SO-rich media. Obviously, the variation is not large and one might argue that it is the result of experimental error rather than of a specific behaviour of the COOH group. It turns out, however, that eq. [6] was never found to apply correctly when NH^+/N equilibria activated by a COOH group are involved in the correlations. The failure of 3-amino benzoïc acid (28) and urocanic acid (29) to enter the general relationships established for anilinium and imidazolium cations, respectively, is very illustrative for this situation. This suggests that the solvation of the COOH substituent is affected by the addition of Me_2SO to such an extent that it modifies the pK_a variations brought about by the solvent effect on the NH^+/N equilibria. This would explain why our data for nicotinic and isonicotinic acids cannot be satisfactorily analysed on the basis of the NH^+/N acidity behaviour of the common pyridinium cation. Interestingly, the log value of the solvent activity coefficients γ_t for the transfer of acetic acid from water to 90% Me_2SO has been measured: $\log \gamma_t = -1{,}5$ (41). Such a value supports the idea that the solvent change must affect the role of the COOH group. The abnormal behaviour of the 3-$CONH_2$ pyridinium cation may be explained along similar lines.

Other pyridinium compounds whose ionization does not fit the Hammett relations of eq. [6] are the 2-amino and 4-amino pyridinium cations.

Interestingly, an unexpected ionization behaviour of these compounds was previously observed in nonaqueous (42) and aqueous (43) solutions as well as in the gas phase (44). This was explained in terms of a strong contribution of the iminium structures **1** and **2** to the stabilization of the parent cations (42–44).

[2] Supplementary material mentioned in the text can be purchased from: The Depository of Unpublished Data, Document Delivery, CISTI, National Research Council Canada, Ottawa, Canada K1A 0S2

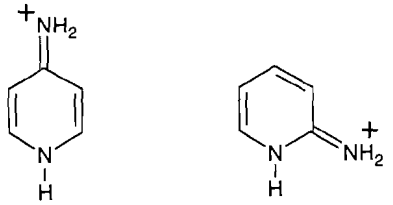

1 2

It turns out, however, that this explanation is not consistent with our finding that the 4-*N*,*N*-dimethylaminopyridinium cation obeys nicely the correlations of eq. [6]. On the other hand, it has been shown that 4-aminopyridine essentially exists in the amino form **3** in aqueous (ref. 33, pp. 152–154; refs. 45, 46) as well as in Me_2SO (47, 48) solution. Hence, an explanation of the peculiar ionization behaviour of the 4-amino (and 2-amino) pyridinium cation on the basis of a strong dependence of the tautomeric equilibrium of eq. [9] upon the Me_2SO concentration does not appear very attractive.

[9] 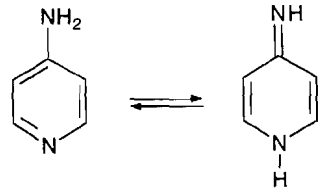

3 4

In contrast, it is well known that the solvation of a primary ammonium group is very important and strongly affected by a transfer from a protic to a dipolar aprotic solvent. Thus, the log value of the solvent activity coefficient γ_t for the transfer of the *n*-butylammonium cation from water to 90% Me_2SO is -2.8 (41), indicating a much stronger stabilization of this species in Me_2SO rich mixtures. This suggests that the contribution of the NH_3^+ substituent must counteract to some extent the increase in acidity observed for other pyridinium cations. This behaviour is actually observed in Table 2 since the decrease in the pK_a values is $\cong$2.0 for pyridinium cations obeying eq. [6] but only $\cong$1.19 and 1.36 for the 4-amino and 2-amino pyridinium cations.

Our feeling is therefore that the abnormal behaviour of the two cations is for the most part the reflection of these solvation effects.

Experimental

Materials

Pyridine and pyrimidine derivatives were commercially available products that were purified according to standard recrystallization or distillation procedures.

Water and dimethyl sulfoxide (Chimiphar) were purified and their mixtures prepared as described earlier (49, 50).

Acidity constant measurements

Thermodynamic pK_a values were determined by potentiometry at 20°C, using an electronic pH meter (Tacussel Isis 20 000) equipped with a Tacussel TB/HA glass electrode and a Tacussel C8 saturated calomel electrode. The experimental procedure was previously described in detail (28, 29, 39, 49, 50).

References

1. T. Khan, J.C. Hallé, M.P. Simonnin, and R. Schaal. J. Phys. Chem. **81**, 587 (1977).
2. H.H. Jaffé. J. Am. Chem. Soc. **77**, 4445 (1955).
3. R.W. Green and H.K. Tong. J. Am. Chem. Soc. **78**, 4896 (1956).
4. P.O. Lumme. Suom. Kemistil. **30B**, 168 (1957).
5. A. Albert. J. Chem. Soc. 1020 (1960).
6. D.L. Hughes, J.J. Bergan, and E.J.J. Grabowski. J. Org. Chem. **51**, 2579 (1986).
7. C.D. Leake (*Editor*). Biological actions of dimethyl sulfoxide. Ann. N.Y. Acad. Sci. **141**, 1–671 (1967).
8. W.L. Reynolds. Prog. Inorg. Chem. **12**, 1 (1970).
9. S.W. Jacob, M. Bischel, and R.J. Herschler. Curr. Theor. Res. **6**, 134 (1964).
10. S.W. Jacob and R.J. Herschler (*Editors*). Biological actions of dimethyl sulfoxide. Ann. N.Y. Acad. Sci. **243**, 1–508 (1975).
11. J. Crosby, R. Stone, and G.E. Lienhard. J. Am. Chem. Soc. **92**, 2891 (1970).
12. F. Gruege, G. Girault, S. Coustal, J. Lascombe, and P. Rumpf. Bull. Soc. Chim. Fr. 3889 (1970).
13. A. Albert, R. Goldacre, and J.N. Phillips. J. Chem. Soc. 2240 (1948).
14. I.R. Bellobono and M.A. Monetti. J. Chem. Soc. Perkin Trans. 2, 790 (1973).
15. K. Clarke and K. Rothwell. J. Chem. Soc. 1885 (1960).
16. A. Fischer, W.J. Galloway, and J. Vaughan. J. Chem. Soc. B, 3591 (1964).
17. A.V. Willi. Helv. Chim. Acta, **37**, 602 (1954).
18. E.B. Hughes, H.H.G. Jellinieck, and B.A. Ambrose. J. Phys. Colloid. Chem. **53**, 410 (1949).
19. A. Albert and J.N. Phillips. J. Chem. Soc. 1294 (1956).
20. F.M. Menger, T.D. Singh, and F.L. Bayer. J. Amer. Chem. Soc. **98**, 5011 (1976).
21. P. Demerseman, C. Pene, G. Colin, R. Royer, R. Reynaud, and P. Rumpf. Bull. Soc. Chim. Fr. 1366 (1972).
22. D.J. Brown, B.T. England, and J.M. Lyall. J. Chem. Soc. C, 226 (1966).
23. J. Riand, M.Th. Chenon, and N. Lumbroso-Bader. J. Am. Chem. Soc. **99**, 6838 (1977).
24. R.L. Benoit, M.J. Mackinnon, and L. Bergeron. Can. J. Chem. **59**, 1501 (1981).
25. Z. Pawlak and R.G. Bates. J. Solution Chem. **4**, 817 (1975).
26. R.G. Bates, L. Johnson, and R.A. Robinson. Chem. Anal. (Warsaw), **17**, 479 (1972).
27. K. Yates and G. Welch. Can. J. Chem. **50**, 474 (1972).
28. J.C. Hallé and R. Schaal. Anal. Chem. Acta, **60**, 197 (1972).
29. J.C. Hallé, C. Pichon, and F. Terrier. J. Biol. Chem. **259**, 4142 (1984).
30. I.M. Kolthoff, M.K. Chantooni, Jr., and S. Bhowmik. J. Am. Chem. Soc. **90**, 23 (1968).
31. J.C. Hallé, R. Gaboriaud, and R. Schaal. Bull. Soc. Chim. Fr. 2047 (1970).
32. A.J. Parker. Chem. Rev. **69**, 1 (1969).
33. J. Elguero, C. Marzin, A.R. Katritzky, and P. Linda. Adv. Heterocycl. Chem. Suppl. 1 (1976).
34. R. Gaboriaud, I. Mentré, and R. Schaal. C. R. Seances Acad. Sci. Ser. C: **286**, 1093 (1969).
35. J.J. Christensen, D.P. Wrathall, R.M. Izatt, and D.O. Tolman. J. Phys. Chem. **71**, 3001 (1967).
36. J.C. Hallé, F. Terrier, and R. Gaboriaud. Bull. Soc. Chim. Fr. 1231 (1973).
37. L.P. Hammett. Physical organic chemistry. McGraw-Hill Publications, New York. 1940. Chap. VII.

38. J.C. Hallé. C. R. Seances Acad. Sci. Ser. C: **271**, 1109 (1970).
39. J.C. Hallé, R. Harivel, and R. Gaboriaud. Can. J. Chem. **52**, 1774 (1974).
40. J.A. Gowland and G.H. Schmid. Can. J. Chem. **47**, 2953 (1969).
41. C.F. Bernasconi and P. Paschalis. J. Am. Chem. Soc. **108**, 2969 (1986).
42. J.P. Dorie, S. Odiot, and M.L. Martin. C. R. Acad. Sci. Paris, **274C**, 2022 (1972).
43. C.L. Liotta, E.M. Perdue, and H.P. Hopkins. J. Am. Chem. Soc. **96**, 7308 (1974).
44. D.H. Aue, H.M. Webb, W.R. Davidson, P. Toure, H.P. Hopkins, Jr., S.P. Moulik, and D.V. Jahagirdar. J. Am. Chem. Soc. **113**, 1770 (1991).
45. M.J. Cook, A.R. Katritzky, P. Linda, and R.D. Jack. Chem. Commun. 510 (1971).
46. S.O. Chua, M.J. Cook, and A.R. Katritzky. J. Chem. Soc. Perkin Trans. 2, 2111 (1973).
47. J.C. Craig, Jr. and D.E. Pearson. J. Heterocycl. Chem. **5**, 631 (1968).
48. J.M. Cox, J.A. Elvidge, and D.E.H. Jones. J. Chem. Soc. 1423 (1964).
49. J.C. Hallé, R. Gaboriaud, and R. Schaal. Bull. Soc. Chim. Fr. 1851 (1969).
50. J.C. Hallé. Ph.D. Thesis, Paris (1971); CNRS A.O. 5780.

Asymmetric synthesis of taxol and taxotère side chains by enolate hydroxylation

Stephen Hanessian and Jean-Yves Sancéau

Abstract: We report an asymmetric synthesis of the taxol and taxotère side chains by hydroxylation of enolates derived from N-substitued methyl 3-amino-3-phenyl propionate with the oxodiperoxymolybdenum (pyridine) (hexamethyl phosphoric triamide) complex (MoOPH).

Key words: taxol and taxotère side chains, hydroxylation.

Résumé : Nous décrivons une synthèse asymétrique des chaînes latérales du taxol et du taxotère par hydroxylation des énolates dérivés d'esters de l'acide 3-amino-3-phénylpropionique L-homo-phénylglycine au moyen du complexe oxodiperoxopyridino (hexaméthylphosphoramido) molybdène (MoOPH).

Mots clés : chaines latérales du taxol et du taxotère, hydroxylation.

Introduction

Taxol **1**, a complex diterpene isolated from the bark of *Taxus brefivolia* (1), and taxotère **2** a semi-synthetic analog (2), are currently considered to be among the most promising anticancer agents (3) (Fig. 1). Their clinically demonstrated effectiveness has stimulated considerable effort in total and analog synthesis (3), as well as in the development of efficient syntheses of the (2*S*,3*R*)-3-phenyl isoserine ester moiety at C-13 that is crucial for bioactivity. The synthetic approaches to this amino acid are centered around the use of chiral glycidate esters (4), opening of β-lactam rings derived from cycloaddition reactions (5), aldol condensations (6), and homologation of *(S)*-phenylglycine (7), intermediates derived from asymmetric dihydroxylation (8), or enzymes (9). With a few exceptions (4*a*, 4*d*), the methods involving glycidic esters and dihydroxycinnamic esters have relied principally on azide ion as a source of nitrogen. To the best of our knowledge only two methods are based on the introduction of the 2-hydroxyl group by hydroxylation of an enolate (10*a*,*b*). Our recent studies on stereocontrolled oxidation of enolates (11) derived from L-aspartic and glutamic acid derivatives (12) prompted us to extend our methodology to the synthesis of the taxol and taxotère side chains. In this paper we describe a stereocontrolled synthesis of methyl esters **6***a* and **6***b* by direct oxidation of β-aminoesters **5***a* and **5***b* using MoOPH as an electrophilic source of oxygen (Scheme 1).

Results

Methyl 3-amino-3-phenyl propionate **4** of high enantiomeric purity (>95%) was obtained from the corresponding acid **3** by resolution with D-tartaric acid following a literature procedure (13*a*). Benzoylation of **4** with benzoyl chloride, or treatment with di-*tert*-butyl dicarbonate in the presence of sodium bicarbonate furnished the N-protected derivatives **5***a* and **5***b* in 75% yield in each case.

Initially, we investigated the hydroxylation of the enolate dianions of **5***a* and **5***b* using racemic 2-phenylsulfonyl-3-phenyloxaziridine (14). Davis et al (10*b*) recently reported that reaction of the lithium dianion of **5***a* generated in the presence of LDA and LiCl with (+)-(camphorsulfonyl)oxaziridine at −100°C to −78°C afforded a preponderance of the desired *syn* isomer **6***a* (*syn/anti* 86:14). In an independent study, we had observed that treatment of the potassium enolate (KHMDS, −78°C to −25°C) of **5***a* with 2-phenylsulfonyl-3-phenyloxaziridine at −60°C led to a 86:14 *syn/anti* mixture in 65% yield. However, similar treatment of the potassium enolate of **5***b* proceeded with only moderate diastereoselectivity in favor of the *anti* isomer (*syn/anti* 40:60) in 62% yield. To clarify this intriguing reversal of selectivity, other metals were examined as counterions. Although the sodium enolate generated with NaHMDS gave a similar ratio (*syn/anti* 35:65), the use of LiHMDS furnished the highest *anti* selectivity (*syn/anti* 10:90). The sense of chiral induction with **5***a* can be rationalized according to Davis et al. (10*b*) where the potassium enolate, which may exist as an eight-membered ring **I** (Scheme 2), is preferentially attacked from the less hindered face of the

Fig. 1.

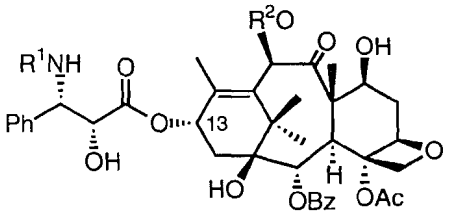

R^1= PhCO, R^2= Ac Taxol **1**
R^1=*t*-BuOCO, R^2= H Taxotère **2**

Received August 25, 1995.

S. Hanessian[1] and J.-Y. Sancéau. Department of Chemistry, Université de Montréal, P.O. Box 6128, Succ. Centre-ville, Montréal, QC H3C 3J7, Canada.

[1] Author to whom correspondence may be addressed. Telephone: (514) 343-6738. Fax: (514) 343-5728. E-mail: hanessia@ere.umontreal.ca

Scheme 1.

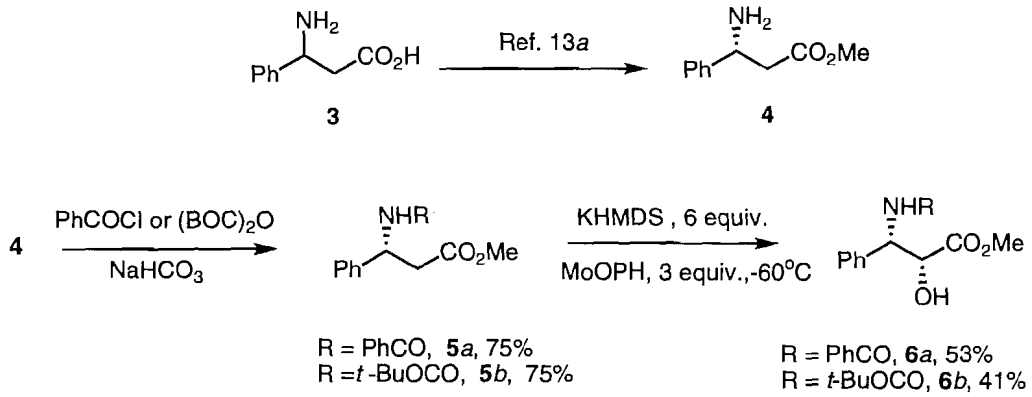

Scheme 2.

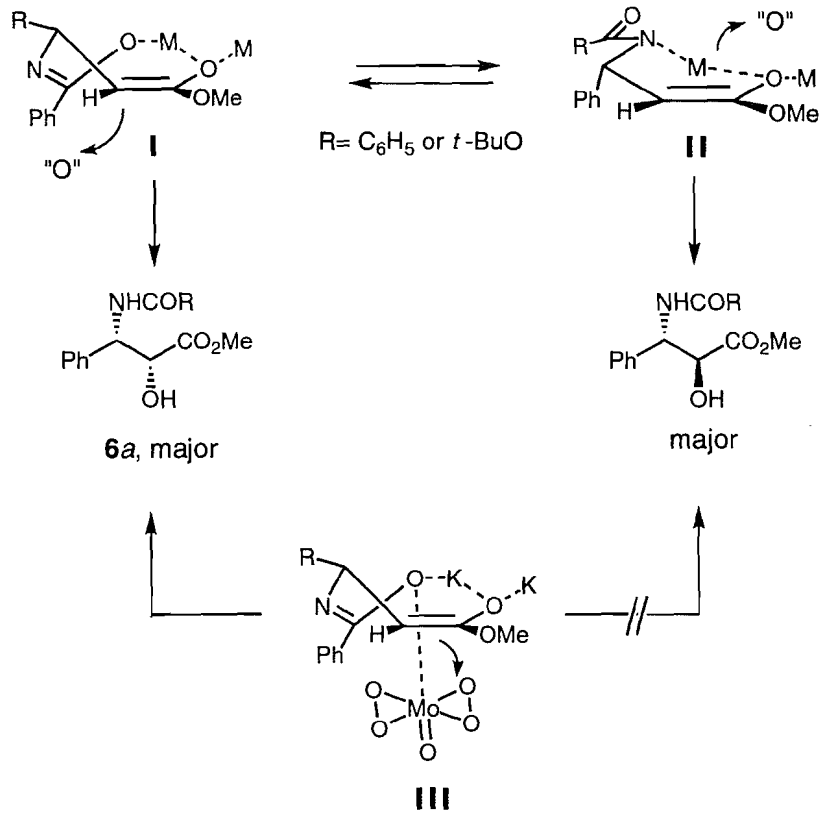

enolate, resulting in the formation of the *syn* hydroxylated product **6***a*. On the other hand, it is possible that the enolates of the carbamate derivative **5***b* preferentially adopt a six-membered ring chelate **II** resulting in a reversal of selectivity.

To improve the *syn* selectivity, we examined hydroxylations of **5***a* and **5***b* with MoOPH (15) in anticipation of an "internal" delivery of oxygen (12). Reaction of the potassium enolate derivative of **5***a* (KHMDS, −78°C to −25°C) with MoOPH (3 equiv.) was carried out at −60°C to give **6***a* as a 86:14 *syn/anti* mixture in 83% after column chromatography. The minor *anti* isomer can be removed almost quantitatively by one recrystallization from $CHCl_3$, yielding the expected amino acid **6***a* in 53% yield. The enantiomeric purity of this material was determined to be >97% by ^1H NMR and ^{19}F NMR analysis of its Mosher ester (16). Interestingly, treatment of the potassium enolate of **5***b* with MoOPH also proceeded with *syn* selectivity (*syn/anti* 86:14) in 65% yield. The taxotère side chain **6***b* could be isolated as a single diastereoisomer after two chromatographic purifications in 41% yield (ee >95% determined by analysis of ^1H NMR and ^{19}F NMR of Mosher ester derivative). The preponderance of the *syn* product in hydroxylations of **5**a and **5***b* with MoOPH can be rationalized by an initial coordination of the MoOPH reagent with the amide or carbamate groups (N or O) followed by an intramolecular delivery of oxygen as depicted in Scheme 2, expression **III** (12).

Previous examples of related enolate hydroxylations have utilized chiral non-racemic oxaziridine reagents derived from camphor (10*a*,*b*). As mentioned above, the Davis method (10*b*) generates the lithium enolate in the presence of lithium chloride (−42°C), and temperatures of −100°C to −78°C are needed for the stereoselective hydroxylation. Davies and co-

workers (10*a*), on the other hand, produce the *anti* isomer as a result of a mismatched reagent combination, which has to be inverted by a Mitsunobu protocol to give the desired *syn* product.

In summary, we have demonstrated that MoOPH can be an alternative reagent to provide the side-chain amino acids in taxol and taxotère in enantiomerically pure form. In both examples of hydroxylation, it was necessary to use more than stoechiometric amounts of base in order to achieve the yields quoted above.

Experimental

Tetrahydrofuran was distilled over benzophenone and potassium prior to use. Analytical thin-layer chromatography (TLC) was carried out on Merck Kieselgel silica gel 60 F_{254} glass plates. ^{1}H nuclear magnetic resonance spectra at 400 MHz were obtained on a Bruker WH-400 spectrometer. ^{1}H multiplicities are recorded by use of the following abbreviations: s, singlet; d, doublet; m, multiplet; br, broad; *J*, coupling constant (Hz). High-resolution FAB mass spectra were obtained by means of Kratos MS5OTCTA and AEI-MS 902 spectrometers at the Université de Montréal. Optical rotations were measured on a Perkin–Elmer 241 polarimeter at 25°C.

Melting points were measured on Büchi apparatus and are uncorrected. Column chromatography was done using the flash technique (17).

(3*R*)-Methyl-3-amino-3-phenylpropionate (4)

The procedure described by Wasserman and Berger (13*a*) for the preparation of (3*S*)-**4** was followed. A solution of (±)-**4** (3.8 g, 21.2 mmol) in MeOH was added in one portion to a refluxing solution of D-tartaric acid in MeOH (20 mL). After cooling overnight at −5°C, the white crystals were filtered off, mp 168–169°C; $[\alpha]_D$ −16.9 (*c* 3, H_2O). Recrystallization of this material from MeOH (20 mL) gave the D-tartrate salt (35–40% yield), which was recrystallized to constant physical properties; mp 169–170°C; $[\alpha]_D$ 19.3 (*c* 3, H_2O) (lit. (13*b*) mp 169–171°C; $[\alpha]_D$ −20.2 (*c* 7, H_2O)); ^{1}H NMR (D_2O) δ: 3.15 (dd, 2H), 3.67 (s, 3H), 4.49 (s, 2H), 7.47 (s, 5H). A solution of the above salt (3.72 g, 11.3 mmol) was treated with 1 N NaOH, affording **4** (1.7 g, 84%) as a colorless oil; bp 175–180°C (5 Torr (1 Torr = 133.3 Pa), Kugelrohr); $[\alpha]_D$ +11.6 (neat); (lit. (13*b*) $[\alpha]_D$ +12.1 (neat); lit. (13*c*) $[\alpha]_D$, +22.3 (*c* 1.99, $CHCl_3$)). ^{1}H NMR ($CDCl_3$) δ: 1.77 (s, 2H), 2.6 (d, 2H), 3.67 (s, 3H), 4.4 (m, 1H), 7.33–7.34 (m, 5H). The enantiomeric purity was detemined to be >95% by ^{1}H and ^{19}F NMR analysis of the corresponding Mosher ester derivative.

(3*R*)-*N*-Benzoyl-methyl-3-amino-3-phenylpropionate (5*a*)

To a stirred emulsion of **4** (204 mg, 1.14 mmol) and $NaHCO_3$ (163 mg) in CH_2Cl_2–H_2O (2:2 mL) was added freshly distilled benzoyl chloride (192 mg, 1.36 mmol). After vigorous stirring overnight, the aqueous phase was extracted three times with CH_2Cl_2 (20 mL). The combined organic layers were washed with brine, dried ($MgSO_4$), and evaporated. The resulting white solid was recrystallized from CH_2Cl_2–Et_2O (1:3), giving white needles of **5***a*, (244 mg, 75%); mp 120–121°C; $[\alpha]_D$ −20.2 (*c* 1.17, $CHCl_3$). ^{1}H NMR ($CDCl_3$) δ: 3 (dd, *J* = 5.6 Hz, *J* = 15.7 Hz, 2H), 3.65 (s, 3H), 5.64 (dd, *J* = 5.6 Hz, *J* = 8.4 Hz, 1H), 7.34–7.35 (m, 8H), 7.83–7.86 (d, 2H). MS (EI) *m/z*: 105 (100), 178 (15), 210; HRMS calcd. for $C_{17}H_{17}NO_3$: 283.3268; found: 283.2103.

(3*R*)-*N*-(*tert*-Butoxycarbonyl)-methyl-3-amino-3-phenylpropionate (5*b*)

To a stirred emulsion of **4** (767 mg, 4.3 mmol) and $NaHCO_3$ (363 mg) in CH_2Cl_2–H_2O (2:2 mL) was added di-*tert*-butyl dicarbonate (938 mg, 4.3 mmol). After vigorous stirring overnight, the aqueous phase was extracted three times with CH_2Cl_2 (20 mL). The combined organic layers were washed with brine, dried ($MgSO_4$), and evaporated. The resulting white solid was purified by column chromatography with 30% EtOAc – hexanes to provide **5***b* (905 mg, 75%) as white needles, mp 92–94°C; $[\alpha]_D$ +28 (*c* 1.1, $CHCl_3$); ^{1}H NMR ($CDCl_3$) δ: 1.4 (s, 9H), 2.82 (m, 2H), 3.6 (s, 3H), 5.1 (br s, 1H), 5.45 (br s, 1H), 7.2–7.4 (m, 5H); MS (EI) *m/z*: 83, 106, 150, 163, 223; HRMS calcd. for $C_{11}H_{13}NO_4$ (M – isobutylene)$^+$: 223.1332; found: 223.0845.

(2*R*,3*S*)-*N*-Benzoyl-3-phenylisoserine methyl ester (6*a*)

To a solution of KHMDS (0.5 M in toluene, 40 mL, 20 mmol, 6 equiv.) in dry THF (10 mL) was added dropwise at −78°C a solution of **5***a* (1g, 3.5 mmol) in THF (30 mL). The reaction mixture was warmed up to −25°C, stirred at this temperature, and then cooled back to −78°C. Freshly prepared MoOPH (15) (2.9 g, 5.25 mmol) was added in one portion. The resulting green solution was stirred at −60°C for 3 h, then quenched with saturated Na_2SO_3 (10 mL) followed by saturated NH_4Cl. The mixture was warmed up to room temperature and stirred until dissolution of the solids. The aqueous layer was extracted with THF (25 mL). The combined organic layers were washed successively with a mixture of 10% HCl – brine (1:1, 10 mL), 2% Na_2CO_3, brine, and dried over Na_2SO_4. After removal of the solvent, flash chromatography with 5% ether in CH_2Cl_2 gave unreacted ester **5***a* (50 mg), then **6***a* (86:14 *syn/anti* mixture by ^{1}H NMR, 833 mg, 84% yield based on consumed ester **5***a*). Recrystallization of this mixture from $CHCl_3$ yielded white needles of taxol side chain methyl ester **6***a* (560 mg, 53%), mp 180–181°C; $[\alpha]_D$ −47.5 (*c* 0.99, MeOH) (lit.(1) mp 184–185°C; $[\alpha]_D$ −49.6; lit.(4*g*) mp 184–185°C; $[\alpha]_D$ −48.1). ^{1}H NMR ($CDCl_3$) δ: 3.25 (br s, 1H), 3.86 (s, 3H), 4.65 (d, *J* = 1.83 Hz,1H), 5.76 (dd, *J* = 9.15 Hz, *J* = 1.83 Hz, 1H), 6.98 (d, *J* = 9.2 Hz, 1H); 7.3–7.6 (m, 8H), 7.7–7.8 (d, 2H). ^{1}H NMR and ^{19}F NMR analysis of this material showed the presence of small amounts of the *anti* diastereoisomer (<5%) and confirmed the enantiomeric purity (>97%).

(2*R*,3*S*)-*N*-(*tert*-Butoxycarbonyl)-3-phenylisoserine methyl ester (6*b*)

To a solution of KHMDS (0.5 M in toluene, 24 mL, 12 mmol, 6 equiv.) in dry THF (10 mL) was added dropwise at −78°C a solution of **5***b* (558 mg, 2 mmol) in THF (30 mL). The reaction mixture was warmed up to −25°C, stirred at this temperature, and then cooled back to −78°C. Freshly prepared MoOPH (1.3 g, 6 mmol, 3 equiv.) was added in one portion. The resulting green solution was stirred at −60°C for 3 h, then quenched with saturated Na_2SO_3 (10 mL) followed by saturated NH_4Cl. The mixture was warmed up to room temperature and stirred until dissolution of the solids. The aqueous layer was extracted with THF (25 mL). The combined organic layers were washed successively with a mixture of 10% HCl – brine (1:1, 10 mL),

2% Na_2CO_3, and brine, and dried over Na_2SO_4. After removal of the solvent, flash chromatography with 1% ether in CH_2Cl_2 gave **6***b* (86:14 *syn/anti* mixture by ^1H NMR) (383 mg, 65% yield based on consumed ester **5***b*). Two chromatographic purifications of this mixture with 20% EtOAc – hexanes provided the taxotère side–chain methyl ester **6***b* (240 mg, 41%) as white needles, mp 128–129°C; $[\alpha]_D$ −6.6 (*c* 1.1, $CHCl_3$) (lit. (4*g*) mp 130.5–131.5°C; $[\alpha]_D$ −7 (*c* 1.2, $CHCl_3$)). ^1H NMR ($CDCl_3$) δ: 1.4 (br s, 9H), 3.12 (br s, 1H), 3.84 (s, 3H), 4.47 (br s, 1H), 5.21 (d, 1H), 5.4 (d, 1H), 7.3–7.6 (m, 8H), 7.25–7.4 (m, 5H). ^1H NMR and ^{19}F NMR analysis of this material showed the presence of only one diastereisomer and confirmed the enantiomeric purity (>95%).

Acknowledgements

We thank the Natural Sciences and Engineering Research Council of Canada (NSERCC) and le Fonds pour la formation de chercheurs et l'aide à la recherche (FCAR) for generous financial assistance.

References

1. M.C. Wani, H.L. Taylor, M.E. Wall, P. Coggon, and A.T. McPhail. J. Am. Chem. Soc. **93**, 2325 (1971).
2. D. Guénard, F. Guéritte-Voegelin, and P. Potier. Acc. Chem. Res. **26**, 160 (1993).
3. For total syntheses of taxol, see: (*a*) K.C. Nicolaou, Z. Yang, J.J. Liu, H. Ueno, P.G. Nantermet, R.K. Guy, C.F. Clairbone, J. Renaud, E.A. Couladouros, K. Paulvannan, and E.J. Sorensen. Nature, **367**, 630 (1994); K.C. Nicolaou, H. Veno, J.-J. Liu, P.G. Nauternet, Z. Yan, J. Renaud, K. Paulvannan, and R. Chadha. J. Am. Chem. Soc. **117**, 653 (1995) and previous references; (*b*) R.A. Holton, C. Somoza, H.-B. Kim, F. Liang, R.J. Biediger, P.-D. Boatman, M. Shindo, C.C. Smith, S. Kim, H. Nadizadeh, Y. Suzuki, C. Tao, P. Vu, S. Tang, P. Zhang, K.K. Murthi, N.L. Gentile, and J.H. Liu. J. Am. Chem. Soc. **116**, 1597 (1994); (*c*) J.J. Masters, J.T. Link, L.B. Snyder, W.B. Young, and S. Danishefsky. Angew. Chem. Int. Ed. Engl. **34**, 1723 (1995); for reviews on biological properties, synthetic approaches, and semi-syntheses of taxol and taxotère, see: (*a*) K.C. Nicolaou, W.M. Dai, and R.K. Guy. Angew. Chem. Int. Ed. Engl. **33**, 15 (1994); (*b*) A.N. Boa, P.R. Jenkins, and N.J. Lawrence. Contemp. Org. Synth. **1**, 47 (1994).
4. (*a*) R.P. Srivastava, J.K. Zjawiony, J.R. Peterson, and J.D. McChesney. Tetrahedron: Asymmetry, **5**, 1683 (1994); (*b*) D.-M. Gou, Y.-C. Liu, and C.-S. Chen. J. Org. Chem. **58**, 1287 (1993); (*c*) A. Commerçon, D. Bézard, F. Bernard, and J.D. Bourzat. Tetrahedron Lett. **33**, 5185 (1992); (*d*) L. Deng and E.N. Jacobsen. J. Org. Chem. **57**, 4320 (1992); (*e*) J.-N. Denis, A. Correa, and A.E. Greene. J. Org. Chem. **55**, 1957 (1990); (*f*) H. Hönig, P. Seufer-Wasserthal, and H. Weber. Tetrahedron, **46**, 3841 (1990); (*g*) J.-N. Denis, A.E. Greene, A.A. Serra, and M.-J. Luche. J. Org. Chem. **51**, 46 (1986).
5. (*a*) A. Commerçon and J.D. Bourzat. Tetrahedron Lett. **34**, 6049 (1993); (*b*) C.S. Swindell and M. Tao. J. Org. Chem. **58**, 5889 (1993); (*c*) C. Palomo, J.M. Aizpurua, J.I. Miranda, A. Mielgo, and J.I. Odriozola. Tetrahedron Lett. **34**, 6325 (1993); (*d*) V. Farina, S.I. Hauck, and D.G. Walker. Synlett, 761 (1992); (*e*) I. Ojima, I. Habus, and M. Zhao. J. Org. Chem. **56**, 1681 (1991); (*f*) G.I. Georg, P.M. Mashava, E. Akgün, and M.W. Milstead. Tetrahedron Lett. **32**, 3151 (1991); (*g*) C. Palomo, A. Arieta, F.P. Cossio, J.M. Aizpurua, A. Mielgo, and N. Aurrekoetxea. Tetrahedron Lett. **31**, 6429 (1990).
6. (*a*) A.M. Kanazawa, J.-N. Denis, and A.E. Greene. J. Org. Chem. **59**, 1238 (1994); (*b*) J. Chem. Soc. Chem. Commun. 2591 (1994); (*c*) K. Hattori and H. Yamamoto. Tetrahedron, **50**, 2785 (1994); (*d*) C. Mukai, I.J. Kim, E. Furu, and M. Hanaoka. Tetrahedron, **49**, 8323 (1993; (*e*) K. Hattori, M. Miyata, and H.Yamamoto. J. Am. Chem. Soc. **115**, 1151 (1993).
7. (*a*) A. Dondoni, D. Perrone, and T. Semola. Synthesis, 181 (1995); (*b*) J.-N. Denis, A. Correa, and A.E. Greene. J. Org. Chem. **56**, 6939 (1991).
8. (*a*) A.M.P. Koskinen, E.K. Karvinen, and P.J. Siirilä. J. Chem. Soc. Chem. Commun. 21 (1994); (*b*) Z.-M. Wang, H.C. Kolb, and K.B. Sharpless. J. Org. Chem. **59**, 5104 (1994).
9. (*a*) R. Brieva, J.Z. Crich, and C.J. Sih. J. Org. Chem. **58**, 1068 (1993); (*b*) R.N. Patel, A. Banerjee, J.M. Howell, C.G. McNamee, D. Brozozowski, D. Mirfakhrae, V. Nanduri, J.K. Thottathil, and L.J. Szarka. Tetrahedron: Asymmetry, **4**, 2069 (1993).
10. (*a*) M.E. Bunnage, S.G. Davies, and C.J. Goodwin. J. Chem. Soc. Perkins Trans 1, 2385 (1994); (*b*) F.A. Davis, R.T. Reddy, and R.E. Reddy. J. Org. Chem. **57**, 6387 (1992).
11. M.P. Gore and J.C. Vederas. J. Org. Chem. **51**, 3700 (1986); R. Gamboni and Ch. Tamm. Tetrahedron Lett. **27**, 3999 (1986); W. Oppolzer and P. Dudfield. Helv. Chim. Acta, **68**, 216 (1985); D.A. Evans, M.M. Morrissey, and R.L. Dow. J. Am. Chem. Soc. **107**, 4346 (1985); F.A. Davis, L.C. Vishwakarma, J.M. Billmers, and J. Finn. J. Org. Chem. **49**, 3243 (1984); E. Vedejs, D.A. Engler, and J.E. Telschow. J. Org. Chem. **43**, 188 (1978); G.M. Rubottom, J.M. Gruber, R. Marrero, H.D. Juve, Jr., and C.W. Kim. J. Org. Chem. **48**, 4940 (1983); H.H. Wasserman and B.H. Lipshutz. Tetrahedron Lett. 1731 (1975); G.W. Moersch and M.L. Zwiesler. Synthesis, 647 (1971).
12. S. Hanessian and B. Vanasse. Can. J. Chem. **71**, 1401 (1993); F.J. Sardina, M.M. Paz, E. Fernandez-Megia, R.F. de Boer, and M. Pilar Alvarez. Tetrahedron Lett. **33**, 4637 (1992); C.W. Jefford, J.B. Wang, and Z.H. Lu. Tetrahedron Lett. **34**, 7557 (1993); R. Gamboni, P. Mohr, N. Sarcevic, and C. Tamm. Tetrahedron Lett., **26**, 203 (1985).
13. (*a*) H.H. Wasserman and G.D. Berger. Tetrahedron, **39**, 2459 (1983); (*b*) H. Pietsch. Tetrahedron Lett. **27**, 2789 (1972); (*c*) for a recent asymmetric synthesis of (−)-**4**, see: J. Jiang, K.K. Schumacher, M. Joulie, F.A. Davis, and R.E. Reddy. Tetrahedron Lett. **35**, 2121 (1994).
14. L.C. Vishwarkarma, O.D. Slunger, and F.A. Davis. Org. Synth. **66**, 203 (1986).
15. E. Vedejs and S. Larsen. Org. Synth. **64**, 127 (1984).
16. H.S. Mosher and J.A. Dale. J. Am. Chem. Soc. **95**, 502 (1973).
17. W.C. Still, M. Kahn, and A. Mitra. J. Org. Chem. **43**, 2923 (1978).

Correlation analysis of reactivity in the addition of substituted benzylamines to β-nitrostyrene

Neeta Jalani, Seema Kothari, and Kalyan K. Banerji

Abstract: The kinetics of addition of a number of *ortho*-, *meta*-, and *para*-substituted benzylamines to β-nitrostyrene (NS) in acetonitrile have been studied. The reaction is first order with respect to NS. The order with respect to the amine is higher than one. It has been shown that the reaction follows two mechanistic pathways, uncatalyzed and catalyzed by the amine. The Arrhenius activation energy for the catalyzed path is negative, indicating the presence of a pre-equilibrium (k_1, k_{-1}) leading to the formation of a zwitterion. The values of the rate constant, k_1, for the nucleophilic attack have been determined for 28 benzylamines. The rate constant k_1 was subjected to correlation analysis using Charton's LDR and LDRS equations. The polar regression coefficients are negative, indicating the formation of a cationic species in the transition state. The reaction is subject to steric hindrance by *ortho* substituents.

Key words: nucleophilic addition, benzylamines, correlation analysis, kinetics, alkene.

Résumé : On a étudié la cinétique de l'addition d'un certain nombre de benzylamines *ortho*-, *méta*- et *para*-substituées sur le β-nitrostyrène (NS) en solution dans l'acétonitrile. La réaction est du premier ordre en NS. L'ordre par rapport à l'amine est supérieur à un. On a montré que la réaction suit deux voies mécanistiques, l'une qui n'est pas catalysée et l'autre qui est catalysée par l'amine. L'énergie d'activation d'Arrhénius pour la voie catalysée est négative; ceci indique la présence d'un pré-équilibre (k_1, k_{-1}) conduisant à la formation d'un zwitterion. On a déterminé les valeurs pour les constantes de vitesse, k_1, pour l'attaque nucléophile par 28 benzylamines. Les constantes de vitesses, k_1, ont été soumises à une analyse de corrélation à l'aide des équations LDR et LDRS de Charton. Les coefficients de régression polaire sont négatifs, ce qui indique qu'il y a formation d'une espèce cationique dans l'état de transition. La réaction est sujette à l'empêchement stérique des substituants en *ortho*.

Mots clés : addition nucléophile, benzylamines, analyse de corrélation, cinétique, alcène.

[Traduit par la rédaction]

Introduction

Synthetic and mechanistic studies of additions to an activated carbon–carbon double bond are of immense importance. A number of reports about the addition of charged nucleophiles to activated systems have been published (1–4). However, not many reports are available about the addition of neutral nucleophiles to activated double bonds (5–10). In this paper, we report the addition of a number of monosubstituted benzylamines to β-nitrostyrene (NS). Attempts have been made to correlate rate and structure in this reaction. Mechanistic aspects are discussed.

Experimental

Materials

NS was prepared by the reported method (11). Its purity was checked by melting point. The preparation, purification, and specification of the substituted benzylamines have already been described (12). Acetonitrile was purified by the usual methods (13).

Received November 7, 1995.

N. Jalani, S. Kothari, and K.K. Banerji.[1] Department of Chemistry, Jai Narain Vyas University, Jodhpur 342 005, India.

[1] Author to whom correspondence may be addressed.

Product analysis

Benzylamine (5.85 g, 0.05 mol) and NS (1.49 g, 0.01 mol) were made up to 100 mL in acetonitrile and kept for ca. 12 h to ensure completion of the reaction. The solvent was removed by distillation under reduced pressure. The product was characterized as 1-benzylamino-1-phenyl-2-nitroethane [PhCH($PhCH_2NH$)CH_2NO_2] on the basis of its ^1H NMR spectrum. The ^1H NMR spectrum (in $CDCl_3$) of the product exhibited signals for the CH and CH_2 groups at δ 3.25 [PhCH($PhCH_2NH$)-] and 4.0 (-CH_2NO_2), respectively.

Kinetic measurements

The reaction was studied under pseudo-first-order conditions by keeping a large excess (×10 or greater) of benzylamine over NS. The solvent was acetonitrile. The reaction was followed spectrophotometrically by monitoring the decrease in NS concentration at 311 nm for ca. 80% reaction. The pseudo-first-order rate constant, k_{obs}, was evaluated from the linear ($r > 0.990$) plot of log [NS] versus time. Duplicate kinetic runs showed that the rate constants were reproducible to within ±3%.

Results and discussion

Rate laws and other data were obtained for all the compounds investigated. Since the results are similar, only representative data are reproduced here.

Fig. 1. Plot of k_{obs}/[amine] versus [amine] for the reaction of β-nitrostyrene with benzylamine.

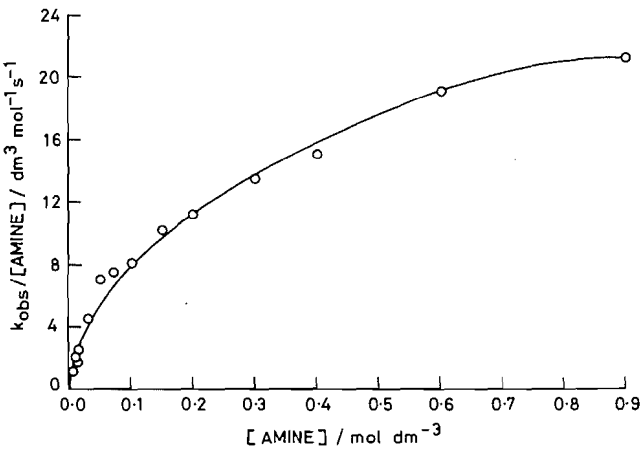

The overall reaction may be represented as eq. [1].

[1] $ArCH_2NH_2 + Ph—CH=CH(NO_2) \rightarrow Ph—CH(NHCH_2Ar)—CH_2(NO_2)$

The reaction is first order with respect to NS. Further, the pseudo-first-order rate constant, k_{obs}, does not vary with the initial concentration of NS. Values of k_{obs} increase with an increase in the concentration of amine and the apparent order in [amine] is higher than one. Results are given in Tables 1 and 2, respectively.

A plot of k_{obs}/[amine] versus [amine] is curvilinear (Fig. 1) with a decrease in slope with increase in amine concentration. However, at low [amine] (≤0.05 mol dm^{-3}), the dependence of k_{obs} on the amine concentration has the following form:

[2] $k_{obs}/[amine] = k + k_c\,[amine]$

This indicates that the addition of benzylamine to NS is catalyzed by a second molecule of the amine and k and k_c are the rate constants of the uncatalyzed and catalyzed reactions, respectively. The values of k and k_c were determined at different temperatures and the activation parameters evaluated are recorded in Table 3. It is observed that while the rate for the uncatalyzed path (k) increases with a rise in temperature, the rate for the catalyzed path (k_c) decreases. Thus the enthalpy of activation of the catalytic route is negative. This may be explained by assuming the presence of a pre-equilibrium in the reaction so that k and k_c are not the rate constants of elementary processes but are composite values.

It is seen that eq. [2] describes the dependence of k_{obs} on amine concentration only for low amine concentration. When the amine concentration is increased, the slope of the curve showing the dependence of the ratio k_{obs}/[amine] on [amine] decreases regularly (downward curvature). Thus a mechanism involving formation of a zwitterionic intermediate in the pre-equilibrium with its subsequent decomposition into the product, via a proton transfer, by two parallel routes, i.e., catalyzed and uncatalyzed, is proposed (Scheme 1). This assumption is also supported by observed large negative values of the entropy of activation. As the formation of the zwitterionic intermediate involves a high degree of charge distribution, solvation of two charged sites must result in large entropy losses.

Scheme 1.

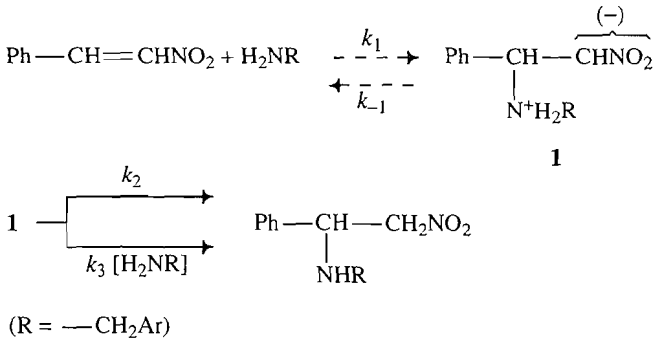

The application of the steady-state treatment to this mechanism gives eq. [3].

[3] $$k_{obs}/[amine] = \frac{k_1\,(k_2 + k_3[amine])}{k_{-1} + k_2 + k_3[amine]}$$

Calculation of rate constants

The linear dependence of k_{obs}/[amine] on amine concentration suggests that $k_{-1} \gg k_3$[amine]. Further, $k_2 \leq k_{-1}$ because, if $k_2 \gg k_{-1}$, no catalysis will be observed as the nucleophilic attack is the rate-determining step, i.e., $k_{obs}/[amine] = k_1$. In the analysis of a kinetic equation of type [3] the condition $k_{-1} \gg k_2 + k_3$[amine] has generally been observed (14) and the observed second-order rate constant can be described by eq. [4], which is similar to eq. [2].

[4] $k_{obs}/[amine] = (k_1/k_{-1})(k_2 + k_3[amine])$

Thus, the constants k and k_c are expressed by eqs. [5] and [6], respectively.

[5] $$k = \frac{k_1 k_2}{k_{-1}}$$

[6] $$k_c = \frac{k_1 k_3}{k_{-1}}$$

At $k_{-1} \approx k_3$[amine] a curvilinear dependence of the second-order rate constant on the amine concentration (≥0.07 mol dm^{-3}) occurs according to eq. [3].

For reactions of the amines in which the difference between the constants k_1 and k is not less than one order of magnitude, the approximation [7] is quite acceptable (8).

[7] $$\frac{1}{(k_{obs}/[amine] - k)} \approx \frac{1}{k_1} + \frac{1}{k_c[amine]}$$

A plot of $(k_{obs}/[amine] - k)^{-1}$ against $[amine]^{-1}$ is a straight

Table 1. Dependence of rate on the concentration of NS.[a]

10^5 [NS]/mol dm^{-3}	4.0	5.0	8.0	10.0	15.0	20.0
10^5 k_{obs}/s^{-1}	19.5	18.9	19.2	19.1	18.7	19.0

[a][Benzylamine] = 0.01 mol dm^{-3}; T = 298 K.

Table 2. Dependence of rate on the concentration of benzylamine.[a]

[Amine]/mol dm^{-3}	0.005	0.008	0.01	0.015	0.03	0.05	0.07
10^5 k_{obs}/s^{-1}	6.15	13.1	19.1	38.7	137	357	521
[Amine]/mol dm^{-3}	0.1	0.15	0.2	0.3	0.4	0.6	0.9
10^5 k_{obs}/s^{-1}	815	1545	2240	4050	6000	11400	19000

[a]10^5 [NS] = 10.0 mol dm^{-3}; T = 298 K.

Table 3. Rate constants at different temperatures and activation parameters for the addition of benzylamine to NS[a] (data processed by eq. [2]).

T/K	10^3 k/dm^3 mol^{-1} s^{-1}	k_e/dm^6 mol^{-2} s^{-1}
288	3.16	1.59
298	6.38	1.28
308	9.81	1.07
318	17.2	0.84
$\Delta H^{\ddagger}$/kJ mol^{-1}	40.0 ± 1.6	−18.4 ± 0.6
$\Delta S^{\ddagger}$/J mol^{-1} K^{-1}	−154 ± 5	−305 ± 2
$\Delta G^{\ddagger}$/kJ mol^{-1}	85.8 ± 1.3	72.4 ± 0.4

[a][Amine] = 0.005–0.05 mol dm^{-3}.

line. The inverse of the intercept gives the rate constant, k_1, of the nucleophilic attack by amine on NS.

Correlation analysis of reactivity

The kinetics of the addition of benzylamine and 27 mono-substituted benzylamines to NS were studied. The kinetics were similar in all cases. The rate constants, k_1, at different temperatures were evaluated. The activation parameters were also calculated. The results are reported in Table 4.

The values of log k_1 at 288 K and at 318 K of the 28 amines are linearly related (r^2 0.9983, slope 0.8275 ± 0.0069). The value of the isokinetic temperature, obtained from the slope of this plot (15), is 636 ± 3 K. The linear correlation implies that all the amines react with the same mechanism (15). Further, a linear isokinetic relationship is a necessary condition for the validity of linear free energy relationships.

In the 1980s, Charton and Charton (16) introduced a triparametric LDR equation for the quantitative description of structural effects on chemical reactivities. It has the advantage of not requiring a choice of parameters, as the same three substituent constants are reported to cover the entire range of electrical effects of substituents. In this work we have applied the LDR equation, eq. [8], to the rate constant, k_1.

$$[8] \quad \log k_1 = L\sigma_1 + D\sigma_d + R\sigma_e + h$$

Here, σ_1 is a localized (field and (or) inductive) effect parameter, σ_d is the intrinsic delocalized (resonance) electrical effect parameter when active site electronic demand is minimal, and σ_e represents the sensitivity of the substituent to change in electronic demand by the active site. The latter two substituent parameters are related by eq. [9].

$$[9] \quad \sigma_D = \eta\sigma_e + \sigma_d$$

where η represents the electronic demand of the reaction site, which is given by $\eta = R/D$, and σ_D represents the delocalized electrical parameter of the diparametric LD equation.

For *ortho*-substituted compounds, it is necessary to account for the possibility of steric effects and Charton (16), therefore, modified the LDR equation to the LDRS equation, eq. [10], where υ is the well-known Charton's steric parameter based on van der Waals radii (17).

$$[10] \quad \log k_1 = L\sigma_1 + D\sigma_d + R\sigma_e + S\upsilon + h$$

The rates of addition of the *ortho*-, *meta*-, and *para*-substituted benzylamines showed excellent correlations with the LDR/LDRS equations (Table 5). All three series of substituted benzylamines meet the requirement of minimum number of substituents for analysis by the LDR and LDRS equations (16). We have used the standard deviation (sd), the coefficient of multiple determination (R^2), and Exner's (18) parameter ψ as measures of the goodness of fit.

Comparison of the L and D values for the substituted benzylamines shows that the addition of *para*-substituted benzyl-

Table 4. Rate constants, k_1, at different temperatures and activation parameters for the addition of substituted benzylamines to NS.

Subst.	k_1/mol dm^{-3} s^{-1} 288 K	298 K	308 K	318 K	$\Delta H^{\ddagger}$ kJ mol^{-1}	$\Delta S^{\ddagger}$ J mol^{-1} K^{-1}	$\Delta G^{\ddagger}$ kJ mol^{-1}
H	0.94	1.51	2.45	4.00	34.2 ± 0.6	−127 ± 2	71.9 ± 0.5
p-Me	1.35	2.11	3.38	5.43	32.8 ± 0.7	−129 ± 2	71.1 ± 0.6
p-OMe	1.57	2.58	4.07	6.53	33.5 ± 0.4	−124 ± 1	70.7 ± 0.3
p-F	0.50	0.88	1.46	2.45	37.6 ± 0.3	−120 ± 1	73.3 ± 0.2
p-Cl	0.43	0.76	1.28	2.15	38.2 ± 0.2	−120 ± 1	73.7 ± 0.2
p-NO_2	0.08	0.17	0.32	0.57	47.2 ± 2.5	−102 ± 3	77.5 ± 0.6
p-CF_3	0.20	0.37	0.67	1.15	42.0 ± 0.1	−113 ± 1	75.5 ± 0.1
p-COOMe	0.28	0.48	0.88	1.50	40.4 ± 0.8	−116 ± 3	74.8 ± 0.6
p-Br	0.40	0.70	1.20	2.02	38.6 ± 0.8	−119 ± 1	73.9 ± 0.2
p-NHAc	1.05	1.74	2.80	4.57	34.7 ± 0.4	−125 ± 1	71.6 ± 0.3
o-Me	0.64	1.06	1.76	2.91	35.9 ± 0.5	−124 ± 2	72.8 ± 0.4
o-OMe	0.81	1.38	2.36	3.94	37.7 ± 0.4	−116 ± 1	72.2 ± 0.3
o-F	0.27	0.50	0.92	1.61	42.9 ± 0.2	−107 ± 1	74.7 ± 0.2
o-Cl	0.16	0.29	0.57	0.95	43.3 ± 0.9	−110 ± 3	76.0 ± 0.7
o-Br	0.13	0.25	0.46	0.83	44.5 ± 0.1	−108 ± 1	76.4 ± 0.1
o-NO_2	0.04	0.08	0.17	0.30	49.3 ± 0.9	−101 ± 3	79.2 ± 0.7
o-CF_3	0.044	0.09	0.17	0.31	46.9 ± 0.3	−108 ± 1	79.0 ± 0.2
o-COOMe	0.11	0.21	0.36	0.67	42.8 ± 0.8	−115 ± 3	76.9 ± 0.6
o-NHAc	0.33	0.58	1.01	1.74	39.7 ± 0.4	−117 ± 1.4	74.3 ± 0.3
m-Me	1.32	2.07	3.28	5.28	32.6 ± 0.7	−130 ± 2	71.2 ± 0.6
m-OMe	1.37	2.18	3.57	5.85	34.4 ± 0.8	−124 ± 3	71.0 ± 0.6
m-F	0.42	0.73	1.28	2.22	39.8 ± 0.6	−115 ± 2	73.8 ± 0.5
m-Cl	0.37	0.65	1.16	2.02	40.6 ± 0.6	−113 ± 2	74.0 ± 0.5
m-I	0.47	0.82	1.43	2.45	39.4 ± 0.4	−115 ± 2	73.5 ± 0.3
m-NO_2	0.08	0.16	0.31	0.58	47.8 ± 0.2	−100 ± 1	77.6 ± 0.1
m-CF_3	0.18	0.33	0.60	1.07	42.7 ± 0.4	−111 ± 1	75.7 ± 0.3
m-COOMe	0.26	0.47	0.84	1.47	41.5 ± 0.3	−113 ± 1	74.9 ± 0.3
m-NH_2	3.04	4.50	6.99	11.0	30.2 ± 0.9	−132 ± 3	69.2 ± 1

Table 5. Temperature dependence of the reaction constants for the addition of substituted benzylamines to NS.

T/K	*L*	*D*	*R*	*S*	η	R^2	sd	ψ	P_D	P_S
***para*-Substituted**										
288	−1.38 ±0.03	−1.05 ±0.03	−0.85 ±0.17	—	0.810	0.9985	0.02	0.01	43.2	—
298	−1.23 ±0.02	−0.99 ±0.02	−0.88 ±0.14	—	0.889	0.9988	0.02	0.01	44.6	—
308	−1.15 ±0.02	−0.91 ±0.02	−0.88 ±0.14	—	0.967	0.9985	0.02	0.01	44.2	—
318	−1.10 ±0.02	−0.88 ±0.02	−0.86 ±0.13	—	0.977	0.9985	0.02	0.01	44.4	—
***meta*-Substituted**										
288	−1.41 ±0.03	−0.98 ±0.02	−0.91 ±0.16	—	0.929	0.9984	0.02	0.01	41.0	—
298	−1.29 ±0.04	−0.90 ±0.03	−0.85 ±0.20	—	0.944	0.9980	0.02	0.01	41.1	—
308	−1.18 ±0.01	−0.86 ±0.01	−0.83 ±0.06	—	0.965	0.9977	0.02	0.01	43.2	—
318	−1.10 ±0.03	−0.82 ±0.02	−0.80 ±0.16	—	0.976	0.9976	0.02	0.01	42.7	—
***ortho*-Substituted**										
288	−1.51 ±0.01	−1.05 ±0.01	−0.93 ±0.06	−0.68 ±0.01	0.886	0.9998	0.01	0.02	41.0	21.0
298	−1.40 ±0.01	−0.99 ±0.01	−0.83 ±0.05	−0.62 ±0.01	0.838	0.9999	0.01	0.02	41.4	20.6
308	−1.25 ±0.02	−0.96 ±0.02	−0.80 ±0.14	−0.61 ±0.02	0.833	0.9992	0.02	0.02	43.4	21.6
318	−1.21 ±0.01	−0.94 ±0.01	−0.78 ±0.02	−0.59 ±0.01	0.829	0.9999	0.01	0.02	43.7	21.5

amines is more susceptible to the delocalization effect than to the localized effect. However, the addition of *ortho*- and *meta*-substituted compounds exhibited a greater dependence on the field effect. In all cases, the magnitude of the reaction constants decreases with an increase in the temperature, pointing to a decrease in selectivity with increase in temperature.

All three regression coefficients, L, D, and R, are negative, indicating an electron-deficient reaction center in the transition state of the reaction. The positive value of η adds a negative increment to σ_d (eq. [9]), increasing the donor effect of the substituent where σ_d is negative and decreasing the acceptor effect where σ_d is positive. The substituent is, therefore, better able to stabilize a cationic reaction site. This also supports the presence of an electron-deficient center in the transition state of the rate-determining step. The negative value of S indicates that the reaction is subjected to steric hindrance by the *ortho* substituent. This may be due to steric hindrance of the *ortho* substituent to the approach of amines to NS.

We evaluated the significance level for all the three/four independent variables by determining the Student's t function for each coefficient (19). The significance level was found to be >99.99%. Thus all the parameters are required to explain the effect of structure on the reactivity of amines towards NS. There is no significant collinearity between the various substituent constants in all three series.

The percent contribution (17) of the delocalized effect, P_D, is given by eq. [11].

$$[11] \quad P_D = \frac{(|D| \times 100)}{(|L| + |D|)}$$

Similarly, the percent contribution of the steric parameter (17) to the total effect of the substituent, P_S, was determined by using eq. [12].

$$[12] \quad P_S = \frac{(|S| \times 100)}{(|L| + |D| + |S|)}$$

The values of P_D and P_S are also recorded in Table 5. The value of P_D for the addition of *para*-substituted benzylamines is ca. 44.1% whereas its values for the *meta*- and *ortho*-substituted amines are ca. 41.7 and 42.4%, respectively. It is seen that the P_D values for the *ortho* and *para* series are in the normal range (17) but that for the *meta*-series is somewhat more than the usual range (28 ± 5). This shows that from the *meta* position the delocalized effects are felt more strongly than expected. Presently,. no explanation of this observation is available. The value of P_S shows that there is considerable steric effect on the reaction. This is indicative of a high degree of C—N bond formation in the transition state of the first step of the reaction.

In many studies of nucleophilic additions to alkenes, the reactivity of substituted alkenes has been studied. We could not find any report on the reactivity of substituted benzylamines. The addition of primary and secondary amines to *trans*-(2-furyl)nitroethylene, in acetonitrile, exhibits (8) kinetics similar to those observed in the present case and is reported to follow similar mechanistic pathways. However, Kada et al. (7) observed a first-order dependence on amine concentration in the addition of secondary amines to 5-substituted *trans*-(2-furyl)nitroethylene.

Acknowledgements

Thanks are due to the University Grants Commission (India) for financial support.

References

1. M.J. Kamlet and D.J. Glower. J. Am. Chem. Soc. **78**, 4556 (1956).
2. B.A. Fiet and A. Zilka. J. Org. Chem. **28**, 406 (1963); B.A. Fiet, J. Sinnreich, and A. Zilka. J. Org. Chem. **28**, 3245 (1963).
3. W.G. Daries, E.W. Hardisty, T.P. Nevell, and R.H. Peters. J. Chem. Soc. B, 998 (1970).
4. C.F. Bernasconi and D.F. Shunck. J. Org. Chem. **57**, 2365 (1992), and refs. cited therein.
5. C.F. Bernasconi and R.A. Rentfrow and P.R. Tia. J. Am. Chem. Soc. **108**, 4541 (1986).
6. C.F. Bernasconi and M. Panda. J. Org. Chem. **52**, 3042 (1987).
7. R. Kada, V. Knoppova, J. Kova, and I. Malenakova. Collect. Czech. Chem. Commun. **49**, 2496 (1984).
8. A.F. Popov, I.F. Perepichka, and L.I. Kostenko. J. Chem. Soc. Perkin Trans. 2, 395 (1989).
9. C.F. Bernasconi and R.B. Killion. J. Org. Chem. **54**, 2878 (1989).
10. A. Shunmugasundaram, L. Thanulingam, and R. Murugesan. Indian J. Chem. Sect. A, **30**, 609 (1991).
11. D.E. Worrell. Organic syntheses. Vol. 1. *Edited by* H. Gilman and A. Blatt. Wiley, New York. 1941. p. 413.
12. K.K. Banerji. J. Chem. Soc. Perkin Trans. 2, 1015 (1988).
13. D.D. Perrin, W.L. Armarego, and D.R. Perrin. Purification of organic compounds. Pergamon Press, London. 1966.
14. Z. Rappoport. Acc. Chem. Res. **14**, 7 (1981); D.R. Palleros and N.S. Nudelman. J. Chem. Soc. Perkin Trans. 2, 1277 (1984); N.S. Nudelman and D.R. Palleros. J. Chem. Soc. Perkin Trans. 2, 479 (1985).
15. O. Exner. Prog. Phys. Org. Chem. **10**, 411 (1973).
16. M. Charton and B. Charton. Bull. Soc. Chim. Fr. 199 (1988), and references cited therein.
17. M. Charton. J. Org. Chem. **40**, 407 (1975).
18. O. Exner. Collect Czech. Chem. Commun. **31**, 3222 (1966).
19. R.L. Wine. Statistics for scientists and engineers. Prentice Hall, New Delhi. 1966. 253.

Reflections on the outer-sphere mechanism of electron transfer[1]

Thomas W. Swaddle

Abstract: The quantitative efficacy of the Stranks–Marcus–Hush theory of volumes of activation $\Delta V^{\ddagger}$ for outer-sphere electron transfer between metal complexes in solution is assessed. The theory predicts $\Delta V^{\ddagger}$ accurately for several couples in aqueous solution, but is satisfactory for polar nonaqueous solvents only at pressures of ca. 100 MPa and above, and accuracy is not improved when the molecular nature of the solvent is allowed for through the Mean Spherical Approximation approach. At low pressures, the calculations become numerically unstable when the isothermal compressibility of the solvent is high and its relative permittivity is low, particularly for the more highly charged couples. For aqueous systems, departures from the predicted $\Delta V^{\ddagger}$ afford insights into the role of the counterions, the incursion of inner-sphere pathways, the enhanced reactivity of $Co^{III/II}$ cage complexes relative to conventional chelates, and the question of "spin forbiddenness" of electron transfer processes that involve a large change in spin multiplicity.

Key words: redox kinetics, inorganic reaction mechanisms, pressure effects, Marcus–Hush theory, activation volumes.

Résumé : On a évalué l'efficacité quantitative de la théorie de Stranks–Marcus–Hush des volumes d'activation, $\Delta V^{\ddagger}$, pour le transfert d'électrons de la couche extérieure entre des complexes métalliques en solution. La théorie prédit d'une façon précise les $\Delta V^{\ddagger}$ pour plusieurs couples en solutions aqueuses, mais pour les solvants non aqueux elle n'est satisfaisante qu'à des pressions d'environ 100 MPa et plus et sa précision n'est pas améliorée lorsqu'on tient compte de la nature moléculaire du solvant par le biais de l'approche d'une approximation sphérique moyenne. À de faibles pressions, les calculs deviennent numériquement instables lorsque la compressibilité isotherme du solvant est élevée et que sa permittivité relative est faible, particulièrement pour les couples les plus chargés. Pour les systèmes aqueux, les déviations par rapport aux valeurs de $\Delta V^{\ddagger}$ prédites fournissent des renseignements sur le rôle des contre-ions, sur les incursions de voies impliquant les sphères internes, l'augmentation de la réactivité des complexes de cage du $Co^{III/II}$ par rapport aux chélates conventionnels et la question de l'«empêchement par les spins» de processus de transferts d'électrons qui impliquent un grand changement dans la multiplicité des spins.

Mots clés : cinétique rédox, mécanismes de réactions inorganiques, effets de pression, théorie de Marcus–Hush, volumes d'activation.

[Traduit par la rédaction]

Introduction

For almost 30 years, my research group at The University of Calgary has maintained an interest in pressure effects in solution chemistry in a variety of contexts, including the elucidation of reaction mechanisms. The following short review will consider how high-pressure kinetics impinge upon an area in which Henry Taube has made seminal contributions, viz., the mechanisms of electron transfer processes in solution. Taube, with his student Russell Hunt (1), was also the first to use the effect of pressure P on reaction rate constants k as a mechanistic criterion in coordination chemistry, showing that the volume of activation $\Delta V^{\ddagger}$ ($= -RT(\partial \ln k/\partial P)_T$) for solvent water exchange on $Co(NH_3)_5OH_2^{3+}$ is +1.2 $cm^3\ mol^{-1}$, consistent with an S_N1 or $\mathbf{I_d}$ mechanism for this process. The pressure effect, however, is disappointingly small in this particular case, and this may explain why Taube did not pursue high-pressure kinetics further after leaving The University of Chicago. Nevertheless, during a visit to The University of Calgary in 1966, Taube responded most encouragingly to my question as to whether further high-pressure studies in inorganic solution chemistry would be worthwhile, and this has been a major theme in my research group ever since.

Probably the best known of Taube's scientific contributions is his elegant demonstration (2, 3) of the existence of a dichotomy between *inner-sphere* (ligand bridged) and *outer-sphere* mechanisms of electron transfer between transition metal complexes in solution, a possibility mooted as early as 1940 but not actually established until Taube's unequivocal study appeared in 1953 (4). Taube's approach depended upon the reduction of a substitution-inert oxidant to a labile product, concomitantly with oxidation of a labile reductant to an inert product; then, if electron transfer occurs via a bridging ligand X^{n-} (e.g., $X^{n-} = Cl^-$), that ligand becomes trapped in the first coordination sphere of the oxidized species:

Received October 30, 1995.

T.W. Swaddle.[2] Department of Chemistry, The University of Calgary, Calgary, AB T2N 1N4, Canada.

[1] This article is based upon a lecture presented at The University of Saskatchewan's *Taube Fest* on October 7, 1995, and is dedicated to Professor Henry Taube in gratitude for his friendship, encouragement, and scientific leadership.

[2] Telephone: (403) 220-5358. Fax: (403) 289-9488. E-mail: swaddle@acs.ucalgary.ca

[1] $$\underset{\text{inert}}{Co^{III}(NH_3)_5X^{(3-n)+}} + \underset{\text{labile}}{Cr(H_2O)_6^{2+}} \longrightarrow \{(NH_3)_5Co\cdots X\cdots Cr(OH_2)_5\}^{(5-n)+} + H_2O$$

$$\xrightarrow{H^+} \underset{\text{labile}}{Co(aq)^{2+}} + 5NH_4^+ + \underset{\text{inert}}{Cr^{III}(H_2O)_5X^{(3-n)+}}$$

Where X^{n-} is incapable of bridging (e.g., X = NH_3), a relatively slow outer-sphere electron transfer process occurs instead, and X does not appear in the oxidized product. If, however, both the reductant and its oxidized product are labile on the time scale of the redox experiment, this distinction is inapplicable. Furthermore, an outer-sphere mechanism can be unequivocally assigned only if ligand substitution rates on *both* reactants are much slower than the redox process. Candlin and Halpern (5), searching for alternative mechanistic criteria, recognized that the inner- and outer-sphere mechanisms differ in that the former requires expulsion of a first coordination sphere ligand (water, in eq. [1]) in the activation process, and so should be characterized by a more positive $\Delta V^{\ddagger}$ than would be expected for a corresponding outer-sphere path. Using pressure equipment left by Taube in Chicago, they found $\Delta V^{\ddagger}$ values ranging from +8 to +14 $cm^3\ mol^{-1}$ for the reduction of various $Co^{III}(NH_3)_5X^{(3-n)+}$ by $Fe(aq)^{2+}$, suggesting an inner-sphere mechanism.

This begs the question, however, of just what $\Delta V^{\ddagger}$ values would be expected for a genuine outer-sphere process. Donald R. Stranks, with whom I collaborated from 1970 until his untimely death in 1986, attacked this question (6) using the Marcus–Hush theory of outer-sphere electron transfer rates (7, 8). Some refinements of Stranks' treatment have subsequently been proposed (9), and in this article we assess the quantitative success of this approach.

Adaptation of the Marcus–Hush theory of electron transfer kinetics

In its simplest form, Marcus–Hush theory relates k for outer-sphere electron transfer to a free energy of activation $\Delta G^{\ddagger}$, which may be expressed in terms of a reorganizational energy λ and the free energy change ΔG^0 for the redox reaction, and a collision frequency Z appropriate for a bimolecular reaction in solution:

[2] $$k = Z \exp(-\Delta G^{\ddagger}/RT)$$

[3] $$\Delta G^{\ddagger} = (\lambda/4)[1 + (\Delta G^0/\lambda)]^2 = (\lambda/4) + \tfrac{1}{2}\Delta G^0 + \{(\Delta G^0)^2/4\lambda\} \approx (\lambda/4) + \tfrac{1}{2}\Delta G^0, \text{ if } \Delta G^0 << \lambda$$

The reorganizational energy comprises an internal contribution λ_{IR}, arising from the readjustment of the geometries (usually taken to mean the metal–ligand bond distances, which usually shorten on oxidation of the metal center and lengthen on its reduction) of the two reactants necessary for electron transfer to be possible, and a contribution λ_{SR} from the reorganization of the solvent. The Coulombic work of bringing the reactants together and medium (Debye–Hückel) effects should also be included in $\Delta G^{\ddagger}$ and Z. In current practice (10–12) Z is replaced by $K_{PREC}\kappa_{el}\nu_n$, where K_{PREC} is the formation constant for the assembly of a precursor complex of the reactants, κ_{el} is the electronic transmission coefficient (= 1 for adiabatic electron transfer), and ν_n is the nuclear frequency.

For *self-exchange* reactions, i.e., those involving no net chemical change ($\Delta G^0 = 0$), the pressure derivative of $-\ln k$ so calculated then gives a theoretical volume of activation $\Delta V_{CALC}^{\ddagger}$ (9):

[4] $$\Delta V_{CALC}^{\ddagger} = \Delta V_{IR}^{\ddagger} + \Delta V_{SR}^{\ddagger} + \Delta V_{DH}^{\ddagger} + \Delta V_{COUL}^{\ddagger} + \Delta V_{PREC}^{\ddagger}$$

where $\Delta V_{IR}^{\ddagger}$, $\Delta V_{SR}^{\ddagger}$, $\Delta V_{DH}^{\ddagger}$, $\Delta V_{COUL}^{\ddagger}$, and $\Delta V_{PREC}^{\ddagger}$ are, respectively, the contributions of internal reorganization, solvent reorganization, medium (Debye–Hückel) effects, the Coulombic work terms (i.e., the free energy component of the precursor formation constant K_{PREC}), and the pre-exponential part of K_{PREC} to the overall volume of activation.

Internal reorganization is often the major contributor to $\Delta G^{\ddagger}$ and hence the most significant influence upon k, since the atomic nuclei of both the oxidant and the reductant in self-exchange must be displaced away from their equilibrium positions towards a common geometry — usually implying bond lengthening and shortening, respectively — before electron transfer can occur. Exceptions occur when the oxidized and reduced species have similar bond lengths to their precursors (e.g., in the $Fe(phen)_3^{3+/2+}$ self-exchange)[3], when electron transfer is expected to be very fast. In contrast, *internal reorganization should make only a very small contribution* $\Delta V_{IR}^{\ddagger}$ *to* $\Delta V_{CALC}^{\ddagger}$, because expansion of the oxidant and the contraction of the reductant as they go to the transition state will effectively cancel. Stranks (6) used Hush's potential function to estimate $\Delta V_{IR}^{\ddagger} \approx +0.6\ cm^3\ mol^{-1}$ for most $ML_n^{(z+1)+/z+}$, this small contribution (barely outside experimental error) reflecting compressibility differences between the initial and transition states. As we shall see below, however, the possibility remains that pressure may hinder or favor the attainment of a special configuration of one of the reactants that provides a particularly efficient channel for electron transfer, in which case $\Delta V_{IR}^{\ddagger}$ would no longer be negligible.

The solvent reorganization contribution to $\Delta V_{CALC}^{\ddagger}$

[5] $$\Delta V_{SR}^{\ddagger} = (N_A e^2/16\pi\varepsilon_0)[\{(2r_1)^{-1} + (2r_2)^{-1} - \sigma^{-1}\} \times \{\partial(n^{-2} - D^{-1})/\partial P\}_T - (n^{-2} - D^{-1})\beta/3\sigma]$$

depends upon the effective radii r_1 and r_2 of the reactants (conveniently assumed to be pressure independent and roughly the same, r), the separation σ of the reactants at the maximum probability of electron transfer (usually assumed to be $r_1 + r_2$), the isothermal compressibility β of the solvent, its static dielectric constant or relative permittivity D, and its high-frequency dielectric constant, which is taken to be the square of the refractive index n; the other symbols have their usual SI meanings. It can be seen that eq. [5] will be dominated by n^{-2} for strongly polar solvents, i.e., those with high D, but the Pekar factor ($n^{-2} - D^{-1}$) and its pressure derivative may become numerically poorly defined for solvents of low polar-

[3] phen = 1,10-phenanthroline; en = 1,2-diaminoethane; $hfac^-$ = 1,1,1,5,5,5-hexafluoropentan-2,4-dionate (hexafluoroacetylacetonate); sep = sepulchrate = 1,3,6,8,10,13,16,19-octaazabicyclo[6.6.6]eicosane; [9]$aneS_3$ = 1,4,7-trithiacyclononane; diamsar = diaminosarcophagine = 1,8-diamino-3,6,10,13,16,19-hexaazabicyclo[6.6.6]eicosane; $edta^{4-}$ = 1,2-ethanedinitrilotetraacetate; terpy = 2,2′:6′,2″-terpyridyl.

Table 1. Calculated contributions to $\Delta V^{\ddagger}$ for self-exchange of a typical couple $ML_n^{3+/2+}$.[a]

Solvent	P (MPa)	β (10^{-10} Pa^{-1})	$\Delta V_{SR}^{\ddagger}$ (cm^3 mol^{-1})	$\Delta V_{DH}^{\ddagger}$ (cm^3 mol^{-1})	$\Delta V_{COUL}^{\ddagger}$ (cm^3 mol^{-1})	$\Delta V_{CALC}^{\ddagger}$ (cm^3 mol^{-1})	$\Delta\beta^{\ddagger}$ (cm^3 mol^{-1} MPa^{-1})
Water	0	4.5	−7.5	1.3	−3.4	−7.9	−0.020
	100	3.6	−6.1	1.1	−2.8	−6.4	−0.013
	200	3.0	−5.1	0.8	−2.2	−5.1	−0.012
Methanol	0	11.6	−18.3	9.9	−20.7	−25.6	−0.253
	100	5.7	−9.1	5.1	−10.8	−12.8	−0.063
	200	3.9	−6.2	3.4	−7.3	−8.5	−0.029
Acetone	0	12.6	−18.4	26.0	−47.6	−36.2	−0.483
	100	6.1	−9.3	10.1	−18.3	−15.4	−0.087
	200	4.2	−6.4	6.2	−11.3	−9.8	−0.036

[a] $[ML_n^{2+}] = [ML_n^{3+}] = 0.001$ mol kg^{-1} ($I = 0.009$ mol kg^{-1}), $r = 500$ pm, $\sigma = 1.0$ nm, $a = 800$ pm, $T = 25°C$, $\Delta V_{IR}^{\ddagger} = 0.6$ cm^3 mol^{-1}.

ity. Since the pressure dependences of both n and D are related to β (9), it follows that $\Delta V_{SR}^{\ddagger}$ is determined largely by β and will also, like β, be pressure dependent.

The consequences of these points are illustrated by Table 1, which shows that the calculation of $\Delta V_{SR}^{\ddagger}$ for water is numerically stable because D is high and, like β for this solvent, not markedly dependent on pressure over the customary experimental range (0–200 MPa). On the other hand, $\Delta V_{SR}^{\ddagger}$ for the less polar solvents methanol and acetone assumes large, numerically unstable values at low pressure that quickly fall with rising pressure because β is large and strongly pressure dependent, and this calculated behavior is typical of organic solvents in general.

The contributions to $\Delta V_{CALC}^{\ddagger}$ from ionic strength (I) and Coulombic effects

$$[6]\quad \Delta V_{DH}^{\ddagger} = \{RTz_1z_2CI^{1/2}/(1 + BaI^{1/2})^2\} \times [(\partial \ln D/\partial P)_T(3 + 2BaI^{1/2}) - \beta)]$$

$$[7]\quad \Delta V_{COUL}^{\ddagger} = (N_A z_1 z_2 e^2/4\pi\varepsilon_0\sigma)(\partial D^{-1}/\partial P)_T$$

are significant when neither of the reactant charge numbers z_1 and z_2 is zero, but are numerically of opposite sign (involving derivatives of ln D and D^{-1}, respectively) and tend to cancel.[4] This cancellation is fortuitously almost exact for a variety of solvents at the typical working ionic strength of $I \approx 0.1$ mol L^{-1} (14), but the values of $\Delta V_{DH}^{\ddagger}$ and $\Delta V_{COUL}^{\ddagger}$, for example, for acetone at ambient pressure and 25°C are numerically very large at this ionic strength (+49.7 and −47.6 cm^3 mol^{-1}, respectively) so that their cancellation and the calculation of $\Delta V_{CALC}^{\ddagger}$ are numerically unstable, i.e., highly sensitive to inadequacies of either the theory or the data used in the computation. This computational instability is clearly seen for solvents of low D and high β in Table 1, in which we consider minimal practical concentrations of reactants without supporting electrolyte.

[4] In Stranks' original presentation of the theory (6), the sign of $\Delta V_{DH}^{\ddagger}$ was reversed (13), giving an apparent agreement of $\Delta V_{CALC}^{\ddagger}$ with experiment for the few studies then available, including the aqueous $Co(en)_3^{3+/2+}$ exchange,[3] which, as we shall see below, is actually an anomalous case. This early apparent success of theory diverted attention from the problem of pressure effects on electron transfer kinetics for some years.

$\Delta V_{PREC}^{\ddagger}$ contributes only about +1 to +3 cm^3 mol^{-1} to the total $\Delta V_{CALC}^{\ddagger}$ listed in Table 1.

A further complication is that, in any one-electron transfer, at least one partner must be charged, so that, in solvents of low D in particular, ion pairing with counterions is to be expected at elevated ion concentrations. The extent of ion pairing can, in principle, be calculated from the Fuoss equation (9), but the consequences of such pairing are not obvious. Wherland (15) notes that ion pairs formed by cationic reactants in nonaqueous solvents are generally less reactive in electron transfer than the free ions, so that the experimental $\Delta V^{\ddagger}$ can be expected to be more negative than $\Delta V_{CALC}^{\ddagger}$ (since pressure breaks up ion pairs by favoring solvation of the separated ions), but the *extent* to which the ion pairs are less reactive is not calculable — the approximation made in some of our published work (9, 16), that ion pairs are inactive, is likely too extreme, although in those specific instances this makes little difference. On the other hand, electron transfer in *anionic* couples such as $MnO_4^{-/2-}$ (17) and $Fe(CN)_6^{3-/4-}$ (18) in aqueous solution shows strong catalysis by cations, and gives experimental $\Delta V^{\ddagger}$ values that are much more positive than $\Delta V_{CALC}^{\ddagger}$ even after allowing for the anticipated electrostatic effect of pairing on $\Delta V_{COUL}^{\ddagger}$.

Self-exchange reactions in nonaqueous solutions

The upshot of these considerations is that the foregoing adaptation of Marcus–Hush theory is unlikely to be satisfactory for nonaqueous systems. $\Delta V_{CALC}^{\ddagger}$ is numerically unstable for typical organic solvents at low pressures, does not allow for the unpredictable effects of possible ion pairing at practical ionic strengths, and furthermore has a very strong pressure dependence, i.e., a substantial compressibility coefficient of activation $\Delta\beta^{\ddagger} = -(\partial\Delta V^{\ddagger}/\partial P)_T$ (Table 1), that is not observed in practice. For example, Fig. 1 compares the theoretical and experimental pressure dependences of ln k in methanol for the $Ru(hfac)_3^{0/-}$ exchange[3] (19), which should be particularly amenable to theoretical treatment since z_1 and, therefore, $\Delta V_{DH}^{\ddagger}$ and $\Delta V_{COUL}^{\ddagger}$ are all zero and ion pairing effects should be minimal. The theoretical plot, however, is markedly curved and unrepresentative of the experimental ln k values, which are linearly dependent upon P within the error limits. The data

Fig. 1. Pressure effect on the logarithm of the rate constant for the $Ru(hfac)_3^{0/-}$ exchange in methanol-d_4 at 25.3°C. Total Ru concentrations (kg mol^{-1}): 0.060 (open circles), 0.026 (filled circles). Solid curve: calculated pressure effect. Broken line: linear least-squares fit of the data (19).

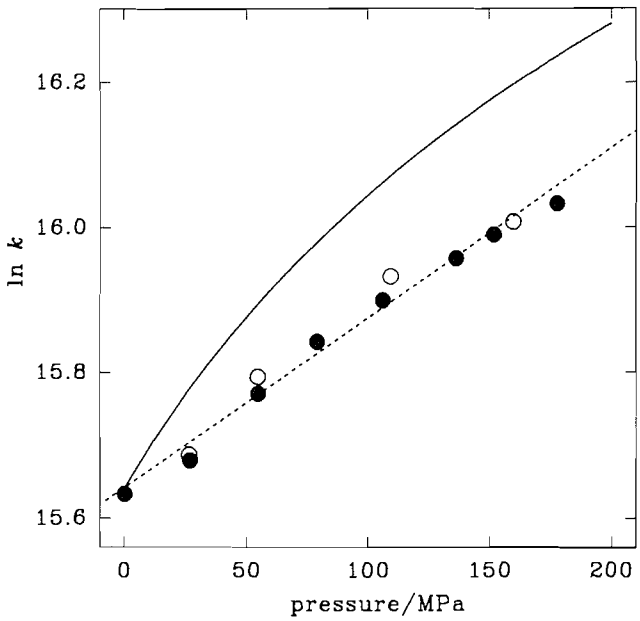

Fig. 2. Pressure effect on the logarithm of the rate constant for the $Fe(\eta^5\text{-}C_5H_5)_2^{+/0}$ self-exchange in acetonitrile at 0°C. Solid curve: calculated pressure effect. Broken line: linear least-squares fit of the data of Hunt and co-workers (20).

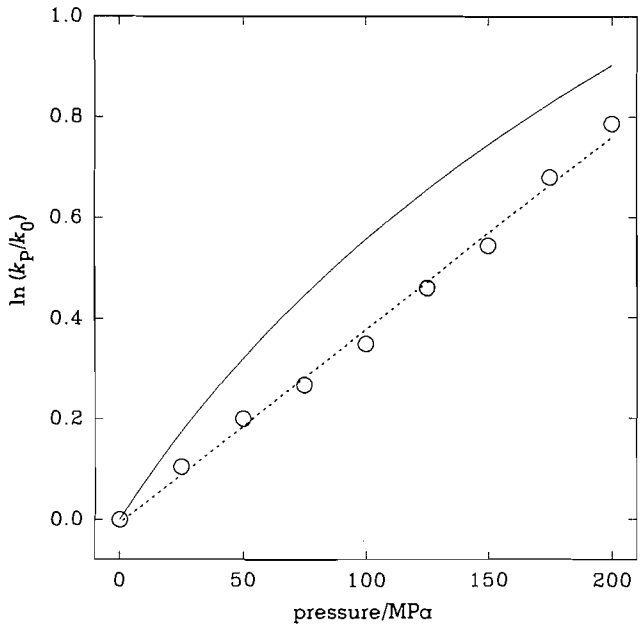

of Hunt et al. (ref. 20 and personal communication) for the ferrocene–ferricenium exchange in acetonitrile present a similar picture (Fig. 2). As Table 1 shows, however, $\Delta\beta^{\ddagger}$ is even more strongly dependent on pressure than is $\Delta V_{CALC}^{\ddagger}$. Thus, the intuitive expectation, that by taking further derivatives of a quantity with respect to pressure we should arrive at one which is sensibly pressure independent, is entirely wrong; the problem of finding a "good" parameter to summarize pressure effects simply gets worse. The situation is analogous to the sharp temperature dependences found for the experimental heat capacities of activation (the temperature derivative of the enthalpy of activation) for aquation of $Co(NH_3)_5X^{(3-n)+}$ (X^{n-} = Br^- and SO_4^{2-}) (21).

Table 1 and Figs. 1 and 2 do suggest, however, that the theory could be applied satisfactorily to organic solvents of moderate dielectric constant (i.e., those for which ion pairing is not expected to be dominant) *if attention were confined to the upper part of the pressure range.* The various parameters of Table 1 appear to be converging towards common values at high pressures for both aqueous and nonaqueous media. Furthermore, in the upper pressure range, the calculated ln k vs. P plots in Figs. 1 and 2 are roughly linear and parallel to the linear least-squares fit of the experimental data, i.e., the observed and calculated $\Delta V^{\ddagger}$ are actually in good agreement at elevated pressures. This can be explained by noting that solvents that are highly compressible in the bulk (i.e., that have much free volume) lose some of this high compressibility locally when solvating solute molecules or ions, which may be regarded as fillers of interstitial space in a quasi-lattice of solvent. As Hupp and co-workers (22) have shown, it is the *local* solvent environment of the reactants that determines $\Delta V_{SR}^{\ddagger}$, the most important contributor to $\Delta V_{CALC}^{\ddagger}$.

Unfortunately, development of this concept requires a full molecular dynamics computational treatment, and this is probably not feasible at present.[5] Besides, the traditional approach, in which phenomena are related to particular bulk properties of the various media, affords some conceptual satisfaction. As a compromise, the molecular nature of the solvent can be introduced into the dielectric-continuum Marcus–Hush theory through the Mean Spherical Approximation (MSA) approach (24–26). We find (27), however, that $\Delta V_{CALC}^{\ddagger}$ values so calculated are not sufficiently different from those computed as above to warrant the added mathematical complexity, except with solvents of very low D such as chloroform (but in those cases complications from ion pairing are expected to undermine the usefulness of the theory).

Wherland's recent review (15) deals with the general problem of electron transfer dynamics in nonaqueous systems, and also documents the extensive high-pressure kinetic studies made by him and his co-workers by NMR line-broadening on $Mn(CNR)_6^{2+/+}$ (R = various alkyl or aryl groups), ferrocene-ferricenium, cobalt(III/II) clathrochelate, and other self-exchange reactions in a variety of organic solvents. The problems noted above are again manifest to varying degrees in the quantitative interpretation of the $\Delta V^{\ddagger}$ measurements.

[5] M. Hilczer and M. Tachiya (23) report a molecular dynamics computer simulation of electron transfer in acetonitrile that predicts rate constants some 10^4-fold slower than does simple Marcus–Hush theory for small driving forces $-\Delta G^0$, and moves the Marcus "inverted" region (where $-\Delta G^0$ exceeds the reorganizational energy barriers, and further increases in $-\Delta G^0$ should result in *reduced* rates) beyond the experimentally accessible range. No computation of $\Delta V^{\ddagger}$ has yet been reported.

Table 2. Volumes of activation at 100 MPa for self-exchange in "well-behaved" $ML_n^{(z+1)+/z+}$ couples in aqueous media.[a]

Couple	I (mol kg^{-1})	T (°C)	$\Delta V^{\ddagger}$ (cm^3 mol^{-1})	$\Delta V_{CALC}^{\ddagger}$ (cm^3 mol^{-1})	Ref.
$Fe(H_2O)_6^{3+/2+}$	0.5	2.0	−11.1 ± 0.4[b]	−10.4	28
$Fe(phen)_3^{3+/2+}$	0.3	3.0	−2.2 ± 0.1[c]	−2.5[d]	29
$Co([9]aneS_3)_2^{3+/2+}$	0.1	25.0	−4.8 ± 0.2[c]	−5.3	30
$Co(sep)^{3+/2+}$	0.2	25.0	−6.4 ± 0.2[e]	−6.4	30
$Co(diamsar)^{3+/2+}$	0.1	25.0	−10.5 ± 0.6[e]	−7.3	31
$Co(diamsarH_2)^{5+/4+}$	0.63	25.0	−9.4 ± 0.9[e]	−9.2	31

[a] $\Delta V_{IR}^{\ddagger}$ taken as +0.6 cm^3 mol^{-1} except as indicated.
[b] By radioisotope sampling at high pressure.
[c] By high-pressure NMR line broadening.
[d] $\Delta V_{IR}^{\ddagger}$ taken as zero.
[e] By high-pressure stopped-flow circular dichroism change.

Self-exchange reactions in aqueous solution: "well-behaved" couples

Table 1 does give confidence in the quantitative applicability of eqs. [4]–[7] to *aqueous* systems, for which β is small and shows relatively little pressure dependence, and for which D is large enough to minimize ion pairing and generate realistic values for $\Delta V_{SR}^{\ddagger}$, $\Delta V_{DH}^{\ddagger}$, and $\Delta V_{COUL}^{\ddagger}$. A small pressure dependence of $\Delta V_{CALC}^{\ddagger}$ is still predicted, but in most cases is unlikely to emerge beyond the experimental uncertainty over the usual 0–200 MPa range, so we may treat the experimental $\Delta V^{\ddagger}$ from an apparently linear ln k vs. P relationship as an *average* over this pressure range and compare it with $\Delta V_{CALC}^{\ddagger}$ for the mid-range pressure, 100 MPa.

Table 2 lists those aqueous self-exchange reactions[3] for which, to date, $\Delta V^{\ddagger}$ has been found to agree well with the predictions of eqs. [4]–[7] at 100 MPa (agreement is only fair in the $Co(diamsar)^{3+/2+}$ case). These "well-behaved" couples include not only $Co([9]aneS_3)_2^{3+/2+}$, in which both the Co^{II} and the Co^{III} are in the low-spin state, but also the cage complexes $Co(sep)^{3+/2+}$, $Co(diamsar)^{3+/2+}$, and $Co(diamsarH_2)^{5+/4+}$, in all of which the Co^{II} partner is in the high-spin state, i.e., in which the electron transfer process involves a large change in spin multiplicity, quartet→singlet and vice-versa. We return to this point below. Other salient points are the conformity to predictions of both 5+/4+ and 3+/2+ charge types, and also of the couple $Fe(H_2O)_6^{3+/2+}$, which has been thought to behave anomalously (32, 33) and for which an inner-sphere (aqua bridged) self-exchange mechanism has been proposed (32, 34), a possibility that the pressure result rules out. Finally, since the theory assumes adiabatic electron transfer, the self-exchange reactions listed in Table 2 are evidently fully adiabatic or close to it; non-adiabatic behavior should be revealed in $\Delta V^{\ddagger}$ values that are significantly more negative than predicted (9).

Self-exchange reactions in aqueous solution: "anomalous" couples

In contrast, Table 3 lists aqueous self-exchange reactions for which $\Delta V^{\ddagger}$ differs sharply from the theoretical value for an adiabatic outer-sphere process. In most cases, however, a reason for the discrepancy can be identified; in other words, $\Delta V^{\ddagger}$ serves as a criterion of a mechanistic anomaly in these instances. For the $Fe_{aq}^{3+/2+}$ exchange via the conjugate base $Fe(H_2O)_5OH^{2+}$, the measured $\Delta V^{\ddagger}$ is inconsistent with an outer-sphere process, but is precisely that calculated for an inner-sphere pathway in which a water ligand is expelled from the labile $Fe(H_2O)_6^{2+}$ and the OH^- ligand acts as a bridge between the Fe centers (cf. eq. [1]) (28). This interpretation receives support from Stranks' fragmentary report of $\Delta V^{\ddagger}$ for the analogous $Cr_{aq}^{3+/2+}$ exchange, in which the measurable exchange rate is carried by the conjugate base pathway and ligand bridging by OH^- has been demonstrated by oxygen isotope transfer (6).[6] Thus, Candlin and Halpern's contention (5), that $\Delta V^{\ddagger}$ can be used to distinguish between inner- and outer-sphere mechanisms of electron transfer, is vindicated.

The gross failure of theory to predict $\Delta V^{\ddagger}$ for the aqueous $Co(en)_3^{3+/2+}$ and $Co(phen)_3^{3+/2+}$ exchanges (Table 3) stands in contrast to the successes for $Co([9]aneS_3)_2^{3+/2+}$ and the $Co^{3+/2+}$ cage complexes (Table 2). It has long been argued that $Co^{III/II}$ exchanges in which the Co^{II} partner is high-spin ($^4T_{1g}$ ground state in O_h symmetry) and the Co^{II} low-spin ($^1A_{1g}$) are slow because of the large change in spin multiplicity accompanying electron transfer. Either the electron transfer occurs non-adiabatically (10–12) from ground state to ground state with a large multiplicity change, or there is a fast (39) but unfavorable high-spin to low-spin Co^{II} pre-equilibrium with adiabatic electron transfer between the low-spin Co^{II} and Co^{III} species. We have, in the past (16, 35, 36), favored the first explanation of the anomalously negative $\Delta V^{\ddagger}$ values for the $Co(en)_3^{3+/2+}$, $Co(phen)_3^{3+/2+}$, and "Co(edta)$^{2-/-}$" exchanges,[7] as nonadiabaticity would make a calculable negative volume contribution

[6] The exact conditions of Stranks' experiments were never reported. Neither is it clear whether the measured $\Delta V^{\ddagger}$ value given in ref. 6 refers to the pressure dependence of an experimental rate constant (first order in Cr^{III} (total) and Cr^{II}, inversely first order in $[H^+]$), or to exchange between the actual conjugate species $Cr(H_2O)_5OH^{2+}$ and Cr^{2+}; in the former case, 3.8 ± 0.7 cm^3 mol^{-1} should be subtracted from $\Delta V^{\ddagger}$ to allow for the volume change accompanying conjugate base formation (38), bringing $\Delta V^{\ddagger}$ into excellent agreement with the value calculated for an inner-sphere process, as in the $Fe^{III/II}$ case (28).

[7] Under the experimental conditions, the Co^{II} partner exists as $Co(Hedta)OH_2^-$, but the volume changes associated with deprotonation of pendant arm and the aqua ligand can be allowed for in $\Delta V_{CALC}^{\ddagger}$ (36).

Table 3. Some "anomalous" volumes of activation at 100 MPa for self-exchange in $ML_n^{(z+1)+/z+}$ couples in aqueous media.

Couple	I (mol kg^{-1})	T (°C)	$\Delta V^{\ddagger}$ (cm^3 mol^{-1})	$\Delta V_{CALC}^{\ddagger}$ (cm^3 mol^{-1})[a]	Ref.
$Fe(H_2O)_5OH^{2+}/Fe_{aq}^{2+}$	0.5	2.0	+0.8 ± 0.9[b]	−11	28
$Cr(H_2O)_5OH^{2+}/Cr_{aq}^{2+}$	?	?	+4.2 ± 1.1[b]	−11	6
$Co(en)_3^{3+/2+}$	0.5	65.0	−15.5 ± 0.8[b,c]	−5.3	16
$Co(phen)_3^{3+/2+}$	0.1(NO_3^-)	25.0	−16.0 ± 0.7[d]	−1.7	35
	0.1(Cl^-)	25.0	−17.6 ± 0.7[d]	−2.2	35
"$Co(EDTA)^{-/2-}$"	0.5	85.0	−3.2 ± 0.3[b]	+4.7[e]	36
$MnO_4^{-/2-}$	1.1	45.0	−17 ± 2[c,f]	−9[g]	17
$Na^+,MnO_4^{-/2-}$	1.1	45.0	+3 ± 1[f]	−6[g,h]	17
$K^+,MnO_4^{-/2-}$	1.1	45.0	−1 ± 1[f]	−6[g,h]	17
$(K^+)_3,Fe(CN)_6^{3-/4-}$	0.5	25.0	+22 ± 2[f]	−5[g,h]	18
$Tl(H_2O)_6^{3+/+}$	1.1	30.0	−13.2 ± 1.0[b,c,i]	−6.3[i,j]	6, 37

[a]This work; $\Delta V_{IR}^{\ddagger}$ taken as +0.6 cm^3 mol^{-1} except as indicated.
[b]By radioisotope sampling at high pressure.
[c]$\Delta V^{\ddagger}$ shows some pressure dependence.
[d]By high-pressure stopped-flow circular dichroism change.
[e]Includes deaquation and deprotonation of $Co(Hedta)OH_2^-$, the form of the Co^{II} complex under the reaction conditions.
[f]By high-pressure NMR.
[g]$\Delta V_{IR}^{\ddagger}$ taken as zero.
[h]Includes an estimate of the Coulombic effect of ion association.
[i]Limiting value at zero pressure.
[j]$\Delta V_{IR}^{\ddagger}$ taken as +3.3 cm^3 mol^{-1} (6); assumes rate-controlling step is a one-electron transfer giving $2Tl(H_2O)_6^{2+}$.

of the right magnitude with reasonable values of the distance scaling factor (9). However, the recent recognition (31) that the cage complexes $Co(sep)^{3+/2+}$ and $Co(diamsar)^{3+/2+}$ conform to our adaptation of Marcus–Hush theory and yet behave very differently from the smaller complexes $Co(en)_3^{3+/2+}$, from which they are derived, forces the conclusion that all these couples undergo self-exchange adiabatically. The Co^{II} spin pre-equilibrium explanation is therefore now preferred, but suffers from the lack of any experimental information on the thermodynamics of the relevant pre-equilibria, although less than 1% low-spin Co^{II} would account for the observed rates (31). Binstead and Beattie found a volume of reaction of −10 cm^3 mol^{-1} for the high-spin to low-spin magnetic isomerism of $Co(terpy)_2^{2+}$ (40),[3] and, although this result may be complicated to a minor extent by dechelation equilibria (31), it is of the order required to account for the anomalies in $\Delta V^{\ddagger}$ for $Co(en)_3^{3+/2+}$ and $Co(phen)_3^{3+/2+}$.

It might be argued that the main difference in general properties between the "anomalous" $Co^{III/II}$ couples of Table 3 and the "well-behaved" $Co^{III/II}$ couples of Table 2 is that the Co^{II} species of the former category are all labile on the time scale of electron transfer, and therefore may offer an inner-sphere alternative to the outer-sphere path that is the only one available to the cage complexes. Such an inner-sphere alternative, however, would lead to the $Co(en)_3^{3+/2+}$ exchange being markedly *faster* than its $Co(sep)^{3+/2+}$ analogue, whereas it is *slower* by a factor of 10^5. Furthermore, as we have seen, $\Delta V^{\ddagger}$ for an inner-sphere process will be markedly more *positive* than for an analogous outer-sphere mechanism, whereas the anomalous Co couples of Table 3 all show $\Delta V^{\ddagger}$ values much more *negative* than are found for the obligate outer-sphere $Co^{III/II}$ exchanges of Table 2.

It remains for us to explain why the low-spin/high-spin $Co^{III/II}$ cage couples of Table 2 should undergo self-exchange relatively rapidly, and why the $\Delta V^{\ddagger}$ values conform so well to theoretical expectations for adiabatic outer-sphere processes. It should first be noted that the Co—N bond length differences between the Co^{III} and Co^{II} members of a couple are much the same (19–21 pm) for all the CoN_6-type complexes of Tables 2 and 3 (31), so that the explanations must be found elsewhere. Geue and Sargeson (ref. 41, and personal communication) answer the first question by pointing out that molecular mechanics calculations show that the cage complexes are strained, and hence destabilized, in their ground states, so that the transition states for electron transfer are more energetically accessible. An alternative explanation (probably equivalent, in the last analysis) is that geometrical (e.g., Jahn–Teller) distortions accompany the spin multiplicity change as bidentate chelate Co^{II} complexes approach the transition state, thereby contributing to the Franck–Condon energy barrier to electron transfer, but are suppressed in the rigid cage complexes (31). This latter explanation also gives an easy rationalization of the $\Delta V^{\ddagger}$ values — if the tendency of the complexes to distort while changing spin state is suppressed, there will be little associated volume change, and eqs. [4]–[7] are applicable without modification. It should also be remembered that Marcus–Hush theory treats the reactants as hard spheres, and this is likely a poor representation of the Co complexes of Table 3 but a good one for the cage complexes of Table 2. In any event, an important inference arises from all of this: *large spin multiplicity changes do not in themselves inhibit electron transfer appreciably*; rather, it is the associated geometrical distortions, where these can occur freely, that retard the reaction.

The ability of cations to catalyze anion–anion electron transfer is well established, and leads to anomalously *positive* values of $\Delta V^{\ddagger}$ (as for $MnO_4^{2-/-}$ and $Fe(CN)_6^{3-/4-}$, Table 3). The effect of cations on $\Delta V^{\ddagger}$ and k is much greater than can be accounted for by their calculated influence on the Coulombic and Debye–Hückel terms, so an actual electronic involvement of the counterion is implied. Curiously, for the cation-independent $MnO_4^{-/2-}$ pathway, $\Delta V^{\ddagger}$ is more negative than predicted, probably because of the unusually small size of the reactants. The molecular nature of the solvent may be asserting itself here, although the MSA approach actually gives a somewhat poorer prediction of $\Delta V^{\ddagger}$ than eqs. [4]–[7] (27). Treatment of the environment of the small precursor complex as an ellipsoidal cavity, rather than two spherical cavities, in the solvent can rationalize the surprisingly negative $\Delta V^{\ddagger}$ (17), but there is a distasteful arbitrariness in this procedure.

The final entry in Table 3 is enigmatic. The $Tl(H_2O)_6^{3+/+}$ exchange may involve either a one-electron endergonic process forming $2Tl(H_2O)_6^{2+}$, with scrambling on reconversion to thallium(I) and -(III), or a simultaneous two-electron exchange. For the one-electron process, Stranks (6) pointed out that, as for any electron transfer reaction involving net chemical change, a term involving the thermodynamic reaction volume ΔV^0 for the formation of $2Tl^{2+}$ must be added to eq. [4]:

$$[8]\quad \Delta V_{CALC}^{\ddagger} = \Delta V_{IR}^{\ddagger} + \Delta V_{SR}^{\ddagger} + \Delta V_{DH}^{\ddagger} + \Delta V_{COUL}^{\ddagger} + \Delta V_{PREC}^{\ddagger} + \lambda^{\ddagger}\Delta V^0$$

where $\lambda^{\ddagger} = 0.5 + \Delta G^0/8(\Delta G_{SR}^{\ddagger} + \Delta G_{IR}^{\ddagger}) = 0.72$ in this case. Stranks' calculations (6) appeared to give $\Delta V_{CALC}^{\ddagger}$ for a single-electron mechanism in excellent agreement with the observed value, whereas $\Delta V_{CALC}^{\ddagger}$ for a two-electron step was 12 $cm^3\ mol^{-1}$ more negative. These numbers, however, incorporate $\Delta V_{DH}^{\ddagger}$ with the sign reversed, and an estimated ΔV^0 of $-9.3\ cm^3\ mol^{-1}$ for the hypothetical formation of $2Tl^{2+}$ as compared with $-2.4\ cm^3\ mol^{-1}$ from a model now available (42), so that the experimental $\Delta V^{\ddagger}$ falls between the theoretical values for the one- and two-electron paths. At least, $\Delta V^{\ddagger}$ rules out an inner-sphere mechanism.

Outer-sphere reactions involving net chemical change

If $\Delta V_{11}^{\ddagger}$ and $\Delta V_{22}^{\ddagger}$ for the self-exchange reactions

$$[9]\quad A + A^+ \rightarrow A^+ + A \qquad (k_{11}, \Delta V_{11}^{\ddagger})$$

$$[10]\quad B + B^+ \rightarrow B^+ + B \qquad (k_{22}, \Delta V_{22}^{\ddagger})$$

can be calculated as above, then it becomes possible to calculate $\Delta V_{12}^{\ddagger}$ for the cross reaction

$$[11]\quad A + B^+ \rightarrow A^+ + B \qquad (k_{12}, K_{12}, \Delta V_{12}^{\ddagger}, \Delta V_{12}^0)$$

from an adaptation (43, 44) of Marcus' "cross relation" (eqs. [12]–[14]) (10), if K_{12} (the equilibrium constant for reaction [11], obtainable from its standard electrode potential change ΔE) and ΔV_{12}^0 (its volume of reaction, obtainable from the pressure dependence of ΔE (45–47)) are known:

$$[12]\quad k_{12} = (k_{11}k_{22}K_{12}f)^{1/2}W$$

$$[13]\quad \ln f = [\ln K_{12} + (w_{12} - w_{21})/RT]^2/4[\ln(k_{11}k_{22}/Z_{11}Z_{22}) + (w_{11} + w_{22})/RT]$$

$$[14]\quad \ln W = (w_{11} + w_{22} - w_{12} - w_{21})/2RT$$

$$[15]\quad \Delta V_{12}^{\ddagger} = [(\Delta V_{11}^{\ddagger} + \Delta V_{22}^{\ddagger} + \Delta V_{12}^0)/2] + C$$

$$[16]\quad C = [X\Delta V_{12}^0 \ln K_{12} - 2(\ln K_{12})^2(\Delta V_{11}^{\ddagger} + \Delta V_{22}^{\ddagger} - \Delta V_{11}^{w} - \Delta V_{22}^{w})]/X^2$$

$$[17]\quad X = 4[\ln(k_{11}k_{22}/Z_{11}Z_{22}) + (w_{11} + w_{22})/RT]$$

where w_{ij} are work terms with associated volume effects ΔV_{ij}^{w}. If ΔE is small, eqs. [12]–[14] and [15]–[17] are much simplified:

$$[18]\quad k_{12} = (k_{11}k_{22}K_{12})^{1/2}$$

$$[19]\quad \Delta V_{12}^{\ddagger} = (\Delta V_{11}^{\ddagger} + \Delta V_{22}^{\ddagger} + \Delta V_{12}^0)/2$$

Tests of eqs. [15]–[17] or [19] are elusive, as one must choose a system for which $\Delta V_{11}^{\ddagger}$ and $\Delta V_{22}^{\ddagger}$ are known and accountable for theoretically (Table 2), and for which k_{12} and ΔV_{12}^0 are measurable. The problem is usually that the high-pressure techniques (48, 49) available for the measurement of k_{12}, notably stopped-flow spectrophotometry, cannot produce reliable rate constants $>10^5\ L\ mol^{-1}\ s^{-1}$, so that eq. [18] limits the choice of participating couples to ones with fairly slow self-exchange rates and a rather small ΔE. The stability of the reactants and products over the relatively long duration of high-pressure experiments is another common source of difficulties. To date, a convincing test of eq. [15] has been possible with only one reaction: the reduction of $Fe(H_2O)_6^{3+}$ by $Co([9]aneS_3)_2^{2+}$, for which $\Delta V_{12}^{\ddagger}$ was predicted to be $-14.7\ cm^3\ mol^{-1}$ at 100 MPa, and values of -13.7 (ClO_4^- medium) and $-15.9\ cm^3\ mol^{-1}$ ($CF_3SO_3^-$) were found (43). With $Co(sep)^{2+}$ as reductant, the driving force was excessive (1.03 V) and eq. [15] failed, but so did the cross relation (eqs. [12]–[14]) — indeed, it is surprising that this reaction is just slow enough to be followed by stopped-flow spectrophotometry. Murguia and Wherland (44) have used equations similar to [15]–[17] to estimate $\Delta V^{\ddagger}$ for self-exchange of some Co clathrochelates from $\Delta V_{12}^{\ddagger}$ data.

An alternative approach involves the calculation of all the components of eq. [8] as outlined above, and van Eldik and coworkers (50) have successfully accounted for $\Delta V_{12}^{\ddagger}$ for the reduction of aqueous $Co(terpy)_2^{3+}$ by $V(H_2O)_6^{2+}$ ($\Delta V_{12}^{\ddagger} = -1.8\ cm^3\ mol^{-1}$) in this way.

Conclusions

For simple outer-sphere electron transfer reactions in aqueous media, $\Delta V^{\ddagger}$ can be satisfactorily calculated from the appropriate equations [4]–[8] and [15]–[17]. Where these fail, one can infer that some special mechanistic feature is operative, or that the reaction is inner-sphere. $\Delta V^{\ddagger}$ data help explain the enhanced redox reactivity of Co(III/II) cage complexes vis-à-vis the analogous "open" chelates, and show that large

changes in spin multiplicity in outer-sphere electron transfer do not *in themselves* limit redox rates — such reactions are not "spin forbidden". For polar nonaqueous media, eqs. [4]–[7] reproduce $\Delta V^{\ddagger}$ adequately at 100 MPa or more, but tend to overestimate it at low pressures, particularly when the solvent has a high isothermal compressibility. When the relative permittivity of the solvent is low, the calculations become numerically unstable, especially where the reactants carry high charges, but in such cases ion pairing becomes important, with unpredictable consequences.

Acknowledgements

I thank my collaborators, whose names appear in the list of references, for their indispensable contributions, and the Natural Sciences and Engineering Research Council of Canada for continued support of our work through research and equipment grants.

References

1. H.R. Hunt and H. Taube. J. Am. Chem. Soc. **80**, 2642 (1958).
2. H. Taube, H. Myers, and R.L. Rich. J. Am. Chem. Soc. **75**, 4118 (1953).
3. H. Taube and H. Myers. J. Am. Chem. Soc. **76**, 2103 (1954).
4. H. Taube. Electron transfer reactions of complex ions in solution. Academic Press, New York. 1970. Chap. 2.
5. J.P. Candlin and J. Halpern. Inorg. Chem. **4**, 1086 (1965).
6. D.R. Stranks. Pure Appl. Chem. **38**, 303 (1974).
7. R.A. Marcus. J. Chem. Phys. **24**, 966 (1956); **24**, 979 (1956); **26**, 867 (1957). Discuss. Faraday Soc. **29**, 21 (1960). Faraday Discuss. Chem. Soc. **74**, 7 (1982).
8. N.S. Hush. Trans. Faraday Soc. **57**, 557 (1961).
9. T.W. Swaddle. Inorg. Chem. **29**, 5017 (1990).
10. R.A. Marcus and N. Sutin. Biochim. Biophys. Acta, **811**, 265 (1985).
11. N. Sutin. Prog. Inorg. Chem. **30**, 441 (1983).
12. N. Sutin, B.S. Brunschwig, C. Creutz, and C. Winkler. Pure Appl. Chem. **60**, 1817 (1988).
13. S. Wherland. Inorg. Chem. **22**, 2349 (1983).
14. T.W. Swaddle, J. Mol. Liquids, **65/66**, 237 (1995).
15. S. Wherland. Coord. Chem. Rev. **123**, 169 (1993).
16. W.H. Jolley, D.R. Stranks, and T.W. Swaddle. Inorg. Chem. **29**, 385 (1990).
17. L. Spiccia and T.W. Swaddle. Inorg. Chem. **26**, 2265 (1987); **27**, 4080 (1988).
18. H. Takagi and T.W. Swaddle. Inorg. Chem. **31**, 4669 (1991).
19. H. Doine and T.W. Swaddle. Inorg. Chem. **27**, 665 (1988).
20. K. Kirchner, S.-Q. Dang, M. Stebler, H.W. Dodgen, S. Wherland, and J.P. Hunt. Inorg. Chem. **28**, 3606 (1989).
21. A.M. Newton and T.W. Swaddle. J. Phys. Chem. **79**, 795 (1975).
22. (*a*) R.L. Blackbourne and J.T. Hupp. J. Phys. Chem. **92**, 2817 (1988); (*b*) M.D. Todd, Y. Dong, and J.T. Hupp. Inorg. Chem. **30**, 4687 (1991).
23. M. Hilczer and M. Tachiya. J. Mol. Liquids, **64**, 113 (1995).
24. P.G. Wolynes. J. Chem. Phys. **86**, 5133 (1987).
25. I. Rips, J. Klafter, and J. Jortner. J. Chem. Phys. **88**, 3246 (1988); **89**, 4288 (1988).
26. W.R. Fawcett and L. Blum. Chem. Phys. Lett. **187**, 173 (1991).
27. H.D. Takagi and T.W. Swaddle. Chem. Phys. Lett. **248**, 207 (1996).
28. W.H. Jolley, D.R. Stranks, and T.W. Swaddle. Inorg. Chem. **29**, 1948 (1990).
29. H. Doine and T.W. Swaddle. Can. J. Chem. **66**, 2763 (1988).
30. H. Doine and T.W. Swaddle. Inorg. Chem. **30**, 1858 (1991).
31. R.D. Shalders and T.W. Swaddle. Inorg. Chem. **34**, 4815 (1995).
32. J.T. Hupp and M.J. Weaver. Inorg. Chem. **22**, 2557 (1983).
33. U. Fürholz and A. Haim. Inorg. Chem. **24**, 3091 (1985).
34. P. Bernhard, L. Helm, A. Lüdi, and A.E. Merbach. J. Am. Chem. Soc. **107**, 312 (1985).
35. M.R. Grace and T.W. Swaddle. Inorg. Chem. **32**, 5597 (1993).
36. W.H. Jolley, D.R. Stranks, and T.W. Swaddle. Inorg. Chem. **31**, 507 (1992).
37. M.G. Adamson and D.R. Stranks. Chem. Commun. 648 (1967).
38. T.W. Swaddle and P.-C. Kong. Can. J. Chem. **48**, 3223 (1970).
39. J.K. Beattie. Adv. Inorg. Chem. **32**, 2 (1988).
40. R.A. Binstead and J.K. Beattie. Inorg. Chem. **25**, 1481 (1986).
41. R.J. Geue, R. Pizer, and A.M. Sargeson. Abstracts of papers, 183rd National Meeting of the American Chemical Society, Las Vegas, Nevada, April 1982: INOR 62.
42. T.W. Swaddle and M.K.S. Mak. Can. J. Chem. **61**, 473 (1983).
43. M.R. Grace, H. Takagi, and T.W. Swaddle. Inorg. Chem. **33**, 1915 (1994).
44. M.A. Murguia and S. Wherland. Inorg. Chem. **30**, 139 (1991).
45. H. Doine, T.W. Whitcombe, and T.W. Swaddle. Can. J. Chem. **70**, 81 (1992).
46. J. Sachinidis, R.D. Shalders, and P.A. Tregloan. J. Electroanal. Chem. **327**, 219 (1992); Inorg. Chem. **33**, 6180 (1994).
47. J. Sun, J.F. Wishart, R. van Eldik, R.D. Shalders, and T.W. Swaddle. J. Am. Chem. Soc. **117**, 2600 (1995).
48. M. Kotowski and R. van Eldik. Coord. Chem. Rev. **93**, 19 (1989).
49. T.W. Swaddle. Can. J. Phys. **73**, 258 (1995).
50. B. Bänsch, P. Martinez, and R. van Eldik. J. Phys. Chem. **96**, 234 (1992).

Standard state heat capacities of aqueous electrolytes and some related undissociated species[1]

Loren G. Hepler and Jamey K. Hovey

Abstract: Uses of heat capacities of solutions of electrolytes are reviewed, with a particular emphasis on the standard state partial molar heat capacities and their applications to calculations of the effects of temperature on equilibrium constants, electrode potentials, enthalpies, and entropies. Methods of obtaining these standard partial molar heat capacities are summarized, followed by comparisons of values obtained in different ways. Many of the "best" such heat capacities are collected and then used as the basis for establishing single-ion heat capacities based on the convention that $C_p^{\circ}(H^+) = 0$, followed by illustrations of the convenient use of these quantities. Finally, there is brief discussion of theoretical analysis of these standard partial molar heat capacities in relation to ion–solvent interactions.

Key words: heat capacities, electrolytes; aqueous solutions, heat capacities; thermodynamics, electrolytes.

Résumé : On présente une revue de l'utilisation des capacités calorifiques de solutions d'électrolytes en insistant d'une façon particulière sur les capacités calorifiques molaires partielles dans l'état standard et leurs applications aux calculs des effets de la température sur les constantes d'équilibre, les potentiels d'électrode, les enthalpies et les entropies. On résume les méthodes d'obtenir ces capacités calorifiques molaires partielles standard et on présente ensuite un comparaison des diverses valeurs obtenues d'après les diverses manières. Plusieurs des «meilleures» propriétés, comme les capacités calorifiques, ont été rassemblées et ont ensuite été utilisées comme base pour l'établissement des capacités calorifiques d'un seul ion en se basant sur la convention que $C_p^{\circ}(H^+) = 0$; elles sont suivies par des illustrations sur l'utilisation commode de ces quantités. Enfin, on présente une brève discussion de l'analyse théorique de ces capacités calorifiques molaires partielles standard en relation avec les interactions ion–solvant.

Mots clés : capacités calorifiques, électrolytes, solutions aqueuses; thermodynamique.

[Traduit par la rédaction]

Introduction

Knowledge of heat capacities of pure substances is useful because such heat capacities can be used in a wide variety of thermodynamic calculations, many of which involve the effects of changing temperature on other thermodynamic properties such as Gibbs energies and related equilibrium constants, enthalpies, and entropies. The principle of these calculations and methods of carrying them out have been reviewed in many texts dealing with chemical thermodynamics.

Received October 31, 1995.

L.G. Hepler.[2] Department of Chemistry, and Department of Chemical Engineering, University of Alberta, Edmonton, AB T6G 2G2 Canada.
J.K. Hovey. Institut fur Mineralogie und Petrologie, Sonneggstrasse 5, Eidgenössische Technische Hochschule (ETH)-Zentrum, CH-8092 Zurich, Switzerland.

[1] This paper, part of which was presented by L.G.H. at the "*Taube Fest*" on 7 October 1995 at the University of Saskatchewan, is dedicated to Henry Taube.

[2] Author to whom correspondence may be addressed. Telephone: (403) 492-2762. Fax: (403) 492-8231.

Although it has been known for a long time that similar calculations for aqueous solutions of electrolytes could be useful, the general paucity of required experimental results severely limited these kinds of applications. In recent years, however, advances in calorimetry have made it practical to obtain reliable and accurate heat capacities of dilute aqueous solutions, thereby leading to the partial molar heat capacities needed for the kinds of calculations mentioned above.

In the remainder of this Introduction, we will provide words and equations (to be used later) to call attention to some of the uses of partial molar heat capacities: (*i*) We provide a review of experimental methods and illustrate methods of calculating the standard state partial molar heat capacities that will form the principal part of the rest of this paper. (*ii*) We provide a critical review of standard state partial molar heat capacities of aqueous inorganic electrolytes (also acetate ion, Ac^-) and a few non-ions such as HAc(aq), NH_3(aq), CO_2(aq), SO_2(aq), H_2S(aq), and H_3PO_4(aq, undissociated). (*iii*) We select "best" values of standard state partial molar heat capacities and provide specific illustrations of some of their uses. (*iv*) We refer briefly to uses of heat capacities in connection with theoretical attempts to improve or extend knowledge of ion–solvent interactions.

To introduce the need for the heat capacities that are the focus of this paper, we begin with the van't Hoff equation:

[1] $(\partial \ln K/\partial T)_p = \Delta_r H^\circ/RT^2$

Making the approximation that the standard state enthalpy of reaction, $\Delta_r H^\circ$, is a constant (independent of temperature), integration of eq. [1] leads to

[2] $\ln K = -(\Delta_r H^\circ/RT) + I$

in which I is a constant of integration.

Equation [2] is often useful over small ranges of temperature, but is generally inadequate for wide or even moderate ranges of temperature. One illustration of the inadequacy of this equation is provided by the observation that ln K is (for temperature-independent $\Delta_r H^\circ$) predicted to be a linear function of $1/T$, increasing or decreasing forever as the temperature increases or decreases, which is contrary to the reality that values of K and thence ln K for many reactions involving aqueous electrolytes pass through a minimum or maximum with changing temperature. The explanation for this kind of failure of eq. [2] is that $\Delta_r H^\circ$ is not generally a constant (independent of temperature), but depends on temperature as shown below.

Effects of temperature on $\Delta_r H^\circ$ and also on $\Delta_r S^\circ$ are described by the following equations:

[3] $(\partial \Delta_r H^\circ/\partial T)_p = \Delta_r C_p^\circ$

[4] $(\partial \Delta_r S^\circ/\partial T)_p = \Delta_r C_p^\circ/T$

Here we have used $\Delta_r C_p^\circ$ to represent the change in heat capacity for a chemical reaction, which is related to the heat capacities of the reactants and products of reaction by

[5] $\Delta_r C_p^\circ = \Sigma C_p^\circ(\text{products}) - \Sigma C_p^\circ(\text{reactants})$

For aqueous solutes, the relevant heat capacity denoted by C_p° is the standard state partial molar heat capacity.

Equations [3] and [4] shows that $\Delta_r H^\circ$ and $\Delta_r S^\circ$ are independent of temperature only in the special (unusual!) case in which $\Delta_r C_p - 0$. Because heat capacities generally depend on temperature, consider various approaches to making use of eq. [3] in combination with eq. [1]. One approach (others are discussed later) is to express the heat capacity of each substance or ion in terms of an empirical power series, such as

[6] $C_p^\circ = a + bT + cT^2 + \ldots$

Combination of equations [5] and [6] leads to

[7] $\Delta_r C_p^\circ = \Delta a + (\Delta b)T + (\Delta c)T^2 + \ldots$

We now illustrate the principle of making use of heat capacities by cutting off eq. [7] after the Δa term, which means that we are (for now) considering $\Delta_r C_p^\circ$ to be independent of temperature. In this case, integration of eq. [3] leads to

[8] $\Delta_r H^\circ = \Delta H_i + (\Delta a)T$

in which ΔH_i is a constant of integration. Insertion of eq. [8] in eq. [1] and integration leads to

[9] $\ln K = -(\Delta H_i/RT) + [(\Delta a)(\ln T)/R] + I$

in which I is another constant of integration.

Equation [9] corresponds to a nonlinear dependence of ln K on $1/T$. Further, it can be shown by differentiating eq. [9] with respect to temperature and setting the resulting derivative equal to zero that there is some temperature at which ln K is either a minimum or a maximum, which is a very substantial improvement over eq. [2]. It will be shown later that using a constant (independent of temperature) value of $\Delta_r C_p^\circ$ leads to remarkably accurate calculations of equilibrium constants over wide ranges of temperature, which justifies part of our focus on heat capacities at just one temperature (298.15 K). It will also be shown that such calculations can be extended to much wider ranges of temperature by making use of heat capacities that have been measured over relatively small ranges of temperature.

Rather than carry out the differentiation of eq. [9] as mentioned above to obtain the temperature at which the value of K passes through a maximum or minimum, we proceed in another way. Integrating eq. [3] between limits of $T = 298$ K and some T_m at which the value of K goes through a maximum or minimum, we obtain

[10] $\Delta_r H^\circ(\text{at } T_m) - \Delta_r H^\circ(\text{at } T = 298 \text{ K}) = \Delta_r C_p^\circ(T_m - 298)$

Setting $\Delta_r H^\circ(\text{at } T_m) = 0$ (because this corresponds to a maximum or minimum in ln K vs. $1/T$), we obtain the following simple equation that relates the temperature at which the value of K passes through a maximum or minimum to the values of $\Delta_r H^\circ$ and $\Delta_r C_p^\circ$ at just one temperature (298 K):

[11] $T_m = -[\Delta_r H^\circ(\text{at } T = 298 \text{ K})/\Delta_r C_p^\circ] + 298 \text{ K}$

Much of the rest of this paper is devoted to collection of C_p° values for $T = 298.15$ K, with a few illustrations of their uses; we will also cite measurements leading to C_p° values at other temperatures and their uses.

Although the focus in this paper is on the standard state partial molar heat capacities represented here by C_p°, non-standard state (for $m > 0$) partial molar heat capacities are also useful. Here we only mention that these non-standard state partial molar heat capacities are related to the temperature dependence of enthalpies of dilution and thence to the temperature dependence of activity coefficients and osmotic coefficients, as reviewed by Millero (1).

Experimental and calculation methods

One approach to obtaining standard state partial molar heat capacities is to solve eq. [1] for $\Delta_r H^\circ$, differentiate with respect to temperature, and combine with eq. [2] to obtain

[12] $\Delta_r C_p^\circ = R[2T(\partial \ln K/\partial T)_p + T^2(\partial^2 \ln K/\partial T^2)_p]$

Because of the magnification of uncertainties and errors associated with two differentiations, this approach is useful only when there are very accurate values for the equilibrium constant over a wide range of temperature. Our focus here is on other methods of obtaining standard state partial molar heat capacities of solutes.

Most of the standard state partial molar heat capacities that we will be considering have been derived from calorimetric

results expressed in terms of apparent molar heat capacities, $C_{p,\phi}$, which are defined in terms of measured quantities as

[13] $C_{p,\phi} = [C_p(\text{soln}) - n_1 C_{p,1}^*]/n_2$

In this defining equation, $C_p(\text{soln})$ represents the heat capacity of a solution containing n_1 moles of water and n_2 moles of solute and $C_{p,1}^*$ represents the molar heat capacity of water. The apparent molar heat capacity is related to the partial molar heat capacity of solute (C_p) by

[14] $C_p = C_{p,\phi} + n_2(\partial C_{p,\phi}/\partial n_2)$

At infinite dilution we have $n_2 = 0$ and thence the important relationship

[15] $C_p^\circ = C_{p,\phi}^\circ$

in which C_p° represents the standard state partial molar heat capacity of solute and $C_{p,\phi}^\circ$ represents the value of the apparent molar heat capacity that is obtained on extrapolation to $n_2 = 0$, corresponding to extrapolation to a composition of zero molality.

Apparent molar heat capacities of dilute solutions of strong electrolytes are represented accurately by equations of the form

[16] $C_{p,\phi} = C_p^\circ + (\omega)^{3/2} A_C(\rho_1^\circ)^{1/2}(m)^{1/2} + B_C\omega m$

in which C_p° represents the value of $C_{p,\phi}$ at $m = 0$ (see eq. [15]), A_C is derived from the Debye–Hückel theory and the dielectric constant of water, ρ_1° represents the density of water, m represents the molality, B_C is an adjustable parameter, and ω is defined by

[17] $\omega = 0.5\Sigma\nu_1(z_i)^2$

in which the ν_i are the subscripts in the chemical formula $A_{\nu+}B_{\nu-}$ and the z_i are the formal charges of the ions.

The experimental problems associated with obtaining accurate values of $C_{p,\phi}$ for dilute solutions are formidable because the difference between $C_p(\text{soln})$ and $n_1 C_{p,1}^*$ is very small compared with either $C_p(\text{soln})$ or $n_1 C_{p,1}^*$. It follows that accurate values of $C_{p,\phi}$ for dilute solutions can be obtained only from the results of extremely accurate measurements or from results of accurate measurements that lead reasonably directly to values of the difference represented by $[C_p(\text{soln}) - n_1 C_{p,1}^*]$ in the numerator of eq. [13]. The twin calorimeters designed, built, and used by Randall, Rossini, Gucker, and a few others, as reviewed by Parker (2), provided data of this kind and permitted the evaluation of the first reasonably accurate values of $C_{p,\phi}^\circ$ for aqueous electrolytes.

More recently, however, the Picker flow calorimeter (3) has permitted more accurate measurements to be made more rapidly, leading to most of the $C_{p,\phi}$ and derived C_p° values to be considered here. The clever principle of the original Picker calorimeter that was designed and built for measurements at or near 25°C has been adapted by Picker for measurements up to about 150°C and by Smith-Magowan and Wood (4) and others to permit measurements to much higher temperatures (and pressures).

Several publications (5–8) have reported consideration of and remedies for small systematic errors that may be present in flow calorimeters. In one of these papers Desnoyers et al. (5) also provide a useful summary of C_p° values that were obtained during the first few years of use of the Picker calorimeter in Desnoyers' laboratory.

Use of eq. [16] for evaluation of C_p° from measured values of $C_{p,\phi}$ at several molalities requires that we know the value of A_C from the Debye–Hückel theory. Because A_C depends on the second derivative of the dielectric constant of water with respect to temperature, there have been some uncertainties in choosing a "best" value. We therefore review briefly the results of several recent calculations.

Before going on to consider specific results, it is well to point out that some previous authors have written another version of eq. [16] in terms of $A_C(c)^{1/2}$ in which c represents concentration (molarity) rather than in terms of molality and $A_C(\rho_1^\circ)^{1/2}(m)^{1/2}$ as in our eq. [16]. Further, some authors have derived Debye–Hückel parameters that are appropriate to partial molar properties, while others have derived these parameters to be appropriate to apparent molar properties as in our eq. [16]. It is necessary to consider these complications and also lack of uniformity in symbols used to represent various quantities in making use of results of different authors. Because our eq. [16] contains the product $A_C(\rho_1^\circ)^{1/2}$, we will express results of various calculations in terms of this product.

Leduc et al. (9) have used published dielectric constants and densities of water to obtain values of $A_C(\rho_1^\circ)^{1/2}$ for several temperatures, including the value 28.95 J K^{-1} $mol^{-3/2}$ $kg^{1/2}$ for 25°C. Similar calculations have been reported by Perron et al. (10) for several temperatures; they have reported nearly the same value as above for 25°C. More recently, Pitzer and coworkers (11), Ananthaswamy and Atkinson (12), Archer and Wang (13), and Spitzer et al. (14) have reconsidered the temperature dependence of the dielectric constant of water and have carried out calculations of the various parameters to be used in Debye–Hückel equations for heat capacities and also other thermodynamic properties for wide ranges of temperatures. Results of all of these later calculations (11–14) are consistent with a "best" value of $A_C(\rho_1^\circ)^{1/2}$ from about 12–23% larger than the value from Desnoyers and colleagues (9, 10) that is given above.

In the favourable cases of electrolytes of 1:1 charge type for which we have accurate values of $C_{p,\phi}$ for sufficiently dilute solutions, choosing different reasonable (in the range cited above) values of $A_C(\rho_1^\circ)^{1/2}$ leads to very small differences in calculated values of C_p°, but for higher charge type electrolytes (14) or when results of accurate measurements are not available for sufficiently dilute electrolytes, choice of value for the Debye–Hückel parameter can have a significant effect on the value of the derived C_p°.

As will be seen later, most of the C_p° values that are selected as "best" for $T = 298.15$ K are based on measurements with Picker-type calorimeters and data analysis based on eq. [16] or similar equations. A simple and commonly adopted procedure for using eq. [16] is based on rearranging to obtain

[18] $C_{p,\phi} - (\omega^{3/2} A_C(\rho_1^\circ)^{1/2}(m^{1/2}) = C_p^\circ + B_C\omega m$

A graph of the quantity represented by the left side of eq. [18]

against m leads to a straight line, with the intercept at $m = 0$ being the value of C_p°.

Another approach that has proven useful is based on eq. [3] and enthalpies of reaction that have been measured at several temperatures. Early applications (15, 16) of this method involved calorimetric measurements leading to the standard enthalpies of ionization of aqueous benzoic acid at several temperatures (10–40°C). More recently and of more importance for our present purpose, Cobble, Criss, and others have used a method based on eq. [3] to obtain useful values of C_p° for several electrolytes over wide ranges of temperature, as first reported by Criss and Cobble (17). Their calorimetric measurements led to values of the standard state enthalpy of solution, $\Delta_S H^\circ$, of sodium chloride in water as represented by

[19] $\quad NaCl(cr) = Na^+(aq) + Cl^-(aq)$

at 13 temperatures ranging from 0.02°C to 95.18°C. The values of $\Delta_S C_p^\circ$ obtained as the derivative of $\Delta_S H^\circ$ with respect to temperature (see eq. [3]) can be expressed as

[20] $\quad \Delta_S C_p^\circ = C_p^\circ(Na^+,Cl^-) = C_p^\circ(NaCl)$

in which $C_p^\circ(Na^+,Cl^-)$ and $C_p^\circ(NaCl)$ represent the standard state partial molar heat capacity of aqueous sodium chloride and the molar heat capacity of NaCl(cr) at the temperature of interest. Because values of C_p° for NaCl(cr) were already known, Criss and Cobble (17) were able to obtain values of $C_p^\circ(Na^+,Cl^-)$ that were reported over the temperature range from 0 to 100°C. Gardner et al. (18) have carried out similar measurements at 114.25, 149.90, and 199.50°C and have combined these results with those from Criss and Cobble (17) to obtain values of $C_p^\circ(Na^+,Cl^-)$ that are reported over the 0–200°C range of temperatures. The method used in these two investigations (17, 180 and also others to be cited later has been called the "integral heat" method.

Bernarducci et al. (19) used still another method of obtaining a value for C_p°, based on combining a value of $C_{p,\phi}$ for a concentrated solution (relatively easy to measure) with the temperature dependence of the enthalpy of dilution to $m = 0$ for this same concentrated solution. They have applied this method to $FeCl_2(aq)$. Although their reported uncertainty (± 30 J K^{-1} mol^{-1}) in C_p° for 25°C is considerably larger than uncertainties attributed to values of C_p° for many electrolytes based on results of measurements with the Picker calorimeter or as derived from several applications of the "integral heat" method, it is likely that the method used by Bernaducci et al. (19) can also be applied usefully to some systems.

Analysis of heat capacity data for systems in which there is an identifiable chemical equilibrium requires consideration of what is now often called the "relaxation" contribution to the total heat capacity. An early example was provided by McCollum (20), who measured heat capacities of the system in which the equilibrium represented by $N_2O_4(g) = 2\ NO_2(g)$ contributes to the total measured heat capacity. Later, Randall and Taylor (21) wrote "If a reaction — for example, the dissociation of bisulfate ion into hydrogen and sulfate ions — is more complete at a higher temperature than at a lower, then the heat corresponding to the additional fraction of bisulfate dissociated at the higher temperature will be measured as though it were a part of the heat capacity of the solution." They (21) had recognized an important problem, but did not continue with any detailed thermodynamic calculations.

The first specific considerations and applications (22, 23) of relaxation contributions to the measured heat capacities of aqueous solutions were followed by many more, which will be cited later in connection with specific electrolytes. Here we call attention to general treatments by Mains et al. (24) and Blandamer et al. (25).

The principle of a relaxation contribution to a measured heat capacity can be illustrated by consideration of a simple imaginary system in which there is a temperature-dependent equilibrium between two isomeric forms of the same "substance," with these two isomeric forms mixing to form an ideal solution so that we need not be concerned here with such complications as activity coefficients, enthalpies of dilution, or the difference between $\Delta_r H$ and $\Delta_r H^\circ$. The chemical equilibrium in this imaginary system is represented by

[21] $\quad A = B \qquad K = f(1 - f)$

in which f represents the fraction of total substance that is in the B isomer form. The measured heat capacity of a system containing one mole is

[22] $\quad C_{p,meas} = (Q/\Delta T) = (1 - f)C_{p,A}^* + fC_{p,B}^* + (\Delta f/\Delta T)\Delta_r H$

in which $C_{p,A}^*$ and $C_{p,B}^*$ represent the heat capacities of the pure isomeric forms A and B, respectively. Because the changes in temperature in most measurements of heat capacities of solutions are small, it is common to replace $(\Delta f/\Delta T)$ with the differential equivalent, (df/dT), and thence obtain an analytical (rather than an equally useful and correct numerical) representation of the relaxation contribution to the total heat capacity. There is also the intangible matter of scientific beauty, which some of us see in an analytical representation. To evaluate the relaxation contribution, which is the last term on the right side of eq. [22], we begin by solving eq. [21] for f and then differentiating with respect to temperature to obtain

[23] $\quad df/dT = (dK/dT)/(1 + K)^2 = (K/K)(dK/dT)/(1 + K)^2$
$= K(d \ln K/dT)/(1 + K)^2 = K\Delta_r H^\circ/RT^2(1 + K)^2$

Using this last expression with the last term in eq. [22] and recognizing that $\Delta_r H^\circ = \Delta_r H$ for this ideal solution system, we obtain

[24] $\quad C_p^{rel} = K(\Delta_r H^\circ)^2/RT^2(1 + K)^2$

for the (always positive) relaxation contribution to the heat capacity.

Evaluation of C_p^{rel} for systems of nonideal electrolytes must include considerations of activity coefficients and their dependence on temperature (related to enthalpies of dilution) and to the distinction between $\Delta_r H$ and $\Delta_r H^\circ$ (also related to enthalpies of dilution), but the general principle is the same as outlined here for our simple imaginary ideal system. After values of C_p^{rel} have been calculated for an electrolyte system, these values are then subtracted from the experimental values of $C_{p,\phi}$ to obtain the $C_{p,\phi}$(species) values that are then combined with some version of the Debye–Hückel theory (such as eq. [16]) to obtain the standard state partial molar heat capacities

represented by C_p° to be used in various thermodynamic calculations of equilibrium constants, etc.

Because the details of calculation of C_p^{rel} are different for nearly every system that has been investigated, we do not try to illustrate any "typical" calculation. Instead, each reference cited here that involves any specific calculation of C_p^{rel} is followed by the symbol (C_p^{rel}) in the list of references.

Values of standard state partial molar heat capacities of aqueous solutes for T = 298.15 K and some of their uses

As background for our selection of "best" values for C_p° of aqueous solutes for 298.15 K, we begin by considering probable accuracies and uncertainties in values obtained in different ways.

It is now clear from experimental results and analysis reported in several publications already cited, in a recent analysis by Criss and Millero (26), and in other publications to be cited later that nearly all of the C_p° values derived from results of measurements with the Picker calorimeter have smaller uncertainties than do C_p° values derived from earlier measurements cited by Parker (2). Although we are not making use of the heat capacities for dilute solutions that have been cited by Parker (2), it is worth emphasizing that many of the results she has cited for more concentrated solution are still quite useful for other purposes.

Our considerations of the differences between C_p° values for the same solute reported by different users of Picker calorimeters and for a few solutes by the same users at different times provide one basis for estimating the experimental uncertainties to be associated with these values. Another contribution to the total uncertainty of C_p° values comes from the method of extrapolation to m = 0. As stated earlier in this paper, one common method for doing this extrapolation is based on eqs. [16] and [18]. But it should be recognized that other extrapolations that are consistent with the Debye–Hückel limiting law can also be justified; one such method of extrapolation, based on equations developed by Pitzer, has been used by Criss and Millero (26) because that formulation is well suited to combination with other thermodynamic quantities for calculation of the effect of temperature on activity coefficients. The difference in values of C_p° obtained by way of different extrapolation procedures is very small when there are values of $C_{p,\phi}$ for sufficiently dilute solutions, but becomes larger when such values are unavailable and extrapolations must be based on experimental results for less dilute solutions. All of these considerations lead us to suggest that total uncertainties in a few values of C_p° based on measurements with the Picker calorimeter may be as small as ± 1 J K^{-1} mol^{-1}, but most of these total uncertainties are in the range ± 2 to ± 4 J K^{-1} mol^{-1} for temperatures close to 25°C. For those systems for which it is necessary to make measurements on solutions of mixed electrolytes or for which C_p^{rel} is large, total uncertainties may be larger than ± 4 J K^{-1} mol^{-1}.

An illustration that provides partial justification for the uncertainty estimates above and that also leads to an estimate of uncertainties to be associated with values of C_p° obtained by application of the "integral heat" method can be based on consideration of values of C_p° for NaCl(aq) at 25°C.

The enthalpies of solution at several temperatures measured by Criss and Cobble (17) led them to $C_p^\circ = -79.1$ J K^{-1} mol^{-1} for NaCl(aq) at 25°C. The compilation by Desnoyers et al. (5), based only on measurements in their laboratory, lists $C_p^\circ = -84.4$ J K^{-1} mol^{-1} for NaCl(aq); their tabulated conventional single ion heat capacities lead to a calculated $C_p^\circ = -84$ J K^{-1} mol^{-1}. Criss and Millero (26) have analyzed several sets of reported values of $C_{p,\phi}$ and have obtained $C_p^\circ = -82.85$ J K^{-1} mol^{-1}; their tabulated single ion heat capacities lead to a calculated $C_p^\circ = -83.31$ J K^{-1} mol^{-1}. Hovey (27) has cited five values of C_p° ranging from -83.7 to -85.5 J K^{-1} mol^{-1}, with an average $C_p^\circ = -84.3$ J K^{-1} mol^{-1}; his tabulated single ion heat capacities lead to a calculated $C_p^\circ = -84.4$ J K^{-1} mol^{-1}. Clarke and Glew (28) have reviewed heat capacities and also other thermodynamic properties of NaCl(aq) over a range of temperatures and have selected $C_p^\circ = -83.94$ J K^{-1} mol^{-1} for NaCl(aq) at 298.15 K as the best value for overall consistency. Altogether, it now seems reasonable to select $C_p^\circ = -84$ J K^{-1} mol^{-1} as a "best" value for NaCl(aq) at 25°C, with a total uncertainty ± 1 J K^{-1} mol^{-1}. It therefore follows that the total uncertainty in the $C_p^\circ = -79.1$ J K^{-1} mol^{-1} reported by Criss and Cobble (17) is at least ± 4 J K^{-1} mol^{-1}. Further consideration of the calculations reported by Clarke and Glew (28) lead to the more specific estimate that the C_p° values from Criss and Cobble (17) for NaCl(aq) at temperatures up to about 100°C have probable uncertainties larger than ± 5 J K^{-1} mol^{-1} but smaller than ± 10 J K^{-1} mol^{-1}. Although these estimated uncertainties for C_p° values obtained by the integral heat method are larger than estimated uncertainties in C_p° values based on results of modern flow calorimetry, it is clear that C_p° values based on the integral heat method are accurate enough to be very useful.

Further support for the estimated uncertainty range for values of C_p° based on the integral heat method is provided by comparison of C_p° values for CsI(aq), for which we have -153.1 J K^{-1} mol^{-1} from Mitchell and Cobble's (29) application of the integral heat method and the probably more accurate -145.0 J K^{-1} mol^{-1} from flow calorimetry (5).

The comparisons of values of C_p° from the integral heat method with values of C_p° from modern flow calorimetry that we have cited have been chosen partly because of the importance of NaCl(aq) and partly to provide illustrations to support our estimates of uncertainties; it should not be assumed that these reasonable estimates of uncertainties represent established or even probable errors in the values of C_p° based on the integral heat method. For example, Mastroianni and Criss (30) have applied the integral heat method to obtain values of C_p° for $NaClO_4$(aq) over the range 0–95°C, including $C_p^\circ = 17.6$ J K^{-1} mol^{-1} for 25°C, which is in good agreement with C_p° = 15.2 and 16.6 J K^{-1} mol^{-1} from two sets of measurements (31, 32) with Picker flow calorimeters.

Jekel et al. (33) measured enthalpies of solution of $GdCl_3$(cr) at several temperatures and used these results to calculate $C_p^\circ = -435$ J K^{-1} mol^{-1} for $GdCl_3$(aq) at 25°C. Xiao and Tremaine (34) have made measurements with a flow calorimeter, leading to C_p° values for $Gd(ClO_4)_3$(aq), $La(ClO_4)_3$(aq), and $LaCl_3$(aq), which in turn lead to a calculated $C_p^\circ = -452$ J K^{-1} mol^{-1} for $GdCl_3$(aq) at 25°C. The difference (17 J K^{-1} mol^{-1}) between these two values of C_p° for $GdCl_3$(aq) that have been obtained in different ways is consistent with estimates of uncertainties already given here for 1:1

electrolytes because of the larger uncertainties in extrapolating to $m = 0$ for 3:1 electrolytes than for 1:1 electrolytes.

One use of standard state partial molar heat capacities is illustrated by beginning with calculation of $\Delta_r C_p^\circ$ for ionization of water as in

[25] $H_2O(liq) = H^+(aq) + OH^-(aq)$

For this calculation we use

[26] $\Delta_r C_p^\circ = C_p^\circ(H^+,X^-) + C_p^\circ(M^+,OH^-) - C_p^\circ(Na^+,X^-) - C_p^*(H_2O)$

Singh et al. (35) have applied eq. [26] by using their C_p° values for the electrolytes (HCl, NaCl, NaOH), (HBr, NaBr, NaOH), (HCl, KCl, KOH), and (HBr, KBr, KOH) to obtain $\Delta_r C_p^\circ = -214.1$, -215.7, -215.4, and -215.8 J K^{-1} mol^{-1}. Later C_p° values from Singh et al. (31) for aqueous $HClO_4$ and $NaClO_4$ led to $\Delta_r C_p^\circ = -213.8$ J K^{-1} mol^{-1}. Also, C_p° values from Enea et al. (36) for aqueous HNO_3, $NaNO_3$, and KNO_3 led to $\Delta_r C_p^\circ = -214.7$ and -214.6 J K^{-1} mol^{-1}. The average of all seven of these values is $\Delta_r C_p^\circ = -214.9$ J K^{-1} mol^{-1}. Because all of the heat capacities used in these calculations were obtained in the same laboratory, using the same flow calorimeter and the same experimental procedures, followed by the same kind of extrapolations to $m = 0$, some of whatever systematic errors were present have been cancelled in the subtraction of C_p° values shown in eq. [26].

It should also be mentioned that Allred and Woolley (7) have made flow calorimetric measurements in another laboratory, leading to values of C_p° for HCl(aq), NaCl(aq), and NaOH(aq) at 25°C (also two other temperatures). Their values of C_p° lead to $\Delta_r C_p^\circ = -216.8$ J K^{-1} mol^{-1} for ionization of water at 25°C, in satisfactory agreement with the values listed in the preceding paragraph.

On the basis of the eight value for $\Delta_r C_p^\circ$ of ionization of water cited (7, 31, 35, 36) in the two preceding paragraphs, we choose $\Delta_r C_p^\circ = -215$ J K^{-1} mol^{-1} as the best available value for ionization of water at 298 K. Because conventional single-ion heat capacities are based on $C_p^\circ(H^+) = 0$ and the molar heat capacity of pure water is known with excellent accuracy, this chosen best value for $\Delta_r C_p^\circ$ leads directly to a "best" conventional value for $C_p^\circ(OH^-)$ and is therefore a helpful start on compiling a useful collection of these single-ion heat capacities, to which we turn after one illustration of a use of heat capacities.

Earlier, we derived eq. [9] for the dependence of the equilibrium constant on temperature when $\Delta_r C_p^\circ$ is taken to be a constant, independent of temperature. Using the known value of $\Delta_r H^\circ$ at 298.15 K in eq. [8] permits evaluation of the constant of integration ΔH_i. Using the chosen value of $\Delta_r C_p^\circ = \Delta a$ with the known value of the equilibrium constant K at T = 298.15 K permits evaluation of the other constant of integration (I) and thence yields an equation that permits calculation of a value for the equilibrium constant at any temperature T. We carried out these calculations for several temperatures in the range 273–573 K (0–300°C) and found that the values of pK(calculated) differ by less than 0.02 from the best experimental values previously selected (37) for this temperature range. We also use our selected value of $\Delta_r C_p^\circ = -215$ J K^{-1} mol^{-1} and $\Delta_r H^\circ = 55\,815$ J mol^{-1} (37, 38) in eq. [11] to calculate $T_m = 557$ K (250°C) as the temperature where the equilibrium constant for ionization of water passes through a maximum. This calculated temperature is about 35° higher than the actual temperature (37) at which K passes through a maximum. Here we are not concerned with the small effect of the difference between $p = 1$ atm (or 1 bar) and the saturation pressure for $t > 100$°C, which has been discussed elsewhere (37).

It is possible to improve on the calculations summarized above by recognizing that C_p° values for electrolytes do depend on temperature and that $\Delta_r C_p^\circ$ also depends on temperature. Using $\Delta_r C_p^\circ = f(T)$ in eq. [3] leads to a more complicated version of eq. [8], which is then substituted in eq. [1] to obtain a more complicated version of eq. [9]. Later in this paper we cite some examples of such calculations, but it is worth emphasizing now that the simpler calculations described here, which are based on a constant (independent of temperature) $\Delta_r C_p^\circ$, are accurate enough over wide ranges of temperature to be useful for many purposes.

Tables 1–4 contain our selections of what we regard as "best" values for standard state partial molar heat capacities (C_p°) for $T = 298.15$ K for a large number of inorganic electrolytes and for a few "neutrals" (undissociated H_3PO_4, CO_2, SO_2, H_2S, NH_3) and one organic (acetic acid) that are related to electrolytes under consideration in this paper. All of the heat capacities listed in these tables are based on heat capacities of solutions that have been measured relative to the heat capacity of pure water, using modern flow calorimeters of the type developed by Picker et al. (3). Although we believe there are good reasons for basing our selections of best standard state partial molar heat capacities on heat capacities measured with flow calorimeters, we emphasize that heat capacities obtained in other ways are also useful. Some illustrations of such alternative heat capacities are provided in the following paragraphs.

Allred and Woolley (44) have used flow calorimetry to obtain standard state partial molar heat capacities of $NH_4^+Cl^-(aq)$ and $NH_3(aq)$; their results have been heavily weighted in selecting the values for these solutes that are listed in Tables 1 and 4, respectively. Allred and Woolley (44) have used their heat capacities in obtaining $\Delta_r C_p^\circ$ for

[27] $NH_4^+(aq) = H^+(aq) + NH_3(aq)$

at three temperatures. We select $\Delta_r C_p^\circ = 9$ J K^{-1} mol^{-1} as the best value (independent of temperature near 298 K) that can be derived from their results. We also note that Oloffson (65) has made calorimetric measurements leading to $\Delta_r H^\circ$ for reaction [27] at seven temperatures in the range 278–418 K and has derived (using eq. [3]) a temperature-independent $\Delta_r C_p^\circ = 11$ J K^{-1} P. Although it is likely that the uncertainty in the $\Delta_r C_p^\circ$ from measured heat capacities is slightly smaller than the uncertainty in the value derived by application of eq. [3] to enthalpies of reaction at several temperatures, the comparison cited here provides convincing evidence that the "integral heat" method based on eq. [3] can provide first-rate results.

Allred and Woolley (44) also used flow calorimetry to obtain standard state partial molar heat capacities of $Na^+,Ac^-(aq)$ and HAc(aq). On the basis of their results, we have selected (Table 4) $C_p(HAc) = 170$ J K^{-1} mol^{-1} as the best available value for 298.15 K. Two earlier calorimetric investi-

Table 1. Standard state partial molar heat capacities ($C_p°$)[a] of 1:1 aqueous electrolytes at 298.15 K.

Solute	$C_p°$	References	Solute	$C_p°$	References
H^+,Cl^-	−126	5, 7, 26, 35, 39	K^+,Cl^-	−114	5, 6, 26, 35
H^+,Br^-	−132	26, 35	K^+,Br^-	−119	5, 6, 35
H^+,NO_3^-	−71	36, 40, 41	K^+,I^-	−109	5
H^+,ClO_4^-	−26	31, 40, 41	K^+,OH^-	−127	35, 45
H^+,HSO_4^-	−18	55	K^+,NO_3^-	−60	36
Li^+,Cl^-	−65	5	K^+,ClO_3^-	−43	32
Li^+,Br^-	−69	5	K^+,BrO_3^-	−77	32
Li^+,OH^-	−77	45	K^+,IO_3^-	−59	32, 36
Na^+,F^-	−75	5	K^+,MnO_4	+1	47
Na^+Cl^-	−84	5, 7, 28, 35, 46	K^+,HCO_3^-	−38	52
Na^+,Br^-	−88	5, 35	K^+,HSO_3^-	+2	52
Na^+,I^-	−77	5	$K^+,HCrO_4^-$	+15	52
Na^+OH^-	−97	5, 7, 35, 45	Rb^+,F^-	−125	5
Na^+,NO_3^-	−29	32, 36	Rb^+,Cl^-	−136	5
Na^+,ClO_3^-	−17	32	Rb^+,Br^-	−139	5
Na^+,ClO_4^-	+16	31, 32	Rb^+,I^-	−132	5
Na^+,BrO_3^-	−50	32	Cs^+,F^-	−139	5
Na^+,IO_3^-	−30	47	Cs^+,Cl^-	−149	5
Na^+,TcO_4^-	+28	48	Cs^+,Br^-	−155	5
Na^+,ReO_4^-	+28	48	Cs^+,I^-	−145	5
Na^+,HCO_3^-	−11	50–52	NH_4^+,Cl^-	−56	5, 32, 44
Na^+,HSO_3^-	+40	52, 54	NH_4^+,Br^-	−67	5
$Na^+,Al(OH)_4^-$	+139	49	NH_4^+,ClO_4^-	+47	32
$Na^+,H_2PO_4^-$	+8	50, 53	NH_4^+,NO_3^-	−2	32
Na^+,HS^-	−51	43	Ag^+,NO_3^-	−37	57
Na^+,Ac^-	+68	5, 44	Ag^+,ClO_4^-	+11	57
K^+,F^-	−104	5			

[a]Units for $C_p°$ are J K^{-1} mol^{-1}.

gations (66, 67) led to $C_p°(HAc) = 165$ and 167 J K^{-1} mol^{-1}, each with larger uncertainty than the value we have selected, but in satisfactory agreement with the selected value. Allred and Woolley (44) used their heat capacities in calculating $\Delta_r C_p° = (-143 \pm 3)$ J K^{-1} mol^{-1} for the reaction represented by

[28] $HAc(aq) = H^+(aq) + Ac^-(aq)$

Olofsson (68) made calorimetric measurements leading to values of $\Delta_r H°$ at five temperatures in the range 274–373 K and used eq. [3] to derive $\Delta_r C_p° = (-143 \pm 5)$ J K^{-1} mol^{-1} for reaction [28]. Once again a comparison shows that calorimetrically measured heat capacities and calorimetrically measured enthalpies at several temperatures can lead to results that are in excellent agreement with each other, it being probable that the uncertainties are smaller for directly measured heat capacities than for heat capacities derived by way of eq. [3].

Table 5 contains our selections of "best" standard state partial molar heat capacities for single ions, all based on the common convention that sets $C_p°(H^+) = 0$. Using our previously selected $\Delta_r C_p° = -215$ J K^{-1} mol^{-1} for ionization of water with this convention and the accurately known molar heat capacity of water leads to $C_p°(OH^-) = -140$ J K^{-1} mol^{-1}. Then the value for $C_p°(Na^+,OH^-)$ listed in Table 1 leads to a value for $C_p°(Na^+)$. A further step is to use this value for $C_p°(Na^+)$ with the $C_p°(Na^+,Cl^-)$ listed in Table 1 to calculate a value for $C_p(Cl^-)$. There are, however, other routes to obtain these $C_p°$(ion) values. For example, the value for $C_p°(H^+,Cl^-)$ leads directly to a value for $C_p°(Cl^-)$, which can then be used with $C_p°(Na^+,Cl^-)$ to obtain a value for $C_p°(Na^+)$. We have considered a large number of these alternative routes to values for various $C_p°$(ion) and have selected those values that give the best overall fits to the $C_p°$ values listed in Tables 1–3, with allowance made for estimated uncertainties in the $C_p°$ values.

We have already illustrated how $C_p°$ values (only for T = 298.15 K) can be used in calculating the equilibrium constant for ionization of water over a wide range of temperatures. Similar calculations, using only $C_p°$ values for T = 298.15 K, have been carried out for other equilibria in several of the references (for examples see refs. 43, 50, 54, and 56) already cited.

Although we have chosen here to carry out calculations of equilibrium constants over a wide range of temperature by combining eqs. [1], [3], and [8] to obtain eq. [9], this same calculation can be done by combining eq. [8] with

[29] $\Delta_r S° = \Delta S_i + \Delta_r C_p° \ln T$

that is based on integration of eq. [4], to obtain $\Delta_r G° = \Delta_r H° - T\Delta_r S°$. Further use of this $\Delta_r G°$ in $\Delta_r G° = -RT \ln K$ permits

Table 2. Standard state partial molar heat capacities (C_p°)[a] of 1:2 and 2:1 aqueous electrolytes at 298.15 K.

Solute	C_p°	References	Solute	C_p°	References
$2Na^+,SO_4^{2-}$	−190	5, 62	$Mn^{2+},2Cl^-$	−259	47
$2Na^+,S_2O_3^{2-}$	−164	62	$Mn^{2+},2NO_3^-$	−156	60
$2Na^+,S_2O_8^{2-}$	−29	62	$Mn^{2+},2ClO_4^-$	−62	59
$2Na^+,MoO_4^-$	−123	62	$Fe^{2+},2ClO_4^-$	−78	27
$2Na^+,WO_4^{2-}$	−110	62	$Co^{2+},2Cl^-$	−279	58
$2Na^+,SO_3^{2-}$	−178	54	$Co^{2+},2NO_3^-$	−170	60
$2Na^+,CO_3^{2-}$	−216	50	$C^{2+},2ClO_4^-$	−81	59
$2Na^+,HPO_4^{2-}$	−168	50, 53	$Ni^{2+},2Cl^-$	−294	57
$2K^+,SO_4^{2-}$	−254	5, 40, 62	$Ni^{2+},2NO_3^-$	−186	60
$2K^+,S_2O_8^{2-}$	−84	62	$Ni^{2+},2ClO_4^{2-}$	−93	59
$2K^+,CrO_4^{2-}$	−244	56, 62	$Cu^{2+},2NO_3^-$	−161	60
$2K^+,Cr_2O_7^{2-}$	−105	56	$Cu^{2+},2ClO_4^-$	−72	58
$Mg^{2+},2Cl^-$	−268	5	$Zn^{2+},2NO_3^-$	−165	60
$Mg^{2+},2ClO_4^-$	−66	58	Zn^{2+},ClO_4^-	−73	59
$Mg^{2+},2NO_3^-$	−160	60	$Cd^{2+},2NO_3^-$	−152	58
$Ca^{2+},2Cl^-$	−281	5, 46, 58	$Cd^{2+},2ClO_4^-$	−57	59
$Ca^{2+},2ClO_4^-$	−77	59	$Hg^{2+},2ClO_4^-$	−67	61
$Ca^{2+},2NO_3^-$	−170	60	$Pb^{2+},2ClO_4^-$	−107	61
$Sr^{2+},2Cl^-$	−289	5	$UO_2^{2+},2ClO_4^-$	−8	42
$Ba^{2+},2Cl^-$	−300	5			

[a]Units for C_p° are J K^{-1} mol^{-1}.

Table 3. Standard state partial molar heat capacities (C_p°)[a] of 1:3, 1:4, and 3:1 aqueous electrolytes at T = 298.15 K.

Solute	C_p°	References
$3Na^+,PO_4^{3-}$	−369	50, 53
$3K^+,Fe(CN)_6^{3-}$	−215	14
$4K^+,Fe(CN)_6^{4-}$	−475	14
$Al^{3+},3Cl^-$	−497	63,[b] 64
$Al^{3+},3NO_3^-$	−331	63,[b] 64
$Cr^{3+},3NO_3^-$	−240	14
$La^{3+},3Cl^-$	−477	14, 34
$La^{3+},3ClO_4^-$	−177	34
$Gd^{3+},3ClO_4^-$	−148	34

[a]Units for C_p° are J K^{-1} mol^{-1}.
[b]The calculations of C_p° reported in this paper were based on measured heat capacities that were reported by Hovey and Tremaine in ref. 64.

Table 4. Standard state partial molar heat capacities (C_p°)[a] of "neutrals" in aqueous solution at T = 298.15 K.

Solute	C_p°	References
H_3PO_4(aq, undissoc.)	+94	50
CO_2(aq)	+243	52
SO_2(aq)	+195	52
H_2S(aq)	+178	43
NH_3(aq)	+75	44
HAc(aq)	+170	44

[a]Units for C_p° are J K^{-1} mol^{-1}.

calculation of $K = f(T)$ as already done in another way. Similarly, combination of $\Delta_r G^\circ = \Delta_r H^\circ - T\Delta_r S^\circ$ for a cell reaction with $\Delta_r G^\circ = -nFE^\circ$ permits convenient calculations of standard state cell potentials (E°) over wide ranges of temperatures.

Heat capacities of aqueous solutions at temperatures other than T = 298.15 K

Heat capacities of solutions of several electrolytes have been measured over temperature ranges from 10 to 55°C. Results of such measurements permit evaluation of the parameters in various equations for $C_p^\circ = f(T)$, which then permit extrapolation to much higher temperatures. The Helgeson–Kirkham–Flowers (69) and Holmes–Mesmer (70) equations have been used many times for this purpose. An example of this kind of calculation using C_p° values for the temperature range 10–55°C for calculations that extend to 350°C is provided by Hovey et al. (55) for the second dissociation constant of sulfuric acid.

A clear illustration of the predictive power of the Helgeson–Kirkham–Flowers (HKF) and Holmes–Mesmer (HM) equations mentioned above is provided by consideration of values of $C_p^\circ[Na^+,Al(OH)_4^-]$. Hovey et al. (49) measured these heat capacities at four temperatures in the range 10–55°C and used the HKF equation to estimate heat capacities at much higher temperatures. Then Caiani et al. (71) measured these heat capacities at five temperatures in the range 53–245°C. Still

Table 5. Conventional[a] standard state partial molar heat capacities[b] of aqueous ions at T = 298.15 K.

Ion	C_p°	Ion	C_p°	Ion	C_p°
H^+	0	Pb^{2+}	−55	Ac^-	+26
Li^+	+62	UO_2^{2+}	+44	MnO_4^-	−11
Na^+	+42	Al^{3+}	−119	TcO_4^-	−14
K^+	+12	Cr^{3+}	−27	ReO_4^-	−14
Rb^+	−9	La^{3+}	−99	$Al(OH)_4^-$	+97
Cs^+	−23	Gd^{3+}	−70	$HCrO_4^-$	+3
NH_4^+	+69	OH^-	−140	$H_2PO_4^-$	−34
Ag^+	+35	F^-	−116	CO_3^{2-}	−300
Mg^{2+}	−16	Cl^-	−126	SO_3^{2-}	−262
Ca^{2+}	−27	Br^-	−132	SO_4^{2-}	−276
Sr^{2+}	−37	I^-	−121	$S_2O_3^{2-}$	−248
Ba^{2+}	−48	NO_3^-	−71	$S_2O_8^{2-}$	−110
Mn^{2+}	−10	ClO_4^-	−26	CrO_4^{2-}	−268
Fe^{2+}	−26	ClO_3^-	−57	$Cr_2O_7^{2-}$	−129
Co^{2+}	−28	BrO_3^-	−90	MoO_4^{2-}	−207
Ni^{2+}	−42	IO_3^-	−71	WO_4^{2-}	−194
Cu^{2+}	−20	HCO_3^-	−52	HPO_4^{2-}	−253
Zn^{2+}	−22	HSO_3^-	−4	PO_4^{3-}	−495
Cd^{2+}	−8	HSO_4^-	−18	$Fe(CN)_6^{3-}$	−251
Hg^{2+}	−15	HS^-	−93	$Fe(CN)_6^{4-}$	−523

[a]Based on $C_p^\circ(H^+) = 0$.
[b]Units for C_p° are J K^{-1} mol^{-1}.

more recently, Chen et al. (72) have measured $\Delta_r H^\circ$ at five temperatures in the range 100–150°C for the reaction represented by

[30] $Al(OH)_3(cr) + OH^-(aq) = Al(OH)_4^-(aq)$

and applied eq. [3] to obtain values of $\Delta_r C_p^\circ$ and thence values of $C_p^\circ[Na^+,Al(OH)_4^-)]$. Although the complete collection of C_p° values based on these three sets of calorimetric measurements leads to the most accurate representation of the thermodynamic properties of this system, it is important to note that the high-temperature heat capacities predicted (49) on the basis of measurements over the relatively narrow range 10–55°C are in good agreement with the heat capacities that were measured or calculated via eq. [3] later.

As previously mentioned, we have not tabulated C_p° values from Criss, Cobble, and colleagues obtained by way of the integral heat method in selecting the "best" values for T = 298.15 K because we believe that values based on modern flow calorimetry are more accurate. But it should be recognized that their values for C_p° for several electrolytes are the best values available for $T > 298$ K and can be used for various calculations of the sort already described here and that have been described by Criss, Cobble, and colleagues.

Wood and colleagues at the University of Delaware have used a flow calorimeter of the type described in 1981 (4) for measurement of many heat capacities at high temperatures and also at various pressures, including measurements at temperatures above the critical temperature of water. Many of their results have been cited by Wood et al. (73). Other measurements have been reported for (H^+, Cl^-) to 140°C by Tremaine et al. (39), for [Na^+, OH^-] to 250°C by Simonson et al. (74), and for hydrolyzed and unhydrolyzed solutions of aluminum chloride by Conti et al. (75). We also mention that researchers at Brigham Young University have made calorimetric measurements leading to values of $\Delta_r H^\circ$ for several reactions at high temperatures and thence to useful values of $\Delta_r C_p^\circ$ for these high temperatures. All of these (and other) heat capacities for high temperatures are now sufficient in number and quality to justify a detailed review that cannot be included here.

Theoretical considerations of heat capacities of aqueous electrolytes

Theoretical analysis of C_p° values for aqueous electrolytes can contribute to our knowledge of ion–water interactions. Early efforts in this direction were reported by Zwicky (76) and by Everett and Coulson (77). More recent reports by Leyendekkers (78) and by Sen (79) illustrate two other approaches. Wood et al. (new work and a review are included in ref. 73) have worked on both theory and measurements to obtain information about partial molar heat capacities (also other thermodynamic properties) for aqueous electrolytes over a range of temperatures and pressures, including near and above the critical conditions for water. One theoretical prediction and experimental verification (80) is that the partial molar heat capacities of electrolytes approach $-\infty$ as T_c is approached from lower temperatures and approach $+\infty$ as T_c is approached from higher temperatures. We also mention that Oelkers et al. (81) have reviewed and extended earlier work by Helgeson and colleagues, such as that leading to the HKF equation (69).

Jolicoeur and Mercier (82), Conway (83) Tremaine et al. (84), French and Criss (85), and Abraham and Marcus (86) have reported methods of estimating "absolute" (rather than conventional) values of single ion heat capacities. It has been pointed out clearly and correctly in several of these papers that it may be appropriate to consider conventional ionic heat capacities when only ions of these same charge are being compared with each other (for example, to learn about the effects of ionic size on heat capacity), but it is necessary to consider "absolute" ionic heat capacities when comparing ions having different charges or when one is concerned with any quantitative theoretical analysis of heat capacities of hydration.

We also mention that Abraham and Marcus (86) and Criss and Millero (26) have provided useful reviews of standard state partial molar heat capacities of aqueous electrolytes. The first of these reviews (86) that was published in 1986 was concerned with both inorganic and organic electrolytes. Although parts of this review are now out of date because of research done in the past decade, the part that is devoted to organic electrolytes is still the best available review. In addition, there is a detailed discussion of the effects of ion–water interactions (hydration) on heat capacities. The more recent report by Criss and Millero (26) was concerned only with 1:1 electrolytes and is focussed on using heat capacities over a range of compositions as part of the evaluation of activity coefficients and osmotic coefficients as a function of both temperature and composition.

Acknowledgements

We thank the Natural Sciences and Engineering Research Council of Canada for support of our research on heat capaci-

ties. J.K.H. thanks the Swiss National Science Foundation for support via grant 2100-037559·93-1. Finally, we are pleased to thank our colleagues, who have been cited in several references, for all of their direct and indirect contributions to our work in his area.

References

1. F.J. Millero. *In* Activity coefficients in electrolyte solutions. Vol. 2. *Edited by* R.M. Pytkowicz. CRC Press, Boca Raton, Fla. 1980. Chap. 2.
2. V.B. Parker. Thermal properties of aqueous 1:1 electrolytes. NSRDS-NBS 2. U.S. Government Printing Office, Washington, D.C. 1965.
3. P. Picker, P-A. Leduc, P.R. Philip, and J.E. Desnoyers. J. Chem. Thermodyn. **3**, 631 (1971).
4. D. Smith-Magowan and R.H. Wood. J. Chem. Thermodyn. **13**, 1047 (1981).
5. J.E. Desnoyers, C. de Visser, G. Perron, and P. Picker. J. Solution Chem. **5**, 605 (1976).
6. I.V. Olofsson. J. Chem. Thermodyn. **11**, 1005 (1979).
7. G.C. Allred and E.M. Woolley. J. Chem. Thermodyn. **13**, 147 (1981).
8. D.E. White and R.H. Wood. J. Solution Chem. **11**, 223 (1982).
9. P-A. Leduc, J-L. Fortier, and J.E. Desnoyers. J. Phys. Chem. **78**, 1217 (1974).
10. G. Perron, N. Desrosiers, and J.E. Desnoyers. Can. J. Chem. **54**, 2163 (1976).
11. L.F. Silvester and K.S. Pitzer. J. Phys. Chem. **81**, 1822 (1977); D.J. Bradley and K.S. Pitzer. J. Phys. Chem. **83**, 1599 (1979).
12. J. Ananthaswamy and G. Atkinson. J. Chem. Eng. Data, **29**, 81 (1984).
13. D.G. Archer and P. Wang. J. Phys. Chem. Ref. Data, **19**, 371 (1990).
14. J.J. Spitzer, I.V. Olofsson, P.P. Singh, and L.G. Hepler. Can. J. Chem. **57**, 2798 (1979).
15. T.L. Cottrell, G.W. Drake, D.L. Levi, K.S. Tully, and J.A. Wolfenden. J. Chem. Soc. 1016 (1948).
16. L.P. Fernandez and L.G. Hepler. J. Phys. Chem. **63**, 110 (1959).
17. C.M. Criss and J.W. Cobble. J. Am. Chem. Soc. **83**, 3223 (1961).
18. W.L. Gardner, R.E. Mitchell, and J.W. Cobble. J. Phys. Chem. **73**, 2025 (1969).
19. E.E. Bernaducci, L.R. Morss, and A.R. Miksztal. J. Solution Chem. **8**, 717 (1979).
20. E.D. McCollum. J. Am. Chem. Soc. **49**, 28 (1927).
21. M. Randall and M.D. Taylor. J. Phys. Chem. **45**, 959 (1941).
22. E.M. Woolley and L.G. Hepler. Can. J. Chem. **55**, 158 (1977). (C_p^{rel}).
23. C. Jolicoeur, L-L. Lemelin, and R. Lapointe. J. Phys. Chem. **83**, 2806 (1979). (C_p^{rel}).
24. G.J. Mains, J.W. Larson, and L.G. Hepler. J. Phys. Chem. **88**, 1257 (1984). (C_p^{rel}).
25. M.J. Blandamer, J. Burgess, and J.M.W. Scott. J. Chem. Soc. Faraday Trans. 1, **80**, 2881 (1984); M.J. Blandamer and J. Burgess. J. Chem. Soc. Faraday Trans. 1, **81**, 1495 (1985); M.J. Blandamer, J. Burgess, and J.M.W. Scott. Annu. Rep. Chem. Soc. **84**, 77 (1987). (C_p^{rel}).
26. C.M. Criss and F.J. Millero. J. Phys. Chem. **100**, 1288 (1996).
27. J.K. Hovey. Ph.D. Thesis, University of Alberta, Edmonton, Canada. 1988.
28. E.C.W. Clarke and D.N. Glew. J. Phys. Chem. Ref. Data, **14**, 489 (1985).
29. R.E. Mitchell and J.W. Cobble. J. Am. Chem. Soc. **86**, 5401 (1964).
30. M. Mastroianni and C.M. Criss. J. Chem. Eng. Data, **17**, 222 (1972).
31. P.P. Singh, K.G. McCurdy, E.M. Woolley, and L.G. Hepler. J. Solution Chem. **6**, 327 (1977).
32. A. Roux, G.M. Musbally, G. Perron, J.E. Desnoyers, P.P. Singh, E.M. Woolley, and L.G. Hepler. Can. J. Chem. **56**, 24 (1978).
33. E.C. Jekel, C.M. Criss, and J.W. Cobble. J. Am. Chem. Soc. **86**, 5404 (1964).
34. C. Xaio and P.R. Tremaine. Presented at the 50th Calorimetry Conference, Gaithersburg, Md., U.S.A. July, 1995. Submitted for publication. (C_p^{rel}).
35. P.P. Singh, E.M. Woolley, K.G. McCurdy, and L.G. Hepler. Can. J. Chem. **54**, 3315 (1976).
36. O. Enea, P.P. Singh, E.M. Woolley, K.G. McCurdy, and L.G. Hepler. J. Chem. Thermodyn. **9**, 731 (1977).
37. G. Olofsson and L.G. Hepler. J. Solution Chem. **4**, 127 (1974).
38. J.D. Cox, D.D. Wagman, and V.A. Medvedev (*Editors*). CODATA key values for thermodynamics. Hemisphere Publ. Corp., New York. 1989.
39. P.R. Tremaine, K. Sway, and J.A. Barbero. J. Solution Chem. **15**, 1 (1986).
40. J.K. Hovey, L.G. Hepler, and P.R. Tremaine. Thermochim. Acta, **126**, 245 (1988).
41. J.K. Hovey and L.G. Hepler. Can. J. Chem. **67**, 1489 (1989).
42. J.K. Hovey, C. Nguyen-Trung, and P.R. Tremaine. Geochim. Cosmochim. Acta, **53**, 1503 (1989).
43. J.A. Barbero, K.G. McCurdy, and P.R. Tremaine. Can. J. Chem. **60**, 1872 (1982).
44. G.C. Allred and E.M. Woolley. J. Chem. Thermodyn. **13**, 155 (1981).
45. A.H. Roux, G. Perron, and J.E. Desnoyers. **62**, 878 (1984).
46. G. Perron, A. Roux, and J.E. Desnoyers. Can. J. Chem. **59**, 3049 (1981).
47. J.J. Spitzer, I.V. Olofsson, P.P. Singh, and L.G. Hepler. Thermochim. Acta, **28**, 155 (1979).
48. R.J. Lemire, P.P.S. Saluja, and A.B. Campbell. J. Solution Chem. **21**, 507 (1992).
49. J.K. Hovey, L.G. Hepler, and P.R. Tremaine. J. Phys. Chem. **92**, 1323 (1988).
50. J.W. Larson, K.G. Zeeb, and L.G. Hepler. Can. J. Chem. **60**, 2141 (1982). (C_p^{rel}).
51. J.C. Peiper and K.S. Pitzer. J. Chem. Thermodyn. **14**, 613 (1982). (C_p^{rel}).
52. J.A. Barbero, L.G. Hepler, K.G. McCurdy, and P.R. Tremaine. Can. J. Chem. **61**, 2509 (1983). (C_p^{rel}).
53. H. Bianchi and P.R. Tremaine. J. Solution Chem. **24**, 439 (1995). (C_p^{rel}).
54. G.C. Allred, J.W. Larson, and L.G. Hepler. Can. J. Chem. **59**, 1068 (1981). (C_p^{rel}).
55. J.K. Hovey and L.G. Hepler. J. Chem. Soc. Faraday Trans. **86**, 2831 (1990). (C_p^{rel}).
56. J.K. Hovey and L.G. Hepler. J. Phys. Chem. **94**, 7821 (1990). (C_p^{rel}).
57. P.P. Singh, J. Spitzer, R.M. McKay, K.G. McCurdy, and L.G. Hepler. Thermochim. Acta, **24**, 111 (1978).
58. J.J. Spitzer, P.P. Singh, K.G. McCurdy, and L.G. Hepler. J. Solution Chem. **7**, 81 (1978).
59. J.J. Spitzer, P.P. Singh, I.V. Olofsson, and L.G. Hepler. J. Solution Chem. **7**, 623 (1978).
60. J.J. Spitzer, I.V. Olofsson, P.P. Singh, and L.G. Hepler. J. Chem. Thermodyn. **11**, 233 (1979).
61. J.K. Hovey, L.G. Hepler, and P.R. Tremaine. J. Chem. Thermodyn. **20**, 595 (1988).
62. I.V. Olofsson, J.J. Spitzer, and L.G. Hepler. Can. J. Chem. **56**, 1871 (1978).
63. L. Barta and L.G. Hepler. Can. J. Chem. **64**, 353 (1986).
64. J.K. Hovey and P.R. Tremaine. Geochim. Cosmochim. Acta, **50**, 453 (1986).
65. G. Olofsson. J. Chem. Thermodyn. **7**, 507 (1975).

66. J. Konicek and I. Wadso. Acta Chem. Scand. **25**, 1541 (1971).
67. C. Casanova, E. Wilhelm, J-P.E. Grolier, and H.V. Kehiaian. J. Chem. Thermodyn. **13**, 241 (1981).
68. G. Olofsson. J. Chem. Thermodyn. **16**, 39 (1984).
69. H.C. Helgeson, D.H. Kirkham, and G.C. Flowers. Am. J. Sci. **281**, 1249 (1981).
70. H.F. Holmes and R.E. Mesmer. J. Phys. Chem. **87**, 1242 (1983).
71. P. Caiani, G. Conti, P. Gianni, and E. Matteoli. J. Solution Chem. **18**, 447 (1989).
72. Q. Chen, Y. Xu, and L.G. Hepler. Can. J. Chem. **69**, 1685 (1991).
73. R.H. Wood, R.W. Carter, J.R. Quint, V. Majer, P.T. Thompson, and J.R. Boccio. J. Chem. Thermodyn. **26**, 225 (1994).
74. J.M. Simonson, R.E. Mesmer, and P.S.Z. Rogers. J. Chem. Thermodyn. **21**, 561 (1989).
75. G. Conti, P. Gianni, and E. Matteoli. Geochim. Cosmochim. Acta, **56**, 4125 (1992).
76. F. Zwicky. Proc. Natl. Acad. Sci. U.S.A. **12**, 86 (1926).
77. D.H. Everett and C.A. Coulson. Trans. Farada Soc. **36**, 633 (1940).
78. J. Leyendekkers. J. Chem. Soc. Faraday Soc. **76**, 1206 (1980).
79. U. Sen. Can. J. Chem. **69**, 440 (1991).
80. D.E. White, R.H. Wood, and D.E. Biggerstaff. J. Chem. Thermodyn. **20**, 159 (1988).
81. E.H. Oelkers, H.C. Helgeson, E.L. Shock, D.A. Sverjensky, J.W. Johnson, and V.A. Pokrovskii. J. Phys. Chem. Ref. Data, **24**, 1401 (1995).
82. C. Jolicoeur and J-C. Mercier. J. Phys. Chem. **81**, 85 (1977).
83. B.E. Conway. J. Solution Chem. **7**, 721 (1978).
84. P.R. Tremaine, N.H. Sagert, and G.J. Wallace. J. Phys. Chem. **85**, 1977 (1981).
85. R.N. French and C.M. Criss. J. Solution Chem. **11**, 625 (1982).
86. M.H. Abraham and Y. Marcus. J. Chem. Soc. Faraday Trans. 1, **82**, 3255 (1986).

Effect of ligand structure, solvent, and temperature on the electrochemical behavior of polyarene–iron complexes

Alaa S. Abd-El-Aziz, Christine R. de Denus, Karen M. Epp, Simone Smith, Richard J. Jaeger, and David T. Pierce

Abstract: The electrochemical investigation of a number of polyarene–iron complexes ($[\mathbf{3}]^{2+}$–$[\mathbf{9}]^{5+}$) containing etheric, sulphide, and sulphone bridges indicated that there were various degrees of interaction based on the nature of the bridging heteroatoms. While the electrochemical investigation of all etheric complexes showed that the metallic moieties behaved as isolated redox centers, it was found that there was electronic communication (ca. 70–80 mV) for the isomeric sulphide complexes $[\mathbf{4}]^{2+}$ and $[\mathbf{6}]^{2+}$. The rate constant of the following chemical reaction (k_f) was calculated for some of these complexes and it was found that these rates were affected by the nature of the solvent, the bridging ligand, and the temperature. At various temperatures, k_f indicated a higher degree of stability for complexes containing sulphide bridges than for those containing etheric bridges, especially at room temperature. The effect of a strong coordinating solvent, such as acetonitrile, on the k_f of complex $[\mathbf{3}]^{2+}$ indicated that the substitution of the arene ligand with acetonitrile molecules proceeded as a dissociative mechanism. Controlled potential coulometry was also used to verify the transfer of two electrons in the first reduction process of the di-iron complexes.

Key words: cyclopentadienyliron, cyclic voltammetry, arene complexes, isolated and interacting redox centers.

Résumé : L'étude électrochimique d'un certain nombre de complexes polyarène–fer ($[\mathbf{3}]^{2+}$–$[\mathbf{9}]^{5+}$) contenant des ponts éthérés, sulfures et sulfones indique qu'il existe divers degrés d'interactions selon la nature des hétéroatomes créant les ponts. Même si l'étude électrochimique de tous les complexes éthérés ont montré que les portions métalliques se comporte comme des centres rédox isolés, il a été observé qu'il y a de la communication électronique (environ 70–80 mV) pour les complexes sulfurés isomères $[\mathbf{4}]^{2+}$ et $[\mathbf{6}]^{2+}$. On a calculé la constante de vitesse de la réaction chimque suivante (k_f) pour quelques-uns de ces complexes et on a trouvé qu'elles sont affectées par la nature du solvant, du coordinat servant de pont et par la température. À diverses températures, les valeurs de k_f indique que les complexes contenant des ponts sulfures sont plus stables que ceux contenant des ponts éthérés, particulièrement à la température ambiante. L'effet d'un solvant pouvant effectuer une forte coordination, tel que l'acétonitrile, sur la valeur k_f du complexe $[\mathbf{3}]^{2+}$ indique que la substitution du coordinat arène par de l'acétonitrile se produit par un mécanisme dissociatif. On a aussi utilisé de la coulométrie à potentiel contrôlé pour vérifier le transfert de deux électrons dans le premier processus de réduction des complexes di-fer.

Mots clés : cyclopentadiénylfer, voltampérométrie cyclique, complexes arènes, centres rédox isolés interagissants.

[Traduit par la rédaction]

Introduction

Over the past few decades, the electrochemical behavior of organometallic materials has been the focus of interest of many chemists (1–6). Recent development in this field is due to the wide range of applications of these redox systems with specific interest being given to the arene complexes in light of their promising electrochemistry (7–14). The oxidation/reduction properties of oligomeric and polymeric materials have led to a thorough investigation of the electron transfer reactions in these complexes (15–23). This interest stems from the ability of these systems to exhibit mixed valency (3, 4, 24–27) and conductivity (28), as well as to sometimes act as electron reservoirs that initiate electron-transfer chain catalysis (1, 29–36).

Since the development of η^6-arene-η^5-cyclopentadienyliron complexes, numerous electrochemical studies have shown that these complexes undergo two successive one-electron reductions (1, 7–9, 37–41). The first reduction is chemically reversible and produces the neutral 19 e^- complex where the second reduction step leads to an anionic 20 e^- complex. It has been reported that the reversibility of the second reduction step is dependent on the nature of the arene or cyclopentadienyl rings (1, 8, 9, 41). Although Solodovnikov et al. have reported the formation of an extremely unstable 21 e^- dia-

Received November 6, 1995.

A.S. Abd-El-Aziz,[2] C.R. de Denus, K.M. Epp, and S. Smith. Department of Chemistry, University of Winnipeg, Winnipeg, MB R3B 2E9, Canada.
R.J. Jaeger and D.T. Pierce. Department of Chemistry, University of North Dakota, Grand Forks, ND 58202, U.S.A.

[1] This paper is dedicated to Nobel Laureate Professor Henry Taube; it was presented at the University of Saskatchewan at the *Taube Fest*, October 1995, in celebration of Professor Henry Taube's contribution to Inorganic Chemistry.

[2] Author to whom correspondence may be addressed. Telephone: (204) 786-9335. Fax: (204) 786-1824. E-mail: abdelaziz@uwinnipeg.ca

nionic complex for the (naphthalene)FeCp system (42), it is the neutral arene systems that are the most important electron reservoirs and could be useful as catalysts in the reduction of other species existing in the solution via homogeneous charge transfer (43, 44). Electrolysis of this class of arene complexes led to the decoordination of the arenes and the formation of ferrocene as well as zerovalent iron (45–50).

There has been a tremendous effort to study the electrochemistry of bi- and polymetallic complexes because of the possible communication of the metallic species via the backbone of the coordinating ligands (7, 17, 20–25). The type of metal present as well as the bridging ligands often dictates whether the metal centers are interacting with, or isolated from, one another. The electrochemical studies of polyferrocenyl complexes demonstrate communication for the silicon-bridged species that is not evident in the case of the methylene-bridged analogues (20–23). In addition, Bard and coworkers have shown that, for the dicyclopentadienyliron phenanthroline complex, the planar polycyclic ligand allows for electrochemical communication to occur between the metal centers (7). The degree of communication is often determined by the separation of formal potentials (ΔE^0) measured by cyclic voltammetry (CV) (51). In an analogous manner, for a molecule with one redox center the CV would be the same as that for one containing multiple isolated redox centers (52). For such large systems with isolated redox centers, the electrochemical technique of controlled potential coulometry is often employed to determine the number of electrons involved in the electron transfer process (53–55).

Recently, we reported on the electrochemical behavior of a variety of cyclopentadienyliron-substituted benzenes and polycyclic and heterocyclic complexes (8, 9). It was found that the first reduction was chemically reversible in all the complexes while the second was dependent on the experimental conditions. We now wish to report on the effect of solvent, temperature, and bridging ligand for a series of isomeric bi- and poly-(cyclopentadienyliron) complexes with etheric, sulphide, and sulphone bridges. For some of these complexes, the rate constants of the following chemical reaction have also been determined.

Experimental

Chemicals

Organic solvents acetone (AC), acetonitrile (AN), and dimethyl sulfoxide (DMSO), were dried over calcium hydride for 2 days and were purified by distillation prior to their use. High-quality *N,N'*-dimethylformamide (DMF, Aldrich; Burdick and Jackson Brand, Baxter Scientific) was purged with purified dinitrogen and stored over Linde molecular sieves 4 Å (Strem Chemicals). Tetra-*N*-butylammonium perchlorate (TBAP) was received from Fluka and was used as the supporting electrolyte. Tetra-*N*-butylammonium hexafluorophosphate ($TBAPF_6$) was used as the supporting electrolyte for all coulometry and voltammetry associated with bulk-scale electrolysis, and was prepared by metathesis of tetra-*N*-butylammonium iodide (Aldrich) and ammonium hexafluorophosphate (Ozark–Mahoning) in acetone followed by recrystallization from ethanol. The η^6-arene-η^5-cyclopentadienyliron complexes used in this study were prepared according to previously described methods (56–58).

Electrochemical measurements

Cyclic voltammetric experiments were performed using a conventional three-electrode cell. The working electrode was either a platinum disk electrode (ca. 2 mm diam.) or a glassy carbon disk electrode (ca. 3 mm diam.). A quasi-reference electrode (Ag/AgCl) was utilized. However, ferrocene was added at the end of each experiment and served as the reference redox couple. The auxiliary electrode in these studies was a Pt wire. Temperatures from 293 to 233 K were obtained by means of a Dry Ice – acetone slush bath in a Dewar flask. The concentration of the complex was 2.0 mM, while that of the supporting electrolyte was 0.1 M. Before measurements, solutions were deaerated by passing high-purity nitrogen through them and the experiment was run under a blanket of purified nitrogen. An EG&G Princeton Applied Research model 263A potentiostat, interfaced with a microcomputer, was used in all experiments. CV simulations were run using the Digisim simulation program, version 2.0, from Bioanalytical Systems Incorporated.

All coulometry and voltammetry measurements associated with bulk-scale electrolysis experiments (conducted at the Chemistry Department, University of North Dakota) were performed with a three-electrode cell that was controlled by an EG&G Princeton Applied Research model 273 potentiostat. Electrolysis currents were recorded for a user-specified applied potential and were acquired over more than 300 s with a time interval of less than 0.5 s. The current–time set for each electrolysis was digitally integrated to yield total charge passed to within less than $\pm 1.0\%$ of comparable, electronically integrated currents. Stirred solution voltammograms were recorded before and after electrolysis to analyze for solution composition and were performed with a potential sweep rate of 0.02 V/s.

Bulk-scale electrolysis experiments were performed with the analyte at 3 mM concentration in 50 mL of DMF/0.1M $TBAPF_6$. Solutions were contained within a sealed electrochemical cell that was constantly purged with purified nitrogen and was cooled by partial immersion in a Dry Ice – acetone slush bath. Rapid stirring during electrolysis and voltammetry immediately before and after electrolysis was performed with a magnetic stir bar that was rotated at a constant rate at the cell bottom. The working electrodes used for controlled-potential coulometry were high surface area cylinders and were composed of either platinum mesh or reticulated vitreous carbon. A small platinum disk electrode (ca. 2 mm diam.) or larger glassy carbon disk electrode (ca. 3 mm diam.) was used as the working electrode for all voltammetry. The counter electrode in all cases was a platinum-mesh cylinder that was contained within a large, separate compartment containing DMF/0.1M $TBAPF_6$ in ionic contact with the analyte solution through a medium porosity glass frit. A silver wire coated with silver chloride acted as a quasi-reference electrode in DMF/0.1M $TBAPF_6$ and was separated from solution within a smaller fritted compartment. At the conclusion of each experiment, the quasi-reference potential was correlated to the potential of the ferrocene/ferrocinium couple (Fc/Fc^+) by addition of ferrocene to the solution.

Results and discussion

Our previous studies of monoiron arene complexes have shown two successive reduction steps for this class of cyclo-

Table 1. CV parameters for complexes $[1]^+$–$[9]^{5+}$ at T = 253 K, v = 0.2 V/s, Pt working electrode, in DMF with $E_{1/2}$ vs. $FeCp_2$.

Complex number	*E*pa	*E*pc	$E_{1/2}$
$[1]^+$	−1.69	−1.84	−1.77
$[2]^+$	−1.62	−1.76	−1.69
$[3]^{2+}$	−1.70	−1.87	−1.79
$[4]^{2+}$	−1.64	−1.86	−1.75
$[5]^{2+}$	−1.58	−1.81	−1.70
$[6]^{2+}$	−1.61	−1.75	−1.68
$[7]^{2+}$	−1.47	−1.60	−1.54
	−1.74	−1.89	−1.82
$[8]^{2+}$	−1.48	−1.69	−1.59
$[9]^{5+}$	−1.68	−1.83	−1.76

pentadienyliron arene complex (8, 9). The first reduction appeared to be chemically reversible at various temperatures when a HMDE was employed as the working electrode. In the present study, we have examined the electrochemistry of a number of arene complexes in DMF medium (Fig. 1) using platinum and (or) glassy carbon working electrodes. It was found that for the monometallic complexes ($[1]^+$, $[2]^+$) the chemical reversibility of the 18 e^-/19 e^- couple was dependent on the temperature and the nature of the substituent on the complexed arene. The first reduction at a platinum working electrode for these systems was chemically reversible at 253 K for both $[1]^+$ and $[2]^+$, leading to the formation of the stable 19 e^- complexes as outlined in Table 1. In contrast, studies at room temperature (293 K) indicated that although complex $[2]^0$ remained chemically stable, complex $[1]^0$ decomposed rapidly. A second wave for the reduction of the neutral 19 e^- complexes to the anionic 20 e^- complexes was also observed when a glassy carbon working electrode was used. This 19 e^-/20 e^- couple for complex $[2]^{0/-}$ was found to be chemically reversible ($E_{1/2}$ = −2.48 vs. Fc/Fc^+) at room temperature. These results are consistent with measurements reported previously (9).

Polyether complexes

Polyether complexes ($[3]^{2+}$–$[9]^{5+}$) also show two separate reduction steps, with the CV response being dependent on the nature of the complex, working electrode material, temperature, and solvent. It was found that for the oxygen-bridged arene complex $[3]^{2+}$, the chemical reversibility of both reduction steps was greatly dependent on the temperature and the solvent. At 293 K the first reduction (36 e^-/38 e^-) was partially chemically reversible while the second (38 e^-/40 e^-) was chemically irreversible. As the temperature was decreased to 233 K, the first process became chemically reversible as

Fig. 1. Complexes studied by cyclic voltammetry and controlled potential electrolysis.

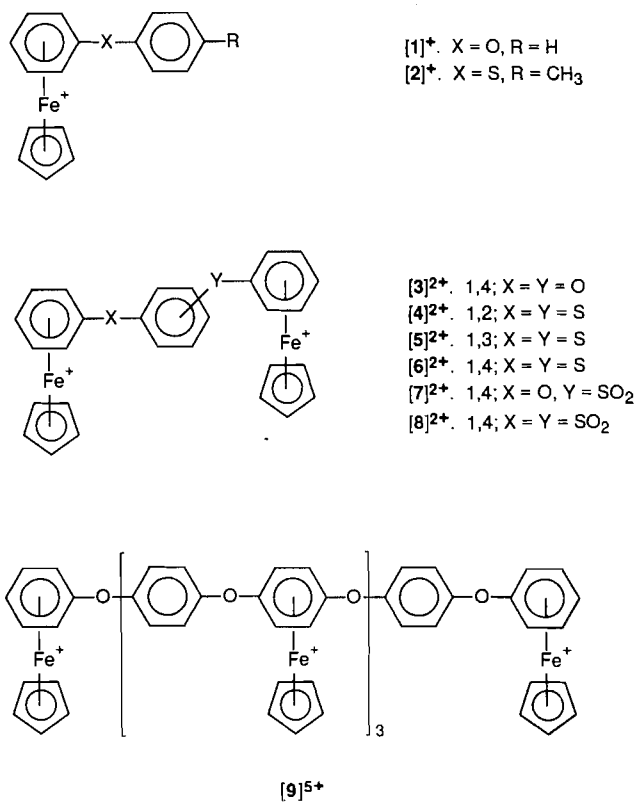

shown in Fig. 2 and was recorded as a single wave at $E_{1/2}$ = −1.75 V vs. Fc/Fc^+. This suggested that the stability of the 38 e^- species formed by the first reduction increased with a decrease in temperature. In contrast to this behavior, the 40 e^- product from the second reduction remained unstable at all temperatures (293–233 K) and time frames (0.05–1.0 V/s) investigated. As indicated in Scheme 1, we are proposing that the bimetallic $[3]^{2+}$ complex reduces in two distinct steps and that in each step the complex adds two electrons. Since CV's of $[3]^{2+}$ are very similar in shape to those of the monoiron analogue ($[1]^+$), we are further proposing that the complex possesses electronically isolated iron centers on the time scale of our CV measurements. By this mechanism, each two-electron reduction is actually composed of separate one-electron reductions that occur in rapid succession at each iron site.

Such a mechanism is in agreement with previous findings for other complexes with noninteracting metal centers (52, 59, 60). However, conclusive evidence for two electrons being transferred in the first reduction process was obtained for $[3]^{2+}$ by controlled potential coulometry of a solution containing

Scheme 1.

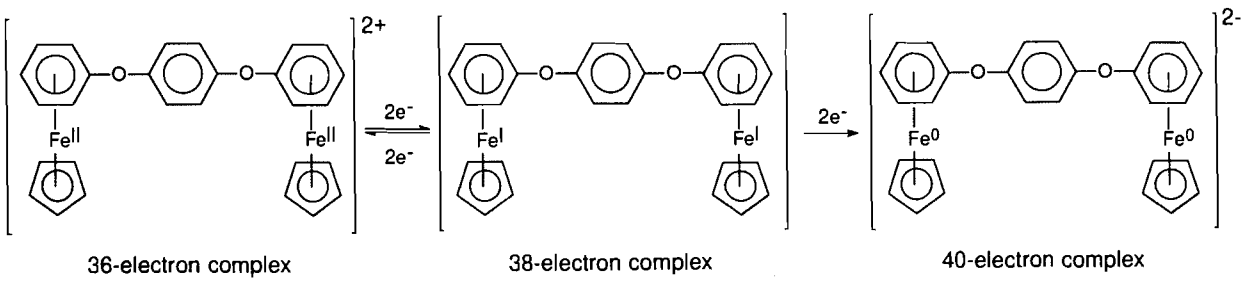

Fig. 2. Cyclic voltammogram at glassy carbon of 2.0 mM complex $[\mathbf{3}]^{2+}$ in DMF containing 0.1 M TBAP at 233 K; $v = 0.2$ V/s.

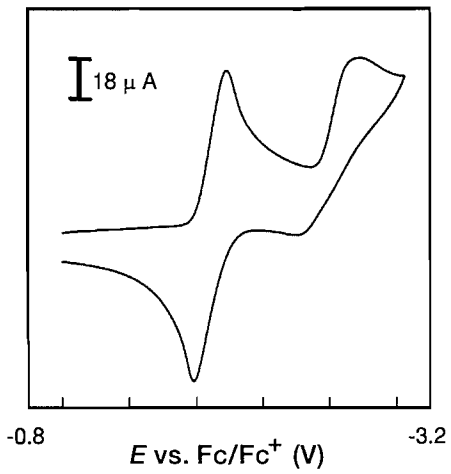

Fig. 3. Stirred solution voltammograms of 3.0 mM complex $[\mathbf{3}]^{2+}$ at 243 K in DMF/0.1 M $TBAPF_6$ recorded (*a*) before and (*b*) after partial electrolysis ($Q = 5.05$ C) at an applied potential of -1.93 V vs. Fc/Fc^+. Voltammograms were recorded with the same platinum disk working electrode and stirring rate.

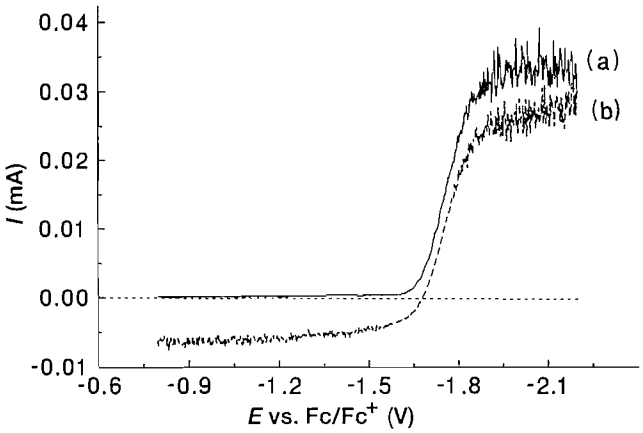

0.149 mmol of the complex at a large platinum mesh electrode. Plateau currents measured from stirred solution voltammograms (Fig. 3) recorded before and after a partial electrolysis at an applied voltage of -1.93 V vs. Fc/Fc^+ demonstrated that 18.1% of the complex was reduced without noticeable decomposition. From the 5.05 C of charge passed during electrolysis, an apparent *n*-value of 1.94 equiv./mol was determined. Electrolysis experiments that were extended to greater conversions demonstrated noticeable decomposition of the reduced complex, even at the lowest temperature of 228 K. Accurate coulometry was not possible with higher conversions because one or more of the decomposition products irreversibly adsorbed and passivated all electrode surfaces. Adsorption of these product(s) was especially severe at carbon electrode surfaces.

Solvent studies

The solubility of the dicationic complex $[\mathbf{3}]^{2+}$ in a number of solvents other than DMF (e.g., DMSO, AN, and AC) allowed for the examination of the electrochemical behavior of this sample complex and its reduced forms under a variety of conditions. It was observed that at 293 K the first reduction step was chemically irreversible in both AN and DMSO, while it was partially chemically reversible in the other two solvents at various CV scan rates (0.05–1.0 V/s). As the temperature was lowered to 253 K, the chemical reversibility of the 36 e^-/38 e^- couple increased in DMF, AN, and AC as indicated in Fig. 4. While it has been found that $[\mathbf{3}]^0$ may either undergo a second reduction or react with the solvent, the rate constants for the decomposition of the 38 e^- complex in a variety of solvents were analyzed in this work using the method described by Nicholson and Shain (61). By this method, the pseudo-first-order rate constant of the following chemical reaction was calculated at a variety of scan rates (0.05–1.0 V/s) with the average rate being reported with a standard deviation between 10 and 30%. It was found that the rate constant at 253 K was small for both AC ($k_f = 0.024$ s^{-1}) and DMF ($k_f = 0.037$ s^{-1}) while it was much greater for AN ($k_f = 0.577$ s^{-1}). This behavior may be attributed to the fact that AN is a stronger coordinating solvent to this class of arene cyclopentadienyliron complexes and that ligand substitution with the 38 e^- $[\mathbf{3}]^0$ complex is enhanced.

Fig. 4. Cyclic voltammogram at Pt of 2.0 mM complex $[\mathbf{3}]^{2+}$; $v = 0.2$ V/s at 253 K in (*a*) DMF containing 0.1 M TBAP; (*b*) AC containing 0.1 M TBAP; (*c*) AN containing 0.1 M TBAP.

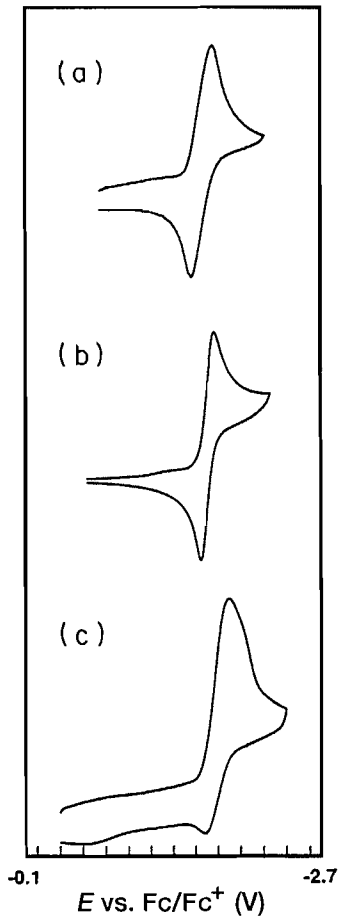

Decoordination studies

To further investigate the effect of solvent on the kinetics of the following chemical reaction, complex $[\mathbf{3}]^{2+}$ was dissolved

Fig. 5. The rate constant of following chemical reaction k_f vs. concentration of AN, 2.0 mM complex $[\mathbf{3}]^{2+}$ in DMF containing 0.1 M TBAP.

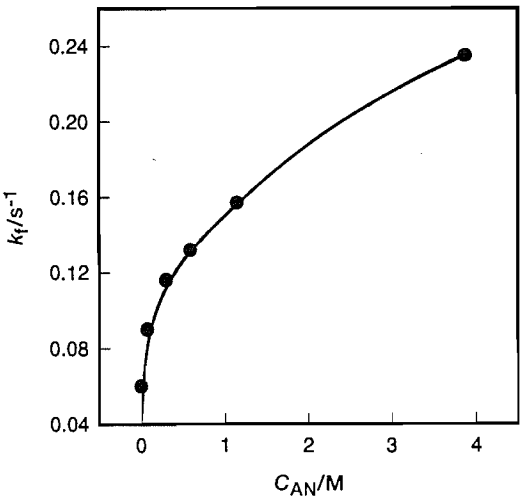

in DMF and CVs were recorded after consecutive additions of AN to the electrochemical cell. The experiment was performed at 243 K due to the high chemical reversibility demonstrated by the 36 e^-/38 e^- couple in DMF at this temperature. Under these conditions, the couple showed a marked decrease in chemical reversibility as the solution concentration of AN was increased. This result clearly indicated that the neutral complex reacts with AN in some form of rate-limiting, ligand-substitution reaction. Such reactions were noted previously by Darchen, who showed that decoordination of monoiron complexes may result in the presence of a strong donor ligand such as $P(OMe)_3$, $CN(C_4H_9)$, or AN (45, 47).

Evidence for this type of substitution reaction was obtained by plotting the pseudo-first-order decomposition rate constant measured for the $[\mathbf{3}]^{2+/0}$ couple (61) against the concentration of AN (Fig. 5). The nonlinearity of the plot indicates a deviation from second-order behavior at high AN concentrations and thus the decomposition reaction was certainly not an associative process in which AN formed a transient coordinate intermediate with the neutral complex. A more chemically reasonable mechanism, and one which qualitatively fits the kinetic data in Fig. 5, was a dissociative interchange mechanism whereby $[\mathbf{3}]^0$ at least partially dissociates the arene ligand, and simultaneously adds one or more AN molecules (62). It should be noted, however, that distinguishing this mechanism from a completely dissociative process is not possible without activation parameters and that participation of a low-coordinate, fully dissociated intermediate during the decomposition reaction cannot be entirely ruled out (63). Because the ultimate fate of the AN-substituted product has been shown by CV in this work and by analysis in previous bulk electrolysis experiments (8, 9) to be neutral ferrocene and a decomplexed iron species, the reaction scheme given in Mechanism I has been proposed to explain the overall decomposition process associated with the $[\mathbf{3}]^{2+/0}$ couple. We have also been able to isolate and characterize these products using ^1H and ^{13}C NMR.

Although most of the experimental work reported herein centers on bimetallic systems ($[\mathbf{3}]^{2+}$–$[\mathbf{8}]^{2+}$), we have explored the electrochemical behavior of the pentairon polyether com-

Mechanism 1.

$$[\{(C_6H_5O)Fe^{II}Cp)\}_2C_6H_4]^{2+} + 2e^- \rightleftharpoons [\{(C_6H_5O)Fe^{I}Cp)\}_2C_6H_4]$$

$$[\{(C_6H_5O)Fe^{I}Cp)\}_2C_6H_4] + nS \xrightarrow{k} 2\,[S_n(Fe^{I}Cp)] + [(C_6H_5O)_2C_6H_4]$$

$$2\,[S_n(Fe^{I}Cp)]_2 \xrightarrow{\text{fast}} Fe^{II}(Cp)_2 + Fe^0 + 2nS$$

plex $[\mathbf{9}]^{5+}$. Our initial findings have shown that this complex exhibits voltammetry that is similar to the mono- and di-iron aryl ether complexes $[\mathbf{1}]^{2+}$ and $[\mathbf{3}]^{2+}$, namely, two distinct reduction processes centered at ca. −1.8 and −2.8 V vs. Fc/Fc^+. However, stability of the pentairon complex following the first reduction process appears to be much lower than that for either the mono- or di-iron analogues. Although this lower stability has made characterization of this redox process difficult, we are presently working towards characterizing the nature of the decomposition reaction and determining if indeed a total of five electrons are transferred to the complex during the first reduction step. Certainly, single reductive processes with such large multiplicity are decidedly rare. However, proof of such a system would indicate that these materials have a great deal of promise to behave as electron reservoirs.

Disulphide complexes

CV studies of bimetallic $CpFe^+$ complexes have been extended further to include sulphur-bridged aromatic compounds ($[\mathbf{4}]^{2+}$–$[\mathbf{6}]^{2+}$). Unlike the oxygen-bridged complex $[\mathbf{3}]^{2+}$, the sulphur-bridged complexes appear to show some measurable electronic communication between the iron centers on the CV time scale. In the case of the *o*- and *p*-substituted disulphide complexes ($[\mathbf{4}]^{2+}$ and $[\mathbf{6}]^{2+}$), two closely spaced processes are observed for the 36 e^-/38 e^- reduction waves corresponding to the reduction processes, which may be distinguished. Based on previous work by Bard and coworkers, it has been postulated that, for similar complexes, one metal moiety undergoes a reduction, which is closely followed by the reduction of the second metal moiety at a more negative potential (7). The presence of the sulphur bridge allows the increase in the electron density of the first iron moiety to be dispersed across to the second metal moiety, making it slightly more difficult to be reduced. Clearly, the behavior observed in the cyclic voltammetric results for $[\mathbf{4}]^{2+}$ and $[\mathbf{6}]^{2+}$ suggests that there is a small degree of electronic interaction between the two metals due to the presence of the sulphur bridge (64). The actual degree of communication can be gauged from the measured difference in formal potentials of the two one-electron reductions (ΔE^0). However, because waves for the distinct 36 e^-/37 e^- and 37 e^-/38 e^- reductions were severely overlapped for both $[\mathbf{4}]^{2+}$ and $[\mathbf{6}]^{2+}$, digital simulation of the CV wave shapes was used to extract the ΔE^0

Fig. 6. Cyclic voltammograms at Pt of 2 mM complex $[6]^{2+}$ in DMF containing 0.1 M TBAP; v = 0.1 V/s at 253 K. Simulated (bottom) and experimental (top).

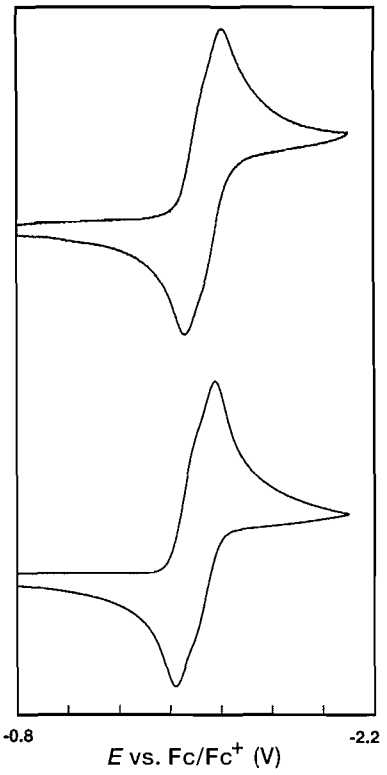

values. Simulation for complex $[6]^{2+}$ is shown in Fig. 6 along with the corresponding experimental voltammogram. Although small, the formal potential separations of ca. 70–80 mV measured for both complexes indicated a limited degree of electronic communication through the sulphur–arene bridge that was approximately the same for *para* and *ortho* substitution. Contrastingly, CV of the *meta* analogue $[5]^{2+}$ showed no measurable difference between formal potentials of its 36 e^-/37 e^- and 37 e^-/38 e^- couples, probably due to some electronic effects, and therefore behaved as if the iron centers were electronically isolated on the CV time scale.

As with the ether-bridged complex $[3]^{2+}$, the sulphide-bridged systems ($[4]^{2+}$–$[6]^{2+}$) also demonstrated instability of their 38 e^- species that caused solvent substitution and arene loss. However, the instability appeared to be much less pronounced for the sulphur analogues. Figure 7 compares the stability of the reduced complexes $[3]^0$ and $[5]^0$ in DMF. Although both 38 e^- species are unstable at room temperature, the sulphur-bridged analogue survives approximately five times longer than the ether-bridged species.

Sulphone complexes

The final group of bimetallic systems to be investigated in this work were complexes containing sulphone bridges ($[7]^{2+}$ and $[8]^{2+}$). Previous studies have shown that reduction of monoiron sulphones occurs at positive potentials of analogous aryl ether bridged complexes (9). Figure 8 compares voltammograms for the bimetallic sulphone $[8]^{2+}$, bimetallic ether $[3]^{2+}$, and the mixed bimetallic complex $[7]^{2+}$ recorded separately but in the same medium at 233 K. As found with the sulphide–arene bridged complexes $[4]^{2+}$ and $[6]^{2+}$, the bimetallic sulphone shows a small but finite potential separation between the 36 e^-/37 e^- and 37 e^-/38 e^- couples, suggesting some electronic communication between the iron centers of the molecule on the time scale of the CV measurement. A greater discrimination of the couples is observed for $[7]^{2+}$. However, this large formal potential separation of nearly 200 mV between the 36 e^-/37 e^- and 37 e^-/38 e^- couples was primarily due to the thermodynamically different iron environments and not to significantly enhanced electronic communication between the two centers. This clear observation of two one-electron reductions in the mixed complex lends further support to our claim that the initial reduction processes for all of our bimetallic complexes involve overall two-elecron reductions to 38 e^- species.

Fig. 7. Plot of temperature vs. the rate constant of the following chemical reaction for bimetallic complexes $[3]^{2+}$ and $[5]^{2+}$ in DMF.

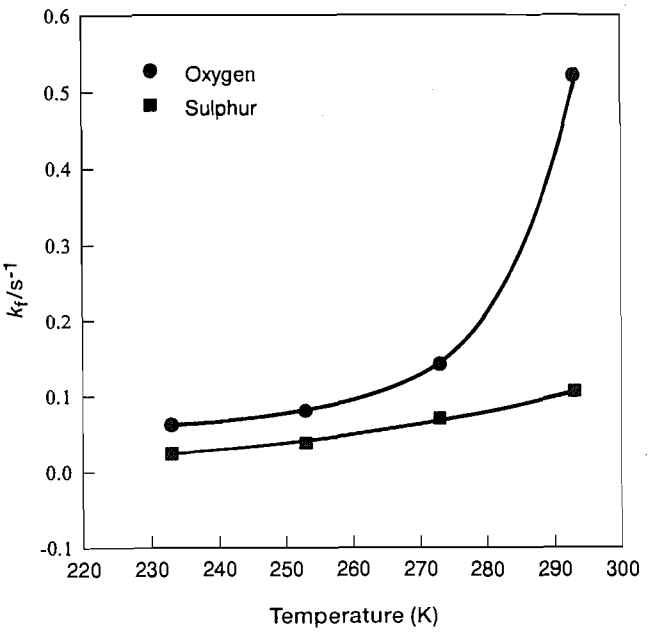

Conclusion

These electrochemical studies have clearly shown the effect of the bridging ligand on the communication between the two metallic centers in bis(cyclopentadienyliron) arene systems. For the etheric complexes ($[3]^{2+}$ and $[9]^{5+}$) it was found that the iron centers were isolated in all cases, and that the rate of the following chemical reaction increased with both an increase in temperature and the number of iron centers present. A series of isomeric di-iron sulphide complexes ($[4]^{2+}$–$[6]^{2+}$) were also studied and it was determined that electrochemical recognition was apparent for complexes $[4]^{2+}$ and $[6]^{2+}$, with a ΔE^0 of 70–80 mV, while complex $[5]^{2+}$ did not show this behavior. Comparison of the rate constants of the following chemical reaction between complexes $[3]^{2+}$ and $[5]^{2+}$ indicated that this rate was dependent on the temperature, and it was accelerated for the etheric system. This suggested that the stability of the neutral species was approximately five times greater in the complexes with a sulphide bridge. It was also found that the electrochemical behav-

Fig. 8. Cyclic voltammogram at Pt; $\upsilon = 0.2$ V/s; 233 K: (*a*) complex $[8]^{2+}$ in DMF containing 0.1 M TBAP; (*b*) complex $[3]^{2+}$ in DMF containing 0.1 M TBAP; (*c*) complex $[7]^{2+}$ in DMF containing 0.1 M TBAP.

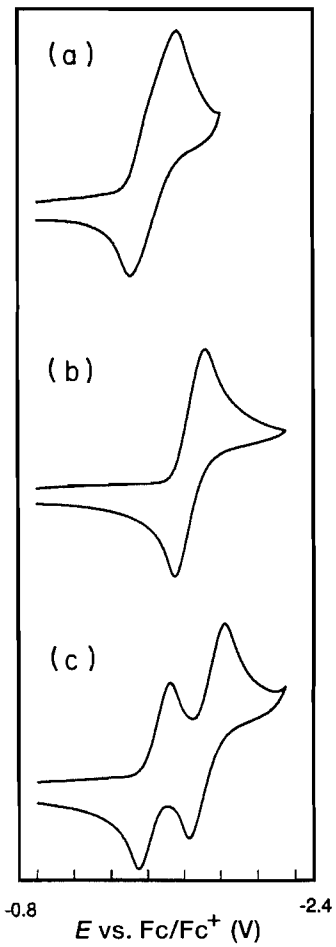

ior of complex $[3]^{2+}$ was greatly influenced by the solvent present. The effect of solvent on the kinetics was investigated using AN as the coordinating ligand, and it was found that there was a dependence of the following chemical reaction on the concentration of AN present. Controlled potential coulometry was used to determine that there were two electrons being transferred in the initial reduction step to produce the neutral radical species. Further evidence for a two-electron transfer was given by the investigation of complex $[7]^{2+}$, which contained a mixed oxygen–sulphone bridge. This complex indicated that two electrons were being transferred with a large ΔE^0 (200 mV) between the two reduction waves present, which led to a 38 e^- complex.

Acknowledgments

Financial support for this work provided by the Natural Sciences and Engineering Research Council of Canada (NSERC), American Chemical Society – Petroleum Research Fund, and Manitoba Hydro is gratefully acknowledged. C.R.D. thanks NSERC for a post-graduate scholarship. C.R.D. and K.M.E. (graduate students, University of Manitoba) also thank the Department of Chemistry, University of Manitoba.

References

1. D. Astruc. Electron transfer and radical processes in transition-metal chemistry. VCH, New York. 1995.
2. D.H. Evans. Chem. Rev. **90**, 739 (1990).
3. W.E. Geiger. Prog. Inorg. Chem. **33**, 275 (1985).
4. W.E. Geiger and N.G. Connelly. Adv. Organomet. Chem. **24**, 87 (1985).
5. N.G. Connelly and W.E. Geiger. Adv. Organomet. Chem. **23**, 1 (1984).
6. R.E. Dessy and L.A. Bares. Acc. Chem. Res. **5**, 415 (1972).
7. R.Q. Bligh, R. Moulton, A.J. Bard, A. Piorko, and R.G. Sutherland. Inorg. Chem. **28**, 2652 (1989).
8. A.S. Abd-El-Aziz, K. Winkler, and A.S. Baranski. Inorg. Chim. Acta, **194**, 207 (1992).
9. A.S. Abd-El-Aziz, A.S. Baranski, A. Piorko, and R.G. Sutherland. Inorg. Chim. Acta, **147**, 77 (1988).
10. D.T. Pierce and W.E. Geiger. J. Am. Chem. Soc. **114**, 6063 (1992).
11. L.I. Denisovich and S.P. Gubin. Russ. Chem. Rev. **46**, 27 (1977).
12. R. M. Neilsen and M. J. Weaver. Organometallics, **8**, 1636 (1989).
13. W.J. Bowyer and W.E. Geiger. J. Am. Chem. Soc. **107**, 5657 (1985).
14. J.D.L. Holloway and W.E. Geiger. J. Am. Chem. Soc. **101**, 2038 (1979).
15. J. Heinze. Top. Curr. Chem. **152**, 1 (1990).
16. J. Lukkari and J. Kankare. Synth. Met. **48**, 181(1992).
17. R. Moulton, T.W. Weidman, K.P.C. Vollhardt, and A.J. Bard. Inorg. Chem. **25**, 1846 (1986).
18. D. Albagli, G. Bazan, R.R. Schrock, and M.S. Wrighton. Mol. Cryst. Liq. Cryst. **216**, 123 (1992).
19. A.D. Hunter and A.B. Szigety. Organometallics, **8**, 2670 (1989).
20. I. Manners. Adv. Mater. **6**, 68 (1994).
21. D. A. Foucher, C. H. Honeyman, J. M. Nelson, B. Z. Tang, and I. Manners. Angew. Chem. Int. Ed. Engl. **32**, 1709 (1993).
22. P. F. Brandt and T. B. Rauchfuss. J. Am. Chem. Soc. **114**, 1926 (1992).
23. V. V. Dement'ev, F. Cervantes-lee, l. Parkanyi, H. Sharma, and K. H. Pannell. Organometallics, **12**, 1983 (1993).
24. D. Obendorf, H. Schottenberger, and C. Reiker. Organometallics, **10**, 1293 (1991).
25. M. Lacoste, H. Rabaa, D. Astruc, N. Ardoin, F. Varret, J-Y. Saillard, and A. Le Beuze. J. Am. Chem. Soc. **112**, 9548 (1990).
26. M.-H. Desbois and D. Astruc. Organometallics, **8**, 1841 (1989).
27. V. Guerchais and D. Astruc. J. Organomet. Chem. **316**, 335 (1986).
28. G.B. Richter-Addo and A.D. Hunter. Inorg. Chem. **28**, 4063 (1989).
29. M. Lacoste, F. Varret, L. Toupet, and D. Astruc. J. Am. Chem. Soc. **109**, 6504 1987).
30. M.-H. Desbois and D. Astruc. New J. Chem. **13**, 595 (1989).
31. C. Moinet, E. Roman, and D. Astruc. J. Electroanal. Chem. **121**, 241 (1981).
32. D. Astruc. Angew. Chem. Int. Ed. Engl. **27**, 643 (1988).
33. M. Chanon and M.L. Tobe. Angew. Chem. Int. Ed. Engl. **21**, 1 (1982).
34. D. Astruc. Top. Curr. Chem. **160**, 47 (1991).
35. J.-N. Verpeaux, M.-H. Desbois, A. Madonik, C. Amatore, and D. Astruc. Organometallics, **9**, 630 (1990).
36. D. Astruc. Acc. Chem. Res. **19**, 377 (1986).
37. R.G. Sutherland. J. Organomet. Chem. Lib. **3**, 311 (1977).
38. R.G. Sutherland, M. Iqbal, and A. Piorko. J. Organomet. Chem. **302**, 3007 (1986).

39. A.N. Nesmeyanov, N.A. Vol'kenau, L.S. Shilovtseva, and V.A. Petrokova. J. Organomet. Chem. **61**, 329 (1973).
40. N. El Murr. J. Chem. Soc. Chem. Commun. 251 (1981).
41. A.N. Nesmeyanov, L.I. Denisovich, S.P. Gubin, N.A. Vol'kenau, E.I. Sirotkina, and I.N. Bolesova. J. Organomet. Chem. **20**, 169 (1969).
42. S.P. Solodovnikov, N.A. Vol'Kenau, and L.C. Shilovtseva, Izv. Akad. Nauk SSSR, Ser. Khim. **8**, 1733 (1985).
43. A. Buet, A. Darchen, and C. Moinet. J. Chem. Soc. Chem. Commun. 447 (1979).
44. D. Astruc. New J. Chem. **16**, 305 (1992).
45. A. Darchen. J. Chem. Soc. Chem. Commun. 768 (1983).
46. D.C. Boyd, D.A. Bohling, and K.R. Mann. J. Am. Chem. Soc. **107**, 1641 (1985).
47. A. Darchen. J. Organomet. Chem. **302**, 389 (1986).
48. A.S. Abd-El-Aziz, A. Piorko, A.S. Baranski, and R.G. Sutherland. Synth. Commun. **19**, 1865 (1989).
49. R.G. Sutherland, A.S. Abd-El-Aziz, A. Piorko, A.S. Baranski, and C.C. Lee. Synth. Commun. **19**, 189 (1989).
50. C. Moinet, E. Roman, and D. Astruc. J. Electroanal. Chem. **121**, 241 (1981).
51. D. E. Richardson and H. Taube. Inorg. Chem. **20**, 1278 (1981).
52. J.B. Flanagan, S. Margel, A.J. Bard, and F.C. Anson. J. Am. Chem. Soc. **100**, 4248 (1978).
53. J.M. Mevs, T. Gennett, and W.E. Geiger. Organometallics, **10**, 1229 (1991).
54. A.J. Bard and L.R. Faulkner. Electrochemical methods: fundamentals and applications. John Wiley and Sons, New York. 1980.
55. D.T. Sawyer and J.L. Roberts. Experimental electrochemistry for chemists. John Wiley and Sons, New York. 1974.
56. R.L. Chowdhury, C.C. Lee, A. Piorko, and R.G. Sutherland. Synth. React. Inorg. Met.-Org. Chem. **15**, 1237 (1985).
57. A.S. Abd-El Aziz, K.M. Epp, C.R. de Denus, and G. Fisher-Smith. Organometallics, **13**, 2399 (1993).
58. A.S. Abd-El-Aziz, C.R. de Denus, M. Zaworotko, and L.R. MacGillvray. J. Chem. Soc. Dalton Trans. 3375 (1995).
59. R.D. Rieker, I. Tucker, S.N. Milligan, D.R. Wright, B.R. Willeford, L.J. Radonovich, and M.W. Eyring. Organometallics, **1**, 938 (1982).
60. N. Van Order, Jr., W.E. Gieger, T.E. Bitterwolf, and A.L. Rheingold. J. Am. Chem. Soc. **109**, 5680 (1987).
61. R.S. Nicholson and I. Shain. Anal. Chem. **36**, 706 (1964).
62. R.B. Jordan. Reaction mechanisms of inorganic and organometallic systems. Oxford University Press, New York. 1991.
63. R.G. Wilkins. Kinetics and mechanisms of reactions of transition metal complexes. VCH, New York. 1991.
64. J. Heinze. Angew. Chem. Int. Ed. Engl. **23**, 831 (1984).

Electron transfer kinetics of cobaloxime complexes[1]

Kefei Wang and R.B. Jordan

Abstract: The rates of oxidation of $Co^{II}(dmgBF_2)_2(OH_2)_2$ by $Co^{III}(NH_3)_5X^{2+}$ (X = Br^-, Cl^-, and N_3^-) have been studied at 25°C in 0.10 M $LiClO_4$. The rate constants are 50 ± 9, 2.6 ± 0.2, and 5.9 ± 1.0 M^{-1} s^{-1} for X = Br^-, Cl^-, and N_3^-, respectively, in 0.01 M acetate buffer at pH 4.7. The relative rates are consistent with the inner-sphere bridging mechanism established earlier by Adin and Espenson for the analogous reactions of $Co^{II}(dmgH)_2(OH_2)_2$. The rate constants with $Co^{II}(dmgBF_2)_2(OH_2)_2$ typically are $\sim 10^3$ times smaller and this is attributed largely to the smaller driving force for the $Co^{II}(dmgBF_2)_2(OH_2)_2$ complex. The outer-sphere oxidations of cobalt(II) sepulchrate by $Co^{III}(dmgH)_2(OH_2)_2^+$ (pH 4.76–7.35, acetate, MES, and PIPES buffers) and $Co^{III}(dmgBF_2)_2(OH_2)_2^+$ (pH 3.3–7.42, chloroacetate, acetate, MES, and PIPES buffers) have been studied. The pH dependence gives the following rate constants (M^{-1} s^{-1}) for the species indicated: (1.55 ± 0.09) × 10^5 ($Co^{III}(dmgBF_2)_2(OH_2)_2^+$); (5.5 ± 0.3) × 10^3 ($Co^{III}(dmgH)_2(OH_2)_2^+$); (3.1 ± 0.5) × 10^2 ($Co^{III}(dmgH)_2(OH_2)(OH)$); (2.5 ± 0.3) × 10^2 ($Co^{III}(dmgBF_2)_2(OH_2)(OH)$). The known reduction potentials for cobalt(III) sepulchrate and the diaqua complexes, and the self-exchange rate for cobalt(II/III) sepulchrate, are used to estimate the self-exchange rate constants for the dioximate complexes. Comparisons to other reactions with cobalt sepulchrate indicates best estimates of the self-exchange rate constants are $\sim 2.4 \times 10^{-2}$ M^{-1} s^{-1} for $Co^{II/III}(dmgH)_2(OH_2)_2$ and $\sim 5.7 \times 10^{-3}$ M^{-1} s^{-1} for $Co^{II/III}(dmgBF_2)_2(OH_2)_2$.

Key words: electron transfer, cobaloxime, inner sphere, outer sphere, self-exchange.

Résumé : Opérant à 25°C, en solutions à 0,10 M de $LiClO_4$, on a étudié les vitesses d'oxydation du $Co^{II}(dmgBF_2)_2(OH_2)_2$ par du $Co^{III}(NH_3)_5X^{2+}$ (X = Br^-, Cl^- et N_3^-). Les constantes de vitesse sont de 50 ± 9, 2,6 ± 2 et 5,9 ± 1,0 respectivement pour X = Br^-, Cl^- et N_3^- dans un tampon acétate à 0,01 M, à un pH de 4,7. Les constantes de vitesse sont en accord avec un mécanisme de formation de pont dans la couche interne démontrée antérieurement par Adin et Espenson pour les réactions analogues du $Co^{II}(dmgH)_2(OH_2)_2$. Les constantes de vitesse pour le $Co^{II}(dmgBF_2)_2(OH_2)_2$ sont en général 1000 moins rapides et on attribue ce résultat principalement à une force motrice plus faible pour le complexe du $Co^{II}(dmgBF_2)_2(OH_2)_2$. On a aussi étudié es oxydations dans la couche externe du sépulcrate de cobalt(II) par le $Co^{III}(dmgH)_2(OH_2)_2^+$ (pH de 4,76 à 7.35, tampons acétate, MES et PIPES) et par le $Co^{III}(dmgBF_2)_2(OH_2)_2^+$ (pH de 3,3 à 7,42, tampons chloroacétate, acétate, MES et PIPES). Les relations avec le pH conduisent aux constantes de vitesse suivantes (M^{-1} s^{-1}) pour les espèces indiquées : (1,55 ± 0,09) × 10^5 ($Co^{III}(dmgBF_2)_2(OH_2)_2^+$); (5,5 ± 0,3) × 10^3 ($Co^{III}(dmgH)_2(OH_2)_2^+$); (3,1 ± 0,5) × 10^2 ($Co^{III}(dmgH)_2(OH_2)(OH)$); (2,5 ± 0,3) × 10^2 ($Co^{III}(dmgBF_2)_2(OH_2)(OH)$). On a utilisé les potentiels connus de réduction du sépulcrate de cobalt(III) et des complexes diaqua ainsi que la vitesse d'autoéchange pour le sépulcrate de cobalt(II/III) pour évaluer les constantes de vitesse d'autoéchange pour les complexes dioximates. Des comparaisons avec d'autres réactions du sépulcrate de cobalt indiquent que les meilleures évaluations des constantes de vitesse d'autoéchange sont d'environ 2,4 × 10^{-2} M^{-1} s^{-1} pour le $Co^{II/III}(dmgH)_2(OH_2)_2$ et d'environ 5,7 × 10^{-3} M^{-1} s^{-1} pour le $Co^{II/III}(dmgBF_2)_2(OH_2)_2$.

Mots clés : transfert d'électrons, cobaloxime, sphère interne, sphère externe, autoéchange.

[Traduit par la rédaction]

Introduction

The bis(dimethylglyoximato)cobalt(II) complexes ($Co^{II}(dmgH)_2$) are models for the B_{12r} state of coenzyme B_{12} (1). They are mild reducing agents, and the electron transfer can be either by an inner-sphere or an outer-sphere mechanism,

Received November 16, 1995.

K. Wang and R.B. Jordan.[2] Department of Chemistry, University of Alberta, Edmonton, AB T6G 2G2, Canada.

[1] This paper is dedicated to Professor Henry Taube on the occasion of the celebration, at the University of Saskatchewan, of his many accomplishments.

[2] Author to whom correspondence may be addressed. Telephone: (403) 492-5551. Fax: (403) 492-8231. E-mail: Bob.Jordan@Ualberta.ca

Scheme 1.

$$(H_3N)_5Co^{III}X + (H_2O)_2Co^{II}L \xrightleftharpoons{fast} (H_3N)_5Co^{III}\text{-}X\text{-}Co^{II}(OH_2)L + H_2O$$

$$(H_3N)_5Co^{III}\text{-}X\text{-}Co^{II}(OH_2)L \xrightarrow{k_{et}} (H_3N)_5Co^{II}\text{-}X\text{-}Co^{III}(OH_2)L$$

$$(H_3N)_5Co^{II}\text{-}X\text{-}Co^{III}(OH_2)L \xrightarrow{fast} Co^{II} + 5NH_3 + XCo^{III}(OH_2)L$$

depending on the nature of the oxidant. It has been shown (2) that the oxidation of $Co^{II}(dmgH)_2(OH_2)_2$ by $Co^{III}(NH_3)_5X^{2+}$ (X = halide and pseudohalide) proceeds by the classical X-bridged inner-sphere pathway (3) shown in Scheme 1 (L = $(dmgH)_2$, charges are omitted) by identifying the bridge-transferred product $Co^{III}(dmgH)_2(X)(OH_2)$.

Part of the present study concerns the rates of oxidation of $Co^{II}(dmgBF_2)_2(OH_2)_2$ by $Co^{III}(NH_3)_5X^{2+}$ (X = Br^-, Cl^-, and N_3^-). A comparison of these results with those of Adin and

[1] 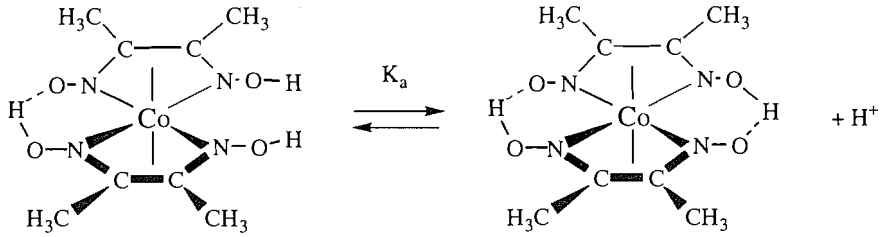

1 2

Espenson (2) on $Co^{II}(dmgH)_2(OH_2)_2$ provides some measure of the effect of the -BF_2 substituents on the inner-sphere reactivity of these systems.

Studies of the reduction of the cobalt(III) derivatives have yielded less definitive mechanistic results. Prince and Segal (4), Balasubramanian et al. (5), and Dayalan and Vijayaraghavan (6) have studied the reduction of various $Co^{III}(dmgH)_2(L)_2^+$ and $Co^{III}(dmgH)_2(X)(L)$ (X = halide or pseudohalide, L = amine or pyridine) complexes by aqueous V^{2+}, Fe^{2+}, and Cr^{2+}. These studies were done in acidic media (pH < 3), and the $[H^+]$ dependence of the reaction rate was used as an important criterion to assign the mechanism. The $[H^+]$ dependence is attributed to protonation equilibrium of the $dmgH^-$ ligand, possibly as shown in eq. [1]. If eq. [1] is a rapidly maintained pre-equilibrium, then the apparent second-order rate constant is given by eq. [2],

$$[2] \qquad k_2 = \frac{k_0 K_a + k_H[H^+]}{K_a + [H^+]}$$

where k_H and k_0 are specific rate constants for reduction of the protonated (**1**) and unprotonated (**2**) complexes, respectively. In general, reductions by V^{2+} are either independent or first order in $[H^+]$ and may be controlled by substitution on $V(OH_2)_6^{2+}$ in some cases. The reactions with $Fe(OH_2)_6^{2+}$ show independent and inverse $[H^+]$ dependencies and the rate order is $I^- > Br^- > Cl^-$ for the reduction of $Co^{III}(dmgH)_2(py)(X)$ (6). This order is opposite to that for reduction of the $Co^{III}(NH_3)_5X^{2+}$ complexes, and was suggested as evidence for bridging through the oximate rather than the halide ligand. The $[H^+]^{-1}$ dependence of the Fe^{2+} reduction of $Co^{III}(dmgH)_2(py)(X)$ (6) also was taken to support such an oximate ligand bridged pathway. The bridged intermediate may be pictured as in **3**, which has some precedent from the complexation of $Co^{III}(dmgH)_2(OH_2)_2^+$ by aqueous iron(III) (7).

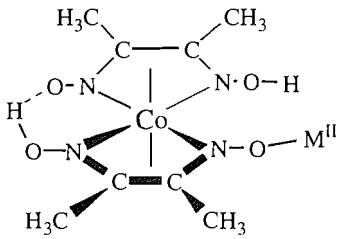

3

The most definitive criterion for establishing an inner-sphere mechanism is to identify the bridging ligand transferred product (3, 8). This is best done with Cr^{2+} as the reducing agent because the Cr^{III} product is substitution inert and can be separated and identified by standard methods. Unfortunately, only rather limited studies of this type have been done. Segal and Prince studied the $Cr^{2+} + Co^{III}(dmgH)_2(NH_3)_2^+$ reaction ($k_2 = 40 + 780 \times [H^+]$ M^{-1} s^{-1}, 25°C) and initially reported no bridge-transferred product, but later (4*c*) separated, by ion-exchange chromatography, a fraction containing $dmgH^-$ and Cr^{3+}. Balasubramanian and Vijayaraghavan (5*b*) did a product study for the Cr^{2+} reductions of $Co^{III}(dmgH)_2(N_3)(NH_3)$ and $Co^{III}(dmgH)_2(N_3)_2^-$ and reported the product ratios $Cr(dmgH)^+/CrN_3^{2+}$ of 2:1 and 1:2, respectively. These results indicate competitive bridging by the azide and oximate ligands, with the latter being more important for the neutral complex. However, it remains possible that the $Cr(dmgH)^+$ was produced by oxidation of a Cr^{2+}–dmgH complex during product analysis.

The main inconsistency between these studies is in the magnitude of K_a (eq. [1]). Prince and Segal (4) determined an approximate value of 0.25 M for $Co^{III}(dmgH)_2(NH_3)_2^+$; Balasubramanian et al. (5) and Dayalan and Vijayaraghavan (6) find values of $(1–7) \times 10^{-3}$ M for various $Co^{III}(dmgH)_2(X)(L)$ species. This difference might be ascribed to the charge on the complexes, but Adin and Espenson (9) had found earlier that $K_a \approx$ Å 0.3 M for various neutral alkyl species, $Co^{III}(dmgH)_2(R)(OH_2)$.

There are no reports of definite outer-sphere reductions of the cobaloxime(III). However, outer-sphere reductions of structurally similar Co(III) tetraaza macrocyclic complexes have been studied extensively by Endicott and co-workers (10–14). In these complexes, the tetraaza ligands form a square-planar chelating ring binding to the Co cation, with the two axial positions of Co occupied by water ligands. The cross reactions between these $Co^{III}(N_4)(OH_2)_2^{3+}$ and $Co^{II}(N'_4)(OH_2)_2^{2+}$ (N_4 and N'_4 represent different tetraaza macrocyclic ligands) are supposed to be outer sphere, and the cross-reaction rates have been determined and used with Marcus theory to calculate the rates for the electron self-exchange. The self-exchange rates were discussed in terms of the Franck–Condon barrier, which is the inner-sphere reorganization energy resulting from the bond length changes accompanying the electron-transfer process. In addition to being structurally analogous to the tetraaza complexes, the cobalt(II)–dioximes are also low spin, and provide further examples to test the effect of this feature on Co(III)/Co(II) self-exchange rates. Most Co(III)/Co(II) exchanges involve high-spin cobalt(II) and there has been some disagreement (15–22) on the influence of the spin state change on the electron exchange rate.

The present study reports the first outer-sphere reduction of $Co^{III}(dmgH)_2^+$ and $Co^{III}(dmgBF_2)_2^+$ by using the cobalt(II) sepulchrate ion ($Co(sep)^{2+}$) as the reducing agent. In $Co(sep)^{2+}$ (**4**), the cobalt(II) ion is encapsulated within a macrocyclic ligand cage.

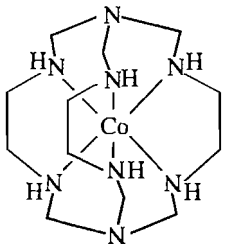

4

The cage ligand prevents substitution on the cobalt(II) ion, so that the electron-transfer from $Co(sep)^{2+}$ to the cobaloximes(III) must be via an outer-sphere mechanism. The observed reaction rates are used to estimate the cobaloxime(III)/(II) electron self-exchange rates by the Marcus cross relationship and the results are compared to those of various $Co(N_4)(OH_2)_2^{3+/2+}$ complexes.

Experimental section

Materials

$Co(dmgBF_2)_2{\cdot}2H_2O$ was prepared according to Bakac et al. (23) $[Co^{III}(dmgH)_2(OH_2)_2]ClO_4$ was prepared by the method of Ablov et al. (24–26) through a series of cobaloxime(III) intermediates as described below.

$[Co^{III}(dmgH_2)(dmgH)Cl_2]{\cdot}2H_2O$, trans-*dichlorobis(dimethylglyoximato)cobalt(III) (ref. 24)*

A finely ground mixture of 2.38 g (0.01 mol) of $CoCl_2{\cdot}6H_2O$ (Fisher) and 2.32 g (0.01 mol) of dimethylglyoxime ($dmgH_2$, Fisher), was treated with ~15 mL of water and the slurry was stirred on a hot plate at 70–80°C for 15 min. The heating was turned off and 3–4 mL of H_2O_2 (30%, Fisher) were added slowly with stirring . The excess H_2O_2 was removed by boiling the solution for about 10 min, and ~30 mL of concentrated HCl (36%, BDH) was added to yield a dark-green precipitate. The mixture was cooled to room temperature, and then in an ice bath. The solid product was collected on a sintered glass filter and washed twice with dilute HCl (5% v/v), ethanol, and diethyl ether. Yield: 80%. The product was formulated as $[Co^{III}(dmg_2H_3)Cl_2]{\cdot}2H_2O$ according to the elemental analysis. Anal. calcd. for $[Co(C_4H_6O_2N_2)_2H_3Cl_2]{\cdot}2H_2O$: C 24.2, H 4.78, N 14.1, Cl 17.9; found: C 24.4, H 4.88, N 13.9, Cl 18.2. The NMR spectrum of this complex in d_6-DMSO shows methyl protons at 2.35 ppm and water as a broad peak at 7.5 ppm. The methyl proton resonance is shifted 0.44 ppm downfield from that in $dmgH_2$ (1.91 ppm). The shift upon coordination of $dmgH^-$ to cobalt(III) is consistent with the reported value of ~0.4 ppm for other cobaloxime(III) complexes (27).

$[Co^{III}(dmgH)_2Cl(H_2O)]$, trans-*chloroaquabis(dimethylglyoximato)cobalt(III)*

This product was prepared by aquation of $[Co^{III}(dmg_2H_3)Cl_2]{\cdot}2H_2O$ (22). The dichloro salt (1.8 g) was covered with 6–8 mL of boiling water and the mixture was stirred for 20 min on a steam bath, and then cooled in ice. The greenish yellow solid obtained by filtration was washed twice with ice-cold water, ethanol, and diethyl ether. Yield: 75–85%.

$[Co^{III}(dmgH)_2(OH)(OH_2)]$, trans-*hydroxoaquabis(dimethylglyoximato)cobalt(III) (ref. 23)*

$[Co^{III}(dmgH)_2Cl(OH_2)]$ (1.4 g) was covered with ~4 mL of a cold aqueous saturated Na_2CO_3 solution, and the mixture was stirred until the color changed from a yellowish green to gray-yellow. The precipitate was collected by filtration, washed twice with small amounts of cold water and cold ethanol, and finally with diethyl ether. Yield: 55%.

$[Co^{III}(dmgH)_2(OH_2)_2]ClO_4{\cdot}H_2O$, trans-*diaquobis(dimethylglyoximato)cobalt(III) perchlorate (ref. 26)*

When 0.7 g of $[Co(dmgH)_2(OH)(OH_2)]$ was dissolved in 4 mL of 2 M $HClO_4$, a yellowish brown solid precipitated, and more was formed when a few drops of concentrated $HClO_4$ were added. The product was collected by filtration, and washed twice with small amounts of ice-cold water and methanol, and finally with diethyl ether. Yield: 35%. The product was formulated based on the elemental analysis. Anal. calcd. for $[Co(C_4H_7O_2N_2)_2(OH_2)_2]ClO_4{\cdot}H_2O$: C 21.7, H 4.55, N 12.7; found: C 21.6, H 4.62, N 12.4. The NMR spectrum in d_6-DMSO shows the methyl protons at 2.54 ppm, and the water protons as a broad peak at 7.4 ppm. The electronic spectrum has a maximum at 240 nm with a molar absorptivity coefficient of 2.2×10^4 M^{-1} cm^{-1}, consistent with the values of 2.1×10^4 M^{-1} cm^{-1} (240 nm) and 1.95×10^4 M^{-1} cm^{-1} (238 nm) reported by Heckman and Espenson (28) and Kita and Jordan (29), respectively. Reduction of this complex in aqueous solution with amalgamated zinc under an argon atmosphere produces a bright yellow solution of $Co^{II}(dmgH)_2(OH_2)_2$. This species has a distinctive absorption maximum at 462 nm, with a molar absorptivity coefficient of 3.42×10^3 M^{-1} cm^{-1}, in agreement with a reported value of 3.40×10^3 M^{-1} cm^{-1} (28).

Solutions of $Co^{III}(dmgBF_2)_2(OH_2)_2^+$ were prepared by electrolysis of $Co^{II}(dmgBF_2)_2(OH_2)_2$ immediately before use. The electrolysis was done in an H-shaped electrolysis cell, with a sintered glass filter (10–20 μm) separating the anode and cathode compartments. The cathode was $Cu^{2+}(aq)/Cu$, and the anode was Pt in the $Co^{II}(dmgBF_2)_2$ solution. $LiClO_4$ (Amend) was added as the supporting electrolyte at a concentration of 0.09 M in both compartments. To avoid diffusion of Cu^{2+} ion into the anode compartment, the small amount of $Cu(NO_3)_2$ solution was carefully placed with a dropper at the bottom of the cathode compartment, and only the anode tube was stirred during the electrolysis. The electrolysis was carried out at ~1 V and 0.4–0.6 mA for 0.5–1 h, during which time most of the yellow color of the $Co^{II}(dmgBF_2)_2$ solution faded. If acetate buffer was required for the kinetic studies, the buffer was added to the solution of $Co^{II}(dmgBF_2)_2$ at pH ~ 4.7. The pH was adjusted with NaOH to the desired values for kinetic studies after the electrolysis.

The two halopentaamminecobalt(III) complexes, $[(H_3N)_5CoCl](ClO_4)_2$ (30) and $[(H_3N)_5CoBr](ClO_4)_2$ (30), and the azidopentaamminecobalt(III) complex $[(H_3N)_5CoN_3]Cl_2$ (31) were prepared according to the published methods.

1,3,6,8,10,13,16,19-Octaazabicyclo[6.6.6]eicosanecobalt-(III) trichloride (cobalt(III) sepulchrate trichloride, or $Co(sep)Cl_3$) was obtained from Aldrich, and the solution of $Co(sep)^{2+}$ was prepared by reduction of the cobalt(III) sepulchrate solution over amalgamated zinc under argon.

Redistilled water was used in all preparations and kinetic studies. Other chemicals used in the preparations are of reagent or analytical grade. For buffer preparations, sodium acetate was from Fisher, chloroacetic acid from BDH, and MES hydrate and PIPES from Aldrich.

Kinetic measurements

All kinetic runs were carried out at 25 ± 0.2°C. The ionic strength was maintained at 0.100 M with $LiClO_4$, and the total buffer concentration is 0.01 M. Acetate buffer was used in the studies of $Co^{II}(dmgBF_2)_2(OH_2)_2$ with $(H_3N)_5CoX^{2+}$, and the pH was kept at 4.72 ± 0.02 for all runs. Other buffers, MES, PIPES, and chloroacetic acid, were used in appropriate pH ranges in the studies of the cobaloxime(III)–$Co(sep)^{2+}$ system. The pH of each solution was measured with a Corning 125 pH meter.

The absorbance decrease due to the oxidation of $Co^{II}(dmgBF_2)_2(OH_2)_2$ by $(H_3N)_5CoCl^{2+}$ and $(H_3N)_5CoN_3^{2+}$ was followed on a Hewlett Packard 8451 diode array spectrophotometer at 454 nm, with the oxidant in excess. A 5.0 cm cylindrical spectrophotometer cell was used, and the reactant solutions were degassed with argon before measurement. The absorbance–time data (80 points over 3–4 half-lives) were analyzed by least squares to obtain the first-order rate constants. The reported second-order rate constants are the average of three measurements at different $(H_3N)_5CoX^{2+}$ concentrations.

The reaction between $(H_3N)_5CoBr^{2+}$ and $Co^{II}(dmgBF_2)_2(OH_2)_2$ was observed on a stopped-flow spectrophotometer (Cantech Scientific Ltd) at 454 nm. The data (256 points/trace) were collected to an MS-DOS 486 computer and at least 150 points for each trace were analyzed by least squares to give the first-order rate constants. The reported rate constants are the averages of at least six runs at each of three oxidant concentrations.

The kinetics of reduction of $Co^{III}(dmgH)_2(OH_2)_2^+$ and $Co^{III}(dmgBF_2)_2(OH_2)_2^+$ by $Co(sep)^{2+}$ were followed by stopped-flow spectrophotometry at 460 nm and 452 nm, respectively, with the $Co(sep)^{2+}$ in excess. The kinetic measurements were performed under anaerobic conditions, since the $Co(sep)^{2+}$ can reduce O_2 in the acidic media to produce H_2O_2, and $Co^{II}(dmgH)_2(OH_2)_2$ is extremely sensitive to O_2 and H_2O_2. The $Co(sep)^{2+}$ solution was transferred to the stopped-flow storage syringe through a serum cap under argon and the cobaloxime(III) solution in the other syringe was capped with a serum cap and degassed with argon for at least 20 min. The reduction of $Co^{III}(dmgH)_2(OH_2)_2^+$ shows biphasic behavior due to the formation and then decomposition of $Co^{II}(dmgH)_2(OH_2)_2$. The absorbance–time profiles were fitted to a biphasic model to obtain the first-order rate constants for the reduction and decomposition.

Results and discussion

Oxidation of $Co^{II}(dmgBF_2)_2(OH_2)_2$ by $(H_3N)_5CoX^{2+}$

For each system, the rate was studied at three cobalt(III) complex concentrations in at least 10-fold excess over the $Co^{II}(dmgBF_2)_2(OH_2)_2$ concentration in 0.01 M acetate buffer at pH 4.72. The observations indicate that the rate is first order in each reactant, and the second-order rate constants k_2 are collected in Table 1 along with the results reported by Adin and Espenson (2) on the oxidation of $Co^{II}(dmgH)_2(OH_2)_2$.

Table 1. Kinetic data for reactions between $(H_3N)_5Co^{III}X^{2+}$ and diaquacobaloximes(II).[a]

	$k_2(M^{-1}\ s^{-1})$[b]	
X^-	$(H_2O)_2Co^{II}(dmgH)_2$[c]	$(H_2O)_2Co^{II}(dmgBF_2)_2$[d]
Br	$(3.2 \pm 0.3) \times 10^5$	50 ± 9
Cl	$(1.4 \pm 0.08) \times 10^4$	2.6 ± 0.2
N_3	$(6.4 \pm 0.3) \times 10^3$	5.9 ± 1.0
NCS	$(1.4 \pm 0.08) \times 10^2$	
OH	$(7.7 \pm 1.5) \times 10^2$	
F	10.5 ± 0.9	

[a]At 25°C in acetate buffer (0.01 M) with μ = 0.10 M by $LiClO_4$.
[b]Errors quoted are one standard deviation.
[c]At 25°C in acetate buffer, from ref. 2.
[d]pH = 4.74.

Adin and Espenson established a bridged inner-sphere mechanism for oxidation of $Co^{II}(dmgH)_2(OH_2)_2$ by $(NH_3)_5CoX^{2+}$ ($Br^- > Cl^- \gg F^-$) by the identification of $Co^{III}(dmgH)_2(X)(OH_2)$ as the exclusive product. They interpreted the variation of k_2 with bridging ligands as the order of stability of the X-bridged precursor complexes following the analysis suggested by Haim (32). The order of k_2 values suggests soft-acid character for the $Co^{II}(dmgH)_2(OH_2)_2$ complex.

A common inner-sphere mechanism for the $Co^{II}(dmgBF_2)_2(OH_2)_2$ and $Co^{II}(dmgH)_2(OH_2)_2$ reductants is consistent with the rate constant ratio $k_{2Br}/k_{2Cl} \approx 20$ for both cobaloxime(II) complexes. For $X = Cl^-$ and N_3^-, the reactivity difference is smaller for both $Co^{II}(dmgBF_2)_2(OH_2)_2$ and $Co^{II}(dmgH)_2(H_2O)_2$, with k_{2Cl}/k_{2N_3} ratio of ~0.4 in the former and ~2 for the latter. The different order may be due to some differences in affinity of Cl^- and N_3^- toward the two cobaloxime(II) complexes. For the outer-sphere reduction of $(H_3N)_5CoX^{2+}$ by $Ru(NH_3)_6^{2+}$ (33), the ratios k_{2Br}/k_{2Cl} and k_{2Cl}/k_{2N_3} of 6 and ~140, respectively, also indicate an inner-sphere mechanism of the cobalt(II) oximes.

The values of k_2 for $Co^{II}(dmgBF_2)_2(OH_2)_2$ oxidations are (1–6) × 10^3 times smaller than those of the $Co^{II}(dmgH)_2(OH_2)_2$ complex. Since the substitution lability for these two cobaloxime(II) complexes is not expected to differ substantially, based on our observed comparable solvent exchange rates for the two complexes (34), the large difference in the k_2 values indicate that the bridge-mediated electron-transfer process is rate controlling in the inner-sphere mechanism. The slower oxidation of $Co^{II}(dmgBF_2)_2(OH_2)_2$ may be due to its less favorable reduction potential of 0.65 V (NHE) compared to 0.36 V (NHE) for $Co^{II}(dmgH)_2(OH_2)_2$. If the Marcus theory (35) prediction of a square-root dependence of the rate on the equilibrium constant is also applicable to these inner-sphere electron transfers, then $Co^{II}(dmgH)_2(OH_2)_2$ is predicted to be ca. 2.8 × 10^2 more reactive. This factor would account in large part for the reactivity difference of the

Table 2. Kinetic results for reactions of cobaloxime(III) with $Co(sep)^{2+}$.[a]

Cobaloxime(III)	k_a or k_b, M^{-1} s^{-1}	pK_a	E° (V)[b]
$(H_2O)_2Co(dmgBF_2)_2^+$	$(1.55 \pm 0.09) \times 10^5$	4.40 ± 0.03	0.36
$(H_2O)_2Co(dmgH)_2^+$	$(5.53 \pm 0.33) \times 10^3$	5.78 ± 0.07	0.65
$(HO)(H_2O)Co(dmgH)_2$	$(3.11 \pm 0.45) \times 10^2$		0.17
$(HO)(H_2O)Co(dmgBF_2)_2$	$(2.46 \pm 0.30) \times 10^2$		0.38

[a]At 25°C with $\mu = 0.10$ M. Errors quoted are one standard deviation.
[b]Estimated as described in text vs. NHE by assuming a $pK_a' = 9$ for $Co^{II}L(OH_2)_2$ (L = $(dmgH)_2$ and $(dmgBF_2)_2$).

Fig. 1. pH dependence of the second-order rate constants for reduction of $Co^{III}(dmgH)_2$ by $Co(sep)^{2+}$ (25°C, $\mu = 0.10$ M, the calculated curve is generated by using parameters in Table 2).

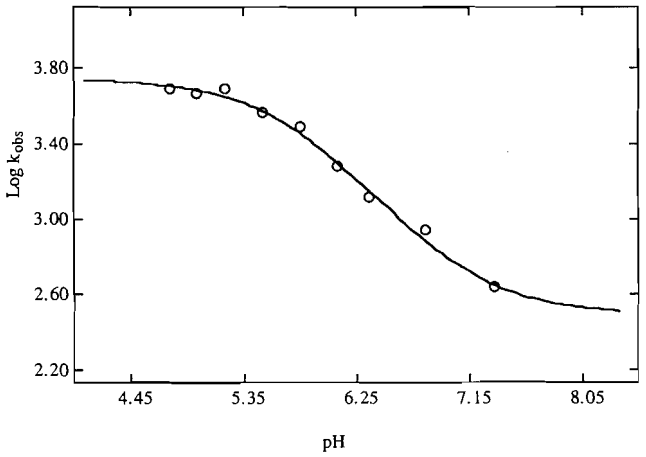

Fig. 2. pH dependence of the second-order rate constants for reduction of $Co^{III}(dmgBF_2)_2$ by $Co(sep)^{2+}$ (25°C, $\mu = 0.10$ M, the calculated curve is generated by using parameters in Table 2).

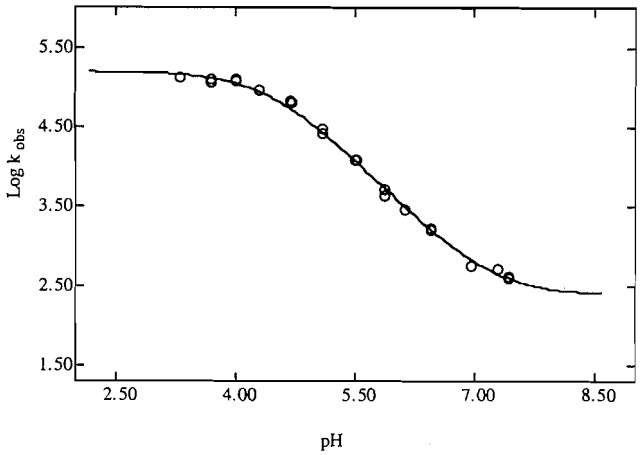

cobaloximes, and the remaining factor of ~10 could be attributed to less favorable precursor complex formation with $Co^{II}(dmgBF_2)_2(OH_2)_2$.

Reduction of cobaloximes(III) by $Co(sep)^{2+}$

The second-order rate constants for reduction of $Co^{III}(dmgH)_2(OH_2)_2^+$ and $Co^{III}(dmgBF_2)_2(OH_2)_2^+$ by cobalt(II) sepulchrate decrease with the acidity, as shown in Figs. 1 and 2, respectively. This dependence suggests an equilibrium involving the dissociation of the proton from the axial coordinated water, as shown in Scheme 2, with the diaqua form more reactive than the hydroxoaqua form.

Scheme 2.

$$(H_2O)_2Co^{III}L^+ \underset{}{\overset{K_a}{\rightleftharpoons}} (HO)(H_2O)Co^{III}L + H^+$$

$$(H_2O)_2Co^{III}L + Co(sep)^{2+} \xrightarrow{k_a} (H_2O)_2Co^{II}L + Co(sep)^{3+}$$

$$(HO)(H_2O)Co^{III}L + Co(sep)^{2+} \xrightarrow{k_b} (HO)(H_2O)Co^{II}L^- + Co(sep)^{3+}$$

L = $(dmgH)_2$ or $(dmgBF_2)_2$

From Scheme 2, the observed second-order rate constant k_{obs} is given by eq. [3]:

$$[3] \qquad k_{obs} = \frac{k_a[H^+] + k_bK_a}{K_a + [H^+]}$$

The values of pK_a, k_a, and k_b, obtained by least-squares analysis of the observed k_{obs} vs. $[H^+]$ data, are given in Table 2, and are used to obtain the calculated curves shown in Figs. 1 and 2.

The pK_a of 5.78 for $Co(dmgH)_2(OH_2)_2^+$ is in reasonable agreement with the value of 5.14 ± 0.02 (at 25°C, in 0.1 M $NaClO_4$) obtained from potentiometric titration by Ablov et al. (36). For $Co(dmgBF_2)_2(OH_2)_2^+$, the pK_a is lower by 1.4 units, as might be expected from the electron-withdrawing effect of the $-BF_2$ substituents in the modified macrocycle. In the pH ranges of our kinetic studies (4.8–7.4 for $Co^{III}(dmgH)_2^+$ and 3.3–7.4 for $Co^{III}(dmgBF_2)_2^+$), neither the ionization of the second proton ($pK_{a2} = 8.38 \pm 0.03$ for $Co^{III}(dmgH)_2(OH_2)_2^+$ (34)) nor the protonation of the dmgH ligand (eq. [1], $pK_a \sim 0.5$ (2) or ~2.5 (3, 4)) seems to have an influence on the k_{obs} measurement.

To analyse the reduction rate constants in terms of Marcus theory, one requires the reduction potentials of the reactants. These are known for $Co(sep)^{3+}$ and for the diaqua complexes, $Co(dmgH)_2(OH_2)_2^+$ and $Co(dmgBF_2)_2(OH_2)_2^+$, but not for the corresponding hydroxo complexes. The latter values have been estimated from the reaction cycle in Scheme 3.

From Scheme 3, the E_2^0 values are given by eq. [4]:

$$[4] \qquad E_2^0 = E_1^0 - 0.059\,(pK_a' - pK_a)$$

where the pK_a values are known from the kinetic results in

Scheme 3.

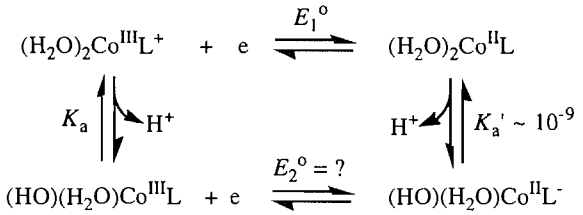

L = $(dmgH)_2$ or $(dmgBF_2)_2$

Table 2, but the pK_a' for diaqua cobaloxime(II) complexes are unknown. A value of $pK_a' = 9$ has been assumed since this is typical for bivalent first-row transition metal ions (37). The E^0 values are given in Table 2.

The self-exchange rate constants for the cobaloxime(III)/(II) couples have been estimated from the Marcus cross relationship (38), eq. [5],

$$[5] \quad k_{12} = (k_{11}k_{22}K_{12}f_{12})^{1/2}W_{12}$$

where k_{12} is the cross-reaction rate constant ($= k_{obs}$), k_{11} and k_{22} are the self-exchange rates for oxidant and reductant, and K_{12} is the equilibrium constant of the cross reaction. The f_{12} and work term corrections (W_{12} and w_{ij}) have been calculated from the following equations (39):

$$[6] \quad \ln f_{12} = \frac{[\ln K_{12} + (w_{12} - w_{21})/RT]^2}{4\ln(k_{11}k_{22}/Z^2) + (w_{11} + w_{22})/RT}$$

$$[7] \quad W_{12} = \exp[-(w_{12} + w_{21} - w_{11} - w_{22})/2RT]$$

$$[8] \quad w_{ij} = \frac{(4.225 \times 10^3)z_iz_j}{r(1 + 0.3285r\sqrt{\mu})}$$

where Z is the collision frequency, taken to be 1×10^{11}

Table 3. Summary of redox reactions of $Co(sep)^{3+/2+}$ with various reactants with known self-exchange rates.[a]

Reactant	E_1^0, V (NHE)	k_{11}, M^{-1} s^{-1}		k_{12}, M^{-1} s^{-1}	
		obsd.	calcd.	obsd.	calcd.
$Co(en)_3^{3+}$	−0.18[b]	3.0×10^{-5} [c]	2.3×10^{-5}	5.0×10^{-2} [d]	5.8×10^{-2}
$Co([9]aneN_3)_2^{2+}$	−0.41[e]	1.4×10^{-1} [f]	5.2×10^{-1}	5.0[f]	13
$Co(sar)^{2+}$	−0.43[b]	2.1[b]	0.13	20[b]	80
$Co(dimsarH_2)^{5+}$	0.03[b]	2.4×10^{-2} [b]	2.0×10^{-2}	1.5×10^2 [b]	1.6×10^2
$Ru(NH_3)_6^{3+}$	0.05[g]	6.7×10^3 [h]	0.39×10^3	1.4×10^4 [i]	3.9×10^4
$Co(NH_3)_6^{3+}$	0.06[j]	4×10^{-7} [k]	0.48×10^{-7}	0.15[j]	0.44
$Co(terpy)_2^{3+}$	0.26[f]	4.0×10^2 [l]	0.93×10^2	1.5×10^5 [f]	3.1×10^5
$Co(bipy)_3^{3+}$	0.32[m]	20[l]	4.8×10^{-2}	1.0×10^4 [n]	20×10^4
$Co(phen)_3^{3+}$	0.38[l]	6.7[o]	3.2×10^{-3}	0.48×10^4 [j]	22×10^4
$Co([14]aneN_4)(OH_2)_2^{3+}$	0.42[p]	2.2×10^{-4} [p,q]	0.5×10^{-4}	1.6×10^3 [j]	3.4×10^3
$Co(Me_4[14]tetraeneN_4)(OH_2)_2^{3+}$	0.56[p]	14×10^{-3} [p,q]	0.14×10^{-3}	1.7×10^4 [j]	17×10^4
$Co(Me_2pyo[14]trieneN_4)(OH_2)_2^{3+}$	0.57[p]	2.5×10^{-2} [p,q]	0.16×10^{-2}	5.4×10^4 [j]	23×10^4
$Co(Me_2[14]\text{-}dieneN_4\text{-}13\text{-}one)(OH_2)_2^{3+}$	0.60[p]	1.2×10^{-3} [p,q]	0.15×10^{-3}	3.0×10^4 [j]	9.1×10^4
$Co(dmgH)_2(OH_2)_2^+$	0.36[r]	(2.4×10^{-2})[t]	2.4×10^{-3}	5.5×10^3	
$Co(dmgBF_2)_2(OH_2)_2^+$	0.65[s]	(5.7×10^{-3})[t]	5.7×10^{-4}	1.5×10^5	

[a]At 25°C and μ = 0.1 M unless otherwise indicated. The self-exchange rates (k_{22}) for $Co(sep)^{3+/2+}$ used are 3.5 and 5.1 M^{-1} s^{-1} at μ = 0.1 and 0.2 M, respectively (ref. 43).

[b]At μ = 0.2 M (ref. 44).

[c]Adjusted to μ = 0.2 using the μ dependence of $Co(sep)^{3+/2+}$ and the value of 5×10^{-5} M^{-1} s^{-1} (μ = 0.5) from ref. 45.

[d]μ = 0.2, ref. 14.

[e]Reference 46.

[f]Reference 47.

[g]Reference 48.

[h]Extrapolated with $\Delta H^* = 5$ kcal mol^{-1} from measurements at 4°C (ref. 49).

[i]Adjusted to μ = 0.1 as in footnote *c* from 3.5×10^4 (μ = 0.5) (ref. 50).

[j]Reference 16.

[k]Extrapolated using $\Delta S^* = -31$ kcal mol^{-1} K^{-1} (as for $Co(en)_3^{3+/2+}$) and ionic strength factor of 0.2 from 8×10^{-6} at 40°C in 2.5 M $CF_3SO_3^-$ (ref. 51).

[l]Reference 52.

[m]Reference 53.

[n]At μ = 0.2, from ref. 50.

[o]Reference 54.

[p]Reference 12.

[q]Adjusted from μ = 1.0 to μ = 0.2 as in footnote *c*.

[r]Reference 28.

[s]Reference 22.

[t]Estimated as described in text.

Table 4. Summary of self-exchange rates (25°C) for low-spin Co(III)/(II) complexes.

Complex	k_{11}, M^{-1} s^{-1}	Δd, Å
$Co([9]aneS_3)_2^{3+}$	9.5×10^4 [a]	0.07[b]
$Co(azacapten)^{3+}$	4.5×10^3 [c]	0.06(N), 0.1(S)[c]
$Co(dmgH)_2(OH_2)_2^+$	$\sim 2.4 \times 10^{-2}$ [d]	~ 0.31(O)[e]
$Co(dmgBF_2)_2(OH_2)_2^+$	$\sim 5.7 \times 10^{-3}$ [d]	~ 0.31(O)[e]
$Co(Me_4[14]tetraeneN_4)(OH_2)_2^{3+}$	1.4×10^{-2} [f] (5.0×10^{-2} [g])	0.38(O)[e]
$Co(Me_2[14]\text{-}dieneN_4\text{-}13\text{-}one)(OH_2)_2^{3+}$	1.2×10^{-3} [f] (4.4×10^{-3} [g])	0.43(O)[e]
$Co(Me_6[14]4,11\text{-}dieneN_4)(OH_2)_2^{3+}$	1.3×10^{-5} [f] (4.5×10^{-5} [g])	0.57(O)[e]
$Co([14]aneN_4)(OH_2)_2^{3+}$	8×10^{-4} [g]	
$Co(Me_2pyo[14]trieneN_4)(OH_2)_2^{3+}$	9.3×10^{-2} [g]	

[a] $\mu = 0.1$ (ref. 55).
[b] Reference 56.
[c] Reference 57.
[d] Calculated from the Marcus cross relationship as described in Table 3. These entries have a different charge type than the others and their relative values are somewhat influenced by the work term correction.
[e] Co—O bond length change, estimated as described in text.
[f] Estimated at $\mu = 0.1$ as described in Table 3.
[g] $\mu = 1.0$ (ref. 12).

M^{-1} s^{-1}, r is the sum of the radii of the reactants in Å, μ is the ionic strength, z_i is the charge on the ion, the numerical constants are for water at 25°C, and w_{ij} values are in cal mol^{-1}.

There has been a good deal of discussion (15–22) about the application of eq. [5] to cobalt(III)/(II) reactions because of the spin state changes involved and the possibility that the reactions are nonadiabatic. If the latter is the case, then a nonadiabatic factor κ of uncertain magnitude may be included on the right-hand side of eq. [5], and calculations of self-exchange rate constants become proportionately uncertain. Most recently, Shalders and Swaddle (22) have concluded that these reactions are essentially adiabatic.

For the specific case of reactions of $Co(sep)^{3+/2+}$, the justification and confidence in calculations based on eq. [5] can be tested by comparing observed and calculated values of k_{11} and k_{12} for systems in which these are known. Such results for 13 systems are summarized in Table 3, where the known k_{11} and k_{22} are used to give a calculated k_{12}, and k_{22} and k_{12} give a calculated k_{11}. For the vast majority of these systems, the observed and calculated values of k_{12} agree within a factor of ≤ 10, although the calculated values are always larger. Since k_{11} depends on $(k_{12})^2$, the calculated k_{11} are ≤ 100 times smaller than the experimental values. The two exceptions are $Co(bipy)_3^{3+}$ and $Co(phen)_3^{3+}$ where the calculated k_{12} is 20 and 50 times, respectively, larger than the experimental value, and the calculated k_{11} are proportionately much smaller. These exceptions might be ascribed to conjugation in the ligand, making self-exchange more favorable than when a reaction partner has no such conjugation. However, this effect does not appear in the terpy system. It should be noted that the first eight cobalt complexes listed in Table 3 have cobalt(II) in the high-spin state, but cobalt(II) is low spin for the remaining entries. There does not appear to be any systematic difference between these two types of systems.

To estimate k_{11} for the cobalt–oxime complexes, one could simply use the k_{11}(calcd.) in Table 3. However, for the other systems, k_{11}(calcd.) is typically 5–10 times smaller than k_{11}(obsd.), so that one might expect as an upper limit for the oximes that the true k_{11}(obsd.) $\approx 10 \times k_{11}$(calcd.) and this estimate has been entered in Table 3.

Endicott et al. (12) studied the variation of self-exchange rates with structure changes for a series of homologous *trans*-$Co(N_4)(OH_2)_2^{3+/2+}$ couples in which both Co(II) and Co(III) are low spin. The self-exchange rates were evaluated from the cross-reaction rates among these complexes. Structural studies have shown that the Co—N bond length changes very little between the Co(III) and Co(II) forms of these complexes, but the axial Co—OH_2 bond lengths are 0.38–0.57 Å longer for Co(II) because the unpaired electron occupies the antibonding d_{z^2} orbital. Endicott et al. attributed the variation of the self-exchange electron-transfer rates to the reorganization energies that result from changes in Co–OH_2 bond length Δd.

The cobaloxime systems are structurally similar to the $CoN_4(OH_2)_2$ complexes in that the equatorial Co—N bond lengths are 1.87–1.89 Å, and are very similar for the Co(III) and Co(II) forms (39). The lengthening of the axial Co—OH_2 bonds (Δd) for Co(II) compared to Co(III) is estimated as 0.31 Å for the $(dmgH)_2$ complex, from the Co—N(py) bond lengths in $Co^{II}(dmgH)_2(py)_2$ (40) and $Co^{III}(dmgH)_2(py)_2^+$ (41). For the $(dmgBF_2)_2$ complex, Co(II)—OH_2 and Co(III)—OH_2 bond lengths can be estimated as 2.28 and 1.97 Å from the Co—O bond lengths in $Co^{II}(dmgBF_2)_2(CH_3OH)_2$ (23) and $Co^{III}(dmgH)_2(X)(OH_2)$ (X = halide ions) (42). Therefore, Δd for both diaqua cobaloxime(II) complexes is estimated to be ~0.31 Å.

For these and other low-spin Co(II)/Co(III) systems, the self-exchange rates and structural change information are collected in Table 4. Our estimates for the cobaloxime complexes seem to conform reasonably with the suggestion of Endicott et al. (12) that larger structural change causes a smaller self-exchange rate constant for $CoN_4(OH_2)_2$ complexes. It is rather more surprising that the structurally quite different $Co([9]aneS_3)_2^{3+}$ and $Co(azacapten)^{3+}$ complexes also seem to follow this trend.

Acknowledgment

The authors thank the Natural Sciences and Engineering Research Council of Canada for financial support.

References

1. B.P. Hay and R.G. Finke. J. Am. Chem. Soc. **108**, 4820 (1986); J. Halpern. Science, **227**, 869 (1985); G.N. Schrauzer. Acc. Chem. Res. **1**, 97, (1968).
2. A. Adin and J.H. Espenson. Inorg. Chem. **11**, 686 (1972).
3. H. Taube, H. Myers, and R.L. Rich. J. Am. Chem. Soc. **75**, 4118 (1953); H. Taube and H. Myers. J. Am. Chem. Soc. **76**, 2103 (1954).
4. (*a*) R.H. Prince and M.G. Segal. Nature, **249**, 246 (1974); (*b*) J. Chem. Soc. Dalton Trans. 330 (1975); (*c*) J. Chem. Soc. Dalton Trans. 1245 (1975).
5. (*a*) G.Balasubramanian and V.R. Vijayaraghavan. Inorg. Chem. Acta, **38**, 49 (1980). (*b*) Inorg. Chem. Acta, **53**, L209 (1981). (*c*) Indian J. Chem. **20A**, 892 (1981). (*d*) G. Balasubramanian, T. Thothadri, and V.R. Vijayaraghavan. Indian J. Chem. **27A**, 997 (1988).
6. A. Dayalan and V.R. Vijayaraghavan. J. Chem. Soc. Dalton Trans. 2491 (1992).
7. A. Bakac and J.H. Espenson. Inorg. Chem. Acta, **30**, L329 (1978).
8. R.B. Jordan. Reaction mechanisms of inorganic and organometallic systems. Oxford University Press, New York. 1991.
9. A. Adin and J.H. Espenson. J. Chem. Soc. Chem. Commun. 653 (1970).
10. D.P. Rellema, J.F. Endicott, and R. Patel. J. Am. Chem. Soc. **94**, 394 (1972).
11. M.D. Glick, J.M. Kuszaj, and J.F. Endicott. J. Am. Chem. Soc. **95**, 5097 (1973).
12. J.F. Endicott, B. Durham, M.D. Glick, T.J. Anderson, J.M. Kuszaj, W.G. Schmonsees, and K.P. Balakrishnan. J. Am. Chem. Soc. **103**, 1431 (1981).
13. J.F. Endicott, B. Durham, and K. Kumar. Inorg. Chem. **21**, 2437 (1982).
14. T. Ramasami and J.F. Endicott. J. Am. Chem. Soc. **107**, 389 (1985).
15. E. Buhks, M. Bixon, J. Jortner, and G. Navon. Inorg. Chem. **18**, 2014 (1979).
16. N. Sutin. Prog. Inorg. Chem. **30**, 441 (1983).
17. J.T. Hupp and M.J. Weaver. J. Phys. Chem. **89**, 2795 (1985).
18. T. Ramasami and J.F. Endicott. J. Phys Chem. **90**, 3740 (1986).
19. S. Larsson, K. Stähl, and M.C. Zerner. Inorg. Chem. **25**, 3033 (1986).
20. D.A. Geselowitz. Inorg. Chim. Acta, **154**, 225 (1988).
21. M.D. Newton. J. Phys. Chem. **95**, 30 (1991).
22. R.D. Shalders and T.W. Swaddle. Inorg. Chem. **34**, 4815 (1995).
23. A. Bakac, M.E. Brynildson, and J.H. Espenson. Inorg. Chem. **25**, 4108 (1986).
24. A.V. Ablov and N.M. Samus. Russ. J. Inorg. Chem. **5**, 410 (1960).
25. A.V. Ablov and N.M. Samus. Dokl. Akad. Nauk SSSR, **113**, 1265 (1957).
26. A.V. Ablov, M.P. Filippov, and N.M. Samus. Dokl. Akad. Nauk SSSR, **133**, 575 (1960).
27. K. Dash. Proc. Indian Natl. Sci. Acad. **55A**, 212 (1989).
28. R.G. Heckman and J.H. Espenson. Inorg. Chem. **18**, 38 (1979).
29. E. Kita and R.B. Jordan. Inorg. Chem. **28**, 1549 (1989).
30. Z. Zhang and R.B. Jordan. Inorg. Chem. **33**, 680 (1994).
31. G.G. Schlessinger. Inorganic laboratory preparations. Chemical Publishing Co. Inc., New York. 1962.
32. A. Haim. Prog. Inorg. Chem. **30**, 273 (1983).
33. H. Diebler and H. Taube. Inorg. Chem. **4**, 1029 (1965).
34. K. Wang and R.B. Jordan. Inorg. Chem. **34**, 5672 (1995).
35. R.A. Marcus. J. Phys. Chem. **67**, 853 (1963).
36. A.V. Ablov, B.A. Bovykin, and N.M. Samus. Russ. J. Inorg. Chem. **11**, 978 (1966).
37. C.F. Baes and R.E. Messmer. The hydrolysis of cations. Wiley, New York. 1976. p. 226.
38. R.A. Marcus and N. Sutin. Biochem. Biophys. Acta, **811**, 265 (1985).
39. K. Zahir, J.H. Espenson, and A. Bakac. J. Am. Chem. Soc. **110**, 5059 (1988).
40. N. Bresciani-Pahor, M. Forcolin, L.G. Marzilli, L. Randaccio, M.F. Summers, and P.J. Toscano. Coord. Chem. Rev. **63**, 1 (1985).
41. G.D. Fallon and B.M. Gatehouse. Cryst. Struct. Commun. **7**, 263 (1978).
42. A.V. Ablov, A.A. Dvorkin, Y.A. Simonov, O.A. Bologa, and T.I. Malinovskii. Dokl. Akad. Nauk SSSR, **217**, 89 (1974).
43. H. Doine and T.W. Swaddle. Inorg. Chem. **32**, 5597 (1991).
44. I.I. Creaser, A.M. Sargeson, and A.W. Zanella. Inorg. Chem. **22**, 4022 (1983).
45. W.H. Jolley, D.R. Stranks, and T.W. Swaddle. Inorg. Chem. **29**, 385 (1990).
46. H.-J. Küppers, A. Neves, C. Pomp, D. Ventur, K. Wieghardt, B. Nuber, and J. Weiss. Inorg. Chem. **25**, 2400 (1986).
47. G.D. Armstrong, J.D. Sinclair-Day, and A.G. Sykes. J. Phys. Chem. **90**, 3686 (1986).
48. H.S. Lim, D.J. Barclay, and F.C. Anson. Inorg. Chem. **11**, 1460 (1972).
49. P.J. Smolenaers and J.K. Beattie. Inorg. Chem. **25**, 2259 (1986).
50. J.F. Endicott, G.R. Brubaker, T. Ramasami, K. Kumar, K. Dwarakanath, J. Cassel, and D. Johnson. Inorg. Chem. **22**, 3754 (1983).
51. A. Hammershoi, D. Geselowitz, and H. Taube. Inorg. Chem. **23**, 979 (1984).
52. R. Farina and R.G. Wilkins. Inorg. Chem. **1**, 514 (1968).
53. U. Furholz and A. Haim. J. Phys. Chem. **90**, 3686 (1986).
54. M.R. Grace and T.W. Swaddle. Inorg. Chem. **32**, 5597 (1993).
55. H. Doine and T.W. Swaddle. Inorg. Chem. **30**, 1858 (1991).
56. W.N. Setzer, C.A. Ogle, G.S. Wilson, and R.S. Glass. Inorg. Chem. **22**, 266 (1983).
57. R.V. Dubs, L.R. Gahan, and A.M. Sargeson. Inorg. Chem. **22**, 2523 (1983).

The chemistry of thujone. XVIII.[1] Homothujone and its derivatives

James P. Kutney, Yong-Huang Chen, and Steven J. Rettig

Abstract: The monoterpene thujone (**1**) is ring expanded regioselectively to provide homothujone (**4**) in order to explore its potential as a chiral starting material. Stereoselective Robinson annulation of homothujone provides an enone intermediate (**5**), further derivatization of which was undertaken to furnish functionalized naphthalenones useful for synthesis of the antifeedant (−)-polygodial and the ambergris fragrance (−)-Ambrox®.

Key words: thujone, homothujone, synthesis, naphthalenones, polygodial, Ambrox.

Résumé : On a effectué une expansion régiosélective de la thujone (**1**) en homothujone (**4**) afin d'explorer ses potentiels comme produit de départ chiral. L'annellation stéréosélective de Robinson réalisée au départ de l'homothujone conduit à une énone intermédiaire, **5**, qui a été transformée en dérivé pour fournir des naphtalénones fonctionnalisées utiles dans la synthèse de l'antiappétant (−)-polygodial et de la fragrance d'ambregris, (−)-Ambrox®.

Mots clés : thujone, homothujone, synthèse, naphtalénones, polygodial, Ambrox.

[Traduit par la rédaction]

Introduction

The logging practice of Western red cedar (*Thuja plicata* Donn) in British Columbia generates a waste material consisting of branches and leaves. This material, also called "slash," can be steam distilled to provide an essential oil containing the monoterpene thujone (**1**) in concentrations of 85–90%, Although this readily available oil can be of use in the perfumery and household chemical industry, higher grade chemical products originating from thujone are of interest in terms of economic benefit and environmental concern. For example, recent synthetic studies from our laboratories have established that thujone is a versatile chiral building block for enantioselective syntheses of biologically active natural products and their analogues including insect juvenile hormone analogues, insecticidal pyrethroids and aryl terpenoids, sesquiterpenes, and steroids (1).

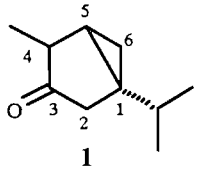

1

Received October 14, 1995.

J.P. Kutney, Y.-H. Chen, and S.J. Rettig. Department of Chemistry, University of British Columbia, 2036 Main Mall, Vancouver, BC V6T 1Z1, Canada.

[1] For a detailed summary of previous studies in this series, see ref. 1.

[2] Author to whom correspondence may be addressed: Tel. and Fax: (604) 822-2710; E-mail: Kutney@unixg.ubc.ca

These diverse studies have revealed that **1**, via its rigid bicyclo[3.1.0]hexane system, affords regio- and stereo-selective reactions such as Robinson annulation to generate chiral synthons for terpene and steroid syntheses, and specific cyclopropyl ring-opening reactions of thujone analogues for a variety of interesting routes to chiral natural products and related compounds, etc.

To further elaborate upon the versatility of this readily available and inexpensive chiral synthon, it was of interest to consider ring expansion of **1** to "homothujone" (**4**) to ascertain whether the latter compound could increase the overall versatility and potential use of thujone in synthetic chemistry.

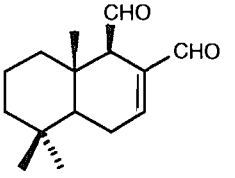

2

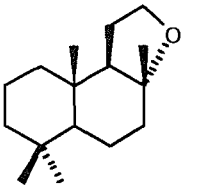

3

Scheme 1 shows the overall plan in which the concept is incorporated to afford functionalized *trans*-fused naphthalenones useful for further elaboration into (−)-polygodial (**2**) and (−)-Ambrox® (**3**). Homothujone (**4**) could be converted to enone **5** by Robinson annulation. Birch reduction of **5** followed by enolate trapping should produce a *trans* ketone **6** and, after reduction, the hydrocarbon **7**. Via a previously established ozonation reaction, **7** would afford **8** and **9**. Finally, acid-catalyzed cyclopropyl ring-opening reactions already developed in our laboratories (2) are expected to convert **8** and **9** to **10** and **11**, respectively. Functional groups in both **11** and **12** would then allow the final elaboration to either (−)-polygodial (**2**) or (−)-Ambrox® (**3**).

Scheme 1. The overall plan to develop the homothujone strategy.

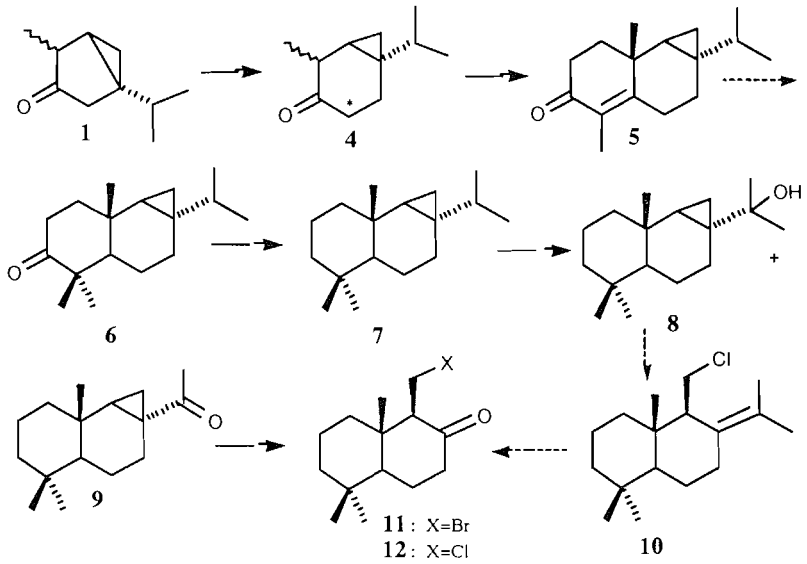

The apparent advantage of the homothujone strategy over previous routes to functionalized naphthalenones is that the *trans* A/B ring fusion could possibly be generated by the Birch reduction directly, rather than through a tedious stereochemical correction sequence from the A/B *cis*-fused systems obtained in earlier studies (1). The homothujone strategy might incorporate 7 of the original 10 carbon atoms present in thujone into potential target molecules in a novel way. In this publication, we would like to report our initial studies on this new strategy.

Results and discussion

Regioselective ring expansion of thujone

The desired regioselective ring expansion of thujone was

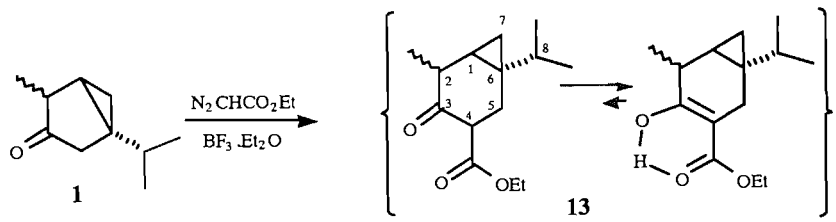

accomplished by treating thujone with ethyl diazoacetate and boron trifluoride etherate under nitrogen at room temperature (3). The β-ketoester 13,[3] which existed mainly in its enol form, was isolated in 70% yield. The mass spectrum of **13** showed a molecular ion at *m/z* 238. The UV spectrum indicated an absorption band at 258 nm (log ε = 3.980) while the IR spectrum displayed a broad hydroxyl absorption at 3370 cm^{-1}, an intense conjugated ester carbonyl stretching absorption at 1655 cm^{-1}, and a weak carbon–carbon double bond stretching absorption at 1615 cm^{-1}. The ^1H NMR spectrum revealed three separate one-proton signals at high field, δ 0.30 (dd, J = 4.4 and 8.8 Hz), 0.39 (t, J = 4.4 Hz), and 0.68 (dd, J = 4.4 and 8.8 Hz), corresponding to the three protons in the cyclopropane ring. Two methyl doublets (J = 5.6 and 4.4 Hz), corresponding to the two methyl groups at the isopropyl side chain, overlapped at δ 0.98 ppm. There were a one-proton multiplet at δ 1.03 ppm corresponding to the methine proton at C8, a methyl doublet (J = 7.2 Hz) at δ 1.24 ppm corresponding to the methyl at C2, and a methyl triplet (J = 6.8 Hz) at δ 1.31 ppm corresponding to the methyl of the ethyl ester group. A two-proton signal of AB type at δ 2.25–2.57 ppm (J = 16 Hz) was assigned to the methylene at C5 while a quartet (J = 7.2 Hz) at δ 2.64 ppm was due to the methine at C2. The J coupling constant between the methine protons at C1 and C2 was zero! A two-proton multiplet at δ 4.21 ppm corresponded to the methylene in the ethyl ester group and a very low-field singlet signal at δ 12.24 ppm was due to the hydroxyl proton in the enol form of **13**.

The spectroscopic data presented above could not differentiate the enol form of **13** from that of **14**, which would be the product of carbon insertion from the more substituted side of the carbonyl function in thujone. Crucial evidence was obtained, however, from the next step, i.e., the decarboxylation of the β-keto ester (**13**).

[3] Because thujone in use was a mixture of α-thujone and β-thujone (10:1), the product **13** was a mixture of two diastereomers in a similar ratio, as revealed by GC. No attempt was made to separate these two diastereomers. The ^1H NMR spectral data presented here represent the characterization of the major α diastereomer while other spectroscopic data are the gross properties of the diastereomeric mixture. This situation remains the same for homothujone **4**.

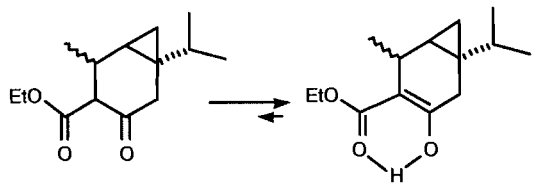

14

Treatment of **13** in moist DMSO with sodium chloride at 140°C for a few hours produced **4**[4] in 95% yield (4). The mass spectrum of **4** showed its molecular ion at *m/z* 166 while the IR spectrum indicated a carbonyl absorption at 1700 cm^{-1}. It is expected that **4** would have the three α protons (to the carbonyl group), that is, C2 and C4, in the region between δ 2.00 ppm and δ 3.00 ppm in the ^1H NMR spectrum whereas **15** available from **14** would reveal four protons in this region. To our surprise, **4** contained four protons in this region: two at δ 2.10 ppm (m), one at δ 2.35 ppm (m), and one at δ 2.47 (dt, J = 3.0 and 8.0 Hz) ppm. A series of decoupling experiments were performed to clarify the situation. Irradiation of the one-proton signal at high field (δ 0.72 ppm), which was assigned to one of the three cyclopropane protons, caused the multiplet at δ 2.47 ppm to collapse into a quartet (J = 8.0 Hz) in addition to the simplification of the complex two-proton signal at high field (δ 0.50 ppm), which was assigned to the two remaining cyclopropane protons. Irradiation of the signal at δ 0.50 ppm resulted only in the collapse of the signal at δ 0.72 ppm. Thus, the signal at δ 0.72 ppm was clearly due to the C1 proton while the signal at δ 2.47 ppm was assigned to the methine proton at C2. Irradiation of the methyl doublet resonance (J = 8.0 Hz) at δ 1.22 ppm led to the collapse of the C2 proton signal into a doublet (J = 3.0 Hz) and irradiation at δ 2.47 ppm transformed the methyl doublet signal at δ 1.22 ppm into a singlet and the C1 proton signal at δ 0.72 ppm into a doublet of doublets (J = 4.8 and 8.8 Hz), further confirming the assignment. The fact that the C2 proton was coupled only to the C1 proton and the methyl protons at δ 1.22 ppm suggested the correct structural assignment to **4** and thus **13**.

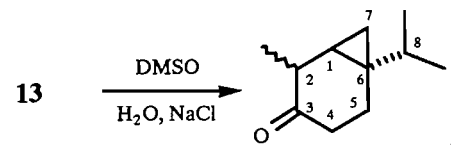

4: a/b

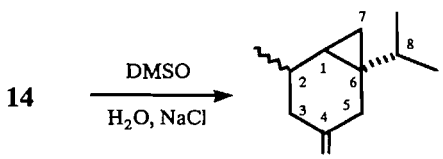

15: a/b

It is noteworthy that the coupling between the C1 proton and the C2 proton in compound **4** (J = 3.0 Hz) was rather different

[4] The product **4** was a mixture of α and β diastereomers (10:1) as indicated by GC. The ^1H NMR data described here represent the characterization of the major α diastereomer while other spectroscopic data are the gross properties of the diastereomeric mixture.

Fig. 1. Conformational analysis of **13**a and **4**a.

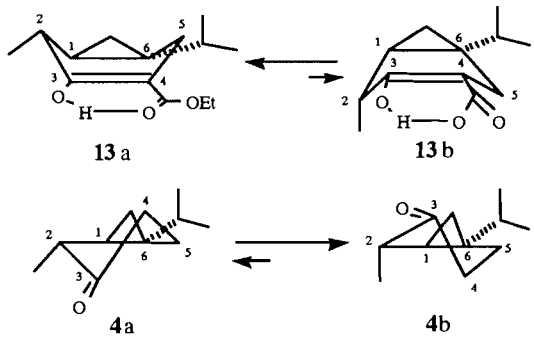

13 a **13** b

4a **4**b

from that in **13** (J = 0 Hz). This can be explained when one considers the possible conformations of these two compounds (Fig. 1). The enol form of compound **13**α[5] can have two boat-like conformers **13**a and **13**b. Conformer **13**b is less stable because of the repulsion between the axial methyl at C2 and the axial hydrogen at C5. Inspection of models reveals a dihedral angle H1–C1–C2–H2 close to 90° in conformer **13**a, which possesses an equatorial methyl group at C2. Therefore, the coupling constant between H1 and H2 is expected to be small. Among the two half-chair conformers of **4**a,[6] **4**b with an axial methyl group is considered more stable because it is devoid of the C2–methyl bond and the C1—H1 bond eclipsing interaction present in **4**a, and the flat nature of the plane involving C2–C1–C6–C5 also greatly reduces the repulsion between the axial methyl at C2 and the axial proton at C4 in **4**b. The dihedral angle H1–C1–C2–H2 is approximately 30° and therefore a larger coupling constant between H1 and H2 is expected.

The insertion reaction of a ketone by ethyl diazoacetate usually takes place from the less substituted or less bulky side. The formation of the reactive conformer shown in Fig. 2 is presumably faster than other possible conformers due to minimal *gauche* steric repulsions (5).

Stereoselective Robinson annulation of homothujone (4)

The Robinson annulation of homothujone (**4**) was carried out by refluxing the starting material with potassium hydroxide, the salt of 1–diethylamino-3–pentanone (ethyl vinyl ketone, EVK equivalent), and one equivalent of iodomethane in ethanol. Enone **5**, as shown, was isolated in 70% yield.

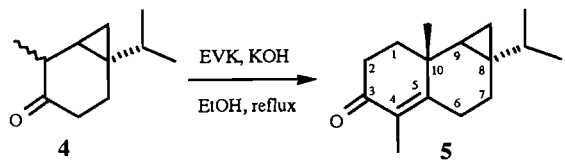

4 **5**

The structure of **5** was further confirmed by a series of NMR experiments. The structure **17**, which might possibly be formed by the ethyl vinyl ketone (EVK) Robinson annulation from the less substituted side of the carbonyl group, is inconsistent with the fact that only two methyl doublets were observed in the spectrum of the isolated product **5**. However,

[5] As indicated in the previous footnotes, the ^1H NMR data thus far described for **13** and **4** represent their α diastereomers only.

[6] See footnote 5.

Fig. 2. Explanation for regioselectivity of the carbon insertion reaction.

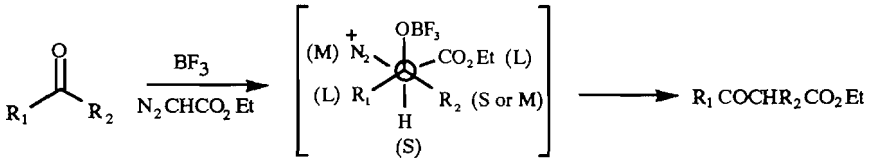

the structure **18**, which was possibly generated from the β-face attack of the more substituted side, could accommodate all the spectroscopic data so far obtained. More evidence was needed to differentiate **5** and **18**.

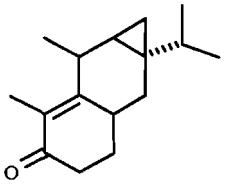

17

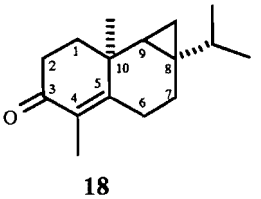

18

Inspection of molecular models reveals that the angular methyl group at C10 has different spatial relationships with the three cyclopropane protons in the diastereomers of **5** and **18**. In the case of **5**, the angular methyl is relatively close to the cyclopropane methylene proton directed into the concave face of the bicyclo[4.1.0]heptane moiety (i.e., H_{in}) but distant from the cyclopropane methine proton (i.e., H9) and the other methylene proton, which is directed away from the concave face of the bicyclo[4.1.0]heptane moiety (i.e., H_{out}). For **18**, the angular methyl is relatively close to H9 but distant from both methylene protons H_{in} and H_{out}. Thus, if the angular methyl is irradiated, a positive NOE enhancement for H_{in} will indicate the presence of **5** while a positive enhancement for H9 will suggest the existence of **18**. Fortunately, the ^{1}H NMR spectrum was fairly well resolved. The methyl singlet signal at δ 1.22 ppm, previously assigned to the angular methyl, was well separated from nearby signals and the three cyclopropane proton signals at high field were also well separated from each other. From a large number of recorded spectra of substituted cyclopropanes, it is generally observed that, in any designated cyclopropane, the magnitude of the vicinal coupling constant for *cis* protons (protons on the same side of a cyclyopropane plane, e.g., H9 and H_{out}) is always larger than that for *trans* protons (e.g., H9 and H_{in}) (6). Since each of the three coupling

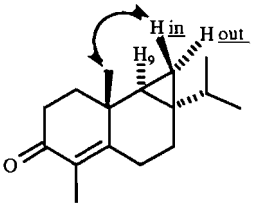

5

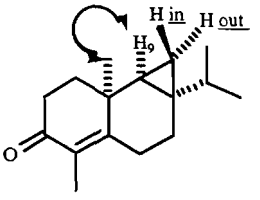

18

constants in the AMX system, for the three cyclopropane protons of **5** or **18**, had to be either 4.8 Hz or 9.6 Hz , the coupling constant between H9 and H_{out} [J (H9,H_{out})] and the coupling constant between H9 and H_{in} [J (H9,H_{in})] should have values 9.6 Hz and 4.8 Hz, respectively, in order to satisfy the relationship: J (H9,H_{out}) > J (H9,H_{in}). J (H_{out},H_{in}) had to be 4.8 Hz to produce a triplet of J = 4.8 Hz observed in the spectrum and this triplet signal was due to H_{in}. Otherwise, if J (H_{out}, H_{in}) were 9.6 Hz, a triplet of J = 9.6 Hz would have been observed and this triplet would have been due to H_{out}. Thus, the consideration of magnitude for coupling constants enabled us to assign the triplet (J = 4.8 Hz) at δ 0.66 ppm to H_{in} but the two doublet of doublets signals at δ 0.30 and 0.50 ppm cannot be assigned further.

A two-dimensional ^{1}H–^{13}C heteronuclear correlation spectrum (2D-HETCOR) further confirmed the assignment. The proton (doublet of doublets) at δ 0.50 ppm correlated intensely with a tertiary carbon at δ 33.00 ppm but weakly with a secondary carbon at δ 12.60 ppm. Both the proton (triplet) at δ 0.66 pm and the proton (doublet of doublets) at δ 0.30 ppm correlated intensely with the secondary carbon at δ 12.60 ppm but not with the tertiary carbon at δ 33.00 ppm. This suggested that the proton (doublet of doublets) at δ 0.50 ppm was due to H9 and the quartet proton at δ 0.30 ppm was due to H_{out}.

The determination of substitution of the above-mentioned carbons was facilitated by an APT (Attached Proton Test) (7) experiment. The carbon at δ 12.60 ppm was assigned as secondary since it was very intense in the off-resonance spectrum and did not invert its phase in the APT spectrum. Among the six carbons of inverse phase (which can be either primary or tertiary carbons) in the APT spectrum, four were sorted out as primary carbons since they had low chemical shifts in the ^{13}C spectrum (δ: 10.35, 18.55, and 19.20 ppm). As shown from the HETCOR spectrum, these four carbons also correlated well with four methyl singlets in the ^{1}H NMR spectrum. Thus, the other two carbons at δ 33.00 and 36.65 ppm must be tertiary carbons.

NOE experiments were then carried out on compound **5.** Irradiation at the angular methyl signal at δ 1.22 ppm resulted in a 4.0% enhancement of H_{in} at δ 0.66 ppm but no enhancement of either H9 or H_{out}. Therefore, the stereochemistry of **5** was finally confirmed. Irradiation of H_{in} at δ 0.66 ppm did not give a clear enhancement of the angular methyl signal but did cause a 10% enhancement of H_{out} and a negative enhancement of H9.

Generation of the *trans*-fused hydrocarbon 7

Having obtained the desired intermediate **5** in good overall yield from thujone, it was appropriate to evaluate some chemistry with this compound. Birch reduction of **5**, followed by iodomethane addition to trap the generated enolate (8), gave the *gem*-dimethylated ketone **6** in low yield (15%). Attempts to improve this reaction by addition of proton donors (i.e., water and *tert*-butanol) during the Birch reduction step, quenching of excess lithium with isoprene, and removal of ammonia prior to iodomethane addition did not prove fruitful. The by-products were relatively nonpolar and difficult to separate from each other.

The mass spectrum of **6** revealed the molecular ion peak at

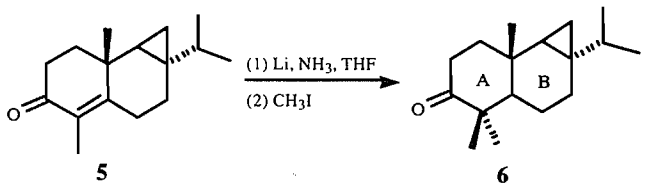

5 6

m/z 248 while the IR spectrum indicated a saturated carbonyl absorption at 1703 cm−1. The A/B ring junction was assigned to be *trans*, in accord with the known stereochemistry of the Birch reduction of 4,5-dehydrodecal-3-ones (9), although insufficient spectroscopic evidence was available for an unambiguous assignment.

To improve the yield of **6** from **5**, an alternative route to **6** was pursued. Reduction of **5** by lithium and ammonia produced a mixture of two compounds **20** and **21** in a ratio of 4:1. Because these two compounds were not convertible by treatment with potassium hydroxide in methanol (monitored by GC), they were judged to be two diastereomers of opposite A/B ring fusion with the major isomer **20** possessing the *trans* ring fusion as that of compound **6**, since both were major products obtained by trapping enolates derived from the Birch reduction of **5**. Compounds **20** and **21** were difficult to separate by column chromatography. The mass spectrum of the mixture (**20** and **21**) indicated a molecular ion at *m/z* 236, while the IR spectrum showed a carbonyl absorption at 1700 cm^{-1}. Catalytic hydrogenation of **5** with 5% Pd-C at room temperature in ethanol generated **20** and **21** at a ratio of 6:1.

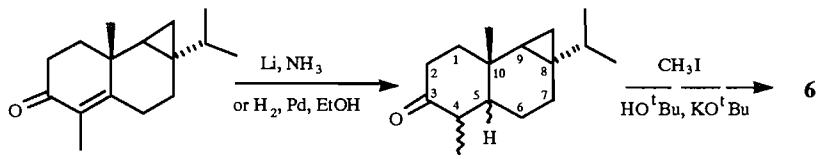

5 20/21

Refluxing the reduction mixture containing **20** and **21** with iodomethane and potassium *tert*-butoxide in anhydrous *tert*-butanol under nitrogen resulted in a complex mixture that did not contain **6**, as indicated by GC. No further attempt was made to elucidate this mixture. The reaction carried out at room temperature gave only recovered starting material.

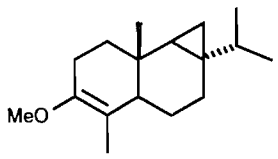

22

Treatment of the mixture of **20** and **21** (6:1) with sodium methoxide and iodomethane produced the enol ether **22** in 54% yield. This compound was characterized by a molecular ion peak at *m/z* 248 in its mass spectrum, and two methyl singlets at δ 1.57 and 3.50 ppm, corresponding to the vinylic methyl and the methoxyl methyl in the ^1H NMR spectrum. The A/B ring junction of **21** was *trans*, the same as that of **6.**

At this point, an alternative sequence to the A/B *trans*-fused hydrocarbon **7**, shown initially via the strategy in Scheme 1, was considered (Scheme 2).

Enone **5** was first methylated to **23** in 60% yield using sodium methoxide in DMSO (10). Decarbonylation of **23** utilizing the Wolf–Kishner–Huang Minlon conditions proceeded smoothly to give **24** in 67% yield.

Treatment of carbon–carbon double bonds by borane to form organoboranes, which are then decomposed with acetic acid to produce saturated C—C bonds, is a useful indirect method of carbon–carbon double bond reduction (11). However, such a treatment of **24** generated a complex mixture that was composed of several compounds, as detected by GC and the ^1H NMR spectrum. When an oxidative treatment of the intermediate organoboranes by basic hydrogen peroxide was carried out, diol **25** and alcohol **26** were isolated in 39% and 29% yield, respectively. The mass spectrum of **25**

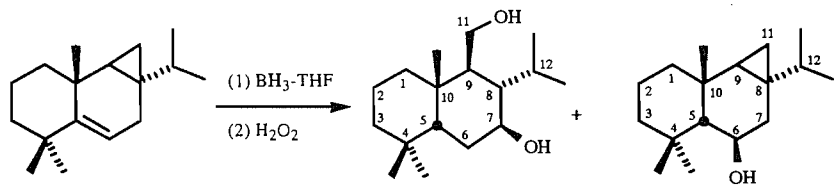

24 25 26

had its molecular ion peak at *m/z* 268 while the IR spectrum indicated an intense hydroxyl absorption near 3500 cm^{-1}. The ^1H NMR spectrum showed three methyl singlets at δ 0.96, 0.98, 1.00 ppm and two methyl doublets at δ 1.01 ppm (J = 7.0 Hz) and 1.15 ppm (J = 7.0 Hz). Two multiplets appearing at δ 3.72 ppm (2H) and 4.04 ppm (1H) corresponded to the the methylene and methine protons attached to C11 and C7. An X-ray structure of **25** (crystallized from methylene chloride) is shown in Fig. 3. The *cis* A/B ring fusion is clearly revealed. Details of the X-ray studies will be published elsewhere.

Alcohol **26** had its molecular ion peak at *m/z* 250 in the mass spectrum and an hydroxyl absorption at 3450 cm^{-1} in the IR spectrum. The ^1H NMR spectrum indicated three multiplets at δ 0.14, 0.45, and 0.64 ppm, corresponding to the three cyclopropane protons. Two methyl doublets appeared at δ 0.85 ppm

Scheme 2. An alternative sequence to hydrocarbon **7**.

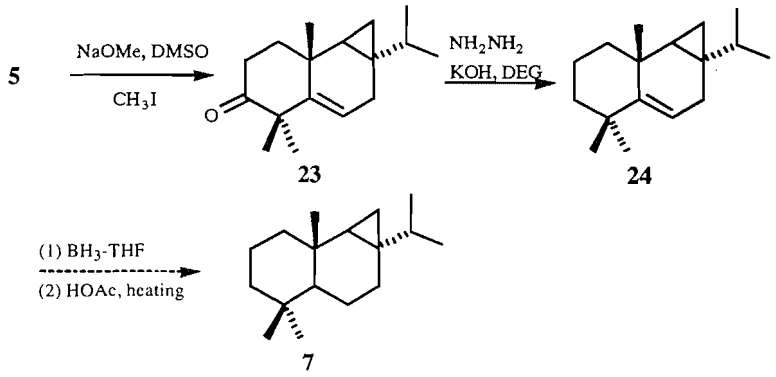

Fig. 3. Single crystal X-ray structure of **25** (PLUTO drawing).

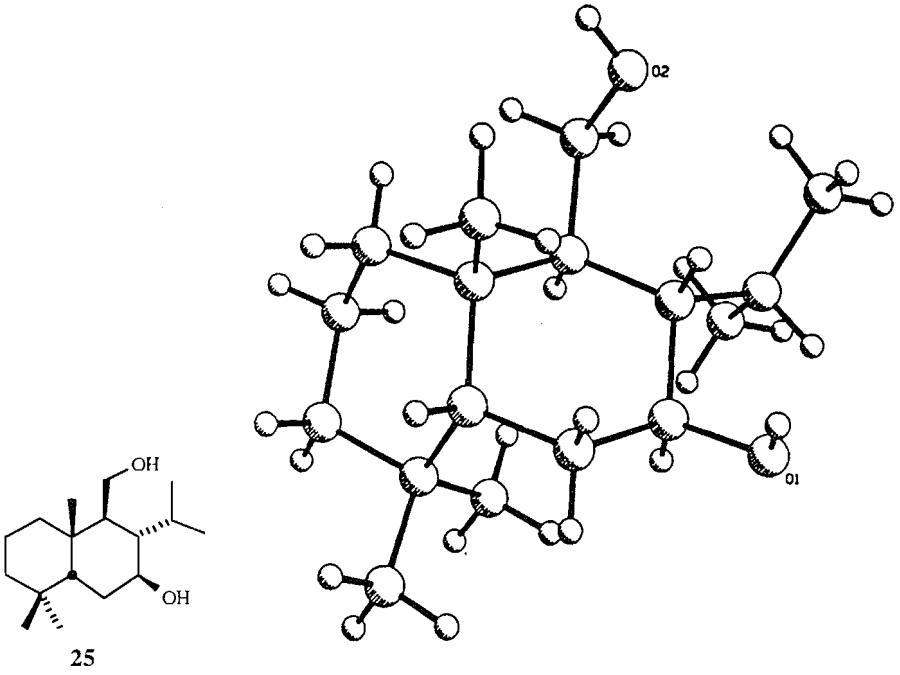

(J = 6.0 Hz) and 0.90 ppm (J = 6.0 Hz) while three methyl singlets were observed at δ 0.98, 1.10, and 1.16 ppm. A doublet of doublets at δ 2.14 ppm (1H, J = 5.2 and 7.4 Hz) was probably due to one of the methylene protons at C7 that was neighboring to the cyclopropane ring). A one-proton complex multiplet at δ 3.87 ppm was assigned to the proton at C6. By analogy to structure **25** and the following mechanistic explanation, the ring fusion of **26** was presumed to be *cis* and the hydroxyl should have β orientation.

The oxidation of **26** by Jones reagent produced ketone **27** in 80% yield.

The mechanism associated with the formation of **25** and **26** is unknown but some specu-lative comments can be put forth. The presence of hydroxyl functions at C7 and C11 in **25** suggest an initial migration of the double bond in **24** to the C6–C7 position and the resultant vinyl cyclopropane function could undergo ring opening and functionalization. The ring opening of vinylcyclopropanes by borane has been previously observed (12) but usually a much more drastic condition is required. It is remarkable that the cleavage reaction of **24** took place at room temperature.

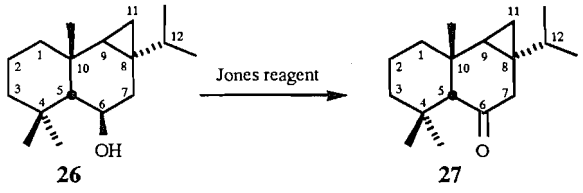

In a final attempt to improve the yield of **6**, the sequence in Scheme 3 was considered and put to an experimental test. Trimethylsilyl enol ether **28** was prepared by trapping the enolate generated in the Birch reduction of **5** with trimethylsilyl chloride (13). The crude product, containing two diastereomers as revealed from the previous enolate trapping with water, was then converted into a mixture of trimethylsilyl cyclopropyl ethers (**29**) using the Simmons–Smith reaction (14, 15). This mixture contained two diastereomers (**29**α and **29**β) that had the newly created cyclopropyl ring α and β oriented. The

Scheme 3. An alternative route to ketone **6.**

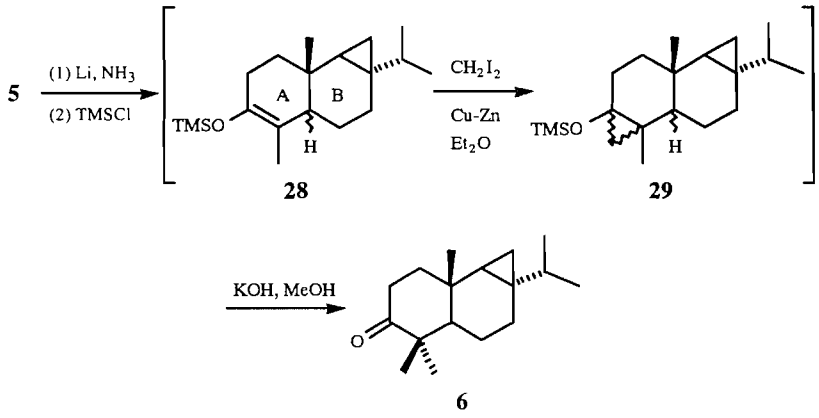

crude product from the Simmons–Smith reaction was hydrolyzed in warm potassium hydroxide – methanol solution without purification (15). A major compound isolated was identified as **6**, previously obtained in the Stork enolate trapping reaction, by comparing their MS, IR, NMR data. The overall yield of **6** from **5** was 45%.

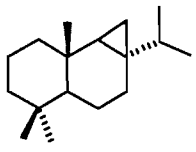

The reduction of **6** by the Wolf–Kishner–Huang Minlon method gave hydrocarbon **7** in 70% yield.

Ozonation of hydrocarbon 7

Ozonation of hydrocarbon **7** in ethyl acetate under conditions similar to those used previously (1) provided an unexpected complex mixture from which ketone **30** (35%) and alcohol **31** (5%) were isolated. The expected functionalization of the isopropyl side chain, as observed in ozonation of other thujone-derived intermediates (1), was not obtained and therefore the compounds **8** and **9** were not isolated.

Ketone **30** in its mass spectrum revealed a molecular ion at

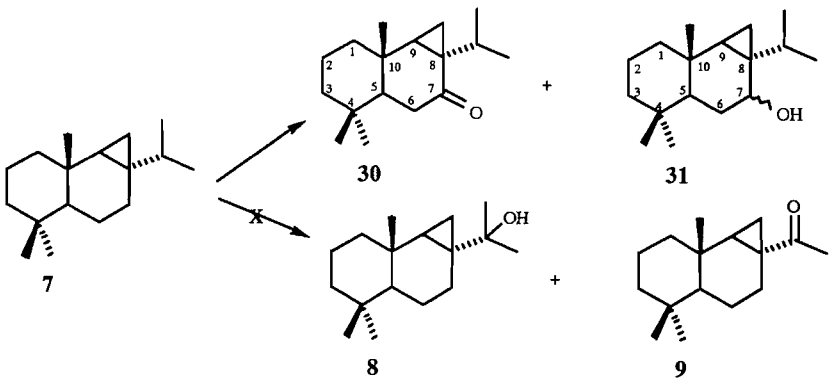

m/z 248 and its IR spectrum displayed a conjugated carbonyl absorption at 1665 cm^{-1}. Its ^1H NMR spectrum indicated two methyl doublets at δ 0.84 ppm (J = 6.6 Hz) and 0.94 ppm (J = 6.6 Hz), corresponding to the two methyl groups of the isopropyl side chain, and three methyl singlets at δ 0.78, 1.11, and 1.30 ppm. A one-proton septet (J = 6.6 Hz) corresponding to the methine proton in the isopropyl side chain appeared at δ 1.84 ppm. A multiplet containing two protons at δ 2.00–2.30 ppm corresponded to the two methylene protons at C6. The corresponding alcohol **31** revealed spectroscopic data consistent with this structural assignment (see Experimental).

It is surprising that the previously observed selective ozonation of thujone derivatives could not be applied to the homothujone derivative **7**. The reasons for this reactivity change are unknown. Generally, a cyclohexane ring is more puckered than a cyclopentane ring. This may allow one of carbon–hydrogen bonds at C7 to be properly oriented towards the cyclopropane ring in **7**. This orientation may then facilitate the participation of the cyclopropyl group in the ozone insertion into this particular carbon–hydrogen bond and the initially formed secondary hydrotrioxide can then be decomposed into either the corresponding ketone or alcohol (16). It is noted here that oxidation of cyclopropyl methylene to cyclopropyl ketone can be effectively accomplished by other oxidizing reagents (17). The regioselective oxidation of homothujone derivatives at the methylene group by other reagents may find applications in a way complementary to the ozonation of thujone derivatives.

Conclusion

In summary, we have initiated studies on a new strategy to develop thujone as a chiral building block, in the context of synthesizing cyclohexane-containing natural products. Regio-

selective ring expansion of thujone was accomplished efficiently to furnish homothujone and the latter was further elaborated stereoselectively into more complex derivatives. Some novel chemistry of homothujone derivatives such as the organoborane-mediated cyclopropane ring opening and the unusual mode of ozonation is starting to demonstrate a departure from that of thujone derivatives retaining the bicyclo[3.1.0]hexane moiety. Such chemical novelty also presents new opportunities to explore efficiently the utility of thujone as a chiral building block and merits further research in the future.

Experimental

Homothujone experimental

Commercially available solvents were used for chromatography without further purification. Petroleum ether refers to the fraction boiling in the range of 30–60°C. Anhydrous diethyl ether and tetrahydrofuran were prepared by distillation from a mixture containing sodium and benzophenone. Anhydrous *n*-pentane was prepared by distillation from phosphorus pentoxide. Anhydrous ethanol was distilled from magnesium. Thujone was distilled from Western red cedar leaf oil, which was generously donated by Intrinsic Research and Development Incorporated.

Unless stated otherwise, all reactions were carried out under a positive pressure of anhydrous nitrogen. Unless otherwise stated, all reaction products were purified by "flash chromatography" using silica gel (230–400 mesh) supplied by E. Merck Co. with air pressure to obtain a suitable flow.

Melting points were measured using a Kofler block melting point apparatus and are uncorrected. Optical rotations were recorded on a Perkin–Elmer 141 automatic polarimeter in chloroform solution using a quartz cell of 10 cm path length with the concentration (in g/100 mL) given in parentheses. The ultraviolet spectra were recorded on Cary 15 or Perkin–Elmer Lambda 4B UV/VIS spectrometers using quartz cells of 1 cm path length. The infrared spectra were recorded on Perkin–Elmer 710, 710B, and 1710 spectrometers in chloroform solution using NaCl cells of 0.1 mm path length or as thin film using NaCl plates. The ^{1}H NMR spectra were obtained from Bruker WH-400 or Varian XL-300 spectrometers with deuteriochloroform as solvent and the chemical shifts are reported in the delta (δ) scale in ppm relative to tetramethylsilane. 13C spectra were taken on Varian XL-300 spectrometers and chemical shifts are reported in the delta (δ) scale in ppm relative to tetramethylsilane. The low- and high-resolution mass spectra were recorded on AEI-MS-9 and KRATOS-MS-50 spectrometers, respectively, using the electron impact ionization method, while the chemical ionization mass spectra were recorded on a Delsi Nermag R10-1 OC spectrometer using ammonia as carrier gas. Elemental analyses were performed by Mr. P. Borda, Microanalytical Laboratory, University of British Columbia.

*[1R-(1α,2α/β,6α)]-4-Ethoxycarbonyl-2-methyl-6-(1-methylethyl)bicyclo[4.1.0]heptan-3-one (**13**, the ketoester form) and [1R-(1α,2α/β,6α)]-4-ethoxycarbonyl-2-methyl-6-(1-methylethyl)bicyclo[4.1.0]hept-3-ene-3-ol (**13**, the enolester form)*

To a cooled solution (0°C) of thujone (**1**) (3.04 g, 20.0 mmol) and boron trifluoride etherate (4.26 g, 30.0 mmol) in anhydrous diethyl ether (25.0 mL), ethyl diazoacetate (3.42 g, 30.0 mmol) in anhydrous diethyl ether (5.0 mL) was added dropwise over a period of 30 min. The resulting solution was stirred under nitrogen at room temperature overnight, made basic with saturated aqueous sodium carbonate solution, and extracted with diethyl ether. The diethyl ether solution was washed with brine, dried over magnesium sulfate, and concentrated *in vacuo*. Column chromatography of the crude product with ethyl acetate:hexanes (1:30, v/v) produced β-ketoester **13** in 70% yield (3.34 g). The physical properties of **13** are as follows: UV (MeOH, c = 20.4 mg/L) $\lambda_{max.}$: 258 nm (log ε = 3.980); IR (film) $\nu_{max.}$: 3370 (O-H stretching), 1655 (C=O stretching), 1615 (C=C stretching) cm^{-1}; ^{1}H NMR (400 MHz, $CDCl_3$) δ: 0.30 (1H, dd, J = 4.4 and 8.8 Hz), 0.39 (1H, t, J = 4.4 Hz), 0.68 (1H, dd, J = 4.4 and 8.8 Hz), 0.98 (6H, two overlapped doublets, J = 5.6 and 4.4 Hz), 1.03 (1H, m), 1.24 (3H, d, J = 7.2 Hz), 1.31 (3H, t, J = 6.8 Hz), 2.25–2.57 (2H, AB type, J = 16 Hz), 2.64 (1H, q, J = 7.2 Hz), 4.21 (2H, m), 12.24 (1H, s); MS *m/z* (relative intensity): 238 (M^+, 35.0%), 192 (79.7%), 177 (66.4%), 149 (100.0%); high-resolution EIMS calcd. for $C_{14}H_{22}O_3$: 238.1569; found: 238.1570.

*[1R-(1α,2α/β,6α)]-2-Methyl-6-(1-methylethyl)bicyclo-[4.1.0]heptan-3-one (**4**)*

To ketoester **13** (2.70 g, 11.3 mmol) in DMSO (20.0 ml) was added sodium chloride (1.20 g, 20.9 mmol) and water (1.0 mL). The resulting mixture was refluxed at 140°C for 4 h, cooled down, diluted with water (40 mL), and extracted with diethyl ether (3 × 25 mL). The ether solution was dried over magnesium sulfate and concentrated in vacuo to give a crude product that was chromatographed with ethyl acetate:hexanes (1:8, v/v). Homothujone **4** was obtained in 96% yield (1.80 g). The physical properties of **4** are as follows: IR(film) $\nu_{max.}$: 3060, 1700 cm^{-1}; ^{1}H NMR (400 MHz, $CDCl_3$) δ: 0.50 (2H, m), 0.72 (1H, m), 0.95 (3H, d, J = 6.4 Hz), 0.98 (3H, d, J = 6.4 Hz), 1.06 (1H, m), 1.22 (3H, d, J = 8.0 Hz), 1.84 (1H, m), 2.10 (2H, m), 2.35 (1H, m), 2.47 (1H, m); EIMS *m/z* (relative intensity): 166 (M^+, 18.3%), 123 (29.7%), 109 (58.0%), 96 (91.2%), 41 (100.0%); high-resolution EIMS, calcd. for $C_{11}H_{18}O$: 166.1358; found: 166.1360.

*[1aR-(1aα,7aβ,7bα)]-1,1a,2,3,6,7,7a,7b-Octahydro-4,7a-dimethyl-1a-(1-methylethyl)-5H-cyclopropa[a]-naphthalen-5-one (**5**)*

Homothujone **4** (341 mg, 2.05 mmol) was mixed with 1–diethylamino-3-pentanone-iodomethane salt (675 mg, 2.26 mmol) in anhydrous ethanol (20.0 mL) under an atmosphere of nitrogen. After the addition of potassium hydroxide (184 mg, ~80% pure, 2.57 mmol), the reaction mixture was heated to reflux for 1 h, cooled down, and diluted with water (30 mL). Petroleum ether (2 × 20 mL) was used to extract the above aqueous mixture. Concentration of the combined petroleum ether solution in vacuo furnished an oil, which was chromatographed to provide **5** in 70% yield (332 mg). The physical properties of **5** are as follows: $[\alpha]_D^{25} = 1.94 \times 10^2$ (c 1.00, $CHCl_3$); UV (MeOH, c 20.0 mg/L) $\lambda_{max.}$: 250 nm ((log ε = 4.133); IR (film) $\nu_{max.}$: 3060, 1660, 1620 cm^{-1}; ^{1}H NMR (400 MHz, $CDCl_3$) d: 0.30 (1H, dd, J = 4.8 and 9.6 Hz), 0.50 (1H, dd, J = 4.8 and 9.6 Hz), 0.66 (1H, t, J = 4.8 Hz), 0.90 (3H, d, J = 7.2 Hz), 0.93 (3H, d, J = 7.2 Hz), 1.01 (1H, m), 1.16 (3H,

s), 1.58 (2H, m), 1.74 (3H, s), 1.82 (1H, m), 1.93 (1H, m), 2.12 (1H, dt, J = 5.2 and 14.0 Hz), 2.35–2.70 (3H, m); EIMS *m/z* (relative intensity): 232 (M+, 57.2%), 217 (18.3%), 189 (60.1%), 161 (100.0%); high-resolution EIMS, calcd. for $C_{16}H_{24}O$: 232.1827; found: 232.2819. Anal. calcd. for $C_{16}H_{24}O$: C 82.70, H 10.41; found: 82.58, H 10.44.

*[1a*R*-(1*α*,7a*β*,7b*α*)]-Decahydro-4,4,7a-trimethyl-1a-(1-methylethyl)-5*H*-cyclopropa[a]naphthalen-5-one (**6**)*

Method A: Ammonia was distilled from sodium to a flask charged with enone **5** (419 mg, 1.81 mmol) under nitrogen. Pieces of lithium metal (13.8 mg, 1.99 mmol, 1.1 equiv.) were added and the resulting dark purple solution was stirred at −33°C for 1 h before iodomethane (1.3 mL) and anhydrous diethyl ether (5.0 mL) were introduced. The Dry Ice – acetone condenser was removed to allow ammonia to evaporate. The reaction mixture was stirred overnight and transferred to a separatory funnel containing water (15 mL) and ether (20 mL). The ether layer was separated, washed with brine (10 mL), and dried over magnesium sulfate. Evaporation of diethyl ether in vacuo resulted in a yellowish oil, which was chromatographed first with ethyl acetate:hexanes (1:15, v/v) and then benzene to furnish ketone **6** in 15% yield (63 mg).

Method B: Ammonia (~20 mL) was distilled from sodium to a solution of enone **5** (1.10 g, 4.74 mmol) in anhydrous ether (10 mL) under nitrogen. Lithium (35 mg, 4.98 mmol, 1.05 equiv.) was added. The dark purple mixture was stirred for 1.5 h at −33°C before freshly distilled trimethylsilyl chloride (1.20 mL, 2.0 equiv.) was injected. The resulting yellowish solution was warmed to room temperature and stirred for 1 h. Evaporation of ammonia and ether gave a yellowish crude oil. Anhydrous ether (10.0 mL) was introduced to the above crude product. Half of the solution (~5.0 mL) thus prepared was transferred to a new dry flask. Zinc–copper couple (powder, 314 mg) and distilled diiodomethane (0.80 mL) were added and the greyish mixture was refluxed overnight. Filtration through a layer of Celite afforded an ether solution, which was condensed to a colorless oil. This oil was then dissolved in methanol (10 mL). After introduction of potassium hydroxide (100 mg, ~80% pure, 1.78 mmol), the solution was refluxed 1 h and cooled down. Evaporation of solvent in vacuo and repeated column chromatography with ethyl acetate:hexanes (1:8, v/v) yielded **6** in 45% (262 mg).

The physical properties of **6** are as follows: $[\alpha]_D^{25}$ −8.3 (*c* 0.42, $CHCl_3$); IR (film) $\nu_{max.}$: 1703 (C=O stretching) cm^{-1}; ^1H NMR (400 MHz, $CDCl_3$) δ: 0.08 (1H, m), 0.35 (2H, m), 0.70–1.55 {20H, including 0.85 (6H, t, J = 2.4 Hz), 1.04 (3H, s), 1.21 (3H, s), 1.22 (3H, s)}, 1.70 (1H, m), 1.85 (1H, m), 2.30 (2H, m), 2.62 (1H, m); EIMS *m/z* (relative intensity): 248 (M^+, 18.6%), 230 (12.0%), 205 (27.2%), 41 (100.0%); high-resolution EIMS, calcd. for $C_{19}H_{28}O$: 248.2140; found: 248.2135.

*[1a*R*-(1*α*,7a*β*,7b*α*)]-Decahydro-4,7a-dimethyl-1a-(1-methylethyl)-5*H*-cyclopropa[a]naphthalen-5-one (**20**)*

Method A: Ammonia (5 mL) was distilled from sodium to a flask containing **5** (151 mg, 0.500 mmol) in anhydrous ether (3.0 mL) under an atmosphere of nitrogen. While the flask was kept at −33°C, small pieces of lithium were added slowly for about 1 h until a blue color persisted. After further stirring for 30 min, ammonium chloride was added to destroy excess lithium and ammonia was evaporated during warming up to room temperature. Concentration of the reaction mixture gave an oil which was chromatographed with ethyl acetate:hexanes (1:8, v/v) to give a mixture of **20** and **21** (124 mg, 82%) at a ratio of 4.3:1 as indicated by gas chromatography.

Method B: The solution of enone **5** (368 mg, 1.59 mmol) in ethanol (15.9 mL) was mixed with 10% palladium – charcoal catalyst (85 mg). The mixture was charged with 1 atm (101.3 kPa) hydrogen at room temperature and stirred for 2 h. Filtration through a layer of Celite gave a colorless solution, which was then concentrated in vacuo. A mixture of **20** and **21** at a ratio 6:1 as shown from GC was thus obtained (350 mg, 95% yield).

The physical properties of **20** are as follows: IR (film) $\nu_{max.}$: 1705 (C=O stretching) cm^{-1}; ^1H NMR (400 MHz, $CDCl_3$) δ: 0.09 (1H, t, J = 5.2 Hz), 0.40 (2H, m), 0.85 (3H, d, J = 6.0 Hz), 0.88 (3H, d, J = 6.0 Hz), 0.93 (3H, J = 8.0 Hz), 1.45 (3H, s), 1.73 (1H, m), 1.87 (1H, m), 2.24 (2H, m), 2.50 (1H, m) 2.89 (1H, m); EIMS *m/z* (relative intensity): 234 (M^+, 30.6%), 219 (16.3%), 191 (20.2%), 41 (100.0%); high-resolution EIMS, calcd. for $C_{16}H_{26}O$: 234.1984; found: 234.1980.

*[1a*S*-(1*α*,7a*β*,7b*α*)]-1,1a,2,4,6,7,7a,7b-Octahydro-4,4,7a-trimethyl-1a-(1-methylethyl)-5*H*-cyclopropa[a]-naphthalen-5-one (**23**)*

To the solution of enone **5** (109 mg, 0.470 mmol) in anhydrous DMSO (5.0 mL) was added sodium methoxide (55 mg, 1.0 mmol, 2.1 equiv.) under nitrogen. After the mixture was stirred for 5 h, iodomethane (100 mL, 1.61 mmol, 4.0 equiv.) was injected. Stirring continued for another 3 h. The reaction mixture was poured into a funnel containing 20 mL water. The aqueous mixture was extracted with hexanes (2 × 15 mL). After drying over magnesium sulfate, evaporation of solvent in vacuo, and chromatography with ethyl acetate:hexanes (1:8, v/v), ketone **23** was obtained (62 mg, 60% yield based on 10% recovery of starting material). The physical properties of **23** are as follows: IR (film) $\nu_{max.}$: 1700 cm^{-1}; ^1H NMR (400 MHz, $CDCl_3$) δ: 0.20 (1H, t, J = 4.0 Hz), 0.39 (1H, dd, J = 4.0 and 10.0 Hz), 0.58 (1H, dd, J = 4.0 and 10.0 Hz), 0.80–1.40 {16 H, m, including 0.94 (6H, d, J = 6.0 Hz), 1.01 (3H, s), 1.18 (3H, s), 1.20 (3H, s)}, 1.84 (1H, m), 1.98 (1H, m), 2.14–2.35 (2H, m), 2.38–2.65 (2H, m), 5.41 (1H, t, J = 4.0 Hz); EIMS *m/z* (relative intensity): 246 (M^+, 36.4%), 231 (42.1%), 218 (5.9%), 203 (50.2%), 105 (100.0%); high-resolution EIMS, calcd. for $C_{17}H_{26}O$: 246.1984; found: 246.1988.

*[1a*S*-(1*α*,7a*β*,7b*α*)]-1a,2,4,5,6,7,7a,7b-Octahydro-4,4,7a-trimethyl-1a-(1-methylethyl)-1*H*-cyclopropa[a]-naphthalene (**24**)*

To the mixture of ketone **23** (500 mg, 2.03 mmol) in diethylene glycol (10 mL) was added potassium hydroxide (422 mg, ~80% pure, 6.02 mmol) and hydrazine hydrate (300 mL, 6.18 mmol) under nitrogen. After refluxing at 100–150°C for 1 h, water and excess hydrazine hydrate were distilled away through a Dean–Stark trap until the temperature reached 250°C. Further refluxing at 200°C continued for 4 h. The reaction mixture was then cooled to room temperature and and diluted with water (20 mL). The aqueous mixture was

extracted with petroleum ether (3 × 10 mL). Evaporation of solvent in vacuo and column chromatograghy with petroleum ether afforded **24** (316 mg, 67%). The physical properties of **24** are as follows: IR (film) $\nu_{max.}$: 3050 (C-H stretching) cm^{-1}; ^1H NMR (400 MHz, $CDCl_3$) δ: 0.15 (1H, m), 0.40 (2H, m), 0.87 (6H, d, J = 6.0 Hz), 1.05 (3H, s), 1.09 (3H, s), 1.16 (3H, S), 5.30 (1H, t, *J* = 4.0 H); EIMS *m/z* (relative intensity): 232 (M^+, 53.4%), 217 (39.3%), 204 (6.7%), 189 (62.1%), 105 (100.0%); high-resolution EIMS, calcd. for $C_{17}H_{28}$: 232.2191; found: 232.2196.

*[1S-(1α,2β,3α,4aα,8aα)]-Decahydro-3-hydroxy-5,5,8a-trimethyl-2-(1-methylethyl)naphthalenemethanol (**25**) and [1aS-(1α,3β,3aβ,7aβ,7bα)]-decahydro-4,4,7a-trimethyl-1a-(1-methylethyl)-3H-cyclopropa[a]naphthalen-3-ol (**26**)*

To the solution of **24** (100 mg, 0.43 mmol) in THF (5.0 mL) at 0°C under nitrogen was added borane (0.35 M in THF, 1.0 mL) in a dropwise manner. The resulting mixture was stirred for 5 h at room temperature and cooled to 0°C again. Aqueous sodium hydroxide solution (3.0 M, 1.0 mL) and hydrogen peroxide solution (aq., 30%, 1.0 mL) were added slowly. The resulting two-phase mixture was warmed to room temperature, stirred for 2 h, and saturated with sodium chloride. The THF layer was separated and the aqueous layer was extracted with ether (5 mL). The organic layers were combined and concentrated in vacuo. Column chromatography of the crude product with ethyl acetate:hexanes (first 1:8 and then 3:7, v/v) generated **25** (45 mg, 39%) and **26** (31 mg, 29%). The physical properties of **25** are as follows: mp = 136–138°C; $[\alpha]_D^{25}$ +23 (*c* 0.84, $CHCl_3$); IR (film) $\nu_{max.}$: 3500 (O-H stretching) cm^{-1}; ^1H NMR (400 MHz, $CDCl_3$) δ: 0.90–1.80 {26H, 0.96806 (3H, s), 0.98 (3H, s), 1.00 (3H, s), 1.01 (3H, d, *J* = 7.0), 1.15 (3H, d, *J* = 7.0)}, 1.97 (2H, m), 2.18 (1H, m), 3.72 (2H, m), 4.04 (1H, m); EIMS *m/z* (relative intensity): 250 ($M^+ - H_2O$, 1.2%), 235 (3.1%), 232 (1.7%), 123 (100%). High-resolution EIMS, calcd. for $C_{17}H_{32}O_2$: 268.2402; found: 268.2215; chemical ionization MS (using NH_3 as carrier gas) *m/z*: 286 ($M + NH_4^+$), 269 ($M + H^+$). Anal. calcd. for $C_{17}H_{32}O_2$: C 76.06, H 12.02; found: C 76.26, H 12.02. The physical properties of **26** are as follows: $[\alpha]_D^{25}$ + 13 (*c* 0.50, $CHCl_3$); IR (film) $\nu_{max.}$: 3400 (O-H stretching), 3060 (cyclopropane C-H stretching) cm^{-1}; ^1H NMR (400 MHz, $CDCl_3$) δ: 0.14 (1H, dd, *J* = 4.4 and 8.8 Hz), 0.45 (1H, dd, *J* = 4.4 and 8.8 Hz), 0.64 (1H, t, *J* = 4.4 Hz), 0.85 (3H, d, *J* = 6.0 Hz), 0.90 (3H, d, *J* = 6.0 Hz), 0.98 (3H, s), 1.10 (3H, s), 1.16 (3H, s), 2.14 (1H, dd, *J* = 7.5 and 15.0), 3.87 (1H, m); EIMS *m/z* (relative intensity): 250 (M^+, 2.1%), 232 (10.5%), 217 (12.8%), 207 (10.6%), 109 (100.0%); high-resolution EIMS, calcd. for $C_{17}H_{30}O$: 250.2297; found: 250.2307.

*[1aS-(1α,3aβ,7aβ,7bα)]-Decahydro-4,4,7a-trimethyl-1a-(1-methylethyl)-3H-cyclopropa[a]naphthalen-3-one (**27**)*

To the solution of alcohol **26** (20 mg, 0.080 mmol) in acetone (2.5 mL) was added Jones reagent (12 M CrO_3 in concentrated sulfuric acid) in a dropwise manner until the mixture changed to a steady orange color. Water (10 mL) was added and the aqueous mixture was extracted with hexanes (2 × 5 mL). Evaporation of solvent in vacuo and column chromatography with ethyl acetate:hexanes (1:8, v/v) afforded **27** (16 mg, 80%). The physical properties of **27** are as follows: IR (film) $\nu_{max.}$: 1700 cm^{-1}; ^1H NMR (400 MHz, C_6D_6) δ: 0.18 (2H, m), 0.53 (1H, m), 0.65 (3H, d, *J* = 7.2 Hz), 0.90 (3H, d, *J* = 7.2 Hz), 0.97 (3H, s), 1.01 (3H, s), 1.19 (3H, s), 2.29 (2H, AB type, *J* = 16.0 Hz). EIMS *m/z* (relative intensity): 248 (M^+, 10.6 %), 233 (2.8%), 205 (5.2%), 177 (9.6%), 109 (100.0%); high-resolution EIMS, calcd. for $C_{17}H_{28}O$: 248.2140; found: 248.2138.

*[1aR-(1α,7aβ,7bα)]-1a,2,3,3a,6,7,7a,7b-Octahydro-4,7a-dimethyl-1a-(1-methylethyl)-5-methoxyl-1H-cyclopropra[a]naphthalene (**22**)*

Ketone **20/21** (6:1, 200 mg, 0.855 mmol), obtained from palladium–charcoal catalyzed hydrogenation of **5**, was treated with sodium hydride (70 mg, 2.0 equiv., 60% in mineral oil) in anhydrous DMSO (5.0 mL) under nitrogen at room temperature for 1 h. Freshly distilled iodomethane (106 mL, 1.71 mmol, 2.0 equiv.) was added rapidly and the resulting mixture was stirred for another hour. The reaction mixture was then poured into water (20 mL) and the aqueous mixture was extracted with hexanes (2 × 15 mL). Evaporation of hexanes in vacuo and column chromatography with ethyl acetate:hexanes (1:8, v/v) gave **22** (91 mg, 54% based on recovery of starting material) and starting material **20/21** (42 mg). The physical properties of **22** are as follows: IR (film) $\nu_{max.}$: 3050, 1680 (C=C stretching) cm^{-1}; ^1H NMR (400 MHz, $CDCl_3$) δ: 0.08 (1H, m), 0.30 (2H, m), 0.70–1.70 {(22H, m,680 including 0.87 (6H, t, *J* = 6.0 Hz), 0.95 (3H, s), 1.60 (3H, s)}, 3.47 (3H, s); EIMS *m/z* (relative intensity): 248 (M^+, 40.2%), 233 (8.4%), 216 (2.9%), 137 (90.2%), 41 (100.0%); high-resolution EIMS, calcd. for $C_{17}H_{28}O$: 248.2140; found: 248.2137.

[1aR-(1α,7aβ,7bα)]-Decadydro-4,4,7a-trimethyl-1a-(1-methylethyl)-1H-cyclopropa[a]naphthalene (7)

Ketone **6** (250 mg, 1.01 mmol) in diethylene glycol (20 mL) was treated with potassium hydroxide (370 mg, 5.28 mmol) and hydrazine monohydrate (270 mL, 5.56 mmol). The mixture was heated at 100–150°C for 1.5 h under nitrogen. The temperature was then gradually raised to 220°C to distill off water and excess hydrazine over a period of 1.5 h. Refluxing continued at 210°C for 4 h. The mixture was cooled down, diluted with water, and extracted with petroleum ether (3 × 20 mL). Evaporation of the solvent in vacuo gave a brown oil, which was chromatographed with petroleum ether through a short column to yield **7** as a colorless oil (175 mg, 75%). The physical properties of **7** are as follows: IR (film) $\nu_{max.}$: 3050 (cyclopropane C-H stretching) cm^{-1}; ^1H NMR (400 MHz, $CDCl_3$) d: 0.07 (1H, m), 0.40 (2H, m), 0.84 (6H, t, *J* = 3.0 Hz), 1.10 (3H, s), 1.20 (3H, s), 1.22 (3H, s); EIMS *m/z* (relative intensity): 234 (M^+, 2.7%), 219 (4.5%), 191 (11.0%), 43 (100.0%); high-resolution EIMS, calcd. for $C_{17}H_{30}$: 234.2348; found: 234.2358.

*[1aS-(1α,7aβ,7bα)]-1,1a,3,3a,4,5,6,7,7a,7b-Decahydro-4,4,7a-trimethyl-1a-(1-methylethyl)-2H-cyclopropra[a]-naphthalen-2-one (**30**) and [1aS-(1α,7aβ,7bα)]-1,1a,3,3a,4,5,6,7,7a,7b-decahydro-4,4,7a-trimethyl-1a-(1-methylethyl)-2H-cyclopropra[a]naphthalen-2-ol (**31**)*

A stream of ozone–oxygen gas was passed through the solution of **7** (200 mg, 0.855 mmol) in ethyl acetate (10.0 mL) at −40°C for 7 h. Oxygen was passed through the solution for 15 min to remove the residual ozone in the solution. The reaction mixture was then treated with dimethyl sulfide (0.5 mL), and extracted with water (10 mL), and with 10% aqueous sodium

bicarbonate solution (10 mL). Removal of solvent in vacuo and chromatography of the crude product with ethyl acetate:hexanes (2:8, v/v) provided ketone **30** (74 mg, 35%) and alcohol **31** (10 mg, 5%). The physical properties of **30** are as follows: IR (film) $\nu_{max.}$: 1665 (C=O stretching) cm^{-1}; ^1H NMR (400 MHz, $CDCl_3$) δ: 0.75–1.35 {23H, m, including 0.78 (3H, s), 0.84 (3H, d, J = 6.6 Hz), 0.97 (3H, d, J = 6.6 Hz), 1.11 (3H, s), 1.30 (3H, s)}, 1.47 (1H, m), 1.63 (1H, m), 1.84 (1H, septet, J = 6.6 Hz), 2.00–2.30 (2H, m); MS *m/z* (relative intensity): 248 (M^+, 18.4%), 233 (15.2%), 205 (23.2%), 177 (42.3%), 41 (100.0%); high-resolution EIMS, calcd. for $C_{17}H_{28}O$: 248.2140; found: 248.2135. The physical properties of **31** are as follows: IR (film) $\nu_{max.}$: 3405 (O-H stretching) cm^{-1}; ^1H NMR (400 MHz, $CDCl_3$) δ: 0.13 (1H, m), 0.45 (2H, m), 0.86 (3H, s), 0.89 (3H, d, J = 6.0 Hz), 0.98 (3H, d, J = 6.0 Hz), 1.10 (3H, s), 1.20 (3H, s), 4.16 (1H, m); EIMS *m/z* (relative intensity): 250 (M^+, 0.8%), 232 (5.3%), 217 (4.5%), 43 (100.0%); high-resolution EIMS, calcd. for $C_{17}H_{30}O$: 250.2297; found: 250.2301.

Acknowledgments

We would like to express our gratitude to the Natural Sciences and Engineering Research Council of Canada for financial support and to Intrinsic Research and Development Inc. for generous samples of Western red cedar leaf oil.

References

1. J.P. Kutney. *In* Stereoselective synthesis (Part I). Vol. 14. *Edited by* Atta-ur-Rahman. Studies in Natural Products Chemistry Series. Elsevier Science Publishers, Amsterdam. 1994. pp. 389–447.
2. Y.H. Chen. Ph.D. Thesis, University of British Columbia. 1992.
3. H.J. Liu and S.P. Majumdar. Synth. Commun. **5**, 125 (1975).
4. (*a*) A.P. Krapcho and A.J. Lovey. Tetrahedron Lett. 957 (1973); (*b*) A.P. Krapcho, J.F. Weimaster, J.M. Elbridge, E.G.E. Jahngen, Jr., A.J. Lovey, and W.P. Stephens. J. Org. Chem. **43**, 138 (1978).
5. W.L. Mock and M.E. Hartman. (*a*) J. Org. Chem. **42**, 459 (1977); (*b*) J. Org. Chem. **42**, 466 (1977).
6. (*a*) L.M. Jackman and S. Sternhall. Applications of nuclear magnetic resonance spectrometry in organic chemistry. 2nd ed. Pergamon Press, Toronto. 1969. pp. 228–229 and p. 286; (*b*) M. Tandon, L.I. Wiebe, and E.E. Knaus. Can. J. Chem. **67**, 1484 (1989).
7. (*a*) J.K.M. Sanders and B.K. Hunter. Modern NMR spectroscopy: a guide for chemists. Oxford University Press, Oxford. 1987; (*b*) A. Derome. Modern NMR Techniques in Chemistry Research. Pergamon Press, New York. 1987.
8. G. Stork, R. Rosen, and N.L. Goldman. J. Am. Chem. Soc. **83**, 2965 (1961).
9. (*a*) D. Caine. Org. React. **23**, 1 (1976); (*b*) G. Stork and S.D. Darling. J. Am. Chem. Soc. **86**, 1761 (1964); (*c*) M.J.T. Robinson. Tetrahedron, **21**, 2475 (1965).
10. D. Caine. *In* Carbon–carbon bond formation. Vol. 4. *Edited by* R.L. Augustine. Marcell Dekker, New York. 1979. pp. 85–352.
11. H.C. Brown and K. Murray. J. Am. Chem. Soc. **81**, 4108 (1959).
12. (*a*) J.B. Pierce and H.M. Walborsky. J. Org. Chem. **33**, 1962 (1968); (*b*) B. Rickborn and S.E. Wood. J. Am. Chem. Soc. **93**, 3940 (1971; (*c*) W.A.G. Graham and F.G.A. Stone. Chem. Ind. (London), 1096 (1957).
13. G. Stork and P.F. Hurdlik. (*a*) J. Am. Chem. Soc. **90**, 4462 (1968); (*b*) J. Am. Chem. Soc. **90**, 4464 (1968).
14. R.D. Smith and H.E. Simmons. Org. Synth. **41**, 72 (1961).
15. (*a*) G.M. Rubottom and M.I. Lopez. J. Org. Chem. **38**, 2097 (1973); (*b*) S. Murai, T. Aya, and N. Sonoda. J. Org. Chem. **38**, 4354 (1973); (*c*) J.M. Conia and G. Girard. Tetrahedron Lett. 2711 (1973).
16. (*a*) Y.M. Hellman and G.A. Hamilton. J. Am. Chem. Soc. **96**, 1530 (1974); (*b*) P.S. Bailey. Ozonation in organic chemistry. Vol. 2. Academic Press, New York. 1982.
17. T. Hasegawa, H. Niwa, and K. Yamada. Chem. Lett. 1385 (1985).

Self-assembly of short and long-chain *n*-alkyl thiols onto gold surfaces: A real-time study using surface plasmon resonance techniques

Reno F. DeBono, Glenn D. Loucks, Deborah Della Manna, and Ulrich J. Krull

Abstract: Gold surfaces coated with monolayers of alkyl thiols are significant in the field of biosensors and chromatography. There is a general concern about the quality of coatings in terms of surface density and voids. The self-assembly of the short-chain hexane (C_6) thiol and long-chain dodecane (C_{12}) and hexadecane (C_{16}) thiols to polycrystalline gold surfaces has been investigated in situ and in real time using surface plasmon resonance (SPR) spectroscopy and surface plasmon microscopy (SPM). The self-assembly was followed based on observed changes in reflectivity at a fixed angle of incidence as a function of time. Our results indicate that the data for hexane, dodecane, and hexadecane thiol adsorption to gold surfaces were best fit by a two-step process rather than a one-step process. The mechanism may involve fast adsorption to the surface to give 80% (C_{12}, C_{16}) or 50% (C_6) coverage followed by a slow (100-fold slower) "rearrangement" of the adsorbed thiol. SPM shows these surfaces to be smooth and homogenous at a 4 μm scale. An understanding of the process of rearrangement could lead to control of the quality of coatings for analytical applications.

Key words: surface plasmon, alkyl thiols, gold, monolayer, kinetics, ellipsometry, microscopy.

Résumé : Les surfaces d'or enduites de monocouches d'alkylthiols présentent de l'intérêt dans le domaine des biosenseurs et de la chromatographie. Il existe une crainte généralisée au sujet de la qualité des enduits en termes de densité et de manques à la surface. Faisant appel à la spectroscopie de résonance des plasmons de surface (RPS) et de la microscopie des plasmons de surface (MPS), on a étudié in situ et en temps réel l'autoassemblage de chaînes courtes (hexane, C_6) et longues (dodécane, C_{12}, et hexadécane, C_{16}) de thiols à des surfaces d'or. On a suivi l'autoassemblage en se basant sur les changements observés dans la réflectivité, à un angle d'incidence fixe, en fonction du temps. Nos résultats indiquent que le meilleur ajustement des données pour les hexane-, dodécane- et hexadécane-thiols correspond à un processus en deux étapes plutôt qu'un processus en une étape. Il est possible que le mécanisme implique une adsorption rapide à la surface, conduisant à une couverture de 80% (C_{12} ou C_{16}) ou de 50% (C_6), qui serait suivie par un «réarrangement» lent (au moins 100 fois plus lent) du thiol adsorbé. La MPS montre que, à une échelle de 4 μm, ces surfaces sont lisses et homogènes. Une compréhension du processus de réarrangement pourrait conduire à une possibilité de contrôle de la qualité des enduits pour des applications analytiques.

Mots clés : plasmons de surface, alkylthiols, or, monocouches, cinétique, ellipsométrie, microscopie.

[Traduit par la rédaction]

Introduction

The development of thin films that provide selective partitioning regions for chemical and biochemical sensors and for chromatographic purposes has led to a significant amount of work into adsorption, chemisorption, and covalent deposition of small molecules, proteins, polymers, and inorganic layers onto solid surfaces (1–6). The organization of organic molecules into monolayer films through self-assembly provides a facile method of preparing surfaces with a well-defined composition, structure, and thickness, and permits the control of chemical and physical properties of the surface. One type of film that exhibits these properties is obtained from the adsorption of *n*-alkyl organosulfur compounds to gold surfaces (7). The self-assembly process is driven through the formation of chemisorptive bonds between the thiol and the gold surface, increased van der Waals interaction between the alkyl chains, and increased entropy of the system as a result of removal of the solvation layer around the thiol molecules (40–45 kcal/mol). When a gold surface is exposed to alkyl thiol solutions an ordered alkyl thiol monolayer forms at the gold surface (8–11). Properties of the deposited film can be modified by varying the length of the hydrocarbon chain and by attachment of different functional groups at the opposite end of the alkyl thiol. Incorporation of functional groups allows the control of the chemical and physical properties at the external surface of the self-assembled membrane. Alkyl thiols with over 10 carbons in the alkyl chain form a densely packed crystalline-like monolayer assembly with an extended all-*trans* alkyl chain tilted 20–30° to the surface normal (12).

Investigations of the kinetics of formation of alkyl thiol monolayers on gold have been reported in the literature (7–10) based on analysis by ellipsometry, contact angle measurements, infrared spectroscopy, X-ray photoelectron spectros-

Received July 25, 1995.[1]

R.F. DeBono, G.D. Loucks, D. Della Manna, and U.J. Krull.[2]
Chemical Sensors Group, Erindale Campus, University of Toronto, 3359 Mississauga Road North, Mississauga, ON L5L 1C6, Canada.

[1] Revision received February 12, 1996.
[2] Author to whom correspondence may be addressed. Telephone: (905) 828-5437. Fax: (905) 569-4388. E-mail: ukrull@tuzo.erin.utoronto.ca

Fig. 1. (*a*) Arrangement for optical excitation of surface plasmons; (*b*) reflected intensity versus angle of incidence for surface plasmon resonance curve.

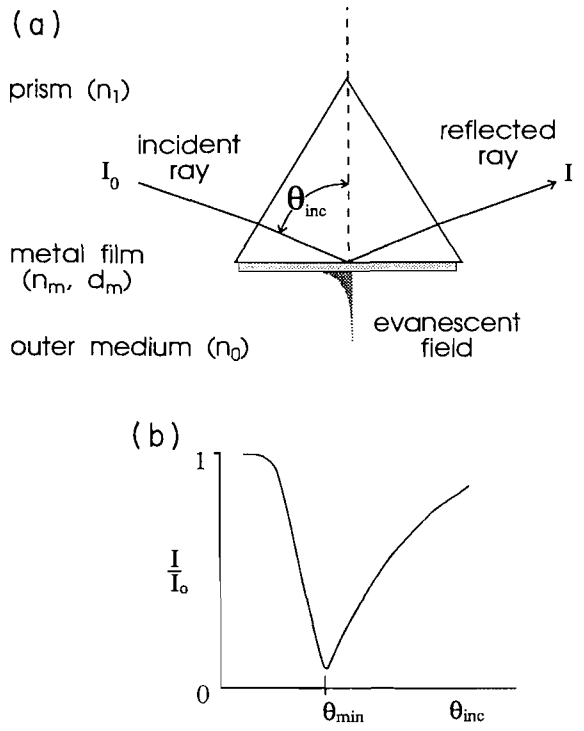

copy, and near-edge X-ray absorption fine structure (NEXAFS). These techniques provide an indication of adsorption kinetics based on the analysis of a series of different samples at different times during the adsorption process. Little information about real-time in situ adsorption has appeared. One approach has been to use a quartz crystal microbalance (QCM). For example, a QCM has been used to directly observe the adsorption/desorption from MeCN and DMF of several long-chain alkyl thiols on gold electrodes (11).

The optical techniques of surface plasmon resonance (SPR) spectroscopy and microscopy (SPM) can be used for the physical characterization and real-time observation of dynamic events in situ at an organic film located in close proximity to a metal surface. An understanding of the self-assembly process will lead to an improved capability for the design of chemically selective surfaces. This work reports a study of self-assembly of hexane, dodecane, and hexadecane thiols from 95% ethanol onto gold surfaces in situ, under static and dynamic solution flow conditions, using SPR and SPM.

Surface plasmon spectroscopy and microscopy

Figure 1*a* shows a prism of refractive index n_1 coated with a thin metal layer with a complex refractive index n_m in contact with a medium of refractive index $n_o < n_1$. Parallel polarized light of wavelength λ passes through the prism at an angle of incidence greater than the critical angle (which is defined by the prism and the outer medium) and reflects at the metal–prism boundary. A reflectivity curve (SPR curve) is produced (Fig. 1*b*) when the angle of incidence is varied while monitoring the reflected intensity. If the metal layer is sufficiently thin (<100 nm) then the reflectivity curve will exhibit a minimum at an angle Θ_{min}. This minimum arises as a result of resonant excitation involving the collective motion of conduction band electrons (surface plasmons), with a coherence length of L_c on the order of 10 μm for gold. Associated with this oscillating charge density wave is a strong evanescent wave with a penetration depth (d_p) into the outer contacting medium (n_o) of approximately 300 nm for λ = 632.8 nm. If an organic film of refractive index n_f is placed between the metal and the outer medium the reflectivity curve will be modified owing to its strong dependence on the environment near the metal surface. If $n_f > n_o$, then Maxwell's equations indicate that the SPR curve will shift to a larger angle of incidence as the thickness of the film (T_f) increases, and the angle of incidence becomes constant when $T_f > d_p$.

The surface plasmon resonance condition is determined by the spatial average of the thickness and refractive index of the organic film as sampled over the coherence length (L_c) near the metal surface. Differences in the profile of the film over distances greater than L_c will be detected as spatially resolved differences in reflected intensity at a fixed angle of incidence and these form the basis of surface plasmon microscopy (13, 14). These differences in intensity provide optical contrast to image regions of different optical mass (refractive index, thickness). Further details concerning the theory of surface plasmon resonance can be found in reviews by Raether (15, 16).

Experimental

Chemicals

Absolute alcohol of pharmaceutical grade was obtained from Consolidated Alcohols (Toronto, Ont.). 95% (v/v) Ethanol was prepared by adding distilled water. All distilled water was obtained using a Milli-Q five-stage cartridge purification system (Millipore, Mississauga, Ont.) and was degassed before use. Diethyl disulfide, 1-hexane thiol, 1-dodecane thiol, and 1-hexadecane thiol were obtained from Aldrich Chemicals (Milwaukee, Wis.) and used as obtained. Stock solutions of 500 μM hexane, hexadecane, and dodecane thiols were prepared with 95% ethanol. Gold metal (99.99% purity) was obtained from DEAK International. Chromium rods were obtained from R.D. Mathis Co., Long Beach, Calif. Premium Quality glass wafers were supplied by Fisher Scientific (Pittsburgh, Pa.).

Equipment

Absorption measurements were done using an HP 8452A diode array spectrophotometer (Hewlett–Packard Company, Palo Alto, Calif.). Ellipsometry was done with an Auto-EL II nulling ellipsometer (Rudolph Research Corporation, Flanders, N.J.) with a 1 mW continuous wave helium–neon laser (632.8 nm) at a fixed angle of incidence of 70.00°. Ellipsometric data were analysed using a "Film 85" software package based on the McCrackin program (17) version 3.0, program 70 to determine the refractive index of the substrate and program 13 to determine the thickness of the alkyl thiol films.

Preparation of silver and gold-coated wafers was done using a Key High Vacuum Products model KV-301 metal vapour deposition instrument (Nesconset, N.Y.) operating at a maximum pressure of 8 μTorr (1 Torr = 133.3 Pa). Substrates

Fig. 2. Surface plasmon spectrometer and microscope.

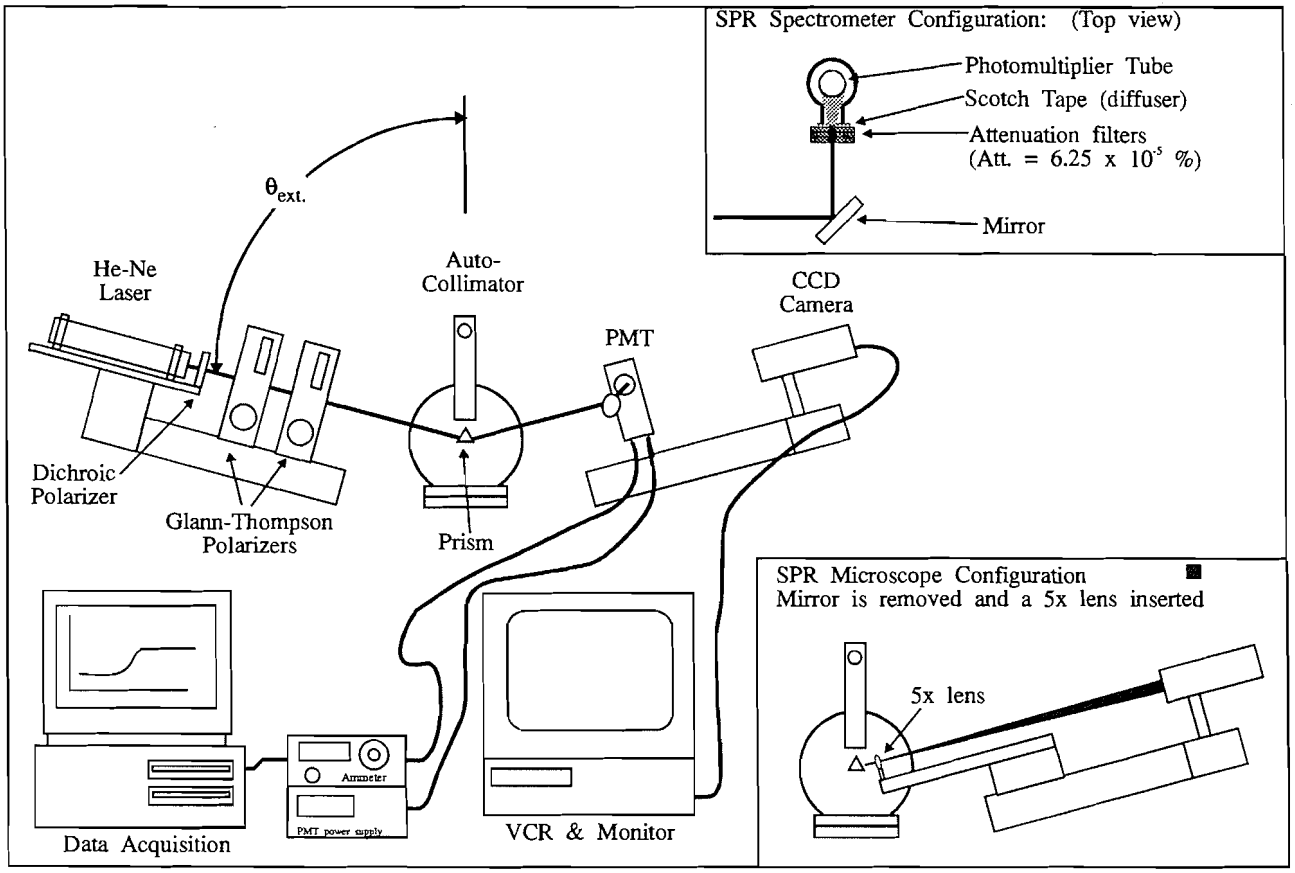

to be coated were positioned 25 cm from a resistively heated molybdenum boat. Thickness and rate of deposition were monitored using a 5 MHz piezoelectric crystal mass balance. Refractive index measurements were done using an Abbé refractometer that was maintained at constant temperature using a water bath. Static contact angle (wettability) estimates were done by imaging a 10 μL drop of distilled water with a monocular microscope that contained a reticule protractor.

Surface plasmon spectrophotometer and microscope

The experimental apparatus used for SPR is shown in Fig. 2. Angular control was achieved by the use of a goniometer from a Rudolph Research ellipsometer. This permitted the angle of incidence to be varied with a precision of 0.005°. The optical source was a 2 mW linearly polarized helium–neon (He-Ne) laser (Spectra Physics, Hughes), which emitted at 632.8 nm with a beam diameter of 2 mm, a divergence of 0.01 mradians, and a stability better than 0.8%. The He–Ne laser was positioned with the plane of polarization at approximately 45°. The optical train consisted of a He–Ne laser, a dichroic polarizer (Melles Griot) set at 45°, and two Glann–Thompson polarizers (referred to as Pol 1 and Pol 2). The optical beam passed though the dichroic polarizer and the Glann–Thompson polarizer, was refracted at the first prism face, and underwent total internal reflection at the prism base. The beam was then refracted again upon exiting the prism and was directed by a mirror (as shown in Fig. 2) through a series of attenuation filters and a diffuser (transparent Scotch™ tape) onto a Hamamatsu R-928 photomultiplier tube (PMT). The PMT current was measured with a Keithley electrometer, and the recorder output of this electrometer was passed to a Metra-Byte 12 bit analog-to-digital board or acquisition of data with an IBM-XT clone. For SPR work, Pol 1 was set at 45.00° while Pol 2 was set at either 0.00° (parallel) or 90.00° (perpendicular). Surface plasmon microscopy required the mirror to be removed and a 5× microscope lens positioned so that the focal point was at the base of the prism as shown in Fig. 2. The scattered light was collected by the lens to produce an image that was captured by a Hitachi KP-111 CCD solid state camera (Nedco, Mississauga, Ont.). The automatic gain control of the CCD camera was disabled. SPM work required careful control of the intensity of the source, which could be achieved by changing the orientation of the Glann–Thompson polarizer (Pol 1).

Procedures

Preparation of glass wafers

Glass slides were cleaned by soaking in a detergent solution in an ultrasonic bath for 1 h at 60°C followed by extensive rinsing in water and drying in an oven (100°C) for several hours. Wafers were then transferred to the vacuum deposition system where a thin layer of chromium (15–30 Å) was deposited at 0.5 Å/s at 5 μTorr. The bell jar was then back-filled with

Fig. 3. Flow cell design.

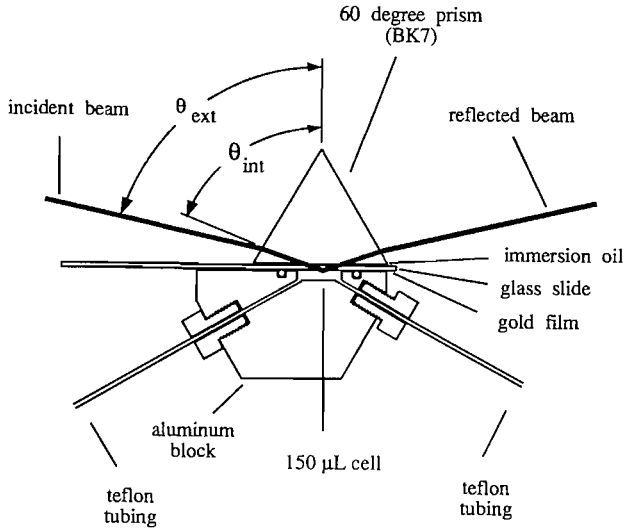

prepurified argon and the chromium rod was exchanged for a molybdenum boat containing gold. During this step, the chromium layer was exposed for a few minutes to atmospheric conditions, resulting in the formation of a thin chromium oxide layer. The system was then evacuated to 5 μTorr and approximately 430 Å of gold was deposited at a rate of 10 Å/s. The percent transmittance for a 10 Å chromium film at 632 nm was 96 ± 3% and for a 430 Å gold film was 6 ± 1%. Wafers were used within 30 min of gold deposition for thiol self-assembly experiments.

Prism and flow-through cell assembly

A 60.00° BK-7 prism (30.00 × 30.00 × 30.00 mm) was optically connected to the gold-coated glass wafer using a matching immersion oil (type B, Cargille Laboratories Inc., n = 1.515). The prism – glass slide assembly was then clamped to an aluminum flow-through cell (150 μL) and with a Viton O-ring pressed against the glass slide (Fig. 3). The Teflon tubing used was refluxed in methanol for 1 month in order to remove leachable contaminants. A Microperspex perisaltic pump (LKB Bromma) was used to pull solution through the cell at 0.30 mL/min for dynamic studies while a 10 mL syringe was used to pull 2 mL of solution for stop-flow studies. The entire assembly was transferred to the sample stage of the SPR apparatus and the autocollimator was used on the portion of the wafer extending past the prism to ensure that the plane of incidence was normal to the glass slide.

SPR reflectivity curves and fixed angle reflectivity measurements

A manual reflectivity scan was obtained by recording the reflected intensity from 70.00° to 90.00° in 0.50° steps for both parallel (I_p) and perpendicular (I_s) polarization modes. The minimum angle of incidence was determined from the parallel polarized scan. From the reflectivity scan a fixed angle of incidence was chosen for the time-dependent measurements. The angle was chosen to be approximately 1° less than the minimum angle, where a compromise between sensitivity and signal-to-noise ratio was achieved. The intensity of the source was recorded at the beginning and end of any time-dependent measurements to verify that drift in laser intensity had not occurred. At the end of the experiment, a second SPR curve was obtained to ensure that the system was working reproducibly. SPM imaging was then done. External angles (θ_{ext}) of incidence were converted to internal angles (θ_{int}) of incidence using the equation:

$$[1] \quad \theta_{int} = \theta_b - \arcsin\left(\frac{\sin(\theta_b - \theta_{ext})}{n_p}\right)$$

where θ_b is the base angle of the prism and n_p is the refractive index of the prism. All angles of incidence reported in the results section are internal angles of incidence.

Determination of normalization factor

All intensity measurements were converted to R_p/R_s reflectivity measurements by multiplying the ratio of I_p/I_s (parallel intensity/perpendicular intensity) by a normalizing factor (NF). The NF corrected for reflectivity losses at the prism faces, mirror, and attenuation filter, and for differential response of the PMT due to movement of the optical beam across the PMT surface as the angle of incidence was varied. The NF was obtained from a reflectivity scan using a blank wafer that was optically connected to the prism. The normalization factor was obtained by dividing the perpendicularly polarized scan (I'_s) by the parallel polarized scan (I'_p):

$$[2] \quad \text{Normalization factor} = I'_s\, I'_p$$

The uncertainty associated with R_p/R_s for each point in the reflectivity curve is 1.5% for $R_p/R_s > 0.10$. R_p/R_s below 0.01 had an absolute error of ±0.0015. This error encompassed the uncertainty associated with the internal angle of incidence of ±0.006° and electrometer noise.

Modelling and fitting program

SPR data were modelled and analyzed using a program developed in Quick Basic 4.5 (SPMOD7). A model based on application of the exact Fresnel equations was used to calculate R_p/R_s for an n-layered system where n could be varied (18). The reflectivity of this system can be described using the Fresnel equations, which can be written as a 2 × 2 matrix for each layer. Combining the two boundaries of one layer then yields a matrix describing the layer. Repeating the process for all the layers results in a product of matrices. An iterative fitting program varied the initial specified parameters by carrying out a one-dimensional minimization along favourable directions in n-dimensional space using Powell's method (19). The best fit was established by use of a chi squared (χ^2) parameter. Error estimates in the fitted values were obtained by varying the specified value until the χ^2 doubled. The final fitting parameter was reported as a normalized $\bar{\chi}^2$, dividing χ^2 by the number of points used in the fitting procedure.

Results and discussion

Surface plasmon resonance spectroscopy and microscopy were used to investigate the self-assembly of alkyl thiols at gold surfaces. The reflectivity curve (Fig. 4) for a 441 Å thick gold film in contact with 95% ethanol has a moderately sharp and well-defined minimum. Hence, a gold surface in contact

Fig. 4. Surface plasmon resonance curves for a bare gold wafer in contact with 95% ethanol and after exposure to 10 μM dodecane thiol. (-----) 95% ethanol; (——) after exposure to 10 μM dodecane thiol.

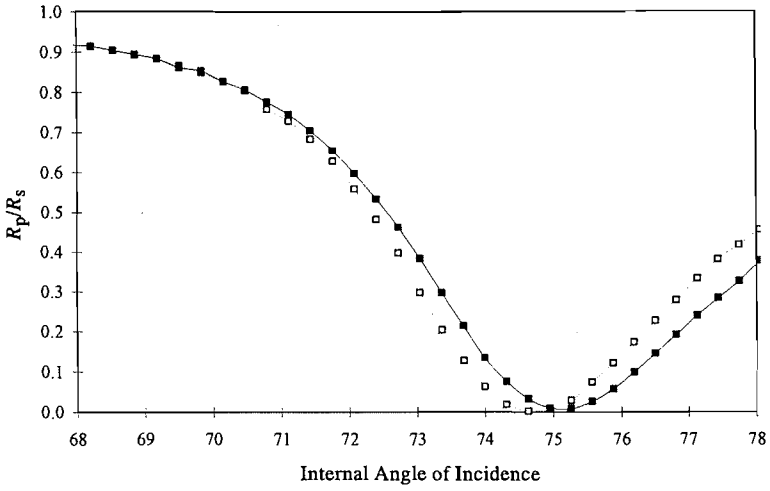

Fig. 5. Reflectivity response (θ = 74.000°) for exposure of the gold surface to 10 μM dodecane thiol in 95% ethanol from $t = 0$ to 1000 s. Delta R_p/R_s obtained by subtracting 0.0812 from R_p/R.

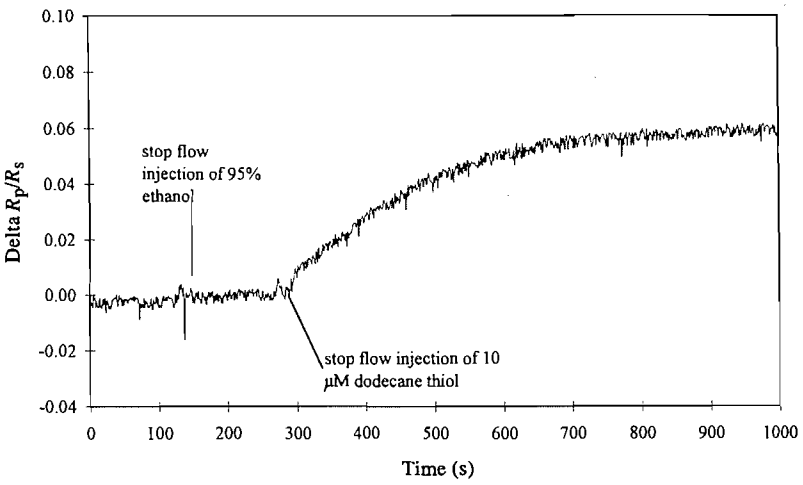

with 95% ethanol is capable of supporting surface plasmons and is expected to show sensitivity to optical mass changes occurring at the metal surface. The full width at half-height of the curve corresponds to a coherence length of 4 μm for the surface plasmon, defining the lateral resolution of this surface for SPM. Freshly prepared gold surfaces had a wettability angle of 48 ± 5°, indicating a partially hydrophobic surface. X-ray photoelectron spectroscopy indicated a thick gold film with no chromium present at the surface.

The UV absorption spectra of a disulfide exhibit two distinct bands at 210 nm and 255 nm while the thiol has one band at 205 nm. Absorption spectra of 500 μM hexane, hexadecane, and dodecane thiol solutions indicate that disulfide contamination did not exist above levels of 0.4% of the parent thiol. Attempts to generate the disulfide from the thiol by bubbling air through a 500 μM hexane thiol solution for 24 h did not generate any observable disulfide. This indicates that these solutions were not susceptible to air oxidation. The presence of disulfides at levels up to 0.4% is not expected to interfere with the adsorption of thiols, since thiol adsorption is favoured over disulfide adsorption onto gold surfaces by a factor of 75 (20). The critical micelle concentration of a lipid such as didodecanyl phosphatidyl choline in water is 400 μM (21). Hexane, dodecane, and hexadecane thiols were used at concentrations between 1 and 100 μM in 95% ethanol. Ethanol exhibits a much higher solvating power than water, hence the presence of micelles at these concentrations is not a consideration.

The reflectivity curves for a bare gold wafer in contact with 95% ethanol after exposure to 10 μM dodecane thiol for 8 h and to 95% ethanol for 15 h under stop-flow conditions are shown in Fig. 4. The change in reflectivity at a fixed angle of incidence of 74.000° upon exposure of the gold surface to 10 μM dodecane thiol is shown in Fig. 5. Exposure of the gold

Table 1. Exposure of gold wafer to 10 μM dodecane thiol.

	Bare gold surface	After exposure to 10 μM dodecane thiol
Contact angle (deg)	47 ± 5	100 ± 5
Ellipsometric measurements: δ	109.14 ± 0.005	107.35 ± 0.03
ψ	42.14 ± 0.07	42.12 ± 0.03
Minimum internal SPR angle	74.726 ± 0.006	75.210 ± 0.006
Reflectivity at 74.000	0.081 ± 0.001	0.160 ± 0.002

Table 2. Relative thickness (Å) of dodecane thiol monolayer.

Basis of relative thickness measurement	After exposure of dodecane thiol for 8 h	After subsequent exposure to 95% ethanol for 15 h
Minimum angle shift		22.2 ± 0.6
Reflectivity shift	16.5 ± 0.3	17.2 ± 0.3
Ellipsometry		16.4 ± 0.5
Theoretical all-*trans* length		17.1

surface to 10 μM dodecane thiol resulted in a rapid increase in reflectivity during the first 300 s, followed by a slow increase over the next 8 h. Exchanging the dodecane thiol solution with a fresh dodecane thiol solution after 8 h resulted in only a very slight increase with time, and replacement of the thiol solution with 95% ethanol resulted in a slight increase of reflectivity. This suggests that the adsorption process is irreversible. The wafer was then removed from the cell and was dried under argon. Subsequent ellipsometric and wettability measurements are summarized in Table 1. The shifts in θ_{min} to a larger angle of incidence, and the increase in reflectivity, are indicative of the formation of an organic layer with a refractive index larger than that of the contacting medium (95% ethanol, n = 1.3606).

Fresnel equations can be used to convert from reflectivity to average thickness based on a multilayer model, where each layer is characterized by its dielectric constant and thickness. The multilayer model consists of Prism/Cr Au organic film/outer medium. The refractive index of the BK-7 prism is 1.515. The chromium layer was treated as a thin absorbing layer with a fixed dielectric constant of 6.26 + i 5.0 and variable thickness. The refractive index of the outer medium, which was 95% ethanol at 20°C, was 1.3606. Fitting of the reflectivity curve of the uncoated gold system using the Fresnel equations permitted accurate determination of chromium layer thickness and the dielectric constant and thickness of the gold layer in situ. Literature values for the dielectric constant of the gold layer can not be used since the dielectric constant of the gold film will show variations depending on preparation conditions. Based on the model for the uncoated gold system, the thickness of the chromium layer was determined to be 21 ± 8 Å and the dielectric constant and thickness of the gold film were $-13.29_{\pm 0.02}$ + i $1.29_{\pm 0.04}$ and 441 ± 3 Å, respectively, with a normalized χ^2 of 1.6. The real part of the dielectric constant of the gold film, which was determined from the SPR experiment, exhibited an absolute magnitude that was 13% larger than the literature value obtained by Johnson and Christy (22) for vacuum-evaporated gold films of −11.7 ± 0.2. The imaginary part of the dielectric constant of gold as determined by SPR agrees within experimental error with the literature value of 1.2 ± 0.1.

Once the dielectric constant of the gold layer had been established, the optical response of this system to the formation of an organic layer on the thin gold film could be determined. It is not possible to simultaneously determine both the refractive index and thickness of the organic layer on the gold surface. However, if the refractive index of the layer is known then the average relative thickness of the layer can be determined. The refractive index of liquid dodecane thiol is 1.46 and of crystalline polyethylene is 1.48. A refractive index of 1.5 was used to determine the relative thickness of the organic monolayers. Table 2 summarizes the relative average thickness values obtained from SPR and ellipsometric measurements for fully formed monolayers.

Good agreement exists between the experimental reflectivity and ellipsometric results, and theoretical all-*trans* length values, while the thickness based on the minimum angle shift is 5 Å larger than expected. The agreement between the theoretical all-*trans* length and the ellipsometrically determined thickness suggests that surface contamination is minimal. Wettability measurements of gold surfaces exposed to the atmosphere for 8 h are typically between 60° and 80°, compared to 47° within 30 min after thiol deposition as observed in these experiments.

During the adsorption process, intermediate surface coverage ($0 < \Phi < 1$) of the adsorbed molecules produced a partially formed monolayer as shown in Fig. 6*a*. The effective refractive index varies from that of the solvent (n = 1.3606) to that of a fully formed monolayer (approximately 1.5). To convert from reflectivity to relative thickness, an assumption must be

Fig. 6. A partially formed monolayer of surface coverage Θ is optically equivalent to a fully formed monolayer of refractive index 1.5000 and relative thickness (T) such that $T = \Theta T_f$. (*a*) A partially formed monolayer of surface coverage Θ and effective refractive index N_{eff} and thickness T_f. (*b*) Fully formed

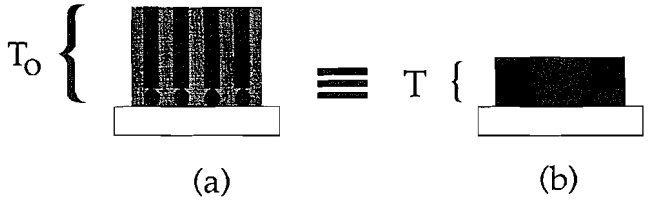

made that a partially formed monolayer is optically equivalent to a fully formed monolayer of refractive index 1.5 and relative average thickness (T) as shown in Fig. 6*b*, such that T is given by:

$$[3] \quad T = \Phi T_f$$

where T_f is the final thickness of the fully formed monolayer. To test the validity of this assumption, the optical response of these two cases for the same surface coverage should be identical. Maxwell–Garnet theory (23) can be used to calculate the effective refractive index (n_{eff}) of the partially formed monolayer. It models this film as a random distribution of small spherical particles embedded in a solvent layer and equates the volume fraction of the film occupied by the particles with surface coverage. This allows the effective refractive index to be given as:

$$[4] \quad n_{eff}^2 = n_{sol}^2 \frac{(1 + 2\Phi B)}{(1 - \Phi B)}$$

where

$$B = \frac{(n_f^2 - n_{sol}^2)}{(n_f^2 + 2n_{sol}^2)}$$

where n_{sol} is the refractive index of the solvent. The reflectivity response of these two cases as a function of surface coverage at a fixed angle of incidence of 73.683° (which is within 1° of the minimum reflectivity for a bare gold surface in contact with 95% ethanol) is shown in Fig. 7. The optical response curves are similar with a maximum difference of 2% occurring at 50% surface coverage. This is well within experimental error and indicates that the assumption associated with eq. [3] is valid, and permits the experimentally determined reflectivity to be converted to average thickness values (Fig. 8).

Kinetics of adsorption

A study of the kinetics and process of alkyl thiol adsorption from ethanolic solutions onto gold has previously been reported. This work made use of NEXAFS (10) to study samples at various reaction times. The results indicated that adsorption occurred in two steps. The first step was rapid (about 10 min for 80% monolayer coverage), and resulted in a monolayer where the alkyl chains were highly entangled. A second slow step (time constant approx. 2 orders of magnitude larger than first step) was suggested to be related to the straightening of alkyl chains. Our work has been directed to an investigation of these processes in real time.

The adsorption process consists of a thiol molecule adsorbing to the surface and forming a chemisorptive bond with the gold surface:

$$[5] \quad RSH + Au \rightarrow RSAu^*$$

Desorption of the adsorbed thiol is assumed to be negligible since the strength of the chemisorptive bond (40–45 kcal/mol) is large. Hence, we will assume that the rate of change of the adsorbed thiol concentration is described by:

$$[6] \quad \frac{d\{RSAu^*\}}{dt} = k[RSH]\{Au\}$$

where $\{RSAu^*\}$ is the surface concentration of the adsorbed thiol and [RSH] is the bulk solution concentration of thiol (i.e., no time-dependent concentration gradient) and $\{Au\}$ is the surface concentration of available sites for thiol adsorption. The parameter $\{Au\}$ can be written as:

$$[7] \quad \{Au\} = \{Au\}_0 - \{RSAu^*\}$$

assuming the mobile precursor model, and that dissociative chemisorption does not apply, where $\{Au\}_0$ is the total concentration of gold sites available for binding with the thiol. Hence, surface coverage (Φ) is represented by the following ratio:

$$[8] \quad \Phi = \{RSAu^*\}/\{Au\}_0$$

Substituting this into eq. [6] gives the rate of change as a function of surface coverage:

$$[9] \quad \frac{d\Phi}{dt} = k[RSH](1-\Phi)$$

Assuming that [RSH] does not change significantly during the course of the adsorption process and combining k[RSH] to give a single rate constant, k_1, integration gives:

$$[10] \quad \Phi = 1 - \exp(-k_1 t)$$

Restating this equation in terms of relative thickness where T is relative thickness at time t and T_1 is the limiting thickness such that:

$$[11] \quad \Phi = T/T_1$$

substitution into eq. [10] and rearranging gives:

$$[12] \quad T = T_1[1-\exp(-k_1 t)]$$

The adsorption kinetics for the dodecane thiol follows a simple model for the first 1000 s with $T_1 = 14.4 \pm 0.8$ Å and $k_1 = (450 \pm 100) \times 10^{-5}$ s^{-1} but breaks down over the next 29 000 s (overall $\bar{\chi}^2 = 2.7$) where a further increase is observed as can be seen in Fig. 8 (note: statistics represent standard deviation of 3 to 6 experiments). Initially, when the thiol adsorbs to the surface, available adjacent gold sites will be blocked from incoming thiol molecules based on simple steric consider-

Fig. 7. The change in reflectivity (Delta R_p/R_s, $(R_p/R_s)_0 = 0.1176$) at a fixed internal angle of incidence 73.683° as a function of increasing surface coverage for two cases. Case I: a (⊟) layer of fixed thickness of 20 Å and variable effective refractive index. Increasing surface coverage results in an increase in the effective refractive index (1.3606 to 1.5000) of the layer based on Maxwell–Garnett theory. Case II: a (■) layer of fixed refractive index (n = 1.5000) and variable thickness. Increasing surface coverage results in an increase in thickness (0 to 20 Å) of the layer $T = \Theta T_0$. Modelling parameters used for bare gold system are prism (n = 1.5000), Cr ($\varepsilon' = 6.25$, $\varepsilon'' = 5$, t = 17 Å), Au($\varepsilon' = -13.23$, $\varepsilon'' = 1.41$, t = 440 Å), and 95% ethanol (n = 1.3606). Error bars correspond to experimental errors arising from reflectivity measurements.

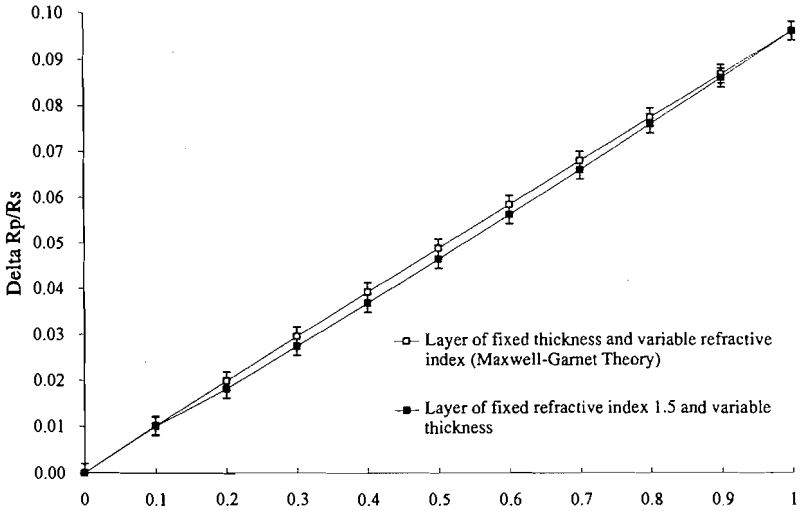

ations. Enthalpy and entropic energy considerations will drive the individually adsorbed thiols to associate into a more ordered assembly with the alkyl chains pointing away from the surface. If association of the individually adsorbed thiols was slow, then the limiting thickness would have broken down much before the first 1000 s.

The gradual increase in average thickness over the next 8 h suggests that a new population of thiol binding sites on the gold surface slowly becomes available, permitting further adsorption, possibly as a result of rearrangement of the adsorbed monolayer on the gold surface. The rate constant of this step, k_2, is experimentally slow and is expected to be independent of solution concentration of the thiol. The integrated rate law of this step is given below.

$$[13] \quad T = T_2\,[1-\exp(-k_2 t)]$$

where T_2 is the limiting average relative thickness increase in Å as a result of the second process. The two rate laws can be directly combined assuming independence of process to give:

$$[14] \quad T = T_1[1 - \exp(-k_1 t)] + T_2[1 - \exp(-k_2 t)]$$

where T_2 is the average thickness (in Å) at time t (in s). Incorporating this second step with $T_2 = 3.5 \pm 0.9$ Å and $k_2 = (4 \pm 2) \times 10^{-5}$ s^{-1} into the model improves the overall fit (overall $\bar{\chi}^2$ = 0.7) between the experimental and theoretical curves between 1000 and 30 000 s as shown in Fig. 9.

The rate of adsorption of thiol to the surface is a function of the concentration and the surface binding as based on the number of available sites and interaction energies. The rate constants k_1 and k_2 were examined by alteration of the reaction conditions. The concentration gradient of dodecane thiol was increased by increasing the solution concentration 10-fold from 10 to 100 μM, and by increasing the rate of thiol delivery to the gold surface through the use of convective delivery by using dynamic flow (0.30 mL/min) conditions. Results are summarized in Table 3.

Increasing the concentration 10-fold increases the rate constant k_1 by a factor of 15 ± 6, suggesting that k_1 is under concentration control. Under dynamic flow conditions of 0.30 mL/min the rate constant k_1 may increase somewhat as a result of convective delivery of thiol to the surface, but this is not definitive given the precision of the results. Increasing the concentration 10-fold only increased k_2 by a factor of 4 ± 2, while using flow conditions did not increase this rate constant any further.

Table 4 summarizes the limiting thickness and rate constants that were measured for dodecane, hexane, and hexadecane thiols under static and dynamic conditions (0.30 mL/min) at 10 μM concentrations. Under static conditions and 10 μM concentration there is no definite correlation between chain length and k_1 and k_2. This is consistent with the assumption that no substantial concentration gradient exists at the interface, and that k_1 is dominated by bulk solution concentration of alkyl thiol. That k_2 is not related to chain length suggests the limiting step to reorganization is not based on van der Waals interactions between the alkyl chains but rather results

Fig. 8. Relative thickness change for exposure of gold surface to 10 μM dodecane thiol in 95% ethanol. "a" Single step adsorption model, $T_1 = 14.4 \pm 0.8$ Å, $k_1 = 450 \pm 100\ s^{-1}$; normalized $\bar{\chi}^2 = 2.7$.

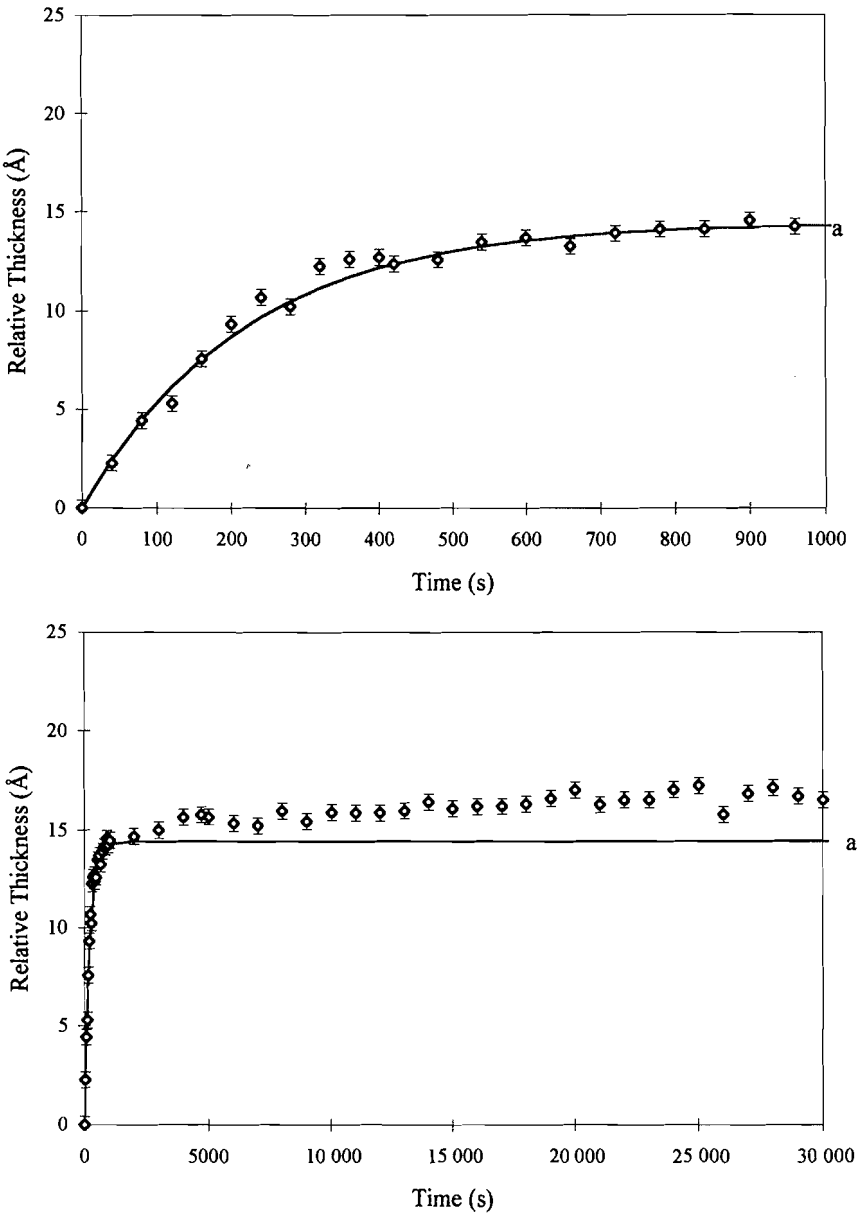

from alterations of the sulfur–gold interaction at the metal surface.

The existence of a two-step mechanism suggests that between 20% (C_{12}, C_{16}) and 50% (C_6) of the surface could be differentially functionalized by removing a wafer after approximately 15 min of exposure to a 10 μM thiol solution (plateau at first adsorption step) and then reimmersing the wafer in a 10 μM thiol solution with a different terminal functional group for 8 h. Alternatively, a higher degree of control could be obtained by exposing the gold surface to a sequential series of thiol solutions via a stop-flow system while using SPR to monitor changes in surface coverage. This approach could prove useful in the functionalization and blocking of surfaces for chemically modified electrochemical detectors in order to enhance selectivity and film stability. It can also serve as a simple method of introducing electroactive mediators.

Ellipsometry and wettability results are summarized in Table 5 for a series of samples prepared concurrently, and allowed to stand for 24 h. The relative thickness of the fully formed hexane thiol layer according to in situ SPR measurements is 2 Å greater than the value obtained from ellipsometric measurements in air (Table 5). For the longer chain alkyl thiols C_{12} and C_{16}, in situ SPR measurements indicate that the films are 7 Å thicker than corresponding ellipsometric measurements. Removal of the alkyl thiol monolayers from a 95% ethanol environment to an air environment results in a decrease in thickness that is larger for the longer chain alkyl thiols and cor-

Fig. 9. Relative thickness change for exposure of gold surface to 10 μM dodecane thiol in 95% ethanol, showing:
first step of adsorption model component "a",

$T_1 = 14.4 \pm 0.8$ Å, $k_1 = (450 \pm 100) \times 10^{-5}$ s^{-1};

second step of adsorption model component "b",

$T_2 = 3.5 \pm 0.9$ Å, $k_2 = (4 \pm 2) \times 10^{-5}$ s^{-1};

and "c", the combined two-step model, normalized $\bar{\chi}^2 = 0.7$.

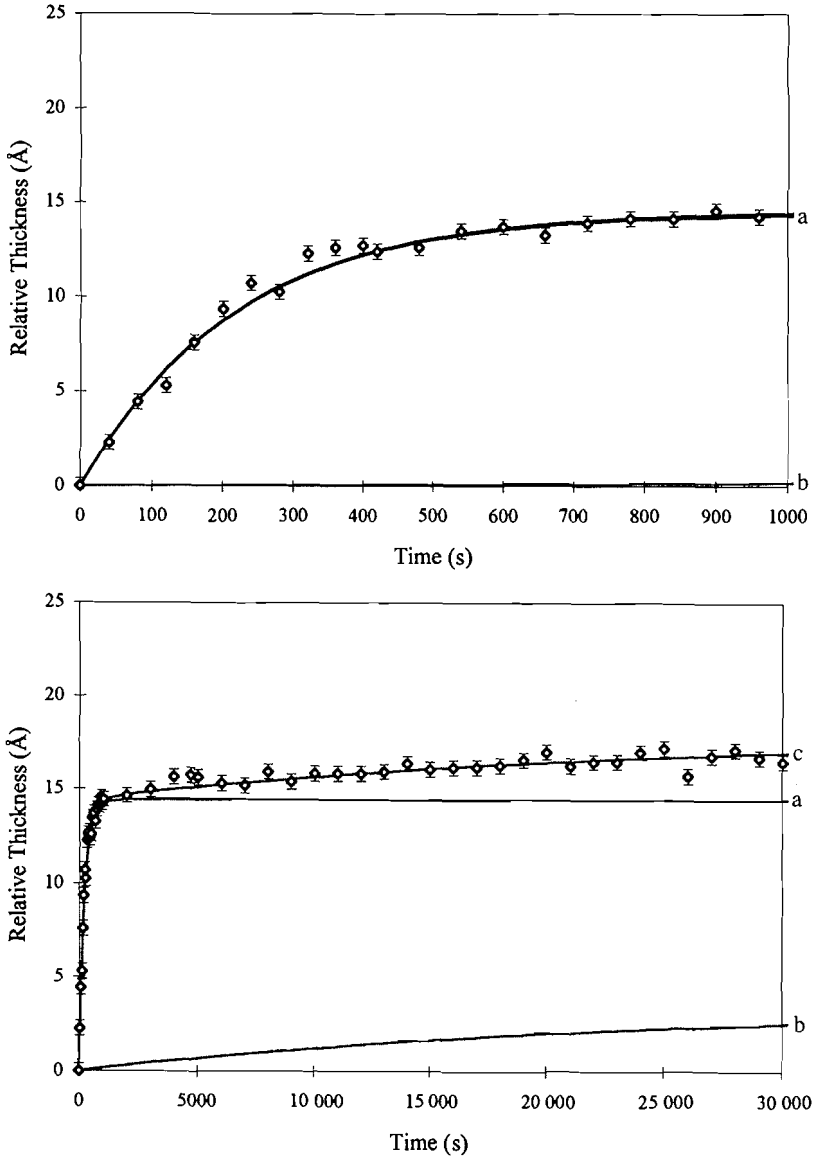

relates with a 15° larger wettability measurement. This may suggest that an ordered layer of solvent may exist between the alkyl chain termini and the bulk solution, which is removed when the wafer is transferred to an air environment. Wettability angles for dodecane thiol and hexadecane thiol are 15° larger than the wettability angle observed for hexane thiol. For long-chain thiols ($n > 10$) the monolayer becomes more structurally homogeneous and densely packed as a result of greater van der Waals interaction between the alkyl chains. This leads to a higher density of methyl groups at the surface and increased hydrophobicity. Ideally, maximization of the van der Waals interaction (a $1/r^6$ distance dependence) between the alkyl chains is expected to result in a 30° tilt in the hydrocarbon chains in order to minimize the interaction distance.

Surface plasmon microscopy was used to search for microscopic structure within the formed alkyl thiol monolayers. No structure was observed for any of the monolayers at the 4 μm resolution level. This suggests that nucleation and growth of these organic layers occurred at the sub-microscopic level and that these films are optically homogenous. These results confirm that application of the Fresnel equations for solving the optical equations is appropriate.

Table 3. Rate constants and limiting thickness from SPR measurements as determined using static and dynamic conditions for adsorption of 10 and 100 μM dodecane thiol from 95% ethanol.

System	Conc. (μM)	T_1 (Å)	T_2 (Å)	$k_1 \times 10^{-5}$ (s^{-1})	$k_2 \times 10^{-5}$ (s^{-1})	$\bar{\chi}^2$
Static	10	14.4 ± 0.8	3.5 ± 0.9	450 ± 100	4 ± 2	0.7
Static	100	22.1 ± 1	7 ± 2	7000 ± 3000	15 ± 4	1.0
Dynamic	100	15.3 ± 1	7 ± 1	14000 ± 5000	10 ± 6	1.2

Table 4. Rate constants and limiting thickness from SPR measurements as determined using static and dynamic conditions for the adsorption of alkyl thiol solutions from 95% ethanol.

Thiol (No. of carbons)	Conc. (μM)	Conditions	T_1 (Å)	T_2 (Å)	$k_1 \times 10^{-5}$ (s^{-1})	$k_2 \times 10^{-5}$ (s^{-1})
Hexane (C_6)	10	Static	4 ± 1	4 ± 1	1300 ± 600	5 ± 3
Dodecane (C_{12})	10	Static	14 ± 1	4 ± 1	450 ± 100	4 ± 2
Hexadecane (C_{16})	10	Static	16 ± 1	5 ± 1	900 ± 300	25 ± 30
Hexadecane (C_{16})	10	0.30 mL/min	20 ± 1	8.0 ± 0.8	1150 ± 70	40 ± 4
Hexadecane (C_{16})	30	0.30 mL/min	20 ± 1	5 ± 1	2700 ± 700	70 ± 30

Table 5. Wettability angle and ellipsometric measurements of surface after exposure to alkyl thiol solutions.

Polycrystalline gold	Wettability angle ±5°	Relative thickness (Å) (ellipsometry) ±10%	Thickness (Å) based on reflectivity ±10%	Theoretical all-*trans* length (Å)
Freshly deposited	48	0		
Hexane thiol	90	11	13	9.6
Dodecane thiol	105	16	23	17.1
Hexadecane thiol	105	23	30	22.1

Conclusions

SPR experiments indicate that hexane, dodecane, and hexadecane thiol adsorption to gold surfaces occurred by a two-step process, with the first step being two orders of magnitude faster than the second step. Fast adsorption to the surface gave 80% (C_{12}, C_{16}) or 50% (C_6) coverage followed by a slow rearrangement of the adsorbed thiol. Growth and formation of domains of thiols were not observed at the microscopic level and the results suggest a relatively homogeneous thiol monolayer.

Acknowledgements

We thank Dr. Gh. Rounaghi for his help with some of the experimental work. We thank the Natural Sciences and Engineering Research Council of Canada for financial support of this work.

References

1. B. Liedberg, B. Ivarsson, and I.J. Lundstrom. Biochem. Biophys. Methods, **9**, 232 (1984).
2. B. Liedberg, I.J. Lundstrom, C.R. Wu, and W.R. Salaneck. J. Colloid Interface Sci. **108**, 123 (1985).
3. W.R. Salaneck, I. Lundstrom, and B. Liedberg. Prog. Colloid Polym. Sci. **70**, 83 (1985).
4. U. Jonsson, M. Malmquist, I. Ronnberg, and L. Berghem. Prog. Colloid Polym. Sci. **70**, 96 (1985).
5. J.J. Pesek and I.E. Leigh (*Editors*). Chemically modified surfaces. Royal Society of Chemistry, London. 1994.
6. I.A. Veliky and R.J.C. McLean (*Editors*). Immobilized biosystems — theory and practical applications. Chapman and Hall, London. 1993.
7. A. Ulman. An introduction to ultrathin organic films from Langmuir–Blodgett to self-assembly. Academic Press, San Diego, Calif. 1991 (and references therein).
8. C.D. Bain, E.B. Troughton, Y.T. Tao, J. Evall, G.M. Whitesides, and R.G. Nuzzo. J. Am. Chem. Soc. **111**, 321 (1989).
9. C.D. Bain, J. Evall, and G.M. Whitesides. J. Am. Chem. Soc. **111**, 7155 (1989).
10. G. Hahner, Ch. Woll, M. Buck, and M. Grunze. Langmuir, **9**, 1955 (1993).
11. T.W. Schneider and D.A. Buttry. J. Am. Chem. Soc. **115**, 12391 (1993).

12. A. Ulman, J.E. Eilers, and N. Tillman. Langmuir, **5**, 1147 (1987).
13. B. Rothehausler and W. Knoll. Nature, **332**, 6115 (1988).
14. W. Hickel and W. Knoll. Thin Solid Films, **187**, 349 (1990).
15. H. Raether. Phys. Thin Films, **9** (1977).
16. H. Raether. Surface plasmons on smooth and rough surfaces and on gratings. Springer, Berlin. 1988.
17. F.L. McCraken. NBS Tech. Note (U.S.), 479 (1969).
18. O.S. Heaven. Optical properties of thin films. Dover, London. 1965.
19. W.H. Press, B.P. Flannery, S.A. Teukolsky, and W.T. Vetterling. Numerical recipes. Cambridge University Press, New York. 1988. p. 294.
20. C.D. Bain, H.A. Biebuyck, and G.M. Whitesides. Langmuir, **5**, 723 (1989).
21. G.D. Fasman (*Editor*). CRC handbook of biochemistry and molecular biology, lipids, carbohydrates and steroids. 3rd ed. CRC Press, Boca Raton, Fla. 1988.
22. P.B. Johnson and R.W. Christy. Phys. Rev. B, **6**, 4370 (1972).
23. R.M.A. Azzam and N.M. Bashara. Ellipsometry and polarized light. Elsevier Science, The Netherlands. 1977. p. 359.

Formal transfers of hydride from carbon–hydrogen bonds. Attempted generation of H_2 by intramolecular protonolyses of the activated carbon–hydrogen bonds of dihydrobenzimidazoles

Philippe Brunet and James D. Wuest

Abstract: Protonolyses of carbon–hydrogen bonds can occur under suitable conditions to produce carbocations and H_2. In an effort to accelerate these fundamental reactions, we have attempted to make them intramolecular by devising compounds in which carbon–hydrogen bonds designed to be particularly good formal donors of hydride are held in close proximity to acidic sites. Dihydrobenzimidazoles **4** and **11** are compounds of this type, since the carbon–hydrogen bonds at C2 are activated as formal donors of hydride by adjacent lone pairs in a dihydroaromatic ring, and acidic anilinium and carboxylic acid groups are held nearby. Unfortunately, this proximity does not lead to the formation of H_2 by protonolysis; instead, other reactions intervene when compounds **4** and **11** are subjected to pyrolysis.

Key words: intramolecular protonolysis of carbon–hydrogen bonds, formal donors of hydride, generation of H_2, dihydrobenzimidazoles.

Résumé : La protonolyse des liaisons carbone–hydrogène peuvent se produire dans des conditions appropriées pour conduire à des carbocations et du H_2. Dans le but d'accélérer les vitesses de ces réactions fondamentales, on a essayé de faire des réactions intramoléculaires en construisant des composés dans lesquels des liaisons carbone–hydrogène comportant des donneurs formels d'hydrures particulièrement bons seront maintenues à faible distance des sites acides. Les dihydrobenzimidazoles **4** et **11** sont des composés de ce type puisque les liaisons carbone–hydrogène en C(2) sont activées comme donneurs formels d'hydrure par les paires non partagées adjacentes du noyau dihydroaromatique alors que les groupes acides anilinium et acide carboxylique sont maintenus à proximité. Malgré cette proximité, la protonolyse ne conduit malheureusement pas à la formation de H_2; quand les composés **4** et **11** sont soumis à une pyrolyse, il y a plutôt intervention d'autres réactions.

Mots clés : protonolyse intramoléculaire de liaisons carbone–hydrogène, donneurs formels d'hydrure, génération de H_2, dihydrobenzimidazoles.

[Traduit par la rédaction]

Introduction

Carbon–hydrogen bonds serve as formal donors of hydride in a variety of well-known redox reactions (1). Of particular practical importance are the formal transfers of hydride from carbon–hydrogen bonds that occur during catalytic cracking and reforming, as well as closely related reactions in which protonolyses of the carbon–hydrogen bonds of simple alkanes by strong acids produce carbocations and H_2 (2). To learn more about these fundamental processes, we have prepared compounds designed to be especially good formal donors of hydride, and we have studied their reactions with acids (3, 4). This work has shown that orthoformamide **1** and related compounds are remarkably reactive substrates for protonolyses, and their activated central carbon–hydrogen bonds react with acids to liberate H_2 and give the corresponding guanidinium ions under surprisingly mild conditions.[3] To further accelerate protonolyses of carbon–hydrogen bonds, we have attempted to make them intramolecular by devising a series of compounds in which similarly activated carbon–hydrogen bonds are held in close proximity to acidic groups (6). In this article, we describe the synthesis and reactions of two dihydrobenz-

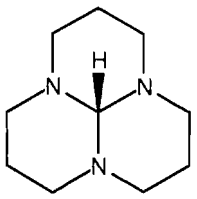

1

Received September 6, 1995.

P. Brunet[1] **and J.D. Wuest.**[2] Département de Chimie, Université de Montréal, Montréal, QC H3C 3J7, Canada.

[1] Fellow of the Ministère de l'Éducation du Québec (1985–1990).

[2] Author to whom correspondence may be addressed. Telephone: (514) 343-6266. Fax: (514) 343-7586.

[3] Few other reactions are known in which protonolyses of carbon–hydrogen bonds generate H_2 (5).

imidazoles that have been designed in this way to undergo intramolecular protonolyses of carbon–hydrogen bonds.

Results and discussion

Acid-catalyzed condensation of *N,N'*-dimethyl-1,2-benzenediamine (7) with 2-(dimethylamino)benzaldehyde (8) produced 2-[2-(dimethylamino)phenyl]-1,3-dimethyl-2,3-dihydro-1*H*-benzimidazole (**2**) in 75% yield. Dihydrobenzimidazole **2** incorporates a carbon–hydrogen bond at C2 able to serve as a

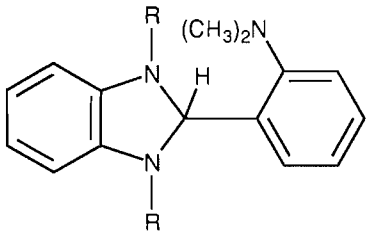

2 (R = CH_3)

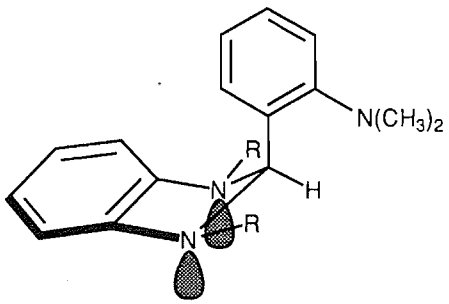

2a (R = CH_3)

particularly effective formal donor of hydride for the following reasons : It is adjacent to two lone pairs in a dihydroaromatic ring, and loss of hydride would generate a stable benzimidazolium ion.[4] The conjugate acid of *N,N*-dimethylaniline is weaker (pK_a 5.1) than that of 1,2-benzenediamine (pK_a 4.5) (9), so protonation of compound **2** should produce a salt in which the hydridic carbon–hydrogen bond of the dihydrobenzimidazole unit is held in close proximity to an acidic dimethylanilinium group. We hoped that this juxtaposition would promote the formation of H_2 by intramolecular protonolysis.

Examination of the IR spectrum of compound **2** in $CHCl_3$ revealed no Bohlmann bands in the region between 2750 and 2400 cm^{-1}, suggesting that the preferred conformation is structure **2a**, in which no lone pairs are antiperiplanar to the carbon–hydrogen bond at C2 (10).[5] Although this observation indicates that the carbon–hydrogen bond at C2 is not notably weakened and polarized by mixing of σ^*_{CH} with adjacent lone-pair orbitals, dihydrobenzimidazole **2** is nevertheless an effective reducing agent.[6] For example, treatment of com-

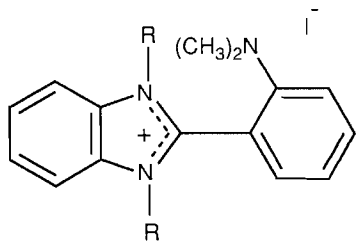

3 (R = CH_3)

pound **2** with methanolic I_2 at 25°C in the presence of K_2CO_3 rapidly produced benzimidazolium iodide **3** in 85% yield.

As expected, addition of aqueous HI to dihydrobenzimidazole **2** in deoxygenated ether provided salt **4** in high yield. Comparison of the ^1H NMR spectra of compounds **2** and **4** confirmed that the principal site of protonation is the nitrogen atom of the dimethylaniline group, since the hydrogens of this

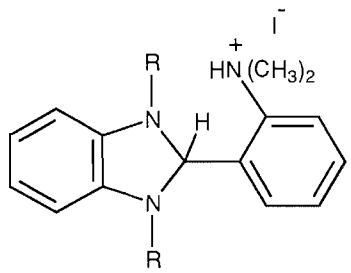

4 (R = CH_3)

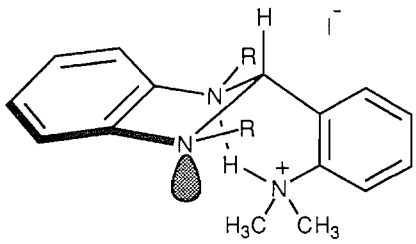

4a (R = CH_3)

group showed important downfield shifts while those of the benzenediamine unit experienced only moderate shifts. Curiously, the hydrogen at C2 appears at δ 5.86 ($CDCl_3$) in dihydrobenzimidazole **2** but is shifted *upfield* to δ 4.83 ($CDCl_3$) in salt **4**. This unexpected shielding presumably arises in part because intramolecular hydrogen bonding now favors conformation **4a**, in which the carbon–hydrogen bond at C2 becomes antiperiplanar to two lone pairs. This conclusion is supported by the presence of a Bohlmann band at 2698 cm^{-1} in the IR spectrum ($CHCl_3$) of salt **4**. Closely similar conformations are known to be preferred by other 2-substituted dihydrobenzimidazoles capable of participating in intramolecular hydrogen bonding (6). Direct evidence for the presence of an intramolecular hydrogen bond was provided by the concentration-independence of the chemical shift of the anilinium hydrogen.

Unfortunately, conformation **4a** is not suitable for the gen-

[4] The estimated hydride affinity of benzimidazolium is 200 kcal/mol (6*d*).

[5] The nitrogen atoms in dihydrobenzimidazoles are known to be distinctly pyramidal (6).

[6] Other dihydrobenzimidazoles are known to be effective reducing agents (11).

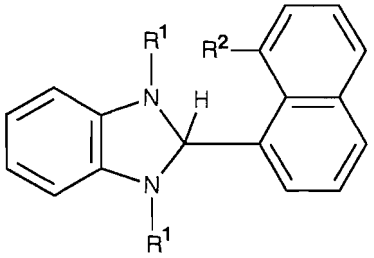

5 (R^1 = CH_3, R^2 = HOOC)

6 (R^1 = CH_3, R^2 = CH_3OOC)

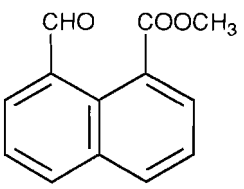

7

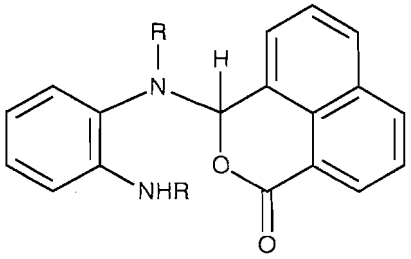

8 (R = CH_3)

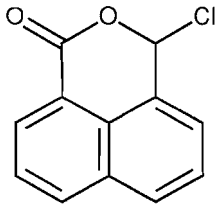

9

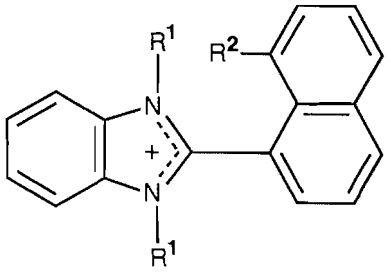

10 (R^1 = CH_3, R^2 = ^-OOC)

eration of H_2 by intramolecular protonolysis of the carbon–hydrogen bond at C2. The carbon–hydrogen bond is activated as a formal source of hydride by two antiperiplanar lone pairs, but the acidic hydrogen of the dimethylanilinium group is not nearby. Although more reactive conformers are presumably accessible, thermal decomposition of salt **4** led only to complex mixtures, and neither H_2 nor benzimidazolium salt **3** could be detected among the products.

A similar molecule designed to be able to undergo intramolecular protonolysis of a carbon–hydrogen bond is dihydrobenzimidazole **5**, which juxtaposes a carboxylic acid and a carbon–hydrogen bond that can serve as a good formal donor of hydride. We attempted to prepare this compound from the corresponding methyl ester **6**, which was obtained in 43% yield by acid-catalyzed condensation of *N,N'*-dimethyl-1,2-benzenediamine (7) with methyl 8-formyl-1-naphthalenecarboxylate (**7**). Ester **7** was made by adding CH_2N_2 to 1,8-naphthaldehydic acid (12), which was synthesized from acenaphthenequinone by a modification of the standard method (13). Unfortunately, basic hydrolysis of ester **6** and subsequent acidification did not provide the expected acid **5**, but gave instead the isomeric aminolactone **8** in 60% yield. Alternatively, compound **8** could be prepared more directly in 80% yield by treating *N,N'*-dimethyl-1,2-benzenediamine (7) in CH_2Cl_2 at 0°C with chlorolactone **9** (14), which was synthesized from 1,8-naphthaldehydic acid by a modification of the standard method (15).

Although aminolactone **8** is not a dihydrobenzimidazole, it nevertheless incorporates a carbon–hydrogen bond activated as a formal donor of hydride by adjacent lone pairs on nitrogen and oxygen. As a result, it is readily oxidized. For example, treatment with methanolic I_2 in the presence of K_2CO_3 provided a 73% yield of internal salt **10**, which is the product expected as a result of intramolecular protonolysis in hypothetical dihydrobenzimidazole **5**. We suspected that compound **8** might be in equilibrium with the desired isomeric dihydrobenzimidazole **5**, so we subjected it to pyrolysis. Unfortunately, thermal decomposition generated only a complex mixture, and neither H_2 nor internal salt **10** was detected among the products.

We reasoned that the closely related dihydrobenzimidazole **11** would be less likely than compound **5** to isomerize to the corresponding isomeric aminolactone. In fact, direct condensation of *N,N'*-dimethylbenzene-1,2-diamine (7) with phthalaldehydic acid gave dihydrobenzimidazole **11** in 87% yield. The presence of a carbonyl band at 1719 cm^{-1} and Bohlmann bands at 2692 and 2637 cm^{-1} in the IR spectrum of compound **11** ($CHCl_3$) provided evidence that the product incorporates a carboxylic acid group and a carbon–hydrogen bond antiperiplanar to two lone pairs on nitrogen. This indicates that the product is in fact compound **11** and not the isomeric aminolactone **12**, and it suggests that intramolecularly hydrogen-bonded structure **11a** is the preferred conformation (6).

Dihydrobenzimidazole **11** is particularly susceptible to oxidation, and it even reacts with atmospheric oxygen at 25°C to produce internal salt **13** (16) in quantitative yield. However, despite the juxtaposition of a hydridic carbon–hydrogen bond and a carboxylic acid in dihydrobenzimidazole **11**, and despite its demonstrated ability to participate in redox reactions, it does not undergo intramolecular protonolysis to form H_2.

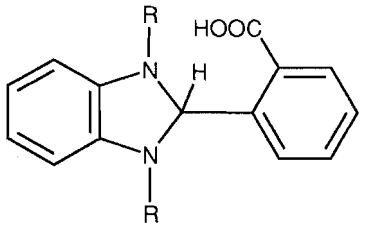

11 (R = CH_3)

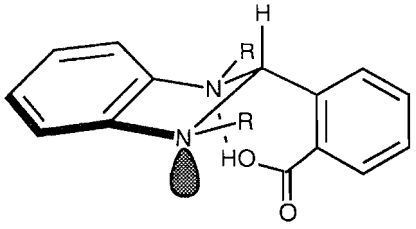

11a (R = CH_3)

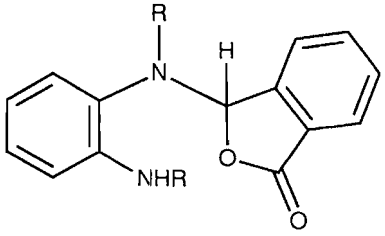

12 (R = CH_3)

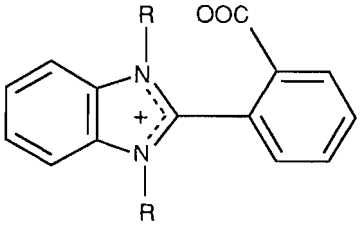

13 (R = CH_3)

Instead, a complex mixture containing three principal components was formed when compound **11** was heated without solvent at 180°C. One of these products, isolated in 32% yield, is internal salt **13**, which is the expected result of intramolecular protonolysis; however, no H_2 could be detected. The other principal products are phthalide (**14**), which was recovered in 19% yield, and bis(benzimidazole) **15**, which was obtained in 14% yield.

We believe that these products result from rearrangement of dihydrobenzimidazole **11** to its less stable aminolactone isomer **12** by a process closely related to the one that intervened in the attempted synthesis of dihydrobenzimidazole **5**. Subsequent protonation then causes cleavage to *N,N'*-dimethyl-1,2-benzenediamine and cation **16**, which is reduced to phthalide by a formal intermolecular transfer of hydride from dihydrobenzimidazole **11**. This transfer yields an equivalent amount of internal salt **13**. Compound **13** and related dimethybenzimidazolium salts are capable of effecting intermolecular methylations (16), ultimately leading to the formation of bis(benzimidazole) **15**, as well as to *N,N,N'*-trimethyl-1,2-benzenediamine and *N,N,N',N'*-tetramethyl-1,2-benzenediamine (17), which are both detected in low yields among the products of pyrolysis. Support for this hypothesis is provided by the observation that a similar pyrolysis of internal salt **13** in the presence of two molar equivalents of *N,N'*-dimethyl-1,2-benzenediamine yielded bis(benzimidazole) **15** and *N,N,N'*-trimethyl-1,2-benzenediamine as major products.

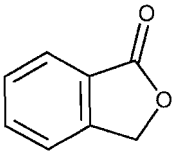

14

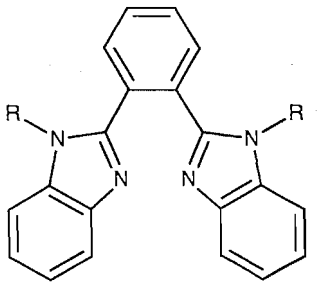

15 (R = CH_3)

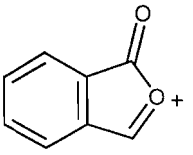

16

Conclusions

By providing structures in which carbon–hydrogen bonds are activated as formal donors of hydride by adjacent lone pairs and are simultaneously held close to acidic sites, dihydrobenzimidazoles **4** and **11** and related compounds are designed to favor the generation of H_2 by intramolecular protonolyses of carbon–hydrogen bonds. Both compounds **4** and **11** are effective reducing agents and react readily in intermolecular redox processes with active oxidants such as I_2 and O_2. Nevertheless, neither undergoes protonolysis of the activated carbon–hydrogen bond, and pyrolysis does not produce detectible quantities of H_2. To be faster than alternative reactions, protonolysis therefore appears to require carbon–hydrogen bonds that are even more highly activated as formal donors of hydride than those in dihydrobenzimidazoles **4** and **11**, or nearby sites that are even more acidic. In pyrolyses of compounds **4** and **11**, other reactions intervene before protonolysis of the activated carbon–hydrogen bonds can take place.

Experimental section

General procedures

Infrared (IR) spectra were recorded on Perkin-Elmer model 783 or 1600 spectrometers. Varian VXR-300, Bruker AMX-300, or Bruker ARX-400 spectrometers were used to obtain ^1H and ^{13}C nuclear magnetic resonance (NMR) spectra. Chemical shifts are reported in parts per million downfield from internal tetramethylsilane (δ). Mass spectra were recording on a Kratos MS-50 TATC instrument or a VG Autospec instrument using chemical ionization (CI), electron impact (EI), or fast atom bombardment (FAB). Melting points were recorded on a Thomas–Hoover capillary apparatus. Elemental analyses were performed by Galbraith Laboratories, Knoxville, Tenn. Flash chromatography was performed in the normal way (18).

Toluene was dried by distillation from sodium, CH_3OH by distillation from magnesium, CH_2Cl_2 by distillation from CaH_2, and ether by distillation from the sodium ketyl of benzophenone. Other commercial reagents were used without further purification.

2-[2-(Dimethylamino)phenyl]-1,3-dimethyl-2,3-dihydro-1*H*-benzimidazole (2)

A solution of *N,N*-dimethyl-1,2-benzenediamine (0.921 g, 6.76 mmol) (7), 2-(dimethylamino)benzaldehyde (1.01 g, 6.77 mmol) (8), and (1*S*)-10-camphorsulfonic acid (0.081 g, 0.35 mmol) in benzene (15 mL) was heated at reflux for 16 h under N_2 in an apparatus fitted with a Dean–Stark trap. The mixture was then washed with 5% aqueous NaOH and water, the organic phase was dried with anhydrous $MgSO_4$, and volatiles were removed by evaporation under reduced pressure. Crystallization of the residue from 95% aqueous C_2H_5OH provided 2-[2-(dimethylamino)phenyl]-1,3-dimethyl-2,3-dihydro-1*H*-benzimidazole (**2**; 1.35 g, 5.05 mmol, 75%) as an analytically pure colorless solid: mp 105–106°C; IR ($CHCl_3$): 2862, 2826, 2790 cm^{-1}; ^1H NMR (400 MHz, $CDCl_3$) δ: 2.63 (s, 6H), 2.75 (s, 6H), 5.86 (s, 1H), 6.43–6.47 (m, 2H), 6.72–6.77 (m, 2H), 7.23 (ddd, ^3J = 7.8 Hz, ^3J = 7.2 Hz, ^4J = 1.3 Hz, 1H), 7.29 (dd, ^3J = 8.1 Hz, ^4J = 1.3 Hz, 1H), 7.39 (ddd, ^3J = 8.1 Hz, ^3J = 7.2 Hz, ^4J = 1.7 Hz, 1H), 7.94 (dd, ^3J = 7.8 Hz, ^4J = 1.7 Hz, 1H); ^{13}C NMR (75 MHz, $CDCl_3$) δ: 33.0, 46.1, 86.1, 105.3, 119.0, 120.1, 124.8, 129.4, 129.4, 134.5, 142.5, 154.9; MS (CI) *m/e*: 268, 267, 252, 147; HRMS (EI) calcd. for $C_{17}H_{22}N_3$: 268.1814; found: 268.1802. Anal. calcd. for $C_{17}H_{21}N_3$: C 76.35, H 7.92, N 15.72; found: C 76.43, H 7.92, N 15.65.

2-[2-(Dimethylamino)phenyl]-1,3-dimethylbenzimidazolium iodide (3)

A stirred mixture of 2-[2-(dimethylamino)phenyl]-1,3-dimethyl-2,3-dihydro-1*H*-benzimidazole (**2**; 73 mg, 0.27 mmol) and K_2CO_3 (54 mg, 0.39 mmol) in CH_3OH (2 mL) was treated dropwise at 25°C with a solution of I_2 (73 mg, 0.29 mmol) in CH_3OH (8 mL). After 1 h, volatiles were removed by evaporation under reduced pressure, the residue was extracted with $CHCl_3$, and the extracts were decolorized with activated carbon. Removal of solvent from the extracts by evaporation under reduced pressure yielded 2-[2-(dimethylamino)phenyl]-1,3-dimethylbenzimidazolium iodide (**3**; 89 mg, 0.23 mmol, 85%) as a yellow solid, which was purified by recrystallization from CH_2Cl_2–benzene: mp 224-226°C; ^1H NMR (400 MHz, $CDCl_3$) δ: 2.59 (s, 6H), 4.01 (s, 6H), 7.18–7.22 (m, 2H), 7.63 (ddd, ^3J = 8.5 Hz, ^3J = 7.3 Hz, ^4J = 1.6 Hz, 1H), 7.63–7.67 (m, 2H), 7.76 (dd, ^3J = 7.7 Hz, ^4J = 1.6 Hz, 1H), 7.95–8.00 (m, 2H); ^{13}C NMR (100 MHz, $CDCl_3$) δ: 33.8, 43.3, 110.4, 113.5, 118.6, 121.7, 127.4, 131.7, 133.0, 134.6, 150.5, 153.3; MS (FAB) *m/e*: 266; HRMS (EI) calcd. for $C_{17}H_{20}N_3 - CH_3$: 251.1422; found: 251.1410.

Hydriodide of 2-[2-(dimethylamino)phenyl]-1,3-dimethyl-2,3-dihydro-1*H*-benzimidazole (4)

A solution of 2-[2-(dimethylamino)phenyl]-1,3-dimethyl-2,3-dihydro-1*H*-benzimidazole (**2**; 113 mg, 0.423 mmol) in deoxygenated ether (1 mL) was stirred at 0°C under N_2 and treated with 57% aqueous HI (90 μL, 0.40 mmol). The precipitated solid was separated by centrifugation, washed with cold absolute C_2H_5OH and ether, and dried in vacuo to give the hydriodide of 2-[2-(dimethylamino)phenyl]-1,3-dimethyl-2,3-dihydro-1*H*-benzimidazole (**4**; 138 mg, 0.349 mmol, 87%) as a beige solid. Recrystallization from CH_2Cl_2–ether under N_2 provided an analytically pure sample: mp 156–157°C (dec.); IR ($CHCl_3$): 2803, 2698 cm^{-1}; ^1H NMR (400 MHz, $CDCl_3$) δ: 2.72 (s, 6H), 3.61 (s, 6H), 4.83 (s, 1H), 6.76–6.80 (m, 2H), 6.93–6.97 (m, 2H), 7.44 (dd, ^3J = 7.6 Hz, ^4J = 1.3 Hz, 1H), 7.61 (dd, ^3J = 7.7 Hz, ^3J = 7.6 Hz, 1H), 7.80 (ddd, ^3J = 8.1 Hz, ^3J = 7.7 Hz, ^4J = 1.3 Hz, 1H), 8.64 (d, ^3J = 8.1 Hz, 1H), 12.16 (bs, 1H); ^{13}C NMR (100 MHz, $CDCl_3$) δ: 34.6, 48.0, 94.5, 110.1, 122.5, 124.3, 126.6, 130.6, 132.3, 133.0, 140.3, 142.9; MS (EI) *m/e*: 267, 252, 147; HRMS (EI) calcd. for $C_{17}H_{22}IN_3 - HI$: 267.1736; found: 267.1726. Anal. calcd. for $C_{17}H_{22}IN_3$: C 51.63, H 5.61; found: C 51.59, H 5.68.

1,8-Naphthaldehydic acid

1,8-Naphthaldehydic acid was prepared by a modification of the standard method (13). A mixture of acenaphthenequinone (10.0 g, 54.9 mmol) and 30% aqueous KOH (70 mL) was heated at 140°C for 20 min in a poly(ethylene) bottle. The resulting blue solution was cooled, diluted with H_2O (180 mL), and acidified with concentrated aqueous HCl. This gave a precipitate that was separated by filtration, washed with H_2O, and dissolved in hot 95% aqueous C_2H_5OH. The resulting solution was decolorized with activated carbon, solvent was removed by evaporation under reduced pressure, and the residue was recrystallized from CH_3CN to give 1,8-naphthaldehydic acid (7.43 g, 37.1 mmol, 68%) as cream-colored needles: mp 166°C (lit. (13) mp 169–171°C); IR (KBr): 3300, 1690 cm^{-1}; ^1H NMR (400 MHz, CD_3CN) δ: 5.79 (s, 1H), 6.81 (s, 1H), 7.64–7.72 (m, 3H), 8.03 (dd, ^3J = 7.6 Hz, ^4J = 1.9 Hz, 1H), 8.24 (dd, ^3J = 8.3 Hz, ^4J = 1.1 Hz, 1H), 8.34 (dd, ^3J = 7.3 Hz, ^4J = 1.1 Hz, 1H); ^{13}C NMR (100 MHz, CD_3CN) δ: 97.0, 121.0, 126.4, 127.5, 127.9, 128.1, 129.4, 130.2, 130.4, 133.0, 134.8, 164.2; MS (CI) *m/e*: 201, 183.

3-Chloro-1*H*,3*H*-naphtho[1,8-*cd*]pyran-1-one (9)

Chloro-1*H*,3*H*-naphtho[1,8-*cd*]pyran-1-one (**9**) was prepared by a modification of the standard method (15). A stirred suspension of 1,8-naphthaldehydic acid (1.08 g, 5.39 mmol) in H_2O (10 mL) was treated dropwise with 1 N aqueous KOH until the solid dissolved. The resulting solution was diluted with H_2O (20 mL) and extracted with CH_2Cl_2, solvent was removed from the aqueous phase by evaporation under

reduced pressure, and the residue was dried at 80°C in vacuo. A suspension of the dried solid in dry toluene (7 mL) was treated with oxalyl chloride (1.75 g, 13.8 mmol). The mixture was stirred at 25°C for 24 h under dry air and then was heated at reflux for 1 h. Volatiles were removed by evaporation under reduced pressure to give a residue of 3-chloro-1*H*,3*H*-naphtho[1,8-*cd*]pyran-1-one (**9**), which was used without purification in subsequent procedures.

Methyl 8-(1,3-dimethyl-2,3-dihydro-1*H*-benzimidazol-2-yl)-1-naphthoate (6)

A solution of *N,N'*-dimethyl-1,2-benzenediamine (1.10 g, 8.08 mmol) (7), methyl 8-formyl-1-naphthoate (**7**; 1.50 g, 7.00 mmol) (12), and (1*S*)-10-camphorsulfonic acid (0.152 g, 0.654 mmol) in deoxygenated benzene (50 mL) was heated at reflux for 17 h under N_2 in an apparatus fitted with a Dean–Stark trap. The mixture was then diluted with benzene and washed with 5% aqueous NaOH, H_2O, and saturated aqueous $CuSO_4$. The organic phase was dried with anhydrous $MgSO_4$, and solvent was removed by evaporation under reduced pressure. Recrystallization of the residue from CH_3CN gave methyl 8-(1,3-dimethyl-2,3-dihydro-1*H*-benzimidazol-2-yl)-1-naphthoate (**6**; 1.00 g, 3.01 mmol, 43%) as a yellow solid: mp 160–161°C; IR ($CHCl_3$); 2867, 2804, 1717 cm^{-1}; ^1H NMR (400 MHz, CD_3CN) δ: 2.54 (s, 6H), 3.89 (s, 3H), 5.84 (s, 1H), 6.37–6.42 (m, 2H), 6.70–6.74 (m, 2H), 7.49 (dd, ^3J = 7.4 Hz, ^3J = 7.1 Hz, 1H), 7.63–7.68 (m, 2H), 7.95 (d, ^3J = 8.0 Hz, 1H), 8.05 (d, ^3J = 8.2 Hz, 1H), 8.41 (d, ^3J = 7.2 Hz, 1H); ^{13}C NMR (100 MHz, CD_3CN) δ: 32.5, 52.8, 87.6, 105.1, 119.0, 124.0, 126.5, 128.5, 128.9, 129.0, 130.0, 130.4, 132.3, 134.1, 135.9, 141.8, 171.7; HRMS (EI) calcd. for $C_{21}H_{20}N_2O_2$ − H: 331.1447; found: 331.1433.

3-[Methyl[(2-methylamino)phenyl]amino]-1*H*, 3*H*-naphtho[1,8-*cd*]pyran-1-one (8)

*Method A. By hydrolysis of methyl 8-(1,3-dimethyl-2,3-dihydro-1*H*-benzimidazol-2-yl)-1-naphthoate (6)*

A solution of methyl 8-(1,3-dimethyl-2,3-dihydro-1*H*-benzimidazol-2-yl)-1-naphthoate (**6**; 358 mg, 1.08 mmol) in THF (4 mL) was treated with 1.1 N aqueous LiOH (10 mL, 11 mmol). The resulting mixture was heated at reflux for 2 h, and then the volatiles were removed by evaporation in vacuo. The dried residue was extracted with $CHCl_3$ (50 mL), and solvent was removed from the extract by evaporation under reduced pressure. The residue was redissolved in deoxygenated H_2O (13 mL) and acidified at 0°C with deoxygenated 1 N aqueous HCl (1.05 mL, 1.05 mmol). The precipitated solid was separated by centrifugation, washed with H_2O, and dried in vacuo to give 3-[methyl[(2-methylamino)phenyl]amino]-1*H*, 3*H*-naphtho[1,8-*cd*]pyran-1-one (**8**; 208 mg, 0.653 mmol, 60%) as a white solid: IR ($CHCl_3$): 3418, 2815, 1711 cm^{-1}; ^1H NMR (400 MHz, CD_3CN) δ: 2.64 (s, 3H), 2.90 (d, ^3J = 3.2 Hz, 3H), 4.63 (bs, 1H), 6.64 (d, ^3J = 7.9 Hz, 1H), 6.72 (m, 1H), 6.78 (s, 1H), 7.13 (m, 1H), 7.60–7.72 (m, 4H), 7.95 (d, ^3J = 8.0 Hz, 1H), 8.14 (dd, ^3J = 8.3 Hz, ^4J = 1.1 Hz, 1H), 8.49 (dd, ^3J = 7.2 Hz, ^4J = 1.1 Hz, 1H); ^{13}C NMR (100 MHz, CD_3CN) δ: 30.5, 34.8, 95.5, 110.0, 116.9, 120.1, 124.9, 125.6, 126.3, 126.5, 127.0, 128.2, 128.3, 128.7, 129.5, 131.9, 133.5, 134.9, 144.6, 164.7; MS (CI) *m/e*: 319, 183; HRMS (FAB) calcd. for $C_{20}H_{18}N_2O_2$ − H: 317.1290; found: 317.1276.

Method B. By the direct reaction of N,N'*-dimethyl-1,2-benzenediamine with 3-chloro-1*H*, 3*H*-naphtho-[1,8-cd]pyran-1-one (9)*

A solution of *N,N'*-dimethyl-1,2-benzenediamine (1.72 g, 12.6 mmol) (7) in dry CH_2Cl_2 (6 mL) was stirred at 0°C under dry N_2 and treated dropwise with a solution of 3-chloro-1*H*, 3*H*-naphtho[1,8-*cd*]pyran-1-one (**9**) in CH_2Cl_2 (10 mL), which was prepared by the procedure described above. The mixture was kept at 25°C for 40 min, diluted with CH_2Cl_2, and washed successively with deoxygenated 5% aqueous NaOH, H_2O, and saturated aqueous $CuSO_4$. The organic phase was dried with anhydrous $MgSO_4$, and volatiles were removed by evaporation under reduced pressure. This yielded a sample of 3-[methyl[(2-methylamino)phenyl]amino]-1*H*, 3*H*-naphtho-[1,8-*cd*]pyran-1-one (**8**; 1.37 g, 4.30 mmol, 80%) identical to the product of method A.

8-(1,3-Dimethylbenzimidazolium-2-yl)-1-naphthoate (10)

A stirred mixture of 3-[methyl[(2-methylamino)phenyl]amino]-1*H*, 3*H*-naphtho[1,8-*cd*]pyran-1-one (**8**; 202 mg, 0.634 mmol) and K_2CO_3 (158 mg, 1.14 mmol) in CH_3OH (5 mL) was treated dropwise at 25°C with a solution of I_2 (169 mg, 0.666 mmol) in CH_3OH (10 mL). After 2 h, volatiles were removed by evaporation under reduced pressure, the residue was extracted with $CHCl_3$, and solvent was removed from the extracts by evaporation under reduced pressure. The residue was redissolved in CH_3OH and decolorized with activated carbon. Evaporation of solvent under reduced pressure left a residue of 8-(1,3-dimethylbenzimidazolium-2-yl)-1-naphthoate (**10**; 146 mg, 0.461 mmol, 73%) as a beige solid, which was purified by recrystallization from CH_3OH–ether: mp 305°C (dec.); IR (KBr): 1597 cm^{-1}; ^1H NMR (300 MHz, D_2O) δ: 3.77 (s, 6H), 7.68–7.76 (m, 2H), 7.76–7.81 (m, 2H), 7.83–7.86 (m, 2H), 7.88–7.94 (m, 2H), 8.16 (dd, ^3J = 7.8 Hz, ^4J = 1.8 Hz, 1H), 8.36–8.42 (m, 1H); ^{13}C NMR (75.4 MHz, D_2O) δ: 32.8, 113.5, 117.6, 126.0, 127.4, 127.5, 127.9, 129.0, 131.0, 132.3, 133.0, 134.8, 135.1, 136.9, 152.1, 176.3; MS (FAB) *m/e*: 317; HRMS (FAB) calcd. for $C_{20}H_{16}N_2O_2$ + H: 317.1290; found: 317.1276.

2-(1,3-dimethyl-2,3-dihydro-1*H*-benzimidazol-2-yl)benzoic acid (11)

In a sealable tube, a solution of *N,N'*-dimethyl-1,2-benzenediamine (0.770 g, 5.65 mmol) (7) in deoxygenated ether (3 mL) was added to a stirred solution of phthalaldehydic acid (0.819 g, 5.46 mmol) in deoxygenated ether (1 mL). This caused the rapid precipitation of a yellow solid. The mixture was kept at 25°C for 15 min, and then volatiles were removed by evaporation in vacuo. Deoxygenated CH_3OH (12 mL) was added to the residue, the mixture was degassed, and the tube was sealed in vacuo. The tube was then heated in an oil bath at 140–150°C until the yellow solid had dissolved. Crystallization occurred when the solution was cooled. The tube was opened under Ar in a glove box, the mother liquors were removed, and the crystals were washed with CH_3OH and dried in vacuo. This provided 2-(1,3-dimethyl-2,3-dihydro-1*H*-benzimidazol-2-yl)benzoic acid (**11**; 1.27 g, 4.73 mmol, 87%) as air-sensitive yellow needles: mp 198–199°C; IR ($CHCl_3$): 2804, 2692, 2637, 1719 cm^{-1}; ^1H NMR (400 MHz, $CDCl_3$) δ: 2.61 (s, 6H), 4.90 (s, 1H), 6.62–6.67 (m, 2H), 6.87–6.91 (m, 2H), 7.45–7.49 (m, 1H), 7.54–7.60 (m, 2H), 8.05–8.10 (m, 1H),

12.4–13.5 (bs, 1H); ^{13}C NMR (100 MHz, $CDCl_3$) δ: 33.9, 95.1, 109.1, 121.8, 130.5, 131.4, 131.9, 133.4, 133.6, 134.7, 140.9, 169.5; MS (CI) *m/e* 269, 267, 253; HRMS (EI) calcd. for $C_{16}H_{16}N_2O_2$: 268.1212; found: 268.1202. Anal. calcd. for $C_{16}H_{16}N_2O_2$: C 71.61, H 6.01, N 10.45; found: C 71.26, H 6.12, N 10.62.

2-(1,3-dimethylbenzimidazolium-2-yl)benzoate (13) (ref. 16)

A solution of 2-(1,3-dimethyl-2,3-dihydro-1*H*-benzimidazol-2-yl)benzoic acid (**11**; 200 mg, 0.745 mmol) in CH_3OH (10 mL) was stirred at 25°C for 1 h under O_2. Volatiles were then removed by evaporation under reduced pressure, and the residue was dried in vacuo. This yielded 2-(1,3-dimethylbenzimidazolium-2-yl)benzoate (**13**; 198 mg, 0.743 mmol, 100%) (16) as a beige solid, which was purified by recrystallization from CH_2Cl_2–ether: mp 275-277°C (lit. (16) mp 294–295°C); IR ($CHCl_3$): 1622 cm^{-1}; ^1H NMR (300 MHz, $CDCl_3$) δ: 3.73 (s, 6H), 7.23 (dd, ^3J = 7.6 Hz, ^4J = 0.7 Hz, 1H), 7.57–7.68 (m, 5H), 7.77 (ddd, ^3J = 7.6 Hz, ^3J = 7.6 Hz, ^4J = 1.3 Hz, 1H), 8.51 (dd, ^3J = 7.8 Hz, ^4J = 0.7 Hz, 1H); ^{13}C NMR (75.4 MHz, $CDCl_3$) δ: 32.0, 112.2, 120.9, 126.2, 127.8, 129.5, 131.6, 131.9, 132.8, 142.6, 156.1, 167.2; MS (CI) *m/e*: 267; HRMS (EI) calcd. for $C_{16}H_{14}N_2O_2$: 266.1055; found: 266.1026.

Pyrolysis of 2-(1,3-dimethyl-2,3-dihydro-1*H*-benzimidazol-2-yl)benzoic acid (11)

One arm of an H-tube was charged with a mixture of *trans*-stilbene (100 mg, 0.55 mmol) and 10% Pd on activated carbon (50 mg) in deoxygenated 95% aqueous C_2H_5OH (2 mL), and the other arm was charged with 2-(1,3-dimethyl-2,3-dihydro-1*H*-benzimidazol-2-yl)benzoic acid (**11**; 47 mg, 0.18 mmol). The tube was sealed, the ethanolic suspension was stirred at 25°C in one arm, and the solid was heated in the other at 185°C for 8 days. The tube was then opened, the suspension was filtered, and solvent was removed from the filtrate by evaporation under reduced pressure. Examination of the residue by ^1H NMR spectroscopy showed that no 1,2-diphenylethane had been formed from *trans*-stilbene and therefore that no H_2 had been generated by the pyrolysis.

In a similar experiment, 2-(1,3-dimethyl-2,3-dihydro-1*H*-benzimidazol-2-yl)benzoic acid (**11**; 250 mg, 0.93 mmol) was pyrolyzed in a sealed tube at 180°C for 150 h. The pyrolysate was taken up in CH_3OH (1.3 mL), and the solution was diluted with H_2O. The aqueous mixture was then extracted with ether and with $CHCl_3$. Volatiles were removed from the aqueous phase by evaporation in vacuo to give a residue of 2-(1,3-dimethylbenzimidazolium-2-yl)benzoate (**13**; 79 mg, 0.30 mmol, 32%). The combined ether extracts were washed with 5% aqueous HCl and dried with anhydrous Na_2SO_4, and volatiles were removed from the dried solution by evaporation under reduced pressure. Flash chromatography (silica, hexane (75%) – ethyl acetate (25%)) of the residue yielded phthalide (**14**; 24 mg, 0.18 mmol, 19%), which was shown by ^1H NMR spectroscopy to be identical with an authentic sample.

The combined acidic washings were made basic by the addition of 50% aqueous NaOH, and the basic mixture was then extracted with CH_2Cl_2. The combined organic extracts were dried with Na_2SO_4, and volatiles were removed from the dried solution by evaporation under reduced pressure. Gradient chromatography (neutral alumina, hexane (80%)/ethyl acetate (20%) – hexane (65%)/ethyl acetate (35%)) of the residue gave 1-methyl-2-[2-(1-methylbenzimidazol-2-yl)phenyl]benzimidazole (**15**; 45 mg, 0.13 mmol, 14%) as a colorless solid. Recrystallization from C_2H_5OH/H_2O (7:3) provided an analytically pure sample: mp 239–240°C; ^1H NMR (300 MHz, $CDCl_3$) δ: 3.27 (s, 6H), 7.13–7.17 (m, 2H), 7.21–7.31 (m, 4H), 7.70–7.74 (m, 2H), 7.77–7.81 (m, 2H), 7.83–7.87 (m, 2H); MS (EI) *m/e*: 338, 323; HRMS (EI) calcd. for $C_{22}H_{18}N_4$: 338.1531; found: 338.1533. Anal. calcd. for $C_{22}H_{18}N_4$: C 78.07, H 5.36, N 16.56; found: C 77.79, H 5.39, N 16.42.

Acknowledgments

We are grateful to the Natural Sciences and Engineering Research Council of Canada and the Ministère de l'Éducation du Québec for financial support.

References

1. J.W. Bunting. Bioorg. Chem. **19**, 456 (1991); C.I.F. Watt. Adv. Phys. Org. Chem. **24**, 57 (1988).
2. J. Sommer, M. Hachoumy, F. Garin, D. Barthomeuf, and J. Vedrine. J. Am. Chem. Soc. **117**, 1135 (1995); J. Sommer and J. Bukala. Acc. Chem. Res. **26**, 370 (1993); G.A. Olah, G.K.S. Prakash, R.E. Williams, L.D. Field, and K. Wade. Hypercarbon chemistry. Wiley-Interscience, New York. 1987; P.-L. Fabre, J. Devynck, and B. Trémillon. Chem. Rev. **82**, 591 (1982); D.M. Brouwer and H. Hogeveen. Prog. Phys. Org. Chem. **9**, 179 (1972).
3. M. Kobayashi and J.D. Wuest. Organometallics, **8**, 2843 (1989); Y. Ducharme, S. Latour, and J.D. Wuest. J. Am. Chem. Soc. **106**, 1499 (1984); Y. Ducharme, S. Latour, and J.D. Wuest. Organometallics, **3**, 208 (1984); A.L. Beauchamp, S. Latour, M.J. Olivier, and J.D. Wuest. J. Am. Chem. Soc. **105**, 7778 (1983).
4. J.M. Erhardt, E.R. Grover, and J.D. Wuest. J. Am. Chem. Soc. **102**, 6365 (1980); J.M. Erhardt and J.D. Wuest. J. Am. Chem. Soc. **102**, 6363 (1980).
5. J.E. McMurry and T. Lectka. J. Am. Chem. Soc. **115**, 10167 (1993); E.C. Ashby, F. Doctorovich, C.L. Liotta, H.M. Neumann, E.K. Barefield, A. Konda, K. Zhang, and J. Hurley. J. Am. Chem. Soc. **115**, 1171 (1993); J.E. McMurry and T. Lectka. J. Am. Chem. Soc. **112**, 869 (1990); E. Berner. Acta Chem. Scand. **B36**, 547 (1982); Z.N. Parnes, M.I. Kalinkin, and D.N. Kursanov. Dokl. Akad. Nauk SSSR, **165**, 1093 (1965).
6. (*a*) P. Brunet and J.D. Wuest. J. Org. Chem. In press; (*b*) F. Montgrain, S.M. Ramos, and J.D. Wuest. J. Org. Chem. **53**, 1489 (1988); (*c*) B. Bachand, S.M. Ramos, and J.D. Wuest. J. Org. Chem. **52**, 5443 (1987); (*d*) S.M. Ramos, M. Tarazi, and J.D. Wuest. J. Org. Chem. **52**, 5437 (1987); (*e*) A.L. Beauchamp, F. Montgrain, and J.D. Wuest. Acta Crystallogr. Sect. C: Cryst. Struct. Commun. **C43**, 1557 (1987).
7. F.A. Neugebauer, B. Funk, and H.A. Staab. Tetrahedron Lett. **35**, 4755 (1994); G.W.H. Cheeseman. J. Chem. Soc. 3308 (1955); R.C. Elderfield and V.B. Meyer. J. Am. Chem. Soc. **76**, 1887 (1954).
8. G. Wulff and G. Wolf. Chem. Ber. **119**, 1876 (1986); D.J. Gale and J.F.K. Wilshire. Aust. J. Chem. **28**, 2447 (1975); K.B. Niewiadomski and H. Suschitzky. J. Chem. Soc. Perkin Trans. 1, 1679 (1975).
9. D.D. Perrin. Dissociation constants of organic bases in aqueous solution. Butterworths, London. 1965.
10. D.C. McKean. Chem. Soc. Rev. **7**, 399 (1976); L.J. Bellamy and D.W. Mayo. J. Phys. Chem. **80**, 1217 (1976); T.A. Crabb, R.F. Newton, and D. Jackson. Chem. Rev. **71**, 109 (1971); F. Bohlmann. Chem. Ber. **91**, 2157 (1958).

11. D.D. Tanner and J.J. Chen. J. Org. Chem. **54**, 3842 (1989); H. Chikashita, S. Nishida, M. Miyazaki, Y. Morita, and K. Itoh. Bull. Chem. Soc. Jpn. **60**, 737 (1987); A.A. Espenbetov, A.F. Pozharskii, Yu. T. Struchkov, and A.N. Suslov. Khim. Geterotsikl. Soedin. 977 (1985); N.T. Berberova, E.P. Ivakhnenko, A.S. Morkovnik, and O. Yu. Okhlobystin. Khim. Geterotsikl. Soedin. 1696 (1979).
12. K. Bowden and A.M. Last. J. Chem. Soc., Perkin Trans. 2, 1144 (1973); K. Bowden and A.M. Last. J. Chem. Soc. Perkin Trans. 2, 345 (1973).
13. J. Cason and J.D. Wordie. J. Org. Chem. **15**, 608 (1950); R.C. Fuson and G. Munn. J. Am. Chem. Soc. **71**, 1870 (1949).
14. K.B. Sloan and S.A.M. Koch. J. Org. Chem. **48**, 635 (1983).
15. J. Suszko and S. Kinastowski. Rocz. Chem. **41**, 523 (1967).
16. W.W. Paudler and A.G. Zeiler. J. Org. Chem. **34**, 2138 (1969).
17. G. Friedmann, M. Brini, P. Ederle, J. Gasser, P.-J. Holderith, M. Vernois, and J.-M. Widmaier. Bull. Soc. Chim. Fr. 706 (1970); H.C. Brown and K.L. Nelson. J. Am. Chem. Soc. **75**, 24 (1953).
18. W.C. Still, M. Kahn, and A. Mitra. J. Org. Chem. **43**, 2923 (1978).

Ground- and excited-state properties of some naphthoflavyliums

Mourad Elhabiri, Paulo Figueiredo, Florian George, Jean-Paul Cornard, André Fougerousse, Jean-Claude Merlin, and Raymond Brouillard

Abstract: A series of five, structurally related, substituted 2-phenyl-benzopyrylium (flavylium) salts were synthesized and characterized by NMR, absorption, and fluorescence techniques. Their hydration and deprotonation constants were obtained through thermodynamic and relaxation kinetic methods. Metallic complexation with the two compounds possessing a catechol group and its effect on the fluorescence intensity was also studied. The ground state properties of the five pigments are correlated with the theoretical data collected through AM1 molecular orbital calculations.

Key words: naphthoflavylium synthesis, hydration and deprotonation constants, fluorescence, metallic complexation, molecular orbital calculations.

Résumé : Cinq sels de 2-phényl-benzopyrylium (flavylium) ont été synthétisés et caractérisés par leurs spectres de RMN, d'absorption et de fluorescence. Les constantes d'hydratation et de déprotonation ont été déterminées par des méthodes thermodynamiques et cinétiques. La complexation de certains métaux avec les deux composés possédant un groupe catéchol et l'effet de ce type de complexe sur l'intensité de fluorescence ont également été étudiés. Les propriétés de l'état électronique fondamental des cinq pigments sont en bon accord avec les données théoriques obtenues par les calculs d'orbitales moléculaires selon la méthode AM1.

Mots clés : synthèse de cations naphthoflavylium, constantes d'hydratation et de déprotonation, fluorescence, complexation métallique, calcul d'orbitales moléculaires.

Introduction

Diversely substituted 2-phenyl-benzopyrylium salts (henceforth referred to as flavylium salts) are frequently found in nature as the yellow to blue coloured pigments of most flowers and fruits (1, 2). They are the aglycone forms of a family of natural colourants, commonly known as anthocyanins (3), which have been consumed by humanity without any apparent unhealthy effects and have thus attracted the attention of numerous scientists for their use as an alternative to the hazardous synthetic dyes (4, 5). Unfortunately, the colourant properties of anthocyanins are somewhat unreliable under the physico-chemical conditions required for their possible use as food additives, namely mildly acidic pH values and interactions with an essentially aqueous environment (6–8). Indeed, in these conditions the flavylium form, which is usually stable at pH lower than 2, undergoes a hydration reaction (Scheme 1) leading to the formation of colourless forms. Moreover, both the coloured and colourless forms are susceptible to thermal and photochemical degradation (9, 10). Several recent studies have, for these reasons, addressed the problem of the stabilization of such colourants in aqueous solution through the formation of molecular complexes with a wide array of natural compounds (1, 2, 11–23).

An alternative path for the obtention of stable coloured pigments is through laboratory synthesis of anthocyanin analogues possessing simple substituent groups, such as OH, CH_3O, phenyl, etc., in key positions of the molecule (24–31) in order to provide not only the widest possible range of colours but also to protect the flavylium cation against nucleophilic attack in the pH domain referred to above (~3 to 5). Some of these synthetic flavylium compounds have revealed very interesting excited-state characteristics, namely fluorescence and photochromic properties (10, 25, 32–34).

With the objective of evaluating the influence on stability brought about by the introduction of different substituents in key positions of the flavylium skeleton, five compounds were synthesized: 2-benzo-naphtho[2,1-*b*]pyrylium chloride (**1**), 2-((3′,4′-dihydroxy)-benzo)-naphtho[2,1-*b*]pyrylium chloride (**2**), 2-((3′,4′-dihydroxy)-benzo)-3-*O*-methyl-naphtho[2,1-*b*]-pyrylium chloride (**3**), 2-naphtho-naphtho[2,1-*b*]pyrylium chloride (**4**), and 2-benzo-naphtho[1,2-*b*]pyrylium chloride (**5**), Scheme 2. The extended conjugated π-systems of these molecules prompted us also to study their emissive properties and to correlate them with the degree of rigidity predicted by semi-empirical molecular orbital calculations for their molecular structures.

Results

Thermodynamic and kinetic measurements in aqueous media

The electronic absorption spectra of flavylium cations present,

Received December 8, 1995.

M. Elhabiri, P. Figueiredo, F. George, A. Fougerousse, and R. Brouillard.[1] Laboratoire de chimie des polyphénols, Centre national de la recherche scientifique, Unité de recherche associée n° 31, Université Louis Pasteur, Institut de Chimie, 4, rue Blaise Pascal, 67008 Strasbourg, France.
J.-P. Cornard and J.-C. Merlin. Laboratoire de spectrochimie infrarouge et Raman, Centre national de la recherche scientifique, Unité propre de recherche A 2631 L), Université des sciences et technologies de Lille, Bâtiment C5, 59655 Villeneuve d'Ascq Cédex, France.

[1] Author to whom correspondence may be addressed. Telephone: (33) 88 41 60 92. Fax: (33) 88 41 60 81. E-mail: brouil@chimie.u-strasbg.fr

Scheme 1.

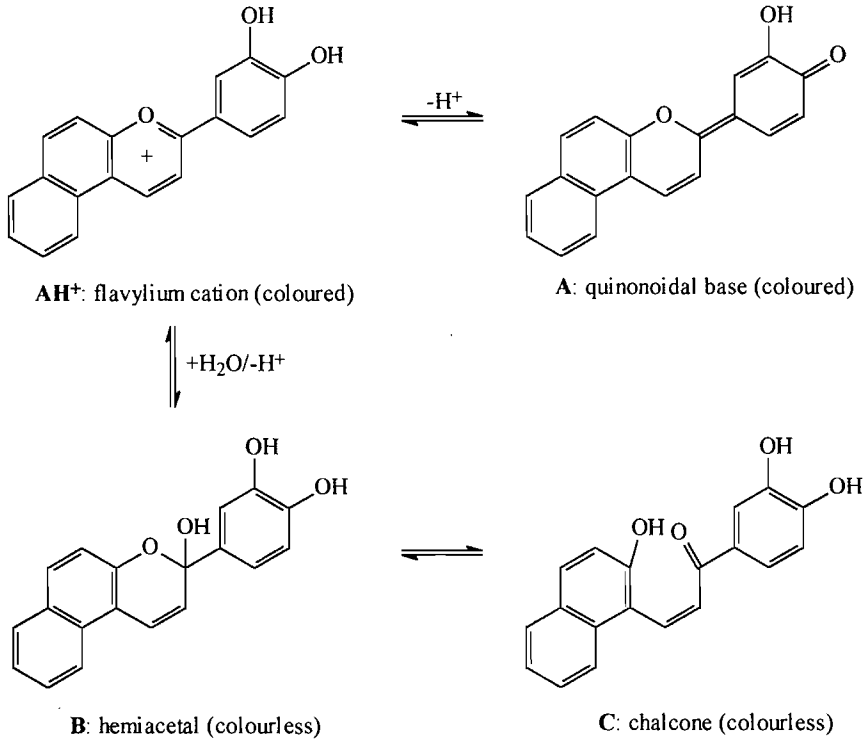

Scheme 2.

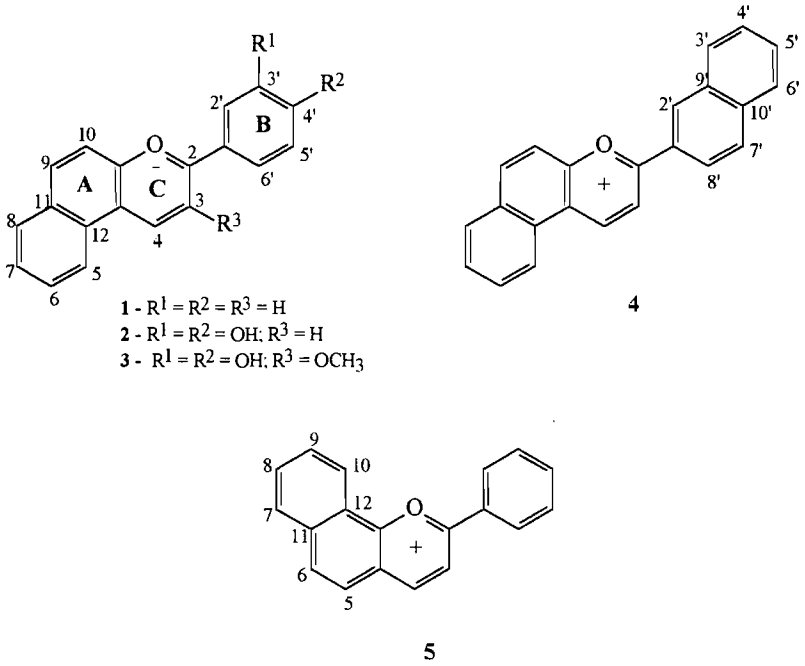

as a characteristic feature, a band in the visible spectral range, whose shape, maximum wavelength, and intensity are functions of the substitution pattern of the chromophoric system (26, 28, 31). Figure 1 reflects the spectral changes brought about by the introduction of different substituents in the same basic structure (β-naphthoflavylium, **1**). Going from **1** to **3**, it can be seen that the presence of the two hydroxyl groups in 3′ and 4′ produces a bathochromic shift from 444 nm to 484 nm and that further addition of the 3-*O*-methyl produces an even larger shift to 502 nm. The shape and intensity of the absorbance bands are also affected by the presence of different types of substituents even when they are linked to the same positions in the basic flavylium molecule (cf. compounds **2** and **4**).

The transformations undergone by these compounds in mildly acidic aqueous solution can be summarized by the equilibria

Fig. 1. Electronic absorption spectra of compounds **1–4**. pH = 1.0. Aqueous solutions with 4% MeOH.

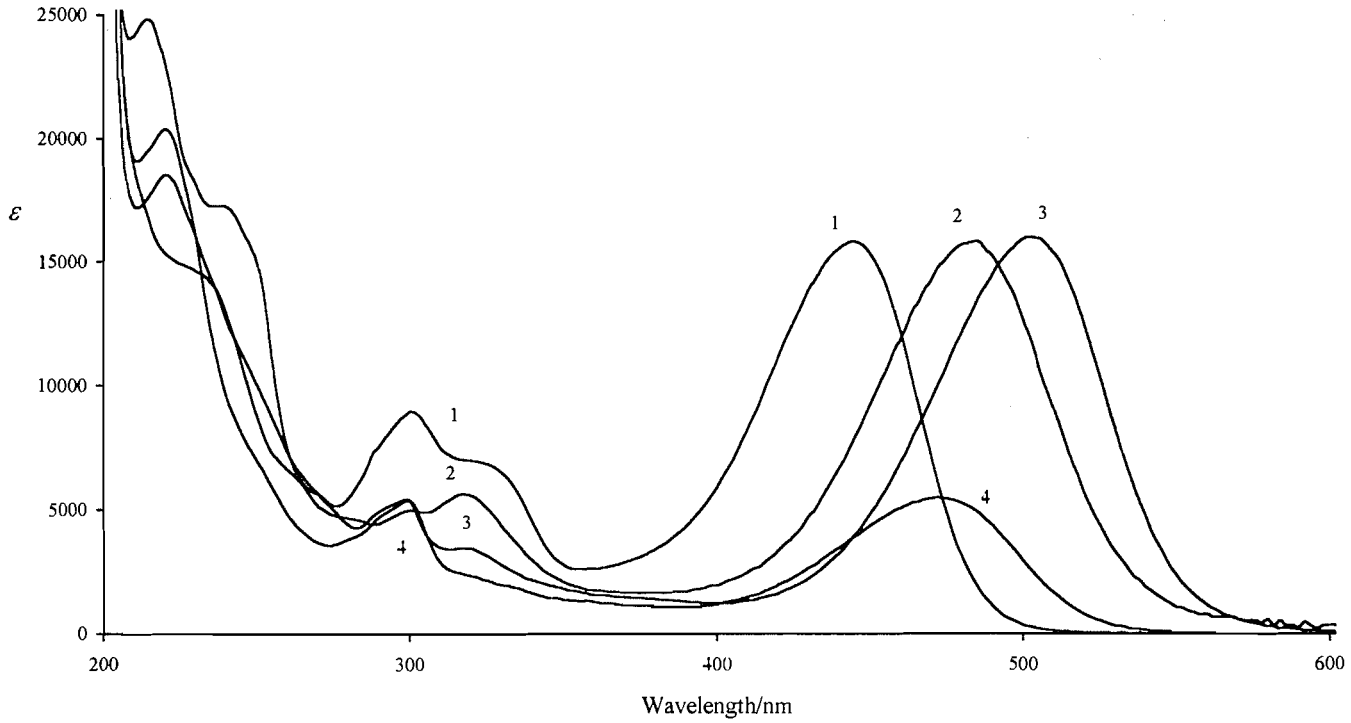

[1] $AH^+ \underset{}{\overset{K_a}{\rightleftharpoons}} A + H^+$

[2] $AH^+ + H_2O \underset{}{\overset{K_h}{\rightleftharpoons}} (B + C) + H^+$

For the sake of simplicity, in eq. [2] the equilibria of hemiacetal (B) formation and subsequent ring opening to form the chalcone C are written as a whole since the second process occurs in a very fast step (35, 36). The increase in pH in aqueous solutions of these compounds with the subsequent attainment of the equilibrium described in eq. [2] produces significant modifications on the electronic spectra of the pigments (Fig. 2), notably a decrease in intensity of the visible band. This fact allows the obtention of a global value of $K' = K_a + K_h$, through a plot of $D_0/(D_0 - D)$ as a function of $[H^+]$, according to eq. [3] (20, 21, 23). Such a plot will give a straight line with an intercept/slope ratio equal to $K_h + K_a$.

$$[3] \quad \frac{D_0}{D_0 - D} = \frac{K_h + K_a}{K_h + K_a(1 - r_A)} + \frac{[H^+]}{K_h + K_a(1 - r_A)}$$

In eq. [3] D_0 represents the absorption of a strongly acidic (pH <1) pigment solution, D the absorption of a solution at a given, less acidic, pH, and r_A stands for the ratio of the molar absorption coefficients $\varepsilon_A/\varepsilon_{AH}{}^+$.

An alternative and complementary method to obtain the values of the equilibrium constants is by performing pH jumps, from very acidic to less acidic pH values, in aqueous solutions of the pigments, and measuring the resulting exponential decay of the visible absorption, which essentially reflects the relaxation of the pH-dependent equilibrium [2] according to an apparent first-order kinetics. The first-order rate constant k for [B] variation (defined by $d\Delta[B]/dt = -k\Delta[B]$) is directly delivered by the spectrophotometer software and can be represented by

$$[4] \quad k = k_2[H^+] + \frac{k_1}{1 + K_a/[H^+]}$$

where $k_1/k_2 = K_h$, i.e., k_1 is the hydration rate constant and k_2 the constant for the reverse process. Rearranging eq. [4] into eq. [5] allows the obtention of a $(K_a + K_h + [H^+])/k$ vs. $1/[H^+]$ straight-line plot with a slope equal to K_a/k_2 and an intercept of $1/k_2$. This leads directly to the values for k_2 and K_a, and through a combination with the results obtained from eq. [3], K_h and k_1 immediately follow. The theoretical treatment that permits the obtention of equilibrium rate constants is given in full detail in ref. 21.

$$[5] \quad \frac{K_a + K_h + [H^+]}{k} = \frac{1}{k_2} + \frac{K_a}{k_2}\frac{1}{[H^+]}$$

Table 1 reports the calculated hydration and deprotonation constants for pigments **1–4**.

Fluorescence properties

Most anthocyanins and some synthetic flavylium salts are known to exhibit fluorescence from all forms existing in mildly acidic aqueous solutions and even in some organic solvents (10, 25, 37, 38). However, all natural anthocyanins possess only very weak fluorescence intensities and poor fluorescence quantum yields, the same being true for the sim-

Fig. 2. Electronic absorption spectra of **3** as a function of pH. Concentration = 2.8×10^{-5} M; $T = 25$°C. pH = 1.1 (*a*), 2.5 (*b*), 2.7 (*c*), 3.0 (*d*), and 3.4 (*e*).

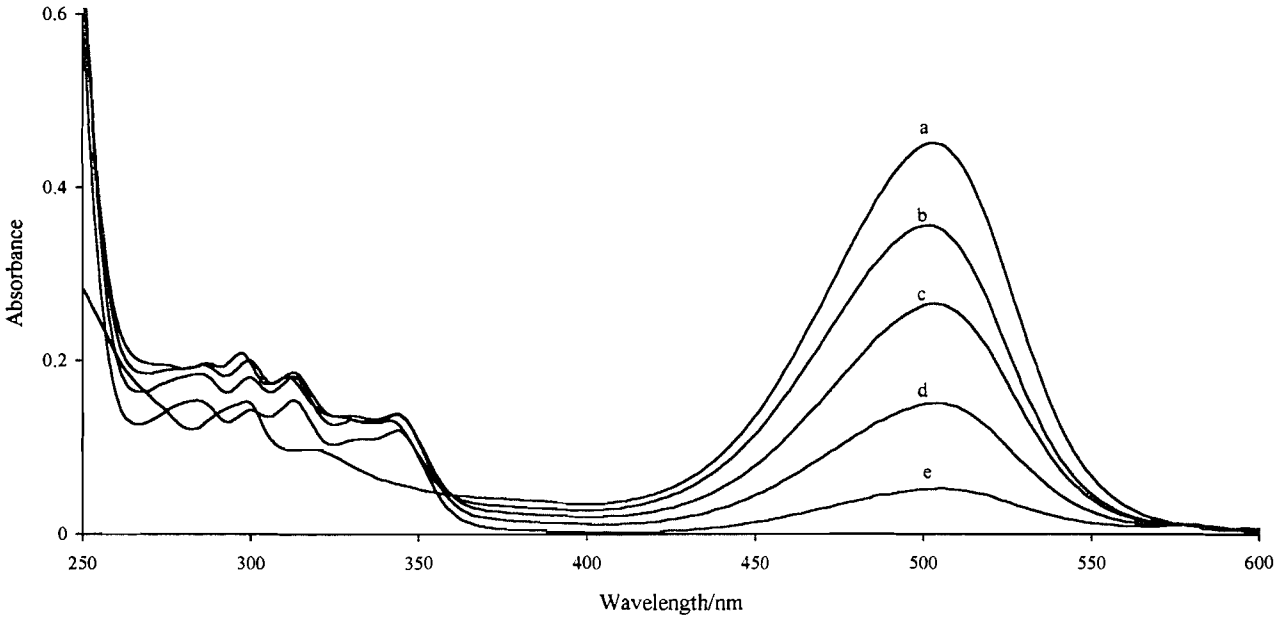

Table 1. Thermodynamic and kinetic parameters for pigments **1–4** in aqueous solution. $T = 25$°C.

Compound	K_h (pK_h)	K_a/M^{-1} (pK_a)
1	1.02×10^{-3} (2.99)	—
2	—	1.41×10^{-4} (3.85)
3	1.51×10^{-3} (2.82)	6.76×10^{-5} (4.17)
4	4.32×10^{-3} (2.365)	—

Table 2. Calculated parameters for compounds **1–5**. AM1 parametrization.

Compound	S_2^N	Torsion angle[a] (°)
1	0.254	0.30
2	0.257	0.32
3	0.239	19.42
4	0.257	0.21
5	0.356	25.67

[a]Between rings C and B.

ple synthetic analogues studied so far. The extended conjugated systems of all pigments reported in this work and their planar molecular structures, especially in the cases of **1**, **2**, and **4** (Table 2), seemed to forecast a possible increase in emission intensity when compared to the above-mentioned pigments. Figure 3 compares the emission spectra of the flavylium forms of compounds **1–3** and **5**, where an influence of the substituents on emission intensity and wavelength is visible. Indeed, compounds **1**, **2**, and **3**, although absorbing at different wavelengths, emit at the same wavelength but the emission intensity of **2** is 500 times lower than that of **1**, and **3** is still less emissive. When compared to **1**, compound **5**, which can be considered as its isomer, is characterized by a strong Stokes shift in acidic methanolic solution, from 534 to 642 nm. Compound **4** also exhibits an emission band at 534 nm, its relative intensity being intermediate between those of **1** and **2**, in spite of being a more conjugated system.

Solvent effect

It is well known that flavylium forms of anthocyanic pigments present a negative solvatochromic behaviour, i.e., a displacement of the visible absorption band towards longer wavelengths with a reduction in medium polarity (39). Absorption and fluorescence emission spectra of pigments **1**, **4**, and **5** were thus performed in several solvents, ranging in polarity from chloroform to water, to assess the solvent influence on absorption and emission wavelengths and intensities of this particular type of flavylium salts. The solvents used were, in order of increasing polarity, chloroform, dichloromethane, formic acid, methanol, and water/HCl. The changes in absorption spectra caused by variation in medium polarity in **4** are presented in Fig. 4. Considerable changes in band shape can be observed, first the disappearance of the typical flavylium absorption and the clear vibrational structure at lower wavelength in methanol, which is also slightly perceptible both in chloroform and dichloromethane. In the cases of chloroform and dichloromethane, the typical bathochromic shift due to medium polarity on the flavylium absorption band is accompanied by the formation of a shoulder at ca. 420 nm. The two other pigments (**1** and **5**) show similar behaviour, notably a bathochromic shift with decreasing medium polarity and the appearance of structured absorbance bands in methanolic solution.

In what concerns fluorescence emission, a hypsochromic shift is observed when decreasing the medium polarity. Furthermore, strong differences of behaviour can be observed between the two isomers **1** and **5**, when comparing their fluo-

Fig. 3. Fluorescence emission spectra of **1**, λ_{EX} = 445 nm; **2**, λ_{EX} = 485 nm; **3**, λ_{EX} = 500 nm; and **5**, λ_{EX} = 600 nm. Acidic methanolic solutions.

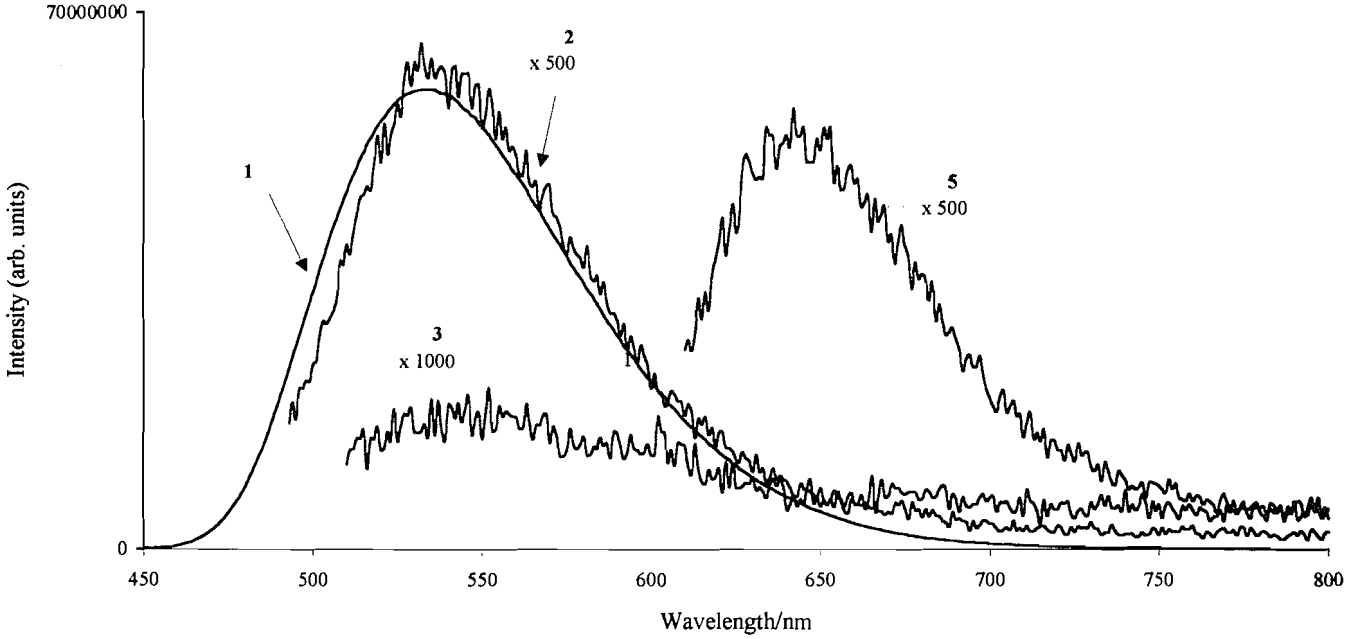

Fig. 4. Absorption spectra of **4** in H_2O, pH = 1.0 (*a*), CH_3OH (*b*), HCOOH (*c*), CH_2Cl_2 (*d*), and $CHCl_3$ (*e*). 3.25 × 10^{-4} M, T = 25°C. Inset: variation of λ_{max} as a function of medium polarity.

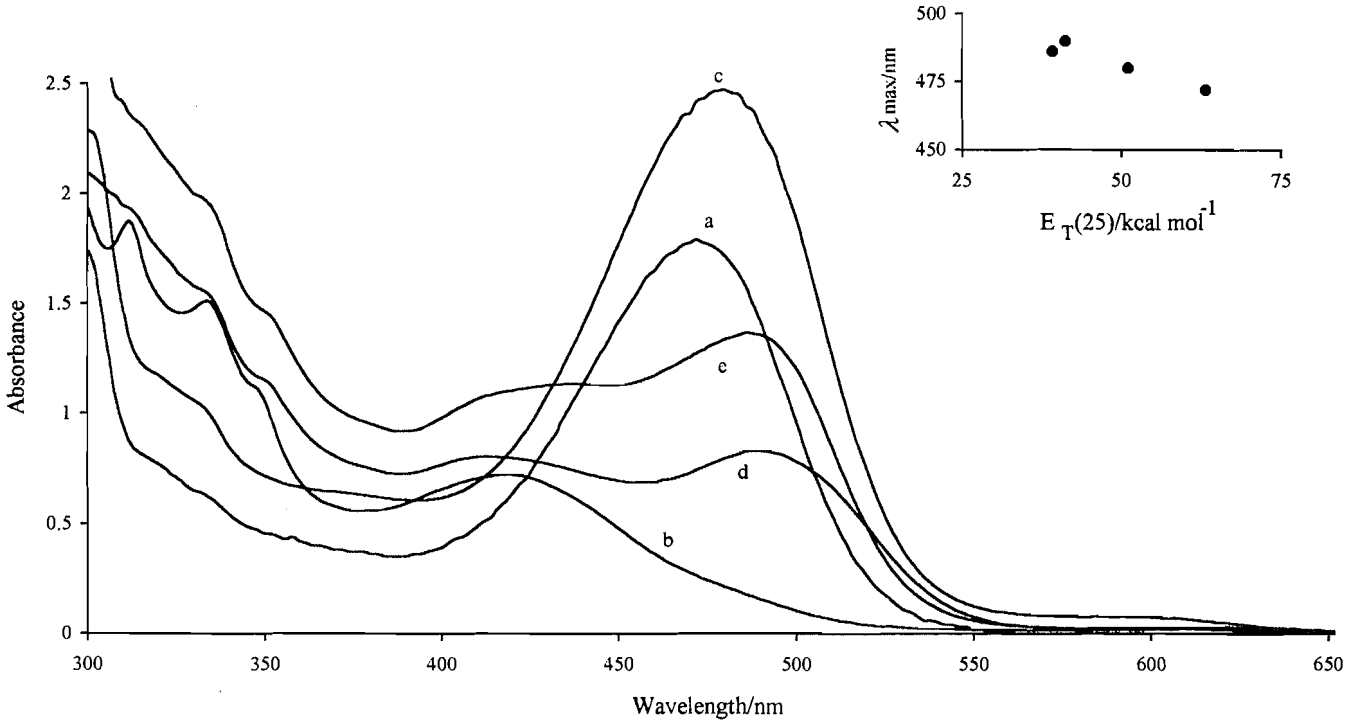

rescence properties in solvents of different polarity. In methanol both **1** and **5** show low-intensity emission bands, when excited at the maximum visible wavelength of their respective flavylium forms, this intensity strongly increasing when a few drops of concentrated formic acid are added to the solution. But in dichloromethane solutions, while **1** produces emission bands more intense than those found in acidic methanol, **5** displays only very weak fluorescence bands.

Photochromic behaviour

Certain synthetic flavylium salts, in mildly acidic aqueous media (3 < pH < 4), have shown interesting photochromic

Fig. 5. Fluorescence emission spectra of **2** in H_2O, pH ≈ 4.0, (*a*) without Al^{3+}, and (*b*) with Al^{3+}.

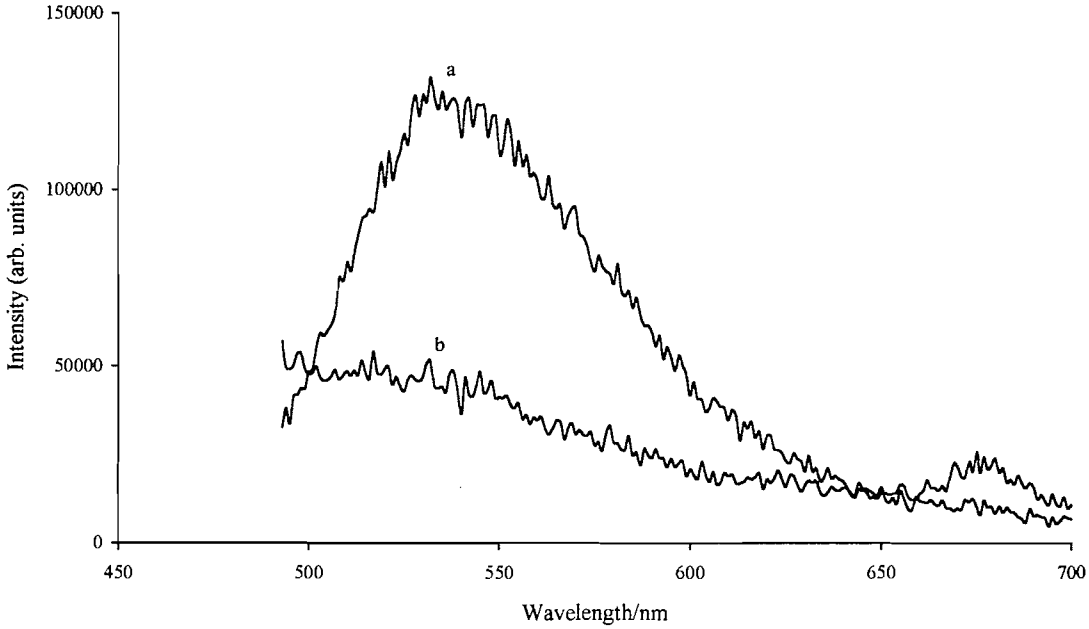

Scheme 3.

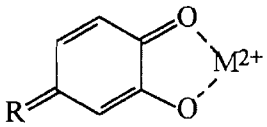

properties with either gain or loss of colour under light irradiation and the inverse behaviour in the dark (10, 32, 34). This prompted us to investigate the photochromic behaviour of the five naphthoflavyliums here reported. Yet, only pigment **3** revealed a manifest photochromic effect with loss of colour when submitted to irradiation, and a partial colour recovery in the dark. Colour recovery was not complete since side reactions of thermal and photo degradation occur.

Metallic complexation

Chelation between some small di- and trivalent metals and anthocyanins possessing a catechol group in ring B has been reported (1, 22, 40, 41) and discussed on the basis of phenolic proton(s) loss to form a quinonoidal structure (Scheme 3), which will be responsible for the bathochromic shift always observed. To our knowledge, no work has been done on the fluorescence properties of these metal complexes. This prompted us to investigate the fluorescence emission changes when europium(III) or aluminium(III) salts are added to stabilized solutions of compounds **2** and **3**.

For both compounds, the addition of a solution of $AlCl_3$ in large excess produces a bathochromic shift of 60 nm in the visible absorption band and a strong decrease of the fluorescence intensity at 534 nm characteristic of the flavylium cation, which is in accordance with the deprotonation model proposed above. Moreover, a faint emission band appears at 675 nm (Fig. 5) and 690 nm, respectively, for **2** and **3**, which becomes more intense when the solution is excited at the new maximum wavelength of the complex.

Discussion

Thermodynamic and kinetic measurements in aqueous media

The spectral changes shown in Fig. 1, namely, the bathochromic shifts observed between pigments **1**, **2**, and **3**, can be attributed to the increase in electron donor strength of the substituting OH and OCH_3 groups. A similar phenomenon is known to occur with natural, largely substituted, anthocyanins, which tend to absorb at longer wavelengths than the parent aglycones (2).

The equilibrium constants obtained through application of eqs. [3] and [5] are presented in Table 1. No values are displayed for pigment **5**, due to its insolubility in aqueous solution. In the cases of molecules **1** and **4**, which possess no OH group and thus cannot permit deprotonation (eq. [1]), K_h is directly obtained from eq. [3] and is equal to K'.

From the analysis of Table 1, it can be inferred that compound **4** is the most susceptible to hydration (lower pK_h), while **2** seems to suffer only a negligible water attack. This is evidenced by the fact that we can obtain the value for only a single equilibrium constant and is further stressed by the subtraction of the flavylium contribution (37) from the absorption spectra as a function of the pH. This results only on the rise of a new band with a maximum wavelength at ca. 555 nm, which is the same maximum wavelength obtained for a fresh solution of **2** at pH 7, where the quinonoidal base is the dominant species. Moreover, an isosbestic point at ca. 530 nm is observed, supporting the existence of only two forms in equilibrium. Since no other absorptions, attributable to the hemiacetal and (or) the chalcone forms, appear as a result of the subtraction, the value found for the equilibrium constant is assigned to K_a.

The greater or lower reactivity towards nucleophilic water attack can be correlated with the charge density in C-2 (given

by the parameter S_2^N), obtained through molecular orbital calculations. Examination of Table 2 allows the conclusion that an increase in S_2^N is accompanied by a diminution in pK_h. This confirms that, for these naphtho derivatives, the hydration reaction occurs in the same manner as that reported for common flavylium salts (2, 28). There is, however, an exception represented by compound **4**, which presents only a small increase in S_2^N relative to **1**, but has a considerably lower pK_h. A tentative explanation for this behaviour is given by taking into account the large absolute hardness value (η) that was computed, through molecular orbital calculations, for pigment **1** (3.31 eV) as compared to the value obtained for compound **4** (3.05 eV). This parameter is defined as $\eta = (E_{LUMO} - E_{HOMO})/2$ and is usually a reliable criterion for predicting reactivity, i.e., the larger the LUMO–HOMO gap the lower the reactivity of the molecule (31). The greater reactivity of **4** may therefore reflect a less aromatic character of this compound relative to **1** in spite of the presence of an additional benzene fragment in **4** (see below the discussion of the fluorescence properties).

Fluorescence properties

The spectra depicted in Fig. 3 demonstrate the influence that is brought about by different substituents on emission intensity and wavelength. The difference in emission intensity among pigments **1–3** may be due to the formation of a twisted intramolecular charge transfer state (TICT) in the excited state, caused by the presence of the OH groups in the case of **2** and further enhanced by the loss of coplanarity in **3** (Table 2). Some authors have already verified that, for similar molecules, the rigidity and consequent coplanarity of the moiety connected to C-2 of the benzopyrylium fragment has a marked influence on their fluorescence properties (25, 42–44). The formation of this TICT state can be viewed as a deactivation channel for the fluorescence emission.

The observed Stokes shift between **1** and **5** (Fig. 3) is attributable to the strong electron-donating properties of the benzyl moiety on position 11 of the latter (25). A strong bathochromic shift from 444 nm to 600 nm is also observed on the absorption spectra of these two compounds.

The structure of compound **4** (Scheme 2) leads us to anticipate a strong fluorescence emission. However, this is not observed. As stated before, it exhibits an emission intensity lower than **1**. This molecule is a good example that it is not simply by combining a great number of benzene fragments that a molecule becomes more aromatic, as demonstrated by the smaller $E_{LUMO} - E_{HOMO}$ gap (28) obtained from molecular orbital calculations applied to **4**. This gap, which is a good measure of the aromaticity of a molecule, was computed as 3.05 eV, compared to 3.31 eV for **1**.

Solvent effect

The insert of Fig. 4 depicts the existing correlation between E_T at 25°C (45) and the maximum wavelength of compound **4** in several solvents, the same relation holding for the two other compounds tested (**1** and **5**). This relation reflects the negative solvatochromic behaviour of these three naphthoflavyliums.

The existence of vibrational bands in the UV region of the absorption spectra, observed for compounds **1**, **4** (Fig. 4), and **5** in methanolic solution, should have their origin in the formation of a methoxy adduct to position 2 (see Scheme 2) of the chromophore, since when such a solution is quickly acidified to pH 1 a spectrum similar to the one observed in aqueous acidic solution is obtained. This methoxy adduct will thus be a methanolic analogous to the hemiacetal formed upon hydration of the flavylium cation, in aqueous medium.

Scheme 4.

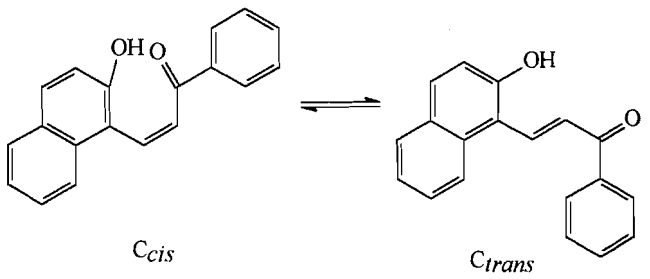

The appearance of a shoulder next to the typical visible absorption band, in chloroform and dichloromethane solutions (Fig. 4), may be caused by a rigidization of the molecular structure in these less polar solvents.

The hypsochromic shift observed in fluorescence emission spectroscopy when the medium polarity is lowered, which appears to be in contradiction with the bathochromic shift observed in absorption spectra, can be explained by a greater delocalization of the positive charge in the excited state than in the ground state. This leads to a smaller stabilization of S_1 relative to S_0 by solvents of high polarity. Since the polarizability of S_1 is greater than that of S_0, less polar solvents stabilize the latter and result in a hypsochromic shift of the emission wavelength.

Finally, it may be the presence of a substituent in position 11, in pigment **5**, responsible for the creation of a deactivation channel, more effective in less polar solvents, that would account for the low intensity of emission displayed by this compound in dichloromethane solution, when compared to its isomer **1**.

Photochromic behaviour

The photochromic properties here reported for compound **3**, in mildly acidic aqueous solutions, seem to be typical of some 3-substituted flavylium based pigments that form the colourless *cis*-chalcone (cf. Scheme 4) as the more stable isomer in the ground state (32, 46). Light irradiation allows us to overcome the energy barrier necessary to displace the equilibrium towards the *trans* isomer (also colourless). The *trans*-chalcone, thus formed in the excited state as the more stable isomer, does not possess the ability to cyclize and reform the flavylium cation according to the set of equilibria depicted in Scheme 1. The displacement of these equilibria towards *trans*-chalcone accumulation results therefore in a loss of colour. This reaction is thermally reversed in the dark.

The inverse process does also occur with some, 3-unsubstituted, flavylium compounds (34), i.e., stabilization of the *trans*-chalcone in the ground state with the irradiation producing a *trans*→*cis* photoisomerization with consequent recyclization of the *cis*-chalcone to reform the flavylium cation. This reaction is also reversed in the dark.

Metallic complexation

The new emission bands observed at 675 and 690 nm (Fig. 5) upon excitation of aqueous solutions of, respectively, compounds **2** and **3** in the presence of Al(III), although having the

Scheme 5.

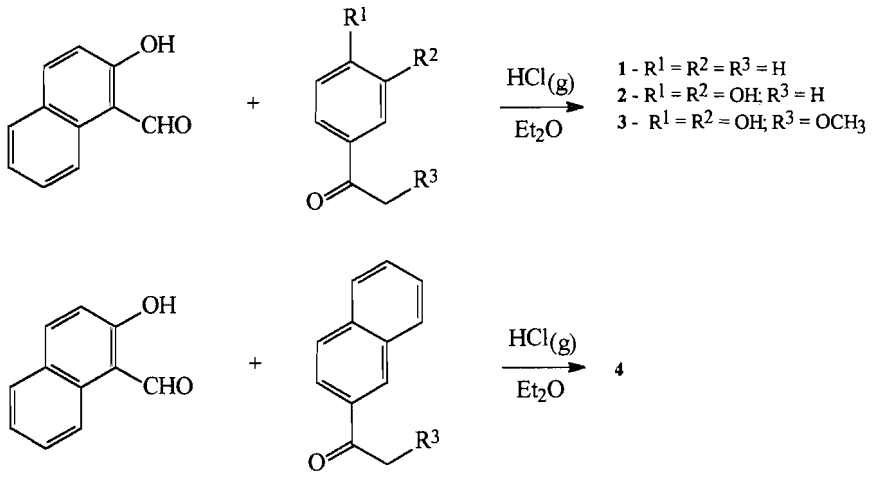

same maximum wavelength as those of a fresh solution of the pigments at neutral pH (where the quinonoidal base is the predominant form in solution), are less intense. This fact may be explained by a quenching process as a consequence of aluminium complexation. Such quenching effect is increased when europium(III) replaces aluminium, since in this case no new emission band accompanies the decrease in the flavylium cation emission.

Conclusion

Ground-state properties of a series of structurally related pigments are shown to be strongly dependent on the substitution pattern and on the greater or lesser coplanarity and aromaticity of the molecule. Commonly, the stronger the electron donor character of the substituent(s), the greater the observed bathochromic shift. The twisting of the B ring relative to the rest of the molecule seems to act in the same direction. Concerning excited-state properties, it is the substitution pattern that seems to play the most significant role. Notably, substitution in position 11 seems to have a profound impact, namely, producing a significant Stokes shift. The other substitution patterns studied do not affect the emission wavelength, but the fluorescence intensity strongly decreases with the presence of donor substituents, through the possible formation of a nonfluorescent TICT state, indicating that nonsubstituted and planar compounds, like **1**, are good candidates for highly aromatic and fluorescent molecules.

Computational

Molecular orbital calculations, using AM1 parametrization (47) were performed on a Escom P100 PC, using the HyperChem program (version 4, Hypercube, Inc., Ont. Canada).

Experimental

Fast atom bombardment (FAB) mass spectrometry was carried out either on a LBK 9000S or on a Thomson THN 208 instrument. Electron-spray ionization (ESI) mass spectrometry was carried out with a Bio-Q quadripole instrument. NMR spectra were recorded at 27°C on a Bruker AM-400 spectrometer operating at 400.14 MHz for ^{1}H and on a Bruker WP-200SY operating at 50 MHz for ^{13}C. Standard pulse frequences and

Scheme 6.

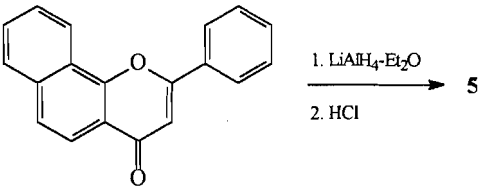

phase cycling scheme (48) were used to record ^{1}H–^{1}H COSY (49, 50). Samples (4–8 mg/mL) were prepared in $(CD_3)_2SO$–CF_3COOD (98:2), CD_3CN–CF_3COOD (98:2). Residual signals of the solvent were used as internal chemical shift reference. Electronic absorption spectra were acquired using a Hewlett–Packard diode-array spectrometer fitted with a quartz cell (d = 1 cm) equipped with a stirring magnet. A constant temperature in the cell was obtained by use of a Lauda water-thermostated bath. The temperature was measured in the spectrometer cell with a Cormak thermocouple and was kept at 25 ± 0.1°C throughout this work. Fluorescence emission spectra were recorded on a SPEX F111 Fluorolog and on a molecular microprobe operating in a way that favours observation of the flavylium emission bands (51). Solutions used in fluorescence measurements always had an absorbance of 0.2 at the excitation wavelength. The pH was measured with a Metrohm 654 pH-meter equipped with a micro-electrode. Milli-Q water was used in all aqueous sample preparations. All other solvents were of analytical grade except for fluorescence measurements where spectroscopic grade solvents were used. 2′-*O*-Methyl-3,4-dihydroxyacetophenone and 3,4-dihydroxyacetophenone were prepared from 2′-chloro-3,4-dihydroxyacetophenone, according to ref. 22. All other reagents used throughout the synthesis were of synthetic or analytical grade and used as received.

This particular class of benzopyrylium salts was prepared by two different methods. The first consists of acidic condensation of an appropriate aldehyde with a ketone (52) (Scheme 5). In the second, the synthesis proceeds through the reduction of the carbonyl group of a flavone by $LiAlH_4$ followed by a treatment with hydrochloric acid (Scheme 6).

General procedure for compounds 1–4

An equimolar solution of the suitable ketone and aldehyde

precursors was vigorously stirred in distilled diethyl ether oxide. Gaseous hydrogen chloride was gently bubbled (3 h) into the mixture to favour solubilization when the initial products presented weak solubilities. Precipitation of coloured crystals occurred after some minutes and was completed by keeping the reaction mixture at −20°C overnight. Crystals were washed several times with distilled diethyl ether oxide and dryed under vacuum.

*2-Benzonaphtho[2,1-*b*]pyrylium chloride (**1**)*
Total yield is 55%. UV–VIS ($CHCl_3$) λ_{max} (nm): 244, 301, 330, 456. ^{1}H NMR (CD_3CN/TFA) δ (ppm): 10.74 (1H, d, J = 9.2 Hz, H4), 9.51 (1H, d, J = 9.2 Hz, H3), 9.12 (2H, d, J = 2.2/7.5 Hz, H2′, H6′), 8.63–8.32 (5H, complex signals, H3′, H4′, H5′, H6, H7), 9.49 (1H, d, J = 9.0 Hz, H5), 8.84 (1H, d, J = 9.3 Hz, H8), 8,82 (1H, d, J = 9.2 Hz, H9), 9.37 (1H, d, J = 9.3 Hz, H10). ESI-MS *m/z*: 257.1 for $C_{19}H_{13}O$.

*2-((3′,4′-Dihydroxy)benzo)naphtho[2,1-*b*]pyrylium chloride (**2**)*
Total yield is 55%. UV–VIS (HCl 0.1 M) λ_{max} (nm): 240, 300, 320, 486. ^{1}H NMR (DMSO/TFA signals assigned by ^{1}H–^{1}H COSY) δ (ppm): 10.07 (1H, d, J = 9.2 Hz, H4), 8.98 (1H, d, J = 9.2 Hz, H3), 8.17 (1H, dd, J = 2.3/8.5 Hz, H6′), 8.02 (1H, d, J = 2.2 Hz, H2′), 7.13 (1H, d, J = 8.6 Hz, H5′), 8.85 (1H, d, J = 9.3 Hz, H5), 7.97 (1H, t, J = 8.0 Hz, H6), 7.87 (1H, t, J = 8.2 Hz, H7), 8.24 (1H, d, J = 9.4 Hz, H8), 8.26 (1H, d, J = 9.3 Hz, H9), 8.71 (1H, d, J = 9.3 Hz, H10). FAB-MS *m/z*: 289.3 for $C_{19}H_{13}O_3$ (100 M^+), 579.2 (observation of a dimer, which can also be noticed by a deviation to the law of Beer–Lambert, when concentrations superior to 2×10^{-5} M were used).

*2-((3′,4′-Dihydroxy)benzo)-3-*O*-methylnaphtho[2,1-*b*]-pyrylium chloride (**3**)*
Total yield is 75%. UV–VIS (HCl 0.1 M) λ_{max} (nm): 240, 300, 320, 504. ^{1}H NMR (DMSO/TFA signals assigned by ^{1}H–^{1}H COSY) δ (ppm): 9.45 (1H, s, H4), 8.27 (1H, dd, J = 2.3/8.8 Hz, H6′), 8.10 (1H, d, J = 2.3 Hz, H2′), 7.07 (1H, d, J = 8.7 Hz, H5′), 4.34 (3H, s), 7.04 (1H, d, J = 7.9 Hz, H5), 7.81 (1H, t, J = 8.1 Hz, H6), 7.90 (1H, t, J = 8.1 Hz, H7), 8.16 (1H, d, J = 9.0 Hz, H8), 8.14 (1H, d, J = 9.0 Hz, H9), 8.43 (1H, d, J = 9.0 Hz, H10). ESI-MS *m/z*: 319.34 for $C_{20}H_{15}O_4$.

*2-Naphthonaphtho[2,1-*b*]pyrylium chloride (**4**)*
Total yield is 60%. UV–VIS (CH_3COOH) λ_{max} (nm): 252, 300, 476. ^{1}H NMR (CD_3CN/TFA) δ (ppm): 10.74 (1H, d, J = 9.2 Hz, H4), 9.51 (1H, d, J = 9.2 Hz, H3), 9.12 (2H, d, J = 2.2/7.5 Hz, H2′, H6′), 8.63–8.32 (5H, complex signals, H3′, H4′, H5′, H6, H7), 9.49 (1H, d, J = 9.0 Hz, H5), 8.84 (1H, d, J = 9.3 Hz, H8), 8.82 (1H, d, J = 9.2 Hz, H9), 9.37 (1H, d, J = 9.3 Hz, H10). FAB-MS *m/z*: 307.1 for $C_{23}H_{15}O$ (100 M^+), 615.2 (once again observation of a dimer).

*2-Benzonaphtho[1,2-*b*]pyrylium chloride (**5**)*
α-Naphthoflavone (200 mg, 0.73 mmol) was dissolved in 10 mL of a mixture of diethyl ether oxide and toluene and 1.1 equivalent of $LiAlH_4$ (20 mg) was added. The solution was kept under reflux for 2 h, diluted with ethyl acetate, and washed with two portions (each 50 mL) of water. The organic phase was then acidified with hydrochloric acid. The solution turned green and was concentrated under vacuum. The pyrylium salt was purified on a silica column, first with $CHCl_3$ as eluent and after with $CHCl_3$–CH_3COOH (95.5). Total yield is 35%. UV–VIS (CH_3COOH–$CHCl_3$, 1:1) λ_{max} (nm): 244, 297, 383, 425, 604. ^{1}H NMR (CD_3CN/TFA) δ (ppm): 10.54 (1H, d, J = 9.2 Hz, H4), 8.84 (1H, d, J = 9.2 Hz, H3), 8.32–7.71 (10H, complex signals, H2′, H3′, H4′, H5′, H6′, H6, H7, H8, H9, H10), 8.79 (1H, d, J = 9.0 Hz, H5). FAB-MS *m/z*: 257.1 (100 M^+) for $C_{19}H_{13}O$.

Acknowledgments

The authors would like to thank Prof. F. Pina, from Universidade Nova de Lisboa, for some preliminary fluorescence measurements. P. Figueiredo wishes also to thank the European Union for a post-doc grant ERBCHBICT9441610.

References

1. T. Goto and T. Kondo. Angew. Chem. Int. Ed. Engl. **30**, 17 (1991).
2. R. Brouillard and O. Dangles. *In* The flavonoids, advances in research since 1986. *Edited by* J.B. Harborne. Chapman and Hall, London. 1993. pp. 565–588.
3. J.B. Harborne and R.J. Grayer. *In* The flavonoids, advances in research since 1980. *Edited by* J.B. Harborne. Chapman and Hall, London. 1988. pp. 1–20.
4. J.J. Macheix and A. Fleuriet. *In* Polyphenolic phenomena. *Edited by* A. Scalbert. INRA Editions, Versailles. 1993. pp. 157–163.
5. F.J. Francis. *In* Polyphenolic phenomena. *Edited by* A. Scalbert. INRA Editions, Versailles. 1993. pp. 209–220.
6. R. Brouillard and J.E. Dubois. J. Am. Chem. Soc. **99**, 1359 (1977).
7. R. Brouillard and B. Delaporte. J. Am. Chem. Soc. **99**, 8461 (1977).
8. R. Brouillard, B. Delaporte, and J.E. Dubois. J. Am. Chem. Soc. **100**, 6202 (1978).
9. P. Furtado, P. Figueiredo, H.C. Neves, and F. Pina. J. Photochem. Photobiol. A: **75**, 113 (1993).
10. P. Figueiredo. Ph.D. Thesis. Universidade Nova de Lisboa (1994).
11. R. Brouillard. Phytochemistry, **22**, 1311 (1983).
12. R. Brouillard, G. Mazza, Z. Saad, A.M. Albrecht-Gary, and A. Cheminat. J. Am. Chem. Soc. **111**, 2604 (1989).
13. T. Hoshino and T. Goto. Tetrahedron Lett. **31**, 1593 (1990).
14. G. Mazza and R. Brouillard. Phytochemistry, **29**, 1097 (1990).
15. P. Rüedi and B. Hutter-Beda. Bull. Liaison — Groupe Polyphenols, **15**, 332 (1990).
16. Y. Cai, T.H. Lilley, and E. Haslam. J. Chem. Soc. Chem. Commun. 380 (1990).
17. T.V. Mistry, Y. Cai, T.H. Lilley, and E. Haslam. J. Chem. Soc. Perkin Trans. 2, 1287 (1991).
18. O. Dangles and R. Brouillard. Can. J. Chem. **70**, 2174 (1992).
19. O. Dangles and R. Brouillard. J. Chem. Soc. Perkin Trans. 2, 247 (1992).
20. O. Dangles, N. Saito, and R. Brouillard. Phytochemistry, **34**, 119 (1993).
21. O. Dangles, N. Saito, and R. Brouillard. J. Am. Chem. Soc. **115**, 3125 (1993).
22. O. Dangles, M. Elhabiri, and R. Brouillard. J. Chem. Soc. Perkin Trans. 2, 2587 (1994).
23. P. Figueiredo, M. Elhabiri, K. Toki, N. Saito, O. Dangles, and R. Brouillard. Phytochemistry, **41**, 301 (1996).
24. G.A. Iacobucci and J.G. Sweeny. Tetrahedron, **39**, 3005 (1983).
25. G. Hauke, P. Czerney, C. Igney, and H. Hartmann. Ber. Bunsen-Ges. Phys. Chem. **93**, 805 (1989).

26. J. Baranac, D. Amić, and V. Vukanović. J. Agric. Food Chem. **38**, 932 (1990).
27. D. Amić, J. Baranac, and V. Vukanović. J. Agric. Food Chem. **38**, 936 (1990).
28. D. Amić and J. Baranac. Croat. Chem. Acta, **64**, 27 (1991).
29. G. Rastelli, L. Costantino, and A. Albasini. J. Mol. Struct. **279**, 157 (1993).
30. O. Dangles, and H. Elhajji. Helv. Chim. Acta, **77**, 1595 (1994).
31. D. Davidović-Amić, D. Amić, and N. Trinajstić. Croat. Chem. Acta, **67**, 163 (1994).
32. L. Jurd. Tetrahedron, **25**, 2367 (1969).
33. M.C. Wigand, O. Dangles, and R. Brouillard. Phytochemistry, **31**, 4317 (1992).
34. P. Figueiredo, J.C. Lima, H. Santos, M.C. Wigand, R. Brouillard, A.L. Maçanita, and F. Pina. J. Am. Chem. Soc. **116**, 1249 (1994).
35. R.A. McClelland, D.B. Devine, and P.E. Sorensen. J. Am. Chem. Soc. **107**, 5459 (1985).
36. R. Brouillard and J. Lang. Can. J. Chem. **68**, 755 (1990).
37. P. Figueiredo, F. Pina, L. Vilas-Boas, and A.L. Maçanita. J. Photochem. Photobiol. A: **52**, 411 (1990).
38. J.C. Lima, P. Danesh, P. Figueiredo, F.S. Pina, and A. Maçanita. Photochem. Photobiol. **59**, 412 (1994).
39. E.S. Sadlowski. Ph.D. Thesis, Colorado State University, Fort Collins, Colo. 1985.
40. K. Takeda, Y. Yamashita, A. Takahashi, and C.F. Timberlake. Phytochemistry, **29**, 1089 (1990).
41. T. Kondo, K. Yoshida, A. Nakagawa, T. Kawai, H. Tamura, and T. Goto. Nature (London), **358**, 515 (1992).
42. N. Filipescu, S.K. Chakrabarti, and P.G. Tarassoff. J. Phys. Chem. **77**, 2276 (1973).
43. S. Tripathi, M. Simalty, and J. Kossanyi. Tetrahedron Lett. **26**, 1995 (1985).
44. V. Wintgens, S. Tripathi, J. Pouliquen, and J. Kossanyi. J. Photochem. **32**, 81 (1986).
45. C. Reichardt. Angew. Chem. Int. Ed. Engl. **4**, 29 (1965).
46. H. Santos, D.L. Turner, J.C. Lima, P. Figueiredo, F. Pina, and A.L. Maçanita. Phytochemistry, **33**, 1227 (1993).
47. M.J.S. Dewar, E.G. Zoebisch, E.F. Healy, and J.J.P. Stewart. J. Am. Chem. Soc. **107**, 3902 (1985).
48. W.E. Hull. *In* Two-dimensional NMR spectroscopy: applications for chemists and biochemists. *Edited by* W.R. Croasmun and R.M.K. Carlson. VCH Publishers, New York. 1987.
49. W.P. Aue, E. Bartoldi, and R.R. Ernst. J. Chem. Phys. **71**, 4546 (1979).
50. A. Bax and R. Freeman. J. Magn. Reson. **44**, 542 (1981).
51. A. Statoua, J.C. Merlin, R. Brouillard, and M. Delhaye. C.R. Acad. Sci. Paris, **296**, 1397 (1983).
52. J. Andrieux, B. Bodo, and D. Molho. Bull. Soc. Chim. Fr. 3421 (1973).

Detection of Newcastle disease virus using an evanescent wave immuno-based biosensor

William E. Lee and H. Gail Thompson

Abstract: A fibre-optic-based evanescent wave biosensor has been used for the detection of virus. Polyclonal antibody directed against the model analyte, Newcastle disease virus, was covalently immobilized on aminosilane-coated quartz fibres, which served as the capture and concentration element of the sensor system. Radiolabelling studies demonstrated a high degree of antibody attachment to the quartz solid support. Maximal coverage could be attained with antibody solution as low as 10 μg/mL and carbonyldiimidazole as the cross-linking agent. Fluorescein-labelled anti-NDV served as the detector antibody in a sandwich format. Assay times were approximately 15 min with a limit of detection of about 2 ng of purified virus in 0.2 mL sample volume. The biosensor detection system possesses several desirable characteristics such as a limited number of mechanical components, a multiple use active surface, and low baseline variation, which indicate that it has the potential to serve as an on-line continuous monitoring device of an automated or semi-automated detection system.

Key words: fibre optic, biosensor, fluorescence, evanescence, immunoassay, antibody, Newcastle disease virus.

Résumé : On a utilisé un biosenseur d'onde évanescence basé sur une fibre optique pour la détection de virus. L'anticorps polyclonal dirigé contre l'analyte modèle, le virus de la maladie de Newcastle, a été immobilisé d'une façon covalente sur des fibres de quartz recouvertes d'aminosilane qui servent d'élément de capture et de concentration pour le système de senseur. Des études de radiomarquages ont démontré un degré élevé d'attachement des anticorps sur le support solide de quartz. Une couverture maximale peut être obtenue avec une solution contenant de l'anticorps à une concentration aussi faible que 10 μg/mL et du carbonyldiimidazole comme agent de réticulation. Les temps de dosage sont d'environ 15 min, avec une limite de détection d'environ 2 ng de virus purifié dans un volume de 0,2 mL d'échantillon. Le système de détection du biosenseur possède plusieurs caractéristiques souhaitables, telles qu'un nombre limité des composants mécaniques, une surface active qui peut être réutilisée et une faible variation de la ligne de base; ceci indique qu'il a le potentiel pour servir comme appareil permettant de faire une évaluation continue, en circuit, dans un système de détection automatisé ou semi-automatisé.

Mots clés : fibre optique, biosenseur, fluorescence, évanescence, immunodosage, anticorps, virus de la maladie de Newcastle.

[Traduit par la rédaction]

Introduction

In the present paper we describe an immunoassay utilizing a fibre optic wave guide sensor and evanescent wave spectroscopy (1) for the detection and quantitation of virus in liquid samples. The phenomenon of evanescence is associated with total internal reflection and occurs when light is reflected at an interface where the refractive index decreases by a step value (1.46 to 1.33 for the quartz–water interface (2)). At the reflection point the confined or guided light generates a localized electromagnetic field (evanescent wave) in the adjacent medium that decreases in magnitude exponentially with distance from the interface. Thus the exterior surface of the optical fibre is electromagnetically coupled to the core and can act as an active sensor. The effective depth of penetration at the quartz–water interface is about one wavelength, i.e., less than 1 μm for visible light (2), and so fluorescently labelled molecules at or near the surface can be selectively excited. The evanescence effect allows for a high level of discrimination between fluorescent probe molecules immobilized on the surface and unbound probes in the bulk solution that do not interact significantly with the evanescent wave.

We have used Newcastle disease virus (NDV), an avian paramyxovirus, as the model analyte. In this assay system, quartz fibres are coated with aminosilane to which the capture element, polyclonal anti-NDV, is covalently immobilized. Sandwich immunoassays are carried out in a stepwise manner: target analyte is introduced to the capture surface, followed by fluorescein-labelled anti-NDV. The output signals are measured by monitoring the rise in fluorescence emitted from the fibre core. For comparison purposes, in order to determine the effectiveness of the antibody immobilization procedures, the same quartz fibres were used as a solid support for ELISA (enzyme-linked immunosorbent assay (3)) of NDV. It was found that the treated quartz fibres, when installed in the reaction cell of the fibre optic sensor, provide analyte recognition and sample concentration. Assays can be carried out in a flow-through manner by alternately pumping analyte and detector antibody through the cell. Individual assays required about 15 min to complete. The limits of detection were approximately 2 ng of purified virus.

Received September 18, 1995.

W.E. Lee[1] and H.G. Thompson. Defence Research Establishment Suffield, P.O. Box 4000, Medicine Hat, AB T1A 8K6, Canada.

[1] Author to whom correspondence may be addressed. Telephone: (403) 544-4706. Fax: (403) 544-3388. e-mail:wlee@dres.dnd.ca

Materials and methods

Equipment

The fibre-optic wave guide (FOWG) was manufactured by

ORD Inc. (North Salem, N.H.) and has been described previously (4). The fibres were made of optical grade quartz, 1 mm diameter, 6 cm length, and were purchased from ORD Inc. The light source in the FOWG was a 4 W quartz halogen lamp, and the photodetector was a Hamamatsu S1087-01 photodiode. Excitation and emission wavelengths were 485 and 530 nm, respectively. The liquids were driven through the flow cell by means of a Cole Parmer peristaltic pump, model 7553-30, with two pump heads, 7013 and 7014. The output of the photodetector was connected to a Hewlett Packard model 7015B XY recorder for data collection. A Beckman model 4000 γ-radiation counter was used to measure the radioactivity of ^{125}I. The same optical grade quartz fibres, as described above, were used as solid support for the enzyme immunoassays.

Reagents

Reagent grade acetone, methanol, chloroform, toluene, and 3-aminopropyltriethoxysilane (APTES) were obtained from Aldrich Chemical Co. (Milwaukee, Wis.). Phosphate-buffered saline (PBS) tablets, bovine serum albumin (fat free), fluorescein-labelled anti-guinea pig IgG from rabbit, anti-human IgG from goat, dimethyl sulfoxide, carbonyldiimidazole, and fluorescein isothiocyanate were obtained from Sigma Chemical Co. (St Louis, Mo.). Polystyrene Immulon-1 flat-bottom microtiter plates were purchased from Dynatek Laboratories (Chantily, Va). Purified La Sota NJ strain of NDV was grown from seed stock obtained from the American Type Culture Collection (Rockville, Md.) in embryonated hen eggs (5), purified by density gradient centrifugation (6), and suspended in PBS pH 7.0. Polyclonal antibody was purified from guinea pig serum using ammonium sulfate precipitation, followed by ion exchange chromatography. Anti-NDV was custom conjugated with horseradish peroxidase by Jackson ImmunoResearch Laboratories (West Grove, Pa.). The substrate reagents for the horseradish peroxidase, H_2O_2 and 2,2-azino-di(3-ethylbenzthiaoline) sulfonate (ABTS), were obtained from Kirkegaard and Perry (Gaithersburg, Md.). ^{125}I-labelled anti-human IgG from goat was obtained from Dupont. Protein concentrations were determined using a Coomassie blue assay kit (BioRad, Mississauga, Ont.) and IgG protein standards (Bio-Rad).

Silanization of quartz fibres

Quartz optical fibres (1 mm × 6 cm, 40 in total) were placed in a 15 × 90 mm glass receiver. The fibres were washed three times with acetone, three times with water, and twice with nitric acid (15%, v/v). The fibres were covered with nitric acid (15%), a condenser was installed, and the apparatus was placed in a Reacti-Therm heating module (Pierce Chemical Co., Rockford, Ill.) with the upper portion of the receiver wrapped in cotton batting. The fibres were heated for 2 h at reflux temperature. Afterwards, the fibres were rinsed thoroughly with water, then methanol, and dried in a convection oven for 2 h at 100°C. Two boiling chips were added to the glass receiver and the fibres were refluxed for 1 h in dry chloroform.

The fibres were rinsed three times with dry toluene. A 20% (v/v) solution of APTES in dry toluene was added in sufficient amount to cover the fibres. The receiver tube was closed with a glass stopper and secured with metal springs. The vial was placed on a Nutator shaker (Clay Adams, Parsippany, N.J.) and rotated gently overnight at room temperature. The fibres were rinsed repeatedly with dry toluene, then dried in the Reacti-Therm block under a stream of dry nitrogen. The coated fibres were stored in screw-cap polystyrene test tubes inside a desiccator. Elemental analysis of the silanized quartz surfaces by X-ray photoelectron spectroscopy indicated that the coverages were approximately 45–50% of the surface area (K. Kallury, personal communication). Ellipsometry data gave a thickness of approximately 11 Å, indicating that the coating was primarily monolayer silane (K. Kallury, personal communication).

Covalent attachment of antibodies to quartz fibres

Quartz fibres that had been previously treated with APTES were placed in glass test tubes (12 × 75 mm), about 10–15 fibres per tube, then 2 mL of 0.5 M carbonyldiimidazole in dimethyl sulfoxide was added to each tube. The test tubes were covered with Parafilm and incubated for 2 h at room temperature; gentle agitation was provided by a Nutator shaker. The supernatant solution was then decanted. The activated fibres were first washed three times with dimethyl sulfoxide, then three times with acetone, and finally dried at room temperature under a stream of dry nitrogen for 15 min. Once activated, quartz fibres were never stored, they were always immediately coupled with antibody by the following procedure.

If the antibody had been stored in sodium azide or some other stabilizer, preservative, or buffer that would react with the activated fibre, it was necessary first to purify the antibody solution by dialysis prior to the linking reaction. The antibody to be linked was then diluted to the working concentration (up to 100 μg/mL) in PBS pH 7.4. The activated fibres were placed in polystyrene 12 × 75 mm snap-cap test tubes (no more than 20 fibres per tube). Sufficient antibody solution to cover the fibres (0.5 mL) was added and the tubes were incubated at 4°C overnight with agitation provided by a Nutator shaker. After the coupling reaction was completed, the antibody solution was decanted. The fibres were washed three times with 0.1 M ethanolamine pH 8.5 and then were incubated with gentle shaking for 2 h at room temperature in the same solution. Finally, the antibody-linked fibres were washed three times with PBS. The fibres could be stored in buffer at 4°C for several days, or longer if the storage medium contained 0.02% sodium azide or merthiolate.

Conjugation of antibodies with fluorescein isothiocyanate

The procedure used to conjugate anti-NDV IgG with fluorescein isothiocyanate was similar to methods previously described (7). An aliquot of anti-NDV IgG (guinea pig) solution, 0.5 mL at 12 mg/mL, was diluted to 6 mL with 0.15 M sodium phosphate buffer, pH 9.0, to give a concentration of 1 mg/mL. A stock solution of fluorescein isothiocyanate (FITC), 1 mg/mL in 0.15 M sodium phosphate buffer, pH 9.0, was prepared. A volume of 10 μL FITC solution per mg of protein, in this case 60 μL, was added to the antibody solution. The pH was adjusted to 9.5 by the addition of 0.1 M sodium phosphate solution, pH 12.0. The reaction mixture was stirred for 1 h at room temperature while maintaining the pH at 9.5. The reaction mixture, about 10 mL total volume, was transferred to dialysis tubing and stirred overnight in a large flask containing 3.5 L of PBS. The PBS solution was changed and stirring continued for an additional 3 h. After dialysis, a uv–vis absorbance spectrum was recorded and a

Coomassie blue protein assay carried out. The A_{280} and A_{495} readings indicated a mole ratio of fluorescein to protein (F/P) of 2.3. The recovery of protein was about 85%. The FITC-conjugated antibody solution was stored frozen at −20°C in 1 mL aliquots.

Enzyme immunoassay on quartz solid support

Quartz fibres previously treated with APTES were cut using a small-bore tube cutter (Scientific Systems Inc., State College, Pa.) and sorted to 3 (±0.3) mm in length. Rubber gloves were used when handling the coated fibres. Capture antibody was covalently linked to the fibre segments according to the above-described procedures. The concentration of the capture antibody solution was 50 μg/mL. Blocking of the fibres was achieved by three successive 1 h incubations and washing with BSA-containing diluent buffer at 37°C. The fibres were placed in the wells of microtitre plates (one fibre per well). The antigen, NDV, was reconstituted in diluent buffer. Aliquots (200 μL) were incubated in the microtitre wells with the capture antibody-coated fibres for 1 h at 37°C. After incubation with NDV, the fibres were washed three times with PBS. Detector antibody (peroxidase-conjugated anti-NDV) was diluted 1/500 in diluent solution. Aliquots (200 μL) of diluted detector antibody were added to the wells containing the quartz fibres and the fibres were incubated for 1 h at 37°C. The fibres were washed several times with wash solution. Freshly prepared substrate, a mixture of ABTS and H_2O_2 solutions, was added, 200 μL per well, and the plate was placed on a Nutator shaker and allowed to develop at room temperature for 30 min. The absorbance of the reacted substrate in the wells was measured in a microtiter plate reader (Molecular Devices, Sunnyvale, Calif.) at 405 nm. The presence of the fibres in the wells did not affect the absorbance readings if the fibres were positioned away from the centres of the wells.

Fluorescence assays of NDV on the fibre-optic wave guide

Assays on the FOWG employed two methods to introduce antigen to the detector system. In one method, fibres coated with capture antibody were set into polystyrene test tubes, one fibre per tube, 0.5 mL of diluted NDV solution was added to each tube, and the tubes were sealed with polystyrene caps. The tubes were placed on their sides on the platform of a Nutator shaker and incubated at room temperature for 5 min. After incubation the fibres were rinsed three times with wash solution. A single fibre was installed in the flow cell of the FOWG. The cell was flushed with wash solution for 1 min and a baseline output signal was obtained during the flushing procedure. After the baseline had been recorded, detector antibody (FITC-labelled anti-NDV) solution was pumped through the flow cell and the resulting fluorescence signal was obtained by monitoring the voltage output of the photodetector with respect to time using the XY recorder. In the second method, the quartz fibres were incubated with NDV in the flow cell of the FOWG. That is, an antibody-coated fibre was installed in the flow cell and a 0.2 mL aliquot of diluted NDV solution was injected into the cell. After 5 min incubation, the flow cell was flushed with wash solution for 1 min. A baseline was obtained while wash solution was flowing through the system, then the detector antibody was introduced by means of the pump and the signal was recorded with respect to time by the XY recorder.

Fig. 1. Radioactivity (counts per minute, $n = 5$) of quartz fibres resulting from covalent fixation of a mixture of native/^{125}I-labelled immunoglobulin G (20/1, w/w).

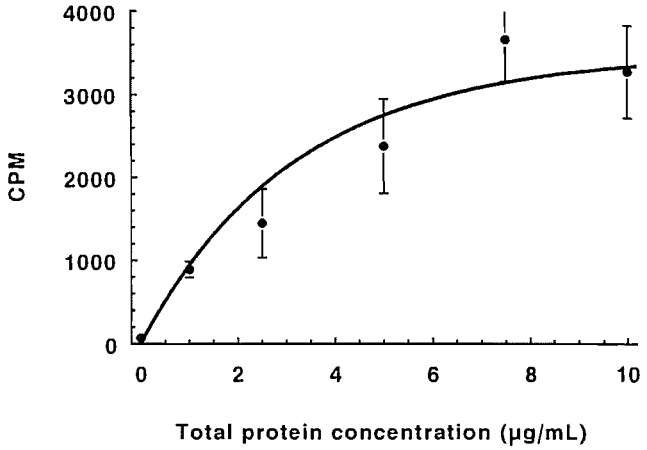

Fig. 2. Standard curve of radioactivity (cpm) versus spiked samples of ^{125}I-labelled goat IgG. Aliquots (1 mL) of labelled antibody were delivered to vials and counted.

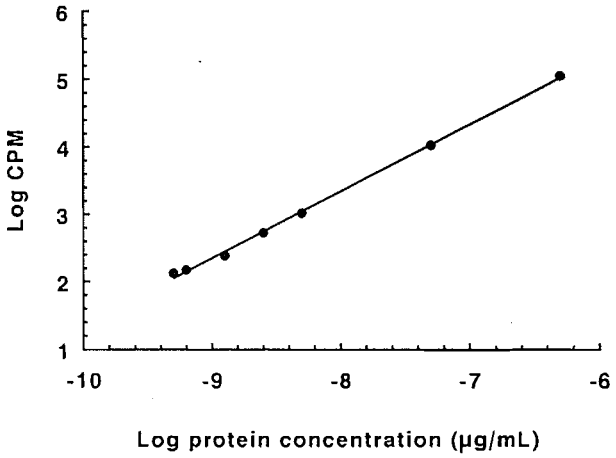

Results

Immobilization of antibodies on silanized quartz fibres

To measure the amount of antibody covalently immobilized by carbonyldiimidazole reaction on the quartz surface, activated silane-coated fibres were reacted with a mixture of ^{125}I-labelled goat anti-human IgG and native goat anti-human IgG. The radioactivity levels of the antibody-coated fibres were determined and the data are shown in Fig. 1. The relative amount of protein immobilized, taken as the γ irradiation emanating from the fibres, initially increased with increasing protein concentration and reached a plateau in the range of 7–10 μg/mL. The experiment was carried out using a ratio of 20/1 (w/w), native to ^{125}I-labelled anti-human IgG. Immobilization experiments with ratios ranging from 10/1 to 1000/1 produced similar results, i.e., a plateau in counts between 5 and 10 μg/mL.

It was possible to calculate the extent of protein coverage from the initial radioactivity of the stock radio-labelled antibody, the radioactivity of the protein coated fibre, and the ratio of native to labelled antibody. We have taken the molecular weight of IgG as 160 000 Da (8) and the specific volume of globular protein as 0.73 (9). By comparison of the radioactiv-

Table 1. Covalent fixation of protein to quartz.

Total protein conc. (μg/mL)[a]	% ^{125}I-labelled[b]	cpm (sd)[c]	Total protein per fibre (g)[d]	Protein coverage (ng/mm^2)[e]
100	1	220 (50)	1.02×10^{-7}	1.6
100	5	505 (72)	4.7×10^{-8}	0.75
100	10	858 (204)	4.0×10^{-8}	0.63
50	5	530 (185)	4.9×10^{-8}	0.78
50	10	664 (67)	3.1×10^{-8}	0.49
25	1	237 (55)	1.1×10^{-7}	1.8
25	5	323 (134)	3.0×10^{-8}	0.48
10	1	194 (40)	9.1×10^{-8}	1.4
10	5	384 (111)	3.6×10^{-8}	0.57

[a]Labelled plus nonlabelled.
[b]Percentage by weight of ^{125}I-labelled protein.
[c]Mean counts per minute (standard deviation, $n = 5$).
[d]20 × 1 mm diam. fibre, surface area = 63 mm^2.
[e]Mean protein coverage 0.94 (0.51) ng/mm^2.

Fig. 3. Immunoassay of NDV using quartz as the solid support. Capture antibody was covalently attached to the solid phase. The LOD was taken to be the sample that produced a signal in excess of the background plus two standard deviations. For this assay the LOD was about 0.5–1.0 ng NDV in a total sample volume of 0.1 mL.

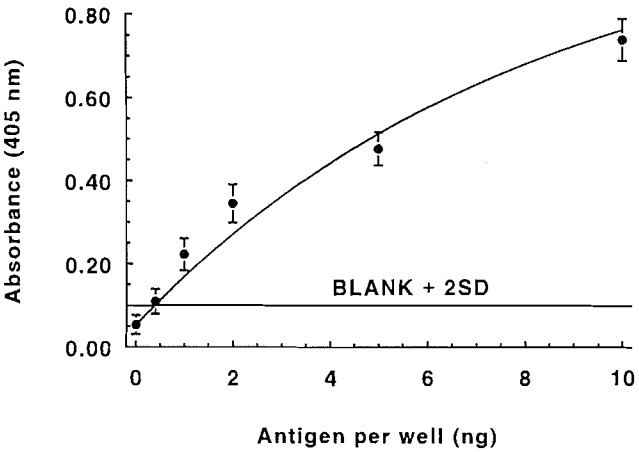

ity (cpm) of the protein-coated fibres (Table 1) with that of a standard curve of ^{125}I-labelled antibody (Fig. 2), the total amount of protein immobilized was calculated to be about 1 ng/mm^2. This latter value represents protein coverage of the fibres of about 20% of the surface area.

Enzyme immunoassay on quartz solid support: response of antibody-coated quartz fibres

Polyclonal antibody directed against NDV was covalently immobilized on quartz fibres (1 mm diam., cut to 3 mm length) according to the above-described methods. The fibres were placed in the wells (one per well) of microtitre plates. Consecutive incubations (30 min in duration) of antigen (NDV) and detector antibody (anti-NDV horse radish peroxidase conjugate) were carried out, substrate solution was added, and the absorbance was determined at 405 nm. The results of an assay are shown in Fig. 3. The lower limit of detection (LOD), taken to be the intersection of the background plus two standard deviations with the dose response curve, was about 0.5 ng (5 ng/mL for 0.1 mL sample). The detection limits were comparable to a colorometric microplate ELISA of NDV (10). These results suggest that the antibody-coating methods produce fibres suitable as capture elements that can be subsequently employed in a fibre-optic sensor. A similar enzyme immunoassay for NDV employing capture antibody noncovalently adhered (physiosorbed) to quartz fibres was less sensitive, having an LOD of about 20–50 ng (W. Lee, unpublished results).

Response of the fibre-optic wave guide

An experiment to determine the active area of the quartz fibre contained in the FOWG flowcell was carried out. Guinea pig immunoglobulin (anti-NDV) was covalently immobilized on quartz fibres and solutions of fluorescein-labelled second antibody (anti-guinea pig IgG from rabbit) were incubated with the fibres in test tubes. Sections of the fibre of increasing lengths were treated with the second antibody solution. The output of the FOWG increased in an approximately linear fashion with the length of fibre treated with the fluorescein-labelled second antibody. The data indicated that the active portion of the optical fibre extended essentially along its whole length (Fig. 4).

The immunosensor capability of the FOWG is shown in Fig. 5. Fibres coated with anti-NDV were treated with increasing amounts of NDV analyte. Detector antibody (fluorescein-labelled anti-NDV) was then pumped through the flow cell. For the blank sample (no NDV), there was a small increase in signal that corresponded to the fluorescein-labelled antibody in the flow cell passing through the evanescent zone of the fibre (Fig. 5). When the flow of detector antibody was interrupted and buffer solution passed through the system, the output signal decreased to approximately its initial value. For the second sample, a fibre incubated with NDV solution (17 ng/mL) was inserted into the flow cell. When detector antibody was pumped through the flow cell, there was a substantial increase in output signal. After the flow of detector antibody was interrupted and wash solution introduced, a small decrease in signal was observed. For fibres incubated in NDV solutions of 100 and 1000 ng/mL, the output signals increased

Fig. 4. Determination of the active area of the quartz fibre in the FOWG. Fibres were covalently coated with guinea pig IgG and then incubated with fluorescein-labelled anti-guinea pig IgG (0.005 μg/mL) with varying lengths of the fibre exposed to the second antibody.

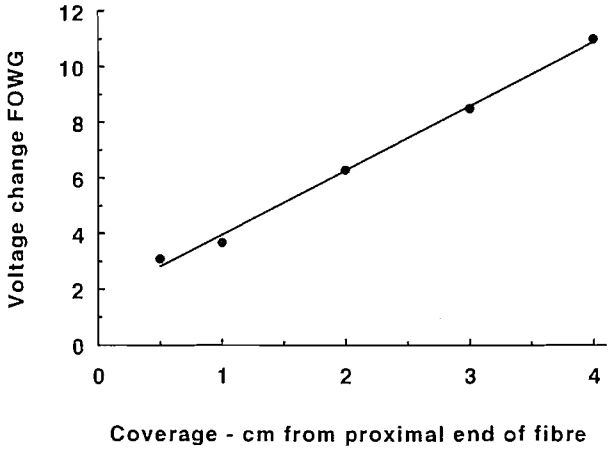

Fig. 5. Response of FOWG to NDV. The quartz fibre was incubated with NDV solution (0.5 mL) at room temperature. After incubation the fibre was washed with PBS. A baseline was recorded while flowing PBS through the flow cell. Detector antibody solution (fluorescein-labelled gp anti-NDV, 1 μg/mL) was pumped through the flow cell at a rate of 1.2 mL/min. A separate fibre was used for each run.

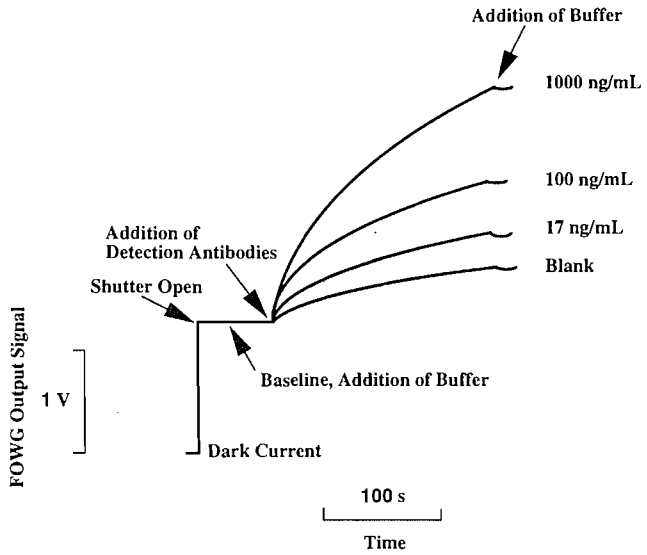

accordingly upon introduction of detector antibody. Higher concentrations of NDV yielded larger output signals (i.e., voltage changes).

Biosensor assay of NDV

Plots of the slopes (dv/dt) versus added NDV are more revealing. The slopes of the individual xy recording (e.g., data in Fig. 5), 1 min after introduction of detector antibody, were plotted against added NDV. A dose response is shown in Fig. 6. Signals were recorded over a range of about 2–250 ng. The limit of detection, taken to be the lowest amount of NDV that produces a signal two standard deviations above the background

Fig. 6. FOWG standard curve on NDV. The slopes of the output traces (e.g., Fig. 5) were determined 1 min after addition of detector antibody (0.5 μg/mL). The data points and error bars represent the mean standard deviation of three samples. A separate fibre was used for each determination. The background (blank) was taken to be the signal output produced by the detector antibody alone, with no analyte present.

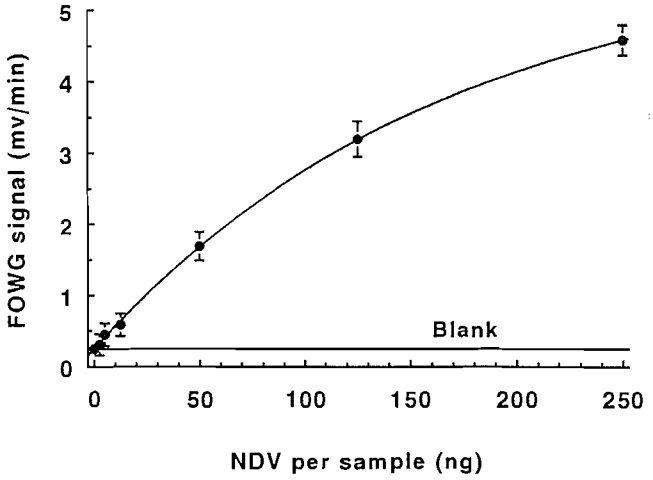

Fig. 7. FOWG assay of NDV carried out on a single fibre. The data points and error bars represent the mean standard deviation of three samples. The analyte sample was incubated for 5 min, detector antibody concentration was 2 μg/mL. The LOD was about 1 ng (volume 0.2 mL). The background (blank) was taken to be the signal output produced by the detector antibody alone, with no analyte present.

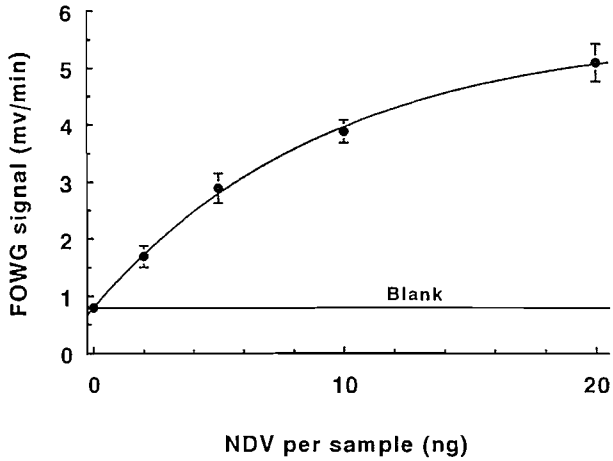

(blank sample), was about 2–3 ng. For the data shown in Fig. 6, each individual run (i.e., addition of NDV, followed by fluorescein-labelled anti-NDV) was carried out on a separate fibre. The reproducibility from fibre to fibre as indicated by the coefficient of variation (sd/mean) was about 0.15–0.20.

After a single run, only a fraction of the binding sites for antigen were occupied; the major portion of the available binding sites on the fibre remained vacant. It was possible to use a single fibre for repetitive assays of the same antigen provided the binding capacity was not overloaded. Between runs, the flow cell was flushed first with wash buffer solution for about 3 min, followed by a solution of 2 μg/mL guinea pig

anti-NDV for 5 min. The latter was the same antibody used for detection but without the fluorescein label and its effect was to block any free epitope sites on the NDV antigen captured during the previous run. Successive 200 μL aliquots of NDV solution were introduced to the flow cell and incubated for 5 min. After incubation the flow cell was flushed with wash solution for 1 min to establish a new baseline and then with fluorescein-labelled antibody to produce a signal. The results of a repetitive assay on a single fibre are shown in Fig. 7. The LOD for the assay was about 1.5 ng and the coefficient variations were about 0.10. For comparison, an immunofiltration assay of NDV that used a silicon sensor gave LODs in the order of 0.5–1.0 ng per 100 μL sample (11).

Discussion

This work describes a fibre-optic-based biosensor for a model virus. Detection of nanogram quantities of NDV was achieved using anti-NDV antibodies immobilized on aminosilane-coated fibres and fluorescein-labelled anti-NDV. Quartz, being composed primarily of silicon dioxide, is relatively chemically inert, save for extreme conditions. Such conditions are too harsh to maintain protein in an active state and so direct reaction of antibodies to quartz is not practical. To overcome this problem, 3-aminopropyltriethoxysilane was reacted with the quartz fibres at high temperature under anhydrous conditions. This procedure results in a covalently attached monolayer covering of silane. Proteins can be readily bonded to the modified fibre through the carboxyl function. In this work carbonyldiimidazole was used as the linking agent, although other protein fixative compounds are commercially available (12, 13). Radiolabelling studies indicated that maximal amounts of antibody, covering up to 20% of the fibre surface, could be covalently immobilized using antibody solution as low as 5–10 μg/mL.

One of the principle advantages of a fibre-optic biosensor is the flow-through design that can provide continuous on-line monitoring of liquid samples. Thus, the sensor has the potential to be incorporated into an automated or semiautomated system. Flow-through systems can include such features as a limited number of mechanical components, reusable solid support, low variations of background or negative control signals, and the potential for multi-recognition elements on a single fibre. Miniaturization and durability are achievable through the use of solid state electro-optic components. Immuno-based fibre-optic biosensors have been successfully employed in detection of proteins (14, 15, 16) and whole cells (17). Other applications of fibre-optic sensors include molecular recognition by receptors (18, 19), enzymes (20), and gene probes (21).

In conclusion, the feasibility of performing immunoassay for intact virus on a fibre-optic wave biosensor has been demonstrated. The limits of detection were about 2 ng for a 10 min assay at room temperature. The assays were further characterized by high reproducibility and low background.

Acknowledgements

We would like to thank Professor Michael Thompson and Dr. Krishna Kallury of the University of Toronto for carrying out the X-ray photoelectron spectroscopy and elipsometry experiments on the quartz surfaces and for many helpful discussions. In addition, we thank the molecular biology group at Defence Research Establishment Suffield for assistance with the antibody and virus preparations. This work has been carried out with the support of the Department of National Defence.

References

1. R.B. Thompson and F.S. Ligler. *In* Biosensors with fiber optics. *Edited by* D.L. Wise and L.B. Wingard. Humana Press Inc., Cliffton, N.J. 1991. pp. 111–138.
2. W.F. Love, L.B. Button, and R.E. Slovacek. *In* Biosensors with fibreoptics. *Edited by* D.L. Wise and L.B. Wingard. Humana Press Inc., Clifton, N.J. 1991. p. 147.
3. E. Engvall and P. Perlann. Immunology, **8**, 871 (1971).
4. T.R. Glass, S. Lackie, and T. Hirschfeld. Appl. Opt. **26**, 2181 (1987).
5. R.A. Hawkes. *In* Diagnosis procedures for viral, rickettsial and chlamydial infections. 5th ed. *Edited by* E.H. Lennette and N.J. Schmidt. American Public Health Assoc., Washington, D.C. 1979. pp. 3–48.
6. R.E. Fulton, J.P. Wong, Y.M. Siddiqui, and M.-S. Tso. J. Virol. Methods, **22**, 149 (1988).
7. T.H. The and T.E.W. Feltkamp. Immunology, **18**, 875 (1970).
8. E. Harlow and D. Land. Antibodies: a laboratory manual. Cold Spring Harbor Laboratory, Cold Spring Harbor, N.Y. 1988.
9. C.R. Cantor and P.R. Schimmel. Biophysical chemistry. Vol. II. Freeman, San Francisco. 1984. p. 554.
10. R.E. Fulton, N.P. Erhardt, and R.I. Frank. Suffield Report 435. Defence Research Establishment Suffield, Ralston, Alberta. 1986.
11. W.E. Lee, H.G. Thompson, J.G. Hall, R.E. Fulton, and J.P. Wong. J. Immunol. Methods, **166**, 123 (1993).
12. P. Tijseen. Practice and theory of enzyme immunoassays. Elsevier, New York. 1985. pp. 221–278.
13. S.S. Wong. Chemistry of protein conjugation. CRC Press Inc., Boca Raton, Fla. 1991.
14. R.A. Ogert, L.C. Shriver-Lake, and F.S. Ligler. Proc. SPIE – Int. Soc. Opt. Eng. **1885**, 1112 (1993).
15. L.C. Shriver-Lake, R.A. Ogert, and F.S. Ligler. Sens. Actuators, B: **11**, 239 (1993).
16. P. Kumar, J.T. Colston, J.P. Chambers, E.D. Rael, and J.J. Valdes. Biosens. Bioelectron. **9**, 57 (1994).
17. F.S. Ligler, J.P. Golden, L.C. Shriver-Lake, R.A. Ogert, D. Wijesuria, and G.P. Anderson. ImmunoMethods, **3**, 122 (1993).
18. K.R. Rogers, J.J. Valdes, and M.E. Eldefrawi. Anal. Biochem. **182**, 353 (1989).
19. K.R. Rogers, J.J. Valdes, and M.E. Eldefrawi. Biosens. Bioelectron. **6**, 1 (1991).
20. J. Hlavay, S.D. Haemmerli, and G.G. Guilbault. Biosens. Bioelectron. **9**, 189 (1994).
21. C.R. Graham, D. Leslie, and D.J. Squirrell. Biosens. Bioelectron. **7**, 487 (1992).

Excess partial molar enthalpies of alkane-mono-ols in aqueous solutions

Steven Hiroshi Tanaka, Hikari Infinity Yoshihara, Alice Wen-Chi Ho, Frankie W. Lau, Peter Westh, and Yoshikata Koga

Abstract: Excess partial molar enthalpies, H_A^E, of methanol, ethanol, and 1- and 2-propanols in aqueous solutions were measured directly, accurately, and in small increments in mole fraction at 25°C. From these data, the solute–solute enthalpic interactions, $H_{AA}^E \equiv N(\partial H_A^E/\partial n_A)$, were evaluated for each alcohol. These data indicate that three distinctively different mixing schemes, I, II, and III exist, as was the case for aqueous 2-butoxyethanol previously studied in our laboratory. The transition from mixing scheme I to II appears to take place gradually within a small composition range. As the hydrophobic moiety becomes smaller from 2-butoxyethanol to methanol, the locus of the transition moves to a higher value in mole fraction of the alcohol. At the same time, the range of transition becomes wider and the solute–solute enthalpic interaction weaker.

Key words: excess partial molar enthalpies in aqueous solutions, methanol, ethanol, 1-propanol, 2-propanol, enthalpic interaction, transition of mixing scheme.

Résumé : Opérant à 25°C et procédant par de faibles augmentations dans les fractions molaires, on a mesuré directement et d'une façon précise les enthalpies molaires partielles en excès, H_A^E, pour des solutions aqueuses de méthanol, d'éthanol et des 1- et 2-propanols. Utilisant ces données, on a évalué pour chaque alcool les interactions enthalpiques soluté–soluté, $H_{AA}^E \equiv N(\partial H_A^E/\partial n_A)$. Ces données suggèrent l'existence de trois schémas différents de mélanges, I, II et III, comme ce fût le cas pour le 2-butoxyéthanol étudié antérieurement dans notre laboratoire. Il semble que la transition du schéma de mélange I vers II se produit graduellement, à l'intérieur d'une faible plage de composition. Quand les portions hydrophobes deviennent plus petites en allant du 2-butoxyéthanol vers le méthanol, le foyer de la transition se déplace vers des valeurs plus élevés de la fraction molaire de l'alcool. En même temps, l'intervalle de transition devient plus grand et l'interaction enthalpique soluté–soluté devient plus faible.

Mots clés : enthalpies molaires partielles en excès en solutions aqueuses, méthanol, éthanol, propan-1-ol, propan-2-ol, interaction enthalpique, schéma de transition de mélange.

Introduction

Extensive thermodynamic studies have been carried out in this laboratory on aqueous solutions of *tert*-butyl alcohol (hereafter abbreviated as TBA) (1–5, 16) and 2-butoxyethanol (BE) (6–16). In particular, the excess partial molar enthalpies of the alcohol (A), H_A^E (A = TBA or BE), were measured directly, accurately, and in small increments in the mole fraction of A, x_A. They are replotted in Fig. 1. As a result, the excess enthalpic solute–solute interaction, H_{AA}^E,

$$[1] \quad H_{AA}^E \equiv N(\partial H_A^E/\partial n_A) = (1 - x_A)(\partial H_A^E/\partial x_A)$$

can be evaluated with a reasonable accuracy. H_{AA}^E signifies the effect of an additional molecule of A on the excess partial molar enthalpy of the existing A. Hence, if H_{AA}^E is negative, an additional A makes the enthalpic situation of A more favorable. Thus, one may state that the A–A interaction is attractive in terms of enthalpy. The value of H_{AA}^E then indicates the degree of such an interaction. Conversely, if $H_{AA}^E > 0$, the enthalpic A–A interaction is repulsive. Note that H_A^E is a sec-

Received November 8, 1995.

S.H. Tanaka, H.I. Yoshihara, A.W.-C. Ho, F.W. Lau, P. Westh,[1] and Y. Koga.[2] Department of Chemistry, The University of British Columbia, 2036 Main Mall, Vancouver, BC V6T 1Z1, Canada.

[1] Permanent address: Department of Chemistry, University of Copenhagen, Copenhagen, Denmark.

[2] Author to whom correspondence may be addressed. Telephone: (604) 822-3491. Fax: (604) 822-2847. E-mail: koga@chem.ubc.ca

Fig. 1. The excess partial molar enthalpies of *tert*-butyl alcohol and 2-butoxyethanol, H_A^E, (A = TBA or BE). ○: TBA at 26.9°C, ref. 1. □: BE at 25°C, ref. 6. The arrows indicate the apparent transition points from mixing schemes I to II and II to III for BE–H_2O.

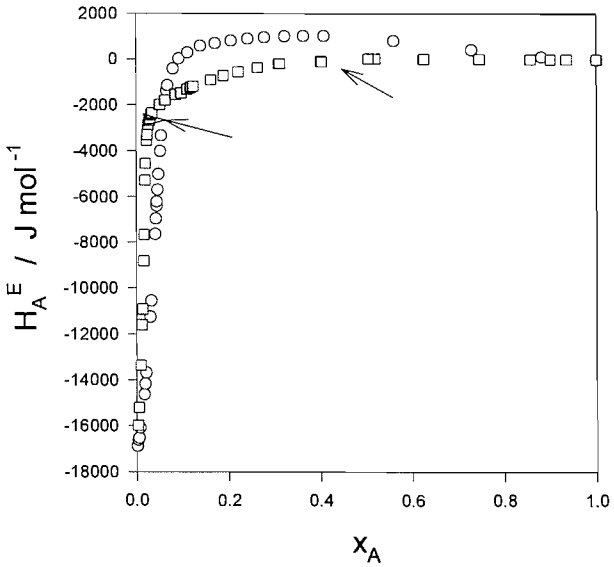

Fig. 2. The enthalpic solute–solute interaction, H_{AA}^{E}. ○: *tert*-butyl alcohol (TBA) at 26.9°C, ref. 1. □: 2-Butoxyethanol (BE) at 25°C, ref. 6. The lines are drawn as a guide. The thick straight line in the range $0.065 < x_{TBA} < 0.12$ in Fig. 2*a* shows the existence of mixing scheme II in TBA–H_2O.

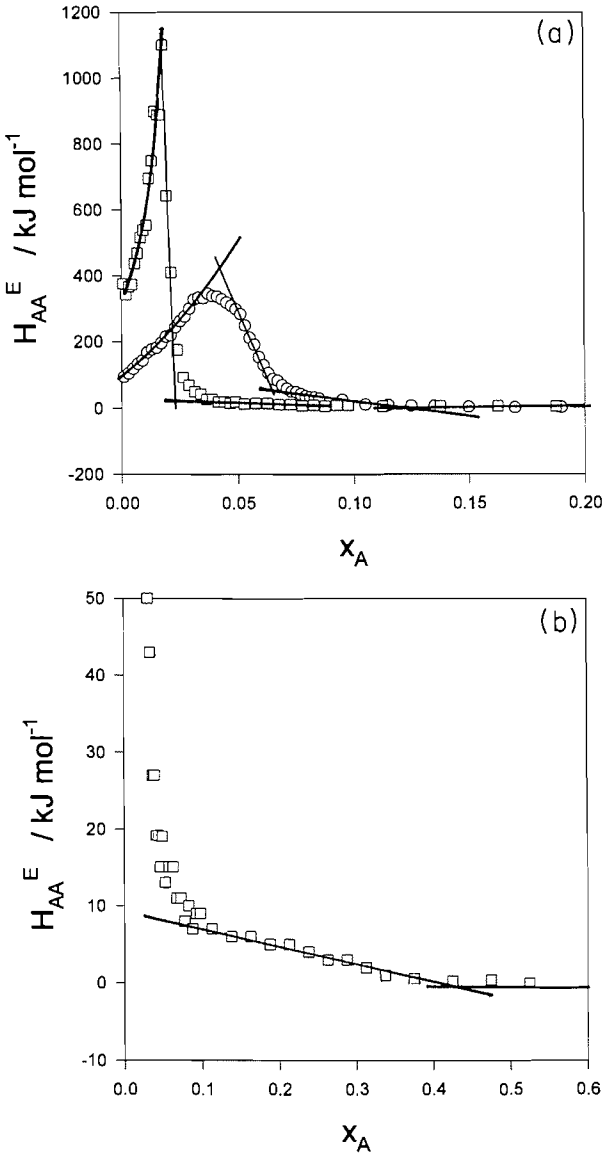

ond derivative of the Gibbs energy, hence H_{AA}^{E} is a third derivative.

Using various derivatives including those mentioned above, it was found (1–16) that the mixing scheme, the way in which the solute A and the solvent H_2O mix with each other, changes qualitatively at $x_{TBA} \approx 0.045$ for TBA–H_2O and at $x_{BE} \approx 0.0175$ for BE, both at 25°C. The threshold is characterized by anomalies in all the third derivatives of the Gibbs energy that have been investigated so far, including peaks in H_{AA}^{E} as shown in Fig. 2. For TBA–H_2O, the value of H_{AA}^{E} at the maximum reached 350 kJ mol^{-1}, while that of BE–H_2O was 1100 kJ mol^{-1}. For both cases, the mixing scheme operating in region I ($0 < x_{TBA} < 0.045$, $0 < x_{BE} < 0.0175$) is not inconsistent with the classical picture of "iceberg formation." Namely, it was concluded (16) that the solute enhances the hydrogen bond network of H_2O in the immediate vicinity, but diminishes the hydrogen bond probability in the bulk away from the solute. However, percolation of the hydrogen bond network (17) is still retained. That is, the hydrogen bond network is connected throughout the entire bulk at any instance. Region II is characterized by small and linearly decreasing values of H_{AA}^{E} up to about $x_{BE} \approx 0.46$, as shown in Fig. 2*b*. Mixing scheme II operative in this region was interpreted as consisting of two kinds of clusters, rich in each component. Hence, the hydrogen bond network is no longer percolated. Region III ($0.46 < x_{BE}$) is characterized by zero H_{BE}^{E} (Fig. 1) and almost zero excess partial molar entropy, S_{BE}^{E}. It was therefore concluded that the solute molecules cluster together, perhaps in a micellar form (6–16). The occurrence of three distinct regions in BE–H_2O is apparent even in the behavior of H_{BE}^{E} without calculating H_{AA}^{E}, as shown by the arrows in Fig. 1. For TBA–H_2O, on the other hand, there is no clear indication of the existence of region II (hence mixing scheme II) in the x_A dependence of H_A^{E}. The behavior of H_{AA}^{E}, however, shows the existence of mixing scheme II as shown by a thick straight line between $0.065 < x_{TBA} < 0.12$ in Fig. 2a. The clearer indication of region II for BE–H_2O may reflect the fact that there is the phase separation with LCST ($x_{BE} = 0.06$ and 50°C) close to the temperature of investigation. In fact, it was argued that mixing scheme II is such that the solution is "preparing" for the phase separation when the temperature becomes high enough (6–16). For TBA–H_2O, a phase separation is not apparent under normal pressures. It is known, however, that liquid–liquid phase separation with LCST occurs, when salt is added to TBA–H_2O (18).

Similar studies on aqueous solutions of dimethyl sulfoxide (DMSO) (19), 2-butanone (BUT) (20), and isobutyric acid (IBA) (21) also showed the existence of mixing schemes I, II, and III. In these cases, the transitions from I to II were found to be accompanied by a step anomaly in H_{AA}^{E} as depicted in Fig. 3*b* for BUT–H_2O, and IBA–H_2O, and in Fig. 3*c* for DMSO. Figure 3*a* represents a peak anomaly, as was the case for BE–H_2O mentioned above. For BE–H_2O, most third derivatives showed peak anomalies (Fig. 3*a*) (6–10, 13–16), while $(\partial C_p/\partial T)$, another third derivative, showed a step anomaly (Fig. 3*b*), at the same threshold (11, 12). It was thus argued (16) that whether an anomaly takes the form of a peak or a step is not intrinsically important. Rather, it is the dependence of H_{AA}^{E} on x_A in region I that dictates the type of anomaly when the transition from mixing scheme I to II occurs. Namely, whether H_{AA}^{E} or any third derivative increases (case a), stays constant (case b), or decreases (case c) as a function of x_A, within region I, decides the shape of the anomaly. Furthermore, we suggest that the width from point X to Y in Fig. 3 signifies the region in which the transition takes place. The narrower this width, the sharper the transition. In the limit of the zero width, the transition point will be mathematically singular. Thus, it may be more appropriate to define the nominal transition threshold as the middle point M, shown in Fig. 3. For BE–H_2O, the peak, point X, has been taken as the threshold for most of the third derivatives (6–10, 13–16), except for $(\partial C_p/\partial T)$ mentioned above, in which case point M was taken (11, 12, 16). Since peaks are very sharp for BE–H_2O, the difference in the threshold value is negligible whether point X or M is chosen.

The differences in terms of H_A^{E} and H_{AA}^{E} between BE and

Fig. 3. A sketch of the dependence of a third derivative on the mole fraction of alcohol, x_A, for mixing schemes I, II, and III, and the transitions thereof. The transition from mixing scheme I to II starts at point X and ends at Y. The mid point M is the nominal transition point. See text.

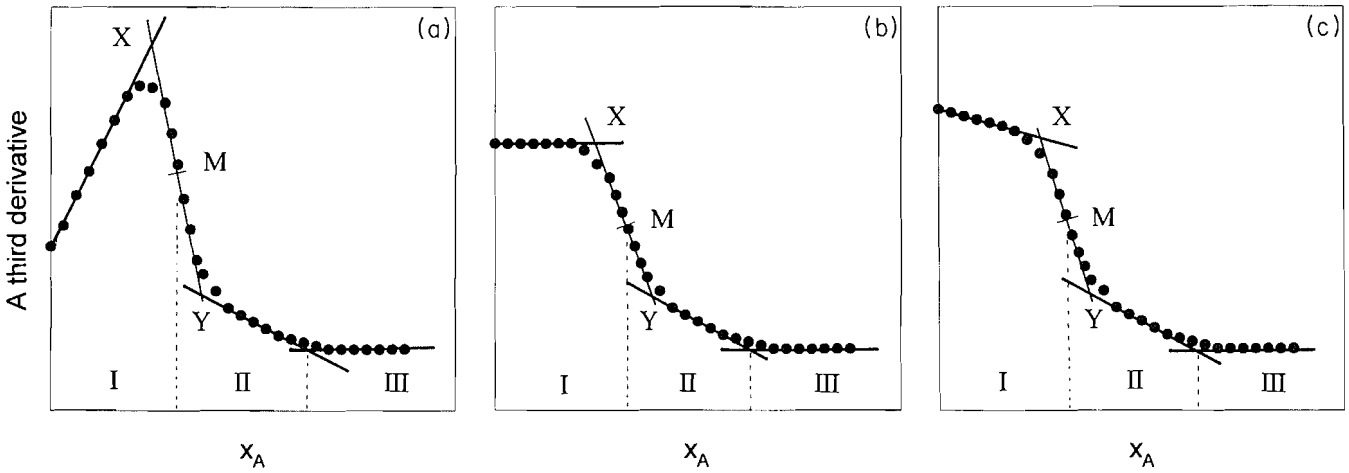

TBA are due to the properties of the individual solute. An obvious difference between the two is the size of the hydrophobic moiety, both being mono-ols. Hence, in the present work, we study aqueous solutions of methanol (ME), ethanol (ET), and 1- and 2-propanols (1P and 2P), in order to further elucidate the effects of hydrophobic moiety on the mixing scheme. While a more complete picture should await the data of other second and third derivatives, we report here the excess partial molar enthalpies, H_A^E, and the enthalpic A–A interactions, H_{AA}^E, and what can be deduced from such data.

Experimental

H_2O used was triply distilled immediately before use. Methanol (99.9+%, GLC), 1-propanol (99.5+%, HPLC), and 2-propanol (99.5+%, HPLC) were supplied by Aldrich. Ethanol was refluxed over Na metal, distilled, and stored over 3A molecular sieve. H_2O content in ethanol was found to be less than 0.7 mol% by Karl–Fischer titration. For determination of the excess partial molar enthalpies, two titration calorimeters were used: an LKB Bromma 8700, and a similar equipment constructed in this laboratory. Details of the latter are described elsewhere (18). The accuracy was estimated to be ±0.05 kJ mol^{-1} at worst.

Results and discussion

The values of H_A^E for A = ME, ET, 1P, or 2P are listed in Table 1 and plotted in Figs. 4–7, as a function of the mole fraction of solute, x_A. Existing data, H_A^E, although scarce, are also shown. As is evident from the figures, the general agreement between our data and the existing data is reasonable. For 1P–H_2O, the excess (integral) molar enthalpies, H_m^E, were determined in small increments in x_{1P} (~0.001) (26). Using these data, graphical differentiation was performed to obtain H_A^E, A = 1P. Namely, a smooth curve was drawn through the measured data points, the values of H_m^E on the curve were read off at the intervals $\delta x_A = 0.002$, the values of $(\partial H_m^E/\partial x_A)$ were approximated by those of $(\delta H_m^E/\delta x_A)$, and the values of H_A^E were calculated by

$$[2] \quad H_A^E = H_m^E + (1 - x_A)(\partial H_m^E/\partial x_A), \text{ (A = 1P)}$$

Fig. 4. The excess partial molar enthalpies of methanol, H_{ME}^E, at 25°C. ○: This work, □: ref. 22; △: ref. 23; ▽: refs. 24 and 27.

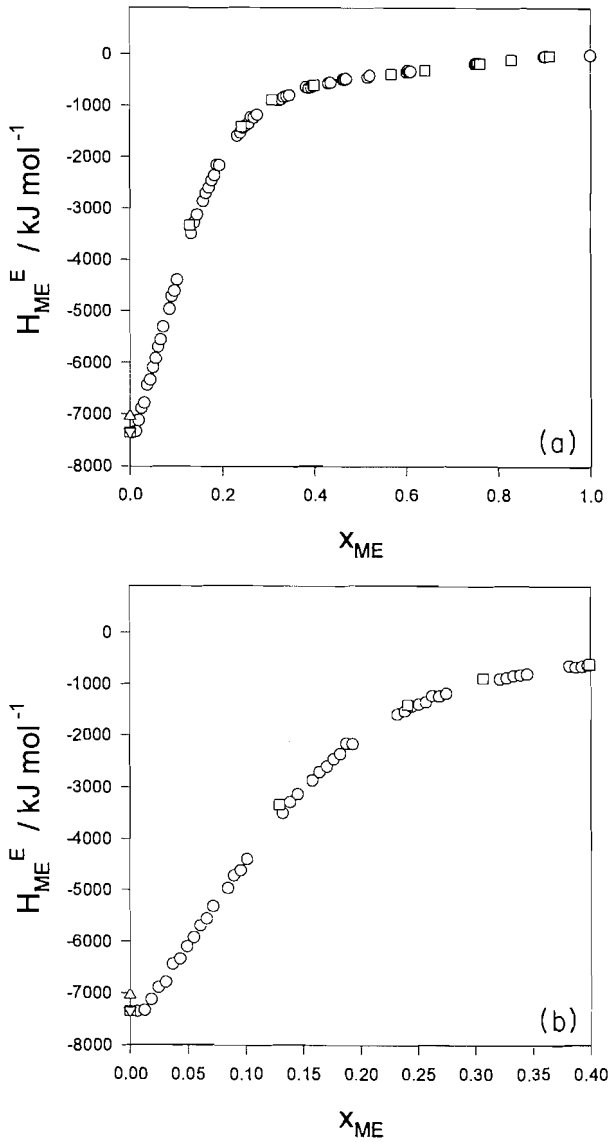

Table 1. The excess partial molar enthalpies of alkane-mono-ols in aqueous solutions, H_A^E, at 25°C. x_A is the mole fraction of alcohol, A = methanol (ME), ethanol (ET), 1- and 2-propanol (1P and 2P). H_A^E, with A = ME, ET, 1P, and 2P, are in the units of kJ mol^{-1}. The uncertainty in H_A^E is less than 0.05 kJ mol^{-1}.

ME–H_2O		ET–H_2O		1P–H_2O		2P–H_2O	
x_A	H_A^E [a]	x_A	H_A^E	x_A	H_A^E	x_A	H_A^E
0.006 087	−7.35	0.003 553	−9.99	0.003 301	−10.26	0.000 504	−13.04
0.012 36	−7.33	0.006 197	−9.88	0.006 702	−9.92	0.001 530	−13.08
0.018 37	−7.11	0.008 672	−9.88	0.010 13	−9.73	0.002 688	−13.10
0.024 59	−6.88	0.011 10	−9.74	0.016 98	−9.09	0.004 079	−12.98
0.030 73	−6.78	0.013 49	−9.70	0.020 25	−8.70	0.007 227	−12.76
0.036 67	−6.43	0.015 89	−9.54	0.023 60	−8.12	0.009 289	−12.61
0.043 14	−6.33	0.018 37	−9.35	0.026 95	−7.68	0.011 65	−12.51
0.049 17	−6.09	0.041 44	−7.87	0.030 45	−7.14	0.031 30	−9.93
0.055 13	−5.91	0.044 00	−7.78	0.033 79	−6.58	0.033 81	−9.72
0.060 84	−5.69	0.061 87	−6.34	0.037 04	−5.93	0.036 05	−9.36
0.066 43	−5.55	0.064 46	−6.09	0.040 20	−5.37	0.038 18	−9.06
0.072 08	−5.30	0.067 11	−5.88	0.043 35	−4.71	0.040 34	−8.69
0.084 82	−4.96	0.070 05	−5.63	0.046 56	−4.09	0.053 44	−6.32
0.089 88	−4.72	0.073 22	−5.36	0.049 68	−3.48	0.056 01	−5.90
0.095 54	−4.61	0.075 77	−5.24	0.052 31	−2.83	0.058 63	−5.43
0.1012	−4.39	0.078 23	−5.12	0.055 41	−2.33	0.060 92	−4.97
0.1322	−3.94	0.078 64	−5.35	0.058 54	−1.79	0.062 89	−4.58
0.1387	−3.28	0.080 61	−4.76	0.061 67	−1.31	0.075 37	−2.67
0.1452	−3.13	0.081 47	−5.07	0.064 67	−0.93	0.077 31	−2.52
0.1581	−2.86	0.082 94	−4.74	0.067 68	−0.62	0.079 34	−2.18
0.1642	−2.70	0.085 48	−4.45	0.070 73	−0.31	0.081 45	−1.92
0.1708	−2.59	0.088 18	−4.27	0.073 71	−0.10	0.1161	0.09
0.1768	−2.45	0.091 08	−4.13	0.076 71	0.10	0.1181	0.24
0.1823	−2.35	0.094 07	−3.84	0.079 59	0.22	0.1202	0.37
0.1877	−2.15	0.096 97	−3.58	0.082 50	0.39	0.1223	0.38
0.1931	−2.15	0.099 81	−3.43	0.085 36	0.48	0.1244	0.47
0.2322	−1.58	0.1019	−3.31	0.088 26	0.54	0.1264	0.51
0.2386	−1.53	0.1024	−3.32	0.091 13	0.62	0.1561	0.78
0.2448	−1.43	0.1051	−3.09	0.094 60	0.65	0.1582	0.73
0.2508	−1.39	0.1079	−2.73	0.097 41	0.70	0.1603	0.79
0.2570	−1.34	0.1107	−2.59	0.1002	0.73	0.1635	0.79
0.2626	−1.22	0.1111	−2.77	0.1030	0.76	0.1677	0.76
0.2688	−1.23	0.1142	−2.67	0.1058	0.81	0.2120	0.84
0.2749	−1.18	0.1174	−2.45	0.1085	0.82	0.2129	0.85
0.3216	−0.89	0.1205	−2.21	0.1141	0.85	0.2160	0.82
0.3275	−0.87	0.1267	−1.95	0.1168	0.87	0.2333	0.82
0.3333	−0.83	0.1368	−1.45	0.1195	0.87	0.2399	0.73
0.3392	−0.81	0.1399	−1.37	0.1196	0.93	0.2473	0.72
0.3449	−0.79	0.1431	−1.23	0.1223	0.87	0.2518	0.82
0.3822	−0.63	0.1589	−0.78	0.1327	0.88	0.2548	0.76
0.3877	−0.66	0.1619	−0.71	0.1425	0.92	0.2559	0.72
0.3928	−0.65	0.1719	−0.52	0.1471	0.92	0.2600	0.82
0.3979	−0.62	0.1753	−0.45	0.1515	0.93	0.2642	0.70
0.4304	−0.57	0.1787	−0.39	0.1794	0.92	0.2682	0.78
0.4353	−0.55	0.1819	−0.32	0.1835	0.93	0.2723	0.82
0.4619	−0.49	0.1852	−0.27	0.1877	0.93	0.2762	0.77
0.4652	−0.49	0.1884	−0.28	0.1916	0.92	0.2856	0.90
0.4687	−0.48	0.1916	−0.24	0.2293	0.87	0.2923	0.90
0.5163	−0.45	0.1948	−0.17	0.2333	0.87	0.2984	0.88
0.5207	−0.41	0.1979	−0.13	0.2373	0.89	0.3041	0.87
0.6014	−0.34	0.2011	−0.09	0.2412	0.87	0.3094	0.83
0.6041	−0.31	0.2042	−0.07	0.2450	0.89	0.3148	0.87
0.6069	−0.34	0.2072	−0.04	0.2841	0.84	0.3201	0.81
0.6096	−0.33	0.2101	−0.01	0.2882	0.84	0.3254	0.82

Table 1 (*continued*).

ME–H_2O		ET–H_2O		1P–H_2O		2P–H_2O	
x_A	H_A^E [a]	x_A	H_A^E	x_A	H_A^E	x_A	H_A^E
0.7509	−0.18	0.2712	0.21	0.2922	0.84	0.3826	0.80
0.7528	−0.17	0.2748	0.22	0.2967	0.81	0.3881	0.76
0.7549	−0.16	0.2780	0.18	0.3446	0.76	0.3936	0.78
0.7570	−0.16	0.2811	0.23	0.3485	0.75	0.3990	0.70
0.9002	−0.04	0.2842	0.21	0.3525	0.76	0.4045	0.71
0.9012	−0.04	0.3651	0.22	0.3565	0.74	0.4098	0.68
0.9022	−0.04	0.3683	0.20	0.4041	0.70	0.4778	0.58
0.9033	−0.03	0.3715	0.21	0.4081	0.65	0.4834	0.58
1	0.00	0.3747	0.21	0.4120	0.65	0.4889	0.51
		0.4483	0.11	0.4161	0.64	0.4943	0.65
		0.4514	0.14	0.4549	0.59	0.4996	0.52
		0.4546	0.11	0.4585	0.59	0.5628	0.47
		0.4577	0.11	0.46231	0.57	0.5685	0.46
		0.4609	0.09	0.4678	0.53	0.5738	0.42
		0.4640	0.11	0.4714	0.56	0.5790	0.44
		0.4857	0.07	0.5142	0.47	0.5841	0.38
		0.4907	0.06	0.5179	0.47	0.6526	0.34
		0.4956	0.06	0.5214	0.43	0.6578	0.32
		0.5003	0.05	0.5249	0.44	0.6630	0.29
		0.5043	0.06	0.5285	0.43	0.6680	0.29
		0.5093	0.05	0.5694	0.36	0.6727	0.28
		0.5136	0.05	0.5727	0.34	0.7729	0.16
		0.5414	0.03	0.5760	0.34	0.7767	0.13
		0.5441	0.03	0.5793	0.32	0.7805	0.12
		0.5491	0.02	0.6157	0.26	0.7840	0.12
		0.5528	0.02	0.6189	0.26	0.7876	0.11
		0.5904	−0.03	0.6221	0.25	0.9634	−0.02
		0.5955	−0.04	0.6250	0.26	0.9643	0.00
		0.5977	−0.02	0.6281	0.23	1	0.00
		0.6192	−0.05	0.6793	0.14		
		0.6215	−0.06	0.6822	0.11		
		0.6239	−0.08	0.6850	0.10		
		0.6261	−0.06	0.6877	0.11		
		0.6283	−0.06	0.7318	0.03		
		0.6306	−0.07	0.7343	0.03		
		0.6534	−0.08	0.7367	0.04		
		0.6556	−0.08	0.7392	0.04		
		0.6578	−0.08	0.7874	−0.03		
		0.6599	−0.08	0.7895	−0.03		
		0.6620	−0.09	0.7916	−0.03		
		0.6865	−0.10	0.7936	−0.04		
		0.6886	−0.11	0.8756	−0.06		
		0.6906	−0.10	0.8772	−0.06		
		0.6925	−0.10	0.8783	−0.06		
		0.6943	−0.10	0.9260	−0.05		
		0.7196	−0.11	0.9269	−0.05		
		0.7214	−0.11	0.9631	−0.03		
		0.7231	−0.11	0.9636	−0.04		
		0.7249	−0.11	1	−0.03		
		0.7534	−0.11				
		0.7551	−0.12				
		0.7567	−0.12				
		0.7849	−0.09				
		0.7884	−0.10				
		0.7914	−0.11				

Table 1 (*concluded*).

ME–H_2O		ET–H_2O		1P–H_2O		2P–H_2O	
x_A	H_A^E [a]	x_A	H_A^E	x_A	H_A^E	x_A	H_A^E
		0.7928	−0.10				
		0.8249	−0.09				
		0.8262	−0.09				
		0.8275	−0.09				
		0.8290	−0.09				
		0.8639	−0.07				
		0.8665	−0.07				
		0.8696	−0.07				
		0.8728	−0.06				
		0.9462	−0.02				
		0.9476	−0.02				
		0.9489	−0.01				
		1	0.00				

[a]kJ mol^{-1}, ±0.05 kJ mol^{-1}.

The results are shown in Fig. 6. As is evident from Fig. 6*b*, the values of H_A^E thus calculated were in reasonable agreement with the measured values except at the low concentration end of the mole fraction scale, which is expected for any set of H_m^E data of high quality. For ET–H_2O, Ott et al. (25) fitted the following function to the data of H_m^E:

$$[3]\quad H_m^E = x_{ET}(1 - x_{ET})[\exp(-\alpha x_{ET})\Sigma b_j(1 - 2x_{ET})^j + \{1 - \exp(-\alpha x_{ET})\}\Sigma c_k(1 - 2x_{ET})^k]$$

with j = 0–2 and k = 0–4. We note that eq. [3] contains an exponential term, which is normally avoided as a fitting function. Using eq. [3], the excess partial molar enthalpy of ET, H_{ET}^E, was calculated by eq. [2] with A = ET. The results are shown in Fig. 5. The agreement with our data is good, including the low x_A region. Therefore, eq. [3] turned out to be a good choice as a fitting function. We note that an exponential term can be differentiated repeatedly. This property may have some bearing on the success of eq. [3] in leading to good values of H_{ET}^E.

The values of H_A^E extrapolated to $x_A = 0$ are listed in Table 2. These values signify the change in the enthalpic situation for the first molecule of A from its pure environment to the aqueous medium, i.e., the solute–solvent interaction at infinite dilution. If, aside from the direct interaction of the hydroxyl group of alcohol with H_2O, the mode of dissolution is dictated by the nonpolar moiety, the general trend in H_A^E from methanol to 2-butoxyethanol may be understandable, although the increments do not scale proportionally with the changes in size. These values of H_A^E at $x_A = 0$ may be interpreted with respect to various imaginary processes: cavity formation in H_2O, removal of alcohol from the pure liquid, insertion into the cavity, and subsequent modification of the hydrogen bond network of H_2O. The absolute value of the enthalpy involved in each step can be an order of magnitude larger than the combined result. It is quite feasible that the resulting value of H_A^E at $x_A = 0$ can be rather insensitive to the size of the hydrophobic moiety, while the enthalpy change involved in each process may depend sharply on it. This indicates the limitation of discussing details of the mixing scheme by using H_A^E data alone.

Table 2. H_A^E at infinite dilution.

A	H_A^E at $x_A = 0$[a]
Methanol	−7.4
Ethanol	−10.2
1-Propanol	−10.4
2-Propanol	−13.1
tert-Butyl alcohol	−17.0[b]
2-Butoxyethanol	−17.0[c]

[a]kJ mol^{-1}.
[b]Reference 1.
[c]Reference 6.

The enthalpic A–A interactions, H_{AA}^E, were calculated graphically from the smoothed curves drawn through the measured data points using eq. [1]. They are plotted in Figs. 8, 9, and 10. The peak loci and their maximum values are listed in Table 3. The size difference in the nonpolar moiety is amplified in the values of H_{AA}^E at the peak. If these peaks represent approximately the point at which mixing scheme I starts to break down, as has been established for BE–H_2O (6–16), the maximum values of H_{AA}^E signify the A–A interaction between the two "hydrated" A molecules at their closest possible distance. Such an interaction is no doubt operational via the H_2O layers modified by the solute A. Hence the maximum values of H_{AA}^E listed in Table 3 represent the influence of A on the hydrogen bond network of H_2O in its immediate vicinity, which is probed by bringing another "hydrated" A to its closest possible vicinity.

When x_A is very small, the peculiar nature of H_2O associated with the hydrogen bond network must be retained. As x_A increases, however, such peculiar nature will eventually be lost and H_2O behaves as an ordinary polar solvent, giving rise to mixing scheme II. For BE–H_2O, it has been well established

Fig. 5. The excess partial molar enthalpies of ethanol, H_{ET}^{E}, at 25°C. ○: This work; □: ref. 22, ▽: refs. 23 and 27; ◇: ref. 24; △: calculated using the fitting function, eq. [3] for H_m^E in ref. 25. Equation [3] turned out to be a good choice, leading to good values of H_{ET}^{E}.

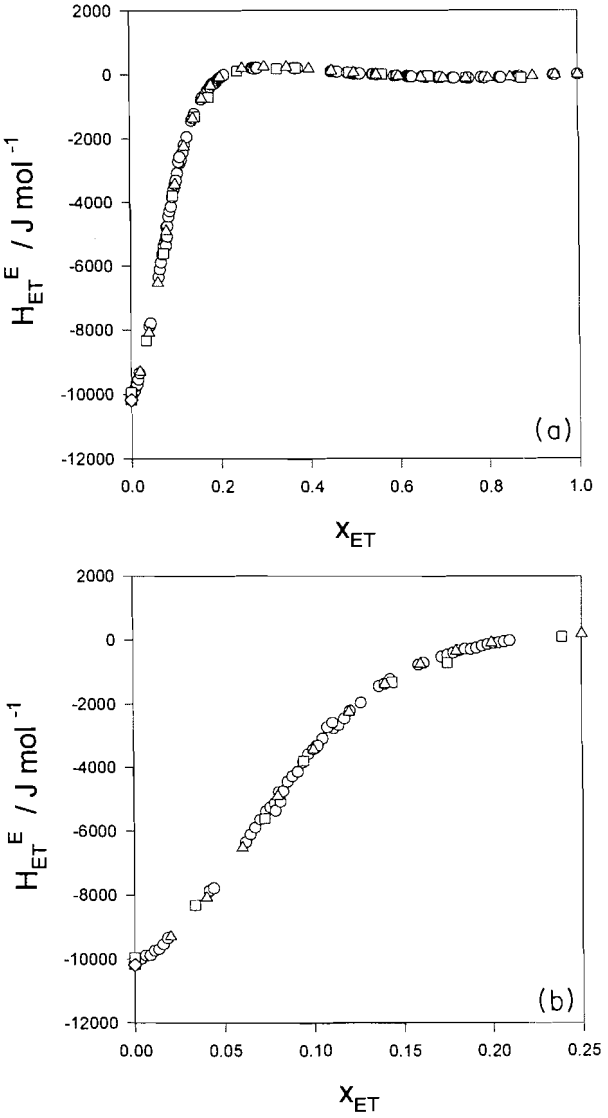

Fig. 6. The excess partial molar enthalpies of 1-propanol, H_{1P}^{E}, at 25°C. ○: This work; □: refs. 24 and 27; △: Graphically calculated using the data of H_m^E in ref. 26. See text.

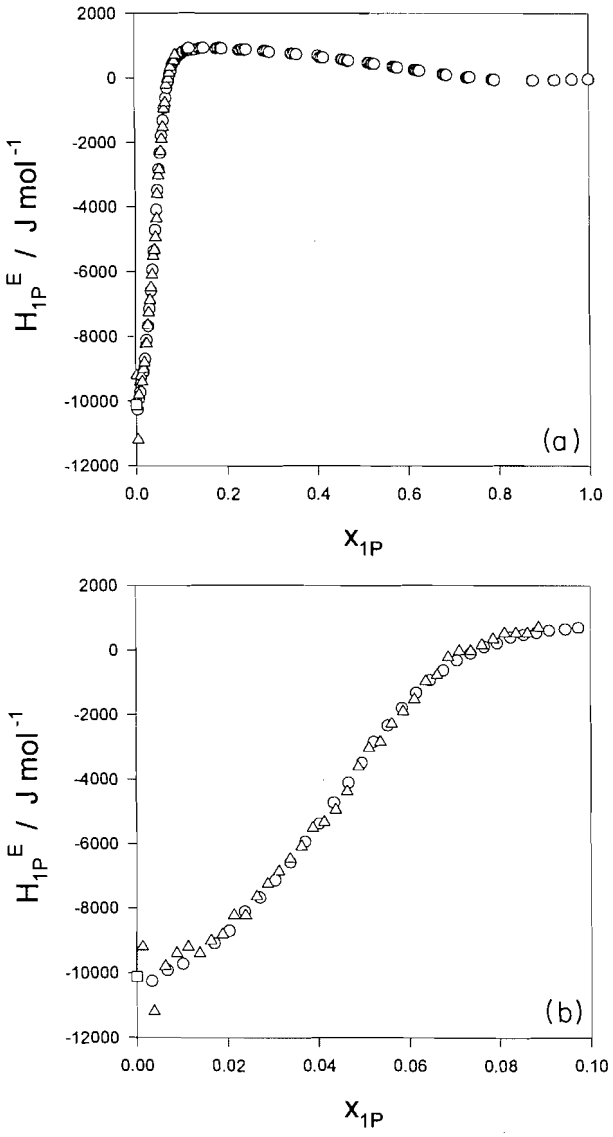

that mixing scheme II does indeed exist and the transition from I to II is rather abrupt. For TBA–H_2O, the transition seems gradual, as seen in Fig. 2. For other alcohols, we tentatively drew the lines representing mixing scheme II as shown in Figs. 8, 9, and 10, and determined points X, Y, and M accordingly. They are listed in Table 3. Since the values of H_A^E are smaller by tenfold in this region than those at $x_A = 0$, an accurate evaluation for H_{AA}^{E} is problematic. Hence, at least a tenfold improvement in sensitivity is required for calorimetry for an unequivocal conclusion on the subtle dependence of H_{AA}^{E} in this region. Nevertheless, we suggest tentatively that mixing scheme II is present in all cases studied, and that the transition from I to II takes place rather gradually, more so, the smaller the hydrophobic moiety. The observation that the transition from I to II takes place over a small composition interval (Table 3) may reflect nonuniformity in hydrogen bond strength in H_2O. If the transition is indeed associated with the loss of percolation in the hydrogen bond network (16), the percolation threshold is reached for the strongest hydrogen bond at point X in Fig. 3, and at point Y for the weakest ones.

The mixing scheme boundary between I and II for BE–H_2O was found to coincide with the incongruent melting point of the addition compound, $BE(H_2O)_{38}$, which was suggested to be a clathrate (28), thus hinting that mixing scheme I may be regarded as "preparing" for the formation of a clathrate solid when the temperature becomes low enough. The trend in the nominal transition point, point M in Table 3, as the hydrophobic moiety becomes larger from ME to BE, can be understood in terms of the number of H_2O participating in the formation of a clathrate. The smaller the hydrophobic moiety, the fewer H_2O molecules are required, hence the larger the threshold value in x_A.

Fig. 7. The excess partial molar enthalpies of 2-propanol, H_{2P}^{E}, at 25°C. ○: This work; □: ref. 23; △: ref. 24.

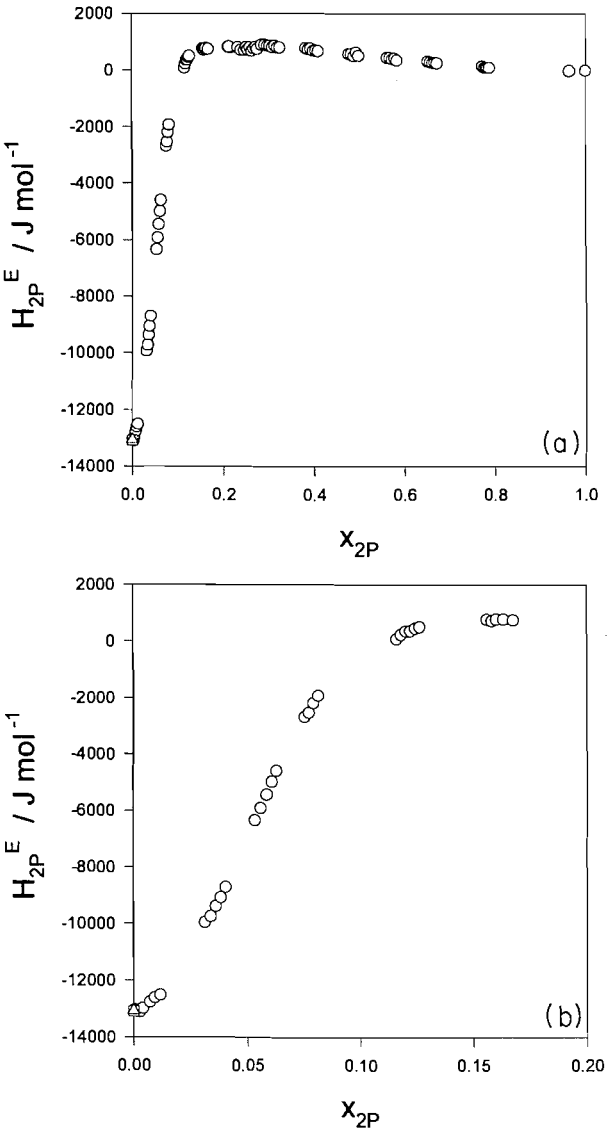

Fig. 8. The enthalpic solute–solute interaction, H_{AA}^{E}, at 25°C. ○: Ethanol (ET); □: 1-propanol (1P).

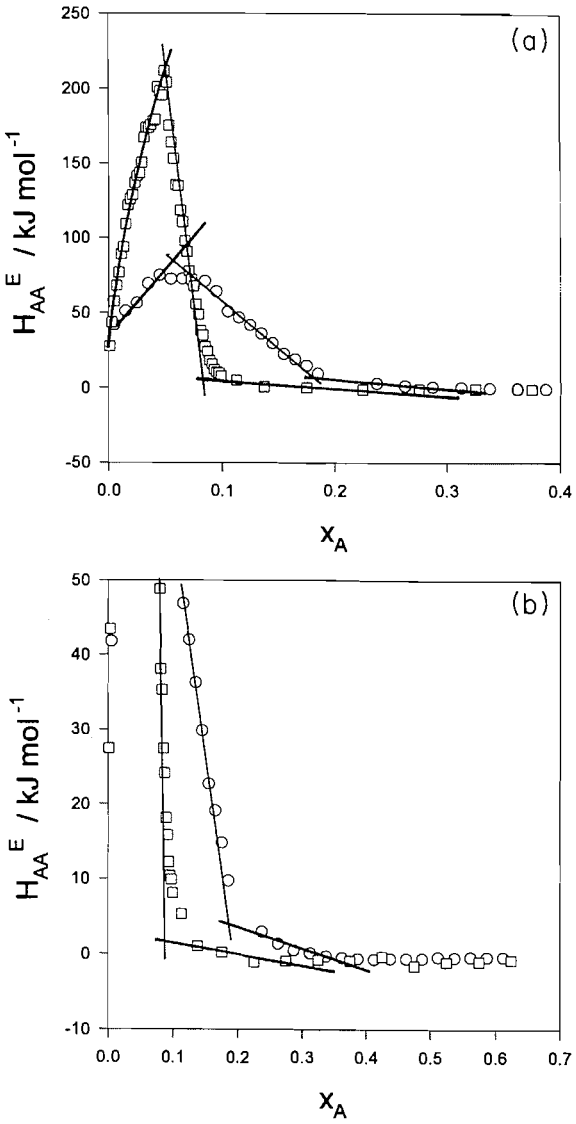

Table 3. The peak loci and their maximum values of H_{AA}^{E} for methanol, ethanol, 1- and 2-propanols, *tert*-butyl alcohol, and 2-butoxyethanol in aqueous solution.

A	x_A (peak)	H_{AA}^{E} (peak)	Range of transition (from X to Y)		Transition point (nominal)
Methanol	0.05	32 ± 3[a]	0.07	0.25	0.16
Ethanol	0.06	73 ± 5	0.06	0.19	0.125
1-Propanol	0.05	210 ± 10	0.05	0.09	0.07
2-Propanol	0.055	180 ± 10	0.05	0.11	0.08
tert-Butyl alcohol	0.04	350 ± 20[b]	0.045	0.065	0.055
2-Butoxyethanol	0.0175	1100 ± 50[c]	0.017	0.021	0.019

[a]kJ mol^{-1}.
[b]Reference 1.
[c]Reference 6.

Fig. 9. The enthalpic solute–solute interaction, H_{AA}^{E}, at 25°C, for 2-propanol.

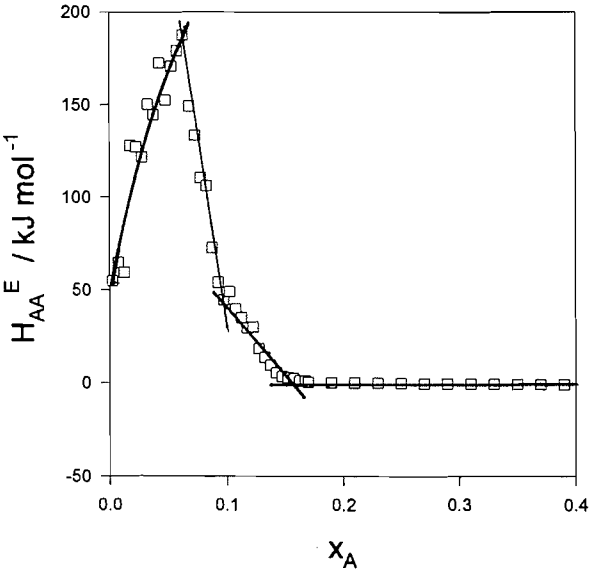

Fig. 10. The enthalpic solute–solute interaction, H_{AA}^{E}, at 25°C, for methanol.

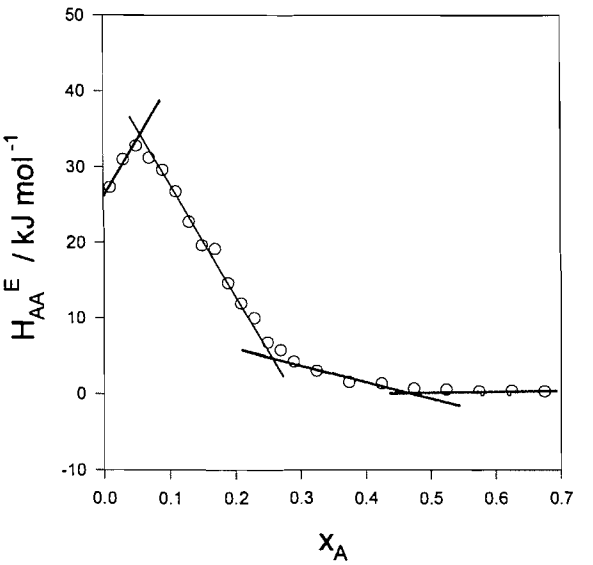

Other third derivatives, including the entropic interaction function S_{AA}^{E}, must be collected before more unequivocal conclusions can be drawn. Another very useful datum is the excess partial molar enthalpy of the solvent water, H_{W}^{E}, and its interaction, H_{WW}^{E}, or equivalently in a binary system, H_{WA}^{E}. The Gibbs–Duhem relation dictates that

$$[4] \quad x_A H_{AA}^{E} + (1 - x_A) H_{WA}^{E} = 0$$

Thus, a peak in H_{AA}^{E}, i.e., $(\partial H_{AA}^{E}/\partial x_A) = 0$, if H_{AA}^{E} is *differentiable at this point*, does not necessarily match with a peak in H_{WA}^{E}. But if the peak is indeed a singular point and hence H_{AA}^{E} is not differentiable, then H_{WA}^{E} also must be singular, although H_{WA}^{E} does not always take the form of a peak. Preliminary data of H_{W}^{E} obtained using a highly sensitive titration calorimeter, MicroCal OMEGA, indicated that H_{WA}^{E} for ET–H_2O showed a peak at about $x_A = 0.1$, near the midpoint M (see Table 3), rather than at the peak in H_{AA}^{E}. For 1P–H_2O, on the other hand, the peak in H_{WA}^{E} is at about $x_A = 0.06$, close to the peak of H_{AA}^{E}, reflecting the narrowness of the transition region. A series of careful measurements of H_{W}^{E}, among other data, are necessary for establishing whether mixing scheme II does indeed exist, exactly at which composition the transition from I to II occurs, and how wide the transition region is.

Acknowledgment

This research was supported by the Natural Sciences and Engineering Research Council of Canada in the form of a research grant to Y. K., and undergraduate summer research awards to A. I. Y. (1993) and to S. H. T. (1994). P. W. thanks the National Danish Research Council for a postdoctoral fellowship.

References

1. Y. Koga. Can. J. Chem. **66**, 1187 (1988).
2. Y. Koga. Can. J. Chem. **66**, 3171 (1988).
3. Y. Koga, W.W.Y. Siu, and T.Y.H. Wong. J. Phys. Chem. **94**, 7700 (1990).
4. Y. Koga, T.Y.H. Wong, and W.W.Y. Siu. Thermochim. Acta, **169**, 27 (1990).
5. Y. Koga. Chem. Phys. Lett. **111**, 176 (1984).
6. W. Siu and Y. Koga. Can. J. Chem. **67**, 671 (1989).
7. Y. Koga, W.W.Y. Siu, and T.Y.H. Wong. J. Phys. Chem. **94**, 3879 (1990).
8. Y. Koga. J. Phys. Chem. **95**, 4119 (1991).
9. Y. Koga, J. Kristiansen, and Aa. Hvidt. J. Chem. Thermodyn. **25**, 51 (1993).
10. Y. Koga. J. Phys. Chem. **96**, 10466 (1992).
11. P. Westh, Aa. Hvidt, and Y. Koga. Chem. Phys. Lett. **217**, 245 (1994).
12. T. Atake and Y. Koga. Netsu Sokutei (Calorim. Therm. Anal. Jpn.), **21**, 130 (1994).
13. J.V. Davies, F.W. Lau, L.T.N. Le, J.T.W. Lai, and Y. Koga. Can. J. Chem. **70**, 2659 (1992).
14. Y. Koga, K. Tamura, and S. Murakami. J. Solution Chem. **24**, 1127 (1995).
15. Y. Koga, K. Nishikawa, K. Yoshino, I. Tanaka, Y.Xu, and Y. Amemiya. Chem. Phys. Lett. **228**, 53 (1994).
16. Y. Koga. Nippon Kessho Gakkaishi (J. Crystallogr. Soc. Jpn.), **37**, 172 (1995): J. Phys. Chem. In press.
17. H.E. Stanley and J. Teixeira. J. Chem. Phys. **73**, 3404 (1980).
18. G.W. Euliss and C.M. Sorensen. J. Chem. Phys. **80**, 4767 (1984).
19. J.T.W. Lai, F.W. Lau, D. Robb, P. Westh, G. Nielsen, C. Trandum, Aa. Hvidt, and Y. Koga. J. Solution Chem. **24**, 89 (1995).
20. T.Y.H. Wong, K.C. Wong-Moon, L.J. Beach, Y.-F. Chuang, and Y. Koga. J. Phys. Chem. **96**, 10025 (1992).
21. W.W.Y. Siu, T.Y.H. Wong, L.C.F. Chau, and Y. Koga. Can. J. Chem. **69**, 1065 (1991).
22. G.L. Bertrand, F.J. Millero, C.-H. Wu, and L.G. Hepler. J. Phys. Chem. **70**, 699 (1966).
23. V. Dohnal, A.H. Roux, and V. Hynek. J. Solution Chem. **23**, 889 (1994).
24. E.M. Arnett, W.B. Kover, and J.V. Carter. J. Am. Chem. Soc. **91**, 4028 (1969).
25. J.B. Ott, C.E. Stouffer, G.V. Cornett, B.F. Woodfield, C. Guanquan, and J.J. Christensen. J. Chem. Thermodyn. **19**, 337 (1987).
26. M.I. Davis and E.S. Ham. Thermochim. Acta, **190**, 251 (1991).
27. D. Hallen, S.-O. Nilsson, W. Rothschild, and I. Wadso. J. Chem. Thermodyn. **18**, 429 (1986).
28. Y. Koga, T. Tanaka, T. Atake, P. Westh, and Aa. Hvidt. Bull. Chem. Soc. Jpn. **67**, 2393 (1994).

Rhenium complexes of *P,P,P′,P′*-tetrakis-(*o*-hydroxyphenyl)diphosphinoethane

Hongyan Luo and Chris Orvig

Abstract: Preparation of the hydrochloride salt of a new potentially hexadentate ligand precursor *P,P,P′,P′*-tetrakis(*o*-hydroxyphenyl)diphosphinoethane dihydrochloride (abbreviated $H_4P_2O_4{\cdot}2HCl$) is described. From $H_4P_2O_4{\cdot}2HCl$, neutral $[Re_2O_2Cl_2(PPh_3)_2(\mu\text{-}P_2O_4)]$ and dianionic $[Re_2O_2Br_4(\mu\text{-}P_2O_4)]^{2-}$ dinuclear rhenium(V) complexes were synthesized. The complexes have been characterized by elemental analysis, infrared spectroscopy, mass spectrometry, and $^1H/^{31}P\{^1H\}$ NMR spectra. $^{31}P\{^1H\}$ NMR revealed that only one isomer, presumably the *anti*, was present for $[Re_2O_2Cl_2(PPh_3)_2(\mu\text{-}P_2O_4)]$, and that two isomers, both *anti* and *syn* isomers, were observed for $[Re_2O_2Br_4(\mu\text{-}P_2O_4)]^{2-}$. The coligands ($PPh_3$ for the former, Br^- for the latter) of both complexes underwent ligand exchange with pyridine.

Key words: rhenium, *P,P,P′,P′*-tetrakis(*o*-hydroxyphenyl)diphosphinoethane, dimer, isomers.

Résumé : On décrit la préparation de sels d'un nouveau précurseur d'un coordinat potentiellement hexadentate, les dichlorhydrates de *P,P,P′,P′*-tétrakis(*o*-hydroxyphényl)diphosphinoéthane ($H_4P_2O_4{\cdot}2HCl$). À partir du $H_4P_2O_4{\cdot}2HCl$, on a synthétisé les complexes dinucléaires du rhénium neutre $[Re_2O_2Cl_2(PPh_3)_2(\mu\text{-}P_2O_4)]$ et dianionique $[Re_2O_2Br_4(\mu\text{-}P_2O_4)]^{2-}$. On a caractérisé les complexes par analyse élémentaire, spectroscopie infrarouge, spectrométrie de masse et spectroscopie RMN du $^1H/^{31}P\{^1H\}$. Les spectres RMN du $^{31}P\{^1H\}$ ont révélé qu'un seul isomère, probablement l'isomère *anti*, est présent dans le $[Re_2O_2Cl_2(PPh_3)_2(\mu\text{-}P_2O_4)]$ alors que deux isomères, les deux isomères *anti* et *syn*, sont présents dans le $[Re_2O_2Br_4(\mu\text{-}P_2O_4)]^{2-}$. Les co-coordinats ($PPh_3$ du premier et Br^- du dernier) des deux complexes subissent des échanges de coordinats avec la pyridine.

Mots clés : rhénium, *P,P,P′,P′*-tétrakis(*o*-hydroxyphényl)diphosphinoéthane, dimère, isomères.

[Traduit par la rédaction]

Introduction

The easy preparation of mixed (PO_2/HPO_2) complexes, $[MO(PO_2)(HPO_2)]$ (M = Re or Tc), from the direct interaction of a salt of bis(*o*-hydroxyphenyl)phenylphosphine ($H_2PO_2{\cdot}HCl$) with MO_4^-, suggests that this dihydroxylated phosphine is effective both as a reducing and a ligating agent, and that the combination of anchoring phenolate oxygen atoms and the softer phosphine P atoms stabilizes Re and Tc metal(V) centers (1). The ligand can both coordinate and reduce the metal center, a distinct advantage when considering potential ^{99m}Tc-radiopharmaceuticals where the only convenient source of ^{99m}Tc is $^{99m}TcO_4^-$ from a $^{99}Mo/^{99m}$Tc generator.

Deutsch and co-workers, working on Tc complexes with bidentate phosphine ligands such as DMPE, DEPE, DPPE (2, 3), showed that stable complexes of Tc in oxidation states from one to five can be formed with these ligands and auxiliary oxo or halo donor ligands. In our extended studies of functionalized phosphines, a novel, potentially hexadentate tetraprotic ligand, the dihydrochloride salt of *P,P,P′,P′*-tetrakis(*o*-hydroxyphenyl)diphosphinoethane ($H_4P_2O_4{\cdot}2HCl$) that contains two soft phosphine phosphorus donors and four hard phenolate oxygen anchors, has been synthesized. The classic hexadentate tetraprotic ligand, H_4edta, an N_2O_4 ligand, is known to form Tc complexes with such stoichiometries as $[TcO(edta)]^-$ (4) and $[Tc(\mu\text{-}O)(edta)]_2$ (5).

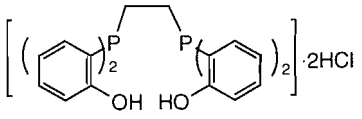

$H_4P_2O_4 \cdot 2HCl$

It was of interest to investigate the coordination chemistry of Tc/Re with this P_2O_4 donor set diphosphine ligand before pursuing the labeling of this ligand with ^{99m}Tc and evaluating its potential as an imaging agent. The results of the studies with Re are presented in this paper. Work with Tc is in progress and the results will be published elsewhere.

Experimental

Materials and methods

All chemicals were reagent grade and were used as received: phenol, PPh_3, dimethoxymethane, *n*-butyllithium, TMEDA (*N,N,N′N′*-tetramethylethylenediamine) (all above from Aldrich), $Cl_2PCH_2CH_2PCl_2$ (6), and NH_4ReO_4 (a gift from Johnson–Matthey, Inc.), $HCl_{(g)}$ (Matheson). $C_6H_5OCH_2OCH_3$ (mom-protected phenol) was prepared according to a published procedure (7), as was $[(n\text{-}Bu)_4N][ReOBr_4]$ (8).

Mass spectra were obtained with either a Kratos MS 50

Received December 5, 1995.

H. Luo[1] **and C. Orvig.**[2] Department of Chemistry, University of British Columbia, 2036 Main Mall, Vancouver, BC V6T 1 Z1, Canada.

[1] Current address: Department of Chemistry, University of Alberta, Edmonton, AB T6G 2G2, Canada.

[2] Author to whom correspondence may be addressed. Telephone: (604) 822-4449. Fax: (604) 822-2847. Internet: ORVIG@CHEM.UBC.CA

(electron impact ionization, EIMS) or a Kratos Concept II H32Q instrument (Cs^+-LSIMS with positive or negative ion detection). Only the most intense peaks are given where consistent isotopic patterns were observed. Infrared spectra were recorded as KBr pellets in the range 4000–400 cm^{-1} on a Perkin–Elmer PE 783 spectrophotometer and were referenced to polystyrene. Microanalyses were performed by Mr. P. Borda in this department. ^1H NMR spectra (300 MHz, 400 MHz, or 500 MHz) were recorded on Varian XL 300, Bruker WH-400 (^1H–^1H COSY), or Bruker AMX-500 ($^1H\{^{31}P\}$) spectrometers, respectively, with δ referenced to external TMS. $^{31}P\{^1H\}$ NMR spectra (81 MHz or 121 MHz) were recorded on Bruker AC-200E or Varian XL 300 spectrometers, respectively, with δ referenced to external H_3PO_4. The assignments were based on those for the unbound ligand and by comparison between analogous complexes.

(o-$C_6H_4OCH_2OCH_3$)$_2$$PCH_2CH_2P$($o$-$C_6H_4OCH_2OCH_3$)$_2$·0.5 H_2O ($(mom)_4P_2O_4$·0.5H_2O, mom = CH_2OCH_3)

This was prepared from $C_6H_5OCH_2OCH_3$ by modifying the procedure for $Ph_2P(o\text{-}C_6H_4\text{-}OCH_2OCH_3)$ ((mom)PO) (9). To an ice-cooled solution of methoxymethyl phenyl ether (21.8 g, 0.16 mol) in ca. 200 mL petroleum ether (bp 35–65°C, dried with anhydrous Na_2SO_4 overnight) was added a solution of 100 mL of 1.6 M n-BuLi in hexanes and 18.05 g TMEDA in 50 mL petroleum ether under N_2. The mixture was stirred for 4 h at room temperature. A yellow precipitate formed from the orange solution. This mixture was heated to ca. 40°C with stirring, and subsequently cooled to 0°C, at which point $Cl_2PCH_2CH_2PCl_2$ (9.30 g, 0.40 mol) in 20 mL petroleum ether was then added via a syringe. The mixture was stirred overnight, during which time it warmed to room temperature. The solvents were removed by rotary evaporation and to the residue was added Na_2HPO_4 (0.5 M, 200 mL). The reaction mixture was then extracted with Et_2O (2 × 200 mL) followed by $CHCl_3$ (2 × 100 mL). All the organic layers were combined, concentrated to a reddish oil under low pressure, diluted with MeOH (ca. 25 mL), and stored at −4°C overnight. A yellowish crude product was filtered off, washed with cold methanol (2 × 10 mL), and dried in vacuo. The yield of the off-white product was 11.5 g (45% based on $C_6H_5OCH_2OCH_3$). IR (cm^{-1}, KBr disk): 3060 (m, aromatic $\nu_{C\text{-}H}$); 3000–2800 (m, $\nu_{C\text{-}H}$, methyl and methylene of mom group); 1590, 1577, 1475, 1452, 1445, 1407 (all s). ^1H NMR ($CDCl_3$, 300 MHz): 7.24 (t, 4H, p-H), 7.14 (dd, 4H, o'-H), 7.03 (d, 4H, m-H), 6.91 (t, 4H, m'-H), 5.04 (s, 8H, OCH_2O), 3.17 (s, 12H, OCH_3), 2.28 (dd, 4H, backbone-CH_2). $^{31}P\{^1H\}$ NMR ($CDCl_3$, 121 MHz): −31.7 (s). Mass spectrum (EI), m/z: 638 ($[(mom)_4P_2O_4]^+$), 623 ($[(mom)_4P_2O_4 - CH_3]^+$). Anal. calcd. (found) for $C_{34}H_{41}O_{8.5}P_2$: C 63.06 (63.19), H 6.38 (6.24).

P,P,P',P'-Tetrakis(o-hydroxyphenyl)diphosphinoethane dihydrochloride salt ($H_4P_2O_4$·2HCl)

This was prepared from $(mom)_4P_2O_4$ by modifying the procedure for $Ph_2P(o\text{-}C_6H_4OH)$ or HPO (9). Anhydrous HCl gas was bubbled overnight, via a dispersion tube, into a stirred solution of $(mom)_4P_2O_4$ (7.36 g, 11.5 mmol) in 350 mL anhydrous methanol. (The white suspension dissolved to give a clear solution after 1 h, but became cloudy again overnight.) A fine white solid was removed by filtration, washed with ethanol (2 × 20 mL), and dried in vacuo. The yield was 3.95 g (74% based on $(mom)_4P_2O_4$). No recrystallization was necessary to obtain an analytically pure sample. IR (cm^{-1}, KBr disk): 3300–2500 (vs, b, $\nu_{O\text{-}H}$ and $\nu_{C\text{-}H}$); 1590, 1495, 1450 (all vs). ^1H NMR (DMSO-d_6, 300 MHz): 10.8 (br s, 4H, OH), 7.6–7.3 (overlapped multiplets, 8H), 7.0–6.8 (multiplet, 8H), 2.6 (br s, 4H, backbone-CH_2). $^{31}P\{^1H\}$ NMR (121 MHz): 43.5 (s, DMSO-d_6): −36.4 (s, py-d_5). EIMS, m/z: 462 ($[H_4P_2O_4]^+$), 368 ($[H_4P_2O_4 - C_6H_6O]^+$). Anal. calcd. (found) for $C_{26}H_{26}Cl_2O_4P_2$: C 58.33 (58.21), H 4.90 (4.84), Cl 13.24 (13.07).

[$Re_2O_2Cl_2(PPh_3)_2(\mu\text{-}P_2O_4)$]

A mixture of $ReCl_4(PPh_3)_2$ (168 mg, 0.20 mmol), $H_4P_2O_4$·2HCl (109 mg, 0.20 mmol), and 8 drops of Et_3N in 15 mL ethanol was brought to reflux overnight. After the mixture was cooled to room temperature, a greenish yellow precipitate was isolated by centrifugation, washed with Et_2O, and dried in vacuo for 4 h. The yield was 40 mg (67%). The product was soluble in pyridine and DMSO (decomposes), slightly soluble in chloroform, but insoluble in diethyl ether. IR (cm^{-1}, KBr disk): 3060 (m, $\nu_{C\text{-}H}$); 1590, 1440 (both vs); 965 (s, $\nu_{Re=O}$). ^1H NMR (300 MHz, py-d_5): 7.70 (dd, 12H, o-H on PPh_3), 7.50 (dd, 2H), 7.40–7.20 (overlapped multiplets, 18H, m and p-H on PPh_3), 7.20 (d, 2H), 7.10 (d, 2H), 6.75 (m, 2H), 6.65 (t, 2H), 6.40 (t, 2H), 6.30 (t, 2H), 5.80 (dd, 2H), 2.85 (m, 2H, ethylene-H_A and -$H_{A'}$), 2.00 (d, 2H, ethylene-H_B and -$H_{B'}$). $^{31}P\{^1H\}$ NMR (81 MHz, py-d_5): 15.7, −11.3. LSIMS: m/z: 1459 ($[M + 1]^+$), 1423 ($[M - Cl]^+$), 1196 ($[M - PPh_3)]^+$), 1161 ($[M - Cl - PPh_3]^+$), 1124 ($[M - 2Cl - PPh_3]^+$), 645 ($[Re(P_2O_4)]^+$), 263 ($PPh_3 + 1$). Anal. calcd. (found) for $C_{62}H_{50}Cl_2O_6P_4Re_2$: C 51.07 (50.76), H 3.46 (3.59), Cl 4.86 (4.65).

[(n-Bu)$_4$N]$_2$[$Re_2O_2Br_4(\mu\text{-}P_2O_4)$]·$Me_2CO$

To a mixture of [(n-Bu)$_4$N][$ReOBr_4$] (77.6 mg, 0.10 mmol), [(n-Bu)$_4$N]Br (151 mg, 0.45 mmol), and $H_4P_2O_4$·2HCl (55.5 mg, 0.10 mmol) was added 20 mL toluene, and the mixture was refluxed for 2 h. From the resulting green oil, a green solid was precipitated with i-PrOH. Recrystallization from acetone gave emerald green crystals of the acetone solvate that were filtered, washed with cyclohexane, and dried in vacuo overnight. The yield was 31 mg (35%). The product was soluble in ethanol, acetone, chloroform, and dichloromethane, but insoluble in diethyl ether or cyclohexane. IR (cm^{-1}, KBr disk): 3060 (m, $\nu_{C\text{-}H}$); 2980, 2780 (s, $\nu_{C\text{-}H}$ of the n-Bu group), 960 (s, $\nu_{Re=O}$). ^1H NMR (500 MHz, acetone-d_6): 7.9–7.6 (overlapped m, 4H), 7.22 (t, ^1H), 7.16 (t, ^1H), 7.1–6.9 (overlapped m, 4H), 6.78 (t, 1H), 6.7–6.6 (overlapped m, 2H), 6.55 (t, ^1H), 6.2 (overlapped m, 2H), 4.14 (m, 2H, ethlyne-H_A and -$H_{A'}$), 3.45 (t, 16H, α-H of the n-Bu group), 2.65 (d, 2H, ethylene-H_B and -$H_{B'}$), 1.70 (quintet, 16H, β-H of the n-Bu group), 3.45 (sextet, 16H, γ-H of the n-Bu group), 0.95 (t, 24H, Me-H of the n-Bu group). $^{31}P\{^1H\}$ NMR (81 MHz, acetone-d_6): 18.0 (major); 17.0 (minor). LSIMS (+), m/z: 242 ($[(n\text{-}Bu)_4N]^+$), 645 ($[Re(P_2O_4)]^+$), 662 ($[ReO(HP_2O_4)]^+$); LSIMS (−), m/z: 645 ($[Re(P_2O_4)]^-$), 661 ($[ReO(P_2O_4)]^-$), 769 ($[ReO(P_2O_4) + 108]^-$). Anal. calcd. (found) for $C_{61}H_{98}Br_4N_2O_7P_2Re_2$: C 42.46 (42.62), H 5.72 (5.47), N 1.62 (1.71).

Scheme 1.

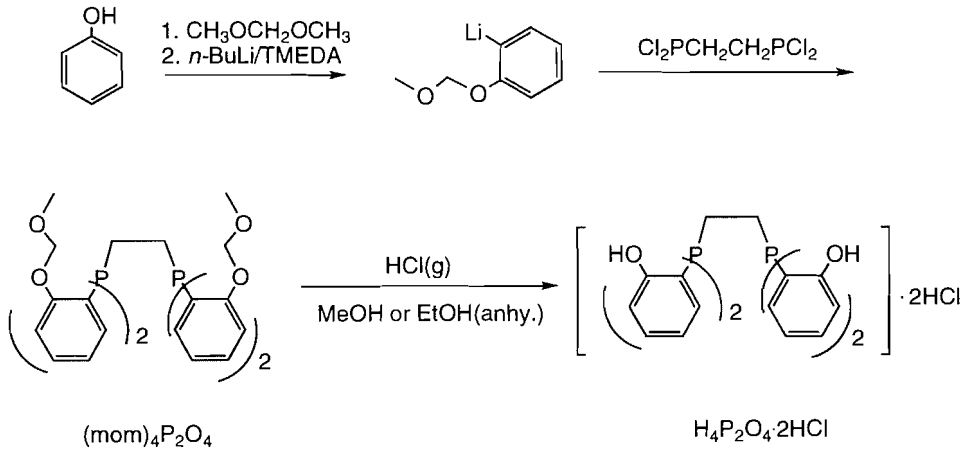

Results and discussion

$H_4P_2O_4 \cdot 2HCl$

The new potentially hexadentate ligand $H_4P_2O_4 \cdot 2HCl$ was synthesized in a manner similar to that used to obtain the potentially tridentate $H_2PO_2 \cdot HCl$ (1). After protecting the phenol hydroxy group as a methoxymethyl (mom) ether (9), the mom-protected phenol was *ortho*-lithiated at low temperature under N_2, and 4 equivalents of it were then reacted with $Cl_2PCH_2CH_2PCl_2$ to give the mom-protected intermediate, $(mom)_4P_2O_4$. Upon treatment with anhydrous HCl gas in methanol or ethanol, the expected functionalized diphosphine was obtained as the dihydrochloride salt (Scheme 1).

For the intermediate, $(mom)_4P_2O_4$, the EIMS shows the expected parent ion peak (*m/z*: 638, $[(mom)_4P_2O_4]^+$), along with fragments formed from the parent ion by the loss of $-CH_3$, $-OCH_3$, $-CH_2OCH_3$, and $-OCH_2OCH_3$ groups. In the $^{31}P\{^1H\}$ NMR spectrum ($CDCl_3$), a singlet at -31.7 ppm, typical for a phosphine P, is present (10). The ^1H NMR spectrum shows four hydrogen resonances at 7.24, 7.14, 7.03, and 6.91 ppm in the aromatic range, corresponding to *p*-, *o'*-, *m*-, and *m'*-*H* of the phenyl ring[3] (assigned from a ^1H–^1H COSY spectrum). The resonances corresponding to methyl and methylene H atoms of the mom protecting group, appear as singlets at 5.04 and 3.17, respectively. The two methylene H nuclei in each mom group of $(mom)_2PO_2$ gave an AB quartet (1), indicating nonequivalence of the two methylene hydrogens because of prochirality. This was not the case with $(mom)_4P_2O_4$, however; the four chemically equivalent backbone H atoms give a doublet of doublets due to unequal coupling to the two P nuclei.

As was seen in $H_2PO_2 \cdot HCl$ (1), the formulation of a hydrochloride salt for its hexadentate analogue $H_4P_2O_4 \cdot 2HCl$ is supported by the elemental analysis and by the ^{31}P chemical shift, characteristic of a phosphonium P (10) at +43.5 ppm in DMSO-d_6. This salt dissociated in its ligand-exchange reactions (vide infra) and in basic solution, as is indicated by the chemical shift of -36.4 ppm in the $^{31}P\{^1H\}$ NMR spectrum in py-d_5. EIMS shows the presence of $[H_4P_2O_4]^+$. The ^1H NMR spectrum in DMSO-d_6 shows four overlapped H resonances in the aromatic region and a broad backbone H resonance at 2.6 ppm with the expected integral ratio.

[3] This is designated as in the following diagram:

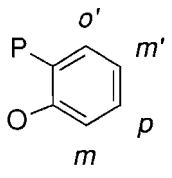

Synthesis of complexes

The phosphine hydrochloride salt $H_4P_2O_4 \cdot 2HCl$, when deprotonated by a base, reacted with $[ReCl_4(PPh_3)_2]$ forming a dinuclear complex $[Re_2O_2Cl_2(PPh_3)_2(\mu\text{-}P_2O_4)]$. Aerial oxidation was responsible for oxidizing Re(IV) to Re(V). In another trial without added base, the ligand did not react with the Re precursor; red crystals obtained from this trial were identified by X-ray crystallography as a partially oxidized mixture of *trans*-$[ReCl_4(PPh_3)_2]$ and *trans*-$[ReOCl_3(PPh_3)_2]$ (11, 12). A dinuclear dianionic complex $[Re_2O_2Br_4(\mu\text{-}P_2O_4)]^{2-}$ (as a $[(n\text{-}Bu)_4N]^+$ salt) was formed from the reaction of $[(n\text{-}Bu)_4N][ReOBr_4]$ with the ligand and added $[(n\text{-}Bu)_4N]Br$ in the absence of added base. These observations, taken together, suggest that an extra driving force is necessary to push forward the substitution reaction of $H_4P_2O_4$ with a precursor that contains PPh_3, consistent with observations reported for H_2PO_2 (1). In addition, chelation of the $P_2O_4^{4-}$ ligand to a single Re center is clearly not favored.

Both the dimetallic Re complexes are air stable in the solid state, and were characterized by elemental analysis, infrared spectroscopy, mass spectrometry, and $^1H/^{31}P\{^1H\}$ NMR spectroscopy. IR measurements confirmed the presence of Re=O multiple bonds and ensured that the multidentate ligands were coordinated as evidenced by the absorptions shifted in comparison with the free ligands. Both ^1H NMR and $^{31}P\{^1H\}$ spectra were very useful in verifying the diastereomeric structures of $[Re_2O_2Cl_2(PPh_3)_2(\mu\text{-}P_2O_4)]$ and $[(n\text{-}Bu)_4N]_2[Re_2O_2Br_4(\mu\text{-}P_2O_4)]$ (vide infra).

Dinuclear (P_2O_4) Re complexes

Mass spectrometric data confirmed formation of dinuclear complexes when the expected parent ions and (or) their fragments were found, while microanalysis established the formulation of both compounds. The parent ion

Fig. 1. $^{31}P\{^1H\}$ NMR spectra (81 MHz) showing reactivity of the dinuclear complexes to pyridine (* decomposition products). (*a*) $[Re_2O_2Cl_2(PPh_3)_2(\mu\text{-}P_2O_4)]$ in py-d_5; (*b*) *a* after standing for 6 months; (*c*) *b* after being heated to 100°C then cooled to room temperature; (*d*) $[(n\text{-}Bu)_4N]_2[Re_2O_2Br_4(\mu\text{-}P_2O_4)]$ in acetone-d_6; (*e*) *d* after 3 drops of py-d_5 were added; (*f*) *e* after being heated to 60°C then cooled to room temperature.

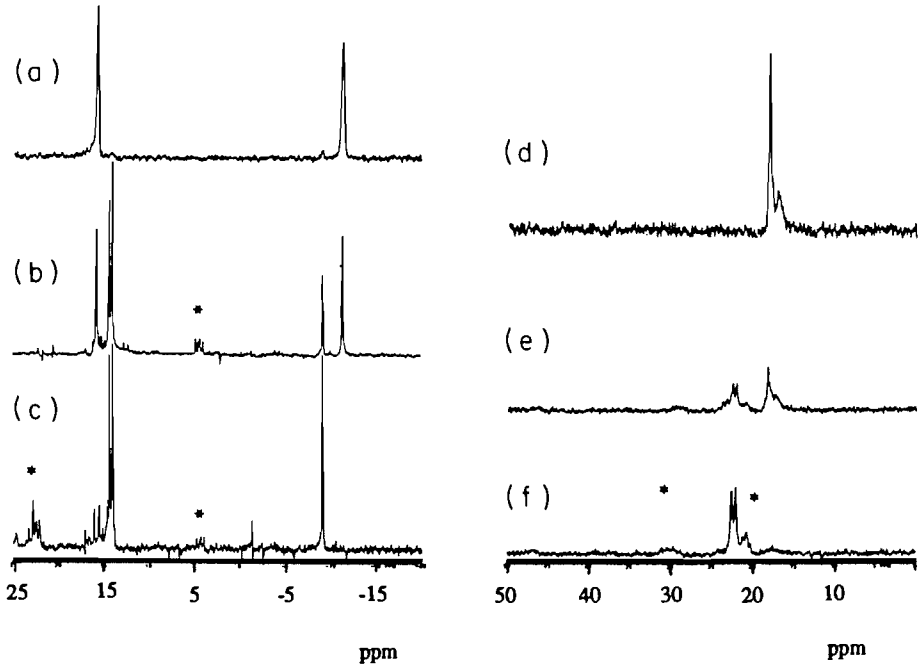

$[Re_2O_2Cl_2(PPh_3)_2(\mu\text{-}P_2O_4) + 1]^+$ (*m/z* = 1459) was present in the +LSIMS spectrum of $[Re_2O_2Cl_2(PPh_3)_2(\mu\text{-}P_2O_4)]$; however, the stronger peaks were *m/z* = 263 (PPh_3), 645 ($[Re(P_2O_4)]^+$), and 1161 ($[M - Cl - PPh_3]^+$ or $[Re_2O_2Cl(PPh_3)(\mu\text{-}P_2O_4)]^+$), indicating that the monodentate Cl^- or PPh_3 ligands were subject to dissociation from the complex under the ionization conditions. For the positive ion detection mode LSIMS spectrum of $[(n\text{-}Bu)_4N]_2[Re_2O_2Br_4(\mu\text{-}P_2O_4]$, *m/z* = 242 ($[(n\text{-}Bu)_4N]^+$) was intense, and a much weaker peak for $[Re(P_2O_4)]^+$ was also found; in the negative ion detection mode, *m/z* = 79 (Br^-) was the most intense peak, with fragments found at *m/z* = 661 ($[ReO(P_2O_4)]^-$) and 769 ($[ReO(P_2O_4) + 108]^-$). The mass of 108 is that of the matrix, thioglycerol ($C_3H_8O_2S$). The dianionic parent ion $[Re_2O_2Br_4(\mu\text{-}P_2O_4)]^{2-}$ did not show in the negative ion mode, presumably due to a very strong interaction with the very polar matrix, thioglycerol, preventing the volatilization of the dianion.

There were similarities in the IR spectra of the two dinuclear complexes. Strong C–H stretching vibrations at 2960 and 2880 cm^{-1}, diagnostic for $[(n\text{-}Bu)_4N]^+$, were observed for $[(n\text{-}Bu)_4N]_2[Re_2O_2Br_4(\mu\text{-}P_2O_4)]$. Below 2000 cm^{-1}, almost all the absorptions in the spectrum of $[(n\text{-}Bu)_4N]_2[Re_2O_2Br_4(\mu\text{-}P_2O_4)]$ were observed in the spectrum of $[Re_2O_2Cl_2(PPh_3)_2(\mu\text{-}P_2O_4)]$ as well. The Re=O stretches for $[(n\text{-}Bu)_4N]_2[Re_2O_2Br_4(\mu\text{-}P_2O_4)]$) and $[Re_2O_2Cl_2(PPh_3)_2(\mu\text{-}P_2O_4)]$) were found at 960 and 965 cm^{-1}, respectively, in the normal range for six-coordinate $Re^V{=}O$ complexes (13). The additional bands in $[Re_2O_2Cl_2(PPh_3)_2(\mu\text{-}P_2O_4)]$ originated from PPh_3 bound to the Re(V) center.

A seven-coordinate complex, as formed from Tc(V) and $edta^{4-}$ (4), did not seem feasible for Re(V) with $P_2O_4^{4-}$. In $[TcO(edta)]^-$, the two neutral tertiary amine N atoms are approximately opposite the oxo ligand, the Tc—N bonds being somewhat lengthened by the *trans* influence (14). Thus, one consideration for $P_2O_4^{4-}$ is that the phosphine P atom, which is much softer than the amine N atom, will be found in *cis* positions relative to the oxo group to avoid the *trans* influence (as soft, neutral donors usually do). The phenolate rings of $P_2O_4^{4-}$ are also considerably less flexible than the carboxylate arms of $edta^{4-}$.

The $^{31}P\{^1H\}$ NMR spectrum of $[Re_2O_2Cl_2(PPh_3)_2(\mu\text{-}P_2O_4)]$ showed two peaks of equal intensity, diagnostic for two nonequivalent phosphorus centers (Fig. 1*a*). This suggested that the two $\mu\text{-}P_2O_4^{4-}$ P nuclei were equivalent, as were the two PPh_3 P nuclei. Consistent with this, in the ^1H NMR spectrum (Fig. 2) there were eight types of aromatic hydrogen nuclei for the PO-phenyl rings of the complex, indicating that the four phenolate rings of the $\mu\text{-}P_2O_4^{4-}$ ligand were in two different environments, each including two equivalent rings. In this aromatic region, a doublet of doublets (7.70 ppm, *o*-H) and overlapped multiplets (~7.3 ppm, *m*-H and *p*-H) were also present, corresponding to the phenyl H nuclei of PPh_3 (Fig. 2). The four H and two P nuclei on the ethylene backbone form an AA′BB′XX′ spin system (one per diastereomer) because of chirality at the metal centre (Fig. 3, *anti*). The *syn* diastereomer was not present for this neutral dinuclear complex (vide infra). The appearance of two resonances (one triplet-like, the other doublet-like) corresponding to the H_A and H_B nuclei was complicated because of multiple couplings.

For $[(n\text{-}Bu)_4N]_2[Re_2O_2Br_4(\mu\text{-}P_2O_4)]$, two peaks were observed in the $^31P\{^1H\}$ spectrum, one major and one minor, at 18.0 and 17.0 ppm, respectively (Fig. 1*d*). In the ^1H NMR spectrum, there were more than eight signals for the PO-phe-

Fig. 2. ^{1}H NMR spectra of $[Re_2O_2Cl_2(PPh_3)_2(\mu\text{-}P_2O_4)]$ (top, in py-d_5, 300 MHz) and $[(n\text{-}Bu)_4N]_2[Re_2O_2Br_4(\mu\text{-}P_2O_4)]$ (bottom, in acetone-d_6, 400 MHz), (# solvent or HOD; * impurity).

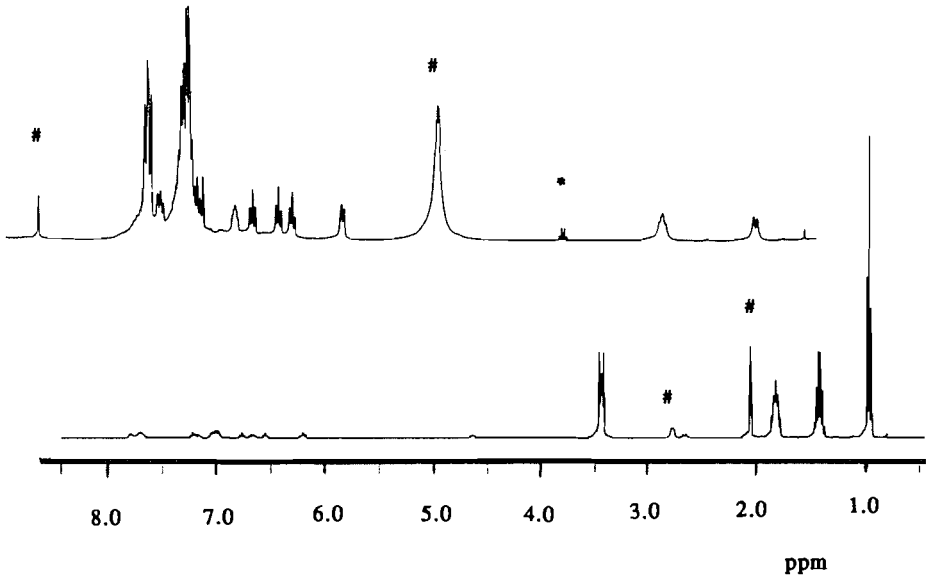

Fig. 3. Diastereomers of the dinuclear complexes showing the AA'BB'XX' system of the backbone (4H, 2P) in each.

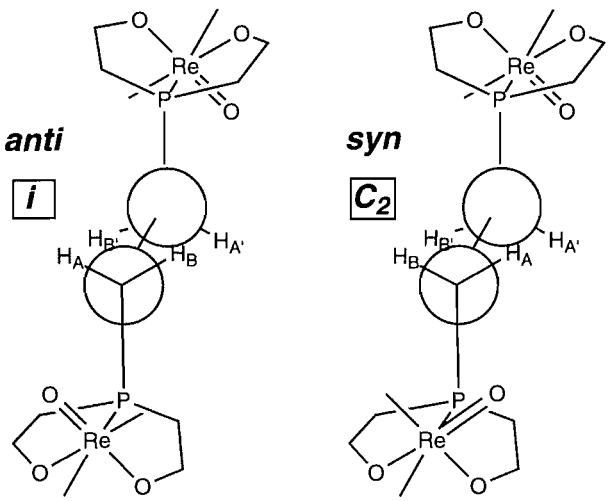

nyl rings in the complex (Fig. 2). In fact, 16 H signals (some of them overlapped) in the aromatic region (6.0–8.0 ppm) were correlated into four groups by a ^{1}H-^{1}H COSY experiment (Fig. 4), indicating that there were four PO-phenyl ring environments (numbered ring 1 to ring 4 as shown in Fig. 4). The H resonances corresponding to the *o'*-H of the four PO-phenyl rings were identified in the ^{1}H{^{31}P} NMR spectrum (each simplified from a multiplet to a doublet upon decoupling as shown in Fig. 5). The ^{1}H NMR signals corresponding to rings 1 and 4 were stronger in intensity than those of rings 2 and 3, and the ^{31}P NMR signal at 18.0 ppm was more intense than that at 17.0 ppm. Taken together, these data indicate that there are one major and one minor isomer present in the $[(n\text{-}Bu)_4N]_2[Re_2O_2Br_4(\mu\text{-}P_2O_4)]$ sample. In the ^{13}C{^{1}H} NMR spectrum, only eight signals were observed in the aromatic region, tentatively assigned to the major isomer eight PO-phenyl ring carbon atoms that had hydrogen atoms attached; those of the minor isomer, and quaternary carbons in both isomers, were not observed because the sample was too dilute. For the ethylene H nuclei, a similar AA'BB'XX' spin system was observed for $[(n\text{-}Bu)_4N]_2[Re_2O_2Br_4(\mu\text{-}P_2O_4)]$, and H_A and H_B were found to be coupled strongly to each other. The chemical shifts for the C_2H_4 ethylene H nuclei of the backbone of each isomer coincide since only two resonances are present. Upon phosphorus decoupling, both H_A and H_B signals appeared as doublets.

Two models, *anti* (*i*) and *syn* (C_2), proposed for the dinuclear complexes are shown in Fig. 3. Assumptions with adequate precedent have been used to formulate these models: neutral P donor(s) are *cis* to the Re=O, and the PO_2 donor set of each end of $P_2O_4^{4-}$ is facially coordinated. Both assumptions are based on the coordination of PO_2^{2-} in *fac*-$[ReZCl(PPh_3)(PO_2)]$ (Z = O or NPh) (1). In fact, P *trans* to M=O, M≡N, or M=NR has not been observed for complexes of this type (M = Re or Tc) incorporating phosphine (11, 15–22) or functionalized phosphine (1, 23, 24) ligands; the P donors are always *cis*.

The two models can be described as *syn* and *anti* with respect to the two Re=O groups, and they have C_2 and *i* symmetry, respectively (Fig. 3). With aid of a 3-D model, it is easy to reason why there is only one isomer for $[Re_2O_2Cl_2(PPh_3)_2(\mu\text{-}P_2O_4)]$, while there are two isomers for $[(n\text{-}Bu)_4N]_2[Re_2O_2Br_4(\mu\text{-}P_2O_4)]$, as shown in the ^{31}P NMR spectra (Figs. 1*a* and 1*d*, respectively). $[Re_2O_2Cl_2(PPh_3)_2(\mu\text{-}P_2O_4)]$ exists presumably as the *anti* isomer (*i* symmetry); the *syn* isomer is not feasible because of the two bulky PPh_3 groups. For this complex, a proposal with the two P donors *trans* to each other can also be rejected because the mutual P–P coupling is quite small. Either arrangement with the two P donors *trans* or *cis* to each other is possible based on modeling and has actually been observed for the complexes *fac*-$[ReZCl(PPh_3)(PO_2)]$ (Z = O or NPh) (1). In modeling $[Re_2O_2Br_4(\mu\text{-}P_2O_4)]^{2-}$, both *syn* and *anti* isomers are found to

Fig. 4. The proposed isomers and the ^1H–^1H COSY spectrum (400 MHz) of $[(n\text{-}Bu)_4N]_2[Re_2O_2Br_4(\mu\text{-}P_2O_4)]$ (aromatic region); the correlated H resonances are designated by the same number as the respective PO phenyl ring.

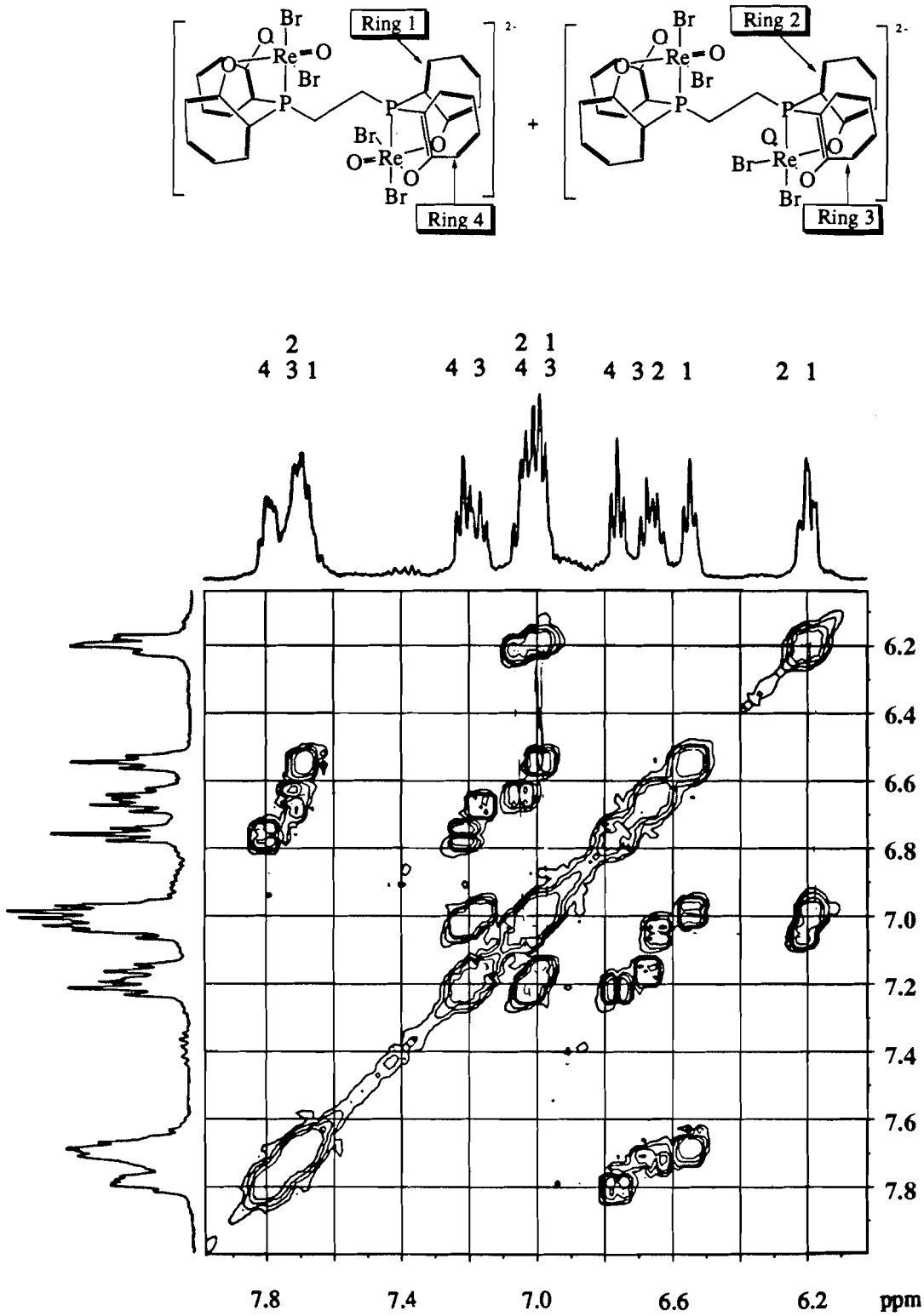

be feasible as Br^- is much less bulky, and this might be the case as indicated by the NMR results.

The two P signals at 15.7 and −11.3 ppm in the $^{31}P\{^1H\}$ NMR spectrum (Fig. 1*a*) for $[Re_2O_2Cl_2(PPh_3)_2(\mu\text{-}P_2O_4)]$ are assigned to the P nuclei of the $\mu\text{-}P_2O_4^{4-}$ and PPh_3 ligands, respectively. Phenolato-anchored phosphine P nuclei experience a greater deshielding effect than the PPh_3 ligand in such complexes as $[ReZCl(PO_2)(PPh_3)]$ (Z = O or NPh) (1), due to

Fig. 5. ^1H (top) and $^1H\{^{31}P\}$ (bottom) NMR spectra (500 MHz) of $[(n\text{-}Bu)_4N]_2[Re_2O_2Br_4(\mu\text{-}P_2O_4)]$ (aromatic and ethylene regions).

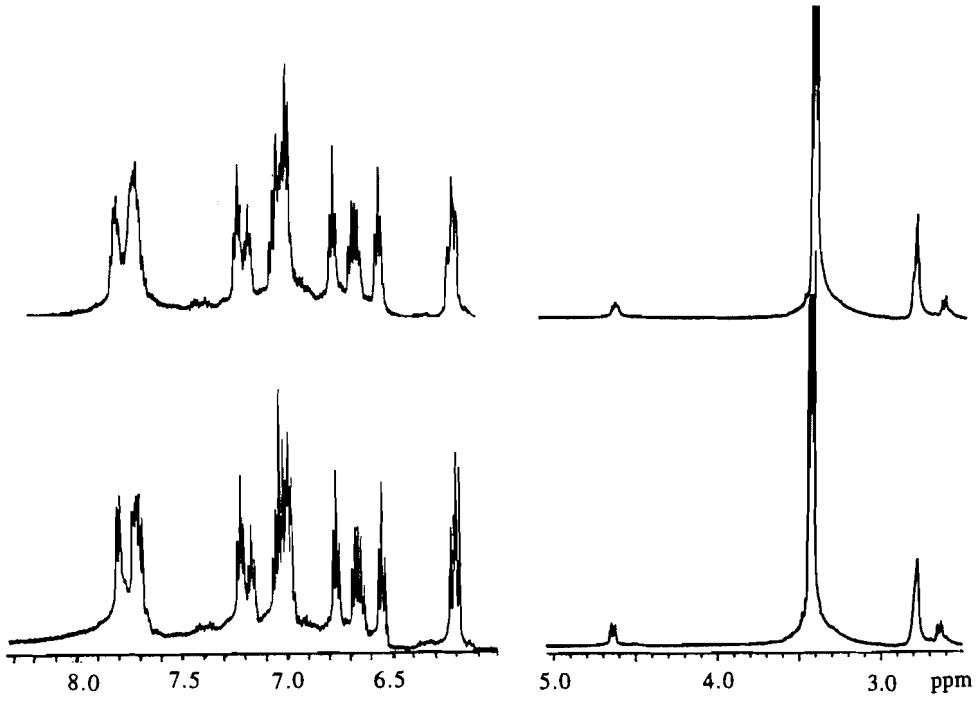

stronger donation (25). This $\mu\text{-}P_2O_4^{4-}$ P chemical shift was found to be quite close to that of $[(n\text{-}Bu)_4N]_2[Re_2O_2Br_4(\mu\text{-}P_2O_4)]$, at 18.0 (major) and 17.0 (minor) ppm (Fig. 1*d*). Further support for this assignment is depicted by Fig. 1*c*, where the PPh_3 P signal is identified by its replacement with py-d_5.

Reactivity with pyridine

The replacement of PPh_3 in $[Re_2O_2Cl_2(PPh_3)_2(\mu\text{-}P_2O_4)]$ with pyridine (py-d_5) was monitored in the $^{31}P\{^1H\}$ NMR spectrum by the appearance of a free PPh_3 singlet at −9.1 ppm, and by the decrease in intensity of the upfield P signal (−11.3 ppm, bound PPh_3) in the original spectrum (Fig. 1*c*). The substitution is very slow (Fig. 1*b*); however, after the solution was heated to 100°C and then cooled to room temperature, the substitution was complete, at which time the bound PPh_3 P signal (−11.3 ppm) disappeared completely, and the downfield P signal (15.7 ppm) was replaced by two singlets (14.3 and 14.0 ppm). Clearly, the PPh_3 ligands in the complex are labile and the assignment of the bound PPh_3 in the original $^{31}P\{^1H\}$ NMR spectrum is verified. No attempt was made to fully characterize the new complex formed with pyridine; however, *syn* and *anti* isomers would be consistent with the appearance of the two singlets at 14.3 and 14.0 ppm.

Pyridine (py-d_5, 3 drops) was added to $[(n\text{-}Bu)_4N]_2[Re_2O_2Br_4(\mu\text{-}P_2O_4)]$ in acetone-d_6. Changes in the ^{31}P resonances were also observed in the $^{31}P\{^1H\}$ NMR spectrum: the original peaks were reduced in intensity, while two new singlets appeared (Fig. 1*e*). After heating to 60°C for 10 min and then cooling to room temperature (the solution changed to yellowish green from the original emerald green), these spectral changes were complete, whereupon the original P signals (18.0 and 17.0 ppm) disappeared completely, giving rise to two singlets at 22.1 and 22.6 ppm (Fig. 1*f*). The dianionic complex is also labile to substitution. Again, similar *syn* and *anti* isomers would be consistent with the substituted products.

Conclusion

The hydrochloride salt of a new ligand, the potentially hexadentate and tetraprotic $H_4P_2O_4{\cdot}2HCl$, was synthesized and characterized. With this salt, neutral $[Re_2O_2Cl_2(PPh_3)_2(\mu\text{-}P_2O_4)]$ and dianionic $[Re_2O_2Br_4(\mu\text{-}P_2O_4)]^{2-}$ dinuclear rhenium(V) complexes were synthesized and characterized. The rigidity of the ligand frame and (or) *trans* influence make it impossible for all the donor atoms to bind a single $Re^V{=}O$ centre. However, this ligand can bridge two Re(V) centers, incorporating monodentate oxo, chloro, and PPh_3 ligands to complete the coordination sphere of each Re(V). These complexes are important since they provide useful information about the coordination preference of the $P_2O_4^{4-}$ ligand. Work on the $^{99}Tc/^{99m}Tc$ complex of this ligand and its radiopharmaceutical chemistry is in progress.

Acknowledgments

We wish to thank the Natural Sciences and Engineering Research Council of Canada, the British Columbia Health Research Foundation, and the Du Pont Merck Pharmaceutical Company for operating grants, Johnson Matthey, Inc. for NH_4ReO_4, and Mr. G. Clentsmith and Professor M. D. Fryzuk for a sample of $Cl_2PCH_2CH_2PCl_2$.

References

1. H. Luo, I. Setyawati, S.J. Rettig, and C. Orvig. Inorg. Chem. **34**, 2287 (1995).
2. E. Deutsch. Radiochim. Acta, **63**, 195 (1993).

3. E. Deutsch, A.R. Ketring, K. Libson, J.-L. Vanderheyden, and W.W. Hirth. Nucl. Med. Biol. **16**, 191 (1989).
4. G. Bandoli, U. Mazzi, E. Roncari, and E. Deutsch. Coord. Chem. Rev. **44**, 191 (1982).
5. H.B. Burgi, G. Anderegg, and P. Blauenstein. Inorg. Chem. **20**, 3829 (1981).
6. R.J. Burt, J. Chatt, W. Hussain, and G.J. Leigh. J. Organomet. Chem. **182**, 203 (1979).
7. J.P. Yardley and H. Fletcher 3rd. Synthesis, 244 (1976).
8. F.A. Cotton and S.J. Lippard. Inorg. Chem. **5**, 9 (1966).
9. T.B. Rauchfuss. Inorg. Chem. **16**, 2966 (1977).
10. J.C. Tebby. *In* Phosphorus-31 NMR spectroscopy in stereochemical analysis. *Edited by* J.G. Verkade and L.D. Quin. VCH, Deerfield Beach, Fla. 1987. p. 1.
11. A.-M. Lebuis and A.L. Beauchamp. Can. J. Chem. **71**, 441 (1993).
12. H. Luo, S.J. Rettig, and C. Orvig. Acta Crystallogr. In press.
13. W.A. Nugent and J.M. Mayer. Metal–ligand multiple bonds. John Wiley & Sons, New York. 1988. p. 116.
14. M.J. Clarke and P.H. Fackler. Struct. Bonding (Berlin), **50**, 57 (1982).
15. T. Nicholson, A. Davison, J.A. Zubieta, Q. Chen, and A.G. Jones. Inorg. Chim. Acta, **230**, 205 (1995).
16. M. Abrams, S.K. Larsen, S.N. Shaikh, and J. Zubieta. Inorg. Chim. Acta, **185**, 7 (1991).
17. U. Abram, B. Lorenz, L. Kaden, and D. Scheller. Polyhedron, **7**, 285 (1988).
18. E. Forsellini, U. Casellato, R. Graziani, M.C. Carletti, and L. Magon. Acta Crystallogr. Sect. C: Cryst. Struct. Commun. **C40**, 1795 (1984).
19. L. Kaden, B. Lorenz, K. Schmidt, H. Sprinz, and M. Wahren. Isotopenpraxis, **17**, 174 (1981).
20. G. Rouschias. Chem. Rev. **74**, 531 (1974).
21. J. Chatt, J.D. Garforth, N.P. Johnson, and G.A. Rowe. J. Chem. Soc. 1012 (1964).
22. K.A. Conner and R.A. Walton. *In* Comprehensive coordination chemistry. Vol. 4. *Edited by* G. Wilkinson, R.D. Gillard, and K.A. McCleverty. Pergamon, Oxford. 1987. p. 125.
23. F. Refosco, F. Tisato, G. Bandoli, C. Bolzati, A. Dolmella, A. Moresco, and M. Nicolini. J. Chem. Soc. Dalton Trans. 605 (1993).
24. F. Tisato, F. Refosco, A. Moresco, G. Bandoli, A. Dolmella, and C. Bolzati. Inorg. Chem. **34**, 1779 (1995).
25. R.V. Parish. NMR, NQR, EPR, and Mossbauer spectroscopy in inorganic chemistry. 1st ed. *In* Ellis Horwood Ser. Inorg. Chem. *Edited by* J. Burgess. Ellis Horwood, New York. 1990.

An unusual fatty acid and its glyceride from the marine fungus *Microsphaeropis olivacea*[1]

Chao-Mei Yu, Jonathan M. Curtis, Jeffrey L.C. Wright, Stephen W. Ayer, and Ziba R. Fathi-Afshar

Abstract: Two new metabolites (**1** and **2**) were isolated from the marine fungus *Microsphaeropsis olivacea*. The structures were elucidated, through analysis of the spectroscopic data, as an unusual methyl-branched unsaturated fatty acid, 10-methyl-9*Z*-octadecenoic acid (**1**), and the glyceride (**2**). The locations of the double bond and the methyl branching were determined from the electron impact (EI) mass spectrum of the picolinyl derivative of **1** and from MS/MS data on the hydrogenation products of **1** and **2**.

Key words: *Microsphaeropsis olivacea*, marine fungus, methyl-branched unsaturated fatty acid, picolinyl ester.

Résumé : On a isolé deux nouveaux métabolites (**1** et **2**) à partir du champignon marin *Microsphaeropsis olivacea*. Faisant appel à des données spectroscopiques, on a établi que les structures sont associées à un acide gras insaturé portant un méthyle comme chaîne latérale, l'acide 10-méthyloctadéc-9*Z*-ènoïque (**1**) et de son glycéride (**2**). Les positions des doubles liaisons et de la ramification méthyle ont été déterminées par spectrométrie de masse par impact électronique sur le dérivé pinacolyle du composé **1** et par des données de SM/SM sur les produits d'hydrogénation des composés **1** et **2**.

Mots clés : *Microsphaeropsis olivacea*, champignons marins, acide gras insaturé portant une ramification méthyle.

[Traduit par la rédaction]

Introduction

Terrestrial microorganisms have long been a traditional source of biologically active metabolites but, after extensive studies, it is increasingly difficult to discover new bioactive agents from this source. In contrast, marine microorganisms are attracting more attention as sources of novel bioactive compounds. These ocean-life forms likely evolved different physiological and biosynthetic capabilities to survive in the unique marine environment at increased salinity and pressure, variable temperatures, and different nutrient compositions. Such capabilities may result in the production of metabolites not found previously in terrestrial microorganisms (1).

Our search for new pharmaceutical-lead compounds from marine microbes led us to investigate the metabolites of the marine fungus *Microsphaeropsis olivacea* (strain SF-10), isolated from a Florida sponge, and to the discovery of a new methyl-branched and unsaturated fatty acid (**1**) and its monoglyceride (**2**) (Fig. 1). In this paper, we describe the production, isolation and structure elucidation of **1** and **2** through their chemical and spectroscopic analyses.

Received January 22, 1996.

C.-M. Yu[2] and Z.R. Fathi-Afshar. SynPhar Laboratories Inc., #2 Taiho Alberta Center, 4290-91A Street, Edmonton, AB T6E 5V2, Canada.
J.M. Curtis, J.L.C. Wright, and W. Ayer. Institute for Marine Biosciences, National Research Council of Canada, Halifax, NS B3H 3Z1, Canada.

[1] NRCC No. 39697.
[2] Author to whom correspondence may be addressed.

Results and discussion

Metabolite **1**, a colorless oily compound, was isolated from the EtOAc extract of the culture filtrate of *M. olivacea*. The molecular formula of $C_{19}H_{36}O_2$ was determined from the high-resolution EI mass spectrum. The ^{1}H NMR spectrum indicated that this compound is an unsaturated linear fatty acid, but the unusual structural feature of an olefinic methyl branch (δ_H 1.65, d, 1.2 Hz) encouraged us to complete the structural elucidation. The multiplicity of the individual carbons was obtained by ^{13}C NMR data (Table 1) and DEPT experiments, indicating 1 terminal methyl group, 1 olefinic methyl group, a trisubstituted double bond (thereby implying the branching position of the olefinic methyl group), 14 methylene groups, and a carboxyl carbon (δ_C 178.11) that was supported by a characteristic infrared absorption at 1733 cm^{-1}. The HMQC experiment showed connectivities between the carbons and protons with the exception of C-4–C-7 and C-13–C-17. This is due to the extensive overlaps of the methylene proton resonances in the range δ 1.29–1.31, which correspond to 18 protons.

In the ^{1}H–^{1}H COSY spectrum, the resonance at δ 2.26 was assigned to the methylene protons H_2-2 adjacent to the carboxyl group, based on chemical shift considerations and supported by the long-range C/H correlation with C-1 in the HMBC experiment. This methylene group was also coupled with H_2-3 (δ 1.59), which in turn was coupled with other methylene groups (δ 1.29–1.31) indicating the connectivity of CH_2-2/CH_2-3/other CH_2 groups. In the HMBC experiment the methylene protons at H_2-2 and H_2-3 were observed to have $^3J_{CH}$ correlation with two methylene carbons C-4 (δ 30.29) and C-5 (δ 30.37), respectively, which established the partial

Fig. 1. The structures of metabolites (**1**, **2**) and their derivatives (**3**, **4**, **5**).

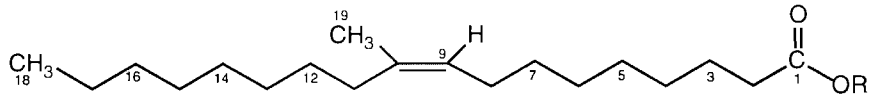

1, R = H; **2**, R = $-CH_2CH(OH)CH_2OH$; **3**, R = $-CH_2$-(N)

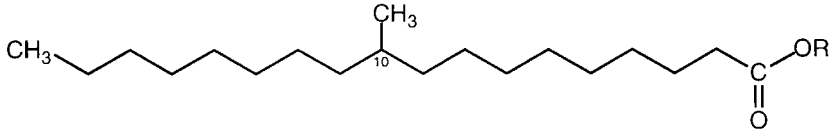

4, R = H; **5**, R = $-CH_2CH(OH)CH_2OH$

Table 1. ^1H and ^{13}C NMR data (CD_3OD) for metabolites **1** and **2**.

	1		**2**	
Position	$\delta^{13}C$ (ppm)	δ^1H (ppm)	$\delta^{13}C$ (ppm)	δ^1H (ppm)
1	178.11	—	175.50	—
2	35.18	2.26 (t)	34.94	2.34 (t)
3	26.19	1.59 (m)	26.01	1.61 (m)
4	30.29[a]	1.29–1.31 (m)	30.22[a]	1.29–1.31 (m)
5	30.37[a]	1.29–1.31 (m)	30.35[a]	1.29–1.31 (m)
6	30.46[b]	1.29–1.31 (m)	30.45[c]	1.29–1.31 (m)
7	31.16[a]	1.29–1.31 (m)	31.17[a]	1.29–1.31 (m)
8	28.78	1.97 (m)	28.79	1.97 (m)
9	126.34	5.11 (t)	126.34	5.11 (m)
10	136.36	—	136.37	—
11	32.60	2.01 (t)	32.60	2.01 (t)
12	29.10	1.37 (m)	29.09	1.37 (m)
13	30.29[b]	1.29–1.31 (m)	30.28[c]	1.29–1.31 (m)
14	30.61[b]	1.29–1.31 (m)	30.60[c]	1.29–1.31 (m)
15	30.66[b]	1.29–1.31 (m)	30.66[c]	1.29–1.31 (m)
16	33.08[a]	1.29–1.31 (m)	33.07[a]	1.29–1.31 (m)
17	23.75[a]	1.29–1.31 (m)	23.75[a]	1.29–1.31 (m)
18	14.45	0.89 (t)	14.45	0.90 (t)
19	23.64	1.65 (d)	23.63	1.65 (d)
1′	—	—	66.48	4.05 (dd), 4.13 (dd)
2′	—	—	71.15	3.80 (m)
3′	—	—	64.07	3.54 (dd), 3.55 (dd)

[b,c]Assignments with the same superscript may be interchanged.
[a]Assigned from the HMBC spectrum.

structure -$CH_2CH_2CH_2CH_2COOH$ and the assignments of C-4 and C-5.

From further interpretation of the ^1H–^1H COSY data, it was found that an olefinic methine proton H-9 (δ 5.11) showed adjacent coupling with H_2-8 (δ 1.97) and allylic couplings with the olefinic methyl group H_3-19 (δ 1.65) as well as H_2-11 (δ 2.01). Each of H_2-8 and H_2-11 was further coupled with other methylene groups of the long hydrocarbon chain at δ 1.29–1.31. The HMBC between C-7/H_2-8, C-10/H_2-8, C-9/H_2-11, C-9/H_3-19, C-10/H_2-11, C19/H_2-11, and C-12/H_2-11 helped in the assignment of C-7, and provided further support for the observed ^1H–^1H COSY correlations and determined the partial structure -$CH_2CH_2C(CH_3)$=$CHCH_2CH_2$-.

The final partial structure of $CH_3CH_2CH_2$- was identified from the HMBC from both C-16 (δ 33.08) and C-17 (δ 23.75) to the terminal methyl group H_3-18 (δ 0.89). Therefore, the combined NMR data led to a structural formula of **1** as $CH_3CH_2CH_2(CH_2)_nCH_2CH_2(CH_3)C$=$CHCH_2CH_2(CH_2)_mC$ $H_2CH_2CH_2CH_2COOH$ where n and m could not be determined from the NMR data alone.

Fig. 2. The low-resolution EI mass spectrum of **3** from GC/MS analysis.

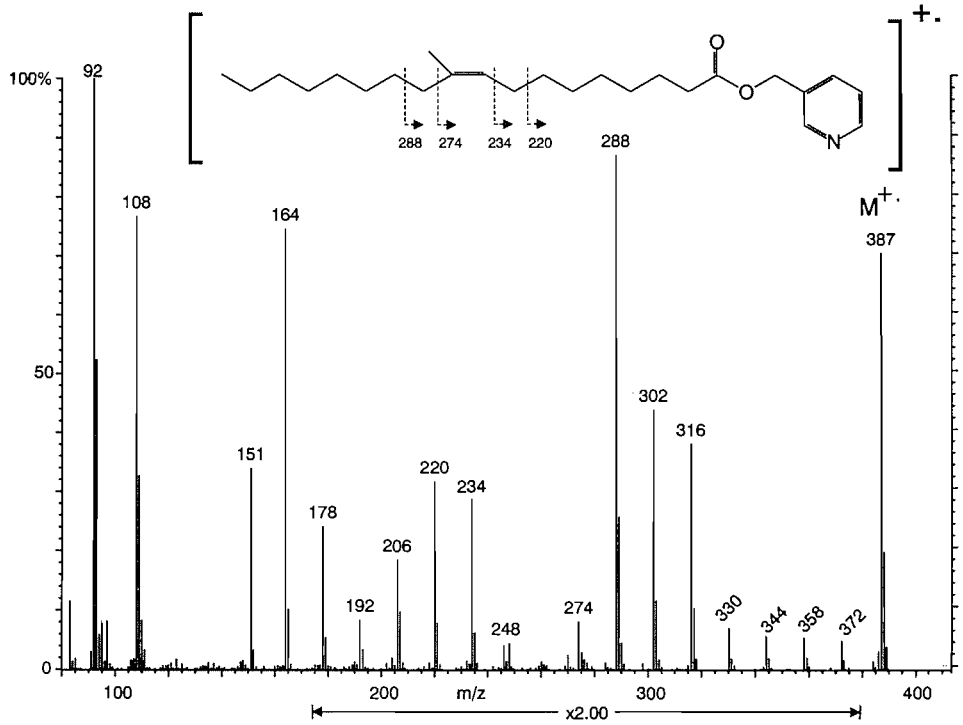

The major difficulties usually encountered in the structure elucidation of long-chain fatty acids by NMR involve the determination of the positions of methyl branching and double bonds. However, location of the double bonds and methyl branching in long-chain fatty acids can be achieved via EIMS analysis of derivatives that strongly localize the charge, for example, on a pyridine ring (2). In this case, the 3-picolinyl ester (**3**) of **1** was prepared (3), and GC/MS analysis of **3** showed the expected molecular ion at *m/z* 387 (Fig. 2). It was anticipated that a diagnostic difference of 40 mass units, corresponding to the trisubstituted double bond -(CH_3)C=CH-, would be found between adjacent ions in the series of charge-remote fragmentations (2). In general, the fragment ions corresponding to vinylic cleavages are of relatively low intensity whereas those due to cleavage at the allylic positions are more intense (2). Furthermore, an enhancement in fragment ion intensity for cleavage at the allylic position on the distal side of the double bond is expected (4). This behavior is clearly seen for **3** in Fig. 2 where the difference of 40 mass units between *m/z* 234 and 274 establishes the location of the double bond. In addition, the enhanced intensity of the peak at *m/z* 288, due to fragmentation at the allylic position, confirms that the weaker peak at *m/z* 274 is indeed due to fragmentation adjacent to the double bond.

Thus, the GC/MS analysis of the 3-picolinyl ester of **1** unambiguously assigned the position of the double bond as Δ^9. However, the data cannot distinguish between a branching position for the methyl group at either C-9 or C-10. To establish this, it was necessary to reduce **1** to the methyl-branched saturated derivative **4**. As previously reported (5), under appropriate conditions for collision-induced decomposition, molecular carboxylate anions of such saturated fatty acids undergo charge-site-remote fragmentations (in an analogous manner to picolinyl ester derivatives of fatty acids in the positive ion mode), resulting in a series of fragment ions characteristic of the alkyl chain. Thus, from the electrospray MS/MS spectrum (Fig. 3) of the $[M - H]^-$ ion of **4** at *m/z* 297, the position of methyl branching was determined by a mass difference of 28 (-$CH(CH_3)$-) rather than 14 (-CH_2-) between the adjacent fragment ions *m/z* 183 and *m/z* 155, proving that the methyl branch is at C-10.

Metabolite **2** was isolated from the CH_2Cl_2 extract from mycelium of *M. olivacea* as a colorless oily compound. The ^1H and ^{13}C NMR data (Table 1) showed signals almost identical with those of **1** except for the additional characteristic signals of a glycerol moiety (H_2-1′: 4.05 (dd), 4.13 (dd); H-2′: 3.80 (m) and H_2-3′: 3.54 (dd), 3.55 (dd)). This suggested that **2** was the glyceride ester of **1**. Further support for this hypothesis was provided by the high-resolution EI mass spectrum, which indicated the expected molecular formula of $C_{22}H_{42}O_4$ plus accurate mass measurement for the fragment ion at *m/z* 278 measured as the formula $C_{19}H_{34}O$ corresponding to the loss of a glycerol molecule. Analysis of **2** by electrospray mass spectrometry in the positive ion mode gave major peaks at *m/z* 371 (MH^+), 393 ($[M + Na]^+$), and 353 ($[MH - H_2O]^+$). The MS/MS spectrum of the MH^+ ion (Fig. 4*a*) shows a major fragment ion at *m/z* 279, once again due to loss of a glycerol moiety, plus a minor fragment at *m/z* 297, which is the protonated fatty acid. The position of the substituted double bond is recognized as Δ^9, the same as that of **1**, from the MS/MS spectrum of the $[M + Na]^+$ ion (Fig. 4*b*). The observed series of charge-remote fragment ions from *m/z* 378 down to *m/z* 294 are due to losses of increasingly large neutral fragments incorporating varying numbers of methylene groups, and the 68 mass unit difference between *m/z* 294 and 226 indicated cleavage at the allylic positions. Interestingly, there is a change in

Fig. 3. The negative ion electrospray MS/MS spectrum of the $[M - H]^-$ ion of **4**.

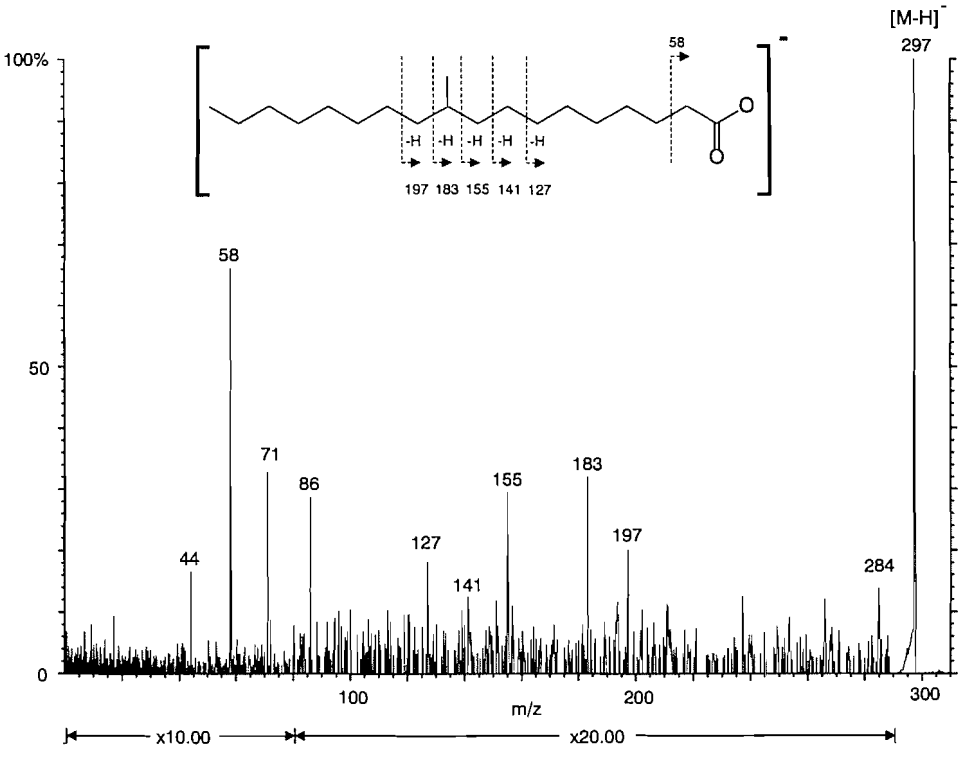

the dominant fragmentation mode, from simple radical cleavage giving rise to the series from *m/z* 294 to 378 to one involving loss of a hydrogen to give the fragment ions at *m/z* 225, 197, 183, and 169. The position of the methyl branch in **2** was verified by the preparation of the hydrogenation product (**5**) (Fig. 1) and subsequent MS analysis. This gave an $[M - H]^-$ ion at *m/z* 371 in the negative ion electrospray mass spectrum. The MS/MS fragmentation of this ion exhibited only one fragment ion at *m/z* 297, which is the stable carboxylate anion formed by loss of the glyceride moiety. The MS/MS spectrum of this fragment ion at *m/z* 297 (which was present in the electrospray mass spectrum of **5**) shows fragmentation identical to that of **4** (Fig. 3), confirming that the methyl group is located at C-10.

The stereochemistry of the double bond in **1** and **2** was established as *Z* configuration from the NOESY spectrum, which showed the through-space correlations between H_3-19 and H-9, H_3-19 and H_2-12, and between H-9 and H_2-7. Based on these combined data, the structures of 10-methyl-9*Z*-octadecenoic acid and 2,3-dihydroxypropyl-10-methyl-9*Z*-octadecenate were assigned to **1** and **2** respectively (Fig. 1).

Different fatty acids possessing an olefinic methyl branch, such as 7-methyl-7-hexadecenoic acid and 7-methyl-6*E*-hexadecenoic acid, have been reported from whale oil (6) and sponge (7), respectively. To our knowledge, **1** and **2** are the first examples of fungal fatty acids having a methyl branch on a *cis*- double bond. Branched methyls can be introduced in fatty acids through the addition of C_1 units, such as *S*-adenosyl methionine, or by introduction of an isoprenoid unit. This fatty acid probably arose through the former biosynthetic pathway.

Experimental

General experimental procedures

NMR spectra were recorded in CD_3OD using a Bruker AMX 500 spectrometer equipped with a Bruker X-32 computer using UXNMR software. Chemical shifts are expressed relative to internal standard (CD_3OD: δ_H 3.30 ppm, δ_C 49.00 ppm). The IR spectrum was measured using a Bomem FT-IR spectrometer (model DA3.02) using a solid film of sample deposited on an AgCl window, and the UV spectrum was obtained using a Hewlett–Packard 1090 HPLC equipped with diode array detector. All EIMS experiments (GC/MS and high-resolution EI) were performed using a VG Organic ZAB-EQ mass spectrometer. GC/MS analysis was carried out on a Hewlett–Packard 5890 Series II GC with a J & W DB225 GC column (30 m × 0.25 mm i.d., 0.25 mm phase thickness). All electrospray and MS/MS experiments were performed using a VG Organic AutoSpec-oaTOF hybrid double-focusing orthogonal acceleration time-of-flight mass spectrometer. MS/MS experiments used a collision energy of 400 eV and Xe collision gas. 3-Pyridylcarbinol was purchased from Aldrich Chemical Company, Milwaukee, Wis.

Fermentation

The producing microorganism identified as *Microsphaeropsis olivacea* was isolated from a marine sponge, *Agelus sp.*, collected off Sombrero Key East, Florida. One loopful of a culture of *M. olivacea* (strain F-10) from an agar slant was used to inoculate five 500-mL Erlenmeyer flasks, each containing media (100 mL) composed of 2.5% glucose and 2.5% pharma-

Fig. 4. The positive ion electrospray MS/MS spectra of **2**: (*a*) $[M + H]^+$, (*b*) $[M + Na]^+$.

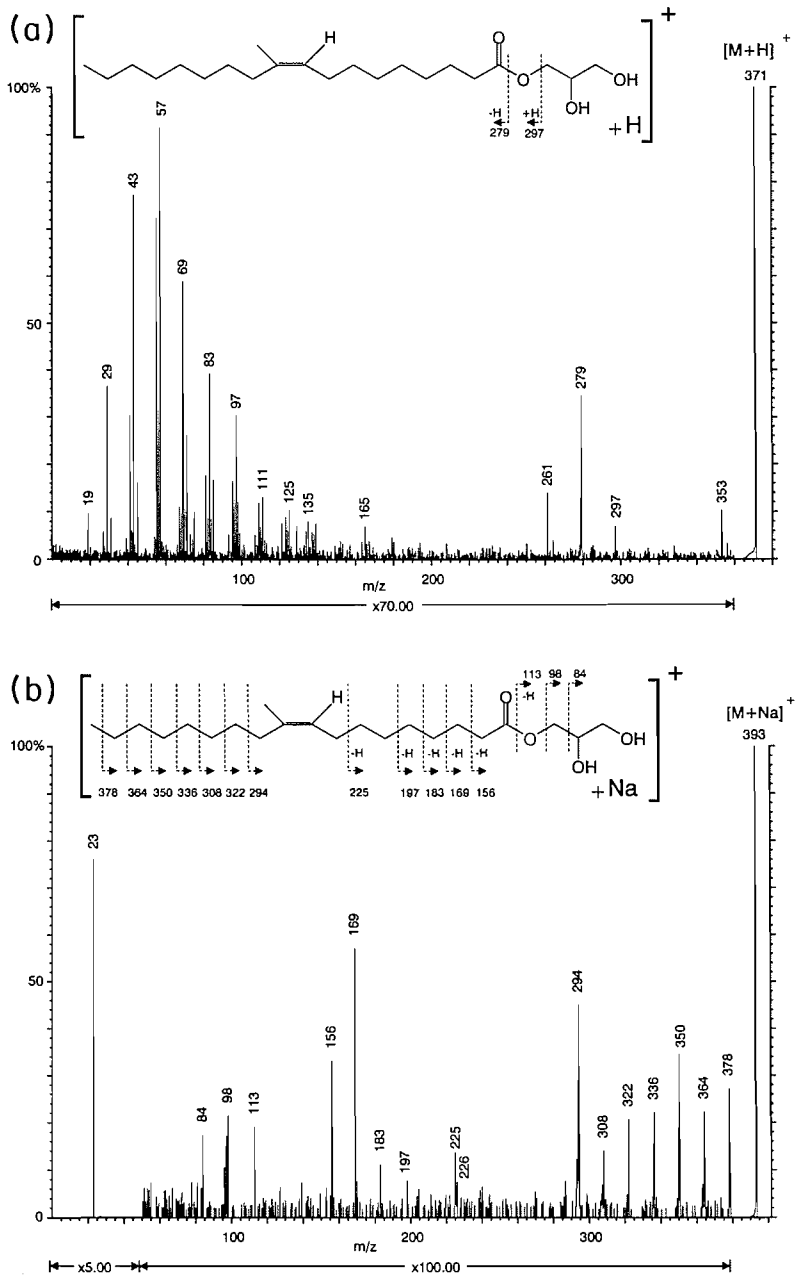

media, and incubated on a rotary shaker (210 rpm) for 3 days at 25°C. The broth (5 mL) of this seed culture was inoculated into each of 60 500-mL Erlenmeyer flasks containing production medium (100 mL) composed of 2% molasses, 3% dextrin, 1.5% fish meal, and 1.5% pharmamedia. The fermentation was carried out under the same conditions for 7 days. The culture broth was filtered, respectively, through a cloth filter and a Millipore filter with pore size of 0.8–8.0 μm. The mycelium was lyophilized for the extraction.

Extraction and isolation

*Isolation of **1** from the EtOAc extract of the culture filtrate*
The crude extract (650 mg) was subjected to reversed phase flash column chromatography on Bakerbond® C-18 eluting with an increasing step gradient of methanol in H_2O (60–100%). The fraction eluted with 95% MeOH was rechromatographed on Bakerbond® C-18 eluting with 85% acetonitrile in H_2O. Final purification of **1** was achieved using normal phase flash column chromatography (Merck silica gel 60) and elution with CH_2Cl_2/MeOH (9.3:0.7) to yield 7 mg of **1**.

*Isolation of **2** from the CH_2Cl_2 extract of the mycelia*
This extract (6 g) was obtained through partition of the MeOH extract of the mycelia between H_2O and CH_2Cl_2. It was subjected to flash column chromatography on Merck LiChroprep® RP-18 with gradient elution of MeOH in H_2O (25–100%), and then with MeOH and CH_2Cl_2 (1:1). The fraction

eluted by MeOH was fractionated by a flash column on Bakerbond® C-18 using acetonitrile/H_2O gradient (50–100%). The fraction eluted with 80% acetonitrile was further purified through a flash column on Merck silica gel 60 using hexane and EtOAc (2:3). The fraction containing mainly **2** was finally purified by a flash column on Bakerbond® C-18 eluting with 95% MeOH, to obtain 7.4 mg of the pure metabolite **2**.

Metabolite 1: A colorless oil; R_f value 0.16, TLC on Merck silica gel precoated plate in CH_2Cl_2–MeOH (9.5:0.5); UV (MeOH) λ_{max}: 210 nm; IR (film) cm^{-1}: 3448, 2930, 2858, 1733, 1458. HREIMS, $C_{19}H_{36}O_2$ ($M^{+\bullet}$) *m/z*: 296.2703 (+ΔM 1.2 mmu). ^1H and ^{13}C NMR spectral data are given in Table 1.

Picolinyl derivatization of 1: A small quantity of **1** (0.33 mg) in a 1.0 mL Reacti-Vial™ was treated with 175 μL of thionyl chloride at 100°C for 10 min. The reaction solution was blown down to dryness with a N_2 stream, and then treated with 165 μL of 20% 3-pyridylcarbinol in acetonitrile. The mixture was reacted for 1 min at 100°C. The reaction product (**3**) was identified by GC/MS analysis, *m/z* 387 ($M^{+\bullet}$) and fragment ions shown in Fig. 2.

Hydrogenation of 1: 0.25 mg of **1** was hydrogenated in MeOH over a catalytic amount of PtO_2. The hydrogenation product (**4**) was directly analysed by negative ion electrospray MS: *m/z*: 297 ($[M - H]^-$) and fragment ions shown in Fig. 3.

Metabolite 2: A colorless oil; R_f value 0.23, TLC on Merck silica gel precoated plate in CH_2Cl_2–MeOH (9.5:0.5); UV (MeOH) λ_{max}: 210 nm; IR (film) cm^{-1}: 3400, 2925, 2855, 1740, 1458. HREIMS, $C_{22}H_{42}O_4$ ($M^{+\bullet}$) *m/z*: 370.3085 (ΔM –0.2 mmu), $C_{19}H_{34}O$ $[(M - C_3H_8O_3)^{+\bullet}]$ *m/z* 278.2612 (ΔM –0.3 mmu). Positive ion electrospray MS gave *m/z* 371 (MH^+), 393 ($[M + Na]^+$), and 353 ($[MH - H_2O]^+$). The MS/MS spectra of *m/z* 371 and 393 are shown in Fig. 4. ^1H and ^{13}C NMR spectral data are given in Table 1.

Hydrogenation of 2: 0.50 mg of **2** was hydrogenated in MeOH over a catalytic amount of PtO_2. The hydrogenation product (**5**) was directly analysed by negative ion electrospray, MS *m/z* (%): 371 ($[M - H]^-$, 100), 297 (23). The MS/MS spectrum of the fragment ion *m/z* 297 is virtually identical to that given as Fig. 3 for M^- of **4**.

Acknowledgments

The authors would like to thank R.G. Ackman, Canadian Institute of Fisheries Technology, Halifax, for helpful discussion and information, Kenneth H.N. Chan, Margaret G. Flack, Marshall Greenwell, and Ping Seto for their technical assistance, John A. Walter for useful comments regarding the NMR data, and Don Brewer for the taxonomic identification of *M. olivacea*.

References

1. W. Fenical and P.R. Jensen. *In* Marine biotechnology. Vol. 2. Pharmaceutical and bioactive natural products. *Edited by* D.H. Attaway and O.R. Zaborsky. Plenum Press, New York. 1993. pp. 419–457.
2. D.J. Harvey. Spectrosc. Int. J. **8**, 211 (1990).
3. D.J. Harvey. Biomed. Mass Spectrom. **9**, 33 (1982).
4. W.W. Christie, E.Y. Brechany, and R.T. Holman. Lipids, **22**, 224 (1987).
5. K.B. Tomer, F.W. Crow, and M.L. Gross. J. Am. Chem. Soc. **105**, 5487 (1983).
6. J.C. Pascal and R.G. Ackman. Lipids, **10**, 478 (1975).
7. N.M. Carballeira and J. Restituyo. J. Nat. Prod. **54**, 315 (1991).

Dissociation constants of host–guest complexes of alkyl-bearing compounds with β-cyclodextrin and "hydroxypropyl-β-cyclodextrin"

Oswald S. Tee, Timothy A. Gadosy, and Javier B. Giorgi

Abstract: Dissociation constants (K_d) of host–guest complexes formed from β-cyclodextrin or "hydroxypropyl-β-cyclodextrin" (β-CD and Hp-β-CD) and several types of aliphatic guests (alcohols, alkanesulfonate ions, alkylamines, and α-amino acids), with up to eight carbons in a chain, are reported. These constants were determined by inhibition kinetics and by a spectrofluorometric displacement method based on competition with 1-anilino-8-naphthalenesulfonate ion as a fluorescent probe. The value of K_d for a particular amine is close to that for the corresponding alcohol. For linear alkyl derivatives, there are strong correlations between pK_d ($= -\log K_d$) and the chain length of the guest, with slopes around 0.5, complementing trends that were noted earlier. Furthermore, the strengths of binding of various aliphatic derivatives to β-CD and to Hp-β-CD are close, with K_d values for the two CDs usually being within a factor of 2 of each other. Overall, for the binding of over 50 alkyl-bearing derivatives, there is a good correlation of pK_d for Hp-β-CD with that for β-CD, with unit slope. These observations imply that the binding of simple aliphatic guests to Hp-β-CD is not greatly influenced by the modification of the hydroxyl groups on the primary side of the β-CD cavity but this may not be true for longer aliphatic derivatives ($>C_8$) or for aromatics that penetrate farther into the CD cavity.

Key words: cyclodextrins, host–guest complexes, dissociation constants.

Résumé : On a mesuré les constantes de dissociation (K_d) de complexes hôte–invité formés à partir de β-cyclodextrines ou d'«hydroxypropyl-β-cyclodextrine» (β-CD et Hp-β-CD) et plusieurs types d'invités aliphatiques (alcools, ions alcanesulfonates, alkylamines et acides α-aminés) comportant jusqu'à huit atomes de carbone. On a déterminé ces constantes par l'inhibition de la cinétique et par une méthode de déplacement spectrofluorométrique qui est basée sur une compétition avec l'ion 1-anilino-8-naphtalènesulfonate comme sonde fluorescente. La valeur du K_d pour une amine donnée est très proche de la valeur pour l'alcool correspondant. Pour les dérivés alkyles linéaires, il existe une forte corrélation entre le pK_d ($= -\log K_d$) et la longueur de la chaîne de l'invité; les pentes de 0,5 sont un complément aux tendances notées antérieurement. De plus, les forces de liaison de divers dérivés aliphatiques à la β-CD et à la Hp-β-CD sont très semblables; les valeurs de K_d pour les deux CD sont généralement à l'intérieur d'un facteur de deux l'une par rapport à l'autre. Dans l'ensemble, pour la liaison de plus de 50 dérivés portant des groupes alkyles, il existe une bonne corrélation entre le pK_d de la Hp-β-CD et celui de la β-CD et la pente est égale à l'unité. Ces observations impliquent que la liaison d'invités aliphatiques simples à la Hp-β-CD n'est pas beaucoup influencée par la modification des groupes hydroxyles sur le côté primaire de la cavité de la β-CD; ceci n'est toutefois pas vrai avec les dérivés comportant des chaînes aliphatiques plus longues ($>C_8$) ou pour les dérivés aromatiques qui pénètrent plus dans la cavité de la CD.

Mots clés : cyclodextrines, complexes hôte–invité, constantes de dissociation.

[Traduit par la rédaction]

Introduction

A key feature of Supramolecular Chemistry is non-covalent binding between the constituents of supermolecules (1, 2). Moreover, non-covalent assembly of carefully chosen precursors is easier and faster than conventional synthesis as a means of developing novel catalytic systems and new materials (3). Better understanding of the interactions responsible for non-covalent binding, and their relative importance to molecular recognition, requires knowledge of complexation constants and how they vary with host–guest structure and the medium (2, 4). The present paper reports dissociation constants of complexes formed between two cyclodextrins (CDs) (5) and some aliphatic derivatives in water. Most of the values were specifically required for ongoing studies of the effects of cyclodextrins on reactivity (6–8), while others were obtained for comparative purposes or for future use.

Received January 31, 1995.[1]

O.S. Tee,[2] T.A. Gadosy,[3] and J.B. Giorgi.[4] Department of Chemistry and Biochemistry, Concordia University, Montréal, QC H3G 1M8, Canada.

[1] Revision received January 29, 1996.
[2] Author to whom correspondence may be addressed. Telephone: (514) 848-3348. Fax: (514) 848-2868.
[3] Holder of an NSERC post-graduate scholarship (1991–1995).
[4] Holder of NSERC summer student awards (1993, 1994).

[1] $A + B \underset{K_d}{\overset{K_f}{\rightleftharpoons}} A{\cdot}B$

There are many ways of estimating dissocation constants (K_d) or formation constants ($K_f = 1/K_d$), based on the alteration of some chemical or physical property that is brought about by complexation (eq. [1]) (9). However, for any particular equilibrium the choice between different methods may not be easy since each one has its own specific requirements and limitations. For example, direct spectrophotometric methods require that either A or B or the complex A·B has a suitable absorption, and that there is a well-behaved, measureable spectral change that accompanies complexation. Likewise, the use of inhibition kinetics (10) requires a probe reaction that is not interfered with by the "inhibitor," except by competitive inhibition (11). A further requirement is that the site on the host occupied by the inhibitor/guest is basically the same as that involved in the probe reaction; otherwise the inhibition is not truly "competitive" and misleading results will be obtained (8, 11).

A different type of limitation, one that is common to many analytical methods, is due to the requirement or assumption of very unequal host and guest concentrations ($[A]_0 \gg [B]_0$ or $[B]_0 \gg [A]_0$). This inequality allows for a mathematical simplification inherent to various "graphical" treatments (e.g., Benesi–Hildebrand, Eadie, and Scatchard plots (9)) but often it is a condition that is difficult or even impossible to fulfil. One improvement in the present work results from removal of this constraint. The other main improvement results from nonlinear fitting of saturation data to an appropriate hyperbolic function, rather than the traditional use of a double-reciprocal plots, with their statistical deficiencies (12), or of other methods based on linearization of the data (9).

Methods and results

Using inhibition kinetics, we have determined dissociation constants for complexes of various aliphatic alcohols with β-cyclodextrin (β-CD) and "hydroxypropyl-β-cyclodextrin" (Hp-β-CD) (5). The method is based on the retarding effect of a CD-binding species on the rate of basic cleavage of *m*-nitrophenyl acetate (mNPA) by a CD (8*c*, 10).

Given that there is hydrolysis of the ester (S) in the basic medium, eq. [2], and cleavage through an ester·CD complex, eq. [3], the dependence of the rate constant for ester cleavage on [CD] is as given by eq. [4]. From experiments over a range of CD concentration, [CD], one finds values of k_u, k_c, and K_S, preferably by nonlinear fitting of eq. [4] (6).[5]

[2] $S \xrightarrow{k_u}$ products

[3] $S + CD \underset{K_S}{\rightleftharpoons} S{\cdot}CD \xrightarrow{k_c}$ products

[4] $$k_{obs} = \frac{(k_u K_S + k_c[CD])}{(K_S + [CD])}$$

[5] $[CD] = (k_{obs} - k_u)K_S/(k_c - k_{obs})$

Rearrangement of eq. [4] leads to an expression for [CD] in terms of k_{obs} (eq. [5]), from which one can estimate [CD], as long as k_{obs} is determined under the same conditions as k_u and k_c. In the presence of an inhibitor (I) that also binds to the CD (eq. [6]) the concentration of unbound CD is reduced and k_{obs} is decreased in accord with eq. [4], if $k_c > k_u$, as in the present case. Traditionally (9, 10), experiments are carried out with high $[I]_0 \gg [CD]_0$ so that the approximation $[CD] = [CD]_0 K_d/(K_d + [I]_0)$ is reasonably valid. Between this expression and eq. [5], [CD] can be eliminated to give an equation relating k_{obs} and $[I]_0$ that is suitable for the graphical estimation of K_d.

[6] $CD + I \underset{K_d}{\rightleftharpoons} CD{\cdot}I$

A major problem with the above approach is that it is not always convenient or even possible to maintain the condition that $[I]_0 \gg [CD]_0$, particularly when the inhibitor has a low solubility in water, which is usually the case with species that bind strongly to CDs. Our approach removes requirement of the inequality by calculating K_d values at various $[I]_0$, directly. Using eq. [5], we estimate [CD] for a given $[I]_0$, and then calculate $[CD{\cdot}I] = [CD]_0 - [CD]$, and $[I] = [I]_0 - [CD{\cdot}I] = [I]_0 - ([CD]_0 - [CD])$, taking account of mass balance. Substitution of these concentrations into $K_d = [CD][I]/[CD{\cdot}I]$ leads to an estimate of the desired dissociation constant (eq. [7]). This procedure is carried out for several different $[I]_0$ and the estimates are averaged. The calculations are conveniently carried out using commercial spreadsheet software (see Experimental).

[7] $K_d = [CD]([I]_0 - [CD]_0 + [CD])/([CD]_0 - [CD])$

Table 1 contains K_d values for 18 alcohols and 5 alkanesulfonate ions binding to β-CD and Hp-β-CD, most of which were determined by the inhibition method just outlined. It also contains values taken from the literature, particularly those for β-CD, that were obtained in other ways (13–15).

The inhibition of mNPA cleavage also works well for the binding of aliphatic ketones,[6] but we did not use it for complexes formed by CDs and alkylamines because amines react with esters in basic solution.[7] To circumvent this problem, we developed a methodology based on competition for the CD between a guest and a fluorescent probe, which in the present case is the 1-anilino-8-naphthalenesulfonate anion (ANS). Mathematically, it is similar to the inhibition method, but with specific particularities.

In aqueous solution, the fluorescence of ANS is very weak but in nonpolar media it is much stronger. Likewise, when ANS is bound to CDs (eq. [8]) its fluorescence intensity is enhanced (16) and for 1:1 binding[8] the relative fluorescence F_{rel} (= I_{obs}/I_0) varies with [CD] in accord with eq. [9] (9).

[5] Note that a usual condition of the experiments to characterize the saturation kinetics is that $[S]_0 > [SCD] \ll [CD]$, so that one can set [CD] equal to $[CD]_0$ in eq. [4]. Likewise, for the inhibition experiments, $[S]_0$ is kept low, so that it does not significantly affect [CD] compared to the effect of the added inhibitor. See last paragraph of the Experimental.

[6] O.S. Tee, A.A. Fedortchenko, P.G. Loncke, and T.A. Gadosy. J. Chem. Soc. Perkin Trans. 2. In press.

[7] In fact, it was studies of the effects of CDs on ester aminolysis (cf. 7*g*, 7*h*) that required us to determine K_d values for {amine·CD} complexes.

[8] Since we were primarily concerned with the quantitation of 1:1 binding, we have avoided conditions (long alkyl chains, very high [CD]) that tend to give rise to 2:1 (CD:guest) binding.

Table 1. Dissocation constants of guest-cyclodextrin complexes, determined by the inhibition kinetics method.[a]

Guest	K_d, mM	
	Hp-β-CD	β-CD[b,c]
(*a*) Alcohols[b]		
EtOH	2100 ± 200	1070
n-PrOH	319 ± 7	269
n-BuOH	64.0 ± 1.0	56 ± 1, 60
n-PentOH	16.6 ± 1.1	16
n-HexOH	4.37 ± 0.13	4.4 ± 0.1, 4.6
n-HeptOH	1.51 ± 0.13	1.41
iso-PrOH	279 ± 16	263
iso-BuOH	40.4 ± 4.1	24
iso-PentOH	9.28 ± 0.47	5.6
2-BuOH	83.6 ± 2.8	65
2-PentOH	41.4 ± 2.3	32
2-HexOH	13.2 ± 1.4	10.5
3-PentOH	32.3 ± 0.6	45
tert-BuOH	40.1 ± 2.2	21
neo-PentOH	2.86 ± 0.18	1.74
cycloPentOH	10.7 ± 0.9	8.3
cycloHexOH	2.19 ± 0.04	1.8 ± 0.2, 1.49 ± 0.08, 2.0
$MeOCH_2CH_2OH$	1200 ± 58	602
(*b*) Alkanesulfonate ions[c,d]		
$BuSO_3^-$	105 ± 1.1	89 ± 3
$PentSO_3^-$	26.6 ± 1.1, 67	16.7
$HexSO_3^-$	9.54 ± 0.23, 8.9	5.6
$HeptSO_3^-$	3.38 ± 0.27, 1.8	2.3
$OctSO_3^-$	1.07 ± 0.13, 0.91	0.97

[a]At 25°C, in aqueous solution. All of the values for Hp-β-CD were determined, in this work, in a phosphate buffer of pH 11.6.

[b]Most of the values for alcohols and β-CD were determined by Matsui et al., using a spectral displacement method (13). The remaining values (those given with errors) were determined earlier in this laboratory, by the inhibition method (8*c*).

[c]All but one of the values for RSO_3^- and β-CD are taken from Satake et al. who used a conductimetric method (14*a*,*b*). Very similar results were obtained by Park and Song, using an ANS fluorescence probe method (14c). Earlier experiments in this laboratory on the binding of these ions to α-CD, using the inhibition method (8*c*), gave results in reasonable agreement with those from conductimetry (14*a*,*b*).

[d]Reinsborough and co-workers (15) found similar values of K_d for RSO_3^- binding to Hp-β-CD, using fluorescent probe displacement and conductimetry.

$$[8]\quad ANS + CD \underset{K_{ANS}}{\rightleftharpoons} ANS{\cdot}CD$$

$$[9]\quad F_{rel} = \frac{(F_0 K_{ANS} + F_c[CD])}{(K_{ANS} + [CD])}$$

Figure 1 shows observed data and calculated curves for the effects of β-CD, γ-CD, and Hp-β-CD on the relative fluorescence of ANS in aqueous solution and Table 2 contains the appropriate constants derived from nonlinear fitting of eq. [9] to the data. As seen in Fig. 1, binding ANS to β-CD and γ-CD causes substantial increases in its fluorescence and these may be used as the basis of competition experiments (14*c*, 17–23).

Fig. 1. Effects of added cyclodextrins on the fluorescence of ANS in aqueous solution at pH 11.60: β-CD, ▼; Hp-β-CD, ■; γ-CD, □. Note that the vertical scale on the left is for Hp-β-CD and that it is 16 times greater than that on the right for the others two CDs. The actual data for Hp-β-CD extend to [Hp-β-CD] = 20 mM.

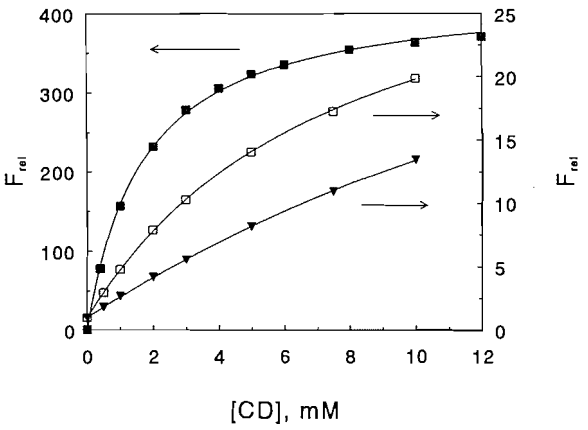

Table 2. Effects of cyclodextrins on the fluorescence of the 1-anilino-8-naphthalenesulfonate ion (ANS) due to complexation.[a]

CD	F_c	K_{ANS}, mM	
		This work	Literature values (ref.)
β-CD	46.7 ± 1.7	26.8 ± 1.3	9.1–90[b]
Hp-β-CD	430 ± 2	1.71 ± 0.04	
γ-CD	34.5 ± 0.4	7.81 ± 0.17	0.79(22), 3.6(19)

[a]At 25°C, in an aqueous phosphate buffer (0.2 M) of pH 11.6. Values of F_c and K_{ANS} were obtained from nonlinear fitting of eq. [9] to relative fluorescence data ($F_{rel} = I_{obs}/I_0$), with $F_0 = 1$ (see Fig. 1).

[b]Literature values of K_{ANS} (in mM) are: 9.1 (21), 11 (20, 23), 12 (14*c*), 13 (17*b*), 15 (22), 16 (18), 17 (17*a*), 90 (19).

On the other hand, ANS binding to α-CD is much weaker and the resulting fluorescence increase is small (16), making it less suitable as a probe, in our experience.[6] By contrast, the binding of ANS to Hp-β-CD is stronger than that to β-CD and it brings about a very large enhancement in fluorescence (Fig. 1).

The literature contains several values of K_{ANS} for the complexation by β-CD (Table 2, footnote *b*), ranging from 9 to 90 mM, but most fall within 13±4 mM. We have settled on a value of 27 mM as being appropriate for our conditions (pH 11.6, 0.2 M phosphate buffer), whereas colleagues have obtained more "normal" values of 10.5±1.3 and 16.4±1.5 mM at lower pH and lower ionic strength.[9] ANS binding under our conditions is discussed further in the experimental section.

When another guest is added to a solution of ANS and a CD, the amount of free CD is reduced, so that some of the CD-bound ANS dissociates, and the ANS fluorescence diminishes, as shown in the examples in Fig. 2. From such decreases, the free [CD] can be estimated from eq. [10], obtained by rearrangement of eq. [9]. Substitution of these CD

[9] S.R. Mikkelsen, S. Rubio and Q. Tan, unpublished results.

Fig. 2. Examples of the effects of amines on the ANS fluorescence in the presence of Hp-β-CD, in aqueous solution at pH 11.6: *n*-propylamine, ●; *n*-butylamine, □; cyclopentylamine, ■; cyclohexylamine, ◆.

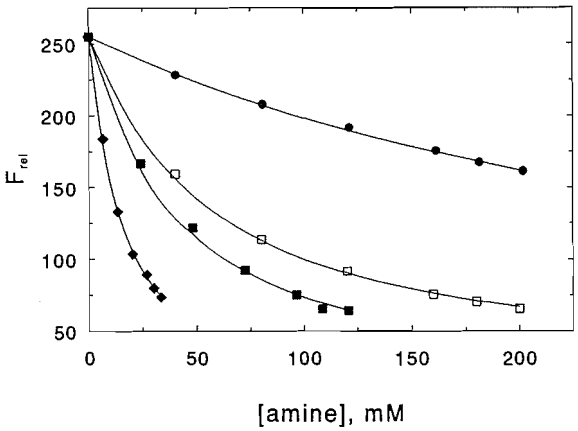

Table 3. Estimation of a dissociation constant by displacement of the fluorescent probe, ANS. Guest = *n*-butylamine; $[ANS]_0$ = 0.075 mM; for β-cyclodextrin, with $[CD]_0$ = 10.0 mM.[a]

$[Guest]_0$, mM	I_{obs}	F_{rel}	[CD], mM	[CD·guest], mM	[guest], mM	K_d, mM
0	0.030 9	13.40	9.980[b]	—	—	—
40	0.019 3	8.37	5.153	4.835	35.18	37.6
80	0.013 8	5.99	3.281	6.711	73.32	35.8
120	0.011 1	4.81	2.440	7.554	112.5	36.3
160	0.009 14	3.96	1.858	8.137	152.0	34.7
180	0.008 55	3.71	1.688	8.308	171.8	34.9
200	0.007 95	3.45	1.517	8.479	191.6	34.3
					Average:	35.6
					Standard deviation:	± 1.2

[a]At 25°C, in aqueous solution at pH 11.60. Individual K_d values were obtained from eq. [7] (with $[I]_0$ = $[guest]_0$), using [CD] values estimated from eq. [10] and F_{rel} in column 3. See the Experimental for more details.
[b]Less than $[CD]_0$ = 10.00 mM due to depletion of CD by binding to ANS. For [CD] = 9.98 mM, a reference fluorescence F_{ref} (= 13.40) was calculated from eq. [9] and the observed intensities were scaled to this, giving F_{rel} in column 3.

concentrations into eq. [7], for each of several $[guest]_0$, leads to estimates of K_d for the guest and these estimates are averaged. Again, the calculations can be most easily carried out in a spreadsheet, an example of which is given in Table 3.

$$[10] \quad [CD] = (F_{rel} - F_0)K_{ANS}/(F_c - F_{rel})$$

As a test of the above fluorescent probe method under our conditions, we looked first at the effects of some alcohols on ANS fluorescence in the presence of β-CD and Hp-β-CD and found values of K_d that are in reasonable to good agreement with those determined in other ways (Table 4 (*a*)). We then applied the method to the binding of several alkylamines and related derivatives, and obtained the K_d values presented in Table 4 (*b*). For the purposes of comparison, Table 4 also contains values that were found in the literature (13, 17, 23–25).

We have also used the fluorescence method to find K_d values for the binding of α-amino acids to β-CD, for the purposes of studies of the reaction of these nucleophiles with esters in the presence of CDs (cf. ref. 26). Our attempts were only partially successful in that smaller derivatives appear to bind weakly, if at all. However, derivatives with larger alkyl or aryl substitutents at the α-carbon of the amino acid bind strongly enough to cause significant decreases in ANS·CD fluorescence, analysis of which afforded the dissociation constants given in Table 4 (*c*).

We have had only limited success using the fluorescent probe method for the binding of ketones to CDs.[6] In general, we have found inhibition kinetics easier to use and to give more reproducible results, perhaps because it is less susceptible to trace impurities (which may quench fluorescence) and to instrumental fluctuations.

Discussion

In earlier work (6, 7*c*, 14*c*) it was noted that the strength of binding of several *n*-alkyl derivatives to CDs, expressed by $pK_d = -\log K_d$, increases monotonically with alkyl chain length, for up to about eight carbons.[10] Similar correlations are found in the present results for both β-CD and Hp-β-CD, and these are summarized in Table 5, along with some others for comparison. The data for β-CD are plotted in Fig. 3.

For reasons given earlier (7*c*), correlations of pK_d with chain length (N) may be treated as linear free energy relationships (LFERs) whose slopes are measures of the sensitivity of binding to structural change in the guests. In the present case, the slopes are in the range 0.4–0.6 (Table 5, Fig. 3), corresponding to free energy increments of 0.55–0.82 kcal/mol for each CH_2 group that is sequestered by the CD. These increments are close to those (0.7–0.9 kcal/mol) found for the transfer of simple aliphatics from water to organic solvents (27). Given this observation, one might infer that hydrophobic interactions (27) largely determine the binding of aliphatics to CDs in aqueous solution but one must recognize that the size and surface area of alkyl chains also increase linearly with *N*, so that van der Waals interactions (4) may contribute to the chain length dependence, as well. Consistent with this latter view, we have found that the binding of nitrophenyl alkanoate esters to both α-CD and β-CD shows a significant, but reduced, dependence on chain length in 60% aqueous DMSO, even though hydrophobic effects are largely absent in this medium (28).

We now compare the binding of aliphatics to Hp-β-CD and β-CD, to see the effects of hydroxypropylation of the primary hydroxy groups of β-CD. For a given *n*-alkylamine, the strength of binding to the two CDs is very similar, being marginally greater for β-CD (Table 4). Both CDs show good linear correlations of pK_d with the chain length of the alkylamines, with similar slopes of ~0.5 (Table 5), and so the pK_d values for binding to β-CD and to Hp-β-CD are strongly correlated (r = 0.997), with near unit slope (0.95 ± 0.05). In

[10] At greater chain lengths, complications set in. First, the chain length dependence of pK_d levels off (6, 7*c*, 7*f*, 14, 15), presumably because of the finite depths of the CD cavities. Second, the intrusion of 2:1 (CD:guest) binding becomes increasingly significant, even at fairly low [CD] (e.g., 7*b*, 7*d*, 7*e*, 14*c*).

Table 4. Dissociation constants of guest–cyclodextrin complexes determined by the displacement of a fluorescent probe.[a]

	K_d, mM			
	β-CD		Hp-β-CD	
Guest	This work	Lit[b]	This work	Lit[c]
(*a*) Alcohols[d]				
n-PrOH	241 ± 9	269	173 ± 18	319
n-PentOH	13.9 ± 1.2	16	15.8 ± 0.5	16.6
n-HexOH	4.84 ± 0.18	4.6	5.41 ± 0.10	4.37
iso-PrOH	246 ± 16	263	255 ± 18	279
cycloHexOH	2.10 ± 0.38[e]	2.0	3.66 ± 0.23	2.19
(*b*) Amines[f]				
n-Propylamine	108 ± 5	111[g]	141 ± 4	
n-Butylamine	35.6 ± 1.2	100,[g]333[h]	42.2 ± 2.2	
n-Pentylamine	11.4 ± 0.2		13.7 ± 0.8	
n-Hexylamine	2.62 ± 0.27		4.81 ± 0.36	
n-Heptylamine	0.955 ± 0.041		1.32 ± 0.05	
n-Octylamine	[i]		0.519 ± 0.023	
n-HexNMe$_2$	6.68 ± 0.37		3.59 ± 0.35	
Cyclopentylamine	13.5 ± 2.1		16.1 ± 0.9	
Cyclohexylamine	1.83 ± 0.24		5.21 ± 0.26[j]	
HO(CH$_2$)$_3$NH$_2$			561 ± 11	
Morpholine	56.3 ± 6.2	59[h]		
N-Methylmorpholine	23.7 ± 2.1			
N-Ethylmorpholine	16.6 ± 0.7			
Piperidine		20[h]	19.4 ± 1.4	
(*c*) α-Amino acids[k]				
L-Alanine	v. large			
L-Valine	255 ± 15			
L-Leucine	107 ± 5			
L-Cysteine	>1000			
L-Tryptophan	45.1 ± 1.6			
L-Tyrosine	55.8 ± 10.0			
L-Phenylalanine	19.8 ± 2.1			
DL-Norvaline	~2500			
DL-Norleucine	158 ± 30			

[a]At 25°C, in aqueous buffers, as noted below.

[b]The literature values for alcohols and β-CD were obtained by a dye displacement method (13).

[c]From inhibition kinetics, carried out at pH 11.6, taken from Table 1.

[d]In a 0.2 M phosphate buffer of pH 11.6.

[e]Earlier workers (17, 20, 23) obtained values of 2.0, 1.4, and 2.2 mM, using similar methods based on the displacement of the ANS.

[f]Five of the amines (*n*-propyl, *n*-butyl, *n*-pentyl, cyclopentyl, cyclohexyl) were studied in their own buffers, adjusted to pH 11.6. The other amines were determined in the phosphate buffer of pH 11.6.

[g]Obtained by Kano et al. (24) using the dye displacement method (13*a*).

[h]Determined by an indicator displacement method, using *p*-nitroaniline (25).

[i]Forms a complex that precipitates from solution.

[j]From an experiment with [amine]$_0$ = 0–33.4 mM. Since the cited value did not lead to acceptable analysis in an aminolysis experiment, a second experiment, with [amine]$_0$ = 0–28.6 mM, was carried out, but it gave the same value: K_d = 5.21 ± 0.59 mM.

[k]In a buffer of the amino acid, adjusted to pH = 9.88.

Table 5. Chain length dependence of the binding of aliphatic guests to cyclodextrins. Correlations between pK_d and the alkyl chain length, N.[a]

Guests	CD	N	Slope ± s.d.	r	Note
ROH	β-CD	3–7	0.568 ± 0.016	0.999	*b*
	Hp-β-CD	3–7	0.582 ± 0.024	0.997	*c*
RCH(OH)Me	β-CD	1–4	0.450 ± 0.039	0.993	*b*
	Hp-β-CD	1–4	0.428 ± 0.030	0.995	*c*
RCO_2^-	β-CD	3–7	0.554 ± 0.018	0.998	*d*
RSO_3^-	β-CD	4–8	0.479 ± 0.041	0.989	*e*
	Hp-β-CD	4–8	0.488 ± 0.014	0.999	*c*
RNH_2	β-CD	3–7	0.524 ± 0.015	0.999	*c*
	Hp-β-CD	3–8	0.490 ± 0.008	0.999	*c*
RCOMe	β-CD	1–6	0.459 ± 0.010	0.999	*f*
	Hp-β-CD	1–6	0.456 ± 0.012	0.999	*f*

[a]In aqueous solution at 25°C. The slope, standard deviation (s.d.), and correlation coefficient (r) are taken from linear least-squares analysis of pK_d against N.
[b]Based on results given by Matsui et al. (13). For the 1-alkanols, the points for methanol and ethanol were not included because we suspect that their K_d values are distorted due to the binding of more than one guest molecule, since this is evident at high [guest].[9]
[c]From K_d values determined in this work (Table 1 or Table 4).
[d]From K_d values determined in earlier studies in this laboratory (8).
[e]Based on data given in Table 1, taken largely from Satake et al. (14).
[f]Results submitted for publication.[6]

Fig. 3. Correlations of the binding of linear aliphatics to β-CD with alkyl chain length, N. The points are R-OH, Δ; RCH(OH)Me, ■; R-CO_2^-, □; RSO_3^-, ▲; R-NH_2, ●; R-COMe, ◇. There are similar correlations for Hp-β-CD (see Table 5).

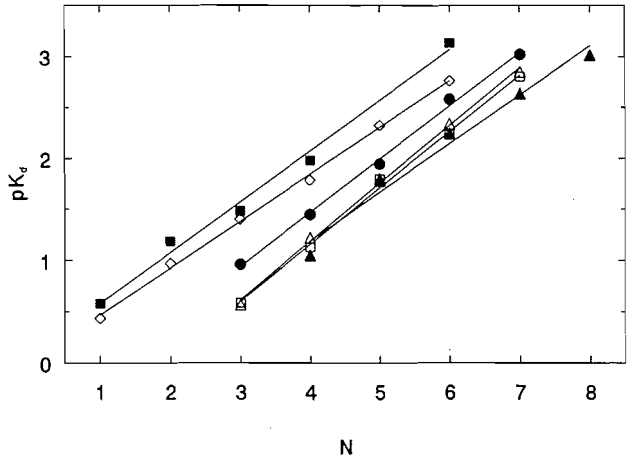

fact, similar correlations are found for other alkyl derivatives, and in a communication (29) we noted a strong correlation between the pK_d values for a collection of 28 aliphatics binding to β-CD and Hp-β-CD, with unit slope. With the addition of new results, this correlation can now be extended to 54 derivatives, comprising 18 alcohols, 10 aryl alkanoates, 5 alkanesulfonate ions, 8 amines, and 13 ketones,[6] for which the slope = 1.01 ± 0.03, intercept = −0.11 ± 0.14, and r = 0.983 (Fig. 4). The collection of guests includes some branched and cyclic compounds (e.g., Tables 1 and 4) and without these the

Fig. 4. Correlation between the binding of aliphatics to Hp-β-CD and to β-CD. The solid diagonal line is for pK_d (Hp-β-CD) = pK_d (β-CD); the adjacent broken line is the actual correlation line (see text). The points are as follows: nitrophenyl alkanoates, ◇; alcohols, ◆; RSO_3^-, Δ; amines, ■; ketones, □.

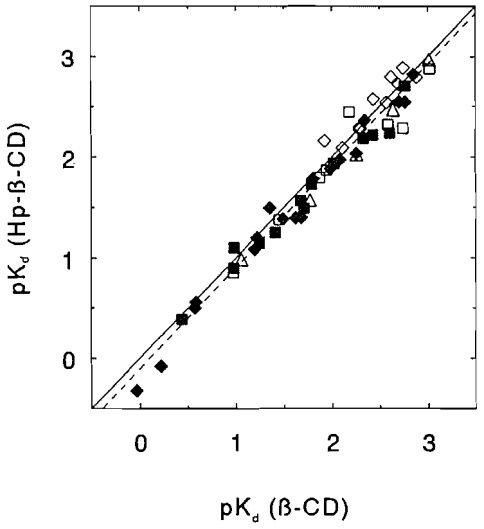

correlation is decidedly better (r = 0.991, 42 points), but the slope is essentially unchanged (1.04 ± 0.02). Thus, to a very good approximation, the strength of binding of simple aliphatics to β-CD and Hp-β-CD is the same, and the closeness of the K_d values for the two CDs implies that the guests enter from the wider opening of the CD cavity that is rimmed by secondary hydroxy groups (5), and that the guests do not penetrate far enough into the cavity to interact strongly with the groups on the other side.

Apparently, a similar situation exists for other types of guests binding to Hp-β-CD. For example, 4-(2-pyridylazo)-*N*,*N*-dimethylaniline binds equally well to Hp-β-CD and β-CD (30), as do the tetraphenylborate ion and BF_4^- (15). For two naphthalene derivatives, 1- and 2-naphthyl acetate, binding to Hp-β-CD is about twice as strong as that to β-CD (31). By contrast, we note that ANS binds to Hp-β-CD 16 times more strongly than to β-CD (Table 2) but for a related fluorescent probe, 2-*p*-toluidino-6-naphthlenesulfonate ion, binding by Hp-β-CD is only slightly (about 15%) stronger (15*b*).

Recently, Hamasaki et al. (32) prepared substituted CDs that are functionalized with a *p*-dimethylaminobenzamido group in place of one of the primary hydroxyls. These derivatives exhibit TICT fluorescence, which can be altered by the binding of guests in the CD cavities. Of relevance to the present discussion, we note their β-CD derivative binds aliphatic alcohols 1.4 to 4 times stronger than unfunctionalized β-CD. So, as with Hp-β-CD, the modification on the primary side of β-CD does not cause a large positive or negative effect on the inclusion of guests, even though it is envisaged that inclusion of the guest forces the fluorophoric group out of the cavity and into the bulk medium (32). The effects of "capping" of the primary side of the β-CD cavity are more variable, depending on the nature of the "cap" and the type of guest that is included, but in many cases the effects on the strength of binding are relatively small (33).

In addition to the correlations discussed above, other fea-

Table 6. Example of estimation of a dissociation constant by inhibition kinetics. Inhibitor = *n*-BuOH; $[Hp\text{-}\beta\text{-}CD]_0$ = 2.00 mM; ester = mNPA; k_u = 0.0502 s^{-1}; k_c = 0.956 s^{-1}; K_S = 6.98 mM.[a]

$[I]_0$, mM	k_{obs}, s^{-1}	k_{scal}, s^{-1}	[CD], mM	[PI], mM	K_d, mM
0	0.237	0.252	2.00	0.00	—
20.0	0.200	0.213	1.53	19.53	62.9
40.0	0.175	0.186	1.23	39.23	63.2
60.0	0.158	0.169	1.05	59.05	65.4
80.0	0.144	0.153	0.89	78.89	63.8
100.0	0.134	0.142	0.79	98.79	64.7
				Average:	64.0[b]
				Standard deviation	±1.0

[a]At 25°C, in 0.2 M aqueous phosphate buffer of pH 11.6. For this $[CD]_0$, the expected k_{calc} = 0.252 s^{-1} and so k_{obs} is scaled to this, as follows: $k_{scal} = k_{obs}(0.252)/(0.237)$. It should be understood that the actual spreadsheet carried more significant figures.

[b]For this set of data the graphical method also works very well, giving K_d = 64.7 ± 0.8 mM.

tures of the present results are noteworthy. For example, K_d for *n*-HexNMe$_2$ binding to Hp-β-CD is virtually the same as that for *n*-HexNH$_2$ and Hp-β-CD. In fact, this type of situation is common since the K_d values for alcohols (ROH), alkanoate ions (RCO_2^-), and alkanesulfonate ions (RSO_3^-) having the same alkyl groups are comparable (Fig. 3), and the binding of the analogous amines (RNH_2) is only slightly stronger (Tables 1 and 4, Fig. 3). Also, all the alkyl derivatives show very similar sensitivities to changes in chain length (Table 5). Taken together, these similarities must mean that the binding of such aliphatic guests is almost solely due to inclusion of their alkyl groups and that the hydrophilic end groups of the bound guests are sufficiently outside the CD cavity that they do not interact strongly with its rim. These are useful observations that may be utilized to estimate K_d values prior to their determination.

Conclusions

In this work, and in earlier studies (6, 7*c*–*f*), we have noted various correlations of pK_d with alkyl chain length, as well as the strong correlation between the pK_d values for the binding of alkyl-bearing compounds to Hp-β-CD and β-CD, with unit slope (Fig. 4). Such correlations have great predictive value for the purposes of planning experiments and for estimating K_d values that may be difficult to determine. At the same time, in combination with other types of studies (4), they may provide information about modes of binding and contribute to our understanding of the factors involved in host–guest complexation in aqueous solution.

Experimental

The cyclodextrins were purchased from Aldrich and from Wacker Chemie, and were used as received. The "hydroxypropyl-β-cyclodextrin" had an average molecular weight of 1500, corresponding to alkylation of six of the seven primary OH groups of β-CD by 2-hydroxypropyl groups. We found no appreciable difference in the behaviour of Hp-β-CD from the two suppliers. Most of the other reagents were purchased from Aldrich and used as supplied.

For the inhibition method of determining K_d, the kinetics of the cleavage of mNPA in the presence of several concentrations of inhibitor ([inhibitor]) were followed by monitoring the first-order appearance of the nitrophenolate ion at 390 nm, in a stopped-flow spectrophotometer with the temperature of the cell kept at 25.0±0.1°C, as previously (8*c*). The rate constants for various $[inhibitor]_0$ were analyzed as outlined in the main text, using a spreadsheet to do the calculations, as shown by the example given in Table 6.

To determine dissociation constants of amine·CD complexes we used competition between the amines and the fluorescent probe ANS for the CD (17–23). First, dissociation constants (K_{ANS}) for the CD·ANS complexes were determined in a basic solution, the same as that to be used with the amines. A solution containing a CD (0–20 mM for β-CD or γ-CD; 0–40 mM for Hp-β-CD) in a 0.4 M sodium phosphate – NaOH buffer of pH 11.60, and a solution containing 200 μM ANS were mixed (1:1) in a stopped-flow apparatus, yielding final concentrations half of the foregoing. The observation cell was irradiated at 383 nm, and the fluorescence was measured at either 474 nm (β-CD), 468 nm (Hp-β-CD), or 473 nm (γ-CD). These wavelengths may not correspond to the actual fluorescence maxima of the CD·ANS complexes, but they were found to be the best for our apparatus, an Applied Photophysics SX17MV spectrofluorimeter. Uncorrected fluorescence values, obtained as the averages of several scans, were then converted into relative fluorescence, using $F_{rel} = I_{obs}/I_0$, where I_0 is the fluorescence intensity at zero [CD]. Analysis of the F_{rel} values at several [CD] (Fig. 1) were carried out by nonlinear regression of eq. [9] (34), giving the fitted constants F_c and K_{ANS} in Table 2.

Several experiments were carried out on the binding of ANS to β-CD, with variable results. Depending on the range of [β-CD] used, we obtained K_{ANS} values ranging from 12 to 50 mM, but most were between 20 and 35 mM, with the highest values coming from experiments where [β-CD] was taken up to 30 mM.[11] In general, we found that eq. [9] gave good fits to the fluorescence data only when [β-CD] <15 mM, probably because of the intrusion of 2:1 binding at high [CD]. Accordingly, we have used the value of 26.8 ± 1.3 mM, obtained from the data with [CD] in the range 0–10 mM, as shown in Fig. 1, and we restricted all further experiments to the same [β-CD] range. By contrast, ANS with Hp-β-CD gave well-behaved fluoresecence data for [CD] up to 20 mM (Fig. 1).

Dissociation constants for the amines complexing with β-CD or Hp-β-CD were obtained as follows. Solution 1 contained the amine and, where necessary, 10 mM β-CD. For most of the amines, this solution was prepared in a 0.4 M phosphate buffer, and adjusted to pH 11.60. In the case of *n*-propylamine, *n*-butylamine, *n*-pentylamine, cyclopentylamine, and cyclohexylamine, the solutions were prepared in water and set to pH 11.60, using the amine as the buffering species. Solution 2 contained CD (β-CD, 10 mM or Hp-β-CD, 5.0 mM) and ANS in water. Both solutions were then mixed to

[11] The normal solubility of β-CD in water is about 16 mM (5), but higher concentrations are attainable in a strong phosphate buffer of pH 11.6.

give final concentrations of 10 mM β-CD + 50–100 μM ANS or 2.5 mM Hp-β-CD + 25 μM ANS. Amine concentrations, which were governed primarily by solubility, varied between 0 and 250 mM (3-amino-1-propanol) and 0 and 5.2 mM (*n*-octylamine). The mixed solution in the observation cell of the spectrofluorimeter, maintained at 25.0 ± 0.1°C, was irradiated at 383 nm, and the fluorescence intensity (I_{obs}) was taken as the average of several scans at 474 nm (β-CD) or 468 nm (Hp-β-CD) for each $[amine]_0$.

For estimation of K_d values (e.g., Table 3), the observed fluorescence intensities, I_{obs} (column 2, Table 3), must first be scaled to bring them into line with the previous ANS/CD "calibration" curves described by eq. [9] with the parameters in Table 2. From the initial $[ANS]_0$ and $[CD]_0$, the actual [ANS] was calculated by solving the quadratic that is obtained by expansion of:

$$K_{ANS} = [ANS][CD]/[CD \cdot ANS]$$
$$= [ANS]([CD]_0 - ([ANS]_0 - [ANS]))/([ANS]_0 - [ANS])$$

Using this [ANS], [CD] was then found from $[CD]_0 - ([ANS]_0 - [ANS])$ and a reference fluorescence (F_{ref}) was evaluated from eq. [9]. This F_{ref} was set equivalent to the observed fluorescence intensity with no guest present (I_{ng}), and the other I_{obs} were converted to relative fluorescence values using $F_{rel} = I_{obs}.F_{ref}/I_{ng}$ (column 3, Table 3). These values of F_{rel} were then used to calculate values of [CD] from eq. [10] for the various $[guest]_0$ (column 4, Table 3), from which estimates of K_d were obtained using eq. [7] (column 7, Table 3). All of these manipulations were carried out in a spreadsheet designed for the purpose.

Dissociation constants for complexation of the amino acids by β-CD were also determined as above, with minor differences. The solutions were set to pH 9.88, to correspond to other experiments (26), using the amino acid as the buffering species. The concentration ranges of the α-amino acids varied between 0 and 200 mM (L-valine, L-cysteine, and DL-norvaline) and 0 and 5.0 mM (L-tyrosine).

Prompted by a referee's comment, we have referred to a paper by Selvidge and Eftink (*9a*) in which they point out some of the same problems that we do and they present an analysis of the use of various concentrations, $[guest]_0$ and $[probe]_0$, in relation to the strengths of guest and probe binding. When they estimate guest binding constants, using their equations [10]–[12], they correct for [probe·CD]. So do we in the fluorescence method, but it only makes a difference of 1% *at most*, for the lowest $[guest]_0$ of the strongest binding guest that was studied. When using the inhibition method, developed earlier (*8a,b*), we did not make this correction, but even there it would only make a difference of 2% in the worst case. The major difference between our approach and that of Selvidge and Eftink (*9a*) is that they used double-reciprocal plots to find the binding constants of their spectroscopic probes, whereas we prefer to use nonlinear fitting.

Acknowledgement

We thank the Natural Sciences and Engineering Research Council of Canada for an operating grant, a post-graduate scholarship, summer student awards, and an equipment grant. We also thank Professor Susan Mikkelsen for several helpful discussions.

References

1. J.-M. Lehn. Science (Washington, D.C.), **227**, 849 (1985); Angew. Chem. Int. Ed. Engl. **27**, 89 (1988).
2. (*a*) F. Vögtle. Supramolecular chemistry. John Wiley & Sons, Chichester, U.K. 1991; (*b*) H.-J. Schneider and H. Dürr (*Editors*). Frontiers in supramolecular organic chemistry and photochemistry. VCH, Weinheim. 1990.
3. (*a*) F.M. Menger and Z.X. Fei. Angew. Chem. Int. Ed. Engl. **33**, 346 (1994); (*b*) F.M. Menger and S.J. Lee. J. Am. Chem. Soc. **116**, 5987 (1994); (*c*) G.M. Whitesides, E.E. Simanek, J.P. Mathias, C.T. Seto, D.N. Chin, M. Mammen, and D.M. Gordon. Acc. Chem. Res. **28**, 37 (1995).
4. (*a*) I. Tabushi. Acc. Chem. Res. **15**, 66 (1982); (*b*) H.-J. Schneider. Angew. Chem. Int. Ed. Engl. **30**, 1417 (1991); (*c*) H.-J. Schneider, V. Rudiger, and O.A. Raevsky. J. Org. Chem. **58**, 3648 (1993); (*d*) H.-J. Schneider. Chem. Soc. Rev. **23**, 227 (1994).
5. (*a*) M.L. Bender and M. Komiyama. Cyclodextrin chemistry. Springer-Verlag, New York. 1978; (*b*) W. Saenger. Angew. Chem. Int. Ed. Engl. **19**, 344 (1980); (*c*) J. Szejtli. Cyclodextrins and their inclusion complexes. Akademiai Kiado, Budapest. 1982; (*d*) G. Wenz. Angew. Chem. Int. Ed. Engl. **33**, 803 (1994).
6. (*a*) O.S. Tee. Carbohydr. Res. **192**, 181 (1989); (*b*) Adv. Phys. Org. Chem. **29**, 1 (1994).
7. (*a*) O.S. Tee and B.K. Takasaki. Can. J. Chem. **63**, 3540 (1985); (*b*) O.S. Tee and X.-X. Du. J. Org. Chem. **53**, 1837 (1988); (*c*) O.S. Tee, C. Mazza, and X.-X. Du. J. Org. Chem. **55**, 3603 (1990); (*d*) O.S. Tee and X.-X. Du. J. Am. Chem. Soc. **114**, 620 (1992); (*e*) T.A. Gadosy and O.S. Tee. J. Chem. Soc. Perkin Trans. 2, 715 (1994); J. Chem. Soc. Perkin Trans. 2 (1994), 2609; (*f*) O.S. Tee and T.A. Gadosy. J. Chem. Soc. Perkin Trans. 2, 2191 (1994); (*g*) J. Chem. Soc. Perkin Trans. 2, 2307 (1994); (*h*) T.A. Gadosy and O.S. Tee. J. Chem. Soc. Perkin Trans. 2, 71 (1995).
8. (*a*) O.S. Tee and J.J Hoeven. J. Am. Chem. Soc. **111**, 8318 (1989); (*b*) O.S. Tee and M. Bozzi. J. Am. Chem. Soc. **112**, 7815 (1990); (*c*) O.S. Tee, M. Bozzi, J.J. Hoeven, and T.A. Gadosy. J. Am. Chem. Soc. **115**, 8990 (1993); (*d*) O.S. Tee, M. Bozzi, N. Clement, and T.A. Gadosy. J. Org. Chem. **60**, 3509 (1995); (*e*) T.A. Gadosy and O.S. Tee. Can. J. Chem. **74**, 745 (1996).
9. (*a*) L.A. Selvidge and M.R. Eftink. Anal. Biochem. **154**, 400 (1986); (*b*) K.A. Connors. Binding constants: the measurement of molecular complex stability. John Wiley & Sons, New York. 1987.
10. (*a*) R.L. VanEtten, J.F. Sebastian, G.A. Clowes, and M.L. Bender. J. Am. Chem. Soc. **89**, 3242 (1967); (*b*) R.L. VanEtten, G.A. Clowes, J.F. Sebastian, and M.L. Bender. J. Am. Chem. Soc. **89**, 3253 (1967).
11. A. Fersht. Enzyme structure and mechanism. 2nd ed. W.H. Freeman, New York. 1985.
12. J.E. Dowd and D.S. Riggs. J. Biol. Chem. **249**, 863 (1965).
13. (*a*) Y. Matsui and K. Mochida. Bull. Chem. Soc. Jpn. **52**, 2808 (1979); (*b*) Y. Matsui, T. Nishioka, and T. Fujita. Top. Curr. Chem. **128**, 61 (1985).
14. (*a*) I. Satake, T. Ikenoue, T. Takeshita, K. Hayakawa, and T. Meda. Bull. Chem. Soc. Jpn. **58**, 2746 (1985); (*b*) I. Satake, S. Yoshida, K. Hayakawa, T. Meda, and Y. Kusumoto. Bull. Chem. Soc. Jpn. **59**, 3991 (1986); (*c*) J.W. Park and H.J. Song. J. Phys. Chem. **93**, 6454 (1989).
15. (*a*) C.D. Lavandier, M.P. Pelletier, and V.C. Reinsborough. Aust. J. Chem. **44**, 457 (1991); (*b*) M.D. Johnson and V.C. Reinsborough. Aust. J. Chem. **45**, 1961 (1992).

16. F. Cramer, W. Saenger, and H.-Ch. Spatz. J. Am. Chem. Soc. **89**, 14 (1967).
17. I. Tabushi, K. Shimokawa, N. Shimizu, H. Shirakata, and K. Fujita. J. Am. Chem. Soc. **98**, 7855 (1976); I. Tabushi, N. Shimizu, T. Sugimoto, M. Shiozuka, and K. Yamamura. J. Am. Chem. Soc. **99**, 7100 (1977).
18. W.M. Müller, W. Werner, and F. Vögtle. J. Inclusion Phenom. **3**, 471(1985).
19. V. Crescenci, A. Gamini, A. Palleschi, and R. Rizzo. Gazz. Chim. Ital. **116**, 435 (1986).
20. Y. Matsui, K. Ogawa, S. Mikami, M. Yoshimoto, and K. Mochida. Bull. Chem. Soc. Jpn. **60**, 1219 (1987).
21. G.C. Catena and F.V. Bright. Anal. Chem. **61**, 905 (1989).
22. H.-J. Schneider, T. Blatter, and S. Simova. J. Am. Chem. Soc. **113**, 1996 (1991).
23. Y. Aoyama, Y. Nagai, J. Otsuki, K. Kobayashi, and H. Toi. Angew. Chem. Int. Ed. Engl. **31**, 745 (1992); Y. Aoyama, J. Otsuki, Y. Nagai, K. Kobayashi, and H. Toi. Tetrahedron Lett. **33**, 3775 (1992).
24. K. Kano, I. Takenoshita, and T. Ogawa. J. Phys. Chem. **86**, 1833 (1982).
25. M. Barra, R.H. de Rossi, and E.B. de Vargas. J. Org. Chem. **52**, 5004 (1987).
26. M. Barra and R.H. de Rossi. Can J. Chem. **69**, 1124 (1991).
27. (*a*) C. Tanford. The hydrophobic effect: formation of micelles and biological membranes. 2nd ed. John Wiley & Sons, New York. 1980; (*b*) M.H. Abraham. J. Am. Chem. Soc. **104**, 2085 (1982); J. Chem. Soc. Faraday Trans. 1, **80**, 153 (1984); (*c*) W. Blokzijl and J.B.F.N. Engberts. Angew. Chem. Int. Ed. Engl. **32**, 1545 (1993).
28. O.S. Tee, C. Mazza, R. Lozano-Hemmer, and J.B. Giorgi. J. Org. Chem. **59**, 7602 (1994).
29. O.S. Tee, T.A. Gadosy, and J.B. Giorgi. J. Chem. Soc. Perkin Trans. 2, 1705 (1993).
30. P.M. Demont and V.C. Reinsborough. Aust. J. Chem. **44**, 759 (1991).
31. O.S. Tee and M.J. Boyd. J. Chem. Soc. Perkin Trans. 2, 1237 (1995).
32. K. Hamasaki, H. Ikeda, A. Nakamura, A. Ueno, F. Toda, I. Suzuki, I. Suzuki, and T. Osa. J. Am. Chem. Soc. **115**, 5035 (1993); K. Hamasaki, A. Ueno, F. Toda, I. Suzuki, and T. Osa. Bull. Chem. Soc. Jpn. 67, 516 (1994).
33. J. Emert and R. Breslow. J. Am. Chem. Soc. **97**, 670 (1975); R. Breslow, M.F. Czarniecki, J. Emert, and H. Hamaguchi. J. Am. Chem. Soc. **102**, 762 (1980); K. Fujita, A. Shinoda, and T. Imoto. J. Am. Chem. Soc. **102**, 1161 (1980).
34. P.R. Bevington. Data reduction and error analysis for the physical sciences. McGraw–Hill, New York. 1969; N.R. Draper and H. Smith. Applied regression. 2nd ed. John Wiley & Sons, New York. 1981.

Spectator catalysis in the cleavage of *p*-nitrophenyl acetate and *p*-nitrophenyl hexanoate by "hydroxypropyl-β-cyclodextrin"

Timothy A. Gadosy and Oswald S. Tee

Abstract: Aliphatic alcohols that form host–guest complexes with "hydroxypropyl-β-cyclodextrin" retard the cleavage of *m*-nitrophenyl acetate by hydroxypropyl-β-cyclodextrin in basic aqueous solution, due to competitive inhibition. By contrast, these same species do not inhibit the reaction of *p*-nitrophenyl acetate and *p*-nitrophenyl hexanoate to the same extent and, in some cases, the addition of alcohols serves to increase the rate of reaction. The observed reaction kinetics require the presence of a process that has *one* molecule of the "potential inhibitor" in the transition state for ester cleavage. Rate constants, k_a, for the reaction of the {ester·hydroxypropyl-β-cyclodextrin} complexes with a series of potential inhibitors show a strong dependence on the ability of the potential inhibitor to bind to the cyclodextrin. On the other hand, rate constants for the kinetically equivalent reaction of the ester with the {cyclodextrin·potential inhibitor} complex show little dependence on the alcohol structure and they vary over a very limited range. The negative logarithms of the apparent dissociation constant of the potential inhibitor from the transition state show a strong dependence on the ability of the potential inhibitor to bind to hydroxypropyl-β-cyclodextrin, indicating that the binding of the potential inhibitor in the initial state and the transition state is similar. It is concluded that the cleavage of *p*-nitrophenyl acetate and *p*-nitrophenyl hexanoate by hydroxypropyl-β-cyclodextrin in the presence of 14 potential inhibitors can occur with the ester largely outside of the hydroxypropyl-β-cyclodextrin cavity during the transition state, allowing the cavity to be occupied by a molecule of potential inhibitor.

Key words: cyclodextrin, spectator catalysis, esterolysis.

Résumé : À cause d'une inhibition compétitive, les alcools aliphatiques qui forment des complexes hôtes–invités avec l'«hydroxypropyl-β-cyclodextrine» retardent le clivage de l'acétate de *m*-nitrophényle par l'hydroxypropyl-β-cyclodextrine en solution basique aqueuse. Par opposition, ces mêmes espèces n'inhibent pas la réaction de l'acétate de *p*-nitrophényle et de l'hexanoate de *p*-nitrophényle de la même façon et, dans certains cas, l'addition d'alcools sert même à augmenter la vitesse de la réaction. Les résultats cinétiques observés suggèrent l'existence d'un processus qui comporte *une* molécule d'«inhibiteur potentiel» dans l'état de transition du clivage de l'ester. Les constantes de vitesse, k_a pour les réactions des complexes {ester·hydroxypropyl-β-cyclodextrine} avec une série d'inhibiteurs potentiels montre une forte dépendance sur l'habilité de l'inhibiteur potentiel à se lier à la cyclodextrine. Par ailleurs, les constantes de vitesse pour la réaction cinétiquement équivalente de l'ester avec le complexe {cyclodextrine·inhibiteur potentiel} ne présente qu'une faible dépendance sur la structure de l'alcool et leurs variations ne sont que très faibles. Les logarithmes négatifs des constantes de dissociations apparentes des inhibiteurs potentiels à partir de l'état de transition montrent une forte dépendance sur l'habilité de l'inhibiteur potentiel à se lier à l'hydroxypropyl-β-cyclodextrine; ceci indique que la fixation de l'inhibiteur potentiel dans l'état initial est semblable à l'état de transition. On en conclut que le clivage de l'acétate de *p*-nitrophényle et de l'hexanoate de *p*-nitrophényle par l'hydroxypropyl-β-cyclodextrine en présence de 14 inhibiteurs potentiels peut se produire alors que l'ester est nettement à l'extérieur de la cavité de l'hydroxypropyl-β-cyclodextrine durant l'état de transition; ceci permet à la cavité d'être occupée par une molécule d'inhibiteur potentiel.

Mots clés : cyclodextrine, catalyse en spectateur, estérolyse.

[Traduit par la rédaction]

Introduction

The cleavage of phenyl esters by cyclodextrins (CDs) in basic aqueous media has been studied extensively over the last several years (1–11). Of particular interest to us is the cleavage of nitrophenyl alkanoates (8, 10, 11) since these compounds provide a convenient series of substrates differing in acyl chain length or position of the nitro substituent, which allows one to probe both initial state and transition state binding as a function of structural or hydrophobic differences. We have shown previously that the *m*-nitrophenyl esters are more reactive than their *para* isomers towards α-CD, β-CD, and "hydroxypropyl-β-cyclodextrin" Hp-β-CD[3] (8, 10). These results support a mechanism whereby the carbonyl group of the *meta* ester (**1**)

Received July 6, 1995.[1]

T.A. Gadosy and O.S. Tee.[2] Department of Chemistry and Biochemistry, Concordia University, 1455 De Maisonneuve Blvd. W., Montreal, QC H3G 1M8, Canada.

[1] Revision received January 29, 1996.
[2] Author to whom correspondence may be addressed. Telephone: (514) 848-3348. Fax: (514) 848-2868.

[3] We note that for the nitrophenyl esters reacting with Hp-β-CD the difference in reactivity between the *meta* and *para* isomers decreases with increasing alkyl chain length, and that *p*-nitrophenyl decanoate is more reactive than its *meta* isomer (10).

Scheme 1.

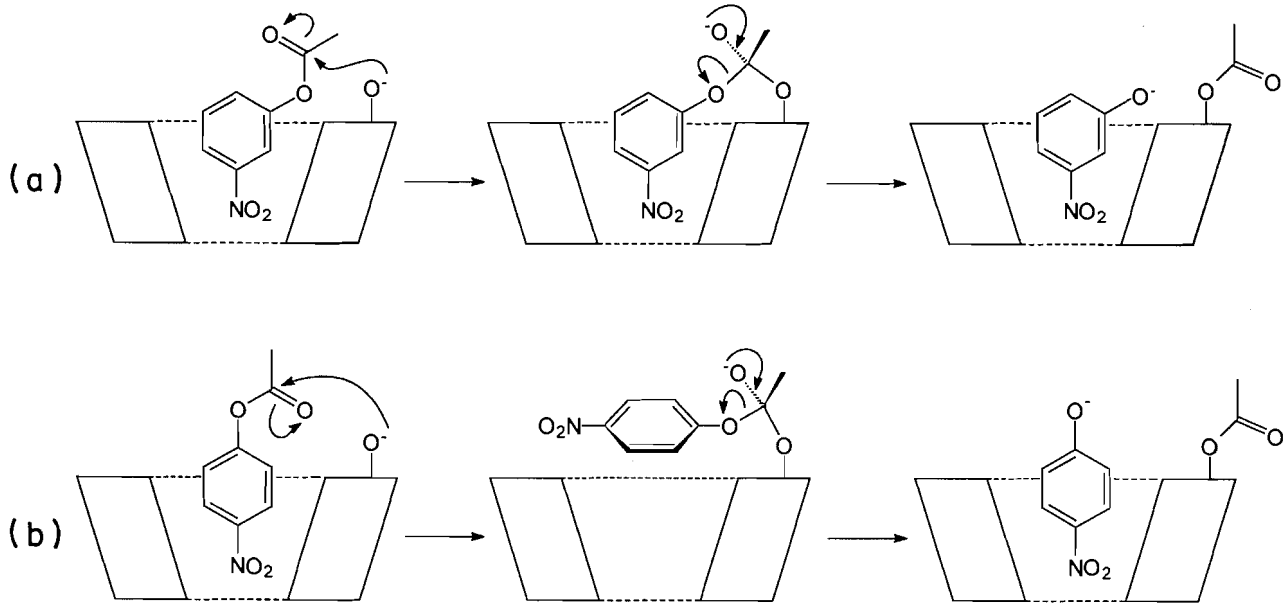

is closer to an ionized hydroxy group than in the case of the *para* esters (**2**). This conclusion is also supported by NMR data, which indicate that the O=C···OH distance is greater in the {*p*-ester·CD} complex than in the {*m*-ester·CD} complex (12). Likewise, the rate enhancement afforded to the cleavage reaction is inversely dependent on the carbonyl–hydroxy group separation (13).

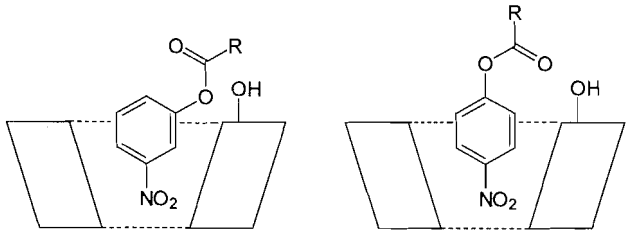

1 **2**

Saturation kinetics and NMR data (12) have shown that the *p*- and *m*-nitrophenyl acetates are bound initially via aryl group inclusion. The *meta* ester is bound to the CD in such a way that the carbonyl group is better oriented for the rate-limiting nucleophilic attack of an ionized CD hydroxy group on the carbonyl carbon of the ester (Scheme 1*a*). However, for the *para* ester to undergo nucleophilic attack, the ester must first lift out of the CD cavity, to bring the carbonyl group closer to the ionized hydroxy group (Scheme 1*b*) (14). This means that the CD cavity is virtually empty[4] during the transition state for ester cleavage. It is conceivable, therefore, that a species with the correct geometry and size might be able to occupy the cavity during the transition state of the cleavage reaction.

It has been shown that the cleavage of *m*-nitrophenyl acetate (mNPA) by α-CD and β-CD is inhibited by molecules such as simple aliphatic alcohols, alkanoate ions, and alkanesulphonate anions. On the other hand, the analogous cleavage of *p*-nitrophenyl acetate (pNPA) in the presence of such "potential inhibitors" (PIs) is retarded to a much lesser degree, and it is even *accelerated* in some instances. This finding is consistent with a situation where the binding of a PI does not allow the normal transition state geometry of the cleavage of mNPA (Scheme 1*a*), but the binding of the PI has little or no effect on the cleavage of pNPA, since the ester is outside the CD cavity during the transition state (Scheme 1*b*) (14).

Both *m*- and *p*-nitrophenyl alkanoates, longer than the acetate and propionate, bind to α-, β-, and Hp-β-CD by inclusion of their acyl chains. The stability of the {ester·CD} complexes shows a strong dependence on the ester chain, with the negative logarithm of the binding constant increasing linearly with the acyl chain length (8, 10). For cleavage of these esters by CDs the mode of transition state binding is not as simple. The *meta* esters show very little dependence of transition state binding on acyl chain length, consistent with a situation in which aryl inclusion is important in the transition state (**3**). The *para* esters, on the other hand, show very little dependence of transition state binding on chain length up to about the hexanoate, after which the transition state binding shows a strong dependence on ester chain length. This behaviour is evidence of a switch in mode of transition state binding from aryl group inclusion (**3**) to acyl group inclusion (**4**) (8, 10) as the acyl chain is lengthened beyond C_5.

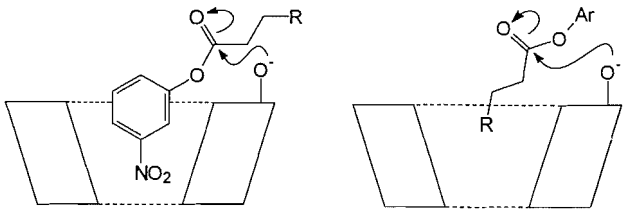

3 **4**

It has also been demonstrated that the cleavage of *p*-nitrophenyl hexanoate (pNPH) by β-CD is not inhibited by the presence of various PIs (15), although the ester is bound by its acyl chain in both the initial state and the transition state. Not only is the reaction not inhibited, it is *catalyzed* by many alco-

[4] In this case we use the term "empty" to mean a lack of any species, other than water, in the cavity.

hols acting as the PI, which means that in the transition state the ester is oriented in such a way that the binding of the PI does not interfere with formation of the transition state and that it can actually lead to a more reactive geometry. The involvement of a molecule of PI is supported by the observation of saturation kinetics that indicate the formation of a 1:1:1 {pNPH·β-CD·PI} complex (15).

The strengths of binding of small molecules containing simple alkyl groups (e.g., alcohols, alkanoate esters, alkanesulphonate ions) to Hp-β-CD are essentially identical to those for binding to β-CD (16, 17) but larger compounds may bind to Hp-β-CD much more tightly than to β-CD (18). For example, 1,8-anilinonaphthalenesulphonate ion (1,8-ANS) is bound more tightly to Hp-β-CD than to β-CD by more than an order of magnitude (17). However, the size of the guest alone cannot account for the difference in binding strengths to these two CDs, since 4-(2-pyridylazo)-*N*,*N*-dimethylaniline complexes with β-CD and Hp-β-CD with dissociation constants of 2.9 and 3.3 mM, respectively (19). Because of the similarity in binding behaviours of alcohols and of alkanoate esters to β-CD and Hp-β-CD (16), we were interested in seeing whether transition state binding in the cleavage of pNPA and pNPH by Hp-β-CD in the presence of PIs is also similar to that for the parent CD or if there is a substantial difference. Some difference was anticipated since the cleavage of nitrophenyl esters by Hp-β-CD is less efficient than that by β-CD (10).

The aim of this paper is to demonstrate how alcohols mediate the cleavage of pNPA and pNPH by Hp-β-CD, and to compare these results with those obtained previously for α-CD and β-CD.

Results

We have examined the effect of various alcohols, containing three to six carbons, on the rates of cleavage of pNPA and pNPH in basic aqueous solution containing Hp-β-CD. The reactions were carried out in a 0.20 M phosphate buffer at pH 11.60. Before discussing the results, we review the pertinent kinetic models used to understand them.

The esters (S) undergo cleavage in the basic medium, eq. [1], and through an ester·CD complex (S·CD), eq. [2], or its kinetic equivalent, so that the dependence of k_{obs} on CD concentration ([CD]) is given by eq. [3], where K_s is a dissociation constant.

$$[1]\quad S \xrightarrow{k_u} \text{Products}$$

$$[2a]\quad S + CD \underset{K_s}{\rightleftharpoons} S{\cdot}CD$$

$$[2b]\quad S{\cdot}CD \xrightarrow{k_c} \text{Products}$$

$$[3]\quad k_{obs} = \frac{k_u K_s + k_c[CD]}{K_s + [CD]}$$

The addition of an inert PI, capable of binding to CD, eq. [4], reduces the concentration of free CD, and k_{obs} is reduced in accord with eq. [3], assuming $k_c > k_u$.

$$[4]\quad CD + PI \underset{K_I}{\rightleftharpoons} CD{\cdot}PI$$

In the CD-mediated cleavage of *m*-nitrophenyl acetate (mNPA) the addition of a PI causes a reduction in the k_{obs}, which obeys the model for competitive inhibition just presented. Analysis of the dependence of k_{obs} on PI concentration by a method described in detail elsewhere (14, 17) allows for the determination of the dissociation constant (K_I) of the CD·PI complex. Values of K_I obtained in this way for PIs binding with α-CD and β-CD (14) generally agree well with results in the literature obtained by other methods (14, 16, 17, 20). The K_I values for alcohols (Table 1) and alkanesulphonate anions binding to Hp-β-CD were also determined by this method and they are reported elsewhere (16, 17).

Table 1. Constants for the cleavage of *p*-nitrophenyl acetate by "hydroxypropyl-β-cyclodextrin" in the presence of various alcohols.[a]

ROH	K_I, mM	k_a, M^{-1} s^{-1}	k_b, M^{-1} s^{-1}	K_{TS}, mM
1–PrOH	319	0.349	13.6	983
iso-PrOH	279	0.432	14.7	795
2–BuOH	83.6	0.851	8.70	403
1–BuOH	64.0	1.18	9.23	291
2–PenOH	41.4	1.21	6.14	282
tert-BuOH	40.1	1.31	6.42	262
iso-BuOH	37.6	1.58	7.24	218
1–PenOH	16.7	3.03	6.18	113
2–HexOH	13.2	–[b]	–[b]	–[b]
c-PenOH	10.7	5.00	6.53	68.6
iso-PenOH	9.28	6.76	7.67	50.7
1-HexOH	4.56	7.39	4.12	46.4
neo-PenOH	2.86	11.6	4.07	29.5
c-HexOH	2.19	17.4	4.67	19.7

[a]Reactions carried out in 0.2 M phosphate buffer, pH 11.60 at 25.0°C. Values of K_I are taken from Matsui and Mochida (20).
[b]Not determined because 2-HexOH inhibited the reaction, see text.

For the present study only aliphatic alcohols of three to six carbons were examined as PIs. They span a wide structural variety, including straight and branched chain (primary, secondary, and tertiary), as well as cyclic alcohols. Overall, the 14 alcohols studied span two orders of magnitude in K_I, providing a range of ability to bind to Hp-β-CD. The addition of these alcohols to the reaction medium of the cleavage of pNPA and pNPH by Hp-β-CD did not inhibit the reaction in the manner required for competitive inhibition, with 2-hexanol (2-HexOH) and the cleavage of pNPA being the sole exception (vide infra). In some cases the addition of PI caused a slight depression in k_{obs} , while in others there was a distinct *acceleration* (Figs. 1 and 2).

As stated above, 2-HexOH did inhibit the reaction of pNPA in the presence of Hp-β-CD. Analyzing the dependence of k_{obs} on [PI] affords a K_I for the {2–HexOH·Hp-β-CD} complex of 14.0 ± 0.9 mM, which is indistinguishable from the value obtained from the inhibition of the cleavage of mNPA (13.2 ± 1.4 mM). It is interesting to note that 2-HexOH did not inhibit the cleavage of pNPA in the presence of β-CD, although it binds to β-CD with similar strength, K_I = 11 mM (14, 20).

In analyzing our data for PI-mediated cleavage, we have taken as our working hypothesis that a reaction occurs between the PI and the ester·CD complex, eq. [5]. Combining

Fig. 1. The effect of alcohols on the cleavage of pNPA by Hp-β-CD. The symbols are ■, i-PrOH; ●, 2-PenOH; ▼, neo-PenOH. The solid lines were calculated using eq. [6] and the appropriate constants found in Tables 1 and 3. The broken lines are those expected for competitive inhibition, calculated using eq. [3] and [CD], corrected for {CD·PI} formation. Likewise, [PI] on the horizontal axis is corrected.

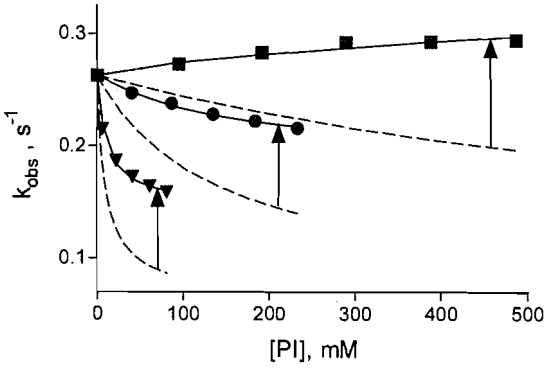

Fig. 2. The effect of alcohols on the cleavage of pNPH by Hp-β-CD. The symbols are ■, i-PrOH; ●, 2-PenOH; ▼, neo-PenOH. The solid lines were calculated using eq. [6] and the appropriate constants found in Tables 1 and 3. The broken lines are those expected for competitive inhibition, calculated using eq. [3] and [CD], corrected for {CD·PI} formation. Likewise, [PI] on the horizontal axis is corrected.

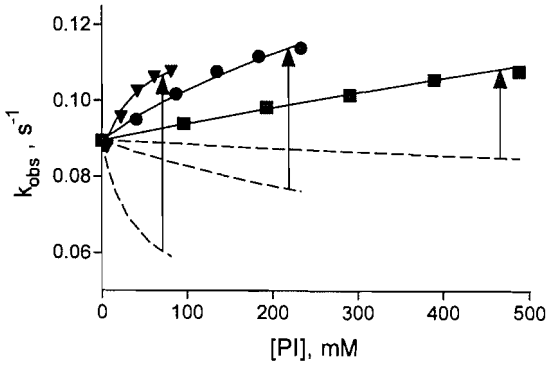

eq. [5] with the two for the reaction in the absence of PI (eqs. [1] and [2]) the expression for k_{obs} is now as described by eq. [6].

$$[5]\quad S\cdot CD + PI \xrightarrow{k_a} \text{Products} + PI$$

$$[6]\quad k_{obs} = \frac{k_u K_s + (k_c + k_a[PI])[CD]}{K_s + [CD]}$$

Equation [6] is not particularly convenient since it is both nonlinear and bivariate but it is made more tractable by linearization, which also brings about a separation of variables, as in eq. [7]. This manipulation amounts to correcting the observed rate constant for the background reaction and the binding of the substrate to the CD, leaving only the terms due to reactions with the CD. Proper use of either eqs. [6] or [7] requires that the amounts of free CD and free PI are employed. These can be calculated from the initial concentration of both species, knowing K_I (7, 14, 21).

Table 2. Constants for the cleavage of *p*-nitrophenyl hexanoate by "hydroxypropyl-β-cyclodextrin" in the presence of various alcohols.[a]

ROH[b]	k_a, M^{-1} s^{-1}	k_b, M^{-1} s^{-1}	K_{TS}, mM
1–PrOH	0.104	21.0	891
iso-PrOH	0.0593	11.9	1570
2-BuOH	0.209	11.0	445
1-BuOH	0.237	9.52	393
2-PenOH	0.253	6.57	368
tert-BuOH	0.205	5.18	454
iso-BuOH	0.336	7.94	277
1-PenOH	0.653	6.85	142
c-PenOH	1.02	6.86	91.0
iso-PenOH	1.06	6.21	87.4
1-HexOH	1.38	3.96	67.3
neo-PenOH	2.06	3.71	45.1
c-HexOH	3.01	4.15	30.9
2-HexOH	1.06	9.29	87.8

[a]As in Table 1.
[b]Values of K_I for the alcohols are given in Table 1.

$$[7]\quad k_{corr} = \frac{k_{obs}(K_s + [CD]) - k_u K_s}{[CD]} = k_c + k_a[PI]$$

According to eq. [7], variations in k_{corr} with [PI] should be linear and the slope equals the rate constant k_a. Several examples of this analysis are shown in Fig. 3 and the linearity of the plots indicates that the assumption of only one molecule of the PI being involved in the transition state is valid. Tables 1 and 2 summarize the k_a values obtained for pNPA and pNPH reacting with Hp-β-CD in the presence of 13 and 14 alcohols, respectively.

The k_a values increase markedly with the ability of the alcohol to bind to Hp-β-CD. For the cleavage of pNPA by Hp-β-CD they range from 0.35 to 17 M^{-1} s^{-1}, an increase of almost 50-fold. These values are decidedly lower than those observed in the case of β-CD, which ranged from 2.8 to 83 M^{-1} s^{-1} (14). For the cleavage of pNPH by Hp-β-CD the k_a values range from 0.10 to 1.1 M^{-1} s^{-1}, an increase of only a factor of 11, whereas for reaction with β-CD, the k_a values varied from 1.4 to 61 M^{-1} s^{-1}, a 44-fold range (21). This difference may be associated with the fact that β-CD forms reactive {S·CD·PI} complexes, whereas there was no evidence for ternary complex formation with Hp-β-CD (vide infra).

Discussion

The results reported above support a cleavage pathway involving the ester (pNPA or pNPH), Hp-β-CD, and *one* molecule of PI. Since the alcohols span a variety of structural types it is unlikely that they interact in a covalent manner; it is more likely that they act as inert space fillers, or "spectators," simply occupying the CD cavity during the transition state for ester cleavage. This same conclusion was drawn for the analogous processes involving α- and β-CD (14, 21) and in the case of pNPA it is consistent with a mechanism for ester cleavage that has the ester largely outside the CD cavity during the

Fig. 3. Examples of the linear dependence of k_{corr} on [PI] (eq. [7]) for the cleavage of pNPA (*A*) and pNPH (*B*) by Hp-β-CD, for the same data as presented in Figs. 1 and 2, respectively. For such plots, [PI] must be corrected for the formation of {CD·PI}. The symbols are the same as in Figs. 1 and 2.

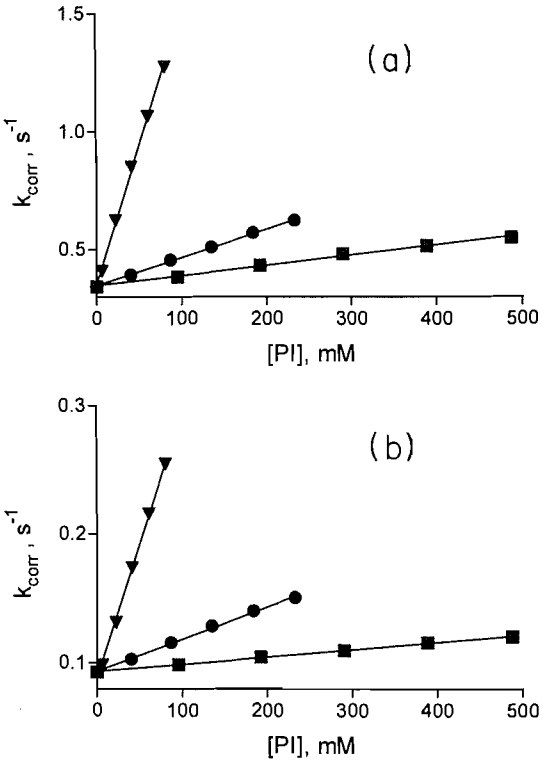

transition state (Scheme 1*b*). For the cleavage of pNPH, we must consider a situation where the acyl portion of the ester is either completely outside of the cavity, or intrudes only slightly, which is different from what seems to happen in the absence of PI (**4**). As detailed below, our analysis of the data with the various PIs supports this interpretation.

The rate constants for the reaction of the PI with the S·CD complex (k_a) increase regularly for pNPA and pNPH as the ability of the PI to bind to the CD increases (Tables 1 and 2). For each ester, there is a good linear free energy relationship[5] (LFER) between the rate constants and the dissociation constants for the CD·PI complexes (eqs. [8] and [9], where $pK_I = -\log K_I$):

[8] pNPA, $\log k_a = 0.77pK_I - 0.87$ ($N = 13$, $r = 0.992$)

[9] pNPH, $\log k_a = 0.74pK_I - 1.52$ ($N = 14$, $r = 0.979$)

These LFERs support the hypothesis that the PI is bound inside the CD cavity during the transition state and the slopes of ~0.75 indicate that its mode of binding is similar to that in the CD·PI complex. The fact that the slopes of the two relationships are almost the same strongly suggests that the involvement of the PI in the two cases is very similar, although the two esters themselves may interact differently in the transition state. Most probably the transition state for the cleavage of both esters is one where the ester resides largely *outside* the CD cavity.

The slope of eq. [9] for the reaction of pNPH with Hp-β-CD is the same as that of the analogous reaction with β-CD (0.75), and lower than that observed with α-CD (1.02) (21). These slopes indicate that the 2-hydroxypropyl groups on the primary side of the CD do not influence the dependence of k_a on the ability of the PI to bind to the CD, whereas altering the width of the CD cavity appears to play a more significant role. This difference can be ascribed to the wider cavities of β-CD and Hp-β-CD allowing the PI to "move around" in the transition state, which decreases the sensitivity of the transition state binding to the nature of the PI because the CDs can more easily accommodate the ester.

The results in the case of pNPA are somewhat different. The slope of the LFER in eq. [8] (0.77) falls in between those observed for β-CD (0.67) and α-CD (1.02) (14). The larger slope for Hp-β-CD means that the cleavage of pNPA is more sensitive to the ability of the PI to bind to Hp-β-CD than to β-CD. This is consistent with a mechanism whereby the pNPA sits outside of the cavity in order for the nucleophilic attack to occur, orienting the phenyl ring directly above the CD cavity (Scheme 1*b*), thereby forcing the PI further down into the CD cavity, where it would come into contact with the 2-hydroxypropyl groups to a greater extent, thus giving a stronger dependence of log k_a on pK_I. The absence of this "extra sensitivity" in the cleavage of pNPH is in agreement with a transition state similar to **4** where the acyl group is oriented towards the CD cavity but largely or completely outside of it. Therefore, the PI would not be forced down further into the CD cavity to bring it into contact with the 2-hydroxypropyl groups, and the behaviour with Hp-β-CD would be similar to that observed with β-CD, as is the case.

Since the PI seems to be bound to the CD in more or less the same way in the initial and transition states, it may be more appropriate to consider the reaction as taking place between the ester and the CD·PI complex (eq. [10]), which is kinetically indistinguishable from that in eq. [5]:

[10] $S + CD{\cdot}PI \xrightarrow{k_b} \text{Products} + PI$

The rate constant for this process can be determined from that for the third-order reaction of S + CD + PI → products ($k_3 = k_a/K_s = k_b/K_I$), using $k_b = k_aK_I/K_s$, and values calculated in this manner are given in Tables 1 and 2.

The values of k_b do not show as much variation with the alcohol as k_a, and they fall within much narrower ranges, 4.0–15 M^{-1} s^{-1} for pNPA and 3.7–21 M^{-1} s^{-1} for pNPH, with most of them being within the ranges of 4–9 M^{-1} s^{-1} and 4–10 M^{-1} s^{-1}, respectively. These values are lower than those for the analogous reactions with β-CD (14, 21), and lower than the second-order rate constant for the reaction of Hp-β-CD with the esters, $k_2 = k_c/K_s$ (Table 3), but they are consistent with the reaction as described in eq. [10], as long as the ester is mainly outside of the cavity during the transition state, so that the PI may be accommodated (transition states **5** for pNPA; **6** for pNPH).

To examine further the transition state binding we have used a method developed by Kurz (23), which allows one to

[5] Although we are aware that the reliability of LFERs has been recently brought into question (22), we feel that they are valid tools for the analysis of physical organic data and continue to use them.

Table 3. Parameters for the cleavage of pNPA and pNPH by CDs.[a]

Ester	CD	k_u, s^{-1}	k_c, s^{-1}	K_s, mM	k_2, M^{-1} s^{-1}
pNPA[b]	Hp-β	0.0653	0.343	8.18	41.9
pNPH[b]	Hp-β	0.0444	0.0932	1.59	58.6
pNPA[c]	β	0.0772	0.660	7.92	83.3
pNPH[d]	β	0.0451	0.137	1.60	85.6

[a]Values of k_c and K_s were estimated by nonlinear fitting of eq. [3].
[b]Reference 10.
[c]Reference 14.
[d]Reference 21.

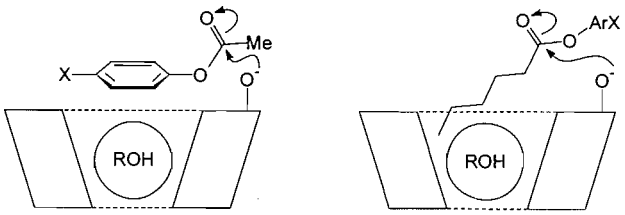

5 6

estimate the stabilization imparted to the transition state by the catalyst in a catalyzed reaction. This method affords an *apparent* dissociation constant of the transition state containing the catalyst into the transition state for the uncatalyzed reaction and the catalyst. It has been widely used by enzymologists (24) and by us for the analysis of CD-mediated processes (8–11, 14, 21, 25 and references therein).

Applying transition state theory to the reaction in eq. [2*b*], we obtain an expression for the rate of reaction given by eq. [11]:

$$[11] \quad \text{rate} = k_c[\text{S}\cdot\text{CD}] = \nu[\text{TS}]$$

and likewise we obtain eq. [12] for the PI-mediated reaction in eq. [5]:

$$[12] \quad \text{rate} = k_a[\text{S}\cdot\text{CD}][\text{PI}] = \nu[\text{TS}\cdot\text{PI}]$$

Dividing eq. [11] by eq. [12] yields an expression for the apparent dissociation of the PI from the PI-containing transition state (eq. [13]), in terms of the known constants k_c and k_a (or k_2 and k_3) [14]:

$$[13] \quad \text{TS} + \text{PI} \underset{K_{TS}}{\rightleftharpoons} \text{TS}\cdot\text{PI}$$

$$[14] \quad K_{TS} = \frac{[\text{TS}][\text{PI}]}{[\text{TS}\cdot\text{PI}]} = \frac{k_c}{k_a} = \frac{k_2}{k_3}$$

The values of K_{TS} for the cleavage of pNPA and pNPH by Hp-β-CD in the presence of PIs are shown in Tables 1 and 2. Using either formalism in eq. [14] for the calculation of K_{TS} is acceptable since $k_2 = k_c/K_s$ and $k_3 = k_a/K_s$.

As discussed in detail elsewhere (25), variations in the values of pK_{TS} (= $-\log K_{TS}$) can be used as a probe of transition state binding. In this study we look at LFERs between pK_{TS} for

Fig. 4. Correlation of transition-state binding (pK_{TS}) of alcohols with pK_I for the binding of the alcohols to Hp-β-CD. Solid squares are for the cleavage of pNPA and open squares are for pNPH cleavage.

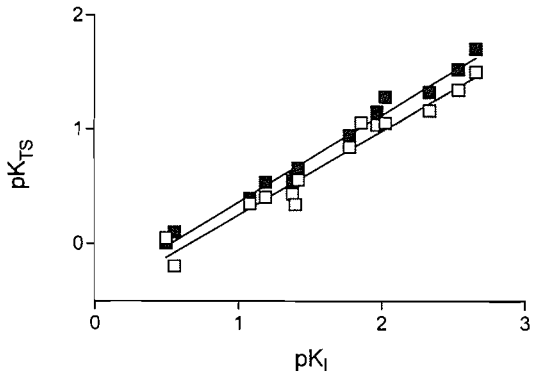

the transition state binding in {TS·PI} and pK_I for the initial state binding in the CD·PI complex. For the cleavage of pNPA and pNPH by Hp-β-CD in the presence of a large number of alcohols we found:

$$[15] \quad \text{pNPA}, \quad pK_{TS} = 0.77pK_I - 0.41 \quad (N = 13, r = 0.992)$$

$$[16] \quad \text{pNPH}, \quad pK_{TS} = 0.74pK_I - 0.49 \quad (N = 14, r = 0.979)$$

These two correlations are shown in Fig. 4. Except for the intercept terms, the equations are identical to those in eqs. [8] and [9] since $K_{TS} = k_c/k_a$ and k_c is a constant for a particular ester reacting with Hp-β-CD (Table 3).

We interpret the similarity between the slope and intercept term of eqs. [15] and [16] to indicate that the binding of the PI in the initial state and the transition state is similar for the alcohol-mediated cleavage of both esters. Although both sets of data in Fig. 4 are almost coincident, this does not necessarily imply that the esters are included in the CD cavity to the same extent during the transition state. Since the intercepts of both eqs. [15] and [16] are so similar it is possible that the PIs are in identical environments during the alcohol-mediated cleavage, which would necessitate the placement of the ester completely outside of the CD cavity; on the other hand, it is possible that the similarity is fortuitous and the result of interactions involving both the ester and the distal 2-hydroxypropyl groups. With β-CD there is a definite difference between the two corresponding correlations: pNPA, $pK_{TS} = 0.67pK_I + 0.19$ (14); pNPH, $pK_{TS} = 0.75\ pK_I + 0.53$ (21). Not only are the slope and intercept terms different for β-CD than for Hp-β-CD, but the PI is bound more tightly in the cleavage of pNPH than pNPA, which is opposite to that observed with Hp-β-CD, and pK_{TS} has a different dependence on pK_I in the cleavage of the two esters.

One of the major contributing factors to the difference observed between β- and Hp-β-CD for the cleavage of pNPH may be the formation of ternary {S·CD·PI} complexes. Such complexes were apparent in the PI-mediated cleavage of pNPH by β-CD (21), but no evidence of ternary complex formation was observed with any of the alcohols and pNPH + Hp-β-CD. Tee et al. found that in the transition state the alcohol is bound in a manner very similar to the ternary complex, although the binding in the transition state is weaker (21). The

dependences of pK_{TS} on pK_I for the PI-mediated cleavage of pNPH by both β- and Hp-β-CD are the same, but the transition state binding for β-CD is stronger. This observation substantiates the claim that the ester is included in the transition state for the cleavage of pNPH by β-CD, but not in the cleavage by Hp-β-CD. The exact origin of these differences is unclear but they are most probably due to the 2-hydroxypropyl groups on the primary side of the Hp-β-CD cavity preventing the formation of the ternary complex involving pNPH.

The differences between the cleavage of pNPA by β-CD and Hp-β-CD in the presence of PIs are not so easy to explain. We know that pNPA and the alcohols studied bind to β-CD and Hp-β-CD with equal strengths (16) and so it has been concluded that the binding occurs to the wider side of the CD cavity (16, 17). Presumably the alcohols approach the CD cavity from the wider secondary face of the cavity, since the hydroxypropyl groups on the primary face do not appear to affect the binding. For a molecule of alcohol to be included in the CD cavity, one or more molecules of water must be excluded. If, during the rate-limiting step, water molecules are required to move in or out of the cavity via the narrow side of the cavity, then the 2-hydroxypropyl groups may retard this process and lead to a less stable transition state. Such an effect in the case of pNPH would mean that both water transport and lack of ternary complex formation play significant roles in the transition state destabilization of the cleavage pNPH by the Hp-β-CD, relative to β-CD.

Conclusions

This paper presents data that show that the cleavage of pNPA and pNPH by Hp-β-CD can occur with a molecule of a PI in the CD cavity. Although both esters bind to Hp-β-CD, as evidenced by saturation kinetics (10), and pNPH is included in the CD cavity during the transition state for the cleavage reaction in the absence of PI (10), it does not necessarily follow that the esters are in the CD cavity during the transition state for the PI-mediated cleavage. The PI may allow for the formation of a transition state of different geometry, which may be more or less reactive. It is clear from the present and earlier results that the inclusion of a PI in the transition state for the cleavage of pNPA and pNPH does not necessarily inhibit the reaction, and that the effect of the PI depends on the size and shape of both the ester, the PI, and the CD.

We conclude that the esters are largely outside of the CD cavity during the transition state for the PI-mediated cleavage of pNPA and pNPH by Hp-β-CD. We note that there are differences between the cleavage of these esters by β-CD and Hp-β-CD, while the only structural differences between the two CDs are the 2-hydroxypropyl groups on the Hp-β-CD, which are by all accounts located away from the centre of activity. Although the exact nature of the effect due to the 2-hydroxypropyl groups is unclear, they may act to restrict the movement of species in and out of the CD via the narrow side of the cavity, which may be necessary to allow for the inclusion of the PI during the transition state.

Experimental

We used Hp-β-CD that has an average molecular weight of 1500, from the Aldrich Chemical Company, without further purification. This material corresponds to a β-CD where about six of the seven hydrogens on the primary hydroxy groups have been replaced by 2-hydroxypropyl groups. The *p*-nitrophenyl acetate and hexanoate were purchased from Sigma and used as received.

The alcohols used as PIs were purchased from Aldrich and were of the highest grade available. After prolonged storage, some secondary alcohols formed peroxides; this was tested for by mixing several millilitres of the alcohol with a saturated solution of KI. If peroxides are present I_2 and I_3^- are formed, giving the solution a yellow colour. Solutions found to contain peroxides were either distilled prior to use or replaced with a fresh supply. **Warning:** the distillation of alcohols containing peroxides must be watched *very* carefully, so as to prevent the distillation flask from boiling dry, which may lead to an explosion.

All reactions were carried out in a 0.20 M phosphate buffer at pH 11.60 and 25.0 ± 0.1°C. The reactions were initiated by mixing equal volumes of phosphate buffer (0.40 M) containing the PI with a solution containing Hp-β-CD (40 or 4.0 mM) and ester ($[pNPA]_o$ = 100 μM; $[pNPH]_o$ = 50 μM). The final concentrations of all species were half of these, after mixing.

The kinetics of ester cleavage were followed by monitoring the first-order appearance of *p*-nitrophenolate ion at 405 nm, using an Applied Photophysics SX17MV stopped-flow spectrophotometer, as described previously (11, 26). The pseudo first-order rate constants, k_{obs}, were determined by fitting a single exponential equation to the absorbance data, using software provided by the instrument manufacturer. The determination of k_{obs} was repeated 5 to 10 times and the values were averaged.

Our analysis based on eq. [7] requires the use of known values of k_u, k_c, and K_s, which were available from previous work (Table 3).

Acknowledgements

We are grateful to the Natural Sciences and Engineering Research Council of Canada (NSERC) for an operating and equipment grant (to O.S.T.), as well as a post-graduate scholarship (to T.A.G.).

References

1. (*a*) J. Szejtli. Cyclodextrins and their inclusion complexes. Akademiai Kiado, Budapest, 1982; (*b*) W. Saenger. Angew. Chem. Int. Ed. Engl. **19**, 344 (1980); (*c*) M. Bender and M. Komiyama. Cyclodextrin chemistry. Springer Verlag, New York. 1978.
2. (*a*) R.L. VanEtten, J.F. Sebastian, G.A. Clowes, and M.L. Bender. J. Am. Chem. Soc. **89**, 3242 (1967); (*b*) R.L. VanEtten, G.A. Clowes, J.F. Sebastian, and M.L. Bender. J. Am. Chem. Soc. **89**, 3253 (1967).
3. (*a*) M. Komiyama and M.L. Bender. J. Am. Chem. Soc. **100**, 4576 (1978); (*b*) Bull. Chem. Soc. Jpn. **53**, 1073 (1980); (*c*) M. Komiyama and S. Inoue. Bull. Chem. Soc. Jpn. **53**, 3334 (1980); (*d*) G.M. Bonora, R. Fornasier, P. Scrimin, and U. Tonellato. J. Chem. Soc. Perkin Trans. 2, 367 (1985).
4. Y. Matsui, T. Nishioka, and T. Fujita. Top. Curr. Chem. **128**, 61 (1985).
5. O.S. Tee and B.K. Takasaki. Can. J. Chem. **63**, 3540 (1985).
6. O.S. Tee and X.-X. Du. J. Org. Chem. **53**, 1837 (1988).
7. O.S. Tee and J.J. Hoeven. J. Am. Chem. Soc. **111**, 8318 (1989).
8. O.S. Tee, C. Mazza, and X.-X. Du. J. Org. Chem. **55**, 3603 (1990).

9. O.S. Tee and X.-X. Du. J. Am. Chem. Soc. **114**, 620 (1992).
10. T.A. Gadosy and O.S. Tee. J. Chem. Soc. Perkin Trans. 2, 715 (1994).
11. O.S. Tee and T.A. Gadosy. J. Chem. Soc. Perkin Trans. 2, 2191 (1994)
12. M. Komiyama and H. Hirai. Chem. Lett. 1471 (1980).
13. M. Komiyama and M.L. Bender. *In* The chemistry of enzyme action. *Edited by* M.I. Page. Elsevier, Amsterdam. 1984.
14. O.S. Tee, M. Bozzi, J.J. Hoeven, and T.A. Gadosy. J. Am. Chem. Soc. **115**, 8990 (1993).
15. O.S. Tee and M. Bozzi. J. Am. Chem. Soc. **112**, 7815 (1990).
16. O.S. Tee, T.A. Gadosy, and J.B. Giorgi. J. Chem. Soc. Perkin Trans. 2, 1705 (1993).
17. T.A. Gadosy, O.S. Tee, and J.B. Giorgi. Can. J. Chem. **74**, 736 (1996).
18. R.P. Frankewich, K.N. Thimaiah, and W.L. Hinze. Anal. Chem. **63**, 2924 (1991).
19. P.M. Demont and V.C. Reinsborough. Aust. J. Chem. **44**, 759 (1991).
20. Y. Matsui and K. Mochida. Bull. Chem. Soc. Jpn. **52**, 2808 (1979).
21. O.S. Tee, M. Bozzi, N. Clement, and T.A. Gadosy. J. Org. Chem. **60**, 3509 (1995).
22. (*a*) S. Hoz. Acta Chem. Scand. **46**, 503 (1992); (*b*) S. Hoz. *In* Abstracts of the 77th Canadian Society for Chemistry Conference (abstract no. 121), Canadian Society for Chemistry, Ottawa. 1994.
23. J.L. Kurz. J. Am. Chem. Soc. **85**, 987 (1963); Acc. Chem. Res. **5**, 1 (1972).
24. (*a*) R. Wolfenden. Acc. Chem. Res. **5**, 10 (1972); (*b*) G.E. Leinhard. Science (Washington, D.C.), **180**, 149 (1973); (*c*) W.P. Jencks. Adv. Enzymol. **43**, 219 (1975); (*d*) R.L. Schowen. *In* Transition states in biochemical processes. *Edited by* R.D. Gandour and R.L. Schowen. Plenum, New York. 1978.
25. (*a*) O.S. Tee. Adv. Carbohydr. Res. **192**, 181 (1989); (*b*) Adv. Phys. Org. Chem. **29**, 1 (1994).
26. O.S. Tee and T.A. Gadosy. J. Chem. Soc. Perkin Trans. 2, 2307 (1994).

Studies on the interaction of selenite and selenium with sulphur donors. Part 4. Thiosulfate[1]

Shermin Rahim and John Milne

Abstract: Raman and Se-77 NMR spectroscopy confirm that when selenous acid is reduced by thiosulfate in water selenopentathionate and tetrathionate are formed.

$$H_2SeO_3 + 4S_2O_3^{2-} + 4H^+ = Se(S_2O_3)_2^{2-} + S_4O_6^{2-} + 3H_2O$$

Depending upon the stoichiometry and pH, two isomers of the selenopentathionate ion, O- and S-bonded, are formed. Insufficiently acid solutions cause decomposition to selenium and tetrathionate ion.

$$Se(S_2O_3)_2^{2-} = Se + S_4O_6^{2-}$$

Fresh solutions prepared from crystalline sodium selenopentathionate and water undergo slow decompositon. NMR and Raman spectra show the presence of both the O-bonded and S-bonded linkage isomers. The O-bonded isomer facilitates the formation of tetrathionate. Addition of thiosulfate to selenotrithionate solution or sulfite to selenopentathionate solution yields trithionate with no indication of dithionate or tetrathionate formation. This suggests that simple S—S bond formation at selenium does not occur but that there may be direct attack of the incoming ligand on the attached ligand.

Key words: selenite, thiosulfate, selenopentathionate, Se-77 NMR, Raman spectroscopy, linkage isomerism.

Résumé : Les spectroscopie Raman et RMN du ^{77}Se confirment que, lorsque l'acide séléneux est réduit par le thiosulfate dans l'eau, il se forme des séléno-pentathionate et tétrathionate.

$$H_2SeO_3 + 4S_2O_3^{2-} + 4H^+ = Se(S_2O_3)_2^{2-} + S_4O_6^{2-} + 3H_2O$$

Suivant la stoechiométrie et le pH, les deux isomères de l'ion sélénopentathionate, liés par O et par S, se forment. Des solutions insuffisamment acides provoquent une décomposition en sélénium et en ion tétrathionate.

$$Se(S_2O_3)_2^{2-} = Se + S_4O_6^{2-}$$

Des solutions fraîchement préparées à partir de sélénopentathionate de sodium et de l'eau se décomposent lentement. Les spectres Raman et de RMN indiquent la présence des deux isomères liés par O et par S. L'isomère lié par O facilite la formation de tétrathionate. L'addition de thiosulfate à une solution de sélénotrithionate ou de sulfite à une solution de sélénopentathionate conduit à la formation de trithionate et il n'y a aucune indication de formation de dithionate ou de tétrathionate. Ces résultats suggèrent qu'il ne se produit pas de formation d'une liaison S—S simple au niveau du sélénium, mais qu'il peut se produire une attaque du coordinat qui arrive sur le coordinat qui est attaché.

Mots clés : sélénite, thiosulfate, sélénopentathionate, RMN du ^{77}Se, spectroscopie Raman, isomérie de liaison.

[Traduit par la rédaction]

Received December 13, 1995.

S. Rahim and J. Milne.[2] Ottawa–Carleton Chemistry Institute, Department of Chemistry, University of Ottawa, Ottawa, ON K1N 6N5, Canada.

[1] Part 3: see ref. 10.

[2] Author to whom correspondence may be addressed. Telephone: (613) 562-5728. Fax: (613) 562-5170. E-mail: jmilne@oreo.chem.uottawa.ca

Introduction

The formation of the selenopentathionate ion, $Se(S_2O_3)_2^{2-}$, was first reported by Norris and Fay (1, 2). The anion was produced by the reduction of selenous acid with thiosulfate in acid solution and the reaction was used as the basis of an iodimetric method of analysis for selenites.

[1] $H_2SeO_3 + 4S_2O_3^{2-} + 4H^+ = Se(S_2O_3)_2^{2-} + S_4O_6^{2-} + 3H_2O$

Crystalline selenopentathionates were prepared by Foss (3, 4), using this reaction, and the X-ray structure determination of barium selenopentathionate dihydrate showed that the selenium is S-bonded and occupies the central position in the anion (5). Reaction [1] parallels that of selenous acid with thiols (6) and with thiocyanic acid (7),[3]

[2] $H_2SeO_3 + 4RSH = RSSeSR + RSSR + 3H_2O$

and their mechanisms (8, 9) are no doubt closely related. Reactions of selenous acid with sterically hindered thiols (8) and with sulfite ion (10) both produce -SSeS- analogues but the oxidation products are exceptional. Hindered thiols produce significant amounts of thiosulfonate, RSO_2SR, in addition to disulfide, and sulfite yields sulfate instead of dithionate ion. Although the formation of the selenopentathionate anion and the reaction stoichiometry have been established for reaction [1], spectroscopic methods have not been used and the precise nature of the sulphur oxoanion is not known. Moreover, the possibility of linkage isomerism, like that observed for selenotrithionate ion (10) and for thiosulfato–metal coordination complexes (11), has not been explored for the selenopentathionate ion. For these reasons, we undertook an investigation of reaction [1] by Raman and Se-77 NMR spectroscopy.

Experimental section

Materials

Freshly ground vitreous selenium (BDH; >99.5%), sodium thiosulfate (BDH), and sodium sulfite (BDH), were all used directly. Selenium dioxide (Aldrich) was analyzed before use by titration against standard NaOH. Distilled water, purged of oxygen by passage of nitrogen, was used thoughout.

Preparations

Sodium selenopentathionate 3-hydrate and sodium pentathionate 1.5-hydrate were prepared by the standard literature methods (3, 12). The 0.375 M tetrathionate solution was made up from a sodium thiosulfate solution and the stoichiometrically required amount of potassium triiodide solution, which were mixed dropwise at ambient temperature. The mixtures of selenous acid, sodium thiosulfate, and sulfite were made up at 0°C from deoxygenated aqueous solutions of the sodium salt and SeO_2.

Methods

The Se-77 NMR spectra were measured with a Bruker AMX 500 spectrometer operating at 95.47 MHz. A 30° tip angle was used with a 0.3 s acquisition time and no pulse delay. Between 1000 and 4000 transients were collected for each spectrum with a resolution of 3 Hz/data point. A line broadening of 5 Hz was applied and the signal-to-noise ratio was between 5 and 100, depending upon the signal. All signal line widths were estimated to lie between 3 and 20 Hz. The samples were contained in 10 mm diameter precision NMR tubes and the probe temperature was held at 5°C. All chemical shifts were measured by sample replacement with respect to saturated selenous acid in water at 22°C (13). The chemical shifts are all listed relative to $\delta(Me_2Se) = 0.0$ ppm ($\delta(Me_2Se) = \delta(H_2SeO_3) + 1300$ ppm (13)).

Raman spectra were measured with a Jobin–Yvon Ramanor HG.2S monochromator in conjunction with a PAR/Hamamatsu photon-counting system. The spectra were excited with the krypton ion line at 647.1 nm and the slits were fixed at 1600 μm, giving a resolution of better than 7 cm^{-1} at 1000 cm^{-1}. Quantitative spectra were measured at ambient temperature (23°C) and normalized against 1.0 M perchloric acid for which the 930 cm^{-1} band was taken to have an intensity of 6.45 cm^2 L mol^{-1} (14).

Results and discussion

Selenothiosulfate, $SeS_2O_3^{2-}$, formation constant

Elemental selenium dissolves to a very small extent in thiosulfate solutions (56 mg in 100 mL 2.0 M sodium thiosulfate) to produce a colourless solution. The formation constant for the reaction,

[3] $S_2O_3^{2-} + Se = SeS_2O_3^{2-}$

was determined by gravimetry and found to be 3.6×10^{-3} at 23°C. Selenothiosulfate formation is much less extensive than formation of the selenothiolate anion formed with 2-hydroxyethanethiolate, $HOCH_2CH_2S^-$ ($K = 0.47$ at 23°C), reflecting the decreased basicity of the terminal sulphur attached to an $[SO_3^{2-}]$ moiety relative to that of sulphur attached to $[CH_2CH_2OH^-]$. The concentration of the selenothiosulfate ion was too small for observation of an NMR signal by routine Se-77 NMR or Raman spectroscopy.

Reaction of selenite and thiosulfate

The Se-77 NMR spectrum of a 1:4:4 molar ratio solution of $SeO_2/Na_2S_2O_3/HCl$ ($c(SeO_2) = 0.5$ M), prepared by dropwise addition of a $Na_2S_2O_3$ solution to SeO_2 in HCl at 0°C, exhibits a single chemical shift at 774.3 ppm, which lies in the range of chemical shifts for Se(II) bound to two sulphur neighbours (10). The Raman spectrum of a solution prepared in the same way but with $c(SeO_2) = 0.43$ M is shown in Fig. 1 (trace B). This spectrum shows no peaks due to thiosulfate or sulfate ion. The Raman spectrum of a 0.38 M solution of sodium tetrathionate prepared by iodine oxidation of thiosulfate ion is shown in Fig. 1 (trace A). The appearance of the characteristic $S_4O_6^{2-}$ peak at 1045 cm^{-1}, to the high-frequency side of the selenopentathionate peak at 1031 cm^{-1}, and the peaks at 310 and 135 cm^{-1} in trace B is consistent with complete reaction of selenous acid and thiosulfate in acid solution as shown in eq. [1]. The other $S_4O_6^{2-}$ peaks are masked by selenopentathionate peaks at 263, 397, 520, 652, and 1237 cm^{-1}. The Raman spectrum of a 1.0 M solution of selenopentathionate, made up from the sodium salt and taken immediately after preparation,

[3] C.J. Milne and J. Milne. Manuscript in preparation.

Fig. 1. Raman spectra. Trace A: 0.375 M $S_4O_6^{2-}$; trace B: 1:4:4 $SeO_2/S_2O_3^{2-}$/HCl molar ratio ($c(SeO_2)$ = 0.43 M); trace C: 1.00 M $Na_2Se(S_2O_3)_2$ (spectrum taken immediately after makeup); trace D: crystalline $Na_2Se(S_2O_3)_2 \cdot 3H_2O$.

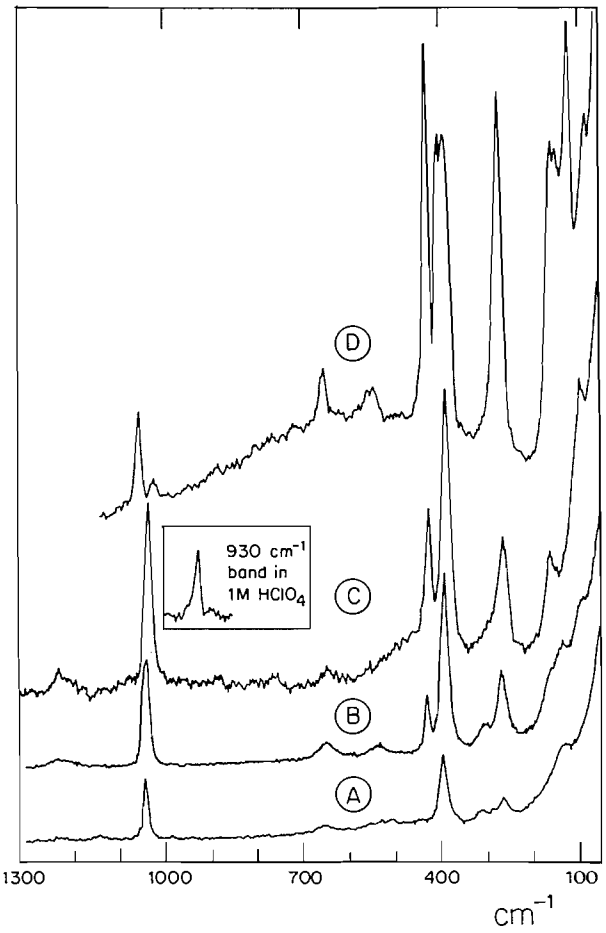

is given in trace C of Fig. 1 and that of crystalline $Na_2Se(S_2O_3)_2$ is given in trace D. The spectrum in trace B parallels that of the $Se(S_2O_3)_2^{2-}$ ion in traces C and D when allowance is made for the presence of the $S_4O_6^{2-}$.

The Raman spectral bands for the selenopentathionate ion in solution and in the sodium salt are listed in Table 1, along with a tentative assignment of the modes, according to the principal atomic motion that is taking place. The spectra of the pentathionate ion in solution and solid are also listed. The symmetric and asymmetric stretching and deformation modes for the [SO_3] units (1031–1053 cm^{-1}, 1210–1235 cm^{-1}, 632–652 cm^{-1}, 520–545 cm^{-1}) and the δ(SSO) mode (304–310 cm^{-1}) are assigned by comparison with similar modes in the thiosulfate ion (1004 cm^{-1} ($\nu_s(SO_3)$), 1106 cm^{-1} ($\nu_a(SO_3)$), 670 cm^{-1} ($\delta_s(SO_3)$), 538 cm^{-1} ($\delta_a(SO_3)$), 339 cm^{-1} (δ(SSO)) (15)). No attempt has been made to distinguish between in-phase and out-of-phase members of these modes, which lie relatively close together for each spectrum within each vibrational mode description, nor has the effect of local symmetry lowering on the doubly degenerate modes been considered. The symmetric stretching mode of the SSeS chain (263–269 cm^{-1}) is readily identified in the spectra by its intensity and by comparison with the related mode in the selenotrithionate ion (285 cm^{-1} (10)). The slightly lower frequency in the spectrum of $Se(S_2O_3)_2^{2-}$ may be attributed to the greater mass of the groups attached to the selenium in $Se(S_2O_3)_2^{2-}$ compared to $Se(SO_3)_2^{2-}$. The most intense observed bands in the spectra of both anions (385–431 cm^{-1}) are assigned to the symmetric and asymmetric, or in- and out-of-phase SS stretching modes (distal SS bonds in the spectrum of the $S_5O_6^{2-}$ ion). The frequencies of these bands are to be compared to the SS stretching frequency in the $S_2O_3^{2-}$ ion (447 cm^{-1} (15)). For the pentathionate, the sharp peaks in the range 480–500 cm^{-1} are assigned to the proximal SS stretching modes ($\nu(SS)_{prox}$). These modes are expected to lie to higher frequency than the distal SS stretching modes based upon the relative SS bond distances (16) as determined in crystalline $BaS_5O_6 \cdot 2H_2O$ (5) (d(SS)(distal) = 2.14 Å; d(SS)(proximal) = 2.04 Å). The predicted frequencies for these distances are 360 (distal) and 470 (proximal) cm^{-1} (16). The bands at 143–162 cm^{-1} in the spectrum of the selenopentathionate and 196–288 cm^{-1} in the pentathionate probably arise from $\delta(SChS)_s$, judging from their strength. The remaining low-frequency bands are assigned to torsional and lattice modes.

The Se-77 NMR spectrum of sodium selenopentathionate dissolved in 1:1 H_2O/HOAc by volume gives a single resonance at 775.8 ppm comparable with the chemical shift observed for the solution with 1:4:4 $SeO_2/Na_2S_2O_3$/HCl molar ratio (774.3 ppm). The signal in acidic solutions lies 107 ppm below the signal for selenotrithionate ion (881 ppm (10)), consistent with greater shielding as a result of binding to sulphur of lower oxidation state in the selenopentathionate compared to the sulphur in selenotrithionate. These acidic solutions are stable over a period of hours but neutral or basic solutions are less stable and precipitate elemental Se, usually within minutes. The variable stability of these solutions is not understood at present but preparation at 0°C improves their stability. A solution of 1:1 $SeO_2/Na_2S_2O_3$ molar ratio ($c(SeO_2)$ = 0.10 M) gives an NMR spectrum consisting of three signals at 770.2, 826.5, and 1310.5 with peak area ratio of 5.0/1.1/18. The deshielded signal arises from selenite ion (13) and the two signals with lower shifts belong to Se(II) species. The ratio of the intensities of the Se(IV) and Se(II) peaks is observed to be 3.0 to 1.0, which corresponds to the stoichiometry required by the reaction

$$[4]\quad H_2SeO_3 + S_2O_3^{2-} = 1/4S_4O_6^{2-} + 1/4Se(S_2O_3)_2^{2-} + 1/2HSeO_3^- + 1/4SeO_3^{2-} + 3/4H_2O$$

Apparently reaction [1] goes to completion but is limited by the amount of thiosulfate present. Two Se(II) species are formed in this solution. The Se-77 NMR spectrum of a 1.0 M solution of selenopentathionate ion, made up in water from crystalline sodium selenopentathionate at room temperature, shows only two signals at 775.0 and 832.5 ppm with intensity ratio 12.6/1.2, respectively, indicating the presence of the same species as in the 1:1 $SeO_2/S_2O_3^{2-}$ mixture. No selenium precipitation occurred in this solution during the period of time necessary for both Se-77 and Raman (vide infra) spectra to be recorded.

Two kinds of isomerism might be expected to occur in pentathionates, (*i*) rotational isomerism, which has been reported in crystalline solids for a variety of trichalcogen chains, where the terminal attached groups, [SO_3] groups in this case, may lie *cis* or *trans* with respect to the three-chalcogen plane (17,

Table 1. Raman spectra of solutions of mole ratio 4:4:1 $HCl/Na_2S_2O_3/SeO_2$ ($c(SeO_2)$ = 0.43 M), $Na_2S_4O_6$ (c = 0.375 M), $Na_2Se(S_2O_3)_2$ (c = 1.0 M), and solid $Na_2Se(S_2O_3)_2 \cdot 3H_2O$ (frequencies in cm^{-1}).

4:4:1 $HCl/Na_2S_2O_3/SeO_2$ (c_{Se} = 0.43 M)	$Na_2S_4O_6$ (0.375 M)	$Na_2Se(S_2O_3)_2$[a] (1.0 M)	$Na_2Se(S_2O_3)_2$[b] (solid)	$Na_2S_5O_6$ (0.50 M)	$Na_2S_5O_6$ (solid)	Assignment for $Ch(S_2O_3^{2-})$ (Ch = S, Se)
—	—	—	89(1)	—	83(8)	
90(1)	—	93(1)	107(5)	95(1)	118(2)	
137(1)	135(2)	—	—	—	—	
160(1)	—	162(2)	143(3) 157(3)	196(2) 288(2)	206(3) 284(4)	δ(SChS)
268(4)	263(2)	264(4)	269(10)	—	—	$\nu(SChS)_s$
—	—	295(1, sh)	—	—	—	
308(1)	310(1)	—	—	310(1)	304(1)	δ(SSO)
392(10)	397(10)	389(10)	388(9) 401(9)	391(10)	385(10)	ν(SS)
431(3)	—	426(4)	428(10)			
				500(2)	480(1) 500(3)	$\nu(SS)_{prox}$
532(1)	520(1)	525(2, sh, br)	545(1, sh)	—	538(0)	$\delta(SO_3)_a$
652(1, br)	652(1, br)	648(1, br)	652(2)	640(1, br)	632(1, br)	$\delta(SO_3)_s$
1040(5)	1044(10)	1035(7)	1020(2) 1053(3)	1031(9)	1034(3)	$\nu(SO_3)_s$
1235(1, br)	1235(1, br)	1210(1, br) 1229(1)	1210(0)	1230(1, br)	—	$\nu(SO_3)_a$

[a]Spectrum taken immediately after solution preparation.
[b]Spectrum recorded up to 1300 cm^{-1}.

18) and (*ii*) S- and O-bonded linkage isomerism, where the $[S_2O_3]$ moiety may be bound to the central chalcogen by sulfur or oxygen. This latter type of isomerism has been observed for the selenotrithionate ion (10) in solution and S- and O-bonded isomers have been reported in Co(III) complexes (11*a*) although there is some controversy in this latter case (11*d*). The barrier to rotation about an SS bond has been estimated to be 21 kJ mol^{-1} (19). Moreover, rotation about the SS bond in 1,2-dithiane is rapid on the proton NMR time scale at ambient temperatures (20). Rotation about SeS bonds is expected to be less hindered than that about SS bonds and the observation of two Se-77 NMR peaks in the spectrum of the selenopentathionate ion is unlikely to arise from this type of isomerism. The NMR spectra are best accounted for by the formation of S- and O-bonded linkage isomers, of which three are possible.

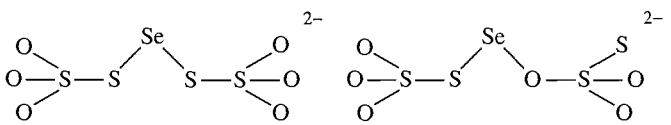

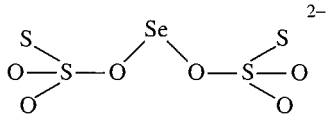

The signal at 775 ppm is due to the [SS] isomer and that at 832.5 ppm, to either the [OS] or [OO] isomer. In the selenotrithionate isomers the signal for the [OO] isomer is 310 ppm less shielded than that of the [SS] isomer and that of the [OS] isomer is only 78 ppm less shielded. On this basis, since the second signal in the spectrum of the sodium selenopentathionate solution is only 58 ppm less shielded, it probably arises from the [OS] isomer. Further support for this interpretation comes from work by Kice, Wilson, and Espinola (21), who report the chemical shift for *t*-BuSOSeSBu-*t* at 854 ppm. The presence of S- and O-bonded isomers is supported by the Raman spectrum shown in Fig. 2 of the same 1.0 M sodium selenopentathionate solution used for the NMR experiment. This spectrum shows two strong bands, at 882 and 1089 cm^{-1}, in addition to those shown for the [SS] isomer in Fig. 1 (trace C). These bands correspond, respectively, to the single bond SO and the symmetric SO_2 stretching modes of the O-bonded thiosulfate moiety and may be compared with the related modes for the H_2SO_4 molecule (ν(S-O) = 910, $\nu_s(SO_2)$ = 1137 cm^{-1} (15)). Furthermore, comparison of the intensities of the remaining strong bands at 318, 391, 430, and 1033 cm^{-1}, relative to that of the 1 M $HClO_4$ normalization band in the spectra in both figures, shows that the bands assigned to the [SS] isomer have decreased in intensity as would be expected with the formation of the isomer. The spectrum of the O-bonded isomer should also exhibit characteristic bands corresponding to ν(SeO) and ν(SS(terminal)). These are probably overlapped with the $\delta(SO_3)$ modes in the spectrum in Fig. 2. Selenium oxygen single bond stretching lies in the region of 650 cm^{-1} in the selenotrithionate ion (10) but SS(terminal) stretching vibrations are much more variable, appearing near 450 cm^{-1} in thiosulfate ion (15) and at 758 cm^{-1} in SSF2 (22). The weak band at 1280 cm^{-1} arises from $\nu_a(SO_2)$ of the O-bonded thiosulfate group in the [OS] isomer.

Fig. 2. Raman spectrum of 1.00M $Na_2Se(S_2O_3)_2$, taken 5 h after makeup.

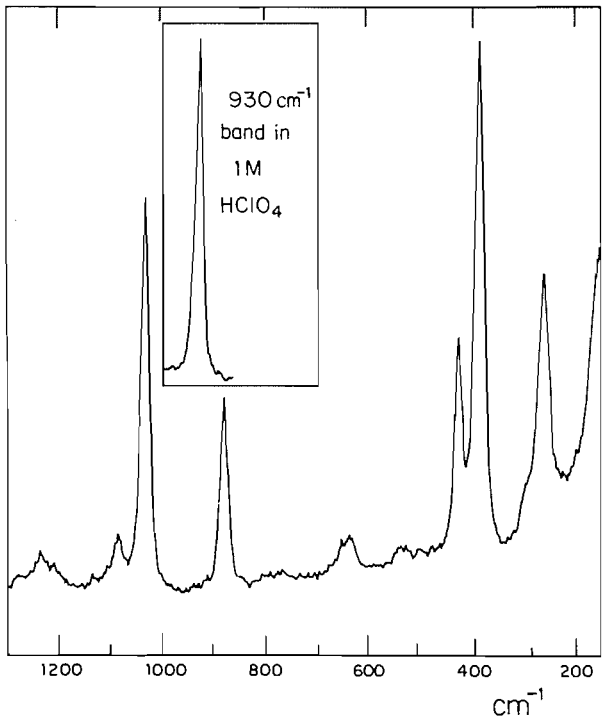

Fig. 3. Raman spectra of 0.48 M $K_2S_3O_6$ (trace A), a mixture of 0.50 M $Na_2Se(S_2O_3)_2$ and Na_2SO_3 (trace B), and a mixture of 0.29 M $Na_2Se(SO_3)_2$ and SO_4^{2-} (see text) and 0.87 M $Na_2S_2O_3$ (trace C).

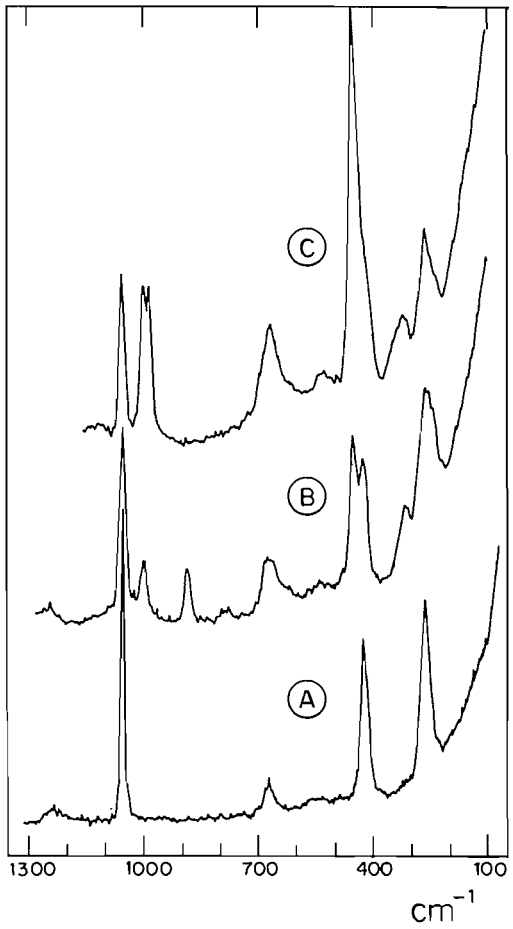

Reactions of excess sulphur donor anions with selenopenta- and selenotri-thionates

It is well known that the addition of excess sulphur donor to -SSeS- species causes decomposition to elemental selenium and the corresponding -SS- species (9). Kinetic studies have shown that nucleophilic attack on the three-chalcogen chain for bis(alkylthio)selenides (23) may occur at Se or S. The addition of thiosulfate in excess of that required for reaction [1] produces, over a period of days, copious amounts of elemental selenium. The Raman spectrum of the filtrate from the solution shows the characteristic bands of the tetrathionate anion at 395 and 1040 cm^{-1} with reduced intensity of the selenopentathionate spectrum. No evidence of other polythionates was found. To find out more about the mechanism of attack of excess sulphur donor on selenopolythionate anions, the reactions of selenopentathionate with sulfite and selenotrithionate with thiosulfate were studied. The Raman spectrum of a solution 0.50 molar in sodium selenopentathionate and sodium sulfite, which was mixed and left to stand for 24 h then filtered, is given in Fig. 3, trace B. The characteristic peaks of the [SS] isomer of the selenopentathionate anion at 389 and 1035 cm^{-1} are missing but some of the [OS] isomer is present, judging from the presence of peaks at 882 and 1089 cm^{-1}. It would be of great interest to locate the frequency of the SS stretching band in this isomer. This mode would be expected to be strong but we can only conclude that it is hidden by the envelope at 400–490 cm^{-1}. The remaining bands are readily assigned to thiosulfate (335, 450, 535, 673, and 1000 cm^{-1}) and trithionate (263, 427, 672, and 1053 cm^{-1}, trace A in Fig. 3). The broad band near 675 cm^{-1} consists of $[SO_2]$ deformation modes, and the envelope around 440 cm^{-1} contains SS stretching modes, from the [OS] isomer of selenopentathionate, thiosulfate, and trithionate ions. The breadth of the band at 1052 cm^{-1}, compared to that in the spectrum of the trithionate ion (trace A), shows that there is some contribution to this peak also from selenopentathionate. No band at 397 cm^{-1}, which would be resolved from the peak at 430 cm^{-1} under the conditions used, is observed, indicating the absence of significant concentrations of tetrathionate ion. The spectrum indicates that decomposition is occurring by the reaction

[5] $Se(S_2O_3)_2^{2-} + SO_3^{2-} = S_3O_6^{2-} + S_2O_3^{2-} + Se$

This result appears to support a mechanism in which electrophilic attack by sulfite takes place at the sulphur attached to Se, similar to the nucleophilic attack of thiolate proposed for bis(alkylthio) selenides (23). In another possible mechanism, which has been proposed (9), SS links between the ligands (SO_3^{2-} and $S_2O_3^{2-}$) would be formed by rearrangement of the three-coordinate intermediate, $Se(SO_3)(S_2O_3)_2^{4-}$, resulting in the formation of elemental selenium and either $S_4O_6^{2-}$ and SO_3^{2-} or $S_3O_6^{2-}$ and $S_2O_3^{2-}$. Such a mechanism would be facilitated by the near proximity of the ligands in the three-

coordinate complex. Given equivalent opportunity for SS bond formation, the ratio of $S_4O_6^{2-}$ to $S_3O_6^{2-}$ from such a three coordinate complex would be 1:2. However, if the attack occurred at one of the sulphurs of the SSeS chain, trithionate would be produced exclusively, as observed. Electrophilic attack may occur on the chain sulphur of the [SS] isomer or on the terminal sulphur of the [OS] isomer to form trithionate. In view of the low formation constant for $SeS_2O_3^{2-}$, the species left after trithionate formation, elemental selenium would be precipitated, releasing thiosulfate.

$$[6]\quad O_3SSSeSSO_3^{2-} \xrightarrow{SO_3^{2-}} O_3SSSO_3^{2-} + SeSSO_3^{2-}$$

$$[7]\quad SeSSO_3^{2-} = Se + SSO_3^{2-}$$

A third mechanism, which involves nucleophilic attack by the chain sulphur of the selenopentathionate ion on S(IV) in the O-bonded sulfite ligand of the complex, is discussed below.

Addition of excess sodium thiosulfate to a solution of sodium selenotrithionate, made by the reaction (10)

$$[8]\quad H_2SeO_3 + 2HSO_3^- + SO_3^{2-} \longrightarrow Se(SO_3)_2^{2-} + SO_4^{2-} + 2H_2O$$

also produced large amounts of elemental Se. The Raman spectrum of the solution ($c(Se(SO_3)_2^{2-}$ = 0.29 M; $c(S_2O_3^{2-})$ = 0.87 M), filtered after a day of standing, is given in Fig. 3, trace C. No characteristic strong peaks for the selenotrithionate ion at 236, 285, and 1030 cm^{-1} (10) appear in the spectrum, showing that reaction is complete. Judging from the absence of any peaks at 387, 882, and 1032 cm^{-1}, selenopentathionates are not present in significant amounts. Foss (4) has reported that thiosulfate ion displaces sulfite from selenotrithionate to give selenopentathionate,

$$[9]\quad Se(SO_3)_2^{2-} + 2S_2O_3^{2-} = Se(S_2O_3)_2^{2-} + 2SO_3^{2-}$$

but this is not supported by the Raman spectra. The spectrum is readily accounted for by the presence of sulfate (980 cm^{-1}, reaction [8]), trithionate (263, 427, 1053 cm^{-1}, trace A, Fig. 3), thiosulfate (339, 447, 538, 1004 cm^{-1} (15)), which was present in stoichiometric excess, and selenosulfate (310 cm^{-1} (10)).

$$[10]\quad Se(SO_3)_2^{2-} + S_2O_3^{2-} \rightarrow S_3O_6^{2-} + SeSO_3^{2-}$$

$$[11]\quad SeSO_3^{2-} = Se + SO_3^{2-}$$

The small amount of sulfite present as a result of equilibrium [11] (K = 2 (10)) is not detected because of the low intensity of sulfite modes (I(970 cm^{-1}) = 3.5 cm^2 L mol^{-1} and I(480 cm^{-1}) = 1.5 cm^2 L mol^{-1}) and overlap with strong bands of other anions present. The broad peak at 670 cm^{-1} has contributions from [SO_3] deformations for all sulphur-containing ions present. The presence of $SeSO_3^{2-}$ ion is only detected because of the very great intensity of the SeS stretching mode at 310 cm^{-1} (10), which appears on the side of the SSO deformation mode of the $S_2O_3^{2-}$ ion at 340 cm^{-1}. It is unlikely that the products of reaction [10] are produced by direct nucleophilic attack of thiosulfate ion on the sulfite sulphur of the S-bonded selenotrithionate ion for steric reasons. However, if some of the $Se(SO_3)_2^{2-}$ ion was present as the O-bonded isomer, then direct attack could occur.

Conclusions

The reaction of selenous acid with thiosulfate ion parallels that of other sulphur donors such as thiols and thiocyanic acid. The selenopentathionate ion in solution exhibits linkage isomerism like that of the selenotrithionate ion but it appears that only SSeS and OSeS linkages are formed for the selenopentathionate, compared to all three possible linkages to selenium in the case of selenotrithionate (10). The compounds isolated from these solutions show only SSeS linkages. No evidence for such linkage isomerism is observed in the case of the analogous pentathionate and trithionate ions in solution.[4] Solutions of selenopentathionate undergo slow decomposition to produce elemental selenium and tetrathionate ion and this process probably proceeds via the O-bonded isomer, which only appears in solutions of selenopentathionate upon standing and before decomposition to give elemental selenium. This isomerization step would provide a plausible intermediate for the process, with a terminal sulphur atom that could attack the proximal sulphur of the neighbouring thiosulfate group, producing tetrathionate. A similar mechanism accounts for the formation of trithionate in solutions of thiosulfate and selenotrithionate, where the sulfite sulphur is exposed to nucleophilic attack by thiosulfate via the O-bonded selenotrithionate isomer. A similar mechanism would be possible for the selenopentathionate/sulfite reaction and this is particularly attractive inasmuch as the sulfite coordination to Se(II) in the SeO_2/sulfite reaction takes place initially over oxygen (10). The importance of Se in these mechanisms, i.e., the initial coordination of sulfite or thiosulfate to selenium in the three-chalcogen chain of the selenopolythionate ions, seems likely in view of the relative inertness of the central sulphur in trithionate to attack by thiosulfate to form tetrathionate in these studies. It might be expected that, if the reaction proceeded by direct attack on sulphur as proposed in other studies (23), the susceptibility of the proximal sulphur in selenopentathionate and pentathionate ions would be comparable. This aspect should be checked and, obviously, further Raman studies and rate studies will be needed to reveal the details of these reactions.

Acknowledgements

Sheila Ball is thanked for some preliminary preparative experiments and Raj Capoor for recording the Se-77 NMR spectra. The Natural Sciences and Engineering Research Council of Canada is thanked for financial support.

References

1. J.T. Norris and H. Fay. Am. Chem. J. **18**, 703 (1895).
2. J.T. Norris and H. Fay. Am. Chem. J. **23**, 119 (1900).
3. O. Foss. Inorg. Synth. **7**, 88 (1963).
4. O. Foss. Acta Chem. Scand. **3**, 435 (1949).
5. O. Foss and O. Tjomsland. Acta Chem. Scand. **8**, 1701 (1954).
6. H.E. Ganther. Biochemistry, **7**, 2898 (1968).
7. S.M. Ohlberg and P.A. van der Meulen. J. Am. Chem. Soc. **75**, 997 (1953).

[4]J. Milne, unpublished data.

8. J.L. Kice, T.W.S. Lee, and S. Pan. J. Am. Chem. Soc. **102**, 4448 (1980).
9. W. Amaratunga and J. Milne. Can. J. Chem. **72**, 2506 (1994).
10. S. Ball and J. Milne. Can. J. Chem. **73**, 716 (1995).
11. (*a*) R.J. Restivo, G. Ferguson, and R.J. Balahura. Inorg. Chem. **16**, 167 (1977); (*b*) H. Ruben, A. Zalkin, M.O. Faltens, and D.H. Templeton. Inorg. Chem. **13**, 1836 (1974); (*c*) A.R. Murdock, T. Tyree, W. Otterbein, L. Kinney, M. Carreras, and J.N. Cooper. Inorg. Chem. **24**, 3674 (1985); (*d*) D.E. Peters and R.T.M. Fraser. J. Am. Chem. Soc. **87**, 2758 (1965); (*e*) I. Baldea and G. Niac. Inorg. Chem. **7**, 1232 (1968).
12. G. Brauer. Handbook of preparative inorganic synthesis. Vol. I. Riley, New York. 1963. p. 401.
13. J. Milne. Magn. Reson. Chem. **31**, 652 (1993).
14. J. Milne and P. Lahaie. Inorg. Chem. **18**, 3180 (1979).
15. H. Siebert. Anwendungen der Schwingungsspektroskopie in der Anorganischen Chemie. Springer, Berlin. 1966.
16. R. Steudel., Top. Curr. Chem. **102**, 158 (1982).
17. O. Foss. Acta Chem. Scand. **7**, 1220 (1953).
18. S.M. Ohlberg and A. Vaughan. J. Am. Chem. Soc. **76**, 2649 (1954).
19. L. Pauling. Proc. Natl. Acad. Sci. U.S.A. **35**, 495 (1949).
20. G. Claeson, G.M. Androes, and M. Calvin. J. Am. Chem. Soc. **82**, 4428 (1960).
21. J.L. Kice, D.M. Wilson, and J.M. Espinola. J. Org. Chem. **56**, 3520 (1991).
22. A. Haas and H. Willner. Spectrochim. Acta, Part A: **35A**, 953 (1979).
23. J.L. Kice and H. Slebocka-Tilk. J. Am. Chem. Soc. **104**, 7123 (1982).

Mixed alkali effect in sodium thiocyanate – potassium thiocyanate – acetamide melt systems

Sekh Mahiuddin

Abstract: Electrical conductivity and molar volume of the $0.25[x\text{NaSCN} + (1-x)\text{KSCN}] + 0.75\text{CH}_3\text{CONH}_2$ systems were measured as functions of temperature (≈293.15–358.15 K) and composition ($x = 0.0 - 1.0$ mol fraction). Temperature dependence of the electrical conductivity was non-Arrhenius in nature and has been analysed by using the Vogel–Tammann–Fulcher (VTF) equation. Molar volume data were fitted to an equation similar to the VTF equation based on the free volume model. Molar volumes and intrinsic volumes were found to be additive in nature. Electrical conductivity isotherms deviate from linearity in different fashion for different temperature regions. The onset of the mixed alkali effect is governed by the anion polarization effect, by a contribution of the auto-dissociated molten acetamide, and by polymeric-type solvated ions.

Key words: electrical conductivity, sodium thiocyanate, potassium thiocyanate, acetamide, mixed alkali effect.

Résumé : On a mesuré les conductivités électriques et les volumes molaires des systèmes $0{,}25[x\text{NaSCN} + (1-x)\text{KSCN}] + 0{,}75\text{CH}_3\text{CONH}_2$ en fonction de la température (d'environ 293,15 à 358, 15 K) et de la composition. La relation entre la température et la conductivité électrique n'est pas du type Arrhénius et on l'a analysée en utilisant l'équation de Vogel–Tammann–Fulcher (VTF). Les données de volumes molaires ont été ajustées à une équation semblable à celle de VTF basée sur le modèle des volumes libres. On a trouvé que les volumes molaires et les volumes intrinsèques sont de nature additive. La déviation des isothermes de conductivité électrique par rapport à la linéarité varient de manières différentes suivant les diverses régions de température. Le début de l'effet des alcalins mixtes est gouverné par l'effet de polarisation de l'anion, par une contribution de l'acétamide fondu autodissocié et par le type d'ions solvatés polymériques.

Mots clés : conductivité électrique, thiocyanate de sodium, thiocyanate de potassium, acétamide, effet d'alcalins mixtes.

[Traduit par la rédaction]

Introduction

A pronounced deviation from additivity in the form of minima or maxima is generally observed in ionic and mass transport properties as the concentration of one of the alkali ions is progressively changed in a glass or melt medium (1–6) while the total alkali ion concentration is kept constant. This phenomenon is usually referred to as the mixed alkali effect (MAE). Physical properties that have been used to detect the MAE are conductivity, dielectric loss, viscosity, chemical durability, and internal friction (1, 2). A similar phenomenon has also been observed for metal cation pairs (7) with a large difference in ionic radii between the two ions. The mixed alkali effect, a particular example of the general phenomenon of the mixed cation effect, is well documented (1–3). Although there are many theories to explain the MAE, no theory explains all the data.

A significant MAE has been observed in electrical conductivity and (or) viscosity isotherms for oxide glass systems (1, 2) having an inherent rigid network structure. On the other hand, in systems containing hydrate melt as medium (5, 6) the MAE in conductivity and (or) viscosity isotherms has been detected but to a lesser extent (ca. 4%). Recently, interest has arisen in looking for the MAE in molecular liquid media (8–11) where no rigid network structure exists and deviations (minima or maxima) in electrical conductivity have been observed. Moynihan (4) suggested that the MAE may only be observed in systems with high viscosity and conductivity. On the other hand, Easteal and Emson (12) suggested, based on their studies, that the MAE becomes significant when the total alkali metal ion concentration in the system is high.

Molten acetamide is a good nonaqueous solvent for many inorganic salts due to its dipolar nature (13), and molten acetamide–electrolyte binary systems have a tendency to form supercooled liquid (14). It has been reported that Na^+ ion forms a polymeric type of solvated ion of low ionic mobility with acetamide (15). It would be interesting to study the behaviour of the electrical conductivity of Na/KSCN–acetamide systems with respect to composition and temperature and to determine whether significant MAEs can be observed in the electrical conductivity isotherms, in comparison to Na/KSCN in hydrate melts (5, 6) and aqueous (10) media. In the present communication, the purpose is to investigate the MAE in $0.25[x\text{NaSCN} + (1-x)\text{KSCN}] + 0.75\text{CH}_3\text{CONH}_2$ by measuring density and electrical conductivity as functions of composition and temperature. This system possesses high conductivity and supercooling properties, which are the criteria (4) for detecting the MAE.

Received October 25, 1995.

S. Mahiuddin.[1] Material Science Division, Regional Research Laboratory, Jorhat-785 006, Assam, India.

[1] Fax: 0376 321158.

Experimental section

Both NaSCN (LOBA, extra pure) and KSCN (BDH, LR grade) were recrystallized twice from distilled water and dried over P_2O_5 in a vacuum desiccator. Acetamide (SD, LR grade) was recrystallized twice from hot methanol. Final drying was done in a vacuum desiccator over fused calcium chloride. To avoid exceeding the solubility of both NaSCN (≃30 mol%) and KSCN (≃28 mol%) in molten acetamide, total alkali ion concentration was kept at 0.25 mol fraction. Six samples were prepared.

Densities (ρ) of all solutions were measured accurate to 0.01% by using a precalibrated single-stem pyknometer (≃9.5 cm^3). Electrical conductivity (κ) measurements were made by using a Precision Component Analyser-6425 (Wayne Kerr) operating in the 2.5×10^{-9} to 10 S range with a sensitivity ±0.01 nS, and platinized platinum electrodes (cell constant = 113.2 m^{-1}) with a field frequency of 1.5 kHz. The sample was put in a glass tube with ground joint and the measuring cell was well fitted to prevent diffusion of moisture. The sample tube was purged with dry nitrogen and the test sample was introduced under nitrogen atmosphere. All the measurements were made as functions of composition ($x = 0.0 - 1.0$ mol fraction) and temperature (≃293.15–358.15 K). A Schott-Geräte thermostat type CT-1450 was used to maintain the temperature of the measurements to ±0.02 K.

Results and discussion

Measured density values of 0.25 [xNaSCN + (1 − x)KSCN] + 0.75CH_3CONH_2 are linear functions of temperature and are presented in Table 1. The electrical conductivity (κ) and molar volume (V) of the present systems as functions of temperature and composition are presented in Table 2.

The measured conductivity values were found to exhibit non-Arrhenius variation with temperature, with ≃17–28% deviation within the temperature range of the study. The following equation of the Vogel–Tammann–Fulcher (VTF) type has often been used successfully to fit conductivity data, and this is again the case with the present systems.

$$[1] \quad \kappa = A \exp[-B/(T - T_0)]$$

Here A and B are constant parameters and T_0 is the ideal glass transition temperature. The best-fit values of A, B, and T_0 obtained by least squares are listed in Table 3.

The onset of the MAE in the present systems has been examined by plotting T_0, A, and B versus x in Fig. 1. It is interesting to observe the nature of the variation of T_0 as a function of composition with both positive (in the Na^+-ion-rich region) and negative (in the K^+-ion-rich region) deviations. In general, either negative or positive deviations in T_g or T_0 with alkali ion concentration have been reported for mixed alkali systems in hydrate melts (4–6) or molecular liquids (8–11) but a system with both positive and negative deviations in T_0 has not yet been reported. For x = 1.0, the system represents the binary system 0.25NaSCN + 0.75CH_3CONH_2 with T_0 = 210.1 K, which is in reasonable agreement with T_g = 234 K (14) reported for the system 0.225NaSCN + 0.775CH_3CONH_2. The observed variation of T_0, A, and B with x (Fig. 1) reveals that the systems exhibit MAE. A probable mechanism for the peculiar variation of T_0 with x will be examined below.

Table 1. Least-squares fitted values of the density equation, $\rho = a - b(T - 273.15)$ for the 0.25[xNaSCN + (1 − x)KSCN] + 0.75CH_3CONH_2 systems.

x	a/kg m^{-3}	b/kg m^{-3} K^{-1}	σ^a
0.0	1227.5 ± 0.1	0.7258 ± 0.0024	0.09
0.2	1222.4 ± 0.1	0.7539 ± 0.0031	0.07
0.4	1218.6 ± 0.2	0.7684 ± 0.0041	0.11
0.6	1213.2 ± 0.2	0.7875 ± 0.0040	0.11
0.8	1212.3 ± 0.1	0.7847 ± 0.0031	0.09
1.0	1206.3 ± 0.2	0.7889 ± 0.0036	0.10

[a]Root-mean-square deviation.

Fig. 1. Variation of T_0, A, and B with composition, x, for the 0.25[xNaSCN + (1 − x)KSCN] + 0.75CH_3CONH_2 systems.

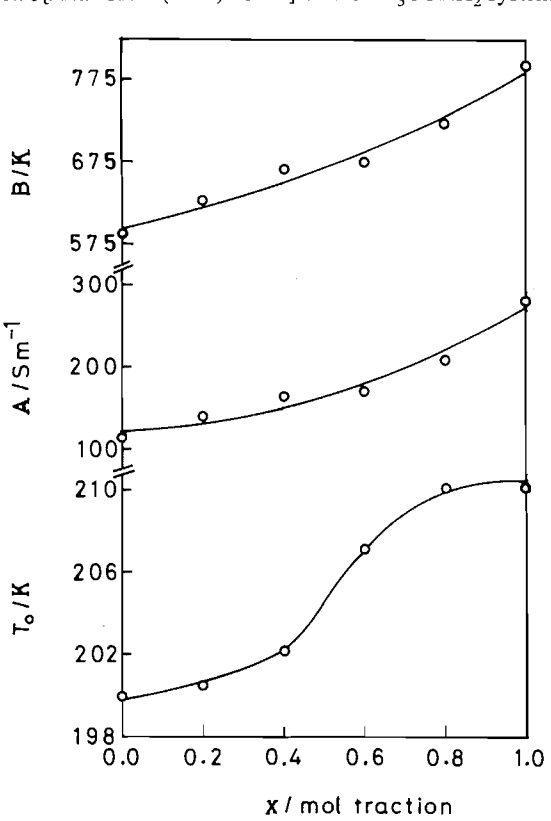

The conductivities of the present systems also vary nonlinearly with the molar volume. Molar volume dependence of the conductivity is explained by using the following equation, similar to eq. [1], derived based on the free volume model:

$$[2] \quad \kappa = A' \exp[-B'/(V - V_0)]$$

where A' and B' are constant parameters and V_0 is the intrinsic volume. The best-fit values of A', B', and V_0 are illustrated and presented in Fig. 2 and Table 4, respectively. From Fig. 2 it is apparent that V_0 decreases linearly with x. However, A' and B' vary nonlinearly with x. The composition dependence of A' and B' can be represented with reasonable accuracy by empirical equations of a polynomial type $A' = 80.03 + 6.53x +$

Table 2. Electrical conductivity and molar volume[a] data for the $0.25[x\text{NaSCN} + (1 - x)\text{KSCN} + 0.75\text{CH}_3\text{CONH}_2$ systems.

	κ/S m^{-1} and (V × 10^6/m^3 mol^{-1})					
T/K	x = 0.0	x = 0.2	x = 0.4	x = 0.6	x = 0.8	x = 1.0
358.15	2.7418 (58.84)	2.5725 (58.52)	2.2640 (58.08)	1.9694 (57.74)	1.5785 (57.07)	1.3234 (56.68)
353.15	2.4371 (58.66)	2.2694 (58.33)	1.9773 (57.89)	1.7003 (57.54)	1.3390 (56.88)	1.1054 (56.48)
348.15	2.1439 (58.48)	1.9834 (58.15)	1.7079 (57.70)	1.4501 (57.34)	1.1189 (56.68)	0.9084 (56.29)
343.15	1.8694 (58.30)	1.7145 (57.96)	1.4575 (57.51)	1.2201 (57.14)	0.9214 (56.49)	0.7347 (56.09)
338.15	1.6246 (58.12)	1.4648 (57.77)	1.2272 (57.32)	1.0109 (56.95)	0.7451 (56.30)	0.5823 (55.90)
333.15	1.3879 (57.94)	1.2349 (57.59)	1.0200 (57.13)	0.8245 (56.76)	0.5919 (56.11)	0.4520 (55.71)
328.15	1.1630 (57.76)	1.0273 (57.40)	0.8333 (56.95)	0.6611 (56.57)	0.4606 (55.92)	0.3432 (55.52)
323.15	0.9674 (57.59)	0.8411 (57.22)	0.6685 (56.76)	0.5196 (56.38)	0.3505 (55.73)	0.2540 (55.34)
318.15	0.7899 (57.41)	0.6758 (57.04)	0.5261 (56.58)	0.3993 (56.19)	0.2599 (55.55)	0.1830 (55.15)
313.15	0.6329 (57.24)	0.5325 (56.86)	0.4050 (56.39)	0.2991 (56.00)	0.1876 (55.36)	0.1278 (54.97)
308.15	0.4957 (57.07)	0.4094 (56.68)	0.3034 (56.21)	0.2177 (55.82)	0.1305 (55.18)	0.0862 (54.78)
303.15	0.3809 (56.90)	0.3075 (56.50)	0.2211 (56.03)	0.1542 (55.63)	0.0883 (54.99)	0.0562 (54.60)
301.45				0.1362 (55.57)		
301.25						0.0473 (54.53)
301.15		0.2731 (56.43)				
300.65		0.2644 (56.41)				0.0448 (54.51)
300.15	0.3214 (56.79)				0.0688 (54.89)	
299.85				0.1226 (55.51)		
298.15	0.2873 (56.72)	0.2246 (56.32)	0.1584 (55.85)	0.1056 (55.45)	0.0572 (54.82)	0.0346 (54.42)
294.05	0.2249 (56.59)					
293.15			0.1078 (55.68)			
288.15			0.0710 (55.50)			

[a]Molar volume data are given in parentheses.

Table 3. Best-fit values of the parameters of eq. [1] for the $0.25[x\text{NaSCN} + (1 - x)\text{KSCN}] + 0.75\text{CH}_3\text{CONH}_2$ systems.

x	T_0/K	A/S m^{-1}	B/K	Std. dev. in ln κ
0.0	200.0 ± 1.1	111.7 ± 4.7	585.4 ± 10.4	0.006
0.2	200.5 ± 0.6	138.8 ± 6.0	627.0 ± 10.4	0.005
0.4	202.2 ± 1.1	163.8 ± 8.9	666.0 ± 13.0	0.006
0.6	207.2 ± 2.3	169.4 ± 18.5	671.2 ± 26.5	0.006
0.8	210.1 ± 1.1	210.2 ± 12.4	723.1 ± 13.8	0.005
1.0	210.1 ± 1.1	283.6 ± 18.3	793.3 ± 15.1	0.006

$75.92x^2$ and $B' \times 10^5 = 1.759 + 0.560x + 0.192x^2$ with standard deviations 4.87 and 0.025, respectively. In Fig. 2 the variation of molar volume with composition is also shown for different temperatures.

In $K^+ - Na^+$ mixed alkali systems the K^+ ion has a smaller ionic potential than the Na^+ ion. In the K^+-ion-rich region, the K^+ ion behaves like an inert solute in the medium. As the K^+ ions are progressively replaced by Na^+ ions, Na^+ ions interact with acetamide and result in a polymeric-type solvated ion (15). The variation of V with x (Fig. 2) reveals that the polymeric solvated ion does not seem to cause detectable deviation in the molar volume of the present systems.

On the other hand, the molar volumes of the present systems are linear functions of temperature of the form

$$[3]\quad V = V' + b'T$$

where V' and b' are constant parameters at a particular composition and are presented in Table 5. As the system has an inherent tendency to supercool (14), the temperature dependence of the molar volume may also be represented as

$$[4]\quad V = V_0 + b'(T - T_0)$$

Comparison of eqs. [3] and [4] gives

$$[5]\quad V' = V_0 - b'T_0$$

The values of the intrinsic volume, V_0, calculated from eq. [5]

Fig. 2. Plots of V_0, A', B', and V vs. x for the 0.25 [xNaSCN + (1 − x)KSCN] + 0.75CH_3CONH_2 systems (open and closed circles are observed and solid lines represent calculated values, respectively).

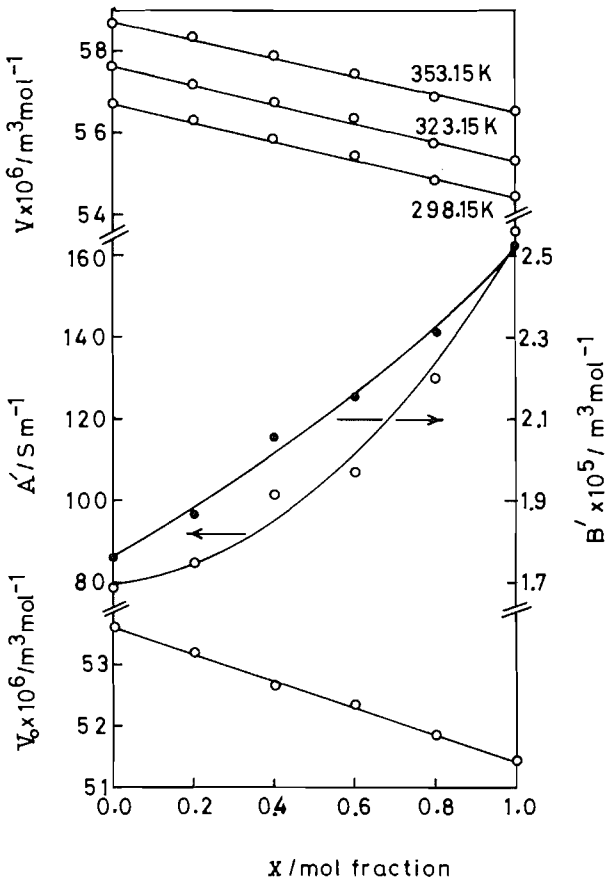

at different compositions using the values of T_0 (eq. [1] and Table 3) and the values of V' and b' (eq. [3] and Table 5) are also presented in Table 4. It is apparent from Table 4 that the V_0 calculated from eq. [5] are reasonably comparable (within 0.8%) with those from eq. [2]. Equilibrium properties such as molar volume and intrinsic volume are additive in nature and vary linearly with composition in spite of the fact that the nature of the composition dependence of T_0 for the present system is not the same throughout.

To examine the MAE in the present system, the composition dependence of the conductivity isotherms is depicted in Fig. 3. An equation of the following type (8) has been used for the concentration dependence of the electrical conductivity:

$$[6] \quad \kappa = a_1 \exp(b_1 x + c_1 x^2)$$

where a_1, b_1, and c_1 are constant parameters. Computed values of the parameters are presented in Table 6. A reasonably good fit has been obtained (Table 6 and Fig. 3).

It is very interesting to note the nature of the variation of conductivity with x above and below ≃323.15 K. The deviation of the κ isotherm from additivity in the temperature range 358.15–353.15 K is positive (≃4.6%, which is more than the uncertainties involved in the experimental data) and is pronounced in the K^+-ion-rich region. Such positive deviation

Table 4. Best-fit values of the paremeters of eq. [2] for the 0.25[xNaSCN + (1 − x)KSCN] + 0.75CH_3CONH_2 systems.[a]

x	A' (S m^{-1})	$B' \times 10^5$ (m^3 mol^{-1})	$V_0 \times 10^6$ (m^3 mol^{-1})	Std. dev. in ln κ
0.0	78.26 ± 4.39	1.758 ± 0.046	53.59 ± 0.05 (53.27)	0.007
0.2	84.61 ± 1.99	1.864 ± 0.019	53.18 ± 0.02 (52.74)	0.003
0.4	101.7 ± 5.5	2.051 ± 0.043	52.68 ± 0.04 (52.31)	0.006
0.6	106.9 ± 2.9	2.151 ± 0.022	52.34 ± 0.02 (51.98)	0.007
0.8	129.9 ± 6.2	2.308 ± 0.037	51.83 ± 0.03 (51.51)	0.007
1.0	165.5 ± 8.7	2.524 ± 0.040	51.44 ± 0.03 (51.11)	0.008

[a]Values of the intrinsic volumes, V_0, calculated from eq. [5] are given in parentheses.

Table 5. Least-squares fitted values of the parameters of eq. [3] for the 0.25[xNaSCN + (1 − x)KSCN] 0.75CH_3CONH_2 systems.

x	$V' \times 10^6$ (m^3 mol^{-1})	$b' \times 10^8$ (m^3 mol^{-1} K^{-1})	$\sigma \times 10^8$ [a]
0.0	46.24 ± 0.04	3.516 ± 0.011	0.92
0.2	45.40 ± 0.03	3.660 ± 0.009	0.68
0.4	44.84 ± 0.04	3.691 ± 0.014	1.13
0.6	44.10 ± 0.04	3.804 ± 0.013	1.02
0.8	43.62 ± 0.04	3.751 ± 0.012	0.97
1.0	43.22 ± 0.04	3.754 ± 0.014	1.04

[a]Root-mean-square deviation.

decreases progressively with decrease in temperature and becomes negative (≃27% in the Na^+-ion-rich region). The deviations (positive and negative) from additivity as observed in the electrical conductivity (Fig. 3) may be attributed to the onset of the MAE in the present system.

From Fig. 3 it is apparent that the nature of the variation of κ with x varies with temperature. There is no clear transition, such as that reported in the Arrhenius plot of viscosity for the 0.225NaSCN + 0.775CH_3CONH_2 binary system (14). On the contrary, the κ vs. x isotherms of the 0.3[xKSCN + (1 − x)NaSCN] + $Ca(NO_3)$ 2·4.06H_2O (5), 0.3[xNaSCN + (1 − x)KSCN] + 0.7 $Na_2S_2O_3$·5.1H_2O (6), and [xNaSCN + (1 − x) KSCN] + RH_2O (10) systems are reported to exhibit a negative deviation from additivity. Similarly $NaNO_3$ – hydrate melt (16), –water (9), and –glycerol (8) systems also exhibit negative deviation in κ vs. x isotherms, and the anion polarization model (APM) (17, 18) has been used to explain the MAE on the electrical conductivity. Berchiesi et al. (14) suggested that the transition at ca. 293 K in the Arrhenius plot of the viscosity may be due to a change in liquid structure. Since our temperature range for the study is above and around 293 K, the nature of the deviation in conductivity isotherms above and below ≃323.15 K (Fig. 3) may be of different origin.

Fig. 3. Plots of conductivity isotherms versus composition for the $0.25[x\text{NaSCN} + (1 - x)\text{KSCN}] + 0.75\text{CH}_3\text{CONH}_2$ systems (circles and solid curves represent observed and calculated values (from eq. [6]), respectively, and broken lines represent the additive property).

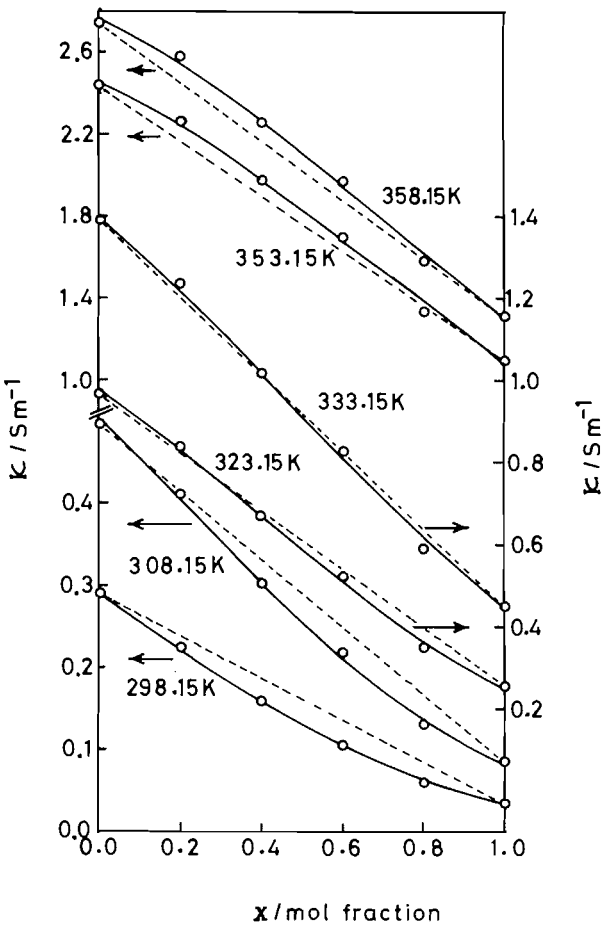

Table 6. Least-squares fitted values of the parameters of eq. [6] for the $0.25[x\text{NaSCN} + (1 - x)\text{KSCN}] + 0.75\text{CH}_3\text{CONH}_2$ systems.

T/K	a_1	b_1	c_1	Std. dev. in ln κ
298.15	0.2902	−1.1118	−1.0439	0.039
308.15	0.5015	−0.9087	−0.8785	0.035
323.15	0.9764	−0.6665	−0.6998	0.027
333.15	1.3990	−0.5554	−0.5914	0.023
353.15	2.4566	−0.3631	−0.4493	0.018
358.15	2.7635	−0.3313	−0.4182	0.018

Fig. 4. Variation of activation energy, E_κ, with composition for the $0.25[x\text{NaSCN} + (1 - x\text{KSCN}] + 0.75\text{CH}_3\text{CONH}_2$ systems (circles and solid curves represent observed and calculated values (from the polynomial equation up to the second degree), respectively).

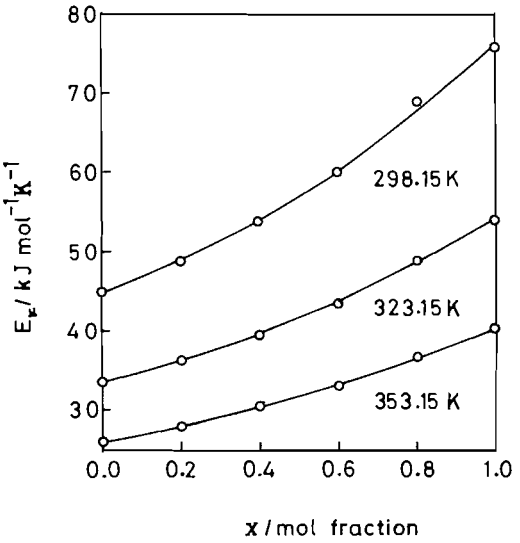

It is reported that molten acetamide, like water, under goes auto-dissociation into $(CH_3CONH_3)^+$ and $(CH_3COHN)^-$ ions (13). The positive deviation (≈4.6%) in conductivity in the K^+-ion-rich region above 323.15 K is due to the contribution of $(CH_3CONH_3)^+$ and $(CH_3CONH)^-$ ions and the higher mobility of the K^+ ion. In the Na^+-ion-rich region, according to the anion polarization model (APM) (17, 18), the SCN^- ion becomes more polarized towards Na^+ than towards K^+ due to its smaller ionic size, resulting in a decrease in the ionic mobility and, in turn, the conductivity. A similar magnitude of the deviation (≈4%), either positive or negative, was observed for Na^+–K^+ mixed alkali systems in hydrate melts (5, 6) or molecular liquid (8) as solvent. The negative deviation in conductivity (≈27%) in the Na^+ -ion-rich region below ≈323.15 K may be governed by two factors: firstly, due to the greater polarization of SCN^- on the Na^+ ion causing a decrease in the ionic mobility, and secondly, interaction of Na^+ ion with acetamide resulting in a polymeric type of solvated ion (15) with further decrease in ionic mobility. As a result a rigid structure with very high relaxation time prevails in the Na^+-ion-rich region in the present system (15, 19). Therefore, the high relaxation time, which is also one of the criteria (4) for the onset of MAE, together with the polarization effect causes maximum negative deviation in the electrical conductivity in the Na^+-ion-rich region. At the intermediate temperature (≈323.15 K) the above effects are almost counterbalanced and the variation of conductivity with composition becomes nearly linear.

The overall nature of variation of electrical conductivity with composition over the entire temperature range of the study (Fig. 3) is also reflected in the variation of T_0 with x (Fig. 1). It has been suggested (6) that the positive or negative deviations in κ would cause negative or positive deviations in T_0. Similar trends in T_0 and κ with x (Figs. 1 and 3) prevail in the present systems and the above explanation may also be applicable for the nature of the variation of T_0 vs. x.

To detect MAE further in the present systems, the activation energy, E_κ, for ion conduction has been calculated from the following relation

$$[7] \quad E_\kappa = \text{BR}[T/(T - T_0)]^2$$

where R is the gas constant. Values of the B and T_0 parameters required to calculate E_κ have been taken from Table 3. The activation energy for ion conduction varies smoothly with x (Fig. 4) in spite of the fact that the variation of T_0 with x is not the same throughout. The activation energy for the system

with $x = 1.0$ at $T = 298.15$ K is reasonably comparable with the average activation energy for the $NaSCN–CH_3CONH_2$ system studied by Berchiesi et al. (14). Therefore, the composition dependence of the B parameter appears to dominate over the variation of T_0 with x to govern the composition dependence of the activation energy.

From the nature of the variation of T_0, B, κ, and E_κ with composition (Figs. 1, 3, and 4) it may be concluded that the MAE exists in the present systems even though the systems are volumetrically ideal in nature. In addition to the polarization effect of the SCN^- ion towards the Na^+ ion, the auto-dissociation of molten acetamide and the polymeric-type solvated Na^+ ion with less ionic mobility also contribute towards positive and negative deviations in the electrical conductivity.

Acknowledgements

The author thanks Dr. Anil C. Ghosh, Director, and Dr. P.C. Borthakur, Head, Material Science Division, for encouragement and interest in this work. Grateful thanks are expressed to the Deutsche Gesellschaft für Technische Zusammenarbeit (GTZ) GmbH, and DAAD, Germany, for the gift of equipment.

References

1. J.O. Isard. J. Non-Cryst. Solids, **1**, 295 (1969).
2. D.E. Day. J. Non-Cryst. Solids, **21**, 343 (1976).
3. M.D. Ingram. Phys. Chem. Glasses, **28**, 215 (1987).
4. C.T. Moynihan. J. Electrochem. Soc. **126**, 2144 (1979).
5. P. Sangma, S. Mahiuddin, and K. Ismail. J. Phys. Chem. **88**, 2378 (1984).
6. S.S. Islam and K. Ismail. J. Chem. Eng. Data, **35**, 348 (1990).
7. A.H. Dietzel. Phys. Chem. Glasses, **24**, 172 (1983), and references therein.
8. S. Mahiuddin. Can. J. Chem. **72**, 2286 (1994).
9. R.L. Gupta and K. Ismail. Can. J. Chem. **68**, 2115 (1990).
10. R.L. Gupta and K. Ismail. J. Chem. Eng. Data, **36**, 142 (1991).
11. D. Teeters and C.M. Hill. Solid State Ionics, **72**, 122 (1994).
12. A.J. Easteal and M.C. Emson. J. Phys. Chem. **84**, 3330 (1980).
13. D.H. Kerridge. Chem. Soc. Rev. **17**, 181 (1988).
14. G. Berchiesi, G. Vitali, P. Passamonti, and R. Płowiec. J. Chem. Soc. Faraday Trans. 2, **79**, 1257 (1983).
15. R. Płowiec, A. Amico, and G. Berchiesi, J. Chem. Soc. Faraday Trans. 2, **81**, 217 (1985).
16. S.S. Islam and K. Ismail. Can. J. Chem. **66**, 242 (1988).
17. C.T. Moynihan and R.W. Laity. J. Phys. Chem. **68**, 3312 (1964).
18. C.T. Moynihan. *In* Ionic interactions. Vol. 1. *Edited by* S. Petrucci. Academic Press, New York. 1971. p. 261.
19. G. Berchiesi, G. Vitali, R. Powiec, and S. Barocci. J. Chem. Soc. Faraday Trans. 2, **85**, 635 (1989).

Propargyl calix[4]arenes and their complexes with silver(I) and gold(I)

Wei Xu, Jagadese J. Vittal, and Richard J. Puddephatt

Abstract: A calix[4]arene **1***b* has been substituted at the lower rim by reaction with propargyl bromide to give either the 1,3- bis(propargyl) derivative **2***b*, which is formed regioselectively, or the tetrakis(*O*-propargyl)calix[4]arene **3** under different reaction conditions. The molecular structure of **2***b* has been characterized by X-ray analysis (monoclinic, space group $P2_1/c$, $Z = 4$, $a = 10.960(1)$, $b = 24.302(3)$, $c = 10.673(1)$ Å, $\beta = 112.99(8)°$, $R = 0.0516$). The molecules of **2***b* in the crystal are arranged in a "head-to-head, tail-to-tail" manner with a phenyl substituent of one molecule partly enclosed in the bowlic cavity of another. Since the two $OCH_2C{\equiv}CH$ groups are accessible, **2***b* can be polymerized by heating to 250°C and the polymerized propargyl calix[4]arene derivatives are stable up to 460°C. Compound **3** exists as a mixture of conformers, the ratio of partial cone to 1,3-alternate conformations being 4:1 or 2:1, dependent on the preparative conditions. These propargyl calix[4]arene derivatives can be further derivatized to form silver(I) or gold(I) alkynyl units by reaction with $AgNO_3$ or $[AuCl(SMe_2)]$, respectively, and base. Further reaction of these transition metal complexes with phosphines yields calixarene derivatives with two metal-phosphine units at the lower rim of the calix[4]arene bowl.

Key words: calix[4]arene, propargyl, gold, silver, polymer.

Résumé : On a substitué un calix[4]arène. **1***b*, sur sa portion inférieure en le soumettant à une réaction avec du bromure de propargyle qui conduit au dérivé 1,3-bis(propargyle), **2***b*, qui se forme régiosélectivement, ou au tétrakis(*O*-propargyl)calix[4]arène, **3**, sous des conditions réactionnelles différentes. La structure moléculaire du composé **2***b* a été caractérisée par diffraction des rayons X (monoclinique, groupe d'espace $P2_1/c$, $Z = 4$, $a = 10,960(1)$, $b = 24,302(3)$ et $c = 10,673(1)$ Å, $\beta = 112,99(8)°$ et $R = 0,0516$). Dans le cristal, les molécules de **2***b* sont arrangées de façon « tête à tête, queue à queue » avec un substituant phényle d'une molécule partiellement entouré dans la cavité d'une autre. Puisque les deux groupes $OCH_2C{\equiv}CH$ sont accessibles, le produit **2***b* peut être polymérisé par chauffage à 250°C et les dérivés polymérisés propargyl calix[4]arène sont stables jusqu'à 460°C. Le composé **3** existe sous la forme de conformères pour lesquels le rapport des conformations à cône partiel/alterné-1,3 est de 4 : 1 ou de 2 : 1 suivant les conditions de préparation. On peut préparer de nouveaux dérivés de ces dérivés propargyl calix[4]arènes de façon à former des unités argent(I) ou or(I) alcynyles par réactions respectivement avec du $AgNO_3$ ou du $[AuCl(SMe)_2]$ en présence de base. Des réactions ultérieures de ces complexes de métaux de transition avec des phosphines fournissent des dérivés de calixarène comportant deux unités métal-phosphine dans la partie inférieure du bol du calix[4]arène.

Mots clés : calix[4]arène, propargyle, or, argent, polymère.

[Traduit par la rédaction]

Introduction

Calix[4]arenes are useful building blocks for more complicated molecules with unusual properties (1) and the hydroxyl substituents that are usually present are very useful for chemical modification. General procedures have been developed for regio- and stereoselective functionalization at the lower rim of calix[4]arenes such as *tert*-butylcalix[4]arene, **1***a* (2–6). However, it has proved to be more difficult to study the regio- and stereo-selectivity of reactions of the parent calix[4]arene, **1***b*. The derivative 1,3-bis(*O*-propargyl)-*tert*-butylcalix[4]arene, **2***a*, has been reported (6) and such compounds are of interest as potential encapsulating ligands for transition metal ions by coordination to the alkynyl substituents (7). This paper reports the regioselective synthesis of a new 1,3-dipropargyl calix[4]arene derivative **2***b* and a tetrapropargyl calix[4]arene derivative **3**, together with a study of their conformations, conformational mobility, thermal properties, and ability to form complexes with silver(I) and gold(I).

Received November 21, 1995.

W. Xu, J.J. Vittal, and R.J. Puddephatt.[1] Department of Chemistry, University of Western Ontario, London, ON N6A 5B7, Canada.

[1] Author to whom correspondence may be addressed. Telephone: (519) 679-2111, ext. 6336. Fax: (519) 661-3022. E-mail:pudd@julian.uwo.ca

Results and discussion

Regioselective synthesis and structure of 1,3-bis(*O*-propargyl)calix[4]arene, 2*b*

Calix[4]arenes are readily converted into a wide variety of derivatives at the lower ring by alkylation of the phenolic groups (8). In this way, the 1,3-bis(*O*-propargyl)calix[4]arene **2***b* was prepared regioselectively in high yield (92%) from propargyl bromide and calix[4]arene **1***b* in a 1:2 ratio in acetone solution in the presence of potassium carbonate as shown in Scheme 1. The ^1H NMR spectrum of **2***b* exhibited an AB

Scheme 1.

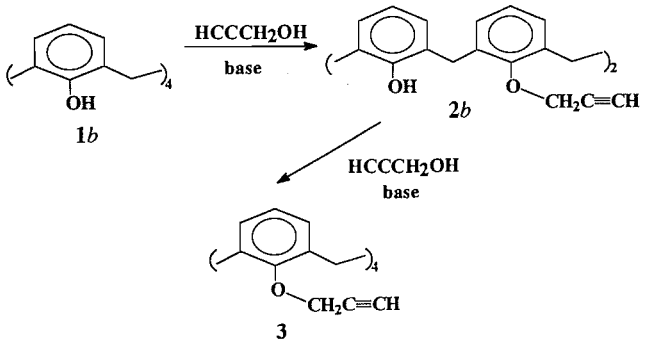

pattern for the bridging methylene groups at δ 3.40 and 4.40 ppm ($^2J_{HH}$ = 14 Hz), a triplet for the acetylenic proton at 2.58 ppm ($^4J_{HH}$ = 4 Hz), a doublet for the methylene groups of the propargyl units at 4.25 ppm ($^4J_{HH}$ = 4 Hz), an A_2B system for the aromatic protons at 6.66–7.08 ppm, and a singlet for the phenolic protons at 7.05 ppm (confirmed by D_2O exchange). These data, together with the ^{13}C NMR evidence, show that **2***b* in solution exists in the cone conformation (1).

The conformation of **2***b* in the solid state was determined by an X-ray structure determination. The 1,3-bis(*O*-propargyl)calix[4]arene **2***b* adopts the cone conformation in a distorted form as shown in Fig. 1. The two benzene rings bearing propargyl groups are almost parallel to each other (interplanar angle 2.28(1)°), while the two phenolic rings have a relatively large interplanar angle (77.7(1)°) and are tilted to place the two hydroxy groups almost inside the cavity with a small O...O separation of 2.9 Å. This arrangement allows intramolecular hydrogen bond formation between proximal hydroxy and ether groups with OH..O distances of 2.0–2.3 Å. These hydrogen bonds are probably responsible for holding the molecule in the cone conformation (8*a*). There are a number of related dihydroxycalixarenes, which display similar hydrogen bonding, of which a bis(*O*-cyanomethyl) analog is particularly striking (6*a*). In addition to these intramolecular hydrogen bonds, there is structural evidence for weak intermolecular "tail-to-tail" hydrogen bonds between C≡C-H..OH groups of adjacent molecules, leading to chains of molecules (Fig. 2*b*). These are examples of so-called "soft" CH..O hydrogen bonds (8*b*). Finally, a phenyl group of each calixarene molecule is partially enclosed in the bowlic cavity of a neighboring molecule (Fig. 2*a*), thus creating "head-to-head" association that leads to blocking of the entrance to the cavity. Small molecule inclusion, which has often been observed in 1,3-dialkylated *tert*-butylcalix[4]arenes, is therefore not present in **2***b*. Bond lengths and angles are unexceptional and are summarized in Table 1.

Synthesis and conformations of the tetrakis(*O*-propargyl)calix[4]arene 3

The calixarene **2***b* did not react with excess propargyl bromide and base at room temperature (7), but either **1***b* or **2***b* did react with excess propargyl bromide in refluxing acetone in the presence of K_2CO_3 to give the new tetrapropargyl calix[4]arene derivative **3**. At short reaction times, a mixture of products representing various stages of alkylation were present but, after 1 day, complete conversion to the tetrakis(*O*-propargyl)calix[4]arene **3** occurred. After 24 and 48 h reflux,

Table 1. Selected interatomic distances (Å) and angles (°) in **2***b*

(*a*) Bond lengths (Å)

O(1)—C(16)	1.374(3)	O(2)—C(36)	1.372(3)
C(1)—C(2)	1.154(5)	C(2)—C(3)	1.450(5)
C(3)—O(3)	1.442(3)	O(3)—C(4)	1.402(3)
C(5)—C(37)	1.522(4)	C(9)—C(10)	1.523(5)
C(10)—C(11)	1.515(4)	C(15)—C(17)	1.515(4)
C(17)—C(25)	1.509(4)	C(21)—C(22)	1.167(4)
C(22)—C(23)	1.471(4)	C(23)—O(4)	1.438(3)
O(4)—C(24)	1.405(3)	C(29)—C(30)	1.520(4)
C(30)—C(31)	1.520(4)	C(35)—C(37)	1.514(4)

(*b*) Bond angles (°)

C(1)-C(2)-C(3)	178.6(4)	O(3)-C(3)-C(2)	112.7(3)
C(4)-O(3)-C(3)	116.4(2)	C(9)-C(4)-O(3)	119.6(3)
C(5)-C(4)-O(3)	117.8(3)	C(6)-C(5)-C(37)	119.4(3)
C(4)-C(5)-C(37)	122.2(3)	C(8)-C(9)-C(10)	120.6(3)
C(4)-C(9)-C(10)	122.2(3)	C(11)-C(10)-C(9)	113.1(3)
C(12)-C(11)-C(10)	121.6(3)	C(16)-C(11)-C(10)	120.9(3)
C(14)-C(15)-C(17)	121.1(3)	C(16)-C(15)-C(17)	120.6(2)
O(1)-C(16)-C(15)	121.2(2)	O(1)-C(16)-C(11)	116.9(2)
C(25)-C(17)-C(15)	112.1(2)	C(21)-C(22)-C(23)	177.0(3)
O(4)-C(23)-C(22)	113.1(2)	C(24)-O(4)-C(23)	114.3(2)
C(25)-C(24)-C(29)	123.0(2)	C(25)-C(24)-O(4)	117.7(2)
C(29)-C(24)-O(4)	119.2(2)	C(26)-C(25)-C(17)	120.0(3)
C(24)-C(25)-C(17)	122.9(2)	C(28)-C(29)-C(30)	120.1(3)
C(24)-C(29)-C(30)	122.5(2)	C(32)-C(31)-C(36)	117.8(3)
C(32)-C(31)-C(30)	122.2(3)	C(36)-C(31)-C(30)	119.9(2)
C(34)-C(35)-C(37)	120.8(3)	C(36)-C(35)-C(37)	122.2(3)
O(2)-C(36)-C(31)	116.2(2)	O(2)-C(36)-C(35)	121.4(2)
C(35)-C(37)-C(5)	113.3(2)		

the calix[4]arene **3** was present as a mixture of the partial cone and 1,3-alternate conformers in 2:1 and 4:1 ratios, respectively. Clearly, in the absence of hydroxyl groups to take part in hydrogen bonding, the cone conformation is no longer preferred and so there is a major difference from **2***b* in this respect.

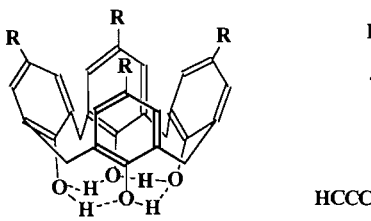

1*a*: R = Bu^t; **1***b*: R = H

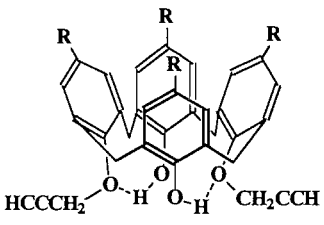

2*a*: R = Bu^t; **2***b*: R = H

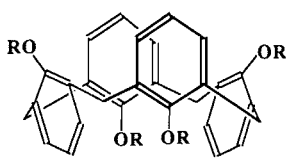

1,3-Alternate

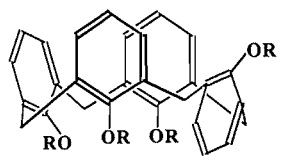

Partial Cone

3: R = $CH_2C{\equiv}CH$

Fig. 1. A view of the molecular structure of **2***b*, showing the cone conformation and intramolecular OH..O hydrogen bonding.

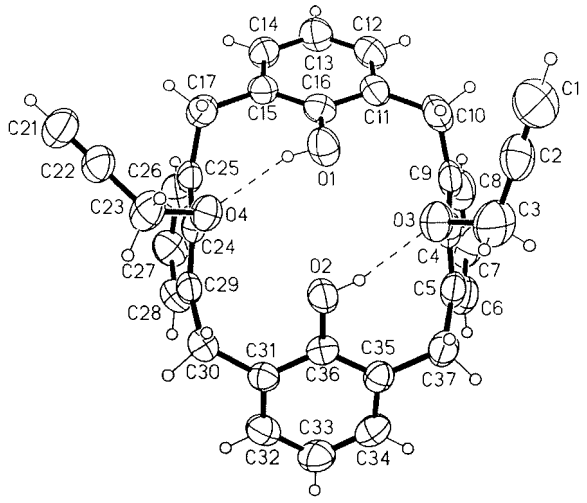

Scheme 2.

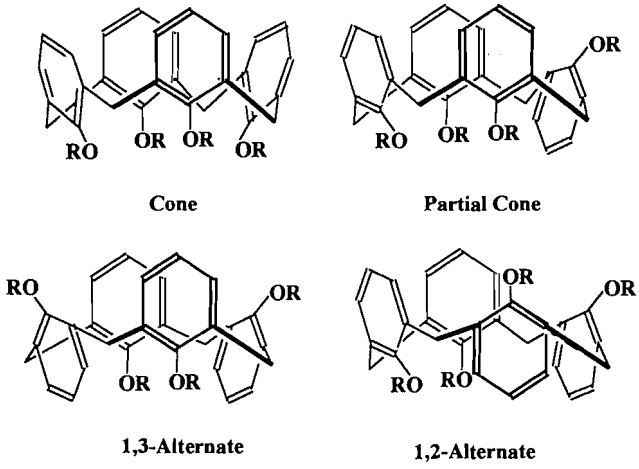

Many tetrakis(*O*-alkyl)calix[4]arene derivatives (though only if the alkyl group is smaller than propyl) are conformationally flexible at room temperature. A schematic representation of the four possible conformers of tetrakis(*O*-propargyl) calixarene with the different orientations of the phenyl rings of the cyclic tetramer is shown in Scheme 2. It has been established that the conformations of calix[4]arenes can be determined by the splitting pattern of the $ArCH_2Ar$ methylene protons in the ^1H NMR spectra and by the number of peaks in the ^{13}C NMR spectra (6, 8). The conformational isomerism of **3** is demonstrated from the observation that the ratio of 1,3-alternate to partial cone conformer is dependent on the conditions of formation, and this observation also shows that the interconversion between conformers is very slow at room temperature. In agreement with the latter conclusion, the ^1H NMR spectrum of **3** recorded at room temperature at 300 MHz showed sharp signals with no evidence of exchange broadening (Fig. 3). The ^1H NMR spectrum in the methylene region is particularly informative (Fig. 3). The minor 1,3-alternate conformer has higher symmetry and gives rise to single resonances of equal intensity due to the CH_2 groups of the propargyl (H^1, 4.08 ppm, d, J(HH) = 4 Hz) and CH_2Ar_2 (H^2, 3.76 ppm, s) groups. The major partial cone conformer has lower symmetry and its spectrum is correspondingly more complex. There are two nonequivalent CH_2Ar_2 groups and each has nonequivalent protons CH^aH^b, thus giving rise to four resonances labelled H^{3a}, H^{3b}, H^{4a}, H^{4b}. There are three nonequivalent propargyl groups in a 1:1:2 ratio, and the CH_2 protons of the last propargyl groups are also nonequivalent. Each CH_2 resonance appears as a doublet due to the coupling $^4J(CH_2CCH)$. Hence there are four resonances, two appearing as doublets (H^5, H^6) and two (H^{7a}, H^{7b}) as more complex multiplets due to the extra coupling $^2J(H^{7a}H^{7b})$. The ratio of partial cone to 1,3-alternate conformer was 4:1 as determined by integration of the spectra, and the spectral assignments are in agreement with those for similar compounds (8). The ^{13}C NMR spectra in both the $ArCH_2Ar$ and OCH_2CCH regions (Experimental section) provided a further diagnostic tool to confirm that the only conformations present are the partial cone and 1,3-alternate at room temperature (9).

It has previously been reported that the conformation of *O*-alkylated calixarenes can be frozen as a single conformation, the partial cone, by complexation with the silver cation, which binds to two arene groups and one ether group (10). In agreement, addition of silver(I) trifluoroacetate to a solution of **3** gave the tetrakis(*O*-propargyl)calix[4]arene–silver(I) complex **4**, which was shown by its ^1H NMR spectrum to exist only as the partial cone conformer. Hence weak binding of the silver cation probably occurs as shown in **4** and not by binding to the C≡C bonds of the propargyl substituents (11).

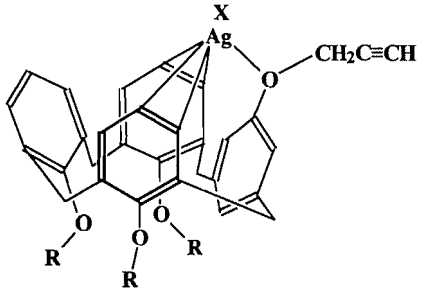

4: R= CH_2CCH; X = O_2CCF_3

Polymerization of the propargyl calix[4]arene derivatives

It is known that the dipropargyl derivatives of bisphenols are attractive building blocks for resins for use as advanced composites, adhesives, coatings, and electronics applications (12). Hence polymerization of the propargyl calix[4]arenes was studied (13). The polymerization of **2***a* or **2***b* was performed by heating in diphenyl ether for 6 h at 120°C and then for 2 h at 150–160°C without a catalyst (12, 13). The polymerization proceeded without evolution of any volatiles and produced a solid thermoset resin **5**. The polymer **5** is soluble in many organic solvents and is neither hygroscopic nor moisture sensitive. The molecular weight of **5***a*, as estimated by gel permeation chromatography (GPC) with THF as eluent and using polystyrene standards, was M_w = 56 000 with a polydispersity (M_w/M_n = 3.2). Differential scanning calorimetry (DSC) measurements of the poly(1,3-(*O*-propargyl)-*tert*-butylcalix[4]-arene), **5a**, shows an exceptionally high glass transition temperature, T_g, of the polymer at 250°C (14). TGA of the polymer **5***a* in air (Fig. 4) shows that decomposition with weight loss occurs above 460°C, which is slightly higher than for its

Fig. 2. Intermolecular interactions in **2***b*: (*a*) The head-to-head arrangement, showing mutual aryl group inclusion. (*b*) The tail-to-tail association involving C≡CH..O hydrogen bonding.

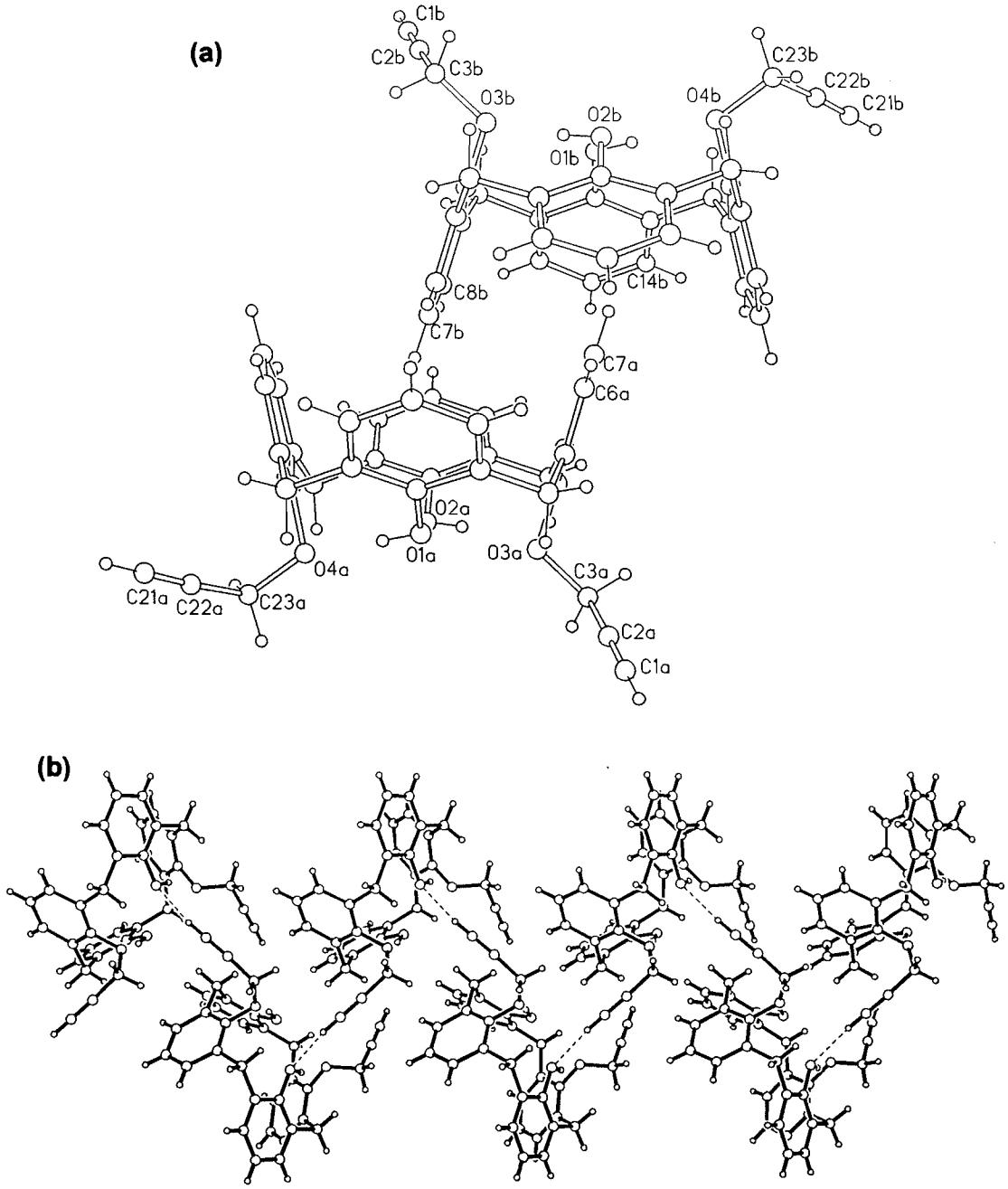

precursor **2***a* (440°C). Clearly, the propargyl calix[4]arene polymer has excellent thermal stability. The polymer is formed through opening of the triple bonds of the propargyl groups. Thus, **5***a* gave broad ^{1}H NMR resonances at δ = 1.0, 2.1 and 3.7, 6.3, and 7.0 which are assigned to the *t*-Bu, CH_2, =CH, and aromatic protons, respectively. In agreement, the FTIR showed the absence of alkyne groups, with no bands corresponding to the bands of **2***a* due to $\nu_{CC\text{-}H}$ = 3289 cm^{-1} (s) or $\nu_{C\equiv C}$ = 2120 cm^{-1} (w).

Complexes of 2 and 3 with transition metals

There is much current interest in the properties of calix[4]arenes as ligands (13, 15–18) and so the synthesis of alkynylmetal complexes from the propargylcalix[4]arenes was studied. Treatment of **2***a* with [AuCl(SMe_2)] in the presence of sodium acetate as base gave the digold(I) complex **6***a*. The ^{1}H NMR spectrum of **6***a* is broad but the observation of only two broad signals due to the methylene protons of the calixarene at 3.4 and 4.2 ppm, one broad resonance due to the methylene protons of the propargyl groups at 4.3 ppm, and one broad Bu^t resonance at 1.1 ppm indicates that **6***a* is primarily in the cone conformation. The FTIR spectrum showed the absence of a CC-H proton (disappearance of the band due to ν_{CCH} at 3275 cm^{-1}) and the presence of a new weak band due

Fig. 3. The ^{1}H NMR spectrum of compound **3** in the methylene region.

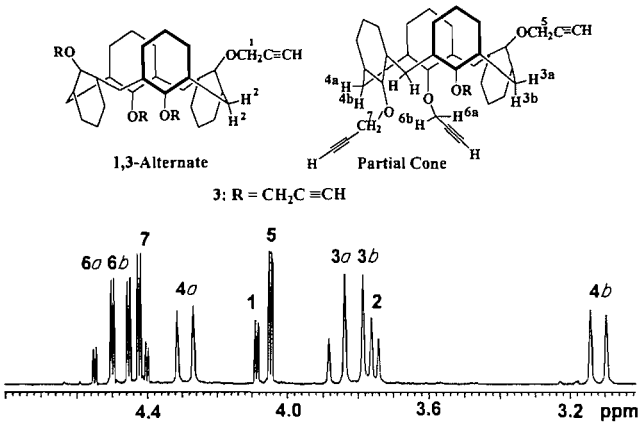

Fig. 4. (*a*) TGA of **2***a*; (*b*) TGA of polymeric **2***a*.

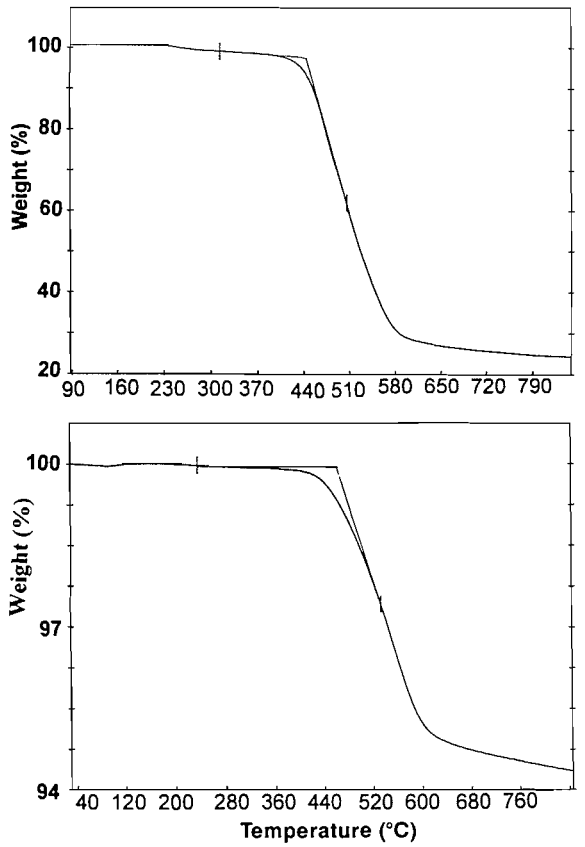

to $\nu_{C\equiv CAu}$ at 1988 cm^{-1}. Alkynylgold(I) complexes are usually oligomeric or polymeric $(RC\equiv CAu)_n$ to allow the gold(I) centres to be linear 2-coordinate. Complex **6***a* could be of this type or each gold(I) centre could be weakly ligated by oxygen donors present in the calixarene skeleton; since **6***a* is soluble in organic solvents it is probably not polymeric (19). In similar ways, **2***a* reacted with silver nitrate and ammonia to give **6***b*, and **3** reacted with $[AuCl(SMe_2)]$ and sodium acetate to give complex **7** as shown in Scheme 3.

Further reaction of these propargylmetal complexes **6** and **7** with either monodentate or bidentate phosphine ligands gave the corresponding complexes **8** and **9** as shown in Scheme 3. The complexes **8***a*–**8***d* are in the cone conformation and have C_2 symmetry, with the two metal-phosphine units at the lower rim of the calix[4]arene. The resonances in the ^{1}H NMR spectra due to the CH_2 groups serve as spectroscopic probes, and clearly indicate the cone conformation. The complexes **9***a* and **9***b* give similar ^{1}H NMR resonances as for their precursor **3**, indicating that the complexation of the propargyl groups does not change the conformation and that there is still a mixture of the partial cone and 1,3-alternate conformations, which do not easily interconvert. The complexes **8** and **9** do not exhibit the inclusion behaviour that is typical of other calixarenes (1), perhaps because the bulky metal-phosphine substituents at the lower rim cause the aryl rings to which they are bound to tilt in such a way as to close access to the top of the bowl (20).

Conclusion

This work has shown that the calixarene **1***b* can be functionalized with two or four propargyl groups at the lower rim and that the reaction to give the dipropargyl derivative is regioselective. Preliminary studies indicate that silver(I) can be incorporated into the propargylcalix[4]arenes either by weak π-bonding to the arene groups or, in the presence of base, by forming σ-bonded propargylsilver(I) groups. Gold(I) also forms propargyl derivatives containing two or four gold atoms. Clearly there is potential for further derivatization of these propargylcalix[4]arenes with metal substituents but it may prove difficult to develop useful inclusion chemistry. In this sense, the incorporation of propargyl groups at the upper rim is preferred and the synthesis and coordination chemistry of such compounds is planned.

Experimental section

The precursor compounds 5,11,17,23-tetra-*tert*-butylcalix[4]arene, **1***a* (21), calix[4]arene **1***b* (22), 5,11,17,23-tetra-*tert*-butyl-25,27-bis(propargyl)calix[4]arene, **2***a* (7), and $[AuCl(SMe_2)]$ (19) were prepared by literature methods. Molecular modeling was carried out using PCMODEL.[2] NMR spectra were collected by using a Varian Gemini 300 spectrometer. ^{1}H and ^{13}C NMR chemical shifts were measured relative to partially deuterated solvent peaks, but are reported relative to tetramethylsilane. ^{31}P NMR chemical shifts were determined relative to 85% H_3PO_4 as external standard. IR spectra were recorded as Nujol mulls using a Bruker IFS32 FTIR spectrometer. The molecular weights of poly[1,3-(*O*-propargyl)-*tert*-butylcalix[4]arene] and of poly[1,3-(*O*-propargyl)calix[4]-arene] were measured by GPC using THF as solvent and polystyrene standards for calibration. Elemental analyses were performed by Galbraith Laboratories, Knoxville, Tenn. Mass spectra were recorded by using a Finnegan mat 8230 mass spectrometer.

1,3-Di-*O*-propargylcalix[4]arene, 2*b*

A solution of calix[4]arene **1***b* (0.5 g, 1.18 mmol) and $BrCH_2CCH$ (0.5 g, 4.2 mmol) in acetone (100 mL) and K_2CO_3 (1.2 g, 8.7 mmol) were stirred for 12 h at 20°C. The solvents

[2] PCMODEL Molecular Modeling Software, version 4.2, Serena Software, 1992.

Scheme 3.

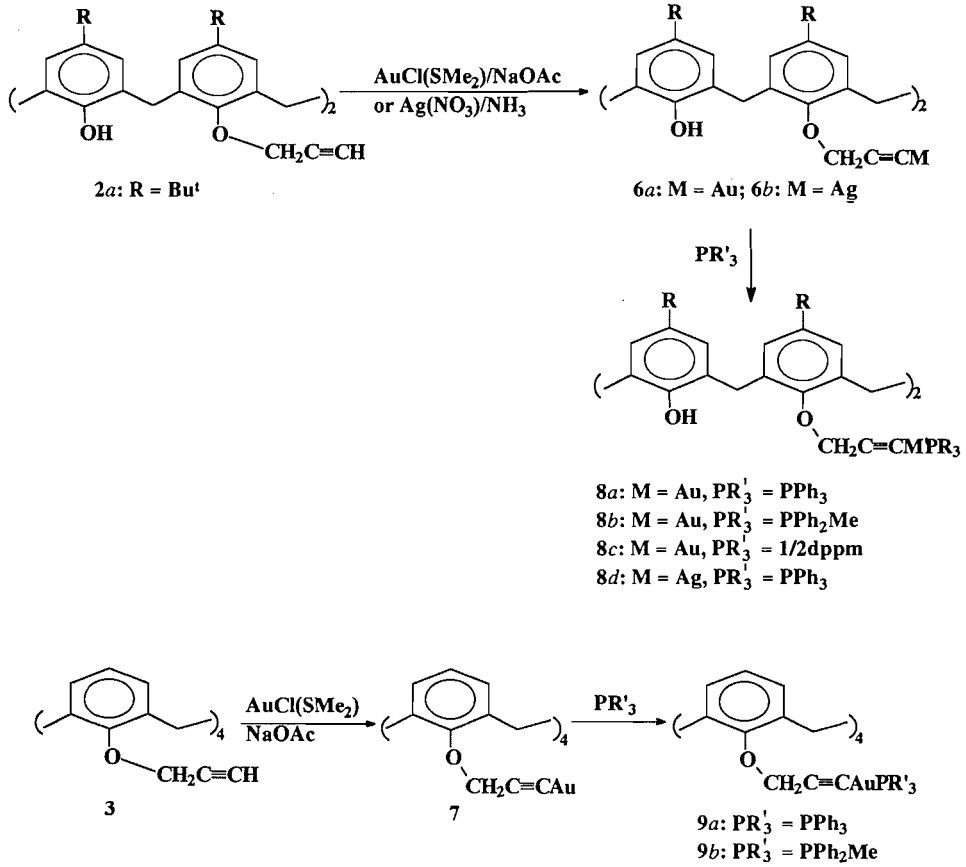

were removed under vacuum and the residue was extracted using chloroform (20 mL). **2***b* can be further purified by crystallization, by slow diffusion of methanol into a chloroform solution. The light yellow crystals of **2***b* (0.54 g, 92%) were collected by filtration, washed with hexane (3 × 20 mL), and dried under vacuum, mp 182–184°C. Spectroscopic data for **2***b*: FTIR: ν_{OH} = 3423 cm^{-1} (s), ν_{CCH} = 3275 cm^{-1} (s), ν_{CC} = 2118 cm^{-1} (w). NMR in $CDCl_3$, δ(^{1}H): 2.58 (t, $^4J_{HH}$ = 4 Hz, 2H, CC*H*), 3.40, 4.40 (ABq, $^2J_{HH}$ = 13 Hz, 8H, ArCH_2Ar), 4.80 (d, $^4J_{HH}$ = 4Hz, 4H, OC*H*), 6.66–6.73 (m, 4H, Ar*H*), 6.85 and 6.82 (s, 4H, Ar*H*), 7.08 and 7.06 (s, 4H, Ar*H*), 7.05 (s, 2H, O*H*). δ(^{13}C): 63.46 (*C*H_2CCH), 31.85 (Ar*C*H_2Ar), 78.32 (CH$_2$*C*CH), 153.03, 151.37, 133.42, 129.01, 128.56, 128.26, 125.75, 119.25 (Ar). EI-MS, *m/e*: 500; calcd. for $C_{34}H_{28}O_4$: 500.

Single crystal X-ray analysis of 2*b*

Single crystals of complex **2***b* were obtained as described above. A suitable crystal with dimensions of 0.42 × 0.35 × 0.22 mm was selected, mounted at the end of a glass fibre, and used for the experiments. The diffraction experiments were carried out using a Siemens P4 diffractometer with the XSCANS software package[3] using graphite monochromated Mo K radiation at 23°C. The cell constants were obtained by centering 25 high-angle reflections (20.7 ≤ Θ ≤ 21.7°). The Laue symmetry 2/*m* was determined by merging symmetry equivalent reflections. A total of 5666 reflections were collected in the Θ range 2.0–25.0° (−13 ≤ h ≤ 1, −1 ≤ *k* ≤ 28, −12 ≤ *l* ≤ 12) in Θ–2Θ scan mode at variable scan speeds (2–10 deg/min). Background measurements were made at the ends of the scan range. Three standard reflections were monitored at the end of every 297 reflections collected. An empirical absorption correction was applied to the data. The maximum and minimum transmission factors are 0.956 and 0.939, respectively. The space group $P2_1/c$ was determined from the systematic absences (*h*0*l*, *l* = 2*n* + 1 and 0*k*0, *k* = 2*n* + 1). The data processing, solution, and the initial refinements were done using the SHELXTL-PC programs (23). The final refinements were performed using SHELXL-93 software programs (24). Anisotropic thermal parameters were refined for all the non-hydrogen atoms. The hydrogen atoms were not directly located but were included in the calculated positions for the purpose of structure factor calculations only. In the final least-squares refinement cycles on F^2 the model converged at R_1 = 0.0516, wR_2 = 0.1046, and GOf = 1.008 for 2659 observations with $F_o \geq 4\sigma(F_o)$, 366 parameters, and R_1 = 0.1101, wR_2 = 0.1288 for all 4612 data. In the final difference Fourier synthesis the electron density fluctuates in the range 0.17 to −0.17 e Å^{-3}, of which the top peak was associated with O(1) at a distance of 1.06 Å. There is no shift in the mean or the maximum shift/esd in the final cycles. A secondary extinction coefficient was refined to 0.0035(5). Experimental detail and crystal data are summarized in Table 2. The positional and thermal parameters, bond distances and angles, the anisotropic thermal parameters,

[3] "XSCANS", Siemens Analytical X-Ray Instruments Inc., Madison, 1990.

Table 2. Crystal data and experimental details.

Empirical formula	$C_{34}H_{28}O_4$
Formula weight	500.56
Temperature	23°C
Wavelength	0.71073 Å
Crystal system	Monoclinic
Space group	$P2_1/c$
Unit cell dimensions	a = 10.960(1) Å
	b = 24.302(3) Å
	c = 10.673(1) Å
	β = 112.99(8)°
Volume	2177.6(4) Å^3
Z	4
Density, calculated, observed	1.270, 1.29(5) g cm^{-3}
Absorption coefficient	0.082 mm^{-1}
F(000)	1056
Independent reflections	4613 (R(int) = 0.0231)
Refinement method	Full-matrix least squares on F^2
Data/restraints/parameters	2659/0/366
Goodness-of-fit (GOF) on F^2	1.022
Final R indices ($I > 2\sigma(I)$)	$R1$ = 0.0516, $wR2$ = 0.1046
R indices (all data)	$R1$ = 0.1101, $wR2$ = 0.1288

$R1 = \Sigma(\|F_o\| - \|F_c\|)/\Sigma|F_o|$; $wR2 = [\Sigma w(F_o^2 - F_c^2)^2/\Sigma wF_o^4]^{1/2}$; GOF = $[\Sigma w(F_o^2 - F_c^2)^2/(n - p)]^{1/2}$, where n is the number of reflections and p is the number of parameters refined.

hydrogen atom coordinates, and selected torsion angles have been deposited as supplementary material.[4]

Tetrakis(*O*-propargyl)calix[4]arene, 3

A mixture of **1***b* (0.5 g, 1.18 mmol) and $BrCH_2CCH$ (1 g, 8.4 mmol) in acetone (100 mL) and K_2CO_3 (2 g, 14.5 mmol) was stirred and heated to reflux for 48 h. The cooled reaction mixture was processed exactly as described in preparation of **2***b* to afford a tetrakis(*O*-propargyl)calix[4]arene **3** (5.6 g, 82%). Spectroscopic data of **3:** NMR in CD_2Cl_2: *1,3-alternate conformer*, δ(^{1}H, ppm): 2.43 (t, 4 H, $^4J_{HH}$ = 4 Hz, CC*H*), 4.00 (d, $^4J_{HH}$ = 4 Hz, 4H, OCH_2), 3.76 (8H, ArCH_2Ar), 7.42–6.33 (m, Ar*H* of both 1,3-alternate and partial cone conformers). δ(^{13}C, ppm): 74.1 (O*C*H$_2$CCH), 59.2 (OCH$_2$*C*CH), 80.6 (OCH$_2$*C*CH), 37.6 (Ar*C*H$_2$Ar), 154.4 (O*Ar*), *partial cone conformer*, δ(^{1}H, ppm): 2.52 (t, 1H, ^4J(HH) = 4 Hz, CC*H*), 2.49 (t, 2H, ^4J(HH) = 4 Hz, CC*H*), 2.19 (t, 1H, ^4J(HH) = 4 Hz, CC*H*), 4.3 and 3.1 (AB q, 4H, $^2J_{HH}$ = 14 Hz, ArCH_2Ar), 3.85 and 3.77 (AB q, 4H, $^2J_{HH}$ = 14 Hz, ArCH_2Ar), 4.52 and 4.44 (AB q, 4H, $^4J_{HH}$ = 4 Hz, $^2J_{HH}$ = 14 Hz, OCH_2), 4.42 (d, $^4J_{HH}$ = 4 Hz, 2H, OCH_2), 4.04 (d, $^4J_{HH}$ = 4 Hz, 2H, OCH_2). δ(^{13}C, ppm): 75.1 (O*C*H$_2$CCH), 58.4 (OCH$_2$*C*CH), 59.9 (OCH$_2$*C*CH), 61.3 (OCH$_2$*C*CH), 81.6 (OCH$_2$*C*CH), 80.8 (OCH$_2$*C*CH), 80.3 (OCH$_2$*C*CH), 32.2 (Ar*C*H$_2$Ar), 36.4 (Ar*C*H$_2$Ar), 156.6 (O*Ar*), 156.0 (O*Ar*), 155.5 (O*Ar*), 138.00, 134.76, 134.32, 133.97, 133.19, 131.48, 131.31, 130.72, 130.59, 129.34, 129.08, 128.76, 123.68, 1213.57, 123.20, 122.98, 122.75, 122.51, 122.40 (*Ar*). The ratio of the two conformers was determined from the integration of resonances due to the C≡CH protons to be 4:1. FTIR: ν_{CCH} = 3289 cm^{-1} (s), ν_{CC} = 2120 cm^{-1} (w), EI-MS, *m/e*: 576, 537; calcd. for $C_{40}H_{32}O_4$: 576, M − CH_2CCH: 537. Anal. calcd. for $C_{40}H_{32}O_4$: C 83.3, H 5.6, found: C 83.5, H 5.2%.

Tetrakis(*O*-propargyl)calix[4]arene-Ag(CF_3COO), 4

A mixture of **3** (0.2 g, 0.35 mmol) and Ag(CF_3COO) (0.08 g, 0.36 mmol) in acetone (100 mL) was stirred for 2 h at room temperature. The product **4** (0.26 g, 93%) was precipitated by adding methanol (10 mL). Spectroscopic data of **4:** FTIR: ν_{CCH} = 3289 cm^{-1} (s), ν_{CC} = 2120 cm^{-1} (w). ^{1}H NMR in $CDCl_3$: δ: 2.20 (t, 1H, $^4J_{HH}$ = 4 Hz, CC*H*), 2.50 (t, 2H, $^4J_{HH}$ = 4 Hz, CC*H*), 2.54 (t, 1H, $^4J_{HH}$ = 4 Hz, CC*H*); 4.29 and 3.12 (AB q, 4H, $^2J_{HH}$ = 21 Hz, ArCH_2Ar), 3.82 (AB q, 4H, $^2J_{H\text{-}H}$ = 21 Hz, ArCH_2Ar), 4.48 (AB q, 4H, $^4J_{HH}$ = 4 Hz, $^2J_{HH}$ = 24 Hz, OCH_2), 4.46 (d, $^4J_{HH}$ = 4 Hz, 2H, OCH_2), 4.04 (d, $^4J_{HH}$ = 4 Hz, 2H, OCH_2); 6.46–7.42 (m, 12H, Ar*H*). Anal. calcd. for $C_{42}H_{32}AgO_6F_3$: C 63.3, H 4.0; found: C 63.0, H 3.8%.

Poly[1,3-(*O*-propargyl)calix[4]arene), 5

A solution of **2** (0.5 g) in Ph_2O (10 mL) was heated to 120°C for 6 h and then heated to 150–160°C for another 2 h under nitrogen atmosphere, to give an orange-brown hard resin (0.5 g) after evaporation of the Ph_2O. The polymer was purified by dissolving the solid obtained above in THF (2 mL) and then precipitating with MeOH (20 mL). The precipitate **5** was a yellow solid, which was dried under vacuum. Spectroscopic data of *poly[1,3-(*O*-propargyl)-*tert*-butylcalix[4]arene*, **5***a*: FTIR: ν_{OH} = 3370 cm^{-1} (s). ^{1}H NMR in $CDCl_3$: δ: 1.1 (br, Bu^t), 2.1 (br, ArCH_2Ar), 3.2 (br, ArCH_2Ar) 3.4 (br, OCH_2), 6.3 (br, =C*H*), 7.0 (br, Ar and O*H*). Spectroscopic data of *poly(1,3-(*O*-propargyl)calix[4]arene)*, **5***b*: FTIR: ν_{OH} = 3370 cm^{-1} (s). ^{1}H NMR in $CDCl_3$; δ: 2.2 (br, ArCH_2Ar), 3.3 (br, 8H, ArCH_2Ar), 3.4 (br, 4H, OCH_2), 6.1 (br, =C*H*), 7.0 (br, 10H, Ar and O*H*).

1,3-Bis(*O*-propargylsilver)tetra-*tert*-butylcalix[4]arene, 6*b*

A solution of **2***a* (0.5 g, 0.69 mmol) in THF (5 mL) was mixed with a solution of $AgNO_3$ (0.235 g, 1.38 mmol) in ammonia (10 M, 5 mL) and the mixture was stirred for 3 h. The product precipitated as the volume of solvent was reduced, and was purified by dissolving in CH_2Cl_2 (5 mL) and then precipitating by addition of MeOH (20 mL). The yellow product was filtered, washed with MeOH, and dried under vacuum. FTIR: ν_{CC} = 2058 cm^{-1} (w). ^{1}H NMR in $CDCl_3$, δ: 1.1 (br, m, 36H, Bu^t), 3.4 (br, ArCH_2Ar), 4.2 (br, 4H, ArCH_2Ar), 4.2 (br, 4H, OCH_2), 7.0 (br, 10H, Ar and O*H*). Anal. calcd. for $C_{50}H_{58}Ag_2O_4$: C 64.0, H 6.2; found: C 63.7, H 5.9%. Complex **6***a* was prepared in a similar way but using [AuCl(SMe$_2$)] with NaOAc as base. Spectroscopic data for *1,3-bis(*O*-propargylgold)tetra-*tert*-butylcalix[4]arene*, **6***a*: FTIR: ν_{CC} = 2015 cm^{-1} (w). ^{1}H NMR in $CDCl_3$, δ: 1.1 (br, m, 36H, Bu^t), 3.4 (br, 4H, ArCH_2Ar), 4.2 (br, 8H, ArCH_2Ar and OCH_2), 7.0 (br, 10H, Ar and O*H*). Anal. calcd. for $C_{50}H_{58}Au_2O_4$: C 53.8, H 5.2; found: C 54.0, H 5.3%. Complex **7** was prepared in a similar way from the calixarene **3**. Spectroscopic data for

[4] These supplementary data can be purchased from: The Depository of Unpublished Data, Document Delivery, CISTI, National Research Council Canada, Ottawa, Canada K1A 0S2. Structure factor amplitudes are no longer being deposited and may be obtained directly from the author. Tables of positional parameters, bond distances and angles, and hydrogen atom coordinates have also been deposited with the Cambridge Crystallographic Data Centre, and can be obtained on request from The Director, Cambridge Crystallographic Data Centre, University Chemical Laboratory, 12 Union Road, Cambridge, CB2 1EZ, U.K.

tetrakis(O-propargylgold)calix[4]arene, **7**: FTIR: ν_{CC} = 2002 cm^{-1} (w). ^1H NMR in $CDCl_3$, δ: 1.1 (br, m, 36H, Bu^t), 3.4 (br, 4H, $ArCH_2Ar$), 4.2 (br, 4H, $ArCH_2Ar$), 4.3 (br, 8H, OCH_2), 7.0 (br, 8H, Ar). Anal. calcd. for $C_{40}H_{28}Au_4O_4$: C 35.3, H 2.1; found: C 35.0, H 2.0%.

1,3-Bis{*O*-propargyl(triphenylphosphine)gold}tetra-*tert*-butylcalix[4]arene, 8*a*

Triphenylphosphine (0.094 g, 0.36 mmol) was added to a solution of complex **6***a* (0.2 g, 0.18 mmol) in CH_2Cl_2 (10 mL) and the mixture was stirred for 1 h. The product was precipitated by adding MeOH (20 mL), then filtered, washed with MeOH, and dried under vacuum. FTIR: ν_{CC} = 2147 cm^{-1} (w). NMR in $CDCl_3$: δ(^1H, −40°C): 0.86 (s, 18H, Bu^t), 1.28 (s, 18H, Bu^t), 3.30 and 4.53 (AB q, 8H, $^2J_{HH}$ = 13 Hz, $ArCH_2Ar$), 4.87 (d, 4H, $^4J_{PH}$ = 2 Hz, OCH_2), 6.66, 6.80, 7.02 (8H, Ar), 7.57–7.24 (m, 30H, PPh), 9.5 (s, 2H, OH); δ(^{31}P, −40°C): 39.2 (s, PPh_3). Anal. calcd. for $C_{86}H_{88}Au_2O_4P_2$: C 62.9, H 5.4; found: C 62.6, H 3.8%.

The complex *1,3-bis{*O*-propargyl(methyldiphenylphosphine)gold}tetra*-tert-*butylcalix[4]arene*, **8***b* was prepared in a similar way: FTIR: ν_{CC} = 2129 cm^{-1} (w). NMR in $CDCl_3$, δ(^1H): 0.88 (s, 18H, Bu^t), 1.29 (s, 18H, Bu^t), 2.02 (d, 6H, $^2J_{PH}$ = 8 Hz, PMe), 3.32 and 4.54 (AB q, 8H, $^2J_{HH}$ = 13 Hz, $ArCH_2Ar$), 4.87 (s, 4H, OCH_2), 6.68, 6.89, 7.04 (8H, Ar), 7.62–7.38 (m, 20H, PPh), 8.76 (s, 2H, OH); δ(^{31}P): 22.4 (s, $PMePh_2$). Anal. calcd. for $C_{76}H_{84}Au_2O_4P_2$: C 60.2, H 5.6; found: C 59.9, H 5.8%. The complex *{1,3-bis(8O-propargyl)[μ-bis(diphenylphosphinomethane)digold]}tetra*-tert-*butylcalix[4]arene*, **8***c*, was prepared similarly. FTIR: ν_{CC} = 2129 cm^{-1} (w). NMR in $CDCl_3$, δ(^1H, −40°C): 1.10 (s, 18H, Bu^t), 1.20 (s, 18H, Bu^t), 3.35 and 4.54 (AB q, 8H, $^2J_{HH}$ = 14 Hz, $ArCH_2Ar$), 3.77 (t, 4H, $^2J_{PH}$ = 8 Hz, PCH_2P), 4.72 (s, 4H, OCH_2), 7.63–6.5 (m, 28H, Ar and PPh), 8.76 (s, 2H, OH); δ(^{31}P, −40°C): 29.7 (s, dppm). Anal. calcd. for $C_{75}H_{80}Au_2O_4P_2$: C 60.0, H 5.4; found: C 59.6, H 5.7%. The complex *1,3-bis{*O*-propargyl(triphenylphosphine)silver}tetra*-tert-*butylcalix[4]arene*, **8***d* was prepared similarly. FTIR: ν_{CCH} = 2101 cm^{-1} (w). NMR in $CDCl_3$, δ(^1H): 0.95 (s, 18H, Bu^t), 1.32 (s, 18H, Bu^t), 3.36 and 4.40 (AB q, 8H, $^2J_{HH}$ = 14 Hz, $ArCH_2Ar$), 4.75 (s, 4H, OCH_2), 7.42–6.33 (m, 38H, Ar, PPh and OH); δ(^{31}P, 22°C): 29.0 (s, br); δ(^{31}P, −60°C): 7.0 (m, ^1J(AgP) = 67 Hz). Anal. calcd. for $C_{86}H_{88}Ag_2O_4P_2$: C 70.6, H 4.4; found: C 70.2, H 4.6%. The complex *tetrakis{*O*-propargyl(triphenylphosphine)gold}calix[4]arene*, **9***a* was prepared similarly. FTIR: ν_{CC} = 2131 cm^{-1} (w). NMR in $CDCl_3$: *1,3-alternate conformer*, δ(^1H): 4.29 (s, 8H, OCH_2), 3.70 (8H, $ArCH_2Ar$), 7.6–6.2 (m, Ar*H* of both 1,3-alternate and partial cone conformers); δ(^{31}P, 22°C): 42.7 (s, br, PPh_3); δ(^{31}P, −80°C): 41.0 (s, PPh_3); *partial cone conformer*: 3.07 and 4.20 (AB q, 4H, $^2J_{HH}$ = 14 Hz, $ArCH_2Ar$), 3.83 and 4.49 (AB q, 4H, $^2J_{HH}$ = 14 Hz, $ArCH_2Ar$), 4.51 and 4.98 (AB q, 4H, $^2J_{HH}$ = 14 Hz, OCH_2), 4.59 (s, 2H, OCH_2), 4.67 (s, 2H, OCH_2); δ(^{31}P, −80°C): 42, 43, 44 (s, PPh_3), Anal. calcd. for $C_{112}H_{88}Au_4O_4P_4$: C 55.8, H 3.7; found: C 55.5, H 3.8%. The complex *tetrakis{*O*-propargyl(methyldiphenylphosphine)gold}calix[4]arene*, **9***b* was prepared similarly. FTIR: ν_{CC} = 2131 cm^{-1} (w). NMR in $CDCl_3$: *1,3-alternate conformer*, δ(^1H): 4.28 (s, 8H, OCH_2), 3.70 (8H, $ArCH_2Ar$), 7.7–6.22 (m, Ar*H* of both 1,3-alternate and partial cone conformers); *partial cone conformer*: 3.00 and 4.50 (AB q, 4H, $^2J_{HH}$ = 14 Hz, $ArCH_2Ar$), 3.84 and 4.38 (AB q, 4H, $^2J_{HH}$ = 14 Hz, $ArCH_2Ar$), 4.50 and 4.90 (AB q, 4H, $^2J_{HH}$ = 14 Hz, OCH_2), 4.58 (s, 2H, OCH_2), 4.67 (s, 2H, OCH_2); δ(^{31}P, 22°C): 40.1 (s, br, $PMePh_2$). Anal. calcd. for $C_{92}H_{80}Au_4O_4P_4$: C 51.1, H 3.0; found C 50.7, H 2.6%.

Acknowledgments

We thank the Natural Sciences and Engineering Research Council of Canada (NSERC) for financial support.

References

1. M. Takeshita and S. Shinkai. Bull. Chem. Soc. Jpn. **68**, 1088 (1995); V. Boehmer. Angew. Chem. Int. Ed. Engl. **34**, 713 (1995); H.E. Katz. *In* Inclusion compounds. Vol. 4. *Edited by* J.L. Atwood, J.E.D. Davies, and D.D. MacNicol. Oxford University Press, New York. 1991. Chap. 9; C.D. Gutsche. *In* Calixarenes. R. Soc. Chem. Monogr. in Supramolecular Chemistry, Cambridge, U.K. 1989; A. McKervey and V. Boehmer. Chem. Br. 724 (1992); S. Shinkai. Tetrahedron, **49**, 8933 (1993); K.M. O'Connor, D.W.M. Arrigan, and G. Svehla. Electroanalysis (NY), **7**, 205 (1995); J. Vicens and V. Boehmer. *In* Calixarenes: a versatile class of macrocyclic compounds. Kluwer Academic Publishers, Dordrecht. 1990.
2. K. Araki. J. Synth. Org. Chem. Jpn. **53**, 22 (1995); D.V. Khasnis, J.M. Burton, J.D. McNeil, C.J. Santini, H.M. Zhang, and M. Lattman. Inorg. Chem. **33**, 2657 (1994); H. Deligoz and M. Yilmaz. Solvent Extr. Ion Exch. **13**, 19 (1995).
3. W. Xu, R.J. Puddephatt, Lj. Manojlovic-Muir, K.W. Muir, and C.S. Frampton. J. Incl. Chem. **19**, 277 (1994).
4. B.R. Cameron, F. van Veggel, and D.N. Reinhoudt. J. Org. Chem. **60**, 2802 (1995).
5. C.D. Gutsche and L.-G. Lin. Tetrahedron, **42**, 1633 (1986); C.D. Gutsche and P.F. Pagoria. J. Org. Chem. **50**, 5795 (1985).
6. (*a*) E.M. Collins, M.A. McKervey, E. Madigan, M.B. Moran, M. Owens, G. Ferguson, and S.J. Harris. J. Chem. Soc. Perkin Trans. 1, 3137 (1991); (*b*) B. Berger, V. Bohmer, E. Paulus, A. Rodriguez, and W. Vogt. Angew. Chem. Int. Ed. Engl. **31**, 96 (1992); (*c*) P.D.J. Grootenhuis, P.A. Kollman, L.C. Groenen, D.N. Reinhoudt, G.J. van Hummel, F. Ugozzoli, and G.D. Andreetti. J. Am. Chem. Soc. **112**, 4165 (1990); (*d*) P.D. Beer, J.P. Martin, and M.G.B. Drew. Tetrahedron, **48**, 9917 (1992); (*e*) V. Bohmer, G. Ferguson, J.F. Gallagher, A.J. Lough, M.A. McKervey, E. Madigan, M.B. Moran, J.P. Phillips, and G. Williams. J. Chem. Soc. Perkin Trans. 1, 1521 (1993).
7. A. Arduini, A. Pochini, A.R. Sicuri, A. Secchi, and R. Ungaro. Gazz. Chim. Ital. **124**, 129 (1994).
8. (*a*) F. Bottino and S. Pappalardo. J. Inclusion Phenom. Mol. Recognit. Chem. **19**, 85 (1994); (*b*) D. Braga, F. Grepioni, K. Biradha, V.R. Pedireddi, and G.R. Desiraju. J. Am. Chem. Soc. **117**, 3165 (1995).
9. C. Jaime, J. de Mendoza, P. Prados, P.M. Nieto, and C. Sanchez. J. Org. Chem. **56**, 3372 (1991).
10. W. Xu, R.J. Puddephatt, Lj. Manojlovic-Muir, and K.W. Muir. Organometallics, **13**, 3054 (1994).
11. A. Ikeda, H. Tsuzuki, and S. Shinkai. J. Chem. Soc. Perkin Trans. 2, 2073 (1994).
12. S. J. Harris, G. Barrett, and M.A. McKervey. J. Chem. Soc. Chem. Commun. 1224 (1991).
13. (*a*) H. Deligoz, M. Tavasli, and M. Yilmaz. J. Polym. Sci. Part A: Polym. Chem. **32**, 2961 (1994); H. Deligoz and M. Yilmaz. J. Polym. Sci. Part A: **33**, 2851 (1995).
14. S. Dirlikov and Y. Feng. Int. SAMPE Electron. Conf. **3**, 169 (1989).
15. J.W. Steed, R.K. Juneja, R.S. Burkhalter, and J.L. Atwood. J. Chem. Soc. Chem. Commun. 2205 (1994).

16. D.V. Khasnis, J.M. Burton, J.D. McNeil, H.M. Zhang, and M. Lattman. Phosphorus Sulfur Silicon, **87**, 93 (1994).
17. A. Decian, J. Fischer, and L. Toupet. Bull. Soc. Chim. Fr. **132**, 166 (1995).
18. X. Delaigue, M.W. Hosseini, N. Kyritsakas, A. Decian, and J. Fischer. J. Chem. Soc. Chem. Commun. 609 (1995).
19. R.J. Puddephatt. The chemistry of gold. Elsevier, Amsterdam. 1978.
20. A. Tamaki and J.K. Kochi. J. Organomet. Chem. **64**, 411 (1974).
21. C.D. Gutsche and M. Iqbal. Org. Synth. **68**, 234 (1989).
22. C.D. Gutsche, B. Dhawan, J.A. Levine, K.H. No, and L.J. Bauer. Tetrahedron, **39**, 409 (1983).
23. G.M. Sheldrick. SHELXTL-PC Software. Siemens Analytical X-Ray Instruments Inc., Madison, Wis. 1990.
24. G.M. Sheldrick, SHELXL-93. Dept. Anorg. Chemie, University of Goettingen, Goettingen, Germany, 1993.

Kinetic energy analysis of atomic multiplets. II. $s^m d^n$ configurations

Toshikatsu Koga, Hidenori Aoki, and Ajit J. Thakkar

Abstract: A kinetic energy analysis of total energy differences in 822 atomic multiplets arising from $s^m d^n$ ($m = 0,1,2$; $n = 2$–8) electronic configurations is performed within the nonrelativistic, restricted Hartree–Fock framework. For the 444 multiplets arising from the d^n and $s^2 d^n$ configurations of 27 atoms in groups 2–10, a very good linear correlation between the total energy difference and the kinetic energy difference of the outermost d-electrons is demonstrated. For the 378 multiplets arising from the sd^n configuration, on the other hand, a good linear correlation is obtained provided that the multiplets are classified into groups based on spin multiplicity.

Key words: kinetic energy, atomic multiplets, $s^m d^n$ configurations, Hartree–Fock approximation.

Résumé : Une analyse de l'énergie cinétique des différences de l'énergie totale de 822 multiplets atomiques dérivant de configurations électroniques $s^m d^n$ ($m = 0,1$ ou 2; $n = 2$–8) a été réalisée dans le cadre restreint, non relativiste de Hartree–Fock. Pour les 444 multiplets dérivant des configurations d^n et $s^2 d^n$ des 27 atomes des groups 2–10, on a obtenu une très bonne corrélation linéaire entre la différence de l'énergie totale et la différence de l'énergie cinétique des électrons d des couches les plus extérieures. Par ailleurs, pour les 378 multiplets dérivant de la configuration sd^n, on a obtenu une bonne corrélation à la condition que les multiplets soient classifiés en groupes basés sur la multiplicité de leurs spins.

Mots clés : énergie cinétique, multiplets atomiques, configurations $s^m d^n$, approximation de Hartree–Fock.

[Traduit par la rédaction]

Introduction

Using numerical Hartree–Fock data, we recently examined (1) the correlation of the total energy E with the kinetic energy $T(nl)$ of electrons in a particular atomic orbital nl in 115 atomic multiplet states arising from the $s^m p^n$ ($m = 1,2$; $n = 2$–4) electronic configurations of 20 main group atoms. We found (1) that, despite non-negligible contributions from the core electrons, there *is* a reasonably accurate linear relationship between the kinetic energy difference ΔT of the electrons in open subshells and the total energy difference ΔE, though the proportionality constant depends on both the atom and electron configuration.

Our study (1) was motivated by an earlier one[2] that used electron momentum distributions for the interpretation of Hund's rules. Kinetic energies T are just one half of the second moments $\langle p^2 \rangle$ of the radial electron momentum density. The theoretical background of our kinetic energy analysis of atomic multiplets is the virial theorem (2), which holds exactly for both exact and Hartree–Fock wave functions:

$$[1a] \quad E = -T = V/2$$

where V is the potential energy. Application of eq. [1a] to two states gives

$$[1b] \quad \Delta E = -\Delta T = \Delta V/2$$

which relates the total energy difference to the differences in the two components. Equation [1] implies that the total energy E can be analyzed using either of its two components, T or V. There is no unique decomposition of the potential energy V into orbital contributions because the potential energy operator has a two-electron component. On the other hand, choosing the kinetic energy T has the advantage that it permits an unambiguous decomposition into orbital contributions since the kinetic energy operator is a one-electron operator. The kinetic energy analysis allows us to focus on the electrons in open subshells thus obtaining insight, albeit at the expense of exactness.

In this paper, we extend the kinetic energy analysis to atomic multiplets arising from $s^m d^n$ electronic configurations with $m = 0,1,2$, and $n = 2$–8. A total of 822 multiplet states are examined for 27 atoms from groups 2–10. For the multiplets arising from the d^n and $s^2 d^n$ configurations, we demonstrate an accurate linear correlation between the total energy difference ΔE and the kinetic energy difference $\Delta T(d)$ of electrons in unfilled d- subshells; thus $\Delta E = -a\Delta T(d)$ where a is a positive constant common to all the multiplets from a chosen configuration of an atom. The Pearson correlation coefficients are greater than 0.999 in most cases. In the case of multiplets from the sd^n configuration, we again obtain an accurate linear relationship in the form $\Delta E = -a\Delta T(d) + b$, where a is a positive

Received June 1, 1994.

This paper is dedicated to Professor Richard F.W. Bader on the occasion of his 65th birthday.

T. Koga and H. Aoki. Department of Applied Chemistry, Muroran Institute of Technology, Muroran, Hokkaido 050, Japan. **A.J. Thakkar.**[1] Department of Chemistry, University of New Brunswick; Fredericton, NB E3B 6E2, Canada.

[1] Author to whom correspondence may be addressed. Telephone: (506) 453-4629. Fax: (506) 453-4981. E-mail: ajit@unb.ca

[2] A.J. Thakkar and A.L. Wonfor. Unpublished.

Table 1. Number of multiplets examined.

Z	Atom	d^n	sd^n	s^2d^n	Total
20	Ca	5	—	—	5
21	Sc	8	7	—	15
22	Ti	16	16	5	37
23	V	16	24	8	48
24	Cr	16	32	16	64
25	Mn	8	24	16	48
26	Fe	5	16	16	37
27	Co	—	7	8	15
28	Ni	—	—	5	5
38	Sr	5	—	—	5
39	Y	8	7	—	15
40	Zr	16	16	5	37
41	Nb	16	24	8	48
42	Mo	16	32	16	64
43	Tc	8	24	16	48
44	Ru	5	16	16	37
45	Rh	—	7	8	15
46	Pd	—	—	5	5
56	Ba	5	—	—	5
57	La	8	7	—	15
72	Hf	16	16	5	37
73	Ta	16	24	8	48
74	W	16	32	16	64
75	Re	8	24	16	48
76	Os	5	16	16	37
77	Ir	—	7	8	15
78	Pt	—	—	5	5
Total		222	378	222	822

constant as before but b is an additional constant that depends not only on the chosen configuration and atom but also on the spin multiplicities of both the multiplets and their parent d^n multiplets. Hartree atomic units are used throughout this paper.

Computational details

All our numerical Hartree–Fock calculations were carried out with an enhanced version of the MCHF72 program (3). The required multiplet energy expressions were taken mainly from Slater (4) and Condon and Odabasi (5). Our total energies were converged to 10 significant figures and various orbital properties to 7 or more significant figures. Errors in the virial ratio V/T were less than 1×10^{-10}, which guarantees the applicability of our basic equations [1*a*] and [1*b*].

We chose 27 atoms from groups 2–10 in the fourth (Ca through Ni), fifth (Sr through Pd), and sixth (Ba through Pt excluding Ce–Lu) periods of the periodic table for our analysis of multiplet states arising from d^n, sd^n, and s^2d^n electronic configurations. The configurations with n = 1,9,10 were excluded since they lead to only one or two energy levels. The numbers of multiplets examined in this study are summarized in Table 1 for each atom and each configuration.

Fig. 1. Linear correlation between ΔE and $-\Delta T(d)$ for the multiplets arising from the d^n configuration.

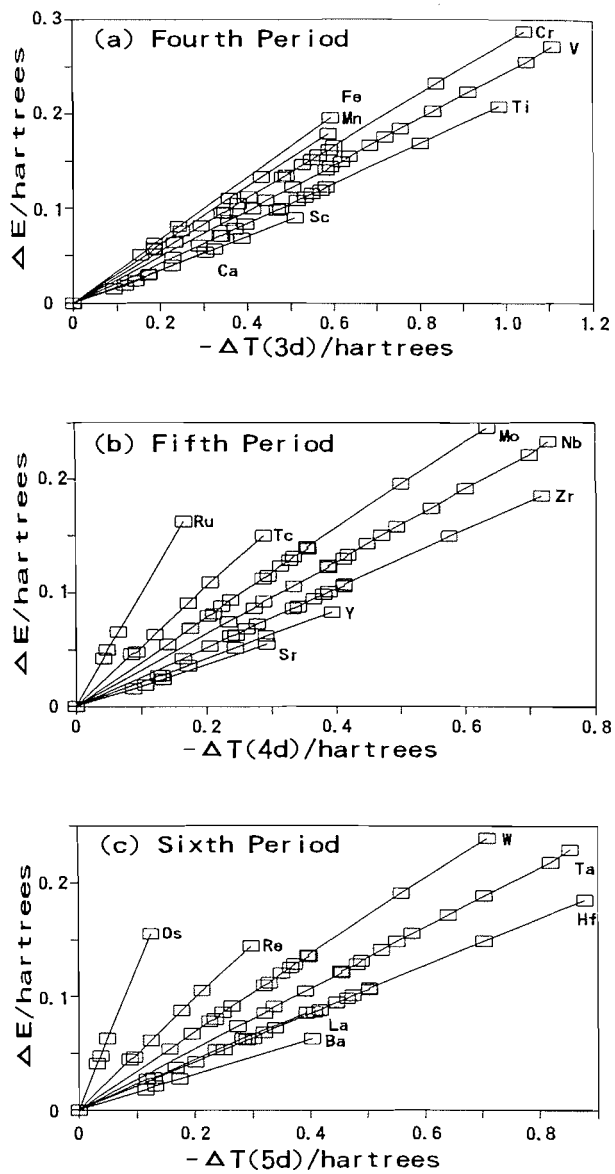

3. Results and discussion

3.1 d^n Configuration

Configurations of this type lead to 222 multiplet states. For each atom, we examined the total energy difference ΔE and the kinetic energy difference $\Delta T(d)$ of electrons in the outermost unfilled d subshell relative to the corresponding quantities for the ground state of the same configuration. Figure 1 shows that the correlation between ΔE and $-\Delta T(d)$ is surprisingly good for all 21 atoms. We then performed least-squares fits of the data to the simple linear equation,

$$[2] \quad \Delta E = -a\Delta T(d)$$

The proportionality constants a and the correlation coefficients R are summarized in Table 2. All the correlation coefficients (except that for Ca) are larger than 0.999, showing that the linear fits are accurate. The proportionality constants increase

Table 2. Correlation between the total energy difference ΔE and the kinetic energy difference $\Delta T(d)$ of the outermost d electrons for the 222 multiplet states arising from the d^n configuration. The proportionality constant a in the equation $\Delta E = -a\Delta T(d)$ is given together with the correlation coefficient R.

		Fourth period				Fifth period				Sixth period			
Configuration	No. of states	Z	Atom	a	R	Z	Atom	a	R	Z	Atom	a	R
d^2	5	20	Ca	0.170 40	0.997 74	38	Sr	0.185 65	0.999 28	56	Ba	0.155 85	0.999 89
d^3	8	21	Sc	0.173 67	0.999 83	39	Y	0.212 00	0.999 90	57	La	0.220 05	0.999 53
d^4	16	22	Ti	0.209 27	0.999 88	40	Zr	0.259 39	0.999 92	72	Hf	0.211 52	0.999 91
d^5	16	23	V	0.243 43	0.999 90	41	Nb	0.318 58	0.999 89	73	Ta	0.267 97	0.999 90
d^6	16	24	Cr	0.275 48	0.999 97	42	Mo	0.390 82	0.999 84	74	W	0.341 06	0.999 84
d^7	8	25	Mn	0.305 15	0.999 94	43	Tc	0.525 19	0.999 74	75	Re	0.489 91	0.999 85
d^8	5	26	Fe	0.330 70	0.999 96	44	Ru	0.989 12	0.999 66	76	Os	1.254 25	0.999 92

Table 3. Correlation between the total energy difference ΔE and the kinetic energy difference $\Delta T(d)$ of the outermost d electrons for the 222 multiplet states arising from the s^2d^n configuration. The proportionality constant a in the equation $\Delta E = -a\Delta T(d)$ is given together with the correlation coefficient R.

		Fourth period				Fifth period				Sixth period			
Configuration	No. of states	Z	Atom	a	R	Z	Atom	a	R	Z	Atom	a	R
s^2d^2	5	22	Ti	0.220 55	0.998 69	40	Zr	0.225 13	0.997 89	72	Hf	0.179 03	0.997 76
s^2d^3	8	23	V	0.268 59	0.999 61	41	Nb	0.295 67	0.999 13	73	Ta	0.240 93	0.999 08
s^2d^4	16	24	Cr	0.298 46	0.999 63	42	Mo	0.353 16	0.999 02	74	W	0.294 93	0.998 93
s^2d^5	16	25	Mn	0.329 12	0.999 91	43	Tc	0.435 61	0.999 67	75	Re	0.376 37	0.999 61
s^2d^6	16	26	Fe	0.350 07	0.999 90	44	Ru	0.538 60	0.999 50	76	Os	0.490 89	0.999 40
s^2d^7	8	27	Co	0.373 53	0.999 91	45	Rh	0.793 05	0.999 76	77	Ir	0.830 99	0.999 81
s^2d^8	5	28	Ni	0.391 76	0.999 94	46	Pd	2.954 87	0.999 49	78	Pt	−7.479 55	0.950 35

with the number of d electrons in the same period, with a minor exception in the first three atoms of the sixth period. However, there seems to be no simple relationship between the value of a and the number of d electrons. Since the values of a are quite different from 1, it is clear that the kinetic energy differences of the core electrons are far from negligible (1). However, adding the kinetic energy contributions from inner electrons such as those in the np subshell does not improve the quality of the fits significantly. Equation [2] captures the essentials of the physics and leads to good fits.

3.2 s^2d^n Configuration

Similarly, we examined the correlation between ΔE and $-\Delta T(d)$ for the 222 multiplets arising from s^2d^n configurations. Figure 2 shows that there is a very accurate linear correlation. The quality of the correlation is similar to that found earlier (1) for the s^2p^n configuration although there are more multiplets in the s^2d^n configuration. Table 3 lists the results of a regression analysis of the data using the linear formula [2]. The correlation coefficients are larger than 0.999 in most cases; exceptions are found for Ti, Zr, Pt, and Hf. The Pt atom is a special exception in that its proportionality constant a is negative. This means that ΔE increases with increases in $\Delta T(d)$ rather than with decreases in $\Delta T(d)$ as anticipated from eq. [1b]. A finer analysis for Pt shows that $\Delta T(4d)$, from the 10 electrons in the filled $4d$ subshell, is larger than $\Delta T(5d)$, and $-\Delta T(4d)$ has the expected positive correlation with ΔE. Similarly, for the Rh, Pd, and Ir atoms, $\Delta T(d)$ for the inner d subshell closest to the outermost d subshell is larger than for the outermost d subshell, but the reason for this remains unclear.

3.3 sd^n Configuration

We examined the 378 multiplet states arising from the sd^n configurations of 21 atoms for a correlation between the total energy difference ΔE and the kinetic energy difference $\Delta T(d)$ of the outermost d subshell. However, we could not find any good correlation between ΔE and $-\Delta T(d)$ for any atom. The situation is illustrated in Fig.3 (a) for the Cr atom, which has the most multiplets.

In multiplets arising from sp^n configurations, $\Delta T(sp) = \Delta T(s) + \Delta T(p)$ has a reasonably accurate linear correlation with ΔE, although $\Delta T(p)$ alone does not (1). Thus, we examined the correlation of $\Delta T(sd) = \Delta T(s) + \Delta T(d)$ with ΔE, where $\Delta T(s)$ is the kinetic energy difference for the singly occupied s orbital. However, since the magnitude of $\Delta T(s)$ is more than 10 times smaller than that of $\Delta T(d)$, this did not lead to any essential improvement in the correlation between ΔE and ΔT.

Finally, we made a careful analysis of the data and found that if all the multiplets from an sd^n configuration of an atom are grouped according to their spin multiplicity $2S + 1$ and the spin multiplicity $2S' + 1$ of their parent d^n multiplets, then a linear relationship,

$$[3] \quad \Delta E = -a\Delta T(d) + b$$

works very nicely. The constant a is common to all the mul-

Fig. 2. Linear correlation between ΔE and $-\Delta T(d)$ for the multiplets arising from the s^2d^n configuration.

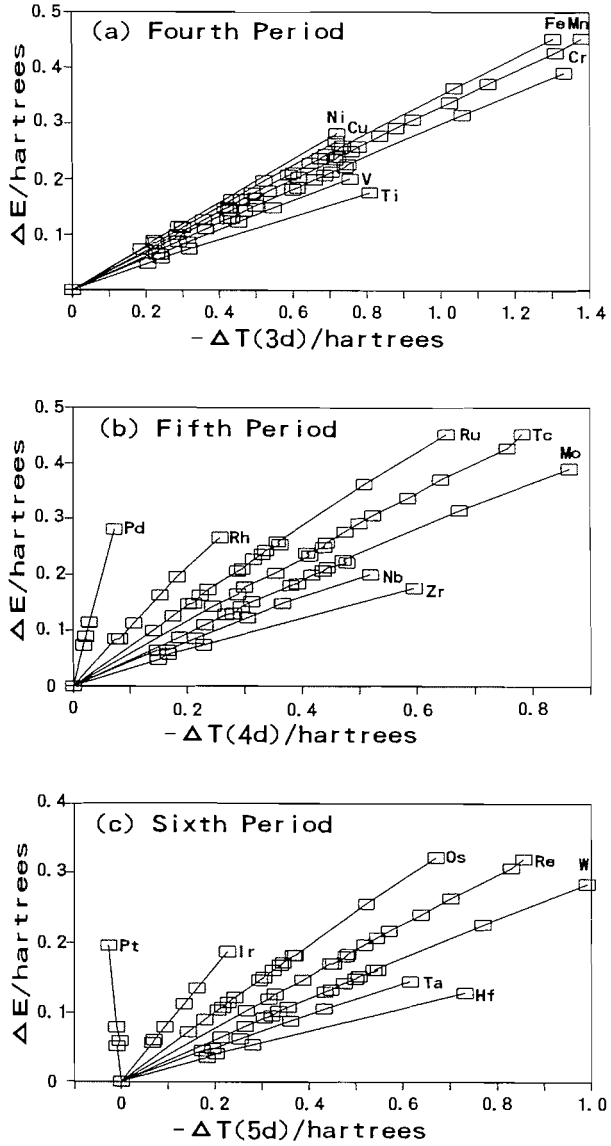

tiplets corresponding to a chosen configuration and atom, but the other constant b also depends on the spin multiplicities $2S + 1$ and $2S' + 1$, but not the orbital multiplicity $2L + 1$. Figure 3(*b*) illustrates some linear correlations between ΔE and $-\Delta T(d)$, obtained by the grouping of multiplets, for the Cr atom. Using the same procedure, we can obtain similar correlations for all the other atoms. Three more examples are given in Fig. 4 for the sd^2 multiplets of Sc, the sd^3 multiplets of Zr, and the sd^4 multiplets of Ta. Note that the sd^n and sd^{10-n} multiplets have a similar profile in the correlation between ΔE and $-\Delta T(d)$ due to the particle–hole relationship. Table 4 summarizes the constants a and b together with the correlation coefficient R for 21 atoms. All the correlation coefficients are larger than 0.999 and the linear relationship [3] is as accurate as eq. [2] for the d^n and s^2d^n multiplets.

An ad hoc explanation is possible for the success of the spin multiplicity grouping of sd^n multiplets. As we observed in Fig. 1 and Table 2, all the d^n multiplets are on a straight line. Addition of an electron to an s orbital causes a splitting of the original d^n multiplet into two new multiplets according to the spin quantum number ($m_s = +1/2$ or $-1/2$) of the s electron. Further more, the width of the splitting depends on the spin multiplicity of the parent d^n multiplet. Thus we need two spin multiplicities $2S + 1$ and $2S' + 1$ to characterize the correlation between ΔE and $-\Delta T(d)$ of sd^n multiplets. This splitting mechanism can be observed roughly in Fig. 3(*b*) by drawing lines that are $(2S + 1)$-weighted "averages" of two lines with the same $2S' + 1$. The two average lines corresponding to $2S' + 1 = 2$ and 4 and the average point from $2S' + 1 = 6$ all lie on a single line passing through the origin.

Fig. 3. Correlation between ΔE and $-\Delta T(d)$ for the multiplets arising from the sd^5 configuration of the Cr atom. (*a*) Without grouping. (*b*) With grouping based on the spin multiplicities $(2S + 1)/(2S' + 1)$.

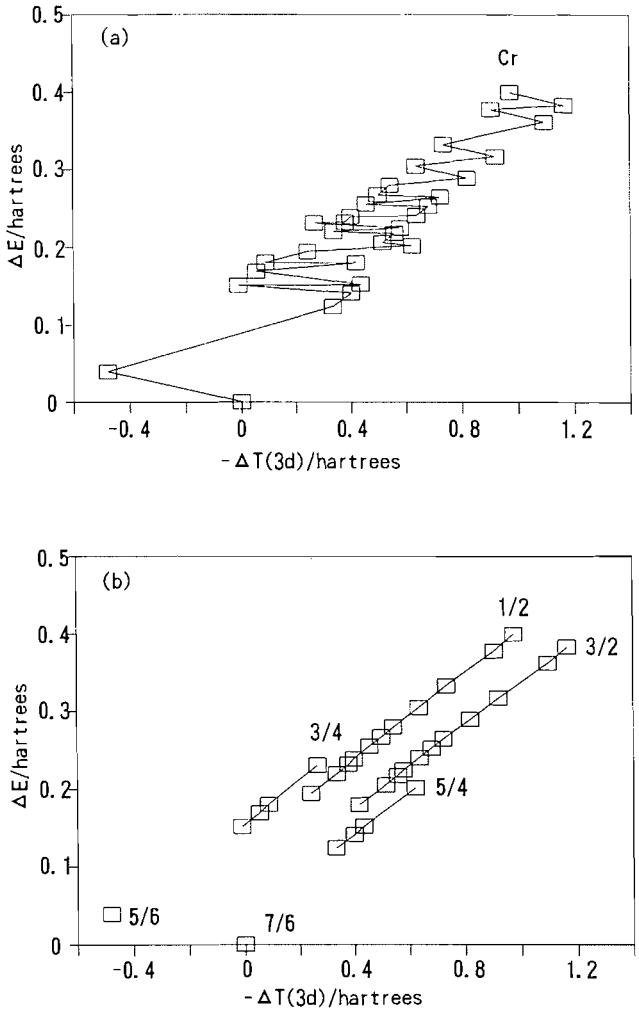

4. Concluding remarks

Using numerical Hartree–Fock calculations, we have shown that there is a very accurate linear correlation between ΔE and $-\Delta T(d)$ of 822 atomic multiplets arising from the s^md^n electronic configurations of 27 atoms. For the d^n and s^2d^n multiplets, the correlation can be expressed by $\Delta E = -a\Delta T(d)$ using a single parameter a. For the sd^n multiplets, an additional parameter b is needed because of the interaction of two open

Table 4. Correlation between the total energy difference ΔE and the kinetic energy difference $\Delta T(d)$ of the outermost d electrons for the 378 multiplet states arising from the sd^n configuration. Parameters a and b in the equation $\Delta E = -a\Delta T(d) + b$ are given together with the correlation coefficient R. Multiplet states are classified based on their spin multiplicities $2S + 1$ and their parent d^n spin multiplicities $2S' + 1$.

			Fourth period					Fifth period					Sixth period				
Configuration	$2S + 1/2S' + 1$	No. of states	Z	Atom	a	b	R	Z	Atom	a	b	R	Z	Atom	a	b	R
sd^2	4/3	2	21	Sc	0.134 02	0.000 93	1.000 00	39	Y	0.157 72	0.001 65	1.000 00	57	La	0.192 82	0.001 46	1.000 00
	2/1	3				0.029 89	0.999 83				0.036 19	0.999 79				0.037 04	0.999 69
	2/3	2				0.083 35	1.000 00				0.104 81	1.000 00				0.101 19	1.000 00
sd^3	5/4	2	22	Ti	0.197 73	−0.000 20	1.000 00	40	Zr	0.230 88	0.000 63	1.000 00	72	Hf	0.185 78	0.000 82	1.000 00
	3/2	6				0.030 27	0.999 72				0.043 62	0.999 43				0.045 63	0.999 41
	1/2	6				0.092 74	0.999 66				0.129 07	0.999 23				0.134 70	0.999 18
	3/4	2				0.116 03	1.000 00				0.164 82	1.000 00				0.173 07	1.000 00
sd^4	6/5	1	23	V	0.236 05	0	—	41	Nb	0.283 82	0	—	73	Ta	0.234 51	0	—
	4/3	7				0.032 57	0.999 81				0.051 16	0.999 56				0.054 89	0.999 56
	2/1	8				0.064 75	0.999 78				0.099 44	0.999 49				0.106 45	0.999 49
	2/3	7				0.125 45	0.999 82				0.191 01	0.999 54				0.205 06	0.999 52
	4/5	1				0.141 67	—				0.220 02	—				0.132 80	—
sd^5	7/6	1	24	Cr	0.276 02	0	—	42	Mo	0.358 65	0	—	74	W	0.304 28	0	—
	5/4	4				0.031 28	0.999 80				0.057 07	0.999 46				0.064 00	0.999 52
	3/2	11				0.063 51	0.999 86				0.112 37	0.999 59				0.125 41	0.999 61
	1/2	11				0.129 29	0.999 86				0.220 96	0.999 59				0.245 39	0.999 61
	3/4	4				0.155 62	0.999 83				0.265 86	0.999 55				0.295 90	0.999 61
	5/6	1				0.171 50	—				0.294 89	—				0.214 45	—
sd^6	6/5	1	25	Mn	0.303 75	0	—	43	Tc	0.441 78	0	—	75	Re	0.390 08	0	—
	4/3	7				0.033 50	0.999 87				0.065 85	0.999 64				0.076 67	0.999 74
	2/1	8				0.067 25	0.999 89				0.129 46	0.999 65				0.150 35	0.999 71
	2/3	7				0.130 97	0.999 88				0.247 67	0.999 68				0.287 34	0.999 77
	4/5	1				0.153 31	—				0.289 83	—				0.337 08	—
sd^7	5/4	2	26	Fe	0.334 62	−0.000 12	1.000 00	44	Ru	0.628 76	−0.000 11	1.000 00	76	Os	0.605 09	−0.000 38	1.000 00
	3/2	6				0.033 44	0.999 90				0.082 75	0.999 68				0.106 18	0.999 88
	1/2	6				0.101 04	0.999 90				0.242 29	0.999 70				0.308 32	0.999 91
	3/4	2				0.130 83	1.000 00				0.310 35	1.000 00				0.393 90	1.000 00
sd^8	4/3	2	27	Co	0.355 12	0.000 38	1.000 00	45	Rh	1.438 47	0.000 20	1.000 00	77	Ir	2.633 58	−0.003 77	1.000 00
	2/1	3				0.034 79	0.999 99				0.174 20	0.999 94				0.422 88	0.999 83
	2/3	2				0.101 26	1.000 00				0.489 39	1.000 00				1.173 57	1.000 00

Fig. 4. Linear correlation between ΔE and $-\Delta T(d)$. (*a*) The multiplets arising from the sd^2 configuration of Sc. (*b*) The multiplets arising from the sd^3 configuration of Zr. (*c*) The multiplets arising from the sd^4 configuration of Ta.

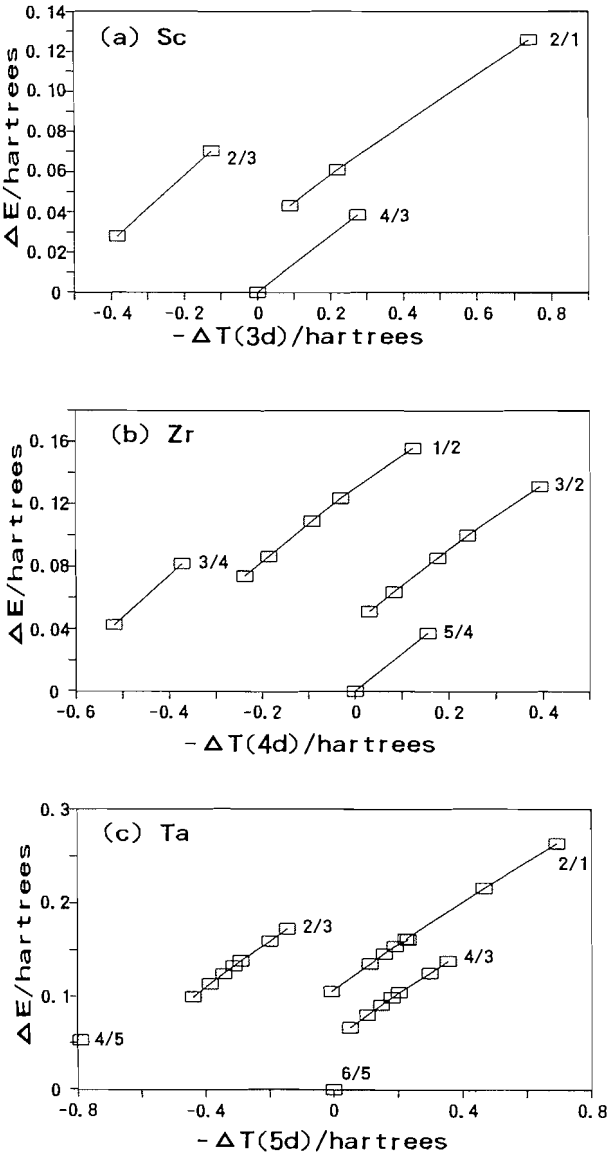

shells, and the correlation is expressed by $\Delta E = -a\Delta T(d) + (b)$. These linear relationships are quite accurate, as indicated by correlation coefficients greater than 0.999 in most cases.

The reciprocal nature of momentum and position space suggests that ΔE may also be correlated with $\Delta\langle r\rangle_d$, the difference in the radii of the outermost d orbitals, instead of $\Delta T(d) = \Delta\langle p^2/2\rangle_d$. We have verified for several atoms that this is approximately true, although the correlation is less accurate with $\Delta\langle r\rangle_d$ than with $\Delta T(d)$. Moreover, the theoretical basis is less firm for the correlation of ΔE with $\Delta\langle r\rangle_d$. Of course, correlations involving other measures of change in orbital size such as $\Delta\langle r^2\rangle_d$ are also possible.

Finally, it would be interesting to examine whether the accurate linear relationship observed within a nonrelativistic framework persists in a relativistic one, particularly for atoms in the sixth period.

Acknowledgments

This work was supported in part by a Grant-in-Aid for Scientific Research from the Ministry of Education of Japan and in part by the Natural Sciences and Engineering Research Council of Canada.

References

1. T. Koga and A.J. Thakkar. Int. J. Quantum Chem. In press.
2. S.T. Epstein. The variation method in quantum chemistry. Academic, New York. 1974.
3. C. Froese-Fischer. Comput. Phys. Commun. **4**, 107 (1972).
4. J.C. Slater. Quantum theory of atomic structure. Vol 2. McGraw–Hill, New York. 1960.
5. E.U. Condon and H. Odabasi. Atomic structure. Cambridge University Press, Cambridge. 1980.

Dispersion formulas for real- and imaginary-frequency-dependent hyperpolarizabilities

David M. Bishop

Abstract: The dynamic second hyperpolarizability for real frequencies, $\gamma_{\|}(-\omega_\sigma;\omega_1,\omega_2,\omega_3)$ in the limit $\omega_i \rightarrow 0$ can be expressed as $\gamma_{\|}^{0} + A_{\|}^{0}\omega_L^2$, where $\omega_L^2 = \omega_\sigma^2 + \omega_1^2 + \omega_2^2 + \omega_3^2$ and $\gamma_{\|}^{0}$ is the frequency-independent (static) quantity; the parallel subscript (||) indicates that the polarization and electric fields all lie along the same axis. In this paper the coefficient $A_{\|}^{0}$ is evaluated exactly for the H atom and very accurately for H^-, He, and Li^+. A similar analysis is carried out for $\gamma_{\|}(-i\omega;i\omega,0,0)$ in the limit $\omega \rightarrow \infty$.

Key words: nonlinear optics, hyperpolarizabilities, dispersion formulas.

Résumé : On peut exprimer la deuxième hyperpolarisabilité dynamique de fréquences réelles, $\gamma_{\|}(-\omega_\sigma;\omega_1,\omega_2,\omega_3)$ dans la limite $\omega_i \rightarrow 0$, peut être exprimée sous la forme $\gamma_{\|}^{0} + A_{\|}^{0}\omega_L^2$, dans laquelle $\omega_L^2 = \omega_\sigma^2 + \omega_1^2 + \omega_2^2 + \omega_3^2$ et $\gamma_{\|}^{0}$ est la quantité (statique) indépendant de la fréquence; l'indice parallèle (||) indique que la polarisation et les champs électriques sont situés dans le même axe. Dans ce travail, on a fait une évaluation exacte de $A_{\|}^{0}$ pour l'atome d'hydrogène et d'une façon précise pour H^-, He et Li^+. On a effectué une analyse semble pour $\gamma_{\|}(-i\omega;i\omega,0,0)$, dans la limite $\omega \rightarrow \infty$.

Mots clés : optique non linéaire, hyperpolarisabilités, formules de dispersion.

[Traduit par la rédaction]

Introduction

Hyperpolarizabilities govern nonlinear optical processes and as such are of much current interest, both theoretically and experimentally. They describe molecular behaviour in the presence of static or oscillating (optical) electric fields and for a detailed introduction the reader is referred to three recent special-issue publications (1–3). In this paper we are concerned with the relationships between the second hyperpolarizabilities and the frequencies of the defining electric fields, i.e., the dispersion. It is well known (4–6) that this property, for real frequencies, can be expressed as

$$[1] \qquad \gamma_{\|}(\omega) = \gamma_{zzzz}(-\omega_\sigma;\omega_1,\omega_2,\omega_3) = \gamma_{\|}^{0} + A_{\|}^{0}\omega_L^2 + O(\omega^4)$$

in the limit that $\omega_i \rightarrow 0$, where $\omega_L^2 = \omega_\sigma^2 + \omega_1^2 + \omega_2^2 + \omega_3^2$ and $\omega_\sigma = \omega_1 + \omega_2 + \omega_3$. Since we will only be considering atoms, the atomic axis z can double as the laboratory axis and $\gamma_{\|}(\omega)$ can also be interpreted as the isotropic or mean value of γ. There have, however, been no *direct* calculations of the coefficient $A_{\|}^{0}$, though values have been obtained by fitting $\gamma_{\|}(\omega)$ values. In this paper we show how $A_{\|}^{0}$ can be found analytically and exactly for the H atom, as well as obtaining accurate values for H^-, He, and Li^+.

In the limit $\omega \rightarrow \infty$, the standard second hyperpolarizability for imaginary frequencies can be written as:

$$[2] \qquad \gamma_{\|}(i\omega) = \gamma_{zzzz}(-\omega;i\omega,0,0) = A_{\|}^{\infty}\omega^{-2} + O(\omega^{-4})$$

At the other limit ($\omega \rightarrow 0$) the relationship in eq. [1] can still be applied. This particular, imaginary-frequency, second hyperpolarizability is of interest since it regulates the dispersion-polarizability coefficients that govern the nonclassical contribution to the change in electronic polarizability due to long-range interactions between colliding atoms (7).[2] The constant $A_{\|}^{\infty}$ turns out to be zero but its components, to be discussed later, are not and they are of some use as a check on calculations of $\gamma_{\|}(i\omega)$.

Both $\gamma_{\|}(\omega)$ and $\gamma_{\|}(i\omega)$ can be written in a sum-over-electronic-states (SOS) formulation and this leads to a positive and a negative contribution

$$[3] \qquad \gamma_{\|}(\omega) = \gamma_{\|}^{(+)}(\omega) - \gamma_{\|}^{(-)}(\omega)$$

$$[4] \qquad \gamma_{\|}(i\omega) = \gamma_{\|}^{(+)}(i\omega) - \gamma_{\|}^{(-)}(i\omega)$$

Received July 28, 1995.

This paper is dedicated to Professor Richard F.W. Bader on the occasion of his 65th birthday: both a colleague and a friend as well as a fellow lover of algebra.

D.M. Bishop.[1] Department of Chemistry, University of Ottawa, Ottawa, ON K1N 6N5, Canada.

[1] Telephone: (613) 562-5181. Fax: (613) 562-5170. E-mail: dmbse@uottawa.ca

[2] There is a misprint in eq. (13) of this reference in the fourth line: replace "$-\omega_m\omega_\sigma(\omega_2+\omega_3)$" by "$-\omega_m\omega_3(\omega_2+\omega_3)$".

Coefficients $A_{\parallel}^{0(+)}$, $A_{\parallel}^{0(-)}$, $A_{\parallel}^{\infty(+)}$, and $A_{\parallel}^{\infty(-)}$ can be attached to these contributions. The SOS definitions of $\gamma_{\parallel}^{(+)}(\omega)$, $\gamma_{\parallel}^{(-)}(\omega)$, etc. are, in their most general form (7, 8):

[5] $$\gamma_{zzzz}^{(+)}(-\omega_\sigma;\ \omega_1,\ \omega_2,\ \omega_3) = \hbar^{-3}\Sigma_P\Sigma_m\Sigma_n{}'\Sigma_p\langle 0|z|m\rangle\langle m|z|n\rangle\langle n|z|p\rangle\langle p|z|0\rangle/(\omega_m-\omega_\sigma)(\omega_n-\omega_2-\omega_3)(\omega_p-\omega_3)$$

[6] $$\gamma_{zzzz}^{(-)}(-\omega_\sigma;\ \omega_1,\ \omega_2,\ \omega_3) = \hbar^{-3}\Sigma_P\Sigma_m\Sigma_n\langle 0|z|m\rangle\langle m|z|0\rangle\langle 0|z|n\rangle\langle n|z|0\rangle/(\omega_m-\omega_\sigma)(\omega_n-\omega_3)(\omega_n+\omega_2)$$

[7] $$\gamma_{zzzz}^{(+)}(-i\omega_\sigma;\ i\omega_1,\ i\omega_2,\ i\omega_3) = \hbar^{-3}\Sigma_P\Sigma_m\Sigma_n{}'\Sigma_p\langle 0|z|m\rangle\langle m|z|n\rangle\langle n|z|p\rangle\langle p|z|0\rangle \times [\omega_m\omega_n\omega_p-\omega_m(\omega_2+\omega_3)\omega_3-\omega_n\omega_\sigma\omega_3-\omega_p\omega_\sigma(\omega_2+\omega_3)]/(\omega_m{}^2+\omega_\sigma{}^2)(\omega_n{}^2+(\omega_2+\omega_3)^2)(\omega_p{}^2+\omega_3{}^2)$$

[8] $$\gamma_{zzzz}^{(-)}(-i\omega_\sigma;\ i\omega_1,\ i\omega_2,\ i\omega_3) = \hbar^{-3}\Sigma_P\Sigma_m\Sigma_n\langle 0|z|m\rangle\langle m|z|0\rangle\langle 0|z|n\rangle\langle n|z|0\rangle \times [\omega_m\omega_n{}^2+\omega_m\omega_2\omega_3+\omega_n\omega_\sigma\omega_2-\omega_n\omega_\sigma\omega_3]/(\omega_m{}^2+\omega_\sigma{}^2)(\omega_n{}^2+\omega_3{}^2)(\omega_n{}^2+\omega_2{}^2)$$

In these equations $\omega_\sigma = \omega_1 + \omega_2 + \omega_3$, z is the electric dipole moment operator, and Σ_P infers a summation over the 24 permutations of $-\omega_\sigma$, ω_1, ω_2, and ω_3 or their imaginary analogues. The prime on the sum over n in eqs. [5] and [7] indicates the exclusion of the electronic ground state (0); for m or $p = 0$, $\langle 0|z|0\rangle = 0$ for atoms, so inclusion or not of the ground state makes no difference. ω_m is the circular electronic transition frequency between the mth excited state, with wave function $|m\rangle$, and the ground state, with wave function $|0\rangle$.

Use of the binomial theorem allows expansion of the energy denominators in eqs. [5] and [6] and we can then collect the terms that are quadratic in the optical frequencies ω_σ, ω_1,.... This leads to the coefficients of $\omega_L{}^2(= \omega_\sigma{}^2 + \omega_1{}^2 + \omega_2{}^2 + \omega_3{}^2)$ being

[9] $$A_{\parallel}^{0(+)} = 12X(-2,\ 0,\ 0) + 8X(0,-2,\ 0) + 8X(-1,-1,\ 0) + 2X(-1,\ 0,-1)$$

and

[10] $$A_{\parallel}^{0(-)} = 6Y(-3)Y(-2) + 14Y(-1)Y(-4)$$

where

[11] $$X(i,\ j,\ k) = \Sigma_m\Sigma_n{}'\Sigma_p\langle 0|z|m\rangle\langle m|z|n\rangle\langle n|z|p\rangle \times \langle p|z|0\rangle E_m{}^{i-1}E_n{}^{j-1}E_p{}^{k-1}$$

and

[12] $$Y(k) = \Sigma_m\langle 0|z|m\rangle\rangle m|z|0\rangle E_m{}^k$$

In eqs. [11] and [12] $E_m = \hbar\omega_m$ is the energy of the mth excited state relative to the ground state energy ε_g. $Y(k)$ are half the usual sum rules, i.e., $S(k-1) = 2Y(k)$. In deriving eqs. [9] and [10], use has been made of the symmetry between the indices m and p.

For $\gamma_{\parallel}^{\infty(+)}$ and $\gamma_{\parallel}^{\infty(-)}$, we can extract from eqs. [7] and [8] those terms with a ω^{-2} dependence as $\omega \rightarrow \infty$. This gives

[13] $$A_{\parallel}^{\infty(+)} = 8X(2,\ 0,\ 0) + 4X(0,\ 2,\ 0) - 8X(1,\ 1,\ 0)$$

and

[14] $$A_{\parallel}^{\infty(-)} = 4Y(1)Y(-2) + 4Y(-1)Y(0)$$

The degree of dispersion in the limiting cases of $\omega \rightarrow 0$ for $\gamma_{\parallel}(-\omega_\sigma;\omega_1,\omega_2,\omega_3)$ and of $\omega \rightarrow \infty$ for $\gamma_{\parallel}(-i\omega;i\omega,0,0)$ is thus dictated by the values of $X(i,j,k)$ and $Y(k)$. In the next section we show how these may be found exactly for the H atom.

Hydrogen atom

The trick to obtaining exact values for $X(i,j,k)$ and $Y(k)$ is to be able to make the energy denominators or numerators disappear. This can be rigorously accomplished for the H atom. Then the next step is to use the closure rule, $\Sigma_m|m\rangle\langle m| = 1$, so the summations disappear, and finally to carry out the simple integration that remains.

The first step requires the following relations, where $\varepsilon_g = -1/2$ au, is the ground state energy of the H atom and $\psi_0 = e^{-r}/\sqrt{\pi}$ the corresponding wave function,

[15] $$(H_0-\varepsilon_g)z\psi_0 = r^{-1}z\psi_0$$

[16] $$(H_0-\varepsilon_g)f_1 = z\psi_0$$

[17] $$(H_0-\varepsilon_g)f_2 = f_1$$

[18] $$(H_0-\varepsilon_g)f_3 = f_2$$

[19] $$(H_0-\varepsilon_g)zf_1 = (z^2/4r)(-r^2+4r+2)\psi_0 - f_1/z + zf_1/2$$

[20] $$(H_0-\varepsilon_g)g_1 = zf_1 - \langle 0|z|f_1\rangle\psi_0 = zf_1 - (9/4)\psi_0$$

[21] $$(H_0-\varepsilon_g)g_2 = g_1 - \langle 0|z|g_1\rangle\psi_0 = g_1 - (81/16)\psi_0$$

[22] $$(H_0-\varepsilon_g)h_1 = zf_2 - \langle 0|z|f_2\rangle\psi_0 = zf_2 - (43/8)\psi_0$$

Equations [16]–[18] are definitions of the functions f_1, f_2, and f_3 and they may be obtained from these equations by using the method of Coulson (9); f_1 is also the negative of the first-order perturbation wave function for a perturbing operator z. Likewise, eqs. [20]–[22] define the functions g_1, g_2, and h_1 and g_1 is the second-order perturbation wave function for a perturbing operator z. Solution of eqs. [16]–[18] and [20]–[22] gives:

[23] $$f_1 = z(r+2)\psi_0/2$$

[24] $f_2 = z(2r^2 + 11r + 22)\psi_0/12$

[25] $f_3 = z(6r^3 + 62r^2 + 287r + 574)\psi_0/144$

[26] $g_1 = r^2[(r^2 + 6r + 18) + (2r^2 + 10r + 15)P_2]\psi_0/24$

[27] $g_2 = r^2[3(4r^3 + 45r^2 + 270r + 810) + (24r^3 + 222r^2 + 818r + 1227)P_2]\psi_0/1440$

[28] $h_1 = r^2[(8r^3 + 85r^2 + 430r + 1290) + (16r^3 + 158r^2 + 662r + 993)P_2]\psi_0/720$

where $P_2 = (3\cos^2\theta - 1)/2$. Equations [23]–[25] are in accord with those of Dalgarno and Kingston (10).

Let us now consider, as an example, the term $X(-2,0,0)$ where the energy denominator is $E_m{}^3E_nE_p$. By replacing $z\psi_0$ in $\langle p|z|0\rangle$ by $(H_0 - \varepsilon_g)f_1$, eq. [16], and then using the Hermitean properties of the operator, E_p will be cancelled. Doing the same thing for $\langle 0|z|m\rangle$, but three times in succession, will remove $E_m{}^3$. This leaves

[29] $X(-2, 0, 0) = \Sigma_m\Sigma_n{}'\Sigma_p\langle f_3|m\rangle\langle m|z|n\rangle\langle n|z|p\rangle\langle p|f_1\rangle/E_n$

Use of closure for the sums over m and p, which is now possible, gives

[30] $X(-2, 0, 0) = \Sigma_n{}'\langle f_3|z|n\rangle\langle n|z|f_1\rangle/E_n$

and, with eq. [20], we obtain

[31] $X(-2, 0, 0) = \Sigma_n{}'\langle f_3|z|n\rangle\langle n|g_1\rangle$
$= \langle f_3|z|g_1\rangle - \langle f_3|z|0\rangle\langle 0|g_1\rangle$

The second term in the last step takes care of the exclusion from the summation over n of the ground state. The integration is now trivial and for the H atom:

[32] $X(-2, 0, 0) = 119539/192 - (319/24)(81/16)$

In a similar fashion:

[33] $X(0, -2, 0) = \langle g_1|g_2\rangle - \langle g_1|0\rangle\langle 0|g_2\rangle$
$= 1640867/3840 - (81/16)(771/64)$

[34] $X(-1, -1, 0) = \langle f_2|z|g_2\rangle - \langle f_2|z|0\rangle\langle 0|g_2\rangle$
$= 2015191/384 - (43/8)(771/64)$

[35] $X(-1, 0, -1) = \langle h_1|z|f_2\rangle - \langle h_1|0\rangle\langle 0|z|f_2\rangle$
$= 1264709/1920 - (1285/96)(43/8)$

[36] $X(2, 0, 0) = \langle 0|z^2r^{-1}|g_1\rangle - \langle 0|z^2r^{-1}|0\rangle\langle 0|g_1\rangle$
$= 243/32 - (1/2)(81/16)$

[37] $X(0, 2, 0) = \langle zf_1|H_0 - \varepsilon_g|zf_1\rangle$
$= 241/16$

[38] $X(1, 1, 0) = \langle 0|z^3|f_1\rangle - \langle 0|z^2|0\rangle\langle 0|z|f_1\rangle$
$= 99/8 - (1)(9/4)$

The much simpler terms $Y(k)$ require closure only once (after the energies have been eliminated) and are given by:

[39] $Y(1) = \langle 0|z^2r^{-1}|0\rangle$

[40] $Y(0) = \langle 0|z^2|0\rangle$

[41] $Y(-1) = \langle f_1|z|0\rangle$

[42] $Y(-2) = \langle f_2|z|0\rangle$

[43] $Y(-3) = \langle f_3|z|0\rangle$

[44] $Y(-4) = \langle f_2|f_2\rangle$

These terms were evaluated previously in ref. 10; they can also be found from the recursion relation in ref. 11.

The exact values of all the required functions are collected in Table 1. Using eqs. [9] and [10], we then find, in atomic units,

$$A_{\parallel}{}^{0(+)} = 693509/48$$

and

$$A_{\parallel}{}^{0(-)} = 95145/64$$

With the value (12) of $\gamma_{\parallel}{}^0 = 10665/8$ this means that

[45] $\gamma_{\parallel}(\omega) = \gamma_{\parallel}{}^0[1 + (2488601/255960)\omega_L{}^2]$

in the limit $\omega_i \to 0$ for the H atom. The quotient in eq. [45] is approximately 9.722617, which is in complete agreement with the result in ref. 4 that was found by fitting known calculated $\gamma_{\parallel}(\omega)$ values to eq. [1].

For the limiting expression for $\gamma_{\parallel}(i\omega)$, we use eqs. [13] and [14] and find $A_{\parallel}{}^{\infty(+)} = A_{\parallel}{}^{\infty(-)} = 79/4$ and thus both the positive and negative parts of $\gamma_{\parallel}(i\omega)$ drop off with respect to ω^{-2} at the same rate and cancel.

It might be mentioned that all the calculations so far reported were performed on a TI-37 Galaxy Solar calculator.

Two-electron systems

To obtain the same properties for the two-electron systems H^-, He, and Li^+, we used accurate variational wave functions, since no analytic ones exist. The $X(i,j,k)$ and $Y(k)$ were found in the same fashion that we have previously used for the calculation of the static and dynamic second hyperpolarizabilities themselves: the sums-over-states were in each

Table 1. Values of $X(i,j,k)$, $Y(k)$, and $A_{\|}$ in atomic units.[a]

	H	H^-	He	Li^+
$X(-2,0,0)$	213239/384	3.075 11 (9)	4.024 540	0.282 712 (−2)
$X(0,-2,0)$	5626703/15360	2.594 61 (9)	2.765 692	0.185 992 (−2)
$X(-1,-1,0)$	3533087/7680	2.892 48 (9)	3.396 009	0.232 508 (−2)
$X(-1,0,-1)$	2253143/3840	3.282 54 (9)	4.265 112	0.298 413 (−2)
$X(2,0,0)$	81/16	2.621 11 (3)	0.932 471	0.469 404 (−1)
$X(0,2,0)$	241/16	7.895 98 (3)	3.092 820	0.156 682
$X(1,1,0)$	81/8	5.236 55 (3)	1.864 872	0.938 772 (−1)
$Y(1)$	1/2	1	1	1
$Y(0)$	1	7.484 25	0.752 498	0.286 017
$Y(-1)$	9/4	1.030 82 (2)	0.691 596	0.962 266 (−1)
$Y(-2)$	43/8	1.885 77 (3)	0.707 510	0.352 808 (−1)
$Y(-3)$	319/24	4.005 01 (4)	0.771 070	0.136 107 (−1)
$Y(-4)$	9673/288	9.339 02 (5)	0.874 944	0.542 432 (−2)
$A_{\|}^{0(+)}$	693509/48	8.736 31 (10)	106.118 3	0.733 737 (−1)
$A_{\|}^{0(-)}$	95145/64	1.800 91 (9)	11.744 75	0.101 887 (−1)
$\gamma_{\|}^{0}$	10665/8	8.025 28 (7)	43.104	0.242 865
$A_{\|}^{0}/\gamma_{\|}^{0}$	2488601/255960	1.066 16 (3)	2.189 44	0.260 17
$A_{\|}^{\infty(+)}$	79/4	1.066 04 (4)	4.912 07	0.251 23
$A_{\|}^{\infty(-)}$	79/4	1.062 90 (4)	4.911 74	0.251 21

[a]The atomic unit of the second hyperpolarizability is $e^4a_0^4E_h^{-3}$ and it is equivalent to 6.23538 × 10^{-65} C^4 m^4 J^{-3}. Numbers in parentheses are the powers of 10 by which the entry is to be multiplied.

case replaced by sums over a pseudo-spectral series (8). The wave functions, which were explicitly electron correlated, were a generalization of those of Thakkar and Smith (13) and Thakkar (14):

$$[46]\quad \Psi^L(r_1, r_2, r_{12}, \theta_1, \theta_2, \phi_1, \phi_2) = \sum_{l_1,l_2}\sum_{k=1}^{N^{l_1l_2}} C_k^{l_1l_2}(1+P_{12})r_1^{l_1}r_2^{l_2}\mathcal{Y}_{Ll_1l_2}^{M_L}(\hat{r}_1, \hat{r}_2)\exp(-\alpha_k^{l_1l_2}r_1 - \beta_k^{l_1l_2}r_2 - \gamma_k^{l_1l_2}r_{12})$$

where, in vector-coupling notation:

$$[47]\quad \mathcal{Y}_{Ll_1l_2}^{M_L}(\hat{r}_1, \hat{r}_2) = \sum_{m_1,m_2}(l_1m_1l_2m_2|l_1l_2LM_L) \times Y_{l_1}^{m_1}(\hat{r}_1)\,Y_{l_2}^{m_2}(\hat{r}_2)$$

and r_1, θ_1, and ϕ_1 are the coordinates of electron 1; r_{12} is the interelectronic separation and Y_l^m are spherical harmonics. The nonlinear parameters were chosen in a pseudorandom fashion and, as before, 140, 140, and 190 functions were used to describe the ^1S, ^1P, and ^1D states, respectively, for He (15). For H^-, 200, 150, and 175 functions were used (16) and, for Li^+, 100, 100, and 150 functions (17).

The integral evaluations and sums lead to the results for $X(i,j,k)$ and $Y(k)$, which are given in Table 1. Combined, they produce the dispersion coefficients $A_{\|}^{0(+)}$, etc., which are also shown in this table. Once again, in all three cases, the positive and negative parts of $\gamma_{\|}(i\omega)$ tail off with respect to ω^{-2} in exactly the same way (within numerical accuracy). It is not immediately apparent from eqs. [13] and [14] why this should be so and it is not, in general, true for $\gamma_{\perp}(i\omega)$. In the Appendix a proof is given. The value of $A_{\|}^{0}/\gamma_{\|}^{0}$ for He was found before (15) by fitting $\gamma_{\|}(\omega)$ values; the result, 2.189, agrees perfectly with the result here. Since all measurements of $\gamma_{\|}(\omega)$ are reported as relative to the calculated value for He, there is no experimental value of $A_{\|}^{0}/\gamma_{\|}^{0}$ of He with which to compare.

To conclude, we have evaluated exactly for the H atom the limiting dispersion in the second hyperpolarizability for both real and imaginary frequencies. For H^-, He, Li^+ we have done the same thing but with resort to nonexact, though accurate, variational wave functions.

Acknowledgements

I thank Dr. Janusz Pipin for providing me with the two-electron results for $X(i,j,k)$ and $Y(k)$ and the Natural Sciences and Engineering Research Council of Canada for financial support.

References

1. M. Evans, and S. Kielich (*Editors*). Modern nonlinear optics. Adv. Chem. Phys. **85** (1993).
2. D.M. Burland (*Editor*). Optical nonlinearities in chemistry. Chem. Rev. **94** (1994).
3. M.A. Ratner (*Editor*). Int. J. Quantum Chem. (Special issue on molecular nonlinear optics) **43** (1992).
4. D.M. Bishop. Phys. Rev. Lett. **61**, 322 (1988).
5. D.M. Bishop. Chem. Phys. Lett. **153**, 441 (1988).
6. D.M. Bishop. J. Chem. Phys. **90**, 3192 (1989).
7. D.M. Bishop and J. Pipin. J. Chem. Phys. **97**, 3375 (1992); **99**, 4875 (1993).

8. D.M. Bishop. Adv. Quantum Chem. **25**, 1 (1994).
9. C.A. Coulson. Proc. R. Soc. Edinburgh, Sect. A: Math. Phys. Sci. **61**, 20 (1941).
10. A. Dalgarno and A.E. Kingston. Proc. R. Soc. London, Ser. A: **259**, 424 (1960).
11. R.J. Bell. Proc. Phys. Soc. London, **92**, 842 (1967).
12. G.L. Sewell. Proc. Cambridge Philos. Soc. **45**, 678 (1949).
13. A.J. Thakkar and V.H. Smith, Jr. Phys. Rev. A: Gen. Phys. **15**, 1 (1977).
14. A.J. Thakkar. J. Chem. Phys. **75**, 4496 (1981).
15. D.M. Bishop and J. Pipin. J. Chem. Phys. **91**, 3549 (1989).
16. J. Pipin and D.M. Bishop. J. Phys. B: At. Mol. Opt. Phys. **25**, 17 (1992).
17. D.M. Bishop and M. Rérat. J. Chem. Phys. **91**, 5489 (1989).

Appendix

The proof that $A_{\|}^{\infty(+)} = A_{\|}^{\infty(-)}$ can be most easily shown for the H atom; the generalization for any other atom follows in a straightforward way. We will require the following identity:

[A1] $(H_0 - \varepsilon_g)z\psi = z(H_0 - \varepsilon_g)\psi - \partial\psi/\partial z$

and thus:

[A2] $(H_0 - \varepsilon_g)z\psi_0 = -\partial\psi_0/\partial z$

Also, from the odd integral derivatives, we have:

[A3] $\partial\langle 0|z|0\rangle/\partial z = 2\langle(\partial\psi_0/\partial z)|z|0\rangle + 1 = 0$

[A4] $\partial\langle f_1|z|f_1\rangle/\partial z = 2\langle(\partial f_1/\partial z)|z|f_1\rangle + \langle f_1 f_1\rangle = 0$

[A5] $\partial\langle 0|z|g_1\rangle/\partial z = \langle(\partial\psi_0/\partial z)|z|g_1\rangle + \langle 0|g_1\rangle + \langle 0|z|(\partial g_1/\partial z)\rangle = 0$

First we will show that $2X(2,0,0) = X(1,1,0)$. From eq. [36], using eqs. [A2] and [A3], we find

[A6] $X(2,0,0) = -\langle(\partial\psi_0/\partial z)|z|g_1\rangle - \langle 0|g_1\rangle/2$

or, alternatively, using the Hermitean properties, and eqs. [A1], [A5], and [20]:

[A7] $X(2,0,0) = \langle 0|z|(H_0 - \varepsilon_g)(zg_1)\rangle - \langle 0|g_1\rangle/2 = \langle 0|z^2|(H_0 - \varepsilon_g)g_1\rangle - \langle 0|z|(\partial g_1/\partial z)\rangle - \langle 0|g_1\rangle/2$

$$= \langle 0|z^3|f_1\rangle - (9/4)\langle 0|z^2|0\rangle + \langle(\partial\psi_0/\partial z)|z|g_1\rangle + \langle 0|g_1\rangle/2$$

Addition of eqs. [A6] and [A7] gives $X(1,1,0)$ as displayed in eq. [38], hence

[A8] $2X(2,0,0) = X(1,1,0)$

With this relationship, we now need to show that

$$A_{\|}^{\infty(+)}/4 = X(0,2,0) - X(1,1,0) = \langle zf_1|(H_0 - \varepsilon_g)(zf_1)\rangle - \langle 0|z^3|f_1\rangle + Y(-1)Y(0)$$

is equal to

$$A_{\|}^{\infty(-)}/4 = \langle f_1|f_1\rangle/2 + Y(-1)Y(0)$$

This is done by the following relations, using eqs. [16], [A1], and [A4]:

$$\langle zf_1|(H_0 - \varepsilon_g)(zf_1)\rangle - \langle 0|z^3|f_1\rangle = \langle zf_1|(H_0 - \varepsilon_g)(zf_1)\rangle - \langle(H_0 - \varepsilon_g)f_1|z^2|f_1\rangle = \langle zf_1|(H_0 - \varepsilon_g)(zf_1)\rangle - \langle f_1|z^2|(H_0 - \varepsilon_g)f_1\rangle$$

$$= \langle z^2 f_1|(H_0 - \varepsilon_g)f_1\rangle - \langle zf_1|\partial f_1/\partial z\rangle - \langle f_1|z^2|(H_0 - \varepsilon_g)f_1\rangle = -\langle zf_1|\partial f_1/\partial z\rangle = \langle f_1 f_1\rangle/2.$$

Topological properties of the electronic structures of the reactants, transition states, and products of the reactions of the hydroxyl radical with the series $C_2H_nF_{6-n}$, n = 1–6

Jaime M. Martell, James B. Tee, and Russell J. Boyd

Abstract: Properties of the bond critical points, including the electron density and its Laplacian, and distances to bonded nuclei, for all species (reactants, transition states, and products) in the reactions of the hydroxyl radical with the series $C_2H_nF_{6-n}$, n = 1–6 were calculated using Bader's atoms-in-molecules methodology. The electron density and its Laplacian at the bond critical points correlate with bond strength, as measured by bond dissociation energies. The positions of the bond critical points vary with the electronegativity of surrounding atoms. Charge development in the course of the reactions was monitored using Mulliken population analysis at the HF/6-31G(d), HF/6-311G(d,p)//HF/6-31G(d), MP2/6-311G(d,p)//HF/6-31G(d), and HF/6-311G(d,p)//MP2/6-31G(d,p) levels of theory, and natural population analysis and Bader population analysis at the highest common level of theory, MP2/6-311G(d,p)//HF/6-31G(d). In general, there is a buildup of charge in the transition states, concentrated near the reaction centre, which dissipates somewhat as the reaction proceeds to products. The description of charge transfer varies somewhat with the three methods.

Key words: topological properties, atomic charges, charge development, reactions of the hydroxyl radical with fluorinated ethanes.

Résumé : Faisant appel à la méthodologie des atomes dans les molécules de Bader, on a calculé les propriétés des points critiques des liaisons, y compris la densité électronique et son laplacien, ainsi que les distances entre les noyaux liés pour toutes les espèces (réactifs, états de transition et produits) des réactions du radical hydroxyle avec la série $C_2H_nF_{6-n}$ dans laquelle n = 1–6. La densité électronique et son laplacien aux points critiques de la liaison donnent une bonne corrélation avec la force de la liaison telle que mesurée par les énergies de dissociation. Les positions des points critiques des liaisons varient avec l'électronégativité des atomes avoisinants. Le développement de la charge au cours des réactions est déterminé en faisant appel à une analyse de population de Mulliken aux niveaux HF/6-31G(d), HF/6-311G(d,p)//HF/6-31G(d), MP2/6-311G(d,p)//HF/6-31G(d) et HF/6-311G(d,p)//MP2/6-31G(d,p), à une analyse naturelle de population et à une analyse de population de Bader au niveau les plus élevé de la théorie, MP2/6-311G(d,p)//HF/6-31G(d). En général, il se produit une accumulation de charge dans les états de transition; elle est concentrée près de la région centre et elle se dissipe un peu au fur et à mesure que la réaction progresse vers les produits. La description du transfert de charge varie un peu avec les trois méthodes.

Mots clés : propriétés topologiques, charges atomiques, développement de la charge, réactions du radical hydroxyle avec d'éthanes fluorés.

[Traduit par la rédaction]

1. Introduction

Charge development at the transition state (TS) is central to chemistry because most reactions involve electron transfer in the TS. This concept has been investigated theoretically for S_N2 reactions involving charged nucleophiles (1). Experimental studies must look at indirect evidence such as the effect of substituents on the reaction rate. One of the most extensively studied reaction classes is hydrogen abstractions, such as is being considered here. These show interesting effects, for example, the attack of substituted toluenes by bromine radicals correlates (2) with σ^+, and polar effects are even observed in abstractions by alkyl radicals (3). These results show that charged species need not be involved for charge to have a significant effect on the reaction. The reactions of hydroxyl radicals (OH) with hydrofluorinated ethanes (HFEs) are formally charge neutral, but significant charge development at the TS is expected due to the influence of the electronegative oxygen atom.

Bader et al. (4, 5) have developed a theory of "atoms in molecules," in which the gradient vector field and the scalar field of the electron density $\rho(\boldsymbol{r})$ are used to study the bonds, atomic interactions, reactivities, and stabilities of molecular systems. The essential topological properties of the electron density, $\rho(\boldsymbol{r})$, can be summarized by the complete specification of its critical points at which $\nabla\rho(\boldsymbol{r}) = 0$. A critical point, $\boldsymbol{r}_c$, is classified according to its rank and signature (4*a*). The rank λ of a

Received July 11, 1995.

This paper is dedicated to Professor Richard F.W. Bader on the occasion of his 65th birthday.

J.M. Martell,[1] J.B. Tee, and R.J. Boyd.[2] Department of Chemistry, Dalhousie University, Halifax, NS B3H 4J3, Canada.

[1] Walter C. Sumner Fellow and NSERC Predoctoral Scholar.
[2] Author to whom correspondence may be addressed. Telephone: (902) 494-8883. Fax: (902) 494-1310. E-mail: boyd@chem1.chem.dal.ca

critical point equals the number of non-zero eigenvalues of the Hessian matrix of $\rho(\boldsymbol{r}_c)$, while the signature σ is the algebraic sum of the signs of the eigenvalues, and the classification is written as (λ,σ). If the eigenvalue is positive its associated eigenvector or gradient path (the path of steepest ascent) originates at, and is directed away from, the critical point. For negative eigenvalues the gradient path terminates at, and is directed toward, the critical point.

In the case of a nondegenerate critical point, four types of critical points are possible: (3,−3), which usually occurs only at a nucleus; (3,+3), a cage critical point; (3,+1), a ring critical point; and (3,−1), a bond critical point. Only bond critical points are considered in this study.

The Laplacian of the electron density,

$$[1] \quad \nabla^2\rho(\boldsymbol{r}) = \frac{\partial^2\rho}{\partial x^2} + \frac{\partial^2\rho}{\partial y^2} + \frac{\partial^2\rho}{\partial z^2}$$

identifies the regions of space wherein the electron density is locally concentrated or depleted. In three dimensions, when $\nabla^2\rho(\boldsymbol{r}) < 0$, then $\rho(\boldsymbol{r})$ is greater than its average value at neighbouring points, and when $\nabla^2\rho(\boldsymbol{r}) > 0$, $\rho(\boldsymbol{r})$ is less than its average value at neighbouring points. Thus a minimum in $\nabla^2\rho(\boldsymbol{r})$ with a negative value means that the electron density is locally concentrated in that region of space, even though the electron density itself exhibits no corresponding maximum. Studies of molecular systems using the properties of $\nabla^2\rho(\boldsymbol{r})$ show that a bond can be characterized in terms of the bond path and the electron density at the bond critical point, $\rho(\boldsymbol{r}_c)$ (6). Also, the magnitude of the electron density at the bond critical point provides a measure of the bond strength (7, 8).

Three methods are used in this study for calculating atomic charges. The Mulliken method (9) is computationally very inexpensive, but suffers at least conceptually because the overlap populations are divided equally between two bonded atoms, irrespective of their relative electronegativities. Thus, it tends to underestimate electron populations on electronegative atoms. Natural population analysis is carried out in terms of localized electron-pair "bonding" units. It is also relatively inexpensive, and has the advantage of being essentially basis-set independent. Bader and Nguyen-Dang (4*b*) devised an electron density partitioning method in which an atom in a molecule is defined as a real space surrounded by a zero-flux surface, and the space occupied by the atom is referred to as the atomic basin. The atomic charge of an atom is obtained by integrating $\rho(\boldsymbol{r})$ over the atomic basin to obtain its average electron population N, and then subtracting this from the nuclear charge Z, i.e., $Q = Z - N$. While this method is conceptually more rigorous, it requires much more human and computer effort, and has been criticized for overestimating the electron population on electronegative atoms (10). For Mulliken population analysis (MPA) four levels of theory were employed: HF/6-31G(d), HF/6-311G(d,p)//HF/6-31G(d), MP2/6-311G(d,p)//HF/6-31G(d), and HF/6-311G(d,p)//MP2/6-31G(d,p). This allowed the investigation of the effects of increased basis-set size, electron correlation, and use of electron correlation in geometry optimizations, respectively (starting from a base theory of HF/6-31G(d)). For natural population analysis (NPA) and Bader population analysis (BPA), only the highest common level of theory used on all the species (MP2/6-311G(d,p)//HF/6-31G(d)) was employed.

2. Computational methods

Ab initio MO calculations were carried out with the GAUSSIAN 90 (11) and GAUSSIAN 92/DFT (12) program packages, employing the optimized geometries of the reactants (13, 14), transition states (15, 16), and products (14, 17) as published previously. The NBO program[3] (included as link 607 of GAUSSIAN 92) was used to calculate the NPA charges.

The topological analysis calculations were performed using a vectorized version of the PROAIM (18) program package. Wave function files from the highest common level of theory employed in this study (MP2/6-311G(d,p)//HF/6-31G(d)) were used as input. For each bond a (3,−1) critical point was located. Integration of atomic charges was performed for each atom, using 96 ϕ and 64 θ planes outside of the β sphere, and the maximum values of 140 points per surface path and 80 basic gradient paths. Threshold values of 0.001 and 0.002 were used for the volume calculation, and the primitive cutoff algorithm was employed.

3. Results and discussion

A. Properties of bond critical points

Properties of bond critical points for reactants, transition states, and products, are given in Tables 1, 2, and 3, respectively. In general, the electron densities at the bond critical points, $\rho(\boldsymbol{r}_c)$ increase with increasing substitution of the species by fluorine atoms, as expected, since these atoms are electron rich and thus increase the overall electron density. This may also be due to a contraction of the molecule: if the C—C distance shortens, as it does with increasing fluorine substitution (13, 14), $\rho(\boldsymbol{r}_c)$ would likely increase. Given the same number of fluorines, values of $\rho(\boldsymbol{r}_c)$ are affected by substitution patterns.

For C—C bond critical points, $\rho(\boldsymbol{r})$ tends to be larger when the fluorine substituents are divided as evenly as possible between the two carbons; this trend applies to reactants, transition states, and products, although the trend is weak in the latter. For the product radicals, and the transition states, there is also a trend to higher values for higher substitution on the β-carbon.

In contrast to the C—C case, values of $\rho(\boldsymbol{r})$ at C—F bond critical points are larger for species where as many fluorines as possible are on one carbon. A second trend is for higher values at α-carbons for transition states and products, although the first trend will take precedence, e.g., in CF_3-CHF values are higher on the highly substituted β-carbon.

Trends in $\rho(\boldsymbol{r})$ at C—H bond critical points are varied. For reactants and products, there is the general trend to increasing values with increasing fluorine substitution and, within a molecule, to larger values on the more substituted carbon. For transition states, values are again higher on the more substituted carbon, but the correlation of higher values with increasing number of fluorines is weaker. Values at β-carbons are lower when there is a β-fluorine *gauche* to the reaction centre. For the special case of the critical bond at the bond being broken in the TS (C1—H1 in Table 2), values are much lower than for other C—H bonds. The predominant trend here is for values to increase with the number of α-fluorines, with a secondary trend for lower values as the number of β-fluorines

[3] E.D. Glendening, A.E. Reed, J.E. Carpenter, and F. Weinhold. NBO Version 3.1.

Table 1. Properties of bond critical points for reactants.

Bond[a]	$\rho(r_c)^b$	$\nabla^2\rho(r_c)^b$	$r_A{}^c$	$r_B{}^c$
OH ($C_{\infty v}$)				
O—H	0.3790	−2.7717	0.776	0.183
C_2H_6 (D_{3d})				
C—C	0.2512	−0.6697	0.764	0.764
C—H	0.2833	−1.0236	0.676	0.410
CH_2F—CH_3 (C_s)				
C_α—C_β	0.2680	−0.7680	0.780	0.732
C—F	0.2295	0.5015	0.437	0.935
C_α—H_α	0.2991	−1.1402	0.688	0.395
C_β—$H_{\beta 0}$	0.2824	−1.0187	0.677	0.408
C_β—$H_{\beta 1}$	0.2848	−1.0323	0.680	0.404
CH_2F—CH_2F (C_2)[d]				
C—C	0.2826	−0.8580	0.752	0.752
C—F	0.2348	0.5029	0.436	0.931
C—H_g	0.2997	−1.1440	0.693	0.389
C—H_t	0.2997	−1.1325	0.689	0.394
CHF_2—CH_3 (C_s)				
C_α—C_β	0.2804	−0.8489	0.805	0.697
C_α—F_α	0.2530	0.3911	0.431	0.915
C_α—H_α	0.3137	−1.2505	0.700	0.379
C_β—$H_{\beta 0}$	0.2856	−1.0370	0.685	0.398
C_β—$H_{\beta 1}$	0.2852	−1.0361	0.681	0.402
CF_3—CH_3 (C_{3v})				
C_α—C_β	0.2845	−0.8926	0.841	0.658
C_α—F_α	0.2763	0.2283	0.428	0.897
C_β—H_β	0.2875	−1.0506	0.685	0.396
CHF_2—CH_2F (C_1)[d]				
C_α—C_β	0.2903	−0.9152	0.781	0.725
C_α—$F_{\alpha g}$	0.2547	0.4119	0.430	0.913
C_α—$F_{\alpha t}$	0.2590	0.4034	0.429	0.909
C_α—H_α	0.3143	−1.2566	0.704	0.374
C_β—F_β	0.2374	0.5171	0.434	0.928
C_β—$H_{\beta gt}$	0.3008	−1.1529	0.693	0.388
C_β—$H_{\beta gg}$	0.3008	−1.1516	0.696	0.385
CF_3—CH_2F (C_s)				
C_α—C_β	0.2932	−0.9489	0.815	0.692
C_α—$F_{\alpha 0}$	0.2769	0.2455	0.427	0.897
C_α—$F_{\alpha 1}$	0.2823	0.2375	0.426	0.892
C_β—F_β	0.2437	0.4990	0.433	0.922
C_β—H_β	0.3022	−1.1632	0.697	0.383
CHF_2—CHF_2 (C_{2h})				
C—C	0.2977	−0.9663	0.755	0.755
C—F	0.2612	0.4084	0.429	0.907
C—H	0.3145	−1.2599	0.708	0.370
CF_3—CHF_2 (C_s)				
C_α—C_β	0.2991	−0.9836	0.790	0.727
C_α—$F_{\alpha 0}$	0.2879	0.2437	0.424	0.887
C_α—$F_{\alpha 1}$	0.2831	0.2433	0.425	0.891
C_β—F_β	0.2668	0.3861	0.428	0.903
C_β—H_β	0.3156	−1.2690	0.709	0.368

[a]Only bonds that are unique by symmetry are given. C_α denotes the most highly substituted carbon. An atom labelled with 0 is in the symmetry plane, 1 is not. See Fig. 1 of ref. 13 for individual geometries.
[b]In atomic units.
[c]For bond A—B, r_A and r_B are the distances, in Å, from the bond critical point to atoms A and B, respectively.
[d]The designations g and t indicate the atom is *gauche* or *trans*, respectively, to a fluorine.

Table 2. Properties of bond critical points for transition states.

Bond[a]	$\rho(r_c)^b$	$\nabla^2\rho(r_c)^b$	$r_A{}^c$	$r_B{}^c$
C_2H_6 + OH[d]				
H1—O	0.1723	−0.1257	0.348	0.870
O—H2	0.3796	−2.7384	0.771	0.184
C1—H1	0.1578	−0.2879	0.866	0.434
C1—C2	0.2572	−0.6981	0.777	0.736
C1—H3/4	0.2877	−1.0493	0.682	0.400
C2—H5	0.2809	−1.0063	0.679	0.409
C2—H6/7	0.2854	−1.0371	0.680	0.404
CH_3—CH_2F + OH				
H1—O	0.1763	−0.1314	0.346	0.864
O—H2	0.3785	−2.7481	0.773	0.182
C1—H1	0.1671	−0.3299	0.878	0.421
C1—C2	0.2716	−0.7870	0.793	0.707
C1—H3	0.3008	−1.1486	0.695	0.385
C1—F4	0.2398	0.5737	0.432	0.922
C2—H5	0.2825	−1.0166	0.683	0.404
C2—H6	0.2848	−1.0346	0.682	0.402
C2—H7	0.2861	−1.0413	0.684	0.399
CH_2F—CH_3 + OH t				
H1—O	0.1794	−0.1701	0.338	0.863
O—H2	0.3788	−2.7462	0.772	0.182
C1—H1	0.1524	−0.2629	0.874	0.438
C1—C2	0.2713	−0.7824	0.750	0.755
C1—H3	0.2891	−1.0584	0.687	0.393
C1—H4	0.2884	−1.0544	0.684	0.396
C2—F5	0.2295	0.4791	0.438	0.936
C2—H6	0.3013	−1.1562	0.691	0.389
C2—H7	0.3011	−1.1547	0.691	0.390
CH_2F—CH_3 + OH g				
H1—O[e]				
O—H2	0.3778	−2.7615	0.775	0.180
C1—H1	0.1525	−0.2599	0.879	0.438
C1—C2	0.2733	−0.7923	0.739	0.763
C1—H3	0.2887	−1.0551	0.686	0.394
C1—H4	0.2872	−1.0464	0.685	0.395
C2—H5	0.2979	−1.1317	0.692	0.392
C2—F6	0.2277	0.4958	0.438	0.937
C2—H7	0.3011	−1.1542	0.692	0.389
CH_2F—CH_2F + OH t				
H1—O	0.1809	−0.1609	0.340	0.859
O—H2	0.3776	−2.7511	0.774	0.181
C1—H1	0.1628	−0.3089	0.884	0.424
C1—C2	0.2840	−0.8640	0.768	0.729
C1—H3	0.3011	−1.1519	0.699	0.380
C1—F4	0.2453	0.5872	0.430	0.917
C2—F5	0.2342	0.4790	0.437	0.931
C2—H6	0.3004	−1.1513	0.694	0.388
C2—H7	0.3012	−1.1552	0.695	0.385
CH_2F—CH_2F + OH g				
H1—O	0.1843	−0.1839	0.335	0.856
O—H2	0.3772	−2.7638	0.776	0.179
C1—H1	0.1610	−0.2978	0.890	0.424
C1—C2	0.2844	−0.8643	0.760	0.737
C1—H3	0.2997	−1.1421	0.697	0.383
C1—F4	0.2475	0.5841	0.429	0.915
C2—H5	0.2987	−1.1369	0.695	0.387
C2—H6	0.3005	−1.1517	0.693	0.388
C2—F7	0.2330	0.4929	0.437	0.932

Table 2 (*continued*).

Bond[a]	$\rho(r_c)$[b]	$\nabla^2\rho(r_c)$[b]	r_A[c]	r_B[c]
CHF_2—CH_3 + OH g,t				
H1—O	0.1869	−0.2182	0.330	0.855
O—H2	0.3778	−2.7608	0.775	0.180
C1—H1	0.1500	−0.2483	0.883	0.439
C1—C2	0.2842	−0.8635	0.710	0.787
C1—H3	0.2892	−1.0595	0.689	0.390
C1—H4	0.2892	−1.0591	0.690	0.389
C2—F5	0.2549	0.3724	0.431	0.913
C2—H6	0.3157	−1.2668	0.704	0.374
C2—F7	0.2518	0.3828	0.432	0.916
CHF_2—CH_3 + OH g,g				
H1—O	0.1881	−0.2300	0.328	0.854
O—H2	0.3777	−2.7633	0.776	0.180
C1—H1	0.1484	−0.2401	0.888	0.439
C1—C2	0.2837	−0.8602	0.706	0.790
C1—H3	0.2896	−1.0623	0.688	0.391
C1—H4	0.2893	−1.0595	0.689	0.389
C2—H5	0.3126	−1.2428	0.704	0.376
C2—F6	0.2577	0.3805	0.430	0.911
C2—F7	0.2513	0.3774	0.432	0.917
CH_3—CF_2H + OH[d]				
H1—O	0.1821	−0.1580	0.340	0.857
O—H2	0.3778	−2.7497	0.774	0.181
C1—H1	0.1717	−0.3483	0.893	0.410
C1—C2	0.2781	−0.8396	0.821	0.675
C1—F3/4	0.2634	0.4577	0.426	0.903
C2—H5	0.2837	−1.0238	0.687	0.398
C2—H6/7	0.2874	−1.0511	0.686	0.396
CF_3—CH_3 + OH				
H1—O	0.1919	−0.2577	0.323	0.850
O—H2	0.3777	−2.7621	0.776	0.180
C1—H1	0.1470	−0.2333	0.892	0.440
C1—C2	0.2878	−0.9007	0.671	0.824
C1—H3	0.2913	−1.0744	0.692	0.386
C1—H4	0.2908	−1.0710	0.693	0.385
C2—F5	0.2781	0.2034	0.428	0.896
C2—F6	0.2748	0.2102	0.429	0.899
C2—F7	0.2811	0.2136	0.427	0.893
CHF_2—CH_2F + OH g,t				
H1—O	0.1874	−0.2034	0.332	0.853
O—H2	0.3778	−2.7578	0.775	0.181
C1—H1	0.1599	−0.2921	0.893	0.425
C1—C2	0.2912	−0.9135	0.741	0.761
C1—H3	0.3015	−1.1556	0.702	0.376
C1—F4	0.2477	0.5998	0.429	0.915
C2—F5	0.2583	0.3777	0.430	0.910
C2—F6	0.2603	0.3961	0.429	0.908
C2—H7	0.3156	−1.2684	0.707	0.370
CHF_2—CH_2F + OH g,g				
H1—O	0.1893	−0.2201	0.329	0.851
O—H2	0.3773	−2.7641	0.776	0.179
C1—H1	0.1580	−0.2809	0.897	0.425
C1—C2	0.2910	−0.9112	0.734	0.768
C1—H3	0.3016	−1.1563	0.700	0.378
C1—F4	0.2499	0.5986	0.428	0.913
C2—H5	0.3132	−1.2483	0.707	0.372
C2—F6	0.2607	0.4000	0.429	0.908
C2—F7	0.2569	0.3867	0.430	0.911

Table 2 (*concluded*).

Bond[a]	$\rho(r_c)$[b]	$\nabla^2\rho(r_c)$[b]	r_A[c]	r_B[c]
CH_2F—CHF_2 + OH				
H1—O	0.1898	−0.2121	0.330	0.850
O—H2	0.3770	−2.7605	0.776	0.179
C1—H1	0.1656	−0.3156	0.905	0.414
C1—C2	0.2879	−0.9003	0.789	0.714
C1—F3	0.2673	0.4889	0.425	0.899
C1—F4	0.2687	0.4773	0.424	0.898
C2—H5	0.2997	−1.1439	0.698	0.383
C2—H6	0.3029	−1.1690	0.697	0.382
C2—F7	0.2373	0.5096	0.435	0.928
CF_3—CH_2F + OH				
H1—O	0.1924	−0.2411	0.325	0.847
O—H2	0.3772	−2.7622	0.776	0.180
C1—H1	0.1569	−0.2744	0.901	0.426
C1—C2	0.2944	−0.9421	0.706	0.798
C1—H3	0.3028	−1.1166	0.704	0.374
C1—F4	0.2540	0.5882	0.427	0.909
C2—F5	0.2817	0.2140	0.427	0.893
C2—F6	0.2829	0.2321	0.426	0.892
C2—F7	0.2836	0.2243	0.426	0.891
CHF_2—CHF_2 + OH				
H1—O	0.1917	−0.2237	0.328	0.847
O—H2	0.3769	−2.7589	0.776	0.180
C1—H1	0.1646	−0.3096	0.907	0.414
C1—C2	0.2941	−0.9410	0.768	0.742
C1—F3	0.2723	0.4895	0.423	0.895
C1—F4	0.2729	0.4865	0.423	0.894
C2—F5	0.2640	0.3745	0.429	0.905
C2—H6	0.3162	−1.2742	0.709	0.368
C2—F7	0.2629	0.3894	0.429	0.906
CF_3—CHF_2 + OH				
H1—O	0.2063	−0.3948	0.311	0.852
O—H2	0.3699	−2.5308	0.763	0.192
C1—H1	0.1467	−0.2034	0.918	0.414
C1—C2	0.2809	−0.7922	0.754	0.763
C1—F3	0.2776	0.1802	0.436	0.882
C1—F4	0.2813	0.2006	0.434	0.879
C2—F5	0.2846	−0.0396	0.439	0.876
C2—F6	0.2913	−0.0392	0.438	0.874
C2—F7	0.2923	−0.0358	0.438	0.874

[a]All species are asymmetrical, except where noted. For numbering scheme, see Fig. 2 of ref. 15 for C_2H_6 + OH, and Fig. 1 of ref. 16 for other species. The designations g and t refer to the hydrogen being abstracted as *gauche* or *trans*, respectively, to a β-F.

[b]In atomic units.

[c]For bond A—B, r_A and r_B are the distances, in Å, from the bond critical point to atoms A and B, respectively.

[d]C_s symmetry.

[e]Bond critical point not found.

increases. Values are also slightly lowered when there are β-fluorines *gauche* to H1.

For the bond critical point of the bond being formed (H1—O in Table 2), the magnitudes of $\rho(r)$ are again low. Higher values are seen when there are β-fluorines *gauche* to H1, and for increasing substitution on the β-carbon, except for CH_2F—CHF_2 + OH being higher than CHF_2—CH_2F + OH.

In contrast, $\rho(r_c)$ values in the hydroxyl group are much larger, and have very different trends. There is a weak trend to

Table 3. Properties of bond critical points for products.

Bond[a]	$\rho(r_c)$[b]	$\nabla^2\rho(r_c)$[b]	r_A[c]	r_B[c]
H_2O (C_{2v})				
O—H	0.3842	−2.7953	0.767	0.181
C_2H_5 (C_s)				
C_α—C_β	0.2628	−0.7198	0.761	0.737
C_α—H_α	0.2880	−1.0395	0.677	0.398
C_β—$H_{\beta 0}$	0.2783	−0.9882	0.681	0.410
C_β—$H_{\beta 1/2}$	0.2834	−1.0235	0.678	0.407
CH_2F—CH_2 (C_1)				
C_α—C_β	0.2774	−0.8072	0.733	0.756
C_α—$H_{\alpha 1}$	0.2891	−1.0475	0.684	0.390
C_α—$H_{\alpha 2}$	0.2884	−1.0440	0.680	0.394
C_β—$F_{\beta 1}$	0.2320	0.4757	0.437	0.934
C_β—$H_{\beta 0}$	0.2950	−1.1105	0.692	0.395
C_β—$H_{\beta 2}$	0.2980	−1.1327	0.691	0.393
CH_3—CHF (C_1)				
C_α—C_β	0.2742	−0.7936	0.779	0.711
C_α—$F_{\alpha 1}$	0.2436	0.7171	0.427	0.913
C_α—$H_{\alpha 2}$	0.2983	−1.1216	0.689	0.387
C_β—$H_{\beta 0}$	0.2840	−1.0296	0.680	0.404
C_β—$H_{\beta 1}$	0.2799	−0.9980	0.684	0.405
C_β—$H_{\beta 2}$	0.2842	−1.0285	0.683	0.402
CH_2F—CHF (a) (C_1)				
C_α—C_β	0.2879	−0.8771	0.757	0.725
C_α—$F_{\alpha 2}$	0.2501	0.7331	0.425	0.916
C_α—$H_{\alpha 1}$	0.2996	−1.1322	0.693	0.381
C_β—$F_{\beta 0}$	0.2308	0.4240	0.440	0.935
C_β—$H_{\beta 1}$	0.2998	−1.1467	0.691	0.390
C_β—$H_{\beta 2}$	0.3005	−1.1507	0.694	0.386
CHF_2—CH_2 (C_1)				
C_α—C_β	0.2883	−0.8780	0.706	0.778
C_α—$H_{\alpha 1}$	0.2906	−1.0604	0.684	0.389
C_α—$H_{\alpha 2}$	0.2905	−1.0589	0.687	0.386
C_β—$F_{\beta 0}$	0.2517	0.3267	0.434	0.917
C_β—$F_{\beta 2}$	0.2555	0.3732	0.431	0.913
C_β—$H_{\beta 1}$	0.3141	−1.2543	0.702	0.377
CH_3—CF_2 (C_s)				
C_α—C_β	0.2780	−0.8358	0.809	0.682
C_α—F_α	0.2632	0.5771	0.424	0.899
C_β—$H_{\beta 0}$	0.2819	−1.0106	0.687	0.400
C_β—$H_{\beta 1/2}$	0.2867	−1.0468	0.684	0.398
CF_3—CH_2 (C_s)				
C_α—C_β	0.2927	−0.9176	0.670	0.813
C_α—H_α	0.2924	−1.0732	0.689	0.382
C_β—$F_{\beta 0}$	0.2759	0.1703	0.430	0.898
C_β—$F_{\beta 1/2}$	0.2785	0.2011	0.428	0.896
CHF_2—CHF (a) (C_1)				
C_α—C_β	0.2952	−0.9289	0.730	0.760
C_α—$F_{\alpha 2}$	0.2535	0.7462	0.424	0.904
C_α—$H_{\alpha 1}$	0.2999	−1.1373	0.698	0.376
C_β—$F_{\beta 0}$	0.2585	0.3834	0.430	0.910
C_β—$F_{\beta 2}$	0.2558	0.3390	0.433	0.913
C_β—$H_{\beta 1}$	0.3149	−1.2625	0.706	0.372
CH_2F—CF_2 (C_s)				
C_α—C_β	0.2892	−0.9068	0.786	0.705
C_α—F_α	0.2692	0.5966	0.422	0.893
C_β—F_β	0.2373	0.4374	0.437	0.929
C_β—H_β	0.3019	−1.1618	0.696	0.384

Table 3 (*concluded*).

Bond[a]	$\rho(r_c)$[b]	$\nabla^2\rho(r_c)$[b]	r_A[c]	r_B[c]
CF_3—CHF (C_1)				
C_α—C_β	0.2983	−0.9559	0.699	0.793
C_α—$F_{\alpha 1}$	0.2602	0.7367	0.423	0.898
C_α—$H_{\alpha 2}$	0.3015	−1.1499	0.699	0.373
C_β—$F_{\beta 0}$	0.2807	0.2213	0.427	0.894
C_β—$F_{\beta 1}$	0.2799	0.1842	0.428	0.895
C_β—$F_{\beta 2}$	0.2844	0.2056	0.426	0.891
CHF_2—CF_2 (C_s)				
C_α—C_β	0.2933	−0.9337	0.763	0.741
C_α—F_α	0.2725	0.6029	0.421	0.891
C_β—F_β	0.2650	0.3750	0.428	0.904
C_β—H_β	0.3125	−1.2428	0.710	0.371
CF_3—CF_2 (C_s)				
C_α—C_β	0.2976	−0.9613	0.733	0.774
C_α—F_α	0.2778	0.5978	0.420	0.886
C_β—$F_{\beta 0}$	0.2846	0.1920	0.427	0.891
C_β—$F_{\beta 1/2}$	0.2875	0.2134	0.425	0.888

[a]Only bonds that are unique by symmetry are given. The α-C is the radical centre. Atom numbering scheme is as in Fig. 1 of ref. 17. See Fig. 1 of ref. 14 for individual geometries.
[b]In atomic units.
[c]For bond A—B, r_A and r_B are the distances, in Å, from the bond critical point to atoms A and B, respectively.

decreasing values with increasing substitution, and lower values are seen when there are β-fluorines *gauche* to H1. It should be noted that the range of values is small, 0.3769−0.3796.

Most of the above trends are consistent with $\rho(r_c)$ providing a measure of bond strength (7). Thus, the forming and breaking bonds have particularly low values. Higher values are seen in C—X bonds for more highly substituted carbons. For transition states, the intramolecular hydrogen bond formed when there is a β-fluorine *gauche* to the reaction centre (16) leads to higher $\rho(r_c)$ values for C_β—H_β and H1—O bonds, the latter at the expense of the hydroxyl bond.

An exception is provided by C—C bonds. If bond dissociation energy (BDE) is used as a measure of bond strength, then C—C bonds are stronger when there is a greater electronegativity difference between the two groups (as observed in the reactant ethanes (13, 14)), but the same trend is not seen in the $\rho(r_c)$ values. As well, the $\rho(r_c)$ values do not correlate with the C—C bond lengths.

Many of the trends in the electron densities are seen again in the Laplacian of the electron density, $\nabla^2\rho(r)$. For most bonds in this study $\nabla^2\rho(r)$ is negative at the bond critical point, indicating a local concentration of charge. All C—F bonds have positive values, except for slightly negative values in the CF_3 group of the CF_3—CHF_2 + OH TS. The anomalous values of $\nabla^2\rho(r)$ for the C—F bonds derive from the unique behaviour of the Laplacian distributions for fluorine atoms, where the electron density is tightly bound and very localized in all of its compounds (ref. 5, p. 274).

For the C—C critical points, the trends are particularly similar to those for the electron density, with the following exceptions: in the products, the trend to larger magnitudes for more symmetrically substituted radicals, which was weak for the

electron densities, is now more effective (see for example the cases for $C_2H_2F_3$); for transition states, there is a strong dependence on the number of fluorines, but no consistent trends with substitution patterns.

The trends in $\nabla^2\rho(r)$ values for C—F bond critical points are at variance with their $\rho(r)$ trends, and also vary with category, i.e., reactants, products, or transition states. For reactants, within a molecule the higher values are on the less substituted carbon. Higher values are also seen in symmetrically substituted molecules, and there is a general trend to higher values with increasing number of fluorines. For transition states, values are usually higher on the α-carbon, with an exception for $CH_2F—CHF_2$ + OH. On both α- and β-carbons, $\nabla^2\rho(r_c)$ decreases with increasing number of fluorines on that carbon. For products, within a radical much larger values are seen at the α-carbon. For isomers with the same number of fluorines, $\nabla^2\rho(r_c)$ is higher in the case where fluorines are distributed as evenly as possible between the carbons; this trend is particularly pronounced for values at the β-centre.

Values of $\nabla^2\rho(r)$ at C—H bond critical points are almost always more negative on the more highly substituted carbon, and as fluorine substitution as a whole increases. For transition states, magnitudes on the β-carbon are lower for hydrogens *gauche* to the reaction centre. Magnitudes of $\nabla^2\rho(r_c)$ for C1—H1 are much lower than for other C—H bonds. They are higher when there are α-fluorines, but decrease when there are β-fluorines. There is no dependence on the total number of fluorines.

For H1—O, $\nabla^2\rho(r_c)$ is more negative when there are β-fluorines, especially if they are *gauche* to H1. There is a general increase in magnitude with increasing substitution. Magnitudes of $\nabla^2\rho(r_c)$ for O—H2 are by far the highest of any bond types in this study. Starting from the parent C_2H_6 + OH reaction, values increase for monosubstituted systems, then are fairly steady (between −2.7497 and −2.7641) when there are two or more fluorines, with more negative values when there are β-fluorines, particularly if they are *gauche* to H1.

A relatively large negative value of $\nabla^2\rho(r_c)$ together with a relatively large $\rho(r_c)$ value indicate a strong covalent bond (ref. 5, 290). Thus, it is again seen that the forming and breaking bonds are weak, and bonds are stronger when there is a high degree of substitution by electronegative fluorine atoms, and for cases of intramolecular hydrogen bonding. Particularly strong bonds are seen in the hydroxyl units.

On the other hand, the positive values of $\nabla^2\rho(r)$ seen at the C—F bond critical points do not indicate that these are weak bonds. Rather, as a result of charge transfer in these polar bonds, the bond critical point moves closer to the carbon nucleus (see below) and the associated bonded charge concentration now lies within the boundary of the fluorine atom (ref. 5, p. 278).

The sum of the distances (r_A and r_B) from the bond critical point to the associated nuclei is usually longer than the bond length, due to curvature in the bond path (the bond critical point will only lie on the internuclear axis if this axis coincides with an axis of symmetry (19)). These distances can be used as a one-dimensional indication of the size of the atom within the molecule and, assuming fairly constant bond (or bond path) lengths, trends in the absolute difference between r_A and r_B for a given bond type can be used as an indication of substituent effects on that bond type.

For C—C bonds, the larger atom is the more highly substituted one, and for transition states and products α-carbons are larger in case of equal substitution. For reactants, the $r_A - r_B$ difference is seen to increase with an increasing difference in the fluorine substitution at the two carbons, and with the total number of fluorines.

For C—F bonds, the $r_A - r_B$ difference decreases slightly with increasing number of fluorines. For transition states and products, the difference is larger at β-carbons.

For C—H bonds, the $r_A - r_B$ difference is larger at the more substituted carbon, at least for reactants and transition states, and for the latter larger differences are seen at the α-carbon when there is equal substitution at the two carbons. For products, the difference in a given radical is largest at the α-carbon, except when there are two β-fluorines. For reactants and products there is a general increase in $r_A - r_B$ differences with increasing substitution.

For the bond in the hydroxyl unit, whose length is remarkably constant through the series (16), the $r_A - r_B$ difference is also nearly constant, except for $CF_3—CHF_2$ + OH, where the bond critical point is closer to the oxygen atom than it is in other transition states.

There is a larger variance in lengths for the bonds being broken (C1—H1) and formed (H1—O) at the TS. Here a better measure of substituent effects on a bond type is the relative length from the critical point to the nearest atom. For H1—O this is fairly constant (28 ± 0.6%). More variance is seen for C1—H1 (31.1–33.4%), with a slight trend to lower values with increasing substitution. For a given number of fluorines, lower values are seen for the TS where they are distributed as evenly as possible between the two carbons.

The above results in the position of the bond critical point are consistent with those seen previously for binary hydrides (20). There it was noted that the position of r_c correlated, although not in a linear fashion, to the electronegativity of the non-hydrogen atom, i.e., as the electronegativity increased, r_c moved closer to the hydrogen (this correlation led to a method for calculating group electronegativities (21). Here, r_c is closer to the least electronegative atom, or to the atom which has less electronegative substituents. Thus, the carbon atom with the largest atomic basin is that which is more substituted with fluorines, or is closer to the incoming oxygen. The same factors lead to smaller hydrogen atoms.

B. Atomic charges

Atomic charges calculated by MPA at four levels of theory, and by NPA and BPA at the MP2/6-311G(d,p)//HF/6-31G(d) level, for all heavy atoms plus the hydrogen being abstracted, are given in Table 4. Starting from the base theory of HF/6-31G(d), the following trends can be seen as the level of theory is increased. Employing a larger basis set (6-311G(d,p)) has dramatic effects, usually reducing the magnitude of the charge. Including electron correlation at the MP2 level has varying effects depending on the atom, similar to previous results (22, 23). Carbon atoms become more negative or less positive. Hydrogens usually become more positive, with some exceptions for more highly substituted species, where the positive charge lessens slightly. Oxygens become less negative in OH and H_2O, and more negative in transition states, with the degree of difference increasing with the number of α-fluorines. Fluorines are less negative, by about 0.8. When electron correlation is employed in the geometry optimizations, varying effects are seen. In general, the change in charge is greater

Table 4. MPA atomic charges at four levels of theory, and NPA and BPA atomic charges at the MP2/6-311G(d,p)//HF/6-31G(d) level.

Atom[a]	HF/6-31G(d)	HF/6-311G(d,p) //HF/6-31G(d)	MP2/6-311G(d,p) //HF/6-31G(d)	HF/6-311G(d,p) //MP2/6-31G(d,p)	NPA	BPA
OH						
O	−0.443	−0.252	−0.239	−0.251	−0.376	−0.595
C_2H_6						
C	−0.477	−0.257	−0.310	−0.256	−0.532	0.162
H	0.159	0.086	0.103	0.085	0.177	−0.054
C_2H_6 + OH						
C_α	−0.460	−0.278	−0.315	−0.307	−0.345	−0.006
C_β	−0.487	−0.252	−0.210	−0.245	−0.568	0.166
H	0.403	0.221	0.256	0.191	0.311	0.295
O	−0.757	−0.443	−0.464	−0.340	−0.747	−0.907
H_2O						
O	−0.864	−0.500	−0.476	−0.497	−0.869	−1.196
H	0.432	0.250	0.238	0.248	0.435	0.598
CH_3—CH_2						
C_α	−0.327	−0.250	−0.263	−0.249	−0.234	−0.016
C_β	−0.496	−0.249	−0.308	−0.248	−0.613	0.164
CH_2F—CH_3						
C_α	−0.520	−0.285	−0.341	−0.282	−0.583	0.157
C_β	0.111	0.211	0.123	0.213	0.140	0.705
F_β	−0.428	−0.360	−0.283	−0.376	−0.383	−0.719
H_β	0.162	0.073	0.083	0.088	0.130	−0.040
$H_{\alpha 0}$	0.181	0.101	0.103	0.102	0.188	−0.028
$H_{\alpha 1/2}$	0.157	0.087	0.116	0.076	0.188	−0.024
CH_2F—CH_3 + OH t						
C_α	−0.491	−0.310	−0.349	−0.334	−0.381	−0.004
C_β	0.127	0.233	0.137	0.232	0.104	0.724
F_β	−0.409	−0.357	−0.275	−0.377	−0.372	−0.714
H	0.292	0.209	0.242	0.183	0.313	0.305
O	−0.693	−0.431	−0.448	−0.337	−0.738	−0.907
CH_2F—CH_3 + OH g						
C_α	−0.505	−0.304	−0.340	−0.324	−0.397	−0.004
C_β	0.107	0.201	0.106	0.193	0.097	0.699
F_β	−0.413	−0.363	−0.280	−0.390	−0.382	−0.719
H	0.333	0.221	0.250	0.197	0.319	NA[b]
O	−0.709	−0.430	−0.444	−0.351	−0.742	NA[b]
CH_2F—CH_2 C_1						
C_α	−0.358	−0.275	−0.289	−0.271	−0.272	−0.010
C_β	0.101	0.222	0.128	0.225	0.059	0.718
F_β	−0.397	−0.356	−0.280	−0.372	−0.377	−0.716
CH_3—CH_2F + OH						
C_α	0.119	0.157	0.070	0.146	0.271	0.570
C_β	−0.526	−0.272	−0.331	−0.268	−0.615	0.167
F_α	−0.375	−0.330	−0.237	−0.373	−0.356	−0.716
H	0.305	0.203	0.242	0.168	0.287	0.304
O	−0.707	−0.434	−0.470	−0.332	−0.766	−0.905
CH_3—CHF						
C_α	0.214	0.168	0.095	0.174	0.318	0.599
C_β	−0.544	−0.269	−0.329	−0.266	−0.654	0.162
F_α	−0.368	−0.307	−0.224	−0.322	−0.361	−0.720
CH_2F—CH_2F						
C	0.076	0.182	0.092	0.186	0.089	0.717
F	−0.406	−0.346	−0.271	−0.361	−0.372	−0.711
H_g	0.155	0.075	0.082	0.080	0.138	−0.013
H_t	0.176	0.090	0.097	0.095	0.145	0.006

Table 4 (*continued*).

Atom[a]	HF/6-31G(d)	HF/6-311G(d,p) //HF/6-31G(d)	MP2/6-311G(d,p) //HF/6-31G(d)	HF/6-311G(d,p) //MP2/6-31G(d,p)	NPA	BPA
$CH_2F—CH_2F$ + OH t						
C_α	0.080	0.128	0.040	0.118	0.229	0.590
C_β	0.090	0.204	0.108	0.205	0.057	0.733
F_α	−0.368	−0.314	−0.221	−0.354	−0.342	−0.708
F_β	−0.399	−0.345	−0.264	−0.363	−0.363	−0.706
H	0.289	0.192	0.229	0.163	0.288	0.309
O	−0.695	−0.425	−0.461	−0.327	−0.760	−0.903
$CH_2F—CH_2F$ + OH g						
C_α	0.080	0.136	0.054	0.131	0.223	0.604
C_β	0.075	0.182	0.086	0.171	0.054	0.718
F_α	−0.364	−0.309	−0.217	−0.343	−0.339	−0.706
F_β	−0.402	−0.350	−0.268	−0.377	−0.370	−0.710
H	0.322	0.205	0.237	0.185	0.292	0.321
O	−0.706	−0.422	−0.454	−0.339	−0.756	−0.904
$CH_2F—CHF$						
C_α	0.191	0.140	0.067	0.149	0.289	0.623
C_β	0.053	0.208	0.108	0.213	0.010	0.728
F_α	−0.365	−0.287	−0.203	−0.299	−0.342	−0.712
F_β	−0.389	−0.351	−0.276	−0.369	−0.373	−0.706
$CHF_2—CH_3$						
C_α	−0.559	−0.298	−0.355	−0.292	−0.619	0.166
C_β	0.634	0.549	0.412	0.559	0.663	1.287
F_β	−0.399	−0.322	−0.246	−0.338	−0.373	−0.721
$H_{\alpha 0}$	0.199	0.115	0.127	0.118	0.105	0.000
$H_{\alpha 1/2}$	0.184	0.105	0.119	0.107	0.201	−0.015
H_β	0.155	0.067	0.069	0.077	0.197	0.017
$CHF_2—CH_3$ + OH gt						
C_α	−0.541	−0.321	−0.358	−0.339	−0.421	0.014
C_β	0.638	0.556	0.412	0.559	0.624	1.296
F_g	−0.391	−0.325	−0.245	−0.354	−0.372	−0.720
F_t	−0.380	−0.314	−0.234	−0.332	−0.361	−0.716
H	0.328	0.218	0.246	0.199	0.319	0.321
O	−0.701	−0.420	−0.433	−0.341	−0.732	−0.908
$CHF_2—CH_3$ + OH gg						
C_α	−0.535	−0.310	−0.346	−0.334	−0.427	0.017
C_β	0.625	0.537	0.394	0.543	0.623	1.291
$F_{\beta 1}$	−0.376	−0.309	−0.230	−0.327	−0.362	−0.717
$F_{\beta 2}$	−0.390	−0.325	−0.245	−0.355	−0.372	−0.720
H	0.341	0.221	0.246	0.207	0.319	0.329
O	−0.703	−0.416	−0.431	−0.339	−0.727	−0.904
$CHF_2—CH_2$ C_1						
C_α	−0.372	−0.274	−0.285	−0.264	−0.271	0.027
C_β	0.611	0.571	0.423	0.582	0.581	1.305
$F_{\beta 1}$	−0.374	−0.321	−0.245	−0.341	−0.368	−0.716
$F_{\beta 2}$	−0.386	−0.317	−0.244	−0.334	−0.367	−0.718
$CH_3—CHF_2$ + OH						
C_α	0.639	0.483	0.341	0.492	0.771	1.200
C_β	−0.555	−0.285	−0.344	−0.282	−0.643	0.180
F_α	−0.369	−0.292	−0.200	−0.324	−0.346	−0.715
H	0.341	0.195	0.233	0.169	0.269	0.319
O	−0.754	−0.422	−0.472	−0.323	−0.771	−0.897
$CH_3—CF_2$						
C_α	0.700	0.489	0.356	0.512	0.788	1.250
C_β	−0.582	−0.275	−0.337	−0.271	−0.681	0.174
F_α	−0.353	−0.284	−0.205	−0.301	−0.360	−0.717

Table 4 (*continued*).

Atom[a]	//HF/6-31G(d)	HF/6-311G(d,p) //HF/6-31G(d)	MP2/6-311G(d,p) //HF/6-31G(d)	HF/6-311G(d,p) //MP2/6-31G(d,p)	NPA	BPA
CF_3—CH_3						
C_α	−0.589	−0.310	−0.372	−0.300	−0.641	0.198
C_β	1.104	0.806	0.614	0.838	1.102	1.932
F	−0.377	−0.287	−0.214	−0.305	−0.360	−0.721
H	0.205	0.122	0.133	0.126	0.207	0.010
CF_3—CH_3 + OH						
C_α	−0.570	−0.330	−0.369	−0.351	−0.443	0.061
C_β	1.092	0.814	0.616	0.838	1.064	1.952
$F_{\beta 1}$	−0.355	−0.280	−0.203	−0.299	−0.349	−0.716
$F_{\beta 2}$	−0.366	−0.291	−0.214	−0.320	−0.360	−0.721
$F_{\beta 3}$	−0.351	−0.274	−0.198	−0.293	−0.349	−0.717
H	0.339	0.223	0.247	0.212	0.320	0.331
O	−0.397	−0.408	−0.425	−0.330	−0.721	−0.899
CF_3—CH_2						
C_α	−0.446	−0.281	−0.297	−0.267	−0.289	0.078
C_β	1.092	0.838	0.634	0.868	1.019	1.960
$F_{\beta 0}$	−0.362	−0.286	−0.212	−0.304	−0.355	−0.717
$F_{\beta 1/2}$	−0.361	−0.284	−0.212	−0.300	−0.354	−0.719
CHF_2—CH_2F						
C_α	0.042	0.165	0.072	0.171	0.061	0.729
C_β	0.589	0.521	0.380	0.533	0.622	1.313
F_α	−0.393	−0.339	−0.265	−0.352	−0.365	−0.706
$F_{\beta 1}$	−0.391	−0.318	−0.242	−0.333	−0.367	−0.715
$F_{\beta 2}$	−0.380	−0.307	−0.232	−0.322	−0.360	−0.712
$H_{\alpha 1}$	0.175	0.094	0.099	0.100	0.146	0.013
$H_{\alpha 2}$	0.187	0.101	0.105	0.107	0.150	0.027
H_β	0.170	0.083	0.082	0.095	0.113	0.042
CHF_2—CH_2F + OH gg						
C_α	0.043	0.115	0.033	0.110	0.197	0.634
C_β	0.599	0.522	0.377	0.523	0.589	1.324
F_α	−0.358	−0.302	−0.211	−0.334	−0.333	−0.702
$F_{\beta 1}$	−0.378	−0.312	−0.231	−0.340	−0.360	−0.713
$F_{\beta 2}$	−0.371	−0.303	−0.223	−0.320	−0.353	−0.711
H	0.328	0.207	0.236	0.195	0.291	0.332
O	−0.697	−0.402	−0.442	−0.324	−0.744	−0.894
CHF_2—CH_2F + OH gt						
C_α	0.031	0.101	0.013	0.096	0.199	0.618
C_β	0.616	0.548	0.404	0.555	0.593	1.347
F_α	−0.363	−0.308	−0.216	−0.346	−0.338	−0.704
$F_{\beta 1}$	−0.375	−0.306	−0.227	−0.325	−0.353	−0.708
$F_{\beta 2}$	−0.372	−0.302	−0.223	−0.324	−0.353	−0.710
H	0.317	0.205	0.237	0.182	0.290	0.323
O	−0.692	−0.406	−0.443	−0.318	−0.749	−0.898
CHF_2—CHF						
C_α	0.152	0.134	0.057	0.147	0.262	0.668
C_β	0.584	0.553	0.404	0.566	0.551	1.337
F_α	−0.348	−0.280	−0.198	−0.292	−0.335	−0.706
$F_{\beta 1}$	−0.379	−0.311	−0.236	−0.329	−0.361	−0.709
$F_{\beta 2}$	−0.379	−0.310	−0.236	−0.325	−0.359	−0.713
CH_2F—CHF_2 + OH						
C_α	0.598	0.474	0.332	0.481	0.730	1.248
C_β	0.046	0.170	0.076	0.159	0.033	0.739
$F_{\alpha 1}$	−0.343	−0.277	−0.186	−0.310	−0.334	−0.706
$F_{\alpha 2}$	−0.351	−0.286	−0.194	−0.320	−0.335	−0.707
F_β	−0.395	−0.340	−0.259	−0.366	−0.361	−0.706
H	−0.311	0.195	0.227	0.182	0.274	0.336
O	−0.703	−0.408	−0.456	−0.322	−0.762	−0.895

Table 4 (*continued*).

Atom[a]	HF/6-31G(d)	HF/6-311G(d,p) //HF/6-31G(d)	MP2/6-311G(d,p) //HF/6-31G(d)	HF/6-311G(d,p) //MP2/6-31G(d,p)	NPA	BPA
$CH_2F—CF_2$						
C_α	0.694	0.462	0.325	0.487	0.744	1.291
C_β	0.034	0.204	0.103	0.210	−0.006	0.761
F_α	−0.356	−0.268	−0.189	−0.283	−0.361	−0.707
F_β	−0.379	−0.336	−0.264	−0.351	−0.344	−0.696
$CF_3—CH_2F$						
C_α	0.019	0.151	0.054	0.162	0.036	0.787
C_β	1.091	0.790	0.593	0.821	1.059	1.977
F_α	−0.381	−0.323	−0.252	−0.336	−0.354	−0.697
$F_{\beta 0}$	−0.378	−0.287	−0.214	−0.302	−0.356	−0.716
$F_{\beta 1/2}$	−0.372	−0.273	−0.202	−0.288	−0.347	−0.712
H	0.196	0.108	0.111	0.116	0.155	0.035
$CF_3—CH_2F$ + OH						
C_α	0.005	0.088	−0.000		0.175	0.680
C_β	1.082	0.815	0.614		1.030	2.013
F_α	−0.349	−0.292	−0.202		−0.325	−0.695
$F_{\beta 1}$	−0.349	−0.273	−0.196		−0.342	−0.708
$F_{\beta 2}$	−0.348	−0.271	−0.194		−0.342	−0.712
$F_{\beta 3}$	−0.349	−0.272	−0.197		−0.341	−0.710
H	0.326	0.208	0.236		0.291	0.335
O	−0.690	−0.397	−0.436		−0.741	−0.890
$CF_3—CHF$						
C_α	0.129	0.126	0.043	0.143	0.241	0.736
C_β	1.057	0.828	0.623	0.861	0.990	2.008
F_α	−0.334	−0.264	−0.183	−0.274	−0.322	−0.696
$F_{\beta 1}$	−0.353	−0.276	−0.199	−0.294	−0.343	−0.710
$F_{\beta 2}$	−0.357	−0.279	−0.208	−0.294	−0.348	−0.714
$F_{\beta 3}$	−0.348	−0.269	−0.205	−0.284	−0.347	−0.710
$CHF_2—CHF_2$ t						
C	0.563	0.507	0.364	0.523	0.589	1.349
F	−0.373	−0.302	−0.229	−0.316	−0.355	−0.708
H	0.190	0.097	0.093	0.110	0.120	0.063
$CHF_2—CHF_2$ + OH						
C_α	0.585	0.463	0.319		0.701	1.290
C_β	0.589	0.526	0.381		0.566	1.384
$F_{\alpha 1}$	−0.337	−0.269	−0.179		−0.324	−0.697
$F_{\alpha 2}$	−0.341	−0.273	−0.182		−0.324	−0.699
$F_{\beta 1}$	−0.365	−0.293	−0.216		−0.342	−0.699
$F_{\beta 2}$	−0.370	−0.301	−0.221		−0.349	−0.706
H	0.296	0.189	0.221		0.271	0.336
O	−0.695	−0.403	−0.456		−0.760	−0.890
$CHF_2—CF_2$						
C_α	0.666	0.469	0.327	0.500	0.724	1.362
C_β	0.561	0.546	0.397	0.559	0.533	1.396
F_α	−0.332	−0.262	−0.185	−0.277	−0.348	−0.702
F_β	−0.366	−0.295	−0.224	−0.309	−0.339	−0.706
$CF_3—CHF_2$						
C_α	0.542	0.494	0.346	0.515	0.565	1.416
C_β	1.040	0.788	0.587	0.822	1.027	2.036
F_α	−0.363	−0.289	−0.219	−0.303	−0.345	−0.700
$F_{\beta 0}$	−0.342	−0.262	−0.192	−0.275	−0.336	−0.703
$F_{\beta 1/2}$	−0.351	−0.273	−0.202	−0.287	−0.345	−0.708
H	0.188	0.106	0.100	0.120	0.123	0.071

Table 4 (*concluded*).

Atom[a]	HF/6-31G(d)	HF/6-311G(d,p) //HF/6-31G(d)	MP2/6-311G(d,p) //HF/6-31G(d)	HF/6-311G(d,p) //MP2/6-31G(d,p)	NPA	BPA
CF_3—CHF_2 + OH						
C_α	0.531	0.423	0.275		0.673	1.211
C_β	0.068	0.813	0.611		1.007	1.921
$F_{\alpha 1}$	−0.327	−0.258	−0.168		−0.315	−0.619
$F_{\alpha 2}$	−0.335	−0.268	−0.180		−0.325	−0.614
$F_{\beta 1}$	−0.344	−0.264	−0.189		−0.332	−0.632
$F_{\beta 2}$	−0.338	−0.259	−0.183		−0.331	−0.638
$F_{\beta 3}$	−0.341	−0.263	−0.187		−0.333	−0.638
H	0.322	0.202	0.230		0.275	0.394
O	−0.689	−0.384	−0.437		−0.749	−0.942
CF_3—CF_2						
C_α	0.660	0.461	0.311	0.498	0.698	1.433
C_β	1.083	0.832	0.624	0.864	0.969	2.075
F_α	−0.335	−0.249	−0.174	−0.262	−0.327	−0.694
$F_{\beta 0}$	−0.361	−0.267	−0.198	−0.282	−0.338	−0.701
$F_{\beta 1/2}$	−0.356	−0.264	−0.195	−0.278	−0.337	−0.707

[a]The α-C is always that written on the right. Atom labelling scheme is generally the same as in Table 3.
[b]A bond critical point was not found for the forming H–O bond, rendering the charge integrations for these atoms meaningless.

for greater geometry changes, and on the oxygen atoms.

The BPA charges are often much larger than the MPA values, and in cases of moderate magnitudes the signs are often different. While experiment cannot give us numbers with which to compare, given their opposing trends noted above with regard to electronegative atoms, the two methods should give results on either side of the expected "actual charges." Simple chemical intuition is not always reliable in judging the relative accuracy of the results. For example, in all the commonly used electronegativity scales carbon is slightly more electronegative than hydrogen, so it is reasonable to expect that in ethane the carbons should have a slight negative charge and the hydrogens should be slightly positive. This is the case for the MPA results, but the opposite situation is seen in the BPA results. However, the dipole moment derivatives for methane correspond to to a bond dipole in the sense C^+—H^- (24), and this conclusion is supported by an analysis (25) of NPA charges (which do not have the basis set quality dependence of MPA charges; on the other hand, NPA does predict a negative charge on the carbons in ethane, as seen in Table 4). A more general conclusion is that MPA leads to the wrong charge distribution in most C—H bonds (26). The high ionic character for C—F bonds as indicated by the BPA charges also seems surprising at first. However, carbon and hydrogen have roughly the same electronegativity, and it is generally recognized that hydrogen fluoride has a large ionic character.

The NPA charges for oxygens and hydrogens are intermediate between the other two methods, although charges on the latter tend to be close to those obtained by either one of MPA or BPA. Charges on fluorines tend to be close to one of the MPA values, usually either at the HF/6-31G(d) or HF/6-311G(d,p)//MP2/6-31G(d,p) level. The greatest variance is seen with the carbon charges, which tend to be more negative or less positive than with the other methods.

For individual atom types, the following trends are noted at the various levels of theory. With MPA and BPA, charges at α-carbons are more negative than at β-carbons, except when the number of α-fluorines is greater than the number of β-fluorines. With NPA, β-carbons are more negative, except if the number of β-fluorines is greater than the number of α-fluorines. With MPA, β-fluorines are usually more negative than α-fluorines, except when there are more fluorines on the β-carbon. Similar trends are observed with NPA, with fewer exceptions. With BPA, there is less variance, and the trends are sometimes opposite. For example, in CH_2F—CHF, MPA gives more negative results for the β-fluorine, but at BPA the more negative value is for the α-fluorine. Charges on hydrogens roughly correlate with the electronegativity of nearby atoms, i.e., as the number of nearby electronegative atoms increases, so does the positive charge on the hydrogen. Charges on oxygen atoms are smallest in the reactant (OH), largest in the product (H_2O), and vary little in the TS, at least with BPA and MPA, and for the latter, smaller magnitudes are seen when MP2 geometries are used. There is more variance in the NPA charges, with magnitudes tending to increase with the number of α-fluorines.

C. Charge development in the reactions

The changes in atomic charges from the reactant to the transition state, and from the transition state to the product, are given for each reaction by the MPA, NPA, and BPA methods, at the MP2/6-311G(d,p)//HF/6-31G(d) level of theory, in Table 5. In going from the reactant to the transition state, C_α always becomes more negative with the BPA method. MPA results are smaller by a factor of up to 10, and the change is often positive when there are no α-fluorines. With NPA, C_α always becomes more positive, and the magnitude is usually larger than with BPA. Less drastic changes are seen at C_β, which in most cases has a slight positive change, and there is better agreement between BPA and MPA. With NPA the change is negative, and the magnitude, while smaller than that for C_α, is still larger than for the other methods.

Table 5. Change in atomic charges from reactants to transition state, and from transition state to products, at MP2/6-311G(d,p)//HF/6-31G(d) level of theory.

		$\Delta Q_{r\to ts}$			$\Delta Q_{ts\to p}$		
Reaction[a]	Atom	MPA	NPA	BPA	MPA	NPA	BPA
C_2H_6 + OH	C_α	−0.005	0.187	−0.168	0.052	0.111	−0.010
	C_β	0.000	−0.036	0.004	0.002	−0.045	−0.002
	H	0.153	0.134	0.349	−0.018	0.124	0.303
	O	−0.225	−0.371	−0.312	−0.012	−0.122	−0.289
CH_2F—CH_3 + OH t	C_α	−0.008	0.202	−0.161	0.060	0.109	−0.006
	C_β	0.014	−0.036	0.019	−0.009	−0.045	−0.006
	F_β	0.008	0.011	0.005	−0.005	−0.005	−0.002
	H	0.139	0.125	0.345	0.004	0.122	0.293
	O	−0.209	−0.362	−0.312	−0.028	−0.131	−0.289
CH_2F—CH_3 + OH g	C_α	0.001	0.186	−0.161	0.051	0.125	−0.006
	C_β	−0.017	−0.043	−0.006	0.022	−0.038	0.019
	F_β	0.003	0.001	0.000	0.000	0.005	0.003
	H[b]	0.134	0.131		0.012	0.116	
	O[b]	−0.205	−0.366		−0.046	−0.127	
CH_3—CH_2F + OH	C_α	−0.053	0.131	−0.135	0.025	0.047	0.029
	C_β	0.010	−0.032	0.010	0.002	−0.039	−0.005
	F_α	0.046	0.027	0.003	0.013	−0.005	−0.004
	H	0.159	0.099	0.328	−0.004	0.148	0.294
	O	−0.231	−0.390	−0.310	−0.006	−0.103	−0.291
CH_2F—CH_2F + OH t	C_α	−0.052	0.140	−0.127	0.027	0.060	0.033
	C_β	0.016	−0.032	0.016	0.000	−0.047	−0.005
	F_α	0.050	0.030	0.003	0.018	0.000	−0.004
	F_β	0.007	0.009	0.005	−0.012	−0.010	0.000
	H	0.132	0.143	0.322	0.009	0.147	0.289
	O	−0.222	−0.384	−0.308	−0.015	−0.109	−0.293
CH_2F—CH_2F + OH g	C_α	−0.038	0.134	−0.113	0.013	0.066	0.019
	C_β	−0.006	−0.035	0.001	0.014	−0.044	0.010
	F_α	0.054	0.033	0.005	0.014	−0.003	−0.006
	F_β	0.003	0.002	0.001	−0.008	−0.003	0.004
	H	0.155	0.154	0.315	0.001	0.143	0.277
	O	−0.215	−0.380	−0.309	−0.022	−0.113	−0.292
CHF_2—CH_3 + OH gt	C_α	−0.003	0.198	−0.152	0.073	0.150	0.013
	C_β	0.000	−0.039	0.009	0.011	−0.043	0.009
	F_g	0.001	0.001	0.001	0.001	−0.007	0.002
	F_t	0.012	0.012	0.005	−0.011	0.005	0.000
	H	0.127	0.118	0.336	−0.008	0.116	0.277
	O	−0.194	−0.356	−0.313	−0.043	−0.137	−0.288
CHF_2—CH_3 + OH gg	C_α	0.009	0.192	−0.149	0.061	0.156	0.010
	C_β	−0.018	−0.040	0.004	0.029	−0.042	0.014
	$F_{\beta1}$	0.016	0.011	0.004	−0.015	−0.006	0.001
	$F_{\beta2}$	0.001	0.001	0.001	0.001	0.005	0.002
	H	0.119	0.214	0.329	−0.008	0.116	0.269
	O	−0.192	−0.351	−0.309	−0.045	−0.142	−0.292
CH_3—CHF_2 + OH	C_α	−0.071	0.108	−0.087	0.015	0.017	0.050
	C_β	0.011	−0.024	0.014	0.007	−0.038	−0.006
	F	0.046	0.027	0.006	−0.005	−0.014	−0.002
	H	0.164	0.072	0.302	0.005	0.166	0.279
	O	−0.233	−0.395	−0.302	−0.004	−0.098	−0.299
CF_3—CH_3 + OH	C_α	0.003	0.198	−0.137	0.072	0.352	0.017
	C_β	0.002	−0.038	0.020	0.018	−0.083	0.008
	$F_{\beta1}$	0.011	0.011	0.005	−0.009	−0.006	−0.001
	$F_{\beta2}$	0.000	0.000	0.000	0.002	0.006	0.002
	$F_{\beta3}$	0.016	0.011	0.004	−0.014	−0.005	−0.002

Table 5 (*concluded*).

Reaction[a]	Atom	$\Delta Q_{r\to ts}$ MPA	NPA	BPA	$\Delta Q_{ts\to p}$ MPA	NPA	BPA
	H	0.114	0.113	0.321	−0.009	0.115	0.267
	O	−0.186	−0.345	−0.304	−0.051	−0.148	−0.297
CHF_2—CH_2F + OH gg	C_α	−0.039	0.136	−0.095	0.024	0.065	0.034
	C_β	−0.003	−0.033	0.011	0.027	−0.071	0.013
	F_α	0.054	0.032	0.004	0.013	−0.002	−0.004
	$F_{\beta 1}$	0.011	0.007	−0.001	−0.005	−0.001	0.004
	$F_{\beta 2}$	0.009	0.007	0.004	−0.013	−0.006	−0.002
	H	0.131	0.141	0.305	0.002	0.144	0.266
	O	−0.203	−0.368	−0.299	−0.034	−0.125	−0.302
CHF_2—CH_2F + OH gt	C_α	−0.059	0.138	−0.111	0.044	0.063	0.050
	C_β	0.024	−0.029	0.034	0.000	−0.042	−0.010
	F_α	0.049	0.027	0.002	0.018	0.003	−0.002
	$F_{\beta 1}$	0.015	0.014	0.004	−0.009	−0.008	−0.001
	$F_{\beta 2}$	0.009	0.007	0.005	−0.013	−0.006	−0.003
	H	0.138	0.144	0.310	0.001	0.145	0.275
	O	−0.204	−0.373	−0.303	−0.033	−0.120	−0.298
CH_2F—CHF_2 + OH	C_α	−0.048	0.108	−0.065	−0.007	0.014	0.043
	C_β	0.004	−0.028	0.010	0.027	−0.039	0.022
	$F_{\alpha 1}$	0.046	0.026	0.006	−0.003	−0.027	−0.001
	$F_{\alpha 2}$	0.048	0.032	0.008	0.005	−0.026	0.000
	F_β	0.006	0.004	0.000	−0.005	0.017	0.010
	H	0.145	0.161	0.294	0.011	0.161	0.262
	O	−0.217	−0.386	−0.300	−0.020	−0.107	−0.301
CF_3—CH_2F + OH	C_α	−0.054	0.139	−0.107	0.043	0.066	0.056
	C_β	0.021	−0.029	0.036	0.009	−0.040	−0.005
	F_α	0.050	0.029	0.002	0.019	0.003	−0.001
	$F_{\beta 1}$	0.006	0.014	0.004	−0.003	−0.001	−0.002
	$F_{\beta 2}$	0.020	0.005	0.004	−0.014	−0.006	−0.002
	$F_{\beta 3}$	0.005	0.006	0.002	−0.008	−0.006	0.000
	H	0.125	0.136	0.300	0.002	0.144	0.263
	O	−0.197	−0.365	−0.295	−0.040	−0.128	−0.306
CHF_2—CHF_2 + OH	C_α	−0.045	0.112	−0.059	0.008	0.023	0.072
	C_β	0.017	−0.023	0.035	0.016	−0.033	0.012
	$F_{\alpha 1}$	0.050	0.031	0.011	−0.006	−0.024	−0.005
	$F_{\alpha 2}$	0.047	0.031	0.009	−0.003	−0.024	−0.003
	$F_{\beta 1}$	0.013	0.013	0.009	−0.008	0.003	−0.007
	$F_{\beta 2}$	0.008	0.006	0.002	−0.003	0.010	0.000
	H	0.128	0.151	0.273	0.017	0.164	0.262
	O	−0.217	−0.384	−0.295	−0.020	−0.109	−0.306
CF_3—CHF_2 + OH	C_α	−0.071	0.108	−0.205	0.036	0.025	0.222
	C_β	0.024	−0.020	−0.115	0.013	−0.038	0.154
	$F_{\alpha 1}$	0.051	0.030	0.081	−0.006	−0.012	−0.075
	$F_{\alpha 2}$	0.039	0.020	0.086	0.006	−0.002	−0.080
	$F_{\beta 1}$	0.003	0.004	0.071	−0.009	−0.006	−0.069
	$F_{\beta 2}$	0.019	0.014	0.070	−0.012	−0.006	−0.069
	$F_{\beta 3}$	0.015	0.012	0.070	−0.008	−0.004	−0.069
	H	0.130	0.152	0.323	0.008	0.160	0.204
	O	−0.198	−0.373	−0.347	−0.039	−0.120	−0.254

[a]As written, the second carbon is attached to the reaction centre (α). The g and t designations refer to the abstracted H being *gauche* or *trans*, respectively, to a β-F.

[b]BPA numbers not available since the bond critical point for the forming H—O bond was not found.

Fluorines attached to the α-carbon become slightly more positive, by about 0.05 with MPA, about 0.03 with NPA, and <0.01 with BPA. For β-fluorines little change is seen, with relatively larger $\Delta Q_{r\rightarrow ts}$ values with MPA and NPA. The abstracted hydrogen becomes more positive, in relative order BPA > MPA ≈ NPA, and the oxygen more negative, with magnitudes in relative order NPA > BPA > MPA.

The above MPA and BPA results are consistent with the influence of the incoming, electronegative oxygen atom, which will draw electron density away from the hydrogen. The impending loss of a relatively electropositive substituent, and (or) an electrostatic effect from the oxygen atom, leaves more electrons at the α-carbon, and a concomitant slight decrease in charge at the remaining substituents. A slightly different picture emerges from the NPA results, where the α-carbon becomes more positive. The oxygen atom again plays a prime role, with the carbon atom losing electron density due to an inductive effect. However, since the positive change on the carbon is greater than the positive change on the hydrogen, it is likely that other forces are at play as well.

As the reaction proceeds to products, the oxygen atom moves away from the ethyl radical, so its influence is no longer felt, and many of the changes in atomic charges are reversed. In going from TS to product, C_α always becomes more positive with MPA (except in $CH_2F—CHF_2 + OH$), in some cases more than compensating for the buildup of charge at the TS. With NPA, C_α continues to become more positive. The BPA changes are smaller, with varying signs. If the change in charge from reactant to product is considered, BPA always predicts that C_α is more negative in the product (except in the case of $CF_3—CHF_2$ + OH), consistent with the increase in electronegativity in going from an sp^3- to sp^2-hybridized carbon.

The MPA results for C_β usually continue the trend to positive changes observed in going from reactant to TS, and with NPA it continues to become more negative. Signs for the BPA changes vary, and the magnitude is often smaller than for MPA, with $CF_3—CHF_2$ + OH again being a notable exception.

For α-fluorines, the trend of MPA results to more positive values, which was seen for the change from reactant to TS, continues but with slightly smaller values, and a few exceptions where the value is slightly negative. With BPA, and NPA in most cases, the values of $\Delta Q_{ts\rightarrow p}$ are slightly negative. All three methods give very small magnitudes for β-fluorine values.

For the reacting hydrogen atom, the BPA method continues the trend to more positive charge, although the effect is smaller than before. It also continues to become more positive with NPA, with the effect having about the same magnitude as for reactants to transition states. Much smaller magnitudes are seen in the MPA results, where the sign of the change varies. The oxygen atom undergoes similar trends as for reactants to transition states, with the effect again being much smaller with MPA.

A general trend seen in these results is that there is a buildup of charge in the TS, concentrated near the reaction centre. The charge buildup on α-carbon atoms dissipates somewhat as the reaction proceeds to products, with MPA and BPA. With NPA, the buildup of positive charge continues. For other atoms the buildup or depletion of charge continues, but the effect is smaller.

4. Conclusions

The magnitudes of the electron density and its Laplacian at the bond critical points are in most cases correlated with the bond strength, as measured by bond dissociation energies. The position of the bond critical point varies with the electronegativity of the surrounding atoms.

The three methods used to calculate atomic charges give somewhat different descriptions of electron transfer in the reactions. In general, there is a buildup of charge in the TS, concentrated near the reaction centre. As the reaction proceeds to products the charge buildup on the α-carbon dissipates somewhat, while for other atoms the buildup or depletion of charge continues, but at a lesser rate.

Of the three methods used to calculate atomic charges, BPA is the most sophisticated, but MPA appears to give more realistic results, at least when relative atomic electronegativities are considered. However, the BPA results are consistent with bond polarities determined in previous studies, and they give a reasonable picture of the charge development in the reactions. The NPA results are in many cases intermediate between the other two, but appear to overestimate charge transfer on carbon atoms.

Acknowledgements

Financial support for this work was provided by the Natural Sciences and Engineering Research Council (NSERC) of Canada, in the form of operating, equipment, and infrastructure grants (to R.J.B.), a postgraduate scholarship (to J.M.M.), and an undergraduate student research award (to J.B.T.). We are grateful for useful suggestions from Zheng Shi and Jian Wang. We thank Richard Bader's group for technical support for the PROAIM programs.

References

1. Z. Shi and R.J. Boyd. J. Am. Chem. Soc. **113**, 1072 (1991).
2. S.S. Kim, S.Y. Choi, and C.H. Kong. J. Am. Chem. Soc. **85**, 4234 (1985).
3. K. Héberger. J. Phys. Org. Chem. **7**, 244 (1994).
4. (*a*) R.F.W. Bader, Y. Tal, S.G. Anderson, and T.T. Nguyen-Dang. Isr. J. Chem. **19**, 8 (1980); (*b*) R.F.W. Bader and T.T. Nguyen-Dang. Adv. Quantum Chem. **14**, 63 (1981); (*c*) R.F.W. Bader, T.T. Nguyen-Dang, and Y. Tal. Rep. Prog. Phys. **44**, 893 (1981); (*d*) R.F.W. Bader and H. Essén. J. Chem. Phys. **80**, 1943 (1984).
5. R.F.W. Bader. Atoms in molecules: a quantum theory. Clarendon Press, Oxford. 1990.
6. K.B. Wiberg, R.F.W. Bader, and C.D.H. Lau. J. Am. Chem. Soc. **109**, 985 (1987).
7. R.F.W. Bader, T.H. Tang, Y. Tal, and F.W. Biegler-König. J. Am. Chem. Soc. **104**, 946 (1982).
8. (*a*) R.J. Boyd. *In* Studies in organic chemistry. Vol. 31. *Edited by* M. Kobayashi. Elsevier Scientific, Amsterdam. 1987. p. 485; (*b*) O. Knop, R.J. Boyd, and S.C. Choi. J. Am. Chem. Soc. **110**, 7299 (1988).
9. R.S. Mulliken. J. Chem. Phys. **23**, 1833 (1955).
10. C.L. Perrin. J. Am. Chem. Soc. **113**, 2865 (1991).
11. M.J. Frisch, M. Head-Gordon, G.W. Trucks, J.B. Foresman, H.B. Schlegel, K. Raghavachari, M.A. Robb, J.S. Binkley, C. Gonzalez, D.J. DeFrees, D.J. Fox, R.A. Whiteside, R. Seeger, C.F. Melius, J. Baker, R.L. Martin, L.R. Kahn, J.J.P. Stewart, S. Topiol, and J.A. Pople. GAUSSIAN 90, Gaussian Inc., Pittsburgh, Pa. 1990.

12. M.J. Frisch, G.W. Trucks, H.B. Schlegel, P.M.W. Gill, B.G. Johnson, M.W. Wong, J.B. Foresman, M.A. Robb, M. Head-Gordon, E.S. Repogle, R. Gomperts, J.L. Andres, K. Raghavachari, J.S. Binkley, C. Gonzalez, R.L. Martin, D.J. Fox, D.J. DeFrees, J. Baker, J.J.P. Stewart, and J.A. Pople. GAUSSIAN 92/DFT, Gaussian Inc., Pittsburgh, Pa., 1993.
13. J.M. Martell and R.J. Boyd. J. Phys. Chem. **96**, 6287 (1992).
14. J.M. Martell, R.J. Boyd, and Z. Shi. J. Phys. Chem. **97**, 7208 (1993).
15. J.M. Martell, A.K. Mehta, P.D. Pacey, and R.J. Boyd. J. Phys. Chem. **99**, 8661 (1995).
16. J.M. Martell and R.J. Boyd. J. Phys. Chem. **99**, 13402 (1995).
17. J.M. Martell, R.J. Boyd, and L.A. Eriksson. J. Phys. Chem. **99**, 623 (1995).
18. F.W. Biegler-König, R.F.W. Bader, and J. Tang. J. Comput. Chem. **3**, 317 (1982).
19. G. Runtz, R.F.W. Bader, and R.R. Messer. Can. J. Chem. **55**, 3040 (1977).
20. (*a*) K.E. Edgecombe. Ph.D. Thesis, Dalhousie University, 1987; (*b*) R.J. Boyd and K.E. Edgecombe. J. Comput. Chem. **8**, 489 (1987); (*c*) K.E. Edgecombe and R.J. Boyd. Int. J. Quantum Chem. **29**, 959 (1986).
21. (*a*) R.J. Boyd and K.E. Edgecombe. J. Am. Chem. Soc. **110**, 4182 (1988); (*b*) S.L. Boyd and R.J. Boyd. J. Am. Chem. Soc. **114**, 1652 (1992).
22. L.-C. Wang and R.J. Boyd. J. Chem. Phys. **90**, 1083 (1989).
23. R.J. Boyd and L.-C. Wang. J. Comput. Chem. **10**, 367 (1989).
24. K.B. Wiberg and J. Wendoloski. J. Phys. Chem. **88**, 586 (1984).
25. A.E. Reed and F. Weinhold. J. Chem. Phys. **84**, 2428 (1986).
26. J. Cioslowski. J. Am. Chem. Soc. **111**, 8333 (1989).

Analysis of magnesium–carbon bonding in magnesium anthracene systems[1]

Ralf Stegmann and Gernot Frenking

Abstract: Ab initio calculations at the MP2/3-21G(*) level of theory have been carried out for the magnesium–anthracene complexes 9,10-magnesiumanthracene·$3H_2O$ (**1**) and the 9-methyl (**2**), dimethyl (**3**), and 9,10-bis(methylsilyl) (**4**) substituted derivatives. The theoretically predicted geometries of the anthracene ligands are also reported. The calculated geometries of **1–4** are in very good agreement with experimental values for the corresponding THF complexes. The Mg—$C_{9,10}$ bonds of the bridged structures are rather long and the anthracene ligands are folded by ~40° along the C_9–C_{10} line in the complexes. Analysis of the electronic structure shows clearly that the Mg—$C_{9,10}$ bonds should be considered as purely ionic. This is revealed by topological analysis of the electron density distribution and its associated Laplacian. The electron density at the Mg—$C_{9,10}$ bond critical points $\rho(\boldsymbol{r}_b)$ is very low and the Laplacian $\nabla^2\rho(\boldsymbol{r}_b)$ and the energy density H_b have positive values. The ionic nature of the Mg—$C_{9,10}$ bond is also indicated by the natural bond order (NBO) analysis, which gives a Lewis structure with two lone pairs at C_9 and C_{10} but no Mg—$C_{9,10}$ bonds. The NBO method gives a charge donation from Mg to the anthracene ligand of nearly two. The theoretically predicted NMR chemical shifts using the GIAO method give ^{13}C resonances for the complex **1** and for anthracene and anthracene dianion that are in good agreement with experimental values.

Key words: magnesium–anthracene complexes, ab initio calculations, analysis of magnesium–carbon bonding.

Résumé : On a effectué des calculs ab initio au niveau MP2/3-21(G*) de la théorie pour les complexes suivants du magnésium avec des anthracènes : 9,10-magnésiumanthracène·$3H_2O$ (**1**) et pour les dérivés substitués 9-méthyl- (**2**), 9,10-diméthyl- (**3**) et 9,10-bis(méthylsilyl)- (**4**). On rapporte aussi les géométries prédites par la théorie pour les coordinats anthracènes. Les géométries calculées des composés **1–4** sont en bon accord avec les valeurs expérimentales des complexes correspondants avec le THF. Les liaisons Mg—$C_{9,10}$ des structures pontées sont relativement fortes et les coordinats anthracènes sont repliés d'environ 40° le long de la droite reliant C_9 à C_{10} dans les complexes. L'analyse de la structure électronique montre clairement que les liaisons Mg—$C_{9,10}$ devraient être considérées comme purement ioniques. Cette conclusion est révélée par l'analyse topologique de la distribution de la densité électronique et du laplacien qui lui est associé. La densité électronique aux points critiques de la liaison Mg—$C_{9,10}$, $\rho(\boldsymbol{r}_b)$ est très faible et le laplacien, $\nabla^2\rho(\boldsymbol{r}_b)$ ainsi que la densité d'énergie, H_b, ont des valeurs positives. La nature ionique de la liaison Mg—$C_{9,10}$ est aussi indiquée par l'analyse NBO qui conduit à une structure de Lewis comportant deux paires non partagées en C_9 et en C_{10}, mais pas des liaisons Mg—$C_{9,10}$. La méthode NBO conduit à un don de charge du Mg au coordinat anthracène de pratiquement deux. Les déplacements chimiques en RMN prédits d'un point de vue théorique à l'aide de la méthode GIAO conduisent à des résonances en ^{13}C pour le complexe **1** et pour l'anthracène et le dianion de l'anthracène qui sont en bon accord avec les valeurs expérimentales.

Mots clés : complexes magnésium–anthracène, calculs ab initio, analyse des liaisons magnésium–carbone.

[Traduit par la rédaction]

Introduction

In 1965, Ramsden found that elementary magnesium reacts with anthracene in tetrahydrofuran (THF) to form an orange compound, which has the magnesium atom in a bridging position between the C_9 and C_{10} position (1). The discovery made by Ramsden remained in a dormant stage, until in 1980 Bogdanovic et al. found that magnesium anthracene systems can be used for the hydrogenation of magnesium under very mild conditions (2). This finding triggered numerous experimental studies about the properties and application of these synthetically and industrially interesting compounds (3–5). It was found that magnesium anthracene compounds are excellent reducing agents for transition metal salts, and that they can be used to prepare Grignard components in a very convenient way.

The key to the fascinating chemistry of the magnesium-anthracene system is the unusual Mg—C bond. X-ray structure analyses of the magnesiumanthracene·3THF complex and substituted derivatives show that the magnesium atom is usually pentacoordinate with three THF molecules surrounding the Mg atom (5). The Mg—$C_{9,10}$ bond distances are very long (2.2–2.35 Å) and the C_9-Mg-C_{10} bond angle is very sharp (71°–79°). The anthracene moiety of the complex is folded along the C_9–C_{10} line by 26°–45°. The complexes with bulky

Received October 4, 1995.

This paper is dedicated to Professor Richard F.W. Bader on the occasion of his 65th birthday.

R. Stegmann and G. Frenking.[2] Fachbereich Chemie, Philipps-Universität Marburg, Hans-Merrwein-Strasse, D-35043 Marburg, Germany.

[1] Theoretical Studies of Organometallic Compounds. XX. Part XIX: ref. 21.

[2] Author to whom correspondence should be addressed. Fax: Int.+6421-282189. Internet: frenking@ps1515.chemie.uni-marburg.de

trimethylsilyl substituents at C_9 and C_{10} have only two THF molecules around the Mg atom (5).

Scheme 1.

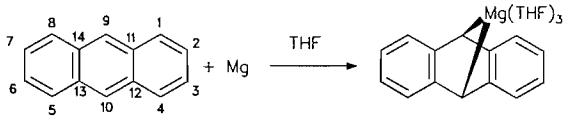

The Mg—C bonding in these complexes appears not to be very strong. The equilibrium between magnesium and anthracene and the adduct is temperature dependent and can be strongly influenced by substituents in the 9 and 10 positions (3). At 0°C, the equilibrium between magnesium and anthracene in THF and the complex is nearly 100% on the adduct side, while at 60°C the equilibrium is strongly shifted toward the starting materials (3*h*). An interesting observation is that at 60°C the equilibrium of the parent compound is only 23% on the complex side, and while one methyl group in the C_9 position enhances the product concentration to 51%, two methyl groups at C_9 and C_{10} reduce the complex concentration to only 5% (Scheme 1) (3*h*).

The nature of the Mg—C bonding in magnesium anthracene systems is not fully understood. The low thermal stability of magnesium anthracene systems speaks against a significant covalent contribution. Since the NMR data of the magnesium–anthracene complexes differ significantly from those of the dianion of Li_2[anthracene] (6), Bogdanovic concluded that an ionic structure can be ruled out (3*f*). The dominant feature of the NMR spectrum of Li_2[anthracene] is the strong shift of the ^{13}C resonances of $C_{9,10}$ towards higher field by 49.8 ppm relative to anthracene (6). The ^{13}C signals of $C_{9,10}$ of Mg-anthracene·3THF are shifted to even higher fields by 68.5 ppm (3*f*). A higher charge concentration at $C_{9,10}$ in the Mg complex than in the anthracene dianion was regarded by Bogdanovic as an unlikely reason for the larger high-field shift. This author interpreted the ^{13}C signals of $C_{9,10}$ as indicating a change in the hybridization of $C_{9,10}$ towards sp^3 (3*f*). Bogdanovic suggested ionic–covalent resonance forms for the description of the Mg—$C_{9,10}$ bonds (Scheme 2). It should be noted that resonance forms such as **b** and **c** should not be very important, because the anthracene moiety is strongly bent along the $C_{9,10}$ line.

Scheme 2.

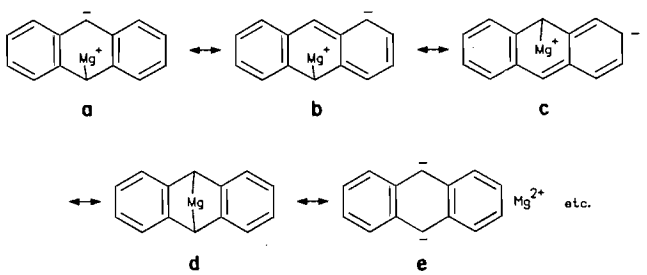

There has been no theoretical investigation of the structure and bonding of these compounds. In this paper we report the theoretically predicted geometries of the parent compound 9,10-magnesiumanthracene·$3H_2O$ (**1**) using ab initio quantum mechanical methods at the Hartree–Fock and MP2 levels of theory. The water ligand has been taken to mimic THF. We also report theoretical results for the substituted derivatives 9-methyl- (**2**), 9,10-dimethyl- (**3**), and 9,10-(methyl)silyl-magnesiumanthracene·$3H_2O$ (**4**). The latter compound was taken as model for 9,10-(trimethyl)silyl-magnesiumanthracene·$3H_2O$), which could not be calculated for computational reasons. The focus of this study is the analysis of the Mg—C bonding interactions. To this end we employed topological analysis of the electron density distribution $\rho(r)$, its gradient field $\nabla\rho(r)$, and the associated Laplacian $\nabla^2\rho(r)$ developed by Bader (7). The electronic structure of the complexes has also been examined by using the natural bond orbital (NBO) method developed by Weinhold and co-workers (8).

Table 1. Calculated and experimental Mg—$C_{9,10}$ bond distance (Å) of **1**

Method	Mg—$C_{9,10}$
PM3	1.930
HF/3-21G(*)	2.223
HF/6-31G**	2.246
MP2/3-21G(*)	2.219
MP2/6-31G**	2.238
Exp.[a]	2.25–2.33

[a]Reference 5*a*.

Method

The geometry of **1** has been optimized at the Hartree–Fock (HF) and MP2 (Møller–Plesset perturbation theory terminated at second order) (9) levels of theory using 3-21G(*) and 6-31G** basis sets (10). Geometry optimizations have also been carried out with the semiempirical method PM3 using the actual Mg parameters (11). The harmonic vibrational frequencies have been calculated at HF/3-21G(*) using analytical second derivatives. The geometries of **2**–**4** and the anthracene species **5**–**8** were optimized at MP2/3-21G(*). The calculated geometry of **1** was not very different when larger basis sets were employed. Because this study focusses on the structure and not the energy of the molecules, calculations at the MP2/3-21G(*) level of theory are sufficient. The program TURBOMOLE was used for the geometry and energy calculations (12). The NMR chemical shifts were calculated using the direct version of the GIAO method (13). The HF/GIAO calculations were carried out with a DZ + P basis set (14). For topological analysis of the electron density distribution the programs EXTREME, SCHUSS, GRIDV, and CONTOUR were employed (15). The NBO calculations (8) were carried out with the program Gaussian 92 (16).

Results and discussion

The optimized structures of the complexes **1**–**4** and anthracenes **5**–**8** are shown in Fig. 1. Table 1 shows the Mg—$C_{9,10}$ bond lengths of **1** calculated at PM3, HF/3-21G(*), HF/6-31G**, MP2/3-21G(*), and MP2/6-31G**. It is obvious that the Mg—$C_{9,10}$ bond distance using the semiempirical method PM3 is much too short, while the ab initio values are in good agreement with experiment. Table 2 gives the theoretical and experimental geometries of **1**–**8**. The ab initio calculations give geometries that are in good agreement with experimental values. It should be noted that the experimental

Fig. 1. Optimized geometries (MP2/3-21G(*)) of the magnesium–anthracene complexes **1–4** and the anthracene ligands **5–8**.

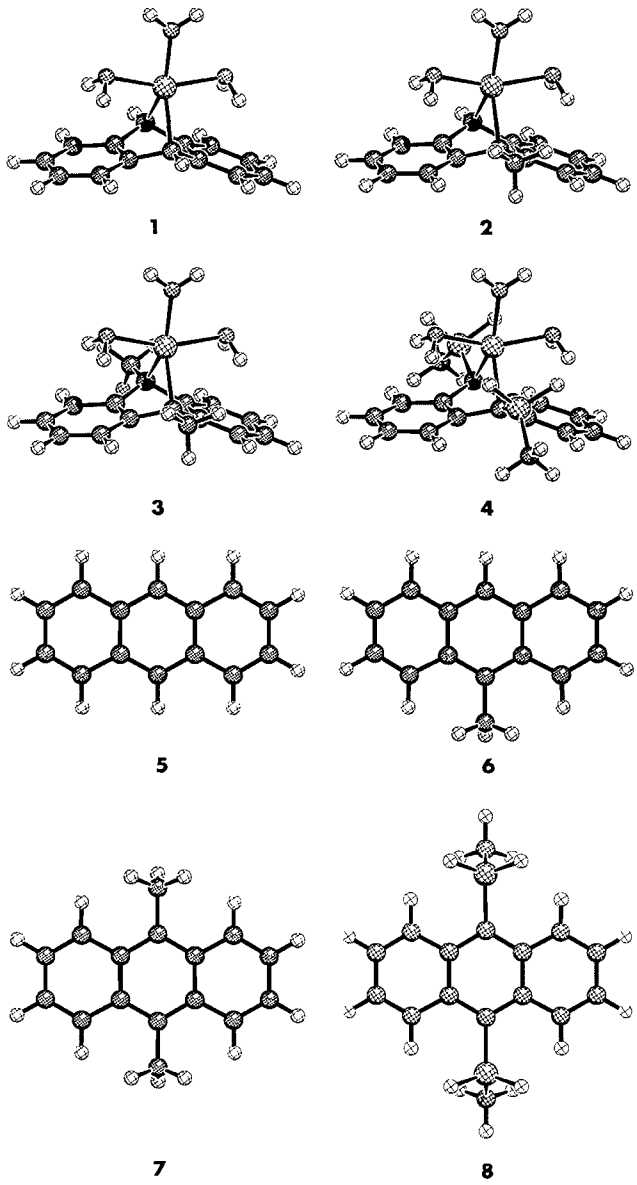

data deduced from X-ray structure analysis are subject to disorder and solid-state effects.

The anthracene moiety of complexes **1–4** is folded along the C_9–C_{10} line. The value of the folding angle depends upon the definition of the vectors forming the angle, τ. We took the midpoints of the lines connecting C_{13}–C_{14}, C_9–C_{10}, and C_{11}–C_{12} as one definition of the folding angle τ (τ_1), and the midpoints of C_5–C_8, C_9–C_{10}, and C_1–C_4 as another definition, which is denoted τ_2. The folding angle of **1** is then calculated to be $\tau_1 = 47.3°$ and $\tau_2 = 38.2°$ (Table 2). Experimentally, two different molecules in the disordered crystal structures were found, for which the angles between the two phenylene planes were reported as $\tau = 26.6°$ and 30.6° (*5a*). The folding angle of the 1,4-dimethyl derivative of **1** has experimentally been reported with a value of $\tau = 40.95°$ (*5b*), which is in good agreement with the calculated value. Similar values of $\tau = 41.2°$ (*5d*) and $\tau = 45°$ (*5c*) have been reported for the trimethylsilyl derivative of **1**. It should be noted that the phenylene rings in the two crystal forms of **1** are slightly bent (*5a*).

The calculated Mg—$C_{9,10}$ distances of **1–4** are in good agreement with the observed values. The experimental Mg—$C_{9,10}$ bond lengths of **1** show some scattering, due to the disorder of the crystal (*5a*). The calculations predict that the Mg—$C_{9,10}$ bond lengths of the 9,10-substituted complexes **2–4** have slightly *shorter* bond lengths than the parent compound **1**. The calculated C_9-Mg-C_{10} angle is not very different for the four complexes. The theoretical values are between 76.1° (**1**) and 77.5° (**3**). This is in good agreement with the experimental results, which show bond angles C_9-Mg-C_{10} between 70.9° and 78.2° (5). It should be kept in mind that the experimental results refer to THF complexes, while the calculated structures have water molecules as ligands.

The effect of substituents at the $C_{9,10}$ position upon the C—C bond lengths of anthracene is negligible (Table 2). It is interesting to compare the calculated C—C bond lengths of the anthracene moieties in the complexes **1–4** with those of anthracene (**5**) and anthracene dianion ($\mathbf{5}^{2-}$). The C_1–C_2 distance of **5** (1.379 Å) becomes longer in $\mathbf{5}^{2-}$ (1.428 Å). Slightly shorter C_1—C_2 distances than in $\mathbf{5}^{2-}$ are calculated for the complexes **1–4** (1.413–1.414 Å). The C_2–C_3 bond length of **5** (1.438 Å) becomes shorter in $\mathbf{5}^{2-}$ (1.401 Å) and it changes little in the complexes (1.403–1.407 Å). The C_1–C_{11} bond length of **5** (1.442 Å) becomes slightly shorter in $\mathbf{5}^{2-}$ (1.430 Å) and reduces even more in the complexes (1.412–1.415 Å). The largest change is found for the C_9—C_{11} bond, which becomes much longer, from 1.410 Å in **5** to 1.430 Å in $\mathbf{5}^{2-}$ and 1.497–1.499 Å in **1–4**. The C_{11}—C_{12} bond length of **5** (1.453 Å) becomes longer in $\mathbf{5}^{2-}$ (1.472 Å) but then it becomes shorter in the complexes **1–4** (1.443–1.449 Å). The changes in the C—C distances from **5** and $\mathbf{5}^{2-}$ to the complexes indicate an enhanced aromatic conjugation within the two outer phenylene rings, while C_9 and C_{10} change towards singly bonded carbon atoms. The bond length alternation in the outer phenyl rings is clearly reduced in **1–4** as compared to **5** and $\mathbf{5}^{2-}$ (Table 2).

We come to the analysis of the magnesium–carbon bonding in the complexes **1–4**. Figure 2 shows the contour line diagrams of the Laplacian distribution for the four compounds in the C_9-Mg-C_{10} plane. For comparison, we show also the Laplacian distribution for the anthracene dianion ($\mathbf{5}^{2-}$) using the geometry of the folded anthracene moiety of **1** (Fig. 2*e*). The areas of charge depletion ($\nabla^2\rho(r) > 0$) are indicated by broken lines, and the areas of charge concentration ($\nabla\rho(r) < 0$) are shown by solid lines. The magnesium atom is characterized by a large area of charge depletion. The shape of the Laplacian distribution around Mg indicates clearly that there is no charge concentration in the valence region. The metal atom has lost its valence electrons. There is an area of charge concentration at C_9 and C_{10} pointing toward the magnesium atom. This area of charge concentration is larger in the complex **1** than in the isolated anthracene dianion moiety (compare Figs. 2*a* and 2*e*). Visual inspection of the Laplacian distribution shows that the Mg—$C_{9,10}$ bonds are strongly polar. Also, the Mg—O bond is characterized by charge concentration at the oxygen end and charge depletion at the magnesium. Unlike C_9 and C_{10}, the charge concentration at the oxygen atom shows little deformation towards the Mg atom. This is reasonable, because oxygen

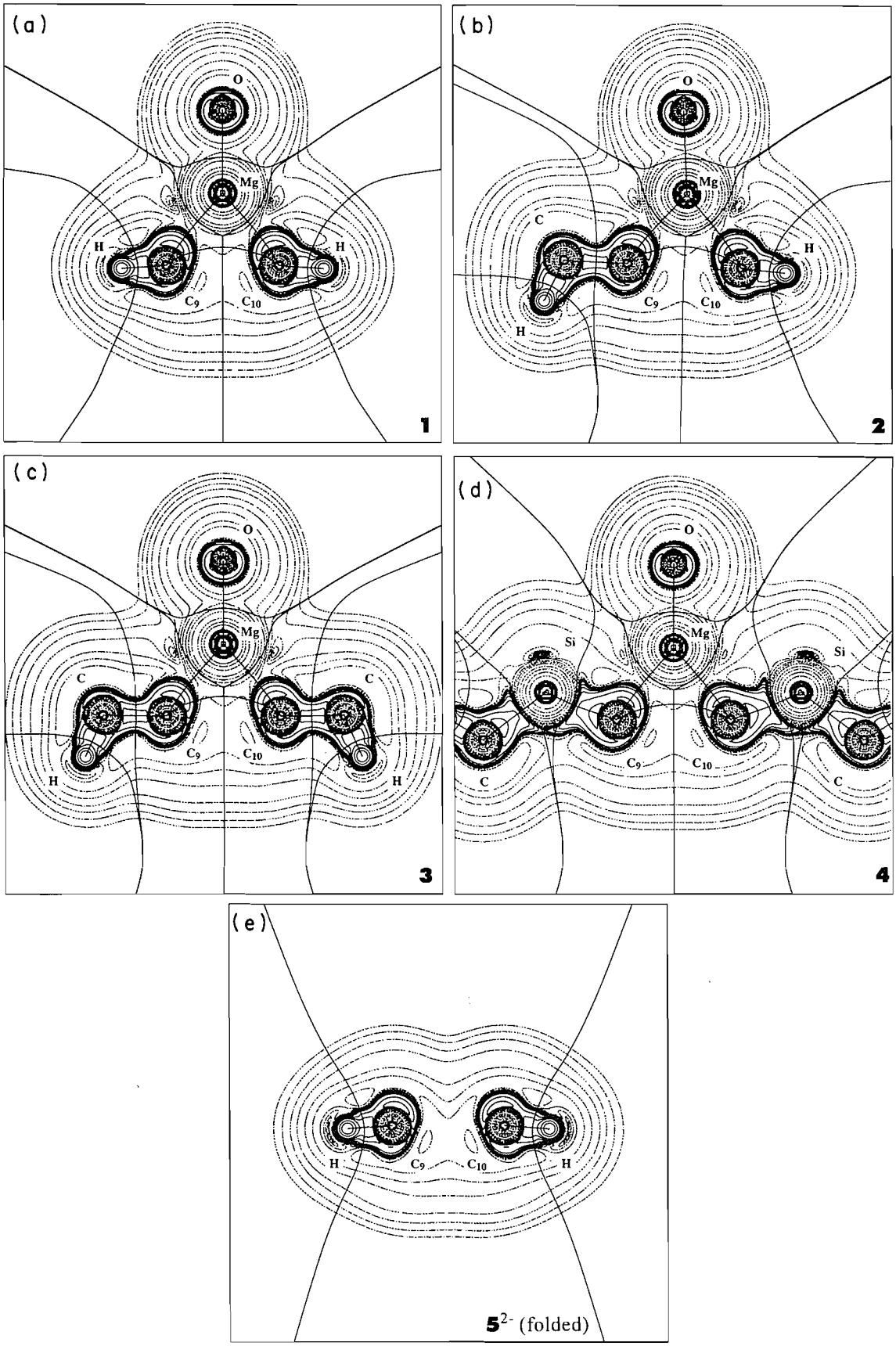

Fig. 2. Contour line diagrams of the Laplacian distribution $\nabla^2\rho(\boldsymbol{r})$ at MP2/3-21G(*). The diagrams are plotted in the C_9–Mg–C_{10} plane. The values $\nabla^2\rho(\boldsymbol{r})$ represented by the contour lines are (in hartrees) 0.001 for the outermost line, then 0.002, 0.004, 0.008, 0.02, 0.04, etc. Figures (*a*)–(*d*) show the complexes **1**–**4**. Figure (*e*) shows the anthracene dianion using the geometry of the anthracene ligand in **1**. Broken lines indicate charge depletion ($\nabla^2\rho(\boldsymbol{r}) > 0$), solid lines indicate charge concentration ($\nabla^2\rho(\boldsymbol{r}) < 0$). The solid lines connecting the atomic nuclei are the bond paths, the solid lines separating the atomic nuclei indicate the zero-flux surfaces in the plane. The crossing points of the bond paths and zero-flux surfaces are the bond critical points $\boldsymbol{r}_b$.

is more electronegative and less polarizable than carbon. The difference between the very polar Mg—$C_{9,10}$ and Mg—O bonds and the truly covalent C—H, C—C (**2** and **3**, Figs. 2*b* and 2*c*), and C—Si bonds (**4**, Fig. 2*d*) becomes obvious by comparing the Laplacian distribution in the interatomic region. The C—H, C—C, and C—Si bonds show continuous areas of charge concentration between the bonded atoms.

Figure 2 shows not only bond paths for the Mg—C_9 and Mg—C_{10} bonds in **1**–**4**, but there is also a bond path between the carbon atoms C_9 and C_{10}. In addition, there is a ring critical point for the C_9MgC_{10} moiety. It follows that topological analysis of the electron density distribution assigns a cyclic structure to the C_9MgC_{10} moiety of **1**–**4**. A closer examination of Fig. 2 shows that the C_9–C_{10} bond path is bent inward, and that the bond critical point is close to the ring critical point. Such a situation is typical for the opening of a three-membered ring. A merging of the C_9–C_{10} bond critical point $\boldsymbol{r}_b$ and the ring critical point $\boldsymbol{r}_c$ would yield a singularity in ρ, which is called a catastrophe point in the configuration space (ref. 7, p. 114).

The relationship between structure diagrams obtained from critical point bond paths and classical chemical bonds has been discussed in detail by Bader (7). Here it is sufficient to say that a bond path does not necessarily indicate a chemical bond. Two helium atoms, which are 100 Å away, are still connected by a bond path, and they have a bond critical point. It is possible, however, to distinguish within the atoms-in-molecules theory (7) between *shared interactions*, which are typical for covalent bonds, and *closed-shell interactions*, which are typical for ionic bonds and van der Waals interactions. It has been shown that for shared interactions (covalent bonding) between two atoms the Laplacian at the bond critical point $\nabla^2\rho(\boldsymbol{r}_b)$ is negative and large in magnitude, and that the electron density at the bond critical point $\rho(\boldsymbol{r}_b)$ is also large in magnitude (ref. 7, p. 290f). For closed-shell interactions it holds that $\nabla^2\rho(\boldsymbol{r}_b) > 0$ and $\rho(\boldsymbol{r}_b)$ is relatively small. It has also been shown that the energy density at the bond critical point H_b is negative for covalent bonds, while it is zero or slightly positive for closed-shell interactions (17).

Table 3 shows the calculated results of the topological analysis for **1**–**4**. For the C_1–C_2 and C_9–C_{11} ring bonds of **1** it is found that $\nabla^2\rho(\boldsymbol{r}_b) < 0$, $\rho(\boldsymbol{r}_b)$ is rather large, and $H_b < 0$. These values are typical for covalent bonds. The results of the topological analysis for the C_9–C_{10}, Mg–O, and Mg–$C_{9,10}$ interactions are clearly different. The values for $\nabla^2\rho(\boldsymbol{r}_b)$ are positive and the magnitude of $\nabla^2\rho(\boldsymbol{r}_b)$ and $\rho(\boldsymbol{r}_b)$ is much lower than for the C—C ring bonds. The H_b values for the Mg—O and Mg—$C_{9,10}$ bonds are positive, while the C_9–C_{10} interactions have slightly negative values (Table 3). It follows that *the topological analysis of the electron density distribution classifies the Mg—$C_{9,10}$ bonds as purely ionic*! We checked if the results of the topological analysis change significantly when a larger basis set is employed. To this end we repeated the calculations at the MP2 level using a 6-31G(*) basis set for $C_{9,10}$ and Mg at the MP2/6-31G(**) optimized geometry. For the other atoms a 3-21G basis set was employed. The energy density and the Laplacian at the Mg—$C_{9,10}$ bond critical points changed only slightly, and the values were still positive (H_b = 0.007 hartree/Å^3, $\nabla^2\rho(\boldsymbol{r}_b)$ = 4.398 e/Å^5).

There is additional theoretical evidence for a classification of the Mg—$C_{9,10}$ bonds of Mg-anthracene as purely ionic bonds. The NBO analysis (8) of the wave function gives the charge distribution and the most important Lewis structure of the molecule. We examined the wave functions of **1**–**4** at the MP2/3-21G(*) level. The most important result of the NBO analysis is that there is no Mg—C bond in the optimal Lewis structure! The NBO results give two lone pairs at C_9 and C_{10}. It follows that the resonance form **e** shown in Scheme 2 gives the best representation of the magnesium–anthracene complexes. The hybridization at $C_{9,10}$ is very interesting. The NBO analysis indicates that the lone pairs at $C_{9,10}$ in complexes **1**–**4** are nearly pure *p* AOs, while the bonds to the neighbouring carbon atoms are essentially sp^2 hydridized (Table 4). The hybridization at $C_{9,10}$ is nearly the same in the planar equilibrium form $\mathbf{5}^{2-}$, in the folded geometry, and finally in the complex ligand. The calculated charge distribution (Table 4) indicates that the partial charge of the Mg–anthracene complexes at $C_{9,10}$ is significantly larger than in anthracene^{2-}, which is in agreement with the Laplacian distribution shown in Figs. 2*a* and 2*e*. This is a reasonable result, because the charge is delocalized in the π-system of planar anthracene^{2-}, while it is more localized at the lone pairs of $C_{9,10}$ in the folded anthracene moiety of **1**–**4**. Table 4 shows that the partial charges at $C_{9,10}$ increase from planar $\mathbf{5}^{2-}$ (−0.40 e) to folded $\mathbf{5}^{2-}$ (−0.46 e). The electron transfer from $Mg(H_2O)_3$ to the anthracene ligand leads to a further increase of the negative partial charge at $C_{9,10}$ (Table 4). The NBO analysis indicates that the $Mg(H_2O)_3$ moiety donates 1.67–1.78 electrons to the anthracene part. The Mg—$C_{9,10}$ overlap-weighted bond order is very low. It follows that the NBO analysis supports the interpretation of the Mg—$C_{9,10}$ bonding in magnesium–anthracene complexes as ionic with negligible covalent contributions. The NBO analysis of the wave function using 6-31G(*) basis sets at $C_{9,10}$ and Mg gave very similar results. The most important Lewis structure had no Mg—$C_{9,10}$ bond. We enforced a Lewis structure with Mg—$C_{9,10}$ bonds. The polarization of the Mg—$C_{9,10}$ bonds was 6.8% at Mg and 93.2% at $C_{9,10}$. This result shows that covalent contributions to the Mg—$C_{9,10}$ bonds are indeed negligible.

We calculated the NMR chemical shifts of the complex **1**, anthracene (**5**), and anthracene dianion ($\mathbf{5}^{2-}$) at the optimized (planar) geometry and with the frozen geometry taken from **1**. The latter form is 15.3 kcal/mol (MP2/3-21G(*)) higher in energy than the planar form. The calculated and experimental ^{13}C chemical shifts of the THF complex are shown in Table 5.

Table 2. Geometry data of structures **1–8** at the MP2/3-21G(*) level of theory. Bond distances in angstrom, bond angles in degrees, folding angle τ in degrees. Experimental values for the THF complexes are given in parentheses.

Structure	Symmetry	Mg—$C_{9,10}$	C_9-Mg-C_{10}	Mg—O_1	Mg—$O_{2,3}$	C_1—C_2	C_2—C_3	C_1—C_{11}	C_9—C_{11}	C_{11}—C_{12}	τ[c]	Ref.
1	C_{2v}	2.219	76.1	2.005	2.132	1.413	1.407	1.412	1.497	1.443	47.3; 38.2	
		(2.25–2.33)	(70.9–71.9)	(2.059–2.065)	(2.028–2.091)	(1.330–1.403)	(1.362–1.396)	(1.365–1.402)	(1.465–1.487)	(1.414–1.428)	(26.6–30.6)	5*a*[d]
2	C_s	2.215[a]–2.212[b]	76.8	2.003	2.137	1.414	1.405	1.415	1.499	1.446	47.3; 37.9	
3	C_{2v}	2.207	77.5	2.003	2.138	1.414	1.403	1.414	1.498	1.449	48.3; 39.4	
4	C_{2v}	2.217	76.7	2.006	2.118	1.413	1.406	1.414	1.499	1.446	45.8; 36.4	
		(2.215–2.222)	(78.1)	(2.013–2.015)		(1.368–1.384)	(1.373–1.383)	(1.398–1.407)	(1.471–1.491)	(1.425–1.428)	(41.2)	5*c*[e]
		(2.233–2.234)	(78.2)	(1.997–2.021)		(1.380–1.407)	(1.377–1.391)	(1.374–1.405)	(1.498–1.509)	(1.430–1.442)	(45.0)	5*b*[e]
5	D_{2h}					1.379	1.438	1.442	1.410	1.453		
						(1.352–1.357)	(1.418)	(1.427)	(1.393–1.398)	(1.437)		18
$\mathbf{5}^{2-}$	D_{2h}					1.428	1.401	1.430	1.430	1.472		
6	C_s					1.380	1.435	1.445	1.423	1.455		
7	C_{2v}					1.378	1.431	1.445	1.420	1.458		
8	C_{2v}					1.378	1.430	1.445	1.430	1.458		

[a]Mg—C_9.

[b]Mg—C_{10}.

[c]Folding angle at the anthracene moiety along the C_9–C_{10} line. The two calculated values refer to two different definitions of τ. The first value τ_1 is given by the midpoint of C_{13}-C_{14}, C_9-C_{10}, C_{11}-C_{12}. The second value τ_2 is given by C_5-C_8, C_9-C_{10}, C_1-C_4.

[d]Magnesiumanthracene·3 THF.

[e]Magnesium-9,10-bis-trimethylsilylanthracene·2 THF.

Table 3. Results of the topological analysis of the electron density distribution at the MP2/3-21G(*) level of theory[a]

Structure	Bond	$\rho(r_b)$	$\nabla^2\rho(r_b)$	H_b	R_{ab}	Δr_{ab}
1	Mg—$C_{9,10}$	0.257	5.854	0.050	2.219	0.902
	C_9—C_{10}	0.166	1.365	−0.027	2.735	1.435
	C_9—C_{11}	1.582	−13.013	−1.471	1.497	0.703
	C_1—C_2	1.874	−18.275	−1.976	1.413	0.600
	Mg—O_1	0.268	10.015	0.105	2.005	0.869
	Mg—$O_{2,3}$	0.215	7.488	0.087	2.132	0.894
2	Mg—C_9	0.264	6.007	0.049	2.215	0.899
	Mg—C_{10}	0.259	5.938	0.051	2.212	0.901
	C_9—C_{10}	0.167	1.277	−0.039	2.750	1.457
	Mg—O_1	0.271	10.068	0.105	2.003	0.869
	Mg—$O_{2,3}$	0.213	7.384	0.086	2.137	0.895
3	Mg—$C_{9,10}$	0.267	6.113	0.049	2.207	0.898
	C_9—C_{10}	0.169	1.200	−0.034	2.763	1.460
	Mg—O_1	0.271	10.056	0.105	2.003	0.869
	Mg—$O_{2,3}$	0.213	7.342	0.086	2.138	0.896
4	Mg—$C_{9,10}$	0.255	5.920	0.050	2.217	0.902
	C_9—C_{10}	0.179	1.493	−0.030	2.750	1.424
	Mg—O_1	0.269	9.916	0.104	2.006	0.870
	Mg—$O_{2,3}$	0.223	7.704	0.087	2.118	0.891

[a]Electron density at the bond critical point $\rho(r_b)$ (e/Å^3), energy density at the bond critical point H_b (hartree/Å^3), Laplacian at the bond critical point $\nabla^2\rho(r_b)$ (e/Å^5), bond distance R_{ab} (Å), distance of the bond critical point for the bond A—B from atom A Δr_{ab} (Å).

The theoretically predicted ^{13}C resonance signals for **5** are in very good agreement with experiment. For the ^{13}C signals of $C_{9,10}$ of the dianion $\mathbf{5}^{2-}$ the calculations predict a shift towards higher field by 61.4 ppm, from 126.6 ppm to 65.2 ppm (Table 5). This is in reasonable agreement with the experimentally observed shift from 126.2 ppm for **5** to 75.1 ppm for Li_2[anthracene]. It should be noted that the latter compound is taken as reference for free $\mathbf{5}^{2-}$, although the structure of the compound is not known. The HF/GIAO calculation for $\mathbf{5}^{2-}$ using the folded geometry of the anthracene moiety of **1** gives a surprising result. The calculations predict that the ^{13}C signals of the planar and folded anthracene dianion are nearly the same (Table 5). A particularly surprising result is the calculated resonances for $C_{9,10}$. Although the charge distribution and the C—C bond lengths of $C_{9,10}$ are clearly different between the planar equilibrium geometry $\mathbf{5}^{2-}$ and in the complex **1**, the ^{13}C signals differ only by 1.1 ppm (Table 5). We want to point out that previous theoretical analyses of the correlation between the electronic structure and the NMR chemical shifts of numerous molecules suggest that *there is generally no correlation between partial charges and NMR resonances* (20). The chemical shift is very sensitive to the electronic structure of the molecule and there are many factors that can strongly influence the position of the NMR resonance. There seems to be a fortuitous cancellation of the diamagnetic and paramagnetic contributions to the ^{13}C resonances of $C_{9,10}$ that leads to nearly identical values for planar and folded $\mathbf{5}^{2-}$.

The HF/GIAO calculations for the ^{13}C signals of $C_{9,10}$ predict a further shift, by 24.5 ppm, towards higher field from planar $\mathbf{5}^{2-}$ to **1** (Table 5). This is in agreement with the experimentally observed high-field shift of 17.4 ppm from 75.1 ppm for $\mathbf{5}^{2-}$ to 57.7 ppm for **1**. Thus, the calculated ^{13}C signals for the compounds given in Table 5 reproduce the experimentally observed resonances quite well.

Summary

The ab initio calculations at the MP2/3-21G(*) level of theory predicted for the magnesium–anthracene complexes **1**–**4** are in very good agreement with X-ray structure analyses of the related THF complexes. Inspection of the electronic structure of the complexes using topological analysis of the electron density distribution and its associated Laplacian shows clearly that the Mg—$C_{9,10}$ bonds should be considered as purely ionic. This follows from the Laplacian distribution of the compounds and the calculated values for the charge density and energy density at the Mg—$C_{9,10}$ bond critical points. An ionic character of the Mg—$C_{9,10}$ bonds is also suggested by the NBO analysis, which gives a Lewis structure with two lone pairs at C_9 and C_{10} and no Mg—C bonds. The NBO calculations predict that the partial charge of the anthracene moiety is nearly −2. The HF/GIAO calculations give ^{13}C NMR signals for the magnesium–anthracene complex **1**, anthracene, and anthracene dianion that are in good agreement with experimental values.

Acknowledgments

It is a pleasure to acknowledge continuous support by the Bader group in providing the programs for the topological analysis of the electron density distribution. This work has been supported by the Deutsche Forschungsgemeinschaft (SFB 260-D19 and Graduiertenkolleg Metallorganische Chemie) and by the Fonds der Chemischen Industrie. Excellent services by the computer centers HRZ Marburg, HRZ Giessen, HHLRZ Darmstadt, and KFA Jülich are gratefully acknowledged.

Table 4. NBO results for the partial charges q, Mg—$C_{9,10}$ bond orders P_{AB},[a] and hybridization of $C_{9,10}$ at the MP2/3-21G(*) level of theory.

	q								P_{AB}	Hybridization			
										$C_{9,10}$–C_{11}		C_9(lp)	
Structure	Mg	C_9	C_{10}	C_1	C_2	C_{11}	O_1	$O_{2,3}$	$Mg(H_2O)_3$	Mg—$C_{9,10}$	%s ($C_{9,10}$)	%p ($C_{9,10}$)	%s	%p
1	+1.50	−0.75	−9.75	−0.28	−0.26	−0.06	−0.93	−0.94	+1.67	0.19	34.2	65.9	1.9	98.1
2	+1.52	−0.53	−0.74	−0.29	−0.26	−0.06	−0.93	−0.94	+1.68	0.17[c]	33.8[c]	66.2[c]	1.3[c]	98.7[c]
										0.19[d]	34.1[d]	65.9[d]	1.9[d]	98.1[d]
3	+1.53	−0.53	−0.53	−0.29	−0.26	−0.05	−0.93	−0.94	+1.69	0.17	33.8	66.2	1.3	98.7
4	+1.61	−0.99	−0.99	−0.27	−0.26	−0.04	−0.94	−0.94	+1.78	0.11	31.4	68.7	1.0	99.0
5		−0.17	−0.17	−0.20	−0.23	−0.06					35.0	65.0	No lone pair	
5^{2-}		−0.40	−0.40	−0.35	−0.32	−0.04					35.8	64.2	0.0	100.0
5^{2-} (folded)[b]		−0.46	−0.46	−0.31	−0.31	−0.05					35.4	64.6	0.5	99.5

[a]Atom–atom overlap-weighted NBO bond order.
[b]Using the frozen geometry of the anthracene ligand of **1**.
[c]C_9.
[d]C_{10}.

Table 5. Calculated (HF/GIAO) and experimental ^{13}C NMR chemical shifts δ_C (ppm) of **1**, **5**, and $\mathbf{5}^{2-}$. Experimental values are given in parentheses.

	δ_C				
Structure	C_1	C_2	C_9	C_{11}	Ref.
1	117.6	122.6	40.7	157.3	
	(114.1)	(118.1)	(57.7)	(145.9)	3*f*
5	129.7	126.2	126.6	135.8	
	(128.1)	(125.3)	(126.2)	(131.7)	19
$\mathbf{5}^{2-}$	101.0	104.6	65.2	167.9	
	(101.1)	(114.2)	(75.1)	(150.0)	6*a*
$\mathbf{5}^{2-}$ (folded)[a]	105.3	106.6	66.3	169.1	

[a]Using the frozen geometry of the anthracene ligand of **1**.

References

1. H.E. Ramsden. U.S. Patent 3 354 190, 1967; Chem. Abstr. **68**, 114744 (1968).
2. B. Bogdanovic, S. Liao, M. Schwickardi, P. Sikorsky, and B. Spliethoff. Angew. Chem. Int. Ed. Engl. **19**, 818 (1980).
3. (*a*) B. Bogdanovic. Angew. Chem. Int. Ed. Engl. **24**, 262, (1985); (*b*) B. Bogdanovic, N. Janke, C. Krüger, K. Schlichte, and J. Treber. Angew. Chem. Int. Ed. Engl. **26**, 1025 (1987); (*c*) B. Bogdanovic, N. Janke, C. Krüger, R. Mynott, K. Schlichte, and U. Westeppe. Angew. Chem. Int. Ed. Engl. **24**, 960 (1985); (*d*) B. Bogdanovic, K. Schlichte, and U. Westeppe. Chem. Ber. **121**, 27 (1988); (*e*) B. Bogdanovic, N. Janke, H.-G. Kinzelmann, and U. Westeppe. Chem. Ber. **121**, 33 (1988); (*f*) B. Bogdanovic,, S.-t. Liao, R. Mynott, K. Schlichte, and U. Westeppe. Chem. Ber. **117**, 1378 (1984); (*g*) B. Bogdanovic,, N. Janke, and H.-G. Kinzelmann. Chem. Ber. **123**, 1507 (1990); (*h*) B. Bogdanovic, N. Janke, H.-G. Kinzelmann, K. Seevogel, and J. Treber. Chem. Ber. **123**, 1529 (1990); (*i*) B. Bogdanovic. Acc. Chem. Res. **21**, 261 (1988), and further references cited therein.
4. (*a*) S. Harvey, P.C. Junk, C.L. Raston, and G. Salem. J. Org. Chem. **53**, 3134 (1988); (*b*) M.J. Gallagher, S. Harvey, C.L. Raston, and R.E. Sue. J. Chem. Soc. Chem. Commun. 289 (1988); (*c*) S. Harvey and C.L. Raston. J. Chem. Soc. Chem. Commun. 652 (1988); (*d*) S. Itsuno, G.D. Darling, H.D.H. Stöver, and J.M.J. Fréchet. J. Org. Chem. **52**, 4644 (1987).
5. (*a*) L.M. Engelhardt, S. Harvey, C.L. Raston, and A.H. White. J. Organomet. Chem. **341**, 39 (1988); (*b*) H. Lehmkuhl, A. Shakoor, K. Mehler, C. Krüger, K. Angermund, and Y.-H. Tsay. Chem. Ber. **118**, 4239 (1985); (*c*) T. Alonso, S. Harvey, P.C. Junk, C.L. Raston, B.W. Skelton, and A.H. White. Organometallics, **6**, 2110 (1987).
6. (*a*) K. Müllen. Helv. Chim. Acta, **59**, 1357 (1976); (*b*) V.I. Mamatyuk and V.A. Koptyuk. Zh. Org. Khim. **13**, 818 (1977).
7. R.F.W. Bader. Atoms in molecules: a quantum theory. Oxford University Press, Oxford. 1990.
8. A.E. Reed, L.A. Curtiss, and F. Weinhold. Chem. Rev. **88**, 899 (1988).
9. (*a*) C. Møller and M.S. Plesset. Phys. Rev. **46**, 618 (1934); (*b*) J.S. Binkley and J.A. Pople. Int. J. Quantum Chem. **9**, 229 (1975).
10. (*a*) J.S. Binkley, J.A. Pople, and W.J. Hehre. J. Am. Chem. Soc. **102**, 939 (1980); (*b*) M.S. Gordon, J.S. Binkley, J.A. Pople, W.J. Pietro, and W.J. Hehre. J. Am. Chem. Soc. **104**, 2797 (1982); (*c*) W.J. Pietro, M.M. Francl, W.J. Hehre, D.J. Defrees, J.A. Pople, and J.S. Binkley. J. Am. Chem. Soc. **104**, 5039 (1982); (*d*) W.J.

Hehre, R. Ditchfield, and J.A. Pople. J. Chem. Phys. **56**, 2257 (1972); (*e*) P.C. Hariharan and J.A. Pople. Theor. Chim. Acta, **28**, 213 (1973); (*f*) M.S. Gordon. Chem. Phys. Lett. **76**, 163 (1980).
11. J.J.P. Stewart. J. Comput. Chem. **10**, 209, 221 (1989).
12. (*a*) M. Häser and R. Ahlrichs. J. Comput. Chem. **10**, 104 (1989); (*b*) R. Ahlrichs, M. Bär, M. Häser, H. Horn, and C. Kölmel. Chem. Phys. Lett. **162**, 165 (1989); (*c*) H. Horn, H. Weiß, M. Häser, M. Ehrig, and R. Ahlrichs. J. Comput. Chem. **12**, 1058 (1991); (*d*) M. Häser, J. Almlöf, and M.W. Feyereisen. Theor. Chim. Acta, **79**, 115 (1991).
13. (*a*) R. Ditchfield. Mol. Phys. **27**, 789 (1974); (*b*) K. Wolinski, J.F. Hinton, and P. Pulay. J. Am. Chem. Soc. **112**, 8251 (1990); (*c*) M. Häser, R. Ahlrichs, H.P. Baron, P. Weiss, and H. Horn. Theor. Chim. Acta, **83**, 455 (1992).
14. (*a*) T.H. Dunning. J. Chem. Phys. **66**, 1382 (1977); (*b*) S. Huzinaga. Approximate atomic wave functions. University of Alberta, Edmonton, Alberta. 1971.
15. F.W. Biegler-König, R.F.W. Bader, and T.J. Ting-Hua. J. Comput. Chem. **3**, 317 (1982).
16. M.J. Frisch, G.W. Trucks, M. Head-Gordon, P.M.W. Gill, M.W. Wong, J.B. Foresman, H.B. Schlegel, K. Raghavachari, M.A. Robb, J.S. Binkley, C. Gonzalez, R. Martin, D.J. Fox, D.J. DeFrees, J. Baker, J.J.P. Stewart, and J.A. Pople. Gaussian 92, Revision C. Gaussian Inc., Pittsburg, Pa. 1992.
17. D. Cremer and E. Kraka. Angew. Chem. Int. Ed. Engl. **23**, 62 (1984).
18. V.I. Ponomarev and G.V. Shilov. Kristallografiya, **28**, 674 (1983).
19. I.I. Schuster. J. Org. Chem. **46**, 5110 (1981).
20. W. Kutzelnigg, U. Fleischer, and M. Schindler. NMR: Basic Princ. Prog. **23**, 165 (1990).
21. A.W. Ehlers, S. Dapprich, S.F. Vyboishchikov, and G. Frenking. Organometallics. **15**, 105 (1996).

The 1,2,3,5-ditelluradiazolyl [HCN_2Te_2] species. Theoretical characterizations of the cation, radical, and radical dimers

William M. Davis and John D. Goddard

Abstract: Dithia- and diselena-diazolyl radicals (HCN_2E_2 E = S, Se) and dimers are important building blocks in the design of low-dimensional molecular conductors. Research on the tellurium-based analogues is much rarer. This work reports the molecular and electronic structures of the cation, radical, and radical dimers of 1,2,3,5-ditelluradiazolyl using ab initio theory including electron correlation by Møller–Plesset perturbation theory up to partial fourth order (MP4SDQ). A face-to-face C_{2v} dimer is predicted to be bound with respect to two radicals by approximately 18 kcal/mol. A C_{2h} dimer also has been studied and is ca. 2 kcal/mol less stable than the C_{2v} conformer. Relaxing symmetry constraints on the dimers led to more energetically stable structures at the Hartree–Fock level but the C_{2v} structure remains the most stable at a level of theory including electron correlation effects. The results for the Te compounds along with our earlier research on the S and Se analogues provide predictions for the geometries, vibrational frequencies, and ionization potentials for the Te species to assist in future experiments.

Key words: tellurium, ab initio, ditelluradiazolyl, dimers, binding.

Résumé : Les radicaux dithia- et disélénadiazolyles (HCN_2E_2, E = S, Se) et leurs dimères sont des blocs de construction importants dans le développement de conducteurs moléculaires de faibles dimensions. Des recherches sur des analogues ayant le tellure comme base sont beaucoup plus rares. Dans ce travail, on a calculé les structures moléculaires et électroniques du cation, du radical et des radicaux dimères du 1,2,3,5-ditelluradiazolyle en utilisant la théorie ab initio, y compris la corrélation d'électrons par la théorie des perturbations de Møller–Plesser jusqu'au quatrième ordre partiel (MP4SDQ). Il est prévu qu'un dimère face à face C_{2v} sera lié par environ 18 kcal/mol par rapport aux deux radicaux. On a aussi étudié un dimère C_{2h} et il est moins stable que le conformère C_{2v} par environ 2 kcal/mol. Au niveau de Hartree–Fock, des contraintes de symétrie de relaxation appliquées aux dimères ont conduit à des structures énergétiquement plus stables, mais la structure C_{2v} demeure la plus stable à un niveau de la théorie qui inclut les effets de corrélation d'électrons. Les résultats pour les composés du Te en relation avec nos études antérieures sur les analogues du S et du Se conduisent à des prédictions au sujet des géométries, aux fréquences vibrationnelles et aux potentiels d'ionisation des espèces du Te qui pourront aider dans des expériences futures.

Mots clés : tellure, ab initio, ditelluradiazolyle, dimères, fixation.

[Traduit par la rédaction]

Introduction

Much research on molecular conductors is based on the use of charged π-radicals, either in the form of charge transfer salts such as TTF-TCNQ (tetrathiafulvalene-tetracyano *p*-diquinodimethane) or radical ion salts such as those based on the TMTSF (tetramethyltetraselenafulvalene) and TTF donors (1). An alternative approach involves the use of neutral rather than charged radicals. Interest in the development of molecular conductors based on these neutral π-radicals has driven recent experimental and theoretical studies of various heterocyclic thiazyl and selenazyl radicals. In particular, derivatives of 1,2,3,5-dithia- and 1,2,3,5-diselenadiazolyl [RCN_2E_2]·**1b** represent "building blocks" (2) that, in the solid state, adopt stacked structures with nearly equal monomer–monomer distances. As with any one-dimensional structure with a half-filled electronic band, these stacked radicals are prone to a Peierls instability, i.e., a tendency to dimerize (3).

This paper presents theoretical studies of the tellurium radicals, **1b**, their dimers, and the corresponding cations, **1a**. It represents a continuation of our theoretical examination of the dichalcogen diazolyl system HCN_2E_2 (E = S, Se, Te). Our earlier results on the S and Se analogues were in good agreement with available experimental data (4).

Our theoretical approach to these main group heterocycles concerns itself with the prediction of the geometries of the radical dimers to suggest possible solid state structures. In addition, the binding energy of the dimer with respect to the

Received November 21, 1995.

This paper is dedicated to Professor Richard F.W. Bader on the occasion of his 65th birthday.

W.M. Davis and J.D. Goddard.[1] Guelph–Waterloo Centre for Graduate Work in Chemistry, Department of Chemistry and Biochemistry, University of Guelph, Guelph, ON N1G 2W1, Canada.

[1] Author to whom correspondence may be addressed. Telephone: (519) 824-4120, ext. 3102. Fax: (519) 824-7771. E-mail: jgoddard@uoguelph.ca

monomeric radical (4) is of interest. The predicted vibrational and photoelectron spectra (2) should aid in the eventual experimental characterization of the tellurium compound.

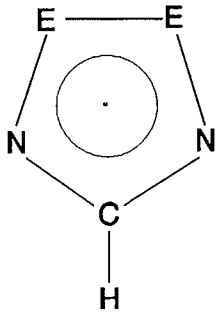

E = S, Se, or Te

1a = +, **1b** = ·

Computational methods

All-electron Hartree–Fock results were obtained using Gaussian 90 (5) or Gaussian 92 (6). The split valence 3-21G* basis set encoded into the program for carbon, nitrogen, and hydrogen was used. The 3-21G* basis set for tellurium was taken from Dobbs and Hehrey (7) and Huzinagay (8) and includes six *d*-type polarization functions.

The effective core potential Hartree–Fock predictions also were performed with Gaussian 90 (5) and Gaussian 92 (6). For tellurium, relativistic effective core potentials (RECPs) were chosen along with energy-optimized shared exponent valence Gaussian basis sets. The RECPs had been generated from relativistic Dirac–Fock atomic orbitals, rather than standard Hartree–Fock orbitals as is the case for the ECPs for the first and second row atoms. The Hay–Wadt LANL1DZ basis set (9) encoded within the Gaussian 90 and 92 programs was chosen. This basis set employs a full split-valence basis set for the first row elements (e.g., C, N) and a {core} plus six valence electron representation for tellurium. To augment this basis set, a set of six Cartesian *d*-type polarization functions was added to tellurium. In these core potential calculations, the exponents for the six *d* polarization functions for tellurium were taken from Jaisen and Stevens (10). This augmented basis set will be referred to as LANL1DZ*.

Stationary points at the SCF level were found using energy gradient methods and the geometry optimization algorithms of Schlegel (11) and Baker (12). The nature of these stationary points was confirmed by determining the SCF harmonic vibrational frequencies using analytical second-derivative methods for the all-electron approach and numerical differences of analytical first derivatives for the core potential based methods. The SCF harmonic vibrational frequencies were scaled (13) by 0.90 when used as predictions of the experimental anharmonic frequencies. This empirical reduction of double-zeta or larger basis set SCF vibrational frequencies by approximately 10% is well established (13).

Electron correlation effects on relative energies were included in the all-electron and effective core potential calculations using Møller–Plesset perturbation theory (14) to second (MP2), third (MP3), and partial fourth order (including single, double, and quadruple excitations (MP4SDQ)). Disk space limitations prohibited an extension to full fourth order, i.e., MP4SDTQ.

Fig. 1. Optimized geometries for the ditelluradiazolium cation from closed shell Hartree–Fock theory.

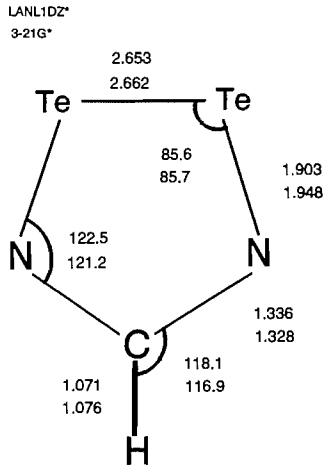

Results and discussion

This study predicts the properties and structures of the prototypal 1,2,3,5-ditellura radical **1b** and cation **1a** at levels comparable to our earlier study of the sulfur and selenium heterocycles (4). These earlier predictions were in good agreement with available experiments (4). Theoretical studies of the isolated dimers also provide a first step towards understanding the associated dimers in any solid state structure that might be adopted by the ditelluradiazolyl radical.

Geometries

Optimized geometries of the ditelluradiazolium cation

The optimized geometries of this closed shell cation in its $^1A_1$ ground electronic state are shown in Fig. 1. The effects of basis set were tested by comparing the all-electron 3-21G* geometry with the effective core potential LANL1DZ* structure. These differences are rather small, the largest being the Te—Te distance, which varies by about 3% from the all-electron result, changing from 2.662 Å (3-21G*) to 2.653 Å (LANL1DZ*). The Te—N distances change from 1.948 Å with the all-electron method to 1.903 Å with the core potential. These slight changes in geometry may be due to the relativistic parametrization of the effective core potential basis set for Te (9).

The structural changes that accompany ionization of the $^2A_2$ radical **1b** to the $^1A_1$ cation **1a** are of relevance to photoelectron spectroscopy. These geometry changes can all be related to the bonding/antibonding properties of the a_2 singly occupied molecular orbital (SOMO, **2**). This orbital is both Te—N and Te—Te antibonding within the five-membered ring. Accordingly, the Te—Te and Te—N bond distances of the radical are shortened significantly upon ionization. To a first approximation, the removal of an electron from the a_2 SOMO should not affect the C—N distances as the carbon atom lies in a nodal plane. Ionization of **1b** nonetheless produces a small increase in the C—N distance within the ring. There have been

Fig. 2. Optimized geometries for the ditelluradiazolyl radical with the unrestricted Hartree–Fock model.

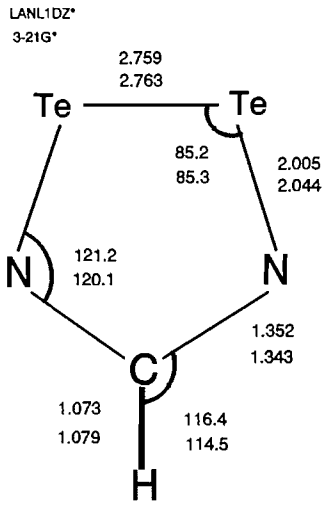

Fig. 3. Optimized geometries for the C_{2v} conformation of the ditelluradiazolyl dimer.

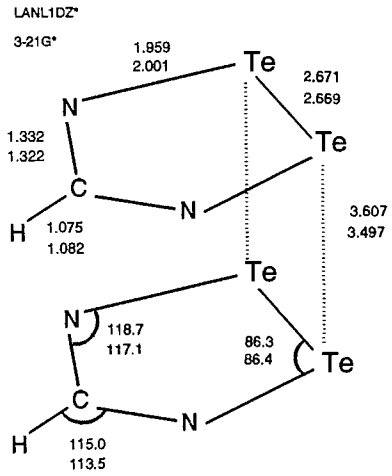

no experimental studies to date on the Te containing cation or on closely similar compounds. There clearly would be difficulties in obtaining sufficient vapor pressure of the tellurium compound to obtain a gas phase photoelectron spectrum.

Optimized geometries of the ditelluradiazolyl radical and dimers

To assess the geometrical changes upon dimerization of the radicals, optimized structures of both the isolated radicals and their corresponding dimers were determined. The radicals were restricted to C_{2v} symmetry to reduce the computational burden. However, checks of this restriction were made by predicting the harmonic vibrational frequencies. Further discussion is given below and it is simply noted here that the C_{2v} monomer is a minimum energy structure at the UHF level. Two conformations were considered for the dimers, the "face-to-face" C_{2v} and "back-to-back" C_{2h} structures. For the dimers the C_{2v} and C_{2h} symmetry constraints were relaxed in order to assess the energetic stabilization that might occur with the removal of symmetry constraints. The monomer rings themselves were constrained to be overall planar in all the dimer calculations. The conformations of the dimers and any symmetry restrictions were chosen with reference to the experimentally observed X-ray crystallographic structures of the sulfur and selenium diazolyl dimers (4).

For the predicted structures, the agreement between the two basis sets at the Hartree–Fock level is very good. Figure 2 presents the UHF optimized geometries of the ditelluradiazolyl radical. The results for this radical (2.76 Å (Te—Te), 2.01–2.04 Å (Te—N), and 1.34–1.35 Å (N—C)) can be used as a prediction for future gas phase experiments on the structure of this compound. A rough comparison of the Te—N bond distance with some recently available experimental results (Te—N = 1.918 Å (15), Te—N = 1.966 Å (16)) can be made. These comparisons are only approximate as the available experimental results are for rather different compounds (15, 16). (Spin contamination in the UHF treatment of the radicals might have geometrical consequences. The value of S^2 for the Te radical with the 3-21G* basis was 1.044 while the proper value for a pure doublet is 0.75. However, the major effect as revealed by

Fig. 4. Optimized geometries for the C_{2h} conformation of the ditelluradiazolyl dimer.

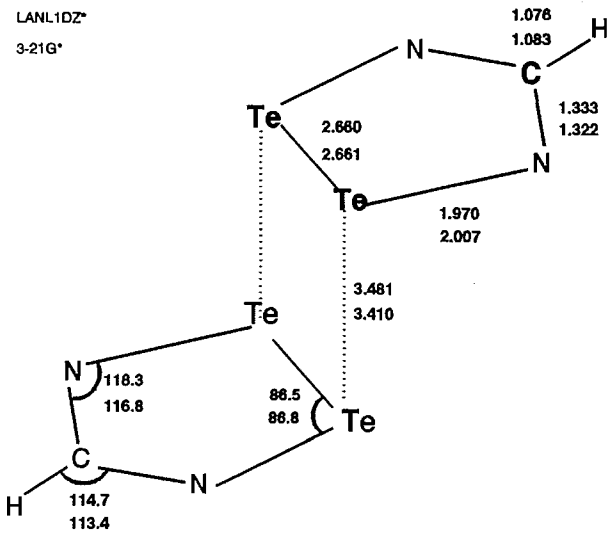

restricted open shell studies on a structure constrained to have C_{2v} symmetry (of Fig. 7) is to shorten the distances in the rings slightly. The C—N distance decreases from 1.34 to 1.32 Å comparing the UHF and ROHF structures of the radical.) It is interesting to speculate how the inclusion of electron correlation by Møller–Plesset perturbation theory or in a density functional model would change the radical geometries. Preliminary results[2] with a core potential plus split valence polarized basis set and the B3LYP approach predicted r(Te–Te) = 2.725 Å, r(Te–N) = 1.986 Å, and r(C–N) = 1.351 Å within 1% agreement with the Hartree–Fock results shown in Fig. 2. Electron correlation does not appear to be affecting the geometry qualitatively.

[2] W.M. Davis. To be published.

Fig. 5. Optimized geometries for the distorted C_{2v} conformation of the ditelluradiazolyl dimer.

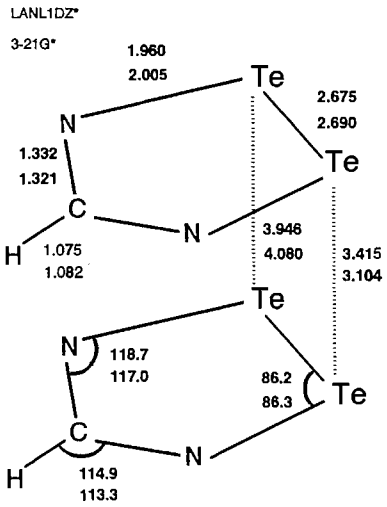

Fig. 6. Optimized geometries for the distorted C_{2h} conformation of the ditelluradiazolyl dimer.

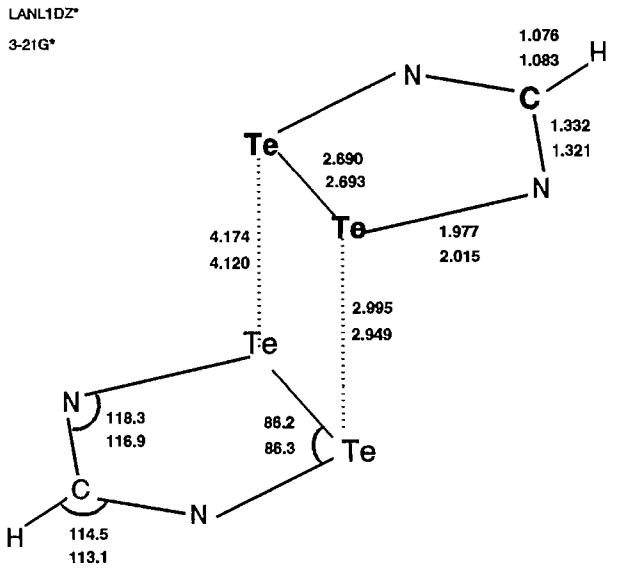

Fig. 7. Results for the geometries and the relative energies of the C_{2v} and C_s forms of the ditelluradiazolyl radical at the restricted open shell Hartree–Fock level of theory.

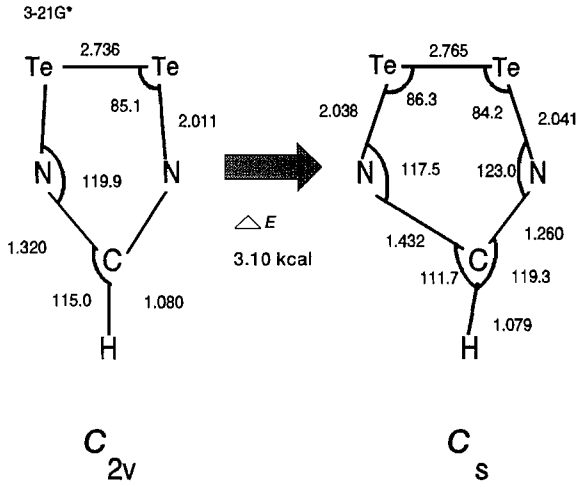

Table 1. Hartree–Fock vibrational frequencies[a] for the ditelluradiazolium cation.

Mode	(Intensity)[b]	LANL1DZ*	3-21G*
a_2	(0)	202	215
a_1	(0.1)	270	260
b_2	(5.3)	292	282
b_1	(44)	508	511
a_1	(3)	584	599
b_2	(125)	596	610
a_1	(10)	723	731
b_1	(7.8)	964	986
b_2	(123)	1128	1084
a_1	(33)	1247	1211
b_2	(9.5)	1315	1319
a_1	(9.2)	3100	3029

[a]All SCF harmonic vibrational frequencies were scaled by 0.90.
[b]The reported IR intensities are the average of the two computed values (in km/mol) with the two basis sets.

The theoretical structures of the tellurium dimer are more complex and are summarized in Figs. 3–6. As the Te—N antibonding a_2 singly occupied molecular orbital (SOMO) **2** of the radical is involved in the dimerization, the individual rings have reduced antibonding character upon dimerization. Consequently, the Te—N distances shorten slightly, as do the intramolecular Te—Te bond lengths. For the C_{2v} and C_{2h} structures, the distance between the rings is predicted to be in the range 3.5–3.6 Å. With the B3LYP method and a core potential plus split valence polarized basis set, the interannular distance is predicted to be 3.525 Å, which is qualitatively similar to that found at the Hartree–Fock level. When symmetry constraints are relaxed, the dimer adopts a "short–long" structure with two rather different interannular distances as shown in Figs. 5 and 6. In all cases, the monomer retains its essential structure within the dimers as revealed by very limited changes in the bond lengths and bond angles upon dimerization. For tellurium, which has a van der Waals radius of ca. 2.06 Å (17), the monomer–monomer distance is significantly shorter than twice this van der Waals radius in both the C_{2v} and C_{2h} dimers. The lower symmetry dimers have one Te—Te distance that is approximately twice the van der Waals radii of tellurium. These lower symmetry dimers appear to have adopted a structure with only one significant interannular Te–Te interaction.

Restricted open shell Hartree–Fock (ROHF) results

ROHF studies on the radicals were carried out with this version of the Hartree–Fock method and showed that the C_{2v} structure was not a minimum. A distortion to C_s symmetry was energetically favourable (see Fig. 4). This situation is reminiscent of the doublet instability problem, the most

Table 2. Hartree–Fock vibrational frequencies[a] for the ditelluradiazolyl radical.

Mode	(Intensity)[b]	LANL1DZ*	3-21G*
a_2	(0)	156	147
a_1	(0.1)	186	197
b_2	(11)	254	247
b_1	(25)	401	409
a_1	(0.8)	448	471
b_2	(37)	495	516
a_1	(0)	703	713
b_1	(7)	848	869
b_2	(0.8)	1086	999
a_1	(15)	1118	1087
b_2	(0.6)	1311	1320
a_1	(11)	3051	2981

[a]All SCF harmonic vibrational frequencies were scaled by 0.90.
[b]The reported IR intensities are the average of the two computed values (in km/mol) with the two basis sets.

Table 3. Hartree–Fock vibrational frequencies[a] for the C_{2v} ditelluradiazolyl dimer.

Mode	(Intensity)[b]	LANL1DZ*	3-21G*
b_1	(3.3)	43i	66i
a_2	(0)	26	20
b_2	(0.2)	64	47
a_1	(0)	69	59
a_2	(0)	59	65
a_1	(0)	73	84
b_1	(0.1)	195	176
b_2	(16)	194	208
a_2	(0)	221	209
a_1	(0.2)	199	215
b_1	(17)	270	264
a_2	(0)	275	266
b_2	(2.3)	454	453
a_1	(1.2)	476	473
b_2	(271)	490	503
a_1	(0.1)	515	528
b_1	(94)	540	555
a_2	(0)	539	555
b_2	(72)	739	760
a_1	(0.5)	744	764
b_2	(3.8)	967	978
a_1	(0)	968	983
b_2	(193)	1183	1145
a_1	(17)	1193	1156
b_1	(46)	1243	1236
a_2	(0)	1276	1277
b_1	(1.6)	1311	1305
a_2	(0)	1338	1315
b_2	(39)	3044	2953
a_1	(9.2)	3046	2957

[a]All SCF harmonic vibrational frequencies were scaled by 0.90.
[b]The reported IR intensities are the average of the two computed values (in km/mol) with the two basis sets.

Table 4. Hartree–Fock vibrational frequencies[a] for the C_{2h} ditelluradiazolyl dimer.

Mode	(Intensity)[b]	LANL1DZ*	3-21G*
a_u	(5)	74i	90i
a_u	(1)	27	20i
a_u	(1)	36	38
a_g	(0)	56	62
a_g	(0)	63	64
a_g	(0)	107	111
a_g	(0)	188	186
a_u	(0)	196	190
a_u	(20)	197	210
a_g	(0)	203	219
a_u	(19)	268	263
a_g	(0)	271	265
a_u	(3)	450	457
a_g	(0)	469	468
a_u	(263)	479	497
a_g	(0)	501	520
a_g	(0)	531	552
a_u	(83)	534	554
a_u	(47)	745	765
a_g	(0)	748	768
a_u	(7)	972	984
a_g	(90)	972	984
a_u	(260)	1177	1145
a_g	(0)	1184	1153
a_u	(78)	1260	1252
a_g	(0)	1272	1273
a_u	(0)	1316	1307
a_g	(0)	1328	1313
a_u	(62)	3034	2943
a_g	(0)	3034	2943

[a]All SCF harmonic vibrational frequencies were scaled by 0.90.
[b]The reported IR intensities are the average of the two computed values (in km/mol) with the two basis sets.

famous example being that of the allyl radical (18–21). This distortion at the ROHF level can be viewed as due to a second-order Jahn–Teller (SOJT) effect. The ROHF solution isolates two geometries that might be associated with the "resonance structures" but a C_{2v} minimum results when the spin restriction is released and UHF is employed. The energy difference between the C_s and C_{2v} structures is quite small (approximately 3 kcal/mol favoring the C_s forms) despite fairly significant changes in geometrical parameters such as the C—N bond lengths. These ROHF results suggest that the Te–N rings may distort easily.

Infrared and UV–photoelectron spectra

The theoretical infrared spectra of the cation and the radical are presented in Tables 1 and 2. As can be seen from the infrared intensities, only four bands of appreciable intensity are predicted at approximately $505(b_1)$, $605(b_2)$, $1110(b_2)$, and $1230(a_1)$ cm^{-1} for the cation. For the radical, three bands of appreciable intensity are predicted at approximately $405(b_1)$, $505(b_2)$, and $1100(a_1)$ cm^{-1}.

The theoretical spectra of the Te dimers are presented in

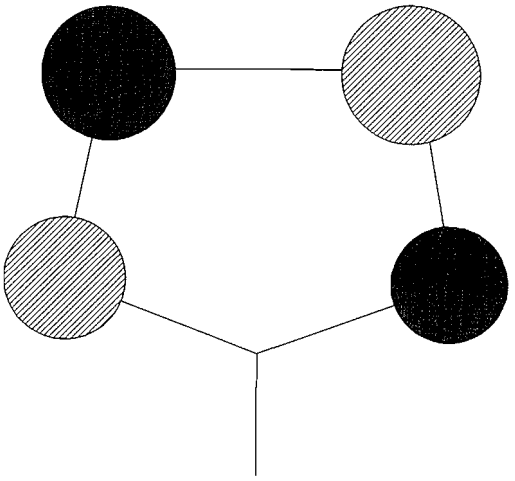

Table 5. Hartree–Fock vibrational frequencies[a] for the lower symmetry face-to-face ditelluradiazolyl dimer.

Mode	(Intensity)[b]	LANL1DZ*	3-21G*
a	(0)	39i	23i
a	(0)	23	30
a	(0)	58	57
a	(0)	64	61
a	(0)	69	67
a	(0)	71	92
a	(2)	192	196
a	(7)	195	196
a	(0)	198	201
a	(3)	219	201
a	(18)	271	263
a	(3)	274	263
a	(9)	451	446
a	(2)	474	465
a	(203)	487	490
a	(7)	512	509
a	(5)	538	550
a	(68)	539	552
a	(47)	739	760
a	(4)	744	765
a	(5)	967	977
a	(0)	968	981
a	(135)	1182	1141
a	(15)	1191	1148
a	(136)	1251	1273
a	(52)	1276	1279
a	(23)	1314	1310
a	(62)	1338	1314
a	(24)	3043	2949
a	(8)	3045	2952

[a]All SCF harmonic vibrational frequencies were scaled by 0.90.
[b]The reported IR intensities are the average of the two computed values (in km/mol) with the two basis sets.

Table 6. Hartree–Fock vibrational frequencies[a] for the lower symmetry back-to-back ditelluradiazolyl dimer.

Mode	(Intensity)[b]	LANL1DZ*	3-21G*
a	(2)	22i	20i
a	(1)	22	16
a	(1)	33	38
a	(0)	54	60
a	(0)	79	80
a	(0)	103	114
a	(4)	163	160
a	(0)	180	193
a	(6)	186	199
a	(1)	209	207
a	(19)	266	260
a	(2)	266	260
a	(24)	446	450
a	(0)	459	457
a	(147)	467	482
a	(5)	480	496
a	(5)	520	541
a	(63)	523	543
a	(22)	745	766
a	(2)	747	768
a	(7)	971	982
a	(0)	973	983
a	(109)	1174	1142
a	(0)	1178	1146
a	(50)	1275	1281
a	(145)	1276	1283
a	(38)	1331	1312
a	(84)	1339	1319
a	(41)	3030	2937
a	(0)	3031	2937

[a]All SCF harmonic vibrational frequencies were scaled by 0.90.
[b]The reported IR intensities are the average of the two computed values (in km/mol) with the two basis sets.

Table 7. Predicted photoelectron spectrum of the ditelluradiazolyl radical using the 3-21G* basis set (ionization potentials in eV).

Orbital	(Character)	Koopmans' IP[a]
a_2	(π)	7.08
b_1	(π)	9.24
a_1	(σ)	9.72
b_2	(σ)	10.94
a_1	(σ)	11.28
a_2	(π)	12.41
b_2	(σ)	13.82
b_1	(π)	14.92
a_1	(σ)	16.24

[a]Koopmans' ionization potentials were scaled by 0.92. The UHF α orbital eigenvalues were used.

Tables 3–6. In all cases, there exists one small imaginary frequency of less than 90i cm^{-1} that correlates with breaking of the ring's planarity, which was enforced in our study. The predicted infrared spectrum of the more stable C_{2v} structure indicates six intense peaks in the 300–3000 cm^{-1} region occurring at 495(b_2), 547(b_1), 750(b_2), 1165(b_2), 1240(b_1), and 3000(b_2) cm^{-1}.

The predicted photoelectron spectrum for the ditelluradia-

Table 8. Predicted total and binding energies[a] for the ditelluradiazolyl radical and dimers.

	Radical	C_{2v} Dimer	C_{2h} Dimer	Distorted C_{2v} dimer	Distorted C_{2h} dimer
Total energies					
LANL1DZ*					
HF	−162.976 49	−325.864 71	−325.868 09	−325.864 75	−325.870 95
MP2	−163.437 27	−326.969 97	−326.963 70	−326.967 28	−326.944 05
MP3	−163.453 93	−326.927 56	−326.926 51	−326.925 93	−326.915 78
MP4SDQ	−163.476 68	−326.978 16	−326.975 17	−326.977 77	−326.969 41
3-21G*					
HF	−13 313.0296	−26 625.9762	−26 625.9807	−26 625.9783	−26 625.9851
MP2	−13 313.5173	−26 627.1315	−26 627.1261	−26 627.1165	−26 627.1052
Binding energies (with ZPVE[b] correction)					
LANL1DZ*					
HF		−52.9	−50.8	−52.9	−49.0
MP2		+62.4	+58.4	+60.7	+46.1
MP3		+14.9	+14.2	+13.8	+7.5
MP4SDQ		+18.1	+16.2	+17.8	+12.6
3-21G*					
HF		−49.5	−46.7	−48.2	−46.5
MP2		+60.8	+57.4	+51.4	+44.3

[a]Binding energies in kcal/mol, total energies in atomic units (au). A positive binding energy indicates that the dimer is bound with respect to two radicals.

[b]ZPVE = zero point vibrational energy.

zolyl radical is presented in Table 7. Koopmans' theorem indicates that the first ionization potential will be lower than for the S or Se radicals and should appear at ca. 7.08 eV. The remaining Koopmans' thoerem predictions for the ionization energies in the range of 7 to 17 eV are at 9.24, 9.72, 10.94, 11.28, 12.41, 13.82, 14.92, and 16.24 eV. All these ionization energies are shifted about 1 eV to higher energy than the corresponding peaks predicted for the Se compound (4).

Energetics

The energetics of dimerization of the radicals proved very sensitive to the theoretical method employed (Table 8). As a radical recombination reaction, the SCF approach will not be quantitatively accurate, therefore electron correlation effects must be included (22). At a low order of Møller–Plesset perturbation theory (MP2) our earlier work (4) showed the C_{2v} sulfur dimer to be bound by ca. 42 kcal/mol and the C_{2v} selenium dimer by a larger amount, ca. 58 kcal/mol. At the same level of theory, the C_{2v} tellurium dimer is predicted to be bound by ca. 61 kcal/mol. These binding energies include the changes in zero point vibrational energies between the two radicals and the dimer. However, upon extending the theory to higher levels, namely to third (MP3) and partial fourth (MP4SDQ) order, the binding energies using the LANL1DZ* and 3-21G* basis sets change to ca. 6.4 and 4.0 kcal/mol (with the ZPVE correction included) for the sulfur species (4). Similar changes are observed for the diselena- and ditellura-diazolyl radical dimers. For the tellurium compounds, computer resources were only sufficient to determine the MP3 and MP4SDQ energies using the LANL1DZ* basis set. The calculated binding energies for the ditelluradiazolyl radical dimer using this basis set were ca. 14.9 (MP3) and 18.1 kcal/mol (MP4SDQ). Comparing these results with the LANL1DZ* and 3-21G* results on the sulfur dimer, the binding energy of the tellurium species using the 3-21G* basis set is estimated to be in the neighbourhood of 15 kcal/mol. Thus, the tellurium dimer is predicted to be more strongly bound by approximately 10 kcal/mol relative to the sulfur dimer. The small binding energies for the tellurium compounds are consistent with the limited structural changes predicted between the monomer and the dimer (vide supra).

To ascertain if the C_{2v} dimer is indeed the most stable, the binding energies of three other dimers were predicted. At the Hartree–Fock level, the distorted C_{2h} dimer is the most stable of the four dimers studied. However, upon extending the theory to include electron correlation effects, MP4SDQ, the C_{2v} dimer is marginally more stable by ca. 0.3 kcal/mol.

Conclusions

This study extends our earlier theoretical research on the Group 16 elements S and Se to include Te. At the Hartree–Fock level, the agreement between the two basis sets, all-electron and ECP, for the structures is very good. Differences noted between the all-electron and effective core potential results probably can be attributed to the relativistic parametrization of the core potential for Te and the neglect of such effects in the 3-21G* basis set.

Vibrational frequency analyses of the cation and radical monomers showed that both are minima in C_{2v} symmetry.

Table 9. Experimental and theoretical results for the dithiadiazolyl and diselenadiazolyl analogues (from ref. 4) along with predictions for the ditelluradiazolyl species (HCN_2E_2; E = S, Se, Te).

	E							
	S			Se			Te	
	LANL1DZ*	3-21G*		LANL1DZ*	3-21G*		LANL1DZ*	3-21G*
Geometries								
Cation								
EE	2.031	2.027		2.293	2.263		2.653	2.662
EN	1.577	1.571		1.719	1.739		1.903	1.948
CN	1.339	1.335		1.337	1.331		1.336	1.328
EEN	94.5	93.8		90.5	91.1		85.8	85.7
ENC	117.3	117.3		119.3	117.8		122.5	121.2
Radical								
EE	2.121	2.125		2.388	2.352		2.759	2.763
EN	1.659	1.660		1.811	1.830		2.005	2.044
CN	1.351	1.344		1.352	1.343		1.352	1.343
EEN	94.0	94.4		90.1	90.8		85.2	85.3
ENC	115.5	115.3		117.5	116.0		121.2	120.1
C_{2v} dimer			Expt.			Expt.		
E--E	3.154	3.026	3.11	3.311	3.072	3.28	3.607	3.497
EE	2.075	2.071	2.07	2.323	2.269	2.33	2.671	2.679
EN	1.639	1.635	1.64	1.780	1.803	1.80	1.959	2.001
CN	1.332	1.323	1.32	1.332	1.322	1.32	1.332	1.322
EEN	94.5	94.4	95	90.9	91.8	91.5	86.3	86.4
ENC	114.5	114.2	113	115.9	113.7	112	115.0	113.5
Koopmans' first ionization potential (scaled by 0.92)								
		8.27	7.87		7.72	7.71		7.08
Selected vibrational frequencies (scaled by 0.90)								
Cation								
b_1	592	608	563	552	559	528	508	511
b_2	819	786	808	685	686	685	596	610
a_1	1297	1260	1377	1266	1224	1221	1247	1211
Radical								
b_2	704	670	757	582	593		495	516
a_1	845	890	900	1131	1098		1118	1087
C_{2v} dimer								
b_2	683	664	742	556	561	559	490	503
b_1	736	705	780	617	622	623	540	555
b_2	1238	1213	1214	775	814	721	739	760

The radical dimers all have at least one imaginary frequency. The common imaginary mode in all the dimers corresponds to a breaking of the imposed constraint of planarity of the rings.

Predictions of the binding energy of the two radicals to give the radical dimer indicate that the Te species will be more strongly bound than the corresponding S and Se species. The C_{2v} dimer is probably the most stable of the four possible dimers studied in this work. These predictions for the ditelluradiazolyl system can be used to guide further experiments.

Finally, we briefly compare our predictions for the tellurium compounds with our earlier results (4) on the sulfur and selenium analogues. Key results are summarized in Table 9 along with the available experimental data (4) for the sulfur and selenium compounds. Our predictions of the same properties for the tellurium species should be approximately as reliable as those for the sulfur and selenium compounds.

Acknowledgements

Financial support of this research by the Natural Sciences and Engineering Research Council of Canada (NSERC) is gratefully acknowledged.

References

1. J.R. Ferraro and J.M. Williams. Introduction to synthetic molecular conductors. Academic Press, New York. 1987.
2. A.W. Cordes, R.C. Haddon, and R.T. Oakley. The chemistry of inorganic ring systems. *Edited by* R. Steudel. Elsevier, Amsterdam. 1992. p. 295.
3. R.T. Oakley. Prog. Inorg. Chem. **36**, 299 (1988).
4. A.W. Cordes, C.D. Bryan, W.M. Davis, R.H. deLaat, S.H. Glarum, J.D. Goddard, R.C. Haddon, R.G. Hicks, D.K. Kennepohl, R.T. Oakley, S.R. Scott, and N.P.C. Westwood. J. Am. Chem. Soc. **115**, 7232 (1993).
5. M.J. Frisch, M. Head-Gordon, G.W. Trucks, J.B. Foresman, H.B. Schlegel, K. Raghavachari, M. Robb, J.S. Binkley, C. Gonzalez, D.J. Defrees, D.J. Fox, R.A. Whiteside, R. Seeger, C.F. Melius, J. Baker, R.L. Martin, L.R. Kahn, J.J.P. Stewart, S. Topiol, and J.A. Pople. Gaussian 90, Revision F. Gaussian, Inc., Pittsburgh, Pa. 1990.
6. M.J. Frisch, G.W. Trucks, M. Head-Gordon, P.M.W. Gill, M.W. Wong, J.B. Foresman, B.G. Johnson, H.B. Schlegel, M.A. Robb, E.S. Replogle, R. Gomperts, J.L. Andres, K. Raghavachari, J.S. Binkley, C. Gonzalez, R.L. Martin, D.J. Fox, D.J. Defrees, J. Baker, J.J.P. Stewart, and J.A. Pople. Gaussian 92, Revision B. Gaussian Inc., Pittsburgh, Pa. 1992.
7. K.D. Dobbs and W.J. Hehre. J. Comput. Chem. **7**, 359 (1986).
8. S. Huzinaga. Gaussian basis sets for molecular calculations. Elsevier, New York. 1984.
9. P.J. Hay and W.R. Wadt. J. Chem. Phys. **82**, 284 (1985).
10. P.G. Jaisen and W.J. Stevens. J. Chem. Phys. **83**, 2984 (1985).
11. H.B. Schlegel. J. Comput. Chem. **3**, 214 (1982).
12. J. Baker. J. Comput. Chem. **7**, 385 (1986).
13. N.C. Handy, J.F. Gaw, and E.D. Simandiras. J. Chem. Soc. Faraday Trans. 2, **83**, 1577 (1987).
14. C. Møller and M.S. Plesset. Phys. Rev. **46**, 618 (1934).
15. H.W. Roesky, J. Munzenberg, R. Bohra, and M. Noltemeyer. J. Organomet. Chem. **418**, 339 (1991).
16. M. Bjorgvinsson, T. Heinze, H.W. Roesky, F. Pauer, D. Stalke, and G.M. Sheldrick. Angew. Chem. Int. Ed. Engl. **30**, 1677 (1991).
17. A. Bondi. J. Phys. Chem. **68**, 441 (1964).
18. J.M. McKelvey and G. Berthier. Chem. Phys. Lett. **41**, 476 (1976).
19. J. McKelvey and W.J. Hehre. Mol. Phys. **25**, 983 (1973).
20. J. Paldus and A. Veillard. Mol. Phys. **35**, 445 (1978).
21. D. Feller, E.R. Davidson, and W.T. Borden. J. Am. Chem. Soc. **106**, 2513 (1984).
22. W.J. Hehre, L. Radom, P.v.R. Schleyer, and J.A. Pople. Ab initio molecular orbital theory. Wiley, New York. 1986. pp. 277–279.

A unified approach to dynamic NMR based on a physical interpretation of the transition probability

Alex D. Bain and G.J. Duns

Abstract: A general theory of the effect of dynamics (relaxation and (or) exchange) on NMR spectra is presented. This theory is based on a reexamination of the transition probability. The classic expression for this is as the square of the transition moment, but we feel it is useful to separate the square into two separate terms. In the generalization presented here, we show that one of these terms corresponds to the share of the initial magnetization that each spin coherence receives at the start of the experiment. The second term is how much that coherence contributes to the total detected signal. The final intensity is the product of these two factors. For a static spectrum, these two terms are complex conjugates, so the product is real and we recover the standard transition probability. When there is dynamics, the product becomes complex, so the time evolution includes oscillatory and dispersive terms. This means that a dynamic spectrum is still a sum of individual transitions, but the lineshapes are distorted in phase, intensity, position, and linewidth by the dynamic process. In this paper we develop the general theory, and illustrate it with a calculation of the classic problem of mutual exchange in an AB spin system.

Key words: NMR spectroscopy, transition probability, chemical exchange, kinetics.

Résumé : On présente une théorie générale de l'effet des processus dynamiques (relaxation et (ou) échange) sur les spectres RMN. Cette théorie est basée sur un réexamen de la probabilité de transition. L'expression classique pour ceci implique le carré du moment de transition; toutefois, on croit qu'il est utile de séparer le carré en deux termes. Dans la généralisation présentée ici, on montre que l'un de ces termes correspond à la partie de la magnétisation initiale que chaque cohérence de spin reçoit au début de l'expérience. Le second terme est un reflet de la partie de cette cohérence qui contribue au signal qui est détecté. L'intensité finale est le produit de ces deux facteurs. Pour un spectre statique, ces deux termes sont des conjugués complexes et le produit est donc réel; on récupère donc la probabilité de transition standard. Quand le spectre est dynamique, le produit devient complexe et l'évolution avec le temps comprend des termes oscillatoires et de dispersion. Ceci signifie qu'un spectre dynamique est encore une somme de transitions individuelles, mais, à cause du processus dynamique, les formes des bandes sont déformées par la phase, l'intensité, la position et la largeur de la bande. Dans ce travail, on a développé la théorie générale et on l'a illustrée à l'aide d'un calcul du problème classique de l'échange mutuel dans un système de spins AB.

Mots clés : RMN spectroscopie, probabilité de transition, échange cinétique, cinétique.

[Traduit par la rédaction]

Introduction

Dynamic Nuclear Magnetic Resonance (1–4) means NMR in which spin relaxation and (or) chemical exchange contribute to the spectra, in a nontrivial way. If the rates of these processes are quite different from frequency separations in the spectrum, dynamic effects can be easily calculated (or ignored). However, as more complex systems are studied, and more sophisticated experiments are developed, it is becoming clear that dynamics should be included from the start of any description of an NMR spectrum.

Received September 6, 1995.

This paper is dedicated to Professor Richard F.W. Bader on the occasion of his 65th birthday.

A.D. Bain[1] **and G.J. Duns.** Department of Chemistry, McMaster University, 1280 Main Street West, Hamilton, ON L8S 4M1, Canada.

[1] Author to whom correspondence may be addressed. Telephone: (905) 525-9140. Fax: (905) 522-2509. E-mail: bain@mcmaster.ca

The title we have used here is a conscious reference to Binsch's classic work (5) on the subject. Indeed, many of the individual components of what we describe have been published elsewhere. We feel, however, that it is useful and important to bring together familiar concepts with those that may be novel to a given reader. This will produce a unified picture in which dynamic spectra are treated in the same way as other NMR spectra.

The foundation of this effort is a reexamination of the transition probability. In this part of the work, there is little that is exclusively nuclear or magnetic about the spectroscopy. The discussion could equally apply to any form of coherent spectroscopy, but we formulate it in terms of NMR. A familiar example is shown in Fig. 1, which shows the lineshape due to mutual exchange in an AB system. It is clear that the static spectrum of an AB spin system at equilibrium is made up of four transitions whose intensities are proportional to the transition probabilities. All the other spectra in Fig. 1 are of the same spin system, with different rates of mutual exchange. The traditional approach to exchange has been to treat these as single lineshapes — to calculate the total signal at any given

Fig. 1. NMR lineshapes of an AB spin system undergoing mutual exchange. The heavy, top line represents the total lineshape, and the lighter lines the four individual components. The parameters of the spin system are as follows: the chemical shift difference between the sites is 86 Hz, the coupling constant is 13 Hz, and T_2 for each site is 5 s. Starting from the bottom, the rates of exchange, in s^{-1}, are 0.1, 5, 25, 125, 625, 3125. Note that the vertical scale in the fourth spectrum from the bottom (rate = 125 s^{-1}) has been multiplied by 4 to show the lineshape more clearly. In the top two spectra, the two main components are almost coincident, and the two minor components are almost zero.

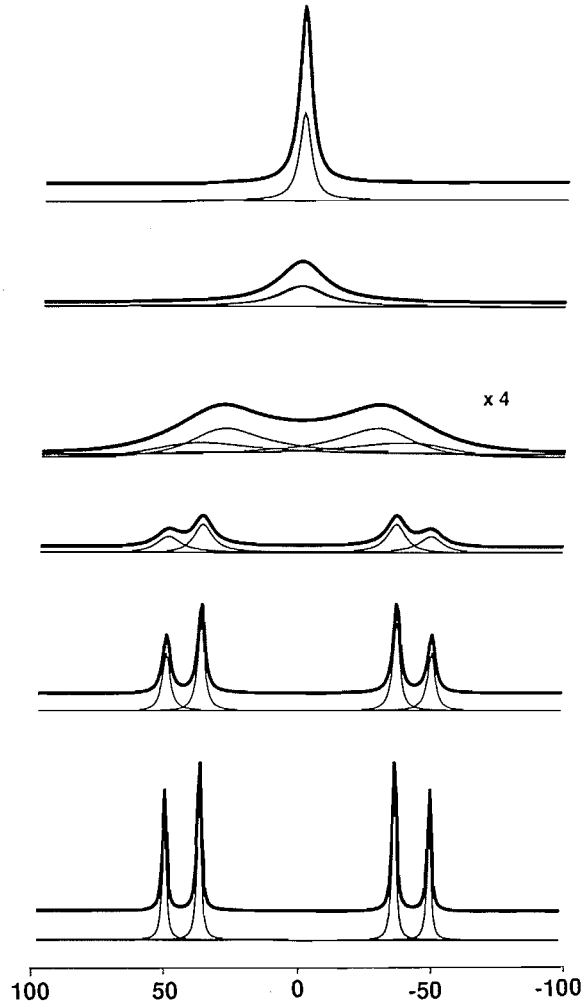

frequency. The dynamic spectra are then traced as a function of frequency (6–13). Johnston (14) has recently published a detailed discussion of these methods. They are, in some way, reminiscent of a continuous wave spectrometer, since they calculate the total signal. In contrast, we prefer (15) to regard all these spectra as the sum of four transitions (16). The signal at any given frequency is the sum of the contributions of the four lines. Furthermore, we deal with the four transitions in the time domain, as we would do with a pulse Fourier transform spectrum. The results are the same, of course, but the reformulation simplifies and clarifies the solution.

To define the transitions in Fig. 1, we need to go back and examine the transition probability. This is usually given by time-dependent perturbation theory (17), or Fermi's Golden Rule No. 2 (18). If ϕ_i is the initial state, ϕ_f the final state, and I_x the perturbation, then the transition probability is given in eq. [1]. Two factors make up the transition probability, and they are complex conjugates, so the intensity is real. In the generalization presented in this paper, these two factors have a physical interpretation: they are the projections of the individual transitions along the total magnetization. In a dynamic system, the two factors are not complex conjugates, so the lineshapes in Fig. 1 are more complex. In spite of this, we may still treat them as transitions, as in the static case.

$$[1] \quad \text{Transition probability} \propto |\langle\phi_f|I_x|\phi_i\rangle|^2 = \langle\phi_f|I_x|\phi_i\rangle^*\langle\phi_f|I_x|\phi_i\rangle$$

In a pulse NMR experiment, the z magnetization is flipped into the xy plane, and the individual transitions start to precess. During the detection, the total xy magnetization is measured as a function of time. We will show that one of the factors in eq. [1] comes from the fact that the total z magnetization (converted to xy magnetization by the first pulse) must be divided amongst the individual NMR coherences. Each line in the spectrum gets its share before it starts precessing. The other factor comes from how visible each transition is to the detector. In a static 1D spectrum, these factors may be different for each line in the spectrum, but they are complex conjugates so the intensity of each line is always real. If we have a pulse experiment, the spin manipulations fit "between" these two factors. The initial magnetization is divided into the individual coherences, these are manipulated by the pulse sequence, and then the signal is detected. In a dynamic system the two factors are no longer equal, and the transition probability has both real and imaginary parts. The real and imaginary terms give the intensity and phase distortions that are common in pulse experiments. All the spectra in Fig. 1 are made up of four transitions; the only difference is the character of the transition probability.

Basic theory

The fundamental equation for this work is the equation of motion for the density matrix (19), as in eq. [2].

$$[2] \quad i\frac{h}{2\pi}\frac{\partial}{\partial t}\rho = [H, \rho]$$

It is more convenient to reexpress this equation in Liouville space (19–21), in which the density matrix becomes a vector, and the commutator with the Hamiltonian becomes the Liouville superoperator. We will use bold-face upper-case italic letters to denote superoperators. Equation [2] becomes eq. [3].

$$[3] \quad i\frac{h}{2\pi}\frac{\partial}{\partial t}\rho = \boldsymbol{L}\rho$$

If we use frequency units ($h/2\pi = 1$), then the formal solution to eq. [3] is given in eq. [4], in which exp( ) denotes the exponential of a matrix.

$$[4] \quad \rho(t) = \exp(-i\boldsymbol{L}t)\rho(0)$$

Relaxation or chemical exchange can be easily added in Liouville space, by including a Redfield matrix, $\boldsymbol{R}$, for relaxation, or a kinetic matrix, $\boldsymbol{K}$, to describe exchange. This restricts this particular description to first-order kinetics in the reaction. The equation of motion becomes eq. [5].

$$[5] \quad \rho(t) = \exp(-i\boldsymbol{L} - \boldsymbol{R} - \boldsymbol{K})t\,\rho(0)$$

In NMR, we detect the magnetization in the xy plane, so we may say that we always measure the expectation value of the I_x operator. This is just the unweighted sum of all the I_{xi} operators for the individual spins i. It may be a function of several time variables, including the time during the acquisition, but it is always given by eq. [6].

$$[6] \quad \langle I_x(t)\rangle = \mathrm{trace}(I_x\rho(t))$$

In Liouville space, both the density matrix and the I_x operator become vectors. The scalar product of these Liouville space vectors is the trace of their product as operators. Therefore, the NMR signal, as a function of a single time variable, t, is given by eq. [7], in which the parentheses denote a Liouville space scalar product.

$$[7] \quad \text{NMR signal} = (I_x|\,\rho(t))$$

We start at equilibrium. In the high-temperature approximation, the equilibrium density operator is proportional to the sum of the I_z operators, which we will call F_z. If there are multiple exchanging sites with unequal populations, p_i, the sum is a weighted one, as in eq. [8].

$$[8] \quad F_x = \sum_{i=1}^{n} p_i I_{xi}$$

We assume that a simple, nonselective pulse has been used at the start of the experiment. This rotates the equilibrium z magnetization onto the x axis. Note that neither the equilibrium state nor the effect of the pulse depend on the dynamics or the details of the spin Hamiltonian (chemical shifts and coupling constants). The equilibrium density matrix is proportional to F_z. After the pulse the density matrix is therefore given by F_x, and it will evolve as in eq. [4] or [5]. If we substitute eq. [5] into eq. [7], we get the NMR signal as a function of time t, as given by eq. [9]. In this equation we distinguish the sum of the operators weighted by the equilibrium populations, F_x, from the unweighted sum, I_x. The detector sees each spin (but not each coherence!) equally well.

$$[9] \quad \text{NMR signal} = (I_x|\exp\{(-i\boldsymbol{L} - \boldsymbol{R} - \boldsymbol{K})t\}F_x)$$
$$= (I_x|\exp\{(-i\boldsymbol{L} - \boldsymbol{R} - \boldsymbol{K})t\}\,|F_x)$$

This equation can be solved several ways (22). One method involves diagonalizing the Liouville matrix, $i\boldsymbol{L} + \boldsymbol{R} + \boldsymbol{K}$. If $\boldsymbol{U}$ is the matrix with the eigenvectors as columns, and Λ is the diagonal matrix with the eigenvalues down the diagonal, then we can write eq. [9] as eq. [10]. This is similar to other eigenvalue problems in quantum mechanics, such as the transformation to normal coordinates in vibrational spectroscopy.

$$[10] \quad \text{NMR signal} = (I_x|U^{-1}\exp(-i\Lambda t)U|F_x)$$

Note that the Liouville matrix, $i\boldsymbol{L} + \boldsymbol{R} + \boldsymbol{K}$ may not be Hermitian, but it can still be diagonalized. Its eigenvalues and eigenvectors are not necessarily real, however, and the inverse of U may not be its complex-conjugate transpose. If we allow complex numbers in it, eq. [10] is a general result. Since Λ is a diagonal matrix we can expand in terms of the individual eigenvalues, λ_j. We can also apply $\boldsymbol{U}^{-1}$ ("backwards") to I_x, and obtain eq. [11]. This is the fundamental result on which this paper is based.

$$[11] \quad \text{NMR signal} = \sum_j (U^{-1}I_x)_j^*(UF_x)_j \exp(i\lambda_j t)$$

Practical considerations

For a single spin-1/2, the solution to eq. [11] is very easy. There are three coherences: the z magnetization and the two counter-rotating xy magnetizations. Both $\boldsymbol{L}$ and $\boldsymbol{R}$ are diagonal, so eq. [11] separates into three one-dimensional equations. For the z magnetization, the matrix element of $\boldsymbol{L}$ is zero, and that of $\boldsymbol{R}$ is $1/T_1$, so it behaves as $e^{-t/T1}$. For the xy magnetizations, the matrix elements of $\boldsymbol{L}$ are $+/-\omega$, and that of $\boldsymbol{R}$ is $1/T_2$. The xy magnetizations behave as $e^{i\omega t}e^{-t/T2}$.

For a general system, these sets of equations are huge, as written. For n spins-1/2, the density matrix has 2^{2n} elements, so the Liouville matrix has 2^{4n} elements. However, we can separate all the density matrix elements according to coherence level (23), that is, how many quanta are in the associated transition. In this case, the matrices block, and the largest single block is the one corresponding to the single-quantum transitions. This single-quantum block is precisely the matrix that Binsch deals with (11, 12). In general, there is an equation like [11] for each order of coherence. The amount of calculation needed in this approach is similar to standard density matrix methods.

The quantities $(\boldsymbol{U}^{-1}I_x)_j$ and $(\boldsymbol{U}F_x)_j$ in eq. [11] are projections of the eigenvector j along I_x. From the above equations, we can interpret these as follows. The term $(\boldsymbol{U}F_x)_j$ is the amount that the transition j received from the total x magnetization, created from the equilibrium state, and $(\boldsymbol{U}^{-1}I_x)_j$ is how much that transition contributes to the observed signal. These two terms may not be equal, as we will see in exchanging systems. An informal way of thinking about these terms is to consider the transition moment, $\langle\phi_f|I_x|\phi_i\rangle$. If we consider that the ket-bra operator $|\phi_f\rangle\langle\phi_i|$ represents the transition, then the transition moment is the projection of the transition operator along the I_x operator.

In the usual preparation–evolution–detection paradigm, neither the preparation nor the detection depend on the details of the Hamiltonian, except in special cases. Starting from equilibrium, a hard pulse gives a density matrix that is just proportional to F_z. The detector picks up only the unweighted sum of the spin operators, I_x. It is only during an evolution (perhaps between sampling points in an FID) that we must divide these totals amongst the various lines in the spectrum. Therefore, one of the factors in the transition probability represents the conversion from preparation to evolution; the other factor represents the conversion back from evolution to detection.

Equations [10] and [11] are the basic equations we will work with. For instance, they say that any time-domain NMR

signal is the sum of decaying oscillations (15). This is obvious from the fact that it is described by a first-order differential equation, but eq. [11] gives a way of calculating the values of these exponentials for any system, static or dynamic. The distinctions amongst different types of spectra lie in the eigenvalues and eigenvectors of the Liouville matrix $iL + R + K$. Equation [11] describes static spectra, spin relaxation, and spectra showing the effects of chemical exchange or T_2 relaxation, in a single, unified picture.

Static spectra

If we have no dynamics ($K = 0$, and R only a perturbation), then the Liouville matrix is Hermitian and all the eigenvalues are pure imaginary. We can restrict our attention to the block containing the single-quantum transitions, and diagonalize that matrix. The positions of the lines in the spectrum are given by the eigenvalues and the intensities are governed by how much the eigenvector overlaps with I_x. The amount that an individual transition receives and the amount it contributes are equal, and the transition probability is their product. This is exactly Banwell and Primas' "direct method," in which they solve for the transitions directly (24), rather than for the energy levels. Because of the size of the matrices, this is not an efficient way of simulating a static spectrum. However, the philosophy of dealing directly with the observables is very important.

For an example, the AB spin system has a Liouville matrix given in eq. [12]. The coupling constant is J, and we may assume that $\omega_B = -\omega_A = -\delta/2$, so that δ is the frequency difference between the two sites. We define the usual angle, θ, for the AB system by the equation $\tan(\theta) = J/2\delta$. The Liouville space basis used here is the superspin equivalent of the four product operators (I_x^A, $I_x^A I_z^B$, I_x^B, $I_x^B I_z^A$), and a set of rules for calculating these elements are given elsewhere.[2]

$$[12]\quad \begin{pmatrix} i\omega_A & iJ/2 & 0 & -iJ/2 \\ iJ/2 & i\omega_A & -iJ/2 & 0 \\ 0 & -iJ/2 & i\omega_B & iJ/2 \\ -iJ/2 & 0 & iJ/2 & i\omega_B \end{pmatrix}$$

The four eigenvalues, which give the positions of the lines, are $+/- J/2 +/- ((J/2)^2 + (\delta/2)^2)^{1/2}$, as you expect for an AB system. The matrix of eigenvectors as columns is given in eq. [13], in which $c = \cos(\theta)$, $s = \sin(\theta)$ and δ is defined above.

$$[13]\quad \text{Eigenvectors} = \begin{pmatrix} c & s & c & s \\ c & s & -c & -s \\ -s & c & s & -c \\ -s & c & -s & c \end{pmatrix}$$

In the basis used in eq. [12], the total x magnetization is proportional to the vector (1,0,1,0). Taking the dot product with the eigenvectors shows that the outer lines get ($\cos\theta - \sin\theta$) from the total, whereas the inner lines get ($\cos\theta + \sin\theta$). The squares of these terms give the familiar AB system intensities: ($1 - \sin 2\theta$) and ($1 + \sin 2\theta$).

T_1 relaxation and evolution in coupled spin systems

The approach described above has always been the standard approach for T_1 relaxation in coupled spin systems (25) relaxation matrix analysis for NOESY spectra (26, 27), and experiments on slow chemical exchange (28–31). We are dealing with the block of the density matrix corresponding to z magnetizations. The oscillation frequencies are all zero, so only the Redfield or kinetic matrix survives. This is symmetric, or at least can be made so (28). In a T_1-type experiment, we do not measure the z magnetizations directly, but their dynamics during the delay follows eq. [10]. We take linear combinations of the z magnetizations that decay exponentially, as in eq. [11], and let them decay (32, 33). Werbelow and Grant have used the analogy of normal modes (25), mentioned above. At the end of the delay, we transform the linear combinations back into the familiar z magnetizations that correspond to the lines in the spectrum.

In principle, the Redfield matrix could connect every density matrix element with every other one. However, we can usually ignore elements that connect two coherences with different frequencies. For the z magnetizations, which are all degenerate in frequency, the off-diagonal elements of R are crucial for explaining observed effects. For the other elements of the density matrix, L has non-zero diagonal and off-diagonal elements that, we often assume, dominate the elements of R. Therefore, we diagonalize L and then calculate the diagonal element of R, which we call $1/T_2$. This implies that the xy magnetization decays as a single exponential. However, if there are degenerate transitions, off-diagonal elements must be included, and multi-exponential decay will be observed. For instance, methyl groups pass through multiple-quantum filters easily (34) because of such relaxation effects.

Chemical exchange and scalar relaxation

If the elements of a relaxation or kinetic matrix become comparable with frequency differences in the spectrum, distortions appear in the spectrum. Chemical exchange is perhaps the most familiar example, but when relaxation becomes very efficient (as in viscous solutions), similar effects occur. In this case, the matrix $iL + R + K$ must be non-Hermitian, since its diagonal elements have both real and imaginary parts. Therefore, the eigenvalues and eigenvectors may have complex values, and the inverse of U is no longer its adjoint. Now the precession in eq. [11] has both a real and imaginary part: the real part gives the decay rate, and the imaginary part gives the frequency. The intensity and phase of each line are given by the transition probabilities calculated from the components of the eigenvectors along I_x, as in eq. [11].

In this case, the concept of a transition is generalized. The transition gets a certain amount of coherence from the initial x magnetization, but this is not equal to how much it contributes to the detected signal. Also, each coherence is not necessarily on the x axis at the start of the precession, at least formally. For a static spectrum they all start together, but not for a dynamic

[2] The SIMPLTN program is available from A.D.B. at e-mail address given in footnote 1.

spectrum. The overall spectrum is still in-phase, as we well know. The phase of the full spectrum is determined by the sum of the real and imaginary parts of each component of the FID at $t = 0$. This is the trace of $\boldsymbol{iL} + \boldsymbol{R} + \boldsymbol{K}$. We can add a constant to the diagonal without disturbing the eigenvectors, so we add an imaginary number to cancel out the imaginary part of the trace. In some sense, this is like zero-order phasing in a FT spectrum.

For example, two-site equally populated exchange is described by the matrix in eq. [14]. The two lines are at +/− δ/2, and k is the exchange rate.

$$[14] \quad \begin{pmatrix} i\delta/2 - k & k \\ k & -i\delta/2 - k \end{pmatrix}$$

Following Reeves and Shaw (16), we can define two parameters, α and β, as in eq. [15].

$$[15] \quad \alpha = \sqrt{k^2 - (\delta/2)^2} \qquad \beta_{\pm} = \frac{\alpha \pm i\delta/2}{k}$$

With these definitions, one possibility for the matrix with the eigenvectors as columns is given in eq. [16], and its inverse in eq. [17].

$$[16] \quad \boldsymbol{U} = \begin{pmatrix} 1 & 1 \\ -\beta_- & \beta_+ \end{pmatrix}$$

$$[17] \quad \boldsymbol{U}^{-1} = \frac{k}{2\alpha} \begin{pmatrix} \beta_+ & -1 \\ \beta_- & 1 \end{pmatrix}$$

These expressions, used in eq. [5] in our preliminary communication (15), give the Reeves and Shaw expressions, which give the familiar Gutowsky and Holm formula.

Another example of these phenomena is the mutual exchange in an AB spin system. This is a classic example, with an analytical solution. We can start with the Liouville matrix for the AB spin system in eq. [12], and then we include the terms that represent spins leaving site A and going to site B. The result is given in eq. [18]. If we set $\omega_B = -\omega_A = -\delta/2$, the symmetry of the matrix allows us to break it into two 2 × 2 complex matrices, which can be diagonalized analytically. The resulting lineshapes match the published solutions (35).

$$[18] \quad \begin{pmatrix} i\omega_A - k & iJ/2 & k & -iJ/2 \\ iJ/2 & i\omega_A - k & -iJ/2 & k \\ k & -iJ/2 & i\omega_B - k & iJ/2 \\ -iJ/2 & k & iJ/2 & i\omega_B - k \end{pmatrix}$$

For more complex systems, the matrices are larger and the calculation of the matrix elements may be more complex, but the formalism is the same. Binsch uses the same matrix as in eq. [18], and extracts the same eigenvalues and eigenvectors. The difference between this work and that of Binsch is that he calculates the total signal as a function of frequency (6), following Gordon's method (6). We believe it is better to leave the signal as a sum of absorption and dispersion lines.

One advantage of this approach is that it simplifies viewing the results. The position, linewidth, phase, and intensity of each line are strong functions of the exchange rate, but they are still determined by the real and imaginary magnetizations at time zero, and the frequency and decay rate. A simulated FID can be calculated from these parameters, in the format of a commercial NMR program. The powerful processing and display routines can be used to compare the simulation with real data, and to plot the comparisons. Furthermore, recent advances in fitting spectra in the time-domain (36) can be applied directly to exchanging systems.

General pulse experiments

Equation [11] provides the basis for a general description of pulse NMR experiments. For simple experiments with hard pulses, the evolution of the spin system during a delay is the only part that involves the static Hamiltonian. The equilibrium state, the effect of a pulse, and the detection all are independent of chemical shifts and couplings. We extract the spectrum by observing the time dependence of the total x magnetization as a function of time. For a single pulse experiment, this is simply the acquisition time. For higher dimensionality, there are more time variables, but no significant complication.

The description of the effect of a pulse is straightforward. Since it does not depend on the spin system, simple rules based on commutation relations or Wigner matrices will work. If the pulses are effectively instantaneous, the calculation is easy (37).

During a delay, the description of the evolution depends on the spin system. For a weakly coupled system, the way that the product operators evolve in time is familiar. For two weakly coupled spins, the single-quantum coherence oscillates back and forth between I_x and I_xI_z (37). For strongly coupled systems, the evolution is more complex (38), and it is worthwhile to consider another basis for Liouville space. The superspin formalism (21) takes this approach, and switches to what is called the Hamiltonian basis for the evolution. This is also the approach taken in the SIMPLTN program.[2] The evolution is then calculated using eq. [11].

Note that this is a completely general approach. The eigenvectors of $\boldsymbol{iL} + \boldsymbol{R} + \boldsymbol{K}$, in the matrix $\boldsymbol{U}$, provide a change of basis for the density matrix. The evolution then proceeds as in eq. [11], in which the eigenvalues are completely general. If they are pure imaginary, then we have the oscillations at the resonant frequencies. If they are pure real, we are dealing with a T_1-type experiment, and the eigenvalues are the relaxation rates. If the eigenvalues have a real and an imaginary part, then we have line broadening and dynamic frequency shifts that are characteristic of this regime.

This approach provides a rigorous description of the effect of dynamics on pulse experiments. Relaxation and other dynamic effects are often added *post facto* in many theories. Since eq. [11] is general, we can use it to explore the effect of exchange on pulse experiments, or the utility of pulse experiments applied to exchanging systems (39–42).

Conclusions

This reformulation of the transition probability provides a

general and concise picture of dynamic NMR. The fundamental equations are [10] and [11], and these are determined by the eigenvalues and the eigenvectors of the Liouville matrix. The eigenvalues give the position and widths of the lines in the spectrum. The eigenvectors determine the transition moments, which give us the intensities and the phases of the lines. Together, these determine all the dynamics of the system: evolution during a delay, relaxation of either the z or xy magnetizations or of the lineshapes in chemically exchanging systems. Of course, any other formalism must give the same answers as the one presented here. The choice of formalism is partly aesthetic, and we feel that this generalization of the superspin approach gives a particularly neat solution.

Much of this theory is implicit in the earlier work cited here. For the particular case of chemical exchange lineshapes, the method does not significantly change the calculation. Both the present work and the standard method involve the diagonalization of the same non-Hermitian matrix. However, the physical interpretation of the transition probability clarifies the picture considerably.

One practical advantage is in the analysis of dynamic spectra. The simulation can be presented in the format of the raw experimental FID, so comparisons are simplified. Much development has gone into the development of fitting procedures for spectra. These use a variety of methods to fit the frequency, width, and position of a series of lines to either the time-domain or frequency-domain data. If the phase is added to list of parameters, all these methods can be applied to exchange lineshapes as well. In general, we feel it is useful to bring all these different approaches to dynamic NMR together, to produce a single, unified 'theory'.

Acknowledgements

We would like to thank Dr. K.D. Sales and Dr. G.E. Hawkes at Queen Mary and Westfield College for their hospitality and their comments. Dr. Ruth Lynden-Bell provided some very helpful encouragement and criticisms. Dr. I. Najfeld and Dr. E.R. Johnston sent copies of their work prior to publication. The work was supported by the Natural Sciences and Engineering Research Council of Canada (NSERC).

References

1. J. Sandstrom. Dynamic NMR spectroscopy. Academic Press, London. 1982.
2. L.M. Jackman and F.A. Cotton. Dynamic nuclear magnetic resonance spectroscopy. Academic Press, New York. 1975.
3. J.I. Kaplan and G. Fraenkel. NMR of chemically exchanging systems. Academic Press, New York. 1980.
4. J.J. Delpuech. Dynamics of solutions and fluid mixtures by NMR. Wiley, Chichester. 1995.
5. G. Binsch. J. Am. Chem. Soc. **91**, 1304 (1969).
6. R.G. Gordon and R.P. McGinnis. J. Chem. Phys. **49**, 2455 (1968).
7. C.S. Johnson. Adv. Magn. Reson. **1**, 33 (1965).
8. H.S. Gutowsky and C.H. Holm. J. Chem. Phys. **25**, 1228 (1956).
9. H.M. McConnell. J. Chem. Phys. **28**, 430 (1958).
10. R.M. Lynden-Bell. Prog. Nucl. Magn. Reson. Spectrosc. **2**, 163 (1967).
11. D.A. Kleier and G. Binsch. J. Magn. Reson. **3**, 146 (1970).
12. D.S. Stephenson and G. Binsch. J. Magn. Reson. **30**, 625 (1978).
13. D.S. Stephenson and G. Binsch. J. Magn. Reson. **32**, 145 (1978).
14. E.R. Johnston. Concepts Magn. Reson. **7**, 219 (1995).
15. A.D. Bain and G.J. Duns. J. Magn. Reson. Ser. A, **112**, 258 (1995).
16. L.W. Reeves and K.N. Shaw. Can. J. Chem. **48**, 3641 (1970).
17. R.K. Harris. Nuclear magnetic resonance spectroscopy. Pitman Books Limited, London. 1983.
18. L.I. Schiff. Quantum mechanics. 3rd ed. McGraw Hill, New York. 1968.
19. R.R. Ernst, G. Bodenhausen, and A. Wokaun. Principles of nuclear magnetic resonance in one and two dimensions. Clarendon Press, Oxford. 1987.
20. U. Fano. *In* Lectures on the many body problem. Vol 2. *Edited by* E.R. Caianiello. Academic Press, New York. 1964. pp. 217–239.
21. A.D. Bain. Prog. Nucl. Magn. Reson. Spectrosc. **20**, 295 (1988).
22. I. Najfeld and T.F. Havel. Adv. Appl. Math. **16**, 321 (1995).
23. A.D. Bain. J. Magn. Reson. **56**, 418 (1984).
24. C.N. Banwell and H. Primas. Mol. Phys. **6**, 225 (1963).
25. L.G. Werbelow and D.M. Grant. Adv. Magn. Reson. **9**, 190 (1977).
26. R. Boelens, T.M.G. Koning, G.A. vander Marel, J.H. vanBoom, and R. Kaptein. J. Magn. Reson. **82**, 290 (1989).
27. B.A. Borgias and T.L. James. J. Magn. Reson. **87**, 475 (1990).
28. J.J. Led and H. Gesmar. J. Magn. Reson. **49**, 444 (1982).
29. M. Grassi, B.E. Mann, B.T. Pickup, and C.M. Spencer. J. Magn. Reson. **69**, 92 (1986).
30. D.R. Muhandiram and R.E.D. McClung. J. Magn. Reson. **71**, 187 (1987).
31. A.D. Bain and J.A. Cramer. J. Magn. Reson. Ser. A, **103**, 217 (1993).
32. H. Shimizu and S. Fujiwara. J. Chem. Phys. **34**, 1501 (1961).
33. E. L. Mackor and C. MacLean. Prog. Nucl. Magn. Reson. Spectrosc. **3**, 129 (1967).
34. N. Muller, G. Bodenhausen, and R.R. Ernst. J. Magn. Reson. **75**, 297 (1987).
35. S. Alexander. J. Chem. Phys. **37**, 967 (1962).
36. H. Gesmar, J.J. Led, and F. Abildgaard. Prog. Nucl. Magn. Reson. Spectrosc. **22**, 255 (1990).
37. O.W. Sorensen, G.W. Eich, M.H. Levitt, G. Bodenhausen, and R.R. Ernst. Prog. Nucl. Magn. Reson. Spectrosc. **16**, 163 (1983).
38. L.E. Kay and R.E.D. McClung. J. Magn. Reson. **77**, 258 (1988).
39. D.R. Muhandiram and R.E.D. McClung. J. Magn. Reson. **76**, 121 (1988).
40. L.W. Reeves. *In* Dynamic nuclear magnetic resonance spectroscopy. *Edited by* L.M. Jackman and F.A. Cotton. Academic Press, New York. 1975. pp. 83–130.
41. H.S. Gutowsky, R.L. Vold, and E.J. Wells. J. Chem. Phys. **43**, 4107 (1965).
42. E.J. Wells and H.S. Gutowsky. J. Chem. Phys. **43**, 3414 (1965).

Non-additivity of intermolecular forces in helium and beryllium clusters

O. Novaro

Abstract: New results on nonadditive effects on small beryllium clusters are presented using the LCAO-MO-SCF method including variational and perturbational (MP-4) configuration effects. Three- and four-body contributions to the interaction energy of these clusters are dominant, and are used to explain the very different behaviour of bulk beryllium as compared to liquid helium. This is relevant because the atomic ground states of Be and He are strikingly similar ($1s^2 2s^2$: $^1S_0$ and $1s^2$: $^1S_0$) and also He_2 and Be_2 share the honour of being the two hardest-to-detect dimers in the whole periodic system. The similitude is lost for larger He_n and Be_n systems because the former, as was shown by R.F.W. Bader 25 years ago, have very small three-body energies (≤1%). Be_n clusters will be shown here to have three-body energies that actually outweigh the pairwise additive ones. The consequences of this are discussed.

Key words: intermolecular forces, non-additivity, He and Be clusters.

Résumé : Utilisant la méthode LCAO-MO-SCF, y compris des effets variationnels et perturbationnels (MP-4) de configuration, on a obtenu de nouveaux résultats sur les effets non additifs de petits agrégats de béryllium qui ont été obtenus. Les contributions de trois et quatre corps à l'énergie d'interaction de ces agrégats sont dominants. On utilise cette observation pour expliquer le comportement différent du béryllium em masse par rapport à celui de l'hélium liquide. Ceci présente de l'intérêt parce que les états atomiques fondamentaux du Be et du He sont remarquablement semblables ($1s^2 2s^2$:$^1S_2$ et $1s^2$:$^1S_0$) et aussi parce que le He_2 et le Be_2 se partagent l'honneur d'être les deux dimères les plus difficiles à détecter dans tout le système périodique. À cause du fait, démontré il y a près de 25 ans par R.F.W. Bader, que les premiers ont de très faibles énergies à trois corps (≤1%) la similitude est perdue pour les systèmes He_n et Be_n plus gros. On montrera ici que les agrégats de Be_n possèdent des énergies à trois corps qui l'emporte sur ceux qui sont additifs par paire. On discute des conséquences de ces conclusions.

Mots clés : forces intermoléculaires, non-additivité, agrégats de He et Be.

[Traduit par la rédaction]

Introduction

Certainly the hardest-to-detect elementary dimers are He_2 and Be_2. As recently as 1984 Bondybey (1) could correctly state that the properties of Be_2 remained virtually unknown. The first experimental observation of a He_2 bound state (a single bound state, in fact) is even more recent (2, 3). This makes the helium dimer the weakest molecular bond (4), incomparably more so than any other noble gas dimer. In fact, a recent study by a Canadian laboratory (5) proposes that He($1s^2$) and Be($2s^2$) should have the most similar bonding properties where their X_2 and XH molecules are concerned. On the other hand, the bulk properties of beryllium, a semi-metal, are completely different from those of the noble gases, with the case of helium (a liquid even at the lowest temperatures) having no conceivable similarity to solid Be. Here we look for the answer to the following question: why do the similarities found between noble gas and beryllium dimers completely disappear in large aggregates of these elements? The answer lies in the three-body effects of the Be_3 versus the He_3, Ne_3, etc. trimers, as we shall try to show here.

Received September 19, 1995.

This paper is dedicated to Professor Richard F.W. Bader on the occasion of this 65th birthday.

O. Novaro.[1] Instituto de Física, Universidad Nacional Autonoma de México A.P.20-364, México 01000 D.F., México.

[1] Member of El Colegio Nacional.

The first fully ab-initio study of three-body nonadditive effects was carried out by R.F.W. Bader et al. (6) (the definition of nonadditive contributions to the energy will be discussed in the following section). They reached the following conclusion: nonadditive contributions to the energy of He_3 calculated at the LCAO-MO-SCF level of approximation, were 10 times larger than estimated before by perturbation treatments (7). Still, their relative role in He_3 binding was at most a few percent of the pairwise additive contributions (6). KoČos and LeČ (8) confirmed these results to be valid at the Hartree–Fock limit. The convergence of the many-body expansion for He_n clusters was first tested by Novaro and Beltrán-López (9) at this same level of accuracy. Much more recently, high level ab-initio calculations 910) have again confirmed that many-body nonadditive interactions are a few percent of the pairwise additive contributions for small He_n clusters.

As concerns Be_3 and Be_4, they were studied by Novaro and KoČos (11), also at the LCAO-MO-SCF level, who found that nonadditive effects were quite large, large enough in fact to make the convergence of the many-body expansion (see following section) doubtful at best. We here present recent results (12) at the CI level for Be_n clusters that confirm that the main difference between bulk He and Be is based on their nonadditive energies.

Method

In the quantum mechanical study of the total energy of an *n*-

particle system, the interaction energy is computed as the total energy of the system minus the energy of its constituents:

$$[1] \quad E_{int}(n) = E(n) - \sum_{i=1}^{n} E_i$$

where E_i is the calculated energy (at the same level of precision as the calculation of $E(n)$) for the i^{th} particle of the system. The interaction energy $E_{int}(n)$ in turn can be divided in terms of different order interactions within the system. One can define the interactions between pairs, triplets, etc. up to interactions involving n particles simultaneously. By defining the sum of the calculated energies of the n individual particles as the one-body energy:

$$[2] \quad E_1(n) = \sum_{i=1}^{n} E_i$$

we can go on to define the two-body energy of the system as:

$$[3] \quad E_2(n) = \sum_{i<j}^{\{n\}} E_{ij}$$

the three-body energy as:

$$[4] \quad E_3(n) = \sum_{i<j<k}^{\{n\}} E_{ijk}$$

the four-body energy as:

$$[5] \quad E_4(n) = \sum_{i<j<k<l}^{\{n\}} E_{ijkl}$$

To obtain $E_2(n)$ we sum up the interaction energy of all pairs from which the individual particle energies are subtracted. To obtain $E_3(n)$ we similarly add the interactions of all triplets from which the component pair and individual particle energies are subtracted, and so on. Through these definitions the interaction energy of an n-particle system can be expressed as a finite sum

$$[6] \quad E_{int}(n) = E_2(n) + E_3(n) + E_4(n) + \ldots\ldots E_n(n)$$

This is the many-body expansion of the interaction energy and it will be considered to be convergent if the higher order terms are systematically smaller than the lower order terms. In fact, in many applications to study large aggregates, the hypothesis that E_3 (n) and higher terms are negligible with respect to E_2 (n) is postulated uncritically.

We here, on the contrary, want to calculate E_3 (n), etc. with the highest possible precision. We must stress that eq. [6] provides an exact representationof the interaction energy of an n-particle system. Only the level of approximation with which the different terms are calculated limits the precision within E_{int} (n) is given.

For the case of small Be and Li clusters, previous calculations at the SCF level already exist for the multibody expansion. To go beyond the SCF level we here use the Møller–Plesset perturbation theory approximation to the correlation energy corrections. We do these calculations utilizing the Gaussian-92 program (13) on UNAM's Cray-YMP4/468 computer. The basis set used is the Gaussian-92 internal 6-311+G(3df) having one diffuse p-function, three 5d-functions, and one 7f-function. The frozen-core approximation of the correlation energy is obtained at the fourth-order Møller–Plesset approximation.

Fig. 1. Potential energy curves for the beryllium and lithium dimers.

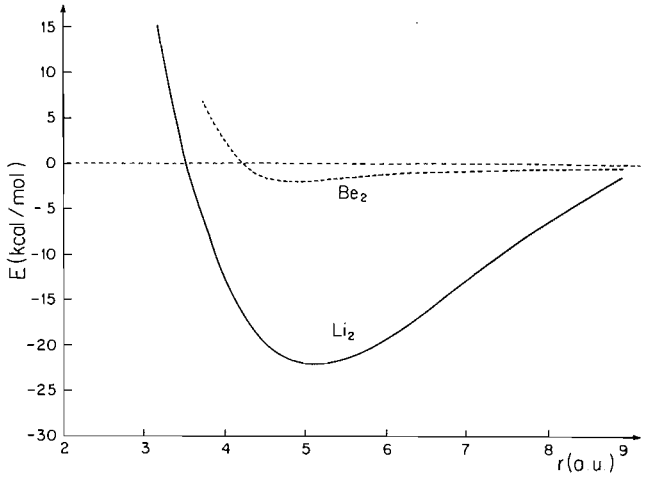

In reality the computational cost added to the calculation of the total energy of an n-particle system by calculating its different m-body contributions given in eq. [6] is not high because $m \leq n$ and $E_m(n)$ implies much less computer memory than $E(n)$ itself. On the other hand, the individual m-body terms contained in the sum:

$$E_m(n) = \sum_{i<j<\ldots<m}^{\{n\}} E_{ij\ldots m}$$

all have different geometries so several configurations for the triplets, quartets, etc. have to be calculated.

Results

Using the method described in the preceding section, we calculated the interaction energies of the Be_2, Be_3, Be_4, and Li_2, Li_3, Li_4 systems as well as their pairwise additive and many-body nonadditive contributions. These energies are given in Table 1. The first thing we notice is that the Be dimer is very slightly bound, especially compared to the Li dimer. This is also evident in Fig. 1, which shows for Li_2 a deep potential energy well with steep walls towards both the united-atom and the separated-atom limits. For Be_2, in contrast, a very shallow well, as well as a very flat potential energy curve, is evident. In fact, the Be_2 curve resembles noble gas dimer curves, very different from that of Li_2. But as we look at the other numbers in Table 1, the differences between beryllium and lithium seemingly diminish. As concerns the interaction energy, for Be_3 it already is quite similar to that for Li_3 and for Be_4, in fact, it is even more attractive than for Li_4.

Also notable is the very poor convergence of the many-body expansion for both lithium and beryllium. In Li_3 three-body repulsions already cancel over 50% of the pair attractions. Li_4 is even more extreme as $E_3(n)$ is larger in magnitude

Table 1. Many-body decomposition of the interaction energy $E_{int}(n)$ onto pairwise $E_2(n)$, three-body $E_3(n)$, and four-body $E_4(n)$ contributions, for the Be_2, Be_3, Be_4, Li_2, Li_3, and Li_4, clusters.

Cluster Be_n, Li_n	Total energy $E(n)$	$E_{int}(n)$	$E_2(n)$	$E_3(n)$	$E_4(n)$	Total non-additive contribution
Be_2	−29.229 29	−0.002 89	−0.002 89	—	—	—
Be_3	−43.881 26	−0.041 15	−0.000 75	−0.040 40	—	−0.040 40
Be_4	−58.600 40	−0.146 72	+0.031 50	−0.210 80	−0.032 58	−0.178 22
Li_2	−14.899 16	−0.035 09	−0.035 09	—	—	—
Li_3	−22.344 43	−0.048 32	−0.096 93	−0.048 61	—	+0.048 61
Li_4	−29.829 83	−0.101 66	−0.163 42	−0.178 82	−0.117 06	+0.061 76

and opposite in sign to the pair energy $E_2(n)$. This means that all of the attraction of Li_4 may be considered due to the four-body term $E_4(n)$. If we pause to consider that there is only one quartet inscribed in Li_4 versus four triplets and six pairs, it becomes evident that for larger clusters higher order nonadditive terms in the many-body expansion will always dominate the pairwise additive energies.

In the case of Be_n clusters the situation is even more striking. For Be_3 almost all of the interaction energy $E_{int}(n)$ comes from the three-body term. As would be expected from the noble-gas-like potential energy curve for Be_2, pairwise attractions are always very small; it is only the comparatively large three-body attractions that make Be_3 stable, with some 20 times larger binding energy than Be_2. In the case of Be_4 this is even more evident as all of the stabilization is due to three-body attractions. The pairwise term in fact is repulsive. This means simply that the equilibrium positions of the four beryllium nuclei are determined by the strong three-body attractions, making the inscribed dimers somewhat short, so short that each Be–Be distance falls on the repulsive part of the curve in Fig. 1. But even these pair repulsions are smaller than the repulsive four-body term. The main result, however, is that for Be_4 clusters the stabilization comes entirely from three-body interactions. We can safely generalize: Be_n cluster geometries and stabilities are mainly determined by nonadditive forces. This is in absolute contrast with He_n clusters for which nonadditive effects are very small. We shall see the consequences of this in the following section.

Discussion

We have seen that nonadditive contributions to the binding energy of the smallest Be_n clusters ($n \geq 3$) are decisive. For medium-size clusters ($n \geq 5$) one can observe the fact that three-body contributions to the total binding energy are larger than pairwise (two-body) contributions has become a rule, rather than an exception. Let us pause for a moment to consider the consequences of this fact. Two-body energies are directly associated with the chemical bond between two individual partners in a given cluster. Three-body energies are not localized on a particular bond. They really correspond to the change in the distance and the energy of any bond between two partners introduced by a third one. They are by their very definition delocalized. The fact that three-body terms are so large in beryllium has great consequences.

For helium, we have known since the work of Bader et al. (6) that three-body effects, while non-negligible, are a small correction of the total energy. Thus we may conclude that the "weakest and weirdest molecular bond (4): He_2" may only lead to the very weakly bound bulk behaviour of liquid helium even at temperatures near 0 K.

The second weakest elementary chemical bond, Be_2, does not prepare us for the bulk beryllium metal properties at room temperature. This is because Be_2 does not contain the main cause of the metal stability: the quite large three-body energy appears only for beryllium trimers and beyond. Dominant in size, delocalized in nature, it is in essence the image of a metallic bond-in-the-making even for the small Be_3, Be_4 molecules.

Although the language of nonadditivity is not too familiar, what we have concluded above is of course not a new concept. We have seen in the previous section, for instance, that the nonadditivity for Li_n clusters is also quite large. We could make a parallel discussion about H and Li, with apparently quite indistinguishable and ($1s^1$: and $1s^2 2s^1$:$2S_{1/2}$) ground states. Yet H_2 is tightly bound while H_3 is very unstable. In contrast, the change from Li_2 to Li_3 and beyond is only a straightforward tendency to the classical metal bond in lithium. The argument of the presence of the empty $2p^0$ subshell in Li in regard to this tendency is too well known to merit any further comment here. Naturally, for Be the $2p^0$ subshell should play a quite similar role.

In short, the answer to our original question: since He_2 and Be_2 have similar bonding properties, why are bulk beryllium and helium so utterly different? has an obvious answer. The many body effects are very different in both cases. By the expression "many-body effects" we are not speaking of 10^{24} particles interacting. We in fact are referring to much smaller system. Many-body effects are already dominant for the small "metallic" Be_3 and Li_3 clusters.

Acknowledgements

A quarter of a century has elapsed since I met Richard Bader during his first trip to Mexico, invited by our mutual friend Virgilio Beltrán. For a person with a fresh Ph.D. and new research responsibilities and projects, it was an invaluable and invigorating experience to collaborate with Richard, a brilliant and enthusiastic scientist with whom we established the first ab-initio study of three-body nonadditive effects. His irrepressible energy (even though he was particularly sensitive to the high altitude of Mexico City) and the pleasure of sharing quality moments with our families linger on in my memory. Even though I have since pursued other fields of research, my

curiosity about nonadditive effects has not waned and in fact it has given me the chance of collaborating with several friends in different countries, like John Murrell, Wlodek KoČos, Ludwig Bruch, Feng Wen-Lin, Enrico Clementi, Ilya Kaplan, and others. Curiously, with Richard Bader our opportunities for scientific and even personal contacts have been scarce. My loss. I always, however, have followed his many successes in research and his growing scientific stature and my admiration for him is ever increasing. I sincerely congratulate the authors of this initiative to honour Richard Bader and hope that this very modest contribution on my part to this special volume of the Canadian Journal of Chemistry serves to add my sincere homage to this exceptional scientist and friend.

I would also like to thank Ilya Kaplan and Jorge Hernández for the use of the beryllium results that will appear in more extended form in a joint paper. To Ilya I am further indebted for his reading of and comments on this manuscript and, in general, for his unselfish help. I also acknowledge financial support from Conacyt and DGAPA to this line of research.

References

1. V.E. Bondybey. Chem. Phys. Lett. **109**, 436 (1984).
2. F. Luo, G.C. McBane, G. Kim, C.F. Giese, and W.R. Gentry. J. Chem. Phys. **98**, 3564 (1993); J. Chem. Phys. **100**, 4023 (1994).
3. W. Schöllkopf and J.P. Toenies. Science, **266**, 1345 (1994).
4. W.R. Gentry. Proc. Annu. Meet. Am. Phys. Soc. San José, Calif. **40**(1), 269 (1995). Paper F22-3.
5. P.J. Bruno, G.A. DiLabio, and J.S. Wright. J. Phys. Chem. **96**, 6269 (1992).
6. R.F.W. Bader, O. Novaro, and V. Beltrán-López. Chem. Phys. Lett. **8**, 568 (1971).
7. J.N. Murrell, M. Randic, and D.R. Williams. Proc. R. Soc. London, Ser. A: **284**, 566 (1966).
8. W. KoČos and A. LeČ. Int. J. Quantum Chem. **10**, 545 (1972).
9. O. Novaro and V. Beltrán-López. J. Chem. Phys. **56**, 815 (1972).
10. C.A. Parish and C.E. Dykstra. J. Chem. Phys. **98**, 437 (1993).
11. O. Novaro and W. KoČos. J. Chem. Phys. **67**, 5066 (1977).
12. I. Kaplan, J. Hernández, I.O. Blake, and O. Novaro. Phys. Rev. A. In press.
13. M.J. Frisch, G.W. Trucks, M. Head-Gordon, P.M.W. Gill, M.W. Wong, J.B. Foresman, B.G. Johnson, H.B. Schlegel, M.A. Robb, E.S. Replogle, R. Gomperts, J.L. Andres, J.L. K. Raghavachari, J.S. Binkley, C. González, R.L. Martin, D.J. Fox, D.J. Defrees, J. Baker, J.J.P. Stewart, and J.A. Pople. Gaussian 92, Revision C.4. Gaussian Inc., Pittsburgh, Pa. 1992.

On the differential geometry of interatomic surfaces

Paul L.A. Popelier

Abstract: Using differential geometry, we propose the total curvature of interatomic surfaces to characterize bonds. In this way visual interpretations of interatomic surfaces are now rigorously quantified. The analysis of the intrinsic geometry of an interatomic surface is implemented in the program MORPHY 2.0. It is shown that the total curvature depends on anionic polarizability, electronegativity differences, and steric effects determined by the total chemical environment of the bonded atoms in question. In general the proposed index measures the external chemical distortion of an atom in a molecule. It can be used in the context of uniform electric fields and in conformational studies.

Key words: interatomic surfaces, differential geometry, total curvature.

Résumé : Utilisant la géométrie différentielle, on propose la courbature totale des surfaces interatomiques pour caractériser les liaisons. De cette façon, des interprétations visuelles des surfaces interatomiques sont maintenant rigoureusement quantifiées. L'analyse de la géométrie intrinsèque d'une surface interatomique est introduite dans le programme MORPHY 2.0. Il a été démontré que la courbature totale dépend de la polarisabilité anionique, des différences d'électronégativité et des effets stériques déterminés par l'environnement chimique total des atomes en question qui sont liés. En général, l'indice proposé mesure la distorsion chimique externe d'un atome dans une molécule. On peut l'utiliser dans le contexte de champs électriques uniformes et dans des études conformationnelles.

Mots clés : surfaces interatomiques, géométrie différentielle, courbature totale.

[Traduit par la rédaction]

1. Introduction

The gradient vector field of the charge density ρ is the carrier of the topological information hidden in molecules, complexes, and crystals. It naturally partitions these systems into atomic basins, each of which adopts a particular shape governed by the *total* charge density. In the course of the last two decades many publications in the field of "Atoms in Molecules" (AIM) have shown pictures of gradient vector fields of ρ revealing a wealth of atomic shapes.

It emerges that some shapes recur repeatedly like the signature of an atom in a given chemical environment (1). On the other hand, it also appears that the geometry of the interatomic surfaces (IAS) that bound the atomic basin is very sensitive to the full chemical environment of the atom.

In view of these observations, the introduction of a measure to quantitatively characterize the shape of an IAS would be timely. For that purpose we propose to use concepts from a mathematical branch called differential geometry since it rigorously provides intrinsic properties of geometrical objects using calculus.

First, selected differential geometrical concepts are briefly reviewed and immediately illustrated with a simple (parametrized) model surface. In Sect. 3.1 we concisely expound on how the analytical expression for an interatomic surface is constructed. Some technical details on the computation of the total curvature C are given in Sect. 3.2. The last section (Sect. 4) presents various data sets of total curvatures for small molecules. The meaning of this measure is interpreted for a series of ionic lithium compounds and related to the behaviour of the IAS in a uniform electric field. Inspecting the hydride series AH_n, it is suggested that charge transfer influences the total curvature. It is demonstrated by means of a series of 10 methyl derivatives that C does not solely parallel charge transfer. Finally, it is shown that our index can be used in conformational studies (e.g., ethane).

2. Mathematical concepts

Differential geometry is the study of geometric figures using the methods of calculus. In particular, the introductory theory investigates curves and surfaces embedded in three-dimensional Euclidean space (2). It is a vast and rich area of mathematics (3–5) from which we will selectively sample and review the elements neccessary for the present investigation. Although most elegant and compact, we have chosen not to formulate the following equations along the lines of tensor analysis.

It can be proven that a curve in three-dimensional space is uniquely determined by two local invariant quantities, curvature and torsion, as functions of arc length. Similarly, a surface is uniquely determined by local invariant quantities called the first and second fundamental forms. In the following brief review, $\boldsymbol{x} = \boldsymbol{x}(u, v)$ denotes a coordinate patch on a sufficiently differentiable surface. For convenience we introduce the notation $\boldsymbol{x}_u \equiv \partial \boldsymbol{x}/\partial u$ and $\boldsymbol{x}_v \equiv \partial \boldsymbol{x}/\partial v$, such that

Received October 12, 1995.

This paper is dedicated to Professor Richard F.W. Bader on the occasion of his 65th birthday.

P.L.A. Popelier.[1] University Chemical Laboratory, Lensfield Road, Cambridge CB2 1EW, U.K.

[1] Present address: Department of Chemistry, University of Manchester Institute of Science and Technology, PO Box 88, Manchester M60 1QD, United Kingdom. Telephone: 44-161-2004511. Fax: 44-161-2367677. E-mail: pla@umist.ac.uk

Fig. 1. Representation of two simple surfaces described by the model equation [2] (see text). The left surface corresponds to $\alpha = 1$ and $\beta = -1$ and is hyperbolic. The right surface is elliptic and has been generated with both parameters α and β set to 1. The origin of each surface is marked by a black dot.

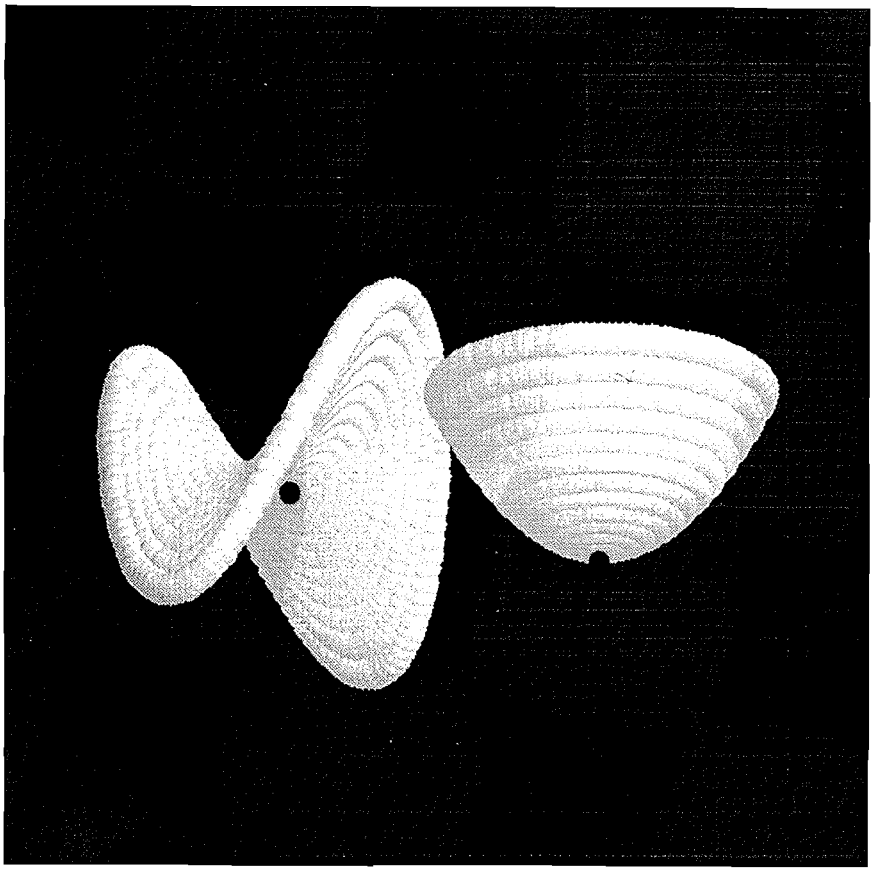

$d\boldsymbol{x} = \boldsymbol{x}_u du + \boldsymbol{x}_v dv$. The function I_1 defined below is called the *first fundamental form* of $\boldsymbol{x}$.

$$[1] \qquad \begin{aligned} I_1 &= (\boldsymbol{x}_u \cdot \boldsymbol{x}_u)du^2 + 2(\boldsymbol{x}_u \cdot \boldsymbol{x}_v)du dv + (\boldsymbol{x}_v \cdot \boldsymbol{x}_v)dv^2 \\ &= E du^2 + 2F du dv + G dv^2 \end{aligned}$$

where $E = \boldsymbol{x}_u \cdot \boldsymbol{x}_v$, $F = \boldsymbol{x}_u \cdot \boldsymbol{x}_v$, and $G = \boldsymbol{x}_v \cdot \boldsymbol{x}_v$. The quantities E, F, and G are called the *first fundamental coefficients.*

As a direct illustration of the developed theory we will compute essential quantities defined by these and following equations for a simple model surface described by:

$$[2] \qquad \boldsymbol{x}(u, v) = u\boldsymbol{e}_1 + v\boldsymbol{e}_2 + (\alpha u^2 + \beta v^2)\boldsymbol{e}_3$$

where $\boldsymbol{e}_1$, $\boldsymbol{e}_2$, and $\boldsymbol{e}_3$ are the unit vectors of a global axis system, u, v are the independent variables, and α, β are parameters introducing the appropriate flexibility to illustrate certain surface characteristics semiquantitively. Figure 1 represents two examples of simple surfaces described by eq. [2]. The left surface corresponds to $\alpha = 1$, $\beta = -1$ and the right one to $\alpha = 1$, $\beta = 1$.

Clearly, using the first derivatives

$$[3] \qquad \begin{aligned} \boldsymbol{x}_u &= \boldsymbol{e}_1 + 2\alpha u \boldsymbol{e}_3 \\ \boldsymbol{x}_v &= \boldsymbol{e}_2 + 2\beta v \boldsymbol{e}_3 \end{aligned}$$

we obtain for the first fundamental coefficients:

$$[4] \qquad \begin{aligned} E &= \boldsymbol{x}_u \cdot \boldsymbol{x}_u = 1 + 4\alpha^2 u^2 \\ F &= \boldsymbol{x}_u \cdot \boldsymbol{x}_v = 4\alpha\beta uv \\ G &= \boldsymbol{x}_v \cdot \boldsymbol{x}_v = 1 + 4\beta^2 v^2 \end{aligned}$$

The first fundamental form I_1 is positive definite and depends only on the surface and not on the particular representation. The first fundamental coefficients themselves are not invariant under a parameter transformation. Denoting the dimensions of u and v by D_u and D_v, respectively, and knowing that components of $\boldsymbol{x}$ are expressed in units of length or L, it is clear that components of $\boldsymbol{x}_u$ have the dimension L/D_u. The dimensions of E, F, and G are L^2/D_u^2, L^2/D_uD_v, L^2/D_v^2, respectively.

An important intermediate quantity is $EG - F^2$ and it can be proven that

$$[5] \qquad EG - F^2 = |\boldsymbol{x}_u \times \boldsymbol{x}_v|^2$$

The area A of a surface patch is calculated with the aid of this quantity by the double integral:

$$[6] \qquad A = \int\int \sqrt{EG - F^2}\, du dv$$

In this work, areas of patches on interatomic surfaces approximating this integral are obtained by Gauss–Legendre quadrature. For the model surface this quantity amounts to:

$$[7] \qquad EG - F^2 = 4\alpha^2u^2 + 4\beta^2v^2 + 1$$

In an analogous manner we now proceed to define the *second fundamental form* denoted by I_2 by:

$$[8] \qquad \begin{aligned} I_2 &= -\mathrm{d}\boldsymbol{x}\cdot\mathrm{d}\boldsymbol{N} = -(\boldsymbol{x}_u\mathrm{d}u + \boldsymbol{x}_v\mathrm{d}v)\cdot(\boldsymbol{N}_u\mathrm{d}u + \boldsymbol{N}_v\mathrm{d}v) \\ &= L\mathrm{d}u^2 + 2M\mathrm{d}u\mathrm{d}v + N\mathrm{d}v^2 \end{aligned}$$

where $L = -\boldsymbol{x}_u\cdot\boldsymbol{N}_u$, $M = -\frac{1}{2}(\boldsymbol{x}_u\cdot\boldsymbol{N}_v + \boldsymbol{x}_v\cdot\boldsymbol{N}_u)$, $N = -\boldsymbol{x}_v\cdot\boldsymbol{N}_v$, and $\boldsymbol{N}$ is the unit normal defined by:

$$[9] \qquad \boldsymbol{N} = \frac{\boldsymbol{x}_u \times \boldsymbol{x}_v}{|\boldsymbol{x}_u \times \boldsymbol{x}_v|}$$

The functions L, M, and N are called the *second fundamental coefficients*.

As before, the function I_2 is invariant (in the same sense that I_1 is invariant) under a parameter transformation that preserves the direction of $\boldsymbol{N}$.

Alternative expressions for L, M, and N that we have implemented for this work are

$$[10] \qquad L = \boldsymbol{x}_{uu}\cdot\boldsymbol{N}, \qquad M = \boldsymbol{x}_{uv}\cdot\boldsymbol{N}, \qquad N = \boldsymbol{x}_{vv}\cdot\boldsymbol{N}$$

The results for these newly introduced quantities for the model surface are

$$[11] \qquad \boldsymbol{x}_{uu} = 2\alpha\boldsymbol{e}_3, \qquad \boldsymbol{x}_{uv} = 0, \qquad \boldsymbol{x}_{vv} = 2\beta\boldsymbol{e}_3$$

$$[12] \qquad \boldsymbol{x}_u \times \boldsymbol{x}_v = 2\alpha u\boldsymbol{e}_1 - 2\beta v\boldsymbol{e}_2 + \boldsymbol{e}_3$$

$$[13] \qquad |\boldsymbol{x}_u \times \boldsymbol{x}_v| = (4\alpha^2u^2 + 4\beta^2v^2 + 1)^{-1/2}$$

$$[14] \qquad L = \boldsymbol{x}_{uu}\cdot\boldsymbol{N} = 2\alpha(4\alpha^2u^2 + 4\beta^2v^2 + 1)^{-1/2}$$

$$M = \boldsymbol{x}_{uv}\cdot\boldsymbol{N} = 0$$

$$N = \boldsymbol{x}_{vv}\cdot\boldsymbol{N} = 2\beta(4\alpha^2u^2 + 4\beta^2v^2 + 1)^{-1/2}$$

Since $\boldsymbol{N}$ is dimensionless the dimension of L is L/D_u^2.

A discriminant D defined as $LN - M^2$ determines qualitatively the nature of the surface in the neighbourhood of a point. We can distinguish four cases: a point is elliptic, hyperbolic, parabolic, or planar when D is strictly positive, strictly negative, zero (without L, M, N all being zero), and when $L = M = N = 0$, respectively. It should be pointed out that ellipticity, etc. is a *local* property, i.e., it refers to the character of a single point on a surface, not to the global surface. This classification is again independent of the representation of the surface. The discriminant for our model surface is given by:

$$[15] \qquad LN - M^2 = 4\alpha\beta(4\alpha^2u^2 + 4\beta^2v^2 + 1)^{-1}$$

In the neighbourhood of an elliptic point the surface lies on the same side of the tangent plane at the point. On the other hand, the surface lies on both sides of the tangent plane in the neighbourhood of a hyperbolic point. Such a point is easy to visualize as the center of an ordinary saddle.

The central quantity for our present discussion is the *Gaussian curvature* K at a given point. A convenient definition is

$$[16] \qquad K = \frac{LN - M^2}{EG - F^2}$$

This is again an invariant property of the surface. Since $(EG - F^2) > 0$ the sign of K classifies a point as elliptic, hyperbolic, or parabolic (or planar). It is clear that on each point of a plane the Gaussian curvature K vanishes. Another useful special case is the spherical surface. For every point on a sphere with radius a we have $K = 1/a^2$. It follows from the previous dimensional analysis that the dimension of K for a point on a general surface is indeed $1/L^2$. The Gaussian curvature for the model surface is

$$[17] \qquad K = 4\alpha\beta(4\alpha^2u^2 + 4\alpha^2v^2 + 1)^{-2}$$

As an example we focus on the origin of each surface in Fig. 1. These points are marked by black dots and correspond to $u = v = 0$. Consequently, $K = 4\alpha\beta$ and the classification of the origin depends only on the signs of α and β and on whether they vanish. It then follows that the origin in the left surface is hyperbolic and in the right surface is elliptic. Since the denominator of K and $(4a^2u^2 + 4a^2v^2 + 1)^{-2}$ in eq. [17] is strictly positive, this statement is true for any point on the respective surface, not just the origin. Furthermore, increased values of α or β steepen the surface at the origin and increase the Gaussian curvature, which is in line with geometrical intuition.

When the Gaussian curvature is integrated over a surface S we obtain the *total curvature* C.

$$[18] \qquad C = \int\int_S K\mathrm{d}S$$

It is very important to note that C is dimensionless. It adopts the following analytical form for the model surface.

$$[19] \qquad \begin{aligned} C &= \int\int_R K\mathrm{d}S = \int\int_D K(\boldsymbol{x}(u, v))|\boldsymbol{x}_u \times \boldsymbol{x}_v|\mathrm{d}u\mathrm{d}v \\ &= 4\alpha\beta\int_0^u\int_0^v (4\alpha^2u^2 + 4\alpha^2v^2 + 1)^{-3/2}\mathrm{d}u\mathrm{d}v \end{aligned}$$

If interatomic surfaces were *compact*, characterizing them using the total curvature C would not quite lead to a useful classification. This statement is a corollary of two well-known theorems, as is explained below. According to the Heine–Borel theorem, a surface is compact if and only if it is bounded and closed. A sphere and a torus are examples of compact surfaces. On the other hand, the Gauss–Bonet theorem proves that for compact surfaces (which must be orientable and sufficiently differentiable) the total curvature is just a multiple of π and is a topological invariant. The total curvature of a sphere, for example, is 4π and for a torus is zero. Since interatomic surfaces are not bounded, they are not compact. Therefore the Gauss–Bonet theorem does not apply to them. As a result we do not *necessarily* recover trivial multiples of π when computing C for an IAS.

3. Implementation

3.1 Analytical expression of the surface

An IAS consists of a bundle of gradient paths that originate at infinity and terminate at the so-called *bond critical point* (6). This point is one of the four possible types of critical points (i.e., $\nabla\rho = \mathbf{0}$) and is denoted by $(3,-1)$. It can be regarded as the center of the IAS. Gradient paths are traced by solving the following system of ordinary differential equations given an initial point through which the path is passing:

$$[20] \qquad \frac{d\boldsymbol{r}}{dl} = \frac{\nabla\rho(\boldsymbol{r})}{\|\nabla\rho(\boldsymbol{r})\|}$$

It has been shown before that solving this system with analytical tools is possible but unsatisfactory (7). A more successful scheme solves the ordinary differential equations using a numerical integrator with adaptive step-size control like the Cash–Karp–Runge–Kutta method (8) and then fits Chebyshev polynomials and trigonometric functions to the points on the IAS. Each component $x_i(l,\theta)$ of a point on the surface is then given by the *explicit* parametric equation:

$$[21] \qquad x_i(l,\theta) = \sum_{m,n}^{M,N} (d_{inm}\cos(m\theta) + d'_{inm}\sin(m\theta))T_n(l)$$

where d_{inm}, d'_{inm} are fitted, T_n is the nth degree Chebyshev polynomial, l is the length of a gradient path on the IAS, and θ is an angular coordinate.

The IAS is constructed by following the gradient paths backwards, away from the bond critical point, starting from a set of *initial points*. These initial points form a circle with a small radius r_ε (typically 0.001 atomic units) in the *eigenplane* (7). The Chebyshev fit only extends over the interval $[-l_{max}, 0]$.

The analytical description of the IAS leaves a small puncture near the bond critical point that we have minimalized by setting r_ε to a really small value like 10^{-6}. So, practically, we assume that the IAS is only bounded for large negative l values and not for $l = 0$.

Excellent fits can be obtained with a moderate number of fitting basis functions (fewer than 50). The quality of the fit is measured by quasi-continuous error estimates such as a global root-mean-square value (7). A value of 10^{-4} atomic units (au) or less is quite typical for a surface up to the 10^{-9} au charge density contour surface. This basically means that the analytical expressions perfectly reproduce the numerical surface.

3.2 Calculation of total curvature

Since the availability of an analytical expression for the IAS (7) it has been possible to obtain fast and accurate surface-related derivatives for computing local and integrated surface curvatures. Derivatives of high-order Chebyshev polynomials do not pose problems and are evaluated rapidly.

It is crucial to test the stability of the total curvature C with respect to various parameters. All surfaces have been fitted with Chebyshev polynomials up to order 40 and with a set of 51 trigonometric functions.[2] The relative accuracy of the differential equation integrator was kept at 10^{-4} (for a precise definition see ref. 8, p. 711) and the minimum allowed step size was fixed at 10^{-7} au.

Secondly, the behaviour of C was monitored as a function of the size of the patch on the IAS. In general, interatomic surfaces extend to infinity and a well-behaved total curvature should converge with more negative l values. Tests for the N|H IAS in ammonia show rather slow convergence but stability is essentially reached for $l < -10$ au (the changes in C are of the order of 10^{-4}). The total curvature varies slightly more for the C|O surface in carbon monoxide. It is well known that Gaussian functions do not properly describe the outer regions of a molecule. We must therefore suspect that gradient paths are not very meaningul in zones where the charge density is as low as 10^{-12} au or less, especially at a moderate level of theory like HF/6-31G**. Consequently the local curvature of the IAS in the outer region is not trustworthy. Since the total curvature is a purely geometrical quantity, not weighted by (extremely low) charge densities or their gradient, the outer region will unduly affect C.

This phenomenon has prompted us to compute the total curvature only for a well-defined and reliable patch on the IAS. There is good evidence that the 0.001 au charge density envelope may be considered as the practical edge of the molecule and thus of its constituent atoms. We have fitted a very accurate continuous contour line to points on the IAS where $\rho = 0.001$ au. This smooth and analytical contour line then bounds the IAS everywhere. All total curvature values quoted below have been computed with a grid extending only to the 0.001 au charge density contour level. We believe that results drawn from these numbers genuinely reflect what happens well inside the molecule and should therefore relate to chemical insight.

Finally, the effect of stability of C on the quadrature grid size was explored. Throughout, we use a grid with 60 radial and 120 angular points, which is sufficient.

4. Applications

Before interpreting the data a general comment is worth inserting. The "outer" shape of an atomic basin is determined by the geometry of the interatomic surfaces bounding it. This is the shape we focus on in the following discussion. But an atom also has an "inner" shape, which is determined by the pattern of the gradient vector field inside the atom. One might say that gradient paths distort space. They establish non-Euclidean geodesics and exhibit a Riemannian curvature that characterizes the whole atomic subspace. This is of course the ultimate curvature to be investigated and is therefore the subject of future work.

All wave functions were generated using the program CADPAC (9) using the 6-31G** basis set (10), 6-31GE,[3] and a [13*s*5*p*/4*s*3*p*] set (4) for lithium.

Table 1 presents the total curvature for a set of four ionic closed-shell lithium compounds: LiF, LiH, $LiCH_3$, and LiO^-. Three quantities consistently indicate that these compounds are ionic. The charge density at the bond critical point or ρ_b

[2] The trigonometric basis set is $\{1, \cos(n\theta), \sin(n\theta)\}$, where $n = 1,2,\ldots,25$.

[3] The basis set is obtained from the 6-31G basis set by adding diffuse functions and polarization functions. More details are found in the CADPAC manual.

Table 1. The total curvature C and additional quantities[a] of some ionic lithium compounds computed using two different basis sets.

Molecule	d(Li–A)[b]	ρ_b	$\nabla^2\rho_b$	q(Li)	$L(\Omega)$	C
HF/6-31G**						
LiF	1.537	0.086	0.767	0.910	3×10^{-4}	1.27
LiH	1.616	0.036	0.137	0.898	7×10^{-5}	2.75
$LiCH_3$	2.053	0.043	0.189	0.907	5×10^{-5}	3.05
LiO^-	1.600	0.094	0.786	0.779	3×10^{-4}	2.97
HF/6-31GE						
LiF	1.570	0.077	0.671	0.935	3×10^{-4}	1.49
LiH	1.622	0.038	0.138	0.908	7×10^{-5}	2.70
$LiCH_3$	1.997	0.044	0.186	0.911	9×10^{-5}	2.95
LiO^-	1.575	0.086	0.699	0.850	1×10^{-4}	3.92
MP2/6-31GE						
LiF	1.593	0.073	0.596	0.925	1×10^{-5}	1.68
LiH	1.612	0.038	0.141	0.904	6×10^{-6}	2.64
$LiCH_3$	1.994	0.041	0.181	0.905	3×10^{-4}	3.02
LiO^-	1.678	0.062	0.472	0.831	3×10^{-5}	6.18

[a]All quantities are given in atomic units unless stated otherwise. Symbols are explained in the main text.
[b]The distance between the two nuclei is given in Å.

is about 10 times smaller than for a typical covalent bond. The Laplacian at the bond critical point or $\nabla^2\rho_b$ is positive and the net charge q(Li) is approaching the value of exactly one. This net charge is obtained by integrating the charge density over the atomic basin of lithium and substracting this population from the nuclear charge. The integration error is typically assessed by $L(\Omega)$, which should ideally vanish (12).

It is a good approximation to regard the charge transfer from lithium to the neighbouring atom as constant within the present series since the maximum discrepancy for q(Li) is only 0.085 e using the 6-31GE basis set. This fact is consistent with the earlier observation of Bader and Beddall (13) for wave functions close to the Hartree–Fock limit. As expected, the well-known AIM quantities are quite insensitive to the variation in basis set. This is also true for the total curvature, with the exception of LiO^- where the highly polarizable O^{2-} anion benefits from the better description provided by the extra diffuse functions.

The inclusion of correlation at the MP2 level does not alter the order $LiF < LiH < LiCH_3 < LiO^-$ as ranked by the total curvature C. It is well known that anions are the most affected by correlation, which is reflected by the pronounced changes for LiO^-. It can be seen from Table 1 that all properties d(Li—A), ρ_b, $\nabla^2\rho_b$, and q(Li) vary considerably for this molecule and only marginally for the other molecules in this set. Since the qualitative conclusions of the present study do not alter with electron correlation we will not systematically investigate its effect on the non-ionic compounds discussed below.

Since the present molecules are nearly completely ionic one may view them as a point charge perturbing a polarizable anion. Exact calculations for the polarizability of free anions yield 15.1 au for F^- (14), 206 au for H^- (15), and an infinite value for O^{2-} (16).[4] This is exactly the order reflected by the total curvature computed with the 6-31GE basis set, predicting that the CH_3^- group must be a very polarizable charge cloud. This conclusion is plausible since the basic methyl anion has a diffuse lone pair of strong sp^3 character and because carbon and hydrogen have a virtually identical electronegativity.

Table 2. The influence of a uniform electric field on the total curvature C of the interatomic surface in the hydrogen molecule and hydrogen fluoride.

Field[a]	$C(H_2)$	C(HF)
−0.050	0.146	1.067
−0.010	0.006	1.386
−0.005	0.001	1.425
−0.001	0.000	1.455
0.000	0.000	1.463
0.001	0.000	1.471
0.005	0.001	1.501
0.010	0.006	1.539
0.050	0.146	1.837

[a]The field strength is expressed in au.

Further evidence that the total curvature C is indeed affected by the extent of polarization of an atom emerges from the behaviour of H_2 and HF in a uniform electric field. The results are shown in Table 2 for a field strength E_z along the molecular axis varying from −0.05 to +0.05 au. Hydrogen fluoride shows an excellent linear correlation ($\rho = 0.9997$) between C and E_z, yielding $C = 7.6973\,E_z + 1.4604$. The linear dependence for H_2 is weaker ($\rho = 0.9883$) and here $C = 3.0349\,E_z - 0.0094$. It is tempting to relate the slope of these equations with $\alpha_s(\Omega)$, which was previously introduced (18) as the associated contribution to the polarizability resulting from the shift in interatomic surface. Using the values quoted in ref. 18 for HF and H_2, the difference in response of the IAS to the applied field could be explained semi-quantitatively. The main point, however, of this small excursion is to indicate that C can be used in studying atoms in electric fields and that the polarization of a charge cloud within an atomic basin does change the intrinsic geometry of its bounding IAS.

The next series of molecules constitutes the classic set of hydrides AH_n where A = H, Li, Be, B, C, N, O, F and n varies, producing H_2, LiH, BeH_2, BH_3, methane, ammonia, water and hydrogen fluoride. Detailed three-dimensional pictures of the atoms encompassed by this set have recently been published for the first time (1). Figure 2 shows the C|H IAS in methane and the corresponding contour map for the Gaussian curvature K.

From Table 3 it is seen that the total curvature for the A|H IAS increases steadily as the charge transfer from H to A increases. Since it was shown before that the charge transfer defined by AIM recovers the basic idea underlying electronegativity, it seems plausible to surmise that the total curvature increases with increasing electronegativity.

[4] The species O^{2-} is unstable with respect to decomposition into a free O^- ion and a free electron; see ref. 17.

(a)

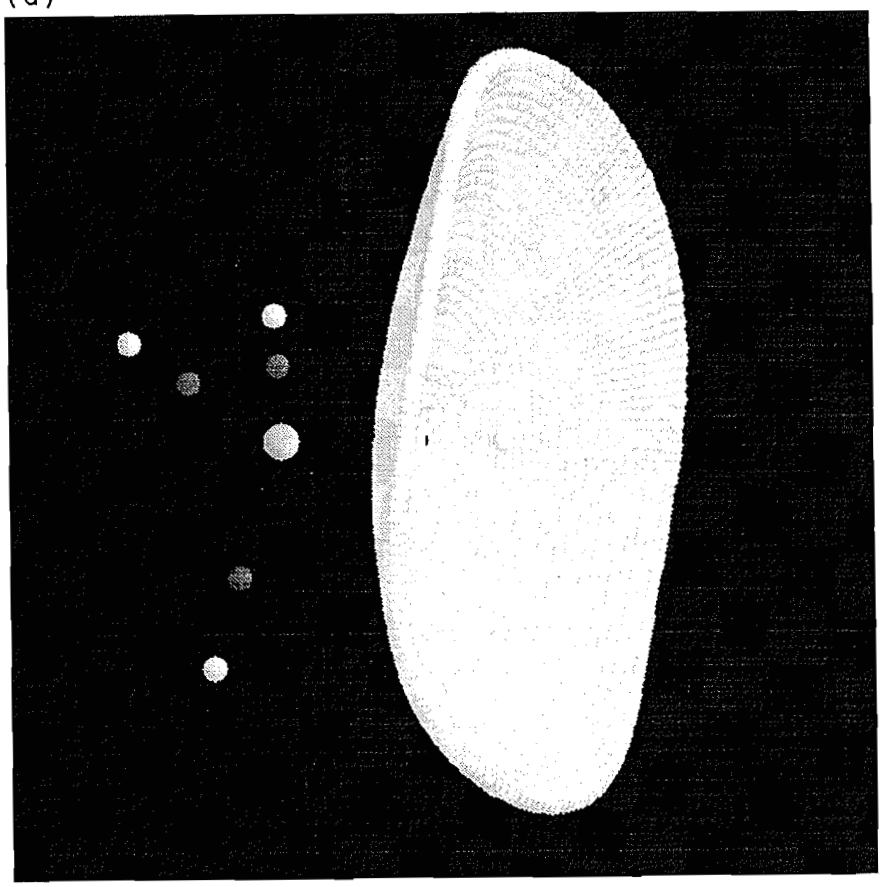

(b)

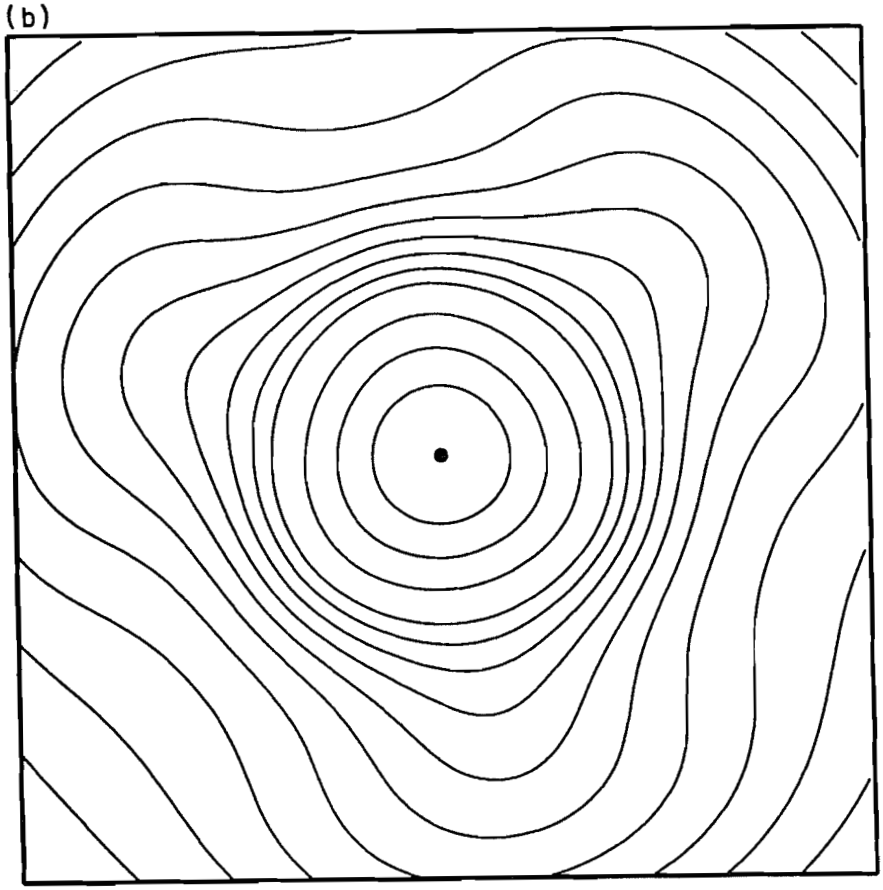

Fig. 2. (*a*) A three-dimensional representation of the C|H interatomic surface in methane. The bond critical points are marked by grey dots. This picture should be compared with the corresponding contour map of Fig. 2*b*. (*b*) A contour map of the Gaussian curvature K of the interatomic surface between C and H in methane. The outer contour line corresponds to a curvature of 0.001 and the contours increase as 0.005, 0.01, 0.015, 0.02, 0.025, 0.03, 0.035, 0.04, 0.045, 0.05, 0.06, 0.07, 0.08, and 0.09. The bond critical point is marked by a dot. Note that the expected threefold symmetry becomes more pronounced towards the outer regions of the interatomic surfaces, which correspond to an l value of about −3.

Table 3. The charge transfer q and the total curvature C and area[a] for the A|H interatomic surface in the second row hydrides AH_n.

Molecules	q(H)	C	Area
H_2	0.000	0.000	28.08
LiH	−0.893	2.741	28.90
BeH_2	−0.873	0.002	35.31
BH_3	−0.718	—[b]	—
CH_4	0.062	0.692	32.00
NH_3	+0.373	1.084	24.88
OH_2	+0.619	1.297	19.18
HF	+0.757	1.463	14.73

[a]The interatomic surface is bounded by a contour line of constant charge density (0.001 au). The area is given in $(au)^2$.
[b]Instabilities in the IAS prevent the computation of a reliable number at present.

Even if charge transfer does influence the total curvature,[5] it cannot be the only effect because the CH bond in methane shows virtually no charge transfer, yet the curvature amounts to 0.692. Similarly, in the $^2\Pi$ diatomic CH the total curvature is reasonable but charge transfer is essentially absent. The series of diatomics, CH, NH, OH, and HF, shows an increase in IAS total curvature resembling that of the present hydride series. These four diatomic molecules are examples of shared interactions characterized by a reasonably large value for ρ_b and a (strongly) negative $\nabla^2\rho_b$ value. In NH, OH, and HF there is an increasing polarization of the shared charge towards the non-hydrogen atom, but the "mechanism" by which this might change the curvature is not clear, the more so because the bond critical point shifts as well in this series.

Because of the symmetry in methane we cannot invoke the fairly large intra-atomic dipole moment of carbon. This measure is the first moment $\boldsymbol{M}(\Omega)$ and determines the displacement of the atom's centroid of negative charge from the position of its nucleus. These contributions will cancel each other in methane and can therefore not be the cause for the shape of the C|H surface.

To shed more light on this matter we have computed the total curvature for several other C—H bonds in saturated hydrocarbons, all of which show negligible charge transfer. In staggered ethane $C = 0.996$ for all six C—H bonds, whereas in the *anti–anti* conformation of propane three types of C—H are found: $C = 1.476$ for hydrogens attached to the central methylene carbon, $C = 1.365$ or $C = 1.022$ for hydrogens attached to a methyl carbon.

It emerges from these observations that the total curvature of C|H interatomic surfaces is very sensitive to the total chemical environment. This becomes intuitively obvious on inspecting Fig. 3. As a rule, a higher number of carbons attached to the carbon of the C|H IAS will increase the total curvature. This measure seems to probe how far atoms that are "pushed" together in a molecule distort each other. "Clashes" with third-party atoms can severely modify the curvature of the IAS between two atoms. This effect has been sufficiently documented in preliminary tests in more "crowded" systems like acetamide and urea. The total curvature for the C|O IAS takes the values −0.116, 0.000, 0.022, 0.174, and 0.242 in formaldehyde, carbon monoxide, formamide, urea, and acetamide, respectively. It can visually be verified that basins that are more distorted at their boundary yield higher total curvature values for their interatomic surface(s). There is no straightforward means of reducing this emerging phenomenon to known physical principles or quantities. The question why the C|H IAS in methane has a considerable curvature is equivalent to asking why this surface simply appears the way it does. One might explain its shape as a compromise between four equally distortable hydrogen atoms covalently bound to a carbon atom with a different distortability.

It is remarkable that the total curvature of the IAS in BeH_2 is almost zero. The shape of this surface is quite similar to the IAS in C≡O, which also has a vanishing total curvature. This is caused by an annihilation of negative contributions to the Gaussian curvature K by positive ones, as shown in Fig. 4.

This similarity can be explained by a common physical ground. Both bonds show a considerable charge transfer, the value for C≡O being 1.33 e. Given that in these molecules there is no "steric" phenomenon influencing the total curvature C and assuming that charge transfer enhances C, we are left with the question why C is nevertheless essentially zero. Carbon monoxide has a large and diffuse (weakly bound) charge distribution on carbon, which leads to a very pronounced polarization opposing the charge transfer moment. This explains the near-zero dipole moment of this molecule. Similarly, berylium has a diffuse valence density, again leading to large atomic polarization. One may hypothesize that the total curvature absorbs both the charge transfer and back-polarization effect.

The fact that the total curvature C is not just mirroring charge transfer is demonstrated by a set of methyl derivatives given in Table 4. In their work on substituent effects of methyl derivatives (19), Wiberg and Breneman have ordered 20 moieties with C_{3v} symmetry according to increasing pop-

[5] Ideally, one wishes to isolate the possible effect of charge transfer on the total curvature C. Constructing a molecule in which two of its atoms show only charge transfer without mutual polarization is virtually impossible unless one resorts to very artificial systems like $LiBe^{5+}$. This species is supposed to eliminate any polarization effect on the IAS and isolate the influence of charge transfer (if present at all) on the total curvature.

Fig. 3. A three-dimensional representation of three C|H interatomic surfaces in the *anti–anti* conformation of propane. The top surface has the highest total curvature (C = 1.476) followed by the bottom (right) one (C = 1.365). The left surface has a much lower total curvature (C = 0.996), identical to the value in the staggered conformation of ethane. This picture provides visual support for the observation that C is very sensitive to the total chemical environment of the atomic basin.

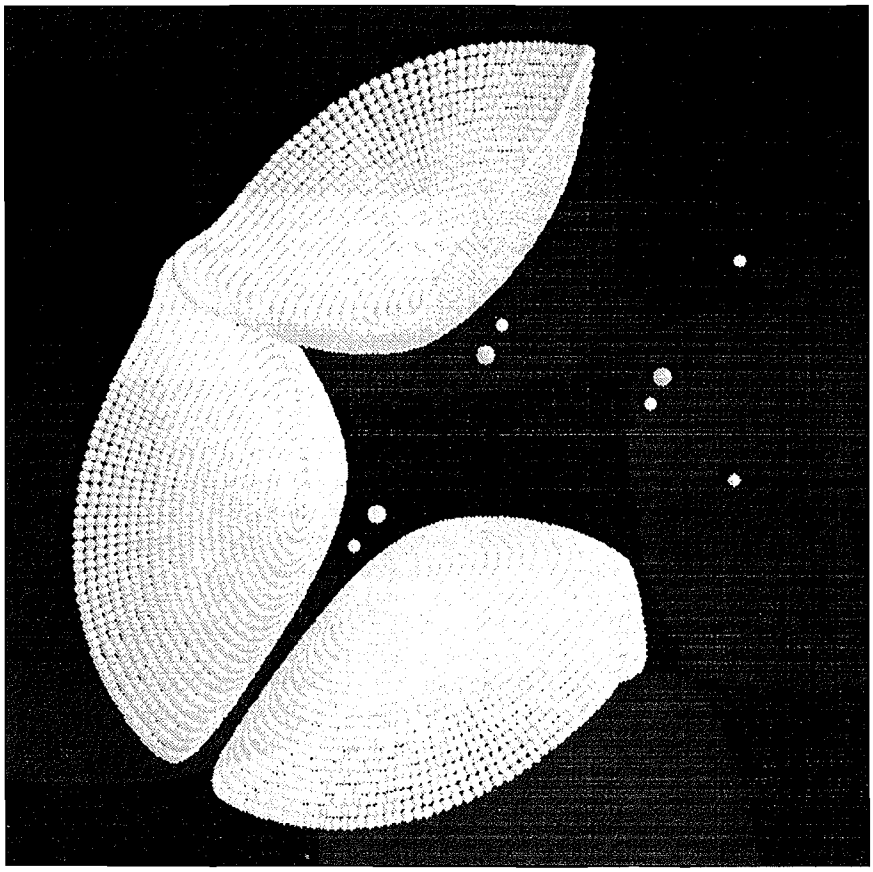

Fig. 4. A relief map of the Gaussian curvature K of the C|O interatomic surface in carbon monoxide. In the outer region of the IAS the curvature practically vanishes, which is the equivalent of near planarity.

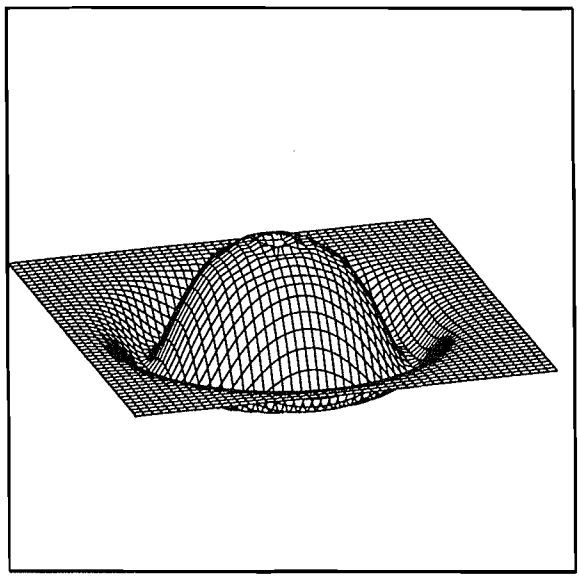

Table 4. The charge transfer q and the total curvature C and area[a] of the C|A[b] interatomic surface in methyl substituted derivatives.

Molecules	C	$q(CH_3)$[c]	Area
CH_3Cl	−0.08	+0.316	42.6
CH_3S^-	−0.08	−0.287	49.3
CH_3 C≡CH	−0.08	+0.362	40.5
CH_3BeH	0.00	−0.875	36.5
CH_3 C≡N	0.03	+0.362	39.4
$CH_3N_2^+$	0.03	+0.840	36.5
CH_3OLi	0.12	+0.618	38.9
CH_3O^-	0.19	+0.474	39.9
CH_4	0.69	+0.061	32.0
CH_3Li	3.05	−0.902	26.4

[a]The interatomic surface is bounded by a contour line of constant charge density (0.001 au). The area is given in $(au)^2$.
[b]The letter "A" represents the atom of the substituent group directly attached to the methyl carbon.
[c]The charge transfer is measured with respect to the population of the whole methyl group, which is 9.000 e. The present values are quoted from ref. 19.

Table 5. The total curvature C and area[a] for the C—C interatomic surface in various conformations of ethane.[b]

τ[c]	ΔE[d]	C	Area
0	12.6	0.000	42.3
15	10.8	−0.054	42.5
30	6.4	−0.168	42.9
45	1.9	−0.267	43.4
60	0.0	−0.304	43.6

[a]The interatomic surface is bounded by a contour line of constant charge density (0.001 au). The area is given in $(au)^2$.
[b]Ethane has been fully optimized at the 6-31G** level only fixing the torsion angles.
[c]This HCCH torsion angle is given in degrees: 0° and 60° correspond to the eclipsed and staggered conformations, respectively.
[d]This energy difference is given in kJ/mol.

ulation of the methyl group. We focus on the IAS between the methyl carbon and the substituent atom attached to it. The 10 molecules we selected from this list fall, broadly speaking, in three categories according to C. The first group has a very small C value with the ionic compound CH_3BeH again showing a vanishing total curvature. Although the population of the methyl group varies considerably in this subset, C is not able to discriminate these systems very well. Under the hypothesis that the total curvature is influenced by charge transfer, polarization, and steric crowding one may speculate that these molecules have enough flexibility to allow these effects to cancel each other and reach an "atomic distortion equilibrium." The two other groups CH_4 and CH_3Li, which have been discussed before, contain only one member.

Finally, we simply point out that the total curvature index can also be applied in conformational analyses. A simple example is reported in Table 5 where the central torsion angle in ethane is varied from 0° to 60°. The total curvature of the C|C surface becomes more negative in a sinusoidal manner on going from the eclipsed to the staggered conformation. The latter IAS is represented in Fig. 5 as an example of a predominantly hyperbolic surface, because for the total curvature (which is an integral) to be negative there must be dominant contributions of surface points with a negative Gaussian curvature.

5. Conclusion

A purely geometrical index is proposed to characterize interatomic surfaces in molecules. This index is called the total curvature C and stems from a rigorous application of differential geometry. It is dimensionless and gauges the intrinsic geometry of a surface regardless of its representation or position in space.

Fig. 5. A three-dimensional representation of the C|C interatomic surface in the staggered conformation of ethane. This surface has a negative total curvature.

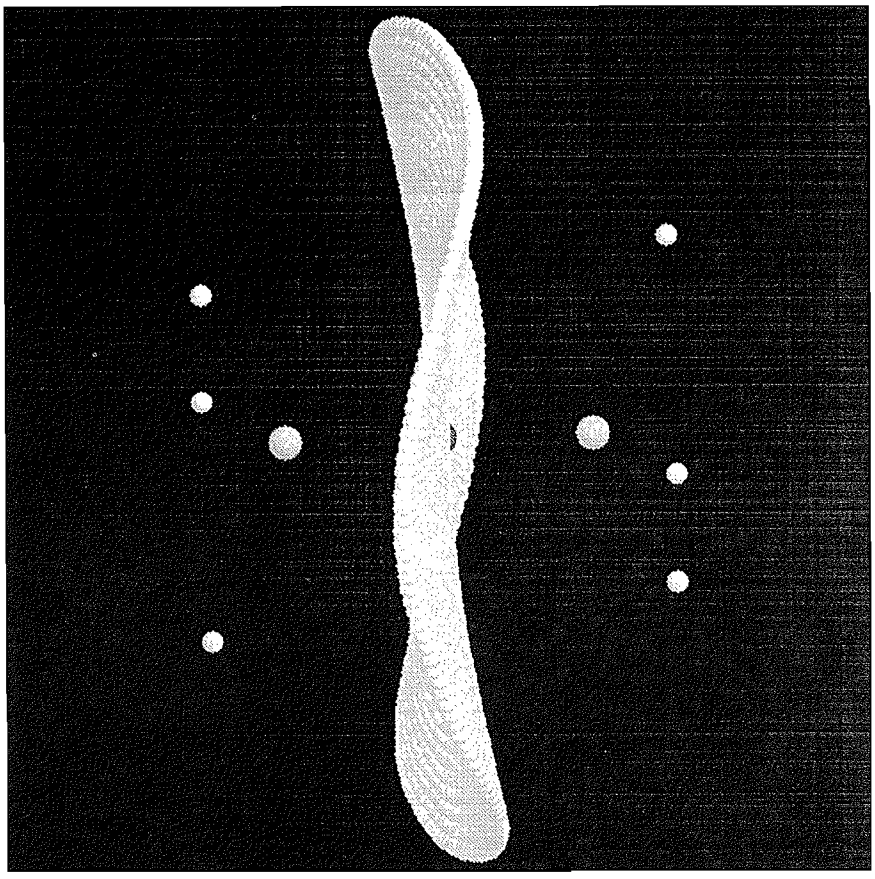

The total curvature measures the chemical distortion of an atom in a molecule, which is a combination of polarization deformation, charge transfer, and steric effects. Although it is a single-bond oriented quantity it is sensitive to the complete chemical environment of the bonded atoms.

For a series of ionic diatomics with a practically constant charge transfer, C measures the distortion of the anion by the positive neighbouring charge. It is conjectured that increasing electronegativity differences between two bonded atoms increases the total curvature of the IAS. Other simultaneous influences on C should be included since the charge transfer in methyl derivatives is not reflected on a one-to-one basis in the total curvature of the IAS between the methyl carbon and the substituent.

The proposed index can be used to probe the response of an IAS in uniform electric fields and can be employed in conformational studies.

It remains speculative whether a straightforward and interesting relationship exists between the HSAB principle (20) and the total curvature.

References

1. R.F.W. Bader, P.L.A. Popelier, and T.A. Keith. Angew. Chem. Int. Ed. Engl. **33**, 620 (1994).
2. M.M. Lipshutz. Differential geometry, Schaum's outline series. McGraw–Hill, New York. 1969.
3. D.J. Struik. Differential geometry. Addison–Wesley, London. 1961.
4. V.I. Arnold. Mathematical methods of classical mechanics. 2nd ed. Springer, New York. 1989.
5. M.P. do Carmo. Differential geometry of curves and surfaces. Prentice-Hall, New Jersey. 1976.
6. R.F.W. Bader. Atoms in molecules. A quantum theory. Clarendon. Oxford. 1990.
7. P.L.A. Popelier. Theor. Chim. Acta, **87**, 465 (1994).
8. W.H. Press, B.P. Flannery, S.A. Teukolsky, and W.T. Vetterling. Numerical recipes. 2nd ed. Cambridge Press, U.K. 1992.
9. CADPAC5: The Cambridge Analytic Derivatives Package Issue 5, Cambridge, 1992. A suite of quantum chemistry programs developed by R.D. Amos with contributions from I.L. Alberts, J.S. Andrews, S.M. Colwell, N.C. Handy, D. Jayatilaka, P.J. Knowles, R. Kobayashi, N. Koga, K.E. Laidig, P.E. Maslen, C.W. Murray, J.E. Rice, J. Sanz, E.D. Simandiras, A.J. Stone, and M.D. Su.
10. R. Krishnan, J.S. Binkley. R. Seeger, and J.A. Pople. J. Chem. Phys. **72**, 650 (1980).
11. F.B. van Duijneveldt. IBM Research Report. RJ 945. 1971.
12. F.W. Biegler-König, R.F.W. Bader, and T.-H. Tang. Comput. Chem. **3**, 317 (1982).
13. R.F.W. Bader and P.M. Beddall. J. Chem. Phys. **56**, 3320 (1972).
14. C. Nellin, B.O. Roos, A.J. Sadlej, and P.E.M. Siegbahn. J. Chem. Phys. **77**, 3607 (1982).
15. R.M. Glover and F. Weinhold. J. Chem. Phys. **65**, 4913 (1976).
16. P.W. Fowler and P.A. Madden. Phys. Rev. B, **29**, 1035 (1984).
17. R.E. Watson. Phys. Rev. **111**, 1108 (1958).
18. K.E. Laidig and R.F.W. Bader. J. Chem. Phys. **93**, 7213 (1990).
19. K.B. Wiberg and C. Breneman. J. Am. Chem. Soc. **112**, 8765 (1990).
20. R.G. Pearson. J. Chem. Educ. **64**, 561 (1987).

Theoretical examination of the Diels–Alder reaction of 1,3-butadiene with cyclopentadiene and 2*H*-phosphole

Steven M. Bachrach and Laureta M. Perriott

Abstract: All Diels–Alder reactions between 1,3-butadiene and cyclopentadiene or 2*H*-phosphole have been examined at the MP4SDQ/6-31G*//HF/6-31G* level. There is remarkable similarity between the two systems. The thermodynamic product is the bicyclo[4.2.0]nonadiene while the kinetic product is the norbornene product. There is a slight kinetic preference for the *endo* addition and for the butadiene to be in the *s-trans* conformation. Except for the case where butadiene is the diene component and addition is *endo*, the reactions are concerted and synchronous. In these other two cases, the reaction is stepwise with a diradical intermediate.

Key words: phosphole, Diels–Alder reaction, topological electron density analysis.

Résumé : On a étudié toutes les réactions de Diels–Alder entre le buta-1,3-diène et le cyclopentadiène ou le 2*H*-phosphole au niveau MP4SDQ/6-31G*//HF/6-31G*. Il existe une similarité remarquable entre les deux systèmes. Le produit thermodynamique est le bicyclo[4.2.0]nonadiène alors que le produit cinétique est le produit norbornène. Il y a une légère préférence cinétique en faveur de l'addition *endo* et pour que le butadiène soit dans la conformation *s-trans*. À l'exception du cas où le butadiène agit comme butadiène et que l'addition est *endo*, toutes les réactions sont concertées et synchrones. Dans ces deux autres cas, la réaction se fait par étape avec un intermédiaire diradicalaire.

Mots clés : phosphole, réaction de Diels–Alder, analyse topologique de la densité électronique.

[Traduit par la rédaction]

Introduction

The Diels–Alder reaction of phosphaalkenes has been a subject of intense study (1, 2). A wide variety of these reactions have been carried out; however, there are limited examples where the phosphaalkene acts as the dienophile. The propensity for phosphaalkenes to dimerize limits its use as a dienophile. One significant exception is the chemistry of 2*H*-phospholes (3).

Mathey et al. first demonstrated the Diels–Alder chemistry of 2*H*-phosphole in the attempted reaction of a 1*H*-phosphole with diphenylacetylene (Scheme 1) (4). The actual recovered product appeared to arrive from the Diels–Alder reaction of a 2*H*-phosphole with the acetylene. Mathey suggested that a facile [1,5]-phenyl shift precedes the Diels–Alder reaction. We recently examined this reaction using theoretical methods and found a low barrier for the [1,5]-hydrogen shift for 1*H*-phosphole (5). Furthermore, the activation energy for the Diels–Alder reaction of 2*H*-phosphole with acetylene is less than the barrier for the hydrogen shift (6), supporting Mathey's mechanism.

Scheme 1.

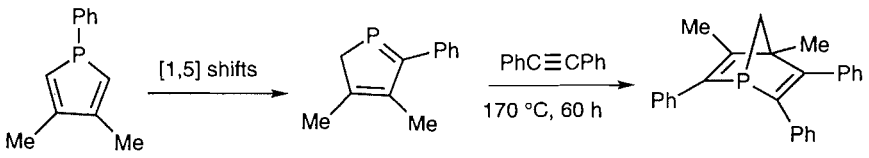

As further proof of the intermediacy of 2*H*-phosphole, Mathey reports the reaction of the phosphole with 2,3-dimethyl-1,3-butadiene, recovering the Diels–Alder product where the phosphole acts as the dienophile, with addition across the P=C bond (Scheme 2) (4). Further experiments have shown this propensity for 2*H*-phosphole to act as the dienophile in reactions with conjugated systems (7, 8).

Scheme 2.

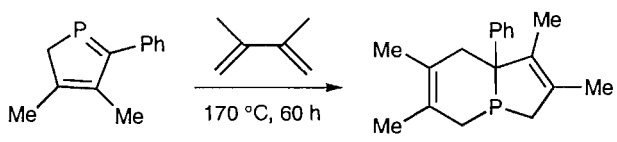

Received September 28, 1995.

This paper is dedicated to Professor Richard F.W. Bader on the occasion of his 65th birthday.

Steven M. Bachrach[1] **and Laureta M. Perriott.** Department of Chemistry, Northern Illinois University, DeKalb, IL 60115, U.S.A.

[1] Author to whom correspondence may be addressed. Telephone: (815) 753-6863; Fax: (815) 753-4802; E-mail: smb@smb.chem.niu.edu

Scheme 3.

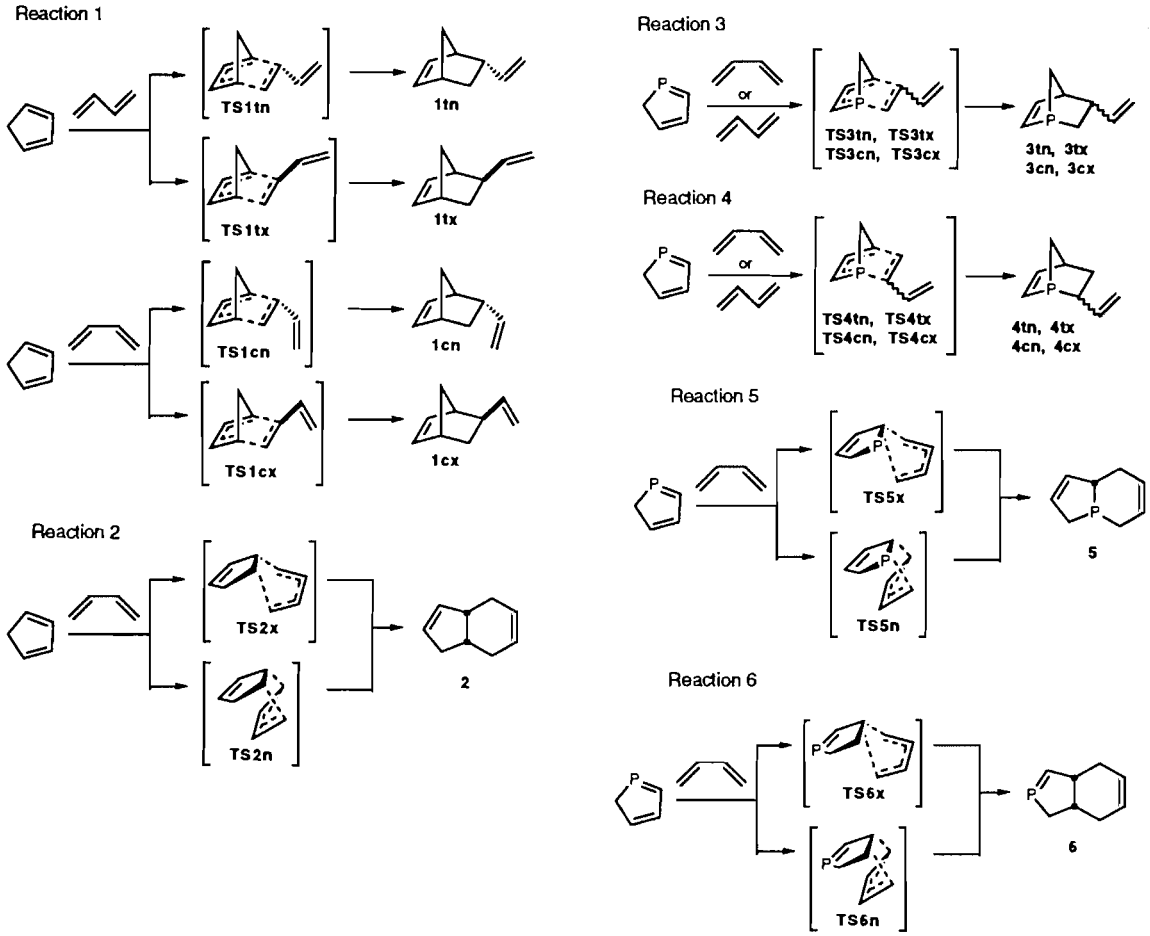

Continuing our theoretical examination of the pericyclic reactions of phosphaalkenes (6, 9–13), we report here ab initio calculations on the Diels–Alder reaction of 2*H*-phosphole with 1,3-butadiene (Scheme 3). We have examined all possible reactions: 2*H*-phosphole (diene) + 1,3-butadiene (dienophile), Reactions 3 and 4, which have differing regiochemistry; 2*H*-phosphole (dienophile) + 1,3-butadiene (diene) with addition across the C=P bond, Reaction 5; and 2*H*-phosphole (dienophile) + 1,3-butadiene (diene) with addition across the phosphole C=C bond, Reaction 6. As a comparison, we examined the hydrocarbon analogue: the Diels–Alder reaction of cyclopentadiene (diene) + 1,3-butadiene (dienophile), Reaction 1, and the reaction of cyclopentadiene (dienophile) + 1,3-butadiene (diene), Reaction 2. We have examined the *endo* vs. *exo* selectivity of product formation and the *cis* vs. *trans* selectivity of the 1,3-butadiene. Using the topological electron density method of Bader (14), we assess the degree of bond formation in the transition states and judge the synchronicity of these reactions.

The only applicable experimental result (4) is the reaction shown in Scheme 2, which shows a clear preference for the phosphole to act as the dienophile with addition across its C=P bond. Mathey did report that another minor unidentified compound was produced.

There have been two important theoretical studies of related systems. Li and Houk (15) examined the dimerization of 1,3-butadiene at the RHF and CASSCF levels. The concerted reaction is found to be about 5 kcal mol^{-1} more favorable than the biradical pathway. In addition, the TS with the dienophilic butadiene in the *trans* conformation is 0.8 kcal mol^{-1} lower in energy than the *cis* conformation. (Houk's earlier study of the Diels–Alder reaction between butadiene and acrolein indicated a slight preference for the *cis* conformation of acrolein (16).) At the CASSCF(6,6) level, the *exo* TS is 0.2 kcal mol^{-1} below the *endo* TS, contrary to the experimental evidence, which indicates a slight preference for *endo* selectivity. Jorgensen, Lim, and Blake (17) examined the Diels–Alder reaction of cyclopentadiene with isoprene and cyclopentadiene. They find a distinct preference for the *cis* conformation of isoprene and *endo* selectivity. All studies have indicated that the concerted pathways show some degree of synchronicity, based on the distances of the forming σ-bonds. We will compare our results with these previous theoretical studies.

Computational methods

The structures of all species involved in Reactions 1–6 were completely optimized at the HF/6-31G* level. The nature of these geometries was confirmed with analytical frequencies; all ground states had all real frequencies and the transitions states had one and only one imaginary frequency. The geometries of the transitions states are drawn in Figs. 1 and 2, while those of the products are drawn in Figs. 3 and 4.

Fig. 1. HF/6-31G* optimized geometries of **TS1–TS2**. All distances are in Å.

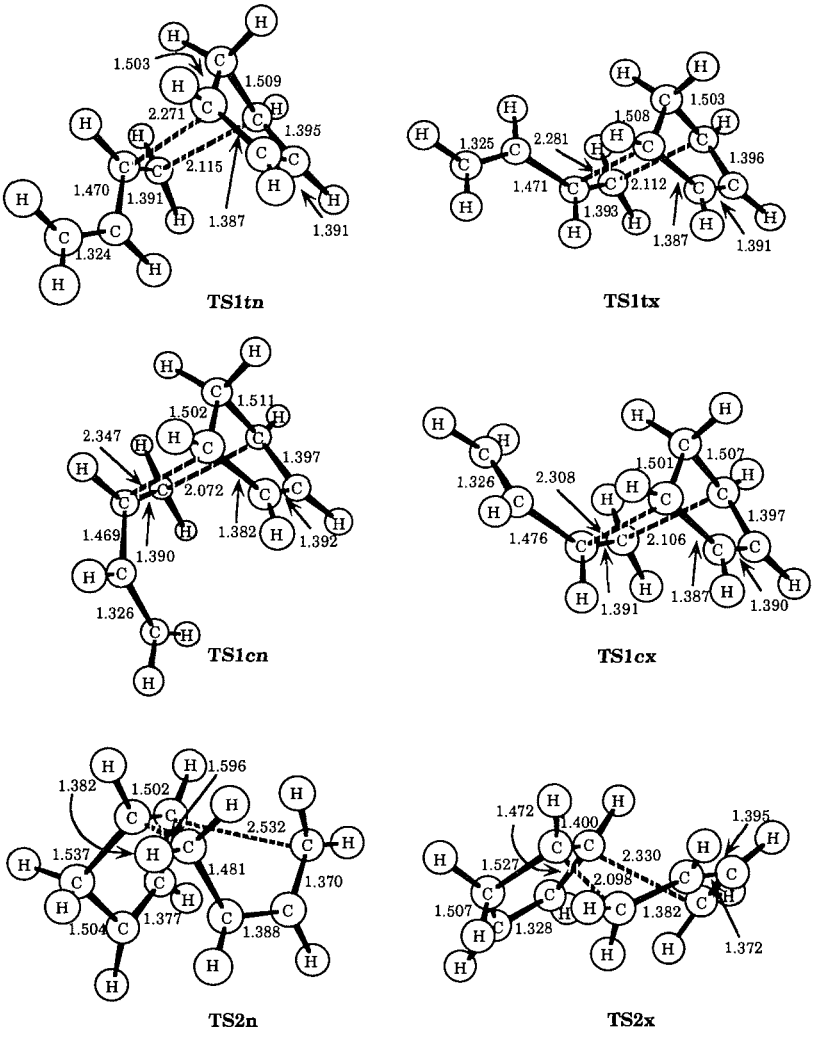

The activation energy of Diels–Alder reactions is known to be sensitive to electron correlation (11, 17–19). Activation energies are dramatically overestimated at HF and underestimated at MP2. However, the HF and MP2 optimized geometries of TSs for Diels–Alder reactions do not differ substantially. Therefore, we have obtained single-point energies at MP4SDQ/6-31G*//HF/6-31G*. Previous studies have shown that computations at this level are adequate to describe the systems under study in this report. Reaction energies are listed in Table 1 and activation energies are given in Table 2.

As described below, the *endo* transition states of Reactions 2 and 6 appear to have biradical character. To better treat these states, Reactions 2 and 6 (through *endo* TSs) were reexamined at UHF/6-31G*. Both reactions were found to have an intermediate state (**INT2** and **INT6**) and transition states leading to and from the intermediate. **INT2** was optimized at UMP2/6-31G* since it could not be located on the UHF surface. Since the main focus of this paper is the concerted mechanism, we report only the UHF energies.

All energy calculations were performed using GAUSSIAN92 (20) or GAUSSIAN94 (21).

Table 1. Reaction energies (kcal mol^{-1}) for Reactions 1–6.

Reaction	Product	HF	MP4	E_{rel}(MP4)
1	**1tn**	−12.67	−22.96	12.44
	1tx	−12.32	−22.64	12.76
	1cn	−10.87	−21.54	13.86
	1cx	−10.77	−21.45	13.95
2	**2**	−27.38	−35.40	0.00
3	**3tn**	−20.07	−25.84	7.06
	3tx	−19.44	−25.34	7.56
	3cn	−18.27	−24.35	8.55
	3cx	−18.02	−24.12	8.78
4	**4tn**	−19.61	−25.46	7.44
	4tx	−19.26	−25.13	7.77
	4cn	−18.02	−24.23	8.67
	4cx	−18.13	−24.25	8.65
5	**5**	−28.37	−31.73	1.17
6	**6**	−23.68	−32.90	0.00

Fig. 2. HF/6-31G* optimized geometries of **TS3**-**TS6**. All distances are in Å.

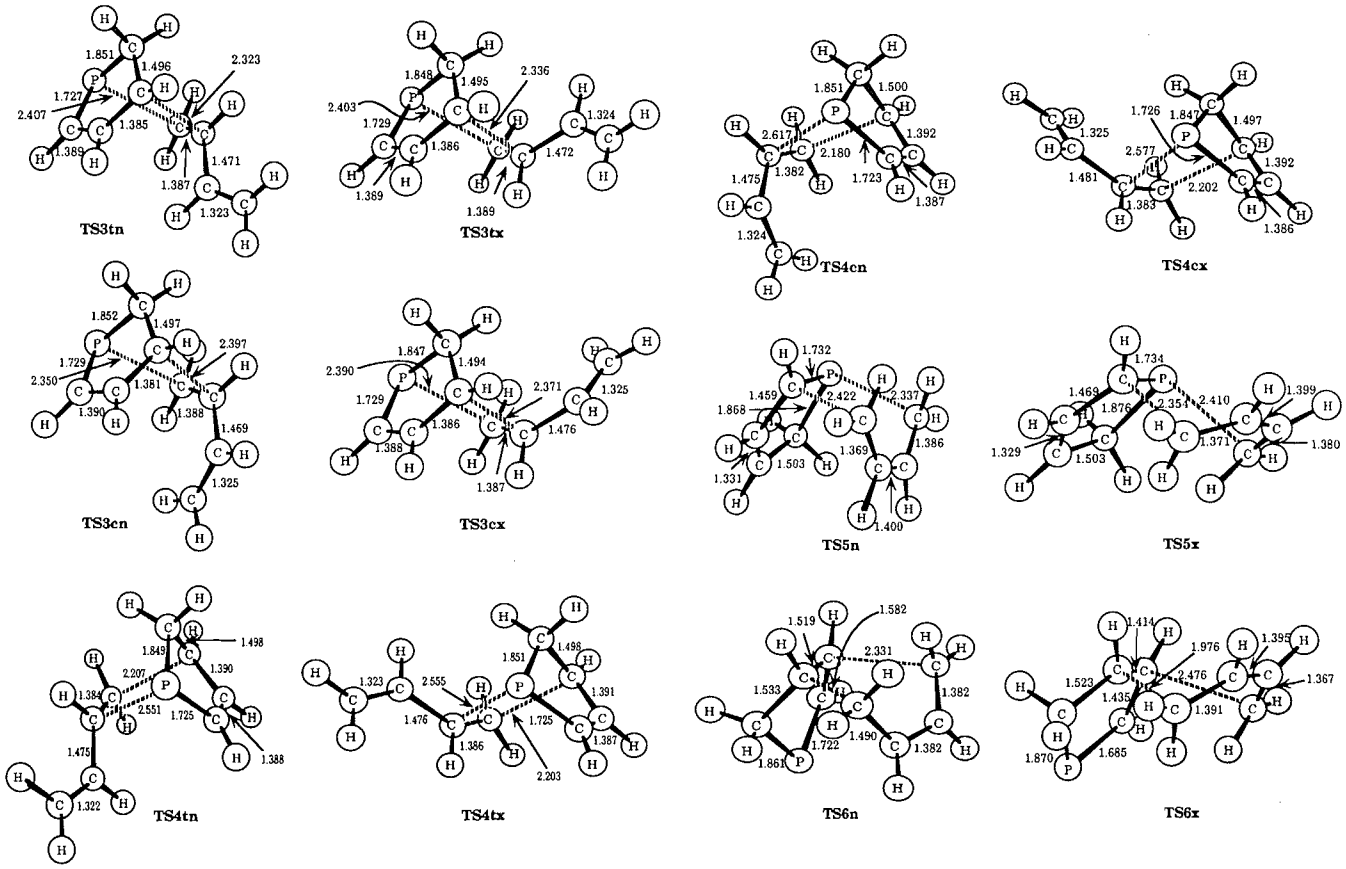

Table 2. Activation energy (kcal mol^{-1}) for Reactions 1–6.

Reaction	TS	HF	MP4	E_{rel}(MP4)
1	**TS1tn**	44.01	26.10	0.00
	TS1tx	44.42	26.34	0.24
	TS1cn	45.20	26.72	0.62
	TS1cx	46.08	27.48	1.38
2	**TS2n**	47.06[a]	23.61[a]	−2.49[a]
	TS2x	49.28	30.72	4.62
3	**TS3tn**	30.61	16.71	0.00
	TS2tx	31.00	16.89	0.18
	TS3cn	31.78	17.38	0.67
	TS3cx	32.59	18.05	1.34
4	**TS4tn**	32.02	17.85	1.14
	TS4tx	32.51	18.10	1.39
	TS4cn	33.10	18.54	1.83
	TS4cx	33.35	18.62	1.91
5	**TS5n**	33.32	18.69	1.98
	TS5x	36.23	21.97	5.26
6	**TS6n**	35.06[a]	14.71[a]	−2.00[a]
	TS6x	48.94	29.67	12.96

[a]RHF/6-31G* results indicate biradical character for these TSs and are likely to be erroneous. See text for discussion.

Table 3. Bond orders for **TS1** using eq. [1].

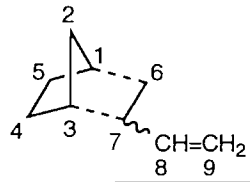

Bond	TS1tn	TS1tx	TS1cn	TS1cx
1–2	1.09	1.09	1.08	1.09
2–3	1.11	1.11	1.11	1.12
7–8	1.22	1.21	1.22	1.19
8–9	2.00	2.00	1.98	1.98
3–4	1.62	1.62	1.65	1.62
4–5	1.57	1.58	1.58	1.58
1–5	1.57	1.57	1.57	1.57
6–7	1.57	1.56	1.57	1.57
1–6	0.31	0.31	0.32	0.32
3–7	0.28	0.28	0.27	0.27
Sum[a]	6.91	6.92	6.96	6.93

[a]Sum of bond orders of active bonds (rows 5–10).

The electron density was analyzed using the topological electron density method of Bader (14). The value of the electron density at critical points ($\rho(r_c)$) was evaluated using a locally modified version of EXTREME (22). Bond orders n were obtained using the empirical relationship eq. [1]. Bond orders are reported in Tables 3–6.

Fig. 3. HF/6-31G* optimized geometries of **1–2**. All distances are in Å and relative energies of **2** are (MP4) in kcal mol^{-1}.

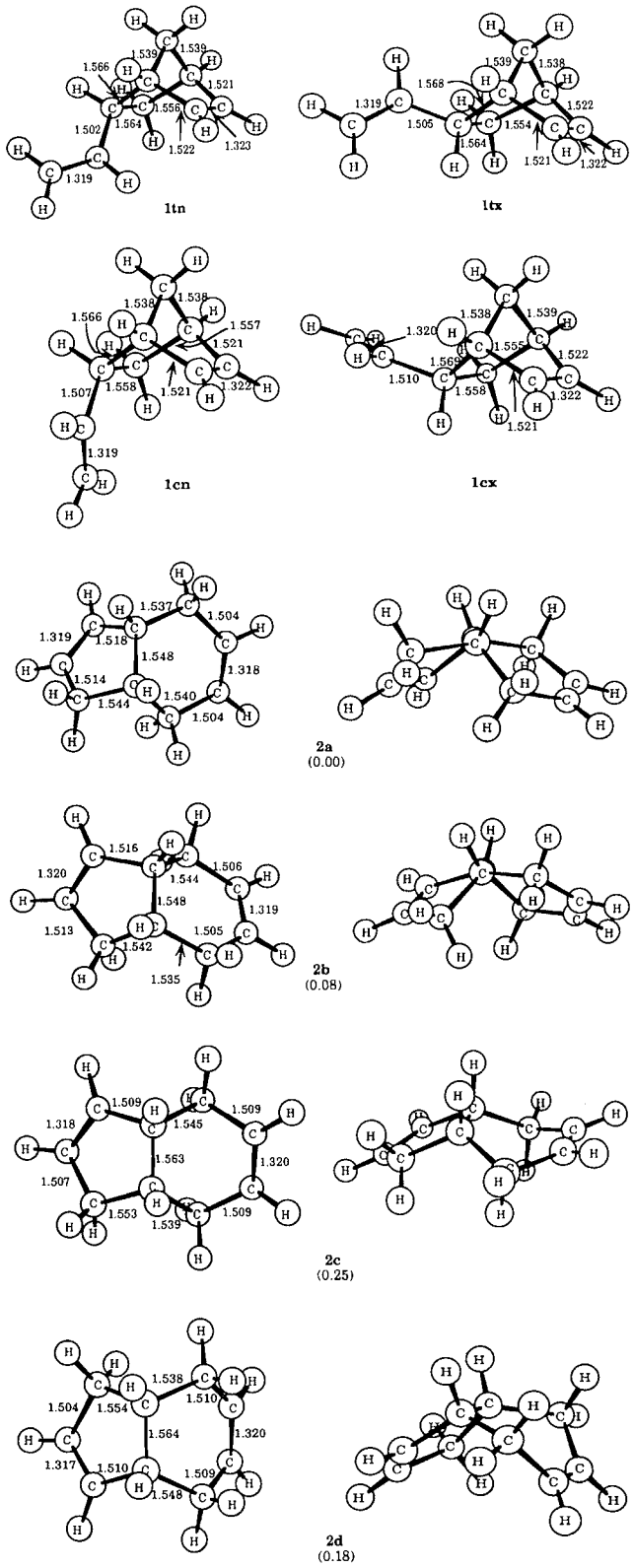

Table 4. Bond orders for **TS2** using eq. [1].

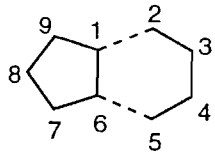

Bond	TS2n	TS2x
1–9	1.01	1.02
8–9	1.10	1.09
7–8	1.69	2.01
6–7	1.64	1.21
1–6	1.12	1.55
1–2	0.80	0.31
5–6	0.25	0.28
2–3	1.18	1.62
3–4	1.60	1.55
4–5	1.69	1.68
Sum[a]	6.64	6.99

[a]Sum of bond orders of active bonds (rows 5–10).

[1] $n(\text{X—Y}) = \exp(A[\rho(r_c) - B])$

X—Y (ref.)	A	B
C—C (23)	6.458	0.252
C—P (24)	19.628	0.153

Results

Reaction 1

For the reaction of cyclopentadiene with butadiene where butadiene acts as the dienophile, four TS are possible, leading to four different products. The reaction of *trans*-1,3-butadiene with cyclopentadiene can proceed through an *endo* TS (**TS1tn**, where **t** indicates *trans*-1,3-butadiene and **n** indicates *endo* orientation) or an *exo* TS (**TS1tx**, where **x** indicates *exo*). The reaction of *cis*-1,3-butadiene can also proceed through an *endo* (**TS1cn**, where **c** indicates *cis*-1,3-butadiene) or *exo* (**TS1cx**) TS. The four products differ by having an *endo* or *exo* vinyl group that is either *s-cis* (**1cn** and **1cx**) or *s-trans* (**1tn** and **1tx**) to the saturated two-carbon bridge. These possibilities are shown in Scheme 3.

The geometries of these four products are very similar (Fig. 3). In fact, the variation in any C—C distance among the four isomers is less than 0.005 Å. All distances and angles are in expected ranges for typical C—C and C=C bonds and norbornene systems. The most stable isomer is **1tn**, which lies 1.42 kcal mol^{-1} below its rotational isomer **1cn** and 0.32 kcal mol^{-1} below its *exo* isomer. Presumably, poor steric interactions in both **1cn** and **1cx** reduce the energy difference between these two isomers to only 0.09 kcal mol^{-1}, compared to the difference of 0.32 kcal mol^{-1} between **1tn** and **1tx**. Formation of the most stable isomer (**1tn**) is exothermic, with reaction energy (using *trans*-1,3-butadiene) of −22.96 kcal mol^{-1} (Table 1).

Table 5. Bond orders for **TS3** and **TS4** using eq. [1].

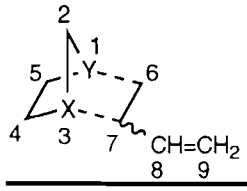

TS3: X=CH, Y=P
TS4: X=P, Y=CH

Bond	TS3tn	TS3tx	TS3cn	TS3x	TS4tn	TS4tx	TS4cn	TS4cx
1–2	1.06	1.06	1.06	1.09	1.11	1.11	1.10	1.11
2–3	1.12	1.12	1.11	1.12	1.06	1.04	1.04	1.07
7–8	1.23	1.21	1.23	1.19	1.20	1.19	1.20	1.17
8–9	2.00	2.00	1.98	1.98	2.01	2.01	1.99	1.99
3–4	1.64	1.64	1.67	1.64	1.57	1.57	1.58	1.55
4–5	1.57	1.57	1.57	1.58	1.58	1.58	1.59	1.59
1–5	1.57	1.57	1.58	1.56	1.62	1.61	1.61	1.61
6–7	1.59	1.58	1.59	1.59	1.61	1.60	1.63	1.61
1–6	0.15	0.15	0.17	0.15	0.29	0.29	0.29	0.29
3–7	0.28	0.27	0.26	0.26	0.12	0.12	0.11	0.11
Sum[a]	6.80	6.78	6.84	6.78	6.79	6.77	6.81	6.76

[a]Sum of bond orders of active bonds (rows 5–10).

Table 6. Bond orders for **TS5** and **TS6** using eq. [1].

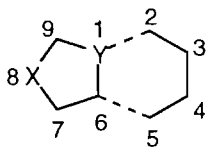

TS5: X=CH, Y=P
TS6: X=P, Y=CH

Bond	TS5n	TS5x	TS6n	TS6x
1–9	1.00	0.96	1.01	1.02
8–9	1.08	1.08	1.00	0.94
7–8	2.00	2.01	1.57	1.73
6–7	1.25	1.20	1.62	1.35
1–6	1.51	1.51	1.07	1.48
1–2	0.17	0.15	0.85	0.36
5–6	0.26	0.26	0.27	0.25
2–3	1.59	1.63	1.15	1.58
3–4	1.53	1.54	1.67	1.56
4–5	1.72	1.69	1.62	1.71
Sum[a]	6.78	6.78	6.63	6.94

[a]Sum of bond orders of active bonds (rows 5–10).

We located four transition states, corresponding to the different paths shown in Scheme 3. Overall, the geometries of the four isomeric TSs of Reaction 1 are also very similar. The bond distances in the butadiene and cyclopentadiene fragments vary by less than 0.007 Å among the isomers. The forming bonds between the two fragments are of different lengths; the forming bond to the carbon bearing the vinyl group is longer than the other forming bond in all four TSs. This asymmetry is slightly greater in the *cis* isomers (difference in bond distances of about 0.20 Å) than in the *trans* isomers (difference of 0.16 Å).

There is remarkable synchronicity in these TSs. The bond distances of the partially broken/formed double bonds in the butadiene and cyclopentadiene fragments vary by less than 0.1 Å. This is even more apparent when examining the bond orders (Table 3). The bond orders for these bonds only vary from 1.56 to 1.62. The bond order of the forming σ-bonds is about 0.3. Summation of the bond orders of these active bonds is nearly 7 in all four TSs, suggesting a synchronous concerted reaction.

The most favorable TS for Reaction 1 is **TS1tn** with an activation energy of 26.10 kcal mol^{-1}. **TS1tx** lies only 0.24 kcal mol^{-1} higher, and **TS1cn** is only 0.38 kcal mol^{-1} higher still. The preference for *endo* over *exo* approach is 0.24 kcal mol^{-1} in the *trans* case and 0.76 kcal mol^{-1} in the *cis* case.

While there is no experimental data to which we can directly compare these results, we can compare our calculations with theoretical results of related systems. Jorgensen, Lim, and Blake (17) have examined the reaction of cyclopentadiene with isoprene at MP3/6-31G*//HF/6-31G*. The geometries of the TSs for the reaction of cyclopentadiene with isoprene are very similar to ours, particularly the distances of the forming σ-bonds. The larger differences in these bond lengths in the *cis* isomers relative to the *trans* isomers are found in the isoprene case. Energetic preference for the *endo* approach is indicated in both the isoprene and our butadiene studies. However, in the isoprene reaction, the lowest TS is the *endo-cis* isomer, favored by 0.53 kcal mol^{-1} over the *endo-trans* isomer. Houk and co-workers noted a preference of the *endo-cis* TS over the *endo-trans* of 0.6 kcal mol^{-1} in the reaction of butadiene with acrolein (16) (but at a much lower computational method). In the dimerization of cyclopentadiene, Jorgensen et al. found an *endo* preference of 2.71 kcal mol^{-1} (17). Clearly, the preference for *endo* over *exo* is confirmed, but the selection of *cis* over *trans* is not corroborated, though the energy differences in all cases is very small.

Reaction 2

The reaction of cyclopentadiene with butadiene, where cyclopentadiene acts as the dienophile, can proceed through two isomeric transition states, **TS2n** with an *endo*

approach or **TS2x** having an *exo* approach, as shown in Scheme 3.

We located four rotamers of the product **2**. **2a** and **2b** have the six-membered ring in the chair conformation and a staggered relationship across the fused bond. **2c** and **2d** have a boat conformation for the six-membered ring and a near eclipsed relationship across the fused bond. **2c** can be thought of as the direct product of an *endo* attack, while **2d** is the product from *exo* attack. The lowest energy rotamer is **2a**, and as expected, the boat conformers are somewhat higher in energy. The reaction energy is -35.40 kcal mol^{-1}. The experimental value for this reaction is not known. We can estimate the heat of formation of bicyclo[4.3.0]-3,7-nonadiene using Benson's group equivalents (25) (with the strain estimate of cyclopentene and cyclohexene) and with the experimental values for cyclopentadiene and 1,3-butadiene estimate the enthalpy of reaction to be -34 kcal mol^{-1}. Product **2a** is 12.44 kcal mol^{-1} more stable than **1tn**.

The bond lengths in the four rotamers of **2** differ only in the fused bond length. In the lower energy chair conformers this bond is 1.548 Å long, which increases to 1.564 Å in the higher energy boat conformers. This increase reduces the eclipsing interactions across this bond in **2c** and **2d** and accounts for the higher energy of the boat conformers.

The geometries of the two transition states **TS2n** and **TS2x** are drawn in Fig. 1. The bond distances in **TS2x** are similar to those found in **TS1** and related Diels–Alder TSs. There is little bond alternation in the butadiene fragment, and the dienophilic double bond has a similar distance. The other bonds of the cyclopentadiene fragment have begun to adjust to the loss of conjugation between the original double bonds. The forming C—C σ-bond distances are 2.330 and 2.098 Å, very similar to the forming distances in **TS1**. The shorter distance is to the carbon of the cyclopentadiene adjacent to the saturated carbon. The bond orders for **TS2x** indicate a synchronous TS. The forming/breaking double bonds have bond orders ranging from 1.55 to 1.68 and the sum of the active bond orders is 6.99. The activation energy through **TS2x** is 30.72 kcal mol^{-1}, or 4.62 kcal mol^{-1} greater than through **TS1tn**. In other words, **TS2** has a perfectly ordinary structure.

The same cannot be said for **TS2n**. The length of the dienophilic C—C bond of cyclopentadiene is 1.502 Å, compared to 1.400 Å in **TS2x**. The butadiene fragment has one long C—C bond (1.481 Å) and then two adjacent shorter bonds (1.388 and 1.370 Å), compared to the non-alternation in **TS2x**. Most striking are the distances for the forming two σ-bonds: 1.596 and 2.532 Å. These distances suggest one C—C bond is nearly formed in the TS and the second has barely begun to form. The geometry suggests a biradicaloid structure, where one new σ-bond has formed, creating two separated allylic systems. The bond orders support this notion. The shorter of the forming σ-bonds has a bond order of 0.80, and the "allylic" C—C bonds have bond orders from 1.60 to 1.69. The sum of the active bond orders is only 6.64, a significant loss of "bonds" in this TS. Since it is well known that biradical structures are poorly described at RHF, we will revisit this structure in a later section.

The activation energy for Reaction 2 through **TS2x** is 30.72 kcal mol^{-1}, 4.62 kcal mol^{-1} higher than the activation energy for Reaction 1.

Reaction 3

Analogous to Reaction 1, the Diels–Alder reaction of 2*H*-phosphole with butadiene as the dienophile proceeds through four stereoisomeric transition states. In addition there is also the regioselection of the vinyl group ending up adjacent to the carbon bridgehead (Reaction 3) or the phosphorus bridgehead (Reaction 4).

Of the four isomeric products of Reaction 3, the lowest energy is **3tn**, which is 0.50 kcal mol^{-1} more stable than the *exo* isomer. The *cis* isomer **3cn** lies 1.49 kcal mol^{-1} above the *trans* isomer, while **3cx** lies 0.23 kcal mol^{-1} higher still. This ordering (and the energy differences) are similar to the hydrocarbon case **1**. The geometries of **3** (shown in Fig. 4) are as expected, with little variation among the four isomers, and are similar to **1**, outside of the substitution of P for C at the bridgehead.

The four isomeric TSs are drawn in Fig. 2. The active C—C bonds that are either breaking or forming a π-bond vary from 1.385 to 1.390 Å, a remarkably small range, among the four isomers, while the active P—C distance varies only from 1.727 to 1.729 Å. The forming C—C σ-bond distance is 2.33 Å in the *trans* TSs and 2.38 Å in the *cis* TSs while the forming C—P σ-bond distance is shorter in the *cis* TSs than in the *trans* TSs. This reflects the steric interaction between the vinyl group and the cyclopentadiene fragment that lengthens the C—C distance in the *cis* isomer, which compensates by having a shorter C—P distance. These C—C distances are a bit longer than in **TS1** due to the longer C—P bond that is being formed in **TS3**, relative to the two C—C bonds being formed in **TS1**.

While it is clear from the active C—C distances that the TS appears synchronous, it is difficult to judge whether the C—P distances are also formed/broken to the same extent. The use of bond orders allows for direct comparison of different bond types, such as in this case. The bond orders for the active bonds involved in the π-bonds range from 1.56 to 1.67 only. The sum of the active bond orders is about 6.80. We have previously seen that the estimated bond order for partial C—P bonds is too low (6, 13), and an increased value would move the bond order sum to near 7. Just as for the hydrocarbon case, the TSs for Reaction 3 appear synchronous.

The smallest activation energy is through **TS3tn**, with a barrier of 16.71 kcal mol^{-1}. The barrier through **TS3tx** is only 0.18 kcal mol^{-1} higher, while the *cis* TSs are higher still. Again we see a preference for the *endo* over *exo* TS and for *trans* over *cis* conformation of the butadiene fragment. The relative order of the four TSs for Reactions 1 and 3 are identical, with nearly identical energy differences between the isomers. However, the barrier for the phosphorus case is nearly 10 kcal mol^{-1} lower than the hydrocarbon. This difference is in accord with our previous studies of phospha Diels–Alder reactions (6, 11, 12).

Reaction 4

The Diels–Alder reaction of 2*H*-phosphole with butadiene as the dienophile can proceed through four different TSs to give four isomeric products with the vinyl group adjacent to the phosphorus. The lowest energy product is **4tn**; the *exo* isomer is 0.33 kcal mol^{-1} higher in energy and the *cis* isomers are 0.90 kcal mol^{-1} higher still. **4tn** is 0.38 kcal mol^{-1} higher than **3tn**. The difference in energy between *endo* and *exo* isomers is

Fig. 4. HF/6-31G* optimized geometries of **3–6**. All distances are in Å and relative energies of **5** and **6** (MP4) are in kcal mol^{-1}.

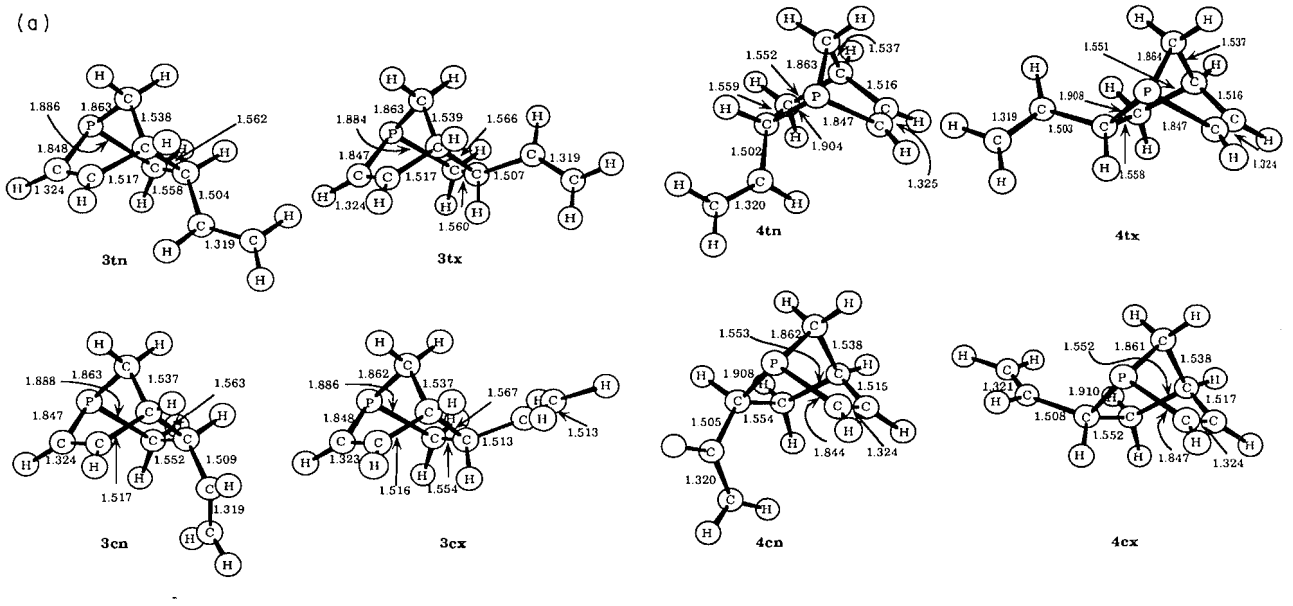

reduced in **4** compared to **3**, especially in the *cis* case. In **4**, the vinyl group is adjacent to the phosphorus and therefore farther removed from the norbornene framework than in **3**, where it is adjacent to the carbon bridgehead. This increased separation diminishes the difference in steric interactions between the vinyl group and either the methylene or ethylene bridge. The geometries of the isomers of **4** are quite similar to each other and to the isomers of **3**.

Just as for the **TS3**, the geometries of **TS4** display a synchronous reaction. The active C—C double bonds have similar length in all four structures, which are also identical to the distances in **TS3**. Bond orders for the active bonds, including the P=C bond, range from 1.55 to 1.63 only, and the sum of the active bond orders is about 6.8.

The partially formed P—C bond distance is about 2.55 Å in the *trans* isomers and 2.6 Å in the *cis* isomers. These are longer than in **TS3**, reflecting the interaction of the vinyl group adjacent to the phosphorus in **TS4** vs. that adjacent to the carbon bridgehead in **TS3**.

TS4tn is the lowest energy TS for Reaction 4, with a barrier of 17.85 kcal mol^{-1}. As for Reactions 1 and 3, there is a slight preference for *trans* over *cis* and *endo* over *exo* TSs. **TS4tn** lies 1.14 kcal mol^{-1} above **TS3tn**.

Reaction 5

The Diels–Alder reaction of 1,3-butadiene with 2*H*-phosphole as the dienophile can occur via addition across the C=P (Reaction 5) or the C=C (Reaction 6) bond. We located three conformations of the product **5**, two boat conformers that correspond to direct *endo* **5a** and *exo* **5c** approach and a chair conformer **5b** (Fig. 4). The lowest energy conformer is **5a**. The reaction energy is −31.73 kcal mol^{-1}, nearly 6 kcal mol^{-1} more exothermic than Reaction 3.

The *endo* **TS5n** is 3.28 kcal mol^{-1} lower than **TS5x**, but it is 1.98 kcal mol^{-1} higher than **TS3tn**. The activation barrier for Reaction 5 is therefore about 10 kcal mol^{-1} lower than in Reaction 2, again showing the effect of replacing carbon with phosphorus in a Diels–Alder reaction.

The structure of **TS5x** is typical for phospha Diels–Alder reactions. There is little alternation in the butadiene fragment. The forming C—C and C—P distances fall in typical ranges. The bond orders of the active π-bonds range from 1.51 to 1.69, a little larger scatter than the other TSs examined here. The sum of the active bond orders is 6.78. With a slightly larger, more realistic, value for the forming C—P bond, this sum is close to the ideal value of 7.

The structure of **TS5n** is more unusual. While there is little alternation in the butadiene fragment, the bond orders for the active π-bonds range from 1.51 to 1.73, a wider range than usual. Further, the forming C—C distance is longer than the forming C—P distance, which is very short, only 2.337 Å. The active bond order sum is the same as for **TS5x**.

Reaction 6

Reaction 6 is the Diels–Alder reaction of 1,3-butadiene with 2*H*-phosphole as the dienophile, with addition across its C=C. The active bonds in this reaction are identical to Reaction 2; the difference is the "spectator" role of the C=P vs. the C=C bond. We located two chair conformations of the product **6**, but could not find any boat structures. The reaction energy is −32.90 kcal mol^{-1}, and is the most exothermic of the Diels–Alder reactions of 1,3-butadiene and 2*H*-phosphole.

The geometry of **TS6x** is as expected, except for the slightly short forming C—C distance of 1.976 Å. Otherwise, the structure shows only small alternation in butadiene and standard bond lengths. The bond orders in **TS6x** indicate the least synchronous of the concerted reactions examined here. The bond orders of the active π-bonds range from 1.48 to 1.71; nevertheless the sum of the bond orders is 6.94. Bond order is conserved, which is expected of a concerted reaction. The activation energy through **TS6x** is 29.67 kcal mol^{-1}, by far the largest value of any Diels–Alder reaction of 2*H*-phosphole with butadiene. However, this barrier is about 1 kcal mol^{-1} less than for the analogous reaction, Reaction 2.

Just as the geometry of **TS2n** indicated possible biradical character, the structure of **TS6n** also appears to have biradical

Fig. 4 (*concluded*).

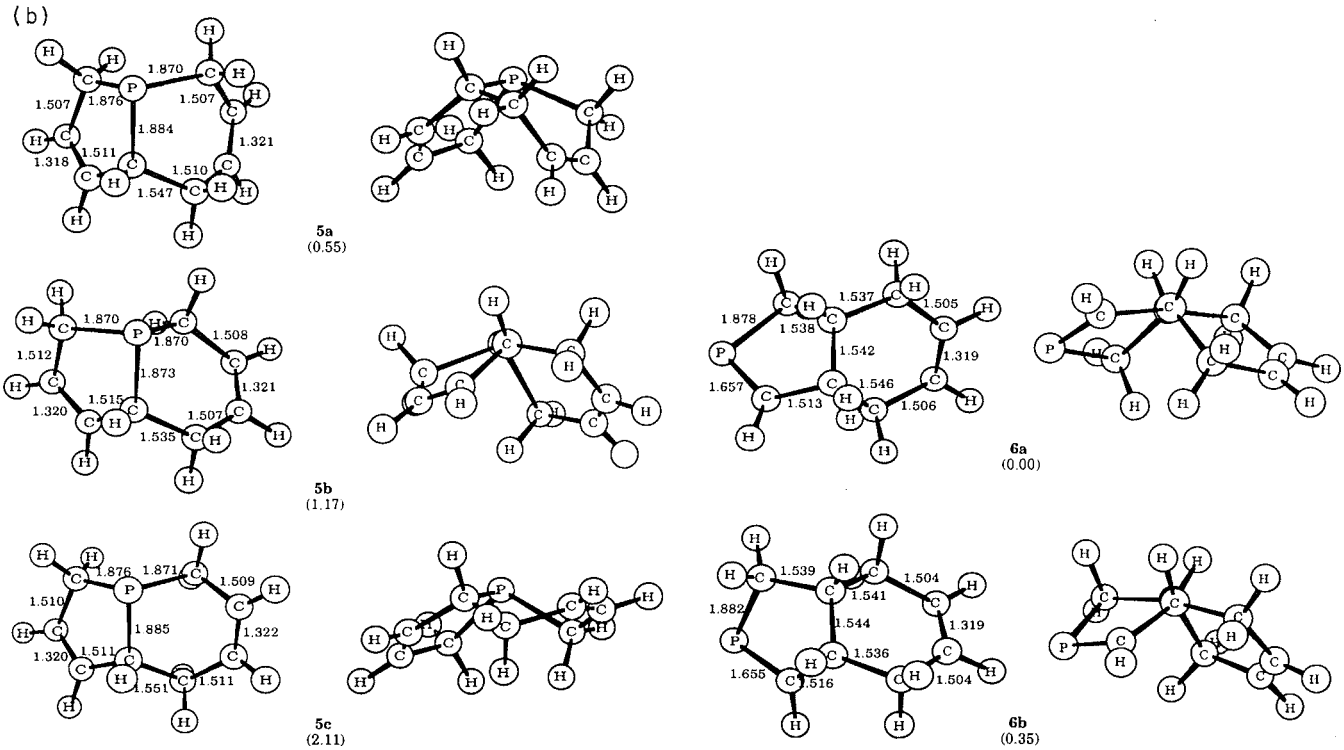

character. Since the active bonds for these two TSs are identical, this similarity is not unexpected. The butadiene fragment has two C—C bonds of length 1.382 Å (an allylic system) and the C—C bond adjacent to the forming C—C σ-bond is 1.490 Å, just short of a standard single bond distance. The distance of the original C=C in phosphole is 1.519 Å. The two forming C—C single bonds have lengths 1.582 Å (nearly fully formed) and 2.331 Å. The bond orders reflect this biradical character as well. The new, short C—C bond has order 0.85. The allylic system in butadiene shows bond orders of 1.67 and 1.62, while the allylic system in phosphole, which includes the C—P bond, has bond orders of 1.57 and 1.62. This *endo* TS is best examined at the UHF level, which will be discussed below.

UHF analysis of reactions 2 and 6

The RHF calculations of Reactions 2 and 6 proceeding through the *endo* TSs strongly suggest biradical character. We therefore decided to reexamine these two reactions at the UHF level, which is more appropriate for treatment of biradical systems. Since the main focus of this work is the concerted Diels–Alder reaction, and given the enormous computational demands for examining all these reactions for biradical intermediates, etc., we have examined these two reactions at the UHF level only.

Before proceeding to the UHF results, we wish to note one additional unusual aspect of the RHF TSs for these two reactions. Tracing the intrinsic reaction coordinate (IRC) for the two TSs indicates that these TSs do not connect the presumed reactant with product. Rather, **TS2n** connects **1cn** with **2** and **TS6n** connects **4cn** with **6**. One should keep in mind that these results are for the RHF surface, which is likely to be totally inappropriate for describing these two reactions.

Reexamination of Reaction 2 at UHF/6-31G* led to the reaction sequence shown in Scheme 4. A stable intermediate **INT2** could not be located at UHF, but was optimized at UMP2/6-31G*. A TS leading from reactants to **INT2** was located (**TS2n′**) as was the TS connecting **INT2** with product (**TS2n″**). The optimized structures are drawn in Fig. 5. The critical geometric features of these structures are the distances of the forming bonds between the two fragments. In **TS2n′**, the distance between one terminal C of butadiene and the C adjacent to the saturated carbon of cyclopentadiene is 2.100 Å, while there is no interaction between the other end of the addends. In **INT2** the one new C—C bond has essentially formed (1.564 Å) while the other still has not begun to form. Finally, in **TS2n″**, the second new bond has begun, indicated by a distance of 2.286 Å.

The activation energy (UHF/6-31G*) to reach **TS2n′** is 21.6 kcal mol^{-1}. **INT2** lies 2.4 kcal mol^{-1} above reactants. **TS2n‴** is 10.3 kcal mol^{-1} above the intermediate, or 12.7 kcal mol^{-1} above reactants.

A similar situation arises for Reaction 6 at UHF/6-31G*, also shown in Scheme 4. Again, a stable intermediate was located (**INT6**) along with TSs leading to (**TS6n′**) and from (**TS6n″**) this intermediate. The progress of the reaction can be monitored via the forming bond distances. The first bond formed is between the terminal carbon of butadiene and the carbon of cyclopentadiene adjacent to the saturated center. This distance is 2.119 Å in **TS6n′** and the bond is formed in **INT6**, having a distance of 1.552 Å. The second bond is not formed at all by **INT6** but begins to form in **INT6n″**, with a separation of 2.207 Å. These structures are drawn in Fig. 5.

TS6n′ lies 19.4 kcal mol^{-1} above reactants, while **INT6** is actually more stable than reactants, lying 3.3 kcal mol^{-1} below

Scheme 4.

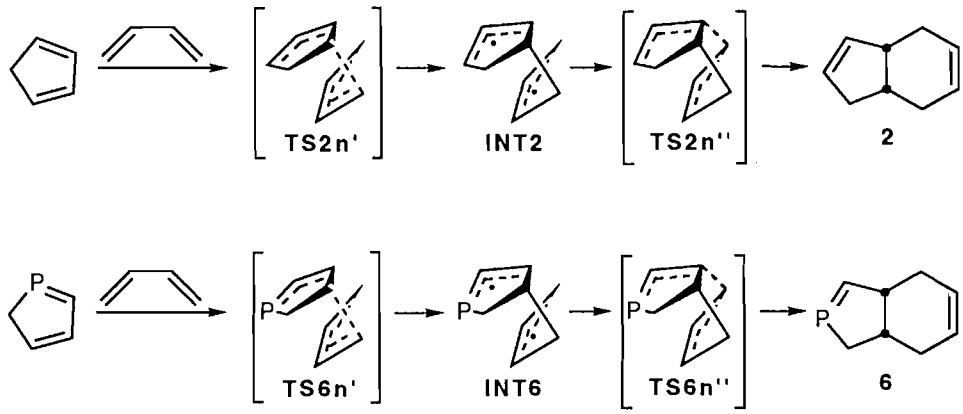

Fig. 5. UHF/6-31G* optimized geometries of transition states and intermediates from Scheme 5. All distances are in Å and relative energies are in kcal mol^{-1}.

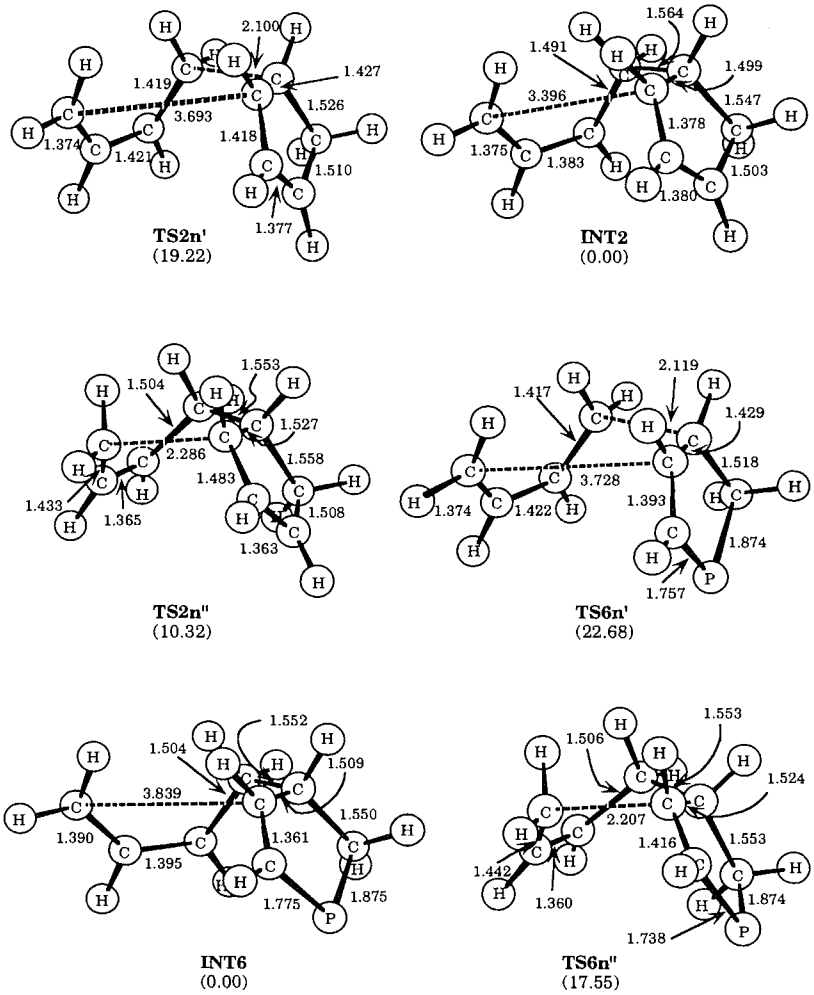

reactants. The barrier for the second step is 17.6 kcal mol^{-1}, or in other terms, **TS6n″** lies 14.3 kcal mol^{-1} above reactants.

At UHF/6-31G*, Reactions 2 and 6 forming the *endo* product proceed through a two-step process. In the first step, one new C—C single bond is formed, creating a stable biradical, which then forms the second new bond in the second step.

Discussion

We first examine the reactions for which we located concerted TS, i.e., excluding the reactions through **TS2n** and **TS6n**. The Diels–Alder reaction of cyclopentadiene with 1,3-butadiene can proceed in two ways, with either reagent acting as the

diene or dienophile. The reaction with butadiene as the dienophile (Reaction 2) is favored under thermodynamic control, which is understandable in terms of the greater ring strain in the norbornene product **1** than the bicyclic product **2**. The reaction where butadiene acts as the dienophile (Reaction 1) is kinetically favored. For normal, electron-demand, Diels–Alder reactions, the rate is dependent on the dienophile LUMO energy. The LUMO of butadiene is lower than in cyclopentadiene, making it the better dienophile. For Reaction 1 there is slight preference for *endo* selectivity and the *trans* conformation of the butadiene. This selectivity is consistent with previous calculations.

Products **5** and **6** are more stable than **3** and **4**, analogous to the hydrocarbon case. However, the energy difference is smaller in the former case. This is likely attributable to the decreased ring strain energy in **3** and **4** relative to **1** since phosphorus occupies the bridgehead position in the former compounds, and is better suited to accommodate the small ring angles than is carbon.

Products **3** and **4** are kinetically favored over **5** and **6**, again similar to the hydrocarbon case. The activation energy for Reactions 3, 4, and 5 (*exo* only) are about 10 kcal mol^{-1} less than for Reactions 1 and 2. A principle reason is the high HOMO and extremely low LUMO (0.0750 eV) of 2*H*-phosphole, making this reagent extremely reactive, particularly noticeable in the low activation energy of the reaction leading to **5n**. The activation energy for Reaction 6 is very similar to those of Reactions 1 and 2, where the active bonds all involve just carbon.

There is a distinct preference for *endo* selectivity in all of the phosphole reactions, though this selectivity is reduced in Reaction 4. The longer distance between the vinyl group and the five-membered ring in Reaction 4 compared to that in Reaction 3 dampens the discrimination. Reaction through the *trans* conformation of butadiene is also slightly favored in the reactions of phosphole. Again, this is consistent with the hydrocarbon results.

All of the concerted TSs are remarkably synchronous based on both bond distances (where appropriate comparisons can be drawn) and empirical bond orders. Perhaps most intriguing are the results of the reactions of phosphole. Even though the symmetry has been substantially broken by the phosphorus substitution, and the forming σ-bonds have very different lengths, the bond orders of the forming/breaking π-bonds are very close. The new σ-bonds have bond orders that match the degree of bond making/breaking at the other active bonds. This is best seen in the conservation of bond order between reactant, TS, and product.

The stepwise, biradical pathway for the Diels–Alder reactions has been shown to be about 10 kcal mol^{-1} less favorable than the concerted pathway for the reaction of 1,3-butadiene with ethylene and 5 kcal mol^{-1} less favorable in the dimerization of 1,3-butadiene (15). For the reactions examined in this study, the stepwise pathway will be further stabilized due to the possible formation of two allylic radicals. While detailed examination of the stepwise vs. concerted reactions is beyond the scope of this paper, two of the reactions examined here clearly proceed by the biradical pathway.

The reactions proceeding through **TS2n** and **TS6n** are distinctly different from the others. These transition states strongly suggest a biradical pathway. Our low-level investigation of the biradical pathway for both reactions confirms a biradical intermediate and therefore a two-step reaction mechanism. Our methods do not allow for direct energetic comparisons between the concerted (RHF) and biradical (UHF) energies, but it is clear that the biradical pathway is preferred for these two cases, since we were unable to locate a concerted TS.

Reactions 2 and 6, which proceed through the *exo* TSs, can proceed in a concerted fashion, providing some indication of the delicate balance between the competing mechanisms. In the *endo* TSs, there is sufficient steric interaction in the concerted approach to favor the stepwise mechanism, which diminishes the steric interactions and provides for stabilization of the two radical centers through allylic delocalization. The steric interactions are small enough in the *exo* TSs for the concerted TS to occur.

The most striking aspect of this study is how similar the results are for the phosphole and cyclopentadiene reactions. For both systems, kinetic control leads to the norbornene product and thermodynamic control leads to the bicyclo[4.3.0]nonadiene product. There is a slight preference for the *endo* TS and also for the butadiene (as dienophile) to react in the *trans* conformation. The TSs are concerted and synchronous, except for the case where butadiene is the diene and addition is *endo*. For this situation, both phosphole and cyclopentadiene react in a stepwise fashion. The only difference of note is the lower activation energies for the reactions of phosphole. The C=P double bond reacts analogously to the C=C double bond, except that its smaller bond energy leads to reduced activation barriers.

Finally, the calculated results are consistent with the experimental results. The reaction shown in Scheme 2 is conducted at high temperature (170°C) and for 5 days (4). The observed product corresponds with our thermodynamic product and, under these conditions, thermodynamic control is likely to prevail.

Conclusion

A major theme of our research program has been to explore the mechanistic changes brought on by replacing carbon with phosphorus in pericyclic reactions. In this paper, we explore the effects of replacing a carbon in cyclopentadiene with phosphorus. There is near-perfect similarity in the predications of the stereochemistry, energetics, and mechanistic path for these two systems. Thermodynamic preference is for formation of the bicyclo[4.3.0]nonadiene product, while kinetic preference is for the norbornene product. The *endo* TSs are lower in energy than *exo* TSs, with preference for the butadiene to be in the *trans* conformation. For the reaction of butadiene as the diene component and *endo* orientation, the reaction with both cyclopentadiene and 2*H*-phosphole proceeds through a stepwise, biradical mechanism; otherwise all reactions have concerted TSs, which show synchronous bond formation/cleavage. These results are in agreement with our previous studies, strongly indicating that the C=P double bond behaves identically to the C=C double bond in pericyclic reactions.

Acknowledgments

Acknowledgment is made to the Donors of the Petroleum

Research Fund, administered by the American Chemical Society, and to the National Science Foundation for support of this work. We are also grateful for a generous grant of computer time on the SGI Power Challenge at the National Center for Supercomputing Applications in Urbana, Ill, where many of these calculations were performed.

References

1. M. Regitz and O.J. Scherer. Multiple bonds and low coordination in phosphorus chemistry. Georg Thieme Verlag, Stuttgart, Germany. 1990.
2. F. Mathey. Acc. Chem. Res. **25**, 90 (1992).
3. F. Mathey. Chem. Rev. **88**, 429 (1988).
4. F. Mathey, F. Mercier, and C. Charrier. J. Am. Chem. Soc. **103**, 4595 (1981).
5. S.M. Bachrach. J. Org. Chem. **58**, 5414 (1993).
6. S.M. Bachrach. J. Org. Chem. **59**, 5027 (1994).
7. G. de Lauzon, C. Charrier, H. Bonnard, F. Mathey, J. Fischer, and A. Mitschler. J. Chem. Soc. Chem. Commun. 1272 (1982).
8. C. Charrier, H. Bonnard, G. de Lauzon, and F. Mathey. J. Am. Chem. Soc. **105**, 6871 (1983).
9. S.M. Bachrach and M. Liu. J. Org. Chem. **57**, 209 (1992).
10. S.M. Bachrach and M. Liu. J. Org. Chem. **57**, 2040 (1992).
11. S.M. Bachrach and M. Liu. J. Org. Chem. **57**, 6736 (1992).
12. S.M. Bachrach and D.C. Mulhearn. First Electronic Computational Chemistry Conference — CD ROM. *Edited by* S.M. Bachrach, D.B. Boyd, S.K. Gray, W. Hase, and H.S. Rzepa. ARInternet, Landover, Md. 1996.
13. U. Salzner and S.M. Bachrach. J. Am. Chem. Soc. **116**, 6850 (1994).
14. R.F.W. Bader. Atoms in molecules - a quantum theory. Oxford University Press, Oxford. 1990.
15. Y. Li and K.N. Houk. J. Am. Chem. Soc. **115**, 7478 (1993).
16. R.J. Loncharich, F.K. Brown, and K.N. Houk. J. Org. Chem. **54**, 1129 (1989).
17. W.L. Jorgensen, D. Lim, and J.F. Blake. J. Am. Chem. Soc. **115**, 2936 (1993).
18. R.D. Bach, J.J.W. McDouall, and H.B. Schlegel. J. Org. Chem. **54**, 2931 (1989).
19. K.N. Houk, R.J. Loncharich, J.F. Blake, and W.J. Jorgensen. J. Am. Chem. Soc. **111**, 9172 (1989).
20. M.J. Frisch, G.W. Trucks, M. Head-Gordon, P.M.W. Gill, M.W. Wong, J.B. Foresman, B.G. Johnson, H.B. Schlegel, M.A. Robb, E.S. Replonge, R. Gomperts, J.L. Andres, K. Raghavachari, J.S. Binkley, C. Gonzales, R.L. Martin, D.L. Fox, D.J. Defrees, J. Baker, J.J.P. Stewart, and J.A. Pople. Gaussian, Inc., Pittsburgh, Pa. 1992.
21. M.J. Frisch, G.W. Trucks, H.B. Schlegel, P.M.W. Gill, B.G. Johnson, M.A. Robb, J.R. Cheeseman, T. Keith, G.A. Petersson, J.A. Montgomery, K. Raghavachari, M.A. Al-Laham, V.G. Zakrzewski, J.V. Ortiz, J.B. Foresman, J. Cioslowski, B.B. Stefanov, A. Nanayakkara, M. Challacombe, C.Y. Peng, P.Y. Ayala, W. Chen, M.W. Wong, J.L. Andres, E.S. Reploge, R. Gomperts, R.L. Martin, D.L. Fox, J.S. Binkley, D.J. Defrees, J. Baker, J.J.P. Stewart, M. Head-Gordon, C. Gonzales, and J.A. Pople. Gaussian, Inc., Pittsburgh, Pa. 1995.
22. F.W. Biegler-Konig, R.F.W. Bader, and T.H. Tang. J. Comput. Chem. **3**, 317 (1982).
23. T.S. Slee. *In* Modern models of bonding and delocalization. *Edited by* J.F. Liebman and A. Greenberg. VCH Publishers, New York. p. 69.
24. S.M. Bachrach. J. Mol. Struct. (THEOCHEM), **255**, 207 (1992).
25. S.W. Benson. Thermochemical kinetics. Wiley–Interscience, New York. 1976.

Inner-shell excitation spectroscopy of aniline, nitrobenzene, and nitroanilines

Cássia C. Turci, Stephen G. Urquhart, and Adam P. Hitchcock

Abstract: Oscillator strengths for C 1s, N 1s, and O 1s excitation spectra of aniline, nitrobenzene, and the isomeric nitroanilines have been derived from inner-shell electron energy loss spectroscopy recorded under low momentum transfer conditions (>2.5 keV impact energy and small scattering angle, $\theta \leq 2°$). Extended Hückel Molecular Orbital (EHMO) calculations carried out within the equivalent core analogy are used to aid spectral interpretation. These spectra are used to investigate the sensitivity of core excitation spectroscopy to charge transfer interactions in aromatic molecules that have both electron-donating and electron-withdrawing substituents. Strong multielectron excitation features were not found, although these had been anticipated from photoemission studies. The C 1s $\rightarrow \pi^*$ and N 1s $(NH_2) \rightarrow \pi^*$ spectral features of the nitroanilines are found to be strongly dependent on the substitution pattern (*ortho*, *meta*, or *para*).

Key words: electronic structure, inner-shell excitation, nitroanilines, EHMO calculations.

Résumé : En se basant sur la spectroscopie de la perte d'énergie des électrons des couches internes dans des conditions de faible transfert du moment (énergie d'impact >2,5 keV et faible angle de diffusion, $\theta \leq 2°$), on a dérivé les forces d'oscillateur des C 1s, N 1s et O 1s pour les spectres d'excitation de l'aniline, du nitrobenzène et des nitroanilines isomères. Comme aide à l'interprétation spectrale, on a utilisé des calculs d'orbitales moléculaires de Hückel étendues (OMHE) effectués à des conditions correspondantes à celle de l'analogie équivalente à celles des couches internes. On a utilisé ces spectres pour étudier la sensibilité de la spectroscopie d'excitation des couches intérieures aux interactions de transfert de charge dans des molécules qui portent à la fois des substituants électrodonneurs et électroattracteurs. On n'a pas observé de caractéristiques de fortes excitations multiélectroniques, même si on les avait anticipées sur la base des études de photoémission. On a observé que les caractéristiques spectrales des transitions C 1s $\rightarrow \pi^*$ et N 1s $(NH_2) \rightarrow \pi^*$ des nitroanilines dépendent fortement des positions (*ortho*, *méta* ou *para*) des substituants.

Mots clés : structure électronique, excitation des couches intérieures, nitroanilines, calculs d'OMHE.

[Traduit par la rédaction]

I. Introduction

This study was motivated by observations in the early 1980s of intense satellite structures in the N 1s X-ray photoelectron spectra of gas phase and condensed *para*-nitroaniline and related compounds (1–11). The X-ray photoelectron spectrum (XPS) of solid *para*-nitroaniline exhibits a single sharp line attributed to N 1s(NH_2)[2] ionization and a 2 eV doublet with approximately equal intensity components initially attributed to N 1s(NO_2) ionization. Early interpretations (1) suggested that the lower binding energy component of the two peaks attributed to N 1s(NO_2) ionization was actually a multiconfigurational state in which N 1s(NO_2) ionization combined with a $\pi \rightarrow \pi^*$ excitation resulted in a state at *lower* energy than that of the one-electron N 1s(NO_2) ionization i.e., a *shake-down* satellite. This unusual situation was ascribed to a facile intramolecular charge transfer in this classic push–pull, donor–acceptor species. However, the N 1s XPS spectrum of gas phase *para*-nitroaniline was found to have a single broad N 1s(NO_2) peak (2) that, upon better resolution, was shown to consist of an asymmetric peak structure (6). Further work involving comparisons of vapour and solid state XPS spectra of *para*-nitroaniline (2, 6, 9, 11), and quantum calculations (4–6, 12) led to alternate spectral interpretations, including a more conventional *shake-up* picture in which the main line, one-electron N 1s(NO_2) ionization was attributed to the lower energy component of the doublet and the intense satellite at 2 eV higher energy was attributed to a $(NH_2) \rightarrow (NO_2)$ charge-transfer satellite of the N 1s(NH_2) line. Differences between the gas and solid state N 1s XPS were attributed to intermolecular charge transfer (9, 10, 12, 13) or hydrogen bonding effects in the solid (6).

The presence of the intense shake (charge transfer) satellites in the N 1s (and to a lesser extent, the O 1s) XPS led us to wonder whether the donor–acceptor character of disubstituted benzenes such as nitroaniline might give rise to analogous intense multielectron satellite structures in the core excitation spectra. Core excitation spectra might be expected to show satellite features closely related to those in core ionization

Received September 20, 1995.

This paper is dedicated to Professor Richard F.W. Bader on the occasion of his 65th birthday.

C.C. Turci. Instituto de Química, Universidade Federal do Rio de Janeiro, Rio de Janeiro, RJ, Brazil, 21910-900 and Department of Chemistry, McMaster University, Hamilton, ON L8S 4M1, Canada.

S.G. Urquhart and A.P. Hitchcock.[1] Department of Chemistry, McMaster University, Hamilton, ON L8S 4M1, Canada.

[1] Author to whom correspondence may be addressed. Telephone: (905) 525-9140, ext. 24749. Fax: (905) 521-2773. E-mail: aph@mcmaster.ca

[2] The core level involved is indicated by this notation. The character of the upper level of a given transition is indicated by a subscript, e.g., π^*_{NO}.

when the same core hole is involved. However, the discrete core excited states are neutral and the excited electron can have strong shielding effects such that the electron reorganization (charge transfer) that leads to XPS satellite lines may be strongly suppressed. Thus, rather than dramatic shake-up features analogous to those seen in XPS, there might be threshold onsets at the energy of the XPS shake-up signal superimposed on other spectral features in the continuum region of the core excitation spectrum (similar to those identified in the core spectra of some simple molecules such as CO and N_2 (14)), but there may not be any strong, sharp-line, multi-electron excitations built upon the main 1s $\rightarrow \pi^*$ discrete transitions. The initial motivation of our study was then to determine which of these two scenarios the experimental spectrum most resembled.

Another interesting theme of the core excitation spectroscopy of these molecules is the dependence of the C 1s $\rightarrow \pi^*$ structure on the nature of the disubstitution pattern (*ortho* versus *meta* versus *para*). While the core excitation spectra of several homo disubstituted benzenes have been studied previously (15, 16), to our knowledge this is the first study of the core spectra of a hetero disubstituted benzene. The pattern of unoccupied π^* orbitals will be affected by π^* electronic interaction between the NH_2 and NO_2 substituents through the ring-π^* system which, in turn, will depend on the substitution pattern. This, along with changes in the C 1s chemical shifts, should be reflected in the C 1s $\rightarrow \pi^*$ signals. If a characteristic signature for *ortho*, *meta*, and *para* substitution patterns can be identified, this could be useful with regard to analytical applications of NEXAFS spectroscopy, such as polymer microanalysis (16, 17).

In this work, inner-shell electron energy loss spectroscopy (ISEELS) has been used to record the C 1s, N 1s, and O 1s spectra of the three isomeric nitroanilines. In addition, the core spectra of nitrobenzene and aniline have been measured, in order to use spectral comparisons to aid assignment. The experimental conditions (high impact energy and small scattering angle) are such that the ISEELS spectra are expected to exhibit the same spectral features with similar relative intensities as those of the corresponding photoabsorption spectra. To our knowledge, aniline is the only one of these species for which core excitation spectra have been reported earlier (18–20), namely, X-ray absorption (NEXAFS) studies of the condensed multilayer solid.

The experimental spectra are reported on absolute oscillator strength scales using a previously developed conversion scheme (21). Extended Hückel (EHMO) calculations and a simple semiempirical molecular orbital method (22–24), carried out within the equivalent ionic core virtual orbital model (EICVOM) (25, 26), have been used to assist spectral assignments and to explore aspects of the virtual molecular orbital electronic structure of these species.

II. Experiment

The gas phase ISEELS spectrometer employed in these experiments has been described in detail previously (27). Basically, it is a high-vacuum apparatus consisting of an electron gun, sets of electrostatic deflector plates for beam steering, beam current monitors, a gas cell, a post collision deceleration lens, a hemispherical electrostatic energy analyzer, and a single electron counting detection system. The detector pulses are processed by standard electronics (preamplifier, amplifier, discriminator) and are counted by a microcomputer that also scans the analyzer voltages and stores the acquired data. The spectrometer is operated under conditions of small momentum transfer where the electronic excitations are dominated by electric-dipole-allowed transitions. The impact energy is 2.5 keV plus the energy loss and the scattering angle is ~2°C. The overall spectral resolution was typically in the range of 0.6–0.8 eV full width at half maximum (fwhm), although the C 1s spectrum of aniline was recorded with a resolution of 0.45 eV.

All samples were obtained commercially; aniline from BDH, nitrobenzene from Baker, and nitroanilines (*ortho*, *meta*, *para*), from Eastern. All samples had a stated purity better than 98%. They were run without further purification, except aniline and nitrobenzene, which were submitted to multiple freeze–pump–thaw cycles to remove any dissolved impurity gases or highly volatile components prior to their use. The least volatile samples, *para*-nitroaniline (mp 149°C), *meta*-nitroaniline (mp 114°C), and *ortho*-nitroaniline (mp 75°C) were placed inside a small glass tube attached directly to the collision cell of the spectrometer. For the *para* and *meta* compounds, the tube was gently heated with an internally mounted quartz–halogen bulb, while the end plates of the gas cell were water cooled to trap the vaporized sample and avoid insulating deposits on sensitive parts of the spectrometer. The aniline and nitrobenzene samples were sufficiently volatile to be introduced into the gas cell through a leak valve from a flask at low vacuum. Multiple spectra were obtained to confirm reproducibility.

The energy-loss scale was calibrated by recording the spectrum of a mixture of the unknown and a suitable reference molecule. The C 1s and O 1s spectra were calibrated using the C 1s $\rightarrow \pi^*$ (290.74(4) eV) (28, 29) and the O 1s $\rightarrow \pi^*$ (535.4(2) eV) (30) transitions of CO_2. The N 1s spectra were calibrated using the N 1s $\rightarrow \pi^*$ (401.10(2) eV) transition of N_2 (28, 29). The signal associated with a particular core edge was isolated from the underlying valence-shell ionization continuum by subtracting a smooth curve determined from a curve fit of the function $a(E - b)^c$ to the pre-edge experimental signal. These background subtracted spectra were then converted to absolute oscillator strength scales using a method described and tested previously (21).

III. EHMO calculations

Extended Hückel molecular orbital (EHMO) calculations were used to predict the core excitation spectra using the equivalent ion core virtual orbital model (EICVOM) (25, 26), as described previously (31–33). In the EICVOM method the localization and reorganization effects associated with core excitation are simulated by replacing the core excited atom with the element of one larger nuclear charge (the equivalent core approximation) and the valence electron count is corrected by adding a positive charge. The virtual orbital energies of the ground state of the cation are interpreted as the relative energies (approximate term values) of core $\rightarrow$ valence excited states while the intensities of each transition are assumed to be proportional to the sum of the square of the coefficients of the electric dipole coupled (2p) atomic orbitals on the 1s excited atom for each virtual MO (Σc^2_{N2p} for C 1s excitation, Σc^2_{O2p}

for N 1s excitation, and Σc^2_{F2p} for O 1s excitation). Extended Hückel calculations were performed with the CACAO molecular program (34) using the default EHMO parameters. The CACAO program provides pictures of the orbitals involved in the transitions that help to identify the spatial characteristics of the core excited electron density. The molecular geometries used in the calculation were ground-state experimental geometries taken from the literature (35).

To account for site-dependent core-hole localization effects on the virtual MOs (15) and the different chemical shifts in the 1s energies, the EHMO calculation of each spectrum is constructed from the results of calculations of the equivalent core analogy species with the core hole at all possible distinguishable sites (e.g., for *para*-nitroaniline, four distinct C 1s sites and two distinct N 1s sites). The core excitation spectrum for each site is constructed from the MO coefficients of all of the unoccupied MOs, with a peak at each eigenvalue assigned an area equal to the 2p density at the core excited atom (as given by twice the reduced charge matrix element (33)) and a width related to the eigenvalue. The experimentally observed line widths have been used as a guide to selecting fixed line widths in four ranges of eigenvalues, with gradually increasing line widths to account for the decreasing lifetime of higher energy continuum states.

Two procedures were explored for matching the EHMO to the absolute experimental energy scale. In the first one the zero of the eigenvalue scale for each component was set to the measured or estimated ionization potential (IP) (2, 36). The components were then added and the sum was shifted to match experiment at the prominent lowest energy π^* resonance. In the second procedure each site spectrum was placed on an absolute excitation energy scale by setting the strongest 1s $\rightarrow$ π^* feature in each site spectrum to the energy of the assigned experimental feature (table 8 provides details). The weighted sum of the individual site spectra (e.g., for C 1s in nitrobenzene, a 2:2:1:1 sum of C 1s(2,6), C 1s(3,5), C 1s(4), and C 1s(C-NO_2); see Fig. 2) was then the EHMO 1s spectrum for that species. The intensity of the EHMO spectrum was then scaled so that the integrated 1s $\rightarrow$ π^* intensity for experiment and EHMO was the same. To simulate the nonresonant part of the spectrum, an oscillator strength continuum component, generated from the tabulated values for the atom (37), was added. The second procedure, that in which the components are matched individually to experiment, gave more satisfactory agreement with experiment. This approach was used to calculate the spectra of each core level of all five molecules (a total of 14 predicted spectra).

IV. Results

A. C 1*s* spectra

A.1 Aniline and nitrobenzene: monosubstituted models

The main features of the C 1s spectra of all five molecules of this study can be readily related to those of benzene (38). First we discuss the spectra of the two singly substituted benzenes, which act as models for the nitroanilines. Figure 1 compares the C 1s spectra of aniline and nitrobenzene with that of benzene. The energies, term values, and proposed assignments of the spectral features of aniline are presented in Table 1 along with results from the literature (19, 20), while the values for

Fig. 1. C 1s oscillator strength spectra of aniline and nitrobenzene, compared to that of benzene (38). All of the spectra were derived from energy loss spectra recorded under near-dipole scattering conditions (2800 eV impact energy, 2° scattering angle) with 0.7 eV fwhm resolution. The hatched lines indicate the measured IPs (36). The insert is an expansion and curve fitting of the first π^* peak in nitrobenzene.

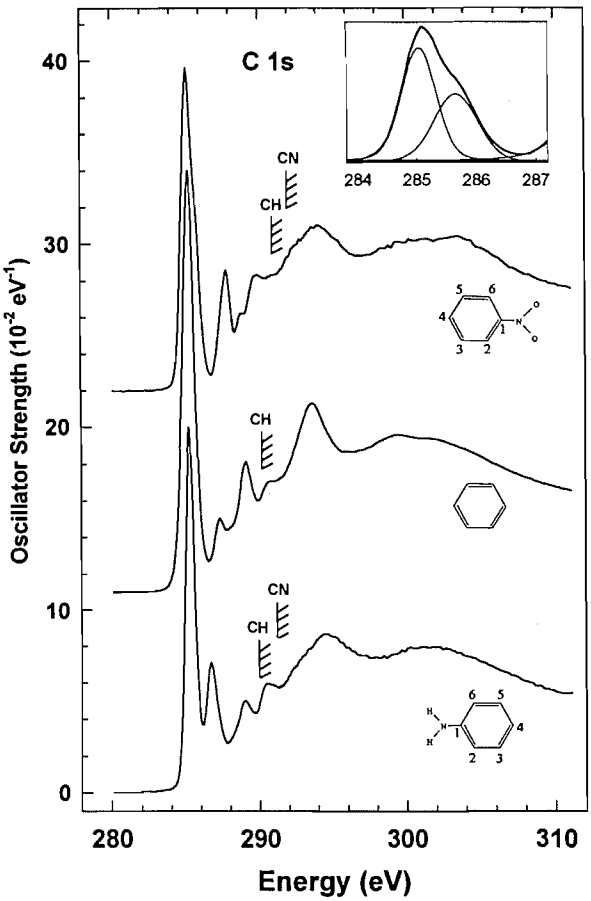

nitrobenzene are presented in Table 2. (Note that the tables only list the spectral features that can be readily observed in the accompanying figures. A number of weaker shoulders, which can be detected on closer examination, have not been tabulated. Our orientation in this study is to explain the main features and their chemical trends. We believe an exhaustive interpretation of all core excitation features is best delayed until higher resolution data are acquired).

Since the orbitals of the amine group interact very little with those of the π manifold, the C 1s $\rightarrow$ π^* region of aniline should be relatively similar to that of benzene, modified mainly by the chemical shift of the C 1s(C-N) site and possibly by a splitting of the e_{2u} ($\equiv 1\pi^*$) orbital of benzene. The lowest energy peak in the C 1s spectrum of aniline is a relatively narrow symmetric line (0.8 eV fwhm) while there is a second band at 1.5 eV higher energy. Based on the similarity of the separation of these first two bands to the separation of the C 1s(C-H) and C 1s(C-N) IPs (1.0 eV (36)), we attribute the second component to the C 1s(C-N) $\rightarrow$ $1\pi^*$ transition. The third resolved peak, that at 289.0 eV, is attributed to the C 1s(C-H) $\rightarrow$ $2\pi^*$ transition (correlating with the b_{2g} ($\equiv 2\pi^*$)

Table 1. Energies (eV), term values (eV), and proposed assignments for features in the 1s spectra of aniline.

(*a*) C 1s.

Gas (this work)		Solid (NEXAFS)		Term value[a]		Assignment	
No.	E (±0.1 eV)	E^b(eV)	E^c(eV)	T_{CH}	T_{CN}	C-H	C-N
1	285.2[d]	285.4	285.4	5.0		$1\pi^*(4b_1)$[e]	
2	286.7	286.9	286.8		4.6		$1\pi^*(4b_1)$
3	289.0	288.7		1.2		$2\pi^*(5b_1)$/3p	
4	290.5	290.6			0.8		$2\pi^*(5b_1)/\sigma^*_{CNH}$
IP	290.2[f]					IP	
IP	291.3[f]						IP
5	294.5	294.5		−3.7		$1\sigma^*$	
6	302(1)	303		−11		$2\sigma^*$	

(*b*) N 1*s*.

No.	*E* (±0.1 eV)	TV	Assignment
1 (sh)	400.7	4.6	3s
2	402.2[d]	3.1	$3p/\pi^*_{NH}(4b_1)$
3 (br)	404	1.3	σ^*_{NH}
IP	405.3[f]		IP
4	407.6	−2.3	σ^*_{CN}

[a]TV = E − IP (derived using values for gas phase excitation energies).
[b]From ref. 19, C 1s spectrum of solid aniline, a multilayer on Ag (110).
[c]From ref. 20.
[d]Calibration: C 1s −5.51(3) eV relative to CO_2 (π^*); N 1s +1.1(1) relative to N_2 (π^*).
[e]Solomon et al. (19) attribute the first feature to a combination of $\pi^*(2a_2)$ and $\pi^*(4b_1)$ excitations. Otherwise all other assignments are the same as given above.
[f]IPs from ref. 36.

orbital of benzene). There is debate concerning the assignment of the corresponding feature in benzene. Both experimental and theoretical studies provide evidence that the final state at 289 eV in benzene is one in which the one-electron ($C\ 1s^{-1}$, $\pi^*(b_{2g})$) configuration is heavily mixed with the ($C\ 1s^{-1}$, π^{-1}, π^{*2}) multi-electron excited configuration (39–41). By analogy to benzene, it is likely that the 289 eV feature in aniline may also contain contributions from multi-electron ($C\ 1s^{-1}$, π^{-1}, π^{*2}) excitations. We do not see any evidence in the aniline C 1s spectrum for the splitting of the $1\pi^*(e_{2u})$ into $2a_2$ and $4b_1$ levels, expected from the reduction of symmetry from that of benzene. According to the electron transmission spectrum of aniline (42) this splitting is of the order of 0.5 eV, which should be detectible. However, transitions to the $2a_2$ orbital are found from quantum calculations to have negligible intensity (see Sect. A.2).

The situation is rather different in nitrobenzene since the π and π^* orbitals of the nitro group interact with those of the ring. Essentially, four π^* orbitals must be considered in the spectral assignments of the C 1s spectrum of nitrobenzene (and also in the nitroanilines) — the three intrinsic π^* orbitals of the ring plus the π^*_{NO} — whereas only the three π^* orbitals of the ring are involved in aniline. While the nitrobenzene spectrum superficially resembles that of benzene, in fact there are marked differences. In particular, if the C 1s spectrum was analogous to that of aniline there should be a C 1s(C-N) → $1\pi^*$ peak around 286.1 eV, about 1 eV above the main C 1s(C-H) → π^* line at 285.1 eV since the C 1s(C-H)/C 1s(C-N) chemical shift is 1.0 eV (36). No such peak exists. However, there is a high-energy shoulder on the first peak, with a separation of 0.64 eV (see the insert to Fig. 1), which is effectively the C 1s(C-N) → $1\pi^*$ transition, but with a significant shift to lower energy because of mixing of the $1\pi^*_{C=C}$ and π^*_{NO} orbitals. In fact, the EHMO calculations (see next section) indicate that interaction of the $1\pi^*_{C=C}$ and π^*_{NO} orbitals has a major effect on all of the C 1s → π^* transitions, such that the second, fully resolved peak in the C 1s spectrum of nitrobenzene (287.8 eV) also arises from C 1s(C-H) → $1\pi^*/\pi^*_{NO}$ transitions. The C 1s → $2\pi^*$ transitions are relatively unchanged from those in benzene and aniline and are attributed to the peak at 288.8 eV and part of the broader signal at 289.7 eV.

At higher energy, the C 1s continua of aniline and nitrobenzene are relatively similar, each exhibiting a two-peaked pattern very similar to that of benzene (38). These features are attributed to C 1s → $\sigma^*_{C\text{-}C}$ transitions. According to the bond length correlation (43), which relates the position of 1s → σ^*_{XY} transitions referenced to the ionization threshold to the X—Y bond length, there should also be C 1s → σ^*_{CNH} (aniline) and C 1s → σ^*_{CNO} (nitrobenzene) features appearing around 291 eV. Broader structures in this region are so assigned in each species. The term value of the σ^*_{CN} feature in aniline is 1.6 eV smaller than that in nitrobenzene, consistent with the shorter C—N bond length in aniline (1.431 Å) than that in nitrobenzene (1.478 Å) (43).

A.2 EHMO results for aniline and nitrobenzene

Table 3 summarizes a selection of the EHMO results for the π^* resonances for aniline and nitrobenzene. Figure 2 com-

Table 2. Energies (eV), term values (eV), and proposed assignments for features in the 1s spectra of nitrobenzene.

(*a*) C 1s.

No.	Energy (±0.1 eV)	Term value T_{CH}	Term value T_{CN}	Assignment $C_{2,6}$-H	Assignment $C_{3,5}$-H	Assignment C_4-H	Assignment C_1-N
1	285.1[a]	6.0		$1\pi^*(4b_1)$	$1\pi^*(5b_1)$	$1\pi^*(4b_1)$	
2 (sh)	285.7		6.4				$1\pi^*(5b_1)$
3	287.8	3.3		$1\pi^*(5b_1)$		$1\pi^*(5b_1)$	
4	288.8		3.3		$2\pi^*(6b_1)$		
5	289.7		2.4	$2\pi^*(6b_1)$		$2\pi^*(6b_1)$	$2\pi^*(6b_1)$, σ^*_{CNO}
IP	291.1[b]			IP	IP	IP	
IP	292.1[b]						IP
6	294.0	−2.4		←	$1\sigma^*$	→	
7	302(1)	−10		←	$2\sigma^*$	→	
8	328(2)	−36			EXAFS		

(*b*) N 1s.

No.	Energy	TV	Assignment
1	403.8[a]	7.7	π^*_{NO}
2	408.3	3.2	$3p/\pi^*_{mix}$[c]
3	409.5	2.0	4p
IP	411.5[b]		IP
4	413.2	−1.7	σ^*_{CN}, $\sigma^*_{NO}(+)$
5	418.5(3)	−7	$\sigma^*_{NO}(-)$

(*c*) O 1s.

No.	Energy	TV	Assignment
1	530.9[a]	7.6	π^*_{NO}
2	534.0	4.5	π^*_{mix}[c]
3	538.0	0.5	$\sigma^*_{NO}(-)$
IP	538.5[b]		IP
4	541.3	−2.8	$\sigma^*_{NO}(+)$

[a]Calibration: C 1s −5.65(3) eV; N 1s +2.67(2) relative to N_2 π^*; O 1s −4.46(6) eV relative to CO_2 π^*.

[b]IPs from ref. 36.

[c]π^*_{mix} refers to a higher energy MO of π^* symmetry with both π^*_{NO} and $\pi^*_{C=C}$ character.

pares the experimental C 1s spectrum of nitrobenzene with that predicted from the EHMO-EICVOM calculations. In addition to illustrating the methodology used to align the individual site components with experimental data, this figure nicely reveals the important role of $\pi^*_{C=C}$ and π^*_{NO} orbital mixing in the C 1s spectrum. According to EHMO, the main π^* contribution for C_1 and $C_{3,5}$ excitations is from the $\pi^*(5b_1)$ orbital, which is an admixture of the π^*_{NO} and $\pi^*_{C=C}$ orbitals. However, at both the C_4 and $C_{2,6}$ sites, there is significant contribution from both the $4b_1$ and $5b_1$ orbitals, with each of these MOs having a combined $\pi^*_{C=C}$ and π^*_{NO} character. There is no significant contribution from the $3a_2$ component (derived from splitting of the e_{2u} orbital of benzene) at any C 1s site. At higher energy there is a small contribution from C 1s $\pi^*(6b_1)$ transitions at each site. Thus, EHMO suggests that the relatively simple experimental spectrum arises from the C 1s(C-H)/C 1s(C-N) chemical shift and a complex overlap of transitions to the $4b_1$ and $5b_1$ orbitals, which have a site-dependent mix of $\pi^*_{C=C}$ and π^*_{NO} character.

As illustrated in Fig. 2, the EHMO predictions for nitrobenzene are in reasonable agreement with experiment in the π^* region (284–288 eV). There is less satisfactory agreement in the region of the continuum onset (288–291 eV), in part because EHMO cannot reproduce spatially extended Rydberg states. There is also disagreement between calculation and experiment in the region of the continuum resonances (and this is true for all species of this study). These resonances are related to 1s excitations to high-lying σ^* MOs, which in some cases have a relatively localized character associated with specific structural aspects of the molecule (43). EHMO often predicts the correct pattern of high-energy σ^* features, but typically places the σ^* resonances at higher energies and with significantly distorted intensities. This could be related to inadequacies of EHMO and other semi-empirical quantum

Table 3. Energies and LCAO-MO coefficients at the core excited atom in π* orbitals of aniline and nitrobenzene from EHMO-EICVOM calculations.

Aniline

MO sym	*E*(eV) ground state	N 1s		MO sym[a]	C 1s(2, 6)		C 1s(3, 5)		C 1s(4)		C 1s(C-N)	
		E	c^2(O2p)		*E*	c^2(N2p)	*E*	c^2(N2p)	*E*	c^2(N2p)	*E*	c^2(N2p)
$5b_1$	4.42	4.51	0.004	$5b_1(2\pi^*)$	5.10	0.029	4.97	0.023	4.94	0.021	5.25	0.031
$4b_1$	7.86	8.04	0.011	$2a_2(1\pi^*)$	7.91	0.002	7.97	0.002	8.29	0.000	8.29	0.000
$2a_2$	8.29	8.29	0.000	$4b_1(1\pi^*)$	9.20	0.095	9.38	0.121	9.00	0.109	9.17	0.137

Nitrobenzene

MO sym	*E*(eV) ground state	O 1s		N 1s		MO sym	C 1s(2, 6)		C 1s(3, 5)		C 1s(4)		C 1s(C-N)	
		E	c^2(F2p)	*E*	c^2(O2p)		*E*	c^2(N2p)	*E*	c^2(N2p)	*E*	c^2(N2p)	*E*	c^2(N2p)
$6b_1$	4.55	4.55	0.001	4.67	0.004	$6b_1(2\pi^*)$	5.21	0.029	5.09	0.022	5.05	0.020	5.37	0.031
$5b_1$	7.81	7.84	0.003	8.11	0.014	$3a_2(1\pi^*)$	7.85	0.002	7.94	0.004	8.35	0.000	8.35	0.000
$3a_2$	8.35	8.35	0.000	8.35	0.000	$5b_1(1\pi^*, \pi^*_{NO})$[b]	9.17	0.076	9.41	0.119	8.84	0.089	9.01	0.124
$4b_1$	10.56	10.83	0.024	11.86	0.201	$4b_1(\pi^*_{NO}, 1\pi^*)$[b]	10.80	0.040	10.56	0.000	10.82	0.043	10.57	0.003

[a]{$\pi^*(2a_2)$, $\pi^*(4b_1)$} correlates with the e_{2u} orbital while $2\pi^*(5b_1)$ correlates with the b_{2g} orbital in benzene.
[b]The $4b_1$ and $5b_1$ orbitals are a site-dependent mix of the b_1 component derived from the $1\pi^*$ (e_{2u}) and the $1\pi^*_{NO}$ (b_1) orbital of the NO_2 group.

Fig. 2. EHMO predicted C 1s spectrum of nitrobenzene compared to experiment. The full C 1s EHMO spectrum is the sum of the indicated constituent components and a nonresonant ionization signal estimated from that tabulated for atomic carbon (37), aligned at the C 1s IPs. The EHMO component spectra were aligned with experiment at the approximate position of the main π^* resonance, with exact values chosen to obtain the best visual agreement with experiment (see Table 8).

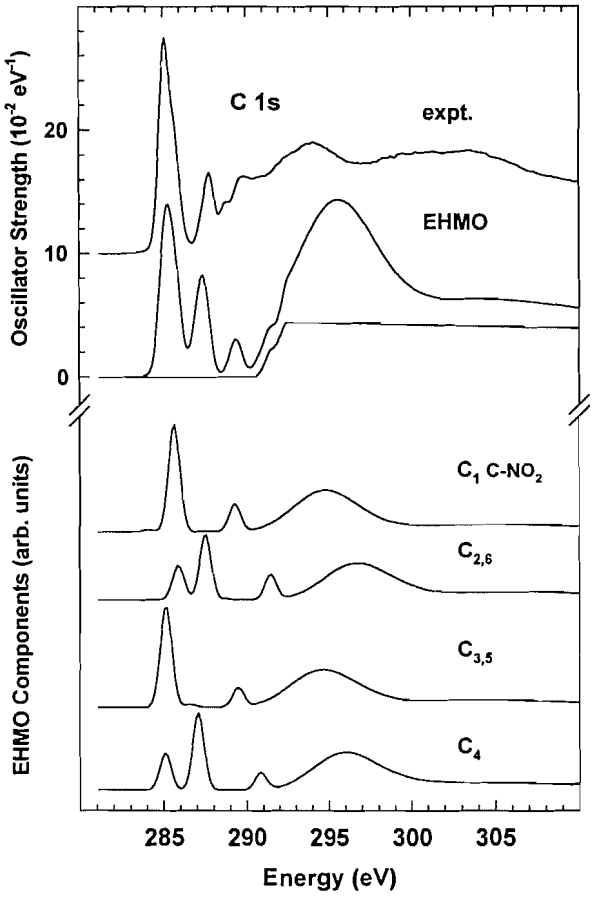

calculations (44) at treating high-energy molecular orbitals. Interestingly, while EHMO overestimates the energy of high-lying σ^* levels, CNDO (44) appears to predict the corresponding levels at energies below those observed experimentally.

The EHMO results for aniline (Table 3, Fig. 3) are a close match to the qualitative spectral description given in the preceding section. The C 1s spectrum of gaseous aniline presented in this work is very similar to the C 1s NEXAFS spectrum of a multilayer of solid aniline on Ag(110) (19). The energies and assignments of the spectral features are generally in agreement with the present work. Solomon et al. (19) and Luo et al. (20) attributed the peaks at 286.9 and 288.7 eV in the NEXAFS spectrum of solid aniline to the presence of the NH_2 group, which, leads to chemical shifts in the C 1s levels and lifts the degeneracy of the $1\pi^*(e_{2u})$ molecular orbitals of benzene. The NEXAFS spectrum of solid aniline has been interpreted by Luo et al. (20) on the basis of high-level multiconfigurational self-consistent field (MCSCF) calculations, in which both relaxation and correlation effects are taken into account. One notable difference among these three studies of C 1s excited aniline is that we and Luo et al. (20) attribute the

Fig. 3. (*a*) C 1s spectra of aniline, the isomeric nitroanilines, and nitrobenzene in the region of the C 1s $\rightarrow \pi^*$ excitation, predicted from EHMO calculations. See the text and Table 8 for details of the line widths and shifts used to construct the predicted spectra. (*b*) Corresponding region of the experimental C 1s oscillator strength spectra.

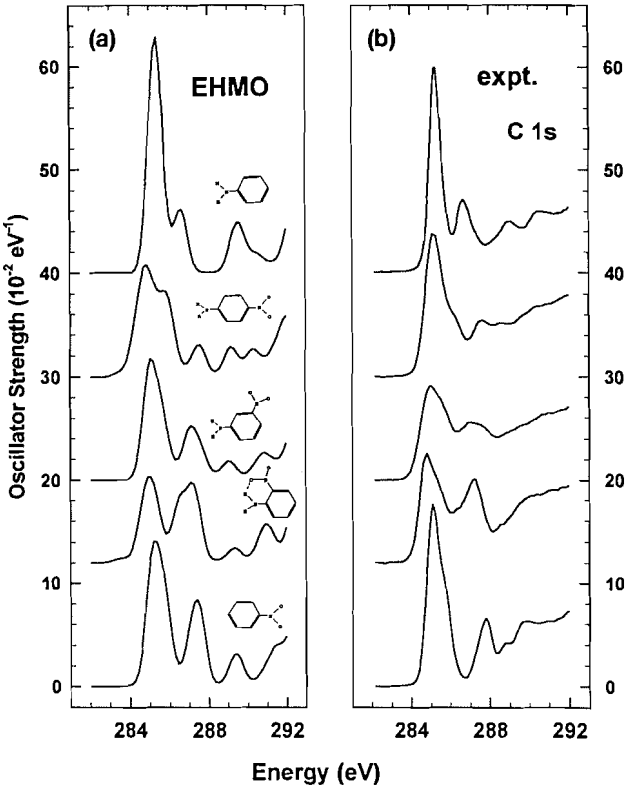

lowest energy peak to C 1s (C-H) $\rightarrow \pi^*$ $(4b_1)$ transitions whereas Solomon et al. (19) have attributed it to combined C 1s $\rightarrow \pi^*(2a_2)$ and C 1s $\rightarrow \pi^*(4b_1)$ transitions. Although C 1s $\rightarrow \pi^*(a_2)$ transitions are allowed at the $C_{2,6}$ and $C_{3,5}$ sites in C_{2v} symmetry, both the EHMO and MCSCF calculations indicate that these have negligible intensity (see Table 3). Another interesting aspect of the EHMO results for aniline (and nitrobenzene) is that there is a reversal in ordering of the a_2/b_1 components associated with the $1\pi^*_{C=C}$ orbital between the ground and N 1s/ O1s states (where $a_2 < b_1$), and all of the C 1s excited states (where $b_1 < a_2$) . The reversal occurs because the C 1s core hole stabilizes the $\pi^*_{C=C}(b_1)$ orbital by 1.1–1.4 eV (see Table 3), but not the a_2 orbital. The "avoidance" of the core hole by the a_2 orbital is the reason there is no contribution from C 1s $\rightarrow \pi^*(a_2)$ transitions. Thus, on the basis of both energetics and intensities, EHMO indicates the main C 1s $\rightarrow \pi^*$ intensity is associated with the b_1 orbitals and not the a_2 orbital.

Table 4 compares our C 1s EHMO predictions of the lower energy π^* features of aniline with those from the MCSCF calculations reported by Luo et al. (20). The MCSCF calculations also indicate that transitions to the $\pi^*(a_2)$ orbital have negligible intensities. They show that the lowest core excited state is the $\{C\ 1s(3, 5)^{-1}, \pi^*(4b_1)\}$ state, which is almost degenerate (ΔE = 0.03 eV) with the $\{C\ 1s(2, 6)^{-1}, \pi^*(4b_1)\}$ state. The energy shift of the $\{C\ 1s(3, 5)^{-1}, \pi^*(4b_1)\}$, $\{C\ 1s(4)^{-1}, \pi^*(4b_1)\}$, and $\{C\ 1s(C\text{-}N)^{-1}, \pi^*(4b_1)\}$ states relative to the

Table 4. Relative spacings of C 1s → π* transitions for aniline from experiment and calculation.

C 1s.

		EHMO calculation		Relative E		
C no.	IP(eV)[a]	−ε(eV)	E(eV)[b]	EHMO[c]	MCSCF (20)	Expt. (this work)
1(C-NH_2)	291.3	9.17	282.1	1.3	1.15	1.5
2,6	290.2	9.20	281.0	0.2	0.03	(<0.2)[d]
3,5	290.2	9.38	280.8	0	0	0
4	290.2	9.00	281.2	0.4	0.29	(<0.2)[d]

[a]From XPS (36).
[b]Assumes −ε from EHMO is equal to the term value. Typically this overestimates the transition energy by about 4 eV (see Table 8).
[c]E_{rel} is the energy relative to the C 1s(3, 5) → 1π*($4b_1$) transition.
[d]The splitting attributable to this separation is not detected. This value is an upper bound based on the 0.45 eV resolution of our ISEELS system and that of <0.2 eV in the NEXAFS study (20).

Fig. 4. C 1s oscillator strength spectra of the *ortho*-, *meta*-, and *para*-nitroaniline, compared to a simulation that is the sum of the C 1s spectra of nitrobenzene (shifted by −0.1 eV) and aniline (shifted +0.8 eV) minus that of benzene (shifted by +0.5 eV) (the shifts are the IP shifts). See Fig. 1 for experimental details.

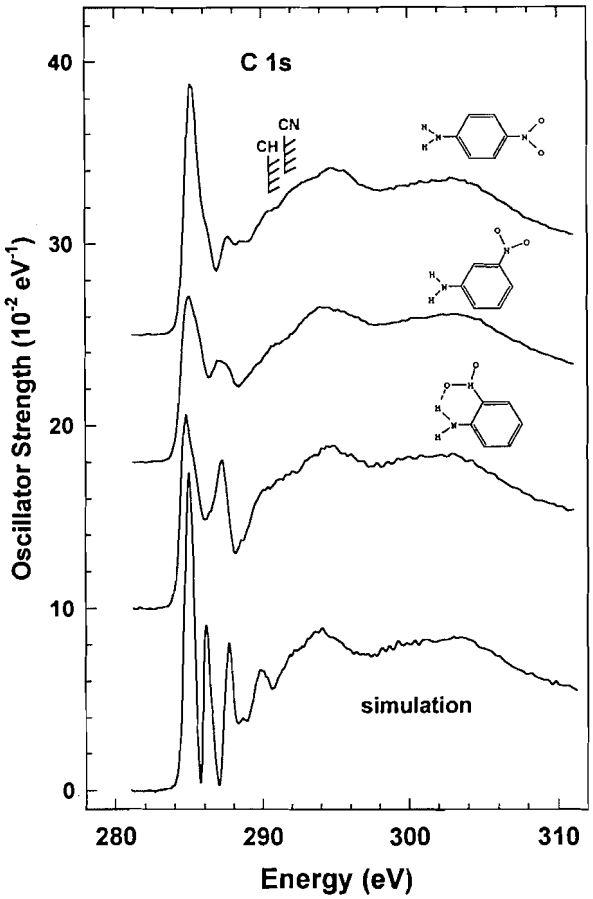

lowest core excited state are also presented in Table 4. Overall the EHMO results agree very well with those from MCSCF calculations. Based on the energy differences between different core-excited states, Luo et al. (20) assigned the first resonance (285.4 eV) to $C_{2,3,4}$ → π*($4b_1$) transitions and the second resonance (286.8 eV) to C 1s(C-N) → π*($4b_1$) transitions, as in the present work. Our calculations indicate that the 290.5 eV feature, which lies above the C 1s(C-N) IP, is the C 1s(C-N) → π*($5b_1$) transition, as first proposed by Solomon et al. (19).

A.3 C 1s spectra of nitroanilines

The C 1s spectra of the isomeric nitroanilines are presented in Fig. 4, while the energies, term values, and proposed assignments are given in Tables 5, 6, and 7. The C 1s chemical shifts of nitroanilines have not been measured although an average C 1s IP of 291.1 eV for *para*-nitroaniline has been reported (2). Based on this value and the shifts between the C 1s(C-H) and the C 1s(C-N) IPs of 1.1 eV for aniline and 1.0 eV for nitrobenzene, we estimate the C 1s IPs of all three nitroanilines as 290.8 eV (C 1s(C-H)) and 291.8 eV (C 1s(C-N)).

If there was negligible interaction between the nitro and amine groups, one might expect the C 1s spectra of the nitroanilines to be similar to a weighted sum of the C 1s spectra of aniline and nitrobenzene as proposed by the "building block" approach (18). Figure 4 includes a comparison to a simulation of the spectrum generated in this manner. The substantial difference between the simulation and any of the nitroaniline spectra in the region of the π* structure indicates that the two substituents interact electronically to affect the unoccupied π* structure. Thus the details of the C 1s spectra provide insight into the donor–acceptor (push–pull) interactions between the NH_2 and NO_2 groups, through their influence on the carbon 2p contributions to the π* orbitals. Because the π^*_{NO} and $\pi^*_{C=C}$ levels of the three nitroanilines will interact in a manner similar to that in nitrobenzene, the spectral features are best explained using the nitrobenzene assignments as a model.

We attribute the first band (285–286 eV) in each of the nitroanilines to C 1s(C-H) → 1π* transitions and the second band (286.5–288.5 eV) to the superposition of C 1s(C-N) → 1π* and C 1s(C-H) → 2π* transitions. Both bands are structured in all three molecules, which is likely the effect of chemical shifts in the C 1s IPs, as well as shifts in state energies associated with the influence of the core-hole location on the energy of the π* orbitals. The C 1s continuum shape in all three nitroanilines is rather similar and can be readily interpreted as the doubly peaked structure of benzene with additional contribution from C 1s → σ^*_{CNO}, σ^*_{CNH} transitions around 290–292 eV. Further details of the ($C\ 1s^{-1}$, π*) spec-

Table 5. Energies (eV), term values (eV), and proposed assignments for features in the 1s spectra of *ortho*-nitroaniline.

(*a*) C 1s.

No.	Energy (±0.1 eV)	Term value T_{CH}	Term value T_{CN}	Assignment[c] $C_{3,5}$-H	$C_{4,6}$-H	C_1-NO_2	C_2-NH_2
1	284.9[a]	5.9		$1\pi^*(6b_1)$	$1\pi^*(5b_1)$		
2(sh)	285.3		6.5				$1\pi^*(5b_1)$
3(sh)	286.4	4.4			$1\pi^*(6b_1)$		
4	287.3		4.5			$1\pi^*(6b_1)$	$1\pi^*(6b_1)$
5(w)	288.6		3.2	$2\pi^*(7b_1)$, 3p			
6	290.5	0.3	1.3		$2\pi^*(7b_1)$	$2\pi^*(7b_1)$, σ^*_{CNO}	$2\pi^*(7b_1)$
IP	290.8[b]			IP	IP		
IP	291.8[b]					IP	IP
7	291.8(4)	0					σ^*_{CNH}
8	294.7		−3.4	←	$1\sigma^*$	→	
9	302(1)		−11	←	$2\sigma^*$	→	

(*b*) N 1s.

No.	Energy (±0.1 eV)	Term value T_{NH}	Term value T_{NO}	Assignment N-H	N-O
1	400.5	5.5		π^*_A[d]	
2	401.8	4.2		π^*_B[d]	
3 (sh)	403.0	3.0		3p	
4	403.8[a]		7.4		π^*_{NO}
IP	406.0[b]			IP	
5 (br)	406.5(9)	−0.5		σ^*_{CNH}	
6	409.2(5)		2		σ^*_{CNO}
IP	411.2[b]				IP
7	413.5		−2.3		$\sigma^*_{NO}(+)$
8	419		−8		$\sigma^*_{NO}(-)$

(*c*) O 1s.

No.	Energy	TV	Assignment
1	531.0[a]	6.9	π^*_{NO}
2(w)	534.0	3.9	π^*_{mix}[e]
IP	537.9[b]		IP
3	538.0	−0.1	$\sigma^*_{NO}(-)$
4	541.5	−3.6	$\sigma^*_{NO}(+)$

[a]Calibration: C 1s −5.83(3) eV; N 1s: +2.72(2) relative to N_2 π^*. O 1s −4.43(6) eV relative to CO_2 π^*.
[b]IPs estimated from those of *para*-nitroaniline (2).
[c]Symmetry labels from C_{2v} group.
[d]See Fig. 8 for sketches of these orbitals.
[e]π^*_{mix} refers to a higher energy MO of π^* symmetry with both π^*_{NO} and $\pi^*_{C=C}$ character.

tral assignments are provided by the EHMO results, which give insight into core-hole relaxation and delocalization effects.

Figure 3 plots an expansion of the experimental C 1s spectra for all five species in the π^* region between 284 and 290 eV, in comparison to the EHMO predictions. Table 8 lists the alignments that were used to generate each of the EHMO spectral predictions. If EHMO is a good tool for predicting core excitation on a relative energy scale, the "EHMO error" (SHIFT − IP) should be rather similar for all sites. Indeed the shifts are quite similar, with an average value of 4.1(1) eV, corresponding to a systematic overstabilization of the orbital energies, similar to that found for EHMO core excitation predictions in other systems (15, 32, 33). There are a few larger deviations, with the extrema of the EHMO errors being values of 2.2 and 5.5 eV for the C 1s(1) and C 1s(2) sites of *meta*-nitroaniline. It is possible these larger deviations are related to errors in the estimated IPs. Alternatively they may give insight into unusual, site-specific aspects of the electronic structure.

Figure 3 emphasizes that the C 1s → π^* signal varies con-

Table 6. Energies (eV), term values (eV), and proposed assignments for features in the 1s spectra of *meta*-nitroaniline.

(*a*) C 1s.

No.	Energy (±0.1 eV)	Term value T_{CH}	Term value T_{CN}	Assignment[c] $C_{2,4}$-H	C_5-H	C_6-H	C_1-NO_2, C_3-NH_2
1	285.1[a]	5.7		$1\pi^*(5b_1)$	$1\pi^*(6b_1)$	$1\pi^*(5b_1)$	
2(sh)	285.4		6.4				$1\pi^*(6b_1)$
3	286.8	4.0		$1\pi^*(6b_1)$		$1\pi^*(6b_1)$	
4	287.4		4.4				
5	289.6		2.2				$2\pi^*(7b_1)$
6	290.6	0.2	1.2	$2\pi^*(7b_1)$	$2\pi^*(7b_1)$		σ^*_{CNH},σ^*_{CNO}
IP	290.8[b]			IP	IP		
IP	291.8[b]					IP	IP
7	294.5		−3.3	←		$1\sigma^*$	→
8	304(1)		−13	←		$2\sigma^*$	→

(*b*) N 1s.

No.	Energy (±0.1 eV)	Term value T_{NH}	Term value T_{NO}	Assignment N-H	N-O
1	401.6	4.4		π^*_A[d]	
2 (sh)	402.5	3.5		π^*_B[d]	
3	403.6[a]		7.6		π^*_{NO}
IP	406.0[e]			IP	
4 (br)	406.2(9)	−0.2		σ^*_{CNH}	
5	408.5		2.7		σ^*_{CNO}
IP	411.2[e]				IP
6	412.8		−1.6		$\sigma^*_{NO}(+)$
7	418		−7		$\sigma^*_{NO}(-)$

(*c*) O 1s.

No.	Energy	TV	Assignment
1	530.9[a]	7.0	π^*_{NO}
2	534.0	3.9	π^*_{mix}
IP	537.9[b]		IP
3	538.0	−0.1	$\sigma^*_{NO}(-)$
4	541.2	−3.3	$\sigma^*_{NO}(+)$

[a]Calibration: C 1s −5.66(3) eV; N 1s: +2.52(2) relative to N_2 π^*; O 1s −4.52(6) eV relative to CO_2 π^*.

[b]C 1s and O 1s IPs estimated from those of *para*-nitroaniline.

[c]Symmetry labels from C_{2v} group.

[d]See Fig. 8 for sketches of these orbitals.

[e]N 1s IPs estimated from those of *p*-nitroaniline (2). The solid state XPS data (48) suggest the ΔIP N 1s (NO_2 – NH_2) of *meta* is 0.7 eV higher than that in *para*, with identical NH_2 IPs. However, this gives an unreasonably large term value for the π^*_{NO} state. Thus we believe the reported *meta–para* difference (48) is specific to the solid state, as suggested in comparisons of gas and solid paranitroaniline (11–13). We assume that the N 1s IPs of all three isomers are the same in the gas phase.

siderably with the substitution pattern. Some of these changes can be attributed to variations in the C 1s energies as the position of the two electronegative substituents changes. However, additional effects, in particular changes in the electronic communication between the two substituents, are clearly important factors. Overall EHMO gives good agreement with the experimental spectra, giving confidence that the relative orbital energies and LCAO compositions predicted by EHMO are reasonable. The orbital characters of the component lines give insight into spectral assignments, in particular addressing the roles of (*i*) the C 1s chemical shifts; (*ii*) the contributions of the "$1\pi^*$" and "$2\pi^*$"; (*iii*) the site-dependent mixing of the $\pi^*_{C=C}(b_1)$ and $\pi^*_{NO}(b_1)$ components, in setting the detailed spectral shape of the C 1s → π^* signals. It is important to observe that, although the symmetry of the ground state and excited state conformations of *ortho*- and *meta*-nitroaniline is

Table 7. Energies (eV), term values (eV), and proposed assignments for features in the 1s spectra of *para*-nitroaniline.

(*a*) C 1s.

No.	Energy (±0.1 eV)	Term value T_{CH}	Term value T_{CN}	Assignment[c] $C_{2,6}$-H	$C_{3,5}$-H	C_1-NO	C_4-NH_2
1	285.2[a]	5.6		$1\pi^*(5b_1)$	$1\pi^*(6b_1)$		
2	286.1		5.7			$1\pi^*(6b_1)$	$1\pi^*(5b_1)$
3	287.7	3.1		$1\pi^*(6b_1)$, 3p			
4	288.6	2.2	3.2		$1\pi^*(7b_1)$, 3p	$1\pi^*(7b_1)$, 3p	$1\pi^*(6b_1)$, 3p
5	290.2(4)	0.6	1.6	$2\pi^*(7b_1)$		σ^*_{CNO}	
IP	290.8[b]			IP	IP		
IP	291.8[b]					IP	IP
6	292.4	−0.6					$2\pi^*(7b_1)$, σ^*_{CNH}
7	294.5		−3.2	←	$1\sigma^*$	→	
8	303(1)		−12	←	$2\sigma^*$	→	

(*b*) N 1s.

No.	Energy (±0.1 eV)	Term value T_{NH}	Term value T_{NO}	Assignment N-H	Assignment N-O
1	401.6	4.4		π^*_A[c]	
2 (sh)	402.8	3.2		π^*_B[c]	
3	403.8[a]		7.4		π^*_{NO}
4 (sh)	405	1		4p	
IP	406.0[d]			IP	
5 (sh)	407.6(4)	−1.6		σ^*_{CNH}	
6 (br)	409.1		2.1		σ^*_{CNO}
IP	411.2[d]				IP
7	412.7		−1.5		$\sigma^*_{NO}(+)$
8	418		−7		$\sigma^*_{NO}(-)$

(*c*) O 1s.

No.	Energy	TV	Assignment
1	530.9[a]	7.0	π^*_{NO}
2	534.0	3.9	π^*_{mix}
IP	537.9[d]		IP
3	538	−0.1	$\sigma^*_{NO}(-)$
4	541.2	−3.3	$\sigma^*_{NO}(+)$

[a]Calibration: C 1s −5.55(3) eV; N 1s: +2.66(2) relative to N_2 π^*; O 1s −4.39(6) eV relative to CO_2 π^*.
[b]IPs derived from the average IP of 291.1 eV (2), the estimated C 1s(C-H)/C 1s(C-N) chemical shift, and the relative numbers of C-H and C-N ring carbons.
[c]See Fig. 8 for sketches of these orbitals.
[d]From XPS (2).

C_s, C_{2v}-based labels for the *para* isomer are used in the following discussion because of the similarity of the shapes of the C 1s MOs involved in the π^* transitions. As with nitrobenzene the EHMO component spectra indicate that the first four spectral features are a superposition of a number of 1s → $\pi^*(b_1)$ transitions at the distinct C 1s sites. In each case the $\pi^*(b_1)$ orbital has both $\pi^*_{C=C}$ and π^*_{NO} character. For C_1 (C-NO_2) and C_5 excitations in all three isomeric nitroanilines, C_3 excitation for *ortho*- and *para*-nitroaniline, and C-NH_2 excitation for the *meta* isomer, the C 1s → $\pi^*(6b_1)$ transition dominates. For the other sites (C_2 for *meta*- and *para*-nitroanilines, C_4 for *ortho*- and *meta*-nitroanilines, C-NH_2 for *ortho*- and *para*-nitroanilines, and the C_6 site for all nitroanilines) there is significant contribution from both the $6b_1$ and $5b_1$ orbitals. At higher energy there is a small contribution from C 1s → $7b_1$ ($2\pi^*$) transitions at all sites. In all three nitroanilines (as in nitrobenzene) the EHMO results suggest this $2\pi^*$ contribution comes about 0.5 eV higher in energy than in aniline or benzene. However these calculations do not take into account mixing with a doubly excited configuration ($C1s^{-1}$, π^{-1}, π^{*2}) that may shift the $2\pi^*$ transition to lower energy. The EHMO predicted spectra (Fig. 3) are consistent with our proposed

Table 8. Alignment of EHMO and experimental results.

(*a*) C 1s.

	Aniline			*para*-Nitroaniline			*meta*-Nitroaniline			*ortho*-Nitroaniline			Nitrobenzene		
C 1s	Shift[a]	IP[b]	Err[c]	Shift	IP	Err	Shift	IP	Err	Shift	IP	Err	Shift	IP	Err
1	295.7	291.3	4.4(NH_2)	294.7	291.8	2.9(NO_2)	294.0	291.8	2.2(NO_2)	296.2	291.8	4.4(NO_2)	294.4	292.1	2.3(NO_2)
2	294.6	290.2	4.4	295.2	290.8	4.4	296.3	290.8	5.5	296.2	291.8	4.4(NH_2)	296.7	291.3	5.4
3	294.6	290.2	4.4	294.3	290.8	3.5	295.0	291.8	3.2(NH_2)	293.9	290.8	3.1	294.5	291.0	3.5
4	294.6	290.2	4.4	296.1	291.8	4.3(NH_2)	295.8	290.8	5.0	295.3	290.8	4.5	295.9	291.2	4.8
5	294.6	290.2	4.4	294.3	290.8	3.5	294.0	290.8	3.2	293.9	290.8	3.1	294.5	291.0	3.5
6	294.6	290.2	4.4	295.2	290.8	4.4	295.9	290.8	5.1	295.4	290.8	4.6	296.7	291.3	5.4

(*b*) N1s and O 1s.

	Aniline			*para*-Nitroaniline			*meta*-Nitroaniline			*ortho*-Nitroaniline			Nitrobenzene		
Edge	Shift	IP	Err	Shift	IP	Err	Shift	IP	Err	Shift	IP	Err	Shift	IP	Err
N 1s(NO_2)	—	—	—	415.5	411.2	4.3	415.5	411.2	4.3	414	411.2	2.8	415.6	411.5	4.1
N 1s(NH_2)	410.0	405.3	4.7	410.0	406.0	4.0	409.4	406.0	3.4	409.8	406.0	3.8	—	—	—
O 1s	—	—	—	541.7	537.9	3.8	541.9	537.9	4.0	541.8	537.9	3.9	541.9	538.5	3.4

[a]The energy added to the EHMO eigenvalues to generate the absolute energy scale for this spectral component.

[b]From XPS or estimated. See Tables 1, 2, 5, 6, 7.

[c]Err = shift − IP. If EHMO eigenvalues were equal to negative term values this quantity would be 0.

Fig. 5. N 1s oscillator strength spectra of nitrobenzene, aniline, and methyl amine (digitized from ref. 45), derived from ISEELS. The hatched lines indicate IPs estimated from XPS (36). See Fig. 1 caption for experimental details.

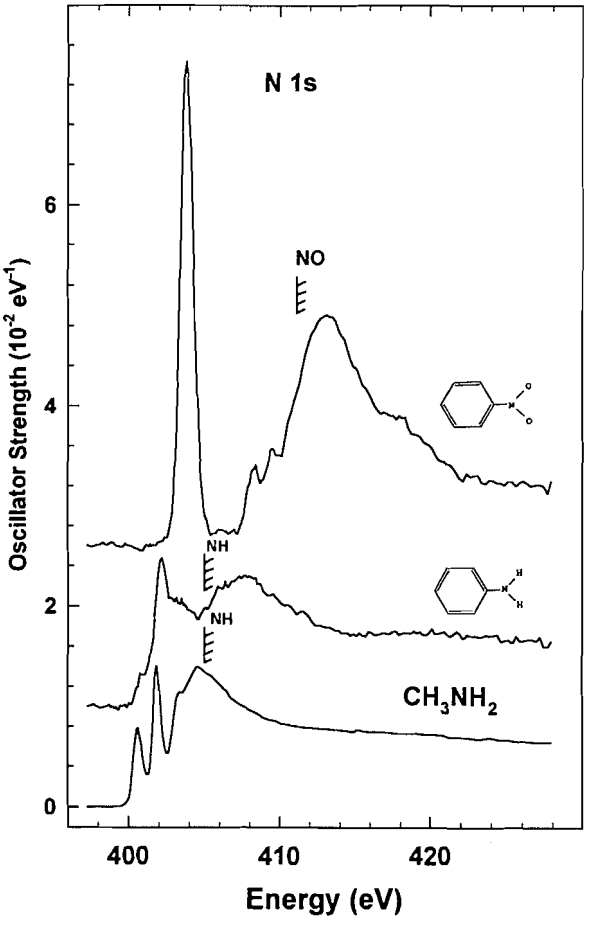

Fig. 6. N 1s oscillator strength spectra of the isomeric nitroanilines compared to a simulation that is the sum of the N 1s spectra of nitrobenzene (shifted by −0.3 eV) and aniline (shifted +0.7 eV), aligned at the estimated N 1s(NH_2) and N 1s(NO_2) IPs (2), which are indicated by the hatched lines.

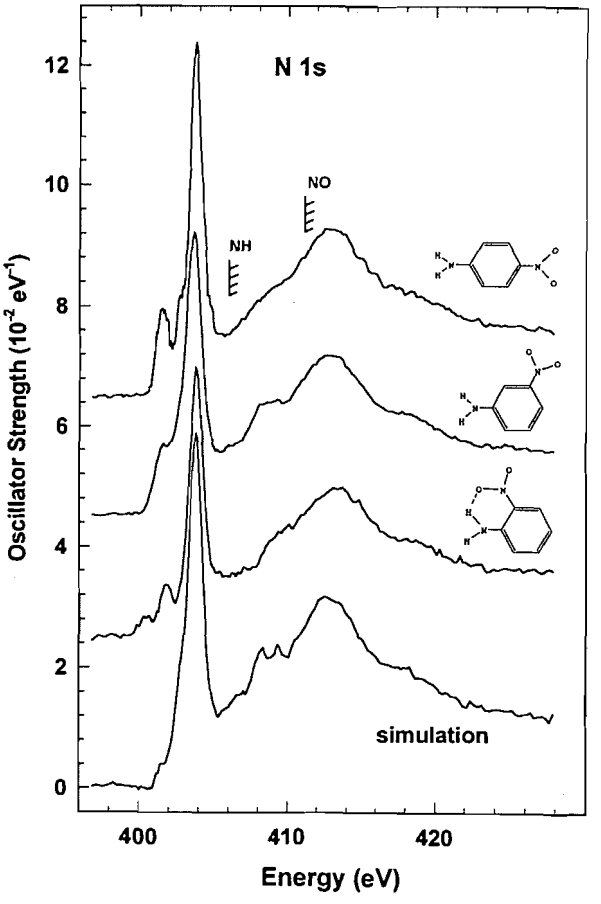

assignments of the experimental spectra, which are outlined in detail in Tables 5–7.

B. N 1*s* spectra

B.1 Aniline and nitrobenzene: monosubstituted models

Figure 5 plots the N 1s spectra of nitrobenzene and aniline. The N 1s spectrum of methyl amine (digitized from ref. 45) is also plotted in order to investigate possible effects of delocalization of the ring π^* orbitals onto the amine group. Energies, term values, and proposed assignments are given in Tables 1 and 2.

The dramatic difference between the N 1s spectra of aniline and nitrobenzene is associated with the essentially saturated character of the NH_2 group and the unsaturated character of the NO_2 group. Thus the N 1s spectrum of nitrobenzene is dominated by the strong N 1s $\rightarrow \pi^*_{NO}$ transition at 403.8 eV whereas the discrete structure in the N 1s spectrum of aniline is much weaker and can be interpreted as mainly Rydberg/σ^*_{NH} in character, as supported by the similarity of the discrete regions of the N 1s spectra of aniline and methyl amine. The N 1s continuum of aniline exhibits a broad feature centered at 407.6 eV, which is attributed to the N 1s $\rightarrow \sigma^*_{CN}$ resonance. It occurs at higher energy than the corresponding σ^*_{CN} resonance in methyl amine (404.6 eV), consistent with the shorter C—N bond length in aniline (1.431 Å) as compared to that in methyl amine (1.465 Å). Nitrobenzene has its main σ^*_{NO} resonance at 413.2 eV, with a weaker second resonance at 418.5 eV. According to the bond length correlation (43) there should only be a single N 1s $\rightarrow \sigma^*_{NO}$ resonance. However, this ignores delocalization effects, which, in molecules like CO_2 and NO_2, leads to a breakdown of the local bond picture of core excitation (46). Thus the higher energy band at ~418 eV is attributed to a second σ^*_{NO} resonance. The two σ^*_{NO} resonances are analogous to the σ_g^* and σ_u^* resonances in CO_2 (46), i.e., orbitals that can be described as positive and negative combinations of two localized σ^*_{NO} orbitals (see Sect. C for further discussion and a comparison to the corresponding O 1s $\rightarrow \sigma^*_{NO}$ features). The lower energy continuum band in nitrobenzene (413.2 eV) will also contain contributions from N 1s $\rightarrow \sigma^*_{CN}$ excitations. The positions predicted from the bond length correlation for the σ^*_{NO} and σ^*_{CN} resonances are 413 eV and 411 eV, respectively (R_{N-O} = 1.218 Å, R_{C-N} = 1.478 Å), in reasonable agreement with experiment.

B.2 N 1s spectra of nitroanilines

The N 1*s* spectra of the nitroanilines are presented in Fig. 6 while the energies, term values, and proposed assignments are summarized in Tables 5–7. Figure 6 also contains a simulated

spectrum, which is the sum of the N 1s spectra of aniline shifted up by 0.7 eV, and nitrobenzene shifted down by 0.3 eV, to account for differences in the IPs. As with the C 1s spectral simulation, if there was negligible interaction between the two substituents one would expect the measured N 1s spectra of the nitroanilines to be similar to this simulated spectrum. The poor agreement, particularly in the region below 403 eV, indicates there is significant electronic interaction between the NH_2 and NO_2 groups. The deviations from the simulated spectrum are thus a manifestation of the donor–acceptor character of nitroanilines.

While the main features of the N 1s spectra of the three isomeric nitroanilines are similar (because of the dominance of the strong N 1s(NO_2) components) there are significant differences in the weak features between 400 and 403 eV that are associated with N 1s(NH_2) excitations. The main spectral feature around 404 eV is clearly the π^*_{NO} resonance. The N 1s continuum contains three broad resonances. The broad, lower energy feature, which is considered to extend from 406 to 410 eV, corresponds to the N 1s $\rightarrow \sigma^*_{CNH}$ transition in aniline and the σ^*_{CNO} resonance in nitrobenzene. The two higher energy features (~413, ~418 eV) correspond to the two continuum resonances in nitrobenzene. With regard to our initial motivation to search for evidence for strong shake-up effects analogous to those seen in XPS, if there was an abrupt threshold onset to the {N 1s$(NH_2)^{-1}$, (π^{-1}, π^*)} shake-up process this would appear as a continuum rise around 414 eV. While there are indications of a weak shoulder at this energy, particularly in the *ortho* and *para* species, these signals are quite weak. Clearly multi-electron excitations are much weaker than the corresponding $\pi \rightarrow \pi^*$ satellite signal in core ionization of nitroanilines (11, 12).

Although the main features of the N 1s spectra can be interpreted in terms of N 1s(NO_2) excitation as outlined above, there are notable differences among the N 1s(NH_2) signals in the nitroanilines. From XPS (1–11) the N 1s(NH_2) component is expected to be more sensitive than the N 1s(NO_2) component to charge transfer interactions between the amine and nitro groups. Of course, these interactions will depend on the substitution pattern. Clearly the lower energy part of the N 1s spectrum is strongly dependent on the pattern of substitution. Initially we were puzzled as to how to interpret this part of the N 1s spectra. If the peaks at 401.6–401.8 eV are correlated with the lowest energy N 1s $\rightarrow$ 3s peak in aniline (which is suggested by similarity in term value), then there is a large intensity enhancement. One then has difficulty in assigning the weak peak observed around 400 eV in *ortho*-nitroaniline. Alternatively one could correlate the 401.6 eV peak in the nitroanilines to the main discrete N 1s $\rightarrow$ 3p/π^* peak in aniline and the 400 eV peak to the lowest energy (3s) band in aniline. With this assignment the absence of the (3s) peak in the *meta* and *para* isomers is puzzling. Neither of these trial assignments are considered acceptable. A different and more satisfactory interpretation is provided by comparison with the EHMO calculations.

B.3 Comparison to N 1s EHMO predicted spectra

Figure 7 plots expanded presentations of the N 1s spectra of the five molecules, in comparison to the N 1s predictions from EHMO. As with the C 1s region, there is reasonable agreement between calculation and experiment. The N 1s spectra are

Fig. 7. (*a*) N 1s spectra of aniline, the isomeric nitroanilines, and nitrobenzene in the region below the N 1s IP, predicted from EHMO calculations. See the text and Table 8 for details of the line widths and shifts used to construct the predicted spectra. (*b*) Corresponding experimental N 1s oscillator strength spectra.

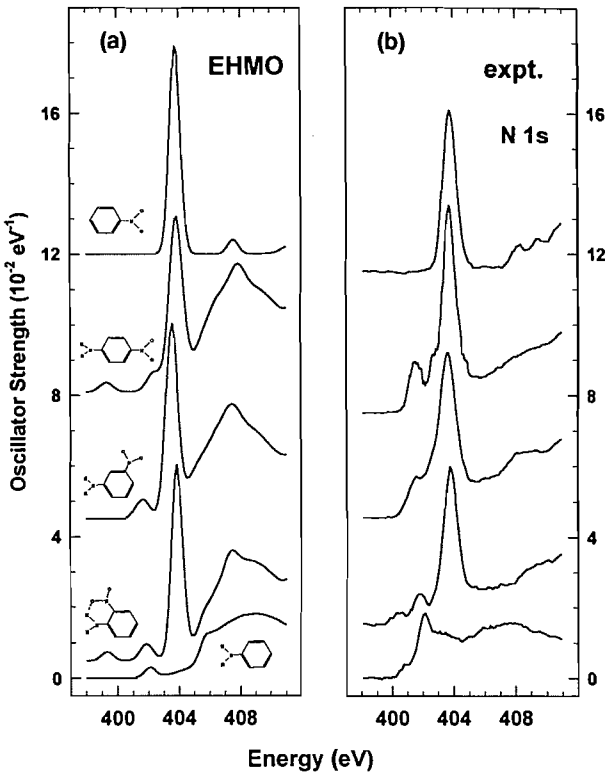

dominated by the strong π^*_{NO} and σ^*_{NO} resonances. EHMO predicts the N 1s(NO_2) component spectra contain a weak, higher energy π^* state of mixed $\pi^*_{NO}/\pi^*_{C=C}$ character that probably corresponds to the well-resolved band at 408.3 eV in nitrobenzene. The corresponding feature in the nitroanilines may exist in the 408–410 eV region but it would be masked by the N 1s(NH_2) $\rightarrow \sigma^*_{CNH}$ and N 1s(NO_2) $\rightarrow \sigma^*_{CNO}$ transitions. A similar, higher energy π^* feature is seen in the EHMO and experimental O 1s spectra (see Fig. 10 and Sect. C). While the N 1s(NO_2) $\rightarrow \pi^*_{NO}$ transition dominates the N 1s edge, there are features clearly attributable to N 1s(NH_2) excitation that EHMO reproduces quite well. In particular, the experimental pattern of the weaker features below 404 eV is also found in the calculated spectrum, with two low-lying N 1s(NH_2) peaks predicted by EHMO in *ortho*- and *para*-nitroaniline but only one in *meta*-nitroaniline. To better understand the origin of these signals it is useful to examine the MOs involved and their dependence both on substitution pattern and on the presence or absence of conjugation.

Figure 8 presents an expansion of the EHMO predictions of the N 1s(NH_2) component of the spectrum of *ortho*-, *meta*-, and *para*-nitroaniline calculated with the hydrogen atoms of the NH_2 group in the plane (the minimum energy conformation) and with the NH_2 group rotated by 90°. In addition Fig. 8 presents schematic MO diagrams of the low-energy π^* orbitals in these N 1s(NH_2) core excited species. In the planar geometry EHMO indicates there are two π^* bands with the

Fig. 8. Comparison of EHMO spectral predictions for N 1s(NH_2) → π* excitations of (*a*) *ortho*-, (*b*) *meta*-, and (*c*) *para*-nitroaniline. The upper trace in each panel is the predicted spectrum for the planar geometry while the lower trace is that calculated with the NH_2 rotated 90°, to place the H atoms out of the plane of the ring. Sketches for the lower energy π* orbitals are shown. These MO plots are projections of the 2pπ density with the diameter of the circles proportional to the 2pπ LCAO coefficient. The intensity of the peaks in the EHMO predicted spectrum is proportional to the 2pπ density on the core excited NH_2.

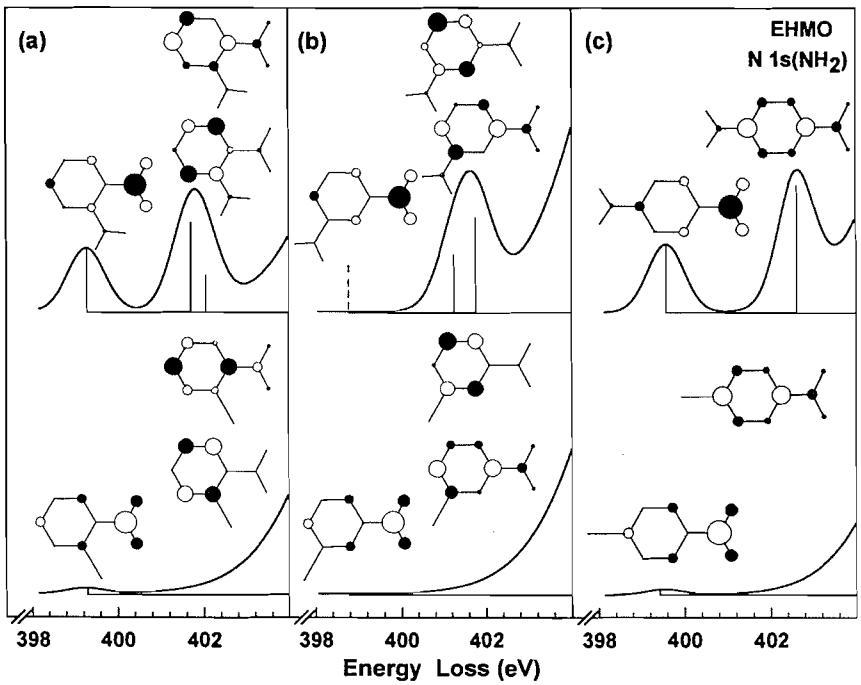

lower energy component being mainly π^*_{NO} while the higher energy component is mostly $\pi^*_{C=C}$ in character. In (planar) *meta*-nitroaniline there is only one N 1s(NH_2) → π* peak because the lower energy N 1s(NH_2) → π^*_{NO} excitation has zero intensity. When the NH_2 group is rotated by 90°, the π* delocalization is broken, the N 2p contribution to the π* orbital disappears, and the transitions are predicted to have essentially zero intensity. The EHMO results indicate that the intensity of N 1s(NH_2) → π* features in the nitroanilines and related molecules are sensitive to molecular geometry in a way that may be helpful in conformational analysis.

The agreement between EHMO and experiment for these N 1s(NH_2) excitations is surprisingly good, especially when one notes that the N 1s spectra of methylamine and aniline indicate there are significant contributions from N 1s(NH_2) → Rydberg transitions that EHMO cannot reproduce. The EHMO results for aniline (lowest curve in Fig. 7) indicate the $1\pi^*_{C=C}$ orbital has some density on the NH_2 group. This component increases considerably when the nitro group is added. The two low-lying N 1s(NH_2) excitations in *ortho*- and *para*-nitroaniline are reproduced by EHMO although the predicted separation of the two N 1s(NH_2) → π* components is larger than found experimentally. It is interesting to compare the N 1s spectra of nitroanilines with that of phenylurea (16). In both species a planar geometry leads to some $\pi^*_{C=C}$ density at the NH nitrogen atom. However the N 1s → $\pi^*_{C=C}$ transitions are much stronger in nitroaniline than in phenylurea, probably because of the strong charge-transfer coupling of the NO_2 and NH_2 groups through the ring π and π* orbitals.

It is also of interest to consider how the donor–acceptor character of these molecules is reflected in other aspects of the EHMO calculations of the core excitation spectra. Table 9 lists the total (valence electron) energy for planar and nonplanar geometries of the nitroanilines as well as a summary of the behaviour of the HOMO–LUMO gaps for different positions of the core hole in aniline, nitrobenzene and *ortho*-, *meta*-, and *para*-nitroanilines. In the neutral nitroaniline molecules the HOMO is localized on the carbons and the NH_2 (donor) substituent while the LUMO is localized on the ring and the NO_2 (acceptor) group. This expresses the donor–acceptor nature of the compound. The HOMO–LUMO gap is notably smaller in *meta*- relative to *ortho*- or *para*-nitroaniline, consistent with the less favourable situation with regard to "resonance stabilization" of the π-charge transfer (47).

The creation of a core hole changes the electron distribution in different ways. If an N 1s core hole is created on the NH_2 group, the levels with large NH_2 character are stabilized relative to those levels localized on the carbon ring or on the NO_2 group. In this situation, the charge distribution in the HOMO changes while that in the LUMO has practically the same shape as in the neutral molecules. At the same time, placing the core hole on the donor substituent increases the HOMO–LUMO gap. On the other hand, if the core hole is created on the N or O of the NO_2 group, the orbitals with NO_2 character

Table 9. Total (valence electron) energy and HOMO–LUMO gaps of neutral and core-excited aniline, nitrobenzene, and *ortho*-, *meta*- and *para*-nitroaniline from EHMO.

(*a*) Total valence electron energy, $-E$(eV).

	NH_2 in-plane			NH_2 out-of-plane		
Compound	G.S	N 1s(NH_2)	N 1s(NO_2)	G.S.	N 1s(NH_2)	N1s(NO_2)
o-Nitroaniline	981.62	998.88	996.37	981.24	998.66	995.67
m-Nitroaniline	981.82	998.86	996.34	981.32	998.66	995.73
p-Nitroaniline	981.96	998.91	996.80	981.34	998.67	995.80

(*b*) HOMO–LUMO gaps ($-\Delta E_{H\text{-}L}$ (eV)).
(*B.1*) N 1s.

	NH_2 in-plane			NH_2 out-of-plane		
Compound	G.S	N 1s(NH_2)	N 1s(NO_2)	G.S.	N 1s(NH_2)	N1s(NO_2)
Aniline	3.82	4.22	—	—	—	—
Nitrobenzene	2.24	—	0.94	—	—	—
o-Nitroaniline	1.62	1.93	0.68	1.69	2.09	0.46
m-Nitroaniline	1.37	1.82	0.23	1.73	2.03	0.50
p-Nitroaniline	1.70	2.02	0.87	1.78	2.17	0.51

(*B.2*) O 1s.

	NH_2 in-plane		NH_2 out-of-plane	
Compound	G.S	O1s	G.S.	O1s
o-Nitroaniline	1.62	1.43[a]	1.69	1.46
m-Nitroaniline	1.37	1.12	1.73	1.48
p-Nitroaniline	1.70	1.54	1.78	1.52

[a]In *ortho*-nitroaniline there is a 0.02 eV difference in $\Delta E_{H\text{-}L}$ when the O 1s hole is moved from the O atom closer to the NH_2 group to that farther from the NH_2 group. In all other cases, $\Delta E_{H\text{-}L}$ was the same for O 1s holes on each O atom.

are stabilized. In this situation the HOMO–LUMO gap decreases, facilitating the intramolecular donor → acceptor charge transfer with respect to the neutral state. In both types of core excitation the *meta* species follows a similar pattern but the HOMO–LUMO gap is smaller, reflecting less resonance stabilization. While the changing HOMO–LUMO gaps in calculations carried out on the "in-plane" geometry reflect the donor–acceptor aspect of these molecules, the situation is markedly different when the calculation is carried out with the NH_2 group rotated to remove $\pi_{C=C}/\pi_{NO}$ delocalization onto the NH_2. In the nonplanar geometry the changes with core-hole location parallel those seen in the in-plane geometry, but the HOMO–LUMO gap is similar in all three isomers. This is consistent with removing the π-delocalization component of the charge transfer.

C. O 1s spectra

Figure 9 plots the O 1s spectra of the nitroanilines and nitrobenzene, while the energies, term values, and proposed assignments of the spectral features are given in Tables 2, 5, 6 and 7. The O 1s spectra for all four species are very similar. They are dominated by the strong O 1s → π^*_{NO} transition at 531 eV. At 534 eV there is a weak feature that could be either a Rydberg state (3s, based on its term value) or a weak excitation to a higher energy π* orbital. On the basis of the EHMO results we assign the 534 eV feature to a second O 1s → π* transition. Figure 10 plots expanded regions of the O 1s spectra in comparison to the O 1s EHMO spectra. As with the C 1s and N 1s spectra, there is good agreement between the EHMO predictions and the experimental O 1s spectra. EHMO predicts a dominant O 1s → π^*_{NO} feature and a relatively strong second O 1s → π^*_{mix} transition (π^*_{mix} is an orbital of mixed π^*_{NO} and $\pi^*_{C=C}$ character). The predicted π^*_{mix} feature likely corresponds to the weak signal at 534 eV in the experimental spectrum. The O 1s EHMO spectra were also determined for the molecules with the NO_2 group rotated by 90°. In this case the π^*_{mix} feature disappears, confirming that the 534 eV feature involves π^*_{NO} delocalization onto the ring.

The O 1s continuum has two broad resonances at 538 and 541 eV, with the higher more intense than the lower energy peak. While EHMO calculations are relatively poor at predicting the *positions* of continuum features, the general shape is often reasonable and thus the calculations can provide some insight into spectral assignments. According to the EHMO calculations there are three main contributions to each of the N 1s and O 1s continua. Figure 11 plots the molecular orbitals for N 1s(NO_2) and O 1s excited *para*-nitroaniline (the EHMO results for the 1s continua are similar for the *ortho* and *meta*

Fig. 9. O 1s oscillator strength spectra of the isomeric nitroanilines and nitrobenzene derived from ISEELS. IPs from XPS (2, 36). See Fig. 1 caption for experimental details.

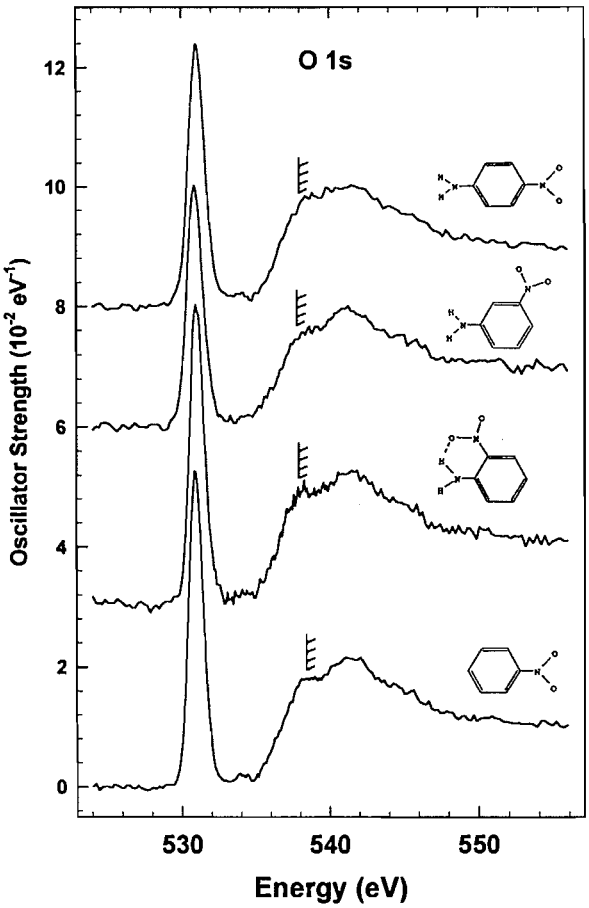

Fig. 10. (*a*) O 1s spectra of nitrobenzene and the isomeric nitroanilines in the region below the O 1s IP, predicted from EHMO calculations. See the text and Table 8 for details of the line widths and shifts used to construct the predicted spectra. (*b*) corresponding experimental O 1s oscillator strength spectra.

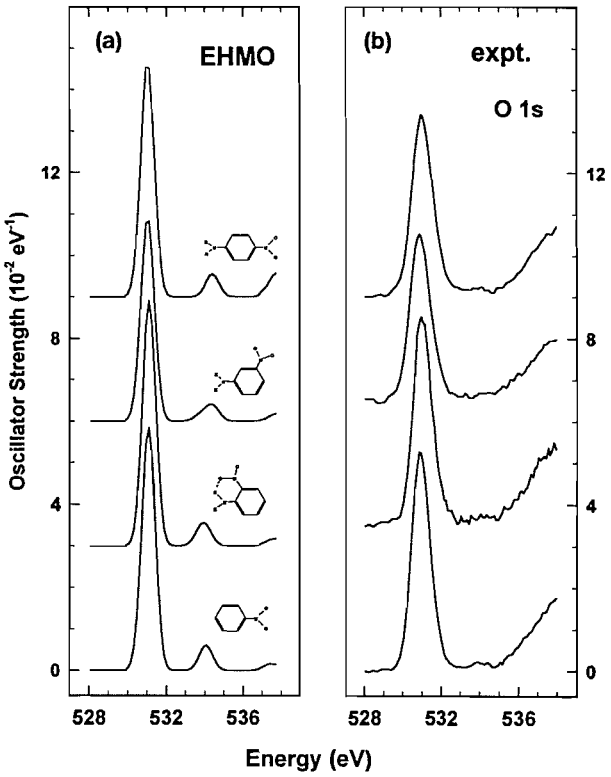

isomers). The figure shows only that portion of the MO which is critical to the core excitation under consideration. The two most intense contributions are mainly σ^*_{NO} in character, where $\sigma^*_{NO}(-)$ and $\sigma^*_{NO}(+)$ are (+/-) and (+/+) linear combinations of localized σ*(N-O) basis functions. These are analogous to the σ_u^* and σ_g^* resonances that are observed in the O 1s spectrum of CO_2 (46). In *para*-nitroaniline these continuum orbitals have a partial π^*_{CN} and σ^*_{CN} in addition to a σ^*_{NO} character according to the EHMO calculations. In the N 1s spectrum the σ^*_{NO} features are attributed to the peaks around 413 and 418 eV. Interestingly, relative to the situation in the O 1s spectrum, $\sigma^*_{NO}(+)$ is at much lower energy than $\sigma^*_{NO}(-)$ in the N 1s spectra and thus the $\sigma^*_{NO}(-)/\sigma^*_{NO}(+)$ ordering predicted by EHMO for the O 1s spectrum is reversed to a $\sigma^*_{NO}(+)/\sigma^*_{NO}(-)$ ordering in the N 1s continuum. This is because, in the presence of a N 1s core hole, there is strong mixing with the σ^*_{CN} orbital, which leads to a much lower energy of the $\sigma^*_{NO}(+)$ orbital in N 1s core-excited than O 1s core-excited nitroanilines. The reversal of $\sigma^*_{NO}(+)/\sigma^*_{NO}(-)$ orbital ordering predicted by EHMO is a plausible explanation of the change in the relative intensities of the continuum features between the N 1s and O 1s spectra.

V. Summary

The C 1s, N 1s, and O 1s electron energy loss spectra of aniline, nitrobenzene, and *ortho*-, *meta*-, and *para*-nitroaniline have been recorded under dipole conditions and converted to oscillator strengths. The spectra do not exhibit any unusual features attributable to exceptionally strong shake-down or shake-up processes, associated either with multi-electron excitations or with the threshold of the shake-up process observed in XPS. This is consistent with electronic shielding from the core-excited electron providing strong damping of the charge-transfer relaxation process believed to give rise to signal from shake-up ion states in the XPS (1–11). Assignments for all spectral features have been proposed through a combination of analysis of systematic trends and comparison to EHMO results. The EHMO results do not reproduce completely all characteristics of the experimental spectra, but they are very useful for providing a good understanding of the effect of the core hole and for giving important insight into the interpretation of the core excitation spectra. A minor revision has been suggested to a previous assignment of the C 1s NEXAFS spectrum of solid aniline (19). The low-energy N 1s(NH_2)→ π* features in the N 1s spectra of the nitroanilines were found to be remarkably sensitive to the substitution pattern and the extent of π-delocalization. While some aspects of the π* signals in the C 1s and N 1s spectra may be characteristic of ring substitution patterns it is difficult to generalize from this example because of effects specific to the nitro-

Fig. 11. Sketches of selected high-energy molecular orbitals of σ^*_{NO} character in the region of the C-NO_2 group derived from extended Hückel calculations of N 1s(NO_2) and O 1s excited *para*-nitroaniline. In each case these three orbitals are the only significant contributions to continuum resonance intensity. The vertical lines indicate the relative spacing of the orbital eigenvalues for each core excited species. A shift of 10 eV was applied between the N 1s(NO_2) and O 1s energy scales. Each orbital has large $\sigma^*_{C=C}$ components in addition to those plotted.

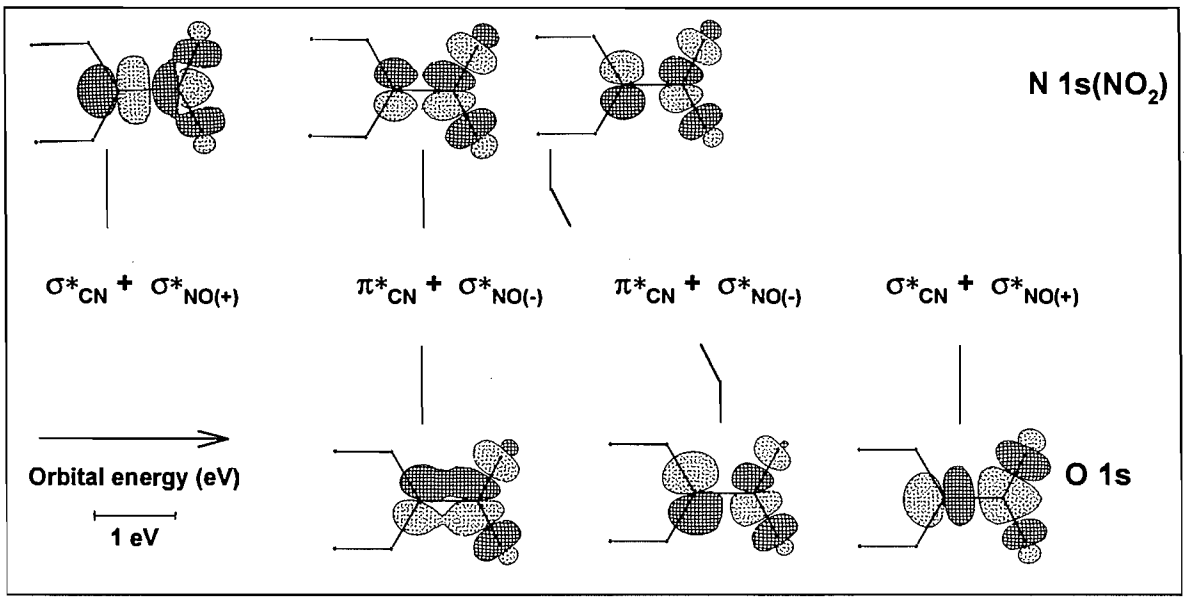

anilines, namely strong $\pi^*_{C=C}/\pi^*_{NO}$ mixing and electronic interaction through the ring π/π^* system between the donor and acceptor groups of the nitroanilines.

Acknowledgements

This work has been supported financially by the Natural Sciences and Engineering Research Council (NSERC) (Canada). C.C.T. thanks CNPq (Brazil) for support of a fellowship and S.G.U. acknowledges support of an Ontario Graduate Scholarship. We thank Dr. Meali for providing the EHMO program.

References

1. W. Domcke, L.S. Cederbaum, J. Schirmer, and W. Von Niessen. Phys. Rev. Lett. **42**, 1237 (1979).
2. M.S. Banna. Chem. Phys. **45** 383 (1980); A.R. Slaughter, M.S. Banna, and C.A. McDowell. Chem. Phys. Lett. **98**, 531 (1983).
3. M. Guerra, D. Jones, F.P. Colonna, G. Distefano, and A. Modelli. Chem. Phys. Lett. **98**, 522 (1983).
4. P.Å. Malmquist, S. Svensson, and H. Ågren. Chem. Phys. **76**, 429 (1983).
5. P.C. Ford and I.H. Hillier. Chem. Phys. Lett. **92**, 141 (1982).
6. H. Ågren, B.O. Roos, P.S. Bagus, U. Gelius, P.A. Malmquist, S. Svensson, R. Maripuu, and K. Siegbahn. J. Chem. Phys. **77**, 3893 (1982).
7. R. Nakagaki, D.C. Frost, and C.A. McDowell. J. Electron Spectrosc. Relat. Phenom. **22**, 289 (1981).
8. G. Distefano, M. Guerra, D. Jones, A. Modelli, and F.P. Colonna. Chem. Phys. **52**, 389 (1980).
9. R.W. Bigelow, R.J. Weagley, and H.-J. Freund. Chem. Phys. Lett. **82**, 305 (1981).
10. G. Distefano, M. Guerra, F.P. Colonna, D. Jones, G. Consiglio, and D. Spinelli. Chem. Phys. **72**, 267 (1982).
11. H.-J. Freund, A.R. Slaughter, S.M. Ballina, M.S. Banna, R.W. Bigelow, B. Dick, J. Lex, and H.M. Deger. J. Chem. Phys. **81**, 2535 (1984).
12. R.W. Bigelow and H-J. Freund. Chem. Phys. Lett. **77**, 261 (1981).
13. H.-J. Freund and R.W. Bigelow. Chem. Phys. **55**, 407 (1981); Phys. Scr. **T17**, 50 (1987).
14. G.R. Wight, C.E. Brion, and M.J. Van der Wiel. J. Electron Spectrosc. Relat. Phenom. **1**, 457 (1972, 1973).
15. A.P. Hitchcock, S.G. Urquhart, and E.G. Rightor. J. Phys. Chem. **96**, 8736 (1992).
16. S.G. Urquhart, A.P. Hitchcock, R.D. Leapman, R.D. Priester, and E.G. Rightor. J. Polym. Sci. Part B: Polym. Phys. **33**, 1593 (1995); S.G. Urquhart, A.P. Hitchcock, R.D. Priester, and E.G. Rightor. J. Polym. Sci. Part B: Polym. Phys. **33**, 1603 (1995).
17. H. Ade and B. Hsiao. Science, **262**, 1427 (1993); H. Ade, X. Zhang, S. Cameron, C. Costello, J. Kirz, and S. Williams. Science, **258**, 972 (1992).
18. J. Stöhr. NEXAFS spectroscopy. Springer, Berlin. 1992.
19. J.L. Solomon, R.J. Madix, and J. Stöhr. Surf. Sci. **255**, 12 (1991).
20. Y. Luo, H. Ågren, J. Guo, P. Skytt, N. Wassdahl, and J. Nordgren. Phys. Rev. A: At. Mol. Opt. Phys. **52**, 3730 (1995).
21. A.P. Hitchcock and D.C. Mancini. J. Electron Spectrosc. Relat. Phenom. **67**, 1 (1994).
22. R. Hoffmann. J. Chem. Phys. **39**, 1397 (1963).
23. R. Hoffmann. J. Chem. Phys. **40**, 2474 (1963).
24. I.N. Levine. Quantum chemistry. 4th ed. Prentice Hall, New York. 1991.
25. W.H.E. Schwarz. Chem. Phys. **11**, 217 (1975).
26. J.A. Tossel. Chem. Phys. **154**, 211 (1991).
27. A.P. Hitchcock. Phys. Scr. **T31**, 159 (1990).
28. R.N.S. Sodhi and C.E. Brion. J. Electron Spectrosc. Relat. Phenom. **34**, 363 (1984).

29. C.E. Brion, S. Daviel, R. Sodhi, and A.P. Hitchcock. AIP Conf. Proc. **94**, 429 (1982).
30. A.P. Hitchcock and I. Ishii. J. Electron Spectrosc. Relat. Phenom. **42**, 11 (1987).
31. E. Rühl, A.T. Wen, and A.P. Hitchcock. J. Electron Spectrosc. Relat. Phenom. **57**, 137 (1991).
32. A.T. Wen, E. Rühl, and A.P. Hitchcock. Organometallics, **11**, 2559 (1992).
33. J.T. Francis and A.P. Hitchcock. J. Phys. Chem. **96**, 6598 (1992).
34. C. Meali and D. Proserpio. J. Chem. Educ. **67**, 399 (1990).
35. Structure data of free polyatomic molecules. Vol. 7. Landolt Bornstein: New Series II. Springer, Berlin. 1976.
36. T. Ohta, T. Fujikawa, and H. Kuroda. Bull. Chem. Soc. Jpn. **48**, 2017 (1975).
37. B.L. Henke, P. Lee, T.J. Tanaka, R.L. Shimabukuro, and B.K. Fujikawa. At. Data Nucl. Data Tables, **27**, 1 (1982).
38. J.A. Horsley, J. Stöhr, A.P. Hitchcock, D.C. Newbury, A.L. Johnson, and F. Sette. J. Chem. Phys. **83**, 6099 (1985).
39. W.H.E. Schwarz, T.C. Chang, U. Seeger, and K.H. Hwang. Chem. Phys. **117**, 73 (1987).
40. M. Bader, J. Haase, K.-H. Frank, C. Ocal, and A. Puschmann. J. Phys. (Paris), **47**, C8-491 (1986).
41. H. Ågren, O. Vahtras, and V. Carravetta. Chem. Phys. **196**, 47 (1995).
42. S.W. Staley and A.E. Howard. Tetrahedron, **42**, 6269 (1986).
43. F. Sette, J. Stöhr, and A.P. Hitchcock. J. Chem. Phys. **81**, 4906 (1984).
44. E. Lindholm, L. Åsbrink, and S. Ljunggren. J. Phys. Chem. **95**, 3923 (1991).
45. R.N.S. Sodhi and C.E. Brion. J. Electron Spectrosc. Relat. Phenom. **36**, 187 (1985).
46. A.P. Hitchcock and J. Stöhr. J. Chem. Phys. **87**, 3523 (1987).
47. T.W. Graham Solomons. Organic chemistry. 2nd ed. John Wiley & Sons, New York. 1980.
48. S. Pignataro and G. Distefano. J. Electron Spectrosc. Relat. Phenom. **2**, 171 (1973).

Cohesive properties of metals as determined from atomic charge densities

Yoram Tal

Abstract: A direct relation between the charge density of a free atom, $\rho_a(r)$, and the cohesive energy of the corresponding metal is proposed. This relation is based on an approximation for the metallic charge density, $\rho_m(r)$, that is constructed from $\rho_a(r)$ through $\rho_m(r) \cong \rho_a(r) + \bar{\rho}$ where $\bar{\rho} = \Omega_0^{-1} \int_{R_0}^{\infty} \rho_a(r) d^3r$, Ω_0 being the atomic volume of the metallic atom, and R_0 the corresponding Wigner–Seitz radius. The cohesive energy E_{coh} is then related to $\bar{\rho}$ through $E_{coh} \cong (3/10)(3\pi^2)^{2/3}\Omega_0\bar{\rho}^{5/3}$. A systematic study of 29 metallic elements including the 3*d* and 4*d* transition elements shows that the proposed relation is, in general, at least as accurate as recent ab initio results. In the same fashion, an expression for the metallic bulk modulus is derived. This expression requires, in addition to $\bar{\rho}$, the values of $\rho_a(R_0)$ and its first derivative $\rho'_a(R_0)$. The computed bulk moduli are, again, at least as good as the ab initio ones for the set of metallic elements studied.

Key words: cohesive energies, bulk moduli, charge density, transition elements.

Résumé : On propose une relation directe entre la densité de charge d'un atome libre $\rho_a(r)$ et l'énergie de cohésion du métal correspondant. Cette relation est basée sur une approximation pour la densité de charge métallique, $\rho_m(r)$, que l'on peut construire à partir de $\rho_a(r)$ par l'équation $\rho_m(r) \cong \rho_a(r) + \bar{\rho}$ dans laquelle $\bar{\rho} = \Omega_0^{-1} \int_{R_0}^{\infty} \rho_a(r) d^3r$, Ω_0 est le volume atomique de l'atome métallique et R_0 est le rayon correspondant de Wigner–Seitz. On peut alors relier l'énergie de cohésion, E_{coh}, à $\bar{\rho}$ par l'équation $E_{coh} \cong (3/10)(3\pi^2)^{2/3}\Omega_0\bar{\rho}^{5/3}$. Une étude systématique de 29 éléments métalliques, y compris les éléments de transition 3*d* et 4*d*, montre que la relation proposée est, en général, au moins aussi précise que les résultats ab initio récents. De la même manière, on a dérivé une expression pour le module du métal à l'état global. Pour cette expression, il faut les valeurs de $\rho_a(R_0)$ et de sa première dérivé $\rho'_a(R_0)$, en plus des valeurs de $\bar{\rho}$. Encore une fois, les valeurs calculées pour ce module, pour l'ensemble d'éléments métalliques étudiés, sont en un accord au moins aussi bon que celles obtenues par des calculs ab initio.

Mots clés : énergies de cohésion, module global, densité de charge, éléments de transition.

[Traduit par la rédaction]

Introduction

The idea of using free atom information to explain the cohesive properties of metals is perhaps as old as the theory of cohesion itself. The free electron theory of metals (1–3) is the first example of such an approach, where atomic valency considerations were used to distinguish between frozen ionic cores and the free electron gas formed by the valence electrons. Wigner and Seitz (4) later made a more detailed application of this idea by using a frozen core potential to calculate the energy band and cohesive properties of metallic sodium. This approach of Wigner and Seitz has subsequently evolved into a more formal pseudopotential theory (5).

A different application of atomic data is exemplified by the overlapping charge density (OCD) model (6), in which a model crystal potential is constructed from a superposition of atomic charge densities. In a recent review paper on self-consistent energy band calculations, Koelling (7) discusses the OCD model and points out that it is actually a prescription for a model charge density. It is a reasonably good prescription, one might add, since the difference between the exact metallic charge density and the superposition of the corresponding atomic charge densities is usually much smaller than either of these charge densities.

Closely related to the OCD model is the renormalized atom (RA) method (8). This method may similarly be considered a prescription for constructing a model charge density from atomic orbitals, although in practice the total charge density is never used in the calculation of cohesive properties. The success of the RA method in predicting cohesive energies may largely be attributed to a fortunate cancellation of energy terms that occurs because of the "frozen" potential condition (9). On the other hand, the method requires a careful choice of the various terms that enter the cohesive energy expression, in order to get an effective cancellation of terms.

A more direct approach to the calculation of cohesive energies has recently been taken by Chelikowsky (10), who has been able to accurately predict such quantities (for simple metals) solely from atomic kinetic energy terms.

The present paper combines, in a way, many of the ideas outlined above. First, an approximation to the charge density difference between the metallic and atomic charge densities is constructed solely from the free atom charge density and the radius of the metallic Wigner–Seitz cell. This charge density difference is then used to determine the cohesive properties of metals.

Theory

The Wigner–Seitz cell of a metallic atom is first approximated by a sphere whose radius is defined by $R = (3\Omega/4\pi)^{1/3}$, where

Received September 15, 1995.

This paper is dedicated to Professor Richard F.W. Bader on the occasion of his 65th birthday.

Y. Tal.[1] Rafael, Computer vision and image processing section, P.O. Box 2250 (39), Haifa, Israel.

[1] Fax: 972-4-9906576

Ω is the atomic cell volume. The metallic charge density is, to first ap-proximation, a sum of atomic charge densities. Conservation of charge therefore implies that the net increase in electronic charge per Wigner–Seitz cell with respect to the unbounded state is

$$[1] \quad N_m = \int_R^\infty \rho_a(r) d^3r$$

where $\rho_a(r)$ is the charge density of the free atom. The total electronic charge within each cell must, of course, equal the nuclear charge in order to preserve the electroneutrality of the system.

A further simplifying assumption, concerning the nature of the charge distribution in the metal, can be made on the basis of previous experience. It turns out that the charge density difference $\delta\rho(r) = \rho_m(r) - \rho_a(r)$, $\rho_m(r)$, being the metallic charge density, is essentially constant. This statement is substantiated by both ab initio (11) and model (6) calculations. Accordingly, one can write

$$[2] \quad \delta\rho(r) \cong \bar{\rho} \equiv N_m/\Omega$$

which means that, to first order, the metallic charge density differs from the corresponding atomic density by a uniformly spread charge $\bar{\rho}$ whose magnitude is determined by the Wigner–Seitz radius, eqs. [1] and [2].

As in the overlapping charge density (OCD) model (6, 7), which uses a similar idea to construct the metallic potential, one still has to define the appropriate atomic configuration whose charge density is to be used in eq. [1]. This issue will be discussed in the next section.

Having established an approximation for $\delta\rho(r)$, one next wishes to calculate the energy difference associated with it, namely, the cohesive energy. Because of the virial theorem, which has the same form for both the free atom and the metallic atom in its equilibrium geometry, i.e., $E = -T$, one has

$$[3] \quad E_{coh} \equiv E_a - E_m{}^0 = T_m{}^0 - T_a \equiv E_k{}^0$$

(the superscript 0 denotes the equilibrium geometry of the metal). Only kinetic energy differences need be calculated. Note that eq. [2] implies $\rho_m(r) = \rho_a(r) + \bar{\rho} > \rho_a(r)$ which is consistent with $E_k > 0$. Finally, E_k may be estimated from a free electron model in which the additional N_m electrons per unit cell are considered to occupy an energy band above the bound atomic levels. The Fermi level of this band is given by

$$[4] \quad E_F = \frac{1}{2}(3\pi^2\bar{\rho})^{2/3}$$

and the corresponding kinetic energy difference is therefore

$$[5] \quad E_k = C_k N_m \bar{\rho}^{2/3}$$

where $C_k = (3/10)(3\pi^2)^{2/3}$. Atomic units are used here and throughout the manuscript unless otherwise specified.

Equations [1]–[3] yield an explicit expression for the cohesive energy of a monoatomic metal in terms of the free atom charge density and the Wigner–Seitz radius, namely,

$$[6] \quad E_{coh} = \frac{3}{10}(3\pi^2)^{2/3}\Omega_0^{-2/3}\left\{\int_{R_0}^\infty \rho_a(r) d^3r\right\}^{5/3}$$

where Ω_0 is the equilibrium atomic cell volume and R_0 is the corresponding Wigner–Seitz radius.

When Ω differs from Ω_0 the virial theorem no longer holds in its simple form, eq. [3], and one should write, instead

$$[7] \quad E \equiv E_m - E_a = E_k + E_v$$

where E_k is given by eq. [5] and E_v is the potential energy difference between the metallic and the free atom. The magnitude of E_v is irrelevant to the calculation of cohesive energies since $E_v^0 = -2E_k^0$ as previously discussed. It is necessary, however, to know its derivatives with respect to Ω in order to calculate bulk moduli. This point will be discussed towards the end of this section. We now turn to calculate the derivatives of E_k with respect to Ω.

Let $x \equiv \rho_a(R)/\bar{\rho}$ and $y \equiv -R\rho'_a(R)/\bar{\rho}$ where $\rho_a(R)$ is the value of ρ_a at $r = R$ and $\rho'_a(R)$ is the first derivative of ρ_a at R. With these definitions the following relations are easily derived

$$[8a] \quad \frac{dN_m}{dR} = -4\pi R^2 \rho_a(R)$$

$$[8b] \quad \frac{d\bar{\rho}}{dR} = -\frac{3}{R}\bar{\rho}[1 + x]$$

$$[8c] \quad \frac{dx}{dR} = \frac{1}{R}[3x(x + 1) - y]$$

The kinetic contributions to the pressure and to the bulk modulus are consequently given by

$$[9] \quad P_k = -\frac{dE_k}{d\Omega} = \frac{5}{3}C_k\bar{\rho}^{5/3}\left(x + \frac{2}{5}\right)$$

$$[10] \quad B_k = -\Omega\frac{dP_k}{d\Omega} = \frac{10}{9}C_k\bar{\rho}^{5/3}\left[(x + 1)^2 + \frac{1}{2}y\right]$$

One recognizes in eqs. [9] and [10] the well-known free electron gas expressions, slightly modified by the fact that the number of free electrons depends on Ω. If this dependence is ignored, then $x = y = 0$ and the free electron formulas are recovered. It turns out that as $R \to 0$ both x and y become negligibly small.

Equation [10] might be used as a rough approximation to the bulk modulus, but it usually gives too large values. To get better results one needs to consider the nature of E_v. In the spirit of the free electron assumption made earlier it seems reasonable to assume that E_v originates from an exchange–correlation interaction of the free electron gas. In doing so one implicitly assumes that all the additional Coulombic interactions, which result from the superposition of atomic charge densities, cancel each other. In other words, the net effect of such a superposition is, approximately, a constant shift in the potential. If this is the case one may calculate the exchange–correlation effect on the free electron bulk modulus by using

Fig. 1. Cohesive energies of metals. Asterisks connected by solid lines represent experimental values. Dotted lines represent theoretical values of MJW (+), and of the present work (○).

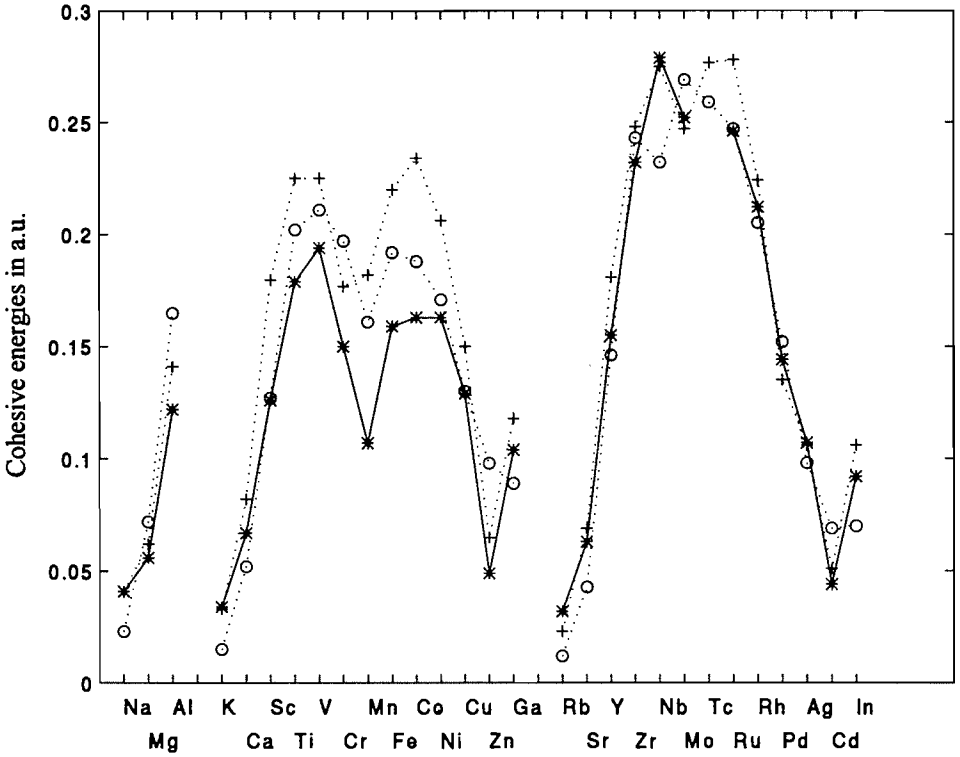

Fig. 2. Bulk moduli of metals. Asterisks connected by solid lines represent experimental values. Dotted lines represent theoretical values of MJW (+), and of the present work (○).

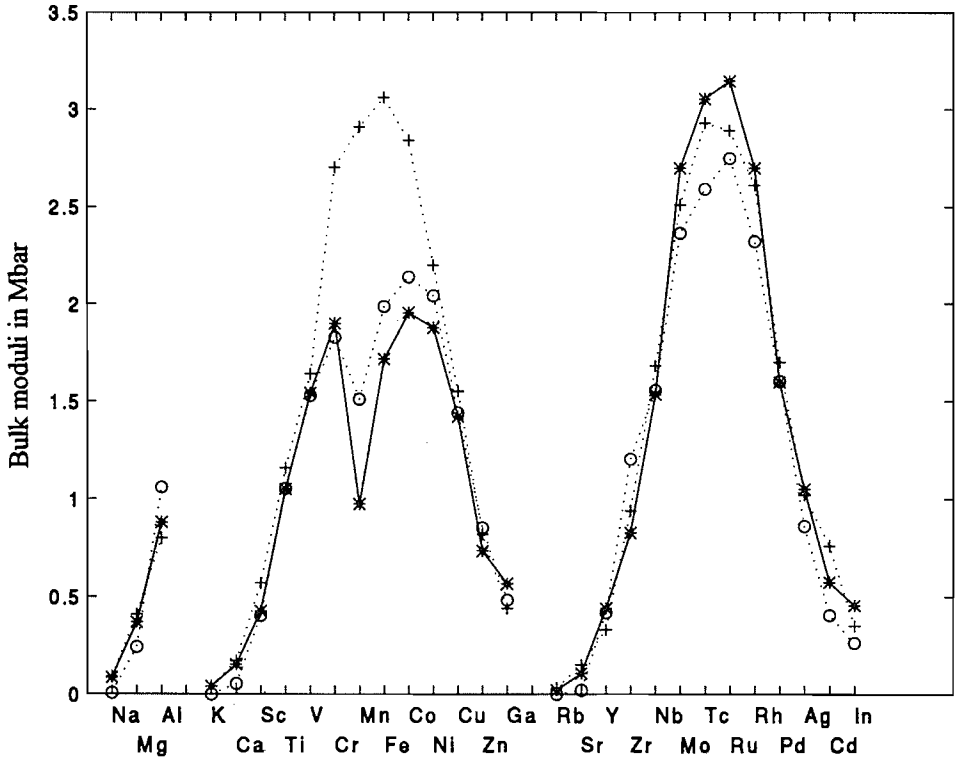

Table 1. Calculated cohesive properties.[a]

		Ω_0	N_m	$\rho(R)$	x	y	E_{coh}	r_s	λ	B_k	B
Na	$3s^1$	254.5	0.511	1.201	0.5983	1.725	0.023	4.918	1.147	0.1024	0.007
Mg	$3s^2$	151.4	0.813	4.160	0.7748	2.714	0.072	3.543	1.112	0.6965	0.241
Al	$3s^23p^1$	109.9	1.182	7.910	0.7354	2.728	0.165	2.810	1.091	2.152	1.058
K	$4s^1$	481.3	0.500	0.708	0.6816	2.168	0.015	6.124	1.175	0.0392	−0.007
Ca	$4s^2$	291.1	0.874	2.442	0.8129	2.854	0.052	4.300	1.131	0.2766	0.053
Sc	$4s^23d^1$	168.7	1.198	4.924	0.6933	2.253	0.127	3.227	1.103	0.9838	0.403
Ti	$4s^23d^2$	120.3	1.383	7.509	0.6532	2.154	0.202	2.749	1.089	2.094	1.054
	$4s^13d^3$	120.3	1.187	6.103	0.6186	2.274	0.157	2.892	1.094	1.600	0.761
V	$4s^13d^4$	93.48	1.281	8.661	0.6320	2.448	0.211	2.592	1.085	2.863	1.528
Cr	$4s^13d^5$	80.63	1.305	10.63	0.6567	2.642	0.240	2.452	1.081	3.951	2.214
	$4s^03d^6$	80.63	1.161	9.398	0.6527	2.971	0.197	2.550	1.084	3.373	1.827
Mn	$4s^13d^6$	82.84	1.185	10.16	0.7101	2.944	0.200	2.555	1.084	3.479	1.881
	$4s^03d^7$	82.84	1.040	8.926	0.7109	3.293	0.161	2.669	1.087	2.912	1.510
Fe	$4s^13d^7$	78.95	1.134	10.64	0.7408	3.157	0.192	2.552	1.083	3.669	1.986
Co	$4s^13d^8$	74.72	1.093	11.19	0.7645	3.335	0.188	2.536	1.083	3.928	2.138
Ni	$4s^13d^9$	73.42	1.027	11.09	0.7930	3.538	0.171	2.574	1.084	3.800	2.041
Cu	$4s^13d^{10}$	78.92	0.897	9.564	0.8410	3.858	0.130	2.759	1.090	2.871	1.439
Zn	$4s^23d^{10}$	99.35	0.829	7.918	0.9486	4.345	0.098	3.058	1.098	1.924	0.852
Ga	$5p^1$	132.4	0.875	5.835	0.8825	4.119	0.089	3.305	1.105	1.225	0.483
Rb	$5s^1$	598.9	0.475	0.595	0.7495	2.626	0.012	6.700	1.187	0.0279	−0.009
Sr	$5s^2$	373.6	0.861	1.984	0.8614	3.184	0.043	4.697	1.141	0.1907	0.021
Y	$5s^24d^1$	194.7	1.380	5.060	0.7141	2.449	0.146	3.230	1.103	1.021	0.418
Zr	$5s^24d^2$	139.9	1.640	8.267	0.7049	2.550	0.243	2.730	1.089	2.376	1.204
	$5s^14d^3$	139.9	1.443	7.259	0.7037	2.856	0.196	2.850	1.092	1.987	0.961
Nb	$5s^24d^3$	119.2	1.717	10.64	0.7382	2.844	0.292	2.549	1.084	3.558	1.928
	$5s^14d^4$	119.2	1.495	9.509	0.7582	3.258	0.232	2.670	1.087	2.999	1.555
Mo	$5s^14d^5$	102.7	1.541	11.98	0.7983	3.593	0.269	2.515	1.083	4.311	2.364
Tc	$5s^14d^6$	97.25	1.474	12.86	0.8487	3.978	0.259	2.507	1.082	4.710	2.590
Ru	$5s14d^7$	92.54	1.403	13.49	0.8901	4.325	0.247	2.507	1.082	4.997	2.748
Rh	$5s^14d^8$	93.70	1.262	12.62	0.9374	4.717	0.205	2.607	1.085	4.373	2.321
Pd	$5s^14d^9$	99.67	1.080	10.71	0.9890	5.150	0.152	2.803	1.091	3.252	1.602
Ag	$5s^14d^{10}$	111.9	0.871	8.143	1.046	5.644	0.098	3.131	1.100	2.010	0.861
Cd	$5s^14d^{10}$	142.9	0.776	6.020	1.109	5.793	0.069	3.529	1.111	1.156	0.404
In	$6p^1$	179.2	0.856	4.696	0.9827	4.930	0.070	3.683	1.115	0.8139	0.259

[a]All values, except for bulk moduli are in atomic units. Values of $\rho(R)$ are in milli atomic units. Values of bulk moduli are in Mbar. The values of Ω_0 were taken from ref. 11. Values of N_m were computed from eq. [1]. Values of E_{coh} were computed from eq. [6]. Values of λ, B_k, and B were computed from eqs. [12], [10], and [11], respectively.

the Hedin–Ludqvist relation.

$$[11] \quad B = B_k[1 - \alpha\xi\cdot\lambda(r_s)]$$

where $r_s = ((3/4)\pi\bar{\rho})^{1/3}$ and

$$[12] \quad \lambda(r_s) = 1 + \frac{b\xi}{1+\xi}$$

Here $\xi = r_s/a$, $\alpha = (4/9\pi)^{1/3}(a/\pi)$ where a and b are numerical constants whose values are $a = 21$ and $b = 0.7734$. A similar application of eq. [11] was successfuly made by Moruzzi et al. (11) in treating the muffin-tin interstitial charge as a free electron gas.

Results and discussion

Atomic charge densities of 29 metallic elements were computed using the relativistic self-consistent field program of Liberman et al. (12). The electronic configuration was, in most cases, the free atom experimental ground state configuration. This choice was made, in particular, for all the simple metals having only S and P valence electrons. In such cases the ground state is distinct both experimentally and computationally. The transition metal elements, however, possess at least two nearly degenerate configurations, namely, $d^{n-1}s^1$ and $d^{n-2}s^2$. Furthermore, it turns out that the ground state energy of the Kohn–Sham Hamiltonian is none of the above but, in general, a $d^{n-x}s^x$ configuration where x is a non-integral number. These difficulties were discussed in other papers and the conclusion seems to be that, in general, the $d^{n-1}s^1$ configuration is

a preferable choice for a model density calculation (8). This configuration was therfore used here with only few exceptions. Three of these exceptions occur at the beginning of the d series, namely, at Ti, Zr, and Nb. For these elements both $d^{n-1}s^1$ and $d^{n-2}s^2$ configurations were calculated. The other two exceptions are Cr and Mn for which the $d^n s^0$ configuration was included in addition to the $d^{n-1}s^1$ configuration.

Having obtained the appropriate free atom chrge densities it is a simple matter to apply eq. [6] in order to get cohesive energies. The results are displayed in Fig. 1 along with the experimental values and the theoretical results of Moruzzi et al. (11). The accuracy of the present results is comparable with, or even slightly better than, the best ab initio calculations.

In general, the largest relative errors are found when E_{coh} is small and second-order effects are expected to become important. Hence in both Na and K only ~50% of E_{coh} is recovered by the present model. On the other hand, for large values of E_{coh} the present model seems to be working surprisingly well. Note, in particular, the 3d series for which the present results are considerably better than the ab initio results.

A similar pattern is observed for the bulk moduli displayed in Fig. 2. The overall agreement of the present results with experimental data is striking, particularly in view of the relatively large errors in the ab initio results for the 3d transition metal series. It was found, however, that eq. [11] does not work well for small values of B_k. Hence, for values of $B_k < 0.3$ Mbar it is much better to use B_k itself as an approximation for B rather than to apply eq. [11].

Table 1 displays some numerical results of the present calculation. Consider, in particular, the values of N_m (eq. [1]), which in the present theory play the role of the number of valence electrons, N_v, in other theories. Yet the values of N_m hardly resemble the values usually assigned to N_v. A possible reason for this apparent discrepancy is that "valence electrons" is a rather loose term, which helps in singling out the significant contributions to cohesion within the framework of a single particle model, but is much less successful than N_m in predicting the *net* cohesive effect.

Certainly, one should not be too naive to think that the success of the present model is totally unrelated to some fortunate cancellation of errors. Yet, it may perhaps create some hope that within density functional theory one might be able to find a direct relation between charge density differences and cohesive properties.

References

1. P. Drude. Ann. Phys. **1**, 566 (1900).
2. A. Sommerfeld. Z. Phys. **47**, 1 (1928).
3. F. Seitz. The modern theory of solids. McGraw-Hill, New York. 1940.
4. E. Wigner and F. Sietz. Phys. Rev. **43**, 804 (1933).
5. W.A. Harrison. Pseudopotentials in the theory of metals. W.A. Benjamin, New York. 1966.
6. L.F. Mattheiss. Phys. Rev. **133**, 184 (1964).
7. D.D. Koelling. Rep. Prog. Phys. **44**, 139 (1981).
8. (*a*) R.E. Watson, H. Ehrenreich, and L. Hodges. Phys. Rev. Lett. **24**, 829 (1970); (*b*) L. Hodgess, R.E. Watson, and E. Ehrenreich. Phys. Rev. B: Solid State, **5**, 3953 (1972); (*c*) C.D. Gelatt, Jr., H. Ehrenreich, and R.E. Watson. Phys. Rev. B: Solid State, **15**, 1613 (1977).
9. J. Ashkenazi. Phys. Rev. B: Condens. Matter, **26**, 1512 (1982).
10. J.R. Chelikowsky. Phys. Rev. Lett. **47**, 387 (1981).
11. V.L. Moruzzi, J.F. Janak, and A.R. Williams. Calculated electronic properties of metals. Pergamon, New York. 1978.
12. D.A. Liberman, D.T. Cromer, and J.T. Waber. Comput. Phys. Commun. **2**, 107 (1971).

Applications and evaluation of IGAIM ^{13}C and ^{1}H chemical shift calculations for unsaturated hydrocarbons and organolithium compounds

Nick Henry Werstiuk and Jiangong Ma

Abstract: Wave functions obtained at the RHF/6-31+G(d) level of theory were used with the new method IGAIM (individual gauges for atoms in molecules) developed by Keith and Bader to calculate the isotropic ^{13}C and ^{1}H NMR chemical shifts of a group of neutral molecules (bicyclo[3.2.1]octa-2,6-diene (**1**), bicyclo[3.2.1]oct-6-ene (**2**), bicyclo[2.2.1]hepta-2,5-diene (**3**), benzene (**4**)), carbanions (prop-2-en-1-yl (allyl) (**5**), bicyclo[3.2.1]octa-3,6-dien-2-yl (**8**)), and lithium complexes (prop-2-en-1-yllithium (**6**) and its dimer **7**, bicyclo[3.2.1]octa-3,6-dien-2-yllithium (**9**)). The theoretical isotropic ^{13}C NMR chemical shifts of the neutral molecules, relative to the calculated value for TMS(tetramethylsilane), are in excellent agreement with the experimental values, with differences between the sets of data ranging from +4.9 to −7.1 ppm. For the same group of compounds the theoretical ^{1}H shifts are lower than the experimental values by increments ranging between 0.4 and 1.29 ppm. For allyllithium, which exists as an unsymmetrical fluxional dimer, the theoretical averaged ^{13}C shifts are larger, 2.6 ppm for the terminal carbons and 16.7 ppm for the central carbon, than the experimental values. In the case of **8**, originally considered to be a bishomoaromatic species, the theoretical ^{13}C chemical shifts of its Li^{+} complex **9** differ from the experimental ones for THF-solvated **9** by values that range from +6.2 to −15.0 ppm. Yet, the relative theoretical chemical shifts — of special importance is the fact that the carbons of the vinylene bridge of this compound are unusually shielded relative to the parent diene **1** — correlate with the experimental data. The ^{1}H chemical shifts calculated for the hydrocarbons **1**, **2**, **3**, **4** and the lithium complexes **7** and **9** range from 0.08 to 1.38 ppm less than the experimental values. To gain information on whether variations in charge density play a significant role in determining the magnitudes of the chemical shifts, we used AIMPAC calculations to obtain the atom electron populations of diene **1**, **5**, **6**, dimer **7**, **8**, and **9**. We find no obvious correlation between the charges on the carbon atoms and the ^{13}C shifts for this set of compounds.

Key words: IGAIM, calculations, ^{13}C and ^{1}H chemical shifts, unsaturated hydrocarbons, organolithium compounds.

Résumé : On a utilisé les fonctions d'onde obtenues au niveau RHF/6-31+G(d) de la théorie en relation avec la nouvelle méthode JIADM (jauges individuelles pour les atomes dans les molécules) développée par Keith et Bader pour calculer les déplacements chimiques isotropes en RMN du ^{1}H et du ^{13}C d'un groupe de molécules neutres (bicyclo[3.2.1]octa-2,6-diène (**1**), bicyclo[3.2.1]oct-6-ène (**2**), bicyclo[2.2.1]hepta-2,5-diène (**3**), benzène (**4**)), de carbanions (prop-2-èn-1-yle (allyle) (**5**), bicyclo[3.2.1]octa-3,6-dièn-2-yle (**8**)) et de complexes du lithium (prop-2-èn-1-yllithium (**6**) et son dimère **7**, bicyclo[3.2.1]octa-3,6-dièn-2-yllithium (**9**)). Les déplacements chimiques théoriques isotropes en RMN du ^{13}C des molécules neutres, relatifs aux valeurs calculées pour le TMS (tétraméthylsilane), sont en bon accord avec les valeurs expérimentales; les différences entre les ensembles de données varient de +4,9 à −7,1 ppm. Pour le même groupe de composés, les déplacements théoriques des ^{1}H sont plus faibles que les valeurs expérimentales par des incréments variant de 0,4 à 1,29 ppm. Pour l'allyllithium qui existe sous la forme d'un dimère en fluxion asymétrique, les déplacements théoriques moyens du ^{13}C sont plus élevés (2,6 ppm pour les carbones terminaux et 16,7 ppm pour l'atome de carbone central) que les valeurs expérimentales. Dans le cas du produit **8**, qui avait originalement été considéré comme une espèce bishomoaromatique, les déplacements chimiques théoriques du ^{13}C de son complexe avec le lithium, **9**, diffèrent des valeurs expérimentales pour le composé **9** solvaté par du THF par des valeurs allant de +6,2 à −15,0 ppm. Malgré tout, les déplacements chimiques théoriques relatifs — ce qui présente le plus d'importance est le fait que les carbones du pont vinylène de ce composé sont inhabituellement blindés par rapport au diène parent, **1** — présentent une corrélation avec les données expérimentales. Les déplacements chimiques calculés du ^{1}H pour les hydrocarbures **1**, **2**, **3** et **4** et les complexes avec le lithium, **7** et **9**, se situent à des valeurs allant 0,08 à 1,38 ppm plus faibles que les valeurs expérimentales. Afin d'obtenir de l'information sur le rôle que jouent les variations dans la densité de charge dans la détermination des amplitudes des déplacements chimiques, on a fait appel à des calcul de AIMPAC pour déterminer les populations électroniques des

Received November 6, 1995.

This paper is dedicated to Professor Richard F.W. Bader on the occasion of his 65th birthday.

N.H. Werstiuk[1] and J. Ma. Department of Chemistry, McMaster University, Hamilton, ON L8S 4M1, Canada.

[1] Author to whom correspondence may be addressed. Telephone: (905) 525-9140. Fax: (905) 522-2509. E-mail: werstiuk@mcmaster.ca

atomes de diène **1**, **5** et **6**, de dimère **7**, **8** et **9**. On n'a pas trouvé de corrélations évidentes entre les charges sur les atomes de carbone et les déplacements chimiques du ^{13}C de cet ensemble de composés.

Mots clés : JIADM, calculs, déplacements chimiques du ^{1}H et du ^{13}C, hydrocarbures insaturés, composés organolithiens.

[Traduit par la rédaction]

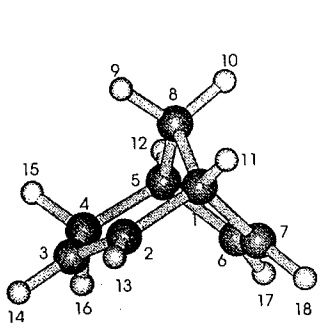

1

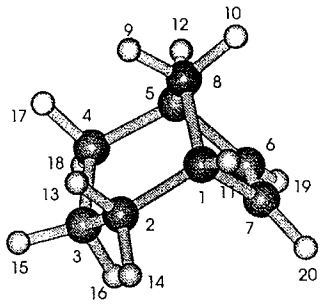

2

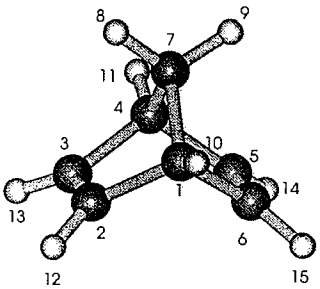

3

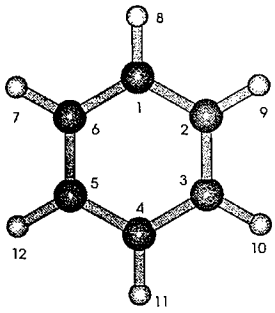

4

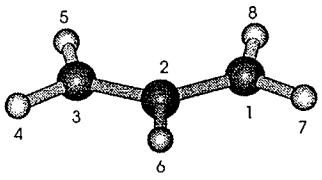

5

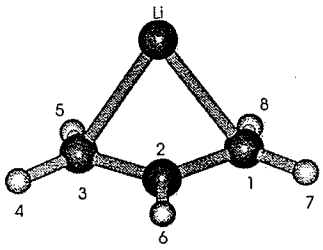

6

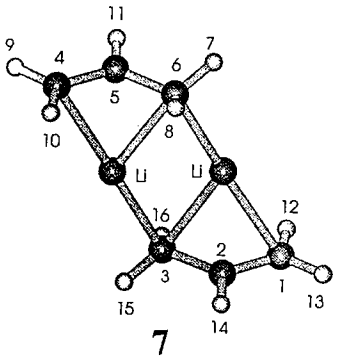

7

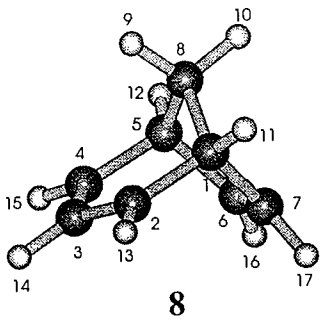

8

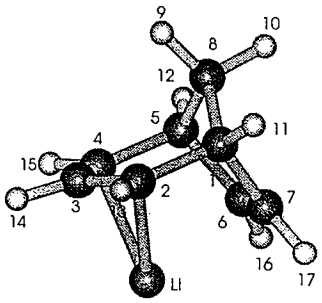

9

Introduction

The bicyclo[3.2.1]octa-3,6-dien-2-yl anion (**8**) has attracted the attention of chemists for over 30 years. Apart from the historical interest, this anion has been the object of a number of studies aimed at determining whether it is homoaromatic (1–3). The enhanced kinetic and thermodynamic acidities of the allylic hydrogens of bicyclo[3.2.1]octa-2,6-diene (**1**) and the unusual chemical shifts of the hydrogens and carbons of the vinylene bridge of its lithium complex **9** solvated with THF (the hydrogens are shielded by 1.98 and 2.51 ppm and the carbons by 39.7 and 49.6 ppm relative to the **1**) were taken as evidence that the anion is bishomoaromatic. It was estimated from the ^{1}H NMR data that **8** had 30–40% of the ring current of benzene. Anion **8** has also been the subject of a number of theoretical studies (4–7). While the results of one of the theoretical studies (6) were used to support the initial interpretation of the experimental data, Lindh et al. (7) concluded, as did two other groups of researchers (4, 5), that the interactions between unoccupied and occupied orbitals necessary to achieve bicycloaromaticity do not take place, in their view, because the distance between the interacting bridges is too large. They suggested that the dominant interaction at the equilibrium distance is electrostatic in nature and proposed that the unusual chemical shifts arise from a through-bond redistribution of charge and not from the bishomoaromaticty of **8**.

Our long-standing interest in the chemistry of carbanions, especially in the factors controlling their stability, coupled with the fact that there are a number of methods available — including IGAIM (individual gauges for atoms in molecules)

recently developed by Keith and Bader (8) — for calculating magnetic response properties such as shieldings and magnetic susceptibilities (9) led us to study of a group of the unsaturated hydrocarbons **1**, **2**, **3**, **4**, the carbanions **5** and **8**, and their lithium complexes **6**, **7** and **9** with a relatively small basis set (6-31+G(d)). We chose the IGAIM method because Keith and Bader showed that IGAIM yields absolute carbon shieldings that agree better with experimental values than those obtained by conventional CHF calculations using the same basis set (8). Our objectives were twofold. Firstly, we set out to establish whether the IGAIM method is useful for calculating ^{13}C and ^{1}H chemical shifts of relatively large molecules with a relatively small basis set — as pointed out by Jørgensen and co-workers recently (10), this information is not available — and, in the same instance begin to gain some understanding of the NMR spectroscopy exhibited by **9**. In this connection, we also obtained the atom charges of **1**, **5**, **6**, **7**, **8**, and **9** with the AIMPAC suite of programs developed by Bader and co-workers (11). In the event that we found IGAIM to be useful for calculating chemical shifts at the 6-31+G(d) level of theory, we planned to carry out a theoretical study of the magnetic susceptibilties of benzene, **1**, **8**, and **9** at the same level of theory, the goal being to analyze the atom susceptibilities on the basis of basin and surface components. Bader and Keith showed that this approach gives information on the flux in current through interatomic surfaces, namely ring currents, induced by a magnetic field (12). In this paper we report the theoretical isotropic ^{13}C and ^{1}H chemical shifts obtained with IGAIM along with the atom charges calculated with AIMPAC and correlate the results with available experimental NMR data.

Computational method

The derivation and detailed description of the IGAIM method are documented in a paper published by Keith and Bader (8). The optimized equilibrium geometries of the compounds were calculated at the RHF/6-31+G(d) level of theory with GAUSSIAN 92 (13). Perturbed wave functions were obtained for these geometries with CADPAC (14), and PROAIMV (11) was used to calculate the magnetic response properties. The atom electron populations were obtained with PROAIMV and PROMEGA (11). All calculations were carried out on IBM RS/6000 model 530, 350, and 320H workstations.

Results and discussion

Calculations on hydrocarbons

We carried out the calculations at the RHF/6-31+G(d) level of theory because (*a*) it is necessary to include diffuse functions on heavy atoms when carrying out calculations on carbanions, (*b*) we wished to establish whether IGAIM calculations on fairly large molecules with a relatively small basis set yield chemical shifts that correlate with experimental data, and (*c*) at the time this study was carried out the scratch disk space available for CADPAC calculations was limited to 2 GB for each temporary file. We studied **1** because it is necessary to track the changes in ^{13}C and ^{1}H chemical shifts in going from **1** to **8** and **9**. Bicyclooctene **2** was studied because it is the dihydro analogue of **1** and its experimental ^{13}C chemical shifts have been published. While norbornadiene (**3**) was studied because its olefinic carbons are unusually deshielded, benzene was studied because it is the archtypical aromatic system that exhibits a large ring current. The total energies of **1–9** obtained at the 6-31+G(d) level of theory are given in Table 1.

Table 1. Total energies of compounds.

Compound	Total energy[a]
1	−308.079 31
2	−308.726 85
3	−315.575 84
4	−116.425 19
5	−84.867 19
6	−247.899 61
7	−230.711 09
8	−269.659 26
9	−309.914 50

[a]In hartrees, calculated at the HF/6-31+G(d)//6-31+G(d) level of theory.

Keith and Bader showed that increasing the size of the basis set (the uncontracted Gaussian basis set [13s8p5d] and 6-311++G(2d,2p) were used) produced only small changes in the shieldings (8). Thus, we expected to find a good correlation between the theoretical chemical shifts and the experimental values for the compounds of interest to us. Because gas-phase absolute chemical shieldings (σ)[2] relative to the bare nucleus are obtained with IGAIM, the theoretical isotropic ^{13}C (Table 2) and ^{1}H chemical shifts (δ) (Table 3) of the unsaturated hydrocarbons including benzene are referenced to the calculated gas-phase ^{13}C and ^{1}H shieldings of tetramethylsilane(TMS) obtained at the same level of theory. The IGAIM isotropic chemical shifts calculated in this way were compared to the values obtained in solution. It is important to note here that the differences between the gas phase and solution chemical shifts of neutral compounds, in general, are small: for ^{13}C the differences usually are in the range of 1 to 2 ppm; for ^{1}H the differences usually fall in the region of 1 ppm unless hydrogen bonding is involved (17).

It is seen that the differences between the theoretical and the experimental solution ^{13}C shifts of the hydrocarbons **1**, **2**, **3**, and **4** range from +9.9 to −7.1 ppm (Table 2). Even so, the correlation between the theoretical and experimental ^{13}C chemical shifts of **1**, **2**, **3**, and **4** is remarkably good (Fig. 1) with the correlation coefficient being 0.999. Of significance is the fact that the relative theoretical chemical shifts of the vinylic carbons of **1**, **2**, and **3** — in this compound the carbons are unusually deshielded — follow the experimental values exactly. The IGAIM ^{13}C chemical shift of benzene, the archtypical aromatic system, is identical to the gas-phase experimental value (Table 2). This result indicates that IGAIM calculations at the 6-31+G(d) level of theory will be useful for studying the magnetic response properties of aro-

[2] The NMR chemical shift is a tensorial property. IGAIM calculations yield the three principle components, which are averaged to obtain the isotropic shifts. Ideally, the IGAIM principle components should be compared with the experimental values if they are available (15, 16).

Table 2. Theoretical and experimental isotropic ^{13}C absolute shieldings (σ)and chemical shifts (δ).

Compound	Nucleus	IGAIM σ	IGAIM δ^a	Expt. δ	Δexpt. – IGAIM
	C1	166.7	36.5	39.5[b]	3.0
	C2	64.9	138.3	134.9	−3.4
	C3	76.2	127.1	124.8	−2.3
	C4	176.4	26.8	29.6	2.8
1	C5	168.3	34.9	39.8	4.9
	C6	68.1	135.1	131.0	−4.1
	C7	57.5	145.7	140.6	−5.1
	C8	161.5	41.7	41.6	−0.1
	C1	168.1	35.2	39.5[c]	4.3
	C2	180.2	23.0	23.5	2.5
	C3	185.9	17.3	18.7	1.4
	C4	180.2	23.0	25.5	2.5
2	C5	168.1	35.2	39.5	4.3
	C6	65.9	137.3	132.1	−5.2
	C7	65.9	137.3	132.1	−5.2
	C8	159.9	43.3	45.1	1.8
	C1	156.0	47.3	50.9[d]	3.6
	C2	52.6	150.6	143.5	−7.1
	C3	52.6	150.6	143.5	−7.1
3	C4	47.3	47.3	50.9	3.6
	C5	52.6	150.6	143.5	−7.1
	C6	52.6	150.6	143.5	−7.1
	C7	130.0	73.2	75.5	2.3
4	C1	72.1	131.2	128.5[e]	2.7
				130.9[f]	0.3

[a]Referenced to TMS; the theoretical ^{13}C absolute shielding (σ) of TMS calculated at the 6-31+G(d) basis is 203.2. The experimental value is 188.1 (33).
[b]Reference 27.
[c]Reference 28.
[d]Reference 29.
[e]Reference 30.
[f]Reference 17.

matic systems. There is an excellent linear correlation (the correlation coefficient is 0.992) between the theoretical and experimental ^1H chemical shifts of **1**, **3**, and **4** (Table 3, Fig. 2) as well, although the calculated chemical shifts are systematically low by around 1 ppm. Except for the bridgehead hydrogens of **1** and **3**, the relative chemical shifts of the hydrogens correlate closely with the experimental values.

Calculations on the allyl and bicyclo[3.2.1]octa-3,6-dien-2-yl anions and their lithium salts

To establish whether IGAIM can be used to calculate chemical shifts of carbanions and their lithium complexes with the 6-31+G(d) basis, we studied the allyl and bicyclo[3.2.1]octa-3,6-dien-2-yl anions **5** and **8** and their lithium complexes **6**, **7**, and **9** without including solvent molecules such as H_2O or THF. Our first goal was to determine the degree to which Li^+ complexation, and dimer formation in the case of **5**, affects the ^{13}C shieldings of carbanions **5** and **8**, and to establish whether the theoretical chemical shifts correlate with the experimental data available for **7** and **9**. Figures 3(*a*), 3(*b*), and 3(*c*) display the optimized equilibrium geometrical structures of **6**, **7**, and **9**, respectively, labelled with selected geometrical parameters. In going from **5** to **6** there is a slight increase in the C1—C2 bond length (the value for **5** is given in parentheses) and C1 and C3 are pyramidalized as indicated by the H4,C3,C2,H6 and H5,C3,C2,H6 dihedral angles. The atom charges of **5**, **6**, **7**, **8**, and **9** calculated from the electron populations obtained with AIMPAC are summarized in Figs. 4(*a*), 4(*b*), and 4(*c*). The values given in parentheses in 4(*a*) and 4(*c*) are the charges for the uncomplexed anions **5** and **8**, respectively. From the data given in Table 4 is seen that in going from **5** to **6** the chemical shifts of the terminal carbons and the central carbon atom increase by 10.5 and 15.2 ppm, even though the electron populations of terminal carbons C1 and C3 and the center carbon C2 increase by 0.067 and 0.101, respectively (Fig. 4(*a*)). It is clear that there is no relationship between charge density and the ^{13}C chemical shifts of the allyl anion (18). Other factors play a more important role (19). As is seen from atom charges shown in Fig. 4(*a*), the electron populations of the carbons increase at the expense of the hydrogens. While the results of an earlier ^{13}C NMR study were interpreted on the basis that allyllithium is an ionic monomeric species (20), cryoscopic

Table 3. Theoretical and experimental istropic ^{1}H absolute shieldings (σ) and chemical shifts (δ).

Compound	Nucleus	IGAIM σ	IGAIM δ[a]	Expt. δ	Δδ expt. – IGAIM
1	H9	27.69	1.26	1.66[b]	0.40
	H10	27.74	1.21	1.90	0.69
	H11	27.67	1.28	2.57	1.29
	H12	27.38	1.56	2.57	1.01
	H13	23.98	4.97	5.92	0.95
	H14	24.78	4.16	5.15	0.99
	H15	23.98	1.41	2.17	0.76
	H16	27.94	1.01	1.79	0.78
	H17	24.21	4.74	5.65	0.91
	H18	23.66	5.29	6.18	0.89
3	H8	27.41	1.54	1.98[c]	0.44
	H9	27.41	1.54	1.98	0.44
	H10	26.65	2.30	3.52	1.22
	H11	26.65	2.30	3.52	1.22
	H12	23.02	5.92	6.72	0.80
	H13	23.02	5.92	6.72	0.80
	H14	23.02	5.92	6.72	0.80
	H15	23.02	5.92	6.72	0.80
4	H7	22.97	5.99	7.3[d]	1.3

[a]In ppm units; referenced to the theoretical ^{1}H absolute shielding (σ) (28.95 ppm) of TMS calculated at the 6-31+G(d) basis.
[b]Reference 3.
[c]Reference 31.
[d]Reference 32.

Table 4. Theoretical and experimental isotropic ^{13}C absolute shieldings (σ) and chemical shifts (δ).

Compound	Nucleus	IGAIM σ	IGAIM δ[a]	Expt. δ	Δδ expt. – IGAIM
5	C1	158.8	44.4		
	C2	53.3	149.9		
	C3	158.8	44.4		
6	C1	148.3	54.9		
	C2	38.1	165.2		
	C3	148.3	54.9		
7	C1	123.9	53.6[b]	51.0[c]	−2.60
	C2	39.6	163.7	147.0	−16.7
	C3	177.4	53.6	51.0[c]	−2.60
	C4	124.0			
	C5	39.6			
	C6	177.3			

[a]Referenced to the theoretical ^{13}C absolute shielding (σ) (203.2) of TMS calculated at the 6-31+G(d) basis. The experimental value is 188.1 (33).
[b]Average values of C1, C3, C4, and C6 and C2 and C5 of the static structure.
[c]At 298 K; ref. 21.

measurements and variable temperature ^{13}C isotopic perturbation NMR studies established that allyllithium exists as a fluxional, unsymmetrical dimer in THF over a wide temperature range (21). Consequently, we studied **7** with IGAIM. Because of hardware limitations, we could not solvate the dimer with THF or even H_2O. The optimized geometrical structure of **7** along with selected parameters is displayed in Fig. 3(*b*). As was found in earlier ab initio studies at the 3-21G level of theory (22, 23) and confirmed by the isotopic perturbation NMR experiments, the dimer has C_i symmetry. The geometri-

Fig. 1. Plot of theoretical versus experimental ^{13}C chemical shifts: **1** (○); **2** (×); **3** (+); **4** (*).

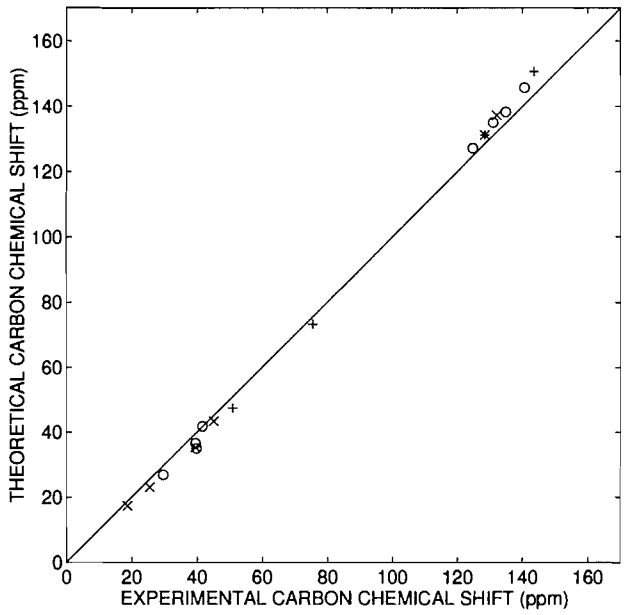

Fig. 2. Plot of theoretical versus experimental ^{1}H chemical shifts: **1** (○); **3** (+); **4** (*).

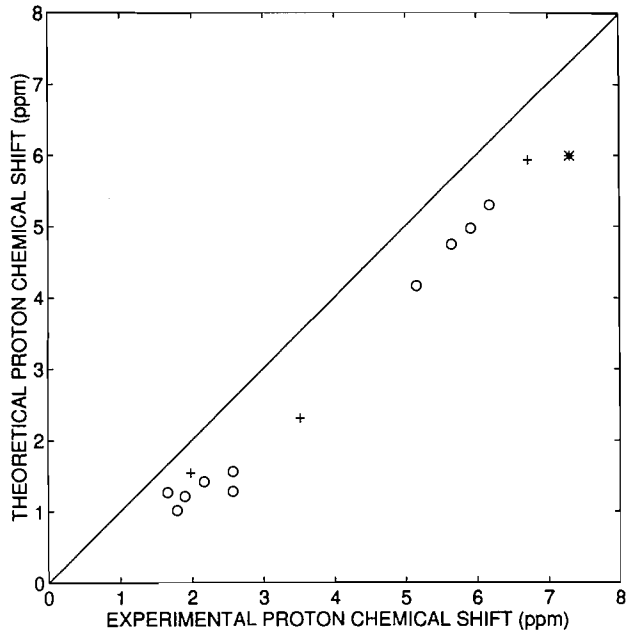

cal parameters and chemical shifts we obtained in this study correlate closely with those obtained in the earlier IGLO study of **7** (23). The atom charges calculated with AIMPAC (Fig. 4(*b*)) show that there is a substantial difference (0.242 and 0.247 au) in the charges of the methylene carbons. This is also the case for the hydrogens. Yet the average values, −0.350 and −0.352, are virtually identical to the carbon-atom charges calculated for the methylene carbons of **6**. The charges on C2 and C5 and on the lithiums are also close to the values obtained for **6**. The theoretical absolute shieldings and chemical shifts, which are referenced to the theoretical absolute ^{13}C shielding of the methyl group of TMS, are given in Table 4. While the terminal carbons (compare C1 and C4 with C3 and C6) of the allyl fragments of the static dimer **7** differ in chemical shift by 53.4 ppm, there is an excellent correlation between averaged ^{13}C chemical shifts and the experimental values obtained for **7** in THF solution. That the averages of the theoretical chemical shifts of C1, C3, C4, and C6, and C2 and C5 correlate with the nmr data even at 107 K, a temperature at which the "inside" (H8, H10, H12, and H16) and "outside" (H7, H9, H13, and H15) hydrogens do not equilbrate, is in keeping with the view that allyl groups of **7** undergo a helicopter-type rotation (20). The relationship between the theoretical and experimental ^{13}C chemical shifts is displayed graphically in Fig. 5. The theoretical ^{1}H chemical shifts of the **5**, its lithium complex **6**, and the unsymmetrical dimer **7** along with the experimental data for **7** are given in Table 5. It is seen that the average of the theoretical chemical shifts of the "outside" hydrogens (H7, H9, H13, and H15) and of **7** is smaller than the average of the "inside" (H8, H10, H12, and H16) ones. While these average values are 0.35 and 0.57 ppm less than the experimental values obtained at 37°C, the relative chemical shifts are in accord with assignments made on the basis of vicinal coupling constants by West et al. (24). The relationship beween the theoretical and experimental shifts is shown graphically in Fig. 6. It is interesting to note that the hydrogens of the C3 and C6 methylene groups of the static structure are considerably more shielded (2 ppm) than the hydrogens of the C1 and C4 methylenes. This is undoubtedly due to the fact that (*a*) there is a significant degree of pyramidalization at C3 and C6 of the dimer, and (*b*) the electron populations of C3 and C6 and the associated hydrogens are larger than the populations of the the C1 and C4 methylenes (Fig. 4(*b*)).

The optimized equilibrium geometrical structure of bicyclo[3.2.1]octa-3,6-dien-2-yllithium (**9**) labelled with selected geometrical parameters is displayed as Fig. 3(*c*). The lithium cation is located in the *endo* position in keeping with the X-ray diffraction structure of **9** solvated with one molecule of TMEDA (25). Hardware limitations precluded studies on **9** solvated with H_2O, THF, or TMEDA. Even so, there is good agreement between the geometrical parameters calculated for **9** and the X-ray diffraction data obtained for TMEDA-solvated **9**, which turns out to be an unsymmetrical species. The largest differences between the theoretical and experimental geometrical parameters are seen in the C5–C6 (**9**, 1.531 Å; TMEDA-solvated **9**, 1.508 Å), C1–C7 (**9**, 1.531; TMEDA-solvated **9**, 1.512), Li–C2 (**9**, 2.219; TMEDA-solvated **9**, 2.440), Li–C3 (**9**, 2.068; TMEDA-solvated **9**, 2.194), and Li–C4 (**9**, 2.219; TMEDA-solvated **9**, 2.515) internuclear distances. Selected geometrical parameters of the free anion **8** are given in parentheses in Fig. 4(*c*). There are only slight changes in the geometrical structure when **8** is converted into **9**. In keeping with the results obtained for conversion of **5** into **6**, the electron populations of the carbons (C2 (Δ0.150 au), C3(Δ0.119 au), and C4(Δ0.150 au)) of the allylic unit of **8** increase substantially when it is converted into **9** (Fig. 4(*c*)). As was found for the allyl anion, this occurs predominately at the expense of hydrogens attached to these carbons, although the other hydrogens and the bridgehead carbons C1 and C5 relinquish electrons as well. Noteworthy is the fact that the

Fig. 3. (*a*) Optimized equilibrium geometical structure of **6** with internuclear distances in Å; (*b*) optimized equilibrium geometical structure of **7**; (*c*) optimized equilibrium geometical structure of **9**.

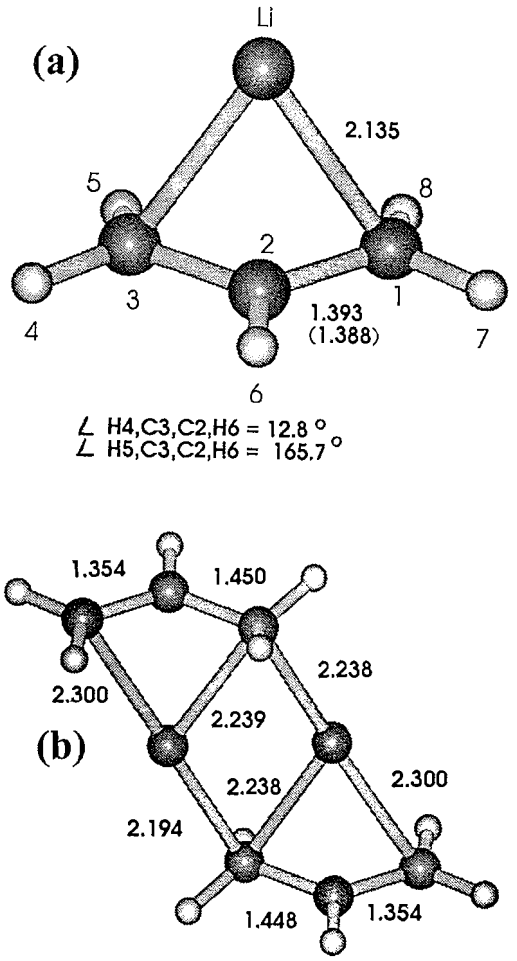

Fig. 4. (*a*) Atom charges of **6**; (*b*) atom charges of **7**; (*c*) atom charges of **9**.

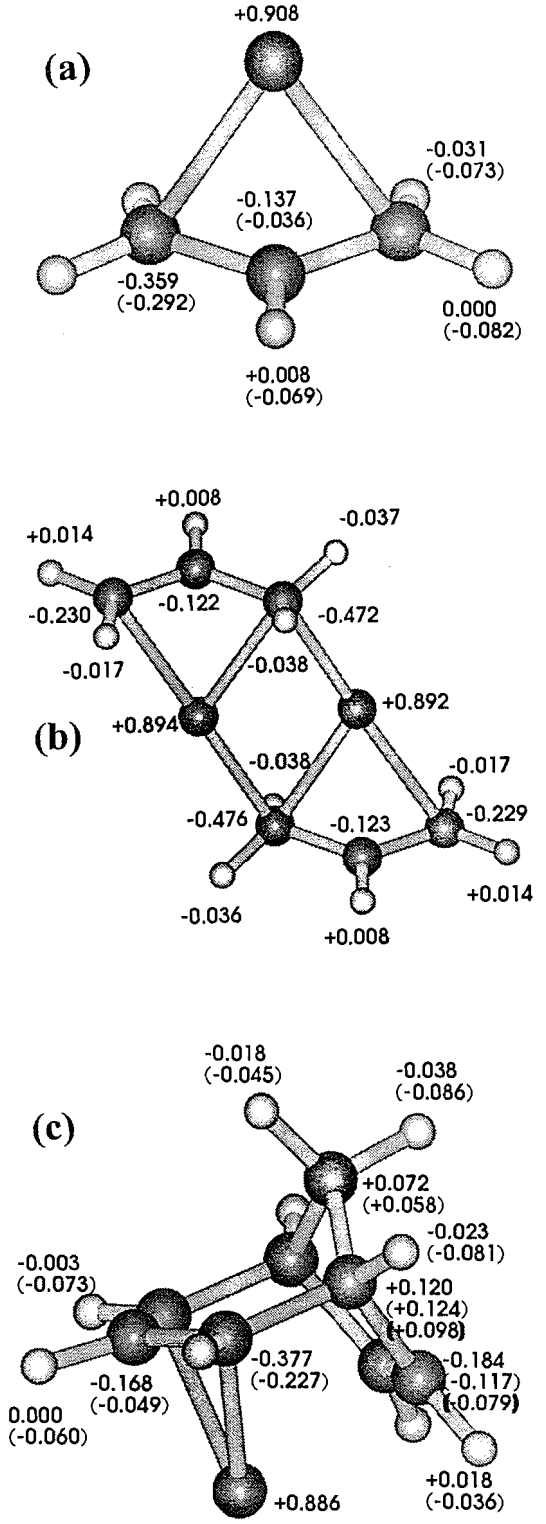

carbons of the vinylene bridge, C6 and C7, also gain electrons (0.067 au) when **8** is converted into **9** (see Fig. 4(*c*)). These carbons also gain 0.046 and 0.038 electrons, respectively, when the parent diene **1** (the value for C7 of **1** is shown in square brackets) is converted into **8**. Overall, carbons C6 and C7 of **1** gain 0.113 and 0.105 electrons, respectively, when **1** is converted into **9**, predominately from the bridgehead carbons C1 and C5 and hydrogens H16 and H17 of the vinylene bridge. Also noteworthy is the fact that C2, C3, and C4 of the allylic unit of **9** bear virtually the same charges as the carbons

Fig. 5. Plot of theoretical versus experimental ^{13}C chemical shifts of **7** (○) and **9** (×).

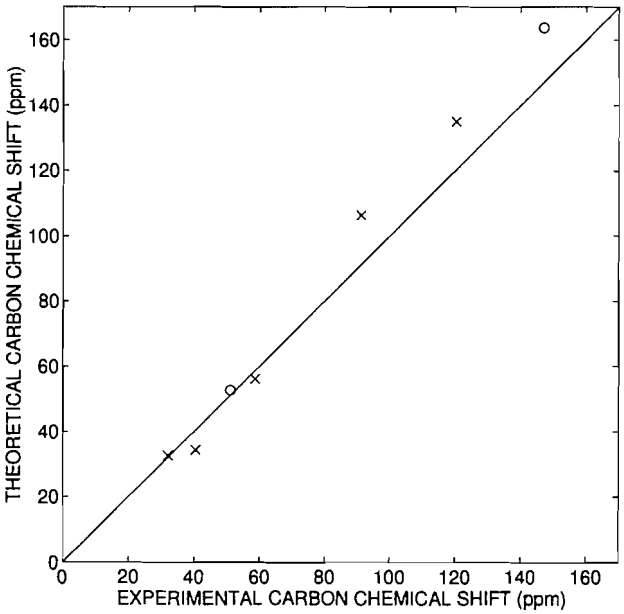

Fig. 6. Plot of theoretical versus experimental ^{1}H chemical shifts of **7** (○) and **9** (×).

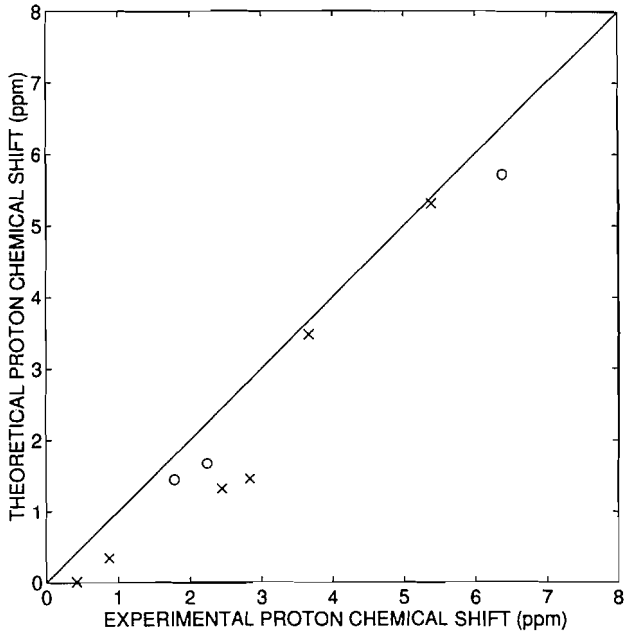

Table 5. Theoretical and experimental isotropic ^{1}H absolute shieldings (σ) and chemical shifts (δ).

Compound	Nucleus	IGAIM σ	IGAIM δ[a]	Expt. δ	Δδ expt. − IGAIM
	H4	28.78	0.17		
	H5	26.56	2.39		
5	H6	24.19	4.76		
	H7	28.78	0.17		
	H8	26.56	2.39		
	H4	27.73	2.32		
	H5	26.85	2.09		
6	H6	22.71	6.24		
	H7	27.73	1.21		
	H8	26.85	2.09		
	H7	28.54	1.67[b]	2.24[e]	0.57
	H8	28.48	1.43[c]	1.78	0.35
	H9	26.51	5.71[d]	6.38	0.67
	H10	26.10			
	H11	23.24			
7	H12	28.48			
	H13	26.51			
	H14	23.24			
	H15	28.52			
	H16	28.44			

[a]Referenced to the theoretical ^{1}H absolute shielding (σ) (28.95) of TMS calculated at the 6-31+G(d) basis.
[b]Average value of H8, H10, H12, and H16 of the static structure.
[c]Average value of H7, H9, H13, and H15 of the static structure.
[d]Average value of H11 and H14 of the static structure.
[e]At 298 K; ref. 24.

of the Li^+ complex **6** or the averaged charges of **7**, not what would be expected if **9** is bishomoaromatic. The theoretical ^{13}C chemical shifts of **8** and **9** along with the solution experimental values (26) for THF-solvated **9** are given in Table 6. The relationship (the correlation coefficient is 0.997) between the theoretical and experimental data for **7** and **9** is shown graphically in Fig. 5. As was found for the allyl anion, complexation with Li^+ results in an increase in the chemical shifts

Table 6. Theoretical and experimental isotropic ^{13}C absolute shieldings (σ) and chemical shifts (δ).

Compound	Nucleus	IGAIM σ	IGAIM δ^a	Expt. δ	$\Delta\delta$ expt. – IGAIM
8	C1	163.6	39.7		
	C2	150.6	52.6		
	C3	70.1	131.1		
	C4	150.6	52.6		
	C5	163.6	39.7		
	C6	97.4	105.9		
	C7	97.4	105.9		
	C8	164.7	38.5		
9	C1	169.0	34.3	40.5[b]	6.2
	C2	147.1	56.2	58.7	2.5
	C3	68.2	135.0	120.4	−14.6
	C4	147.1	56.2	58.7	2.5
	C5	169.0	34.3	40.5	6.2
	C6	96.9	106.3	91.3	−15.0
	C7	96.9	106.3	91.3	−15.0
	C8	170.7	32.5	32.0	−0.5

[a]In ppm units; referenced to theoretical ^{13}C absolute shielding (σ) (203.2) of TMS calculated at the 6-31+G(d) basis. The experimental absolute shielding is 188.1 (33).
[b]Reference 26.

Table 7. Theoretical and experimental isotropic ^{1}H absolute shieldings (σ) and chemical shifts (δ).

Compound	Nucleus	IGAIM σ	IGAIM δ^a	Expt. δ	$\Delta\delta$ expt. – IGAIM
8	H9	28.27	0.68		
	H10	28.85	0.10		
	H11	27.83	1.12		
	H12	27.83	1.12		
	H13	27.67	1.28		
	H14	24.26	4.69		
	H15	27.67	1.28		
	H16	26.10	2.85		
	H17	26.10	2.85		
9	H9	28.94	0.01	0.42[b]	0.41
	H10	28.61	0.34	0.87	0.53
	H11	27.63	1.32	2.45	1.13
	H12	27.63	1.32	2.45	1.13
	H13	27.48	1.46	2.84	1.38
	H14	23.64	5.31	5.39	0.08
	H15	27.48	1.46	2.84	1.38
	H16	25.46	3.48	3.67	0.19
	H17	25.46	3.48	3.67	0.19

[a]In ppm units; referenced to the theoretical ^{1}H absolute shielding (σ) (28.95) of TMS calculated at the 6-31+G(d) basis.
[b]Reference 3.

of the methylene carbons C2 and C4. The theoretical chemical shifts of the bridgehead carbons C1 and C5 change only marginally even though the electron populations of these carbons decrease in going from **1** to **9**. The 9.6 ppm decrease in chemical shift of C8 found experimentally in going from **1** to THF-solvated **9** is accurately reproduced by the IGAIM calculations. The greatest differences between the calculated values for **9** and experimental values for THF-solvated **9** are found for C6 and C7 of the vinylene bridge and C3 of the allylic unit (Table 6). The calculated chemical shifts of C6 and C7 — they are not sufficiently shielded — are too large by 15.0 and 14.6 ppm, respectively (Table 6). Even so, the calculated increases in the shieldings of C6 and C7 of **1** in going to **9** are 28.8 and 39.4 ppm, respectively, in reasonable agreement with the increases (37.9 and 49.6 ppm) found experimentally when **1** is converted into THF-solvated **9**. Given the fact that there is no clear correlation between the changes in electron populations of C1, C3, C5, and C8 and the variations in the ^{13}C chemical

shifts when **1** is converted into **9**, it is unlikely that the increases in electron populations of C6 and C7 are the major source of the increase in shielding experienced by these carbons.

The theoretical ^{1}H chemical shifts of **8** and **9** along with the experimental values for the THF-solvated **9** are given in Table 7 and displayed graphically in Fig. 6. The correlation coefficient of the data for **7** and **9** is 0.979. It is seen that the relative chemical shifts are in accord with the experimental values although the differences between the two sets of data range between 0.08 and 1.38 ppm. The shielding of H16 (1.07 ppm) and H17 (1.52 ppm) found calculationally in going from **1** (the atom charges of H16 and H17 are 0.022 and 0.027 au) to **9** (the atom charges of H16 and H17 are 0.018 au) is in keeping with the experimental findings that H16 and H17 are shielded by 1.98 and 2.51 ppm, respectively, when **1** is converted into THF-solvated **9**. It is also of interest to note that the relative chemical shifts of H9 and H10 only correlate with the experimental data when **8** is converted into its Li^+ complex **9**, showing that Li^+ exhibits a long-range effect when complexed with **8**.

Conclusions

IGAIM calculations at the 6-31+G(d) level of theory give ^{13}C and ^{1}H chemical shifts of unsaturated hydrocarbons — including benzene, the archtypical aromatic system — and unsaturated organolithium compounds that correlate well with experimental data. This result suggests that the IGAIM method will be generally useful for calculating magnetic response properties of these classes of compounds with the 6-31+G(d) basis. Changes in theoretical chemical shieldings do not correlate with variations in electron populations.

Acknowledgement

Financial support by the Natural Sciences and Engineering Council of Canada is gratefully acknowledged.

References

1. J.M. Brown and J.L. Occolowitz. J. Chem. Soc. Chem. Commun. 376 (1965).
2. J.M. Brown. J. Chem. Soc. Chem. Commun. 638 (1967).
3. S. Winstein, M. Ogliaruso, M. Sakai, and J.M. Nicholson. J. Am. Chem. Soc. **89**, 3656 (1967).
4. J.B. Grutzner and W.L. Jorgensen. J. Am. Chem. Soc. **103**, 1372 (1981).
5. E. Kaufmann, H. Mayr, J. Chandrasekhar, and P.v.R. Schleyer. J. Am. Chem. Soc. **103**, 1375 (1981).
6. J.M. Brown, R.J. Elliott, and W.G. Richards. J. Chem. Soc. Perkin Trans. 2, 485 (1982).
7. R. Lindh, B.O. Roos, G. Jonsall, and P. Ahlberg. J. Am. Chem. Soc. **108**, 6554 (1986).
8. T.A. Keith and R.F.W. Bader. Chem. Phys. Lett. **194**, 1 (1992).
9. D.B. Chestnut. Annu. Rep. NMR Spectrosc. **21**, 51 (1989).
10. K. Ruud, H. Skaane, T. Helgaker, K.L. Bak, and P. Jørgensen. J. Am. Chem. Soc. **116**, 10135 (1994).
11. F.W. Biegler-Konig, R.F.W. Bader, and T.-H. Tang. J. Comput. Chem. **317**, 13 (1982).
12. R.F.W. Bader and T.A. Keith. J. Chem. Phys. **99**, 3683 (1993).
13. M.J. Frisch, M. Head-Gordon, G.W. Trucks, J.B. Foresman, H.B. Schlegel, K. Raghavachari, M.A. Robb, J.S. Binkley, C. Gonzalez, D.J. De Frees, D.J. Fox, K.A. Whiteside, R. Seeger, G.F. Melius, J. Baker, R.L. Martin, L.R. Kahn, J.J.P. Stewart, S. Topiol, and J.A. Pople. Gaussian 92. Gaussian, Inc., Pittsburgh, Pa. 1992.
14. R.D. Amos and J.E. Rice. CADPAC: the Cambridge Analytic Derivatives Package, Cambridge, U.K.
15. C.W. Kirby, M.D. Lumsden, and R.E. Wasylishen. Can. J. Chem. **73**, 604 (1995).
16. G. Wu, M.D. Lumsden, G.C. Ossenkamp, K. Eichele, and R.E. Wasylishen. J. Chem. Phys. **99**, 15806 (1995).
17. W. Kutzelnigg, U. Fleischer, and M. Schindler. NMR, **23**, 105 (1990).
18. W. Kutzelnigg, C. van Willen, U. Fleischer, R. Franke, and T. van Mourik. NATO ASI Ser., Ser. C: **386**, 141 (1993).
19. A.J. Jones, D.M. Grant, J.G. Russell, and G. Fraenkel. J. Phys. Chem. **73**, 1624 (1969).
20. J.P.C.M. van Dongen, H.W.D. van Dijkman, and M.J.A. de Bie. Recl. Trav. Chim. Pays-Bas, **93**, 29 (1974).
21. W.R. Winchester, W. Bauer, and P.v.R. Schleyer. J. Chem. Soc. Chem. Commun. 178 (1987).
22. N.J.R.v.E. Hommes, M. Bhhl, P.v.R. Schleyer, and Y-D. Wu. J. Organomet. Chem. **409**, 307 (1991).
23. M. Bühl, N.J.R.v.E. Hommes, P.v.R. Schleyer, U. Fleischer, and W. Kutzelnigg. J. Am. Chem. Soc. **113**, 2459 (1991).
24. P. West, J.I. Purmort, and S.V. McKinley. J. Am. Chem. Soc. **90**, 797 (1968).
25. N. Hertkorn, F.H. Köhler, G. Müller, and G. Reber. Angew. Chem. Int. Ed. Engl. **5**, 25 (1986).
26. M. Christl, H. Leininger, and D. Brückner. J. Am. Chem. Soc. **109**, 4843 (1983).
27. F.H. Köhler and N. Hertkorn. Chem. Ber. **116**, 3274 (1983).
28. J.B. Stothers, J.R. Swenson, and C.T. Tan. Can. J. Chem. **53**, 581 (1975).
29. R. Bicker, H. Kessler, and G. Zimmerman. Chem. Ber. **111**, 3200 (1978).
30. R.M. Silverstein, G.C. Bassler, and T.C. Morrill. Spectrometric identification of organic compounds. 4th ed. Wiley, New York. 1988.
31. C.T. Pouchert. The Aldrich Library of NMR Spectra. 1, 57.
32. C.T. Pouchert. The Aldrich Library of NMR Spectra. 1, 733.
33. A.K. Jameson and C.J. Jameson. Chem. Phys. Lett. **134**, 461 (1987).

Some results on the electrostatic energy of ionic crystals

Hanno Essén and Arne Nordmark

Abstract: We define a class of ionic cyrstals, the alternating Bravais lattice ionic crystals, which has the NaCl and CsCl structures as members. We calculate the electrostatic energy of finite pieces and study the convergence to the macroscopic Madelung limit. For the one-parameter family of trigonal lattices we calculate the dependence of the electrostatic energy on the parameter. The NaCl and CsCl structures correspond to minima, the CsCl minimum being deeper. This is due to long-range effects; for small clusters the NaCl structure is favored. We also study the Madelung constant of simple cubic lattices as a function of spatial dimension, and discuss the results. We finally calculate the electrostatic repulsion of two constant unit charge distributions in the unit cube. This quantity, a six-dimensional integral, can be integrated analytically five times, leaving a simple one-dimensional integral to be done numerically.

Key words: ionic crystal, Madelung constant, ionic cluster, electrostatic energy.

Résumé : On définit une classe de cristaux ioniques, les cristaux ioniques de maille de Bravais alternante, dont font partie le NaCl et le CsCl. On a calculé l'énergie électrostatique de piéces finies et on a étudié la convergence vers la limite macroscopique de Madelung. Pour la famille à un paramétre des mailles trigonales, on a calculé la dépendance de l'énergie électrostatique sur le paramètre. Les structures du NaCl et du CsCl correspondent à des minima, celui du CsCl étant plus profond. Ceci est le résultat d'effets à longue distance; pour de petits agrégats, la structure du NaCl est celle qui est favorisée. On a aussi étudié la constante de Madelung de mailles cubiques simples en fonction de la dimension spatiale et on discute des résultats. On a finalement calculé la répulsion électrostatique des distributions unitaires de charge à deux constantes dans unité de cube. Cette quantité, une intégrale à six dimensions, peut être intégrée analytiquement cinq fois; on obtient une intégrale simple unidimensionnelle à être intégrée d'une façon numérique.

Mots clés : cristal ionique, constante de Madelung, agrégat ionique, énergie électrostatique.

[Traduit par la rédaction]

1. Introduction

The subject of the electrostatic energy of ionic crystals is an old one and much work has followed the pioneering efforts by Madelung (1). This paper is partly didactic and attempts to clarify known results, and partly presents results that we believe to be new.

Most of the work on these problems, including the present, uses the assumption that the ions can be treated as point charges. This is valid provided they are non-overlapping spherical charge distributions. It was not really until the pioneering work by Richard Bader that these assumptions were put on a sound theoretical basis (2). Bader's work shows that one can rigorously partition molecules and crystals into atoms and find the shape and charge of these.

We start by defining a class of ionic crystals, the alternating Bravais lattice (ABL) ionic crystals. It includes two of the most common types of such crystals, the NaCl and CsCl structures. For this class we are able to give some explicit formulas for the electrostatic energy, some of which we believe to be new. We study how the electrostatic energy (per molecule) of finite clusters converges to a macroscopic limit. We suggest an efficient numerical method to calculate the Madelung constants of this class. We then calculate this constant as a function of the parameter of the one-parameter family of orthorhombic (trigonal) lattices. This function throws some light on the interrelation between the NaCl and CsCl structures. We find that for small clusters the NaCl structure is energetically favored while CsCl has the largest Madelung constant and thus has lower energy in the macroscopic limit.

We also consider the dependence on the spatial dimension of the energy of small ionic clusters and of the Madelung constant. We find that, for the simple cubic case, these grow monotonically with dimension n, but eventually very slowly. Finally we calculate a related quantity of physical interest: the electrostatic interaction energy of constant charge distributions in a cube.

Received June 27, 1995.

This paper is dedicated to Professor Richard F.W. Bader on the occasion of his 65th birthday.

H. Essén[1] and A. Nordmark. Department of Mechanics, Royal Institute of Technology, S-100 44 Stockholm, Sweden.

[1] Author to whom correspondence may be addressed. Telephone: 46-8-790-8759. Fax: 46-8-796-9850. E-mail: hanno@mech.kth.se

2. Alternating Bravais lattice ionic crystals

Consider a Bravais lattice with basis vectors $\boldsymbol{a}_1$, $\boldsymbol{a}_2$, $\boldsymbol{a}_3$. We call a crystal an *alternating Bravais lattice* (ABL) *ionic crystal* when there is an ion of charge

$$[1] \qquad q(i, j, k) = (-1)^{i+j+k}$$

at

$$\boldsymbol{r}(i, j, k) = i\boldsymbol{a}_1 + j\boldsymbol{a}_2 + k\boldsymbol{a}_3$$

The meaning of this definition is that as one goes along a line defined by a lattice basis vector the charges alternate in sign. That is, along the line $\boldsymbol{r}(\lambda) = \lambda\boldsymbol{a}_1 + j_0\boldsymbol{a}_2 + k_0\boldsymbol{a}_3$ there are charges $q(i) = q_0(-1)^i$ at integer values, $\lambda = i$, of the parameter.

It should be immediately clear that the NaCl crystal is an example of an ABL ionic crystal. With lattice basis vectors of the simple cubic (sc) lattice,

[2] $$\boldsymbol{a}_1 = \boldsymbol{e}_1 \equiv (1, 0, 0),\ \boldsymbol{a}_2 = \boldsymbol{e}_2 \equiv (0, 1, 0),$$

$$\boldsymbol{a}_3 = \boldsymbol{e}_3 \equiv (0, 0, 1)$$

the NaCl structure is obtained. It is only a little less obvious that the CsCl crystal also can be obtained. The lattice basis vectors of the body-centered cubic (bcc) lattice,

[3] $$\boldsymbol{a}_1 = \frac{1}{\sqrt{3}}(-1, 1, 1),\ \boldsymbol{a}_2 = \frac{1}{\sqrt{3}}(1, -1, 1),$$

$$\boldsymbol{a}_1 = \frac{1}{\sqrt{3}}(1, 1, -1)$$

are then the appropriate ones. Since there is a continuous transformation between these two sets of lattice basis vectors, and indeed between any two sets of lattice basis vectors, one may regard all ABL ionic crystals as, in a sense, topologically equivalent. In particular, one can take a unified view of the two standard structures (NaCl and CsCl) and study transformations between them. The zinc blende structure is not in the ABL class.

3. Electrostatic energy

The electrostatic (Coulomb) interaction energy of N^3 ions of charge $q(i,j,k)$ at positions $\boldsymbol{r}(i,j,k)$ is

[4] $$\Phi_N = \frac{1}{2}\sum_{ijk=1}^{N}{\sum_{lmn=1}^{N}}' \frac{q(i, j, k)q(l, m, n)}{|\boldsymbol{r}(i, j, k) - \boldsymbol{r}(l, m, n)|}$$

The prime on the sum means that the terms with zero denominator are excluded. If we have an ABL arrangement of the ions we can use eq. [1] and get

[5] $$\Phi_N(\boldsymbol{a}_1, \boldsymbol{a}_2, \boldsymbol{a}_3) = \frac{1}{2}\sum_{ijk=1}^{N}{\sum_{lmn=1}^{N}}' \times \frac{(-1)^{i+j+k+l+m+n}}{|(i-1)\boldsymbol{a}_1 + (j-m)\boldsymbol{a}_2 + (k-n)\boldsymbol{a}_3|}$$

for the total electrostatic energy. In the macroscopic limit when N becomes large this quantity will go to minus infinity. If we divide it by the number of (neutral) molecules, $N^3/2$, we get the electrostatic energy per molecule in the form

[6] $$\phi_N(\boldsymbol{a}_1, \boldsymbol{a}_2, \boldsymbol{a}_3) = \frac{2}{N^3}\Phi_N(\boldsymbol{a}_1, \boldsymbol{a}_2, \boldsymbol{a}_3)$$

and this should have a finite macroscopic limit

[7] $$\phi = \lim_{N\to\infty} \phi_N$$

Note that N should be even if the macroscopic piece is to be neutral; otherwise it has charge minus one, but this does not affect convergence.

The sum in eq. [5] is a six-dimensional sum. It is seen, however, to depend essentially only on differences between summation indices. If we put

[8] $$I = i - l,\ J = j - m,\ K = k - n$$

some calculation shows that the energy per molecule can be rewritten

[9] $$\phi_N = \frac{1}{N^3}\sum_{IJK=-(N-1)}^{(N-1)}{}' \times \frac{(-1)^{I+J+K}(N - |I|)(N - |J|)(N - |K|)}{|I\boldsymbol{a}_1 + J\boldsymbol{a}_2 + K\boldsymbol{a}_3|}$$

The full interaction energy can thus be written as this three-dimensional sum (over $(2N-1)^3 - 1$ terms). The total charge of the ions summed over, including the positive one in the middle, is -1 for even N and $+1$ for odd. The transformation of the summation indices done here is analogous to the transformation to center-of-mass and relative coordinates that is well known from the two-body problem (compare Sect. 9, especially formula [44]).

4. Relation to the Madelung constant

In ionic crystals one usually estimates the energy of an ion in the crystal by means of the Madelung (1) constant. This constant is thus the sum of all electrostatic interaction energies of the ion with all the other ions of the crystal. There is a large literature on the calculation of Madelung constants. For a review see Tosi (3). Johnson and Templeton (4) give the values of this constant for many structures. For modern methods of calculation see Christiansen et al. (5). For a careful investigation of the mathematics of lattice sums in general, see Glasser and Zucker (6).

The general conclusion is that calculation of Madelung constants is a difficult problem. Slow convergence and dependence on order of summation are a few of the problems (Borwein et al. (7)). It is of special importance to avoid summing in such a way that there is a dipole moment (Smith (8)) and to sum over neutral chunks. With ABL crystals these problems can be handled in a unified and natural way. The sum should simply be over a parallelepiped with edges parallel to the lattice basis vectors $(\boldsymbol{a}_1, \boldsymbol{a}_2, \boldsymbol{a}_3)$ placed symmetrically around the central ion. Such a sum can be written

[10] $$\alpha_M = -\sum_{ijk=-M}^{M}{}' \frac{(-1)^{i+j+k}}{|i\boldsymbol{a}_1 + j\boldsymbol{a}_2 + k\boldsymbol{a}_3|}$$

and the macroscopic limit of these sums,

[11] $$\alpha = \lim_{M\to\infty} \alpha_M$$

Table 1. This table illustrates the slow convergence of ϕ_N and α_N to the two traditional Madelung constants for the NaCl and CsCl structures.

N	$-\phi_N$(NaCl)	$-\phi_N$(CsCl)	α_{N-1}(CsCl)
2	1.456 029 925 6300	1.424 077 966 6800	2.263 010 770 3212
4	1.628 723 191 4176	1.603 719 655 2523	1.947 351 124 0847
8	1.693 917 644 6892	1.683 696 940 0257	1.848 352 785 3331
16	1.721 993 913 6163	1.722 980 563 5781	1.804 086 719 3739
32	1.735 064 935 0971	1.742 731 582 3887	1.783 047 012 0754
64	1.741 382 517 4569	1.752 673 339 8033	1.772 780 083 5976
128	1.744 490 021 4990	1.757 665 856 0027	1.767 707 540 3185
256	1.746 031 364 4517	1.760 168 170 9412	1.765 186 223 1587
512	1.746 798 986 0756	1.761 420 924 3686	1.763 929 269 4904
Extrapolated	1.747 564 60	1.762 674 78	1.762 674 78

is thus the Madelung constant α. Usually it is assumed that the nearest neighbor distance, R_n, is 1 and we will adopt this convention.

The sequence $\alpha_M (M = 2, 3, \ldots)$ converges monotonically to the appropriate Madelung constant. For the NaCl structure this sum is over cubic "shells" and for CsCl is it over the corresponding rhombohedral "shells." When Madelung constants are looked at from the conventional point of view these two crystals appear very different (8).

It is interesting to note that for $M = N - 1$ the two sums [9] and [10] go over the corresponding terms and that, in fact,

$$[12] \qquad \phi_N = -\alpha_{N-1} + \text{"surface terms"}$$

Here "surface terms" represent sums in which increased weight is given to terms near the surface of the parallelepiped. As N grows larger the relative importance of these decreases and the two sequences have the same limits (apart from sign):

$$[13] \qquad \phi = -\alpha$$

This is a natural result that normally has been taken for granted, but we have checked it numerically and it holds. For an example see Table 1. Since the sum [10] is simpler than [9], this result can be used to speed up calculation of ϕ. On the other hand, while the sequences ϕ_N give a measure of the energy of finite (parallelepipedal) clusters of $N^3/2$ molecules, the unconverged Madelung sums α_M are of no particular physical significance.

5. Numerical considerations

Nowadays it is easy to try plug formula [9] or [10] into a computer to find the relevant limit. The convergence is, however, quite slow. This has physical reasons. Convergence means that the surface terms of eq. [12] become negligible. But volume varies as N^3 and surface area like $8N^2$, so N must, of course, be quite large before $8N^2$, and corresponding physical surface effects, can be neglected in comparison with N^3.

Ewald (9) developed analytic methods for speeding up the convergence and many methods have been suggested since then. We have used a method for convergence improvement introduced by Shanks (10), as reported by Levin (11). This method extrapolates a sequence ϕ_N to the limit ϕ by making certain assumptions about the analytical behavior of the terms. We found that it gives values for Madelung constants, accurate to four digits, cheaply and with very little programming. A little extra effort is needed to find the following, nine-digit-accurate, values for the usual Madelung constants

$$[14] \qquad \alpha(\text{NaCl}) = 1.747\,564\,60$$

$$[15] \qquad \alpha(\text{CsCl}) = 1.762\,674\,78$$

Here there is an uncertainty of one in the last digit. The convergence can be studied in Table 1.

For the simple cubic NaCl structure one can find a much faster and more accurate path to the Madelung constant based on analytical formulae of Borwein et al. (7). This is discussed in Sect. 8. At present, however, these do not extend to non-cubic lattices.

The ϕ_N values of Table 1 show that, for small N (up to ~16, or 2048 molecules) the NaCl structure is energetically favored compared to the CsCl structure, while for higher N the opposite is true. This physically relevant fact cannot be obtained from the corresponding Madelung sequences; the α_N for CsCl are larger than those for NaCl for all N.

6. A one-parameter lattice family

To compare different lattices in a reliable way one should find a continuous path between them. We thus study the one-parameter family of trigonal (rhombohedral) lattices that have the lattices [2] and [3] as members. Hoppe (12) was the first to do this; we do it in a somewhat different way that follows naturally from the ABL concept.

We first put

$$[16] \qquad \boldsymbol{\varepsilon}_1 = \boldsymbol{e}_1,\ \boldsymbol{\varepsilon}_2 = \frac{1}{2}(-1, \sqrt{3}, 0),\ \boldsymbol{\varepsilon}_3 = \frac{1}{2}(-1, -\sqrt{3}, 0)$$

for three unit vectors 120° apart in the xy-plane, so that $\boldsymbol{\varepsilon}_i \cdot \boldsymbol{\varepsilon}_j = -1/2$, $(i \neq j)$. We can now define the family of lattice (unit length) basis vectors

$$[17] \qquad \boldsymbol{a}_1(\theta) = \sqrt{2/3}(\sqrt{1 - \cos\theta}\,\boldsymbol{\varepsilon}_i + \sqrt{1/2 + \cos\theta}\,\boldsymbol{e}_3), \qquad i = 1, 2, 3$$

Table 2. This table illustrates some properties of the one-parameter family of trigonal lattices for different values of the parameter θ.

θ(deg)	cos θ	$V(\theta)$	$R_n(\theta)$	$\alpha(\theta)$	Lattice type	Crystal
0	1	0	0	$-\infty$?	Half-line	—
15	0.966	0.058	0.261	−9.527	—	—
45	0.707	0.455	0.765	−0.0396	—	—
60	1/2	0.707	1	1.2357	fcc	—
75	0.259	0.913	1	1.6532	—	—
90	0	1	1	1.7476	sc	NaCl
104	−0.242	0.893	1	1.7182	—	—
109.47	−1/3	0.770	1	1.7627	bcc	CsCl
115	−0.423	0.559	0.681	1.4601	—	—
120	−1/2	0	0	1.3863	Plane	—

depending on the parameter θ. They are all of length one, $|\boldsymbol{a}_i(\theta)| = 1$, and all make the same angle θ

$$[18] \qquad \boldsymbol{a}_i(\theta)\cdot\boldsymbol{a}_j(\theta) = \cos\theta \quad (i \neq j)$$

with one another. The volume of the parallelepiped spanned by these vectors is given by

$$[19] \qquad V(\theta) = \boldsymbol{a}_1\cdot(\boldsymbol{a}_2 \times \boldsymbol{a}_3) = (1 - \cos\theta)\sqrt{1 + 2\cos\theta}$$

and the surface area is $A(\theta) = 8|\boldsymbol{a}_1 \times \boldsymbol{a}_2| = 8 \sin\theta$.

Since we are interested in the nearest neighbor normalized Madelung constants we also note that the nearest neighbor distance in this lattice family is given by

$$[20] \qquad R_n(\theta) = \begin{cases} \sqrt{2 - 2\cos\theta} & \text{for } 0 < \theta < 60° \\ 1 & \text{for } 60° \leq \theta \leq 109°.47 \\ \sqrt{3 + 6\cos\theta} & \text{for } 109°.47 < \theta < 120° \end{cases}$$

Thus $R_n = 1$ for all angles between 60° and 109°.47 (the "tetrahedral angle"), since for these values the nearest neighbor is along a lattice vector $\boldsymbol{a}_i$. The new nearest neighbor that appears below θ = 60° is one of the same charge. At θ = 109°.47, which corresponds to the CsCl structure, the new nearest neighbor is of opposite charge. Some relevant values of θ and the corresponding lattices are listed in Table 2.

7. Energy of orthorhombic ABL crystals

Let $\phi_N(\boldsymbol{a}_1, \boldsymbol{a}_2, \boldsymbol{a}_3)$ be defined by eq. [9]. By means of the lattice family of the previous section we now define

$$[21] \qquad \phi_N(\theta) \equiv R_n(\theta) \cdot \phi_N(\boldsymbol{a}_1(\theta), \boldsymbol{a}_2(\theta), \boldsymbol{a}_3(\theta))$$

Here we have introduced a nearest neighbor normalization so that

$$[22] \qquad \lim_{N\to\infty} \phi_N(\theta) = \phi(\theta) = -\alpha(\theta)$$

is the (negative) nearest neighbor normalized Madelung constant. The physical model underlying the nearest neighbor normalization is that of hard sphere (billiard ball) ions. For such a model system the electrostatic potential energy is the full potential energy.

Fig. 1. Plot of the function φ(θ). The two minima correspond to the NaCl structure (at θ = 90°) and the CsCl structure (at θ = 109°.47). These minima clearly have different characters.

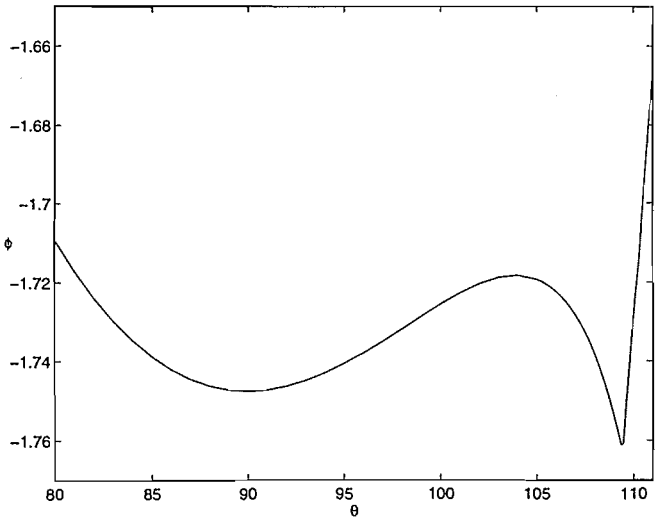

The function $\phi_2(\theta)$, which represents the electrostatic energy of four molecules (8 ions), can be calculated explicitly and is given by

$$[23] \qquad \phi_2(\theta) = -R_n(\theta)\frac{3}{2}\left(2 - \frac{1}{\sqrt{2 + 2\cos\theta}} - \frac{1}{\sqrt{2 - 2\cos\theta}} + \frac{1}{2\sqrt{3 - 2\cos\theta}} + \frac{1}{6\sqrt{3 + 6\cos\theta}}\right)$$

This function has a global minimum at θ = 90° where its value is −1.456. It has a shallow local minimum at θ = 109°.47 where it is −1.424. Between these two minima there is a local maximum at θ = 109°.27; the value of the function at this point is only 2×10^{-5} higher than at θ = 109°.47 (the calculations were done using Maple (13)). In practice this means that the NaCl structure is the only stable structure for this system. As we saw in Table 1 the NaCl structure is predicted to be the electrostatically most stable up to $N \approx 16$.

In Fig. 1 we have plotted the function φ(θ) near its relevant minima. It shows a local minimum at θ = 90°, corresponding

to the NaCl structure. There is a local maximum at roughly $\theta = 104°$ which is 0.0455 higher than the global minimum at $\theta = 109°.47$, the CsCl structure. We see that the two minima are very different. The CsCl minimum is very narrow and sharp. Its shape is determined by the fact that a new nearest neighbor appears at this angle; if it were not for the nearest neighbor normalization the function would go down to minus infinity towards $\theta = 120°$. Our results agree with those of Hoppe (12) who calculated the same curve using a different, but equivalent, parameter.

It has been known for a long time that substances that have the NaCl structure can go into the CsCl structure when pressure is applied. Conversely, CsCl changes into the NaCl structure at high temperatures (see Tosi (3) or Pauling (14) and references therein). The curve in Fig. 1 gives some feeling for the electrostatics going on in these transitions.

8. The electrostatic energy of simple cubic ABL clusters and crystals as a function of dimension

It is of some interest to note that one can easily generalize the concept of ABL ionic crystals from spatial dimension three to any (integer) spatial dimension. Here, of course, only dimensions one and two of direct physical interest, but higher dimensions may be of interest to illustrate the general trend.

In this section we will limit ourselves to the simple cubic case, so formula [9] becomes

$$[24] \qquad \phi_N = \frac{1}{N^3} {\sum_{IJK=-(N-1)}^{(N-1)}}' \times \frac{(-1)^{I+J+K}(N-|I|)(N-|J|)(N-|K|)}{\sqrt{I^2+J^2+K^2}}$$

If now consider only the smallest, $N = 2$, cluster (or molecule), the generalization of this formula to arbitrary dimension n is

$$[25] \qquad \phi_2(n) = F(n,0) = \frac{1}{2^n} {\sum_{i_1=-1}^{1}} \cdots {\sum_{i_n=-1}^{1}}' \times \frac{(-1)^{\sum_{k=1}^n i_k} \prod_{k=1}^n (2-|i_k|)}{\sqrt{\sum_{k=1}^n i_k^2}}$$

The direct calculation of this quantity by means of nested summation loops rapidly becomes unwiedly as n increases. We shall calculate it by means of a recursion method.

We start by defining

$$[26] \qquad F(n,j) = \frac{1}{2^n} {\sum_{i_1=-1}^{1}} \cdots {\sum_{i_n=-1}^{1}} \times \frac{(-1)^{\sum_{k=1}^n i_k} \prod_{k=1}^n (2-|i_k|)}{\sqrt{\sum_{k=1}^n i_k^2 + j}}$$

for $n, j > 0$. We also define

$$[27] \qquad F(0,0) = 0 \quad \text{and} \quad F(0,j) = \frac{1}{\sqrt{j}}$$

Table 3. This table lists the electrostatic energies, $\phi_2(n)$, of neutral ionic hypercubic molecules of dimension n and the Madelung constants $\alpha(n)$ of simple cubic ABL crystals. The spatial dimensions n = 1–6, n = 10, 50, and 100 are given and the results are accurate to 14 digits.

n	$-\phi_2(n)$	$\alpha(n)$
1	1.000 000 000 000 00	1.381 971 451 866 13
2	1.292 893 218 813 45	1.615 542 626 712 83
3	1.456 029 925 629 98	1.747 564 594 633 18
4	1.566 760 389 639 21	1.839 399 084 045 05
5	1.649 648 475 530 74	1.909 337 815 618 77
6	1.715 436 948 530 18	1.965 557 039 009 08
⋮	⋮	⋮
10	1.890 851 969 665 06	2.118 310 501 384 82
50	2.371 200 612 411 97	2.553 231 760 698 21
100	2.551 846 198 763 93	2.721 232 274 628 21

and then find the recursive relation

$$[28] \qquad F(n,j) = F(n-1,j) - F(n-1,j+1), \; n > 0, \; j \geq 0$$

for these sums. The quantities of interest, $F(n,0)$, can then easily be generated. They will correspond to the electrostatic energy of neutral hypercubic ionic molecules of dimension n. Some results are given in Table 3.

The Madelung constant for a simple cubic ABL crystal of dimension n can be defined as

$$[29] \qquad \alpha(n) = (-1)^n \lim_{M\to\infty} {\sum_{i_1=-M}^{M}} \cdots {\sum_{i_n=-M}^{M}}' \frac{(-1)^{i_1+\ldots+i_n}}{\sqrt{\sum_{k=1}^n i_k^2}}$$

(compare eq. [10]). Here the prime indicates that the term with $i_1 = i_2 = \ldots = i_n = 0$ is to be excluded. In the case $n = 1$ one obtains (Kittel (15))

$$[30] \qquad \alpha(1) = (-1) {\sum_{k=-\infty}^{\infty}}' \frac{(1-)^k}{k} = 2\sum_{k=1}^{\infty}(-1)^{k+1}\frac{1}{k} = 2\log 2 \approx 1.38197$$

but for higher dimensions there is no obvious analytic result. In direct numerical calculations the number of terms would be roughly $(2M)^n$ so a calculation would rapidly become very cumbersome for large n. Borwein et al. (7) have, however, using theta functions and the Mellin transform, derived the analytical expression

$$[31] \qquad \alpha(n) = \frac{1}{\sqrt{\pi}} \int_0^\infty \left\{ \left[\sum_{k=-\infty}^{\infty} (-1)^k \exp(-k^2 t) \right]^n - 1 \right\} \frac{dt}{\sqrt{t}}$$

for the simple cubic Madelung constant as a function of n. (It follows from eq. (28) in ref. 7.) This formula is easily programmed and gives the numerical results of Table 3.

The number of nearest neighbors with opposite charge increases by two for each dimension. It is thus not surprising that the Madelung constants increase with n, as we find. The increase, however, becomes smaller with each new dimen-

sion and, formula [31] can be used to show that the asymptotic behavior is given by

$$[32] \qquad \alpha(n) \asymp \frac{2}{\sqrt{\pi}}\sqrt{\log n}$$

For large n the increase is thus very slow. Table 3 shows that the difference between the Madelung constant and $-\phi_2(n)$ decreases with increasing n. This means that the lattice summation converges more rapidly in higher dimensions. Physically this seems natural as the field produced by a neutral hypercube must correspond roughly to a multipole field one order higher for each new dimension.

9. The interaction energy of two constant charge distributions in a cube

Consider the electrostatic energy of a system of $\mathcal{N}$ (positive) charged particles of charge q at $\boldsymbol{r}_i$. This electrostatic energy is

$$[33] \qquad \Phi = \sum_{i<j}^{\mathcal{N}} \frac{q^2}{r_{ij}}$$

Assume that the number $\mathcal{N}$ is large and that the particles are evenly distributed (randomly or in some ordered way) in a cubic region of side L. We can then estimate this energy using the continuum approximation, i.e., we assume that we are dealing with the self-interaction of a charge density $\rho = (\mathcal{N}q)/L^3$ (constant inside the cube and zero outside). We can thus write

$$[34] \qquad \Phi \approx \frac{1}{2} C_c \frac{(\mathcal{N}q)^2}{L}$$

where C_c is a dimensionless number that we now proceed to calculate. This number is of interest in the theory of ionic crystals but is also of interest in other areas of solid state theory (16).

Consider two electrons of charge e in a cubic box of side length L. Assume that both electrons have constant charge density

$$[35] \qquad \rho = e/L^3$$

in this box. The Coulomb, electrostatic, interaction energy of these charge distributions is then:

$$[36] \qquad \left[\int_{r_1 \in \Omega_L^1} \left(\int_{r_2 \in \Omega_L^2} \frac{dV_2}{|\boldsymbol{r}_1 - \boldsymbol{r}_2|} \right) dV_1 \right] \left(\frac{e}{L^3}\right)^2 \equiv C_c \frac{e^2}{L}$$

Here Ω_L^a $(a = 1,2)$ denote the cubic regions over which the integration variables, $\boldsymbol{r}_a = (x_a, y_a, z_a)$, take their values. We now introduce units so that $e = L = 1$. These regions are then

$$[37] \qquad \Omega^a = \{(x_a, y_a, z_a);$$

$$0 < x_a < 1,\ 0 < y_a < 1,\ 0 < z_a < 1\}, \qquad a = 1, 2$$

and the energy can simply be expressed as

$$[38] \qquad C_c = \int_{\Omega^1} \int_{\Omega^2} \frac{dV_1 dV_2}{|\boldsymbol{r}_1 - \boldsymbol{r}_2|}$$

or, alternatively, in the form

$$[39] \qquad C_c = \int_0^1 \int_0^1 \int_0^1 \int_0^1 \int_0^1 \int_0^1 \times \frac{dx_1 dy_1 dz_1 dx_2 dy_2 dz_2}{\sqrt{(x_1 - x_2)^2 + (y_1 - y_2)^2 + (z_1 - z_2)^2}}$$

which shows explicitly that this is a six-dimensional integral.

To calculate this integral we first transform to center-of-mass and relative coordinates for the two "electrons":

$$[40] \qquad \boldsymbol{r} = \boldsymbol{r}_1 - \boldsymbol{r}_2$$

$$[41] \qquad \boldsymbol{R} = \frac{1}{2}(\boldsymbol{r}_1 + \boldsymbol{r}_2)$$

For the x-components we then have explicitly

$$[42] \qquad x = x_1 - x_2, \qquad x_1 = X + \frac{1}{2}x$$

$$\Longleftrightarrow$$

$$[43] \qquad X = \frac{1}{2}(x_1 + x_2), \qquad x_2 = X - \frac{1}{2}x$$

and similarly for the y- and z-components. This transformation makes the three integrations over $\boldsymbol{R} = (X, Y, Z)$ trivial and the result is the three-dimensional integral

$$[44] \qquad C_c = \int_{-1}^1 dx \int_{-1}^1 dy \int_{-1}^1 dz \frac{(1 - |x|)(1 - |y|)(1 - |z|)}{\sqrt{x^2 + y^2 + z^2}}$$

(compare formula [9]). Because of symmetry this gives

$$[45] \qquad C_c = 8 \int_0^1 dx \int_0^1 dy \int_0^1 dz \frac{(1 - x)(1 - y)(1 - z)}{\sqrt{x^2 + y^2 + z^2}}$$

We now transform first to cylindrical coordinates

$$[46] \qquad x = \rho \cos\varphi, \qquad y = \rho \sin\varphi$$

Because of a further symmetry the integral now becomes

$$[47] \qquad C_c = 16 \int_0^{\pi/4} d\varphi \int_0^{1/\cos\varphi} \rho d\rho \int_0^1 dz \times \frac{(1 - \rho\cos\varphi)(1 - \rho\sin\varphi)(1 - z)}{\sqrt{\rho^2 + z^2}}$$

Finally we transform to spherical coordinates by means of the transformation

$$[48] \qquad z = r\cos\theta, \qquad \rho = r\sin\theta$$

We must now split the integration over θ into two integrals because of the corner at $z = 1$, corresponding to $\theta = \arctan(1/\cos\varphi)$. We thus get

$$[49] \qquad C_c = 16 \int_0^{\pi/4} d\varphi \times \left\{ \left[\int_0^{\arctan(1/\cos\varphi)} \sin\theta\, d\theta \int_0^{1/\cos\theta} r^2 dr + \int_{\arctan(1/\cos\varphi)}^{\pi/2} \sin\theta\, d\theta \int_0^{1/(\cos\varphi \sin\theta)} r^2 dr \right] \times \frac{(1 - r\sin\theta\cos\varphi)(1 - r\sin\theta\sin\varphi)(1 - r\cos\theta)}{r} \right\}$$

Here the r-integrations are trivial. The θ-integrations can be done analytically and we have used Maple (13) to do them. The result is

$$[50] \qquad C_c = 16 \int_0^{\pi/4} \Phi_c(\varphi) d\varphi$$

where the integrand is the function

$$\begin{aligned}[51] \qquad \Phi_c(\varphi) = \frac{1}{120}[&5\cos(\varphi)^5 \ln(\sqrt{\cos(\varphi)^2+1}+1) \\ &- 5\cos(\varphi)^5 \ln(\cos(\varphi)) + 4\cos(\varphi)^5 \sin(\varphi) \\ &- 4\cos(\varphi)^4 \sin(\varphi)\sqrt{\cos(\varphi)^2+1} \\ &- 5\cos(\varphi)^4 \sin(\varphi)\ln(\cos(\varphi)) \\ &+ 5\cos(\varphi)^4 \sin(\varphi)\ln(\sqrt{\cos(\varphi)^2+1}+1) \\ &- 20\cos(\varphi)^4 + 15\cos(\varphi)^3\sqrt{\cos(\varphi)^2+1} \\ &- 3\sin(\varphi)\sqrt{\cos(\varphi)^2+1}\cos(\varphi)^2 - 6\sin(\varphi) \\ &+ 10\cos(\varphi) + 6\sin(\varphi)\sqrt{\cos(\varphi)^2+1} \\ &- 20\ln(\sqrt{\cos(\varphi)^2+1} - \cos(\varphi))\cos(\varphi)^2 \\ &+ 10\sin(\varphi)\ln(\sqrt{\cos(\varphi)^2+1} - \cos(\varphi))\cos(\varphi) \\ &- 10\sqrt{\cos(\varphi)^2+1}\cos(\varphi)]/\cos(\varphi)^4 \end{aligned}$$

This formula is taken (almost) directly from Maple output; to get it one must use *simplify* with "*assume* $\cos(\varphi) > 0$."

The final φ-integration can not be done analytically by Maple, but it turns out that the function Φ_c is nearly constant (it varies with roughly 10%) over the interval 0–$\pi/4$. It is thus easy to get very accurate numerical results. Maple, with the default ten-digit accuracy, gives

$$[52] \qquad C_c = 1.882\,312\,645$$

and this is the desired constant. We have checked the calculation by using other, more straightforward, numerical methods.

10. Conclusions

Electrostatic interactions are at the root of many subtle and long-range effects in crystals and molecules. They indicate that it is physically difficult to regard the energy of some three-dimensional region as arising locally within that region. This is also connected with the lack of transferability of the Bader atoms (ions), a problem that was discussed by Bader and Becker (17) from a different point of view.

In this paper we have discussed various aspects of the electrostatic interaction energy. In particular we have studied the (macroscopic) Madelung constants for a class of ionic crystals, and the electrostatic interaction energies for finite clusters. One unusual aspect of our treatment is that we have shown that the electrostatic energy can be reduced to a simple sum over the crystal which differs from the Madelung sums by the presence of "surface terms." We also believe that some of our other results are either new or, at least, represent a novel way of viewing these problems.

Acknowledgments

This research has come about in the tolerant and open-minded climate of Prof. Martin Lesser's research group at the Department of Mechanics at KTH. This group has many similarities to Prof. Richard Bader's group where one of us (H.E.) spent two years as a post doc in 1981–1982. We would also like to thank one of the referees of the Canadian Journal of Chemistry for useful comments and references. These led to the discovery of an error in an earlier version of this manuscript.

References

1. E. Madelung. Phys. Z. **19**, 524 (1918).
2. R.F.W. Bader. (1994) Atoms in molecules, a quantum theory. Clarendon Press, Oxford. 1994. Sect. 6.4. p. 195.
3. M.P. Tosi. Solid State Phys. **16**, 1 (1964).
4. Q.C. Johnson and D.H. Templeton. J. Chem. Phys. **34**, 2004 (1961).
5. D. Christiansen, J.W. Perram, and H.G. Petersen. J. Comput. Phys. **107**, 403 (1993).
6. M.L. Glasser and I.J. Zucker. Theor. Chem. Adv. Perspect. **5**, 67 (1980).
7. D. Borwein, J.M. Borwein, and K.F. Taylor. J. Math. Phys. **26**, 2999 (1985).
8. E.R. Smith. Proc. R. Soc. London, Ser. A: **375**, 475 (1981).
9. P.P. Ewald. Ann. Phys. **64**, 253 (1921).
10. D. Shanks. J. Math. Phys. (Cambridge, Mass.), **34**, 1 (1955).
11. D. Levin. Int. J. Comput. Math. **3**, 371 (1973).
12. R. Hoppe. Angew. Chem. **78**, 52 (1966).
13. B.W. Char et al. First leaves: A tutorial introduction to Maple V. Springer-Verlag, New York. 1992.
14. L. Pauling. The nature of the chemical bond. 3rd ed. Cornell University Press, Ithaca, New York. 1960. pp. 519–520.
15. C. Kittel. Introduction to solid state physics. 5th ed. John Wiley & Sons, Inc., New York. 1976. p. 90.
16. H. Essén. Phys. Scr. **52**, 388 (1995).
17. R.F.W. Bader and P. Becker. Chem. Phys. Lett. **148**, 452 (1988).

The role of hydrogens in stabilizing organic ions

Kenneth B. Wiberg, Paul von Rague Schleyer, and Andrew Streitwieser

Abstract: The changes in electron density that result from processes in which ions are formed were examined using both electron density difference maps and calculations of electron populations using Bader's theory of atoms in molecules. The processes include the loss of an electron from a neutral precursor forming a radical cation, the loss of an electron from a free radical forming a carbocation, the addition of a proton to ammonia, the addition of an electron to a free radical forming a carbanion, and the loss of a proton from a neutral precursor forming an anion. In the reactions forming cations, the new positive charge resides mainly at the hydrogens, and the heavy atoms generally gain electron density. The anion-forming reactions lead to negative charge being shared among atoms but, again, much of the charge appears at the hydrogens. $\sigma-\pi$ polarization is an important feature of the charge distribution in all of the ions. There is an advantage to placing the charge at the periphery of an ion since this will minimize its electrostatic energy.

Key words: electron density, anions, cations, radical cations, $\sigma-\pi$ polarization.

Résumé : Faisant appel à des cartes de différences de densité électronique ainsi qu'à des calculs de densités de population dans le cadre de la théorie des atomes dans des molécules, on a étudié les changements dans la densité électronique qui découlent de processus dans lesquels il se forme des ions. Les processus comprennent la perte d'un électron par un précurseur neutre conduisant à un cation radical, la perte d'un électron par un radical libre conduisant à la formation d'un carbocation, l'addition d'un proton à de l'ammoniac, l'addition d'un électron à un radical libre conduisant à la formation d'un carbanion et la perte d'un proton d'un précurseur neutre conduisant à la formation d'un anion. Dans les réactions conduisant à des cations, la nouvelle charge positive réside principalement au niveau des hydrogènes et généralement les atomes lourds subissent un gain de densité électronique. Lors des réactions conduisant à la formation d'anions la charge négative est partagée parmi les atomes, mais, encore une fois, la plus grande partie de la charge apparaît sur les hydrogènes. La polarisation $\sigma-\pi$ est une caractéristique importante de la distribution de charge dans tous ces ions. Il y a un avantage à placer la charge à la périphérie d'un ion puisque ceci a tendance à minimiser son énergie électrostatique.

Mots clés : densité électronique, anions, cations, radicaux cations, polarisation $\sigma-\pi$.

[Traduit par la rédaction]

1. Introduction

It is well established that charged species are stabilized by spreading the charge over as large a surface area as possible (1). In organic ions, this suggests that a considerable part of the charge should be transferred to the hydrogens at the periphery of the ion. The hydrogens should be a good source for electron density since they have a small nuclear charge and cannot hold onto their electron density as well as other atoms with larger nuclear charges. They may also be able to accept some electron density in the formation of anions. This report will be concerned with the role hydrogens play in the stabilization of ions.

Several processes that form positively or negatively charged ions were examined using ab initio molecular orbital theory. The structural parameters for the compounds and ions were obtained via MP2 (2) or Becke3LYP (3) geometry optimizations. Both procedures correct for electron correlation, and generally give similar relative energies and charge distributions. The 6-31G* basis set was used for saturated compounds and carbocations, and 6-31+G* was used for compounds and ions having lone pairs. The analysis of the charge distribution was made either using Bader's theory of atoms in molecules (AIM) (4) to obtain electron populations, or using electron density difference plots between the ions and their neutral precursors.

2. Formation of radical cations via photoelectron spectroscopy

Photoelectron spectroscopy is a process in which a radical cation is formed via the loss of an electron from a neutral precursor (5). It is a vertical excitation, and so it is appropriate to use the same geometry for the precursor and the ion. The MP2/6-31G* wave functions for the two species were converted into three-

Received October 20, 1995.

This paper is dedicated to Professor Richard F.W. Bader on the occasion of his 65th birthday.

K.B. Wiberg.[1] Department of Chemistry, Yale University, New Haven, CT 06520, U.S.A.
P.v.R. Schleyer. Institut für Organische Chemie, Friedrich-Alexander Universität, Erlangen-Nürnberg, D-8250 Erlangen, Germany.
A. Streitwieser. Department of Chemistry, University of California, Berkeley, CA 94720, U.S.A.

[1] Author to whom correspondence may be addressed. Telephone: (203) 432-5160. Fax: (203) 432-6144. E-mail: wiberg%kbwgpx@biomed.med.Yale.edu

Fig. 1. Change in electron density distribution on going from (*a*) ethane using the highest CH bonding orbital, (*b*) ethane using the highest C—C bonding orbital, and (*c*) ethene using its π orbital to their radical cations calculated at the MP2/6-31G* level. The contour level is 0.005 e/au^3. Loss of electron density is indicated by broken contours.

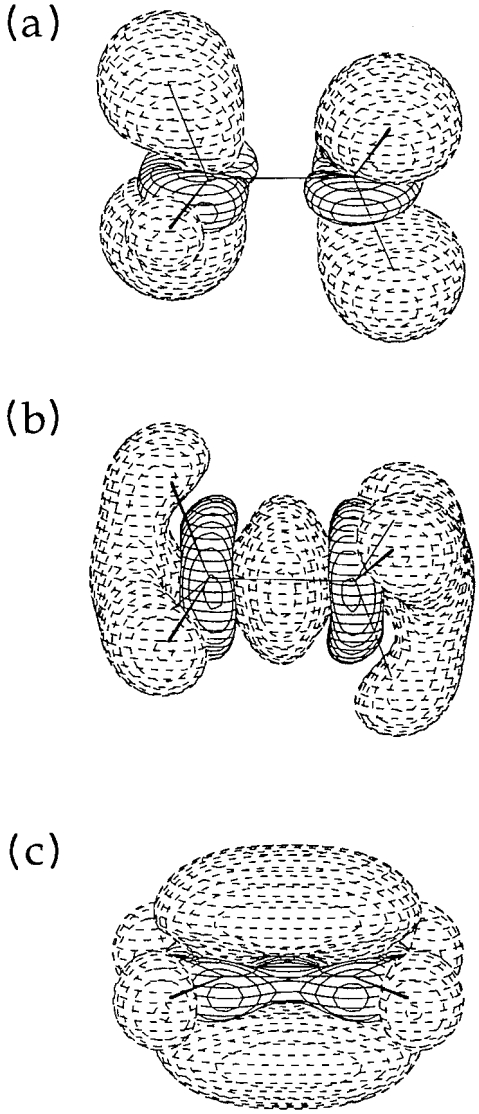

dimensional arrays of electron density, and the distribution for the neutral compound was subtracted from that of the radical cation. The difference density was visualized as a 3-D plot.

Ethane provides a good example of this approach. The highest occupied MO's of ethane are a pair of degenerate CH bonding orbitals. The difference density between ethane and the radical cation formed by removal of an electron from one of these MO's is shown in Fig. 1*a* where the broken contours indicate regions that lose electron density on going to the radical cation, and solid contours show regions that gain density. As expected, electron density is lost from the hydrogens but, at the same time, the carbons gain some electron density. Separate integrations of the regions in the figure that have gained and lost electron density found a 0.122*e* gain by the carbons and a 1.122*e* loss by the hydrogens.

The electron populations may also be derived using Bader's theory of atoms in molecules (AIM) in which the electron density is integrated within atomic volume elements defined by zero-flux surfaces (4). Each hydrogen of ethane has 0.981*e*. With this radical cation, the hydrogen populations are not equal because of the loss of symmetry in taking an electron from one of a pair of degenerate orbitals. Two of the hydrogens have 0.847*e* and the other four have 0.739*e* for a net loss of 1.24*e* at the hydrogens. Thus, both methods agree that more than one electron is taken from the hydrogens in forming the radical cation.

The next ethane MO is associated with the C—C bond. The difference density between ethane and the radical cation formed by loss of an electron from this MO is shown in Fig. 1*b*. Loss is seen at the C—C bond and also at the hydrogens, but the carbons again gain charge density. Integration of the regions in Fig. 1*b* indicates a 0.12*e* gain at each carbon, a 0.32*e* loss at the C—C bond, and a 0.15*e* loss at each hydrogen. Thus, even for this MO, the hydrogens contribute 90% of the electron that is lost in the photoionization.

The AIM electron populations were calculated for this radical cation. Each hydrogen has 0.797*e*, for a loss of 0.18*e* on going to the radical cation. It can be seen that the two methods are in good agreement.

Ethene provides another interesting example. Here, the lowest energy radical cation is formally derived by the loss of one of the π electrons. Will charge be taken from the hydrogens in this case? Figure 1*c* shows that this is the case, and that the electron density near the carbons is again increased. Integration of the electron loss and gain regions in Fig. 1*c* showed that 0.180*e* is gained in the vicinity of the carbons, and that 1.180*e* is lost at the hydrogens and the carbon π orbital. The loss of electron density at the hydrogens is also seen in the AIM populations. Each hydrogen of ethene has 0.946*e*, and each hydrogen of the radical cation had 0.780*e*, for a loss of 0.166*e* on going to the radical cation. Thus, the hydrogens contribute about 66% of the electron that is lost on photoionization.

This procedure was also applied to several cyclic hydrocarbons: cyclopropane, bicyclo[1.1.0]butane, bicyclo[1.1.1.]pentane, and [1.1.1]propellane (Fig. 2) (6). Again, the broken contours indicate regions that lose electron density on going to the radical cation, and the solid contours indicate regions that have gained density.

In agreement with the ethane result, the electron density loss is found largely at the hydrogens and in the bonding regions, and the carbons again gain electron density in the process. With cyclopropane, the difference density is not symmetrical with respect to the three C—C bonds because in forming the radical cation the electron is taken from one of a pair of degenerate orbitals, leading to incipient Jahn–Teller distortion. Here, the electron is taken from two of the bent C—C bonds and from the hydrogens, and at shorter distances from the nuclei the carbons gain electron density. The changes for bicyclobutane are similar, except that the central C—C bond becomes a major source of the lost electron.

The difference density for bicyclo[1.1.1]pentane (Fig. 2*c*) shows that the bridgehead protons lose considerable electron density on going to the radical cation. Some density is lost from the C—C bonds, but at shorter distances from the nuclei the carbons gain electron density. With [1.1.1]propellane (Fig.

Fig. 2. Change in electron density distribution on going from cycloalkanes to their vertical radical cations calculated at the MP2/6-31G** level. The contour level is 0.005 e/au^3. The compounds are: (*a*) cyclopropane; (*b*) bicyclo[1.1.0]butane; (*c*) bicyclo[1.1.1]pentane; and (*d*) [1.1.1]propellane. The HOMO of cyclopropane is degenerate, and only one of the pair of possible radical cations is depicted, maintaining the cyclopropane geometry.

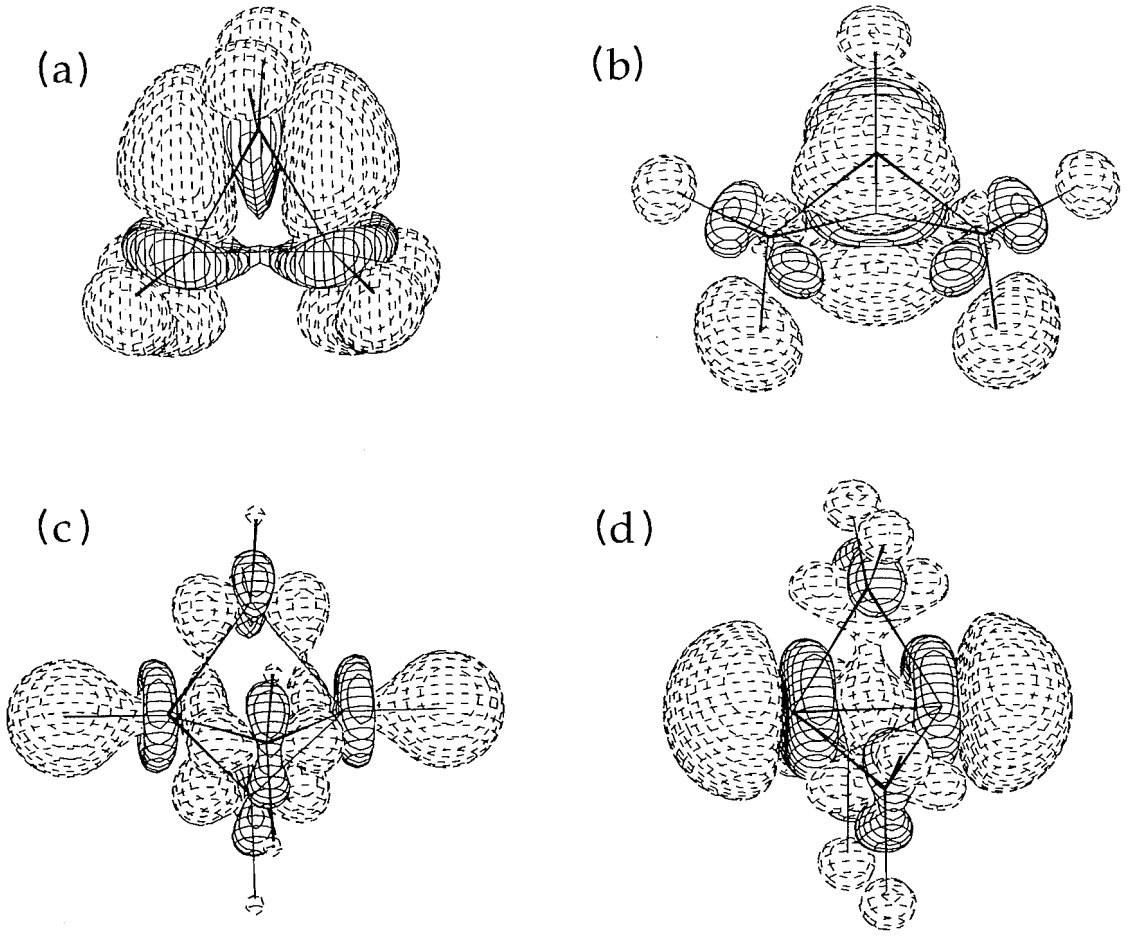

2*d*) much electron density is lost from the nonbonded density near the bridgehead carbons.

To make the changes more quantitative, the positive and negative regions in Fig. 2 were integrated, giving the results shown in Table 1. In each case, there is a sizable positive sum corresponding to the increases in electron density in the regions near the carbon atoms.

The atomic charges also were obtained using AIM, and the carbon and hydrogen charges were separately summed. These data also are given in Table 1. Again, it is seen that much of the decrease in electron density on going to the cation is seen at the hydrogens. In most cases, the carbons have a much smaller decrease in electron density, and in the case of bicyclo[1.1.1]pentane, C1 is calculated to have in increase in electron density. The small loss seen at most carbons is due to the volume element used in the AIM integrations that includes some of the volume near the carbons for which there is a loss of electron density.

Both methods of examining the changes in electron density agree that the hydrogens provide a large part of the loss in density on going to the cations.

3. Protonation of ammonia

A simple example of the conversion of a neutral molecule to a charged ion is found in the protonation of ammonia. The changes in electron density on protonation have been examined making use of the Mulliken population analysis, and it was concluded that most of the positive charge appears at the hydrogens (7). In view of the difficulties sometimes associated with the Mulliken populations (8), it seemed appropriate to examine this process using other methods of analysis.

There is relatively little change in structure in this process (Table 2), and so it is reasonable to use the ammonium ion geometry for both the ion and for the location of the nitrogen and three hydrogens of ammonia. The use of the same nuclear coordinates for both species is essential since otherwise large shifts in charge density resulting from the nuclear motions will confuse the interpretation of the electron density difference plots. Both the MP2 and B3LYP levels of theory were used, and there were no significant differences between them with regard to structure or relative energies. To be sure that the small change in geometry between the equilibrium structure of

Table 1. Charge shifts on forming radical cations.
(*a*) Integration of electron density differences.

Compound	Positive sum	Negative sum
Cyclopropane	0.221	−1.221
Bicyclo[1.1.0]butane	0.207	−1.206
Bicyclo[1.1.1]pentane	0.232	−1.230
[1.1.1]Propellane	0.235	−1.235

(*b*) From AIM electron populations.

Compound	Atom[a]	Shift
Cyclopropane	C[b]	0.037 × 3 = 0.112
	H[b]	0.146 × 6 = 0.888
Bicyclo[1.1.0]butane	C1	0.085 × 2 = 0.170
	H	0.129 × 2 = 0.258
	C2	0.006 × 2 = 0.012
	Ha	0.113 × 2 = 0.226
	Hb	0.167 × 2 = 0.334
Bicyclo[1.1.1]pentane	C1	−0.050 × 2 = −0.100
	H	0.261 × 2 = 0.522
	C2	0.006 × 3 = 0.018
	H	0.094 × 6 = 0.564
[1.1.1]Propellane	C1	0.135 × 2 = 0.270
	C2	0.064 × 3 = 0.192
	H	0.090 × 6 = 0.538

[a]In each case C1 is the bridgehead carbon and C2 is a methylene carbon.
[b]Average values for the radical cation. There is a small difference in population among the atoms due to incipient Jahn–Teller distortion.

ammonia and the structure based on ammonium ion has no effect, the AIM atomic charges were calculated (Table 2). The changes in the hydrogen charges are only 0.002*e*, which is negligible.

The change in electron density in this process is shown in Fig. 3 where loss is shown by broken contours and gain is shown by solid contours. The MP2 and B3LYP wave functions gave essentially the same plot. It can be seen that the three hydrogens of ammonia lose electron density on protonation, and that both the added proton and the nitrogen nucleus gain density. Thus, the nitrogen, which has a significant negative charge in ammonia because of its higher electronegativity as compared to hydrogen, retains its negative charge in the ion, and in fact increases it slightly despite the overall positive charge in the ion. The increase in electron density at nitrogen on protonation is also seen in the AIM nitrogen atomic charges given in Table 2.

The changes in electron density shown in Fig. 3 may be made more quantitative by integrating the positive and negative regions. With the B3LYP wave functions, the region that gains electron density (the added proton and the nitrogen) corresponds to 0.56*e*, and the other region corresponds to a loss of 0.56*e*. This is in good accord with the populations given in Table 2. For the three hydrogens of ammonia there is a loss of 3 × (0.532 − 0.365) or 0.50*e*. With the MP2 wave functions, integration of the regions in Fig. 2 give 0.49*e* gain and loss, respectively. The AIM populations give a loss for the ammonia hydrogens of 3 × (0.537 − 0.374) or 0.50*e*. The increase in electron density at nitrogen on protonation is small (0.03*e*), but that is expected since it already has a considerable negative charge because of its electronegativity. The important conclusion is that all of the added positive charge (and a little more) appears at the hydrogens.

Fig. 3. Change in electron density distribution on going from ammonia to ammonium ion calculated at the MP2/6-31+G* level. The contour level is 0.001 e/au^3. Note the loss of electron density at the three original hydrogens and the gain in electron density at the nitrogen and the added hydrogen.

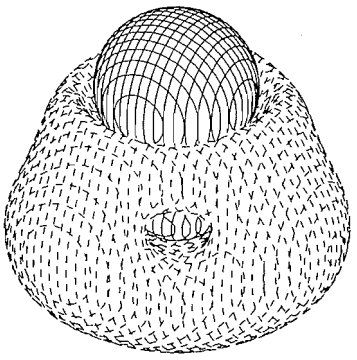

4. Formation of carbocations from free radicals

With carbon compounds, the largest charge transfer from the hydrogens would be expected in the formation of carbocations. This has been examined by Bader via a comparison of the AIM charges in the carbocation and the hydrocarbon precursors (9). He found that the hydrogens do receive much of the positive charge in the formation of the carbocations.

The shift in electron density on forming these ions is most readily studied by considering the loss of an electron from a radical. Since both species have three-coordinate carbons, it is reasonable to use the same geometry for both. The stabilization of cations is more dependent on the details of their structures than in the case of the radicals, and so the cation geometries will be used for both species. The loss of an electron from methyl radical, isopropyl radical, *tert*-butyl radical, and allyl radical has been studied, and the results are visualized in Fig. 4.

Again, it can be seen that the electron is taken from the hydrogens and the *p*-orbital that contained the odd electron, and that in other regions the carbons gain electron density on going to the cations. The magnitude of the changes in Fig. 4 were obtained by integrating separately the positive and negative regions, giving the results shown in Table 3.

The methyl cation is by far the least stable of the simple carbocations. Integration of the regions in Fig. 4 indicate that 1.2 electrons are taken from the hydrogens and the carbon *p*-orbital, and that the other carbon orbitals gain 0.2*e*. The AIM populations suggest that 0.89*e* is taken from the hydrogens and 0.11*e* is taken from the carbon. The difference between the two estimates of the charge shift is that the AIM procedure includes the carbon *p*-orbital along with the region shown with solid contours in Fig. 4. As a result, it includes part of the region in which charge density is lost.

Fig. 4. Change in electron density distribution on going from (*a*) methyl radical, (*b*) allyl radical, (*c*) isopropyl radical, and (*d*) *tert*-butyl radical to the corresponding carbocations via the loss of an electron. The calculations used the MP2/6-31G** level of theory, and the contour level is 0.005 e/au^3.

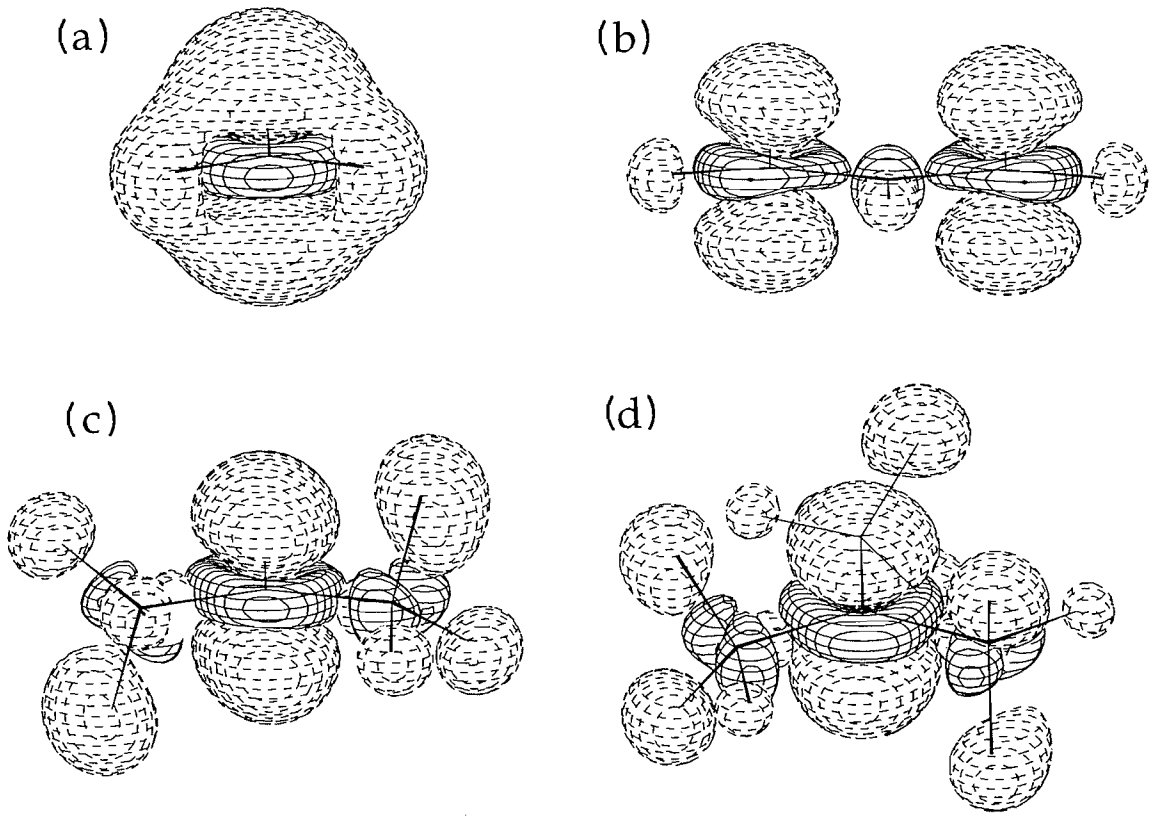

Table 2. Structures and energies of NH_3 and NH_4^+.[a]

Species	Level[b]	Energy	r(XH)	∠(HXH)	q_H	q_X
NH_4^+	B3LYP	−56.90612	1.028	109.5	0.532	−1.126
NH_3	B3LYP	−56.56698	1.016	108.2	0.365	−1.096
NH_3(at NH_4^+)	B3LYP	−56.56647	1.028	109.5	0.366	−1.097
NH_4^+	MP2	−56.73826	1.022	109.5	0.537	−1.149
NH_3	MP2	−56.39581	1.011	108.1	0.372	−1.115
NH_3(at NH_4^+)	MP2	−56.39533	1.022	109.5	0.374	−1.122

[a]Total energies are given in hartrees, bond lengths in Å, bond angles in degrees, and AIM charges (q) in electrons.
[b]All calculations used the 6-31+G** basis set.

Table 3. Changes in electron density on going from radicals to cations derived by integration of 3D difference density plots.

Compound	Electron loss	Electron gain
Methane	1.158	0.160
Isopropyl	1.194	0.195
tert-Butyl	1.228	0.230
Allyl	1.180	0.183
Cyclopropylcarbinyl	1.222	0.223
Cyclobutyl	1.205	0.206

The important conclusion is that much of the positive charge appears at the hydrogens that are in the nodal plane of the empty carbon p-orbital. When the electron is removed from the half-filled p-orbital of the radical, the increased electronegativity of the carbon leads to charge withdrawal from the hydrogens via the σ-bonds. Thus, the conversion of the radical to the cation involves considerable reorganization of charge density.

The isopropyl cation is the simplest secondary cation, and it is considerably more stable than the methyl cation Experimental nmr data are consistent with the theoretical structure (10), which has been found to have C_2 symmetry with a hydrogen on one methyl group aligned with one side of the empty car-

Table 4. Percent decreases in population at carbon and hydrogen on going from the radical to the cation based on AIM populations.

Compound	Position	% at H	% at C
Methyl[a]		65.3	34.7
Isopropyl[b]	C2	15.8	11.9
	C1	81.9	−9.6
tert-Butyl[b]	C2	6.3	
	C1	107.8	−14.1
Allyl[b]	C2	11.4	6.5
	C1	52.5	29.6

[a]The decreases with respect to methane are 76% from the hydrogens and 24% from the carbons.
[b]C2 is the cationic site.
[c]C2 is the central carbon.

bon *p*-orbital and a hydrogen of the second methyl aligned with the other side of the *p*-orbital.

An examination of Fig. 3 shows that the hydrogens that are aligned with the *p*-orbital suffer a greater loss of electron density than the other pairs of hydrogens, as would be expected from the usual hyperconjugation picture. However, all of the hydrogens, including the one attached to the cationic center, suffer loss of charge density. Integrations of the separate regions in Fig. 4 found 1.19*e* was taken from the set of hydrogens and the carbon *p*-orbital and 0.19*e* was gained by the other carbon orbitals.

The AIM analysis also found large changes in the charges for the hydrogens. The methyl carbons are calculated to gain electron population on going to the cation, whereas the cationic carbon loses electron population (Table 4).

The *tert*-butyl cation is quite similar to the isopropyl cation. The structure used in this study had C_{3h} symmetry for convenience in presentation. At the MP2/6-31G* level, it was calculated to be a transition state, but with a very low imaginary frequency (70*i* cm^{-1}). The minimum was slightly distorted from this symmetry, and has a negligibly lower energy (11). The charge integrations (Table 3) show the same pattern as found with the isopropyl cation. Here, 1.23*e* are taken from the hydrogens and the carbon *p*-orbital and 0.23*e* are gained by the other carbon orbitals. The AIM populations show that the central carbon gains electron population on going from the radical to the cation, and that the methyl carbons lose a small amount of electron population. The hydrogens are again a major source of the electron density that is lost on going to the cation.

With the allyl cation, the formation from the allyl radical leads to a net loss of 0.53*e* from the four hydrogens at the terminal methylene groups, and 0.30*e* from the methylene carbons. This is especially interesting in that these hydrogens are in the nodal plane of the π system, and thus the loss of electron density must involve σ–π polarization, as also found with the methyl cation. The loss of electron density from these hydrogens also is clear in Fig. 4.

5. Formation of carbanions from radicals

The conversion of a radical to an anion by the addition of an electron is the converse of the process used in studying the carbocations. Here, the radicals are not as pyramidal as the anions, but the change in charge density on going to the more strongly pyramidal structure should be small for the radicals. The application of this method to the simple carbanions is questionable since they are not bound species, and can decrease their energies by the loss of an electron (12). However, there are some carbanions that are stable species in the gas phase. This includes vinyl anion (13), cyclopropyl anion (14), bicyclo[1.1.0]butyl-1 anion (15), and allyl anion (16). The formation of these ions from the corresponding radicals, using the anion geometries for the latter, led to the electron density shifts shown in Fig. 5.

Table 5. Changes in electron density on going from radicals to anion derived by integration of 3D difference density plots.

Compound	Electron loss	Electron gain
Allyl anion	0.141	1.140
Bicyclobutyl-1 anion	0.206	1.204
Cyclopropyl anion	0.182	1.179
Vinyl anion	0.166	1.164

In each case, the largest change in electron density is found at the carbanion lone pairs. There are large charge shifts to the hydrogens in vinyl anion, but near the carbons there is a loss of density. This is the opposite of what was found in the formation of carbocations from radicals where the carbons gained electron density despite the overall loss of an electron. A gain of electron density at the hydrogens is found for all of the compounds in Fig. 5. The positive and negative regions in the figure were integrated giving the values shown in Table 5. It is interesting to compare the effects of removing an electron (Fig. 4*b*) and adding an electron to an allyl radical (Fig. 5*b*).

The AIM electron populations for the four anions and the corresponding radicals are given in Table 6. The large charge shifts for the carbons formally bearing the positive charge are due to the formation of the anionic lone pair. However, with the exception of allyl anion, only about one third of the charge is found at this carbon and the rest is distributed over the other carbons and the hydrogens.

6. Formation of anions by proton abstraction

The removal of a proton from methane to form methide ion is formally the reverse of the protonation of ammonia, and it also was examined (Table 7). An important difference from the ammonia case is that the carbon and hydrogen have similar electronegativities, and there is little charge separation in methane. In methide ion, the electron density released by the lost proton is found at both the hydrogens and the carbon, and the AIM populations show that 42% of the charge appears at the hydrogens and 58% at the carbon.

The abstraction of protons from ammonia or water are related processes (Table 8). Here, the central atoms have a higher electronegativity than the hydrogens and, as a result, they have a relatively large negative charge. As a further result, one might expect that it would be relatively difficult to

Fig. 5. Change in electron density on going from a (*a*) vinyl radical, (*b*) allyl radical, (*c*) cyclopropyl radical, and (*d*) bicyclo[1.1.0]butyl-1 radical to the corresponding anions by the addition of an electron, calculated at the MP2/6-31+G** level. The contour level is 0.001 e/au^3.

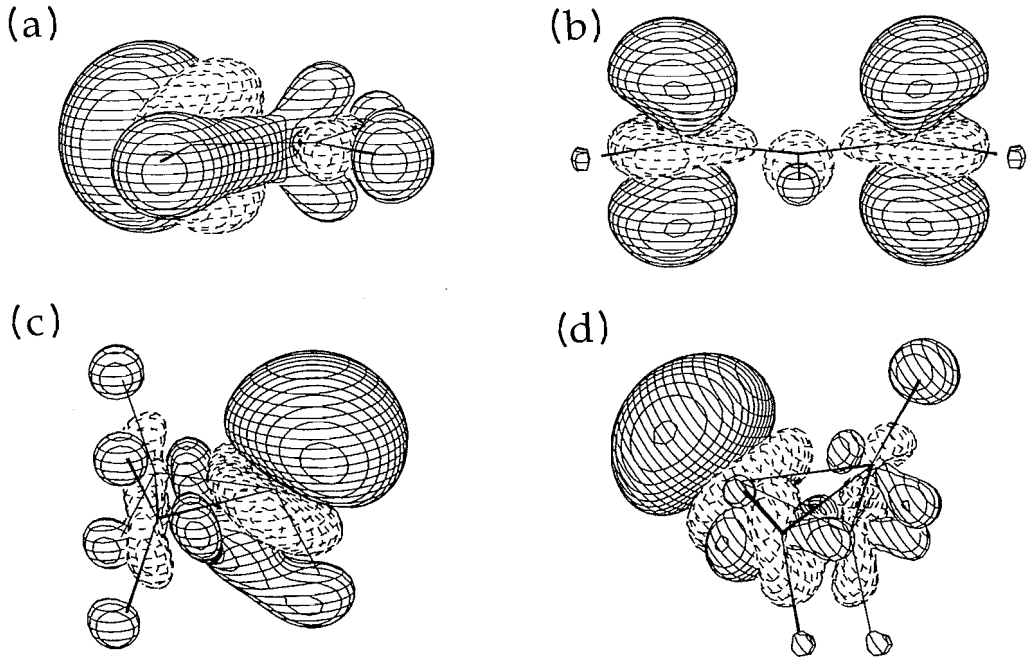

add additional electron density to them. The data in Table 8 support this expectation. In the abstraction of a proton from ammonia, 73% of the electron density from the proton appears at the remaining hydrogens, and only 27% appears at the nitrogen. Similarly, in the abstraction of a proton from water, 75% of the electron density from the proton appears at the hydrogen and 25 % appears at the oxygen.

The more interesting ions are those formed by the ionization of carboxylic acids and enols. A number of these compounds have been examined,[2] and we will examine formic acid and 5-hydroxypentadienal here.

The changes in electron distribution in the ionization of these compounds was examined using the average structures so that the effect of moving nuclear charges would not overwhelm the shifts in the distributions. The changes in charge are shown in Fig. 6. In the conversion of formic acid to formate ion, the electron density originally associated with the acid proton (~0.5*e*) is about equally distributed between the aldehydic proton and the two oxygens. The electron density difference plot for the conversion of hydroxypentadienal to its enolate ion shows that much of the negative charge appears at the carbon-bound protons even though they are in the nodal plane of the π system. This is also found in the changes in AIM and NPA electron populations on going from the hydroxyaldehyde to its anion (17).

7. Conclusions

In the conversion of neutral precursors to the corresponding cations or anions, hydrogens accept much of the charge, even when the charge is formally associated with a π system and the hydrogens are in the nodal plane of this system. This is espe-

[2] The details of this investigation will be presented elsewhere (17).

Fig. 6. Change in electron density on going from (*a*) formic acid and (*b*) 5-hydroxypentadienal to their anions by the loss of a proton, calculated at the MP2/6-31+G** level. Only the regions that gain charge density are shown. In each case, the original carbonyl group is at the right.

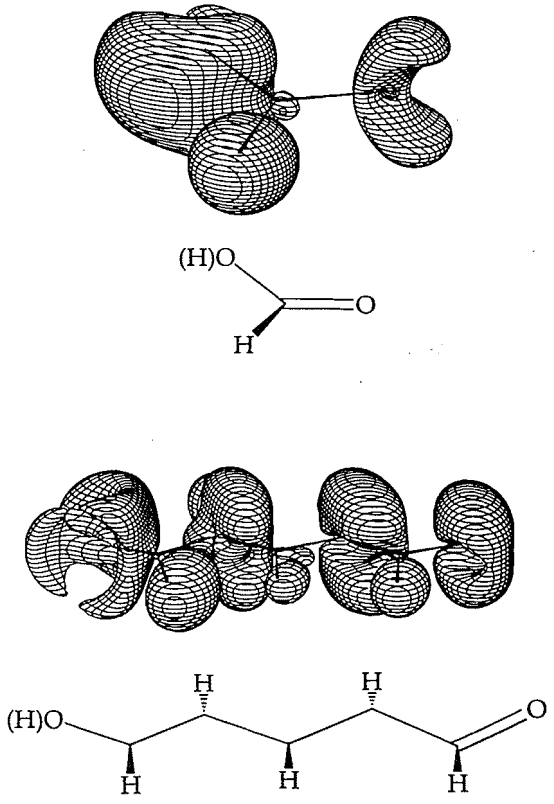

Table 6. Changes in AIM electron populations on going from radicals to anions.

Compound	Atom	Anion	Radical	Change
Vinyl	C1	6.472	6.136	0.336
	H	1.084	0.874	0.210
	C2	6.330	6.200	0.161
	Ha	1.071	0.895	0.176
	Hb	1.043	0.926	0.117
Allyl	C1	6.055	6.049	0.006
	Ha	1.027	0.948	0.079
	Hb	6.406	6.149	0.256
	C2	1.030	0.922	0.108
	H	1.024	0.931	0.093
Cyclopropyl	C1	6.462	6.102	0.360
	H	1.064	0.912	0.152
	C2	6.168	6.125	0.043
	Ha	1.023	0.931	0.092
	Hb	1.045	0.937	0.108
Bicyclo[1.1.0]butyl-1	C1	6.392	6.104	0.288
	C2	6.132	6.042	0.090
	Ha	1.107	0.936	0.081
	Hb	1.042	0.947	0.095
	C3	6.234	6.174	0.060
	H	0.993	0.872	0.121

Table 7. Structures and energies of CH_4 and CH_3^-.[a]

Species	Level[b]	Energy	r(XH)	∠(HXH)	q_H	q_X
CH_4	B3LYP	−40.52614	1.093	109.5	−0.012	0.047
CH_3^-	B3LYP	−39.84738	1.104	110.2	−0.148	−0.555
CH_3^- (at CH_4)	B3LYP	−39.84711	1.093	109.5	−0.156	−0.531
CH_4	MP2	−40.36595	1.086	109.5	−0.058	0.231
CH_3^-	MP2	−39.68627	1.096	110.6	−0.151	−0.546
CH_3^- (at CH_4)	MP2	−39.68596	1.086	109.5	−0.210	−0.371

[a]Total energies are given in hartrees, bond lengths in Å, bond angles in degrees, and AIM charges (q) in electrons.
[b]All calculations used the 6-31+G** basis set.

Table 8. Structures and energies of NH_3, NH_2^-, H_2O, and HO^-.[a]

Species	Level[b]	Energy	r(XH)	∠(HXH)	q_H	q_X
NH_3	B3LYP	−56.56698	1.016	108.2	0.365	−1.096
NH_2^-	B3LYP	−55.90925	1.033	102.9	0.180	−1.364
NH_3	MP2	−56.39581	1.011	108.1	0.372	−1.115
NH_2^-	MP2	−55.73454	1.028	103.4	0.197	−1.398
H_2O	B3LYP	−76.43405	0.965	105.8	0.583	−1.166
HO^-	B3LYP	−75.80343	0.970		0.421	−1.420
H_2O	MP2	−76.23589	0.963	105.5	0.594	−1.187
HO^-	MP2	−75.60471	0.969		0.442	−1.441

[a]Total energies are given in hartrees, bond lengths in Å, bond angles in degrees, and AIM charges (q) in electrons.
[b]All calculations used the 6-31+G** basis set.

cially true in the formation of cations where the hydrogens bear much of the charge, and the heavier atoms generally gain electron density despite the development of an overall positive charge. The change in charge in the formation of anions is not as dramatic but, in many cases, the majority of the negative charge is found at the hydrogens.

In the conversion of a radical to a carbocation, an electron is taken from the carbon making it more electronegative. As a result, there is a tendency for the carbon to contract the electron density in its σ bonds, leading to an increase in electron density in these regions. The opposite is seen when an electron is added to a radical to form a carbanion. Here, the carbon becomes less electronegative and electron density in its σ bonds becomes dispersed, leading to a decrease in density in these regions. The origin of the shifts in electron density resulting from the addition or loss of a proton is not as obvious, but in each case the MO that is involved will have a significant component at the first-row element that is involved, and thus its electronegativity can be modified, leading to the effects described above.

Although there is formal σ–π separation in many cases, σ–π polarization is an important factor in determining electron distributions in ions. When π electrons move in one direction, the σ electrons tend to move in the opposite direction so as to minimize electron repulsion. The neglect of this polarization in the application of resonance concepts and FMO arguments will lead to incorrect conclusions about electron distributions.

Calculations

The ab initio calculations were carried out using Gaussian 95 (18). The AIM integrations were done using PROAIM (19). The 3D plots, along with their integration, were made using CASGEN (20).

Acknowledgment

This investigation was supported by grants from the National Science Foundation.

References

1. E.M. Purcell. Electricity and magnetism. Vol. 2. 2nd ed. McGraw–Hill, New York. 1985.
2. C. Møller and M.S. Plesset. Phys. Rev. **46**, 618 (1934).
3. P.J. Stephens, F.J. Devlin, C.F. Chabalowski, and M.J. Frisch. J. Phys. Chem. **98**, 11623 (1994); A.D. Becke. J. Chem. Phys. **98**, 5648 (1993); C. Lee, W. Yang, and R.G. Parr. Phys. Rev. B: Condens. Matter, **37**, 785 (1988).
4. R.F.W. Bader. Atoms in molecules. A quantum theory. Clarendon Press, Oxford. 1990.
5. D.W. Turner, C. Baker, C.R. Baker. Molecular photoelectron spectroscopy. Wiley, New York. 1970.
6. K.B. Wiberg, C.M. Hadad, S. Sieber, and P.v.R. Schleyer. J. Am. Chem. Soc. **114**, 5820 (1992).
7. A. Greenberg, R. Winkler, B.L. Smith, and J.F. Liebman. J. Chem. Educ. **58**, 367 (1982).
8. R.S. Mulliken and P. Politzer. J. Chem. Phys. **55**, 5135 (1971); D.D. Grier and A. Streitwieser. J. Am. Chem. Soc. **104**, 3556 (1982).
9. R.F.W. Bader. Can. J. Chem. **64**, 1036 (1986).
10. W. Koch, B. Liu, and P.v.R. Schleyer. J. Am. Chem. Soc. **111**, 3479 (1989); P.v.R. Schleyer, W. Koch, B. Liu, and U. Fleisher. J. Chem. Soc. Chem. Commun. 1098 (1989); P.v.R. Schleyer, P. Buzek, and B. Liu. Croat. Chim. Acta, **65**, 655 (1992).
11. S. Sieber, P. Buzek, P.v.R. Schleyer, W. Koch, and J.W. de M. Carneiro. J. Am. Chem. Soc. **115**, 259 (1993).
12. P.v.R. Schleyer, G.W. Spitznagel, and J. Chandrasekhar. Tetrahedron Lett. **27**, 4411 (1986); C.H. DePuy, V.M. Bierbaum, and R. Damrauer. J. Am. Chem. Soc. **106**, 4051 (1984).
13. K.K. Anderson and S.R. Kass. Tetrahedron Lett. **30**, 3045 (1989).
14. H.M. Walborsky and J.M. Motes. J. Am. Chem. Soc. **92**, 2445 (1970).
15. P.K. Chou and S.R. Kass. J. Am. Chem. Soc. **110**, 7899 (1988).
16. K.B. Wiberg, C.M. Breneman, and T.J. LePage. J. Am. Chem. Soc. **112**, 61 (1990).
17. K.B. Wiberg, J. Ochterski, and A. Stretwieser. J. Am. Chem. Soc. Submitted.
18. M.J. Frisch, G.W. Trucks, H.B. Schlegel, P.M.W. Gill, B.G. Johnson, M.A. Robb, J.R. Cheeseman, T. Keith, G.A. Petersson, J.A. Montgomery, K. Raghavachari, M.A. Al-Laham, V.G. Zakrzewski, J.V. Ortis, J.B. Foresman, J. Cioslowski, B.B. Sefanov, A. Nanayakkara, M. Challacombe, C.Y. Peng, P.Y. Ayala, W. Chen, M.W. Wong, J.L. Andres, E.S. Replogle, R. Gomperts, R.L. Martin, D.J. Fox, J.S. Binkley, D.J. Defrees, J. Baker, J.P. Stewart, M. Head-Gordon, C. Gonzalez, and J.A. Pople. Gaussian 95, Development Version (Rev. B.1). Gaussian, Inc., Pittsburgh, Pa. 1995.
19. F.W. Biegler-König, R.F.W. Bader, T.-H. Tang. J. Comput. Chem. **3**, 317 (1982).
20. P.R. Rablen and C.M. Hadad. Yale University.

The theory of atoms in molecules as a tool to investigate the reactivity of tetraphosphacubane

O. Mó and M. Yáñez

Abstract: Bader's theory of atoms in molecules is used to rationalize the gas-phase reactivity of tetraphosphacubane vs. H^+, Li^+, Na^+, and Be^{2+}. For this purpose we have used MP2 densities obtained at the 6-31G(d,p) level. The characteristics of the C—P bonds of tetraphosphacubane are discussed. The Laplacian of its electron charge density shows that both phosphorus and carbon atoms are active centers for electrophilic substitutions. This is consistent with the fact that both phosphorus and carbon protonated species are minima of the potential energy surface. The strong charge redistribution associated with carbon protonation explains the enhanced stability of the carbon protonated species with respect to the phosphorus protonated one. The Laplacian field also shows the existence of a cavity inside the cage surrounded by high electronic density that can stabilize a cation of the appropriate size. Our results confirm that Li^+ and Be^{2+} fulfil this requirement and the corresponding complexes, where the cation is located inside the cage, are minima of the corresponding potential energy surface. Na^+ is far too large and a similar structure is a saddle point of the potential energy surface.

Key words: atoms-in-molecules theory, tetraphosphacubane, reactivity, cationization.

Résumé : On a utilisé la théorie de Bader des atomes dans les molécules pour rationaliser la réactivité en phase gazeuse du tétraphosphacubane vs. H^+, Li^+, Na^+ et Be^{2+}. À cette fin, on a utilisé les densités MP2 obtenues au niveau 6-31G(d,p). On discute des caractéristiques des liaisons C—P du tétraphosphacubane. La laplacien de sa densité de charge électronique montre que les atomes tant de carbone que de phosphore sont des centres actifs pour les substitutions électrophiles. Ceci est en accord avec le fait que les espèces protonées, tant phosphorées que carbonées, correspondent à des minima de la surface de l'énergie potentielle. La forte redistribution de charge associée à la protonation du carbone explique la stabilité accrue des espèces protonées carbonées par rapport aux espèces protonées phosphorées. Le champ du laplacien démontre aussi l'existence d'une cavité à l'intérieur de la cage, entourée par une densité électronique élevée qui peut stabiliser un cation d'une taille appropriée. Nos résultats confirment que le Li^+ et le Be^{2+} remplissent ces conditions et les complexes correspondants, dans lesquels le cation se trouve à l'intérieur de la cage, sont des minima des surfaces d'énergie potentielles correspondantes. Le Na^+ est beaucoup trop gros et une structure semblable est un col sur la surface d'énergie potentielle.

Mots clés : théorie des atomes dans les molécules, tétraphosphacubane, réactivité, cationisation.

[Traduit par la rédaction]

Introduction

The reactivity of tetraphosphacubane is of particular interest since, in principle, it might be affected by its likely high strain energy. In fact, tetraphosphacubane can be considered as the result of substituting the carbon atoms in alternative corners of cubane, which has a very high strain energy (1–4) although it is thermally stable, by phosphorus atoms. On the other hand, all efforts to synthesize 1,3,5,7-tetraazacubane have failed, probably because the presence of four nitrogen atoms in alternative corners of the cube would imply a significant increase of the strain energy, which as mentioned above is already very high (ca. 165 kcal/mol) for cubane. On the contrary, the tetra-*tert*-butyl substituted derivative of 1,3,5,7-tetraphosphacubane was recently synthesized by M. Regitz and co-workers (5), which is probably an indication that substitution of carbon by phosphorus leads to a certain alleviation of the strain of the system. Since tetraphosphacubane is a quite novel species, we have considered it of interest to investigate its intrinsic reactivity, i.e., its reactivity toward some monocations in the absence of any interaction with the solvent. Along this line, we have studied (6), very recently, the protonation of the tetra-*tert*-butyl substituted derivative of 1,3,5,7-tetraphosphacubane in the gas phase. This *in concert* experimental and theoretical study (6) showed tetraphosphacubane to be an unexpectedly strong carbon base. In this paper we shall try to illustrate that the atoms-in-molecules theory of Bader (7) provides useful information either to rationalize the behaviour of tetraphosphacubane with respect to different closed-shell cations, namely, H^+, Li^+, Na^+, and Be^{2+}, or to describe the charge redistributions that take place upon cationization. We shall have the opportunity to illustrate, once more, that Bader's theory is a very versatile tool for characterizing ion–molecule interactions (8–14) and, in particular, to investigate bond acti-

Received October 2, 1995.

This paper is dedicated to Professor Richard F.W. Bader on the occasion of his 65th birthday.

O. Mó and M. Yáñez.[1] Departamento de Química, C-9, Universidad Autónoma de Madrid, Cantoblanco, 28049-Madrid, Spain.

[1] Author to whom correspondence may be addressed. Telephone: 34-1-397-4953. Fax: 34-1-397-4187. E-mail: MYANEZ@vm1.sdi.uam.es

Fig. 1. Numbering of atoms used throughout this work. M^+ stands for metal cation.

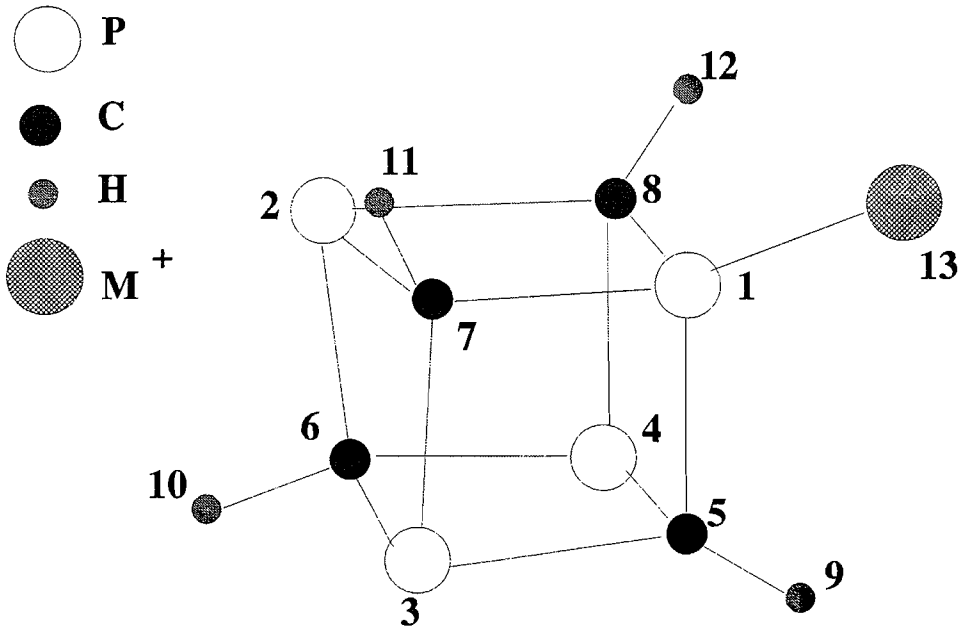

vations produced by protonation (9) or metal cation association in the gas phase (10–14). Although, as mentioned above, only the 1,3,5,7-tetra-*tert*-butyltetraphosphacubane has been synthesized, we shall limit our theoretical treatment to the unsubstituted parent compound for the sake of economy.

Computational details

The geometries of the complexes of tetraphosphacubane (**1**) with Li^+, Na^+, and Be^{2+} were optimized at the HF/6-31G(d,p) level. The corresponding vibrational frequencies were evaluated by means of analytical second-derivative techniques, in order to classify the stationary points of the potential energy surfaces as minima or saddle points and to evaluate the corresponding zero point vibrational energies (ZPE), which were scaled by the empirical factor 0.893. These geometries were then refined at the MP2/6-31G(d,p) level to account for electron correlation effects. The MP2 densities so obtained were then used for the corresponding Bader's topological analysis. The MP2/6-31G(d,p) optimized geometries of tetraphosphacubane (**1**) and those of the corresponding phosphorus and carbon protonated species, namely, **1PH**$^+$ and **1CH**$^+$, were taken from ref. 6. The binding energies were evaluated at the MP2/6-31G(d,p) level after including the corresponding ZPE corrections.

These standard ab initio calculations were carried out by using the Gaussian-90 (15) and Gaussian-92 (16) series of programs.

The bonding of the neutral species as well as that of the different cations included in this study was investigated by means of a topological analysis of the electronic charge density, ρ, and its Laplacian, $\nabla^2\rho$. As has been shown by Bader et al. (17–19), $\nabla^2\rho$ identifies regions of space where the electronic charge is locally depleted ($\nabla^2\rho > 0$) or built up ($\nabla^2\rho < 0$). We have also located the relevant bond critical points (bcp), i.e., points where the electronic charge density is minimum along the bond path and maximum in the other two directions, because the values of ρ and $\nabla^2\rho$ at these points offer quantitative information on the strength and nature of the bonding. Furthermore, the values of the negative curvatures (λ_1, λ_2) allow us to define the ellipticity of the bond as $\varepsilon = 1 - \lambda_1/\lambda_2$. This topological analysis was carried out by using the AIMPAC series of programs.[2]

The numbering of atoms used throughout this paper is given in Fig. 1. For the sake of consistency we are assuming that phosphorus association takes place systematically at P1. It should be mentioned that all the cations investigated were found to be symmetric with respect to the P1P2C6C5 plane. This also applies to carbon-attached species provided that association takes place at C5.

Results and discussion

Neutral tetraphosphacubane

The MP2/6-31G(d,p) optimized structure of tetraphosphacubane (r_{P-C} = 1.895 Å, CPC = 83.7°, PCP = 96.0°) agrees reasonably well with the X-ray crystal structure of tetra-*tert*-butyltetraphosphacubane (1) (r_{P-C} = 1. 881 Å, CPC = 85.6°, PCP = 94.4°), the differences being likely due to both the effects of the *t*-Bu substituents and the crystal packing. Topological analysis of its charge density reveals the existence of a significant ring strain since the bond path angles are significantly larger than the geometrical ones, in particular, those about phosphorus atoms (see Table 1). This seems to be in agreement with its high ring strain energy, which according to the recent estimations of Bachrach and Perriot (4) is ca. 63 kcal/mol. It is also interesting that the charge densities at the P—C bond critical points (see Table 2) are very close to those

[2] The AIMPAC programs package was provided by J. Cheeseman and R.F.W. Bader.

Table 1. Bond path angles and geometrical bond angles (within parentheses) for the systems included in this study. All values in degrees.

Angle	1	1PH$^+$	1CH$^+$	1Li$^+$	1Be^{2+}	1Na$^+$	1Li$^+$b	1Be^{2+}b	1Na$^+$b
C8-P1-C7	91.5	101.1	92.1	94.6	104.2	94.1	82.3	76.2	82.1
	(83.7)	(91.8)	(86.6)	(86.5)	(93.3)	(86.0)	(81.6)	(79.5)	(82.8)
P1-C7-P2	97.5	92.0	92.2	95.3	87.5	95.7	89.2	83.9	85.1
	(96.0)	(92.1)	(91.6)	(94.7)	(91.1)	(95.0)	(97.8)	(99.6)	(96.8)
C7-P2-C8		90.4	96.4	90.6	91.3	90.7			
		(83.9)	(80.3)	(83.7)	(84.5)	(83.6)			
P1-C5-P3		92.2	—	95.3	87.6	95.7			
		(92.3)		(94.7)	(91.2)	(94.9)			
C5-P3-C7		90.4	98.1	90.6	91.2	90.7			
		(83.8)	(97.5)	(83.7)	(84.4)	(83.7)			
P3-C7-P1		92.3	118.1	95.3	87.6	95.7			
		(92.3)	(121.7)	(94.7)	(91.2)	(94.9)			
C7-P1-C5		100.9	—	94.6	104.1	94.1			
		(91.6)		(86.5)	(93.2)	(86.1)			
C7-P2-C6		91.2	101.9	91.3	89.9	91.4			
		(83.2)	(91.5)	(83.5)	(81.9)	(83.5)			
P2-C6-P3		97.7	93.4	97.3	98.6	97.4			
		(97.7)	(92.4)	(96.7)	(99.4)	(96.6)			
C6-P3-C7		91.2	95.2	91.3	89.9	91.4			
		(83.2)	(87.6)	(83.5)	(81.9)	(83.5)			
P3-C7-P2		97.8	80.6	98.2	100.8	98.2			
		(95.0)	(87.4)	(95.6)	(95.8)	(95.6)			
P4-C5-P3		97.8	97.5	98.2	100.8	98.2			
		(95.2)	(98.2)	(95.6)	(95.8)	(95.6)			
C5-P3-C6		91.1	88.5	91.3	89.8	91.4			
		(83.0)	(81.2)	(83.5)	(81.9)	(83.5)			
P3-C6-P4		97.7	97.9	97.3	98.6	97.4			
		(97.9)	(96.4)	(96.7)	(99.4)	(96.6)			

reported in ref. 20 for typical P—C single bonds. As was found for phosphaalkenes (20), the ellipticity of the P—C linkages is small but not zero, indicating that there is some axial distortion of density, due to a certain delocalization of the charge into the corresponding four-membered ring.

In Fig. 2*a* we present the Laplacian of the charge density evaluated in the diagonal plane that bisects the cube. The existence is apparent of nonbonded charge concentrations close to the phosphorus atoms, which are associated with phosphorus lone pairs, but also in the vicinity of the carbon atoms. These regions correspond to sites most susceptible to electrophilic attack (8). This is in agreement with previous findings (6) that indicate that both phosphorus and carbon protonated species are stable cations. Furthermore, as we shall discuss in forthcoming sections, the strong charge redistribution that takes place upon protonation at the carbon atom will be responsible for the enhanced stability of the carbon protonated species (6). There is another interesting feature in Fig. 2*a* which is worth noticing: the existence of a cavity inside the cage, with negligibly small electron charge density, but surrounded by the electronic clouds associated with the P—C linkages. In Fig. 2*b* we present an alternative view of this cavity by showing the Laplacian of the charge density in a plane that contains three of the phosphorus atoms of the system. As we shall discuss later, this cavity may accommodate a cation of the appropriate size leading to a body-centered metal cation complex.

Protonated species

The bonding characteristics of phosphorus and carbon protonated species are summarized in Tables 1 and 2. Several points should be singled out for comment. As has been discussed in ref. 9, in protonation processes there is a large charge transfer from the basic center to the incoming proton. This implies an enhancement of the electronegativity of the basic center, which tries to recover part of this charge by polarizing or depleting, depending on the electronegativity of the other atoms bonded to it, the other bonds in which it participates. If the basic center is the most electronegative one it will depopulate the bond, which accordingly will become longer and weaker. If, on the contrary, the basic center is not the most electronegative one it would only polarize the bonding charge toward it, with the result that the charge density at the bonding

Table 2. Bonding characteristics of the systems included in this study. All values in atomic units.

Bond		1	1PH$^+$	1CH$^+$	1Li$^+$	1Be^{2+}	1Na$^+$	1Li$^+$b	1Be^{+2}b	1Na$^+$b
P1—C7	ρ	0.143	0.170	0.158	0.153	0.166	0.151	0.117	0.112	0.078
	$\nabla^2\rho$	−0.127	−0.085	0.180	−0.120	−0.131	−0.119	−0.149	−0.106	−0.020
	ε	0.120	0.055	0.184	0.063	0.027	0.076	0.110	0.513	0.042
P1–C5			0.170	—	0.153	0.166	0.151			
			−0.089		−0.120	−0.135	−0.119			
			0.055		0.063	0.027	0.076			
P2–C6			0.146	0.154	0.146	0.147	0.145			
			−0.156	−0.120	−0.136	−0.173	−0.134			
			0.107	0.065	0.117	0.086	0.118			
P2–C7			0.135	0.139	0.140	0.131	0.140			
			−0.173	−0.222	−0.128	−0.189	−0.125			
			0.120	0.048	0.130	0.111	0.129			
P3–C5			0.135	0.155	0.140	0.131	0.140			
			−0.171	−0.095	−0.128	−0.187	−0.126			
			0.122	0.096	0.130	0.112	0.129			
P3–C6			0.146	0.146	0.146	0.147	0.145			
			−0.157	−0.109	−0.136	−0.173	−0.133			
			0.107	0.109	0.117	0.086	0.118			
P3–C7			0.135	0.115	0.140	0.131	0.140			
			−0.170	−0.160	−0.128	−0.186	−0.126			
			0.122	0.058	0.130	0.112	0.129			
P1–X			0.175	0.269[a]	0.021	0.058	0.016	0.057 (0.073)[b]	0.070 (0.089)[b]	0.050 (0.066)[b]
			−0.109	−0.919	0.083	0.025	0.065	0.300 (0.481)	0.264 (0.524)	0.261 (0.456)
			0.001	0.000	0.000	0.000	0.000	0.000 (0.000)	0.024 (0.000)	0.000 (0.000)
C5–H		0.278	0.281	0.278	0.280	0.281	0.280	0.284	0.281	0.283
		−0.980	−1.029	−0.995	−1.003	−1.056	−0.998	−1.074	−1.116	−1.080
		0.000	0.008	0.013	0.008	0.014	0.007	0.000	0.000	0.000

[a]C5—H bond formed upon protonation.
[b]Values within parentheses correspond to the bonding between the metal cation and the carbon atom.

region would increase and the bond would become reinforced. The second case exists when protonation takes place at the phosphorus atom of tetraphosphacubane. Hence, the charge densities at the P1—C5, P1—C7, and P1—C8 bond critical points increase (see Table 2) and the corresponding bond lengths become shorter than in the neutral (1.802 vs. 1.895 Å). The aforementioned polarization effect implies a decrease in the valence charge density about C5, C7, and C8. These atoms recover part of this charge by depopulating the other C—P linkages in which they participate (C7—P2, C5—P3, C8—P4) (see Table 2), which accordingly become slightly longer (1.934 Å) than in the neutral. The remaining linkages of the system are not significantly affected (see Table 2 and Fig. 3*a*).

The enhancement of the electronegativity of P1 upon protonation is necessarily reflected in an increase of the *s* character of the hybrids involved in the P—C linkages. As a consequence, the bond angles about P1 increase significantly (see Table 2). This implies that the protonated phosphorus moves closer to the centre of the cage, and the P1-C7-P2 and P1-C8-P2 bond angles must decrease accordingly (see Table 2). The angles about the other phosphorus and carbon atoms do not change significantly. It must be observed, however, that in the **1PH$^+$** species the bond path angles are still significantly greater than the geometrical ones, indicating that the phosphorus protonated species retains much of the strain present in the neutral.

When protonation takes place at carbon, the situation is completely different. The basic center (C5) is now the most electronegative one and it recovers part of the charge transferred to the incoming proton by depopulating the C5—P1 bond. This effect is clearly seen by comparing Figs. 2*a* and 3*b*, which present the Laplacian of the charge density evaluated in the diagonal plane that bisects the cube, for the neutral and the carbon protonated species, respectively. This comparison shows that the charge depletion at the P1—C5 bonding region is so large that the bond breaks apart, the P1—C5 distance being 3.2 Å (6). This bond fission alleviates significantly the strain of the system, which is reflected in a dramatic increase of the P3-C7-P1 and C5-P3-C7 bond angles (see Table 1). As a consequence, the carbon protonated species becomes about 10 kcal/mol more stable than the phosphorus protonated one (6). The P1—C5 bond fission also implies hybridization changes at both centers that are particularly important at P1, which becomes dicoordinated while C5 maintains its tetraco-

Fig. 2. Laplacian of the charge density of tetraphosphacubane in (*a*) a diagonal plane bisecting the cube; (*b*) a plane that contains three phosphorus atoms. Positive values of $\nabla^2\rho$ are denoted by solid lines and negative values by broken lines. Contour values, in au, are ±0.05, ±0.25, ±0.50, ±0.75, and ±0.95. The arrows indicate nonbonded charge concentrations most susceptible to electrophilic attack.

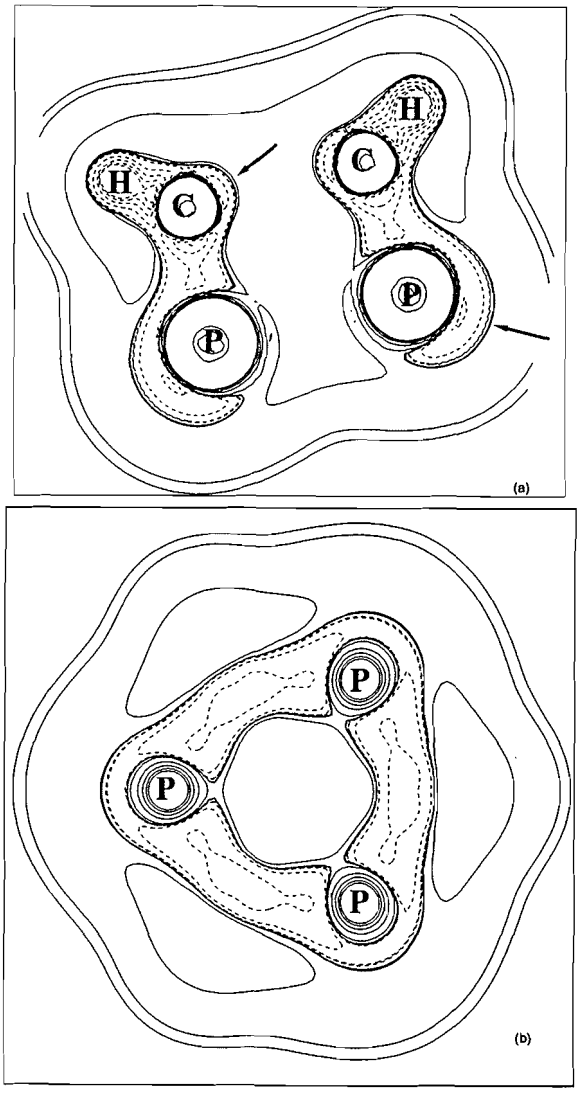

Fig. 3. Laplacian of the charge density in a diagonal plane bisecting the cube for (*a*) phosphorus-protonated tetraphosphacubane; (*b*) carbon-protonated tetraphosphacubane. Same conventions as in Fig. 2.

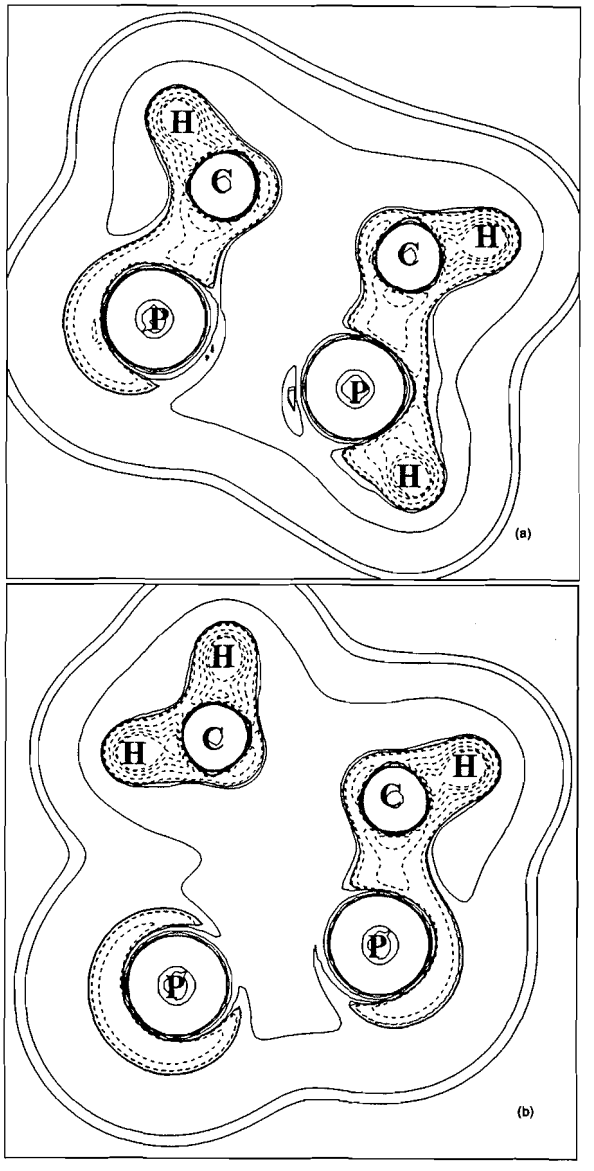

ordination. The consequence is a sizeable strengthening of the P1—C7 and P1—C8 linkages and a parallel weakening of the P3—C7 and P4—C8 bonds (see Table 2).

It is worth noting that the protonated species in which the proton is located at the centre of the cage is not a minimum but a saddle point of the potential energy surface. This is not an unexpected result since is well known that proton attachment is followed by the formation of a covalent linkage, which is strongly favoured when the interaction involves nonbonded charge concentrations such as those exhibited by phosphorus and carbon atoms. Since nonbonded charge concentrations are not found in the charge density that surrounds the centre of the cube cavity, the imaginary vibrational frequencies try to displace the proton outside the cage, in order to favour the interaction with the aforementioned charge concentrations.

Metal cation complexes

The MP2/6-31G(d,p) optimized structures of complexes of tetraphosphacubane with Li^+, Be^{2+}, and Na^+ are shown schematically in Fig. 4. We shall first discuss the alkali metal cation complexes. It can be seen that when the metal cations are located outside the cage only the phosphorus attached complexes, namely, **1Li**$^+$, **1Na**$^+$, are stable. This is consistent with the fact that the molecular electrostatic potential of tetraphosphacubane shows attractive regions only at the phosphorus lone pairs (21), if one takes into account that the interactions of alkali cations with neutral compounds are essentially electrostatic. The Laplacian of the charge density for **1Li**$^+$ (see Fig. 5*a*) and the bonding characteristics of this complex confirm this picture. The charge density at the P—Li^+ bond critical point is small and the Laplacian positive as in typical

Fig. 4. MP2/6-31G(d,p) optimized structures for tetraphosphacubane–X (X = Li^+, Na^+, Be^{2+}) complexes. Bond lengths in Å. The bond angles are given in Table 1. Same conventions as in Fig. 1.

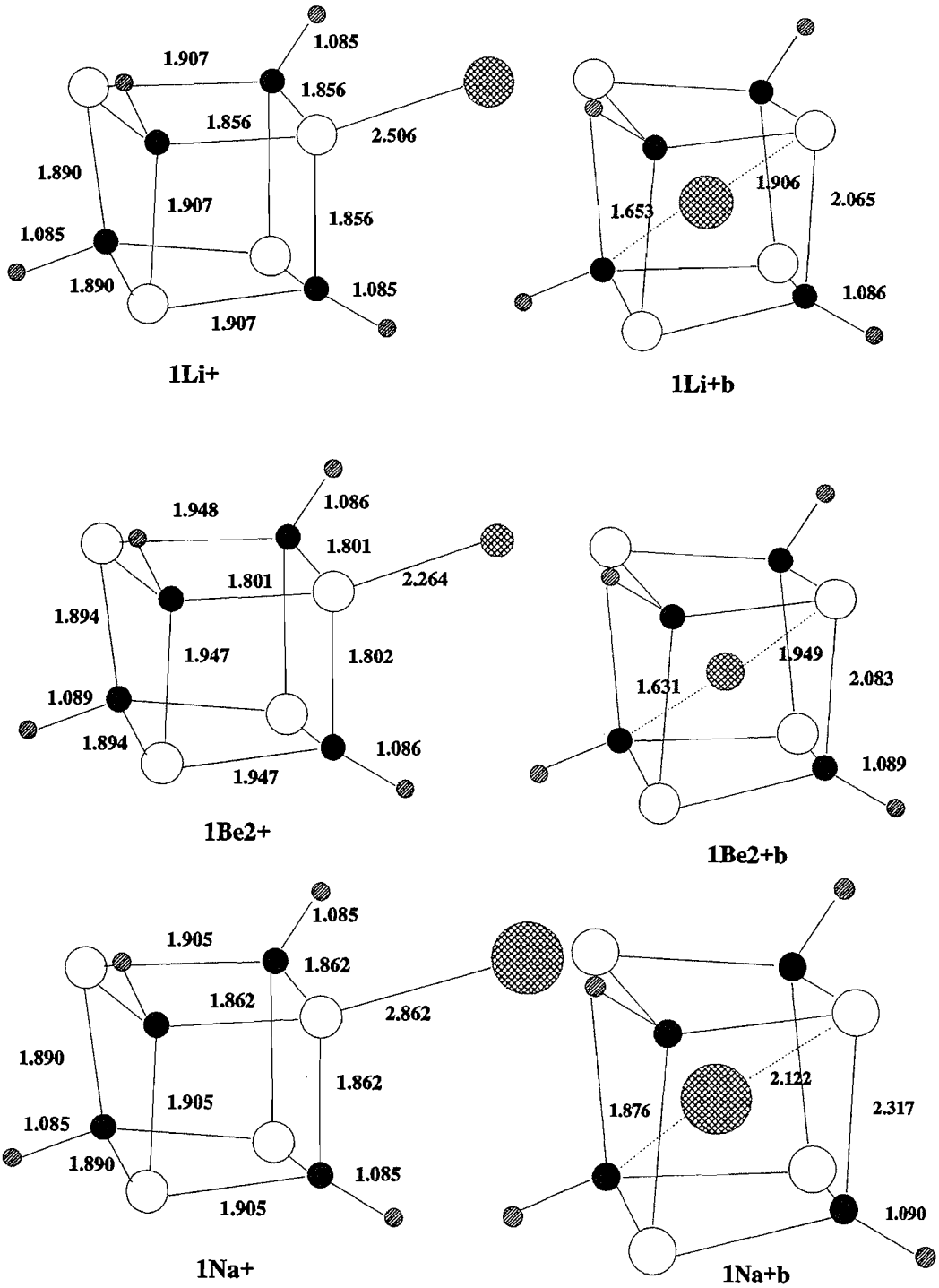

closed-shell interactions. Something similar applies to the **1Na**$^+$ complex. The smaller charge density at the P—Na bond critical point is consistent with a Na^+ binding energy (20.4 kcal/mol) smaller than that found for Li^+ complexes (29.3 kcal/mol). The situation is completely different when the attacking ion is Be^{2+}. As illustrated in Fig. 5*b*, the attachment of Be^{2+} to phosphorus involves charge transfer toward the metal dication that is reflected in a negative value of the Laplacian of the charge density in the P—Be bonding region. The most important consequence is that while the charge redistribution of the neutral upon Li^+ or Na^+ association is small, that found upon Be^{2+} association is quantitatively similar to that found upon protonation (see Tables 1 and 2). It must be observed, however, that the distortions of the bond angles are

Fig. 5. Laplacian of the charge density in a diagonal plane bisecting the cube for (*a*) the **1Li$^+$** complex; (*b*) the **1Be^{2+}** complex. Same conventions as in Fig. 2.

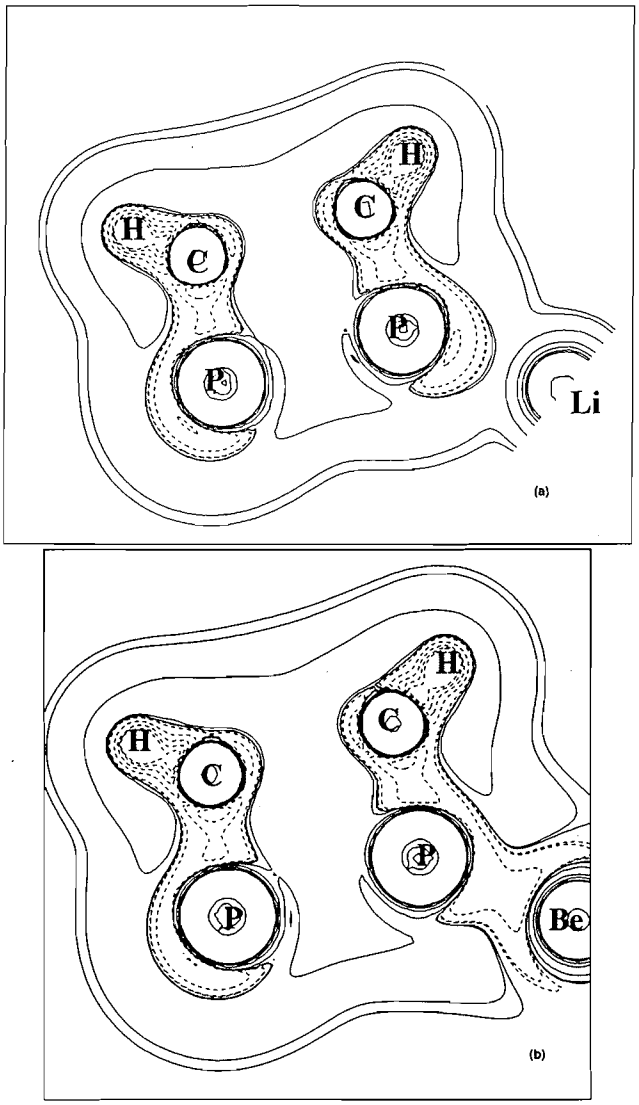

Fig. 6. Laplacian of the charge density in a diagonal plane bisecting the cube for (*a*) the **1Li$^+$b** complex; (*b*) the **1Be^{2+}b** complex. Same conventions as in Fig. 2.

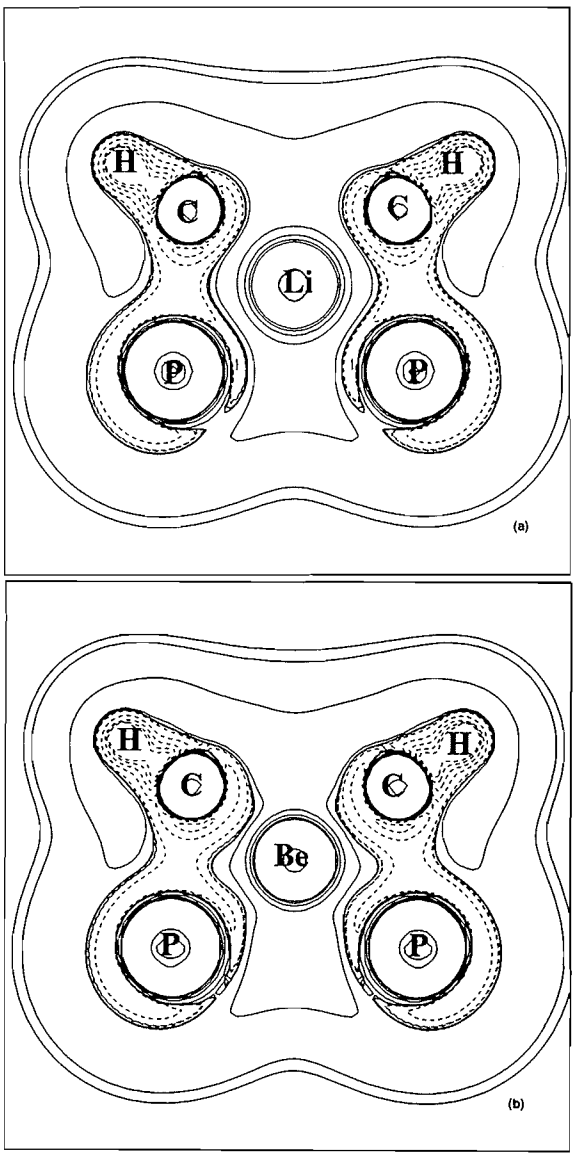

larger for Be^{2+} association than for proton attachment (see Table 1). This is easily understood if one takes into account that in both **1PH$^+$** and **1Be^{2+}** there is a large charge transfer from the neutral to the cation, which reduces significantly the positive charge of the latter. However, while in the **1PH$^+$** species the net positive charge at the proton is rather small (about +0.1), in **1Be^{2+}** the net positive charge at the Be atom is still quite high (about +0.9). This high positive charge is then responsible for an enhancement of the hybridization changes at the basic center, which becomes strongly polarized toward the metal. These effects are mirrored in a significantly large Be^{2+} binding energy (208.5 kcal/mol).

Similarly to what was found upon protonation, Be^{2+} also yields more stable carbon-attached complexes than the phosphorus-attached species **1Be^{2+}**. However, Be^{2+} association implies stronger structural reorganizations than those mentioned above for protonation and, for the sake of conciseness, will not be discussed here.

One of the most significant results of our theoretical survey is that species **1Li$^+$b** and **1Be^{2+}b**, where Li^+ and Be^{2+} are located at the center of the cage cavity, are minima of the potential energy surface, while this was not the case for H^+. As discussed above, this would be expected on the grounds of the different nature of the ion–molecule interactions when the ion is Li^+ or H^+. Since for Li^+ these interactions are essentially electrostatic, the Coulombic attraction between the metal cation and the electronic cloud that surrounds the cavity (see Fig. 6*a*) stabilizes the system. This is confirmed by the existence of bond critical points between Li^+ and the carbon and the phosphorus atoms of the cage (see Table 2). However, since Li^+ is

Fig. 7. Laplacian of the charge density of the **1Be^{2+}b** complex in a plane containing three phosphorus atoms. Same conventions as in Fig. 2.

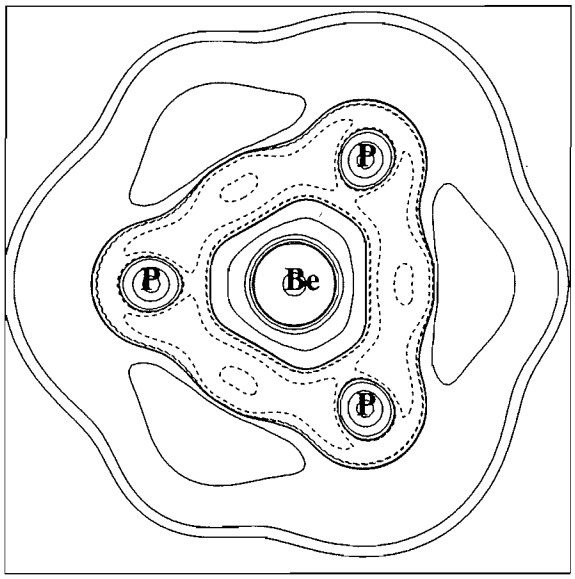

not a point charge, there is a certain repulsive interaction between its $1s^2$ shell of electrons and the electronic charge density around the cavity that leads to an enlargement of the cage. The obvious consequence, as shown in Table 2, is that the charge density at the P—C bond critical points considerably decreases and the P—C linkages become weaker than in the neutral. From the energetic point of view the destabilization of the P—C bonds is not counterbalanced by the attractive interaction between the cation and the charge around the cavity and the formation of species **1Li$^+$b** becomes endothermic with respect to tetraphosphacubane + Li^+.

Since the ionic radius of Na^+ is significantly greater than that of Li^+, the increase of the cage size in **1Na$^+$b** is dramatic (see Fig. 4). As illustrated in Table 1, the P—C bonds become strongly depopulated and the tetraphosphacubane system strongly destabilized. As a consequence the **1Na$^+$b** species is not a minimum of the potential energy surface.

There are significant differences between the **1Li$^+$b** and **1Be^{2+}b** species that are apparent when comparing the Laplacian fields of both complexes (see Figs. 6*a* and 6*b*), and which are due to the strong polarizations caused by Be^{2+}. As shown in Fig. 6*b*, this is reflected in a migration of electronic charge density from the P—C bonding regions into the interior of the cage. As a consequence the charge density at the P—C bond critical points decreases and the bonds become longer, but at the same time the accumulation of electronic charge around the cavity favours a stabilizing interaction with the metal cation. The result is that the **1Be^{2+}b** species is a minimum of the potential energy surface about 172 kcal/mol more stable than tetraphosphacubane + Be^{2+}. It is worth noting that the polarization caused by Be^{2+} is clearly anisotropic as reflected by the deformation undergone by the cavity (See Fig. 7). Actually the distances between the metal cation and the phosphorus atoms in **1Be^{2+}b** are greater than those found for **1Li$^+$b**, while the contrary holds for the metal cation – carbon distances (see Fig. 4). This is so because, as illustrated in Fig. 1*a*, the charge concentrations around the phosphorus atoms point to the outside the cage, while those around the carbon atoms are closer to the center of the cage, favouring interactions with the metal cation.

Conclusions

We have analyzed the reactivity of tetraphosphacubane by using the theory of atoms in molecules. The characteristics of the C—P bonds of tetraphosphacubane are very similar to single P—C bonds in phosphaalkenes. The differences between bond path angles and geometrical bond angles clearly show that the system presents a non-negligible ring strain. The Laplacian of its electron charge density shows that both phosphorus and carbon atoms are active centers for electrophilic substitutions. This is consistent with the fact that both phosphorus and carbon protonated species are minima of the potential energy surface. The strong charge redistribution associated with carbon protonation results in the fission of one of the P—C bonds in which the protonated carbon atom participates. The consequence of this is a significant alleviation of the strain of the system that results in an enhanced stability of carbon protonated species with respect to phosphorus protonated forms. A similar behaviour is found as far as Be^{2+} association is concerned, although charge polarizations are greater than those found upon protonation. An inspection of the electron charge density and its Laplacian indicates that upon either H^+ or Be^{2+} association there is a strong charge transfer from the neutral to the incoming ion. However, in the latter case the net positive charge of Be atom in the complex is still very high (close to unity) and therefore this center still significantly polarizes the rest of the molecule.

The Laplacian field of neutral tetraphosphacubane also shows the existence of a cavity inside the cage surrounded by high electronic density that can stabilize a cation of the appropriate size. Our results confirm that Li^+ and Be^{2+} fulfil this requirement, and the corresponding complexes, where the cation is located at the center of the cage, are minima of the corresponding potential energy surface. Na^+ is far too large and a similar structure is a saddle point of the potential energy surface. The strong polarization caused by Be^{2+} is high enough to considerably stabilize this structure with respect to the isolated systems. For Li^+ this is not the case and the formation of the body-centered complex is endothermic with respect to tetraphosphacubane + Li^+.

Acknowledgements

This work has been partially supported by the DGICYT Project No. PB93-0289-C02-01. We thank A.I. González for valuable suggestions.

References

1. A. Greenberg and J.F. Liebman. Strained organic molecules. Academic Press, New York. 1978.
2. J.D. Cox and G. Pilcher. Thermochemistry of organic and organometallic compounds. Academic Press, New York, 1970.
3. M.D. Newton. *In* Modern theoretical chemistry. *Edited by* H.F. Schaefer III. Plenum Press, New York. 1977.

4. S.M. Bachrach and C.M. Perriott. Tetrahedron Lett. **34**, 6365 (1993).
5. T. Wettling, J. Schneider, O. Wagner, C.G. Kreiter, and M. Regitz. Angew. Chem. **101**, 1035 (1989); Angew. Chem. Int. Ed. Engl. **28**, 1013 (1989); T. Wettling, B. Geißler, R. Schneider, S. Barth, P. Binger, and M. Regitz. Angew. Chem. **104**, 761 (1992); Angew. Chem. Int. Ed. Engl. **31**, 758 (1992).
6. J.L.-M. Abboud, J. Elguero, M. Herreros, R. Notario, O. Mó, M. Regitz, and M. Yáñez. J. Org. Chem. Submitted.
7. R.F.W. Bader. Atoms in molecules. A quantum theory. Oxford University Press, New York. 1990.
8. R.F.W. Bader, P.J. MacDougall, and C.D.H. Lau. J. Am. Chem. Soc. **106**, 1594 (1984).
9. M. Alcamí, O. Mó, M. Yáñez, J.L.-M. Abboud, and J. Elguero. Chem. Phys. Lett. **172**, 471 (1990).
10. M. Alcamí, O. Mó, M. Yáñez, F. Anvia, and R.W. Taft. J. Phys. Chem. **94**, 4726 (1990).
11. A. Luna, O. Mó, and M. Yáñez. J. Mol. Struct. (Theochem), **310**, 135 (1994).
12. A. Luna and M. Yáñez. J. Phys. Chem. **97**, 10659 (1993).
13. J. Tortajada, E. Leon, A. Luna, O. Mó, and M. Yáñez. J. Phys. Chem. **98**, 12919 (1994).
14. A. Luna, O. Mó, and M. Yáñez. Chem. Phys. Lett. **197**, 581 (1992).
15. M.J. Frisch, M. Head-Gordon, G.W. Trucks, J.B. Foresman, H.B. Schlegel, K. Raghavachari, M.A. Robb, J.S. Binkley, C. Gonzalez, D.J. Defrees, D.J. Fox, R.A Whiteside, R. Seeger, C.F. Melius, J. Baker, R.L. Martin, L.R. Kahn, J.J.P. Stewart, S. Topiol, and J.A. Pople. Gaussian 90. Gaussian Inc., Pittsburgh, Pa. 1990.
16. M.J. Frisch, G.W. Trucks, M. Head-Gordon, P.M.W. Gill, M.W. Wong, J.B. Foresman, B.G. Johnson, H.B. Schlegel, M.A. Robb, E.S. Repogle, R. Gompers, J.L. Andres, K. Raghavachari, J.S. Binkley, C. Gonzalez, R. L. Martin, D.J. Fox, D.J. Defrees, J. Baker, J.J.P. Stewart, and J. A. Pople. Gaussian 92, Revision D.2. Gaussian Inc., Pittsburgh, Pa. 1992.
17. R.F.W. Bader and C. Chang. J. Phys. Chem. **93**, 2946 (1989).
18. R.F.W. Bader and H. Essén. J. Chem. Phys. **80**, 1943 (1984).
19. R.F.W. Bader and T.T. Nguyen-Dang. Rep. Prog. Phys. **44**, 893 (1981).
20. S.M. Bachrach. J. Comput. Chem. **10**, 392 (1989).
21. K. Jayasuriya. J. Mol. Struct. (Theochem), **256**, 17 (1992).

An ab initio study on the insertion reactions of CH ($X^2\Pi$) with NH_3, H_2O, and HF

Zhi-Xiang Wang, Ruo-Zhuang Liu, Ming-Bao Huang, and Zhonghua Yu

Abstract: The mechanisms of the reactions of CH ($X^2\Pi$) with NH_3, H_2O, and HF have been studied by means of ab initio molecular orbital calculations incorporating electron correlation with Møller–Plesset perturbation theory up to the second order. For each of the three CH reactions, the insertion path has been found in the potential energy surface; in the calculated insertion path there exists an intermediate complex prior to the transition state that has a lower energy than the reactants. Energetic results indicate that insertion paths are favourable channels for these CH reactions, which is in line with proposals based on kinetic experiments.

Key words: CH radical, ammonia, water, hydrogen fluoride, reaction mechanism.

Résumé : On a étudié les mécanismes des réactions du CH ($X^2\Pi$) avec le NH_3, le H_2O et le HF en faisant appel à des calculs d'orbitales moléculaires ab initio incorporant une corrélation d'électrons avec la théorie de Møller–Plesset jusqu'au deuxième ordre. Pour chacune des trois réactions du CH, on a trouvé la réaction d'insertion dans chacune des surfaces d'énergie potentielle; de plus, dans chaque voie d'insertion calculée, il existe un complexe intermédiaire antérieur à l'état de transition qui possède une énergie inférieure à celle des réactifs. Les résultats énergétiques indiquent que les voies d'insertion sont des canaux favorables pour ces réactions des CH; ceci est en accord avec les propositions basées sur des expériences cinétiques.

Mots clés : CH radical, NH_3, H_2O, HF, mécanisme des réactions.

[Traduit par la rédaction]

Introduction

Methylidyne (CH) is known to be one of the most reactive of all free radicals (1), and is important in combustion and planetary atmospheric chemistry. The reactions of the CH radical with numerous small molecules have been studied by kinetic experiments (1). However, reported theoretical studies on the CH reactions are very few. To our knowledge, reactions of CH with H_2 (2), C_2H_4 (3), CH_4 (4), and N_2 (5) have been theoretically studied. The CH + H_2 reaction was studied by several theoretical groups (2) and it is well known that accurate ab initio calculations predicted the non-least-motion path to be much more favourable than the least-motion path for the CH ($X^2\Pi$) + H_2 insertion reaction. The theoretical study of Gosavi et al. (3) for the CH ($X^2\Pi$) + C_2H_4 reaction indicated that, in agreement with experiment, the energy barrier for the addition reaction was zero if an asymmetric non-least-motion path was followed. The theoretical study of Yu et al. (4) for the CH + CH_4 reaction predicted a complicated and unexpected mechanism. The CH + N_2 reaction was also studied by several theoretical groups (5) and the predicted mechanisms seem to be very complicated. These studies all show unexpected situations and complexities in the reaction paths.

We have been interested in the reactions of CH ($X^2\Pi$) with the XH_n molecules (X = C, N, O, and F with n = 4, 3, 2, and 1, respectively). For these CH reactions, two mechanistic paths (channels) could be assumed: (*i*) the insertion reaction path, methylidyne insertion (with its C-atom) into one X—H bond of the molecule, leading to CH_2XH_{n-1}; and (*ii*) the abstraction reaction path, leading to CH_2 + XH_{n-1}. Experimental studies (6–8) have suggested that the insertion reaction path is the dominant channel for these CH reactions (no reported experimental study on the CH + HF reaction) because of the weak endothermicity of the abstraction reaction. In 1993, two of us investigated the CH + CH_4 reaction by ab initio molecular orbital (UHF) calculations (4), and the results indicated that, for this CH reaction, the assumed insertion path did not seem to exist and the most favorable channel was an abstraction – addition reaction path, which was not in line with that proposed by experiment (6).

We studied the mechanisms of the CH reactions with NH_3, H_2O, and HF by ab initio molecular orbital calculations incorporating electron correlation with unrestricted Møller–Plesset perturbation theory up to second order (UMP2) (9). In the present paper, we report our UMP2 studies on the mechanisms of the three CH reactions, and also discuss the mechanism of the CH reaction with CH_4.

The important goals of the present study were: (*i*) to find the insertion reaction paths in the CH + XH_n (X = N, O, and F) potential energy surfaces, and (*ii*) to then show that the insertion paths are energetically favorable (dominant).

Received October 26, 1995.

This paper is dedicated to Professor Richard F.W. Bader on the occasion of his 65th birthday.

Z.-X. Wang and R.-Z. Liu.[1] Department of Chemistry, Beijing Normal University, Beijing 100875, People's Republic of China. **M.-B. Huang and Z. Yu.** Graduate School, Academia Sinica, P.O. Box 3908, Beijing, 100039, People's Republic of China.

[1] Author to whom correspondence may be addressed.

Calculations details

The UMP2 calculations were carried out with the GAUSSIAN 86 (10) suite of programs using extended 3-21G (11) and polarized 6-31G** (12) basis sets. All the stationary points along the reaction paths were scanned in the geometry optimization calculations with analytic gradient methods at both the UMP2/3-21G and UMP2/6-31G** levels. They were characterized as minima (intermediate complexes) or saddle points (transition states) by means of frequency analysis calculations at the UMP2/3-21G level. In searching the stationary points, geometry optimizations at the UHF level with the 6-31G* basis (12) were also performed. The UMP2/6-31G** optimized geometries and energies are used throughout the text unless otherwise noted.

Results and discussion

1. Insertion reaction paths

The solid-line parts of the potential energy curves shown in (*a*), (*b*), and (*c*) of Fig. 1 represent the UMP2/6-31G** insertion reaction paths of the CH reactions with NH_3, H_2O, and HF, respectively. The insertion products (H_2C–XH_{n-1}) are denoted as 4a, 4b, and 4c, and the transition states of the insertion paths as 3a, 3b, and 3c, respectively. The species 2a, 2b, and 2c represent the intermediate complexes (HC–XH_n) appearing in the insertion paths of the three CH reactions, respectively. The energies of *n*a, *n*b, *n*c (n = 2, 3, and 4) relative to the respective reactants (1a, 1b, and 1c) are given in Fig. 1, and the geometrical parameters of these nine species are given in Fig. 2, together with the UMP2/3-21G and UHF/6-31G* parameters. The insertion paths of these three CH reactions were also found in the UMP2/3-21G potential energy surface. The skeletons of the UMP2/3-21G potential energy curve describing the reaction paths (insertion reactions and subsequent reaction steps) are similar to the UMP2/6-31G** curves shown in Fig. 1.

We examined the geometry evolution of the systems along the insertion paths of the CH reactions with NH_3 and H_2O, for which we looked at the geometries at the stationary points and also those at certain points in between. The UMP2/3-21G geometry optimization calculations were performed at six *Z*-values (the *Z*-parameter, fixed in the optimization, is the distance between the C-atom and the center of the attacked X—H bond) corresponding to the points I, J (2a or 2b), K, L (3a or 3b), M, and N (4a or 4b) on the curves (see Fig. 1). The triangles, shown in Fig. 3(*a*), are the main parts of the six optimized geometries for the CH + NH_3 system, and those shown in Fig. 3(*b*) are for the CH + H_2O system. It is shown in Fig. 3 that, as the *Z*-value decreases, the X—H distance becomes longer and the X—C and C—H distances become shorter, finally leading to the breaking of the X—H bond and simultaneous formation of the X—C and C—H bonds. For all three reaction systems studied, the UMP2/3-21G IRC (intrinsic reaction coordinate) calculations were performed starting at the transition states (3a, 3b, and 3c). In each case, the system, following the calculated IRC, goes downhill to the intermediate complex (2a, 2b, or 2c) in the negative direction of the IRC, and to the insertion product (4a, 4b, or 4c) in the positive direction, which further confirms that the intermediate complex exists prior to the transition state in the path of the insertion reaction for each of the three CH reactions. In 1987, Yates et al. (13) found, in the HF and MPn potential energy surfaces of the CH_2–NH_3 and CH_2–OH_2 systems, two species that could be considered as intermediate complexes in the insertion reactions of $CH_2(^1A_1)$ with NH_3 and H_2O, respectively. In 1991, Sudhakar and Lammertsma (14) reported their theoretical (HF and MPn) studies on singlet nitrene insertion into H_2O and HF, and they found the complexes HN–OH_2 and HN–FH in the insertion reaction paths. These previous studies support our predictions of the existence of intermediate complexes in the insertion paths.

The energetic results for the insertion reaction paths are given in Table 1. Insertion products 4a, 4b, and 4c are predicted to be –103.9, –99.2, and –97.0 kcal/mol more stable than reactants 1a, 1b, and 1c, respectively. The value of –99.2 kcal/mol is reasonably comparable with the available experimental value of –86.2 kcal/mol (8) for the heat of the CH + H_2O reaction. Transition states 3a and 3b are predicted to be 11.4 and 6.2 kcal/mol lower in energy than the respective reactants 1a and 1b, which is line with the experimental facts that the CH + NH_3 and CH + H_2O reactions both have (small) negative activation energies (7, 8). The transition state 3c also has a lower energy than the reactants 1c. The UMP2/6-31G** energetic results definitely indicate that the insertion paths represent the favourable reaction channel for these three CH reactions (see below). The energetic results including the zero-point energy corrections are also given in Table 1, and the changes in the relative energies are small and, as expected, have no effect on the above conclusion for the mechanisms of the reactions.

The energies and geometric parameters, calculated at the UMP2/3-21G and UHF/6-31G* levels, for *n*a, *n*b, and *n*c (n = 2–4) are given in Table 1 and Fig. 2, respectively. The UHF/3-21G and UMP2/6-31G* calculations were also performed for some of the stationary points. The UMP2 calculations with the 3-21G and 6-31G* basis sets predict negative relative energies for the insertion transition states 3a, 3b, and 3c, as with the 6-31G** basis. Due to correlation effects, the UHF energies for these transition states were very high, leading to positive relative energies. As shown in Fig. 2, the UHF/6-31G* values for the C—X distances in 2b and 2c are unreasonably large. Transition state 3c was not found int he UHF/6-31G* calculations.

The intermediate complexes

Intermediate complexes 2a, 2b, and 2c are predicted to be 31.4, 14.3, and 7.2 kcal/mol more stable than reactants 1a, 1b, and 1c, and to be 20.0, 8.1, and 3.7 kcal/mol lower in energy than insertion transition states 3a, 3b, and 3c, respectively (Table 1). Sudhakar and Lammertsma (14) investigated the interactions in the complexes HN–OH_2 and HN–FH, and they were considered as donor–acceptor complexes. In the structures of 2a, 2b, and 2c (Fig. 2), the relatively long C—X distances imply that the three species are only complexes; and the near-orthogonal HCX angles and the orientations of the XH bonds imply that a carbon *p*-orbital is directed at the lone pair (or one of the lone pairs) on the X-atom. The CH radical has two carbon *p*-orbitals perpendicular to its H—C bond, one being singly occupied (SOMO) and the other empty. We found that the SOMO in each of the complexes is just a carbon *p*-orbital perpendicular to the HCX plane, which indicates that there is no interaction between the SOMO of CH and the

Fig. 1. A schematic diagram of the potential energy curves of CH($X^2\Pi$) reactions with NH_3 (*a*), H_2O (*b*), and HF (*c*). The solid-line parts of the curves represent the insertion reactions. The values in parentheses are the UMP2/6-31G** relative energies in kcal/mol.

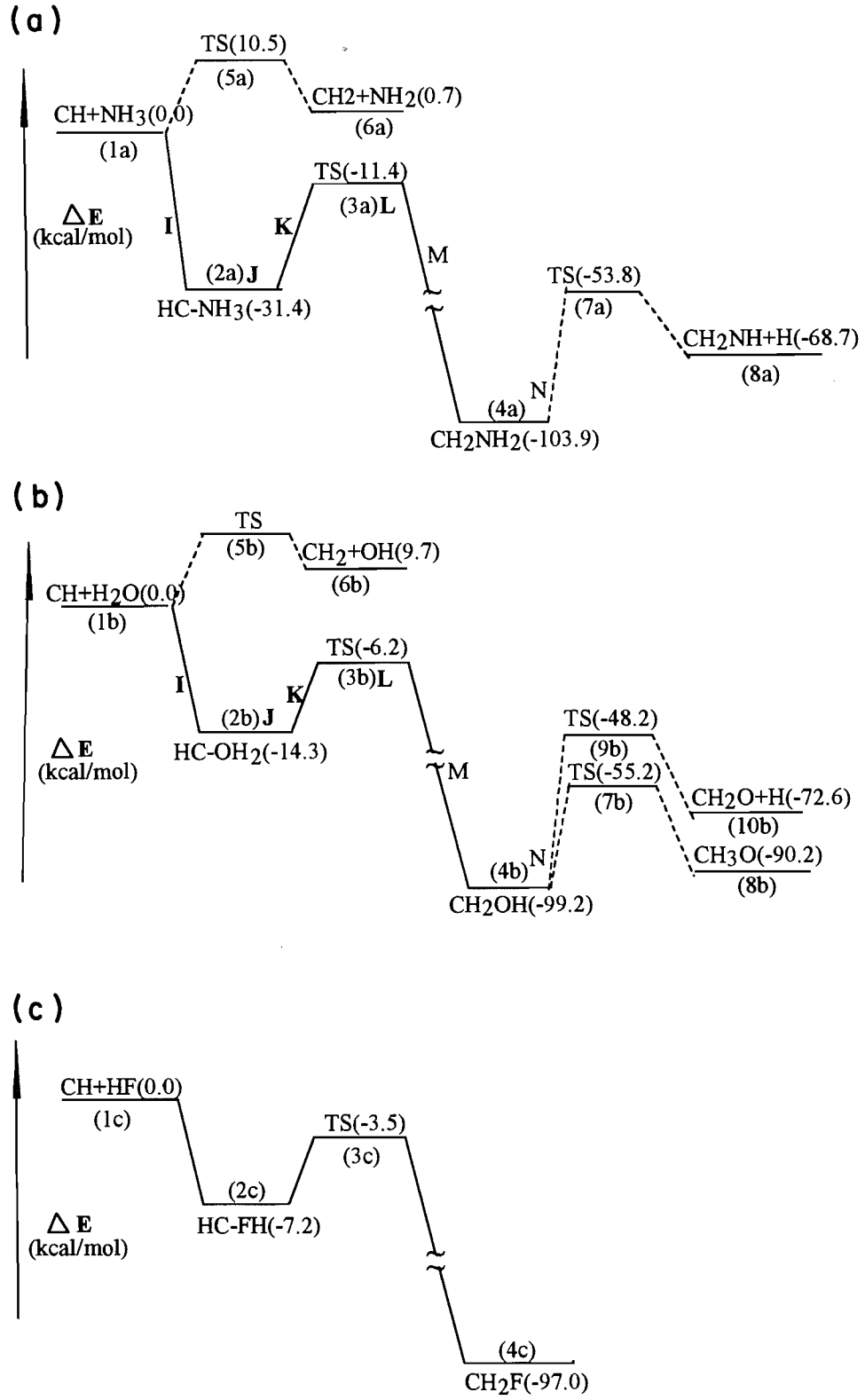

orbital with lone-pair electrons on the X-atom and that the empty carbon *p*-orbital is only directed at the lone-pair orbital. The interaction between the empty *p*-orbital and the lone-pair orbital causes the lone-pair donation to the empty *p*-orbital, which stabilizes complexes 2a, 2b, and 2c. The binding energies of 2a, 2b, and 2c toward the respective reactants are 31.4,

Table 1. Relative energies (in kcal/mol) for the intermediate complexes, transition states, and products of CH ($X^2\Pi$) reactions with NH_3 H_2O, and HF.

	Level				
	UHF/6-31G*	UMP2/3-21G	UMP2/6-31G**	UMP2/6-31G** + ZPE[a]	Exptl.
CH + NH_3 (1a)	0.0	0.0	0.0	0.0	0.0
	(−94.449 29)[b]	(−94.083 11)	(−94.738 00)		
HC–NH_3 (2a)	−16.7	−37.8	−31.4	−26.5	
TS (3a)	16.0	−12.5	−11.4	−9.2	
CH_2NH_2(4a)	−86.2	−103.2	−103.9	−98.3	
TS (5a)	15.9	5.3	10.5	8.7	
CH_2 + NH_2 (6a)	−18.7	−6.6	0.7	−2.0	7.0[c]
TS (7a)	−41.0	−55.2	−53.8	−53.7	
CH_2NH+H (8a)	−48.5	−70.5	−68.7	−70.0	−53.0[c]
CH + H_2O (1b)	0.0	0.0	0.0	0.0	0.0
	(−114.275 68)	(−113.808 00)	(−114.573 53)		
HC–OH_2 (2b)	−7.5	−25.5	−14.3	−12.0	
TS (3b)	21.3	−12.7	−6.2	−4.9	
CH_2OH (4b)	−83.5	−101.0	−99.2	−93.4	−86.2[d]
TS (5b)	16.9	—	—	—	
CH_2 + OH (6b)	−17.6	−7.8	9.7	8.4	17.6[d]
TS (7b)	−34.5	−55.7	−55.2	−52.6	
CH_3O (8b)	−91.0	−101.5	−90.2	−83.7	−80.7[d]
TS (9b)	−39.6	−57.0	−48.2	−48.0	
CH_2O + H(10b)	−55.8	−69.9	−72.6	−71.2	−60.0[d]
CH + HF (1c)	0.0	0.0	0.0	0.0	0.0
	(138.267 84)	−(137.682 24)	(−138.547 78)		
HC–FH (2c)	−5.7	−15.9	−7.2	−5.8	
TS (3c)	—	−10.4	−3.5	—	
CH_2F (4c)	−84.3	−103.2	−97.0	−91.2	

[a]The UHF/6-31G* zero-point energies scaled by a factor of 0.9.
[b]Values in parentheses are the total energies in au.
[c]From ref. 7.
[d]From ref. 8.

14.3, and 7.2 kcal/mol, respectively, and the decreasing order could be rationalized by the fact that the higher the electronegativity of the X-atom, the more difficult it is to donate its lone-pair electrons. Due to the basis set superposition errors, the stability of these intermediate complexes is probably somewhat overestimated.

The CH + CH_4 reaction

As mentioned above, the insertion path for the CH + CH_4 reaction was not found in the previous theoretical study (4), where the UHF method was used and C_s symmetry was assumed for the system. In the present study, we reinvestigated the CH + CH_4 reaction at the UMP2/3-21G level with no symmetry constraint for the system. We tried many ways of approach for the insertion, but we found no species like 2a or 3a and did not find the assumed insertion path. We claim that the complex (HC–XH_n) does not exist for the CH + CH_4 system because there is no lone pair on CH_4. If the insertion path for the CH + CH_4 reaction indeed exists, the path would have a completely different feature from the insertion paths for the CH reactions with NH_3, H_2O, and HF.

Subsequent reaction steps

In (*a*) and (*b*) of Fig. 1, the broken-line sections, starting at 4a and 4b, of the potential energy curves describe the reaction steps subsequent to the insertion reactions of CH with NH_3 and H_2O, respectively. The energetic results for the reaction steps studied are given in Table 1, and the geometrical parameters of the transition states and the products for these reaction steps are given in Fig. 4.

The reaction step subsequent to the insertion reaction of CH with NH_3 is the dissociation of an H-atom from the N-center of 4a via transition state 7a (Fig. 1). The products 8a (CH_2NH + H) are predicted to be 35.2 kcal/mol less stable than 4a, and the calculated energy barrier is 50.1 kcal/mol. However, the energies of 7a and 8a are still much lower than the energy of the reactants 1a. The energy difference between 8a and 1a of −68.7 kcal/mol is comparable with the experi-

Fig. 2. Optimized structures of the intermediate complexes (2), transition states (3), and products (4) for CH ($X^2\Pi$) insertion reactions with NH_3 (*a*), H_2O (*b*), and HF (*c*). The upper values are the UMP2/6-31G** geometric parameters, and the mid and lower values are the UMP2/6-31G** and UHF/6-31G* ones, respectively. Bond lengths are given in Å and angles in degrees.

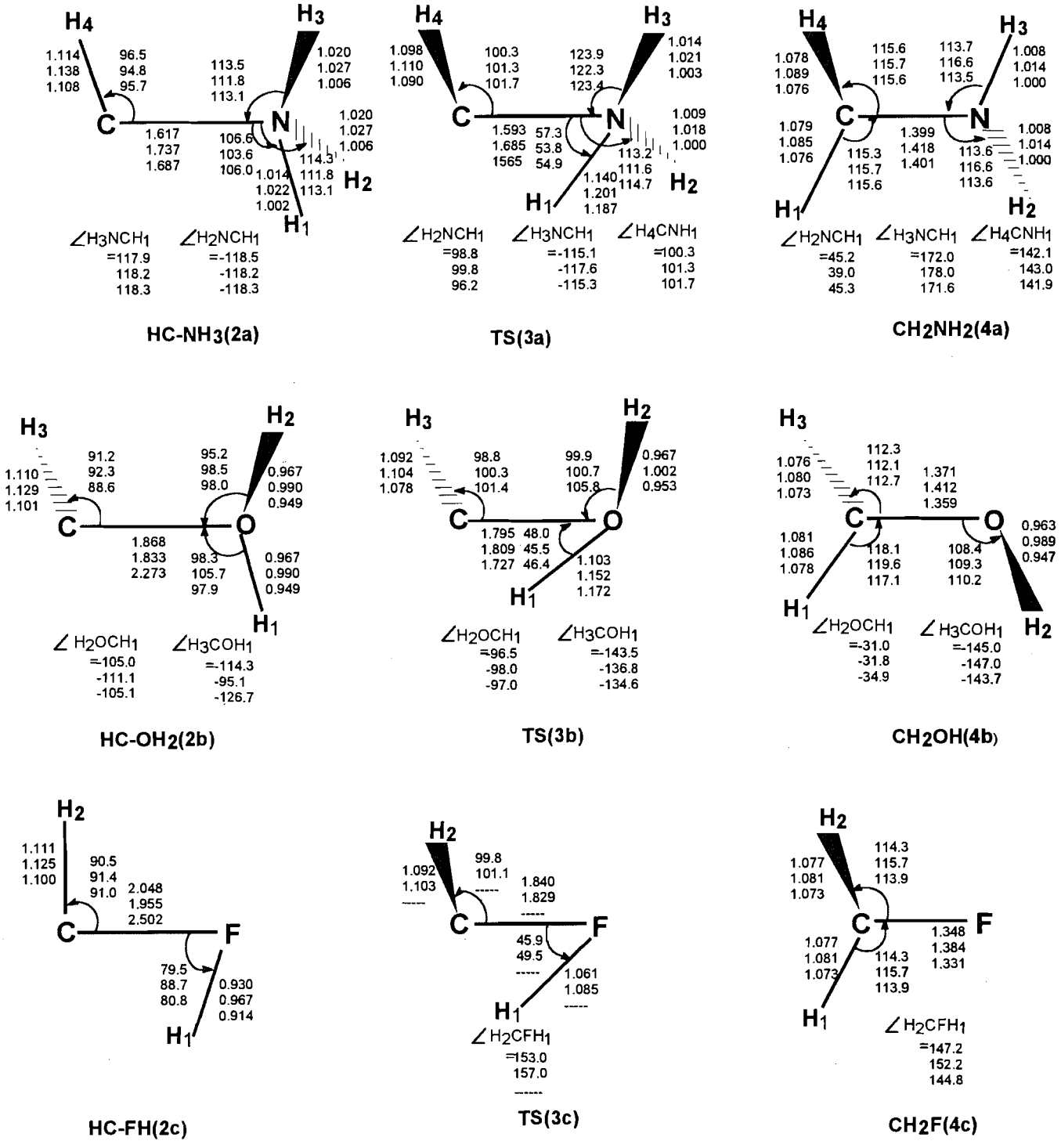

mental value of –53.0 kcal/mol for the heat of the CH + NH_3 reaction (7).

Two channels, as the reactions subsequent to the insertion reaction of CH with H_2O, were studied (Fig. 1). One channel represents the dissociation of the H-atom from the O-center of 4b via transition state 9b, leading to products 10b (CH_2O + H), and other represents hydrogen migration from the O-center to the C-center of 4b via a transition state 7b, leading to product 8b (CH_3O (C_s, $^2A'$)). The energetic results (Table 1) indicate that 7b, 8b, 9b, and 10b all have much lower energies than 1b,

Fig. 3. Structures of ΔCXH (X = N (*a*) and O (*b*)) abstracted from the UMP2/3-21G geometries of the CH + XH_n systems optimized at fixed *Z*-values corresponding to the points I, J, K. L, M, and N in (*a*) and (*b*) of Fig. 1. The parameter *Z* is the distance between the C-atom and the center of the XH distances. Distances are given in Å and the UMP2/3-21G energies (Δ*E*) relative to the reactants in kcal/mol.

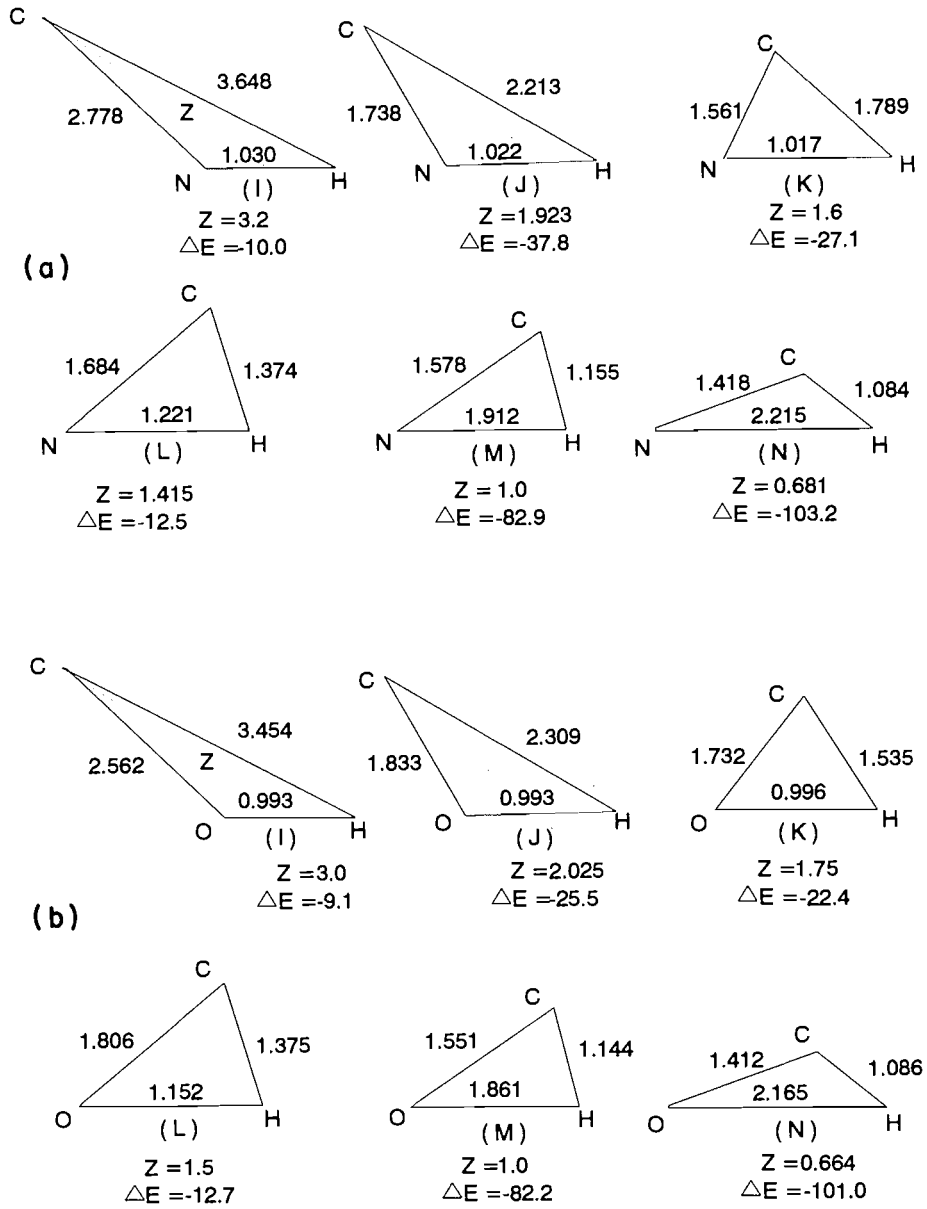

and that the migration reaction is more favorable than the decomposition reaction, which is in agreement with experiment (8). The species 4b, 7b, 8b, 9b, and 10b and related reactions (rearrangements and decompositions) were previously studied by many groups (15–18) at various levels of theory. For this portion of the potential energy surface, the energetic and geometrical results of the present study are comparable with those reported in the previous studies. In the theoretical study of Saebø et al. (15) for the rearrangement of CH_3O to CH_2OH, the geometries of 4b, 7b, 8b, 9b, and 10b were optimized at the UHF levels and the UMP3/6-31G** energies were calculated at the UHF/6-31G** geometries. For the relative energies of 7b, 8b, 9b, and 10b (to 4b) our (UMP2/6-31G** + ZPE) values are close to their respective (UMP3/6-31G**//UHF/6-31G** + ZPE) values, and their optimized geometries are close (or identical) to our respective UHF/6-31G* geometries. In the theoretical study of Walch (16), accurate CASSCF calculations with a large basis set were performed for 7b and 8b. Our (UMP2/6-31G** + ZPE) relative energy value for 7b to 8b is 31.1 kcal/mol, which is comparable with the CASSCF value of 30.1 kcal/mol (16). Our UMP2/6-31G** values for the C—O bonds in the structures of 7b and 8b (Fig. 4) are about 0.03 Å smaller than the CASSCF values (16), and our value of 1.228 Å for the C—H (the migrating one) distance in the structure of 7b (TS) (Fig. 4) is 0.047 Å smaller than the CASSCF value (16). However, the UMP2/6-

Fig. 4. Optimized structures of the transition states (7a, 7b, and 9b) and products (CH_2NH, CH_2O,and CH_3O) for the reaction steps subsequent to the insertion of CH with NH_3 and H_2O. The upper values are the UMP2/6-31G** geometric parameters, and the mid and lower values are the UMP2/3-21G and UHF2/6-31G* ones, respectively. Bond lengths are given in Å and angles in degrees.

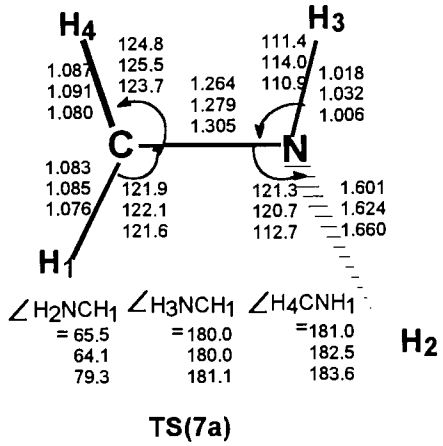

TS(7a)

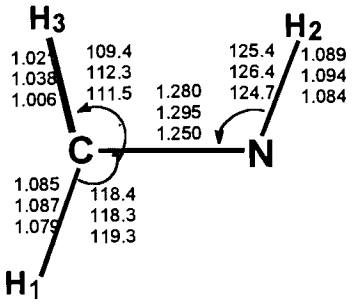

CH_2NH

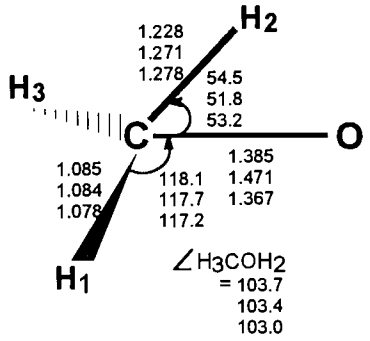

TS(7b)(Cs)

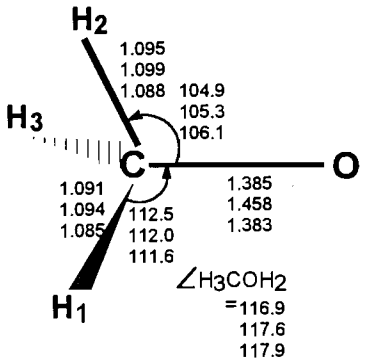

CH_3O(8b)(Cs)

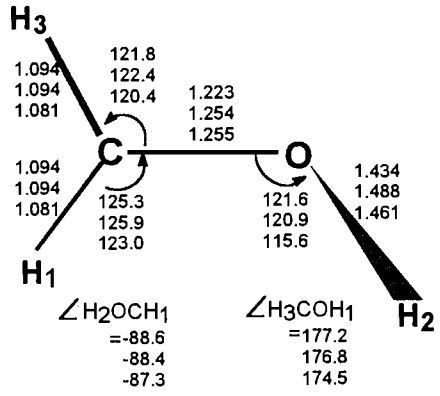

TS(9b)

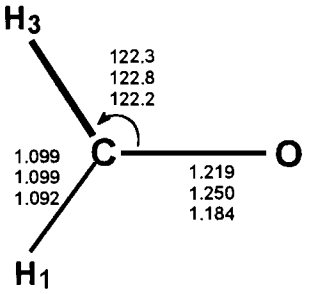

CH_2O

31G** values for the other geometrical parameters in the structures of 7b and 8b are quite close to the respective CASSCF values. In the theoretical study of Bauschlicher et al. (17), the relative energy of 8b to 4b was predicted to be 7.0 kcal/mol, which is closer to the experimental value of 5.5 kcal/mol (8) than our UMP2/6-31G** + ZPE value of 9.7 kcal/mol.

The spin contaminations in the wave functions of the intermediates and transition states, appearing along the paths of the three insertion reactions including the subsequent steps, are small and thus the UHF and UMP2 calculations are valid from the methodological point of view.

2. Abstraction reaction paths

Based on the results reported above, it could already be concluded that the CH reactions with NH_3, H_2O, and HF all have their feasible insertion paths that are strongly exothermic and have transition states with negative relative energies. However, we still calculated the abstraction paths of the CH reactions with NH_3 and H_2O, and the calculated paths are represented by the broken-line curves starting at 1a and 1b shown in (*a*) and (*b*) of Fig. 1, respectively. The abstraction products ($XH_{n-1} + CH_2$ (X^3B_1)) are denoted as 6a and 6b, and the transition states as 5a and 5b, respectively. At the UMP2/6-31G** level (Table 1), the abstraction products are predicted to be slightly less stable than the respective reactants, which is in agreement with experiment (7, 8). The calculated energy differences between the products and the reactants are small values of 0.7 and 9.7 kcal/mol, respectively, which are both about 7.0 kcal/mol smaller than the respective experimental values (7, 8) for the heats of the two abstraction reactions. Calculations at higher levels would lead to better quantitative agreements. The UHF/6-31G* and UMP2/6-31G relative energies for 6a and 6b (Table 1) have the wrong signs. Transition state 5a is predicted to be 10.5 kcal/mol higher in energy than 1a. Transition state 5b was found only in the UHF/6-31G* calculations. Spin contaminations in the wave functions of 5a and 5b are large ($\langle s^2 \rangle \approx 1.35$). This is probably because these doublet transition states are connected with products consisting of a triplet and a doublet species.

Summary

For CH ($X^2\Pi$) reactions with NH_3, H_2O, and HF, insertion reaction paths have been found in the potential energy surfaces. In the insertion path calculated for each of these CH reactions there exists an intermediate complex prior to the transition state. The energetic results indicate that these insertion reactions are all strongly exothermic and all have transition states with negative energies relative to the respective reactants. The present study supports the proposal of the experimental workers (7, 8) that the insertion path is the dominant channel for CH reactions with NH_3 and H_2O.

Acknowledgments

We appreciate the financial support of this work that was provided by the National Natural Science Foundation Committee of China.

References

1. W.A. Sanders and M.C. Lin. *In* Chemical kinetic of small organic radicals, Vol. III. Reactions of special radicals. *Edited by* Z. Alfassi. CRC Press, Boca Raton, Fla. 1988.
2. (*a*) B.R. Brooks and H.F. Schaefer III. J. Chem. Phys. **67**, 5146 (1977); (*b*) T.H. Dunning, L.B. Harding, R.A. Baic, R.A. Eades, and R.L. Shepard. J. Phys. Chem. **90**, 344 (1986); (*c*) T.H. Dunning and L.B. Harding. *In* Theory of chemical reaction dynamics. Vol. I; *Edited by* M. Baer. CRC Press, Boca Raton, Fl. 1985. (*d*) M. Aoyagi, R. Shepard, A.F. Wagner, T.H. Dunning, and F.B. Brown. J. Phys. Chem. **94**, 3236 (1990).
3. R.K. Gosavi, I. Safarik, and O.P. Strausz. Can. J. Chem. **63**, 1689 (1985).
4. Z.-H. Yu, C. Chen, and M.-B. Huang. Can. J. Chem. **71**, 512 (1993).
5. (*a*) M.R. Manaa and D.R. Yarkony. J. Chem. Phys. **95**, 1808 (1991); (*b*) Chem. Phys. Lett. **188**, 352 (1992); (*c*) S.P. Walch. Chem. Phys. Lett. **208**, 214 (1993); (*d*) J.M.L. Martin and P.R. Taylor. Chem. Phys. Lett. **209**, 143 (1993).
6. (*a*) J.E. Butler, J.W. Fleming, L.P. Goss, and M.C. Lin. Chem. Phys. **56**, 355 (1981); (*b*) M.R. Berman and M.C. Lin. Chem. Phys. **82**, 435 (1983).
7. (*a*) S. Zabarnick, J.W. Fleming, and M.C. Lin. Chem. Phys. **132**, 407 (1989); (*b*) K.H. Becker, B. Engelhardt, H. Geiger, R. Kurtenbach, and P. Wissen. Chem. Phys. Lett. **210**, 135 (1993).
8. S. Zabarnick, J.W. Fleming, and M.C. Lin. Symp. (Int.) Combust. [Proc.] 21st. The Combustion Institute. 1986. p. 713.
9. (*a*) C. Møller and M.S. Plesset. Phys. Rev. **46**, 618 (1934); (*b*) J. A. Pople, J.S. Binkley, and R. Seeger. Int. J. Quantum Chem. Symp. **10**, 1 (1976).
10. M.J. Frisch, J.S. Binkley, H.B. Schlegel, K. Raghavachari, C.F. Melius, R.L. Martin, J.J.P. Stewart, F.W. Bobrowicz, C.W. Rohlfing, L.R. Kahn, L.R. DeFrees, R. Seeger, R.A. Whiteside, D.J. Fox, E.M. Fleuder, and J.A. Pople. GAUSSIAN 86. Carnegie–Mellon Quantum Chemistry Publishing Unit, Pittsburg, Pa. 1986.
11. J.S. Brinkley, J.A. Pople, and W.J. Hehre. J. Am. Chem. Soc. **102**, 939 (1980).
12. P.C. Hariharan and J.A. Pople. Theor. Chem. Acta, **28**, 213 (1973).
13. B.F. Yates, W.J. Bouma, and L. Radom. J. Am Chem. Soc. **109**, 2250 (1987).
14. P.V. Sudhakar and K. Lammertsma. J. Am. Chem. Soc. **113**, 5210 (1991).
15. S. Saebø, L. Radom, and H.F. Schaefer III. J. Chem. Phys. **78**, 845 (1983).
16. S.P. Walch. J. Chem. Phys. **98**, 3076 (1993).
17. C.W. Bauschlicher, Jr., S.R. Langhoff, and S.P. Walch. J. Chem. Phys. **96**, 450 (1992).
18. J. Fossey and J. Sorba. THEOCHEM, **186**, 305 (1989).

Calculation of static molecular properties in the framework of the unitary group based coupled cluster approach

Josef Paldus and Xiangzhu Li

Abstract: The recently developed and implemented state selective, fully spin-adapted coupled cluster (CC) method that employs a single, yet effectively multiconfigurational, spin-free reference and the formalism of the unitary group approach (UGA) to the many-electron correlation problem, has been employed to calculate static electric properties of various open-shell (OS) systems using the finite field (FF) technique. Starting with the lithium atom, the method was applied at the first-order interacting space single and double excitation level (CCSD(is)) to several first- and second-row hydrides having OS ground state, namely to the CH, NH, OH, SiH, PH, and SH radicals. In the case of NH we also considered three OS excited states. In all cases the dipole moment and polarizability were determined using a high quality basis set and compared with the experiment, whenever available, as well as with various configuration interaction results and other theoretical results that are available from the literature. The agreement of our CCSD(is) values with experiment is very satisfactory except for the $^3\Sigma^-$ ground state of the NH radical, where the experimentally determined dipole moment is too small. No experimental data are available for the corresponding polarizabilities. It is also shown that the FF technique is not suitable for calculations of higher order static properties, such as the hyperpolarizability β and γ tensors. For this reason we formulate the linear response version of our UGA-based CCSD approach and discuss the aspects of its future implementation.

Key words: static molecular properties, dipole moments, polarizabilities, free radicals, unitary group based coupled cluster method, linear response theory, finite field technique.

Résumé : On a utilisé la méthode des «coupled cluster» («CC») complètement adaptée aux spin et sélective des états, développée et mise en place récemment, qui n'utilise qu'une référence sans spin, mais qui est malgré tout effectivement multiconfigurationnelle, ainsi que le formalisme de groups unitaires («UGA») au problème de la corrélation de plusieurs électrons pour calculer les propriétés statiques de divers systèmes en couches ouvertes («OS») en utilisant la technique du champ fini («FF»). En commençant avec l'atome de lithium, on a appliqué cette méthode au premier niveau d'interaction de l'espace des configurations singulièrement et doublement excitées (CCSD(is)) pour plusieurs hydrures des deux premières couches possédant un état fondamental OS, soit les radicaux CH, NH, OH, SiH, PS et SH. Dans le cas du NH, on a aussi considéré trois états excités OS. Dans tous les cas, on a déterminé le moment dipolaire et la polarisabilité en utilisant un ensemble de base de bonne quantité et, dans tous les cas où cela était possible, on les a comparés avec les données expérimentales ainsi qu'avec les divers résultats d'interactions de configuration et d'autres résultats théoriques disponibles dans la littérature. L'accord entre nos valeurs de CCSD(is) et les valeurs expérimentales est satisfaisant, à l'exception de ceux pour l'état fondamental $^3\Sigma^-$ du radical NH pour lequel la valeur expérimentale est trop faible. Il n'y a pas de données expérimentales disponibles pour les polarisabilités correspondantes. Il a été démontré que la technique «FF» n'est pas appropriée pour les calculs des propriétés statiques d'ordre supérieur, tels que les tenseurs d'hyperpolarisabilité β et γ. C'est la raison pour laquelle on formule la version de la réponse linéaire à notre approche «CCSD» qui repose sur l'approche «UGA» et on discute les aspects de sa réalisation pratique dans l'avenir.

Mots clés : propriétés moléculaires statiques, moments dipolaires, polarisabilités, radicaux libres, groupe unitaire basé sur la méthode des agrégats couplés, théorie de la réponse linéaire, technique du champ fini.

[Traduit par la rédaction]

Received October 5, 1995.

This paper is dedicated to Professor Richard F.W. Bader, with friendship and affection, on the occasion of his 65th birthday.

J. Paldus[1,2] and X. Li. Department of Applied Mathematics, University of Waterloo, Waterloo, ON N2L 3G1, Canada.

[1] Also at: Department of Chemistry and Guelph–Waterloo Center for Graduate Work in Chemistry – Waterloo Campus, University of Waterloo, Waterloo, ON N2L 3G1, Canada.

[2] Author to whom correspondence may be addressed. Telephone: (519) 888-4567, ext. 6267. Fax: (519) 746-4319. E-mail: paldus@theochem.uwaterloo.ca

1. Introduction

An ab initio determination of static and dynamic molecular properties is very useful in a wide range of both theoretical and practical applications. This is particularly the case for nonlinear optical properties that are closely related with various hyperpolarizabilities (see, for example, ref. 1), but also for molecular electric and magnetic multipole moments that play an important role in diverse spectroscopic studies (2) as well as in the determination of long-range components of intermolecular interaction potentials (3). Very recently, for example, molecular polarizabilities were employed to rationalize an alignment and trapping of molecules in intense laser fields, enabling one to enhance dynamical resolution of collisional or spectroscopic experiments (4). While in the past most of the quantum chemical methodology and computations concentrated on the determination of molecular energetics and structure, more recent developments often focus on property determination as well.

In the framework of the coupled clustered (CC) methodology (5, 6) which proved to be very successful in computations of correlated electronic energies, particularly for nondegenerate closed shell (CS) ground states (6), as well as the closely related many-body perturbation theory (MBPT) (7), a number of different approaches have been exploited for this purpose. These include direct evaluation of expectation values of the operator characterizing the given property (5*b*, 8), variational and bivariational approaches (9), a stationary Lagrangian technique (10), a linear response (LR) theory (6*b*, 11) and related approaches (12, 13), as well as methods using a uniform finite field (FF) or a field generated by a set of strategically placed point charges (14). The direct evaluation of expectation values leads to a nonterminating series expansion (5*b*) that is rather cumbersome to handle (8) and could lead to serious convergency problems in quasidegenerate cases when the magnitude of some cluster amplitudes can be appreciable (cf., however, ref. 8*d*). Similar problems also plague some stationary response methods (9). The last methods (i.e., uniform FF or point charge generated field methods) are easiest to implement, since they can directly employ the existing codes for the electronic energy calculations. However, the FF methods have their limitations when considering higher order properties, as we shall indicate later on. These problems can be circumvented by employing suitable multipolar fields of point changes (14*a*–*e*), as first proposed by McLean and Yoshimine (15) and extensively used even in other than CC approaches (see, e.g., ref. 16).

One of the most appealing approaches of great generality is undoubtedly the LR theory, which can handle not only static properties of various orders, but also the dynamic or frequency-dependent ones. This approach, first outlined in the context of the CC method by Monkhorst (11*a*), requires only a single calculation of the correlation energy and cluster amplitudes for each geometry followed by the solution of a recursive set of linear equations for higher and higher order properties. A recent implementation of this approach in our laboratory (17), within the context of CS orthogonally spin-adapted CCSD (CC method restricted to singly and doubly excited cluster components) formalism (18), enabled very promising applications when computing higher order properties.[3] Even for the second hyperpolarizability tensor we were able to generate the entire property surface,[3] which is required when considering rovibrational effects and computing rovibrationally averaged property values for individual rotational and vibrational states (19).

While considerable progress is being made for CS systems, as we just outlined, the computation of properties (even of static ones) for open shell (OS) molecular systems with more than three electrons is sorely lacking (8*g*, 13*d*–*f*, 20). The principal reason for this state of affairs is the lack of suitable OS CC methodology. Although the proper multireference CC approaches of either the valence universal or state universal types have been formulated, and several of their variants even implemented (for an overview, see refs. 6 and 21), their complexity and the cognate practical difficulties associated with intruder state problem, multiplicity of solutions, or symmetry breaking make their implementation limited even when considering molecular energetics. As far as we are aware, the only properly spin-adapted multireference CC property calculation, using the state universal approach, was recently carried out in our laboratory for the lowest singlet state of methylene (20). Otherwise, most CC approaches to OS systems exploit the simple single reference CCSD approach based on the unrestricted Hartree–Fock (UHF) reference. This very simple and straightforward approach does indeed often provide very useful results in spite of its inherent limitations and conceptual drawbacks (see e.g. ref. 22). Even when the UHF reference is heavily spin contaminated, the spin impurity of the resulting CC wave function is usually greatly reduced (23) and the computed energies are little affected. However, when calculating other properties, the residual spin contamination can play a significant role. For example, even small spin impurities can cause a significant error in calculated vibrational frequencies, since the magnitude of this error is a function of the derivative of the mean value of the total spin $\langle S^2 \rangle$ with respect to the molecular geometry (24). In any case, the choice of a suitable UHF solution as a reference is not unambiguous, since for a certain range of geometries several UHF solutions may exist, and the energetically lowest one may not correspond to the ground state potential energy curve (22). Most importantly, however, the UHF-based CC method is restricted to high-spin states and cannot be used to describe the important case of low-spin, OS singlet states. Similar problems are, of course, encountered in other post-Hartree–Fock approaches that employ the UHF reference, such as the finite order MBPT method (25).

In view of the challenge of handling the OS systems using the CC methodology, we have recently introduced (26) and implemented (27) a single reference, yet effectively multi-configurational, CC approach exploiting a spin-free formalism of the so-called unitary group approach (UGA) (28), or Clifford algebra UGA (CAUGA) (29) and bonded tableau approach (30) to the many-electron correlation problem. Our existing experience (22, 31, 32) indicates a great practical usefulness of this formalism in the handling of many OS sys-

[3] A.E. Kondo, P. Piecuch, and J. Paldus. J. Chem. Phys. In press.

tems, particularly the high-spin doublet and triplet states as well as low-spin OS singlets (involving two OS orbitals). It is thus desirable to explore the potentialities of this formalism in property calculations as well. Although our ultimate goal is to formulate and implement the UGA-based CC version of the LR method, we will first investigate the performance of the UGA-CCSD approximation using the FF technique. For this reason we investigate several static properties for a few first- and second-row hydrides in their OS ground states using the UGA-CCSD FF method. In addition, we also consider the ground state of Li and several excited states of the NH radical, where experimental information concerning the dipole moment is available. These results will not only attest to the reliability of the UGA-based CCSD method for property calculations, but also provide the much needed benchmark values for the testing of various versions of the LR approach based on this method that we intend to develop in the future.

In the next section we thus briefly outline the UGA-based CCSD method employed and its implementation. In Sect. 3 we apply this method, using the FF approach, to a few OS species and compare the calculated property values with the available experimental ones as well as with other computations. The LR approach within the context of UGA-CC formalism is then outlined and discussed in Sect. 4.

2. UGA-based CC method

The single reference CC methods rely on the cluster expansion of the exact wave function $|\Psi\rangle$,

$$[1] \qquad |\Psi\rangle = e^T|\Phi\rangle,$$

where $|\Phi\rangle$ designates an independent particle model reference configuration, represented by a single antisymmetrized product of spin orbitals, and T is the cluster operator, which can be expressed as a linear combination of a suitable set $\{G_I\}$ of excitation operators G_I,

$$[2] \qquad T = \sum_I t_I G_I$$

with t_I labelling the corresponding cluster amplitudes. The excitation operators G_I may then be conveniently represented as products of unitary group generators (33).

In contrast to the standard single reference CC approach, when $|\Phi\rangle$ is represented by an independent particle model (usually Hartree–Fock) single determinantal configuration wave function, the UGA-based formalism employs a spin-free reference representing in general a multi-configurational state. This reference state can be labeled by a Gel'fand, Weyl, or Paldus tableau (28), or by a two-box CAUGA or bonded tableau (29, 30). In the CS case, the resulting approach can be shown to be equivalent to the standard (orthogonally) spin-adapted CC formalism (26). However, in OS cases, the spin-free CC Ansatz [1] is unique to the UGA-CC theory and is not equivalent to some spin-adapted version of molecular spin orbital-based Ansätze.

Adopting thus the spin-free Ansatz [1], we can formally proceed as in the standard single reference case, except that we can no longer exploit the diagrammatic techniques (6, 7*a*, 34) but have to rely solely on the algebraic formalism. Nonetheless, rather than exploiting the second quantization formalism, we can employ directly the unitary group approach (28–30). Starting from the time-independent, spin-free form of the Schrödinger equation for the electronic Hamiltonian H,

$$[3] \qquad H|\Psi\rangle = E|\Psi\rangle$$

and exploiting the cluster expansion [1], we obtain after premultiplying with the inverse operator $\exp(-T)$ the basic equation

$$[4] \qquad e^{-T}He^T|\Phi\rangle = E|\Phi\rangle$$

The projection onto the reference state $|\Phi\rangle$ yields the standard expression for the energy, namely

$$[5] \qquad E = \langle e^{-T}He^T\rangle = \langle H\rangle + \langle [H, T]\rangle + \tfrac{1}{2}\langle [[H, T], T]\rangle + \cdots$$

and the projection on the excited configurations $G_I|\Phi\rangle$ gives the energy-independent CC equations

$$[6] \qquad \langle G_I^\dagger e^{-T}He^T\rangle = 0$$

where $\langle X\rangle$ designates the reference state mean value of an operator X

$$[7] \qquad \langle X\rangle := \langle\Phi|X|\Phi\rangle$$

and $[X, Y]$ the commutator of X and Y,

$$[8] \qquad [X, Y] = XY - YX$$

In contrast to the standard CS case, where the energy expression involves at most bilinear terms in monoexcited cluster amplitudes and only linear terms in biexcited amplitudes, the general OS case may contain even quartic terms thanks to the presence of partially occupied valence or active orbitals in the reference $|\Phi\rangle$. Thus, for the correlation energy $\Delta E \equiv E - \langle H\rangle$ we obtain (26, 27)

$$[9] \qquad \Delta E = \sum_I e_I^{(1)} t_I + \sum_{IJ} e_{IJ}^{(2)} t_I t_J + \sum_{IJK} e_{IJK}^{(3)} t_I t_J t_K + \sum_{IJKL} e_{IJKL}^{(4)} t_I t_J t_K t_L$$

where the general coefficient has the form

$$[10] \qquad e_{IJ\cdots M}^{(n)} = \frac{1}{n!}\langle [\cdots [[H, G_I], G_J], \cdots G_M]\rangle = \frac{1}{n!}\langle HG_IG_J\cdots G_M\rangle$$

The last equality is implied by the fact that

$$[11] \qquad G_I^\dagger|\Phi\rangle = 0$$

since the excitation operators G_I always annihilate at least one core orbital or create at least one virtual orbital.

The corresponding CC equations [6], determining the cluster amplitudes t_I, can involve up to eight commutators and have the general form

$$[12] \qquad \langle G_I^\dagger e^{-T} H e^T \rangle = a_I + \sum_J b_{IJ} t_J + \sum_{J \le K} c_{IJK} t_J t_K + \cdots = 0$$

The absolute, linear, and bilinear coefficients are then given by the following expressions

$$[13] \qquad a_I = \langle G_I^\dagger H \rangle$$

$$[14] \qquad b_{IJ} = \langle G_I^\dagger [H, G_J] \rangle = \langle G_I^\dagger H G_J \rangle - \langle G_I^\dagger G_J H \rangle$$

and

$$[15] \qquad c_{IJK} = [2(1+\delta_{JK})]^{-1} \langle G_I^\dagger ([[H, G_J], G_K] + [[H, G_K], G_J]) \rangle$$

Defining

$$[16] \qquad \tilde{c}_{IJK} = \langle G_I^\dagger H G_J G_K \rangle + \langle G_I^\dagger G_J G_K H \rangle - 2\langle G_I^\dagger G_J H G_K \rangle$$

we can write

$$[17] \qquad c_{IJJ} = \tfrac{1}{2} \tilde{c}_{IJJ}$$

and

$$[18] \qquad c_{IJK} = \tfrac{1}{2}(\tilde{c}_{IJK} + \tilde{c}_{IKJ}), \qquad (K \neq J)$$

The terms involving higher order commutators can be similarly handled. However, in our implementation of the UGA-CCSD approach, which we briefly describe below, we consider at most bilinear terms in CC equations [12], while considering all the terms when evaluating the energy, eq. [9]. Note, however, that the quartic energy term involves only semi-internal monoexcitations and the cubic term at least a pair of such monoexcitations. Similarly, the n-commutator term in CC equations [12] must involve at least $\max\{(2n-8), 0\}$ semi-internal monoexcitations, the remaining amplitudes being either semi-internal biexcitations or all-external monoexcitations. The possible types of nonlinear terms appearing in CCSD equations [12] that arise from n-commutator terms of eq. [6] and involve n excitation operators G_I and n corresponding cluster amplitudes t_I, $2 \le n \le 8$, are listed in Table 1. These n-linear terms are characterized by the number of semi-internal and all-external mono- and bi-excited cluster amplitudes involved. Clearly, we can safely neglect most of the higher than bilinear terms, since they primarily involve semi-internal monoexcitations, or high orders of other terms corresponding to high-order MBPT contributions. In the present version of our codes, at most bilinear terms ($n < 3$) are considered.

Numerous applications carried out so far, and their comparison with the exact full configuration interaction (FCI) results or highly precise data, justify the truncation scheme employed and described above (22, 27, 31, 32). However, it would be worthwhile to explore the role of certain higher order terms in greater detail, particularly for highly stretched geometries. In this work, we shall restrict our attention to geometries that are close to the equilibrium one.

Table 1. List of distinct types of n-linear terms in CCSD equations [12] for $n \ge 2$.

n	Possible terms[a]				
2	(2000)	(1100)	(0200)	(0020)	(0002)
		(1010)	(0110)	(0011)	
		(1001)	(0101)		
3		(1200)	(0300)	(0030)	(0003)
		(1110)	(0210)	(0021)	
		(1101)	(0201)	(0012)	
		(1020)	(0120)		
		(1011)	(0111)		
		(1002)	(0102)		
4		(1102)	(0400)	(0040)	(0004)
		(1012)	(0301)	(0031)	
		(1003)	(0220)	(0022)	
			(0211)	(0013)	
			(0202)		
			(0121)		
			(0112)		
			(0103)		
5		(1004)	(0212)	(0032)	(0005)
			(0203)	(0023)	
			(0122)	(0014)	
			(0113)		
			(0104)		
6			(0204)	(0024)	(0006)
			(0114)	(0015)	
			(0105)		
7			(0106)	(0016)	(0007)
8					(0008)

[a]Each n-linear contribution originating from an n-commutator term comprising n excitation operators and cluster amplitudes is labelled by a quadruple of integers (n_1, n_2, n_3, n_4), $n = n_1 + n_2 + n_3 + n_4$, whose components n_i indicate the number of all-external biexcitations (n_1), semi-internal biexcitations (n_2), all-external monoexcitations (n_3), and semi-internal monoexcitations (n_4) involved.

To select a suitable set of excitation operators, we exploit the group chain

$$[19] \qquad U(n_c + n_v + n_a) \supset U(n_c) \times U(n_v) \times U(n_a)$$

where n_c, n_v, and n_a designate the number of core, virtual, and active orbitals, respectively. Recall that the core and virtual orbitals are, respectively, doubly occupied and unoccupied in the reference, while the active orbitals are singly occupied. In this way, the invariance of our formalism with respect to separate unitary transformations within each orbital group (ie., core, active, and virtual) is assured.

In actual applications we truncate the cluster operator expansion [2] at the biexcited level. However, since some of the excitation operators G_I also involve active (or valence) orbitals, which are only partially occupied in the reference $|\Phi\rangle$, we should also include in our set of singly (S) and doubly (D) excited configurations so-called pseudo-single and pseudo-double ones, which involve up to four UGA orbital generators

(in the triplet case; otherwise at most three orbital generators). However, higher than rank two biexcitations usually play a rather unimportant role, at least for near equilibrium geometries. We have in fact examined two distinct approximations (32*b*), namely, the full single and double (SD) excitation space approximation [CCSD(f)], involving all S and D as well as pseudo-single and pseudo-double excitations (the latter represented by rank 3 or rank 4 excitation operators), and the so-called (first-order) interacting space (is) approximation [CCSD(is)], restricting our set of excitation operators to the first-order interacting space, represented by at most rank 2 operators. It turns out that in the vicinity of equilibrium geometries these two approximations differ very little (usually by a few microhartrees) but, even for significantly stretched geometries, this difference does not exceed a few millihartrees (32*b*). Thus, unless we wish to explore the structures with highly stretched bonds (where the method may fail to converge anyway if $|\Phi\rangle$ no longer represents a suitable zero order approximation), the CCSD(is) approximation is adequate.

The explicit form of the excitation operators G_I for the three important cases, namely the high-spin doublet and triplet states (involving one and two OS orbitals, respectively) and the low-spin OS singlet case (involving two OS orbitals) may be found in ref. 27 (for the high-spin cases, see also ref. 26*c*). These operators represent irreducible tensor operators adapted to the chain [19] and generate orthonormal states. Since we have to distinguish a considerable number of these operators (up to 30 in the most involved triplet case), the derivation of the explicit expressions for various coefficients appearing in our CC equations [12] and in the expression for the energy, eq. [9], is very laborious. To facilitate this derivation and to avoid possible errors, we have designed a set of codes that carry out this procedure automatically. This software is described in greater detail in ref. 27, and it generates the FORTRAN codes that set up and solve the UGA-CCSD equations and evaluate the corresponding energy. These codes were carefully tested by duplicating the algebraic derivations by hand in the doublet and OS singlet cases, as well as by careful numerical studies (27).

3. Static property calculations using the UGA-CCSD FF method

To test the capability of our UGA-based CCSD method, as implemented in our codes (27), to provide reliable values of at least low-order static properties for OS systems, we employ the FF approach and examine a few test examples involving states of different multiplicity. These results will also serve us as benchmark values when implementing and testing various versions of the LR approach, which we briefly outline in Sect. 4.

Systems examined and computational details

The systems that we examine in this work comprise the lithium atom (Li), first-row diatomic hydrides methylidene (CH), imidogen, or nitrene (NH) and hydroxyl (OH) radicals, and the second-row hydrides silylidine (SiH), phosphinidene (PH), and sulfhydryl or mercapto (SH) radicals. All of these systems have an OS ground state that is amenable to our UGA-based CC approach. The ground state equilibrium bond lengths were taken from ref. 35 (see Tables 3 and 5). In addition to the ground states of the above-mentioned systems, we also examine three degenerate excited states of NH, namely the states $a^1\Delta$, $A^3\Pi$, and $c^1\Pi$ whose experimental electric dipole moments are known (36). The experimental bond lengths for these excited states were taken from ref. 35 (see Table 6).

Computations of molecular properties generally require large high-quality basis sets, preferably designed specifically for this purpose. We have chosen two different types of basis sets for our investigations. The first type is represented by the POL1 basis sets of Sadlej (37), which are medium-sized polarized basis sets that are specifically tailored for the high-level correlated calculations of molecular electrostatic properties. For the first-row atoms (C, N, and O), this is a [5*s*3*p*2*d*] basis set, for the second-row atoms (Si, P, S) a [7*s*5*p*2*d*] set, and for hydrogen a [3*s*2*p*] set. Basis sets of the second type, which we employed for the first-row hydrides, are due to Widmark et al. (38). In contrast to the property-oriented POL1 bases, these are high-quality, all-purpose basis sets consisting of atomic natural orbitals (ANO) obtained from correlated atomic calculations, as first advocated by Almlöf and Taylor (39). Experience shows that the ANO basis sets can efficiently account for the molecular many-electron correlation effects. The ANO basis set that is relevant for the first-row hydrides is of the [6*s*5*p*3*d*2*f*/4*s*3*p*2*d*] quality.

For the ground states we always employed the ROHF solution as a reference, while for the excited states of NH, the ground state ROHF orbitals were used. In all cases we rely on Cartesian Gaussian functions, thus using 6 *d* and 10 *f* components. In all our OS CCSD calculations we employ the first-order interacting space approximation (40), as already noted in Sect. 2. For the sake of comparison, we also carried out various limited CI computations, in particular CISD(is) (CI interacting space singles and doubles), CISD$^+$, and CISDT$^+$, using the GAMESS system of programs (41).[4] In all post-HF calculations, only valence electrons were correlated (with the exception of the Li atom, in which case all three electrons were correlated). The ROHF calculations were also carried out using the GAMESS program package.

Properties considered

To calculate static electric properties, such as dipole moments, or dipole polarizabilities or hyperpolarizabilities, we employ the finite field (FF) method (42). The energy change ΔE when the system is submerged in a homogeneous electric field $\boldsymbol{F} \equiv (F_x, F_y, F_z)$ can be written as

$$[20] \quad \Delta E \equiv E(\boldsymbol{F}) - E(\boldsymbol{0}) = -\mu_i F_i - (1/2!)\alpha_{ij}F_iF_j - (1/3!)\beta_{ijk}F_iF_jF_k - (1/4!)\gamma_{ijkl}F_iF_jF_kF_l - \cdots$$

where the summation over repeated indices is implied, $E(\boldsymbol{0})$

[4] The CI program for high-spin multiplicity generates some extra CSFs of higher excitation order. Hence various CI approaches will be referred to as CISD$^+$, CISDT$^+$, etc.

designates the energy with no field present, and $F_i (i = x, y, z)$ are the field components. For linear diatomic hydrides in a uniform electric field along the molecular axis (chosen to be the z-axis, $\boldsymbol{F} = (0, 0, F)$), the above expression [20] simplifies to

$$[21] \quad \Delta E = -\mu F - (1/2)\alpha_{zz}F^2 - (1/6)\beta_{zzz}F^3 - (1/24)\gamma_{zzzz}F^4 - \cdots$$

Thus, once we know the functional dependence of E or ΔE on F, the dipole moment μ, the parallel polarizability component $\alpha \equiv \alpha_{zz}$, etc., can be evaluated as, respectively, the first, second, etc., derivative of the energy with respect to the applied field. While there is only one dipole moment component for linear molecules, the number of independent components of the polarizability tensor deserves a comment. Besides the diagonal (or axial) components, the mixed ones, such as α_{xz}, also generally represent useful quantities. Moreover, for degenerate OS states, such as Π or Δ states, one has to distinguish between different perpendicular diagonal components, namely $\alpha_{xx}(\Pi_x) = \alpha_{yy}(\Pi_y)$ and $\alpha_{xx}(\Pi_y) = \alpha_{yy}(\Pi_x)$, while only one such component exists for nondegenerate Σ states. For the sake of simplicity, we examine in this paper only the most important parallel polarizability component $\alpha \equiv \alpha_{\parallel} \equiv \alpha_{zz}$. A complete investigation of other polarizability components will be presented elsewhere.

When considering a very weak field F, we can truncate expansion [21] at the quadratic term. Within such an approximation, we can then evaluate μ and α if we know the energy for at least two different field strengths, in addition to the zero field energy in case of α. Thus, choosing the fields $F_z = \pm F$, the μ and α are given by

$$[22] \quad \mu = [\Delta E(-F) - \Delta E(F)]/2F = [E(-F) - E(F)]/2F$$

$$-\alpha = [\Delta E(-F) + \Delta E(F)]/F^2 = [E(-F) + E(F) - 2E(0)]/F^2$$

In the case of hydrides, we have chosen the field strength to be $F = \pm 0.002$ au. Using fields of this magnitude, the μ and α obtained from formulas [22], which rely on the smallest number of calculations for different fields, turned out to be almost identical with values that were obtained when using the information for four or more nonzero fields. It should also be noted that for $F = \pm 0.002$ au, we require that our energies are precise to at least 4×10^{-8} au if we wish to compute α with an error not exceeding 10^{-2} au. Thus, in all our calculations, the energies were converged to within 10^{-8} au or better. We must also mention that the dipole moment of a hydride XH is defined in such a way that H is in the positive direction assuming that X is located at the origin.

As we pointed out earlier, a very important characteristic of the UGA-based CC method is its ability to handle the low-spin, OS singlet states, which are inaccessible to the standard UHF-based CC or MBPT approaches. For this reason, we have chosen two excited OS singlet states of NH, namely the $c^1\Pi$ and $a^1\Delta$ states, in order to illustrate this feature of our UGA-CCSD approach. We wish to point out that while both the $^1\Pi_x$ and $^1\Pi_y$ components of the $^1\Pi$ state are OS singlets, only the xy component of the $^1\Delta$ state is an OS singlet state.

Table 2. Total energy (E) and dipole polarizability (α) (both in au) of the Li atom obtained with various methods.

Method	E	α
SCF/ANO	−7.432 710	170.1
CISD(is)/ANO	−7.461 621	118.2
FCI/ANO	−7.461 651	165.1
CCSD(is)/ANO	−7.461 622	165.1
UMP4-P(E[2/1])[a]	−7.475 692	164.5
CCSD(T)-B95[a]	−7.477 1456	164.2
Hylleraas-CI[b]	−7.478 0601	164.1
Experiment	−7.478 0624[c]	164 ± 3[d]

[a]Reference 44.
[b]Reference 45.
[c]The most recent nonrelativistic estimate of the exact energy (46).
[d]Reference 43.

Of course, only one component of the $^1\Pi$ state needs to be considered in our case.

Results and discussion

We start by considering a simple atomic system, the lithium atom. This enables us to easily obtain the full configuration interaction (FCI) results (that are equivalent to CISDT in this case, since we deal with a three-electron system), representing the exact solution within the N-electron subspace generated by the chosen set of atomic orbitals (AOs), even when employing fairly large basis sets. The computed total energy and dipole polarizability obtained with various methods and the atomic natural orbital (ANO) basis $[6s5p3d2f]$ (38) are compared with the experimental values in Table 2. It is noteworthy that the uncorrelated SCF values of the polarizability (α = 170.1 au) is much closer to the FCI result (α = 165.1 au) than is the limited CISD(is) result (α = 118.2 au). CISD(is) should represent a very good approximation is this case, since the system allows, at most, triexcitations. In fact, the CISD(is) approach recovers almost the entire correlation energy (99.896%) in this case, yet gives a significantly lower polarizability than does even the uncorrelated SCF approximation. Interestingly enough, our UGA-CCSD(is) approach, which improves the total energy relative to the CISD(is) approach by only one microhartree (thus yielding 99.900% of the correlation energy), gives practically the exact value for the polarizability (α = 165.1 au), which is also very close to the experimental value (43). This is a clear indication of the fact that the CCSD(is) wave function is much better than the CISD(is) one, even though both methods employ the same set of excitation operators. Of course, due to the nonlinearity of the CC Ansatz, the effective excited state manifold is much larger in the CCSD(is) case.

For the sake of comparison, we also include in Table 2 the results of two recent theoretical studies of the Li atom. The first employs the fourth-order MBPT and the standard UHF-based CCSD(T) methods with a very large basis set (44), while the second one relies on the combined configuration interaction and Hylleraas methods (45). It is very encouraging that the CCSD(is) polarizability is very close to the result provided by these extensive calculations, all of these

falling within the experimental limits. A comparison with the most recent estimate of the total energy (46) indicates, however, that the fairly large ANO basis set has not yet reached the basis set limit, since our FCI and CCSD(is) energies are about 17 mhartree short of the "experimental" limit. Of course, from the methodological viewpoint, the agreement of the CCSD(is) quantities with the FCI results is most relevant.

The computation of the hyperpolarizability, particularly when using the FF method, is considerably more challenging. Our attempt to determine $\gamma \equiv \gamma_{zzzz}$ using the FF approach was in fact unsuccessful. For example, relying on FCI energies,[5] we get $\gamma = 6.2 \times 10^4$ au using the fields $F = \pm 0.002$ and ± 0.004 au, but only $\gamma = 2.1 \times 10^4$ au with smaller fields $F = \pm 0.001$ and ± 0.002 au. Employing yet smaller fields ($\pm 5 \times 10^{-4}$ and $\pm 10^3$ au) gives $\gamma = 4 \times 10^3$ au. The same unstable behaviour is found when employing CCSD energies. In fact, our recent exploration of mathematical and numerical properties of expansions like [21], using the linear response based CCSD approaches, seems to indicate a fundamental problem of the FF approach when considering higher order properties.[6]

We next considered the first-row diatomic hydrides having a doublet or triplet ground state. The total energies, dipole moments, and polarizabilities obtained with both the POL1 and ANO basis sets at the experimental geometries (35) using various methods are summarized in Table 3, and compared with the available experimental values (47–52) in the case of dipole moments. These results enable us to draw a number of interesting conclusions concerning the role of the correlation effects, the use of relaxed (R) vs. nonrelaxed (N) orbitals, and the size of the basis set employed.

The correlation effects may change the computed dipole moments by about 0.1–0.2 D, causing about 10–15% error, which is hardly acceptable when striving for high-quality dipole moments. The same holds for polarizabilities. The computed dipole moments monotonically decrease with the increasing amount of correlation that is accounted for via higher and higher order of excitations. For the POL1 basis, the largest limited single reference CI that we were able to carry out on our Silicon Graphics (Challenge L) minicomputer is CISDT$^+$ (41). In all cases, the CCSD(is) results are very close to the CISDT$^+$ ones. As might be expected with the CC approach (see, for example, ref. 20), the orbital relaxation effects are not significant, amounting to 0.002, 0.005, and 0.012 D for CH, NH, and OH, respectively. The same holds for polarizabilities, where the changes due to the orbital relaxation are in the range of 0.11 to 0.18 au.

While the dipole moments monotonically decrease with the increasing order of excitations that are included in CI calculations, the polarizabilities change in a less regular manner. The SCF α values are first lowered when the correlation due to the singles and doubles is introduced via CISD(is), only to be subsequently increased when the triple excitations are accounted for, as in the CISDT$^+$ method. Thus, generally, we observe the following order of polarizabilities.

$$[23] \qquad \alpha[\text{CISD(is)}] < \alpha(\text{SCF}) < \alpha(\text{CSDT}^+) \approx \alpha[\text{CCSD(is)}]$$

[5] We used the GAMESS package (41) to compute the FCI energies.
[6] P. Piecuch and J. Paldus. Unpublished results.

Table 3. Total energy E (in au), dipole moment μ (in D), and polarizability α (in au) for the ground state of first-row diatomic hydrides CH, NH, and OH.

Basis	Method	E	μ	α
CH($X\,^2\Pi$), R_e = 1.1199 Å[a]				
POL1	SCF	−38.273 128	1.568	15.25
	CISD(is)	−38.383 262	1.407	14.04
	CISD$^+$	−38.383 636	1.398	14.43
	CISDT$^+$	−38.386 837	1.353	16.44
	CCSD(is), R	−38.386 356	1.359	16.22
	CCSD(is), N	−38.386 356	1.361	16.33
ANO	SCF	−38.279 543	1.573	15.35
	CISD(is)	−38.410 048	1.443	13.62
	CISD$^+$	−38.410 659	1.438	13.97
	CCSD(is), R	−38.413 650	1.410	16.02
Expt.			1.46 ± 0.06[b]	
NH($X\,^3\Sigma^-$), R_e = 1.0362 Å[a]				
POLI	SCF	−54.970 684	1.606	10.75
	CISD(is)	−55.105 755	1.514	10.11
	CISD$^+$	−55.106 730	1.499	10.78
	CISDT$^+$	−55.110 396	1.487	11.80
	CCSD(is), R	−55.109 380	1.497	11.64
	CCSD(is), N	−55.109 380	1.492	11.80
ANO	SCF	−54.978 212	1.611	10.73
	CISD(is)	−55.143 962	1.545	9.57
	CISD$^+$	−55.145 514	1.536	10.15
	CCSD(is), R	−55.148 382	1.535	11.35
Expt.			1.38 ± 0.07[c]	
OH($X\,^2\Pi$), R_e = 0.969 66 Å[a]				
POLI	SCF	−75.411 121	1.758	7.81
	CISD(is)	−75.583 404	1.639	7.38
	CISD$^+$	−75.583 939	1.632	7.61
	CISDT$^+$	−75.588 221	1.628	8.65
	CCSD(is), R	−75.589 187	1.631	8.59
	CCSD(is), N	−75.589 187	1.619	8.77
ANO	SCF	−75.420 990	1.757	7.78
	CISD(is)	−75.645 372	1.661	6.85
	CISD$^+$	−75.646 178	1.657	7.06
	CCSD(is), R	−75.652 908	1.650	8.36
Expt.			1.655[d]	

[a] Reference 35.
[b] Reference 47.
[c] Reference 52.
[d] Reference 51.

so that the uncorrelated SCF value is always closer to the exact result than is the CISD(is) value. Again, the CCSD(is) polarizabilities are very close to the CISDT$^+$ values, as was the case for dipole moments. We should emphasize here, however, that the CISDT$^+$ method employs a much larger excited state manifold than does CCSD(is). In cases considered here, the dimensions of the CISDT$^+$ spaces are in fact more than 10 times larger than those of the corresponding CCSD(is) or CISD(is) problems. Clearly, the CCSD(is) procedure represents the optimal choice when computing dipole moments as well as polarizabilities.

The choice of a suitable basis set is clearly very crucial

Table 4. Optimized bond length R_e (in Å), vibrational frequency ω_e (in cm^{-1}), dipole moment μ (in D), and polarizability α (in au) at the optimized geometries for the ground state of CH($X\ ^2\Pi$), NH($X\ ^3\Sigma^-$), and OH ($X\ ^2\Pi$), obtained with various basis sets.

Molecule	Method	R_e	ω_e	μ	α
CH	CCSD/6-31G*	1.131	2826	[a]	[a]
	CCSD/POL1	1.1505	2772	1.304	16.90
	CCSD/ANO	1.1182	2872	1.413	15.99
	Expt.	1.1199[b,c]	2859[b,c]	1.46 ± 0.06[d]	
NH	CCSD/6-31G*	1.048	3234	[a]	[a]
	CCSD/ANO	1.0344	3317	1.536	11.31
	Expt.	1.0362[b]	3282[b]	1.38 ± 0.07[e]	
OH	CCSD/6-31G*	0.983	3658	[a]	[a]
	CCSD/ANO	0.9672	3783	1.649	8.33
	Expt.	0.9697[b]	3738[b]	1.655[f]	

[a]Not computed.
[b]Reference 35.
[c]More recent experimental values by Bernath are R_e = 1.119 83(2) Å and ω_e = 2860.4118(98) cm^{-1} (ref. 53).
[d]Reference 47.
[e]Reference 52.
[f]The most accurate experimental result (ref. 51).

when computing electric properties. Both basis sets employed by us, i.e., POL1 and ANO, are sufficiently large and flexible to provide meaningful results for a comparison with experiment. In general, the uncorrelated results are much less sensitive to the basis set choice than are highly correlated ones. Thus, the difference between the computed dipole moments when using the POL1 and ANO basis sets is only about 5×10^{-3} D at the SCF level, but almost an order of magnitude larger at the correlated level (0.05, 0.04, and 0.02 D for CH, NH, and OH, respectively). A similar observation can be made for the polarizability.

The results of Table 3 were obtained for the experimental geometries. To find out how much these differ from the theoretical values for the basis sets employed, we also present in Table 4 the computed equilibrium geometries and harmonic vibrational frequencies, as well as the corresponding dipole moments and polarizabilities. In this case, only the CCSD(is) results with the ANO basis set are shown. For a comparison, we also included the geometries and harmonic frequencies obtained with the 6-31G* basis set,[7] and for the CH ground state also with the POL1 basis set. The latter result clearly indicates that the POL1 basis set, which is specifically tailored for the electrostatic property calculations, is not suited for the structure and energetics determinations. Indeed, the CCSD/POL1 geometry is inferior even to the CCSD/6-31G* geometry (differing from the experimental value by 0.03 and 0.01 Å, respectively) and, similarly, for the corresponding harmonic frequencies (87 and 33 cm^{-1}, respectively). The CCSD/POL1 equilibrium bond length being too large implies a too small dipole moment. Introducing the core correlation (although this is not recommended for the POL1 basis), the equilibrium bond length shrinks a little to 1.149 Å. Clearly, with this property-dedicated basis set it is best to employ the experimental geometry. For this reason, we performed the geometry optimization for the NH and OH ground states only with the ANO basis set (Table 4).

The CCSD/ANO geometries for the CH, NH, and OH ground states, shown in Table 4, agree well with experiment (being, respectively, 0.0017, 0.0018, and 0.0025 Å shorter than the experimental values) and represent a significant improvement over the CCSD/6-31G* values, which are longer by 0.011–0.013 Å. The computed CCSD/ANO harmonic frequencies are also in good agreement with experiment (the differences being 13, 35, and 45 cm^{-1}). Since the optimized bond lengths are close to the experimental ones, the dipole moments and polarizabilities obtained for these theoretical geometries differ very little from those based on experimental geometries (cf. Tables 3 and 4).

The computed CH dipole moment (1.413 D) falls within the experimental error bounds (1.46 ± 0.06 D) (47). The dipole moment in the electronic and vibrational ground state of OH was measured by several groups (48–51). The most recently determined rotationally resolved values, obtained with the molecular beam electric resonance technique by Peterson et al. (51), are μ = 1.6549 D for $\Omega = J = 1/2$ and μ = 1.65520 D for $\Omega = J = 3/2$ (we report them as 1.655 D in our tables). Our CCSD/ANO result of μ = 1.649 D agrees well with these results. In view of the availability of these precise, rotationally resolved experimental results, it will be interesting to obtain the corresponding rovibrationally corrected values, as we did for other systems (19*b*).

The least satisfactory agreement between the CCSD/ANO and experimental (52) dipole moments is found for the NH $^3\Sigma^-$ ground state (1.536 vs. 1.38 ± 0.07 D, respectively). In fact, all ab initio calculations that we are aware of (cf. Table

[7] X. Li and J. Paldus. J. Chem. Phys. In press.

Table 5. Total energy E (in au), dipole moment μ (in D), and polarizability α (in au) for the ground states of second-row diatomic hydrides SiH, PH, and SH, obtained with the polarized basis sets POL1.

Method	E	μ	α
SiH($X\ ^2\Pi$), R_e = 1.5201 Å[a]			
SCF	−289.426 915	0.270	39.26
CISD(is)	−289.520 653	0.123	32.86
CISD$^+$	−289.521 033	0.119	33.73
CISDT$^+$	−289.524 369	0.091	39.12
CCSD(is), R	−289.523 815	0.093	38.81
CCSD(is), N	−289.523 815	0.092	38.93
PH($X\ ^3\Sigma^-$), R_e = 1.4223 Å[a,b]			
SCF	−341.282 190	0.532	29.29
CISD(is)	−341.394 162	0.466	24.73
CISD$^+$	−341.395 201	0.446	26.47
CISDT$^+$	−341.399 680	0.410	29.71
CCSD(is), R	−341.398 207	0.417	29.53
CCSD(is), N	−341.398 207	0.415	29.70
SH($X\ ^2\Pi$), R_e = 1.340 Å[a,c]			
SCF	−398.067 569	0.870	22.89
CISD(is)	−398.207 937	0.823	19.05
CISD$^+$	−398.208 590	0.814	19.79
CCSD(is), R	−398.214 272	0.774	23.41
CCSD(is), N	−398.214 272	0.776	23.55
Expt.		0.758,[d] 0.62[e]	

[a]Reference 35.
[b]More recent experimental value by Ram and Bernath is R_e = 1.422 18 Å (ref. 54).
[c]Most recent experimental value is R_e = 1.340 614(4) Å (ref. 55).
[d]Reference 57.
[e]Reference 56.

Table 6. Total energy E (in au), dipole moment μ (in D), and polarizability α (in au) for several excited states of NH, obtained with the polarized basis sets POL1 and ground state, nonrelaxed ROHF orbitals.

Method	E	μ	α
$a\ ^1\Delta$, R_e = 1.034 Å[a]			
CISD(is)	−55.040 954	1.499	11.93
CISD$^+$	−55.041 781	1.484	10.71
CISDT$^+$	−55.045 400	1.470	11.88
CCSD(is), N	−55.044 907	1.473	12.12
Expt.		1.49 ± 0.06[b]	
$A\ ^3\Pi$, R_e = 1.0369 Å[a]			
CISD(is)	−54.957 932	1.161	9.56
CISD$^+$	−54.960 128	1.219	10.22
CISDT$^+$	−54.970 261	1.216	11.30
CCSD(is), N	−54.969 270	1.216	11.38
Expt.		1.31 ± 0.03[b]	
$c\ ^1\Pi$, R_e = 1.110 Å[a]			
CISD(is)	−54.892 165	1.544	10.64
CISD$^+$	−54.897 468	1.652	11.48
CISDT$^+$	−54.903 262	1.595	12.70
CCSD(is), N	−54.902 336	1.588	12.91
Expt.		1.70 ± 0.07[b]	

[a]Reference 35.
[b]Reference 36.

7) report $\mu \geq 1.5$ D. This fact, as well as the senescence of the experimental result, suggest that it would be worthwhile to reexamine the latter.

We next considered the second-row hydrides SiH, PH, and SH in their ground electronic states, using only the POL1 basis set. The results are summarized in Table 5 and exhibit behaviour similar to that of the first-row hydrides. Thus, the computed dipole moments monotonically decrease with the increasing order of excitations included in CI calculations and the CCSD(is) results are again close to the CISDT$^+$ ones, namely,

$$[24] \quad \mu(\text{SCF}) > \mu[\text{CISD(is)}] > \mu[\text{CISD}^+] > \mu[\text{CISDT}^+] \approx \mu[\text{CCSD(is)}]$$

This decrease in the dipole moment value with the increasing correlation is most pronounced in smaller systems, namely in the SiH case, where the SCF value is about three times as large as the CISDT$^+$ result that we employ as our benchmark. For other systems, the differences between the SCF and CISDT$^+$ dipole moments are not so startling and usually do not exceed 30% (see Tables 3 and 5). This was to be expected, since the smaller the dipole moment, the more critical is the electronic charge distribution and thus the correlation effects.

The behaviour of the computed polarizabilities is also similar to that found for the first-row hydrides. The CISD(is) polarizabilities are thus smaller than either the SCF and CISDT$^+$ ones, and the CCSD(is) method rectifies the shortcomings of the CISD(is) method and yields very close results as found with the computationally demanding CISDT$^+$ method. We also note that the effect of orbital relaxation is again very small when using the CCSD(is) approach.

To our knowledge, there are no experimental data available for the dipole moments in the SiH and PH ground states. For SH, two values have been published: μ = 0.62 D by Carrington et al. (56) and μ = 0.758 D by Meerts and Dymanus (57). Our CCSD(is) value of μ = 0.774 D is closer to the latter, more recent, experimental result. Unfortunately, no experimental information is available concerning the polarizabilities, either for the first- or for the second-row hydrides considered.

Finally, we compute the dipole moment and polarizability for the three degenerate excited states of NH using the POL1 basis set and the experimental equilibrium geometry (Table 6). We have seen above that the orbital relaxation played an insignificant role when we examined the ground states of first- and second-row hydrides. It is thus interesting to examine the performance of our UGA-CCSD methods for excited states, while using the nonrelaxed ground state orbitals. Such orbitals, being neither variationally reoptimized for the excited state considered, nor for the applied perturbing electric field, are clearly as far removed from the "ideal" ones as one can get. It is thus very gratifying to see that our CCSD(is) method, employing the ground state, nonrelaxed orbitals, yields reasonably good dipole moments and polar-

Table 7. Comparison of dipole moments (in D) of first- and second-row diatomic hydrides, obtained by various theoretical methods, with experiment.

Method	CH	NH	OH	SiH	PH	SH
SR-CI	1.438[a]	1.526[b]	1.634[d]	0.077[e]	0.410[a]	0.814[a]
		1.587[c]	1.657[a]	0.160[f]		
		1.536[a]		0.091[a]		
MR-CI		1.511[g]	1.645[h]	0.123[i]	0.403[j]	0.734[k]
		1.48[g]				
CEPA	1.430[l]	1.578[l]	1.650[m]	0.141[l]	0.481[l]	0.810[l]
			1.642[m]			0.743[k]
H_v	1.424[n]	1.579[o]	1.71[p]	0.122[q]	0.452[q]	0.769[q]
CPF				0.118[f]		
CCSD(is)[a]	1.413	1.536	1.649	0.093	0.417	0.774
Expt.	1.46 ± 0.06[r]	1.38 ± 0.07[s]	1.655[t]			0.758[u]
						0.620[v]

[a]Present work.
[b]Reference 61.
[c]Reference 62.
[d]Reference 65.
[e]Reference 69.
[f]Reference 70.
[g]Reference 63. μ = 1.48 D is the vibrationally average v = 0 result.
[h]Estimated from ref. 66.
[i]Reference 71.
[j]Reference 73.
[k]Reference 74.
[l]Reference 58.
[m]Reference 67.
[n]Reference 59.
[o]Reference 64.
[p]Estimated from ref. 68.
[q]Reference 72.
[r]Reference 47.
[s]Reference 52.
[t]Reference 51.
[u]Reference 57.
[v]Reference 56.

izabilities (see Table 6), as a comparison with the CISDT+ results or with the experimental values (for the dipole moments) indicates. The fact that we can use nonrelaxed ground state orbitals for the computation of excited state properties is of considerable practical significance, not only for reasons of economy, but also because of the difficulties that one encounters when trying to converge the SCF orbitals for the excited states to a sufficiently high accuracy.

In concluding this section, let us compare our UGA-CCSD(is) dipole moments for the first- and second-row hydrides considered with those obtained by other methods that account for correlation effects in a different way (see Table 7). These methods include the single reference CI, multi- reference CI, coupled electron pair approximation (CEPA) or its variants, coupled pair functional (CPF), and effective valence Hamiltonian (H_v) methods. The latter represents essentially a version of a quasidegenerate MBPT. The results obtained with these various methods for the dipole moment of CH (refs. 58–60), NH (58, 61–64), OH (58, 65–68), SiH (58, 69–72), PH (58, 72, 73), and SH (58, 72, 74) in their ground electronic states are summarized in Table 7 together with our UGA-CCSD(is) results. Al the results for CH are within the experimental error bounds, the CCSD(is) value being the smallest of them all. Likewise, all results for OH are in good agreement with the very accurate experimental value (51) (a rather high value obtained with the H_v method is most likely due to a relatively small basis set employed). Our CCSD value differs by only 0.005 D and belongs amongst the most accurate theoretical results. For SH, all ab initio dipole moments favor the measurements of Meerts and Dymanus (57). Unfortunately, no experimental data are available for the remaining second-row hydrides, SiH and PH. The theoretical results for SiH range between 0.077 and 0.160 D, a rather large spread, although most seem to favor the narrower range between 0.09 and 0.12 D. Similarly, the values for PH range from 0.403 to 0.481 D.

Finally, let us discuss the results for the ground state of NH, where we find a rather serious disagreement between the theoretical and experimental data. As the results assembled in Table 7 indicate, and as already mentioned above, all ab initio dipole moments are in this case larger than 1.5 D. Thus, all these results fall well beyond the reported experimental error bounds of 1.38 ± 0.07 D (52). Clearly, the rovibrational averaging can lower the purely electronic values given in Table 7. Such an averaging was carried out for the MRCI dipole moment and amounted to 0.03 D (63). This decreased the MR CI electronic value of 1.511 D to 1.48 D (for the vibrationless v = 0 level), which is still too large. Clearly, the existing discrepancy between the computed and measured dipole moment of the NH ground state is of concern and should be clarified.

4. LR approach with UGA-CC formalism

We now outline the LR method within the framework of the UGA-based CC approach. The LR method based on the standard CC approach, as first outlined by Monkhorst (11*a*) and Dalgaard and Monkhorst (11*b*), was recently explicitly formulated (17) in the context of the orthogonally spin-adapted CCSD method (18) and fully implemented and tested in our CC codes (17, 19). The most recent version is capable of providing reliable values even for high-order static proper-

ties, such as the second hyperpolarizability, over the whole range of molecular geometries for which the standard CS CCSD approach is applicable, in contrast to the FF methods, which become particularly troublesome for large internuclear separations (footnote 3). Moreover, the LR formalism can be generalized to handle dynamic properties.

We will essentially follow the development as outlined in ref. 17. However, we can no longer use the diagrammatic technique (34) to obtain the required explicit expressions and will have to rely on an algebraic formalism. We must also account for the fact that in the OS case the excitation operators G_I no longer commute. Finally, since our UGA-based CC formalism can handle rather general OS situations, we also do not employ the normal product form of the Hamiltonian.

Starting with the unperturbed problem [3], we consider the perturbed Hamiltonian

$$[25] \qquad H(\lambda) = H + \lambda W$$

where the perturbation W represents the property we are interested in. We thus look for the solution of the corresponding Schrödinger equation

$$[26] \qquad H(\lambda)|\Psi(\lambda)\rangle = E(\lambda)|\Psi(\lambda)\rangle$$

assuming the following general cluster ansatz for $|\Psi(\lambda)\rangle$,

$$[27] \qquad |\Psi(\lambda)\rangle = e^{T(\lambda)}|\Phi\rangle$$

with

$$[28] \qquad T(\lambda) = \sum_I t_I(\lambda) G_I$$

We further assume a power series expansion for the relevant quantities in terms of the perturbation parameter λ, namely,

$$[29] \qquad E(\lambda) = \sum_{i=0}^{\infty} E^{(i)} \lambda^i$$

and

$$[30] \qquad T(\lambda) = \sum_{i=0}^{\infty} T^{(i)} \lambda^i$$

or, equivalently,

$$[31] \qquad t_I(\lambda) = \sum_{i=0}^{\infty} t_I^{(i)} \lambda^i$$

Clearly, the unperturbed problem of Sect. 2 results for $\lambda = 0$ and is characterized by the energy $E^{(0)} \equiv E(0)$ and cluster amplitudes $t_I^{(0)} \equiv t_I(0)$. We also note that in contrast to the CS case (17), when the cluster operators $T^{(i)}$ representing various orders in perturbation expansion [30] commute, in general OS situations we have that $[G_I, G_J] \neq 0$, unless at least one excitation operator is all-external, i.e., does not involve active or valence orbitals. Consequently, we cannot express the wave operator $\exp(T(\lambda))$ as a product of exponential factors, $\exp T^{(i)}$, as we did in the CS case (cf. eq. [30] of ref. 17). Nonetheless, since we employ a single spin-free configuration state $|\Phi\rangle$ as a reference, we can still benefit from the property [11].

Proceeding then as in the unperturbed case, we arrive at the general equation of type [4] or, equivalently

$$[32] \qquad \{H(\lambda) + [H(\lambda), T(\lambda)] + \tfrac{1}{2}[[H(\lambda), T(\lambda)], T(\lambda)] + \cdots\}|\Phi\rangle = E(\lambda)|\Phi\rangle$$

Expanding in powers of λ, we see immediately that the absolute term, resulting for $\lambda = 0$, recovers the unperturbed CC problem of Sect. 2. We can thus assume the zero-order quantities $E^{(0)}$ and $t_I^{(0)}$ to be known. The LR equations then result from the linear terms in λ. For the energy increment $E^{(1)}$, giving the desired expectation value of the considered property $\langle\Psi(0)|W|\Psi(0)\rangle/\langle\Psi(0)|\Psi(0)\rangle = E^{(1)}$, we thus find

$$[33] \qquad E(1) = \langle W\rangle + \sum_{i\geq 1}\langle\{H, T\}_i^{(1)} + \{W, T\}_i^{(0)}\rangle$$

where we introduced the symbol for the symmetrized sum of the kth order commutator terms

$$[34] \qquad \{X, T\}_k^{(i)} = (k!)^{-1} \times \sum_{i_1+i_2+\cdots+i_k=i} [\cdots[[X, T^{(i_1)}], T^{(i_2)}], \cdots, T^{(i_k)}]$$

For example,

$$[35] \qquad \{H, T\}_3^{(1)} = \tfrac{1}{6}([[[H, T^{(0)}], T^{(0)}], T^{(1)}] + [[[H, T^{(0)}], T^{(1)}], T^{(0)}] + [[[H, T^{(1)}], T^{(0)}], T^{(0)}])$$

while

$$[36] \qquad \{H, T\}_1^{(1)} = [H, T^{(1)}]$$

and

$$[37] \qquad \{W, T\}_1^{(0)} = [W, T^{(0)}]$$

Similarly, the corresponding LR CC equations determining the $t_I^{(1)}$ amplitudes have the form

$$[38] \qquad \left\langle G_I^{\dagger}\left[W + \sum_{i\geq 1}(\{H, T\}_i^{(1)} + \{W, T\}_i^{(0)})\right]\right\rangle = 0$$

In view of eq. [11], we can write again for the property value

$$[39] \qquad E^{(1)} = \langle W\rangle + \langle WT^{(0)}\rangle + \tfrac{1}{2}\langle WT^{(0)}T^{(0)}\rangle + \langle HT^{(1)}\rangle + \tfrac{1}{2}\langle H(T^{(0)}T^{(1)} + T^{(1)}T^{(0)})\rangle + \cdots + \frac{1}{24}\langle H[(T^{(0)})^3T^{(1)} + (T^{(0)})^2T^{(1)}T^{(0)} + \cdots + T^{(1)}(T^{(0)})^3]\rangle$$

assuming that W is a one-electron operator.

In CC equations [38], which are linear in the unknown cluster amplitudes $t_I^{(1)}$, we can again have up to eight commutators for the H-containing terms and six for the terms involving W. Again, these high-order terms can only involve semi-internal monoexcitations. Assuming that we employ an ROHF reference (restricted OS HF), the monoexcited $t_I^{(0)}$ amplitudes should be small, and thus the high-order terms

involving their products should be negligible. We recall that a similar situation arises in the zero-order (unperturbed) level of approximation, where the consideration of at most bilinear terms in CCSD equations provides very good results. It will thus be necessary to find out to which extent this feature extends to the LR methods.

Considering various terms in LR CC equations [38] we see again that the linear and bilinear terms (in mixed zero- and first-order amplitudes) can be handled in the same way as the zero-order amplitude terms in the unperturbed case. For example, considering bilinear terms involving the Hamiltonian we find that

$$
\begin{aligned}
[40] \qquad \langle G_I^\dagger \{H, T\}_2^{(1)}\rangle &= \tfrac{1}{2}\langle G_I^\dagger([[H, T^{(0)}], T^{(1)}] \\
&\quad + [[H, T^{(1)}], T^{(0)}])\rangle \\
&= \tfrac{1}{2}\langle G_I^\dagger \{H(T^{(0)}T^{(1)} + T^{(1)}T^{(0)}) \\
&\quad + (T^{(0)}T^{(1)} + T^{(1)}T^{(0)})H \\
&\quad - 2(T^{(0)}HT^{(1)} + T^{(1)}HT^{(0)})\}\rangle \\
&= \tfrac{1}{2}\sum_{J,K} t_J^{(0)} t_K^{(1)} \langle G_I^\dagger \{H(G_J G_K + G_K G_J) \\
&\quad + (G_J G_K + G_K G_J)H - 2(G_J H G_K \\
&\quad + G_K H G_J)\}\rangle \\
&= \sum_{J\le K} (t_J^{(0)} t_K^{(1)} + t_K^{(0)} t_J^{(1)}) c_{IJK}
\end{aligned}
$$

where c_{IJK} are again defined by eqs. [16]–[18]. Thus, for up to bilinear terms the existing codes generating the required coefficients in both CC equations [40] and in the energy expression [39] can be directly exploited. Of course, when evaluating the corresponding terms involving W, we must employ the corresponding one-electron integrals $\langle\mu|w|\nu\rangle$.

The role of higher than bilinear terms in CC equations (although always linear in $t_I^{(1)}$ amplitudes) must also be addressed. Hopefully, most of these higher order terms will turn out to be of little importance, similarly to the unperturbed case.

Acknowledgement

Continued support by the Natural Sciences and Engineering Research Council of Canada (J.P.) is greatly appreciated.

References

1. (*a*) Optical Nonlinearities in Chemistry. Chem. Rev. **94**, No. 1 (1994); (*b*) M. Evans and S. Kielich (*Editors*). Modern nonlinear optics, Parts 1–3. Adv. Chem. Phys. **85** (1993).
2. (*a*) C.H. Townes and A.L. Schawlow. Microwave spectroscopy. McGraw–Hill, London. 1955; (*b*) W.S. Benedict and L.D. Kaplan. J. Chem. Phys. **30**, 388 (1959); (*c*) W.S. Benedict and R. Herman. J. Quant. Spectrosc. Radiat. Transfer, **3**, 265 (1963); (*d*) B. Th. Berendts and A. Dymanus. J. Chem. Phys. **48**, 1361 (1968); (*e*) **49**, 2632 (1968); (*f*) F.H. DeLeeuw and A. Dymanus. J. Mol. Spectrosc. **48**, 427 (1973).
3. (*a*) A.D. Buckingham. Adv. Chem. Phys. **12**, 107 (1967); (*b*) *In* Intermolecular interactions: from diatomics to biopolymers. *Edited by* B. Pullman. Wiley. Chichester. 1978. pp. 1–67; (*c*) H. Margenau and N.R. Kestner. Theory of intermolecular forces. Pergamon. New York. 1971; (*d*) A. van der Avoird, P.E.S. Wormer, F. Mulder, and R.M. Berns. Top. Curr. Chem. **93**, 1 (1980); (*e*) P. Piecuch. *In* Molecules in physics, chemistry and biology. Vol. 2. Physical aspects of molecular systems. *Edited by* J. Maruani. Kluwer, Dordrecht. 1988. pp. 417–505; (*f*) B. Jeziorski, R. Moszyński, and K. Szalewicz. Chem. Rev. **94**, 1887 (1994).
4. B. Friedrich and D. Herschbach. Phys. Rev. Lett. **74**, 4623 (1995).
5. (*a*) J. Čížek. J. Chem. Phys. **45**, 4256 (1966); (*b*) Adv. Chem. Phys. **14**, 35 (1969); (*c*) J. Čížek and J. Paldus. Int. J. Quantum Chem. **5**, 359 (1971); (*d*) J. Paldus, J. Čížek, and I. Shavitt. Phys. Rev. A: Gen. Phys. **5**, 50 (1972).
6. (*a*) R.J. Bartlett. J. Phys. Chem. **93**, 1697 (1989); (*b*) J. Paldus. *In* Methods in computational molecular physics. NATO ASI Ser., Ser. B: **293**, 99 (1992); (*c*) *In* Relativistic and electron correlation effects in molecules and solids. NATO ASI Ser., Ser. B: **318**, 207 (1994); (*d*) R.J. Bartlett and J.F. Stanton. *In* Reviews in computational chemistry. Vol. 5. *Edited by* K.B. Lipkowitz and D.B. Boyd. VCH Publishers, New York. 1994. pp. 65–169; (*e*) R.J. Bartlett. *In* Modern electronic structure theory. *Edited by* D.R. Yarkony. World Scientific, Singapore. 1995. pp. 1047–1131.
7. (*a*) J. Paldus and J. Čížek. Adv. Quantum Chem. **9**, 105 (1975); (*b*) I. Hubač and P. Čársky. Top. Curr. Chem. **75**, 97 (1978); (*c*) R. Krishnan and J.A. Pople. Int. J. Quantum Chem. **14**, 91 (1978); (*d*) R.J. Bartlett. Annu. Rev. Phys. Chem. **32**, 359 (1981).
8. (*a*) J. Noga and M. Urban. Theor. Chim. Acta, **73**, 291 (1988); (*b*) R.J. Bartlett and J. Noga. Chem. Phys. Lett. **150**, 29 (1988); (*c*) M. Urban, G.H.F. Diercksen, A.J. Sadlej, and J. Noga. Theor. Chim. Acta, **77**, 29 (1990); (*d*) B. Jeziorski and R. Moszyński. Int. J. Quantum Chem. **48**, 161 (1993).
9. (*a*) S. Pal. Phys. Rev. A: Gen. Phys. **33**, 2240 (1986); (*b*) **34**, 2682 (1986); (*c*) **39**, 2712 (1989); (*d*) **42**, 4385 (1990); (*e*) K.B. Ghose and S. Pal. Phys. Rev. A: Gen. Phys. **36**, 1539 (1987); (*f*) **45**, 1518 (1992); (*g*) S. Pal and K.B. Ghose. Curr. Sci. **63**, 667 (1992); (*h*) K.B. Ghose, P.G. Nair, and S. Pal. Chem. Phys. Lett. **211**, 15 (1993); (*i*) N. Vaval, K.B. Ghose, and S. Pal. J. Chem. Phys. **101**, 4914 (1994).
10. (*a*) H. Koch, H.J.Aa. Jensen, P. Jørgensen, T. Helgaker, G.E. Scuseria, and H.F. Schaefer III. J. Chem. Phys. **92**, 4924 (1990); (*b*) R. Kobayashi, H. Koch, and P. Jørgensen. J. Chem. Phys. **101**, 4956 (1994).
11. (*a*) H.J. Monkhorst. Int. J. Quantum Chem. Quantum Chem. Symp. **11**, 421 (1977); (*b*) E. Dalgaard and H.J. Monkhorst. Phys. Rev. A: Gen. Phys. **28**, 1217 (1983).
12. (*a*) H. Sekino and R.J. Bartlett. Int. J. Quantum Chem. Quantum Chem. Symp. **18**, 255 (1984); (*b*) M. Takahashi and J. Paldus. J. Chem. Phys. **85**, 1496 (1986).
13. (*a*) Z.W. Liu and H.P. Kelly. Theor. Chim. Acta, **80**, 307 (1991); (*b*) H. Koch and P. Jørgensen. J. Chem. Phys. **93**, 3333 (1990); (*c*) H. Koch, R. Kobayashi, A. Sanchex de Merás, and P. Jørgensen. J. Chem. Phys. **100**, 4393 (1994); (*d*) S. Pal. Phys. Rev. A: Gen. Phys. **39**, 39 (1989); (*e*) Int. J. Quantum Chem. **41**, 443 (1992); (*f*) P.G. Szalay and R.J. Bartlett. J. Chem. Phys. **101**, 4936 (1994).
14. (*a*) G. Maroulis and A.J. Thakkar. J. Chem. Phys. **88**, 7623 (1988); (*b*) **92**, 812 (1990); (*c*) A.J. Thakkar. Phys. Rev. A: Gen. Phys. **40**, 1130 (1989); (*d*) E.F. Archibong and A.J. Thakkar. Chem. Phys. Lett. **173**, 579 (1990); (*e*) G. Maroulis. J. Chem. Phys. **101**, 4949 (1994); (*f*) H. Sekino and R.J. Bartlett. Int. J. Quantum Chem. Quantum Chem. Symp. **21**, 487 (1987).
15. (*a*) A.D. McLean and M. Yoshimine. J. Chem. Phys. **46**, 3682 (1967); (*b*) **47**, 1927 (1967); (*c*) **47**, 3256 (1967).
16. (*a*) D.M. Bishop and G. Maroulis. J. Chem. Phys. **82**, 2380 (1985); (*b*) G. Maroulis and D.M. Bishop. Chem. Phys. Lett.

114, 182 (1985); (*c*) **128**, 462 (1986); (*d*) Theor. Chim. Acta, **69**, 161 (1986), and references therein.
17. A.E. Kondo, P. Piecuch, and J. Paldus. J. Chem. Phys. **102**, 6511 (1995).
18. (*a*) J. Paldus. J. Chem. Phys. **67**, 303 (1977); (*b*) P. Piecuch and J. Paldus. Theor. Chim. Acta, **78**, 65 (1990); (*c*) Int. J. Quantum Chem. **36**, 429 (1989).
19. (*a*) P. Piecuch, A.E. Kondo, V. Špirko, and J. Paldus. J. Chem. Phys. **104**, 4699 (1996); (*b*) V. Špirko, P. Piecuch, A.E. Kondo, and J. Paldus. J. Chem. Phys. **104**, 4716 (1996).
20. P. Piecuch and J. Paldus. J. Phys. Chem. **99**, 15354 (1995).
21. D. Mukherjee and S. Pal. Adv. Quantum Chem. **20**, 292 (1989).
22. X. Li and J. Paldus. J. Chem. Phys. **103**, 6536 (1995).
23. J.F. Stanton. J. Chem. Phys. **101**, 371 (1994).
24. F. Jensen. Chem. Phys. Lett. **169**, 519 (1990).
25. P. Čársky and I. Hubač. Theor. Chim. Acta, **80**, 407 (1991).
26. (*a*) J. Paldus and X. Li. *In* Symmetries in science VI: From the rotation group to quantum algebras. *Edited by* B. Gruber. Plenum Press, New York. 1993. pp. 573–592; (*b*) X. Li and J. Paldus. Int. J. Quantum Chem. Quantum Chem. Symp. **27**, 269 (1993); (*c*) B. Jeziorski, J. Paldus, and P. Jankowski. Int. J. Quantum Chem. **56**, 129 (1995).
27. X. Li and J. Paldus. J. Chem. Phys. **101**, 8812 (1994).
28. (*a*) J. Paldus. J. Chem. Phys. **61**, 5321 (1974); (*b*) *In* Theoretical chemistry: advances and perspectives. Vol. 2. *Edited by* H. Eyring and D. Henderson. Academic Press, New York. 1976. pp. 131–290; (*c*) *In* Mathematical frontiers in computational chemical physics. *Edited by* D.G. Truhlar. Springer-Verlag, Berlin. 1988. pp. 262–299; (*d*) *In* Contemporary mathematics. Vol. 160. *Edited by* P. Olver and N. Kamran. American Mathematical Society, Providence. R.I. 1994. pp. 209–236.
29. (*a*) J. Paldus and C.R. Sarma. J. Chem. Phys. **83**, 5135 (1985); (*b*) J. Paldus, M.-J. Gao, and J.-Q. Chen. Phys. Rev. A: Gen. Phys. **35**, 3197 (1987); (*c*) J. Paldus, S. Rettrup, and C.R. Sarma. J. Mol. Struct. (Theochem.), **199**, 85 (1989); (*d*) X. Li and J. Paldus. Int. J. Quantum Chem. **41**, 117 (1992).
30. X. Li and Q. Zhang. Int. J. Quantum Chem. **36**, 599 (1989).
31. (*a*) X. Li, P. Piecuch, and J. Paldus. Chem. Phys. Lett. **224**, 267 (1994); (*b*) P. Piecuch, X. Li, and J. Paldus. Chem. Phys. Lett. **230**, 377 (1994).
32. (*a*) X. Li and J. Paldus. Chem. Phys. Lett. **231**, 1 (1994); (*b*) J. Chem. Phys. **102**, 8897 (1995); (*c*) **102**, 2013 (1995); (*d*) **102**, 8059 (1995); (*e*) **103**, 1024 (1995).
33. J. Paldus and B. Jeziorski. Theor. Chim. Acta, **73**, 81 (1988).
34. J. Paldus. Diagrammatic methods for many-fermioin systems. University of Nijmegen, Nijmegen, The Netherlands. 1981.
35. K.P. Huber and G. Herzberg. Molecular spectra and molecular structure. Vol 4. Constants of diatomic molecules. Van Nostrand Reinhold, New York. 1979.
36. T.A.R. Irwin and F.W. Dalby. Can. J. Phys. **43**, 1766 (1965).
37. (*a*) A.J. Sadlej. Collect. Czech. Chem. Commun. **53**, 1995 (1988); (*b*) Theor. Chim. Acta, **79**, 123 (1991).
38. P.O. Widmark, P.A. Malmqvist, and B.O. Roos. Theor. Chim. Acta, **77**, 291 (1990).
39. J. Almlöf and P.R. Taylor. J. Chem. Phys. **86**, 4070 (1987).
40. (*a*) A. Bunge. J. Chem. Phys. **53**, 20 (1970); (*b*) A.D. McLean and B. Liu. J. Chem. Phys. **58**, 1066 (1973).
41. GAMESS. M.W. Schmidt, K.K. Baldridge, J.A. Boatz, S.T. Elbert, M.S. Gordon, J.H. Jensen, S. Koseki, N. Matsunaga, K.A. Nguyen, S.J. Su, T.L. Windus, together with M. Dupuis and J.A. Montgomery. J. Comput. Chem. **14**, 1347 (1993).
42. H.D. Cohen and C.C.J. Roothaan. J. Chem. Phys. **43**, S34 (1965).
43. R.W. Molof, H.L. Schwarz, T.M. Miller, and B. Bederson. Phys. Rev. A: Gen. Phys. **10**, 1131 (1974).
44. G. Maroulis and A.J. Thakkar. J. Phys. B: Mol. Opt. Phys. **22**, 2439 (1989); N. El-Bakali Kassimi and A.J. Thakkar. Phys. Rev. A: At. Mol. Opt. Phys. **50**, 2948 (1994).
45. J. Pipin and D.M. Bishop. Phys. Rev. A: At. Mol. Opt. Phys. **45**, 2736 (1992).
46. O. Jitrik and C.F. Bunge. Phys. Rev. A: At. Mol. Opt. Phys. **43**, 5804 (1991).
47. D.H. Phelps and F.W. Dalby. Phys. Rev. Lett. **16**, 3 (1966).
48. F.X. Powell and D.R. Lide. J. Chem. Phys. **42**, 4201 (1965).
49. D.H. Phelps and F.W. Dalby. Can. J. Phys. **43**, 144 (1965).
50. W.L. Meerts and A. Dymanus. Chem. Phys. Lett. **23**, 45 (1973).
51. K.I. Peterson, G.T. Fraser, and W. Klemperer. Can. J. Phys. **62**, 1502 (1984).
52. E.A. Scarl and F.W. Dalby. Can. J. Phys. **52**, 1429 (1974).
53. P.F. Bernath. J. Chem. Phys. **86**, 4838 (1987).
54. R.S. Ram and P.F. Bernath. J. Mol. Spectrosc. **122**, 275 (1987).
55. R.S. Ram, P.F. Bernath, R. Engleman, Jr., and J.W. Brault. J. Mol. Spectrosc. **172**, 34 (1995).
56. A. Carrington, D.H. Levy, and T.A. Miller. J. Chem. Phys. **47**, 3801 (1967).
57. W.L. Meerts and A. Dymanus. Astrophys. J. **187**, L45 (1974); Can. J. Phys. **53**, 2123 (1975).
58. W. Meyer and P. Rosmus. J. Chem. Phys. **63**, 2356 (1975).
59. H. Sun and K.F. Freed. J. Chem. Phys. **88**, 2659 (1988).
60. G.C. Lie, J. Hinze, and B. Liu. J. Chem. Phys. **59**, 1872 (1973); **59**, 1887 (1973).
61. P.J. Hay and T.H. Dunning. J. Chem. Phys. **64**, 5077 (1976).
62. C.F. Bender and E.R. Davidson. Phys. Rev. **183**, 23 (1969).
63. E.M. Goldfield and K.P. Kirby. J. Chem. Phys. **87**, 3986 (1987).
64. J.K. Park and H. Sun. Chem. Phys. Lett. **211**, 618 (1993).
65. S.I. Chu, M. Yoshimine, and B. Liu. J. Chem. Phys. **61**, 5389 (1974).
66. S.R. Langhoff, C.W. Bauschlicher, and P.R. Taylor. J. Chem. Phys. **86**, 6992 (1987).
67. H.J. Werner, P. Rosmus, and E.A. Reinsch. J. Chem. Phys. **79**, 905 (1983).
68. H. Sun, Y.S. Lee, and K.F. Freed. Chem. Phys. Lett. **150**, 529 (1988).
69. W.D. Allen and H.F. Schaefer III. Chem. Phys. **108**, 243 (1986).
70. L.G.M. Pettersson and S.R. Langhoff. Chem. Phys. Lett. **125**, 429 (1986).
71. M. Larsson. J. Chem. Phys. **86**, 5018 (1987).
72. J.K. Park and H. Sun. Chem. Phys. Lett. **195**, 469 (1992).
73. J. Senekowitsch, P. Rosmus, H.J. Werner, and M. Larsson. Z. Naturforsch. A: Phys. Phys. Chem. Kosmophys. **41A**, 719 (1986).
74. J. Senekowitsch, H.J. Werner, P. Rosmus, E.A. Reinsch, and S.V. ONeil. J. Chem. Phys. **83**, 4661 (1985).

Solvent isotope effects as a probe of general catalysis and solvation in phosphoryl transfer

Clinton D. Bryan, K. Barbara Schowen, and Richard L. Schowen

Abstract: Phosphoryl transfer to methanol from tris(*p*-nitrophenyl) phosphate (PNNN), methyl bis(*p*-nitrophenyl) phosphate (PMNN), and dimethyl *p*-nitrophenyl phosphate (PMMN) exhibits general base catalysis by acetate ion but no detectable catalysis by acetic acid. For PNNN, acetate catalysis produces normal solvent isotope effects k_{ROH}/k_{ROD} of 1.68 ± 0.01 at high ionic strength (0.475) and 1.77 ± 0.04 at low ionic strength (0.048). A linear proton inventory indicates most simply that the isotope effect arises from a one-proton catalytic bridge in the transition state, although this model cannot strongly be distinguished from a generalized solvation effect. Reactions of methoxide ions produce slight inverse isotope effects k_{ROD}/k_{ROH} of 1.1–1.2, far smaller than the inverse effect of about 2.5 expected for complete and uncompensated desolvation of the reactant-state methoxide ion. The transition state is thus stabilized by substantial interaction with the solvent. The proton inventory for the least reactive substrate PMMN (relative rate constant 1) is suggestive of transition-state stabilization by a combination of one-proton catalytic bridge(s) and distributed sites, while the proton inventory for the most reactive substrate PNNN (relative rate constant 1388) suggests only generalized transition-state solvation (many distributed sites); the proton inventory for PMNN, a substrate of intermediate reactivity (relative rate constant 60), suggests an intermediate situation. The data are consistent with a model in which transition states with exterior concentrations of charge favor stabilization of the charge by isotope-fractionating one-proton bridges, while transition states with distributed charge favor stabilization of the charge by many distributed sites.

Key words: phosphoryl transfer, proton inventories, solvent isotope effects.

Résumé : Le transfert d'un phosphoryle à du méthanol à partir du phosphate de tris(*p*-nitrophényle) (PNNN), du phosphate de méthyle et de bis(*p*-nitrophényle) (PMNN) et du phosphate de diméthyle et de *p*-nitrophényle (PMMN) est sujet à de la catalyse générale des bases, par l'ion acétate, mais sans catalyse détectable par l'acide acétique. Pour le PNNN, la catalyse par l'acétate conduit à des effets isotopiques du solvant qui sont normaux, k_{ROH}/k_{ROD} de 1,68 ± 0,01 à force ionique élevée (0,475) et de 1,77 ± 0,04 à une force ionique plus faible (0,048). Un inventaire linéaire des protons indique de la façon la plus simple que l'effet isotopique découle d'un pont catalytique à un hydrogène dans l'état de transition, même s'il n'est pas facile de distinguer ce modèle d'un effet généralisé de solvatation. Les réactions des ions méthanolates conduisent à de légers effets isotopiques inverses, k_{ROD}/k_{ROH} de 1,1 à 1,2, beaucoup plus faible que l'effet inverse d'environ 2,5 attendu pour une désolvatation complète et non compensée de l'ion méthylate dans l'état de réactif. L'état de transition est donc stabilisé par une interaction importante avec le solvant. L'inventaire de proton pour le substrat le moins réactif, PMMN (constante relative de vitesse de 1), suggère qu'il y a stabilisation de l'état de transition par une combinaison de pont(s) catalytique(s) à un proton et de sites distribués alors que l'inventaire de proton pour le substrat le plus réactif (PNNN, constante de vitesse relative de 1388) ne suggère qu'une solvatation généralisée de l'état de transition (plusieurs sites distribués); l'inventaire de proton pour le PMNN, un substrat de réactivité intermédiaire (constante de vitesse relative de 60), suggère l'existence d'une situation intermédiaire. Les données sont en accord avec un modèle dans lequel les états de transition avec des concentrations extérieures de charge favorisent une stabilisation de la charge par des ponts à un hydrogène provoquant un fractionnement de l'isotope alors que les états de transition comportant un distribution de la charge favorisent une stabilisation de la charge par les divers sites distribués.

Mots clés : transfert de phosphoryle, inventaires de protons, effets isotopiques du solvant.

[Traduit par la rédaction]

Received October 4, 1995.

This paper is dedicated to Professor Richard F.W. Bader on the occasion of his 65th birthday.

Clinton D. Bryan,[1] K. Barbara Schowen, and Richard L. Schowen.[2] Department of Chemistry, University of Kansas, Lawrence, KS 66045-0046, U.S.A.

[1] Current address: Department of Physical Science, Cameron University, Lawton, OK 73505, U.S.A.
[2] Author to whom correspondence may be addressed. Telephone: (913) 864-4080. Fax: (913) 864-5349. E-mail: rschowen@kuhub.cc.ukans.edu

Introduction

A vital scientific contribution of Professor Richard Bader was made already in his doctoral research with C. Gardner Swain, at the Massachusetts Institute of Technology. Building upon their panoramic critique of preceding studies in reaction kinetics and mechanism, the chemistry and physics of isotopes, and the spectroscopy and thermodynamics of solutions, Bader, Swain, and Edward R. Thornton produced a deeply detailed and complete theory of isotopic solvent effects and of reaction rates in mixtures of isotopic solvents (1–4). Two of us (K.B.S. and R.L.S.) count ourselves among those "present at the Creation" (or shortly thereafter) and have been profoundly influenced by these and others of Richard Bader's contributions throughout a period now approaching 40 years. It is with a spirit of gratitude that we present this paper describing a current application of isotopic solvent effects to the issue of the *Canadian Journal of Chemistry* celebrating the scientific contributions of Richard Frederick William Bader.

Displacement at phosphorus at the phosphate level of oxidation is of particular importance in biochemistry, where it dominates bioenergetics, the formation and decomposition of the genetic materials DNA and RNA, the regulation of protein properties accompanying transmembrane signal transduction, and many other vital processes. In mechanistic chemistry, the understanding of the mechanism of the reaction remains a subject of vigorous investigation and debate. A comprehensive background on all aspects of this broad subject may be derived from the magisterial review of Thatcher and Kluger (5).

Solvent isotope effects provide an entry to the examination of two aspects of phosphoryl-transfer mechanistic chemistry: (*i*) the role of general acid–base catalysis (where the catalytic proton bridge may be expected to generate an isotope effect), and (*ii*) the desolvation or solvation of centers that lose or develop solvation sites of sufficient basicity to produce hydrogen-isotope fractionation.

Biochemical phosphoryl transfer reactions are sometimes hydrolytic, as in the dephosphorylation of phosphoproteins, but they often involve transfer from phosphoryl donors to non-water nucleophiles: examples include the formation of 2′,3′ cyclic phosphoryl derivatives in the cleavage of RNA by ribonucleases, the formation of phosphoryl serine and tyrosine residues in regulatory events, and the self-splicing of RNA molecules. In these cases, alcoholysis reactions at phosphate centers are occurring either intramolecularly or within catalyst–substrate complexes.

We report here some transition-state structural and energetic features of the phosphate alcoholysis reactions illustrated in Fig. 1. These reactions bear some relationship to the ribonuclease reaction just described, although the systems studied here are artificially activated by use of *p*-nitrophenoxy leaving groups in place of the alkoxy leaving groups present in the natural systems.

Results

General-base catalysis of the methanolysis of PNNN and PMNN

The rate of methanolysis of tris(*p*-nitrophenyl) phosphate (PNNN) was examined (as described in the Experimental section) in methanolic acetate buffers as a function of both buffer ratio and total buffer concentration. Figure 2 shows plots of observed rate constants vs. total buffer concentration at five different buffer ratios (the data are given in Table S1 of the supplementary material[3]). It is not visually obvious but the dependences show a slight upward curvature, probably resulting from a specific salt effect that accompanies replacement of sodium acetate by sodium bromide; thus small negative intercepts with large errors are calculated, as reported in Table S2.[3] When the intercepts were constrained to be zero as in Fig. 2, little change in the mean values of the second-order rate constants resulted and the rate constants thus calculated were used subsequently.

A plot (Fig. 3) of the buffer catalysis constant vs. fraction of base in the buffer shows catalysis to arise only from acetate ion. In these buffers, the reaction is therefore general-base cat-

Fig. 1. The reaction with methanol of the three substrates studied in this work.

$$OP(OAr)(OR^1)(OR^2) + CH_3OH \rightarrow OP(OCH_3)(OR^1)(OR^2) + ArOH$$

Ar = *p*-nitrophenyl
PNNN: $R^1 = R^2 = Ar$
PMNN: $R^1 = Ar$, $R^2 = CH_3$
PMMN: $R^1 = R^2 = CH_3$

Fig. 2. Observed first-order rate constants for the methanolysis of PNNN as a function of total buffer concentration in acetic acid–sodium acetate buffers at 25.0°C and ionic strength of 0.475 adjusted with sodium bromide. The mole fraction of sodium acetate in the buffer is 0.2 (bottom curve, filled circles), 0.3 (open squares), 0.5 (filled triangles), 0.7 (open triangles), 0.8 (filled squares).

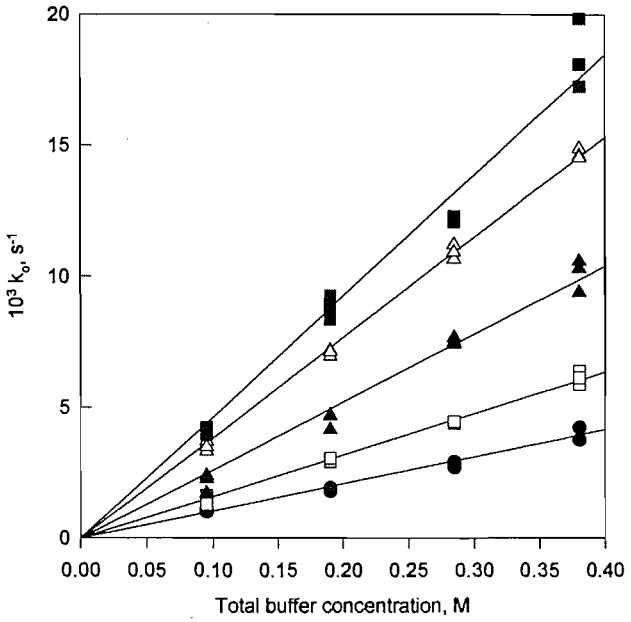

[3] Sets of original data are deposited with the National Research Council of Canada and can be purchased from: The Depository of Unpublished Data, Document Delivery, CISTI, National Research Council Canada, Ottawa, Canada K1A 0S2.

Fig. 3. Second-order rate constants for acetate – acetic acid buffer catalysis (slopes of the lines in Fig. 2) as a function of the mole fraction of acetate base in the buffer. The data indicate that acetate and not acetic acid is the catalytic component of the buffer.

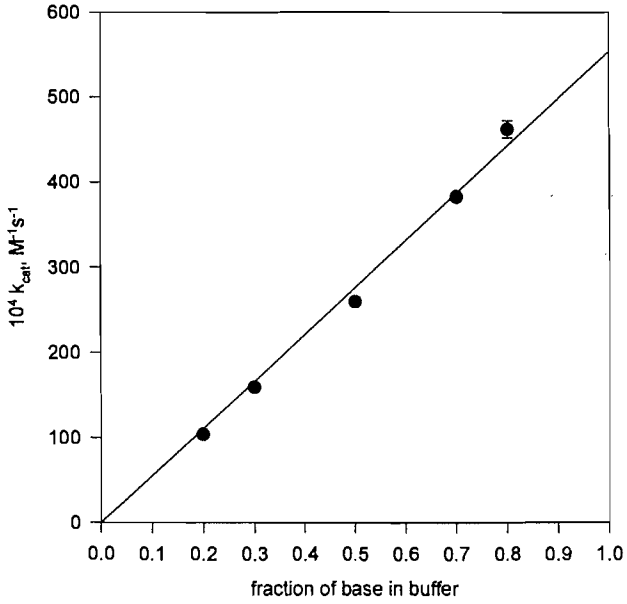

alyzed and not general-acid catalyzed. The value of the second-order rate constant for acetate ion general catalysis is $(5.54 \pm 0.11) \times 10^{-2}\ M^{-1}\ s^{-1}$.

A brief examination was made of the buffer catalysis of the methanolysis of dimethyl *p*-nitrophenyl phosphate (PMMN) by a 1:1 buffer of acetic acid and sodium acetate at total buffer concentrations of 0.5, 0.7, and 0.95 M without added salt (Table S3[3]). Assuming acetate ion to be the sole catalyst, its second-order rate constant is $(2.25 \pm 0.22) \times 10^{-4}\ M^{-1}\ s^{-1}$.

Solvent isotope effect and proton inventory for the acetate-catalyzed methanolysis of PNNN

The rate constants for general-base catalysis by acetate ion of the methanolysis of PNNN in CH_3OH, CH_3OD, and binary mixtures of the isotopic solvents were obtained from the observed first-order rate constants in 1:1 buffers of acetic acid and sodium acetate. It was assumed that, as in CH_3OH, acetate was the sole catalyst in the deuterated solvents (otherwise an infinite inverse isotope effect for acetic acid catalysis would be required). The first-order rate constants are presented in Table S4[3] (for an ionic strength of 0.475 maintained by added sodium bromide) and in Table S5[3] (for an ionic strength of 0.048 maintained by added sodium nitrate). The acetate ion catalytic constants are given in Tables 1 and 2.

Solvent isotope effects and proton inventories for the methoxide ion promoted methanolysis of PNNN, PMNN, and PMMN

In Tables S6, S7, and S8 of the supplementary material[3] are given first-order rate constants for methoxide ion promoted methanolyses of PNNN, PMNN, and PMMN in CH_3OH, CH_3OD, and binary mixtures of the isotopic solvents. In a manner reminiscent of the behavior in acetate buffers described above, the plots of first-order rate constants against sodium methoxide concentration exhibited a small upward curvature so that when the data were fitted to a straight line, small but definite negative intercepts with large errors were calculated. A reasonable explanation is a specific salt effect resulting from the replacement of bromide ion by methoxide ion. When the intercepts were constrained to be zero, only modest effects on the calculated second-order rate constants resulted. Values obtained in this way were therefore employed in subsequent considerations. The results of these calculations are presented for the reactions of PNNN, PMNN, and PMMN, respectively, in Tables 3, 4, and 5.

Table 1. Calculated second-order rate constants at fraction of base 0.5 for the acetic acid – sodium acetate buffer-catalyzed methanolysis of PNNN in binary mixtures of methanol-*h* (mole fraction $1 - n$) and methanol-*d* (mole fraction n), at 25.0 ± 0.1°C (μ = 0.475, maintained with added sodium bromide).

n(D)	$10^4\ k_B$ (SD)[a] $M^{-1}\ s^{-1}$	10^5 Intercept (SD)[a,b]	$10^4\ k_B$ (SD)[a,c] $M^{-1}\ s^{-1}$
0.00	284 (10)	−70 (30)	260 (5)
0.40	211 (6)	14 (16)	217 (3)
0.50	208 (7)	− 2 (19)	208 (3)
0.60	184 (8)	−14 (22)	189 (3)
0.99	161 (3)	−17 (9)	155 (2)

[a]SD = Standard Deviation.
[b]Average intercept = $(-12 \pm 31) \times 10^{-5}$.
[c]Calculated with intercept constrained to be zero.

Table 2. Calculated second-order rate constants at fraction of base 0.5 for acetic acid – sodium acetate buffer-catalyzed methanolysis of PNNN in binary mixtures of methanol-*h* (mole fraction $1 - n$) and methanol-*d* (mole fraction n) at 25.0 ± 0.1°C (μ = 0.048, maintained with added sodium nitrate).

n(D)	$10^4\ k_B$ (SD)[a] $M^{-1}\ s^{-1}$	10^5 Intercept (SD)[a,b]	$10^4\ k_B$ (SD)[a,c] $M^{-1}\ s^{-1}$
0.00	381 (11)	4.3 (9.4)	385 (4)
0.40	314 (10)	0.6 (8.1)	314 (2)
0.50	300 (10)	−2.9 (8.0)	297 (2)
0.60	285 (7)	3.5 (5.8)	289 (2)
0.99	225 (5)	−5.3 (4.3)	218 (1)

[a]SD = Standard Deviation.
[b]Average intercept = $(0.04 \pm 3.67) \times 10^{-5}$.
[c]Calculated with intercept constrained to be zero.

Discussion

Transition-state stabilization in general-base catalyzed methanolysis of *p*-nitrophenyl phosphate esters

General base catalysis of these reactions by acetate ion can in principle occur in any of the following catalytic modes:
(*i*) *nucleophilic mode*, in which the acetate ion displaces *p*-nitrophenoxide ion to form a rapidly solvolyzed acetyl phosphate intermediate;
(*ii*) *protolytic mode*, in which a transition state for attack by

Table 3. Calculated second-order rate constants for the sodium methoxide promoted methanolysis of PNNN in binary mixtures of methanol-*h* (mole fraction $1 - n$) and methanol-*d* (mole fraction n) at 25.0 ± 0.1°C (μ = 0.095, maintained with added sodium bromide).

n(D)	k_M (SD)[a] M^{-1} s^{-1}	10^4 Intercept (SD)[a,b]	k_M (SD)[a,c] M^{-1} s^{-1}
0.00	62 (3)	−37 (10)	63 (2)
0.20	64 (2)	−9 (9)	62 (1)
0.40	63 (3)	7 (13)	64 (1)
0.60	60 (4)	20 (10)	66 (2)
0.80	66 (4)	16 (14)	70 (2)
0.97	66 (4)	20 (20)	71 (2)

[a]SD = Standard Deviation.
[b]Average intercept = (2.8 ± 20.14) × 10^{-4}.
[c]Calculated with intercept constrained to be zero.

Table 4. Calculated second-order rate constants for the sodium methoxide promoted methanolysis of PMNN in binary mixtures of methanol-*h* (mole fraction $1 - n$) and methanol-*d* (mole fraction n) at 25.0 ± 0.1°C (μ = 0.095, maintained with added sodium bromide).

n(D)	k_M (SD)[a] M^{-1} s^{-1}	10^4 Intercept (SD)[a,b]	k_M (SD)[a,c] M^{-1} s^{-1}
0.00	2.74 (0.02)	−10 (10)	2.71 (0.01)
0.20	2.79 (0.01)	10 (20)	2.80 (0.02)
0.40	2.88 (0.07)	8 (22)	2.90 (0.03)
0.60	3.07 (0.05)	−5 (43)	3.06 (0.05)
0.80	3.26 (0.04)	−17 (16)	3.21 (0.02)
0.98	3.32 (0.03)	−1 (15)	3.32 (0.02)

[a]SD = Standard Deviation.
[b]Average intercept = (−2.5 ± 9.5) × 10^{-5}.
[c]Calculated with intercept constrained to be zero.

Table 5. Calculated second-order rate constants for the sodium methoxide promoted methanolysis of PMMN in binary mixtures of methanol-*h* (mole fraction $1 - n$) and methanol-*d* (mole fraction n) at 25.0 ± 0.1°C (μ = 0.095, maintained with added sodium bromide).

n(D)	10^2 k_M (SD)[a] M^{-1} s^{-1}	10^5 Intercept (SD)[a,b]	10^2 k_M (SD)[a,c] M^{-1} s^{-1}
0.00	4.66 (0.07)	−4 (1)	4.54 (0.02)
0.20	5.03 (0.08)	−10 (2)	4.71 (0.05)
0.40	5.10 (0.10)	−8 (2)	4.85 (0.04)
0.50	5.15 (0.04)	−7 (1)	4.93 (0.04)
0.60	5.30 (0.07)	−9 (2)	5.03 (0.04)
0.80	5.82 (0.04)	−18 (4)	5.22 (0.10)
0.99	6.12 (0.17)	−20 (2)	5.46 (0.09)

[a]SD = Standard Deviation.
[b]Average intercept = (−11 ± 5) × 10^{-5}.
[c]Calculated with intercept constrained to be zero.

Fig. 4. Three forms of transition-state stabilization for protolytic general-base catalysis of nucleophilic displacement at phosphate-phosphorus. Note that all structures are isomeric and thus kinetically indistinguishable. (*a*) Proton bridging from an attacking nucleophile ROH to a general base B (class n or "classical general-base" catalysis). (*b*) Proton bridging from the conjugate acid of the general base B to the departing leaving-group ArO^- (class e or "specific-base general-acid" catalysis). This is often thought to be probable only if leaving-group departure is occurring in the rate-limiting transition state, as in a concerted displacement reaction. (*c*) Proton bridging from the conjugate acid of the general base B to the P═O oxygen (another form of class e or "specific-base general-acid" catalysis). This is often thought to be probable only if leaving-group departure is not occurring in the rate-limiting transition state, as in formation of a trigonal-bipyramidal adduct.

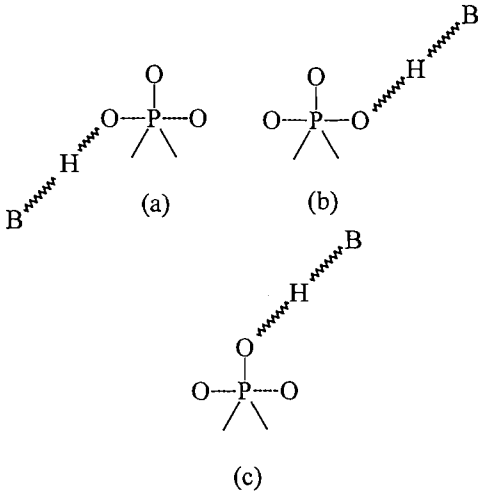

methanol is stabilized through a protonic bridge between an acetate anion and a nucleophilic center in the remainder of the transition state; a protolytic transition state may have several isomeric structures, illustrated in Fig. 4 (for nomenclature, see ref. 6):

(*a*) *protolytic mode class n* (Fig. 4*a*), in which acetate ion accepts a proton bridge from a nucleophilically attacking methanol molecule (often called "classical general-base catalysis");

(*b*) *protolytic mode class e* (Fig. 4*b*,*c*), in which acetic acid donates a proton bridge to a center in the transition state for methoxide ion nucleophilic attack at phosphorus, the most likely acceptor sites being the P═O oxygen or the *p*-nitrophenoxide oxygen (the former more likely if a trigonal-bipyramidyl intermediate is forming, the latter more likely if the displacement reaction is concerted).

The nucleophilic mode is expected to produce only small isotope effects (see below for expected magnitudes) from generalized solvation changes between reactants and transition state, while the various protolytic modes are expected to generate larger isotope effects from the proton in the bridging site of the transition state. In principle, this protonic bridge may be formed of a proton that is "in flight," undergoing transfer in a manner coupled in the reaction coordinate to other bonding changes in the transition state, or it may be stabilizing the transition state through a relatively strong kind of hydrogen bond-

Fig. 5. Proton inventories for the acetate ion general-base catalyzed methanolysis of PNNN at ionic strengths 0.048 (maintained with sodium nitrate) and 0.475 (maintained with sodium bromide). The solid circles represent the experimental data from Tables 1 and 2; where error bars are not visible, they lie within the space of the symbol. The data are buffer catalysis constants at fraction of base 0.5. The solid curves are linear and correspond to one-proton catalysis and to linear least-squares best fits of the data ($10^4 k_B$ (M^{-1} s^{-1}) = (384 ± 3) [1 − n + n(0.565 ± 0.012)] for the upper curve; $10^4 k_B$ (M^{-1} s^{-1}) = (259 ± 3) [1 − n + n(0.585 ± 0.002)] for the lower curve). The dotted curves are exponential and are least-squares fits with no constraints ($10^4 k_B$ (M^{-1} s^{-1}) = (388 ± 7) (0.579 ± 0.020)^n for the upper curve; $10^4 k_B$ (M^{-1} s^{-1}) = (263 ± 4) (0.597 ± 0.019)^n for the lower curve. The dash-dot curves are exponential representations with the rate constant in methanol-h and the isotope effect constrained to the values obtained in the linear best fit.

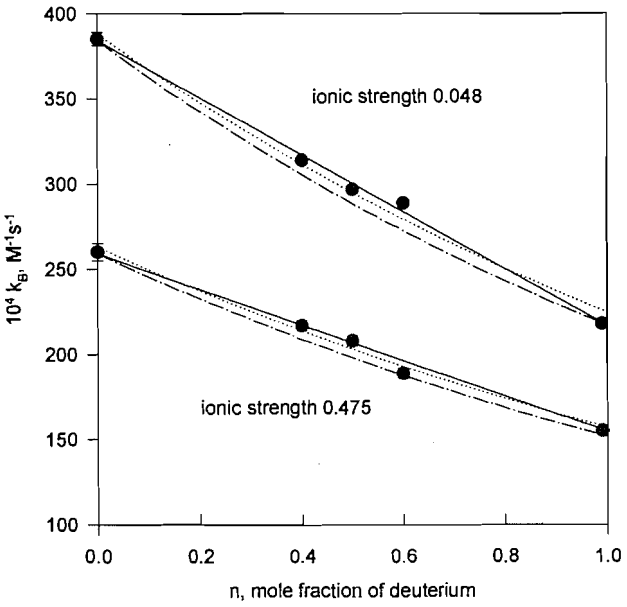

ing but not participating in the reaction-coordinate motion. The "in flight" proton bridge might be expected to generate larger, and the hydrogen-bonding proton bridge smaller isotope effects (for the question of whether the proton in general acid–base protolytic catalysis need be considered "in flight," see refs. 7–9).

The isotope effects observed in this work for acetate ion catalysis of the methanolysis of PNNN are 1.77 ± 0.04 (low ionic strength) and 1.68 ± 0.01 (high ionic strength). These would generally be regarded as indicative of protolytic catalysis rather than nucleophilic catalysis, although prudence suggests that they be seen as borderline cases. However, if the isotope effects derive completely from a one-proton protolytic bridge, they should generate a linear *proton inventory* (10–14), i.e., plot of rate constant vs. mole fraction of deuterium in mixtures of methanol-*h* and methanol-*d*. If, on the other hand, the isotope effects arise from generalized solvation changes, they should give an exponential proton inventory. This treatment assumes that the relatively weakly basic acetate ion produces negligible isotope fractionation so that the entire solvent isotope effect derives from transition-state sites.

Figure 5 shows the data compared with linear and exponential models. The solid curves describe the linear, protolytic model and are obviously consistent with the data at both ionic strengths. The dotted curves represent unconstrained exponential fits to the data, and are equally consistent with the data at both ionic strengths. Thus, the proton-inventory data do not rigorously distinguish protolytic from nucleophilic catalysis. However, the dash-dot lines provide a suggestive indication that protolytic catalysis may be at work. In these exponential, generalized-solvation models, the rate constants in methanol-*h* and methanol-*d* have been constrained to the values from the linear fit, which are closer to the measurements at the low and high limits of deuteration. These models clearly make a poorer fit to the data than the linear models. We therefore conclude that the more probable mode of catalysis is protolytic but that contributions from nucleophilic catalysis or another generalized-solvation model cannot be rigorously excluded. The protolytic catalysis model may apply as well to the observation of Bel'skii et al. (15) that triethanolamine catalysis of the ethanolysis of diphenyl *p*-nitrophenyl phosphate produces a solvent isotope effect of 2.

The data show that any one-proton bridge that is present is producing an isotope effect no larger than the observed isotope effect of 1.7–1.8: the observed isotope effect is not the resultant of a much larger effect from the proton bridge, partly cancelled by inverse solvent isotope-effect contributions arising from "tightly bound" sites in the solvation sphere of the transition state. An isotope effect from a one-proton catalytic bridge can be as small as 1.7–1.8 in at least two ways: (*a*) the proton may be "in flight" but very asymmetrically disposed between donor and acceptor atoms (16); (*b*) the proton may be in a stable potential with a structure that generates some isotope fractionation, such as the kind of hydrogen bond observed by Kreevoy and Liang (17), a suggestion originally made by Eliason and Kreevoy (18) and others (19) and lately revived under the rubric of "low-barrier hydrogen bonds (20)." Our data cannot distinguish these concepts, although we favor the latter hypothesis for reasons earlier presented (9). *We conclude from these data that a major part of the isotope effect of 1.7–1.8 is associated with a one-proton catalytic bridge in the transition state, with possible contributions from generalized solvation changes.*

Transition-state stabilization in methoxide ion promoted methanolysis of *p*-nitrophenyl phosphate esters

The simplest view of methoxide ion promoted methanolysis of PNNN, PMNN, and PMMN is that methoxide ion is bonding to P in the transition state, with its charge appearing chiefly (*a*) on the oxygen of the P═O group if a hypervalent adduct is forming (such an adduct should expel the ArO leaving group quite rapidly, so formation of the adduct should be the rate-limiting step), or (*b*) on the oxygen of the ArO leaving group (perhaps also on the oxygen of the P═O) if a concerted displacement is occurring. Methanol molecules could be interacting at any of these sites to stabilize the negative charge. On one model, the individual interactions might be quite numerous, weak, and generate only small isotope fractionation at each site; we refer to this model as a "solvation only" model. On the other hand, methoxide ion may be playing the same role in transition-state stabilization that is played by acetate ion in the buffer-catalyzed reaction: there may be transition-

state stabilization (at any of the three sites in Fig. 4) by means of a one-proton bridge. We call this model a "proton-bridge plus solvation model," since more diffuse solvation may also be occurring.

Methoxide ion itself is triply solvated by methanol molecules that generate substantial isotope fractionation (21–24). Each site has a deuterium fractionation factor (10–14) of 0.74 (expressing the deuterium preference relative to an average site in the bulk methanol solvent, so that protium is preferred in the three solvating sites by a factor of 1/0.74 = 1.35). Kresge's formulation (25) can be used to express this reactant-state contribution and the transition-state contribution to the partial solvent isotope effect k_n/k_0. Here k_n is the rate constant in a mixed isotopic solvent with mole fraction n of CH_3OD; k_0 is then the rate constant in methanol-h (n = 0). The result is shown in eq. [1] and eq. [2], where TSC means "transition-state contribution" and RSC means "reactant-state contribution."

$$[1] \quad k_n/k_0 = \text{TSC/RSC} = \text{TSC}/(1 - n + n[0.74])^3$$

$$[2] \quad k_0\,(\text{TSC}) = k_n\,(1 - n + n[0.74])^3$$

A plot of the right-hand side of eq. [2] vs. n can then be used to explore the number of isotope-fractionating sites and the size of the associated isotope effects in the transition states for the methoxide ion promoted methanolysis of PNNN, PMNN, and PMMN. Such plots are shown in Figs. 6, 7, and 8, respectively.

First it should be noted that the observed isotope effects are only slightly inverse for all three substrates, while complete liberation of the three methanol molecules solvating the reactant-state methoxide ion with no compensating effects in the transition state would have produced an inverse solvent isotope effect of $(1/0.74)^3 = 2.47$. Therefore, in all three cases, the transition state includes one or more strongly isotope-fractionating sites that prefer protium over deuterium.

Two plausible, limiting models may readily be generated for such interactions, as described above. On a "solvation only" model, there could be large numbers of sites each generating a quite small amount of isotope fractionation. This model will generate (10–14) an exponential dependence on n (eq. [3], where k_1 is the rate constant in CH_3OD). On a "proton bridge plus solvation" model, one site could be generating isotope fractionation analogous to that in the acetate-catalysis transition state, while the remaining sites could be numerous and diffuse. This situation corresponds to eq. [4], where we have arbitrarily taken the one-proton bridge to generate an isotope effect of 1.5.

$$[3] \quad k_n\,[1 - n + n(0.74)]^3 = k_0\,(k_1/k_0)^n$$

$$[4] \quad k_n\,[1 - n + n(0.74)]^3 = k_0\,[1 - n + n/(1.5)](1.5\,k_1/k_0)^n$$

In Figs. 6, 7, and 8, the "solvation only" model of eq. [3] is plotted as the solid curve and the "proton bridge plus solvation" model of eq. [4] as a dotted curve. Clearly the data lie very close to the predictions of both models, which are only slightly different, so no reliable distinction is possible. On the other hand, a suggestive trend can be noted by comparing the results in the three figures. For the most reactive substrate

Fig. 6. Proton inventory of the transition-state contribution to the solvent isotope effects for methoxide-promoted methanolysis of PNNN, $k_M[1 - n + n(0.74)]^3$. The solid curve is exponential and corresponds to the least-squares best fit to the data, $k_M = 63(0.463 \pm 0.006)^n$. It represents a model in which the entire transition-state contribution to the solvent isotope effect is ascribed to generalized solvation effects. The dotted curve is a plot of the equation, $k_M = 63\,[1 - n + (n/1.5)](0.70)^n$, corresponding to a model that ascribes an isotope effect of 1.5 to a one-proton catalytic bridge analogous to that for acetate catalysis and the remainder of the isotope effect to generalized solvation effects.

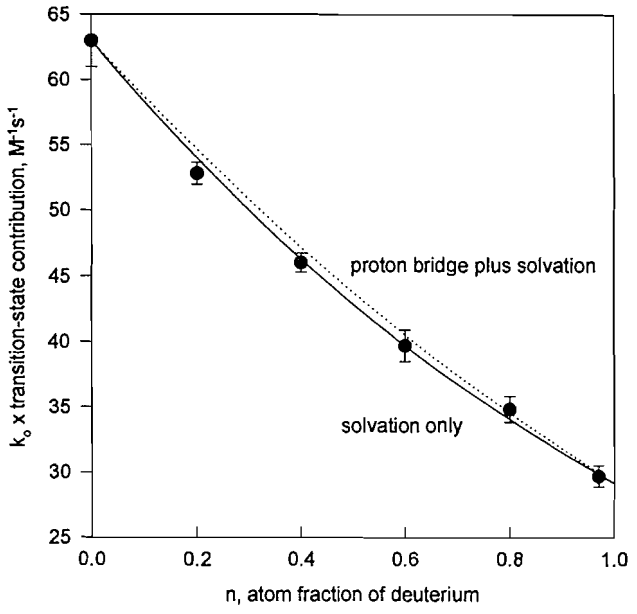

PNNN (Fig. 6), the experimental points for the most part lie on or below the curve for "solvation only." For the least reactive substrate, PMMN (Fig. 8), the experimental points lie a good deal closer to the "proton bridge plus solvation" model. For the substrate of intermediate reactivity, PMNN (Fig. 7), the experimental points lie between the curves for the two models.

We interpret these results as consistent with a relationship between *charge concentration* and *one-proton catalytic bridging*. For the least reactive substrate PMMN, where the negative charge is least stabilized by and least dispersed over the non-reacting phosphorus ligands and is thus most concentrated on the three sites (Fig. 4) at which one-proton catalytic bridging is expected, the data lie closest to a model that includes a one-proton bridge. For the most reactive substrate PNNN, where the non-reacting ligands can most effectively disperse the charge, the data lie closest to a model in which the solvating interactions are distributed over many sites, with little isotope fractionation at any single site. The choice of 1.5 as the value of the isotope effect for the one-proton bridge, although arbitrary, is reasonable. Values greater than 1.5 force the dotted curve toward linearity and a poorer fit to the data; values less than 1.5 force the curve down toward that of the pure solvation model.

For the most reactive substrate PNNN, a comparison can be made between the methoxide ion promoted reaction and the acetate ion catalyzed reaction. The methoxide ion reaction

Fig. 7. Proton inventory of the transition-state contribution to the solvent isotope effects for methoxide-promoted methanolysis of PMNN, $k_M[1 - n + n(0.74)]^3$. The solid curve is exponential and corresponds to the least-squares best fit to the data, $k_M = 2.71(0.513 \pm 0.005)^n$. It represents a model in which the entire transition-state contribution to the solvent isotope effect is ascribed to generalized solvation effects. The dotted curve is a plot of the equation, $k_M = 2.71\ [1 - n + (n/1.5)](0.77)^n$, corresponding to a model that ascribes an isotope effect of 1.5 to a one-proton catalytic bridge analogous to that for acetate catalysis and the remainder of the isotope effect to generalized solvation effects.

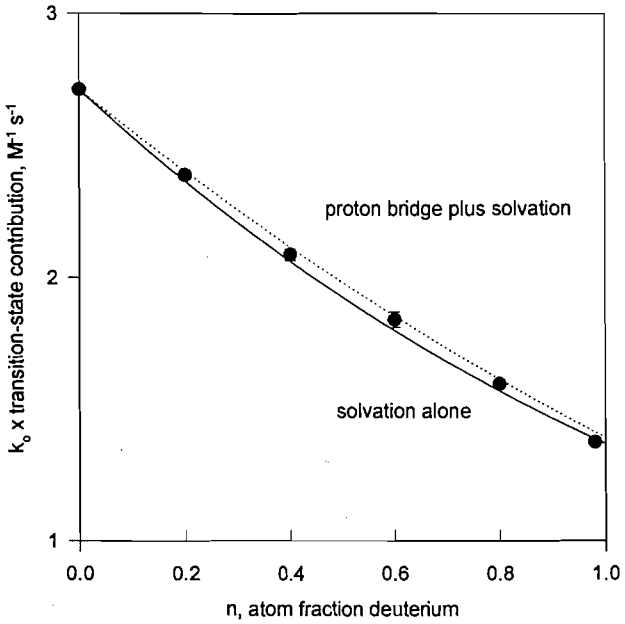

Fig. 8. Proton inventory of the transition-state contribution to the solvent isotope effects for methoxide-promoted methanolysis of PMMN, $100k_M[1 - n + n(0.74)]^3$. The solid curve is exponential and corresponds to the least-squares best fit to the data, $100k_M = 4.54(0.502 \pm 0.005)^n$. It represents a model in which the entire transition-state contribution to the solvent isotope effect is ascribed to generalized solvation effects. The dotted curve is a plot of the equation, $100k_M = 4.54\ [1 - n + n/(1.5)](0.75)^n$, corresponding to a model that ascribes an isotope effect of 1.5 to a one-proton catalytic bridge analogous to that for acetate catalysis and the remainder of the isotope effect to generalized solvation effects.

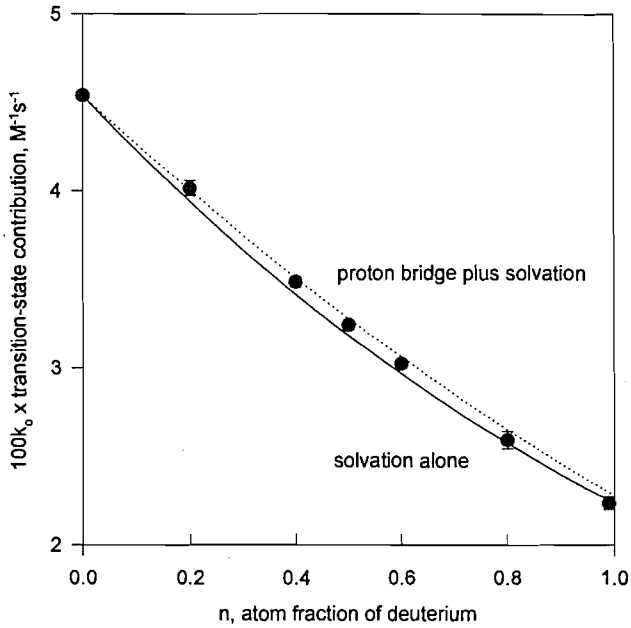

obeys a "solvation only" model, suggesting that methoxide ion attacks as a nucleophile rather than serving as a protolytic general-base catalyst for attack of one of its solvating methanol molecules. Acetate ion, on the other hand, we suggest to serve as a protolytic catalyst for attack of one of its solvating methanol molecules rather than to attack directly as a nucleophile. Thus our suggestion holds that between the strong nucleophile methoxide ion (direct attack, "solvation only") and the weak nucleophile acetate ion (one-proton catalysis of methanol attack), the mechanism changes from nucleophilic catalysis (strong nucleophile) to protolytic catalysis (weak nucleophile). This in turn implies that the protolytic mechanism is less sensitive to nucleophile basicity (smaller Brönsted ß) than the nucleophilic mechanism, and that the nucleophile therefore bears a larger part of the overall unit negative charge in the protolytic than in the nucleophilic transition state. While we have no direct evidence on the point, such a situation appears entirely possible.

We conclude from these data that proton-bridge stabilization of transition states, as in protolytic general acid–base catalysis, tends to be associated with concentrations of charge, probably on the exterior periphery of the transition state, while stabilization through generalized or distributed solvation interactions, relatively numerous and with small isotope fractionation at individual sites, tends to occur in transition states with dispersed charge.

Experimental section

Materials

Anhydrous sodium nitrate (Merck), sodium bromide (Fisher Scientific), and sodium acetate (Fisher Scientific) were stored in a vacuum oven for no less than 2 days at 120–150°C before use; glacial acetic acid (Fisher Scientific) was used as obtained. Methanol (Fisher Scientific and MCB Reagents), acetonitrile (MCB Reagents), and dichloromethane were distilled through a 48 cm Vigreux column after storage over 4A molecular sieves for no less than 2 days. Methanol-*d* (Aldrich Gold Label) was used as obtained. Tris(*p*-nitrophenyl) phosphate (Sigma; PNNN) was used as obtained.

Methyl bis(*p*-nitrophenyl) phosphate (PMNN) and dimethyl *p*-nitrophenyl phosphate (PMMN) were prepared according to Hamilton et al. (26). To PNNN in dichloromethane was added 0.1 M methoxide solution, slowly (1 drop in 10 s) with vigorous stirring, as reaction progress was monitored by TLC. When PNNN was no longer observed, the solution was immediately extracted five times with 10% aqueous potassium carbonate solution and stored 24 h over sodium sulfate. PMNN was recrystallized from 5:12 chloroform – carbon tetrachloride solution (mp 140.5–141.5°C (lit. (26) mp 141–143°C)). Methoxide addition 10-fold faster, followed by extraction with water and 1% sodium carbonate, drying, and evaporation of the dichloromethane, produced a yellow oil. PMMN was

obtained by vacuum distillation through a short-path apparatus (bp 152°C at 0.54 Torr (lit. (27) bp 151°C at 0.51 Torr)). (1 Torr = 133.3 Pa.)

Extinction coefficients

Extinction coefficients were determined in methanol for each component of the reaction mixtures monitored, and in methanolic acetate buffers and sodium methoxide solutions for some materials. The values are given in Table S9 of the supplementary material.[3]

Kinetics procedure

The solvolysis kinetics were determined spectrophotometrically using a personal-computer-interfaced Perkin–Elmer 555 recording spectrophotometer. Temperature was controlled at 25.0°C using a thermostatted cell holder. Buffer or sodium methoxide solutions (950 μL) were thermally equilibrated in a 1.0 cm cuvet for no less than 3 minutes. To initiate reaction, 50 μL of a stock solution of substrate (in acetonitrile) was injected with a pipetter or syringe. The reaction was monitored at 315 nm (acetate buffers) or 388 nm (sodium methoxide solutions), and the data collected by a computer program package developed by the Instrumentation Design Laboratory of the University of Kansas.

Solutions

Acetate buffers were prepared by dilution of weighed samples of the components with appropriate volumes of methanol. Appropriate volumes of these stock solutions were mixed to prepare buffer solutions of desired acid–base ratio. Volumes of stock solutions of sodium nitrate or sodium bromide were added to maintain the desired ionic strength. Sodium methoxide solutions (about 0.1 M) were prepared by weighing sodium under cyclohexane, then washing the metal with methanol, and dissolving it in degassed absolute methanol (Dry Ice – acetone bath). Solutions were standardized against dried potassium biphthalate or against 2-phenylquinoline-4-carboxylic acid (cinchophen) in dimethylformamide–benzene with exclusion of moisture and carbon dioxide. Substrate stock solutions were prepared by weight in dried distilled acetonitrile.

Treatment of data

The generation of *p*-nitrophenol in a solution initially containing only PNNN deviates slightly from an exponential time course because the product PMNN also generates *p*-nitrophenol and PMMN, which in turn generates *p*-nitrophenol. A similar deviation is seen in reactions of PMNN. In principle, the system can be described as a sequence of three irreversible reactions. However, PNNN is around 25 times more reactive than PMNN, which is about 60 times more reactive than PMMN. Thus the absorbance change associated with reactions of PNNN and PMNN can be described as a first-order process with a small zero-order correction (eq. [5]):

$$[5] \quad [\mathrm{ArOH}]_t = [\mathrm{R}]_0(1 - e^{-kt} + at)$$

Here R refers to either PNNN or PMNN, k is the rate constant for reaction of R, and a is the rate constant for reaction of the product formed from R (i.e., PMNN or PMMN, respectively). Least-squares fitting of the data to eq. [5] gives good values of k and values of a that are not inconsistent with the values obtained from the corresponding first-order reaction but which were not used further.

References

1. C.G. Swain and R.F.W. Bader. Tetrahedron, **10**, 182 (1960).
2. C.G. Swain, R.F.W. Bader, and E.R. Thornton. Tetrahedron, **10**, 200 (1960).
3. C.G. Swain and E.R. Thornton. J. Am. Chem. Soc. **83**, 3884 (1961).
4. C.G. Swain and E.R. Thornton. J. Am. Chem. Soc. **83**, 3890 (1961).
5. G.R.J. Thatcher and R. Kluger. Adv. Phys. Org. Chem. **25**, 99 (1989).
6. W.P. Jencks. Acc. Chem. Res. **9**, 425 (1976).
7. C.G. Swain, D.A. Kuhn, and R.L. Schowen. J. Am. Chem. Soc. **87**, 1553 (1965).
8. R.L. Schowen. Prog. Phys. Org. Chem. **9**, 275 (1972).
9. R.L. Schowen. *In* Mechanistic principles of enzyme activity. *Edited by* J.F. Liebman and A. Greenberg. VCH, New York. 1988. pp. 119–168.
10. K.B. Schowen. *In* Transition states of biochemical processes. *Edited by* R.D. Gandour and R.L. Schowen. Plenum Press, New York. 1978. Chap. 6.
11. R.L. Schowen. *In* Isotope effects on enzyme-catalyzed reactions. *Edited by* W.W. Cleland, M.H. O'Leary, and D.B. Northrop. University Park Press, Baltimore, Md. 1977. pp. 64–99.
12. K.S. Venkatasubban and R.L. Schowen. Crit. Rev. Biochem. **17**, 1 (1984).
13. F.J. Alvarez and R.L. Schowen. Isot. Org. Chem. **7**, 1 (1987).
14. D.M. Quinn and L.D. Sutton. *In* Enzyme mechanism from isotope effects. *Edited by* P.F. Cook. CRC Press, Boca Raton, Fla. 1991. pp. 73–126.
15. V.E. Bel'skii, L.A. Kudryavsteva, K.A. Derstuganova, S.B. Federov, and B.E. Ivanov. Zh. Obshch. Khim. **50**, 1997 (1980).
16. J. Sühnel and R.L. Schowen. *In* Enzyme mechanism from isotope effects. *Edited by* P.F. Cook. CRC Press, Boca Raton, Fla. 1991. pp. 3–35.
17. M.M. Kreevoy and T.M. Liang. J. Am. Chem. Soc. **102**, 3315 (1980).
18. R. Eliason and M.M. Kreevoy. J. Am. Chem. Soc. **100**, 7037 (1978).
19. M. Hegazi, D.M. Quinn, and R.L. Schowen. *In* Transition states of biochemical processes. *Edited by* R.D. Gandour and R.L. Schowen. Plenum Press, New York. 1978. p. 370.
20. W.W. Cleland and M.M. Kreevoy. Science, **264**, 1887 (1994).
21. V. Gold and S. Grist. J. Chem. Soc. B: 1665 (1971).
22. V. Gold and S. Grist. J. Chem. Soc. B: 1672 (1971).
23. V. Gold and S. Grist. J. Chem. Soc. B: 1682 (1971).
24. V. Gold and S. Grist. J. Chem. Soc. B: 1685 (1971).
25. A.J. Kresge. Pure Appl. Chem. **8**, 243 (1964).
26. S.E. Hamilton, N.P. Dudman, J. DeJersey, J.K. Stoops, and B. Zerner. Biochim. Biophys. Acta, **377**, 82 (1975).
27. A.M. De Roos and H. Toet. Recl. Trav. Chim. Pays-Bas, **77**, 946 (1958).

Orthogonal effective atomic orbitals in the topological theory of atoms

I. Mayer

Abstract: A simple formalism has been developed permitting us to extract, from the molecular wave functions, the *effective orthogonal atomic orbitals* characterizing the actual state of the atom in the molecule within the framework of Bader's topological theory of atoms. This may give important conceptual connections between the SCF wave functions obtained in the large-scale ab initio calculations, or even at the Hartree–Fock limit, and the traditional atomic orbital picture. The method is based on some partial orthogonality properties of the non-orthogonal localized molecular orbitals constructed by requiring a maximal weight in the given atomic domain, or in another selected molecular fragment. (The use of such localized orbitals may also be of independent interest.)

Key words: effective atomic orbitals, atomic orbitals from molecular wave functions, non-orthogonal localized orbitals, topological theory of atoms, Bader's theory of atoms in molecules.

Résumé : On a mis au point un formalisme simple qui permet d'extraire, à partir des fonctions d'ondes moléculaires, les *orbitales atomiques orthogonales effectives* qui caractérisent l'état réel de l'atome dans la molécule dans le cadre de la théorie topologique des atomes de Bader. Cette possibilité peut conduire à des relations conceptuelles importantes entre les fonctions d'onde en champ autocohérent obtenues lors de calcules ab initio à grande échelle, ou même dans les limites de Hartree–Fock, et les représentations traditionnelles des orbitales atomiques. La méthode est basée sur quelques propriétés d'orthogonalité partielle des orbitales moléculaires localisées, mais non orthogonales, construites en imposant une hauteur maximale dans un domaine atome donné ou dans un autre fragment moléculaire choisi. (L'utilisation de telles orbitales localisées peut aussi avoir un intérêt par lui-même.)

Mots clés : orbitales atomiques effectives; orbitales atomiques dérivés de fonctions d'ondes moléculaires; orbitales moléculaires localisées, non orthogonales; théorie atomique topologique; théorie de Bader des atomes dans les molécules.

[Traduit par la rédaction]

1. Introduction

The atomic orbital concept is of central importance in our understanding of the basic properties of molecules. The notion that atoms enter molecules with their $1s$, $2s$, $2p$, etc. orbitals (or their hybrids) is so fundamental that its importance can hardly be overestimated: our general picture about the electronic (and also geometrical, etc.) structure of molecular systems is mainly based on this qualitative, but extremely fruitful, application of quantum mechanics. However, as the computational schemes of quantum chemistry developed, it became more and more difficult to find direct links between the results of large-scale ab initio calculations and traditional atomic orbital (AO) concepts. Energetic considerations became paramount, often hiding the atomic nature of the chemical problems.

Bader's topological theory of atoms (see ref. 1) represented a very important step towards establishing a firm theoretical basis for the chemist's view on molecules as consisting of *atoms*, which is something additional to the picture of molecules representing merely assemblies of electrons and nuclei. The aim of the present paper is to show that in the framework of Bader's theory one can also regain the traditional AO description by an *a posteriori* analysis of the large-basis ab initio SCF results (or even the wave functions corresponding to the Hartree–Fock limit) producing the *effective* — distorted but still orthogonal — atomic orbitals by which the atom in question participates in formation of the molecular orbitals. To do this, we shall develop a non-orthogonal localized orbital analysis using an "extrinsic" localization criterion: maximizing the weight of each localized molecular orbital (LMO) within the selected part of the space. The orthogonal AOs are then obtained by applying the results to the special case of individual atomic domains and utilizing some partial orthogonality properties of the non-orthogonal LMOs introduced. This permits introduction of the concept of effective AOs within the molecule in a *basis-independent* manner. The present approach represents a generalization of the recent one (2) involving Mulliken's population analysis.[2] Numerical applications of the latter showed full agreement with the traditional AO picture: for all "ordinary" compounds

Received July 28, 1995.

This paper is dedicated to Professor Richard F.W. Bader on the occasion of his 65th birthday.

I. Mayer.[1] Central Research Institute for Chemistry of the Hungarian Academy of Sciences, H-1525 Budapest, P.O. Box 17, Hungary.

[1] Telephone: +361-325-7900. Fax: +361-325-7554. E-mail: mayer@cric.chemres.hu

[2] The analogy is, however, somewhat different from that seen (3) in the case of bond order and valence indices.

one obtains as many molecular orbitals appreciably localized on the given atom as are contained in the classical "minimal basis" for that atom (2). One may also expect similar results in the framework of Bader's theory.

It should be noted that by selecting fragments consisting of two (or more, if necessary) adjacent atomic domains, the present formalism permits one to obtain localized bonding orbitals, etc. as well, which may also be of independent interest. However, it must be stressed once again, that — contrary to more customary localization schemes performing *unitary* transformation of the canonical MO — we do not require the different LMOs to be orthogonal to each other. In fact, the single Slater-determinant SCF wave function is invariant (up to an insignificant constant factor) with respect to any *nonsingular* linear transformations among the occupied orbitals, not only to the unitary ones, and the conservation of orbital orthogonality is only a matter of convenience but not that of essence. At the same time the use of non-orthogonal LMOs permits distinguishing between delocalization effects of "physical" and "mathematical" type (4) — the former correspond to the actual interactions in the system studied, while the latter are simply due to the orthogonality requirement and give rise to so-called orthogonality tails in the LMOs, reducing the degree to which a given LMO is localized on the corresponding molecular fragment.

2. Equations for determining the localized orbitals

We start with considering a general (non-singular but not necessarily unitary) transformation of the occupied molecular orbitals, permitting each LMO φ_i^l to be maximally localized in the respective molecular domain X_i, selected for it. If we introduce the notation $\langle\varphi|\psi\rangle_{X_i}$ for the integration restricted to the volume Ω_i of the domain X_i,

$$[1] \qquad \langle\varphi|\psi\rangle_{X_i} = \int_{\Omega_i} \varphi^*(\boldsymbol{r})\psi(\boldsymbol{r})\mathrm{d}v$$

then the relative weight of the localized orbital φ_i^l in the domain X_i is given by

$$[2] \qquad M_i = \frac{\langle\varphi_i^l|\varphi_i^l\rangle_{X_i}}{\langle\varphi_i^l|\varphi_i^l\rangle}$$

Because there is no restriction concerning the unitary character of the localization transformation, each LMO can be determined independently, so we may require the fulfillment of the condition

$$[3] \qquad \delta M_i = 0$$

for each orbital separately.

The localized orbitals φ_i^l are obtained from the canonical orbitals φ_i^c by a linear transformation characterized by the transformation matrix $\boldsymbol{A}$:

$$[4] \qquad \varphi_i^l = \sum_{j=i}^{n} A_{ji}\varphi_j^c$$

n being the number of the occupied orbitals. The only restriction is $\det(\boldsymbol{A}) \neq 0$. If we define the ith column of matrix $\boldsymbol{A}$ as an n-dimensional vector $\boldsymbol{a}^i$ (its elements are $a_j^i = A_{ji}$), a trivial derivation gives (in matrix notations)

$$[5] \qquad M_i = \frac{\boldsymbol{a}^{i\dagger}\boldsymbol{Q}^i\boldsymbol{a}^i}{\boldsymbol{a}^{i\dagger}\boldsymbol{a}^i}$$

where the elements of the n by n matrix $\boldsymbol{Q}^i$ are defined as

$$[6] \qquad Q_{jk}^i = \langle\varphi_j^c|\varphi_k^c\rangle_{X_i}$$

and orthonormalization of the canonical orbitals φ_i^c has been utilized. From eq. [5] one obtains, in a standard manner, that the requirement $\delta M_i = 0$ is equivalent to the Hermitian n by n matrix eigenvalue equation

$$[7] \qquad \sum_{j=1}^{n} Q_{kj}^i a_j^i = M_i a_k^i$$

for determining the coefficients $A_{ki} = a_k^i$ to be substituted into eq. [4].

3. Analogy with the LMOs derived from Mulliken's population analysis and alternative forms of the equations

In practical calculations one uses the finite basis expansion

$$[8] \qquad \varphi_j^c = \sum_{\mu=1}^{m} c_{j,\mu}^c \chi_\mu$$

for the canonical orbitals, where the $c_{j,\mu}^c$ are the LCAO coefficients and χ_μ is the μth basis orbital, and searches the localized orbitals φ_i^l in a similar form:

$$[9] \qquad \varphi_i^l = \sum_{\mu=1}^{m} c_{i,\mu}^l \chi_\mu$$

In light of the above derivations, the relationship between the LCAO coefficients of the localized and canonical orbitals can be given as

$$[10] \qquad c_{i,\mu}^l = \sum_{j=1}^{n} a_j^i c_{j,\mu}^c$$

or, in matrix form,

$$[11] \qquad \boldsymbol{c}_i^l = \sum_{j=1}^{n} a_j^i \boldsymbol{c}_j^c$$

where $\boldsymbol{c}_i^l$ and $\boldsymbol{c}_j^c$ are the m-dimensional vectors formed from the LCAO coefficients of orbitals φ_i^l and φ_j^c, respectively.

Substituting the expansion [8] into the definition (eq. [6]) of the matrix elements Q_{jk}^i, one gets

$$[12] \qquad Q_{jk}^i = \sum_{\mu,\nu} c_{j,\mu}^{c*} S_{\mu\nu}^i c_{k,\nu}^c$$

where the elements of the matrix $\boldsymbol{S}^i$ are obtained by integrating the products of the basis functions in the volume of domain $\boldsymbol{X}_i$ only:

[13] $$S^i_{\mu\nu} = \langle\chi_\mu|\chi_\nu\rangle_{X_i} = \int_{\Omega_i} \chi^*_\mu(\boldsymbol{r})\chi_\nu(\boldsymbol{r})\mathrm{d}v$$

Equation [12] very much resembles a similar quantity that appeared (2) in the case when non-orthogonal LMOs were required to have a maximal *net* Mulliken's population on the fragment selected (the so-called Magnasco–Perico localization criterion (5)). However, in that case the restriction was related not to the volume of integration but to the summation indices:

[14] $$Q^{i(M-P)}_{jk} = \sum_{\mu,\nu\in X_i} c^{c*}_{j,\mu} S_{\mu\nu} c^{c}_{k,\nu}$$

where the notation $\mu, \nu \in X_i$ indicates that the sum should be taken over the basis orbitals assigned to fragment X_i. The two definitions would lead to the same result in the limiting case when each basis orbital differs appreciably from zero only within its "own" atomic domain. In practice, however, one can expect some deviation between the matrices $\boldsymbol{Q}^i$ calculated by using these two definitions, because there is no direct counterpart of Mulliken's overlap population in the topological theory of atoms.

The analogy between the two approaches is very straightforward; one has only to observe that in the framework of Mulliken's population analysis (i.e., if the Magnasco–Perico criterion is used), the matrix $\boldsymbol{L}^i\boldsymbol{S}\boldsymbol{L}^i$ is a perfect analogue of matrix $\boldsymbol{S}^i$ above. Here $\boldsymbol{L}^i$ is the "cut-off" matrix (2): its block corresponding to the basis functions of fragment X_i is a unit matrix and all other elements are zero:

[15] $$L^i_{\mu\nu} = \begin{cases} \delta_{\mu\nu} & \text{if } \mu, \nu \in X_i; \\ 0 & \text{otherwise} \end{cases}$$

This means that a number of considerations described in ref. 2 can be adapted to our present case simply by replacing the matrix product $\boldsymbol{L}^i\boldsymbol{S}\boldsymbol{L}^i$ by matrix $\boldsymbol{S}^i$ defined above.[3] Therefore, we need not repeat in detail some of the derivations but may refer to those in ref. 2.

We introduce again the usual LCAO "density matrix"[4] $\boldsymbol{P}$:

[16] $$\boldsymbol{P} = \sum_{j=1}^{n} \boldsymbol{c}^c_j \boldsymbol{c}^{c\dagger}_j$$

and consider the variational problem $\delta M_i = 0$ with respect to the variations $\delta\boldsymbol{c}^l_i$ of the LMO coefficient vector $\boldsymbol{c}^l_i$. The variations $\delta\boldsymbol{c}^l_i$ are not quite arbitrary, because the orbital φ^l_i should remain in the subspace of occupied orbitals even after the variation is performed. Therefore, the most general *permitted* variation of vector $\boldsymbol{c}^l_i$ has the form of a projection (2): $\delta\boldsymbol{c}^l_i = \eta\boldsymbol{PSd}$, where $\boldsymbol{d}$, is an arbitrary m-dimensional vector and η is a variational parameter tending to zero. Then, repeating the derivations in ref. 2 we arrive at the alternative form of equations as

[17] $$\boldsymbol{PS}^i\boldsymbol{c}^l_i = M_i\boldsymbol{PSc}^l_i$$

or, because $\boldsymbol{c}^l_i = \boldsymbol{PSc}^l_i$ (the localized orbitals φ^l_i lie completely in the subspace of occupied orbitals):

[18] $$\boldsymbol{PS}^i\boldsymbol{c}^l_i = M_i\boldsymbol{c}^l_i$$

This is an eigenvalue equation for the non-Hermitian matrix $\boldsymbol{PS}^i$, which can be transformed to the generalized eigenvalue equation of a Hermitian matrix by utilizing once again the relationship $\boldsymbol{c}^l_i = \boldsymbol{PSc}^l_i$, and multiplying the equation by matrix $\boldsymbol{S}$:

[19] $$\boldsymbol{SPS}^i\boldsymbol{PSc}^l_i = M_i\boldsymbol{Sc}^l_i$$

Similarly to the case discussed in ref. 2, eqs. [17], [18], and [19] are equivalent to each other and to eq. [7] for all solutions corresponding to non-zero eigenvalues $M_i \neq 0$.

4. Partial orthogonality properties: definition of orthogonal atomic hybrids in a molecule

The non-orthogonal localized orbitals determined by the scheme discussed above have the following partial orthogonality properties analogous to those in ref. 2.

1. The localized orbitals corresponding to *the same* fragment (atomic domain) X_i are automatically orthogonal to one another in the case of different localization criteria (eigenvalues) M_i. (In the case of degenerate eigenvalues they can be chosen to be orthogonal.)

[20] $$\langle\varphi^{l(j)}_i|\varphi^{l(k)}_i\rangle = \sum_l a^{i(j)*}_l a^{i(k)}_l = \sum_{\mu,\nu} c^{l(j)}_{i,\mu} S_{\mu\nu} c^{l(k)}_{i,\nu} = \delta_{jk}$$

Here the additional indices j and k are introduced in order to distinguish between the different solutions of eqs [7], or [17]–[19], corresponding to *the same* fragment (domain) X_i. The orthogonality, eq. [20], follows from the fact that the localized orbitals can be obtained from the canonical ones by solving the Hermitian eigenvalue equation [7].

2. In the case of different eigenvalues M_i, the localized orbitals corresponding to the same fragment have also orthogonal "truncations" within the fragment X_i. This means that defining the functions

[21] $$\psi^{(j)}_i(\boldsymbol{r}) = \begin{cases} \varphi^{l(j)}_i(\boldsymbol{r}) & \text{if } \boldsymbol{r} \in \Omega_i; \\ 0 & \text{otherwise} \end{cases}$$

one has

[22] $$\langle\psi^{(j)}_i|\psi^{(k)}_i\rangle \equiv \langle\varphi^{l(j)}_i|\varphi^{l(k)}_i\rangle_{X_i} = M^{(j)}_i\delta_{jk}$$

Proof: The integral $\langle\varphi^{l(j)}_i|\varphi^{l(k)}_i\rangle_{X_i}$ can be transformed as

[23] $$\begin{aligned}\langle\varphi^{l(j)}_i|\varphi^{l(k)}_i\rangle_{X_i} &= \left\langle \sum_{p=1}^{n} a^{i(j)}_p\varphi^c_p \middle| \sum_{q=1}^{n} a^{i(k)}_q\varphi^c_q \right\rangle_{X_i} \\ &= \sum_{p,q=1}^{n} a^{i(j)*}_p \langle\varphi^c_p|\varphi^c_q\rangle_{X_i} a^{i(k)}_q \\ &= \sum_{p,q=1}^{n} a^{i(j)*}_p Q^i_{pq} a^{i(k)}_q\end{aligned}$$

[3] This cannot of course, be applied directly to the formulae in which the non-orthogonal LMOs are expressed as linear combinations of some columns of matrix $\boldsymbol{P}$.

[4] This nomenclature is not quite fortunate, as the true LCAO representation of the first-order density matrix in the case of an overlapping basis is matrix $\boldsymbol{PS}$, rather than simply $\boldsymbol{P}$ (6). This means, for instance, that $\boldsymbol{PS}$ is the matrix of projection on the subspace of the occupied orbitals.

Utilizing the fact that, according to eq. [7], $\boldsymbol{a}^{i(j)}$ and $\boldsymbol{a}^{i(k)}$ are *orthonormalized* eigenvectors of the Hermitian matrix $\boldsymbol{Q}^i$:

$$\sum_{q=1}^{n} Q^i_{pq} a^{i(k)}_q = M^{(k)}_i a^{i(k)}_p$$

we have

$$[24] \qquad \langle \varphi^{|(j)}_i | \varphi^{|(k)}_i \rangle_{X_i} = M^{(k)}_i \sum_{p=1}^{n} a^{i(j)*}_p a^{i(k)}_p = M^{(k)}_i \delta_{jk}$$

Q.E.D.

The "truncated" orbitals $\psi^{(j)}_i$ can be, therefore, considered as orthogonal atomic hybrids characterizing the atom within the molecule; it might be reasonable to renormalize them by multiplying by the factor $(M^{(j)}_i)^{-1/2}$. A detailed study of orbitals with significant M_i values on individual atoms can provide useful information about the electronic state and *chemical* nature of a given atom in a given molecule. Even if a large basis set is used, the number of hybrids with non-negligible M_i values is expected to remain small;[5] the orbitals and M_i values should quickly converge to their Hartree–Fock limits. (We stress once again in this connection the *basis-independent* nature of the basic definition, eq. [7], expressed solely in terms of the *canonical* molecular orbitals.)

3. As the atomic hybrids $\psi^{(j)}_i$ and $\psi^{(k)}_l$ corresponding to different domains (atoms) X_i and X_l differ from zero in *disjunct* parts of the 3-dimensional space, these orbitals are also automatically orthogonal to each other. This means that *the overlap effects are absorbed in the distortions of the individual hybrids*, so the latter should differ considerably from those in the free atoms.[6] At the same time, this additional orthogonality may permit us to have a new look at the classical VB, etc. theories in which all the orbitals were considered orthogonal, and to get a better understanding of their unquestionable success in qualitative explanation of different chemical phenomena.

[5] As noted in the Introduction, if the criterion based on Mulliken's population analysis was used, there were as many hybrids with non-negligible M_i values on each atom as the number of orbitals in the conventional minimal basis set of that atom (2).

[6] It may be also of considerable interest to select fragment X_i as the *union* of atomic domains for chemically bonded atoms; then bonding orbitals of the respective chemical bonds can also be explicitly studied.

5. Conclusions

This paper was not intended to solve the quantum mechanical problems of the topological theory of atoms, but only to extract some additional, chemically meaningful, information from such solutions, assumed to be already accomplished. Accordingly, we have derived equations permitting us to determine non-orthogonal localized molecular orbitals having a maximal weight in the given atomic domain, or in another selected molecular fragment. (The approach is analogous to a recent one in which the localization criterion was defined as the maximal net Mulliken's population on the fragment in question.) These non-orthogonal localized orbitals have some interesting partial orthogonality properties: the orbitals corresponding to the same fragment and their *truncations* to the given fragment are mutually orthogonal. This permits one to define, in the framework of Bader's topological theory of atoms, the *effective* — distorted but still orthogonal — atomic orbitals by which the atom in question participates in formation of the molecular orbitals. The orbitals determined in this manner may give important conceptual connections between the SCF wave functions obtained in the large-scale ab initio calculations, or even at the Hartree–Fock limit, and the traditional atomic orbital picture.

Acknowledgement

This work was supported in part by the Hungarian Research Fund (OTKA No. T 15838).

References

1. R.F.W. Bader and T.T. Nguyen-Dang. Adv. Quantum Chem. **14**, 63 (1981).
2. I. Mayer. Chem. Phys. Lett. **242**, 499 (1995).
3. J.G. Ángyán, M. Loos, and I. Mayer. J. Phys. Chem. **98**, 5244 (1994).
4. I. Mayer. Chem. Phys. Lett. **89**, 390 (1982).
5. V. Magnasco and A. Perico. J. Chem. Phys. **47**, 971 (1967).
6. I. Mayer. J. Mol. Struct. (Theochem), **225**, 1 (1992).

Electrostatic properties of ammonium fluoride and deuterated ice-I_h

C.G. van Beek, J. Overeem, J.R. Ruble, and B.M. Craven

Abstract: New single crystal X-ray diffraction data have been collected at reduced temperature (120 K) and high resolution ($\sin\theta/\lambda \leq 1.34$ Å^{-1}) for ammonium fluoride and for heavy ice-I_h (D_2O) in order to determine the detailed electron density distribution in these structures. The crystals are isostructural. Ammonium fluoride, NH_4F, is hexagonal with space group $P6_3mc$, $a = 4.4365(3)$, $c = 7.1672(5)$ Å, $Z = 2$. Ice-I_h, D_2O, is hexagonal with space group $P6_3/mmc$, $a = 4.4950(5)$, $c = 7.3170(10)$ Å, $Z = 4$. The X-ray data were collected with Nb-filtered Mo$K\alpha$ radiation ($\lambda = 0.7093$ Å). Refinements with Stewart's rigid pseudoatom model gave $R(F^2) = 0.016$ for 292 reflections for NH_4F and $R(F^2) = 0.023$ for 296 reflections for ice-I_h. Hydrogen nuclear positions and mean-square displacements were taken from previous neutron diffraction studies. The structures each contain two crystallographically distinct H(D) atoms, namely, those with N-H or O-D directed along the c-axis and those that are directed tetrahedrally with respect to c. For NH_4F, maps of the total electron density, the total electrostatic potential, and the values of the Laplacian at the bond critical points show that the bonding interactions involving both kinds of H atom are the same within experimental error. Similar results are obtained for ice-I_h, although there are complications and limitations owing to the disorder in the structure. Nevertheless, the pseudoatom model enables the electron density distribution to be determined for an ordered water molecule isolated from the crystal structure. The estimated molecular dipole moment for water in ice-I_h is 2.1 debye.

Key words: electron density, bond critical points, hydrogen bonding, water dipole moment.

Résumé : Opérant à température réduite (120 K) et utilisant une haute résolution ($\sin\theta/\lambda \leq 1{,}34$ Å^{-1}), on a recueilli de nouvelles données de diffraction des rayons X concernant le fluorure d'ammonium et la glace lourde-I_h (D_2O) dans le but de déterminer la distribution détaillée de la densité électronique dans ces structures. Les cristaux sont isostructuraux. Le fluorure d'ammonium, NH_4F, est hexagonal, groupe d'espace $P6_3mc$, avec $a = 4{,}4365(3)$, et $c = 7{,}1672(5)$ Å, $Z = 2$. La glace lourde-I_h (D_2O) est hexagonale, groupe d'espace $P6_3/mmc$, avec $a = 4{,}4950(5)$ et $c = 7{,}3170(10)$ Å, $Z = 4$. Les données de rayons X ont été obtenues à l'aide d'un rayonnement Mo$K\alpha$ filtré par du Nb ($\lambda = 0{,}7093$ Å). Les affinements à l'aide du modèle du pseudoatome rigide de Stewart a conduit à une valeur de $R(F^2) = 0{,}016$ pour 292 réflexions pour NH_4F et de $R(F^2) = 0{,}023$ pour 296 réflexions pour la glace-I_h. On a utilisé les positions des noyaux hydrogènes ainsi que les déplacements quadratiques moyens qui avaient été obtenus lors d'études de diffractions de neutrons antérieures. Les structures contiennent chacune deux atomes H(D) cristallographiquement distincts, à savoir ceux du N-H ou du O-D qui sont orientés le long de l'axe c et ceux qui sont orientés tétraédriquement par rapport à c. Pour le NH_4F, les cartes de la densité électronique totale, du potentiel électrostatique total et les valeurs du laplacien aux points critique de liaison montrent que les interactions de liaison impliquant chacun des types d'atome H sont les mêmes aux erreurs expérimentales près. Des résultats semblables ont été obtenus pour la glace-I_h, même s'il y a des complications et des limitations résultant du désordre dans la structure. Malgré tout, le modèle du pseudoatome lourd permet de déterminer la distribution de la densité électronique dans des molécules d'eau isolées de la structure du cristal. Le moment dipolaire moléculaire évalué pour l'eau dans l'eau I_h est de 2,1 debye.

Mots clés : densité électronique, points critique de liaison, liaison hydrogène, moment dipolaire de l'eau.

[Traduit par la rédaction]

Introduction

The crystal structure of ordinary ice, designated ice-I_h, has been the subject of many experimental and theoretical studies (1). Ammonium fluoride has been subject to far fewer studies although it has special interest since it is isostructural with ice-I_h (Fig. 1) and it is the only substance known to form solid solutions with ice-I_h. The two substances also form the crystal complexes $NH_4F{\cdot}H_2O$ and $(NH_4F)_4{\cdot}H_2O$ (2).

In 1927, Zachariasen (3) determined the arrangement of the N/F framework in ammonium fluoride, using X-ray diffraction. The structure is hexagonal in the polar space group $P6_3mc$, with each N and F atom at the center of a tetrahedron, as in the wurtzite configuration. The hydrogen positions in ammonium fluoride were determined by Adrian and Feil (4) using both X-ray and neutron diffraction. The arrangement of the oxygen atoms in ice-I_h was first determined by Barnes (5) in 1929, using X-ray diffraction. The O atoms replace N and F

Received October 19, 1995.

This paper is dedicated to Professor Richard F.W. Bader on the occasion of his 65th birthday.

C.G. van Beek, J. Overeem,[1] J.R. Ruble, and B.M. Craven.[2] Department of Crystallography, University of Pittsburgh, Pittsburgh, PA 15260, U.S.A.

[1] Permanent address: Chemical Physics Laboratory, University of Twente, PO Box 217, 7500 AE Enschede, The Netherlands.

[2] Author to whom correspondence may be addressed. Telephone: (412) 624-9300. Fax: (412) 624-1882. E-mail: craven@vms.cis.pitt.edu

Fig. 1. The atomic configuration in the crystal structures of ammonium fluoride (left) and ice-I_h (right). The crystallographic *c*-axis runs from the bottom to the top of the page.

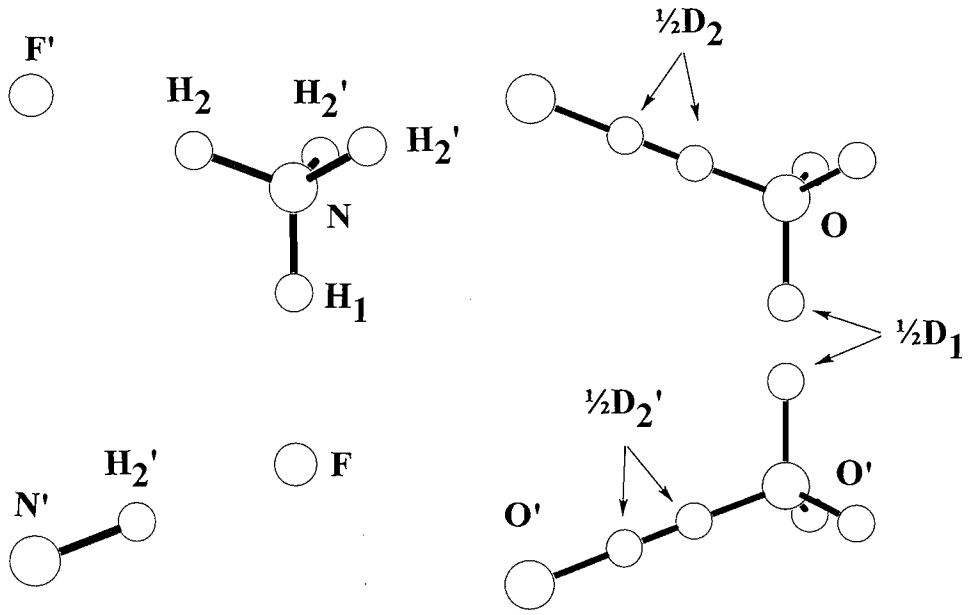

in the NH_4F structure, giving rise to the centrosymmetric space group $P6_3/mmc$. The arrangement of the hydrogen atoms in ice-I_h was determined in 1953 by Owston (6) and then more precisely by Peterson and Levy (7) who carried out a neutron diffraction study on deuterated ice-I_h. These studies confirmed the disordered half-hydrogen model proposed by Pauling (8). In this model, each hydrogen atom is statistically distributed over two equilibrium positions between O···O nearest neighbors. More recent careful diffraction studies of ice-I_h have been carried out by Goto, Hondo, and Mae using X-rays (9) and by Kuhs and Lehmann using neutrons (1). Additional disorder in ice-I_h has been proposed. Chidambaram (10) invoked additional disorder of the H atoms so that the hydrogen bonds would be bent and the H-O-H bond angles would be smaller and similar to the value in the vapor phase. Kuhs and Lehmann (1) proposed disorder for the O atoms to explain the O—H bond length in ice-I_h being longer (0.02–0.05 Å) than values obtained from molecular orbital calculations and spectroscopic data.

A consideration of geometrical aspects brings out the similarities in the structures of ammonium fluoride and ice-I_h. Both are based on a wurtzite-type structure with a tetrahedral configuration of hydrogen bonds about each heavy atom center. Our study draws attention to important chemical differences that are based on the charge density distribution in these structures.

Ammonium fluoride, experimental

A crystal selected from a commercial sample obtained from J. T. Baker Chemical Co. was mounted on a glass fiber with the *c*-axis close to the φ-axis of the Enraf–Nonius CAD-4 diffractometer. To minimize ice formation on the crystal, the diffractometer was placed in a sealed box with a constant supply of dry air into the box. The crystal was kept at a nominal temperature of 120 K in a stream of nitrogen gas. Throughout the data collection the temperature was monitored (± 1 K) using a thermocouple located about 8 mm upstream from the crystal. X-ray data were collected using niobium-filtered Mo$K\alpha$ radiation (λ = 0.7093 Å). Unit cell dimensions (see Abstract) were obtained from a least-squares fit of $\sin^2\theta_{hkl}$ for 25 reflections measured at four symmetry equivalent positions. Bragg intensities were measured using ω/2θ scans for all reflections with $\sin\theta/\lambda \leq 1.34$ Å^{-1} in an octant of reciprocal space (*h* and *k* from 0 to 11, *l* from 0 to 19). The intensities of three monitor reflections were measured every 6000 s of the data collection. Integrated intensities were obtained from the scan profiles using the method of Lehmann and Larsen (11) and the data processing computer programs of Blessing (12). The integrated intensities were internally scaled by factors ranging from 0.979 to 1.007 that were obtained from the observed variations of the monitor reflections during the course of the data collection. A total of 1084 reflections were collected. Averaging gave 513 independent reflections with an internal agreement factor, R_{int} (F_o^2) = 0.019.

Ammonium fluoride, structure refinement

The electronic charge density distribution in the crystal structure was determined by full-matrix least-squares refinement based on the rigid pseudoatom model of Stewart (13). X-ray scattering factors for the pseudoatom *K*-shells of N and F^- were assumed to be those of Hartree–Fock isolated atoms (14). Scattering factors for the spherical component of the *L*-shell of N and F^- were constructed from a linear combination of Slater-type Roothaan–Hartree–Fock atomic wave functions (15). For these spherical valence shells, a variable radial contraction parameter, κ, was introduced (16). Pseudoatom higher multipole terms, as well as the radial scattering factor for H, were assigned a single Slater-type radial function. These functions had a fixed standard value (17) for the radial exponent (α = 7.37 Å^{-1} for N and α = 4.69 Å^{-1} for H). No

higher multipoles were introduced for F^-.[3] The initial nuclear positions and mean-square displacements for the least-squares refinement were taken from the previous neutron study (4). As in previous studies, the origin for the unit cell was defined by placing F at ($\frac{1}{3}$, $\frac{2}{3}$, 0). For H, positional and mean-square displacement parameters were not refined.

The refinement was carried out with the computer program POP (19). The function $\Sigma w\Delta^2$ was minimized, where $\Delta = |F_o^2| - |F_c^2|$, and $w = 1/\sigma^2(F_o^2)$ with $\sigma^2(F_o^2) = \sigma_{cs}^2 + (0.02F_o^2)^2$, where σ_{cs}^2 is the variance due to counting statistics. The structure model involved a total of 20 variables, consisting of the overall scale factor applied to the *K*-shell scattering, κ(F), κ(N), positional and anisotropic mean square displacement parameters for F and N, monopole population parameters for F, N, and H, and for N (but not F) all symmetry-allowed higher multipole population parameters up to octapoles and for H up to dipoles. There was also an isotropic extinction parameter *g* assuming a type II crystal with Lorentzian mosaicity (20). Initially the refinement included all 513 independent reflections, but many of the reflections at high resolution were insignificant in terms of their standard deviations. Reflections having sin θ/λ > 1.00 Å^{-1} and with intensity less then 3σ were omitted and the refinement was then completed with the remaining 292 reflections. Convergence was obtained with $R_w(F^2) = 0.041$, $R(F^2) = 0.016$, and goodness-of-fit = 1.00.[4] The final value $g = 0.29(8)\ 10^4$ rad^{-1} indicated that extinction effects were not serious. The largest correction for a Bragg intensity was a decrease of 6%. The final values for the pseudoatom parameters are given in Table 1*a*. The corresponding atomic distances and angles are in Table 2*a*. During the refinement there were no constraints on the monopole populations p_v; that is, on the number of valence electrons for each pseudoatom. After the refinement, $\Sigma p_v = 15.8(3)$ valence shell electrons, as compared with 16 for a neutral unit cell. The population parameters in Table 1*a* have been scaled to give a neutral unit cell. Both κ(F) and κ(N) are slightly greater than 1.0, indicating a slight contraction of the valence electron density as compared with an isolated Hartree–Fock atom.

Ice-I_h, experimental

The experimental procedures for ice-I_h were very similar to those used for ammonium fluoride. A single crystal of heavy ice-I_h was grown from a sample containing about 89% D_2O.[5] The crystal, having length 0.4 mm and diameter 0.5 mm, was grown with repeated zone melting and freezing in a glass capillary bathed in a stream of cold nitrogen gas. The capillary was already mounted on the diffractometer. Throughout the data collection the crystal was kept at a nominal temperature 120(1)K. Unit cell dimensions (see Abstract) were determined using Mo *K*α radiation in the same way as for ammonium fluoride. Intensity data were collected for all reflections having sin θ/λ ≤ 1.34 Å^{-1} in the hemisphere of reciprocal space with $0 \le h \le 12$, $-12 \le k \le 12$, and $-19 \le l \le 19$. The integrated intensities were internally scaled by factors ranging from 0.975 to 1.018 that were derived from the observed variations in the intensities of the monitor reflections throughout the data collection. An absorption correction (μ = 0.0991 mm^{-1}) was applied (21) that gave correction factors from 1.038 to 1.043. A total of 2358 reflections were collected. Averaging gave 550 independent reflections with an internal agreement factor of $R_{int}(F_o^2) = 0.037$.

Ice-I_h, structure refinement

The refinement procedure was very similar to that used for ammonium fluoride. After an initial refinement using all reflections, those having sin θ/λ > 1.00 Å^{-1} and with intensity less than 3σ were omitted and the refinement was completed with the remaining 296. X-ray atomic scattering factors were derived as described above (14, 15). The higher multipole terms for O were assigned a fixed standard value for the radial exponent of α = 8.50 Å^{-1} (17). The O atoms were assumed to be ordered while half-H atoms were assumed to be disordered according to the Pauling model (8). The initial nuclear positions and mean square displacements were the values for D_2O obtained from neutron diffraction by Kuhs and Lehmann (1). The structure model involved 21 variables consisting of the overall scale factor applied to the *K*-shell scattering, positional and mean-square displacement parameters for O, together with all symmetry-allowed third- and fourth-order displacement parameters as defined in the Gram–Charlier formalism, and all symmetry-allowed multipole parameters up to octapoles for O and up to dipoles for H. A κ-parameter for O was included initially but later was excluded since the value was not significantly different from unity. An isotropic extinction parameter was introduced assuming a type II crystal with Lorentzian mosaicity (20), but extinction was found to be only marginally significant ($\rho = 0.14(8) \times 10^{-3}$ mm). Convergence was obtained with $R_w(F^2) = 0.045$, $R(F^2) = 0.023$, and goodness-of-fit = 1.08. The final values for the structure parameters are in Table 1*b*. The anharmonic third- and fourth-order displacements for O are not listed since all final values were within 1.5σ of zero except $C^{333} = -1.9(8) \times 10^{-9}$ Å^3. After the refinement, the total number of electrons in the asymmetric unit of the structure consisted of the two O-atom *K*-shell electrons, together with the number of valence shell electrons given by the unconstrained sum $p_v(O) + 0.5p_v(D1) + 1.5p_v(D2) = 8.25(11)$. Thus the total number of *K*- and *L*-shell electrons is close to the value 10 that is required for a neutral unit cell. There is further discussion below concerning the atomic charges on the O and H atoms when disorder is taken into account. The population parameters listed in Table 1*b*, have been scaled to give 8 valence shell electrons in the asymmetric unit. Final atomic distances and angles are in Table 2*b*.

Discussion

For an idealized hexagonal packing of equal spheres, the unit cell axial ratio *c*/*a* = 1.6330. The observed ratio is 1.6155 for

[3] In polar space groups, such as $P6_3mc$, instability can be introduced in the least-squares structure refinement owing to strong correlations between electron population parameters for certain pairs of odd-order multipole terms (18). For ammonium fluoride, this problem is avoided by assuming F^- to be spherical.

[4] $R(F^2) = \Sigma|\Delta|/\Sigma|F^2|$, $R_w(F^2) = [\Sigma w\Delta^2/\Sigma(wF^2)^2]^{1/2}$, goodness-of-fit = $[\Sigma w\Delta^2/(m_{obs}-n_{param})]^{1/2}$; where $\Delta = |F_{obs}|^2 - |F_{calc}|^2$.

[5] The composition is estimated by comparison with results of a neutron diffraction study of barbituric acid dihydrate in which the same D_2O sample was used for deuteration. This is unpublished work, which we carried out in collaboration with Dr W.T. Klooster.

Table 1. Pseudoatom parameters. Atoms in the asymmetric unit conform to those used in previous work (1, 4, 7). Positional parameters x, y, z are fractional coordinates in the unit cell. Mean-square displacement parameters U^{ij} are given in Å^2 units and correspond to the expression $T = 2\pi^2\sum_{ij}h_ih_ja^{*i}a^{*j}U^{ij}$. Values without estimated standard deviations (in parentheses) are symmetry constrained. Electron population parameters p_v, d_1, etc., correspond to normalized multipole terms as described by Epstein, Ruble, and Craven (22) and are referred to the crystal cartesian axes a, b^*, c. Multipole terms not listed have zero value.

(*a*) Ammonium fluoride. Nuclear positions and mean-square displacements for H1 and H2 are taken from the neutron diffraction study by Adrian and Feil (4). Valence shell radial contraction parameters have values κ(F) = 1.036(6) and κ(N) = 1.015(14).

	Atom			
Parameter	F	N	H1	H2
x	0.3333	0.3333	0.3333	0.4614(8)
y	0.6667	0.6667	0.6667	0.5386
z	0	0.3777(1)	0.2337(10)	0.4270(5)
U^{11}	0.0156(2)	0.0144(3)	0.028(3)	0.0256(8)
U^{22}	0.0156	0.0144	0.028	0.0256
U^{33}	0.0163(4)	0.0150(5)	0.015(4)	0.027(4)
U^{12}	0.0078	0.0072	0.014	0.0164(8)
U^{13}	0	0	0	−0.0012(9)
U^{23}	0	0	0	0.0012
p_v	7.75(10)	5.3(2)	0.80(6)	0.72(3)
d_1	0	0	0	−1.4(3)
d_2	0	0	0	0.81(27)
d_3	0	0.2(5)	2.3(6)	−0.69(16)
q_5	0	0.1(4)		
o_2	0	−1.7(3)		
o_7	0	−2.5(4)		

(*b*) Ice-I_h. Atomic parameters are based on the half-hydrogen model (8). Nuclear positions and mean-square displacements for D1 and D2 are taken from the neutron diffraction study by Kuhs and Lehmann (1).

	Atom		
Parameter	O	D1	D2
Site factor:	1.0	0.5	1.5
x	0.3333	0.3333	0.4545(4)
y	0.6667	0.6667	0.9090
z	0.0617(3)	0.1988(5)	0.0170(2)
U^{11}	0.0186(8)	0.0346(2)	0.0343(2)
U^{22}	0.0186	0.0346	0.0366(2)
U^{33}	0.0190(9)	0.0250(2)	0.0239(1)
U^{12}	0.0093	0.0173	0.0172
U^{13}	0	0	0.0054(3)
U^{23}	0	0	0.0054
p_v	6.25(9)	0.82(5)	0.89(4)
d_2	0	0	−2.5(3)
d_3	0.5(4)	−2.3(4)	1.4(3)
q_5	−0.8(3)		
o_2	−0.3(2)		
o_7	0.8(2)		

Table 1 (*concluded*).
(*c*) Average water molecule from ice-I_h. Pseudoatom parameters are with respect to a molecular cartesian axial system with *X* along the internal D-O-D bisector and *Z* normal to the plane of D_2O. Axes are of length 1 Å.

	Atom		
Parameter	O	D1	D2
x	0	0.577	0.577
y	0	−0.816	0.816
z	0	0	0
p_v	6.26	0.87	0.87
d_1	0.0	−1.6	−1.6
d_2	0.0	−2.3	2.3
o_2	−2.3	0.0	0.0
o_5	−0.8	0.0	0.0

Table 2. Interatomic distances (Å) and angles (°). Positional parameters for H and D atoms are from neutron diffraction (1, 4).

Ammonium fluoride		Ice-I_h	
N···F	2.7071(2)	O···O^{iv}	2.755(5)
N···F^{i}	2.7076(7)	O···O^{v}	2.748(2)
N—H_1	1.032(7)	O—D_1	1.003(5)
N—H_2	1.045(4)	O—D_2	0.999(3)
F···N···F^{i}	108.89(2)	O^{iv}···O···O^{v}	109.20(14)
F^{i}···N···F^{ii}	110.06(1)	O^{v}···O···O^{vi}	109.75(7)
H_1-N-H_2	108.7(2)	D_1-O-D_2	109.1(2)
H_2-N-H_2^{iii}	109.2(2)	D_2-O-D_2^{vii}	109.8(2)
N-H_2···F^{i}	178.6(3)	O-D_2···O^{v}	179.9(2)

Symmetry-related positions:

i:	2/3, 1/3, 1/2
ii:	2/3, 4/3, 1/2
iii:	x, $2x$, z
iv:	1/3, 2/3, 1/2 − z
v:	2/3, 4/3, −z
vi:	2/3, 1/3, −z
vii:	x, 1 − x, z

ammonium fluoride, indicating a slight deviation from ideality. Consequently, there must be slight departures from a regular tetrahedral configuration of hydrogen bonds. For ice-I_h the axial ratio is 1.6278, close to the ideal value. From Table 2, it can be seen that the two crystallographically independent heavier atom hydrogen-bonding distances in each structure are the same within experimental error (N···F, 2.7071(2) and 2.7076(7) Å; O···O, 2.755(5) and 2.748(2) Å). However, pairs of angles F···N···F and O···O···O, which in a regular tetrahedral arrangement would be 109.47°, are observed to be 108.89(2)° and 110.06(1)° in ammonium fluoride and 109.20(14)° and 109.75(7)° in ice-I_h. Thus, in ammonium fluoride, the distortion from ideality is realized as differences in hydrogen bond angles rather than distances.

The bond distances and angles presently obtained for ammonium fluoride and ice-I_h (Table 2) are similar to those previously reported (1, 4, 7). They will not be discussed further except to point out that the values are uncorrected for the effects of atomic mean-square displacements. For ice-I_h these effects might arise from the static disorder of O and H as well as the atomic thermal vibrations (1, 10). In carrying out the charge density analysis, we assume Stewart's rigid pseudoatom model (13), in which the charge distribution is carried rigidly on the pseudoatom nuclei. The model does not require a distinction between static and dynamic nuclear displacements.

In ammonium fluoride, the monopole population (p_v) of the fluoride is 7.75(10) instead of 8 for a true ion. Thus, according to the pseudoatom model, the crystal structure is ionic with the anion and cation carrying net charges of $\pm 0.75e$.

In ice-I_h the D-atom disorder gives rise to uncertainty in the experimental value for the net charge on a particular water molecule. The disorder allows six possible water molecule configurations about each O-atom site because there are six ways to choose two corners from a tetrahedron. Presumably these configurations occur with equal probability. Three molecules are of the type D1-O-D2 and three are of the type D2-O-D2′. Taking values of p_v from Table 2*b*, the net valence shell charges are $\Sigma p_v = 7.96(11)$ for the first type of molecule and 8.03(11) for the second. Within experimental error, these charges are the same as the value 8 required for a neutral molecule. However, this calculation neglects the possibility that the O atom may have a different value for p_v in the two kinds of water molecule. It is only the average that is constrained to the experimental value of 6.25. We consider that any real difference in the two kinds of water molecules will be very small and therefore, in the following, we assume that the water molecules are all electrically neutral and are chemically identical.

We assume an isolated averaged water molecule with *2mm* point symmetry that is referred to a Cartesian axial system with x along the twofold axis and z normal to the molecular plane. With this system and using the nomenclature of Epstein, Ruble, and Craven (22), the only higher multipole terms for the O atom that are symmetry allowed are d_1, q_1, q_5, o_1, and o_5. The molecule is then rotated in six different ways into the cartesian axial system a, b^*, c as used in the crystal structure refinement. Each rotation is made to correspond with one of the six configurations for water molecules that share a common O-atom site. After each rotation, the population parameter for a multipole term with respect to the crystal axes is given as a linear combination of values for all multipoles of the same order when referred to the molecular axes (23). After summing the results of these rotations, giving them all equal weight, a set of linear equations is obtained that can be solved to obtain the electron population parameters for the isolated molecule in terms of the experimental values for the disordered structure (Table 1*b*). In this way it is shown that, for the O atom, d_1, q_1, and q_5 are small and can be set to zero while the octapole terms have values $o_1 = -3.2$ and $o_5 = -0.8$. These multipole populations, together with average values for the H-atom coordinates and population parameters (Table 1*c*), were used to derive electrostatic properties for an ordered water molecule extracted from the ice-I_h crystal structure. Following the procedure of Stewart (24), we obtain a molecular dipole moment for water in ice-I_h (2.1 debye) that is in good agree-

Table 3. Bond critical point data for ammonium fluoride. Fractional coordinates (x, y, z) are given for the (3, −1) bond critical points. The standard deviations are isotropic estimates (Å units) of the position of the bond critical points. The electron density at the bond critical point $\rho(r)$ is in units e Å^{-3} and the Laplacian of the electron density at the bond critical point $\nabla^2\rho(r)$, which is the trace of the Hessian matrix, is in units e Å^{-5}. The principal values of the Hessian matrix are λ_1, λ_2, and λ_3.

Bond	x	y	z	e.s.d.	$\rho(r)$	$\nabla^2\rho(r)$	λ_1	λ_2	λ_3
N–H_2	0.4241	0.5726	0.4137	0.004	2.01(7)	−20(2)	30	−25	−25
N–H_1	0.3333	0.6667	0.2736	0.005	2.24(12)	−24(3)	32	−28	−28
F···H_2	0.5316	0.4685	0.4493	0.009	0.22(2)	5.3(3)	7.7	−1.2	−1.2
F···H_1	0.3333	0.6667	0.1547	0.016	0.20(5)	5.7(8)	7.8	−1.0	−1.0

Fig. 2. The total charge density in the crystal structures. Contours are at intervals 0.2 e Å^{-3} beginning at 0.2 e Å^{-3}. The crystallographic c-axis runs from the bottom to the top of the page. The nuclear positions are marked as "+". (*a*) Ammonium fluoride in the plane through H2-N-H1. (*b*) Ice-I_h in the plane through D2-O-D1.

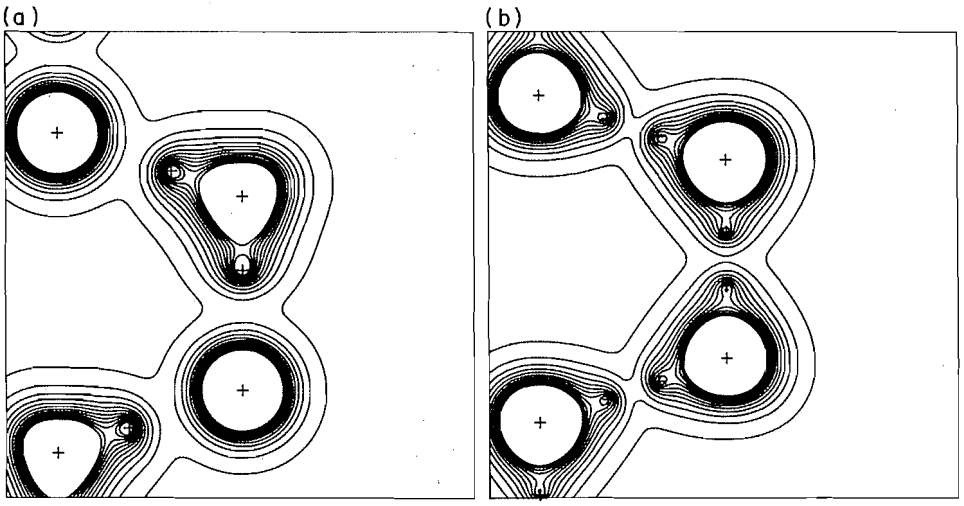

ment with the values 2.3(3) debye obtained for the water molecule in cytosine monohydrate (25) and 1.83 debye obtained for water vapor using microwave spectroscopy (26).

Figure 2 shows the total charge density in the crystal structures of ammonium fluoride and ice-I_h with all atoms stationary. In ice-I_h, the charge density is for an averaged unit cell using the half-hydrogen model. In both structures, regardless of the H-atom disorder in ice-I_h, it can be seen that the total density around the crystallographically distinct H1 (or D1) and H2 or (D2) is remarkably similar. The total density in ammonium fluoride has been analysed further by determining the positions of the bond critical points (Table 3). As pointed out by Bader and Essén (27), these are the (3, −1) critical points that occur in the total density $\rho(r)$, at the saddle point along the bond path between pairs of nuclei. Table 3 also lists the Laplacian of the total density at the bond critical points. The Laplacian can be written as $\nabla^2\rho(r) = \lambda_1 + \lambda_2 + \lambda_3$, where λ_i are the three principal values of the curvature of $\rho(r)$ in order of decreasing magnitude. Because of the saddle point, λ_1 is positive while λ_2 and λ_3 are negative. In ammonium fluoride, each H atom is associated with two bond critical points, one in the covalent N—H bond and the other in the H···F hydrogen bond. In each covalent bond, the Laplacian is negative, corresponding to a local concentration of charge, while in each hydrogen bond the Laplacian is positive, corresponding to a local depletion. The difference in sign is an indication of the difference between a covalent and an ionic or closed-shell interaction. It can be seen from Table 3 that at the (3, −1) critical points associated with the two different H atoms in ammonium fluoride, the respective values of $\rho(r)$, $\nabla^2\rho(r)$, and λ_i are the same within experimental error. These values are also similar to those obtained for the N—H bond in the crystal structure of 1-methyluracil (28).

Because of the disorder of the D atoms, analysis of the critical points in the crystal structure of ice-I_h would not be meaningful. However, using the parameters from Table 1*c*, we have mapped $\rho(r)$ for the average water molecule isolated from ice-I_h and have located the (3, −1) critical point in the O—D bond. The critical point is 0.75 Å from the O atom. At the critical point, $\rho(r) = 2.55$ e Å^{-3}, $\nabla^2\rho(r) = -31$ e Å^{-5}, $\lambda_1 = 45$ e Å^{-5} and $\lambda_2 = \lambda_3 = -38$ e Å^{-5}.

The total electrostatic potential in the crystal structure of

Fig. 3. The electrostatic potential in the crystal structure of ammonium fluoride. The section is the same as in Fig. 2*a*. Contours are at intervals 0.07 e $Å^{-1}$ beginning at -1.30 e $Å^{-1}$. Dashed contours are used for regions of electronegativity. (*a*) The total electrostatic potential. (*b*) The total electrostatic potential after the removal of the contribution of one fluoride ion (center, bottom).

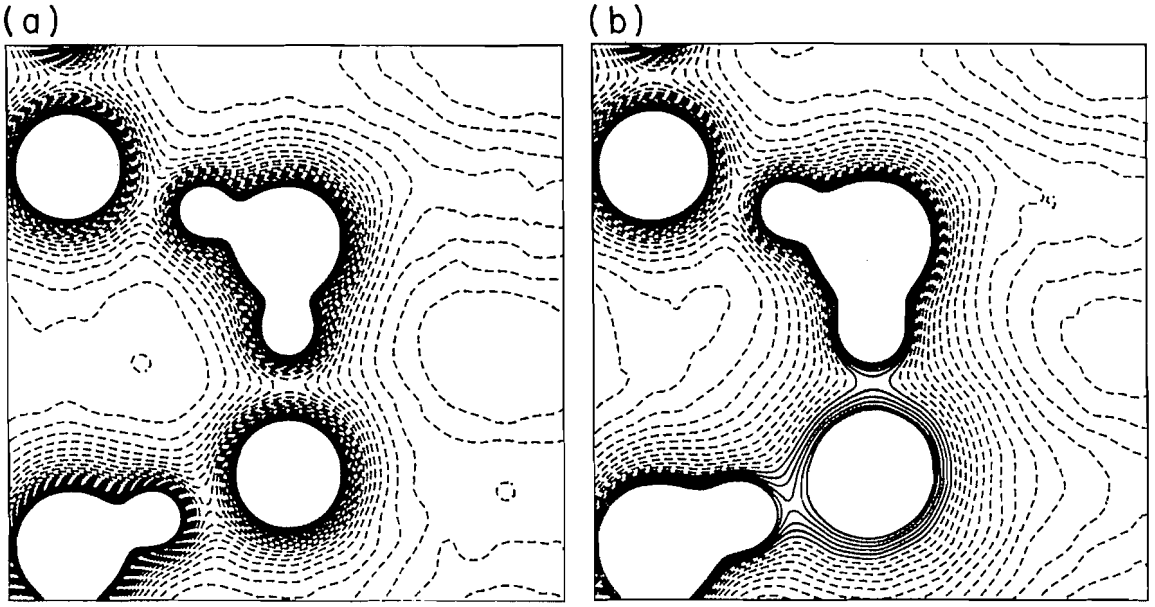

Fig. 4. The electrostatic potential of an averaged water molecule isolated from the crystal structure of ice-I_h. Contours are at intervals 0.05 e $Å^{-1}$ with broken contours representing the region of electronegativity. (*a*) The potential in the molecular plane. (*b*) The potential in the plane normal to the molecular plane and containing the D-O-D bisector. The O—D bonds project towards the bottom of the page.

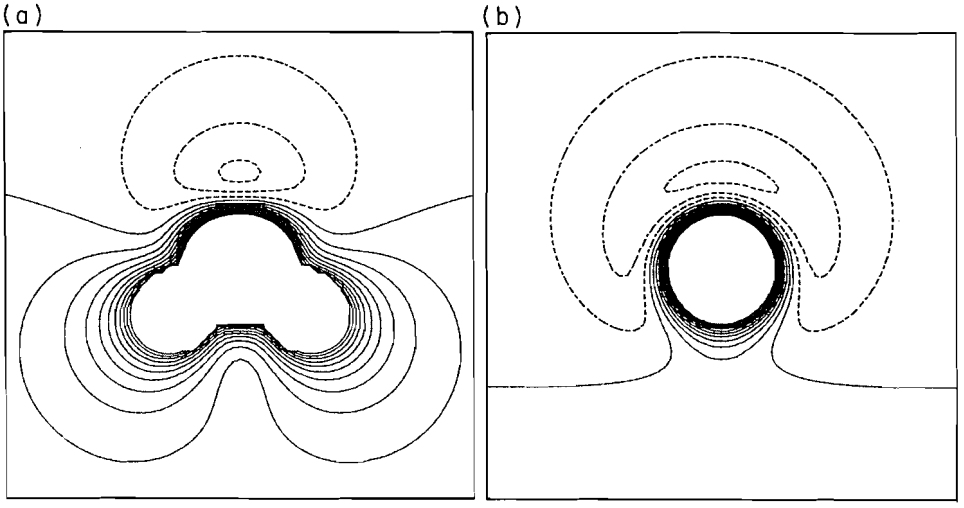

ammonium fluoride (Fig. 3) has been obtained using the procedure described by Stewart (29). The contribution to the potential at short range around each atom center is derived from the nucleus acting as a point charge and from the wave function for the neutral spherical Hartree-Fock atom (30). The lattice sum for the long-range contribution is obtained by a difference Fourier synthesis with coefficients $\Delta F_H/s_H^2$, where $s_H = \sin \vartheta_{hkl}/\lambda$ and $\Delta F_H = F_{ps} - F_{hf}$ where the subscript *ps* refers to the structure factor for the complete pseudoatom model and *hf* for an assembly of neutral spherical Hartree Fock atoms. The mean inner potential, which corresponds to the Fourier term with $H = 0$, is obtained only approximately because in a polar structure such as ammonium fluoride this term is affected by the nature of the surface charges on the crystal. Thus the total potential is subject to uncertainty in the level of the zero contour.

From Fig. 3*a*, it can be seen that the total potential is electronegative in the cavities between the ions and has bridges that are less electronegative along the hydrogen bonds. In Fig. 3*b*, the potential is shown when a vacancy in the crystal is sim-

ulated by subtracting the contribution of a single fluoride ion. The structure is not permitted to relax around the vacancy. As expected, the vacancy has enhanced electropositivity. There is also a tetrahedral deformation of the potential around the vacancy owing to the electropositivity of the surrounding ammonium ions.

We have not attempted to map the total potential for the ice-I_h structure because of the disorder. However, in Fig. 4*b*, we show the total potential for the average water molecule isolated from ice-I_h. The potential was computed from the pseudoatom parameters in Table 1*c* and from Hartree–Fock wave functions (15) using the procedure described by Stewart and Craven (30). There is an electronegative feature associated with the lone pair region of the O atom. This is a single unresolved minimum (-0.16 e Å^{-1}) that extends on both sides of the molecular plane.

As a subject for further study, we conclude that the pseudoatom model might be useful in calculating the electrostatic properties of hypothetical structures involving icelike structures with ordered water molecules and also for studying the effect that the incorporation of ammonium fluoride might have on inducing order in the ice-I_h structure.

Acknowledgement

This work was supported by grant GM-39513 from the U. S. National Institutes of Health.

References

1. W.F. Kuhs and M.S. Lehmann. *In* Water Science Reviews **2**, Cambridge University Press, Cambridge, New York. 1985. p. 1.
2. A. Tranquard and G. Coffy. C.R. Acad. Sci. **270**, 416 (1970).
3. W. Zachariasen. Z. Phys. Chem. **127**, 218 (1927).
4. H.W.W. Adrian and D. Feil. Acta Crystallogr. Sect. A: Cryst. Phys. Diffr. Theor. Gen. Crystallogr., **A25**, 438 (1969).
5. W.H. Barnes. Proc. R. Soc. London, Ser. A: **125**, 670 (1929).
6. P.G. Owston. J. Chim. Phys. **50**, C-13 (1953).
7. S.W. Peterson and H.A. Levy. Acta Crystallogr. **10**, 70 (1957).
8. L. Pauling. J. Am. Chem. Soc. **57**, 2680 (1935).
9. A. Goto, T. Hondoh, and S. Mae. J. Chem. Phys. **93**, 1412 (1990).
10. R. Chidambaram. Acta Crystallogr. **14**, 467 (1961).
11. M.S. Lehmann and F.K. Larsen. Acta Crystallogr. Sect. A: Cryst. Phys. Diffr. Theor. Gen. Crystallogr. **A30**, 580 (1974).
12. R.H. Blessing. Crystallogr. Rev. **1**, 3 (1987).
13. R.F. Stewart. Acta Crystallogr. Sect. A: Cryst. Phys. Diffr. Theor. Gen. Crystallogr. **A32**, 565 (1976).
14. D.T. Cromer and J.T. Waber. *In* International tables for X-ray crystallography. Vol. IV. Kynoch Press, Birmingham. 1974. p. 71.
15. E. Clementi and C. Roetti. At. Data Nucl. Data Tables, **14**, 177 (1974).
16. P. Coppens, T.N. Guru Row, P. Leung, E.D. Stevens, P.J. Becker, and Y.W. Yang. Acta Crystallogr. Sect. A: Cryst. Phys. Diffr. Theor. Gen. Crystallogr. **A35**, 63 (1979).
17. W.J. Hehre, R.F. Stewart, and J.A. Pople. J. Chem. Phys. **51**, 2657 (1969).
18. M. Terpstra, B.M. Craven, and R.F. Stewart. Acta Crystallogr. Sect. A: Found. Crystallogr. **A49**, 685 (1993).
19. B.M. Craven, H.-P. Weber, X.M. He, and W.T. Klooster. The POP procedure: computer programs to derive electrostatic properties from Bragg diffraction data. Technical Report, Department of Crystallography, Univ. of Pittsburgh. 1987.
20. P.J. Becker and P. Coppens. Acta Crystallogr. Sect. A: Cryst. Phys. Diffr. Theor. Gen. Crystallogr. **A30**, 129 (1974).
21. N.W. Alcock. *In* Crystallographic computing. Munksgaard, Copenhagen. 1970. p. 271.
22. J. Epstein, J.R. Ruble, and B.M. Craven. Acta Crystallogr. Sect. B: Struct. Crystallogr. Cryst. Chem. **B38**, 140 (1982).
23. D.T. Cromer, A.C. Larsen, and R.F. Stewart. J. Chem. Phys. **65**, 336 (1976).
24. R.F. Stewart. J. Chem. Phys. **58**, 1668 (1973).
25. H.-P. Weber and B.M. Craven. Acta Crystallogr. Sect. B. Struct. Sci. **B46**, 532 (1990).
26. T.R. Dyke and J.S. Muenter. J. Chem. Phys. **59**, 3125 (1973).
27. R.F.W. Bader and H. Essén. J. Chem. Phys. **84**, 1943 (1984); R.F.W. Bader. *In* Atoms in molecules, a quantum theory. Clarendon Press, Oxford. 1994. Chap. 2.
28. W.T. Klooster, S. Swaminathan, R. Nanni, and B.M. Craven. Acta Crystallogr. Sect. B: Struct. Sci. **B48**, 217 (1992).
29. R.F. Stewart. God. Jugoslav. Cent. Kristalogr. **17**, 1 (1982).
30. R.F. Stewart and B.M. Craven. Biophys. J. **65**, 998 (1993).

Cyclobutene photochemistry. Adiabatic photochemical ring opening of alkylcyclobutenes

William J. Leigh, J. Alberto Postigo, and K.C. Zheng

Abstract: The photochemistry of the *cis* and *trans* isomers of a series of dimethylbicyclo[*n*.2.0]alk-(*n*+2)-enes (*n* = 2–5) (bicyclic cyclobutene derivatives in which the C=C bond is shared by the two rings) in pentane solution is described. Irradiation of these compounds using monochromatic 193- or 214-nm light sources results in ring opening to yield the corresponding 1,2-bis(1-ethylidene)cycloalkanes (C_4–C_7) in high chemical and quantum yields. In all cases, the reaction proceeds with a high (70–90%) degree of disrotatory stereoselectivity. Quantum yields for direct *cis,trans* photoisomerization of the isomeric *E,E*- and *E,Z*-1,2-bis(1-ethylidene)cycloalkanes have also been determined. The product distributions from irradiation of the cyclobutenes are wavelength dependent, but for 214-nm excitation the isomeric diene distributions obtained from cyclobutene ring opening agree fairly closely with those calculated from the quantum yields for *cis,trans* photoisomerization of the isomeric dienes on the assumption that the process involves purely disrotatory ring opening to yield a single diene isomer in the lowest excited singlet state. The results are consistent with an orbital-symmetry-controlled, adiabatic mechanism for ring opening.

Key words: photochemistry, cyclobutene, electrocyclic, adiabatic, conical intersection, orbital symmetry.

Résumé : On décrit la photochimie des isomères *cis* et *trans* d'une série de diméthylbicyclo[*n*.2.0]alc-(*n*+2)-ènes (*n* = 2–5) (dérivés cyclobutènes bicycliques dans lesquels la liaison C=C est partagée entre deux cycles) en solution dans le pentane. L'irradiation de ces composés utilisant des sources de lumière monochromatique (193 ou 214 nm) provoque une ouverture de cycle qui conduit aux 1,2-bis(1-éthylidène)cycloalcanes (C_4–C_7) correspondants avec des rendements chimiques et quantiques élevés. Dans tous les cas, la réaction se produit avec un degré élevé (70–90%) de stéréosélectivité disrotatoire. On a déterminé les rendements quantiques pour la photoisomérisation *cis/trans* des *E,E*- and *E,Z*-1,2-bis(1-éthylidène)cycloalcanes. Les distributions des produits dérivant de l'irradiation des cyclobutènes dépendent de la longueur d'onde, mais, pour l'excitation à 214 nm, les distributions des dienes isomères obtenues pour l'ouverture de cycle du cyclobutène sont en assez bon accord avec ceux calculés à partir des rendements quantiques pour la photoisomérisation *cis/trans* des dienes isomères en supposant que le processus implique une ouverture de cycle strictement disrotatoire pour conduire à un seul diène isomère dans l'état singulet excité le plus bas. Les résultats sont en accord avec un mécanisme, pour l'ouverture de cycle, qui serait adiabatique et sous contrôle d'une symétrie des orbitales.

Mots clés : photochimie, cyclobutène, électrocyclique, adiabatique, intersection conique, symétrie d'orbitales.

[Traduit par la rédaction]

Introduction

The photochemical ring opening of simple alkylcyclobutenes in solution is known to proceed nonstereoselectively (1–5). While this appears to be quite general, there is increasing evidence to suggest that orbital symmetry factors (which predict that ring opening should proceed with disrotatory stereospecificity (6)) *do* play a role in the reaction. Firstly, isolated examples for which a high degree of disrotatory stereoselectivity is observed have been reported (7–9). Secondly, the UV resonance Raman spectrum of cyclobutene has been proposed to be consistent with initial *disrotatory* rotation of the C_1—C_4 and C_2—C_3 bonds immediately after excitation to the lowest excited singlet state (10) (this interpretation has recently been questioned, however (11)). Finally, we have recently reported a study of (C_3/C_4) substituent effects on the quantum yield for ring opening of 1,2-dimethylcyclobutene (12). This study indicates that *syn*-dimethyl substitution at C_3/C_4 reduces the absolute and relative (to cycloreversion) quantum yields for ring opening in a manner that is consistent with the process involving *initial* excited state disrotation about the C_1—C_4 and C_2—C_3 bonds of the cyclobutene ring. Each of these suggest that the photochemical ring opening of cyclobutene at least begins on the (disrotatory) pathway predicted by orbital symmetry selection rules.

Photopericyclic reactions are conventionally explained in terms of the avoided crossing model of Van der Lugt and Oosterhoff, in which stereospecific product formation results from internal conversion to the ground state surface at an

Received September 19, 1995.

This paper is dedicated to Professor Richard F.W. Bader on the occasion of his 65th birthday.

W.J. Leigh,[1] J.A. Postigo, and K.C. Zheng. Department of Chemistry, McMaster University, Hamilton, ON L8S 4M1, Canada.

[1] Author to whom correspondence may be addressed. Telephone: (905) 525-9140, ext. 23715. Fax: (905) 522-2509. E-mail: leigh@mcmaster.ca

Scheme 1.

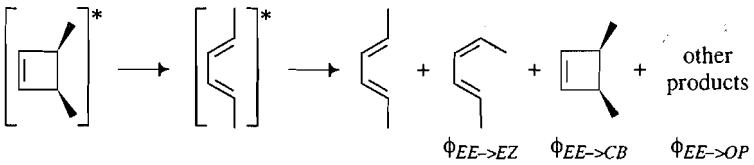

[1] $(EE/EZ)_{\text{from CB}} = (1 - \phi_{EE->EZ} - \phi_{EE->CB} - \phi_{EE->OP})/\phi_{EE->EZ}$

avoided crossing (the pericyclic minimum) between the ground and excited state surfaces for the photochemically allowed (thermally forbidden) pathway (13, 14). This is the mechanistic model that is traditionally employed to explain, for example, why conjugated dienes undergo photochemical ring closure with a high degree of disrotatory stereospecificity (15). If it is valid — and recent theoretical work suggests it is not (16–19) — then the ultimate formation of formally-forbidden diene isomers must be due to some intervening process that competes with internal conversion at the avoided crossing for disrotatory interconversion. The possibilities that have been considered include (1, 9): (*i*) internal conversion to upper vibrational levels of the ground state (before the pericyclic minimum is reached), from which conrotatory ring opening ensues (1, 12); (*ii*) internal conversion to biradicaloid geometries on the diene ground state surface, from which torsional relaxation yields a mixture of isomeric dienes (20); and (*iii*) complete disrotatory ring opening on the excited state surface to yield fully open diene(s) in the first excited singlet state (i.e., adiabatically), followed by decay to the ground state by *cis,trans* isomerization (1, 9, 20). Another, recently suggested possibility is that excited-to-ground state internal conversion occurs via one or more *conical intersections* (geometries where the excited and ground state surfaces are degenerate) (21–23), after which the loss in disrotatory stereochemistry occurs on the ground state surface (17). According to calculations, the approach of the excited molecule to the conical intersection geometry involves rupture of the C_3—C_4 bond (cyclobutene numbering) and substantial twisting about *all three* of the remaining C—C bonds in the cyclobutene/1,3-butadiene framework (17).

Of these, the adiabatic ring-opening mechanism is potentially the easiest to test experimentally. According to this mechanism, a given cyclobutene, appropriately labelled with substituents at C_3 and C_4 in order to track the stereochemistry of the process, will open in purely disrotatory fashion to yield a single (vide infra) diene isomer in the lowest excited singlet state (see Scheme 1). The excited product would then decay to the ground state, yielding *its* characteristic mixture of products. In principle, this characteristic mixture should be the same as that obtained when the diene itself is irradiated directly in solution. Thus, the experimental study of this mechanism would involve comparing isomeric diene distributions obtained from cyclobutene ring opening to distributions calculated from the quantum yields for direct photoisomerization of the corresponding orbital-symmetry-allowed diene isomer. The relevant expression is given by eq. [1], which relates the observed *EE/EZ* diene ratio from ring opening of an appropriate *cis*-disubstituted cyclobutene ($(EE/EZ)_{\text{from CB}}$) to the quantum yields for formation of the *EZ*-diene ($\phi_{EE\rightarrow EZ}$), cyclobutene ($\phi_{EE\rightarrow CB}$), and other products ($\phi_{EE\rightarrow OP}$) from direct irradiation of the *EE*-diene.

The main difficulty with applying this analysis to most of the cyclobutenes that have been studied results from the fact that the photochemistry of aliphatic dienes is conformation-dependent (24–27). Clearly, cyclobutene ring opening would be expected to yield the excited diene in an *s-cis* conformation, so it is the excited state behaviour of the *s-cis* diene conformer that must be known for a reliable analysis of the product distributions obtained from cyclobutene ring opening. Since most acyclic dienes exist preferentially in the *s-trans* conformation in solution at room temperature, they are poor models for the excited state behaviour of dienes under the conditions in which they are (presumably) formed by cyclobutene ring opening; thus, an analysis of this type is meaningless for monocyclic cyclobutenes and their corresponding dienes. A second potential difficulty is that in the case of *cis*-3,4-disubstituted cyclobutenes, there are two stereochemically distinct disrotatory ring-opening modes available, one leading to *E,E*-diene and the other leading to the *Z,Z* isomer. Should ring opening occur by both modes competitively, then an analysis of the type represented in Scheme 1 would clearly not be expected to model the observed diene distribution accurately. Fortunately, however, *Z,Z*-dienes are formed in extremely low yields from irradiation of every *cis*-3,4-disubstituted cyclobutene that has been reported (3, 5), so that this potential difficulty can be safely neglected. Presumably, the preferred formation of the *E,E*- over the *Z,Z*-diene isomer can be attributed to the different steric requirements of the two possible disrotatory ring opening modes (12).

We have recently described our preliminary efforts to test the adiabatic mechanism for photochemical cyclobutene ring opening (9, 28). These studies employed cyclobutene derivatives whose isomeric dienes are *structurally constrained* to exist in the *s-cis* conformation, in order to minimize difficulties associated with the conformational factors noted above. The first study involved a comparison of the diene distributions obtained from ring opening of the isomeric bicyclic cyclobutenes *cis*- and *trans*-**1c** (eq. [2]) with values calculated from the quantum yields for direct photoisomerization of the corresponding isomeric *s-cis* dienes *E,E*- and *E,Z*-**2c** (9). Comparison of the observed diene distributions from irradiation of **1c** with the so-calculated values (see Scheme 1) indicate that the adiabatic mechanism satisfactorily describes the isomeric diene distribution from photochemical ring opening of *cis*-**1c**, but it does not in the case of the *trans* isomer (9).

A second, potentially more precise type of comparison employs an asymmetrically substituted *cis*-cyclobutene, whose corresponding (*s-cis*) *E,E*-diene photoisomerizes to yield two *E,Z* isomers in a characteristic ratio (28). This sys-

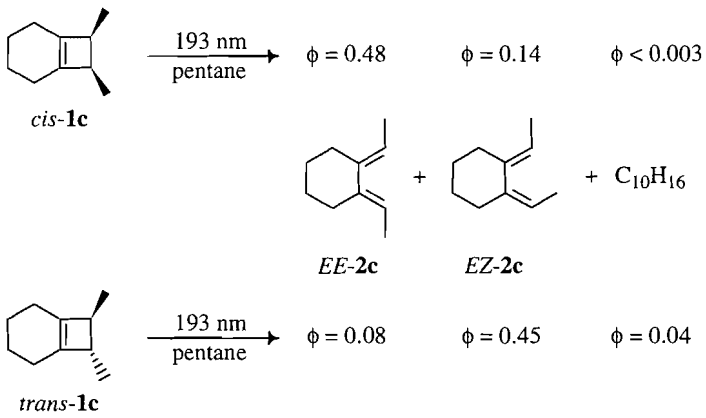

tem has the advantage that quantum yield determinations are unnecessary; the validity of the adiabatic mechanism can be tested by simply comparing product ratios from irradiation of the cyclobutene with those from irradiation of the corresponding allowed diene isomer. The system reported is *cis*-2,2,6,7-tetramethylbicyclo-[3.2.0]hept-1[5]-ene (**3**), whose irradiation (214 nm) in pentane solution yields a mixture of *E,E*-, *E,Z*-, and *Z,E*-1,2-bis(ethylidene)-3,3-dimethylcyclopentane (**4**; see eq. [3]). As predicted by the adiabatic mechanism, the relative yields of *E,Z*- and *Z,E*-**4** obtained from irradiation of **3** (*EZ*/*ZE* = 1.30 ± 0.12) are identical to those obtained in the direct irradiation (254 nm) of *E,E*-**4** (*EZ*/*ZE* = 1.25 ± 0.11) within experimental error. The distribution of allowed and forbidden dienes ([*EE*-**4**]/[*EZ*-**4** + *ZE*-**4**] = 2.4 ± 0.3) is similar to that obtained from irradiation of *cis*-6,7-dimethylbicyclo-[3.2.0]-hept-1[5]-ene (*cis*-**1b**) at the same wavelength ([*EE*-**2b**]/[*EZ*-**2b**] = 2.0 ± 0.3; see eq. [4]), which in turn agrees with the ratio predicted from quantum yields for photoisomerization of *EE*-**2b** (see eq. [1]) within experimental error. This is the best evidence for the validity of the adiabatic ring-opening mechanism that has been obtained to date.

In addition to proceeding cleanly and yielding a predictable mixture of isomeric dienes, the ring opening of these compounds shows the additional unusual feature of proceeding in remarkably high quantum efficiency compared to those of other compounds that have been studied (3, 4, 12). Clearly, some aspect of the unique structures of these molecules is responsible for reducing the rate of nonproductive excited state decay relative to that of ring opening. Three basic differences between the structures of these compounds and simple monocyclic cyclobutenes can be noted: increased ring strain, decreased rotational flexibility of the substituents on the cyclobutene double bond, and decreased central-bond torsional flexibility in the isomeric 1,3-diene products (9). The latter possibility is related to the ability of the system to allow C_1–C_2 torsion during ring opening, which is required according to the conical intersection model for the process (17). Experimental evidence for the importance of such torsional modes in the photochemical ring opening of cyclobutene has been reported by Mathies and co-workers (10).

In the present work, we report the results of a more comprehensive study of the photochemical ring opening of specially

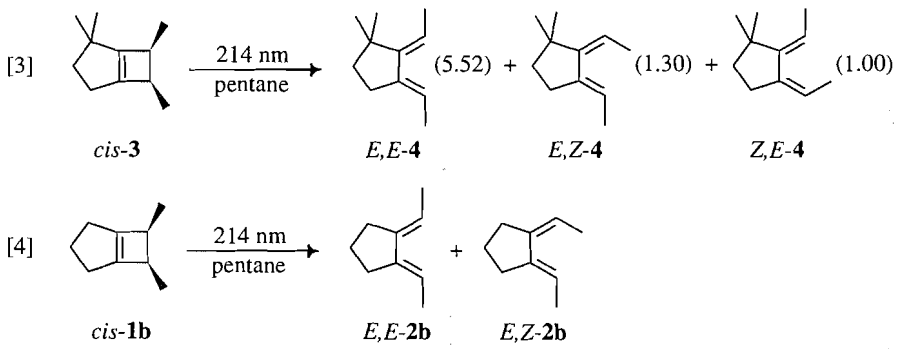

constrained cyclobutene derivatives. Primarily, we wished to attempt to identify the factors that are responsible for the anomalous photobehavior of **1b,c** with respect to ring opening, and to test the adiabatic mechanism for this process in a more detailed and systematic way. We thus report the photochemistry of the series of compounds **1a–d** in hydrocarbon solution with monochromatic 193- and 214-nm light sources. We also report complete details of a study of the photochemistry of the series of isomeric *E,E*- and *E,Z*-1,2-bis-(ethylidene)cycloalkanes **2a–d**. Preliminary results for three members of this series of dienes have been reported previously (9, 29).

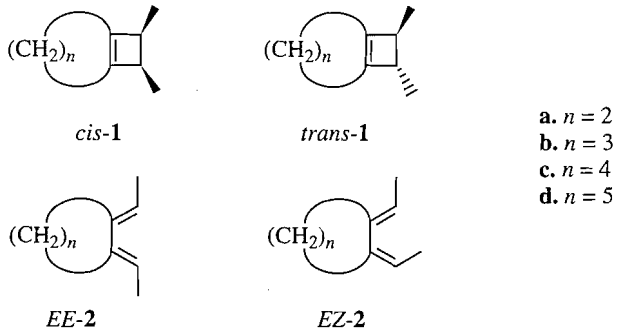

Results

The dienes *E,E*-**2** were prepared by zirconocene-mediated intramolecular coupling of the corresponding dialkynes **5** (n = 2–5; eq. [5]) (30, 31). Exhaustive irradiation of the *E,E*-diene (254 nm) was then carried out to afford isomeric mixtures consisting largely of the *E,E*- and *E,Z*-dienes and the *cis* and *trans*-substituted cyclobutenes, which were separated and purified

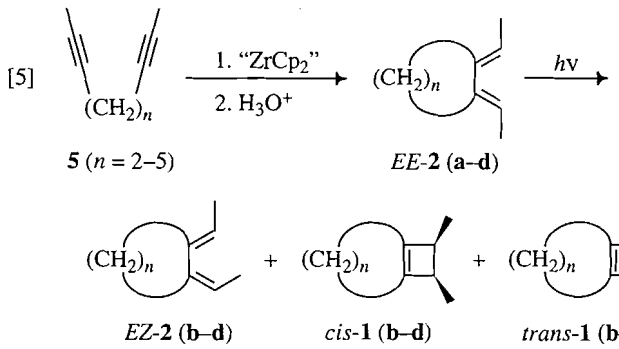

by semi-preparative gas chromatography. The irradiation mixtures usually also contained several other minor products; these were all determined to be isomers of **1** and **2** by GC/MS, but were isolated and rigorously identified in only certain cases (see experimental section). The *Z,Z* isomers of **2b–d** were tentatively identified by GC/MS, on the basis of comparisons of retention times and mass spectra (relative to the other components of the mixtures) to *Z,Z*-**2a**, which is a known compound and was isolated and rigorously identified from the exhaustive irradiation of *E,E*-**2a**. Because these compounds were minor components of extremely complex reaction mixtures, however, they were not isolated and rigorously identified.

While the first step in this procedure was successful for the synthesis of all four *E,E*-dienes in the series, the subsequent photoisomerization as a means of generating the desired cyclobutene derivatives was useful only for **2b–d**. In the case of *E,E*-**2a**, direct irradiation led to *cis,trans* photoisomerization and the formation of several minor products whose yields were similar to those of the desired cyclobutene derivatives. Thus, *cis*- and *trans*-**1a** were synthesized by photocyclization of 3,4-dimethyl-1,2-bis-(methylidene)cyclobutane (**7**), which was prepared as a mixture of isomers by zirconocene-mediated cyclization of the dialkyne **6** (eq. [6]) followed by bis-desilylation. This procedure led to excellent chemical yields of the desired cyclobutenes **1a**, which in spite of their rather substantial lability toward polymerization could be separated and purified by semi-preparative GC, and stored under liquid nitrogen until required.

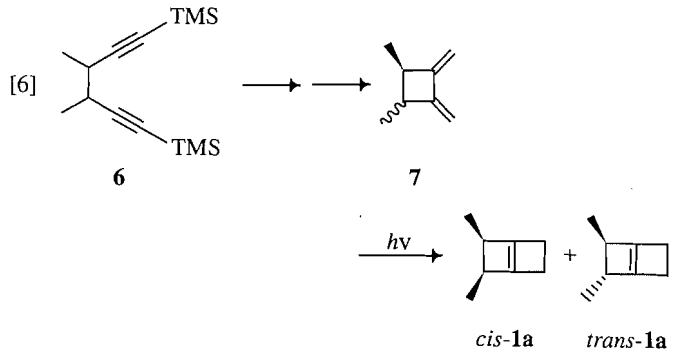

The structures of **1a–d** and **2a–d** were assigned on the basis of their mass, infrared, and high-resolution ^{1}H and (except for **1a**) ^{13}C NMR spectra (see experimental section). The *cis* and *trans* isomers of **1a–d** are readily distinguishable on the basis of ^{1}H and ^{13}C NMR spectroscopy; the present series of compounds exhibit the same spectral regularities with C_3/C_4 stereochemistry as has been reported previously for other systems (20, 32). Ultraviolet absorption spectra of *cis*- and *trans*-**1a–d**, and *E,E*- and *E,Z*-**2a–d**, were recorded in deoxygenated pentane solution at 23°C, and are shown in Figs. 1 and 2, respectively.

Direct irradiation of deoxygenated, ca. 0.02 M pentane solutions of **1b–d** with the pulses from an Ar/F_2 excimer laser (193 nm; 15 ns; 20 mJ; 0.5 Hz repetition rate) resulted in the clean formation of *E,E*- and *E,Z*-**2b–d** as the major products. In the irradiations of the *trans* isomers, minor amounts of the compounds identified (tentatively; vide supra) as *Z,Z*-**2b–d** were also formed, as indicated by comparison of the GC and GC/MS characteristics of the photolysates to those of the crude mixtures from direct irradiation of the *E,Z*-dienes. No other products were observed in yields greater than ca. 3% in any case. Quantum yields for formation of the three products from **1b–d** were determined from the slopes of concentration vs. laser dose plots, using the ring opening of bicyclo[4.2.0]oct-6-ene (**1**) as actinometer for 193-nm irradiations. Representative plots of this type are shown for *cis*- and *trans*-**1d** in Fig. 3.

Irradiation of deoxygenated, ca. 0.02 M pentane solutions of **1a–d** with 214-nm light was carried out using a Zn resonance lamp as the light source. The photolyses of **1b–d** were carried out with vigorous stirring of the solutions, and were monitored over a 0.1–4% conversion range. Relative product yields were calculated from the initial slopes of concentration vs. time plots, examples of which are shown in Fig. 4 for *cis*- and *trans*-**1d**. Quantum yields for ring opening of *cis*- and *trans*-**1a** were determined on unstirred solutions with 214-nm excitation, using the initial slopes of product concentration vs. time plots to determine product yields, and uranyl oxalate actinometry to determine light intensities (12).

Table 1 lists the quantum yield data from irradiation of **1a–d** at 214 nm and **1b–d** at 193 nm. The table also lists *EE*/*EZ* diene ratios from *cis*- and *trans*-**1a–d** and *EE*/*ZZ* diene ratios from *trans*-**1a–c** (the yield of the *Z,Z*-diene from *trans*-**1d** was too low to be determined); these were calculated from the slopes of concentration vs. time plots as described above.

Fig. 1. Ultraviolet absorption spectra of *cis* (——) and *trans* (– · – · –) **1a–d** in deoxygenated pentane solution at 23°C.

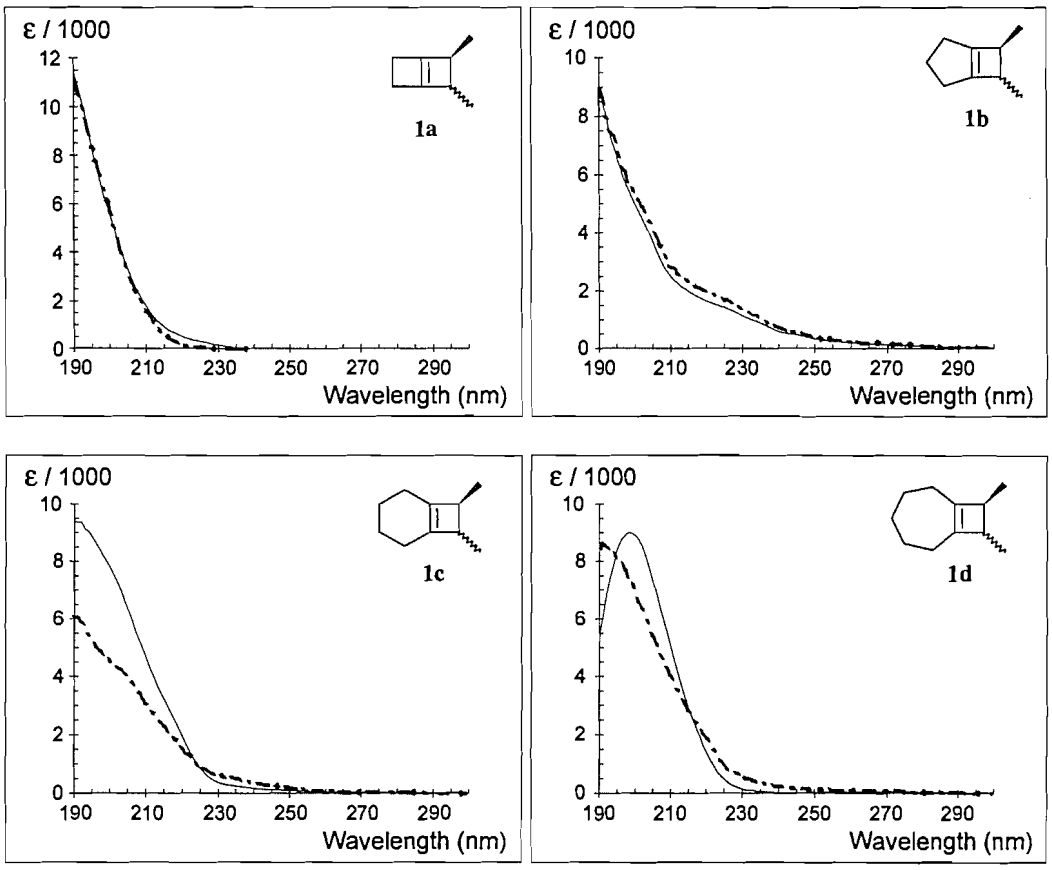

Table 1. Quantum yields for diene formation[a] and isomeric diene ratios[b] from 193- or 214-nm irradiation of deoxygenated 0.02 M pentane solutions of *cis*- and *trans*-**1a–d**.

Compound	$\phi_{EE\text{-}2}$	$\phi_{EZ\text{-}2}$	ϕ_{total}	(*EE*-**2**/*EZ*-**2**)^{193}	(*EE*-**2**/*ZZ*-**2**)^{193}	(*EE*-**2**/*EZ*-**2**)^{214}	(*EE*-**2**/*ZZ*-**2**)^{214}
cis-**1a**	0.55 ± 0.04	0.32 ± 0.06	0.87	*n.d.*	*n.d.*	1.7	[c]
cis-**1b**	0.42 ± 0.05	0.17 ± 0.03	0.59	2.5	[c]	2.0	[c]
cis-**1c**	0.48 ± 0.06	0.14 ± 0.02	0.62	3.4	[c]	4.1	[c]
cis-**1d**	0.68 ± 0.05	0.075 ± 0.008	0.75	9.1	[c]	5.6	[c]
trans-**1a**	0.066 ± 0.009	0.61 ± 0.04	0.68	*n.d.*	*n.d.*	0.11	10.0 ± 1.0
trans-**1b**	0.065 ± 0.008	0.59 ± 0.07	0.66	0.11	3.0 ± 0.6	0.45	4.3 ± 0.4
trans-**1c**	0.08 ± 0.02	0.45 ± 0.06	0.57	0.18	7.3 ± 1.4	0.29	8.6 ± 0.8
trans-**1d**	0.19 ± 0.03	0.67 ± 0.05	0.86	0.28	[c]	0.21	[c]

[a]Quantum yields for product formation from *cis*- and *trans*-**1a** were determined using filtered 214-nm excitation and uranyl oxalate actinometry. Those for product formation from **1b–d** were determined using 193-nm excitation and bicyclo[4.2.0]oct-7-ene actinometry.

[b]Calculated from the initial slopes of product concentration versus irradiation dose plots; errors were calculated from the standard deviations of the slopes; *n.d.* = not determined.

[c]*Z,Z*-**2** was not formed in sufficient yield to enable determination of the yield.

A control experiment was performed, in which a deoxygenated pentane solution containing 0.015 M *cis*-**1c** and 0.0011 M 1,3-cyclooctadiene (**8**) was irradiated (193 nm) to ca. 4.5% conversion of the cyclobutene. At these low conversions, isomerization of **8** to *cis,trans*-1,3-cyclooctadiene (the major product of irradiation of **8** (33)) could not be detected in the photolysate within our detection limits (ca. 10^{-6} M). Analogous results were obtained in the irradiation (214 nm) of *cis*- and *trans*-**1d**, employing low concentrations of *E,E*-**2b** as the standard.

As mentioned above, direct irradiation of *E,E*- and *E,Z*-**2a–d** in deoxygenated pentane solution led predominantly to

Fig. 2. Ultraviolet absorption spectra of *E,E* (——) and *E,Z* (·····) **2a–d** in deoxygenated pentane solution at 23°C.

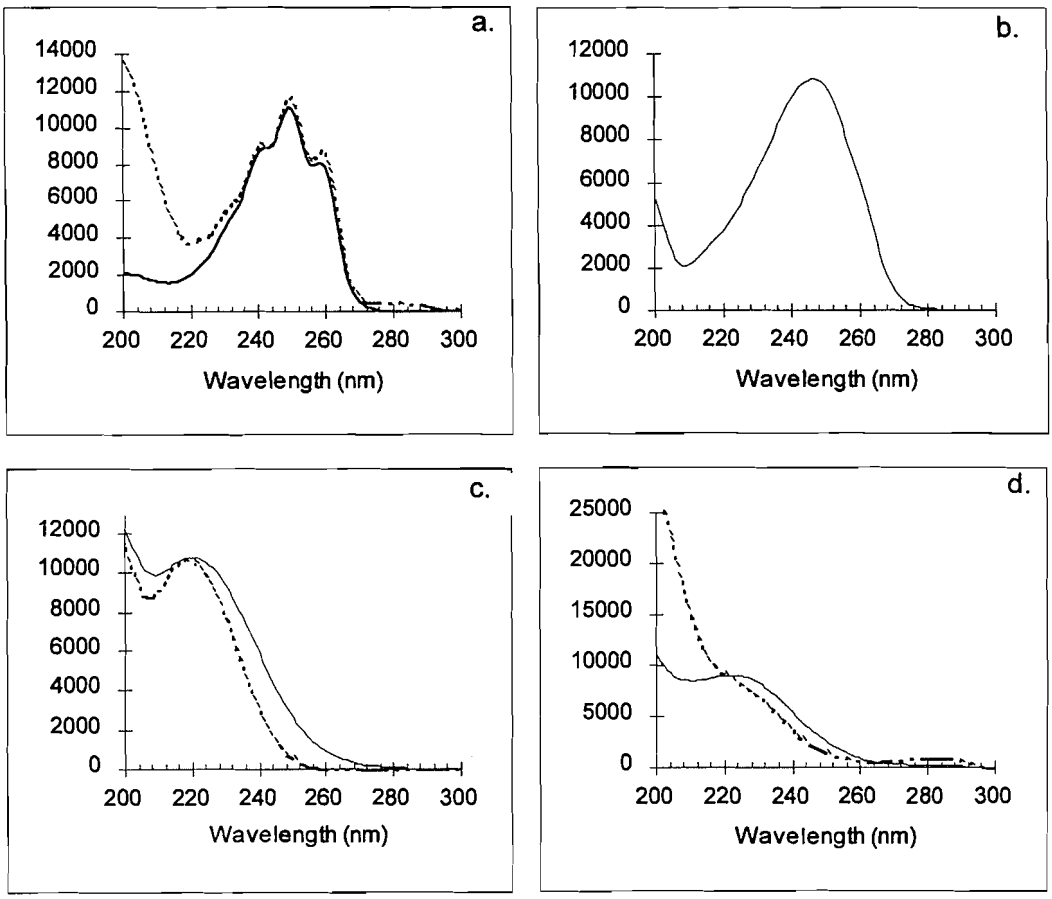

Table 2. Quantum yields for direct *cis,trans* photoisomerization and the formation of cyclobutene (**1**) and "other products" from 254-nm irradiation of deoxygenated 0.02 M pentane solutions of *E,E*- and *E,Z*-**2a–d**.[a]

Compound	$\phi_{EE\text{-}EZ}$	$\phi_{EZ\text{-}EE}$	$\phi_{EE\text{-}1}$[b]	$\phi_{EZ\text{-}1}$[c]	$\Sigma\phi_{OP}(EE)$[d]	$\Sigma\phi_{OP}(EZ)$[d]
2a	0.12 ± 0.02	0.11 ± 0.03	< 0.005	< 0.005	< 0.005	0.011 ± 0.005[e]
2b	0.24 ± 0.02	0.39 ± 0.04	0.10 ± 0.02	0.13 ± 0.01	0.06 ± 0.01	0.17 ± 0.03
2c	0.20 ± 0.03	0.27 ± 0.03	0.05 ± 0.01	0.019 ± 0.004	0.06 ± 0.02	0.06 ± 0.01
2d	0.21 ± 0.03	0.14 ± 0.06	0.15 ± 0.02	0.12 ± 0.06	0.05 ± 0.01	0.06 ± 0.01

[a]Determined by potassium ferrioxalate actinometry. The ZZ-dienes were rigorously identified only for Z,Z-**2a**.
[b]Quantum yield for formation of *cis*-**1** from *E,E*-**2**.
[c]Quantum yield for formation of *trans*-**1** from *E,Z*-**2**.
[d]Estimated total quantum yield for formation of unknown products from *E,E*- ($\Sigma\phi_{OP}(EE)$) and *E,Z*- ($\Sigma\phi_{OP}(EZ)$) **2**.
[e]Quantum yield for formation of *Z,Z*-**2a** from the *E,Z* isomer. No other products are formed, within the limits of our detection method.

cis,trans photoisomerization and the stereospecific formation of *cis*- and *trans*-**1a–d** (from *E,E*- and *E,Z*-**2a–d**, respectively). Other products were also formed in yields of ≤10% in some cases, but these were not rigorously identified. In the cases of *E,Z*-**2b** and **2c**, the most prominent of the minor photoproducts were those tentatively identified as the corresponding *Z,Z*-diene isomers, on the basis of GC/MS and GC retention time comparisons to *Z,Z*-**2a**, which was isolated and rigorously identified (vide supra). Irradiation of *E,Z*-**2d** yielded *E,E*-**2d** and *trans*-**1d** quite cleanly, and a minor product tentatively identifiable as *Z,Z*-**2d** could be detected only after extensive irradiation of the solution. Quantum yields for *cis,trans* photoisomerization and formation of **1a–d** and other minor products were determined in deoxygenated pentane solution (ca. 0.02 M) using potassium ferrioxalate actinometry. Quantum yields for the formation of minor products (*Z,Z*-**2** and all other unidentified products) were estimated in each case by GC (assuming equal response factors to the averages of those of the identified products) at ca. 5% conversion of starting material. Table 2 lists the results of these experiments.

Fig. 3. Product concentration versus laser dose plots for the formation of *E,E* (■) and *E,Z* (◆) **2d** from the photolysis (193 nm) of *cis* (A) and *trans* (B) 8,9-dimethylbicyclo[5.2.0]non-1[7]-ene (**1d**) in deoxygenated pentane solution at 23°C. The laser intensity was not the same in the two experiments.

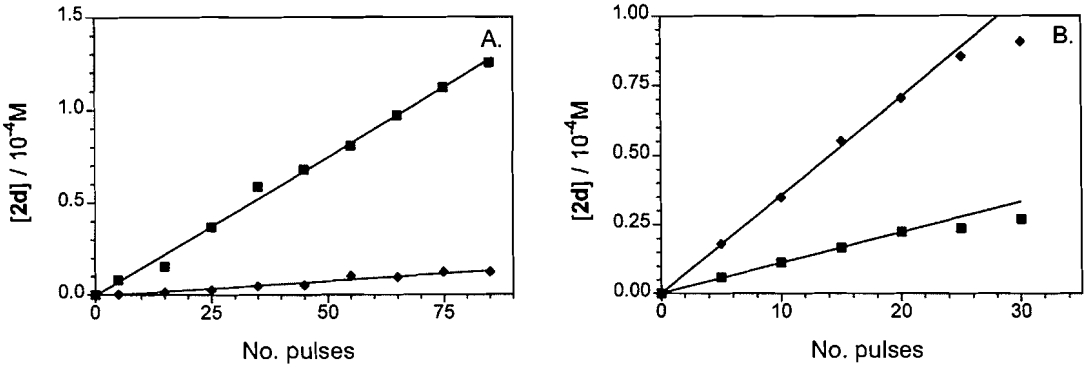

Fig. 4. Product concentration versus irradiation time for the formation of *E,E* (■) and *E,Z* (◆) **2d** from the photolysis (214 nm) of *cis* (A) and *trans* (B) 8,9-dimethylbicyclo[5.2.0]non-1[7]-ene (**1d**) in deoxygenated pentane solution at 23°C.

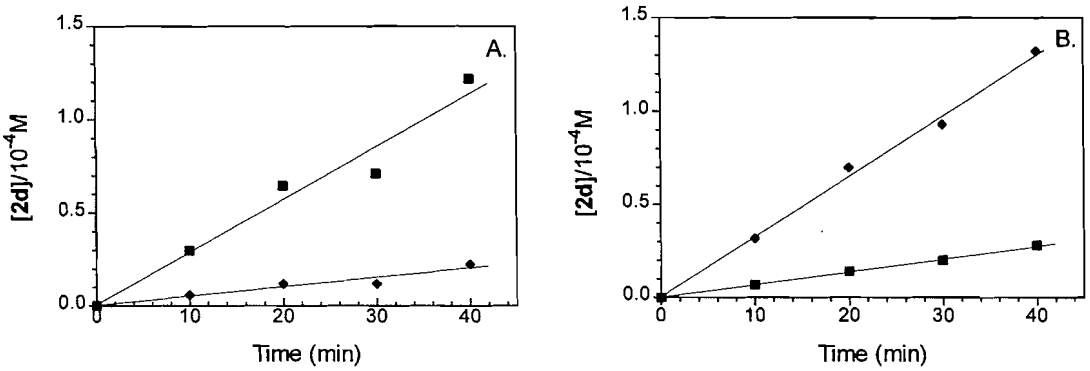

Discussion

The solution-phase UV absorption spectra of the series of bicyclic cyclobutene derivatives **1a–d** (Fig. 1) exhibit interesting trends. We previously reported spectra of several monocyclic alkylcyclobutene derivatives with *cis*- and *trans*-dimethyl substitution at C3/C4, and noted that those of the *cis* isomers are red-shifted with respect to those of the *trans* isomers (32). This was attributed to a stereochemical effect on the relative extinction coefficients of the π,π^* and Rydberg(π,R(3*s*))-like absorption bands. This is particularly noticeable in the gas phase UV spectra of these compounds, where the latter are considerably more intense than in the solution phase spectra. In solution, these absorption bands are sufficiently reduced in intensity that the result is an apparent broadening and red shift in the position of the prominent band in the spectra of the *cis* isomers compared to that in the spectra of the *trans* isomers. Similar differences are observed in the solution phase spectra of *cis*- / *trans*-**1d** and *cis*- / *trans*-**1c**, while the effect is absent altogether in the spectra of *cis*- and *trans*-**1a,b**. We do not understand the origins of the stereochemical effect on the spectra of monocyclic and relatively unstrained bicyclic alkylcyclobutenes such as **1c,d**, but it is interesting to note that the effect is truncated in the more highly strained members of the present series of compounds. It is clear that incorporation of the cyclobutenyl double bond into a second cycloalkyl ring has a significant effect on the UV absorption spectrum of the cyclobutenyl chromophore, to an extent that depends on the size of the ancillary ring.

The UV spectra of the isomeric dienes (Fig. 2) are consistent with an increasing amount of torsional flexibility about the central bond with increasing ancillary ring size throughout the series. For both **2a** and **2b** the long-wavelength bands in the spectra of the *E,E* and *E,Z* isomers are almost perfectly superimposable and exhibit maxima at ~250 nm, consistent with the molecules having planar, *s-cis* conformations that are roughly the same for the *E,E* and *E,Z* isomers. The spectra of the higher members of the series show maxima at shorter wavelengths, consistent with their preferred conformations having twisted *s-cis* geometries. The spectra of *E,E*-**2b** and **2c** are slightly red-shifted, but otherwise similar to those of the parent 1,2-dimethylenecycloalkanes (34).

Direct irradiation of *cis*- and *trans*-**1a–d** leads to ring opening to the isomeric dienes (**2a–d**) with a high degree of disrotatory stereoselectivity in each case (Table 1). None of these compounds undergo formal [2+2]-cycloreversion to any detectable extent, presumably because this process would lead to the formation of the corresponding, highly strained C_4–C_7

Table 3. Observed[a] and calculated[b] diene ratios from irradiation of *cis*-**1** in pentane solution at 23°C.

cis-**1**	$^{193}(EE\text{-}\mathbf{2}/EZ\text{-}\mathbf{2})_{obs}$	$^{214}(EE\text{-}\mathbf{2}/EZ\text{-}\mathbf{2})_{obs}$	$(EE\text{-}\mathbf{2}/EZ\text{-}\mathbf{2})_{c,calc}$
1a	*n.d.*	1.7 ± 0.2	8 ± 1
1b	2.5 ± 0.4	2.0 ± 0.4	2.2 ± 0.4
1c	3.4 ± 0.4	4.1 ± 0.3	3.7 ± 0.4
1d	9.1 ± 0.9	5.6 ± 0.9	3.7 ± 0.8

[a]Observed diene distributions from irradiation (193 and 214 nm) of *cis*-**1** (see Table 1); calculated from the slopes of concentration vs. time plots for the formation of *EE*- and *EZ*-**2**; *n.d.* = not determined.

[b]Expected diene ratios calculated using the quantum yield data in Table 2 and eq. [1].

Table 4. Observed[a] and calculated[b] diene ratios from irradiation of *trans*-**1** in pentane solution at 23°C.

trans-**1**	$^{193}(EZ\text{-}\mathbf{2}/EE\text{-}\mathbf{2})_{obs}$	$^{214}(EZ\text{-}\mathbf{2}/EE\text{-}\mathbf{2})_{obs}$	$(EZ\text{-}\mathbf{2}/EE\text{-}\mathbf{2})_{t\text{-}2,calc}$	$^{193}(EE\text{-}\mathbf{2}/ZZ\text{-}\mathbf{2})_{obs}$	$^{214}(EE\text{-}\mathbf{2}/ZZ\text{-}\mathbf{2})_{obs}$	$(EE\text{-}\mathbf{2}/ZZ\text{-}\mathbf{2})_{t\text{-}2}$
a	—	9.1 ± 1.1	8.0 ± 0.9	*n.d.*	10.0 ± 1.0	9.1 ± 1.5
b	9.1 ± 1.2	2.2 ± 0.3	1.4 ± 0.2	3.0 ± 0.6	4.3 ± 0.4	3.7 ± 0.7
c	5.6 ± 0.7	3.5 ± 0.4	2.6 ± 0.4	7.3 ± 1.4	8.6 ± 0.8	9.2 ± 1.8
d	3.6 ± 0.4	4.8 ± 0.8	5.6 ± 1.1	[c]	[c]	[c]

[a]Observed diene distributions from irradiation (193 and 214 nm) of *trans*-**1** (see Table 1); calculated from the slopes of concentration vs. time plots for the formation of *EE*-, *EZ*-, and *ZZ*-**2**; *n.d.* = not determined.

[b]Expected *EZ*/*EE*-diene ratios calculated using the quantum yield data in Table 2 and eq. [1] ($(EZ\text{-}\mathbf{2}/EE\text{-}\mathbf{2})_{t\text{-}2,calc}$), and *EE*/*ZZ* diene ratios obtained from direct irradiation of *E,Z*-**2** ($(EE\text{-}\mathbf{2}/ZZ\text{-}\mathbf{2})_{t\text{-}2}$).

[c]*ZZ* isomer was not formed in sufficient yield to enable yield determination.

cycloalkyne (35, 36). Another noteworthy feature of the present results is that *cis*- and *trans*-**1a** undergo ring-opening regiospecifically to yield the various geometric isomers of **2a**. In principle, **1a** has two ring opening modes available: one involving cleavage of the (unsubstituted) C5—C6 bond to yield **7**, and one involving cleavage of the (substituted) C2—C3 bond to yield **2a**. The fact that only the latter occurs in detectable yield is consistent with previous results that indicate that the efficiency of photochemical cyclobutene ring opening depends to some extent on the strength of the cyclobutenyl C3—C4 bond (12, 20).

The possibility that the overall nonstereoselectivity of photochemical ring opening might be explained by a mechanism in which purely disrotatory ring opening occurs adiabatically is suggested by the experimental results of Michl, Yang, and co-workers (37, 38), which demonstrated that direct irradiation of Dewar naphthalene (38) and Dewar anthracene (37) affords the corresponding aromatic hydrocarbons in the lowest excited singlet states. This was evidenced by the observation of the characteristic fluorescence of the aromatic hydrocarbons upon excitation of the corresponding Dewar isomers in solution.

If ring opening of alkylcyclobutenes proceeds in stereospecific, disrotatory fashion to yield a single diene isomer in the lowest excited singlet state, the final distributions of *E,E*- and *E,Z*-diene isomers obtained by irradiation of *cis*- and *trans*-**1a–d** should be determined by the excited state decay characteristics of the initially formed (allowed) diene isomer. These characteristics are given in quantitative form as the ratio of the quantum yields for productive vs. nonproductive decay of the diene (9, 28). Thus, the relevant equation for calculation of the expected distribution of *EE*- and *EZ*-dienes from irradiation of the *cis* cyclobutenes ($(EE/EZ)_{c,calc}$) is given in Scheme 1 (eq. [1]), which assumes that ring opening yields the *E,E*-diene to the exclusion of the other formally allowed product, the *Z,Z* isomer. That this assumption is reasonable follows from the fact that extremely low yields of *Z,Z*-dienes are observed in the photolyses of every *cis*-dimethyl substituted alkylcyclobutene that has yet been reported (3–5). The results of these calculations are listed in Table 3 along with the observed *EE*/*EZ* diene ratios from irradiation of *cis*-**1a–d** with the 193- and 214-nm light sources.

A similar equation can be employed to calculate the expected *EZ*/*EE* diene ratios from irradiation of the *trans* cyclobutenes ($(EZ/EE)_{t,calc}$). In these cases, the *E,Z*-diene is the only formally allowed ring-opening product, so no assumptions regarding the initial excited state product distribution are necessary in order to simplify the calculation. These compounds actually provide additional mechanistic information over that obtainable from the *cis* isomers, in that *two* detectable products are formed upon excited state decay of the *E,Z*-dienes: the *E,E*- and *Z,Z*-diene isomers. The adiabatic ring-opening mechanism would predict that, in these cases, the *EE*/*ZZ* diene distribution from ring opening of a *trans*-3,4-disubstituted cyclobutene should be identical to the *EE*/*ZZ* distribution from direct irradiation of the corresponding *E,Z*-diene (28). Table 4 summarizes the observed *EZ*/*EE* and *EE*/*ZZ* diene ratios from direct irradiation of *trans*-**1a–d**, along

with the expected *EZ/EE* ratios (according to eq. [7]) and the *EE/ZZ* diene ratios obtained in the direct irradiation of *E,Z*-**2a–d**.

As can be seen from inspection of Tables 3 and 4, the degree of agreement between the observed and calculated isomeric diene ratios varies for the two excitation wavelengths. For 214 nm excitation, the calculated and observed *EE/EZ* diene ratios agree within experimental error in seven cases out of eight (i.e., in all cases but *cis*-**1a**). In the cases of the *trans* isomers (**1a–c**), the similarity in the diene distributions from direct irradiation of cyclobutene and *E,Z*-diene extends as well to the *EE/ZZ* diene ratios, although the errors in these ratios are somewhat large due to the fact that the *Z,Z*-dienes are formed in relatively low yields in each case. The *EE/ZZ* ratio could not be determined reliably for *trans*-**1d**, as the yield of the *ZZ*-diene is extremely low in this case; irradiation of *E,Z*-**2d** also yields *Z,Z*-**2d** in unusually low yield, however.

For the most part, the present data support a mechanism in which ring opening occurs in purely disrotatory fashion to *first* yield the allowed diene isomer in the same electronic excited state that is populated upon direct excitation of the particular diene isomer and that is responsible for *cis,trans* isomerization; once formed, the excited diene then relaxes to form its characteristic mixture of products. In fact, this conclusion can be stated in more general terms. *The data support a mechanism in which ring opening occurs on the excited state surface in disrotatory fashion, but decay to the ground state surface(s) for product formation does not occur at the classical avoided crossing for cyclobutene–butadiene interconversion. Rather, it occurs at the same place(s), yielding a similar product distribution, as is(are) involved when the allowed diene isomer is itself excited directly.*

The behaviour of one compound in the series (*cis*-**1a**) is very clearly different from the others, in that its isomeric diene distribution is not modelled accurately by the excited state decay characteristics of the corresponding disrotatory diene (*E,E*-**2a**). We do not believe that the anomalously low disrotatory stereoselectivity observed in this case is due to an experimental artifact resulting from secondary irradiation of the *E,E*-diene. While ruling this out is admittedly more difficult to do in this case because of the shorter wavelength cutoff in the UV absorption spectrum of *cis*-**1a** compared to those in the spectra of **1b–d**, we note that irradiation of *trans*-**1a** (which should be subject to similar problems) leads to very high yields of *E,Z*-**2a** (there is, furthermore, no significant difference in the quantum yields for *cis,trans* photoisomerization of *E,E*- and *E,Z*-**2a** (29)). One possible explanation is that ring opening by the pathway leading to the *Z,Z*-diene isomer is much more important in *cis*-**1a** than in *cis*-**1b–d**; this would lead to a lower *EE/EZ* diene ratio than that predicted from consideration of the quantum yields for photoisomerization of the *E,E*-diene alone, due to isomerization of the *Z,Z*-diene to the *E,Z* isomer. Such behaviour could result from the considerably higher degree of ring strain afforded by the ancillary cyclobutyl ring (compared to that afforded by the ancillary rings in *cis*-**1b–d**), which might outweigh the normally dominant steric effects between the C_3–C_4 methyl groups and reduce the discrimination between the two possible disrotatory ring-opening modes. This explanation seems unlikely, however, given the sheer magnitude of the difference between the calculated and observed *EE/EZ* ratios for this compound (a simple calculation reveals that the yield of *E,Z*-**2a** formed by the *Z,Z*-diene route would have to be four times greater than that formed by the *E,E*-diene route, in order to account for the difference between the observed and calculated *EE/EZ* diene ratios). Besides, one would also expect that the observable yield of the *Z,Z*-diene should be significant if this were true, and such is not the case.

There is an intriguing wavelength dependence observed in the diene distributions throughout the two series of compounds **1b–d**, as is clear from inspection of Tables 3 and 4. With 214-nm excitation, the observed *EE/EZ* diene distributions very closely match those expected on the basis of the adiabatic ring-opening mechanism, as discussed above. On the other hand, the observed ratios for 193-nm excitation clearly deviate from the expected values in some cases, and the data reveal different trends in the variations in the degree of deviation throughout the two series of compounds. For the *cis* compounds, the deviation from expected behaviour increases with ancillary ring size (being largest for **1d**), while it decreases accordingly for the *trans* compounds. In both cases, the deviation occurs in the direction of a *higher* degree of overall disrotatory stereospecificity than the adiabatic mechanism can account for.

Comparison with theoretical models

In terms of the avoided crossing model for excited state pericyclic reactions, the data suggest that in the ring-opening reaction, conversion to the ground state at the avoided crossing does not occur; the excited molecule proceeds instead to the fully open geometry corresponding to the lowest excited singlet state of the symmetry-allowed diene isomer. The excellent agreement between observed and expected diene distributions further suggests that ring opening by the symmetry-forbidden conrotatory pathway does not occur to a significant extent.

This is consistent with the theoretical calculations of Devaquet and co-workers (14) and Morihashi and Kikuchi (39), which suggest that there may be a relatively small barrier between the pericyclic (2^1A_g) minimum for excited singlet state disrotatory ring opening/closure and the lowest Franck–Condon excited singlet (^1B_u) state of *s-cis* 1,3-butadiene (39). The barrier arises as a result of an allowed crossing of the ^1B_u and 2^1A_g states at intermediate geometries for ring closure of the diene. The pericyclic minimum (at which the cyclobutenyl C3—C4 is *partially* broken) occurs on the doubly excited 2^1A_g surface, access to which must involve internal conversion from the initially populated excited state of either cyclobutene (in ring opening) or 1,3-butadiene (in ring closure). Morihashi and Kikuchi determined that the probability of internal conversion from the pericyclic minimum to the ground state, while substantially higher than that on the conrotatory side, is quite low ($\sim 10^{-4}$) (39). Thus, these calculations suggest that full formation of electronically excited *s-cis* diene by disrotatory ring opening could occur competitively with internal conversion to the ground state surface at the pericyclic minimum, providing that such a barrier is small enough.

This model for photopericyclic reactions contains the implicit assumption that product selection in a photochemical reaction occurs *on the excited state surface* after initial relaxation to the favored equilibrium geometry; i.e., that the formation of different products in a photochemical reaction involves motion along different reaction coordinates on the excited

state surface (18). Thus, the formation of *E,Z*-diene by *disrotatory* ring opening of a *cis*-3,4-disubstituted cyclobutene can only result if electronically excited *E,E*-diene is fully formed *prior* to decay to the ground state by *cis,trans* isomerization. The ramifications of these statements are actually easier to understand from the point of view of diene photochemistry: the mixture of products that is normally formed from irradiation of an *s-cis* diene (geometric isomers, cyclobutene, and the *s-trans* conformer in acyclic systems) results from partitioning amongst different *excited state* reaction coordinates, according to the avoided crossing model.

Recent theoretical calculations by Bernardi, Robb, Olivucci and their co-workers suggest a fundamentally different mechanism for such reactions, in which product formation results from evolution along a *single* (preferred) excited state reaction coordinate (21, 23). Decay to the ground state surface then occurs at a single *conical intersection* of the ground and excited state potential energy surfaces to yield a mixture of products that is dictated by the structure of the molecule at the conical intersection, the atomic trajectories that are activated as the excited molecule approaches it, and various barriers that the molecule encounters on the ground state surface as it cascades to stable products. Thus, the formation of *all* the products of direct irradiation of an *s-cis* diene is proposed to be due to funnelling through a single conical intersection of the doubly excited (2^1A_g) and ground (1^1A_g) state potential energy surfaces. At the $2^1A_g/1^1A_g$ conical intersection calculated for *s-cis* butadiene, the molecule is twisted about all three carbon–carbon bonds; the termini (the C1—C2 and C3—C4 bonds in 1,3-butadiene) are twisted in disrotatory fashion, while the central (C2—C3) bond is effectively twisted by ca. 52° as a result of pyramidalization at C2 or C3 (16, 18, 19). One particularly intriguing aspect of this mechanism is the suggestion that torsion about the terminal double bonds of a diene is *accompanied by* torsional motions about the *central* (single) bond. This contrasts expectations based on the avoided crossing model, in which *cis,trans* photoisomerization and disrotatory ring closure are both assumed to involve planarization of the four-carbon framework. We have recently published preliminary experimental evidence that provides tentative support for the importance of central bond torsional motions, and hence for the conical intersection mechanism, in the *cis,trans* photoisomerization of constrained *s-cis* dienes (29).

It seems reasonable to expect that ring opening of cyclobutene should proceed by a pathway that involves internal conversion to the ground state surface at the same conical intersection as is proposed to be involved in the photochemistry of *s-cis* 1,3-butadiene: that which is characterized by disrotatory twisting of the incipient diene double bonds *and* twisting of the central bond. In terms of reaction products, one would expect a distribution that bears a strong resemblance to that obtained from direct excitation of the corresponding diene. In general, an exact match would not be expected if the product distribution depends on the direction of approach to the conical intersection, since this would most reasonably be expected to be different for the cyclobutene and the diene.

The striking similarities in the isomeric diene distributions obtained from cyclobutene ring opening (with 214-nm excitation) and direct diene irradiation, which are observed in all but one of the present series of compounds, may indicate that, in fact, the direction of approach to the conical intersection is *approximately the same* for a given cyclobutene and its corresponding disrotatory diene. This would be the case if ring opening occurs in disrotatory fashion on the ^1B_u surface, after which rapid crossing to the 2^1A_g surface and procession to the $2^1A_g/1^1A_g$ conical intersection occurs by an identical route to that followed when the diene is excited directly.

While there is agreement that the UV resonance Raman spectrum of cyclobutene indicates there to be activation of central (C=C) bond torsional modes within a few tens of femtoseconds after excitation of the molecule (10, 11), our results suggest that large-scale motions of this type are not required for efficient ring opening. If they were, one might expect there to be *some* observable difference in the photobehaviour of **1a–d** as the incipient flexibility of the system changes throughout the series as a function of ancillary ring size. Except for *cis*-**1a**, this does not appear to be the case. There is no variation throughout the series in the degree of agreement between observed and "expected" product distributions (for 214-nm excitation), nor is there any variation in the overall quantum yields for ring opening. Furthermore, the quantum yields for ring opening of **1a–d** are unusually high, compared to monocyclic systems. These considerations suggest that (large-scale) central bond torsion can only be important *after* the ring-opening stage of the reaction (on the excited state surface) is complete.

The conical intersection model is better able to account for the observation of higher disrotatory stereoselectivity with higher excitation energy than is the avoided crossing model; higher energy excitation could provide access to a different pathway for approach of the excited molecule to the conical intersection, one that results in a higher degree of disrotatory stereoselectivity in product formation. An alternate explanation is that the higher excitation energy populates an upper electronic excited state, whose involvement somehow results in a higher degree of disrotatory stereoselectivity. We can provide no reasonable explanation (using either theoretical model) for the difference in the trends in the wavelength dependence of the *cis* and *trans* isomers of this series of compounds.

Summary and conclusions

The isomeric *s-cis* diene distributions obtained from irradiation of alkylcyclobutenes that are structurally constrained at the cyclobutenyl C=C (central) bond are, for the most part, dictated by the excited state decay characteristics of a *single* diene isomer — that which forms by adiabatic ring opening by the disrotatory pathway predicted by orbital symmetry selection rules. Thus, the overall nonstereoselectivity of the reaction is most likely the result of *stereospecific* ring opening to yield an *electronically excited* product. Both the avoided crossing and conical intersection models for photopericyclic reactions can account for the qualitative aspects of the present data, but the latter appears to do so more completely than the former.

Other aspects of the photochemistry of aliphatic dienes are potentially exploitable for further verification of the adiabatic mechanism for excited state cyclobutene ring opening, and to further address the validity of theoretical models for the process. These include photochemical *s-cis* → *s-trans* conformer interconversion (in acyclic systems) and cyclobutene forma-

tion. The former should be detectable using matrix isolation techniques, while the latter could be probed by monitoring photoracemization of an optically active cyclobutene or the interconversion of isomeric cyclobutenes, which are both linked to a single diene isomer via disrotatory ring closure. Experiments of these types are in progress.

Experimental

^{1}H NMR spectra were recorded on Bruker AM300 or AM500 spectrometers, while ^{13}C NMR spectra were recorded at 125.6 MHz on the Bruker AM500; all were recorded in deuteriochloroform (or where noted, carbon tetrachloride) solution and are reported in parts per million downfield from tetramethylsilane. Condensed phase infrared spectra were recorded on a BioRad FTS40 infrared spectrometer as neat samples or in carbon tetrachloride solution (where noted). GC/FTIR analyses were carried out using the same spectrometer, interfaced to a Hewlett–Packard 5890 gas chromatograph via a BioRad GC/C 32 interface and equipped with a DB-17 megabore capillary column (30 m × 0.53 mm; Chromatographic Specialties). Gas chromatographic analyses were carried out using a Hewlett–Packard 5890 gas chromatograph equipped with a flame ionization detector, a Hewlett–Packard 3790 recording integrator, and both conventional heated and cold on-column injectors. A DB-1 microbore capillary column (15 m × 0.2 mm; Chromatographic Specialties, Inc.) was employed in conjunction with the latter, while a DB-1 megabore capillary column (30 m × 0.53 mm; Chromatographic Specialties, Inc.) or a HP-17 megabore capillary column (15 m × 0.53 mm, Hewlett–Packard, Inc.) were used with the conventional injector. GC/MS analyses were performed using a Hewlett–Packard 5890 gas chromatograph equipped with a HP-5971A mass selective detector and a DB-1 microbore capillary column (12 m × 0.2 mm; Chromatographic Specialties, Inc.). Exact masses were determined using a VGH ZABE mass spectrometer, and employed a mass of 12.000 000 for carbon.

Semi-preparative gas chromatographic separations employed a Varian 3300 gas chromatograph equipped with a thermal conductivity detector, a Hewlett–Packard 3390A recording integrator, and one of the following stainless steel columns: (*a*) 20% TCEP on 80/100 Chromosorb PNAW (20 ft × 1/4 in., Chromatographic Specialties, Inc.); (*b*) 20% TCEP on 80/100 Chromosorb PNAW (6 ft × 1/4 in., Chromatographic Specialties); or (*c*) 3.8% UC-W982 on 80/100 Supelcoport (24 ft × 1/4 in., Supelco, Inc.).

Ultraviolet absorption spectra were recorded using a Perkin–Elmer Lambda 9 spectrometer which is interfaced with an IBM PS2 model 30-286 and controlled by software supplied by the manufacturer. The spectrometer sample compartment was continuously flushed with dry nitrogen, and the sample and reference were deoxygenated with a stream of argon prior to recording the spectrum.

Pentane (Baker Photrex), hexanes (Fisher Reagent), *n*-nonane (Matheson, Coleman & Bell), and uranyl sulfate trihydrate (Alfa Ventron) were used as received from the suppliers. Tetrahydrofuran (Caledon Reagent) was dried over calcium hydride and distilled from sodium/benzophenone. Hexamethylphosphoramide, *n*-butyllithium (2.5 M in hexane), zirconocene dichloride, iodomethane, *n*-decane, *cis,cis*-1,3-cyclooctadiene, and 1,8-nonadiyne were used as received from Aldrich Chemical Co. Cerium(IV) sulfate tetrahydrate (Aldrich) was recrystallized three times from distilled water. 1,7-Octadiyne, 1,6-heptadiyne (Wiley Organics), and 1,5-hexadiyne (Lancaster) were purified by alumina column chromatography using hexanes as the eluant. 2,6-Octadiyne, 2,7-nonadiyne, 2,8-decadiyne, and 2,9-undecadiyne were prepared according to the procedure of Negishi et al. (30), and purified by alumina column chromatography (hexanes eluant). Oxalic acid (BDH Reagent) was recrystallized three times from water. Uranyl oxalate was prepared according to the published procedure and recrystallized three times from water (40).

Synthetic photolyses employed a Rayonet photochemical reactor fitted with 12 253.7-nm lamps and a merry-go-round apparatus. Deoxygenated solutions were irradiated in a 30-mL capacity quartz cell.

The (*E,E*)-1,2-bis(ethylidene)cycloalkanes (*E,E*-**2a–d**) were prepared according to the published procedures (30, 31). The *E,Z*- and *Z,Z*- diene isomers and the bicyclic cyclobutenes *cis*- and *trans*-**1b–d** were prepared by 253.7-nm irradiation of deoxygenated 2 M pentane solutions (10.0 mL) of the corresponding *E,E* isomer. For isolation of the dienes, the irradiations were stopped after the photostationary state had been reached; more extensive irradiation times were employed for the synthesis of the cyclobutenes **1b–d**. Following irradiation, the solvent was removed by distillation and the mixtures were passed through an alumina column, eluting with hexane. Following concentration of the solutions by careful distillation, isolation and further purification were achieved by preparative gas chromatography using column (*b*). Analytical and spectroscopic data for these compounds are similar to published data for all three isomers of **2a** (vide infra) (31, 41), *E,E*- and *E,Z*-**2b** (31, 42), *E,E*- and *E,Z*-**2c** (9, 31), and *E,E*-**2d** (31). The following lists complete spectroscopic data for all new or tentatively identified compounds (*Z,Z*-**2b**, *Z,Z*-**2c**, *E,Z*-**2d**, and *Z,Z*-**2d**), as well as previously unpublished data for the others.

(E,E)-1,2-Bis(ethylidene)cyclobutane (E,E-***2a***) (31, 41): IR (gas): 2961 (m), 2929 (m), 2855 (m), 1578 (m), 1561 (s), 1416 (w), 1314 (w), 1068 (s), 1011 (s); ^{1}H NMR, δ: 1.51 (d, J = 6.9 Hz, 6H), 2.49 (br s, 4H), 5.43 (q, J = 6.5 Hz, 2H); ^{13}C NMR, δ: 13.21, 24.99, 111.47, 141.60; MS, *m/z* (*I*): 108 (45), 93 (86), 91 (96), 79 (100), 77 (83), 66 (16), 65 (17), 53 (12), 51 (39), 39 (51), 27 (41).

(E,Z)-1,2-Bis(ethylidene)cyclobutane (E,Z-***2a***) (41): IR (gas): 2962 (m), 2929 (m), 2855 (m), 1470 (s), 1382 (s), 1261 (s), 1097 (s), 1015 (s); ^{1}H NMR, δ: 1.61 (d, 3H, J = 7.0 Hz), 1.72 (d, J = 7.0 Hz, 3H), 2.48 (br s, 4H), 5.11 (cplx q, J = 7.0 Hz, 1H), 5.57 (cplx q, J = 7.0 Hz, 1H); ^{13}C NMR, δ: 13.94, 14.60, 24.98, 26.42, 116.07, 117.29, 140.22, 142.47; MS, *m/z* (*I*): 108 (33), 93 (81), 91 (89), 79 (100), 77 (97), 53 (31), 51 (49), 39 (76), 27 (51).

(Z,Z)-1,2-Bis(ethylidene)cyclobutane (Z,Z-***2a***) (41): IR (gas): 2963 (m), 2928 (m), 2866 (m), 1602 (m), 1448 (w), 1412 (w), 1261 (s), 1097 (s), 1015 (s); ^{1}H NMR, δ: 1.77 (d, J = 7.1 Hz, 6H), 2.41 (br s, 4H), 5.06 (q, J = 7.1 Hz, 2H); MS, *m/z* (*I*): 108 (44), 93 (79), 91 (84),79 (100), 77 (95), 65 (41), 53 (27), 51 (42), 39 (67), 27 (46).

(E,E)-1,2-Bis(ethylidene)cyclopentane (E,E-**2b**) (31, 42): IR (gas): 2961 (m), 2928 (s), 2855 (m), 1678 (m), 1561 (s), 1261 (s), 1101 (m), 1068 (s), 1011 (s); ^{1}H NMR, δ: 1.51 (quintet, 2H), 1.60 (d, J = 7.0 Hz, 6H), 2.23 (t, 4H), 5.21 (m, 2H); ^{13}C NMR, δ (CCl_4): 14.8, 23.8, 30.4, 111.1, 141.1; MS, *m/z* (*I*): 122 (75), 107 (45), 105 (25), 94 (35), 93 (75), 79 (50), 77 (80), 67 (35), 65 (30), 55 (25), 41 (40).

(E,Z)-1,2-Bis(ethylidene)cyclopentane (E,Z-**2b**) (42): IR (gas): 2941 (s), 2872 (m), 1641 (w), 1450 (m), 909 (m); UV (pentane), λ_{max} (ε): 249 nm (9900 M^{-1} cm^{-1}); ^{1}H NMR, δ: 1.61 (quintet, 2H), 1.74 (d, 3H), 1.79 (d, 3H), 2.35 (cplx, 4H), 5.48 (m, 1H), 5,77 (m, 1H); ^{13}C NMR, δ: 15.10, 15.41, 23.78, 31.09, 36.42, 116.06, 120.32, 141.10.

(Z,Z)-1,2-Bis(ethylidene)cyclopentane (Z,Z-**2b**; identification tentative): MS, *m/z* (*I*): 122 (21), 107 (39), 105 (20), 95 (13), 94 (45), 93 (83), 79 (50), 77 (55), 67 (47), 65 (30), 55 (40), 41 (30).

cis-*6,7-Dimethylbicyclo[3.2.0]hept-1(5)-ene* (cis-**1b**) (43): IR (gas): 2965 (s), 2900 (s), 2868 (m), 1459 (w), 1380 (w), 1337 (w), 795 (m); ^{13}C NMR, δ: 14.11, 26.32, 29.81, 38.67, 153.34; MS, *m/z* (*I*): 122 (17), 107 (21), 93 (55), 91 (38), 79 (45), 77 (35), 65 (31), 51 (34), 39 (51).

trans-*6,7-Dimethylbicyclo[3.2.0]hept-1(5)-ene* (trans-**1b**) (43): IR (gas): 2966 (s), 2901 (s), 2865 (m), 1460 (w), 1383 (w), 1331 (w), 790 (m); ^{13}C NMR, δ: 17.50, 26.20, 29.75, 44.62, 152.60; MS, *m/z* (*I*): 122 (25), 107 (20), 93 (61), 91 (43), 79 (44), 77 (37), 65 (33), 51 (41), 39 (45).

(E,E)-1,2-Bis(ethylidene)cyclohexane (E,E-**2c**) (9, 30, 31): IR (gas): 2959 (m), 2939 (s), 2857 (s), 1443 (m), 1375 (w), 1235 (w), 1001 (w), 905 (w), 843 (w), 808 (w); ^{1}H NMR, δ: 1.58 (d, 6H), 1.59 (m, 4H), 2.16 (br s, 4H), 5.26 (q, 2H); ^{13}C NMR, δ: 12.90, 26.29, 27.95, 115.71, 142.03; MS, *m/z* (*I*): 136 (45), 121 (10), 107 (45), 93 (50), 91 (65), 79 (100), 77 (50), 67 (20), 65 (20), 53 (20), 51 (19), 39 (40).

(E,Z)-1,2-Bis(ethylidene)cyclohexane (E,Z-**2c**) (9): IR (neat): 3035 (w), 2935 (s), 2860 (s), 1442 (m), 1375 (w), 1238 (w), 993 (m), 907 (m), 837 (s), 807 (m); ^{1}H NMR, δ: 1.60 (d, 3H), 1.60 (m, 4H), 1.67 (d, 3H), 2.10 (m, 2H), 2.74 (m, 2H), 5.12 (cplx, 2H); ^{13}C NMR, δ (CCl_4): 12.69, 14.11, 27.19, 27.94, 28.66, 37.89, 116.48, 118,85, 137.39, 142.16; MS, *m/z* (*I*): 136 (30), 121 (15), 107 (45), 93 (50), 91 (75), 79 (100), 77 (50), 67 (25), 65 (27), 53 (16), 51 (16), 41 (21), 39 (43).

(Z,Z)-1,2-Bis(ethylidene)cyclohexane (Z,Z-**2c**; identification tentative): MS, *m/z* (*I*): 136 (33), 121 (8), 107 (85), 105 (39), 93 (40), 91 (39), 79 (100), 77 (65), 67 (30), 65 (32), 39 (15).

cis-*7,8-Dimethylbicyclo[4.2.0]oct-1(6)-ene* (cis-**1c**) (9): IR (neat): 2905 (br, s), 1465 (m), 1438 (s), 1375 (m), 1363 (m), 1315 (m), 1233 (m), 1125 (m), 1017 (w), 968 (w), 928 (w), 885 (w), 815 (w), 805 (w); ^{1}H NMR, δ: 0.94 (d, 6H), 1.62 (m, 4H), 1.75 (d, 2H), 1.86 (d, 2H), 2.78 (cplx q, 2H); ^{13}C NMR, δ (CCl_4): 13.19, 22.34, 22.92, 40.48, 144.74; MS, *m/z* (*I*): 136 (22), 121 (17), 107 (40), 105 (13), 93 (51), 91 (59), 79 (100), 77 (46), 67 (21), 65 (18), 53 (20), 51 (19). 41 (25), 39 (43).

trans-*7,8-Dimethylbicyclo[4.2.0]oct-1(6)-ene* (trans-**1c**) (9): IR (neat): 2917 (br, s), 2840 (s), 1443 (s), 1438 (m), 1327 (m), 1291 (m), 1260 (m), 1223 (m), 1123 (w), 1043 (w), 967 (m); ^{1}H NMR, δ: 1.08 (d, 6H), 1.60 (m, 2H), 1.66 (m, 2H), 1.77 (d, 2H), 1.85 (d, 2H), 2.19 (cplx q, 2H); ^{13}C NMR, δ (CCl_4): 16.94, 22.44, 23.04, 46.42, 143.69; MS, *m/z* (*I*): 136 (23), 121 (19), 107 (48), 105 (17), 93 (57), 91 (46), 79 (100), 77 (48), 67 (24), 65 (18), 53 (25), 51 (20), 41 (31), 39 (50).

(E,E)-1,2-Bis(ethylidene)cycloheptane (E,E-**2d**) (30, 31): IR (gas): 3034 (w), 2392 (s), 2868 (m), 1870 (w), 1647 (w), 1452 (m), 1384 (w), 1346 (w), 1315 (w), 1035 (w), 977 (w), 840 (w), 806 (w); ^{1}H NMR, δ: 1.45–1.55 (m, 6H), 1.56 (d, 6H), 2.21 (m, 4H), 5.37 (q, 2H); ^{13}C NMR, δ: 13.03, 27.78, 29.38, 31.80, 117.40, 146.06; MS, *m/z* (*I*): 150 (52), 135 (16), 121 (41), 107 (37), 105 (21), 93 (96), 91 (75), 79 (100), 77 (62), 67 (38), 55 (18), 53 (28), 39 (50). 27 (31).

(E,Z)-1,2-Bis(ethylidene)cycloheptane (E,Z-**2d**): IR (gas): 2968 (m), 2931 (s), 2864 (m), 2681 (w), 1457 (m), 1384 (w), 1350 (w), 957 (w), 822 (w), 798 (w); ^{1}H NMR, δ: 1.51 (br s, 6H), 1.59 (d, 3H), 1.63 (d, 3H), 2.16–2.22 (m, 4H), 5.22 (sextet, 2H); ^{13}C NMR, δ: 14.04, 14.95, 27.42, 29.46, 29.52, 29.68, 38.00, 117.38, 121.33, 140.27, 145.31; MS, *m/z* (*I*): 150 (56), 135 (18), 121 (43), 107 (39), 105 (21), 93 (97), 91 (69), 81 (28), 79 (100), 77 (60), 69 (3), 67 (41), 55 (17), 53 (29), 39 (54), 27 (30). Exact Mass, calcd. for $C_{11}H_{18}$: 150.1409; found: 150.1418.

(Z,Z)-1,2-Bis(ethylidene)cycloheptane (Z,Z-**2d**; identification tentative): MS, *m/z* (*I*): 150 (6), 135 (33), 121 (71), 107 (83), 93 (100), 91 (87), 79 (100), 77 (83), 67 (41), 65 (32), 53 (25), 41 (27), 39 (49), 29 (20), 27 (28).

cis-*8,9-Dimethylbicyclo[5.2.0]non-1(7)-ene* (cis-**1d**): IR (gas): 3087 (w), 2971 (w), 2932 (s), 2866 (m), 1641 (w), 1452 (m), 993 (w), 913 (m); ^{1}H NMR, δ: 0.90 (d, J = 7 Hz, 6H), 1.49 (cplx m, 4H), 1.65 (cplx m, 2H), 1.88 (cplx m, 2H), 2.02 (cplx. m, 2H), 2.57 (br q, 2H); ^{13}C NMR, δ: 13.11, 28.31, 29.04, 29.67, 38.35, 145.12; MS, *m/z* (*I*): 150 (27), 135 (16), 121 (34), 107 (35), 105 (18), 93 (90), 91 (69), 81 (51), 79 (100), 77 (61), 67 (51), 63 (9), 55 (23), 53 (32), 39 (63), 27 (36). Exact Mass, calcd. for $C_{11}H_{18}$: 150.1409; found: 150.1418.

trans-*8,9-Dimethylbicyclo[5.2.0]non-1(7)-ene* (trans-**1d**): IR (gas): 2966 (m), 2920 (s), 2866 (m), 1459 (m), 1378 (w), 977 (w), 831 (w), 815 (w); ^{1}H NMR, δ: 1.02 (d, J = 7 Hz, 6H), 1.51 (br s, 4H), 1.58 (cplx m, 4H), 1.95 (cplx m, 4H); ^{13}C NMR, δ: 16.96, 28.53, 29.07, 29.69, 44.11, 146.22; MS, *m/z* (*I*): 150 (33), 135 (17), 121 (39), 107 (42), 105 (22), 93 (99), 91 (77), 81 (25), 79 (100), 77 (61), 67 (39), 65 (25), 55 (16), 53 (25), 39 (52), 27 (29). Exact Mass, calcd. for $C_{11}H_{18}$: 150.1409; found: 150.1409.

The irradiation of *E,Z*-**2b,c** also yielded minor amounts of hydrogen migration products, which were identified as 1-ethyl-2-vinylcyclopentene from *E,Z*-**2b**, and 2-ethyl-3-ethylidenecyclohexene from *E,Z*-**2c**:

1-Ethyl-2-vinylcyclopentene: ^{1}H NMR, δ: 0.98 (t, 3H, J = 7 Hz), 1.80 (t, 2 H), 2.22 (cplx q, 2 H), 2.44 (cplx, 2H), 4.97 (cplx t, 1 H), 5.02 (cplx m, 1 H), 6.65 (dd, 1 H); ^{13}C NMR, δ:

12.87, 21.41, 32.43, 36.26, 112.37, 131.04, 133.31, 144.51; MS, *m/z* (*I*): 122 (20); 107 (23); 93 (60); 91 (64); 79 (100); 77 (53); 65 (17); 51 (15); 39 (27); 27 (17).

2-Ethyl-3-ethylidenecyclohexene: ^{1}H NMR, δ: 1.02 (t, 3H, *J* = 7.2 Hz), 1.63 (br t, 2H), 1.67 (d, 3H, *J* = 6.8 Hz), 2.09 (br m, 2H), 2.14 (cplx q, 2H), 2.26 (br t, 2H), 5.43 (q, 1H); 5.49 (br t, 1 H); ^{13}C NMR, δ: 13.01, 13.41, 22.59, 25.44, 25.52, 25.72, 115.78, 123.04, 135.09, 138.57. MS, *m/z* (*I*): 136 (25); 121 (7); 107 (100); 93 (31); 91 (97); 79 (99); 77 (55); 65 (21); 51 (17); 41 (18); 39 (30).

Preparation of cis- *and* trans-*2,3-dimethylbicyclo[2.2.0]hex-1(4)-ene* (cis- *and* trans-***1a***)

In a flame-dried, 150-mL two-necked flask, fitted with an addition funnel, magnetic stirrer, reflux condenser, and nitrogen inlet, were placed (±)-2,3-butanediol di-*p*-tosylate (19.90 g, 0.05 mol) and tetrahydrofuran (50.0 mL). The system was purged with dry nitrogen and then cooled with an external isopropanol – Dry Ice bath to −78°C, after which a solution of lithium trimethylsilylacetylide (generated from trimethylsilylacetylene (9.82 g, 0.1 mol) and *n*-butyllithium) in tetrahydrofuran (25 mL) was added dropwise over a period of 1 h with vigorous stirring. The resulting solution was stirred for an additional hour at −78°C, allowed to warm to room temperature, and then quenched with ice (20 g) and extracted with pentane (3 × 10 mL). The combined extracts were dried with sodium sulfate, filtered, and the solvent was evaporated to yield a colourless oil that was tentatively identified as 3,4-dimethyl-1,6-bis(trimethylsilyl)-1,5-hexadiyne (4.75 g, 0.019 mol, 38%) on the basis of its ^{1}H NMR and mass spectra: ^{1}H NMR, δ ($CDCl_3$): 0.11 (s, 9H), 1.71 (d, 3H), 5.01 (q, 1H); MS, *m/z* (*I*): 235 (13), 207 (3), 162 (75), 161 (43), 156 (2), 147 (22), 138 (13), 110 (14), 96 (14), 83 (12), 81 (11), 73 (100), 59 (12), 43 (11). The material was used without further purification in the following step.

In a flame-dried, 50-mL two-necked flask fitted with magnetic stirrer, addition funnel, reflux condenser, and gas inlet were placed zirconocene dichloride (2.92 g, 0.01 mol) and tetrahydrofuran (15 mL). The system was purged with dry nitrogen and cooled to −78°C with an external Dry Ice bath. A solution of *n*-butyllithium (0.02 mol) in tetrahydrofuran (5 mL) was added dropwise with stirring over a period of 1 h. After stirring at −78°C for an additional hour, a deoxygenated solution of 3,4-dimethyl-1,6-bis(trimethylsilyl)-1,5-hexadiyne (2.50 g, 0.01 mol) in tetrahydrofuran (5 mL) was added to the reaction mixture by means of a double-headed needle. The resulting solution was stirred at −78°C for an additional 3 h, warmed to room temperature, quenched with ice (20 g), and extracted with pentane (3 × 10 mL). The extracts were combined, the solvent was evaporated, and the residue (1.74 g) was dissolved in dichloromethane (10 mL) and placed in a 25-mL roundbottom flask. Trifluoroacetic acid (3.0 mL) was added and the mixture was stirred for 12 h at room temperature. The resulting brown reaction mixture was quenched with water (10.0 mL) and extracted with pentane (3 × 5 mL). The extracts were combined, dried over sodium sulfate, filtered, carefully distilled to remove the solvent, and finally bulb-to-bulb distilled under vacuum to yield a colourless liquid (0.73 g, 66%) that contained two major isomeric products according to GC/MS analysis. Small (ca. 10 mg) quantities of the two components were isolated by semi-preparative GC (column *c*), and identified as *cis*- and *trans*-3,4-dimethyl-1,2-(bis)-methylenecyclobutane (*cis*- and *trans*-**7**) on the basis of comparison of their ^{1}H NMR spectra to the published data (41).

The remaining portion of the mixture from above was dissolved in pentane (5 mL), placed in a quartz irradiation tube, and sealed with a rubber septum. The solution was deoxygenated with a stream of N_2, and photolysed (253.7 nm) to ca. 70% conversion. GC and GC/MS analysis indicated the formation of two major products, which were isolated and purified by semi-preparative GC (column *a*), and identified as *cis*- and *trans*-**1a** on the basis of their GC retention times, ^{1}H NMR, UV, and mass spectra (see below). As is also known to be the case for the parent compound, bicyclo[2.2.0]hex-1(4)-ene, *cis*- and *trans*-**1a** are relatively unstable compounds, with half-lives of ca. 15 h in pentane solution (1×10^{-2} M) at 25°C. The samples were stored under liquid nitrogen prior to their use in photolysis experiments.

cis-*2,3-Dimethylbicyclo[2.2.0]-hex-1(4)-ene* (cis-***1a***): IR (gas): 2962 (s), 2929 (s), 2872 (m), 2855 (m), 1450 (w), 1381 (w), 1353 (w), 1261 (m), 1101 (m); ^{1}H NMR, δ: 1.60 (d, *J* = 6.5 Hz, 6H), 1.76 (cplx m, 4H), 2.21 (q, *J* = 7.2 Hz, 2H); MS, *m/z* (*I*): 108 (39), 93 (78), 91 (83), 79 (100), 77 (94), 66 (24), 65 (29), 53 (29), 51 (41), 39 (63), 27 (41).

trans-*2,3-Dimethylbicyclo[2.2.0]-hex-1(4)-ene* (trans-***1a***): IR (gas): 2962 (s), 2929 (s), 2872 (w), 2856 (w), 1451 (w), 1261 (m); ^{1}H NMR, δ: 1.60 (d, *J* = 6.5 Hz, 6H), 1.76 (cplx m, 4H), 2.14 (cplx m, 2H); MS, *m/z* (*I*): 108 (40), 93 (96), 91 (96), 79 (95), 77 (100), 66 (23), 65 (27), 53 (33), 51 (44), 39 (64), 27 (42).

Quantitative photolyses employed a Rayonet photochemical reactor fitted with a merry-go-round and two 253.7 nm lamps, a 16-W Phillips 93106E Zn resonance lamp (214 nm) either alone or in conjunction with a 214 nm interference filter (Acton Research Corp. 214-B-ID), or the unfocussed pulses from a Lumonics 510 excimer laser containing Ar/F_2/He mixtures (193 nm, ca. 15 ns, 20 mJ, 0.5 Hz repetition rate). Solutions were contained in 5-mm quartz tubes sealed with rubber septa for 214 nm or 253.7 nm photolyses, or 1 × 2.5-cm round Suprasil UV cells (sealed with rubber septa) for 193 nm photolyses, and were deoxygenated with a stream of dry nitrogen or argon prior to irradiation. *n*-Decane was employed as an internal GC standard in all cases; the VPC detector responses were calibrated using solutions of known concentrations of substrate and standard. The solutions were vigorously stirred with a magnetic stirrer during the photolyses.

Quantum yields for product formation from 253.7 nm irradiation of dienes **2a–d** were carried out by ferrioxalate actinometry (44, 45), using 0.02 M solutions in pentane, and are the averages of triplicate single point determinations taken at conversions of 10% or less.

Quantum yields for product formation from 214-nm irradiation of *cis*- and *trans*-**1a** were carried out on unstirred solutions, using the initial slopes of product concentration vs. time plots to determine product yields, and uranyl oxalate actinometry (40, 44, 46) to determine light intensities.

Quantum yields for product formation from 193-nm irradiation of cyclobutenes **1b–d** were determined using the irradiation of bicyclo[4.2.0]oct-7-ene as the actinometer (1).

Irradiation of substrate and actinometer were followed as a function of light dose between 0.5 and 5% conversion, and quantum yields were determined from the slopes of concentration vs. time plots after correction of the raw data with the corresponding GC response factors.

Acknowledgments

We gratefully acknowledge the assistance of the McMaster University Regional Centre for Mass Spectrometry for Exact Mass determinations, the Natural Sciences and Engineering Research Council of Canada for equipment and operating grants, and M. Olivucci for helpful discussions.

References

1. K.B. Clark and W.J. Leigh. J. Am. Chem. Soc. **109**, 6086 (1987).
2. W.G. Dauben and J.E. Haubrich. J. Org. Chem. **53**, 600 (1988).
3. W.J. Leigh. Can. J. Chem. **71**, 147 (1993).
4. W.J. Leigh. Chem. Rev. **93**, 487 (1993).
5. W.J. Leigh. *In* CRC Handbook of organic photochemistry and photobiology. *Edited by* W.G. Horspool and P.-S. Song. CRC Press, Inc., Boca Raton, Fla. 1995. p. 123.
6. R.B. Woodward and R. Hoffmann. The conservation of orbital symmetry. Verlag-Chemie, Weinheim. 1970.
7. J. Saltiel and L.S. Ng Lim. J. Am. Chem. Soc. **91**, 5404 (1969).
8. W.J. Leigh and K. Zheng. J. Am. Chem. Soc. **113**, 2163 (1991).
9. W.J. Leigh and K. Zheng. J. Am. Chem. Soc. **113**, 4019 (1991).
10. M.K. Lawless, S.D. Wickham, and R.A. Mathies. J. Am. Chem. Soc. **116**, 1593 (1994).
11. F. Negri, G. Orlandi, F. Zerbetto, and M.Z. Zgierski. J. Chem. Phys. **103**, 5911 (1995).
12. W.J. Leigh and J.A. Postigo. J. Am. Chem. Soc. **117**, 1688 (1995).
13. W.T.A.M. Van der Lugt and L.J. Oosterhoff. J. Am. Chem. Soc. **91**, 6042 (1969).
14. D. Grimbert, G. Segal, and A. Devaquet. J. Am. Chem. Soc. **97**, 6629 (1975).
15. W.G. Dauben, R.L. Cargill, R.M. Coates, and J. Saltiel. J. Am. Chem. Soc. **88**, 2742 (1966).
16. F. Bernardi, S. De, M. Olivucci, and M.A. Robb. J. Am. Chem. Soc. **112**, 1737 (1990).
17. F. Bernardi, M. Olivucci, I.N. Ragazos, and M.A. Robb. J. Am. Chem. Soc. **114**, 2752 (1992).
18. M. Olivucci, I.N. Ragazos, F. Bernardi, and M.A. Robb. J. Am. Chem. Soc. **115**, 3710 (1993).
19. P. Celani, F. Bernardi, M. Olivucci, and M.A. Robb. J. Chem. Phys. **102**, 5733 (1995).
20. W.J. Leigh, K. Zheng, and K.B. Clark. J. Org. Chem. **56**, 1574 (1991).
21. F. Bernardi, M. Olivucci, and M.A. Robb. Acc. Chem. Res. **23**, 405 (1990).
22. J. Michl and V. Bonacic-Koutecky. Electronic aspects of organic photochemistry. John Wiley & Sons, New York. 1990. p. 225.
23. M.A. Robb. Pure Appl. Chem. **67**, 783 (1995).
24. J. Saltiel, L. Metts, and M. Wrighton. J. Am. Chem. Soc. **92**, 3227 (1970).
25. W.G. Dauben and E.G. Olsen. J. Org. Chem. **45**, 3377 (1980).
26. J. Saltiel and J.L. Charlton. *In* Rearrangements in ground and excited states. Vol. III. *Edited by* P. De Mayo. Academic, New York. 1980. p. 25.
27. M.E. Squillacote and T.C. Semple. J. Am. Chem. Soc. **112**, 5546 (1990).
28. W.J. Leigh, J.A. Postigo, and P.C. Venneri. J. Am. Chem. Soc. **117**, 7826 (1995).
29. W.J. Leigh and J.A. Postigo. J. Chem. Soc. Chem. Commun. 1836 (1993).
30. E. Negishi, S.J. Holmes, J.M. Tour, J.A. Miller, F.E. Cederbaum, D.R. Swanson, and T. Takahashi. J. Am. Chem. Soc. **111**, 3336 (1989).
31. W.A. Nugent, D.L. Thorn, and R.L. Harlow. J. Am. Chem. Soc. **109**, 2788 (1987).
32. W.J. Leigh, K. Zheng, and K.B. Clark. Can. J. Chem. **68**, 1988 (1990).
33. W.J. Nebe and G.J. Fonken. J. Am. Chem. Soc. **91**, 1249 (1969).
34. W.J. Bailey and W.B. Lawson. J. Am. Chem. Soc. **79**, 1444 (1957).
35. H. Meier. *In* Advances in strain in organic chemistry. Vol. I. *Edited by* B. Halton. Jai Press, Ltd., Greenwich, Conn. 1991. p. 215.
36. R.P. Johnson and K.J. Daoust. J. Am. Chem. Soc. **117**, 362 (1995).
37. N.C. Yang, R.V. Carr, E. Li, J.K. McVey, and S.A. Rice. J. Am. Chem. Soc. **96**, 2297 (1974).
38. R.V. Carr, B. Kim, J.K. McVey, N.C. Yang, W. Gerhartz, and J. Michl. Chem. Phys. Lett. **39**, 57 (1976).
39. K. Morihashi and O. Kikuchi. Theor. Chim. Acta, **67**, 293 (1985).
40. D.H. Volman and J.R. Seed. J. Am. Chem. Soc. **86**, 5095 (1964).
41. J.J. Gajewski and C.N. Shih. J. Org. Chem. **37**, 64 (1972).
42. R. Sustmann, P. Daute, R. Sauer, A. Sommer, and W.S. Trahanovsky. Chem. Ber. **122**, 1551 (1989).
43. H.J. Kuhn, S.E. Braslovsky, and R. Schmidt. Pure Appl. Chem. **61**, 187 (1989).
44. N.J. Bunce. *In* CRC Handbook of organic photochemistry. Vol. I. *Edited by* J.C. Scaiano. CRC Press, Inc., Boca Raton, Fla. 1989. p. 241.
45. N.J. Bunce, J. LaMarre, and S.P. Vaish. Photochem. Photobiol. **39**, 531 (1984).
46. J.N.J. Pitts, J.D. Margerum, R.P. Taylor, and W. Brim. J. Am. Chem. Soc. **77**, 5499 (1955).

On the stability of endohedral rare gas fullerenes

Dennis P. Clougherty

Abstract: The stability of $He@C_{60}$ and $Ne@C_{60}$ is discussed in the context of a spherical model where the carbon atoms are smeared out into a uniform shell. The electronic properties of the 60 π-electrons together with those of the central atom are treated in the Thomas–Fermi approximation. Simple electrostatic reasoning elucidates the nature of the radial stability of the complex. A method to include nonspherical corrections is outlined. Possible bonding topologies of the central atom and the C_{60} cage are discussed, as well as the relevance of these topologies to incipient central atom distortions.

Key words: fullerenes, Thomas–Fermi, dopeyball, $He@C_{60}$, $Ne@C_{60}$.

Résumé : On discute de la stabilité des $He@C_{60}$ et $Ne@C_{60}$ dans le contexte d'un modèle sphérique dans lequel les atomes de carbone sont répartis dans une coquille uniforme. On a traité les propriétés électroniques des 60 électrons π avec ceux de l'atome central par l'approximation de Thomas–Fermi. Un raisonnement électrostatique simple permet d'élucider la nature de la stabilité radiale du complexe. On décrit une méthode permettant d'inclure des corrections non sphériques. On discute des topologies de liaison possibles de l'atome central et de la cage C_{60} ainsi que de ces topologies par rapport aux distorsions qui naissent de l'atome central.

Mots clés : fullerènes, Thomas–Fermi, dopeyball, $He@C_{60}$, $Ne@C_{60}$.

[Traduit par la rédaction]

I. Introduction

An interesting consequence of the closed cage structure of C_{60} is that atoms and molecules may be trapped inside, forming endohedral complexes ("dopeyballs"). A variety of such complexes have been produced (1) where the dopant may be a metallic or a rare gas atom/cluster. The electronic structure and mechanical stability of two such endohedral rare gas complexes, $He@C_{60}$ and $Ne@C_{60}$, are considered here.

It has previously been noted (2) that the high symmetry of the C_{60} cage suggests the following geometrical approximation: the one-electron potential of icosahedral symmetry is replaced with its spherical average. Physically, the nuclear charge together with the charge from the core electrons is smeared out into a thin spherical shell of uniform surface charge density and radius R. Such a fictitious molecule — "spherene" — has complete spherical symmetry.

In the case of metallofullerenes such as $Na@C_{60}$, it has been shown (3) that the equilibrium position of the dopant is not at the center of the cage, consequently reducing the symmetry of the complex. For rare gas dopants, however, it was previously asserted (1) that there is no such symmetry reduction. Additionally, previous calculations (4) on $Ne@C_{60}$ indicate that the dopant is stable at the center. Consequently, given the large coordination number of the gas atom and the lack of a distortion from the high symmetry configuration, endohedral rare gas fullerenes seem to be good candidates for the spherical approximation.

The endohedrally doped spherene is treated in the Thomas–Fermi approximation. It is anticipated that the highly delocalized π-electrons of the cage and the closed shell configuration of the gas atom are well suited to such a statistical description. This method of treating high symmetry molecules was originally suggested by March (5).

The cage is parametrized by the radius R and valence electron number N, while the gas atom has nuclear charge Z and an equal number of electrons. The total electron density is calculated using the Thomas–Fermi equations, subject to the shell boundary conditions.

The total energy of the system is calculated for a variety of radii. A stable equilibrium radius is obtained, when the cage self-energy is computed from the system of ionic point charges, rather than from the continuum model. A method of treating nonspherical corrections is outlined. Lastly, possible central atom distortions are discussed in the context of the Bader molecular graphs arising from the electron density.

II. Thomas–Fermi theory of dopeyballs

The nuclear potential from the central atom and the cage atoms can be expanded in a multipole series as

$$[1] \qquad V_n(r) = \sum_{\ell,m} \frac{1}{r^{\ell+1}} \sqrt{\frac{4\pi}{2\ell+1}}\, Q_{\ell m} Y^*_{\ell m}(\Omega)$$

$Q_{\ell m}$ is the 2^ℓ-pole moment, given by

Received October 11, 1995.

This paper is dedicated to Professor Richard F.W. Bader on the occasion of his 65th birthday.

D.P. Clougherty.[1] Department of Physics, University of Vermont, Burlington, VT 05405, U.S.A.

[1] Telephone: (802) 656-0063 or -2644. Fax: (802) 656-0817. E-mail: dpc@holstein.physics.uvm.edu

[2] $$Q_{\ell m} = eR^{\ell}\sqrt{\frac{4\pi}{2\ell+1}}\sum_i Y_{\ell m}(\Omega_i) + Ze\delta_{\ell 0}$$

where Z is the atomic number of the rare gas atom of interest. From the icosahedral symmetry of the molecule, it has been shown (2) that the first three nonvanishing multipole moments are for ℓ =0, 6, 10. As the occupied one-electron states have an effective $\ell = 5$, it is not necessary to consider $\ell > 10$ multipole terms in first-order perturbation theory.

The spherical approximation consists of retaining only the $\ell = 0$ term in the multipole expansion. The error introduced can be estimated by consideration of the relevant dimensionless parameters

[3] $$\alpha_{\ell m} = \left|\sqrt{\frac{4\pi}{2\ell+1}}\,\frac{Q_{\ell m}}{R^{\ell}Q_{00}}\right|$$

The following values are found as functions of Z: $\alpha_{6,0} = 0.026/(1+Z)$, $\alpha_{6,5} = 0.020/(1+Z)$, $\alpha_{10,0} = 0.021/(1+Z)$, and $\alpha_{10,5} = 0.034/(1+Z)$. As $\alpha_{\ell m} << 1$ for $\ell \leq 10$, it may be concluded that the spherical approximation is justified for such a high symmetry structure, and one-electron splittings under the true icosahedral symmetry can be treated perturbationally.

With spherical symmetry imposed, the endohedral cluster is quasi-atomic in form. The 60 π-electrons of the cage plus the Z electrons of the central atom are now treated in the Thomas–Fermi (TF) approximation where the $Z+N$ electrons see a point charge of Ze at the origin and a uniform shell of charge Ne and radius R. The methodology follows that of March (5).

At temperature $T = 0$, the dimensionless TF equation without exchange is given by

[4] $$\frac{d^2\phi}{dx^2} = \frac{\phi^{3/2}}{x^{1/2}}$$

x is the distance from the center of the shell in units of

[5] $$b = \frac{1}{4}\left[\frac{9\pi^2}{2Z}\right]^{1/3} a_0$$

where a_0 is the Bohr radius of hydrogen. ϕ is related to the potential in the usual way

[6] $$V(r) = \frac{Ze}{r}\,\phi(x)$$

Equation [4] is supplemented with the boundary conditions: $\phi(0) = 1$, and

[7] $$\phi'(X^-) - \phi'(X^+) = \frac{N}{ZX}$$

where X is the shell radius in dimensionless units and differentiation is with respect to x. Additionally, ϕ itself is continuous over its domain, and $\phi \rightarrow 0$ as $x \rightarrow \infty$.

III. Numerical results

$\phi(r)$ is found by numerical integration of eq. [4] subject to the above boundary conditions. The charge density $n(r)$ and total electronic energy E_e are subsequently obtained from $\phi(r)$, as

Fig. 1. Radial electron density for Ne@C_{60} (in units of $10/b$) vs. x for $R = 7.36a_0$.

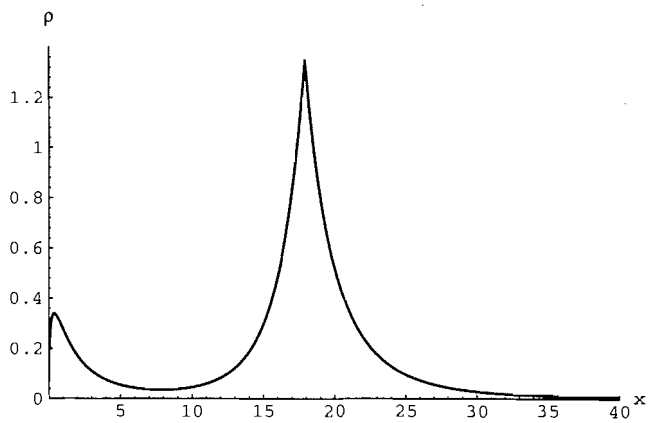

[8] $$n(x) = \frac{Z}{4\pi b^3}\left[\frac{\phi(x)}{x}\right]^{3/2}$$

and

[9] $$E_e = \frac{3Z^2e^2}{7b}\left[\phi'(0) + \frac{4N}{3Z}\,\frac{\phi(X^-)}{X} - \frac{N}{3Z}\,\phi'(X^-) - \left(\frac{N}{Z}\right)^2\frac{1}{X} - \frac{7N}{3Z}\,\frac{1}{X}\right]$$

as was obtained by March. The radial electron density of Ne@C_{60} is given as an example in Fig. 1.

The electronic energy E_e is found for various values of the dimensionless cage radius X in the cases of Z = 2 and 10, corresponding to He@C_{60} and Ne@C_{60}, respectively. As the boundary condition for ϕ at the shell explicitly depends on Z, E_e will not have simple "atomic" scaling with Z ($E_e \sim Z^{7/3}$).

If we add to E_e the electrostatic self-energy of the continuum shell, U, it is found that this total energy $E = E_e + U$ does not have a minimum for finite X, in accord with Teller's no-binding theorem (6) for molecules in TF theory. The continuum shell self-energy is too large and dominates E_e. However, if the self-energy is evaluated as a sum over point ions distributed on the shell surface, an energy minimum at finite shell radius is found. The spherical approximation is abandoned for the purpose of calculating the potential energy for the nuclear configuration.

The self-energy of the nuclear configuration may be written in the form

[10] $$U = \frac{ZNe^2}{bX} + c\,\frac{N^2e^2}{bX}$$

where c is a dimensionless number, computed from the actual equilibrium coordinates of C_{60}. It was previously (2) computed as $c = 0.43101$.

The total energies for He@C_{60} and Ne@C_{60} as a function of the shell radius are displayed in Figs. 2 and 3. The resulting equilibrium radii, R_0, are listed in Table 1, together with the total energies for the equilibrium configuration. Previous results for C_{60} are provided for comparison.

The expansion of the equilibrium cage radius with in-

Fig. 2. Total energy E (Ry) for He@C_{60} vs. shell radius R (Bohr).

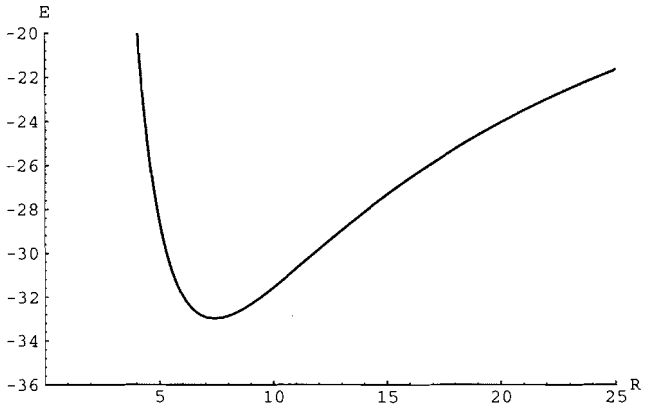

Fig. 3. Total energy E (Ry) for Ne@C_{60} vs. shell radius R (Bohr).

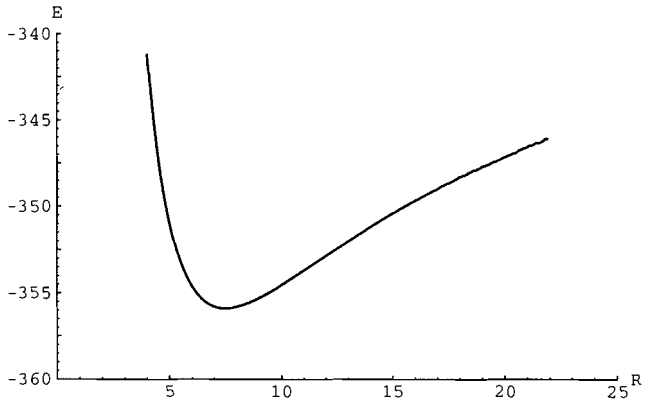

Table 1. Minimum total energies E (Ry), equilibrium radii R (Bohr), for $Z = 0, 2, 10$.

Z	R	E
0[a]	7.35	−25.313
2	7.41	−32.98
10	7.64	−356.30

[a]Reference 2.

creasing Z is observed, in agreement with a previous restricted Hartree–Fock calculation (4). It should, however, be noted that c is a result of the detailed atomic positions in C_{60}. Certainly, distortions that do not preserve the relative positions of cage ions will give rise to changes in c and, consequently, to changes in R_0. It is also interesting to note that the monotonic increase of R_0 with Z does not follow the "atomic size" scaling relation ($D \sim Z^{-1/3}$).

The shell equilibrium can be understood from electrostatic considerations. At equilibrium, the centrifugal force on the shell resulting from self-interaction is balanced by the centripetal force exerted on the shell by the charge contained inside the shell. The total charge contained inside the shell at equilibrium is $-cNe \approx -25.86e$, and the total number of electrons inside the shell is $(Z+cN)$. Thus we see that endohedral fullerenes whose central atoms have higher Z require more electrons inside the shell to maintain equilibrium.

IV. Beyond spherene

While approximating the discrete cage ions by a uniform spherical shell is a valid approximation with regard to the total energy, it is the corrections to the spherical average that contain all the information regarding the bonding. The spherical approximation reduces the complex to a one-dimensional system. The consequent critical points in the electron density consist of only minima and maxima, and an analysis of the bonding topology requires consideration of the effects of the nuclear multipole moments $\ell > 0$. A method for finding the electron density corrugations of endohedral fullerenes is given below.

To treat these nonspherical contributions, one must return to the general TF equation,

$$[11] \qquad \nabla^2 V = \beta V^{3/2} - 4\pi\rho_+$$

where $\beta = \dfrac{32\pi^2 e^2}{3h^3}(2m)^{3/2}$ and ρ_+ is the (positive) nuclear charge density.

ρ_+ can be expressed as a sum of spherical harmonics,

$$[12] \qquad \rho_+(\boldsymbol{r}) = Ze\delta(\boldsymbol{r}) + \frac{\delta(r-R)}{r^2}\frac{Ne}{4\pi} + \Delta\rho$$

where

$$[13] \qquad \Delta\rho = \frac{\delta(r-R)}{r^2}\sum_{\substack{\ell,m \\ \ell\geq 1}} R^{-\ell}\sqrt{\frac{2\ell+1}{4\pi}}\, Q_{\ell m}\, Y_{\ell m}(\Omega)$$

The potential V is now written as

$$[14] \qquad V(\boldsymbol{r}) = V_0(r) + \zeta(\boldsymbol{r})$$

where V_0 is the spherically averaged solution and ζ results from consideration of the higher order multipole moments. It is assumed that ζ is much smaller than V_0. Thus, eq. [11] leads to a linearized equation for ζ

$$[15] \qquad \nabla^2\zeta = \frac{3}{2}\beta V_0^{1/2}\zeta - 4\pi\Delta\rho$$

Equation [15] is of the form of the single particle Schrödinger equation at zero energy with a central "potential," $\frac{3}{2}\beta V_0^{1/2}$, which is everywhere positive, and a nonhomogeneous boundary term. ζ may be expanded in spherical harmonics inside and outside $r = R$, and the boundary term gives rise to a discontinuity in the radial derivative of ζ. Thus,

$$[16] \qquad \zeta(\boldsymbol{r}) = \sum_{\ell m}\zeta_{\ell m}(r)Y_{\ell m}(\Omega)$$

where $\zeta_{\ell m}$ satisfies the following

$$[17] \qquad \left(\frac{d^2}{dr^2} - \frac{3}{2}\beta V_0^{1/2} - \frac{\ell(\ell+1)}{r^2}\right) r\zeta_{\ell m}(r) = 0$$

and is subject to the following boundary conditions

$$[18] \quad r\zeta_{\ell m} \rightarrow 0, \qquad \text{as } r \rightarrow 0$$

$$[19] \quad r\zeta_{\ell m} \rightarrow 0, \qquad \text{as } r \rightarrow \infty$$

$$[20] \quad \frac{\mathrm{d}}{\mathrm{d}r}(r\zeta_{\ell m})\Big|_{r=R^-}^{R^+} = -R^{-\ell-1}\sqrt{4\pi(2\ell+1)}Q_{\ell m}$$

As the effective "potential" in eq. [17] is positive for all r, only exponential solutions are possible for ζ. Without a discontinuity in the radial derivative, only the trivial solution would satisfy the boundary conditions at the origin and at infinity. Thus, $\zeta_{\ell m}$ is non-zero only when $Q_{\ell m}$ is non-zero. The first nonspherical corrections to the potential and the electron density then are at $\ell = 6$, 10. Not surprisingly, these ℓ values correspond to irreducible representations of the rotation group that contain the trivial representation (A_g) of I_h. It is interesting to note that the centrifugal term in the effective "potential" will reduce the contributions from large ℓ to the density.

V. Structure and bonding

The simplest bonding configuration consistent with the symmetry constraints is that of 60 bonds between the central atom and the carbon atoms in the cage. However, a second possibility was proposed on the basis of an ab initio calculation (4) on Ne@C_{60}. There, it was found that with the Ne atom in the center of the cage, 30 bond paths exist, starting on the Ne atom and terminating on the carbon–carbon double bond points. Is this a stable configuration with respect to central atom displacement?

While the total energy calculations in ref. 4 indicate that Ne is in a stable equilibrium at the center of the cage, unless the bond point at the carbon–carbon double bond is a nonnuclear attractor (8) ("pseudoatom"), it would seem that the bonding topology found in ref. 4 may correspond to that of the metastable state described by Bader (7) as a "conflict structure."

Given that the Na^+ is isoelectronic with Ne, and that Na^+ in $Na^+@C_{60}$ does distort along a fivefold axis, a similiar instability in Ne@C_{60} would seem possible. The possible incompatibility of the molecular graph with the total energy calculations indicates that additional study is warranted, and central atom distortions in rare gas endohedral fullerenes remain as an intriguing possibility.

Acknowledgments

Acknowledgment is made to the Donors of The Petroleum Research Fund, administered by the American Chemical Society, for support of this research.

References

1. D.S. Bethune, R.D. Johnson, J.R. Salem, M.S. deVries, and C.S. Yannoni. Nature, **366**, 123 (1993).
2. D.P. Clougherty and X. Zhu. J. Chem. Phys. Submitted.
3. J. Liu, S. Iwata, and B. Gu. Phys. Rev. B: Condens. Matter, **50**, 5552 (1994).
4. J. Cioslowski and E.D. Fleischmann. J. Chem. Phys. **94**, 3730 (1991).
5. N.H. March. Proc. Cambridge Philos. Soc. **48**, 665 (1952).
6. E. Teller. Rev. Mod. Phys. **34**, 627 (1962).
7. R.F.W. Bader. Acc. Chem. Res. **18**, 9 (1985).
8. W.L. Cao, C. Gatti, P.J. MacDougall, and R.F.W. Bader. Chem. Phys. Lett. **141**, 380 (1987).

Local energy and chemical potential equations and the exchange-correlation potential

N.H. March

Abstract: Local energy and chemical potential equations are considered in some detail in relation to low-order density matrices. Some asymptotic properties can be extracted in exact form. The spatial derivative of the chemical potential equation referred to above yields the external force, defined as the (negative of the) gradient of the potential energy of the nuclear framework. This quantity, by utilizing the differential virial theorem, can be expressed as a sum of three terms: (*i*) a Laplacian contribution known explicitly in terms of the ground-state electron density; (*ii*) a kinetic part derivable from the "near-diagonal" behaviour of the first-order density matrix; and (*iii*) a term from electron–electron interactions, that involves the electronic pair correlation function. Following the work of Holas and March, this allows the exchange-correlation potential of density functional theory to be expressed in terms of low-order density matrices. Finally, scaling of electron–electron interactions is briefly considered, as well as the adiabatic connection formula in density functional theory. Such scaling arguments lead to a kinetic correction to the Harbola–Sahni form of the exchange-only potential.

Key words: external force, first-order density matrix, electronic pair function.

Résumé : On considère en détail les équations de l'énergie locale et des potentiels chimiques en relation avec des densités de matrices d'ordre peu élevé. On peut extraire quelques propriétés asymptotiques dans une forme exacte. La dérivé spatiale de l'équation du potential chimique mentionné plus haut fournit le force externe, définie comme la valeur négative du gradient de l'énergie potentielle du squelette nucléaire. Cette quantité, en utilisant le théorème de la différentielle viriale, peut être exprimée sous la forme de la somme de trois termes : (*i*) une contribution d'un laplacien connue explicitement en termes de densité électronique de l'état fondamental; (*ii*) un partie cinétique que l'on peut dériver à partir du comportement «practiquement diagonal» de la matrice de densité du premier ordre et (*iii*) une partie des interactions électron–électron qui implique la fonction de corrélation d'une paire électronique. À la suite du travail de Holas et March, ceci permet d'exprimer le potentiel de corrélation d'échange de la théorie de la densité fonctionnelle en termes de matrices de densité d'ordre peu élevé. Finalement, on considére briévement la possibilité d'échelonner les interactions électron–électron ainsi que la formula de connexion adiabatique dans la théorie de la densité fonctionnelle. De tels arguments d'échelonnage conduisent à une correction cinétique à la forme de Harbola–Sahni du potentiel uniquement d'échange.

Mots clés : force externe, densité du premier ordre, fonction d'une paire électronique.

[Traduit par la rédaction]

1. Introduction

Richard Bader spent a year in Europe around 1980, and half of that period in the Theoretical Chemistry Department in Oxford. I hope we were not too sleepy when Richard arrived: we were certainly wide awake when he left!! For me, that visit and the friendship that built up as a result were very important. We found opportunity to interact, even though Richard was very busy with "Atoms in Molecules" theory (1) and paid many visits to other departments in the U.K. and Europe during his stay. Two things resulted directly from our scientific collaboration: (*i*) a joint contribution in Physics Letters (2) that addressed the question of the relation of the chemical potential μ of density functional theory to the ionization potential I and (*ii*) a short piece in my review (3) on "Topology of Molecular Charge Distributions," a topic I could not have included at that time without his help and advice. These two things have influenced my own thinking a lot and will provide some focal points for the present article in this issue honouring Richard.

Let us start by contrasting the local chemical potential equation, referred to in (*i*) above, with the local energy equation. The first of these equations is the Euler–Lagrange equation of density functional theory (DFT) while the second comes directly from the many-electron Schrödinger equation. In both cases the discussion below will be confined almost exclusively to the ground state, and the second equation referred to above can be viewed as expressing the ground-state energy E of the atom or molecule under consideration as $E = H\Psi/\Psi$, with H the many-electron Hamiltonian. Of course, the N-electron wave function Ψ should be antisymmetrical in the interchange of space plus spin coordinates for any pair of electrons (spin will usually be suppressed below

Received September 27, 1995.

This paper is dedicated to Professor Richard F.W. Bader on the occasion of his 65th birthday.

N.H. March.[1] 6, Northcroft Road, Egham, Surrey TW20 ODU, England.

[1] Emeritus Professor, Oxford University, England.

for notational convenience). But whereas the local chemical potential equation can be written formally as

$$[1] \qquad \mu = \text{K.E}|_r + \text{P.E}|_r$$

where the kinetic and potential terms, dependent on a single position vector $\boldsymbol{r}$, are to be defined precisely below; the local energy E above involves N vectors. However, by introducing low-order density matrices, we shall show that considerable reduction of these variables is also again feasible (4, 5).

2. Definitions of density matrices and local energy equation

Let us first define the density matrices in terms of the many-electron wave function (6–8). Then an alternative, and of course equivalent, definition will be given in the language of second quantization and this will be employed to derive the local energy in terms of density matrices.

The second-order density matrix $\gamma_2(\boldsymbol{r}_1,\boldsymbol{r}_2;\boldsymbol{r}'_1,\boldsymbol{r}'_2)$ is defined from the normalized, anti-symmetric N-electron wave function by

$$[2] \qquad \gamma_2(\boldsymbol{r}_1, \boldsymbol{r}_2; \boldsymbol{r}'_1, \boldsymbol{r}'_2) = \frac{N(N-1)}{2} \int \Psi^*(\boldsymbol{r}_1, \boldsymbol{r}_2, \boldsymbol{r}_3 \ldots \boldsymbol{r}_N) \times \Psi(\boldsymbol{r}'_1, \boldsymbol{r}'_2, \boldsymbol{r}_3 \ldots \boldsymbol{r}_N)\mathrm{d}\boldsymbol{r}_3 \ldots \mathrm{d}\boldsymbol{r}_N$$

The other central quantity for the present study is the first-order density matrix $\gamma(\boldsymbol{r}_1,\boldsymbol{r}'_1)$. This is defined by

$$[3] \qquad \gamma(\boldsymbol{r}_1, \boldsymbol{r}'_1) = N \int \Psi^*(\boldsymbol{r}_1, \boldsymbol{r}_2 \ldots \boldsymbol{r}_N) \times \Psi(\boldsymbol{r}'_1, \boldsymbol{r}_2 \ldots \boldsymbol{r}_N)\mathrm{d}\boldsymbol{r}_2 \ldots \mathrm{d}\boldsymbol{r}_N$$

The basic quantity of density functional theory (DFT) — the electron number density $n(\boldsymbol{r})$ — is evidently the diagonal element $\gamma(\boldsymbol{r},\boldsymbol{r})$ of the first-order density matrix. The diagonal element of the second-order matrix is the important electronic pair correlation function $n_2(\boldsymbol{r},\boldsymbol{r}') = \gamma_2(\boldsymbol{r},\boldsymbol{r}';\boldsymbol{r},\boldsymbol{r}')$. For a single determinant ground-state wave function, such as obtains in the Slater–Kohn–Sham reference system or in the Hartree–Fock method, the first-order density matrix is idempotent, i.e., $\gamma^2 = \gamma$. For a fully interacting electronic assembly, this equality is replaced by the inequality $\gamma^2 < \gamma$ reflecting the Pauli Principle requirements.

2.1 Alternative and equivalent definitions: second quantized form

Following Dawson and March (4), we define as an alternative to eqs. [2] and [3] the first- and second-order density matrices in the language of second quantization as ($1 \equiv \boldsymbol{r}_1$ etc):

$$[4] \qquad \gamma(1; 1') = \langle N|\psi^+(1')\psi(1)|N\rangle \equiv \langle\psi^+(1')\psi(1)\rangle$$

and

$$[5] \qquad \gamma_2(1, 2; 1', 2') = \langle N|\psi^+(1')\psi(2')\psi(2)\psi(1)|N\rangle \equiv \langle\psi^+(1')\psi(2')\psi(2)\psi(1)\rangle$$

The three-particle or third-order density matrix constitutes an obvious generalization of the definitions [4] and [5].

Next one defines the time-dependent operator

$$[6] \qquad \psi(1, t) = \mathrm{e}^{iHt/\hbar}\psi(1)\mathrm{e}^{-iHt/\hbar}$$

which obeys the equation of motion

$$[7] \qquad ih\frac{\partial\psi(1, t)}{\partial t} = [\psi(1, t), H]$$

In this eq. [7], H denotes the second quantized Hamiltonian for interacting electrons moving in the external field generated by the nuclear framework. Employing this form of H, together with eq. [7], one is led to the result

$$[8] \qquad i\hbar\frac{\partial\psi(1, t)}{\partial t} = \frac{-\hbar^2}{2m}\nabla_1^2\psi(1, t) + V_n(1)\psi(1, t) + \int u(1-2)\psi^+(2, t)\psi(2, t)\psi(1, t)\mathrm{d}2$$

It can readily be proved that

$$[9] \qquad \gamma(1, t; 1', t) = \langle\psi^+(1', t)\psi(1, t)\rangle$$

is time independent for the Hamiltonian H defined above. Setting therefore its time derivative to zero, and using eq. [8] plus definitions one finds

$$[10] \qquad \frac{-\hbar^2}{2m}(\nabla_1^2 - \nabla_{1'}^2)\gamma(1, 1') + [V_n(1) - V_n(1')]\gamma(1, 1') + \int [u(1-2) - u(1'-2)]\gamma_2(1, 2; 1', 2)\mathrm{d}2 = 0$$

Further use of the quantity

$$[11] \qquad \left[i\hbar\frac{\partial}{\partial t}\langle\psi^+(1', t)\psi(1, t)\rangle\right]_{t=0} \equiv \langle\psi^+(1')\psi(1)H\rangle - \langle\psi^+(1')H\psi(1)\rangle$$

and eq. [8] leads then, after some further manipulation, to the desired result

$$[12] \qquad E\gamma(1:1') = \{\hat{t}_1 + V_n(\mathbf{1})\}\gamma(1:1') + 2\int \mathrm{d}2\{\hat{t}_2 + V_n(\mathbf{2}) + u(12)\}\gamma_2(\mathbf{12}; \mathbf{1'2'}) + 3\int \mathrm{d}\mathbf{2}\,\mathrm{d}\mathbf{3}\,u(\mathbf{23})\gamma_3(\mathbf{123}; 1'23)$$

Here $\hat{t}_i$ denotes simply $-\frac{1}{2}\nabla_i^2$. Next we integrate both sides of eq. [12] over $\mathrm{d}\mathbf{1}$ (after replacing $1'$ by 1)

$$[13] \qquad EN = \int \mathrm{d}\mathbf{1}\{\hat{t}_1 + V_n(\mathbf{1})\}\gamma(\mathbf{1}:1') + 2\int \mathrm{d}\mathbf{1}\,\mathrm{d}\mathbf{2}\{\hat{t}_2 + V_n(\mathbf{2}) + u(12)\}\gamma_2(\mathbf{12}; \mathbf{12'}) + 3\int \mathrm{d}\mathbf{1}\,\mathrm{d}\mathbf{2}\,\mathrm{d}\mathbf{3}\,u(\mathbf{23})\gamma_3(\mathbf{123}; 123)$$

Using reduction properties of density matrices, we can

rewrite eq. [13] as

$$[14]\qquad EN = \left(1+2\frac{N-1}{2}\right)\int \mathrm{d}\mathbf{1}\{\hat{t}_1 + v(1)\}\gamma(\mathbf{1};\mathbf{1}') + \left(2+3\frac{N-2}{3}\right)\int \mathrm{d}\mathbf{1}\,\mathrm{d}\mathbf{2}\,u(\mathbf{12})\gamma_2(\mathbf{12};\mathbf{12})$$

i.e., the well-known expression for the total energy in terms of γ and γ_2.

Having established that eq. [12] leads back to the correct result, eq. [14], for the total energy of the N-electron system, the final step in obtaining the local energy equation paralleling the chemical potential eq. [1] is to put $\mathbf{1}' = 1$ in eq. [12] and to divide both sides by the electron density $n(\boldsymbol{r})$. Then one has the local energy equation, with $t(\boldsymbol{r})$, the kinetic energy density, as (9, 10)

$$[15]\qquad E = \frac{t(\boldsymbol{r})}{n(r)} + V_n(\boldsymbol{r}) + 2\int \mathrm{d}2(\hat{t}_2 + V_n(2) + u(12))\gamma_2(12;12')/n(r) + 3\int \mathrm{d}2\,\mathrm{d}3\,u(23)\gamma_3(123;1'23)/n(r)$$

As already anticipated, this equation now expresses the local energy E, constant throughout the charge cloud of the molecule, as a sum of terms, each of which depends only on a single vector $\boldsymbol{r}$, just as in eq. [1] for μ, but which involve individually density matrices up to, and including, order 3.

One obvious use of eq. [15] would be to test an approximate many-electron wave function of an atom. One would have to integrate the wave function down according to eq. [3], but once the density matrices are known one would want to know how great was the variation with position $\boldsymbol{r}$ of the right-hand side of eq. [15].

Below, however, we shall explore the consequences of eq. [15] in the Hartree–Fock limit.

2.2 Local energy equation: reduction via Hartree–Fock approximation

As Dawson and March (4) emphasized, the Hartree–Fock (HF) approximation introduced into the local energy equation leads to the cancellation of the energy E from that equation. We can then write, in HF theory, with $V_n(\boldsymbol{r})$ the potential energy of the nuclear framework and $V_e(\boldsymbol{r})$ that created electrostatically by the ground-state electron density $n(\boldsymbol{r})$:

$$[16]\qquad t(\boldsymbol{r}) + V_n(\boldsymbol{r})n(\boldsymbol{r}) + V_e(\boldsymbol{r})n(\boldsymbol{r}) - \varepsilon_x(\boldsymbol{r}) = \frac{-\hbar^2}{2m}\int \gamma(\boldsymbol{r},\boldsymbol{r}_2)\nabla^2_{r_2}\gamma(\boldsymbol{r}_2,\boldsymbol{r}) + \int V_n(\boldsymbol{r}_2)\gamma^2(\boldsymbol{r},\boldsymbol{r}_2)\mathrm{d}\boldsymbol{r}_2 - \int u(|\boldsymbol{r}_3-\boldsymbol{r}_2|)\gamma(\boldsymbol{r},\boldsymbol{r}_2)\gamma(\boldsymbol{r}_3,\boldsymbol{r})\mathrm{d}\boldsymbol{r}_2\mathrm{d}\boldsymbol{r}_3 + \int u(|\boldsymbol{r}_3-\boldsymbol{r}_2|)\gamma^2(\boldsymbol{r},\boldsymbol{r}_2)n(\boldsymbol{r}_3)\mathrm{d}\boldsymbol{r}_2\mathrm{d}\boldsymbol{r}_3$$

The left-hand side involves terms that are evidently clear-cut contributions of the form of energy densities; e.g., $t(\boldsymbol{r})$ is the kinetic and $\varepsilon_x(\boldsymbol{r})$ the exchange contribution.

If we now therefore integrate this eq. [16] we find, by making use of the idempotency of the HF first-order density matrix $\gamma(\boldsymbol{r},\boldsymbol{r}_1)$, for the sum of total kinetic plus exchange energies $T+A$:

$$[17]\qquad T + A = \int \gamma(\boldsymbol{r}_2,\boldsymbol{r}_3)\times\left[\frac{-\hbar^2}{2m}\nabla^2_{r_2}\gamma(\boldsymbol{r}_2,\boldsymbol{r}_3) - u(|\boldsymbol{r}_3-\boldsymbol{r}_2|)\right]\mathrm{d}\boldsymbol{r}_2\mathrm{d}\boldsymbol{r}_3$$

One can now drop the integration over $\boldsymbol{r}_3$ to write

$$[18]\qquad t(\boldsymbol{r}) + \varepsilon_x(\boldsymbol{r}) = \int \gamma(\boldsymbol{r}_2,\boldsymbol{r})\times\left[\frac{-\hbar^2}{2m}\nabla^2_{r_2}\gamma(\boldsymbol{r}_2,\boldsymbol{r}) - u(|\boldsymbol{r}-\boldsymbol{r}_2|)\right]\mathrm{d}\boldsymbol{r}_2 + \text{term integrating to zero through all space}$$

This is a somewhat different form from the more conventional expression given by Dawson and March (4).

3. Asymptotic results for exchange and kinetic energies

We shall discuss in this section, motivated by the forms of the local energy equation, and especially eqs. [15] and [18], the asymptotic behaviour far from all nuclei of the kinetic energy density $t(\boldsymbol{r})$ and the exchange energy density $\varepsilon_x(\boldsymbol{r})$. Taking the latter, and working in the Hartree–Fock approximation, one has

$$[19]\qquad A = \int \varepsilon_x(\boldsymbol{r})\mathrm{d}\boldsymbol{r} = -\frac{1}{4}e^2\int\frac{\gamma(\boldsymbol{r},\boldsymbol{r}_1)^2}{|\boldsymbol{r}-\boldsymbol{r}_1|}\mathrm{d}\boldsymbol{r}\,\mathrm{d}\boldsymbol{r}_1$$

The writer, in earlier work (11), defined $\varepsilon_x(\boldsymbol{r})$ by

$$[20]\qquad \varepsilon_x(\boldsymbol{r}) = -\frac{1}{4}e^2\int\frac{\gamma(\boldsymbol{r},\boldsymbol{r}_1)^2}{|\boldsymbol{r}-\boldsymbol{r}_1|}\mathrm{d}\boldsymbol{r}_1$$

which clearly, from eq. [19], integrates to yield the total exchange energy A, as any definition of the exchange energy density must. Furthermore $\varepsilon_x(\boldsymbol{r})$ is always negative at all $\boldsymbol{r}$.

Now we are interested in the asymptotic behaviour of $\varepsilon_x(\boldsymbol{r})$ at large r. As was pointed out in ref. 11, one can, for sufficiently large $\boldsymbol{r}$, inside the integral in eq. [20], neglect $\boldsymbol{r}_1$ relative to $\boldsymbol{r}$. Then using the idempotency of the Hartree–Fock first-order density matrix, we find the asymptotic result

$$[21]\qquad \varepsilon_x(\boldsymbol{r})|_{r\to\infty} = -\frac{1}{2}\frac{e^2}{r}n(\boldsymbol{r})$$

a result that has also been discussed by Umrigar and Gonze (12).

Turning briefly to the kinetic energy density $t(\boldsymbol{r})$, we note that the asymptotic form was determined by Tal and Bader (13), the large r form corresponding to eq. [21] for exchange being

$$[22]\qquad t(\boldsymbol{r}) = In(\boldsymbol{r})$$

where I is the (exact) ionization potential. It is relevant here to add that the limiting form of the kinetic energy density as $\boldsymbol{r}$ tends to zero was discussed by Bader and Beddall (14).

4. Force theorems in relation to local chemical potential equation

For simplicity we start from the one-dimensional case.

4.1 Equation of motion of density matrix: one dimensional without interactions

March and Young (15) gave a treatment of force by starting from the equation of motion of the density matrix. These workers were dealing with one-dimensional motion of N electrons moving independently in a common potential energy $V(x)$. Then, putting the electron–electron interaction $u = 0$ in eq. [10], one is led to the one-dimensional equation of motion:

$$[23] \qquad \frac{\partial^2\gamma(x, x')}{\partial x^2} - \frac{\partial^2\gamma(x, x')}{\partial x'^2} = \frac{2m}{\hbar^2}[V(x) - V(x')]\gamma(x, x')$$

Introducing sum and difference coordinates $\xi = \frac{1}{2}(x+x')$ and $\eta = \frac{1}{2}(x-x')$, eq. [23] becomes

$$[24] \qquad \frac{\partial^2}{\partial\xi\partial\eta}\gamma(\xi, \eta) = \frac{2m}{\hbar^2}[V(\xi+\eta) - V(\xi-\eta)]\gamma(\xi, \eta)$$

Expanding about the diagonal $\eta = 0$, and using the definition of kinetic energy density $t(x)$ already discussed, March and Young obtained the so-called differential form of the virial theorem

$$[25] \qquad \frac{\partial t}{\partial x} = -\frac{1}{2}n(x)\frac{\partial V(x)}{\partial x} + \frac{1}{8}\frac{\partial^3 n}{\partial x^3}$$

They pointed out that by multiplying by x and integrating through the whole of space one recovered the usual virial theorem: of course an integral relation rather than the point-to-point relation, eq. [25].

The recent work of Holas and March (16) has led one to reinterpret this equation [25] as an expression for the force $-\partial V/\partial x$:

$$[26] \qquad -\frac{\partial V}{\partial x} = \frac{2}{n(x)}\frac{\partial t(x)}{\partial x} - \frac{1}{4n(x)}\frac{\partial^3 n(x)}{\partial x^3}$$

This scalar equation for the force $f = -\partial V/\partial x$ is evidently the sum of two parts. One, called f_L for reasons to emerge below, is determined solely by the electron density $n(x)$ as

$$[27] \qquad f_L = -\frac{1}{8n(x)}\frac{\partial^3 n(x)}{\partial x^3}$$

while the other is evidently a kinetic contribution, say f_K. Though formal density functional theory assures us that the kinetic energy density t is indeed also a functional of $n(x)$, that remains unknown at the time of writing. These expressions f_L and f_K will be generalized below to their vector counterparts for interacting electrons in three dimensions.

However, before doing so, it is of interest to provide here some historical background, involving intimately the research of Richard Bader. The derivation of a local form of the quantum-mechanical virial theorem for the general case of a time-dependent system was given by Bader (17). His argument was based on the divergence equations satisfied by the spatial components of the energy–momentum tensor of the Schrödinger field. The result was written in terms of what is now called the quantum stress tensor. This derivation was reviewed and expanded upon by Bader and Nguyen-Dang (18). Bader's own book (1) presents in fact a detailed account of the variational derivation of the atomic statement of the virial theorem and its differential or local form. In the above sources, the integrated and differential statements of the virial theorem are related to the corresponding integrated and local theorems for the Ehrenfest force. These theorems, and corresponding theorems for any observable, are derived from a single fundemental variational principle. Anticipating the following section, we finally note that variational derivations lead naturally to the quantum stress tensor, whereas (see eq. [28] below) the recent paper of Holas and March (16), to be described, works with the related kinetic energy density tensor.

4.2 Differential virial theorem for interacting electrons in three dimensions

We wish to effect the generalization of eq. [25] to interacting electrons. Then, in three dimensions a differential virial theorm represents an exact, local (at space point $\boldsymbol{r}$) relation involving the external potential $v(\boldsymbol{r})$, the e–e interaction potential $u(\boldsymbol{r},\boldsymbol{r}')$, the diagonal elements of the 1st and 2nd order density motion (DMs), $n(\boldsymbol{r})$ and $n_2(\boldsymbol{r},\boldsymbol{r}')$, and the 1st order DM$\gamma(\boldsymbol{r}_1;\boldsymbol{r}_2)$ "close to its diagonal," for a particular system. As Holas and March (16) have shown, it is a very useful tool for establishing various exact relations for a many-electron system. The mentioned dependence on γ may be written in terms of the kinetic energy density tensor, defined as

$$[28] \qquad t_{\alpha\beta}(\boldsymbol{r}; [x]) = \frac{1}{4}\left(\frac{\partial^2}{\partial r'_\alpha \partial r''_\beta} + \frac{\partial^2}{\partial r'_\beta \partial r''_\beta}\right) \times \gamma(\boldsymbol{r}+\boldsymbol{r}'; \boldsymbol{r}+\boldsymbol{r}'')|_{\boldsymbol{r}'=\boldsymbol{r}''=0}$$

This is a real, symmetric tensor, the trace of which is the non-negative kinetic energy density (scalar)

$$[29] \qquad t(\boldsymbol{r}; [\gamma]) = \sum_{\alpha=1}^{3} t_{\alpha\alpha}(\boldsymbol{r}; [\gamma]) \geq 0$$

leading to the global kinetic energy

$$[30] \qquad T = \langle\Psi|\hat{T}|\Psi\rangle = \tilde{T}[\gamma] = \int d^3 r t(\boldsymbol{r}; [\gamma])$$

The differential virial theorem, obtained in refs (16) and (19), has the form

$$[31] \qquad n(\boldsymbol{r})\frac{\partial}{\partial r_\alpha}v(\boldsymbol{r}) + 2\int d^3 r' n_2(\boldsymbol{r}, \boldsymbol{r}')\frac{\partial}{\partial r_\alpha}u(\boldsymbol{r}, \boldsymbol{r}') - \frac{1}{4}\nabla^2\frac{\partial}{\partial r_\alpha}n(\boldsymbol{r}) + 2\sum_\beta \frac{\partial}{\partial r_\beta}t_{\alpha\beta}(\boldsymbol{r}; [\gamma]) = 0$$

No assumptions concerning potentials $u(\boldsymbol{r},\boldsymbol{r}')$ and $v(\boldsymbol{r})$ (like

Coulombic character), except that they lead to bounded solutions Ψ of the Schrödinger equation, were involved in obtaining relation [31]. The density matrices occurring there: $n_2(\boldsymbol{r},\boldsymbol{r}')$, $\gamma(\boldsymbol{r};\boldsymbol{r}')$, and $n(\boldsymbol{r})$ are generated from the normalized Ψ as set out in Sect. 2 above.

It should be mentioned also that no assumption concerning the nature (as GS or excited-state) of the solution Ψ or a degeneracy of its energy level E was invoked in the derivation of eq. [31] by Holas and March (16, 19).

4.3 Force equation for interacting electrons related to local chemical potential equation

The differential virial theorem, eq. [31] can be rewritten following ref. 16 as

$$[32] \qquad \boldsymbol{\nabla}\, v(\boldsymbol{r}) = -\boldsymbol{f}(\boldsymbol{r};\,[u,\,n,\,\gamma,\,n_2])$$

where the following "force" field has been introduced:

$$[33] \qquad \boldsymbol{f}(\boldsymbol{r};\,[u,\,n,\,\gamma,\,n_2]) = \left\{ -\frac{1}{4}\,\boldsymbol{\nabla}\,\nabla^2 n(\boldsymbol{r}) + z(\boldsymbol{r};\,[\gamma]) + 2 \times \int \mathrm{d}^3 r'\, n_2(\boldsymbol{r},\boldsymbol{r}')\,\boldsymbol{\nabla}\, u(\boldsymbol{r},\boldsymbol{r}') \right\} \Big/ n(\boldsymbol{r})$$

with the vector field z having components z_α defined in terms of the kinetic energy density tensor in eq. [28] by

$$[34] \qquad z_\alpha(\boldsymbol{r};\,[\gamma]) = 2 \sum_\beta \frac{\partial}{\partial r_\beta}\, t_{\alpha\beta}(\boldsymbol{r};\,[\gamma])$$

The first term on the right-hand side of eq. [33] involves the Laplacian (L) of the electron density $n(\boldsymbol{r})$. This is then the vector generalization of the scalar f_L introduced in eq. [27]. The term with the vector field z is evidently kinetic, the generalization to vector form of the force f_K discussed in one dimension earlier. That discussion was for independent electrons. Due to the inclusion of electron–electron interaction $u(\boldsymbol{r},\boldsymbol{r}') = e^2/|\boldsymbol{r}-\boldsymbol{r}'|$, there is now a third vectorial contribution to the "total" force $\boldsymbol{f}$ in eq. [32]: namely the electron–electron (ee) $\boldsymbol{f}_{ee}$ given in terms of the electronic pair function $n_2(\boldsymbol{r},\boldsymbol{r}')$ and the interaction u by

$$[35] \qquad \boldsymbol{f}_{ee} = \frac{2}{n(\boldsymbol{r})} \int \mathrm{d}^3 r'\, n_2(\boldsymbol{r},\boldsymbol{r}')\,\boldsymbol{\nabla}\, u(\boldsymbol{r},\boldsymbol{r}')$$

This is the point to relate to the local chemical potential equation, but now in the form

$$[36] \qquad \mu = \frac{\delta F}{\delta n(\boldsymbol{r})} + V_n(\boldsymbol{r})$$

where F is the universal, as yet unknown, functional of $n(\boldsymbol{r})$ introduced by Hohenberg and Kohn (20), with $V_n(\boldsymbol{r})$ the nuclear potential energy only, in contrast to the form in eq. [1]. Differentiating with respect to $\boldsymbol{r}$, and noting again that μ is constant throughout the entire electronic cloud, one recognizes that the force $\boldsymbol{f}$ above has the alternative form

$$[37] \qquad \boldsymbol{f} = \frac{\partial}{\partial \boldsymbol{r}} \left\{ \frac{\delta F}{\delta n(\boldsymbol{r})} \right\}$$

This equation therefore demonstrates that the force $\boldsymbol{f}$ is a functional of the ground-state density, as is to be anticipated, in fact, from the formal theory of Hohenberg and Kohn (20). Unfortunately, of the three terms comprising $\boldsymbol{f}$ above, only f_L is presently known explicitly in terms of the density $n(\boldsymbol{r})$. f_K, the kinetic contribution to the force, involves the "near-diagonal" behaviour of the first-order density matrix $\gamma(\boldsymbol{r},\boldsymbol{r}')$ while evidently, from eq. [35], the electron–electron force term $\boldsymbol{f}_{ee}$ depends on the diagonal element of the second-order density matrix, i.e., the pair function $n_2(\boldsymbol{r},\boldsymbol{r}')$. Nevertheless, it is useful to proceed to extract the exact exchange-correlation potential $V_{xc}(\boldsymbol{r})$ of density functional theory, defined through the third form of chemical potential equation:

$$[38] \qquad \mu = \frac{\delta T_s}{\delta n(\boldsymbol{r})} + V_{\mathrm{Hartree}}(\boldsymbol{r}) + V_{xc}(\boldsymbol{r})$$

Here T_s is the single-particle kinetic energy only, correlation kinetic energy being subsumed into $V_{xc}(\boldsymbol{r})$, which is related to the exchange-correlation energy E_{xc} by the functional derivative relation

$$[39] \qquad V_{xc}(\boldsymbol{r}) = \frac{\delta E_{xc}}{\delta n(\boldsymbol{r})}$$

T_s is customarily calculated via the Slater–Kohn–Sham (SKS) orbitals, which in turn can be utilized to construct, for this reference system, an idempotent density matrix $\gamma_{SKS}(\boldsymbol{r},\boldsymbol{r}')$ already referred to.

5. Exact expression for the exchange-correlation potential

Equation [32] may be viewed as a differential equation for the potential $v(\boldsymbol{r})$. Because $\boldsymbol{f}(\boldsymbol{r}) = -\boldsymbol{\nabla}\, v(\boldsymbol{r})$, the force field $\boldsymbol{f}(\boldsymbol{r})$ is conservative. Therefore, following Holas and March (16) the potential at point $\boldsymbol{r}_0$, say, is the work done in bringing an electron from infinity to $\boldsymbol{r}_0$ against the force field $\boldsymbol{f}(\boldsymbol{r})$:

$$[40] \qquad v(\boldsymbol{r}_0) = -\int_\infty^{\boldsymbol{r}_0} \mathrm{d}\boldsymbol{r} \cdot \boldsymbol{f}(\boldsymbol{r})$$

Since $\boldsymbol{f}(\boldsymbol{r})$ is conservative, the value of the line integral in eq. [40] does not depend on the path of integration chosen. Note that eq. [43] has been written such that $v(\infty) = 0$: a standard choice of gauge for the potential.

By calculating $\boldsymbol{f}$ in the exact fully interacting system and subtracting the same force, but now calculated with exact density matrices in $\boldsymbol{f}$ being replaced by SKS reference density matrices, Holas and March (16) construct $V_{xc}(\boldsymbol{r})$ as a line integral in terms of density matrices. This is a formally exact result, but while it avoids the need for functional differentiation such as is exhibited in eq. [39], to turn it into a density functional theory requires the solution of a difficult many-electron problem. This involves as the first step the relation between the first- and second-order density matrices of a fully interacting electronic assembly. However, a start has already been made on this problem (21–23).

5.1 Exchange-only potential: scaling of electron–electron interactions

Though the exact result above may seem very formal, it was stressed by Holas and March (16) that if the simplest con-

ceivable approximation was then made, namely, to replace all interacting density matrices with their SKS counterparts, then one regained the Harbola–Sahni (24) exchange-only potential. Though their potential is known to be often very accurate, it is nevertheless true that the approximations made in the formally exact line integral result destroy the rigorous path-independence property.

Therefore, very recently, Levy and March (25) generalized the Holas–March (16) work to include the scaling of the electron–electron interactions such that e^2/r_{ij} becomes $\lambda e^2/r_{ij}$. By then taking an appropriate limit of the exact exchange correlation for general λ between 0 and 1, as λ tends to zero, they exhibit the kinetic correction to the Harbola–Sahni result that is required to restore the path independence. Some approximate arguments are given in ref. 25 that throw light on the reasons why this kinetic "correction" is often only a small fraction of the Harbola–Sahni contribution to the exchange-only potential.

5.2 Adiabatic connection formula

In the context of electron–electron scaling, we shall briefly summarize below recent work by Levy et al. (26) on the so-called adiabatic connection formula for the exchange-correlation energy. The formula relates, via integration between 0 and 1 (see eq. [41] below), the potential energy U_{xc} at coupling parameter λ, to the total exchange-correlation energy E_{xc} in eq. [39]. Levy et al. (26) find a linear approximation in λ to become exact in the Thomas–Fermi–Dirac limit of atoms and molecules with large numbers of electrons.

The early references on the idea of an adiabatic connection include those of Harris and Jones (27), Langreth and Perdew (28), Gunnarsson and Lundqvist (29), Levy (30), and Harris (31). Following the route set out, for instance, in the book by Parr and Yang (8), the exchange-correlation energy functional can be written as

$$[41] \qquad E_{xc}[n] = \int_0^1 d\lambda U_{xc}^{\lambda}[n]$$

In this equation, $U_{xc}^{\lambda}[n]$ is defined by

$$[42] \qquad U_{xc}^{\lambda}[n] = \langle \Psi_n^{\lambda} | V_{ee} | \Psi_n^{\lambda} \rangle - J[n]$$

Here $U_{xc}^{\lambda}[n]$ is the potential energy contribution to $E_{xc}[n]$ and $J[n]$ is the Coulomb energy. $\hat{V}_{ee}$ is the electron–electron repulsion operator, and Ψ_n^{λ} is the wave function of a Hamiltonian $\hat{H}_{\lambda}$ that represents a system in which the electron–electron interaction is scaled with λ as discussed already:

$$[43] \qquad \hat{H}_{\lambda} = \hat{T} + \lambda V_{ee} + \sum_i V_{\lambda}(\boldsymbol{r}_i)$$

It also minimizes, for fixed electron density n, the constrained search expression of Levy (32, 33). In the above approach, $n(\boldsymbol{r})$ is to be interpreted as the exact density of the fully interacting ($\lambda = 1$) electronic assembly.

Becke (34) has used the above approach in the context of a two-point integration formula. He writes eq. [41] as (35):

$$[44] \qquad E_{xc}[n] \sim \frac{1}{2}(U_{xc}^0 + U_{xc}^1)$$

where U_{xc}^0 is the exchange energy associated with the SKS reference first-order density matrix while U_{xc}^1 is the potential enery contribution to the exchange-correlation energy of the fully interacting system. This all led Becke to his half-and-half functional, which was the forerunner of his valuable three-parameter functional (36). It is the revival of interest in adiabatic scaling that has led Levy et al. (26) to examine some scaled Hamiltonians in the context of Thomas–Fermi theory and to introduce some new elements into the adiabatic connection approach in SKS theory. For instance, these authors provide a formula that enables use to be made of nonlocal exchange-correlation potential energies, such as those from gradient expansions, for U_{xc}^1 in eq. [44].

6. Discussion and summary

The spatial derivative of the formal chemical potential, eq. [36], yields the external force. By combining this with the differential virial theorem, a force balance equation emerges, the sum of Laplacian, kinetic, and electron–electron force terms appearing. While, in principle, from the theorems of DFT, these are functionals of the ground-state electron density $n(\boldsymbol{r})$, only for the Laplacian contribution is that functional known. However, as Holas and March (16) have shown, the kinetic term is fixed by the "near-diagonal" first-order density matrix. The third, electron–electron interaction term is determined by the diagonal form of the second-order density matrix, i.e., the electronic pair function $n_2(\boldsymbol{r},\boldsymbol{r}')$.

Integrating this equation yields an exchange-correlation potential in the form of a line integral, such as given in eq. [40]. The simplest approximation then leads back to the Harbola–Sahni exchange-only potential, which is, however, known to be path dependent. Levy and March (25) have exhibited, by generalizing the Holas–March result to include the scaling parameter λ, the kinetic correction that, when added to the Harbola–Sahni result, restores the required path independence in the exchange-only potential.

More briefly, the local energy equation has also been discussed and has motivated a discussion of the asymptotic forms of exchange (11) and kinetic energy densities (19) far from nuclei. Finally, new avenues also seem to be opening up in connection with scaling of the strength of the electron–electron interactions, and in particular through adiabatic connection formulae. These involve the potential energy of the exchange-correlation energy, the functional derivative of which was shown by March and Bader (2) to determine the "correction" to the ionization potential I in the chemical potential equation. In the adiabatic connection formulae, one can now use nonlocal exchange correlation potential energies, usually through gradient approximations. Richard Bader was ahead of his time, of course, in recognizing the central role of $\nabla n(\boldsymbol{r})$, and the Laplacian $\nabla^2 n(\boldsymbol{r})$ in problems of molecular electronic structure (1). In the context of the present work, in which density functional theory is approached via density matrices (15, 16), it is highly relevant also to point here to Richard Bader's philosophy regarding the one-electron density matrix. This is summarized in his very recent paper "Chemistry and the Near-Sighted Nature of the One-Electron Density Matrix" (37).

Acknowledgments

The writer is most grateful to Dr A. Holas (Warsaw) for

much fruitful collaboration, and numerous invaluable discussions on the general area embraced by the present paper. My thanks are also due to Professors M. Levy and N.C. Handy for generously involving me in electron–electron interaction scaling theory. The Leverhulme Trust (U.K.) is thanked for financial support. Finally, both referees are to be acknowledged for contributing very helpful and constructive comments on the original manuscript. All their comments are now embodied in the final version.

References

1. R.F.W. Bader. Atoms in molecules: a quantum theory. Clarendon Press, Oxford. 1990.
2. N.H. March and R.F.W. Bader. Phys. Lett. **78A**, 242 (1980).
3. N.H. March. Theor. Chem. (London), **4**, 92 (1981).
4. K.A. Dawson and N.H. March. J. Chem. Phys. **81**, 5850 (1984).
5. L. Cohen and C. Frishberg. Phys. Rev. A: Gen. Phys. **13**, 927 (1976); J. Chem. Phys. **65**, 4234 (1976).
6. P.O. Löwdin, Phys. Rev. **97**, 1474 (1955).
7. P.O. Löwdin. Rev. Mod. Phys. **34**, 80 (1962).
8. R.G. Parr and W. Yang. Density functional theory of atoms and molecules. University Press, Oxford. 1989.
9. A. Holas and N.H. March. Proc. Paris Conf. on Density functional theory. 1995. Int. J. Quantum Chem. To appear.
10. A. Holas and N.H. March. *In* Topics in current chemistry. *Edited by* R. Nalewajski. Springer, Berlin. 1996.
11. N.H. March. Phys. Rev. A: Gen. Phys. **36**, 5077 (1987).
12. C.J. Umrigar and X. Gonze. Phys. Rev. A: At. Mol. Opt. Phys. **50**, 3827 (1994).
13. Y. Tal and R.F.W. Bader. Int. J. Quantum Chem. Symp. **12**, 153 (1978); A. Holas and N.H. March. J. Mol. Struct. (Theochem). In press.
14. R.F.W. Bader and P.M. Beddall. J. Chem. Phys. **56**, 3320 (1972).
15. N.H. March and W.H. Young. Nucl. Phys. **12**, 237 (1959).
16. A. Holas and N.H. March. Phys. Rev. A: At. Mol. Opt. Phys. **51**, 2040 (1995).
17. R.F.W. Bader. J. Chem. Phys. **73**, 2871 (1980).
18. R.F.W. Bader and T.T. Nguyen-Dang. Adv. Quantum Chem. **14**, 63 (1981).
19. A. Holas and N.H. March. J. Mol. Struct. (Theochem), **121**, 239 (1994).
20. P. Hohenberg and W. Kohn. Phys. Rev. [Sect.] B, **136**, 864 (1964).
21. W.R. Thorson, J.H. Choi, and R.B. Hake. Int. J. Quantum Chem. Symp. **1S**, 487 (1967).
22. C. Valdemoro. Phys. Rev. A: At. Mol. Opt. Phys. **45**, 4462 (1992).
23. D.J. Klein and N.H. March. J. Mol. Struct. (Theochem). In press.
24. M.K. Harbola and V. Sahni. Phys. Rev. Lett. **62**, 489 (1989).
25. M. Levy and N.H. March. to be published.
26. M. Levy, N.H. March, and N.C. Handy. J. Chem. Phys. **104**, 1989 (1996).
27. J. Harris and R.O. Jones. J. Phys. F: Met. Phys. **4**, 1170 (1974).
28. D.C. Langreth and J.P. Perdew. Phys. Rev. B: Condens. Matter, **21**, 5469 (1980).
29. O. Gunnarsson and B.I. Lundqvist. Phys. Rev. B: Solid State, **13**, 4274 (1976).
30. M. Levy. *In* Density functional theory. *Edited by* J. Keller and J.L. Gasquez. Springer-Verlag, New York. 1983.
31. J. Harris. Phys. Rev. A: Gen. Phys. **29**, 1648 (1984).
32. M. Levy. Proc. Natl. Acad. Sci. U.S.A. **76**, 6062 (1979).
33. M. Levy. Phys. Rev. A: Gen. Phys. **26**, 1200 (1982).
34. A.D. Becke. J. Chem. Phys. **98**, 1372 (1993).
35. A.D. Becke. J. Chem. Phys. **88**, 1053 (1988).
36. A.D. Becke. J. Chem. Phys. **98**, 5648 (1993).
37. R.F.W. Bader. Int. J. Quantum Chem. **56**, 409 (1995).

Topologically partitioned dynamic polarizabilities using the theory of atoms in molecules

Christof Hättig, Georg Jansen, Bernd A. Heß, and János G. Ángyán

Abstract: Frequency-dependent distributed polarizabilities have been determined from time-dependent Hartree–Fock calculations, using the partitioning of the molecular space suggested by Bader's topological theory of atoms in molecules. The basis set dependence of the distributed dynamic polarizabilities is analyzed in terms of the first few Cauchy moments, for the carbon monoxide, water, cyanogen, urea and benzene molecules. Two alternative relocalization schemes have been considered in order to reduce the number of distributed dynamic polarizability parameters. The first one, closely related to the atomic polarizability model of Bader, leads to atomic charge–dipole and dipole–dipole polarizabilities, describing the response of the molecular charge distribution to a uniform external field, in terms of atomic charges and dipoles. The second scheme, similar to that suggested by Stone, retains the fully distributed description of the dynamic charge-flow polarizabilities, while all two-center dipole–dipole and charge–dipole contributions are condensed in one-center dynamic dipole–dipole polarizabilities.

Key words: Bader-partitioning, distributed dynamic polarizabilities, Cauchy-moments, benzene, polarizability of; urea, polarizability of.

Résumé : Faisant appel à des calculs de Hartree–Fock dépendant du temps et utilisant la partition de l'espace moléculaire suggérée par la théorie topologique des atomes dans les molécules de Bader, nous avons déterminé des polarisabilités dynamiques distribuées. L'influence de la base a éte analysé en termes des premiers moments de Cauchy pour les molécules suivantes : monoxyde de carbone, eau, cyanogène, urée et benzène. Afin de réduire le nombre des paramètres de polarisabilité dynamique distribuée, deux méthodes alternatives de relocalisation ont été considérées. La première, qui est fortement apparentée au modèle de polarisabilité atomique de Bader, conduit aux polarisabilités atomiques charge–dipôle et dipôle–dipôle décrivant la réponse de la distribution de charge moléculaire à un champ externe uniforme en termes de charges et de dipôles atomiques. Le deuxième méthode, semblable à celle suggérée par Stone, maintient la description totalement distribuée des polarisabilités dynamique de flux de charges, alors que toutes les contributions dipôle–dipôle et charge–dipôle à deux centres sont réduites à des polarisabilités dynamiques dipôle–dipôle à un centre.

Mots clés : méthode de partition de Bader, polarisabilités dynamiques distribuées, moments de Cauchy, polarisabilité du benzène, polarisabilité de l'urée.

[Traduit par la rédaction]

I. Introduction

Frequency-dependent (dynamic) multipole polarizabilities, which describe the response of a molecular system under the influence of a time-dependent external multipolar field, play an important role in the interpretation of many physical phenomena. They contain information concerning, for example, the refractive index, Rayleigh scattering cross sections, and Raman intensities (1, 2), etc. Dynamic polarizabilities, taken at imaginary frequencies, can be used to calculate long-range dispersion coefficients (3), which are of outstanding importance in the theory of intermolecular interactions. Since dynamic polarizability tensors are difficult to measure experimentally, there is an increasing demand for the reliable theoretical calculation of their components.

The dynamic charge density susceptibility function, $\alpha(\boldsymbol{r},\boldsymbol{r}';\omega)$, describes the linear response of a molecular charge distribution to an arbitrary time-dependent external field (4). The multipole components of a molecular dynamic polarizability tensor, $\alpha_{lm,l'm'}(\omega)$, are related to the dynamic charge density susceptibility function via the following relationship:

$$[1] \qquad \alpha_{lm,l'm'}(\omega) = \int\int \mathrm{d}\boldsymbol{r}\mathrm{d}\boldsymbol{r}' R^0_{lm}(\boldsymbol{r})\alpha(\boldsymbol{r},\boldsymbol{r}';\omega)R^0_{l'm'}(\boldsymbol{r}')$$

Received October 13, 1995.

This paper is dedicated to Professor Richard F.W. Bader on the occasion of his 65th birthday.

C. Hättig and B.A. Heß. Institut für Physikalische und Theoretische Chemie, Universität Bonn, Wegelerstr. 12, D-53115 Bonn, Germany.
G. Jansen and J.G. Ángyán.[1] Laboratoire de chimie théorique, Université Henri Poincaré, Unité de recherche associée au Centre national de la recherche scientifique, nº 510, B.P. 239, F-54506 Vandœuvre-lès-Nancy Cedex, France.

[1] Author to whom correspondence may be addressed. Fax: +33.83.91.25.30. E-mail: angyan@lctn.u-nancy.fr

where $R^0_{lm}(\boldsymbol{r}) = R_{lm}(\boldsymbol{r} - \boldsymbol{R}_0)$ is a regular solid harmonics, taken with respect to the molecular origin $\boldsymbol{R}_0$. Obviously, by taking the above integral over the molecular volume, a certain amount of information about the details of the spatial distribution of response properties is lost. This can be a nuisance, especially in the case of relatively large, extended molecular systems. The difficulty can partially be circumvented by the concept of *distributed* polarizabilities (5), by attributing specific response parameters to atoms and to pairs of atoms (or functional groups) in the molecule. The formal definition of distributed dynamic polarizabilities involves double integration over the volumes Ω_A and Ω_B, corresponding to atoms or functional groups of the molecule:

$$[2] \qquad \alpha^{AB}_{lm,l'm'}(\omega) = \int_{\Omega_A}\int_{\Omega_B} d\boldsymbol{r}d\boldsymbol{r}' R^A_{lm}(\boldsymbol{r})\alpha(\boldsymbol{r},\boldsymbol{r}';\omega)R^B_{l'm'}(\boldsymbol{r}')$$

Once the atomic volumes, Ω_A, are defined, we have, by virtue of eq. [2], an exact partitioning of the total dynamic polarizabilities, eq. [1]. Thus the response of the molecular charge density to an external non-uniform field is described by atomic charges, dipoles (multipoles, $^{ind}Q^A_{lm}$, in general), induced by a set of multipolar field components, $F^B_{l'm'}$, acting at atom B. Accordingly, we can speak of charge–charge (charge-flow) polarizabilities, corresponding to atomic charges induced by the differences in the external potential at different atoms, charge–dipole polarizabilities, describing the atomic charge induced by the external field at different atoms, etc. Charge–multipole polarizabilities satisfy the following sum rule (5):

$$[3] \qquad \sum_A \alpha^{AB}_{00,lm} = 0$$

reflecting the fact that the effect of an external perturbation cannot change the total charge of the system.

The theory of atoms in molecules (AIM) of Bader (6, 7) constitutes an excellent general framework to partition properties of molecular systems into atomic contributions. Atomic regions, Ω_A, surrounded by the atomic surface, $S_A(\boldsymbol{r})$, are defined in an unambiguous manner on the basis of the topological features of the electron density, by the zero-flux condition $\nabla\rho(\boldsymbol{r}) \cdot \boldsymbol{n}(\boldsymbol{r}) = 0$ for $\forall \boldsymbol{r} \in S_A(\boldsymbol{r})$. Application of the principle of stationary action to these atomic regions, in fact open quantum subsystems, leads to a complete quantum mechanical description of their properties. Furthermore, it has been shown (6) that the topological definition of atoms and functional groups (as an assembly of atoms) allows one to maximize the transferability of their properties between various systems.

Application of the topological definition of atoms to partition static (zero-frequency) polarizabilities leads to a consistent set of distributed static polarizability parameters, free of any physically unjustified basis set dependence (8). In fact, distributed polarizability parameters, as obtained by various basis set partitioning schemes, were not stable enough with respect to extension of the basis set: for example, in extended basis sets the charge-flow polarizabilities became extremely large (9). Topologically partitioned polarizabilities do not vary more strongly with the basis set than do the total polarizability components. Furthermore, a recent study on a series of hydrocarbons confirms the transferability of these topologically distributed static polarizabilities (10). Calculation of intermolecular induction energies has shown that the fully distributed description leads to reasonable interaction energies even in those cases where the molecule-centered expansion of electrostatic and induction energies fails completely (11) (e.g., for the cyanogen dimer).

One-center atomic polarizabilities have been investigated recently by Bader and co-workers (12–14) by finite perturbation techniques. In contrast to the fully distributed polarizabilities, which, due to their nonlocal character, are able to describe the charge density response to a non-uniform external field, Bader's atomic polarizabilities

$$[4] \qquad \alpha^{A,mol}_{lm,l'm'}(\omega) = \int_{\Omega_A}\int d\boldsymbol{r}d\boldsymbol{r}' R^A_{lm}(\boldsymbol{r})\alpha(\boldsymbol{r},\boldsymbol{r}';\omega)R^0_{l'm'}(\boldsymbol{r}')$$

give the atomic multipole, $^{ind}Q^A_{lm}$ induced by an external field component $F_{l'm'}$ applied globally to the molecule at its origin. Therefore it is justified to call these quantities "atom–molecule" polarizabilities. For example, the application of a uniform external field F_β gives rise to induced atomic charges and dipoles, which are described by the $\alpha^{A,mol}_{q\beta}$ and $\alpha^{A,mol}_{\alpha\beta}$ charge–dipole and dipole–dipole atom–molecule polarizabilities. To cope with empirical additivity schemes, based on atomic dipole–dipole polarizabilities, the charge–dipole contributions have to be converted to atomic dipole–dipole polarizabilities (13). Unfortunately, there is no unique way to do that; therefore each case should be carefully examined in order to obtain chemically meaningful atomic polarizabilities, as has been done for hydrocarbons (14). Although Bader's atomic polarizabilities are conceptually very helpful in developing additivity and transferability schemes for atomic and group contributions, they are probably less appropriate for the calculation of intermolecular interactions, where molecules are subject to non-uniform external fields.

The present paper extends our earlier study of distributed static polarizabilities (8) to their dynamic counterparts. After a brief overview of the most important working equations, we are going to examine the basis-set sensitivity of topologically partitioned dynamic polarizability components, represented by their Cauchy moments. Since the main goal of our study is to explore the behaviour of the topological partitioning scheme, it has been judged sufficient to calculate Cauchy moments at the simple TDHF (time-dependent Hartree–Fock) level. A simple algorithm, inspired by the scheme proposed by Le Sueuer and Stone (15), is given for partial relocalization of the fully distributed nonlocal Cauchy moments, allowing us to reduce considerably the number of parameters characterizing the dynamic response properties of a molecular system.

II. Method

In full analogy with its molecular counterpart, a distributed dynamic polarizability component for real wave functions, taken at the real frequency, ω, is defined as

$$[5] \qquad \alpha^{AB}_{lm,l'm'}(\omega) = \sum_{n\neq 0} \frac{2(E_n - E_0)\langle 0|\hat{Q}^A_{lm}|n\rangle\langle n|\hat{Q}^B_{l'm'}|0\rangle}{(E_n - E_0)^2 - \omega^2}$$

$$= \sum_{n\neq 0} \frac{f^{AB}_{lm,l'm'}(n)}{(E_n - E_0)^2 - \omega^2}$$

and it can be expanded in a Cauchy power series:

$$[6] \qquad \alpha^{AB}_{lm,l'm'}(\omega) = \sum_{k=0}^{\infty} \omega^{2k} S^{AB}_{lm,l'm'}(-2k-2)$$

where the distributed Cauchy moments (16), $S^{AB}_{lm,l'm'}(k)$, are given by the sum-over-states formula:

$$[7] \qquad S^{AB}_{lm,l'm'}(k) = \sum_{n\neq 0} (E_n - E_0)^k f^{AB}_{lm,l'm'}(n)$$

and $f^{AB}_{lm,l'm'}(n)$ denotes the generalized oscillator strengths of the transition between the ground and the nth electronic state $|n\rangle$, with energy E_n. Static polarizabilities correspond to Cauchy moments of order -2:

$$\alpha^{AB}_{lm,l'm'}(0) = S^{AB}_{lm,l'm'}(-2)$$

In the time-dependent Hartree–Fock approximation the dynamic polarizability components can be obtained by solving the following generalized eigenvalue problem (17):

$$[8] \qquad (\boldsymbol{A}+\boldsymbol{B})C_n = \omega^2_{on}(\boldsymbol{A}-\boldsymbol{B})^{-1}C_n$$

for the TDHF excitation energies, ω_{on} and amplitudes, C_n, which are normalized according to $C_n^T(\boldsymbol{A}-\boldsymbol{B})C_n = 1$. The matrices $\boldsymbol{A}$ and $\boldsymbol{B}$ are defined in terms of occupied i,j and virtual a,b orbitals, as usual:

$$[9] \qquad A_{ia,jb} = (\varepsilon_a - \varepsilon_i)\delta_{ab}\delta_{ij} + 2(ai|jb) - (ab|ij)$$

$$B_{ia,jb} = 2(ai|bj) - (bi|ja)$$

The generalized oscillator strengths are given in this approach by

$$[10] \qquad f^{AB}_{lm,l'm'}(n) = 2\sum_{ia}(i|\hat{Q}^A_{lm}|a)C_{ia,n}\sum_{jb}(j|\hat{Q}^B_{l'm'}|b)C_{jb,n}$$

and they can be used directly to calculate dynamic polarizabilities at a given frequency ω, with the help of expressions [5] and [7], respectively.

The atomic multipole moment operators, $\hat{Q}^A_{lm}$, are defined by their matrix elements:

$$[11] \qquad (i|\hat{Q}^A_{lm}|a) = \int_{\Omega_A} d\boldsymbol{r}\phi^*_i(\boldsymbol{r})R^A_{lm}(\boldsymbol{r})\phi_a(\boldsymbol{r})$$

where the volume of integration extends over the atomic basin, limited by a zero-flux surface of the unperturbed molecule.

Total molecular Cauchy moments can be calculated either by replacing the atomic transition integrals in expression [11] by molecular ones, or by reconstituting them from distributed Cauchy moments via translation of the atomic components to the common molecular origin (5).

A series of molecules, carbon monoxide, water, cyanogen, urea, and benzene, has been selected to study the basis-set sensitivity of the frequency-dependent distributed polarizabilities, by examining the behavior of Cauchy moments in five different contracted Gaussian type orbital (CGTO) basis sets.

Fig. 1. Orientation of the molecules in the coordinate frame.

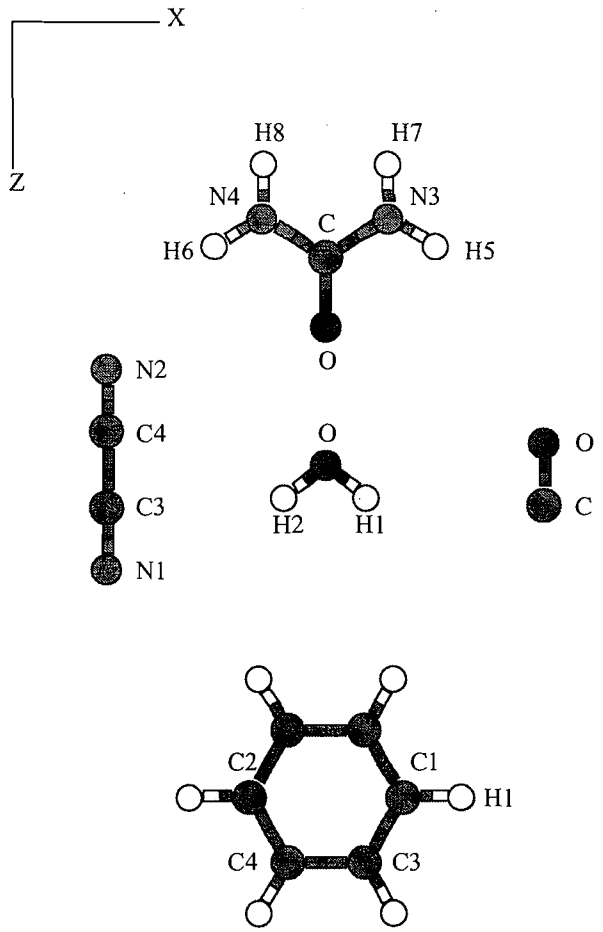

Calculations on CO, H_2O, cyanogen (NCCN), and benzene were done at their experimental gas-phase geometries (18–20). In the case of urea, a planar geometry was used, determined by low-temperature neutron-diffraction measurements (21) of the crystal. The orientation of the molecules is defined in Fig. 1.

Self-consistent field (SCF) calculations were performed with the MOLCAS program (22). We have used the 6-31G** valence double-zeta polarization, the 6-311G(2d,2p) valence triple-zeta double polarization, and the 6-311++G(2d,2p) valence triple-zeta double polarization plus diffuse functions basis sets. The polarization basis set of Sadlej (23), optimized for molecular polarizabilities and electrostatic properties, consists of (6s4p)/[3s2p] and (10s6p4d)/[5s3p2d] contracted sets for H and other atoms, respectively. The largest basis set in our study was derived from that of Widmark et al. (24) by keeping the same exponents. Only the innermost three s- and two p-functions were contracted for the hydrogen atom, resulting in a (8s4p)/[6s3p] CGTO set, and for the other atoms we contracted only the innermost five s-, four p-, and two d-functions, thus yielding (14s9p4d)/[10s6p3d] sets. This basis set contains also the diffuse functions essential for a reliable prediction of polarization properties. Except for the case of 6-31G** basis set, five-component d-functions were always employed.

Table 1. Cauchy moments (in au) calculated with various basis sets, compared to CDOSD, experimental, or theoretical values.

Component	6-31G**	6-311G(2d,2p)	6-311++G(2d,2p)	[5s3p2d]	[10s6p3d]	Literature
CO						
$S_{xx}(-2)$	7.766	9.335	10.069	11.089	11.255	11.89[a]
$S_{xx}(-4)$	28.686	31.833	38.432	41.459	41.806	46.61[a]
$S_{xx}(-6)$	207.822	219.815	270.726	275.343	277.421	301.4[a]
$S_{zz}(-2)$	12.237	12.759	14.313	14.435	14.447	15.46[a]
$S_{zz}(-4)$	26.557	28.821	40.581	41.178	41.224	51.56[a]
$S_{zz}(-6)$	68.251	77.617	143.372	145.178	145.770	275.7[a]
$\bar{S}(-2)$	9.256	10.476	11.484	12.204	12.299	13.08[a]
$\bar{S}(-4)$	27.976	30.829	39.148	41.365	41.612	48.26[a]
$\bar{S}(-6)$	161.298	172.415	228.275	231.955	233.537	292.9[a]
H_2O						
$S_{xx}(-2)$	7.024	7.945	8.269	9.167	9.153	9.68[b]
$S_{xx}(-4)$	16.145	16.215	17.613	20.894	20.716	
$S_{xx}(-6)$	49.603	47.597	52.015	60.631	60.145	
$S_{yy}(-2)$	2.928	4.873	6.681	7.821	7.855	9.19[b]
$S_{yy}(-4)$	4.623	11.244	21.747	25.679	25.884	
$S_{yy}(-6)$	30.644	80.289	152.013	164.178	170.006	
$S_{zz}(-2)$	5.108	6.519	7.180	8.488	8.438	9.47[b]
$S_{zz}(-4)$	11.514	14.030	17.814	22.637	22.276	
$S_{zz}(-6)$	45.422	58.102	81.464	93.415	92.753	
$\bar{S}(-2)$	5.020	6.446	7.377	8.492	8.482	9.642[c]
$\bar{S}(-4)$	10.761	13.830	19.058	23.070	22.959	35.42[c]
$\bar{S}(-6)$	41.890	61.996	95.164	106.075	107.635	240.1[c]
NCCN						
$S_{xx}(-2)$	13.467	17.345	18.618	21.128	21.635	
$S_{xx}(-4)$	34.741	39.111	51.580	63.180	62.464	
$S_{xx}(-6)$	174.000	170.119	260.312	287.172	279.676	
$S_{zz}(-2)$	48.388	48.818	52.487	52.694	52.682	
$S_{zz}(-4)$	239.897	247.833	293.798	295.554	295.975	
$S_{zz}(-6)$	1407.708	1493.164	1916.611	1933.662	1940.971	
$(NH_2)_2CO$						
$S_{xx}(-2)$	27.592	31.048	33.070	35.910	35.947	38.152[d]
$S_{xx}(-4)$	77.715	91.748	113.048	127.305	127.379	
$S_{xx}(-6)$	338.232	431.891	645.837	722.183	729.192	
$S_{yy}(-2)$	12.211	17.556	22.654	24.451	24.465	26.007[d]
$S_{yy}(-4)$	13.128	30.385	67.873	73.931	73.737	
$S_{yy}(-6)$	35.348	129.243	401.943	425.506	426.063	
$S_{zz}(-2)$	30.018	32.239	35.491	37.269	37.252	39.661[d]
$S_{zz}(-4)$	89.383	94.754	127.309	138.619	138.591	
$S_{zz}(-6)$	452.368	487.789	801.181	871.198	879.491	
Benzene						
$S_{xx}(-2)$	70.536	74.869	78.528	80.216		
$S_{xx}(-4)$	417.986	463.618	543.681	560.331		
$S_{xx}(-6)$	4128.978	4834.773	6286.459	6408.163		
$S_{yy}(-2)$	21.382	31.929	44.817	45.784		
$S_{yy}(-4)$	21.857	59.189	205.160	210.467		
$S_{yy}(-6)$	43.236	253.599	1696.201	1750.928		
$\bar{S}(-2)$	54.151	60.556	67.291	68.739		67.79[e]
$\bar{S}(-4)$	285.943	328.808	430.841	443.710		430.4 [e]
$\bar{S}(-6)$	2767.064	3307.715	4756.373	4855.751		4932[e]

[a]CDOSD data (27).
[b]From rotational Raman spectra (30).
[c]CDOSD data (28).
[d]RAS-SCF linear response calculations (31).
[e]CDOSD data (29).

Cauchy moments and dynamic polarizabilities at fixed values of the frequency were calculated with a self-written TDHF program that uses the necessary transformed two-electron integral blocks produced by either a nonstandard link after a closed-shell SCF run of Gaussian 92 (25), or by the MOLCAS-2 suite of programs (22). Our code makes use of eq. [8] and thus inversion of the $(\boldsymbol{A} - \boldsymbol{B})$ matrix is required. This becomes prohibitive for cases with many single excitations. Due to the implementation of Abelian point group symmetries in our code (available when working with MOLCAS), we were able to treat all molecules even with the large [10s6p3d] basis set, except for benzene, where this basis set had to be left out. The occupied/virtual one-electron integral blocks of the distributed moments were generated by a modified version of the Proaim program (26).

III. Results and discussion

The first three molecular Cauchy moments, $S(-2), S(-4)$, and $S(-6)$, which enter in the power series expansion for the dynamic polarizability as calculated by the five basis sets, are listed in Table 1. In the case of CO, H_2O, and C_6H_6 they are compared with the available data obtained by the CDOSD (constrained dipole oscillator strength distribution) method of Meath and co-workers (27–29). Anisotropic static polarizabilities were taken from the experimental data of Murphy (30) for water, and from the theoretical calculations of Sanchez de Merás et al. (31) for urea. In the TDHF calculations on CO and H_2O even the largest-basis results remain significantly smaller than the CDOSD values and the error is enhanced with increasing order of the Cauchy moments. In the case of CO the Sadlej polarization and the [10s6p3d] basis calculations have about −13 and −21% error with respect to the CDOSD results for the mean $S(-4)$ and $S(-6)$ Cauchy moments. The errors are much larger in the case of the water molecule: they are 35 and 55%, respectively. This is in agreement with the observation of Spackman, who underlined the relatively poor quality of the higher Cauchy moments (32), calculated by the TDHF method. Electron correlation, taken into account, for example, by the recently developed time-dependent MP2 (TDMP2) approach, can bring these Cauchy moments into closer agreement with experiment (33, 34). The TDHF results for benzene are in remarkably good agreement with recent CDOSD data. The errors in the mean Cauchy moments of order −2, −4, and −6 are +0.7%, +0.1%, and −3.6% with the 6-311++G(2d,2p) basis set, while they are +1.4%, +3.1%, and +1.5% when using the [5s3p2d] basis set of Sadlej. The good quality of the higher Cauchy moments is probably partly due to the success of the TDHF method in reproducing the first dipole-allowed excitation energy in reasonable agreement with the experiment (6.56 eV calculated vs. 6.9 eV) and partly to the overwhelming importance of the charge-flow contribution to the static *and* dynamic polarizabilities (see below).

The basis set dependence of the higher $S(-4)$ and $S(-6)$ Cauchy moments is similar to that of the static polarizability, $S(-2)$, but the effects are more pronounced. Out-of-plane polarizability components are influenced much more by the quality of the basis set than are the in-plane components. In CO the parallel Cauchy moment components are in reasonable agreement with CDOSD values (below 10%), while the perpendicular ones are in error by 20 and 47%! In the water molecule $S_{yy}(-2)$ varies by a factor of 2.7 between the smallest and the largest basis set, while the higher-order Cauchy moment, $S_{yy}(-6)$, is enhanced by a factor of 5.7. In urea and benzene the approximately twofold enhancement of the out-of-plane static polarizability increases to a 12- and 40-fold enhancement, respectively. The in-plane polarizability components are relatively insensitive to the choice of basis set.

Coming now to the distributed models, selected distributed dipole–dipole Cauchy moment components have been plotted against the basis set quality in Figs. 2 and 3 for the two smallest systems, CO and H_2O. In addition to the static polarizability, $S(-2)$, and the $S(-6)$ Cauchy moment, the $S(0)$ Cauchy moments are also represented in these figures. Zeroth-order Cauchy moments correspond to the high-frequency limit of the multipolar dynamic polarizability components. The $S_{1,1}(0)$ dipolar components, according to the Thomas–Reiche–Kuhn (TRK) sum rule (35), are equal to the total number of electrons in the molecule. For SCF wave functions the TRK sum rule is satisfied in the basis set limit, therefore $S_{\alpha\alpha}(0)$ can be considered as a measure of the basis set completeness in the subspace of dipole excitations.

The general trends observed in the two molecules represented in Figs. 2 and 3 are identical, and they remain the same for the other three molecules, not represented here. Although the TRK sum rule is relatively poorly satisfied for the [5s3p2d] polarization basis set, this basis describes the static polarizability as well as the higher Cauchy moments in very good agreement with the larger [10s6p3d] basis. In fact, this basis set has been optimized by Sadlej to faithfully reproduce molecular polarizabilities, while the description of compact p- and d-orbitals, important for good fulfillment of the TRK sum rule, is less complete. This observation is in agreement with the experience of Mulder and Meath (36), who found that the importance of the core basis set in reproducing various sum rules increases with increasing Cauchy order.

Distributed atom–atom dipole polarizabilities, represented in Fig. 4, vary with the basis set quality in a similar way as the total polarizability components. One could expect that basis set effects would be reflected mostly by distributed dipole–dipole polarizabilities, while charge-flow terms would be reasonably described even by a relatively poor basis set. Distributed static polarizabilities confirm this rule (cf. Fig. 4), but the same is not necessarily true for higher Cauchy moments, i.e., for the frequency dependence of the polarizabilities. The increase in magnitude of the $S(-6)$ charge–charge and charge–dipole Cauchy moments for CO between the 6-311G(2d,2p) and 6-311++G(2d,2p) basis sets in Fig. 4 indicates that diffuse functions are indispensable for their good description.

Analysis of the different kinds of fully distributed terms becomes more and more complicated in larger molecules, due to the increasing number of parameters. Therefore one should envisage some "relocalization" scheme, which simplifies the model but preserves the advantages of the distributed description. As a first step in this direction, we analyzed the various kinds of distributed contributions to the molecular dipole–dipole Cauchy moments.

The molecular dynamic dipole–dipole polarizability, as

Fig. 2. Distributed dipole–dipole Cauchy moments for CO.

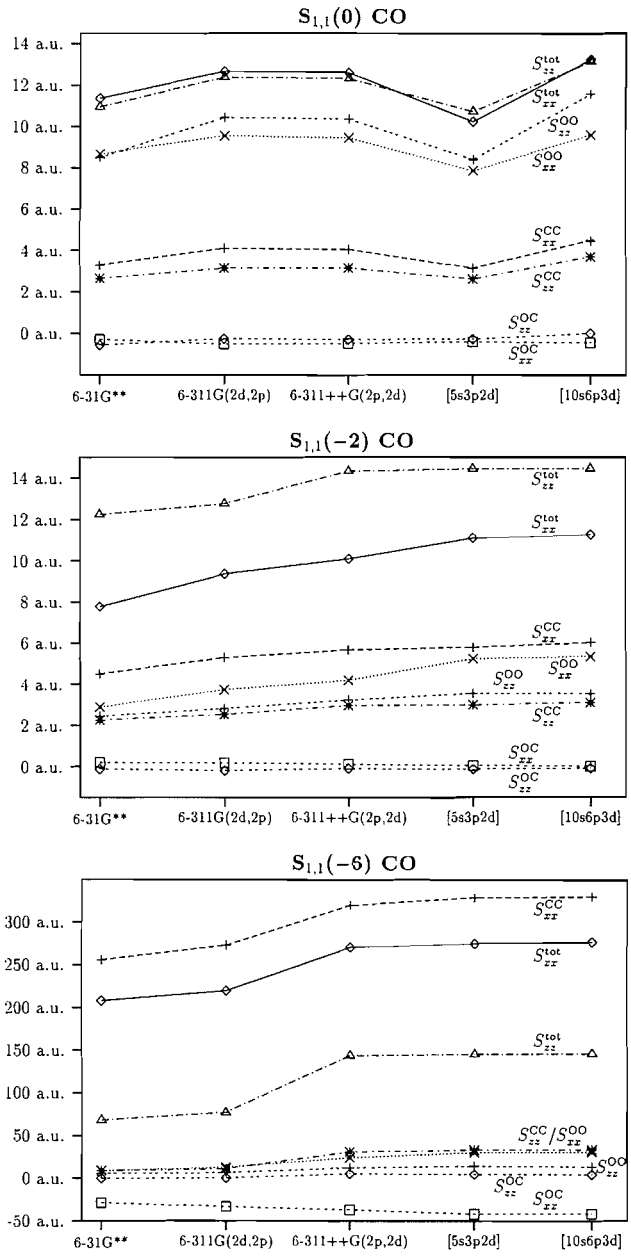

Fig. 3. Distributed dipole–dipole Cauchy moments for H_2O.

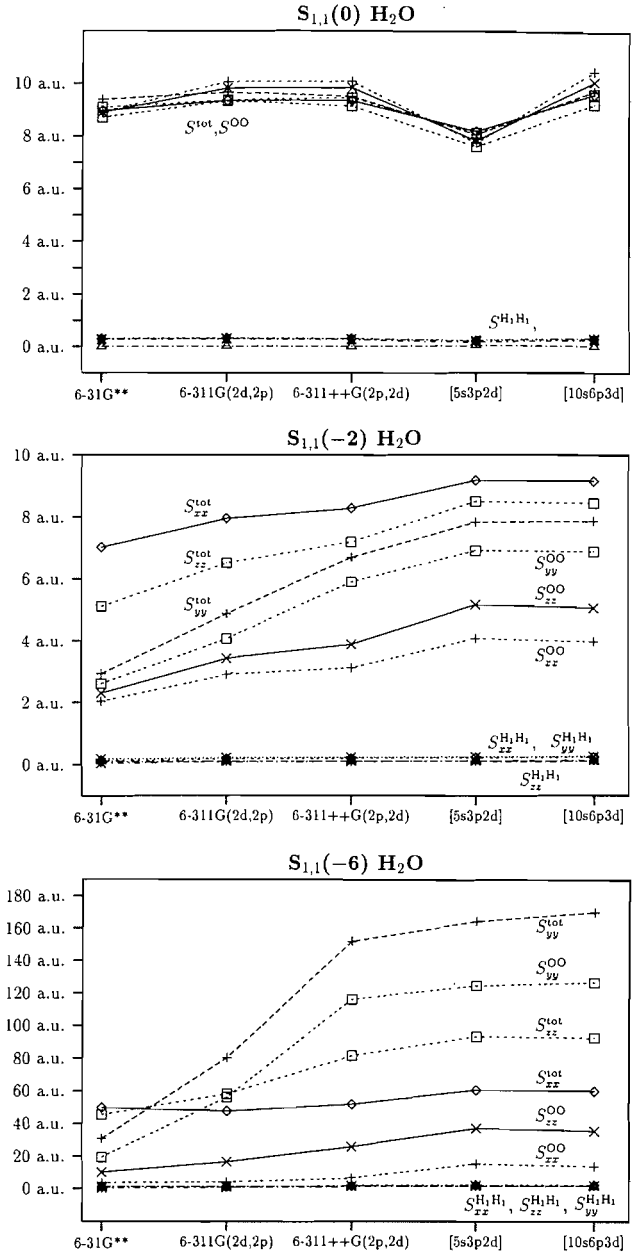

well as the corresponding Cauchy moments, can be broken down into various kinds of distributed components:[2]

$$[12]\qquad \alpha_{\alpha\beta}(\omega) = \alpha_{\alpha\beta}^{[\mu\mu,1-c]}(\omega) + \alpha_{\alpha\beta}^{[\mu\mu,2-c]}(\omega) + \alpha_{\alpha\beta}^{[q\mu]}(\omega) + \alpha_{\alpha\beta}^{[qq]}(\omega)$$

where Greek subscripts $\alpha\beta$ stand for the Cartesian components x, y, z, and the one- and two-center dipole–dipole, the charge–dipole and charge–charge contributions are defined as:

$$[13]\qquad \alpha_{\alpha\beta}^{[\mu\mu,1-c]}(\omega) = \sum_{A} \alpha_{\alpha\beta}^{AA}(\omega)$$

$$[14]\qquad \alpha_{\alpha\beta}^{[\mu\mu,2-c]}(\omega) = \sum_{A} \sum_{B\neq A} \alpha_{\alpha\beta}^{AB}(\omega)$$

$$[15]\qquad \alpha_{\alpha\beta}^{[q\mu]}(\omega) = \sum_{A} \sum_{B} R_{\alpha}^{A} \alpha_{q\beta}^{AB}(\omega) + \alpha_{\alpha q}^{AB}(\omega) R_{\beta}^{B}$$

$$[16]\qquad \alpha_{\alpha\beta}^{[qq]}(\omega) = \sum_{A} \sum_{B} R_{\alpha}^{A} \alpha_{qq}^{AB}(\omega) R_{\beta}^{B}$$

[2] For the sake of simplicity, the formulae in the text are written for the polarizabilities, $\alpha_{\alpha\beta}$, but they are valid *mutatis mutandis* for the corresponding Cauchy moments.

Fig. 4. Distributed charge-flow Cauchy moments for CO and H_2O.

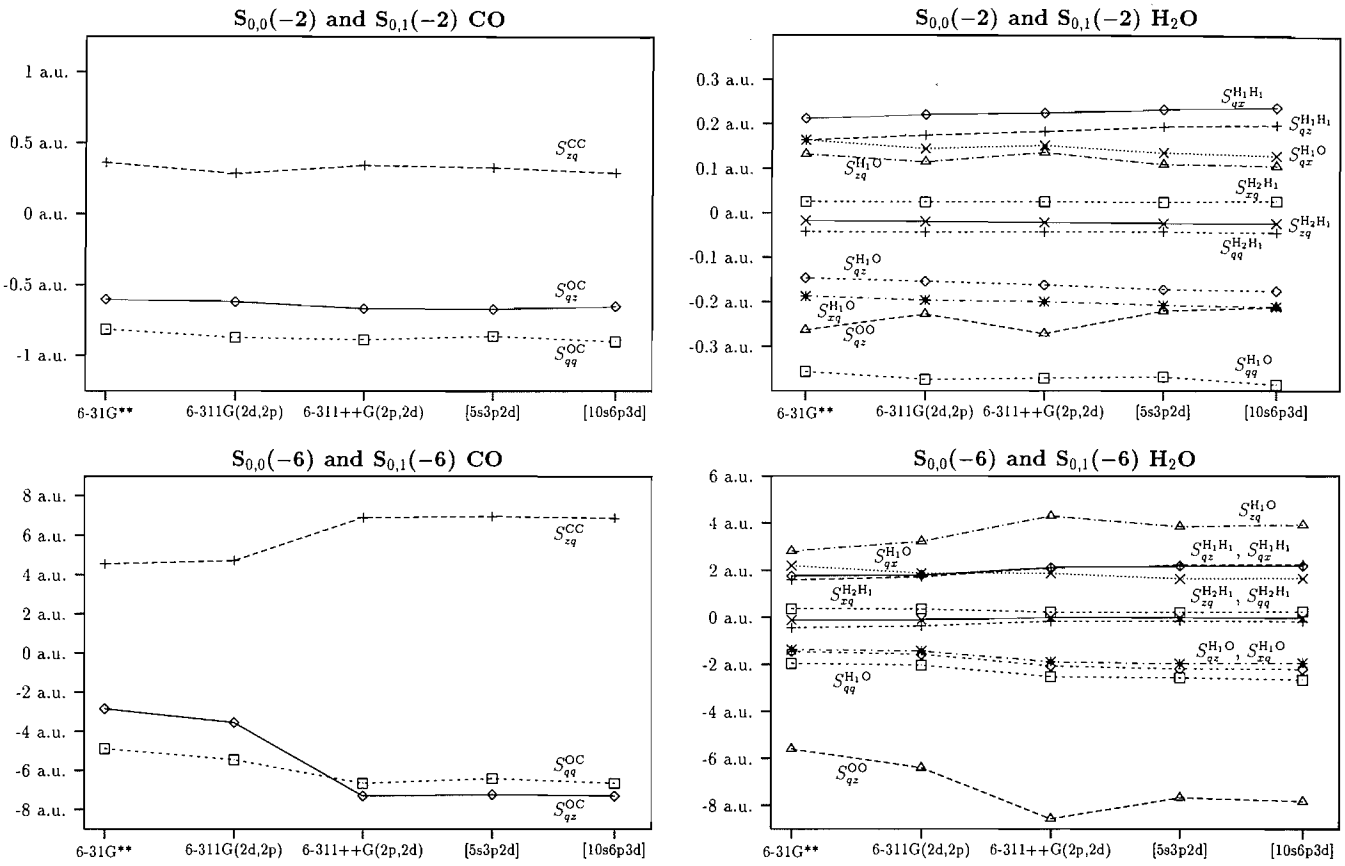

and R_α^A is the α component of the vector from the molecular origin to the Ath atom. Contribution of the different terms depends on the chemical system and on the geometry, as is exemplified by the data for water and benzene molecules in Table 2, calculated with the polarization basis set of Sadlej.

Out-of plane molecular polarizabilities have only one- and two-center dipole–dipole components, since no atomic charge transfer is possible in this direction. The one-center contribution is always considerably larger than the two-center one, although the latter becomes increasingly important for higher order Cauchy moments in all cases. The charge-flow contribution to in-plane polarizabilities is always significant, and it even becomes the most important term for conjugated systems like benzene (and also for cyanogen), where it accounts for 80% of the total in-plane dipole polarizability. The distributed charge–dipole Cauchy moments contribute by 10–30% to the total molecular quantities, and their importance increases for higher orders.

The basis set dependence of distributed components in the larger systems, cyanogen and urea, is illustrated in Figs. 5 and 6, by regrouping all dipole–dipole and charge–dipole contributions in a single term, $S^{[\mu]}(k)$, and denoting the sum of charge–charge contributions by $S^{[q]}(k)$. In the case of the static polarizability, $S(-2)$, the sum of charge–charge terms is quite insensitive to the basis set and, in agreement with the experience obtained by detailed analysis of the smaller systems, the basis set variation of the total Cauchy moments is reflected by the sum of distributed dipole–dipole and charge–dipole Cauchy moments. The situation changes considerably for the contributions to the $S(-6)$ Cauchy moments. Here, the basis set dependence of the charge–charge terms is of comparable importance to that of the dipolar contributions, and diffuse functions are imperatively needed for a good reproduction of charge-flow contributions to higher Cauchy moments as well.

The data discussed above can serve as a starting point in appreciating the advantages or disadvantages of different partial relocalization schemes of distributed polarizabilities and Cauchy moments. Let us consider first the "atom–molecule" polarizabilities. The total molecular dynamic polarizabilities can be reconstituted from dipole–dipole and charge–dipole atom–molecule polarizabilities in the following manner (the argument ω will be omitted for the sake of notational simplicity):

$$[17] \qquad \alpha_{\alpha\beta} = \sum_A (\alpha_{\alpha\beta}^{A,mol} + R_\alpha^A \alpha_{q\beta}^{A,mol})$$

where

$$[18] \qquad \alpha_{\alpha\beta}^{A,mol} = \sum_B \alpha_{\alpha\beta}^{AB} + \alpha_{\alpha q}^{AB} R_\beta^B$$

$$[19] \qquad \alpha_{q\beta}^{A,mol} = \sum_B \alpha_{q\beta}^{AB} + \alpha_{qq}^{AB} R_\beta^B$$

Table 2. Decomposition of total Cauchy moments for water and benzene molecules calculated with the Sadlej [5s3p2d] polarization basis set. Numbers in parentheses indicate the percentage contribution to the total reconstituted Cauchy moment from distributed one- and two-centered dipole–dipole, dipole–charge, and charge–charge contributions.

αβ	k	$S_{\alpha\beta}^{[dd,1\text{-}c]}(k)$	$S_{\alpha\beta}^{[dd,2\text{-}c]}(k)$	$S_{\alpha\beta}^{[qd]}(k)$	$S_{\alpha\beta}^{[qq]}(k)$	$S_{\alpha\beta}^{total}(k)^a$	$S_{\alpha\beta}^{full}(k)$
H_2O							
xx	−2	4.5603	0.4973	2.2581	1.8506	9.1663	9.1669
		(49.75)	(5.43)	(24.63)	(20.19)	(−0.01)	
yy	−2	7.1535	0.6663	0.0000	0.0000	7.8198	7.8211
		(91.48)	(8.52)	(0.00)	(0.00)	(−0.02)	
zz	−2	5.6120	0.7248	1.2452	0.9054	8.4874	8.4879
		(66.12)	(8.54)	(14.67)	(10.67)	(−0.01)	
xx	−6	19.2028	6.4873	23.0117	11.8993	60.6010	60.6306
		(31.69)	(10.70)	(37.97)	(19.64)	(−0.05)	
yy	−6	128.0793	35.9794	0.0000	0.0000	164.0587	164.1782
		(78.07)	(21.93)	(0.00)	(0.00)	(−0.07)	
zz	−6	41.6719	18.6769	26.7305	6.3165	93.3958	93.4152
		(44.62)	(20.00)	(28.62)	(6.76)	(−0.02)	
C_6H_6							
xx	−2	15.5331	0.8625	4.1356	59.6587	80.1899	80.2164
	−2	(19.37)	(1.08)	(5.16)	(74.40)	(−0.03)	
yy	−2	42.0741	3.6293	0.0000	0.0000	45.7035	45.7836
	−2	(92.06)	(7.94)	(0.00)	(0.00)	(−0.17)	
xx	−6	431.6299	−107.4498	1661.8356	4414.3488	6400.3644	6408.1626
	−6	(6.74)	(−1.68)	(25.96)	(68.97)	(−0.12)	
yy	−6	1452.5266	285.9955	0.0000	0.0000	1738.5221	1750.9281
	−6	(83.55)	(16.45)	(0.00)	(0.00)	(−0.71)	

[a]The number in parentheses below the $S_{\alpha\beta}^{total}$ indicates the percentage error with respect to $S_{\alpha\beta}^{full}$, the Cauchy moment calculated with analytic molecular multipole transition integrals (last column).

A selected set of significant components of the Cauchy moments $S_{\alpha\beta}^{A,mol}(k)$ as well as of $S_{q\beta}^{A,mol}(k)$ are listed in Table 3. The atom–molecule charge–dipole polarizabilities are relatively large for atoms at the extremities of the molecule, such as the nitrogen in cyanogen, the oxygen in urea, and the hydrogens in benzene. An interesting feature, already remarked by Bader and co-workers in the case of hydrocarbons, is the counter-polarization of "buried" atoms, such as the carbon in cyanogen and in urea: the induced dipole is in the opposite direction with respect to the applied field on the molecule.

A more conventional model, including exclusively atomic dipole–dipole polarizabilities, could be obtained by transforming the charge–dipole terms to atomic dipole–dipole contributions. Taking the molecular center of mass as the molecular origin, a set of atomic polarizabilities can be obtained (cf. the term in parentheses in eq. [17] that can be compared to other models available in the literature. For example, Åstrand et al. proposed a polarizable intermolecular potential for the urea molecule, in which an isotropic polarizability was assigned to each atom (37). A similar model can be constructed from our atom–molecule polarizabilities, using eq. [17]. The mean polarizability of urea, corresponding to the model of Åstrand et al. ($\alpha(C) = 0.0$, $\alpha(O) = 9.62$, $\alpha(N) = 2.63$, $\alpha(H_{cis}) = \alpha(H_{trans}) = 2.14$), is 23.44 au, i.e., practically identical to our 6-31G** result. Taking this basis set, we obtain a model, that is quite similar to theirs: ($\alpha(C) = 0.20$, $\alpha(O) = 6.40$, $\alpha(N) = 3.71$, $\alpha(H_{cis}) = \alpha(H_{trans}) = 2.32$). With the Sadlej polarization basis set, the qualitative features of the model remain unchanged: the polarizability of the carbon is practically zero, and the hydrogen polarizability (coming mainly from induced charge contributions) is about 2.5 au. However, the mean polarizabilities of the O and N atoms are considerably enhanced: they are 9.45 and and 6.21 au, respectively, reflecting the better quality of this basis set.

Atom–molecule polarizabilities have two main drawbacks. First, the external field is supposed to be uniform, which is a considerable restriction for the study of the intermolecular interaction of larger molecules, where a really nonlocal picture would be more appropriate. Second, the charge–dipole parameter cannot be combined in a simple, origin-independent way (the atomic contributions obtained from eq. [17] depend on the choice of the molecular origin) with the atomic dipole–dipole polarizability, except in some special cases.

A closer look at the expression for atom–molecule charge–dipole polarizability shows that only the charge-flow terms are responsible for the impossibility of assigning it to atomic dipole polarizabilities in an origin-independent way. A straightforward solution to this problem, already suggested by Le Sueur and Stone (15), is to keep charge-flow polarizabilities fully distributed, and relocalize only the dipole–dipole and charge–dipole terms, which can be done in a strictly origin-independent way. After a little algebra, using the sum rule, eq. [3], one gets the following expression for the relocalized atomic dipole polarizability:

Fig. 5. Breakdown of the molecular dipole–dipole Cauchy moments to distributed charge–charge ($S^{[q]}_{\alpha\beta}$) and dipole–dipole plus charge–dipole ($S^{[\mu]}_{\alpha\beta}$) contributions ($S^{[q]}_{\alpha\beta} + S^{[\mu]}_{\alpha\beta} = S^{tot}_{\alpha\beta}$) for cyanogen.

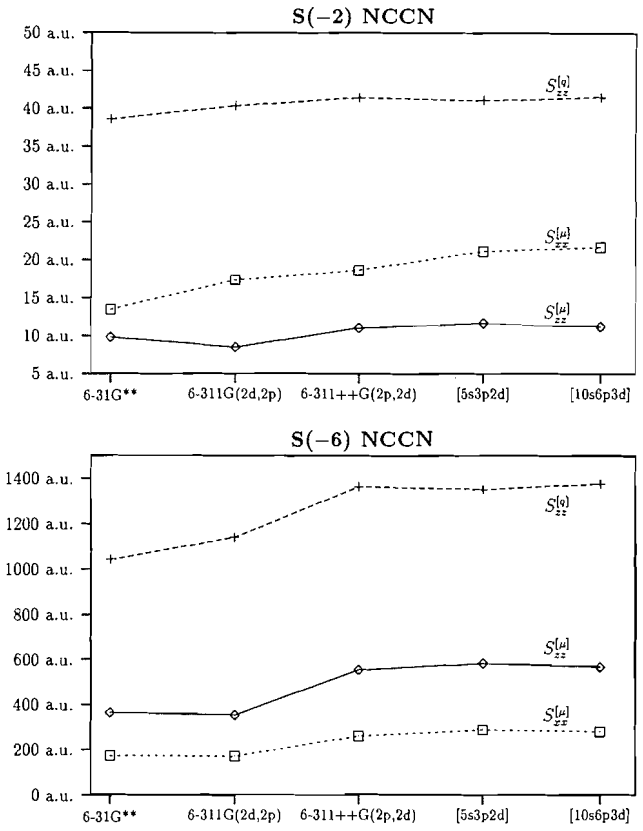

$$[20]\qquad \tilde{\alpha}^{A}_{\alpha\beta} = \frac{1}{2}\sum_{B}(\alpha^{AB}_{\alpha\beta} + \alpha^{BA}_{\alpha\beta}) + r^{AB}_{\alpha}(\alpha^{AB}_{q\beta} - \alpha^{BA}_{q\beta}) + r^{AB}_{\beta}(\alpha^{BA}_{\alpha q} - \alpha^{AB}_{\alpha q})$$

with $\boldsymbol{r}^{AB} = \boldsymbol{R}^{A} - \boldsymbol{R}^{B}$, the vector of interatomic distance. In this scheme all two-center charge–dipole and dipole–dipole terms are distributed in an equal manner between the centers in question. The resulting atomic dipole polarizability tensors are symmetric, unlike the atom–molecule polarizabilities, for which $\alpha^{A,mol}_{\alpha\beta} \neq \alpha^{A,mol}_{\beta\alpha}$. The charge-flow and the relocalized atomic Cauchy moments according to expression [20] are listed in Tables 4 and 5, respectively.

The charge–charge Cauchy moments (Table 4) are expected to be significant mainly between covalently bonded atoms: chemical bonds are natural paths for transferring electrons in a molecule. (A consistent formulation of the covalent bond order using the topological definition of atoms in molecules has been discussed in ref. 38.) The relative magnitude of charge-flow Cauchy moments for pairs of formally nonbonded atoms seems to increase with the order (e.g., N1–C3 compared to N2–C3 in urea, or the *meta* (C1–C4) charge flow in benzene). Several of the examples discussed here (cyanogen, urea, benzene) are conjugated systems, where surprisingly high charge flow may take place between quite distant atoms. For example, the end-to-end N1–N2 charge flow in cyanogen is larger than the charge flow between the first neighbor C3 and C4 atoms. This is already true for $S^{AB}_{qq}(-2)$, and the difference becomes even more important for the moments $S^{AB}_{qq}(-4)$ and $S^{AB}_{qq}(-6)$. Similar trends can be observed for benzene and urea.

Fig. 6. Breakdown of the molecular dipole–dipole Cauchy moments for urea.

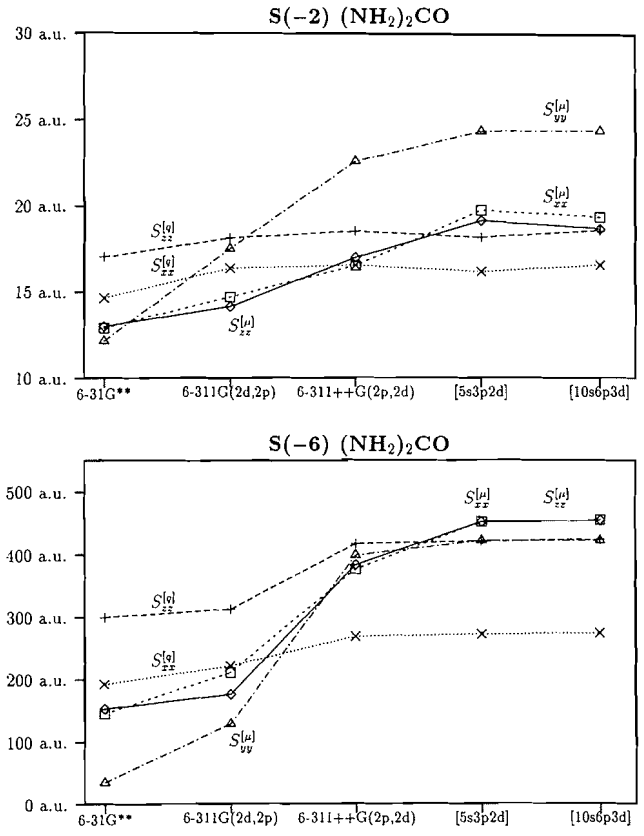

Atomic dipole–dipole polarizabilities according to eq. [20] are larger than the corresponding atom–molecule dipole–dipole polarizabilities, since they include the totality of the charge–dipole contributions. Nevertheless, the main qualitative features are similar: negative in-plane polarizabilities for "buried" atoms and relatively small positive out-of-plane components. Hydrogen atoms have consistently small dipole–dipole atomic Cauchy moments ($S(-2)$ usually smaller than 1 au), when connected to the electronegative O and N atoms, but in benzene the component along the C—H bond becomes larger than 2 au. According to these observations a "united atom" description for the XH_n functional groups might be a reasonable model. In the same spirit, the water molecule could be regarded as a single dipole – polarizable oxygen site, bearing about 75% of the total molecular polarizability, and an additional charge transfer contribution between the oxygen and the hydrogen atoms.

IV. Summary and conclusions

We have shown that the atoms-in-molecules theory of Bader constitutes an appropriate framework for partitioning dy-

Table 3. Atomic Cauchy moments relocalized according to eq. [17] as calculated with the [5s3p2d] polarization basis of Sadlej.

Atom	αβ	$k = -2$	$k = -4$	$k = -6$	Atom	αβ	$k = -2$	$k = -4$	$k = -6$
CO					**$(NH_2)_2CO$**				
C	qz	2.840	8.157	27.890	O	qz	4.040	20.536	157.946
C	xx	5.816	34.816	286.874	O	xx	5.720	16.794	103.316
C	zz	4.281	13.838	52.718	O	yy	6.300	15.136	46.390
					O	zz	5.823	23.333	153.960
O	qz	−2.841	−8.161	−27.906					
O	xx	5.251	6.528	−12.216	C	qz	−0.299	−2.995	−29.198
O	zz	4.097	9.941	32.967	C	xx	−0.246	−1.072	−6.497
					C	yy	1.167	2.035	4.219
NCCN					C	zz	−0.353	−1.511	−10.652
N1	qz	7.022	41.509	275.900					
N1	xx	7.423	22.710	107.027	N3	qx	1.300	7.114	52.473
N1	zz	4.982	21.733	129.246	N3	qz	−0.731	−5.069	−47.188
					N3	xx	4.174	15.123	89.123
C3	qz	−2.388	−17.403	−121.326	N3	xz	−0.746	−7.251	−68.018
C3	xx	3.133	8.831	36.272	N3	yy	7.580	24.726	152.727
C3	zz	0.019	4.156	34.704	N3	zx	−0.601	−5.258	−42.308
					N3	zz	3.236	9.087	52.246
H_2O									
O	qz	−1.380	−3.965	−17.777	H5	qx	1.540	4.181	15.247
O	xx	4.687	9.022	22.934	H5	qz	0.507	0.338	−4.694
O	yy	7.240	23.153	142.193	H5	xx	1.162	3.995	17.230
O	zz	5.777	14.218	54.700	H5	xz	0.167	0.228	−2.622
					H5	yy	0.390	1.453	13.102
H1	qx	1.042	2.627	8.181	H5	zx	0.365	1.843	10.407
H1	qz	0.690	1.982	8.888	H5	zz	0.452	0.723	0.812
H1	xx	0.750	2.176	7.131					
H1	yy	0.290	1.257	10.933	H7	qx	0.328	2.087	15.299
H1	zz	0.591	2.013	9.507	H7	qz	−1.646	−4.043	−12.518
H1	xz	0.329	1.363	6.725	H7	xx	0.468	0.846	2.176
H1	zx	0.459	1.711	6.222	H7	xz	−0.088	−0.406	−1.368
					H7	yy	0.451	1.920	19.847
					H7	zx	−0.294	−2.128	−16.780
					H7	zz	1.320	4.516	18.070
C_6H_6					**C_6H_6**				
C1	qx	2.444	30.750	439.660	H1	qx	2.997	14.410	123.512
C1	xx	1.707	14.894	193.089	H1	xx	2.492	15.159	132.166
C1	yy	6.340	29.408	230.630	H1	yy	1.280	5.526	59.166
C1	zz	0.958	8.358	109.510	H1	zz	0.998	−1.210	−49.735

namic polarizabilities and leads to a physically consistent set of atom–atom parameters describing the nonlocal response of the molecular charge density to a time-dependent external field. The basis set dependence of distributed dynamic polarizabilities has been studied through their first three distributed Cauchy moments, which vary in parallel with the total Cauchy moments when improving the basis set quality.

In the case of static polarizabilities ($S(-2)$ Cauchy moments) the basis set dependence is manifested almost exclusively in the distributed dipole–dipole contributions, and charge-flow terms are quite well described by relatively poor basis sets. Nevertheless, diffuse functions seem to be important for the description of higher order charge–charge Cauchy moments. Static charge–charge polarizabilities between distant pairs of atoms may be quite large in conjugated systems and in all cases the importance of charge-flow Cauchy moments between nonbonded and (or) distant atoms increases with increasing order.

Two alternative schemes have been considered to "relocalize" the fully distributed, nonlocal dynamic polarizabilities. The atom–molecule polarizabilities, closely related to the atomic polarizabilities recently studied by Bader and coworkers, describe induced atomic charges and dipoles of a molecule in a uniform external field. Description of the response in non-uniform fields is possible only by considering higher rank (e.g., charge–quadrupole, dipole–quadrupole, charge–octupole., etc.) atom–molecule polarizabilities, with all the pitfalls of the single-centered Taylor expansion of the external field for spatially extended systems. The other model, which retains all charge-flow terms fully distributed and relocalizes only the charge–dipole contributions, is better suited to the description of molecules in non-uniform fields.

Table 4. Selected atomic charge–charge Cauchy moments calculated with the Sadlej basis.

A	B	−2	−4	−6	A	B	−2	−4	−6
CO					**H_2O**				
O	C	−0.864	−2.029	−6.424	O	O	0.739	1.419	5.153
NCCN					H1	H1	0.411	0.829	2.742
N1	N1	1.796	7.859	46.904	H1	O	−0.369	−0.709	−2.576
C3	C3	1.735	3.809	16.131	**$(NH_2)_2CO$**				
C3	N1	−1.256	−4.501	−24.785	C	C	0.912	1.156	3.942
C4	C3	−0.437	−0.259	−2.133	O	C	−0.385	−1.075	−7.581
N2	N1	−0.499	−4.309	−32.909	O	O	1.034	4.387	33.777
C3	N2	−0.042	0.952	10.788	N3	O	−0.211	−1.122	−10.099
C_6H_6					N3	C	−0.242	−0.055	1.467
C1	C1	2.389	13.142	211.131	N3	N3	1.405	2.550	12.162
C2	C1	−0.316	−8.224	−185.061	N4	N3	−0.124	−0.394	−2.248
C3	C1	−0.800	−7.159	−150.812	H5	N3	−0.375	−0.345	0.157
C4	C1	0.103	5.264	139.301	H5	N4	−0.022	−0.067	−0.135
H1	H1	0.868	2.291	12.929	H7	N3	−0.402	−0.417	−0.263
C1	H1	−0.421	1.054	32.952	H5	H5	0.545	0.961	2.536
C1	H2	−0.055	−1.401	−31.303	H7	H7	0.583	1.110	3.524
C1	H3	−0.102	−1.116	−23.644					

Table 5. Relocalized atomic Cauchy moments according to eq. [20] as calculated with the [5s3p2d] polarization basis of Sadlej.

Atom	αβ	−2	−4	−6	Atom		−2	−4	−6
CO					**$(NH_2)_2CO$**				
C	*xx*	5.816	34.816	286.874	C	*xx*	−0.174	−1.289	−17.168
C	*zz*	4.975	17.709	67.547	C	*yy*	1.167	2.035	4.219
O	*xx*	5.251	6.528	−12.216	C	*zz*	0.062	0.631	1.573
O	*zz*	5.532	14.237	48.385	O	*xx*	6.613	25.564	180.699
H_2O					O	*yy*	6.300	15.136	46.390
O	*xx*	5.280	10.491	28.593	O	*zz*	6.502	30.927	217.008
O	*yy*	7.240	23.153	142.193	N3	*xx*	4.679	17.992	103.108
O	*zz*	6.156	15.303	59.565	N3	*xz*	−0.463	−6.177	−57.070
H1	*xx*	1.018	3.259	10.055	N3	*yy*	7.580	24.726	152.727
H1	*yy*	0.290	1.257	10.933	N3	*zz*	4.157	13.532	84.676
H1	*zz*	0.713	2.796	13.757	H5	*xx*	1.239	5.434	24.629
H1	*xz*	0.515	2.254	10.090	H5	*xz*	0.236	0.952	1.554
NCCN					H5	*yy*	0.390	1.453	13.102
N1	*xx*	7.423	22.710	107.027	H5	*zz*	0.696	2.115	7.816
N1	*zz*	6.140	36.533	255.015	H7	*xx*	0.726	2.799	16.462
C3	*xx*	3.133	8.831	36.272	H7	*xz*	−0.201	−1.910	−16.255
C3	*zz*	−0.312	6.251	35.749	H7	*yy*	0.451	1.920	19.847
					H7	*zz*	1.429	6.002	24.104
C_6H_6					**C_6H_6**				
C1	*xx*	2.334	25.515	351.294	H1	*xx*	2.179	19.741	199.755
C1	*zz*	0.970	12.261	137.368	H1	*zz*	1.370	2.065	−26.243
C1	*yy*	6.340	29.408	230.630	H1	*yy*	1.280	5.526	59.166

Considering the increasing importance of distant charge-flow contributions with increasing Cauchy order, this second model seems to be more appropriate for the relocalization of distributed dynamic polarizabilities.

The main use of distributed dynamic polarizabilities, which have been characterized in the present study by their various Cauchy moments, is in the field of intermolecular interactions. We have recently developed an efficient computational scheme for obtaining multicentered multipolar dispersion energies. In the case of relatively small molecules, where the dipolar approximation is valid, one can obtain reliable dispersion energies by the CDOSD method (39). Theoretically calculated distributed dynamic polarizabilities allow us to extend the practical utility of the multipolar approximation to larger systems as well. To attain this goal the accuracy of the polarizability calculations has to be improved by

including electron correlation (for example by the TDMP2 method (33)) and the number of independent polarizability components has to be kept at a reasonably low level by the application of appropriate relocalization schemes. Work in these directions is in progress.

Acknowledgments

One of the authors (G.J.) is indebted to the Humboldt Foundation (Bonn) for the Feodor Lynen fellowship and to the CNRS. B.A.H and C.H. thank the Deutsche Forschungsgemeinschaft for financial support of this work through the Sonderforschungsbereich 334.

References

1. L.D. Barron. Mol. Spectrosc. (Chem. Soc. London), **4**, 96 (1976).
2. G.C. Tabisz. Mol. Spectrosc. (Chemical Society, London), **6**, (1979).
3. P. Arrighini. Lect. Notes Chem. **25** (1981).
4. K.L.C. Hunt. J. Chem. Phys. **78**, 6149 (1983).
5. A.J. Stone. Mol. Phys. **56**, 1065 (1985).
6. R.W.F. Bader. Atoms in molecules — a quantum theory. University of Oxford Press, Oxford. 1990.
7. R.F.W. Bader. Chem. Rev. **91**, 893 (1991).
8. J.G. Ángyán, G. Jansen, M. Loos, C. Hättig, and B.A. Heß. Chem. Phys. Lett. **219**, 267 (1994).
9. C.R. Le Sueur and A.J. Stone. Mol. Phys. **78**, 1267 (1993).
10. A.J. Stone, C. Hättig, G. Jansen, and J.G. Ángyán. Mol. Phys. In press.
11. G. Jansen, C. Hättig, B.A. Heß, and J.G. Ángyán. Mol. Phys. In press.
12. R.F.W. Bader. J. Chem. Phys. **91**, 6989 (1989).
13. K.E. Laidig and R.F.W. Bader. J. Chem. Phys. **93**, 7213 (1990).
14. R.F.W. Bader, T.A. Keith, K.M. Gough, and K.E. Laidig. Mol. Phys. **75**, 1167 (1992).
15. C.R. Le Sueur and A.J. Stone. Mol. Phys. **83**, 293 (1994).
16. J.O. Hirschfelder, W.B. Brown, and S.T. Epstein. Adv. Quantum Chem. **1**, 255 (1964).
17. F. Visser, P.E.S. Wormer, and P. Stam. J. Chem. Phys. **79**, 4973 (1983).
18. W.S. Benedict, N. Gailar, and E.K. Plyler. J. Chem. Phys. **24**, 1139 (1956).
19. G. Herzberg. Molecular spectra and molecular structure. Vol. 3. Electronic spectra and electronic structure of polyatomic molecules. Van Nostrand, Princeton, N.J. 1966.
20. K.P. Huber and G. Herzberg. Molecular spectra and molecular structure. Vol. 4. Constants of diatomic molecules. Van Nostrand, Princeton, N.J. 1979.
21. S. Swaminathan, B.M. Craven, and R.K. McMullan. Acta Crystallogr. Sect. B: Struct. Sci. **B40**, 300 (1984).
22. K. Anderson, M.R.A. Blomberg, M.P. Fülscher, V. Kellö, R. Lindh, P.-Å. Malmquist, J. Noga, J. Olsen, B.O. Roos, A.J. Sadlej, P.E.M. Siegbahn, M. Urban, and P.-O. Widmark. MOLCAS version 3, University of Lund, Sweden. 1994.
23. A.J. Sadlej. Collect. Czech. Chem. Commun. **53**, 1995 (1988).
24. P.-O. Widmark, P.-A. Malmquist, and B.O. Roos. Theor. Chim. Acta, **77**, 291 (1990).
25. M.J. Frisch, G.W. Trucks, M. Head-Gordon, P.M.W. Gill, M.W. Wong, J.B. Foresman, B.G. Johnson, H.B. Schlegel, M.B. Robb, E.S. Replogle, R. Gomperts, J.L. Andres, K. Raghavachari, J.S. Binkley, C. Gonzalez, R.L Martin, D.J. Fox, D.J. Defrees, J. Baker, J.J.P. Stewart, and J.A. Pople. Gaussian 92, Revision D1. Gaussian, Inc., Pittsburgh, Pa. 1992.
26. F.W. Biegler-König, R.W.F. Bader, and T.H. Tang. J. Comput. Chem. **3**, 317 (1982).
27. A. Kumar and W.J. Meath. Chem. Phys. **189**, 467 (1994).
28. G.D. Zeiss and W.J. Meath. Mol. Phys. **33**, 1155 (1977).
29. A. Kumar and W.J. Meath. Mol. Phys. **75**, 311 (1992).
30. W. Murphy. J. Chem. Phys. **67**, 5877 (1977).
31. A.M. Sanchez de Merás, H.J.Aa. Jensen, P. Jørgensen, and J. Olsen. Chem. Phys. Lett. **186**, 379 (1991).
32. M.A. Spackman. J. Chem. Phys. **94**, 1288 (1991).
33. C. Hättig and B.A. Heß, Chem. Phys. Lett. **233**, 359 (1995).
34. C. Hättig and B.A. Heß. J. Phys. Chem. **100**, 6243 (1996).
35. H.A. Bethe and E.E. Salpeter. Quantum mechanics of one- and two-electron atoms. Springer Verlag, Berlin. 1957.
36. F. Mulder and W.J. Meath. Mol. Phys. **42**, 629 (1981).
37. P.-O. Åstrand, A. Wallquist, G. Karlström, and P. Linse. J. Chem. Phys. **100**, 1262 (1994).
38. J.G. Ángyán, M. Loos, and I. Mayer. J. Phys. Chem. **98**, 5244 (1994).
39. W.J. Meath and A. Kumar. Int. J. Quantum Chem. Symp. **24**, 501 (1990).

Coherent control of electrons in molecules

Andre D. Bandrauk, Hengtai Yu, and Eric E. Aubanel

Abstract: Coherent superposition of electronic states can be achieved by simultaneous laser excitation at different frequencies. As an example, the three-level system is examined in order to demonstrate the possibility of phase control of electron transfer in molecules. Ab initio calculations are used to illustrate the principle in a charge transfer molecule DMBAN, 4-(*N*,*N*-dimethylamino)benzonitrile.

Key words: laser control, charge transfer electrons.

Résumé : On peut effectuer une superposition cohérente d'états électroniques par une excitation simultanée au laser à différentes fréquences. À titre exemple, on a examiné le système à trois niveaux afin de démontrer la possibilité de contrôle de phase du transfert d'électron dans des molécules. On a utilisé des calculs ab initio pour illustrer le principe dans une molécule à transfert de charge, le 4-(*N*,*N*-diméthylamino)benzonitrile (DMABN).

Mots clés : contrôle de laser, électrons de transfert de charge.

[Traduit par la rédaction]

I. Introduction

Control of photochemical processes has focused on controlling via relative laser beam phases the detailed dynamics of photodissociations of molecules (1–3). There has recently been interest in the possibilities of controlling electrons. Thus high-order harmonic generation in atoms and molecules was shown theoretically to be controllable by superpositions of laser beams of different frequency and phase, as a result of the phase control of electron trajectories upon ionization (4, 5). This numerical demonstration of electron control lead to the highly innovative idea of generating attosecond (subfemtosecond) pulses by using superpositions of elliptically and linearly polarized light in order to control electron recollision with the parent ion (5, 6). Recently we showed that one can control electron transfer, ET, in photodissociating Cl_2 molecules by using a symmetry-breaking excitation scheme with ω and 2ω photons (4–7). Such a scheme has now been demonstrated experimentally to provide a useful means of controlling currents in quantum wells (8), which have strong analogies to molecular systems.

In the present work we investigate the use of optically induced quantum coherence effects, which can be achieved using moderately intense laser fields, well below intensities $I = 10^{13}$ W/cm^2, above which considerable ionization will then occur (9, 10). A well-known coherent effect in atomic quantum optics is the creation of the so-called dark state (11), which is a special dressed superposition state of excited states and is uncoupled from the ground state. We shall focus on the phase dependence of coherent superpositions of the three-level system, called the V-system in atomic physics (12, 13), in order to illustrate the basic principle of **phase-dependent electron transfer**. We then use ab initio calculation of the lowest excited states of a charge transfer (CT) molecular system: DMBAN, 4(*N*,*N*-dimethylamino)benzonitrile, illustrated in Fig. 1. Previous ab initio calculations on this system (14) have shown the existence of ion-pair states in the excited states of this molecule. Thus using electron distributions in DMBAN obtained from ab initio (with CI) calculations we have examined the feasibility of creating laser-induced charge redistributions in order ot control ET, or equivalently CT, in such large molecular systems via the phase of the exciting laser beams. Conditions for such electron control scenarios in large systems are discussed with reference to the ab initio results presented here.

Fig. 1. Coordinate system of DMABN.

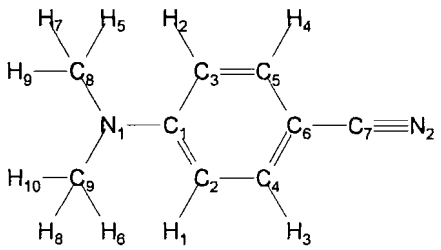

II. Phase control in a three-level V system

Previous studies of the coherences induced in a three-level V-system, Fig. 2, have shown the occurrence of dark states that are completely uncoupled from the initial ground states as a consequence of radiative nonlinear coherent properties of such systems during the laser excitation (11–13). We examine here the phase dependence of such systems and explore in the next section their possible application to controlling ET, or equivalently CT, in large molecules.

Received October 12, 1995.

This paper is dedicated to Professor Richard F.W. Bader on the occasion of his 65th birthday.

A.D. Bandrauk,[1] H. Yu and E.E. Aubanel. Laboratoire de chimie théorique, Faculté des sciences, Université de Sherbrooke, Sherbrooke, QC J1K 2R1, Canada.

[1] Author to whom correspondence may be addressed. Telephone: (819) 821-7098. Fax: (819) 821-8017. E-mail: bandrauk@gauss.chimie.usherb.ca

Fig. 2. Resonant three-level V system with appropriate Rabi frequencies Ω, transition moments μ, and laser field amplitudes E.

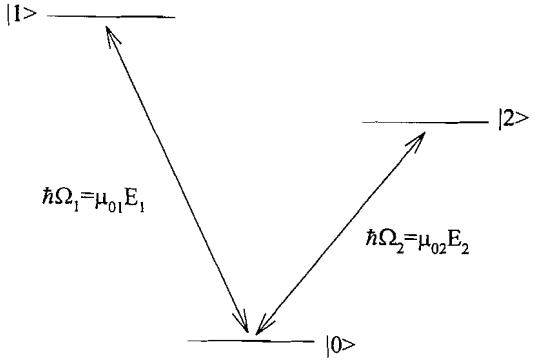

We limit ourselves here to the resonant case, whereas the nonresonant case (13) will be described in detail elsewhere (15). Figure 2 illustrates the resonant V configuration in which one assumes simultaneous excitation from an initial ground state $|0\rangle$ to two nondegenerate excited states $|1\rangle$ and $|2\rangle$ with Rabi frequencies Ω_1 and Ω_2, where $\hbar\Omega_2 = \mu_{01}E_2$, $\hbar\Omega_2 = \mu_{02}E_2$, μ is the transition moment, and E is the field amplitude. For a real time-dependent field, $E(t) = E\cos(\omega t+\phi) = (E/2)(e^{i(\omega t+\phi)}+e^{-i(\omega t+\phi)})$, in the rotating wave approximation, RWA, one retains only the resonant field $(E/2)(e^{i(\omega t+\phi)}$ contribution. This leads to a time-independent Hamiltonian in the dressed state representation (9, 13),

$$[1] \qquad H = \frac{1}{2}\begin{pmatrix} 0 & \Omega_1 e^{i\phi_1} & \Omega_2 e^{i\phi_2} \\ \Omega_1 e^{-i\phi_1} & 0 & 0 \\ \Omega_2 e^{-i\phi_2} & 0 & 0 \end{pmatrix}$$

where ϕ_1 and ϕ_2 are the phases of the two laser beams E_1 and E_2. Defining an effective three-level Rabi frequency

$$[2] \qquad \Omega = (\Omega_1^2 + \Omega_2^2)^{1/2}$$

one obtains the following three dressed states or eigenmodes of the three-level laser–molecule system (n =photon number),

$$[3] \qquad |\alpha\rangle = 2^{-1/2}\left[|0, n_1, n_2\rangle + \frac{\Omega_1}{\Omega}e^{-i\phi_1}|1, n_1-1, n_2\rangle + \frac{\Omega_2}{\Omega}e^{-i\phi_2}|2, n_1, n_2, -1\rangle\right]$$

$$[4] \qquad E_\alpha = \frac{\hbar\Omega}{2}$$

$$[5] \qquad |\beta\rangle = 2^{-1/2}\left[-|0_1, n_1, n_2\rangle + \frac{\Omega_1}{\Omega}e^{-i\phi_1}|1, n_1-1, n_2\rangle + \frac{\Omega_2}{\Omega}e^{-i\phi_2}|2, n_1, n_2-1\rangle\right]$$

$$[6] \qquad E_\beta = -\frac{\hbar\Omega}{2}$$

$$[7] \qquad |\gamma\rangle = -\frac{\Omega_2}{\Omega}e^{i\phi_2}|1, n_1-1, n_2\rangle + \frac{\Omega_1}{\Omega}e^{i\phi_2}|2, n_1, n_2-1\rangle$$

$$[8] \qquad E_\gamma = 0$$

where $E_{\alpha(\beta,\gamma)}$ are the dressed state energies of the laser–molecule system. We note that the states $|\alpha\rangle$ and $|\beta\rangle$ are Stark shifted by $\pm\hbar(\Omega/2)$, so that the frequency separation between these two dressed states is the effective Rabi frequency Ω defined in eq. [2]. Both states reflect the Rabi-induced superposition of all three electronic states that are phase dependent. The state $|\gamma\rangle$ is the dark state, which remains unshifted and does not contain the initial state $|0\rangle$. Clearly the state $|\gamma\rangle$ will never be populated from the ground state $|0\rangle$ in the V-configuration. As a consequence the total wave function can be written as combinations of $|\alpha\rangle$ and $|\beta\rangle$ only:

$$[9] \qquad |\psi(t)\rangle = 2^{-1/2}(|\alpha\rangle e^{\frac{-i\Omega t}{2}} - |\beta\rangle e^{\frac{i\Omega t}{2}})$$

satisfying the initial condition $|\psi(0)\rangle = |0, n_1, n_2\rangle$, i.e., the ground state. Thus at times $\tau = \pi/\Omega$, one has the superpositions

$$[10] \qquad |\psi(\tau)\rangle = -i2^{-1/2}(|\alpha\rangle + |\beta\rangle)$$

$$= -i\left(\frac{\Omega_1}{\Omega}e^{-i\phi_1}|1, n_1-1, n_2\rangle + \frac{\Omega_2}{\Omega}e^{-i\phi_2}|2, n_1, n_2-1\rangle\right)$$

One observes that at such times, i.e., at $\tau = \pi/\Omega$, the laser-induced coherent state is a pure superposition of the excited state $|1\rangle$ and $|2\rangle$ only, the relative sign of these amplitudes can be controlled by the relative laser phase difference $(\phi_2 - \phi_1)$. To see this more succinctly, we specialize further to the particular case,

$$[11] \qquad \Omega_1 = \Omega_2 = 2^{-1/2}\Omega$$

This can be achieved by varying the laser field amplitudes E_1 and E_2 so that $\mu_{01}E_1 = \mu_{02}E_2$. In this case one recovers the simply transparent result,

$$[12] \qquad |\psi(\tau)\rangle = -i2^{-1/2}(e^{-i\phi_1}|1, n_1-1, n_2\rangle + e^{-i\phi_2}|2, n_1, n_2-1\rangle)$$

Thus if $\phi_1 = \phi_2 = \phi$, one obtains

$$[13] \qquad |\psi^+(\tau)\rangle = -i2^{-1/2}(e^{-i\phi}(|1, n_1-1, n_2\rangle + |2, n_1, n_2-1\rangle)$$

If $\phi_1 = \phi_2 = \pi$, one now has

$$[14] \qquad |\psi^-(\tau)\rangle = -i2^{-1/2}e^{-i\phi}(|1, n_1-1, n_2\rangle - |2, n_1, n_2-1\rangle)$$

We observe that at times $\tau = \pi/\Omega$, one can create new excited state amplitudes that are simple sums or differences of the original excited states. For molecules, this implies that one should be able to prepare simple superpositions of delocalized molecular orbitals and thus create more localized electronic states leading to laser-induced CT.

We designate the states $|\psi^\pm(\tau)\rangle$ as our target states and

Table 1. Optimized geometry of DMABN using 3-21G basis sets.

Bond length (Å)			
C_1—C_2	1.407	C_7—N_2	1.141
C_2—C_4	1.373	C_1—N_1	1.375
C_4—C_6	1.388	C_8—N_1	1.463
C_6—C_7	1.423	C_2—H_1	1.076
C_4—H_3	1.080	C_8—H_5	1.188
Valence angle (degree)			
$C_3C_1C_2$	115.86	$C_1C_2C_4$	121.89
$C_2C_4C_6$	121.31	$C_4C_6C_7$	121.14
$N_1C_1C_2$	122.07	$C_8N_1C_1$	124.35

examine their time evolution from the occupation probability:

$$[15] \qquad P^{\pm}(t) = |\langle\psi^{\pm}(\tau)|\psi(t)\rangle|^2$$

The resulting time-dependent occupation probability of the target states $|\psi^{\pm}(\tau)\rangle$ is readily obtained from eqs. [13]–[15].

$$[16] \qquad P^{\pm}(t) = \tfrac{1}{2}\sin^2\left(\frac{\Omega t}{2}\right)[1 \pm \cos(\phi_2 - \phi_1)]$$

We conclude by observing that in order to obtain complete selectivity of one state or another, i.e., $P^{\pm}(t) = 1$, then: (*i*) the phases of the two lasers must be locked, i.e., $\phi_2 - \phi_1 = 0$ or $= \pi$; (*ii*) the occurrence time of the selectivity is $t_n = (2n+1)\tau = [(2n+1)\pi]/\Omega$. Thus two essential parameters enter into the controllability of the system: the Rabi frequency Ω, which depends on transition moments μ and field E amplitudes, and finally the phase difference ϕ between the two laser beams or pulses. We observe furthermore from eq. [10] that a special feature of the three-level V system is that in the general case the total system oscillates between the ground state $|0\rangle$ and the coherent linear superpositions of $|1\rangle$ and $|2\rangle$ defined by $|(\psi(\tau)\rangle$, eq. [10]. In fact, the general state (eq. [9] can be written as

$$[17] \qquad |\psi(t)\rangle = |0\rangle\cos\left(\frac{\Omega t}{2}\right) - i|\psi(\tau)\rangle\sin\left(\frac{\Omega t}{2}\right)$$

thus showing that at recursion times $t_n = (2n+1)(\pi/\Omega)$, one is indeed in the general coherent state $|\psi(\tau)\rangle$, eq. [10], whereas times $t_m = 2m(\pi/\Omega)$, one is in the ground state, $|0\rangle$. In the next section we examine laser-induced electron density redistributions in a large molecule DMABN based on preparation of the coherent state $|\psi(\tau)\rangle$, eq. [10].

III. AB initio simulations

DMABN is the prototype of CT molecules, in which the formation of a twisted intramolecular charge transfer state is well documented from fluorescence studies. Thus from the red shifts of the fluorescence in polar solvents, it is inferred that the dimethylamino group (see Fig. 1) undergoes a 90° internal rotation with respect to the aromatic ring and an electron is completely transferred from the amino group to the benzonitrile moiety because the conjugation between the amino lone pair and the π orbitals in the aromatic ring is absent (16, 17). The time for such rotation has been estimated to be at least 40 picoseconds (ps) (16).

The static electronic properties of DMABN are calculated here by ab initio methods using the GAMESS program (18). The molecular geometry is reoptimized with split-valence shell 3-21G basis sets (19) using previous results (STO-3G, ref. 14) as a starting point and supposing the molecule has C_s symmetry. The optimized results for the planar geometry are given in Table 1. All energies in the ground state and the first five low-lying excited states are calculated by configuration interaction (CI) methods. MINI4 basis sets (20) are used for all hydrogen and two carbon atoms in the methyl groups, and MINI4+double zeta basis sets (21) are used for all other atoms. There are 39 occupied MOs in DMABN with 78 electrons; 34 orbitals with lower orbital energies were considered as the internal orbitals and the remaining 5 occupied MOs with higher orbital energies and the lowest 5 virtual MOs were included in the CI computations with single and double excitations. The number of symmetry-adapted (C_s) configurations is more than 60 000 for the basis sets mentioned above. The calculated energies are −452.7952, −452.5149, −452.4810, −452.4216, −452.4096, and −452.3958 au for the ground state and the first five low-lying excited states, respectively. This gives the first excitation energy 5.5 eV of state S_1. This value is overestimated by 2.5 eV compared with the experimental excitation energy of ~4 eV (14). The second excited state S_3 can be reached by 8.5 eV from the ground state.

To classify clearly molecular orbital symmetry, so that we can easily simulate ET, DMABN is regarded as C_{2v} symmetry. This way the last three occupied MOs that are used for CI calculations are assigned to symmetries $4b_1(37)$ with mainly character of the N lone pair and triple bond C≡N, $1a_2(38)$ with mainly π character in the aromatic ring, and $5b_1(39)$ of mainly N lone pair character. Similar considerations apply to the lowest two virtual MOs $6b_1(40)$ (lone pair) and $2a_2(41)$ (π character in aromatic ring). It can be seen from an analysis of the coefficients of electronic configuration state functions (CSF) in the CI calculations that the first excited state S_1 is characterized mainly by the two CSF transitions: $5b_1(39) \rightarrow 1a_2(41)$ and $1a_2(38) \rightarrow 6b_1(41)$ in the planar geometry, corresponding to $^1B_2$ symmetry. In fact it is obtained by $n\pi^*$ plus πn^* transitions. The second S_2 and third S_3 excited states are characterized by the three CSF transitions $5b_1(39) \rightarrow 6b_1(41)$ and $4b_1(37) \rightarrow 6b_1(39)$, which correspond to nn^* transitions, and $1a_2(38) \rightarrow 2a_2(41)$, which is a $\pi\pi^*$ transition. Both S_2 and S_3 excited states have the same symmetry $^1A_1$ as does the ground state. Hence they are easily accessible by laser excitation from the ground state. For the sake of convenience, we call these three CSF Φ_A, Φ_B, and Φ_C in the following text.

Now we want to simulate the ET from the N lone pair on the amino group to the triple bond C≡N in the DMABN. Because the first excited state S_1 has different symmetry from the ground state and is formed by the $n\pi^*$ (or πn^*) transition, ideal ET from the amino group to the triple bond can be achieved by considering the exited states S_2 and S_3 only. To construct the coherent state, we assume that the S_2 and S_3 state wave functions Ψ_I and Ψ_{II} can be expressed as a linear combination of the three electronic CSF, Φ_A, Φ_B, and Φ_C:

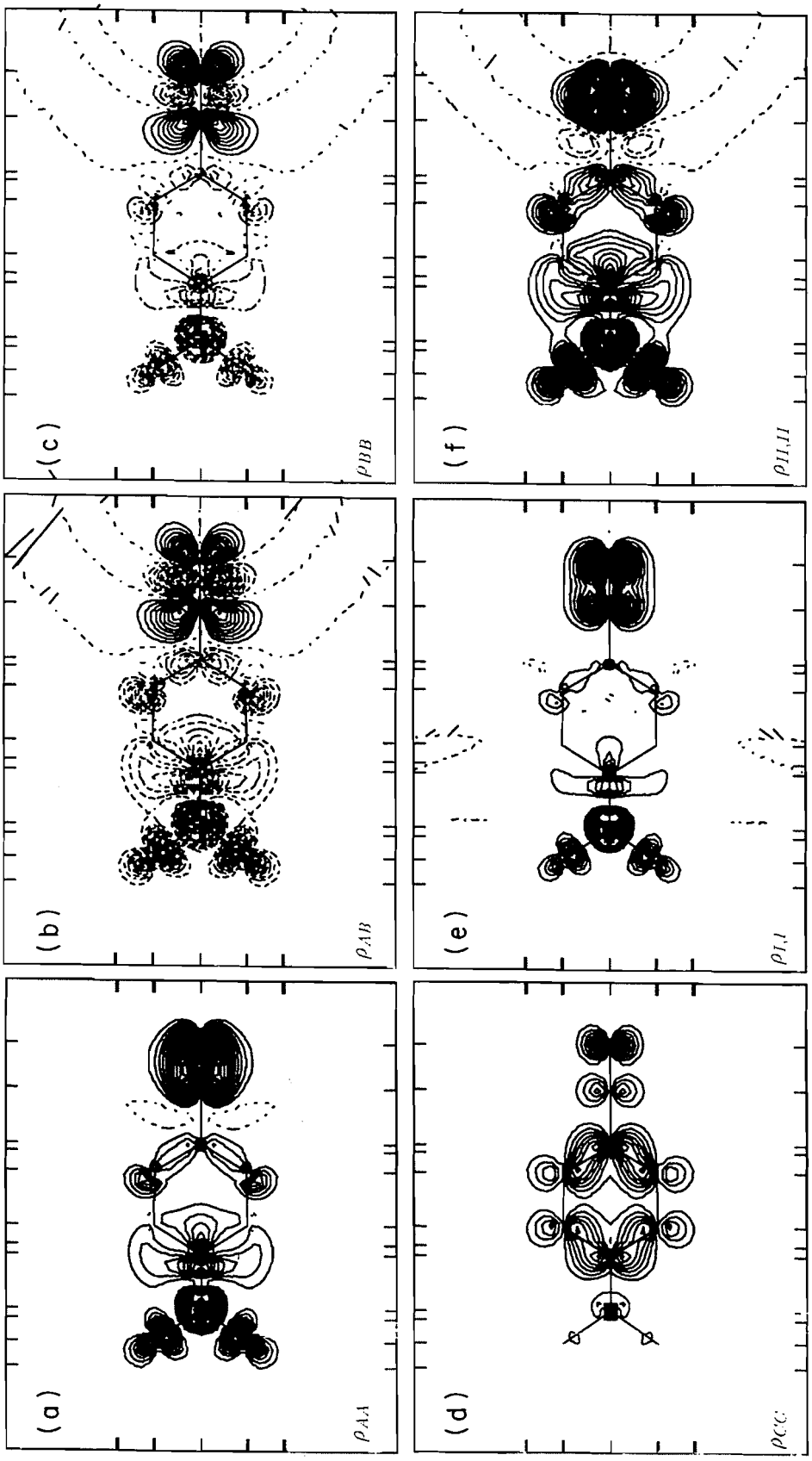

Fig. 3. Density maps of initial wave states: (*a*) ρ_{AA}, (*b*) ρ_{AB}, (*c*) ρ_{BB}, (*d*) ρ_{CC}, (*e*) $\rho_{I,I}$, and (*f*) $\rho_{II,II}$.

[18] $|\Psi_I\rangle = a_1\Phi_A + b_1\Phi_B + c_1\Phi_C$

and

[19] $|\Psi_{II}\rangle = a_2\Phi_A + b_2\Phi_B + c_2\Phi_C$

where a_i, b_i, $c_i (i = 1, 2)$ are the coefficients of CSF in the CI calculations. The calculated values are $a_1 = 0.9635$, $b_1 = 0.1088$, $c_1 = -0.2447$, and $a_2 = -0.4400$, $b_2 = 0.8859$, $c_2 = -0.1467$ after renormalization to eliminate other CSF contributions. Here $|\Psi_I\rangle$ and $|\Psi_{II}\rangle$ correspond to $|1, n_1-1, n2\rangle$ and $|2, n_1, n2_1\rangle$ in eq. [10]. As mentioned above, ET can be controlled by two factors: laser field amplitudes E and the phase difference ϕ between the two laser beams or pulses. According to eq. [10], the coherent state can be written as

[20] $|\Psi_{co}\rangle = C_I e^{-i\phi_1}\Psi_I + C_{II}e^{-i\phi_2}\Psi_{II}$

where C_I and C_{II} are the coefficients related to the laser amplitudes E and ϕ_1, ϕ_2 are the phases of the two laser fields. For simplicity without losing generality, eq. [20] can be rewritten as

[21] $|\Psi_{co}\rangle = \Psi_I + \alpha e^{-i\phi_1}\Psi_I$

where ϕ is the phase difference between the two laser field and α is the coefficient related to the laser amplitude E through RAbi frequency Ω. Putting eqs. [18] and [19] into eq. [21], $|\Psi_{co}\rangle$ becomes

[22] $|\Psi_{co}\rangle = a_1\Phi_A + b_1\Phi_B + c_1\Phi_C + \alpha e^{i\phi}(a_2\Phi_A + b_2\Phi_B + c_2\Phi_C)$

Thus the coherent state density is

[23] $\rho_{co} = \Psi^*_{co}\Psi_{co} = A\rho_{AA} + B\rho_{BB} + C\rho_{CC} + AB\rho_{AB}$

where

[24]
$$A = a_1^2 + (\alpha a_2)^2 + 2\alpha a_1 a_2 \cos(\phi)$$
$$B = b_1^2 + (\alpha b_2)^2 + 2\alpha b_1 b_2 \cos(\phi)$$
$$C = c_1^2 + (\alpha c_2)^2 + 2\alpha c_1 c_2 \cos(\phi)$$
$$AB = 2[a_1 b_1 + \alpha^2 a_2 b_2 + \alpha(a_2 b_1 + a_1 b_2)\cos(\phi)]$$

In deriving eq. [23], we have eliminated $\Phi^*_A\Phi_C$ and $\Phi^*_B\Phi_C$ contributions because they are the transition densities between different symmetries (Φ_C is $\pi\pi^*$ character), which are regarded as zero. The configuration densities are obtained from the wave functions of the excited states S_2 and S_3. Thus we obtain from eqs. [18] and [19] (see also ref. 14):

[25]
$$\rho_{AA} = [b_2^2\rho_{I,I} - 2b_1 b_2\rho_{I,II} + b_1^2\rho_{II,II} - (b_1c_2 - c_1b_2)^2\rho_{CC}]/\text{norm}$$
$$\rho_{BB} = [a_2^2\rho_{I,I} - 2a_1 a_2\rho_{I,II} + a_1^2\rho_{II,II} - (a_1c_2 - c_1a_2)^2\rho_{CC}]/\text{norm}$$
$$\rho_{AB} = -[a_2 b_2\rho_{I,I} - (a_1b_2 + a_2b_1)\rho_{I,II} + a_1b_1\rho_{II,II} - (a_1c_2 - c_1a_2)(b_1c_2 - c_1b_2)\rho_{CC}]/\text{norm}$$

Fig. 4. Density maps obtained by changing α or laser field amplitudes E: (*a*) $\alpha = 2.19$, (*b*) $\alpha = -0.12$ (*c*) $\alpha = -1.67$.

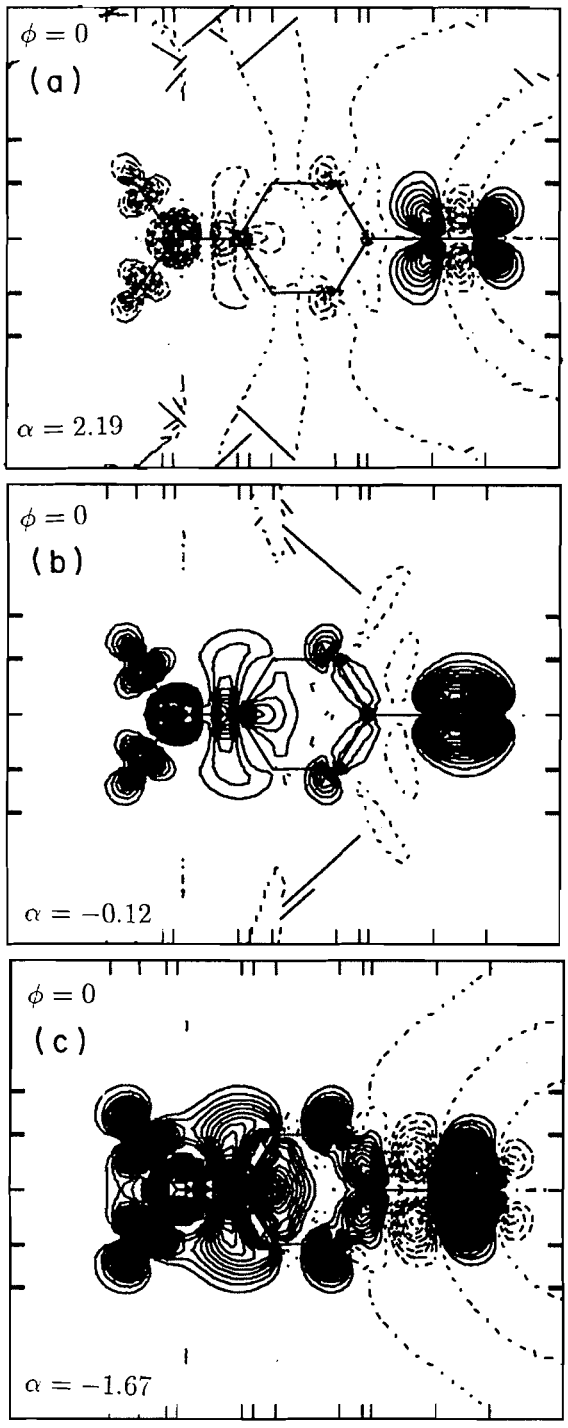

where norm $= (a_1b_2 - b_1a_2)^2$, and $\rho_{I,I}$, $\rho_{I,II}$, and $\rho_{II,II}$ are the densities of S_2 and S_3 and the transition density between these two states, respectively. In deriving eq. [25], ρ_{AC} and ρ_{BC} are considered to be zero as explained above. Putting eq. [25] into eq. [23] we can obtain explicit formula for ρ_{co}, and laser-induced ET can be simulated by changing α and ϕ.

It should be indicated that the excited state S_2 (or S_3) contains 10 active orbitals, 5 occupied and 5 virtual MOs, i.e., 10 electrons are involved in the CI calculations. All

Fig. 5. Density maps obtained by changing the phase difference ϕ at $\alpha = -0.12$ (Fig. 4*b*): (*a*) 45°, (*b*) 90° (*b*) 135° (*d*) 180°.

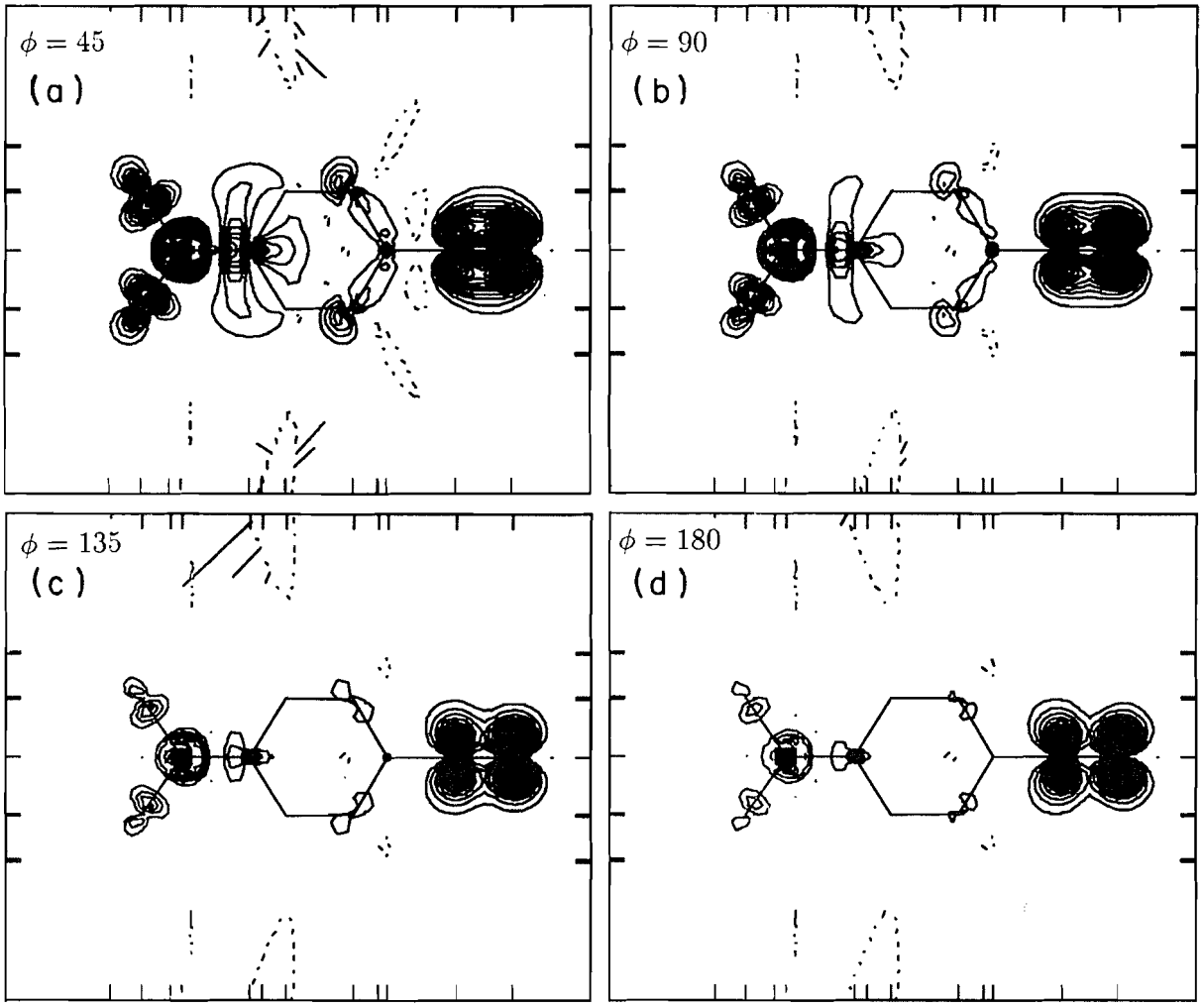

wave functions we obtain are renormalized and the corresponding density maps are calculated for 10 active electrons. The molecule DMABN is placed in the zx plane and density maps are drawn in the same plane.

The initial state density maps of various wave functions are given in Fig. 3*a–f* for ρ_{AA}, ρ_{AB}, ρ_{BB}, ρ_{CC}, $\rho_{I,I}$, and $\rho_{II,II}$, respectively. It can be seen that the density ρ_{AA} is similar to that of $\rho_{I,I}$, and ρ_{AB} similar to $\rho_{II,II}$, as these reflect the dominant coefficients. For example, Φ_A has the largest coefficient in Ψ_I while on the other hand Φ_B has the largest coefficient in Ψ_{II}. Both represent mainly $nn*$ transitions. ρ_{CC} represents mainly a $\pi\pi^*$ transition as shown in Fig. 3*d*. Transition densities ρ_{AB} between Φ_A and Φ_B are not very large although they are of the same symmetry.

The density maps that correspond to a change in α related to laser amplitudes E are given in Fig. 4*a–c*. When $\alpha = -(a_1/a_2) = 2.19$ and $\phi = 0$, from eqs. [18] and [19], Φ_A is cancelled in Ψ_I and Ψ_{II}. The resulting density map is formed mainly from Φ_B and Φ_C, and is illustrated in Fig. 4*a*. In this case the transferred electrons are concentrated mostly on the triple bond C≡N. We can make Φ_B disappear in Ψ_I and Ψ_{II} by choosing $\alpha = -(b_1/b_2) = -0.12$ with $\phi = 0$. The corresponding map contains mainly Φ_A and Φ_C configurations and is given in Fig. 4*b*. It is similar to ρ_{AA} shown in Fig. 3*a* because Φ_A now plays a principle role in Ψ_I and Ψ_{II}. When we cancel the contribution of configuration state Φ_C with $\alpha - (c_1/c_2) = -1.67$ and $\phi = 0$, the map contains mainly Φ_A and Φ_B. The corresponding map, Fig. 4*c*, shows a strong electron density, mainly concentrated on the N lone pair in the amino group and the triple bond C≡N. This reflects the negative coefficients of Φ_C in Ψ_I and Ψ_{II}. The ET effects shown in Fig. 4 correspond therefore to changes in the laser field amplitude E only through the factor α.

Now we demonstrate the effect of laser phase difference ϕ on ET. The ideal scenario to see how electrons can be transferred from the N lone pair in the amino group to the triple bond C≡N in DMABN involves cancelling the Φ_B state in Ψ_I and Ψ_{II}. Thus when $\phi = 0$, the corresponding map is the same as shown in Fig. 4*b*. The new maps for $\phi = 45°$, 90°, 135° and 180° are given in Fig. 5*a– d*. Comparing Figs. 4*b* and 5, one observes that ET begins to occur at $\phi = 90°$, gradually attaining a maximum at $\phi = 180°$, Fig. 5*d*. In the

latter case, one is essentially changing the sign of α from -0.12 to 0.12, thus enhancing the presence of the Φ_B state function, a nn^* transition.

IV. Conclusions

We have shown that simultaneous laser excitation of different electronic states in CT systems can be used to transfer electrons between different functional groups, e.g., amino to nitrile. This is achieved by varying appropriately configuration state function coefficients through laser amplitudes E. Varying relative phases ϕ of the laser fields will help to enhance ET effects in large molecules. Clearly, as shown from eq. [17], the ET effect only persists during the laser illumination, i.e., at the recursion times $\tau_n = (2n + 1)(\pi/\Omega)$. Since $\Omega(\text{cm}^{-1}) \simeq 10^{-3}I(\text{W/cm}^{-2})\mu$ (au) (9), for a 10 au transition moment μ and intensity $I = 10^8$ W/cm^2, we thus obtain $\Omega \simeq 100$ cm^{-1} and $\tau = \pi/\Omega = 10^{-12}$ s = 1 ps. Considering that DMABN undergoes an internal rotation after 40 ps in order to stabilize the CT state (16, 17), the above calculation shows that laser-induced ET should be feasible with moderate intensity (10^8 W/cm^2) picosecond pulses. Another condition is that the total molecular rotation rate must be smaller than the Rabi frequency Ω. In the present case this condition is satisfied. One should therefore expect molecular alignment along the laser fields (7), since one is exciting both states S_2 and S_3 using transition moments that are parallel to the CT process, i.e., from N to C≡N (see Fig. 1). This will enhance the electron transfer control described in the present work.

V. Acknowledgments

We thank Professor J.D. Goddard for providing GAUSSIAN 92 CI results of DMABN. We thank the Natural Sciences and Engineering Research Council of Canada for support of the present research.

References

1. P. Brumer and M. Shapiro. Chem. Phys. Lett. **126**, 541 (1986); J. Chem. Phys. **84**, 4103 (1986).
2. M. Shapiro, J. Hepburn, and P. Brumer. Chem. Phys. Lett. **149**, 451 (1988).
3. P. Brumer and M. Shapiro. *In* Molecules in laser fields. *Edited by* A.D. Bandrauk. M. Dekker, New York. 1984. Chap. 6.
4. T. Zuo, A.D. Bandrauk, M. Ivanov, and P.B. Corkum. Phys. Rev. A: At. Mol. Opt. Phys. **51**, 3991 (1995).
5. M. Ivanov, P.B. Corkum, T. Zuo, and A.D. Bandrauk. Phys. Rev. Lett. **74**, 2939 (1995).
6. P.B. Corkum, N.H. Burnet, and M. Ivanov. Opt. Lett. **19**, 1870 (1994).
7. E.E. Aubanel and A.D. Bandrauk. Chem. Phys. Lett. **229**, 169 (1994); Chem. Phys. **198**, 159 (1995).
8. E. Dupont and P.B. Corkum. Phys. Rev. Lett. **74**, 3596 (1995).
9. A.D. Bandrauk (*Editor*). Molecules in laser fields. M. Dekker, New York. 1984. Chap. 1.
10. P. Dietrich, D.T. Strickland, M. Laberge, and P.B. Corkum. *In* Molecules in laser fields. *Edited by* A.D. Bandrauk. M. Dekker, New York. 1984. Chap. 4.
11. B.W. Shore. The theory of coherent atomic excitation. Wiley, New York. 1990. p. 824.
12. M. Lindberg and R. Binder. Phys. Rev. Lett. **75**, 1403 (1995).
13. D.A. Cardimona. Phys. Rev. A: At Mol. Opt. Phys. **41**, 5016 (1990).
14. S. Kato and Y. Amatatsu. J. Chem. Phys. **92**, 7241 (1990).
15. A.D. Bandrauk, H. Yu, and E. Aubanel. In preparation.
16. J. Hicks, M. Vandersall, Z. Babarogic, and K. Eisenthal. Chem. Phys. Lett. **116**, 18 (1981).
17. O. Kajimoto, M. Futakami, T. Kobayashi, and K. Yamasaki. J. Phys. Chem. **92**, 18 (1981).
18. M.W. Schmidt, K.K. Baldridge, J.A. Boatz, J.H. Jensen, S. Koseki, M.S. Gordon, K.A. Nguyen, T.L. Windus, and S.T. Elbert. QCPE Bull. **10**, 52 (1990).
19. J.S. Binkley, J.A. Pople, and W.J. Hehre. J. Am. Chem. Soc. **102**, 939 (1980).
20. H. Tatewaki and S. Huzinaga. J. Comput. Chem. **1**, 205 (1980).
21. T.H. Dunning, Jr. and P.J. Hay. *In* Methods of electronic structure theory. *Edited by* H.F. Shaefer III. Plenum Press, New York. 1977. Chap. 1.

Current-density dependent exchange-correlation functionals

Axel D. Becke

Abstract: Previous models for exchange (Becke and Roussel, Phys. Rev. A: **39**, 3761 (1989)) and for correlation (Becke, J. Chem. Phys. **88**, 1053 (1988)) are, in a simple and natural way, generalized to include explicit dependence on current density $\boldsymbol{J}$. First-principles incorporation of $\boldsymbol{J}$ into exchange-correlation density functionals, as proposed here, is crucial for further progress in the study of magnetic effects in density-functional theory.

Key words: density-functional theory, exchange-correlation functionals, current density.

Résumé : Des modèles antérieures d'éxchange (Becke et Roussel, Phys. Rev. A: **39**, 3761 (1989)) et de corrélation (Becke, J. Chem. Phys. **88**, 1053 (1988)) sont généralisés d'une façon simple et naturelle de façon à inclure la dépendance explicite sur la densité du courant, $\boldsymbol{J}$. Telle que proposée ici, l'incorporation sur la base de principes premiers de $\boldsymbol{J}$ dans les fonctionnelles de la densité de la corrélation d'éxchange est cruciale pour les progrès futurs dans l'étude des effets magnétiques de la théorie de la densité fonctionnelle.

Mots clés : théorie de la densité fonctionnelle, fonctionnelles de la corrélation d'éxchange, densité de courant.

[Traduit par la rédaction]

Introduction

There has been a call in recent density-functional literature for exchange-correlation approximations with explicit dependence on *current* density $\boldsymbol{J}$ as well as the density itself (1, 2). Such functionals are required for proper description of magnetic properties of electronic systems. The formalities of current-density-functional theory have been discussed by Vignale, Rasolt, and Geldart (1). A first-principles derivation of the $\boldsymbol{J}$-dependent exchange-correlation energy in inhomogeneous systems, however, is still lacking. In this note, we present such a derivation.

The various ingredients of this work have, in fact, already been published. Indeed, a related $\boldsymbol{J}$-dependent correlation-only functional may be found in ref. 3. Here, we generate a new, $\boldsymbol{J}$-dependent exchange functional by combining the $\boldsymbol{J}$-dependent exchange-hole curvature formula of Dobson (3, 4) with the hydrogenic exchange-hole model of Becke and Roussel (5). Then, we generate a new correlation functional by generalizing an old correlation model from 1988 (6).

Exchange

The exchange-hole model of Becke and Roussel is based on the following analytic form inspired by the hydrogenic atom (see ref. 5 for details):

$$[1] \qquad \rho_{X\sigma}(\boldsymbol{r}, s) = \frac{a}{16\pi bs}\left[(a|b-s|+1)e^{-a|b-s|} - (a|b+s|+1)e^{-a|b+s|}\right]$$

where $\rho_{X\sigma}$ is the σ-spin exchange charge density, and the arguments $(\boldsymbol{r}, s)$ denote spherical average on a shell of radius s centred on the reference point $\boldsymbol{r}$. This model exchange charge density is always positive definite and properly normalized by construction. Two parameters a and b need to be specified at each reference point. If the leading two terms of the Taylor expansion (around $\boldsymbol{r}$) of the model $\rho_{X\sigma}$ are equated to those of the exact $\rho_{X\sigma}$ at each reference point,

$$[2] \qquad \rho_{X\sigma}(\boldsymbol{r}, s) = \rho_\sigma + Q_\sigma s^2 + \ldots$$

then a parameter-free exchange approximation is obtained. Equating values at $s = 0$ yields the condition

$$[3] \qquad a^3 e^{-ab} = 8\pi\rho_\sigma$$

and equating curvatures Q_σ gives

$$[4] \qquad a^2 b - 2a = 6bQ_\sigma/\rho_\sigma$$

whose solution will be outlined momentarily.

For a system with zero current density, the exact exchange-charge curvature Q_σ is given by (5, 7):

$$[5] \qquad Q_\sigma = \tfrac{1}{6}[\nabla^2\rho_\sigma - 2\tau_\sigma + \tfrac{1}{2}(\nabla\rho_\sigma)^2/\rho_\sigma]$$

where the *kinetic* energy density τ_σ is defined as follows (notice that we do not include a 1/2 factor in the definition):

$$[6] \qquad \tau_\sigma = \sum_k \nabla\psi^*_{k\sigma} \cdot \nabla\psi_{k\sigma}$$

Solution of eqs. [3] and [4] proceeds by introduction of a

Received October 11, 1995.

This paper is dedicated to Professor Richard F.W. Bader on the occasion of his 65th birthday.

A.D. Becke.[1] Department of Chemistry, Queen's University, Kingston, ON K7L 3N6, Canada.

[1] Telephone: (613) 545-2634. Fax: (613) 545-6669. E-mail: beckea@qucdn.queensu.ca

new variable $x = ab$; then seeking the (unique) root of the 1D nonlinear equation

$$[7] \qquad \frac{xe^{-2x/3}}{(x-2)} = \tfrac{2}{3}\pi^{2/3}\rho_\sigma^{5/3}/Q_\sigma$$

by an iterative Newton–Raphson scheme (5). Finally, setting

$$[8] \qquad b^3 = \frac{x^3e^{-x}}{8\pi\rho_\sigma}$$

the exchange potential $U_{X\sigma}$ at reference point $\boldsymbol{r}$ is given by

$$[9] \qquad U_{X\sigma} = -(1 - e^{-x} - \tfrac{1}{2}xe^{-x})/b$$

and the total σ-spin exchange energy is

$$[10] \qquad E_{X\sigma} = \frac{1}{2}\int \rho_\sigma U_{X\sigma} d^3\boldsymbol{r}$$

Though not expressible in closed analytical form, this entire procedure is readily automated. We demonstrate in ref. 5 that the resulting exchange energies of atomic systems are significantly better than the LSDA (local spin-density approximation), but not as good as those of the best GGAs (generalized gradient approximation).

The curvature expression of eq. [5] is valid for systems of zero current density only. Dobson has pointed out that the generalization to non-zero currents is simple (3, 4). With the present definition of τ_σ, as given by eq. [6], we find that (see the Appendix)

$$[11] \qquad Q_\sigma = \tfrac{1}{6}[\nabla^2\rho_\sigma - 2\tau_\sigma + \tfrac{1}{2}(\nabla\rho_\sigma)^2/\rho_\sigma + 2\boldsymbol{J}_\sigma^2/\rho_\sigma]$$

where

$$[12] \qquad \boldsymbol{J}_\sigma = -\frac{i}{2}\sum_k [\psi_{k\sigma}^*\nabla\psi_{k\sigma} - \psi_{k\sigma}\nabla\psi_{k\sigma}^*]$$

is the (paramagnetic) σ-spin current density in atomic units. A $\boldsymbol{J}$-dependent extension of the Becke–Roussel exchange approximation is now obvious. Simply replace eq. [5] for Q_σ with eq. [11]. The resulting functional depends explicitly on ρ, $\nabla\rho$, $\nabla^2\rho$, τ, and $\boldsymbol{J}$. It is entirely free of empirical parameters, and its $\boldsymbol{J}$ dependence is incorporated in a first-principles manner.

Correlation

Our dynamical correlation model of ref. 6 (see also ref. 8) yields two correlation functionals: one for opposite-spin pairs,

$$[13] \qquad E_C^{opp} = -0.8\int \rho_\alpha\rho_\beta z_{\alpha\beta}^2\left[1 - \frac{\ln(1+z_{\alpha\beta})}{z_{\alpha\beta}}\right]d^3\boldsymbol{r}$$

and another for parallel-spin pairs,

$$[14] \qquad E_C^{\sigma\sigma} = -0.01\int \rho_\sigma\left\{\tau_\sigma - \frac{1}{4}\frac{(\nabla\rho_\sigma)^2}{\rho_\sigma}\right\} \times z_{\sigma\sigma}^4\left[1 - \frac{2}{z_{\sigma\sigma}}\ln\left(1 + \frac{z_{\sigma\sigma}}{2}\right)\right]d^3\boldsymbol{r}$$

where τ_σ is the same kinetic-energy density as above. Parameters $z_{\alpha\beta}$ and $z_{\sigma\sigma}$ are correlation "lengths" or "ranges" characterizing the sizes of the opposite and parallel-spin dynamical correlation holes, respectively. We approximate these as follows (see ref. 8):

$$[15] \qquad z_{\sigma\sigma'} = |c_{\sigma\sigma'}(U_{X\sigma}^{-1} + U_{X\sigma'}^{-1})|$$

where $U_{X\sigma}$ is the σ-spin exchange potential as in the previous section, and the correlation range constants $c_{\alpha\beta}$ and $c_{\sigma\sigma}$ have values (8)

$$[16] \qquad c_{\alpha\beta} = 0.63, \qquad c_{\sigma\sigma} = 0.88$$

Thus, if the $\boldsymbol{J}$-dependent Q_σ of eq. [11] is used to obtain $U_{X\sigma}$, then a $\boldsymbol{J}$-dependent correlation approximation naturally arises.

Even more importantly, however, the prefactor

$$[17] \qquad \left\{\tau_\sigma - \frac{1}{4}\frac{(\nabla\rho_\sigma)^2}{\rho_\sigma}\right\}$$

in the parallel-spins functional, eq. [14], needs to be modified in the case of non-zero current densities. If the derivation of ref. 6 is repeated using the generalized Q_σ of eq. [11], we obtain the appropriate $\boldsymbol{J}$-dependent extension of the σσ correlation energy:

$$[18] \qquad E_C^{\sigma\sigma} = -0.01\int \rho_\sigma\left\{\tau_\sigma - \frac{1}{4}\frac{(\nabla\rho_\sigma)^2}{\rho_\sigma} - \frac{\boldsymbol{J}_\sigma^2}{\rho_\sigma}\right\} \times z_{\sigma\sigma}^4\left[1 - \frac{2}{z_{\sigma\sigma}}\ln\left(1 + \frac{z_{\sigma\sigma}}{2}\right)\right]d^3\boldsymbol{r}$$

To summarize: the total dynamical correlation energy E_C is the sum

$$[19] \qquad E_C = E_C^{opp} + E_C^{\alpha\alpha} + E_C^{\beta\beta}$$

where E_C^{opp} is given by eq. [13], $E_C^{\alpha\alpha}$ and $E_C^{\beta\beta}$ are given by eq. [18], and the exchange potentials $U_{X\sigma}$ required in eq. [15] are generated from the $\boldsymbol{J}$-dependent Q_σ of eq. [11] via the Becke–Roussel procedure of the previous section.

Conclusions

Exchange and correlation functionals with explicit dependence on current-density $\boldsymbol{J}$ have been developed from first principles by slight modification of existing models (5, 6, 8). No empiricism whatsoever has been employed. Self-consistent computations with the Becke–Roussel functional (5), the foundation of this work, have recently become possible (9). We hope that incorporation of its $\boldsymbol{J}$ dependence, as developed here, will soon follow.

References

1. G. Vignale, M. Rasolt, and D.J.W. Geldart. Adv. Quantum Chem. **21**, 235 (1990).
2. S.M. Colwell and N.C. Handy. Chem. Phys. Lett. **217**, 271 (1994).
3. J.F. Dobson. J. Phys.: Condens. Matter, **4**, 7877 (1992).

4. J.F. Dobson. J. Chem. Phys. **98**, 8870 (1993).
5. A.D. Becke and M.R. Roussel. Phys. Rev. A: Gen. Phys. **39**, 3761 (1989).
6. A.D. Becke. J. Chem. Phys. **88**, 1053 (1988).
7. A.D. Becke. Int. J. Quantum Chem. **23**, 1915 (1983).
8. A.D. Becke. Int. J. Quantum Chem. Quantum Chem. Symp. **28**, 625 (1994).
9. R. Neumann, R.H. Nobes, and N.C. Handy. Mol. Phys. **87**, 1 (1996).

Appendix

Derivation of the exchange-charge curvature Q_σ, as defined in eq. [2], is relatively straightforward. The exchange charge $\rho_{X\sigma}(\boldsymbol{r}_1, \boldsymbol{r}_2)$ is related to the σ-spin orbitals by (see refs. 5 and 7)

$$[A1] \qquad \rho_{X\sigma}(\boldsymbol{r}_1, \boldsymbol{r}_2) = \left| \sum_k \psi^*_{k\sigma}(\boldsymbol{r}_1)\psi_{k\sigma}(\boldsymbol{r}_2) \right|^2 / \rho_\sigma(\boldsymbol{r}_1)$$

where $\boldsymbol{r}_1$ is taken as the reference point and $\boldsymbol{r}_2$ is the variable. Q_σ, the coefficient of the quadratic term in the Taylor expansion of the spherically averaged $\rho_{X\sigma}$ about $\boldsymbol{r}_1$, is equal to (7)

$$[A2] \qquad Q_\sigma(\boldsymbol{r}_1) = \tfrac{1}{6}\nabla^2_{(2)}\rho_{X\sigma}(\boldsymbol{r}_1, \boldsymbol{r}_2)|_{\boldsymbol{r}_2=\boldsymbol{r}_1}$$

with the Laplacian acting on variable $\boldsymbol{r}_2$ only. The indicated manipulations produce eq. [11] relatively easily.

Strongly bound doubly excited states of Be_2

Pablo J. Bruna and James S. Wright

Abstract: The triplet and singlet potential curves of Be_2 generated by single and double excitations from $2\sigma_u$ into $3\sigma_g$ and (or) $1\pi_u$ are studied with a multireference configuration interaction (MRD-CI) method. Relative to $X^1\Sigma_g^+(2\sigma_g^2 2\sigma_u^2)$ with $R_e = 4.72$ bohr and $\omega_e = 258$ cm^{-1} (calculated here), these *antibonding MO* → *bonding MO* excitations lead to average decreases in bond distance (in bohr) of 0.55 ($2\sigma_u \rightarrow 3\sigma_g$), 0.88 ($2\sigma_u \rightarrow 1\pi_u$), 0.93 ($2\sigma_u^2 \rightarrow 3\sigma_g 1\pi_u$), and 1.22 ($2\sigma_u^2 \rightarrow 1\pi_u^2$). The increase in vibrational frequencies ranges from 240 to 600 cm^{-1}. The $3\sigma_g$ MO is found to be less bonding than $1\pi_u$, confirming predictions made by Bader et al. The experimental states $A^1\Pi_u$ and $B^1\Sigma_u^+$ correspond to doubly excited $1^1\Pi_u(2\sigma_u^2 \rightarrow 3\sigma_g 1\pi_u)$ and singly excited $1^1\Sigma_u^+(2\sigma_u \rightarrow 3\sigma_g)$, respectively. The $1^3\Sigma_g^-$ and $1^1\Delta_g$ states, both $2\sigma_u^2 \rightarrow 1\pi_u^2$, preserve their doubly excited structure up to dissociation. Within the Franck–Condon region, $1^3\Pi_u$ changes from bound ($2\sigma_u^2 \rightarrow 3\sigma_g 1\pi_u$) to repulsive (mixed $2\sigma_u \rightarrow 1\pi_g/2\sigma_g \rightarrow 1\pi_u$), thereby creating the unusual situation of a strongly bound potential (short R_e, high ω_e) with an adiabatic dissociation energy near zero. The singlet counterpart $1^1\Pi_u$, however, behaves regularly as its doubly excited character is maintained up to large R(Be—Be).

Key words: ab initio calculations, beryllium dimer, doubly excited states, electronic transitions, potential curves.

Résumé : Faisant appel à une méthode d'interaction de configuration à multiréférences («MRD-CI»), on a étudié les courbes de potentiel triplet et singulet du Be_2 généré par des excitations simple et double de $2\sigma_u$ en $3\sigma_g$ et (ou) $1\pi_u$. Relatives à $X^1\Sigma_g^+(2\sigma_g^2 2\sigma_u^2)$ avec $R_e = 4{,}72$ bohr et $\omega_e = 258$ cm^{-1} (calculé ici), ces excitations d'*OM antiliantes* → *OM liantes* conduisent à des diminutions moyennes des distances de liaisons (en bohr) de 0,55 ($2\sigma_u \rightarrow 3\sigma_g$), 0,88 ($2\sigma_u \rightarrow 1\pi_u$), 0,93 ($2\sigma_u^2 \rightarrow 3\sigma_g 1\pi_u$) et 1,22 ($2\sigma_u^2 \rightarrow 1\pi_u^2$). L'augmentation de fréquences vibrationnelles varient de 240 à 600 cm^{-1}. On a trouvé que les OM $3\sigma_g$ sont moins liantes que les $1\pi_u$, ce qui confirme les prédictions faites par Bader et al. Les états expérimentaux $A^1\Pi_u$ et $B^1\Sigma_u^+$ correspondent respectivement aux états doublement excité $1^1\Pi_u(2\sigma_u^2 \rightarrow 3\sigma_g 1\pi_u)$ et simplement excité $1^1\Sigma_u^+(2\sigma_u \rightarrow 3\sigma_g)$. Les états $1^3\Sigma_g^-$ et $1^1\Delta_g$, qui correspondent tous les deux à $2\sigma_u^2 \rightarrow 1\pi_u^2$, conservent leur structure doublement excitée jusqu'à la dissociation. Dans la région de Franck–Condon, le $1^3\Pi_u$ se change de liée ($2\sigma_u^2 \rightarrow 3\sigma_g 1\pi_u$) à répulsive ($2\sigma_u \rightarrow 1\pi_g/2\sigma_g \rightarrow 1\pi_u$), ce qui crée la situation inhabituelle d'un potentiel fortement lié (valeurs de R_e courte et de ω_e élevée) accompagnée d'une énergie de dissociation adiabatique pratiquement égale à zéro. La contrepartie singulet, $1^1\Pi_u$, se comporte toutefois d'une façon régulière alors que son caractère doublement excité est maintenu jusqu'à une valeur élevée de R(Be—Be).

Mots clés : calculs ab initio, dimère du béryllium, états doublement excités, transitions électroniques, courbes de potentiel.

[Traduit par la rédaction]

1. Introduction

The nature of the bonding in the $X^1\Sigma_g^+(2\sigma_g^2 2\sigma_u^2)$ state of Be_2, formally with a zero bond order, has been the topic of many theoretical studies (1–13). An increase in the net bond order due to mixing with the double excitation $2\sigma_u^2 \rightarrow 3\sigma_g^2$ is responsible for the weakly bound character of the Be_2 ground state (7, 12).

Much less attention has been paid to the equilibrium properties and bonding features of excited states. Bender and Davidson (2) reported several potential curves, without specifying spectroscopic data or electronic configurations. Local spin density (LSD) calculations by Jones (4) analyzed five states ($1^{3,1}\Sigma_u^+$, $1^{3,1}\Pi_g$, $1^3\Sigma_g^-$), while a single-reference (SD)-CI study by Gosavi and Strausz (9) focused on triplets ($1^3\Sigma_u^+$, $1^3\Pi_{g,u}$, $1^3\Sigma_g^-$). These two papers gave partial insight into structures and equilibrium parameters, but the data are not accurate enough for spectroscopic purposes.

Experimentally, two dipole-allowed excited states are known (14), e.g., $A^1\Pi_u$ at 2.66 eV and $B^1\Sigma_u^+$ at 3.44 eV (T_e's). The bonding character of A is stronger than that of B, as pointed out by 3.74 versus 4.16 bohr for R_e, and 686 versus 511 cm^{-1} for ω_e. These values are to be compared with 4.63 bohr and 276 cm^{-1} measured for $X^1\Sigma_g^+$ (14).

Bondybey (14) speculated that $B^1\Sigma_u^+$ and $A^1\Pi_u$ are, respectively, described by the configurations $2\sigma_g^2 2\sigma_u 3\sigma_g$ ($2\sigma_u \rightarrow 3\sigma_g$ with respect to $X^1\Sigma_g^+$) and $2\sigma_g 2\sigma_u^2 1\pi_u$ ($2\sigma_g \rightarrow 1\pi_u$). The relatively tight structure assigned to $B^1\Sigma_u^+$ seems plausible as the $2\sigma_u \rightarrow 3\sigma_g$ excitation increases the bond order. However, it is difficult to justify assigning $2\sigma_g \rightarrow 1\pi_u$ to $A^1\Pi_u$ (with a measured ΔR_e of −0.89 bohr relative to $X^1\Sigma_g^+$) since for this bonding → bonding excitation the bond order remains formally unchanged. Also, it seems unusual for an excitation from the low-lying $2\sigma_g$ MO to lie about 1.0 eV

Received October 23, 1995.

This paper is dedicated to Professor Richard F.W. Bader on the occasion of his 65th birthday.

P.J. Bruna[1] and J.S. Wright. Ottawa–Carleton Chemistry Institute, Carleton University, Ottawa, ON K1S 5B6, Canada.

[1] Author to whom correspondence may be addressed. Present address: Department of Chemistry, University of New Brunswick, Fredericton, NB E3B 6E2, Canada. Telephone: (506) 453-4781. Fax: (506) 453-4981. E-mail: fg01@jupiter.sun.csd.unb.ca

below that from $2\sigma_u$. Obviously, the $A^1\Pi_u$ assignment needs revision.

Because of the weakly bound character of ground state Be_2, the stability of its doubly excited states is expected to be quite substantial. As shown in various studies from the authors (15–21), particular excited states of X_2 molecules (with 3–8 valence electrons (VEs)) are strongly bound, i.e., they have shorter bond distances and higher vibrational frequencies than in the ground state. (For simplicity, the valence MOs $2\sigma_g$, $2\sigma_u$, $3\sigma_g$, $1\pi_u$, and $1\pi_g$ are hereafter labeled as σ_g, σ_u, σ'_g, π_u, and π_g, respectively.) The so-called strongly bound doubly excited states (SBDES) arise from $\sigma_u^2 \rightarrow (MO)^2$ excitations, with MO^2 corresponding to σ'^2_g, π_u^2, or $\sigma'_g\pi_u$. As the final configurations have *a maximal number of bonding electrons (highest bond order)*, an increase in bond strength upon excitation is understandable. As shown later, the experimental $A^1\Pi_u$ state is in fact an SBDES representative, confirming earlier speculations (22).

This work has been carried out with two goals in mind. First, to follow the changes in bonding for all low-lying excited states of Be_2 generated by single and double excitations from the antibonding σ_u into the bonding σ_g and π_u MOs. Second, to provide reliable potential curves for the interpretation of past and future experimental studies on the electronic spectrum of Be_2.

2. Technical details

The *sp* valence AOs on Be consist of the 10*s*/5*s* and 5*p*/2*p* subsets from Huzinaga (23) and Dunning and Hay (24) optimized for the $^1S_g(s^2)$ and $^3P_u(sp)$ atomic states, respectively. The 5*p* set of primitives given by Dunning (24) is contracted to 311. Additional AOs on Be include one *s* (α = 0.026), one *p* (α = 0.021) and three uncontracted *d* species (α = 0.3, 0.1, and 0.03). Rydberg AOs, with exponents of 0.012 (*s*), 0.01 (*p*), and 0.008 (*d*), are placed at the midpoint of the Be—Be bond. The exponents of the additional AOs have been estimated from the data given in ref. 24, except for the two most compact *d* species whose exponents are taken from ref. 5.

The configuration-interaction calculations are carried out with the MRD-CI method (25). The MOs used for the CI expansions are those corresponding to $1^5\Sigma_u^-(\sigma_g\sigma_u\pi_u^2)$. Exploratory calculations using $X^1\Sigma_g^+(\sigma_g^2\sigma_u^2)$ MOs were more demanding technically, i.e., a large number of reference configurations was needed, and, very often, high-lying states were poorly described ($\Sigma c^2 < 90\%$).

The frozen-core approximation has been used (no excitation from $1\sigma_g^2$ or $1\sigma_u^2$, and the complementary highest lying species discarded), leaving 78 MOs to describe valence correlation. The number of reference configurations ranges from 50 to 60, leading to a total of about 60 000 symmetry-adapted functions (SAFs) on average. Using a configuration selection threshold of 2 microhartree, the diagonalized CI spaces vary from 6000 to 10 000 SAFs. The total and relative energies to be reported correspond to those extrapolated to zero selection threshold and then corrected by the multi-reference analog of the Langhoff–Davidson correction (26).

3. Dissociation channels

The composition and relative energies of the first four dissociation channels are summarized in Table 1. The experimental spacings (27) are reproduced quite well.

Channels II (triplets) and III (singlets), each containing one $s \rightarrow p$ excited atom, give rise to singly excited configurations. Channel IV (quintets, triplets, and singlets), composed of two $s \rightarrow p$ states, is the lowest that generates doubly excited states. Interestingly, the $1^3\Sigma_g^-$ and $^1\Delta_g$ states, both correlating with channel IV, may preserve their doubly excited character over the whole range of bond distances.

Fig. 1. Potential curves of low-lying triplet excited states of Be_2.

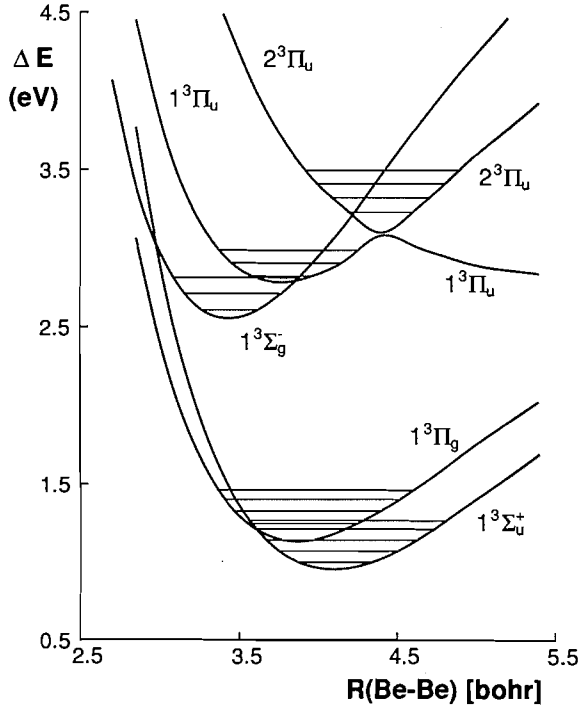

4. Excited states

Potential curves are shown in Figs. 1 (triplets) and 2 (singlets), with spectroscopic data being compiled in Tables 2 and 3.

4.1 Triplet states

The first two triplets, $1^3\Sigma_u^+(\sigma_u \rightarrow \sigma'_g)$ and $1^3\Pi_g(\sigma_u \rightarrow \pi_u)$, arise from single excitations. An R_e of 4.09 bohr for $1^3\Sigma_u^+(\sigma_u\sigma'_g)$ versus 3.87 bohr for $1^3\Pi_g(\sigma_u\pi_u)$ indicates that π_u is more bonding than σ'_g. Their mimina lie energetically close (T_e's of 0.90 and 1.08 eV, Table 2).

The next two triplets correspond to the doubly excited states $1^3\Pi_u(\sigma_u^2 \rightarrow \sigma'_g\pi_u)$ at 2.73 eV and $1^3\Sigma_g^-(\sigma_u^2 \rightarrow \pi_u^2)$ at 2.50 eV. Once again, it is noted that σ'_g exhibits weaker bonding than π_u, as pointed out by an R_e of 3.76 bohr for $1^3\Pi_u(\sigma'_g\pi_u)$ versus 3.43 bohr for $1^3\Sigma_g^-(\pi_u^2)$. The bonding features associated with SBDES species are best exemplified by $1^3\Sigma_g^-(\pi_u^2)$, a state having the shortest R_e and highest ω_e (860 cm^{-1}) among all low-lying states of Be_2.

$1^3\Pi_u$ exhibits unusual features (Fig. 1). Specifically, near its minimum, this state is characterized by a well-bound potential (R_e = 3.76 bohr, ω_e= 677 cm^{-1}). However, a T_e value of 2.73 eV, being identical with the location of channel II (Table

Fig. 2. Potential curves of low-lying singlet excited states of Be_2.

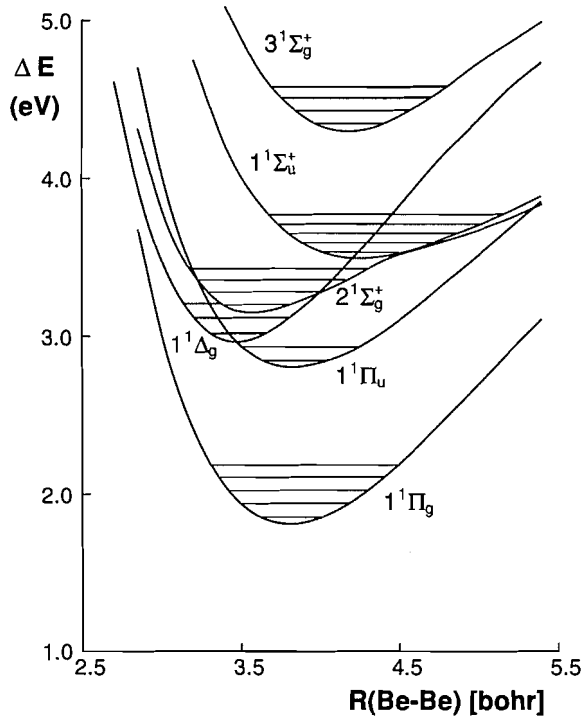

1), results in an adiabatic dissociation energy D_e near zero (Table 2). This peculiar behaviour is caused by a crossing near 4.25 bohr with $2^3\Pi_u$, a repulsive state mainly arising from $\sigma_u \rightarrow \pi_g$ at very short R. Past 4.40 bohr, $1^3\Pi_u$ acquires a mixed, singly excited character $\sigma_u \rightarrow \pi_g/\sigma_g \rightarrow \pi_u$, as expected for a state correlating with channel II.

The dissociation barrier of $1^3\Pi_u$ amounts to 0.32 eV, accommodating up to 4 vibrational levels. The existence of this avoided crossing remained unnoticed in earlier studies (2, 4, 9).

Due to that crossing, the structure of $2^3\Pi_u$ complementary changes from $\sigma_u \rightarrow \pi_g$ at short R to $\sigma_u^2 \rightarrow \sigma'_g\pi_u$ at large R. When compared with other states (including the ground state), the mixed singly/doubly excited composition of $2^3\Pi_u$ near equilibrium results in an anomalous relationship between bond distance and vibrational frequency, e.g., large R_e (4.36 bohr) but high ω_e (720 cm^{-1}).

4.2 Singlet states

The lowest singlet excited states correspond to $1^1\Pi_g(\sigma_u \rightarrow \pi_u)$ at T_e = 1.76 eV, and $1^1\Pi_u$ (mainly $\sigma_u^2 \rightarrow \sigma'_g\pi_u$) at 2.76 eV. Since doubly excited $1^1\Pi_u$ has some contribution of the repulsive $\sigma_u \rightarrow \pi_g$ excitation, its potential curve is not as strongly bound as expected. In fact, both $1^1\Pi_g$ and $1^1\Pi_u$ have comparable values of R_e and ω_e (≈3.82 bohr, ≈680 cm^{-1}, Table 3).

Worth noting, the potential curve of doubly excited $1^1\Pi_u$ (Fig. 2) shows a regular behaviour, in contrast to that of $1^3\Pi_u$ having a maximum near 4.25 bohr (Fig. 1).

Slightly above $1^1\Pi_u$ one finds two SBDES, namely, $1^1\Delta_g$ at 2.89 eV and $2^1\Sigma_g^+$ at 3.11 eV. Both arise from the double excitation $\sigma_u^2 \rightarrow \pi_u^2$, like the $1^3\Sigma_g^-$ state. While R_e and ω_e values of 3.49 bohr and 841 cm^{-1} for $1^1\Delta_g$ are as high as for $1^3\Sigma_g^-$, those for $2^1\Sigma_g^+$ indicate a weaker bonding (larger R_e and smaller ω_e, Table 3). This feature is due to contribution of $\sigma_u^2 \rightarrow \sigma'^2_g$ to the $2^1\Sigma_g^+$ wave function — a double excitation increasing the bond strength to a lesser degree than $\sigma_u^2 \rightarrow \pi_u^2$, in line with the observed bonding differences between σ'_g and π_u.

The $3^1\Sigma_g^+$ potential, with T_e = 4.26 eV, interacts with $2^1\Sigma_g^+$ near 4.25 bohr. To some extent, $3^1\Sigma_g^+$ exhibits the same anomalous behaviour as $2^3\Pi_u$, i.e., large bond length (4.17 bohr) but a relatively deep potential (644 cm^{-1}). Such anomalies arise in both cases from avoided crossings between states of the same symmetry.

Since the $2^1\Sigma_g^+$–$3^1\Sigma_g^+$ interaction is not as sharp as that between $1^3\Pi_u$ and $2^3\Pi_u$, none of these singlets develop a potential barrier. The avoided crossing is reflected, however, in a change in the curvature of $2^1\Sigma_g^+$ around 4.25 bohr (Fig. 2). Also worth mentioning is that while the $3^1\Sigma_g^+$ minimum arises from the intersection of two doubly excited states (one strongly bound but the other much less so), the $2^3\Pi_u$ minimum arises from the mixing between singly and doubly excited states (repulsive and bound, respectively).

The $1^1\Sigma_u^+(\sigma_u \rightarrow \sigma'_g)$ state is predicted at T_e = 3.45 eV, in very good agreement with an experimental gas phase value of 3.44 eV (14). An earlier study in inert matrices by Brom et al. (22) reported 0-0 transition energies (in eV) of 3.54 (Ne) and 3.43 eV (Ar). As seen in Fig. 2, the $1^1\Sigma_u^+$ minimum lies close to v' = 5 of the lower lying $2^1\Sigma_g^+$ state, with the possible existence of perturbations.

A $1^3\Sigma_u^+$–$1^1\Sigma_u^+$ splitting of 2.55 eV near equilibrium is almost identical with the energy separation between channels II and III (Table 1), thus explaining why both potential curves run nearly parallel to each other.

5. Comparison with previous studies

Theoretical and experimental results from the literature are summarized in Table 4. There are no data available on $2^3\Pi_u$, $1^1\Delta_g$, and $2,3^1\Sigma_g^+$ for comparison. Changes in R_e and ω_e relative to the ground state are given in Table 5 as ΔR_e and $\Delta\omega_e$.

Only one experimental and two theoretical works have been devoted to the excited states. Data on $1^3\Sigma_u^+$ have also been reported in refs. 2 and 28. Compared with the LSD results (4), this study finds similar values of R_e and ω_e (maximal deviations of 0.07 bohr and 55 cm^{-1}) but higher excitation energies. The discrepancy is quite substantial for $1^1\Sigma_u^+$, with a ΔE of 3.45 versus 1.55 eV (Table 4). On the other hand, the R_e data from a previous SDCI study (9) are similar to ours, but the present transition energies are up to 0.30 eV smaller.

For the $X^1\Sigma_g^+$ ground state, the MRD-CI results for R_e, ω_e, and D_e are in line with prior theoretical estimates, most of them giving bond distances about 0.1 bohr too long and vibrational frequencies ≈ 30 cm^{-1} too small. A recent study by Røeggen and Almlöf (10*b*) reproduces the experimental very closely (Table 4); their work also gives a complete list of earlier theoretical studies.

The present R_e values for $1^1\Pi_u(A^1\Pi_u)$ and $1^1\Sigma_u^+(B^1\Sigma_u^+)$ also overestimate experimental data by about 0.1 bohr. Due to error compensations, however, the measured ΔR_e and $\Delta\omega_e$ are well reproduced (Table 5).

For $1^1\Pi_u(A^1\Pi_u)$, a predicted T_e value of 2.76 eV is about 0.10 eV too high. This state arises from the double excitation

Table 1. Low-lying dissociation channels of Be_2.

Channel	Be + Be	ΔE (eV)		Molecular states
I, $s^2 + s^2$	$^1S_g + {}^1S_g$	0.00[a]	0.00[b]	$X^1\Sigma_g^+$
II, $sp + s^2$	$^3P_u + {}^1S_g$	2.73	2.73	$1^3\Sigma_{g,u}^+$, $1^3\Pi_{g,u}$
III, $sp + s^2$	$^1P_u + {}^1S_g$	5.28	5.34	$2^1\Sigma_g^+$, $1^1\Sigma_u^+$, $1^1\Pi_{g,u}$
IV, $sp + sp$	$^3P_u + {}^3P_u$	5.45	5.46	$3,4^1\Sigma_g^+$, $2,3^3\Sigma_u^+$, $1^3\Sigma_g^-$, $1^1\Sigma_u^-$, $2^3\Pi_{g,u}$, $2^1\Pi_{g,u}$, $1^1\Delta_g$, $1^3\Delta_u$, $1,2^5\Sigma_g^+$, $1^5\Sigma_u^-$, $1^5\Pi_{g,u}$, $1^5\Delta_g$

[a]Experimental data from ref. 27.
[b]This work. Total energy for Be (^1S_g): −14.618 16 hartree (SD-CI, 2 VEs).

Table 2. Spectroscopic parameters of the triplet states of Be_2 correlating with dissociation channels II–IV.

State[a]	T_e (eV)	R_e (bohr)	ω_e (cm^{-1})	$\omega_e x_e$ (cm^{-1})	B_e (cm^{-1})	α_e (cm^{-1})	D_e (eV)
$1^3\Sigma_u^+(\sigma_u \rightarrow \sigma_g')$	0.90	4.09	606	3.9	0.803	0.009	1.83 (II)
$1^3\Pi_g(\sigma_u \rightarrow \pi_u)$	1.08	3.87	640	5.2	0.892	0.011	1.65 (II)
$1^3\Sigma_g^-(\sigma_u^2 \rightarrow \pi_u^2)$	2.50	3.43	860	5.3	1.131	0.009	2.96 (IV)
$1^3\Pi_u(\sigma_u^2 \rightarrow \sigma_g'\pi_u)$ 70 $(\sigma_g \rightarrow \pi_u)$ 15	2.73	3.76	677	6.1	0.944	0.009	0.00 (II)
$2^3\Pi_u(\sigma_u \rightarrow \pi_g)$ 65 $(\sigma_u^2 \rightarrow \sigma_g'\pi_u)$ 20	3.14	4.36	720	4.8	0.689	−0.001	2.32 (IV)

[a]Relative weights (in per cent) given for states with a mixed composition near equilibrium.

Table 3. Spectroscopic parameters of the singlet states of Be_2 correlating with dissociation channels I–IV.

State[a]	T_e (eV)	R_e (bohr)	ω_e (cm^{-1})	$\omega_e x_e$ (cm^{-1})	B_e (cm^{-1})	α_e (cm^{-1})	D_e (eV)
$X^1\Sigma_g^+(\sigma_g^2\sigma_u^2)$	0.00	4.72	258	23.5	0.603	0.052	0.095 (I)
$1^1\Pi_g(\sigma_u \rightarrow \pi_u)$	1.76	3.81	705	4.0	0.924	0.009	3.58 (III)
$1^1\Pi_u(\sigma_u^2 \rightarrow \sigma_g'\pi_u)$ 65 $(\sigma_u \rightarrow \pi_g)$ 16	2.76	3.83	655	4.7	0.913	0.011	2.58 (III)
$1^1\Delta_g(\sigma_u^2 \rightarrow \pi_u^2)$	2.89	3.49	841	6.3	1.098	0.010	2.57 (IV)
$2^1\Sigma_g^+(\sigma_u^2 \rightarrow \pi_u^2)$ 70 $(\sigma_u^2 \rightarrow \sigma_g'^2)$ 10	3.11	3.57	692	15.9	1.049	0.029	2.23 (III)
$1^1\Sigma_u^+(\sigma_u \rightarrow \sigma_g')$	3.45	4.25	495	5.2	0.739	0.010	1.89 (III)
$3^1\Sigma_g^+(\sigma_u^2 \rightarrow \sigma_g'^2)$ 30 $(\sigma_u^2 \rightarrow \pi_u^2)$ 30, $(\sigma_g^2\sigma_u^2)$ 10	4.26	4.17	644	4.9	0.760	0.004	1.20 (IV)

[a]Footnote *a*, Table 2.

$\sigma_u^2 \rightarrow \sigma'_g\pi_u$ rather than $\sigma_g \rightarrow \pi_u$, as proposed by Bondybey (14). Such a doubly excited structure was already suggested in ref. 22.

Vibrationally excited $1^1\Pi_u$ may be perturbed by both $1^1\Delta_g$ and $2^1\Sigma_g^+$ (Fig. 2). Dipole-allowed transitions between these u and g states lie in the near infrared region. In principle, absorption from $1^1\Pi_u$ opens the possibility of spectroscopically studying both (upper) doubly excited states, although both transitions may be of low intensity.

Bondybey speculated that $1^1\Pi_g$ should be the lowest excited singlet of Be_2, which is confirmed by this study. The transition energies $1^1\Pi_u \rightarrow 1^1\Pi_g$ and $1^1\Sigma_u^+ \rightarrow 1^1\Pi_g$ are predicted to be 1.0 and 1.69 eV, respectively. Such small values explain Bondybey's failure in detecting $1^1\Pi_g$ via decay

Table 4. Comparison of the spectroscopic parameters of selected states of Be_2 with literature data.[a]

State	T_e	R_e	ω_e	D_e	Reference
$X^1\Sigma_g^+$ $(\sigma_g^2\sigma_u^2)$	0.00	4.72	258	0.095 (I)	TW
		4.63	276	0.098	Expt., 14
		4.73	—	0.088	6
		4.75	—	0.081	7
		4.70	242	—	8
		4.73	—	0.091	10*a*
		4.63	212	0.102	11
		4.73	225	0.094	13
		4.67	—	0.101	10*b*
$1^3\Sigma_u^+$ $(\sigma_u \rightarrow \sigma_g')^b$	0.90	4.09	606	1.83 (II)	TW
	0.75	4.16	550	2.33	4
	0.86	4.05	—	1.71	9
$1^3\Pi_g$ $(\sigma_u \rightarrow \pi_u)$	1.08	3.87	640	1.65 (II)	TW
	0.85	3.84	640	2.23	4
	1.23	3.90	—	1.33	9
$1^1\Pi_g$ $(\sigma_u \rightarrow \pi_u)$	1.76	3.81	705	3.58 (III)	TW
	1.30	3.82	650	4.33	4
$1^3\Sigma_g^-$ $(\sigma_u^2 \rightarrow \pi_u^2)$	2.50	3.43	860	2.96 (IV)	TW
	2.07	3.39	890	3.74	4
	2.79	3.47	—	2.61	9
$1^3\Pi_u$ $(\sigma_u \rightarrow \pi_u)$	2.73	3.76	677	0.00 (II)	TW
	2.83	3.80	—	−0.48	9
$1^1\Pi_u$ $(\sigma_u^2 \rightarrow \sigma_g'\pi_u)$	2.76	3.83	655	2.58 (III)	TW
$(A^1\Pi_u)$	2.66	3.74	686	2.71	Expt., 14
$1^1\Sigma_u^+$ $(\sigma_u \rightarrow \sigma_g')$	3.45	4.25	495	1.89 (III)	TW
$(B^1\Sigma_u^+)$	3.44	4.16	511	1.94	Expt., 14
	1.55	4.21	540	4.08	4

[a] T_e and D_e in eV, R_e in bohr, and ω_e in cm^{-1}.
[b] R_e = 4.12 bohr and ω_e = 914 cm^{-1} (28); R_e = 4.10 bohr and ω_e = 677 cm^{-1} (2).

Table 5. Excitations in Be_2. Values in brackets are experimental results (ref. 14).

Excitation	State	T_e (eV)	ΔR_e[a] (bohr)	$\Delta\omega_e$[a] (cm^{-1})
$\sigma_u \rightarrow \sigma_g'$	$1^3\Sigma_u^+$	0.90	−0.63	348
	$1^1\Sigma_u^+$	3.45	−0.47	237
	$1^1\Sigma_u^+$	[3.44]	[−0.47]	[235]
$\sigma_u \rightarrow \pi_u$	$1^3\Pi_g$	1.08	−0.85	382
	$1^1\Pi_g$	1.76	−0.91	447
$\sigma_u^2 \rightarrow \sigma_g'\pi_u$	$1^3\Pi_u$	2.73	−0.96	419
	$1^1\Pi_u$	2.76	−0.89	397
	$1^1\Pi_u$	[2.66]	[−0.89]	[409]
$\sigma_u^2 \rightarrow \pi_u^2$	$1^3\Sigma_g^-$	2.50	−1.29	602
	$1^1\Delta_g$	2.89	−1.23	583
	$2^1\Sigma_g^+$	3.11	−1.15	434
$\sigma_u^2 \rightarrow \sigma_g'^2$	$3^1\Sigma_g^+$	4.26	−0.55	386

[a] Relative to the ground state (Table 3).

$1^1\Pi_u \rightarrow 1^1\Pi_g$ or $1^1\Sigma_u^+ \rightarrow 1^1\Pi_g$, as both emission systems lie beyond the spectral range studied by him (from 2 to 3 eV).

Nothing is experimentally known about the triplet states. The near-infrared transition $1^3\Sigma_u^+ \leftrightarrow 1^3\Pi_g$ ($\sigma'_g \leftrightarrow \pi_u$) at 0.18 eV is expected to be rather weak (small ΔE, ΔR_e = 0.22 bohr). Doubly excited $1^3\Sigma_g^-$ cannot be detected in emission as there are no lower lying triplets of the appropiate symmetry. On the other hand, the (weak) infrared absorption band $1^3\Pi_u \leftarrow 1^3\Sigma_g^-$ (ΔE = 0.23 eV, ΔR_e = 0.34 bohr) might have an irregular structure reflecting the $1^3\Pi_u$–$2^3\Pi_u$ crossing, with the possible existence of a continuum due to $1^3\Pi_u$ predissociation.

The absorption transition $1^3\Pi_u \leftarrow 1^3\Pi_g$ (ΔE = 1.65 eV, $\Delta R_e = -0.11$ bohr) may exhibit similarly complex structure. However, this band system has more favorable Franck–Condon factors than does $1^3\Pi_u \leftarrow 1^3\Sigma_g^-$ (cf. Fig. 1).

6. Discussion

Five triplet and six singlet excited states of Be_2, all having

minima below 5 eV, are predicted to be bound. From the eight states generated by channels II and III, only $1^3\Sigma_g^+$(II) is repulsive.

The singly excited states, four in total, arise from $\sigma_u \rightarrow \sigma'_g$ ($1^3\Sigma_u^+$, $1^1\Sigma_u^+$) and $\sigma_u \rightarrow \pi_u$ ($1^3\Pi_g$, $1^1\Pi_g$). Their potential curves have relatively deep minima (Tables 2 and 3). In fact, the lowest lying excited singlet, $1^1\Pi_g$, has a dissociation energy D_e of ca. 3.6 eV, the largest among all states studied. When compared with a D_e of about 0.10 eV for the ground state (Table 4), this represents a tremendous increase in bond strength upon (single) substitution of an antibonding σ_u by a bonding π_u MO.

Interestingly, *seven* excited states (three triplets and four singlets) exhibit a SBDES character $\sigma_u^2 \rightarrow \sigma'^2_g$, $\sigma'_g\pi_u$, or π_u^2 near equilibrium. Their high bond order is reflected by the correspondingly short R_e and high ω_e values. The $1^3\Sigma_g^-(\sigma_u^2 \rightarrow \pi_u^2)$ minimum, for example, occurs at an interatomic distance about 25% shorter than for the ground state; the strong bonding is also manifested by an increase in ω_e of about 300%, and a D_e near 3.0 eV (Table 2).

The stabilities and equilibrium properties of the low-lying excited states of Be_2 are determined by the relative bonding properties of the σ_u, σ'_g, and π_u MOs. As shown in ref. 3, the charge density of σ_u is shifted toward both nuclei, i.e., it is almost zero within the bond, maximal at each Be atom, and still relatively high behind the nuclei. The σ'_g species exhibits a less localized distribution, as the amount of charge density *outside* the bond is practically the same as that *inside* it (see Fig. 2 in ref. 3).

A detailed analysis of orbital forces carried out by Bader et al. (1) for the ground states of N_2, O_2, and F_2 (all having σ_u, σ'_g, and π_u doubly occupied) came to the conclusion that while σ_u is strongly antibonding, σ'_g should be better classified as nonbinding rather than binding. The π_u MO is strongly bonding. The spectroscopic data of the excited states of Be_2 presented in Sect. 5 also indicate that σ'_g is less bonding than π_u.

The triplet–singlet splittings of the excited states $\sigma_u\sigma'_g$, $\sigma_u\pi_u$, and $\sigma'_g\pi_u$ reflect the differences in MO charge distributions. At the monodeterminant level, a splitting is given by twice the value of the corresponding exchange integral, K_{ab}. A small (large) K_{ab} arises when both open-shell MOs *a* and *b* are localized in different (similar) regions of space.

The predicted values (in eV) are 2.55 for $1^{3,1}\Sigma_u^+(\sigma_u\sigma'_g)$, 0.68 for $1^{3,1}\Pi_g(\sigma_u\pi_u)$, and 0.03 for $1^{3,1}\Pi_u(\sigma'_g\pi_u)$. The large $^{3,1}\Sigma_u^+$ splitting results from both σ_u and σ'_g lying in the molecular axis as well as having appreciable density in the same area (outside the bond). A smaller splitting of 0.68 eV for $1^{3,1}\Pi_g(\sigma_u\pi_u)$ is in line with π_u being perpendicular to the bond axis as well as with the significant amount of π_u density around each Be atom, where σ_u is mainly localized. Finally, the quasidegeneracy observed for the $\sigma'_g\pi_u$ states corroborates the fact that, within the bond, σ'_g has much less density than does π_u. Since $1^3\Pi_u$ has some contribution of $\sigma_u \rightarrow \pi_g$, the true $\sigma'_g\pi_u$ splitting might be slightly larger.

Although near equilibrium both states mainly arise from $\sigma'_g\pi_u$, the different behaviour shown by the potential curves of $1^3\Pi_u$ and $1^1\Pi_u$ is striking (Figs. 1 and 2). The reason for this deviation lies in the relative location of their dissociation channels. Specifically, $1^3\Pi_u$ and $1^1\Pi_u$ correlate with channels II ($\approx$ 2.83 eV) and III ($\approx$ 5.28 eV), respectively. Both channels give rise to singly excited states only, whereas the lowest one generating doubly excited states corresponds to channel IV at 5.45 eV (triplets *and* singlets).

Evidently, an asymptotic separation ΔE_a of only 0.17 eV between singly and doubly excited channels (III–IV) makes it possible for $1^1\Pi_u$ to maintain its doubly excited character over a wide R(Be—Be) range. Conversely, a higher asymptotic ΔE_a of 2.72 eV between $1^3\Pi_u$(II) and $2^3\Pi_u$(IV) causes $1^3\Pi_u$ to become singly excited around 4.25 bohr. Another factor for such a mixed composition within the Franck–Condon region is that the $1^3\Pi_u$ minimum lies energetically as high as channel II, so that the crossing of $\sigma_g^2\sigma'_g\pi_u$ with $\sigma_g^2\sigma_u\pi_g$ and $\sigma_g\sigma_u^2\pi_u$ takes place earlier than for $1^1\Pi_u$. As seen in Fig. 1 for $1^3\Pi_u$, the change in structure occurs suddenly; in that area, the interacting configurations are interrelated by the double excitations $\sigma'_g\pi_u \leftrightarrow \sigma_u\pi_g$ and $\sigma_g\sigma'_g \leftrightarrow \sigma_u^2$, respectively.

The states $1^3\Sigma_g^-$ and $1^1\Delta_g$ (both $\sigma_u^2 \rightarrow \pi_u^2$) are peculiar in the sense that they keep a doubly excited character up to large R values. Similar behaviour is shown by other diatomics with less than 4 VEs, e.g., the states $1^4\Sigma_g^-(\sigma_g\pi_u^2)$ of Be_2^+ (21) and $1^3\Sigma_g^-(\pi_u^2)$ of Li_2 (29). In all these cases, the lowest dissociation channel in which *both* atoms are $s \rightarrow p$ excited (a precondition for generating doubly excited states $\sigma^2 \rightarrow \pi_u^2$, with σ = σ_g or σ_u) constitutes, at the same time, *the lowest channel giving rise to* Σ_g^- *states* (channel III in Li_2, VI in Be_2^+, and IV in Be_2). In contrast, for systems with 5 VEs, there always exists a lower lying, singly excited channel that also generates Σ_g^- states. Hence, a SBDES of type $\sigma_u^2 \rightarrow \pi_u^2$ at short R becomes singly excited at large R, as, for example, the $1^4\Sigma_g^-(\sigma_g^2\sigma'_g\pi_u^2)$ state of B_2^+ (16, 17). For 6–8 VE systems, the region in which a given state retains its SBDES character is even more constricted, as previously discussed for B_2 (15–17), C_2^+, and C_2 (15, 18, 19).

Selected Be_2 states may be generated via photodetachment upon the bound states $X^2\Pi_u(\sigma_g^2\sigma_u^2\pi_u)$ and $A^2\Sigma_g^+(\sigma_g^2\sigma_u^2\sigma'_g)$ of Be_2^- (30). For example, the $X^1\Sigma_g^+$ state can be obtained by $\pi_u \rightarrow \infty$ ionization relative to $X^2\Pi_u$, or by $\sigma'_g \rightarrow \infty$ relative to $A^2\Sigma_g^+$. As the ground state of Be_2^- has an R_e about 0.45 bohr shorter than that of Be_2, the photodetachment spectrum $X^1\Sigma_g^+ \leftarrow X^2\Pi_u$ could provide valuable information about higher vibrational levels of Be_2, as well as about the dissociative continuum.

Similarly, $\sigma_u \rightarrow \infty$ ionization from $X^2\Pi_u$ of Be_2^- generates $1^3\Pi_g$ and $1^1\Pi_g$ of Be_2, both states being prevented by the selection rules from combining with the $X^1\Sigma_g^+$ ground state (i.e., difficult to detect spectroscopically). The same ionization process $\sigma_u \rightarrow \infty$ relative to $A^2\Sigma_g^+$ leads to $1^3\Sigma_u^+$ and $1^1\Sigma_u^+$ of Be_2.

7. Summary and conclusions

While no less than *forty-five* theoretical papers have been published about the $X^1\Sigma_g^+$ potential (Table 1 in ref. 10*b*), only *three* have focused on the excited states of Be_2. However, the scope of the data reported in the latter studies is rather limited (see Introduction). To remedy such a situation, in this work all low-lying states of Be_2 generated by single and double excitations, from σ_u into σ'_g and (or) π_u relative to the ground state $X^1\Sigma_g^+$, have been studied with the MRD-CI method and an extended AO basis set.

Seven of the eight states correlating with channels II and III are well bound (Tables 2 and 3); only $1^3\Sigma_g^+$(II) is repulsive.

Doubly excited states arising from channel IV (both atoms $s \rightarrow p$ excited) are particularly stable ($1^3\Sigma_g^-$ and $^1\Delta_g$). In line with predictions made by Bader et al. (1) for heavier first-row diatomics, the $3\sigma_g$ MO of Be_2 is less bonding than $1\pi_u$.

The increase in bond order affected by these *antibonding* → *bonding* excitations is supported by the predicted values for the spectroscopic constants of the excited states, which invariably follow a common trend: short R_e, high ω_e and large D_e (the only exception being doubly excited $1^3\Pi_u$). In detail, the R_e values range from 3.43 ($1^3\Sigma_g^-$) to 4.36 bohr ($2^3\Pi_u$), ω_e from 495 ($1^1\Sigma_u^+$) to 860 cm^{-1} ($1^3\Sigma_g^-$), and D_e from 1.20 ($3^1\Sigma_g^+$) to 3.58 eV ($1^3\Pi_g$). The increase in bonding with respect to $X^1\Sigma_g^+$ is evident, with $R_e = 4.63$ bohr, $\omega_e = 276$ cm^{-1}, and $D_e \approx 0.10$ eV (experimental, ref. 14).

From the 11 excited states of Be_2 lying below 5 eV and having a bound character, only $1^1\Pi_u(A)$ at 2.66 eV and $1^1\Sigma_u^+(B)$ at 3.44 eV have been observed experimentally (14, 22). (N.B.: for all singlet states studied here, dipole-allowed transitions into or from the ground state are therefore currently known.) The T_e values above underline the importance of double excitations for a diatomic with few VEs such as Be_2 — the detected A state (mainly $\sigma_u^2 \rightarrow \sigma'_g\pi_u$) is about 0.8 eV more stable than B (singly excited $\sigma_u \rightarrow \sigma'_g$).

Besides $1^1\Pi_u(A)$ of Be_2 (observed in emission), a few other SBDES cases are also experimentally known, namely $1^3\Sigma_g^-$ ($\sigma_g^2 \rightarrow \pi_u^2$) of Li_2 (29), $2^3\Pi_u(\sigma_u^2 \rightarrow \sigma'_g\pi_u)$ of B_2 (16, 17, 20, 31, 32), $2^2\Sigma_g^+(\sigma_u^2 \rightarrow \pi_u^2)$ of C_2^+, and $E^1\Sigma_g^+(\sigma_u^2 \rightarrow \sigma'^2_g)$ of C_2 (15, 18, 19, 33, 34). These doubly excited states have been detected either indirectly via perturbations ($1^3\Sigma_g^- - 2^3\Pi_g$ in Li_2) or directly via emission or absorption spectroscopy (B_2, C_2^+, C_2).

In Be_2, possible routes for detecting $1^3\Sigma_g^-$, $1^1\Delta_g$, and $2^1\Sigma_g^+$ are provided by the transitions $1^3\Pi_u$–$1^3\Sigma_g^-$ and $1^1\Delta_g$, $2^1\Sigma_g^+$–$1^1\Pi_u$; all these band systems lie in the near infrared. To detect $1^3\Sigma_g^-$ via perturbations with $1^3\Pi_g$ seems difficult since, as seen in Fig. 1, at the $1^3\Sigma_g^-$ minimum the vibrationally excited $1^3\Pi_g$ state lies close to its dissociation continuum.

We hope that the present spectroscopic parameters will serve as a guideline for modeling future experimental studies on those electronic states of Be_2 not yet observed. With the same goal in mind, an analysis of radiative data (Frank–Condon factors, oscillator strengths, radiative lifetimes) for several dipole-allowed transitions, particularly between excited states, is to be reported elsewhere.[2]

Acknowledgment

The authors thank B. Meng for his help at the first stage of the calculations as well as Dr. G.H. Lushington (UNB, Fredericton) for critical comments. Financial support from the Natural Sciences and Engineering Research Council of Canada is gratefully acknowledged.

References

1. R.F.W. Bader, W.H. Henneker, and P.E. Cade. J. Chem. Phys. **46**, 3341 (1967).
2. C.F. Bender and E.R. Davidson. J. Chem. Phys. **47**, 4972 (1967).
3. K.D. Jordan and J. Simons. J. Chem. Phys. **67**, 4027 (1977).
4. R.O. Jones. J. Chem. Phys. **71**, 1300 (1979).
5. M.R.A. Blomberg, P.E.M. Siegbahn, and B.O. Roos. Int. J. Quantum. Chem. Symp. **14**, 229 (1980).
6. B.H. Lengsfield, A.D. McLean, M. Yoshimine, and B. Liu. J. Chem. Phys. **79**, 1891 (1983).
7. R.J. Harrison and N.C. Handy. Chem. Phys. Lett. **98**, 97 (1983); **123**, 321 (1986).
8. C.W. Bauschlicher and H. Partridge. J. Chem. Phys. **80**, 334 (1984).
9. R.K. Gosavi and O.P. Strausz. Can. J. Chem. **66**, 2034 (1988).
10. (*a*) I. Røeggen, K. Morokuma, and K. Yamashita. Chem. Phys. Lett. **140**, 349 (1987); (*b*) I. Røeggen and J. Almlöf. Int. J. Quantum Chem. In press.
11. G.A. Peterson and W.A. Shirley. Chem. Phys. Lett. **160**, 494 (1989); W.A. Shirley and G.A. Peterson. Chem. Phys. Lett. **181**, 588 (1991).
12. M.B. Lepetit and J.P. Malrieu. Chem. Phys. Lett. **169**, 285 (1990); A. Goursot, J.P. Malrieu, and D.R. Salahub. Theor. Chim. Acta, **91**, 225 (1995).
13. S. Evangelisti, G.L. Bendazzoli, and L. Gagliardi. Chem. Phys. Lett. **185**, 47 (1994).
14. V.E. Bondybey and J.H. English. J. Chem. Phys. **80**, 568 (1984); V.E. Bondybey. Chem. Phys. Lett. **109**, 436 (1984).
15. J.S. Wright and P.J. Bruna. Chem. Phys. Lett. **156**, 533 (1989).
16. P.J. Bruna and J.S. Wright. J. Chem. Phys. **91**, 1126 (1989); J. Phys. Chem. **94**, 1774 (1990).
17. P.J. Bruna and J.S. Wright. J. Chem. Phys. **93**, 2617 (1990); J. Mol. Struct. (Theochem), **210**, 243 (1990).
18. P.J. Bruna and J.S. Wright. Chem. Phys. **157**, 111 (1991); J. Phys. Chem. **96**, 1630 (1992).
19. P.J. Bruna and J.S. Wright. J. Mol. Struct. (Theochem), **230**, 213 (1991).
20. P.J. Bruna and J.S. Wright. J. Phys. B: At. Mol. Opt. Phys. **26**, 1819 (1993).
21. B. Meng, P.J. Bruna, and J.S. Wright. Mol. Phys. **79**, 1305 (1993); P.J. Bruna, B. Meng, and J.S. Wright. J. Mol. Spectrosc. **159**, 79 (1993).
22. J.M. Brom, W.D. Hewett, and W. Weltner. J. Chem. Phys. **62**, 3122 (1975).
23. S. Huzinaga. J. Chem. Phys. **42**, 1293 (1965).
24. T.H. Dunning. J. Chem. Phys. **55**, 716 (1971); T.H. Dunning and P.J. Hay. Modern theoretical chemistry. Vol. 3. *Edited by* H.H. Schaefer. Plenum, New York. 1977.
25. R.J. Buenker and S.D. Peyerimhoff. Theor. Chim. Acta, **35**, 33 (1974); **39**, 217 (1975); R.J. Buenker, S.D. Peyerimhoff, and W. Butscher. Mol. Phys. **35**, 771 (1978); R.J. Buenker. Studies in physical and theoretical chemistry: current aspects of quantum chemistry. Vol. 21. Elsevier, Amsterdam. 1982; R.J. Buenker and R.A. Phillips. J. Mol. Struct. (Theochem), **123**, 291 (1985).
26. R.J. Buenker, S.D. Peyerimhoff, and P.J. Bruna. *In* Computational organic chemistry. *Edited by* I.G. Csizmadia and R. Daudel. Reidel, Dordrecht. 1981. p. 55.
27. C. Moore. Atomic energy levels. U.S. Govt., Washington, D.C. 1971.
28. B.J. Ransil and S. Fraga. J. Chem. Phys. **35**, 669 (1961).
29. A. Yiannopoulou, B. Ji, L. Li, M. Li, K. Urbanski, A.M. Lyyra, W.C. Stalley, and G.-H Jeung. J. Chem. Phys. **101**, 3581 (1994).
30. P.J. Bruna, G.A. DiLabio, and J.S. Wright. J. Phys. Chem. **96**, 6269 (1992).
31. C.R. Brazier and P.G. Carrick. J. Chem. Phys. **96**, 8684 (1992).
32. M. Hachey, S.P. Karna, and F. Grein. J. Phys. B: At. Mol. Opt. Phys. **25**, 1119 (1992).
33. L.J. van De Burgt and M.C. Heaven. J. Chem. Phys. **87**, 4235 (1987).
34. K. Huber and G. Herzberg. Molecular spectra and molecular structure. IV. Constants of diatomic molecules. Van Nostrand-Reinhold, New York. 1979.

[2] P.J. Bruna and J.S. Wright, to be published.

Density-functional calculation of core-electron binding energies of glycine conformers

Delano P. Chong

Abstract: Our recent procedure of computing accurate core-electron binding energies (CEBEs) with density-functional theory is applied to glycine conformers in this work. The procedure uses the unrestricted generalized transition-state model and a combined functional of Becke's 1988 exchange with Perdew's 1986 correlation. When a large basis set such as Dunning's correlation-consistent polarized valence quadruple zeta set is used, the average absolute deviation from experiment for the CEBEs of the most stable conformer of glycine is only 0.2 eV, compared with 18 eV for Koopmans' theorem.

Key words: core-electron binding energies, density-functional theory, glycine.

Résumé : Dans ce travail, on a appliqué le procédure que l'on a développée récemment pour calculer avec précision les énergie de liaison des électrons de coeur («CEBE») à l'aide de la théorie de la densité fonctionnelle. La méthode utilise le modèle généralisé et sans restriction de l'état de transition et une fonctionnelle combinée de l'échange de Becke de 1988 avec la corrélation de Perdew de 1986. Quand on utilise un ensemble de base large, comme l'ensemble zêta quadruple, à valence polarisée et en accord avec la corrélation de Dunning, la déviation absolue moyenne des CEBE du conformère le plus stable de la glycine par rapport aux valeurs expérimentales n'est d'environ que de 0,2 eV par comparaison avec les 18 eV pour le théorème de Koopmans.

Mots clés : énergie de liaison des électrons, théorie de la densité fonctionelle, glycine.

[Traduit par la rédaction]

Introduction

Although the gas-phase structure of glycine may be very different from that in the solid (in a zwitterionic form) or in aqueous solutions, it is of great interest and importance in radio astronomy. In the last few years, there have been several studies of the geometry and conformations of glycine (1, 2). The two low-lying conformers, often called conformers **I** and **II**, differ in the nature of the intramolecular hydrogen bond, as shown in Fig. 1. Based on microwave spectroscopy, Godfrey and Brown (1) recently concluded that there is no discrepancy between theory and experiment as far as the structures of conformers **I** and **II** are concerned.

On the other hand, we recently (3, 4) discovered a density-functional (DF) procedure of computing accurate core-electron binding energies (CEBEs) with an average absolute deviation from experiment of about 0.23 eV. The procedure used the unrestricted generalized transition-state (uGTS) model and an exchange-correlation potential labeled as B88-P86, made from Becke's 1988 exchange functional (5) and Perdew's 1986 correlation functional (6). The uGTS model for ionization from orbital k approximates the nonrelativistic ionization energy by

[1] $$I_{nr} = -0.25\ \varepsilon_k(0) - 0.75\ \varepsilon_k(2/3)$$

where $\varepsilon_k(\lambda)$ is the orbital energy when λ electron has been removed from orbital k. Before comparison is made with experimental I_{obs}, relativistic corrections C_{rel} were added to the computed I_{nr} values. A simple estimate of C_{rel} is given (4) by

[2] $$C_{rel} = KI_{nr}^{N}$$

with $K = 2.198 \times 10^{-7}$ and $N = 2.178$, when both I_{nr} and C_{rel} are in eV.

In 1988, Slaughter and Banna (7) reported the CEBE spectrum of glycine vapor. The objective of the present study is to apply our tested procedure to compute the CEBEs of conformers **I** and **II** of gas-phase glycine and to compare the results with the observed X-ray photoelectron spectrum (7).

Preliminary calculations

In most of our studies, we used the deMon DF program (8), which approximates some integrands with auxiliary basis functions. The set of auxiliary basis functions recommended by the authors is (4,4;4,4) for O and (3,1;3,1) for H. The meaning of $(j,k;m,n)$ has been given elsewhere (9, 10). Test calculations with a slightly larger auxiliary set (5,4;5,4) for O and (4,1;4,1) for H showed negligible effects. In contrast, neither Gaussian92 (11) nor CADPAC5 (12) employs fitting functions. Because the evaluation of CEBEs in our uGTS model requires the DF orbital energies, we benchmarked a deMon calculation on H_2O against those using Gaussian92 and CADPAC5.

In all benchmark calculations, we used the experimental geometry of H_2O (13), the local density approximation based

Received October 20, 1995.

This paper is dedicated to Professor Richard F.W. Bader on the occasion of his 65th birthday.

D.P. Chong.[1] Department of Chemistry, 2036 Main Mall, University of British Columbia, Vancouver, BC V6T 1Z1, Canada.

[1] Telephone: (604) 822-5754. Fax: (604) 822-2847. E-mail: chong@theory.chem.ubc.ca

Fig. 1. Two low-lying conformers of glycine.

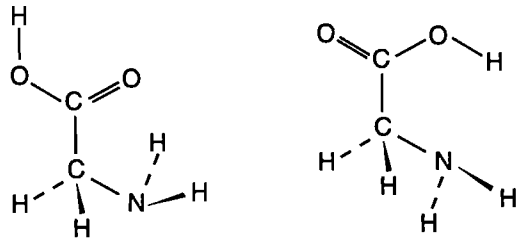

Conformer I Conformer II

Table 1. Comparison of total energy E (in hartree), orbital energies ε (in hartree), and dipole moment μ (in debye) from benchmark calculations on neutral H_2O with local density approximation and cc-pVTZ basis set.

	Gaussian92[a,b]	CADPAC5[a]	deMon[c]
$E + 75$	−0.897 61	−0.897 65	−0.899 16
$\varepsilon(1a_1)$	−18.595 96	−18.595 97	−18.597 48
$\varepsilon(2a_1)$	−0.914 18	−0.914 18	−0.915 76
$\varepsilon(1b_2)$	−0.476 66	−0.476 66	−0.478 83
$\varepsilon(3a_1)$	−0.330 67	−0.330 67	−0.331 37
$\varepsilon(1b_1)$	−0.254 21	−0.254 21	−0.255 11
μ	1.945 5	1.945 4	1.955 5

[a]96 radial points × 2048 angular points per atom.
[b]With SVWN5 functional. The corresponding entries for the SVWN functional are −0.09282, −18.61478, −0.93258, −0.49494, −0.34887, −0.27239, and −1.9488, respectively.
[c]32 radial points × 194 angular points per atom, (4,4;4,4) and (3,1;3,1) auxiliary basis.

on the Slater exchange term with the correlation function of Vosko, Wilk, and Nusair (14) (SVWN), and the correlation-consistent polarized valence triple-zeta (cc-pVTZ) basis of Dunning and co-workers (15, 16). As in our earlier calculations (3, 4), only *s*-, *p*-, and (six-component) *d*-type basis functions were used. For numerical quadrature in deMon, we used the extra-fine grid, which consists of 32 radial points × 194 angular points per atom. For calculation with Gaussian92 and CADPAC5, we specified 96 radial points × 2048 angular points per atom.

The results of our preliminary calculations are summarized in Table 1, from which several conclusions can be drawn. Both Gaussian92 and CADPAC5 computations have converged as far as numerical quadrature is concerned and there are small numerical errors associated with deMon calculations, possibly due to the lack of *f*-type functions in the auxiliary basis. However, in light of the gain in computing speed, errors of 0.0015 eV in orbital energies and 0.01 debye in dipole moments seem to be tolerable.

Results and discussion

For conformers **I** and **II** of glycine, we used the CCSD/DZP geometry obtained by Hu et al. (2), the correlation-consistent polarized valence quadruple-zeta basis set (cc-pVQZ) of Dunning and co-workers (15, 16), the B88-P86 functional (5, 6)

Table 2. Comparison of relative energy ΔE (in kcal mol^{-1}), and dipole moment μ (in debye) of conformers **I** and **II** of neutral glycine.[a]

	Method	ΔE	μ_A	μ_B	μ_{total}
Conformer **I**	HAM/3	(0)	1.901	0.951	2.125
	AM1	(0)	0.855	0.563	1.024
	CCSD/DZP[b]	(0)	1.14	0.48	1.24
	DF[c]	(0)	1.001	0.685	1.213
	Expt.	(0)	1.0[d]		
Conformer **II**	HAM/3	−39.2	7.858	2.384	8.212
	AM1	12.6	4.985	1.312	5.155
	CCSD/DZP[b]	1.43	5.69	1.06	5.79
	DF[c]	1.68	5.514	0.873	5.583
	Expt.	1.4 ± 0.4[d]	4.5[e]	<1[e]	

[a]All calculations were done at the CCSD/DZP geometry reported by Hu et al. in ref. 2. The components μ_A and μ_B are along the principal axes of the conformers.
[b]Reference 2.
[c]B88-P86/cc-pVQZ.
[d]Reference 19.
[e]Reference 20.

mentioned above, internal auxiliary basis set of (4,4;4,4) and (3,1;3,1), and an extra-fine grid for numerical integrations. Again, any atomic orbital basis function of *f*-type or higher angular momentum was excluded from our calculations. The relative energy and components of the dipole moment are compared in Table 2. The results obtained by using semi-empirical MO methods HAM/3 (17) and AM1 (18) are also included in Table 2 for comparison. It can be seen that our procedure, which can be labeled B88-P86/cc-pVQZ//CCSD/DZP, leads to results with accuracy comparable to that from CCSD/DZP (2).

Finally, we applied our uGTS model to compute the CEBEs of conformers **I** and **II** of the glycine molecule. The results are summarized in Table 3. Instead of adding the estimated relativistic corrections C_{rel} to the calculated I_{nr} to compare with the observed CEBEs, it is more convenient to subtract C_{rel} from I_{obs} and compare the results with various calculated I_{nr} values. The computed CEBEs for conformer **I** agree better with experiment than those for conformer **II**: every calculated CEBE for conformer **II** deviates more from experiment than the corresponding one for conformer **I** (as are the average and maximum absolute deviations), confirming the conclusion that **I** is the more stable conformer. It can also be seen that we have succeeded in applying our reliable method to compute accurate CEBEs for glycine.

Acknowledgment

This work was supported by the Natural Sciences and Engineering Research Council of Canada. We also thank Dr. D.R. Salahub for an early version of the deMon DF program, Dr. M. Cohen for performing the CADPAC calculations, Dr. V. Barone for an interface program to feed deMon basis sets into the Gaussian program, and Dr. N. Cann for implementing it at U.B.C.

Table 3. Comparison of core-electron binding energies (in eV) of glycine conformers **I**[a] and **II**[a] with experiment.

	Obsd.[b]	Obsd.$-C_{rel}$[c]	KT[d] **I**	HAM/3 **I**	DF[e] **I**	DF[e] **II**
H_2NCH_2COOH	292.25	292.20	307.10	287.04	292.31	292.56
H_2NCH_2COOH	295.15	295.10	310.28	293.01	294.92	294.57
H_2NCH_2COOH	405.58	405.47	423.32	401.04	405.57	406.44
H_2NCH_2COOH	538.2	538.0	559.49	536.54	538.19	538.58
H_2NCH_2COOH	540.0	539.8	561.03	538.70	540.14	539.32
Avg. abs. dev.		(0)	18.1	2.8	0.2	0.6

[a]All calculations were done at CCSD/DZP geometry.
[b]Reference 7.
[c]For estimated relativistic corrections C_{rel}, see eq. [2].
[d]Koopmans' theorem (RHF/DZP/ /CCSD/DZP) results from C.-H. Hu, private communications.
[e]B88-P86/cc-pVQZ.

References

1. P.D. Godfrey and R.D. Brown. J. Am. Chem. Soc. **117**, 2019 (1995), and references therein.
2. C.-H. Hu, M. Shen, and H.F. Schaefer III. J. Am. Chem. Soc. **115**, 2923 (1993).
3. D.P. Chong. Chem. Phys. Lett. **232**, 486 (1995).
4. D.P. Chong. J. Chem. Phys. **103**, 1842 (1995).
5. A.D. Becke. Phys. Rev. A: Gen. Phys. **38**, 3098 (1988).
6. J.P. Perdew. Phys. Rev. B: Condens. Matter, **33**, 8822 (1986).
7. A.R. Slaughter and M.S. Banna. J. Phys. Chem. **92**, 2165 (1988).
8. A. St-Amant and D.R. Salahub. Chem. Phys. Lett. **169**, 387 (1990); A. St-Amant. Ph.D. Thesis, University of Montreal (1991).
9. P. Dufy, D.P. Chong, and M. Dupuis. J. Chem. Phys. **102**, 3312 (1995).
10. D.P. Chong. Chin. J. Phys. **30**, 115 (1992).
11. M.J. Frisch, G.W. Trucks, H.B. Schlegel, P.M.W. Gill, B.G. Johnson, M.W. Wong, J.B. Foresman, M.A. Robb, M. Head-Gordon, E.S. Replogle, R. Gomperts, J.L. Andres, K. Raghavachari, J.S. Binkley, C. Gonzalez, R.L. Martin, D.J. Fox, D.J. Defrees, J. Baker, J.J.P. Stewart, and J.A. Pople. Gaussian92/DFT. Gaussian, Inc., Pittsburgh, Pa. 1993.
12. R.D. Amos, I.L. Alberts, J.S. Andrews, S.M. Colwell, N.C. Handy, D. Jayatilaka, P.J. Knowles, R. Kobayashi, N. Koga, K.E. Laidig, P.E. Maslen, C.W. Murray, J.E. Rice, J. Sanz, E.D. Simandiras, A.J. Stone, and M.-D. Su. CADPAC5, Cambridge. 1992.
13. K.-L. Hellwege (*Editor*). Landolt–Börnstein numerical data and functional relationships in science and technology. New Series, Group II, Vol. 7. Springer, Berlin. 1976.
14. S.J. Vosco, L. Wilk, and M. Nusair. Can. J. Phys. **58**, 1200 (1980).
15. T.H. Dunning, Jr. J. Chem. Phys. **90**, 1007 (1989).
16. R.A. Kendall, T.H. Dunning, Jr., and R.J. Harrison. J. Chem. Phys. **96**, 6796 (1992).
17. L. Åsbrink, C. Fridh, and E. Lindholm. Chem. Phys. Lett. **52**, 63 (1977); **52**, 68 (1977); **52**, 72 (1977).
18. M.J.S. Dewar, E.G. Zoebisch, E.F. Healy, and J.J.P. Stewart. J. Am. Chem. Soc. **107**, 3902 (1985).
19. R.D. Suenram and F.J. Lovas. J. Am. Chem. Soc. **102**, 7180 (1980).
20. R.D. Brown, P.D. Godfrey, J.W.V. Storey, and M.P. Bassez. J. Chem. Soc. Chem Commun. 547 (1978).

Atoms in molecules from the exact one-electron wave function

Geoffrey Hunter

Abstract: Use of the electron amplitude (i.e., the square root of the electron density) in place of the electron density in Bader's topological theory of atoms in molecules, is shown to lead to identical definitions of bond paths and interatomic surfaces. The concepts of regions of charge concentration and depletion, derived from the Laplacian of the electron density, become the concepts of classically allowed and forbidden regions of space when derived from the Laplacian of the electron amplitude, because the latter is the wave function in the exact Schrödinger equation for (any) one electron in the many-electron molecule. However, the domains of corresponding regions are different, the size and depth of a classically allowed region always being larger than the corresponding region of charge concentration; in some cases there is no region of charge concentration corresponding to a classically allowed region. The surface between the outermost allowed and forbidden regions of space provides a definition of the size and shape of the molecule. This definition of the outermost surface of the electronic charge cloud (the molecular envelope) is exact apart from quantum mechanical tunelling. Hence it is proposed as a basis for molecular graphics; i.e., as the unique, non-arbitrary, and, in principle, exact definition of the size and shape of a molecule.

Key words: electron density, quantum chemistry, molecular graphics.

Résumé : On montre que l'utilisation de l'amplitude électronique (c'est-à-dire la racine carrée de la densité électronique), au lieu de la densité électronique dans la théorie topologique de Bader des atomes dans les molécules, conduit à des définitions identiques pour les chemins de liaison et pour les surfaces interatomiques. Les concepts de régions avec concentration et épuisement de charge sont dérivés du laplacien de la densité électronique; lorsqu'on les dérive du laplacien de l'amplitude électronique, compte tenu du fait que ce dernier est une fonction d'onde dans l'équation exacte de Schrödinger pour tout électron d'une molécule à plusieurs électrons, ils deviennent des concepts de régions de l'espace qui sont classiquement permises et défendues. Les domaines qui correspondent aux régions sont toutefois différents, la taille et la profondeur d'une région classiquement permise étant toujours plus grande que la région correspondante de la concentration de charge; dans quelques cas, il n'existe pas de région de concentration de charge correspondant à une région classiquement permise. La surface entre les régions les plus extérieures permises et les régions de l'espace qui sont interdites fournit une définition de la taille et de la forme de la molécule. Cette défintion de la surface la plus extérieure du nuage de la charge électronique (l'enveloppe moléculaire) est exacte à part de l'effet tunnel de la mécanique quantique. Il est donc proposé comme base pour des graphiques moléculaire, c'est-à-dire comme la définition unique, non arbitraire et, en principe, la définition exacte de la taille et de la forme de la molécule.

Mots clés : densité électronique, chimie quantique, graphiques moléculaires.

[Traduit par la rédaction]

Introduction

The theory of atoms in molecules has been developed by R.F.W. Bader and his associates (1). This theory provides mathematical tools for interpreting the electron density distribution in a molecule in terms of the traditional concepts of chemistry; i.e., in terms of bonds between atoms. The theory provides a precise definition of the bond path[2] between, and the surface separating, a pair of bonded atoms; at the point where the path and the surface intersect the gradient of the electron density is zero.[3] The principal utility of the theory is for the interpretation of electronic wave functions of molecules produced as the results of ab initio calculations.[4]

Received October 2, 1995.

This paper is dedicated to Professor Richard F.W. Bader on the occasion of his 65th birthday.

G. Hunter.[1] Department of Chemistry, York University, Toronto, ON M3J 1P3, Canada.

[1] Telephone: (416) 736-5306. Fax: (416) 736-5936. E-mail: ghunter@yorku.ca

[2] A line (possibly curved but usually straight) between the nuclei of the bonded atoms.

[3] It is a saddle-point, a (3,-1) critical point of the density (ref. 1, p. 19).

[4] Recent advances in X-ray diffraction (keeping the crystal at a very low temperature and analysis of the scattering data in terms of a multipole expansion of the electron density) are now yielding atoms in molecules analyses that are comparable in accuracy with those obtained from ab initio wave functions (2).

In this respect it is a better theory of molecular structure than the valence-bond and molecular orbital theories, because it is applicable to *any* wave function (including correlated wave functions) regardless of any orbital construction or decomposition of the wave function.

The exact one-electron model of molecular structure (3) is an application of the general theory of conditional probability amplitudes in wave mechanics (4). It is closely related to the theory of atoms in molecules, since the exact one-electron wave function is (except for a normalization constant equal to the number of electrons, N) simply equal to the square root of the electron density (ref. 3, eq. (8)):[5]

$$[1] \qquad \rho(r|R) = N\left[\psi(r|R)\right]^2 \qquad \psi(r|R) = +\sqrt{\rho(r|R)/N}$$

in which r represents the three coordinates of a single electron, and R represents all of the nuclear coordinates. For the sake of brevity, and by analogy with the term **electron density**, this exact one-electron wave function (the square-root of the electron density in a many-electron system) will henceforth be referred to as the *electron amplitude*.

The purpose of this article is to discuss the similarities and differences between the models of molecular structure based, respectively, upon the topology of the electron density, and upon the topology of the square root of the electron density. It turns out that the definitions of the bond path and of the interatomic surface are identical for the two models. The important differences between the two models stem from the fact that the square root of the density, $\psi(r|R)$ satisfies a one-electron Schrödinger equation (3):

$$[2] \qquad -\frac{\hbar^2}{2m_e}\nabla^2\psi(r|R) + U(r|R)\psi(r|R) = E(R)\psi(r|R)$$

in which $U(r|R)$ is the effective potential for the motion of the single electron within[6] the many-electron molecule, and $E(R)$ is the total electronic energy.[7] This one-electron Schrödinger equation [2] has been derived in different ways by several different authors (3, 5–7). We used it originally in application to the ground state of the helium atom (8).

2. The exact one-electron model

It is important to realize that the Schrödinger equation satisfied by $\psi(r|R)$ is obtained from the full many-electron, electronic Schrödinger equation of the whole molecule (by the algebra of conditional probability amplitudes) without any approximation whatsoever (4, 9). Thus this Schrödinger equation for the motion of one electron within the many-electron system is, in principle *exact*,[8]. In computational practice the accuracies of the electron amplitude $\psi(r|R)$ and of the potential energy function $U(r|R)$ depend upon the accuracy of the many-electron wave function from which they are computed. Many-electron computations based upon high quality basis sets with allowance for electron correlation will yield correspondingly accurate one-electron wave functions and potentials.

This exact one-electron Schrödinger equation [2] provides an exact dynamical model of the motion of any one electron in the many-electron system. No such dynamical model is known for the electron density itself (9). In particular, the exact one-electron model yields a definition of the surface enclosing the molecule (and of each atom within the molecule) as the turning surface within which the electron would be confined if it were a classical particle.[9] This surface is appropriately called the **molecular envelope**, a name that was coined by Richard Bader *circa* 1985.

3. Critical points of $\rho(r|R)$ and $\psi(r|R)$

The topology of a scalar field such as $\rho(r|R)$ or $\psi(r|R)$ is revealed by the gradient of the field and especially through the critical points where the gradient is zero (ref. 1, Chap. 2).[10] The gradient of a scalar field is, of course, a vector field, and at each point in space the components of the gradient will be 3 independent (say x,y,z) first derivatives of the scalar at the specified point; these components specify both the magnitude of the gradient and its direction, the latter being the direction in which the scalar field is increasing or decreasing most rapidly.

Since $\rho(r|R) = N\left[\psi(r|R)\right]^2$ it follows by the elementary rules of differentiation that:

$$[3] \qquad \nabla\rho(r|R) = 2N\psi(r|R)\nabla\psi(r|R)$$

or

$$\frac{\nabla\rho(r|R)}{\rho(r|R)} = 2\,\frac{\nabla\psi(r|R)}{\psi(r|R)}$$

Note: When plotting the gradient to display its topology our experience has been that the second form of this equation is preferable to the first form; the range of values of $\nabla\rho(r|R)/\rho(r|R)$ is less than that of $\nabla\rho(r|R)$ itself because it is essentially a semi-log plot: $\nabla\rho(r|R)/\rho(r|R) = \nabla\ln[\rho(r|R)]$.

Thus the gradient vector field of $\rho(r|R)$ is equal to the gradient vector field of $\psi(r|R)$ multiplied by the scalar field $2N\psi(r|R)$. Furthermore, multiplication of a vector by a scalar produces another vector in the same direction if the scalar is positive, and in the opposite direction if it is negative, and since the scalar field $\rho(r|R)$ is positive everywhere (as is its positive square root $\psi(r|R)\sqrt{N}$), it follows that the gradient of $\rho(r|R)$ and the gradient of $\psi(r|R)$ *point in the same direction everywhere*; they only differ in magnitude. Specifically the critical points of $\rho(r|R)$ will thus be identical with the critical points of $\psi(r|R)$.

---

[5] The positive square root of $\rho(r|R)$ is chosen since the phase factor of $\psi(r|R)$ is arbitrary.

[6] That is, after averaging over the motion of the other electrons as explained in ref. 3.

[7] All of the quantities are parametrically dependent upon the nuclear coordinates R as is usual in the Born–Oppenheimer approximation.

[8] That is, exact within the framework of the non-relativistic, Born–Oppenheimer approximations commonly used in theoretical chemistry.

[9] That is, in the absence of quantum mechanical tunelling.

[10] The domains where $\nabla\rho(r|R) = 0$ are *points*, because this vector equation is equivalent to the 3 scalar equations: $\partial\rho/\partial x = 0$, $\partial\rho/\partial y = 0$, $\partial\rho/\partial z = 0$, and 3 constraints on a function of 3 variables produces a domain of single points.

The geometrical nature of the critical points is characterized by the signs of the eigenvalues of the Hessian matrix; i.e., the matrix of second derivatives of the original scalar (ref. 1, pp.16–19). Determination of the eigenvalues of the Hessian matrix is equivalent to a transformation to coordinates for which all cross-derivatives of the form $\partial^2\rho(r|R)/\partial x\partial y$ are zero at the critical point being characterized (ref. 1, p. 47).

The **rank** of a critical point is the number of non-zero eigenvalues (1–3) and its **signature** is the sum of the signs of the eigenvalues. Stable critical points[11] are of rank 3 and are of 4 kinds: a maximum or minimum (all 3 eigenvalues negative or positive), and two kinds of saddle (2 eigenvalues negative or positive with the third of opposite sign).

It is not immediately obvious that the Hessian matrix of $\rho(r|R)$ has eigenvalues with the same signs as those of $\psi(r|R)$, because their second derivatives are related, in general, as follows:

$$[4] \qquad \frac{\partial^2\rho(r|R)}{\partial x\partial y} = 2N\left\{\psi(r|R)\frac{\partial^2\psi(r|R)}{\partial x\partial y} + \frac{\partial\psi(r|R)}{\partial x}\frac{\partial\psi(r|R)}{\partial y}\right\}$$

and for a diagonal derivative:

$$[5] \qquad \frac{\partial^2\rho(r|R)}{\partial x^2} = 2N\left\{\psi(r|R)\frac{\partial^2\psi(r|R)}{\partial x^2} + \left(\frac{\partial\psi(r|R)}{\partial x}\right)^2\right\}$$

However, at a critical point, r_c, *all* the first derivatives of $\rho(r_c|R)$ and $\psi(r_c|R)$ are zero (regardless of the orientation of the coordinate axes, x, y, z) , and hence the second terms on the right-hand sides of eqs. [4] and [5] are zero. Hence eq. [4] becomes simply:

$$[6] \qquad \frac{\partial^2\rho(r_c|R)}{\partial x\partial y} = 2N\psi(r_c|R)\frac{\partial^2\psi(r_c|R)}{\partial x\partial y}$$

and thus we see that each second derivative of $\rho(r_c|R)$ is equal to the corresponding derivative of $\psi(r_c|R)$ multiplied by the positive scalar factor $2N\psi(r_c|R)$. Furthermore this scalar factor is *the same* for all 10 second derivatives and hence we conclude that the Hessian matrix of $\rho(r_c|R)$ is equal to the Hessian matrix of $\psi(r_c|R)$ multiplied by this common scalar factor.

Such a common scalar factor will only multiply the eigenvalues of the matrix by the factor, and since the factor is positive everywhere, it follows that the eigenvalues of the Hessian of $\rho(r_c|R)$ have the same signs as those of the Hessian of $\psi(r_c|R)$ at every critical point of $\rho(r_c|R)$ (and of $\psi(r_c|R)$ since they have the same critical points).

In summary: the above analysis leads to the conclusion that the critical points of $\psi(r|R)$ are identical with those of $\rho(r|R)$ in both location (the coordinates r_c) and geometrical nature (i.e., rank and signature).

[11] Stability against small changes to the density distribution is important for characterizing the critical points of a stable molecule, because the ever-present nuclear vibrations cause such changes.

Interpretation

A **trajectory** of the gradient vector field $\nabla\rho(r|R)$ is a (generally curved) line in 3-dimensional space traced out by following the direction of the vector $\nabla\rho(r|R)$ from any given starting point, and from all subsequent points along it (ref. 1, p. 22). Different starting points will usually produce different trajectories, and two different adjacent trajectories will be locally parallel (in the limit as their distance apart tends to zero). Thus by definition two different trajectories cannot meet anywhere except at the critical points of $\rho(r|R)$ where the direction of $\nabla\rho(r|R)$ is undefined. Trajectories thus originate and terminate at critical points of $\rho(r|R)$. Many trajectories originate at infinity where there is a spherical shell throughout which $\nabla\rho(r|R) = 0$, and many trajectories terminate at atomic nuclei, where the direction of $\nabla\rho(r|R)$ is undefined even though its magnitude is finite.

The gradient of the electron amplitude $\nabla\psi(r|R)$ is proportional to the electron's local momentum, $\boldsymbol{p}$, at each point in space:

$$[7] \qquad \boldsymbol{p} = \frac{\hbar}{i}\frac{\nabla\psi(r|R)}{\psi(r|R)}$$

Thus a trajectory of the gradient vector field $\nabla\psi(r|R)$ traces out the path that an electron would follow starting from any given point on the path.[12]

Between every pair of bonded atoms there is a (3,-1) critical point where the electron's momentum is zero so that the direction of its motion at this point is undefined (ref. 1, pp.23–24). The **bond path** between the two atoms consists of two trajectories that originate at this critical point and terminate at the two nuclei; if the electron was at the critical point it would move along one of the trajectories that make up the bond path towards the corresponding nucleus.[13]

The **interatomic surface** is the locus of all trajectories that terminate at the bond critical point; the electron's local momentum has no component perpendicular to this surface. The surface is orthogonal to the bond path at the bond critical point. If the electron were in this surface it would move along a trajectory in the surface until it came to rest at the bond critical point.

The bond critical point is a maximum of $\rho(r|R)$ and $\psi(r|R)$ when approached along any trajectory within the interatomic surface; it is a minimum along the two trajectories that make up the bond path.

4. The Laplacians of $\rho(r|R)$ and $\psi(r|R)$

The Laplacian of $\rho(r|R)$ (or of $\psi(r|R)$) is the divergence of its gradient:

[12] Division by the scalar field does not change the direction of $\nabla\psi(r|R)$. This quasi-physical conclusion is, however, subject to the local momentum, eq. [7], being *imaginary* for real (bound state) wave functions $\psi(r|R)$ because of the factor of i in the quantum mechanical momentum operator.

[13] These descriptions of the electron's motion are not to be taken literally in the sense of classical trajectories; the quantum mechanical uncertainty principle does not allow for the simultaneous specification of the electron's position and momentum. Nevertheless this electron-momentum interpretation of the trajectories has conceptual merit.

$$[8] \qquad \text{div grad}\,\rho = \nabla.\nabla\rho(r|R) = \nabla^2\rho(r|R) = \frac{\partial^2\rho(r|R)}{\partial x^2} + \frac{\partial^2\rho(r|R)}{\partial y^2} + \frac{\partial^2\rho(r|R)}{\partial z^2}$$

It is equivalently the sum of the diagonal elements of the Hessian matrix of $\rho(r|R)$, which[14] is equal to the sum of the eigenvalues of the Hessian matrix. Thus the Laplacian of $\rho(r|R)$ (and of $\psi(r|R)$) is a scalar field whose value is independent of the coordinate system.

As noted above in introducing eq. [4], the Laplacians of $\rho(r|R)$ and $\psi(r|R)$ are not generally simply proportional to each other; this simplicity only pertains at the critical points where the gradients of $\rho(r|R)$ and $\psi(r|R)$ are zero. From eqs. [8] and [5] the relationship between the Laplacians can be expressed by the following equivalent equations:

$$\nabla^2\rho(r|R) = 2N\left\{\psi(r|R)\nabla^2\psi(r|R) + \left[\nabla\psi(r|R)\right]^2\right\}$$

$$[9] \qquad \frac{\nabla^2\rho(r|R)}{\rho(r|R)} = 2\left\{\frac{\nabla^2\psi(r|R)}{\psi(r|R)} + \left[\frac{\nabla\psi(r|R)}{\psi(r|R)}\right]^2\right\}$$

$$\frac{\nabla^2\psi(r|R)}{\psi(r|R)} = \frac{1}{2}\frac{\nabla^2\rho(r|R)}{\rho(r|R)} - \left[\frac{\nabla\rho(r|R)}{2\rho(r|R)}\right]^2$$

where eq. (3) has been used to derive the last of these alternative forms.

The Laplacian of $\psi(r|R)$ is proportional to the local kinetic energy of the electron as is apparent from the Schrödinger equation [2] satisfied by $\psi(r|R)$. Thus in atomic units[15] the expression for the electron's local kinetic energy is:

$$[10] \qquad \text{Kinetic energy} = -\frac{1}{2}\frac{\nabla^2\psi(r|R)}{\psi(r|R)} = -\frac{1}{4}\frac{\nabla^2\rho(r|R)}{\rho(r|R)} + \frac{1}{8}\left[\frac{\nabla\rho(r|R)}{\rho(r|R)}\right]^2$$

which is essentially eq. (15) of ref. 3.[16] It is especially noteworthy that the second term of the right hand-side of this equation (being a quantity squared) always makes a positive contribution to the electron's local kinetic energy. It is this term that produces significant differences between the topologies of the Laplacians of $\psi(r|R)$ and $\rho(r|R)$.

Atomic shell structure

Bader has described the topology of the Laplacian of $\rho(r|R)$ in terms of charge concentration and depletion (ref. 1, p. 252); electronic charge is locally depleted in regions of space where $\nabla^2\rho(r|R) > 0$, and locally concentrated where $\nabla^2\rho(r|R) < 0$.

Calculations based upon this concept were carried out on many atoms by Shi and Boyd (10), and by Sagar et al. (11), and have been summarized by Bader (ref. 1, p. 256). These calculations revealed spherical shells of charge concentration separated by shells of charge depletion and, for elements within the first two periods of the periodic table, the shell structure thus revealed was in one to one correspondence with the shell structure predicted by the Bohr model of the hydrogen atom and the aufbau principle, by which there can be $2n^2$ electrons in each "shell of electrons" ($n = 1, 2, 3, \ldots$),[17] the total number of electrons being equal to the atomic number of the element. The calculations revealed that "at most five shells are seen" (11) based upon the topology of $\rho(r|R)$.

Sagar et al. conducted a parallel study of atomic shell structure based upon the topology of $\nabla^2\psi(r|R) = \nabla^2\sqrt{\rho(r|R)/N}$ (12). They noted that the computed topology of $\nabla^2\psi(r|R)$ was "very similar in nature" to that of $\nabla^2\rho(r|R)$, "the significant difference being that $\nabla^2\psi(r|R)$ displays all seven shells in the heavier elements of the periodic table," whereas (as noted above) $\nabla^2\rho(r|R)$ only displays five shells. This difference is directly attributable to the second (always positive) term on the right-hand side of eq. [10].

In a later study Kohout et al. (13) used relativistic wave functions to compare the atomic shell structures predicted by $\nabla^2\rho(r|R)$, $\nabla^2\sqrt{\rho(r|R)}/\sqrt{\rho(r|R)}$, and $\nabla\rho(r|R)/\rho$. They concluded that there were no topological differences between relativistic and non-relativistic results, and that $\nabla^2\rho(r|R)$ does not resolve the valence shell of heavy atoms, while $\nabla^2\psi(r|R) = \nabla^2\sqrt{\rho(r|R)}$ does show a valence maximum for heavy atoms, but in the case of transition elements this maximum occurs in a (classically forbidden) region of negative kinetic energy.[18] They also concluded that the electron momentum $\nabla\rho(r|R)/\rho$ (eq. [7], equal to $\nabla\psi(r|R)/\psi$ by eq. [3]) describes the complete shell structure in all cases.

In addition to being a better predictor of *atomic* shell structure than $\nabla^2\rho(r|R)$, the Laplacian of $\psi(r|R) = \sqrt{\rho(r|R)/N}$ also displayed a classically allowed outer region in the electron density of the ammonium radical (ref. 3, p. 204) corresponding to this radical's extra electron, whereas the Laplacian of $\rho(r|R)$ computed from the same ab initio wave function did not display a corresponding region of charge concentration.

Interpretation

The computed differences between the topologies of the Laplacians of the electron density, $\rho(r|R)$, and the electron amplitude, $\psi(r|R) = \sqrt{\rho(r|R)/N}$, also reflect their different interpretation. Regions of space where $\nabla^2\psi(r|R) > 0$ correspond to the electron's local kinetic energy being negative

[14] from the properties of matrices.

[15] In which $\hbar = m_e = 1$.

[16] Bader presented this equation in his book (ref. 1, p. 102) in the context of a one-electron atom or molecule.

[17] That is, a separate shell of charge concentration for each principal quantum number, n, occupied in the atom.

[18] This is consistent with the supplementary conclusion of Sagar et al. (12) that: "the outermost zero-extremum is not displayed in the transition elements; i.e., where d-orbital filling is present." That is, the kinetic energy, eq. [10], displays the complete expected shell structure (a shell of positive kinetic energy for each occupied principal quantum number n) for all elements of the periodic table except the transition elements, in which the outermost shell is displayed as a maximum in the kinetic energy but in a classically forbidden (i.e., negative kinetic energy) region.

and hence such a region is a classical forbidden region of space. On the other hand, where $\nabla^2\psi(r|R) < 0$ the electron's local kinetic energy is positive and the region of space is classically allowed.

These classically allowed and forbidden regions of space are separated by surfaces where $\nabla^2\psi(r|R) = 0$.[19] These are the classical turning surfaces of the electron's motion; in classical mechanics the electron's kinetic energy would decrease as it approached such a surface, and it would be zero when it is on the surface. It would then turn around and accelerate into the classically allowed region of space.

5. The molecular envelope

The outermost surface where the electron's kinetic energy is zero is the surface within which it is confined except for quantum mechanical tunnelling; if the electron were a classical particle it would never go outside of this outermost turning surface.[20] Thus this surface is an unequivocal definition of the size and shape of the molecule's cloud of electronic charge surrounding the nuclei. Within the constraints on determinism imposed by the uncertainty principle, it appears to be the best possible unambiguous definition of molecular size and shape, whereas other definitions rely upon arbitrarilly chosen contours such as those having a particular value of the electron density. Furthermore, it is pertinent to recall that the one-electron model, within which this outermost turning surface is defined, is in principle exact.

This non-arbitrary definition of molecular size and shape is appropriately called the **molecular envelope**. In view of its non-arbitrary and in-principle exact nature, it appears to be potentially an excellent basis for molecular graphics. The results already computed and reported for diatomic molecules (3) encourage the further development and application of this well-defined concept of molecular size and shape.

6. Atoms defined as quantum sub-spaces

One of the later developments in Bader's theory of atoms in molecules is the concept that each atomic region of space (delimited by the interatomic surfaces through which the component of the gradient of the density is zero) can be regarded as an independent quantum subsystem, independent of the other subsystems except for the matching boundary conditions at each interatomic surface (ref. 1, Chap. 8).

This concept arises from a consideration of Schwinger's variational derivation of Schrödinger quantum mechanics for which the natural boundary condition (ref. 1, p. 152) at the surface of the sub-space is that the gradient of the wave function, $\nabla\psi(r|R)$, must be tangent to the surface everywhere.[21] This requisite boundary condition for the Schwinger variational principle to be applicable may be regarded as a fundamental definition of an atom as an independent quantum sub-system (ref. 1, p. 402).

It is apparent that the exact one-electron Schrödinger equation [2] is the pertinent Schrödinger equation within each atomic sub-space. Furthermore, it is a reasonable conjecture that the rather erudite mathematics involved in the development of the concept of the atomic sub-spaces[22] may be simplified by regarding the electron amplitude, $\psi(r|R)$, rather than the density, $\rho(r|R)$, as the fundamental amplitude that is being varied according to the principle of least action.

Discussion

The conclusion from the above analysis and discussion, is that basing Bader's atoms in molecules topological analysis of electronic wave functions upon the square root of the electron density (rather than upon the density itself) has merit, and in some respects appears to be superior both conceptually and in terms of computed results. The fundamental reason for this may be that quantum mechanics is a theory of amplitudes rather than one of densities.

It should be noted that in computational practice it is never necessary to actually compute the square root of the density, since the topology of $\psi(r|R)$ is revealed by $\nabla\psi(r|R)/\psi(r|R)$ and $\nabla^2\psi(r|R)/\psi(r|R)$; these topological functions are conveniently computed from the density and its first and second derivatives using eq. [3] and [10].

Thus the proposition that $\psi(r|R)$ is a better basis for the atoms in molecules analysis than $\rho(r|R)$ can be explored with only a very small amount of extra computing and plotting. Indeed efficiency dictates that the computations for $\psi(r|R)$ and $\rho(r|R)$ should be carried out in parallel in the same computer program; very few additional lines of computer code are needed, and the corresponding results can be output and plotted consecutively. This is, in fact, how the results reported in 1986 [3] were obtained — by slightly modifying a computer program in the laboratory of Richard Bader at McMaster University.

In view of the ease with which the above proposition can be explored, it is surely desirable to compute the Laplacians of both $\rho(r|R)$ and $\psi(r|R)$ whenever an atoms in molecules analysis is carried out.

At this juncture many results based upon $\rho(r|R)$ have already been published, whereas very few corresponding results based upon $\psi(r|R)$ have been obtained. The above proposition must, of course, in the spirit of science[23] remain tentative until many comparative computational results have been obtained. The trend already observed in previously

[19] The domains where $\nabla^2\psi(r|R) = 0$ are *surfaces*, because this scalar equation places a single constraint on the function, thus reducing the domain from 3 to 2 dimensions.

[20] At large distances from the nuclei the electron's kinetic energy tends to a negative asymptotic limit equal to minus the ionization energy of the molecule (4, 6). This asymptotic limit is independent of the path by which the electron leaves the molecule, but different paths will have different gradients $\nabla^3\psi/\psi$ that are proportional to the local force necessary to move the electron along the path. Thus ionization will preferentially occur by a path along which the maximum force is minimal.

[21] Equivalently that the scalar product of $\nabla\psi(r|R)$ with a normal to the surface should be zero everywhere.

[22] Defined as being enclosed by the surfaces perpendicular to which $\nabla\rho(r|R) = \nabla\psi(r|R) = 0$.

[23] That is, that ideas are always subject to the scrutiny of experiments, in this case computational experiments.

computed results (3, 12, 13) does, however, encourage the exploration of the proposition in future calculations.

Last but not least, the conceptual basis of using $\psi(r|R) = \sqrt{\rho(r|R)/N}$, based as it is upon the exact one-electron Schrödinger equation [2], offers an exact atoms in molecules analysis firmly based in all the well-established concepts of quantum mechanics as applied in chemistry, without appealing to auxiliary concepts such as charge concentration and depletion.

Acknowledgements

Computations are underway to apply the above analytical methods to molecules, specifically to generate the molecular envelopes of molecules that exhibit hindered rotation or steric hindrance to see if the molecular envelope definition of molecular size and shape is a good predictor of experimental properties. The ultimate objective is to establish an accurate, well-defined basis for molecular graphics. This work is being carried out by A.A. Ahari, with whom discussions about the conceptual aspects contributed to the writing of this article. Similar discussions with Dr. W.T. Chan are also gratefully acknowledged. Financial and logistic support for this work was provided by York University, and by Glenamadda Enterprises, Inc. An incisive review of the original manuscript by an anonymous referee contributed to the completeness and clarity of this article.

References

1. R.F.W. Bader, Atoms in molecules: a quantum theory. Oxford University Press, Oxford. 1990.
2. R. Destro and F. Merati. Acta. Crystallogr. Sect. B: Struct. Sci. **B51**, 559 (1995).
3. G. Hunter. Int. J. Quantum Chem. **29**, 197 (1986).
4. G. Hunter. Int. J. Quantum Chem. **9**, 237 (1975).
5. M. Levy, J.P. Perdew, and V. Sahni. Phys. Rev. A: Gen. Phys. **30**, 2745 (1984).
6. E.N. Lassettre. J. Chem. Phys. **83**, 1709 (1985).
7. N.H. March. Phys. Lett. **113A**, 66 (1985).
8. G. Hunter and C.C. Tai. Int. J. Quantum Chem. **19**, 1041 (1982).
9. G. Hunter. *In* Density matrices and density functionals. *Edited by* R. Erdahl and V.H. Smith, Jr. D. Reidel Publishing Company, Dordrecht. 1987. pp. 583–596
10. Z. Shi and R.J. Boyd. J. Chem. Phys. **88**, 4375 (1988).
11. R.P. Sagar, A.C.T. Ku, V.H. Smith, Jr., and A.M. Simas. J. Chem. Phys. **88**, 4367 (1988).
12. R.P. Sagar, A.C.T. Ku, V.H. Smith, Jr., and A.M. Simas. Can. J. Chem. **66**, 1005 (1988).
13. M. Kohout, A. Savin, and H. Preuss. J. Chem. Phys. **95**, 1928 (1991).

Study of NO and CO dissociation on the (100) Cu surface using density functional theory and the topological analysis of the electronic density and its Laplacian

Yosslen Aray and Jesús Rodríguez

Abstract: Molecular orbital ab initio Hartree–Fock, post-Hartree–Fock at the MP2 and QCISD levels, and density functional theory calculations of the dipole moment, the topology of the electronic density, $\rho(r)$, and its Laplacian, $\nabla^2\rho(r)$, for CO and NO molecules are reported. The results obtained confirm that density functional methods provide remarkably good electronic properties and a good description of the topology of $\rho(r)$ and $\nabla^2\rho(r)$. The Becke exchange functional with the correlation functional of Lee, Yang, and Parr was used to calculate the electronic density of the (100) Cu surface. Topological analysis of $\rho(r)$ shows that the crystal graph corresponds to square pyramids between the atoms of the top of the surface and the atoms of the second layer. The topological analysis of $-\nabla^2\rho$ shows that the atomic graph of the Cu surface exhibits one (3,−3) local charge concentration surrounded by four (3,+1) local charge depletion points. Additionally, there is a (3,+3) local depletion in the midpoint between each of four contiguous Cu atoms corresponding to the active site for the adsorption of the (3,−3) local charge concentration on the C atom of the CO or the N atom of the NO molecule. The larger value of the $-\nabla^2\rho$ at the nonbonded charge concentration on the atoms and the geometrical configuration of these critical points favor the interaction of the NO over the CO molecule with the (100) Cu surface. This result is in accord with the known reaction barriers for these molecules.

Key words: density functional theory, Laplacian of the electronic density, (100) Cu surface, carbon monoxide, nitrogen monoxide, molecular graph, atomic graph.

Résumé : Utilisant des calculs d'orbitales moléculaires ab initio de Hartree–Fock, aux niveaux post-Hartree–Fock MP2 et QCISD, et des calculs de la théorie de la densité fonctionnelle, on a évalué les moments dipolaires et la topologie de la densité électronique, $\rho(r)$ et son laplacien, $\nabla^2\rho(r)$, des molécules de CO et de NO. Les résultats obtenus confirment que les méthodes de la densité fonctionnelle conduisent à des propriétés électroniques particulièrement bonnes ainsi qu'à une bonne description de la topologie de $\rho(r)$ et de $\nabla^2\rho(r)$. On a utilisé la fonctionnelle d'échange de Becke avec la corrélation fonctionnelle de Lee, Yang et Parr pour calculer la densité électronique de la surface (100) du Cu. L'analyse topologique de $\rho(r)$ montre que le graphe du cristal correspond à des pyramides carrées entre les atomes au sommet de la surface et les atomes de la deuxième couche. L'analyse topologique de $\nabla^2\rho$ montre que le graphe atomique de la surface du Cu présente une concentration locale de charge (3,−3) entourée par quatre points (3,+1) présentant une déficience de charge. De plus, il y a une déficience locale de charge (3,+3) à la mi-distance entre chacun des quatre atomes de Cu contigus qui correspondent au site actif pour l'adsorption de la concentration locale de charge (3,−3) sur l'atome de carbone du Co ou sur l'atome d'azote de la molécule de NO. La valeur plus élevée du $-\nabla^2\rho$ à la concentration de charges non-liées sur les atomes ainsi que la configuration géométrique à ces points critiques favorisent toutes les deux l'interaction du NO par rapport à celle de la molécule de CO sur la surface (100) du Cu. Ce résultat est en accord avec les barrières connues à la rotation de ces molécules.

Mots clés : théorie de la densité fonctionnelle, laplacien de la densité électronique, surface (100) du Cu, monoxyde de carbone, monoxyde d'azote, graphe moléculaire, graphe atomique.

[Traduit par la rédaction]

Received October 2, 1995.

This paper is dedicated to Professor Richard F.W. Bader on the occasion of his 65th birthday.

Y. Aray[1] and J. Rodríguez. Centro de Quimica, Instituto Venezolano de Investigaciones Cientificas, IVIC, Apartado 21827, Caracas 1020-A, Venezuela.

[1] Author to whom correspondence may be addressed. Telephone: 58 2 5011337. Fax: 58 2 501 1350. E-mail:yaray@quimica.ivic.ve

Introduction

The properties of a molecular charge distribution are summarized in terms of its critical points (CP) (1). These are points where the gradient vector field, $\nabla\rho(\boldsymbol{r})$, vanishes and they are classified by the $\rho(\boldsymbol{r})$ curvatures or three eigenvalues λ_i (i = 1, 2, and 3) of the Hessian matrix ($H_{ij} = \partial^2\rho(\boldsymbol{r})/\partial x_i \partial x_j$). There are, in molecules and crystals, four types of these extremes that, labeled by their rank (number of non-zero eigenvalues) and signature (excess number of positive over negative eigenvalues), are maxima (3,−3), minima (3,+3), and saddles (3,+1) and (3,−1). The (3,−3) points occur generally at the nuclear positions so that each nucleus is a three-dimensional point attractor in the vector field spanned by $\nabla\rho(\boldsymbol{r})$. The region transversed by the gradient paths that terminate at a given attractor is called the basin of the attractor. A (3,−1) CP is found between every pair of neighboring nuclei. It represents both local maxima in two directions and a local minimum in a third and is called a bond critical point. The gradient paths associated with the negative eigenvalues at the (3,−1) point define the zero flux that partitions the molecule or crystal into unique fragments. Therefore, the set of surfaces formed by all (3,−1) points partitions the system into a collection of chemically identifiable regions called atomic basis (2). These are the most transferable pieces one can define in an exhaustive partitioning of the real space (1). The unique pair of trajectories associated with the positive eigenvalue at the (3,−1) CP define a line linking the nuclei along which the charge density is a maximum with respect to any neighboring line. It is called a bond path and its presence provides the necessary and sufficient conditions for the existence of a bond (1). The network of bond paths corresponding to the ground state charge density defines a molecular graph and the structure of a molecule or a crystal. A bond path determines and characterizes all of the atomic interactions in a given system (3, 4) and has proven useful in the analysis of physical properties of insulators, metals, and alloys (3–6).

The reactivity of molecules is reflected in the topology of the Laplacian of the charge density, $\nabla^2\rho(\boldsymbol{r})$ (7–10). The Laplacian of any scalar field such as $\rho(\boldsymbol{r})$ determines where the field is locally concentrated ($\nabla^2\rho(\boldsymbol{r}) < 0$), and locally depleted ($\nabla^2\rho(\boldsymbol{r}) < 0$) (1). The atomic Laplacian (11, 12) exhibits alternating shells of charge concentration and charge depletion equal in number to the number of quantum shells. The outer shell of charge concentrations (VSCC) contains a spherical surface over which $\rho(\boldsymbol{r})$ is maximally concentrated. The distribution of the $\nabla^2\rho(\boldsymbol{r})$ over this surface in the free atom is uniform if one assumes that the nucleus has a negligible electric quadrupole moment. The formation of bonds produces changes in this distribution, and the VSCC of a bound atom exhibits localized concentrations of charge that mimic in number, relative position, and size the pairs of electrons assumed in the Lewis model, topological features that are absent from the relatively simple topology exhibited by the density itself. The structure of the Laplacian for an atom in a molecule (10), called its atomic graph, is most easily visualized in terms of the polyhedron defined by the maxima in $-\nabla^2\rho(\boldsymbol{r})$, a polyhedron whose vertices (V), edges (E), and faces (F) satisfy Euler's formula

$$V - E + F = 2$$

The maxima define the vertices V; the unique pairs of trajectories that originate at (3,−1) critical points and terminate at neighboring vertices define the edges, E; and the (3,+1) critical points define the faces F. The face critical points define the centers of local depletions in the valence-shell charge concentration or VSCC. A Lewis acid–base reaction corresponds to aligning a charge concentration (CC) on the base with a charge depletion (CD) on the acid, that is, by directing a vertex of the atomic graph on the base atom at a face of the polyhedron on the acid. This is a general phenomenon that is observed in many different kinds of interactions (1), examples being the formation of hydrogen bonds (13), the alignment of chlorine molecules in the solid (4), and the adsorption of molecules on surfaces (14–16). The Laplacian of the electronic density provides a physical model that guides one in the determination of the sites of adsorption and the geometry of approach of the substrate relative to the surface site, and predicts whether the interaction will correspond to physi- or chemisorption (14).

Density functional theory (DFT) plays a role of increasing importance in the calculations of ground states of molecules and solids (17–21). The electron correlation, important for many systems such as transition metals, is included in the DFT computational scheme: the Kohn–Sham (KS) equations. Using (18) a nonrigorous approximation to the exchange and correlation energy of an interacting system, KS methodology leads to a scheme analogous to the Hartree method but containing the major part of the effects of exchange and correlation. The resulting KS equations are similar to the Hartree–Fock (HF) equations but do not need multireference representations, which increase the computational requirements and make post-HF methods impractical for large systems.

In this work, the topological analysis of the electron density and its Laplacian, using the charge distribution obtained from DFT calculations, was applied to study the structure of the Cu (100) surface and its reactivity towards CO and NO molecules. These are two examples of interesting catalytic reactions (22). The CO dissociation (23) is important in the production of hydrocarbons from carbon monoxide and hydrogen, components of a synthesis gas. Copper clusters are an important component of DENOX (22), a new class of automotive exhaust catalyst. Comparisons between HF, post-HF, and DFT results are presented.

Methodology

The calculations were carried out with the Gaussian 94 (24) program using the 6-311+G(d,p) (25) basis set. The molecular orbital calculations were performed at HF, Møller–Plesset perturbation (MP2), and quadratic CI (including triple and quadruple terms (QCISD)) levels. In the DFT case, the Becke exchange functional (26) and the correlation functional of Lee, Yang, and Parr (LYP) (27), which includes both local and nonlocal terms (BLYP), and Becke's three-parameter hybrid method with the LYP correlation functional (B3LYP) (28) were used. The topology of $\rho(\boldsymbol{r})$ and $\nabla^2\rho(\boldsymbol{r})$ was analyzed using the Aimpac-94 package.[2]

[2] R.F.W. Bader. Department of Chemistry, McMaster University, Hamilton, Ontario, Canada. 1994.

Table 1. Dipole moment of CO and NO molecules (debye).

		μ_z	
Basis set	Method	CO (μ_{exp} = 0.12)	NO (μ_{exp} = 0.15)
6-311+(d,p)	HF	−0.299	−0.207
6-311+(d,p)	MP2	0.287	0.167
6-311+(d,p)	QCISD	0.090	0.105
6-311+(d,p)	BLYP	0.133	0.154
6-311+(d,p)	B3LYP	0.072	0.099

Table 2. Topological properties (au) of $\rho(r)$ at the bond critical points for the (*a*) CO and (*b*) NO molecules.

(*a*) CO

Method	r_C	r_O	λ_1	λ_2	λ_3	$\rho(r)$	$\nabla^2\rho$	λ_1/λ_3
HF	0.714	1.415	−1.741	−1.741	4.324	0.491	0.842	0.403
MP2	0.727	1.424	−1.515	−1.515	3.794	0.469	0.764	0.399
QCISD	0.723	1.416	−1.590	−1.590	3.959	0.479	0.779	0.402
BLYP	0.737	1.415	−1.555	−1.555	3.491	0.479	0.381	0.395
B3LYP	0.727	1.403	−1.656	−1.656	3.860	0.493	0.548	0.429

(*b*) NO

Method	r_N	r_O	λ_1	λ_2	λ_3	$\rho(r)$	$\nabla^2\rho$	λ_1/λ_3
HF	0.769	1.340	−1.839	−1.562	1.131	0.640	−2.270	1.626
MP2	0.848	1.295	−1.629	−1.349	0.992	0.601	−1.986	1.642
QCISD	0.880	1.309	−1.470	−1.363	0.921	0.572	−1.912	1.596
BLYP	0.920	1.281	−1.470	−1.376	1.131	0.563	−1.715	1.300
B3LYP	0.879	1.290	−1.563	−1.432	1.026	0.588	−1.969	1.523

Table 3. Value of $-\nabla^2\rho(r)$ at the (3,−3) critical points in the atomic valence shell of the (*a*) CO and (*b*) NO molecules.

(*a*) CO

Method	O(nonbonded)	O(bonded)	C(nonbonded)
HF	5.095	4.624	1.470
MP2	4.918	4.576	1.234
QCISD	4.574	4.896	1.264
BLYP	4.746	4.477	1.260
B3LYP	4.854	4.619	1.308

(*b*) NO

Method	O(nonbonded)	O(bonded)	N(bonded)	N(nonbonded)
HF	5.518	3.737	2.491	2.733
MP2	4.631	3.442	1.993	2.814
QCISD	5.344	3.334	1.953	2.538
BLYP	5.097	3.236	1.870	2.518
B3LYP	5.165	3.387	2.015	2.574

CO and NO molecules

To study the accuracy of the charge density produced by the different methods of calculation, the electric dipole moment, the topological properties of $\rho(r)$, and the local charge concentration in the VSCC for the CO and NO molecules were calculated. The results are reported in Tables 1–3. The molecular geometry in the ground state was optimized in all of the cases. The HF value of the dipole, as it is known, is not correct (29), not only in magnitude but in sign. The experimental dipoles of

CO (30) and NO (30) are 0.12 and 0.15 D in the direction $^{-}C–O^{+}$ and $^{-}N–O^{+}$ while HF results are 0.299 and 0.27, respectively, in the reverse direction $^{+}C–O^{-}$ and $^{+}N–O^{-}$. Inclusion of electronic correlation orients the dipole correctly but the errors are also around 30% in MP2, QCISD, and B3LYP. There is only a small difference between the dipole calculated from the BLYP and the experimental value in both molecules. In spite of these large variations observed in the dipole moments, the topological properties of the electronic density show only small changes (see Table 2). The DFT methods follow the same trend shown by the MO post-HF methods. In general, the curvatures of $\rho(\boldsymbol{r})$ at the critical points reported by the other methods decrease (around 10%) with respect to the HF values. The two negative (λ_1 and λ_2) curvatures measure the degree of contraction of $\rho(\boldsymbol{r})$ perpendicular to the bond towards the critical point while the positive curvature (λ_3) measures the degree of contraction parallel to the bond and away from the critical point towards each of the neighboring nuclei. When the negative curvatures dominate, electronic charge is locally concentrated in the region of the CP, resulting in a sharing of electronic charge by both nuclei forming the bond. These interactions, referred to as shared interactions, are characteristic of the covalent or polar bond and are characterized by large values of $\rho(\boldsymbol{r})$, $\lambda_1/\lambda_3 > 1$, $\nabla^2\rho < 0$ at the CP, and by the large negative value of the potential energy in the internuclear region. If the positive curvature is dominant, the electronic density is concentrated separately in each of the atomic basins and the interaction, referred to as a closed-shell interaction, is dominated by the relatively large positive contributions to the kinetic energy of the system. In this case, ρ is relatively low in value, $\lambda_1/\lambda_3 < 1$, and $\nabla^2\rho > 0$ at the CP. Table 2 shows that in NO there is a shared interaction while in CO there is an intermediate-type interaction characteristic of a polar bond, i.e., ρ is relatively large although $\nabla^2\rho > 0$ and $\lambda_1/\lambda_3 < 1$.

The value of the (3,−3) critical points of the CO and NO molecule are reported in Table 3. Contour maps obtained with the BLYP method are shown in Fig. 1. In CO, the O VSCC distribution shows two local charge concentrations located along the C—O bond direction. One is facing the carbon atom (Vb), while the other is found in the opposite side of the shell forming a nonbonded local charge concentration (Vnb). A ring of degenerate critical points of the (2,0) type in a plane perpendicular to the C–O direction completes the O atomic graph. The carbon atom exhibits only one local charge concentration (Vnb), which is located in the nonbonded region. A torus of charge depletion around the internuclear axis with a ring of degenerate points is found in the C VSCC. We can see in Table 3 that, similar to $\rho(\boldsymbol{r})$, the inclusion of electronic correlation decreases the value of the Laplacian at the critical point. The variations are more pronounced in the carbon nonbonded region (14%) than in the O nonbonded region (10%). The DFT shows again the same trend as the MO post-HF methods.

As is expected from the electronic ground state (π^2) of the NO molecule, the topology of the Laplacian distribution is significantly different from that of the CO molecule (see Fig. 1*b*). The ground state of NO has the open-shell configuration $(1\sigma)^2(2\sigma)^2(3\sigma)^2(4)\sigma^2(5\sigma)^2(1\pi)^4(2\pi)$ so that the extra electron in the 2π molecular orbital, which is mostly located in a plane, destroys the axial symmetry. In NO, both the N and O VSCC show three local maxima, two nonbonded forming an angle of 120° with the bond direction and one located in the bond

Fig. 1. Laplacian distribution for (*a*) carbon monoxide and (*b*) nitrogen monoxide. Solid contours denote negative values of $\nabla^2\rho$, that is, concentrations of electronic charge; broken contours, regions of charge depletion. (3,−3) Critical points or local charge concentrations are denoted by dots. In (*a*), the black arrow points out the torus of charge depletion on the C atom and the white the ring of degenerate points in the O atom.

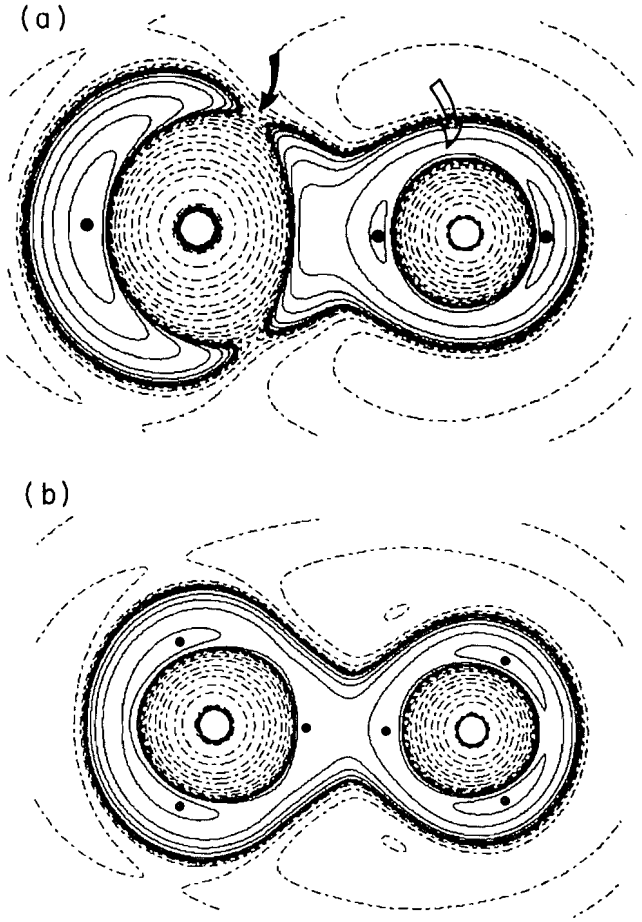

region. Three (3,−1) critical points lie on the same plane of the (3,−3) forming two faces, one above and the other below the plane, with two (3,+1) capping the atomic graph. In contrast to the CO case, the inclusion of correlation produces larger changes in the bonded region than in the nonbonded region. Most of the variations occur at the b critical point of the N atom which shows around 22% decrease in its value. The previous results and discussion confirm that the DFT methods provide remarkably good values of the electronic properties and a good description of the topology of the electronic density and its Laplacian.

According to Bader's theory (1), the active sites in a molecule are associated with the critical points of $-\nabla^2\rho$ of the VSCC. In a chemical reaction, the V critical point or local charge concentration of some atom in a general base reacts with the F or local charge depletion of the VSCC of another atom in a general acid. The carbon and nitrogen monoxide can act as a base by means of the Vnb of the O or C (N) atoms, respectively. In both molecules the Vnb's of the O atom are characterized by a large radial curvature, μ_3 (489.82 and

Table 4.

(*a*) Data for critical points in $\rho(r)$ for the (100) Cu surface.

Critical point	λ_1	λ_2	λ_3	$\rho(r)$	$\nabla^2\rho$
Cu—Cu bond	−0.028	−0.027	0.144	0.031	0.088
Ring	−0.011	0.039	0.041	0.020	0.068
Cage	0.007	0.007	0.021	0.008	0.034

(*b*) Data for critical points in the Laplacian of $\rho(r)$ in the Cu atom on the (100) Cu surface.

Critical points	$-\nabla^2\rho$
One (3,−3) above surface	60.988
One (3,−3) below surface	60.945
Four (3,−3) in surface	61.250
Four (3,−1) above surface	58.604
Four (3,−1) in surface	57.779
Four (3,−1) below surface	57.204
Four (3,+1) above surface	56.992
Four (3,+1) below surface	57.023
One (3,+3) in the middle of each four Cu atoms	+0.022

479.17 at the BLYP level in CO and NO, respectively), which measures the degree of contraction of $\rho(r)$ along the radial direction towards the nuclei, and by much smaller perpendicular curvatures that limit the radial extension ($\mu_1 = \mu_2 = -7.67$ in CO and $\mu_1 = -17.37$ and $\mu_2 = -13.46$ in NO). The μ_3 of the Vnb on the C is 61.33 au and $\mu_1 = \mu_2 = -2.95$ au. Thus, the O atom of CO and NO acts as a hard base while the C acts a soft base. The N of NO with $\mu_3 = 173.42$, $\mu_1 = -9.38$, and $\mu_2 = -4.51$ is a harder base than the C atom of CO. In contrast with CO, in the Laplacian distribution of NO there is no torus of charge depletion in the N density encircling the internuclear axis. This torus provides the region for nucleophilic attack in CO or molecules that contain CO groups. The lack of such a torus in the N atom indicates that a nucleophilic attack is less likely in NO.

The DFT offers simplification in handling the electronic correlation using single-particle density instead of the many determinants considered in the post-HF method (18), so it is relatively easy to study complex systems such as transition metals. In the following section we study an example of one of these complex systems: the (100) Cu surface.

(100) Cu surface

The most stable phase (31) of bulk Cu is cubic fcc and belongs to the *Fm3m* space group with $a = 3.577$ Å. Each atom is linked by bond paths to 12 neighboring atoms. There are no interactions with the second neighbors (6) so the bond path defined by the (3,−1) CPs midway between nearest neighbors forms an octahedron with a cage critical point at the center and eight ring critical points at the faces (Fig. 2*a*). The packing of these polyhedra gives rise to the Cu fcc structure. The lack of translational symmetry in the direction orthogonal to the surface can be dealt with by approximating the semi-infinite crystal by a finite slab of several layers of Cu atoms. It is known (32) that the (100) Cu surface reconstructs only to a small extent, so the surface relaxation effects on the charge distribution are expected to be small. For this reason, a slab of two layers was modeled with a Cu_{13} cluster, illustrated in Fig. 2*b* with the geometrical parameters of the bulk form. Each atom of the surface has eight nearest neighbors and four next-nearest neighbors at distances of 2.529 and 3.577 Å, respectively. The structure, as determined by the gradient vector field map, Fig. 3, is a truncated form of that found for the bulk form with bond paths linking each surface Cu atom to its eight neighbors. The top atoms of the surface form square pyramids with the atoms of the second layer. A contour map of the electron density of the top atoms is shown in Fig. 4. The parameters for the CPs of $\rho(r)$ of one of these pyramids are reported in Table 4. The relatively small values of the density, ρb, and the positive values for $\nabla^2\rho$ are characteristic of closed-shell interactions. Such interactions are dominated by the Pauli principle, which leads to a depletion of electron density in the interatomic surface and hence to low values of ρb. The accompanying separate accumulation of electron density in the basin of each atom results in the value of $\nabla^2\rho$ being dominated by its single positive curvature parallel to the bond path.

The values of the Laplacian at the position of the VSCC critical points for the Cu atoms of the top are given in Table 4. The atomic graph for these atoms has six vertices, two along the axis perpendicular to the surface, one above (L_u) and other below the surface (L_d) and four (L_i with $i = 1, ..., 4$) in the plane along the Cu—Cu bonds. These CPs are linked by 12 edges, 4 between the L_u and L_i, four between L_d and L_i, and four linking the L_i's. Thus, the atomic graph of the Cu atoms is an octahedron with eight faces joining the vertices, four above the surfaces and four below it. There is a (3,+1) CP in the middle of each face. These critical points denote the position where the Laplacian attains its least negative value in the shell described by the atomic graph. In addition to the CPs forming the Cu atomic graph, a Laplacian contour map of the (100) Cu surface shows (see Fig. 5) the presence of a (3,+3) critical point of $-\nabla^2\rho$ in the midpoint of each four Cu atoms. This represents the site of maximum charge depletion on the surface and around the Cu atoms.

Fig. 2. (*a*) Model of the bulk Cu illustrating the crystal graph, an octahedron, corresponding to the fcc structure. (*b*) Diagram of the Cu13, cluster model of a two-layer slab of the (100) surface.

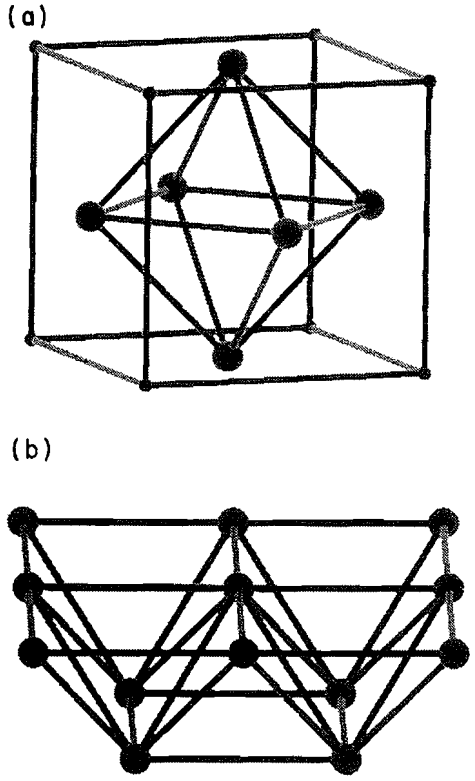

Fig. 3. Trajectories traced out by gradient vectors of the electron density, trajectories of $\nabla\rho$, in the top of the (100) Cu surface. The region of space traversed by trajectories that terminate at a given nucleus where $\rho(r)$ is a local maximum (denoted by open circle) defines the basin of the atom. A unique pair of trajectories originates at each bond critical point (denoted by dots) defining a line of maximum electron density linking bonded nuclei, the bond path. The arrows point out the (3,+1) or ring critical points.

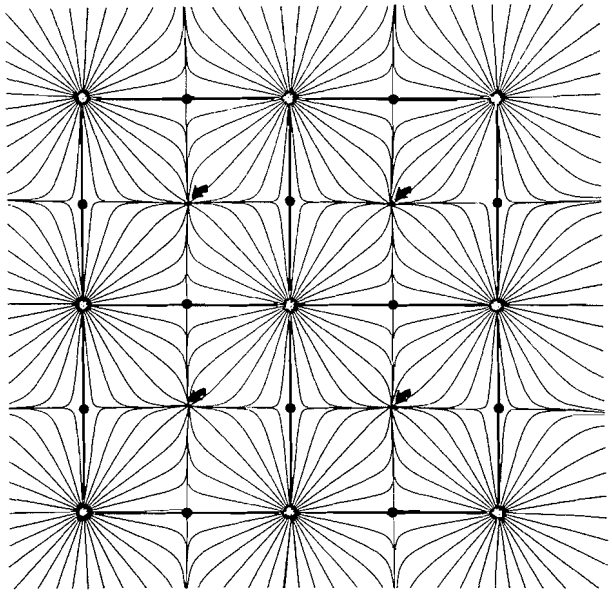

Fig. 4. Contour map of $\rho(r)$ in the top of the (100) Cu surface overlaid with interatomic surfaces, as defined by the gradient vector field in Fig. 3.

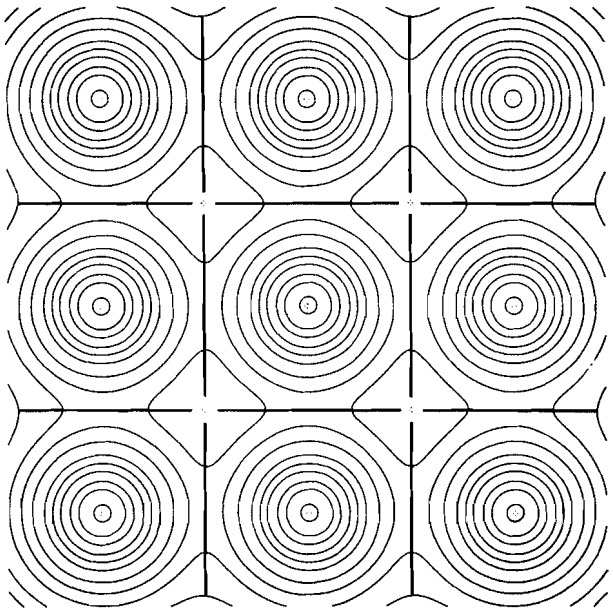

The adsorption pathway of CO and NO on Cu (100) can be anticipated from the topology of $-\nabla^2\rho$. The perpendicular bonding on Cu would require that a CC on the CO molecule interacts with a CC (a repulsive interaction) on the surface, so the CO deviates towards the midpoint of four Cu atoms where the greatest interaction with the faces of the atomic graph above the surface and the (3,+3) CP is reached. Due to the interaction of the CC at the oxygen atom with another nearest CC (3,+3) on the surface and the interaction of the torus of charge depletion on C with CC on the Cu atom, the molecule tilts toward the metal surface and finally the bond will be broken. This suggestion is in accord with recent studies (22) of the transition states of this dissociation for several reaction paths using the same cluster models of the (100) Cu surface. The lateral localization (see Fig. 1*b*) and the larger value of $-\nabla^2\rho$ of the nonbonded CC at the atoms in NO (see Table 4) with respect to those in CO favors the interactions of the NO molecule over those of CO with the (100) Cu surface. This prediction is in agreement with the value of the energy barriers for NO dissociation (30 kcal/mol) and CO dissociation (88 kcal/mol) on the 100 Cu surface (22).

Conclusions

In a variety of calculations for CO and NO molecules it was found that the DFT method using the Becke exchange functional and the correlation functional of Lee, Yang, and Parr (LYP), BLYP, generates more accurate values of the dipole moment than both the post-HF method and Becke's three-parameter hybrid method with the LYP correlation functional, B3LYP. This latter functional yields a result similar to the MP2 and QCISD methods.

Fig. 5. Laplacian distribution of $\nabla^2\rho$ of the (100) Cu surface. Solid contours denote negative values of $\nabla^2\rho$, that is, concentrations of electronic charge; broken contours, regions of charge depletion. The black arrows point out the (3,+3) critical points in the middle of each four Cu atoms.

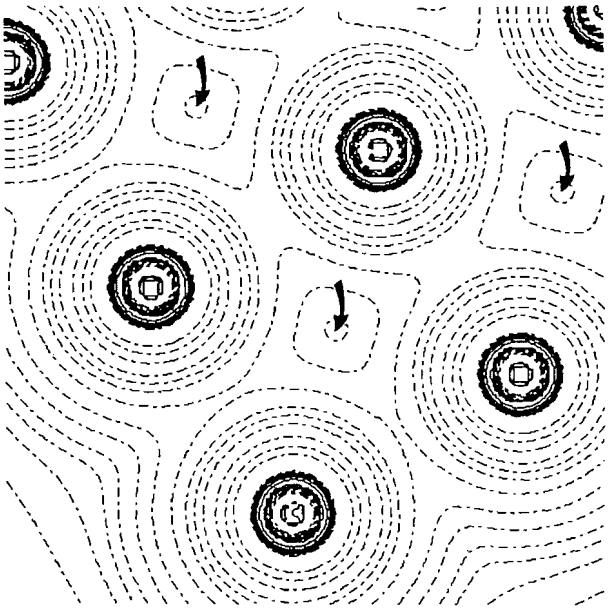

The values of the topological properties of $\rho(r)$ and $-\nabla^2\rho$ at the critical points for CO and NO molecules follow the same trend shown by the MO post-HF methods. The topology of the $\rho(r)$ and its Laplacian is maintained (same number and type of critical points) but, in general, the inclusion of the electronic correlation decreases (around 10–20%) the value of these quantities with respect to the HF values. These results confirm that the DFT method provides remarkably good electronic properties and a good description of the topology of the electronic density and its Laplacian.

The topology of $-\nabla^2\rho$ not only predicts the active site but also the correct trend for the adsorption and dissociation of CO and NO molecules on the (100) Cu surface. This and earlier work (1, 14–16) demonstrates the potential usefulness of the topology of the Laplacian of the electron density in determining the conditions governing the reactivity of surfaces and in locating the active centers for the adsorption of either Lewis bases or acids.

Acknowledgments

The authors thank Dr. Juan Rivero Charlton for his valuable help in computational and linguistic matters and Y.A. wishes to acknowledge the kind hospitality provided by Dr. R.F.W. Bader and the Department of Chemistry of McMaster University during the 1994 summer.

References

1. R.F.W. Bader. Atoms in molecules — a quantum theory. Oxford University Press, Oxford. 1990.
2. R.F.W. Bader. Phys. Rev. B: Condens. Matter, **49**, 13348 (1994).
3. P.F. Zou and R.F.W. Bader. Acta Crystallogr. Sect. A: Found. Crystallogr. **A50**, 714 (1994).
4. V.G. Tsirelson, P.F. Zou, T-H. Tang, and R.F.W. Bader. Acta Crystallogr. Sect. A: Found. Crystallogr. **A51**, 143 (1995).
5. M.E. Eberhart, M.M. Donovan, J.M. McLaren, and D.P. Clougherty. Prog. Surface Sci. **3**, 1 (1991).
6. M.E. Eberhart, D.P. Clougherty, and J.M. McLaren. J. Mater. Res. **8**, 438 (1993).
7. R.F.W. Bader and H. Essén. J. Chem. Phys. **80**, 1943 (1984).
8. R.F.W. Bader, P.J. MacDougall, and C.D.H. Lau. J. Am. Chem. Soc. **106**, 1594 (1984).
9. R.F.W. Bader and P.J. MacDougall. J. Am. Chem. Soc. **107**, 6788 (1985).
10. R.F.W. Bader, P.L.A. Popelier, and C. Chang. J. Mol. Struct. (THEOCHEM), **255**, 145 (1992).
11. R.P. Sagar, A.C.T. Ku, and V.H. Smith, Jr. J. Chem. Phys. **88**, 4367 (1988).
12. Z. Shi and R.J. Boyd. J. Chem. Phys. **88**, 4375 (1988).
13. M.T. Carrol, C. Chang, and R.F.W. Bader. Mol. Phys. **63**, 387 (1988).
14. Y. Aray and R.F.W. Bader. Surface Sci. In press.
15. Y. Aray, F. Rosillo, and J. Murgich. J. Am. Chem. Soc. **116**, 10639 (1994).
16. Y. Aray, J. Rodriguez, J. Murgich, and F. Ruette. J. Phys. Chem. **97**, 8393 (1993).
17. S. Lundqvist and N.H. March (*Editors*). Theory of inhomogeneous electron gas. Plenum Press, New York. 1983.
18. R.G. Parr and W. Yang. Density-functional theory of atoms and molecules. Oxford University Press, New York. 1989.
19. J.P. Perdew, J.A. Chevary, S.H. Vosko, K.A. Jackson, M.R. Pederson, D.J. Singh, and C. Fiolhais. Phys. Rev. B: Condens. Matter, **46**, 6671 (1992).
20. J. Andzelm and E. Wimmer. J. Chem. Phys. **96**, 1280 (1992); J. Andzelm, J. Baker, A. Scheiner, and M. Wrinn. Int. J. Quant. Chem. **56**, 734 (1995).
21. R.O. Jones and O. Gunnarsson. Rev. Mod. Phys. **61**, 689 (1989).
22. M.A. van Daelen, Y.S. Li, J.M. Newsan, and R.A. van Santen. Chem. Phys. Lett. **226**, 100 (1994).
23. P. Biloen and W.H.H. Sachtler. Adv. Catal. **30**, 165 (1981).
24. M.J. Frisch, G.W. Trucks, H.B. Schlegel, P.M.W. Gill, B.G. Johnson, M.A. Robb, J.R. Cheeseman, T. Keith, G.A. Peterson, J.A. Montgomery, K. Raghavachari, M.A. Al-Laham, V.G. Zakrzewski, J.B. Ortiz, J.B. Foresman, C.Y. Peng, P.Y. Ayala, W. Chen, M.W. Wong, J.L. Andres, E.S. Replogle, R. Gomperts, R.L. Martin, B.J. Fox, J.S. Binkley, D.J. Defrees, J. Baker, J.O. Steward, M. Head-Gordon, C. Gonzalez, and J.A. Pople. Gaussian 94, Revision B.3. Gaussian, Inc., Pittsburgh, Pa.
25. R. Krishnan, M.J. Frisch, and J.A. Pople. J. Chem. Phys. **72**, 4244 (1980).
26. A.D. Becke. J. Chem. Phys. **88**, 2547 (1988).
27. C. Lee, W. Yang, and R.G. Parr. Phys. Rev. B: Condens. Matter, **37**, 786 (1988).
28. A.D. Becke, J. Chem. Phys. **98**, 1372 (1993).
29. W.J. Hehre, L. Radom, P.R. Schleyer, and J.A. Pople. Ab initio molecular orbital theory. John Wiley, New York. 1986. p. 325.
30. H.B. Gray. Electrons and chemical bonding. W.A. Benjamin, New York. 1965. p. 70.
31. V.L. Moruzzi, J.F. Janak, and A.R. Williams. Calculated electronic properties of metals. Pergamon, New York. 1978.
32. H.L. Davis and J.R. Noonan. Surface Sci. **126**, 245 (1983).

Delocalized bonding in tetrahedral organo-transition metal clusters: an EHMO study of metal vertex rotations in $Co_2Fe(CO)_9S$, $CpMoCo_2(CO)_8CR$, and in $Cp_2Mo_2(CO)_4(RC{\equiv}CR)$

Krisztina L. Malisza, Lijuan Li, and Michael J. McGlinchey

Abstract: Molecular orbital calculations at the extended Hückel level are used to rationalize the barriers to vertex rotation in the tetrahedral metal cluster complexes $FeCo_2(CO)_9S$, **2**, and $(C_5H_5)MoCo_2(CO)_8CH$, **3**. It is shown that, in accord with experimental observations on **2**, rotation of an $Fe(CO)_3$ fragment through 60° brings about a weakening of the metal–metal bonding interactions within the $FeCo_2$ triangle. In the $MoCo_2$ cluster, **3**, rotation of the $CpMo(CO)_2$ fragment about an axis joining the molybdenum to a central point within the tetrahedron gives rise to three minima in which the cyclopentadienyl ring is oriented *proximal* or *distal* relative to the capping carbynyl moiety, or in the plane of the three metals. The rotation trajectory of the $CpMo(CO)_2$ vertices in $Cp_2Mo_2(CO)_4(HC{\equiv}CH)$, **4**, has been elucidated by means of a Bürgi–Dunitz analysis of the X-ray crystal structures of a series of related clusters in which the $CpMo(CO)_2$ units exhibit a range of orientations. The calculations suggest that the barriers to vertex rotations in **4** are primarily of steric rather than electronic origin.

Key words: metal clusters, vertex rotations, EHMO calculations.

Résumé : On a utilisé des calculs d'orbitales moléculaires au niveau de Hückel étendu pour rationaliser les barrières à la rotation aux sommets des complexes d'agrégats métalliques tétraédriques, $FeCo_2(CO)_8S$, **2**, et $(C_5H_5)MoCo_2(CO)_8CH$, **3**. Il a été démontré que, en accord avec les observations expérimentales sur le composé **2**, la rotation de 60° d'un fragment $Fe(CO)_3$ provoque un affaiblissement des interactions de liaison métal–métal dans le triangle $FeCo_2$. Dans l'agrégat $MoCo_2$, **3**, une rotation du fragment $CpMo(CO)_2$ autour d'un axe reliant le molybdène à un point central à l'intérieur du tétragone conduit à trois minima dans lesquels le noyau cyclopentadiényle prend des orientations *proximale* et *distale* par rapport à la portion carbynyle servant de cap ou une orientation dans le plan des trois métaux. Faisant appel à une analyse de Bürgi–Dunitz des structures cristallines par diffraction des rayons X d'une série d'agrégats apparentés dans lesquels les unités $CpMo(CO)_2$ présentent un ensemble d'orientations, on a élucidé la trajectoire de la rotation des sommets $CpMo(CO)_2$ dans le $Cp_2Mo_2(CO)_4(HC{\equiv}CH)$, **4**. Les calculs suggèrent que l'origine des barrières à la rotation aux sommets dans le composé **4** sont principalement de nature stérique plutôt qu'électronique.

Mots clés : agrégats de métaux, rotations aux sommets, calculs d'OM de Hückel étendues.

[Traduit par la rédaction]

Introduction

Molecular orbital calculations at the Extended Hückel level have proven invaluable in gaining an understanding of the structure and reactivity of organo-transition metal clusters. In particular, the fragment approach pioneered by Hoffmann and his colleagues (1, 9) lends itself beautifully to this chemistry since it allows us to take advantage of the picturesque symmetry of these systems. In recent years, we have used these concepts to rationalize the structures of a number of clusters, many of which exhibit stereochemical nonrigidity on the NMR time scale (2–4). Since these simple EHMO methods could be successfully used (5) to account for the fluxional character of five-vertex square-based pyramidal molecules such as **1**, we chose to extend them to encompass the phenomenon of metal vertex rotations in tetrahedral tri- and di-metallic clusters **2** through **4**. We have selected two systems for which reliable experimental data are available: (*a*) the interchange of axial and equatorial carbonyl ligands within the $Fe(CO)_3$ and $Co(CO)_3$ vertices of $FeCo_2(CO)_9S$, **2**, and (*b*) rotation of the $(C_5H_5)Mo(CO)_2$ fragment in $(C_5H_5)MoCo_2(CO)_8CH$, **3**. Moreover, the $(C_5H_5)Mo(CO)_2$ vertex rotation process in dimolybdenum-alkyne clusters, **4**, has been analyzed by means of the Bürgi–Dunitz trajectory technique in which appropriately selected X-ray crystal structures are used to provide a series of "snapshots" of the reaction pathway.

Received November 9, 1995.

This paper is dedicated to our friend and colleague Professor Richard F.W. Bader on the occasion of his 65th birthday. We appreciate his remarkable insight into the nature of chemical interactions.

K.L. Malisza, L. Li,[1] and M.J. McGlinchey.[1] Department of Chemistry, McMaster University, Hamilton, ON L8S 4M1, Canada.

[1] Authors to whom correspondence may be addressed. Telephone: (905) 525-9140. Fax: (905) 522-2509. E-mail: mcglinc@mcmaster.ca

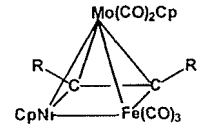

1

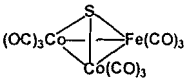

2

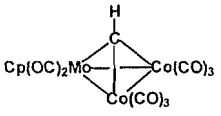

3

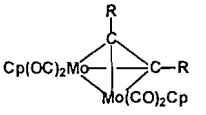

4

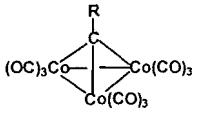

5a

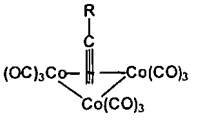

5b

The bonding within the four vertex atoms in tetrahedral organo-transition metal clusters continues to attract attention. The edge-localized model of $RCCo_3(CO)_9$, **5a**, yields electron counts of 8 and 18, respectively, for the carbon and cobalt atoms. In contrast, the core and valence shell photoelectron spectra of such systems have been rationalized in terms of a carbyne-capped metal triangle, as in **5b** (6). Similarly, a variety of inner-shell spectroscopic measurements have been interpreted by using the latter model (7).

According to Wade's rules (8), a tetrahedral cluster can be regarded either as a *nido*-trigonal bipyramid or as an electron-precise four-vertex system. The barriers toward local rotation of the ML_n vertices provide a probe for the degree of edge-localized bonding. We here present a molecular orbital analysis of the vertex rotations in a series of mixed metal clusters and compare these calculations to the available experimental data.

Results and discussion

$M(CO)_3$ rotation in $FeCo_2(CO)_9S$

As shown in Fig. 1, metal triangles such as $[Co_3(CO)_9]^{3+}$, **6**, or $[Fe_3(CO)_9]$, **7**, give rise to a low-lying set of three filled orbit-

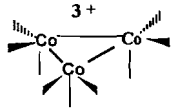

6

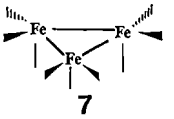

7

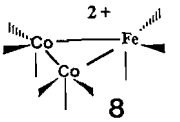

8

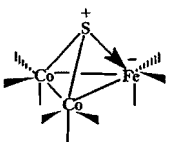

9

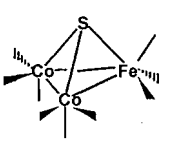

10

Fig. 1. Frontier orbitals of an $M_3(CO)_9$ fragment. (The symbols in square brackets correspond to the labelling used by Saillard (5) for heterometallic triangles of the type $M_2M'L_9$.)

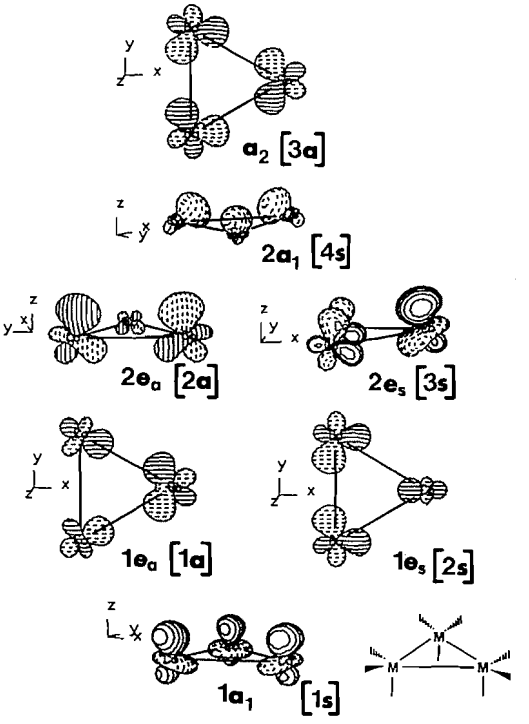

als ($1a_1$ and $1e$) and, at somewhat higher energy, a set of three vacant orbitals ($2a_1$ and $2e$) that serve to accept electron density from capping ligands. There is also an a_2 orbital (made up primarily of out-of-phase d_{xy} orbitals) that is metal–metal antibonding in character. In $Co_3(CO)_9S$, this a_2 orbital does not find a symmetry match with the frontier orbitals of the sulfur cap and is singly occupied in the cluster, as shown in Fig. 2.

Replacement of a $Co(CO)_3$ vertex in the tricobaltnonacarbonyl triangle by a different metal fragment such as $(C_5H_5)Mo(CO)_2$ or $Fe(CO)_3$ lowers the symmetry from C_{3v} to C_s and splits the degeneracies of the $1e$ and $2e$ orbital pairs. Thus the localization of the frontier orbitals on the three metal vertices can change quite markedly. This premise was used previously to rationalize the orientations of alkyne moieties in heterometallic M_3C_2 clusters, **1** (5). (We here follow the notation adopted in Saillard's paper on trimetallic systems (5); the symmetric (s) and antisymmetric (a) labels are used to correlate frontier orbitals in homometallic (M_3L_9) and heterometallic ($M_2M'L_9$) metal triangles.)

Compared to the situation in $[Co_3(CO)_9]^{3+}$, **6**, the localization of the acceptor set of frontier orbitals in the heterometallic fragment $[FeCo_2(CO)_9]^{2+}$, **8**, is much more heavily weighted towards the iron atom than to its cobalt partners. Typically, in the $2e_a$ orbital, which has 22.5% localization on each cobalt in **6**, the distribution in **8** is calculated to be 28% on Fe and only 19% on each cobalt. More importantly, the $3s$ orbital in **8** (which is poised to accept electron density from the p_x orbital of the capping moiety) is now 51% localized on Fe with less than 10% on each cobalt; this is considerably perturbed from that found for the corresponding orbital, $2e_s$, in the tricobalt fragment **6**, which has 42% localization on Co(1)

Fig. 2. Frontier orbital interactions in $Co_3(CO)_9S$ and $FeCo_2(CO)_9S$.

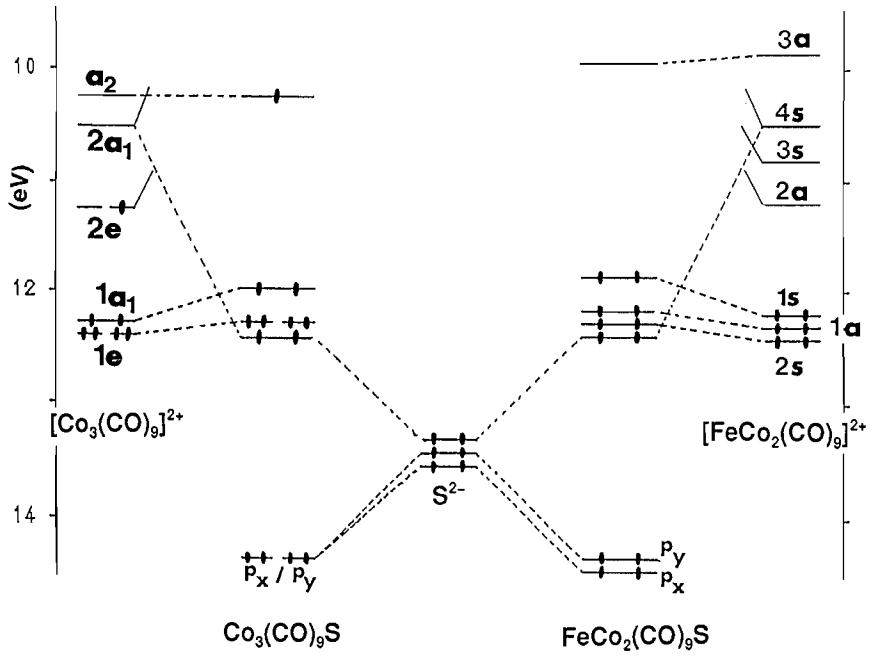

and 13% on each of Co(2) and Co(3). In contrast, the $2e_a$ orbital, which interacts with the p_y donor orbital from the capping sulfur, has only a negligible contribution from Co(1) in **6** (or from Fe in **8**) and so remains almost unchanged. Concomitantly, the filled orbital set arising from the metal triangle is correspondingly more heavily weighted towards the cobalt vertices in **8**.

We see in Fig. 2 not merely that the orbital degeneracies present in $Co_3(CO)_9S$ have been lifted in $FeCo_2(CO)_9S$, **2**, but also that the major π-type interactions, viz. sulfur p_x with *3s* and sulfur p_y with *2a*, are now different in magnitude. This enhanced splitting of the bonding components of the metal–sulfur π-interactions may be attributed to the greater contribution of the iron atom to the *3s* acceptor orbital.

To summarize, the interactions of the $1a_1$ and *1e* filled orbital set with p_x, p_y, and p_z, respectively, of sulfur are rather small since the overlaps are poor. The principal differences in bonding between the tricobalt and iron–dicobalt clusters can be traced to the preferential localization of the $2e_s$ orbital of the metal triangle on Fe. In effect, it is not a gross oversimplification to draw a structure **9** in which the sulfur donates an electron pair to iron, which thereby achieves an 18-electron configuration. To the extent that we choose to believe the charge distribution given by the EHMO calculation, we gain some support for a structure such as **9** when we note that the $Fe(CO)_3$ fragment is more negative than each of the $Co(CO)_3$ units by almost 0.5 electrons. This model focusses charge along the sulfur–iron vector and places the metal in a pseudo-octahedral environment. Now, if we allow local rotation of the $Fe(CO)_3$ vertex so as to interchange the axial and equatorial carbonyl ligands, this must proceed via the trigonal-prismatic geometry **10**. (To simplify the problem, and to take maximum advantage of symmetry, the starting molecular geometry for $Co_3(CO)_9S$ (and for $FeCo_2(CO)_9S$) is an idealized version of the crystallographically determined structure (10). Thus, the experimentally observed OC-Co-CO angles differ by only $\approx 2°$ and so we have imposed local C_{3v} symmetry on each $M(CO)_3$ vertex.)

In Fig. 3 we show the result of rotating through 60° either of the $M(CO)_3$ fragments in $FeCo_2(CO)_9S$, **2**, so as to orient the axial ligand *proximal* with respect to the sulfur cap while the two equatorial ligands are now in *distal* positions. It is apparent that the greater barrier must be surmounted when rotating the $Fe(CO)_3$ vertex from the pseudo-octahedral to the trigonal-prismatic geometry. Figure 3 also reveals that this barrier can be traced primarily to the behaviour of the *1a* orbital (corresponding to $1e_a$ in the homometallic clusters), which is destabilized by the rotation process. The remaining orbitals are but little affected since they either lie along the rotation axis or have only a small contribution from the vertex undergoing rotation. In contrast, the component of the *1a* orbital that was originally a d_{xy} orbital on iron is transformed during the rotation into a hybrid with predominant d_{yz} character. One can see from Fig. 4 that this results in a markedly diminished interaction between the iron and the two cobalt atoms; consequently, there is a loss of metal–metal bonding in the plane of the metal triangle. Overall, the EHMO calculations support the idea of a sizeable barrier to $Fe(CO)_3$ rotation (9 kcal mol^{-1}) and a somewhat more modest energetic requirement (5 kcal mol^{-1}) for the $Co(CO)_3$ vertex to spin about its threefold axis.

Experimental data describing the fluxional behavior of $FeCo_2(CO)_9S$, **2**, have been furnished by Aime who showed that the initial ^{13}CO singlet (at +30°C) exhibits a 6:3 splitting at −80°C (11). Clearly, intermetal exchange of the carbonyls has slowed and one sees the six equivalent ligands on cobalt and three bonded to iron. At −100°C the $Fe(CO)_3$ resonance shows a well-resolved 2:1 pattern demonstrating unequivocally that local rotation of the tricarbonyliron fragment has a sufficiently large barrier to slow this process on the NMR time scale. In contrast, the cobalt carbonyl resonance remains a

Fig. 3. Walsh diagram depicting variations in orbital energy levels upon rotation of a $Co(CO)_3$ or an $Fe(CO)_3$ vertex in $FeCo_2(CO)_9S$, **2**. (The broken line represents the change in total electronic energy.)

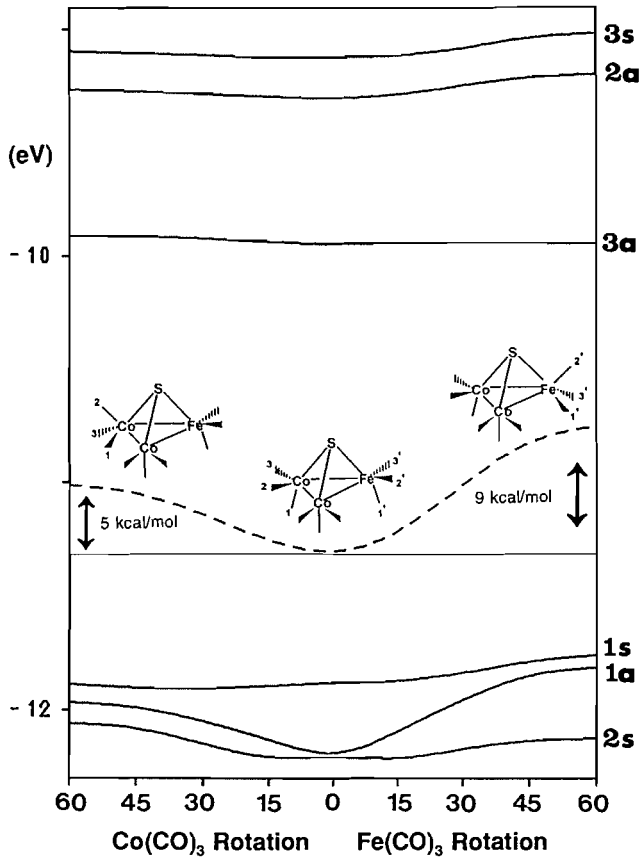

sharp singlet at all accessible temperatures. These results are in excellent accord with the energy barriers derived from the EHMO calculations.

$(C_5H_5)Mo(CO)_2$ rotation in $(C_5H_5)MoCo_2(CO)_8CR$ clusters

Let us turn now to the question of rotation of the $(C_5H_5)M(CO)_2$ vertex (M = Mo or W) in trimetallic clusters such as $(C_5H_5)MoCo_2(CO)_8CH$, **3**. When the tetrahedral clusters $(C_5H_5)MoCo_2(CO)_8C$-phenyl, **11**, and $(C_5H_5)WCo_2(CO)_8C$-tolyl, **12**, were first synthesized, both Beurich and Vahrenkamp (12) and Stone and co-workers (13) pointed out that there were too many ν_{CO} bands in the infrared spectra to be assigned to a single isomer. Subsequently, Sutin et al. (14) reported that the low-temperature ^{13}C NMR spectrum of $(C_5H_5)MoCo_2(CO)_8C\text{-}CO_2{}^iPr$ revealed the presence of two species that were assigned as those rotamers in which the cyclopentadienyl ring was sited (*i*) below the trimetallic plane, as in **3a**, and (*ii*) above the metal triangle and *proximal* to the carbynyl capping group, as in **3b** (see Fig. 5). The rotational barrier for the interconversion of rotamers **3a** and **3b** is approximately 8.5–9.5 kcal mol^{-1} depending on the nature of the substituents at the carbynyl capping position and within the cyclopentadienyl ring (14). The clusters **11** and **12** reported by Vahrenkamp (12) and by Stone (13) adopt structural type **3a** and, very recently, the latter rotamer, viz. **3b**, has been characterized X-ray crystallographically for the particular case of $(C_5Me_5)MoCo_2(CO)_8C\text{-}CO_2{}^iPr$, **13** (15).

Before attempting to calculate the relative energies of the various rotameric structures on the $(C_5H_5)MoCo_2(CO)_8CH$ hypersurface, one must select a viable rotation axis about which to spin the $(C_5H_5)Mo(CO)_2$ fragment. We were guided in this problem by the powerful concepts developed by Bürgi and Dunitz, who showed that a succession of static X-ray structures can give information about the dynamics of a reaction (16). For decades X-ray crystallography has been recognized as the method *par excellence* for the determination of molecular structures. The Bürgi–Dunitz approach allows us to extract dynamic information by careful scrutiny of a series of related crystal structures. As an example of the beautiful results that have emerged from Dunitz's laboratory, we note that the distribution of crystal structures of more than 60 $(C_6H_5)_3P$-X fragments in many different environments can be related to the "two-ring flip" mechanism by which these chiral propeller-like moieties can undergo racemization (17). These ideas were extended into the organometallic arena by Crabtree and Lavin who showed that carbonyl migration between two metal atoms proceeds via a trajectory in which a linear terminal ligand proceeds through a series of increasingly more bent

Fig. 4. The effect on the *1a* frontier orbital in $FeCo_2(CO)_9S$, **2**, upon rotating the $Fe(CO)_3$ vertex through 60°.

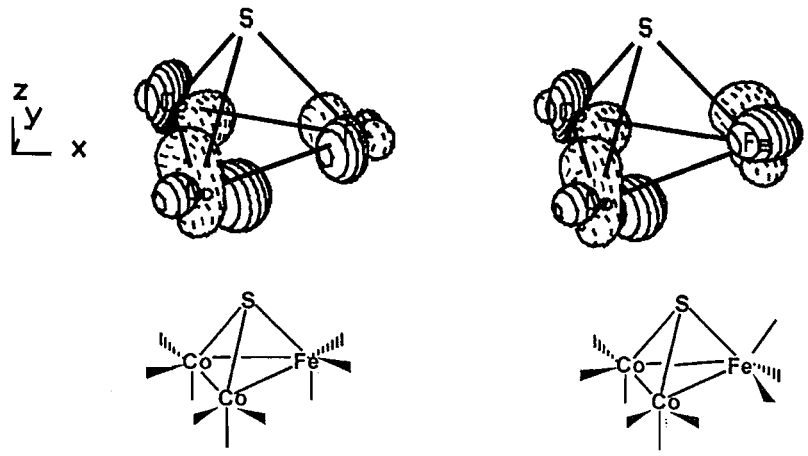

Fig. 5. Rotamers of $CpMo(CO)_2Co_2(CO)_6CR$, **3**; the views are analogous to Newman projections of staggered and eclipsed ethanes.

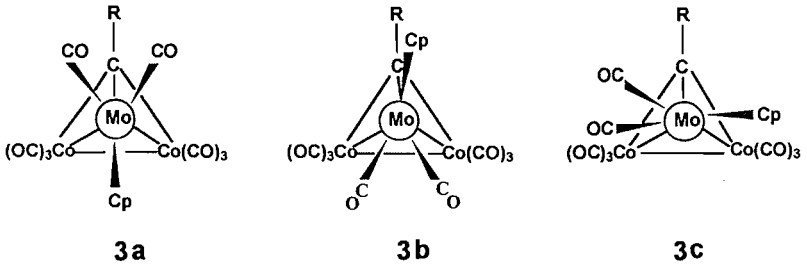

Fig. 6. X-ray crystallographically characterized clusters **12**, **14**, and **15**. Their Newman-type projections correspond to the $CpMoCo_2(CO)_8CR$ rotamers **3a**, **3b**, and **3c**, respectively, as indicated by the labels in square brackets.

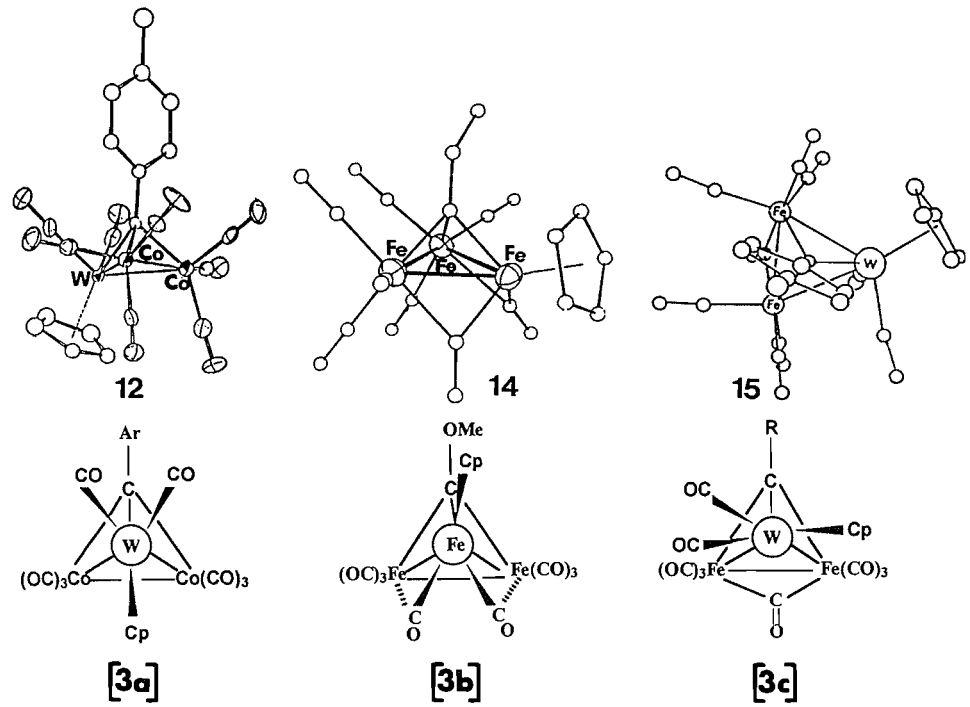

semi-bridging structures to a symmetrically bridging situation (18). Subsequently, this approach was used in an analysis of a series of organometallic derivatives of triphenylsilanol (19). Furthermore, in a study from this laboratory it has been reported that the calculated pathway for antarafacial migration of a CH_2^+ fragment between the molybdenum sites in cation clusters of the type $[Cp_2Mo_2(CO)_4(RC{\equiv}C\text{-}CR_2)]^+$ is paralleled beautifully by the available structural data on such cations (20).

To gain some understanding of the dynamic behavior of the $CpMoCo_2(CO)_8CR$ system, we therefore required several crystal structures in which the $CpM(CO)_2$ unit was oriented differently with respect to the trimetallic plane. As mentioned previously, two essentially identical X-ray structures of type **3a** have been reported (12, 13) and also one of type **3b**. Another molecule closely analogous to **13** is the $(C_5H_5)Fe_3(CO)_8C$-OMe cluster **14** reported by Aitchison and Farrugia (21), and shown in Fig. 6. Finally, we were aware of the structure of the $(C_5H_5)WFe_2(CO)_9C$-tolyl cluster **15** in which the tungsten-to-cyclopentadienyl vector is almost exactly in the plane of the metals, as in **3c** (22). The crucial parameter to note here is the angle made by the $Cp_{centroid}$–metal axis with a line joining this metal to the centre of the cobalt–cobalt (or iron–iron) vector. This angle is 125.5° in **11** and **12**, it becomes 141° in **15**, and opens up to 156°(160°) in **13**(**14**). These values are consonant only with rotation of the $CpM(CO)_2$ fragment about an imaginary line connecting the metal atom to the centre of the cluster.

To be more precise, this imaginary center "**X**" is located as follows: we see from Fig. 7 that, assuming the $CpMo(CO)_2$ vertex executes a simple rotation about the axis defined by the line **X**–Mo, the locus of the centroid of the cyclopentadienyl ring will define a circle. The lowest point "Cp_a" corresponds to structure **3a** for which the angle Cp_a-Mo-**Y** is 125.5° (in **11** and **12**), where "**Y**" is the midpoint of the cobalt–cobalt bond. The highest point "Cp_b" corresponds to structure **3b** for which

Fig. 7. Calculation of the point "**X**" in $CpMo(CO)_2Co_2(CO)_6CH$ (see text).

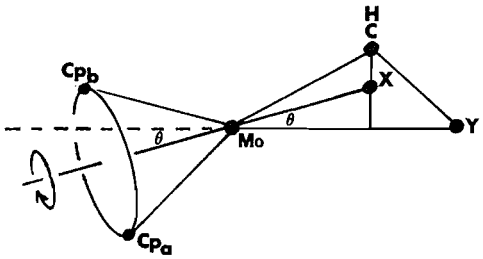

Fig. 8. Frontier orbital interactions in $CpMo(CO)_2Co_2(CO)_6CH$.

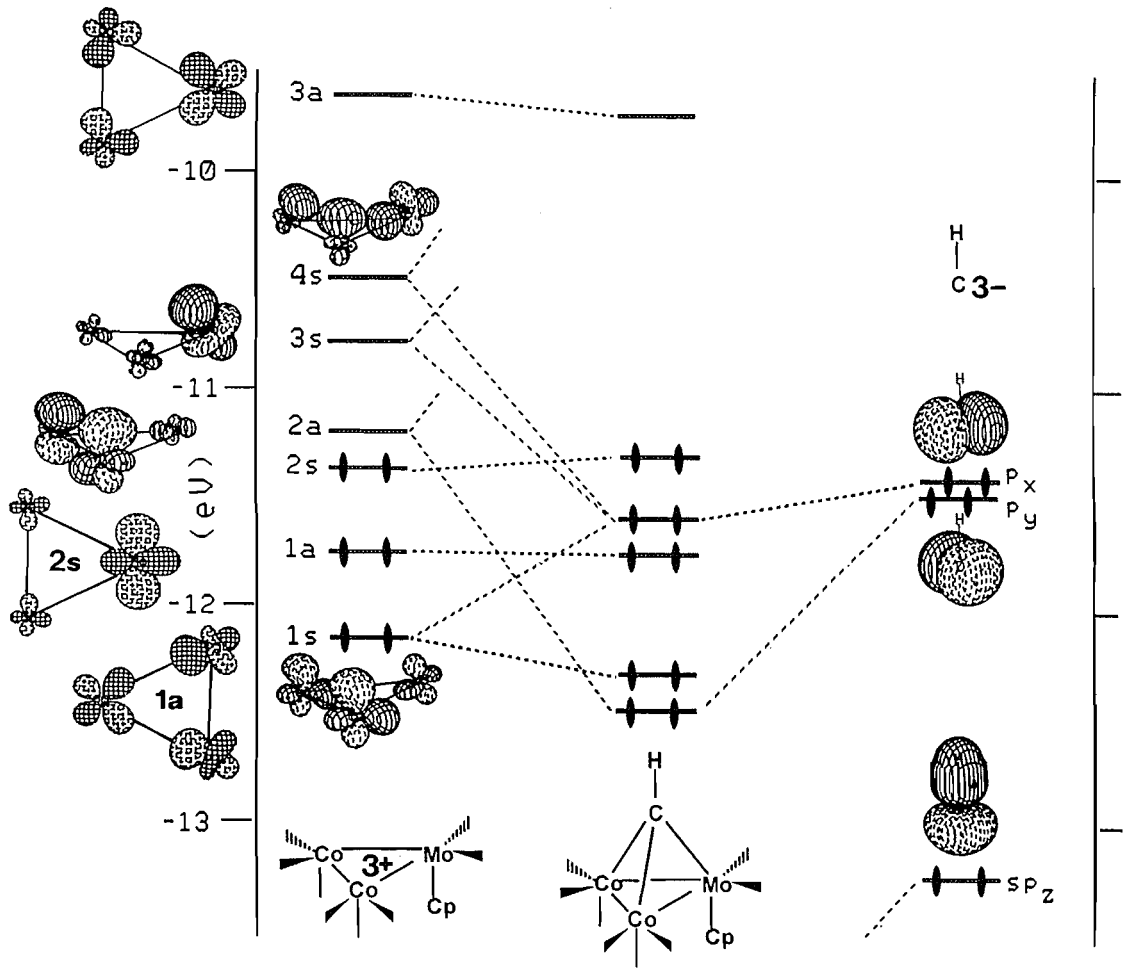

the angle Cp_b-Mo-**Y** is 156° (in **13**). The angle θ in Fig. 7 can thus be evaluated as 15.3°, and so the point **X** can be located vertically below the capping carbon atom.

Such a scenario provides support for the Wade–Mingos delocalized model of cluster bonding (23) rather than one in which there is localized bonding along the edges of the tetrahedron. As a consequence of this analysis, the energies of the rotamers derived by following the trajectory depicted in Fig. 7, i.e., from **3a** to **3b** in Fig. 5, were evaluated by using the EHMO method. The frontier orbitals of the $(C_5H_5)Mo(CO)_2$ moiety have previously been described by Schilling, Hoffmann, and Lichtenberger (24). As with the trimetallic fragments $[Co_3(CO)_9]^{3+}$, **6**, and $[FeCo_2(CO)_9]^{2+}$, **8**, discussed already, the $[(C_5H_5)Mo(CO)_2Co_2(CO)_6]^{3+}$ unit gives rise to a set of three low-lying filled frontier orbitals and also three vacant orbitals (see Fig. 8) that can readily form one σ and two π bonds with the capping carbyne moiety.

A simple rotation of the $(C_5H_5)Mo(CO)_2$ vertex while holding the rest of the molecular geometry constant yields a barrier of more than 40 kcal mol^{-1}; this value arises as a result of unfavorable steric interactions between the cyclopentadienyl and carbonyl ligands on the molybdenum with the carbonyls

attached to cobalt. However, one must recall that, while the barrier to $CpMo(CO)_2$ rotation was sufficiently large that the process becomes slow on the NMR time scale at low temperatures, local rotation of the $Co(CO)_3$ vertices continued unabated. Consequently, the calculations were repeated such that rotation of the $CpMo(CO)_2$ vertex was carried out in 15° increments and the tricarbonylcobalt fragments were each rotated independently so as to give the minimum energy conformation for each point on the curve. At this juncture, the calculated barrier plummeted to 13 kcal mol^{-1}, a value more in line with the experimentally observed barrier of ca. 10 kcal mol^{-1} (14). (It may be relevant to note that Pepermans et al. reported that the perpendicular-to-parallel rotation of the alkyne in $(HC{\equiv}CH)Co_2(CO)_6$ is a forbidden process with a suitably high activation energy barrier. However, when the cobalt carbonyls were allowed to twist concomitant with the alkyne rotation, the barrier was drastically reduced (25).) We reiterate that in the present calculation the $Co(CO)_3$ moieties maintain their local threefold symmetry and all bond lengths are unchanged. Doubtless, if the entire molecular geometry were to be energy minimized at each point of the calculation, one might then reduce this barrier even closer to the experimental value.

These data show that there is a substantial barrier to rotation of the molybdenum vertex and this must be primarily an electronic effect since any potential steric problems can be alleviated via facile rotation of the cobalt carbonyl fragments. Moreover, we note that as the rotation angle of the molybdenum vertex approaches 180°, i.e., towards structure **3b**, it is energetically favorable (to the tune of ≈2 kcal mol^{-1}) to allow the molybdenum carbonyls to become semi-bridging as has been found crystallographically for **13** (15).

In summary, it is evident that there are two strongly favored rotamers of $(C_5H_5)Mo(CO)_2Co_2(CO)_8CH$, both of which possess mirror symmetry: the molybdenum vertex may be oriented with the cyclopentadienyl group below the trimetallic plane, as in **3a**, or above and *proximal* to the carbyne as in **3b**. In the latter case, the molybdenum carbonyls adopt semi-bridging postures and this rotamer is favored when the cyclopentadienyl group is strongly electron donating, as in $(C_5Me_5)Mo(CO)_2Co_2(CO)_6CR$. There is an example of a molecule — the $(C_5H_5)WFe_2(CO)_9C$-tolyl cluster **15** — in which the vertex is rotated through 90°, but the two $Fe(CO)_3$ units are linked by a bridging carbonyl (22). This molecule would be an interesting candidate for a detailed variable-temperature NMR study.

$(C_5H_5)Mo(CO)_2$ rotation in $[(C_5H_5)Mo(CO)_2]_2C_2R_2$ clusters

The NMR fluxionality of alkyne complexes of the type $[(C_5H_5)Mo(CO)_2]_2(RC{\equiv}CR)$ was first investigated by Cotton, who noted that two independent mechanisms were operative (see Fig. 9). The lower energy process involved a pairwise interchange of a terminal carbonyl ligand environment on one molybdenum with a semi-bridging CO on the other metal. The second, and higher energy, process equilibrated the environments of the two cyclopentadienyl groups by a mechanism that must involve some degree of $CpMo(CO)_2$ vertex rotation (26). It is this latter phenomenon that we wish to address.

The dimolybdenum-alkyne clusters originally synthesized by Cotton possess a semi-bridging carbonyl ligand and this structural feature, together with the twisting of the cyclopentadienyl groups, renders the clusters asymmetric.[2] Since that time, many clusters of the type $Cp_2M_2(CO)_4(\boldsymbol{A}{\equiv}\boldsymbol{B})$ have been characterized, where M = Mo or W, and ***A*** and ***B*** are atoms or molecular fragments isolobal (28) with CH. These include systems containing such vertices as P (29), As (30), S^+ (31), O^+ (32), $Co(CO)_3$ (33), $Ir(CO)_3$ (34), etc. In particular, Sullivan and Rheingold have shown that the diarsenic cluster $[(C_5H_5)Mo(CO)_2]_2As_2$, **16**, adopts C_2 symmetry, at least in the solid state (30). Thus the two carbonyl ligands on each molybdenum in **16** are nonequivalent and so, in principle, the barrier to oscillation of the two $(C_5H_5)Mo(CO)_2$ vertices should be measurable by using variable-temperature ^{13}C NMR techniques.

As with the molybdenum–dicobalt tetrahedral clusters discussed above, the $(C_5H_5)Mo(CO)_2$ vertices in $Cp_2M_2(CO)_4(\boldsymbol{A}{\equiv}\boldsymbol{B})$ systems can be considered to oscillate via rotation about a line joining the molybdenum to a point "**X**" within the tetrahedron. This point **X** must be positioned above the midpoint of the Mo–Mo bond along the pseudo-C_2 axis of the molecule; however, establishing its location was a nontrivial exercise and required a Bürgi–Dunitz analysis of the trajectory of the ring-centroid of the cyclopentadienyl fragment. Fortunately, since Cotton's original report (26) of the structure and fluxionality of $[(C_5H_5)Mo(CO)_2]_2(HC{\equiv}CH)$, **4**, there have been more than 20 crystallographically characterized tetrahedral clusters of the general type $Cp_2M_2(CO)_4(\boldsymbol{A}{\equiv}\boldsymbol{B})$, and selected parameters for a number of these clusters are collected in Table 1.

As shown above for $(C_5H_5)MoCo_2(CO)_8CH$ and related trimetallic clusters, the axis of rotation of the $CpMo(CO)_2$ vertex is relatively straightforward to visualize since we have crystallographic data for the two extreme structures **3a** and **3b**, both of which have C_s symmetry. Thus, the **X**–Mo axis about which vertex rotation occurs can be readily defined. Now, for molecules possessing an alkyne bonded transverse to the Mo–Mo vector, we need X-ray crystal structures for which the centroid of the cyclopentadienyl ring lies in the plane defined by the two molybdenum atoms and the midpoint of the C≡C bond. However, the crystallographic data available are all for molecules in which the cyclopentadienyl group has been twisted out of this plane. The problem then becomes one of taking the coordinates of the Cp centroids in the numerous structures of the type $[(C_5H_5)Mo(CO)_2]_2(\boldsymbol{A}{\equiv}\boldsymbol{B})$ and defining the best circle that passes through, or close to, these points.

To this end, the structures of 11 tetrahedral clusters of the type $[(C_5H_5)M(CO)_2]_2(\boldsymbol{A}{\equiv}\boldsymbol{B})$ were selected that closely fit the following criteria: (*a*) the dihedral angle between the M≡M and $\boldsymbol{A}{\equiv}\boldsymbol{B}$ vectors was ≈90°; (*b*) there were no obvious perturbing effects such as the strong bonding interaction of a molybdenum carbonyl with another vertex. This latter criterion eliminated $Cp_2Mo_2(CO)_4Ir_2(CO)_6$ (34). Thus the atomic coordinates for the molecules where $\boldsymbol{A}{\equiv}\boldsymbol{B}$ is

[2] When one of the alkyne substituents is inherently chiral, such as a terpenoid or steroidal group, then the four carbonyl ligands will always yield four ^{13}CO resonances even when all fluxional processes are rapid. At lower temperatures, one sees four ^{13}CO absorptions for each diastereomer. For some recent examples, see ref. 27.

Fig. 9. Fluxional processes that interchange semi-bridging and terminal carbonyl ligands in $Cp_2Mo_2(CO)_4(RC{\equiv}CR')$. Note the pairwise character of the terminal to semi-bridging carbonyl environments.

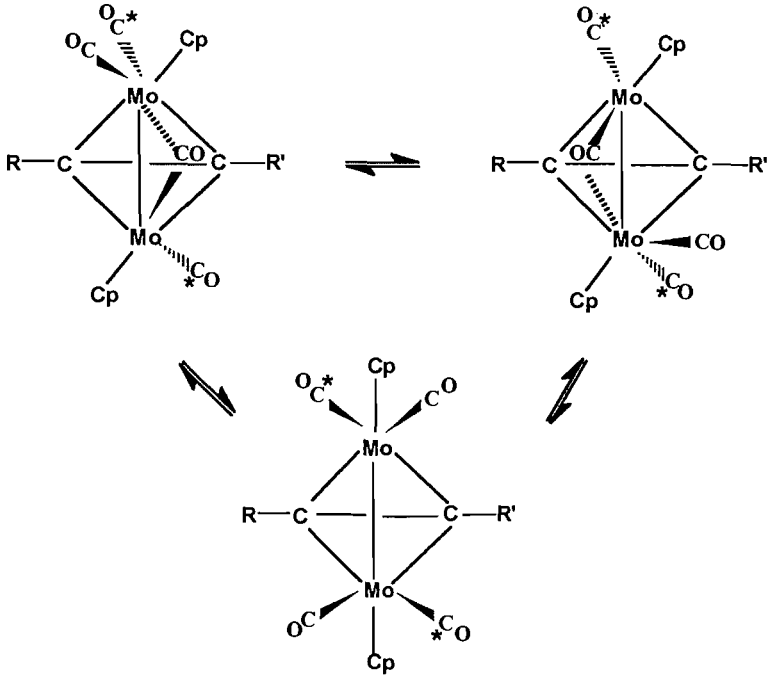

$RC{\equiv}CR'$, $RC{\equiv}P$, $RC{\equiv}BR'$, $RC{\equiv}Co(CO)_3$, $P{\equiv}P$, $As{\equiv}As$, $O{\equiv}Fe(CO)_3$, or $S{\equiv}Ru(CO)_3$ were entered into the molecular modelling program ALCHEMY[3] and the following parameters were evaluated for both $CpM(CO)_2$ vertices in each molecule: (*i*) the angles $Cp_{centroid}$-M-M and $Cp_{centroid}$-M-C(=O), (*ii*) the torsion angles $Cp_{centroid}$-M-M-$Cp_{centroid}$ and **Q**-**R**-M-$Cp_{centroid}$, where the dummies **Q** and **R** are the midpoints of the ***A***—***B*** and M—M bonds, respectively, as shown in Fig. 10.

As is evident from Table 1, the angles $Cp_{centroid}$-M-C(=O) average 114.3° ± 3.7° for 22 different $CpM(CO)_2$ vertices. This consistency bears witness to the fact that the $(C_5H_5)Mo(CO)_2$ or $(C_5H_5)W(CO)_2$ moiety has a remarkably well-defined geometry and may be regarded as a transferable fragment between clusters, just like the regular functional groups of organic chemistry (35). These molecules were selected as being reasonably representative of tetrahedral clusters in that the dihedral angle between the M–M and ***A***–***B*** vectors was in all cases 90° ± 5°.

In the absence of structurally characterized rotamers in which the $Cp_{centroid}$ lies in the same plane as the two molybdenum (or tungsten) atoms and the bond midpoints **Q** and **R**, it was necessary to extrapolate from the experimentally available data and then estimate a value for θ, i.e., the angle M-M-**X** illustrated in Fig. 10. The original choice of θ = 25° was then refined by use of the molecular modelling program to correlate each M-M-$Cp_{centroid}$ angle and its associated **Q**-**R**-M-$Cp_{centroid}$ torsion angle with the corresponding X-ray derived parameters; that is, the point **X** was located empirically from the crystallographic data, and the best fit is found when θ = 29°.

[3] ALCHEMY: available from Tripos associates, St. Louis, Mo.

It is interesting that the location of the axis of rotation in the dimolybdenum complexes $[(C_5H_5)M(CO)_2]_2$(***A***≡***B***) yields a value of 139° for the angle **X**-Mo-$Cp_{centroid}$. We note that the corresponding angle in the $CpMo(CO)_2Co_2(CO)_6CH$ system is 141°; this again supports the idea of transferability of organometallic vertices between different clusters.

Having established the rotation trajectory for a $CpMo(CO)_2$ vertex, it was possible to carry out EHMO calculations on the rotamers of $[(C_5H_5)M(CO)_2]_2(HC{\equiv}CH)$. We commented previously (27*b*) that racemization of such a cluster can occur either (*a*) by synchronous swivelling of both molybdenum vertices to generate a molecule of C_{2v} symmetry, as in **16** or (*b*) by rotating only one vertex so as to produce a C_s cluster, **17**, in which the cyclopentadienyl rings are oriented in a *syn* manner (see Fig. 11). In the latter case, the other vertex must subsequently swivel to generate the enantiomer of the original molecule. The calculations of the energy barriers for these two processes revealed that (*i*) the most favored rotamer does indeed possess the C_2 geometry found crystallographically for $Cp_2Mo_2(CO)_4As_2$ by Sullivan and Rheingold (30), and (*ii*) the proposed C_{2v} structure **16**, is almost certainly not attainable since it would bring the hydrogens of the cyclopentadienyl groups into direct contact. As Cotton and co-workers have noted (26), these steric constraints are the probable cause of the low symmetry observed even in the parent cluster $Cp_2Mo_2(CO)_4(HC{\equiv}CH)$.

To probe the scenario of independently rotating vertices, EHMO calculations were performed in which one $CpMo(CO)_2$ moiety was maintained at a constant orientation (ϕ) with respect to the alkyne while the other molybdenum vertex was rotated through ω values of 40°–320°. The energy profiles depicted in Fig. 12 reveal minima when the molecule

Table 1. Structural parameters for $Cp_2M_2(CO)_4(A{\equiv}B)$ clusters.

	$Cp_{centroid}$-M-C(=O) (deg)	$Cp_{centroid}$-M-M-$Cp_{centroid}$ (deg)	$Cp_{centroid}$-M-M (deg)	$A{\equiv}B$	M	Ref.
1	110.5 116.3 112.7 114.6	163.5	121.4 160.3	**P≡C**-Me	Mo	40
2	110.9 118.1 112.4 119.9	159.2	121.9 153.9	Ph-**C≡C**-R R = cyclopentenyl	Mo	41
3	109.3 117.6 111.0 114.2	146.1	124.1 157.9	Me-**C≡Co**$(CO)_3$	Mo	33
4	109.6 121.1 109.7 125.2	143.4	121.9 150.3	Me-**C≡C**-R R = norbornyl	Mo	4
5	111.2 116.0 111.4 115.8	84.3	117.8 117.8	**P≡P**	Mo	29
6	113.8 117.2 113.5 116.8	80.3	113.8 114.1	**As≡As**	W	30
7	113.0 116.4 113.2 116.8	78.1	114.3 114.7	**As≡As**	Mo	30
8	112.9 114.2 115.5 122.0	83.5	120.4 123.5	Me-**C≡B**(H)-Et	W	42
9	118.6 119.9 110.5 110.8	84.7	122.5 118.2	Me-**C≡B**-Et	W	42
10	111.8 113.5 109.3 115.8	28.8	144.1 118.1	**S≡Ru**$(CO)_3$	Mo	43
11	111.9 113.1 109.0 114.1	24.4	131.0 151.0	**O≡Fe**$(CO)_3$	Mo	32

Fig. 10. Calculation of the point "**X**" in $[(C_5H_5)M(CO)_2]_2(A{\equiv}B)$ systems (see text).

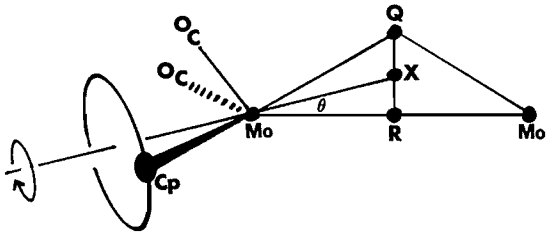

has either approximate C_2 or C_s symmetry. These calculations yield activation energy barriers of ≈15 kcal mol^{-1}, a value in reasonable accord with the experimental data (36). It is noteworthy that the height of the barrier is *extremely* sensitive to minor geometric perturbations; it is necessary to rotate the cyclopentadienyl ligands about their Cp–Mo axes so as to minimize the steric interactions between these rings at each point of the calculated pathway. Attempts to correlate the rotation barrier of the $CpMo(CO)_2$ vertex with the energy profile of any particular frontier orbital were inconclusive and the process appears to be dominated by steric factors. We reiterate that these calculations use a simple "ball-and-socket" model whereby a rigid $(C_5H_5)Mo(CO)_2$ vertex rotates about a clearly defined axis.

The level of agreement between the idealized trajectory of $CpMo(CO)_2$ rotation and the X-ray crystallographically observed structures is manifest evidence of the power of the Bürgi–Dunitz approach for our understanding of molecular dynamics. According to the basic assumptions of the structure correlation method (16), there should be a concentration of sample points (i.e., crystal structures) in the low-energy regions of three-dimensional space. One may thus identify the transition state as lying in the least densely populated stretch of the reaction path. In the present case, this is the region in which the torsion angle between the Mo–$Cp_{centroid}$ vector and the pseudo-C_2 axis approaches 0° or 180°. Figure 12 shows how the crystallographically determined structures do indeed lie primarily in the low-energy regions of the favored pathway found as a result of the EHMO analysis. Once again, it is an impressive confirmation of the Bürgi–Dunitz concept.

Concluding remarks

It is evident that the barriers to rotation of organometallic vertices in clusters, which can be experimentally determined by using variable-temperature NMR methods, are in some cases rationalizable in terms of the energies and symmetries of their frontier orbitals. In particular, the variations between clusters containing homometallic and heterometallic triangular faces can be traced to the degree of localization of the frontier orbitals on the different metallic vertices. It is also shown that use of the structure correlation technique allows the selection of reasonable pathways for fluxional processes. Vertex rotations in $FeCo_2(CO)_9S$ and in $CpMo(CO)_2Co_2(CO)_6CR$ are controlled primarily by electronic factors, and the electronically favored orientations of the organometallic units correlate with those which have been characterized by X-ray crystallography. In contrast, we have been unable to find an electronic rationale to account satisfactorily for the molecular dynamics of $[(C_5H_5)M(CO)_2]_2(HC{\equiv}CH)$ and related molecules that appear to be dominated by steric effects.

Fig. 11. Proposed mechanism of interconversion of enantiomeric clusters via C_S rather than C_{2v} intermediates.

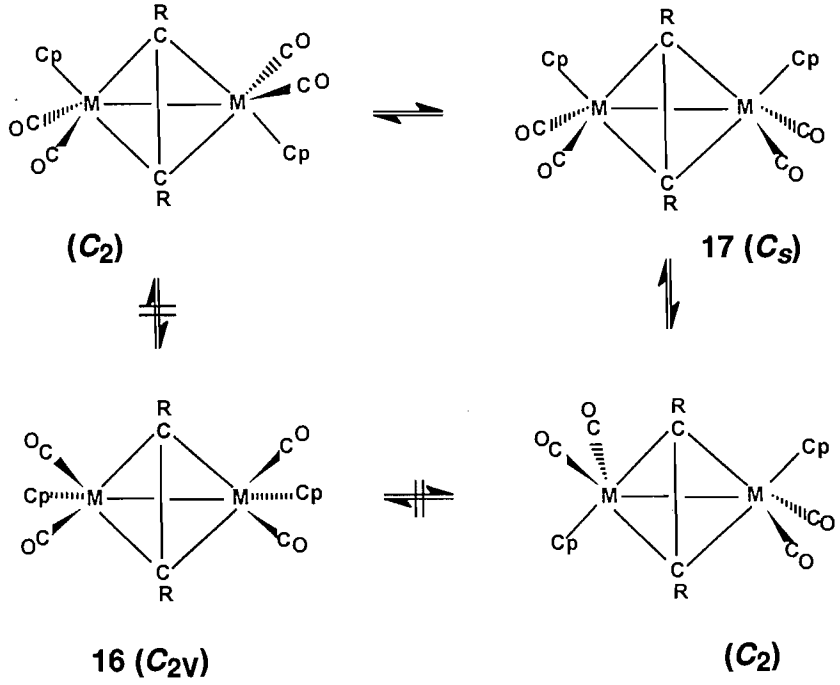

Fig. 12. EHMO-calculated energy profiles corresponding to rotation of only one molybdenum vertex through angle ω while the other $CpMo(CO)_2$ fragment is kept constant, with successive ϕ values ranging from 120° through 145°. The majority of the experimentally observed structures lie in the valleys, and the molecules are numbered as in Table 1.

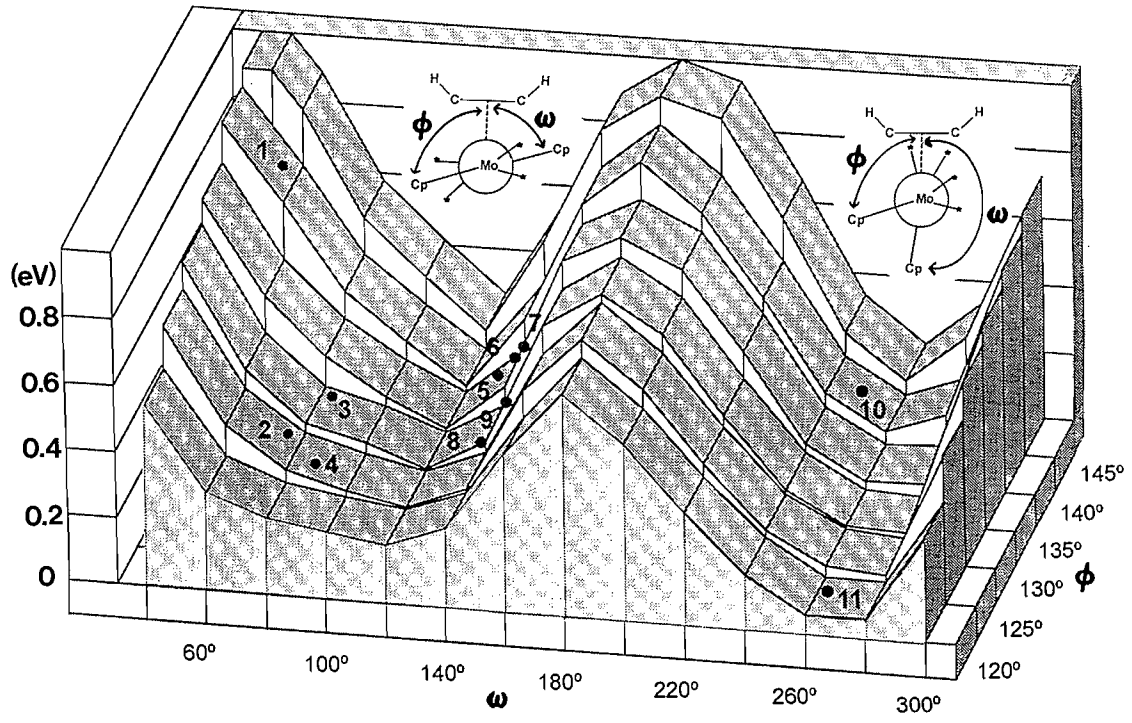

The correlation of X-ray data and fluxional behavior for closely related organometallic clusters could be applied to other situations. An example that could be well worth pursuing is the $RCCo_3(CO)_9$ series of which many have been crystallographically characterized (37). The rotation angles of the $Co(CO)_3$ tripods may tell us whether the intermetallic scram-

bling of the CO ligands over all the metal sites is correlated with rotation of the $Co(CO)_3$ vertices.

Experimental section

Molecular orbital calculations were performed via the extended Hückel method using weighted H_{ij}'s (38); orbital drawings were obtained by use of the program CACAO (39).

Acknowledgements

We thank the Natural Sciences and Engineering Research Council of Canada (NSERC) for financial support, and the reviewers for helpful comments. K.L.M. thanks the Province of Ontario and NSERC for graduate scholarships.

References

1. T.A. Albright, J.K. Burdett, and M. Whangbo. Orbital interactions in chemistry. John Wiley, New York. 1985.
2. M.F. D'Agostino, M. Mlekuz, J. Kolis, B.G. Sayer, C.A. Rodger, J.-F. Halet, J.-Y. Saillard, and M.J. McGlinchey. Organometallics, **5**, 2345 (1986).
3. J.A. Cramer, M.J. McGlinchey, and J.-Y. Saillard. Can. J. Chem. **67**, 1931 (1989).
4. M.F. D'Agostino, C.S. Frampton, and M.J. McGlinchey. J. Organomet. Chem. **394**, 145 (1990).
5. J.-F. Halet, J.-Y. Saillard, R. Lissillour, M.J. McGlinchey, and G. Jaouen. Inorg. Chem. **24**, 218, (1985).
6. S.F. Xiang, A.A. Bakke, H.W. Chen, C.J. Eyermann, J.L. Hoskins, T.H. Lee, D. Seyferth, H.P. Withers, and W.L. Jolly. Organometallics, **1**, 699. (1982).
7. A.P. Hitchcock, M.J. McGlinchey, A.L. Johnson, W.K. Walter, M.P. Jigato, D.A. King, D. Norman, E. Rühl, C. Heinzel, and H. Baumgärtel. J. Chem. Soc. Faraday Trans. **89**, 3331 (1993).
8. (*a*) K. Wade. Chem. Br. **11**, 177 (1975); (*b*) Adv. Inorg. Chem. Radiochem. **18**, 1 (1976).
9. B.E.R. Schilling and R. Hoffmann. J. Am. Chem. Soc. **101**, 3456 (1979).
10. C.H. Wei and L.F. Dahl. Inorg. Chem. **6**, 1229 (1967).
11. S. Aime, L. Milone, R. Rossetti, and P.L. Stanghellini. Inorg. Chim. Acta, **25**, 103 (1977).
12. H. Beurich and H. Vahrenkamp. Angew. Chem. Int. Ed. Engl. **17**, 863 (1978).
13. M.J. Chetcuti, P.A.M. Chetcuti, J.C. Jeffery, R.M Mills, P. Mitrprachachon, S.J. Pickering, F.G.A. Stone, and P. Woodward. J. Chem. Soc. Dalton Trans. 669 (1982).
14. K.A. Sutin, J.W. Kolis, M. Mlekuz, P. Bougeard, B.G. Sayer, M.A. Quilliam, R. Faggiani, C.J.L. Lock, M.J. McGlinchey, and G. Jaouen. Organometallics, **6**, 439 (1987).
15. K.A. Sutin, L. Li, C.S. Frampton, B.G. Sayer, and M.J. McGlinchey. Organometallics, **10**, 2362 (1991).
16. H.-B. Bürgi and J.D. Dunitz. Acc. Chem. Res. **16**, 153 (1983).
17. (*a*) E. Bye, W.B. Schweizer, and J.D. Dunitz. J. Am. Chem. Soc. **104**, 5893 (1982); (*b*) D. Gust and K. Mislow. J. Am. Chem. Soc. **95**, 1535 (1973).
18. R.H. Crabtree and M. Lavin. Inorg. Chem. **25**, 805 (1986).
19. K.L. Malisza, L.C.F. Chao, J.F. Britten, B.G. Sayer, G. Jaouen, S. Top, A. Decken, and M.J. McGlinchey. Organometallics, **12**, 2462 (1993).
20. L. Girard, P.E. Lock, H. El Amouri, and M.J. McGlinchey. J. Organomet. Chem. **478**, 189 (1994).
21. A.A. Aitchison and L.J. Farrugia. Organometallics, **6**, 819 (1987).
22. L. Busetto, J.C. Jeffery, R.M. Mills, F.G.A. Stone, M.J. Went, and P. Woodward. J. Chem. Soc. Dalton Trans. 101 (1983).
23. (*a*) K. Wade. *In* Transition metal clusters. *Edited by* B.F.G. Johnson. Wiley–Interscience, New York. 1980. pp. 193–264; (*b*) D.M.P. Mingos. Adv. Organomet. Chem. **15**, 1 (1977); (*c*) M.J. McGlinchey, M. Mlekuz, P. Bougeard, B.G. Sayer, A. Marinetti, J.-Y. Saillard, and G. Jaouen. Can. J. Chem. **61**, 1319 (1983), and references therein.
24. B.E.R. Schilling, R. Hoffmann, and D.L. Lichtenberger. J. Am. Chem. Soc. **101**, 585 (1979).
25. H. Pepermans, C. Hoogzand, and P Geerlings. J.Organomet. Chem. **306**, 395 (1986).
26. W.I. Bailey, Jr., M.H. Chisholm, F.A. Cotton, and L.A. Rankel. J. Am. Chem. Soc. **100**, 5764 (1978).
27. (*a*) H. El Hafa, C. Cordier, M. Gruselle, Y. Besace, G. Jaouen, and M.J. McGlinchey. Organometallics, **13**, 5149 (1994); (*b*) S. Tondu, G. Jaouen, K.L. Malisza, M.F. D'Agostino, and M.J. McGlinchey. Can. J. Chem. **70**, 1743 (1992).
28. R. Hoffmann. Angew. Chem. Int. Ed. Engl. **21**, 711 (1982).
29. O.J. Scherer, H. Sitzmann, and G. Wolmershäuser. J. Organomet. Chem. **268**, C9 (1984).
30. P.J. Sullivan and A.L. Rheingold. Organometallics, **1**, 1547 (1982).
31. M.D. Curtis and W.M. Butler J. Chem. Soc. Chem. Commun. 998 (1980).
32. C.P. Gibson, J. Huang, and L.F. Dahl. Organometallics, **5**, 1676 (1986).
33. R. Blumhofer, K. Fischer, and H. Vahrenkamp. Chem. Ber. **119**, 194 (1986).
34. M.R. Churchill, C. Bueno, and J.P. Hutchinson. Inorg. Chem. **21**, 1359 (1982).
35. R.F.W. Bader. Atoms in molecules: a quantum theory. Clarendon Press, Oxford. 1994.
36. P. Bougeard, S. Peng, M. Mlekuz, and M.J. McGlinchey. J. Organomet. Chem. **296**, 383 (1985), and references therein.
37. M.I. Bruce. *In* Comprehensive organometallic chemistry. Vol. 9. *Edited by* G. Wilkinson, F.G.A. Stone, and E.W. Abel. Pergamon Press, New York. 1982. p. 1275, and references therein.
38. (*a*) R. Hoffmann. J. Chem. Phys. **39**, 1397 (1963); (*b*) R. Hoffmann and W.N. Lipscomb. J. Chem. Phys. **36**, 2179 (1962); **36**, 3489 (1962); (*c*) J.H. Ammeter, H.-B. Bürgi, J.C. Thibeault, and R. Hoffmann. J. Am. Chem. Soc. **100**, 3686 (1978).
39. C. Mealli and D.M. Proserpio. J. Chem. Educ. **67**, 3399 (1990).
40. G. Becker, W.A. Herrmann, W. Kalcher, G.W. Kriechbaum, C. Pahl, C.T. Wagner, and M.L. Ziegler. Angew. Chem. Int. Ed. Engl. **22**, 413 (1983).
41. K.L Malisza, L. Girard, D.W. Hughes, J.F. Britten, and M.J. McGlinchey. Organometallics, **14**, 4676 (1995).
42. G.A. Carriedo, G.P. Elliot, J.A.K. Howard, D.B. Lewis, and F.G.A. Stone. J. Chem. Soc. Chem. Commun. 1585 (1984).
43. R.D. Adams, J.E. Babin, and M. Tasi. Organometallics, **7**, 219 (1988).

On the accuracy of density functional theory for ion–molecule clusters. A case study of PL_n^+ clusters of the first and second row hydrides

Xabier Lopez, Jesus M. Ugalde, Cecilia Sarasola, and Fernando P. Cossio

Abstract: PL_n^+ clusters (n = 1, 2 and L = NH_3, OH_2, FH, PH_3, SH_2, ClH) in both their triplet and singlet states have been characterized by common approximate density functional methods, SVWN, BVWN, BLYP, and B3LYP. The phosphorus–ligand distances (R), dissociation energies (D_0), triplet–singlet gaps (Δ_{t-s}), and several bond properties, such as the electron density ($\rho(r_c)$), the Laplacian ($\nabla^2\rho(r_c)$), and the local energy density $H(r_c)$ at the bond critical point, were compared with those obtained by accurate ab initio molecular orbital theory, namely, second-order Møller–Plesset (MP2) and G2 theory. In general, it is observed that the local spin density approximation (SVWN) yields stronger bonds than ab initio molecular orbital theory. However, addition of gradient corrections to the exchange functional (BVWN) yields ion–molecule bonds that are too weak. Finally, taking account also of gradient corrections to the correlation functional (BLYP) leads to very close agreement with ab initio results. Among these functionals, Becke's hybrid functional, B3LYP, best fit the second-order Møller–Plesset and G2 data, reproducing the qualitative trends observed for the above-mentioned properties of phosphorus clusters, except for $\nabla^2\rho(r_c)$. This fit is particularly good for distances, dissociation energies, and electron densities at the bond critical point, and both methods show similar deviations of the values of binding energies and triplet–singlet gap with respect to the G2 data. Compared with our most accurate ab initio molecular orbital data, namely G2, significant overbinding for the singlets, larger for one-ligand than for two-ligand complexes, and significant overestimation of the triplet–singlet gap for one-ligand complexes is observed for both methods, namely, B3LYP and MP2. The deviations at the second-order Møller–Plesset level of theory are mainly due to the lack of quadratic configuration interaction (QCI) corrections, and this deficiency is also present to some extent in B3LYP. However, for larger clusters these corrections are smaller, therefore the B3LYP functional is expected to lead to accurate descriptions.

Key words: DFT, Bader analysis, G2, ion–molecule complexes, phosphorus.

Résumé : Faisant appel aux méthodes de densités fonctionnelles SVWN, BVWN, BLYP et B3LYP, on a caractérisé les agrégats PL_n^+ (n = 1 et 2 et L = NH_3, OH_2, FH, PH_3, SH_2, et ClH) dans les états tant triplet que singulet. Les distances phosphore coordinat (R), les énergies de dissociation (D_0), les écarts triplet–singlet (Δ_{t-s}) et plusieurs autres propriétés, telles que la densité électronique ($\rho(r_c)$), le laplacien ($\nabla^2\rho(r_c)$) et la densité locale d'énergie $H(r_c)$ au point critique de liaison ont été comparées avec celles obtenues avec de calculs d'orbitales moléculaires ab initio plus précis, à savoir ceux aux niveaux G2 de la théorie et d'autres de Møller–Plesset du deuxiéme ordre (MP2). En général, on a observé que, par comparaison avec les valeurs obtenues par des calculs d'orbitales moléculaires au niveau de la théorie ab initio, celles obtenues par l'approximation de la densité locale de spin (SVWN) conduit à des valeurs plus élevées pour les forces de liaisons. Toutefois, l'addition de corrections de gradients à l'échange fonctionnel (BCWN) conduit à des liaison ion–molécule qui sont trop faibles. Enfin, si l'on essaye aussi de tenir compte des corrections de gradient dans la corrélation fonctionnelle (BLYP), on arrive à de très bons accords avec les calculs ab initio. Parmi ces corrélations fonctionnelles, le fonctionnelle hybride de Becke, B3LYP, est celle qui s'accorde le mieux avec les donnés de Møller–Plesset du deuxième ordre et de G2 en reproduisant les tendances qualitatives observés pour les propriétés mentionnées plus haut pour les agrégats du phosphores, à l'exception du $\nabla^2\rho(r_c)$. Cet accord est particulièrement bon pour les distances, les énergies de dissociation et les densités électroniques au point critique de la liaison et, par rapport aux données G2, les deux méthodes présentent des déviations semblables pour les valeurs des énergies de fixation et pour l'écart triplet–singulet. Si l'on compare nos résultats avec les données les plus précises d'orbitales moléculaires ab initio, soit G2, on note des surfixations importantes pour les singulets qui sont plus importantes avec les complexes à un coordinat que pour ceux à deux coordinats; avec le deux méthodes, soit B3LYP et MP2, on observe aussi une surévaluation importante de l'écart

Received September 8, 1995.

This paper is dedicated to Professor Richard F.W. Bader on the occasion of his 65th birthday.

X. Lopez,[1] **J.M. Ugalde,**[1] **C. Sarasola, and F.P. Cossío.** Kimika Fakultatea, Euskal Herriko Unibertsitatea, P.K. 1072, 20080 Donostia, Euskadi, Spain.

[1] Authors to whom correspondence may be addressed. Telephone: +3443-216 600. Fax: +3443-212 236. E-mail: ugalde@sq.chu.es

triplet–singulet pour les complexes à un coordinat. Les déviations au niveau de la théorie de Møller–Plesset du deuxiéme ordre sont principalement dues à un manque de corrections pour l'interaction quadratique de configuration (IQC) et cette déficience se retrouve aussi, jusqu'à un certain point, dans B3LYP. Toutefois, pour les agrégats plus volumineux, ces corrections sont plus petites et on peut s'attendre à ce que la fonctionnelle B3LYP conduise à des descriptions précises.

Mots clés : DFT, analyse de Bader, G2, complexes ion–molécule, phosphore.

[Traduit par la rédaction]

1. Introduction

The elucidation and characterization of ionic clusters has been the subject of several theoretical and experimental studies over the last decade (1, 2). Because clusters constitute a bridge between the gas and condensed phases, the study of the formation of cluster ions is relevant to an understanding of such phenomena as nucleation, the development of surfaces, catalysis, solvation, acid–base chemistry, combustion, and atmospheric processes. Clusters are also of great theoretical interest, since a variety of bonds can coexist in the same molecular structure. The majority of common interactions inside a molecule fall more or less into three kinds of interaction: ionic, covalent, or van der Waals (the hydrogen bond could be considered as a special case of van der Waals interactions). The ion–molecule bond of an ionic cluster could be due to any of these interactions, and normally a mixture of them is present. Also, transitions between different kinds of interaction can occur as the clusters grow up, i.e., as the number of ligands attached to the ion increases. Thus, covalent bonds are often characteristic of small clusters, while electrostatic interactions dominate for larger clusters. Undoubtedly, this also depends on the nature of both the ligand and the ion. Soft ligands favor covalent interactions over electrostatic ones, while the opposite is found for hard. Also, open-shell ions tend to favor electronic over electrostatic interactions, since empty orbitals of low energy are available. Apart from electrostatic and covalent binding, van der Waals and hydrogen bonds can also be found, especially when the first solvation shell is completed, and new ligands are bound to the ligands on the first solvation shell. Due to these features, much interest has been focused on the determination of bond properties, such as binding energies and distances, as a function of the size of the clusters, the nature of the ligand, and the hardness of ion involved in the cluster structure.

Inclusion of electron correlation (3–6), at least at the MP2 level, is essential to describe the bonds in such systems, and normally the use of a large basis set is necessary to yield accurate binding energies. This makes the computational cost too expensive. This is especially true in the determination of properties that involve large systems, i.e., determination of magic numbers (maximum number of ligands that the ion admits in its first solvation shell) or the effect of the second coordination shell. In these cases, we have to build up large clusters, which means dealing with a large number of electrons. It is a problem for conventional ab initio methods to treat such large systems, at least with a proper degree of accuracy. Density functional theory (7–11) (DFT) can be a promising alternative to these methods. For a wide range of systems DFT has been found to yield properties (geometries, dissociation energies, and frequencies) comparable in quality to the MP2 results (11). Also, it has been established that DFT yields accurate reaction energies for several chemical processes (12–14), when appropriate nonlocal gradient corrections are included. DFT is computationally less demanding than MP2 or other ab initio methods that include electron correlation, especially for large systems. Thus, these systems could in principle be treated within the framework of DFT with large basis sets, extending the range of clusters amenable to study at an assumable computational cost. However, it is not known how DFT works with ionic clusters. Good results have recently been reported for hydrogen bond systems (15–18), hydrated proton clusters (19), proton transfer systems (20), and some ion–molecule complexes (21) when nonlocal gradient corrections are considered. It would be interesting to compare results between highly accurate ab initio calculations and DFT for different ion–molecules, in order to assess the reliability of DFT for such systems.

We have tested the quality of DFT methods for the description of ionic clusters, by making a comparative study of the previous (22–24) ab initio characterized PL_n^+ clusters (n = 1, 2; L = NH_3, OH_2, FH, PH_3, SH_2, and ClH), for both their singlet and triplet states. Binding energies, ion–molecule bond distances, and bond properties of the bond critical points were characterized using high accuracy ab initio methods (G1 and G2 methodologies (25–27)). Depending on the spin state of the phosphorus, the hardness of the ligand, and the number of ligands bound to the P^+, different kinds of bond were obtained, from covalent to electrostatic. In this paper, we have recalculated the abovementioned properties, employing four different DFT methods (28–32): SVWN, BVWN, BLYP, and B3LYP. We have considered the local spin density approximation in its SVWN form, and have progressively added nonlocal gradient corrections, firstly, only to the exchange, thus BVWN functional, and then to both exchange and correlation with the BLYP functional. We have also applied the hybrid B3LYP functional, which has been proven to yield accurate results for a wide range of chemical systems.[2] It is the aim of this paper to compare the DFT results with the previous ab initio results, in order to test the reliability of DFT in describing such systems, and the accuracy expected for different types of complexes: singlet and triplet spin states, one- and two-ligand complexes. This will provide us with the necessary information about the quality of DFT and, hopefully, will permit us to treat clusters of higher numbers of ligands in future studies.

2. Methods

All the calculations reported here were carried out using the GAUSSIAN92/DFT (33) suites of programs. In the density

[2] See supplement on DFT in Gaussian 92 manual.

Fig. 1. Geometries of the triplet one-ligand complexes calculated at the SVWN, BVWN (in parentheses), BLYP (in square brackets), B3LYP (in curly brackets), and MP2 (underlined) levels of theory, using the 6-31G(d) basis set. Distances are in Å, and angles in degrees. MP2 values have been taken from ref. 24.

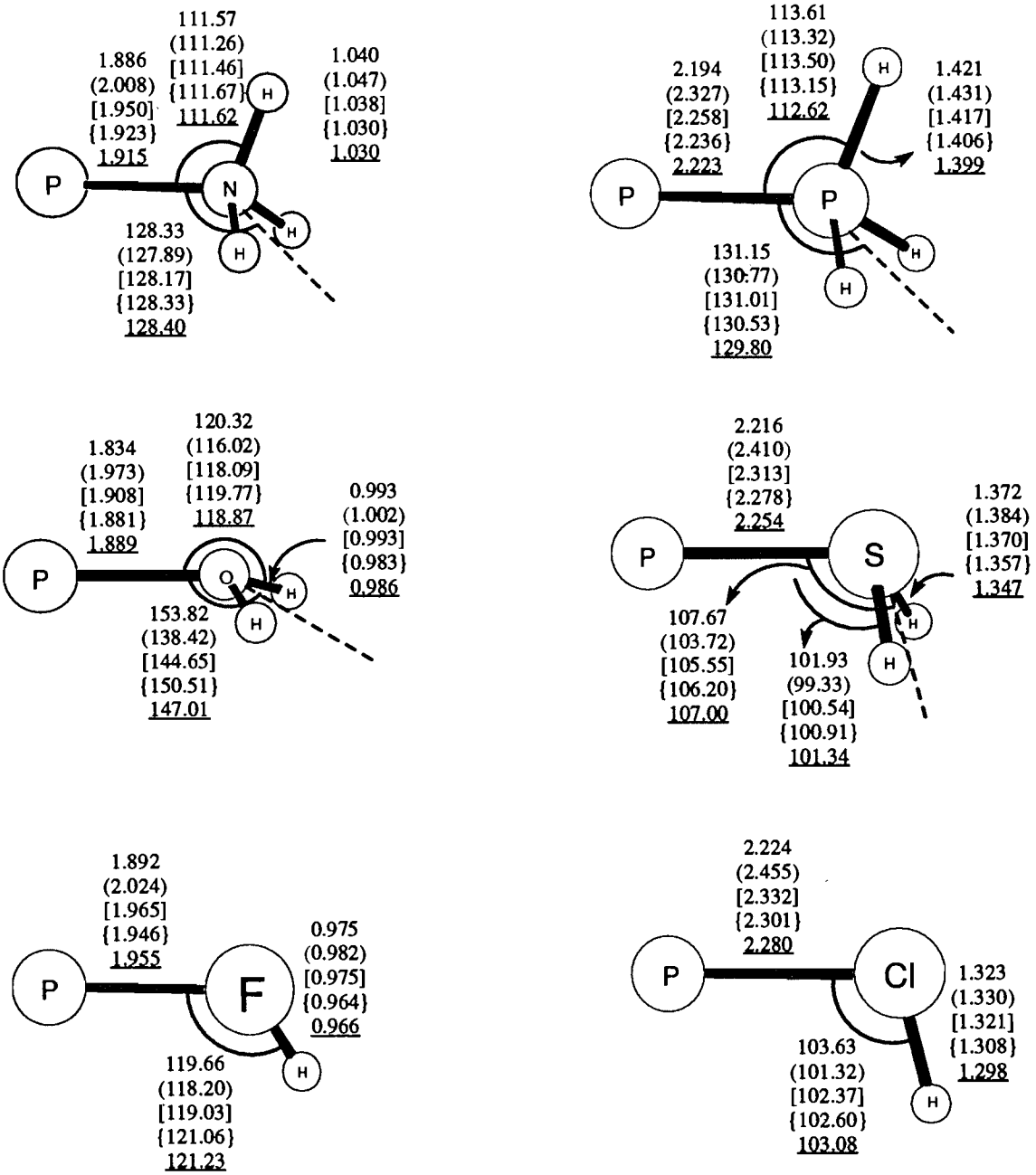

functional theory (DFT) calculations, the Coulombic and the exact exchange integrals were computed analytically and the integrals over the exchange and the correlation functionals were evaluated over numerical grids. Four functionals were employed: (*i*) The SVWN functional, thus, the Slater exchange (28) (local spin density approach, LSDA) and the local correlation of Vosko, Wilk and Nusair (29) (VWN). (*ii*) The BVWN functional, which adds Becke's 1988 exchange functional correction (30). (*iii*) The BLYP functional, which comprises this last Becke's correction plus the gradient-corrected correlation functional of Lee, Yang and Parr (31) (LYP). (*iv*) Finally, we also used the hybrid method consisting of Becke's three-parameter functional (32) in the form

$$[1] \qquad (1-a_0)E_x^{\mathrm{LSDA}}+a_0E_x^{\mathrm{HF}}+a_xE_x^{\mathrm{B88}}+a_cE_c^{\mathrm{LYP}}+(1-a_c)E_c^{\mathrm{VWN}}$$

the values of the parameters being $a_0 = 0.20$, $a_x = 0.72$ and $a_c = 0.81$.

All structures were optimized at the DFT/6-31G(d) level of theory (where DFT is SVWN, BVWN, BLYP, and B3LYP). (For notation of the basis sets see ref. 34.) The optimized geometries, along with the previously obtained MP2 values, can be found in Figs. 1–5. Analytical frequencies at the stationary points were calculated at the DFT/6-31G(d) level of

Fig. 2. Geometries of the singlet one-ligand complexes calculated at the SVWN, BVWN (in parentheses), BLYP (in square brackets), B3LYP (in curly brackets), and MP2 (underlined) levels of theory, using the 6-31G(d) basis set. Distances are in Å, and angles in degrees. MP2 values have been taken from ref. 24.

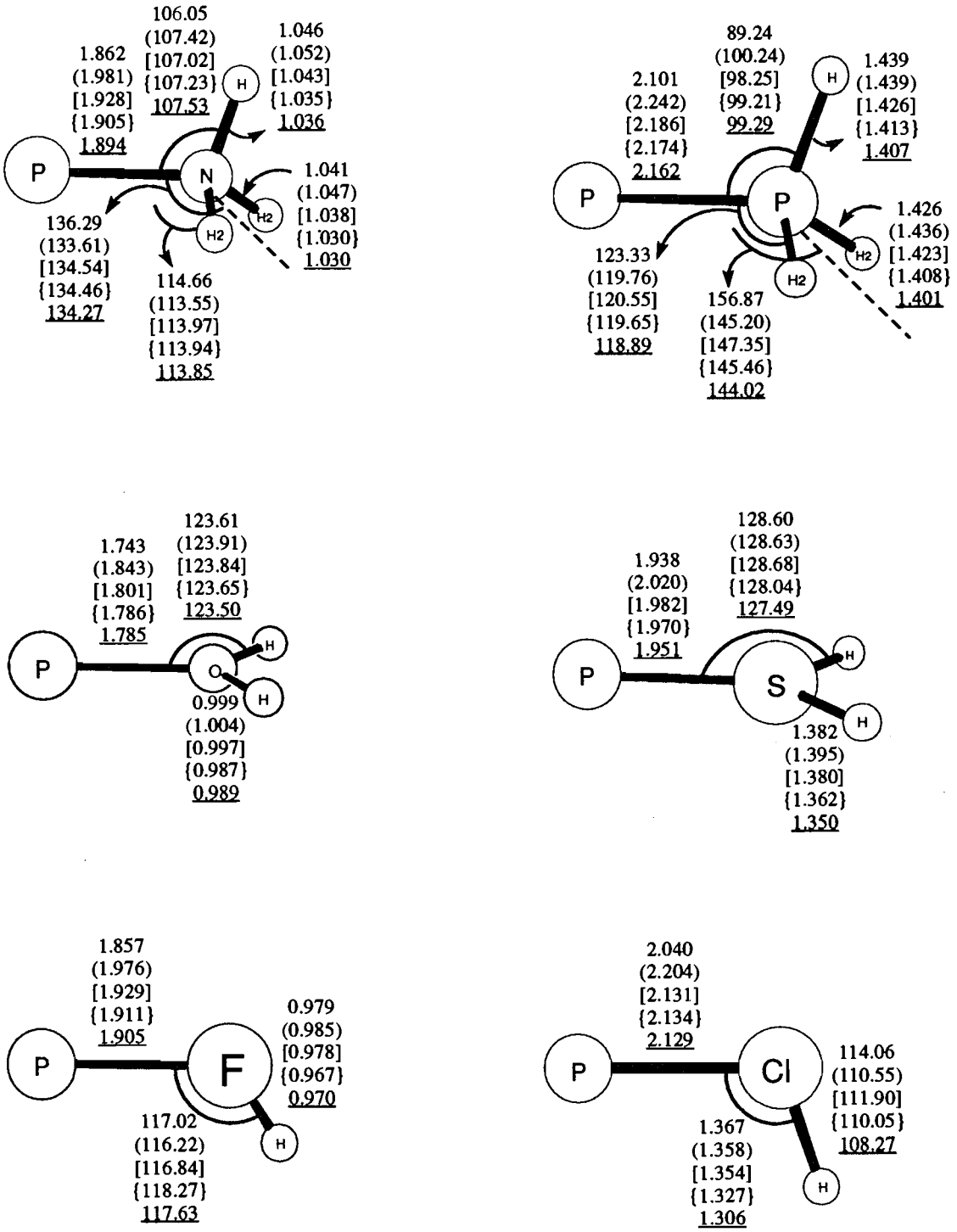

theory and all of them were found to be positive. At these optimized geometries single-point energy calculations with an extended basis set, 6-311+G(3df,2p), were carried out. We recall that this basis set is the largest one employed in G2 theory (25–27). These energies were corrected by the zero point vibrational energy (ZPVE) corrections, evaluated at the DFT/6-31G(d) level of theory. The total energies calculated in this way were employed to evaluate the dissociation energies (D_0) of the PL_n^+ clusters, which are defined as the energy difference between the ion–molecule complexes and their monomers in the appropriate spin state, thus:

[2] $$(D_0)_{PL_n} = -[(E_{PL_n} - (E_{PL_{n-1}} + E_L))]$$

The calculated binding energies for one- and two-ligand com-

Fig. 3. Geometrics of the triplet two-ligand complexes calculated at the SVWN, BVWN (in parentheses), BLYP (in square brackets), B3LYP (in curly brackets), and MP2 (underlined) levels of theory, using the 6-31G(d) basis set. Distances are in Å, and angles in degrees. MP2 values have been taken from ref. 24.

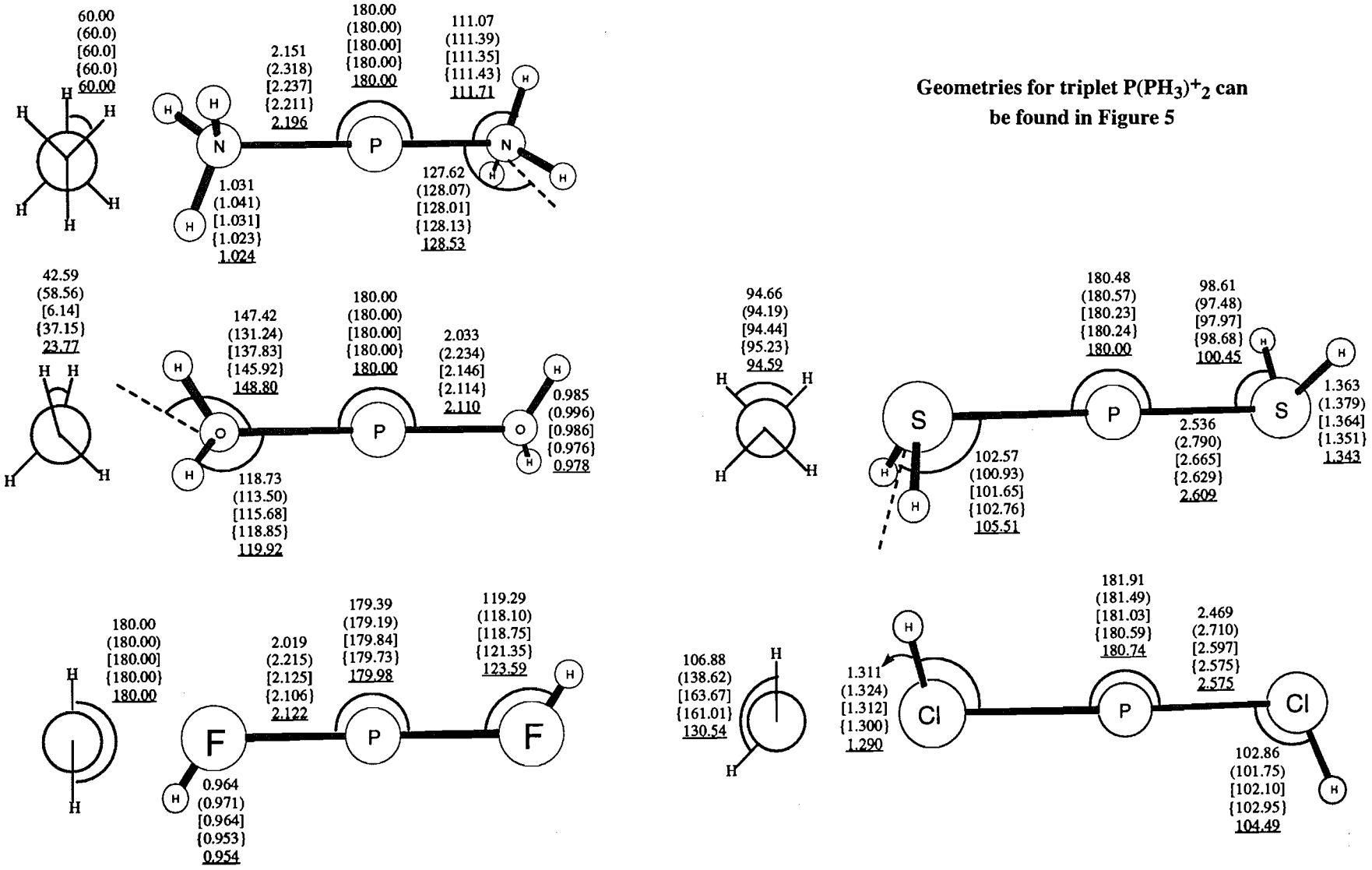

Fig. 4. Geometries of the singlet two-ligand complexes calculated at the SVWN, BVWN (in parentheses), BLYP (in square brackets), B3LYP (in curly brackets), and MP2 (underlined) levels of theory, using the 6-31G(d) basis set. Distances are in Å, and angles in degrees. MP2 values have been taken from ref. 24.

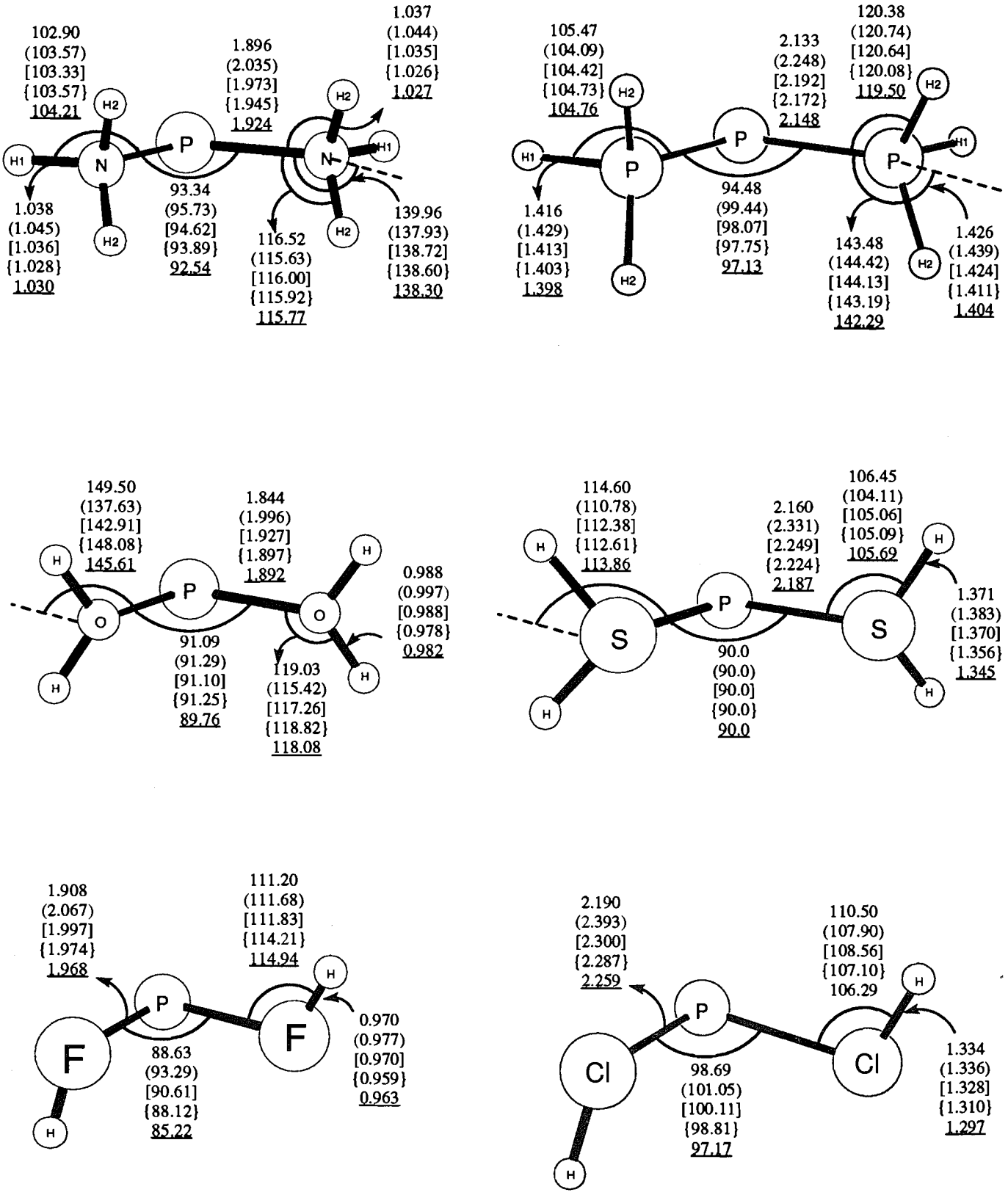

Fig. 5. Geometries of the triplet $P(PH_3)_2^+$ cluster, calculated at MP2 (*a*), SVWN (*b*), BVWN (*c*), BLYP (*d*), and B3LYP (*e*), levels of theory, using the 6-31G(d) basis set. Distances are in Å, and angles in degrees. MP2 values have been taken from ref. 24.

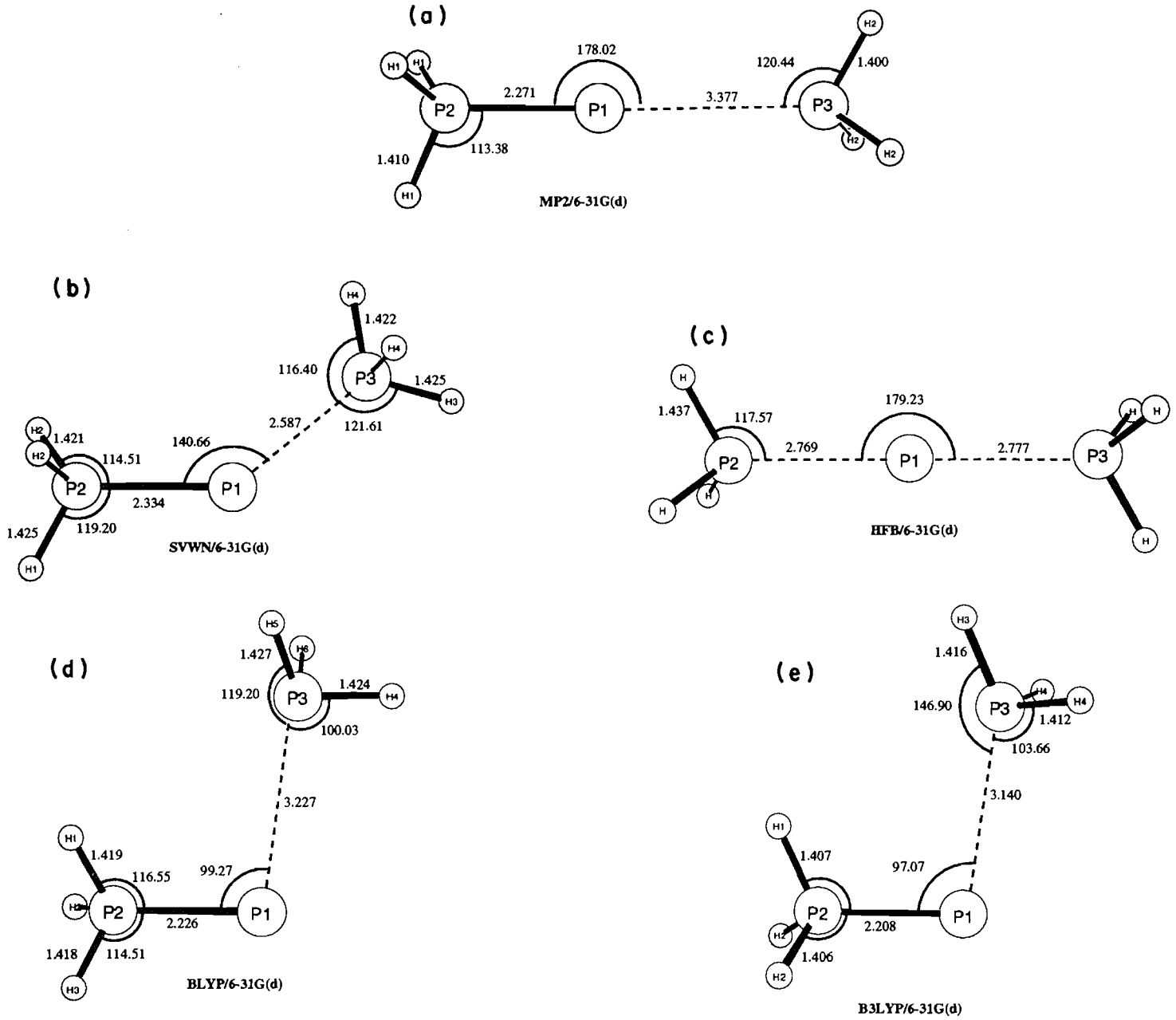

Table 1. D_0 values, in kcal/mol, of the PL_n^+ clusters.

Species		SVWN	BVWN	BLYP	B3LYP	MP2	G2[a]	QCI[a]
$P(NH_3)^+$	$^3A_2$	107.33	76.88	86.33	87.27	86.39	85.80	0.20
	$^1A'$	107.44	78.74	89.25	91.51	91.70	86.43	−3.62
$P(NH_3)_2^+$	$^3A_{2g}$	29.73	17.12	21.31	19.82	19.79	18.49	−0.82
	$^1A_1$	80.36	50.89	59.36	59.09	62.46	55.10	−4.84
$P(OH_2)^+$	$^3A''$	80.10	51.31	60.27	61.06	58.55	57.90	0.05
	$^1A_1$	61.33	38.75	46.74	74.63	72.89	64.84	−6.50
$P(OH_2)_2^+$	^3A	29.69	16.98	21.36	20.37	20.79	19.56	−0.92
	$^1A_1$	87.58	55.90	65.62	39.22	40.44	36.79	−2.13
$P(FH)^+$	$^3A''$	48.22	27.04	33.47	32.71	29.18	28.73	−0.17
	$^1A'$	52.06	25.55	31.81	36.72	33.74	29.13	−4.07
$P(FH)_2^+$	^3V_g	24.23	11.76	16.11	15.79	15.79	15.81	−0.71
	^1A	36.69	23.93	30.27	24.01	23.06	18.23	−4.18
$P(PH_3)^+$	$^3A_2$	106.27	75.10	85.62	86.72	85.84	84.33	0.08
	$^1A'$	87.43	73.23	81.34	95.12	95.23	86.66	−5.53
$P(PH_3)_2^+$	$^3A''$	17.77	5.45	10.19	9.32	6.10	5.80	−0.21
	$^1A_1$	117.30	66.51	80.89	70.29	80.35	70.48	−3.43
$P(SH_2)^+$	$^3A''$	91.08	62.03	71.12	70.37	66.85	66.78	0.37
	$^1A_1$	117.19	79.43	92.06	89.64	87.78	76.89	−7.19
$P(SH_2)_2^+$	^3B_g	22.31	12.77	15.54	13.40	11.87	10.69	−0.54
	$^1A_1$	58.60	35.28	42.71	44.15	47.97	44.66	−0.92
$P(ClH)^+$	$^3A''$	63.74	37.91	45.81	44.49	40.79	40.91	0.31
	$^1A'$	45.18	26.71	60.23	57.83	54.35	47.33	−5.54
$P(ClH)_2^+$	^3A	20.91	10.97	13.61	12.12	11.27	10.38	−0.42
	^1A	78.70	45.96	28.63	28.36	29.23	25.09	−2.24

[a]Values taken from ref. 24.

Table 2. Triplet–singlet gap,[a] in kcal/mol, of the PL_n^+.

Species	SVWN	BVWN	BLYP	B3LYP	MP2	G2[b]	QCI[b]
P^+	−33.45	−45.20	−35.75	−36.57	−40.20	−25.20	6.68
$P(NH_3)^+$	−33.34	−43.35	−32.83	−32.33	−34.89	−24.58	4.20
$P(NH_3)_2^+$	17.30	−9.58	5.22	6.94	7.78	12.03	0.19
$P(OH_2)^+$	−52.22	−57.77	−49.28	−22.99	−25.86	−18.27	1.47
$P(OH_2)_2^+$	5.67	−18.85	−5.02	−4.14	−6.21	−1.03	0.27
$P(FH)^+$	−29.62	−46.69	−37.41	−32.56	−35.64	−24.81	4.12
$P(FH)_2^+$	−17.15	−34.52	−23.25	−24.33	−28.40	−21.66	0.02
$P(PH_3)^+$	−52.29	−47.07	−40.03	−28.17	−30.81	−22.88	2.41
$P(PH_3)_2^+$	47.24	13.99	30.67	32.80	43.45	41.81	−0.80
$P(SH_2)^+$	−7.35	−27.80	−14.82	−17.30	−19.27	−15.09	0.46
$P(SH_2)_2^+$	28.94	−5.29	12.36	13.45	16.82	18.87	0.08
$P(ClH)^+$	−52.01	−56.40	−21.33	−23.22	−26.64	−18.78	2.17
$P(ClH)_2^+$	5.79	−21.41	−6.32	−6.99	−8.68	−4.06	0.35

[a]Notice that when triplet is the ground state the gap takes negative values, whereas positive values are obtained when singlet is the ground state.

[b]Values taken from ref. 24.

plexes have been collected in Table 1. These energies have been also used to evaluate the triplet–singlet gap, which is given in Table 2.

The previously obtained MP2 and G2 values for D_0 and Δ_{t-s} have also been reported in Tables 1 and 2, for comparison with DFT. We recall that G2 energy is the result of several additive corrections made to the MP4/6-311G(d,p)//MP2/6-31G(d) base level energy, which accounts for the deficiencies of this energy in the treatment of basis set and electron correlation. One of these corrections, QCI, has also been reported, since, as we shall see below, it accounts for the main differences between MP2 and G2 dissociation energies, and makes a significant contribution to the differences for Δ_{t-s}. These will be found in Table 6. We note that these corrections are calculated as:

[3] $$\Delta E^{QCI} = [QCISD(T)/6\text{–}311G(d,p)] - [MP4/6\text{–}311G(d,p)]$$

Table 3. $\rho(r_c)$ values, in atomic units, of the PL_n^+ clusters.

Species		SVWN	BVWN	BLYP	B3LYP	MP2[a]
$P(NH_3)^+$	$^3A_2$	0.1180	0.0966	0.1059	0.1092	0.1073
	$^1A'$	0.1228	0.1013	0.1101	0.1128	0.1110
$P(NH_3)_2^+$	$^3A_{2g}$	0.0752	0.0554	0.0636	0.0657	0.0657
	$^1A_1$	0.1116	0.0885	0.0979	0.1010	0.1011
$P(OH_2)^+$	$^3A''$	0.1051	0.0837	0.0923	0.0939	0.0897
	$^1A_1$	0.1192	0.0978	0.1055	0.1070	0.1032
$P(OH_2)_2^+$	^3A	0.0756	0.0533	0.0612	0.0626	0.0608
	$^1A_1$	0.1018	0.0788	0.0878	0.0899	0.0875
$P(FH)^+$	$^3A''$	0.0839	0.0653	0.0723	0.0723	0.0681
	$^1A'$	0.0892	0.0717	0.0780	0.0773	0.0748
$P(FH)_2^+$	^3B_g	0.0681	0.0462	0.0544	0.0543	0.0500
	^1A	0.0826	0.0607	0.0689	0.0694	0.0668
$P(PH_3)^+$	$^3A_2$	0.1139	0.0921	0.1033	0.1085	0.1110
	$^1A'$	0.1309	0.1062	0.1163	0.1197	0.1224
$P(PH_3)_2^+$	$^3A''$	0.0551	0.0399	0.0192	0.0220	0.0129
		0.0864	0.0406	0.1065	0.1114	0.1011
	$^1A_1$	0.1207	0.1005	0.1104	0.1151	0.1190
$P(SH_2)^+$	$^3A''$	0.1017	0.0728	0.0861	0.0918	0.0949
	$^1A_1$	0.1390	0.1209	0.1291	0.1306	0.1309
$P(SH_2)_2^+$	^3B_g	0.0569	0.0362	0.0449	0.0477	0.0483
	$^1A_1$	0.1090	0.0812	0.0937	0.0978	0.1026
$P(ClH)^+$	$^3A''$	0.0880	0.0561	0.0710	0.0749	0.0766
	$^1A'$	0.1179	0.0891	0.1013	0.1002	0.0987
$P(ClH)_2^+$	^3A	0.0544	0.0336	0.0417	0.0429	0.0414
	^1A	0.0917	0.0616	0.0738	0.0751	0.0774

[a]Values taken from ref. 24.

We also carried out Bader's topological analysis (35–38) of the electron density ($\rho(\boldsymbol{r})$), for all the DFT methods, using the AIMPAC series of programs (39), based on the DFT/MC-311G(d,p)//DFT/6-31G(d) electron densities. We will focus on the values of various properties at the bond critical points, such as the electron density ($\rho(r_c)$), the Laplacian ($\nabla^2\rho(r_c)$), and the energy density ($H(r_c)$). These values, along with those for MP2, are given in Tables 3, 4, and 5, respectively.

For the comparison between these methods of certain properties, we will consider the mean deviation between them for a given property. These deviations have been calculated by the sum of absolute differences between two given methods over values obtained for all the clusters, divided by the total number of clusters. We will use the following abbreviation to refer to them: ΔX_j^i is the average deviation of "i" method values with respect to "j" method values for a given property X.

3. Results and discussion

3.1 Geometries

Both MP2 and DFT describe structures with intramolecular parameters similar to those of the free molecules, while ion–molecule distances vary greatly depending on the nature of ligand, the number of ligands, and the spin state of phosphorus atom. The DFT structures, irrespective of the functional employed, show the same trends and symmetries as the MP2 ones, the only exception being triplet $P(PH_3)_2^+$ (Fig. 5). In that sense, one-ligand complexes show shorter P—X distances for the singlets than for the triplets, encountering the largest triplet–singlet difference for P—O and P—S bonds within first- and second-row ligands, respectively. Also, changes in the symmetry point group of the complexes on going from triplets to singlets are similar for DFT and MP2. Thus, PXH_3^+ systems change from C_{3v} to C_s and PXH_2^+ from C_s to C_{2v}. It should be noted that in some cases HF and MP2 point groups were in disagreement; for instance, HF predicted as C_{2v} triplet $P(OH_2)^+$ and a C_s singlet $P(SH_2)^+$. Two-ligands complexes, except for triplet $PH_3)_2^+$, show the same tendencies with DFT and MP2 methods. Thus, the two ligands are equivalent for two-ligand complexes, but while linear complexes of large P—X distances are found for triplet complexes, singlets show angular structures with P—X distances much shorter and closer to the values of the one-ligand complexes. It should also be mentioned that the HF method described a situation of unequivalent ligands for triplet $P(NH_3)_2^+$ and triplet $P(SH_2)_2^+$. The exception in this DFT–MP2 agreement is observed for the description of the P—O and P—F bonds of triplet complexes. While MP2 describes a P—F bond larger than the corresponding P—O bond SVWN, BVWN, and BLYP describe the reverse situation. In this case, the only functional in concordance with MP2 is the hybrid B3LYP functional.

Apart from the good qualitative agreement between DFT and MP2 structures, the quantitative agreement is strongly functional dependent. SVWN tends to give longer ion–molecule bonds than MP2. The inclusion of nonlocal gradient corrections to the exchange functional, the BVWN functional, shorten the bonds, but too much compared with MP2,

Table 4. $\nabla^2\rho(r_c)$ values, in atomic units, of the PL_n^+ clusters.

Species		SVWN	BVWN	BLYP	B3LYP	MP2[a]
$P(NH_3)^+$	$^3A_2$	−0.0021	−0.9442	−0.0422	−0.0070	0.0241
	$^1A'$	0.0197	−0.0534	−0.0407	0.0037	0.0668
$P(NH_3)_2^+$	$^3A_{2g}$	0.0398	0.0588	0.0554	0.0519	0.0519
	$^1A_1$	0.0288	−0.0166	−0.0183	0.0097	0.0686
$P(OH_2)^+$	$^3A''$	0.1269	0.0371	0.0590	0.0981	0.1083
	$^1A_1$	0.3472	0.1584	0.2244	0.2784	0.3150
$P(OH_2)_2^+$	^3A	0.0828	0.0847	0.0904	0.0928	0.0940
	$^1A_1$	0.1265	0.0493	0.0610	0.0924	0.1162
$P(FH)^+$	$^3A''$	0.0896	0.0841	0.0874	0.0935	0.0933
	$^1A'$	0.1068	0.0765	0.0807	0.0991	0.1028
$P(FH)_2^+$	^3B_g	0.1120	0.0966	0.1085	0.1124	0.1128
	^1A	0.0863	0.0902	0.0908	0.0932	0.0940
$P(PH_3)^+$	$^3A_2$	−0.1273	−0.0645	−0.0948	−0.1190	−0.1394
	$^1A'$	−0.1957	−0.1079	−0.1404	−0.1549	−0.1793
$P(PH_3)_2^+$	$^3A''$	0.0303	0.0336	0.0321	0.0349	0.0285
		−0.0306	0.0333	−0.1023	−0.1274	−0.1002
	$^1A_1$	−0.1479	−0.0852	−0.1149	−0.1398	−0.1646
$P(SH_2)^+$	$^3A''$	−0.0668	−0.0003	−0.0256	−0.0484	−0.0695
	$^1A_1$	0.1075	0.0046	0.0492	0.1035	0.1936
$P(SH_2)_2^+$	^3B_g	0.0387	0.0412	0.0428	0.0412	0.0414
	$^1A_1$	−0.0897	−0.0143	−0.0439	−0.0648	−0.0910
$P(ClH)^+$	$^3A''$	−0.0146	0.0429	0.0233	0.0099	−0.0022
	$^1A'$	−0.0570	−0.0290	−0.0600	−0.0417	−0.0706
$P(ClH)_2^+$	^3A	0.0617	0.0583	0.0631	0.0630	0.0647
	^1A	−0.0138	0.0449	0.0278	0.0192	0.0057

[a]Values taken from ref. 24.

Table 5. $H(r_c)$ values, in atomic units, of the PL_n^+ clusters.

Species		SVWN	BVWN	BLYP	B3LYP	MP2[a]
$P(NH_3)^+$	$^3A_2$	−0.0902	−0.0572	−0.0725	−0.0799	−0.0808
	$^1A'$	−0.0960	−0.0646	−0.0788	−0.0843	−0.0840
$P(NH_3)_2^+$	$^3A_{2g}$	−0.0258	−0.0102	−0.0157	−0.0185	−0.0209
	$^1A_1$	−0.0823	−0.0480	−0.0627	−0.0697	−0.0727
$P(OH_2)^+$	$^3A''$	−0.0683	−0.0423	−0.0538	−0.0569	−0.0553
	$^1A_1$	−0.0747	−0.0588	−0.0647	−0.0642	−0.0604
$P(OH_2)_2^+$	^3A	−0.0274	−0.0088	−0.0140	−0.0164	−0.0176
	$^1A_1$	−0.0652	−0.0365	−0.0487	−0.0527	−0.0531
$P(FH)^+$	$^3A''$	−0.0425	−0.0218	−0.0288	−0.0310	−0.0307
	$^1A'$	−0.0487	−0.0281	−0.0349	−0.0364	−0.0379
$P(FH)_2^+$	^3B_g	−0.0204	−0.0064	−0.0103	−0.0112	−0.0107
	^1A	−0.0406	−0.0172	−0.0246	−0.0274	−0.0288
$P(PH_3)^+$	$^3A_2$	−0.0609	−0.0377	−0.0487	−0.0561	−0.0638
	$^1A'$	−0.0829	−0.0515	−0.0630	−0.0690	−0.0782
$P(PH_3)_2^+$	$^3A''$	−0.0111	−0.0045	0.0001	−0.0004	0.0006
		−0.0331	−0.0047	−0.0539	−0.0614	−0.0523
	$^1A_1$	−0.0740	−0.0483	−0.0599	−0.0690	−0.0824
$P(SH_2)^+$	$^3A''$	−0.0514	−0.0223	−0.0337	−0.0417	−0.0501
	$^1A_1$	−0.1175	−0.0956	−0.1058	−0.1073	−0.1079
$P(SH_2)_2^+$	^3B_g	−0.0120	−0.0031	−0.0061	−0.0078	−0.0092
	$^1A_1$	−0.0654	−0.0309	−0.0441	−0.0523	−0.0666
$P(ClH)^+$	$^3A''$	−0.0418	−0.0119	−0.0236	−0.0291	−0.0350
	$^1A'$	−0.0919	−0.0450	−0.0633	−0.0650	−0.0706
$P(ClH)_2^+$	^3A	−0.0103	−0.0011	−0.0039	−0.0049	−0.0052
	^1A	−0.0474	−0.0163	−0.0267	−0.0299	−0.0369

[a]Values taken from ref. 24.

Fig. 6. Plots of the values of P—X distances (*A*), electron density at the P—X bond critical point (*B*), and energy density at the P—X bond critical point (*C*) calculated at B3LYP versus those calculated at MP2. T and S refer to triplet and singlet complexes, respectively, and 1 and 2 to one- and two-ligand complexes. In plot *A*, the data for the anomalous triplet $P(PH_3)_2^+$ have been omitted.

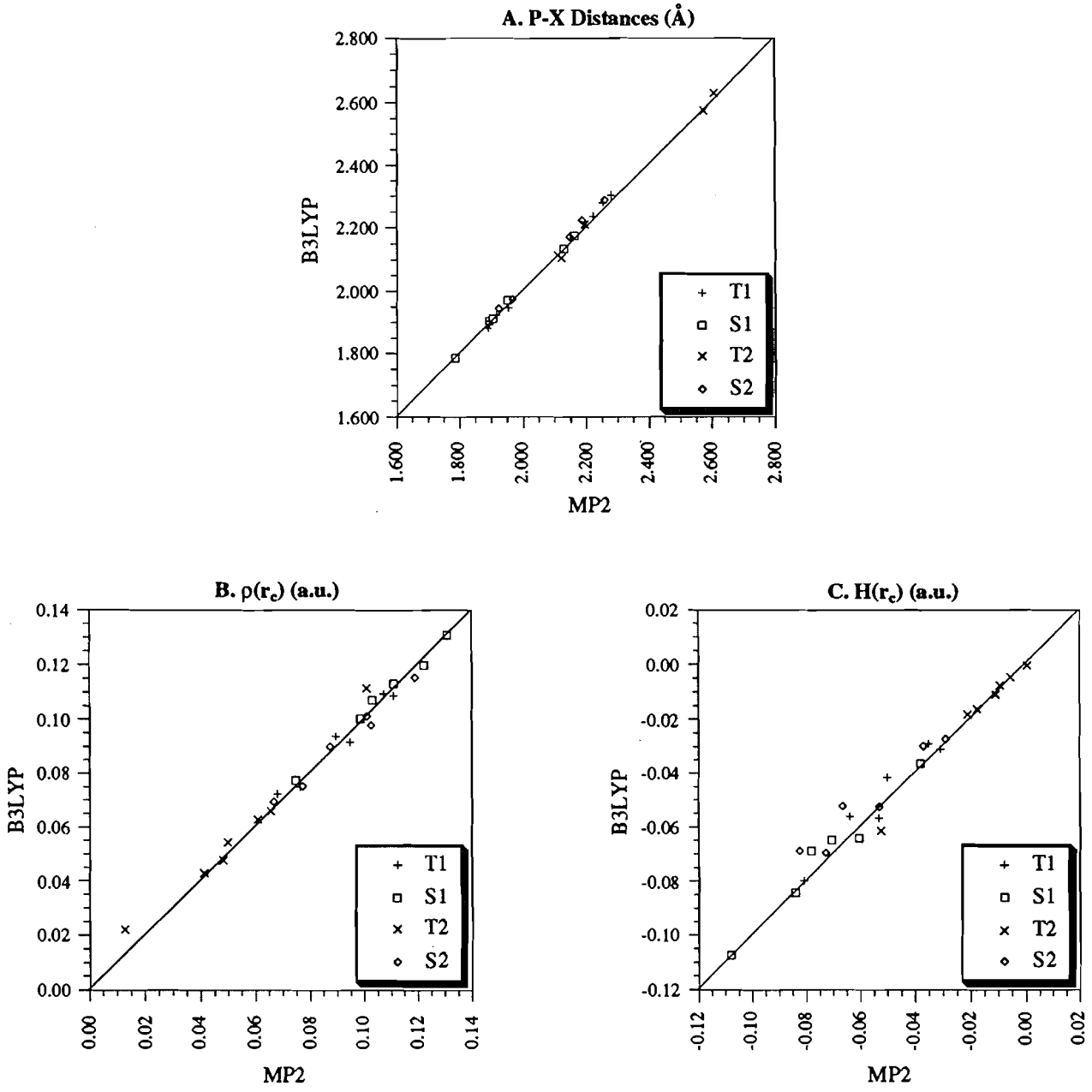

despite the fact that the absolute differences are now diminished. Inclusion of nonlocal gradient corrections to both the exchange and correlation in its BLYP form balances this situation, giving values in quantitative agreement with the MP2 values. The ΔR_{MP2}^{BLYP} is 0.042 Å, without taking into account the anomalous case of triplet $P(PH_3)_2^+$. B3LYP shows a significant improvement of these data and ΔR_{MP2}^{B3} is 0.013 Å. The magnitude of this deviation is maintained quit constant throughout the series, although we are dealing with a great variety of P—X distances and P—X bond types. This can be observed from inspection Figure 6*A*, in which R_{MP2} are plotted versus R_{B3} values. A good fit is obtained for any kind of complex, whether triplet or singlet, or one- or two-ligand complexes. It should also be mentioned that, in general, there is a tendency for the BLYP and B3LYP methods to describe slightly longer bonds than do MP2 methods.

As mentioned, triplet $P(PH_3)_2^+$ constitutes a special case. Its geometries calculated at the different levels of theory can be found in Fig. 5. Contrary to the findings described above, DFT an MP2 describe structures with substantial differences (see Fig. 5). As well, each functional shows different symmetries, except BLYP and B3LYP, which show similar structures. Thus, at the MP2 level of theory (Fig. 5*a*), triplet $P(PH_3)_2^+$ is a linear complex with one ligand strongly bound to the phosphorus, while the other lies at a much greater distance. Instead of that, SVWN describes an angular structure

Fig. 7. The top two charts depicted plots of the dissociation energies calculated at the B3LYP versus those calculated at MP2 (*A*) and G2 levels of theory (*B*). T and S refer to triplet and singlet complexes, respectively, and 1 and 2 to one- and two-ligand complexes. In the bottom two charts, plots of the triplet–singlet gap for B3LYP versus MP2 (*C*) and G2 (*D*) values can be found for phosphorus cation (P^+), one-ligand clusters (One), and two ligand clusters (Two).

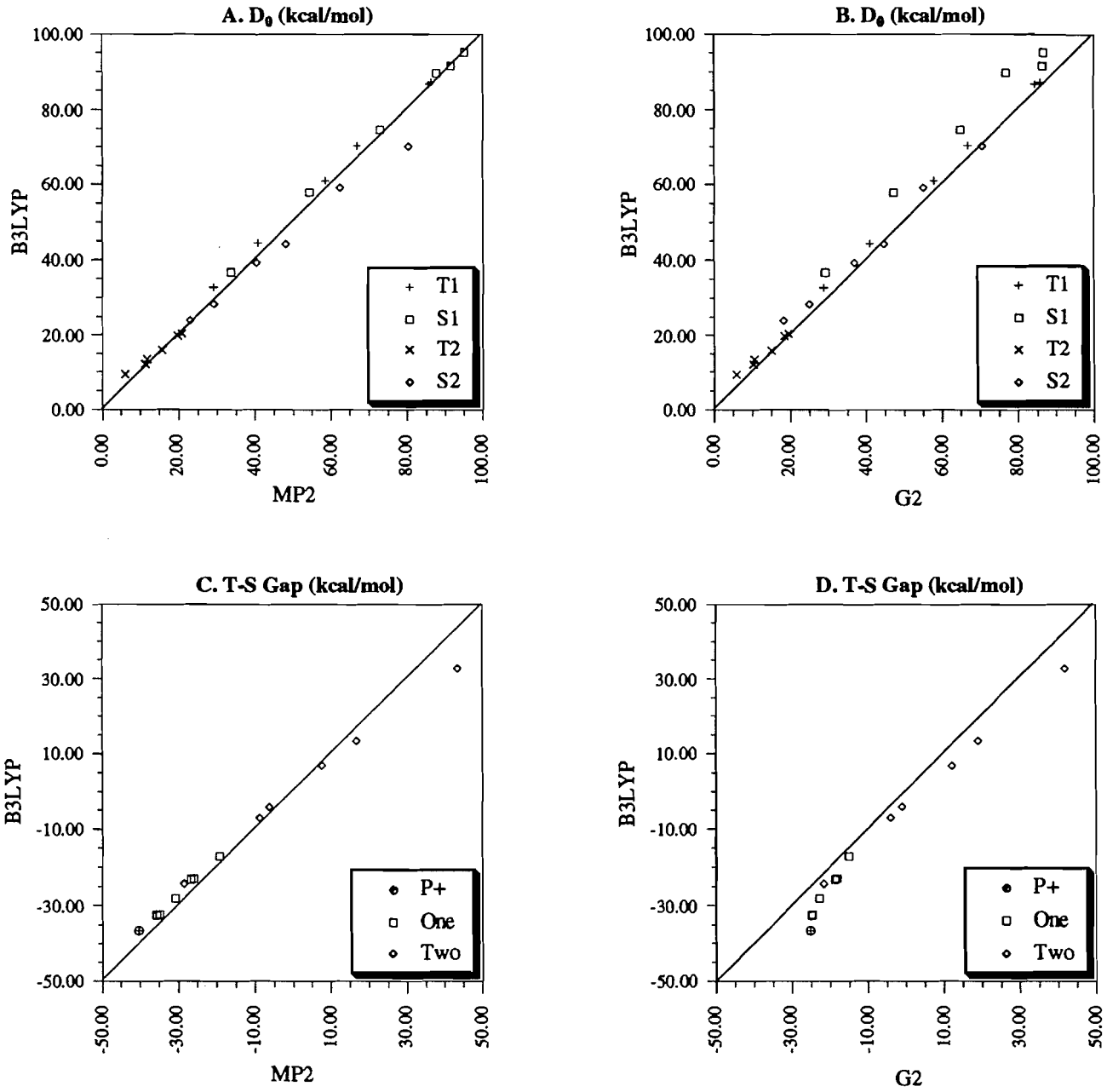

with unequivalent ligands (Fig. 5*b*), but the difference in ion–ligand distance has now decreased to a large extent. BVWN methods describe a linear complex, but with both ligands similarly linked to phosphorus (Fig. 5*c*). BLYP and B3LYP structures are angular with an angle close to 100°. However, as in MP2, one ligand is strongly bound to phosphorus, while the other lies at much longer distances, describing a similar kind of complex for the three methods despite the large difference in the PPP angle.

In summary, DFT geometries show excellent agreement with MP2 ones, when the proper nonlocal gradient corrections are used. Our results for B3LYP show similar values to those for MP2. Triplet $P(PH_3)_2^+$ constitutes the only exception, although a similar kind of complex is described by the BLYP, B3LYP, and MP2 methods.

3.2 Dissociation energies

The dissociation energies calculated with the SVWN, BVWN, BLYP, and B3LYP functionals and the MP2 and G2 methods, along with the QCI energy corrections involved in the G2 method can be found in Table 1. Plots of the B3LYP dis-

sociation energies versus their corresponding MP2 and G2 values are shown in Figs. 7*a* and 7*b*, respectively. Inspection of Table 1 reveals that the SVWN dissociation energies are much larger than their corresponding accurate G2 values. Allowing for gradient corrections in the exchange functional only (BVWN functional) weakens the ion–molecule bonds, hence the calculated D_0 values are now lower than those obtained at the G2 level of theory. Nevertheless, when gradient corrections are implemented for both the exchange and electron correlation functionals (BLYP and B3LYP) the dissociation energies show better agreement with G2 values. In particular, it is worth noting that the average deviation of the B3LYP D_0's with respect to those for MP2 is only 2.17 kcal/mol. However, the average deviation of the B3LYP dissociation energies with respect to the G2 ones is worse, $\Delta D_0^{B3}{}_{G2} = 4.30$ kcal/mol, with the general tendency of the B3LYP to overestimate the G2 dissociation energies although this is strongly dependent on the spin multiplicity and the number of ligands of the cluster. Thus, B3LYP D_0's for the triplets and two-ligand complexes are closer to their corresponding G2 values than singlets and one-ligand complexes, respectively. Remarkably, the same observation is also true for the comparison between the MP2 and G2 dissociation energies. This fact points to the QCI energy corrections as the main source of discrepancies between the MP2, and consequently the B3LYP, and the G2 dissociation energies, for the G2 empirical energy corrections cancel exactly between the two terms of the left-hand side of eq. [2]. Indeed, if both the MP2 and B3LYP dissociation energies are added to the QCI energy correction values of the G2 method, we obtain dissociation energies that lie within 1.5 kcal/mol error bar with respect to the G2 values, for both singlet and triplet complexes, irrespective of whether they have one or two ligands. Recall that we have used the largest G2 basis set, namely the 6-11+G(3df,2p), for the calculation of the dissociation energies within the density functional theory. QCI energy corrections to the total energy of the ions studied in this paper are collected in Table 6.

With the previous comments in mind, we will now discuss each kind of complex (one- and two-ligand, triplet and singlet) separately. Both the quantitative agreement and qualitative common patterns among the various methods used to evaluate the dissociation energy will now be analyzed.

3.2.1 Triplet one-ligand complexes

Let us comment first on the agreement between the MP2 and G2 methods. For triplet one-ligand complexes, MP2 and G2 values match each other reasonably well. Even for phosphine, the worst case, the difference is 1.51 kcal/mol, and for any of the other ligands is less than 1 kcal/mol. Hence, ΔD_{G2}^{MP2} is small, namely, 0.58 kcal/mol. Taking into account that G2 has been proven to yield values in accordance with experimental data by 2 kcal/mol for many chemical systems, we can conclude that MP2 seems to describe these systems properly. This good concordance can be easily understood bearing in mind the comments outlined above. Thus, QCI corrections to the D_0's are small (see Table 1), namely, less than 0.5 kcal/mol in all cases, and consequently a good agreement between MP2 and G2 should be expected.

B3LYP fits G2 data worse than does MP2, with ΔD_{G2}^{B3} 3.03 kcal/mol and ΔD_{MP2}^{B3} 2.51 kcal/mol. However, these results should be regarded as reasonably good matching, since discrepancies with respect to G2 values are always maintained below 4 kcal/mol and the same trends are reproduced by B3LYP and G2 methods for the ligand dependency. The deviation with respect to G2 values increases as we move to the right within each row in the periodic table. In that sense, the best agreement is found for XH_3 systems, and the worst for XH. It should also be taken into account that for these complexes BLYP produces results of similar accuracy to B3LYP and that, despite the bad quantitative results of the SVWN and BVWN functionals, they show the same trends for ligand dependency as the other methods.

Table 6. QCI corrections[a] to the total energy, in millihartrees.

Species		ΔE^{QCI}
P^+	^3P	−1.630
P^+	^1D	−14.399
$P(NH_3)^+$	$^3A_2$	−2.329
	$^1A'$	−9.025
$P(NH_3)_2^+$	$^3A_{2g}$	−1.399
	$^1A_1$	−1.694
$P(OH_2)^+$	$^3A''$	−1.712
	$^1A_1$	−4.054
$P(OH_2)_2^+$	^3A	−0.232
	$^1A_1$	−0.659
$P(FH)^+$	$^3A''$	−1.067
	$^1A'$	−7.636
$P(FH)_2^+$	^3B_g	+0.353
	^1A	−0.684
$P(PH_3)^+$	$^3A_2$	−3.558
	$^1A'$	−7.395
$P(PH_3)_2^+$	$^3A''$	−5.013
	$^1A_1$	−3.735
$P(SH_2)^+$	$^3A''$	−3.364
	$^1A_1$	−4.099
$P(SH_2)_2^+$	^3B_g	−3.648
	$^1A_1$	−3.774
$P(ClH)^+$	$^3A''$	−2.697
	$^1A'$	−6.149
$P(ClH)_2^+$	^3A	−2.599
	^1A	−3.162

[a]Values taken from ref. 24.

3.2.2 Singlet one-ligand complexes

As mentioned earlier, the dissociation energies of singlet states do not compare as well with the G2 ones as those of triplets. There is a marked tendency for both MP2 and B3LYP methods to overbind the ion–molecule complexes with respect to the G2 level of theory, hence ΔD_{G2}^{MP2} and ΔD_{G2}^{B3} are significantly larger, namely, 7.41 and 9.03 kcal/mol, respectively, for the singlet one-ligand complexes. The worst fit to G2 data within each row is observed for XH_2 ligands, being even larger than 10 kcal/mol for SH_2 in both methods. Despite this augmented discrepancy, the accord between MP2 and B3LYP remains, leading to a similar value of the ΔD_{MP2}^{B3} as for the triplets, namely, 1.73 kcal/mol. A substantial part of the enhanced deviation between MP2 and G2 data origi-

nates in the augmented QCI corrections, which are now quite important in contrast with the case for triplet states. These corrections, see Table 1, are largest for XH_2 ligands, 6.50 and 7.19 kcal/mol for OH_2 and SH_2, respectively. This discrepancy is also observed for the B3LYP method, leading to similar trends in the G2–B3LYP discrepancies as in MP2.

In spite of these enhanced deviations, both MP2 and B3LYP reproduce the same trends as the G2 method. In this sense, binding energies increase for all ligands when we go from triplets to singlets, decrease as we go to the right through the periodic table, and larger binding energies are found for second-row hydrides than for first-row ones. However, these trends are not always reproduced by the other functionals. For instance, SVWN, BVWN, and BLYP produce larger binding energies for SH_2 than for PH_3, and for some complexes SVWN, BVWN, and BLYP show larger binding energies for the triplets than for the singlets (see Table 2). Discrepancies also appear if we compare the relative strength of the P—X bond of first-row hydrides with that of the analogous second-row ones. B3LYP, MP2, and G2 binding energies for second-row ligands are larger than for the first-row ones, even though the G2 difference is very low for XH_3 ligands. However, this is not always true for SVWN, BVWN, and BLYP functionals. These facts suggest that B3LYP is the only functional that reproduces the trends of the G2 method, despite the significant overbinding mentioned.

The anomalous results obtained for the singlet $P(OH_2)^+$ should also be mentioned. In this case, the largest binding energy among DFT methods is obtained for the B3LYP functional, namely 74.63 kcal/mol, which compares fairly well with that obtained at the MP2 level of theory, 72.89 kcal/mol, but not so well with the 64.84 kcal/mol value of the G2 method. Surprisingly, the best fit to the G2 value is obtained for the SVWN functional, 61.33 kcal/mol.

3.2.3 Triplet two-ligand complexes

At the G2 level of theory, we can observe a large decrease of D_0's when a second ligand is attached to the phosphorus ion in its triplet state. In fact, the lowest D_0's for all ligands are obtained for these complexes. This lowering was related to a marked lowering of covalency, which even changes the bonding character of the covalent bonds, and it was larger as the covalency of the P—X bond increased. This lowering is also reproduced by all functionals and MP2 theory. A fairly good agreement is found between MP2 and G2; differences are always maintained below 1.4 kcal/mol, so ΔD_{G2}^{MP2} is very small, namely 0.94 kcal/mol. This good agreement should be expected since QCI corrections to D_0's are not significant for triplet two-ligand complexes, see Table 1. Apart from the triplet $P(PH_3)_2^+$, B3LYP shows good concordance with MP2 and G2 results, showing a ΔD_{G2}^{MP2} of only 1.81 kcal/mol. The worst fit is observed for the triplet $P(PH_3)_2^+$; a dissociation energy of 5.80 kcal/mol is obtained for G2 whereas B3LYP predicts 9.32 kcal/mol. We recall that B3LYP and MP2 geometries were quite different in this case. Therefore, it should expected that this disagreement would also be present in the D_0. Along with the good B3LYP–MP2–G2 agreement, the trends for the ligand dependencies of the D_0 are equally well reproduced by these three methods.

With respect to the other functionals, it should be mentioned that SVWN and BVWN show discrepancies in the variation of D_0 with the ligand, with respect to G2. For instance, whereas water is bound slightly more strongly to phosphorus than is ammonia, by 1.07 kcal/mol with G2, ammonia is bound more strongly to phosphorus with the SVWN and BVWN functionals, by 0.04 and 0.14 kcal/mol, respectively. For first-row hydrides, the trends are similar to those described before, thus, SVWN D_0's are larger than the G2 values, BVWN smaller, and BLYP, B3LYP, and MP2 lie in between. However, quite surprisingly, for second-row hydrides the best DFT fit to G2 values is obtained with BVWN, in some cases even better than with MP2. Curiously, for triplet $P(PH_3)_2^+$ a similar value to that with G2 is obtained with BVWN, despite the great disagreement between MP2 and BVWN geometries.

3.2.4 Singlet two-ligand complexes

When we add a second ligand to the singlet one-ligand complexes, the lowering of the dissociation energies is not so pronounced as in the triplet states at the G2 level of theory. Exploration of the bonding properties of the electron density reveals that the loss of covalent character is not so pronounced as in the triplet state, so the nature of the covalent bonds remains unchanged. Nevertheless, binding energies were found to be very similar to those of the one-ligand complexes, and the trends in ligand stability were similar to them, in contrast with the behaviour of the triplets. However, this trend is not equally reproduced by the various methods. Once again, B3LYP, MP2, and G2 show similar patterns; thus, D_0 decreases are predicted as we move to the right through the periodic table and larger binding energies are predicted for second-row ligands than for first-row ones. The other functionals, SVWN, BVWN, and BLYP, present some exceptions to these tendencies. As in the singlet one-ligand complexes, OH_2 is the anomalous case of the first-row hydrides, but now by the opposite effect. These three functionals give too large binding energies compared with G2, even the BVWN functional that often gives smaller ones. SH_2 is also poorly reproduced with SVWN and BVWN functionals. Probably, these discrepancies were transferred from the poor results for singlet PXH_2^+ complexes.

With respect to the quantitative agreement, MP2 and G2 show a worse agreement than for the triplets, MP2 tending to overbind the cluster so that ΔD_{G2}^{MP2} is increased to 5.53 kcal/mol. Phosphine is the worst case and the disagreement is close to 10 kcal/mol. However, these differences are sensibly smaller than for the singlet one-ligand complexes and, in contrast, PXH_2^+ complexes now show the best MP2–G2 fit within each row. Here again, the MP2–G2 discrepancies match the trends of the QCI corrections. Thus, QCI corrections represent a more significant contribution for singlets than for triplets, but lower than singlet one-ligand complexes. Also, they are minima for $P(XH_2)_2$ systems within each row.

Again, B3LYP is the functional that best fits G2 values, even better than that of the MP2 method, so ΔD_{G2}^{B3} is now substantially smaller, namely, 2.70 kcal/mol. Its discrepancies with respect to the G2 data follow a similar trend as the MP2 method, except for phosphine, for which good agreement is found between the B3LYP and G2 methods.

3.3 Triplet-singlet gap

The energy difference between high and low spin states of an ion and the relaxation of this triplet–singlet gap, as cluster growths, measures the strength of the ligand field and its dependence upon the nature of the ligands and the size of the cluster. The two lowest spin states of P^+ are the triplet and the singlet, with the singlet lying 25.20 kcal/mol above the triplet at the G2 level of theory. When one ligand is attached to the phosphorus, stabilization of the singlets is observed although it is not strong enough to allow the singlets to become the ground state. This stabilization is mainly due to the ability of the ligands to interact with the empty $3p$ orbital of the singlet phosphorus cation, which lies perpendicular to the bond direction, and this orbital is occupied by one unpaired electron in the triplet ground state.

First, we will briefly discuss the G2 qualitative trends. For one-ligand complexes, the relaxation of the triplet–singlet gap is maximum for the XH_2 systems (6.93 kcal/mol for water and 10.11 kcal/mol for SH_2) because they have an additional lone pair for π donation to the empty $3p$ orbital of P^+. On the other hand, XH_3 ligands, which have a single lone pair, and very hard bases like FH, have triplet–singlet gaps similar to that of the free P^+. Also, it is observed that relaxation of the triplet–singlet gap is larger for second-row hydrides than for the corresponding first-row ones, an indication of the greater capability of the former to delocalize their electronic charge. For two-ligand complexes, the π donation disappears, since now both the formal empty $3p$ orbitals of the singlet P^+ have their own donating ligand, and the relaxation is totally dominated by the σ donation of the ligands. Therefore, for the two-ligand complexes, the relaxation is larger as we go to the left through the periodic table, being large enough for NH_3, PH_3, and SH_2 two-ligand complexes to allow for singlet ground states, by 12.03, 41.81, and 18.87 kcal/mol, respectively, at the G2 level of theory. Also, for the OH_2 complex, the singlet and triplet states are nearly degenerate, the former being above the latter by only 1.03 kcal/mol.

Values of the triplet–singlet gap (Δ_{t-s}) for P^+ and the 12 ion–molecule complexes calculated at the SVWN, BVWN, BLYP, B3LYP, MP2, and G2 levels of theory are given in Table 2. The plots Δ_{t-s}^{B3} versus Δ_{t-s}^{MP2} and Δ_{t-s}^{G2} are shown in Figs. 7*C* and 7*D*, respectively. As evidence in these figures, P^+ and the one-ligand complexes have a worse B3LYP-G2 agreement than the two-ligand complexes, while the B3LYP–MP2 fit is remarkably good. We will now analyze these two cases separately.

For P^+ and one-ligand complexes, DFT and MP2 methods significantly overestimates Δ_{t-s} with respect to G2 values. The MP2 overestimation can be partially understood by considering both empirical corrections to the energy and QCI corrections made in the G2 method. Empirical corrections are different for singlets and for triplets, since they have different numbers of electron pairs (α and β electrons). These empirical corrections suggest a 2.89 kcal/mol stabilization of the singlets with respect to the triplets and it is constant for P^+ and for any cluster. The origin of the QCI corrections to Δ_{t-s} is the enhanced relaxation of the singlets compared with the triplets when these corrections are accomplished. In that way, a method such as MP2, which does not take them into account, tends to understabilize the singlets, overestimating the triplet–singlet gap. Values of Δ_{t-s}^{QCI} can be found in Table 2. Although they do not account for all the overestimation, they are significant for P^+ and one-ligand complexes, Δ_{t-s}^{QCI} are not homogeneously maintained through all the clusters. Within each row, PXH_2 has the lowest Δ_{t-s}^{QCI}, with PXH_3 and PXH showing very similar ones. Besides, Δ_{t-s}^{QCI} are lowered when we go from first-row hydrides to second-row ones. It should be noted that MP2–G2 differences in Δ_{t-s} follow these trends.

As we can see in Fig. 7*C*, B3LYP presents an analogous behaviour. B3LYP tends to give Δ_{t-s} than MP2, rendering results closer to the G2 values. Nevertheless, B3LYP markedly overestimates the Δ_{t-s}, see Fig. 7*D*. The trends in B3LYP–G2 discrepancies are analogous to those of the MP2 method, suggesting here again that B3LYP and MP2 in some way possess similar shortcomings. Despite these failures, the qualitative trends mentioned before are well reproduced by both methods, and we conclude that similar conclusions could be reached from B3LYP, MP2, and G2 data. In general, the other functionals, SVWN, BVWN, and BLYP, do not only tend to overestimate the triplet–singlet gap, but sometimes they do not reproduce the same qualitative trends of the Δ_{t-s}^{G2}. For instance, the poor results for the $P(OH_2)^+$ system should be noted, or the larger triplet–singlet gap obtained for $P(PH_3)^+$ with respect to that of the free P^+.

For two-ligand complexes, we can see that B3LYP and MP2 agreement with G2 improves, see Table 2 and Figs. 7*C* and 7*D*. Recall that QCI corrections to the energy for two-ligand complexes were similar for triplets and for singlets, so that the Δ_{t-s}^{QCI}'s are negligible, as can be seen in Table 2. In this way, a lower MP2–G2 discrepancy is observed. Also, B3LYP shows the best fit to G2 values (Fig. 7*D*), the only exception being $P(PH_3)_2^+$. For his complex, we obtain a value of 32.80 kcal/mol for Δ_{t-s}^{B3}, whereas 43.45 and 41.81 kcal/mol are obtained with the MP2 and G2 methods, respectively. These discrepancies have to be partially attributed to the large differences in the description of triplet $P(PH_3)_2^+$ made by B3LYP and MP2. We recall that triplet $P(PH_3)_2^+$ is almost twice more stable in B3LYP theory than in MP2 or G2, and different geometries were encountered for it using the B3LYP and MP2 methods. Apart from this disagreement, B3LYP and MP2 reproduce properly the qualitative trends in Δ_{t-s}^{G2} mentioned before. The same is not true for the other functionals; for instance, SVWN stabilizes the singlets too much compared to G2, and for $P(OH_2)_2^+$ and $P(ClH_2)_2^+$ we get singlet ground states instead of the triplet predicted by the G2 method. The inclusion of the gradient corrections only to the exchange, the BVWN functional, favors the triplet, and for $P(NH_3)_2^+$ and $P(SH_2)_2^+$ we get a triplet ground state, instead of the G2 singlet. BLYP gives the same ground state as G2 for any ligand but in general shows a worse fit to G2 data than B3LYP.

3.4 Bonding properties: $\rho(r_c)$, $\nabla^2\rho(r_c)$, and $H(r_c)$

Properties of the bond critical points such as the electron density ($\rho(r_c)$), the Laplacian ($\nabla^2\rho(r_c)$), and the energy density ($H(r_c)$) are usually employed for characterization of the binding mechanism in a great variety of systems. A large value of $\rho(r_c)$ with negative values of $\nabla^2\rho(r_c)$ and $H(r_c)$ are typical features of covalent interactions, whereas smaller

$\rho(r_c)$ and positive values of $\nabla^2\rho(r_c)$ and $H(r_c)$ are common to electrostatic interactions. In previous papers, we used these properties to rationalize the bonding of various phosphorus clusters. We found that $\rho(r_c)$ and $H(r_c)$ were useful for these purposes, whereas analysis of $\nabla^2\rho(r)$ could only lead to some inconsistencies. Looking at $\rho(r_c)$ and $H(r_c)$, it was stated that P^+ behaves as a soft acid for one-ligand complexes and prefers to be bound to the softest bases, for which electronic effects are more favored, than to hard ones (FH), for which electrostatics interaction dominates the bond. Larger covalency, which accounts for the enhanced dissociation energies, was characterized for singlets than for triplets, as denoted by the larger $\rho(r_c)$ and more negative $H(r_c)$ found for the former. For two-ligand complexes, great differences were encountered for triplet and singlets. A huge decrease of $\rho(r_c)$ and an absolute value of $H(r_c)$ was observed for the triplets, denoting the large decrease in covalency occurring for these complexes. The loss of covalency was so high that changes in the shape of the Laplacian could be observed for the most covalent systems. This was the origin of the great lowering of the D_0 values mentioned earlier. Singlet two-ligand complexes did not show such pronounced lowering of $\rho(r_c)$ and the $H(r_c)$ in absolute value, denoting that the binding keeps a great deal of its covalent character.

It would be desirable to know how DFT fits these values, and whether or not it provides reliable information, reproducing the trends commented upon above. Values of $\rho(r_c)$, $\nabla^2\rho(r_c)$, and $H(r_c)$ calculated by the SVWN, BVWN, BLYP, B3LYP, and MP2 methods are depicted in Tables 3, 4, and 5, respectively. Also, we have plotted $\rho(r_c)$ and $H(r_c)$ values of B3LYP versus those of MP2, Figs. 6*B* and 6*C*, respectively. From inspection of Tables 3 and 5, it is clear that SVWN tends to assign greater covalency than MP2, whereas the inclusion of non-gradient corrections to the exchange, BVWN functional, removes electron density form the internuclear region, resulting in lower values of $\rho(r_c)$ and less negative values of $H(r_c)$ than those of MP2. This is the origin of the enhanced and lowered bond strength of the SVWN and BVWN methods, respectively. BLYP and B3LYP lead to intermediate values of $\rho(r_c)$ and $H(r_c)$, closer to the MP2 values. Generally, B3LYP shows a better fit to MP2 values than does BLYP. It can be observed from Fig. 6*B* that this fit is very good, resulting in a small $\Delta\rho^{B3}_{MP2}$, namely, 0.0029. According to this good agreement, the qualitative trends in $\rho(r_c)$ are properly reproduced by the B3LYP method, therefore the same conclusions can be drawn from them. $H(r_c)$ shows a bit worse fit (see Fig. 6*C*) with a ΔH^{B3}_{MP2} of 0.0042. The worst cases are the singlet $P(PH_3)_2^+$ and singlet $P(SH_2)_2^+$, showing sensibly lower absolute values than MP2. Despite this worse fit, the qualitative trends in $H(r_c)$ are also reproduced, so that similar conclusions could also be extracted from these data.

On the contrary, B3LYP $\nabla^2\rho(r)$ has a very bad fit; the mean deviation between B3LYP and MP2 data is 0.0217 and, moreover, it is not the functional with a best fit to the MP2 values. SVWN now shows the best fit, with a mean deviation of 0.0189. Its qualitative trends are similar to those shown by MP2 and, in this sense, the same incoherences, which did not allow us to consider the value of $\nabla^2\rho(r)$ as a reliable sole magnitude to characterize the binding mechanism, are observed. Positive values of the Laplacian are encountered for most of the first-row hydride clusters, whereas values of $\rho(r_c)$, $H(r_c)$, and D_0 denote that some covalency is occurring for these bonds.

4. Concluding remarks

Among the functionals studied here, SVWN, BVWN, BLYP, and B3LYP, the B3LYP has been proven to yield the best fit and overall coherence with the MP2 dissociation energies, phosphorus–ligand distances, triplet–singlet energy gap, and local bond properties, such as the electron and the energy densities at the bond critical points. The local spin density approximation, in its SVWN form, tends to describe too strong bonds. The inclusion of nonlocal gradient corrections solely to the exchange weakens the bonds too much, even though lower absolute deviations for various properties with respect to the accurate G2 method are encountered. The inclusion of nonlocal gradient corrections to both exchange and correlation in its BLYP form balances this situation and much better values are obtained for the above-mentioned properties. However, some incoherent results are obtained, especially for systems containing XH_2 ligands, which disagree with the qualitative trends determined at the G2 level of theory. B3LYP improves these results and removes these incoherences, giving a good fit with MP2 data for R and $\rho(r_c)$ and, except for the $P(PH_3)_2^+$ complex, also for D_0 and Δ_{t-s}. This MP2–B3LYP fit is a bit worse for $H(r_c)$, although overall qualitative agreement remains, and it is fairly bad for $\nabla^2\rho(r)$. For the latter property, the lower mean deviation with MP2 is obtained for the SVWN functional.

In general, the deviations of B3LYP and MP2 methods from G2 dissociation energies and the triplet–singlet gap are similar. Thus, while triplets show quite good accord for D_0, significant overbinding, which is larger for one-ligand than for two-ligand complexes, is obtained for the singlets. The overbinding is largest for XH_2 ligands in one-ligand complexes, but smallest for the same ligands in two-ligand complexes. For MP2, the origin of such deviations can be understood as the result of the QCI relaxation. Our results show that B3LYP bears in some way this deficiency of the MP2 method. Also, we could observe an overestimation of the triplet–singlet gap, favoring the former spin state, of both methods, again partially due to the lack of QCI relaxation. QCI corrections can be considered important only when the occupation of the open shell of the singlet phosphorus changes sensibly, adding a new ligand. This is the case for small clusters, when we add one or two ligands. For bigger clusters, we consider that these effects will be negligible and so, taking into account our results, we can conclude that B3LYP is expected to yield accurate characterizations of the bigger clusters.

5. Acknowledgment

This research has been supported by the University of the Basque Country (Euskal Herriko Unibertsitatea), Grant No. UPV 203.215-EB247/95, and by the Basque Provincial Government of Guipuzcoa (Gipuzkoako Foru Aldundia); one of us (X. Lopez) wishes to thank the Basque Government (Eusko Jaurlaritza) for a grant.

References

1. A.W. Castleman, Jr. and R.G. Keesee. Chem. Rev. **86**, 589 (1986).

2. R.G. Keesee and A.W. Castleman, Jr. J. Phys. Chem. Ref. Data, **15**, 1011 (1986).
3. M. Rosi and C.W. Bauschlicher, Jr. J. Chem. Phys. **90**, 7264 (1989).
4. M. Rosi and C.W. Bauschlicher, Jr. J. Chem. Phys. **92**, 1876 (1990).
5. S.R. Langhoff, C.W. Bauschlicher, Jr., H. Partridge, and M. Sodupe. J. Phys. Chem. **95**, 10677 (1991).
6. J. Kim, S. Lee, S.J. Cho, B.J. Mhin, and K.S. Kim. J. Chem. Phys. **102**, 839 (1995).
7. P. Hohenberg and W. Kohn. Phys. Rev. Sect. B, **136**, 864 (1964).
8. W. Kohn, and L.J. Sham. Phys. Rev. [Sect.] A, **140**, 1133 (1965).
9. R.G. Parr and W. Yang. *In* Density functional theory of atoms and molecules. *Edited by* Oxford University Press, New York. 1989.
10. J.K. Labanowski and J. Andzelm (*Editors*). Density functional methods in chemistry. Springer, Heidelberg. 1991.
11. T. Ziegler. Chem. Rev. **91**, 651 (1991); and references therein.
12. C. Sosa, C. Lee, G. Fitzgerald, and R.A. Eades. Chem. Phys. Lett. **211**, 265 (1993).
13. J. Andzelm and E. Wimmer. J. Chem. Phys. **96**, 1280 (1992).
14. J. Andzelm, C. Sosa, and R.A. Eades. J. Phys. Chem. **97**, 4664 (1993).
15. F. Sim, A. St.-Amant, I. Papai, and D.R. Salahub. J. Am. Chem. Soc. **114**, 4391 (1992).
16. T. Chiavassa, P. Roubin, L. Pizzala, P. Verlaque, A. Alouche, and F. Marcinelly. J. Phys. Chem. **96**, 10659 (1992).
17. K. Kim and K.D. Jordan. J. Phys. Chem. **98**, 10089 (1994).
18. Z. Latajka and Y. Bouteiller. J. Chem. Phys. **101**, 9793 (1994).
19. R.V. Stanton and K.M. Merz, Jr. J. Chem. Phys. **101**, 6658 (1994).
20. D. Wei and D.R. Salahub. J. Chem. Phys. **101**, 7633 (1994).
21. A. Rica and Bauschlicher, Jr. J. Phys. Chem. **98**, 12899 (1994).
22. X. Lopez, J.M. Ugalde, F.P. Cossío, B. Lecea, A. Largo, and C. Barrientos. J. Phys. Chem. **97**, 9337 (1993).
23. X. Lopez, J.M. Ugalde, F.P. Cossío, B. Lecea, A. Largo, and C. Barrietos. J. Phys. Chem. **98**, 3148 (1994).
24. X. Lopez, A. Irigoras, J.M. Ugalde, and F.P. Cossío. J. Am. Chem. Soc. **116**, 10670 (1994).
25. J.A. Pople, M. Head-Gordon, D.J. Fox, K. Raghavachari, and L.A. Curtiss. J. Chem. Phys. **90**, 5622 (1989).
26. L.A. Curtiss, C. Jones, G.W. Trucks, K. Raghavachari, and J.A. Pople. J. Chem. Phys. **93**, 2537 (1990).
27. L.A. Curtiss, K. Raghavachari, G.W. Trucks, and J.A. Pople. J. Chem. Phys. **94**, 7221 (1991).
28. J.C. Slater. *In* Quantum theory of molecules and solids. Vol. 4. The self-consistent field for molecules and solids. McGraw-Hill, New York. 1974.
29. S.H. Vosko, L. Wilk, and M. Nusair. Can. J. Phys. **58**, 1200 (1980).
30. A.D. Becke. Phys. Rev. A: Gen. Phys. **38**, 3098 (1988).
31. C. Lee, W. Yang, and R.G. Parr. Phys. Rev. B: Condens. Matter, **37**, 785 (1980).
32. A.D. Becke. J. Chem. Phys. **98**, 5648 (1993).
33. M.J. Frisch, G.W. Trucks, M. Head-Gordon, P.M.W. Gill, M.W. Wong, J.B. Forseman, B.G. Johnson, H.B. Schlegel, M.A. Robb, E.S. Repogle, R. Gomperts, J.L. Andres, K. Raghavachari, J.S. Binkley, C. Gonzales, R.L. Martin, D.J. Fox, D.J. Defrees, J. Baker, J.J.P. Stewart, and J.A. Pople. Gaussian 92/DFT, Revision F.4. Gaussian Inc., Pittsburgh, Pa. 1992.
34. W.J. Hehre, L. Radom, P.v.R. Schleyer, and J.A. Pople. *In* Ab-initio molecular orbital theory. Wiley Interscience, New York. 1986, and references within.
35. R.F.W. Bader. *In* Atoms in molecules. A quantum theory. Clarendon Press, Oxford. 1990.
36. D. Cremer and E. Kraka. Croat. Chem. Acta, **57**, 1259 (1984).
37. E. Kraka and D. Cremer. *In* Theoretical models of chemical bonding. Vol. 2. The concept of the chemical bond. *Edited by* Z.B. Maksic. Springer Verlag, Berlin. 1990. p. 453.
38. R.J. Boyd and J.M. Ugalde. *In* Computational chemistry. Part A. *Edited by* S. Fraga. Elsevier, Amsterdam. 1992. pp. 273–297.
39. F.W. Biegler-Konig, R.F.W. Bader, and T.H. Tang. J. Comput. Chem. **27**, 1924 (1980).

Molecular charge density analysis

Juergen Hinze, F. Biegler-Konig, and A.G. Lowe

Abstract: It is proposed to analyse the first-order reduced density matrix of a molecular wave function in terms of the first-order reduced density matrices of different states of the constituent atoms. With this an unambiguous partitioning of the molecular charge distribution in terms of the atomic charge distributions is obtained. Simple practical formulae are derived, such that in many ab initio molecular wave function calculations the analysis proposed can be carried out routinely. The results obtained should be useful for the interpretation of molecular wave functions in terms of their atomic constituents, as well as for the determination of atomic form factors to be used in X-ray molecular structure determination. Some simple examples are given, and the results obtained are compared with those obtained using other methods of analysis.

Key words: charge density, density matrix, goodness-of-fit, correlation coefficient, standard deviation.

Résumé : On s'est proposé d'analyser la matrice de densité réduite du premier ordre d'une fonction d'onde moléculaire en termes de matrices de densité réduite du premier ordre de différents états des atomes qui la constituent. De cette façon, on a pu obtenir une partition non ambiguë de la distribution de la charge moléculaire en termes des distributions des charges atomiques. On en a dérivé des formules pratiques simples telles que, dans plusieurs calculs ab initio de fonctions d'onde moléculaires, l'analyse proposée peut être effectuée d'une façon routinière. Les résultats obtenus devraient être utiles pour l'interprétation des fonctions d'onde moléculaires en termes de leurs constituants atomiques, ainsi que pour la détermination de facteurs f atomiques à être utilisés dans la détermination des structures moléculaires par les rayons X. On donne quelques exemples simples et on compare les résultats avec ceux obtenus en utilisant d'autres méthodes d'analyse.

Mots clés : densité de charge, matrice de densité, facteur d'accord, coefficient de corrélation, déviation standard.

[Traduit par la rédaction]

1. Introduction

The analysis of the molecular wave function or the molecular charge density in terms of the corresponding quantities of the constituent atoms has a long history (1–8). The intention is to better understand, on the basis of such an analysis, how much atomic properties predetermine molecular properties and how atomic charges are deformed and modified in the process of molecular formation. In addition, there is the hope of finding criteria for atomic or molecular fragment charge distributions, such that these are transferable and can be used to easily build approximate charge distributions of increasingly larger and more complex molecules. Furthermore, there is the aspiration to derive from the molecular charge distribution information about molecular interactions and reactivity. Foremost in the analysis of the molecular wave function in terms of its atomic contributions ranks the Mulliken population analysis (1) and its variations (9–15) with the aim of achieving a more rational division of the overlap populations. Much insight as well as partial atomic charges can be derived, using these methods; however, they are plagued by the non-uniqueness of the partitioning of the overlap populations. A similar situation obtains in the analysis of the molecular charge density in terms of its atomic contributions (16–22). The use, in these procedures proposed, of spherically averaged atomic "prodensities" makes available significant information; however, it is possible to also determine atomic deformation densities (23, 24). Using these methods requires in general significant extra computational effort, a disadvantage. Also the division of the molecular density into unique atomic regions, being limited by the zero flux surfaces between the atoms (25–30), requires a significant extra computational effort. However, useful chemical insight, which is not always obvious to chemical intuition, has been gained by using this type of analysis of the molecular charge density.

We propose here to analyse the first-order reduced density matrix of the molecule, the diagonal of which is the charge density, in terms of the reduced density matrices of the constituent atoms. We will show that such an analysis is computationally simple in most molecular wave function calculations. The procedure is unique inasmuch as least-squares optimizations are unique, in that they permit a correlation and error analysis of the results obtained. In Sect. 2 we will present a brief definition of the terms used and outline the method proposed. In Sect. 3 we will show the ease with which the required matrix elements can be computed, if a standard basis function method is used to compute the molecular wave function, and in Sect. 4 we will present some

Received December 6, 1995.

This paper is dedicated to Professor Richard F.W. Bader on the occasion of his 65th birthday.

J. Hinze,[1] F. Biegler-König, and A.G. Löwe. Fakultät für Chemie, Universität Bielefeld, 33615 Bielefeld, Germany.

[1] Author to whom correspondence may be addressed. Telephone: 0521-106-2076. Fax: 0521-106-6146. E-mail: juergen@tc1.chemie.uni-bielefeld.de

results obtained. In Sect. 5 we will outline the possibility of a correlation and error analysis of the results and consider the possibility of constructing approximate molecular density matrices of complex molecules, using the corresponding atomic or fragment density matrices.

2. Charge density analysis

Rather than analysing the molecular charge density, $\rho_M(\boldsymbol{r})$, directly, as has been suggested in the past (16–21), we propose to analyse the first-order reduced spatial density matrix, $\rho_M(\boldsymbol{r}',\boldsymbol{r})$, which is defined in terms of the molecular wave function, Ψ_M, for an N particle system as (31, 32):

$$[2.1]\quad \rho_M(\boldsymbol{r}',\boldsymbol{r}) = N\int \mathrm{d}s_1 \int \mathrm{d}\tau_2 \cdots \times \int \tau_N [\Psi_M^{\dagger}(\tau_1',\tau_2,\ldots,\tau_N)\Psi_M(\tau_1,\tau_2,\ldots,\tau_N)]_{s_1'\rightarrow s_1}$$

Here the integration is over the spin variable, s_1, of particle one, and the space-spin variables, $\tau_2,\ldots,\tau_N$, of the remaining particles. The molecular charge density is obtained as the diagonal of the density matrix, i.e.,

$$[2.2]\quad \rho_M(\boldsymbol{r}) = \rho_M(\boldsymbol{r}',\boldsymbol{r})_{\boldsymbol{r}'\rightarrow\boldsymbol{r}}$$

The analysis in terms of the density matrix, rather than the charge density, has the advantage of containing more information, in addition to being simpler, as will be seen below. For the analysis we extremalize the functional

$$[2.3]\quad \chi^2 = \int \mathrm{d}\boldsymbol{r}\left|\rho_M(\boldsymbol{r}',\boldsymbol{r}) - \sum_{AI}\rho_{AI}(\boldsymbol{r}',\boldsymbol{r})w_{AI}\right|^2$$

which represents the absolute value square of the difference between the molecular density matrix and the sum of the density matrices of the constituting atoms A in their different states I, weighted with the as yet unknown coefficients w_{AI}. The dependence on the variable $\boldsymbol{r}'$ disappears in eq. [2.3], because the absolute value of the product of two density matrices means

$$[2.4]\quad |\rho_A(\boldsymbol{r}',\boldsymbol{r})\rho_B(\boldsymbol{r}',\boldsymbol{r})| = \int \mathrm{d}\boldsymbol{r}'\rho_A^{\dagger}(\boldsymbol{r}',\boldsymbol{r})\rho_B(\boldsymbol{r}',\boldsymbol{r})$$

Extremalization of χ^2 with respect to the w_{AI}'s yields the linear set of normal equations

$$[2.5]\quad \boldsymbol{Mw} = \boldsymbol{b}$$

for the determination of the elements w_{AI} of the vector $\boldsymbol{w}$.

The matrix elements to be computed are

$$[2.6]\quad M_{BJ,AI} = \int \mathrm{d}\boldsymbol{r}\int \mathrm{d}\boldsymbol{r}'\rho_{BJ}^{\dagger}(\boldsymbol{r}',\boldsymbol{r})\rho_{AI}(\boldsymbol{r}',\boldsymbol{r})$$

and

$$[2.7]\quad b_{BJ} = \int \mathrm{d}\boldsymbol{r}\int \mathrm{d}\boldsymbol{r}'\rho_{BJ}^{\dagger}(\boldsymbol{r}',\boldsymbol{r})\rho_M(\boldsymbol{r}',\boldsymbol{r})$$

With the auxiliary condition of charge conservation, i.e.,

$$[2.8]\quad \sum_{AI}\int \mathrm{d}\boldsymbol{r}\rho_{AI}(\boldsymbol{r})w_{AI} - N = 0$$

introduced with a Lagrange multiplier λ into the functional to be extremalized, the following somewhat modified linear equation is obtained:

$$[2.9]\quad \begin{pmatrix} \boldsymbol{M} & \boldsymbol{N} \\ \boldsymbol{N}^{\dagger} & 0 \end{pmatrix}\begin{pmatrix} \boldsymbol{w} \\ \lambda \end{pmatrix} = \begin{pmatrix} \boldsymbol{b} \\ N \end{pmatrix}$$

Here the coefficient-matrix $\boldsymbol{M}$ is extended by one row and one column by the vector $\boldsymbol{N}$, the elements of which are given as

$$[2.10]\quad N_{BJ} = \int \mathrm{d}\boldsymbol{r}\rho_{BJ}(\boldsymbol{r})$$

i.e., the number of electrons of the atom B in state J; also ions are admissible. The vector with the elements w_{AI} has as the last element λ, the Lagrange multiplier, and the vector with the elements b_{BJ} has as its last element N, the total number of electrons in the molecule.

3. Computation of the matrix elements

For the computation of the matrix elements, eqs. [2.6] and [2.7], it is possible to use highly accurate density matrices for the various states of the constituent atoms. However, the computation becomes particularly simple if the density matrices of the atomic states are determined using the same basis set that is used in the molecular wave function calculation. Represented in such a common basis, the density matrices are

$$[3.1]\quad \rho(\boldsymbol{r}',\boldsymbol{r}) = \sum_{pq}(\boldsymbol{r}'|\chi_p > D_{pq} < \chi_q|\boldsymbol{r})$$

where the D_{pq}'s are the elements of the first-order reduced density matrix in the space spanned by the basis functions. The number of electrons of such a system is then given as

$$[3.2]\quad N = \int \mathrm{d}\boldsymbol{r}\rho(\boldsymbol{r}',\boldsymbol{r})_{\boldsymbol{r}'\rightarrow\boldsymbol{r}} = tr[\boldsymbol{SD}]$$

where $\boldsymbol{S}$ is the overlap matrix with the elements

$$[3.3]\quad S_{pq} = \langle\chi_p|\chi_q\rangle$$

With this the desired matrix elements become

$$[3.4]\quad M_{IJ} = \int \mathrm{d}\boldsymbol{r}'\int \mathrm{d}\boldsymbol{r}\rho_I(\boldsymbol{r},\boldsymbol{r}')\rho_J(\boldsymbol{r}',\boldsymbol{r})$$

$$[3.5]\quad = \sum_{pqrs}\langle\chi_s|\chi_p\rangle D_{I,pq}\langle\chi_q|\chi_r\rangle D_{J,rs}$$

$$[3.6]\quad = tr[\boldsymbol{SD}_I\boldsymbol{SD}_J]$$

Thus they can be obtained using simple matrix multiplication of matrices that are generally available in a standard molecular wave function calculation. With this, the method suggested becomes particularly simple and could be implemented easily in most molecular wave function programs.

4. Results

In Table 1 we present some results obtained, using the method described. These results were computed, using the

Table 1. Weight coefficients w_i for the atomic density matrices calculated by solving eq. [2.9] and partial charges q computed using the w_i's compared with values^M of a Mulliken population analysis and values^H obtained following the method of Hirsfeld (22).

Molecule	VDZ		STO-3G		Molecule	VDZ		STO-3G	
Atom(conf.)	w_i	q	w_i	q	Atom(conf.)	w_i	q	w_i	q
LiH					**BeH**				
H(s)	1.54	0.54	1.51	0.51	H(s)			1.55	0.55
Li(s)	0.82		0.83		Be(s^2)			0.86	
H(s)	1.46	0.46	1.43	0.43	H(s)			1.16	0.16
Li(s)	0.56	0.28^M	0.57	0.14^M	Be(s^2)			0.10	
Li(p)	0.28	0.42^H	0.29	0.19^H	Be(sp)			0.86	
BH					**CH**				
H(s)	0.85	0.15	0.91	0.09	H(s)	0.72	0.28	0.80	0.20
B(s^2p)	0.99		1.02		C($s^2p\pi$)	1.05		1.03	
H(s)	0.76	0.24	0.83	0.17	H(s)	0.67	0.33	0.75	0.25
B(s^2p)	0.63	0.07^M	0.64	0.13^M	C($s^2p\pi$)	0.60		0.61	
B(sp^2)	0.42	0.05^H	0.39	0.09^H	C($sp^2\pi$)	0.46		0.43	
NH					**OH**				
H(s)	0.68	0.32	0.76	0.24	H(s)	0.60	0.40	0.70	0.30
N($s^2p\pi^2$)	1.05		1.03		O($s^2p\pi^3$)	1.05		1.04	
H(s)	0.65	0.35	0.73	0.27	H(s)	0.58	0.42	0.68	0.32
N($s^2p\pi^2$)	0.59		0.60		O($s^2p\pi^3$)	0.57		0.59	
N($sp^2\pi^2$)	0.46		0.44		O($sp^2\pi^3$)	0.48		0.45	
HCl					**AlH**				
H(s)	0.82	0.18			H(s)	1.10	0.10		
Cl($s^2p\pi^4$)	1.01				Al(s^2p)	0.98			
H(s)	0.79	0.21			H(s)	1.06	0.06		
Cl($s^2p\pi^4$)	0.65	0.14^M		0.17^M	Al(s^2p)	0.77	0.43^M		0.41^M
Cl($sp^2\pi^4$)	0.36	0.16^M		0.15^H	Al(sp^2)	0.22	0.21^H		0.33^H
HF					**HF**				
H(s)	0.54	0.46	0.65	0.35	H(s)	0.38	0.62	0.53	0.47
F($s^2p\pi^4$)	1.05		1.04		F($s^2p\pi^4$)	0.20		0.28	
H(s)	0.53	0.47	0.65	0.35	F($sp^2\pi^4$)	0.10		0.11	
F($s^2p\pi^4$)	0.57	0.27^M	0.60	0.21^M	F($s^2p^2\pi^4$)	0.69		0.59	
F($sp^2\pi^4$)	0.48	0.24^H	0.44	0.14^H					

MOLPRO program (33) STO-3G as well as a valence double zeta (VDZ) basis set, in order to have a comparison to the partial charges calculated by Davidson and Chakravorty (22), using Mulliken population analysis (1) and the method of Hirsfeld (18). To be sure, the data presented here are just preliminary and far from being conclusive. They were computed using density matrices of independent Hartree–Fock calculations for the ground states of the molecules and the various states of the atoms. In the case of atomic open-shell configurations, all states arising from these configurations that can couple to the appropriate molecular state are included in the calculation. In Table 1 the result is reported for the configuration in total, in order not to expand the table unduly. This is also the reason that the Mulliken and Hirsfeld values given for comparison are entered in the free spaces in the column headed by q for the partial charge. The partial charges obtained with all methods are reasonable; however, significant differences can be observed. The differences of the results for the two different basis sets can surely be attributed to the inadequacy of the STO-3G basis to yield a reasonable approximation to the true densities; that is particularly apparent in the case of HF. In addition to the partial charges, the method proposed here also yields information on the s- and p-character the atoms use in bond formation. This becomes significant already in the case of LiH, where Li is found to use 30% p-character in its bond to H, and with the P-state of Li in the analysis the partial charge found is reduced by 20%. Even more drastic, as expected, is the situation of BeH. Here the excited P-state of Be is to almost 90% involved in the formation of BeH with a concomitant drastic reduction in the partial charges obtained if this state is included in the analysis. Also in the hydrides of B through F there is a significant though decreasing use of s-character in the bond formation. That the inclusion of F^- in the anal-

ysis of the density of HF (lower right-hand box of Table 1) leads to a significant increase of the resulting partial charges is another finding that could have been anticipated. To assess conclusively the full potential of the method suggested here for the molecular charge density analysis, a much more exhaustive study, including many more molecules and more atomic states and a larger variety of basis set, will be required. This will be presented in the future; however, it is clear from the results presented that their value could be increased if statistical measures can be obtained to determine the significance of the individual contributions to the total molecular density.

5. Quality estimate of calculated data

To gain confidence in the results produced by solving the normal equation we should be able to answer the following questions:

1. How sensitive are the w_{AI} with respect to errors or changes in the density matrix elements?

2. Does the chosen set of atomic density matrices ρ_{AI} supply us with a suitable approximation of the molecular density matrix ρ_M?

3. Does adding a new atomic state AI improve this approximation significantly?

By assuming a normal distribution of the errors we can use statistical methods (34) to obtain numbers that quantify the answers to our questions.

Let us first consider a standard least-squares problem with n data points given and m coefficients to compute. We want to determine an m vector $\boldsymbol{x}$, which minimizes

$$[5.1] \qquad \chi^2 = \|\boldsymbol{b} - \boldsymbol{A} * \boldsymbol{x}\|_2^2 = \sum_{i=1}^{n} \left(b_i - \sum_{i=1}^{m} A_{ij} x_j \right)^2$$

where $\boldsymbol{A}$ is an nxm matrix and $\boldsymbol{b}$ an n vector.

One way of determining $\boldsymbol{x}$ is by solving the normal system of the minimization problem

$$[5.2] \qquad \boldsymbol{M}\boldsymbol{x} = (\boldsymbol{A}^*\boldsymbol{A})\boldsymbol{x} = (\boldsymbol{A}^*\boldsymbol{b})$$

with an $m \times m$ matrix $M = (A^*A)$.

To obtain a measure of the sensitivity of a solution component x_i with respect to errors in the data points we can calculate the variance of x_i:

$$[5.3] \qquad \sigma^2(x_i) = \sum_{j=1}^{n} \left(\frac{\partial x_i}{\partial b_j} \right)^2$$

By substituting

$$[5.4] \qquad x_i = \sum_{j=1}^{m} (M^{-1})_{ij} b_j$$

into eq. [5.3] we obtain for the variance

$$[5.5] \qquad \sigma^2(x_i) = (M^{-1})_{ii}$$

The positive square root of the variance is called the standard deviation of x_i.

To estimate the "goodness-of-fit" of the data to the model we can introduce the correlation coefficient:

$$[5.6] \qquad R^2 = 1 - \frac{\sum_{i=1}^{n} (b_i - \hat{b}_i)^2}{\sum_{i=1}^{n} (b_i - \bar{b})^2}$$

where

$$[5.7] \qquad \hat{\boldsymbol{b}} = \boldsymbol{M}\boldsymbol{x} \qquad \text{and} \qquad \bar{b} = \frac{\sum_{i=1}^{n} b_i}{n}$$

Note that $R^2 = 1$ in the case of a perfect fit (data points are perfectly correlated) and $R^2 = 0$ if no correlation between the data points can be observed.

Returning to the Charge Density Analysis we see that expression [2.3] for χ^2 closely resembles expression [5.1] but with an infinity of data points. The sums over index i therefore change into integrals over $\boldsymbol{r}$.

The definitions of variance and standard deviations of the w_{AI} as the diagonal elements of the inverted normal matrix $\boldsymbol{M}$ are straightforward, see eq. [2.5] or [2.9]:

$$[5.8] \qquad \sigma^2(w_{AI}) = (M^{-1})_{AI,AI}$$

The term in the numerator of eq. [5.6] is equivalent to our χ^2. The mean value in the denominator vanishes in our case (the mean value over the interval $[-\infty, \infty]$ of any square integrable function is zero). Hence the correlation coefficient of eq. [5.6] generalizes to

$$[5.9] \qquad R^2 = 1 - \frac{\int d\boldsymbol{r} \int d\boldsymbol{r}' |\rho_M(\boldsymbol{r}, \boldsymbol{r}') - \sum_{AI} \rho_{AI}(\boldsymbol{r}, \boldsymbol{r}') w_{AI}|^2}{\int d\boldsymbol{r} \int d\boldsymbol{r}' |\rho_M(\boldsymbol{r}, \boldsymbol{r}')|^2}.$$

After defining standard deviations and correlation coefficients for our problem we are able to answer the questions:

1. The standard deviations $\sigma(w_{AI})$ of eq. [5.8] give us a measure for the sensitivity of the calculated data with respect to perturbations in ρ_M and ρ_{AI}.

2. The correlation coefficient R of eq. [5.9] measures the "goodness-of-fit" of our approximation of ρ_M by the weighted sum of atomic densities ρ_{AI}. The closer R is to 1 the better is our fit of ρ_M.

3. By including another atomic state function ρ_{AI} in our approximation we get a modified correlation coefficient R'. The difference $R' - R$ quantifies the progress we made by including an extra w_{AI}.

It is to be expected that, with the inclusion of an increasing number of excited atomic states in the expansion of the molecular density, the coefficient matrix $\boldsymbol{M}$ of eq. [2.5] or its extension in eq. [2.9] will become singular or nearly so. In this case, a singular value decomposition (35) of the coefficient matrix would permit the elimination of redundant linear combinations of the atomic densities, permitting a focus on the remaining significant contributions.

The method suggested is simple and unique; there is no arbitrariness with respect to the division of overlap densities. With the use of atomic ground and excited state densities, specific M_z components along bonds will have to be used for such states; the method will also give information about atomic deformation densities, dependent on the chemical surrounding of an atom. These deformed atomic densities could

then be used to calculate atomic form factors to be used in X-ray molecular structure determinations. The extent to which such deformed atomic densities or also molecular fragment densities can be transferred and used to construct approximate densities of increasingly complex molecules remains to be investigated (36, 37).

References

1. R.S. Mulliken. J. Chem. Phys. **23**, 1833 (1955); **23**, 1841 (1955); **23**, 2338 (1955); **23**, 2343 (1955).
2. A. Streitwieser. Orbital and electron density diagrams. MacMillan, New York. 1973.
3. J.R. van Wazer and I. Absar. Electron densities in molecules and molecular orbitals. Academic Press, New York. 1975.
4. P. Coppens. Angew. Chem. **89**, 33 (1977).
5. I. Absar and J.R. van Wazer. Angew. Chem. **90**, 87 (1978).
6. P. Becker (*Editor*). Electron and magnetization densities in molecules and crystals. NATO Adv. Study Inst. Ser. Ser. B: **48**, 1980.
7. P. Coppens and M.B. Hall. Electron distribution and the chemical bond. Plenum Press, New York. 1981.
8. R.F.W. Bader. Atoms in molecules, a quantum theory. Clarendon Press, Oxford, U.K. 1990.
9. P.-O. Löwdin. J. Chem. Phys. **21**, 375 (1955).
10. K.R. Roby. Mol. Phys. **27**, 81 (1955).
11. E.R. Davidson. J. Chem. Phys. **46**, 3320 (1967).
12. R. Heinzmann and R. Ahlrichs. Theor. Chim. Acta, **42**, 33 (1976).
13. I. Mayer. Chem. Phys. Lett. **97**, 270 (1983).
14. I. Mayer. Chem. Phys. Lett. **110**, 440 (1984).
15. A.E. Reed, R.B. Weinstock, and F. Weinhold. J. Chem. Phys. **83**, 735 (1985).
16. P. Politzer and R.R. Harris. J. Am. Chem. Soc. **92**, 6451 (1970).
17. S. Srebrenik, R. Pauncz, and H. Weinstein. Chem. Phys. Lett. **32**, 420 (1975).
18. F.L. Hirsfeld. Theor. Chim. Acta, **44**, 129 (1977).
19. M. Yanez, R.F. Stewart, and J.A. Pople. Acta Crystallogr. Sect. A: Crys. Phys. Diffr. Theor. Gen. Crystallogr. **A34**, 641 (1978).
20. P. Coppens. J. Phys. Chem. **93**, 7979 (1989).
21. D.L. Grier and A. Streitwieser. J. Am. Chem. Soc. **104**, 3556 (1982).
22. E.R. Davidson and S. Chakravorty. Theor. Chim. Acta, **83**, 319 (1992).
23. W.H.E. Schwarz, K. Ruedenberg, and L. Mensching. J. Am. Chem. Soc. **111**, 6926 (1989).
24. L. Mensching, W. von Nissen, P. Valtazanos, K. Ruedenberg, and W.H.E. Schwarz. J. Am. Chem. Soc. **111**, 6933 (1989).
25. R.F.W. Bader and P.M. Beddall. J. Chem. Phys. **56**, 3320 (1972).
26. R.F.W. Bader, S.G. Anderson, and A.J. Duke. J. Am. Chem. Soc. **101**, 1389 (1979).
27. R.F.W. Bader, T.T. Nguyen-Dang, and Y. Tal. J. Chem. Phys. **70**, 4316 (1979).
28. R.F.W. Bader, Y. Tal, S.G. Anderson, and T.T. Nguyen-Dang. Isr. J. Chem. **19**, 8 (1980).
29. R.F.W. Bader, T.T. Nguyen-Dang, and Y. Tal. Rep. Prog. Phys. **44**, 893 (1981).
30. E. Kraka. Ph.D. Thesis, Universität zu Köln, 1984.
31. P.-O. Löwdin. Phys. Rev. **97**, 1491 (1955).
32. E.R. Davidson. Reduced density matrices in quantum chemistry. Academic Press, New York. 1976.
33. H.-J. Werner and P.J. Knowles. User's Manual for MOLPRO, University of Sussex, Brighton, U.K. 1991.
34. I.N. Bronstein and K.A. Semendjajew. *In* Taschenbuch der Mathematik. *Edited by* G. Grosche, V. Ziegler, and D. Ziegler. B.G. Teubner, Stuttgart, Leipzig. 1991.
35. W.H. Press, B.P. Flannery, S.A. Teuklowsky, and W.T. Vetterling. Numerical recipes. Cambridge University Press, Cambridge. 1986.
36. P.D. Walker and P.G. Mezey. J. Am. Chem. Soc. **115**, 12423 (1993).
37. P.D. Walker and P.G. Mezey. J. Am. Chem. Soc. **116**, 12022 (1994).

Charge density study with the Maximum Entropy Method on model data of silicon. A search for non-nuclear attractors

R.Y. de Vries, W.J. Briels, D. Feil, G. te Velde, and E.J. Baerends

Abstract: In 1990 Sakata and Sato applied the maximum entropy method (MEM) to a set of structure factors measured earlier by Saka and Kato with the Pendellösung method. They found the presence of non-nuclear attractors, i.e., maxima in the density between two bonded atoms. We applied the MEM to a limited set of Fourier data calculated from a known electron density distribution (EDD) of silicon. The EDD of silicon was calculated with the program ADF-BAND. This program performs electronic structure calculations, including periodicity, based on the density functional theory of Hohenberg and Kohn. No non-nuclear attractor between two bonded silicon atoms was observed in this density. Structure factors were calculated from this density and the same set of structure factors that was measured by Saka and Kato was used in the MEM analysis. The EDD obtained with the MEM shows the same non-nuclear attractors that were later obtained by Sakata and Sato. This means that the non-nuclear attractors in silicon are really an artefact of the MEM.

Key words: Maximum Entropy Method, non-nuclear attractors, charge density, X-ray diffraction.

Résumé : Sakata et Sato (1990) ont appliqué la méthode d'entropie maximale (MEM) sur un ensemble de facteurs de structures mesurés par Saka et Kato à l'aide de la méthode Pendellösung. Ils ont trouvé la présence d'attracteurs non nucléaires, c'est-à-dire de maxima dans la densité entre deux atomes liés. On a appliqué la MEM à un ensemble limité de données de Fourier calculés à partir d'une distribution de densité électronique connue (DDE) du silicium. On a calculé la DDE du silicium à l'aide du programme ADF-BAND. Ce programme qui effectue des calculs de structures électroniques, y compris la périodicité, repose sur la théorie de la densité fonctionnelle de Hohenberg et Kohn. Aucun attracteur non nucléaire entre deux atomes de silicium non liés n'a été observé dans cette densité. On a calculé les facteurs de structure à partir de cette densité et, pour l'analyse MEM, on a utilisé l'ensemble de facteurs de structure qui avait été mesuré par Saka et Kato. Les DDE obtenues avec l'analyse MEM montre la présence des mêmes attracteurs non nucléaires que ceux obtenus par Sakata et Sato. On peut en déduire que les attracteurs non nucléaires dans le silicium sont en réalité des artefacts de l'analyse MEM.

Mots clés : méthode d'entropie maximale, attracteurs non nucléaires, densité de charge, diffraction par rayons X.

[Traduit par la rédaction]

1. Introduction

In the study of the electron density distribution (EDD) with the help of X-ray diffraction, experiment yields a set of intensities. In most, if not all, centrosymmetric crystals, structure factors can be derived from these intensities without any ambiguity in the phases. The most common method of extracting the EDD from an incomplete and noisy set of structure factors is to fit the data to a multipole model (e.g., POP (1), MOLLY (2), and LSEXP (3, 4)). The advantages of a multipole fit over a direct Fourier synthesis are that a multipole fit allows one to overcome the series termination effect, to filter out the noise from the data that were measured, and to extract the static density from the thermally smeared density. A drawback to a multipole fit is the fact that bias is introduced, and random errors are traded for systematic errors (5).

In the past few years, the maximum entropy method (MEM) has been used to obtain the EDD from an incomplete and noisy set of structure factors (e.g., Sakata and Sato (6), Sakata et al. (7), and Takata et al. (8)). The MEM is capable of handling the series termination effect by estimating missing data. The MEM selects the EDD that is closest to an a priori EDD or, in its absence, closest to a uniform distribution. It is believed that all the features that show up in the EDD are supported by the data and that the MEM gives least biased results.

It has been pointed out by Jauch (9) that the EDDs produced with the MEM have to be interpreted with great care. Our MEM study on a hypothetical water crystal (10) confirmed these reservations with respect to the method. In particular we showed that the MEM results yield an unrealistic χ^2-distribution. In case the data is very accurate the struc-

Received September 22, 1995.

This paper is dedicated to Professor Richard F.W. Bader on the occasion of his 65th birthday.

R.Y. de Vries, W.J. Briels, and D. Feil.[1] Chemical Physics Laboratory, University of Twente, PO Box 217, 7500 AE Enschede, The Netherlands.
G. te Velde and E.J. Baerends. Afdeling Theoretische Chemie, Scheikundig Laboratorium der Vrije Universiteit, De Boelelaan 1083, 1081 HV Amsterdam, The Netherlands.

[1] Author to whom correspondence may be addressed.

ture factors are forced to be nearly equal to their measured values and the obtained EDD is independent of the distribution. Therefore, Sakata and Sato (6) did not have similar problems in their MEM study on silicon data since their work was based on highly accurate data. They found a local maximum in the middle of the Si—Si bond. Although this (3, −3) critical point (Bader, ref. 11) was unexpected, no doubt about this non-nuclear attractor was expressed. Recently, a MEM study by Iversen et al. (12) revealed non-nuclear attractors in beryllium. The phenomenon, however, is small and the MEM has not been tested on this level of accuracy by means of model studies. Thus we decided to create a set of structure factors corresponding with a known EDD and to apply the MEM.

To illustrate this we have applied the MEM to data calculated from a known EDD of silicon. This EDD was obtained by means of an electronic structure calculation, including periodicity, with the Amsterdam density functional BAND (ADFBAND) program (13). The results were compared with those obtained by Sakata and Sato (6) who applied the MEM to experimental data on silicon.

2. Method

The maximum entropy principle states that out of all EDDs that satisfy certain constraints one should chose the EDD that maximizes the entropy $\overline{S}$ (because this is the least biased), defined by Jaynes (14) as:

$$[1] \qquad \overline{S} = -\int p(x,y,z) \ln (p(x,y,z)/m(x,y,z))\, dxdydz$$

where

$$[2] \qquad p(x,y,z) = \frac{\rho(x,y,z)}{\int \rho(x,y,z)\, dxdydz}$$

and

$$[3] \qquad m(x,y,z) = m'(x,y,z) \Big/ \int m'(x,y,z)\, dxdydz$$

m' is a prior density for the EDD $\rho(x,y,z)$, i.e., some estimate before the present set of data was used. To calculate the integral in eq. [1] the density is usually represented on a grid ($N_1 \times N_2 \times N_3$), to give:

$$[4] \qquad S = -\sum_{i=1}^{N_1} \sum_{j=1}^{N_2} \sum_{m=1}^{N_3} p_{ijm} \ln (p_{ijm}/m_{ijm})$$

In case the prior density m' is not specified, a uniform distribution is assumed and eq. [4] reduces to

$$[5] \qquad S = -\sum_{i=1}^{N_1} \sum_{j=1}^{N_2} \sum_{m=1}^{N_3} p_{ijm} \ln p_{ijm} + \text{constant}$$

The second term in eq. [5] can be dropped in the maximization process. This is the form we will use since we do not assume any prior information.

The constraints are provided by the experiment and involve the structure factors that were measured. We also constrain the total number of electrons per unit cell to the correct value N:

$$[6] \qquad (V_{cell}/N_1N_2N_3) \sum_{i,j,m} \rho_{ijm} = N$$

The most common way to incorporate the reflections that were measured is by maximizing the entropy subject to

$$[7] \qquad \chi^2 = \sum_{h,k,l} \{[F_{hkl} - D_{hkl}]/\sigma_{hkl}\}^2 = M$$

where D_{hkl} is the measured structure factor, F_{hkl} is the structure factor calculated from the resulting density, σ_{hkl} is the standard deviation of the measurement, and M is the total number of (unique) reflections that were measured. Of course the EDD has to be positive everywhere. This is automatically satisfied since the logarithm of a negative number does not exist.

It has been shown (10) that maximizing the entropy subject to this constraint does not necessarily lead to a proper frequency histogram of reduced differences $(|F_{hkl}| - |D_{hkl}|)/\sigma_{hkl}$ between calculated and observed structure factors. In particular, a few strong low-order structure factors calculated from the EDD obtained by MEM show large deviations (up to 19σ in the model study presented) from the measured values. The value of χ^2 is dominated by these structure factors. This causes the remaining structure factors to be exactly equal to their measured values with disastrous effects on the resulting EDD. The same effect was also observed by Jauch and Palmer (15). The introduction of a weighting scheme as proposed by Feil and co-workers (10) partially solves this problem.

Structure factors can be measured very accurately with the Pendellösung method. In case the error in the measurements is very small the resulting EDD is insensitive to the distribution. The structure factors calculated from the maximum entropy EDD are then forced to have the same value as the measured structure factors. In this case only the series termination effect is dealt with by the MEM.

In the present study we focus on the series termination effect. We have calculated structure factors from a known density and want to apply the MEM with $\sigma_{hkl} = 0$. The program that was used to perform the optimization was based on the algorithm that was presented by Skilling and Bryan (16). A detailed description of this algorithm was given by de Vries, Briels, and Feil (10). Since the use of $\sigma = 0$ leads to calculational problems in applying constraint [7] we have chosen the error to be very small ($\sigma_{hkl} = 0.0005$). The iterations were stopped when $\chi^2 = M$ and $\delta < 5 \times 10^{-4}$ where δ is defined as

$$\delta = \frac{1}{2} \left| \frac{\nabla S}{|\nabla S|} - \frac{\nabla \chi^2}{|\nabla \chi^2|} \right|^2$$

3. Calculation of the EDD and the structure factors

The EDD of silicon was calculated with the program ADFBAND (13). This program performs an electronic structure calculation based on density functional theory (17) taking

Fig. 1. Fourier synthesis of the structure factors for which $\sin(\theta)/\lambda < 5.5$ Å^{-1}. The (static) structure factors were calculated with the program ADF-BAND. Thermal motion was introduced with the program FITTER. Contour intervals are at 0.1 e/Å^3.

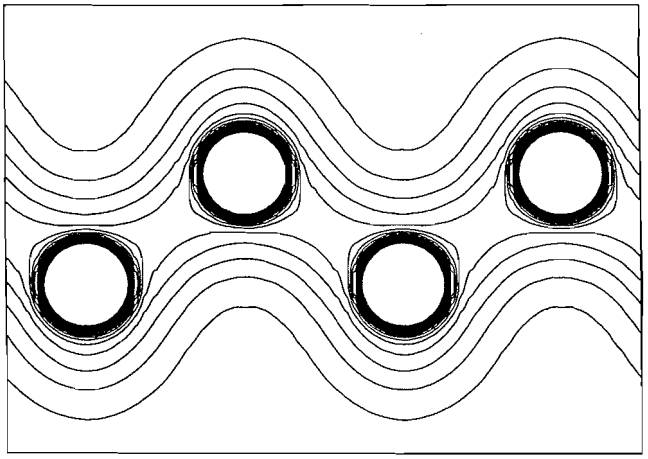

into account the periodicity of the system. For the present purpose it is not important that $\rho(x, y, z)$ be very accurate. It should be a reasonable, but accurately known, density. Once the EDD is known from this calculation, the structure factors can be calculated in a straightforward way by taking the Fourier transformation of the EDD. This will give us the structure factors of the static density. In principle this is very simple. One can calculate the density in the unit cell on a regular, 3-dimensional grid. From this, the structure factors can be calculated using Fast Fourier Transform (FFT) routines. However, the grid that has to be used in this case has to be very dense to make sure that aliasing does not occur in Fourier space. The calculation of the density on all these grid points would simply take too long.

Instead, a different approach is followed that was implemented by Bruning and Feil (18) in the program FITTER. This program contains the following steps:

1. Partition the density according to the stockholder principle (19) to obtain "atomic" densities.
2. Subtract "free" atoms (calculated with the same basis set) from these atomic densities. Since these free atoms are spherically symmetric, their Fourier transform can be easily calculated. The remaining density is referred to as the (atomic) deformation density. It no longer has the problem of "near singularities."
3. Fit the (atomic) deformation densities with suitable functions that can be Fourier transformed analytically.
4. Calculate the Fourier transform of these functions.
5. Add the Fourier transform of the free atoms.
6. Introduce individual atomic thermal motion.
7. Calculate the structure factors by summing the structure factors of all atoms.

In the present study the atomic thermal motion is introduced by multiplying the structure factors with an isotropic temperature factor: $\exp(-B(\sin(\theta)/\lambda)^2$ with $B = 0.4632$ Å^2. This value of B was taken from Spackman (20). Structure factors with $\sin(\theta)/\lambda < 5.5$ Å^{-1} were calculated. A Fourier transform of these structure factors was made to obtain the thermally smeared density, the dynamic density. This is shown in Fig. 1 where the density in the 110 plane of silicon is plotted. Non-nuclear attractors are seen to be absent. We have confirmed this by calculating the electron density along the Si—Si bond: along this line a minimum in the electron density is found. Extension of the set of structure factors by increasing the value of $\sin(\theta)/\lambda$ did not change the EDD. It is easily shown that thermal motion obliterates all information beyond $\sin(\theta)/\lambda = 5.5$ Å^{-1}.

Fig. 2. Fourier synthesis of the same set of structure factors that were measured by Saka and Kato (21). (Structure factors calculated with ADF-BAND and FITTER.) Positive contours are drawn as solid lines, zero contours as dash-dotted lines, and negative contours as dotted lines. The contours are at intervals of 0.8 e/Å^3.

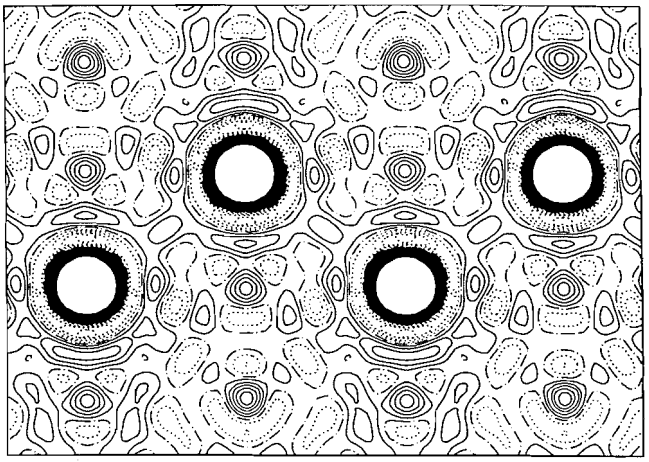

4. Results

A number of MEM calculations was performed using a 64 × 64 × 64 grid to describe the density. The first calculation only involved structure factors with the same h, k, and l values as those measured by Saka and Kato (21). A direct Fourier transformation of these structure factors is shown in Fig. 2. The result of the MEM calculation is shown in Fig. 3. The similarity between the latter density and the density obtained by Sakata and Sato (6), who used experimental data, is striking. To our surprise the same non-nuclear attractors between the silicon atoms appear. However, from Fig. 1, the dynamic density, we know that the midpoint between two bonded atoms is a saddle point.

All structure factors of the dynamic density are known. We can compare them with the values that were "predicted" by the MEM. For a number of structure factors this is shown in Table 1. As can be seen from Table 1, the absolute values of the structure factors predicted by the MEM are, in most cases, smaller than the exact values. Furthermore, the sign of the 622 structure factor is opposite to the sign of the 622 structure factor of the exact density. This is also found when the experimental data are used (comparing the phase of the 622 structure factor with the experimentally determined phase (22)). Sakata and Sato (6) suggested that the 622 structure factor might be affected significantly when the number of pixels is increased. We have done the calculation using a 128 × 128 × 128 grid and found that the value of the 622 reflection hardly changes: $F(622) = -0.0070$.

Fig. 3. The EDD calculated with the MEM from the same structure factors that were used to calculate the EDD of Fig. 2. The contours are at intervals of 0.1 e/Å^3.

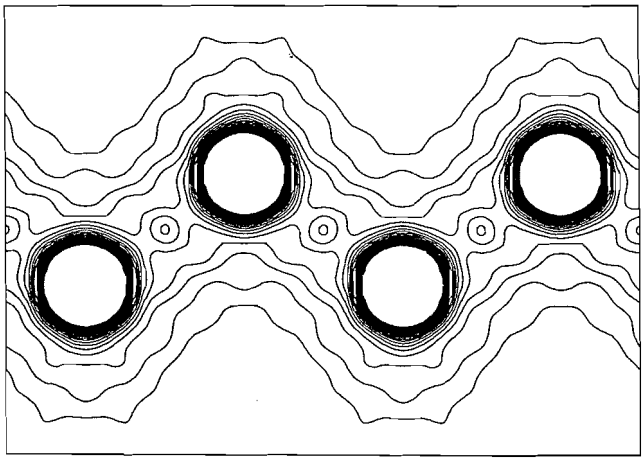

Table 1. The exact values of some structure factors (calculated from the dynamic density) compared with the values that were predicted by the MEM.

hkl			Exact	MEM
2	2	2	1.1547	1.3336
4	4	2	−0.0376	−0.0243
6	2	2	0.0040	−0.0065
9	3	1	−12.9648	−12.8838
7	5	5	11.8025	11.7844
9	3	3	11.7940	11.6661
7	7	1	11.7946	11.8050
8	6	2	15.7646	15.5886
10	2	0	−15.7643	−15.4879
7	7	3	10.7861	10.6664
9	5	1	10.7804	10.5872
9	5	3	9.9016	9.7060
10	4	2	13.2955	12.8175
7	7	5	−9.1149	−8.7348
11	1	1	−9.1227	−8.7003
9	7	1	8.4368	8.1761
9	5	5	−8.4305	−7.9868
10	6	0	11.3806	10.7407

It should be noticed that, although error-free data were used, the contours of the EDD obtained through MEM are still not very smooth. It has been suggested (23) that only a complete sphere of structure factors in reciprocal space should be used in the MEM analysis. This means that the 844 and the 880 structure factors should be omitted from the data set measured by Saka and Kato (21). The result of this calculation is shown in Fig. 4. The contours are indeed much smoother and although it looks like the non-nuclear attractors have disappeared they are still present but do not show on the contour level that was used. One could expect that when all the structure factors (except the forbidden ones) up to the

Fig. 4. The EDD calculated with the MEM from the same structure factors that were used to calculate the EDD of Fig. 2 except for the 844 and the 880 structure factors. The contours are at intervals of 0.1 e/Å^3.

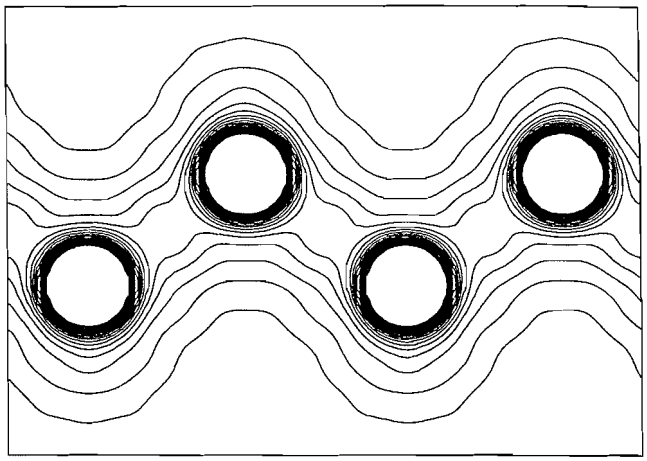

Fig. 5. The EDD calculated with the MEM from all the structure factors up to 880 ($\sin(\theta)/\lambda < 1.05$ Å^{-1}) except the forbidden structure factors. The contours are at intervals of 0.1 e/Å^3.

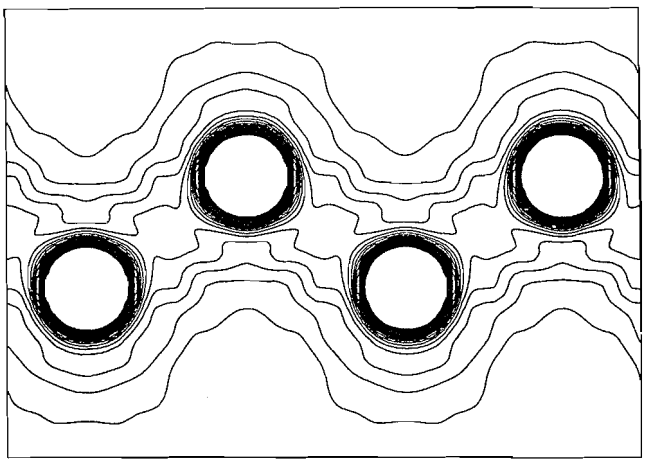

880 reflection (= $\sin(\theta/\lambda) = 1.05$ Å^{-1}, 42 structure factors in total) are used in the MEM analysis, the density should become even smoother. This is shown in Fig. 5. Contrary to expectation, the contours are less smooth than with the MEM optimization shown in Fig. 4. In general, the information of the EDD is not evenly distributed in reciprocal space but occurs in regions of high density. We believe that it is important to include such a high-density region completely in the analysis.

The EDD that is obtained when all the structure factors (except the forbidden ones) for which $\sin(\theta)/\lambda < 1.4$ Å^{-1} (92 structure factors) are included in the optimization is shown in Fig. 6. Figure 7 shows the result when the series cutoff level is extended to the structure factors for which $\sin(\theta)/\lambda <$ 1.7 Å^{-1} (152 structure factors). When we calculate the 222 structure factor from the density that is shown in Fig. 7. we find the value $F(222) = 1.35$. So, although the densities of Fig. 7 and Fig. 1 look very similar, the value of the 222 structure factor is quite different from the exact value.

Fig. 6. The EDD calculated with the MEM from all the structure factors for which $\sin(\theta)/\lambda < 1.4$ Å^{-1} except the forbidden structure factors. The contours are at intervals of 0.1 e/Å^3.

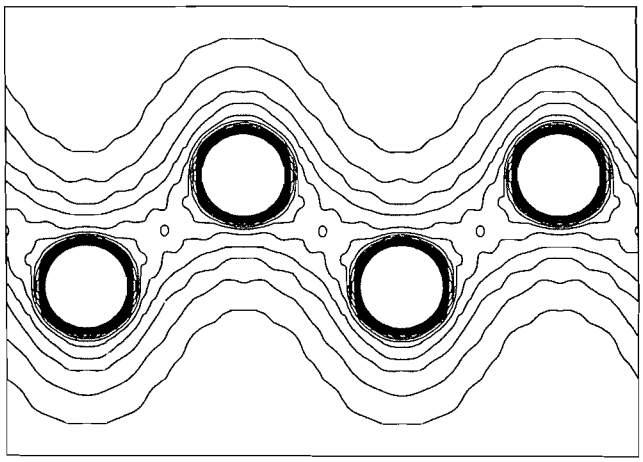

Fig. 7. The EDD calculated with the MEM from all the structure factors for which $\sin(\theta)/\lambda < 1.7$ Å^{-1} except the forbidden structure factors. The contours are at intervals of 0.1 e/Å^3.

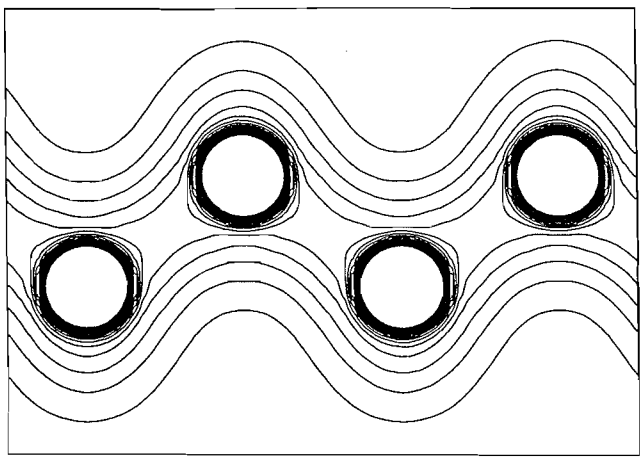

5. Discussion and concluding remarks

The MEM calculation on model data of silicon shows that one has to be very careful when interpreting the EDD obtained by MEM. If we compare both the Fourier synthesis (Fig. 2) of the data and the density obtained by the MEM (Fig. 3) with the original density (Fig. 1) we can say that the MEM deals well with the series termination effect. Minor peaks remain, however, which were not present in the theoretically calculated EDD. In a sense we are the victim of our own success when we interpret the remaining structure as being real physical features. One advantage of the direct Fourier transform of the data is that one will never be tempted to give such an overinterpretation of these little features.

Thus, from remaining maxima obtained by the application of MEM on experimental data one cannot draw conclusions about the presence or absence of non-nuclear attractors in the Si bonds.

The use of a complete sphere in reciprocal space still shows the presence of this non-nuclear attractor but the height of this non-nuclear attractor is much smaller. But a complete sphere is no guarantee that the EDD will be smooth. We have seen that this depends on the range in reciprocal space that is used in the analysis. Increasing the size of the sphere in reciprocal space does not automatically mean that the EDD becomes more smooth.

An interesting option for improving the EDDs obtained by MEM might be the use of prior densities. For instance, by using the sum of "free atoms" as a prior density the method can focus on the deformation density itself.

Acknowledgement

We would like to express our gratitude and admiration to Richard F.W. Bader for the way he taught us the relevance of critical points in charge density analysis.

References

1. B.M. Craven, H.P. Weber, and X. He. Tech. Report TR-87-2, Department of Crystallography, University of Pittsburgh, Pittsburgh, Pa. (1987).
2. N.K. Hansen and P. Coppens. Acta Crystallogr. Sect. A: Cryst. Phys. Diffr. Theor. Gen. Crystallogr. **A34**, 909 (1978).
3. F.L. Hirshfeld. Acta Crystallogr. Sect. B: Struct. Crystallogr. Cryst. Chem. **B27**, 769 (1971).
4. F.L. Hirshfeld. Isr. J. Chem. **16**, 226 (1977).
5. H. Bruning. PhD Thesis. University of Twente, Enschede, The Netherlands. 1992.
6. M. Sakata and M. Sato. Acta Crystallogr. Sect. A: Found. Crystallogr. **A46**, 263 (1990).
7. M. Sakata, T. Uno, M. Takata, and R. Mori. Acta Crystallogr. Sect. A: Found. Crystallogr. **A39**, 47 (1992).
8. M. Takata, Y. Kubota, and M. Sakata. Z. Naturforsch. Teil A, **48**, 75 (1993).
9. W. Jauch. Acta Crystallogr. Sect. A: Found. Crystallogr. **A50**, 650 (1994).
10. R.Y. Vries, W.J. Briels, and D. Feil. Acta Crystallogr. Sect. A: Found. Crystallogr. **A50**, 383 (1994).
11. R.F.W. Bader. Atoms in molecules — A quantum theory. Clarendon Press, Oxford. 1990.
12. B.B. Iversen, F.K. Larsen, M. Souhassou, and M. Takata. Acta Crystallogr. Sect. B: Struct. Sci. **B51**, 580 (1995).
13. G. Velde te and E.J. Baerends. Phys. Rev. B: Condens. Matter, **44**, 7888 (1991).
14. E.T. Jaynes. (Collected Works) Papers on Probability, statistics and statistical physics. *Edited by* R.D. Rosenkrantz. Reidel, Dordrecht, Holland. 1983.
15. W. Jauch and A. Palmer. Acta Crystallogr. Sect. A: Found. Crystallogr. **A49**, 590 (1993).
16. J. Skilling and R.K. Bryan. Mon. Not. R. Astron. Soc. **211**, 111 (1984).
17. P. Hohenberg and W. Kohn. Phys. Rev. [Sect.] B, **136**, 864 (1964).
18. H. Bruning and D. Feil. Acta Crystallogr. Sect. A: Found. Crystallogr. **A48**, 865 (1992).
19. F.L. Hirshfeld. Theor. Chim. Acta, **44**, 129 (1977).
20. M.A. Spackman. Acta Crystallogr. Sect. A: Found. Crystallogr. **A42**, 271 (1986).
21. T. Saka and N. Kato. Acta Crystallogr. Sect. A: Found. Crystallogr. **A42**, 469 (1986).
22. J.Z. Tischler and B.W. Batterman. Phys. Rev. B: Condens. Matter, **30**, 3659 (1984).
23. M. Takata. Sagamore XI. Brest, France. 1994.

Topological studies of the charge density of some group 2 metallocenes $M(\eta^5\text{-}C_5H_5)_2$ (M = Mg or Ca)

Ian Bytheway, Paul L.A. Popelier, and Ronald J. Gillespie

Abstract: Ab initio quantum chemical calculations using both the Hartree–Fock and the B3LYP density functional theory methods have been performed for the group 2 metallocenes $M(\eta^5\text{-}C_5H_5)_2$ (M = Mg or Ca). The topology of the calculated charge density (ρ) and its Laplacian ($\nabla^2\rho$) have been analysed using a new critical point search algorithm in order to understand why $Mg(\eta^5\text{-}C_5H_5)_2$ is linear while $Ca(\eta^5\text{-}C_5H_5)_2$ is bent. The Laplacian of the core of the Ca atom in $Ca(\eta^5\text{-}C_5H_5)_2$ is perturbed by the polarizing field of the cyclopentadienyl ligands and the bent geometry is a consequence of the interactions between the distorted core and the ligand atoms. In the case of $Mg(\eta^5\text{-}C_5H_5)_2$, charge concentration maxima in the Mg core occur along the vectors connecting the metal to the centroids of the cyclopentadienyl ligands irrespective of whether or not the molecule is linear, and the preferred geometry is linear as expected. The results of these calculations demonstrate that the geometries of the group 2 metallocenes can be understood in terms of the repulsive interactions between the ligands and between the ligands and the distorted core of the metal atom.

Key words: atoms in molecules, group 2 metallocenes, VSEPR, charge density, Laplacian of ρ.

Résumé : Utilisant les méthodes de Hartree–Fock ainsi que de la théorie de la densité fonctionnelle B3LYP, on a effectué des calculs ab initio de chimie quantique sur des métallocènes du groupe 2, $M(\eta^5\text{-}C_5H_5)_2$ (M = Mg ou Ca). Afin d'essayer de comprendre pourquoi le $Mg(\eta^5\text{-}C_5H_5)_2$ est linéaire alors que le $Ca(\eta^5\text{-}C_5H_5)_2$ est replié, on a analysé la topologie de la densité de charge calculée (ρ) et de son laplacien ($\nabla^2\rho$) en utilisant un nouvel algorithme pour la recherche du point critique. Le laplacien du noyau de l'atome de Ca du $Ca(\eta^5\text{-}C_5H_5)_2$ est perturbé par le champ polarisant des coordinats cyclopentadiényles et sa géométrie repliée est une conséquence des interactions entre le noyau déformé et les atomes du coordinat. Dans le cas du $Mg(\eta^5\text{-}C_5H_5)_2$, la concentration maximale de la charge dans le noyau du Mg se produit le long des vecteurs reliant le métal aux centroïdes des coordinats cyclopentadiényles que la molécule soit linéaire ou pas et on s'attend alors à une géométrie linéaire qui soit privilégiée. Les résultats de ces calculs démontrent qu'il est possible de comprendre les géométries des métallocènes du groupe 2 en termes d'interactions répulsives entre les coordinats et entre les coordinats et le noyau déformé de l'atome de métal.

Mots clés : atomes dans les molécules, métallocènes du groupe 2, VSEPR, densité de charge, laplacien de ρ.

[Traduit par la rédaction]

Introduction

The factors governing molecular geometry are important and fundamental to our understanding of chemistry – why do molecules prefer some shapes and not others? In trying to answer this question one is struck by the fact that despite the vast number of different molecules, there exist common geometrical motifs that persist even when the constituent atoms of a molecule are changed. Clearly, rules which allow this vast body of information to be classified are of importance to chemistry as they allow us to understand what is known, and make predictions about what is not.

Perhaps the simplest set of rules that can be used to understand and classify molecular geometries are those of the valence shell electron pair repulsion (VSEPR) model (1–3). The VSEPR model requires that we consider the strength of mutual repulsions between the different types of electron pairs present within the molecule in order to obtain its preferred, or energetically most favourable, geometry. The intuitive nature of the VSEPR model is one of its most useful features, and one that has allowed its application to a wide variety of molecules, ranging from those containing main group atoms (1–3) to those containing transition metals (4, 5). The successes of the VSEPR model should, of course, prompt us to study the model in order to understand why it is often so successful, and, likewise, we should seek the reasons for its failures because uncovering these reasons should lead to a deeper understanding of molecular geometry.

The fundamental postulate of the VSEPR model, that molecular shape is determined by repulsions between bonding and nonbonding pairs of electrons, is explained by the Pauli exclusion principle. Electrons are not, however, really local-

Received September 27, 1995.

This paper is dedicated to Professor Richard F.W. Bader on the occasion of his 65th birthday.

I. Bytheway. Department of Physical and Theoretical Chemistry, University of Sydney, Sydney 2006, NSW, Australia.
P.L.A. Popelier. University Chemistry Laboratory, Lensfield Road, Cambridge CB2 1EW, U.K.
R.J. Gillespie.[1] Department of Chemistry, McMaster University, Hamilton, ON L8S 4M1, Canada.

[1] Author to whom correspondence may be addressed. Telephone: (905) 529- 9140, ext. 23307. Fax: (905) 522-2509. E-mail: gillespi@mcmail.cis.mcmaster.ca

ized to form pairs (6, 7), but this idea remains valid if we consider regions in the valence shell where charge is locally concentrated arising from the localization of the Fermi hole (8, 9). Regions where charge is concentrated, which are revealed by the Laplacian of the charge density ($\nabla^2\rho$) (8–10) have played an important role in understanding the VSEPR model, resulting in it being reformulated in terms of electron-pair domains (2, 3, 11, 12) i.e., the regions in the valence shell where charge is locally concentrated.

For many molecules of the main groups, there is excellent agreement between the expected locations of the electron pairs of the VSEPR model and the locations of maximum charge concentration (8–10). Therefore, the physical basis for the VSEPR model is provided by the Laplacian of the charge density (8, 9) in that preferred molecular geometries may be described in terms of the repulsions between these regions of charge concentration rather than between localized pairs of electrons. For example, the geometries of ClF_3 (**1**) and SF_4 (**2**) are both derived from the trigonal bipyramid, in which the bonding and lone pair electrons of the VSEPR model appear as regions of maximum charge concentration and their preferred geometries explained accordingly (8, 9). This relationship between the VSEPR model and $\nabla^2\rho$ is observed for many main group molecules (9), so that one might then ask what the Laplacian of the charge density reveals for molecules which have geometries not accounted for by the VSEPR model.

One such set of counter-examples to the VSEPR model are the YSF_4 (Y = O, NH, or CH_2) (**3**), which are trigonal bipyramidal as predicted; however, taking into consideration the decreasing electronegativity of the series Y = O, NH, CH_2 it might be expected that both equatorial and axial F-S-F bond angles would decrease. Experimentally, it is found that the equatorial bond angle does decrease (13, 14) as expected but the axial bond angles in fact *increase*. Analysis of $\nabla^2\rho$ for these molecules provides a clear picture of the S—Y bonding region, from which it can be seen that the charge concentrations are elliptical with the major axis in the equatorial plane (15). As Y = O, NH, CH_2 the ellipticity increases, resulting in an increased amount of charge concentrated in the equatorial plane (resulting in decreased equatorial F-S-F bond angles) and a decreased amount of charge concentrated in the axial plane (resulting in increased axial F-S-F bond angles). Thus the observed geometries can be thought of as arising from the repulsions between the different types of bonding charge concentrations as revealed by the Laplacian of the charge density.

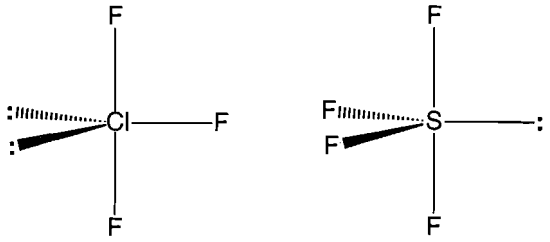

1

2

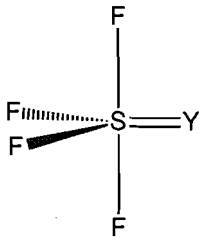

3

The explanation of these apparent exceptions to the VSEPR model in terms of $\nabla^2\rho$ is encouraging and led to the consideration of others, namely the difluorides of group 2. It has been known for some time that the halides of Ca, Sr, and Ba (**4**) are bent (16, 17) and analysis of $\nabla^2\rho$ for these molecules has shown (18) that this bending is a consequence of distortions of the metal atom by the presence of the fluoride ligands. It is usual to think of the central atoms in these molecules as spherical but, as was suggested some time ago (19), metals may be sufficiently polarizable that their cores are distorted in the presence of some ligands. The importance of considering such distortions of the core charge density of transition metals has been noted previously, for example in explaining the deviation of the bond angles in $VOCl_3$ (20) (**5**) and CrO_2Cl_2 (21) (**6**) from the VSEPR predicted angles. In the case of CaF_2, partial condensation of the core electrons into pairs results in a distorted Ca^{2+} core that contains regions of charge concentration, i.e., it is no longer spherical. Interaction between the ligands and these regions of core charge concentrations (CCC) results in the observed nonlinear geometry for this molecule.

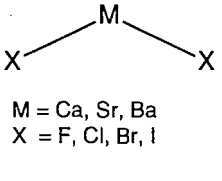

4

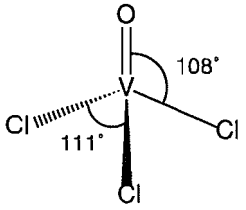

5

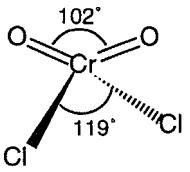

6

A closely related set of molecules are the metallocenes of group 2, for which gas phase electron diffraction experiments have shown that $MgCp_2$ (22) and $MgCp^*_2$ (23, 24) are linear, while $CaCp^*_2$ (23, 24), $SrCp^*_2$, and $BaCp^*_2$ (25, 26) are all bent. In the solid phase $MgCp_2$ (27) is also linear, while $CaCp_2$ (28), $CaCp^*_2$ (29), and $BaCp^*_2$ (30) are all bent, where Cp = cyclopentadienyl, η^5-C_5H_5 and Cp^* = pentamethyl-cyclopentadienyl, η^5-$C_5(CH_3)_5$. Theoretical studies of the bonding and photoelectron spectra (31–33) have been reported for lanthanide metallocenes and the importance of electron correlation in the description of transition metal metallocenes has also been established (34–36). More recently, ab initio calculations of group 2 and lanthanide metallocenes (37) showed that the bending potential in these molecules is small (<1 kcal

mol^{-1}) and, based on natural population analysis, the preference for nonlinear geometries was ascribed to π-type covalent contributions to the metal–cyclopentadienyl bonding. Recently, molecular mechanics methods have been used to explain the bent nature of these molecules (38, 39) by the introduction of an attractive ligand–ligand potential. We present here the results of ab initio calculations using all-electron basis sets for some group 2 metallocenes (MCp_2 where M = Mg and Ca) and study the distortion of the central metal atom by the cyclopentadienyl ligands in order to understand the preferred nonlinear geometry of these molecules.

Theoretical details

The geometries of the MCp_2 (M = Mg and Ca) were optimized with the imposition of C_s symmetry and with the Cp rings staggered with respect to each other. In addition the M-X vector was fixed normal to the C_5 ring, where X will be used throughout to denote the centroid of the Cp ring. Within this framework, all M—C, C—C, and C—H bond lengths were optimized, as was the X-M-X angle. Calculations were performed at both the Hartree–Fock (HF) and the B3LYP density functional methods using all-electron basis sets. The extended Wachters basis set was used for Ca (40) as this was found to give an adequate description of Ca in previous calculations (18) and the standard 6−311G* basis set was used to describe Mg (41). For C and H the standard 6-31G* was used (41) after preliminary results suggested that the addition of the polarization function to carbon was required in order to obtain a bent equilibrium geometry for $CaCp_2$.

Previous calculations of group 2 dihalides have shown that the inclusion of the effects of electron correlation is required in order to obtain nonlinear geometries. The size of the these metallocenes, coupled with our desire to study the distortion of the metal atom, precluded the use of effective core potentials and Möller–Plesset perturbation theory. To examine the effects of electron correlation, density functional calculations incorporating exchange-correlation functionals, as implemented in the GAUSSIAN92/DFT software package (41), were also performed. The B3LYP functional was chosen because of its successful application to a variety of main group molecules giving results of MP2 (or better) quality (42–44). Additionally, the B3LYP calculations allow for a comparison of total charge densities with those calculated at the HF level.

The wave functions obtained from each of the calculations have been analysed within the context of the theory of "Atoms in Molecules" (AIM), and atomic properties have been calculated using the PROAIM program (45).[2] AIM theory, through the topological analysis of the total charge density (ρ) shows how molecules can be divided naturally into their constituent atoms, while the Laplacian of the charge density ($\nabla^2\rho$) reveals where charge is locally concentrated and depleted. Finding the critical points in these scalar fields that have complicated topologies is both a challenging and cumbersome task unless a robust algorithm can be relied upon. In general, the search for critical points in the Laplacian of the charge density would greatly benefit from such an algorithm as it has a more complex topology than that of the charge density. Unravelling the topology of the charge density for the complexes described here, however, poses serious problems for the conventional algorithm.[3] This is a consequence of the use of the Newton–Raphson (NR) method, which requires excellent starting points in order to be successful. This can be explained by considering that the best step $\boldsymbol{h}$ to get from the current point to the critical point is $\boldsymbol{h} = -\boldsymbol{H}^{-1}\boldsymbol{g}$ where $\boldsymbol{H}$ is the Hessian matrix. This step can be re-expressed in terms of the eigenvectors $\boldsymbol{V}_i$ and eigenvalues b_i of the Hessian (of the scalar field) by

$$[1] \quad \boldsymbol{h} = -\sum_{i=1}^{3} F_i \boldsymbol{V}_i / b_i$$

where $F_i = \boldsymbol{V}_i^T\boldsymbol{g}$ is the projection of the gradient $\boldsymbol{g}$ along the local eigenmode $\boldsymbol{V}_i$.

It has been shown previously (46) that the NR method minimizes along eigenmodes with positive Hessian eigenvalues and maximizes along modes with negative eigenvalues. Suppose we wish to locate a transition state on a surface starting in a region where the Hessian has one negative eigenvalue. In such a region the NR step is appropriate because it does exactly what is required: it maximizes along one mode while minimizing along the others. Thus in general the NR method only successfully locates a critical point provided that it starts in a region where the Hessian has the correct structure. For our purposes, this would mean, for example, that starting in a region where the Hessian has a signature of minus one (corresponding to a bond critical point) we could never find a nearby ring critical point, which has a different signature.

This inadequacy of the NR method has been remedied by using the powerful *eigenvector following method* algorithm (47) and its subsequent refinement (48). Its success has recently been proven convincingly (49) in the context of Atoms in Molecules (AIM). The program MORPHY 1.0 (50), which utilizes the *eigenvector following method*, yielded consistent atomic graphs (i.e., the unique trajectories of the gradient of $\nabla^2\rho$ that link the charge concentration maxima (51)) for all systems studied and was also used to prepare all of the different contour plots presented here. This program searches for critical points in a chainlike manner, i.e., the locations of previously found critical points are used to generate suitable starting points in the search for others. The reduced sensitivity to starting conditions has allowed successful use of MORPHY in the study of $\nabla^2\rho$ (S. Johnson, private communication), nevertheless, the topological studies of $\nabla^2\rho$ of the group 2 metals presented here required a huge computational investment.

Results and discussion

Geometries

Optimized bond lengths and angles for the various calculations of $MgCp_2$ and $CaCp_2$ are given in Table 1 and the optimized geometries are shown in Fig. 1. In general, bond lengths and angles calculated using the two methods agree: compared to the B3LYP method, the HF method predicts slightly longer M—C bond lengths and a larger X-M-X angle. Agreement with experiment is also good and both methods predict a linear $MgCp_2$ molecule, and a bent $CaCp_2$ molecule.

[2] The program PROAIM modified by T.A. Keith and J.R. Cheeseman.

[3] Program EXTREME written by K. Laidig (McMaster University, 1989).

Fig. 1. The HF optimized geometries of the $Mg(\eta^5\text{-}C_5H_5)_2$ (top) and $Ca(\eta^5\text{-}C_5H_5)_2$ (bottom).

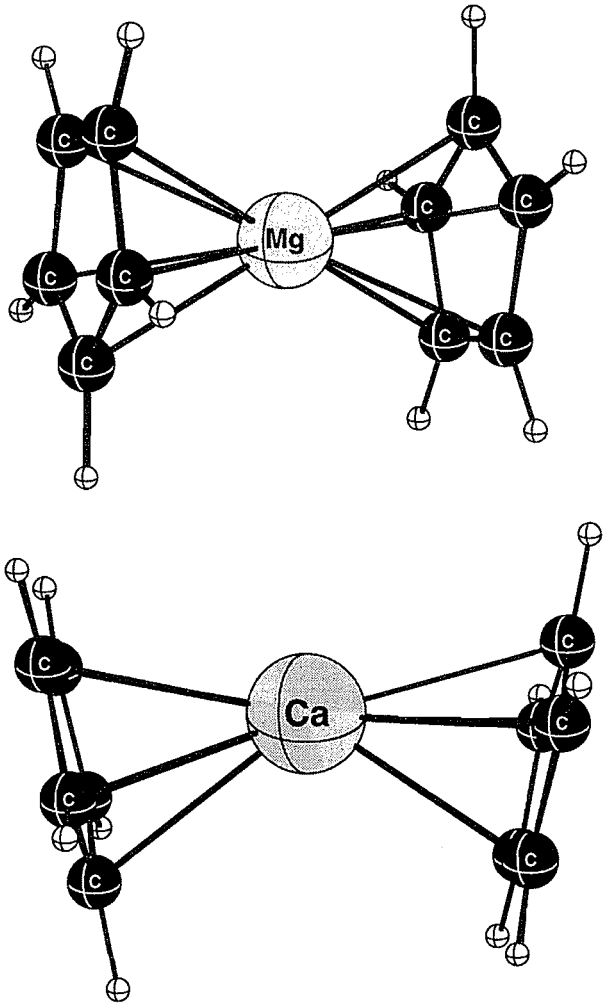

Table 1. Calculated and experimental bond lengths, angles (Å and deg), and relative energies (kcal mol^{-1}) for the linear and bent geometries of the $MgCp_2$ and $CaCp_2$ molecules.

	HF	B3LYP	Gas phase	Solid state
$CaCp_2$				
X-Ca-X[a]	156.9	149.6	154[d,e]	147.7[d,g,h]
r(Ca—X)	2.369	2.317	2.313	2.35
r(Ca—C)	2.655	2.613		2.64
r(C—C)	1.408	1.420		1.41
r(C—H)	1.075	1.085		
X-Ca-X[b]	180.0	180.0		
r(Ca—X)	2.374	2.324		
r(Ca—C)	2.659	2.620		
r(C—C)	1.408	1.420		
r(C—H)	1.075	1.086		
ΔE_L[c]	0.28	1.2		
$MgCp_2$				
X-Mg-X[a]	180.0	180.0	180.0[f]	180.0[g]
r(Mg—X)	2.050	2.022	2.008	
r(Mg—C)	2.376	2.357	2.339	2.28–2.32
r(C—C)	1.411	1.424		1.35–1.41
r(C—H)	1.073	1.084		
X-Mg-X[b]	150.0	150.0		
r(Mg—X)	2.072	2.047		
r(Mg—C)	2.394	2.378		
r(C—C)	1.411	1.422		
r(C—H)	1.073	1.084		
ΔE_L[c]	6.8	6.5		

[a]Equilibrium geometry.
[b]X-M-X fixed during optimization.
[c]Energy required to distort the molecule from the equilibrium X-M-X angle to the fixed value.
[d]Values for $CaCp_2^*$.
[e]References 23 and 24.
[f]Reference 22.
[g]Reference 27.
[h]Reference 29.

Nonequilibrium geometries were also studied in order to obtain some idea of the bending potential for these molecules. The geometry of $MgCp_2$ was optimized using both the HF and B3LYP methods with the X-Mg-X angle constrained at 150°, and the resultant geometries (Table 1) were 6.8 kcal mol^{-1} (HF) and 6.5 kcal mol^{-1} (B3LYP) higher than at the equilibrium geometries. These results are similar to those obtained previously for HF calculations of $MgCp_2$ (26) from which it was estimated that approximately 3.5 kcal mol^{-1} was required to bend the molecule from 180° to 160°.

Bending the $CaCp_2$ molecule from the equilibrium X-Ca-X value to 180° requires much less energy, only 0.3 and 1.2 kcal mol^{-1} at the HF and B3LYP levels, respectively. These energies are also consistent with previous calculations (26, 37), where it was found that the location of a bent equilibrium geometry was basis set and method dependent. The use of reasonably sized all-electron basis sets in the calculations given here may be an important factor in obtaining a bent geometry for $CaCp_2$, and indeed the large number of calculations for the group 2 dihalides (52, 53) and previous calculations of metallocenes (34–36) suggests that these systems are very sensitive to the basis sets and calculational methods chosen. Nevertheless, our results support the contention that $CaCp_2$ is bent but very floppy.

In all of the calculations a staggered arrangement of Cp rings was assumed. Experimental results for $CaCp_2$ suggest that this is reasonable (23, 24), however, on the basis of gas phase electron diffraction data it was not possible to assign either a staggered or eclipsed conformation to $MgCp_2$ (22). Although a staggered conformation was used in this work, the HF energy of the eclipsed conformation was found to be only 0.01 kcal mol^{-1} higher in energy than the staggered conformation (i.e., negligible), in agreement with the experimental finding.

Charge density and bonding

The total charge densities of these group 2 metallocenes are expected to have quite complex topologies, comprising: 10 M—C, 10 C—C, and 10 C—H bond critical points; 10 ring critical points belonging to each M and adjacently connected C atoms; a ring critical point in the plane of each cyclopenta-

Fig. 2. The molecular graph for the linear $MgCp_2$ molecule. The complex topology is apparent, with bond (3, −1), ring (3, +1), and cage (3, +3) critical points all in close proximity.

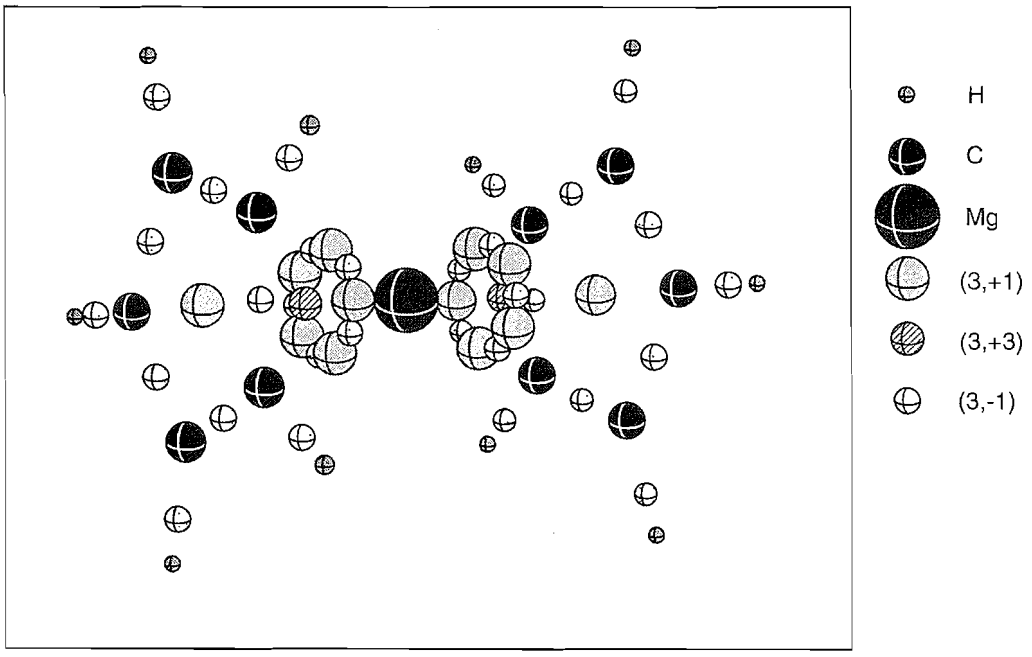

dienyl ligand; and a cage critical point in the region between M and each of the centroids of the cyclopentadienyl rings. All of these critical points are required in order to construct a proper molecular graph that satisfies the Poincaré–Hopf relationship (9) for η^5 coordination of two cyclopentadienyl rings to a metal atom. Initial topological analysis using the Newton–Raphson technique, as implemented by the EXTREME program[3] in the AIMPAC suite of programs, was not successful in the location of the bond and ring critical points between the metal and carbon atoms. The eigenvector following method as implemented in the MORPHY program (49, 50) was successful, however, and the results of the topological analyses are summarized in Table 2. The spatial relationship between the various types of critical points and the atom locations is shown in Fig. 2 for Hartree–Fock optimized $MgCp_2$ molecule; this arrangement of critical points is similar to that found in each of the other total charge density analyses.

The η^5 coordination of the cyclopentadienyl ligands is demonstrated quite clearly by location of bond critical points along all M–C vectors, i.e., bonding occurs between the metal and carbon atoms and *not* between the metal and the centre of the Cp ring. Metal–carbon bond critical points occur at regions of local charge depletion (Table 2) indicative of ionic bonding between these atoms, in accord with that suggested previously (37). Values of ρ and $\nabla^2\rho$ for the different critical points obtained from the HF and B3LYP charge densities are similar; the B3LYP values of ρ at the M—C bond critical points are slightly larger than the analogous HF values, although not significantly so. For $CaCp_2$ the values of ρ at the Ca—C bond critical point are less than was found in $Ca(CH_3)_2$ by approximately 0.015 au (18), indicating that the 10 Ca—C bonds in $CaCp_2$ are not as strong as the two Ca—C bonds in the $Ca(CH_3)_2$ complex. The C—C and C—H nuclei of the cyclopentadienyl ligands are bound via shared interactions, typical of the covalent character expected for these bonds.

Plots of the total charge densities are shown in Fig. 3 for the HF optimized geometries of $MgCp_2$ and $CaCp_2$. For $MgCp_2$ these plots show how the magnesium atom has been distorted from spherical upon complex formation (Fig. 3*a*) and is now more ellipsoidal. The nonspherical shape of the Ca atom is also evident in a similar plot (Fig. 3*b*) while the plot for the Cp ligand in the $MgCp_2$ molecule (Fig. 3*c*) shows quite clearly the atomic boundaries of each atom and the expected ring critical point at the centre of the five-membered ring. Additionally, these plots show how these metallocene molecules may be divided into their constituent atoms.

It is usual to consider the formal charge distribution in these group 2 metallocenes as $M^{2+}(Cp^-)_2$, i.e., analogous with the group 2 dihalides. The AIM atomic charges in these metallocenes were calculated in order to see how much charge may be properly ascribed to the various portions of these MCp_2 molecules, and to see if comparison with the analogous dihalides is indeed warranted. Atomic charges were obtained by integration over the various atomic basins, using the PROMEGA program (45). The charges for $MgCp_2$ indicate a large degree of metal–ligand charge separation, with the Mg atom and Cp ligands having approximate charges of +1.75 and −0.88 respectively (see Table 2). These charges are similar to those obtained previously for MgF_2 (18) and suggest that the ionic model used to describe MgF_2 is applicable to $MgCp_2$. Similarly, charges obtained for the Ca atom and the Cp ligand are of the order of 1.6 and −0.8 respectively, which are similar to the analogous charges obtained previously for CaF_2, CaH_2, and $Ca(CH_3)_2$ (18).

Analysis of $\nabla^2\rho$ for $MgCp_2$

Plots of $\nabla^2\rho$ for the HF optimized (i.e., linear) and bent

Table 2. Values of ρ (ea_0^3), $\nabla^2\rho$ (ea_0^5) at the (3, −1), (3, +1), and (3, +3) critical points in the total charge density, the integrated atomic charges q (e), and values of $\nabla^2\rho$ in the core regions of the metal atom, for the different geometries $MgCp_2$ and $CaCp_2$.

	$MgCp_2$ X-Mg-X = 180°		$MgCp_2$ X-Mg-X = 150°		$CaCp_2$ Optimized X-Ca-X		$CaCp_2$ X-Ca-X = 180°	
	HF	B3LYP	HF	B3LYP	HF	B3LYP	HF	B3LYP
ρ(M—C)	0.026	0.027	0.025	0.026	0.025	0.028	0.025	0.028
r_b(M)[a]	0.960	0.967	0.964	0.974	1.270	1.264	1.270	1.266
$\nabla^2\rho$(M—C)	0.144	0.138	0.137	0.132	0.112	0.116	0.111	0.113
ρ(C—C)	0.308	0.292	0.308	0.293	0.309	0.294	0.309	0.294
$\nabla^2\rho$(C—C)	−0.873	−0.721	−0.877	−0.725	−0.877	−0.727	−0.878	−0.727
ρ(C—H)	0.285	0.275	0.285	0.275	0.283	0.274	0.282	0.272
$\nabla^2\rho$(C—H)	−1.060	−0.949	−1.062	−0.952	−1.038	−0.928	−1.031	−0.925
ρ(M—C—C)[b]	0.026	0.027	0.025	0.025	0.025	0.027	0.025	0.0269
ρ(M—Cp)[c]	0.022	0.023	0.021	0.022	0.018	0.019	0.018	0.019
q(M)	1.752	1.691	1.754	1.687	1.671	1.571	1.681	1.594
$q(C_5H_5)$[d]	−0.884	−0.841	−0.881	−0.850	−0.834	−0.786	−0.838	−0.792
$-\nabla^2\rho$[e]	55.2	54.4	55.3	54.4	4.01(2)	4.03(4)	4.03	4.02
r[f]	0.39	0.39	0.39	0.39	0.90(4)	0.90(4)	0.90	0.90

[a]Distance of the bond critical point from the M atom (M = Mg or Ca) in Å.

[b]Value of ρ at the ring critical point between M and two C atoms of the Cp ring.

[c]Value of ρ at the cage critical point between M and the Cp ligand.

[d]Integrated charges for the individual C and H atoms have been summed to give the net charge of the cyclopentadienyl ligand.

[e]Values at the (3, −3) critical points in $\nabla^2\rho$ for the Mg and Ca core regions. Numbers in parentheses denote the number of critical points with this value.

[f]Distance (in au) of the charge concentration maximum from the nucleus.

(X-M-X = 150°) $MgCp_2$ molecule are shown in Fig. 4. The B3LYP charge densities for these $MgCp_2$ molecules yielded similar results to the HF analysis, and these results are given in Table 2. Two (3, −3) critical points in $\nabla^2\rho$ belonging to the core region of the Mg atom were located along the vectors connecting the Mg atom with the center of the Cp ligands. This is shown clearly in Fig. 4*a*, where the locations of the CCC's are shown relative to the Cp ligands. No charge concentration maxima are located along Mg—C bonds, further illustrated in Fig. 4*b*, and the atomic graph of Mg is essentially the same as that found previously for MgF_2 (18).

A plot of $\nabla^2\rho$ for the Cp ligand is given in Fig. 4*c*, which shows clearly the regions of charge concentration along the C—C and C—H bonds. Each carbon atom has three charge concentration maxima, one along each C—C bond and one along the C—H bond. The apparent maxima in the valence shell of the C atoms visible in Figs. 4*a* and 4*b* are a consequence of the plotting plane chosen, and are not (3, −3) critical points in $\nabla^2\rho$.

It is also of interest to see how the atomic graph of Mg changes as the molecule is bent. At an X-M-X angle of 150° it was found that the two CCC's found in the linear molecule (Fig. 4*a*) followed the direction of bending, with one of the maxima now situated along an Mg—C bond (Fig. 4*d*). This behaviour upon bending was also noted for MgF_2, thus the preferred linear geometry in both molecules (i.e., $MgCp_2$ and MgF_2) can be understood in terms of the minimization of both the ligand–ligand and CCC–ligand interactions.

Analysis of $\nabla^2\rho$ for $CaCp_2$

Plots of $\nabla^2\rho$ for the HF optimized $CaCp_2$ molecule are shown in Fig. 5. Figure 5*a* shows the arrangement of the Cp ligands with respect to the regions of charge concentration in the Ca core, and Fig. 5*b* is plotted in this same plane focussing upon the Ca atom. Four charge concentration maxima were located in this core region, two in the region between the bond paths shown in Fig. 5*b*, and two in the same plane, in the long, narrow region apparent in Fig. 5*b*. These latter two charge concentration maxima are very close (≈0.3 au apart) and upon further bending to an X-M-X angle of 148° they coalesce, giving a total of three CCC maxima (see Fig. 6).

To ensure that no charge concentration maxima had been missed, a complete atomic graph was determined, and only the four maxima shown in Fig. 5*b* were located. This arrangement of charge concentration maxima is related to that found for the HF optimized CaF_2 molecule. This relationship is shown schematically in Fig. 6 where the approximate arrangement of the (3, −3) critical points in the Ca core, with respect to the X (i.e., the centroid of the Cp ligands) and F positions in $CaCp_2$ and CaF_2 respectively, is given. This difference in atomic graphs is probably due to the formation of ligand-opposed charge concentrations in CaF_2, resulting in only two maxima, while the expected 10 ligand-opposed charge concentration maxima here collapse into the arrangement found.

At the HF level linear $CaCp_2$ was found to be approximately 0.3 kcal mol^{-1} higher in energy than the bent molecule. This slight preference for the bent geometry may be understood in

Fig. 3. Plots of the total charge density with interatomic surfaces overlaid for the HF optimized $MgCp_2$ and $CaCp_2$ molecules. In these and following plots, bold asterisks; bold, open circles; and filled squares are used to mark the positions of cage (3, +3), ring (3, +1), and bond (3, −1) critical points in ρ, respectively. Bold labels and filled circles are used to label nuclei in the plotting plane, while outlined atom labels and circles are used denote nuclei that are not in the plotting plane. (*a*) In the plane containing four C nuclei and the Mg nucleus. The overlaid interatomic surfaces show the slightly nonspherical shape of the Mg atom. (*b*) A similar plot for $CaCp_2$ shown in the plane containing the Ca atom and a C atom on each Cp ligand. (*c*) The total charge density in the plane of a cyclopentadienyl ligand showing bond paths and interatomic surfaces.

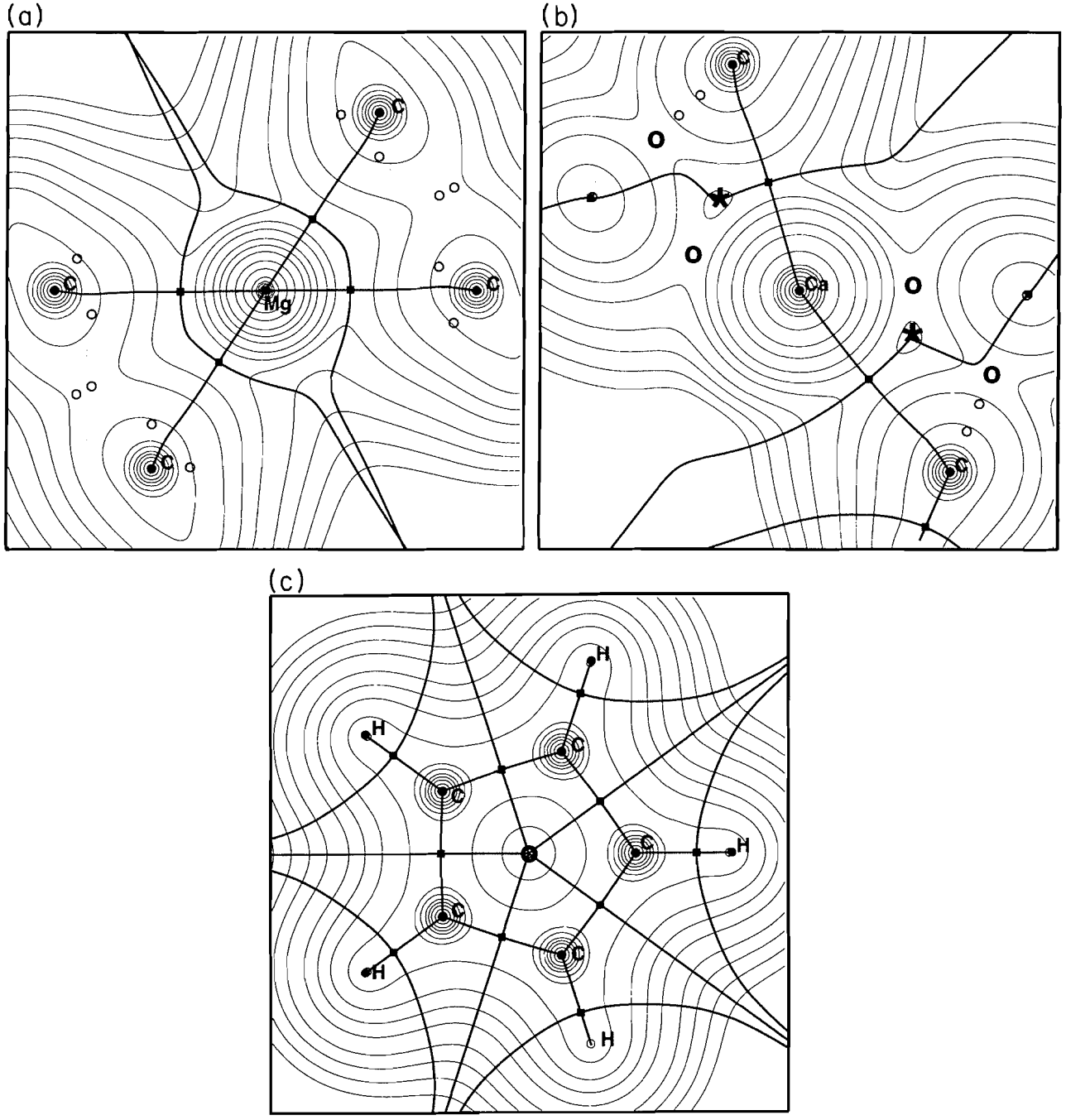

terms of the different distributions of maxima in $\nabla^2\rho$. Figure 7 shows plots of $\nabla^2\rho$ for the linear $CaCp_2$ molecule. The region of core charge concentration is barely visible in Fig. 7*a*, while Fig. 7*b* (plotted in the same plane as Fig. 7*a*) shows the intersection of this plane with the two tori of charge concentration maxima. A plot in the plane of one of these tori of charge concentration is shown in Fig. 7*c*. Five charge concentration maxima were located in this torus and these are staggered with respect to the nearest cyclopentadienyl ring (labelled in Fig. 7*c*). As can be seen in Fig. 7*c*, however, this region of charge

Fig. 4. Plots of the Laplacian of the charge density for the $MgCp_2$ molecule. In this and following plots of $\nabla^2\rho$, regions of charge concentration ($\nabla^2\rho < 0$) are denoted by solid contours and regions of charge depletion ($\nabla^2\rho > 0$) by broken contours. Critical points in ρ are denoted by the same symbols as those used in Fig. 3. (*a*) Linear $MgCp_2$ showing the location of the maxima in $-\nabla^2\rho$ (denoted by the filled circles near the Mg nucleus) in the magnesium core. Note also that the Mg—C bond critical points are in regions of charge depletion. (*b*) $\nabla^2\rho$ plotted in the same plane as that used in Fig. 3*b*. Neither of the magnesium CCC are located in this plane. (*c*) A plot of $\nabla^2\rho$ in the plane of the cyclopentadienyl ligand, showing the covalent C—C and C—H bonds, and the region of charge depletion in the center of the ring. (*d*) A plot of $\nabla^2\rho$ for the bent $MgCp_2$ molecule in the same plane as that shown in (*a*). Note that the CCC are still directed along the Mg–X vector as in the linear molecule.

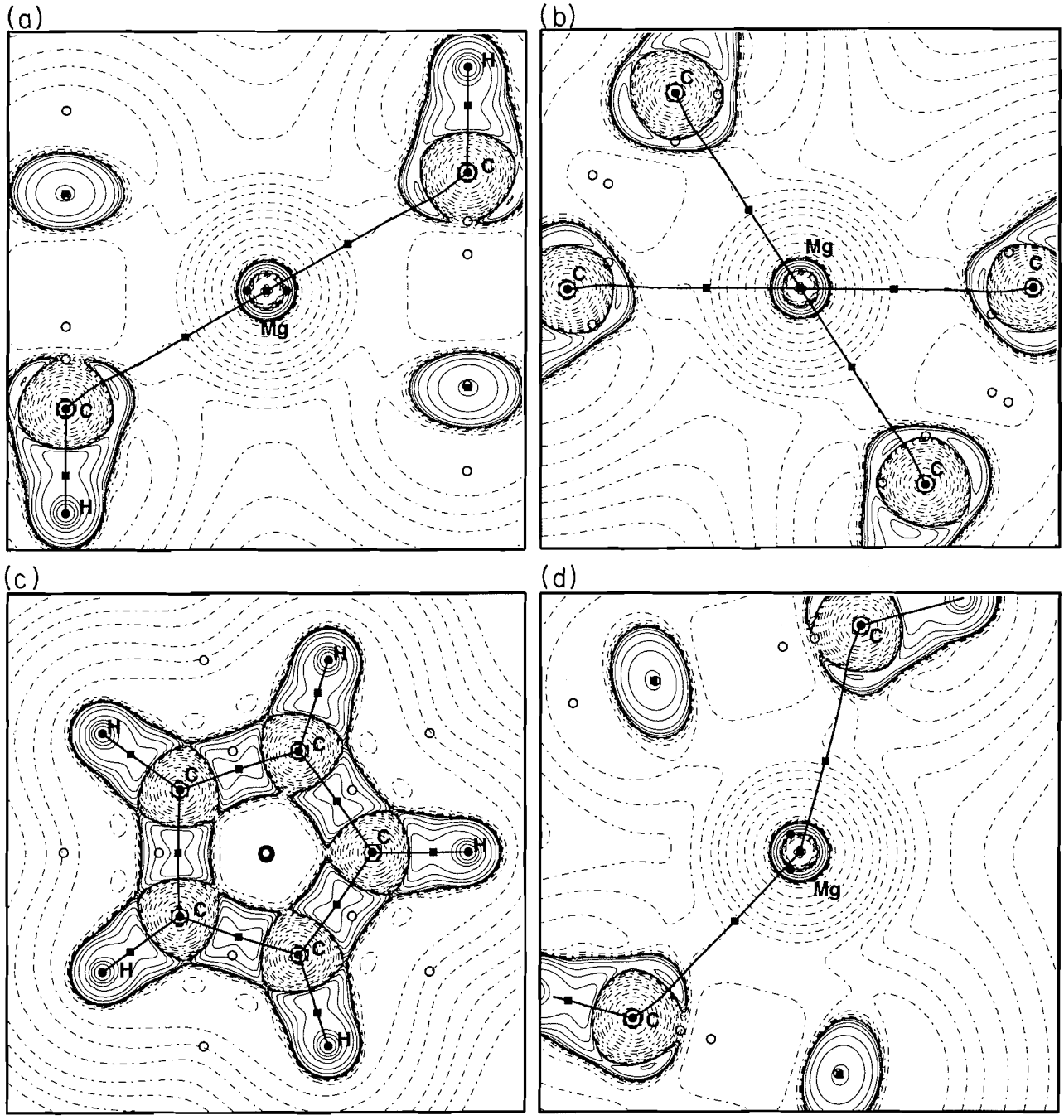

concentration is better described as a torus as the contour value shown is for a $\nabla^2\rho$ value of 0.395 au while the values at the maxima are only 0.402 au. The resolution of the torus of charge concentration into five maxima is a consequence of the D_{5d} symmetry of the molecule. In contrast to the bent molecule then, there are now regions of charge concentration (i.e., both tori) along all 10 Ca—C bonds in the linear molecule, which results in a less favourable geometry.

Previous studies of ρ and $\nabla^2\rho$ have shown that their topologies remain the same upon inclusion of electron correlation and only small quantitative changes at various critical points were noted (54, 55). With this in mind, the topologies of $\nabla^2\rho$

Fig. 5. Plots of $\nabla^2\rho$ for the HF optimized $CaCp_2$ molecule. (*a*) In the same plane as that used previously in Figs. 4(*a*) and 4(*d*) for $MgCp_2$. The region of charge concentration in the calcium core can be seen, although its topology is not evident. (*b*) In the same plane but focussing upon the calcium core region. Four maxima in $-\nabla^2\rho$ were found in this region, two are well defined by the contour chosen (0.39 au) regions and two in the long, narrow region in the middle left of the plot.

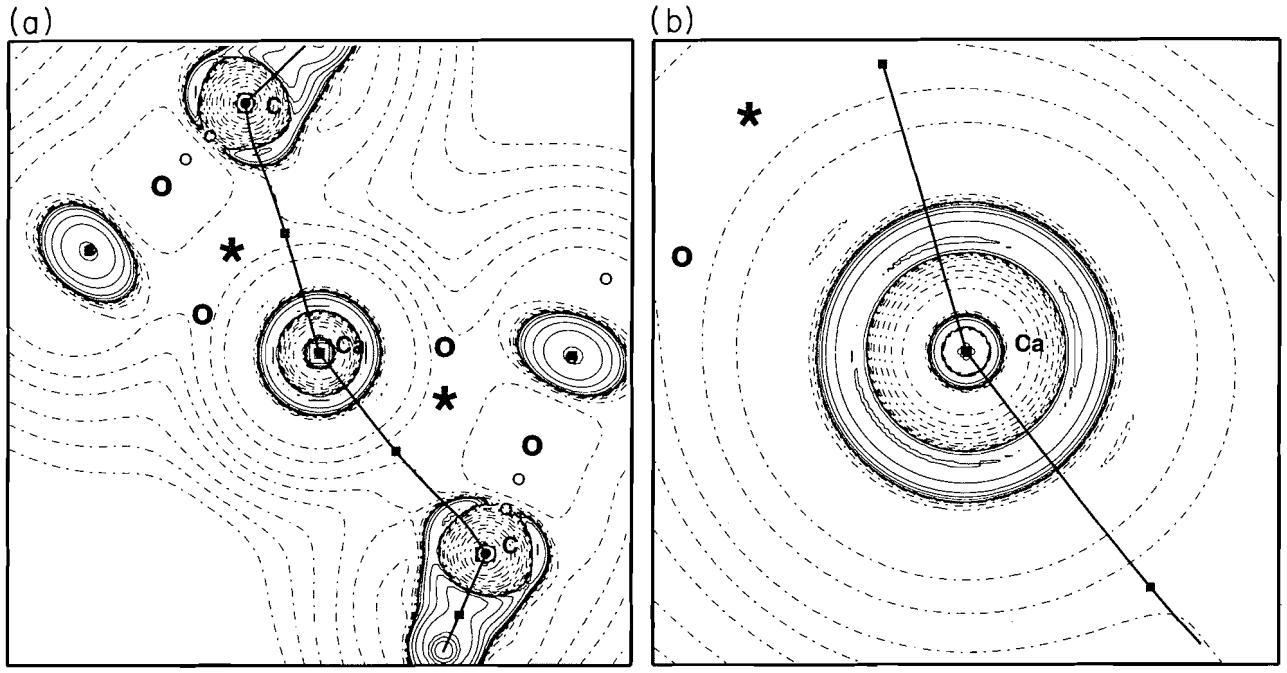

Fig. 6. Schematic representations of the arrangement of charge concentration maxima in the calcium core in both CaF_2 and $CaCp_2$ molecules relative to the fluoride and cyclopentadienyl ligands (X denotes the centroid of the Cp ligand). The approximate positions of charge concentration maxima are denoted by asterisks and are in the plane of the page in all cases except for the B3LYP optimized geometry of $CaCp_2$ (bottom right) in which case + and − symbols denote charge concentration maxima above and below the plane of the page, respectively.

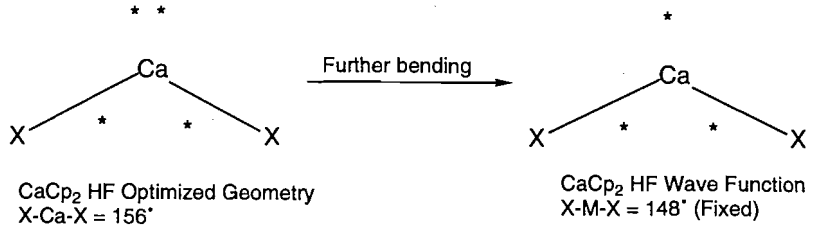

$CaCp_2$ HF Optimized Geometry
X-Ca-X = 156°

$CaCp_2$ HF Wave Function
X-M-X = 148° (Fixed)

CaF_2 HF Optimized Geometry
F-Ca-F = 156°

$CaCp_2$ B3LYP Optimized Geometry
X-M-X = 148°

Fig. 7. Plots of $\nabla^2\rho$ for the linear $CaCp_2$ molecule. (*a*) In the same plane as that used in Fig. 4*a*. (*b*) Focussing on the the calcium core region in this plane. The intersection of this plane with the tori of charge concentration maxima is apparent in this plot. (*c*) Plotted in the plane containing five charge concentration maxima with the C atoms of the nearest Cp ligand labelled. The five maxima are not apparent even though a contour of 0.395 was used and the maxima have values of 0.402 au.

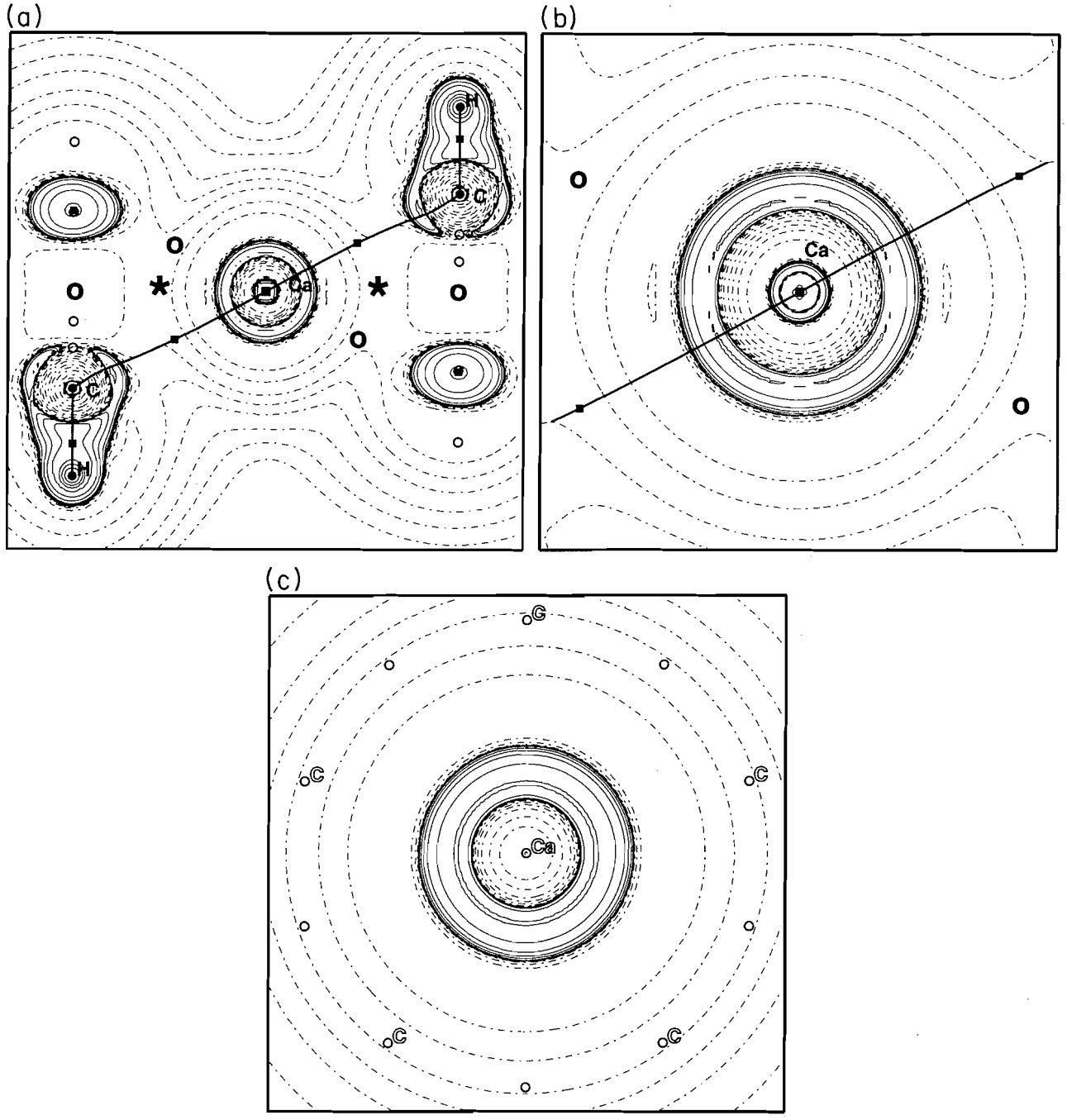

obtained from the B3LYP charge densities were also examined and values of the various (3, −3) charge concentration maxima are given in Table 2. As might be expected, the values of $\nabla^2\rho$ calculated by the two methods are in good agreement with each other, as are the distances from the calcium nucleus to the (3, −3) critical points. There is, however, a small difference in the atomic graphs of Ca given by the two methods. Analysis of the wave function obtained from the B3LYP geometry optimization of $CaCp_2$ revealed a square pyramidal arrangement of charge concentration maxima in the atomic graph of the Ca atom. A summary of the different atomic graphs obtained for the various calculations of $CaCp_2$ are shown in Fig. 6, along with that obtained previously for CaF_2 (18). These diagrams show how the various atomic graphs are related through the joining and splitting of charge concentration maxima.

Fig. 8. Plots of $\nabla^2\rho$ for the B3LYP optimized $CaCp_2$ molecule. (*a*) A view of the molecule plotted in the plane containing three of the calcium CCC maxima. No C or H nuclei are in this plane. (*b*) The calcium core shown in this same plane. The five charge concentration maxima are arranged in the form of a square pyramid, with the apex to the right of the Ca nucleus, and two diametrically opposed maxima shown in the left. (*c*) A plot for this molecule in the plane containing the Ca and two C atoms, i.e., that used in previous plots. $\nabla^2\rho$ in the core region is similar (in gross terms) to that shown in Fig. 5*a*.

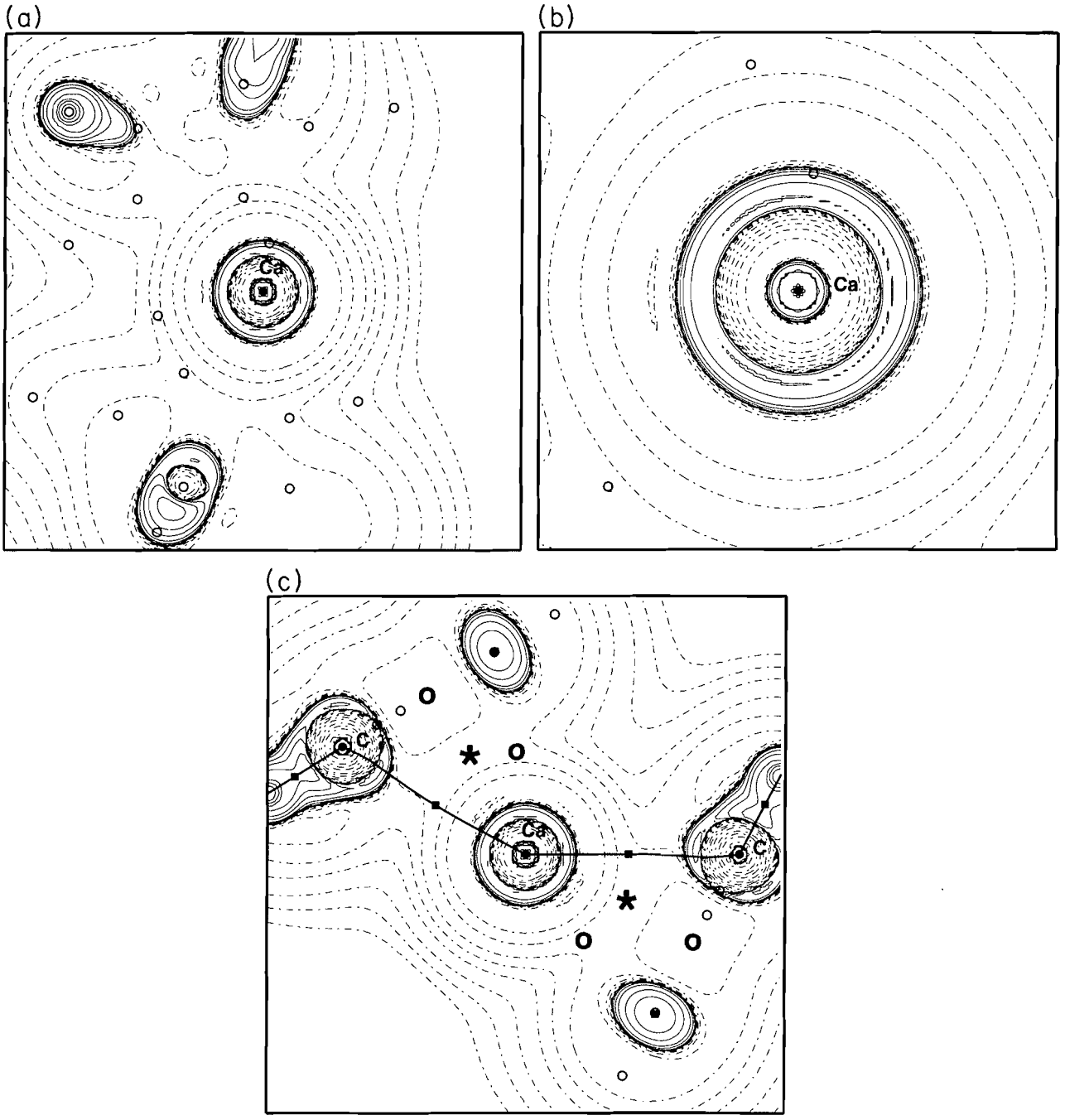

A plot of $\nabla^2\rho$ in the plane defined by the apical and two diametrically opposed charge concentrations is shown in Fig. 8*a*, which shows the relationship between the location of the core charge concentration maxima and the cyclopentadienyl ligands — note that no nuclei lie in this plane. Figure 8*b* is a magnification of the Ca core in the same plane as that used in Fig. 8*a*, where the apical charge concentration maximum is to the right of the Ca nucleus. Finally, a plot of $\nabla^2\rho$ in the same plane as that used in Fig. 5*a* is given in Fig. 8*c*, which shows the gross similarity between the HF and B3LYP results.

Results for the B3LYP calculations of the linear $CaCp_2$ molecule are also similar to the HF results, revealing two tori of charge concentration intersecting the Ca—C bond paths. In this case, however, the 10 charge concentration maxima are

eclipsed with respect to the nearest cyclopentadienyl ligand but, as found previously, the values of $-\nabla^2\rho$ are only marginally larger than the surrounding region of charge concentration. Thus a plot of $\nabla^2\rho$ in the plane of the five charge concentrations nearest a Cp ligand obtained from the linear B3LYP wave function is almost indistinguishable from that given in Fig. 7*c*. Although this finding is slightly different than the HF results, the location of critical points is an artifact of the imposed symmetry, and the explanation for the preferred bent geometry is the same.

Conclusions

The work presented here is part of the continuing exploration of the physical basis for the VSEPR model. We have presented charge density analyses for both magnesium and calcium dicyclopentadienes, and have shown that their preferred geometries can be understood using arguments similar to those used to explain the geometries of both MgF_2 and CaF_2 (18). Metallocene formation results in sufficient distortion of the metal atom such that it can no longer be considered spherical, as is usually assumed in the VSEPR model. It is these interactions between the ligands and the distorted core of the metal atom that play an important part in determining the preferred arrangement of the cyclopentadienyl ligands. Thus the preferred geometry is one in which the various types of interactions (i.e., ligand–ligand, CCC–ligand, and CCC–CCC) are minimized, in keeping with the spirit of the VSEPR model.

It is worth noting, however, that the possibility of attractive interactions between the cyclopentadienyl ligands in these group 2 metallocenes has been suggested (38, 39). In these calculations the group 2 metal atom was assumed to be spherical (39) so that the introduction of a Cp–Cp attractive term is then necessary in order to recover the bent nature of these molecules. On the basis of the results presented here it is not possible to dismiss the possibility of such dispersive (attractive) interactions between the Cp ligands in these molecules, although our explanation has the advantage that it is applicable to situations where such ligand–ligand attractions are not expected (e.g., the heavier group 2 dihalides). In terms of a molecular mechanics model, it seems reasonable to suggest that a potential function that mirrors these CCC–ligand repulsions be incorporated in place of the ligand–ligand attractive potential.

The testing ground for these ideas lies in the realm of experiment because, as we have seen, it is the exceptions to the VSEPR model that have prompted further study, and challenged its underlying assumptions. Within the context of this current work, it would be of interest to see how preferred geometries are affected as the size of the coordinated ligands is increased.

References

1. R.J. Gillespie and R.S. Nyholm. Q. Rev. Chem. Soc. **11**, 339 (1957).
2. R.J. Gillespie and I. Hargittai. The VSEPR model of molecular geometry. Allyn and Bacon, Boston. 1991.
3. R.J. Gillespie. Chem. Soc. Rev. 59 (1992).
4. D.L. Kepert. Inorganic stereochemistry. Springer Verlag, Berlin. 1982.
5. B.W. Clare, M.C. Favas, D.L. Kepert, A.S. May, and N.R. Taylor. J. Organomet. Chem. **478**, 111 (1994).
6. R.F.W. Bader and M.E. Stephens. Chem. Phys. Lett. **26**, 445 (1974).
7. R.F.W. Bader and M.E. Stephens. J. Am. Chem. Soc. **97**, 7391 (1975).
8. R.F.W. Bader, R.J. Gillespie, and P.J. MacDougall. J. Am. Chem. Soc. **110**, 7329 (1988).
9. R.F.W. Bader. Atoms in molecules: a quantum theory. Oxford University Press, Oxford. 1990.
10. R.F.W. Bader, P.J. MacDougall, and C.D.H. Lau. J. Am. Chem. Soc. **106**, 1594 (1984).
11. R.J. Gillespie. Educ. Chem. (1996) In press.
12. R.J. Gillespie and E.A. Robinson. Angew. Chem. Int. Ed. Engl. **35**, 495 (1996).
13. H. Oberhammer and J.E. Boggs. J. Mol. Struct. **56**, 107 (1979).
14. H. Günther, H. Oberhammer, R. Mews, and I. Stahl. Inorg. Chem. **21**, 1872 (1982).
15. R.J. Gillespie, I. Bytheway, R.S. DeWitte, and R.F.W. Bader. Inorg. Chem. **33**, 2115 (1994).
16. M. Hargittai. *In* Stereochemical applications of gas phase electron diffraction. Vol. B. *Edited by* I. Hargittai and M. Hargittai. VCH, New York. 1988. p. 383.
17. M. Hargittai and I. Hargittai. *In* Structures and conformations of non-rigid molecules. *Edited by* J. Laane, M. Dakkouri, B. van der Veken, and H. Oberhammer. NATO ASI Ser. Ser C: **410** (1993).
18. I. Bytheway, R.J. Gillespie, T.-H. Tang, and R.F.W. Bader. Inorg. Chem. **34**, 2407 (1995).
19. R. J. Gillespie. Molecular geometry. Van Nostrand Reinhold, London. 1972.
20. P.J. MacDougall, M.B. Hall, R.F.W. Bader, and J.R. Cheeseman. Can. J. Chem. **67**, 1842 (1989).
21. P.J. MacDougall and M.B. Hall. Trans. Am. Crystallogr. Assoc. **26**, 101 (1990).
22. A. Haaland, J. Lusztyk, J. Brunvoll, and K.B. Starowieyski. J. Organomet. Chem. **85**, 279 (1975).
23. R.A. Andersen, J.A. Boncella, C.J. Burns, R. Blom, and H.V. Volden. J. Organomet. Chem. **312**, C49 (1986).
24. R.A. Andersen, R. Blom, J.M. Boncella, C.J. Burns, and H.V. Volden. Acta Chem Scand. **A41**, 24 (1987).
25. R.A. Andersen, R. Blom, C.J. Burns, and H.V. Volden. J. Chem. Soc. Chem. Commun. 768 (1987).
26. R. Blom, K. Faegri, and H.V. Volden. Organometallics, **9**, 372 (1990).
27. W. Bünder and E. Weiss. J. Organomet. Chem. **92**, 1 (1975).
28. R. Zerger and G. Stucky. J. Organomet. Chem. **80**, 7 (1974).
29. R.A. Williams, T.P. Hanusa, and J.C. Huffman. Organometallics, **9**, 1128 (1990).
30. R.A. Williams, T.P. Hanusa, and J.C. Huffman. J. Chem. Soc. Chem. Commun. 1045 (1988).
31. J.V. Ortiz and R. Hoffmann. Inorg. Chem. **24**, 2095 (1985).
32. R.A. Andersen, J.M. Boncella, C.J. Burns, J.C. Green, D. Hohl, and N. Rösch. J. Chem. Soc. Chem. Commun. 405 (1986).
33. J.C. Green, D. Hohl, and N. Rösch. Organometallics, **6**, 712 (1987).
34. H.P. Lüthi, J.H. Ammeter, J. Almlöf, and K. Faegri. J. Chem. Phys. **77**, 2002 (1982).
35. J. Almlöf, K. Faegri, B.E.R. Schilling, and H.P. Lüthi. Chem. Phys. Lett. **106**, 266 (1984).
36. H.P. Lüthi, Per E.M. Siegbahn, J. Almlöf, K. Faegri, and A. Heiberg. Chem. Phys. Lett. **111**, 1 (1984).
37. M. Kaupp, P. v.R. Schleyer, M. Dolg, and H. Stoll. J. Am. Chem. Soc. **114**, 8202 (1992).
38. T.K. Hollis, J.K. Burdett, and B. Bosnich. Organometallics, **12**, 3385 (1993).
39. T.V. Timofeeva, J.-H. Lii, and N.L. Allinger. J. Am. Chem. Soc. **117**, 7452 (1995).
40. A.J.H. Wachters. J. Chem. Phys. **52**, 1033 (1970).

41. M.J. Frisch, G.W. Trucks, M. Head-Gordon, P.M.W. Gill, M.W. Wong, J.B. Foresman, B.G. Johnson, H.B. Schlegel, M.A. Robb, E.S. Replogle, R. Gomperts, J.L. Andres, K. Raghavachari, J.S. Binkley, C. Gonzalez, R.L. Martin, D.J. Fox, D.J. Defrees, J. Baker, J.P. Stewart, and J.A. Pople. Gaussian 92/DFT, Revision G.1. Gaussian Inc., Pittsburgh, Pa. 1993.
42. V. Barone. Chem. Phys. Lett. **226**, 392 (1994).
43. R.H. Hertwig and W. Koch. J. Comput. Chem. **16**, 576 (1995).
44. C.W. Bauschlicher, Jr. and H. Partridge. Chem. Phys. Lett. **240**, 533 (1995).
45. F.W. Biegler-König, R.F.W. Bader, and T.-H. Tang. J. Comput. Chem. **3**, 317 (1982).
46. J. Simons, P. Jorgensen, H. Taylor, and J. Ozment. J. Phys. Chem. **87**, 2745 (1983).
47. C.J. Cerjan and W.H. Miller. J. Chem. Phys. **75**, 2800 (1981).
48. J. Baker. J. Comput. Chem. **7**, 385 (1986).
49. P.L.A. Popelier. Chem. Phys. Lett. **228**, 160 (1994).
50. P.L.A. Popelier. Comput. Phys. Commun. In press.
51. R.F.W. Bader and P.J. MacDougall J. Am. Chem. Soc. **107**, 6788 (1985).
52. L. Seijo, Z. Barandiarán, and S. Huzinaga. J. Chem. Phys. **94**, 3762 (1991), and references cited therein.
53. D.M. Hassett and C. J. Marsden. J. Mol. Struct. **346**, 249 (1995).
54. C. Gatti, P.J. MacDougall, and R.F.W. Bader. J. Chem. Phys. **88**, 3792 (1988).
55. L.-C. Wang and R.J. Boyd. J. Chem. Phys. **90**, 1083 (1989).

A comparative study of the energetics, structures, and mechanisms of the HCN ↔ HNC and LiCN ↔ LiNC isomerizations

V. Sreedhara Rao, Amrendra Vijay, and A.K. Chandra

Abstract: The potential energy surfaces of the HCN ↔ HNC and LiCN ↔ LiNC isomerization processes were determined by ab initio theory using fully optimized triple-zeta double polarization types of basis sets. Both the MP2 corrections and the QCISD level of calculations were performed to correct for the electron correlation. Results show that electron correlation has a considerable influence on the energetics and structures. Analysis of the intramolecular bond rearrangement processes reveals that, in both cases, H (or Li^+) migrates in an almost elliptic path in the plane of the molecule. In HCN ↔ HNC, the migrating hydrogen interacts with the in-plane π,π^* orbitals of CN, leading to a decrease in the C—N bond order. In LiCN ↔ LiNC, Li^+ does not interact with the corresponding π,π^* orbitals of CN.

Key words: potential energy surfaces, intra-molecular bond rearrangement, bond orders, elliptic path, migration of Li^+.

Résumé : On a déterminé les surfaces d'énergie potentielle des processus d'isomérisation HCN ↔ HNC et LiCN ↔ LiNC à l'aide de la théorie ab initio, en faisant appel à des ensembles de base de type double polarisation, triple zêta, totalement optimisés. Dans le but de corriger la corrélation électronique, on a effectué des corrections MP2 ainsi que des calculs au niveau QCISD. Les résultats montrent que la corrélation électronique a une grande influence sur les énergies et les structures. L'analyse des processus de réarrangement intramoléculaire des liaisons révèle que, dans chacun des cas, H (ou Li^+) migre par une voie pratiquement elliptique dans le plan de la molécule. Dans le réarrangement HCN ↔ HNC, l'hydrogène qui migre interagit avec les orbitales $\pi,\pi p^*$ dans le plan CN conduisant à une diminution de l'ordre de la liaison C—N. Dans LiCN ↔ LiNC, Li^+ n'interagit pas avec les orbitales π,π^* correspondantes du CN.

Mots clés : surfaces d'énergie potentielle, réarrangement intramoléculaire d'une liaison, ordres de liaison, voie elliptique, migration du Li^+.

[Traduit par la rédaction]

Introduction

One of the major goals of quantum chemistry is to predict from ab initial calculations the energetics, structures of molecules, and dynamics of chemical reactions. Of many chemically bound molecules, hydrogen cyanide has been studied extensively, both theoretically and experimentally (1–9). Both hydrogen cyanide and its isomer isocyanide are abundant in interstellar clouds (1). The energetics and structures of the HCN ↔ HNC isomerization process have been investigated in several papers by ab initio methods (2–9). Pau and Hehre (10) observed that the heat of reaction of the HCN ↔ HNC isomerization is 60 ± 8 kJ/mol, where HNC is the less stable. Pearson et al. (2) suggested from SCF calculations using double-zeta plus polarization functions that HNC lies 40 kJ/mol above HCN while the configuration interaction yields 61.3 kJ/mol. The barrier heights for this isomerization were estimated at 168.0 and 146.6 kJ/mol by the SCF and CI methods, respectively (2). The latter value of the barrier height was also obtained from the potential energy surface of Murrell et al. (11). Recent calculations at the single and double excitation coupled-cluster (CCSD) and CCSD(T) levels of theory by Lee and Rendell (12) led to a transition state 187 kJ/mol above the HCN isomer, while HNC was predicted to be 61 ± 4 kJ/mol above HCN. All these studies agree that HCN is linear with the H atom bound to carbon and this is borne out by experiment (13). Detailed calculations by Bowman et al. (14*a*) on the HCN ↔ HNC isomerization using a large atomic natural orbital (ANO) 1-particle basis set with the CCSD(T) theory predicts a barrier of 202.3 kJ/mol and an endothermicity of 61.7 kJ/mol measured from HCN. They have fitted the ab initio potential surface with the Morse potential via the nonlinear least-squares method and obtained the vibrational frequencies for the HCN and HNC. Their results are in good agreement, within 10 cm^{-1}, with the experimental frequencies. The further augmentation of g and f functions (14*b*) on heavy (C, N) and light (H) atoms, respectively, to the ANO basis set reveals closer agreement of the fundamental vibrational frequencies with the experimental data.

Extensive studies of the HCN ↔ HNC isomerization have

Received September 14, 1995.

This paper is dedicated to Professor Richard F.W. Bader on the occasion of his 65th birthday.

V.S. Rao, A. Vijay, and A.K. Chandra.[1] Department of Inorganic and Physical Chemistry, Indian Institute of Science, Bangalore-560 012, India.

[1] Author to whom correspondence may be addressed.
Telephone: (91) (80) 334-4411, ext. 2382.
Fax: (91) (80) 334-1683.
E-mail: akc@hamsadvani.serc.iisc.ernet.in

naturally led to an interest in the LiCN ↔ LiNC isomerization. LiCN is predicted to be linear and to have also an isocyanide structure (15). Besides, the number of valence electron pairs is the same in HCN and LiCN. So the correlation energies of the Li isomers are expected to be close to those of the H isomers. Among the earlier studies of the LiCN ↔ LiNC isomerization, those of Clementi et al. (15) are worth mentioning. They used a Slater-type basis set at the Hartree–Fock level and observed no energy barrier between the LiCN and LiNC linear configurations and that the two molecules have nearly the same energies. Later, Essers et al. (16) performed ab initio SCF calculations using a large polarized Gaussian basis set and observed a small barrier above LiCN for isomerization to LiNC. Experimental studies by Van Vaals et al. (17) via molecular beam microwave spectroscopy confirms the presence of LiNC and its linear structure. Ab initio calculations by von Schleyer et al. (18) predict the presence of another minimum, centered near LiNC, with T-shaped structure. This result has not been confirmed by experiment. Most recent calculations (19) on the LiCN ↔ LiNC isomerization were carried out up to second-order Møller–Plesset perturbation theory, by employing an extended 6-311++G(2d,f) basis set. These results also revealed two linear and one T-shaped structures. The energies of the various structures were found to be very sensitive to electron correlation.

Although ab initio calculations with large basis set including polarization functions are reported, the basis set parameters are not fully optimized. All of the Pople basis sets (20, 21) have larger basis set superposition errors (BSSE) (22) than the Dunning bases (22–24). Therefore the Dunning bases give more accurate energies at the both SCF and CI levels than do the Pople bases. Lee and Rendell (12) used the basis set of triple-zeta double-polarization type (TZ2P) with f functions on hydrogen and g functions on carbon and nitrogen in HCN. Addition of polarization functions generally increases BSSE and optimization of orbital exponents on augmented polarization functions could be tantamount to optimizing BSSE (25). For calculations of LiCN, Makarewicz and Ha (19) used the 6-311++G(2d,f) functions. Grev and Schaefer (26) have studied the 6-311G basis set of Pople and co-workers (27) and observed that this is essentially of the double-zeta quality and should be represented as 63-11G instead of 6-311G. This may be due to collapse of the valence orbitals into the core. The simple comparison of energies calculated with bases of different sizes cannot decide on the quality of the basis set. Rather, the optimum values of the orbital exponents determine the quality of the basis set. The magnitude of the reduced gradient of the energy with respect to the Gaussian exponents

$$|g| = \frac{\sum G_i}{n}$$

where

$$G_i = \frac{\partial E}{\partial \ln \delta_i}$$

and n = number of exponents, has been suggested as a measure of the quality of a basis set by Mezey, Kari, and Csizmadia (28). Recently, Schäfer et al. (29) determined basis sets for several atoms where all the basis set parameters are fully optimized by means of gradient techniques.[2] They noted that Huzinaga's atom-optimized GTO basis sets (30) are, in part, far from being optimized. Even Dunning bases (31) have been found to have large reduced gradients, |g|. Schäfer et al. (29) presented fully optimized basis sets, for several atoms, of relatively small size with least possible loss in accuracy. In this paper we have used their basis sets of the TZ2P type, which are expected to be superior to those created by just contracting atom-optimized GTO sets.

The main purpose of this paper is to determine the energetics, structures, and the minimum energy path for HCN ↔ HNC and LiCN ↔ LiNC isomerizations and to bring out any difference in the mechanisms of these two intramolecular bond-rearrangement processes. Although the energetics of these two processes were studied theoretically earlier, they were reported at different levels of calculation. In this paper, we maintain the same level of calculation for both systems so that a meaningful comparison can be made. We make corrections for electron correlation in our calculations.

2. Computational methodology

For accurate description of chemical bonding one needs the triple-zeta double-polarization (TZ2P) type of basis set for the SCF calculations. In our calculations, we utilized a triple-zeta basis set in full space augmented with two sets of polarization functions on each atom (TZ2P). The basis set parameters for atomic core and valence orbitals were taken from Schäfer et al. (29). The exponents of the polarization functions were taken from Huzinaga (30) and the values of the polarization functions are α_p(H) = 0.388, 1.141; α_p(Li) = 0.044, 0.161; α_d(C) = 0.288, 1.335; and α_d(N) = 0.412, 1.986. To note the effect of higher polarization functions, we augmented the TZ2P set with one set of d functions on H and Li and one set of f functions on C and N (TZ2P(d,f)). The exponents of the d and f functions were taken from Dunning (31) and the values are α_d(H) = 1.057, α_d(Li) = 0.2, α_f(C) = 0.761, and α_f(N) = 1.093. These basis set parameters were optimized in full space (29). The pure spherical harmonic components of the d and f functions were incorporated in the basis sets. We used the Gaussian 92 (32) series of programs for the restricted Hartree–Fock single configuration calculations using the TZ2P and TZ2P(d,f) basis functions. We then made the correlation corrections using Møller–Plesset perturbation theory by treating the correlation part of the Hamiltonian as a perturbation on the Hartree–Fock and treating the energy expansion at the second order (MP2) (33).

We consider the quadratic configuration interaction with single and double excitations (34). This method, called QCISD, was proposed by Pople et al. (34) and has the features of size consistency. These authors claimed that the results of QCISD calculations deviate from that of CCSD in the fifth order. A more recent report (35) reveals that QCISD and CCSD are correct to the fourth order of perturbation in the space of single, double, and quadruple substitutions

[2] These basis functions were obtained via file transfer protocol from the directory with the internet address "tchibm3.chemie.uni-karlsruhe.de" (internet no. 129.13.107.186) using anonymous login.

Fig. 1. The structural parameters R and θ in the X-CN ↔ X-NC bond rearrangement processes (X = H, Li).

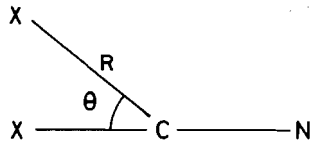

(MP4SDQ). Therefore, the QCISD method may be considered valuable in exploring correlation energies for a wide range of molecules. All the core and valence electrons were considered for electron correlation in both systems.

We consider that, in both the HCN ↔ HNC and LiCN ↔ LiNC isomerization processes, the C—H and C—Li bonds move away from the internuclear axis by the variable angle θ (Fig. 1). Geometry optimizations were carried out analytically at both the SCF and the correlated levels employing Schlegel's technique (36) with an SCF convergence of energy to 10^{-11} au and density to 10^{-9}. At the optimum point, the largest component of the Cartesian gradient vector was less than 10^{-4} hartree/bohr. The first derivatives of the energies were estimated analytically while the force constant matrix elements were evaluated by numerical methods at the QCISD level. The force constant matrix was then diagonalized in mass-scaled Cartesian space to obtain the vibrational frequencies. The saddle point in the isomerization paths was identified by its having only one negative eigenvalue in the force constant matrix.

3. Results and discussion

Energies of HCN, HNC, and the transition state of the HCN ↔ HNC isomerization process obtained at the different levels of calculations are reported in Table 1. Table 2 reports the results of similar calculations for the LiCN ↔ LiNC isomerization. Table 3 gives the optimized structures of the various species observed in the minimum energy paths for the two isomerization processes. The optimized equilibrium structures of HCN, HNC, LiCN, and LiNC are linear. Results show that there is hardly any influence of the additional polarization functions d,f in TZ2P on the energies or the geometrical structures in the HCN ↔ HNC and LiCN ↔ LiNC isomerization processes. On the other hand, electron correlation has a considerable influence on the energetics. Also, at the correlated levels bond lengths are longer than at the SCF level. We observe that the correlation energies in HCN, HNC, LiCN, and LiNC are nearly equal to each other in value. That the correlation energies of the Li isomers are nearly same as those of the H isomers is expected because the number of valence electron pairs is the same. Table 2 shows that at the SCF level LiNC is more stable than LiCN. Clementi et al. (15) also observed that the LiNC structure is more stable than the LiCN structure in the Hartree–Fock model. At the MP2 level of electron correlation, LiCN is more stable than LiNC. This is because the cyanide has a larger correlation energy than isocyanide at the MP2 level. On the other hand, at the QCISD level of calculations LiNC is more stable than LiCN. The linear LiNC equilibrium structure has been confirmed experimentally by molecular beam spectroscopy (17). Our ab initio calculations with corrections for electron correlation reveal three local minima on the potential energy surface of the LiCN ↔ LiNC isomerization. The additional minimum corresponds to a triangular nearly T-shaped structure. Since the energies of the three local minima are very close to each other, the relative stabilities could not be definitely established. Since the energy barrier from this second minimum (T-shaped) to the second transition state is within the error bars of our calculations, no significance is given to the second transition state. Our ab initio calculations with the geometry optimization could not isolate the second transition state between the T-shaped minimum and LiNC. Besides, molecular beam spectroscopy could not detect the T-shaped structure of LiCN. On the other hand, gas phase rotational spectroscopy (37, 38) determined unambiguously the T-shaped structures of NaCN and KCN.

4. HCN ↔ HNC isomerization

Traditional discussions of chemical reaction center on the minimum energy path (MEP), which follows from one minimum over the saddle point to the other minimum. Figure 1 shows the two coordinates R and θ to determine the relative orientations of the migrating atom. In previous papers the C—N bond length was kept fixed during the isomerization process, as it was believed that variation in the C—N bond lengths did not play a crucial role in the reaction. Optimized bond length data in Table 3 reveal that the C—N bond length changes during this isomerization. We select the coordinate θ, which varies monotonically in the course of the reaction, for values of θ varying from 0° to 180°; the optimized values of R are so determined that the energy is minimized. The path of minimum energy is given as a polar graph in Fig. 2*a* where one sees that the path is elliptic but not symmetric about the minor axis. The value of θ at the saddle point is 110°. It should be noted that the value of θ is not very sensitive to the level of calculation. The value of θ obtained by Lee and Rendell for the transition state structure was 104.2°. As the system approaches the transition state, both the C—H and C—N bond lengths increase. The height of the barrier is 187 kJ/mol while the heat of isomerization is 58 kJ/mol at the QCISD level of calculations. Determination of the heat of reaction by Pau and Hehre (10), using ion cyclotron double-resonance spectroscopy, yields 60 kJ/mol, which is in excellent agreement with our QCISD results. The best experimental value of the activation barrier of 145 kJ/mol comes from a semi-empirical potential energy surface of Murrell et al. (11). Lee and Rendell, however, concluded that the PES of Murrell et al. was not accurate in the transition state region and their estimate (12) was 187.3 ± 4.2 kJ/mol. The calculated energy difference between HCN and HNC, where the latter is less stable than the former and there is a large barrier for isomerization from HCN to HNC, explains why HNC was not observed in HCN at room temperature. However, at high temperatures ($T > 900$ K) HNC was observed in equilibrium with HCN (39).

We then consider Mayer's definition of bond order from the standard density matrix (40). The density matrix in the CI calculations is not idempotent and may not give reliable changes in bond order along the minimum energy path (MEP). We consider the density matrix obtained from the single configuration calculations with the MP2 correction using the TZ2P basis functions. In the HCN ↔ HNC isomerization, the C—H bond is broken and an N—H bond is formed. Population analysis shows that the charge on hydrogen is +0.15, so the H—C

Table 1. Energies of HCN, transition state (TS), and HNC in atomic units. The activation barrier E_a and heat of reaction ΔE are in kJ/mol.

	SCF/TZ2P	MP2 = full/TZ2P	SCF/TZ2P(d,f)	MP2 = full/TZ2P(d,f)	QCISD/TZ2P(d,f)
HCN	−92.909 09	−93.263 50	−92.912 62	−93.291 14	−93.257 18
TS	−92.830 87	−93.177 69	−92.833 93	−93.206 14	−93.179 71
HNC	−92.892 19	−93.233 76	−92.896 16	−93.262 26	−93.234 02
E_a[a]	190	213	191	211	187
ΔE[a]	42	77	41	75	58

[a]These numbers include zero point vibrational energy corrections.

Table 2. Energies of LiCN, transition state (TS), T-shaped structure, and LiNC in atomic units. The activation barrier E_a and heat of reaction ΔE are in kJ/mol.

	SCF/TZ2P	MP2 = full/TZ2P	SCF/TZ2P(d,f)	MP2 = full/TZ2P(d,f)	QCISD/TZ2P(d,f)
LiCN	−99.807 11	−100.175 09	−99.810 01	−100.202 44	−100.151 98
TS	−99.801 72	−100.169 44	−99.804 73	−100.197 24	−100.147 19
T-shaped structure	−99.812 72	−100.175 09	Not observed	−100.203 71	−100.155 31
LiNC	−99.814 19	−100.173 36	−99.818 37	−100.201 80	−100.154 95
E_a[a]	11.89	12.82	11.59	11.68	10.57
ΔE[a]	−19.96	3.82	−23.15	1.1	−8.83

[a]These numbers include zero point vibrational energy corrections.

Table 3. The optimized bond lengths (Å) in reactants, transition states (TS), and products in the HCN → HNC and LiCN → LiNC isomerizations.

		SCF/TZ2P	MP2 = full/TZ2P	SCF/TZ2P(d,f)	MP2 = full/TZ2P(d,f)	QCISD/TZ2P(d,f)
HCN	R_{C-H}	1.056	1.063	1.056	1.0615	1.064
	R_{C-N}	1.123	1.163	1.124	1.1620	1.152
TS	R_{C-H}	1.157	1.176	1.154	1.172	1.182
	R_{N-H}	1.457	1.406	1.464	1.410	1.391
	R_{C-N}	1.159	1.184	1.159	1.184	1.187
HNC	R_{N-H}	0.981	0.995	0.983	0.994	0.992
	R_{C-N}	1.144	1.173	1.144	1.172	1.161
LiCN	R_{Li-C}	1.950	1.950	1.950	1.950	1.950
	R_{C-N}	1.138	1.177	1.139	1.177	1.166
TS	R_{Li-C}	1.930	1.930	1.930	1.930	1.930
	R_{C-N}	1.140	1.180	1.140	1.180	1.169
	R_{Li-N}	2.650	2.620	2.120	2.640	2.660
T-shaped structure	R_{Li-C}	2.461	2.123	Not observed	2.116	2.169
	R_{C-N}	1.154	1.186		1.186	1.178
	R_{Li-N}	1.885	1.921		1.915	1.888
LiNC	R_{Li-N}	1.780	1.810	1.780	1.811	1.804
	R_{C-N}	1.150	1.180	1.152	1.182	1.176

Fig. 2. (*a*) An almost elliptic path for hydrogen migration in the HCN ↔ HNC isomerization. The black dots refer to the changed positions of nitrogen during the rearrangement process. The position of the transition state is indicated by TS. (*b*) An almost elliptic path for Li^+ migration in the LiCN ↔ LiNC isomerization. The position of the transition state is indicated by TS.

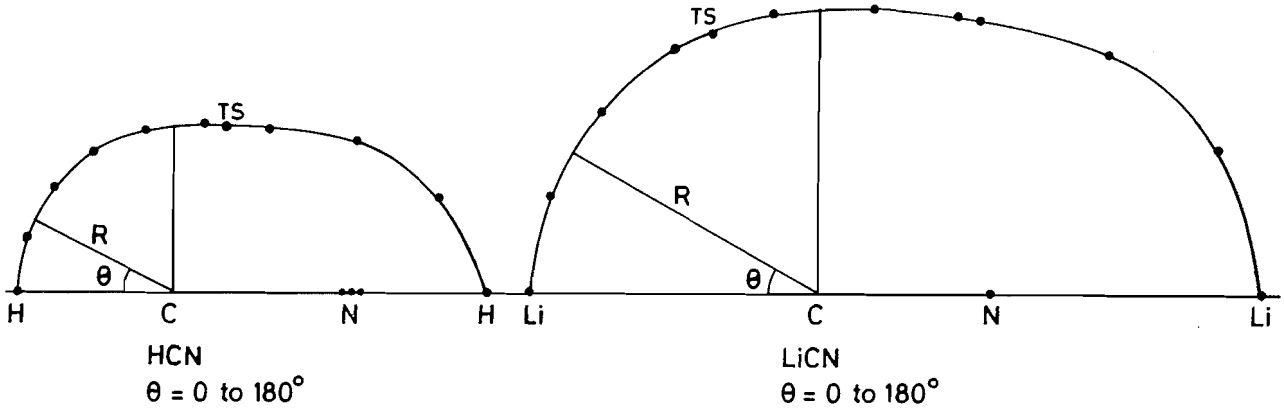

bond in HCN is predominantly covalent. Our bond-order calculations reveal that the sum of the C—H and N—H bond orders is nearly constant and close to unity along the MEP. But the C—N bond is not passive during the isomerization process. Figure 3 shows how the C—N bond order (B_{CN}) changes from a nearly triple bond in HCN to a nearly double bond in HNC. Optimization of bond lengths in our ab initio calculations also shows that the CN bond length increases from 1.16 to 1.18 Å in the transition state. When the hydrogen atom migrates in the plane of the molecule, the orbitals of hydrogen interact with the in-plane π and π^* orbitals of CN, as the distance of H from C in the transition state is only 1.18 Å. This leads to a decrease of the C—N bond order and an increase of energy. Thus, the migration of hydrogen from the carbon end to the nitrogen end via the elliptic path (Fig. 2) involves overcoming a large barrier that may arise primarily from the weakening of the C—N bond, as the C—H bond cleavage and the N—H formation may almost annul each other in the reaction path.

5. LiCN ↔ LiNC isomerization

We have now established that the two Li isomers have nearly the same energies. Population analysis of LiCN at the same level as that of HCN reveals that Li has +0.70 charge and therefore the Li—C bond is predominantly ionic. The path of minimum energy for migration of Li^+ from the C-end to the N-end is once again elliptic but not symmetric about the minor axis (shown in Fig. 2*b*). The orbiting of Li^+ around the C—N bond had also been observed earlier by Clementi et al. (15). Since the bond is ionic, the Coulomb force should dominate the bonding. This force is isotropic and the orbiting of Li^+ around the remainder of the molecule involves no, or very little, expenditure of energy, unlike the orbiting of hydrogen in the HCN ↔ HNC isomerization. This is borne out by our observation of a very low barrier of ~10.6 kJ/mol. The value of θ at the saddle point is nearly ~70° in the LiCN ↔ LiNC isomerization. The saddle point is characterized by its having a negative eigenvalue in the force constant matrix. Since a very low barrier exists between the two linear geometries (LiCN and LiNC), the bending of the Li—C bond from the linear structure becomes very easy. Our force constant calculations reveal that the bending force constant in LiCN is lower than that in HCN. Besides, the calculated bending vibration frequencies of the Li—C and H—C bonds in LiCN and HCN are 175 and 756 cm^{-1}, respectively, at the QCISD/TZ2P(d,f) level.

We then consider the bond orders according to Mayer's definition, following the same level of calculations as that the HCN ↔ HNC isomerization. Mayer's definition leads to a small bond order for an ionic bond. The Li—C bond in the equilibrium linear structure of LiCN has a bond order of 0.47, which decreases while that of Li—N increases along the MEP. On the other hand, the C—N bond order remains constant until the transition state is reached and then decreases until LiNC is formed, where the N—C bond is nearly a double bond. The variation of the C—N bond order with θ is shown in Fig. 3. Optimization of bond length shows that the C—N bond length remains constant at 1.18 Å throughout the reaction path while the Li—C bond initially decreases slightly and then increases in LiNC. When Li^+ migrates along an elliptic path in the plane of the molecule, there is hardly any interaction between the orbitals of Li^+ and the in-plane π,π^* orbitals of CN. This is due to the fact that the atomic radius of Li^+ is only 0.19 Å, which is less than the atomic radius of hydrogen (0.30 Å) (41). As well, the H—C distance in the elliptic path during the migration of hydrogen in the HCN ↔ HNC isomerization is smaller than the Li^+—C distance in the LiCN ↔ LiNC isomerization process.

6. Conclusions

We observe that electron correlation has a considerable influence on the energetics and structures in the HCN ↔ HNC and LiCN ↔ LiNC isomerization processes. The correlation energies in HCN, HNC, LiCN, and LiNC are almost the same. In both isomerization processes, H (or Li^+) migrates in an elliptic path in the plane of the molecule. In HCN the C—H bond is predominantly covalent while the Li—C bond in LiCN is predominantly ionic. In the HCN ↔ HNC isomerization, migration of hydrogen involves overcoming a large barrier. The

Fig. 3. The change of the C—N bond order during the HCN ↔ HNC and LiCN ↔ LiNC isomerization processes. The positions of the transition states are indicated by arrows.

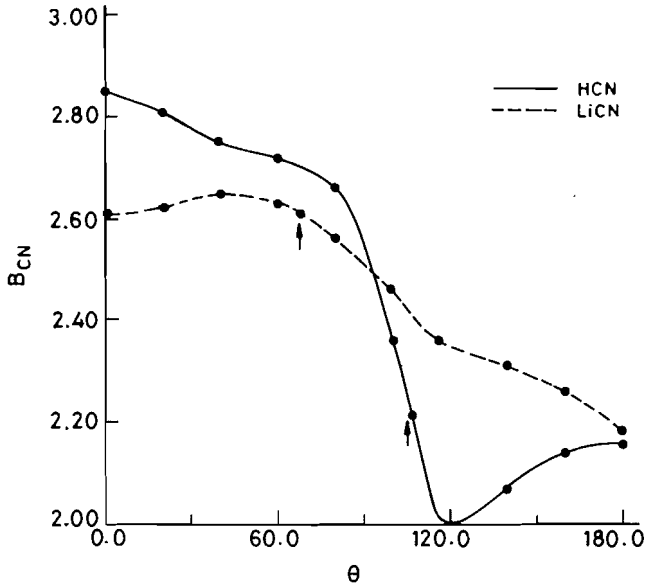

origin of the large barrier lies primarily in the interaction of the migrating hydrogen with the in-plane π,π^* orbitals of the C—N bond, which leads to a decrease of the C—N bond order in the transition state. In the LiCN ↔ LiNC isomerization, the Coulomb force dominates the bonding. Since the Coulomb force is isotropic, migration of Li^+ involves very little or negligible barrier. There is hardly any interaction of Li^+ with the in-plane π,π^* orbitals of the C—N bond until the saddle point is reached.

Acknowledgement

One of the authors (A.K.C.) thanks the Council of Scientific and Industrial Research (Govt. of India) for financial support.

References

1. L.E. Snyder and D. Pull Prau. Am. Acad. Sci. **3**, 388 (1971); B. Zuckerman, M. Morris, P. Palmer, and B.E. Turner. Astrophys. J. Lett. **173**, L.125 (1972); R.L. Snell and A. Wootton. Astrophys. J. **228**, 748 (1979).
2. P.K. Pearson, H.F. Schaefer II, and U. Wahlgren. J. Chem. Phys. **65**, 350 (1975).
3. P.R. Taylor, G.B. Bacskay, N. Hush, and A.C. Hurley. J. Chem. Phys. **69**, 4669 (1978).
4. P.R. Taylor, G.B. Bacskay, N. Hush, and A.C. Hurley. J. Chem. Phys. **69**, 1971 (1978).
5. L.T. Redmon, G.D. Purvis, and R.J. Bartlett. J. Chem. Phys. **72**, 986 (1980).
6. C.E. Dykstra and D. Secrest. J. Chem. Phys. **75**, 3967 (1981).
7. J.A. Pople, K. Raghavachari, M.J. Frisch, J.S. Binkley, and P. von R. Schleyer. J. Am. Chem. Soc. **105**, 6389 (1983).
8. W.D. Ladig, Y. Yamaguchi, and H.F. Schaefer III. J. Chem. Phys. **86**, 3069 (1984).
9. B.H. Besler, G.E. Scuseria, A.C. Scheiner, and H.F. Schaefer III. J. Chem. Phys. **89**, 360 (1988).
10. C.F. Pau and W.J. Hehre. J. Phys. Chem. **86**, 321 (1982).
11. J.N. Murrell, S. Carter, and L.O. Halomen. J. Mol. Spectrosc. **93**, 307 (1982).
12. T.J. Lee and A.P. Rendell. Chem. Phys. Lett. **177**, 491 (1991).
13. G. Winnewisser, A.G. Maki, and D.R. Johnson. J. Mol. Spectrosc. **261**, 395 (1976).
14. (*a*) J.M. Bowman, B. Gazdy, J.A. Bentley, T.J. Lee, and C.E. Dateo. J. Chem. Phys. **99**, 308 (1993); (*b*) T.J. Lee, C.E. Dateo, B. Gazdy, and J.M. Bowman. J. Phys. Chem. **97**, 8937 (1993).
15. E. Clementi, H. Kistenmacher, and H. Popkie. J. Chem. Phys. **58**, 2460 (1973).
16. R. Essers, J. Tennyson, and P.E.S. Wormer. Chem. Phys. Lett. **89**, 223 (1982).
17. J.J. Van Vaals, W.L. Meerts, and A. Dymanus. Chem. Phys., **86**, 147 (1984).
18. P.v.R. Schleyer, A. Sawaryn, E.A. Reed, and P. Hobza. J. Comput. Chem. **7**, 666 (1986).
19. J. Makarewicz and T.K. Ha. J. Mol. Struct. (Theochem), **315**, 149 (1994).
20. R. Ditchfield, W.J. Hehre, and J.A. Pople. J. Chem. Phys. **54**, 724 (1971); W.J. Hehre and W.A. Lathan. J. Chem. Phys. **56**, 5225 (1972).
21. W.J. Hehre, R. Ditchfield, and J.A. Pople. J. Chem. Phys. **56**, 2257 (1972); M.M. Francl, W.J. Pietro, W.J. Hehre, J.S. Binkley, M.S. Gordon, D.J. DeFrees, and J.A. Pople. J. Chem. Phys. **77**, 3654 (1982).
22. E.R. Davidson and D. Feller. Chem. Rev. **86**, 681 (1986).
23. T.H. Dunning. J. Chem. Phys. **53**, 2883 (1970).
24. T.H. Dunning and P.J. Hay. *In* Modern theoretical chemistry. Vol. 2. 1972. Plenum Press, New York.
25. S. Huzinaga. Comput. Phys. Rep. **2**, 279 (1985).
26. R.S. Grev and H.F. Schaefer III. J. Chem. Phys. **91**, 7305 (1989).
27. M.J. Frisch, J.A. Pople, and J.S. Binkley. J. Chem. Phys. **80**, 3265 (1984).
28. P.G. Mezey, R.E. Kari, and I.G. Csizmadia. J. Chem. Phys. **66**, 964 (1977).
29. A. Schäfer, H. Horn, and R. Ahlrichs. J. Chem. Phys. **92**, 2571 (1992).
30. S. Huzinaga. Gaussian basis sets for molecular calculations. V16. Elsevier, Amsterdam. 1984.
31. T.H. Dunning. J. Chem. Phys. **90**, 1007 (1989).
32. A.M.J. Frisch, G.W. Trucks, M.H. Gordon, P.M.W. Gill, M.W. Wong, J.B. Foresman, B.G. Johnson, H.B. Schlegel, M.A. Robb, E.S. Replogle, R. Gomperts, J.L. Anders, K. Raghavachari, J.S. Binkley, C. Gonzalez, R.L. Martin, D.J. Fox, D.J. Defrees, J. Baker, J.J.P. Stewart, and J.A. Pople. Gaussian 92. Gaussian, Inc., Pittsburgh, Pa. 1992.
33. C. Møller and M.S. Plesset. Phys. Rev. **46**, 618 (1934).
34. J.A. Pople, M.H. Gordon, and K. Raghavachari. J. Chem. Phys. **87**, 5968 (1987).
35. K. Raghavachari. Annu. Rev. Phys. Chem. **42**, 615 (1991).
36. H.B. Schlegel. J. Comput. Chem. **3**, 214 (1982).
37. J.J. Val Vaals, W.L. Meerts, and A. Dynamus. Chem. Phys. **82**, 385 (1983).
38. T. Torring, J.P. Beekoy, W.L. Meerts, J. Hoeft, E. Tieman, and A. Dymanus. J. Chem. Phys. **73**, 4875 (1980).
39. A.G. Maki and R.L. Sams. J. Chem. Phys. **75**, 4178 (1981).
40. I. Mayer. Int. J. Quantum Chem. **29**, 73 (1986); **29**, 477 (1986).
41. S. Fraga, J. Karwowski, and K.M.S. Saxena. Handbook of atomic data. Elsevier Scientific Publishing Company, Amsterdam. 1976.

Proton and electron transfers in O•H•O and C•H•O hydrogen-bridged ions: their role in the dissociation chemistry of ionized acetol, $CH_3C(=O)CH_2OH^{\bullet+}$

Paul J.A. Ruttink, Peter C. Burgers, and Johan K. Terlouw

Abstract: Low-energy acetol ions $CH_3C(=O)CH_2OH^{\bullet+}$, **1**, dissociate to $CH_3C(H)OH^+$ and $HC=O^\bullet$ by a double hydrogen transfer (DHT), a common reaction among oxygen-containing radical cations. Recent experimental work has shown that the isotopologue $CH_3C(=O)CH_2OD^{\bullet+}$ specifically loses $HC=O^\bullet$ to produce $CH_3C(D)OH^+$. This finding refutes an earlier postulated attractive mechanism based on the behaviour of **1** in ion–molecule reactions. Using ab initio MO calculations (at the CEPA//RHF/DZP level of theory complemented with valence bond (VB) methods), a low-energy pathway was traced that may explain all of the available experimental observations. It is shown that the unimolecular chemistry of **1** can be understood in terms of two *proton* transfers, taking place in intermediate O•H•O and C•H•O bonded hydrogen-bridged radical cations. The two protons originate from the same moiety and a charge transfer complex is therefore implicated and shown to be involved. These concepts of proton and charge transfer may well be more generally applicable and they do correctly predict the unimolecular chemistry of ionized acetoin, $CH_3C(=O)CH(CH_3)OH^{\bullet+}$ and related α-ketols.

Key words: ab initio calculations, hydrogen-bridged ions.

Résumé : Les ions acétol de basse énergie, $CH_3(C=O)CH_2OH^{\bullet+}$, **1**, se dissocient en $CH_3C(H)OH^+$ et en $HC=O^\bullet$ par un double transfert d'hydrogène (DTH), une réaction courante des cations radicaux contenant de l'oxygène. Des travaux expérimentaux récents ont montré que l'isotopologue, $CH_3(C=O)CH_2OD^{\bullet+}$ perd spécifiquement du $HC=O^\bullet$ pour fournir du $CH_3C(D)OH^+$. Cette observation réfute un mécanisme attrayant proposé antérieurement et qui était basé sur le comportement du composé **1** dans les réactions ion–molécule. Utilisant des calculs d'OM ab initio (au niveau CEPA//RHF/DZP de la théorie avec un complément des méthodes de liaisons de valence), on a pu tracer une voie réactionnelle de basse énergie qui peut expliquer toutes les données expérimentales disponibles. Il a été montré que le chimie unimoléculaire du composé **1** peut se comprendre en termes de deux transferts de *protons* qui se produisent par l'intermédiaire de cations radicaux de liasions hydrogènes pontées O•H•O et C•H•O. Les deux protons ont leur origine dans la même partie de la molécule; il y a donc un complexe de transfert de charge d'impliquer et on l'a démontré. Il est fort possible que ces concepts de transferts de protons et de charges puissent s'appliquer d'une façon générale et ils permettent de prédire correctement la chimie unimoléculaire de l'acétoïne ionisée, $CH_3(C=O)CHCH_3OH^{\bullet+}$ et des α-cétols apparentés.

Mots clés : calculs ab initio, ions de hydrogène-ponté.

[Traduit par la rédaction]

Introduction

"The role of physics in chemistry is to predict what can be observed and to provide an understanding of these observations." So begins Professor R.F.W. Bader an influential review article entitled "A quantum chemical theory of molecular structure and its applications" (1). One of the purposes of the present commemorative paper is to show that nowadays state-of-the-art ab initio molecular orbital (MO) calculations can indeed predict experimental observables and that they can indeed lead to a deeper understanding of the underlying phenomena. In this paper we deal with gas-phase ions, that is to say, solitary species free of solvent molecules, which as such are preeminently suited to study by computational methods. Our case concerns the remarkable dissociation behaviour of acetol radical cations, $CH_3C(=O)CH_2OH^{\bullet+}$, and related systems, for which there appear to be (seemingly) conflicting experimental data that we resolve here by computational methods.

Radical cations obtained by electron impact ionization of organic molecules are renowned for their propensity to rearrange prior to dissociation (for selected reviews see ref. 2).

Received October 12, 1995.

This paper is dedicated to Professor Richard F.W. Bader on the occasion of his 65th birthday.

P.J.A. Ruttink. Theoretical Chemistry Group, Department of Chemistry, University of Utrecht, Padualaan 14, 3584 CH Utrecht, The Netherlands.
P.C. Burgers. Hercules European Research Center BV, Nijverheidsweg 60, 3771 ME Barneveld, The Netherlands.
J.K. Terlouw.[1] Department of Chemistry, McMaster University, 1280 Main Street West, Hamilton, ON, L8S 4M1, Canada.

[1] Author to whom correspondence may be addressed. Telephone: (905) 525-9140, ext. 27111. Fax: (905) 522-2509.

This is especially true for those ions that fragment during flight through the mass spectrometer, the so-called metastable ions, which dissociate with rate constants of $10^5 < k < 10^6$ s^{-1} (3). Indeed, it is frequently observed that the decay of such ions, as reflected by their metastable ion (MI) spectra, can be totally different from the fast fragmentations ($k > 10^6$ s^{-1}), which take place in the ion source of the mass spectrometer and give rise to the conventional electron impact (EI) mass spectrum. A case in point is ionized acetol, $CH_3C(=O)CH_2OH^{\bullet+}$: while its EI mass spectrum consists of structure characteristic peaks at *m/z* 43, $CH_3C{\equiv}O^+$ (100%), *m/z* 31, $^+CH_2OH$ (20%), and *m/z* 15, CH_3^+ (10%) arising from fast C—C cleavages, its MI spectrum is dominated by a completely different signal at *m/z* 45, corresponding to $CH_3C(H)OH^+$ (4–7), obviously the result of a rearrangement process involving the loss of HC=O$^\bullet$.

In the context of ionic rearrangements, hydrogen-bridged radical cations, in particular O·H·O bonded ions, are increasingly being proposed as intermediates to rationalize the seemingly unintelligible dissociation behaviour of oxygen-containing radical cations (2). These proposals were inspired by the growing realization (2) both from experiment and theory that O·H·O bonded radical cations can be thermodynamically as stable as the unrearranged reactant ion, making them energetically attractive intermediates. The first indications that such hydrogen-bridged radical cations might well be very stable species were presented by us in this journal more than 10 years ago (8). Based on MI and collision-induced (CID) dissociation characteristics, it was proposed that loss of C_2H_4 from $ROCH_2CH_2CH_2CH_2OH$ (R = H, CH_3) does not produce, via a least-motion extrusion (9), the conventional structure $ROCH_2CH_2OH^{\bullet+}$ but rather a product ion comprised of vinyl alcohol and ROH, $[CH_2{=}CHOH/ROH]^{\bullet+}$, and the possibility was entertained that the observed product ion might be the "proton bound radical-molecule pair" (8) $^\bullet CH_2C(H){=}O\cdots H^+\cdots O(H)R$, whose dissociation characteristics can be rationalized by consideration of the relative proton affinities (PA) of the radical and molecules involved. Subsequent ab initio MO calculations on the $C_2H_6O_2^{\bullet+}$ potential energy surface (PES) (R = H) (8*b*, 10*a*,*b*) revealed that the O·H·O bridged ion is not only thermodynamically by far the most stable isomer (it is 42 kcal/mol more stable than $HOCH_2CH_2OH^{\bullet+}$), but that it is very stable (by ca. 24 kcal/mol) towards dissociation as well. Its most stable structure was found to be $CH_2{=}C(H)O\text{-}H^{\bullet+}\cdots OH_2$, i.e., with the bridging hydrogen more closely connected to the moiety of higher PA. This interesting ion reappeared recently in an ab initio study concerning the enzyme–coenzyme B_{12} catalyzed dehydration of ethylene glycol (10*c*).

Indeed, it is invariably found, from ab initio MO calculations, that such (necessarily asymmetric) O·H·O bridged radical cations can best be described as H-bridged ion–dipole complexes of the type $A\text{–}H^{\bullet+}\cdots B$ (or $A\text{–}H^+\cdots B^\bullet$), where most of the stabilization energy is provided by ion–dipole attractions. Although the hydrogen bridge furnishes additional stabilization, its main function, as we shall see, is to direct the course of isomerization by allowing a relatively facile *proton* transfer.

Recent evidence has suggested that the C·H·O bonded counterparts of the O·H·O bonded species may, despite their elevated enthalpies, be even more important intermediates in the decay of oxygen-containing radical cations (2, 5, 6, 11, 12). A case in point is acetol's fragmentation to $CH_3C(H)OH^+$ and HC=O$^\bullet$, see above, which has been interpreted in terms of O·H·O bonding on the one hand (6) and C·H·O bonding on the other (5).

In their ion cyclotron resonance (ICR) study Pakarinen et al. (6, 7) found compelling evidence from characteristic ion–molecule reactions that ionized acetol rearranges to the O·H·O species $CH_3C{=}O\cdots H\cdots O{=}CH_2^{\bullet+}$, **4**. It was further proposed that ion **4** undergoes a hydrogen shift prior to the loss of HC=O$^\bullet$ as follows:

[1] $CH_3C(=O)CH_2OH^{\bullet+}$ (**1**) $\rightarrow CH_3C{=}O\cdots H\cdots O{=}CH_2^{\bullet+}$ (**4**)

$\rightarrow CH_3C(H){=}O\cdots H\cdots O{=}CH^{\bullet+}$ (**7**)

$\rightarrow CH_3C(H)OH^+ + HC{=}O^\bullet$

George et al. (5) found this mechanism to be incompatible with their isotopic labelling data: they observed from MS/MS/MS experiments that the hydroxyl hydrogen of **1** appears at the carbenium carbon atom of the product ion and not, as expected from eq. [1], at the oxygen atom. These authors proposed a mechanism, supported by ab initio MO calculations, that involves C·H·O bonding:

[2] $CH_3C(=O)CH_2O\mathbf{D}^{\bullet+}$ (**1**) $\rightarrow CH_3C(=O)\text{-}\mathbf{D}\cdots O{=}CH_2^{\bullet+}$ (**5**)

$\rightarrow CH_3C(\mathbf{D}){=}O\cdots H\cdots O{=}CH^{\bullet+}$ (**7**)

$\rightarrow CH_3C(\mathbf{D})OH^+ + HC{=}O^\bullet$

Goaded by these (seemingly) conflicting experimental results, we decided to investigate by state-of-the-art ab initio MO calculations the minimum energy reaction path for the isomerization–dissociation processes of ionized acetol. We note that ionized acetol's decay is an example of a type of reaction that many a radical cation undergoes, namely double hydrogen transfer (DHT) to produce a protonated molecule.

A prototype species that undergoes such a dissociation and has been the subject of a thorough theoretical investigation (13) is ionized ethane-1,2-diol, which dissociates to $CH_3OH_2^+$ and HC=O$^\bullet$. It appears that the isomerization processes involved can be understood in terms of *proton* (14) (as opposed to hydrogen atom) and electron transfers taking place in intermediate hydrogen-bridged ion–dipole complexes. Interestingly, these are the very processes that are known to occur rapidly in hydrogen-bridged radical cations formed by direct ionization of gas phase clusters (15) (these processes also take place rapidly in ion–molecule encounters, see for example ref. 16, and indeed the proposed intermediates in eqs. [1] and [2] can be considered as such ionized "clusters"). Our calculations suggest a reinterpretation of the seemingly conflicting experimental data for ionized acetol, but when this is done there appears excellent agreement.

Theoretical methods

Ab initio calculations were performed using the program sys-

Scheme 1.

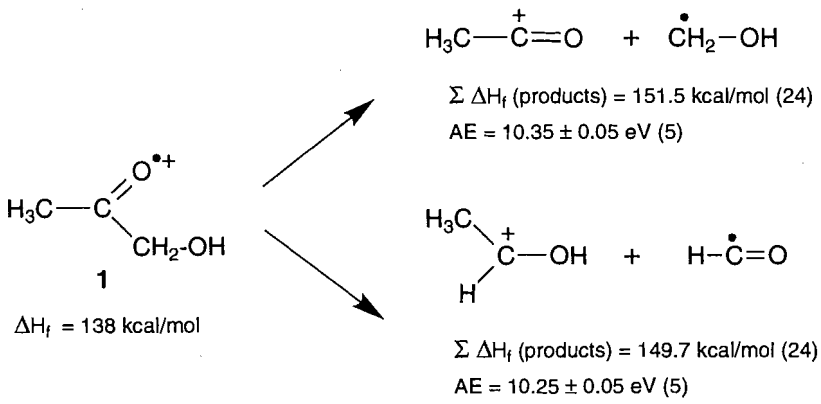

tem GAMESS-UK (17) employing RHF and (MR)CI/CEPA methods (18, 19). Dunning's DZP basis (20) was used throughout. ZPVE corrections were calculated on the RHF level and scaled with 0.9 (21). All minima and transition states were checked for the correct number of imaginary frequencies and the transition states were checked for their connections with the relevant minima. Note that inclusion of electronic correlation and ZPVE contributions may affect the relative energies such that a transition state need not even be higher in energy than the minima it connects. This may happen since transition states are more sensitive to correlation effects than minima and the ZPVE also tends to favour transition states.

The (Pople) size consistency correction procedure (22) for the standard HF-SDCI method was not satisfactory for the present system, since $E[CH_3C(H)OH^+ + HCO^\cdot] - E[CH_3C(H)OH^+] - E[HCO^\cdot]$ yielded 5 kcal/mol. We therefore resorted to single-reference open-shell CEPA calculations using our ATMOL/MR-CEPA program (18), which yielded a much smaller size consistency error (< 1 kcal/mol). However, for some intermediates this procedure suffers from an intruder state problem (23), which means that the solution is unstable, because one of the excited configurations becomes dominant in the wave function during the iterative diagonalization process, thereby destroying the ground state character of the wave function. The appearance of the intruder states is caused by the shifts in the diagonal elements of the excitations, which are used to simulate the effects of the higher excitations on the electronic correlation. This effect can be remedied either by using a multi-configuration reference approach or by switching off the diagonal shift for the intruder states. It appears rather difficult to make a balanced selection of reference configurations, i.e., a selection leading to results of uniform accuracy for the whole PES. Therefore we have used the second approach. In all cases the "dangerous" configurations then appear to have small coefficients (<0.15). This yields results that are acceptable as to the size consistency as well as to the stability of the wave function. The results are given in Table 1.

For the acetol radical cation, the RHF calculations indicate that there exist two minima for the acetol radical cation, one with the charge localized on the carboxyl oxygen and one with the charge localized in an accordingly long CC bond, which acts as the reacting configuration for the formation of complexes involving the $CH_3C{=}O$ and CH_2OH units. The first minimum is probably an artefact of the HF calculation, since the correlated results lead to a lower energy for the geometry corresponding to the HF transition state between the HF minima. This is corroborated by an MP2 geometry optimization, which leads to a long CC bond (13).

Results and discussion

Preliminary considerations

Ionized acetol has two dissociation reactions of low energy requirement, see Scheme 1. Both reactions, as evidenced by appearance energy (AE) measurements, take place at their thermochemical thresholds. Although the AE's are not significantly different, the formation of $CH_3C(H)OH^+$ has the expected lower energy requirement, as this is the dominant peak in the MI spectrum, see above. Note that the average kinetic energy release is very small, $T = 7$ meV (5) and this indicates, according to theory (25, 26) and experiment (27), that the excess energy will be correspondingly small, smaller than the uncertainty in the AE measurements (±50 meV); as a consequence, formation of $CH_3C(H)OH^+$ may well dominate the MI spectrum, even if the AE's are the same within experimental error. The small T value also indicates that there is no reverse term and that the final step most likely involves dissociation of an ion–dipole complex (26).

The energy requirement for the rearrangement–dissociation processes (as measured by the difference in AE and ionization energy (IE)) is only 12 kcal/mol (5); that an ion having such a relatively small activation energy should nevertheless dissociate at a slow rate further attests to dissociation of an intermediate ion–dipole complex (28). It is also clear from the above energetic measurements that the leeway in our ab initio calculations is only 12 kcal/mol.

As mentioned above, the ethane-1,2-diol radical cation, $HOCH_2CH_2OH^{\cdot+}$, also undergoes a double hydrogen transfer to produce $CH_3OH_2^+$ and $HC{=}O^\cdot$, and the associated mechanism has been unravelled by high-level ab initio calculations (13). After detailed calculations (see below), we found that the sequence in Scheme 2, which is very similar to that of ionized ethane-1,2-diol, applies to ionized acetol. The corresponding energy diagram is shown in Fig. 1 and the equilibrium and transition structures are shown in Fig. 2.

O/H/O (ion 4) versus C/H/O(ion 5) bonding

First we deal with the mechanistic proposal by Pakarinen et al.

Table 1. Calculated total energies, zero-point vibrational energies ZPVE (kcal/mol), relative energies E_{rel} (kcal/mol), and experimental heats of formation (kcal/mol) of acetol-type $C_3H_6O_2^{\bullet+}$ ions (equilibrium and transition structures) and some dissociation products.

Isomer	RHF[a]	CEPA[a]	ZPVE	E_{rel}	Expt.[b]
1	−0.565 84	−0.352 52	59.2	−8.0	−12[c]
2	−0.549 27	−0.362 73	59.1	−14.5	−12[d]
3	−0.554 91	−0.341 90	59.5	−1.0	
4	−0.563 23	−0.347 34	57.5	−6.3	
5	−0.547 94	−0.342 11	55.9	−4.4	
6	−0.533 62	−0.330 41	55.7	2.8	< 0[e]
7	−0.568 89	−0.354 89	56.9	−11.5	
TS 1-2	−0.546 56	−0.363 46	57.6	−16.3	
TS 2-3	−0.545 39	−0.352 20	57.2	−9.6	
TS 3-4	−0.549 50	−0.340 77	57.8	−1.8	
TS 4-5	−0.527 74	−0.345 94	53.3	−9.2	
C	−0.527 79 / −0.527 84	−0.334 48	—		
TS 6-7	−0.527 30	−0.343 41	52.9	−7.9	
TS 4-7	−0.480 48	−0.298 53	53.9	21.2	
$CH_3C(H)OH^+ + HC{=}O^{\bullet}$	−0.538 69	−0.334 49	55.5	0.0	0
$CH_3C{=}O^+ + {}^{\bullet}CH_2OH$	−0.534 79	−0.328 80	55.5	3.6	2

[a]Hartrees, +266 for RHF, +267 for CEPA.
[b]Values from ref. 24.
[c]Assuming adiabatic ionization energy (IE_a) corresponds to **1**.
[d]Assuming adiabatic ionization energy (IE_a) corresponds to **2**.
[e]No reverse barrier, see text.

Scheme 2. Proposed reaction mechanism for the loss of $HCO^{\bullet}$ from ionized acetol, **1** (see text for details).

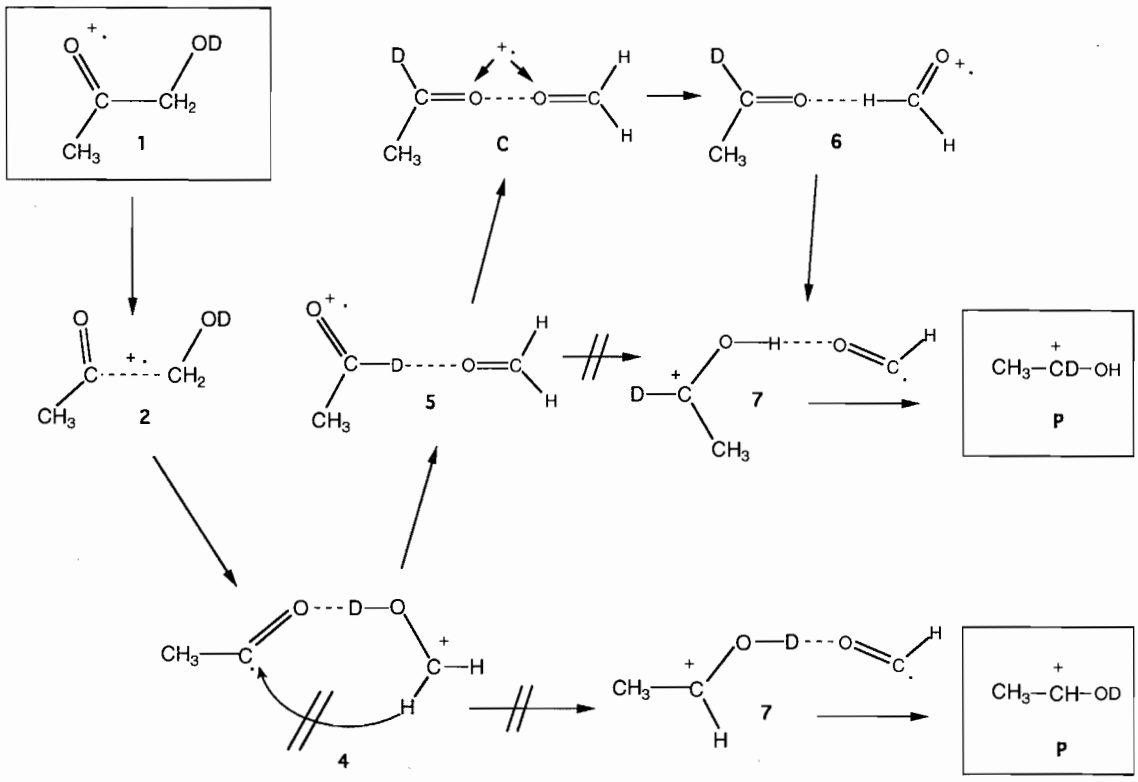

Fig. 1. Theoretical results (CEPA) for the relative energies of the isomers and transition states encountered in the dissociation of acetol radical cations, $CH_3C(=O)CH_2OH^{\bullet+}$. Experimental Appearance Energy of the products as indicated (see text for discussion).

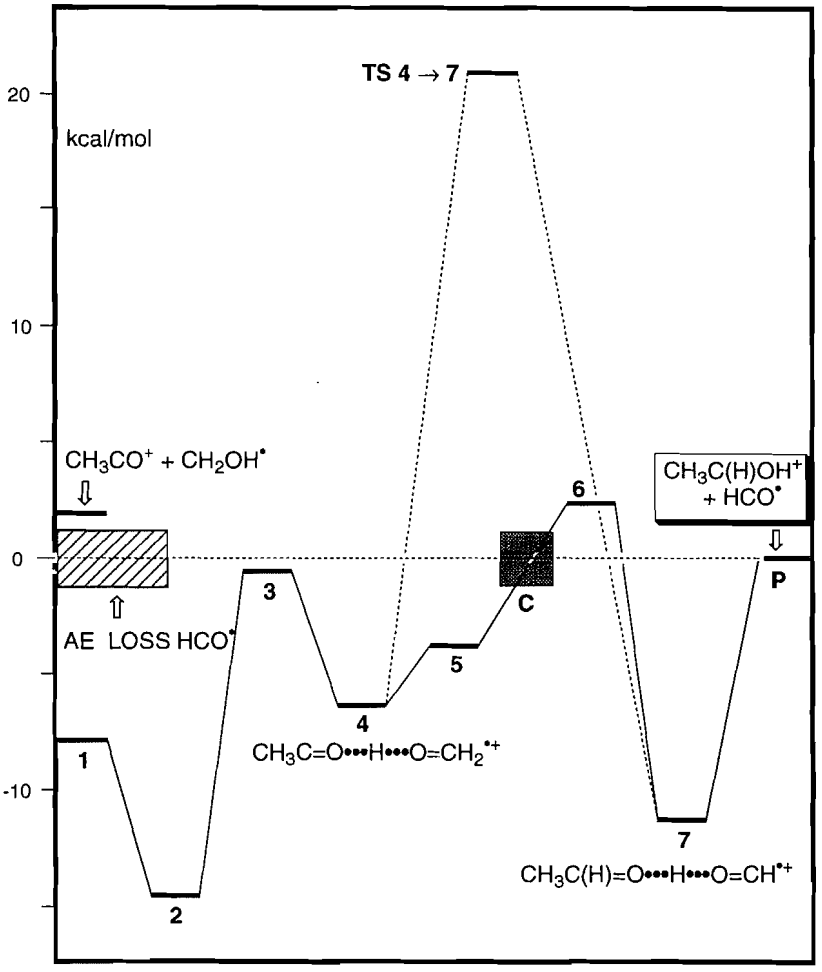

(6). The key intermediate in this proposal is ion **4**, which was proposed to yield the products directly, i.e., **4** → **7**. Our calculations confirm previous computational results (29) that the hydrogen-bridged species **4** is best described as a $^+CH_2OH$ ion interacting through a hydrogen bridge with the acetyl radical dipole, see Fig. 2. Hence this ion is a prime candidate to explain the acetyl *radical* displacement reactions observed for ionized acetol in the ICR experiments of Pakarinen et al. (6). If indeed ion **4** can be generated from **1** below the dissociation limit, then the labelling results of George et al. (5) dictate that **4** does not undergo the hydrogen transfer **4** → **7** depicted in Scheme 2.

According to our calculations, this process indeed has a prohibitively large barrier, see Fig. 1. That this barrier should be large can be understood as follows. As a first step, the bridging deuterium in **4** may be shifted towards the acetyl oxygen atom; since the carbene CH_3-C-OH has a high thermodynamic stability as an ion (30*a*), but not as a neutral (30*b*), this would have to lead to *ionized* CH_3-C-$OD^{\bullet+}$ interacting with the formaldehyde dipole, that is to say, the above deuterium shift would have to be a deuteron, D^+, shift. To produce CH_3-C(H)-OD^+ from the incipient CH_3-$C^{\bullet+}$-OD···O=CH_2 would then require a further hydrogen *atom* shift and there are two reasons why this reaction should have a large barrier. First, this reaction would involve cleavage of a covalent C—H bond in neutral formaldehyde and this requires considerable energy; secondly, to move this H atom to the ionized carbene would require an unfavourable rotation of the formaldehyde dipole.

Alternatively, the above sequence may be reversed, i.e., first one of the C-H hydrogens of the $^+CH_2OD$ ion in **4** is shifted to the acetyl dipole; this would lead to $[CH_3$-C(H)=O···D-O-C-H$]^{\bullet+}$. Again, the incipient carbene, H-C-OD, has a high stability only in its ionized form (31), so that it should bear the charge; hence the above hydrogen shift again would have to be a hydrogen *atom* shift and for the same reason as given above such a shift requires considerable energy, the associated TS (TS **4**→**7**) lying some 20 kcal/mol outside our leeway, see Fig. 1. Thus ion **4** cannot directly lead to the products as shown in eq. [1], in agreement with the experimental findings of George et al. (5).

However, similar arguments can be put forward against the transformation **5** → **7** proposed by George et al. (5). From ion–

Fig. 2. Geometries of the $C_3H_6O_2^{\bullet+}$ isomeric ions and transition states optimized at the RHF/DZP level of theory.

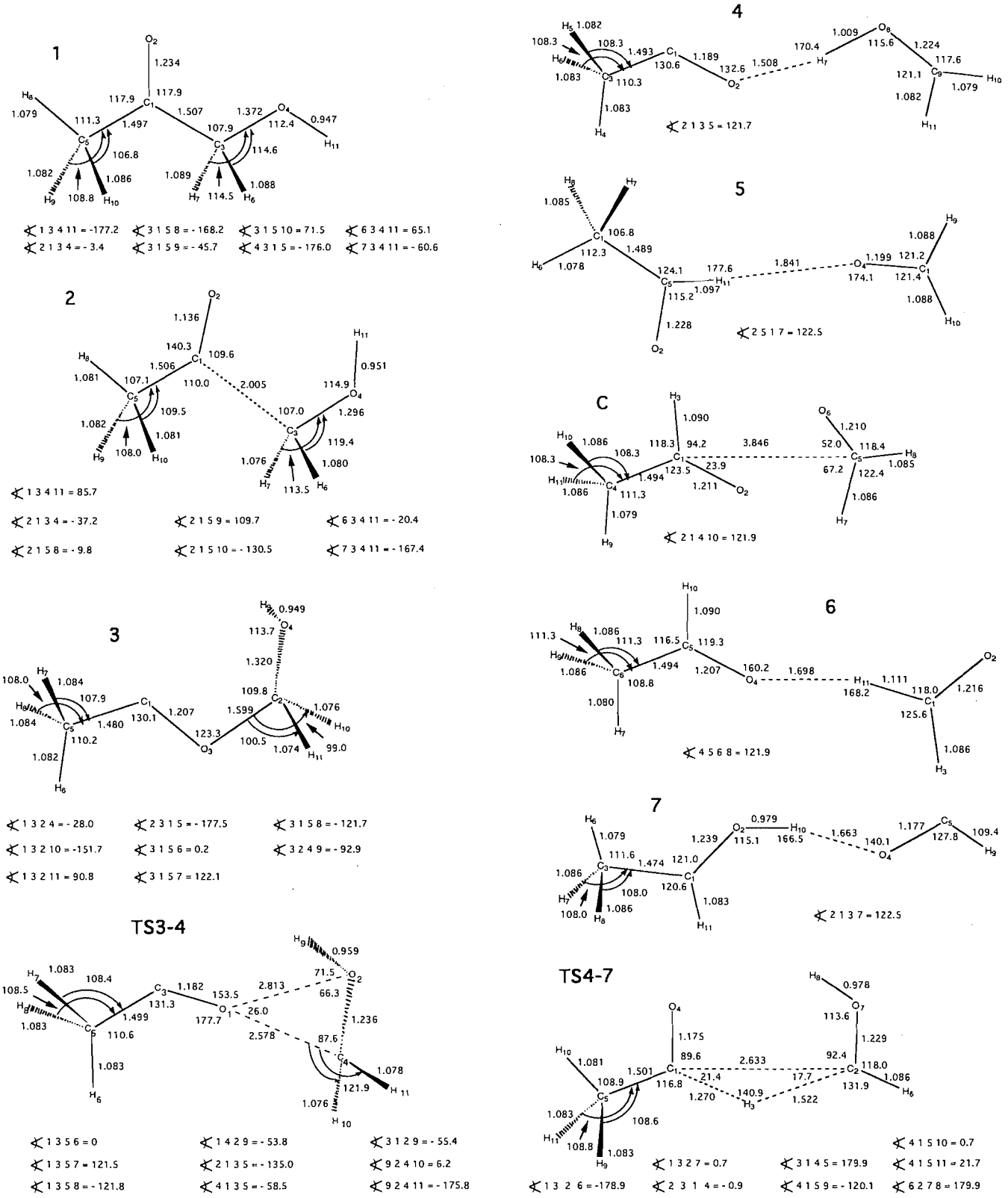

Fig. 3. Proposed isomerization steps involved in the loss of HCO$^{\bullet}$ from ionized acetol, **1**, as visualized by Pluton pictures (see text for details). Orientation: e.g., ion **2**: left-hand side CH_2OH^+, right-hand side $CH_3C{=}O^+$; hydroxyl hydrogen labelled black.

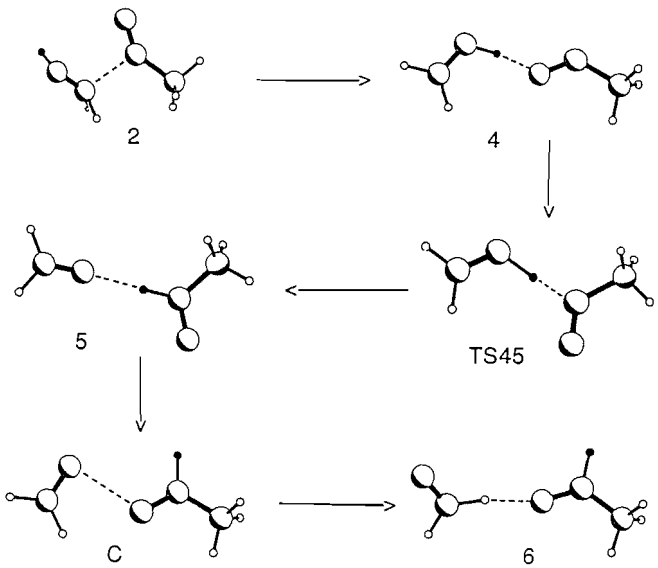

dipole considerations, the charge in **5** must reside on the acetaldehyde moiety, so that the rearrangement **5** → **7** must involve an unfavourable C—H cleavage in neutral formaldehyde, concomitant with a destabilizing rotation of the formaldehyde dipole, and so it is inferred that the transformation **5** → **7** should require considerable energy as well. Note that the above authors did find a low-lying TS (labeled TS**3b**→**5a** in their work) where the formaldehyde group has indeed rotated concomitant with H transfer and which they identified as TS **5**→**7**. However, we have now found that this TS does not connect **7** with **5**, but rather **7** with **6** where the charge is on the formaldehyde group, see Scheme 2.

It therefore appears that neither **4** nor **5** can lead directly to the products at the measured appearance energy and with the observed small kinetic energy release. Nevertheless, there is good experimental evidence that **4** is involved. How then can ion **4** lose HCO$^{\bullet}$?

Rearrangement of ion 4 : $[CH_3\text{-}C{=}O\cdots H\text{-}O{=}CH_2]^{\bullet+}$, 4→5→C→6 (→7)→products

The rearrangement processes of ion **4** leading to the loss of HCO$^{\bullet}$ are visualized as Pluton pictures in Fig. 3. Our calculations indicate that the O/H/O bonded species **4** can rearrange below the dissociation threshold to the C/H/O bonded species **5**. First, the $^+CH_2OH$ moiety undergoes a shuffle along the C=O axis of the acetyl dipole until the configuration TS **4**→**5**, $CH_3\text{-}C(=O)\cdots H\text{-}O{=}CH_2^+$, is reached, which then undergoes a proton transfer to generate **5**. The transition **4**→**5** could be viewed, in principle, as the 1,2-hydrogen shift $CH_3\text{-}C\text{-}OH^{\bullet+} \rightarrow CH_3\text{-}C(H){=}O^{\bullet+}$, catalyzed by the formaldehyde dipole (13, 14). Note, see Table 1, that at the RHF level there is a small barrier for the transition **5**→**4** (10 kcal/mol, including ZPVE contributions). However, with electron correlation (CEPA) this barrier has disappeared, so that the transformation **4**→**5**, which for visualization purposes is depicted as stepwise in Fig. 3, actually occurs smoothly, see energy diagram, Fig. 1. As to the formation of **5**, George et al. (5) found a TS (labelled TS **4a-3b** in that work) that was proposed to connect **2** and **5**. We have found that this TS in actuality connects **4** and **5**, i.e., it is our TS **4**→**5**. So we feel that the sequence **1** → **2** → **4** → **5** presents a more realistic pathway for the formation of **5** than the transformation **2** → **5**.

As mentioned above, the charge in ion **5** is on the acetaldehyde moiety and thus ion **5** cannot yield the desired products directly. We note, however, that in ion **6** the charge is on the formaldehyde group and so **6** can easily donate a proton to the neutral formaldehyde followed by dissociation (**6** → **P**). Ions **5** and **6** can be formed from **5** via the charge transfer complex **C** as follows. We note (see Fig. 1) that ions **5** and **6** have comparable energies. This is so because there is a trade-off between effects arising from the differences in IE's and dipole moments (μ) of acetaldehyde and formaldehyde: the lower IE of acetaldehyde (10.23 eV versus 10.87 eV (32)) favours the charge on the acetaldehyde (ion **5**), whereas the larger dipole moment of acetaldehyde (μ = 2.77 D vs. 2.33 D for fomaldehyde (32)) favours the charge on formaldehyde (ion **6**). Since the acetaldehyde moiety in **5** is charged, it can rotate on the dipole vector of the formaldehyde molecule without loss of too much of the ion–dipole stabilization energy, i.e., only the weak hydrogen bond is sacrificed. That is to say, the relative orientation of the $CH_3CH{=}O$ and $CH_2{=}O$ units is changed (ion–dipole reorientation (33)), such that the dipole vectors of the putative neutral molecules are oriented towards each other. In this situation both choices, i.e., $CH_3\text{-}CH{=}O^{\bullet+}\cdots O{=}CH_2$ and $CH_3\text{-}CH{=}O\cdots O{=}CH_2^{\bullet+}$ will correspond to low-energy situations and such arrangements are acceptable as conformations where the charge transfer may take place easily (**5** → **C** → **6**) (see also the following section on the charge transfer complex).

We can now see why the transition **4** → **5** is necessary to bring about the above charge transfer process. For any charge transfer process $A^{\bullet+}\cdots B \rightarrow A\cdots B^{\bullet+}$ to take place easily, both A and B must represent thermodynamically stable molecules. Now consider ion **4**: this ion could well undergo a shift of the bridging H to generate $CH_3\text{-}C^{\bullet+}\text{-}OH\cdots O{=}CH_2$. This species cannot undergo ion–dipole reorientation and charge transfer along the lines described above, simply because neutral CH_3-C-OH is thermodynamically a high-energy species. This is the reason that the transformation **4** → **5** is necessary.

While we feel that our theoretical calculations (as well as the simple energetic arguments given in the previous section) strongly favour a charge transfer process over the direct dissociation **5** (→ **7**) → **P**, we have no experimental proof of its occurrence, at least not for acetol. However, substituting one of the methylene hydrogen atoms in ionized acetol by $CH_3^{\bullet}$ yields acetoin ions, $CH_3C(=O)CH(CH_3)OH^{\bullet+}$. Ionized acetoin undergoes one unimolecular dissociation to produce $CH_3C(H)OH^+$ (*m/z* 45) + $CH_3C{=}O^{\bullet}$, ostensibly a simple bond cleavage reaction. If the sequence outlined in Scheme 2 also applies to acetoin, i.e., **1**→**4**→**5**→**C**→**6**(→**7**)→**P**, and substituting a methylene hydrogen in **1** by a CH_3 group, then the charge transfer process becomes degenerate, i.e., **5**→**C**→**5**. If such a degenerate process takes place below the dissociation limit, then it is *predicted* (and this prediction, we stress, follows from our ab initio MO calculations) that the labelled pre-

cursor ion $CH_3C(=O^{18})CH(CH_3)OH^{\cdot+}$ should produce $CH_3C(H)OH^+$ (*m/z* 45) and $CH_3C(H)^{18}OH^+$ (*m/z* 47) in a ratio of exactly 1:1. This, as we have recently reported (12) is precisely what is observed experimentally. Equally important are MS/MS/MS experiments (12) on the labelled ion $CH_3C(=O^{18})CH(CH_3)OD^{\cdot+}$. These experiments established that the above acetoin isotopomer generates $CH_3C(D)^{18}OH^+$ (in admixture with CH_3CHOD^+) with the deuterium atom attached to the carbenium carbon atom and not to the oxygen atom, precisely as predicted from our calculations. We therefore feel confident that the acetol radical cation also fragments via a charge transfer complex.

The $[CH_3C(H)=O\cdots O=CH_2]^{\cdot+}$ charge transfer complex: computational aspects

At the end of the reaction sequence a proton transfer from $CH_2=O^{\cdot+}$ to $CH_3C(H)=O$ takes place. The charge localization in the $[CH_3C(H)=O\cdots O=CH_2]^{\cdot+}$ complex will be determined by the relative orientation of the two units. This means that the charge will go to that unit whose dipole moment is directed away from the other unit. Therefore, to create a stable situation for this transfer we have to start with a neutral $CH_3C(H)=O$ and an ionized $CH_2=O$. The dipole of the $CH_3C(H)=O$ is directed toward the charge on the $CH_2=O^{\cdot+}$ unit, ion **6**, which is oriented such that a H-bridge is formed that also stabilizes the complex.

In the intermediate resulting from the first proton transfer, **5**, the charge is located on the $CH_3C(H)=O$ unit, with the dipole of the $CH_2=O$ directed toward the $CH_3C(H)=O^{\cdot+}$. For reasons given above, **5** and **6** have comparable stabilities. However, when we tried to find a transition state for the charge transfer process **5** → **6**, the RHF calculation led to a crossing instead of a saddle point. This situation was also encountered in the dissociation of ethane-1,2-diol (13) (charge transfer between CH_3OH and $CH_2=O$). To find the energetically most favourable geometry for the charge transfer, we optimized the geometry of the transition point within the intersection of the two potential energy surfaces (34). A useful starting geometry for this optimization was obtained by optimizing the complex with the restriction that the -C=O dipole moment vectors are oriented towards each other. This yields the geometry of structure **C**. In this geometry a Valence Bond (VB) calculation (13) was performed involving the two RHF determinants corresponding to the two charge localizations. Since these determinants are degenerate in the transition point, whereas the HF-MO's mutually overlap, the VB calculation will lead to an energy lowering in the neighbourhood of the crossing. As a result the charge transfer process is now described as a continuous process involving an avoided crossing between the two extremes, i.e., structures **5** and **6.** To obtain a final result comparable in accuracy to the results for the other intermediates, we used the Natural Orbitals of the VB function in the final CEPA calculation.

Formation of ion 4, $CH_3C=O\cdots H\cdots O=CH_2^{\cdot+}$, the reaction sequence 1→2→3→4

The calculations by George et al. (5) indicate that, below the dissociation limit, **1** can undergo a 1,4-hydrogen shift to produce the distonic ion $CH_3C^+(OH)CH_2O^{\cdot}$. However, its formation from **1** represents a "cul de sac" isomerization (35) with significant barriers for further rearrangement. This nicely parallels theoretical observations for the distonic ion $H_2O^+CH_2CH_2O^{\cdot}$ generated from ethane-1,2-diol, which too is not the precursor for the O·H·O bonded species.

How then can ion **4** be formed from **1**? Analogous to ethane-1,2-diol, ion **4** could be formed from ion **2**, which is computed to have a long C—C bond (ca. 2 Å) and to lie 6.5 kcal/mol below **1** (this and other results (13) show that in radical cations long bonds can be stronger than short bonds). The C—C bond in ion **2** is a one-electron bond with the charge and radical character both localized in this bond. The possibility therefore exists that the adiabatic Appearance Energy (AE_a) corresponds to **2** and not to **1**. This is the reason, see Fig. 1, that we have anchored the energy levels relative to the products, which are experimentally well known. We note, however, that because of its long C—C bond, the formation of **2** from **1** at the AE_a is not probable kinetically (13).

Starting from ion **2** there is a choice: the lone electron can be transferred to the CH_2OH moiety, and this configuration leads to dissociation to $CH_3C=O^+$ as observed in the conventional mass spectrum, or it can go to the $CH_3C=O$ part. This choice leads to ion **4** as visualized by the Pluton pictures in Fig. 3. Thus after elongation of the C—C bond in **1** to generate **2**, the $^+CH_2OH$ moiety can rotate in the dipole field of the acetyl radical (TS **3** → **4**) to eventually generate **4**, see also Fig. 2. (Along the way the distonic ion **3** is encountered. This ion, which is a minimum at the HF level, has a relatively long O—C bond (ca. 1.6 Å); TS **3** → **4** actually connects **4** with **3** via a torsion motion.) TS **3** → **4** lies close to the experimental energy limit, see Fig. 1.

Thus we have found a low-energy pathway whereby ionized acetol can rearrange to the hydrogen-bridged species **4** via the one-electron bond species **2**. At the same time our results suggest that ion **2** rather than (or in addition to) ion **4** may be responsible for the observed acetyl radical displacement of collisionally cooled ions (6) because, unlike **4**, ion **2** can be spontaneously formed upon ionization, see Fig. 1.

In summary, our calculations lead to the following mechanistic proposal, which is consistent with all of the available experimental data. Upon ionization, acetol relaxes to the one-electron bonded species **2** with a long C—C bond (2 Å). Ion **2** has a choice: the charge can go to the acetyl moiety but then the $\cdot CH_2OH$ dipole is directed away from the charge and is ejected; this leads to $CH_3C=O^+$, *m/z* 43, as observed in the normal mass spectrum. Alternatively, the charge can go to the CH_2-OH unit and now the acetyl dipole has the correct orientation to be attracted by the charge: this choice leads to the O·H·O bonded species **4**, as described above. This species cannot undergo a 1,5-H shift because the necessary orientation of the formaldehyde dipole leads to destabilization. Rather, ions **4** undergo a shuffle (**4** → TS **4** → **5**) and then *proton* transfer to generate the C·H·O bonded species **5**. In ion **5** the charge is on the acetaldehyde moiety. For **5** to undergo a second proton transfer the charge must be moved over to the formaldehyde molecule. This is done via **C**; when the formaldehyde unit has accepted the charge, it can rotate in the acetaldehyde dipole field to produce **6**, which then undergoes *proton* transfer followed by disscociation.

As argued above, the double hydrogen transfer processes that take place in ionized acetol and ethane-1,2-diol can best be viewed as proton (as opposed to hydrogen atom (see for example ref. 36)) transfers and conformations must be sought

to allow such proton transfers. Since the two protons originate from the same moiety a charge transfer complex is implicated; to reach such a complex necessitates C·H·O bonding and this is the reason that the above molecular ions dissociate via C·H·O bonded intermediates, as implicated by experiment.

At the same time, our calculations show that the C·H·O bonded species is most easily formed from the O·H·O bonded ion **4**, rather than directly from **2**, and so a unification of the seemingly conflicting experimental data of Pakarinen et al. (6) (dissociation via O·H·O bonding) and George et al. (5) (fragmentation via C·H·O bonding) is correspondingly manifest: the reactivity experiments (37) of Pakarinen et al. detect **2** and perhaps also **4** (first part of Fig. 1), while the product ion measurements of George et al. detect the higher energy species **5** (second part of Fig. 1). These concepts also offer a mechanistic generalization for the DHT processes observed in related systems including ionized acetoin (12), and methyl glycolate and methyl lactate (11).

Finally we note that ionized acetol is isomeric with ionized methyl acetate, $CH_3C(=O)OCH_3^{\cdot+}$, **8**, and that low-energy ions **8** lose both $CH_3O^{\cdot}$ and $CH_2OH^{\cdot}$ (yielding $CH_3C{\equiv}O^+$) but not $HC{\equiv}O^{\cdot}$. Hence **1** and **8** do not communicate with each other, although ion **4** has been proposed, on the basis of a detailed computational study, to participate as a high-energy transient intermediate in the loss of $CH_2OH^{\cdot}$ from **8** (29). Experimental and computational work to further characterize the behaviour of independently generated ions **4** is in progress.

Acknowledgements

This work was sponsored by the Stichting Nationale Computer Faciliteiten (National Computing Facilities Foundation, NCF) for the use of supercomputer facilities, with financial support from the Nederlandse Organisatie voor Wetenschappelijk Onderzoek (Netherlands Organization for Scientific Research, NWO). J.K.T. thanks the Natural Sciences and Engineering Research Council of Canada (NSERC) for financial support and Dr H.E. Audier, Dr C.A. Kingsmill, and Mr D. Suh for stimulating discussions.

References

1. R.F.W. Bader. Chem. Rev. **91**, 893 (1991).
2. (*a*) N. Heinrich and H. Schwarz. *In* Ion and cluster ion spectroscopy and structure. *Edited by* J.P. Maier. Elsevier, Amsterdam. 1989. p. 329; (*b*) P.C. Burgers and J.K. Terlouw. *In* Specialist Periodical Reports: Mass Spectrometry. *Edited by* M.E. Rose. The Royal Society of Chemistry, London. **10**, 35 (1989); (*c*) L. Radom. Org. Mass Spectrom. **26**, 359 (1991); (*d*) E. Uggerud. Mass Spectrom. Rev. **11**, 389 (1992); (*e*) P. Longevialle. Mass Spectrom. Rev. **11**, 157 (1992); (*f*) T.H. Morton. Org. Mass Spectrom. **27**, 353 (1992); (*g*) R.D. Bowen. Org. Mass Spectrom. **28**, 1577 (1993).
3. P.C. Burgers and J.L. Holmes. Int. J. Mass Spectrom. Ion Processes, **58**, 15 (1984).
4. J.K. Terlouw, J.L. Holmes, and P.C. Burgers. Int. J. Mass Spectrom. Ion Processes, **66**, 239 (1985).
5. M. George, C.A. Kingsmill, D. Suh, J.K. Terlouw, and J.L. Holmes. J. Am. Chem. Soc. **116**, 7807 (1993).
6. A. Pakarinen, K.M. Stirk, P. Vainiotalo, T.A. Pakkanen, and H.I. Kenttämaa. J. Am. Chem. Soc. **115**, 12431 (1993).
7. K.M. Stirk, L.K.M. Kiminkinen, and H.I. Kenttämaa. Chem. Rev. **92**, 1655 (1992).
8. (*a*) J.K. Terlouw, W. Heerma, P.C. Burgers, and J.L. Holmes. Can. J. Chem. **62**, 289 (1984); (*b*) R. Postma, P.J.A. Ruttink, F.B. van Duijneveldt, J.K. Terlouw, and J.L. Holmes. Can. J. Chem. **63**, 2798 (1985).
9. T. Drewello, N. Heinrich, W.P.M. Maas, N.M.M. Nibbering, T. Weiske, and H. Schwarz. J. Am. Chem. Soc. **109**, 4810 (1987).
10. (*a*) R. Postma. Ph. D. Thesis, University of Utrecht (1987); (*b*) R. Postma, S.P. van Helden, J.H. van Lenthe, P.J.A. Ruttink, J.K. Terlouw, and J.L.Holmes. Org. Mass Spectrom. **23**, 503 (1988); (*c*) P. George, J.P. Glusker, and C.W. Bock. J. Am. Chem. Soc. **117**, 10131 (1995).
11. D. Suh, C.A. Kingsmill, P.J.A. Ruttink, P.C. Burgers, and J.K. Terlouw. Int. J. Mass Spectrom. Ion Processes, **146/147**, 305 (1995).
12. D. Suh, P.C. Burgers, and J.K. Terlouw. Int. J. Mass Spectrom. Ion Processes, **144**, L1 (1995).
13. P.C. Burgers and P.J.A. Ruttink. Org. Mass Spectrom. **28**, 1087 (1993).
14. (*a*) D.K. Bohme. Int. J. Mass Spectrom. Ion Processes, **115**, 95 (1992); (*b*) H.E. Audier, D. Leblanc, P. Mourgues, T.B. McMahon, and S. Hammerum. J. Chem. Soc. Chem. Commun. 2329 (1994).
15. (*a*) E.L. Coitino, A. Lledos, R. Serra, J. Bertran, and O.N. Ventura. J. Am. Chem. Soc. **115**, 9121 (1993), and refs. cited therein; (*b*) M. Sodupe, A. Oliva, and J. Bertran. J. Am. Chem. Soc. **117**, 8416 (1995).
16. R.D. Guetter, G.C. Jones, Jr., L.A. Posey, and R.N. Zare. Science, **266**, 259 (1994).
17. M.F. Guest and J. Kendrick. GAMESS users manual. SERC Daresbury Laboratory, CCP/86/1, 1986; M. Dupuis, D. Spangler, and J. Wendolowski. NRCC Software Catalog, Vol. 1, Program No. QG01 (GAMESS), 1980; M.F. Guest, R.J. Harrison, J.H. van Lenthe, and L.C.H. van Corler. Theor. Chim. Acta, **71**, 117 (1987).
18. V.R. Saunders and J.H. van Lenthe. Mol. Phys. **48**, 923 (1983).
19. P.J.A. Ruttink, J.H. van Lenthe, R. Zwaans, and G.C. Groeneboom. J. Chem. Phys. **94**, 7212 (1991).
20. (*a*) T.H. Dunning, Jr. J. Chem. Phys. **53**, 2823 (1970); (*b*) T.H. Dunning, Jr. and P.J. Hay. *In* Modern theoretical chemistry. Vol. 3. Methods of electronic structure theory. *Edited by* H.F. Schaeffer III. Plenum Press, New York. 1977. p. 1.
21. (*a*) J.A. Pople, H.B. Schlegel, R. Krishnan, D.J. DeFrees, J.S. Binkley, M.J. Frisch, R.A. Whiteside, R.F. Hout, Jr., and W.J. Hehre. Int. J. Quantum Chem. Quantum Symp. **15**, 269 (1981); (*b*) R.S. Gren, C.L. Janssen, and H.F. Schaeffer III. J. Chem. Phys. **95**, 5128 (1991); (*c*) J.A. Pople, A.P. Scott, M.W. Wong, and L. Radom. Isr. J. Chem. **33**, 345 (1993).
22. J.A. Pople, R. Seeger, and R. Krishnan. Int. J. Quantum Chem. **11**, 149 (1977).
23. T.H. Schucan and H.A. Weidenmüller. Ann. Phys. (N.Y.) **76**, 483 (1973).
24. S. Lias, J.E. Bartmess, J.F. Liebman, J.L. Holmes, R.D. Levin, and W.G. Mallard. J. Phys. Chem. Ref. Data, **17**, Suppl. 1 (1988).
25. C.E. Klots. J. Chem. Phys. **58**, 5364 (1973).
26. P.J.A. Ruttink. J. Phys. Chem. **91**, 703 (1987).
27. P.C. Burgers and J.L. Holmes. Rapid Commun. Mass Spectrom. **3**, 279 (1989).
28. J-D Shao, T. Baer, J.C. Morrow, and M.L. Fraser-Monteiro. J. Chem. Phys. **87**, 5242 (1987).
29. N. Heinrich, J. Schmidt, H. Schwarz, and Y. Apeloig. J. Am. Chem. Soc. **109**, 1317 (1987).
30. (*a*) J.K. Terlouw, J. Wezenberg, P.C. Burgers, and J.L. Holmes. J. Chem. Soc. Chem. Commun. 1121 (1983); (*b*) C. Wesdemiotis and F.W. McLafferty. J. Am. Chem. Soc. **109**, 4760 (1987).
31. W.J. Bouma, P.C. Burgers, J.L. Holmes, and L. Radom. J. Am. Chem. Soc. **108**, 1767 (1986).

32. D.R. Lide (*Editor*). Handbook of chemistry and physics. 73rd ed. CRC Press, Boca Raton, Fla. 1992.
33. P. Longevialle and O. Lefèvre. Org. Mass Spectrom. **28**, 1083 (1993).
34. N. Koge and K. Morokuma. Chem. Phys. Lett. **119**, 371 (1985).
35. S. Hammerum, T. Vulpius, and H.E. Audier. Org. Mass Spectrom. **27**, 369 (1992).
36. S. Tajima, Y. Nagai, O. Sekiguchi, M. Fujishige, and N. Uchida. J. Am. Soc. Mass Spectrom. **6**, 202 (1995).
37. H.E. Audier, P. Mourgues, D. Leblanc, and S. Hammerum. C.R. Acad. Sci. Paris, Ser. II: Mec. Phys. Chim. Astron. **317**, 27 (1993).

Topological analysis of the electron localization function applied to delocalized bonds

A. Savin, B. Silvi, and F. Colonna

Abstract: What is a local viewpoint of delocalized bonds? We try to provide an answer to this paradoxical question by investigating representative conjugated organic molecules (namely, allyl cation, *trans*-butadiene, and benzene) together with reference nonconjugated systems (ethylene and propene) by means of topological analysis of the electron localization function ELF. The valence attractors of the ELF gradient field are classified according to their synaptic order (i.e., connections with core attractors). The basin populations $\bar{N}$, (i.e., the integrated density over the attractor basins) and their standard deviation, σ, have been calculated and are discussed. The basin populations and their relative fluctuations, defined as $\lambda = \sigma^2/\bar{N}$, are sensitive criteria of delocalization. In the case of well-localized C—C or C=C bonds, $\lambda \sim 0.4$, whereas for delocalized bonds λ increases to about 0.5. Another criterion of delocalization is provided by the basin hierarchy, which is defined from the reduction of the localization domains. For most systems, delocalization occurs not only for neighboring carbon–carbon disynaptic attractor basins, but also for nearest neighbor disynaptic protonated attractor basins.

Key words: electron localization function, topological analysis, delocalization, population analysis.

Résumé : Y a-t-il un point de vue local des liaisons délocalisées ? Nous essayons de répondre à cette question pour le moins paradoxale en examinant une série de molécules organiques conjuguées et de systèmes non-conjugués de référence à l'aide de l'analyse topologique de la fonction de localisation ELF. Ces systèmes sont d'une part le cation allyl, le *trans*-butadiène et le benzène et, d'autre part l'éthylène et le propène. Les attracteurs de valence du champ gradient de ELF sont classés suivant leur order synaptique (c'est à dire, suivant le nombre de connections qu'ils forment avec les cœurs). La population moyenne par bassin, $\bar{N}$, et son écart-type, σ, ont été calculés et font l'objet d'une discussion. Les populations moyennes par bassin et leurs fluctuations relatives, $\lambda = \sigma^2/\bar{N}$, sont des indicateurs sensibles de la délocalisation. Pour des liaisons C—C ou C=C localisées, $\lambda \sim 0.4$ tandis que pour des liaisons plus délocalisées $\lambda \sim 0.5$. La hiérarchie des bassins, définie à partir de la réduction des domaines de localizations, est un autre critère de délocalisation. Dans la plupart des systèmes la délocalisation affecte non seulement les bassins des attracteurs relatifs au squelette carboné mais également les bassins adjacents d'attracteurs disynaptiques protonés.

Mots clés : fonction de localisation d'électrons, analyse topologique, délocalisation, analyse de population.

1. Introduction

The bonding in conjugated organic systems cannot be represented by a definite Lewis structure and is therefore referred as delocalized. Attempts at understanding such systems on the basis of the Lewis theory of valence have given rise to, for example, chimerical structures such as those proposed by Huggins (1), which were rejected with the advent of quantum chemistry. The valence-bond (VB) and molecular orbital (MO) approaches are at the root of the two basic descriptions of these bonds that can be found in textbooks (2). On the one hand is the resonance concept, in which the true ground state wave function of the system is expressed as a linear combination of wave functions corresponding to definite Lewis structures (3), and on the other hand is the MO description in which the bonding orbitals are delocalized over the whole molecule. As mentioned by Coulson (4): "There is an interesting contrast between the VB and MO descriptions of benzene. Both require complete delocalization, but whereas the VB method introduces it by superposition of Kekulé (and other) structures, in the MO method there is nothing that even remotely resembles a structure. This situation warns us once more against any too literal belief in the reality of our structures." This epistemological difficulty is mostly due to the weakness of interpretative methods that give a physical significance to quantities, such as molecular orbitals or valence-bond structures, appearing as intermediate during the course of approximate procedures of solution of the many-body Schrödinger equation.

The analysis of local functions defined within the exact many-body theory, such as the electron densities and deformation densities, is an alternative interpretative strategy that is more consistent with the interpretative postulates of quantum mechanics. The difficulty is then to find a guideline

Received November 1, 1995.

This paper is dedicated to Professor Richard F.W. Bader on the occasion of his 65th birthday.

A. Savin, B. Silvi,[1] and F. Colonna. Laboratoire de chimie théorique (URP 9070), Université Pierre et Marie Curie, 4, Place Jussieu, 75252 Paris cédex 05, France.

[1] Author to whom correspondence may be addressed. Telephone: +31-1-4427-4053. Fax: +31-1-4427-4117. E-mail: silvi@lct.jussieu.fr

allowing an objective partition of the molecular space and to make a link with the ideas widespread in the chemistry community. With respect to the delocalization problem, the question of the description provided by such local theories may seem to be paradoxical. In an early version of the loge theory, delocalization in benzene could be accounted for by the presence of "one loge with six delocalized electrons and extending over the carbon cores" (5). This assumption has not been supported by calculations since the numerical complexity of the determination of the boundaries of such a loge is too high to be feasible. The theory of atoms in molecules (6) provides a partition of the molecular space into atomic basins. Though these basins cannot by themselves provide a picture of the delocalization, the definition of bond orders within this framework (7, 8) provides a proper framework for the discussion of the delocalization.

An alternative partition of the molecular space is provided by topological analysis of the electron localization function ELF (9), which yields basins related to the local pairing of electrons. In this paper, we have investigated by this technique the bonding in simple hydrocarbons containing double and single bonds (namely ethylene, propene, allyl cation, *trans*-butadiene, and benzene) in order to compare the local properties in typical localized and delocalized systems.

2. A sketch of the topological analysis of the ELF function

The topological analysis of molecular space has been pioneered for two decades by Richard Bader (6) who investigated the gradient field of the electron density in order to build a rigorous theory of the chemical bond. Gradient field analysis is the mathematically well-established method allowing "access to a rigorous qualitative thinking" (10). In the particular field of the chemical bond, it can help to objectively define the words used to describe molecules on a microscopic scale. In this respect, Bader's definition of the atom within the molecule exemplifies the possibilities of the method. In principle, gradient field analysis can be applied to any well-defined local function. For us, a well-defined local function is a function of the space coordinate $\boldsymbol{r}$, which can be expressed in the framework of an exact many-body theory. Property densities are defined as the integral over the spin coordinate:

$$[1] \qquad \rho_A(\boldsymbol{r}) = \int \hat{A}\rho(\boldsymbol{x};\boldsymbol{x}')_{\boldsymbol{x}'=\boldsymbol{x}}\mathrm{d}\sigma$$

$\hat{A}$ is the Hermitian operator associated with the property, $\rho(\boldsymbol{x},\boldsymbol{x}')$ is the first-order density matrix (11), and $\boldsymbol{x}$ stands for the space and spin coordinates. They are well-defined local functions whereas orbitals, in many-electron systems, have no physical meaning since they appear as mathematical intermediates during the calculation. Functions of densities of property are also local functions. As examples of well-defined local functions we can mention the electron density and derived quantities such as the molecular electrostatic potential. We have recently shown (9) that a similar analysis applied to a localization function such as that of Becke and Edgecombe (12) provides "a clear demarcation between shared-electron interaction, as in covalent and metallic bonding, and unshared-electron interactions, such as in ionic and hydrogen bonded systems" (13).

2.1. The physical significance of ELF

The ELF function proposed by Becke and Edgecombe (12) was originally defined within the framework of Hartree–Fock (approximate) theory as:

$$[2] \qquad \eta(\boldsymbol{r}) = \frac{1}{1+\left(\frac{D_\sigma}{D_\sigma^0}\right)^2}$$

in which D_σ and D_σ^0 represent the curvature of the electron pair density for electrons of identical σ spins (the Fermi hole) for, respectively, the actual system and a homogeneous electron gas with the same density. D_σ is the Laplacian of the conditional probability calculated from a single determinental Hartree–Fock wave function:

$$[3] \qquad D_\sigma = (\nabla_2^2 P_{\mathrm{cond}}^{\sigma\sigma}(1,2))_{1=2} = \sum_{i=1}^{N} |\nabla\varphi_i|^2 - \frac{1}{4}\frac{|\nabla\rho^\sigma(1)|^2}{\rho^\sigma(1)}$$

As mentioned before (14) this expression is formally identical to the difference between the positive definite local kinetic energy of a system of noninteracting fermions $T_s^\sigma[\rho]$ appearing in the Kohn–Sham equations (15) and that appearing in the von Weizsäcker functional (16).

$$[4] \qquad D_\sigma = T_s^\sigma[\rho] - \frac{1}{4}\frac{|\nabla\rho^\sigma(1)|^2}{\rho^\sigma(1)}$$

As pointed out by Tal and Bader (17), the von Weizsäcker functional (16) is a lower bound to the positive definite local kinetic energy that is locally approached at the Hartree–Fock level when a single orbital makes the dominant contribution to the density in the same region of space. The von Weizsäcker functional is also the positive definite local kinetic energy of a system of noninteracting particles of density ρ^σ for which the Pauli repulsion has been switched off. Therefore, D_σ signifies the local excess of kinetic energy due to the Pauli repulsion. The kinetic interpretation of D_σ (14) is very important because it extends the validity of the ELF function to the ground state of real systems for which $T_s^\sigma[\rho]$ can be exactly evaluated within density functional theory. Therefore, for ground state systems ELF gains the status of a well-defined local function. Furthermore, this definition of ELF allows its determination from knowledge of the electron density alone. Thus, instead of considering the Laplacian of the conditional probability, it is more advantageous to consider D_σ in its kinetic interpretation to redefine ELF. For closed-shell systems, $T_s^\alpha[\rho] = T_s^\beta[\rho] = \frac{1}{2}T_s[\rho]$ and $\rho^\alpha(\boldsymbol{r}) = \rho^\beta(\boldsymbol{r}) = \frac{1}{2}\rho(\boldsymbol{r})$, so:

$$[5] \qquad \begin{aligned} D_\sigma &= \frac{1}{2}T_s[\rho] - \frac{1}{8}\frac{|\nabla\rho(1)|^2}{\rho(1)} \\ D_\sigma^0 &= \frac{3}{10}(3\pi^2)^{2/3}\rho^{5/3}(1) \end{aligned}$$

In these expressions, the σ dependence no longer appears on

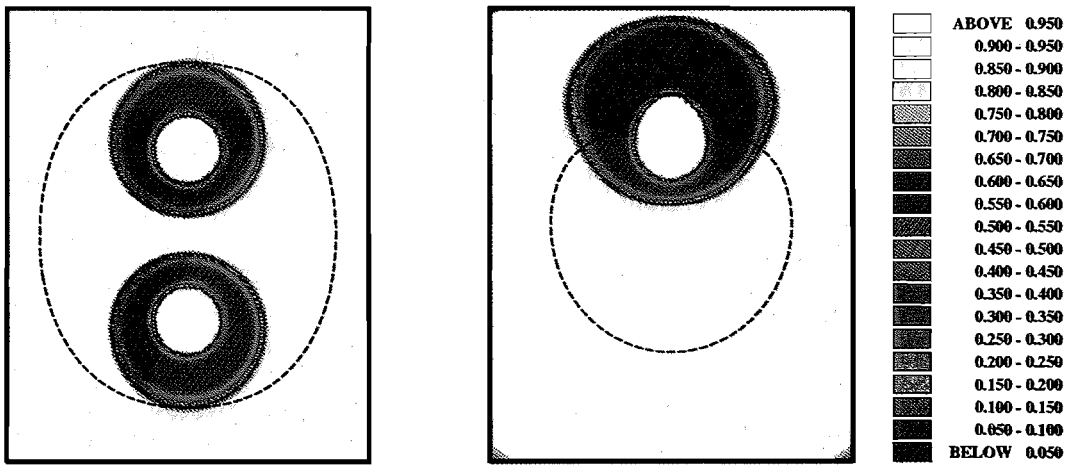

Fig. 1

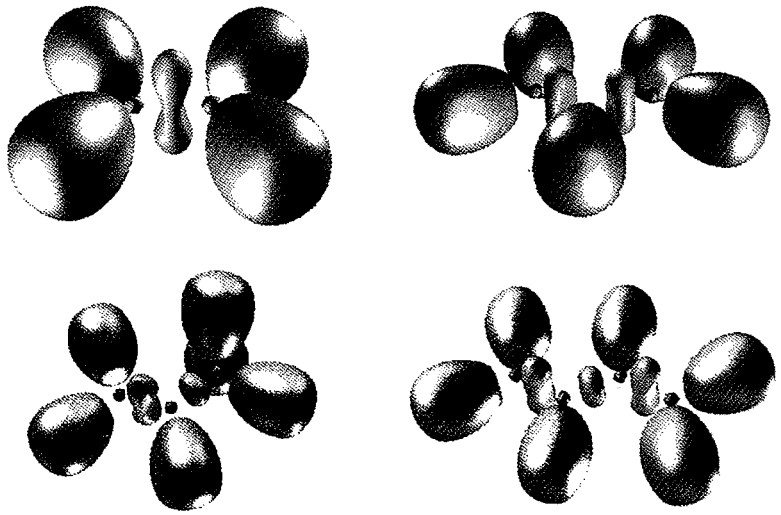

Fig. 2

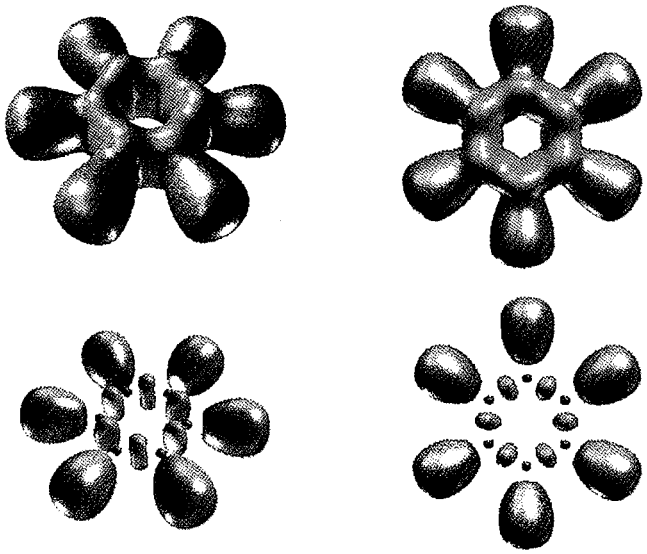

Fig. 3

Plate 1. Fig. 1. Representation of ELF for Li_2 (left) and LiH (right). ELF has been calculated with the density threshold ε set to zero. The value of ELF is given by the color scale. The broken lines correspond to the 10^{-3} e^- bohr^{-3} isodensity contours. **Fig. 2.** $\eta(\boldsymbol{r}) = 0.8$ localization domains of ethylene (top left), propene (bottom left), allyl cation (top right), and *trans*-butadiene (bottom right). The nature of the attractor defining the domain is given by the color code. Magenta: core; green: valence disynaptic; blue: protonated valence disynaptic. **Fig. 3.** The $\eta(\boldsymbol{r}) = 0.5$ and $\eta(\boldsymbol{r}) = 0.8$ localization domains of benzene. Same color code as in Fig. 2.

the right-hand side of the equations and therefore, one may consider D and D^0.[2]

In regions of space where the electron density is very low, the numerical representation of the wave function and of the density is not accurate enough to warrant the reliability of the gradients of local functions. Spurious attractors may appear that are due to computational artefacts such as roundoff errors or to basis set effects. Such troubles arise when D_σ tends to zero faster than $\rho(\boldsymbol{r})$. In practice, one can remove these difficulties by taking an effective ELF written as:

$$[6] \quad \frac{1}{1+\left(\frac{D+\varepsilon}{D^0}\right)^2}$$

ε is chosen such that ELF tends to zero with the density ρ. In actual calculation we use $\varepsilon = 2.87 \times 10^{-5}$. This value constrains ELF to be less than 0.5 for $\rho \leq 10^{-3}$.

ELF is a local measure of the effect of the Pauli repulsion on the kinetic energy density. In the region of space where the Pauli repulsion is weaker than in a uniform electron gas of identical density (we should say, where the local parallel pairing is lower), ELF is close to 1 whereas where the local parallel pairing is higher (and therefore the Pauli repulsion strongly active) ELF is low. For example, in a closed-shell system, though the α and β spin densities are equal everywhere, there are regions of low ELF between high ELF regions.

2.2. The topological analysis of ELF

As ELF is a scalar function, the analysis of its gradient field allows us to locate attractors to which we have given a chemical signification (9). Usually, the attractors of a gradient field[3] are single points as is the case for the gradient field of the density. However, for the ELF function, they can also be circles and spheres if the system belongs to a continuous symmetry group (here, cylindrical and spherical symmetry, respectively). In actual cases, the local symmetry remains very strong and, effectively, circular and spherical attractors can be found in molecules belonging to finite symmetry groups. There are, basically, two types of attractors: core and valence attractors. The attractors are designated according to the presence of a nucleus (except a proton) within their basin. They are either points (K-shell attractors) or spheres for the outer core shells.

To offer an efficient visualization tool, we introduced f-localization domains (9), which we defined as formal bodies bounded by a given isosurface $\eta(\boldsymbol{r}) = f$ and enclosing points for which ELF $> f$. These localization domains[4] are the ELF analogs of Mezey's density domains (18). They are said to be reducible when they contain more than one attractor, irreducible when they contain one attractor. The graphical representation of the irreducible localization domains with color codes associated with the type of attractor provides explanatory pictures of the bonding in molecules and crystals.

A valence attractor is connected to a core attractor when the two following conditions are fulfilled.

(*i*) Their basins are bounded by a part of a common separatrix.

(*ii*) The valence attractor lies within the smallest (reducible or irreducible) valence f-localization domain that totally surrounds the core attractor basin in a chemically relevant region (i.e., within which the electron density is larger than 10^{-3} au (19)).

In principle, a core is always totally encapsulated by at least one valence basin and therefore propositions (*i*) and (*ii*) are redundant when f tends to zero unless the valence localization domains have already merged with a core domain. Figure 1 (see Plate 1) provides an example of the determination of

---

[2] A possible generalization of ELF, which is valid to any stationary state and which preserves the requirements of a well-defined local function, can be achieved by substituting $T_s[\rho]$ by the positive definite local kinetic energy density $G(\boldsymbol{r})$, which refers to interacting particles and is obtained from eq. [1] with $\hat{A} = \nabla_r \nabla_{r'}$:

$$D = \frac{1}{2}G(\boldsymbol{r}) - \frac{1}{8}\frac{|\nabla\rho(\boldsymbol{r})|^2}{\rho(\boldsymbol{r})}$$

D_σ derived accordingly is no longer the local excess of kinetic energy due to the Pauli repulsion but has the meaning of a local excess of kinetic energy due to both Fermi and Coulomb holes. Its physical signification is less clear because eq. [1] is not formally equal to the Laplacian of the single determinental conditional probability. This definition might be, however, useful in actual calculations where correlated wavefunctions and natural orbitals are available instead of Kohn–Sham orbitals.

[3] A gradient dynamical system is a vector field that is defined as the gradient field of a given function called the potential function. By analogy with a velocity field, one can build trajectories that form the phase portrait of the dynamical system. Of particular importance are the sets of points where the gradient vanishes. These critical points are either local minima (repellors), saddle points, or local maxima (attractors) of the potential function. The basin of an attractor is the set of points lying on the trajectories ending in the neighbourhood of this attractor. Basins are separated by manifolds called separatrices.

[4] In topology, a domain is defined as a set of points that satisfies the following property: for any pair of points a and b belonging to the domain, there exists at least a path joining a and b and totally contained in the domain.

Table 1. Nomenclature of valence attractors.

Synaptic order	Nomenclature	Symbol
0	Asynaptic	V
1	Monosynaptic	$V(X_i)$
2	Disnaptic	$V(X_i, Y_j)$
≥3	Polysynaptic	$V(X_i, Y_j, ...)$

the number of cores connected to a valence basin. The ELF maps of Li_2 and LiH are represented in a plane containing the internuclear axis. We expect a valence basin containing the proton and a core basin in LiH, a valence basin and two core basins in Li_2. In LiH, there are two ~0.5 localization domains that are bounded by the brick-red lines: the first one is an elongated disk that is contained in the lithium core basin; the second, corresponding to the space remaining outside of the blue zones of low ELF, is in the valence basin. The separatrix between the two basins lies within the blue ring. For Li_2, there are three such ~0.5 localization domains. In Li_2, any core basin is connected to the valence basin because (*i*) they share a common separatrix and (*ii*) the 10^{-3} au isodensity contour represented by the broken line is totally contained in the ~0.5 localization domain (and *a fortiori* in the 0.3 domain). We should say that the valence attractor (located at the midpoint of the internuclear distance) is connected to the two lithium cores. On the contrary, for LiH, though condition (*i*) is fulfilled, condition (*ii*) is not because the broken line crosses the blue and green zones and, therefore, the separatrix. Inside the 10^{-3} au isodensity, the *f*-bounding isosurface does not close up the core for any value of ELF above the valence-core merging and, thus, the valence protonated attractor is not connected to the lithium core.

The number of cores connected to a given valence attractor determines its synaptic order. To avoid misleading confusion between valence attractors and orbital vocabulary we have been moved to introduce a new nomenclature of valence attractors, which is given in Table 1. Hydrogen is a particular case because it is, with helium, the only coreless atom. Therefore, as in Lewis theory, it has to be considered as an exception. Hydrogenated attractors are intermediate between core and valence attractors. In our description of the chemical bond, an attractor whose basin contains a proton is considered as a valence attractor and will be designated as protonated; to establish its synaptic order the proton is counted as a formal core basin (for example: a C—H bond is characterized by an protonated disynaptic attractor). In the examples represented in Fig. 1 (see Plate 1), the Li_2 valence attractor is disynaptic whereas the LiH valence attractor is protonated and monosynaptic.

In the present paper, the attractors and their basins will be labeled as $T_{[i]}$(atom labels). T denotes the type of attractor, V for valence, C for core; *i* is an optional running number in the case of multiple attractors related to the same atom(s). For example, in the water molecule there is one core attractor for the oxygen *K*-shell labeled C(O), two protonated disynaptic attractors $V(H_1, O)$ and $V(H_2, O)$, and two monosynaptic attractors corresponding to the lone pairs $V_1(O)$ and $V_2(O)$. In ethane, the disynaptic attractor of the C—C bond will accordingly be named $V(C_1, C_2)$.

The classification of bonds previously proposed remains valid with this new nomenclature. The shared electron interaction is characterized by a di- or polysynaptic attractor. The lone pairs of electronegative atoms are monosynaptic attractors.

2.3. Localization basin integrated density and related properties

The partition of the molecular space into basins of attractors allows the calculation of related properties by integration of the densities of property over the basins (20). In particular, for a basin labeled Ω_A, one can define the average population as :

$$[7] \quad \bar{N}(\Omega_A) = \int_{\Omega_A} \rho(\boldsymbol{r})\, d\boldsymbol{r}$$

Within the framework of our theory, these average populations are referred to as core, bond, and nonbonding (i.e., lone pair) populations according to the type of attractor that defines the basin. Such average populations over ELF basins were first calculated by us (21, 22) and recently by Häussermann et al. for intermetallic solids (23). They are not expected to have integral values and the bond populations would be about twice the topologically defined bond orders (7, 8).

The RMS deviation $\sigma(\bar{N};\Omega_A))$ is defined by (24, 25):

$$[8] \quad \sigma^2(\bar{N};\Omega_A)) = \langle N^2\rangle_{\Omega_A} - \langle N\rangle^2_{\Omega_A}$$

It represents the quantum mechanical uncertainty on $\bar{N}(\Omega_A)$. The variance (or fluctuation) σ^2 was investigated by Bader in the framework of atomic basins (26). The variance is expressed in terms of the diagonal elements of the first ($\rho(\boldsymbol{x})$) and second-order ($\pi(\boldsymbol{x}_1,\boldsymbol{x}_2)$) density matrices (11) as:

$$[9] \quad \sigma^2(\bar{N};\Omega) = \int_\Omega d\boldsymbol{x}_1 \int_\Omega d\boldsymbol{x}_2 \pi(\boldsymbol{x}_1,\boldsymbol{x}_2) + \bar{N}(\Omega) - \left[\bar{N}(\Omega)\right]^2$$

in which $\boldsymbol{x}_i$ denotes the space and spin coordinates of the electron labeled *i*. For a single determinental wave function (i.e., Hartree–Fock or Kohn–Sham) $\sigma^2(\bar{N};\Omega)$ is the difference between the basin population and the integral over the basin of the exchange part of the second-order density matrix:

$$[10] \quad \sigma^2(\bar{N};\Omega) = \bar{N}(\Omega) - B(\Omega,\Omega)$$

In terms of the orbitals $\phi_i(\boldsymbol{r})$ and of the occupations n_i^α, n_i^β, $B(\Omega,\Omega)$ is given by:

$$[11] \quad B(\Omega,\Omega) = \sum_i \sum_j (n_i^\alpha n_j^\alpha + n_i^\beta n_j^\beta)\langle\phi_i|\phi_j\rangle_\Omega\langle\phi_j|\phi_i\rangle_\Omega$$

in which

$$[12] \quad \langle\phi_i|\phi_j\rangle_\Omega = \int_\Omega d\boldsymbol{r}\phi_i^*(\boldsymbol{r})\phi_j(\boldsymbol{r})$$

It is also convenient to define the interbasin integrated exchange density:

$$[13] \quad B(\Omega_A,\Omega_B) = \sum_i \sum_j (n_i^\alpha n_j^\alpha + n_i^\beta n_j^\beta)\langle\phi_i|\phi_j\rangle_{\Omega_A}\langle\phi_j|\phi_i\rangle_{\Omega_B}$$

The fluctuation in a superbasin $\Omega_A \cup \Omega_B$ is:

$$[14] \quad \sigma^2(\bar{N};\Omega_A \cup \Omega_B) = \sigma^2(\bar{N};\Omega_A) + \sigma^2(\bar{N};\Omega_B) - 2B(\Omega_A,\Omega_B)$$

and for the whole space

$$[15] \quad \sigma^2(\bar{N};\Omega_A \cup \Omega_B \cup \ldots) = 0$$

It follows from eq. [14] that for independent basins σ^2 is an extensive quantity. Following Bader (26), it is useful to introduce the relative fluctuation

$$[16] \quad \lambda(\Omega) = \sigma^2(\bar{N};\Omega)/\bar{N}(\Omega)$$

which is positive and also expected to be less than 1.

Another criterion of discrimination between basins is provided by the reduction of reducible domains. The reduction of a reducible localization domain occurs at a critical value of the bounding isosurface, over which the domain is split into domains containing fewer attractors. The localization domains are then ordered with respect to the ELF critical values, yielding bifurcations. Starting at a very low ELF value, we find only one localization domain (the whole space for $\eta(\boldsymbol{r}) = 0$) upon increase of the isosurface defining value, we meet a first separation between valence and core domains, and at higher ELF values the valence reducible domain is split in its turn. The hierarchy of the bifurcation can be visualized by a tree-diagram.

3. Results and discussion

The calculations were performed at the DFT level with Gaussian94 software (27). The standard 6-31G** basis set (28) was used in conjunction with Becke exchange (29) and Lee, Yang, and Parr correlation (30) functionals. All structures were fully optimized. The labeling of atoms that will be used to label the attractors of the ELF vector gradient field is given in Fig. 4.

Figure 2 (see Plate 1) displays the $\eta(\boldsymbol{r}) = 0.8$ localization domains of ethylene, allyl cation, and *trans*-butadiene whereas the $\eta(\boldsymbol{r}) = 0.5$ and $\eta(\boldsymbol{r}) = 0.8$ localization domains of benzene are represented in Fig. 3 (Plate 1). The representation provided by the topological analysis of ELF does not correspond to the conventional picture of a double bond made into σ and π bonds. This latter description is not invariant upon a unitary transformation of the molecular orbitals; alternative representations such as "banana double bonds" have been shown to be equivalent (3).

3.1. Ethylene

In ethylene there are two core attractors, labeled $C(C_1)$ and $C(C_2)$, four protonated disynaptic attractors, $V(C_i, H_j)$, and two disynaptic attractors $V_1(C_1, C_2)$ and $V_2(C_1, C_2)$. The attractor basins that surround $C(C_1)$ are $V(C_1, H_1)$, $V(C_1, H_2)$, $V_1(C_1, C_2)$, and $V_2(C_1, C_2)$ whereas around $C(C_2)$ we find $V(C_2, H_3)$, $V(C_2, H_4)$, $V_1(C_1, C_2)$, and $V_2(C_1, C_2)$. Therefore, the $V(C_i, H_j)$ and the $V_i(C_1, C_2)$ are disynaptic, according to the definition given in a previous section. The basin populations, their standard deviation and relative fluctuations are listed in Table 2. The basins of the two disynaptic attractors have been gathered together in the superbasin labeled $V_{1\cup2}(C_1C_2)$. The basin population corresponding to

Fig. 4. Atomic labels of ethylene, propene, allyl cation, *trans*-butadiene, and benzene.

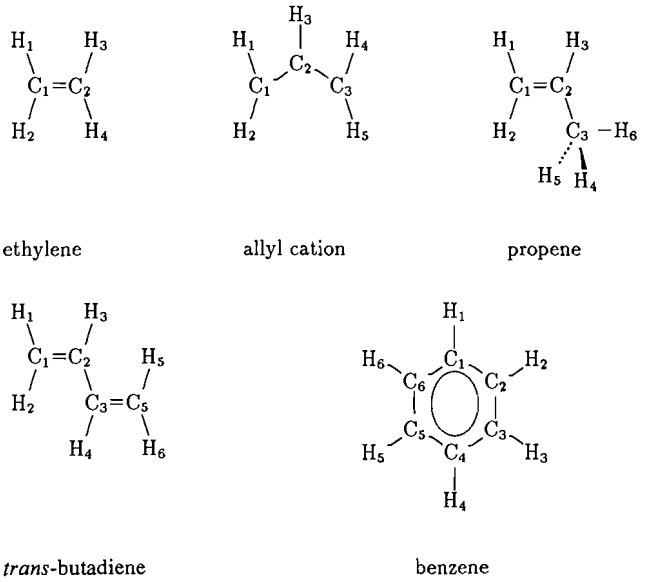

Table 2. ELF value at attractor, basin population, standard deviation, and relative fluctuations of the basin populations of ethylene.

	ELF	$\bar{N}$	$\sigma(\bar{N};\Omega)$	$\lambda(\Omega)$
C(C)	1.0	2.09	0.51	0.12
$V(C_1, H_1)$	1.0	2.04	0.94	0.43
$V(C_1, C_2)$	0.93	1.81	1.12	0.70
$V_{1\cup2}(C_1, C_2)$	0.93	3.62	1.47	0.40

the C=C double bond is less then 4, whereas the core and hydrogen basins are slightly greater than 2. The topological bond orders of Cioslowski and Mixon (7) and of Angyán et al. (8) calculated with the same carbon basis set at the SCF level are, respectively, 1.958 and 1.984. With a 6-31++G** basis these values are reduced to 1.881 and 1.918 whereas the C—H bond order is increased by 0.012 e^-. The discrepancy with our value (1.79) is due in part to different definitions and also to the fact that in our calculation the core population is independently treated. The relative fluctuation in the population of the core basins is low. On the contrary, for basins of the disynaptic attractors of the C=C bond the relative fluctuation is very high (0.7). These two basins are strongly correlated and their aggregation lowers the relative fluctuation from 0.70 to 0.40.

The bifurcation graph (Fig. 5) provides a hierarchy that is consistent with the relative fluctuation values. At $\eta(\boldsymbol{r}) = 0.06$, there is a first partition into core and valence basins. The valence basin is split into two protonated reducible domains $V(C_1, H_1) \cup V(C_1, H_2)$, $V(C_2, H_3) \cup V(C_2, H_4)$, and the $V_{1\cup2}(C_1, C_2)$ one $V_1(C_1, C_2) \cup V_2(C_1, C_2)$ at $\eta(\boldsymbol{r}) = 0.64$. This bifurcation is immediately followed at $\eta(\boldsymbol{r}) = 0.65$ by the reduction of the two protonated domains. Finally, $V_{1\cup2}(C_1, C_2)$ is reduced at $\eta(\boldsymbol{r}) = 0.92$, a value very close to that of the attractors.

Fig. 5. Localization domain reduction tree-diagram of ethylene.

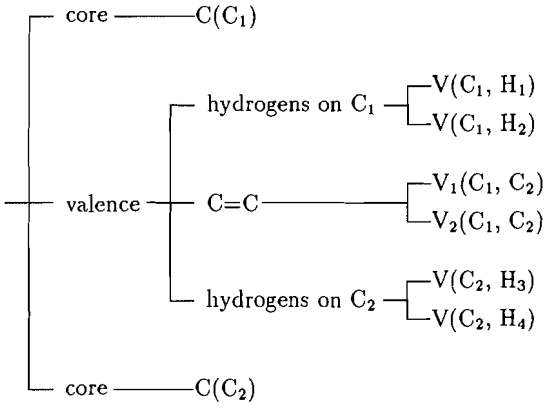

3.2. Propene

The basin populations, their standard deviation, and relative fluctuations of propene are given in Table 3. As for ethylene, the basins of the two disynaptic attractors of the double bond have been merged. The $V_{1\cup2}(C_1, C_2)$ population is larger in propene than in ethylene by 0.1 e^-. The relative fluctuation for this basin, 0.41, is very close to the corresponding value in ethylene. The same value is also found for the $V(C_2, C_3)$ basin, which corresponds to the single C—C bond. The lowering of the molecular symmetry from D_{4h} in ethylene to C_s in propene weakens the correlation between the allylic hydrogen basins; their relative fluctuations decrease by about 0.1. An important correlation remains between the two methyl hydrogens symmetric with respect to the σ plane.

The bifurcation graph of the localization domains of propene is shown in Fig. 6. After the core–valence separation at $\eta(r) = 0.06$, the valence domain undergoes a second separation into three domains at $\eta(r) = 0.65$. These domains correspond to the central carbon hydrogen, the methyl group, and the allyl group. The methyl group domain is reduced at $\eta(r) = 0.67$ into two components $V(C_2, C_3)$ and the domain of the three hydrogens from which the in-plane hydrogen is separated at $\eta(r) = 0.69$, the two out-of-plane being ultimately split for $\eta(r) = 0.70$. On the allyl side, hydrogens detachments occur successively at $\eta(r) = 0.67$ and $\eta(r) = 0.69$ and the reduction of the C=C domain at $\eta(r) = 0.93$.

3.3. Allyl cation

In ethylene and propene the number of attractors is equal to the number of occupied Kohn–Sham orbitals; in allyl cation, there are 10 attractors for 11 doubly occupied orbitals. One disynaptic attractor with a basin population of 2.6 (Table 4) is found for each C—C bond. The value of ELF at the attractor is slightly less than that of the propene single bond. The relative fluctuation for the basins of these attractors, 0.55, is higher than for a double or a single C—C bond in the absence of conjugation, indicating a noticeable delocalization. Delocalization over hydrogen basins is of the order found in propene since the corresponding relative fluctuations are both of the order of 0.30.

The localization domain reduction pattern (Fig. 7) reflects the symmetry of the system. As in propene, the first splitting of the valence domain at $\eta(r) = 0.59$ is due to the detachment of the central carbon hydrogen. The second valence separation ($\eta(r) = 0.645$) involves hydrogens linked to the terminal carbon, which are immediately ($\eta(r) = 0.65$) followed by domains containing the disynaptic C—C attractors. At ($\eta(r) = 0.66$) the domains are totally reduced. It is worth noting that delocalization delays the separation of the $V(C_1, C_2)$ and $V(C_2, C_3)$ domains with respect to the allyl–methyl separation in propene.

Table 3. ELF value at attractor, basin population, standard deviation, and relative fluctuations of the basin populations of propene.

	ELF	$\bar{N}$	$\sigma(\bar{N}; \Omega)$	$\lambda(\Omega)$
C(C)	1.0	2.09	0.51	0.12
$V(C_1, H_1)$	1.0	2.05	0.79	0.31
(C_3, H_4)	1.0	1.98	0.93	0.44
(C_3, H_6)	1.0	1.99	0.75	0.28
$V_{1\cup2}(C_1, C_2)$	0.93	3.68	1.22	0.41
(C_2, C_3)	0.96	1.91	1.0	0.41

Fig. 6. Localization domain reduction tree-diagram of propene.

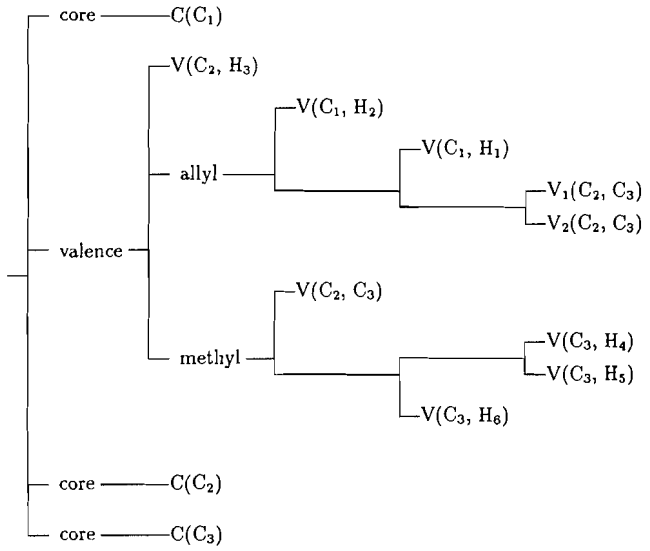

Table 4. ELF value at attractor, basin population, standard deviation, and relative fluctuations of the basin populations of allyl cation.

	ELF	$\bar{N}$	$\sigma(\bar{N}; \Omega)$	$\lambda(\Omega)$
C(C)	1.0	2.09	0.51	0.12
$V(C_1, H_1)$	1.0	2.10	0.78	0.29
$V(C_2, H_3)$	1.0	2.12	0.80	0.30
$V(C_1, C_2)$	0.95	2.60	1.19	0.55

3.4. *trans*-Butadiene

The populations of the attractor basins of *trans*-butadiene, reported in Table 5, show similarities to and differences from

Fig. 7. Localization domain reduction tree-diagram of allyl cation.

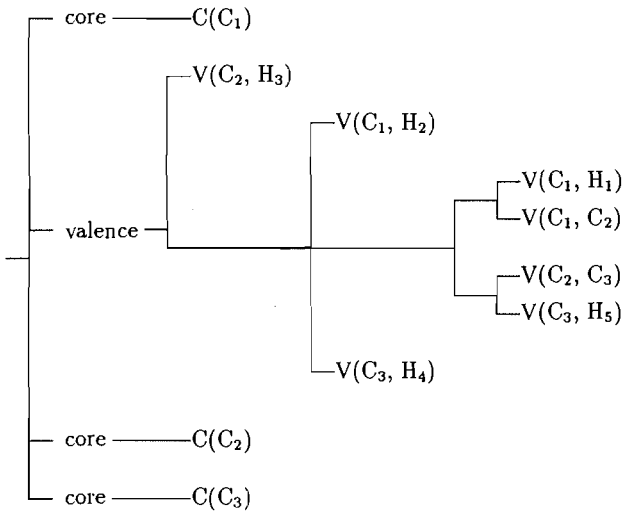

Table 5. ELF value at attractor, basin population, standard deviation, and relative fluctuations of the basin populations of *trans*-butadiene.

	ELF	$\bar{N}$	$\sigma(\bar{N}; \Omega)$	$\lambda(\Omega)$
C(C)	1.0	2.09	0.51	0.12
$V(C_1, H_1)$	1.0	2.05	0.79	0.31
$V(C_2, H_3)$	1.0	2.05	0.79	0.31
$V_{1\cup 2}(C_1, C_2)$	0.93	3.56	1.23	0.42
$V(C_2, C_3)$	0.96	2.17	1.04	0.50

Fig. 8. Localization domain reduction tree-diagram of *trans*-butadiene.

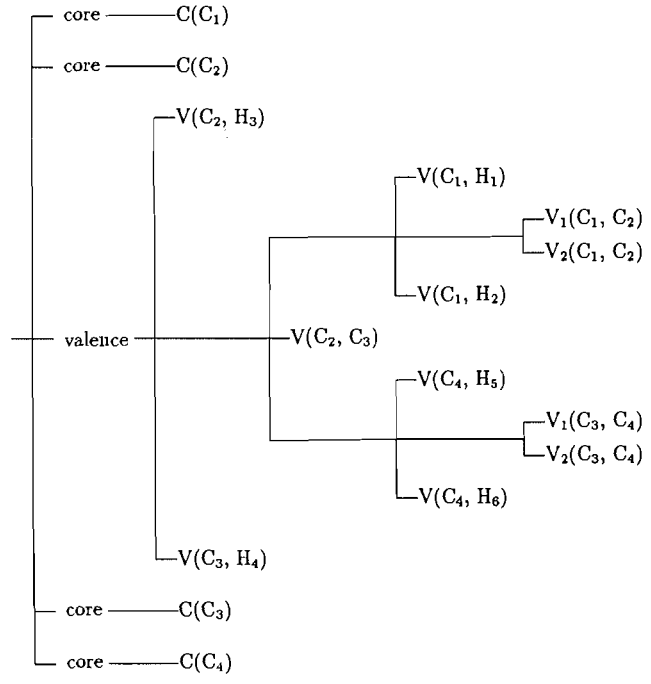

Table 6. ELF value at attractor, basin population, standard deviation, and relative fluctuations of the basin populations of benzene.

	ELF	$\bar{N}$	$\sigma(\bar{N}; \Omega)$	$\lambda(\Omega)$
C(C)	1.0	2.09	0.51	0.12
$V(C_i, C_j)$	0.94	2.83	1.14	0.47
$V(C_i, H_i)$	1.0	2.08	0.80	0.31

that of propene. On the one hand, the ELF values at the attractors are identical in *trans*-butadiene and in propene and the populations of the hydrogen basins are equal to that of the allylic hydrogens; on the other hand, the populations of the double bond attractors are less than that of propene by 1/8 e^-, whereas the single bond basin population is increased by 1/4 e^-. This reorganization of the basin population is an indication of the delocalization along the carbon skeleton. Note also, the increase with respect to propene of the relative fluctuation of the single C—C bond basin.

The localization domain reduction diagram of *trans*-butadiene (Fig. 8) is very similar to that of propene. After the core–valence separation at $\eta(\boldsymbol{r}) = 0.06$, the domains of the protonated disynaptic attractors linked to the carbons of the single bond part from the valence domain at $\eta(\boldsymbol{r}) = 0.63$. The next step, at $\eta(\boldsymbol{r}) = 0.64$, isolates the disynaptic attractor of the C—C single bond from two allylic fragments. At higher ELF values, the two allylic fragments are split in accordance with the way followed in propene, except that the two hydrogen basins are simultaneously detached from the C=C domain.

3.5. Benzene

There are 18 attractors in benzene: 6 core, 6 protonated disynaptic, and 6 C—C disynaptic. Each V(C—C) has a basin population of 2.83 e^-, which compares with the topological bond order, ~ 1.4(7, 8). Delocalization along the skeletal ring is indicated by a rather high relative fluctuation, 0.47 (Table 6). The ELF analysis does not give evidence for any σ and π systems in benzene.

The reduction of the localization domains in benzene, presented in Fig. 9, is very simple and is ruled by the molecular symmetry. At $\eta(\boldsymbol{r}) = 0.06$ the core domains are separated from the valence domain, which undergoes two successive splittings. The first one at $\eta(\boldsymbol{r}) = 0.65$ plucks off the hydrogen, the second, at $\eta(\rho) = 0.68$ unties the $V(C_i, C_j)$ domains.

4. Conclusion

For the electron density produced by a given potential of the nuclei, ELF provides a structuring of the molecular space into basins that may be roughly associated with the electron-pairing regions and have therefore a chemical meaning. The average number of electrons per basin is obtained by integration of the electron density function over the basins. For the systems investigated here, it corresponds roughly to the number of electrons expected on chemical grounds.

Quantum mechanical uncertainty yields standard deviations that typically range from 0.5 for the well-separated

Fig. 9. Localization domain reduction tree-diagram of benzene.

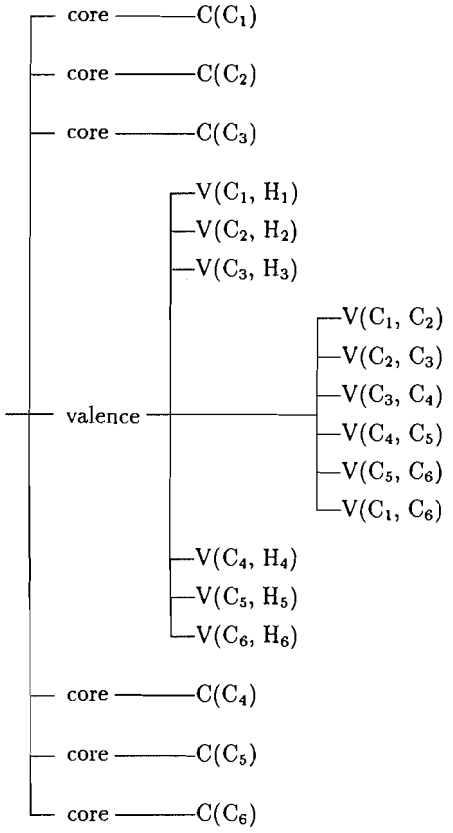

core basins to 1.2 for the valence basins. The core basins are well separated from the valence basins because the value of ELF on the separatrix (i.e., at the border) is always very low, ~0.06. This is not the case between valence basins that are separated at higher ELF values, about 0.6–0.7 for the systems presented here. Following Bader (26), we found that the relative fluctuation is a good measure of the delocalization. It is of the order of 0.1 for core basins, 0.3 for basins of the protonated disynaptic attractor of the C—H bonds, 0.4 for basins related to single and double C—C bonds, and 0.5 for delocalized bonds. Of course, the relative fluctuation is not the only measure of delocalization, which is also reflected by the average basin populations of the C—C bonds (e.g., 2.8 for benzene).

This work illustrates the importance of Richard Bader's contribution to theoretical chemistry. Beyond the theory of Atoms in Molecules, he demonstrated the importance of topological analysis for scrutinizing molecular space and he introduced tools, such as fluctuation analysis, that are very useful complements to the topological approach.

Acknowledgements

The authors gratefully acknowledge M. Kohout's comments on the draft manuscript. The data analyzer software SciAn (31) was used to produce Figs. 2 and 3.

References

1. M.L. Huggins. Science, **55**, 679 (1922).
2. M. Karplus and R.N. Porter. Atoms and molecules. An introduction for students of physical chemistry. W.A. Benjamin, New York. 1970.
3. L. Pauling. The nature of the chemical bond. Cornell University Press, Ithaca, N.Y. 1960.
4. C.A. Coulson. Valence. Oxford University Press, Oxford. 1952.
5. R. Daudel. Quantum theory of the chemical bond. Reidel, Dordrecht. 1974.
6. R.F.W. Bader. Atoms in molecules: a quantum theory. Oxford University Press, Oxford. 1990.
7. J. Cioslowski and S. T. Mixon. J. Am. Chem. Soc. **113**, 4142 (1991).
8. J. Ángyán, M. Loos, and I. Mayer. J. Phys. Chem. **98**, 5244 (1994).
9. B. Silvi and A. Savin. Nature, **371**, 683 (1994).
10. R. Thom. Stabilité structurelle et morphogénèse. Intereditions, Paris. 1972. Structural stability and morphogenesis. W.A. Benjamin, Reading, Mass. 1975.
11. R. McWeeny. Methods of molecular quantum mechanics. Academic Press, London. 1989. pp. 119–124.
12. A.D. Becke and K.E. Edgecombe. J. Chem. Phys. **92**, 5397 (1990).
13. D.L. Cooper. Nature, **371**, 651 (1994).
14. A. Savin, O. Jepsen, J. Flad, O.K. Andersen, H. Preuss, and H.G. von Schnering. Angew. Chem. **31**, 187 (1992).
15. W. Kohn and L.J. Sham. Phys. Rev. [Sect.] A, **140**, 1133 (1965).
16. C.F. von Weizsäcker. Z. Phys. **96**, 431 (1935).
17. Y. Tal and R.F.W. Bader. Int. J. Quantum Chem. **S12**, 153 (1978).
18. P. Mezey. Can. J. Chem. **72**, 928 (1994).
19. R.F.W. Bader, M.T. Carroll, J.R. Cheeseman, and C. Chang. J. Am. Chem. Soc. **109**, 7968 (1987).
20. F.W. Biegler-König, R.F.W. Bader, and T.H. Tang. J. Comput. Chem. **3**, 317 (1982).
21. A. Savin. Second International Conference on Inorganic Chemistry, Sept. 12–15, 1993, Stuttgart, Germany.
22. M. Kohout and A. Savin. Int. J. Quantum Chem. In press.
23. U. Häussermann, S. Wengert, and R. Nesper. Angew. Chem. Int. Ed. Engl. **33**, 2073 (1994).
24. A. Messiah. Mécanique quantique. Tome I. Dunod, Paris. 1962. p. 113.
25. P. Claverie and S. Diner. Localization and delocalization in quantum chemistry. Vol. 2. *Edited by* O. Chalvet et al. Reidel, Dordrecht. 1976.
26. R.F.W. Bader. Localization and delocalization in quantum chemistry. Vol. 1. *Edited by* O. Chalvet et al. Reidel, Dordrecht. 1975.
27. M.J. Frisch, G.W. Trucks, H.B. Schlegel, P.M.W. Gill, B.G. Johnson, M.A. Robb, J.R. Cheeseman, T. Keith, G.A. Petersson, J.A. Montgomery, K. Raghavachari, M.A. Al-Laham, V.G. Zakrzewski, J.V. Ortiz, J.B. Foresman, J. Cioslowski, B.B. Stefanov, A. Nanayakkara, M. Challacombe, C.Y. Peng, P.Y. Ayala, W. Chen, M.W. Wong, J.L. Andres, E.S. Replogle, R. Gomperts, R.L. Martin, D.J. Fox, J.S. Binkley, D.J. Defrees, J. Baker, J.P. Stewart, M. Head-Gordon, C. Gonzalez, and J.A. Pople. Gaussian 94, Revision B.1. Gaussian, Inc., Pittsburgh, Pa. 1995.
28. W.J. Hehre, R. Ditchfield, and J.A. Pople. J. Chem. Phys. **56**, 2257 (1972).
29. A.D. Becke. J. Chem. Phys. **98**, 5648 (1988).
30. C. Lee, Y. Yang, and R.G. Parr. Phys. Rev. B: Condens. Matter, **37**, 785 (1988); B. Miehlich, A. Savin, H. Stoll, and H. Preuss. Chem. Phys. Lett. **157**, 200 (1989).
31. E. Pepke, J. Murray, and T.-Z. Hwu. SciAn. Supercomputer Computations Research Institute, Florida State University, Tallahassee, Fla. 1993.

Approximate kinetic energy density functionals generated by local-scaling transformations

E.V. Ludeña, R. López-Boada, and R. Pino

Abstract: Different stages in the development of density functional theory are succinctly reviewed for the purpose of tracing the origin of the local-scaling transformation version of density functional theory. Explicit kinetic energy functionals are generated within this theory. These functionals are analyzed in terms of several approximations to the local-scaling function and are applied to a few selected first-row atoms.

Key words: density functional theory, kinetic energy density functionals, local-scaling transformations, explicit kinetic energy functionals, kinetic energy of first-row atoms.

Résumé : On fait une revue succincte des divers stades du développement de la théorie de la fonctionnelle de densité dans le but de déterminer l'origine de la version de la théorie de la fonctionnelle de densité basée sur la transformation d'échelle locale. Des fonctionnelles explicites de l'énergie cinétique sont générées à l'intérieur de cette théorie. On analyse ces fonctionnelles en termes de plusieurs approximations à la fonction d'échelle locale et on les applique à quelques éléments choisis de la première période.

Mots clés : théorie de la fonctionnelle de densité, fonctionnelles de densité de l'énergie cinétique, transformations d'échelle locale, fonctionnelles explicites de l'énergie cinétique, énergie cinétique des éléments de la première période.

[Traduit par la rédaction]

1. Introduction

A very demanding problem in density functional theory concerns the adequate treatment of the kinetic energy term of quantum mechanical many-particle systems. Indeed, the problem is so difficult that actual treatments of these systems are carried out within the Kohn–Sham approach where the kinetic energy is handled in terms of noninteracting particles, thus bypassing the construction of the kinetic energy density functional. Nevertheless, both from a fundamental point of view as well as from a practical one, it would be desirable to find this functional or sufficiently accurate approximations to it.

We deal in the present paper with the generation of energy density functionals in the context of the local-scaling transformation version of density functional theory. The latter is a constructive approach that allows one to obtain explicit density functionals, which can be devised to approximate as closely as one wishes the exact functional provided, that is, to ensure that one starts from a good enough "generating" wave function for the system at hand.

In Sect. 2, we review some stages in the development of density functional theory in order to sketch the appropriate background against which to assess the local-scaling transformation version. In Sect. 3, we formulate the general problem of obtaining kinetic energy density functionals by means of these transformations. In Sect. 4, we apply these transformations to selected first-row atoms and investigate various types of approximations that can be introduced both to these functionals and to the generating wave functions. The results presented here should be regarded as first attempts at modelling the kinetic energy functional without having to rely on previous calculations of "generating" wave functions.

2. Stages in the development of DFT

As is well known, density functional theory (1–4) has become one of the most promising methods for dealing with the quantum-mechanical many-particle problem. One may describe its development in terms of the following four stages.

Heuristic stage

This stage was initiated in 1927 in the classical works of Thomas (5) and Fermi (6); it was continued in the thirties by Dirac (7), Wigner (8), and von Weizsäcker (9), and it was further developed in the following decades by Kirzhnitz (10), Hodges (11), and others (12–14). In this stage, within the framework of a "statistical" approximation, the bases were laid for writing heuristic expressions of the energy as a functional of the one-particle density $\rho(\boldsymbol{r})$. Much of the work that

Received October 12, 1995.

This paper is dedicated to Professor Richard F.W. Bader on the occasion of his 65th birthday.

E.V. Ludeña,[1] R. López-Boada, and R. Pino. Instituto Venezolano de Investigaciones Científicas (IVIC), Centro de Química, Apartado 21827, Caracas 1020–A, Venezuela.

[1] Author to whom correspondence may be addressed. Telephone: (582) 501-1320. Fax: (582) 501-1350. E-mail: eludena@quimica.ivic.ve

followed the initial formulation of Thomas and Fermi had to do with how to include inhomogeneous corrections as well as many-particle correlation effects in these energy functionals.

Formal nonconstructive stage

This stage came into being with the formulation in 1964 of the Hohenberg–Kohn theorem (15), which proved the existence of an energy density functional that yields the exact ground-state energy when evaluated at its extremum, i.e., when $\rho(\boldsymbol{r})$ is the exact ground-state density. Although this theorem lent support to the earlier heuristic approach, due to the fact that it is just an existence theorem, it failed to provide the means for a systematic approach to the construction of energy density functionals. Moreover, the Hohenberg–Kohn-based formulation of density functional theory led to a misconception concerning the existence of a "universal" functional that, purportedly, was capable of expressing through the same formula the ground-state energy of any many-electron system, regardless of its number of particles or of its symmetry (the latter, for example, in the case of atoms is described in terms of angular momentum, spin, and parity operators).

The Hohenberg–Kohn theorem establishes a one-to-one correspondence between the exact ground-state one-particle density $\rho_0^v(\boldsymbol{r})$ and the external potential $v(\boldsymbol{r})$. This means, furthermore, that the density also determines the Hamiltonian $\hat{H}_v = \hat{T} + \hat{U} + \sum_{i=1}^{N} v(\boldsymbol{r}_i)$ and hence the exact ground-state wave function Ψ_0^v (through $\hat{H}_v\Psi_0^v = E_0^v\Psi_0^v$). Note, however, that in this "existence" proof, the exact wave function is still the solution to the Schrödinger equation and can be obtained only by solving this equation.

This one-to-one correspondence between the exact one-particle density and the exact ground-state wave function provided a *nonconstructive proof* (16) of the existence of a density functional $E[\rho]$ for the electronic energy. The question of whether it is possible to obtain the energy density functional without having to resort to previous knowledge of the exact wave function is in fact left open in Hohenberg and Kohn's work.

Implicit constructive stage

This question, however, lies at the basis of the density functional theory formulation advanced by Levy (17) (see also Lieb, Payne, and the early work of Percus (18, 19, 33)). The constrained search approach of Levy advocates the *implicit construction* (16) of the functional $E[\rho] = F[\rho] + \int v\rho$, where the auxiliary functional $F[\rho]$ is defined as the internal energy corresponding to the kinetic energy and electron–electron interaction operators:

$$[1] \quad F[\rho] = \min \{\langle \Phi_\rho \,|\, \hat{T} + \hat{U} \,|\, \Phi_\rho \rangle\}, \qquad \Phi_\rho \in \mathscr{L}_N$$

$$= \langle \Phi_\rho^{\min} \,|\, \hat{T} + \hat{U} \,|\, \Phi_\rho^{\min} \rangle$$

Clearly, wave functions appear in Levy's formalism in the definition of $F[\rho]$. Notice that in order to calculate $F[\rho]$ for a given and fixed ρ, the internal energy must be evaluated scanning over all wave functions Φ_ρ (in Hilbert space $\mathscr{L}_N$) that yield the fixed density ρ. Among these wave functions there exists a minimizing wave function $\Phi_\rho^{\min}$, which yields $F[\rho]$.

When the fixed density is selected to be $\rho = \rho_0^v$, i.e., the exact ground-state density, then $F[\rho_0^v] = \langle \Psi_0^v \,|\, \hat{T} + \hat{U} \,|\, \Psi_0^v \rangle$, where the minimizing wave function is the exact ground-state wave function Ψ_0^v.

Certainly, if the exact auxiliary functional $F[\rho_0^v]$ depends upon the exact wave function Ψ_0^v for a particular N-particle system (corresponding to a given external potential $v(\boldsymbol{r})$), it follows that this functional is not "universal," namely, that it is not the same for all N-particle systems. (Gill and Pople (20) have verified the non-universality of the exchange functional for the hydrogen atom — which can be calculated exactly.) This non-universality of the functional $F[\rho]$ (for any fixed density ρ and not only for ρ_0^v) is a consequence of the specificity of the minimizing wave function defining $F[\rho]$. Although the external potential does not appear explicitly in the calculation of this functional, it affects the wave function in view of the fact that the external potential determines the density.

Explicit constructive stage

The implementation of Levy's constrained search approach to density functional theory requires that a procedure be set up such that all wave functions in Hilbert space $\mathscr{L}_N$, yielding a fixed density ρ, are spanned. An interesting approach in this direction was carried out by Zumbach and Maschke (21) who, essentially, by resorting to particular forms of density transformations applied to a plane-wave wave function, were able to obtain energy functionals that depended on the density. The type of reference wave function (based on plane waves) did not allow, however, for an accurate representation of actual systems such as atoms and molecules whose densities vary quite markedly in the intra-shell and inter-shell regions. Another attempt to build approximate functionals based on density transformations was that of Ludeña in 1983 (22). Independently, also Nyden and Parr (23) and Gosh and Parr (24) dealt with this same problem (see also the pioneer work of March and Young (25) and the later work of Kozlowski and March (26)).

Density transformations are generalizations of scaling transformations. There is a long history, which starts with the work of Macke in 1955 (27, 28), of their use in relation to the many-body problem in quantum mechanics (18, 21–25, 27–37). Local-scaling transformations are a particular type of the more general density transformations.

The formalization of the *explicit constructive stage* was brought about through the formulation of the local-scaling transformation version of density functional theory. The initial paper setting up this new approach was that of Petkov, Stoitsov, and Kryachko (1986) (38) (see also ref. 1). The theory was further developed in the works of Kryachko and Ludeña (39) and of Kryachko, Ludeña, and Koga (see ref. 40, and references therein; for some recent developments see refs. 41 and 42).

A constructive formulation that is quite similar to the local-scaling transformation version of density functional theory was advanced independently in 1988 by Cioslowski (43–45; also ref. 16) and it is known as the density-driven approach. The connection between these two approaches was investigated by Kryachko and Ludeña in 1991 (46).

3. Explicit kinetic energy density functionals

There have been many attempts to reduce the kinetic energy, which is a natural functional of the 1-matrix, to a functional of the one-particle density (for a recent review see ref. 47 and references therein). Although functionals that yield an accuracy of 1% have been advanced, chemical precision demands that much more accurate functionals be devised. In this vein, we discuss in the present work the use of local-scaling transformations for the generation of kinetic energy functionals (expressed as functionals of just the one particle-density) and analyze some approximate forms of these functionals. We carry out illustrations for selected first-row atoms.

Local-scaling transformations are generalizations of the well-known scaling transformations. The latter carry a vector $\boldsymbol{r}$ into a transformed vector $\lambda\boldsymbol{r}$, where λ is a constant. The constancy of λ means that the vector $\boldsymbol{r}$ is modified uniformly in each point of the Euclidean space $\mathscr{R}^3$. On the other hand, local-scaling transformations distort the vector $\boldsymbol{r}$ at each point of $\mathscr{R}^3$, so that the transformed vector becomes $\boldsymbol{f}(\boldsymbol{r}) = \lambda(\boldsymbol{r})\boldsymbol{r}$. In this case λ is a function.

As discussed elsewhere (48) local-scaling transformations correspond to density transformations that keep the direction of the transformed vector $\boldsymbol{f}(\boldsymbol{r})$ constant. Thus, they satisfy the following equation relating densities $\rho_1(\boldsymbol{r})$ and $\rho_2(\boldsymbol{r})$ (see ref. 1, Sect. 7.1.d):

$$[2] \quad \rho_2(\boldsymbol{r}) = J(\boldsymbol{f}(\boldsymbol{r});\boldsymbol{r})\rho_1(\boldsymbol{f}(\boldsymbol{r}))$$

where $J(\boldsymbol{f}(\boldsymbol{r});\boldsymbol{r})$ is the Jacobian of the transformation and is given by

$$[3] \quad J(\lambda(\boldsymbol{r})\boldsymbol{r};\boldsymbol{r}) = \begin{vmatrix} \frac{\partial\lambda(\boldsymbol{r})x}{\partial x} & \frac{\partial\lambda(\boldsymbol{r})y}{\partial x} & \frac{\partial\lambda(\boldsymbol{r})z}{\partial x} \\ \frac{\partial\lambda(\boldsymbol{r})x}{\partial y} & \frac{\partial\lambda(\boldsymbol{r})y}{\partial y} & \frac{\partial\lambda(\boldsymbol{r})z}{\partial y} \\ \frac{\partial\lambda(\boldsymbol{r})x}{\partial z} & \frac{\partial\lambda(\boldsymbol{r})y}{\partial z} & \frac{\partial\lambda(\boldsymbol{r})z}{\partial z} \end{vmatrix} = \lambda^3(\boldsymbol{r})[1 + \boldsymbol{r}\cdot\nabla_r \ln\lambda(\boldsymbol{r})]$$

From eqs. [2] and [3] we can obtain the following expression for $\lambda(\boldsymbol{r})$:

$$[4] \quad \lambda(\boldsymbol{r}) = \left[\frac{\rho_2(\boldsymbol{r})}{\rho_1(\lambda(\boldsymbol{r})\boldsymbol{r})(1 + \boldsymbol{r}\cdot\nabla_r \ln\lambda(\boldsymbol{r}))}\right]^{1/3}$$

Equation [4] is a first-order differential equation for the transformation function $\lambda(\boldsymbol{r})$. An iterative solution for $\lambda(\boldsymbol{r})$ can be obtained through:

$$[5] \quad \lambda^{(i)}(\boldsymbol{r}) = \left[\frac{\rho(\boldsymbol{r})}{\rho_g(\lambda^{(i-1)}(\boldsymbol{r})\boldsymbol{r})(1 + \boldsymbol{r}\cdot\nabla_r \ln\lambda^{(i-1)}(\boldsymbol{r}))}\right]^{1/3}$$

with $\lambda^{(0)}(\boldsymbol{r}) = 1$.

Let us now consider the kinetic energy expressed as a functional of the first-order reduced density matrix

$$[6] \quad T[\Psi_\rho] \equiv T[D^1_\rho] = \frac{1}{2}\int d^3\boldsymbol{r}_1 \nabla_{r_1}\nabla_{r'_1} D^1_\rho(\boldsymbol{r}_1,\boldsymbol{r}'_1)|_{r'_1=r_1}$$

where $D^1_\rho(\boldsymbol{r}_1,\boldsymbol{r}'_1)$ is the first-order reduced density matrix associated with the N-particle wave function Ψ_ρ (the latter is a wave function in Hilbert space $\mathscr{L}_N$ that yields the one-particle density $\rho(\boldsymbol{r})$. Our aim is to express eq. [6] as an explicit functional of the one-particle density $\rho(\boldsymbol{r})$. For this purpose, let us also consider the arbitrary and finite orbital set $\{\phi_{g,k}(\boldsymbol{r})\}_{k=1}^m$ with $m > N$ (the subindex g stands for "generating", as we shall denote this orbital set as the "generating" set). Out of this set, let us form the set of N-particle Slater determinants $\{\Phi^g_K\}$ (where K stands for the set of ordered single-particle labels). Let us further consider the generating wave function Ψ_g expanded in terms of the Slater determinants:

$$[7] \quad \Psi_g = \sum_{K=1}^{M} C^g_K \Phi^g_K$$

For the time being, let us consider the expansion coefficients $\{C^g_K\}$ as arbitrary parameters. Denoting by $D^1_g(\boldsymbol{r}_1,\boldsymbol{r}'_1)$ the "generating" 1-matrix associated with Ψ_g, we readily see that in terms of the generating orbital set, it is given by

$$[8] \quad D^1_g(\boldsymbol{r},\boldsymbol{r}') = \sum_{i=1}^{N}\sum_{j=1}^{N} n^g_{ij}\phi_{g,i}(\boldsymbol{r})^*\phi_{g,j}(\boldsymbol{r}')$$

The corresponding "generating" one-particle density is

$$[9] \quad \rho_g(\boldsymbol{r}) == \sum_{i=1}^{N}\sum_{j=1}^{N} n^g_{ij}\phi_{g,i}(\boldsymbol{r})^*\phi_{g,j}(\boldsymbol{r})$$

The local-scaling transformation connecting the "generating" density $\rho_g(\boldsymbol{r})$ and the "final" density $\rho(\boldsymbol{r})$ satisfies eq. [4] with $\rho_1(\boldsymbol{r}) \equiv \rho_g(\boldsymbol{r})$ and $\rho_2(\boldsymbol{r}) \equiv \rho(\boldsymbol{r})$. Moreover, applying this local-scaling transformation to the "generating" orbital set, we obtain the following transformed one-particle set:

$$[10] \quad \phi_{\rho,k}(\boldsymbol{r}) = [J(\lambda(\boldsymbol{r})\boldsymbol{r};\boldsymbol{r})]^{1/2}\phi_{g,k}(\boldsymbol{f}(\boldsymbol{r})) = \left[\frac{\rho(\boldsymbol{r})}{\rho_g(\lambda(\boldsymbol{r})\boldsymbol{r})}\right]^{1/2}\phi_{g,k}(\lambda(\boldsymbol{r})\boldsymbol{r})$$

It can be readily shown that the 1-matrix $D^1_\rho(\boldsymbol{r}_1,\boldsymbol{r}'_1)$ can be written in terms of the transformed orbitals as:

$$[11] \quad D^1_\rho(\boldsymbol{r},\boldsymbol{r}') = \sum_{i=1}^{N}\sum_{j=1}^{N} n^g_{ij}\phi_{\rho,i}(\boldsymbol{r})^*\phi_{\rho,j}(\boldsymbol{r}')$$

Similarly, the one-particle density becomes:

$$[12] \quad \rho(\boldsymbol{r}) == \sum_{i=1}^{N}\sum_{j=1}^{N} n^g_{ij}\phi_{\rho,i}(\boldsymbol{r})^*\phi_{\rho,j}(\boldsymbol{r})$$

It follows from eqs. [10] and [11] that the 1-matrix $D^1_\rho(\boldsymbol{r}_1,\boldsymbol{r}'_1)$ can be rewritten as:

$$[13] \quad D^1_\rho(\boldsymbol{r},\boldsymbol{r}') = \left[\frac{\rho(\boldsymbol{r})\rho(\boldsymbol{r}')}{\rho_g(\lambda(\boldsymbol{r})\boldsymbol{r})\rho_g(\lambda(\boldsymbol{r}')\boldsymbol{r}')}\right]^{1/2} \times D^1_g(\lambda(\boldsymbol{r})\boldsymbol{r},\lambda(\boldsymbol{r}')\boldsymbol{r}')$$

Substituting eq. [13] into eq. [6] one obtains

$$[14]\quad T[D_\rho^1] = \frac{1}{8}\int d^3r \frac{[\nabla_r \rho(r)]^2}{\rho(r)} + \frac{1}{2}\int d^3r \rho(r) \nabla_r \nabla_{r'} \tilde{D}_g^1(f(r), f(r'))|_{r'=r}$$

where $f(r) = \lambda(r)r$ and where $\tilde{D}_g^1$ is the non-local part of the "generating" 1-matrix evaluated at the transformed vectors:

$$[15]\quad \tilde{D}_g^1(f(r_1), f(r_1')) = \frac{D_g^1(f(r_1), f(r_1'))}{[\rho_g(f(r_1))]^{1/2}[\rho_g(f(r_1'))]^{1/2}}$$

Notice that in eq. [14] the first term is the well-known von Weizsäcker contribution (9) to the kinetic energy, which is a local term (49). The second term corresponds to the non-local contribution to the kinetic energy.

To transform eq. [15] into a functional of $\rho(r)$, let us first change, using the chain rule, the derivatives in the second term of eq. [15] (defined with respect to r) to those depending on the vector $f(r) = \lambda(r)r$: $\nabla_r = \nabla_r f \nabla_f$. Because the transformed vector $f(r)$ maintains the same direction as the original one, namely, since $f(r) = f(r)\hat{1}_r$ (where $\hat{1}_r$ is the unit vector along r), one can write

$$[16]\quad \nabla_r = \frac{\partial f(r)}{\partial r}\nabla_f = \frac{r^2}{f^2(r)}\frac{\rho(r)}{\rho_g(f)}\nabla_f$$

Substituting eqs. [18] and [16] into eq. [14], we obtain the following expression for the kinetic energy

$$[17]\quad T[D_\rho^1] = T_W[\rho] + \frac{1}{2}\int d^3r \frac{\rho(r)^3}{\rho_g^3(f(r))}\frac{r^4}{f^4(r)} \times \left[\sum_{i=1}^{m}\sum_{j=1}^{m} n_{ij}^g \nabla_f \phi_{g,i}(f(r)) \nabla_f \phi_{g,j}^*(f(r)) - \frac{1}{4}\frac{(\nabla_f \rho_g(f(r)))^2}{\rho_g(f(r))}\right]$$

Our task of expressing the kinetic energy as a functional of the one-particle density can be accomplished by introducing eq. [4] into eq. [17]. This leads to

$$[18]\quad T[D_\rho^1] = T_W[\rho] + \frac{1}{2}\int d^3r \rho^{5/3}(r) \times (1 + r\cdot\nabla_r \ln\lambda(r))^{4/3}\tau([\rho(r)]; r)$$

where

$$[19]\quad \tau(f(r)) = \frac{1}{\rho_g^{5/3}(f(r))} \times \left[\sum_{i=1}^{m}\sum_{j=1}^{m} n_{ij}^g \nabla_f \phi_{g,i}^*(f(r)) \nabla_f \phi_{g,j}(f(r)) - \frac{1}{4}\frac{(\nabla_f \rho_g(f(r)))^2}{\rho_g(f(r))}\right]$$

A very appealing characteristic of eq. [18] is that the Thomas–Fermi term $\rho^{5/3}(r)$ emerges in a very natural way. In addition, there arises a second factor that depends on the local-scaling function $\lambda([\rho]; r)$. Moreover, these first two factors are "universal" as they depend only on ρ (or $\lambda([\rho]; r)$). The particular traits of the N-body problem are manifested through the form of the "modulating" factor $\tau([\rho(r)]; r)$. Clearly, this factor is not universal since it contains the "generating" orbitals for the particular problem at hand and the "generating" one-particle density $\rho_g(f(r))$.

Table 1. Parameters of the Raffenetti-type RT^a "generating" orbitals for selected first-row atoms.

Atom	α_s RT^a	β_s RT^a	α_p RT^a	β_p RT^a
Li	0.452 246	1.290 937		
Be	0.582 434	1.318 837		
B	0.790 699	1.305 542	0.508 345	1.422 519
F	1.308 402	1.447 490	1.006 690	1.508 533
Ne	1.328 402	1.487 490	1.016 690	1.518 533

Let us note that eq. [18] can be transformed into an explicit, albeit approximate, functional of the one-particle density $\rho(r)$ by replacing $\lambda(r)$ by the first iterative solution, i.e., $\lambda^{(1)}(r)$ in eq. [5] (assuming that $\lambda^{(0)}(r) = 1$):

$$[20]\quad \lambda^{(1)}(r) = (\rho(r)/\rho_g(r))^{1/3}$$

When this is done, the product of the Thomas–Fermi term times the second term in eq. [18] takes the form:

$$[21]\quad \rho(r)^{5/3}(1 + r\cdot\nabla_r \ln(\rho(r)/\rho_g(f))^{1/3})^{4/3}$$

Clearly, these approximations to $\lambda(r)$ (or equivalently to the transformation function $f(r)$) can also be introduced into $\tau([\rho]; r)$. In this manner, we can generate explicit iterative representations of the kinetic energy functional.

4. Calculations and results for first-row atoms

Although the expressions derived in the previous section are general, we shall illustrate the present approach by calculating the Hartree–Fock kinetic energy of selected first-row atoms. In that case, the "orbit-generating" set is $\{\phi_{g,k}(r)\}_{k=1}^N$. The single Slater determinant that we can construct using these locally scaled orbitals is

$$[22]\quad \Phi_\rho^{SD}(r_1, \cdots, r_N) \equiv \frac{\det}{\sqrt{N!}}[\phi_{\rho,1}(r_1)\cdots\phi_{\rho,N}(r_N)]$$

The 1-matrix corresponding to this wave function is

$$[23]\quad D^{1SD}(r, r') = \sum_{j=1}^{N}\phi_j^*(r)\phi_j(r')$$

As in the previous section, this leads to the following expression for the kinetic energy functional

$$[24]\quad T[D_\rho^{1SD}] = T_W[\rho] + \frac{1}{2}\int d^3r \rho^{5/3}(r) \times (1 + r\cdot\nabla_r \ln\lambda(r))^{4/3}\tau_N([\{\phi_{g,i}(f(r)\}_{i=1}^N]; r)$$

where

$$[25]\quad \tau_N([\{\phi_{g,i}(f(r))\}_{i=1}^N]; r) = \frac{1}{\rho_g^{5/3}(f(r))} \times \left[\sum_{j=1}^{N}|\nabla_f \phi_{g,j}(f(r))|^2 - \frac{1}{4}\frac{(\nabla_f \rho_g(f(r)))^2}{\rho_g(f(r))}\right]$$

Table 2. Parameters of the Raffenetti-type RT^b and RT^c "generating" orbitals for selected first-row atoms.

	α_s		β_s		α_p		β_p	
Atom	RT^b	RT^c	RT^b	RT^c	RT^b	RT^c	RT^b	RT^c
Li	0.351 242	0.331 242	1.604 735	1.684 735				
Be	0.447 163	0.467 163	1.659 528	1.689 528				
B	0.581 716	0.631 716	1.659 501	1.679 501	0.509 473	0.519 473	1.802 049	1.812 049
F	1.066 337	1.076 337	1.679 609	1.779 609	0.848 776	0.858 776	1.736 217	1.766 217
Ne	1.183 685	1.203 685	1.683 251	1.703 251	0.929 874	0.939 874	1.683 251	1.753 414

Table 3. Approximate Hartree–Fock energies (in hartrees) corresponding to the sets RT^a, RT^b, and RT^c for selected first-row atoms.

Atom	RT^a	RT^b	RT^c	Hartree–Fock[d]
Li	−7.432 313	−7.432 720	−7.239 994	−7.432 725
Be	−14.573 023	−14.573 014	−14.361 015	−14.573 021
B	−24.527 802	−24.529 049	−24.087 132	−24.529 057
F	−99.407 089	−99.409 204	−93.969 541	−99.409 300
Ne	−128.547 096	−128.546 951	−128.109 877	−128.547 050

[d]Clementi–Roetti results (57).

In the present case, the modulating factor $\tau_N([\{\phi_{g,i}(\lambda(\boldsymbol{r})\boldsymbol{r})\}_{i=1}^N];\boldsymbol{r})$ depends upon the N "generating" orbitals $\{\phi_{g,i}(\boldsymbol{f}(\boldsymbol{r}))\}_{i=1}^N$ evaluated at the transformed vector $\boldsymbol{f}(\boldsymbol{r}) = \lambda(\boldsymbol{r})\boldsymbol{r}$.

We choose Raffenetti-type orbitals (50) as the generating orbitals:

$$[26]\quad R_{ns}([\alpha_s, \beta_s, \{C_{nsj}\}]; r) = \sum_{j=1}^{M} C_{nsj}(2\alpha_s\beta_s^j)^{3/2}/(2)^{1/2}\exp(-\alpha_s\beta_s^j r)$$

for the R_{ns} orbitals and

$$[27]\quad R_{np}([\alpha_p, \beta_p, \{C_{npj}\}]; r) = \sum_{j=1}^{M} C_{npj}(2\alpha_p\beta_p^j)^{5/2}/(24)^{1/2} r\exp(-\alpha_p\beta_p^j r)$$

for the R_{np} orbitals. In the present calculations, we consider three sets of such Raffenetti-type (RT) orbitals: the set RT^a, RT^b, and RT^c. The first set is defined as follows:

$$[28]\quad RT^a \equiv \{\text{Li}: 12s;\quad \text{Be}: 12s;\quad \text{B}: 12s, 8p;\quad \text{F}: 8s, 6p;\quad \text{Ne}: 8s, 6p\}$$

and the sets RT^b and RT^c are given by

$$[29]\quad RT^{b,c} \equiv \{\text{Li}: 6s;\quad \text{Be}: 6s;\quad \text{B}: 4s, 4p;\quad \text{F}: 4s, 4p;\quad \text{Ne}: 4s, 4p\}$$

In Table 1 we list the parameters α_s, β_s, α_p, and β_s that characterize the set RT^a. These parameters were determined by a constrained-density energy optimization of the Hartree–Fock energy within the scheme of local-scaling transformations (51). The fixed Hartree–Fock density was taken to be that of Boyd (52). In Table 2, we list the orbital parameters for the sets RT^b and RT^c. The former is the extended triple-zeta (ETZ) set of Raffenetti (50) and the latter is a variant of this set where the parameters have been chosen arbitrarily. The orbital expansion coefficients for set RT^b are taken from ref. 50, whereas the coefficients of the set RT^c were determined by a Schmidt orthonormalization of the Raffeneti ETZ set. The approximate Hartree–Fock energies obtained from the "generating" orbitals making up the sets RT^a, RT^b, and RT^c are listed in Table 3, where for completeness, we have also included the Clementi–Roetti Hartree–Fock energies.

The energies reported in Table 3 reflect the quality of the wave functions employed (which for simplicity we have restricted to be of the Raffenetti type). In general, we observe that the functions belonging to the set RT^b are closer to the Clement–Roetti Hartree–Fock wave functions (where we assume that the energy is an adequate criterion for measuring "closeness"). By this same criterion, wave functions of set RT^a are farther apart and, clearly, those of set RT^c, i.e., functions with arbitrarily chosen parameters, differ the most from the Clementi–Roetti wave functions.

In Table 4, we list the kinetic energies evaluated by means of eq. [24] for various approximations of the local-scaling function $\lambda(r)$. Note that $\lambda(r) = 1$ corresponds to the zeroth-order iterative solution, namely, $\lambda^{(0)}(r)$ of eq. [5]. Similarly, $\lambda(r) = (\rho/\rho_g)^{1/3}$ is the first-order iterative approximation $\lambda^{(1)}(r)$.

The kinetic energy corresponding to λ_{exact} in Table 4 is precisely $T[D_\rho^{\text{ISD}}]$ of eq. [24] calculated using the locally scaled transformed single Slater determinant given by eq. [22]. Note that the final density for the determination of λ_{exact} is $\rho(r)_{\text{Boyd}}$ [52], that is, a representation of the densities associated with Clementi–Roetti's Hartree–Fock wave functions.

Table 4. Kinetic energies (in hartrees) evaluated by means of eq. [24] for selected first-row atoms using different approximations for the local scaling function $\lambda(r)$.

System		$\lambda = (\rho/\rho_g)^{1/3}$	$\lambda = 1$	$\lambda = \lambda_{exact}$	Hartree–Fock
Li	RT^a	7.412 134	7.421 922	7.432 277	7.432 754[d]
	RT^b	7.432 390	7.432 473	7.432 538	7.432 720[e]
	RT^c	7.902 298	7.571 672	7.462 216	
Be	RT^a	14.573 140	14.572 995	14.572 911	14.573 036[d]
	RT^b	14.572 916	14.572 822	14.572 898	14.573 014[e]
	RT^c	15.241 022	14.914 005	14.580 992	
B	RT^a	24.578 669	24.561 536	24.530 216	24.528 956[d]
	RT^b	24.529 134	24.528 851	24.528 851	24.529 049[e]
	RT^c	25.941 753	25.353 307	24.554 481	
F	RT^a	103.559 724	103.824 327	99.391 608	99.409 140[d]
	RT^b	99.429 323	99.413 514	99.411 240	99.409 204[e]
	RT^c	110.610 110	107.117 744	100.378 220	
Ne	RT^a	132.569 040	133.035 295	128.530 783	128.546 810[d]
	RT^b	128.539 468	128.545 731	128.540 731	128.546 951[e]
	RT^c	130.996 564	130.911 242	128.574 134	

[a,b,c]Raffenetti-type sets defined in text.
[d]Clementi–Roetti results (57).
[e]Raffenetti results for triple-zeta orbitals (50).

Table 5. Kinetic energies (in hartrees) evaluated by means of eq. [30] for selected first-row atoms using different approximations for the local scaling function $\lambda(r)$.

System		$\lambda = (\rho/\rho_g)^{1/3}$	$\lambda = 1$	$\lambda = \lambda_{exact}$	Hartree–Fock
Li	RT^a	7.404 487	7.416 636	7.432 277	7.432 754[d]
	RT^b	7.432 392	7.432 434	7.432 538	7.432 720[e]
	RT^c	7.940 030	7.654 009	7.462 216	
Be	RT^a	14.573 260	14.573 070	14.572 911	14.573 036[d]
	RT^b	14.573 035	14.572 947	14.572 898	14.573 014[e]
	RT^c	15.430 093	14.984 760	14.580 992	
B	RT^a	24.504 964	24.511 238	24.530 216	24.528 956[d]
	RT^b	24.529 340	24.529 148	24.528 851	24.529 049[e]
	RT^c	26.206 812	25.445 378	24.545 992	
F	RT^a	109.411 291	98.626 781	99.391 608	99.409 140[d]
	RT^b	99.402 844	99.407 678	99.411 240	99.409 204[e]
	RT^c	110.833 516	108.175 759	100.378 220	
Ne	RT^a	128.541 870	128.540 327	128.530 783	128.546 810[d]
	RT^b	128.531 380	128.536 863	128.540 731	128.546 951[e]
	RT^c	130.636 095	130.148 266	128.574 134	

[a,b,c]Raffenetti-type sets defined in text.
[d]Clementi–Roetti results (57).
[e]Raffenetti results for triple-zeta orbitals (50).

For this reason, the kinetic energies for the set RT^b in Table 4 do not coincide with the Raffeneti ETZ values listed in the last column of this table. When we use as our " object" densities the ETZ densities of Raffenetti, however, we obtain exactly the Raffenetti ETZ kinetic energy values. Again for λ_{exact}, we observe in Table 4 that the kinetic energy values obtained using the *arbitrary* set RT^c are as good or better than those obtained from improved local-density approximations (53) or even from non-local ones (47, 54). In this sense, the present method clearly shows that it is possible to develop approximations to the kinetic energy functional that are both economical and accurate.

It follows from Table 4 that the use of $\lambda = 1$ introduces slight modifications in the kinetic energy values. These changes are observed to increase for the first-order iterative correction $\lambda = (\rho/\rho_g)^{1/3}$. It is interesting to observe in Table 4 that there arise significant deviations for the kinetic energy values of RT^a of F and Ne for the zeroth- and first-order approximations to λ. Now, these approximations enter either in the second factor $(1 + \boldsymbol{r} \cdot \nabla_r \ln \lambda_{exact}(\boldsymbol{r}))^{4/3}$ or in the third factor $\tau_N([\{\phi_{g,i}(\boldsymbol{f}(\boldsymbol{r})\}_{i=1}^N]; \boldsymbol{r})$ of the kinetic energy expression given by eq. [24]. To assess the relative importance of the terms appearing in eq. [24], we list in Table 5 the kinetic energy values calculated according to the expression

Fig. 1. Behavior of the modulating function $A(r) = r^2\rho_g^{5/3}(f)\tau_N(f)$ for the sets RT^b and RT^c of the lithium atom.

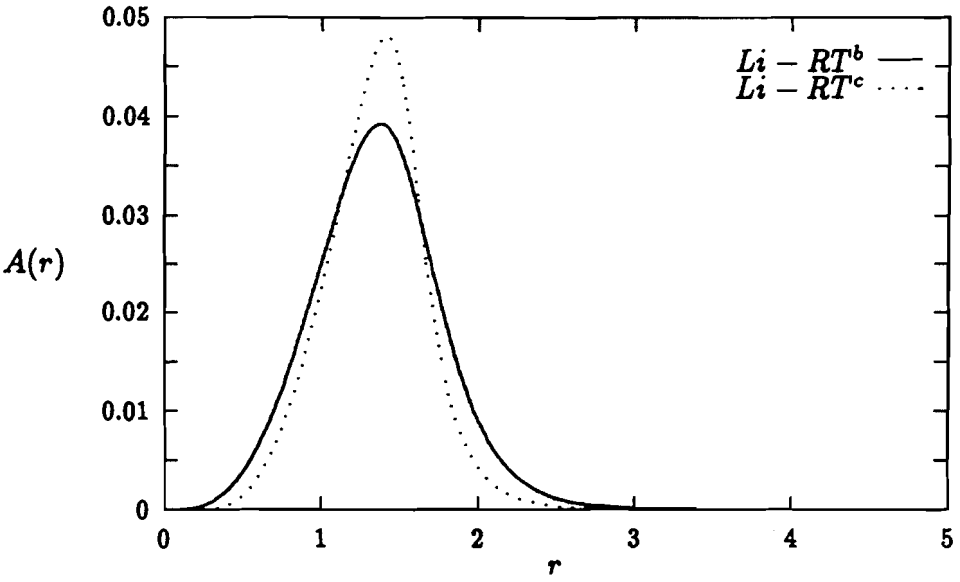

Fig. 2. Behavior of the modulating function $A(r) = r^2\rho_g^{5/3}(f)\tau_N(f)$ for the sets RT^b and RT^c of the neon atom. On the present scale only the first hump is visible.

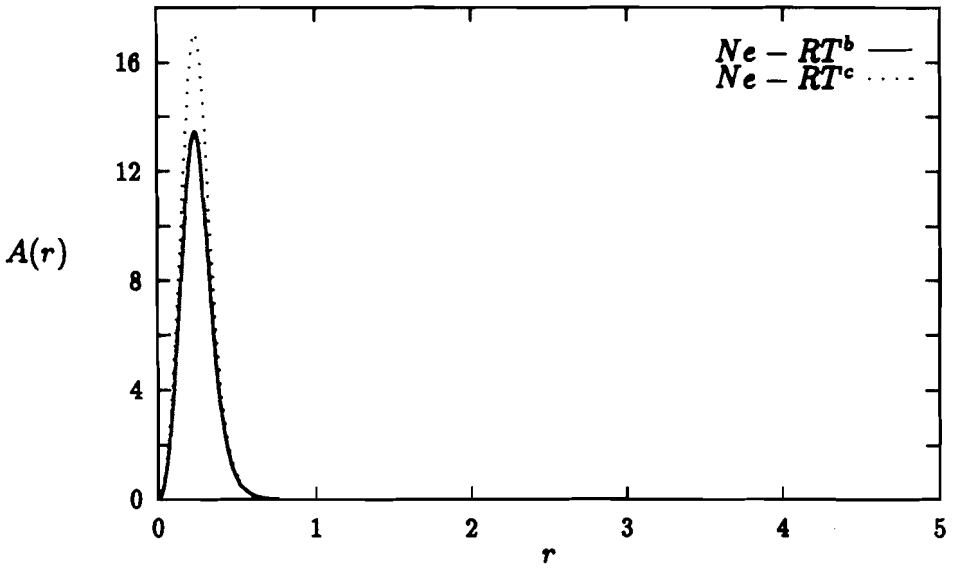

$$[30]\quad T[D_\rho^{\mathrm{LSD}}] = T_W[\rho] + \frac{1}{2}\int d^3\boldsymbol{r}\rho^{5/3}(\boldsymbol{r}) \times (1 + \boldsymbol{r}\cdot\nabla_r \ln\lambda_{\mathrm{exact}}(\boldsymbol{r}))^{4/3}\tau_N([\{\phi_{g,i}(\boldsymbol{f}(\boldsymbol{r})\}_{i=1}^N];\boldsymbol{r})$$

Notice that in the above expression we have introduced λ_{exact} in the second factor such that we are able to make approximations for λ only in the modulating factor τ_N.

In Table 5 we observe that, for example, in the case of the Ne atom, there is a considerable improvement in the kinetic energy values for the set RT^a with respect to equivalent values listed in Table 4. It is clear in this case that the effect of approximating λ is not crucial for the modulating factor τ_N as it is for the second factor of eq. [30]. In fact, we observe that there is an improvement as $T = 132.569040$ (in Table 4) goes into $T = 128.541870$ (in Table 5). That this is not always the case becomes evident when we consider the case of F for the set RT^a for $\lambda = (\rho/\rho_g)^{1/3}$. The kinetic energy becomes worse in Table 5: $T = 109.411291$ as compared to $T = 103.559724$ in Table 4. A possible explanation of this situation may be advanced in terms of a cancellation of errors between the second and third terms in eq. [30].

Fig. 3. Behavior of the modulating function $A(r) = r^2\rho_g^{5/3}(f)\tau_N(f)$ for the sets RT^b and RT^c of the neon atom. The scale is magnified at the tail to enhance the presence of a second hump.

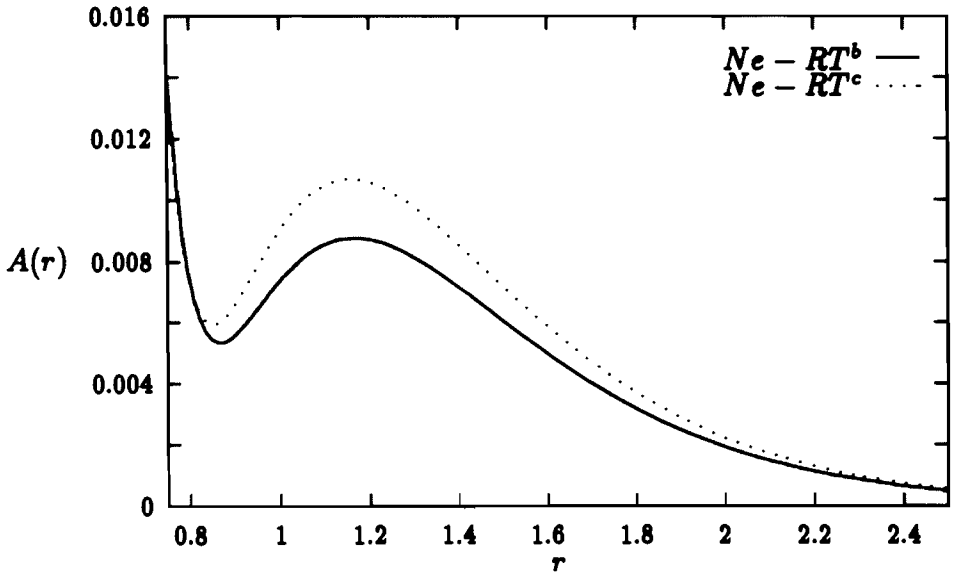

The preliminary results presented in this work demonstrate the subtleties of the kinetic energy functional. It is clear that the modulating factor has to do with the creation of a pointed peak in the intershell region. This can be clearly observed in Fig. 1 where we have plotted $A(r) = r^2\rho_g^{5/3}(f)\tau_N([\{\phi_{g,i}(f(r)\}_{i=1}^N];r)$ vs. r for the sets RT^b and RT^c for the lithium atom. One sees that the form of this function is that of a bell-shaped curve with a maximum located approximately in the intershell region. In Fig. 2 we show the behavior of this function for the Ne atom, again for the RT^b and RT^c sets. Although barely visible in Fig. 2, there is a second hump further out in this atom (as well as in the boron and fluorine atoms studied here, i.e., atoms that possess an L shell). This slight protuberance is illustrated in Fig. 3, for the sets RT^b and RT^c of Ne.

It seems that the presence of the bell-shaped modulating function in the intershell region is a necessary ingredient for the existence of shell structure in atoms. Let us mention that, in contexts different from the present, similar humps had already been observed in the analysis of the kinetic energy density (55, 56). A detailed investigation of the modulating functions and their relationship with shell structure is currently underway. One of the promising possibilities is that of constructing approximate energy density functionals by modelling the modulating factor by some simple function of $\lambda(r)$ (i.e., as a function of the one-particle density).

The results presented here, although preliminary, clearly indicate that it is quite feasible to obtain accurate models for the kinetic energy functional within the context of local-scaling transformations of the density. The elucidation of the subtleties underlying the construction of the kinetic energy functional is, however, an important prerequisite toward this end.

Dedication

It is a pleasure to dedicate this article to Richard Bader on the occasion of his 65th birthday. His undying enthusiasm, his penetrating intelligence, and his love for life are attributes that have shaped him into a very special human being and a highly original scientist.

Acknowledgment

E.V.L. gratefully acknowledges support of this work by the Commission of European Communities through Contract No. CI1*-CT93-0333.

References

1. E.S. Kryachko and E.V. Ludeña. Energy density functional theory of many-electron systems. Kluwer Academic Publishers, Dordrecht. 1990.
2. R.G. Parr and W. Yang. Density functional theory of atoms and molecules. Oxford University Press, Oxford. 1989.
3. R.M. Dreizler and E.K.U. Gross. Density functional theory. Springer-Verlag, Berlin. 1990.
4. N.H. March. Electron density theory of atoms and molecules. Academic Press, New York. 1992.
5. L.H. Thomas. Proc. Cambridge Philos. Soc. **23**, 542 (1927).
6. E. Fermi. Atti. Accad. Naz. Lincei Cl. Sci. Fis., Mat. Nat., Rend. **6**, 602 (1927).
7. P.A.M. Dirac. Proc. Cambridge Philos. Soc. **26**, 376 (1930).
8. E.P. Wigner. Phys. Rev. **46**, 1002 (1934).
9. C.F.von Weizsäcker. Z. Phys. **96**, 431 (1935).
10. D.A. Kirzhnitz. Zh. Eksp. Teor. Fiz. **32**, 115 (1957).
11. C.H. Hodges. Can. J. Phys. **51**, 1428 (1973).
12. B. Grammaticos and A. Voros. Ann. Phys. **129**, 153 (1979).
13. D.R. Murphy. Phys. Rev. A: Gen. Phys. **24**, 1682 (1981).
14. W. Yang. Phys. Rev. A: Gen. Phys. **34**, 4575 (1986).
15. P.C. Hohenberg and W. Kohn. Phys. Rev. [Sect. B], **136**, (1964) 864; P.C. Hohenberg, W. Kohn, and L.J. Sham. Adv. Quantum Chem. **21**, 7 (1990).
16. J. Cioslowski. Adv. Quantum Chem. **21**, 303 (1990).
17. M. Levy. Proc. Natl. Acad. Sci. U.S.A. **76**, 6062 (1979).
18. E.H. Lieb. Int. J. Quantum Chem. **24**, 243 (1983).
19. P.W. Payne. J. Chem. Phys. **71**, 490 (1979).

20. P.M.W. Gill and J.A. Pople. Phys. Rev. A: At. Mol. Opt. Phys. **47**, 2383 (1993).
21. G. Zumbach and K. Maschke. Phys. Rev. A: Gen. Phys. **28**, 544 (1983); **29**, 1585(E) (1984).
22. E.V. Ludeña. J. Chem. Phys. **79**, 6174 (1983).
23. M.R. Nyden and R.G. Parr. J. Chem. Phys. **78**, 4044 (1983).
24. S.K. Ghosh and R.G. Parr. J. Chem. Phys. **82**, 3307 (1985).
25. N.H. March and W.H. Young. Proc. R. Soc. London, **72**, 182 (1958).
26. P.M. Kozlowski and N.H. March. Int. J. Quantum Chem. **36**, 741 (1989).
27. W. Macke. Phys. Rev. **100**, 992 (1955).
28. W. Macke. Ann. Phys. (Leipzig), **17**, 1 (1955).
29. G.G. Hall. Proc. R. Soc. London, **75**, 575 (1960).
30. M.J. Ten Hoor. Int. J. Quantum Chem. **33**, 563 (1988); J. Chem. Educ. **66**, 633 (1989).
31. J. Moser. Trans. Am. Math. Soc. **120**, 286 (1965).
32. T.L. Gilbert. Phys. Rev. B: Solid State, **12**, 2111 (1975).
33. J.K. Percus. Int. J. Quantum Chem. **13**, 89 (1978).
34. J.E. Harriman. Phys. Rev. A: Gen. Phys. **24**, 680 (1981).
35. E.H. Lieb. *In* Physics as natural philosophy: Essays in honor of Laszlo Tisza on his 75th birthday. *Edited by* H. Feshbach and A. Shimony. MIT Press, Cambridge, Mass., 1982. p. 111.
36. E.V. Ludeña. *In* Condensed matter theories. Vol. 1. *Edited by* F.B. Malik. Plenum, New York. 1986. p. 183.
37. E.H. Lieb. *In* Density functional methods in physics. *Edited by* R.M. Dreizler and J. da Providencia. Plenum, New York. 1985. p. 31.
38. I.Zh. Petkov, M.V. Stoitsov, and E.S. Kryachko. Int. J. Quantum Chem. **29**, 149 (1986).
39. E.S. Kryachko and E.V. Ludeña. Phys. Rev. A: At. Mol. Opt. Phys. **43**, 2179 (1991).
40. E.S. Kryachko, E.V. Ludeña, and T. Koga. *In* Methods and techniques in computational chemistry. METECC-94, Vol. B: Medium Size Systems. *Edited by* E. Clementi. STEF, Cagliari, Italy. 1993. p. 23.
41. E.V. Ludeña, E.S. Kryachko, T. Koga, R. López-Boada, J. Hinze, J. Maldonado, and E. Valderrama. *In* Theoretical and computational chemistry: density functional calculations. *Edited by* J.M. Seminario and P. Politzer. Elsevier, Amsterdam. 1995. p. 75.
42. E.V. Ludeña, R. López-Boada, J. Maldonado, E. Valderrama, T. Koga, E.S. Kryachko, and J. Hinze. Int. J. Quantum Chem. **56**, 285 (1995).
43. J. Cioslowski. Phys. Rev. Lett. **60**, 2141 (1988).
44. J. Cioslowski. J. Chem. Phys. **89**, 4871 (1988).
45. J. Cioslowski. Adv. Quantum Chem. **21**, 303 (1990).
46. E.S. Kryachko and E.V. Ludeña. J. Chem. Phys. **95**, 9054 (1991).
47. D.J. Lacks and R.G. Gordon. J. Chem. Phys. **100**, 4446 (1994).
48. E.V. Ludeña and R. López-Boada. Top. Curr. Chem. In press.
49. E.V. Ludeña. J. Chem. Phys. **76**, 3157 (1982).
50. R.C. Raffenetti. J. Chem. Phys. **59**, 5936 (1973).
51. E.V. Ludeña, J. Maldonado, R. López-Boada, T. Koga, and E.S. Kryachko. J. Chem. Phys. **102**, 318 (1995).
52. R.J. Boyd. Can. J. Phys. **55**, 452 (1977).
53. S.K. Ghosh and M.M. Deb. J. Phys. B: At. Mol. Opt. Phys. **49**, 381 (1994).
54. M.D. Glossman, A. Rubio, L.C. Balbás, and J.A. Alonso. Phys. Rev. A: **47**, 1804 (1993).
55. A. Sierraalta and E.V. Ludeña. Int. J. Quantum Chem. Quantum. Chem Symp. **20**, 277 (1986).
56. S.K. Ghosh and L.C. Balbás. J. Chem. Phys. **83**, 5778 (1985).
57. E. Clementi and C. Roetti. At. Data Nucl. Data Tables, **14**, 177 (1974).

Zero-temperature equation-of-motion of electron pair in the BCS theory of superconductivity

Akitomo Tachibana

Abstract: By projecting the BCS ground state of superconducting electron condensate on the N-electron Hilbert space, a real-space equation-of-motion is obtained for the electron pair function $\phi(1, 2)$ at absolute zero temperature ($T = 0$):

$$i\hbar \frac{\mathrm{d}\phi(1,2)}{\mathrm{d}t} = h_\phi(1,2)\phi(1,2)$$

$$h_\phi(1,2) = \frac{1}{2m}\boldsymbol{p}(1)^2 + \frac{1}{2m}\boldsymbol{p}(2)^2 + v_\phi(1,2)$$

$$v_\phi(1,2) = v(1) + v(2) + \frac{e^2}{r_{12}} + \int\left(\frac{e^2}{r_{13}} + \frac{e^2}{r_{23}}\right)\rho^{N-2}(3)\mathrm{d}\tau_3$$

where ρ^{N-2} denotes electron density of the $(N-2)$-electron condensate given as

$$\rho^{N-2}(1) = (N-2)\int|\phi(1,2)|^2\mathrm{d}\tau_2$$

Since the exchange-correlation potential is given as an explicit functional of electron density, this equation represents the fundamental working equation for the new density functional theory of superconductivity. The 2nd-order density matrix $\Gamma^N(1,2|1',2')$ projected on the N-electron Hilbert space satisfies

$$\Gamma^N(1,2|1',2') = \frac{N(N-1)}{2}c^N(1,2)c^{N*}(1',2')$$

$$c^N(1,2) = \frac{1}{\sqrt{2!}}A\phi(1,2)\alpha(1)\beta(2) = \phi(1,2)\frac{1}{\sqrt{2!}}(\alpha(1)\beta(2) - \beta(1)\alpha(2))$$

so that asymptotically

$$\lim_{|R^{\mathrm{CM}}_{1,2} - R^{\mathrm{CM}}_{1',2'}|\to\infty}\Gamma^N(1,2|1',2') = \text{finite}$$

where $R^{\mathrm{CM}}_{1,2}$ denotes the center-of-mass coordinate of electrons e_1 and e_2; this is considered the ODLRO (off-diagonal long-range order) at $T = 0$ projected on the N-electron Hilbert space. A new attractive potential analysis for the two-electron scattering problem (A. Tachibana, Bull. Chem. Soc. Jpn. **66**, 3319 (1993); Int. J. Quantum Chem. **49**, 625 (1994)) is straightforwardly applicable to the present equation-of-motion, and we can also plug in the vibronic interaction for the enhancement of the attractive force. Our approach is purely mathematical and basic, restricted merely at $T = 0$, but proves to serve as a real-space analysis of the pair function itself.

Key words: equation-of-motion of electron pair, BCS theory, superconductivity, electron pair function, density functional theory.

Résumé : En projetant l'état fondamental BCS du condensat superconducteur sur l'espace de Hilbert à N-electron, on obtient un équation du mouvement en espace réel pour la fonction de la paire d'électrons, $\phi(1, 2)$, à la température du zéro absolu ($T = 0$) :

Received October 10, 1995.

This paper is dedicated to Professor Richard F.W. Bader on the occasion of his 65th birthday.

A. Tachibana.[1] Department of Molecular Engineering, Kyoto University, Kyoto 606-01, Japan.

[1] Telephone and Fax: +81-75-753-5932. E-mail: akitomo@scl.kyoto-u.ac.jp

$$i\hbar \frac{d\phi(1,2)}{dt} = h_\phi(1,2)\phi(1,2)$$

$$h_\phi(1,2) = \frac{1}{2m}\boldsymbol{p}(1)^2 + \frac{1}{2m}\boldsymbol{p}(2)^2 + v_\phi(1,2)$$

$$v_\phi(1,2) = v(1) + v(2) + \frac{e^2}{r_{12}} + \int\left(\frac{e^2}{r_{13}} + \frac{e^2}{r_{23}}\right)\rho^{N-2}(3)d\tau_3$$

dans laquelle ρ^{N-2} correspond à la densité électronique du condensat électronique $(N-2)$ obtenu sous la forme de

$$\rho^{N-2}(1) = (N-2)\int|\phi(1,2)|^2 d\tau_2$$

Puisque le potentiel de la corrélation d'échange est donnée sous la forme d'une fonctionnelle explicite de la densité électronique, cette équation est au moins aussi bonne que l'équation de travail fondamentale de la nouvelle théorie fonctionnelle de la densité de la superconductivité. La matrice de densité du deuxième ordre, $\Gamma^N(1,2|1',2')$ projetée sur l'espace de Hilbert à N-électron satisfait les équations

$$\Gamma^N(1,2|1',2') = \frac{N(N-1)}{2}c^N(1,2)c^{N*}(1',2')$$

$$c^N(1,2) = \frac{1}{\sqrt{2!}}A\phi(1,2)\alpha(1)\beta(2) = \phi(1,2)\frac{1}{\sqrt{2!}}(\alpha(1)\beta(2) - \beta(1)\alpha(2))$$

ce qui signifie que, d'une façon asymptotique,

$$\lim_{|R^{CM}_{1,2} - R^{CM}_{1',2'}|\to\infty}\Gamma^N(1,2|1',2') = \text{finite}$$

dans laquelle $R^{CM}_{1,2}$ correspond à la coordonnée du centre de masse des électrons e_1 et e_2 ; ceci est considéré comme l'« ODLRO » (off-diagonal long range-ordre), à $T = 0$ projeté sur l'espace Hilbert à N-électron. Une nouvelle analyse du potentiel attractif pour le problème de la diffusion de deux électrons (A. Tachibana, Bull. Chem. Soc. Jpn. **66**, 3319 (1993); Int. J. Quantum Chem. **49**, 625 (1994)) peut s'appliquer directement à la présente équation de mouvement et on peut y introduire l'interaction vibronique pour l'augmentation de la force attractive. Notre approche est purement mathématique et fondamentale, elle n'est restreinte qu'à $T = 0$, mais il s'avère qu'elle peut même servir dans une analyse de temps réel de la fonction de paire.

Mots clés : équation de mouvement d'une paire d'électron, théorie BCS, superconductivité, fonction d'une paire d'électron, théorie fonctionnelle de la densité.

[Traduit par la rédaction]

I. Introduction

There are two fundamental prerequisites for electrons to reach the superconducting state (1, 2). First, there must be an attractive force between a pair of electrons to form a Boson pair state. According to the conventional picture in the physics of condensed matter, the medium is somehow polarized through interaction with the electron, and the polarization is slow to relax compared with the time scale of the motion of the electron. This retardation works to bind a pair of electrons effectively despite the Coulomb repulsion between them.

Second, there must be a certain value of hopping integral for electrons to delocalize and form a band of finite width. The Boson pairs can then go through a process of condensation, collectively forming a lower energy state like the process of Bose condensation.

In the BCS theory of superconductivity (3), these two actions take place simultaneously, where the BCS ground state demonstrates the strong overlap between the electron pair wave functions $\phi(1, 2)$'s (1).

The aim of this paper is to give a rigorous equation-of-motion for the electron pair function $\phi(1, 2)$ at absolute zero temperature ($T = 0$). This equation is found to be dependent on an explicit function of electron density, so that the application of density functional theory (4) should be of direct interest. As a concrete example, using the jellium model of the background medium and the associated homogeneous electron density, the $\phi(1, 2)$ is found to be given as the Rutherford scattering wave function. Polarization of the medium surely affects the pairing potential; it may strengthen or weaken the electron pairing according to the situation considered (5–8). In particular, the vibronic interaction will be demonstrated to strengthen the electron pairing. The BCS ground state is characterized by the ODLRO (off-diagonal long-range order) (9), so that a mean field theory is of great help in describing the phase transition process itself (1, 3, 10, 11). Our approach is purely mathematical and basic, restricted merely at $T = 0$, but is proven to serve as a real-space analysis of the pair function itself for application to various kinds of present

or future superconductors that are important in the field of materials science (12).

II. Electron pair function

A. Singlet s-wave pairing state of electron gas

The wave function of the pairing state of N (even number assumed) electrons is given as (1, 2):

$$[1] \quad |N\rangle = \frac{1}{\sqrt{N!}} A\phi(1,2)\alpha(1)\beta(2)\phi(3,4)\alpha(3)\beta(4)\cdots \phi(N-1,N)\alpha(N-1)\beta(N)$$

where A denotes the antisymmetrizer and $\phi(i,j)$ denotes the orbital part of the singlet wave function of the electron pair. The $\phi(i,j)$ is symmetric with respect to the interchange of electrons:

$$[2] \quad \phi(j,i) = \phi(i,j)$$

which property is a prerequisite for low-energy stable pair formation as analyzed by Fano (13); this situation has also been analyzed by Wannier (14) in a purely two-electron escape problem from the atomic core (15). This wave function is of course invariant under lattice translation:

$$[3] \quad T\phi(i,j) = \phi(i,j)$$

where T denotes the lattice translation operator (16) for the lattice. In the jellium model, the wave function $\phi(i,j)$ of the electron pair is represented as the superposition of products of one-electron orbitals with which equal and opposite wave vectors are paired; this is in general referred to as time-reversal pairing (1, 2, 17, 18):

$$[4] \quad \phi(i-j) = \sum_k g_k e^{ikr_i} e^{-ikr_j} = \sum_k g_k e^{ik(r_i - r_j)}$$

It should be noted that the s-wave pairing state in the jellium model satisfies

$$[5] \quad \boldsymbol{p}_{ij}\phi(i-j) = 0$$

with $\boldsymbol{p}_{ij}$ being the relative momentum of the ith electron with respect to the jth electron:

$$[6] \quad \boldsymbol{p}_{ij} = \boldsymbol{p}_i - \boldsymbol{p}_j$$

According to the presence of crystal structure of its unique translational symmetry, the Bloch theorem is applied to the pairing wave function. The Bragg reflection may be a possible obstruction to the occurrence of stable electron pairing (1).

B. Electron field operators

The equation-of-motion of the electron field operator is now given for the space spanned by the pairing states of electrons.

Let the electron Hamiltonian be H_e and the time-evolution of the N-electron state $|N(t)\rangle$ be given as

$$[7] \quad i\hbar \frac{d|N(t)\rangle}{dt} = H_e|N(t)\rangle$$

$$[8] \quad H_e = \int a^+(1)h_e(1)a(1)d\tau_1 + \frac{1}{2}\int\int a^+(1)a^+(2)\frac{e^2}{r_{12}}a(2)a(1)d\tau_1 d\tau_2$$

where $a(1)$, $a^+(1)$ denote the electron field operators and $d\tau$ the volume element, and where $h_e(1)$ denotes the one-electron Hamiltonian including the kinetic energy and the nuclear attraction potential $v(1)$:

$$[9] \quad h_e(1) = \frac{1}{2m}\boldsymbol{p}(1)^2 + v(1)$$

C. Equation of motion

The equation-of-motion of the electron field operators $a(1)$, $a^+(1)$ is given as

$$[10] \quad i\hbar \frac{da(1)}{dt} = [a(1), H_e] = h_{ee}(1)a(1)$$

$$[11] \quad i\hbar \frac{da^+(1)}{dt} = [a^+(1), H_e] = -a^+(1)h_{ee}(1)$$

where

$$[12] \quad h_{ee}(1) = h_e(1) + \int \frac{e^2}{r_{13}}\rho(3)d\tau_3$$

with

$$[13] \quad \rho(3) = a^+(3)a(3)$$

Therefore we obtain

$$[14] \quad i\hbar \frac{da(1)a(2)}{dt} = [a(1)a(2), H_e] = \left[h_e(1) + h_e(2) + \frac{e^2}{r_{12}} + \int\left(\frac{e^2}{r_{13}} + \frac{e^2}{r_{23}}\right)\rho(3)d\tau_3\right]a(1)a(2)$$

and its complex conjugate.

Now, the pair function in the 2nd-order density matrix is given as the transition amplitude of $a(1)a(2)$ between the N-electron state vector $|N\rangle$ and some ith $(N-2)$-electron state vector $\langle i^{N-2}|$,

$$[15] \quad c_i^N(1,2) = \langle i^{N-2}|a(1)a(2)|N\rangle$$

The 2nd-order density matrix can then be written as

$$[16] \quad \Gamma^N(1,2|1',2') = \langle N|a^+(2')a^+(1')a(1)a(2)|N\rangle = \sum_i c_i^N(1,2)c_i^{N*}(1',2')$$

Here, it should be noted that we are treating the complete pairing states at $T = 0$, so that the specification i of the state is uniquely determined to be the state with one pair lost:

$$[17] \quad c_i^N(1,2) \propto c^N(1,2) \ : \text{ independent of } i$$

with

[18] $\langle c^N(1,2)|c^N(1,2)\rangle = 1$

and the 2nd-order density matrix can then be written as

[19] $\Gamma^N(1,2|1',2') = \frac{N(N-1)}{2}\, c^N(1,2)c^{N*}(1',2')$

where $N(N-1)/2$ is the degeneracy of the pair function. This is the characteristic situation distinct from the case of the normal state of many-electron systems (19, 20). The pair function is now identified with the singlet wave function of the electron pair given in eq. [2]:

[20] $c^N(1,2) = \frac{1}{\sqrt{2!}} A\phi(1,2)\alpha(1)\beta(2)$

$$= \phi(1,2)\frac{1}{\sqrt{2!}}(\alpha(1)\beta(2) - \beta(1)\alpha(2))$$

Thus the equation-of-motion of the pair function is obtained as

[21] $i\hbar \frac{d\phi(1,2)}{dt} = h_\phi(1,2)\phi(1,2)$

where

[22] $h_\phi(1,2) = \frac{1}{2m}\boldsymbol{p}(1)^2 + \frac{1}{2m}\boldsymbol{p}(2)^2 + v_\phi(1,2)$

[23] $v_\phi(1,2) = v(1)+v(2)+\frac{e^2}{r_{12}}+\int\left(\frac{e^2}{r_{13}}+\frac{e^2}{r_{23}}\right)\rho^{N-2}(3)d\tau_3$

[24] $\rho^{N-2}(3) = \langle N-2|\rho(3)|N-2\rangle$

In the general case of the ODLRO (off-diagonal long-range order) (9), the $\Gamma(1,2|1',2')$ satisfies asymptotically

[25] $\Gamma(1,2|1',2') \approx \alpha_0 c(1,2)c^*(1',2'); \qquad \alpha_0 \gg 1$

so that

[26] $\lim_{|R^{CM}_{1,2} - R^{CM}_{1',2'}|\to\infty} \Gamma(1,2|1',2') = \text{finite}$

where $R^{CM}_{1,2}$ denotes the center-of-mass coordinate of electrons e_1 and e_2. Therefore, eq. [19] is considered the ODLRO at $T = 0$ for the Hilbert space of fixed electron number N.

III. Electron pair potential

The stability of the electron pair is now examined for the potential $v_\phi(1, 2)$ given by eq. [23]. Imagine for the sake of simplicity the jellium model of the background medium for the electron pair and the associated homogeneous electron density for ρ^{N-2}. Then the interelectron interaction is solely governed by the following term $v_{int}(1, 2)$ in $v_\phi(1, 2)$:

[27] $v_\phi(1,2) = v_{int}(1) + v(1) + v(2)$

$$+ \int\left(\frac{e^2}{r_{13}}+\frac{e^2}{r_{23}}\right)\rho^{N-2}(3)d\tau_3$$

with

[28] $v_{int}(1,2) = \frac{e^2}{r_{12}}$

This is because the residual terms in eq. [27], aside from eq. [28], are merely constant under the condition "the jellium model of the background medium for the electron pair and the associated homogeneous electron density for ρ^{N-2}."

Let θ be the angle between the position vectors $\boldsymbol{r}_1$, $\boldsymbol{r}_2$ of the electrons e_1, e_2:

[29] $r_{12} = \sqrt{r_1^2 + r_2^2 - 2r_1 r_2 \cos\theta}$

The "distance" of the electron pair as a whole from the scattering center may be measured by the hyperspherical radius r:

[30] $r = \sqrt{r_1^2 + r_2^2}$

Then using the variable transformation of Wannier (14) as

[31] $r_1 = r\cos\left(\frac{\chi}{2}\right)$

[32] $r_2 = r\sin\left(\frac{\chi}{2}\right)$

with

[33] $0 < \chi < \pi$

eq. [28] reduces to

[34] $v_{int}(1,2) = \frac{e^2}{r\sqrt{1-\sin(\chi)\cos(\theta)}}$

It is easily found that the configuration P defined as

[35] $P : \{\chi = \pi/2, \theta = \pi\}$

corresponds to the minimum of $v_{int}(1, 2)$:

[36] $\left.\frac{\partial v_{int}}{\partial\theta}\right|_P = \left.\frac{\partial v_{int}}{\partial\chi}\right|_P = 0$

[37] $\left.\frac{\partial^2 v_{int}}{\partial\theta^2}\right|_P = \left.\frac{\partial^2 v_{int}}{\partial\chi^2}\right|_P = \frac{1}{4r^2}\frac{e^2}{\sqrt{2}}\, r > 0$

This configuration P exactly dictates the time-reversal configuration for the electron pair with respect to the scattering center: the radial vectors point to mutually opposite directions with the same distance, $r_1 = r_2$, from the scattering center. It should be noted that if the scattering center is identified with the center-of-mass of the electron pair, then the configuration P is mandatory because of s-wave condition eq. [5]. Therefore, we should consider eq. [37] as the stability of the configuration P against small perturbations. If the perturbation to the interelectron potential is of short-range character, then this stability mechanism remains valid because the long-range Coulomb interaction overwhelms in

the asymptotic scattering region. For example, if an electron density fluctuation occurs, the electron pair is stable if such a condition is satisfied. Indeed, for the case of the isolated electron pair problem, the stability of the configuration P has been clearly demonstrated (6–8).

It should be noted that although the resultant equation-of-motion, eq. [21], is that for the usual Rutherford scattering under the condition "the jellium model of the background medium for the electron pair and the associated homogeneous electron density for ρ^{N-2}," which we have adopted here, and therefore the analytical solution is given in any standard textbook, the scattering center is not fixed in space. Instead, by definition of the situation considered, the scattering center is homogeneously distributed in space, so that this verifies the underlying condition "the homogeneous electron density" in its rigorously self-consistent manner.

IV. Vibronic attraction

If the stability of the electron pair as demonstrated in Sect. III is not strong enough, then some subsidiary mechanism should be invoked to ensure time-reversal electron pairing. This is the electron–phonon coupling (1, 3) or instantaneous vibronic coupling (5). In the context of the density functional theory, Kohn, Gross, et al. have explicitly treated this subsidiary force as W in their working equation (21). As a concrete and interesting example of W, we shall in this section explicitly demonstrate the instantaneous vibronic interaction for the subsidiary attractive force in our basic equation, eq. [13]. The vibronic interaction is treated as the internal potential, not the external potential, so that the Mermin entropy principle works and hence our density functional theory remains valid in due course.

According to the theory of the vibronic Hamiltonian (5), let eqs. [7] and [8] be modified as

$$[38]\quad i\hbar\,\frac{\mathrm{d}|N(t)\rangle}{\mathrm{d}t} = H_\kappa|N(t)\rangle$$

$$[39]\quad H_\kappa = H_e + \Delta H_\kappa$$

where ΔH_κ is the vibronic term that is represented by W in ref. 21:

$$[40]\quad \Delta H_\kappa = \frac{1}{2}\sum_{m,n=1}^{f}\sum_{i,j} a^{mn}\hat{a}_i^+\hat{a}_j\left\langle\frac{\partial\psi_i}{\partial q^m}\,|\,\frac{\partial\psi_j}{\partial q^n}\right\rangle - \frac{1}{2}\sum_{m,n=1}^{f}\sum_{i,j,k,l} a^{mn}\hat{a}_i^+\hat{a}_k^+\hat{a}_l\hat{a}_j\left\langle\psi_i|\,\frac{\partial\psi_j}{\partial q^m}\right\rangle\left\langle\psi_k|\,\frac{\partial\psi_l}{\partial q^n}\right\rangle$$

where $\{\psi_i(1)\}_{i=k\sigma}$ denotes an orthonormal complete set of spin functions with $\boldsymbol{k}$ for the momentum and σ for the spin,

$$[41]\quad \langle\psi_i|\psi_{i'}\rangle = \delta_{ii'} = \delta_{kk'}\delta_{\sigma\sigma'}, \qquad i = \boldsymbol{k}\sigma$$

that are used to expand the field operators as follows:

$$[42]\quad a_\sigma(1) = \sum_k \hat{a}_{k\sigma}\psi_{k\sigma}(1)$$

$$a_\sigma^+(1) = \sum_k \hat{a}_{k\sigma}^+\psi_{k\sigma}^*(1)$$

The q^m ($m = 1,2,\ldots, f$) denote the internal coordinates that describe the vibrational motion of nuclei, the degrees of freedom being f, while a^{mn} denotes the kinetic tensor (5). It should be noted that the vibronic Hamiltonian is given in a closed form, namely, we are free from the perturbation series treatment using a small amplitude approximation for nuclear displacements. For the sake of easier application to eq. [13], eq. [39] is rewritten as follows:

$$[43]\quad H_\kappa = \int a^+(1)h_\kappa(1,1')a(1')\mathrm{d}\tau_1\mathrm{d}\tau_{1'} + \frac{1}{2}\int a^+(1)a^+(2)v_\kappa(1,2;1',2')a(2')a(1')\mathrm{d}\tau_1\mathrm{d}\tau_{1'}\mathrm{d}\tau_2\mathrm{d}\tau_{2'}$$

$$[44]\quad h_\kappa(1,1') = h_e(1)\delta(1-1') + \frac{1}{2}\sum_{m,n=1}^{f}\sum_i a^{mn}\frac{\partial\psi_i(1)}{\partial q^m}\frac{\partial\psi_i^*(1')}{\partial q^n} = h_\kappa^*(1',1)$$

$$[45]\quad v_\kappa(1,2;1',2') = \frac{e^2}{r_{12}}\delta(1-1')\delta(2-2') + \frac{1}{2}\sum_{m,n=1}^{f} a^{mn}\kappa_m(1,1')\kappa_n(2,2') = v_\kappa(2,1;2',1') = v_\kappa^*(1'2';1,2)$$

where κ_m is given as

$$[46]\quad \kappa_m(1,2) = \frac{1}{2}\sum_i\{[\pi_m\psi_i(1)]\psi_i^*(2) + \psi_i(1)[\pi_m\psi_i(2)]^*\} = \kappa_m^*(2,1)$$

where π_m denotes the quantum mechanical momentum operator with respect to q^m (5).

It should be noted that the asymptotic behavior of the subsidiary term to the interelectron potential is in general indefinite,

$$[47]\quad \lim_{r_{12},r_{1'2'}\to\infty} v_\kappa(1,2;1',2') = \frac{e^2}{r_{12}} + (\text{indefinite sign}) \text{ terms}$$

However, just for the time-reversal electron scattering, it will be negative definite, as shown in the following eq. [52].

First, the vibronic one-electron equation-of-motion is modified from eq. [10] to

$$[48]\quad i\hbar\,\frac{\mathrm{d}a(1)}{\mathrm{d}t} = [a(1),H_\kappa] = \int h_{\kappa\kappa}(1,3')a(3')\mathrm{d}\tau_{3'}$$

$$[49]\quad h_{\kappa\kappa}(1,3') = h_\kappa(1,3') + \int a^+(4)v_\kappa(1,4;3',4')a(4')\mathrm{d}\tau_4\mathrm{d}\tau_{4'}$$

Second, the vibronic two-electron equation-of-motion is modified from eq. [13] to

$$[50]\quad i\hbar\,\frac{\mathrm{d}a(1)a(2)}{\mathrm{d}t} = [a(1)a(2), H_\kappa]$$
$$= \int h_\kappa(1,3')a(3')a(2)\mathrm{d}\tau_3 + \int h_\kappa(2,3')a(1)a(3')\mathrm{d}\tau_{3'}$$
$$+ \int v_\kappa(2,1;3',4')a(4')a(3')\mathrm{d}\tau_{3'}\mathrm{d}\tau_{4'}$$
$$+ \int v_\kappa(1,4;3',4')a^+(4)a(2)a(4')a(3')\mathrm{d}\tau_{3'}\mathrm{d}\tau_4\mathrm{d}\tau_{4'}$$
$$+ \int v_\kappa(4,2;3',4')a^+(4)a(1)a(4')a(3')\mathrm{d}\tau_{3'}\mathrm{d}\tau_4\mathrm{d}\tau_{4'}$$

Using eq. [45], eq. [50] is rewritten as

$$[51]\quad i\hbar\,\frac{\mathrm{d}a(1)a(2)}{\mathrm{d}t} = \left[h(1)+h(2)+\frac{e^2}{r_{12}}+\int\left(\frac{e^2}{r_{13}}+\frac{e^2}{r_{23}}\right)\rho(3)\mathrm{d}\tau_3\right]a(1)a(2)$$
$$+\frac{1}{2}\sum_{n,m=1}^{f} a^{mn}\left(\begin{array}{l}\displaystyle\sum_i\left(\int\frac{\partial\psi_i(1)}{\partial q^m}\frac{\partial\psi_i^*(3')}{\partial q^n}a(3')a(2)\mathrm{d}\tau_{3'}+\int\frac{\partial\psi_i(2)}{dq^m}\frac{\partial\psi_i^*(3')}{\partial q^n}a(1)a(3')\mathrm{d}\tau_{3'}\right)\\ \quad+\displaystyle\int\kappa_m(2,3')\kappa_n(1,4')a(4')a(3')\mathrm{d}\tau_{3'}\mathrm{d}\tau_{4'}\\ \quad+\displaystyle\int\kappa_m(1,3')\kappa_n(4,4')a^+(4)a(2)a(4')a(3')\mathrm{d}\tau_{3'}\mathrm{d}\tau_4\mathrm{d}\tau_{4'}\\ \quad+\displaystyle\int\kappa_m(4,3')\kappa_n(2,4')a^+(4)a(1)a(4')a(3')\mathrm{d}\tau_{3'}\mathrm{d}\tau_4\mathrm{d}\tau_{4'}\end{array}\right)$$

The attractive force for the time-reversal pair of electrons is observed among the last terms in eq. [51]:

$$[52]\quad \frac{1}{2}\sum_{m,n=1}^{f} a^{mn}\int\kappa_m(2,3')\kappa_n(1,4')\psi_{-k\beta}(4')\psi_{k\alpha}(3')\mathrm{d}\tau_{3'}\mathrm{d}\tau_{4'}$$
$$= -\frac{1}{2}\sum_{m,n=1}^{f} a^{mn}\frac{\partial\psi_{k\alpha}(2)}{\partial q^m}\frac{\partial\psi_{-k\beta}(1)}{\partial q^n}$$

where we have explicitly highlighted the $\{k\alpha, -k\beta\}$ pair. The same conclusion is reached in a different context in ref. 5.

V. Density functional theory

In Sect. III, using a concrete example, we have shown the simple self-consistent picture of the stability of the pairing state. According to eqs. [36] and [37], the BCS ensemble of pairing states is at least "metastable" in constructing the local minimum, if not the global minimum, in the subset of the grand canonical ensemble of electrons. Any tiny but finite relaxation of electron cloud is not mandated at all for a probe electron. This governs even the s-wave pairing; extension to higher angular momentum wave pairing is straightforward using standard partial wave analysis of the Rutherford scattering wave function and the associated spin function. If we need a more powerful attractive force in order to arrive at the global minimum, see for example Sect. IV.

The equation-of-motion of the pair function is obtained in eq. [21]. The potential $v_\phi(1, 2)$ for this equation is given as an explicit functional of electron density, eq. [23], so that eq. [21] becomes the fundamental working equation for the density functional theory of superconductivity (10, 11, 21). The superconducting phase transition process is characterized as the change of description of electron from the independent particle orbital to the pair function as shown in eq. [4]. The self-consistent picture of this change of description should be related to a certain mathematical structure of the Bogoliubov–Valatin transformation (1, 21). A precise description of the change in electron density will also be obtained.

Indeed, in our density functional theory of superconductivity (10, 11), the crucial mathematical strategy was to find the zeros of the order parameter G_k (defined for the quasi particles in eq. [65] below) or, equivalently, the zeros of the weight function w_k (defined in eq. [66] below) in the complex Gaussian plane of the x_k (defined in eq. [57] below), while keeping the order parameter F_k (defined for the electrons in eq. [56] below) nonzero. This is distinct from the BCS ensemble where the zeros of the w_k distribute uniformly on the real positive axis of the x_k, because the G_k is identically zero for the BCS ensemble, which is the very definition of the BCS ensemble according to the mathematical theory of Valatin (22). On the other hand, in the normal grand canonical ensemble that we use, the zeros of the w_k never exactly touch the real positive axis of the x_k. This clarifies our mathematical point of view when the superconducting phase transition is declared to occur if the zeros of the w_k infinitely approach the real positive axis of the x_k (10, 11).

We use the normal grand canonical ensemble, not the BCS ensemble. Thus we can appeal to the Mermin entropy principle and arrive at our own density functional theory where we use analytic continuation of the electron density in the complex Gaussian plane (10, 11). Then, the onset of electron pairing is detected by monitoring the change in the description of the electron density as in the standard Landau approach to phase transition. Therefore, it may be visualized that the manner in which our density functional theory of superconducting phase transition is related to the BCS theory resembles the relation of Lee–Yang theory to the Mayer theory of condensation. Namely, one theory treats the phase transition as the mathematical limit of some thermodynamic function that is under analytic continuation in the complex Gaussian plane, while the other treats it as a completely distinct ensemble in which phase transition has already occurred. Indeed, our density functional theory of superconductivity treats the electron density as under analytic continuation in the complex Gaussian plane. We shall elaborate this as follows, whereby we further relax to allow the complex number for w_k that was restricted to be real in our original paper (10, 11). This permits the logical framework of our density functional theory of superconductivity to be sufficiently complete to be applicable to a more general situation that may occur in the future development of the theory. For example, eq. [72] below is the rigorous expression of the r_k defined in eq. [62] below for the mixing ratio of quasi particles to electrons.

The electron density $\rho(1)$ is the diagonal part of the first-order density matrix, and hence given as

$$[53]\quad \rho(1) = \sum_{\sigma}^{\alpha\beta} \sum_{k} f_{k\sigma} |\psi_{k\sigma}(1)|^2 + \sum_{\sigma}^{\alpha\beta} \sum_{k \neq k'} f_{k'\sigma k\sigma} \psi^*_{k'\sigma}(1) \psi_{k\sigma}(1)$$

$$f_{k\sigma} = f_{k\sigma k\sigma}, \qquad f_{k'\sigma' k\sigma} = \langle \hat{a}^+_{k'\sigma'} \hat{a}_{k\sigma} \rangle$$

in which we have used eqs. [41] and [42].

Using the grand canonical ensemble, the field operators are defined in Fock space where the number of electrons is not fixed, in sharp contrast to Hilbert space where the number of electrons is fixed, say N. In Fock space, therefore, the total electron number is given as the ensemble average,

$$[54]\quad \langle N \rangle = \int \rho(1) d\tau_1 = \sum_{\sigma}^{\alpha,\beta} \sum_{k} f_{k\sigma}$$

Therefore, $f_{k\sigma}$ plays the role of occupation number for $\psi_{k\sigma}$ (1). Moreover, the following probability amplitude of the variable electron number should appear in general:

$$[55]\quad F_{i'i} = \langle \hat{a}_{k'\sigma'} \hat{a}_{k\sigma} \rangle, \qquad F^*_{i'i} = \langle \hat{a}^+_{k\sigma} \hat{a}^+_{k'\sigma'} \rangle$$

which should disappear in a Hilbert space:

$$[56]\quad F_{i'i} = F^*_{i'i} = 0, \qquad \text{in a Hilbert space}$$

It should be noted that in the BCS theory of superconductivity, the following Bogoliubov–Valatin transformation is performed for the description of a collective particle in Fock space:

$$[57]\quad \hat{a}_\kappa = \frac{\hat{c}_\kappa + g^*_k \hat{c}^+_{-\kappa}}{\sqrt{1+x_k}}, \qquad \hat{a}^+_\kappa = \frac{\hat{c}^+_\kappa + g_k \hat{c}_{-\kappa}}{\sqrt{1+x_k}}$$
$$\hat{a}_{-\kappa} = \frac{\hat{c}_{-\kappa} - g^*_k \hat{c}^+_\kappa}{\sqrt{1+x_k}}, \quad \hat{a}^+_{-\kappa} = \frac{\hat{c}^+_{-\kappa} - g_k \hat{c}_\kappa}{\sqrt{1+x_k}}, \quad x_k = |g_k|^2$$

where we used the convention of time-reversal symmetry (22)

$$[58]\quad \kappa = k\alpha \text{ and } -\kappa = -k\beta, \qquad \text{or } \kappa = -k\alpha \text{ and } -\kappa = k\beta$$

Conversely, we get

$$[59]\quad \hat{c}_\kappa = \frac{\hat{a}_\kappa - g^*_k \hat{a}^+_{-\kappa}}{\sqrt{1+x_k}}, \qquad \hat{c}^+_\kappa = \frac{\hat{a}^+_\kappa - g_k \hat{a}_{-\kappa}}{\sqrt{1+x_k}}$$
$$\hat{c}_{-\kappa} = \frac{\hat{a}_{-\kappa} + g^*_k \hat{a}^+_\kappa}{\sqrt{1+x_k}}, \qquad \hat{c}^+_{-\kappa} = \frac{\hat{a}^+_{-\kappa} + g_k \hat{a}_\kappa}{\sqrt{1+x_k}}$$

The new collective particles are also fermions that satisfy the same anticommutation relationship as the original electrons. The occupation numbers of the collective particles are similarly given as

$$[60]\quad d_{k\sigma} = d_{k'\sigma' k\sigma} = \langle \hat{c}^+_{k'\sigma'} \hat{c}_{k\sigma} \rangle$$

The occupation numbers are found to satisfy the difference rule:

$$[61]\quad f_\kappa - f_{-\kappa} = d_\kappa - d_{-\kappa}$$

Now, let us introduce and estimate the ratio of mixing in the level of occupation number as follows:

$$[62]\quad f_\kappa = \frac{d_\kappa + r_k(1 - d_{-\kappa})}{1 + r_k}, \qquad f_{-\kappa} = \frac{d_{-\kappa} + r_k(1 - d_\kappa)}{1 + r_k}$$

where r_k is the ratio of mixing so defined. These satisfy the sum rule:

$$[63]\quad f_\kappa + f_{-\kappa} - 1 = \frac{1 - r_k}{1 + r_k} (d_\kappa + d_{-\kappa} - 1)$$

The converse relationship is found if $r_k \neq 1$; then

$$[64]\quad d_\kappa = \frac{f_\kappa - r_k(1 - f_{-\kappa})}{1 - r_k}, \qquad d_{-\kappa} = \frac{f_{-\kappa} - r_k(1 - f_\kappa)}{1 - r_k}$$

where if $r_k = 1$ the right-hand-side of each equation is indefinite. In order to get the form of r_k, the following probability amplitudes should appear in general:

$$[65]\quad F_k = \langle \hat{a}_{-\kappa} \hat{a}_\kappa \rangle$$
$$G_k = \langle \hat{c}_{-\kappa} \hat{c}_\kappa \rangle$$

which are related in such a way that

$$[66]\quad G_k = \frac{1}{2} \omega_k F_k$$

where ω_k is the weight function thus defined. It should be noted that the BCS ground state (1, 3, 22) is characterized as the zero of G_k, i.e., of ω_k:

$$[67]\quad G_k = 0, \qquad \text{i.e., } \omega_k = 0$$

while

[68] $F_k \neq 0$

for the BCS ground state.

In general, the functional relationship is found to be

[69] $$F_k(g_k)^2 + g_k(1 - f_\kappa - f_{-\kappa}) + \left\{ \frac{1 + x_k}{2}\, \omega_k^* - 1 \right\} F_k^* = 0$$

Taking the complex conjugate of this equation and, next, summing and subtracting with the original equation, we then obtain

[70] $$(g_k F_k + g_k^* F_k^*)(x_k - 1) + 2x_k(1 - f_\kappa - f_{-\kappa}) + \frac{1 + x_k}{2}\,(\omega_k g_k F_k + \omega_k^* g_k^* F_k^*) = 0$$

and

[71] $$g_k F_k - g_k^* F_k^* - \frac{1}{2}\,(\omega_k g_k F_k - \omega_k^* g_k^* F_k^*) = 0$$

After some manipulation, we finally obtain

[72] $$r_k = \frac{g_k F_k + g_k^* F_k^* + \frac{1}{2}\,(\omega_k g_k F_k + \omega_k^* g_k^* F_k^*)}{g_k F_k + g_k^* F_k^* - \frac{1}{2}\,(\omega_k g_k F_k + \omega_k^* g_k^* F_k^*)}\, x_k$$

where of course we assume the nonzero denominator of the right-hand-side expression. It should be noted that the BCS ground state (1, 3, 22) leads to

[73] $r_k = x_k$

for the BCS ground state.

The most significant characteristic of the BCS theory of superconductivity is that eq. [67] holds for any temperature where not only the BCS ground state is involved:

[74] $\omega_k = 0, \qquad$ i.e., $r_k = x_k$

for the BCS ensemble at $T \neq 0$. This is possible only when the electronic state for any electron number N that is involved in the BCS ensemble should possess the same pair function $\phi(1, 2)$ as demonstrated in eq. [1].

To conclude, in our density functional theory of superconductivity (10, 11), the zeros of ω_k were sought for the electron density that is under analytical continuation in the complex Gaussian plane. If the zeros of ω_k infinitely approach the real positive axis of x_k, we can declare that superconducting phase transition has just occurred. In other words, the situation described in eq. [74] holds at that temperature of phase transition in the sense of the "limit." At that limiting situation, the grand canonical ensemble infinitely approaches the BCS ensemble. It should be noted here that the BCS ensemble is not exactly the same as the usual grand canonical ensemble even at the temperature of phase transition. However, the difference is not significant there. Therefore, it is of great interest to study how the BCS wave function given in eq. [1] or, more precisely, how the pair function $\phi(1, 2)$ in it is described in terms of the electron density. As far as the author is aware, the equation-of-motion of the pair function $\phi(1, 2)$ for the BCS ensemble has not been published in the literature, although its derivation is disarmingly easy, as shown in eq. [21]. The potential for the pair function $\phi(1,2)$ is given as an explicit function of the electron density. Thus the deterministic eq. [21] obtained in this work should be the fundamental working equation for density functional theory that allows the continuous analytical description of a superconducting phase transition (10, 11), in which the weight function ω_k that is, in general, complex was assumed to be real.

The power of our theory lies in its predictability, slightly over and above that of BCS theory. First of all, after the superconducting phase transition occurs, our theory reduces to BCS theory. Nothing new happens. Thus the new phenomena should be related to the pre-BCS regime, namely, the gray zone between the normal Fermi liquid and the complete pairing state. Actually, we can predict the presence of the metastable pairing state at temperature T_b, higher than the well-defined critical temperature T_c, where the electronic specific heat C should show a negative jump in sharp contrast to the positive jump at T_c.

Thus, once the electron pair becomes created according to eq. [13] for a certain time-reversal combination, say $\{k\alpha, -k\beta\}$, then even if its lifetime is short, namely, even if it is not in the ground state, the vibronic attractive force will be plugged in as shown in eq. [52]. If this subsidiary attractive force overwhelms the interelectron repulsive force, then a net attractive force will be created and the firm superconducting condensate should be brought about. For metastable electron pairing, the absolute value of the x_k that gives the zero of the ω_k as for the limiting situation of eq. [74] should not be very large. After stable electron pairing is attained, the absolute value of the x_k that gives the zero of the ω_k as for the limiting situation of eq. [74] should be considerably larger. Therefore the $T_b(> T_c)$ in refs. 10 and 11 should be the temperature for metastable electron pairing because it is associated with a small value of x_k, while the T_c associated with a large value of x_k should be that for the complete electron pairing.

The possible consequence in an explanation of certain experimental data will be briefly shown as follows, when we may first show the prediction in Fig. 1, and its experimental evidence in Fig. 2. Experimentally, T_b = 93 K and T_c = 89 K for that sample (23). We cannot predict how high the T_b is, compared with the T_c, until the detailed data pertinent to the sample are available. We can only say at this moment that, mathematically, if it occurs, then Fig. 1 results. Then, the detailed mechanism follows. Figure 3 shows the spectrum of the quasi-particle that is cast in the pairing state. Its temperature dependence is determined by the x in eq. [57], whose functional relationship is deduced by our density functional theory (10, 11). The x itself also depends on temperature as shown in Fig. 4. At $T = T_b$, nonzero x emerges but is not large enough to bind electrons, and at $T = T_c$, the x becomes large enough to form the real bound state of electrons as shown in Fig. 3. Finally, at $T = 0$, the x may converge to a finite value or diverge to infinity, when the behavior is denoted as curve A or B, respectively, in Figs. 3 and 4. The zeros of ω are shown in Fig. 5. For conventional low-T_c superconductors, only those electrons lying in the very vicinity of the Fermi level are combined to form the pairing state, and hence the T_b and T_c may coalesce. This is the reason

Fig. 1. Predicted behavior of the electronic specific heat C as a function of temperature T.

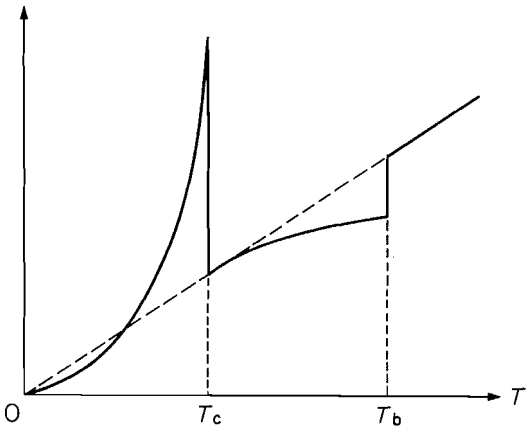

Fig. 2. Experimental evidence of the 93 K anomaly of C for high-T_c (89 K) superconductor.

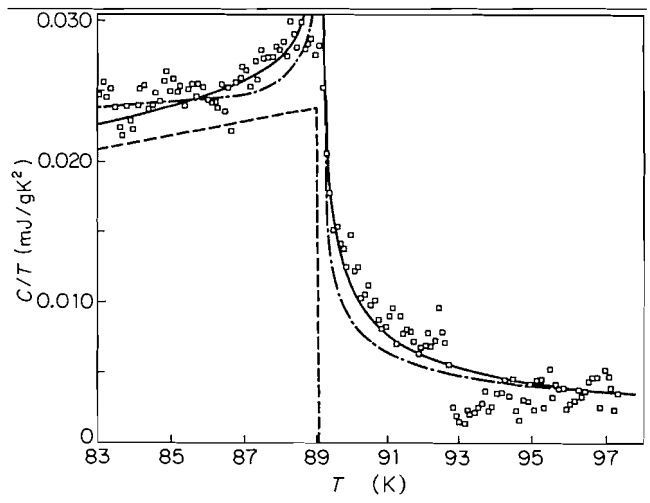

Fig. 3. Predicted behavior of the spectrum of quasi-particle in the pairing state as a function of temperature T.

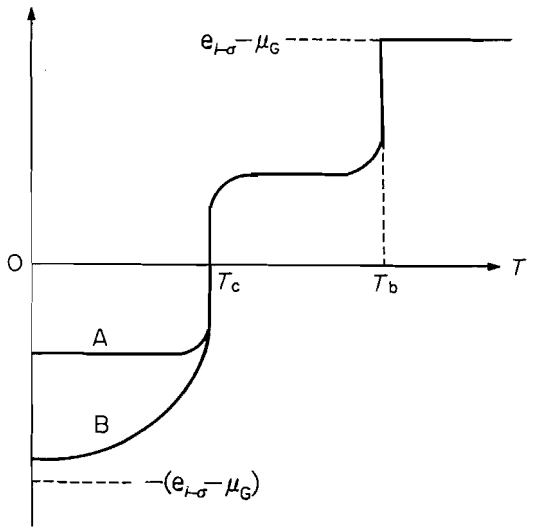

Fig. 4. Assumed behavior of x as a function of temperature T.

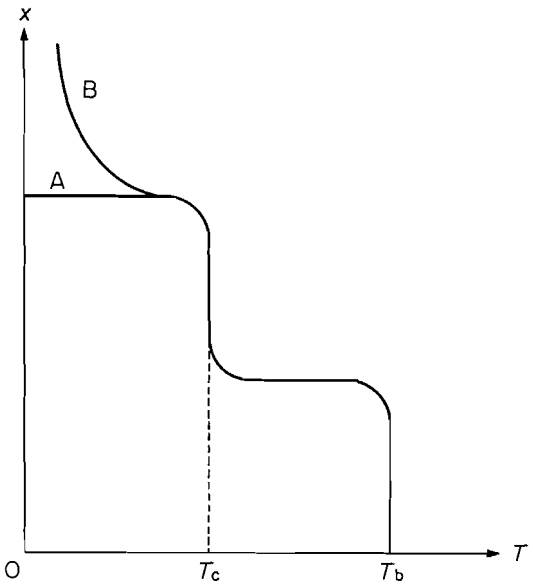

Fig. 5. The distribution of the zeros of ω in the complex Gauss plane of x.

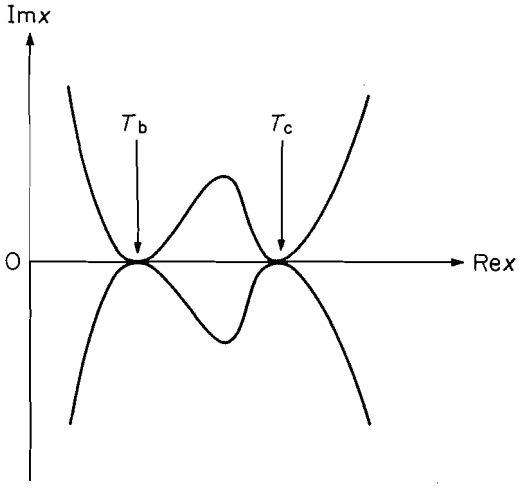

why the T_b anomaly is not observed for conventional low-T_c superconductors.

VI. Conclusion

A rigorous equation-of-motion, eq. [21], is given for the time-reversal electron pair function $\phi(1, 2)$ of the superconducting electron condensate projected on the N-electron Hilbert space at $T = 0$. Since the exchange-correlation potential is given as an explicit functional of electron density, this eq. [21] represents the fundamental working equation for the new density functional theory of superconductivity (10, 11). New stability analysis of the two-electron scattering problem (6–8) is straightforwardly applicable to the present equation-of-motion, and we can directly observe the intrinsic stability

or "rigidity" of the time-reversal electron pair in the superconducting electron condensate (18). The pairing wave function given in eq. [1] was also analyzed in the mean-field theory of superconductivity by Schafroth and Blatt and in the Kohn–Luttinger theory of superconductivity, in the sense that s-wave pairing is, in general, allowed (24–26). Plasmon should strengthen the electron pairing (27). The instantaneous vibronic coupling (5) should, as well, strengthen the attractive force for electron pairing, which is demonstrated explicitly in this paper.

Acknowledgments

This work was supported by a Grant-in-Aid for Scientific Research from the Ministry of Education, Science, and Culture of Japan.

References

1. J.R. Schrieffer. Theory of superconductivity. W.A. Benjamin, Reading, England. 1964.
2. N.W. Ashcroft and N.D. Mermin. Solid state physics. Saunders College, Philadelphia, Pa. 1976.
3. J. Bardeen, L.N. Cooper, and J.R. Schrieffer. Phys. Rev. **108**, 1175 (1957).
4. P. Hohenberg and W. Kohn. Phys. Rev. [Sect.] B, **136**, 864 (1964).
5. A. Tachibana. Phys. Rev. A: Gen. Phys. **35**, 18 (1987).
6. A. Tachibana. Bull. Chem. Soc. Jpn. **66**, 3319 (1993).
7. A. Tachibana. Int. J. Quantum Chem. **49**, 625 (1994).
8. A. Tachibana and H. Inaba. Fullerene Sci. Technol. **2**, 107 (1994).
9. C.N. Yang. Rev. Mod. Phys. **34**, 694 (1962).
10. A. Tachibana. *In* High-temperature superconducting materials. *Edited by* W.E. Hatfield and J.H. Miller, Jr. Marcel Dekker, New York. 1988. p. 99.
11. A. Tachibana. *In* The physics and chemistry of organic superconductors. *Edited by* G. Saito and S. Kagoshima. Springer-Verlag, Heidelberg. 1990. p. 461.
12. W.Y. Liang. *In* The science of superconductivity and new materials. *Edited by* S. Nakajima. World Scientific, Singapore. 1989. p. 161.
13. U. Fano. Rev. Mod. Phys. **64**, 313 (1992).
14. G. Wannier. Phys. Rev. **90**, 817 (1953).
15. J.R. Friedman, X.Q. Guo, M.S. Lubell, and M.R. Frankel. Phys. Rev. A: At. Mol. Opt. Phys. **46**, 652 (1992).
16. C. Kittel. Quantum theory of solids. John Wiley, New York. 1963.
17. P.W. Anderson. J. Phys. Chem. Solids, **11**, 26 (1959).
18. P.W. Anderson. Basic notions of condensed matter physics. Benjamin-Cummings, Menlo Park, Calif. 1984.
19. K.A. Dawson and N.H. March. J. Chem. Phys. **82**, 323 (1985).
20. K.A. Dawson. Phys. Rev. A: Gen. Phys. **32**, 1867 (1985).
21. L.N. Oliveira, E.K.U. Gross, and W. Kohn. Phys. Rev. Lett. **60**, 2430 (1988); W. Kohn, E.K.U. Gross, and L.N. Oliveira. Int. J. Quantum Chem. Symp. **23**, 611 (1989); W. Kohn, E.K.U. Gross, and L.N. Oliveira. J. Phys. Lett. Les Ulis, Fr., **50**, 2601 (1989); O.-J. Wacker, R. Kümmel, and E.K.U. Gross. Phys. Rev. Lett. **73**, 2915 (1994); K. Capelle and E.K.U. Gross. Phys. Lett. A, **198**, 261 (1995); M. Lüders and E.K.U. Gross. Int. J. Quantum Chem. **56**, 521 (1995).
22. J.G. Valatin. Nuovo Cimento, **7**, 843 (1958).
23. S.E. Inderhees, M.B. Salamon, N. Goldenfeld, J.P. Rice, B.G. Pazol, D.M. Ginsberg, J.Z. Liu, and G.W. Crabtree. Phys. Rev. Lett. **60**, 1178 (1988); A. Tachibana. Chemistry (Kagaku: in Japanese), **49**, 698 (1994).
24. M.R. Schafroth. Phys. Rev. **100**, 463 (1955).
25. J.M. Blatt. Theory of superconductivity. Academic, New York. 1964.
26. W. Kohn and J.M. Luttinger. Phys. Rev. Lett. **15**, 524 (1965).
27. Y. Takada. J. Phys. Soc. Jpn. **45**, 786 (1978); Phys. Rev. B: Condens. Matter, **47**, 5202 (1993).

The topology of the valence shell and the electric field gradient at the nitrogen nucleus in aziridines

Félix Rosillo, Yosslen Aray, Jesús Rodríguez, and Juan Murgich

Abstract: The ab initio molecular charge density $\rho(r)$ of substituted aziridines was calculated at the MP2 level for R = -H, -CH_3, -CF_3, -Cl, -NO_2, -CN, -OH, -NO, and -F. The use of the topology of the Laplacian of $\rho(r)$ allowed the analysis of the electric field gradient (EFG) at the nitrogen nucleus directly in terms of its valence shell charge concentration. The EFG changed sign and the orientation of its *y*- and *z*-axes with respect to aziridine when R = -Cl, -NO_2, -CN, -OH, -NO, and -F. The changes in the EFG in these aziridines upon substitution were correlated with those calculated in the valence charge concentrations along the direction of the N—R bond. The sign of the q_{zz} component and the orientation of the principal axes of the EFG tensor were found to be determined by the relative value of the contributions from the charge concentrations at the points in the valence shell along the N—C and N—R bond directions.

Key words: molecular charge distribution, aziridines, Laplacian of the charge density, electric field gradient.

Résumé : On a calculé la densité de charge moléculaire ab initio, $\rho(r)$, d'aziridines substituées au niveau MP2, pour R = -H, -CH_3, -CF_3, -Cl, -NO_2, -CN, -OH, -NO et -F. L'utilisation du laplacien de $\rho(r)$ a permis d'analyser le gradient du champ électrique (GCE) au niveau du noyau d'azote en termes de la concentration de la charge sur les couches de valence. Lorsque R = -Cl, -NO_2, -CN, -OH, -NO et -F, le GCE change de signe et ses axes *y* et *z* changent d'orientation par rapport à l'aziridine. On a pu établir une corrélation entre les changements dans le GCE dans ces aziridines par substitution et ceux calculés dans les concentrations de la charge de valence dans la direction de la liaison N—R. On a trouvé que la composante $q_{z,z}$ et l'orientation des axes principaux du tenseur du GCE sont déterminées par la valeur relative des contributions des concentrations de charge aux points de la couche de valence le long des directions des liaisons N—C et N—R.

Mots clés : distribution de charge moléculaire, aziridines, laplacian de la densité de charge, gradient du champ électrique.

[Traduit par la rédaction]

Introduction

The electric field gradient tensor EFG at the nuclei has been employed extensively (1) in studies of the molecular charge distribution $\rho(r)$. The EFG tensor can be measured by means of NQR, NMR, EPR, and other techniques and has provided important information about $\rho(r)$ in many different types of compounds (1).

Almost all the resulting data have been interpreted in terms of the Mulliken population of localized atomic orbitals (1) or by using molecular orbitals (2) centered at the atom containing the quadrupolar nucleus. Nevertheless, the orbitally based populations are not physical observables as defined by quantum mechanics. It is well known that this type of population analysis is not invariant under unitary transformations. Thus, the interpretation of the EFG obtained with one set of orbitals may be not easily related to, or may even differ from, that obtained with another set. Clearly, information obtained about the charge distribution by means of theories based on arbitrary partitions of subsets of Hilbert space is open to serious questions based on sound quantum mechanical principles. The use of localized orbitals in the interpretation of the EFG presents the additional problem of "tails" located away from the main body of the orbitals (3). These "tails" can make sizable contributions to the EFG and obscure the analysis of more important contributions to it (3).

A better way of obtaining information is the direct interpretation of the EFG in terms of the electronic charge distribution $\rho(r)$ or quantities directly related to it. One of the main advantages of this approach is that $\rho(r)$ is a physical observable and is independent of the orbital model used in its calculation. The EFG present at the nitrogen nucleus has been interpreted in terms of the topology of $\rho(r)$ and its associated fields (4–6) in several N-containing compounds. The study of the distribution of the Laplacian of the charge density $\nabla^2\rho(r)$ allows the location in space of the electronic shells (7). As the EFG present at the nucleus reflects, primarily, the departure from spherical symmetry of its electronic shells (1), a connection between the extremes in the $\nabla^2\rho(r)$ of the valence shell and the

Received November 9, 1995.

This paper is dedicated to Professor Richard F.W. Bader on the occasion of his 65th birthday.

F. Rosillo,[1] Y. Aray, J. Rodríguez, and J. Murgich.[2] Centro de Química, Instituto Venezolano de Investigaciones Científicas (IVIC), Apartado 21827, Caracas 1020A, Venezuela.

[1] On leave from Laboratorio de Química Inorgánica, Departamento de Quimica, Universidad del Zulia, Maracaibo, Venezuela.

[2] Author to whom correspondence may be addressed. Telephone: 58-2-5011337. Fax: 58-2-5011350. E-mail: jmurgich@quimica.ivic.ve

Fig. 1. The generic aziridine molecule.

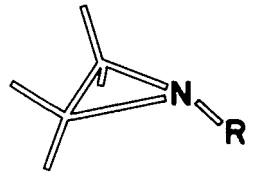

gradient at the quadrupolar nucleus was found for several types of nitrogen coordination (4–6). In this work, the EFG data for the N atom in nine substituted azidiridines (see Fig. 1) has been interpreted in terms of the $-\nabla^2\rho(\boldsymbol{r})$ distribution. Recently three aziridines were studied and the results interpreted in terms of Boys's localized orbitals (8, 9). In the present work, an observable such as $\rho(\boldsymbol{r})$ and a derived quantity such as $\nabla^2\rho(\boldsymbol{r})$ are used in the interpretation of the EFG. This approach has the advantage that the interpretation of the gradient is not linked to any particular orbital description and its conclusions may be tested against other experimental results related to the charge distribution.

Computational methods

The ab initio molecular orbitals at MP2 level calculations for the aziridines (see Fig. 1) were obtained on a Silicon Graphics Indigo^2 R-4400 workstation using the Gaussian 92 program (10) with a 6-31G+(d,p) basis set (11). Optimized geometries were obtained by the SCF gradient method (10) with the 6-31G** set. The topological properties of the Laplacian of the electronic density were calculated with the AIMPAC 94 package.[3]

Theory

The EFG is a traceless, second-rank tensor (1) whose *ij*-th component at the origin is

$$[1] \quad q_{i,j} = \int \frac{\partial^2}{\partial x_i \partial x_j}\left(\frac{\rho(\boldsymbol{r})}{\boldsymbol{r}}\right) \mathrm{d}v$$

where $\rho(\boldsymbol{r})$ is the charge density at point $\boldsymbol{r}$. The principal axes of the EFG tensor are such that $|q_{zz}| \geq |q_{yy}| \geq |q_{xx}|$. The independent components of this tensor are two diagonal terms and three direction cosines linking the principal axes system with an arbitrary frame of reference (1). The nuclear quadrupole coupling constant, e^2qQ/h, (where Q is the nuclear electric quadrupole moment, and $eq = q_{zz}$) plus the asymmetry parameter, $\eta = |(q_{yy} - q_{xx})/q_{zz}|$ are usually determined experimentally (1).

The EFG has the symmetry of its source charges and presents, by definition, even parity (12). Any charge distribution may be divided into its odd and even parity components. Then, due to the parity of the EFG, one has to consider only the contribution of the even part of $\rho(\boldsymbol{r})$ because the other integrates to zero for symmetry reasons (12). In an isolated molecule, the charge distribution of the N atom may be separated into two parts: (*i*) a spherically symmetric core, formed by the nitrogen shells, that is not deformed by bonding; (*ii*) the deformed part represented by the extremes in the charge distribution in the nitrogen valence shell produced by bonding. The spherical core will not generate a field gradient at the N nucleus for symmetry reasons already mentioned (12). The charge from neighboring atoms generates a small EFG because the contribution of the nuclei is mostly compensated by that of the electrons (6). The r^{-3} dependence of the EFG operator (1) further decreases the contribution from those sources that are located away from the shells of the N atom. As we are interested only in the main contributions to the EFG at the nucleus in N atoms of aziridines, we will not consider these contributions here.

The topology of the charge distribution

The topological properties of $\rho(\boldsymbol{r})$ or $\nabla^2\rho(\boldsymbol{r})$ scalar fields are reflected in their critical points (7) $\boldsymbol{r}_c$, (where $\nabla\rho(\boldsymbol{r})$ and $\nabla[\nabla^2\rho(\boldsymbol{r})] = 0$). These points are classified according to their type (*m*, *n*) by stating their rank *m* and signature *n*. The rank is the number of non-zero eigenvalues of the Hessian matrix at $\boldsymbol{r}_c$ while the signature is the algebraic sum of the signs of the eigenvalues (7). Two types of critical points in the $\rho(\boldsymbol{r})$ field are found in the nitrogen valence shell, the (3,−1) saddle points related to the interaction of N with the neighboring atoms and a (3,−3) point representing a maximum at the position of the nucleus. More complex is the topology of the Laplacian field of $\rho(\boldsymbol{r})$ for the N valence shell because it also exhibits (3,+1) saddle points in aziridines. From the topology of the $\nabla^2\rho(\boldsymbol{r})$ field, one can recover the chemical model of the localized bonded and nonbonded pairs (7). Moreover, this type of field helps to characterize the regions of local concentration ($-\nabla^2\rho(\boldsymbol{r}) > 0$) and of depletion ($-\nabla^2\rho(\boldsymbol{r}) < 0$) of the atomic and molecular $\rho(\boldsymbol{r})$ (7).

The $\nabla^2\rho(\boldsymbol{r})$ distribution of a free atom reflects the quantum shell structure by exhibiting the corresponding number of alternating pairs of shells of charge concentration and depletion (7). Upon bonding, local maxima and minima are formed in the valence shell of the bonded atom. The number, type, location, and $-\nabla^2\rho(\boldsymbol{r})$ value at these extremes are functions of the linked atoms. The sets of these extremes in each atom form the basis of its atomic graph. This graph contains information about the atom's Lewis model and displays the connectivity of the extremes of the valence shell (7).

In a free atom, the charge distribution of the valence shell is uniform over the surface of a sphere (7) and the EFG at its nucleus is, by symmetry, equal to zero. In light bonded atoms, the EFG at the nucleus is produced mainly by the departure of the valence shell from spherical symmetry. Then, a connection exists between the local charge extremes that are reflected in the $-\nabla^2\rho(\boldsymbol{r})$ values of the atomic graph and the EFG present at the corresponding nucleus (4–6).

Results

The atomic graph of the N atom of the aziridines studied in this work and shown in Fig. 2 has four (3,–3) critical points in its valence shell charge concentration (VSCC). Two are located in the direction of the ring bond with the -CH_2 groups b_1 and b_2, and one in the direction of substituent R. The fourth critical point is found in the direction of the nonbonded concentration ("lone pair") N_b. These points form a tetrahedral atomic graph in the nitrogen valence shell as seen in Fig. 2. This type of graph is similar to that found for the N atom in

[3] R.F.W. Bader. Private communication, 1993.

Fig. 2. Atomic graph of the $-\nabla^2\rho(\mathbf{r})$ distribution of the valence shell of the N atom in aziridines. The maxima are denoted by a dot (●) and the saddle points by an asterisk (*). The N nucleus is in the center of the sphere and the three covalent bonds and the "lone pair" are shown as parallel lines joining the nucleus with these extremes of the valence shell.

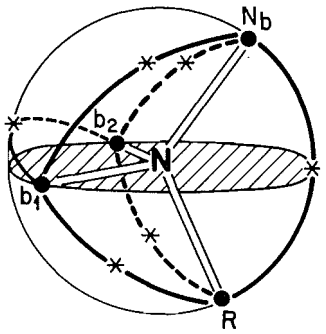

Table 1. Values[a] of the $-\nabla^2\rho(r)$ at some of the critical points of the N valence shell in some substitued aziridines.

Substituent R	N_b	R	b_1
-H	2.986	2.025	1.390
$-CH_3$	3.018	1.695	1.430
-CF3	2.982	1.673	1.483
-Cl	3.115	0.904	1.725
$-NO_2$	2.940	1.160	1.766
-CN	2.989	1.597	1.505
-OH	3.332	0.891	1.833
-NO	2.939	1.467	1.455
-F	3.445	0.504	1.986

[a]All values are in atomic units.

Fig. 3. Orientations of the z- and y-axes in aziridine (H) and in fluoroaziridine (F) with regard to the "lone pair" N_b. These axes are in a plane perpendicular to the ring plane.

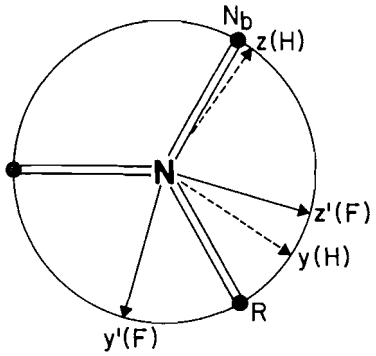

Table 2. Principal components, asymmetry parameter of the electric field gradient at the N nucleus, and the angle Θ between the principal z-axis and the "lone pair" direction in aziridines.[a]

Substituent R	q_{zz}	q_{yy}	q_{xx}	η	Θ
-H	−0.700	0.602	0.097	0.72	7.1
$-CH_3$	−0.723	0.640	0.083	0.77	2.5
$-CF_3$	−0.732	0.724	0.008	0.98	0.6
-Cl	0.940	−0.630	−0.309	0.34	86.7
$-NO_2$	0.908	−0.632	−0.277	0.39	89.2
-CN	0.727	−0.715	−0.013	0.97	98.1
-OH	0.978	−0.701	−0.278	0.43	80.4
-NO	0.609	−0.541	−0.068	0.78	79.1
-F	1.138	−0.626	−0.512	0.10	78.3

[a]All values except Θ are in atomic units. The values of Θ are in degrees.

NH_3 and other symmetrically substituted amines (13). The values of $-\nabla^2\rho(\mathbf{r})$ for the different critical points of the nitrogen VSCC in some aziridines are reported in Table 1.

The charge concentration at the b_i points of the nitrogen graph increased with respect to aziridine for substituents more electronegative than H such as -Cl, $-NO_2$, -CN, -OH -NO, and -F. The values of the $-\nabla^2\rho(\mathbf{r})$ at the N_b point for these aziridines changed only slightly upon substitution while those at the R point showed much larger fluctuations. In another group of aziridines (R = $-CH_3$ and $-CF_3$) substitution produced small changes in the values of $-\nabla^2\rho(\mathbf{r})$ at the N_b points, a decrease in its value at the R point, and a small increase at the b_i points.

Table 2 shows the components of the EFG for the aziridines studied in this work. From this table, one sees that the nitrogen EFG in aziridines may be divided into two different sets: one with $q_{zz} < 0$ (R = -H, $-CH_3$, and $-CF_3$) and another with $q_{zz} > 0$ (R = -Cl, $-NO_2$, -CN, -OH -NO, and -F). The modifications introduced in the nitrogen charge distribution by groups or atoms more electronegative than H produce not only a change in the signs of the components of the EFG tensor, but also a significant reorientation of its axes, as seen in Fig. 3. In the aziridine and in some substituted aziridines (R = $-CH_3$ and $-CF_3$), the z-axis points within a few degrees along the direction of "lone pair" N_b as in several other nonplanar but symmetrical amines (13). When the substituent is more electronegative than H, the z-axis is rotated away from the N_b direction by a significant amount as shown by the Θ values found in Table 2 and in Fig. 3. The principal z- and y-axes in all the aziridines studied in this work are located in a plane perpendicular to the ring plane. When substitution with the more electronegative groups occurs, the z- and y-axes are rotated in that plane in such a way that now the y-axis points close to the N_b point (see Fig. 3).

Discussion

The changes in the EFG upon substitution can be related to the variations in magnitude and position of the nitrogen VSCC points (4–6). It was found in this work that the variations in the position of these points with respect to the N nucleus upon substitution in aziridines are negligible so they do not seem to be the cause of the modifications observed in the EFG.

On the other hand, the values of the $-\nabla^2\rho(\mathbf{r})$ at the b_i points

vary up to 30%, those at the N_b points by only 13%, and at R by a factor of four upon substitution, as seen in Table 1. When substitution occurs, the main changes, as expected, are observed in the charge distribution of the point R of the N valence shell. Nevertheless, changes in this region of the valence shell also propagate (4–6) to concentrations along the N—C bond directions and at the "lone pair" N_b (4–6). A linear correlation between the values of the Laplacian of $\rho(r)$ in these two points for the aziridines shows how the perturbation introduced by substitution propagates to the other part of the valence shell. It was found that $\nabla^2\rho(r)_{b1} = 2.171 - 0.417\nabla^2\rho(r)_R$ with $r = 0.959$. This correlation implies that the decrease in the charge concentration produced by more electronegative atoms or groups at the R point in the N valence shell produces an increase at the points found in both N—C directions. An opposite behavior in these points was found for electron-donating groups such as $-CH_3$ or $-CF_3$. A linear correlation was also obtained between the values of $\nabla^2\rho(r)_R$ and the nonbonded concentration at N_b, with $\nabla^2\rho(r)_{Nb} = 3.477 - 0.298\nabla^2\rho(r)_R$ but with $r = 0.795$. In this case, the charge at the N_b point is increased when the concentration at the R point is decreased although the correlation is not as good as in the other extremes. It is likely that additional factors may influence the values of $\nabla^2\rho(r)$ at the N_b point upon substitution and thus lower the correlation.

The correlations found between the changes in the R point with the other extremes show that substitution at the N position of atoms or groups more electronegative than H in aziridines draws electrons from the ring toward the N valence shell with some additional increase of concentration at the N_b point. The substitution of $-CH_3$ or $-CF_3$ groups produced, instead, a decrease in the charge concentration at the R point and a slight increase in the points along the N—C bond directions while at N_b only small changes were found.

We can summarize the effects of substitution in aziridines as perturbing primarily the valence shell along the N–R direction plus inducing changes at the other extremes. As these extremes are the sources of the EFG, it is reasonable then to assume that the changes found in q_{zz} upon substitution are produced mainly by the variations of the charge concentration at the R point with contributions from the remaining points of the valence shell.

From Tables 1 and 2, we see that the aziridines with $q_{zz} > 0$ have a rather large charge concentration in the N valence shell along the N–R direction and a relatively low value at the b_i points. The opposite behavior is found for the aziridines with $q_{zz} < 0$ as seen in the same tables. A linear regression among the six $q_{zz} > 0$ values and those of the Laplacian at the R point gave $q_{zz} = 1.359 - 0.438\nabla^2\rho(r)_R$ with $r = 0.942$. The same type of analysis for the b_i points in the same aziridines gave $q_{zz} = -0.697 + 0.923\nabla^2\rho(r)_{bi}$ with $r = 0.986$ while for the N_b point, $q_{zz} = -1.378 + 0.723\ \nabla^2\rho(r)_{Nb}$ with $r = 0.828$.

It is expected that the q_{zz} at the nucleus will be generated mainly by the N "lone pair" (1, 2). The other extremes produced by bonding in the N valence shell also contribute to q_{zz} but their contribution is expected to be smaller with regard to that generated by the "lone pair." This later charge concentration represents the largest deviation from the uniform distribution found over the valence shell surface in the free atom. Consequently, it produces an important part of the EFG found in N upon bonding. The other critical points represent, instead, smaller departures as seen in Table 1, and consequently their contribution to the EFG is, in general, smaller. The total EFG tensor contains all these contributions plus a geometrical factor that takes into account the spatial localization of the critical points (13). This geometrical factor reflects the specific type of atomic graph that the N atom has. The existence of the geometrical factor explains why, in certain types of graphs, the contribution of some points is compensated by that produced by others (13). In this case, the total EFG reflects only the presence of the uncompensated critical points. The importance of the geometric factor becomes greater as the number of concentration points in the N valence shell increases. In the high symmetry cases, such as an atomic graph having T_d symmetry (i.e., the N atom in the N^+H_4 ion), the contributions of all the different charge concentration points are equal but the geometric factor cancels them out. For the tetrahedral atomic graph found in the four-coordinated N atom in N^+R_3X compounds, the role of the nonbonded charge concentration is taken by that found along the N—X bond direction (13). The larger the difference between the local maxima in the N–R and N–X directions, the larger was the calculated value of q_{zz}. The geo-metrical factor of a tetrahedral atomic graph is still operative in this case but the charge concentrations in the different points of the valence shell are not equal and a finite EFG is found at the nucleus. In the case of aziridines, we have even larger differences in the charge concentrations than in the N^+R_3X case so that they may generate a larger contribution to the EFG. The geometric factor is the same for the different atoms and groups R, so the changes observed in the orientation and sign of the EFG upon substitution in aziridines are the result of the variations observed in $\rho(r)$ at the different local extremes of the N valence shell. It seems that the values of charge concentration along the N–C and N–R directions are such that $q_{zz} < 0$ for the more electronegative substituents, and the principal y-axis is located near the "lone pair." This is a result of the contributions arising from the uncompensated extremes existing in the tetrahedral atomic graph found in the N valence shell. For the less electronegative substituents or for a more symmetric substitution (13), the z-axis points along or near the "lone pair" direction and the resulting value of q_{zz} is positive.

Conclusions

The use of the topology of $-\nabla^2\rho(r)$ allowed the analysis of the EFG in aziridines directly, in terms of the VSCC present in the N atomic graph. For R = $-CH_3$ and $-CF_3$, the orientation and components of the EFG were similar to those of aziridine. It was found that the q_{zz} component changed sign and the orientation of its z- and y-axes when -Cl, $-NO_2$, -CN, -OH, -NO, and -F substituted the H atom in aziridine. The changes in the EFG in these aziridines were found to be correlated with those in the VSCC point located along the direction of the N—R bonds. The sign of the q_{zz} component and the orientation of the principal axes of the EFG tensor were found to be determined by the relative value of the contributions from the charge concentrations that were at the points in the valence shell along the N—C and N—R bond directions.

References

1. E.A.C. Lucken. Nuclear quadrupole coupling constants. Academic, New York. 1969; J.A.S. Smith. Chem. Soc. Rev. **15**, 225 (1986).

2. F.A. Cotton and C.B. Harris. Proc. Natl. Acad. Sci. U.S.A. **56**, 12 (1966).
3. Y. Aray, R. Gomperts, C. Urdaneta, J. Saavedra, and J. Murgich. Theor. Chim. Acta, **73**, 279 (1987).
4. Y. Aray and J. Murgich. J. Chem. Phys. **91**, 293 (1989).
5. Y. Aray, H. Soscun and J. Murgich. Int. J. Quantum Chem. **25**, 587 (1991).
6. Y. Aray and J. Murgich. J. Chem. Phys. **97**, 9154 (1992).
7. R.F.W. Bader. Atoms in molecules: a quantum theory. Oxford University Press, Oxford, U.K. 1990; R.F.W. Bader, P.L.A. Popelier and A.T. Keith. Angew. Chem. Int. Ed. Engl. **33**, 620 (1994).
8. O.D. Fominykh, M. Yu Balakina, I.D. Morozova, and D. Ya Osokin. J. Mol. Struct. (Theochem), **315**, 229 (1994).
9. O.D. Fominykh, M. Yu Balakina, I.D. Morozova, and D. Ya Osokin. J. Mol. Struct. (Theochem), **279**, 29 (1993).
10. M.J. Frisch, G.W. Trucks, M. Head-Gordon, P.M.W. Gill, M.W. Wong, J.B. Foresman, B.G. Johnson, H.B. Schlegel, M.A. Robb, E.S. Replogle, R. Gomperts, J.L. Andres, K. Raghavachari, J.S. Binkley, C. Gonzalez, R.L. Martin, D.J. Fox, D.J. Defrees, J. Baker, J.J.P. Steward, and J.A. Pople. Gaussian 92, Revision C. Gaussian Inc., Pittsburgh, Pa. 1992.
11. R. Ditchfield, W.J. Hehre, and J.A. Pople. Chem. Phys. **54**, 724 (1970).
12. M.J. Hunt. J. Magn. Reson. **15**, 113 (1974).
13. Y. Aray, J.C. Casilimas, and J. Murgich. J. Phys. Chem. **100**, 5291 (1996).

Quantum chemical valence indices from the one-determinantal difference approach

Roman F. Nalewajski, Janusz Mrozek, and Grzegorz Mazur

Abstract: The recently introduced *quadratic* (two-electron) *valence indices*, ionic and covalent, derived from the Hartree–Fock finite-difference approach, are applied to selected organic and inorganic molecules to demonstrate their utility in monitoring chemical bonding patterns in molecular systems. The indices are defined in terms of differerences between simultaneous probabilities of finding two electrons on specified atoms, calculated from the molecular and *separated-atom-limit* (SAL) wave functions, respectively, in the UHF approximation. The total quadratic valence number represents the overall number of chemical bonds in the system under consideration; it is interpreted as the molecular expectation value of the difference operator of the molecular and SAL density operators. This interpretation leads to a new set of ionic atomic and diatomic valence components; these modified valence numbers are discussed using the two-orbital model in the UHF scheme. A new procedure is proposed for dividing the one-center contributions to the bond valences; it generates effective bond orders in qood agreement with chemical expectations. The new valence quantities are tested on selected typical molecules and prototype hydrogen-bonded dimers. A more extensive study has been carried out on small-ring propellanes, to examine changes in bond valences between bridgehead atoms in selected systems.

Key words: chemical valence: UHF difference approach; chemical bond: two-electron model; bond multiplicities; ionic/covalent bond components; propellanes: valence study.

Résumé : Les *indices de valence quadratique* (deux électrons), ionique et covalente, dérivés de l'approche d'une différence finie de Hartree–Fock, sont appliqués à des molécules organiques et inorganiques choisies afin de démontrer leur utilité dans l'évaluation des patrons de liaison chimique dans des systèmes moléculaires. Les indices sont définis en termes de différences entre des probabilités simultanées de trouver deux électrons sur des atomes donnés et elles sont calculées à partir des fonctions d'onde respectivement moléculaires et à la *limite de la séparation des atomes* (LSA), dans l'approximation UHF. Le nombre de valence quadratique total représente le nombre global de liaisons chimiques dans le système étudié; on l'interprète comme la valeur de l'expectative moléculaire de l'opérateur de la différence des opérateurs de densité moléculaire et LSA. Cette interprétation conduit à un nouvel ensemble de composantes de valence atomique ionique et diatomique; on discute de ces nombres de valence modifiés en faisant appel au modèle à deux orbitales du schéma UHF. Une nouvelle méthode de diviser les contributions provenant d'un centre aux valences de liaison, elle génère des ordres de liaison effectives qui sont en bon accord avec les attentes chimiques. On a évalué les nouvelles valeurs de valence sur des molécules typiques choisies et des dimères prototypes à liaison hydrogènes. Afin d'examiner les changements dans les valences de liaison entre les atomes en tête de pont de systèmes choisis, on a effectué une étude plus étendue sur des propellanes à petits cycles.

Mots clés : valence chimique : UHF; liaison chimique : modèle de deux électrons; multiplicités de liaison; parties constituants de liaison : ionique et covalent; propellanes : étude de valence.

[Traduit par la rédaction]

Introduction

The chemical valence represents a central electronic structure concept reflecting both bond multiplicity and the effective (promoted) states of *atoms-in-molecules* (AIM). It was originally introduced on an intuitive basis (1); later its quantum-mechanical interpretations (2–13) were also developed. The two-electron valence measures (10–14) directly connect to the original, electron-pair concept of Lewis (1) by relating chemical bond orders to changes in the electron pairings in a molecule, relative to those in isolated constituent atoms. This Hartree–Fock difference approach (10–14) compares the two-electron distribution among AIM with the reference *separated atoms limit* (SAL). It provides absolute valence indices (covalent and ionic) reflecting the associated changes in the simultaneous probabilities of finding two electrons on specified atoms. These absolute valence numbers can subsequently be used to calculate relative valences, e.g., changes in bond orders due to ionization or change in the system geometry, by subtracting absolute values of compared systems. These so called *quadratic valence indices* (QVI) (11–14) represent contributions to the overall second-order change in the pair-diagonal two-electron density matrix in a molecule, relative

Received October 13, 1995.

This paper is dedicated to Professor Richard F.W. Bader on the occasion of his 65th birthday, in recognition of his pioneering, "first principles" studies on extracting structure and reactivity information from the electronic density and its Laplacian.

R.F. Nalewajski[1] **and J. Mrozek.** K. Gumiński Department of Theoretical Chemistry, Jagiellonian University, R. Ingardena 3, 30-060 Cracow, Poland.
G. Mazur. Department of Computational Methods in Chemistry, Jagiellonian University, R. Ingardena 3, 30-060 Cracow, Poland.

[1] Author to whom correspondence may be addressed. Telephone: (48-12)-336-377, ext. 212. E-mail: Nalewajs@Trurl.Ch.UJ.edu.Pl

to the SAL. In the one-determinantal (HF or DFT) approximation they can be expressed as quadratic forms in terms of differences of the relevant one-particle *charge-and-bond-order* (CBO) matrix elements in the basis set of *orthogonal atomic orbitals* (OAO). Accordingly, the three-electron, *cubic valence indices* (CVI), measuring contributions to the corresponding third-order change in the diagonal part of the three-electron density matrix, are similarly represented by the corresponding cubic forms of the molecular CBO displacements relative to the SAL. It has been demonstrated (11–14) that these two-electron valence numbers reproduce intuitive chemical expectations quite adequately for typical molecules and model transition states of simple chemical reactions. The corresponding UHF three-electron corrections have been shown to be small (13). Recently (14) the QVI have been implemented in the Kohn–Sham (LSDA) scheme (15). It has been concluded that the novel bond valence measures provide a very useful and easy-to-implement diagnostic tool for monitoring changes in the bonding pattern of both isolated molecules and reactants in a model catalytic system.

The main purpose of the present paper is to examine more closely the expectation value interpretation of the QVI proposed in ref. 14, and to present and test the appropriate schemes for partitioning atomic contributions among the bond valences. The set of typical organic molecules exhibiting various C—C bond multiplicities includes hydrocarbons (acetylene, ethylene, ethane, benzene, and simple propellanes); we also consider the B_2H_6 molecule and simple inorganic dimers of HF and H_2O to test whether the proposed bond multiplicities discriminate between strong chemical interactions and weak hydrogen bonds.

Difference approach to valence indices

The recently proposed set of QVI (11) measures changes in the two-electron simultaneous probability distribution in a molecule, relative to the SAL reference state (^{0}), reflected by the pair-diagonal elements $\Delta\Gamma(\mu,\nu) \equiv \Delta\bar{\Gamma}(\mu\nu|\mu\nu)$, of the spinless two-electron density matrix in the OAO representation $|\boldsymbol{\lambda}\rangle = |\mu,\nu,\ldots\rangle = |\boldsymbol{a},\boldsymbol{b},\ldots\rangle$; throughout the paper the Löwdin normalization is assumed, and $|\boldsymbol{a}\rangle = |a,a',\ldots\rangle$ denotes OAO associated with atom A.

The RHF/LDA QVI (11, 14) have been defined in the framework of the second-order Taylor expansion,

$$[1]\quad \Delta\boldsymbol{\Gamma} \equiv \boldsymbol{\Gamma} - \boldsymbol{\Gamma}^0 = \left\{\sum_{\mu,\nu}^{\mathrm{OAO}} \left(\frac{\partial\boldsymbol{\Gamma}}{\partial P_{\mu\nu}}\right)^0 \Delta P_{\mu\nu}\right\} + \left\{\frac{1}{2}\sum_{\mu,\nu}^{\mathrm{OAO}}\sum_{\rho,\tau}^{\mathrm{OAO}} \Delta P_{\mu\nu}\left(\frac{\partial^2\boldsymbol{\Gamma}}{\partial P_{\mu\nu}\partial P_{\rho\tau}}\right)^0 \Delta P_{\rho\tau}\right\} \equiv \{\Delta\boldsymbol{\Gamma}^{(1)}\} + \{\Delta\boldsymbol{\Gamma}^{(2)}\}$$

in terms of powers of the CBO displacements, $\Delta\boldsymbol{P} \equiv \boldsymbol{P} - \boldsymbol{P}^0$; the related UHF/LSDA QVI are similarly defined by the quadratic expansion of $\Delta\boldsymbol{\Gamma}(\Delta\boldsymbol{P}^\sigma)$, where $\Delta\boldsymbol{P}^\sigma = \boldsymbol{P}^\sigma - \boldsymbol{P}^{0,\sigma}$, $\sigma = \alpha,\beta$, are the corresponding spin-resolved CBO shifts: $\Delta\boldsymbol{P} = \Delta\boldsymbol{P}^\alpha + \Delta\boldsymbol{P}^\beta$. In what follows we denote by $\Delta\boldsymbol{n} = (\Delta n_A, \Delta\boldsymbol{n}_B, \ldots)$ and $\Delta\boldsymbol{q} = (\Delta P_{\mu\mu}, \Delta\boldsymbol{P}_{\nu\nu}, \ldots)$ the corresponding changes in the AIM electron populations and the orbital occupations, respectively. The RHF/LDA QVI monitor the second-order atomic and diatomic contributions to $\Delta\boldsymbol{\Gamma}$,

$$[2]\quad \Delta\boldsymbol{\Gamma}^{(2)}_{\mathrm{RHF}} = \Delta\boldsymbol{\Gamma}(\{\Delta n_A\ \Delta n_B\}, \{(\Delta q_\mu)^2\}, \{(\Delta P_{\mu\nu})^2\})$$

with the obvious slight modification in the UHF case:

$$[3]\quad \Delta\boldsymbol{\Gamma}^{(2)}_{\mathrm{UHF}} = \Delta\boldsymbol{\Gamma}(\{\Delta n_A\ \Delta n_B\}, \{(\Delta q^\sigma_\mu)^2\}, \{(\Delta P^\sigma_{\mu\nu})^2\})$$

This difference approach gives the following expressions for the resulting valence indices:
(*i*) in the RHF/LDA theories:

$$[4]\quad V_A^{\mathrm{ion}} = \frac{1}{2}\left[(\Delta n_A)^2 - \frac{1}{2}\sum_a^A (\Delta q_a)^2\right]$$

$$[5]\quad V_A^{\mathrm{cov}} = -\frac{1}{2}\sum_{a<a'}^{A}\sum^{A} (\Delta P_{aa'})^2$$

$$[6]\quad V_{AB}^{\mathrm{ion}} = \Delta n_A \Delta n_B$$

$$[7]\quad V_{AB}^{\mathrm{cov}} = -\frac{1}{2}\sum_a^A\sum_b^B (\Delta P_{ab})^2$$

(*ii*) in the UHF/LSDA theories:

$$[8]\quad V_A^{\mathrm{ion}} = \frac{1}{2}\left\{(\Delta n_A)^2 - \sum_a^A [(\Delta q_a^\alpha)^2 + (\Delta q_a^\beta)^2]\right\}$$

$$[9]\quad V_A^{\mathrm{cov}} = -\sum_{a<a'}^{A}\sum^{A} [(\Delta P^\alpha_{aa'})^2 + (\Delta P^\beta_{aa'})^2]$$

$$[10]\quad V_{AB}^{\mathrm{ion}} = \Delta n_A \Delta n_B$$

$$[11]\quad V_{AB}^{\mathrm{cov}} = -\sum_a^A\sum_b^B [(\Delta P^\alpha_{ab})^2 + (\Delta P^\beta_{ab})^2]$$

The ionic indices depend solely on $\Delta\boldsymbol{n}$ and $\Delta\boldsymbol{q}$ (diagonal CBO displacements) while the covalent valence numbers are defined exclusively by the diagonal quadratic forms in terms of the off-diagonal CBO displacements, $\mu \neq \nu$. They originate from the Coulombic and exchange parts of $\Delta\boldsymbol{\Gamma}^{(2)}$, respectively. By definition, the negative (positive) QVI contributions, in terms of electronic pairs, are bonding (antibonding).

It has been shown recently (14) that the overall QVI representing the sum of all valence contributions,

$$[12]\quad V = \sum_{\mu,\nu}^{\mathrm{OAO}} \Delta\Gamma^{(2)}_{\mu,\nu} = \sum_A^{\mathrm{AIM}} (V_A^{\mathrm{ion}} + V_A^{\mathrm{cov}}) + \sum_{A<B}^{\mathrm{AIM}}\sum (V_{AB}^{\mathrm{ion}} + V_{AB}^{\mathrm{cov}}) \equiv \sum_A^{\mathrm{AIM}} V_A + \sum_{A<B}^{\mathrm{AIM}}\sum V_{AB}$$

can be given alternative interpretation as the average CBO displacement. For example, in the RHF case

$$[13]\quad V = -\frac{1}{4}\,\mathrm{Tr}(\Delta\boldsymbol{P})^2 = -\frac{1}{2}\,\mathrm{Tr}(\boldsymbol{P}\Delta\boldsymbol{P}) \equiv -\frac{1}{2}\,\langle\Delta\hat{\mathrm{P}}\rangle$$

where $\langle \Delta\hat{P} \rangle$ stands for the molecular expectation value of

$$[14] \quad \Delta\hat{P} = \hat{P} - \hat{P}^0 = N(\hat{\rho} - \hat{\rho}^0) \equiv N\Delta\hat{\rho}$$

and the CBO operators, expressed in terms of the canonical molecular and SAL orbitals, $|\varphi\rangle = |\lambda\rangle C$ and $|\varphi^0\rangle = |\lambda\rangle C^0$, respectively, are

$$[15] \quad \hat{P} = |\varphi\rangle d\langle\varphi| \equiv N\hat{\rho}, \qquad \hat{P}^0 = |\varphi^0\rangle d^0\langle\varphi^0| \equiv N\hat{\rho}^0$$

Here N is the number of electrons, d, d^0 represent the diagonal matrices of molecular orbital occupations, and $\hat{\rho}, \hat{\rho}^0$ are the corresponding density operators. Another interesting expression for V is in terms of the difference between two expectation values of $\Delta\hat{P}$, the SAL and molecular (14):

$$[16] \quad V = \frac{1}{4}\left[\langle\Delta\hat{P}\rangle^0 - \langle\Delta\hat{P}\rangle\right]$$

Here $\langle\Delta\hat{P}\rangle^0 \equiv \mathrm{Tr}\,(P^0\Delta P)$.

The overall valence number of eq. [13] can be naturally decomposed into atomic ($\bar{V}_{AA}$) and diatomic ($\bar{V}_{AB}$) contributions:

$$[17] \quad V = -\frac{1}{4}\sum_{A}^{AIM}\sum_{B}\left[\sum_{a}^{A}\sum_{b}^{B}(\Delta P_{ab})^2\right] \equiv \sum_{A}^{AIM}\sum_{B}\bar{V}_{AB}$$

These modified atomic contributions consist of both ionic and covalent components (see eqs. [4]–[7]),

$$[18] \quad \bar{V}_{AA} = \left[V_A^{ion} - \frac{1}{2}(\Delta n_A)^2\right] + V_A^{cov} \equiv v_A^{ion} + V_A^{cov}$$

thus the new ionic index, v_A^{ion} differs from V_A^{ion} (eq. [4]) by the missing global atomic population term. The modified diatomic contributions are purely covalent:

$$[19] \quad \bar{V}_{AB} + \bar{V}_{BA} \equiv V_{AB}^{cov}$$

so that the global AIM charge contributions of eq. [6] do not appear in this new set of indices:

$$[20] \quad \{v_A^{ion}, V_A^{cov}, V_{AB}^{cov}\}$$

$$V = \sum_{A}^{AIM}(v_A^{ion}, +V_A^{cov}) + \sum_{A<B}^{AIM}\sum V_{AB}^{cov} \equiv \sum_{A}^{AIM} v_A + \sum_{A<B}^{AIM}\sum V_{AB}^{cov}$$

Therefore, this new partitioning scheme recovers the orbitally resolved parts of the RHF/LDA valence numbers of eqs. [4]–[7], without the atomic global population terms that do not contribute to the overall valence V,

$$[21] \quad \sum_{A}^{AIM}\sum_{B}\Delta n_A \Delta n_B = (\Delta N)^2 = 0$$

since both the molecular and SAL states correspond to the same number of electrons: $\Delta N = N - N^0 = 0$.

This new development indicates that one could alternatively consider a set of three types of the RHF/LDA indices of eq. [20], $\{v_A^{ion}, V_A^{cov}, V_{AB}^{cov}\}$, to characterize the bonding structure in a molecule, instead of the four valence numbers of eqs. [4]–[7]. This new set gives rise to the same overall valence and it removes a somewhat arbitrary V_{AB}^{ion} term, which appears in the *absolute valences* even at large distances between two molecular subsystems, to be eventually cancelled when calculating the relative valence indices defined as the difference between the overall valences of the combined system and those of the separated subsystems. Similar modified valence indices are obtained in the UHF/LSDA theory, by removing the global atomic population term in eq. [8] and neglecting the diatomic ionic valence number of eq. [10]. Removal of the global atomic population contributions leaves only valence numbers that are quadratic diagonal forms in terms of the CBO displacements.

The above difference approach introduces a dependence of valence numbers upon the choice of the SAL, with both specific orbital occupations of the open-shell atoms or ions, and the mutual (interatomic) arrangements of spins of unpaired electrons affecting the one-center QVI. This dependence should not come as a surprise, since bond valence (bond order) is the difference quantity with respect to the SAL state. It is common in all chemical processes involving bond formation (bond breaking). As we have shown before (11–14) this dependence can be managed by an appropriate averaging scheme or through a selection of a single, representative reference state in the SAL. For example, one can average the resulting valence quantities over all admissible spin orientations and orbital electron configurations (11–13) or one can adopt the *minimum AIM valence state promotion principle* (14), which selects the promoted (P)-SAL state generating the minimum CBO reorganization in a molecule, measured by the magnitude of the atomic global valence numbers, V_A or v_A (eqs. [12], [20]). The latter, P-SAL perspective, has been shown to generate numerical values of the bond valences in slightly better agreement with chemical intuition (14).

Our definition of $\Delta\hat{P}$ (eq. [14]) gives negative values of the overall and bond valences, in accordance with our previous definitions (10–13). Clearly, a simple change of order of terms in this definition would reverse the signs, thus bringing our sign convention into conformity with other valence definitions.

The underlying main purpose, of a fast extraction of the difference valence numbers from molecular RHF/UHF or LDA/LSDA calculations, is only practical when one fixes the ground-state SAL orbitals φ^0 (from separate atomic calculations), when selecting the P-SAL or averaging over admissible SAL orbital configurations. Such a *frozen SAL orbital approximation* is used throughout the paper.

Typical calculations of the QVI involve molecular calculations, e.g., UHF or LSDA, in a given non-orthogonal basis set $|\chi\rangle$, consisting of specified atomic subsets $\{|\chi_A\rangle\}$, to calculate molecular CBO matrices, and separate atomic calculations in the same atomic basis sets, to determine the SAL CBO information. Symmetrical Löwdin orthogonalizations are carried out to obtain the corresponding OAO data. In principle, both molecular and SAL CBO in the $|\chi\rangle$ basis set should be transformed using the common (molecular) or-

thogonalization transformation, which includes the effects of the AIM overlaps at finite separations. However, this would produce in the SAL the artificial, and unphysical, tails in the atomic wave functions from basis functions of the remaining atoms, thus contradicting the assumed separated (noninteracting) character of atoms in this reference state. Therefore, we have performed separate atomic orthogonalizations in the SAL, including only the atomic overlap blocks, $\langle \chi_A | \chi_A \rangle$, in accordance with vanishing interatomic overlap integrals at infinite (or sufficiently large) separations.

When calculating bond valences, the most important quantities for chemical purposes, one faces the problem of partitioning atomic valence numbers between all bonds in which the atom participates; these bond-order indicators also include the corresponding two-center component(s). Obviously, a partitioning of atomic valences, $v_A = v_A^{cov} + V_A^{ion}$ or $V_A = V_A^{ion} + V_A^{cov}$, is arbitrary. The most obvious, bond partitioning by equally dividing one-center terms, say V_A, among all k_A chemical bonds A—B formed by the atom A, $V_A^{(I)}(AB) = V_A/k_A$, defines the Scheme I of calculating bond valences (13):

$$[22] \quad V_b^{(I)}(AB) \equiv [V_A^{(I)}(AB) + V_B^{(I)}(AB)] + [V_{AB}^{cov} + V_{AB}^{ion}] \equiv [V_{AB}^{(1)}(I)] + [V_{AB}^{(2)}]$$

where $V_{AB}^{(1)}(I)$ and $V_{AB}^{(2)}$ stand for the one- and two-center contributions to the bond valence estimated in this scheme. Obviously, this partitioning requires an advanced knowledge of the bonding pattern, which is generally unavailable. Therefore, one has to have alternative unbiased schemes that do not suffer from this severe limitation.

Another *weighted* (w) division of one-center valence contributions is obtained when one partitions them proportionally to the two-center contributions, $V_A^w(AB) = V_A w_{AB}$, where the weighting factors can be linked either to the total diatomic contribution (Scheme II), $w_{AB} = w_{AB}^{(II)} \equiv V_{AB}^{(2)} / \sum_{C \neq A} V_{AC}^{(2)}$ or to its covalent part only (Scheme III), the total diatomic part in the modified valence indices of eq. [20]: $w_{AB} = w_{AB}^{(III)} \equiv V_{AB}^{cov} / \sum_{C \neq A} V_{AC}^{cov}$. Replacing $V_X^{(I)}(AB)$ by $V_X^w(AB)$ in eq. [22] gives the corresponding weighted bond valences $V_b^{(II)}$ and $V_b^{(III)}$ estimated within Schemes II and III, respectively. These two totally unbiased bond valence measures should reflect more realistically the valence asymmetry between the single and multiple bonds in which a given atom is involved. We shall test numerically all three partitioning schemes on selected molecular systems.

Replacing V_A by v_A in the above three partitioning schemes gives rise to bonding valences corresponding to the new set of valence indices (eq. [20]).

Two-orbital model of a single bond

Following our previous development (10–13), let us consider an illustrative case of the two OAO models corresponding to the singly occupied molecular spin orbitals of the UHF/LSDA approximation:

$$[23] \quad \varphi^\alpha = (a + \gamma b)/(1 + \gamma^2)^{1/2}, \qquad \varphi^\beta = (\delta a + b)/(1 + \delta^2)^{1/2}$$

with $\varphi^\alpha \rightarrow a$, and $\varphi^\beta \rightarrow b$ in the SAL. The two independent parameters γ and δ, to be determined variationally, can be expressed in terms of the electron population and spin polarization on a given atom, say, $q_a = q_a^\alpha + q_a^\beta = 2 - q_b$ and $\sigma_a = q_a^\alpha - q_a^\beta = -\sigma_b$. In terms of these more informative degrees-of-freedom of the system electronic structure, the CBO matrix elements are

$$[24] \quad q_\mu^\alpha = \frac{1}{2}(q_\mu + \sigma_\mu), \qquad q_\mu^\beta = \frac{1}{2}(q_\mu - \sigma_\mu), \qquad \mu = a, b$$
$$P_{ab}^\sigma = (q_a^\sigma q_b^\sigma)^{1/2}, \qquad \sigma = \alpha, \beta$$

Fig. 1. The RHF/LDA ($\sigma_a = 0$) valence diagrams from the two-orbital model.

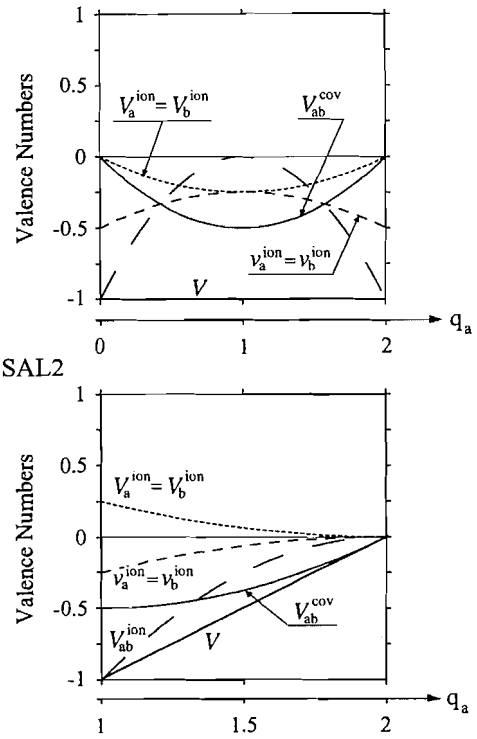

As before (10–13) let us consider the following two choices of the SAL:

(*i*) SAL1 (Å + B̊), defined by $\mathbf{P}^{0,\alpha} = \begin{pmatrix} 1 & 0 \\ 0 & 0 \end{pmatrix}$; $\mathbf{P}^{0,\beta} = \begin{pmatrix} 0 & 0 \\ 0 & 1 \end{pmatrix}$, i.e., $q_a^0 = q_b^0 = 1$ and $\sigma_a^0 = 1 = -\sigma_b^0$, corresponding to a covalent A—B bond;

(*ii*) SAL2 (Ä + B), defined by $\mathbf{P}^{0,\alpha} = \mathbf{P}^{0,\beta} = \begin{pmatrix} 1 & 0 \\ 0 & 0 \end{pmatrix}$, i.e., $q_a^0 = 2, q_b^0 = 0$, and $\sigma_a = \sigma_b = 0$, corresponding to the donor–acceptor (coordination) bond, A → B.

In both SAL cases $\Delta P_{ab}^\sigma = P_{ab}^\sigma$, $\sigma = \alpha, \beta$, due to the vanishing SAL values of these CBO matrix elements, and $\Delta q_a^\alpha = (\sigma_a + q_a - 2)/2$, due to the identical $q_a^{0,\alpha}$ values. The remaining CBO displacements are $\Delta q_a^\beta = q_a^\beta$ [SAL1], $\Delta q_b^\alpha = q_b^\alpha$, and $\Delta q_b^\beta = q_b^\beta$ [SAL2]. Using these CBO shifts and the valence number expressions of eqs. [7]–[11] and [20] allows one to construct the valence diagrams of Figs. 1 and 2 for nonvanishing valence components plotted as functions

Fig. 2. The valence diagrams of the spin polarization ($\sigma \equiv \sigma_a$) dependent V_{ab}^{cov} (panel (*a*)), $v_{a(b)}^{ion}$ (panel (*b*)), and $V_{a(b)}^{ion}$ (panel (*c*)) indices from the two-orbital model.

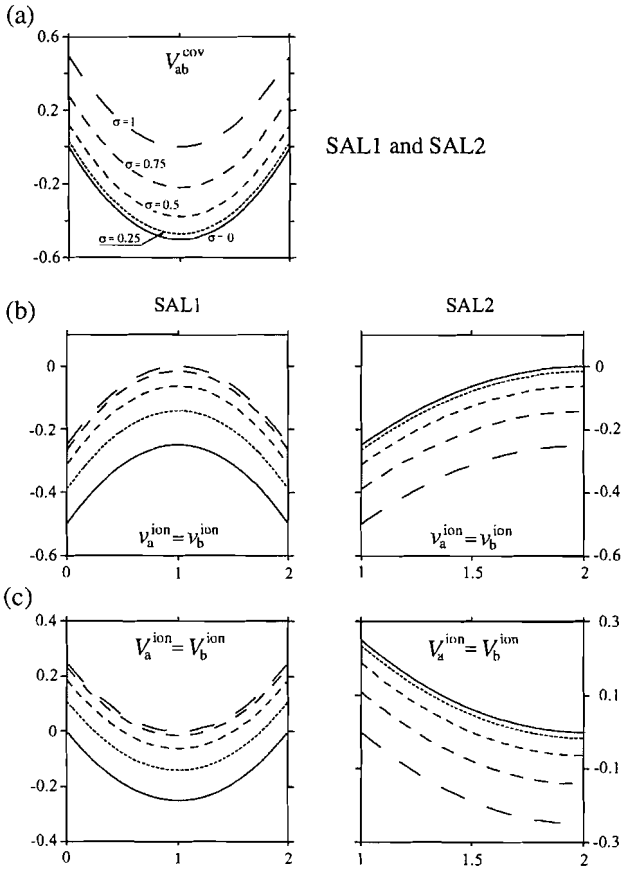

of q_a for the assumed values of σ_a. They correspond to the physically and chemically interesting regions of $0 \leq q_a \leq 2$, $0 \leq \sigma_a \leq 1$ (SAL1), and $1 \leq q_a \leq 2$, $0 \leq \sigma_a \leq 1$ (SAL2). The extreme values of σ_a represent spin equalization (as in SAL2 or in the RHF/LDA limit) and total spin polarization (as in SAL1). The valence diagrams in the RHF/LDA limit of $\sigma_a = \sigma_b = 0$ are shown in Fig. 1.

The resulting model expressions for the difference valence indices in the UHF/LSDA theories are ($V_A^{cov} = V_B^{cov} = 0$)

$$[25] \quad V_{ab}^{cov} = \frac{1}{2}\,[q_a(q_a - 2) + \sigma_a^2] \qquad \text{(SAL1 and SAL2)}$$

$$[26] \quad v_a^{ion} = -\frac{1}{2}\left[\frac{1}{2}\,(q_a^2 + \sigma_a^2) - (\sigma_a + q_a) + 1\right] = v_b^{ion} \qquad \text{(SAL1)}$$

$$[27] \quad V_a^{ion} = v_a^{ion} + (q_a - 1)^2/2 = V_b^{ion} \qquad \text{(SAL1)}$$

$$[28] \quad V_{ab}^{ion} = -(q_a - 1)^2 \qquad \text{(SAL1)}$$

$$[29] \quad v_a^{ion} = -\frac{1}{4}\,[(q_a - 2)^2 + \sigma_a^2] = v_b^{ion} \qquad \text{(SAL2)}$$

$$[30] \quad V_a^{ion} = v_a^{ion} + \frac{1}{2}\,(q_a - 2)^2 = V_b^{ion} \qquad \text{(SAL2)}$$

$$[31] \quad V_{ab}^{ion} = -(q_a - 2)q_b \qquad \text{(SAL2)}$$

By putting $\sigma_a = 0$ one obtains the corresponding RHF/LDA expressions plotted in Fig. 1.

Reference to Fig. 1*a* shows that the model single covalent bond in the limit of the RHF orbitals is partitioned into the diatomic covalent part, V_{ab}^{cov}, which reaches its maximum bonding magnitude at $q_a = q_b = 1$ and vanishes for the lone-pair configurations ($q_a = 2$ or $q_b = 2$), and the equal atomic ionic contributions, $v_a^{ion} = v_b^{ion}$, which exhibit the largest bonding effect when both electrons are localized on a single atom. The bonding atomic contribution at $q_a = q_b = 1$ is due to delocalizations of the α-spin electron (A → B) and the β-spin electron (A ← B), from the total spin separation in the SAL1 to the full spin equilibration ($\sigma_a = \sigma_b = 0$) in the RHF/LDA wave function, eq. [18]. Furthermore, eq. [26] shows (see also Fig. 2) that the spin polarization in a molecule ($0 \leq \sigma_a \leq 1$) raises the RHF/LDA V_{ab}^{cov} and v_a^{ion} curves by $\sigma_a^2/2$ and $\sigma_a(2 - \sigma_a)/4$, respectively, thus diminishing the overall bonding valence of the spin-polarized solution by the net shift σ_a. One can clearly see the competition between the ionic and covalent valences of the model for the changing electronic structure, with a loss of bonding measure in one component being exactly compensated by the complementary increase in the bonding character of the other component.

The role of spin delocalization in the model valences becomes clearer when one examines separately the (α, β)-spin components of the UHF/LSDA expressions for $v_a^{ion} = v_b^{ion}$,

$$[32] \quad v_a^{ion} = -\frac{1}{2}\,[(\Delta q_a^{\alpha})^2 + (\Delta q_a^{\beta})^2] \equiv v_{a,\alpha}^{ion} + v_{a,\beta}^{ion}$$

and V_{ab}^{cov},

$$[33] \quad V_{ab}^{cov} = -[(P_{ab}^{\alpha})^2 + (P_{ab}^{\beta})^2] = V_{ab,\alpha}^{cov} + V_{ab,\beta}^{cov}$$

Expressing the above spin-resolved components in terms of the spin delocalization measures, (q_b^{α}, q_a^{β}) for SAL1, and (q_b^{α}, q_b^{β}) for SAL2, gives:

$$[34] \quad v_{a,\alpha}^{ion} = -\frac{1}{2}\,(q_b^{\alpha})^2, \qquad \text{(SAL1)}$$

$$[35] \quad v_{a,\beta}^{ion} = -\frac{1}{8}\,(q_b^{\alpha} + q_b^{\beta})^2, \qquad \text{(SAL1)}$$

$$[36] \quad v_{a,\sigma}^{ion} = -\frac{1}{2}\,(q_b^{\sigma})^2, \qquad \sigma = \alpha, \beta, \qquad \text{(SAL2)}$$

$$[37] \quad V_{a,b\alpha}^{cov} = q_b^{\alpha}(q_b^{\alpha} - 1)^2, \qquad \text{(SAL1 and SAL2)}$$

$$[38] \quad V_{a,b\beta}^{cov} = q_a^{\beta}(q_a^{\beta} - 1), \qquad \text{(SAL1)}$$

$$= q_b^{\beta}(q_b^{\beta} - 1), \qquad \text{(SAL2)}$$

It follows from the above equations that all nonvanishing model valences are explicitly determined by the degree of CT and spin delocalization. It follows from panels in the first column of Fig. 2 that the increase in the spin polarization $\sigma = \sigma_a$ increases all nonvanishing valence contributions (decreases their bonding character).

Fig. 3. A comparison of the predicted bond and overall valences for selected molecules; the overall valence is listed below the molecular diagram in the last column. Panels (*a*) and (*b*) correspond to the UHF indices of eqs. [8]–[11] for the averaged and promoted SAL reference states, respectively; panels (*c*) and (*d*) refer to the UHF indices of eqs. [9] and [11] and the v_A^{ion} index defined by eq. [18], again for the averaged and promoted SAL choices, respectively. The Scheme I (column I) and the weighted partitioning Schemes II and III (columns II and III) are compared to establish the partitioning schemes or reference state choice giving the best agreement with chemical intuition.

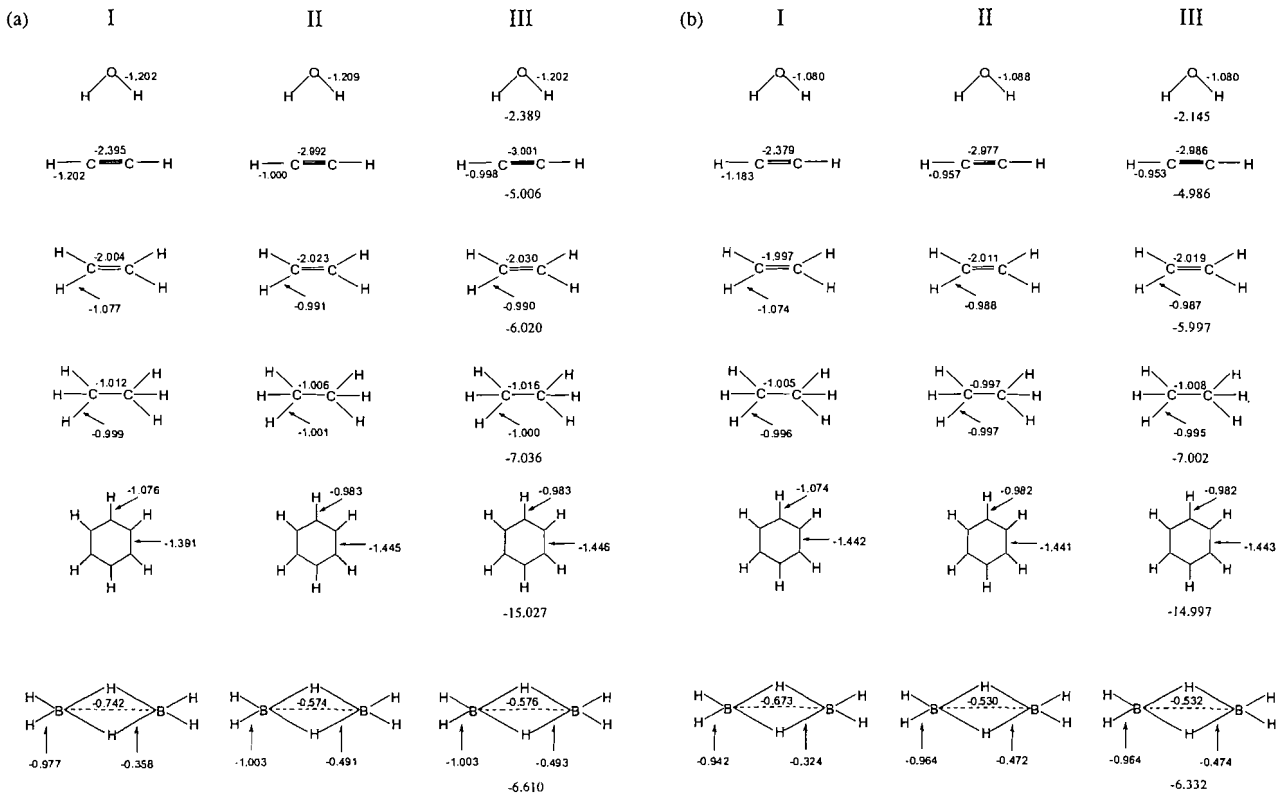

Consider now the SAL2 valence diagrams of Fig. 1*b*, exhibiting the same diatomic covalent curve as that in panel *a* of the figure. Here the atomic ionic contributions $v_a^{ion} = v_b^{ion}$ increase their bonding magnitude with increasing A → B *charge transfer* (CT). However, since the SAL2 already corresponds to the equalized spin distribution, $\sigma_a = \sigma_b = 0$, which is preserved within the RHF/LDA approximation, the ionic bonding is solely due to the CT, and therefore must exactly vanish for $q_a = 2$. We would like to point out (see eq. [29] and Fig. 2) that a given nonvanishing spin polarization ($\sigma_a \neq 0$) increases the bonding character of the ionic components; this shift in ionic valence due to spin polarization is exactly cancelled by an accompanying decrease in the bonding magnitude of the covalent component. Therefore, the overall model valence measure with respect to SAL2 remains unaffected by the spin polarization.

We would like to emphasize that the two sets of indices ($V_a^{ion} = V_b^{ion}, V_{ab}^{ion}, V_{ab}^{cov}$) and ($v_a^{ion} = v_b^{ion}, V_{ab}^{cov}$) are fully equivalent, giving rise to the same overall valence: $V = -1 + \sigma_a$ (SAL1) and $V = -q_b$ (SAL2). The first set is linked to changes in the electron pair distribution, while the second monitors molecularly averaged shifts in the CBO matrix structure, relative to the SAL.

Computational details

The numerical calculations were carried out using the standard GAMESS program (16).[2] STO-6G minimum basis sets were used in the valence calculations for typical molecules reported in Figs. 3 and 4. The remaining systems, including the water and the hydrogen fluoride dimers (Fig. 5), as well as the propellanes (Fig. 6), were studied using the 3-21G basis set (optimized geometries). Löwdin symmetrical orthogonalization was used to determine the molecular and SAL CBO data. Throughout the paper atomic units are used, unless stated otherwise.

Bond valences

In Fig. 3 we compare the predicted overall and bond valences for a set of representative molecules including water, acetylene, ethylene, ethane, benzene, and B_2H_6. The four panels of the figure explore the two SAL options (averaged and promoted) and the two types of ionic indices. Each panel also examines the three partitioning schemes of the atomic valences, denoted by the respective Roman numerals; the weighted Schemes II and III become identical for the new set of three types of indices (eq. [20]), with atomic ionic indices of eq. [18] replacing those defined by eqs. [8] and [10].

[2] See also: General Atomic and Molecular Electronic Structue System GAMESS: user's guide. North Dakota State University, Fargo, N. Dak., and Iowa State University, Ames, Iowa.

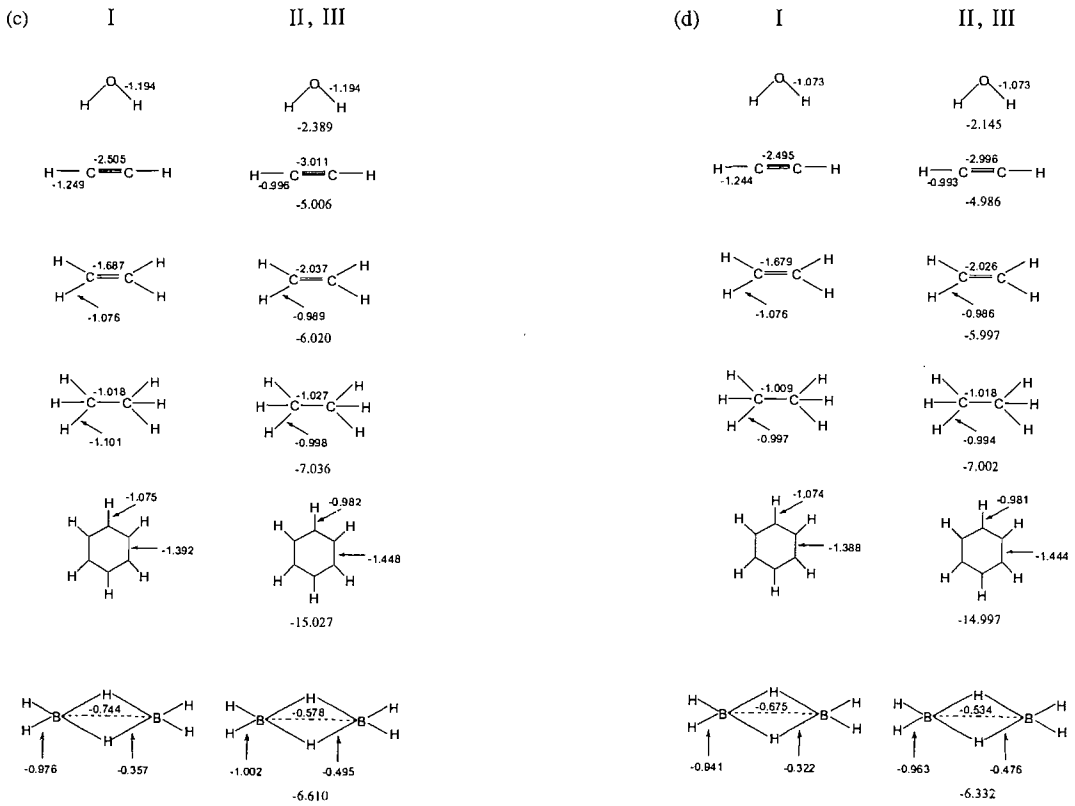

The overall negative valences, as already seen in Figs. 3*a* and *b*, are in good agreement with the total number of bonds predicted by chemists. This is particularly so in hydrocarbons, where the ionic interactions contribute less to the molecular bonding pattern. Larger deviations are observed for water and B_2H_6, which exhibit a more pronounced charge polarization. We would like to emphasize that the result for boron hydride correctly predicts roughly one bonding electron pair for each B-H-B bridging bond. A comparison between the respective overall valences reported in panels *a* and *b* (identical to those in panels *c* and *d*, respectively) shows that the average and promoted SAL approaches generate similar overall valence numbers; thus, specific choice of the reference state only weakly affects the predicted overall valences.

The extra total bonding, beyond the chemical intuitive value, may be attributed to the ionic component. Indeed, the largest deviations from the "chemical" values are detected for water and boron hydride; they are reduced in the P-SAL calculations, relative to the averaged atomic reference state scheme.

A reference to Fig. 3*a* also shows that predictions from the weighted partitioning schemes of atomic valences are in much better agreement with chemical intuition, particularly in the case of acetylene, in which a carbon atom participates in bonds exhibiting extreme (minimum and maximum) multiplicities. A similar conclusion follows from an examination of both the direct (B—B) and H-bridging bonds in B_2H_6. Namely, the approximately half-bond valence predictions for B—B and B—H (bridge) bonds appear to be closer to chemical expectation. We would like to point out that the boron atomic contributions in Scheme I have been equally divided into four BH contributions, thus assuming the absence of a partial direct B—B bond; the very algorithm of Schemes II and III takes into account all atomic pairs, including also the B–B interactions. In ethane molecule Scheme I works well due to a single character of all bonds involving carbon atoms. In general, the predictions in columns II and III are in good agreement with accepted chemical values, with single bonds being identified by approximately one bonding electron pair, a double bond exhibiting roughly two bonding pairs, and the triple bond originating from practically three bonding electron pairs. The bond order in the intermediate case of the C—C bond in benzene is also correctly reproduced. A slightly higher magnitude of the bond valence in the water molecule may be attributed to a more pronounced ionic component; however, as seen in Fig. 3*b*, it is reduced in the P-SAL case (compare also OH valences in Figs. 3*c*, *d*), so that the value −1.2 is partly due to the SAL averaging procedure. In conclusion, a comparison of Fig. 3*a* unequivocally points towards Schemes II and III as the preferred schemes for chemical applications.

The P-SAL results of Fig. 3*b* (columns II and III) are of comparable quality relative to those reported in panel *a*, thus also indicating a relatively weak dependence upon the selected SAL reference state.

A comparison between numerical values of the bond valences reported in Figs. 3*a*, 3*b* and 3*c*, 3*d*, respectively, shows that the predictions following from the two alternative ionic indices are very similar and basically equivalent for all practical purposes.

An additional test of the present valence indices involves a comparison of the nonbonding valences between the benzene ring carbons (Fig. 4). In all SAL and partitioning options the

Fig. 4. The average nonbonding C_{meta}—C_{meta}, C_{para}—C_{para} bond valences in benzene (*a*) and the relevant valence-bond structures (*b*) that can be used to rationalize the observed differences.

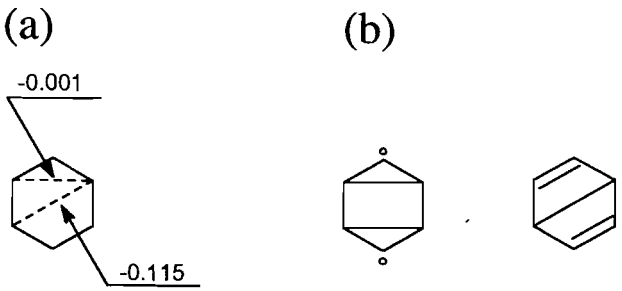

valences between carbons in the mutual *para* positions are much stronger than those predicted for the two carbons in the mutual *meta* positions. This prediction can be rationalized in terms of the relative participation of the valence bond structures shown in Fig. 4. Namely, the *meta–meta* partial bond can be achieved only through the diradical valence structure, in which the π electrons of the two carbons are localized, as in the Wheland intermediate. No such localization is required when one considers the partial *para–para* bond, as in the second covalent structure. Therefore, the diradical configuration is expected to have much higher energy, and thus much lower participation in the ground-state wave function. This explains the observed differences in the cross-ring valences. These preferences are independent of both the SAL and the assumed division of the atomic contributions.

To summarize, we advocate the averaging Schemes II and III for bond valence calculations in general molecular systems, when no a priori information about bonding is available. Scheme I of equally dividing atomic valences, is in fact more subjective than the remaining schemes, since one has to postulate a specific distribution of bonds (without specifying their multiplicity) to use it. In this respect Schemes II and III are totally objective, by not a priori discriminating between any atomic pair in the system under consideration.

We have also examined the prototype hydrogen-bonded dimers of water and hydrogen fluoride, to test how discriminatory are our valence indices in distinguishing between strong chemical and weak hydrogen bonds, respectively. The dimers of hydrogen fluoride in bent (ground state) and linear (hypothetical) arrangements are shown in panels *a* and *b* of Fig. 5; the geometry of the water dimer is shown in Fig. 5*c*. All these structures are UHF 3-21G optimized, with the linear constraint being imposed in the hypothetical model of $(HF)_2$. The figure reports changes in the P-SAL bond valences (Scheme III) obtained from the new valence indices of eq. [20], relative to separated monomers.

The calculated overall valence for the hydrogen fluoride (V[HF] = −1.12) gives the corresponding two separated molecules value V[HF + HF] = −2.23; it can be compared with the corresponding value $V[(HF)_2]$ = −2.34 (bent geometry) and −2.27 (linear geometry). This comparison gives rise to the following values of the relative overall valence measure $\Delta V = V$[dimer] − V[separated monomers]: −0.11 (bent, ground state structure) and −0.03 (linear, displaced structure). These extra valence changes are in qualitative agreement with the corresponding dimerization energies: ΔE = −0.018 66 (bent) and ΔE = −0.015 45 (linear). The relatively small values of the dimerization valence numbers show that present finite-difference indices do indeed discriminate between chemical and hydrogen bonds, predicting bond valences differing by an order of magnitude.

Fig. 5. Changes in the bond valences (P-SAL, Scheme III, ionic valence from eq. [18]) in prototype hydrogen-bonded dimers of HF and H_2O, relative to the separated monomers limit.

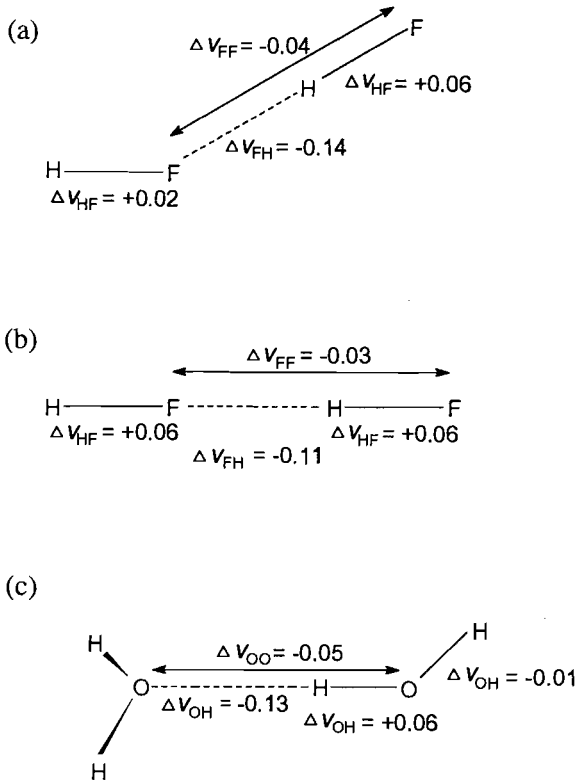

As seen in Fig. 5*a*, most of the extra bonding valence in the bent structure comes from the F--H and F--F intermonomer interactions; these are accompanied by asymmetric changes in the bond valences (both decreasing the bond order) within the interacting monomers. These intramonomer changes should be expected, due to the competition effect between the bond being formed and the intramonomer bonds. Namely, the monomer linked by proton to the other molecule is more destabilized than its bonding partner, since hydrogen can participate in the hydrogen bonding only at the expense of the HF bond; the other monomer linked by fluorine to the hydrogen of the other molecule can form a new bond using the lone-pair electrons, thus less affecting its intramonomer bond.

In the linear dimer (Fig. 5*b*) both monomers are seen to have increased their overall valence (decrease of the bond order) by practically the same amount. This is due to the symmetry constraints preventing a use of the lone-pair p_π orbitals of the hydrogen-bond fluorine, in a new bond with the hydrogen of the other monomer. Thus, the new bond and the associated accumulation of the electron density can be

Fig. 6. Calculated bond valences (for calculation specifications see caption to Fig. 5) in [1.1.1]propellane (*a*), [2.1.1]propellane (*b*), [2.2.1]propellane (*c*), and [2.2.2]propellane (*d*). The numbers in parentheses reported in panel (*a*) correspond to 1,3-diborabicyclo[1.1.1]pentane. The bridgehead atoms are shown as open circles.

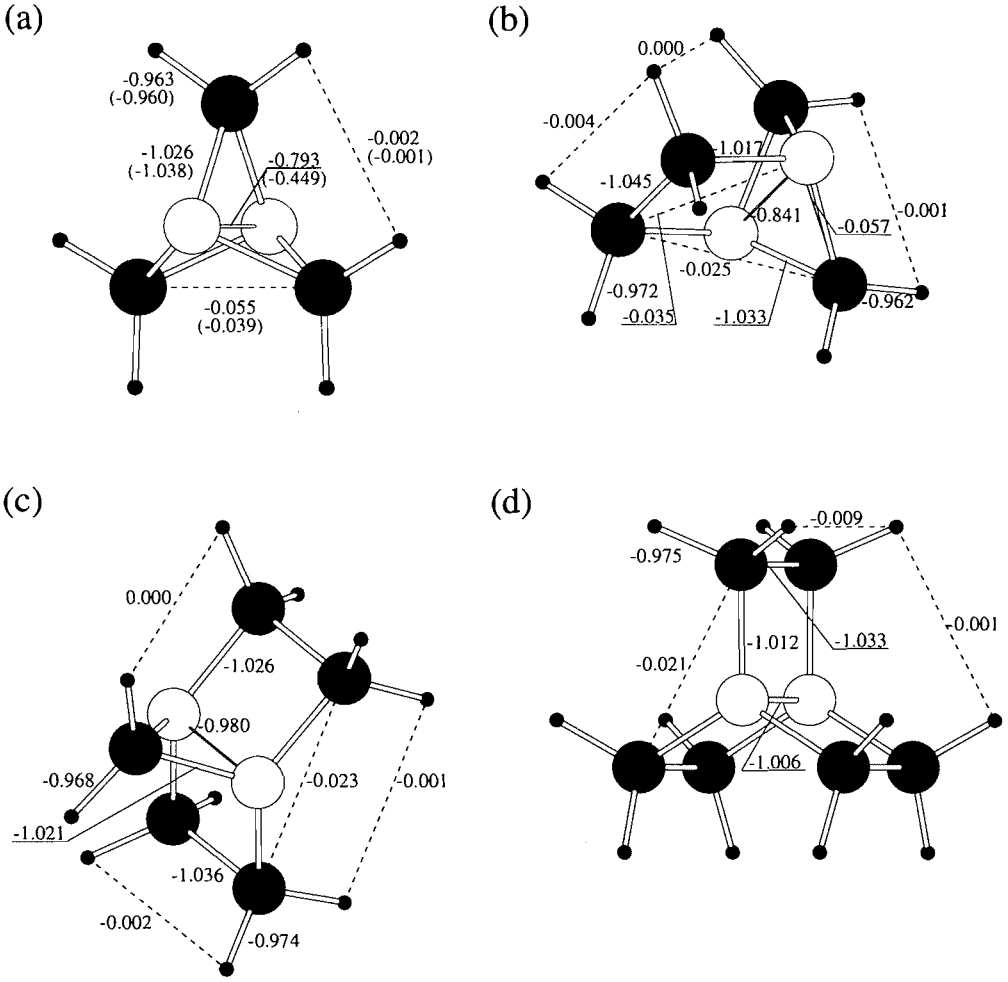

achieved only by partly weakening both the intramonomer bonds.

Similar conclusions follow from the valence numbers of the water dimer reported in Fig. 5*c*. The dimerization energy, $\Delta E = -0.017\ 48$, is due to the corresponding increase in the magnitude of the dimer overall valence relative to the separated monomers value, $\Delta V = -0.10$. This net extra bonding effect is mainly due to the new bonding valence between the terminal, interacting atoms of both monomers, $\Delta V_b^{(III)}(OH) = -0.13$, the interaction between oxygen atoms, $\Delta V_b^{(III)}(OO) = -0.05$, and a small increase in bonding valence of one of the peripheral OH bonds, accompanied by a more pronounced weakening of the other OH bond of the same monomer. The bonds inside the other monomer are practically unaffected by the hydrogen bond, due to the "buffering" influence of the oxygen lone pairs.

These illustrative applications show that typical hydrogen bonds exhibit bonding valence by an order of magnitude smaller than those corresponding to a single chemical bond, in agreement with chemical intuition.

Propellanes

Theoretical studies on properties of the then hypothetical propellane molecule and related derivatives began 10 years prior to the synthesis of [1.1.1]propellane by Wiberg and Walker (17, 18). Research has also been carried out on propellanes containing boron and heavier elements (Si, P, S, Sn, Ge) in bridge and (or) bridgehead positions (19, 20). The computed length of the C1—C3 bond in [1.1.1]propellane (Fig. 6*a*) is very close to that of typical single carbon–carbon bonds; depending on the method used it varies from 1.65 to 1.54 Å. The C1—C3 bond energy estimated by Feller and Davidson (21) by comparing total energies of [1.1.1]propellane and bicyclo[1.1.1]pentane is about 59 kcal/mol, thus amounting to approximately 70% of the corresponding value for a single C—C bond (~84 kcal/mol). The X-ray crystallographic study by Chackrabarti et al. (22) indicates that there is little deformation density between bridgehead carbons; Jackson and Allen (19) have rationalized this through their σ-bridged-π description of the overall C1—C3 bond in [1.1.1]propellane.

However, as pointed out by Wiberg et al. (23), in reality the charge density between bridgehead carbons is around 80% of that corresponding to the C2—C3 bond in *n*-butane; this density accumulation, due mainly to a superposition of atomic densities, can also produce a partial bond between the bridgehead atoms (central bond). Indeed, the Bader analysis (24; see also ref. 25) of the Laplacian of the molecular density indicates a presence of the bond critical point in the [1.1.1]propellane central region (23).

This short outline indicates that the problem of the central bond in propellane systems constitutes a challenging case for testing the utility of the present difference valence indices. Of interest also is how the nature of the central bond changes with both an increase in the bridge sizes (a series of [1.1.1], [2.1.1], [2.2.1], and [2.2.2]propellanes) and the bridge character (2,4,5-trioxa[1.1.1]propellane). We have also examined a change in the bridgehead atoms (1,3-diborabicyclo[1.1.1]pentane and bicyclo[1.1.1]pentane), in which the central bond should disappear in accordance with chemical expectations.

A comparison between the central bond valences of [1.1.1]propellane and bicyclo[1.1.1]pentane, −0.793 and −0.083, respectively, indeed shows a substantial central bond in the first case and its practical absence in the second system. A reference to Fig. 6*a* shows a substantial reduction (−0.449) of the central bond valence magnitude in the 1,3-dibora[1.1.1]cyclopentane representing the propellane system with more electron-deficient bridgeheads. Finally, the corresponding central bond valence in the 2,4,5-trioxa[1.1.1]propellane assumes an intermediate value, −0.666; at the same time the bridge C—O bond valence is strengthened (−1.081).

A reference to Fig. 6 also shows that an enlargement of the bridges leads to a gradual increase in the magnitude of the bridgehead bond valence: −0.793 ([1.1.1]propellane), −0.841 ([2.1.1]propellane), −0.980 ([2.2.1]propellane), and −1.006 ([2.2.2]propellane). Therefore, in the last two systems one can already talk about the single central bond.

To summarize, our present valence predictions clearly identify at least a partial bond between the bridgehead atoms in all these propellane systems, in qualitative agreement with the previous result from the Bader topological analysis (23–25). The present and previous studies convincingly demonstrate a practical utility of this type of quantum mechanical valence indices in rationalizing the network of bonds in a molecule. It also shows that a lack of appreciable changes in the difference density diagrams, $\Delta\rho$, in the region between the bridgehead atoms is not sufficient to claim the absence of the chemical bond. Our results, previous (11–14) and present, convincingly demonstrate that the present simple functions of the CBO displacements relative to the SAL do indeed carry all the relevant chemical information needed to generate the bonding pattern in any molecular system, including molecules, transition states, catalytic systems, etc. This numerical validation constitutes a good prognosis for future routine applications of this difference approach as an inexpensive tool for chemical interpretations, supplementing standard Hartree–Fock or DFT calculations.

Acknowledgment

This work was supported by research grant No. PB 0512/P3/93/05 from the State Committee for Scientific Research in Poland.

References

1. G.N. Lewis. J. Am. Chem. Soc. **38**, 762 (1916); J. Phys. Chem. **1**, 17 (1993).
2. K. Wiberg. Tetrahedron, **24**, 1093 (1968).
3. M.S. Gopinathan and K. Jug. Theor. Chim. Acta, **63**, 497 (1983); **63**, 511 (1983); K. Jug and M.S. Gopinathan. *In* Theoretical models of chemical bonding. Vol. 2. *Edited by* Z.B. Maksić. Springer, Heidelberg. 1990. p. 77, and refs. therein.
4. D.R. Armstrong, P.G. Perkins, and J.J.P. Stewart. J. Chem. Soc. Dalton Trans. 838 (1973); M.A. Natiello and J.A. Medrano. Chem. Phys. Lett. **105**, 180 (1984).
5. A.B. Sannigrahi and T. Kar. Chem. Phys. Lett. **173**, 569 (1990); T. Kar and E.S. Marcos. Chem. Phys. Lett. **192**, 14 (1992).
6. I. Mayer. Chem. Phys. Lett. **97**, 270 (1983); A. Somorgyi and A. Gömöry. Chem. Phys. Lett. **192**, 221 (1992).
7. M.S. Giambiagi, M. Giambiagi, and F.E. Jorge. Theor. Chim. Acta, **68**, 337 (1985); P. Pitanga, M. Giambiagi, and M.S. Giambiagi. Chem. Phys. Lett. **128**, 411 (1986).
8. J. Ciosłowski and S.T. Mixon. J. Am. Chem. Soc. **113**, 4142 (1991).
9. J.G. Angyan and I. Mayer. J. Phys. Chem. **98**, 5244 (1994).
10. R.F. Nalewajski, A.M. Koster, and K. Jug. Theor. Chim. Acta, **85**, 463 (1993).
11. R.F. Nalewajski and J. Mrozek. Int. J. Quantum Chem. **51**, 187 (1994).
12. R.F. Nalewajski, S.J. Formosinho, A.J.C. Varandas, and J. Mrozek. Int. J. Quantum Chem. **52**, 1153 (1994).
13. R.F. Nalewajski and J. Mrozek. Int. J. Quantum Chem. **57**, 377 (1996).
14. R.F. Nalewajski, J. Mrozek, and A. Michalak. Int. J. Quantum Chem. In press.
15. W. Kohn and L.J. Sham. Phys. Rev. [Sect.] A, **140**, 1133 (1965).
16. M. Dupuis, D. Spangler, and J.J. Wendoloski. *In* National resource for computations in chemistry software catalog. Program QGO. University of California, Berkeley. 1980; M.W. Schmidt, K.K. Baldridge, J.A. Boatz, J.H. Jensen, S. Koseki, M.S. Gordon, K.A. Nguyen, T.J. Windus, and S.T. Elbert. QCPE Bull. **10**, 52 (1990). See also: General Atomic and Molecular Electronic Structure System GAMESS: User's Guide (North Dakota State University, Fargo and Iowa State University, Ames).
17. K.B. Wiberg and F.H. Walker. J. Am. Chem. Soc. **104**, 5239 (1982).
18. K.B. Wiberg. Chem. Rev. **89**, 975 (1989).
19. J.E. Jackson and L.C. Allen. J. Am. Chem. Soc. **106**, 591 (1984).
20. K.A. Nguyen, M.T. Carrol, and M.S. Gordon. J. Am. Chem. Soc. **113**, 7924 (1991).
21. D. Feller and E.R. Davidson. J. Am. Chem. Soc. **109**, 4133 (1987).
22. P. Chackrabarti, P. Seiler, J.D. Dunitz, A.-D. Slutter, and G. Szeimies. J. Am. Chem. Soc. **103**, 7378 (1981).
23. K.B. Wiberg, R.F.W. Bader, and C.D.H. Lau. J. Am. Chem. Soc. **109**, 985 (1987); **109**, 1001 (1987).
24. R.F.W. Bader. Chem. Rev. **91**, 893 (1991).
25. R.F.W. Bader. Atoms in molecules: a quantum theory. Clarendon Press, Oxford, U.K. 1990.

Atomic origins of molecular polarizabilities[1]

Keith E. Laidig

Abstract: We demonstrate that the multipole polarizability tensors of a molecule are expressible as a sum of atomic contributions, each of which is based upon the change in the spatial distribution of electronic charge within each atom resulting from the application of electric fields and field gradients. The use of the spatially defined atoms of subsystem quantum mechanics correctly partitions molecular polarizabilities into physically meaningful atomic contributions. It is shown that the origin of any molecular polarizability tensor may be understood from an investigation of these contributions and the general expressions for the summation of atomic components to yield molecular polarizabilities are presented. Their use is demonstrated by the construction and investigation of the axial components of the dipole–dipole, dipole–quadrupole, and quadrupole–quadrupole polarizability tensors of carbon monoxide and carbon sulfide.

Key words: atomic polarizabilities, atoms-in-molecules, molecular polarizabilities.

Résumé : On démontre que les tenseurs de polarisabilité multipolaire d'une molécule peuvent être exprimés sous la forme d'une somme de contributions atomiques, chacune étant basée sur le changement dans la distribution spatiale de la charge électronique dans chaque atome résultant de l'application de champs électriques et de gradients de champs. L'utilisation d'atomes définis dans l'espace de la mécanique quantique d'un sous-système permet de faire une partition correcte des polarisabilités en contributions atomiques ayant une signification physique. On a montré qu'il est possible de comprendre l'origine de tout tenseur de polarisabilité moléculaire en examinant ces contributions et on présente les expressions générales pour la sommation des composantes atomiques qui conduisent aux polarisabilités moléculaires. On démontre leur utilisation en contruisant et en étudiant les composantes axiales des tenseurs des polarisabilités dipôle–dipôle, dipôle–quadripôle et quadripôle–quadripôle du monoxyde de carbone et du sulfure de carbone.

Mots clés : polarisabilités atomiques, atomes dans des molécules, polarisabilités moléculaires.

[Traduit par la rédaction]

Introduction

The significant forces at work during the interaction of two molecules in the "long-range" regime (the distances at which interactions vary as R^{-n}) arise from the interaction of one molecular charge distribution with the electric fields and field gradients produced by the other molecule. This includes electrostatic, inductive, and dispersive interactions (1). The theory of these interactions has been well established and is typically base upon the multipole moments of the molecular charge distribution and the response of these moments to external fields (1). If the external field $\boldsymbol{F}$ is uniform, the dipole moment, μ_α, can be written as a power series in $\boldsymbol{F}$ (2):

$$[1] \qquad \mu_\alpha(\boldsymbol{F}) = \mu_\alpha + \alpha_{\alpha\beta}F_\beta + \tfrac{1}{2}\beta_{\alpha\beta\gamma}F_\beta F\gamma + \tfrac{1}{6}\gamma_{\alpha\beta\gamma\delta}F_\beta F_\gamma F_\delta + \cdots$$

where $\alpha_{\alpha\beta}$ is the linear dipole–dipole polarizability and $\beta_{\alpha\beta\gamma}$ and $\gamma_{\alpha\beta\gamma\delta}$ are the associated quadratic and cubic response tensors, respectively. The latter two terms are also referred to as the first and second hyperpolarizabilities.

The fields generated by an approaching molecule are not uniform, yielding additional distortions of the electronic charge distribution. The dipole moment then also depends on higher order linear polarizabilities that respond to the electric field gradients and field Hessians of the approaching molecule. Expanding μ_α in powers of a non-uniform $\boldsymbol{F}$ yields (2):

$$[2] \qquad \mu_\alpha(\boldsymbol{F}_\beta, \boldsymbol{F}_{\beta\gamma}, \boldsymbol{F}_{\beta\gamma\delta}, \ldots) = \mu_\alpha + \alpha_{\alpha\beta}F_\beta + \tfrac{1}{2}A_{\alpha,\beta\gamma}F_{\beta\gamma} + \tfrac{1}{15}E_{\alpha,\beta\gamma\delta}F_{\beta\gamma\delta} + \cdots$$

where $A_{\alpha\beta,\gamma}$ is the dipole–quadrupole polarizability, $F_{\alpha\beta}$ is the field gradient, etc. Similarly, the quadrupole moment $\Theta_{\alpha\beta}$, is expandable in powers of a non-uniform $\boldsymbol{F}$ as (3)

$$[3] \qquad \Theta_{\alpha\beta}(F_\beta, F_{\beta\gamma}, F_{\beta\gamma\delta}) = \Theta_{\alpha\beta} + A_{\alpha\beta,\gamma}F_\gamma + C_{\alpha\beta,\gamma\delta}F_{\gamma\delta} + \tfrac{1}{15}H_{\alpha\beta,\gamma\delta\epsilon}F_{\gamma\delta\epsilon} + \cdots$$

where $C_{\alpha\beta\gamma\delta}$ is the quadrupole–quadrupole polarizability, and so on.

Aside from their intrinsic interest as the terms which dictate intermolecular interaction, the origins of molecular polarizabilities yield insight into the intramolecular interactions and their change under the influence of external forces and fields. The partitioning of molecular polarizabilities in terms

Received September 28, 1995.

This paper is dedicated to Professor Richard F.W. Bader on the occasion of his 65th birthday.

K.E. Laidig.[2] Department of Medicinal Chemistry, University of Washington, Seattle, WA 98195-7610, U.S.A.

[1] A preliminary account of this work was presented as a poster in the first Electronic Computational Chemistry Conference, 1994.

[2] E-mail: laidig@u.washington.edu

of atomic (3–7) and bond (8–11) contributions have been investigated. As part of our continuing development of a general methodology for the construction and representation of molecular charge distributions and their polarizabilities, we have generalized the expression for the spatial partitioning of molecular polarizabilities into atomic and functional group contributions, based upon the atomic partitioning of subspace quantum mechanics. A similar approach has been presented recently in which the dipole polarizability is evaluated by integration of the polarizability density directly and expanding the contributions into spherical harmonics (12). This approach provided results in general agreement with earlier work using finite fields (3). Here we present a general expression for the spatial partitioning of molecular polarizabilities using Cartesian multipole moments and their changes under the application of finite, uniform fields. The general expression of molecular moments and multipole moments has been presented previously and will form the basis of our development (13).

Theoretical overview

The general expression for an arbitrary moment, $\zeta^{(n)}$, of a distribution of charges, when expanded to consider the nuclei and electrons within the distribution, is

$$[4]\qquad \zeta^{(n)}_{\alpha\beta\gamma\ldots\nu} = \sum_{\Omega} Z^{\Omega} X^{\Omega}_{\alpha} X^{\Omega}_{\beta} X^{\Omega}_{\gamma} \ldots X^{\Omega}_{\nu} - \int r_{\alpha} r_{\beta} r_{\gamma} \ldots r_{\nu} \rho(\boldsymbol{r}) d\tau$$

where Z^{Ω} is the charge on nucleus Ω, X^{Ω}_{α} is the α component of the displacement of nucleus Ω from the origin of the property evaluation, r_{α} is the α component of the displacement vector from the origin, and $\rho(\boldsymbol{r})$ is the electronic charge density in electrons per unit volume. The molecular moment may be expressed in terms of atomic contributions by breaking the integration over all space into integrations over the regions of space associated with each atom within the molecule (13), the atom's basin. Effectively, we are substituting $X^{\Omega}_{\alpha} + r^{\Omega}_{\alpha}$ for r_{α}, where r^{Ω}_{α} is the position vector within the atomic basin and a superscript Ω denotes an atomic-based property or position vector. We also use the notation $P(\alpha\beta\gamma\ldots)$ to imply summation over all permutations of the tensor components; thus $P(\alpha\beta\gamma)X_{\alpha\beta\gamma} = X_{\alpha\beta\gamma} + X_{\alpha\gamma\beta} + X_{\beta\gamma\alpha} + X_{\beta\alpha\gamma} + X_{\gamma\alpha\beta} + X_{\gamma\beta\alpha}$.

The general expression for an arbitrary moment then becomes:

$$\begin{aligned}[5]\qquad \zeta^{(n)}_{\alpha\beta\gamma\ldots\nu} = &\sum_{\Omega} \zeta^{(0)}(\Omega) X^{\Omega}_{\alpha} X^{\Omega}_{\beta} X^{\Omega}_{\gamma} \ldots X^{\Omega}_{\nu} \\ &+ P(\alpha)\zeta^{(1)}_{\alpha}(\Omega) X^{\Omega}_{\beta} X^{\Omega}_{\gamma} \ldots X^{\Omega}_{\nu} \\ &+ P(\alpha\beta)\zeta^{(2)}_{\alpha\beta}(\Omega) X^{\Omega}_{\gamma} \ldots X^{\Omega}_{\nu} \\ &+ \ldots P(\alpha\beta\gamma\ldots\mu)\zeta^{(m)}_{\alpha\beta\gamma\ldots\mu}(\Omega) X^{\Omega}_{\nu} + \zeta^{(n)}_{\alpha\beta\gamma\ldots\nu}(\Omega)\end{aligned}$$

where we're used the following definitions for the various atomic moments:

$$[6]\qquad \zeta^{(0)}(\Omega) = q(\Omega) = Z(\Omega) - \int_{\Omega} \rho(r) d\tau$$

$$[7]\qquad \zeta^{(1)}_{\alpha}(\Omega) = M_{\alpha}(\Omega) = Z(\Omega) - \int_{\Omega} r_{\alpha} \rho(r) d\tau$$

$$[8]\qquad \zeta^{(2)}_{\alpha\beta}(\Omega) = Q_{\alpha\beta}(\Omega) = Z(\Omega) - \int_{\Omega} r_{\alpha} r_{\beta} \rho(r) d\tau$$

We've defined $q(\Omega)$ as the atomic charge, M_{α} is the α component of the atomic first moment, $Q_{\alpha\beta}$ is the $\alpha\beta$ component of the atomic second moment, and so on. Each of these atomic, tensoral contributions to the molecular property tensor is based upon the form of the charge distribution within the basin of the atom and the relative location of that atom from the origin. Any molecular moment may be seen as the tensorial summation of these associated atomic contributions, in that each contribution is based upon the distribution of electronic charge within the associated atom and its relation to the molecular origin.

Molecular multipole moments

Multipole moments represent the anisotropic contributions to the molecular moments of a given rank (1). A general expression of the multipole moments of the charge distributions in terms of its atomic contributions is an extension of the development above. The general expression for a multipole moment is

$$[9]\qquad \xi^{(n)}_{\alpha\beta\gamma\ldots\nu} = \frac{(-1)^n}{(n!)} \left\langle \boldsymbol{r}^{(2n+1)} \nabla_{\alpha} \nabla_{\beta} \nabla_{\gamma} \ldots \nabla_{\nu} \frac{1}{\boldsymbol{r}} \right\rangle$$

which when expanded to explicitly express both nuclear and electronic distributions yields

$$[10]\qquad \xi^{(n)}_{\alpha\beta\gamma\ldots\nu} = \frac{(-1)^n}{(n!)} \left[\sum_{\Omega} Z^{\Omega} \boldsymbol{X}^{(2n+1)} \nabla_{\alpha} \nabla_{\beta} \nabla_{\gamma} \ldots \nabla_{\nu} \frac{1}{\boldsymbol{X}} - \int \boldsymbol{r}^{(2n+1)} \nabla_{\alpha} \nabla_{\beta} \nabla_{\gamma} \ldots \nabla_{\nu} \frac{1}{\boldsymbol{r}} \rho(\boldsymbol{r}) d\tau \right]$$

In parallel with the development above, the expansion of this to atomic-based integration yields

$$\begin{aligned}[11]\qquad \xi^{(n)}_{\alpha\beta\gamma\ldots\nu} &= \sum_{\Omega} [\xi^{\Omega(n)}_{\alpha\beta\gamma\ldots\nu}] \\ &= \frac{(-1)^n}{(n!)} \sum_{\Omega} Z^{\Omega} X^{\Omega^{(2n+1)}} \nabla_{\alpha} \nabla_{\beta} \nabla_{\gamma} \ldots \nabla_{\nu} \frac{1}{X^{\Omega}} \\ &\quad - \int (r^{\Omega} + X^{\Omega})^{(2n+1)} \nabla_{\alpha} \nabla_{\beta} \nabla_{\gamma} \ldots \nabla_{\nu} \\ &\quad + \frac{1}{(r^{\Omega} + X^{\Omega})} \rho(r) d\tau\end{aligned}$$

where the scalars are denoted by a lack of subscript. Once the particular moment has been chosen, the expansion may be completed using the procedures discussed in the previous section for the molecular moments by substitution of the various atomic moments, etc. (13). The quadrupole moment is given here in terms of the atomic contributions as an example:

$$\begin{aligned}[12]\qquad \Theta_{\alpha\beta} &= \sum_{\Omega} [\Theta^{\Omega}_{\alpha\beta}] = \tfrac{1}{2} \sum_{\Omega} [3Q^{\Omega}_{\alpha\beta} - Q^{\Omega}_{\gamma\gamma}\delta_{\alpha\beta}] \\ &= \tfrac{1}{2} \sum_{\Omega} 3\{q(\Omega) X^{\Omega}_{\alpha} X^{\Omega}_{\beta} + M_{\alpha}(\Omega) X^{\Omega}_{\beta} \\ &\quad + M_{\beta}(\Omega) X^{\Omega}_{\alpha} + Q_{\alpha\beta}(\Omega)\} \\ &\quad - \{q(\Omega)(X^{\Omega})^2 + 2X^{\Omega}\langle r^{\Omega}\rangle_{\Omega} + \langle (r^{\Omega})^2\rangle_{\Omega}\}\delta_{\alpha\beta}\end{aligned}$$

Molecular multipole polarizabilities

The response of a molecular charge distribution to the electric field or field gradient of another molecule can be conveniently addressed in terms of changes of the molecular multipole moments, yielding the multipole polarizabilities. Following the development of Buckingham (1), we define the multipole polarizability to be the multipole moment induced by unit magnitude of the appropriate uniform field or field gradient. Given this, the dipole–dipole, dipole–quadrupole, and quadrupole–quadrupole polarizabilities may be respectively expressed as

$$[13] \qquad \alpha_{\alpha,\beta} = \frac{\partial \mu_\alpha}{\partial F_\beta}$$

$$[14] \qquad A_{\alpha,\beta\gamma} = \frac{\partial \mu_\alpha}{\partial F_{\beta\gamma}} = A_{\alpha,\beta\gamma} = \frac{\partial \Theta_{\beta\gamma}}{\partial F_\alpha}$$

$$[15] \qquad C_{\alpha\beta,\gamma\delta} = \frac{\partial \Theta_{\alpha\beta}}{\partial F_{\gamma\delta}}$$

where we use comma to distinguish between the molecular moment and the applied field.

If we consider the polarizabilities as arising from the application of a finite field, each of these response tensors may then be generalized into atomic contributions, as outlined above, yielding

$$[16] \qquad \alpha_{\alpha,\beta} = \sum_\Omega [\alpha^\Omega_{\alpha,\beta}] = \frac{\Delta \mu^\Omega_\alpha}{\Delta F_\beta} = \sum_\Omega \left[\frac{\Delta q(\Omega) X^\Omega_\alpha + \Delta M_\alpha(\Omega)}{\Delta F_\beta} \right]$$

$$[17] \qquad A_{\alpha,\beta\gamma} = \sum_\Omega [A^\Omega_{\alpha,\beta\gamma}]$$

$$= \sum_\Omega \left[\frac{\Delta \mu^\Omega_\alpha}{\Delta F_{\beta\gamma}} \right] = \sum_\Omega \left[\frac{\Delta q(\Omega) X^\Omega_\alpha + \Delta M_\alpha(\Omega)}{\Delta F_{\beta\gamma}} \right]$$

$$= A_{\beta\gamma,\alpha} = \sum_\Omega \left[\frac{\Delta \Theta^\Omega_{\beta\gamma}}{\Delta F_\alpha} \right]$$

$$= \frac{1}{2} \sum_\Omega \frac{3\{\Delta q(\Omega) X^\Omega_\beta X^\Omega_\gamma + \Delta M_\beta(\Omega) X^\Omega_\gamma + \Delta M_\gamma(\Omega) X^\Omega_\beta + \Delta Q_{\beta\gamma}\} - \{\Delta q(\Omega)(X^\Omega)^2 + 2X^\Omega \Delta \langle r^\Omega \rangle_\Omega + \Delta \langle (r^\Omega)^2 \rangle_\Omega\} \delta_{\beta\gamma}}{\Delta F_\alpha}$$

$$[18] \qquad C_{\alpha\beta,\gamma\delta} = \sum_\Omega [C^\Omega_{\alpha\beta,\gamma\delta}] = \sum_\Omega \left[\frac{\Delta \Theta^\Omega_{\alpha\beta}}{\Delta F_{\gamma\delta}} \right]$$

$$= \frac{1}{2} \sum_\Omega \frac{3\{\Delta q(\Omega) X^\Omega_\alpha X^\Omega_\beta + \Delta M_\alpha(\Omega) X^\Omega_\beta + \Delta M_\beta(\Omega) X^\Omega_\alpha + \Delta Q_{\alpha\beta}\} - \{\Delta q(\Omega)(X^\Omega)^2 + 2X^\Omega \Delta \langle r^\Omega \rangle_\Omega + \Delta \langle (r^\Omega)^2 \rangle_\Omega\} \delta_{\alpha\beta}}{\Delta F_{\gamma\delta}}$$

Analogously, the general expression of the linear multipole polarizabilities resulting from nonuniform field is

$$[19] \qquad \frac{\partial \xi^{(n)}_{\alpha\beta\gamma\ldots\nu}}{\partial F_{\tau\nu\ldots\omega}} = \sum_\Omega \left[\frac{\Delta \xi^{\Omega(n)}_{\alpha\beta\gamma\ldots\nu}}{\Delta F_{\tau\nu\ldots\omega}} \right]$$

$$= \frac{(-1)^n}{(n!)} \sum_\Omega \frac{Z^\Omega X^{\Omega(2n+1)} \nabla_\alpha \nabla_\beta \nabla_\gamma \ldots \nabla_\nu \frac{1}{X^\Omega} - \int (r^\Omega + X^\Omega)^{(2n+1)} \nabla_\alpha \nabla_\beta \nabla_\gamma \ldots \nabla_\nu \frac{1}{(r^\Omega + X\Omega)} \Delta\rho(r) d\tau}{\Delta F_{\tau\nu\ldots\omega}}$$

The related expression for the partitioning of nonlinear polarizabilities is

$$[20] \qquad \frac{\partial \xi^{(n)}_{\alpha\beta\gamma\ldots\nu}}{\partial F_\tau \partial F_\nu \ldots \partial F_{\bar{\omega}}} = \sum_\Omega \left[\frac{\Delta \xi^{\Omega(n)}_{\alpha\beta\gamma\ldots\nu}}{\Delta F_\tau \Delta F_\nu \ldots \Delta F_{\bar{\omega}}} \right]$$

$$= \frac{(-1)^n}{(n!)} \sum \frac{Z^\Omega X^{\Omega(2n+1)} \nabla_\alpha \nabla_\beta \nabla_\gamma \ldots \nabla_\nu \frac{1}{X^\Omega} - \int (r^\Omega + X^\Omega)^{(2n+1)} \nabla_\alpha \nabla_\beta \nabla_\gamma \ldots \nabla_\nu \frac{1}{(r^\Omega + X^\Omega)} \Delta\rho(r) d\tau}{\Delta F_\tau \Delta F_\nu \ldots \Delta F_{\bar{\omega}}}$$

The application of this later equation to nonlinear contributions to molecular multipole moments is the subject of ongoing work in our laboratory.

Quantum mechanics of open systems

The reader will note that this derivation of atomic decomposition of molecular polarizabilities has not required that the atom to be used arise from a particular theory or model. It requires only that each atom have a distinct, spatial volume and that the partitioning exhaust all space. The general expansion demonstrates that each order of the Taylor's series expansion depends upon the displacement of the lower order terms. This derivation also demonstrates that the simple charge separation model, often used to describe dipole and higher polarizabilities, is only appropriate when the atoms have spherical charge distributions and thus can not be used in a general manner. We propose that any spatial partitioning of molecular polarizabilities must recover these relationships if the regions defined are to be physically meaningful.

Sub-system quantum mechanics, as implemented in the theory of atoms in molecules (14), generalizes quantum mechanics to sub-systems, atoms or groupings of atoms, within a total system. Atoms are open quantum mechanical systems that exchange electronic charge and momenta with other systems that share their bounding surface. The atom is bounded by a surface through which there is zero flux in the gradient vector field of the charge density at each point on the surface:

$$[21] \qquad \nabla\rho(\boldsymbol{r}) \cdot \boldsymbol{n}(\boldsymbol{r}) = 0$$

This boundary condition appears as a constraint in the generalized variation of the quantum action integral and is equally valid for the total system as well as for each atom within the system (14, 15).

The physical observables, their average values, and the theorems that determine the mechanics of a sub-system in a stationary state are produced in analogy to those for the total system (16–18). For each observable, the associated property density, which is the average of the property over the motions of all the particles within the system, is determined at each point in real space. When integrated over the basin of the atom, this yields the atomic average value of the property. In this manner, the properties and mechanics of the atoms, and indeed the total system, are predicted by quantum mechanics (14).

We have chosen to use sub-system quantum mechanics to provide our spatial partitioning because of the quantum mechanical basis of the atoms so defined (19). It has been demonstrated that the populations defined by the theory of atoms in molecules are physical observables (20). This proof may be generalized to show that any moment of the quantum atom is also a physical observable. Similarly, the atomic contributions to a moment are the sum of expectation values multiplied by the associated displacement vectors. The form of the spatial distribution of charge within each atom is used as the basis to describe the spatial distribution of charge within the molecule. The change in the contributions to the molecular properties made by each atom under the stress of internal or external forces is the result of the changes in these physical observables. This provides a procedure that is applicable to studying the change in the charge density, independent of the way in which the density is represented. It is independent of the form of the wave function, orbital sets, localizations of the orbitals, or choice of basis functions and can be used on experimentally determined charge distributions as well. This brings a physical and quantum mechanical basis to the investigation of the origin of the molecular polarizabilities that might be otherwise difficult to uncover.

In addition to being the expectation values of physical observables, the atomic properties predicted by theory enjoy the advantage of transferability between similar systems, as do all the atomic properties predicted using sub-system quantum mechanics (3, 14, 18, 20–22). As the atoms of theory are defined in real space, they represent the physical characteristics of the charge distribution within the space. And, insofar as two atoms are the same, so too are their contributions to molecular properties. This is the physical basis for the success of the presented work and the theory of atoms in molecules in general, namely, that the form of the charge distribution within a region of space determines the contribution of that region to the properties of the molecule. Thus to the degree that the charge distributions in two atomic basins are the same, so too will be their contributions to the physical properties of the molecule. The atoms bounded by surfaces of zero flux in the gradient vector field of the charge density have been shown to be nearly constant in their properties between different systems and that other choices of surfaces for partitioning decrease the constancy of atomic properties between systems (21, 22).

Methodology

Each molecule was optimized using the 6-311++G** basis (23) with the GAMESS (24) and CADPAC5 (25) program packages. The wave functions were produced at the same level of theory using the ANVIL5 properties package (26) and then analyzed using the AIMPAC (27) program suite. The atomic contributions to the molecular energetics for all the molecules are given below and their summation is accurate throughout the series to 0.0005 electrons in population and within 0.3 kcal/mol in total energies.

The molecular polarizabilities were determined analytically using CADPAC5. The atomic properties were determined from individual wave functions by application of finite electric fields and field gradients along the molecular axis (±0.001 au). The atomic contributions were then determined by finite difference in comparison with the unperturbed values. Only a subset of the tensors is presented and discussed, those components associated with application of fields along the molecular axis. Only the dipole–dipole multipole polarizability is origin independent, but for convenience the center of mass is chosen as the origin of property evaluation. In this work it is our intention to focus upon the properties of the molecular polarizabilities predicted using the HF/6-311++G**//HF/6-311++G** wave function rather than try to reproduce the experimentally observed values.

Results and discussion

The atomic coordinates and properties of the molecules, as well as atomic contributions to the molecular moments, are listed in moments, see Table 1 for carbon monoxide (CO) and Table 2 for carbon sulfide (CS). The total electronic charge density of CO and CS is shown in Figs. 1*a* and 2*a*, respectively, and the Laplacian of the charge density for the two is shown in Figs. 1*b* and 2*b*, respectively. The molecular prop-

Table 1. Atomic properties of carbon monoxide.

CO	Carbon	Oxygen	Atomic sum[a]	Molecular values[a]
Z^{Ω}	−1.193	0.895		
$N(\Omega)$[b]	4.668	9.333	14.000	14.000
$E(\Omega)$	−36.871	−75.901	−112.771	−112.771
$q(\Omega)$	1.333	−1.333	0.000	0.000
$M_z(\Omega)$	1.726	0.983		
$Q_{xx}(\Omega)$	−2.605	−4.951		
$Q_{yy}(\Omega)$	−2.605	−4.951		
$Q_{zz}(\Omega)$	−2.762	−4.967		
μ^{Ω}_z	0.137	−0.209	−0.073	−0.073
Θ^{Ω}_{xx}	1.189	−0.338	0.851	0.852
Θ^{Ω}_{yy}	1.189	−0.338	0.851	0.852
Θ^{Ω}_{zz}	−2.378	0.676	−1.702	−1.703

[a]Atomic sum is the sum of atomic contributions, Molecular value is the independently determined molecular value for the given property. All values are in atomic units.

[b]Z^{Ω} is the atomic coordinate, $N(\Omega)$ is the atomic population, $E(\Omega)$ is the atomic energy, $q(\Omega)$ is the atomic charge, $M_{\alpha}(\Omega)$ is the atomic first moment, $Q_{\alpha\beta}(\Omega)$ is the atomic second moment, μ^{Ω}_{α} is the atomic contribution to the molecular dipole moment, $\Theta^{\Omega}_{\alpha\beta}$ is the atomic contribution to the molecular quadrupole moment.

Table 2. Atomic properties of carbon sulfide.

CS	Carbon	Sulfur	Atomic sum[a]	Molecular values[a]
Z^{Ω}	−1.518	0.570		
$N(\Omega)$[b]	8.045	13.955	22.000	22.000
$E(\Omega)$	−40.025	−394.858	−434.883	−434.883
$q(\Omega)$	−2.045	2.045	0.000	0.000
$M_z(\Omega)$	−0.570	−2.284		
$Q_{xx}(\Omega)$	−6.661	−5.792		
$Q_{yy}(\Omega)$	−6.661	−5.792		
$Q_{zz}(\Omega)$	−6.273	−4.896		
μ^{Ω}_z	2.534	−1.119	1.415	1.415
Θ^{Ω}_{xx}	1.296	0.521	1.817	1.818
Θ^{Ω}_{yy}	1.296	0.521	1.817	1.818
Θ^{Ω}_{zz}	−2.593	−1.042	−3.635	−3.636

[a]Atomic sum is the sum of atomic contributions, Molecular value is the independently determined molecular value for the given property. All values are in atomic units.

[b]Z^{Ω} is the atomic coordinate, $N(\Omega)$ is the atomic population, $E(\Omega)$ is the atomic energy, $q(\Omega)$ is the atomic charge, $M_{\alpha}(\Omega)$ is the atomic first moment, $Q_{\alpha\beta}(\Omega)$ is the atomic second moment, μ^{Ω}_{α} is the atomic contribution to the molecular dipole moment, $\Theta^{\Omega}_{\alpha\beta}$ is the atomic contribution to the molecular quadrupole moment.

Fig. 1. Contour diagrams of (*a*) the total charge density and (*b*) the Laplacian of the carbon monoxide along the molecular axis. The regions of negative Laplacian (in which charge is locally concentrated) are shown in solid lines and those regions of positive Laplacian (in which charge is locally depleted) are shown in broken lines. The bond path joining the two nuclei and the interatomic surface partitioning the molecule into individual atoms are both overlaid upon the contour diagrams. The outer contour value is 0.2×10^{-3} and they increase as 0.4×10^{-3}, 0.8×10^{-3}, 0.2×10^{-2}, etc.

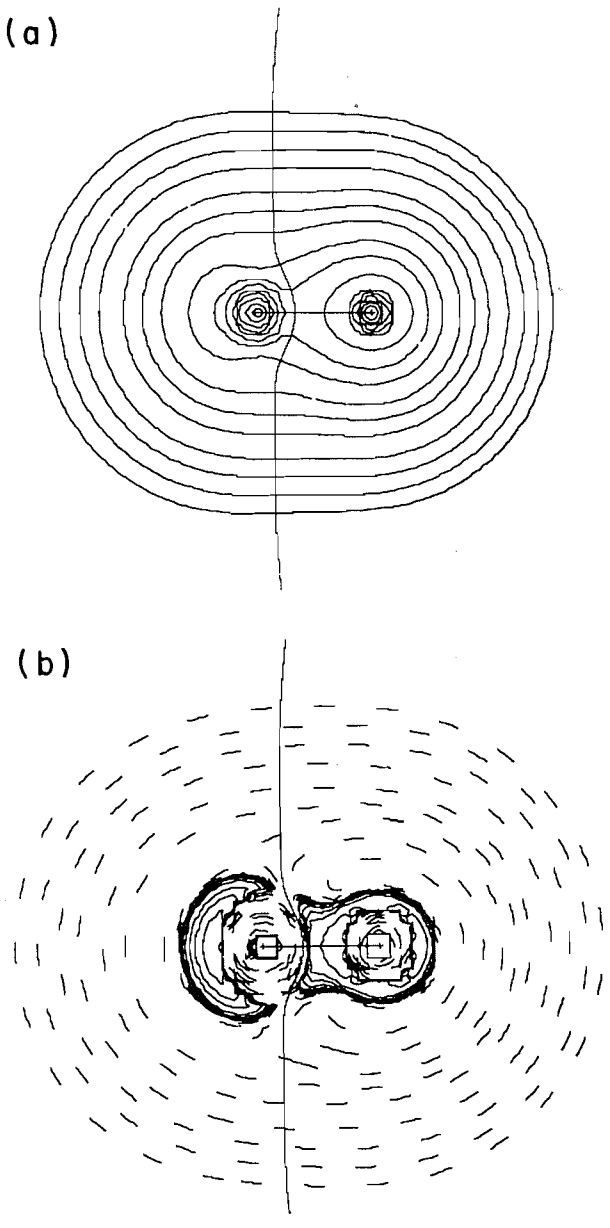

erties are recovered by the summation of atomic contributions to within 2% in general. The molecular polarizabilities are also recovered with summation of the same atomic contributions and their derivatives with respect to applied fields, see Table 3 for CO and Table 4 for CS.

Molecular moments

The origins of the dipole and quadrupole moment of CO and CS have been reported previously (3, 28) and will be briefly reviewed here for clarity. For the dipole moment of CO, the contribution of the transfer of charge from C to the more electronegative O, $q(\Omega)^*X^{\Omega}$, produces a large contribution in the expected direction (recall that the dipole moment, as defined by quantum mechanics, points from the negative "pole" to the positive "pole" (29), opposite to the definition typically used in organic chemistry texts). The nearly

Fig. 2. Contour diagrams of (*a*) the total charge density and (*b*) the Laplacian of the carbon sulfide along the molecular axis. See the caption of Fig. 1.

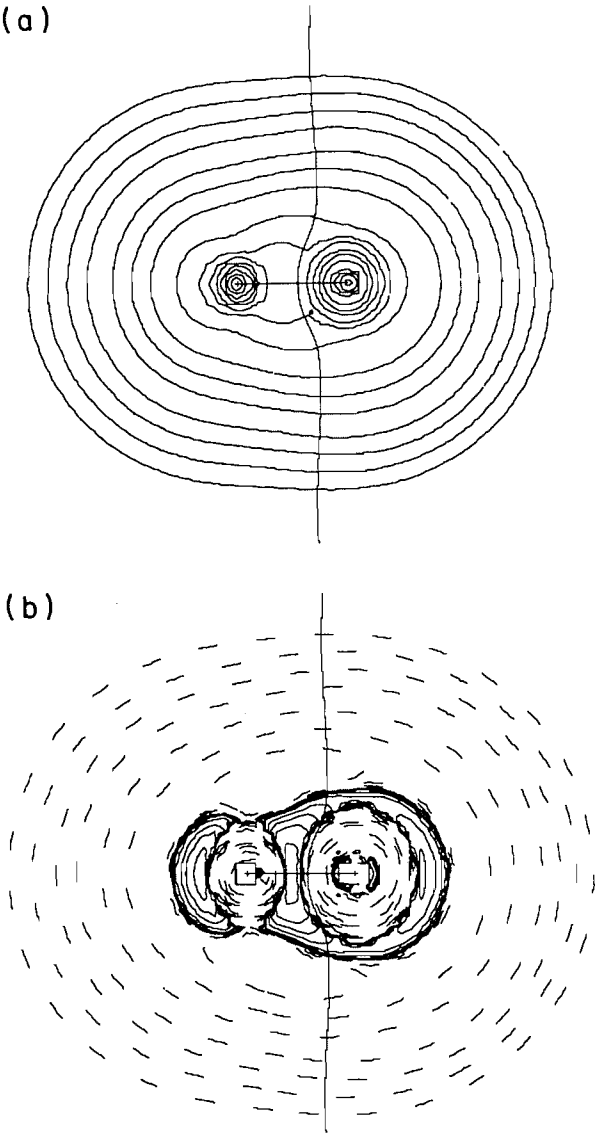

zero dipole moment is the result of the opposing contribution from the large polarization of the remaining charge on C in the opposite direction of the charge transfer. This polarization of charge on carbon can be seen in the Laplacian of the CO charge distribution, Fig. 1*b*, and is the reason for the nucleophilic character of that carbon atom. In the case of CS, the dipole moment has its largest contributions from the transfer of charge from sulfur to carbon. This is offset by a large polarization of sulfur in opposition to the transfer of charge, but this contribution is only ~50% that of the charge transfer to C. The charge density plot of CS in Fig. 2*a* shows that the interatomic surface is much closer to S than to C, which indicates that C is more electronegative than S.

The quadrupole moment of CO is large and negative, indicating that the molecular charge density is preferentially polarized along the molecular axis and contracted along the orthogonal axes. The large transfer of charge from C to O gives

Table 3. Atomic contributions to molecular polarizabilities of carbon monoxide along molecular axis.[a]

CO	Carbon	Oxygen	Atomic sum[a]	Molecular values[a]
$\alpha_{z,z}$	7.947	6.024	13.970	13.995
ΔCT[b]	3.697	2.774	6.470	
ΔM	4.250	3.250	7.500	
$A_{zz,z}$	−21.994	8.168	−13.826	−13.804
ΔCT	−5.038	2.836	−2.202	
ΔM	−11.584	6.646	−4.938	
ΔQ	−12.686	4.800	−7.886	
ΔI	−43.937	26.511	−17.426	
$A_{z,zz}$	−17.509	3.749	−13.759	−13.804
ΔCT	−2.981	−2.282	−5.263	
ΔM	−14.350	5.850	−8.500	
$C_{zz,zz}$	26.73	7.55	34.286	34.240
ΔCT	1.330	−0.577	0.753	
ΔM	12.087	3.213	15.299	
ΔQ	13.100	0.650	13.750	
ΔI	26.083	−5.247	20.863	

[a]All atoms are in atomic units. The subscript notation reads as follows, $\xi_{\alpha\beta,\gamma\delta}$ is the response of the moment $\xi_{\alpha\beta}$ to the applied field, $F_{\gamma\delta}$. For example, $A_{z,zz}$ is the response of the z component of the dipole moment to the application of a field gradient F_{zz}.

[b]ΔCT is the charge transfer contribution, ΔM is the displacement of first moment contribution, ΔQ is the polarization of the second moment contribution, and ΔI is the change in isotopic terms associated with the atomic quadrupole moment. The total contributions of $A_{zz,z}$ and $C_{zz,zz}$ are summed from the atomic contributions as 1/2*(3*(ΔCT + ΔM + ΔQ) − ΔI).

a large charge transfer contribution from C which deemphasizes the polarization along the molecular axis. But this is not as large as the contribution from the displaced first moment contribution from C, as it polarizes away from O. The contributions from the O atom are primarily the result of the atomic second moment of O. Thus, it is the large first moment contribution of C and the second moment of O that determine the negative quadrupole moment of CO. The quadrupole moment of CS is also negative, but roughly half as large as CO. Here, the transfer of charge is from S to C and this results in a large deemphasizing contribution from S, over twice as large as the emphasizing contribution from C. The dominant contribution to polarization along the molecular axis is from the displaced first moment term of S due to the polarization of S away from the C atom. The second moment of S produces half again as large a contribution to Q^{Ω}_{xx} and Q^{Ω}_{yy} as to Q^{Ω}_{zz}, and this dampens the polarization along the axis.

Molecular dipole–dipole polarizability

The axial component of the dipole–dipole polarizability, α_z, of CO has also been discussed (3). Briefly, the atomic contribution of C is larger than that of O, Table 3, with the polarization of the diffuse charge within C providing the largest atomic contribution and the charge transfer contribution, $q(C)^*X^C$, being the next largest. The more tightly held charge in O provides smaller contributions to the polarizability from both transfer of charge and the polarization of charge under the application of an external field.

Table 4. Atomic contributions to molecular polarizabilities of carbon sulfide along molecular axis.[a]

CS	Carbon	Sulfur	Atomic sum[a]	Molecular values[a]
$\alpha_{z,z}$	14.803	9.680	24.482	24.500
ΔCT[b]	11.003	4.130	15.133	
ΔM	3.800	5.550	9.530	
$A_{zz,z}$	9.070	−1.694	7.569	7.567
ΔCT	4.174	−0.588	3.586	
ΔM	2.883	−1.581	1.303	
ΔQ	6.525	−4.213	2.313	
ΔI	22.608	−15.756	6.852	
$A_{z,zz}$	−18.162	25.744	7.582	7.567
ΔCT	4.638	8.094	12.732	
ΔM	−22.800	17.650	−5.150	
$C_{zz,zz}$	36.699	38.408	75.107	74.996
ΔCT	−1.176	3.580	2.404	
ΔM	11.558	15.612	27.170	
ΔQ	15.267	18.467	33.733	
ΔI	3.549	36.158	39.707	

[a]All values in atomic units. The subscripts notation reads as follows, $\xi_{\alpha\beta,\gamma\delta}$ is the response of the moment $\xi_{\alpha\beta}$ to the applied field, $F_{\chi\delta}$. For example, $A_{z,zz}$ is the response of the z component of the dipole moment to the application of a field gradient F_{zz}.

[b]ΔCT is the charge transfer contribution, ΔM is the displacement of first moment contribution, ΔQ is the polarization of the second moment contribution, and ΔI is the change in isotopic terms associated with the atomic quadrupole moment. The total contributions of $A_{zz,z}$ and $C_{zz,zz}$ are summed from the atomic contributions as 1/2*(3*(ΔCT + ΔM + ΔQ) − ΔI).

The dipole–dipole polarizability of CS, Table 4, is nearly twice that of CO. While this is not surprising, the origin of the difference in polarizability along the molecular axis is. The charge transfer term of C is more than twice the magnitude of the other contributions and dominates the molecular tensor. This reflects the ease with which charge may be pushed onto or taken from the less electronegative S. The polarization contribution of S, while large, is only half the charge transfer term of C.

That charge transfer provides large, often dominant contributions to axial polarizabilities has been observed elsewhere (3, 5). This term is crucial in the axial components of both molecular tensors for CO and CS, and is dominating in the latter. This demonstrates that the atomic polarization, while important in describing molecular polarizabilities, is secondary to the transfer of charge between approximately electroneutral atoms within molecules. This term becomes less important as the system becomes more ionic, as in CO. In the limit of ionic interactions, the charge transfer becomes relatively unimportant and the polarization of charge in the atomic basins becomes the dominant contribution (3). Clearly, this has important implications for the design and implementation of representations of molecules for dynamic simulations. Efforts towards inclusion of polarizability within classical force fields would be advised to take into account the differing atomic and functional group origin of these molecular tensors.

Molecular dipole–quadrupole polarizability

The tensor $A_{\alpha,\beta\gamma}$ describes both the change in the quadrupole moment with applied field and the change in the dipole moment with applied electric field gradient. This "cross-term" provides a useful test of the generality of the atomic partitioning described here, as there are two different ways of yielding the same molecular response tensor. The two pathways provide complementary and consistent information about the response of the molecule to external fields.

The quadrupole moments of the two molecules behave differently under the application of an axial electric field. For CO, Table 3, there is an increase in the axial quadrupole component; the molecule polarizes along the axis and contracts along the orthogonal axes. The increased polarization of the charge transfer contribution, the first moment contribution, and the second moment of C along the molecular axis dictate the molecular polarizability. All three of the oxygen contributions are in opposition to this quadrupolar polarization, making contributions to depolarizations along the molecular axis and polarization along the orthogonal axes. This expansion of the torus of charge around the oxygen atom away from the molecular axis cannot overcome the polarizations along the molecular axis by the diffuse charge on the carbon atom. The molecular quadrupole of CS, in contrast, contracts along the molecular axis and expands along the orthogonal axes. The C atom also dominates $A_{zz,z}$ in CS, Table 4, but here provides large contributions for quadrupolar polarization away from the molecular axis. The largest contributions are the charge transfer and the second moments of C. All the contributions from the S atom provide contributions for polarization along the molecular axis with contractions along the orthogonal axes.

Viewing the same tensor as the change in the molecular dipole with applied electric field gradient yields a complementary picture. In CO, the polarization of the C atom along the molecular axis yields the largest contribution to the molecular value. There is a depolarization of O, the same quadrupolar polarization seen in the application of an electric field, but this is roughly one third the size of the C atom's contribution. For CS we find the large dipole depolarization of S is overcome by the large charge transfer contributions of C. The S atom also contributions a large charge transfer contribution in support of the polarization term of C.

For CO, both ways of looking at the tensors find the quadrupolar polarization of O away from the molecular axis overcome by the polarization of the diffuse charge on C along the molecular axis. This diffuse charge concentration, Fig. 1*b*, dictates the response tensors of this molecule. The case of CS is more general in that no single character of the molecule dictates is response to the differing external fields. When under the application of an electric field, which pushes along the molecular axis, the C atom polarizes away from the direction of force. Inspecting Fig. 2*b*, one sees that the bonding charge density within the C basin adjacent to the interatomic surface is distributed such that an axial field will cause that charge to expand away from the molecular axis. (In contrast, the entire bonding charge concentration between C and O is within the basin of O and it is that atom which shows quadrupolar polarization away from the molecular axis.) In the face of a field gradient, which pushes charge so as to yield a quadrupolar polarization of an isolated atom, there

is a large polarization of C along the molecular axis. But the quadrupolar polarization of the S and the charge transfer contributions of both C and S against the direction of the field gradient overcome the contributions of the polarization of C.

Molecular quadrupole–quadrupole polarizability

The effect of a field gradient upon the quadrupole moment yields the quadrupole–quadrupole polarizability tensor, $C_{zz,zz}$, $C_{zz,zz}$ for CS is twice as large as that for CO, primarily through the difference in behavior of O and S. Both molecules experience quadrupole polarizations away from the molecular axis with application of the field gradient, F_{zz}. In both molecules the contributions of the first and second moments of C are large, as the relatively diffuse charge on the C atom polarizes away from the molecular axis in the direction of the field gradient. The tightly held charge of O yields relatively small quadrupolar polarization contributions in CO, while those of the first and second moment contributions of S dominate the tensor in CS. As expected, the less tightly held charge of S yields large polarization contributions through the first and second moment contributions.

Conclusions

Molecular polarizabilities can be partitioned into atomic contributions, each of which depends upon the change in the distribution of electronic charge within the individual atoms under the application of an external field. Each of the atomic contributions is the result of the change in the moments of the individual atoms and there are no other nonphysical terms that emerge within the formalism. The contributions of each atom are based upon the physical observables of that atom, the charge, the first moment, etc., and their change under the application of external fields.

This approach provides a detailed understanding of the origin of molecular polarizabilities based upon the contributions made by atoms and functional groups. This has important implications in the design and development of representations of molecules for mechanical modeling and dynamic simulations. This method will provide one of the foundations of our general methodology for the construction and representation of very large molecules for use in static and dynamic simulation.

Acknowledgments

The author is pleased to acknowledge the financial support provided by Professor Daggett of the Department of Medicinal Chemistry at the University of Washington.

References

1. A.D. Buckingham. *In* Intermolecular interactions: from diatomics to biopolymers. *Edited by* B. Pullman. Wiley & Sons, Chichester. 1978. p. 1.
2. A.D. Buckingham. Adv. Chem. Phys. **12**, 107 (1967).
3. K.E. Laidig and R.F.W. Bader. J. Chem. Phys. **93**, 7213 (1990).
4. J. Applequist. Acc. Chem. Res. **10**, 79 (1977).
5. A.J. Stone. Mol. Phys. **56**, 1065 (1985).
6. C.R. Le Sueur and A.J. Stone. Mol. Phys. **78**, 1267 (1993).
7. C.R. Le Sueur and A.J. Stone. Mol. Phys. **83**, 293 (1995).
8. R.E. Hester. *In* Molecular spectroscopy. Vol. 2. *Edited by* R.F. Barrow, D.A. Long, and D.J. Milen. Chemical Society, London. 1974. p. 439.
9. M. Gusoni, S. Abbate, and G. Zerbi. *In* Vibrational spectroscopy — modern trends. *Edited by* A.J. Barnes and W.J. Orville-Thomas. Elsevier, Amsterdam. 1977. p. 205.
10. M. Gusoni. *In* Advances in infrared and Raman spectroscopy. Vol. 6. *Edited by* R.J.H. Clark and R.E. Hester. Heyden, London. 1980. p. 61.
11. W.B. Person and G. Zerbi (*Editors*). Vibrational intensities in infrared and Raman spectroscopy. Elsevier, Amsterdam. 1982.
12. J.G. Angyán, D. Jansen, M. Loos, C. Hättig, and B.A. Heß. Chem. Phys. Lett. **219**, 267 (1994).
13. K.E. Laidig. J. Phys. Chem. **97**, 12760 (1993).
14. R.F.W. Bader. Atoms in molecules: a quantum theory. Clarendon Press. Oxford. 1990.
15. R.F.W. Bader and T.T. Nguyen-Dang. Adv. Quantum Chem. **14**, 63 (1981).
16. R.F.W. Bader and P.L.A. Popelier. Int. J. Quantum Chem. **45**, 189 (1993).
17. R.F.W. Bader and T.A. Keith. J. Chem. Phys. **99**, 3683 (1993).
18. R.F.W. Bader, P.L.A. Popelier, and T.A. Keith. Angew. Chem. Int. Ed. Engl. **33**, 620 (1994).
19. R.F.W. Bader. Int. J. Quantum Chem. **49**, 299 (1994).
20. R.F.W. Bader and P. Zhou. Chem. Phys. Lett. **191**, 54 (1992).
21. R.F.W. Bader, T.A. Keith, K.M. Gough, and K.E. Laidig. Mol. Phys. **75**, 1164 (1992).
22. R.F.W. Bader and P. Becker. Chem. Phys. Lett. **148**, 452 (1988).
23. R. Krishnan, J.S. Binkley, R. Seeger, and J.A. Pople. J. Chem. Phys. **72**, 650 (1980); P.C. Hariharan and J.A. Pople. Theor. Chim. Acta. **28**, 213 (1973).
24. M.W. Schmidt, K.K. Baldridge, J.A. Boatz, S.T. Elbert, M.S. Gordon, J.H. Jensen, S. Koseki, N. Matsunaga, K.A. Nguyen, S.J. Su, T.L. Windus, M. Dupuis, and J.A. Montgomery. J. Comput. Chem. **14**, 1347 (1993).
25. R.D. Amos, I.L. Alberts, J.S. Andrews, S.M. Colwell, N.C. Handy, D. Jayatilaka, P.J. Knowles, R. Kobayashi, N. Koga, K.E. Laidig, P.E. Maslen, C.W. Murray, J.E. Rice, J. Sanz, E.D. Simandiras, A.J. Stone, and M.D. Su. CADPAC5: The Cambridge Analytic Derivatives Package, issue 5.0. Cambridge. 1992.
26. K.E. Laidig and R.D. Amos. ANVIL5: The Cambridge Analytical Derivatives Wave function Analysis Package. Cambridge. 1992.
27. F.W. Biegler-König, R.F.W. Bader, and T.H. Tang. J. Comput. Chem. **3**, 317 (1982).
28. K.E. Laidig. Chem. Phys. **282**, 167 (1992).
29. P.W. Atkins. Quanta. A handbook of concepts. Oxford University Press, Oxford. 1991.

Analysis of molecular polarizabilities and polarizability derivatives in H_2, N_2, F_2, CO, and HF, with the theory of atoms in molecules

Kathleen M. Gough, Margaret M. Yacowar, Richard H. Cleve, and Jason R. Dwyer

Abstract: Ab initio molecular orbital calculations have been performed on the title molecules at the SCF-HF and MP2 levels to obtain molecular polarizabilities and the derivatives associated with bond stretch. The wave functions from these calculations have been analyzed with the theory of atoms in molecules (AIM). Both the polarizability and its derivative are successfully reconstructed from AIM terms representing the transfer of charge between atoms (CT = charge transfer) and the rearrangement of charge within an atomic basin (AD = atomic dipole). The results for the diatomics are compared to each other and to the alkanes studied previously. Equilibrium polarizabilities are qualitatively explained with reference to atomic electronegativity and type of bonding. While derivatives of the mean molecular polarizability differ by a factor of two at most, individual contributions vary by an order of magnitude. The derivatives along the bond axis for H_2 are $\Delta CT = 2.06$ and $\Delta AD = -0.62 \times 10^{-30}$ C m/V, while for N_2 they are $\Delta CT = 13.77$ and $\Delta AD = -10.00 \times 10^{-30}$ C m/V. The common feature observed is that as the induced dipole due to charge transfer increases, the induced dipole due to changes in the atomic dipole also increases and *opposes* it.

Key words: diatomic molecules, molecular polarizability, molecular polarizability derivative, theory of atoms in molecules, ab initio molecular orbital calculations.

Résumé : Afin d'obtenir les polarisabilités moléculaires et les dérivés associées à l'élongation des liaisons, on a effectué des calculs d'orbitales moléculaires ab initio, aux niveaux SCG-HF et MP2, sur les molécules mentionnées dans le titre. On a analysé les fonctions d'onde obtenues à partir de ces calculs à l'aide de la théorie des atomes dans les molécules (ADM). On a pu reconstituer avec succès la polarisabilité ainsi que sa dérivé à partir de termes d'ADM qui représentent le transfert de charge entre les atomes (TC = transfert de charge) et le réarrangement de la charge à l'intérieur du basin atomique (DA = dipôle atomique). On compare les résultats pour les molécules diatomiques entre eux et avec ceux obtenus antérieurement pour les alcanes. On peut expliquer qualitativement les polarisabilités d'équilibre en faisant référence à l'électronégativité atomique et au type de liaison. Les dérivés de la polarisabilité moléculaire moyenne diffèrent, au plus, par un facteur de deux; toutefois, les contributions individuelles varient par un ordre de grandeur. Pour le H_2, les dérivés le long de l'axe de liaison correspondent à $\Delta TC = 2{,}06$ et $\Delta DA = -0{,}62 \times 10^{-30}$ C m/V, alors que, pour le N_2, elles sont égales à $\Delta TC = 13{,}77$ et $\Delta DA = -10{,}00 \times 10^{-30}$ C m/V. La caractéristique commune observée est que, lorsque le dipôle induit dû au transfert de charge augmente, le dipôle induit dû aux changements dans le dipôle atomique augmente aussi et qu'il s'y *oppose*.

Mots clés : molécules diatomiques, polarisabilité moléculaire, derivé de la polarisabilité moléculaire, théorie des atomes dans les molécules, calculs d'orbitales moléculaires ab initio.

[Traduit par la rédaction]

Introduction

Molecular polarizabilities (α) and their derivatives play an important role in many phenomena. We have been investigating structural and conformational dependencies of derivatives of the mean molecular polarizability ($\partial\bar{\alpha}/\partial r$, where $\bar{\alpha} = (1/3)[\alpha_{xx} + \alpha_{yy} + \alpha_{zz}]$) in hydrocarbons: methane, ethane, propane (1*a*,*b*), butane (1*a*), cyclohexane (1*c*), pentane (1*d*), ethene and ethyne (2), and the methyl halides (CH_3X, X = F, Cl, Br) (3*a*,*b*). The experimental values of the derivatives are obtained from absolute intensity measurements in gas phase Raman spectra, while theoretical values are obtained from ab initio SCF-HF molecular orbital (MO) calculations. Further insight into the nature of the derivatives is obtained by analyzing the resulting wave functions with the theory of atoms in molecules (AIM), introduced by Richard Bader (4, 5). With the AIM analysis, we are able to examine the charge redistribution which constitutes both α and $\partial\bar{\alpha}/\partial r$. Several interesting trends have been discovered that throw serious doubt on the reliability of the bond polarizability model, conventionally used as a means of interpreting Raman scattering intensities (1–3).

Received November 3, 1995.

This paper is dedicated to Professor Richard F.W. Bader on the occasion of his 65th birthday.

K.M. Gough,[1] M.M. Yacowar,[2] R.H. Cleve,[3] and J.R. Dwyer.[2] Department of Chemistry, University of Manitoba, Winnipeg, MB R3T 2N2, Canada.

[1] Author to whom correspondence may be addressed. Telephone: (204) 474-9321. Fax: (204) 275-0905.

[2] Present address: Department of Chemistry, Brock University, St. Catharines, ON L2S 3A1, Canada.

[3] Present address: Department of Physics, University of Guelph, Guelph, ON N1G 2W1, Canada.

There is little experimental information available for molecules larger than methane and, even for small molecules, the theoretical data far outnumber the experimental. In an endeavor to broaden the scope of our study, we have now undertaken a theoretical analysis of five diatomic molecules: H_2, F_2, HF, N_2, and CO. The data on their equilibrium molecular polarizabilities have been well characterized experimentally (6–11) and theoretically (12–23); reasonable basis sets exist for the MO calculations; some data on $\partial\alpha/\partial r$ exist for all five molecules (24–30); and, finally, they embody an interesting range and variety of fundamental characteristics. The equilibrium values of α have already been examined to some extent with AIM (1*a*, 18) with slightly smaller basis sets than those employed in the present work. A study of the distributed atom–atom multipolar polarizability of CO has been reported recently (13) and our equilibrium results are quite similar. Our intent here is to reconsider α, with particular emphasis on a comparison between the equilibrium polarizabilities and the derivatives.

Computational method

Choice of basis set

For accurate calculations of the electronic properties, the basis set must be large and well polarized (12–23). Computational limitations in our previous work (1–3) on small alkanes necessitated the use of a relatively small basis: D95**, the Dunning (31) contraction of the Huzinaga (32) basis set (9*s*5*p*1*d*)/[4*s*2*p*1*d*]. With the diatomics, size and speed of computation presented less of an obstacle, and a new larger basis was sought. A recent article (12) has outlined some guidelines for basis set design and provided an extensive survey of the literature for, among others, H_2 and HF.

We calculated α with a number of published basis sets and selected the polarized set developed by Sadlej (23) specifically for the calculation of electronic properties. Our calculations were performed prior to the publication of the work of Papadopoulos et al. (12); however, we note that this basis set yields values for α that are about as good as theirs, at the SCF-HF level. A useful criterion (19) for the quality of the basis set is the magnitude of $\Delta\alpha = \alpha_{//} - \alpha_{\perp}$ where, for a linear molecule, $\alpha_{xx} = \alpha_{yy} = \alpha_{\perp}$ and $\alpha_{zz} = \alpha_{//}$. A poorly polarized basis set may lead to an apparently good value for $\bar{\alpha}$, due to overestimation of $\alpha_{//}$ and underestimation of $\alpha_{\perp}$. Our choice was based on the energy of the molecule and the magnitudes of both α and $\Delta\alpha$; however, we did not examine higher order properties, which would provide further criteria for assessment.

Electron correlation

Depending on the molecule, electron correlation may have considerable influence on higher order moments. For comparison, our calculations were repeated at the MP2 level, both at the optimized geometries from the SCF-HF calculations and at geometries reoptimized for the MP2 level. It is unfortunate that the version of code for AIM theory currently available (33) does not accommodate electron correlation contributions, restricting the analysis to the SCF-HF wave functions. While this introduces greater uncertainty into the absolute values calculated below, the results provide interesting and useful qualitative information.

Calculation of α and $\partial\bar{\alpha}/\partial r$ through AIM

All MO calculations were performed with Gaussian 90 (34). Geometry optimization preceded the calculation of any electronic properties. The dipole (or linear) polarizability was calculated analytically through the coupled perturbed Hartree–Fock theory implemented in the Gaussian 90 program. Values of the derivatives could be obtained analytically; however, it was our intent to examine both the polarizability and the derivative within the context of the AIM theory. To do this, we require the wave functions for the molecule both in the presence and absence of an electric field (to determine α) and at equilibrium and stretched or compressed bond lengths (to determine $\partial\bar{\alpha}/\partial r$). The procedure followed was the same as that described in earlier work (1*a*–*d*), and we present only a brief synopsis.

The wave functions were obtained from the Gaussian read-write file and analyzed with the AIMPAC suite of programs (33). The AIM theory provides a method for defining the volume of the electronic charge distribution associated with each nucleus in a molecule (5). It has been shown (5) that all properties that may be calculated for the molecule (e.g., electron population, dipole moment, etc.) may be calculated for an atomic basin. Molecular properties are found as the sum of the atomic contributions. The parameters of interest here are (*i*) the atomic electron population: the total number of electrons found within an atomic basin, and (*ii*) the atomic dipole moment: the way in which that charge is distributed throughout the atomic basin.

Molecular polarizability is the measure of the ease with which the charge in a molecule may be displaced in response to an external electric field. The contribution of atom Ω to the ijth element of the molecular polarizability tensor may be written as:

$$[1]\quad \alpha_{ij,\Omega} = \underbrace{\frac{[-(N_i - N_0)]\cdot r_{j,\Omega}}{\mathscr{E}_i}}_{\text{charge transfer}} + \underbrace{\frac{(\mu_{ij} - \mu_{0j})_\Omega}{\mathscr{E}_i}}_{\text{atomic dipole}}$$

where i denotes the direction of the applied field, while 0 implies zero field. The first term represents the charge transferred into or out of the atomic basin due to the applied field; the second term, the change in atomic first moment ($\Delta\mu$). N_i and N_0 are the atomic electron populations for the given fields, r_j is the position on the jth axis, for atom Ω. For the molecules studied here, the internuclear bond is directed along the z-axis, producing a diagonal polarizability tensor, with $\alpha_{xx} = \alpha_{yy} < \alpha_{zz}$.

From calculations of α at the optimized geometry ($r = r_e$) and at $r_e \pm 0.005$, ± 0.010, and ± 0.020 Å, it was verified that the polarizability was changing linearly, to within the precision reported. The derivative is calculated from the numerical difference ($\Delta\alpha_{ij}$) between the polarizability at the equilibrium geometry and that for a geometry in which the nuclei have been displaced by 0.010 Å, divided by the magnitude of the displacement:

$$[2]\quad \partial\alpha_{ij}/\partial r \approx \Delta\alpha_{ij}/\Delta r$$

All AIMPAC calculations were performed at the limits of accuracy possible with the current versions of the code.

Table 1. Polarizability components for H_2, N_2, F_2, CO, and HF in units of 10^{-40} C m^2/V calculated at SCF and MP2 levels, compared to literature values (theoretical and experimental; references in italics).

Molecule	Method (reference)	$\bar{\alpha}$	$\alpha_{//} - \alpha_{\perp}$
H_2	SCF (this work)	0.865	0.371
	AIM from SCF (this work)	0.865	0.370
	MP2 (this work)	0.879	0.393
	Correl. via CCSD (14)	0.861	0.314
	Expt. (10, 12)	0.916, 0.858	0.345
N_2	SCF (this work)	1.837	0.838
	AIM from SCF (this work)	1.838	0.838
	MP2 (this work)	1.950	0.793
	Correl. via CCSD (14)	1.938	0.803
	Expt. (6, 8)	1.967, 1.939	0.782, 0.734
F_2	SCF (this work)	1.269	1.123
	AIM from SCF (this work)	1.267	1.125
	MP2 (this work)	1.358	0.815
	Correl. via SDQ-MPPT (20)	1.400	0.983
	Expt. (11, 20)	1.424	
CO	SCF (this work)	1.987	0.512
	AIM from SCF (this work)	1.990	0.531
	MP2 (this work)	2.197	0.694
	Correl. via CCSD (14)	2.150	0.646
	Expt. (6)	2.031	0.527
HF	SCF (this work)	0.784	0.200
	AIM from SCF (this work)	0.784	0.201
	MP2 (this work)	0.946	0.190
	Correl. via CCSD (14)	0.922	0.193
	Expt. (12, 9)	0.947	0.183, 0.220

Experimental data

Molecular polarizabilities have been measured by a variety of methods (6–11). Polarizability derivatives are obtained from absolute scattering cross sections in Raman spectra (24–27). The $\partial\bar{\alpha}/\partial r$ values require separate measurement of isotropic (or trace) and anisotropic scattering intensities, which in turn require measurement of the differences in the parallel ($I_{//}$) and perpendicular ($I_{\perp}$) components of the Raman scattered light:

[3] $$I_{//} \propto 45(\partial\bar{\alpha}/\partial r)^2 + 4(\partial\gamma/\partial r)^2$$

[4] $$I_{\perp} \propto 3(\partial\gamma/\partial r)^2$$

The anisotropic scattering, $(\partial\gamma/\partial r)$, is more difficult to measure experimentally and the calculation is subject to a greater relative error (1*a–d*, 2), hence our decision to examine only $(\partial\bar{\alpha}/\partial r)$.

Results and discussion

Molecular polarizability

There are three sets of α and $\partial\bar{\alpha}/\partial r$ to be considered: (*a*) experimental values, (*b*) those obtained analytically from the MO program, and (*c*) those constructed from the AIM analysis of the MO wave functions. The latter two should be identical. The degree to which the AIM results recover the analytical values is a measure of the completeness of the integrations over the atomic basins. Since the change in α due to these small displacements is only 1–3% of the equilibrium value, any meaningful analysis of the AIM data on the derivatives can take place only if the recovery of α at each point is better than 99.5%.

The molecular polarizabilities from SCF-HF and MP2 calculations from the AIM analysis of the SCF-HF wave functions for the five molecules are listed in Table 1. Experimental values and selected calculated values from the literature are presented for comparison.

The SCF values obtained with Sadlej's basis set are of comparable quality to those of other calculations at this level. Small differences arise from our use of optimized rather than experimental bond lengths. Overall, the SCF results are quite reasonable, as is the anisotropy ($\alpha_{//} - \alpha_{\perp}$), which is best for H_2 and N_2, and poorest for HF.

Our MP2 results are reported for the bond lengths obtained by reoptimization at this level. All bond lengths are slightly longer, and this alone accounts for about half of the difference between the SCF and MP2 values. As has been noted by others (12), it is clear that the polarizability of H_2 is little altered by the inclusion of electron correlation. N_2 is only changed by about 5%, and CO slightly more; however, electron correlation significantly changes the calculated polarizability for F_2

Table 2. Experimental (references as noted) and calculated values of the derivative of the mean molecular polarizability ($\partial\bar{\alpha}/\partial r$), in units of 10^{-30} C m/V.

Molecule	SCF	SCF-AIM	MP2	Expt.	Ref. no.
H_2	1.53	1.53	1.42	1.36	25
				1.25	28
				1.23–1.3	24
N_2	2.22	2.22	2.01	1.95	24
				1.85	28
F_2	1.63	1.63	1.14	1.02	28
CO	1.56	1.57	1.65	1.50	24
				1.72	28
HF	0.77	—	0.93	1.13	25

Table 3. Breakdown of molecular polarizability and polarizability derivatives in terms of charge transfer and atomic dipole contributions (units: α: 10^{-40} C m^2/V; $\partial\bar{\alpha}/\partial r$: 10^{-30} C m/V).

Molecule	Charge transfer		Atomic dipole		Total	
: property	⊥	//	⊥	//	⊥	//
H_2: α	0	1.058	0.741	0.054	0.741	1.112
$\partial\bar{\alpha}/\partial r$	0	2.86	1.17	−0.62	1.17	2.25
N_2: α	0	1.527	1.558	0.869	1.558	2.396
$\partial\bar{\alpha}/\partial r$	0	13.77	1.45	−10.00	1.45	3.77
F_2: α	0	1.484	0.892	0.533	0.892	2.017
$\partial\bar{\alpha}/\partial r$	0	4.65	0.24	−0.25	0.24	4.40
CO: α	0	1.042	1.814	1.302	1.814	2.344
$\partial\bar{\alpha}/\partial r$	0	2.59	1.02	0.89	1.02	3.48
HF: α	0	0.408	0.716	0.513	0.716	0.921

and HF (10–20%). Any AIM analysis of the polarizability must be considered as less reliable for the latter two compounds.

There is little experimental data available on the polarizability derivatives, particularly the $\partial\bar{\alpha}/\partial r$ values calculated in this work. The best data are presented in Table 2 along with our values calculated at SCF and MP2 levels of theory, and those recovered by the AIM analysis of the SCF wave functions. The error estimates in the experimental data are about 5%. Once again, the results for F_2 and HF are most affected by electron correlation.

In all cases, the AIM analysis enables us to reconstruct the equilibrium molecular polarizability to the level of accuracy required for valid interpretation. For HF, the recovery of non-equilibrium polarizabilities, required for the derivative, was only 98–99%, and interpretation of the AIM derivative data was not considered to be warranted.

AIM analysis of α and $\partial\bar{\alpha}/\partial r$

The breakdown of the polarizability and the polarizability derivatives in terms of charge transfer and atomic dipole components, as given in eq. [1], is presented in Table 3. Both the charge transfer and the atomic dipole contributions to the equilibrium polarizability are positive. This initially appears to be in direct contrast to the situation found with the alkanes, but in fact is not surprising.

In the alkanes, the principal contributions to the molecular polarizability were found to be a large *positive* contribution from charge transfer between the (exterior) hydrogens, a small *positive* contribution from their induced atomic dipoles, and a large *negative* contribution from the atomic dipole of the (interior) carbon atoms. Essentially, the alkanes behave as small units of dielectric material. The presence of an external field causes a surface charge polarization to appear (field-induced charge transfer between exterior atoms) that is balanced in part by the response of the internal atoms to the local external field (field-induced changes in atomic dipole moments). Diatomic molecules exhibit only the positive charge transfer and atomic dipole contributions of exterior atoms.

The $\partial\bar{\alpha}/\partial r$ of H_2 is less than half that of N_2, yet at its equilibrium geometry H_2 exhibits the largest // charge transfer. In contrast, the ⊥ atomic dipole contribution is quite small and

the // atomic dipole contribution is almost negligible. The ⊥ contribution to the polarizability is greatest in N_2 and CO, which are triply and doubly bonded, respectively.

It is interesting to note that while SCF-HF calculations produce a molecular dipole for CO that is opposite to that observed experimentally (35), the molecular polarizability is of reasonable magnitude and sign, as is the derivative. The problem with the dipole moment rests in part with its small size, where a small error in calculated value can result in a sign change. Electron correlation is required to obtain the correct dipole moment (35) but makes a change of only 6% in the derivative. Thus while there is some error in the assignment of the electrons to the nuclei, the shift in electron population in response to an applied field is as expected.

The // charge transfer contribution to the polarizability derivative for H_2 is about 2.9×10^{-30} C m/V and is opposed by a // atomic dipole contribution of about -0.6×10^{-30} C m/V, while the corresponding terms in N_2 are $+13.8 \times 10^{-30}$ and -10.0×10^{-30} C m/V. This is not unlike the behavior found in the alkanes when a CH bond is stretched, in that increases in charge transfer between carbon atoms are generally offset by decreases in the atomic dipoles on the attached hydrogen atoms. However, the similarity is only qualitative. The relative magnitudes of the terms are surprisingly different.

The polarizability derivatives of the diatomics studied here exhibit some general similarities. In all cases, $\bar{\alpha}$ of a molecule increases as the bond is stretched. This arises from an increase in the amount of charge transferred between atoms for a field applied along the bond axis, and an increase in the induced atomic dipoles for a field applied perpendicular to the bond. However, as the amount of charge transfer increases, so too does the induced atomic dipole opposing the charge transfer. Thus the net results are quite similar, despite differences of an order of magnitude in individual terms.

On comparing the homonuclear diatomics, it may be noted that F_2, the most electronegative element with the smallest molecular polarizability, exhibits the smallest tendency to both charge transfer and atomic dipole rearrangement, whether at equilibrium or during the stretching vibration. The only exception is the derivative of the parallel charge transfer contribution, which is about double that in H_2. The derivative (Table 2) is calculated to be the smallest of the four analyzed with AIM. In this, it is similar to HF, where the equilibrium polarizability is found to be quite small and the SCF and MP2 values for the derivative are also small, in agreement with the experimental results. The derivative for F_2 decreases by 30% when electron correlation is included, thus any SCF-HF data should not be overinterpreted. The qualitative results are as expected for this molecule.

Conclusions

The theory of atoms in molecules is found to provide interesting insights into the nature of molecular polarizability and the polarizability derivative. The dipole induced in a molecule by the presence of an external field has been broken down into a dipole contribution due to charge transfer between atomic basins and a contribution due to reorientation of charge within an atomic basin. The polarizability of diatomic molecules is similar to that of the alkanes studied previously, in that, as exterior atoms, both the charge transfer and atomic dipole contributions are positive. Variations in the magnitude of the individual terms may be rationalized in light of the electronegativity of individual atoms and the number of bonds (single, double, or triple). The mean molecular polarizability derivatives differ at most by a factor of two, but individual changes in both charge transfer and atomic dipole terms differ by an order of magnitude. In general, an increase in the charge transfer along a stretched bond is offset, at least in part, by an increase in the atomic dipole *opposing* that of the charge transfer. These findings are quite intriguing, and illustrate the usefulness of the theory of atoms in molecules as a probe of molecular electronic behavior. A most desirable extension to the AIMPAC suite of programs would be the capacity to perform calculations on wave functions that include electron correlation effects.

Acknowledgments

K.M.G. is happy to express her gratitude to Professor Richard Bader, for the two stimulating and enjoyable years she spent as an NSERC post-doctoral fellow in his research group (1987–1989), and for the cordial friendship and assistance which he has offered ever since. R.H.C. is grateful to the Natural Sciences and Engineering Research Council of Canada for an undergraduate summer research award (1994). This work was supported by a grant from the Natural Sciences and Engineering Research Council of Canada.

References

1. (*a*) K.M. Gough. J. Chem. Phys. **91**, 2424 (1989); (*b*) K.M. Gough, H.K. Srivastava, and K. Belohorcová. J. Chem. Phys. **98**, 9669 (1993); (*c*) J. Phys. Chem. **98**, 771 (1994); (*d*) K.M. Gough and H.K. Srivastava. J. Phys. Chem. **100**, 5210 (1996).
2. K.M. Gough and W.F. Murphy. J. Mol. Struct. **224**, 73 (1990) and references therein.
3. G. Sharma. M.Sc. Thesis, Brock University, St. Catharines, Ont., Canada. 1993; M. Upton. B.Sc. Thesis, Brock University, St. Catharines, Ont., Canada. 1995.
4. R.F.W. Bader, T.A. Keith, K.M. Gough, and K.E. Laidig. Mol. Phys. **75**, 1167 (1992).
5. R.F.W. Bader. Atoms in molecules — a quantum theory. Oxford University Press, Oxford. 1990.
6. M.P. Bogaard, A.D. Buckingham, R.K. Pierens, and A.H. White. J. Chem. Soc. Faraday Trans. 1, **74**, 3008 (1978).
7. H.J. Werner and W. Meyer. Mol. Phys. **31**, 855 (1976).
8. G.R. Alms, A.K. Burnham, and W.H. Flygare. J. Chem. Phys. **63**, 3321 (1975).
9. J.S. Meunter. J. Chem. Phys. **56**, 5409 (1972).
10. (*a*) N.J. Bridge and A.D. Buckingham. Proc. R. Soc. London, Ser. A: **295**, 334 (1966); (*b*) J. Chem. Phys. **40**, 2733 (1964).
11. E.U. Franck. Naturwissenschaften, **41**, 37 (1954)
12. M.G. Papadopoulos, J. Waite, and A.D. Buckingham, J. Chem. Phys. **102**, 371 (1995).
13. J.G. Ángyán, G. Jansen, M. Loos, C. Hättig, and B. Heß. Chem. Phys. Lett. **219**, 267 (1994).
14. H. Sekino and R.J. Bartlett. J. Chem. Phys. **98**, 3022 (1993).
15. G.H.F. Diercksen and A.J. Hernandez. J. Mol. Struct. (Theochem), **254**, 191 (1992).
16. G.H.F. Diercksen, J. Oddershede, I. Paidarova, and J.R. Sabin. Int. J. Quantum Chem. **39**, 755 (1991).
17. D.P. Chong and S.R. Langhoff. J. Chem. Phys. **93**, 570 (1990).
18. K.E. Laidig and R.F.W. Bader. J. Chem. Phys. **93**, 7213 (1990).
19. G. Maroulis and A.J. Thakkar. J. Chem. Phys. **88**, 7623 (1988).

20. G. Maroulis and A.J. Thakkar. J. Chem. Phys. **88**, 366 (1989).
21. J. Oddershede and E.N. Svendsen. Chem. Phys. **64**, 359 (1982).
22. G.D. Zeiss and W.J. Meath. Mol. Phys. **33**, 1155 (1977).
23. A.J. Sadlej. Collect. Czech. Chem. Commun. **53**, 1995 (1988).
24. W.F. Murphy, W. Holzer, and H.J. Bernstein. Appl. Spectrosc. **23**, 211 (1969).
25. Y. Le Duff and W. Holzer. J. Chem. Phys. **60**, 2175 (1974).
26. J.M. Hoell, F. Allario, O. Jarrett, Jr., and R.K. Seals. J. Chem. Phys. **58**, 2896 (1973).
27. W.R. Fenner, H.H. Hyatt, J.M. Kellam, and S.P.S. Porto. J. Opt. Soc. Am. **63**, 73 (1973).
28. B. Fontal and T.G. Spiro. Spectrochim. Acta, Part A: **33**, 507 (1977).
29. S.R. Langhoff, C.W. Bauschlicher, Jr., and D.P. Chong. J. Chem. Phys. **78**, 5287 (1983).
30. E.N. Svendsen and J. Oddershede. J. Chem. Phys. **71**, 3000 (1979).
31. T.H. Dunning. J. Chem. Phys. **53**, 2823 (1970); **55**, 716 (1971).
32. S. Huzinaga. J. Chem. Phys. **42**, 1293 (1965).
33. AIMPAC, McMaster University, Hamilton, Ont. 1990; F.W. Biegler-Konig, R.F.W. Bader, and T.H. Tang. J. Comput. Chem. **3**, 317 (1982).
34. M.J. Frisch, M. Head-Gordon, G.W Trucks, J.B. Foresman, H.B. Schlegel, K. Raghavachari, M.A. Robb, J.S. Binkley, C. Gonzalez, D.J. DeFrees, D.J. Fox, R.A. Whiteside, R. Seeger, C.F. Melius, J. Baker, R.L. Martin, L.R. Kahn, J.J.P. Stewart, S. Topiol, and J.A. Pople. Gaussian90, Revision I. Gaussian Inc., Pittsburgh, Pa. 1990.
35. W.J. Hehre, L. Radom, P.v.R. Schleyer, and J.A. Pople. Ab initio molecular orbital theory. John Wiley and Sons, New York. 1986. p. 331.

Charge density in crystalline citrinin from X-ray diffraction at 19 K

Pietro Roversi, Mario Barzaghi, Felicita Merati, and Riccardo Destro

Abstract: For the fungal metabolite citrinin, $C_{13}H_{14}O_5$, the total experimental electron distribution $\rho(\boldsymbol{r})$ and its Laplacian $\nabla^2\rho(\boldsymbol{r})$ have been obtained from an extensive set (36 564 measurements) of single-crystal X-ray diffracted intensities at a temperature of 19 ± 2 K. Relevant steps in data collection and processing are reported. The resulting 7698 independent intensity data have been analysed with a multipole (pseudoatoms) formalism. The topological properties of $\rho(\boldsymbol{r})$ have been determined according to the quantum theory of atoms in molecules. CC and CO bond path lengths have been obtained by numerical integration; their values are found to be well correlated with those of the electron density at the bond critical points. Topological features have been used to characterize the extension of the conjugated system of the molecule, and to confirm the stability of its rings, particularly the two formed by intramolecular H bonds. Maps of $\nabla^2\rho(\boldsymbol{r})$ are presented, showing details in the valence charge distribution and providing a very sensitive tool for analysing dependence of the density on the model adopted to interpret X-ray data. The known chemical reactivity of the molecule towards nucleophiles at a Csp^2 atom is confirmed by the shape of the molecular reactive surface (the zero envelope of $\nabla^2\rho(\boldsymbol{r})$).

Key words: experimental electron density, low-temperature X-ray diffraction, topological analysis, Laplacian of ρ.

Résumé : En se basant sur un ensemble extensif (36 564 mesures) d'intensités de diffraction des rayons X par un cristal unique obtenues à une température de 19 ± 2 K, on a obtenu la distribution expérimentale totale, $\rho(\boldsymbol{r})$, ainsi que son laplacien, $\nabla^2\rho(\boldsymbol{r})$, pour le métabolite de champignon citrinine, $C_{13}H_{14}O_5$. On a ensuite analysé les 7698 données indépendantes d'intensité à l'aide du formalisme multipôle (pseudoatomes). On a déterminé les propriétés topologiques de $\rho(\boldsymbol{r})$ suivant la théorie quantique des atomes dans les molécules. On a déterminé les longueurs des liaisons CC et CO par leur intégration numérique; on a trouvé que leurs valeurs donnent une bonne corrélation avec celles obtenues à partir de la densité électronique des points critiques de liaison. On a utilisé des caractéristiques topologiques pour caractériser l'extension du système conjugué de la molécule et pour confirmer la stabilité de ses noyaux, particulièrement les deux formés par les liaisons hydrogènes intramoléculaires. On présente des cartes de $\nabla^2\rho(\boldsymbol{r})$ qui montrent les détails de la distribution de charge de valence et qui fournissent un outil très sensible pour analyser la dépendance de la densité sur le modèle adopté pour interpréter les données de diffraction des rayons X. En se basant sur la forme de la surface moléculaire réactive (l'enveloppe zéro du $\nabla^2\rho(\boldsymbol{r})$), on a confirmé la réactivité connue de la molécule vis-à-vis des nucléophiles au niveau d'un atome de carbone sp^2.

Mots clés : densité électronique expérimentale, diffraction des rayons X à basse température, diffraction, analyse topologique, laplacien de ρ.

[Traduit par la rédaction]

Introduction

This paper reports the results of a topological study of the *total experimental* charge distribution $\rho(\boldsymbol{r})$ in a medium-size molecule. In particular, the following features of Bader's quantum theory of atoms in molecules, QTAM (1), are explored: (*i*) number and nature of critical points (cp's); (*ii*) values (ρ_b) of the electron density at the bond critical points, and its curvatures (λ's) and Laplacian ($\nabla^2\rho_b$); (*iii*) correlations between ρ_b values and bond path lengths; and (*iv*) topology of rings and ring stability. A brief description is also given of the dependence of some topological features on the model adopted to interpret the X-ray diffraction data. Finally, the relationship between chemical reactivity — in the present case a nucleophilic attack at a C sp^2 atom — and $\nabla^2\rho(\boldsymbol{r})$ is discussed.

We are well aware of the remark (2) that a density obtained from X-ray diffraction data by a multipolar fit is not a pure quantum object, hence differs from the proper quantity dealt with in Bader's theory. However, the topological analysis of such a density can afford very useful information about the ground state of the system under study, provided that all configurations spanned by the nuclei in thermal motion within the crystal belong to the same crystalline structure around equilibrium, so that the corresponding densities all possess equivalent molecular graphs. In other words, if the nuclei do not reach unstable points in configuration space, the network of

Received January 15, 1996.

This paper is dedicated to Professor Richard F.W. Bader on the occasion of his 65th birthday.

P. Roversi, F. Merati,[1] and R. Destro.[2] Dipartimento di Chimica Fisica ed Elettrochimica, Università di Milano, Via Golgi 19, 20133 Milano, Italy.
M. Barzaghi. Centro del CNR per lo Studio delle Relazioni tra Struttura e Reattività Chimica, Via Golgi 19, 20133 Milano, Italy.

[1] Deceased 8 September 1995.
[2] Author to whom correspondence may be addressed. Telephone: 0039-2-26603285. Fax: 0039-2-70638129. E-mail: dest@rs6.csrsrc.mi.cnr.it

Scheme 1.

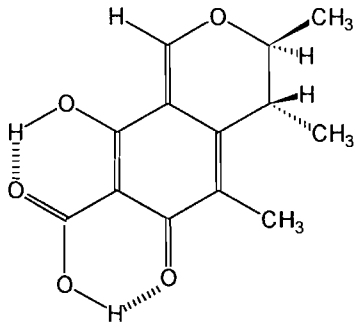

bond paths defining the crystal structure remains unique (1, 3), and the topology of the vibrationally averaged density can be safely assumed to be equivalent, in terms of number and type of cp's, to the one at the equilibrium geometry.

For the quantities used in the topological analysis of $\rho(\boldsymbol{r})$ we have adopted the definitions recently summarized by Bader (4). Numerous applications of the same concepts to the study of experimental electron densities in crystals have already appeared in the literature, e.g., in the case of urea, imidazole, 9-methyladenine, and benzene (2), L-alanine (5), 2-methyl-4-nitroaniline (6), 1-methyluracil (7), molecular chlorine (8), danburite (a borosilicate) (9), *syn*-1,6:8,13-biscarbonyl-[14]annulene (10), and metallic beryllium (11).

To reduce the chances that artifacts, rather than genuine features, be described by the topological analysis of $\rho(\boldsymbol{r})$, extensive sets of high-quality X-ray data are essential. This implies that diffracted intensities must be measured and processed with great and special care. For this reason, we devote part of the paper to a detailed description of some crucial steps of data acquisition and treatment.

As reported below, our X-ray measurements have been performed at temperatures of 17–20 K; an average temperature of 19 K can therefore reasonably be assumed as that of the whole experiment. The great advantages, especially for a detailed structural analysis of organic molecular crystals, of data collection with closed-cycle helium refrigerators, hence at temperatures below 30 K, have been recently discussed (12).

Citrinin (Scheme 1) appears particularly well suited for a study of the electron distribution: the molecule contains a variety of CC and CO bonds, two fused six-membered rings, each formed by six covalent bonds, and two rings of different type, where one of the sides is a rather short, intramolecular hydrogen bond. It has been shown (13) that at room temperature a tautomeric equilibrium occurs in crystals of citrinin, and that at 147 K only one of the two tautomers can be detected by X-ray diffraction experiments. Based on those data, on measurements at 240 K, and on a partial set of intensities diffracted at 20 K, the thermodynamic parameters of the tautomeric equilibrium have been evaluated (14): the presence of structural disorder at 17–20 K, the temperatures of the experiments described in this paper, can be unquestionably excluded.[3]

[3] Very recent results (R. Poupko, Z. Luz, and R. Destro, submitted for publication) of a solid state NMR study have fully confirmed the thermodynamic parameters obtained by X-ray studies alone (14).

Table 1. Crystal data and details of data collection for citrinin at 19 K.

Formula	$C_{13}H_{14}O_5$
M_r	250.25
Space group	Orthorhombic $P2_12_12_1$
Z	4
D_{calcd}(g cm^{-3})	1.428
a (Å)	13.2552(11)
b (Å)	7.2377(7)
c (Å)	12.1360(21)
V (Å^3)	1164.29(25)
Diffractometer	Syntex $P\bar{1}$
Radiation	MoK_α (graphite monochromated)
Scan range (2θ, deg)	2.4 + $S_{\alpha1-\alpha2}$[a]
Scan rate (2θ, deg/min)	3
$(\sin\theta/\lambda)^{Mo}_{max}$ (Å^{-1})	1.14[b]

Set	No. of data	P range (Pa)	T range (K)
hkl	11274	(2×10^{-5})–(1×10^{-4})	19.7–20.2
$hk\bar{l}$	8368	$<10^{-1}$	18.7–19.2
$\bar{h}kl$	8242	(2×10^{-6})–(1×10^{-4})	17.3–18.0
$\bar{h}k\bar{l}$	8680	(2×10^{-6})–(5×10^{-4})	17.2–18.2

[a] $S_{\alpha1-\alpha2}$ is the α_1,α_2 separation in the intensity profile.
[b] Corresponding to $(2\theta)^{max}_{MoK\alpha1}$ = 108°.

Experimental

Pale-yellow crystals of citrinin were grown from an ethanol solution. A specimen was ground to a sphere of radius 0.18 mm and mounted on a four-circle Syntex $P\bar{1}$ diffractometer modified for low-temperature measurements (15). Relevant features, operative conditions, and performance of the instrument have been described elsewhere (16).

Data collection

After a preliminary room-temperature data collection, lowering of the temperature at the sample crystal from 290 to 20 K was achieved in about 100 min, the maximum cooling rate being about 15 K min^{-1} between 90 and 25 K. The temperature was decreased at similar rates in all subsequent cooling operations, after intermediate warming to 290–292 K (see below). A check upon proper alignment of the crystal at low temperature was given by the angular settings for reflections centered at both positive and negative 2θ values.

Four sets of 15 reflections were employed for accurate determination of the cell dimensions. A fit of the $\sin^2\theta$ values for these reflections gave the results reported in Table 1, together with other crystal data and parameters for the data collection. Unit-cell dimensions do not differ significantly from those given in a preliminary report (17).

Intensities were collected by ω–2θ scans and the monochromator was in the configuration corresponding to ε = 90° (18). The X-ray generator was set to nominal values of 50 kV and 25 mA. Seven reflections whose diffracted intensities exceeded the range of linearity of the counter were measured at 30 kV and 3 mA, together with other reflections for subsequent scaling of the data. Four sets of equivalent intensities were collected, with the sample exposed to X-rays for more

than 200 h during each data collection. Warming to room temperature before each set of intensity measurements allowed an appropriate degassing of the chamber, so that the temperature could be kept stable within ±1 K during the recording of each set. A ϕ-shaft with a lower thermal conductivity was employed for the first data collection; hence the temperature in that experiment was higher than in the other three cases (see Table 1). The vacuum shroud was continuously evacuated by a cryogenic pump during data collections 1, 3, and 4, and the pressure within the chamber remained in the range 10^{-4}–10^{-6} Pa, with occasional leakages leading to temporary excursions up to 10^{-1} Pa. During data collection 2 the cryopump broke down, and the cold station of the cryostat itself accomplished the gas condensation; the pressure was accordingly higher, around 10^{-1} Pa.

The intensities of three standards were measured every 47 reflections. Decay at the end of each set of data never exceeded 3% (see below).

Data processing

High-order diffracted intensities are expected to suffer from scan truncation losses due to the finite range of the scan. In the hypothesis that thermal diffuse scattering can be neglected at T<25 K, an appropriate treatment of accurately measured profiles can provide a means of correcting for this well-known systematic error, and achieve a more accurate evaluation of integrated intensities (16, 19, 20). A second, more approximate procedure can be adopted, which employs only average background distributions, and gives a substantially equivalent evaluation of truncation losses under the peak of the reflection profiles (16, 19).

This second procedure was followed in the present case: individual backgrounds of reflections with $I_{net} < 10\sigma(I_{net})$, corresponding to a total of 40 738 measurements from both sides of experimental profiles, were used to evaluate average distributions, where both 2θ and χ dependences were taken into account (16). Background anomalies for 2θ ≅ 10° and 2θ ≅ 30°, typical of the instrumental configuration adopted in our laboratory, also appear in the present case: they have been shown to be due to scattering from the specimen support, that is, a Pyrex glass fiber, 0.15 mm in diameter, and epoxy glue.

We stress the general low level of background for the present experiments, around 3.5 count s^{-1} at high angles, to be compared with values of about 1 count s^{-1} for a tube setting of 45 kV and 15 mA (19), and about 6 count s^{-1} for 50 kV and 30 mA (16). Such an excellent instrumental performance is certainly related to the use of aluminum-coated Kapton foils as windows of the cryostat.

Average backgrounds were substituted for those individually measured, and net intensities recomputed. A contribution was also included, at this stage, to take into account scan truncations at the tails of the intensity profiles. The latter quantity, up to a correction of 4% for the net intensities at higher 2θ values, was evaluated according to previous studies and analyses of experimental profiles (16, 19, 20).

The set of diffracted intensities corrected for scan truncation losses underwent conventional data processing, and yielded the experimental values for structure factor amplitudes. A linear fit of the intensities of the three standards vs. time was performed for each set of data, and corrections for decay computed accordingly. Apart from decay, statistical oscillations did not exceed 2% for all check reflections. Decay from the beginning of the experiment to the end of the fourth data collection amounted to about 10%, and was never higher than 3% within each set of data. High- and low-power measurements were merged after appropriate scaling, the average ratio of intensities common to the two subsets being around 40. Variances due to statistical counting were increased by an additional term, depending on intensity under the peak and velocity of the scan:

$$\sigma^2(I_{net}) = \sigma^2_{sc}(I_{net}) + (0.02 I_{peak} v_{scan})^2$$

The intensities were corrected for Lorentz and polarization factors, but not for absorption, and symmetry-equivalent structure factor amplitudes were then merged, with weights taken as inverse variances of individual measurements, and $\sigma^2(\langle F^2\rangle) = [\sum_{equiv.\ i} 1/\sigma^2(F_i^2)]^{-1}$. Friedel pairs were also merged. Each independent structure factor amplitude came, on average, from 4 measurements, only 19 values being measured but once. The merge index amounted to 1.07%, thus confirming the overall excellent agreement between the different sets of data. Among the resulting 7954 independent structure factor amplitudes, 256 had $|F^2| < 0$, and 5941 (about 75% of the total) had $|F^2| > 6\sigma(F^2)$.

Multipolar refinements

The electron density was modelled with a multipolar expansion of atom-centered functions (21–23), according to the pseudoatom formalism of Stewart (24). An approximate absolute scale factor had been previously determined by a conventional spherical atom refinement. Three different models were adopted for multipolar refinements: they will be denoted A, B, and C in the following.

A: This model employed a multipolar expansion up to the octopolar level on carbon and oxygen atoms. Core and valence monopole one-electron density functions were taken equal to the Hartree–Fock expansions of Clementi (25). Core electron population parameters for all C and O atoms were constrained to be equal. Single exponential functions, $r^n \exp(-\alpha r)$, were adopted as radial parts of the higher multipoles. Values for n were 2, 2, and 3 for dipole, quadrupole and octupole, respectively; values for α were 4.50 and 3.44 $bohr^{-1}$ for O and C, respectively (26).

Positional and anisotropic displacement parameters (ADP's) were varied for all C and O atoms. H atoms were initially given scattering factors taken from the H_2 molecule (27); their positional parameters were varied together with isotropic U's. In the final stages of the refinement, H positions were kept fixed, and generalized scattering factors were employed for these atoms as well (at these later stages, there is no need to readjust H positions, the geometry being virtually unaffected by subsequent changes in the model employed). Expansion of the pseudoatom density for H atoms comprised one monopole and three dipole functions. Radial parts for all poles were again single exponentials, with n = 0,1 for monopole and dipole, respectively, and an α value of 2.48 $bohr^{-1}$ (26). An isotropic extinction parameter, of type I and Lorentzian "mosaic" distribution (28), was also varied. Besides this extinction term, the model comprised 162 positional and displacement parameters and 289 electron population parameters for the 18 non-H atoms of the molecule, plus 14 isotropic U's

and 56 electron population coefficients for H atoms. The total number of variables refined was 522.

B: On passing from model A to model B, only the description of the H atoms was changed. First, ADP's were evaluated for all 14 H nuclei. The procedure, based on a rigid-body fit (29) to the ADP's of the 10 non-H atoms of the two central rings of the molecule, and on spectroscopic information, will be described in detail in a forthcoming paper. As a check of the order of magnitude of the values obtained, equivalent U's were compared with the previously (model A) refined U_{iso}'s: the difference exceeded 3 esd's in only one case, the average $|\Delta/\sigma|$ being 1.6. In model B, positional parameters of the H nuclei were kept fixed at the values refined in early stages of refinement A, and the corresponding ADP's were kept at the calculated values. Quadrupoles were added on the multipolar expansion for the H atoms, with single exponential radial functions having $n = 2$ and $\alpha = 2.48$ bohr^{-1}. The number of variables was thus raised to 578.

C: Six additional refinable parameters were added in this model: a radial scaling parameter κ for the valence monopole radial density function of C atoms; a common α value for their dipole, quadrupole, and octopole functions; two corresponding κ and α parameters for O atoms; an α_H^0 for the monopole and a common α_H^1 value for the dipole and quadrupole radial functions on H atoms. Model C counted up to 584 variables.

All refinements were carried out using the VALRAY set of programs (30). The quantity minimized in the calculations was $\varepsilon = \Sigma w(F_o^2 - kF_c^2)^2$, based on the 7698 reflections with $I > 0$. Weights w were taken as $w = 1/\sigma^2(F_o^2)$. Convergence was assumed when the ratio between $\Delta\varepsilon$ from one cycle to the next and the value of ε itself was smaller than 5×10^{-6}. Full second derivatives were included in the calculation of the Hessian matrix of ε in the last cycles, to obtain accurate esd's in the refined parameters.

Results and discussion

Overall quality of the fits

Statistical comparison of the models

Reliability indexes for the three multipolar refinements are summarized in Table 2. For comparison of models A and B, and of A with C, application of the Hamilton ratio test (31) would not be adequate, in that the parameters of one model are not a subset of the parameters of the other: B and C employ fixed ADP's and refine quadrupoles on H atoms, while in A isotropic U values have been refined and the multipolar expansion is up to the dipole level on the same atoms. A more general statistical test (32) was then performed for the pairs A–B, A–C, and B–C. For each pair, least-squares estimates for the slope λ and its esd σ were obtained for the regression line $z = \lambda x$, with:

$$z = [F_o^2 - 0.5(F_{c1}^2 + F_{c2}^2)]/\sigma(F_o^2)$$

and

$$x = (F_{c1}^2 - F_{c2}^2)/\sigma(F_o^2)$$

where subscripts 1 and 2 denote the first and the second model of the pair. For the B–C pair, values for λ and σ are -0.466 and 0.045, respectively, and similar values were obtained for the other two pairs. A value of λ significantly different from 0 indicates better performance of one of the two models, limiting values being $-\frac{1}{2}$ (better fit by the second model) and $+\frac{1}{2}$ (opposite case). The hypothesis that two models gave equally good fits to the data was then tested making use of Student's t distribution for the ratio $t = |\lambda/\sigma|$. For all three pairs considered (A–B, A–C, B–C), the hypothesis could be rejected at the 0.5% significance level (33), confirming that the R indices of the second model of each pair are indeed significantly smaller than those of the first.

Table 2. Summary of least-squares refinements with models A–C.[a]

Model	A	B	C
N° of observations	7698	7698	7698
N° of parameters	522	578	584
Scale factor	1.0012(14)	1.0066(13)	1.0144(24)
Extinction coefficient[b]	0.318(7)	0.312(7)	0.309(11)
$\varepsilon = \Sigma w\Delta^2$	11258	10714	10106
$\lvert\Delta\varepsilon\rvert/\varepsilon$[c]	2.9×10^{-7}	8.6×10^{-8}	3.9×10^{-6}
$R(F)$	0.0286	0.0281	0.0277
$wR(F)$[d]	0.0168	0.0164	0.0159
$R(F^2)$	0.0229	0.0218	0.0216
$wR(F^2)$	0.0333	0.0325	0.0316
Goodness-of-fit	1.2525	1.2267	1.1919
Max. Δ/σ	0.0018	0.0010	0.0047
Average Δ/σ	<0.0001	<0.0001	<0.0001

[a]Radial parameters were fixed at the standard molecular value in models A and B. In model C final values were: $\kappa_C = 1.001(2)$, $\alpha_C = 3.087(28)$ bohr^{-1}; $\kappa_O = 0.988(1)$, $\alpha_O = 4.50(14)$ bohr^{-1}; $\alpha_H^0 = 2.39(2)$ and $\alpha_H^1 = 3.27(14)$ bohr^{-1}.

[b]In units of 10^{-4} rad^2.

[c]$\Delta\varepsilon = \varepsilon_n - \varepsilon_{n-1}$; n is the number of the last cycle.

[d]Weights equal to $4F^2/\sigma^2(F^2)$.

Agreement as a function of resolution

Scattering at high resolution being dominated by core electrons, only positional and displacement parameters are expected to be sensitive to high-order data: the "effective" observations to parameters ratio (n/p) is in fact resolution dependent, and smaller than the nominal value of 7698/584 = 13.2 (model C). Indeed, a plot of the average ratio $|F_{core}^h|/|F^h|$ vs. resolution range for citrinin reaches unity around $(\sin\theta)/\lambda = 0.626$ Å^{-1}, suggesting that the subset of valence population parameters is in fact determined by a smaller number of observations than the total fitted. For model C, the n/p ratio would be lowered to 1828/420 = 4.35, if valence population parameters only and data up to $(\sin\theta)/\lambda = 0.626$ Å^{-1} were considered. It is precisely in the resolution range where valence multipoles are active that the major differences are observed when comparing residuals for different models. A plot of the root-mean-square (rms) $\Delta F^2/\sigma(F^2)$ values in resolution bins is reported in Fig. 1, where $\Delta F^2 = F_{obs}^2 - F_{calc}^2$. It is apparent that on going from model A to model C, rms values approach unity for reflections in the relatively low-resolution range $0.444 \leq (\sin\theta)/\lambda < 0.808$ Å^{-1}; a comparable improvement of the fit to low-order data upon variation of radial parameters has recently been observed in

Fig. 1. Root-mean-square $\Delta F^2/\sigma(F^2)$ vs. resolution for models A, B, and C. About 450 data were averaged in each resolution bin.

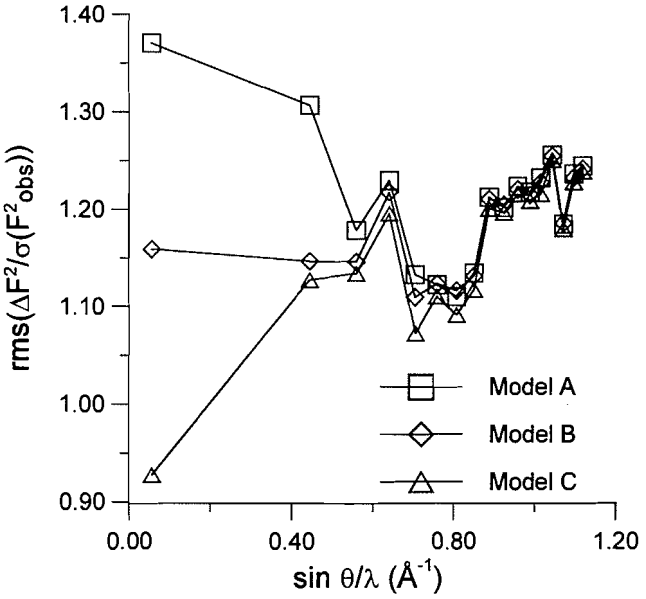

the case of the refinement of X-ray diffraction data at $T = 19$ K for *syn*-1,6:8,13-biscarbonyl[14]annulene (10). Residuals for high-order reflections are less sensitive, on average, to variations of the model. This is in keeping with the fact that the three models differ mainly in the description of valence electron density, while a common set of parameters active at high resolution has been employed. Indeed, virtually identical nuclear positions and displacement parameters for non-H atoms are obtained in the three fits. On passing, we notice that the values in Fig. 1 for high-angle data indicate a possible underestimation of the standard deviations by 15–20%.

It must be noticed that the three fits A, B, and C show negative average values of $\Delta F^2/\sigma(F^2)$ in all 16 resolution bins above (sin θ)/λ = 0.444 Å^{-1}, with an overall $\langle \Delta F^2/\sigma(F^2) \rangle$ of −0.19 in all three cases, while for the 530 reflections at the lowest resolution the average values amount to +0.16, +0.17, and +0.07, respectively, for A, B, and C. Opposite behaviour was observed for a fit performed on data not corrected for scan truncation losses with model B, which gave poorer reliability indexes ($R(F)$ = 0.0384; $wR(F)$ = 0.0208; $R(F^2)$ = 0.0279; $wR(F^2)$ = 0.0382; g.o.f. = 1.379), and instead showed positive values for the average $\Delta F^2/\sigma(F^2)$ at all resolution ranges (overall $\langle \Delta F^2/\sigma(F^2) \rangle$ = +0.20), except for the 480 data of the resolution bin with 0.444 < (sin θ)/λ ≤ 0.560 Å^{-1}, where the average value is −0.017. Diagonal ADP's for non-H atoms for this refinement are 1.8% larger, on average, than those coming from the refinement of the same model B against corrected data ($\langle (U^{ii}_{\text{uncorr}} - U^{ii}_{\text{corr}})/\sigma(U^{ii}_{\text{corr}}) \rangle$ = 1.08). All this might suggest that high angle data have been slightly overcorrected in the treatment of scan truncation losses.

Positivity of the density

The multipolar expansion does not ensure non-negative electron density everywhere in the crystal: a check for positivity of $\rho(\boldsymbol{r})$ was performed by sampling values on a uniform and orthogonal grid in the asymmetric unit, chosen as $0 \leq x \leq \frac{1}{2}$, $0 \leq y \leq 1$, $0 \leq z \leq \frac{1}{2}$, with steps of 0.1 Å along each axis. Far from atomic regions, small negative electron density values were found for models A and B, down to minima of $-0.03(14) \times 10^{-2}$ and $-0.93(54) \times 10^{-2}$ e Å^{-3}, respectively. It is seen that the value for model B, where quadrupolar deformation functions have been added on H atoms, amounts to almost twice its esd, but remains almost negligible. A search for the nuclei closest to the set of very few points having negative density in models A and B revealed that, with no exception, the closest was always a hydrogen nucleus, the distances ranging from 1.071 to 1.521 Å. By contrast, no negative values were found in the asymmetric unit for model C ($\rho_{\text{min}} = 1.98 \times 10^{-3}$ e Å^{-3}). We recall that in model C α^0_H and α^1_H parameters were refined: it is conceivable that the observed (see Table 2) contraction of dipoles and quadrupoles for these atoms, and the concomitant expansion of their monopoles, is mainly responsible for the observed disappearence of the cited regions of negative density in model C.

Correlation coefficients and deconvolution of static/dynamic features

Off-diagonal terms of the inverse of the full Hessian matrix of $\varepsilon = \Sigma w \Delta^2$ give correlation coefficients between the parameters varied. In the present case, coefficients greater than 0.707 in absolute value at the end of the least-squares refinement were rather few, in number 38, 24, and 18, respectively, for models A, B, and C. As was the case for *syn*-1,6:8,13-biscarbonyl[14]annulene (10), the largest correlation was that between the radial scaling parameter κ of the C atoms and the core population coefficient common to all the 18 non-H atoms (coefficient of 0.84). No other parameter involving C atoms has correlation coefficients greater than 0.707 in absolute value. Common to all three refinements are the correlations involving some of the parameters of the O atoms, namely, those between dipole populations and positional parameters (max. value 0.81), and between ADP's and quadrupole populations (up to 0.74).

The substantially small number of significant correlations increases our confidence in the overall reliability of the parameters obtained. We cite also the excellent results derived from the rigid-bond test of Hirshfeld (34) on ADP's from model C: none of the differences between mean-square amplitudes of vibration along the bond direction for all non-H bonded pairs is greater than 0.0006 Å^2, with only the exception of the C6—O7 value, which amounts to 0.0009 Å^2.

All these findings point to a more than satisfactory description of the atomic motions, and hence suggest that the deconvolution of dynamic from static features in the charge density of citrinin has been successfully attained.

Non-centrosymmetry and the phase problem

Odd-order poles that are invariant under crystal-class symmetry are known to give rise to a contribution to the structure factor having a phase shift of π/2 with respect to the sum of contributions from core, valence monopoles, and even-order poles invariant under crystal-class symmetry (ref. 35 and footnote 4). To first-order approximation, and in the limit of a completely negligible contribution from the non-invariant

[4] N.K. Hansen. Private communication.

Fig. 2. ORTEP plot of citrinin at 19 K, with numbering scheme. Ellipsoids at 50% probability level; those for H atoms come from calculated anisotropic displacement parameters (ADP's).

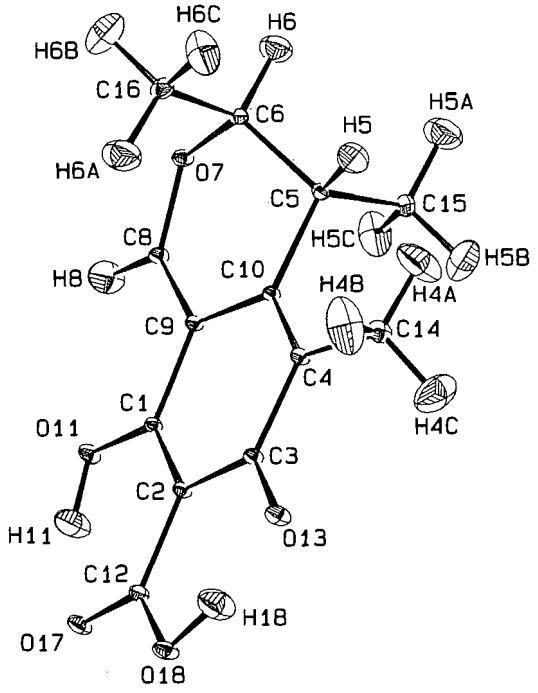

poles, changes in the values of the population coefficients of invariant odd-order poles alter only the phase of the structure factor, without affecting its modulus (P. Roversi, unpublished results). In non-centrosymmetric structures, these population coefficients are therefore ill determined, to an extent depending on the relative amplitude of the contributions from invariant and non-invariant poles to the structure factor. In the present work, the only odd-order poles invariant under point symmetry 222 are the 18 octopolar functions *Oxyz*, centered on C and O atoms, while the total number of non-invariant poles for which population coefficients were refined is 364. For this structure, it could therefore be anticipated that the uncertainties on *Oxyz* values should not be too large. Indeed, esd's for these population coefficients were found to be only 1.5 times greater, on average, than those for non-invariant poles. None of the correlation coefficients between the populations for *Oxyz* centered on different atoms was greater than 0.67 in any of the three fits A, B, and C.

Geometry

An ORTEP plot (36) of the molecule is shown in Fig. 2. Positional parameters and U_{eq}'s at the end of refinement C are listed in Table 3.[5] As already anticipated, the geometry proved relatively insensitive to the choice of multipolar model: three sets equivalent within one esd resulted, for bond distances and angles, from the refinements we carried on.

[5] A table of anisotropic displacement parameters may be purchased from: The Depository of Unpublished Data, Document Delivery, CISTI, National Research Council Canada, Ottawa, Canada K1A 0S2. Structure factor amplitudes are no longer being deposited and may be obtained directly from the authors.

Table 3. Final fractional coordinates and equivalent isotropic displacement parameters[a] for citrinin at 19 K (model C).

Atom	*x*	*y*	*z*	U_{eq} (Å^2)
C1	0.89985(2)	0.23996(4)	0.33310(2)	0.00513(5)
C2	0.98113(2)	0.23009(5)	0.26098(2)	0.00550(5)
C3	0.96434(2)	0.21734(5)	0.14380(2)	0.00580(5)
C4	0.86169(2)	0.20460(5)	0.10091(2)	0.00580(5)
C5	0.67389(2)	0.18691(4)	0.14149(3)	0.00569(5)
C6	0.60738(2)	0.31765(5)	0.20782(3)	0.00609(5)
O7	0.62442(3)	0.29288(5)	0.32716(3)	0.00671(5)
C8	0.71860(2)	0.27049(5)	0.35934(3)	0.00614(5)
C9	0.79891(2)	0.24181(4)	0.28981(2)	0.00511(5)
C10	0.78296(2)	0.21599(4)	0.17282(2)	0.00498(5)
O11	0.91287(3)	0.25056(6)	0.44087(3)	0.00798(6)
C12	1.08447(2)	0.23343(5)	0.30535(3)	0.00660(5)
O13	1.03856(3)	0.21191(6)	0.07789(3)	0.00915(6)
C14	0.85190(3)	0.17588(6)	−0.02116(3)	0.00957(7)
C15	0.64415(3)	−0.01572(5)	0.16000(3)	0.00868(6)
C16	0.62299(3)	0.51904(5)	0.17923(3)	0.00926(7)
O17	1.10119(3)	0.24015(6)	0.40598(3)	0.00919(6)
O18	1.15851(3)	0.22920(7)	0.23367(3)	0.00964(6)
H5	0.6606(6)	0.2230(11)	0.0545(7)	0.01674
H6	0.5283(6)	0.2782(12)	0.1982(6)	0.01731
H8	0.7269(6)	0.2771(13)	0.4494(8)	0.02033
H4A	0.7760(9)	0.1466(15)	−0.0454(7)	0.03176
H4B	0.8788(8)	0.2989(15)	−0.0676(8)	0.03438
H4C	0.9007(8)	0.0635(15)	−0.0482(7)	0.03408
H5A	0.5677(8)	−0.0377(11)	0.1337(8)	0.02621
H5B	0.6933(7)	−0.1076(12)	0.1113(8)	0.02611
H5C	0.6511(7)	−0.0536(10)	0.2462(8)	0.02563
H6A	0.7006(8)	0.5617(12)	0.1928(8)	0.02559
H6B	0.5723(7)	0.6070(12)	0.2297(8)	0.02760
H6C	0.6044(7)	0.5371(10)	0.0939(8)	0.02611
H11	0.9858(8)	0.2481(14)	0.4509(6)	0.02020
H18	1.1217(6)	0.2228(14)	0.1566(8)	0.02169

[a] U_{eq} is defined as 1/3 (U_{11} + U_{22} + U_{33}).

Values for bond lengths and angles from refinement C are reported in Tables 4 and 5. The former table also lists bond distances from ab initio optimizations, performed with GAUSSIAN94 (37) for an isolated molecule. Theoretical values come from HF/6-31G* and density-functional B3LYP calculations (38); details will be published elsewhere.[6] We only comment here on the fact that all C=C, CO, CH, and OH theoretical bond distances show very significant lengthening toward the experimental values on passing from the HF/6-31G* to the density-functional calculation, while the C—C bonds of the conjugated system are shortened, again in closer agreement with the experimental geometry. As for the other C—C bonds, it is seen that in four out of five cases, the B3LYP lengths are in poorer agreement with experiment than are the HF/6-31G* ones. The fifth bond, C4—C14, which is at least in part involved in the conjugated system (see below), behaves in the opposite way.

It is worth noting that CH and OH distances as obtained

[6] M. Barzaghi, F. Merati, P. Roversi, and R. Destro. In preparation.

Table 4. Bond lengths (R_e), bond path lengths (R_b), and bonded radii (R_A and R_B) in citrinin. Å units.

Bond A—B	R_e HF/6-31G*	R_e B3LYP/6-31G*	R_e expt.	R_b	$d \times 10^3$ [a]	R_A	R_B	R_A/R_b
C2—C1	1.3714	1.3897	1.3899(4)	1.3903	13	0.6647	0.7257	0.478
C4—C10	1.3373	1.3624	1.3629(4)	1.3630	3	0.6748	0.6882	0.495
C9—C8	1.3467	1.3681	1.3743(4)	1.3747	4	0.6385	0.7363	0.464
C9—C1	1.4472	1.4471	1.4375(4)	1.4376	2	0.6961	0.7414	0.484
C2—C3	1.4598	1.4531	1.4425(4)	1.4432	13	0.7096	0.7336	0.492
C2—C12	1.4819	1.4787	1.4720(4)	1.4721	5	0.7101	0.7621	0.482
C4—C3	1.4842	1.4782	1.4597(4)	1.4599	3	0.6924	0.7675	0.474
C10—C9	1.4613	1.4550	1.4476(4)	1.4480	5	0.7150	0.7330	0.494
C14—C4	1.5077	1.5055	1.5016(5)	1.5021	7	0.7294	0.7727	0.486
C5—C6	1.5312	1.5369	1.5234(4)	1.5237	7	0.7230	0.8007	0.474
C5—C10	1.5192	1.5212	1.5097(4)	1.5099	2	0.7333	0.7766	0.486
C15—C5	1.5376	1.5435	1.5352(5)	1.5355	9	0.7564	0.7791	0.493
C16—C6	1.5226	1.5260	1.5125(5)	1.5128	3	0.7402	0.7726	0.489
C3—O13	1.2187	1.2557	1.2686(5)	1.2686	6	0.4839	0.7847	0.381
C1—O11	1.3088	1.3257	1.3215(5)	1.3218	6	0.5300	0.7918	0.401
C6—O7	1.4364	1.4665	1.4767(6)	1.4778	23	0.6097	0.8681	0.412
C8—O7	1.3098	1.3262	1.3179(5)	1.3185	16	0.5092	0.8093	0.386
C12—O17	1.2079	1.2405	1.2421(6)	1.2422	4	0.4639	0.7783	0.373
C12—O18	1.3046	1.3217	1.3118(5)	1.3125	8	0.4928	0.8197	0.375
H18—O18	0.9636	1.0077	1.056(10)	1.056	7	0.2778	0.7785	0.263
H11—O11	0.9705	1.0190	0.974(11)	0.976	16	0.2235	0.7522	0.229
H5—C5	1.0818	1.0950	1.101(9)	—	—	(0.411)[b]	(0.690)[b]	(0.373)[b]
H6—C6	1.0802	1.0933	1.093(8)	1.093	3	0.4133	0.6793	0.378
H8—C8	1.0719	1.0852	1.100(9)	—	—	(0.377)[b]	(0.723)[b]	(0.343)[b]
H—C_{meth}(av.)	1.0837	1.0947	1.089(16)	—	—	(0.419)[b]	(0.671)[b]	(0.385)[b]

[a]Distance of critical point from line A–B.
[b]Values refer to geometric distances and not to lengths along the bond path.

from the refinement employing the polarized H scattering factors (27) are in good agreement with average values from neutron diffraction studies (39). The values $d_{H5—C5}$ = 1.101(9) Å and $d_{H6—C6}$ = 1.093(8) Å are to be compared with that for secondary Csp^3—H distances, 1.099(4) Å; the value for $d_{H8—C8}$ = 1.100(9) is slightly longer than the average value 1.077(12) Å from a collection of 14 Csp^2—H bond distances. Methyl group CH distances are here in the range 1.073(10)–1.112(11) Å, all longer than the average neutron value 1.059(30) Å, but the latter quantity includes numerous contributions from experiments at temperatures much higher than 19 K. When only low-temperature neutron work is considered, significantly longer bond distances are usually observed: for example, in the case of 1-methyluracil at 15 K (40), CH bonds are 1.083(2) and 1.088(1) Å long. The OH distances are 0.974(11) Å and 1.056(10), respectively, for the alcoholic and acidic protons of citrinin, in qualitative agreement with the average values from neutron diffraction studies of systems with similar protons: 0.967(10) and 1.015(17) Å. Although these comparisons must be taken with some care (owing to H-bonding effects and temperature dependence of the bond lengths), they certainly indicate that the procedure adopted here, based solely on X-ray data, has led to a very satisfactory location of the H nuclei positions.

Topology of ρ(*r*)

The set of electron population coefficients obtained from the least-squares refinement C was employed to generate the electron density for a molecule extracted from the crystal.[7] Although the density obtained from the experimental data does not, as already noticed, pertain to a pure quantum state, in the following we shall discuss its topology in terms of the usual quantities employed to characterize ab initio densities, such as the number and kind of critical points (i.e., points where $\nabla\rho = 0$), the values of ρ, curvatures, and $\nabla^2\rho$ at the crit-

[7] A discussion of the virtual identity between the density for such an "isolated" molecule and that for the molecule surrounded by the neighbouring ones in the crystal has been presented in the case of L-alanine (41). For citrinin, no differences greater than 0.01 e/Å^3 were observed in density values at the critical points of bonds between non-H atoms, while Laplacian values at the same points showed shifts up to 2.0 esd's toward more negative values at all intramolecular bonds in the crystal.

Table 5. Bond path angles α_b and experimental bond angles α_e (degrees) for non-H atoms in citrinin.

Angle	α_b	α_e	$\Delta\alpha = \alpha_b - \alpha_e$	β_1[a]	β_2[a]
C2-C1-C9	120.40	119.46(2)	0.94	1.76	0.61
C2-C1-O11	120.16	121.66(3)	−1.50	1.76	1.19
C9-C1-O11	119.43	118.86(3)	0.57	0.61	1.19
C1-C2-C12	119.01	119.36(3)	−0.35	2.09	1.40
C1-C2-C3	124.04	120.30(2)	3.76	2.09	3.28
C12-C2-C3	116.92	120.35(2)	−3.43	1.40	3.28
C2-C3-C4	118.10	119.96(2)	−1.86	1.02	1.64
C2-C3-O13	119.63	120.27(3)	−0.64	1.02	1.05
C4-C3-O13	122.26	119.74(3)	2.52	1.64	1.05
C10-C4-C14	125.49	125.03(3)	0.46	0.54	2.48
C10-C4-C3	119.92	118.79(2)	1.13	0.54	1.18
C14-C4-C3	114.57	116.17(2)	−1.60	2.48	1.18
C10-C5-C15	111.14	110.01(3)	1.13	0.62	2.39
C10-C5-C6	107.07	109.54(2)	−2.47	0.62	2.16
C15-C5-C6	118.18	111.56(3)	−1.38	2.39	2.16
C16-C6-C5	115.29	113.47(3)	1.82	1.88	0.18
C16-C6-O7	107.42	108.73(3)	−1.31	1.88	3.96
C5-C6-O7	107.75	110.75(3)	−3.00	0.18	3.96
C6-O7-C8	114.30	116.77(3)	−2.47	1.65	0.94
C9-C8-O7	121.37	124.78(3)	−3.41	1.60	2.39
C1-C9-C10	119.46	119.55(2)	−0.09	0.55	2.21
C1-C9-C8	118.66	119.87(2)	−1.21	0.55	1.83
C10-C9-C8	121.87	120.57(2)	1.30	2.21	1.83
C4-C10-C5	124.34	124.30(2)	0.04	0.71	1.33
C4-C10-C9	121.85	121.60(2)	0.25	0.71	0.94
C5-C10-C9	113.69	113.88(2)	−0.19	1.33	0.94
C2-C12-O17	122.42	121.75(3)	0.67	1.56	0.75
C2-C12-O18	113.54	116.95(3)	−3.41	1.56	2.13
O17-C12-O18	124.03	121.29(4)	2.74	0.75	2.13
C3-O13···H18	98.76	99.87(37)	−1.11	1.64	2.33

[a] $\beta_1(\beta_2)$ = limiting values at the nucleus of the angle between the direction of $\nabla\rho$ on the bond path and the corresponding bond line (see text).

ical points, and bond ellipticities (1). Bonded radii, bond path lengths, and bond path angles will also be considered. All quantities of interest are listed in Tables 4–6.

The critical points of the density were searched via a Newton–Raphson algorithm, starting from a uniform orthogonal grid of points. A set of 35 (3,−1) or bond critical points (bcp's), and 4 (3,+1) or ring critical points (rcp's) was found; together with that of 32 maxima located at the nuclei, this set of critical points obeys the Poincaré–Hopf relationship for an isolated molecule (42). All the conventional covalent bonding interactions are thus recovered, together with the two intramolecular H bonds.

Bond path lengths and bonded radii

In Bader's QTAM, atomic interaction lines are traced by two $\nabla\rho$ trajectories originating from a (3,−1) critical point, and terminating at two neighbouring nuclear attractors. When an ab initio density for an equilibrium nuclear configuration is studied, atomic interaction lines are referred to as bond paths (1, 43). For citrinin, the bond path lengths (R_b) between all

pairs of bonded nuclear attractors were computed by numerical integration; values are reported in Table 4, together with the distances of the bond critical points from the straight lines connecting the nuclei. Values of the bonded radii (R_A and R_B), i.e., the distances *along the bond path* from the bcp to each of the two bonded nuclei, are also listed.

The difference between bond path length (R_b) and conventional bond length (R_e) values amounts here to a fraction of the esd of the latter, and in all cases is less than 0.07% of the value of R_e itself: in other words, all bond paths closely follow the straight line connecting the two nuclear attractors. Only for C6—O7 is the $R_b - R_e$ value moderately significant in terms of the esd of the bond length: $R_e = d_{C6—O7} = 1.4767(6)$ Å vs. $R_b = 1.4778$ Å. Here the bcp is displaced from the line connecting the nuclei by 0.023 Å, corresponding to about 1.6% of the bond length. Thus, this bond is slightly but sensibly curved.

The bonded radii of C atoms in CC bonds are in the range 0.64–0.80 Å; these bcp's are located approximately at the midpoint of the bonds, as is apparent from the R_A/R_b values, none of which is less than 0.47. A shift of the bcp position towards the C nucleus is observed in CO bonds, where the critical points are, on average, at a distance of about $0.39R_b$ from the C atom. This contraction is more pronounced for the keto and carboxylic CO bonds. The bond path lengths could not be successfully integrated for most of the CH bonds: reasons for such a behaviour are under investigation. The distances of the bcp's from the bonded C and H nuclei along the internuclear straight line were then taken as approximated bonded radii. A displacement toward the H nucleus is observed for all CH bcp's, whose distances from the H nucleus amount to $0.38R_e$ on average; an even greater shift in the same direction is shown by the two OH bcp's, at $0.26R_b$ and $0.23R_b$ from H18 and H11, respectively.

Correlation between density at bcp and bond path length

The accumulation of density between bonded nuclei balances the forces arising mainly from nuclear repulsion, and is therefore expected to increase with decreasing bond length (44). The existence of a correlation between ab initio values of the density (ρ_b) at the bond critical point and calculated or experimental equilibrium bond lengths has been demonstrated in a number of molecular systems for a variety of intra- and intermolecular bonds (44, 45*a–d*). Linear and power empirical laws have been employed to fit the data, thus allowing estimates of electron density values (and related properties) from experimental bond lengths: a power law of the form $\rho_b = A \cdot R_e^{-B}$ is the simplest model carrying the correct asymptotic behaviour as the bond length increases, but in some cases very good correlations have been found with the simpler linear model $\rho_b = a \cdot R_e + b$ (45*d*). The empirical correlation laws have been observed to be more closely satisfied in strained systems if bond path lengths instead of geometrical bond lengths are considered (44).

Plots of ρ_b vs. R_b for the 13 CC and 6 CO bonds of citrinin are shown in Figs. 3 and 4, respectively. It must be stressed that no esd's have been computed for bond path lengths nor for positions of the critical points; the esd's for ρ_b values come from the least-squares refinement.

CC bonds: the variation of ρ_b for the 13 CC bonds in citrinin is best represented by the straight line (Fig. 3) in atomic units:

Fig. 3. Values ρ_b of electron density at the CC bond critical points vs. bond path lengths (R_b). Model C, molecule extracted from the crystal. The esd's of ρ_b are reported as vertical bars.

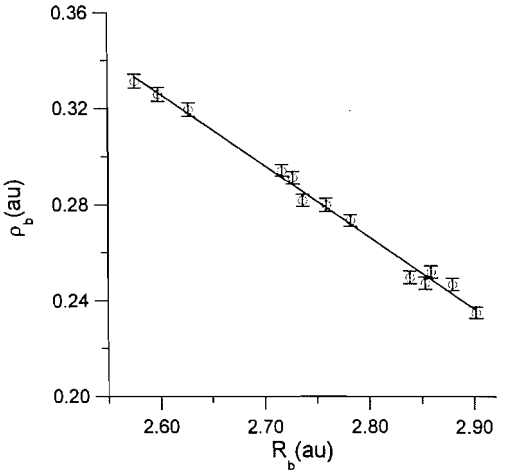

Fig. 4. Same as Fig. 3 for the CO bonds.

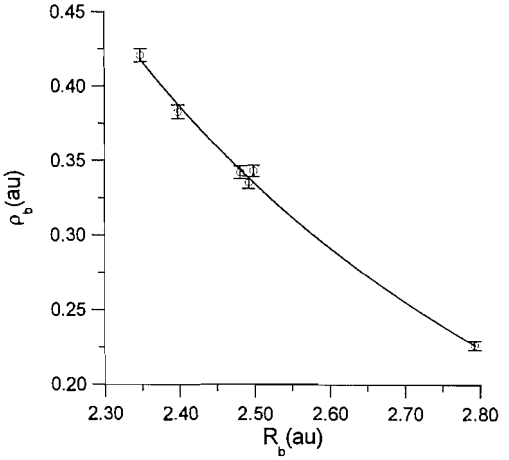

$$\rho_b = -0.297(8) \cdot R_b + 1.099(23)$$

with a correlation coefficient $r = -0.996$ and a rms residual $\sigma = 0.031$. Slope and intercept can be compared with those reported in the literature from a fit of ab initio 6-31G and STO-3G values for ρ_b and CC internuclear distances in ethane, ethylene, benzene, and acetylene (44): the 6-31G fit gave (in au) $a = -0.283$ and $b = 1.043$; the STO-3G fit gave $a = -0.184$, $b = 0.777$. Experimental values for CC bonds in citrinin are therefore in closer agreement with the 6-31G values.

On the basis of ρ_b and R_b values, CC bonds in citrinin can be clearly divided into three groups: C8—C9, C1—C2, and C10—C4, with $\langle\rho_b\rangle = 0.326$ e/(au)^3 and $\langle R_b\rangle = 2.60$ au (1.38 Å); C1—C9, C2—C3, C2—C12, C3—C4, and C9—C10, with $\langle\rho_b\rangle = 0.284$ e/(au)^3 and $\langle R_b\rangle = 2.74$ au (1.45 Å); and C5—C6, C10—C5, C4—C14, C5—C15, and C6—C16, with $\langle\rho_b\rangle = 0.246$ e/(au)^3 and $\langle R_b\rangle = 2.87$ au (1.52 Å). These three subsets may be clearly identified as the formally double and single CC bonds within the extended conjugated system of the molecule, and the single CC bonds not involved in conjugative interactions.

Table 6. Properties[a] of ρ at the bond critical points (bcp's) of citrinin (model C, molecule extracted from crystal).

Bond	ρ_b	λ_1	λ_2	λ_3	$\nabla^2\rho_b$	ε
C1—C2	2.16(2)	−17.20	−13.15	13.22	−17.1(9)	0.309
C4—C10	2.24(2)	−17.96	−13.26	13.34	−17.9(6)	0.355
C8—C9	2.20(2)	−17.55	−13.14	12.82	−17.9(9)	0.336
C1—C9	1.99(2)	−15.19	−12.60	13.44	−14.3(8)	0.206
C2—C3	1.96(2)	−14.94	−12.24	13.72	−13.5(7)	0.220
C2—C12	1.84(2)	−13.69	−11.47	13.45	−11.7(7)	0.194
C3—C4	1.89(2)	−14.25	−11.60	13.45	−12.4(7)	0.229
C9—C10	1.90(2)	−13.83	−11.96	13.68	−12.1(7)	0.156
C4—C14	1.69(2)	−11.52	−10.73	13.33	−8.9(6)	0.070
C5—C6	1.67(2)	−10.97	−10.63	13.17	−8.4(6)	0.032
C5—C10	1.67(2)	−11.20	−10.67	13.21	−8.7(6)	0.050
C5—C15	1.59(2)	−10.19	−9.84	13.44	−6.6(6)	0.035
C6—C16	1.70(2)	−11.45	−11.08	13.39	−9.1(7)	0.034
C3—O13	2.58(3)	−23.00	−20.29	17.88	−25.4(19)	0.134
C6—O7	1.53(2)	−10.31	−9.83	16.97	−3.2(8)	0.050
C8—O7	2.27(3)	−18.87	−17.20	16.50	−19.6(15)	0.097
C1—O11	2.32(2)	−19.90	−17.77	17.43	−20.2(14)	0.120
C12—O17	2.84(3)	−27.24	−24.29	19.27	−32.3(22)	0.121
C12—O18	2.31(3)	−20.27	−17.69	16.58	−21.4(17)	0.145
H5—C5	1.81(3)	−17.12	−16.25	17.82	−15.6(17)	0.053
H6—C6	1.92(3)	−19.18	−17.09	17.58	−18.7(18)	0.122
H8—C8	1.92(3)	−19.90	−19.06	18.58	−20.4(23)	0.044
H14A—C14	1.79(4)	−17.08	−15.46	18.70	−13.8(21)	0.105
H14B—C14	1.76(4)	−16.21	−15.12	18.39	−12.9(19)	0.072
H14C—C14	1.90(3)	−17.44	−16.58	15.86	−18.2(19)	0.051
H15A—C15	1.81(3)	−16.39	−15.65	16.58	−15.5(17)	0.047
H15B—C15	1.87(4)	−17.77	−17.18	18.60	−16.3(20)	0.035
H15C—C15	1.80(3)	−16.17	−15.54	17.44	−14.3(16)	0.041
H16A—C16	1.85(3)	−17.20	−16.64	17.17	−16.7(18)	0.034
H16B—C16	1.81(4)	−17.00	−16.54	17.84	−15.7(19)	0.028
H16C—C16	1.83(3)	−16.92	−16.17	18.12	−15.0(17)	0.047
H11—O11	2.33(7)	−42.75	−40.72	33.68	−49.8(70)	0.050
H18—O18	2.06(6)	−32.76	−30.70	30.03	−33.4(53)	0.067
H11—O17	0.44(19)	−3.39	−2.89	8.54	2.25(6)	0.174
H18—O13	0.65(26)	−6.49	−5.40	11.99	0.10(12)	0.203

[a]Density (ρ_b), curvatures (λ's), Laplacian ($\nabla^2\rho_b$), and ellipticity (ε) of the density at the bcp's are reported. Density values in e Å^{-3}, curvatures and Laplacian in e Å^{-5}. For ρ_b and $\nabla^2\rho_b$ the esd's are in parentheses, and refer to the last significant digit. For comparison with the quantities reported in Figs. 3, 4, and 5, we recall that 1 e Å^{-3} ≡ 0.1482 au, and 1 e Å^{-5} ≡ 0.0415 au.

The linear fit for the six CO bonds gave (in au): $\rho_b = -0.417(29)\ R_b + 1.385(73)$, with $r = -0.990$ and $\sigma = 0.008$ e/(au)^3. A simple exponential was also fitted to the data for these bonds, and the fit improved considerably:

$$\rho_b = 8.433\ R_b^{-3.521}$$

with $r = -0.998$ and $\sigma = 0.011$ e/(au)^3 (Fig. 4). We are not aware of reported correlations for CO bonds in the literature. We stress that differences up to 0.1 Å in the position of bcp's for polar bonds were observed when comparing theoretical and experimental electron densities for L-alanine (41): the dependence of ρ_b on the R_b for CO bonds is therefore expected to be sensibly different if values from ab initio densities are considered.

CH bonds: no correlation could be found for these bonds

between ρ_b and R_e (the latter were used instead of R_b, owing to the already mentioned problems in bond path integration). This may be partly due to the relatively high uncertainty on H positions.

Bond path angles

The bond path angle α_b, defined as the limiting value of the angle subtended at a nucleus by two bond paths, provides a measure of the degree of strain induced on bonding density by the nuclear framework geometry (46). Bond path angles were computed from values of $\nabla\rho$ on the bond paths in vicinity of the nucleus. Values of α_b, and of the corresponding geometrical bond angles α_e at non-H atoms, are reported in Table 5. The differences $\Delta\alpha = \alpha_b - \alpha_e$ and the values of the angle β formed by the geometric bond line and the bond path at the nucleus are also reported in the same table. The β values give further insight into the relative proportions with which the two bond paths considered contribute to the bond angle strain and $\Delta\alpha$ value.

All bond path angles have values very close to the geometric values, and none of the $\Delta\alpha$ is greater in modulus than 4°: the bond strain induced on the molecule of citrinin, if any, can therefore be estimated fairly well on the basis of the geometry of the nuclear framework only. The largest departure of the bond path from the straight bond line occurs at C6 for the C6—O7 bond (β = 3.96°), giving additional evidence of the already mentioned small bending of this bond path, which is more curved on the C6 terminus. The value of $\Delta\alpha$ for the C5-C6-O7 angle is −3°, indicating a slightly larger strain than the geometrical angle would suggest.

Curvature of $\rho(\mathbf{r})$ *at the bcp's*

The eigenvalues λ of the Hessian matrix of ρ at a bcp and the associated eigenvectors are used in topological analysis to characterize chemical interactions (1). The eigenvectors relative to λ_1 and λ_2 define the *minor* and *major axis* of the bond, respectively. Deviation of the bond charge distribution from cylindrical symmetry, as well as conjugative interactions between single and double bonds, may be measured in terms of bond ellipticity at the bcp, $\varepsilon = (\lambda_1/\lambda_2) - 1$, and angles between major axes of neighbouring bonds (1, 46, 47). For citrinin, values of the principal curvatures of ρ at the bcp's (λ's), their sum (i.e., the Laplacian $\nabla^2\rho_b$), and ellipticities ε are reported in Table 6. For the CC and CO bonds, the values of ε and $\nabla^2\rho_b$ are also shown (in au) in Fig. 5.

It is apparent that on the basis of ellipticity and Laplacian values, CC bonds can again be clustered in three groups, as already observed when ρ_b and R_b values were considered. On passing from the single to the double CC bonds of the conjugated system, ellipticities increase, on average, from 0.20 to 0.33 (the average value for ε at the five single CC bonds outside the conjugated system is 0.04). These values reflect an increased contraction of the density towards the bond path with increasing bond order. The increase in λ_1 dominates that in λ_2, and leads to the observed trend for ellipticities: along the minor axis, the density at the bcp's of the double bonds is more curved than at those of the single bonds. The curvature of the density along the major axis (the one relative to λ_2, here directed orthogonally to the plane of the central rings) shows a less marked dependence on the alternation of double and single bonds along the π system. Similar behaviour was reported

Fig. 5. Values ($\nabla^2\rho_b$) of the Laplacian of the electron density at the bond critical point and bond ellipticity (ε) for CC and CO bonds. Model C, molecule extracted from the crystal. The esd's of $\nabla^2\rho_b$ are reported as vertical bars.

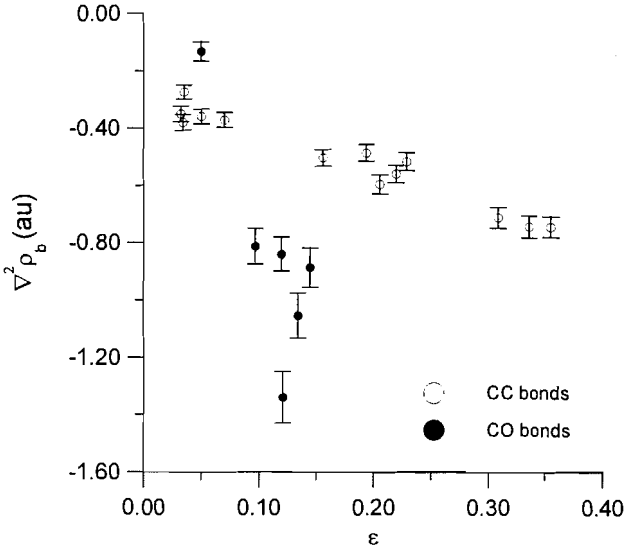

for the curvatures of ab initio ρ at the CC bcp's in the series ethane, benzene, ethylene (47): ε increased mainly because of greater λ_1 values, while λ_2 showed smaller variations with increasing bond order, their sign depending on the basis set adopted. Values of λ_3, the curvature along the direction of the bond, are nearly constant in the 13 CC bonds of citrinin, and remain in the range 12.8–13.7 e Å^{-5}. The observed variation is negligible if compared with the pooled esd of the Laplacian at these bcp's, 0.7 e Å^{-5} (no esd's were calculated for individual curvatures of the density).

For CO bonds, $\nabla^2\rho_b$ values span the range −19.6(15) to −32.3(22), with the exception of C6—O7, by far the longest of all CO bonds, for which the $\nabla^2\rho_b$ value is very close to zero, although still negative. The largest negative Laplacian values are those pertaining to keto and carboxyl C=O bonds, as would be expected on the basis of bond lengths and formal bond order (but ε's are of comparable magnitude for all CO bonds). The large parallel curvatures λ_3 at these two bonds are in keeping with the already observed pronounced displacement of bcp toward the C atoms, and clearly signal greater polarity here than at the alcoholic (C1—O11) and ether (C6—O7 and C8—O7) bonds.

The conjugated system: bond ellipticity and bond overlap

In citrinin, an extensive conjugated system is present, spanning the two fused rings of the molecule. The extension of the π system predicted on the basis of traditional chemical reasoning is confirmed by analysis of the overlap between neighbouring bonds, computed as the scalar product of the eigenvectors of λ_2 at the bcp's (1, 47), or, equivalently, as the angle between the same eigenvectors. Values of such angles smaller than 20° are reported in Fig. 6. Major axes are fairly well aligned for all CC and CO bonds of the planar part of the molecule, while overlap is lost in the C5-C6-O7 portion of the dihydropyrane ring. The overlap of CO bonds seems poorer than the average for the whole π system (this effect was less

Table 7. Topological properties at intramolecular ring critical points. Model C, molecule extracted from the crystal. Units for ρ, λ's, and $\nabla^2\rho$ as in Table 6.

Ring[a]	Σα[b]	d[c] (Å)	ρ	λ_1	λ_2	λ_3	$\nabla^2\rho$	Min ($\lvert r_{rcp} - r_{bcp}\rvert$)[d] (Å)	
R1	360.06	0.013	0.148(6)	−0.28	1.50	1.81	3.03(2)	C2—C3	1.2066
R2	361.83	0.011	0.185(5)	−0.51	1.74	1.88	3.12(2)	C8—C9	1.1773
R3	359.69	0.005	0.177(6)	−0.61	1.76	2.20	3.35(3)	H11···O17	0.8274
R4	360.04	0.047	0.159(6)	−0.50	1.54	2.02	3.06(3)	H18···O13	0.8368

[a]Atoms forming the rings: R1: C1, C2, C3, C4, C10, and C9; R2: C5, C6, O7, C8, C9, and C10; R3: C1, C2, C12, O17, H11, and O11; R4: C12, C2, C3, O13, H18, and O18.
[b]Σα = sum of bcp-rcp-bcp angles.
[c]*d* = distance of the rcp from the least-squares plane through the bcp's along the ring.
[d]Minimum distance from rcp to a bcp of the associated ring.

Fig. 6. Angles (degrees) between eigenvectors of λ_2 at the bond critical points of adjacent bonds. Only values smaller than 20° are reported. Values of the angles are shown between the two bonds to which they refer. Model C, molecule extracted from the crystal.

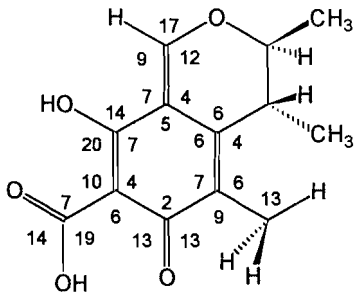

pronounced in models A and B, see discussion below). Interesting and unexpected features arise in connection with the exocyclic C4—C14 bond, linking the methyl group at C14 with the unsaturated system. The bond path length for this bond is the smallest and ellipticity the highest amongst the single C—C bonds of the molecule. Its major axis is aligned almost parallel to those of the C3—C4 and C4—C10 bonds within the ring (angles of 9° and 6°, respectively). These details, however small, may be interpreted as invoking some kind of hyperconjugative interaction (47*a*) of this methyl with the unsaturated system of citrinin, inducing a slight double bond character in what is formally a single bond. It is noticeable that even the major axes of the C14—H4A and C14—C4 bonds are fairly well aligned; the same is observed for the pair of H8—C8 and C8—C9 bonds. Both H4A and H8 atoms approximately lie in the plane of the quinonoid system, torsion angles τ(H8-C8-C9-C1) and τ(H4A-C14-C4-C10) being −7.04(4)° and −7.79(5)°, respectively. We recall that on the basis of the topology of ρ(***r***) at NH bonds, recent ab initio calculations have shown that in crystalline urea conjugation extends across the net of N—H···O bonds (48).

The intramolecular rings and ring critical points

Four six-membered topological rings are present in citrinin: the quinomethide ring R1, the dihydropyrane ring R2 condensed to it, and the two rings formed by the intramolecular hydrogen bonds H11···O17 (R3), and H18···O13 (R4). Topological properties at the corresponding ring critical points (rcp's) are summarized in Table 7. Each of these rcp's lies very close to the least-squares plane passing through the six bcp's along its associated ring; only for the rcp of R4 is this distance as high as 0.047 Å.

The ring R1 shows a remarkable degree of planarity: the maximum distance from the least-squares plane through the six nuclei is 0.037 Å for atom C9. An almost complete overlap between all bonds forming the ring, as already discussed in a previous section, is observed: all major axes are oriented perpendicularly to the ring. The C8-C9-C10-C5 portion of the dihydropyrane ring R2 is also fairly planar, while atoms C6 and O7 are 0.782 and 0.314 Å apart, respectively, from the least-squares plane through the other four atoms. An even greater degree of planarity is exhibited by rings R3 and R4, where no nuclei are further than 0.011 and 0.014 Å from the best plane through the six atoms in each ring.

Incipient ring opening through breaking of a given bond is known to be signalled by displacement of the rcp toward the bcp of that bond: the process occurs by coalescence of these two critical points, with annihilation of one of the positive curvatures at the rcp with a negative curvature at the bcp. An opening of the ring effected via rupture of the bond thus requires the negative curvature λ_2 along the direction pointing toward the rcp to become less and less negative as the rcp and the bcp approach, so that an increase in bond ellipticity at the same bcp is also observed (1, 46, 49).

In citrinin, the relatively high values of ellipticity at the O···H bcp's might suggest potential instability of both R3 and R4 ring structures. The rcp's for these rings are indeed found to be significantly displaced towards the corresponding O···H bcp's, at distances of 0.827 (in R3) and 0.837 Å (in R4), to be compared with values for the average distances from the remaining five bcp's along each ring, 1.187 and 1.172 Å, respectively. (For rings R1 and R2 all distances of the rcp's from the surrounding bcp's are in the range 1.21–1.27 Å and 1.18–1.24 Å, respectively: in both cases the rcp is located virtually in the middle of the six-membered ring.) And yet, values of the density and λ_2 curvatures at the bcp and rcp are sensibly different in both rings R3 and R4. Furthermore, no appreciable alignment is observed between the eigenvector relative to λ_2 at the rcp, and the major axis of the O···H bond.

Table 8. Properties[a] of ρ at the intermolecular bond critical points (bcp's) of citrinin (model C).

Bond	R_c (Å)	R_A (Å)[b]	R_B (Å)[b]	ρ_b	$\nabla^2\rho_b$	ε
H5[c]···O13	2.329(8)	0.946	1.384	0.070(4)	0.97(3)	0.23
H6A···O18[d]	2.399(10)	0.984	1.418	0.070(5)	0.86(3)	0.08
H6C[e]···O11	2.421(9)	1.002	1.423	0.060(4)	0.86(2)	0.05
H8[f]···O17	2.423(9)	1.015	1.410	0.060(3)	0.90(2)	0.14

[a]Density (ρ_b), Laplacian ($\nabla^2\rho_b$), and ellipticity (ε) of the density at the bcp's are reported. Units as in Table 6.
[b]As in note *b* of Table 4.
[c]H5 at $x + 1/2, -y + 1/2, -z$.
[d]O18 at $-x + 2, y + 1/2, -z + 1/2$.
[e]H6C at $-x + 3/2, -y + 1, z + 1/2$.
[f]H8 at $x + 1/2, -y + 1/2, -z + 1$.

These angles amount to 33° and 49°, respectively, for R3 and R4. It can be concluded that the two intramolecularly hydrogen-bonded rings in citrinin are topologically stable.

Dependence of topological properties on models

The overall picture of the bonds involving H atoms, as inferred from the values of the topological properties at the bcp's, more closely resembles that of covalent interactions once ADP's and quadrupoles are introduced to the H atoms, that is, on moving from model A to model B. The bond critical points of CH and OH bonds in model B are shifted toward H nuclei at about 3–8% of the value of their distance from H in model A. Values of ρ_b of CH and OH bonds are increased by 2.3 esd's, on average, and all $\nabla^2\rho_b$ values become more negative by more than 2 esd's. Topological properties at the bcp's of bonds between non-H atoms are instead virtually unchanged: ρ_b increases by about 0.2 esd's, on average, while $\nabla^2\rho_b$ values become more negative by about the same fraction of the associated esd, because of less pronounced parallel and larger perpendicular curvatures.

Figures 7*a* and 7*b* show maps of $-\nabla^2\rho(\boldsymbol{r})$ in a plane through rings R3 and R4, for models A and B, respectively. We recall that charge depletion and charge concentration regions in a given molecule appear as holes and lumps, respectively, in plots of $-\nabla^2\rho(\boldsymbol{r})$: charge is locally concentrated (depleted) in those regions of space where $-\nabla^2\rho$ is positive (negative) (1). The major differences between the pictures of charge concentration and depletion in the two maps are apparent in the regions around atoms H11 and H18: in Fig. 7*b*, the valence shells of these H atoms are connected to those of the bonded O atoms, and their shape is no longer circular (as it is in Fig. 7*a*), but is more realistically elongated toward the hydrogen bond acceptors O17 and O13. On the other hand, the same model B shows a negative region of $-\nabla^2\rho$ between atoms C1 and O11. Also, in the remaining CO bonds a contraction of the valence charge concentration away from the middle of the bond is observed on passing from model A to B, although the valence shells of these C and O atoms are still connected. Both maps show contours at $-\nabla^2\rho = 96.4$ e Å^{-5} (4 au) around the sp^2 atoms O13 and O17, on opposite sides with respect to the direction of the CO bond, and at about 120° from it. Such nonbonded valence charge concentrations correspond to the lone pairs for these atoms (1, 50, 51).

Upon introduction of radial parameters, the picture of all CC and CO bonds of the molecule becomes more polar: $\nabla^2\rho_b$ values become less negative; ellipticities decrease (both λ_1 and λ_2 become less negative, but the latter undergoes a larger percent shift, on average); the average ratio $\lambda_3/(\frac{1}{2}|\lambda_1+\lambda_2|)$ increases from 0.96 to 1.04. A slight loss of conjugation of CO bonds with the rest of the π system is signalled by an increase of the angle giving the overlap, whose average value at O atoms goes from 9.3° (model B) to 14.3° (model C). When comparing the maps of $-\nabla^2\rho(\boldsymbol{r})$ for models B and C (Figs. 7*b* and 7*c*) the increased polarity of the CO bonds is clearly visible: the trend already observed on passing from model A to model B is here enhanced, so that regions of charge depletion now intervene between atoms C3 and O13 and between atoms C12 and O18. Only C12—O17, the shortest of these CO bonds, still shows connected C and O valence charge concentration regions.

Intermolecular contacts and (3,–1) critical points in the crystal

A full topological characterization of the crystal structure, defined as the net of the bond paths obtainable for the density of the solid (3), has not been attempted. Reliable and robust algorithms have recently been proposed that would allow for a complete recovering of the net of critical points of the experimental density in the crystal (52, 53): none of them has been yet implemented in our version of VALRAY. Only a subset of the critical points of the crystalline electron density was therefore found by a conventional Newton–Raphson search.[8] The search was started between all symmetry-unique pairs of nuclei whose distance was smaller than the sum of the van der Waals radii. All pseudoatoms within a contact radius of 5 Å contributed to $\rho(\nabla\rho, \nabla^2\rho)$ at a given point. Iteration was deemed to have reached convergence if none of the components of the calculated shift was higher than 0.001 Å; if no critical point was found after 10 iterations, the search was stopped.

All of the 39 critical points already found when analysing the density of the molecule extracted from the crystal were also recovered in the solid: these critical points are equivalent in number and type, and their positions are virtually the same, as those of the critical points already discussed for the "isolated" molecule. A set of four (3,−1) critical points relative to intermolecular interactions was also recovered. Table 8

[8] For a discussion of the shortcomings of this technique when dealing with systems with non-trivial topology see ref. 52.

Fig. 7. Contour maps (7.2 × 5.0 Å) of $-\nabla^2\rho$ in the plane of rings R3 and R4 of citrinin, molecule extracted from the crystal. The plane is defined by atom C2 and by the (3,−1) critical points of bonds O11—H11 and C2—C12. Origin at the latter bcp. None of the atoms is further than 0.02 Å from the plane. Solid lines: negative Laplacian, contour lines at -4×10^{-1}, -2×10^{-1}, -8×10^{-2}, -4×10^{-2}, -2×10^{-2}, -8×10^{-3} au. Broken lines: positive Laplacian, contour levels at 2×10^{n}, 4×10^{n}, 8×10^{n} au, with n beginning at −2 and increasing in steps of unity up to $n = 0$. Zero contour omitted. (*a*) Model A; (*b*) model B; (*c*) model C.

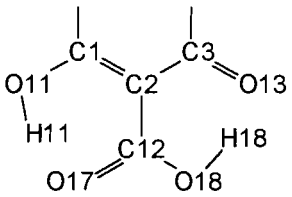

(a)

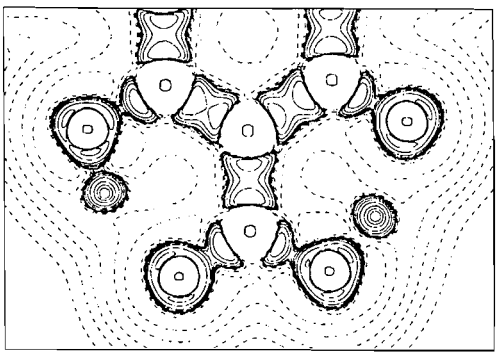

(b)

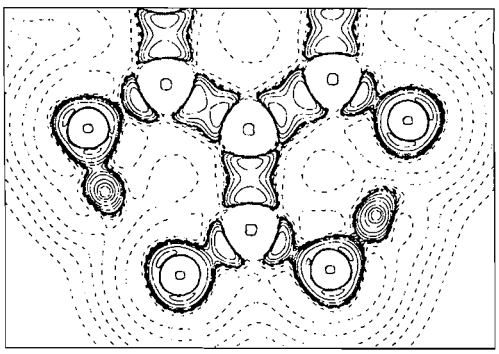

(c)

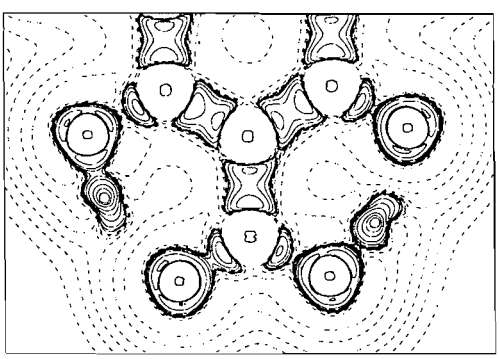

reports the main topological properties at these (3,−1) bcp's, all of which are located in between O and H atoms of neighbouring molecules, with O···H distances of 2.329(8) to 2.423(9) Å. Density values span the range 0.04–0.07 e Å^{-3}; the small and positive values of $\nabla^2\rho_b$ are characteristic of non-shared interactions dominated by the curvature along the internuclear direction. Also for these bonds an inverse relationship is observed between R_e and ρ_b values.

Finally, we mention that 14 (3,+1) and 3 (3,+3) symmetry-unique critical points were also found,[9] the former group including the four intramolecular rcp's. The Poincaré–Hopf relationship governing the type and number of critical points for an extended system (3, 54) is not satisfied by this set of critical points, in that four more cage critical points (3,+3) would be required, if all other cp's are assumed to have been recovered. We mention that the intermolecular (3,+1) and (3,+3) cp's are located in low-density and flat regions within the crystal. Curvatures there are often very close to zero, and the exact rank and signature of the critical point become uncertain.

Chemical reactivity and the molecular reactive surface

When treated with alkali, citrinin (**1**) is known to yield the alcohol (**2**) (55):

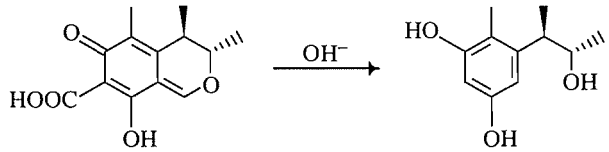

1 **2**

The reaction involves a nucleophilic attack at the C8 carbon atom in the dihydropyrane ring. It has been shown that the geometry of approaching reactants and the relative reactivity of different sites within a given molecule can be rationalized by making use of the distribution of $\nabla^2\rho(\boldsymbol{r})$ (1). We have not yet performed the topological analysis of the Laplacian of the experimental charge density for citrinin. Qualitative evidence about the electrophilic character of a given site can nevertheless be obtained from the values of the Laplacian function alone. A display of the *reactive surface* of the molecule, defined as the $\nabla^2\rho = 0$ isosurface, traces the separation between regions of charge concentration and charge depletion, and gives an effective description of the qualitative affinity of the various molecular portions toward Lewis acids and bases (1, 51).

Figures 8*a* and 8*b* show plots of the reactive surface in the dihydropyrane ring R2 of citrinin, for densities from models C and A, respectively. In both maps the surface shows holes through which the inner zero surfaces between core charge concentration and core charge depletion for some of the C atoms are visible. No valence charge concentration region is encountered while moving away from these atoms along the viewing direction. In both plots, this feature is particularly

[9] A full specification of the atoms forming the rings (cages) associated with the points found would require tracing out the $\nabla\rho$ trajectories from the rcp's (cage cp's) and terminating at the surrounding attractors.

Fig. 8. Isovalue surface of $-\nabla^2\rho$ for citrinin. The surface drawn is the $-\nabla^2\rho = 0$ surface, the reactive surface. The values of the negative Laplacian were sampled on an orthogonal grid in a box of size 4.2 × 4.2 Å, and extending 1.35 Å above and below the plane defined by the atoms C6 and O7, and the ring critical point of the dihydropyrane ring R2. (*a*) Model C; (*b*) model A.

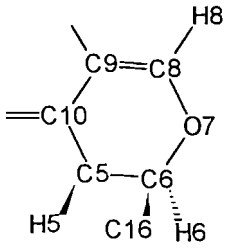

(a)

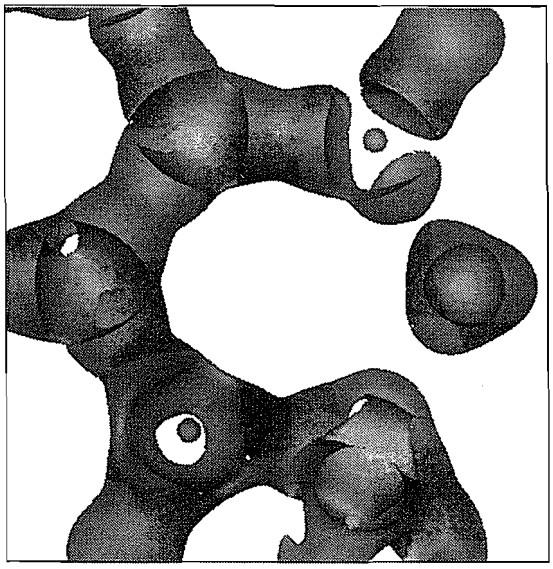

(b)

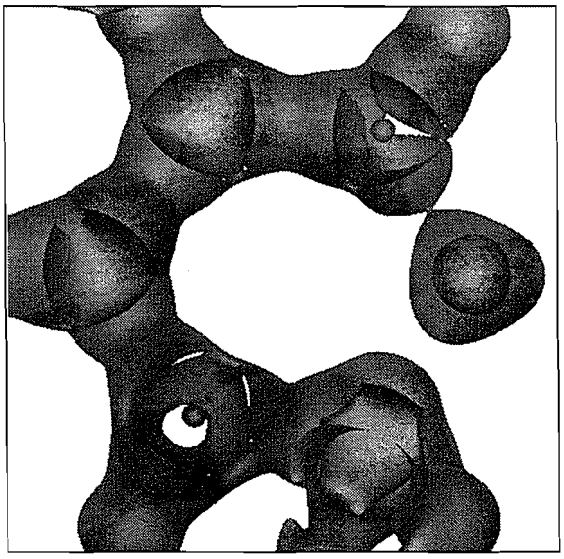

Fig. 9. $-\nabla^2\rho = 0$ isovalue surface for citrinin, isolated molelcule, model C. The values of the negative Laplacian were sampled on an orthogonal grid in a box of size 5.85 × 4.65 Å, and extending 1.35 Å above and below the plane mapped in Fig. 7.

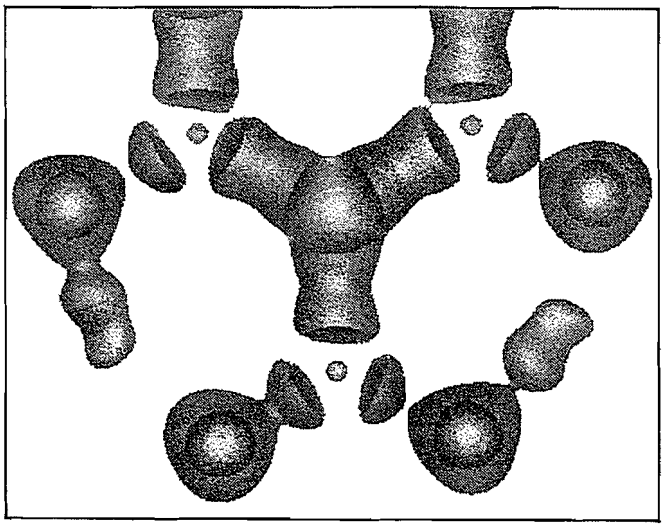

pronounced around atom C8, which is therefore predicted to be the most suitable site for nucleophilic attack in this portion of the molecule. We emphasize the striking difference between this atom and other C atoms in the ring, e.g., C9 (which has similar sp^2 hybridization) or C6 (which is bonded to the same oxygen O7). A completely equivalent image of the reactive surface is obtained when viewing it from the other side of ring R2, again indicating carbon C8 as the most electrophilic site in this ring.

Figure 9 shows the reactive surface (model C) for the molecular portion containing rings R3 and R4. Around all carbon atoms bonded to oxygen in the mapped region, the zero envelope of the Laplacian shows pronounced holes and missing valence charge concentration regions along directions approximately orthogonal to the plane of the rings. As far as can be judged from the display of the reactive surface, these carbon atoms are also indicated as possible sites of nucleophilic attack. It is seen that the experimental picture of the charge density distribution in citrinin is in keeping with the known chemical reactivity of the molecule in alkali, although quantitative predictions about the preferred site of nucleophilic attack must await a thorough analysis of the $-\nabla^2\rho$ field.

Concluding remarks

The wealth of chemical information obtainable from careful and accurate measurement and processing of low-temperature diffraction intensities has been demonstrated in the case of citrinin. Valence deformation terms are sensitive to data up to about 0.8 Å resolution only, but the number and quality of higher order data are essential to attain a satisfactory deconvolution of the dynamic features from the experimental density. Although of minor importance in the system under study, where no significantly strained bonds are present, bond path lengths and bond path angles have been shown to usefully complement the information given by the traditional bond lengths and angles computed from the nuclear geometry.

Other important chemical features of the system under study, such as conjugation and hydrogen bond stability, have been shown to be successfully redescribed in terms of topological quantities at the bcp's of the experimental density. Good agreement with published theoretical results for the inverse correlation between ρ_b and R_b values for CC bonds has been obtained, and a similar relationship for the CO bonds established.

Adoption of calculated ADP's and concomitant multipolar expansion up to the quadrupolar level on H atoms has yielded a more realistic shape of their valence charge concentration region. However, only a variation of the standard radial dependence of monopole and higher poles radial functions could prevent the density from acquiring small negative values in regions far from the non-H atoms.

Topological analysis has proven very valuable in revealing the sometimes subtle dependence of the picture of the density upon the model adopted in interpreting the X-ray data. The tracing of bond paths in the solid and the implementation of robust and automatic algorithms to locate all kinds of critical points and calculate interatomic surfaces in the bulk are the main directions along which we plan our future work, to achieve a complete topological analysis of experimental electron densities.

The picture we obtain for CO bonds in citrinin closely resembles that of polar interactions, with pronounced parallel curvature and considerable contraction of density toward the nuclei. The charge depletion intervening in the middle of these bonds is at variance with ab initio results (1): the shape we find might be an artifact due, at least in part, to inability of our radial functions to fit the density in these bonding regions. Further investigation of the role played by these radial functions in modelling experimental densities is therefore demanded.

For the first time (to our knowledge), a reactive surface has been plotted from values of the Laplacian of an experimental density. The shape of the surface has been found to be in agreement with the known electrophilic character of one of the C atoms of the molecule under study. On the other hand, only a complete analysis of the topology of the Laplacian of the density would allow the charge density study to be of help in rationalizing chemical reactivity in a more quantitative way.

Acknowledgements

One of us (P.R.) wishes to thank for warm hospitality the Medical Research Council – Laboratory of Molecular Biology in Cambridge, England, where part of the computational work was done. We also thank G. Bricogne and C. Gatti for enlightening comments and fruitful discussions. Thanks are also due to C. Scolastico and F. Aragozzini for a generous gift of crystalline citrinin.

References

1. R.F.W. Bader. Atoms in molecules — a quantum theory. Oxford University Press, Oxford, U.K. 1990.
2. R.F. Stewart. *In* The application of charge density reasearch to chemistry and drug design. *Edited by* G.A. Jeffrey and J.F. Piniella. Plenum Press, New York. 1991. pp. 63–101.
3. P.F. Zou and R.F.W. Bader. Acta Crystallogr. Sect. A: Found. Crystallogr. **A50**, 714 (1994).
4. R.F.W. Bader. Trans. Am. Crystallogr. Assoc. **26**, 1 (1990).
5. R. Destro, R. Bianchi, C. Gatti, and F. Merati. Chem. Phys. Lett. **186**, 47 (1991).
6. S.T. Howard, M.B. Hursthouse, C.W. Lehmann, P.R. Mallinson, and C.S. Frampton. J. Chem. Phys. **97**, 5616 (1992).
7. W.T. Klooster, S. Swaminathan, R. Nanni, and B.M. Craven. Acta Crystallogr. Sect. B: Struct. Sci. **B48**, 217 (1992).
8. V.G. Tsirelson, P.F. Zou, T.-H. Tang and R.F.W. Bader. Acta Crystallogr. Sect. A: Found. Crystallogr. **A51**, 143 (1995).
9. J.W. Downs and R.J. Swope. J. Phys. Chem. **96**, 4834 (1992).
10. R. Destro and F. Merati. Acta Crystallogr. Sect. B: Struct. Sci. **B51**, 559 (1995).
11. B.B. Iversen, F.K. Larsen, M. Souhassou, and M. Takata. Acta Crystallogr. Sect. B: Struct. Sci. **B51**, 580 (1995).
12. F.K. Larsen. Acta Crystallogr. Sect. B: Struct. Sci. **B51**, 468 (1995).
13. R. Destro and R.E. Marsh. J. Am. Chem. Soc. **106**, 7269 (1984).
14. R. Destro. Chem. Phys. Lett. **181**, 232 (1991).
15. S. Samson, E. Goldish, and C.J. Dick. J. Appl. Crystallogr. **13**, 425 (1980).
16. R. Destro. Aust. J. Phys. **41**, 503 (1988).
17. R. Destro and F. Merati. Z. Naturforsch. A: Phys. Sci. **48**, 99 (1993).
18. U.W. Arndt and B.T.M. Willis. Single crystal diffractometry. Cambridge University Press, Cambridge. 1966. p. 287.
19. R. Destro and R.E. Marsh. Acta Crystallogr. Sect. A: Found. Crystallogr. **A43**, 711 (1987).
20. R. Destro and R.E. Marsh. Acta Crystallogr. Sect. A: Found. Crystallogr. **A49**, 183 (1993).
21. P. Coppens and P.J. Becker. *In* International tables for crystallography. Vol. C. *Edited by* A.J.C. Wilson. Kluwer Academic Publishers, Dordrecht. 1995. pp. 627–636.
22. P. Coppens. Annu. Rev. Phys. Chem. **43**, 663 (1992).
23. B.M. Craven and R.F. Stewart. Trans. Am. Crystallogr. Assoc. **26**, 41 (1990).
24. R.F. Stewart. Acta Crystallogr. Sect. A: Cryst. Phys. Diffr. Theor. Gen. Crystallogr. **A32**, 565 (1976).
25. E. Clementi. IBM J. Res. Dev. (Suppl.) **9**(2), (1965).
26. W.J. Hehre, R.F. Stewart, and J.A. Pople. J. Chem. Phys. **51**, 2657 (1969).
27. R.F. Stewart, J.J. Bentley, and B. Goodman. J. Chem. Phys. **63**, 3786 (1975).
28. P.J. Becker and P. Coppens. Acta Crystallogr. Sect. A: Cryst. Phys. Diffr. Theor. Gen. Crystallogr. **A30**, 129 (1974).
29. V. Schomaker and K.N. Trueblood. Acta Crystallogr. Sect. B: Struct. Crystallogr. Cryst. Chem. **B24**, 63 (1968).
30. R.F. Stewart and M.A. Spackman. VALRAY users manual. Carnegie-Mellon Univ., Pittsburgh, Pa. 1983.
31. W.C. Hamilton. Acta Crystallogr. **18**, 502 (1965).
32. E. Prince and C.H. Spiegelman. *In* International tables for crystallography. Vol. C. *Edited by* A.J.C. Wilson. Kluwer Academic Publishers, Dordrecht. 1995. pp. 618–624.
33. W.C. Hamilton. *In* Statistics in physical science: estimation, hypothesis testing and least squares. Ronald Press, New York. 1964. pp. 35–49 and pp. 78–81.
34. F. Hirshfeld. Acta Crystallogr. Sect. A: Cryst. Phys. Diffr. Theor. Gen. Crystallogr. **A32**, 239 (1976).
35. M. Terpstra, B.M. Craven, and R.F. Stewart. Acta Crystallogr. Sect. A: Found. Crystallogr. **A49**, 685 (1993).
36. C.K. Johnson. ORTEP. Report ORNL-3794. Oak Ridge National Laboratory, Oak Ridge, Tenn. 1965.
37. M.J. Frisch, G.W. Trucks, H.B. Schlegel, P.M.W. Gill, B.G. Johnson, M.A. Robb, J.R. Cheeseman, T. Keith, G.A. Petersson, J.A. Montgomery, K. Raghavachari, M.A. Al-Laham, V.G. Zakrzewski, J.V. Ortiz, J.B. Foresman, J. Cioslowsky, B.B. Stefanov, A. Nanayakkara, M. Challacombe, C.Y. Peng, P.Y.

Ayala, W. Chen, M.W. Wong, J.L. Andres, E.S. Repogle, R. Gomperts, R.L. Martin, D.J. Fox, J.S. Binkley, D.J. Defrees, J. Baker, J.P. Stewart, M. Head-Gordon, C. Gonzalez, and J.A. Pople. GAUSSIAN94, Revision B.2. Gaussian, Inc., Pittsburgh, Pa. 1995.

38. (*a*) P.J. Stephens, F.J. Devlin, and M.J. Frisch. J. Phys. Chem. **98**, 11623 (1994); (*b*) A.D. Becke. J. Chem. Phys. **98**, 5648 (1993); (*c*) C. Lee, W. Yang, and R.G. Parr. Phys. Rev. B: Condens. Matter, **37**, 785 (1989); (*d*) S.H. Vosko, L. Wilk, and M. Nusair. Can. J. Phys. **58**, 1200 (1980).
39. F.H. Allen, O. Kennard, D.G. Watson, L.Brammer, A.G. Orpen, and R. Taylor. *In* International tables for crystallography. Vol. C. *Edited by* A.J.C. Wilson. Kluwer Academic Publishers, Dordrecht. 1995. pp. 696 and 703.
40. R.K. McMullan and B.M. Craven. Acta Crystallogr. Sect. B: Struct. Sci. **B45**, 270 (1989).
41. C. Gatti, R. Bianchi, R. Destro, and F. Merati. J. Mol. Struct. (THEOCHEM), **255**, 409 (1992).
42. K. Collard and G.G. Hall. Int. J. Quantum Chem. **12**, 623 (1977).
43. R.F.W. Bader and D.A. Legare. Can J. Chem. **70**, 657 (1992).
44. R.F.W. Bader, T.-H. Tang, Y. Tal, and F.W. Biegler-König. J. Am. Chem. Soc. **104**, 946 (1982).
45. (*a*) R.J. Boyd and S.C. Choi. Chem. Phys. Lett. **120**, 80 (1985); (*b*) Chem. Phys. Lett. **129**, 62 (1986); (*c*) R.J. Boyd. *In* Studies in organic chemistry. Vol. 31. *Edited by* M. Kobayashi. Elsevier Science Publishers B.V., Amsterdam. 1987. pp. 485–492; (*d*) O. Knop, R.J. Boyd, and S.C. Choi. J. Am. Chem. Soc. **110**, 7299 (1988).
46. R.F.W. Bader. *In* The chemistry of alkanes and cycloalkanes. *Edited by* S. Patai and Z. Rappoport. Wiley–Interscience, New York. 1992. pp. 27–31.
47. (*a*) R.F.W. Bader, T.S. Slee, D. Cremer, and E. Kraka. J. Am. Chem. Soc. **105**, 5061 (1983); (*b*) D. Cremer, E. Kraka, T.S. Slee, R.F.W. Bader, C.D.H. Lau, T.T. Nguyen-Dang, and P.J. MacDougall. J. Am. Chem. Soc. **105**, 5069 (1983).
48. C. Gatti, V.R. Saunders, and C. Roetti. J. Chem. Phys. **101**, 10686 (1994).
49. P.L.A. Popelier and R.F.W. Bader. J. Phys. Chem. **98**, 4473 (1994).
50. R.F.W. Bader, P.J. McDougall, and C.D.H. Lau. J. Am. Chem. Soc. **106**, 1594 (1984).
51. R.F.W. Bader, P.L.A. Popelier, and C. Chang. J. Mol. Struct. (THEOCHEM), **255**, 145 (1992).
52. P.L.A. Popelier. Chem. Phys. Lett. **228**, 160 (1994).
53. J. Cioslowsky and A. Nanayakkara. Chem. Phys. Lett. **219**, 151 (1994).
54. C.K. Johnson. Am. Crystallogr. Assoc. Winter Meet., Asilomar. 1977. Abstracts p. 30.
55. L. Colombo, C. Gennari, D. Potenza, and C. Scolastico. J. Chem. Soc. Perkin Trans. 1, 2594 (1981).

A theoretical study of some X—H···π hydrogen-bonded complexes using the theory of atoms in molecules

Ting-Hua Tang and Yun-Ping Cui

Abstract: π-Type hydrogen-bonded complexes consisting of hydrogen halide HX (X = Cl, F) and the carbon–carbon triple or double bond of vinyl acetylene (1-buten-3-yne, HC≡C-CH=CH_2) have been studied. The vinyl acetylene molecule contains two possible π-bonding sites (C≡C and C=C). It offers three possible structures of C_4H_4···HX that comprise two T-type bonds to C≡C (*endo* and *exo* approaches) and one T-type bond to C=C (perpendicular approach). The optimized geometries and the hydrogen-bond stabilization energies, based on MP2(FULL)/6-311++G(d,p)//6-31G(d,p) calculations, indicate that the π-type hydrogen bond to a C≡C triple bond leads to a more stable complex than for an analogous bond to C=C. The calculated global minima for the complexes with HF and HCl correspond to the H—X moiety lying along a bisector of the C≡C triple bond in the *endo* approach, predictions that are in good agreement with the reported FTMS results. The topological properties of the electron density distributions of these two systems have been analyzed in terms of the theory of atoms in molecules. The nature of π-type hydrogen bonds has also been discussed using the Laplacian of the electron density, $\nabla^2\rho$. The complexes C_2H_2···HX and C_2H_4···HX as well as the hydrogen-bonded complex consisting of 2-butyne (CH_3-C≡C-CH_3) and HCl were also studied for comparison.

Key words: ab initio calculation, hydrogen bonding, topological analysis of electron density, vinyl acetylene, 2-butyne.

Résumé : On a étudié les complexes à liaisons hydrogènes de type π formés par des halogénures d'hydrogène (HX, X = Cl, F) et la liaison carbone–carbone double ou triple du vinylacétylène (but-1-èn-3-yne, HC≡C-CH=CH_2). La molécule de vinylacétylène comporte deux sites possibles de liaisons π (C≡C et C=C). Il existe trois structures possibles de C_4H_4···HX qui comprennent deux liaisons de type T par rapport à C≡C (approches *endo* et *exo*) et une liaison de type T par rapport à C=C (approche perpendiculaire). Les géométries optimisées et les énergies de stabilisation de la liaison hydrogène, basées sur des calculs MP2(FULL)/6-311++G(d,p)//6-31G(d,p) indiquent que la liaison hydrogène de type π à une liaison triple C≡C conduit à un complexe plus stable que celle pour une liaison C=C analogue. Les minima globaux calculés pour les complexes avec HF et HCl suggèrent que, dans l'approche *endo*, la portion H—X se trouve sur une bissectrice de la liaison triple C≡C, une prédiction qui est en bon accord avec les résultats de FTMS déjà rapportés. On a analysé les propriétés topologiques des distributions de densité électronique de ces deux systèmes en termes de la théorie des atomes dans les molécules. On a discuté de la nature des liaisons hydrogènes de type π en faisant appel au laplacien de la densité électronique, $\nabla^2\rho$. De plus, pour fins de comparaison, on a étudié les complexes C_2H_2···HX et C_2H_4···HX ainsi que le complexe à liaison hydrogène formé entre le but-2-yne (CH_3-C≡C-CH_3) et le HCl.

Mots clés : calculs ab initio, liaison hydrogène, analyse topologique de la densité électronique, vinylacétylène, but-2-yne.

[Traduit par la rédaction]

Introduction

X—H···π type hydrogen-bonded complexes, consisting of a hydrogen halide molecule HX as proton donor and the carbon–carbon multiple bond as proton acceptor, are usually considered to be the initial stage of an electrophilic addition to the alkene or alkyne, with an X-H orientation that is perpendicular to the CC multiple bond. These complexes were studied experimentally by traditional thermal analysis almost four decades ago (1); more recently, for more reliable determinations, by Fourier transform microwave spectroscopy (FTMS) as well as IR spectroscopy in the gaseous state (2–5); and most recently by X-ray scattering in the crystal (6). Theoretically based ab initio calculations have also been reported in the literature (7–10). In our previous study (10), the calculated (MP2/6-31G(d,p)//6-31G(d)) π-type hydrogen-bond stabilization energies for C_2H_2·HF, C_2H_4·HF, C_3H_6·HF, and C_6H_6·HF were reported and the nature of the π-type hydrogen bond was discussed in a preliminary fashion on the basis of topological property analysis of the electron density distribution in the theory of atoms in molecules (AIM) (11). Lin and

Received October 20, 1995.

This paper is dedicated to Professor Richard F.W. Bader on the occasion of his 65th birthday.

T.-H. Tang.[1] Department of Chemistry, McMaster University, Hamilton, ON L8S 4M1, Canada, and Department of Chemistry, Tianjin Normal University, Tianjin 300074, China.
Y.-P. Cui.[2] Department of Chemistry, Tianjin Normal University, Tianjin 300074, China.

[1] Author to whom correspondence may be addressed. Telephone: (905) 525-9140. Fax: (905) 522-2509. E-mail: ttang@mcmail.cis.mcmaster.ca
[2] Current address: Department of Chemistry, University of Waterloo, Waterloo, ON N2L 3G1, Canada.

Bytheway (12) very recently reported the analysis of the Laplacian of the electron density of C_2H_4·HCl, which was then compared with the C_2H_4·ClBr system.

Experimentally, vinyl acetylene (1-buten-3-yne, HC≡C-CH=CH_2), which is a molecule with both double and triple carbon–carbon bonds, has been used to determine which of the two sites and which of the two approaches (*exo* or *endo*) for the C≡C triple bond was the most attractive for T-type hydrogen-bond formation with HCl (4) and HF (5). From these reported FTMS experimental results (4, 5), both HX molecules (X = Cl, F) preferably attach to the C≡C triple bond in vinyl acetylene in an *endo* approach. Also, an X-ray crystal structure determination of 2-butyne·HCl has been reported (6) in which the solid-state T-shape geometry of Cl—H···π type hydrogen bonding was convincingly displayed. It is necessary to deepen our understanding of the structure, the nature of bonding, and the energetics of these π-type hydrogen-bonded complexes. To further characterize the chemical nature of π-type hydrogen bonding in these complexes we have carried out a topological analysis of their electron density, $\rho(\boldsymbol{r})$. The analysis of topological properties of the critical points of ρ and its associated Laplacian $\nabla^2\rho(\boldsymbol{r})$ is a useful tool for the characterization of atomic interactions within molecules (11). It is the purpose of the present paper to give further insight into the details of the bonding in these π-type hydrogen-bonded complexes.

Methods

All geometries were optimized at the 6-31G(d,p) level of theory (13). The hydrogen-bonded stabilization energy is defined in the thermodynamic sense as the difference between the total energy of the hydrogen-bonded complex and the sum of the total energies of the HX (X = F, Cl) and the hydrocarbon molecule that form the complex. The correlation-energy corrections were obtained by using Møller–Plesset perturbation theory at the second-order level (MP2) (14). For π-type hydrogen-bond stabilization energy calculations, single-point MP2(FULL)/6-311++G(d,p) (15) (MP2(FULL)/6-311++G-(2d,2p) for the 2-butyne·HCl complex) calculations, in which all electrons are included, were performed on 6-31G(d,p) fully optimized geometries. All ab initio calculations were performed using GAUSSIAN 90 (16*a*) and GAUSSIAN 92 programs (16*b*).

Recently, inter-, intra-, and π-type hydrogen bonding have been analyzed using the theory of atoms in molecules (AIM) (10, 11, 17) to elucidate the nature of the hydrogen bonding. In this theory, the topological properties of the electron density distribution of a molecule are based on the gradient vector field of the electron density $\nabla\rho(\boldsymbol{r})$, and on the Laplacian of the electron density $\nabla^2\rho(\boldsymbol{r})$. Several excellent reviews have been published (11) on this subject and it has been discussed in detail elsewhere; therefore only a brief description of some selected topological parameters pertinent to the present work is given here. The electron density distribution of a molecule is described by $\rho(\boldsymbol{r}, \boldsymbol{X})$ where $\boldsymbol{r}$ is a vector in ordinary three-dimensional space and $\boldsymbol{X}$ represents a particular set of nuclear coordinates in the space corresponding to the nuclear configurations of the molecule in question. An atom in a molecule is defined as a region of real three-dimensional space bounded by a zero-flux surface. The points on this surface satisfy $\nabla\rho(\boldsymbol{r})\cdot\boldsymbol{n}(\boldsymbol{r}) = 0$ where $\boldsymbol{n}(\boldsymbol{r})$ is the unit vector normal to the surface at $\boldsymbol{r}$. Two interacting atoms in a molecule form a critical point in the electron density, where $\nabla\rho = 0$, called a bond critical point (BCP). The pairs of gradient paths that originate at a BCP and terminate at neighbouring nuclei define a line, called an atomic interaction line, through which electron distribution, $\rho(\boldsymbol{r})$, is a maximum with respect to any lateral displacement. The presence of such a line, linking two nuclei in a molecule, which exists in a minimum energy geometry, implies that two atoms are bonded to one another and in this instance this line is called a bond path. The necessary condition for two atoms to be bonded to one another is therefore that their nuclei be linked by a bond path. The network of bond paths for a molecule in a given nuclear configuration $\boldsymbol{X}$ defines the molecular graph, which essentially is the union of the closures of the bond paths. Such a topological graph usually corresponds to the commonly drawn chemical bond network.

The electron density, $\rho(\boldsymbol{r})$, at the BCP is related to the bond order and therefore to the bond strength (18). The eigenvalues associated with the second derivatives of ρ, at the BCP (λ_1, λ_2, and λ_3) indicate how rapidly the density changes on moving away from the BCP and represent the curvatures of electron density along different directions. For a normal single bond, such as the C—C bond in ethane, the two negative curvatures (λ_1 and λ_2), which are perpendicular to the bond line, are approximately equal. However, if there is a double bond, one curvature (in the direction of the π-bond) will be much smaller than the other. This difference may be described by the ellipticity, ε, of the bond, which is defined as $\varepsilon = \lambda_1/\lambda_2 - 1$, in which λ_2 is the curvature of smaller magnitude. For a single bond, $\lambda_1 \cong \lambda_2$; therefore $\varepsilon \cong 0$. For a double bond, $\lambda_1 > \lambda_2$; therefore $\varepsilon > 0$. For aromatic systems, in general, ε is in between a typical single and a typical double bond. For symmetrical triple bonds, since $\lambda_1 \cong \lambda_2$, ε is equal or close to zero. In practice, the trace or the sum of the second partial derivative values of $\nabla^2\rho(\boldsymbol{r}_b) = \Sigma_{j=1,3}\partial^2\rho\,(\boldsymbol{r}_b)/\partial x_j^2$ at the BCP, denoted by $\boldsymbol{r}_b$, is negative for a covalent interaction. The trace of $\nabla^2\rho(\boldsymbol{r}_b)$ is positive for an interaction between closed-shell systems. A critical point, at which $\rho(\boldsymbol{r})$ has one negative curvature and two positive curvatures, can be defined as a ring critical point. The existence of a ring critical point, at which the density $\rho(\boldsymbol{r})$ is smaller than that of all surrounding BCPs, indicates that the molecule contains a ring structure. Of particular interest to the present study is the Laplacian of the electron density, the quantity at any point, $\nabla^2\rho(\boldsymbol{r}) = \Sigma_{j=1,3}\partial^2\rho(\boldsymbol{r})/\partial^2 x_j^2$, that determines the regions of space wherein the electron density is locally concentrated or depleted. From the definition of a second derivative, one finds that $\rho(\boldsymbol{r})$ is greater than the average of its values over an infinitesimal sphere centered on $\boldsymbol{r}$, when $\nabla^2\rho(\boldsymbol{r}) < 0$, and $\rho(\boldsymbol{r})$ is less than this average when $\nabla^2\rho(\boldsymbol{r}) > 0$. Thus a local maximum (or minimum) in $-\nabla^2\rho(\boldsymbol{r})$ signifies a local concentration (or depletion) of electron density. It has been reported (11, 19) that these magnitudes of $-\nabla^2\rho(\boldsymbol{r})$ can be used to study the preferred orientation of electrophilic and nucleophilic attack. The site of Laplacian depletion favors nucleophilic and the site of Laplacian concentration favors electrophilic attack. Moreover, in some series of closely related molecules the Laplacian can give quantitative formation concerning relative protonation energies (20). On the other hand, the use of the Laplacian $\nabla^2\rho(\boldsymbol{r})$ for the study of hydrogen-bonded complexes has been reported (17*e–i*). This

method is superior to some conventional models (21–23). In the above method using the Laplacian $\nabla^2\rho(r)$, no models are employed and no parameters are used, as it is determined by the electron density, for predicting chemical behaviour of hydrogen-bonded complexes. The numbers, locations, and relative sizes of the bonded and nonbonded concentration of charge in the valence shell of a bonded atom, as determined by the Laplacian of $\rho(r)$, are found to be in generally good agreement with the corresponding properties ascribed to bonded and nonbonded pairs in Gillespie's VSEPR model of molecular geometry (24).

The AIMPAC program[3] was employed for the electron density topological analysis, using the electron densities obtained from the MP2(FULL)/6-311++G(d,p) calculations (MP2-(FULL)/6-311++G(2d,2p) for the 2-butyne·HCl complex).

Results and discussion

1. Optimized geometries and π-type hydrogen-bond energies

For vinyl acetylene, HC≡C-CH=CH_2 (C_4H_4), there are three possible approaches for the incoming HX forming C_4H_4·HX π-type hydrogen-bonded complexes. These are *endo* and *exo* approaches to the carbon–carbon triple bond as well as a perpendicular approach to the carbon–carbon double bond at the other end of the molecule.

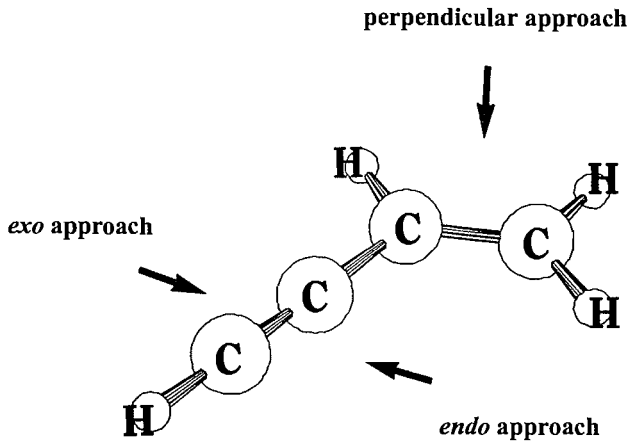

The full geometry optimizations for the aforementioned molecules and their hydrogen-bonded systems were carried out using the 6-31G(d,p) basis set. The results of geometry optimization of the C_4H_4·HX (X = F, Cl) systems, considering different approaches by HX to form C_4H_4·HX complexes, together with the optimized geometries of HX, C_2H_2, C_2H_4, C_4H_4, C_2H_2·HX, C_2H_4·HX, C_4H_6·HCl, are shown in Fig. 1. The hydrogen-bond energies for the 11 systems mentioned above are tabulated in Table 1. It can be seen from the first two columns of Table 1 that increasing the size of the basis set decreases the hydrogen-bond energy. It seems that if the basis set used is smaller, then the basis set superposition error (BSSE) is larger — which erroneously provides an extra stabilization energy. Thus the larger basis set results are more reliable. The third column contains hydrogen-bond energies that include correlation-energy corrections.

[3] Available from Professor R.F.W. Bader's laboratory, McMaster University, Hamilton, ON L8S 4M1, Canada.

It was reported earlier (17*f*, 25) that if the basis set has diffuse functions and polarization functions on each of the atoms, then the BSSEs are quite small and these will not influence the trends in the computed hydrogen-bond energies. From Table 1 it can be seen, very clearly, that the π-type hydrogen bond to the C≡C bond among vinylacetylene·HX (C_4H_4·HX) complexes (**10–15**) leads to a more stable complex than for an analogous complex involving the C=C bond. For the sake of comparison, the hydrogen-bond energies of C_2H_2·HX and C_2H_4·HX complexes (**5–8**) were also calculated. The calculated global minima for these C_4H_4·HX complexes, with HF and HCl (complexes **11** and **14**), correspond to the HX moiety lying along a bisector of the C≡C bond in the *endo* approach. Moreover, in these optimized geometries of complexes **11** and **14**, the $R_{C\equiv C\cdots F}$ equals 3.161 Å and the $R_{C\equiv C\cdots Cl}$ equals 3.824 Å. These predictions are in good agreement with the reported FTMS experimental results (4, 5). Also there is a significant amount of hydrogen-bond energy (−4.87 kcal/mol) for the 2-butyne·HCl (C_4H_6·HCl, **17**) complex. Obviously it is a stable complex that is, in fact, in good agreement with the X-ray determination of its solid-state geometry (6).

2. Molecular graphs of π-type hydrogen-bonded complexes

The topological properties of the electron density distributions of these 11 (**5–8**, **10–15**, **17**) complexes have been analyzed in terms of the theory of atoms in molecules. For these hydrogen-bonded systems the location of all BCPs and attractors were determined,[4] and the molecular graphs were mapped out for the hydrogen-bonded systems studied. These molecular graphs of the C_2H_2·HX, C_2H_4·HX, C_4H_4·HX (X = F, Cl), and C_4H_6·HCl complexes are shown in Fig. 2. As shown in this figure, π-type hydrogen bonding does exist and it is perpendicular to the C≡C and C=C bonds. All of them have the same "conflict type" structure. In particular, it is found, for C_4H_4·HF complexes, that both the *endo* and *exo* approaches lead to complexes that are nearly planar, with the proton of HF directed towards the triple C≡C bond in vinyl acetylene, forming a π-type hydrogen bond. Furthermore, a second hydrogen bond is formed between H of a C—H bond and F of

[4] For the monomers and complexes containing a carbon–carbon triple bond, there is an exceptional local maximum in $\rho(r)$ on the axis between two acetylenic carbons at the 6-31G(d, p) level of theory. For example, in acetylene, there is a local maximum in $\rho(r)$ at the midpoint of the C≡C bond (ρ = 0.4180 au) and two (3, −1) critical points, besides this maximum, at which ρ = 0.4146 au. In better approximations (MP2/6-311++G(d,p) or MP2/6-311++G(2d,2p)) for these monomers and complexes, these spurious maxima are no longer present. Similar results were reported (18*a*) previously for acetylene and its methyl derivative at the STO-3G level of approximation. For a comparison of HF-SCF, CI, and DFT, it was reported recently (26, 27) that the electron density in the BCP regions is overconcentrated by HF-SCF (probably it causes the existence of an exceptional local maximum in $\rho(r)$ on the axis between two acetylenic carbons) and is reduced correctly by DFT. In our further calculations, there is no exceptional local maximum at all in $\rho(r)$ on the axis of the C≡C bond in C_2H_2, $C_2H_2\cdots$HF, and $C_2H_2\cdots$HCl systems using DFT at the B3LYP/6-31G(d,p) level of theory. In the monomer, C_2H_2, there is only one (3, −1) BCP at the midpoint of the C≡C bond, at which ρ = 0.4023 au.

Fig. 1. The 6-31G(d,p) optimized geometries of C_2H_2·HX, C_2H_4·HX, C_4H_4·HX, and C_4H_6·HX hydrogen-bonded complexes and their components: **1**, HF; **2**, HCl; **3**, C_2H_2; **4**, C_2H_4; **5**, C_2H_2·HF; **6**, C_2H_2·HCl; **7**, C_2H_4·HF; **8**, C_2H_4·HCl; **9**, C_4H_4; **10**, C_4H_4·HF (*exo* approach); **11**, C_4H_4·HF (*endo* approach); **12**, C_4H_4·HF (perpendicular approach); **13**, C_4H_4·HCl (*exo* approach); **14**, C_4H_4·HCl (*endo* approach); **15**, C_4H_4·HCl (perpendicular approach); **16**, C_4H_6; and **17**, C_4H_7·HCl. Bond lengths are in Å and angles are in degrees.

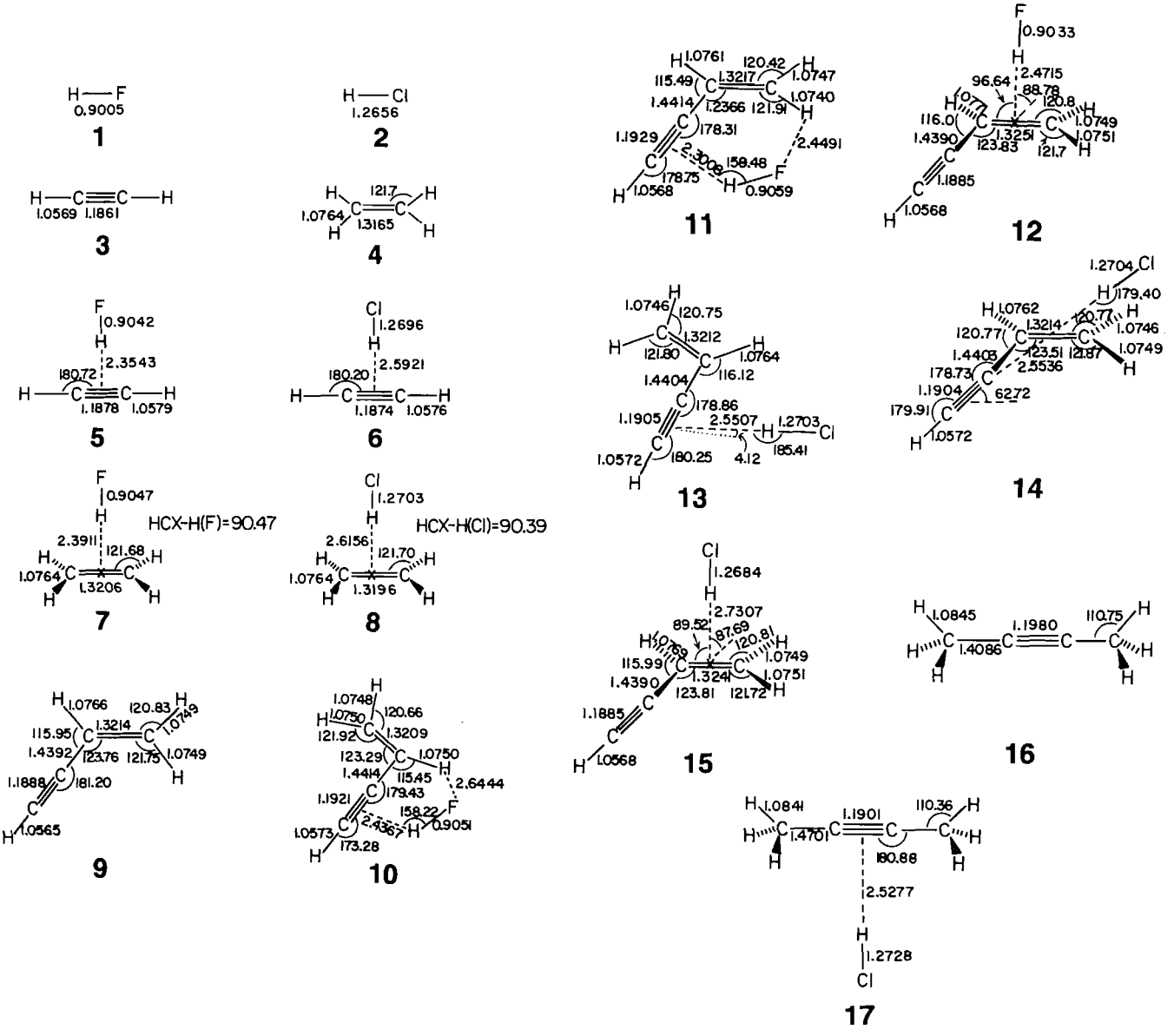

HF and a ring critical point is found, which confirms a ring structure (Figs. 2*e* and 2*f*). No second hydrogen bond is found in the HCl complexes. In Figs. 2*g* and 2*h*, the HX perpendicular approach to the C=C bond yields a hydrogen-bonded system. Since a conflict structure is an unstable structure (11, 18*a*), perturbation from the acetylenic group is strong enough to cause the hydrogen bond path to switch to the carbon of CH_2 and it no longer points towards to the centre of the C=C bond as is the case in C_2H_4·HX (Figs. 2*c* and 2*d*).

3. The nature of π-type hydrogen bonds

The values that are characteristic of hydrogen bonds, associated with the BCPs for C_2H_2·HX, C_2H_4·HX, and C_4H_4·HX (X = F, Cl), are given in Table 2 as computed at the MP2/6-311++G(d,p) level of theory as well as for the C_4H_6·HCl system computed at the MP2/6-311++G(2d,2p) level.

The nature of these hydrogen bonds, both π- and σ-type, can be further investigated from the distributions of the Laplacian of the electron density, $\nabla^2\rho(\boldsymbol{r})$. *Firstly*, in general, at the BCP, covalent bonding (shared interaction) is characterized by $\nabla^2\rho(\boldsymbol{r}_b) < 0$, while the interaction of two closed-shell atoms is characterized by $\nabla^2\rho(\boldsymbol{r}_b) > 0$ (11). Indeed, the values of $\nabla^2\rho(\boldsymbol{r}_b)$, where $\boldsymbol{r}_b$ denotes the BCP of the hydrogen bonds in these complexes, are all positive as in Table 2. These values clearly show that these hydrogen bonds, in the above-mentioned complexes, both π- and σ-type, result from the interaction of two closed-shell systems. *Secondly*, it was reported (17*e*) that in the Lewis base·HX complexes the nonbonded

Table 1. The calculated hydrogen-bond energies (kcal/mol) for the C_2H_2·HX, C_2H_4·HX, C_4H_4·HX (X = F, Cl), and C_4H_6·HCl systems.

System	6-31G(d,p)//6-31G(d,p)	6-311++G(d,p)//6-31G(d,p)	MP2(FULL)/6-311++G(d,p)//6-31G(d,p)
C_2H_2·HF	−3.76	−2.94	−4.24
C_2H_2·HCl	−2.32	−1.51	−3.09
C_2H_4·HF	−3.95	−3.07	−4.16
C_2H_4·HCl	−2.49	−1.56	−3.13
C_4H_4·HF			
C (*endo*) ‖‖···HF	−5.28	−3.20	−4.84
C (*exo*)	−4.59	−2.89	−4.36
C ‖···HF C (perpendicular)	−2.28	−2.23	−3.47
C_4H_4·HCl			
C (*endo*) ‖‖···HCl	−2.60	−1.88	−4.09
C (*exo*)	−2.42	−1.67	−3.81
C ‖···HCl C (perpendicular)	−1.74	−1.21	−3.17
C_4H_6·HCl			
C ‖‖···HCl C	−3.15	−2.27[a]	−4.87[a]

[a]Based on 6-311++G(2d,2p) and MP2(FULL)/6-311++G(2d,2p) calculations.

Table 2. Characteristics of π- and σ-type hydrogen bonds associated with the BCPs for the C_2H_2·HX, C_2H_4·HX, C_4H_4·HX (X = F, Cl), and C_4H_6·HCl[a] systems computed at the MP2(FULL)/6-311++G(d,p)//6-31G(d,p) level of theory.

System	$\rho(r_b)$	$\nabla^2\rho(r_b)$	ε
C_2H_2·HF	0.0110	+0.0375	0.3936
C_2H_2·HCl	0.0083	+0.0221	0.3399
C_2H_4·HF	0.0108	+0.0315	0.5807
C_2H_4·HCl	0.0085	+0.0192	0.5109
C_4H_4·HF			
C (*endo*) ‖‖···HF	0.0121	+0.0404	0.3934
C (*exo*)	0.0119	+0.0413	0.3490
-C-H···FH (*endo*)	0.0083	+0.0310	0.0807
(*exo*)	0.0062	+0.0265	1.0033
C ‖···HF C (perpendicular)	0.0092	+0.0272	0.5517
C_4H_4·HCl			
C (*endo*) ‖‖···HCl	0.0089	+0.0241	0.3841
C (*exo*)	0.0091	+0.0243	0.3260
C ‖···HCl C (perpendicular)	0.0069	+0.0153	0.4935
C_4H_6·HCl			
C ‖‖···HCl C	0.0100	+0.0263	0.2506

[a]Based on MP2(FULL)/6-311++G(2d,2p)//6-31G(d,p) calculations.

Fig. 2. Contour line diagrams of calculated (MP2/6-311++G(d,p)//6-31G(d,p)) Laplacian concentrations and depletions as well as molecular graphs of π-type hydrogen-bonded systems: (*a*) C_2H_2·HF, (*b*) C_2H_2·HCl, (*c*) C_2H_4·HF, (*d*) C_2H_4·HCl, (*e*) C_4H_4·HF (*endo* approach), (*f*) C_4H_4·HF (*exo* approach), (*g*) C_4H_4·HCl (*endo* approach), (*h*) C_4H_4·HCl (*exo* approach), (*i*) C_4H_4·HF (perpendicular approach), (*j*) C_4H_4·HCl (perpendicular approach), (*k*) C_4H_7·HCl. Bond paths denoted by lines, BCPs denoted by solid circles, ring critical points denoted by solid triangles, Laplacian concentrations denoted by solid squares, and Laplacian depletions denoted by open squares (the C_4H_7·HCl system is based on MP2/6-311++G(2d,2p) calculation).

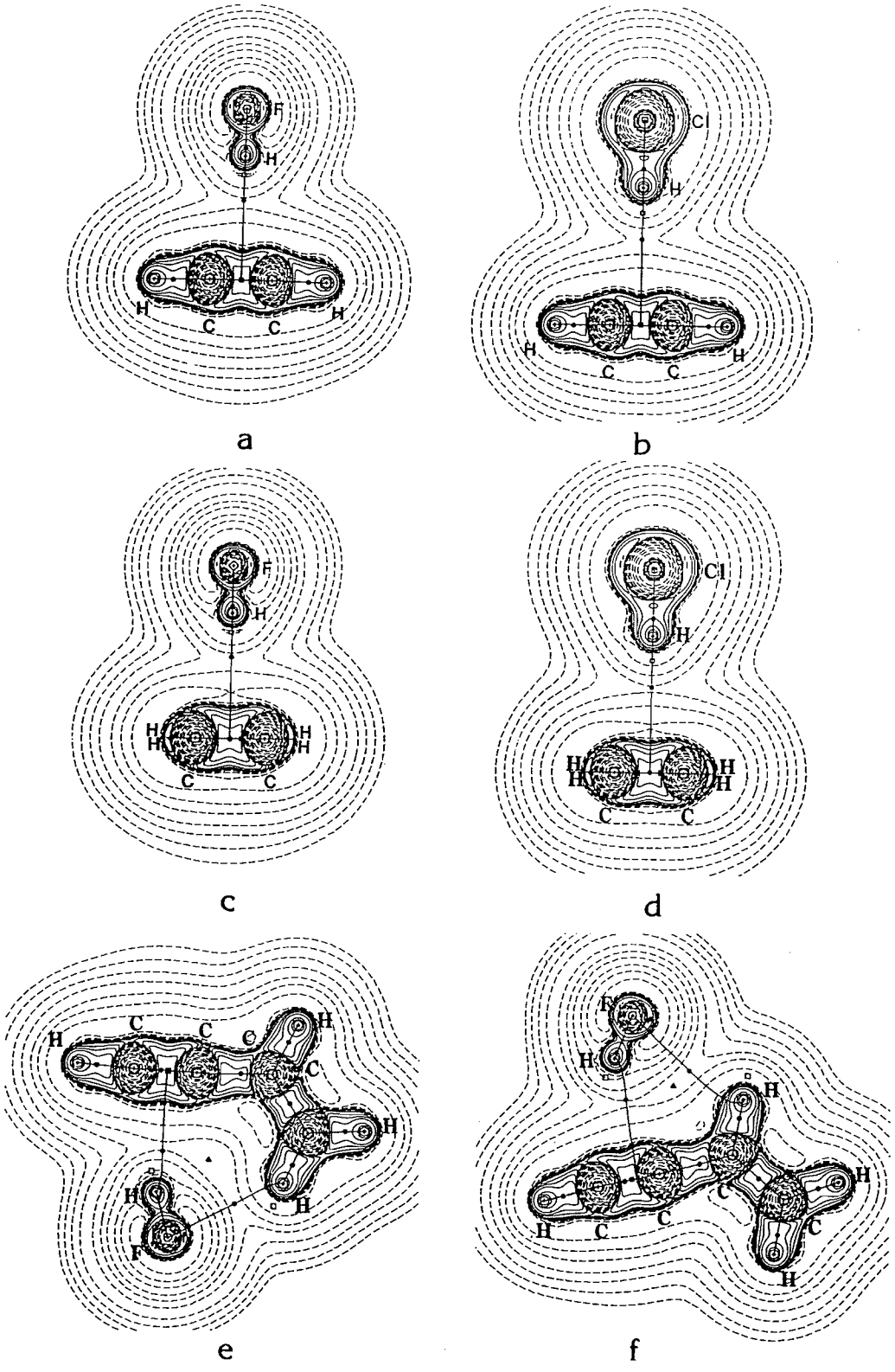

Fig. 2 (*concluded*).

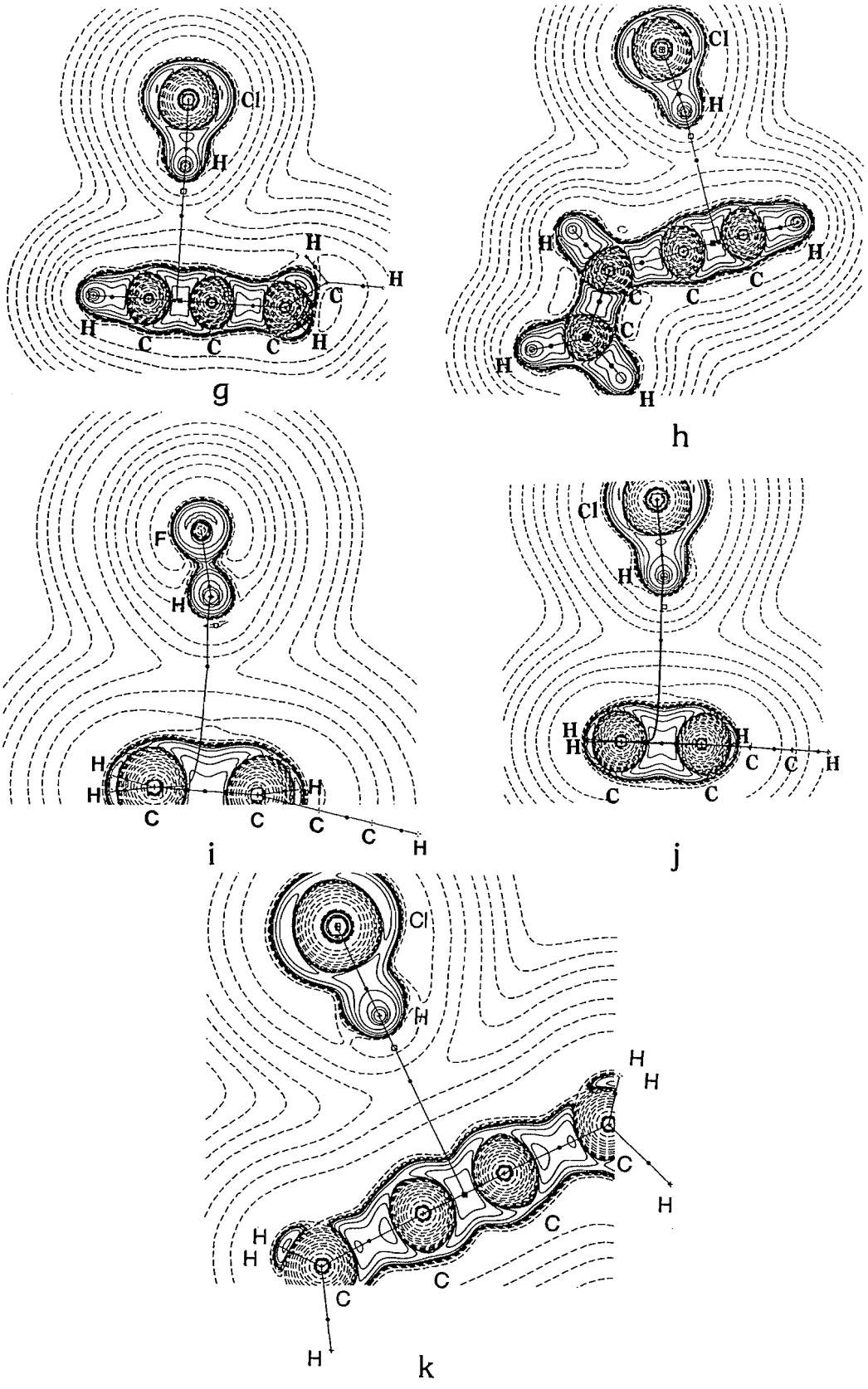

Fig. 3. The Laplacian of electron density profiles along the multiple CC bond in (*a*) C_2H_4, (*b*) C_2H_2, (*c*) C_2H_4·HF, (*d*) C_2H_2·HF.

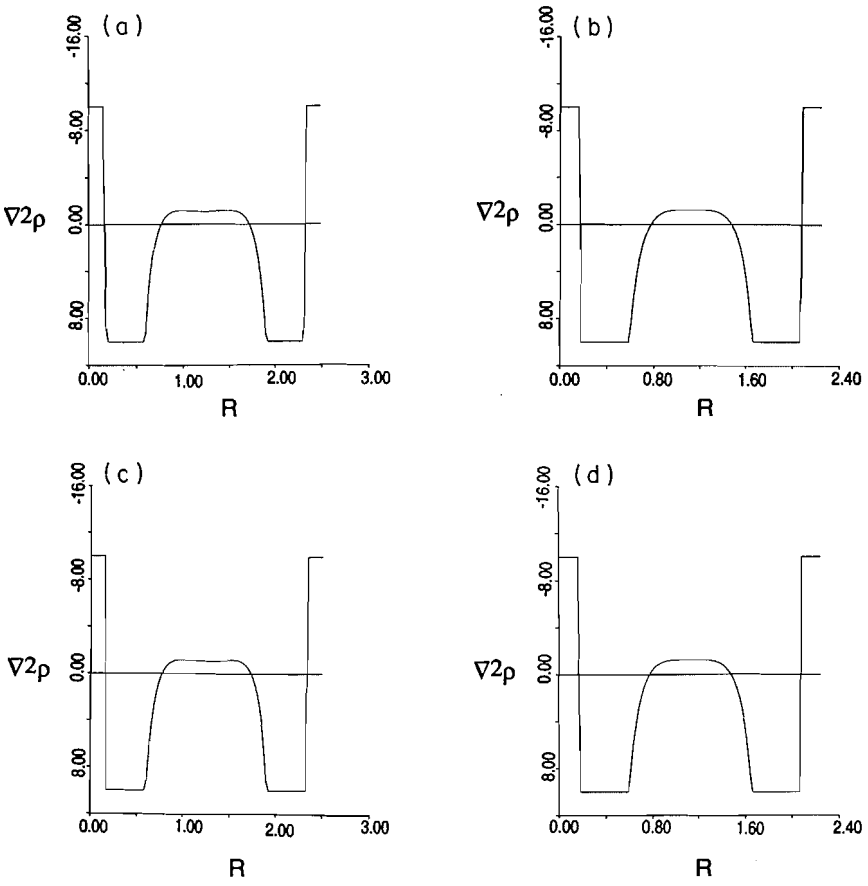

Laplacian concentration (the maximum of $\nabla^2\rho(\boldsymbol{r})$) in the Lewis base is predicted to be the site of electrophilic attack and the approach of the Brønsted acid proton is such as to align the Laplacian depletion (the minimum of $\nabla^2\rho(\boldsymbol{r})$) on H of HX with the chosen Laplacian concentration of the Lewis base. This is the case for σ-type hydrogen bonding. However, in π-type hydrogen bonding there is no nonbonded Laplacian concentration, but bonded Laplacian concentration(s) of the electron density at the multiple carbon–carbon bonds: only one located at the midpoint of the C≡C bond and two Laplacian concentrations close to each carbon of the C=C, respectively. It seems, for C_2H_2·HX and C_2H_4·HX systems, that the direction of attack of the Laplacian depletion on the H of the Brønsted acid, HX, is towards the bonded concentration at the C≡C bond in C_2H_2·HX systems, or equally to two bonded concentrations at the C=C bond in C_2H_4·HX systems (see Fig. 2*a*–2*d*). The Laplacian of the electron density profiles between two carbons along the C=C and C≡C bonds for C_2H_2, C_2H_4, C_2H_2·HF, and C_2H_4·HF systems are shown in Fig. 3. From Fig. 3 it is clear that there is only one Laplacian maximum along the C≡C bond in both the C_2H_2 monomer and the C_2H_2·HF complex but there are two Laplacian maxima present along the C=C bond in both the C_2H_4 monomer and the C_2H_4·HF system. Based on the MP2/6-311++G(d,p)//6-31G(d,p) calculations, further discussion of the nature of π-type hydrogen bonding can be exemplified by the following systems. For the C_2H_2·HF complex (Fig. 2*a*) there is a Laplacian depletion, namely a (3, +3) critical point in $-\nabla^2\rho(\boldsymbol{r})$, located 0.356 Å away from the position of the proton of HF on the HF bond axis and $-\nabla^2\rho(\boldsymbol{r}) = +0.2167$ au. Also, there is a Laplacian concentration, a (3,−3) critical point in $-\nabla^2\rho(\boldsymbol{r})$, located at the midpoint of the C≡C bond (equally 0.594 Å away from each of the carbon atoms with $-\nabla^2\rho(\boldsymbol{r}) = -1.2508$ au). For the C_2H_4·HF complex (Fig. 2*c*), again there is a Laplacian depletion located 0.356 Å away from the proton of HF on the HF bond axis with value of $-\nabla^2\rho(\boldsymbol{r}) = +0.2150$ au. On the other side of the complex, there are two Laplacian concentrations on the C=C bond that are equally 0.522 Å away from each of the carbon atoms on the C=C bond axis, each with a value of $-\nabla^2\rho(\boldsymbol{r}) = -1.1633$ au. For the C_4H_4·HF (*endo* approach) complex (Fig. 2*e*), there is a Laplacian depletion located "outside," 0.350 Å away from the proton of HF on the bond axis of HF, at which the $-\nabla^2\rho(\boldsymbol{r})$ has a value of +0.2307. On the C_4H_4 part of this complex, there is a Laplacian concentration located at the C≡C bond that is 0.624 Å away from the CH carbon and 0.568 Å from the internal acetylenic carbon, with a value of $-\nabla^2\rho(\boldsymbol{r}), = -1.2300$ au. The hydrogen bond path still links to this C≡C bond perpendicularly although the Laplacian concentration is no longer located at the midpoint of this C≡C bond. However, for the C_4H_4·HF (*exo* approach) complex (Fig. 2*f*), there is a Laplacian depletion that is 0.356 Å from H of HF along the bond axis of HF, with value $-\nabla^2\rho(\boldsymbol{r}) =$

+0.2161. On the other part of this complex, a Laplacian concentration is located at the C≡C bond that is 0.622 Å away from the CH carbon and 0.569 Å from the internal acetylenic carbon at which $-\nabla^2\rho(r) = -1.2293$ au. In this case, which is different from the previous, the hydrogen bond path switches to the internal acetylenic carbon. For the C_4H_4·HF (perpendicular approach) complex (Fig. 2*i*), there are two Laplacian concentrations on the C=C bond. One of them is 0.518 Å away from the middle acetylenic carbon atom, with a $-\nabla^2\rho(r)$ value of −1.1805 au, and the second one is 0.524 Å away from the CH_2 carbon, with $-\nabla^2\rho(r) = -1.1380$. There is a Laplacian depletion 0.357 Å away from the proton of HF on the HF bond axis at which $-\nabla^2\rho(r) = +0.2157$. In this complex (**12**), the direction of attack of the Laplacian depletion on the H of the Brønsted acid HF is located towards two different bonded concentrations at the C=C bond of the C_4H_4 part, in an unequal fashion. Most likely the perturbation from the acetylenic group changed the positions and values of these two bonded concentrations and then caused the hydrogen bond path to switch to the carbon atom of the CH_2. *Thirdly*, it is quite clear that in the C_4H_4·HF complexes (**10** and **11**), in both *endo* and *exo* approaches, a second hydrogen bond is formed between H of a C—H and F of HF that is a σ-type hydrogen bond. Finally, it was reported earlier (17*h*, 18*b*) that the ρ value at the BCP is related to the bond order and therefore to the bond strength. From Table 2, the $\rho(r_b)$ values of both π-type and σ-type hydrogen bonds in C_4H_4·HF (*endo* approach, **11**) are larger than in C_4H_4·HF (*exo* approach, **12**). Consequently, it is understandable that complex **11** is energetically more stable than **12**.

Acknowledgement

The calculations were mostly carried out on the HP-750 computer at the Department of Chemistry, University of Toronto. We would like to thank Professor Imre G. Csizmadia for his interest in this work.

References

1. D. Cook, Y. Lupien, and W.G. Schneider. Can. J. Chem. **34**, 957 (1956).
2. W.G. Read and W.H. Flygare. J. Chem. Phys. **76**, 2238 (1982); J.A. Shea and W.H. Flygare. J. Chem. Phys. **76**, 4857 (1982).
3. P. Hobza and R. Zahradnik. Chem. Rev. **88**, 871 (1988).
4. Z. Kisiel, P.W. Fowler, A.C. Legon, D. Devanne, and P. Dixneuf. J. Chem. Phys. **93**, 6249 (1990).
5. Z. Kisiel, P.W. Fowler, and A.C. Legon. Chem. Phys. Lett. **176**, 446 (1991).
6. D. Mootz and A. Deeg. J. Am. Chem. Soc. **114**, 5887 (1992).
7. J.A. Pople, M.J. Frisch, and J.E. Del Bene. Chem. Phys. Lett. **91**, 185 (1982); M.J. Frisch, J.A. Pople, and J.E. Del Bene. J. Chem. Phys. **78**, 4083 (1983).
8. A.M. Sapse and D.C. Jain. J. Phys. Chem. **88**, 4970 (1984).
9. X.-Y. Fu, R.-Z. Liu, and K. Morokuma. J. Mol. Sci. **5**, 21 (1987).
10. T.-H. Tang, W.-J. Hu, D.-Y. Yan, and Y.-P. Cui. J. Mol. Struct. (THEOCHEM), **207**, 319 (1990).
11. (*a*) R.F.W. Bader. Chem. Rev. **91**, 893 (1991); (*b*) Atoms in molecules: a quantum theory. Clarendon Press, Oxford. 1990; (*c*) Acc. Chem. Res. **18**, 9 (1985).
12. Z. Lin and I. Bytheway. Chem. Phys. Lett. **240**, 541 (1995).
13. (*a*) P.C. Hariharan and J.A. Pople. Chem. Phys. Lett. **66**, 217 (1980); (*b*) J.S. Binkley, J.A. Pople, and W.J. Hehre. J. Am. Chem. Soc. **102**, 939 (1980); (*c*) M.S. Gordon, J.S. Binkley, J.A. Pople, W.J. Pietro, and W.J. Hehre. J. Am. Chem. Soc. **104**, 2997 (1982); (*d*) W.J. Pietro, M.M. Francl, W.J. Hehre, D.J. Defrees, J.A. Pople, and J.S. Binkley. J. Am. Chem. Soc. **104**, 5039 (1982).
14. (*a*) R. Krishnan, J.S. Binkley, R. Seeger, and J.A. Pople. J. Chem. Phys. **72**, 650 (1980); (*b*) T. Clark, J. Chandrasekhar, G.W. Spitznagel, and P. von R. Schleyer. J. Comput. Chem. **4**, 294 (1983).
15. C. Møller and M.S. Plesset. Phys. Rev. **46**, 618 (1934).
16. (*a*) M. Frisch, M. Head-Gordon, G.W. Trucks, J.B. Foresman, H.B. Schlegel, K. Raghavachari, M.A. Robb, J.S. Binkley, C. Gonzalez, D.J. Defrees, D.J. Fox, J.J.P. Stewart, S. Topiol, and J.A. Pople. GAUSSIAN 90 (Revision F). Gaussian Inc., Pittsburgh, Pa. 1990; (*b*) M.J. Frisch, G.W. Trucks, M. Head-Gordon, P.M. Gill, M.W. Wong, J.B. Foresman, B.G. Johnson, H.B. Schlegel, M.A. Robb, E.S. Replogle, R. Gomperts, J.L. Andres, K. Raghavachari, J.S. Binkley, C. Gonzalez, R.L. Martin, D.J. Fox, D.J. Defrees, J. Baker, J.J.P. Stewart, and J.A. Pople. GAUSSIAN 92 (Revision C), Gaussian Inc., Pittsburgh, Pa. 1992.
17. (*a*) T.-H. Tang and X.-Y. Fu. Int. J. Quantum Chem. **24**, 317 (1983); (*b*) S.C. Choi and R.J. Boyd. Can. J. Chem. **64,** 2042 (1986); (*c*) R.J. Boyd. Stud. Org. Chem. (Amsterdam), **31**, 485 (1987); (*d*) J.R. Cheeseman, M.T. Carroll, and R.F.W. Bader. Chem. Phys. Lett. **143**, 450 (1988); (*e*) M.T. Carroll, C. Chang, and R.F.W. Bader. Mol. Phys. **63**, 387 (1988); (*f*) Mol. Phys. **65**, 695 (1988); (*g*) T.-H. Tang, D.M. Whitfield, S.P. Douglas, J.J. Krepinsky, and I.G. Csizmadia. Can. J. Chem. **70**, 2434 (1992); (*h*) T.-H. Tang, D.M. Whitfield, S.P. Douglas, J.J. Krepinsky, and I.G. Csizmadia. Can. J. Chem. **72**, 1803 (1994); (*i*) D.M. Whitfield and T.-H. Tang. J. Am. Chem. Soc. **115**, 9648 (1993).
18. (*a*) R.F.W. Bader, T.-H. Tang, Y. Tal, and F.W. Biegler-König. J. Am. Chem. Soc. **104**, 940 (1982); (b) **104**, 946 (1982).
19. (*a*) R.F.W. Bader, P.J. MacDougall, and C.D.H. Lau. J. Am. Chem. Soc. **106**, 1594 (1984); (*b*) R.F.W. Bader and P.J. MacDougall. J. Am. Chem. Soc. **107**, 6788 (1985); (*c*) R.F.W. Bader. Can. J. Chem. **64**, 1036 (1986); (*d*) J.P. MacDougall and R.F.W. Bader. Can. J. Chem. **64**, 1496 (1986); (*e*) R.F.W. Bader and C. Chang. J. Phys. Chem. **93**, 2946 (1989); (*f*) M.T. Carroll, J.R. Cheeseman, R. Osman, and H. Weinstein. J. Phys, Chem. **93**, 5120 (1989); (*g*) Z. Shi and R.J. Boyd. J. Phys. Chem. **95**, 4698 (1991); (*h*) T. Slee and R.F.W. Bader. J. Mol. Struct. (THEOCHEM), **255**, 173 (1992); (*i*) Z. Shi and R.J. Boyd. J. Am. Chem. Soc. **115**, 9614 (1993).
20. T.-H. Tang, W.-J. Hu, D.-Y. Yan, and Y.-P. Cui. J. Mol. Struct. (THEOCHEM), **207**, 327 (1990).
21. A.C. Legon and D.J. Millen. Chem. Rev. **86**, 635 (1986); Acc. Chem. Res. **20**, 39 (1987).
22. J.T. Brobjer and J.N. Murrell. J. Chem. Soc. Faraday Trans. 2, **78**, 1853 (1982).
23. A.D. Buckingham and P.W. Fowler. Can. J. Chem. **63**, 2018 (1985).
24. R.J. Gillespie and I. Hargittai. The VSEPR model of molecular geometry. Allyn and Bacon, Boston, Mass. 1991.
25. S.M. Bachrach and A. Streitwieser. J. Am. Chem. Soc. **106**, 2283 (1984).
26. J. Wang, Z. Shi, R.J. Boyd, and C.A. Gonzalez. J. Phys. Chem. **98**, 6988 (1994).
27. G.I. Csonka, N. Anh, J. Angyan, and I.G. Csizmadia. Chem. Phys. Lett. **245**, 129 (1995).

Topological analysis of the experimental electron density

Vladimir G. Tsirelson

Abstract: Methods of topological analysis of the experimental electron density reconstructed from X-ray diffraction data are described. Their advantages and drawbacks are discussed and the results for organic and inorganic crystalline solids are presented.

Key words: topological analysis, experimental electron density.

Résumé : On décrit des méthodes d'analyse topologique de densités électroniques expérimentales reconstruites à partir de données de diffraction des rayons X. On discute de leurs avantages et de leurs limitations et on présente les résultats obtenus à l'aide de solides cristallins organiques et inorganiques.

Mots clés : analyse topologique, densité électronique expérimentale.

[Traduit par la rédaction]

Introduction

Richard Bader opened a new avenue in chemical physics when he used Schwinger's principle of stationary action (1) for the description of many-electron systems (2, 3). According to this principle, the quantum action integral

$$W_{12}[\Psi] = \int_{t_1}^{t_2} dt \int L(\Psi, \nabla\Psi, \Psi^*, t)d\boldsymbol{r}$$

($L(\Psi, \nabla\Psi, \Psi^*, t)$ is the many-particle Lagrangian density) does not depend upon infinitesimal variation of the state function Ψ within the time interval $t_2 - t_1$; rather, it depends on the action of the infinitesimal generator of transformation at time points t_1 and t_2. Using an additional condition $d\Psi = d\Psi^* = 0$ at finite points of a time interval, Bader has shown that from one universal dynamical principle, $dW_{12} = 0$, one can obtain both equations of motion and expected values of observed quantities as well as determine the expected values of physical characteristics of the fragments of a total system.

For a description of ground state many-electron systems it is sufficient to use the one-particle Lagrangian density, $L(\boldsymbol{r})$. It is connected by the relation

$$[1] \quad L(\boldsymbol{r}) = -(\hbar^2/4m)\nabla^2\rho(\boldsymbol{r})$$

with the ground state electron density (ED) $\rho(\boldsymbol{r})$. Consideration of the virial of the force density results in the expression (4)

$$[2] \quad -L(\boldsymbol{r}) = 2G(\boldsymbol{r})+V(\boldsymbol{r})$$

Received October 31, 1995.

This paper is dedicated to Professor Richard F.W. Bader on the occasion of his 65th birthday.

V.G. Tsirelson.[1] Mendeleev University of Chemical Technology, Moscow 125047, Russia.

[1] Fax: +7-095-2004204. E-mail: tsirelso@mhti.msk.su.

were $G(\boldsymbol{r})$ and $V(\boldsymbol{r})$ are the densities of electron kinetic energy and electron potential energy, respectively, at point $\boldsymbol{r}$. From expressions [1] and [2] there follows a local form of the virial theorem:

$$[3] \quad 2G(\boldsymbol{r}) + V(\boldsymbol{r}) = (\hbar^2/4m)\nabla^2\rho(\boldsymbol{r}).$$

It shows that densities of kinetic and potential energies in any point of position space are related via the Laplacian of ED.

An important role of the ED and its derivatives led Bader to a thorough analysis of the topological properties of ED. The many features of function ρ are described by a number and type of critical points (CP), $\boldsymbol{r}_c$, points at which $\nabla\rho(\boldsymbol{r}_c) = 0$. The type of CP is determined by its rank, l, and signature s. Rank l equal to the number of non-zero eigenvalues of a 3×3 curvature (Hessian) matrix of $\rho(\boldsymbol{r})$. Signature s is a difference between the numbers of positive and negative eigenvalues of this matrix. The ED shows four types of nondegenerate CP with $l = 3$: maxima $(3, -3)$; saddle points $(3, -1)$ and $(3, +1)$; minima $(3, +3)$.

Application of the Gauss theorem (5) to eq. [3] gives

$$[4] \quad \int (2G(\boldsymbol{r}) + V(\boldsymbol{r}))d\boldsymbol{r} = \oint_S \nabla\rho(\boldsymbol{r})\cdot n(\boldsymbol{r})\, dS(\boldsymbol{r})$$

The right-hand side of this expression vanishes in molecules and crystals if the surface S covers them completely or if the ED gradient vector flux through these surfaces is zero. It has been postulated (6) that local ED maxima, corresponding to $(3,-3)$ CP, are present at nuclei positions only.[2] This results from the asymptotic condition describing the local behaviour of true ED near the nuclei (11–13). Since vector $\nabla\rho$ indicates the direction of greatest increase in ED, the ED areas embracing nuclei happen to be separated in many-nuclear systems by the surfaces on which vector $\nabla\rho$ changes its direction. The zero-flux surfaces S are taken as boundaries of bonded atoms, the latter coincide with an atom defined according to the sta-

[2] The existence of the non-nuclear local ED maxima has been discussed in refs. 7–10.

tionary action principle modified by Bader. The Hohenberg–Kohn theorem (14) as well as virial theorem (15) are valid for such atoms and the total energy and other properties of a system are expressed as a sum of atomic contributions.

The pairs of gradient lines starting from the same (3, −1) CP and terminating at two neighbouring nuclei are determined by eigenvectors corresponding to a single positive eigenvalue of the Hessian at this point. They form the atomic interaction lines, along which the ED decreases for any lateral displacements. The saddle point on this line in a stable system is called the bond critical point (BCP). The set of bond lines yields a molecular graph, which thus has a hard physical basis and usually coincides with the structural formula used in the classical chemical theory of molecular structure [16].

Critical points of types (3, +1) and (3, +3) arise only in the presence of rings and cages. A significant number of these points always exist in crystals (17–19).

Three Hessian eigenvalues, $\lambda_1 < \lambda_2 < \lambda_3$, characterize three ED curvatures at the point considered as well as three corresponding mutually orthogonal eigenvectors, u, directed along the principal curvatures. The sign of the $\nabla^2\rho = \lambda_1 + \lambda_2 + \lambda_3$ depends on the relation between these three items. In the (3, −1) BCP, the eigenvalues λ_1 and λ_2, corresponding to eigenvectors normal to the bond line, are negative. The λ_3 is positive and the corresponding eigenvector is directed along the bond line. When $|\lambda_1| + |\lambda_2| > 1$, the ED is concentrated at BCP; in the opposite case the ED is depleted here. Thus, the sign of $\nabla^2\rho$ can be related to the character of the atomic interactions, i.e., the character of the chemical bond. This results in a natural division of the atomic interactions into two types (20). Negative λ_1 and λ_2 values measure the degree of contraction of ED toward the BCP, perpendicular to the bond path. The positive λ_3 value measures the degree of ED contraction toward each of the neighbouring nuclei. If the ED is locally concentrated in the region of the BCP, it is then shared by both nuclei. The local electronic potental energy in the BCP region is more than twice in excess of the local kinetic energy in this case. Such a picture is typical for a covalent bond. If the positive curvature dominates in the BCP, the ED is concentrated in each of atomic basins separately and a relatively large positive contribution to the local kinetic energy of a system takes place. Such closed-shell interactions are usually observed in ionic and hydrogen bonds and van der Waals interactions.

The spatial distribution of the Laplacian of ρ characterizes concentration and depletion of the ED at each point of a system. It reveals the nonevident peculiarities of ED distribution such as shell structure of atoms (21, 22), localized electron pairs (23), etc. and points out areas where the local potential energy dominates in bonded systems. Additionally, the $\nabla^2\rho$ is connected with local electron energy, $H_e(\boldsymbol{r}) = G(\boldsymbol{r}) + V(\boldsymbol{r})$ (15, 24) by the simple expression

$$[5] \quad H_e(\boldsymbol{r}) = [V(\boldsymbol{r}) + (\hbar^2/4m)\nabla^2\rho(\boldsymbol{r})]/2$$

The sign of $H_e(\boldsymbol{r})$ shows whether kinetic or potential energy dominates at a given point of a space: if $V(\boldsymbol{r})$ dominates in the internuclear region, the $H_e(\boldsymbol{r}) < 0$ here and the accumulation of electrons is stabilizing. In a bonded system the local electron energy density is negative at the covalent bond critical points independent of the sign of $\nabla^2\rho$: the relation $(1/4)\nabla^2\rho < |V(\boldsymbol{r})|$ is fulfilled in this case even if $\nabla^2\rho > 0$. Unfortunately, the positive values of $\nabla^2\rho$ and of H are observed in closed-shell interactions at the (3, −1) points, therefore it is impossible, considering $H_e(\boldsymbol{r})$, to separate the ionic, hydrogen, and van der Waals bonds from one another.

Thus, in order to characterize the chemical bond it is necessary to calculate the topological characteristics of ED in a space of the molecule or crystal or, sometimes, only at the critical points.

Topological theory has been applied mainly to analysis of theoretical electron densities, as was reviewed in refs. 2 and 25–28. However, starting from the first earlier work (29, 30), it is increasingly being applied to treatment of the experimental ED obtained from X-ray diffraction data. Topological analysis of the experimental ED has same specificity, which should be taken into account in interpretation of the data obtained. This approach is discussed in the present work.

When the absolute values of kinematic structure amplitudes are obtained from intensities of reflection measured and their phases are calculated with any crystal structural model, the problem of crystal ED reconstruction is reduced to the calculation of the Fourier series with complex structure amplitudes $F(\boldsymbol{H})$ as coefficients, or to fitting some model of ED to these structure amplitudes. Correspondingly, there are three different methods in topological analysis of the experimental ED (29, 31). One of them consists of differentiation of Fourier series with respect to coordinates. The second method consists of the calculation of $\nabla\rho$ and $\nabla^2\rho$ represented as a sum of contributions from spherical atom superposition (promolecule) ED, $\rho_o(\boldsymbol{r})$, in the position space and the Fourier series for deformation ED. The third method is based on the use of the multipole model presenting ED in simple analytical form. Let us consider these approaches in detail.

Calculation of the topological characteristics with Fourier series

Fourier decomposition of the ED has the form

$$[6] \quad \rho(\boldsymbol{r}) = (1/V) \sum_{\boldsymbol{H}} F(\boldsymbol{H}) \exp(-2\pi i \boldsymbol{H}\boldsymbol{r})$$

(V is the unit cell volume). At infinite summation limits in eq. [6], ρ has the same sign over the whole space, and satisfies the condition of electroneutrality of the unit cell: $\int\rho(\boldsymbol{r})\, d\boldsymbol{r} = N$, and, therefore, is N-representable (it can be described by an antisymmetric many-electron wave function (32, 33)).

The experimental ρ is a dynamic function because it includes the thermal motion effect. The question arises: can the topological theory be applied to dynamic ED? The answer, fortunately, is "yes." The molecular graphs for all nuclear configurations in the neighbourhood of equilibrium geometry are equivalent (2). Therefore, the same set of the critical points describes both static and dynamic systems. The quantitative values of topological characteristics depend, of course, on the thermal motion of the nuclei (34, 35). The last point is illustrated the Fig. 1. Hence, for the general case, low-temperature X-ray diffraction data are preferable for obtaining the thermally independent topological characteristics of the ED.

Only a limited number of reflections are measured inside the reciprocal space sphere with $q = (\sin\theta/\lambda) < 1/\lambda$, where λ is the radiation wavelength. At the wavelengths applied in accurate X-ray structure analysis, a resolution in experimental ED

Fig. 1. Influence of the thermal atomic motion on the electron density along the C–C line in the promolecule (the superposition of spherical atoms) of ethylene, C_2H_4 (B is the isotropic thermal parameter of the C atom). Thermal motion diminishes the curvature of the electron density in the interatomic region.

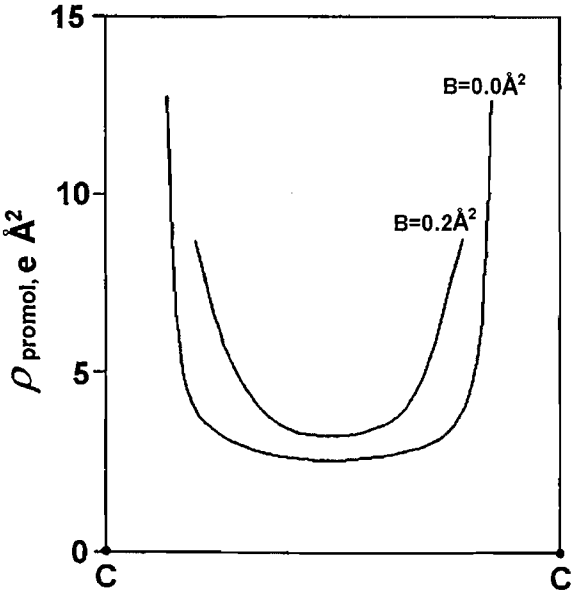

of $\lambda/3 \sim 0.2$ Å is achieved, according to the Rayleigh criterion. This results in false maxima and minima in the ED picture, which are especially significant in those regions of space where ρ varies most rapidly, for instance, near nuclei. These distortions will be much more evident in functions $\nabla\rho$ and $\nabla^2\rho$ (5). Simple extension of the Fourier series by adding theoretical values of structure amplitudes is not effective (36) and leads to an increase of the function variance (37). Moreover, although the derivatives of ρ exist, in fact, a formal differentiation of eq. [6] with respect to x, y, z results in divergent Fourier series for $\nabla\rho$ and $\nabla^2\rho$.

In addition, due to the presence of random errors in the structure amplitudes, the summation of approximate values in the Fourier series, eq. [6] is unstable (38) and the calculation of ρ and its derivatives with this series is a so-called ill-posed problem.

Thus we wish to reconstruct the topological characteristics of the experimental ED distorted by the Fourier series truncation effect and by statistical errors. The Lanczos method of calculating the derivatives of finite Fourier series by averaging over a "false" wave period (39) and the theory of regularization (38) allow one to obtain the mathematically correct solution of this problem. The Lanczos method gives the derivatives of the functions, presented as limited Fourier series, that are as close to the correct ones as is possible at the resolution achieved. For example, writing the second derivative of the Fourier series in a finite-difference form and averaging, we arrive at the following expression (29):

$$[7] \quad \nabla^2\rho(\boldsymbol{r}) = -(4\pi^2/V)\sum M_{hkl}L_{hkl}F(hkl) \times \exp[-2\pi i(hx + ky + lz)]$$

with

Fig. 2. Laplacian of the electron density in fluorite crystal, CaF_2, determined with Fourier series: the map contains the Ca—F ionic bond. The broken lines correspond to points with $\nabla^2\rho > 0$. The lines around atomic centers are omitted.

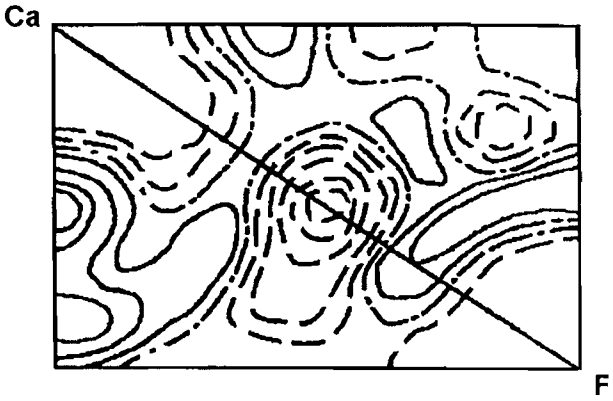

$$[8] \quad L_{hkl} = \sum_i \{\sin^2[\pi h_i/(H_i + 1)]/[\pi h_i/(H_i + 1)]^2\}(h_i/a_i)^2$$

Here $a_i = a, b, c$ are crystal unit cell parameters, and H_i are maximal values of Miller indicies h, k, l in the structure amplitude set. It is seen that the L_{hkl} factors actually provide the convergency of series [7].

The introduction in series [7] the regularising (filtering) factors M_{hkl} (40):

$$[9] \quad M_{hkl} = \begin{cases} |F(hkl)|^2/[|F(hkl)|^2 + \sigma^2(|F(hkl)|] & |F| > \beta\sigma(|F|) \\ 0 & |F| \le \beta\sigma(|F|) \end{cases}$$

according to general theory (38) allows the influence of random errors to diminish. The M-factors smoothly depend on the level of error in the X-ray diffraction data: $\beta < 3$, if the random errors in a structure amplitudes set are distributed according to Gauss' law (which can be checked by means of statistical tests (41)).

The method outlined allows calculation of the best approximation to the "true" Laplacian of ED directly from the X-ray structure amplitudes. The results remain dependent on the series truncation effect, and the shell structure of bonded atoms is lost in this method. At the same time, the ED curvature in the internuclear space is properly reproduced. Studies of fluorite, CaF_2 (29), spinels $MgAl_2O_4$, $CoAl_2O_4$, and $FeAl_2O_4$ (42), and a few garnets (43, 44) have shown that the correct sign of the function $\nabla^2\rho$ is obtained in between atoms. The map of the Laplacian of ρ in the (110) plane of fluorite calculated by formula (7) is shown in Fig. 2. There are no typical "false" waves around the nucleus position in this map ($\sin\theta/\lambda < 1.164$ Å^{-1}); simultaneously, a well-localized area of positive $\nabla^2\rho$ values is observed in the centre of the Ca–F line. In accordance with general theory (2), a depletion of electrons takes place here. Together with location of the negative $\nabla^2\rho$ regions near the ion positions, these are typical features of the ionic bond.

The method discussed was used in ref. 45 to investigate the

weak secondary atomic interactions in spinels $MgAl_2O_4$, $FeAl_2O_4$, and $CoAl_2O_4$. The spinel AB_2C_4 structure (space group *Fd3m*) can be considered as close packing of C-type anions with 2- and 3-valent cations in tetrahedral (A) and octahedral (B) positions, respectively. The magnetic properties of the spinels are usually explained phenomenologically by indirect exchange interactions between A and B sublattices via nonmagnetic anions (46). This indirect exchange leads, as a rule, to antiferromagnetism and, sometimes, in ferrimagnetism. The magnetic ordering in $FeAl_2O_4$ and $CoAl_2O_4$ occurs at very low (helium) temperatures; however, the corresponding true magnetic structures are still unknown. The indirect exchange channel A-O-B-O-A, the A-O-B angle being ~121°, is most probable for spinels with a nonmagnetic B-cation (47). An additional direct exchange channel A-A can, in principle, take place as well (48).The distance between two A cations in spinels is about 3.5 A and direct interaction is weak, nevertheless it should manifest itself in specific ED distribution between the A cations. The deformation ED maps have supported the indirect exchange picture; however, they did not offer an explanation of the interactions in the A-A area of $FeAl_2O_4$ and $CoAl_2O_4$ (49).

Figure 3 presents the $\nabla^2\rho$ distributions between A-A cations in MAl_2O_4 spinels (M = Mg, Fe, Co). The region of positive $\nabla^2\rho$ values is revealed between both nonmagnetic A-cations in Mg-spinel and the magnetic one in Co-spinels. At the same time, negative $\nabla^2\rho$ areas are observed here in $FeAl_2O_4$. It is evident that ED concentrates between magnetic Fe cations and favours the direct A-A interactions in $FeAl_2O_4$. A polarized neutron study is needed to confirm this observation.

Combination of the Fourier and position space presentations

Fourier series truncation and thermal smearing are strong disadvantages of the approach just described. To avoid these drawbacks, the use of a combination of Fourier and position space presentations of ρ was suggested (50). The ED is presented as a sum of the superposition of atoms (promolecule), ρ_0, and deformation ED, δρ. Then, the expression for the Laplacian of ρ has the form

$$[10] \quad \nabla^2\rho(\boldsymbol{r}) = \nabla^2\rho_0(\boldsymbol{r}) + \nabla^2\delta\rho(\boldsymbol{r})$$

The first term on the right-hand of eq. [10] is easily calculated using tabulated atomic wave functions (51) or the Fourier transform of the atomic scattering amplitudes, expressed in parametric form (52). The second term in eq. [10] is presented in the Fourier series form in analogy with eq. [7]. The Fourier series for $\nabla^2\delta\rho$ converges much better than that for $\nabla^2\rho$ and

Fig. 3. Laplacian of ρ between atoms in tetrahedral positions in spinels: (a) $MgAl_2O_4$; (*b*) $FeAl_2O_4$; (*c*) $CoAl_2O_4$. The lines around atomic centers are omitted. The (3, −1) critical points are denoted by signs ⊙.

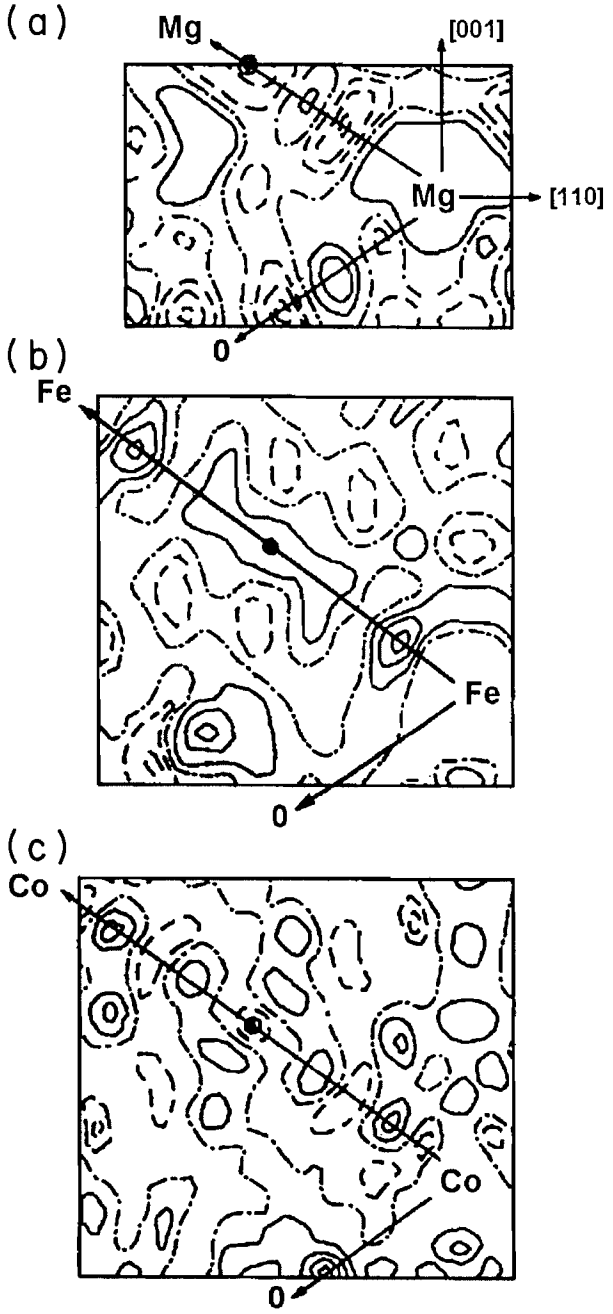

Table 1. Topological characteristics of bonds at (3,−1) critical points for ethane.

Bond	*R*, Å	ρ, e Å^{-3}	$\nabla^2\rho$, e Å^{-5}	λ_1, e Å^{-5}	λ_2, e Å^{-5}	λ_3, e Å^{-5}	ε
C—C (crystal)	1.510	1.61	−16.13	−12.09	−9.25	5.21	0.31
C—C (free)[a]	1.523	1.68	−14.77	−11.62	−11.62	8.47	0.00
C—H (crystal)[b]	0.960	1.55	−8.78	−13.01	−13.01	16.24	0.00
C—H (free)	1.083	1.88	−23.71	−17.47	−17.47	11.07	0.00

[a]The values for free molecule are calculated in the 6-311G** basis set.
[b]The values for C—H bonds have been averaged.

Fig. 4. Laplacian of ρ in ethane: (*a*) experimental map determined by combination of the position and Fourier space presentations for the crystal; (*b*) theoretical distribution for the free molecule ($3-11G^{**}$ basis set has been used).

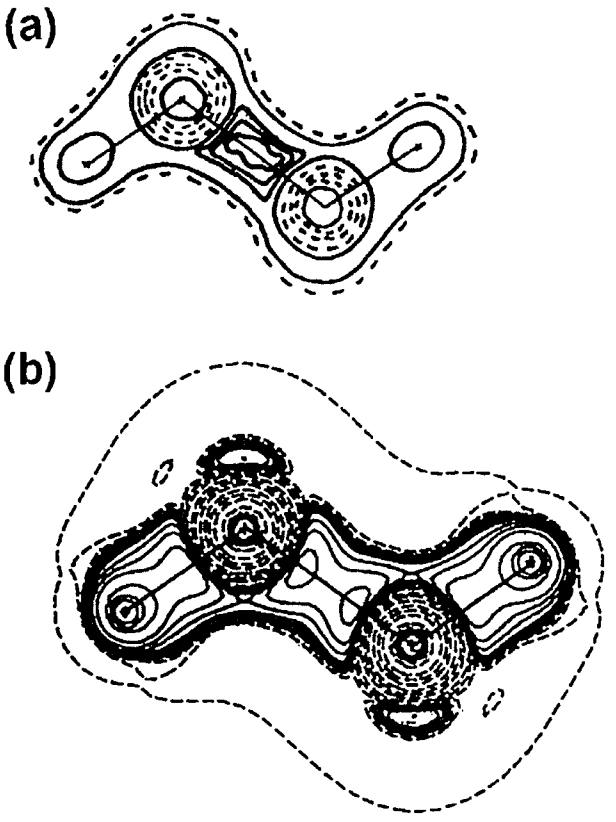

can be regularized in the same manner as the series for ρ. As well, calculations (34, 53) have confirmed Stewart's prediction (54) that the experimental deformation ED, which follows mainly lattice modes and suffers less from thermal smearing, can be considered as near pseudostatic. Moreover, the $\nabla^2\rho$ can be calculated from static model structure amplitudes. Since the ED of the promolecule is calculated as a static function as well, the consequences of thermal smearing are to a great extent rejected for derivatives of ρ.

The approach described was used for the first time in the study of monoclinic modification of ethane, C_2H_6 (55). This compound crystallizes at 90 K and only a small temperature gap exists between the melting point and X-ray measurement temperature of 85 K (56). Therefore the thermal smearing significantly distorts the ED curvature. Despite that, the (3, −1) CP were found on C—C and C—H bonds in crystalline ethane (Table 1) and values of $\nabla^2\rho$ at these points proved to be in agreement with the corresponding values calculated nonempirically for the free molecule. The agreement for C—H bonds is worse due to a larger thermal smearing effect for bonds with a light H atom, as can be expected. The overall experimental picture of the Laplacian of ρ agreed with theory as well (Fig. 4). At the same time, the crystal environment distorts the axial ED symmetry of the formally single bond in the ethane crystal. The quantitative measure of preferential concentration of electrons in a plane perpendicular to the interatomic line is ellipticity $\varepsilon = \lambda_1/\lambda_2 - 1$ (2). If the axes associated with λ_1 and λ_2 are symmetrically equivalent, as in the C—C bond of the free ethane molecule, then $\lambda_1/\lambda_2 = 1$ and $\varepsilon = 0$. However, the experimental ellipticity of this bond in a crystal is different from zero. The eigenvector, directed along the minimal decrease of the ED, deviates only at 15° from the direction toward the nearest-neighbour molecule in the crystal; at the same time the axes of the tensor of the C atom thermal vibra-

Table 2. Topological characteristics of (3,−1) critical points for some bonds in the icosahedron and external bonds in 9-azido-*m*-carborane.[a]

Bond	ρ, e Å^{-3}	$\nabla^2\rho$, e Å^{-5}	λ_1, e Å^{-5}	λ_2, e Å^{-5}	λ_3, e Å^{-5}	ε
C1—H1	1.637	−15.01	16.40	−16.18	−15.24	0.06
C7—H7	1.752	−15.35	16.50	−16.42	−15.43	0.06
B4—H4	1.000	−6.01	5.26	−6.37	−4.90	0.30
B5—H5	1.029	−6.90	4.50	−6.36	−5.04	0.26
N3—N2	3.601	−24.74	26.84	−26.52	−25.05	0.06
N2—N1	2.940	−11.38	30.49	−21.89	−19.98	0.10
B9—N1	1.009	15.03	24.78	−5.10	−4.66	0.10
C1—B5	0.832	−1.43	4.13	−3.99	−1.57	1.55
C1—B2	0.845	−1.46	3.31	−3.96	−0.81	3.87
C1—B4	0.815	−0.86	1.34	−1.58	−0.61	1.57
C7—B1	20.863	−2.65	3.36	−3.84	−2.17	0.77
B4—B3	0.797	−2.30	1.66	−2.97	−0.99	1.97
B3—B8	0.793	−1.48	1.43	−2.14	−0.78	1.76
B4—B9	0.821	−3.32	0.83	−2.12	−2.03	0.04
B8—B9	0.793	−2.19	1.79	−3.12	−0.88	2.55

[a]Low-temperature (160 K) X-ray diffraction data (57) were used.

Fig. 5. Overall view of the 9-azido-*m*-carborane molecule (*a*), distribution of the Laplacian of ρ on the B face of the icosahedron (*b*), and in section through the body of the icosahedron (*c*). The critical points are denoted by signs ■ ((3, +1)) and ▲ ((3, +3)).

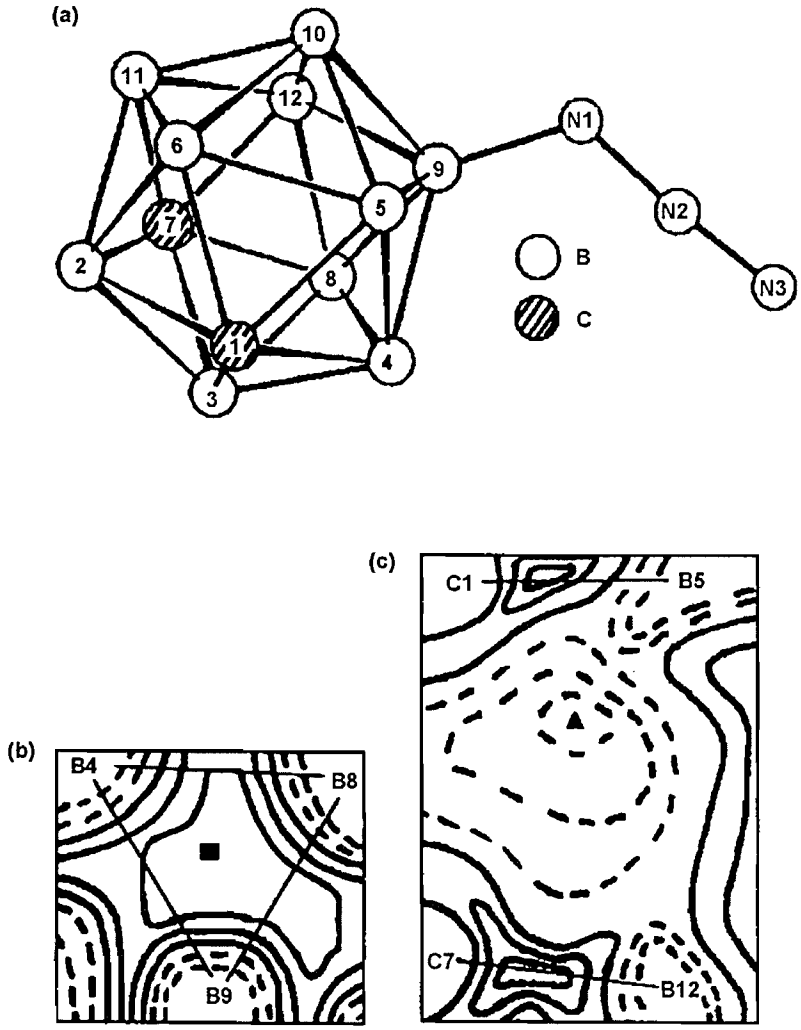

tions are oriented in other directions. Therefore, the ED polarization observed can be treated as a manifestation of intermolecular interaction in solid ethane. Thus, the ellipticity describes the mutual molecule influence as well as the π character of a chemical bond and conjugative and superconjugative effects, as stated in ref. 57.

The molecule of 9-azido-*m*-carborane, N_3-*m*-$C_2B_{10}H_{11}$, depicted in Fig. 5(*a*) is an example of a system where all types of critical points are present. The BCP are found, using the method discussed, on all interatomic lines in three-membered rings forming the icosahedron surface (Table 2) as well as on external B9—N1, N1—N2, and N2—N3 bonds; only the B9—N1 bond is characterized by a positive value of $\nabla^2\rho$ and, therefore, has ionic character. The icosahedron BCP lie outside lines connected to the nuclei in three-membered rings; large ellipticity values are observed at these points. The (3, +1) CP are located near the center of the B_3 rings (Fig. 5(*b*); the ED values at these points differ on average by only 0.08 e A^{-3} from those at the (3, −1) CP. All bonds with participation of the B atom are characterized by a relatively low value of the ED due to an electron deficiency of these bonds. Simultaneously, a small displacement of the ED to the more electronegative C atom is observed. The (3, +3) CP, a local minimum of the ED (ρ = 0.106 e A^{-3}), is sited approximately in the centre of the icosahedron. The Laplacian of the ED here is positive, $\nabla^2\rho$ = 3.87 e A^{-5} (Fig. 5(*c*); correspondingly, the depletion of the ED takes place inside the icosahedron. Thus, topological treatment of the X-ray experimental data (57) shows that the electron cloud is significantly delocalized on the surface of the icosahedron in 9-azido-*m*-carborane, as was predicted in ref. 16. Analysis of more simple *closo*-carboranes on the basis of nonempirical calculations (58) has resulted in the same topological picture.

Topological analysis of the model electron density

The parametric models of the ED, reconstructed by fitting to the experimental structure amplitudes, are to a large extent free from the effects of limited resolution of Fourier series, thermal smearing, and experimental statistical errors (31). One of these

Table 3. The (3,−1) critical points in urea crystal.[a]

Bond	R, Å	ρ, e Å^{-3}	λ_1, e Å^{-5}	λ_2, e Å^{-5}	λ_3, e Å^{-5}	$\nabla^2\rho$, e Å^{-5}	ε	R_A, Å
C—O	1.258	2.536	−23.33	−20.23	24.71	−18.86	0.15	0.427
	1.261	2.568	−24.97	−24.97	42.02	−7.923	0.003	0.411
C—N	1.343	2.538	−27.34	−23.00	12.68	−37.66	0.19	0.440
	1.345	2.352	−21.13	−19.21	12.73	−27.61	0.099	0.451
N—H1	1.005	1.797	−26.77	−25.54	21.88	−30.44	0.05	0.795
	1.009	2.319	−34.81	−33.13	21.13	−46.82	0.047	0.787
N—H2	0.997	1.843	−28.13	−26.93	21.68	−33.37	0.05	0.791
	1.005	2.352	−34.81	−33.37	20.89	−47.30	0.048	0.782
O...H1	2.014	0.159	−0.62	−0.57	2.77	1.58	0.09	1.269
	1.992	0.148	−0.72	−0.72	2.88	1.68	0.072	1.293
O...H2	2.071	0.142	−0.53	−0.52	2.58	1.53	0.02	1.275
	2.058	0.128	−0.48	−0.48	2.64	1.68	0.036	1.299

[a]The experimental and theoretical values are presented in the first and second lines, respectively. R_A is the distance from the first atom in the A–B interaction to the critical point.

Fig. 6. Fragment of the urea crystal.

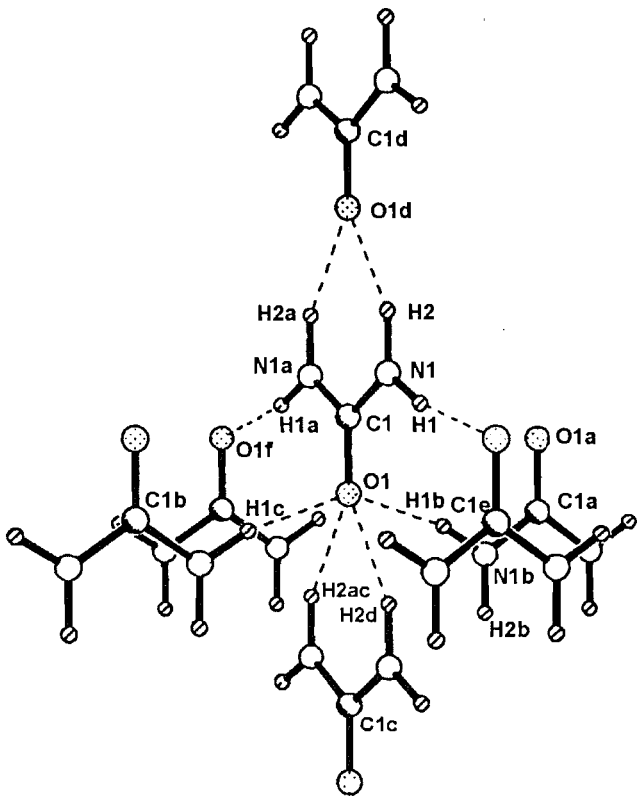

models, the multipole model, describes the ED of a crystal as superposition of the nuclear-centered pseudoatomic electron densities. The valence part of each pseudoatom is presented in the form of a Laplacian series; the radial dependence of each member of the series is described by the function

$$R_l(r) = Nr^{n_l} \exp(-\alpha r)$$

and angle dependence is described by spherical harmonics, $y_{lm}(\theta, \phi)$ (59–61):

$$[11] \quad \rho(\boldsymbol{r}) = \sum_i \{\rho^i_{\text{core}}(\boldsymbol{r}) + \sum_{lm} C^i_{lm} R^i_l(\boldsymbol{r}) y^i_{lm}(\theta, \varphi)\}$$

The electron populations C_{lm} and exponential factors α_l are determined by model refinement over low- and middle-angle X-ray reflections, while thermal parameters are found in the high-angle region. This allows the distortion of electronic parameters by thermal motion to diminish. The derivatives of the ED, presented as expansion [11], can be easily calculated analytically. Therefore, the use of this approach, proposed in refs. 30 and 50, in the topological analysis of the ED is most attractive and is now widely used (see, for example, refs. 31, 36, and 49).

An earlier topological analysis of ethylene, C_2H_4, and acetylene C_2H_2, compounds typical of a covalent bond, carried out by this method in ref. 50 by using low-temperature X-ray diffraction data from refs. 62 and 63, showed a negative sign of the $\nabla^2\rho$ in all BCP. However, agreement between experimental and theoretical topological values was only marginal due to incomplete elimination of the thermal smearing effect. Fortunately, much better agreement is achieved when the thermal motion effect is properly accounted for. Experimental (148 K) (64) and theoretical (65) studies of the urea crystal, CH_4N_2O (Fig. 6), support this statement. As can be seen from Table 3, quantitative agreement of the topological characteristics of both types is observed for this compound.

The interesting point of atomic interactions in solid urea is the unusual hydrogen bond picture. The planar urea molecules, linked in the crystal to each other through O...H2 hydrogen bonds, form indefinite planar types. The latter are connected with adjacent, mutually orthogonal, types by out-of-plane O—H1 hydrogen bonds. Thus, each carbonyl oxygen atom participates in four closed-shell interactions. Topological analysis shows that ED concentrations related to O-atom lone pairs take place in the molecular plane: they are responsible for formation of in-plane hydrogen bonds. The additional O...H1 interactions result from a good alignment of the saddle point sites in the valence shell of the O atom to ED minima near the H1 atoms. Hence, hydrogen bonds of nearly the same lengths may have a different nature.

Intermolecular interaction in the Cl_2 crystal gives another

Fig. 7. Maps of the Laplacian of ρ in molecular layer of crystalline Cl_2: (*a*) theoretical (the 6-21G* basis set), (*b*) calculated from the multipole model fitted to the experimental structure factors. The (3, −1) critical points and topological boundaries of the bonded Cl atom in this layer are shown.

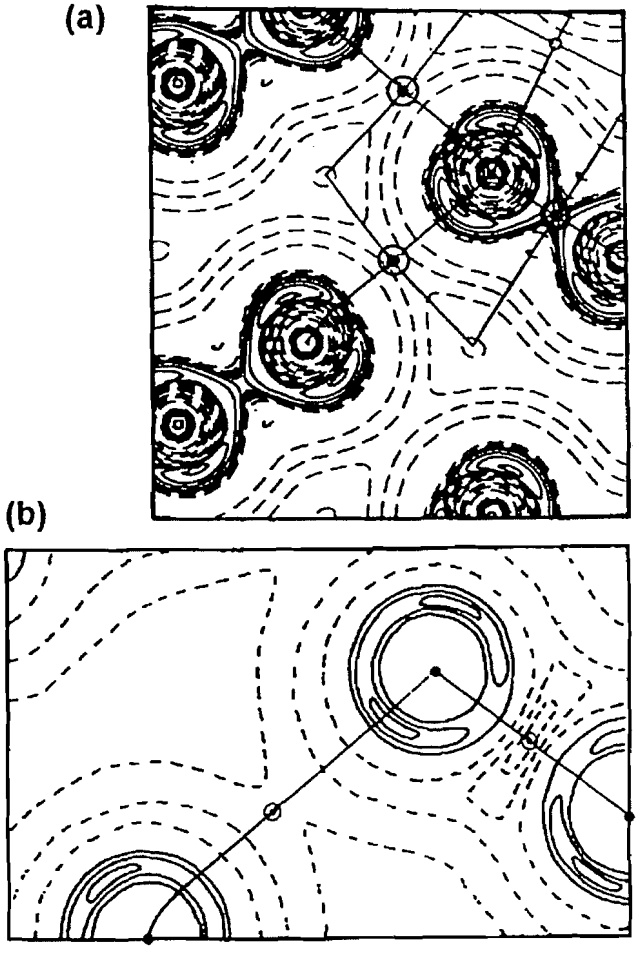

interesting example of closed-shell atomic interactions. The structure of solid chlorine is layered, with molecules in planes parallel to the (100) plane in an orthorhombic unit cell. Short intermolecular contacts of 3.28 Å, a value significantly less than twice the accepted van der Waals radius of 1.8 Å, are observed in the (100) plane. This indicates the presence of a specific intermolecular bonding in the Cl_2 crystal, the structure of which is not described in terms of a nondirectional van der Waals potential. Indeed, it was shown both experimentally and theoretically (19) that an intermolecular interaction line connects the lone-pair charge concentration on each Cl atom with a charge depletion at the end of the neighbouring molecule; each atom participates in two such interactions in the (100) plane (Fig. 7). It is important that topological consideration of the $(Cl_2)_2$ dimer, based on the theoretical ED, allows prediction of a layered structure and geometrical characteristics of the Cl_2 crystal. Additionally, the shape of the Cl atom in both dimer and crystal proved to be far from spherical. The observations mentioned explain why spherical van der Waals potentials are not applicable to a description of the structure of solid Cl_2.

As was noted earlier, topological analysis allowed us to

Fig. 8. Topological characterization of LiF crystal: (*a*) the bond paths and (3, −1) critical points imposed on the experimental electron density; (*b*) theoretical gradient vector field and (3,−1) critical points (20).

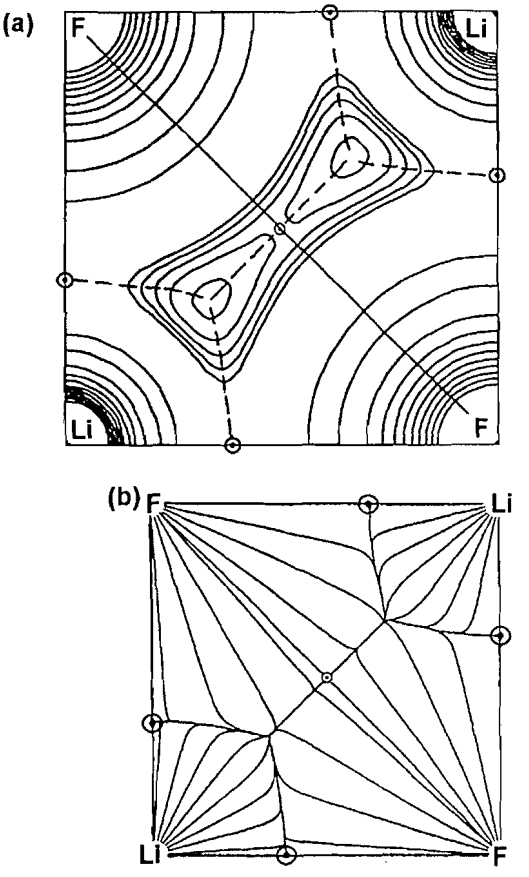

identify the secondary interactions in spinels. This can be done in other ionic crystals as well. The nearest-neighbour F nuclei in LiF, for example, are connected by a set of bond paths (Fig. 8) in addition to the expected Li—F bond paths. The general network of bond paths results in the LiF crystal model consisting of close-packed anions with small cations in the holes. The radii of bonded ions in LiF, determined from the experimental ED as distances to the corresponding BCP along the Li–F lines, are 0.769 (Li^+) and 1.243 Å (F^-). These are very close to the Shannon and Prewitt values of 0.90 and 1.19 Å. Thus, topological analysis can provide a basis for some conclusions that are reached in traditional crystal chemistry.

Concluding remarks

Topological analysis of the experimental electron density supports the main conclusions concerning a description of the chemical bond and intermolecular and secondary interactions in crystals, based on the topological theory of Bader, applied to the theoretical ED. The use of multipole representation of the ED provides semi-quantitative agreement between the experimental and theoretical topological values obtained. Combination of theoretical and experimental approaches in order to approach an understanding of the complicated crystal structures observed in terms of their constituent parts now seems the next problem to be addressed.

Acknowledgements

The author is grateful to Professor R.F.W. Bader for many discussions and hospitality during a stay at his laboratory. I wish to thank the Natural Sciences and Engineering Research Council of Canada for an International Scientific Exchange Award enabling me to visit McMaster University.

References

1. J. Schwinger. Phys. Rev. **82**, 914 (1951).
2. R.F.W. Bader. Atoms in molecules — a quantum theory. Oxford Univ. Press, Oxford. 1990.
3. R.F.W. Bader. Phys. Rev. B: Condens. Matter, **49**, 13348 (1994).
4. R.F.W. Bader. J. Chem. Phys. **73**, 2871 (1980).
5. G. Arfken. Mathematical methods for physicists. Academic Press, Orlando, Fla. 1985.
6. R.F.W. Bader, Y. Tal, S.G. Anderson, and T.T. Nguyen-Dang. Isr. J. Chem. **19**, 8 (1980).
7. C. Gatti, P. Fantucci, and G. Pacchioni. Theor. Chim. Acta, **72**, 433 (1987).
8. W.L. Gao, C. Gatti, P.J. MacDougall, and R.F.W. Bader. Chem. Phys. Lett. **141**, 380 (1987).
9. K.E. Edgecombe, R.O. Esquivel, V.H. Smith, and F. Muller-Plathe. J. Chem. Phys. **97**, 2593 (1992).
10. G.I. Bersuker, C. Peng, and J.E. Boggs. J. Phys. Chem. **97**, 19323 (1993).
11. T. Kato. Pure Appl. Math. Commun. **10**, 151 (1957).
12. W.Z. Bingel. Naturforsch. A: Astrophys. Phys. Phys. Chem. **18A**, 1249 (1963).
13. R.T. Pack and W.B. Brown. J. Chem. Phys. **45**, 556 (1966).
14. R.F.W. Bader and P. Becker. Chem. Phys. Lett. **148**, 452 (1988).
15. R.F.W. Bader and P.M. Beddall. J. Chem. Phys. **56**, 3320 (1972).
16. R.B. King (*Editor*). Chemical applications of topology and graph theory. Elsevier Scientific Publishing, New York. 1983.
17. P.F. Zou and R.F.W. Bader. Acta Crystallogr. Sect. A: Found. Crystallogr. **A50**, 714 (1994).
18. C. Mei, K.E. Edgecombe, V.H. Smith, and A. Heilingbrunner. Int. J. Quantum Chem. 48, 287 (1993).
19. V.G. Tsirelson, P.F. Zou, T.-H. Tang, and R.F.W. Bader. Acta Crystallogr. Sect. A: Found. Crystallogr. **A50**, 143 (1995).
20. R.F.W. Bader and H.J. Essén. Chem. Phys. **80**, 1943 (1984).
21. R.P. Sagar, A.C.T. Ku, V.H. Smith, and A.M. Simas. J. Chem. Phys. **88**, 4367 (1988).
22. Z. Shi and R.J. Boyd. J. Chem. Phys. **88**, 4375 (1988).
23. R.F.W. Bader, R.J. Gillespie, and P.J. MacDougall. J. Am. Chem. Soc. **110**, 7329 (1988).
24. D. Cremer and E. Kraka. Croat. Chem. Acta, **57**, 1259 (1984).
25. R.F.W. Bader, R.J. Gillespie, and P.J. MacDougall. *In* Molecular structure and energetics. *Edited by* J.F. Liebman and A. Greenberg. VCH Publishers, Deerfield Beach, Fla. 1989.
26. E. Kraka and D. Cremer. *In* Theoretical models of chemical bonding. *Edited by* Z.B. Maksič, Springer Verlag, Heidelberg. 1990.
27. R.F.W. Bader. Chem. Rev. **91**, 893 (1991).
28. R.F.W. Bader. *In* The chemistry of alkanes and cycloalkanes. *Edited by* S. Patai and Z. Rappoport. John Wiley and Sons, New York. 1992. p. 1.
29. V.G. Tsirelson and R.P. Ozerov. *In* Application of X-rays to the study of materials. *Edited by* T.I. Malinovsky. Kishinev, Stiintsa. 1986. p. 103.
30. C.D.H. Lau, R.F.W. Bader, K. Hermansson, and Z. Berkovich-Ellin. Sagamore Conf. on charge, spin, and momentum density, 7th. Abstracts. Chem. Scr. **26**, 476 (1986).
31. V.G. Tsirelson and R.P. Ozerov. Electron density and bonding in crystals. IOP Publ., Bristol, U.K. 1996.
32. J. Harriman. Phys. Rev. A: Gen. Phys. **24**, 680 (1981).
33. V. Yu. Kolmanovich and I.M. Reznik. Dokl. Acad. Sci. USSR, **285**, 1100 (1981).
34. M.E. Stephens and P.J. Becker. Mol. Phys. **49**, 65 (1983).
35. M. Kapphahn. Quantum topological treatment of the X-ray diffraction data for molecular crystals. Ph.D. Thesis, Mendeleev University, Moscow. 1989.
36. R.F. Stewart. NATO ASI Ser. Ser. B: **250**, 63 (1991).
37. B. Rees. Acta Crystallogr. Sect. A: Cryst. Phys. Diffr. Theor. Gen. Crystallogr. **A32**, 483 (1979).
38. A.N. Tichonov and V. Ya. Arsenin. Methods in solution of ill-posed problems. Nauka, Moscow. 1986.
39. C. Lanczos. Applied analysis. Prentice Hall, New York. 1957.
40. V.A. Streltsov, V.G. Tsirelson, R.P. Ozerov, and O.A. Golovanov. Sov. Phys. Crystallogr. **33**, 90 (1988).
41. S.C. Abrahams and E.T. Keve. Acta Crystallogr. Sect. A: Cryst. Phys. Diffr. Theor. Gen. Crystallogr. **A27**, 157 (1971).
42. V.A. Streltsov and V.G. Tsirelson. Conf. crystal chemistry of inorganic and coordination compounds, 4th. Abstracts. Buchara, Uzbekistan. 1986.
43. N.N. Lobanov. Accurate X-ray studies of garnets. Ph.D. Thesis. Mendeleev University, Moscow. 1986.
44. N.N. Lobanov, E.L. Belokoneva, and V.G. Tsirelson. Russ. J. Inorg. Chem. **32**, 1740 (1988).
45. V.G. Tsirelson, E.L. Belokoneva, V.A. Streltsov, and M. Yu. Antipin. Sagamore Conf. on charge, spin, and momentum density, 10th. Abstracts. Konstanz, Germany. 1991. p. 141.
46. J. Goodenough. Magnetism and the chemical bond. Metallurgiya Publ., Moscow. 1963.
47. I. Mayer and S. Angelov. Phys. Status Solidi B: **106**, 467 (1981).
48. A.J. Freeman and R.E. Watson. Phys. Rev. **124**, 1439 (1961).
49. V.G. Tsirelson. The chemical bond and thermal atomic motion in crystals. VINITI Publ., Moscow. 1993 (*in Russian*).
50. M. Kapphahn, V.G. Tsirelson, and R.P. Ozerov. Port. Phys., **19**, 213 (1988).
51. E. Clementi and C. Roetti. At. Data Nucl. Data Tables, **14**, 177 (1974).
52. D. Schwarzenbach and N. Tong. Acta Crystallogr. Sect. A: Cryst. Phys. Diffr. Theor. Gen. Crystallogr. **A35**, 652 (1979).
53. J. Epstein and D.J. Swenton. J. Chem. Phys. **77**, 1048 (1982).
54. R.F. Stewart. Chem. Phys. Lett. **49**, 281 (1977).
55. M. Kapphahn, V.G. Tsirelson, and R.P. Ozerov. Dokl. Acad. Sci. USSR, **303**, 444 (1988).
56. G.J.H. van Nes and A. Vos. Acta Crystallogr. Sect. B: Struct Crystallogr. Cryst. Chem. **B34**, 1947 (1978).
57. M. Yu. Antipin, A.V. Polyakov, V.G. Tsirelson, M. Kapphahn, V.V. Grushin, and Yu. T. Struchkov. Organomet. Chem. (USSR), **3**, 421 (1990).
58. R.F.W. Bader and D.A. Legare. Can. J. Chem. **70**, 657 (1992).
59. F.L. Hirshfeld. Acta Crystallogr. Sect. B: Struct. Crystallogr. Cryst. Chem. **B27**, 769 (1971).
60. R.F. Stewart. Acta Crystallogr. Sect. A: Cryst. Phys. Diffr. Theor. Gen. Crystallogr. **A32**, 565 (1976).
61. N. Hansen and P. Coppens. Acta Crystallogr. Sect. A: Cryst. Phys. Diffr. Theor. Gen. Crystallogr. **A34**, 909 (1978).
62. G.J.H. van Nes and A. Vos. Acta Crystallogr. Sect. B: Phys. Diffr. Theor. Gen. Crystallogr. **B35**, 2580 (1979).
63. G.J.H. van Nes and A. Vos. Acta Crystallogr. Sect. B: Phys. Diffr. Theor. Gen. Crystallogr. **B35**, 2593 (1979).
64. V.E. Zavodnik, A.I. Stash, V.G. Tsirelson, R. de Vrijes, and D. Feil. Acta Crystallogr. Sect. A: Found. Crystallogr. Submitted.
65. C. Gatti, V.R. Saunders, and C. Roetti. J. Chem. Phys. **101**, 10686 (1994).

Anisotropic and isotropic triple-dipole dispersion energy coefficients for all three-body interactions involving He, Ne, Ar, Kr, Xe, H_2, N_2, and CO

Sean A.C. McDowell, Ashok Kumar, and William J. Meath

Abstract: Formulae for the computation of isotropic and anisotropic dipolar dispersion energy coefficients, for two-body and three-body interactions involving H_2, N_2, CO, and the rare gases, are presented in an average energy approximation. These coefficients are computed to within 1% of the reliable values for these coefficients, which are obtained by using the relevant dipole oscillator strength distributions, with the exception of a few that are recorded in tabular form. The input data required for these formulae are the isotropic and anisotropic polarizabilities and average energies for the interacting species. The results provide the first reliable anisotropic triple-dipole dispersion energy coefficients for interactions involving molecules.

Key words: non-additive, anisotropic, interaction energies, triple-dipole dispersion energies.

Résumé : On présente des formules permettant de calculer, en approximation d'énergie moyenne, les coefficients d'énergie de dispersion dipolaire isotropique et anisotropique pour des interactions à deux et à trois corps impliquant le H_2, le N_2, le CO et les gaz rares. On peut calculer ces coefficients en deçà de 1% des valeurs fiables pour ces coefficients qui sont obtenues en utilisant les distributions des forces d'oscillateurs dipolaires appropriés, à l'exception d'un certain nombre qui ont été enregistrés sous des formes de tableaux. Les données nécessaires pour ces formules sont les polarisabilités isotropiques et anisotropiques ainsi que les énergies moyennes des espèces qui interagissent. Les résultats fournissent les premiers coefficients fiables d'énergie de dispersion anisotropique à triple dipôle pour des interactions impliquant des molécules.

Mots clés : non additif, anisotropique, énergies d'interaction, énergies de dispersion à triple dipôle.

[Traduit par la rédaction]

1. Introduction

We recently derived a computationally convenient expression for the exact triple-dipole dispersion energy (DDD) for interactions involving linear (Σ-state) molecules (1). It involves the isotropic triple-dipole dispersion energy coefficient for the interaction, C_9, and, in the most general case, seven anisotropic triple-dipole dispersion energy coefficients Γ. The coefficients C_9 and the Γ's are expressed in terms of the isotropic and anisotropic dipole oscillator strengths and excitation energies of the interacting species. Part of the purpose of this paper is to present reliable results for all the triple-dipole dispersion energy coefficients for all three-body interactions involving He, Ne, Ar, Kr, Xe, H_2, N_2, and CO. They are evaluated through the use of available isotropic and anisotropic dipole oscillator strength distributions for the interacting species (2–7).

Rather than present the large number of isotropic and anisotropic triple-dipole dispersion energy coefficients explicitly, average energy approximations (8, 9), which require a minimal amount of input data, are derived for them. The approach is first tested for the isotropic and anisotropic dipole–dipole dispersion energy coefficients for all two-body interactions involving the species of interest (Sect. 2). This average energy approximation is then adapted to the three-body interactions in Sect. 3. The average energy input parameters are listed in tables and consist of the isotropic, parallel, and perpendicular polarizabilities and average energies for each individual atom or molecule. Usually the average energy results reproduce the directly calculated triple-dipole dispersion energy coefficients to within their estimated uncertainty of ~1%. The coefficients are explicitly tabulated only for those cases (26 out of a total of 286 unique coefficients) for which this reliability is not achieved in the average energy approximation. Section 4 contains a brief discussion of our results and a comment on their overall importance.

Received November 2, 1995.

This paper is dedicated to Professor Richard F.W. Bader on the occasion of his 65th birthday.

S.A.C. McDowell,[1] A. Kumar,[2] and W.J. Meath.[1,3] Department of Chemistry, University of Western Ontario, London, ON N6A 5B7, Canada.

[1] Associated with the Centre for Interdisciplinary Studies in Chemical Physics, University of Western Ontario.
[2] Present address: Department of Physics, Meerut University, Meerut, India.
[3] Author to whom correspondence may be addressed. Telephone: (519) 679-2111, ext. 6334. Fax: (519) 661-3022. E-mail: wmeath@julian.uwo.ca

All expressions and results in this paper are in atomic units.

2. A test of an average energy approximation for C_6

Here we test an average energy approximation for the calculation of anisotropic dipole–dipole dispersion energy coefficients with the view toward the extension to the triple-dipole dispersion energy (Sect. 3). The approximation is tested for the various two-body interactions arising from the species He, Ne, Ar, Kr, Xe, H_2, N_2, CO.

The long-range dipole–dipole dispersion energy, which is dependent on the relative orientations of the two interacting linear Σ-state molecules, is given (10, 11) by

$$[1]\quad E^{ab}_{\mathrm{dis},R^{-1}} = -\frac{C_6(a,b)}{R^6} \times \left[1 + \Gamma_{ab}P_2(\cos\theta_a) + \Gamma_{ba}P_2(\cos\theta_b) + \Delta_{ab}\left(\frac{4\pi}{5}\right)\sum_{m=-2}^{m=2}(3-|m|)Y_2^m(\theta_a,\phi_a)Y_2^{-m}(\theta_b,\phi_b)\right]$$

where R is the distance between the interacting molecules, P_2 and Y_2^m are Legendre and spherical harmonic functions of the spherical polar angles (θ_a,ϕ_a) and (θ_b,ϕ_a) specifying the relative orientations of the molecules a and b (as detailed in refs. 11, 12). $C_6(a,b)$ is the isotropic dipole-dipole dispersion energy coefficient (3, 4, 10, 11),

$$[2]\quad C_6(a,b) = \frac{2}{3}\left(C_{ab}^{\parallel,\parallel} + 2C_{ab}^{\parallel,\perp} + 2C_{ab}^{\perp,\parallel} + 4C_{ab}^{\perp,\perp}\right)$$

and

$$[3]\quad \Gamma_{ab} = \frac{2}{3}(C_{ab}^{\parallel,\parallel} + 2C_{ab}^{\parallel,\perp} - C_{ab}^{\perp,\parallel} - 2C_{ab}^{\perp,\perp})/C_6(a,b)$$

$$[4]\quad \Gamma_{ba} = \frac{2}{3}(C_{ab}^{\parallel,\parallel} + 2C_{ab}^{\perp,\parallel} - C_{ab}^{\parallel,\perp} - 2C_{ab}^{\perp,\perp})/C_6(a,b)$$

$$[5]\quad \Delta_{ab} = \frac{2}{3}(C_{ab}^{\parallel,\parallel} - C_{ab}^{\perp,\parallel} - C_{ab}^{\parallel,\perp} + C_{ab}^{\perp,\perp})/C_6(a,b)$$

where the anisotropic dispersion energy coefficients $C_{ab}^{\zeta,\zeta'}$, ζ, $\zeta' = \parallel, \perp$, can be expressed in terms of integrals involving the $\parallel$ and $\perp$ dipole oscillator strength distributions (DOSDs) of the interacting species a and b (3, 4, 10, 11).

Since the DOSDs contain both discrete and continuum contributions, it is computationally more convenient, without loss of accuracy, to evaluate the $C_{ab}^{\zeta,\zeta'}$ coefficients by using pseudo-DOSDs that provide a discrete representation of the original DOSDs for the molecules (3, 4, 12, 13). For molecule a, say, the ζ-component of the pseudo-DOSD is given by $\{E_{k_a}^{\zeta}, f_{k_a}^{\zeta}\}$ where the $E_{k_a}^{\zeta}$ and the $f_{k_a}^{\zeta}$ are the excitation energy – oscillator strength pairs defining the pseudo-DOSD (3, 4, 12, 13). The coefficients $C_{ab}^{\zeta,\zeta'}$ are given by (3, 4)

$$[6]\quad C_{ab}^{\zeta,\zeta'} = \frac{1}{4}\sum_{k_a=1}^{N_a}\sum_{k_b=1}^{N_b}\frac{f_{k_a}^{\zeta}f_{k_b}^{\zeta'}}{E_{k_a}^{\zeta}E_{k_b}^{\zeta'}\left[E_{k_a}^{\zeta}+E_{k_b}^{\zeta'}\right]}$$

If one of the species is isotropic (say a), then $C_{ab}^{\zeta,\zeta'}$ may be written as $C_{ab}^{0,\zeta'}$ and is given by eq. [6] with the ζ-pseudo-DOSD for a replaced by the isotropic atomic DOSD (3, 4).

The Unsöld average energy approximation (8) may now be applied to eq. [6] to give

$$[7]\quad C_{ab}^{\zeta,\zeta'} = \frac{1}{4}\sum_{k_a=1}^{N_a}\sum_{k_b=1}^{N_b}\frac{f_{k_a}^{\zeta}}{(E_{k_a}^{\zeta})^2}\frac{f_{k_b}^{\zeta'}}{(E_{k_b}^{\zeta'})^2}\frac{U_a^{\zeta}U_b^{\zeta'}}{(U_a^{\zeta}+U_b^{\zeta'})} = \frac{1}{4}\alpha_a^{\zeta}\alpha_b^{\zeta'}\frac{U_a^{\zeta}U_b^{\zeta'}}{(U_a^{\zeta}+U_b^{\zeta'})}$$

where U_a^{ζ} is an atomic ($\zeta = 0$) average energy or a molecular ($\zeta = \parallel$ or $\perp$) average energy independent of k_a, and α_a^{ζ} refers to either the isotropic dipole polarizability $\bar{\alpha}_a$ ($\zeta = 0$) or the anisotropic dipole polarizability (for a being a molecule; $\zeta = \parallel$ or $\perp$).

The atomic average energies, U_a and U_b (we drop $\zeta = 0$ for atoms) of atoms a and b, can be related to the isotropic $C_6(a,b)$ dispersion energy coefficient by (9, 14)

$$[8]\quad C_6(a,b) = \frac{3}{2}\frac{U_aU_b}{(U_a+U_b)}\bar{\alpha}_a\bar{\alpha}_b$$

If we now consider the dispersion energy interaction between two like atoms a we obtain from eq. [8]

$$[9]\quad U_a = \frac{4C_6(a,a)}{3\bar{\alpha}_a^2}$$

Thus, we can calculate an average energy for each of the rare gas atoms from reliable values (2, 15, 16) of the isotropic C_6 coefficients and isotropic dipole polarizabilities. For linear Σ-state molecules we introduce average energies, $U_a^{\parallel}$ or $U_a^{\perp}$, which can be determined from $C_{aa}^{\parallel,\parallel}$ and $C_{aa}^{\perp,\perp}$. Using eq. [7]

$$[10]\quad U_a^{\zeta} = \frac{8C_{aa}^{\zeta,\zeta}}{(\alpha_a^{\zeta})^2}$$

where $\zeta = \parallel$ or $\perp$. Thus, we can calculate $U_a^{\parallel}(U_a^{\perp})$ for H_2, N_2, and CO from eq. [10] using reliable values of the anisotropic polarizabilities and the $C_{aa}^{\zeta,\zeta}$ that have been computed from pseudo-DOSDs for the molecules (3, 4).

The atomic and molecular polarizabilities, α_a^{ζ}, and average energies U_a^{ζ}, are listed in Tables 1 and 2. To test the validity of the average energy approximation we compute all the dispersion energy coefficients $C_6(a,b)$, Γ_{ab}, Γ_{ba}, and Δ_{ab} for all two-body interactions involving the rare gases, H_2, N_2, CO through the use of Tables 1 and 2, eq. [7], and eqs. [2]–[5]. The results were then compared with reliable results in refs. 2–4 from which the average energies were obtained for like-species interactions using $C_{aa}^{\zeta,\zeta}$, $\zeta = \parallel$, $\perp$, and $C_6(a,a)$ only.

There are 66 unique two-body dispersion energies for the

Table 1. (*a*) Atomic and (*b*) molecular polarizabilities (in atomic units) (2–4). The isotropic polarizability $\bar{\alpha} = \frac{1}{3}(\alpha^{\parallel} + 2\alpha^{\perp})$.

(*a*)

Polarizability	He	Ne	Ar	Kr	Xe
$\bar{\alpha}$	1.379	2.669	11.08	16.79	27.16

(*b*)

Polarizability	H_2	N_2	CO
$\alpha^{\parallel}$	6.794	14.80	15.46
$\alpha^{\perp}$	4.752	10.21	11.89
$\bar{\alpha}$	5.432	11.74	13.08

Table 2. (*a*) Atomic and (*b*) molecular average energies obtained from like atom–atom and like molecule–molecule dispersion energy interaction coefficients (2–4) (see the main text for definitions and, in particular, eqs. [9] and [10]). All quantities in atomic units.

(*a*)

Average energy	He	Ne	Ar	Kr	Xe
U_a	1.023	1.194	0.6981	0.6129	0.5169

(*b*)

Average energy	H_2	N_2	CO
$U_a^{\parallel}$	0.5049	0.6596	0.6403
$U_a^{\perp}$	0.5780	0.7502	0.6291

interactions considered. Of these, 53 coefficients can be generated, within the claimed 1% uncertainty (2–4), by the average energy approximation. The reliable DOSD results for the remaining 13 coefficients are listed in Table 3, together with the percentage difference ($\leq \sim 2.8\%$) between them and the results obtained from the average energy approximation.

Table 3. Reliable anisotropic dipolar dispersion energy coefficients (3, 4), defined by eqs. [2]–[6], which were not reproduced to within 1% by the average energy approximation through the use of eqs. [2]–[5], [7], and Tables 1 and 2 (see the main text). The percentage difference, $(\frac{\text{reliable}-\text{approximate}}{\text{reliable}}) \times 100\%$, is shown in parentheses. All reliable C_6 coefficients were reproduced to within 1% except the He–Xe (1.3%), Ne–Xe (1.1%), and CO–He (1.02%). All quantities are in atomic units.

a–b		*a–b*	
CO–CO	$\Delta_{ab} = 0.0090$ (1.4%)	H_2–H_2	$\Delta_{ab} = 0.0108$ (1.1%)
CO–N_2	$\Delta_{ab} = 0.0103$ (2.0%)	H_2–N_2	$\Gamma_{ab} = 0.0966$ (−1.2%)
CO–Ne	$\Gamma_{ab} = 0.0916$ (−2.8%)	H_2–Ne	$\Gamma_{ab} = 0.0901$ (−2.5%)
H_2–CO	$\Gamma_{ab} = 0.0976$ (−1.7%)	N_2–N_2	$\Delta_{ab} = 0.0121$ (1.5%)
	$\Delta_{ab} = 0.0094$ (1.6%)	N_2–Ne	$\Gamma_{ab} = 0.0999$ (1.03%)

3. An average energy approximation for the triple-dipole dispersion energy coefficients

In this section the average energy approximation developed for the dipole–dipole dispersion energy coefficient is adapted to the triple-dipole case. Direct use of the average energies obtained in the last section does not yield adequate results for the isotropic and anisotropic triple-dipole dispersion energy coefficients.

An exact computationally viable expression for the triple-dipole dispersion energy (DDD) between three interacting linear Σ-state molecules has been recently developed and may be written (1) as

$$[11]\quad \mathrm{DDD} = \frac{(1+3\cos\theta_A\cos\theta_B\cos\theta_C)C_9(a,b,c)}{R_{ab}^3R_{bc}^3R_{ac}^3}\,\mathrm{Re}[1-\Gamma(a)W(\theta_a,\phi_a,\theta_A,\theta_B)-\Gamma(b)W(\theta_b,\phi_b,\theta_A,\theta_B)$$
$$-\Gamma(c)W(\theta_c,\phi_c,\theta_A,\theta_B)+\Gamma(a,b)W(\theta_a,\phi_a,\theta_b,\phi_b,\theta_A,\theta_B)+\Gamma(a,c)W(\theta_a,\phi_a,\theta_c,\phi_c,\theta_A,\theta_B)$$
$$+\Gamma(b,c)W(\theta_b,\phi_b,\theta_c,\phi_c,\theta_A,\theta_B)-\Gamma(a,b,c)W(\theta_a,\phi_a,\theta_b,\phi_b,\theta_c,\phi_c,\theta_A,\theta_B)]$$

where Re[...] indicates the real part of [...], θ_A, θ_B, θ_C are the internal angles of the triangle formed by the centres of mass of molecules *a*, *b*, and *c*, and R_{ab} represents the distance between molecule *a* and molecule *b*. The coefficients, *W*, are functions of the relative orientations of the interacting molecules (through the spherical polar angles (θ_a,ϕ_a), (θ_b,ϕ_b), (θ_c,ϕ_c)). The C_9 and Γ's are the isotropic and anisotropic triple-dipole dispersion energy coefficients. For complete details see ref. 1.

The isotropic triple-dipole dispersion energy coefficient $C_9(a,b,c)$ is given (1) by

$$[12]\quad C_9(a,b,c) = \frac{1}{9}\left[C_{abc}^{\parallel,\parallel,\parallel} + 2C_{abc}^{\parallel,\parallel,\perp} + 2C_{abc}^{\parallel,\perp,\parallel} + 4C_{abc}^{\parallel,\perp,\perp} + 2C_{abc}^{\perp,\parallel,\parallel} + 4C_{abc}^{\perp,\parallel,\perp} + 4C_{abc}^{\perp,\perp,\parallel} + 8C_{abc}^{\perp,\perp,\perp}\right]$$

where

$$[13]\quad C_{abc}^{\zeta,\zeta',\zeta''} = \frac{1}{2}\sum_{k_a=1}^{N_a}\sum_{k_b=1}^{N_b}\sum_{k_c=1}^{N_c}\frac{f_{k_a}^{\zeta}f_{k_b}^{\zeta'}f_{k_c}^{\zeta''}\left[E_{k_a}^{\zeta}+E_{k_b}^{\zeta'}+E_{k_c}^{\zeta''}\right]}{E_{k_a}^{\zeta}E_{k_b}^{\zeta'}E_{k_c}^{\zeta''}\left[E_{k_a}^{\zeta}+E_{k_b}^{\zeta'}\right]\left[E_{k_a}^{\zeta}+E_{k_c}^{\zeta''}\right]\left[E_{k_b}^{\zeta'}+E_{k_c}^{\zeta''}\right]}$$

with $\zeta, \zeta', \zeta'' = \parallel$ or $\perp$. The anisotropic interaction coefficients appearing in eq. [11] are defined (1) by

[14] $$\Gamma(a) = \frac{1}{9}\left[C_{abc}^{\|,\|,\|} + 2C_{abc}^{\|,\|,\perp} + 2C_{abc}^{\|,\perp,\|} + 4C_{abc}^{\|,\perp,\perp} - C_{abc}^{\perp,\|,\|} - 2C_{abc}^{\perp,\|,\perp} - 2C_{abc}^{\perp,\perp,\|} - 4C_{abc}^{\perp,\perp,\perp}\right]/C_9(a,b,c)$$

[15] $$\Gamma(c) = \frac{1}{9}\left[C_{abc}^{\|,\|,\|} - C_{abc}^{\|,\|,\perp} + 2C_{abc}^{\|,\perp,\|} - 2C_{abc}^{\|,\perp,\perp} + 2C_{abc}^{\perp,\|,\|} - 2C_{abc}^{\perp,\|,\perp} + 4C_{abc}^{\perp,\perp,\|} - 4C_{abc}^{\perp,\perp,\perp}\right]/C_9(a,b,c)$$

[16] $$\Gamma(a,b) = \frac{1}{9}\left[C_{abc}^{\|,\|,\|} + 2C_{abc}^{\|,\|,\perp} - C_{abc}^{\|,\perp,\|} - 2C_{abc}^{\|,\perp,\perp} - C_{abc}^{\perp,\|,\|} - 2C_{abc}^{\perp,\|,\perp} + C_{abc}^{\perp,\perp,\|} + 2C_{abc}^{\perp,\perp,\perp}\right]/C_9(a,b,c)$$

[17] $$\Gamma(b,c) = \frac{1}{9}\left[C_{abc}^{\|,\|,\|} - C_{abc}^{\|,\|,\perp} - C_{abc}^{\|,\perp,\|} + C_{abc}^{\|,\perp,\perp} + 2C_{abc}^{\perp,\|,\|} - 2C_{abc}^{\perp,\|,\perp} - 2C_{abc}^{\perp,\perp,\|} + 2C_{abc}^{\perp,\perp,\perp}\right]/C_9(a,b,c)$$

[18] $$\Gamma(a,b,c) = \frac{1}{9}\left[C_{abc}^{\|,\|,\|} - C_{abc}^{\|,\|,\perp} - C_{abc}^{\|,\perp,\|} + C_{abc}^{\|,\perp,\perp} - C_{abc}^{\perp,\|,\|} + C_{abc}^{\perp,\|,\perp} + C_{abc}^{\perp,\perp,\|} - C_{abc}^{\perp,\perp,\perp}\right]/C_9(a,b,c)$$

where $\Gamma(b)$ is obtained from $\Gamma(a)$, and $\Gamma(a,c)$ from $\Gamma(b,c)$, by interchanging a and b.

Applying the Unsöld average energy approximation (8) to eq. [13] gives (1)

[19] $$C_{abc}^{\zeta,\zeta',\zeta''} = \frac{1}{2}\,\frac{\left[U_a^{\zeta} + U_b^{\zeta'} + U_c^{\zeta''}\right]U_a^{\zeta}U_b^{\zeta'}U_c^{\zeta''}}{\left[U_a^{\zeta} + U_b^{\zeta'}\right]\left[U_a^{\zeta} + U_c^{\zeta''}\right]\left[U_b^{\zeta'} + U_c^{\zeta''}\right]}\alpha_a^{\zeta}\alpha_b^{\zeta'}\alpha_c^{\zeta''} = \frac{1}{2}\,U_{abc}^{\zeta,\zeta',\zeta''}\,\alpha_a^{\zeta}\alpha_b^{\zeta'}\alpha_c^{\zeta''}$$

where the U_a^{ζ}'s are average energies that are yet to be defined.

For three-body interactions involving only atoms the parameter $U_{a,b,c}^{\zeta,\zeta',\zeta''}$ may be replaced by U_{abc} since for isotropic interactions $U_{a,b,c}^{\zeta,\zeta',\zeta''}$ is independent of ζ, ζ', ζ''. Following Stogryn (9), we may now write U_{abc} in terms of the isotropic $C_9(a,b,c)$ coefficient and isotropic polarizabilities,

[20] $$U_{abc} = \frac{2C_9(a,b,c)}{3\bar{\alpha}_a\bar{\alpha}_b\bar{\alpha}_c}.$$

Using this result, U_a for each rare gas atom can be related to $C_9(a,a,a)$ by considering the interaction between three like atoms a. That is

[21] $$U_{aaa} = \frac{3}{8}\,U_a = \frac{2C_9(a,a,a)}{3\bar{\alpha}_a^3}$$

which gives

[22] $$U_a = \frac{16C_9(a,a,a)}{9\bar{\alpha}^3}.$$

Analagous to the two-body interactions involving linear Σ-state molecules (see Sect. 2) we can compute average energies ($U_a^{\|}$,$U_a^{\perp}$) from the anisotropic triple-dipole dispersion energy coefficients ($C_{aaa}^{\|,\|,\|}$, $C_{aaa}^{\perp,\perp,\perp}$). Using eq. [19]

[23] $$U_a^{\zeta} = \frac{16C_{aaa}^{\zeta,\zeta,\zeta}}{3(\alpha_a^{\zeta})^3}$$

where $\zeta = \|$ or $\perp$. The average energy U_a for each rare gas atom can be determined from eq. [22] from reliable values (2, 15, 16) for the isotropic C_9 triple-dipole coefficients and the isotropic polarizabilities. The $U_a^{\|}(U_a^{\perp})$ for H_2, N_2, and CO can be calculated from eq. [23] using reliable values of the anisotropic polarizabilities and the $C_{aaa}^{\zeta,\zeta,\zeta}$ that have been computed from the pseudo-DOSDs for these molecules (3,4).

The atomic and molecular polarizabilities, α_a^{ζ}, and triple-dipole average energies U_a^{ζ}, are listed in Tables 1 and 4, respectively. All the triple-dipole dispersion energy coefficients (C_9 and Γ's) for *all* three-body interactions involving the rare gases H_2, N_2, and CO were computed through the use of Tables 1 and 4, eq. [19], eq. [12], and eqs. [14]–[18]. The results were then compared with reliable values obtained through use of the pseudo-DOSDs (2–4) in eq. [13] (and from which the average energies were obtained for like-species interactions and for $\zeta = \zeta' = \zeta'' = \|$ or $\perp$), and eq. [12] and eqs. [14] – [18].

Table 4. (*a*) Atomic and (*b*) molecular average energies obtained from like atom–atom–atom (2) and like molecule–molecule–molecule (computed here using the DOSDs of refs. 3 and 4 and eq. [13]) triple-dipole dispersion energy interaction coefficients (see the main text for definitions and, in particular, eqs. [22] and [24]). All quantities in atomic units.

(*a*)

Average energy	He	Ne	Ar	Kr	Xe
U_a	0.9988	1.117	0.6771	0.5904	0.4947

(*b*)

Average energy	H_2	N_2	CO
$U_a^{\|}$	0.5002	0.6389	0.6130
$U_a^{\perp}$	0.5676	0.7151	0.5874

There are 286 unique three-body dispersion energy coefficients for the interactions considered. Of these 259 can be generated, to within a 1% uncertainty, by the average energy approximation; the only rare gas atom – rare gas atom – rare gas atom isotropic C_9 coefficient outside this error margin is for the He–He–Xe interaction and it is 1.3% smaller than the reliable value. The reliable DOSD results for the remaining 26 coefficients are listed in Tables 5–7, together with the percentage difference ($\lesssim \sim 3.6\%$) between them and the results obtained from the average energy approximation values.

In Tables 5–7 non-zero triple-dipole dispersion energy coefficients for each type of interaction, e.g., rare gas – rare gas – molecule, rare gas – molecule–molecule, and molecule–

Table 5. Reliable anisotropic triple-dipole dispersion energy coefficients for rare gas – rare gas – molecule interactions, defined by eqs. [12]–[18] and the main text and evaluated using the DOSDs of refs. 2–4, which were not reproduced to within 1% by the average energy approximation through the use of eqs. [12]–[19] and Tables 1 and 4 (see the main text).[a] The percentage difference, $(\frac{\text{reliable}-\text{approximate}}{\text{reliable}}) \times 100\%$, is shown in parentheses. The reliable C_9 coefficients for He–He–CO and He–Ne–CO are 11.47 (1.2%) and 22.78 (1.01%) atomic units, respectively. All quantities are in atomic units.

a–b–c		*a–b–c*	
He–He–CO	$\Gamma(c)$ = 0.0960 (–2.3%)	He–Ne–CO	$\Gamma(c)$ = 0.0957 (–2.9%)
He–Ne–H_2	$\Gamma(c)$ = 0.0997 (–1.2%)	He–Ar–CO	$\Gamma(c)$ = 0.0962 (–1.2%)
Ne–Ne–CO	$\Gamma(c)$ = 0.0953 (–3.6%)	Ne–Ne–H_2	$\Gamma(c)$ = 0.0986 (–1.6%)
Ne–Ne–N_2	$\Gamma(c)$ = 0.1096 (–1.1%)	Ne–Ar–CO	$\Gamma(c)$ = 0.0960 (–1.6%)
Ne–Kr–CO	$\Gamma(c)$ = 0.0960 (–1.2%)		

[a]Only unique non-zero results are included; only $C_9(a, b, c)$ and $\Gamma(c)$ are non-zero.

Table 6. Reliable anisotropic triple-dipole dispersion energy coefficients for rare gas – molecule – molecule interactions, defined by eqs. [12]–[18] and the main text and evaluated using the DOSDs of refs. 2–4, which were not reproduced to within 1% by the average energy approximation through the use of eqs. [12]–[19] and Tables 1 and 4 (see the main text).[a] The percentage difference, $(\frac{\text{reliable}-\text{approximate}}{\text{reliable}}) \times 100\%$, is shown in parentheses. All quantities are in atomic units.

a–b–c		*a–b–c*	
He–CO–CO	$\Gamma(b, c)$ = 0.0093 (–1.9%)	Ne–N_2–CO	$\Gamma(c)$ = 0.0959 (–1.7%)
He–CO–H_2	$\Gamma(c)$ = 0.1044 (–1.1%)	Ne–N_2–H_2	$\Gamma(c)$ = 0.1028 (–1.1%)
He–N_2–CO	$\Gamma(c)$ = 0.0961 (–1.2%)	Ne–CO–CO	$\Gamma(c)$ = 0.0958 (–1.3%)
Ne–CO–H_2	$\Gamma(c)$ = 0.1036 (–1.3%)		$\Gamma(b, c)$ = 0.0092 (–2.6%)

[a]Only unique non-zero results included; the non-zero coefficients are C_9, $\Gamma(b)$, $\Gamma(c)$, and $\Gamma(b, c)$. If $b = c$, $\Gamma(b) = \Gamma(c)$.

Table 7. Reliable anisotropic triple-dipole dispersion energy coefficients for molecule–molecule–molecule interactions, defined by eqs. [12]–[18] and the main text and evaluated using the DOSDs of refs. 2–4, which were not reproduced to within 1% by the average energy approximation through the use of eqs. [12]–[19] and Tables 1 and 4 (see the main text).[a] The percentage difference, $(\frac{\text{reliable}-\text{approximate}}{\text{reliable}}) \times 100\%$, is shown in parentheses. All quantities are in atomic units.

a–b–c		*a–b–c*	
CO–CO–H_2	$\Gamma(a, b, c)$ = 0.0010 (1.1%)	H_2–H_2–N_2	$\Gamma(a, b, c)$ = 0.0015 (1.02%)
CO–H_2–H_2	$\Gamma(a, b, c)$ = 0.0012 (1.3%)	N_2–N_2–H_2	$\Gamma(a, b)$ = 0.0143 (1.04%)
CO–N_2–H_2	$\Gamma(a, b, c)$ = 0.0012 (1.2%)		$\Gamma(a, b, c)$ = 0.0017 (1.3%)
CO–N_2–N_2	$\Gamma(a, b, c)$ = 0.0013 (1.2%)		

[a]Only unique non-zero results included. Three types of interactions need to be considered here, i.e., *a–a–a*, *a–b–b*, and *a–b–c*. For *a–a–a* there are four unique coefficients: C_9, $\Gamma(a)$, $\Gamma(a, a)$, and $\Gamma(a, a, a)$, and for *a–b–b* there are six unique coefficients, namely C_9, $\Gamma(a)$, $\Gamma(b)$, $\Gamma(a, b)$, $\Gamma(b, b)$, and $\Gamma(a, b, b)$. All nine of the triple-dipole dispersion energy coefficients, C_9 and the Γ's, are necessary to describe the *a–b–c* interaction.

molecule–molecule, are given, where an (*a–b–c*) order is implied for each interaction. Interactions involving the same species, in a different *a b c* ordering, are related to these by symmetry. For example, the coefficients for a *c–b–a* interaction are identical to the *a–b–c* interaction coefficients with the *a* and *c* molecules interchanged, so that for the CO–H_2–N_2 (*a–b–c*) interaction $\Gamma(a)$, $\Gamma(c)$, $\Gamma(a, b)$, $\Gamma(b, c)$ are identical to $\Gamma(c)$, $\Gamma(a)$, $\Gamma(c, b)$, $\Gamma(b, a)$, respectively, of the N_2–H_2–CO (*c–b–a*) interaction; the C_9, $\Gamma(b)$, $\Gamma(a, c)$ and $\Gamma(a, b, c)$ coefficients are the same for both interactions.

4. Discussion of results

Reliable results for the isotropic and anisotropic triple-dipole (DDD) dispersion energy coefficients for interactions involving H_2, N_2, CO, and for interactions involving H_2, N_2, CO, and one or two rare gases, have been obtained using literature (2–4) pseudo-dipole oscillator strength distributions for these species. An average energy approximation has been used to (usually) reliably represent the large number of DDD interaction coefficients so obtained.

An average energy approximation has been developed for the isotropic and anisotropic dipole–dipole and triple-dipole dispersion energy coefficients. The required input is the isotropic and anisotropic average energies and polarizabilities of the interacting species, which are provided in tabular form for He, Ne, Ar, Kr, Xe, H_2, N_2, and CO. The average energy approximation expressions, with the provided input, reproduce most of the two- and three-body dispersion energy coeffficients to within the 1% accuracy claimed for the results obtained directly from the isotropic and anisotropic dipole oscillator strength distributions for the interacting species. Fifty-three of the 66 unique two-body dispersion energy coefficients, and 259 out of the 286 unique non-additive three-body dispersion energy coefficients, for all the interactions arising from the rare gases, H_2, N_2, and CO, are reproduced reliably in the average energy approximation. The coefficients not reproduced to within 1% are provided in tabular form (Table 3 and Tables 5–7 for the dipole–dipole and triple-dipole coefficients, respectively). The results in this paper provide the first reliable anisotropic triple-dipole dispersion energies for three-body interactions involving molecules.

The use of the average energy approximation to represent the reliable DOSD results for the triple-dipole dispersion energy clearly works well. It is of interest to discuss, briefly, the principal source of the difficulty in our application of this approach. For interactions involving at least one molecule, our average energy approach yields results for the individual $C_{abc}^{\zeta,\zeta',\zeta''}$ coefficients, defined by eq. [13], that are reliable to within 1% for all cases except $C_{abc}^{0,0,\perp}$, for He–He–CO (1.5%), He–Ne–CO (1.3%), Ne–Ne–CO (1.4%); $C_{abc}^{0,0,\parallel}$(Ne–Ne–H_2) (1.1%); and $C_{abc}^{0,\perp,\perp}$ for He–CO–CO (1.2%) and Ne–CO–CO (1.1%). The principal source of error in obtaining the overall triple-dipole coefficients, defined by eqs. [12]–[18], is due to cumulative errors arising from summing the individual $C_{abc}^{\zeta,\zeta',\zeta''}$ to obtain the overall coefficients. For example, the percent difference of −3.6% between the reliable DOSD and the average energy results for $\Gamma(c)$ for Ne–Ne–CO is due to the accumulation of errors from the individual coefficients $C_{abc}^{0,0,\parallel}$ (0.4%), $C_{abc}^{0,0,\perp}$ (1.4%), and C_9 (1%) occurring in the expression, eq. [15], for $\Gamma(c)$.

It is relevant to mention that the average energies for the dipole–dipole dispersion energy coefficients, Table 2, are different from those for the triple-dipole coefficients, Table 4. Use of Table 2 in the evaluation of the triple-dipole dispersion energy coefficients, in the average energy approximation, leads to significant errors. That is, 251 out of the 286 triple-dipole coefficients so obtained disagree with the reliable values by more than 1%.

Non-additive interaction energies are important for many properties of bulk matter (17–25). The triple-dipole energy is one of many competing non-additive interactions relevant to such properties (24–29). Others include non-additive higher order dispersion energies and non-additive induction energies, the charge overlap corrections to all multipolar non-additive energies, and first order and higher order electron exchange energies (23–30). It is important to quantify as many of these non-additive effects as possible so that experiments can be used to study computationally more difficult non-additive energies (24–26). This paper, see also ref. 1, is a recent contribution towards this goal.

Acknowledgment

This research was supported by a grant from the Natural Sciences and Engineering Research Council of Canada.

References

1. S.A.C. McDowell, A. Kumar, and W.J. Meath. Mol. Phys. **87**, 845 (1996).
2. A. Kumar and W.J. Meath. Mol. Phys. **54**, 823 (1985).
3. W.J. Meath and A. Kumar. Int. J. Quantum Chem. **24**, 501 (1990).
4. A. Kumar and W.J. Meath. Chem. Phys. **189**, 467 (1994).
5. A. Kumar and W.J. Meath. Can. J. Chem. **63**, 1616 (1985).
6. G.D. Zeiss, W.J. Meath, J.C.F. McDonald, and D.J. Dawson. Can. J. Phys. **55**, 2080 (1977).
7. B.L. Jhanwar and W.J. Meath. Chem. Phys. **67**, 185 (1982).
8. A. Unsöld. Z. Phys. **43**, 563 (1927).
9. D.E. Stogryn. Phys. Rev. Lett. **24**, 971 (1970).
10. G.A. Victor and A. Dalgarno. J. Chem. Phys. **50**, 2535 (1969); **53**, 1316 (1970).
11. P.W. Langhoff, R.G. Gordon, and M. Karplus. J. Chem. Phys. **55**, 2126 (1971).
12. D.J. Margoliash and W.J. Meath. J. Chem. Phys. **68**, 1426 (1978).
13. D.J. Margoliash, T.R. Proctor, G.D. Zeiss, and W.J. Meath. Mol. Phys. **35**, 747 (1978).
14. A.D. Buckingham. Adv. Chem. Phys. **12**, 107 (1967).
15. P.J. Leonard and J.A. Barker. Theor. Chem. Adv. Perspect. **1**, 117 (1975).
16. J.A. Barker and P.J. Leonard. Phys. Lett. **13**, 127 (1964).
17. J.A. Barker. *In* Rare gas solids. Vol. 1. *Edited by* M.L. Klein and J.A. Venables. Academic Press, New York. 1976. Chap. 4.
18. B. Guillot. J. Chem. Phys. **91**, 3456 (1989); B. Guillot, R.D. Mountain, and G. Birnbaum. J. Chem. Phys. **90**, 650 (1989); Mol. Phys. **64**, 747 (1988).
19. J.K. Lee, J.A. Barker, and G.M. Pound. J. Chem. Phys. **60**, 1976 (1974).
20. R.J. Bell and I.J. Zucker. *In* Rare gas solids. Vol. 1. *Edited by* M.L. Klein and J.A. Venables. Academic Press, New York. 1976. Chap. 1.
21. W.-K. Liu. Phys. Rev. B: Condens. Matter, **32**, 868 (1985); J. Mahanty. Phys. Rev. B: Condens. Matter, **35**, 4113 (1987).
22. J.J. Salacuse and P.A. Egelstaff. Phys. Rev. A: Gen. Phys. **38**, 4313 (1988).
23. A. Ernesti and J.M. Hutson. Faraday Discuss. **97**, 1 (1994); M.J. Elrod, R.J. Saykally, A.R. Cooper, and J.M. Hutson. Mol. Phys. **81**, 579 (1994); A.R. Cooper and J.M. Hutson. J. Chem. Phys. **98**, 5337 (1993); M.J. Elrod, D.W. Steyert, and R.J. Saykally. J. Chem. Phys. **94**, 58 (1991); M.J. Elrod, D.W. Steyert, and R.J. Saykally. J. Chem. Phys. **95**, 3182 (1991); M.J. Elrod, J.G. Loeser, and R.J. Saykally. J. Chem. Phys. **98**, 5352 (1993).
24. W.J. Meath and R.A. Aziz. Mol. Phys. **52**, 225 (1984); Faraday Discuss. Chem. Soc. **80**, 225 (1985).
25. W.J. Meath and M. Koulis. J. Mol. Struct. Spectrosc. (Theochem), **226**, 1 (1991).

26. Z.C. Zhang, A.R. Allnatt, J.D. Talman, and W.J. Meath. Mol. Phys. **81**, 1425 (1994).
27. A.D. McLean, B. Liu, and J.A. Barker. J. Chem. Phys. **89**, 6339 (1988); J.A. Barker. J. Stat. Phys. **52**, 1359 (1988).
28. R. LeSar. Phys. Rev. B: Condens. Matter, **28**, 6812 (1983); Phys. Rev. Lett. **61**, 2121 (1988).
29. G. Chalasinski, S.M. Cybulski, M.M. Szczesniak, and S. Scheiner. J. Chem. Phys. **91**, 7048 (1989); G. Chalasinski, M.M. Szczesniak, P. Cieplak, and S. Scheiner. J. Chem. Phys. **94**, 2873 (1991), and references therein.
30. S.F. O'Shea and W.J. Meath. Mol. Phys. **28**, 1431 (1974); Mol. Phys. **31**, 515 (1976).

Topological analysis of electron momentum densities and the bond directional principle: the first-row hydrides, AH, and homonuclear diatomic molecules, A_2

Jiahu Wang, B. James Clark, Hartmut Schmider, and Vedene H. Smith, Jr.

Abstract: Topological analysis of electron momentum densities of the first-row hydrides and homonuclear diatomic molecules has been carried out. The densities and their curvatures were calculated from wave functions of near Hartree–Fock quality using a Slater basis. The bond directional principle has been discussed through the topological properties of electron momentum densities. Basis set effects on the topological features have also been addressed.

Key words: electron momentum density, the bond directional principle, topological analysis, first-row hydrides, homonuclear diatomic molecules.

Résumé : On a effectué une analyse topologique des densités des moments électroniques des hydrures et des molécules diatomiques homonucléaires des éléments de la première couche périodique. On a calculé les densités et leurs courbures à partir de fonctions d'onde de qualité se rapprochant de celle de Hartree–Fock, en utilisant une base de Slater. On a discuté du principe de la liaison directionnelle par le biais des propriétés des densités des moments électroniques. On a aussi examiné les effets des ensembles de bases sur les caractéristiques topologiques.

Mots clés : densité du moment électronique, le principe de la liaison directionnelle, hydrures de la première période, molécules diatomiques homonucléaires.

[Traduit par la rédaction]

1. Introduction

Topological analysis of electron densities in position space has received much attention (1). Atoms (2, 3), molecules (1), as well as solids (4, 5) have been investigated. Through the study of the Laplacian at the critical points and the Laplacian distribution of an electron density, information about chemical bonding (6) and chemical reactivity (7) can be obtained. The electron momentum density (EMD), which provides a complementary description of electron motion to the electron charge distribution in position space, has only recently been studied through topological analysis. Sagar et al. (8) reported the topological features of the EMDs of atoms and ions. It has been found that, differing from its position space counterpart, the origin of an EMD is not always a local maximum. Quite often, it is a local minimum (9). More recently, Gadre and co-workers (10, 11) reported the topological properties of the EMDs of a few simple molecules with Gaussian basis sets. These authors have also studied the implication of the additional inversion symmetry (12) of an EMD on its topological properties (13).

Because of their relation to the Compton profile under the impulse approximation, EMDs have been the subject of extensive theoretical studies since the 70s. The development of (e,2e) (also called electron momentum spectroscopy) experiments further stimulated such investigations. Accurate wave functions have been employed to predict the momentum space properties (14, 15) and the agreement between theory and experiment is satisfactory. To facilitate the analysis of EMDs of atoms and molecules and the changes in EMDs upon formation of chemical bonds, Epstein and Tanner (16) have proposed several principles. Among them, the bond directional principle (BDP) has received most attention. The BDP states that "the momentum of an electron in a chemical bond is more likely to be directed perpendicular to than along the bond axis. Furthermore, in the chemical bond there is greater density at low momentum along the bond and greater density at high momentum perpendicular to the bond than was the case in the isolated atoms." Since then, various momentum space quantities, such as zero-point Compton profile anisotropy $\Delta J(0)$ (17–19), $J(0)$ surface (20), kinetic energy anisotropy (21), kinetic energy tensor (22), Husimi second moment of momentum tensor (23), have been chosen

Received January 2, 1996.

This paper is dedicated to Professor Richard F.W. Bader on the occasion of his 65th birthday.

J. Wang. Department of Chemistry, Dalhousie University, Halifax, NS B3H 4J3, Canada.
B.J. Clark, H. Schmider,[1] and V.H. Smith, Jr.[2] Department of Chemistry, Queen's University, Kingston, ON K7L 3N6, Canada.

[1] Present address: Chemistry Department B, Chemical Physics, Technical University of Denmark, DTU-301, 2800 Lyngby, Denmark.
[2] Author to whom correspondence may be addressed. Telephone: (613) 545-2650. Fax: (613) 545-6669. E-mail: smithvh@qucdn.queensu.ca

for the study of the directional characteristics of molecular EMDs. Exceptions to the bond directional principle have been reported (see ref. 24 for a summary). More recently, Tanner (24) has modified the aforementioned BDP and the revised one states: "in a chemical bond in a bound molecule in its equilibrium configuration, there are values $\boldsymbol{p}_m$ of momentum which are more probable, i.e., which correspond to local maxima of $\pi(\boldsymbol{p})$. Those values are determined by both the geometric and electronic symmetries of the molecule. For momenta, $\boldsymbol{p} = \boldsymbol{p}_m + \delta\boldsymbol{p}$, near a maximum it is more likely that $\delta\boldsymbol{p}$ is perpendicular rather than parallel to the bond axis." According to this new interpretation, we should pay attention to the directional characteristics of local maxima or (3, −3) critical points when analyzing an EMD.

The purpose of this paper is to introduce the curvatures of EMDs as an alternative measure of anisotropy of molecular EMDs.

2. Curvatures of EMDs and the BDP

Each topological feature of an EMD is associated with a critical point, $\boldsymbol{p}_c$, in momentum space, where the first derivatives of $\pi(\boldsymbol{p})$, $\nabla\pi(\boldsymbol{p}_c) = 0$. A critical point is characterized by the curvatures of $\pi(\boldsymbol{p})$. The principal axes and their corresponding curvatures at a critical point are obtained as the eigenvectors and the corresponding eigenvalues through the diagonalization of the Hessian matrix of $\pi(\boldsymbol{p}_c)$. The type of a critical point is determined by its rank, ω, and signature, σ, and is labeled by (ω, σ). Rank ω is equal to the number of nonzero curvatures of π, whereas signature σ is simply the algebraic sum of the signs of the curvatures at the critical point. There are four types of nondegenerate critical points: local maxima (3, −3); saddle points (3, −1), saddle points (3, +1), and local minima (3, +3). A critical point with $\omega < 3$ is said to be degenerate.

In the vicinity of a critical point, $\boldsymbol{p}_c$, the EMD can be written as

$$[1]\quad \pi(\boldsymbol{p}_c + \delta\boldsymbol{p}) = \pi(\boldsymbol{p}_c) + \frac{1}{2}\nabla^2\pi(\boldsymbol{p}_c)\delta\boldsymbol{p}^2 + \mathcal{O}(\delta\boldsymbol{p}^3)$$

$$= \pi(\boldsymbol{p}_c) + \frac{1}{2}[\lambda_1\delta p_x^2 + \lambda_2\delta p_y^2 + \lambda_3\delta p_z^2] + \mathcal{O}(\delta\boldsymbol{p}^3)$$

where λ_1, λ_2, and λ_3 are the curvatures of $\pi(\boldsymbol{p})$ at $\boldsymbol{p}_c$. The subscripts x, y, z indicate the three principal axes. δp_i is the projection of $\delta\boldsymbol{p}$ on the axis i.

For linear molecules locating along the z-axis, EMDs display $D_{\infty h}$ symmetry with p_z being the unique axis. Thus, p_z will always be a principal axis. We may choose two mutually orthogonal directions in the plane perpendicular to the p_z axis as the other principal axes, p_x and p_y. Supposing the momentum distributions follow the BDP formulated by Tanner (24), we then have

$$[2]\quad \lambda_3 < \lambda_1 (= \lambda_2)$$

at the (3, −3) critical points.

Due to the inversion symmetry of EMDs, the origin is always a critical point. Through the application of eq. [1], information about the anisotropy of EMDs at small momenta can be obtained.

The present momentum space quantities were obtained with near Hartree–Fock quality wave functions (25, 26) using Slater basis. Since we focus on the BDP of EMDs, only the topological properties at $\boldsymbol{p} = 0$ and local maxima are presented. Atomic units are used throughout this paper.

Fig. 1. The EMDs of the first-row hydrides. The innermost contour value is 1.50, 1.50, 2.50, 1.40, 0.90, 0.64, 0.46, and 1.00 for LiH, BeH, BH, CH, NH, OH, FH, and OH^-, respectively. The remaining contour values, from the outermost, are 0.003, 0.006, 0.01, 0.02, 0.05, 0.2, 0.5, respectively.

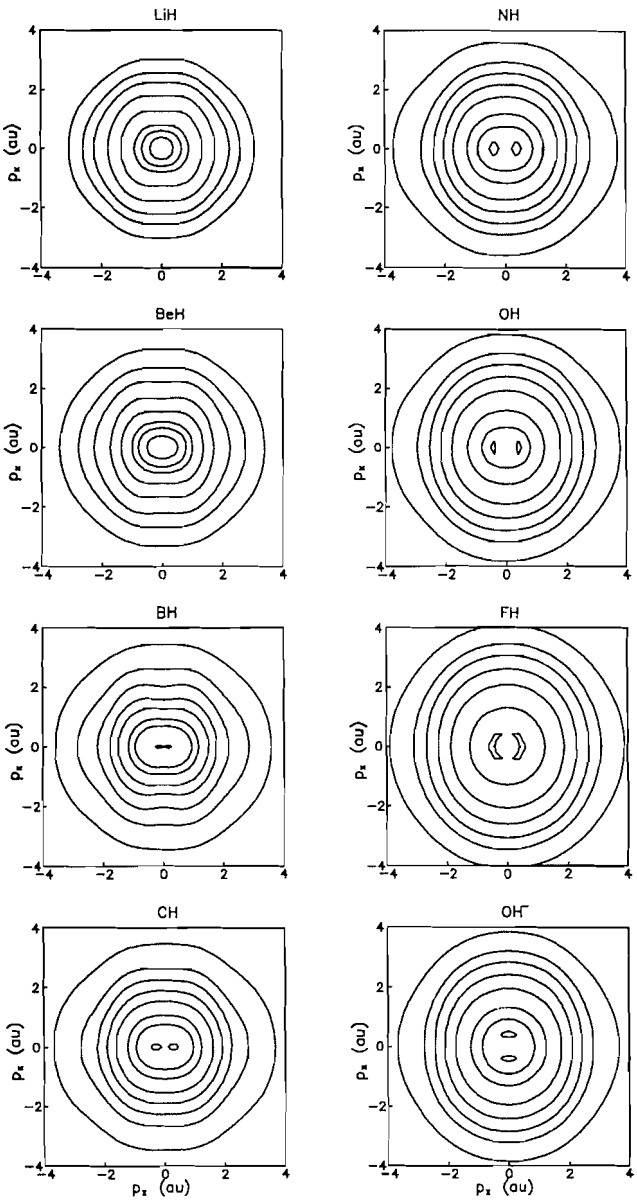

3. EMDs of the first-row hydrides and homonuclear diatomic molecules

Ramirez studied the EMDs of the first-row hydrides (27) and homonuclear diatomic molecules (28) and also discussed the chemical bonding through the EMD difference maps. Contour maps of the EMDs of LiH ($X^1\Sigma^+$), BeH ($X^2\Sigma^+$), BH ($X^1\Sigma^+$), CH ($X^2\Pi$), NH ($X^3\Sigma^-$), OH ($X^2\Pi_i$) and FH ($X^1\Sigma^+$), Li_2 ($X^1\Sigma_g^+$), Be_2 ($^1\Sigma_g^+$), B_2 ($X^3\Sigma_g^-$), C_2 ($X^1\Sigma_g^+$), N_2 ($X^1\Sigma_g^+$), O_2 ($X^3\Sigma_g^-$), and F_2 ($X^1\Sigma_g^+$) at their experimental equilibrium

Fig. 2. The EMDs of H_2 and the first-row homonuclear diatomic molecules. The innermost contour value is 1.00, 5.00, 5.50, 2.50, 1.50, 1.00, 0.92, and 0.64 for H_2, Li_2, Be_2, B_2 C_2, N_2, O_2, and F_2, respectively. The remaining contour values, from the outermost, are 0.005, 0.006, 0.01, 0.02, 0.05, 0.10, 0.20, 0.50, except for H_2. The starting contour value for H_2 is 0.006.

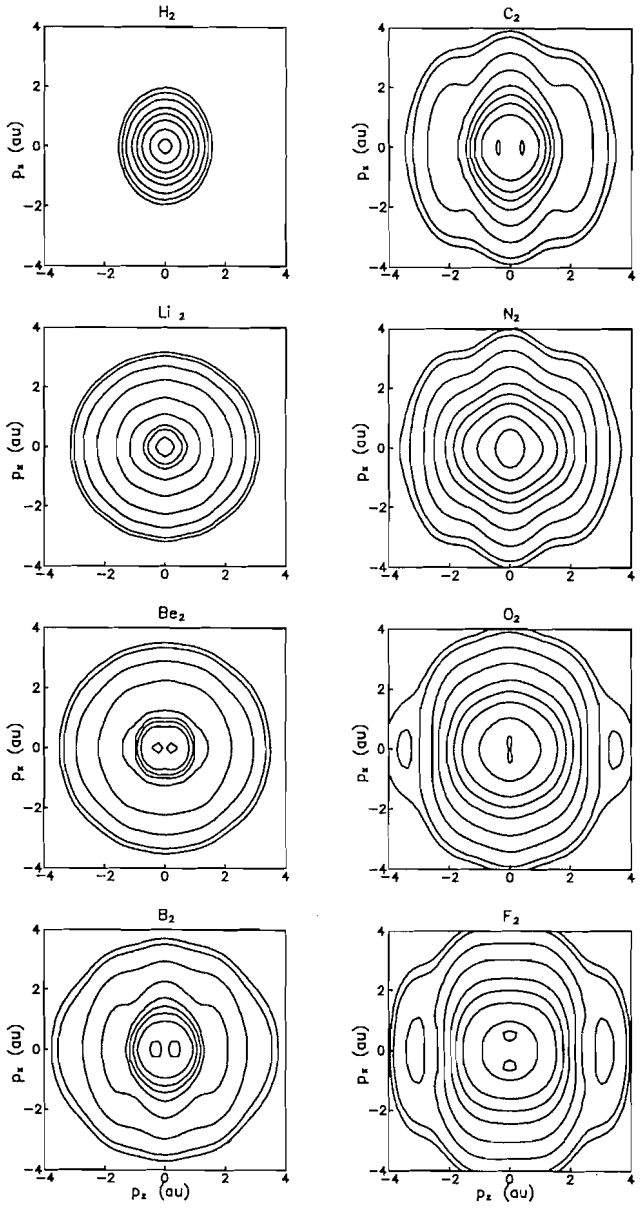

separation (except Be_2 for which experimental data are unavailable) were shown. However, many important features of the EMDs were not presented. We plotted again the EMDs on the p_x–p_z plane for the first-row hydrides and OH^- in Fig. 1 and for H_2 and the first-row homonuclear diatomic molecules in Fig. 2. In addition to those contour values used before (27, 28), we include an extra contour at the innermost region to show the important topological features of each EMD.

Similar to the earlier findings for the first-row hydrides by Ramirez (27), the EMDs tend to be more diffuse from LiH to FH. This behavior is just the opposite to the change in position space. In position space, due to the increase of the nuclear charge of the heavier atom in the hydrides, electrons are more likely to move closer to the heavier atom. In the complementary momentum space, the higher the nuclear charge of the heavier atom, the faster the electrons will move. In other words, it is more probable for electrons to appear at higher momenta.

It is clear that several features of the EMDs in Fig. 1 have been newly revealed. In LiH and BeH, the EMD displays a global maximum at $\boldsymbol{p} = 0$. From the topological point of view, $\boldsymbol{p} = 0$ is a (3, −3) critical point. Starting from BH, the origin is no longer a (3, −3) critical point. The local maxima move away from the origin along the p_z axis except for OH^-, for which the local maxima are located on the plane perpendicular to the p_z axis. More features of the topological properties are addressed in the next section.

Because a variety of chemical bonds can be formed in the homonuclear diatomic molecules, the EMDs in Fig. 2 display more complicated features than in Fig. 1 for the hydrides. Nevertheless, it can be seen that from Li_2 to F_2 (excluding Be_2), electrons are more likely to move perpendicular to than along the bond axis, a tendency that is more obviously portrayed in the EMD of H_2. According to the BDP by Epstein and Tanner (16), this anisotropy signifies the chemical bonding in these molecules. On the other hand, the EMD of an unbound system, Be_2, shows a preference for moving along, rather than perpendicular to, the bond axis. It is also interesting to note the gradual shift of the locations of maxima from Li_2 to F_2. Similar trends can be observed in Fig. 1 as well.

4. Curvature of EMDs at local maxima and the BDP

The topological features of the first-row hydrides and homonuclear diatomic molecules at the origin are summarized in Table 1. Besides BH, the momentum density at the origin, $\pi(0)$, has the same value as reported by Ramirez (27, 28). The $\pi(0)$ of BH has been calculated to be 2.5273, compared to the previous value of 2.5200.

In Table 1, the origin appears as a local maximum for the EMD of H_2, Li_2, N_2, LiH, and BeH. The first four molecules also share the property of $\lambda_3 < \lambda_1$, in agreement with the revised BDP formulated by Tanner (24). BeH is an exception, as previously noted by Tanner (24). For LiH, λ_1 and λ_3 have been found to be very close and this may be traced to the strong ionic character of its molecular structure. Besides being a local maximum, the other three types of nondegenerate critical points all show up in Table 1. According to eq. [1], this may indicate that, in general, there is no preferential direction of electron movement at small momentum regions in a bound system.

As seen from Figs. 1 and 2, several molecules have maximal EMDs away from the origin. The topological properties for those that have (3, −3) critical points along p_z are given in Table 2. Because of the inversion symmetry of EMDs, these critical points are paired by an inversion. The locations of the maxima, however, are dependent on the nuclear charges of the molecule. There is a clear trend for the (3, −3) critical points to move to higher momentum regions from BH

Table 1. Summary of the topological properties of EMDs at the origin.

Molecule	Bond length	$\pi(0)$	Signature	$\lambda_1(=\lambda_2)$	λ_3
H_2	1.4	1.2299	(3, −3)	−8.034	−9.416
Li_2	5.051	18.7836	(3, −3)	−574.985	−710.878
N_2	2.068	1.4079	(3, −3)	−1.011	−6.292
LiH	3.015	3.8198	(3, −3)	−54.948	−55.990
BeH	2.538	3.4007	(3, −3)	−40.617	−15.545
Be_2	4.0	4.9209	(3, −1)	−64.591	165.712
BH	2.336	2.5273	(3, −1)	−24.467	7.202
CH	2.214	1.3440	(3, −1)	−3.806	6.885
NH	1.9614	0.8215	(3, −1)	−0.029	4.752
O_2	2.282	0.9297	(3, +1)	0.953	−4.196
F_2	2.68	0.5883	(3, +1)	1.466	−1.204
B_2	3.005	2.0360	(3, +3)	7.356	54.730
C_2	2.3481	0.9945	(3, +3)	11.000	17.804
OH	1.8342	0.5390	(3, +3)	1.637	2.906
OH^-	1.781	0.6346	(3, +3)	15.219	7.535
FH	1.7328	0.3742	(3, +3)	1.755	1.849

Table 2. Summary of the topological properties of EMDs at the (3, −3) critical points, $\boldsymbol{p}_c = (0, 0, \pm p_z)$.

Molecule	p_z	$\pi(\mathbf{p}_c)$	$\lambda_1(=\lambda_2)$	λ_3
Be_2	0.2602	7.1465	−102.588	−160.799
B_2	0.3295	3.1751	−18.236	−47.885
C_2	0.4177	1.5892	−2.370	−15.474
BH	0.1965	2.5907	−24.797	−10.901
CH	0.3141	1.4873	−6.754	−8.182
NH	0.3928	0.9706	−2.563	−5.032
OH	0.4546	0.6589	−0.618	−2.912
FH	0.5114	0.4696	−0.116	−1.783

Table 3. Summary of the topological properties of EMDs at the (2, −2) degenerate critical points, $\boldsymbol{p}_c = (p_x, p_y, p_z)$.

Molecule	$\sqrt{p_x^2 + p_y^2}$	p_z	$\pi(\boldsymbol{p})$	λ	λ_3
O_2	0.2983	0.0000	0.9490	−1.440	−3.799
F_2	0.5157	0.0000	0.6688	−1.628	−1.165
OH^-	0.4092	0.0000	1.0869	−10.479	−2.410

to FH and from Be_2 to C_2. Of these eight molecules, all but BH (another exceptional case noted by Tanner (24)) have the property that $\lambda_3 < \lambda_1$. This includes also the unbound Be_2 molecule.

The EMDs of O_2, F_2, and OH^- have local maxima in the plane perpendicular to the p_z axis. Because of the cylindrical symmetry of linear molecules, those critical points are degenerate. The rank ω is equal to 2 in this case. The topological properties of these three species are summarized in Table 3. The curvature along the p_z axis is still labeled as λ_3. λ is used to refer to the nonzero curvature in the perpendicular plane. We expect to see $\lambda_3 < \lambda_1$ if the revised BDP is followed. However, only O_2 shows such characteristics.

As the above discussion shows, the revised BDP can account for the EMDs of many bound molecular systems. However, exceptions also exist. More importantly, the revised BDP appears unable to distinguish the unbound molecule from the bound ones.

Before concluding this section, we would like to mention a few words about the basis set effects. Gadre and co-workers (10, 11) carried out the topological analysis of EMDs with double zeta or triple zeta Gaussian basis sets. For N_2, they (10, 11) predicted the origin of the EMD to be a (3, +1) saddle point. The signature of the local maximum was given as (2, −2). These contradict the present and other earlier studies (15, 29). The EMD of OH^- were studied twice (10, 11) using a 4-31G and triple-zeta basis set, respectively. Only the second study (11) located the (2, −2) degenerate local maxima. The first study actually found (3, −3) critical points in the EMD of OH^-. Inconsistent results were also reported for HF (10, 11). EMDs are, in general, quite sensitive to the basis sets used. It is also well known that Gaussian basis sets suffer from the fact that they do not represent the correct asymptotic behavior in position space. This will inevitably affect the description of EMDs in the small-momentum region, the same region where most of the topological features of a molecule are in evidence. We would like to call for caution when studying topological properties of EMDs with Gaussian basis sets.

5. Summary

The electron momentum densities (EMDs) of the first-row hydrides and homonuclear diatomic molecules were calculated with near Hartree–Fock quality wave functions. Important features in the EMDs, which were not shown previously, are presented. The bond directional principle (BDP) was discussed through the curvatures of EMDs at their local maxima. It has been shown that the revised BDP is able to account for the momentum distributions for many bound systems (H_2, Li_2, N_2, LiH, B_2, C_2, CH, NH, OH, FH, O_2). However, exceptions to the revised BDP, including cases of both the bound (BeH, BH, F_2, OH^-) and unbound (Be_2) molecules, are also found. Topological analysis with Gaus-

sian basis sets should be carried out with care as the quality of basis sets can strongly influence the results.

Acknowledgment

Financial support from the Natural Sciences and Engineering Research Council of Canada is gratefully acknowledged. J.W. would like to thank the Killam Trust for a Killam postdoctoral fellowship.

References

1. R.F.W. Bader. Atoms in molecules: a quantum theory. Clarendon Press, Oxford. 1990.
2. R.P. Sagar, A.C.T. Ku, V.H. Smith, Jr., and A.M. Simas. J. Chem. Phys. **88**, 4367 (1988).
3. Z. Shi and R.J. Boyd. J. Chem. Phys. **88**, 4375 (1988).
4. C. Mei, K.E. Edgecombe, V.H. Smith, Jr., and A. Heilingbrunner. Int. J. Quantum Chem. **48**, 287 (1993).
5. P.F. Zuo and R.F.W. Bader. Acta Crystallogr. Sect. A: Found. Crystallogr. **A50**, 714 (1994).
6. R.F.W. Bader and H. Essén. J. Chem. Phys. **80**, 1943 (1984).
7. Z. Shi and R.J. Boyd. J. Phys. Chem. **95**, 4698 (1991).
8. R.P. Sagar, A.C.T. Ku, V.H. Smith, Jr., and A.M. Simas. J. Chem. Phys. **90**, 6520 (1989).
9. W.M. Westgate, A.M. Simas, and V.H. Smith, Jr. J. Chem. Phys. **83**, 4054 (1989).
10. S.A. Kulkarni, S.R. Gadre, and R.K. Pathak. Phys. Rev. A: At. Mol. Opt. Phys. **45**, 4399 (1992).
11. S.A. Kulkarni and S.R. Gadre. Z. Naturforsch. A: Phys. Sci. **48**, 145 (1993).
12. P. Kaijser and V.H. Smith, Jr. *In* Methods and structure in quantum science. *Edited by* J.L. Calais, O. Goscinski, J. Linderberg, and Y. Öhrn. Plenum Press, New York. 1976. pp. 417–426.
13. S.R. Gadre, A.C. Limaye, and S.A. Kulkarni. J. Chem. Phys. **94**, 8040 (1991).
14. A.O. Bawagan, C.E. Brion, E.R. Davidson, and D. Feller. Chem. Phys. **113**, 19 (1987).
15. A.J. Thakkar and W.A. Pedersen. Int. J. Quantum Chem. Symp. **24**, 327 (1990).
16. I.R. Epstein and A.C. Tanner. *In* Compton scattering. *Edited by* B.G. Williams. McGraw–Hill, New York. 1977. pp. 209–233.
17. R.A. Tawil and S.R. Langhoff. Chem. Phys. **63**, 1572 (1975).
18. B.M. Pettitt, R.L. Matcha, and B.I. Ramirez. J. Chem. Phys. **79**, 2913 (1983).
19. A. Rozendaal and E.J. Baerends. Chem. Phys. **95**, 57 (1985).
20. W.J. Janis, P. Kaijser, V.H. Smith, Jr., and M. Whangbo. Mol. Phys. **35**, 1237 (1978).
21. A.J. Thakkar, B.S. Sharma, and T. Koga. J. Chem. Phys. **85**, 2845 (1986).
22. W. Weyrich. Ber. Bunsen-Ges. Phys. Chem. **83**, 797 (1979).
23. J.L. Anchell and J.E. Harriman. J. Chem. Phys. **92**, 2943 (1990).
24. A.C. Tanner. Chem. Phys. **123**, 241 (1988).
25. P.E. Cade and W. Huo. At. Data Nucl. Data Tables, **12**, 415 (1973).
26. P.E. Cade and A.C. Wahl. At. Data Nucl. Data Tables, **13**, 339 (1974).
27. B.I. Ramirez. J. Phys. B: At. Mol. Phys. **15**, 4339 (1982).
28. B.I. Ramirez. J. Phys. B: At. Mol. Phys. **16**, 343 (1983).
29. A.J. Thakkar, A.M. Simas, and V.H. Smith, Jr. J. Chem. Phys. **81**, 2953 (1984).

Oxidative damage to the glycyl α-carbon site in proteins: an ab initio study of the C—H bond dissociation energy and the reduction potential of the C-centered radical

D.A. Armstrong, D. Yu, and A. Rauk

Abstract: The C—H bond dissociation energies ($D_{C—H}$) of a series of model glycyl proteins were derived from selected isodesmic reactions based on high level ab initio calculations. At 298 K, the recommended values of $D_{C—H}$, in kJ mol^{-1} are: NH_2CH_2CHO, 308; $NH_2CH_2C(O)NH_2$, 336; $HC(O)NHCH_2CHO$, 331; $HC(O)NHCH_2C(O)NH_2$, 350; $CH_3C(O)NHCH_2C(O)NH_2$, 347; $HC(O)NHCH_2C(O)NHCH_3$, 349; and $CH_3C(O)NHCH_2C(O)NHCH_3$, 346. The average of the last four values, 348 kJ mol^{-1}, is the predicted bond dissociation energy of the α-C—H bond of a glycyl protein. The reduction potential in aqueous medium at 298 K and pH 7 for the process, $R^\bullet + H^+ + e^- = RH$, where $R^\bullet$ = $XNHCH^\bullet C(O)Y$ and X and Y represent extension of the protein chain, is $E^{0\prime} = 0.8$ V. This result suggests that the α-C—H bond of a glycyl protein is susceptible to attack by RS•, ROO•, tyrosyl, and OH• radicals, whose reduction potentials for the analogous process are higher. The present study has established that the molecule $HC(O)NHCHRC(O)NH_2$ (R = an amino acid side chain) serves as an accurate model for the α-C environment of an amino acid residue in a protein, and that a reliable $D_{C—H}$ value for the α-C—H bond may be obtained from calculations on this model at the B3LYP/6-31G(D) level of theory in conjunction with an isodesmic reaction using neutral glycine as reference.

Key words: glycine, peptide, amino acid, bond energy, radicals, ab initio, computation.

Résumé : On a dérivé les énergies de dissociation de liaisons C—H ($D_{C—H}$) d'une série de protéines glycyles modèles à partir de réactions isodesmiques choisies et reposant sur des calculs ab initio à des niveaux élevés. À 298 K, les valeurs recommandées de $D_{C—H}$, en kJ mol^{-1}, sont : NH_2CH_2CHO, 308; $NH_2CH_2C(O)NH_2$, 336; $HC(O)NHCH_2CHO$, 331; $H(CO)NHCH_2C(O)NH_2$, 350; $CH_3C(O)NHCH_2C(O)NH_2$, 347; $HC(O)NHCH_2C(O)NHCH_3$, 349 et $CH_3C(O)NHCH_2C(O)NHCH_3$, 346. La moyenne des quatre dernières valeurs, 348 kcal kJ mol^{-1}, correspond à la valeur prédite pour l'énergie de dissociation de la liaison α-C—H d'une protéine glycyle. Le potentiel de réduction, en solution aqueuse, à 298 K, à un pH de 7, pour le processus, $R^\bullet + H^+ + e^- = RH$, dans laquelle $R^\bullet$ = $XNHCH^\bullet C(O)Y$ et X et Y correspondent à une extension de la chaîne de la protéine, est $E^{0\prime} = 0{,}8$ V. Ce résultat suggère que la liaison α-C—H d'une protéine glycyle est susceptible d'être attaquée par les radicaux RS•, ROO•, tyrosyles et OH• dont les potentiels de réduction, pour des processus analogues, sont élevés. La présente étude a permis d'établir que la molécule $HC(O)NHCHRC(O)NH_2$ (R = une chaîne latérale d'un acide aminé) est un excellent modèle pour l'environnement α-C d'un résidu d'acide aminé dans une protéine et que l'on peut arriver à une valeur fiable de $D_{C—H}$ pour une liaison α-C—H par des calculs sur ce modèle au niveau B3LYP/-31(D) de la théorie en relation avec une réaction isodesmique, en utilisant de la glycine neutre comme référence.

Mots clés : glycine, acide aminé, énergie de liaison, ab initio, calculs.

[Traduit par la rédaction]

Introduction

Oxidative damage to proteins has been implicated in physiological processes and pathological disorders, such as protein turnover, tissue injury during ischemia–reperfusion, atherosclerosis, and cataractgenesis (1). Oxidation of proteins in the presence of oxygen leads to the formation of alkyl peroxides and (or) hydrogen peroxide, and to peptide cleavage (1– 3). It is generally initiated by hydrogen atom abstraction of OH• radicals, which may be produced intra-cellularly by a Fenton-type reaction or by other radicals formed enzymatically (1, 4–7). Ultraviolet and ionizing radiation may also produce oxidizing radicals (8).

The site at which H-abstraction occurs depends to some extent on the structure and conformation of the protein (1, 8). However, the α-carbon center of exposed amino acid residues is known to be a preferred site of attack (1, 3, 9). Its susceptibility to oxidation has been emphasized in recent experiments with the peptide glutathione (GSH), which show that in basic solutions an H atom can be transferred intramolec-

Received January 23, 1996.

This paper is dedicated to Professor Richard F.W. Bader on the occasion of his 65th birthday.

D.A. Armstrong,[1] D. Yu, and A. Rauk.[1] Department of Chemistry, The University of Calgary, Calgary, AB T2N 1N4, Canada.

[1] Author to whom correspondence may be addressed. Telephone: (403) 220-7207 or 6247. Fax: (403) 220-9488. E-mail: armstron@acs.ucalgary.ca or rauk@acs.ucalgary.ca.

ularly from an α-carbon center to the S-centered GS• radical (10). Because S—H bonds are usually more labile than C—H bonds and hydrogen transfer normally goes from S—H to carbon-centered radicals (8, 11), viz:

[1] $P^{\bullet} + GSH = PH + GS^{\bullet}$

GSH has traditionally been considered to be a protector. The observation of equilibrium lying in the opposite direction means that the dissociation energy of one (or more) of the C—H bonds in GSH is a few kJ mol^{-1} below that of the S—H bond. Dissociation energies of S—H bonds attached to aliphatic structures do not vary widely (12), and that of GSH must be close to 368 kJ mol^{-1}. This places the energy of the above C—H bond below 368 kJ mol^{-1}, somewhat lower than that expected for a secondary or tertiary C—H of a hydrocarbon (~397, ~389 kJ mol^{-1}, respectively, ref. 13). Intramolecular H transfer from α-C—H groups to sulfur has now also been reported in homocysteine and cysteine (14) and 2-mercaptoethanol (15). Also Zhao et al. have shown (14) that S-centered radicals are able to abstract α-C—H hydrogen atoms from the anions of glycine and alanine, and have estimated a value of 356 kJ mol^{-1} for the tertiary α-C—H bond dissociation energy of $H_2NC(CH_3)HCO_2^-$.

The above experimental results all confirm that the X-NH-C(R)H-C(O)-Y structure must contribute to a significant weakening of the α-C—H bond. The presence of the electron-donating -NH group on one side and the electron-withdrawing -CO group on the other identifies the X-NH-C(R)•-C(O)-Y radical as one that will be subject to stabilization by the captodative effect (16–19). However, the relative magnitude of the effect for specific X and Y groups, where the groups represent the extension of the protein backbone, needs to be determined. The object of this paper is to use modern ab initio methods to determine the α-C—H bond dissociation energy for the glycyl residue in a nonterminal (~mid-chain) position of a protein, and also to determine which X and Y groups satisfactorily represent the continuing peptide chain. This will enhance our understanding of the relative susceptibility of the peptide backbone to H-abstraction and oxidative damage, and at the same time provide a practical model for such studies on other amino acid residues.

Calculations carried out with the Gaussian 92 molecular orbital package (20) yield reliable structural information. They can also be used to provide thermochemical data for both closed- and open-shell species. When absolute G2(MP2) energies are used in isodesmic reactions in conjunction with reliable (preferably but not necessarily experimentally determined) heats of formation for related systems, they can be expected to provide thermochemical data that are reliable to within ± 10 kJ mol^{-1} (21). Previously these methods were used by us in detailed investigations of the structure and thermochemistry of glycine (22) and of its ionic and free radical forms in the gas phase (23) and in solution (24). Earlier predictions (16) of the stabilizing effect of the $-NH_2$ and -C(O)OH groups on the α-C—H bond dissociation energy were confirmed (23) and the stabilization was shown to be diminished in the $H_2NCH^{\bullet}CO_2^-$ radical anion. This investigation represents an extension to the more complex glycine polypeptide.

The basis sets required in the ab initio calculations in order to achieve the desired level of accuracy must be 6-31G(D)

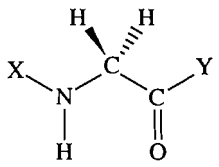

or better. Hence there are limitations to the size of peptide for which calculations at the desired level (G2(MP2)) can be performed, and it was necessary to define the minimum sizes of the X and Y subsections of the polymeric backbone on either side of the $-NH-CH_2-C(O)-$ residue, for which the chemistry at the α-carbon atom would be representative of its actual behavior at a mid-chain point in a large protein. This was a second objective of the present study. At the same time, we decided to determine whether a computationally more economical reduced level procedure that would give the same reliability in isodesmic reaction calculations as the G2(MP2) level could be devised. This became the third objective.

Computational details

All ab initio calculations presented here were performed with the Gaussian 92 molecular orbital packages (20). The geometry optimizations were carried out at the HF/6-31G(D), MP2/6-31G(D), and B3LYP/6-31G(D) (a hybrid HF-DFT procedure) levels as implemented in the Gaussian 92/DFT molecular orbital packages. Vibrational frequencies were calculated at the HF/6-31G(D) level for all the species under study. For systems containing up to six heavy atoms, the correlation corrections were estimated at the G2(MP2) level. The G2(MP2) procedure (25) includes: a geometry optimization with the standard Hartree–Fock method and the 6-31G(D) split-valence basis set (HF/6-31G(D)); a vibrational frequency calculation at the HF optimized geometry; MP2/6-31G(D) geometry optimization; two single-point post-HF calculations, i.e., QCISD(T)/6-311G(D,F) and MP2/6- 311+G(3DF,2P), on the MP2 optimized geometry in order to obtain an accurate estimate of the correlation energy. The vibrational frequencies calculated at the HF/6-31G(D) level were scaled by a factor of 0.89 in considering the zero-point energy.

As a means of reducing residual errors due to basis set and correlation effects, the bond dissociation energies were derived from the heats of isodesmic reactions (26). In the context of bond dissociation energies (BDEs), these reactions can be represented by process [2]:

[2] $P^{\bullet} + HA \rightarrow HP + A^{\bullet}$

in which HP is the species for which the BDE, $D_{C-H}(HP)$, is desired, and HA is a reference molecule for which the BDE, $D_{C-H}(HA)$, is known accurately. For each HP and HA the heat of reaction, $\Delta H_R(2)$, was evaluated from ab initio calculations. $D_{C-H}(HP)$ is then given by:

[3] $D_{C-H}(HP) = D_{C-H}(HA) - \Delta H_R(2)$

The highest accuracy would be achieved if A and P are as similar as possible and the theoretical method is as high as possible. The former point suggests that A also should incorporate captodative effects since these were previously

Fig. 1. Definition of **GLY** and relations between structures under study. $D_{C—H}$ reported in kJ mol^{-1} from isodesmic reactions at the B3LYP/6-31G(D)//B3LYP/6-31G(D) and the G2(MP2) (in parentheses) levels.

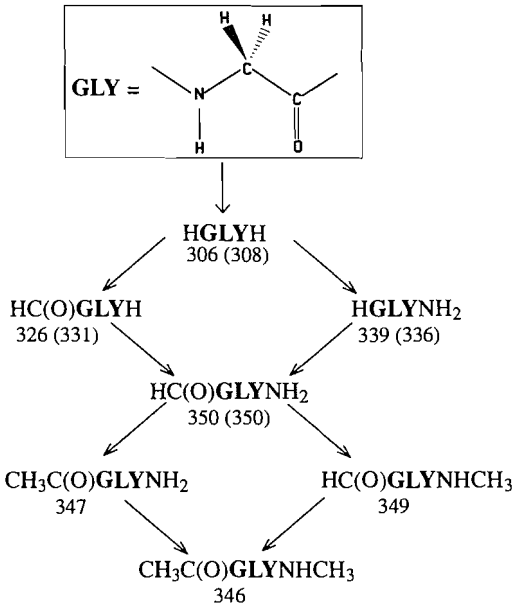

found to incur higher than average errors in calculated heats of formation (23). The latter point suggests that the G2(MP2) procedure (25) should be used.

The limits of application of G2(MP2) are restricted by the requirement of carrying out a QCISD(T) calculation with a large basis set, 6-311G(D,P), the most time-consuming step. Because the G2(MP2) procedure could not be applied to a key compound in the present study, a "reduced" G2(MP2) procedure, G2(MP2)′, was devised and tested. In this, the QCISD(T) and corresponding MP2 calculations were carried out with the smaller 6-31G(D,P) basis set rather than the 6-311G(D,P) basis set of the standard G2(MP2) method (25). The vibrational frequencies and other parameters were treated in the same way as in the standard G2(MP2) method. The reliability of G2(MP2)′ and of calculations at lower levels (MP2 and B3LYP) with respect to the calculation of C—H bond dissociation energies was evaluated by comparisons with G2(MP2) level results for smaller systems.

To obtain $\Delta H_R(2)$ values at 298 K, $H^0_{298}-H^0_0$ were required. These quantities, as well as the entropies needed in the evaluation of reduction potentials, were calculated by standard statistical thermodynamic methods based on the rigid rotor – harmonic oscillator model (27) and using the frequencies obtained at HF/6-31G(D) level. These frequencies are scaled by a factor of 0.89 in the calculation of these thermodynamic functions.

Results and discussion

Structures

The species for which the optimized structures of the peptide and its α-C-centered radical have been calculated are presented in Fig. 1 and Table 1. For simplicity the common fragments, -NH-CH_2-C(O)- and -NH-C$^{\bullet}$H-C(O)- of the parent and radical are denoted as **GLY** and **GLY$^{\bullet}$**, respectively,

Table 1. Vibrational (kJ mol^{-1}) and electronic (hartree) energies.

Species		ZPE HF/6-31G(D)	MP2/6-31G(D)//MP2/6-31G(D)	B3LYP/6-31G(D)//B3LYP/6-31G(D)	G2(MP2)′[a]	G2(MP2)
HGLYH	NH_2CH_2CHO	209.9	−208.529 05	−209.171 94	−208.832 19	−208.835 29
HGLY′H	$NH_2C^{\bullet}HCHO$	172.8	−207.903 74	−208.548 88	−208.212 45	−208.214 87
HGLYNH$_2$	$NH_2CH_2C(O)NH_2$	259.1	−263.751 85	−264.554 63	−264.134 42	−264.137 84
HGLY′NH$_2$	$NH_2C^{\bullet}HC(O)NH_2$	222.4	−263.122 54	−263.919 33	−263.503 81	−263.506 80
HC(O)GLYH	$HC(O)NHCH_2CHO$	239.3	−321.576 76	−322.517 54	−322.024 14	−322.028 35
HC(O)GLY′H	$HC(O)NHC^{\bullet}HCHO$	202.9	−320.942 36	−321.887 40	−321.395 67	−321.399 34
HC(O)GLYNH$_2$	$HC(O)NHCH_2C(O)NH_2$	288.3	−376.800 35	−377.901 45	−377.327 60	
HC(O)GLY′NH$_2$	$HC(O)NHC^{\bullet}HC(O)NH_2$	251.7	−376.166 27	−377.262 02	−376.691 60	
$CH_3C(O)$GLYNH$_2$	$CH_3C(O)NHCH_2C(O)NH_2$	365.5	−415.975 35	−417.224 97		
$CH_3C(O)$GLY′NH$_2$	$CH_3C(O)NHC^{\bullet}HC(O)NH_2$	328.8	−415.342 50	−416.586 45		
HC(O)GLYNHCH$_3$	$HC(O)NHCH_2C(O)NHCH_3$	368.6	−415.961 08	−417.212 70		
HC(O)GLY′NHCH$_3$	$HC(O)NHC^{\bullet}HC(O)NHCH_3$	331.3	−415.327 10	−416.573 18		
$CH_3C(O)$GLYNHCH$_3$	$CH_3C(O)NHCH_2C(O)NHCH_3$	445.8	−455.135 98	−456.536 16		
$CH_3C(O)$GLY′NHCH$_3$	$CH_3C(O)NHC^{\bullet}HC(O)NHCH_3$	408.2	−454.503 21	−455.897 48		

[a]6-31G(D,P) basis set was used in place of 6-311G(D,P) for QCISD(T) and corresponding MP2 calculations in the standard G2(MP2) procedure, see text.

GLY = —N(H)—C(H)(H)—C(=O)— GLY′ = —N(H)—C$^{\bullet}$(H)—C(=O)—

Fig. 2. B3LYP/6-31G(D) optimized structures for $NH_2CH_2C(O)NHCH_3$ and $NH_2C{\cdot}HC(O)NHCH_3$. The filled circles stand for nitrogen, open ones for carbon, and the shielded ones for oxygen atoms, respectively. The small circles represent the hydrogen atoms. The central units of the glycyl residue and its α-C-centered radical are defined by the broken lines. Bond lengths are in angstroms and angles in degrees.

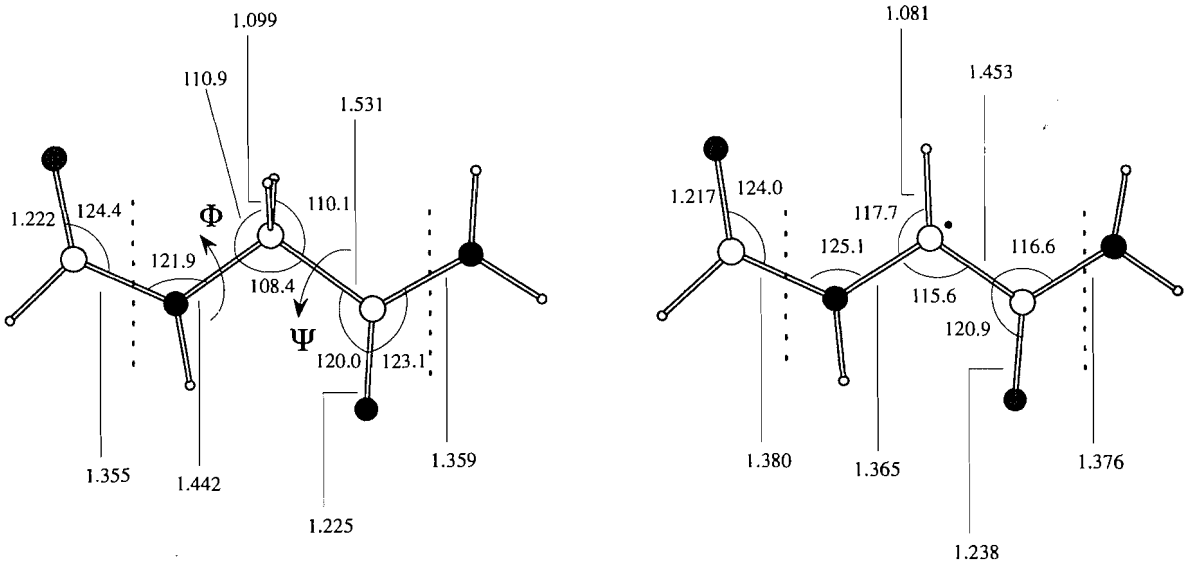

Table 2. S^0_{298} (J K^{-1} mol^{-1}) and $H^0_{298} - H^0_0$ (kJ mol^{-1}).

	S^0_{298}	$H^0_{298} - H^0_0$		S^0_{298}	$H^0_{298} - H^0_0$
HGLYH	291.2	15.4	**HGLY**·H	287.4	14.6
HGLYNH_2	331.7	19.6	**HGLY**·NH_2	317.7	18.3
HC(O)**GLY**H	337.7	19.7	HC(O)**GLY**·H	331.4	18.6
HC(O)**GLY**NH_2	374.5	23.8	HC(O**GLY**·NH_2	364.5	22.8
$CH_3C(O)$**GLY**NH_2	429.1	28.7	$CH_3C(O)$**GLY**·NH_2	412.8	27.6
HC(O)**GLY**$NHCH_3$	416.5	27.9	HC(O)**GLY**·$NHCH_3$	405.8	27.3
$CH_3C(O)$**GLY**$NHCH_3$	468.4	32.7	$CH_3C(O)$**GLY**·$NHCH_3$	455.3	32.2

while the formulae of the increasingly complex X and Y end groups are given explicitly.

The optimized geometric parameters of each species obtained with 6-31G(D) basis sets at the HF, MP2, and B3LYP levels were all similar, indicating that the geometric parameters were not sensitive to the correlation levels. Also the structures of the different species resembled each other in the region of the α-C center. Those of $HC(O)NHCH_2C(O)NH_2$ (HC(O)**GLY**NH_2) and HC(O)NHC·HC(O)NH_2 (HC(O)-**GLY**·NH_2) are presented in Fig. 2 as examples, with the **GLY** and **GLY**· sections defined by broken lines. For all the species, the optimized Ramachandran angles (Φ and Ψ of Fig. 2) have values near 180°. Thus the optimized structures in many cases have C_s symmetry or C_1 symmetry with minor deviation from C_s.

Energies

The vibrational ZPEs evaluated at the HF/6-31G(D) level and the total energies calculated at the B3LYP/6-31G(D) and MP2/6-31G(D) levels are listed in Table 1. For the small systems, **HGLY**H, **HGLY**NH_2, HC(O)**GLY**H, and HC(O)**GLY**NH_2 and their radicals, the energies at the G2(MP2)′ and G2(MP2) levels are also reported.

$H^0_{298} - H^0_0$ and S^0_{298}

The calculated values of $H^0_{298} - H^0_{298}$ are given in Table 2. It may be noted that $H^0_{298} - H^0_0$ for the parent and radical species are usually similar, which means that in most cases the $H^0_{298} - H^0_0$ corrections to $\Delta H_R(2)$ are less than 1 kJ mol^{-1}.

C—H bond dissociation energies (BDEs)

As asserted above, to obtain the most accurate values of the BDEs, the reference molecules used in the isodesmic reaction [2] should be as closely related as possible to the glycyl protein fragments under investigation. Ideally they should have both an adjacent amino group and a carbonyl group so that the special feature of the donor–accepter stabilization can be taken into account. The five reference molecules (HA) adopted for use in reaction [2] and their α-C—H bond dissociation energies (in kJ mol^{-1}), were $CH_3CH_2NH_2$ (374.5), $CH_3C(O)OH$ (407.0), $CH_3C(O)CH_3$ (395.0), $NH_2CH_2C(O)O^-$ (363.0), and $NH_2CH_2C(O)OH$ (331.0). Although none of them has a full -C(O)-NH-CH_2-C(O)-NH-structure, three of the reference molecules manifest at least one of the required aspects, either -$NHCH_2$- ($CH_3CH_2NH_2$), or -$CH_2C(O)$- ($CH_3C(O)CH_3$ and $CH_3C(O)OH$). The value for the BDE of $CH_3CH_2NH_2$ is

Table 3. D_{C-H}(HX) at 298 K in kJ mol^{-1} from isodesmic reactions P$^{\cdot}$ + HA → HP + A$^{\cdot}$.

HP	HA[a]	B3LYP/6-31G(D)//B3LYP/6-31G(D)	MP2/6-31G(D)//MP2/6-31G(D)	G2(MP2)′[b]	G2(MP2)
HGLYH	$NH_2CH_2CH_3$	296.2	328.7	304.7	306.3
	$CH_3C(O)OH$	299.6	326.5	310.0	311.2
	$CH_3C(O)CH_3$	298.3	306.2	305.7	306.4
	$NH_2CH_2C(O)O^-$	297.4	325.1	306.2	307.5
	$NH_2CH_2C(O)OH$	**306.2**	325.7	308.0	308.7
	Average			**306.9**	**308.0**
HGLYNH$_2$	$NH_2CH_2CH_3$	329.2	340.0	333.8	334.7
	$CH_3C(O)OH$	332.5	337.8	339.0	339.6
	$CH_3C(O)CH_3$	331.3	317.5	334.8	334.8
	$NH_2CH_2C(O)O^-$	330.4	336.4	335.3	335.9
	$NH_2CH_2C(O)OH$	**339.2**	337.1	337.0	337.1
	Average			**336.0**	**336.4**
HC(O)**GLYH**	$NH_2CH_2CH_3$	315.7	353.4	328.0	329.1
	$CH_3C(O)OH$	319.1	351.3	333.2	334.1
	$CH_3C(O)CH_3$	317.8	331.0	329.0	329.2
	$NH_2CH_2C(O)O^-$	316.9	349.9	329.5	330.3
	$NH_2CH_2C(O)OH$	**325.7**	350.5	331.2	331.5
	Average			**330.2**	**330.8**
HC(O)**GLYNH$_2$**	$NH_2CH_2CH_3$	339.8	352.3	347.6	
	$CH_3C(O)OH$	343.2	350.1	352.9	
	$CH_3C(O)CH_3$	341.9	329.8	348.6	
	$NH_2CH_2C(O)O^-$	341.0	348.8	349.1	
	$NH_2CH_2C(O)OH$	**349.8**	349.4	350.9	
	Average			**349.8**	

[a] D_{C-H}(HA) at 298 K are 374.5, 407.0, 395.0, 331.0, and 363.0 kJ mol^{-1} for $NH_2CH_2CH_3$, CH_3COOH, CH_3COCH_3, NH_2CH_2COOH, and $NH_2CH_2COO^-$, respectively. See text.

[b] The 6-31G(D,P) basis set was used in place of 6-311G(D,P) for QCISD(T) and corresponding MP2 calculations in the standard G2(MP2) procedure, see text.

based on $\Delta_f H^0_{298}$ for the parent and radical from Lias et al. (28). For CH_3COCH_3, $\Delta_f H^0_{298}$ of the parent (−217.6) was from Lias et al. (28) while the value for the radical (−41.0) was from Orlov et al. (29). The BDE of $CH_3C(O)OH$ is from a critical examination of experimental and theoretical results by Yu et al. (21, 23). The BDE of the glycyl species, $H_2NCH_2C(O)O^-$ and $H_2NCH_2C(O)OH$, which also exhibit the captodative stabilization, are not directly available from experiment, and were derived from G2(MP2) calculations in combination with isodesmic reactions in which two of the present species, $CH_3C(O)OH$ and $CH_3CH_2NH_2$, as well as CH_4 and CH_3NH_2, were used as references (23).

During the course of the investigation it became clear that a very accurate value for the BDE of $HCONHCH_2CONH_2$ (HCO**GLYNH$_2$**) was required, and that the large size prohibited application of the G2(MP2) procedure. For this reason, the G2(MP2)′ procedure was devised (see above). As a method of testing the G2(MP2)′ procedure for the calculation of BDEs, the values of D_{C-H} for $H_2NCH_2C(O)OH$ and $H_2NCH_2C(O)O^-$ were reexamined by the isodesmic reaction method with $CH_3CH_2NH_2$, $CH_3C(O)CH_3$, and $CH_3C(O)OH$ as reference species. The average values with the G2(MP2)′ procedure were the same as previously reported by Yu et al. (23), namely, 331 and 363 kJ mol^{-1} for $H_2NCH_2C(O)OH$ and $H_2NCH_2C(O)O^-$, respectively, using G2(MP2). The maximum difference between the G2(MP2)′ and G2(MP2) results for any one reference was 1 kJ mol^{-1}. The standard deviations of the values for both $H_2NCH_2C(O)OH$ and $H_2NCH_2C(O)O^-$ with the three references were 2.8 kJ for G2(MP2)′, versus 2.7 kJ mol^{-1} for G2(MP2). These results demonstrate that the G2(MP2)′ procedure has basically the same accuracy as G2(MP2) when used in isodesmic reactions, and reconfirm the reliability of the D_{C-H} values for $H_2NCH_2C(O)OH$ and $H_2NCH_2C(O)O^-$.

HGLYH, HGLYNH$_2$, HCOGLYH, and HCOGLYNH$_2$

These four species represent the first steps toward glycyl protein modelling, and the practical limit for which the most accurate theoretical levels are applicable. The values of D_{C-H} from the isodesmic reactions and ab initio energies calculated at different levels are reported in Table 3. For **HGLYH**, **HGLYNH$_2$**, and HC(O)**GLYH** the G2(MP2) and G2)MP2)′ level results with the five isodesmic reactions in columns 5 and 6 all fall in the narrow range of 5.3 kJ mol^{-1}. The maximum difference between the G2(MP2)′ and G2(MP2) values is less than 2 kJ mol^{-1}. For HC(O)**GLYNH$_2$**, where the highest level of calculation was G2(MP2)′, the range is the same, from 347.6 to 352.9 kJ mol^{-1}. These narrow ranges indicate that at these levels the cancellation of residual errors for all of the standards in the isodesmic reactions was very effective. Therefore, the average value over the isodesmic reactions of the G2(MP2) or G2(MP2)′ results, shown in

Table 4. D_{C-H}(HP) at 298 K in kJ mol^{-1} from isodesmic reactions P$^{\cdot}$ + $NH_2CH_2C(O)OH \rightarrow$ HP + $NH_2CHC(O)OH^{\cdot}$.

HP	B3LYP/6-31G(D)//B3LYP/6-31G(D)	MP2/6-31G(D)//MP2/6-31G(D)
HC(O)**GLY**NH_2	349.8	349.8
$CH_3C(O)$**GLY**NH_2	347.4	346.2
HC(O)**GLY**$NHCH_3$	349.0	348.1
$CH_3C(O)$**GLY**$NHCH_3$	346.4	344.6

bold face in Table 3, may be taken as the "standard" against which the level of accuracy of other calculation methods (i.e., B3LYP and MP2) can be examined.

One can anticipate that the more closely bond types are conserved between P$^{\cdot}$ and HA, and HP and A$^{\cdot}$ in reaction [2], the more complete would be the cancellation of residual errors. Breakdown in this process can be expected to show up more strongly as the level of calculation falls, and the results in Table 3 show that this happens at the B3LYP and MP2 levels. The D_{C-H} values for the four model peptide species obtained at the B3LYP/6-31G(D) level have a maximum deviation of 11.8 kJ mol^{-1} and an average of 7.7 kJ mol^{-1}. The corresponding values at the MP2/6-31G(D) level are 16.4 and 9.3 kJ mol^{-1}, respectively. There is therefore some preference for the B3LYP/6-31G(D) level calculations as they are less scattered. At the same time, the D_{C-H}(HP) values derived at the B3LYP/6-31G(D) level with $NH_2CH_2C(O)OH$ as the reference molecule show the least deviation compared with the averaged G2(MP2) results: the maximum difference between B3LYP and G2(MP2)(′) for the four systems is 5.1 kJ mol^{-1} and the average deviation is 2.4 kJ mol^{-1}. Thus, the B3LYP/6-31G(D) level calculations with $NH_2CH_2C(O)OH$ as standard in the isodesmic reaction seem best able to reproduce the correct D_{C-H} values (assumed to be the same as derived with the G2(MP2) and G2(MP2)′ procedures).

It may be noted that in the course of the present study, results from other levels including B3LYP/6-311G(D,P), MP2/6-311G(D,P), MP2/6-311+G(3DF,2P), QCISD(T)/6-31G(D,P), and QCISD(T)/6-311G(D,P), as single calculations at the B3LYP/6-31G(D) or MP2/6-31G(D) optimized geometries, were also examined in detail. In general, using basis sets larger than 6-31G(D) with B3LYP or MP2 methods did not improve the results. Only at the QCISD(T) level did D_{C-H} parallel the G2(MP2) values for all reference isodesmic systems. Thus for larger systems where the QCISD(T) and G2(MP2) calculations are not practical and lower theoretical levels must be used, the most accurate D_{C-H}(HP) values can be derived with the combination of B3LYP/6-31G(D) theoretical level and $NH_2CH_2C(O)OH$ as isodesmic reference. D_{C-H} values thus derived should fall within 10 kJ mol^{-1} of the correct values.

C—H bond dissociation energies of $CH_3C(O)$GLYNH_2, HC(O)GLY$NHCH_3$, and $CH_3C(O)$GLY$NHCH_3$

These three systems represent extension of the protein chain from HC(O)**GLY**NH_2 to include the next α-C in one or both directions (as modelled by a methyl group). Table 4 collects the central C—H bond dissociation energies for HC(O)**GLY**NH_2 as well as $CH_3C(O)$**GLY**NH_2, HC(O)-$NHCH_3$, and $CH_3C(O)$**GLY**$NHCH_3$, derived at the B3LYP/6-31G(D) level with the glycine molecule ($NH_2CH_2C(O)OH$) as the reference. For these four species, the D_{C-H} values at the MP2/6-31G(D) level are consistent with those of B3LYP/6-31G(D), as was also true for H**GLY**NH_2, but not for H**GLY**H and HC(O)**GLY**H (Table 3). The values of D_{C-H} and the implication of these results for choice of protein model are discussed below.

Effects of X and Y Groups on D_{C-H}

As stated in the Introduction, the bond dissociation energy of a secondary C—H bond in an unsubstituted hydrocarbon is ~397 kJ mol^{-1}. The value of 308 kJ mol^{-1} for D_{C-H} for H**GLY**H (Fig. 1) demonstrates the occurrence of a very strong captodative stabilization (~90 kJ mol^{-1}) for the C-centered radical when the electron-donating group is -NH_2 and the electron-withdrawing group is -C(O)H.

It is convenient to use the H**GLY**H structure as a reference point in discussing the systems studied here. Clearly, altering X by adding the electron-withdrawing C—O group will reduce the electron-donating ability of the -NH- group. Indeed, D_{C-H} increases by 20 kJ mol^{-1} when X = H is replaced by X = HC(O) (Fig. 1). Likewise, changing the group attached to the carbonyl from Y = H to Y = NH_2, the better electron donor group, is expected to diminish the electron-withdrawing power of the -C—O- group and raise the BDE. In accord with expectations, D_{C-H} increases by 33 kJ mol^{-1} when Y = H is replaced by Y = NH_2 (Fig. 1). Replacing both groups causes D_{C-H} to increase by 44 kJ mol^{-1}. Since D_{C-H} is the same for HC(O)**GLY**NH_2 and HC(O)**GLY**$NHCH_3$, changing the -NH_2 to -$NHCH_3$ in the Y end group has no further effect. Similarly, altering the electron-withdrawing group on the amino end from X = HC(O)- to X = $CH_3C(O)$-, or making both replacements simultaneously, also has only a small effect. The last results suggest that addition of the methyl groups, which model the α-C of the next amino acid residue in each direction, is not necessary. It is anticipated therefore that the same "chain extending" groups, X = HC(O) and Y = NH_2, would serve to model the α-C environment of all of the other amino acid residues as well.

The value of D_{C-H} for nonterminal glycyl in a long-chain peptide

A primary objective is to obtain a value for D_{C-H} at a nonterminal or mid-chain position in a glycyl peptide. Based on the BDE values given in Fig. 1, it is evident that further extensions of the X and Y groups beyond X = $CH_3C(O)$ and Y = $NHCH_3$ will have minimal, if not negligible, effects. Therefore, the best estimate is D_{C-H} = 348 kJ mol^{-1}, taken as the average of the D_{C-H} values of the four species in Table

4. The uncertainty in this result should not exceed ±10 kJ mol^{-1}. This indicates a stabilization of ~50 kJ mol^{-1} for the glycyl α-C-centered radical. For the reasons discussed above, this is smaller than for free neutral glycine, $H_2NCH_2C(O)OH$ (~66 kJ mol^{-1}), but it is still substantial. It means, for example, that the α-C position will be vulnerable to H atom abstraction by RS•, RO•, and some phenoxyl and peroxyl radicals, for which the parent compounds have bond dissociation energies in excess of 350 kJ mol^{-1} (12, 13). The feasibility of those processes is best examined in terms of the reduction potential, which is estimated below.

Relevance to proteins

The present theoretical procedure predicts the C—H bond dissociation energy of a model protein fragment containing glycine in the gas phase from the difference between the energies of the parent fragment and the corresponding α-C-centred radical, both in their fully relaxed geometries. The effect of an aqueous environment is estimated in the next section. The relaxed geometry of both the radical and neutral glycine-based model correspond to Ramachandran angles (Φ and Ψ of Fig. 2) equal to 180° (planar geometry). The radicals of other amino acids should also have planar geometries, although this will not be true of the neutral species because of the chirality at the α-C centre. In a real protein, the backbone chain may be rigidly anchored by hydrogen bonds that form the secondary and tertiary structure, with Φ and Ψ far from 180°, particularly in the case of α-helical segments (average values, $\Phi = -60°$ and $\Psi = -45°$). A recent survey of 78 protein structures (30) from the Brookhaven Protein Structure Databank (BPSD) (31) revealed many instances of amino acids whose Φ, Ψ values were within 30° of 180°, a region of conformational space close to the β-sheet structure (average values, $\Phi = -150°$ and $\Psi = +150°$). Values close to 180° correspond approximately to minima on the radical potential energy surface but may be far from minima of the undamaged amino acid residue. α-C—H bonds at such sites will be especially weak and susceptible to damage by free radicals generated internally in mitochondria or through the action of external sources of radiation. We have examined 10 proteins from BPSD with different proportions of α-helical and β-sheet structure for instances of glycine with dihedral angles near 180°. These are very common in proteins high in β-sheet content, especially in silk fibroins that also have a high proportion of glycine (and alanine) (32). Indeed, 30% of the glycine (and also of the alanine) residues of one of the theoretical models of silk fibroin of Scheraga and coworkers (33) are within 30° of the locally planar geometry. Since near-planar geometries do not occur in α- helical segments, one may infer that these are less susceptible to oxidative damage than β-sheets. We are examining the effect of angular constraints on α-C—H bond strengths as a function of Φ and Ψ.

The reduction potential of a nonterminal α-C-centered radical in a long-chain peptide

The standard free energy change at 298 K, ΔG^0_{298}, of the reaction:

[4] $XNHCH^{\bullet}C(O)Y_{(g)} + \frac{1}{2}H_{2(g)} = XNHCH_2C(O)Y_{(g)}$

can be estimated from the above values of $D_{C—H}$ together with ΔS^0_{298} (Table 2). ΔG^0_{298} is given by expression [5],

[5] $\Delta G^0_{298} = -D_{C—H} - T\Delta S^0_{298} + \Delta_f H^0_{298}(H^{\bullet}_{(g)})$

The difference in entropy of $XNHCH_2C(O)Y$ and $XNHCH^{\bullet}C(O)Y$ was also estimated from those of $HC(O)\mathbf{GLY}NH_2$, $CH_3C(O)\mathbf{GLY}NHCH_3$, and their radicals (Table 2). $\Delta_f H^0_{298}(H^{\bullet}_{(g)})$ has a value of 218 kJ mol^{-1} (34) and the other correction term $(-T\Delta S^0_{298})$ in eq. [4] amounts to 16.5 and 15.5 kJ mol^{-1}, respectively, for $HC(O)\mathbf{GLY}NH_2$ and $CH_3C(O)\mathbf{GLY}NHCH_3$. The difference between the values for the two peptides is negligible. Using a net correction of 234 kJ mol^{-1}, ΔG^0_{298} for reaction [4] is found to be −114 kJ mol^{-1}.

The free energies of solution of the $XNHCH^{\bullet}C(O)Y$ radical and its $XNHCH_2C(O)Y$ parent are unlikely to differ by more than a few kJ mol^{-1}, so that ΔG^0_{298} for reaction [6]

[6] $XNHCH^{\bullet}C(O)Y_{(aq)} + \frac{1}{2}H_{2(g)} = XNHCH_2C(O)Y_{(aq)}$

can also be estimated to be −114 kJ mol^{-1}. ΔE^0 for this reaction, 1.2 V, is obtained from $-\Delta G^0_{298}/F$, where F is the Faraday constant, and has an uncertainty of less than ±0.2 V. This is also E^0 for the half reaction [7]:

[7] $XNHCH^{\bullet}C(O)Y_{(aq)} + H^+_{(aq)} + e^- = XNHCH_2C(O)Y_{(aq)}$

which was our objective.

Correcting to the pH of 7 gives $E^{0'} = 0.8$ V for reaction [7]. For comparison, RS•, ROO•, and tyrosyl radicals have $E^{0'}$ values in reaction [8]

[8] $R^{\bullet}_{(aq)} + H^+_{(aq)} + e^- = RH_{(aq)}$

of 0.92 V (35, 36), 1.06 V (37), and 0.97 V (38), respectively. Those $E^{0'}$ values indicate that these other radicals, as well as $OH^{\bullet}$ ($E^{0'}(OH^{\bullet}, H^+/H_2O) = 2.3$ V, ref. 39), are potentially able to abstract H atoms from the glycyl α-CH_2 group. Since these radicals are less reactive than OH• due to the smaller driving force, their effects will be more apparent in biological systems, where the radical concentrations are usually lower than in chemical experiments and time scales for reactions are long.

Finally it may be noted that the α-CH group of an N-terminal amino acid is strongly protected by protonation, since this totally destroys the electron-donating ability of the amino group and eliminates the possibility of captodative stabilization of the C-centered radical. As an example, from the results of Armstrong et al. (24) $E^{0'}$ is expected to rise from 0.8 V for reaction [9]

[9] $H_2NCH^{\bullet}CO_2^-{}_{(aq)} + H^+_{(aq)} + e^- = H_2NCH_2CO_2^-{}_{(aq)}$

to 1.5 V on protonation of the amino group (see reaction [10]);

[10] $H_3N^+CH^{\bullet}CO_2^-{}_{(aq)} + H^+_{(aq)} + e^- = H_3N^+CH_2CO_2^-{}_{(aq)}$

This effect of protonation is undoubtedly the reason why H atom transfers from α-CH groups in $H_2NCH_2C(O)$- structures to S-centered radicals only occur at high pH, where the amino groups are deprotonated (10, 14).

Summary

At the present time there are no experimental bond dissociation energies specifically for peptide α-C—H bonds, which could be used in isodesmic reaction [2] to determine $D_{C—H}$ values in proteins. Until they become available, the best approach is therefore to use the glycine molecule, $H_2NCH_2C(O)OH$, which has itself been studied by the isodesmic reaction method. Based on a number of isodesmic reactions involving different experimental data (16, 23) the value of $D_{C—H}$ for glycine is 331 kJ mol^{-1} at 298 K with a standard deviation of 3.5 kJ mol^{-1}. In the present work we have established, by use of high-level theoretical procedures, isodesmic reactions, and convergent molecular modelling, that $D_{C—H}$ for the mid-chain region of a glycyl protein is 348 kJ mol^{-1} at 298 K. The low value of $D_{C—H}$ means that the α-C position will be vulnerable to H atom abstraction by RS$^{\bullet}$, RO$^{\bullet}$, and some phenoxyl and peroxyl radicals, for which the parent compounds have bond dissociation energies in excess of 350 kJ mol^{-1}. This result is also expected in aqueous solution, since the best estimate of E^0 at neutral pH for the bond-forming reaction [7] gives $E^0 = 0.8$ V, which is lower than experimentally determined E^0 values for RS$^{\bullet}$, ROO$^{\bullet}$, tyrosyl, and OH$^{\bullet}$ radicals.

The present work has established that the minimum suitable model for the local environment of the α-C region of an amino acid residue in a protein requires that the CO_2^- group be converted to $C(O)NH_2$ and the NH_2 group be converted to HCONH. In other words, the properties of the α-CH in the molecule, $HC(O)NHCHRC(O)NH_2$, where R is an amino acid side chain, effectively mirror the local properties of a protein.

The B3LYP/6-31G(D) procedure in combination with an isodesmic reaction with the glycine molecule can reliably predict the α-C—H bond dissociation energy of a protein-like molecule. As implemented in the Gaussian package of programs, it is feasible to apply this procedure to all of the other amino acid residues. This work is in progress.

Acknowledgement

The financial support of the Natural Sciences and Engineering Research Council of Canada is gratefully acknowledged.

References

1. E.R. Stadman. Annu. Rev. Biochem. **62**, 797 (1993).
2. R.T. Dean. *In* Oxidative damage and repair: chemical, biological and medical aspects. *Edited by* K.J.A. Davies. Pergamon Press, New York. 1991. pp. 341–347.
3. W.M. Garrison. Radiat. Res. Rev. **3**, 305 (1972).
4. H. Sies. *In* Oxygen stress. Academic Press, London. 1985.
5. M.G. Simic, K.A. Taylor, J.F. Ward, and C. von Sonntag. Oxygen radicals in biology and medicine. Plenum Press, New York. 1988.
6. H. Sies. *In* Oxidative stress — oxidants and anti-oxidants. Academic Press, London. 1991.
7. K.J.A. Davies. Oxidative damage and repair: chemical, biological and medical aspects. Pergamon Press, New York. 1991.
8. C. von Sonntag. The chemical basis of radiation biology. Taylor and Francis, London. 1987.
9. O.J. Mieden and C. von Sonntag. Z. Naturforsch. B: Chem. Sci. **44**, 959 (1989).
10. L. Grierson, K. Hildenbrand, and E. Bothe. Int. J. Radiat. Biol. **62**, 265 (1992).
11. P. Wardman. *In* Atmospheric oxidation and antoxidants. Vol. III. *Edited by* G. Scott. Elsevier, Amsterdam. 1993. pp. 101–127.
12. D. Griller, J.A.M. Simões, and D.D.M. Wayner. *In* Sulfur-centered reactive intermediates in chemistry and biology. *Edited by* C. Chatgilialoglu and K.-D. Asmus. NATO ASI Ser. Plenum Press, New York. 1990. pp. 37–52.
13. D.F. McMillen and D.M. Golden. Annu. Rev. Phys. Chem. **33**, 493 (1982).
14. R. Zhao, J. Lind, G. Merényi, and T. Eriksen. J. Am. Chem. Soc. **116**, 12010 (1994).
15. X. Zhang, N. Zhang, H.-P. Schuchmann, and C. von Sonntag. J. Phys. Chem. **98**, 6541 (1994).
16. G. Leroy, M. Sana, and C. Wilante. J. Mol. Struct. **228**, 37 (1991).
17. F.G. Bordwell, X.-M. Zhang, and M.S. Alnajjar. J. Am. Chem. Soc. **114**, 7623 (1992).
18. H.-G. Viehe, Z. Janousek, R. Merényi, and L. Stella. Acc. Chem. Res. **18**, 148 (1985).
19. R. Sustman and H.-G. Korth. Adv. Phys. Org. Chem. **26**, 131 (1990).
20. M.J. Frisch, G.W. Trucks, M. Head-Gordon, P.M.W. Gill, M.W. Wong, J.B. Foresman, B.G. Johnson, H.B. Schlegel, M.A. Robb, E.S. Replogle, R. Gomperts, J.L. Andres, K. Raghavachari, J.S. Binkley, C. Gonzalez, R.L. Martin, D.J. Fox, D.J. Defrees, J. Baker, J.J.P. Stewart, and J.A. Pople. Gaussian 92, Revision B. Gaussian, Inc., Pittsburgh, Pa. 1992.
21. D. Yu, A. Rauk, and D.A. Armstrong. J. Chem. Soc. Perkin Trans. 2, 2207 (1994).
22. D. Yu, D.A. Armstrong, and A. Rauk. Can. J. Chem. **70**, 1762 (1992).
23. D. Yu, A. Rauk, and D.A. Armstrong. J. Am. Chem. Soc. **117**, 1789 (1995).
24. D.A. Armstrong, A. Rauk, and D. Yu. J. Chem. Soc. Perkin Trans. 2, 553 (1995).
25. L.A. Curtiss, K. Raghavachari, and J.A. Pople. J. Chem. Phys. **98**, 1293 (1993).
26. W.J. Hehre, R. Ditchfield, L. Radom, and J.A. Pople. J. Am. Chem. Soc. **92**, 4796 (1970).
27. D.A. McQuarrie. Statistical thermodynamics. Harper & Row, New York. 1973.
28. S.G. Lias, J.E. Bartmess, J.F. Liebman, J.L. Holmes, R.D. Levin, and W.G. Mallard. J. Phys. Chem. Ref. Data, **17**, Suppl. No. 1 (1988).
29. V.M. Orlov, A.D. Misharev, V.V. Takhistov, and I.I. Ryabinkin. Izv. Akad. Nauk SSSR, Ser. Khim. **7**, 1514 (1988).
30. A. Perczel, M.A. McAllister, P. Császàr, and I.G. Csizmadia. Can. J. Chem. **72**, 2050 (1994).
31. F.C. Bernstein, T.F. Koetzle, G.J.B. Williams, E.F. Meyer, Jr., M.D. Brice, Jr., J.R. Rodgers, O. Kennard, T. Shimanouchi, and M. Tasumi. J. Mol. Biol. **112**, 535 (1977).
32. W. Traub. *In* Peptides, polypeptides and proteins. *Edited by* E.R. Blout, F.A. Bovey, M. Goodman, and N. Lotan. John Wiley and Sons, New York. 1974. p. 146.
33. S.A. Fossey, G. Nemethy, K.D. Gibson, and H.A. Scheraga. Biopolymers, **31**, 1529 (1991).
34. D.D. Wagman, W.H. Evans, V.B. Parker, R.H. Schumm, I. Holow, S.M. Bailey, K.L. Churney, and R.L. Nuttal. J. Phys. Chem. Ref. Data, **11**, Suppl. No. 2 (1982).
35. P.S. Surdhar and D.A. Armstrong. J. Phys. Chem. **90**, 5915 (1986).
36. P.S. Surdhar and D.A. Armstrong. J. Phys. Chem. **91**, 6532 (1987).
37. G. Merényi, J. Lind, and L. Engman. J. Chem. Soc. Perkin Trans. 2, 2551 (1994).
38. M. Faraggi and M.H. Klapper. Chim. Phys. **90**, 711 (1993).
39. P. Wardman. J. Phys. Chem. Ref. Data, **18**, 1637 (1989).

Interpretation of neighboring group interactions in crystal structures. A solid state and quantum-chemical study of "incipient nucleophilic attack" in 2-diazonium benzoic acid and its benzoate[1]

Rainer Glaser and Christopher J. Horan

Abstract: The concept of the Bürgi–Dunitz angle of attack on carbonyls is compatible with the electronic structure of carbonyls. However, it is argued here that the generalization asserted to describe the interaction of nucleophiles with diazonium ions is inappropriate. Distortions in crystal structures of diazonium ions with proximate nucleophiles were interpreted by an incipient nucleophilic attack (INA) on the formally positive-charged N_α. This "N_α attraction model" relies on the assumption that the *formal* charge in the most commonly used Lewis structure of diazonium ions represents *actual* charge. We proposed that the close approach of the proximate nucleophile to the diazonium group occurs to enhance attractive 1,3-(C,N_β)-bridging interactions and despite repulsion between N_α and the proximate oxygen (O_{pr}). The present study combines theoretical analysis of rotamers of 2-diazonium benzoic acid and its conjugate base with experimental results *on the same system* to provide compelling evidence that the more general conclusions drawn from analyses of neighboring group interactions in propenoic acid models are fully warranted. The crystallographic record is more fully consistent with the "1,3-bridging attraction model." Combined analysis of solid state and gas phase structures reveals the intrinsic features due to INA. Both electrostatic models can account for these features but with different postulates about the electron density distribution. While the structural analysis alone cannot distinguish between the alternative interpretations, the study of the electronic structure allows one to clearly differentiate between these competing interpretations. A method (ESI) for the quantitative evaluation of electrostatic neighboring group interactions has been devised and this ESI concept employs atomic electrical moments (charges, dipoles, and quadrupoles) determined via topological electron density analysis. The results of the ESI analysis support the 1,3-bridging attraction model and eliminate the N_α attraction model.

Key words: electrostatic interactions, electron density analysis, atoms in molecules, X-ray crystallography, ab initio molecular orbital theory, incipient nucleophilic attack, bonding models, ESI analysis.

Résumé : Le concept de l'angle d'attaque sur les carbonyles de Bürgi–Dunitz est compatible avec la structure électronique des carbonyles. Il a toutefois été suggéré que la généralisation proposée pour décrire l'interaction des nucléophiles avec les ions diazonium est inappropriée. Les distorsions dans les structures cristallines des ions diazonium avec des nucléophiles à proximité ont été interprétées par une attaque nucléophile incidente (ANI) sur le N_α qui est formellement chargé positivement. Ce «modèle d'attraction N_α» se base sur l'hypothèse que la charge *formelle* dans la structure de Lewis la plus couramment utilisée pour les ions diazonium représente la charge *réelle*. Nous avons proposé que l'approche du nucléophile à faible proximité du groupe diazonium se produit pour augmenter les interactions attractives 1,3-(C,N_β) qui font le pont et malgré la répulsion entre le N_α et l'oxygène à proximité (O_{pr}). La présente étude combine une analyse théorique des rotamères de l'acide 2-diazoniumbenzoïque et de sa base conjuguée avec des résultats expérimentaux *sur le même système* qui fournit des données suggèrent fortement que les conclusions plus générales tirées de l'analyse des interactions des groupes avoisinants dans les modèles de l'acide propénoïque sont pleinement justifiées. Les données cristallographiques disponibles sont en meilleur accord avec le «modèle d'attraction à pont-1,3». Une analyse combinée des structures en phases solide et gazeuse met en relief les caractéristiques intrinsèques dues à l'ANI. Les deux modèles électrostatiques peuvent expliquer ces caractéristiques, mais en se basant sur des postulats différents concernant la distribution de la densité électronique. Même si l'analyse structurale seule ne permet pas de distinguer entre ces interprétations alternatives, l'étude de la structure électronique permet de bien différencier entre ces interprétations en compétition. La méthode (ESI) d'évaluation quantitative des interactions électrostatiques des groupes avoisinants a été mise au

Received October 19, 1995.

This paper is dedicated to Professor Richard F.W. Bader on the occasion of his 65th birthday.

R. Glaser[2] and C.J. Horan. Department of Chemistry, University of Missouri–Columbia, Columbia, MO 65211, U.S.A.

[1] Part 6 in the series "Incipient nucleophilic attack as a probe for the electronic structure of diazonium ions." For parts 1–5, see ref. 1*a–e*.

[2] Author to whom correspondence may be addressed. Telephone: (573) 882-0331. Fax: (573) 882-2754.
E-mail: chemrg@showme.missouri.edu

point et cette méthode fait appel aux moments électriques atomiques (charges, dipôles et quadripôles) déterminés par l'analyse de la densité électronique topologique. Les résultats de l'analyse ESI supportent le modèle d'attraction à pont-1,3 et permet d'éliminer le modèle d'attraction N_α.

Mots clés : interactions électrostatiques, analyse de la densité électronique, atomes dans les molécules, diffraction des rayons X, théorie des orbitales moléculaires ab initio, attaque nucléophile incidente, modèles de liaisons, analyse ESI.

[Traduit par la rédaction]

Scheme 1.

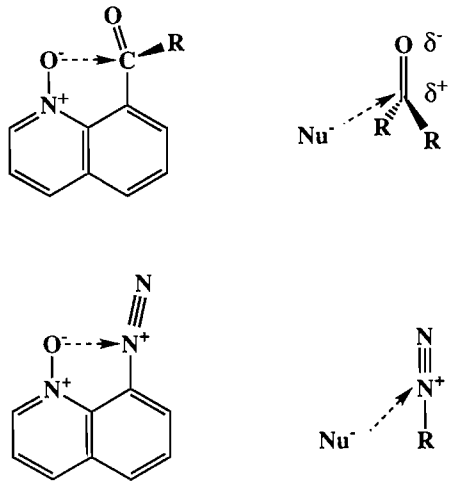

Scheme 2.

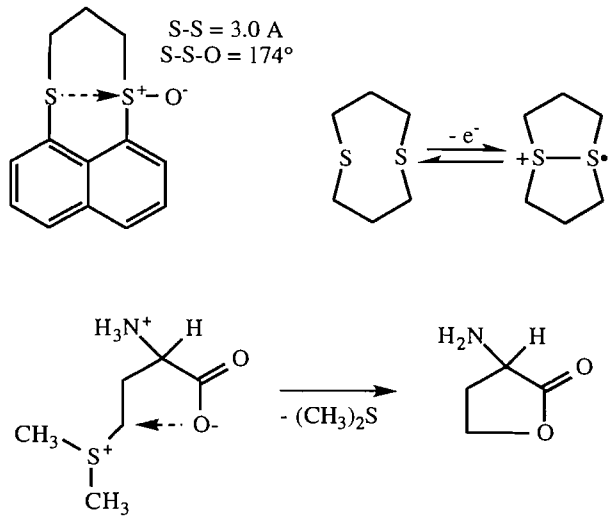

Introduction

The Bürgi–Dunitz angle of attack of a nucleophile on a carbonyl group was first described over 20 years ago (2), the feature was well established, and it is now "common knowledge." The trajectory of a nucleophile approaching a carbonyl in its π plane is not perpendicular but encloses an angle of 109° with the C=O σ-bond (Scheme 1). The angle of attack was determined both by a systematic analysis of crystal structures of compounds that contain either intra- or intermolecular nonbonded interactions between nucleophilic centers and carbonyl groups, and also by quantum-mechanical potential energy surface explorations. It was suggested that chemical reaction paths could be determined by examination of distortions in structural parameters caused by the presence of the two reactive centers in the "frozen" environment of the crystal lattice. Bürgi and Dunitz found the attack angle of 109° to be rather general for various nucleophiles and consistent distortions occurred for carbonyls in different environments. As the nucleophile's distance to the carbonyl decreased, the C=O distance increased and carbonyl C pyramidalization occurred. The idea of an "incipient nucleophilic attack" on a carbonyl center was demonstrated by Dunitz's elegant description of nucleophile–electrophile interactions in 1,8-disubstituted naphthalene and quinoline systems (3). In the seven systems studied, the distortions were consistent and characteristic of an initial nucleophilic attack. There was a splaying outward of the electrophilic carbonyl group and a splaying inward of the proximate nucleophile. The carbonyl carbon was also displaced toward the nucleophile and out of the plane of its three bonded atoms.

The Bürgi–Dunitz model for attack of nucleophiles on carbonyls is easily accepted as it is in agreement with the known electronic structure of carbonyls. The C=O bond is highly polar (4) for reasons of electronegativity and nucleophiles will be attracted to the electron-deficient carbonyl C. The nonperpendicular attack angle might be seen as a reflection of repulsive interactions between the nucleophile and the negatively charged carbonyl O. Because of its simplicity, this model quickly was applied to related systems as well. The attack of a nucleophile on a nitrile group can be discussed from this vantage point since the C≡N and C=O bonds show similar polarities (5). In fact, the concept of incipient nucleophilic attack has been broadened (6) to include not only nucleophilic attack on polar $^{\delta+}CX^{\delta-}$ or $^{\delta+}YO^{\delta-}$ multiple bonds but on all kinds of multiple bonds and to include dative bond formation as well.[3] In Scheme 2, a few examples of incipient nucleophilic attack on electron-deficient S centers are illustrated. The X-ray structure of the monosulfoxide suggests incipient sulfurane formation. The ease of oxidation of the disulfides was explained by incipient S—S bond formation (8). In a study of the directional preference of the approach of nucleophiles to sulfonium ions (9), 22 sulfonium ion crystal structures were analyzed for close contacts and interpreted as representing early stages of either an addition or a displacement reaction. Methylmethionine with its short C···O contact in the crystal exemplifies an early stage of facile conversion to a lactone.

Wallis and Dunitz asserted the generalization that an attack of a nucleophile on an NN triple bond will occur in a similiar fashion as with the carbonyls. Quinoline-8-diazonium-1-

[3] Intramolecular incipient nucleophilic attack on Si centers by aminoaryl groups: see ref. 7.

Scheme 3.

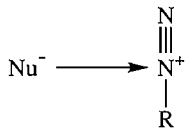

N_α attraction model

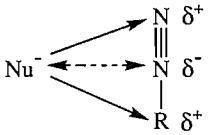

1,3-bridging attraction model

Scheme 4.

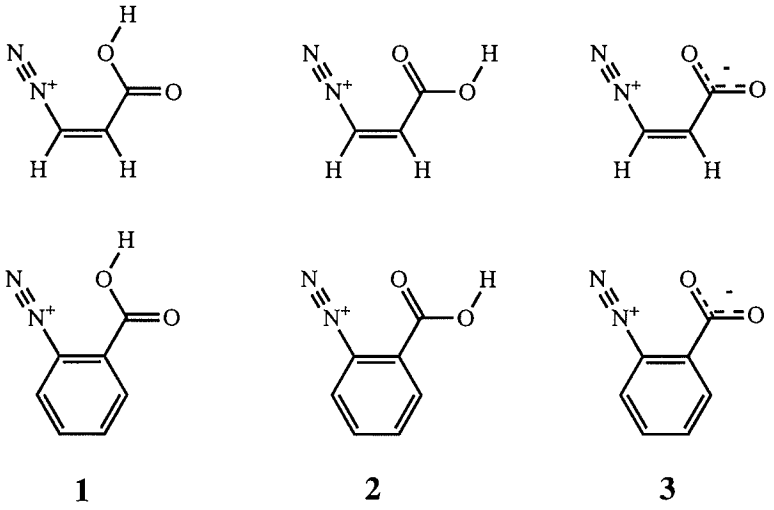

1 **2** **3**

oxide tetrafluoroborate (10) was discussed in complete analogy to the respective carbonyl system (Scheme 1) to argue that an incipient attack would occur at N_α (the central N). Several other cases of incipient nucleophilic attack on diazonium ions will be discussed below. This reasoning reflects the formal similarities of the Lewis structure (11) of diazonium ions with its formally positive-charged N_α and of the C=O bond polarity — this *formal* similarity is illustrated in a compelling fashion in Scheme 1. The explanation of distortions of diazonium ions by incipient nucleophilic attack relies on the assumption that N_α carries a positive charge and postulates an attractive interaction between the nucleophile and N_α (Scheme 3). Hence, this "N_α attraction model" would imply that the *formal* charge in the Lewis structure is a good representation of the *actual* charge distribution. Based on electronic structure analyses of diazonium ions, we argued that this assumption is not warranted and that the simple electrostatic model cannot be correct.

We proposed a bonding model for diazonium ions based on Bader's topological electron density analysis (12, 13) (TEDA) that emphasizes dative C←N bonding between a carbenium ion acceptor and an N_2 group donor that is internally polarized in the fashion $N_\alpha^{\delta-}$—$N_\beta^{\delta+}$ (14). This bonding model has since been shown to be general, fully consistent with all chemical and physical properties of diazonium ions,[4] and we argued for its preferability over purely formal bonding notations such as the Lewis notation (14*d*). In this context, we have been studying incipient nucleophilic attack in diazonium ions to probe their electronic structures. We first reported a theoretical study of neighboring group interactions in the rotamers of 3-diazonium propenoic acid and the zwitterionic conjugate base (1*a*). These systems were particularly suitable as they allowed for a variation of the nucleophilicity of the proximate O-atom (O_{pr}: C-O̲H, C=O̲, C-O̲$^-$) in the proximity of the N_2 group without major skeleton changes. Secondly, an aliphatic unsaturated molecule was selected because it allowed us to study the incipient nucleophilic attack in the *cis* isomer in comparison to the *trans* isomers as reference. We provided compelling evidence that the distortions occur in order to optimize the electrostatic interactions associated with the quadrupolar charge arrangement of the N_2 group and the C—O_{pr} bond. We showed that the close approach of the proximate nucleophile to the diazonium group occurs to enhance attractive 1,3-(C,N_β)-bridging interactions and *despite* N_α–O_{pr} *repulsion* (Scheme 3). We succeeded in the determination of the X-ray structures of the first β,β-disubstituted vinyldiazonium ions (16) but the synthesis and crystallization of β-*mono*substituted vinyldiazonium ions remain elusive. To corroborate our arguments, we thought it necessary to undertake a theoretical and experimental study on the *same* molecule and we resorted to aromatic diazonium systems. The crystal structures of 3-carboxy-2-naphthalenediazonium salt reported by Gougoutas and Johnson (17) were appealing but somewhat large from the viewpoint of computational demands. Hence, we focused on the *ortho*-carboxyl benzenediazonium ions and we report here on the interpretation of the distortions present in their quantum-mechanically determined gas phase structures and their experimental solid state structures. The three gas phase structures considered (Scheme 4) are the rotamer of 2-diazonio

[4] Excellent new monographs are available: see ref. 15.

Table 1. Total energies and vibrational zero-point energies.

		RHF/3-21G			RHF/6-31G*		
No.	Sym.	Energy	VZPE	NI	Energy	VZPE	NI
1	C_s	−523.389 019	77.57	0	−526.353 357	77.14	0
2	C_s	−523.391 896	77.54	0	−526.359 159	77.26	0
3	C_s	−522.966 332	68.55	0	−525.945 001	68.23	0

[a]Total energies in atomic units and vibrational zero-point energies (VZPE) in kcal/mol.
[b]Number of imaginary frequencies, NI.

benzoic acid in which the hydroxyl O is close to N_2, **1**, the other rotamer of this acid, **2**, and the conjugate base 2-diazonium benzoate zwitterion, **3**. We were able to determine the crystal structures of one rotamer of the benzoic acid derivative, the monohydrate of 2-carboxybenzenediazonium chloride (1*b*), **4**·Cl^-·H_2O, and of the conjugate base, the explosive 2-carboxylatobenzenediazonium ion hydrate (1*d*), **6**·H_2O. In addition, we solved the structure of **5**·Cl^-, which can be seen as the 1:1 complex between **4**·Cl^- and **6** (1*c*). The nucleophilicity of the proximate oxygen in **5** should be in between those of **4** and **6**. Details of the solid state structures were communicated (1*b–d*). With the theoretical data, we can now distinguish between intrinsic and packing-related distortions and probe the consistency of the competing explanations. While the structural analysis alone cannot distinguish between the alternative interpretations, a method for the quantitative evaluation of electrostatic neighboring group interactions has been devised for this purpose. The ESI concept employs atomic electrical moments determined via topological electron density analyses and the results of the ESI analysis do provide independent information that strongly supports the 1,3-bridging attraction model and eliminates the N_α attraction model.

Computational methods

Restricted Hartree–Fock (RHF) ab initio calculations were carried out on IBM RS-6000 systems with the program Gaussian92/DFT (18, 19) and electron density analyses were performed on Silicon Graphics Indigo workstations. Geometries were optimized in C_s symmetry and the Hessian matrices were computed analytically for each of the structures to confirm that an extremum had indeed been located and to characterize the stationary structures via the number of negative eigenvalues. Optimizations and vibrational analyses were performed with the basis sets 3-21G and 6-31G*. Total energies and vibrational zero-point energies of **1–3** are listed in Table 1 and their RHF/6-31G* geometries are listed in Table 2 together with the solid state structural data. The electronic structure analyses were performed at the RHF/6-31G* level. Topological and integrated properties were determined using various modules of the Proaim program (20). Graphical representations of the integrated atomic moments were generated with the program Dipoles.[5] The analysis of the electrostatic interactions between neighboring groups was performed with our program ESI[6] and the theoretical background will be discussed below.

Results and discussion

Incipient nucleophilic attack in crystal structures of diazonium ions

In crystal structures of salts of diazonium ions that contain a proximate nucleophile, the N_2 group is bent in a way that was interpreted as the result of *intramolecular* incipient nucleophilic attack on N_α. As with the interpretation of the structure of quinoline-8-diazonium-1-oxide tetrafluoroborate (vide supra), Gougoutas and Johnson (17) attributed distortions in 3-carboxy-2-naphthalenediazonium salts and the corresponding zwitterion **I** mainly to attractive interactions between N_α and the carbonyl O and also between N_β and the counterion. *Intermolecular* incipient nucleophilic attack of sulfonate O on N_α has been discussed for **II** (21). The close O–N_α contact might equally well be explained as the result of minimization of the distances between the sulfonate O and the atoms N_β and $C(N_2)$. The placement of nucleophiles in 1,3-bridging positions is common, and structures are known of several diazonium ions with polyfluoro anions in which the F atoms are placed successively in the two CNN bridging positions and, if both of these are occupied, in the proximity of N_β. The crystal structures of **III** (22) and **IV** (23) both contain F atoms in such bridging positions with nearly equal F–N_α and F–N_β distances. The crystal structure of $PhN_2^+BF_4^-$ (24), **V**, provides an excellent example for the placement of counterions in the proximity of both N_2 group nitrogens and this bridging was regarded as the result of electrostatic interactions of F with N_α and N_β. Haymore and coworkers (25) studied host–guest assemblies **VI** formed by 18-crown-6 ethers and diazonium ions and the crystal structure[7] showed the N_2 group inserted into the cavity of the crown ether such that each O atom assumes a 1,3-bridging position between N_β and C_{ipso}.[8]

[5] R. Glaser. Department of Chemistry, University of Missouri–Columbia, 1990.

[6] R. Glaser, B.S. Chladny, and M.K. Hall. Department of Chemistry, University of Missouri–Columbia, 1994.

[7] B.L. Haymore. Unpublished results. We thank Dr. Haymore for communicating these X-ray data prior to publication.

[8] Similar coordination of a 21-crown-7 ether to 4-methoxybenzene-1-diazonium cation also has been observed: ref 26.

Table 2. Comparison between computed gas-phase geometries and experimental solid state structures.

	Ab initio theory			X-ray crystallography		
Parameter	**1**	**2**	**3**	**4**	**5**	**6**
C1—N2	1.419	1.422	1.424	1.406(3)	1.415(4)	1.406(4)
N2—N3	1.075	1.075	1.075	1.085(3)	1.076(4)	1.090(3)
C1—C4	1.384	1.380	1.394	1.374(3)	1.384(4)	1.386(4)
C4—C5	1.385	1.387	1.373	1.373(4)	1.379(5)	1.376(4)
C5—C6	1.383	1.382	1.398	1.383(4)	1.371(5)	1.389(3)
C1—C7	1.401	1.400	1.382	1.397(3)	1.387(4)	1.398(2)
C6—C8	1.394	1.396	1.381	1.391(3)	1.389(5)	1.385(4)
C7—C8	1.379	1.378	1.390	1.378(3)	1.383(4)	1.387(4)
C7—C13	1.503	1.498	1.561	1.494(3)	1.494(4)	1.526(3)
C13—O14	1.177	1.189	1.231	1.208(3)	1.224(4)	1.250(3)
C13—O15	1.324	1.307	1.210	1.311(3)	1.280(4)	1.239(2)
C4—H9	1.074	1.074	1.074	0.79(3)	1.02(4)	0.95(2)
C5—H10	1.073	1.073	1.074	0.99(3)	1.01(4)	0.98(3)
C6—H11	1.074	1.074	1.075	0.88(3)	0.92(4)	0.98(3)
C8—H12	1.072	1.072	1.072	0.90(3)	0.94(4)	0.99(2)
O15—H16	0.957	0.956		0.99(3)	1.22(2)	
C1-N2-N3	176.89	176.62	170.42	173.3(3)	172.7(3)	174.29(16)
N2-C1-C7	120.86	120.06	119.17	119.49(19)	119.2(3)	118.54(23)
N2-C1-C4	114.70	115.42	115.12	115.64(21)	115.0(3)	116.06(17)
C1-C7-C13	126.11	120.62	121.34	120.98(17)	123.3(3)	122.27(24)
C8-C7-C13	117.86	122.98	123.17	123.07(20)	121.8(3)	122.72(15)
C7-C13-O14	122.59	121.69	111.51	121.40(20)	119.0(3)	115.91(15)
C7-C13-O15	112.61	112.86	114.51	112.69(17)	114.2(3)	115.75(19)
O14-C13-O15	124.80	125.50	133.98	125.85(20)	126.8(3)	128.33(21)
C4-C1-C7	124.44	124.51	125.71	124.78(19)	125.7(3)	125.3(3)
C1-C7-C8	116.02	116.40	115.49	115.87(19)	114.9(3)	115.01(22)
N2-C1-C7-C13	0.00	0.00	0.00	7.4(1)	7.0(2)	5.1(1)
C1-C7-C13-O14	180.00	0.00	0.00	12.3(1)	6.5(2)	25.9(1)
C1-C7-C13-O15	0.00	180.00	180.00	−170.5(2)	−176.2(4)	−154.3(3)

[a]Bond lengths in Å and bond angles and dihedrals in degrees.
[b]Estimated standard deviations are given in parentheses for the solid state data.
[c]Ab initio geometries determined at the RHF/6-31G* level.

Most recently, Wallis, Easton, and Dunitz (10*b*) reported the crystal structures of three 8-substituted naphthalene-1-diazonium ions, **VII**a, and the authors reiterated their previously stated view that the distortions are due to the attack of the electron-rich nucleophiles on the electron-deficient N_α. It was recognized that the functional groups are on opposite sides of the best molecular plane and this observation was said to be indicative of "attractive interactions between an electron-rich atom ... and the α-N atom of the diazonium group." In the earlier paper (10*a*) on the quinoline **VII**b, this feature was thought to disfavor their interpretation and downplayed as it "only increases the O(1)···N(1) separation by 0.017 Å." We pointed out (1*a*) that placing the two functional groups on opposite sides of the plane of the aromatic ring is *not* supportive of the suggested attractive interaction. In the crystal structure of 8-nitronaphthalene-1-diazonium ion, a system that is very closely related to the carboxyl-substituted structures, the NO_2 group is rotated out of the aromatic plane by 33°. This feature was said to assist in decreasing the distance between the nitro O and the diazonium α-N-atom. Certainly, rotating the nitro group out of the plane (and out of conjugation) only increases its distance from the N_2 group and this distortion is clearly not consistent and, in fact, is in contradiction to the idea of an attractive interaction between the nucleophile and N_α.

Neighboring group interactions in 2-diazonium benzoic acid derivatives

Crystal structures

The X-ray structures of the *ortho*-carboxy benzenediazonium ions **4–6** are shown in Fig. 2. Several types of distortions are pertinent to our discussion. The first two concern *in-plane deformations* of bond angles and specifically (*a*) the deviations from CNN linearity and (*b*) the splaying apart of the angles ∠(N_2-C═C) and ∠(C═C-CO_2). Two further types of distortions concern *out-of-plane displacements* of the functional groups and they include (*c*) the positioning of the two functional groups on opposite sides of the molecular plane and

Fig. 1. Examples of incipient nucleophilic attack in crystal structures of diazonium ions (charges on counterions omitted): 3-carboxylate-2-naphthalenediazonium zwitterion (**I**); 2-diazonium-4-phenolsulfonate monohydrate (**II**); *para*-bromobenzene tetrafluoroborate (**III**); *para*-diethylaminobenzenediazonium hexafluorophosphate (**IV**); benzenediazonium tetrafluoroborate (**V**); 18-crown-6 ether complexed benzenediazonium ion (**VI**); naphthalene-1-diazonium ions (**VII**a) and 8-substituted quinoline diazonium ions (**VII**b).

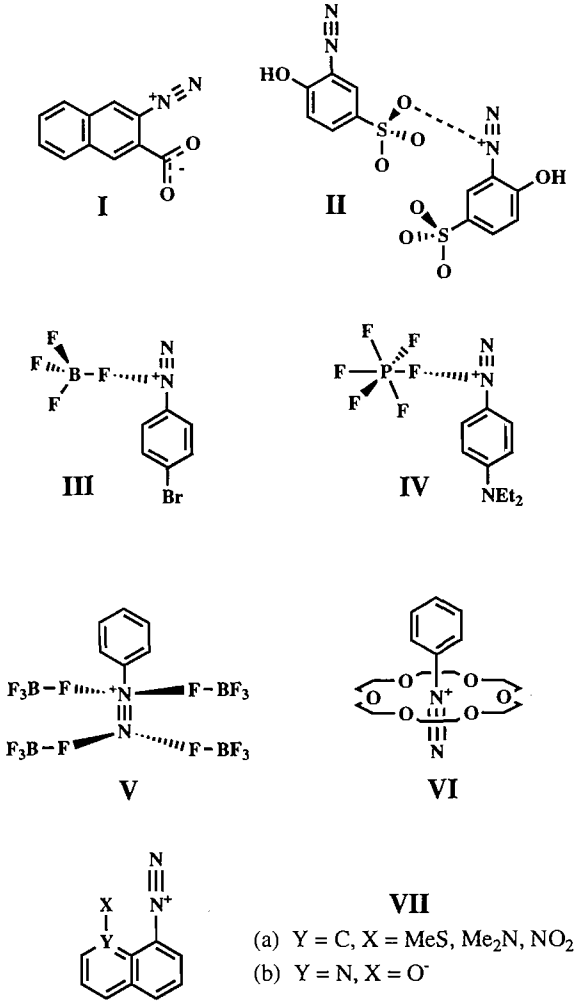

Fig. 2. Perspective view of the cations **4**–**6** contained in 2-carboxybenzenediazonium chloride monohydrate, $\mathbf{4}\cdot Cl^{-}\cdot H_2O$, in the symmetrically H-bridged system formed by 1:1 complex formation between 2-carboxybenzene-diazonium chloride and benzenediazonium-2-carboxylate, $\mathbf{5}Cl^{-}$, and in the 2-carboxylatobenzenediazonium ion hydrate, $\mathbf{6}^{-}H_2O$. Thermal ellipsoids are drawn at the 50% probability level.

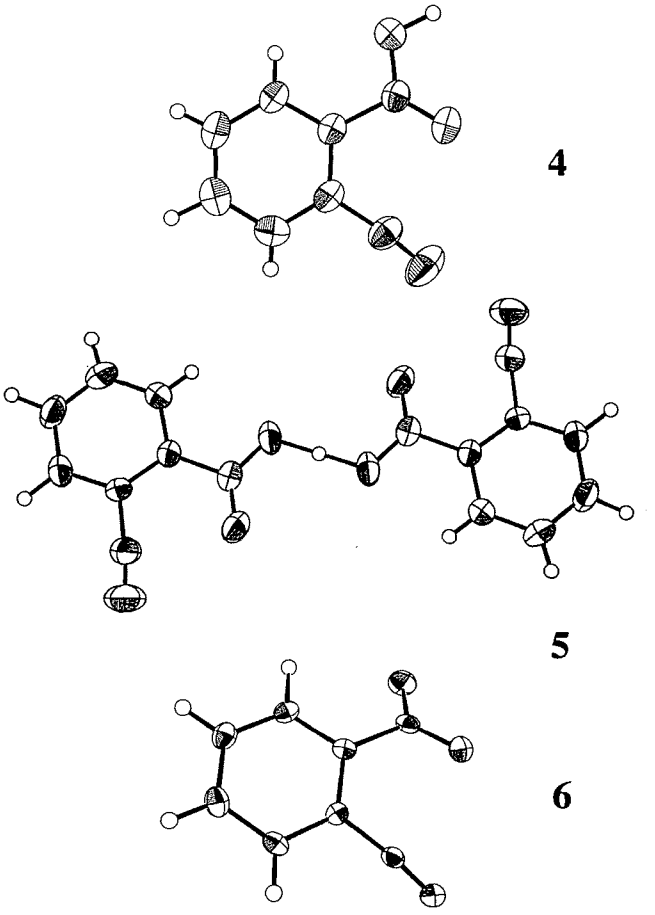

(*d*) the rotation of the carboxyl groups about the C(7)—C(13) bonds.

Primarily, the in-plane deformations were considered as evidence for an attraction between O_{pr} and N_{α}. In **4**–**6**, N_{β} is displaced away from the carboxyl group resulting in deviations of the C(1)-N_{α}-N_{β} skeleton from linearity by 5–7°. Benzenediazonium ions are well known to exhibit widened C-C_{ipso}-C angles at the N_2 bearing C atom (1*c*). It is because of *this* effect on the C(4)-C(1)-C(7) angles (>124.8°) that the other angles at C(1) have to be less than 120°. We find the angles N(2)-C(1)-C(4) and N(2)-C(1)-C(7) to be about 115° and 119°, respectively, and they differ in a way that would position N_{α} *further away* from O_{pr}. The C(1)=C(7)-C(13) angles all are larger than the sp^2 angle of 120°. Hence, considering all of the crystallographic evidence, the in-plane deformations of the angles N(2)-C(1)-C(7) and C(1)-C(7)-C(13) certainly do not allow one to argue in favor of an attraction of O_{pr} to N_{α} but these angle widenings would increase the distance between the two neighboring groups.

The N_2 groups and the carboxyl groups are on opposite sides with regard to the best molecular plane with N(2)-C(1)-C(7)-C(13) dihedral angles of 7.4–5.1° for **4**–**6**. This displacement increases the N_{α}–O_{pr} distance. Another significant dihedral angle describes the carboxyl group rotation out of the plane of the aromatic ring and its value can be as high as 25.9°. These rotational distortions are due to *intermolecular* interactions and, in any case, it is clear that the rotational distortions certainly cannot be interpreted as evidence of N_{α}–O_{pr} attraction since O_{pr} is rotated *away* from the N_2 group.

Fig. 3. Molecular models of the RHF/6-31G* optimized planar minimum structures of **1–3** with integrated atomic charges.

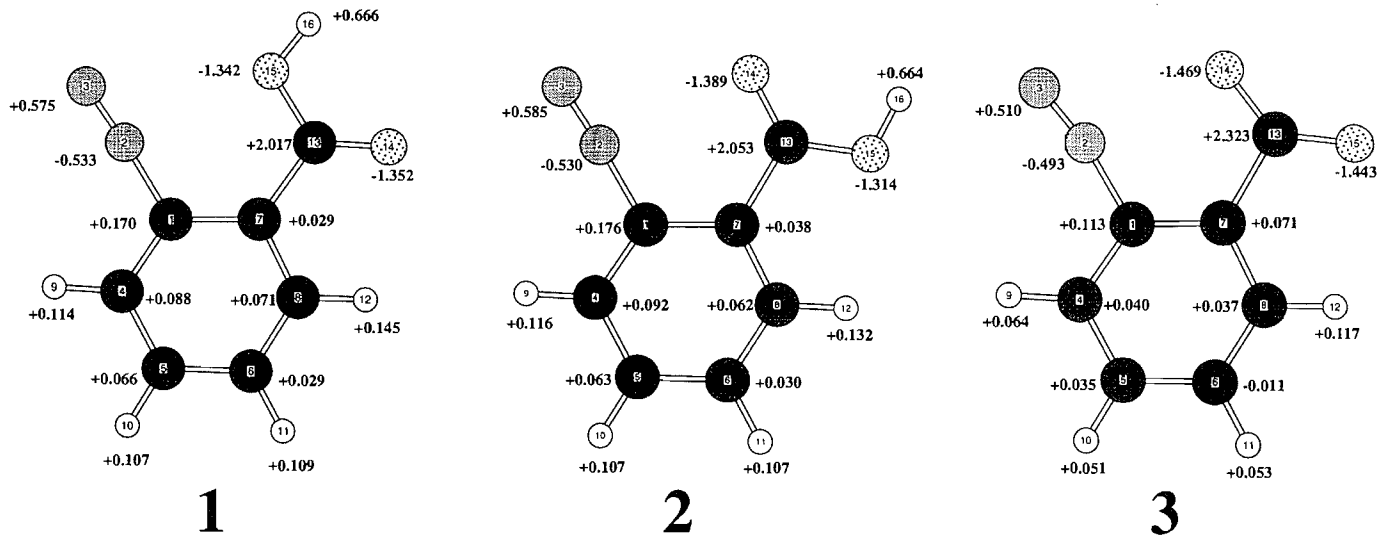

Calculated gas phase geometries

All the optimized planar structures **1–3** are minima[9] (Table 1 and Fig. 3) and we conclude that the out-of-plane distortions for **4–6** are due to packing. Basis set effects on structures are minimal, the agreement between theory and experiment is excellent, and, moreover, corresponding bond lengths in **1–3** differ only slightly (Table 2). The significant in-plane deformations found in **4–6** also occur in **1–3** (Table 2). The C(1)-N_α-N_β backbones are not linear (177° for **1** and **2**, 170.4° for **3**), there is a slight widening of the C(4)-C(1)-C(7) angles to values >124°, and the C(1)-C(7)-C(8) angles of 115.0°±0.5° are larger than in the parent benzenediazonium ion.

Intrinsic INA features and their interpretations

The combined analysis of the solid state and of the gas phase structural data shows that the intrinsic features associated with incipient nucleophilic attack on diazonium ions are the CNN nonlinearity and the widening of the in-plane angles. These features result in the nonbonded distances summarized in Table 3 and we note that the N_α–O_{pr} distances in all systems remain substantially less than the sum of the van-der-Waals radii of N and O (2.9 Å). Both the N_α attraction model and the 1,3-bridging attraction model account for these features with different postulates concerning the electron density distribution. The former explains the kink in the CNN backbone and the short N_α–O_{pr} contact with an attraction of the nucleophile to the positively charged N_α atom. The 1,3-bridging attraction model differs fundamentally in that it reflects the polarity $C(+)N(^{\delta-})N(^{\delta+})$ and it is slightly more complicated as it considers not just the interaction between O_{pr} and N_α, which is repulsive in this model. The C—O_{pr} and N_α—N_β bonds are arranged in a nearly perfectly aligned quadrupolar arrangement with roughly identical N_α–C and N_β–O_{pr} distances. The short N_α–O_{pr} distance results from the optimization of the 1,3-bridging O_{pr}–N_β and O_{pr}–C(N) attractions and N_α–$C(O_{pr})$ attraction as well. Note that the latter interaction provides a straightforward explanation of the kink in the CNN backbone. It is evident that *the structural characteristics can be interpreted based on different assumptions concerning the electronic structures*. A corollary statement would be that structure distortions *alone* do not allow one to make any deductions concerning electron density distribution. On the other hand, the study of the electronic structure will allow one to clearly differentiate between competing interpretation of the structural distortions.

Quantitative evaluation of electrostatic neighboring group interactions

AIM and the ESI concept

Both the N_α attraction model and the 1,3-bridging attraction model are electrostatic in nature. To formulate these models in quantitative terms, one needs to assign electrostatic moments to the atoms and evaluate their interactions. The concept of "atomic charge" is of paramount importance in discussions of all aspects of chemistry and many methods have been proposed to partition molecules into atoms and to assign charges to the atoms. Basis set partitioning and density partitioning methods have been developed (27). To the class of basis set partitioning methods belong, for example, the historically significant Mulliken population analysis and the modern Natural Population Analysis (28). The density partitioning methods do not rely on properties of the Hilbert space but consider directly the observable molecular electron density distribution in Cartesian space. As far as the partitioning of the molecular electron density distribution into atomic components is concerned, two schools of thought seek to recover either "spatially

[9] The conformational preference energy of 3.6 kcal/mol in favor of **2** compared to **1** is nearly the same as for the respective propenoic acid derivatives (3.8 kcal/mol). The proton affinity of 259.9 kcal/mol of **3**, however, is significantly higher than the value of 238.5 kcal/mol (ref. 1*a*) obtained at the same level for the aliphatic system.

Table 3. Theoretical and experimental nonbonded intramolecular interactions.

	Proximate oxygen, O_{pr}			Carboxyl carbon		
No.	C(1)	N_α	N_β	C(1)	N_α	N_β
1	2.839	2.586	2.938	2.589	3.015	3.725
2	2.842	2.575	2.923	2.518	2.876	3.567
3	2.731	2.396	2.826	2.566	2.889	3.639
4	2.855	2.603	3.013	2.516	2.864	3.600
5	2.851	2.594	3.006	2.535	2.901	3.640
6	2.866	2.622	3.020	2.561	2.887	3.600

[a]All values in Å.

extended" or "spatially constrained" atom-shaped objects. The approaches by Parr (29) and by Walker and Mezey (30) exemplify the former and Bader's topological Atoms in Molecules theory (12, 13) (AIM) is the most rigorous formulation of the latter. For the discussion of the majority of chemical problems, the AIM method is especially well suited and its widespread usage emphasizes this point. An aspect of the topological electron density analysis (TEDA) that is particularly appealing concerns its ability to deal with atom anisotropies (31, 32). Many population analyses merely describe atomic charges and few attempts have been made to include higher moments (33). For example, the extended Mulliken electron population analysis proposed by Huzinaga et al. produces a point charge model that correctly reproduces the molecular electric dipole moment (34). There have also been reports on the extensions of the Mulliken population analysis to include atomic polarizations to recover the molecular dipole moment.[10] The topological method allows for a more refined representation of the atom in a molecule since not only the charge but higher atomic moments as well can be determined. We will be interested in charges, dipoles, and quadrupoles of the atoms but still higher moments can also be determined.

Arguments based on charges and electrical moments can become rather involved as many values "with direction" need to be considered. It is thus important to define and discuss parameters that incorporate all of this information. As the basis for such parameters, we are studying the electrostatic interaction energy[11] between atoms i and j, ESI_{ij}, defined by the equation

$$ESI_{ij} = CC_{ij} + CD_{ij} + DD_{ij} + QC_{ij} + QD_{ij} + QQ_{ij}$$

where CC_{ij} is the Coulomb energy between the atomic charges q_i and q_j, CD_{ij} is the sum of the energies associated with the interaction of q_i with atomic dipole μ_j and of q_j with μ_i, and DD_{ij} is the interaction energy between the dipoles μ_i and μ_j. The remaining terms consider the interactions of the atomic quadrupoles with the charges (QC_{ij}), dipoles (QD_{ij}), and quadrupoles (QQ_{ij}).

Topological analysis and determination of electrical moments

The quantitative evaluation of electrostatic neighboring group effects[12] requires knowledge of the ESI_{ij} values, which in turn depend on the atomic properties evaluated by the AIM theory. We have determined all of the topological and integrated atomic properties and pertinent results are summarized in Tables 4 and 5. The analysis begins with the characterization of topological features of the electron density distribution based on the properties of the gradient vector field. The collection of all gradient vector field lines originating at a given atom, the attractor, define the associated zero-flux surfaces as the boundaries of the atoms in the molecules. Bond critical points occur at the intersection between the zero-flux surfaces and the so-called bond paths. A bond path connects two attractors and is defined as the line traced out by following the direction of positive curvature of the electron density (λ_3) beginning at the bond critical point. *In praxis*, one first locates all bond critical points and then traces out the zero-flux surfaces following the directions associated with the two negative principal curvatures of the density, λ_1 and λ_2. Properties of the bond critical points, such as the density at that point, ρ_b, and its distances r_A and r_B from the atoms, are commonly used to characterize electron density distributions and such information is collected in Table 4 for **1–3**. With the atomic regions defined, atomic properties are determined by numerical integration within the basins and this aspect is the most time-consuming step (36). Integrated properties are summarized in Table 5 and include the atomic charge and dipole moments. The directions of the dipole moments are shown in Fig. 4. The atomic quadrupole moments also were determined and employed in the ESI_{ij} evaluations but, for brevity, they are not documented.

Analysis of the data presented in Tables 4 and 5 shows the great similarity of the electronic structures of **1–3** and the respective propenoic acid derivatives. In fact, the electronic structures of aromatic and aliphatic diazonium functions are rather general (14). The N_α basins extend greatly into the C—N bonding region ($F_{CN} \approx 0.31$) and modestly ($F_{N\alpha N\beta} \approx 0.56$) into the N—N bonding region. Fairly typical ρ_b values of about 0.22 and 0.68 are found for all of the C—N and N—N bond critical points. Negative N_α charges in the range from -0.53 to -0.49 are found for **1–3** and the N_β charges are positive, just slightly larger in magnitude, and in the range between +0.51 and +0.58 (Fig. 3). Hence, the N_2 groups exhibit a large internal polarization but only a modest overall charge (< +0.055). The N_2 group polarization and the dative N→C bonding are manifested in the atomic moments of **1–3**. The vector $\mu(N_\alpha)$ is directed toward N_β and the $\mu(N_\beta)$ vector is antiparallel and much larger, and $\mu(C1)$ is directed toward N_α. The electron density within the basins of N_α and N_β is

[10] Compare the discussion of ethylene in ref. 32*b*.

[11] A similar approach was described by Cooper and Stutchbury in their study of hydrogen-bonded van de Waals complexes (35).

[12] Penetration effects are neglected in the present discussion. We found that the electron density between nonbonded atoms provides a good indication for assessing the importance of penetration effects. If the electron density is as low as in the present cases (between N_α and O_{pr}), then the neglect of penetration effects is warranted to a first approximation even though the N_α–O_{pr} distance is less than the sum of the van der Waals radii. One has to keep in mind that the sum of the van der Waals radii provides only a rather crude parameter for the assessment of steric effects because the van der Waals radius of an "N_α in a diazonium ion" is different from "the van der Waals radius of prototypical N" and so forth.

Table 4. Topological characteristics of bond and ring critical points of the electron densities.[a]

No.	A	B	r_A	r_B	F	ρ_b	λ_1	λ_2	λ_3	ε
Molecule 1										
1	C1	N2	0.434	0.984	0.306	0.220	−0.306	−0.258	1.222	0.185
2	N2	N3	0.604	0.471	0.562	0.680	−1.545	−1.512	0.430	0.022
3	C1	C4	0.761	0.623	0.550	0.326	−0.709	−0.564	0.211	0.257
6	C1	C7	0.764	0.637	0.545	0.314	−0.673	−0.539	0.234	0.247
8	C7	C8	0.727	0.651	0.528	0.331	−0.716	−0.584	0.248	0.226
13	C7	C13	0.752	0.751	0.500	0.277	−0.594	−0.542	0.317	0.097
14	C13	O14	0.422	0.902	0.318	0.317	−0.823	−0.777	1.503	0.060
15	C13	O15	0.386	0.791	0.328	0.451	−1.374	−1.200	3.119	0.145
16	O15	H16	0.783	0.172	0.820	0.347	−1.909	−1.882	1.646	0.014
17	N2	O15	1.268	1.323	0.489	0.016	−0.015	−0.013	0.099	0.089
18[b]	C1	C6	1.323	1.390	0.488	0.020	−0.014	0.086	0.095	
19[c]	C1	O15	1.498	1.376	0.521	0.013	−0.009	0.024	0.061	
Molecule 2										
1	C1	N2	0.435	0.986	0.306	0.220	−0.308	−0.267	1.193	0.153
2	N2	N3	0.603	0.471	0.561	0.681	−1.543	−1.520	0.430	0.016
3	C1	C4	0.759	0.621	0.550	0.329	−0.715	−0.567	0.209	0.261
6	C1	C7	0.764	0.637	0.545	0.316	−0.681	−0.545	0.233	0.250
8	C7	C8	0.724	0.653	0.526	0.332	−0.717	−0.582	0.250	0.231
13	C7	C13	0.746	0.751	0.498	0.281	−0.606	−0.553	0.318	0.097
14	C13	O14	0.388	0.800	0.326	0.441	−1.332	−1.194	2.952	0.116
15	C13	O15	0.417	0.890	0.319	0.333	−0.891	−0.854	1.642	0.043
16	O15	H16	0.782	0.173	0.819	0.349	−1.916	−1.890	1.657	0.013
17	N2	O14	1.247	1.333	0.483	0.018	−0.018	−0.016	0.110	0.148
18[b]	C1	C6	1.322	1.388	0.488	0.020	−0.014	0.087	0.095	
19[c]	C1	O14	1.463	1.414	0.508	0.015	−0.012	0.028	0.073	
Molecule 3										
1	C1	N2	0.436	0.988	0.306	0.218	−0.297	−0.256	1.173	0.162
2	N2	N3	0.607	0.467	0.565	0.681	−1.520	−1.516	0.409	0.002
3	C1	C4	0.748	0.646	0.536	0.320	−0.694	−0.554	0.242	0.254
6	C1	C7	0.783	0.598	0.567	0.327	−0.687	−0.584	0.169	0.175
8	C7	C8	0.714	0.676	0.514	0.327	−0.698	−0.598	0.270	0.168
13	C7	C13	0.877	0.683	0.562	0.242	−0.491	−0.467	0.284	0.050
14	C13	O14	0.399	0.831	0.325	0.402	−1.159	−1.089	2.304	0.063
15	C13	O15	0.394	0.815	0.326	0.420	−1.239	−1.135	2.584	0.091
16	N2	O14	1.142	1.254	0.477	0.028	−0.030	−0.028	0.172	0.041
17[b]	C1	C6	1.318	1.375	0.489	0.021	−0.014	0.087	0.097	
18[c]	C1	O15	1.372	1.367	0.501	0.019	−0.015	0.043	0.090	

[a]Distances r_A and r_B in Ångstroms between each critical point and atoms A and B, respectively. F is defined as $F = r_A/(r_A + r_B)$. The electron density at the critical point, ρ_b, is given in e au^{-3}. The curvatures of the electron density at the locations of the critical points, λ_i, are given in e au^{-5}. The ellipticity, ε, is defined as $\varepsilon = \lambda_1/\lambda_2 - 1$ and given for all (3,+1) bond critical points.

[b]The locations of (3,−1) ring critical points within the benzene rings are characterized with respect to C1, the carbon that carries the diazonio function, and the "*para*-carbon".

[c]The locations of (3,−1) ring critical points between functional groups are characterized with respect to C1, the carbon that carries the diazonio function, and the proximate O14 or O15.

polarized into the CN bonding and the lone pair regions, respectively. The -CO_2H groups show large $q(C) \approx +2$, negative OH charges of about −0.66, and carbonyl-O charges of −1.39 (**1**) and −1.34 (**2**) that are more than twice as high. Since the acidic hydrogens carry positive charges of 0.66 in **1** and **2**, deprotonation adds only 0.34 electron to the fragment [$N_2C_6H_4CO_2$]. Since the electron populations of the CO_2 groups *decrease* from −0.68 and −0.65 in **1** and **2**, respectively, to −0.59 in **3** and since $q(N_2)$ remains indifferent, it follows that *deprotonation serves to reduce the electron deficiency in the phenyl ring*. This is quite a remarkable result: In the absence of the proton, it is no longer beneficial to accu-

Table 5. Integrated atomic charges (q), magnitude of the first atomic moments (μ), and atom stabilities (KE).

	1			**2**			**3**		
Atom	q	μ	KE	q	μ	KE	q	μ	KE
C1	+0.170	0.741	37.737 39	+0.176	0.748	37.742 26	+0.113	0.788	37.790 47
N2	−0.533	0.348	55.008 34	−0.530	0.348	55.002 07	−0.493	0.357	54.958 77
N3	+0.575	0.888	53.925 56	+0.585	0.887	53.919 74	+0.510	0.923	53.957 49
C4	+0.088	0.354	37.843 25	+0.092	0.352	37.840 16	+0.040	0.285	37.855 07
C5	+0.066	0.222	37.848 29	+0.063	0.218	37.847 46	+0.035	0.178	37.844 71
C6	+0.029	0.134	37.872 87	+0.030	0.133	37.870 26	−0.011	0.097	37.880 57
C7	+0.029	0.356	37.871 80	+0.037	0.394	37.874 30	+0.071	0.553	37.896 11
C8	+0.071	0.256	37.859 44	+0.062	0.242	37.856 63	+0.037	0.193	37.864 62
H9	+0.114	0.125	0.572 76	+0.116	0.125	0.571 70	+0.064	0.130	0.593 96
H10	+0.107	0.126	0.576 30	+0.107	0.126	0.576 48	+0.051	0.131	0.599 97
H11	+0.109	0.125	0.576 80	+0.107	0.126	0.577 68	+0.053	0.131	0.600 63
H12	+0.145	0.121	0.562 25	+0.132	0.120	0.569 24	+0.117	0.128	0.572 80
C13	+2.017	0.770	36.478 83	+2.053	0.792	36.480 30	+2.323	0.494	36.266 92
O14	−1.342	0.367	75.616 75	−1.389	0.734	75.701 91	−1.469	0.579	75.629 90
O15	−1.352	0.776	75.693 88	−1.314	0.408	75.619 88	−1.443	0.651	75.632 54
H16	+0.666	0.130	0.302 83	+0.663	0.130	0.305 97			
Σ	+0.959		526.347 34	+0.990		526.356 04	−0.002		525.944 53
C_6H_4	+0.928		229.321 15	+0.922		229.326 17	+0.570		229.498 91
N_2	+0.042		108.933 90	+0.055		108.921 81	+0.017		108.916 26
COOH	−0.011		188.092 29	+0.013		188.108 06	−0.589		187.529 36

[a]Deviation between directly calculated molecular energy and the sum over the negative atom kinetic energies (in kcal/mol): 3.77 for **1**, 1.96 for **2**, and 0.29 for **3**.

mulate as much excess density on the CO_2 fragments, and the CO_2 population and the charge on the phenyl ring are both reduced drastically. While the CO_2 population is reduced in **3**, the data in Table 5 also indicate a higher polarization, and the negative charges on O_{pr} (a measure of their nucleophilicity) increase in the order −1.34, −1.39, and −1.47 in going from **1** to **3**. The μ vectors of the carboxyl C-atoms all are more or less parallel to the C—CO_2 bond and directed into the region between the oxygens, and the μ vectors of the carbonyl and carboxylate oxygens are directed away from the carboxyl C. Note that the dipoles $\mu(N_\beta)$ and $\mu(O_{pr})$ are large and antiparallel whereas the dipoles $\mu(N_\alpha)$ and $\mu(O_{pr})$ are parallel to each other.

The similarities and differences between the electronic structures of the aromatic systems **1–3** and of the aliphatic propenoic acid derivatives come clearly to the fore. The electronic structures of the functional groups are very similar and the only significant difference lies with the assignment of positive charge to the hydrocarbon fragments C_6H_4 and C_2H_2 in the two series. While the positive charge necessarily remains local in the C_2H_2 groups, the positive charge is well dispersed in the phenyl groups.

Electrostatic interaction analysis

We determined the interaction terms for **1–3**, and in Tables 6–8 are listed the various electrostatic contributions due to each pair of atoms within the two functional groups together with their sum $\Sigma = ESI_{ij}$. These ESI_{ij} values are shown in Fig. 4. Most importantly, *this analysis provides compelling evidence that the more general conclusions we drew from our analyses of the neighboring group interactions in the propenoic acid models are fully warranted and completely corroborated by the present combined experimental and theoretical studies*. The interaction between N_α and the proximate oxygen nucleophile is repulsive. Strong 1,3-bridging attractions occur between N_β and O_{pr} and C(1) and O_{pr}. It is for these two statements that the interpretation based on the 1,3-bridging attraction model is consistent with the electronic structure while the N_α attraction model is eliminated. At the same time, one also must realize that *every* model presents a simplification. The 1,3-bridging attraction model does describe the dominant interactions in **II–VI**. However, Fig. 4 shows that there are other interactions between the neighboring groups that are quite large and that suggest that one needs to consider the bridging interactions not just of O_{pr} but also of the highly electron-deficient carboxyl-C atom with the atoms of the C-N-N fragment. Substantial repulsions occur between the carboxyl C and N_β and C(1) while there is strong attraction between N_α and the carboxyl C. The overall electrostatic interactions between O_{pr} with C(1) and the N-atoms are −42.0, −48.0, and −34.3 kcal/mol for **1–3**, respectively. The interactions of the carboxyl C with the CNN fragment are +37.1, +47.1, and +21.5 kcal/mol, respectively, for **1–3**. Two observations are noteworthy: The interaction between O_{pr} and the neighboring group is attractive in all cases but it does not parallel O_{pr} nucleophilicity and, similiarly, the interactions of the carboxyl C with the neighboring group all are repulsive but also do not parallel the charge on the carboxyl C. This observation reflects

Table 6. Electrostatic interaction matrix for **1**.

		N2	N3	C7	C13	O14	O15	H16
CC	C1	−21.1	13.0	1.2	43.9	−26.6	−20.9	9.9
CD		−39.5	16.3	4.4	−3.5	−9.8	0.7	2.9
CQ		12.5	−3.1	−2.6	−1.5	1.2	0.4	−0.3
DD		−8.3	3.9	−4.1	0.0	0.1	0.2	0.1
DQ		−4.1	3.6	−1.1	−0.3	0.2	−0.1	0.0
QQ		2.3	0.2	1.8	0.0	0.0	0.0	0.0
Σ		−58.3	34.0	−0.4	38.6	−35.0	−19.7	12.7
CC	N2		−94.6	−2.1	−118.3	91.8	57.1	−33.9
CD			−41.8	−5.5	−0.2	−3.4	6.1	−0.5
CQ			3.8	1.1	0.1	0.2	0.1	0.0
DD			22.8	−0.6	0.2	0.0	0.1	0.0
DQ			33.8	−0.1	−0.1	0.0	0.0	0.0
QQ			3.9	0.0	0.0	0.0	0.0	0.0
Σ			−72.1	−7.3	−118.3	88.5	63.4	−34.4
CC	N3			1.6	103.5	−87.3	−52.9	34.7
CD				3.1	14.5	−8.8	−9.7	3.4
CQ				−0.4	−0.8	−0.1	0.1	0.1
DD				0.6	−0.4	0.5	−0.4	0.1
DQ				0.4	0.1	0.0	0.0	0.0
QQ				0.0	0.0	0.0	0.0	0.0
Σ				5.3	116.8	−95.6	−62.9	38.3
CC	C7				13.0	−5.5	−5.6	2.0
CD					−24.1	−2.2	10.8	−0.1
CQ					−22.1	3.1	4.1	0.7
DD					3.0	0.0	1.2	0.0
DQ					−8.6	−0.2	−1.4	0.1
QQ					−0.3	0.0	0.0	0.0
Σ					−39.0	−4.8	9.2	1.3
CC	C13					−678.7	−769.5	238.0
CD						−91.3	−282.2	27.9
CQ						9.5	14.6	−0.6
DD						−2.6	−21.6	0.7
DQ						−3.4	−12.9	0.1
QQ						0.3	0.2	0.0
Σ						−766.2	−1071.3	266.1
CC	O14						271.6	−310.5
CD							50.0	−43.3
CQ							0.3	−14.0
DD							2.1	−1.1
DQ							−0.1	4.3
QQ							0.0	−0.1
Σ							324.0	−364.7
CC	O15							−129.1
CD								−11.9
CQ								−0.1
DD								−0.1
DQ								0.0
QQ								0.0
Σ								−141.2

[a]Based on integrated charges, dipoles, and quadrupoles determined at RHF/6-31G*.
[b]All values in kilocalories per mole.

that a linear change in one component of a multi-interaction situation does not necessitate a linear response. Secondly, the interactions of O_{pr} and of the carboxyl C with the CNN fragment are of the same magnitude. This observation emphasizes the general problem of *over*simplification in attempts to reduce a complicated scenario to the "essential" parts. Model building and interpretation is thus a matter of *balanced* reasoning. Some models can be eliminated because they are

Table 7. Electrostatic interaction matrix for **2**.

		N2	N3	C7	C13	O14	O15	H16
CC	C1	−21.8	13.7	1.6	47.7	−28.6	−21.2	8.9
CD		−39.7	16.7	4.9	−0.3	−12.2	1.5	0.1
CQ		12.1	−3.1	−2.3	−1.8	1.4	0.4	−0.1
DD		−8.3	3.9	−4.4	−0.2	−0.5	0.0	0.0
DQ		−3.9	3.5	0.2	−0.3	−0.2	0.0	0.0
QQ		2.3	0.2	1.5	0.0	0.0	0.0	0.0
Σ		−59.3	35.0	1.4	45.1	−40.1	−19.3	8.9
CC	N2		−95.8	−2.7	−125.7	95.0	55.4	−25.0
CD			−41.1	−6.2	−1.2	−1.1	3.6	−0.7
CQ			3.5	1.0	0.1	0.0	0.1	0.0
DD			22.6	−0.6	0.2	0.0	0.0	0.0
DQ			33.4	−0.1	−0.1	0.0	0.0	0.0
QQ			3.8	0.0	0.0	0.0	0.0	0.0
Σ			−73.7	−8.6	−126.7	93.9	59.2	−25.7
CC	N3			2.1	111.9	−92.4	−52.4	24.7
CD				3.6	17.7	−9.8	−7.9	2.5
CQ				−0.4	−0.9	−0.1	0.1	0.0
DD				0.7	−0.2	0.5	−0.2	0.0
DQ				0.4	0.1	0.0	0.0	0.0
QQ				0.0	0.0	0.0	0.0	0.0
Σ				6.4	128.6	−101.9	−60.5	27.3
CC	C7				17.1	−7.4	−7.0	2.6
CD					−19.8	−3.6	12.0	−2.7
CQ					−23.3	3.9	3.6	−0.7
DD					2.4	−0.3	0.4	−0.1
DQ					−9.3	−1.2	−0.6	0.1
QQ					−0.3	0.0	0.1	0.0
Σ					−33.3	−8.5	8.4	−0.8
CC	C13					−797.4	−685.5	242.3
CD						−269.9	−108.5	29.5
CQ						13.5	10.6	−0.7
DD						−19.3	−3.6	0.8
DQ						−11.1	−4.3	0.1
QQ						0.2	0.2	0.0
Σ						−1084.0	−790.9	272.0
CC	O14						273.2	−131.5
CD							50.1	−11.2
CQ							0.3	−0.2
DD							2.2	−0.1
DQ							0.0	0.0
QQ							0.0	0.0
Σ							325.7	−143.1
CC	O15							−302.8
CD								−40.2
CQ								−15.1
DD								−0.8
DQ								4.7
QQ								−0.1
Σ								−354.4

inconsistent with the electron density distributions, but there remains the difficult choice of selecting the best model among the ones that are consistent with the electron density distribution.

1,3-Bridging and steric interactions with the 2-position

As can be seen in Fig. 5, there occurs a bond path connecting N_α and the carbonyl-O in the molecular graph of **2**. The electron density at the bond critical point is 0.018 e au^{-3} and it is only marginally higher than the ρ_b value at the ring critical point (0.015 e au^{-3}). Equally small ρ_b values are found for the respective critical points in **1** and **3** (Table 4). What does this feature contribute to the discussion of the neighboring group interactions? Proponents of the N_α attraction model might

Table 8. Electrostatic interaction matrix for **3**.

		N2	N3	C7	C13	O14	O15
CC	C1	−12.9	7.7	1.9	33.9	−20.1	−15.0
CD		−36.7	14.3	2.0	−6.2	−10.4	3.8
CQ		11.9	−2.6	−2.6	−2.2	2.4	0.4
DD		−8.6	4.3	−8.3	0.2	−0.3	0.3
DQ		−4.8	3.7	−4.2	−0.3	−0.2	−0.1
QQ		1.9	0.2	1.9	0.0	0.0	0.0
Σ		−49.2	27.6	−9.2	25.4	−28.5	−10.6
CC	N2		−77.7	−4.8	−131.6	100.4	57.7
CD			−43.9	−4.9	−0.8	−4.7	4.7
CQ			5.1	1.6	−0.7	0.7	0.3
DD			22.3	−0.5	0.1	0.0	0.1
DQ			32.2	−0.3	−0.1	0.0	0.0
QQ			3.6	0.1	0.0	0.0	0.0
Σ			−58.3	−8.8	−133.1	96.5	62.8
CC	N3			3.5	108.2	−88.0	−50.4
CD				2.8	22.1	−15.3	−10.5
CQ				−0.6	−1.0	0.0	0.1
DD				0.5	−0.2	0.6	−0.4
DQ				0.5	0.1	0.1	−0.0
QQ				0.0	0.0	0.0	0.0
Σ				6.7	129.2	−102.6	−61.2
CC	C7				34.9	−14.9	−14.5
CD					−81.0	11.4	24.4
CQ					−3.9	0.9	2.6
DD					5.6	0.9	2.2
DQ					−0.7	−0.3	−0.9
QQ					0.0	0.0	0.0
Σ					−45.1	−1.8	13.8
CC	C13					−920.7	−920.1
CD						−186.1	−217.3
CQ						11.0	11.0
DD						−5.1	−7.1
DQ						−9.0	−10.9
QQ						0.5	0.6
Σ						−1109.4	−1143.8
CC	O14						313.3
CD							55.9
CQ							1.4
DD							2.5
DQ							−0.4
QQ							0.0
Σ							372.7

tend to be guided again by formalities and interpret the "bond path" in support of incipient bond formation between the O_{pr} donor and the electron-deficient N_α acceptor. We address this issue by analysis for consistency with the electron density distribution, by consideration of interaction lines (37) between interacting closed-shell systems, by citation of precedent for the occurrence of interaction lines between sterically interfering groups, and, finally, by citation of precedent for steric interference with the 2-position in optimizations of 1,3-bridging attractions.

The idea of incipient bond formation between the O_{pr} donor and the electron-deficient N_α acceptor is inconsistent with the electronic structures (vide supra). The N_α atom is not an acceptor but it is negatively charged. As the O_{pr} nucleophilicity increases, the negative charge of N_α *decreases* and, moreover, $q(N_\alpha)$ for **1–3** all are *less* negative than $q(N_\alpha) = -0.54$ in the parent benzenediazonium ion (14*d*). These features are not consistent with $O_{pr} \rightarrow N_\alpha$ electron donation but these electron density shifts are consistent with minimization of electron–electron repulsion between N_α and O_{pr}, that is, closed-shell or steric repulsion. The helium dimer is the simplest system for studying closed-shell interactions. Simple logic shows that there must be a "bond path" between the He atoms for *all* distances no matter whether the He atoms are far apart and essentially not bonded, in the region of the bound van-der-Waals dimer, or in the repulsive domain. The occurrence of a line connecting two attractors does not make any statement about the mode of interaction. The line just indicates "an interaction" and the better term for "bond path" is in fact "interaction line." Intramolecular interaction lines between nonconnected closed-shell systems were reported and associated with steric interactions (38).

Allyl alkali metals (39) and some of their heteroanalogues (40) prefer π-complexes in which the metal cation is located in a 1,3-bridging position between the negatively charged termini and above the best molecular plane of the allyl anion. In these cases, the distance between the metal and the C-atom at the 2-position is shorter than the contacts between the metal and the terminal carbons. The 1,3-bridging attraction model is very closely related to, and in fact can be seen as a polarity-reversed analogue of, the allyl metal bonding scenario.

Conclusion

The Bürgi–Dunitz angle of attack presents a useful concept that is easily accepted as it is in agreement with the electronic structure of carbonyls. Successful generalizations to other systems with the same bond polarity have also been described. We have argued, however, that the generalization asserted to describe the interaction of nucleophiles with diazonium ions cannot be correct. The N_α attraction model discussed by the groups of Dunitz and of Gougoutas is based on formal similarities of the C=O bond polarity and of the most commonly used Lewis structure of diazonium ions with its formally positive-charged N_α. This model relies on the assumption that the *formal* charge in the Lewis structure represents the *actual* charge distribution and the results of electronic structure analyses show that this assumption is not warranted.

The brief review of the crystallographic record on diazonium ion salts containing proximate nucleophiles shows that the distortions in their solid state structures are more fully consistent with the 1,3-bridging interaction model than with the N_α attraction model. In particular, combined analysis of solid state and of gas phase structures allows one to identify intramolecular interactions from packing effects and reveals that the intrinsic features associated with INA in diazonium ions are the CNN nonlinearity and the widening of the in-plane angles. Both of the electrostatic models can account for these features but in doing so different postulates are made concerning the electron density distribution. While the structural analysis alone cannot distinguish between the alternative interpretations, the study of the electronic structure allows one to clearly differentiate between competing inter-

Fig. 4. Electrostatic interaction energies ESI_{ij} (in kcal/mol) between pertinent pairs of atoms are shown for **1–3**. Solid (broken) arrows and negative (positive) interaction energies indicate attraction (repulsion). Values given in italics are the charge components CC_{ij} of ESI_{ij}. Atomic dipole moments are superimposed on the structures and they are directed from "o" to "•".

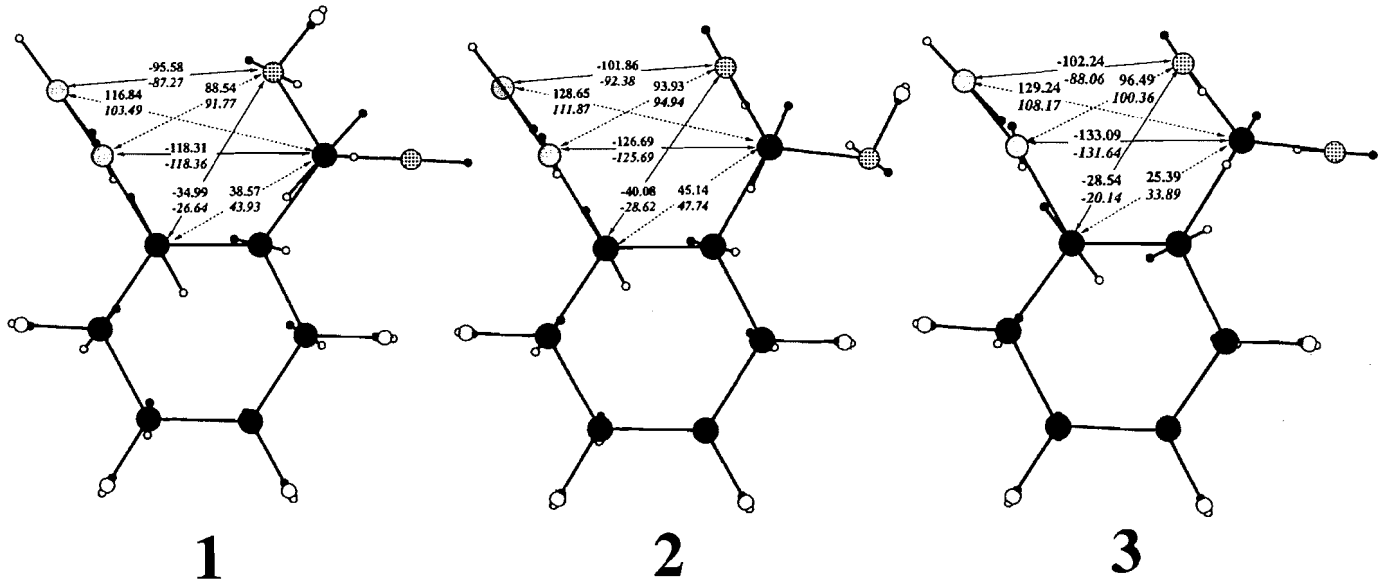

Fig. 5. The molecular graph (the collection of bond paths) of **2** is shown together with the cross sections of the zero-flux surfaces of the gradient vector field of the electron density. A "bond path" occurs between N_α and the proximate oxygen nucleophile.

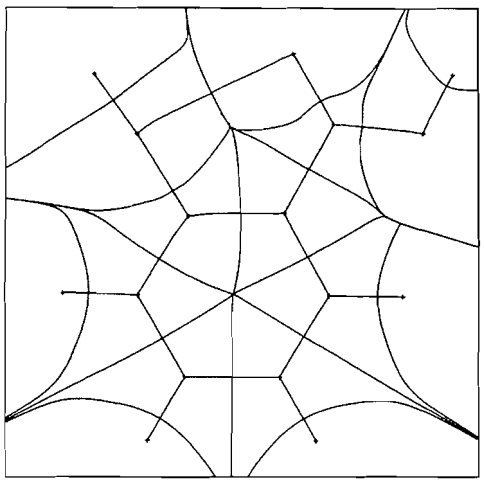

pretations of structural distortions. A method for the quantitative evaluation of electrostatic neighboring group interactions has been devised for this purpose and this ESI concept employs atomic electrical moments determined via topological electron density analysis. The results of the ESI analysis provide independent information that strongly supports the 1,3-bridging attraction model and eliminates the N_α attraction model.

The interpretation of neighboring group effects in crystal structures remains a matter of balanced reasoning. The discussion shows that some models can be eliminated because they are inconsistent with the electron density distributions, but the difficult challenge remains of identifying and selecting the best model among those that are consistent with the electron density distribution. The ESI method should prove particularly valuable for the development of electrostatic models as it is firmly based in quantum chemistry. It is hoped that these electrostatic models will allow for a better understanding of important stereochemical issues in a variety of chemical and biochemical problems.

Acknowledgment

We thank the Donors of the Petroleum Research Fund, administered by the American Chemical Society, and the Research Board as well as the Campus Computing Center of the University of Missouri for support.

References

1. (*a*) R. Glaser, C.J. Horan, E. Nelson, and M.K. Hall. J. Org. Chem. **57**, 215 (1992); (*b*) C.J. Horan, C.L. Barnes, and R. Glaser. Acta Crystallogr. Sect. C: Cryst. Struct. Commun. **C49**, 507 (1993); (*c*) Chem. Ber. **126**, 243 (1993); (*d*) C.J. Horan, P.E. Haney, C.L. Barnes, and R. Glaser. Acta Crystallogr. Sect. C: Cryst. Struct. Commun. **C49**, 1525 (1993); (*e*) R. Glaser, C.L. Mummert, C.J. Horan, and C.L. Barnes. J. Phys. Org. Chem. **6**, 201 (1993).
2. (*a*) H.-B. Bürgi, J.D. Dunitz, and E. Shefter. J. Am. Chem. Soc. **95**, 5065 (1973); (*b*) Acta Crystallogr. Sect. B: Struct. Crystallogr. Cryst. Chem. **B30**, 1517 (1974); (*c*) H.-B. Bürgi, J.D. Dunitz, J.M. Lehn, and G. Wipff. Tetrahedron, **30**, 1563 (1974); (*d*) J.D. Dunitz. Philos. Trans. R. Soc. London, Ser. B: **272**, 99 (1975); (*e*) M. Kaftory and J.D. Dunitz. Acta Crystallogr. Sect. B: Struct. Crystallogr. Cryst. Chem. **B31**, 2912 (1975); (*f*) Acta Crystallogr. Sect. B: Struct. Crystallogr. Cryst. Chem. **B31**, 2914 (1975); (*g*) Acta Crystallogr. Sect. B: Struct. Crystallogr.

Cryst. Chem. **B31**, 2917 (1975); (*h*) Acta Crystallogr. Sect. B: Struct. Crystallogr. Cryst. Chem. **B32**, 1 (1976).
3. W.B. Schweizer, G. Procter, M. Kaftory, and J.D. Dunitz. Helv. Chim. Acta, **61**, 2783 (1978).
4. K.B. Wiberg and K.E. Laidig. J. Am. Chem. Soc. **109**, 5935 (1987).
5. P.N.W. Baxter, J.A. Connor, D.C. Povey, and J.D. Wallis. J. Chem. Soc. Chem. Commun. 1135 (1991).
6. H.-B. Bürgi and V. Shklover. *In* Structure correlation. Vol. 1. *Edited by* H.-B. Bürgi and J.D. Dunitz. VCH Publishers, Inc., New York. 1994. Chap. 7.
7. G.F. Lanneau. Main Group Chem. News, **1**, 16 (1993).
8. (*a*) R.S. Glass, J.L. Broeker, and H. Firouzabadi. J. Org. Chem. **55**, 5739 (1990); (*b*) R.S. Glass, L. Adamowics, and J.L. Broeker. J. Am. Chem. Soc. **113**, 1065 (1991); (*c*) R.S. Glass. Main Group Chem. News, **2**, 4 (1994).
9. D. Britton and J.D. Dunitz. Helv. Chim. Acta, **63**, 1068 (1980).
10. (*a*) J.D. Wallis and J.D. Dunitz. J. Chem. Soc. Chem. Comm. 671 (1984); (*b*) J.D. Wallis, R.J.C. Easton, and J.D. Dunitz. Helv. Chim. Acta, **76**, 1411 (1993).
11. G.N. Lewis. *In* Valence and the structure of atoms and molecules. ACS Monogr. Ser. The Chemical Catalog Company, Inc., New York, New York, 1923.
12. R.F.W. Bader. *In* Atoms in molecules — a quantum theory. Clarendon Press, Oxford, U.K. 1990.
13. (*a*) R.F.W. Bader. Chem. Rev. **91**, 893 (1991); (*b*) Acc. Chem. Res. **18**, 9 (1985); (*c*) R.F.W. Bader, T.T. Nguyen-Dang, and Y. Tal. Rep. Prog. Phys. **44**, 893 (1981).
14. (*a*) R. Glaser. J. Phys. Chem. **93**, 7993 (1989); (*b*) J. Comput. Chem. **11**, 663 (1990); (*c*) R. Glaser, G.S.-C. Choy, and M.K. Hall. J. Am. Chem. Soc. **113**, 1109 (1991); (*d*) R. Glaser and C.J. Horan. J. Org. Chem. **60**, 7518 (1995).
15. (*a*) H. Zollinger. *In* Diazo chemistry I — Aromatic and heteroaromatic compounds. VCH, Weinheim, Germany. 1994; (*b*) *In* Diazo chemistry II — Aliphatic, inorganic, and organometallic compounds. VCH, Weinheim, Germany. 1995.
16. (*a*) R. Glaser, G.S. Chen, and C.L. Barnes. Angew. Chem. **104**, 749 (1992); Angew. Chem. Int. Ed. Engl. **31**, 740 (1992); (*b*) G.S. Chen, R. Glaser, and C.L. Barnes. J. Chem. Soc. Chem. Commun. 1530 (1993).
17. (*a*) J.Z. Gougoutas and J.J. Johnson. J. Am. Chem. Soc. **100**, 5816 (1978); (*b*) J.Z. Gougoutas. Cryst. Struct. Commun. **7**, 183 (1978); (*c*) J. Am. Chem. Soc. **101**, 5672 (1979); (*d*) Cryst. Struct. Commun. **11**, 1305 (1982).
18. M.J. Frisch, G.W. Trucks, H.B. Schlegel, P.M. Gill, P, B.G. Johnson, M.W. Wong, J.B. Foresman, M.A. Robb, M. Head-Gordon, E.S. Replogle, R. Gomperts, J.L. Andres, K. Raghavachari, J.S. Binkley, C. Gonzalez, R.L. Martin, D.J. Fox, D.J. Defrees, J. Baker, J.J.P. Stewart, and J.A. Pople. Gaussian92/DFT, Revision G.2. Gaussian Inc., Pittsburgh, Pa. 1993.
19. W.J. Hehre, L. Radom, P.v.R. Schleyer, and J.A. Pople. *In* Ab initio molecular orbital theory. John Wiley & Sons, New York. 1986.
20. F.W. Biegler-König, R.F.W. Bader, and T.-H. Tang. J. Comput. Chem. **3**, 317 (1982).
21. B. Greenberg and Y. Okaya. Acta Crystallogr. Sect. B: Struct. Crystallogr. Cryst. Chem. **B25**, 2101 (1969).
22. K. Sasvari, H. Hess, and W. Schwarz. Cryst. Struct. Commun. **11**, 781 (1982).
23. R.G. Ball and R.M. Elofson. Can. J. Chem. **63**, 332 (1985).
24. M. Cygler, M. Przybylska, and R.M. Elofson. Can. J. Chem. **60**, 2852 (1982).
25. R.M. Izatt, J.D. Lamb, C.S. Swain, J.J. Christensen, and B.L. Haymore. J. Am. Chem. Soc. **102**, 3032 (1980).
26. P. Groth. Acta Chem. Scand. Ser. A: **35**, 541 (1981).
27. R. Glaser. J. Comput. Chem. **10**, 118 (1989).
28. J.E. Carpenter and F. Weinhold. J. Mol. Struct. (Theochem), **169**, 41 (1988); (*b*) R. Arnaud. J. Comput. Chem. **15**, 1341 (1994), and references cited there.
29. R.G. Parr. Int. J. Quantum Chem. **26**, 687 (1984).
30. P.M. Walker and P.G. Mezey. J. Am. Chem. Soc. **115**, 12423 (1993).
31. R. Glaser and G.S.-C. Choy. J. Am. Chem. Soc. **115**, 2340 (1993).
32. (*a*) T. Slee. J. Am. Chem. Soc. **108**, 7541 (1986); (*b*) R.F.W. Bader, A. Larouche, C. Gatti, M.T. Carroll, P.J. MacDougall, and K.B. Wiberg. J. Chem. Phys. **87**, 1142 (1987).
33. U. Dinur and A.T. Hagler. J. Chem. Phys. **91**, 2949 (1989).
34. (*a*) S. Huzinaga, Y. Sakai, E. Miyoshi, and S. Narita. J. Chem. Phys. **93**, 3319 (1990); (*b*) S. Huzinaga and Y. Narita. Isr. J. Chem. **19**, 242 (1980).
35. D.L. Cooper and N.C.L. Stutchbury. Chem. Phys. Lett. **120**, 167 (1985).
36. R. Glaser and B.L. Harris. J. Mol. Struct. (Theochem), **255**, 45 (1992).
37. R.F.W. Bader and H. Essén. J. Chem. Phys. **80**, 1943 (1984).
38. (*a*) J. Cioslowski and S.T. Mixon. J. Am. Chem. Soc. **114**, 4382 (1992); (*b*) Can. J. Chem. **70**, 443 (1992).
39. N.J.R.v.E. Hommes, M. Bühl, and P.v.R. Schleyer. J. Organomet. Chem. **409**, 307 (1991), and references cited there.
40. (*a*) R. Glaser and A. Streitwieser. J. Org. Chem. **56**, 6612 (1991); (*b*) J. Org. Chem. **54**, 5491 (1989); (*c*) J. Am. Chem. Soc. **111**, 8799 (1989).

Origin of depressed dipole moments in five-membered, unsaturated heterocycles

Keith E. Laidig, Peter Speers, and Andrew Streitwieser

Abstract: The smaller molecular dipole moments of cyclopentadiene, pyrrole, furan, and thiophene, relative to their saturated analogs, are investigated using the HF/6-311++G**//HF/6-311++G** level of theory. Investigation of the atomic origins of the molecular dipole moments demonstrates that the decreased dipole moments of the unsaturated heterocycles result from simple perturbations of the butadiene fragment, rather than a delocalization of hetero-atom lone pairs into the π system. Comparison with the origins of the molecular dipole moments of the saturated analogs shows that a special delocalization mechanism is not necessary.

Key words: ab initio, atoms-in-molecule, electronic effects, delocalization, polarization.

Résumé : Opérant au niveau HF/6-311++G**//HF/6-311++G** de la théorie, on a étudié les moments polaires moléculaires du cyclopentadiène, du pyrrole, du furane et du thiophène qui sont plus faibles par rapport à ceux des leurs analogues saturés. L'étude sur les origines atomiques des moments dipolaires moléculaires démontre que les moments dipolaires plus faibles des hétérocycles insaturés résultent de perturbations simples du fragment butadiène plutôt que d'une délocalisation des paires d'électrons non partagées des hétéroatomes dans le système π. Une comparaison avec les origines des moments dipolaires moléculaires des analogues saturés montre qu'il n'est pas nécessaire de faire appel à un mécanisme spécial de délocalisation.

Mots clés : ab initio, atomes dans les molécules, effets électroniques, délocalisation, polarisation.

[Traduit par la rédaction]

Introduction

Recent investigations into the consequences of methyl carbon deprotonation in methyl vinyl sulfide found that there was little delocalization of electronic charge from the anionic center to the vinyl group in the resulting anion (1). This suggests that the sulfur atom acts as an insulator between the anionic methylene center and the π system of the vinyl fragment, effectively isolating the two moieties (Fig. 1). One surprising implication applies to the physical properties of the five-membered heterocycles, pyrrole, furan, and thiophene, relative to their saturated analogs. Typically, the differences are attributed to a significant delocalization of the hetero-atom lone pairs into the π system of the five-membered ring. This implication prompted the present investigation of the distribution of electronic charge within five-membered heterocycles with an emphasis upon the consequences of delocalization upon the observable physical properties of these molecules (2–5).

One physical property that has often been linked to the delocalization of the hetero lone pairs into π systems is the dipole moment of the unsaturated five-membered ring heterocycles (6). The dipole moments are compared to the saturated analogs in Fig. 2 (7).

The differences have been attributed to a superposition of a π-moment opposed to the σ-moment to give a smaller resulting moment, and in the case of pyrrole a net moment in the opposite direction. The effect in pyrrole is also symbolized by the polarization resonance structures in Fig. 3 that show a dipole moment contribution whose direction is from nitrogen to the ring. The corresponding saturated system has no such mechanism available and so the σ-moment dominates, resulting in less dampening of molecular dipole moment.

Any multipole moment of a molecule may be broken into the contributions of the constituent atoms in a rigorous and physically meaningful manner using subsystem quantum mechanics (8–10). This is done by expanding the $\boldsymbol{r}$-weighted, spatial integration of the electronic charge density in terms of integrations over the spatial regions defined by the boundary conditions of the quantum subsystems, the atoms of the molecule. Explicitly, the dipole moment is broken into two terms, the displacement of charge from the origin, $q(\Omega)X_\alpha{}^\Omega$, and the polarization of the charge within each atom, $M_\alpha(\Omega)$, eq. [1].

$$[1] \quad \mu_\alpha = \sum_\Omega [q(\Omega)X_\alpha{}^\Omega + M_\alpha(\Omega)]$$

Such a breakdown of the molecular moment allows for a detailed investigation of the origins of that moment and its relation to the properties of the atoms of the systems. In the

Received October 5, 1995.

This paper is dedicated to Professor Richard F.W. Bader on the occasion of his 65th birthday.

K.E. Laidig,[1] P. Speers,[2] and A. Streitwieser.[3] Department of Chemistry, University of California, Berkeley, CA 94720-1460, U.S.A.

[1] Current address: Department of Medicinal Chemistry, University of Washington, Seattle, WA 98195-7610, U.S.A. E-mail: laidig@u.washington.edu

[2] Current address: Department of Pharmacy, University of Manchester, Manchester, U.K. E-mail: pspeers@fs1.pa.man.ac.uk

[3] Author to whom correspondence may be addressed. E-mail: astreit@garnet.berkeley.edu

Fig. 1. A depiction of the lack of delocalization in the vinylthiomethyl anion.

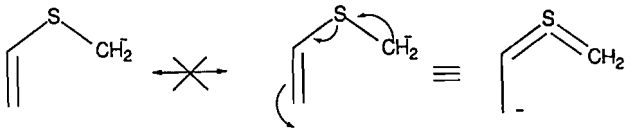

Fig. 2. A depiction of the direction and magnitude of the dipole moments (in D) of the saturated and unsaturated five-membered ring systems. Values shown are for the gas phase except for pyrrolidine (cyclohexane) and tetrahydrothiophene (benzene) (7). Numbers in parentheses are the calculated values from this work. The saturated heterocycles are not planar and their dipole moments do not lie in the plane of the figure.

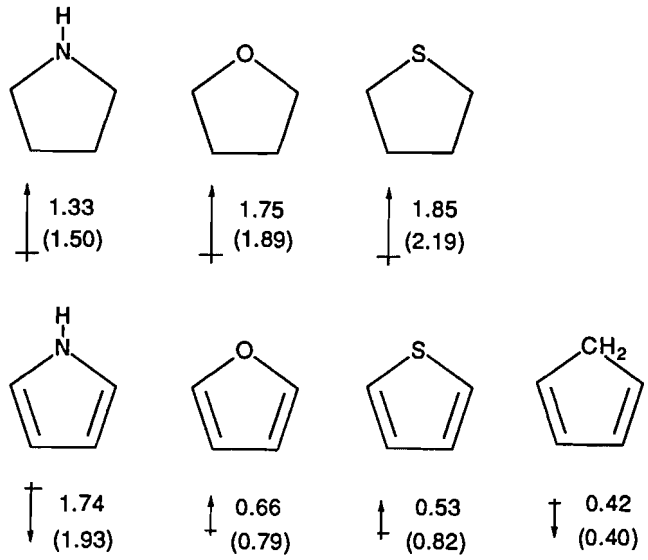

present work we apply this approach to investigate the origin of the depressed dipole moment in unsaturated five-membered ring heterocycles.

Methodology

We consider the unsaturated series, cyclopentadiene, pyrrole, furan, and thiophene, and the corresponding saturated series of cyclopentane, tetrahydropyrrole, tetrahydrofuran, and tetrahydrothiophene, as well as *cis*-butadiene as our prototypical butadienoid fragment. All of the atomic and molecular properties were determined from the triple-zeta, polarized, diffuse, and balanced HF/6-311++G** wave functions (11–14) determined at conformations optimized using the same level of theory. The potential surfaces were characterized via the determination of the analytical second derivatives, and each structure was found to be a minimum on its potential energy surface. The molecular calculations were performed using the Gaussian92 (15) and GAMESS (16) program suites. The HF/6-311++G** wave functions were used to determine the properties of the charge distribution and the atomic properties with the AIMPAC (17) suite of programs. Although the molecular dipole moments of neutral molecules are independent of origin, all dipole moments were determined using the center of mass.

The particular terms used in this study are defined as follows: $q(\Omega)$ is the atomic charge and $M_\alpha(\Omega)$ is the atomic dipole moment. These properties are determined by integration over the space of the atom bounded by zero-flux surfaces of the electronic charge density and the position-weighted charge density, for the atomic population (which is subtracted from the nuclear charge to yield the atomic charge) and the atomic dipole moment, respectively. The atomic contribution each atom makes, M_α^Ω, to the molecular dipole moment is the sum of $q(\Omega)*X_\alpha^\Omega$ and $M_\alpha(\Omega)$. The first term is a charge displacement term, which individually is dependent upon the origin, but whose sum is origin independent. The origin dependence of the individual terms reflects the fact the dipole moment describes the spatial distribution of electronic charge within the molecule. A change of origin does not change the physical distribution of electronic charge within a molecule or within the individual atoms. Instead, an origin shift changes the manner in which the moment, which is a tensor, is expanded mathematically. Clearly, care should be taken in comparing the origin-dependent terms in dissimilar systems. In the present case, the center of mass is a convenient choice since it provides the minimum set of mass-weighted distances to each atom, the molecules are similar in shape and size, and it corresponds to the origin generally used in experiment.

Results

The molecular dipole moments and their atomic contributions are listed in Tables 1 and 2, respectively. The molecular dipole moments reproduce the observed trends, with the dipole moments of the unsaturated systems being depressed relative to the corresponding saturated molecule. The experimental results are given in Fig. 2 (2.542 D = 1 au).

The dipole moment of tetrahydrofuran is dominated by the atomic contribution of the O atom, $M_z^\Omega(O)$. Its contribution is opposed by the contributions of C_α and H_α and is enhanced by those of C_β and H_β. The contribution O makes to the molecular dipole is the sum of a large charge displacement, reflecting the displacement of the large atomic charge from the molecular center of mass, and a small opposing polarization of O back towards the center of the ring. The transfer of charge from

Fig. 3. A depiction of the various resonance isomers of pyrrole.

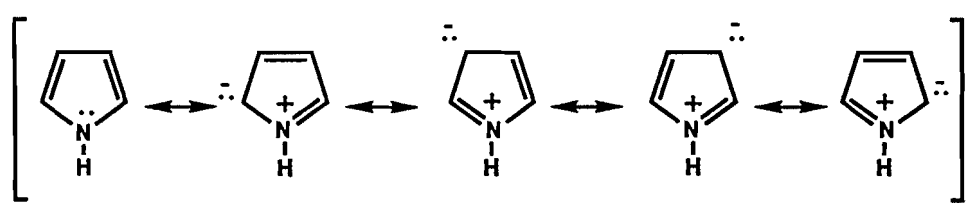

Table 1. The atomic contributions to the molecular dipole moments of the unsaturated pentacycles.[a]

***cis*-Butadiene**

	C_β	C_α	$H_{C\beta}$	$H_{C\alpha}$	$H_{C\alpha}$	Sum	Mol
$q(\Omega)$	0.040	0.064	−0.044	−0.030	−0.038	−0.016	0
Z^Ω	−1.029	0.967	−2.878	0.739	2.876		
$q(\Omega)*Z^\Omega$	−0.041	0.062	0.126	−0.022	−0.312		
$M_z(\Omega)$	−0.044	−0.003	0.100	0.008	−0.101		
M_z^Ω	−0.085	0.059	0.226	−0.014	−0.211	−0.050	−0.012 (−0.03 D)[b]

Cyclopentadiene

	C	C_β	C_α	H_{CH2}	$H_{C\alpha}$	$H_{C\beta}$	Sum	Mol
$q(\Omega)$	0.167	0.017	−0.002	−0.038	−0.029	−0.031	0.001	0.000
Z^Ω	2.335	−1.824	0.554	3.561	1.161	−3.497		
$q(\Omega)*Z^\Omega$	0.390	−0.030	−0.001	−0.136	−0.034	0.107		
$M_z(\Omega)$	−0.039	0.043	−0.025	−0.076	−0.032	0.087		
M_z^Ω	0.351	0.013	−0.026	−0.212	−0.066	0.194	0.156	0.156 (0.40 D) expt. 0.42 D

Furan

	O	C_α	C_β	$H_{C\beta}$	$H_{C\alpha}$	Sum	Mol
$q(\Omega)$	−1.343	0.567	0.085	−0.008	0.027	0.000	0.000
Z^Ω	2.105	0.600	−1.842	−3.442	1.526		
$q(\Omega)*Z^\Omega$	−2.825	0.340	−0.157	0.028	0.042		
$M_z(\Omega)$	0.288	0.618	0.209	0.079	−0.044		
M_z^Ω	−2.537	0.958	0.052	0.107	−0.002	−0.309	−0.309 (−0.79 D) expt. 0.66 D

Thiophene

	S	C_α	C_β	$H_{C\alpha}$	$H_{C\beta}$	Sum	Mol
$q(\Omega)$	0.240	−0.212	0.088	0.019	−0.015	0.000	0.000
Z^Ω	2.167	−0.110	−2.464	0.421	−4.148		
$q(\Omega)*Z^\Omega$	0.519	0.023	−0.217	0.008	0.063		
$M_z(\Omega)$	−0.963	−0.034	0.153	−0.025	0.088		
M_z^Ω	−0.444	−0.011	−0.064	−0.017	0.151	−0.324	−0.323 (−0.82 D) expt. 0.53 D

Pyrrole

	N	H_N	C_α	C_β	$H_{C\beta}$	$H_{C\alpha}$	Sum	Mol
$q(\Omega)$	−1.585	0.470	0.532	0.062	−0.029	−0.008	0.001	0.000
Z^Ω	2.103	3.978	0.617	−1.841	−3.458	1.424		
$q(\Omega)*Z^\Omega$	−3.334	1.870	0.329	−0.115	0.099	−0.011		
$M_z(\Omega)$	0.176	−0.166	0.585	0.188	0.082	−0.049		
M_z^Ω	−3.158	1.704	0.914	0.073	0.181	−0.060	0.761	0.761 (1.93 D) expt. 1.74 D

[a]Only the symmetry-unique atoms are listed, as are only those contributions to non-zero components of the molecular dipole moments. All values are given in atomic units, 1 au = 2.542 D, or in D as indicated. Sum is the sum of atomic contributions and Mol is the molecular value. $q(\Omega)$ is the basin charge, Z^Ω is the z-coordinate, $q(\Omega)*Z^\Omega$ is the charge displacement contribution, $M_z(\Omega)$ is the polarization of each atom within its basin, M_z^Ω is the atomic (basin) contribution to the molecular dipole moment. Experimental values taken from ref. 7.

[b]*cis*-Butadiene is not planar; the direction of the molecular dipole moment has the positive pole at the β-position.

Table 2. The atomic contributions to the molecular dipole moments of the saturated pentacycles.[a]

Tetrahydrofuran	O	C_α	C_β	$H_{C\alpha}$	$H_{C\beta}$	$H_{C\alpha}$	$H_{C\beta}$	Sum	Mol[b]
$q(\Omega)$	−1.297	0.760	0.172	−0.075	−0.048	−0.078	−0.082	0.001	0.000
X^Ω	0.646	−0.253	−0.071	1.667	0.889	−1.628	−2.204		
Z^Ω	2.124	0.832	−1.987	−2.793	1.375	−3.058	1.375		
$q(\Omega)*X^\Omega$	−0.839	−0.193	−0.012	−0.124	−0.043	0.127	0.182		
$q(\Omega)*Z^\Omega$	−2.755	0.633	−0.342	0.208	−0.066	0.238	−0.113		
$M_x(\Omega)$	0.102	0.190	0.019	−0.090	−0.051	0.081	0.112		
$M_z(\Omega)$	0.143	0.381	−0.017	0.051	−0.028	0.061	−0.028		
M_x^Ω	−0.737	−0.003	0.007	−0.214	−0.094	0.208	0.294	−0.340	−0.342
M_z^Ω	−2.612	1.014	−0.359	0.259	−0.094	0.299	−0.141	−0.658	−0.659

Tetrahydrothiophene	S	C_α	C_β	$H_{C\beta}$	$H_{C\alpha}$	$H_{C\beta}$	$H_{C\alpha}$	Sum	Mol[c]
$q(\Omega)$	−0.050	0.059	0.197	−0.070	−0.037	−0.076	−0.054	−0.011	0.000
X^Ω	0.953	−0.548	−0.479	1.220	0.451	−2.074	−2.474		
Z^Ω	2.112	0.205	−2.536	−3.451	0.441	−3.585	0.853		
$q(\Omega)*X^\Omega$	−0.048	−0.033	−0.095	−0.086	−0.016	0.157	0.132		
$q(\Omega)*Z^\Omega$	−0.106	0.012	−0.499	0.243	−0.016	0.271	−0.046		
$M_x(\Omega)$	−0.580	−0.065	0.016	−0.088	−0.044	0.084	0.113		
$M_z(\Omega)$	−0.685	0.002	−0.004	0.058	−0.015	0.064	−0.026		
M_x^Ω	−0.628	−0.098	−0.079	−0.174	−0.060	0.241	0.245	−0.477	−0.480
M_z^Ω	−0.791	0.014	−0.503	0.301	−0.031	0.335	−0.072	−0.704	−0.714

Tetrahydropyrrole	N	H_N	C_α	C_β	$H_{C\beta}$	$H_{C\beta}$	$H_{C\alpha}$	$H_{C\alpha}$	Sum	Mol[d]
$q(\Omega)$	−1.247	0.357	0.604	0.161	−0.090	−0.071	−0.082	−0.077	0.001	0.000
X^Ω	−0.573	−2.462	0.282	0.044	−1.709	−0.789	1.573	2.246		
Z^Ω	2.277	2.388	0.831	−1.988	−2.771	1.336	−3.109	1.309		
$q(\Omega)*X^\Omega$	0.714	−0.879	0.171	−0.137	0.154	0.056	−0.130	−0.172		
$q(\Omega)*Z^\Omega$	−2.839	0.851	1.136	−0.319	0.249	−0.095	0.254	−0.100		
$M_x(\Omega)$	−0.085	0.196	−0.115	−0.023	0.095	0.054	−0.079	−0.110		
$M_z(\Omega)$	−0.200	0.001	−0.317	−0.052	0.049	−0.028	0.068	−0.022		
M_x^Ω	0.629	−0.683	0.056	−0.016	0.249	0.110	−0.209	−0.282	−0.237	−0.244
M_z^Ω	−3.039	0.852	0.819	−0.371	0.298	−0.123	0.322	−0.122	−0.541	−0.538

[a]Only the symmetry-unique atoms are listed, as are only those contributions to non-zero components of the molecular dipole moments. All values are given in atomic units; 1 au = 2.542 D. Sum is the sum of atomic contributions and Mol is the molecular value. Symbols are defined in Table 1. Experimental dipole moments from ref. 7.

[b]Resultant μ = 1.89 D (expt. 1.75 D, g, for lowest vibrational state).

[c]Resultant μ = 2.19 D (expt. 1.85 D, in benzene).

[d]Resultant μ = 1.50 D (expt. 1.33 D, in cyclohexane).

both C_α to the more electronegative O atom causes the charge displacement contribution from C_α to be in opposition to that of the O contribution. As is typical for atoms that lose charge to more electronegative bonded neighbors, the remaining charge within the C_α basin is polarized in opposition to the direction of charge transfer to the bonded O atom, further adding to the opposing contribution of C_α. In the case of C_β, the transfer of charge away from these sp^3 atoms to their more electronegative bonded hydrogens provides a charge displacement contribution in support of that of O ($q(C_\beta)$ is both the opposite sign and on the opposite side of the center of mass, thus its charge displacement contribution is of the same sign as $q(O)*Z^\Omega(O)$).

In furan, the total contribution of the O atom is also the dominant term. The C_α provides an opposing contribution, as does H_β, while H_α and C_β contribute relatively little to the molecular moment. As in the saturated system, the charge transferred from C_α to O yields a strong contribution to the overall molecular polarization towards the O atom. But the atomic polarization of the O atom back towards the center of the ring is twice as large as in tetrahydrofuran. Again, both the charge displacement and atomic polarization contributions from C_α are in opposition to the contribution from oxygen. The sp^2 β carbons of the unsaturated heterocycles are more electronegative than the sp^3 carbons of their saturated counterparts, resulting in less charge transferred to the β hydrogens

Fig. 4. Electronic effects treated as perturbations of butadiene.

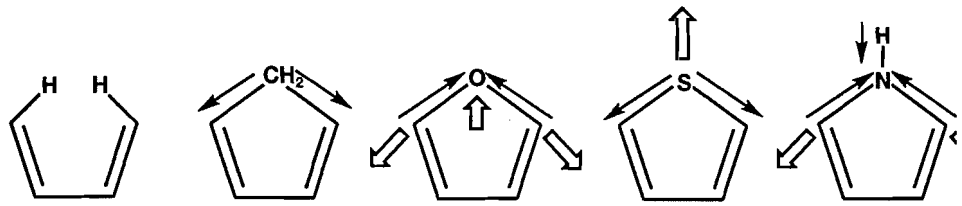

and therefore only small charge displacement contributions to the molecular moment.

The dipole moment of tetrahydrothiophene is dominated by the contribution of large first moment of S, M_z(S), while the nearly neutral atomic charge contributes little. Unlike its O substituted counterpart, the C_α of tetrahydrothiophene makes little contribution to the molecular moment. Since S is roughly electroneutral in comparison to sp^3 C, there is only a small charge transfer from C_α and the first moments of that atom are also small. In common with tetrahydrofuran, the contribution from C_β results from charge transfer to its bonded H atoms and increases the magnitude of molecular polarization towards the S atom.

In the unsaturated thiophene, the atomic first moment M_z(S) is not as large as that in tetrahydrothiophene, but still dominates the contribution from S. The greater electronegativity of the neighboring sp^2 carbons results in a greater withdrawal of charge from S, creating a small dampening charge displacement contribution, $q(S)^* Z^\Omega(S)$. The C_α and C_β make only small contributions and the largest is the dampening coming from H_β, a result of the atom's charge and its displacement from the molecular center of mass.

The largest change in molecular dipole moment between saturated and unsaturated heterocycles is between tetrahydropyrrole and pyrrole. In the saturated system, the charge displacement contribution from N dominates the molecular moment, reflecting that N pulls charge from all three of its bonded neighbors. This effect is dampened by both the charge displacement and polarization contributions from the C_α atoms and a large contribution from H_N. The large amount of charge pulled from H_N and its distance from the center of mass creates this large charge displacement contribution. The C_β atoms provide a charge displacement contribution in the direction of N, in the same manner as in tetrahydrofuran and tetrahydrothiophene.

In pyrrole, the large charge displacement contribution of N is the largest individual term. The large transfer of charge from C_α to N and the strong polarization of the remaining charge on carbon away from N provide large dampening terms. As in the saturated system, the large positive charge of H_N and its distance from the molecular center of mass provide a large charge displacement dampening term $q(H_N)^* Z^\Omega(H_N)$. This dampening is larger in the planar, unsaturated system because the vector contributions are in direct opposition to the contributions of N. In contrast, in the nonplanar saturated system the dampening from H_N is not in direct opposition, but the vectors are less efficiently directed and the projection of this contribution against the N contribution is smaller in magnitude.

As a test of this interpretation of H_N of the nitrogen heterocycles, the dipole moment of protonated furan was calculated using the same level of theory. Our observations would lead to the prediction that protonation of furan should create a large charge displacement term, $q(H_O)^* Z^\Omega(H_O)$, which would contribute in opposition to the molecular dipole moment of furan. Although the dipole moments of such charged species are origin dependent, using the center of mass as the origin provides a common basis for comparison. The resulting dipole moment is heavily dampened (+1.047 au), and indeed is opposite in sign compared to furan; the result shows the behavior predicted.

Discussion

The primary origin of the dampened dipole moments in the unsaturated heterocycles arises from the difference in electronegativity of the sp^2 carbon centers. The greater electronegativity of the sp^2 C_α in the unsaturated molecules reduces the amount of charge transferred to O and to N, and increases the amount of charge withdrawn from S. The increasing charge displacement and the resulting polarizations act to dampen the contributions from the hetero atoms. Similarly, the sp^2 C_β centers do not transfer as much charge to their bonded neighbors and thus do not provide the enhancing contributions to the hetero-atom terms that are seen from the C_β atoms in the saturated analogs.

The dipole moments of the series of unsaturated five-membered heterocycles can be readily understood as simple perturbations of the atomic contributions to the dipole moment of a common butadiene fragment (see Fig. 4) (18).

As listed in Table 1, the dipole moment of *cis*-butadiene is nearly zero. Replacing two of the H atoms with a CH_2 group yields cyclopentadiene, whose dipole moment is small in magnitude and whose center of negative charge is displaced away from the CH_2 group. The replacement of the hydrogens with a less electronegative sp^3 carbon results in charge displacement towards the butadiene group and a resulting small molecular polarization with the positive end of the vector pointing towards the CH_2 group.

Replacing the CH_2 group by O pulls charge from the butadiene fragment. The resulting polarization of the C_α atoms is away from the direction of charge withdrawal. O is slightly polarized towards the direction of charge donation, but this and the contributions from C_α cannot overcome the large charge displacement contributions at O. Thus, the negative pole of the overall dipole moment points towards the O atom. In contrast, replacing the CH_2 group with the less electronegative S allows charge to be pulled into the butadiene fragment. Unlike the CH_2 fragment, the polarizable S can and does polarize away from the direction of charge withdrawal. This large atomic polarization dominates and the negative end of overall dipole moment vector points away from the S atom.

Finally, replacing the CH_2 group by NH again puts an electronegative group in the position to pull charge from the butadiene. In parallel with the origin of the dipole moment in furan, the transfer of charge from C_α and its resulting polarization provide dampening polarizations. But in this case, the withdrawal of charge from H_N puts a relatively large positive charge on the other side of the N atom. This provides a large contribution in opposition to the charge displacement terms of N, ultimately reversing the sign of the molecular dipole moment in comparison to that of furan. This can be clearly seen in the comparison between furan and protonated furan, in which this very mechanism reverses the sign of the molecular dipole moment.

This study demonstrates that the difference in molecular dipole moments between the saturated and unsaturated heterocycles can be readily understood in terms of the transfer of charge between atoms, their geometric relation to the molecular center of mass, and the atomic polarizations. A delocalization mechanism is not required to explain the dampening of the molecular dipole moments; arguments based upon pairwise interactions and their consequences suffice.

Conclusion

The present study has presented a dissection of the molecular dipole moment of five-membered heterocycles into atomic contributions using subspace quantum mechanics. The dipole moments were partitioned into atomic contributions, each of which is a physical observable in the quantum mechanical sense. A detailed comparison of the contributions to the dipole moments of the saturated and unsaturated five-membered ring heterocycles of nitrogen, oxygen, and sulfur shows that the changes of the molecular dipole moments of the unsaturated heterocycles can be readily understood in terms of the transfer of charge between atoms, the geometric relation of the atoms to one another, and the polarization of the atoms. A delocalization mechanism of the π-resonance type such as in Fig. 3 is not necessary to explain the observed dipole moment effects.

Acknowledgments

This work was supported in part by NSF Grants CHE87-21134 and CHE92-21277. Some of the computations made use of the Graphics Facility of the College of Chemistry, which is supported by NIH Grant S10 RR05651-01. We also thank Professor R.F.W. Bader for valuable discussions. P.S. would like to thank Professors M. Rowland and K.T. Douglas, and Glaxo Group Research for support at Manchester; K.E.L. is pleased to acknowledge financial support from Professor V. Daggett of the Department of Medicinal Chemistry at Washington during the preparation of this manuscript.

References

1. P. Speers, K.E. Laidig, and A. Streitwieser. Manuscript in preparation.
2. C.K. Ingold. J. Chem. Soc. 1120 (1933).
3. J. March. Advanced organic chemistry, reactions, mechanisms, and structure. McGraw–Hill, New York. 1977.
4. L.A. Paquette. Principles of modern heterocyclic chemistry. W.A. Benjamin, Inc., New York. 1968.
5. G. Marino. Adv. Heterocycl. Chem. **13**, 235 (1971).
6. H. Lumbroso and C. Carpanelli. Bull. Soc. Chim. Fr. 3198 (1964).
7. A.L. McClellan. Tables of experimental dipole moments. Vol. 2. Rahara Enterprises, El Cerrito, Calif. 1974.
8. R.F.W. Bader, A. Larouche, C. Gatti, M.T. Caroll, P.J. MacDougall, and K.B. Wiberg. J. Chem. Phys. **87**, 1142 (1987).
9. R.F.W. Bader. Atoms in molecules: a quantum theory. Oxford University Press, New York. 1990.
10. K.E. Laidig. J. Phys. Chem. **97**, 12760 (1993).
11. W.J. Hehre, R. Ditchfield, and J.A. Pople. J. Chem. Phys. **56**, 2257 (1972).
12. M.M. Francl, W.J. Pietro, W.J. Hehre, M.S. Gordon, D.J. DeFrees, and J.A. Pople. J. Chem. Phys. **77**, 3654 (1982).
13. P.C. Hariharan and J.A. Pople. Theor. Chim. Acta, **28**, 213 (1973).
14. M.J. Frisch, J.A. Pople, and J.S. Binkley. J. Chem. Phys. **80**, 3265 (1984).
15. M.J. Frisch, G.W. Trucks, M. Head-Gordon, P.M.W. Gill, M.W. Wong, J.B. Foresman, B.G. Johnson, H.B. Schlegel, M.A. Robb, E.S. Replogle, R. Gomperts, J.L. Andres, K. Raghavachari, J.S. Binkley, C. Gonzalez, R.L. Martin, D.J. Fox, D.J. Defrees, J. Baker, J.J.P. Stewart, and J.A. Pople. Gaussian, Inc., Pittsburgh, Pa. 1992.
16. M.W. Schmidt, K.K. Baldridge, J.A. Boatz, S.T. Elbert, M.S. Gordon, J.H. Jensen, S. Koseki, N. Matsunaga, K.A. Nguyen, S. Su, T.L. Windus, M. Dupuis, and J.A. Montgomery, Jr. J. Comput. Chem. **14**, 1347 (1993).
17. F.W. Biegler-König, R.F.W. Bader, and T.H. Tang. J. Comput. Chem. **3**, 317 (1982).
18. N.D. Epiotis, W.R. Chery, F. Bernardi, and W.J. Hehre. J. Am. Chem. Soc. **98**, 4361 (1976).

The anomeric effect in first-row/second-row acetal-like systems

Camilla Scott and Friedrich Grein

Abstract: Ab initio calculations were performed at the HF/6–31+G* level on first-row/second-row neutral, protonated, and anionic acetal-like systems. The neutral and anionic systems are of the general form $XH_mCH_2YH_n^{(-)}$ with XH_m = F, a-OH, s-NH_2, s-CH_3; YH_n = SH, PH_2; and YH_n^- = PH^-, SiH_2^-. For the protonated systems the general form is $XH_m^+CH_2YH_n$, with XH_m^+ = a-FH^+, s-OH_2^+, s-NH_3^+; and YH_n = SH, PH_2. In all cases the hydrogens on Y were rotated about the CY bond, and geometries were optimized for each setting of the YH_n dihedral angles. Following previously developed methods, the electronic part e of the anomeric stabilization was evaluated. For PH_2 rotation, $-e_P$ (e is always negative) is smaller than for corresponding nitrogen systems, whereas for SH rotation the $-e_S$ parameters are larger than for corresponding oxygen systems. In the case of protonated molecules, the energy associated with the reverse anomeric effect was estimated to be −4 kcal/mol for s-$OH_2^+CH_2SH$ and −3 kcal/mol for s-$NH_3^+CH_2SH$. For corresponding phosphorus systems they are close to −2 and −5 kcal/mol, respectively. The π-bonding model applied to neutral species shows that in the case of SH rotation the F and O systems clearly follow the trend of the π-bonded cation $CH_2{=}SH^+$. For PH_2 rotation, however, only the F system can be considered to correlate with such a model.

Key words: anomeric effect, reverse anomeric effect, first-row/second-row atoms, phosphorus, sulfur.

Résumé : On a effectué des calculs ab initio au niveau HF/6-31+G* sur des systèmes de types acétals neutres, protonés et anioniques d'éléments des deux premières périodes. Les systèmes neutres sont de la forme générale $XH_mCH_2YH_n^{(-)}$ pour lesquels XH_m = F, a-OH, s-NH_2, s-CH_3; YH_n = SH, PH_2 et $H_n^{(-)}$ = PH^- et SiH_2^-. Les systèmes protonés sont de la forme générale $XH_m^+CH_2YH_n$ pour lesquels XH_m^+ = a-FH^+, s-OH_2^+, s-NH_3^+ et YH_n = SH et PH_2. Dans tous les cas, on a fait subir une rotation aux hydrogènes sur Y autour de la liaison CY et on a optimisé les géométries pour tous les angles dièdres attribués aux YH_n. Suivant des méthodes développées antérieurement, on a évalué la partie électronique, e, de la stabilisation anomérique. Pour la rotation PH_2, la valeur de $-e_P$ (la valeur de e est toujours négative) est toujours plus faible que celle des systèmes azotés correspondants. Dans les cas de molécules protonées, l'énergie associée à l'effet anomérique inverse a été évaluée à −4 kcal mol^{-1} pour s-$OH_2^+CH_2SH$ et à −3 kcal mol pour le s-$NH_3^+CH_2SH$. Pour les systèmes phosphorés, ces valeurs sont plutôt près de −2 et −5 kcal mol^{-1} respectivement. Le modèle de la liaison π appliqué aux espèces neutres montre que, dans le cas du SH, la rotation des systèmes F et O suit bien la tendance du cation $CH_2{=}SH^+$ impliqué dans une liaison π. Pour la rotation du PH_2, on doit toutefois considérer que seul le système F donne une corrélation avec un tel modèle.

Mots clés : effet anomérique, effet anomérique inversé, éléments des deux premières périodes, phosphore, soufre.

[Traduit par la rédaction]

1. Introduction

The anomeric and related stereoelectronic effects, including some controversies surrounding these effects, have recently been reviewed by Juaristi and Cuevas (1) and Thatcher (2). In its simplest formulation, applicable to acetal-like systems $XH_mCH_2YH_n$, the anomeric effect (ae) stabilizes that conformation for which an sp^3 lone pair on X or Y is antiperiplanar (app) to the polar bond CY or CX, respectively.

Received October 6, 1995.

This paper is dedicated to Professor Richard F.W. Bader on the occasion of his 65th birthday.

C. Scott and F. Grein.[1] Department of Chemistry, University of New Brunswick, Fredericton, NB E3B 6E2, Canada.

[1] Author to whom correspondence may be addressed. Telephone: (506) 453-4776. Fax: (506) 453-4981. E-mail: fritz@unb.ca.

Many ab initio studies have been performed on $XH_mCH_2YH_n$ systems with X and Y being first-row atoms, starting in 1971 with the work by Wolfe et al. (3) and Radom et al. (4). Also, there is a substantial amount of literature on first-row/second-row combinations (e.g., refs. 5, 6). Here, the general consensus is that the ae is still active; however, not as strongly as for their first-row/first-row counterparts. For example, bond separation energies calculated by Schleyer et al. (6) as energies of the reaction $XH_mCH_2YH_n + CH_4 \rightarrow CH_3XH_m + CH_3YH_n$, range from 11 to 18 kcal/mol for first-row/first-row systems (X, Y = N, O, F) while being 1–11 kcal/mol for first-row/second-row combinations (X = N, O, F; Y = P, S, Cl). In these reactions, the number and type of bonds stays the same, but the anomeric effect active in $XH_mCH_2YH_n$ is removed in the products.

In a recent series of papers (7–10), an attempt was made to separate the anomeric stabilization energy into steric, electrostatic, and electronic components. Both an energy decomposition scheme and a scheme based on Fourier analysis showed that the *electronic* component (absolute value) of the anomeric

effect decreases in the order X = F, O, N for fixed Y, as expected, and that it increases with increasing electronegativity difference between X and Y. For example, for X = F, O, N, and Y = O, the parameters e_O are −2.0, −1.0, and −0.7 kcal/mol, whereas for Y = N, the e_N parameters are −3.6, −1.9, and −1.0 kcal/mol.

The same ideas were also applied to corresponding protonated ($XH_{m+1}{}^+CH_2YH_n$) and anionic ($XH_mCH_2YH_{n-1}{}^-$) systems. For protonated molecules, the electronic component of the ae is much larger than for the corresponding neutral systems, due to the higher electronegativity (EN) of the positive ion. Also, an energy component for the reverse anomeric effect (rae), corresponding to the stabilization received by a lone pair on Y in synperiplanar (spp) position due to the positive charge on X, was obtained, with 7–8 kcal/mol for the $OH_2{}^+$/OH, $NH_3{}^+$/OH, and $NH_3{}^+$/NH_2 systems. For example, for $NH_3{}^+CH_2NH_2$, the conformation having the lone pair on NH_2 in spp position is more stable than the corresponding app conformation, indicating the rae to be strong.

For anionic systems $XH_mCH_2NH^-$, the electronic component of the ae lies between the values obtained for the corresponding neutral and protonated systems.

The reason for anomeric stabilization in $XH_mCH_2YH_n$ systems was seen in the tendency of the CH_2YH_n fragment of the molecule to form, as much as possible, a planar structure. If X is more electronegative than Y, electronic charge is moved from YH_n to XH_m, and CH_2YH_n acquires thereby a partial double-bond structure of type $CH_2{=}YH_n{}^+$, which prefers a planar geometry. It can be shown that, under rotation of the YH_n hydrogens about the CY bond, the CY bond distance and the charges on YH_n change in the same way, although not as dramatically, as in a rotation of the YH_n hydrogens around the CY bond in $CH_2{=}YH_n{}^+$. The same π-bonding model also applies to anomeric stabilization of protonated and anionic systems. The anomeric effect, as far as its electronic component is concerned, is driven by the desire of the electropositive fragment of the molecule to become planar. Therefore, and as seen from the Fourier analysis, conformations with a lone pair in spp position are, electronically, as stabilizing as those in antiperiplanar position. Experimental verification of this synperiplanar effect has recently been demonstrated by Deslongchamps and co-workers. (11–13).

In this paper, the analysis of the anomeric effect for systems $XH_mCH_2YH_n{}^{(\pm)}$, as previously performed for X, Y being first-row atoms, will be extended to first-row/second-row combinations. More specifically, X will be a first-row atom (F, O, N, and C for reference), and YH_n will be SH and PH_2 (PH^- and $SiH_2{}^-$ for anionic systems). In all calculations, the hydrogen(s) on Y will be rotated about the C—Y bond, whereas the XH_m group will remain in fixed conformational position. As before, neutral as well as protonated and anionic systems will be dealt with. Despite the fact that there is a greater EN difference between first- and second-row atoms than between corresponding first-row atoms, a weaker anomeric effect is expected since the less electronegative second-row atoms are considered to be relatively poor electron donors.

2. Methods

Geometry optimizations were carried out at the 6-31+G* level using the GAUSSIAN 86 programs (14). All bond lengths and angles, except for specified dihedral angles, were optimized. In particular, the dihedral angles of the XH_m hydrogens were held constant while the YH_n hydrogens were rotated about the C—Y bond.

Table 1. Relative energies ΔE in kcal/mol (first line), optimized C—S distances in Å (second line), and Mulliken charges on SH (third line), obtained by 6-31+G* geometry optimizations on XH_m-CH_2-SH, for SH dihedral angles of 0°, 60°, 120°, and 180°.

XH_m-CH_2-SH	0°	60°	120°	180°
F-CH_2-SH	0.00	−1.15	−3.27	0.51
	1.8185	1.8094	1.7988	1.8253
	0.049	0.056	0.063	0.038
a-OH-CH_2-SH	0.00	−0.05	−2.49	0.05
	1.8193	1.8157	1.8038	1.8245
	0.053	0.052	0.061	0.042
s-NH_2-CH_2-SH	0.00	0.75	−0.62	2.10
	1.8474	1.8524	1.8412	1.8596
	−0.006	−0.014	0.001	−0.018
s-CH_3-CH_2-SH	0.00	1.20	−0.33	1.46
	1.8271	1.8346	1.8241	1.8336
	0.013	0.003	0.008	−0.003

The nonrotating hydrogens of XH_m were held at dihedral angles φ (relative to XCZ; structure **1**) of 0° for a-OH and a-FH^+; at ±120° for s-NH_2 and s-$OH_2{}^+$, and at 0, ±120° for s-CH_3 and s-$NH_3{}^+$. The prefix a stands for anti and s for staggered. The rotating YH_n hydrogens were set to dihedral angles of 0°, 60°, 120°, and 180° for SH and PH^- (relative to YCZ), and to ±60° (0°); 0°, 120° (60°); 60°, 180° (120°), and ±120° (180°) for PH_2 and $SiH_2{}^-$. The numbers in parentheses are the φ values given in the tables, and refer to the midpoint between the two hydrogens. In structure **1**, a-$OHCH_2SH$ for φ = 0, and in structure **2**, s-$NH_2CH_2PH_2$, also for φ = 0, are shown. Structure **3** gives s-$CH_3CH_2PH_2$ for φ = 180°.

The Fourier constants V_1, V_2, and V_3 were calculated from the equation $\Delta E(\phi) = (V_1/2)(1 - \cos\phi) + (V_2/2)(1 - \cos 2\phi) + (V_3/2)(1 - \cos 3\phi)$, using the dihedral angles φ = 0°, 60°, 120°, and 180°.

3. Results

3.1 Neutral systems

Relative energies, C—S bond distances, and Mulliken charges for the XH_mCH_2SH systems are given in Table 1. The trends in relative energies and bond lengths are as expected, with the lowest energy and smallest bond length obtained for the 120° conformer. For the NH_2CH_2SH and CH_3CH_2SH systems the energy lowering from the 0° to the 120° conformer is small, and an energy barrier has developed at 60°. As well, there is little change in bond length. This indicates that the anomeric effect in these systems is weak or nonexistent. A discussion is to follow later.

The Fourier parameters V_1, V_2, and V_3 obtained from the relative energies in Table 1 are given in Table 2. The range of V_3 values lies between 1.51 and 1.64 kcal/mol, which is close to the energy difference of 1.28 kcal/mol between the eclipsed and staggered conformers of CH_3SH calculated at the

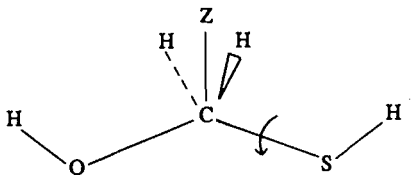

a-OH-CH_2-SH, ϕ(SH) = 0°

1

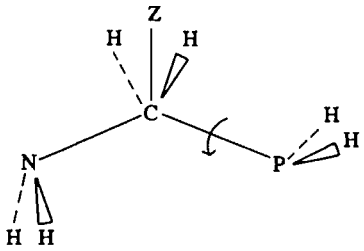

s-NH_2-CH_2-PH_2, ϕ(PH_2) = 0°

2

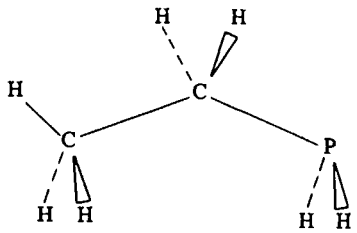

s-CH_3-CH_2-PH_2 ϕ(PH_2) = 180°

3

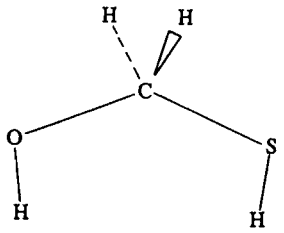

s-OH-CH_2-SH, ϕ(SH) = 180°

4

Table 2. Fourier constants V_1–V_3 in kcal/mol for SH rotation in systems XH_m-CH_2-SH, obtained from relative energies of Table 1.

XH_m-CH_2-SH	V_1	V_2	V_3
F-CH_2-SH	−1.07	−3.29	1.58
a-OH-CH_2-SH	−1.59	−1.73	1.64
s-NH_2-CH_2-SH	0.49	−1.31	1.61
s-CH_3-CH_2-SH	−0.05	−0.39	1.51

6-31+G* level. The V_2 parameter has the greatest (absolute) value for the most electronegative F system and the smallest value for the least electronegative CH_3 system. No such regularity can be found for the V_1 parameter. The energy barrier at 60°, observed for the NH_2 and CH_3 systems, is explained by the V_3 parameter, describing the SH–CH_2 repulsion, being larger in magnitude than V_2, which describes the stabilizing electronic effect.

The relative energies, C—P bond distances, and Mulliken charges for the $XH_mCH_2PH_2$ systems are given in Table 3. The energies are as expected, with the 180° conformer having the lowest energy due to anomeric stabilization occurring at 180°. The greatest energy lowering occurs for the F and a-OH systems, as expected. For the s-NH_2 and s-CH_3 molecules there are 1,3-hydrogen repulsions at 180° that decrease any stabilization received from the anomeric effect at this angle, resulting in smaller energy differences. The C—P bond distances are smallest at the 180° conformer, due to the anomeric effect.

The Fourier values obtained from the relative energies in Table 3 are given in Table 4. The magnitude of V_3 (−2.28 to −2.58 kcal/mol) is close to the energy difference between the staggered and eclipsed conformers of CH_3PH_2, which was calculated to be −1.93 kcal/mol (6-31+G*). The V_2 parameter has the greatest value for the most electronegative XH_m, decreasing to the least electronegative. V_2 is positive due to the anomeric stabilization occurring at 180°.

3.2 Protonated systems and reverse anomeric effect

Tables 5 and 6 give energies, bond distances, charges, and Fourier constants for the protonated systems $XH_m{}^+CH_2SH$ under SH rotation.

As seen from the bond distances, all four conformers of a-FH^+CH_2SH form complexes of type $FH\cdots CH_2{=}SH^+$. Therefore, the calculated Fourier constants do not properly represent the required 1,3-interactions and have been omitted from Table 6. For the other two systems, stabilization at 60° and 120° relative to 0° is obtained, with appropriate changes in bond distances, indicating that the ae is active. This is confirmed by the rather large V_2 values. Later on, the V_1 parameters will be discussed in connection with the reverse anomeric effect.

Table 5 shows that there is no energy barrier at 60° for any of the protonated systems, whereas the NH_2 and CH_3 neutral systems (Table 1) showed such a barrier. The reason is seen in the strong electronic stabilization (V_2) experienced by protonated systems, compared to the rather normal CH_2–SH repulsion (V_3). The same argument applies to the anionic systems, to be discussed below.

Table 3. Relative energies ΔE in kcal/mol (first line), optimized C—P distances in Å (second line), and Mulliken charges on PH_2 (third line), obtained by 6-31+G* geometry optimizations on XH_m-CH_2-PH_2 for PH_2 dihedral angles of 0° (±60), 60° (0°,120°), 120° (60,180), and 180° (± 120°).

XH_m-CH_2-PH_2	0°	60°	120°	180°
F-CH_2-PH_2	0.00	−0.72	1.25	−3.52
	1.8581	1.8582	1.8700	1.8391
	0.153	0.154	0.133	0.138
a-OH-CH_2-PH_2	0.00	−1.86	−0.15	−3.92
	1.8613	1.8565	1.8688	1.8412
	0.148	0.156	0.133	0.131
s-NH_2-CH_2-PH_2	0.00	−1.61	1.25	−2.01
	1.8801	1.8689	1.8855	1.8614
	0.089	0.106	0.083	0.138
s-CH_3-CH_2-PH_2	0.00	−2.01	0.30	−2.22
	1.8683	1.8560	1.8685	1.8525
	0.107	0.113	0.096	0.102

Table 4. Fourier constants V_1–V_3 in kcal/mol for PH_2 rotation in systems XH_m-CH_2-PH_2, obtained from relative energies of Table 3.

XH_m-CH_2-PH_2	V_1	V_2	V_3
F-CH_2-PH_2	−1.03	2.70	−2.49
a-OH-CH_2-PH_2	−1.47	1.27	−2.45
s-NH_2-CH_2-PH_2	0.57	1.10	−2.58
s-CH_3-CH_2-PH_2	0.06	0.34	−2.28

For PH_2 rotation in systems $XH_m{}^+CH_2PH_2$, energy differences, bond distances, charges, and Fourier parameters are given in Tables 7 and 8. As before, the a-FH^+ molecule optimizes to a complex (of type $FH\cdots CH_2{=}PH_2{}^+$) at all four dihedral angles, preventing a useful interpretation of Fourier constants. For the remaining two systems, V_2 parameters of 7.6 and 4.9 kcal/mol are obtained, again much larger than for the corresponding neutral systems.

In previous papers of this series (8, 9), energy estimates were obtained for the reverse anomeric effect (rae) in protonated systems. Briefly, the rae has been defined as the energy of stabilization of the $\phi = 0°$ conformer over the $\phi = 180°$ conformer due to the lone pairs on SH or PH_2 being attracted by the positive charge on X when in *syn* position relative to CX. Therefore, the rae parameter v is V_1 with adjustments made for steric and electrostatic effects between lone pairs and hydrogen atoms on X and Y, as well as for the electronic part of the ae in the case of PH_2 systems. For example, for s-$NH_3{}^+CH_2OH$ (9), for which $\phi = 0°$ is the most stable conformer, v was calculated as $v = -V_1 - 2h + r$ to give about −7 kcal/mol (please note that in ref. 9 $\Delta E(180)$ was used instead of V_1). At 0° the internal hydrogen bond is described by the energy $2h$, and at 180° the 1,3 H–H repulsion is r. As outlined in previous papers, approximate values of 1 and −1 kcal/mol for r and h, respectively, were assumed.

Here, another approach to calculating v parameters will be given, with the purpose of reducing reliance on estimated energy parameters h and r. The problem is to separate v from regular steric and electrostatic energies contained in the Fourier constant V_1. This can be accomplished by comparing $V_1{}^{prot}$ (for the protonated system) with $V_1{}^{neut}$ (corresponding neutral system). Hydrogens and lone pairs on X and Y interact approximately in the same way in the neutral and protonated system, the big difference being the rae.

For X = N and Y = O or S, v can be calculated as $-v = V_1{}^{prot} - V_1{}^{neut}$. As a check, v_O gives $-(9.72 - 0.95) \cong -9$ kcal/mol for s-$NH_3{}^+CH_2OH$, compared with −7 kcal/mol (revised value) in ref. 9. For X = N and Y = N or P, the ae occurs at 180°, so $V_1{}^{prot} - V_1{}^{neut}$ needs to be corrected by the difference $e_+ - e$. Therefore, for s-$NH_3{}^+CH_2NH_2$, $-v_N = V_1{}^{prot} - V_1{}^{neut} + e_N - e_{N^+}$, to result in $v_N \cong -11$ kcal/mol, compared with −10 (revised value) in ref. 9.

In the present case, v_S for s-$NH_3{}^+CH_2SH$ is calculated as $v_S = -(3.61 - 0.5) \cong -3$ kcal/mol, and v_P for s-$NH_3{}^+CH_2PH_2$ is $v_P = -2.64 + 0.57 - 3.7 + 0.8 \cong -5$ kcal/mol. Both values are significantly smaller than for the corresponding OH and NH_2 systems.

For the s-$OH_2{}^+$ systems, v can, unfortunately, not simply be calculated as the difference of the V_1's, since the 1,3-hydrogen and lone-pair interactions of the neutral a-OH system do not match those of the protonated s-$OH_2{}^+$ system. To make the procedure easier, the neutral systems were recalculated with the OH hydrogen in *syn* rather than *anti* position relative to CY. For s-$OHCH_2SH$ (structure **4**), the values $V_1 = 1.01$, $V_2 = -5.40$, and $V_3 = 1.69$ kcal/mol were obtained, whereas for s-$OHCH_2PH_2$ the V's are 1.05, 4.36, and −2.21 kcal/mol. (It should be noted that the V_2's for the s-OH are much larger than for the a-OH molecules.) Now, for s-$OH_2{}^+CH_2SH$, $v_S \cong -\Delta V_1 - h$, to give $-(4.0 + 1.0) + 1.0 = -4$ kcal/mol. For s-$OH_2{}^+CH_2PH_3$, $v_P \cong -\Delta V_1 + r - h + e_P{}^+ - e_P = -1.7$ kcal/mol, using $e_P = -3.3$ kcal/mol, as obtained from V_2. As before, 1 and −1 kcal/mol were chosen for r and h, respectively.

3.3 Anionic systems

The relative energies, C—P bond distances, and Mulliken charges for the anioinic $XH_mCH_2PH^-$ systems are give in Table 9. As expected for a system that receives anomeric stabilization at 120°, the lowest energy, shortest C—P bonds, and most positive (least negative) charges on P are found for the 120° conformer. The greatest energy lowering for 120° occurs for the most electronegative system FCH_2PH^-, and the lowering decreases with decreasing electronegativity of X.

The Fourier parameters for these systems are given in Table 10. The V_3 values have the range of 1.63–1.96 kcal/mol, which is similar to the energy difference between the staggered and eclipsed forms of CH_3PH^-, calculated to be 1.43 kcal/mol (6-31+G*).

The V_2 values reflect the energy lowerings at 120°, with the most negative value of −5.71 kcal/mol for F, progressively decreasing to a value of −1.02 kcal/mol for the least electronegative system $CH_3CH_2PH^-$. All V_1 values are small, close to 0. This implies that steric and electrostatic interactions between X and Y are negligible.

Table 11 contains the relative energies, C—Si bond lengths, and Mulliken charges for the $XH_mCH_2SiH_2{}^-$ systems. The 180° conformers have the lowest energies and shortest C—Si

Table 5. Relative energies ΔE in kcal/mol (first line), optimized C—S/C—X distances in Å (second line), and Mulliken charges on SH (third line), obtained by 6-31+G* geometry optimizations on XH_m^+-CH_2-SH, for SH dihedral angles of 0°, 60°, 120°, and 180°.

XH_m^+-CH_2-SH	0°	60°	120°	180°
a-FH^+-CH_2-SH	0.00	−32.89[a]	−39.46	0.54
	1.7614/2.0743	1.6169/2.9066	1.6174/2.7860	1.7573/2.2663
	0.390	0.565	0.558	0.382
s-OH_2^+-CH_2-SH	0.00	−3.93	−3.76	5.82
	1.8054/1.5148	1.7795/1.5476	1.7709/1.5522	1.8178/1.5172
	0.252	0.276	0.302	0.270
s-NH_3^+-CH_2-SH	0.00	−1.70	−1.59	5.30
	1.8136/1.5062	1.8048/1.5150	1.7958/1.5154	1.8238/1.5055
	0.222	0.224	0.246	0.234

[a]For $\phi = 60°$ the angle CFH was fixed at 109.5°.

Table 6. Fourier constants V_1–V_3 in kcal/mol for SH rotation in systems XH_m^+-CH_2-SH, obtained from relative energies of Table 5.

XH_m^+-CH_2-SH	V_1	V_2	V_3
a-FH^+-CH_2-SH	*a*	*a*	*a*
s-OH_2^+-CH_2-SH	3.99	−9.01	1.83
s-NH_3^+-CH_2-SH	3.61	−5.73	1.69

[a]Calculated Fourier constants are not useful, since all four conformers are optimized as complexes.

Table 7. Relative energies ΔE in kcal/mol (first line), optimized C—P/C—X distances in Å (second line), and Mulliken charges on PH_2 (third line), obtained by 6-31+G* geometry optimizations on XH_m^+-CH_2-PH_2, for PH_2 dihedral angles of 0° (±60°), 60° (0°, 120°), 120° (60°, 180°), and 180° (±120°).

XH_m^+-CH_2-PH_2	0°	60°	120°	180°
a-FH^+-CH_2-PH_2	0.00	−0.59	−0.53	−0.66
	1.6797/2.7860	1.6746/3.0715	1.6759/3.0700	1.6820/2.6381
	0.680	0.655	0.647	0.643
s-OH_2^+-CH_2-PH_2	0.00	3.82	7.38	−0.17
	1.8525/1.5525	1.8679/1.5373	1.8817/1.5435	1.8268/1.5865
	0.347	0.355	0.356	0.387
s-NH_3^+-CH_2-PH_2	0.00	2.05	5.66	0.35
	1.8702/1.5181	1.8724/1.5130	1.8869/1.5149	1.8524/1.5247
	0.303	0.323	0.320	0.334

Table 8. Fourier constants V_1–V_3 in kcal/mol for PH_2 rotation in systems XH_m^+-CH_2-PH_2, obtained from relative energies of Table 7.

XH_m^+-CH_2-PH_2	V_1	V_2	V_3
a-FH^+-CH_2-PH_2	*a*	*a*	*a*
s-OH_2^+-CH_2-PH_2	2.26	7.58	−2.43
s-NH_3^+-CH_2-PH_2	2.64	4.91	−2.29

[a]Calculated Fourier constants are not useful, since all four conformers are optimized as complexes.

distances due to the anomeric stabilization that occurs at this angle.

The Fourier values are given in Table 12. The V_2's are positive, and again decrease with decreasing electronegativity of XH_m. As before, V_1 values are small and do not follow any particular order.

4. Discussion

4.1 Electronic component of anomeric effect

Following the convention of previous papers (7–10), the elec-

Table 9. Relative energies ΔE in kcal/mol (first line), optimized C—P distances in Å (second line), and Mulliken charges on PH (third line), obtained by 6-31+G* geometry optimizations on XH_m-CH_2-PH^-, for PH^- dihedral angles of 0°, 60°, 120°, and 180°.

XH_m-CH_2-PH^-	0°	60°	120°	180°
F-CH_2-PH^-	0.00	−2.42	−4.25	1.89
	1.8928	1.8739	1.8619	1.9037
	−0.767	−0.743	−0.739	−0.793
a-OH-CH_2-PH^-	0.00	−1.20	−3.10	1.74
	1.8981	1.8863	1.8734	1.9073
	−0.772	−0.761	−0.759	−0.802
s-NH_2-CH_2-PH^-	0.00	0.31	−1.37	2.51
	1.9035	1.9041	1.8927	1.9185
	−0.822	−0.839	−0.830	−0.839
s-CH_3-CH_2-PH^-	0.00	0.89	−0.69	1.73
	1.9060	1.9111	1.8990	1.9152
	−0.845	−0.844	−0.840	−0.862

Table 10. Fourier constants V_1–V_3 in kcal/mol for PH rotation in systems XH_m-CH_2-PH^-, obtained from relative energies of Table 9.

XH_m-CH_2-PH^-	V_1	V_2	V_3
F-CH_2-PH^-	0.04	−5.71	1.85
a-OH-CH_2-PH^-	−0.11	−4.03	1.85
s-NH_2-CH_2-PH^-	0.55	−2.38	1.96
s-CH_3-CH_2-PH^-	0.10	−1.02	1.63

Table 11. Relative energies ΔE in kcal/mol (first line), optimized C—Si distances in Å (second line), and Mulliken charges on SiH_2 (third line), obtained by 6-31+G* geometry optimizations on XH_m-CH_2-SiH_2^-, for SiH_2 dihedral angles of 0° (±60°), 60° (0°, 120°), 120° (60°, 180°), and 180° (±120°).

XH_m-CH_2-SiH_2^-	0°	60°	120°	180°
F-CH_2-SiH_2^-	0.00	−0.33	1.40	−3.82
	1.9639	1.9659	1.9779	1.9382
	−0.614	−0.612	−0.654	−0.656
a-OH-CH_2-SiH_2^-	0.00	−1.09	0.70	−3.86
	1.9683	1.9652	1.9779	1.9444
	−0.624	−0.613	−0.661	−0.681
s-NH_2-CH_2-SiH_2^-	0.00	−1.31	−1.59	−1.88
	1.9710	1.9635	1.9805	1.9535
	−0.719	−0.675	−0.705	−0.721
s-CH_3-CH_2-SiH_2^-	0.00	−1.57	−0.56	−2.03
	1.9762	1.9654	1.9785	1.9579
	−0.703	−0.693	−0.712	−0.701

tronic component of the anomeric effect is calculated as 0.75 V_2, and a change of sign is required for PH_2/SiH_2^- rotation. The results are given in Table 13. These *e*-parameters represent the *electronic* part of the anomeric stabilization when the

Table 12. Fourier constants V_1–V_3 in kcal/mol for SiH_2^- rotation in systems XH_m-CH_2-SiH_2^-, obtained from relative energies of Table 11.

XH_m-CH_2-SiH_2^-	V_1	V_2	V_3
F-CH_2-SiH_2^-	−1.39	3.26	−2.43
a-OH-CH_2-SiH_2^-	−0.38	2.31	−2.48
s-NH_2-CH_2-SiH_2^-	0.68	1.44	−2.56
s-CH_3-CH_2-SiH_2^-	0.07	0.68	−2.10

SH or PH^- group is rotated from $\phi = 0°$ (H in app position, no anomeric effect) to $\phi = 120°$ (one lone pair in app position, anomeric effect), or when the PH_2 or SiH_2^- group is rotated from 60° (one H in app position, no ae) to 180° (lone pair in app position, ae).

Table 13 shows that the *e*-parameter drops when the atom X changes from F to C, as expected, reflecting the decreasing electronegativity of the first-row atoms. The *e*-parameters for protonated systems are larger (in magnitude) than for neutral systems, and the anionic systems lie in between. A comparison of the *e*-parameters calculated here for first-row/second-row systems, with those given earlier for first-row/first-row molecules, where both X and Y are F, O, N and C, is most interesting. For both the neutral and protonated SH systems, the electronic parameter *e* is larger (in magnitude) than for the corresponding OH systems. For example, e_S for FCH_2SH is −2.5, whereas e_O for FCH_2OH is −2.0 kcal/mol, and e_S for s-$OH_2^+CH_2SH$ is −6.8 compared with −6.2 kcal/mol for e_O of s-$OH_2^+CH_2OH$. As mentioned in the Introduction, such a trend would be expected on the basis of the larger electronegativity difference between first- and second-row atoms than between first-row atoms (e.g., ΔE_n (F-S) ≅ 1.5, ΔE_n (F-O) ≅ 0.5).

Against this speaks the expected lower electron-donating property of second-row atoms compared with the corresponding first-row atoms. Table 13 shows that the latter quality appears to win out in the phosphorus systems, since $|e_P|$ parameters for neutral and protonated systems are *smaller* than the corresponding $|e_N|$ results.

Based on this analysis, the conclusion can be drawn that sulfur is highly effective in promoting anomeric stabilization, even more effective than oxygen, whereas the capacity of phosphorus for anomeric stabilization is inferior to that of nitrogen. "Effectiveness" refers to the electronic part of the anomeric stabilization only. The total energy lowering between 0° and 120° is larger for XH_mCH_2OH than for XH_mCH_2SH, at least when X = F and O, thanks to larger negative V_1's in the OH case. For example, the energy lowering at 120° is −4.8 kcal/mol for FCH_2OH, and −3.3 kcal/mol for FCH_2SH. Using $\Delta E(120) = 0.75\ (V_1 + V_2)$, with $V_1 = -3.7$, $V_2 = -2.7$ for FCH_2OH, and $V_1 = -1.1$, $V_2 = -3.3$ kcal/mol for FCH_2SH, shows that $V_1 + V_2$ (absolute) is larger for the OH than the SH system, resulting in higher stabilization. It is reasonable to expect the electrostatic and steric 1,3-interactions, reflected in V_1, to decrease with increasing bond distances. However, the increase of the *electronic* interaction of S over O, despite larger bond distances, is unexpected.

When going from NH_2 to PH_2 systems, both $|V_1|$ and V_2 decrease, causing at 180° less stabilization for the PH_2 than the

Table 13. Electronic anomeric parameters e for neutral, protonated, and anionic systems $XH_m^{(+)}CH_2YH_n^{(-)}$ with first- and second-row atoms, in kcal/mol. Numbers in parentheses are for corresponding first-row/first-row systems.

	Neutral		Protonated		Anionic	
XH_m/XH_m^+	SH(OH)	$PH_2(NH_2)$	SH(OH)	$PH_2(NH_2)$	$PH^-(NH^-)$	$SiH_2^-(CH_2^-)$
F/a-FH^+	−2.5	−2.0	—[a]	—[a]	−4.3	−2.4
	(−2.0)	(−3.6)	(−20.5)	(−30.6)	(−16.5)	(−8.1)
a-OH/s-OH_2^+	−1.3	−1.0	−6.8	−5.7	−3.0	−1.7
	(−1.0)	(−1.9)	(−6.2)	(−17.3)	(−5.2)	(−5.3)
s-NH_2/s-NH_3^+	−1.0	−0.8	−4.3	−3.7	−1.8	−1.1
	(−0.7)	(−1.0)	(−3.5)	(−5.7)	(−2.7)	(−3.0)
s-CH_3	−0.3	−0.3	–	–	−0.8	−0.5
			–	–	(−1.0)	(−1.2)

[a]Since complexes were formed at all dihedral angles, e could not be evaluated.

NH_2 system (for X = F,O). Apparently, the electron donating properties of phosphorus are drastically reduced in comparison to sulfur.

In the last two columns of Table 13, the e_P- and $e_{Si}-$ values are shown for the anionic systems involving PH^- and SiH_2^- rotation. It is seen that such parameters are smaller than comparable e_{N-} and e_{C-} values.

4.2 The π-bonding model

For neutral and protonated first-row/first-row molecules $XH_m^+CH_2YH_n$, the π-bonding model showed that for systems undergoing anomeric stabilization, CY bond distances and charges on YH_n change in the same way, however, not as strongly, as those for $CH_2{=}YH_n^+$ when YH_n is rotated about the double bond. This indicates that the anomeric effect is caused by the tendency of the slightly positive CH_2-$YH_n^{(+)}$ fragment of the molecule to assume a near-planar structure.

In Table 14, energy differences, CS distances, and charges on SH are shown for $CH_2{=}SH^+$. The dihedral angle ϕ in $CH_2{=}SH^+$ is defined analogously to ϕ in XH_mCH_2SH compounds (see the CH_2SH moiety in structure **1** for illustration). It is seen that, relative to ϕ = 0, the CS distances decrease for 60° and 120°, and increase again for 180°. This is combined with significant stabilization at 60° and 120°. Relative to ϕ = 0, the charges on SH increase for 60° and 120°, and decrease for 180°. Referring to Table 1, the neutral systems with X = F and O show similar trends, whereas the remaining systems with X = N and C have an increase in CS distance and energy, and a substantial decrease of Q(SH), at 60°. Although the electronic parameter e_S is −1.0 kcal/mol for s-NH_2CH_2SH, the bond distances and energies in this system do not follow the π-bonding trend.

Table 15 gives corresponding data for $CH_2{=}PH_2^+$. Again, the dihedral angle ϕ is defined in the same way as in $XH_mCH_2PH_2$ compounds (see structure **2**). Here, the higher energies and larger CP distances occur at 60° and 120°, as expected. The charge on PH_2 decreases at 60°, and increases thereafter. In line with the weak electronic anomeric effect observed for $XH_mCH_2PH_2$, the energies and bond distances given in Table 3 do not always show the corresponding trend. For the F-system, the correlation of CP distances is good; for a-OH the CP distance at 60° is shorter than at 0°, whereas for the s-NH_2 and s-CH_3 systems a correlation with $CH_2{=}PH_2^+$ is neither seen nor expected.

Table 14. Relative energies ΔE in kcal/mol, optimized C—S distances in Å, and Mulliken charges on SH, for SH rotation in $CH_2{=}SH^+$, obtained from 6-31+G* calculations.

ϕ	0°	60°	120°	180°
ΔE	0.00	−36.36	−42.04	−7.70
R_{CS}	1.7519	1.6298	1.6197	1.7496
Q(SH)	0.422	0.602	0.612	0.585

Table 15. Relative energies ΔE in kcal/mol, optimized C—P distances in Å, and Mulliken charges on PH_2, for PH_2 rotation in $CH_2{=}PH_2^+$, obtained from 6-31+G* calculations.

ϕ	0°	60°	120°	180°
ΔE	0	14.52	5.01	−17.71
R_{CP}	1.6617	1.7047	1.7021	1.6807
$Q(PH_2)$	0.693	0.619	0.705	0.748

A comparison of the trends in stabilization energies and bond distances of the protonated systems given in Tables 5 and 7 with those of $CH_2{=}SH^+$ and $CH_2{=}PH_2^+$ in Tables 14 and 15 shows good agreement for all systems. As mentioned earlier, for protonated systems with fluorine, complexes are formed at all dihedral angles, and the anomeric effect can therefore not be evaluated.

4.3 Reverse anomeric effect in protonated systems

In Table 16, the four estimated values for the reverse ae in first-row/second-row systems are given, and compared with corresponding first-row/first-row values. It should be stressed that there is no straightforward method to calculate rae values, and that the given numbers can only be seen as a rough indication of the energy related to this effect.

Table 16. Estimated values v_S and v_P in kcal/mol for the reverse anomeric effect in systems s-$OH_2^+CH_2YH_n$ and s-$NH_3^+CH_2YH_n$, with YH_n = SH and PH_2. Numbers in parentheses are for corresponding first-row/first-row systems.

	SH(OH)	$PH_2(NH_2)$
s-OH_2^+	−4 (−7.5)	−2 (—)[a]
s-NH_3^+	−3 (−7)[b]	−5 (−10)[b]

[a]No value for O^+/N system available.
[b]Revised value, see text.

Having said this, the v_S and v_P numbers are reasonable, smaller than corresponding v_O and v_N values. The larger C—S/C—P distances compared to C—O/C—N are certainly partly responsible for the decrease in v values. The v_N value for s-$OH_2^+CH_2NH_2$ could not be obtained due to complex formation. The number obtained for s-$OH_2^+CH_2PH_2$ appears to be too small, not reflecting the trend of increasing v's as one goes from S to P.

5. Summary and conclusion

Previous theoretical work on the anomeric effect in acetal-like systems was extended to include the second-row atoms S and P.

The conformational energies obtained by rotating the SH or PH_2 hydrogens about the CY bond (the compounds are written as $XH_mCH_2YH_n$) were subjected to a Fourier analysis, from which the electronic energy portion of the anomeric stabilization was evaluated. Interestingly, for the SH systems this electronic component is *larger* (in absolute terms) than for corresponding OH systems, whereas for PH_2 rotation, the electronic component is *smaller* than for NH_2 rotation.

For molecules protonated on the first-row atom X, the same situation applies. For SH rotation the electronic component is larger (absolute) than for OH, and for PH_2 rotation smaller than for NH_2. The weaker electron-donating properties of phosphorus are also seen in the anionic systems, where PH^- leads to lower electronic stabilizations than NH^-. Judged by the π-bonding model, the anomeric effect is clearly working for SH systems with X = F and O, and for PH_2 systems with X = F. For the N/SH and O/PH_2, N/PH_2 combinations, a weak anomeric effect is still active, whereas for X being C, as expected, there is no more evidence for anomeric stabilization. According to the π-bonding/model and calculated stabilization energies, a strong anomeric effect is working in all protonated systems.

Estimates are also given for energy stabilization due to the reverse ae in protonated systems. Such stabilization is largest when the electron pair on Y is in *syn* position relative to XH_m^+. The v parameters are smaller than for corresponding first-row/first-row systems, likely due to the larger CY bond distances.

In conclusion, the SH group has shown remarkable anomeric stabilization properties for the neutral systems FCH_2SH and $OHCH_2SH$, and for protonated systems $XH_m^+CH_2SH$ with X = F, O, N. On the other hand, stabilization due to PH_2 is much weaker.

Acknowledgements

The authors wish to thank the Natural Sciences and Engineering Research Council of Canada for financial support, and Employment and Immigration Canada for awarding a Challenge grant to C.S.

References

1. E. Juaristi and G. Cuevas. Tetrahedron, **48**, 5019 (1992).
2. G.R.J. Thatcher. ACS Symp. Ser. **539**, 6 (1994).
3. S. Wolfe, A. Rauk, L.M. Tel, and I.G. Czismadia. J. Chem. Soc. B: **136** (1971).
4. L. Radom, W.J. Hehre, and J.A. Pople. J. Am. Chem. Soc. **93**, 289 (1971).
5. B.M. Pinto, H.B. Schlegel, and S. Wolfe. Can. J. Chem. **65**, 1658 (1987).
6. P.v.R. Schleyer, E.D. Jemmis, and G.W. Spitznagel. J. Am. Chem. Soc. **107**, 6393 (1985).
7. F. Grein and P. Deslongchamps. Can. J. Chem. **70**, 604 (1992).
8. F. Grein and P. Deslongchamps. Can. J. Chem. **70**, 1562 (1992).
9. F. Grein. ACS Symp. Ser. **539**, 205 (1994).
10. C. Scott and F. Grein. Can. J. Chem. **72**, 2521 (1994).
11. S. Li, A.J. Kirby, and P. Deslongchamps. Tetrahedron Lett. **34**, 7757 (1993).
12. S. Li and P. Deslongchamps. Tetrahedron Lett. **34**, 7759 (1993).
13. P. Deslongchamps, Y.L. Dory, and S. Li. Can. J. Chem. **72**, 2021 (1994).
14. M.J. Frisch, J.S. Binkley, H.B. Schlegel, K. Raghavachari, C. F. Melius, R.L. Martin, J.J.P. Stewart, F.W. Bobrowicz, C.M. Rohlfing, L.R. Kahn, D.J. DeFrees, R. Seeger, R.A. Whiteside, D.J. Fox, E.M. Fleuder, and J.A. Pople. GAUSSIAN 86, Carnegie-Mellon Quantum Chemistry Publishing Unit, Pittsburgh, Pa. 1984.

From topology to geometry

Mark Eberhart

Abstract: A systematic study of the charge density topologies corresponding to a number of transition metal aluminides with the B2 structure indicates that unstable crystal structures are sometimes associated with uncharacteristic topologies. This observation invites the speculation that the "distance" to a topological instability might relate to a metals phase behavior. Following this speculation, a metric is imposed on the topological theory of Bader, producing a geometrical theory, where it is now possible to assign a distance from a calculated charge density topology to a topological instability. For the cubic transition metals, these distances are shown to correlate with single crystal elastic constants, where the metals that are furthest from an instability are observed to be the stiffest.

Key words: crystal structure, charge density topology, mechanical properties, brittle/ductile failure.

Résumé : Une étude systématique des topologies des densités de charges correspondant à un certain nombre d'aluminures de métaux de transition de structure B2 indique que des structures cristallines instables sont quelquefois associées à des topologies qui ne sont pas caractéristiques. Cette observation nous amène à spéculer que la «distance» par rapport à une instabilité topologique pourrait être reliée à un comportement de la phase des métaux. À la suite de cette spéculation, on impose une «métrique» à la théorie topologique de Bader conduisant à une théorie géométrique grâce à laquelle il est alors possible d'attribuer une distance, par rapport à une topologie d'une densité de charge calculée, à une instabilité topologique. Pour des métaux de transition cubiques, il est démontré qu'il existe une corrélation entre ces distances et les constantes électriques des cristaux. Dans les cas où les métaux se trouvent les plus loin d'une instabilité, on observe qu'ils sont les plus durs.

Mots clés : structure cristalline, topologie des densités de charges, propriétés mécaniques, détaillance fragile/ductile.

[Traduit par la rédaction]

1. Introduction

All of chemistry is based on the molecular structure hypothesis, which simply stated is the following: a molecule or solid is a collection of atoms linked by a network of bonds, and all molecular properties result from this linked system of atoms. Accompanying this hypothesis are a number of models that seek to quantify these concepts of atoms and bonds and to correlate empirically determined properties with the models. While each of the models represents these concepts differently, they have all had considerable success in explaining the observed properties of matter.

Of the many models advanced in support of the molecular structure hypothesis, the most familiar is the Lewis model (1), in which a bond is pictured as a pair of valence electrons shared by two atoms. This representation of a chemical bond and its quantum mechanical extensions of directed valence (2) form the basis for understanding the chemistry of organic molecules. Structural, chemical, spectroscopic, and thermochemical data are interpreted using terms defined within the Lewis model of molecular structure.

Received October 4, 1995.

This paper is dedicated to Professor Richard F.W. Bader on the occasion of his 65th birthday.

M. Eberhart.[1] Department of Metallurgical and Materials Engineering, Colorado School of Mines, Golden, CO 80401, U.S.A.

[1] Telephone: (303) 273-3559. Fax: (303) 273-3795.

While many attempts have been made to interpret metallurgical properties within the framework of the molecular structure hypothesis, none of these attempts can be called totally successful. In my opinion, this lack of success can be attributed to a less than rigorous definition of the metallic bond. However, the topological model of molecular and solid state structure advanced by Bader et al. (3–8) provides a rigorous definition for all classes of chemical bonds, of which the metallic bond is a subset. Believing that such a rigorous description of the metallic bond should provide the starting point for the application of chemical formalism to explain the structure and properties of metallic systems, we have sought a correlation between the topological properties of the charge density of metals and alloys and their respective properties (9–14).

In this paper, I briefly review the topological model of electronic structure developed by Bader, specifically applying this model to metallic crystals. While the Bader model of molecular structure is tremendously powerful, as a topological model it can only be used to compare two structures, where these structures either share the same topology or not. The concept of "distance" between two structures can not be determined from a topological theory. Yet the concept of distance is essential for a complete application of the molecular structure hypothesis. For example, the application of transition state theory is dependent on assessing the "closeness" of an electronic charge distribution to the transition state.

In an attempt to provide a measure by which two electronic charge distributions can be compared, a metric will be introduced that measures the distance from a bond to an instability in that bond. It will be shown that there is a correlation

between this distance and the elastic properties of the metal being modeled. Through the introduction of this metric, the Bader formalism is extended from a topological theory to a geometrical one.

2. Charge density and topology

The Bader model of molecular structure makes use of the total charge density of a molecule or solid to determine its topology. The charge density is a scalar field, $\rho(r)$, which, as with any scalar field, possesses a unique topology. This topology is characterized in terms of its critical points, which are the zeroes of the gradient of the scalar field. There are four kinds of critical points in a three-dimensional space: a local minimum, a local maximum, and two kinds of saddle points. These critical points (cps) are denoted by an index that is the number of positive curvatures minus the number of negative curvatures; for example, a minimum cp has positive curvature in the three orthogonal directions; therefore, it is called a (3, 3) cp, where the first number is simply the number of dimensions of the space, and the second number is the net number of positive curvatures. A maximum would be denoted by (3, −3), since all three curvatures are negative. A saddle point with two of the three curvatures negative is denoted (3, −1), while the other saddle point is a (3, 1) cp.

Bader realized that bonds in molecules can be seen in terms of the topology of $\rho(r)$. A bond path connects two nuclei (where the charge density possesses (3, −3) cps) through a (3, −1) cp such that the charge density is always a maximum with respect to any neighboring path. Other types of critical points can be correlated with other features of molecular structure. A (3, 1) cp must be seen at the center of ring structures like benzene. Accordingly, this critical point is designated as a ring critical point. Cage structures are always characterized by a (3, 3) cp somewhere within the cage, and again have been given the descriptive name of cage critical points. A (3, −3) cp is always seen at a nuclei, but also, on occasion, local maxima are observed that are not associated with an atom; these are called pseudo-atoms.

Figure 1 shows the positions and type of critical points in a (100) plane of Cu. This topology is characteristic of all nonmagnetic FCC allotropic transition metals and therefore is designated as an FCC topology. The (3, −1) cps midway between nearest neighbors are indicative of bonds between these atoms. The bond paths are shown as lines connecting the bound atoms. These bonds form the edges of two types of polyhedra or cages: tetrahedra and octahedra, Fig. 2. At the center of each of these polyhedra is a cage critical point, i.e., a (3, 3) cp, with the octahedral cage critical points shown in Fig. 1. At the center of each of the faces of these two polyhedra are ring critical points. The entire set of critical points define specific bonding polyhedra, the packing of which gives rise to the FCC structure. The **topology** of these polyhedra is determined only by the number of corners, edges, and faces. As a convenience, a polyhedron is denoted by $\{c, e, f\}$. A polyhedron topologically equivalent to a regular tetrahedron will have four corners, six edges, and four faces, {4, 6, 4}. The total charge density will reflect these features with a (3, −3) cp at each corner, a (3, −1) cp along each edge, a (3, 1) cps in each face, and a (3, 3) cp within this polyhedron. The FCC topology is the result of packing two types of polyhedra, a {4, 6, 4} and a {6, 12, 8} (octahedron), with each face of the {4, 6, 4} shared with a {6, 12, 8}. Any structure whose charge density gives rise to the same set of bonding polyhedra, packed in the same manner, is topologically equivalent to the FCC structure.

Fig. 1. The charge density in a (100) plane of Cu. The critical points are marked by type. In this plane two types of critical points are shown, cage and bond critical points.

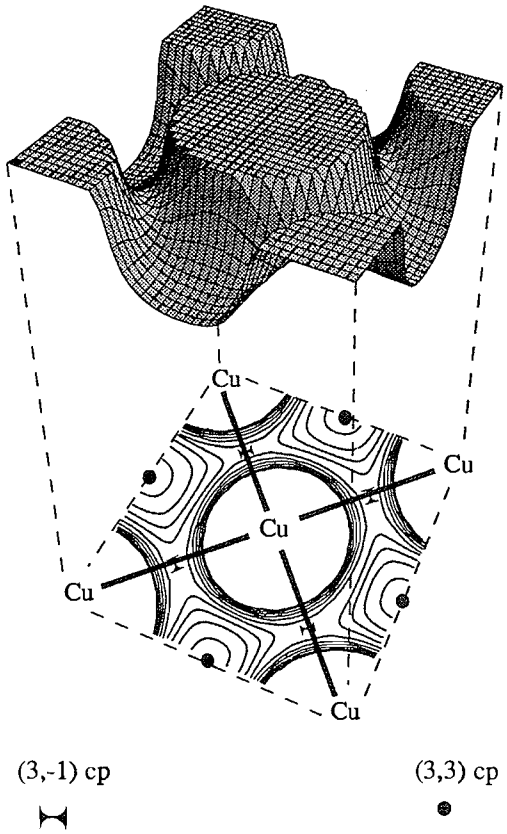

The BCC structure for all nonmagnetic transition metals is characterized by the topology represented by the polyhedron shown in Figure 3. This is a {6, 8, 4} polyhedron. Though it appears to be equivalent to an octahedron, it is not. This polyhedron has no bonds (edges) between second neighbors, rather there are four nonplanar faces.

3. Topologies of the B2 crystal structure

While the FCC and BCC structures of the transition metals appear to give rise to unique topologies, this is not a necessity. For most crystal structures there will be multiple topologies that can give rise to the structure.

As an example, consider the B2 structure: a simple cubic lattice with a two-atom basis. One of these atoms is usually pictured sitting on the corner of the cube with the other located at the body center, Fig. 4. Shown in Fig. 5 are several of the topologies available to the B2 structure. The first of these (**a**) corresponds to the case in which each atom A and B is bound only to its first coordination shell and therefore has 8 bonds from A to B. For such a case the "octahedral holes" of the B2 structure are characterized by local minima, i.e., (3, 3) cps, and the "tetrahedral holes" by ring (3, 1) cps. The B2 structure

Fig. 2. The bonding polyhedra characteristic of the FCC topology.

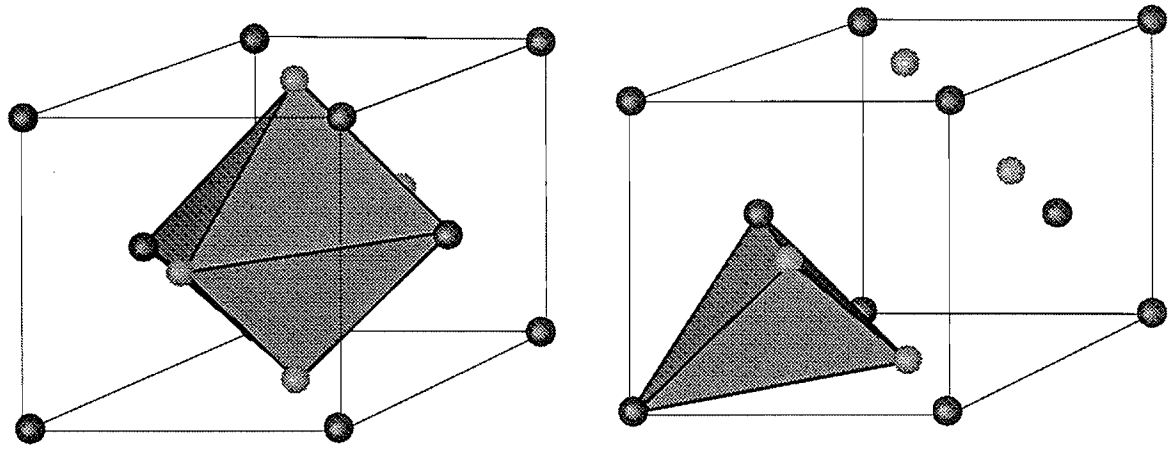

Fig. 3. The bonding polyhedron characteristic of the BCC structure. Note that there are four nonplanar faces.

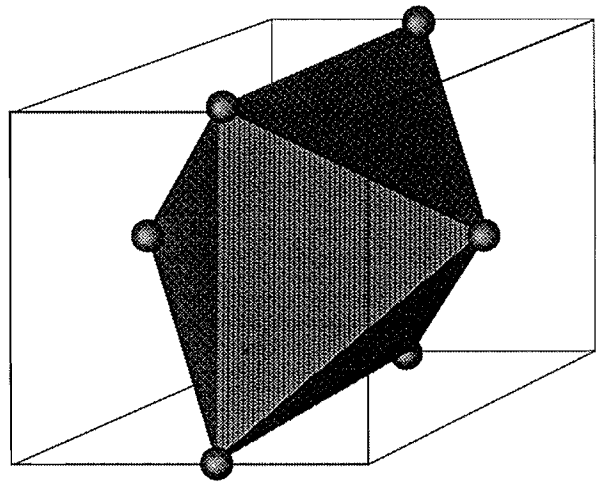

Fig. 4. The B2 crystal structure. This is a simple cubic structure with a two-atom basis. One atom is located at the corner of the cube while the other is at the body center.

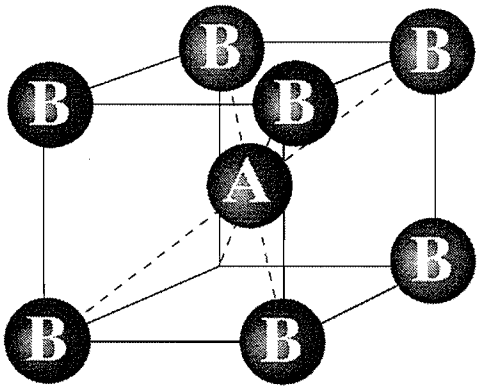

would be the result of packing one type of polyhedron with 6 corners, 8 edges, and 4 faces. Thus the B2 structure, along with one of its allowed charge density topologies, can be conveniently described as having 6 {6, 8, 4} polyhedra at each lattice point of the B2 structure.

An allowed alternative charge density topology would result when either atom A or atom B is bound to its 8 first neighbors and its 6 second neighbors, while the other atom remains bound to only its 8 first neighbors (**b**). For such a case the structure results from the packing of one type of polyhedron. This polyhedron has 5 corners, 8 edges, and 5 faces, i.e., a {5, 8, 5} polyhedron. A description of both the electronic structure and the crystallographic structure is provided by placing 6 {5, 8, 5} polyhedra on either site A or site B of the B2 structure.

Finally, if both atoms A and B are bound to second neighbors (**c**), then the B2 structure along with its charge density topology can be described as resulting from 24 {4, 6, 4} polyhedra on each lattice point. These polyhedra are topologically equivalent to regular tetrahedra.

While each of the charge densities described above is topologically permitted, each is not necessarily energetically permitted. That is, there may be structure–property relationships between charge density topologies and crystallographic structure, through which only specific bonding polyhedra give rise to a particular crystallographic structure. This hypothesis is easily tested by performing quantum mechanical calculations on a number of B2 alloys, some of which are known to be stable and some of which are not, and correlating the resultant charge density topologies with the observed stability of the B2 structure. The series of B2 alloys used for this initial test are the transition metal aluminides TmAl where Tm is Sc, Ti, V, Ni, Re, Ru, Pt, or Pd.

Of the equiatomic transition metal aluminides, the late transition metals Fe through Ni, Ru through Pd, and Re through Pt all form a stable B2 phase, though it is not necessarily the ground state structure. Of the early transition metals, only Sc forms a B2 structure. In between Sc and the late transition metals there is an "island of instability" where the B2 structure is not observed, e.g., TiAl and VAl.

The B2 structure has been assumed for all of the above-mentioned aluminides, where the lattice constant is either

Fig. 5. The bonding polyhedra available to the B2 structure.

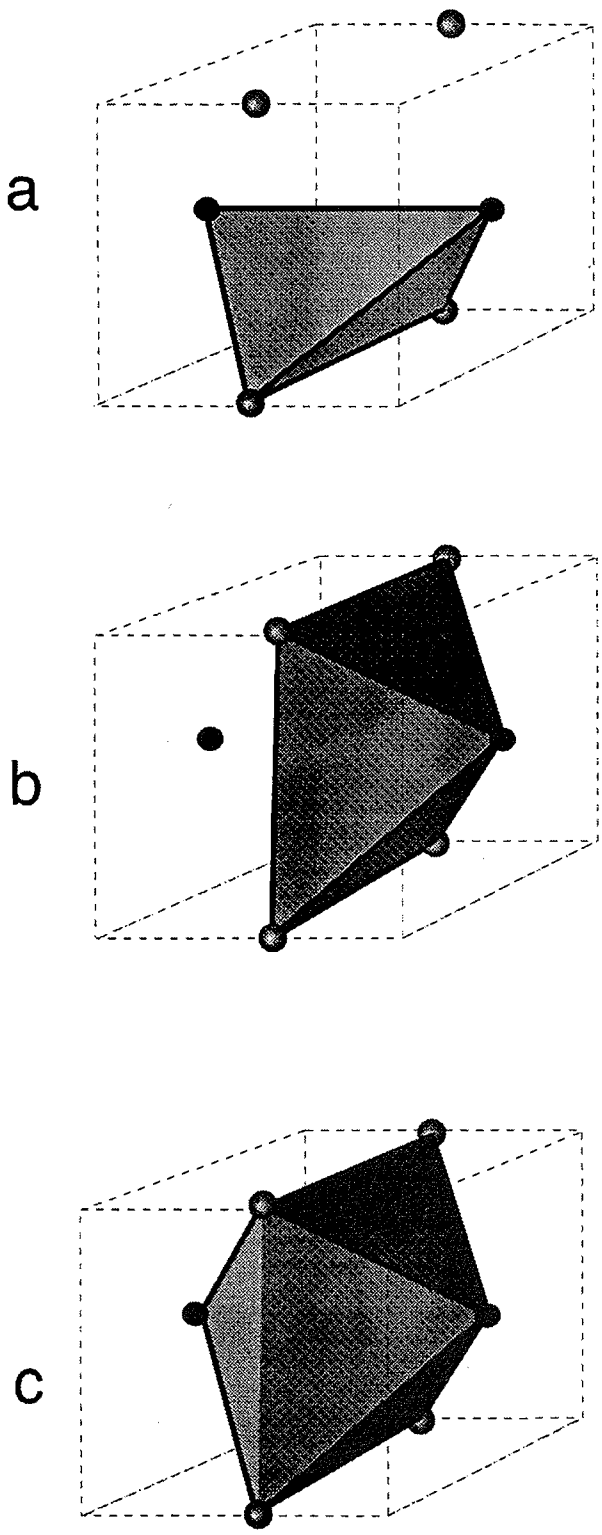

taken from experiment or assumed to be that which will give the same density compared to the observed structure(s) at the equiatomic composition. For each of these calculations, the charge density was determined using the Full Potential Linear Augmented Slater Type Orbital approach (15, 16).

Fig. 6. Distinguishing between the polyhedra of Fig. 5 is easily done by determining the charge density along the broken line shown. A maxima along this line at point *a* corresponds to a bond critical point between transition metal atoms, while a maxima at point *c* corresponds to a bond between aluminum atoms. Maxima at both points correspond to second-neighbor bonds between both types of atoms of the B2 structure.

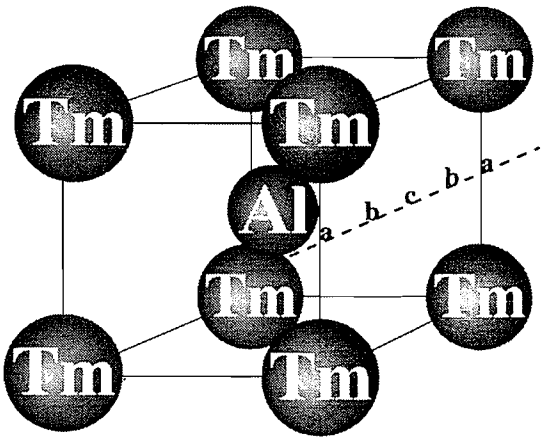

In the B2 structure there are two types of octahedral hole and one type of tetrahedral hole. The octahedral holes are characterized by a fourfold axis where either the A atoms or B atoms are located along this axis. These octahedral holes will be designated by the type of atom lying along the fourfold axis, i.e., either an Al or transition metal octahedral hole.

Each of the different allowed charge densities discussed above can be distinguished by the character of the critical point at the location of the tetrahedral and octahedral holes. If there is more charge density at either of the octahedral holes than at the tetrahedral hole, then one of the topologies resulting in second-neighbor bond formation will be seen, i.e., topologies **b** or **c** of Fig. 5. In turn, the character of the critical point in the center of each of these holes can be determined from a plot of the charge density along the line beginning at a midpoint of one edge of the conventional cubic unit cell and extending to the center of one of the cube faces, Fig. 6. The resultant plot will be sinusoidal in character. The minima along these lines will occur at the location of cage or ring critical points ((3, 3) or (3, 1) cps) and maxima at locations of (3, −1) cps, designating second-neighbor bonds.

The charge density for each of the compounds ScAl, TiAl, VAl, and NiAl along the designated line is shown in Fig. 7. For those compounds that do form the B2 structure, there is a single topology corresponding to second-neighbor bonds between only one of the pairs of atoms. In the case of ScAl the second-neighbor bond is between Al atoms, while in all other cases (both those shown and not shown in Fig. 7) the second-neighbor bond is between the transition metal atoms. In the case of TiAl the topology is consistent with the topology **b** of Fig. 5 and for VAl the topology is consistent with **c** of Fig. 5.

In terms of the topology of the charge density, as one moves from ScAl across the periodic table to NiAl one sees a continuous topological transformation. This transformation can be

Fig. 7. The charge density along the line shown in Fig. 6. Note that AlSc is characterized by second-neighbor bonds between the aluminum atoms while NiAl is characterized by second-neighbor bonds between Ni atoms only. AlV shows both types of second-neighbor bonds.

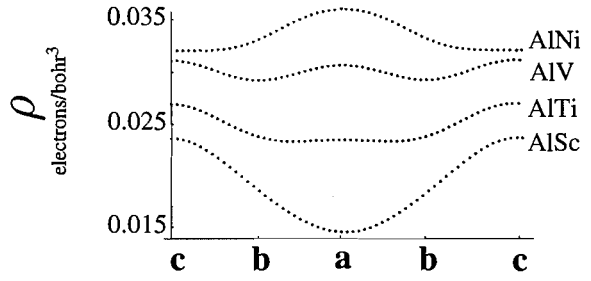

understood to represent a competition for electron density between the two different types of octahedral holes present in the B2 structure. Beginning with ScAl, the Al atoms compete more effectively for second-neighbor electron density than do the Sc atoms. The resulting structure gives rise to local and global minima in the charge density in the Sc octahedral holes and a bond critical point in the center of the Al octahedral holes. For NiAl, the transition metal is now more effectively competing for electron density and the Al octahedral holes have become cage critical points, i.e., global minima. To reach these two extremes, in a continuous fashion, it is necessary to pass through an intermediate region where both atoms of the B2 structure compete more or less equivalently for charge density. At VAl the competition is almost equal with second-neighbor bonds between both types of atoms, the tetrahedral holes becoming the location of the cage critical points, and both octahedral holes marked by (3, −1) cps. It is in this region where the B2 structure is not observed to be stable.

The island of instability can be understood to result from the necessary region of topological transition, bounding the allowed B2 charge density topology. On one side is the region where transition metal octahedral holes are cage critical points, on the other side, Al octahedral holes are cage critical points. There is no way to continuously distort the charge density without passing through a region in which the charge density adopts a unique topology uncharacteristic of stable B2 structures.

Within the topological model of structure, structure becomes a continuous variable, unlike the crystallographic description where structure is a discrete variable. As a continuous variable one would like to assign a "distance" between an observed topology and a topological instability, that is, develop a geometry of the charge density. It is anticipated that this distance will provide information related to the phase behavior of the alloy.

4. A charge density metric

The curvature of the charge density at a point is a tensor, the Hessian of the charge density $\mathscr{H}_{ij}\rho(\boldsymbol{r}) = \partial^2\rho(\boldsymbol{r})/\partial x_i \partial x_j$. This is a symmetric, rank-two tensor having the same transformation properties as the coefficients of a quadratic polynomial, often referred to as the representation quadric. At a bond critical point, one of the eigenvalues of $\mathscr{H}_{ij}\rho(\boldsymbol{r})$ will be positive while the two remaining eigenvalues are negative. The representation quadric at a (3, −1) cp for $-\mathscr{H}_{ij}\rho(\boldsymbol{r})$ is therefore an hyperboloid of one sheet. The 2-D cross section of this hyperboloid normal to the bond path is an ellipse, whose major and minor axes correspond to two of the principal axes of $\mathscr{H}_{ij}\rho(\boldsymbol{r})$, while the third principal axis is always parallel to the bond path.

In the FCC structure, for example, there are bonding cps midway between each pair of first-neighbor atoms. The principal axes of the Hessian tensor with negative curvature extend from this bonding cp toward the octahedral and tetrahedral holes. The curvatures in these directions are denoted here as ρ_{oo} and ρ_{tt}, respectively. The principal axis of positive curvature extends parallel to the bond, by definition. The curvature in this direction is denoted as $\rho_{\parallel\parallel}$. For the BCC structure the eigenvalues of negative curvature are degenerate and are denoted as $\rho_{\perp\perp}$. Table 1 summarizes the values of the principal components of the Hessian tensor at the bond cps for a variety of FCC and BCC metals.

To develop a measure of the distance from a specific charge density to a topological instability, begin by considering the possible topological changes available to a (3, −1) cp, a bond critical point. This critical point can change its character by a change in sign of one of the principal axes of the Hessian tensor at the bond cp. There are two possible changes that will lead to a loss of electron density at the bonding cp. These correspond to a change in sign of the negative eigenvalues. These changes will lead to transformation of a bond critical point to a ring or cage critical point, i.e., a (3, 1) or (3, 3) cp, depending on whether one or two negative eigenvalues changes sign. There is one topological change that will lead to an increase in charge density at a bond cp. This corresponds to a change in sign of the positive eigenvalue, resulting in the formation of a (3, −3) cp, i.e., a pseudo-atom. The topological changes leading to a loss of charge density are defined as electrophobic transformations, while transformations leading to an increase in charge density are defined as electrophilic transformations.

A measure for the distance to either an electrophobic or an electrophilic transformation can be associated with the angle between the directions of zero curvature at a bond critical point and the principal axes of the Hessian of the charge density. Because a bonding cp possesses one axis of positive curvature and two of negative curvature, there must be directions in which the curvature is zero. These directions have a particularly simple geometric interpretation. The representation quadric for the Hessian tensor at a (3, −1) cp is an hyperboloid. Along the line passing through the (3, −1) cp and parallel to the asymptotic surface that bounds this hyperboloid, the curvature is zero. For illustrative purposes consider any plane of the BCC structure that contains two bound atoms, Fig. 8. This plane must contain two of the principal axes of the Hessian tensor: the principal axis of positive curvature and one of the infinite number of degenerate axes of negative curvature. At the (3, −1) cp and lying in this plane there must be a pair of directions in which the curvature is zero. These directions correspond to the asymptotes of an hyperbola formed from the intersection of this plane with the representation quadric of the (3, −1) cp. The slope of the lines that lie in these directions is given by $(\rho_{\parallel\parallel}/\rho_{\perp\perp})^{1/2}$. Figure 8 shows these directions for a variety of BCC and FCC metals.

When the charge density is perturbed, either mechanically

Fig. 8. The directions of zero curvature at a bond critical point for the nonmagnetic FCC and BCC transition metals. Note that for a BCC metal the angle made by the direction of zero curvature with one of the principal axes of the Hessian will be constant regardless of the plane chosen. For FCC metals the angle will vary between two extremes, where one of the extreme planes contains the bond path and the principal axis extending into the tetrahedral hole (the plane shown in the figure) and the other contains the bond path and the principal axis extending into the octahedral hole.

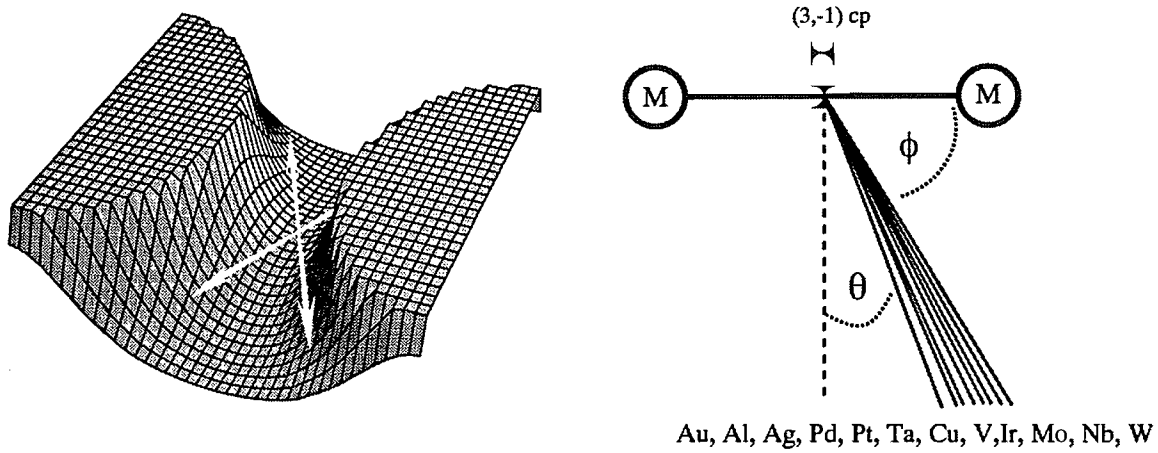

Fig. 9. Left: The correlation between one of the single crystal elastic constants of the BCC metals and the charge-scaled distance to an electrophobic transformation. Right: The same correlation between FCC metals and the charge-scaled distance to an electrophilic transformation.

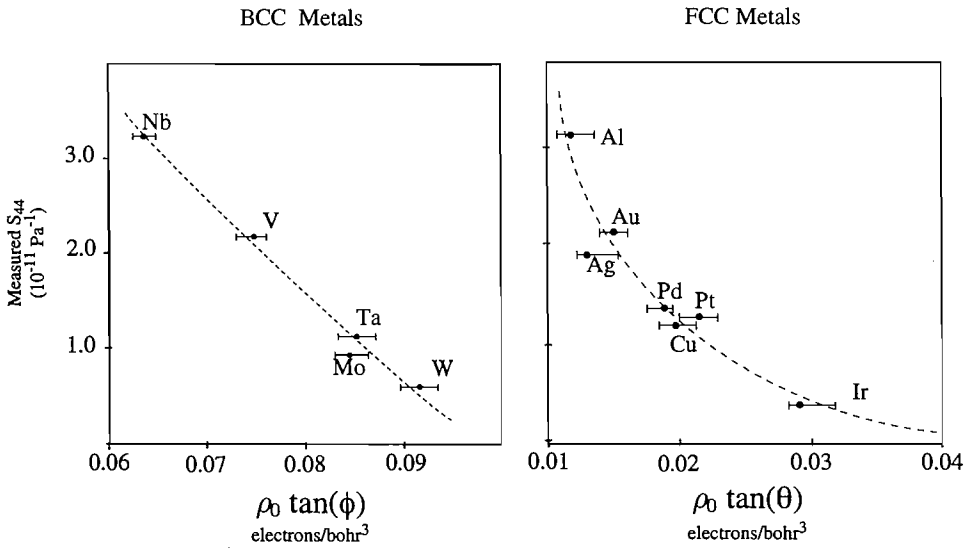

or chemically, the values of the curvature of the charge density at some bonding cps will change and the directions of zero curvature will also change, swinging toward or away from the principal axes of these cps. If these directions of zero curvature should coincide with one of the principal axes of the Hessian of the charge density, then the bond will become unstable and a topological change will follow. Accordingly, one can take the tangent of the angle between these two directions (the direction of zero curvature and one of the principal axes of the Hessian) as a measure of the distance to topological instability. Through this construction, the distance to two different topological instabilities is quantified. These represent the distances to an electrophobic and an electrophilic transformation, i.e., the vanishing of a positive or a negative eigenvalue, respectively. Using the designation in Fig. 8, these distances are given by $\tan(\phi) = (\rho_{\parallel\parallel}/\rho_{\perp\perp})^{1/2}$ and $\tan(\theta) = (\rho_{\perp\perp}/\rho_{\parallel\parallel})^{1/2}$. Table 1 gives the value of $\tan(\theta)$ for the FCC and BCC nonmagnetic transition metals.

The physical significance of these distances can be found by considering the elastic deformations of a metallic lattice. For two metals that deform by the same mechanism, chemical reaction theory dictates that the one that lies closest to an instability, i.e., the transition state, is the one that should be the most compliant (softest). Accordingly, the C_{44} elastic constant

Table 1. Charge density and eigenvalues of the Hessian of the charge density at the bond critical point for nonmagnetic FCC and BCC transition metals. For the purposes of computing the value of the electrophilicity, tan(θ), an average perpendicular eigenvalue is used for the FCC metals given by $\rho_{\perp\perp} = (\rho_{oo} + \rho_{tt})/2$.

Metal	ρ_0	$\rho_{\parallel\parallel}$	$\rho_{tt}(\rho_{\perp\perp})$	$\rho_{oo}(\rho_{\perp\perp})$	$\tan(\theta) = (\rho_{\perp\perp}/\rho_{\parallel\parallel})^{1/2}$
FCC Metals					
Ag	0.0312	0.0893	−0.0140	−0.0140	0.396
Au	0.0402	0.1496	−0.0198	−0.0209	0.369
Cu	0.0421	0.1073	−0.0218	−0.0205	0.444
Ir	0.0626	0.1464	−0.0311	−0.0389	0.489
Pd	0.0434	0.1217	−0.0226	−0.0235	0.435
Pt	0.0536	0.1611	−0.0269	−0.0350	0.438
BCC Metals					
Mo	0.0490	0.0609	−0.0207	−0.0207	0.582
Nb	0.0376	0.0322	−0.0113	−0.0113	0.592
Ta	0.0389	0.0315	−0.0066	−0.0066	0.457
V	0.0348	0.0242	−0.0063	−0.0063	0.510
W	0.0557	0.0697	−0.0258	−0.0258	0.608

(which measures the stiffness of a lattice in response to a specific deformation) of the cubic metals is expected to scale with either $\tan(\phi)/\rho_0$ or $\tan(\theta)/\rho_0$ depending on whether the metal is closer to an electrophobic or electrophilic transformation and where ρ_0 is the value of the charge density at the bond critical point. While the functional form of this relationship is not known, one can expect a power law relationship between the compliance, $S_{44} = 1/C_{44}$, and the distance to instability, as the compliance at zero distance should be infinite and at infinite distance should be zero. Thus S_{44} should vary hypobolically with either $\rho_0 \tan(\phi)$ or $\rho_0 \tan(\theta)$. Figure 9 gives plots showing the relationship between S_{44} and the charge-scaled distance to instability. From these plots one can conclude that the elastic constants of the BCC metals vary as the distance to electrophilic transformations while those of FCC metals vary as the distance to electrophobic transformations.

5. Conclusion

The Bader topological description of the charge density has been reviewed. It has been shown for a single example that unstable crystal structures are sometimes associated with topologies uncharacteristic of the structure. This observation motivated the development of a metric that measures the distance from a calculated charge density topology to topological instabilities. These distances have been found to correlate with the values of the single crystal shear constants for nonmagnetic FCC and BCC metals. Thus the cubic metal elastic constants are seen to be related to the closeness to alternative topologies and the crystallographic structures associated with these charge density topologies, with stiffer metals being further from structural transformations.

References

1. G.N. Lewis. J. Am. Chem. Soc. **38**, 762 (1916).
2. J.C. Slater. Phys. Rev. **37**, 481 (1931); Phys. Rev. **38**, 1109 (1931).
3. R.F.W. Bader and H.J.T. Preston. Int. J. Quantum Chem. **3**, 327 (1969).
4. R.F.W. Bader, P.M. Beddalland, and J. Peslak, Jr. J. Chem. Phys. **28**, 557 (1973).
5. G.R. Runtz, R.F.W. Bader, and R.R. Messer. Can. J. Chem. **55**, 3040 (1977).
6. R.F.W. Bader, T.T. Nguyen-Dang, and Y. Tal. Rep. Prog. Phys. **44**, 893 (1981).
7. R.F.W. Bader and P.J. MacDougall. J. Am. Chem. Soc. **107**, 6788 (1985).
8. P.F. Zou and R.F.W. Bader. Acta Crystallogr. Sect. A: Found. Crystallogr. **A50**, 714 (1994).
9. M.E. Eberhart, M.M. Donovan, J.M. MacLaren, and D.P. Clougherty. Prog. Surf. Sci. **36**, 1 (1991).
10. M.E. Eberhart, J.M. MacLaren, and D.P. Clougherty. Philos. Mag. B: **68**, 455 (1993).
11. M.E. Eberhart, D.P. Clougherty, and J.M. MacLaren. J. Mater. Res. **8**, 438 (1993).
12. M.E. Eberhart, D.P. Clougherty, and J.M. MacLaren. J. Am. Chem. Soc. **115**, 5762 (1993).
13. M.E. Eberhart. Acta Metall. **44**, 2495 (1996).
14. M.E. Eberhart. Philos. Mag. A, **73**, 47 (1996).
15. J.W. Davenport. Phys. Rev. B: Condens. Matter, **29**, 2896 (1984).
16. G.W. Fernando, J.W. Davenport, R.E. Watson, and M. Weinert. Phys. Rev. B: Condens. Matter, **40**, 2757 (1989).

Molecules in high-intensity laser fields

T.-T. Nguyen-Dang, F. Châteauneuf, and S. Manoli

Abstract: The separability of a dressed molecule, a composite molecule + quantized radiation field system, at high field intensities is examined. Various forms of the Hamiltonian describing the dressed molecule are reviewed and are used to assess the zeroth-order separability of the dressed system. A new high-order adiabatic separation between the strongly coupled quantized field and molecular subsystems is derived. Qualitative manifestations of laser-induced molecular structures are discussed within this high-order adiabatic representation.

Key words: dynamics, dressed molecule, intense laser field, adiabatic separation, laser-induced molecular structure.

Résumé : La séparabilité des molécules habillées, super-systèmes «molécule + champ quantifié», est examinée dans un régime de hautes intensités. Différentes formes de l'hamiltonien de la molécule habillée sont rappelées et sont utilisées dans la discussion de la séparabilité dite d'ordre zéro du système habillé. Une séparation adiabatique d'ordre supérieur est démontrée. Des manifestations de la structure moléculaire laser-induite sont discutées qualitativement dans le cadre de cette représentation adiabatique d'ordre supérieur.

Mots clés : dynamique, molécule «habillée», champ laser intense, séparation adiabatique, structure moléculaire laser-induite.

1. Introduction

A central problem in the quantum description of interacting systems is the partitioning of the energy of interaction between the subsystems. In the theory of atoms in molecules developed by Bader et al. (1), these subsystems are molecular fragments defined in three-dimensional real space by the zero-flux surfaces of the molecular charge density, and their interactions are partitioned through the virial of the associated forces, ensuring that a virial theorem is satisfied in each subspace (2). The virial partitioning was introduced with the specific aim of defining atomic fragments within a bound molecular environment, fragments that retain a formal identity in spite of strong interactions with their environment. The same type of problem arises whenever strong interactions between formally defined subsystems prevent the identification of these subsystems as quasi-independent entities with physically meaningful individual properties.

One such problem arises in the study of molecular systems subjected to the influence of intense laser fields. In this problem, the quantized field and the molecule are identified at the outset through attributes associated with the separate entities in an asymptotic, noninteracting situation as subsystems of a composite super system, the dressed molecule (3, 4). This partitioning is thus dictated by the different nature of the two entities and is necessarily a partitioning in Hilbert space as opposed to a partitioning in the real configuration space, as is Bader's virial partitioning of a molecular system. In this sense, the problem may appear easier at first sight; however, it is not clear how one could still speak about the molecule and the field as separate entities at the high intensities delivered by present-day lasers. It is indeed expected that in an intense field a molecule will undergo distortions so strong that it will no longer be recognizable using traditional standards such as the basis states of the isolated field-free molecule. Thus, it was suggested that new molecular states and new species are created by the laser field and are responsible for newly observed phenomena such as the above-threshold ionization (ATI) or dissociation (ATD) of molecules (5–7), their stabilization with respect to ionization, and dissociation at high field intensities (8, 9). Furthermore, the distorted molecule acts as a source of new excitations in the field, giving rise to highly nonlinear effects such as the recently observed high-order harmonic generation phenomenon (10, 11).

Even at low intensities, the problem of separation between the field and the molecule persists since the external field may be of comparable magnitude to the intrinsic electromagnetic field radiated by the moving charges. A distinction between these two types of field that recognizes the inseparability of the molecule from its own field is achieved by a unitary transformation that defines the Pauli–Fierz or Bloch–Nordsieck representation (12–14). This transformation has also been used by Nguyen-Dang and Bandrauk in intense-field molecular dynamics (15, 16). In this paper, this representation is the starting point for the development of a high-order adiabatic separation between the two subsystems of a dressed molecule in the high-field-intensity regime. The

Received November 17, 1995.

This paper is dedicated to Professor Richard F.W. Bader on the occasion of his 65th birthday.

T.-T. Nguyen-Dang,[1] F. Châteauneuf, and S. Manoli.[2]
Département de chimie, Université Laval, Ste-Foy, QC G1K 7P4, Canada.

[1] Author to whom correspondence may be addressed. Telephone: (418) 656-3853. Fax: (418) 656-7916. E-mail: tang@chm.ulaval.ca

[2] Also at Champlain Regional College, St Lawrence Campus, 790 Nérée-Tremblay, Ste-Foy, QC G1V 4K2.

separation is analogous to the adiabatic separation between electrons and nuclei in the usual Born–Oppenheimer treatment of isolated molecules, with the field playing the role of the slow subsystem while the molecule plays the role of the fast one. With no further transformation of the Hamiltonian of the dressed system, such an adiabatic separation would require that the field be slowly varying in time, i.e., that the frequencies of the relevant field modes are smaller than the frequencies characterizing the molecular internal motions. To generalize this type of separation to include the case of a high-frequency field, a subsequent unitary transformation of the Hamiltonian of the dressed molecule is required. This type of transformation was first introduced by Maréchal in the study of proton transfer dynamics in hydrogen-bonded systems (17). It is a correction to the Born–Oppenheimer approximation. Physically, it corresponds to a phase shift between the response of the "fast" subsystem to the motions of the "slow" subsystem, a response that is considered instantaneous in the Born–Oppenheimer approximation. This procedure has subsequently been reformulated to make it noniterative and was applied to the study of energy transfer in model systems of anharmonically coupled oscillators (18, 19). In the present context the resulting separation gives an adiabatic representation that is called high order because a large part of the radiative coupling is implicitly resummed in the formal construction of the adiabatic states, leaving residual, nonadiabatic radiative couplings, which vanish as the intensity increases. Hence, the two subsystems are genuinely separable in the asymptotic limit of an infinite field intensity. At a finite, but sufficiently high intensity, they remain well defined as quasi-separate entities. One of these depends on the usual molecular attributes, such as the masses, charges, and coordinates of the particles, and is called the molecular subsystem or simply the molecule, while the other depends on the field attributes, its normal modes and frequencies, and is called the field subsystem. Due to the very nature of this partitioning in the dressed system's Hilbert space, separate equations of motion are obtained for the two subsystems from whose solutions the total wave function for the dressed system can be constructed.

2. Dressed-molecule Hamiltonian and radiative interactions

2.1. Dressed-molecule Hamiltonian: alternative forms

In the Coulomb gauge (14), a molecular system interacting with a quantized, single-mode radiation field is described by the following Hamiltonian

$$[1]\quad \hat{H} = \hat{T}_N + \hat{H}_{el} + \hat{H}_R - \sum_\alpha \left(\frac{Z_\alpha e}{m_\alpha}\right) \boldsymbol{p}_\alpha \cdot \boldsymbol{A}(\boldsymbol{r}_\alpha) + \sum_i \left(\frac{e}{m_e}\right) \boldsymbol{p}_i \cdot \boldsymbol{A}(\boldsymbol{r}_i) + \sum_\alpha \frac{Z_\alpha^2 e_\alpha^2}{2m_\alpha} \boldsymbol{A}^2(\boldsymbol{r}_\alpha) + \frac{e^2}{2m_e} \sum_i \boldsymbol{A}^2(\boldsymbol{r}_i)$$

where $\hat{T}_N$ is the nuclear kinetic energy operator, $\hat{H}_{el}$ the electronic Hamiltonian, and $\hat{H}_R$ the quantized field Hamiltonian. The remaining terms in eq. [1] describe the interaction of the field with the nuclei (of mass m_α and charge $Z_\alpha e$) and electrons. The quantized field Hamiltonian, $\hat{H}_R$, is

$$[2]\quad \hat{H}_R = \hbar\omega(\hat{a}^\dagger\hat{a} + 1/2)$$

Within the quantized field formalism, the transverse potential vector $\boldsymbol{A}(\boldsymbol{r})$ is an operator expressed in terms of the creation and annihilation operators $\hat{a}^\dagger$ and $\hat{a}$ as (14)

$$[3]\quad \boldsymbol{A}(\boldsymbol{r}) = \left(\frac{\hbar}{2\varepsilon_0\omega V}\right)^{1/2} (\hat{a}e^{i\boldsymbol{k}\cdot\boldsymbol{r}} + \hat{a}^\dagger e^{-i\boldsymbol{k}\cdot\boldsymbol{r}})\boldsymbol{\varepsilon}$$

where $\boldsymbol{\varepsilon}$ is the polarization of the field and $\boldsymbol{k}$ is the wave vector, which is related to the field frequency ω by $\omega = c|\boldsymbol{k}|$. Within the long-wavelength approximation (LWA), the dependence of $\boldsymbol{A}$ on $\boldsymbol{r}$ is neglected and eq. [3] reduces to

$$[4]\quad \boldsymbol{A} = \left(\frac{\hbar}{2\varepsilon_0\omega V}\right)^{1/2} (\hat{a} + \hat{a}^\dagger)\boldsymbol{\varepsilon} = \left(\frac{\hbar}{\varepsilon_0\omega V}\right)^{1/2} \boldsymbol{\varepsilon}\hat{P}$$

where

$$[5]\quad \hat{P} \equiv 2^{-1/2}(\hat{a} + \hat{a}^\dagger)$$

is the unitless, canonical momentum operator of the harmonic oscillator associated with the field mode. The corresponding coordinate operator of this oscillator is

$$[6]\quad \hat{Q} \equiv 2^{-1/2} i(\hat{a}^\dagger - \hat{a}).$$

Note that with these definitions, $[\hat{P}, \hat{Q}] = i$ such that, in the coordinate representation,

$$[7]\quad \hat{P} \equiv i\partial_Q$$

In terms of $\hat{P}$ and $\hat{Q}$, the Hamiltonian for the field, eq. [2], is

$$[8]\quad \hat{H}_R = \frac{\hbar\omega}{2}(\hat{P}^2 + \hat{Q}^2)$$

Introducing the coupling constants

$$[9] \quad \theta_e \equiv \frac{e}{m_e}\left(\frac{\hbar}{\varepsilon_0 \omega V}\right)^{1/2}$$

and

$$[10] \quad \theta_\alpha \equiv -\frac{Z_\alpha e}{m_\alpha}\left(\frac{\hbar}{\varepsilon_0 \omega V}\right)^{1/2}$$

eq. [1] can be rewritten as

$$[11] \quad \hat{H} = \hat{T}_N + \hat{H}_{el} + \frac{\hbar\omega}{2}(\hat{P}^2 + \hat{Q}^2) + \sum_\alpha \theta_\alpha(\boldsymbol{\varepsilon}\cdot\boldsymbol{p}_\alpha)\hat{P} + \theta_e \sum_i (\boldsymbol{\varepsilon}\cdot\boldsymbol{p}_i)\hat{P} + \left(\sum_\alpha \frac{m_\alpha\theta_\alpha^2}{2} + N_e\frac{m_e\theta_e^2}{2}\right)\hat{P}^2$$

where N_e is the number of electrons, such that the radiative interactions denote momentum coupling between the charges and the field. The last term in eq. [11] corresponds to the A^2 terms of eq. [1]. Since the LWA is used, including this term merely gives rise to a renormalization of the mass factor associated with the field oscillator. This term, as well as the momentum coupling terms in eq. [11], can be removed by applying the unitary transformation

$$[12] \quad \hat{U}_{EF} = \exp\left\{\frac{i}{\hbar}\left[\sum_\alpha m_\alpha\theta_\alpha(\boldsymbol{\varepsilon}\cdot\boldsymbol{r}_\alpha) + m_e\theta_e\sum_i(\boldsymbol{\varepsilon}\cdot\boldsymbol{r}_i)\right]\hat{P}\right\}$$

to $\hat{H}$. In this case, the transformed Hamiltonian

$$[13] \quad \hat{H}_{EF} \equiv \hat{U}_{EF}\hat{H}\hat{U}_{EF}^\dagger$$

$$= \hat{T}_N + \hat{H}_{el} + \frac{\hbar\omega}{2}(\hat{P}^2 + \hat{Q}^2) + \omega\left[\sum_\alpha m_\alpha\theta_\alpha(\boldsymbol{\varepsilon}\cdot\boldsymbol{r}_\alpha) + m_e\theta_e\sum_i(\boldsymbol{\varepsilon}\cdot\boldsymbol{r}_i)\right]\hat{Q}$$

has radiative interactions expressed in the so-called Electric Field (EF) gauge (20), since Q is related to the electric field $\boldsymbol{E}$ by

$$[14] \quad \hat{\boldsymbol{E}} = -\omega\frac{m_e\theta_e}{e}\boldsymbol{\varepsilon}\hat{Q} = -\omega\frac{m_\alpha\theta_\alpha}{Z_\alpha e}\boldsymbol{\varepsilon}\hat{Q}$$

Alternatively, the momentum interaction in the Radiation Field (RF) gauge (20) Hamiltonian of eq. [11] can also be removed by using the unitary transformation

$$[15] \quad \hat{U}_{BN} = \exp\left\{-\frac{i}{\hbar}\left[\sum_\alpha\frac{\theta_\alpha}{\omega}(\boldsymbol{\varepsilon}\cdot\boldsymbol{p}_\alpha) + \frac{\theta_e}{\omega}\sum_i(\boldsymbol{\varepsilon}\cdot\boldsymbol{p}_i)\right]\hat{Q}\right\}$$

yielding

$$\hat{H}_{BN} \equiv \hat{U}_{BN}\hat{H}\hat{U}_{BN}^\dagger = \hat{T}_N + \hat{T}_{el} + V_{coul}\left(\left\{\boldsymbol{r}_i - \frac{\theta_e}{\omega}\boldsymbol{\varepsilon}\hat{Q}, \boldsymbol{r}_\alpha - \frac{\theta_\alpha}{\omega}\boldsymbol{\varepsilon}\hat{Q}\right\}\right) + \frac{\hbar\omega}{2}[(1+\Delta)\hat{P}^2 + \hat{Q}^2]$$

where $\Delta = \left(\sum_\alpha m_\alpha\theta_\alpha^2 + N_e m_e\theta_e^2\right)/\hbar\omega$ and $(1+\Delta)$ denotes the renormalization of the field oscillator mentioned previously. Using a subsequent scaling transformation on the field variables alone, which maps $\hat{P}$ onto $(1+\Delta)^{1/4}\hat{P}$ and $\hat{Q}$ onto $(1+\Delta)^{-1/4}\hat{Q}$, and defining the renormalized field frequency $\omega' = \omega(1+\Delta)^{1/2}$, and coupling constants $\theta_k' = (1+\Delta)^{3/4}\theta_k$ ($k = e$ or α), the above equation for $\hat{H}_{BN}$ becomes

$$[16] \quad \hat{H}_{BN} = \hat{T}_N + \hat{T}_{el} + V_{coul}\left(\left\{\boldsymbol{r}_i - \frac{\theta_e}{\omega}\boldsymbol{\varepsilon}\hat{Q}, \boldsymbol{r}_\alpha - \frac{\theta_\alpha}{\omega}\boldsymbol{\varepsilon}\hat{Q}\right\}\right) + \frac{\hbar\omega}{2}(\hat{P}^2 + \hat{Q}^2)$$

exactly, where for clarity ω', θ' have been relabeled ω, θ. The transformation eq. [15] was first introduced by Bloch and Nordsieck (13), and then used by Pauli and Fierz (12) in a general, multimode formulation designed to resolve the so-called infrared divergence problem. At low field intensity, this transformation removes from the transverse field that part which is thought to be tied to the moving charges (14). It is this association of an intrinsic field with the charges that gives a satisfactory solution to the infrared divergence problem through a renormalization of the particles' masses. In intense-field molecular dynamics, it was used

by Nguyen-Dang and Bandrauk (15, 16), who identified the field mode in the Bloch–Nordsieck Hamiltonian, eq. [16], as an additional degree of freedom that parametrizes the electronic Hamiltonian in the same manner as the nuclear coordinates. In the quantized-field formalism, the Bloch–Nordsieck transformation is the counterpart of the Kramers–Henneberger transformation of semiclassical theory (21).

The general relationship between the present time-independent, fully quantum formulation in which the quantized field is included as part of a super system, the dressed molecule, and the semiclassical formulation, in which the field is treated as a classical, time-dependent, external field is established by the Mollow unitary transformation (14, 22, 23) defined as

$$[17]\quad \hat{T}_{\text{Mollow}}(t) = \exp\{i(\text{Re}\lambda(t)\hat{Q} - \text{Im}\,\lambda(t)\hat{P})\}$$

with

$$[18]\quad \text{Re}\lambda(t) = \left(\frac{\hbar}{\varepsilon_0\omega V}\right)^{-1/2} A_{\text{cl}}(t)$$

and

$$[19]\quad \text{Im}\lambda(t) = \left(\frac{\hbar\omega}{\varepsilon_0 V}\right)^{-1/2} E_{\text{cl}}(t)$$

with A_{cl} and $E_{\text{cl}} = -(1/c)\partial_t A_{\text{cl}}$ being the harmonic functions describing the amplitudes of the classical vector potential and electric field, respectively, which for example, may be

$$[20]\quad A_{\text{cl}}(t) = A_0\cos(\omega t), \qquad E_{\text{cl}}(t) = (\omega/c)A_0\sin(\omega t)$$

This transformation leaves the field hamiltonian $\hat{H}_{\text{R}}$ invariant in the sense that

$$[21]\quad \hat{T}_{\text{Mollow}}(t)\hat{H}_{\text{R}}\hat{T}^{\dagger}_{\text{Mollow}}(t) - i\hbar\,\hat{T}_{\text{Mollow}}(t)\partial_t\hat{T}^{\dagger}_{\text{Mollow}}(t) = \hat{H}_{\text{R}}$$

Hence, the results of transforming the various dressed Hamiltonians under $\hat{T}_{\text{Mollow}}$ are

$$[22]\quad \hat{H}(t) = \hat{T}_{\text{N}} + \hat{H}_{\text{el}} + \hat{H}_{\text{R}} + \sum_{\alpha}\left(\frac{Z_\alpha e}{m_\alpha}\right)(\boldsymbol{\varepsilon}\cdot\boldsymbol{p}_\alpha)\boldsymbol{A}_{\text{cl}}(t) + \sum_i\left(\frac{e}{m_{\text{e}}}\right)(\boldsymbol{\varepsilon}\cdot\boldsymbol{p}_i)\boldsymbol{A}_{\text{cl}}(t) + \left\{\sum_\alpha \theta_\alpha(\boldsymbol{\varepsilon}\cdot\boldsymbol{p}_\alpha) + \theta_{\text{e}}\sum_i(\boldsymbol{\varepsilon}\cdot\boldsymbol{p}_i)\right\}\hat{P}$$

for the Hamiltonian of eq. [11],

$$[23]\quad \hat{H}_{\text{EF}}(t) = \hat{T}_{\text{N}} + \hat{H}_{\text{el}} + \hat{H}_{\text{R}} + \left[\sum_\alpha Z_\alpha e(\boldsymbol{\varepsilon}\cdot\boldsymbol{r}_\alpha) - e\sum_i(\boldsymbol{\varepsilon}\cdot\boldsymbol{r}_i)\right]E_{\text{cl}}(t) + \omega\left[\sum_\alpha m_\alpha\theta_\alpha(\boldsymbol{\varepsilon}\cdot\boldsymbol{r}_\alpha) + m_{\text{e}}\theta_{\text{e}}\sum_i(\boldsymbol{\varepsilon}\cdot\boldsymbol{r}_i)\right]\hat{Q}$$

for that of eq. [13], and

$$[24]\quad \hat{H}_{\text{BN}}(t) = \hat{T}_{\text{N}} + \hat{T}_{\text{el}} + V_{\text{coul}}\left(\left\{\boldsymbol{r}_i - \left(\frac{e}{m_{\text{e}}}\right)\boldsymbol{Z}_{\text{cl}}(t) - \frac{\theta_{\text{e}}}{\omega}\,\boldsymbol{\varepsilon}\,\hat{Q}, \boldsymbol{r}_\alpha - \left(\frac{Z_\alpha e}{m_\alpha}\right)\boldsymbol{Z}_{\text{cl}}(t) - \frac{\theta_\alpha}{\omega}\,\boldsymbol{\varepsilon}\,\hat{Q}\right\}\right) + \hat{H}_{\text{R}}$$

for the Bloch–Nordsieck Hamiltonian. In this last equation, $\boldsymbol{Z}_{\text{cl}}(t)$ is defined by

$$[25]\quad \boldsymbol{Z}_{\text{cl}}(t) = \boldsymbol{\varepsilon}\int_0^t A_{\text{cl}}(t')\text{d}t' = \boldsymbol{\varepsilon}\,\frac{1}{\omega}\,A_0\sin(\omega t)$$

The Mollow transformation maps a coherent state of the field corresponding to a classical intense field $\boldsymbol{E}_{\text{cl}}(t)$

$$[26]\quad |\boldsymbol{E}_{\text{cl}}(t)\rangle = \hat{T}_{\text{Mollow}}(t)|0\rangle$$

into the vacuum state so that the residual couplings between the quantized field and the molecule are negligible in comparison to the time-dependent radiative couplings exhibited explicitly in eqs. [22], [23], and [24]. The residual interactions between the molecule and the quantized field are responsible for spontaneous emission while the time-dependent radiative couplings are responsible for stimulated processes (23). In semiclassical theory, only stimulated processes are considered and the residual couplings between the quantized field and the molecule are completly neglected. In a sense, a separation between the quantized field and the molecule has been achieved. As a consequence, the quantized field remains in the vacuum state, i.e., it remains coherent, at all times. In reality, the Mollow transformation only achieves a separation between the nonimportant part of the field (the residual, unexcited quantized field) and the intense field, which becomes a classical time-dependent force that strongly drives the molecular system. The problem of the interaction of this intense field with the charges remains to be solved.

2.2 Molecular structure changes in intense field: Floquet descriptions

One approach to solving the molecular time-dependent Schrödinger equation in semiclassical theory begins with the fact that the time-dependent molecular Hamiltonian in the semiclassical theory is periodic in time with a period $T = 2\pi/\omega$, and exploits the Floquet theorem to express the time-dependent molecular state vector as (24)

$$[27] \quad |\Psi, t\rangle = \exp\left(-\frac{i}{\hbar}\varepsilon_{Fl}t\right)\sum_{n=-\infty}^{+\infty} e^{in\omega t}|\psi_n\rangle$$

yielding a set of coupled equations for the time-independent Floquet components $|\psi_n\rangle$ given by

$$[28] \quad \{\langle\hat{H}_{mol}(t)\rangle_{nn} + n\hbar\omega - \varepsilon_{Fl}\}|\psi_n\rangle = -\sum_{n'\neq n}\langle\hat{H}_{mol}(t)\rangle_{nn'}|\psi_{n'}\rangle$$

where $\hat{H}_{mol}(t)$ is the time-dependent molecular Hamiltonian of eq. [22], or [23] or [24] (with the residual quantized field–molecule interactions neglected), and

$$[29] \quad \langle\hat{H}_{mol}(t)\rangle_{nn'} = \frac{1}{T}\int_{-T/2}^{T/2} dt e^{i(n'-n)\omega t}\hat{H}_{mol}(t)$$

It is from these coupled equations that various forms of the laser-induced effects on the molecular structure were obtained. Figure 1 shows the dressed potential energy surfaces (PESs) of H_2^+ described in a model using just two field-free electronic states, the ground state $1\sigma_g$ and the first excited state $1\sigma_u$. Due to their displacements by the photon energy $n\hbar\omega$, as indicated on the left-hand side of eq. [28], the zeroth-order PESs cross each other at specific values of the internuclear distance R. At these crossings, the radiative couplings between the two electronic states are resonant. Diagonalizing the potential energy matrix, whose off-diagonal terms are the radiative interactions, at each value of R, removes these radiative interactions, and transforms the intersections into avoided crossings (7, 25, 26). This yields a new set of PESs called adiabatic dressed PESs which can support new vibrational states. In the case of the dihydrogen molecular ion illustrated in Fig. 1, the new electronic adiabatic channels and the new vibrational bound states are thought to play an important role in the ATD mechanism of this system (5–7, 27). Laser-induced molecular structure changes of a completely different type have been suggested for a high-frequency field in the Kramers–Henneberger representation where the semiclassical molecular Hamiltonian depends on time through displacements of the position vectors of the particles, as described in eq. [24]. For a high-frequency field, the Floquet blocks corresponding to different values of n in eq. [29] are well separated from each other so that their interactions, denoted by the nondiagonal matrix elements $\langle\hat{H}_{mol}(t)\rangle_{nn'}$ with $n' \neq n$, can be neglected. Restricting the problem to a single Floquet block, the electronic wave function of the molecule is governed by the "dressed" Coulomb potential

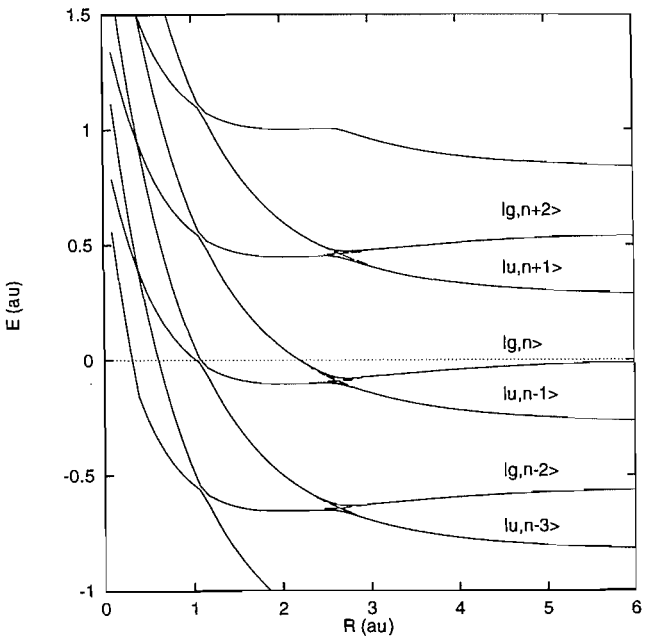

Fig. 1. Adiabatic (solid lines) and diabatic (broken lines) dressed PESs of H_2^+ in a two-state model of the photodissociation of the molecular ion in a field with λ = 164.85 nm, and $I = 4 \times 10^{13}$ W/cm^2. The labels refer to the dressed diabatic states $|K,n\rangle = |K\rangle|n\rangle, K = g,u$.

$$[30] \quad \langle V_{coul}\rangle_{nn} = \frac{1}{T}\int_{-T/2}^{T/2} dt V_{coul}\left(\boldsymbol{r}_i - \left(\frac{e}{m_e}\right)\boldsymbol{Z}_{cl}(t),\ \boldsymbol{r}_\alpha - \left(\frac{Z_\alpha e}{m_\alpha}\right)\boldsymbol{Z}_{cl}(t)\right)$$

As demonstrated by Gavrila and Zaminski (28) for an atomic system, and by Zuo and Bandrauk (29) for one-electron molecular ions, this "dressed" Coulomb potential exhibits new, non-nuclear wells giving rise to what can be described as non-nuclear attractors in the ground state electron density of the molecular system, using the terminology of Bader's topological theory of atoms in molecules (1).

While the current theories discussed in this section highlight the various manifestations of laser-intensity effects on molecular structure, they also point to their limitations: the new states and molecular species created at avoided crossings of dressed PESs are meaningful only insofar as the truncated electronic basis used in this picture is itself meaningful; the effects of the intense field on the ground state electron density as described in the single-block description of the laser-driven molecule using the Kramers–Henneberger frame are limited to high-frequency fields. Moreover, it is not clear how the laser-induced resonances and new bound electronic or vibrational states predicted by these Floquet solutions are prepared from an initially unexcited molecule. However, the central conceptual problem remains the lack of a clear demonstration of a separability of some sort between the molecular system and the intense radiation field. Once established, such a separability will lend support to the identification of laser-induced effects in molecular structure such as those mentioned above as real, observable phenomena.

3. Adiabatic separation at high intensities

3.1. Zeroth-order adiabatic representation

In the Bloch–Nordsieck form of the dressed Hamiltonian, eq. [16], the field-mode appears as an additional degree of freedom which parametrizes the electronic Hamiltonian in the same manner as the nuclear coordinates (15, 16). This suggests an adiabatic separation of the molecule–field system just as the electronic and nuclear motions are separated within the Born–Oppenheimer (BO) approximation. To explore this zeroth-order adiabatic representation, the eigenfunctions $\Psi_{\text{tot}}(\{\boldsymbol{r}_\alpha\}, Q)$ of $\hat{H}_{\text{BN}}$ are expressed in the form of a Born–Huang expansion

$$[31] \quad \Psi_{\text{tot}}(\{\boldsymbol{r}_i, \boldsymbol{r}_\alpha\}, Q) = \sum_I \chi_I(Q)\psi_I(\{\boldsymbol{r}_i, \boldsymbol{r}_\alpha\} \mid Q)$$

in the orthonormal eigenbasis $\{\psi_I(\{\boldsymbol{r}_i, \boldsymbol{r}_\alpha\} \mid Q)\}$ of $\hat{H}_{\text{mol}}(Q)$, i.e.,

$$\hat{H}_{\text{mol}}(Q)\psi_I = \varepsilon_I\psi_I$$

where

$$[32] \quad \hat{H}_{\text{mol}}(Q) \equiv \hat{T}_{\text{N}} + \hat{T}_{\text{el}} + V_{\text{coul}}\left(\left\{\boldsymbol{r}_i - \frac{\theta_e}{\omega}\boldsymbol{\varepsilon}Q,\ \boldsymbol{r}_\alpha - \frac{\theta_\alpha}{\omega}\boldsymbol{\varepsilon}Q\right\}\right)$$

and the parameter Q is the eigenvalue of the operator $\hat{Q}$, i.e., in the coordinate representation implied by the adiabatic scheme, $\hat{H}_{\text{mol}}$ is a local operator with respect to the field mode. The use of eq. [31] gives the following coupled equations for the field wave functions $\chi_I(Q)$

$$[33] \quad (\hat{H}_{\text{R}} + \varepsilon_I - E)\chi_I(Q) = \sum_J \frac{\hbar\omega}{2}\{\langle\psi_I|\partial_{QQ}^2|\psi_J\rangle\chi_J(Q) + 2\langle\psi_I|\partial_Q|\psi_J\rangle\partial_Q\chi_J(Q)\}$$

The adiabatic separation between the field and the charges is obtained by neglecting the nonadiabatic coupling terms in eq. [33]. Since $\hat{H}_{\text{mol}}(Q)$ is exactly a unitary transform (under $\hat{U}_{\text{BN}}$) of the field-free molecular Hamiltonian, its eigenvalues ε_I are independent of Q as are the matrix elements

$$\langle\psi_I|\partial_Q|\psi_J\rangle = -\frac{i}{\hbar}\langle\psi_I^0|\left[\sum_\alpha \frac{\theta_\alpha}{\omega}(\boldsymbol{\varepsilon}\cdot\boldsymbol{p}_\alpha) + \frac{\theta_e}{\omega}\sum_i(\boldsymbol{\varepsilon}\cdot\boldsymbol{p}_i)\right]|\psi_J^0\rangle$$

where the $\{\psi_I^0\}$ denote the field-free molecular eigenfunctions. Defining $\chi_{In}^0(Q)$ to be the field wave functions in this approximation, the $\chi_{In}^0(Q)$ denote the usual photon number states because ε_I is independent of Q. Thus, $\chi_{In}^0(Q) = \langle Q \mid n\rangle$ exactly. Hence, the magnitudes of the neglected nonadiabatic couplings are of the order of

$$[34] \quad -\langle\chi_{In}^0|\langle\psi_I|\partial_Q|\psi_J\rangle\,\partial_Q|\chi_{Jn'}^0\rangle = \frac{1}{\hbar}\langle\psi_I^0|\left[\sum_\alpha \frac{\theta_\alpha}{\omega}(\boldsymbol{\varepsilon}\cdot\boldsymbol{p}_\alpha) + \frac{\theta_e}{\omega}\sum_i(\boldsymbol{\varepsilon}\cdot\boldsymbol{p}_i)\right]|\psi_J^0\rangle\langle n|\hat{P}|n'\rangle = O(\theta_\alpha n^{1/2})$$

This estimate is to be compared with estimates of the radiative couplings in eqs. [11] and [13] when a basis of uncoupled molecule–field states $|\psi_I^0\rangle|n\rangle$ is used

$$[35] \quad \langle\psi_I^0|\left[\sum_\alpha \theta_\alpha(\boldsymbol{\varepsilon}\cdot\boldsymbol{p}_\alpha) + \theta_e\sum_i(\boldsymbol{\varepsilon}\cdot\boldsymbol{p}_i)\right]|\psi_J^0\rangle\langle n|\hat{P}|n'\rangle = O(\theta_\alpha n^{1/2})$$

$$[36] \quad \omega\langle\psi_I^0|\left[\sum_\alpha m_\alpha\theta_\alpha(\boldsymbol{\varepsilon}\cdot\boldsymbol{r}_\alpha) + m_e\theta_e\sum_i(\boldsymbol{\varepsilon}\cdot\boldsymbol{r}_i)\right]|\psi_J^0\rangle\langle n|\hat{Q}|n'\rangle = O(\theta_\alpha n^{1/2})$$

Since the non-adiabatic couplings in eq. [34] are of the same order of magnitude as the radiative potential couplings in eqs. [35] and [36], the adiabatic representation defined by the eigenstates of $\hat{H}_{\text{mol}}(Q)$ does not offer a real advantage over the usual diabatic basis associated with the original RF Hamiltonian, eq. [11], or the EF Hamiltonian, eq. [13]. In fact, none of the three representations gives a convergent description in superintense fields: in the limit $I \to \infty$, i.e., $n \to \infty$, the radiative couplings in eqs. [34]–[36] all diverge. Note that these radiative couplings depend on the coupling constants θ_α, θ_e, and on the photon number n through the combination $\theta_a n^{1/2} (a = \alpha \text{ or } e)$. At low field intensities, for example when n is of the order of unity, the radiative interactions can be treated perturbatively because θ_a is weak ($\theta_e \simeq 10^{-7}$ ms^{-1} for a field with $\omega = 1000$ cm^{-1} in a 1 m^3 cavity; thus, for an electron with a kinetic energy of 10 eV in a field of intensity $I \simeq 1$ W cm^{-2}, the radiative coupling

is of order 10^{-7} eV). Henceforth, any quantity that is of order $(\theta_a n^p)^k$ with $p < 1/2, k \geq 1$ will be considered negligible, and a molecule–field separation with residual couplings that are negligible in this sense will be called a high-order separation.

3.2. High-order adiabatic molecule–field separation

To obtain a partial analytic summation of the nonadiabatic couplings, Maréchal proposed the introduction of a phase shift between the fast and slow motions that accounts for a delay in the response of the fast subsystem to the fluctuations of the slower one (17–19). In the present context, where the molecule is identified as the fast subsystem while the field mode is the slow one, Maréchal's ansatz,

$$[37]\quad \Psi_{\text{tot}}(\{\boldsymbol{r}_\kappa\}, Q) = \mathrm{e}^{-(i/\hbar) f(\{\boldsymbol{r}_\kappa\}, Q)\hat{P}} \Psi^M_{\text{tot}}(\{\boldsymbol{r}_\kappa\}, Q)$$

requires an appropriate function $f(\{\boldsymbol{r}_\kappa\}, Q)$ such that the new total wave function $\Psi^M_{\text{tot}}(\{\boldsymbol{r}_\kappa\}, Q)$ can be written in the form of a BO-like product $\chi_I(Q)\psi_I(\{\boldsymbol{r}_\kappa\} \mid Q)$. Henceforth, to simplify the notation, the subscript κ will denote either electronic or nuclear coordinates. The unitary transformation

$$[38]\quad \hat{U}_{\text{M}} = \exp\{-(i/\hbar) f(\{\boldsymbol{r}_\kappa\}, Q)\hat{P}\}$$

displaces Q by $f(\{\boldsymbol{r}_\kappa\}, Q)/\hbar$ while it leaves the coordinate vectors $\boldsymbol{r}_\kappa$ invariant and transforms the corresponding momenta $\boldsymbol{p}_\kappa$ into

$$[39]\quad \hat{U}_{\text{M}} \boldsymbol{p}_\kappa \hat{U}^\dagger_{\text{M}} \simeq \boldsymbol{p}_\kappa + \boldsymbol{\nabla}_\kappa f \hat{P}$$

If f is independent of, or is weakly dependent on, Q, then $\hat{U}_{\text{M}}$ also leaves the field momentum operator $\hat{P}$ invariant. These transformation properties of $Q, \hat{P}, \boldsymbol{r}_\kappa$, and $\boldsymbol{p}_\kappa$ under $\hat{U}_{\text{M}}$ give

$$[40]\quad \hat{U}_{\text{M}} \hat{H}_{\text{BN}} \hat{U}^\dagger_{\text{M}} = \sum_\kappa \frac{\hat{p}^2_\kappa}{2m_\kappa} + V_{\text{coul}}\left(\left\{\boldsymbol{r}_\kappa - \frac{\theta_\kappa}{\omega}\,\boldsymbol{\varepsilon}\left(Q + \frac{f}{\hbar}\right)\right\}\right) + \omega f Q + \frac{\omega}{2}\frac{f^2}{\hbar}$$
$$+ \frac{\hbar\omega}{2}\left[\left(1 + \sum_\kappa \frac{1}{m_\kappa \hbar\omega}(\boldsymbol{\nabla}_\kappa f)^2\right)\hat{P}^2 + Q^2\right] + \sum_\kappa \frac{1}{2m_\kappa}(\boldsymbol{\nabla}_\kappa f \cdot \boldsymbol{p}_\kappa + \text{h.c.})\hat{P}$$

This is the Hamiltonian governing the dynamics of the dressed system in the new representation, which will be called the Bloch–Nordsieck–Maréchal (BNM) representation. To see how a partial analytic summation of non-adiabatic couplings is possible in this representation, let the new total wave function $\Psi^M_{\text{tot}}(\{\boldsymbol{r}_\kappa\}, Q)$ be expressed in the form similar to that of eq. [31], i.e., as an infinite Born–Huang expansion in terms of the eigenstates of the new molecular Hamiltonian defined by

$$[41]\quad \hat{h}_{\text{mol}}(Q) \equiv \sum_\kappa \frac{\hat{p}^2_\kappa}{2m_\kappa} + V_{\text{coul}}\left(\left\{\boldsymbol{r}_\kappa - \frac{\theta_\kappa}{\omega}\,\boldsymbol{\varepsilon}\left(Q + \frac{f}{\hbar}\right)\right\}\right) + \omega f(\{\boldsymbol{r}_\kappa\}, Q)Q + \frac{\omega}{2}\frac{f(\{\boldsymbol{r}_\kappa\}, Q)^2}{\hbar}$$

This yields the set of coupled equations for the field wave functions $\chi_I(Q)$

$$[42]\quad (\hat{H}_{\text{R}} + \varepsilon_I - E)\chi_I = \sum_J \left\{\left[\langle\psi_I| \sum_\kappa \frac{1}{2m_\kappa}(\boldsymbol{\nabla}_\kappa f . \boldsymbol{p}_\kappa + \text{h.c.})|\psi_J\rangle + \hbar\omega\langle\psi_I|\left(1 + \sum_\kappa \frac{1}{m_\kappa\hbar\omega}(\boldsymbol{\nabla}_\kappa f)^2\right)\hat{P}|\psi_J\rangle\right]\hat{P}\chi_J\right.$$
$$\left. + \langle\psi_I|\left(1 + \sum_\kappa \frac{1}{m_\kappa\hbar\omega}(\boldsymbol{\nabla}_\kappa f)^2\right)\hat{P}^2 + \sum_\kappa \frac{1}{2m_\kappa}(\boldsymbol{\nabla}_\kappa f \cdot \boldsymbol{p}_\kappa + \text{h.c.})\hat{P}|\psi_J\rangle\chi_J + \langle\psi_I| \sum_\kappa \frac{1}{m_\kappa\hbar\omega}(\boldsymbol{\nabla}_\kappa f)^2|\psi_J\rangle\hat{P}^2\chi_J\right\}$$

The nonadiabatic coupling terms in eq. [42] arise from two sources: the parametric dependence of $\hat{h}_{\text{mol}}(Q)$ on Q, eq. [41], and the explicit momentum coupling term induced by the unitary transformation $\hat{U}_{\text{M}}$ in the Hamiltonian of the dressed system, (last term of eq. [40]). The interplay between these allows the partial cancellation of the nonadiabatic couplings, leaving residual interaction terms that are of higher order in the coupling constants θ_κ, or that behave as n^p, where $p < 0$. This partial cancellation determines f and yields a representation of the dressed system in which the total wave function can be written in the form of a BO product denoting an adiabatic response of the molecule to the field oscillations. The nonadiabatic decoupling condition

$$[43]\quad \langle\psi_I| \sum_\kappa \frac{1}{2m_\kappa}(\boldsymbol{\nabla}_\kappa f \cdot \boldsymbol{p}_\kappa + \text{h.c.}) + \hbar\omega\left(1 + \sum_\kappa \frac{1}{m_\kappa\hbar\omega}(\boldsymbol{\nabla}_\kappa f)^2\right)\hat{P}|\psi_J\rangle = 0$$

indicates that the leading term in f is linear in $\boldsymbol{r}_\kappa$ and is of first order in θ_κ. As a consequence, if f is defined in terms of a power series expansion as

$$[44]\quad f(\{\boldsymbol{r}_\kappa\}, Q) = \hbar \sum_\kappa [a_\kappa(\boldsymbol{\varepsilon} . \boldsymbol{r}_\kappa) + b_\kappa(Q)(\boldsymbol{\varepsilon} . \boldsymbol{r}_\kappa)^2 + \ldots]$$

where a_κ is of order θ_κ and b_κ and the coefficients of the higher powers of r_κ are assumed to be much smaller than a_κ, then all terms containing the products $a_\kappa b_\kappa, b_\kappa^2$, and so on can be considered negligible. The $(\nabla_\kappa f)^2$ terms in eqs. [42] and [43] are thus replaced by a_κ^2, so that the last term on the right-hand side of eq. [42] is diagonal and can be absorbed in $\hat{H}_R$. The $(\nabla_\kappa f)^2$ term in the nonadiabatic decoupling condition, eq. [43], is also negligible since $\hat{P}|\psi_J\rangle$ is already of first order in θ_κ. Thus, eq. [43] reduces to

$$[45] \quad \langle\psi_I|\sum_\kappa \frac{1}{2m_\kappa}(\nabla_\kappa f\cdot p_\kappa + \text{h.c.}) + \hbar\omega\hat{P}|\psi_J\rangle = 0$$

which, for $J \neq I$, is

$$[46] \quad \frac{\langle\psi_I|\left[\sum_\kappa \frac{1}{2m_\kappa}(\nabla_\kappa f\cdot p_\kappa + \text{h.c.}), \hat{h}_{\text{mol}}(Q)\right] + i\hbar\omega\partial_Q\hat{h}_{\text{mol}}(Q)|\psi_J\rangle}{\varepsilon_J - \varepsilon_I} = 0$$

Finally, the nonadiabatic decoupling condition requires that

$$[47] \quad \left[\sum_\kappa \frac{1}{2m_\kappa}(\nabla_\kappa f\cdot p_\kappa + \text{h.c.}), \hat{h}_{\text{mol}}(Q)\right] + i\hbar\omega\partial_Q\hat{h}_{\text{mol}}(Q) = 0$$

which represents an implicit equation governing the function f. Satisfying eq. [47] exactly will imply that the eigenvalues ε_I of $\hat{h}_{\text{mol}}$ are independent of Q. In practice, eq. [47] will be satisfied approximately, so that only a weak dependence of ε_I on Q is ensured. Thus, the decoupled equation

$$[48] \quad (\hat{H}_R + \varepsilon_I - E)\chi_I = 0$$

would still describe a simple harmonic oscillator and define field states χ_{In} identified by a photon number n, as in the free field case. As a consequence, a quadratic form of f, as in eq. [44], with $b_\kappa \propto 1/Q$ will correspond to a $n^{-1/2}$ behaviour of b_κ at high intensities, since for the values of n corresponding to these intensities, the decoupled wave functions χ_{In} of the field mode will be strongly localized at large values of $Q, |Q| \simeq n^{1/2}$. With this limited form of f and the further hypothesis that $b_\kappa/m_\kappa = C(Q) \propto 1/Q$, i.e., b_κ/m_κ is a common constant for a given value of Q, eq. [47] becomes

$$[49] \quad 0 = \left\{\omega\partial_Q - \sum_\kappa \frac{\hbar}{m_\kappa}[a_\kappa + 2b_\kappa(\boldsymbol{\varepsilon}.\boldsymbol{r}_\kappa)]\boldsymbol{\varepsilon}.\nabla_\kappa\right\}V_{\text{coul}} - 4\hbar C(Q)V_{\text{coul}} + \hbar\{\omega^2 - 8\hbar\omega C(Q)Q\}\sum_\kappa[a_\kappa(\boldsymbol{\varepsilon}.\boldsymbol{r}_\kappa) + b_\kappa(\boldsymbol{\varepsilon}.\boldsymbol{r}_\kappa)^2]$$
$$- \sum_\kappa \frac{\hbar^2\omega}{m_\kappa}[a_\kappa + 2b_\kappa(\boldsymbol{\varepsilon}.\boldsymbol{r}_\kappa)]\sum_{\kappa'}[a_{\kappa'}(\boldsymbol{\varepsilon}.\boldsymbol{r}_{\kappa'}) + b_{\kappa'}(\boldsymbol{\varepsilon}.\boldsymbol{r}_{\kappa'})^2] - 2\hbar^2\omega C(Q)\left(\sum_\kappa[a_\kappa(\boldsymbol{\varepsilon}.\boldsymbol{r}_\kappa) + b_\kappa(\boldsymbol{\varepsilon}.\boldsymbol{r}_\kappa)^2]\right)^2$$

In writing eq. [49], terms that are independent of r_κ and those that are proportional to $\hat{h}_{\text{mol}}$ have been ignored since the nonadiabatic decoupling condition, eq. [47], is to be satisfied in the sense of off-diagonal matrix elements in the orthonormal eigenbasis $\{|\psi_I\rangle\}$ of $\hat{h}_{\text{mol}}$. In this expression, the last two terms are of order $\theta_\kappa^2 n^0$ and $\theta_\kappa n^{-1/2}$, and they can be neglected. The second term can be removed by setting

$$[50] \quad \frac{b_\kappa}{m_\kappa} \equiv C(Q) = \frac{\omega}{8\hbar Q}$$

which determines b_κ. The remaining parameter in f, a_κ, is determined by the approximate cancellation of the terms involving the Coulomb potential in eq. [49]. The term $4\hbar C(Q)V_{\text{coul}}$ is clearly of order $1/Q$ or $n^{-1/2}$ and can be neglected. At first sight, the same conclusion seems to apply also to the term $(\hbar/m_\kappa)b_\kappa(\boldsymbol{\varepsilon}\cdot\boldsymbol{r}_\kappa)(\boldsymbol{\varepsilon}\cdot\nabla_\kappa V_{\text{coul}})$. However, at this point, it is important to note that, in the Coulomb potential, r_κ is displaced by $(\theta_\kappa/\omega)\boldsymbol{\varepsilon}Q$ to first order in θ_κ. Consequently, a simple relation can be established between $\partial_Q V_{\text{coul}}$ and $\boldsymbol{\varepsilon}\cdot\nabla_\kappa V_{\text{coul}}$:

$$[51] \quad \partial_Q V_{\text{coul}} \simeq -\sum_\kappa \frac{\theta_\kappa}{\omega}\boldsymbol{\varepsilon}\cdot\nabla_\kappa V_{\text{coul}}$$

In addition, due to this displacement, in the eigenbasis $\{|\psi_I\rangle\}$ of $\hat{h}_{\text{mol}}$, it is the term $(\hbar/m_\kappa)b_\kappa(\boldsymbol{\varepsilon}\cdot[\boldsymbol{r}_\kappa - (\theta_\kappa/\omega)\boldsymbol{\varepsilon}Q])(\boldsymbol{\varepsilon}\cdot\nabla_\kappa V_{\text{coul}})$ which gives matrix elements of order $n^{-1/2}$ rather than the term $(\hbar/m_\kappa)b_\kappa(\boldsymbol{\varepsilon}\cdot\boldsymbol{r}_\kappa)(\boldsymbol{\varepsilon}\cdot\nabla_\kappa V_{\text{coul}})$. With this in mind, eq. [49] is rewritten as

$$[52] \quad \sum_\kappa\left(-\theta_\kappa - \frac{\hbar}{m_\kappa}\left[a_\kappa + \frac{2b_\kappa\theta_\kappa}{\omega}Q\right]\right)\boldsymbol{\varepsilon}\cdot\nabla_\kappa V_{\text{coul}} + 2\hbar C(Q)\left\{\sum_\kappa\left(\boldsymbol{\varepsilon}\cdot\left[\boldsymbol{r}_\kappa - \frac{\theta_\kappa}{\omega}\boldsymbol{\varepsilon}Q\right]\right)\boldsymbol{\varepsilon}\cdot\nabla_\kappa V_{\text{coul}} - 2V_{\text{coul}}\right\} = 0$$

Neglecting the term containing $C(Q)$ and using eq. [49], we obtain from eq. [51]

$$[53]\quad a_\kappa = -\frac{5m_\kappa\theta_\kappa}{4\hbar}$$

In summary, in the BNM representation defined by eqs. [37]–[40] with

$$[54]\quad f(\{r_\kappa\},Q) = -\frac{5}{4}\sum_\kappa m_\kappa\theta_\kappa(\boldsymbol{\varepsilon}\cdot\boldsymbol{r}_\alpha) + \frac{\omega}{8Q}\sum_\kappa m_\kappa(\boldsymbol{\varepsilon}\cdot\boldsymbol{r}_\alpha)^2$$

the explicit field–molecule coupling terms induced by $\hat{U}_M$ cancel the most significant nonadiabatic coupling terms. The remaining nonadiabatic coupling terms are either of higher order in θ_κ or behave as n^p where $p < 0$. They should not significantly affect the dynamics of the dressed field–molecule system as described within this BO-type scheme. Thus, in this new high-order adiabatic representation, a genuine separation between the molecular system and the field has been achieved in spite of the strong coupling between these two subsystems as denoted by the interaction terms in the various dressed Hamiltonians, eqs. [11], [13], and [16]. These couplings have been explicitly resummed. The fact that residual nonadiabatic couplings behave as n^p, where $p < 0$, makes this representation particularly suitable for the description of the dynamics of molecules in high-intensity fields. The Maréchal transformation modifies the molecular portion, $\hat{H}_{mol}$, of the total Hamiltonian such that the effective Hamiltonian, $\hat{h}_{mol}$, embodies the effects of the intense field on the molecule yielding laser-induced molecular structure.

4. Laser-induced molecular structure

In the traditional analysis of molecular structure within the BO separation of electronic and nuclear motions, the fast subsystem, the electrons, exerts effective forces on the slow subsystem, the nuclei. These effective forces are derived from new potential functions for the nuclear motions, the well-known BO PESs. The fact that new Hellmann–Feynman forces are dynamically exerted on the slow subsystem by the fast subsystem is true for any zeroth-order adiabatic separation. In contrast, within the high-order adiabatic separation presented in this work, it is the slow subsystem, the field, which exerts an effective force on the fast one, the molecule. This role reversal results from the efficient decoupling between the two subsystems.

The effective force exerted on the molecule by the field gives rise to laser-induced molecular structure, which can be obtained from the eigenfunctions of the effective Hamiltonian, $\hat{h}_{mol}(Q)$. With f given by eq. [54]

$$[55]\quad \hat{h}_{mol}(Q) = \sum_\kappa \frac{\hat{p}_\kappa^2}{2m_\kappa} + V_{coul}\left(\left\{\boldsymbol{r}_\kappa - \frac{\theta_\kappa}{\omega}\boldsymbol{\varepsilon}\left(Q + \frac{f}{\hbar}\right)\right\}\right) - \omega\left[\frac{5}{4}\sum_\kappa m_\kappa\theta_\kappa(\boldsymbol{\varepsilon}\cdot\boldsymbol{r}_\kappa)\right]Q + \left[\frac{\omega^2}{8}\sum_\kappa m_\kappa(\boldsymbol{\varepsilon}\cdot\boldsymbol{r}_\kappa)^2\right] + \frac{\omega}{2}\frac{f^2}{\hbar}$$

The presence of the phase factor f in the Coulomb potential term and the last term of eq. [45] gives rise to higher order corrections that can be neglected; they will not contribute significantly to the laser-induced molecular structure. Thus eq. [45] becomes

$$[56]\quad \hat{h}_{mol}(Q) \simeq \sum_\kappa \frac{\hat{p}_\kappa^2}{2m_\kappa} + V_{coul}\left(\left\{\boldsymbol{r}_\kappa - \frac{\theta_\kappa}{\omega}\boldsymbol{\varepsilon}Q\right\}\right) - \omega\left[\frac{5}{4}\sum_\kappa m_\kappa\theta_\kappa(\boldsymbol{\varepsilon}\cdot\boldsymbol{r}_\kappa)\right]Q + \left[\frac{\omega^2}{8}\sum_\kappa m_\kappa(\boldsymbol{\varepsilon}\cdot\boldsymbol{r}_\kappa)^2\right]$$

It is convenient to rewrite this effective Hamiltonian in terms of the spatial coordinates $\boldsymbol{r}_\kappa$ displaced by $(\theta_\kappa/\omega)\boldsymbol{\varepsilon}Q$ as

$$[57]\quad \hat{h}_{mol}(Q) \simeq \sum_\kappa \frac{\hat{p}_\kappa^2}{2m_\kappa} + V_{coul}\left(\left\{\boldsymbol{r}_\kappa - \frac{\theta_\kappa}{\omega}\boldsymbol{\varepsilon}Q\right\}\right) - \omega\left[\sum_\kappa m_\kappa\theta_\kappa\boldsymbol{\varepsilon}\cdot\left(\boldsymbol{r}_\kappa - \frac{\theta_\kappa}{\omega}\boldsymbol{\varepsilon}Q\right)\right]Q + \frac{\omega^2}{8}\sum_\kappa m_\kappa\left(\boldsymbol{\varepsilon}\cdot\boldsymbol{r}_\kappa - \frac{\theta_\kappa}{\omega}Q\right)^2 - \sum_\kappa m_\kappa\theta_\kappa{}^2Q^2$$

In this way, $\hat{h}_{mol}$ is expressed clearly as the unitary transform of an undisplaced Hamiltonian $\hat{h}'_{mol}$

$$[58]\quad \hat{h}_{mol}(Q) = \exp\left\{-\frac{i}{\hbar}\sum_\kappa \frac{\theta_\kappa}{\omega}(\boldsymbol{\varepsilon}\cdot\boldsymbol{p}_\kappa)Q\right\}\hat{h}'_{mol}(Q)\exp\left\{\frac{i}{\hbar}\sum_\kappa \frac{\theta_\kappa}{\omega}(\boldsymbol{\varepsilon}\cdot\boldsymbol{p}_\kappa)Q\right\}$$

where

$$[59]\quad \hat{h}'_{mol}(Q) \simeq \sum_\kappa \frac{\hat{p}_\kappa^2}{2m_\kappa} + V_{coul}(\{\boldsymbol{r}_\kappa\}) - \omega\sum_\kappa m_\kappa\theta_\kappa\boldsymbol{\varepsilon}\cdot\boldsymbol{r}_\kappa Q + \frac{\omega^2}{8}\sum_\kappa m_\kappa(\boldsymbol{\varepsilon}\cdot\boldsymbol{r}_\kappa)^2 - \sum_\kappa m_\kappa\theta_\kappa{}^2Q^2$$

The last term in this expression can be absorbed into the Hamiltonian for the field and the relationship between $\boldsymbol{E}$ and Q, eq. [14] expressed in the coordinate representation, can be used to give

$$[60]\quad \hat{h}'_{mol}(\boldsymbol{E}) = \sum_\kappa \frac{\hat{p}_\kappa^2}{2m_\kappa} + V_{coul}(\{\boldsymbol{r}_\kappa\}) - \sum_\kappa q_\kappa\boldsymbol{r}_\kappa\cdot\boldsymbol{E} + \frac{\omega^2}{8}\sum_\kappa m_\kappa(\boldsymbol{\varepsilon}\cdot\boldsymbol{r}_\kappa)^2$$

Fig. 2. Profile, along the field polarization, of the Coulomb potential for the single electron in H_2^+ distorted by the potential (*a*) $-e\boldsymbol{r}\cdot\boldsymbol{E} + (\omega^2/8)m(\boldsymbol{\varepsilon}\cdot\boldsymbol{r})^2$ (solid line); (*b*) $-e\boldsymbol{r}\cdot\boldsymbol{E}$ (broken line), induced by a field of wavelength $\lambda = 2270$ nm and intensity $I = 3.2 \times 10^{13}$ W/cm^2. The nuclei are at a fixed internuclear distance of $R = 2.0$ au. The horizontal line at $E = -0.6$ au marks the position of the field-free ground-state energy of the molecule.

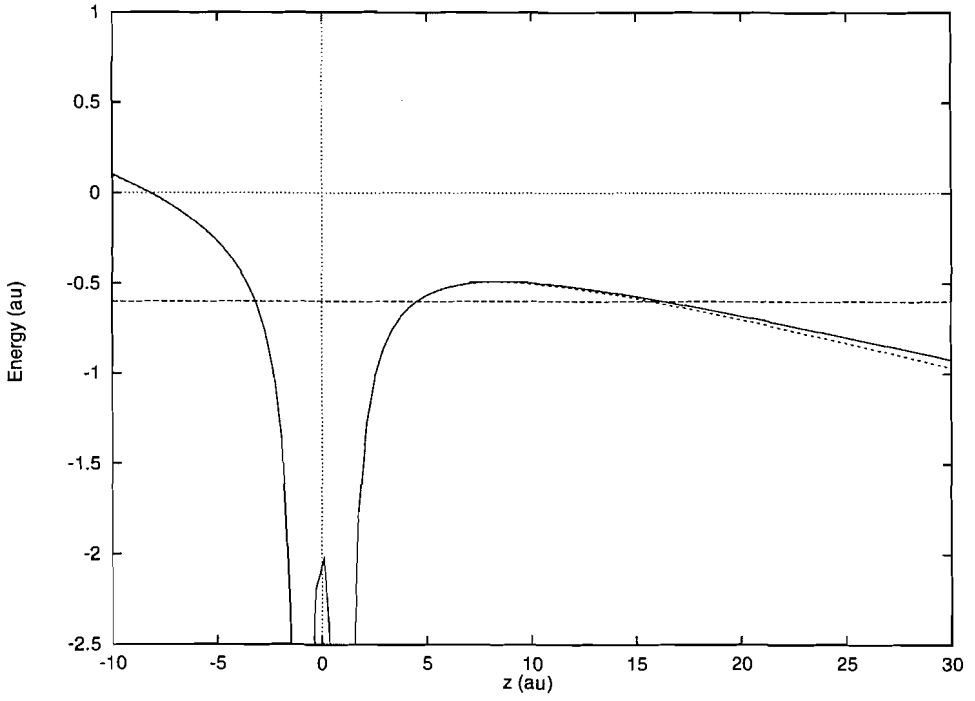

Fig. 3. Profile, along the field polarization, of the Coulomb potential for the single electron in H_2^+ distorted by the potential (*a*) $-e\boldsymbol{r}\cdot\boldsymbol{E} + (\omega^2/8)m(\boldsymbol{\varepsilon}\cdot\boldsymbol{r})^2$ (solid line); (*b*) $-e\boldsymbol{r}\cdot\boldsymbol{E}$ (broken line), induced by a field of wavelength $\lambda = 113.5$ nm and intensity $I = 4.0 \times 10^{15}$ W/cm^2. The nuclei are at a fixed internuclear distance of $R = 2.0$ au. The horizontal line at $E = -0.6$ au marks the position of the field-free ground-state energy of the molecule.

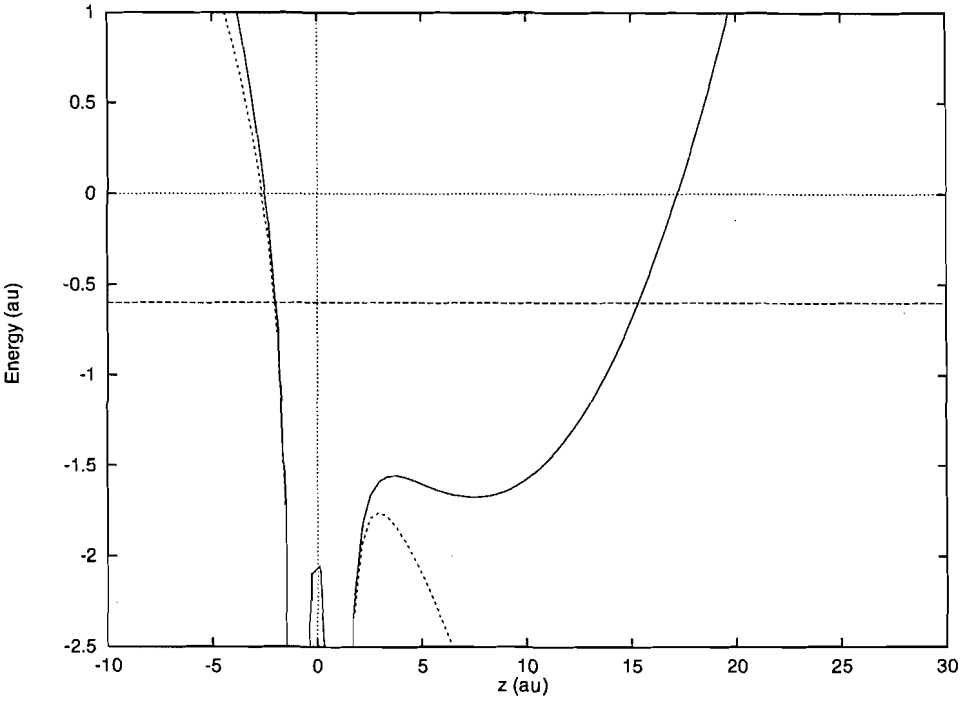

The last two terms in this effective Hamiltonian give rise to the effective force exerted by the field subsystem on the molecular subsystem, which, as discussed previously, are uncoupled in this adiabatic representation. Note that one component of this force appears as an electric field $\boldsymbol{E}$; however, it is not an interaction term between the field and the molecule in the dynamical sense: it no longer couples the eigenstates of $\hat{h}'_{\text{mol}}$ but directly defines them. The instantaneous electric field $\boldsymbol{E}$ is simply a parameter because, as noted previously, Q in $\hat{h}'_{\text{mol}}(Q)$ is the eigenvalue of the operator $\hat{Q}$ and hence, in the coordinate representation, $\boldsymbol{E}$ is a c-number vector. This intensity-dependent force component polarizes the charge distribution whereas the harmonic force component associated with the last term in eq. [60] confines the charges and forces them to oscillate. This term cannot be identified with an effective magnetic force because it is independent of the field intensity. The effects of these two terms on the Coulomb potential felt by the single electron in the dihydrogen ion H_2^+ are illustrated in Figs. 2 and 3. In both figures, the nuclei are at a fixed internuclear distance of $R = R_e$, the equilibrium bond length of H_2^+. In Fig. 2, the dihydrogen ion is in a field of wavelength $\lambda = 2270$ nm and intensity $I = 3.2 \times 10^{13}$ W/cm^2. The broken curves illustrate the effect of the polarization term $-\boldsymbol{er}\cdot\boldsymbol{E}$ alone. At this frequency, this term still dominates the harmonic term and is responsible for the efficient tunnel ionization of the molecular system. However, the effect of the harmonic term is to confine the ionized electron to finite but large distances from the nuclei. The electron oscillates in a shallow well centered far from the nuclei with a frequency imparted by the field. In Fig. 3, the ion is in a field of wavelength $\lambda = 113.5$ nm and intensity $I = 4.0 \times 10^{15}$ W/cm^2. At this higher frequency, it is the harmonic term which gives the dominant character of the laser-induced change in the molecular structure. The polarization term merely displaces the harmonic potential, which, in turn, strongly distorts the Coulomb potential. It is interesting to note that, even for energies that correspond to the field-free ionization continuum, the motion of the electron in a direction parallel to the polarization of the field can be bound. Since the potential well remains open in the other directions, the states describing this situation are resonances, i.e., quasi-bound states. These new quasi-bound states represent states of an electron subjected to oscillations imparted by the field but still under the influence of the Coulomb forces. In the neighborhood of the ground state energy of the field-free molecule, the Coulomb potential is distorted to such an extent that drastic changes can occur in the ground-state molecular charge distribution: A concentration in the charge distribution is expected in the neighborhood of the minimum of the displaced harmonic potential and can give rise to a non-nuclear maximum in the electron distribution. Moreover, the superposition of the harmonic potential with the Coulomb one introduces an asymmetry in the nuclear wells resulting in an asymmetrical electron distribution.

5. Summary and conclusions

From the Bloch–Nordsieck Hamiltonian for the dressed molecule, eq. [16], an adiabatic separation between the field and the molecule has been achieved after a further transformation of the Hamiltonian by the Maréchal unitary operator, eq. [38], whose generator is determined by the nonadiabatic decoupling condition, eq. [47]. Although this condition has been satisfied only approximately, the residual couplings are negligible at high field intensities. Some of these even tend to vanish as the field intensity increases. This trend is due to a $(1/Q)$ dependence of these residual coupling terms and to the well-known localization of the field amplitude at the turning points $Q \propto \pm n^{-1/2}$, for field states with large n that correspond to a high field intensity regime. Thus, the high-order adiabatic representation is only appropriate for high-intensity-field states and denotes an asymptotic separability between the molecule and the field. In this intensity regime, the adiabatic representation identifies genuinely separated molecular and field subsystems in the strongly coupled dressed molecule. The strong modifications of the properties of the molecule in the presence of the intense-field are reflected in the transformation of the molecular hamiltonian from the field free-form, $\hat{H}_{\text{mol}}(Q)$, eq. [32] to the effective form, $\hat{h}_{\text{mol}}$, eq. [55].

The feedback that these modifications have on the field subsystem corresponds to the deformation of the field Hamiltonian $\hat{H}_R$ by $\varepsilon_I(Q)$. As discussed previously, satisfying eq. [47] exactly would imply that the eigenvalues ε_I of $\hat{h}_{\text{mol}}$ are independent of Q. Since eq. [47] had been solved only up to order $\theta_a^2, a = e$ or α, ε_I will depend on Q only through terms that are at least of this order, i.e., the feedback of the changes in molecular structure induced by the laser field on the field is at least of second order in θ_a^2. As of yet, the interesting problem of the feedback that these molecular structure changes have on the quantized field has not been addressed. This problem is being investigated in current work.

Finally, the adiabatic representation developed in this work has a counterpart in semiclassical theory. Indeed, by applying the Mollow transformation to the BNM Hamiltonian, the effective Hamiltonian $\hat{h}_{\text{mol}}(Q)$ can be mapped onto a time-dependent operator that turns out to be approximately an adiabatic invariant, the Lewis invariant (30–32) of the laser-driven molecule treated semiclassically. Since the time evolution is diagonal in the basis of the eigenstates of a Lewis invariant, denoting an adiabatic transport of these eigenstates, an interesting relation exists between the high-order adiabatic molecule–field separation in the present time-independent fully quantized formalism, and the concept of high-order adiabatic time evolution of the molecule in semiclassical theory (33). In this way, laser-induced molecular structures associated with the time-independent effective Hamiltonian $\hat{h}_{\text{mol}}$ can be mapped onto corresponding time-dependent, dynamical molecular structures.

Acknowledgments

Financial support of this research by the Natural Sciences and Engineering Research Council of Canada (NSERCC) and by Québec's Fonds pour la Formation de Chercheurs et l'Aide à la Recherche (FCAR) is gratefully acknowledged.

References

1. R.F.W. Bader, T.T. Nguyen-Dang, and Y. Tal. Rep. Prog. Phys. **44**, 893 (1981).
2. R.F.W. Bader and T.T. Nguyen-Dang. Adv. Quantum. Chem. **14**, 63 (1981).

3. T.F. George, J.H. Zimmerman, J.M. Yuan, J.R. Laing, and P.L. DeVries. Acc. Chem. Res. **10**, 449 (1977).
4. A.D. Bandrauk. Int. Rev. Phys. Chem. **13**, 123 (1994).
5. A. Zavriyev, P.H. Bucksbaum, H.G. Muller, and D.W. Schumacher. Phys. Rev. A: **42**, 5500 (1990).
6. A. Giusti-Suzor, X. He, O. Atabek, and F.H. Mies. Phys. Rev. Lett. **64**, 515 (1990).
7. X. He, O. Atabek, and A. Giusti-Suzor. Phys. Rev. A: Gen. Phys. **38**, 5586 (1988).
8. E.E. Aubanel, J.M. Gauthier, and A.D. Bandrauk. Phys. Rev. A: At. Mol. Opt. Phys. **48**, 2145 (1993).
9. G. Yao and S.I. Chu. Chem. Phys. Lett. **197**, 413 (1992).
10. A. L'Huillier, K.J. Schafer, and K.C. Kulander. J. Phys. B **24**, 3315 (1991).
11. T. Zuo, S. Chelkowski, and A.D. Bandrauk. Phys. Rev. A: At. Mol. Opt. Phys. **48**, 3837 (1993).
12. W. Pauli and M. Fierz. Nuovo Cimento, **16**, 167 (1938).
13. F. Bloch and A. Nordsieck. Phys. Rev. **52**, 54 (1937).
14. C. Cohen-Tannoudji, J. Dupont-Roc, and G. Grynberg. Atom–photon interactions, Wiley–Interscience, New York. 1992.
15. T.T. Nguyen-Dang and A.D. Bandrauk. J. Chem. Phys. **79**, 3256 (1983).
16. T.T. Nguyen-Dang and A.D. Bandrauk. J. Chem. Phys. **80**, 4926 (1984).
17. Y. Maréchal. J. Chem. Phys. **83**, 247 (1985).
18. T.T. Nguyen-Dang and A.D. Bandrauk. J. Chem. Phys. **85**, 7224 (1986).
19. T.T. Nguyen-Dang. J. Chem. Phys. **87**, 2177 (1987).
20. H.R. Reiss. Phys. Rev. A: Gen. Phys. **19**, 1140 (1979).
21. W.C. Henneberger. Phys. Rev. Lett. **21**, 838 (1968).
22. B.R. Mollow. Phys. Rev. A: Gen. Phys. **12**, 1919 (1975).
23. A. Keller and O. Atabek. Phys. Rev. A: At. Mol. Opt. Phys. **48**, 3741 (1993).
24. S.I. Chu. Adv. Chem. Phys. **63**, 739, (1989).
25. T.T. Nguyen-Dang and S. Manoli. Phys. Rev. A: **44**, 5841 (1991).
26. T.T. Nguyen-Dang, F. Châteauneuf, O. Atabek, and X. He. Phys. Rev. A: At. Mol. Opt. Phys. **51**, 1387 (1995).
27. E.E. Aubanel, A. Conjusteau, and A.D. Bandrauk. Phys. Rev. A: At. Mol. Opt. Phys. **48**, R4011 (1993).
28. M. Gavrila and J.Z. Zaminski. Phys. Rev. Lett. **52**, 613 (1984).
29. T. Zuo and A.D. Bandrauk. Phys. Rev. A: At. Mol. Opt. Phys. **51**, R26 (1995).
30. H.R. Lewis, Jr. and W.B. Riesenfeld. J. Math. Phys. **10**, 1458 (1968).
31. J.G. Hartley and J.R. Ray. Phys. Rev. A: Gen. Phys. **24**, 2873 (1981).
32. T.T. Nguyen-Dang, C. Chatelas, and D. Tanguay. J. Chem. Phys. **102**, 1528 (1995).
33. T.T. Nguyen-Dang.J. Chem. Phys. **90**, 2657 (1989).

On the performance of molecular model core potential orbitals in spin-orbit and electron correlation studies

Dietmar Krause and Mariusz Klobukowski

Abstract: The role of improved parametrization and accurate basis sets in model core potentials was studied in calculations of the spin-orbit coupling constants (in PH, AsH, and SbH) and of the electron correlation effects (in P_2, As_2, and Sb_2). An effective method of identifying and removing the intruder quasi-core orbitals from the virtual orbital space was proposed in connection with the post-Hartree–Fock calculations. The results demonstrated that (*a*) the flexible valence basis sets allow evaluation of the spin-orbit effects without resorting to any scaling techniques and (*b*) the intruder quasi-core orbitals, even if left imbedded in the virtual space, have negligible effect on the values of the electron correlation energy.

Key words: effective core potentials, basis sets, spin-orbit effects, electron correlation.

Résumé : On a étudié le rôle d'une paramétrisation améliorée et d'ensembles de base précis dans les modèles des potentiels des noyaux dans les calculs des constantes de couplage spin-orbitale (dans le PH, AsH et le SbH) et les effets de corrélation des électrons (dans P_2, As_2 et Sb_2). En relation avec les calculs post-Hartree–Fock, on propose une méthode efficace d'identifier et d'enlever les orbitales quasi-nucléaires inopportunes de l'espace orbitalaire virtuel. Les résultats ont démontré que (*a*) les ensembles de base à valence flexible permettent d'évaluer les effets spin-orbitale sans faire appel à des techniques scalaires et (*b*) les orbitales quasi-nucléaires inopportunes, même si on les laisse dans l'espace virtuel, n'ont qu'un effet négligeable sur les valeurs de l'énergie de corrélation électronique.

Mots clés : potentiels efficace des noyaux, ensembles de base, effets spin-orbitale, corrélation électronique.

[Traduit par la rédaction]

I. Introduction

Both the model core potential (MCP) method (1, 2) and the widely used effective core potential (ECP) method (3) treat only the valence electrons of an atomic or molecular system explicitly. Two distinctive features of the MCP method make it different from the ECP family of methods: (*a*) the capability of reproducing the full nodal structure of the valence orbitals and (*b*) the use of projection operators. The model potential orbitals not only reproduce the all-electron (AE) valence orbitals in the region around the outermost maximum but they also match the inner part of the AE valence orbitals, resulting in an improved description of the region near nuclei. (Depending on the basis set, the full nodal structure may be maintained in model potential orbitals.) The projection operator technique used in the MCP method shifts the core orbitals into the energy continuum, where in the finite basis set calculations they become mixed with the virtual orbitals.

To probe the region near the nucleus, we studied the spin-orbit coupling of the lowest $^3\Sigma^-$ state of PH, AsH, and SbH. These systems were the subject of a comparative study in the past (4), showing rather uneven performance of the model core potential method. In our present study, the performance of the model potential method is significantly improved by choosing a better parametrization scheme and employing a high-quality basis set.

Furthermore, in previous work (5, 6) we compared the performance of the model core potential method and the ECP method in studies of valence-electron correlation energies in atoms and molecules. Both methods were shown to yield essentially equivalent results. The question arose, however, whether the core orbitals, shifted into the virtual orbital (VO) space by the projection operators, might lead to overestimated correlation energies. Excitations of valence electrons into these quasi-core orbitals have no counterpart in all-electron CI calculations, and it was hoped that the corresponding correlation energies are negligible compared to the overall valence-electron correlation energies. To study the effect of the quasi-core orbitals, we performed CI-SD calculations of P_2, As_2, and Sb_2 with an active virtual orbital space containing only quasi-core orbitals, without quasi-core orbitals, and in full virtual orbital space. To observe the effect of higher excitations, Møller–Plesset calculations up to fourth order were done. For the model core potential calculations, an all-electron basis was employed that enables both

Received November 6, 1995.

This paper is dedicated to Professor Richard F.W. Bader on the occasion of his 65th birthday.

D. Krause[1] **and M. Klobukowski.**[2] Department of Chemistry, University of Alberta, Edmonton, AB T6G 2G2, Canada.

[1] Harry Emmett Gunning Graduate Fellow 1993–1995.
[2] Author to whom correspondence may be addressed. Telephone: (403) 492-2568. Fax: (403) 492-8231. E-mail: mariusz.klobukowski@ualberta.ca

Table 1. Size and contraction of the all-electron well-tempered basis for P, As, and Sb.

Atom	Size	Contraction
P	23*s* 16*p*	(6,12,12,12,11111/ 3,8,8,11111)
As	26*s* 20*p* 14*d*	(9,12,12,12,12,11111/ 3,12,12,12,11111/ 14)
Sb	28*s* 23*p* 17*d*	(5,18,18,18,18,19,11111/ 18,18,18,18,11111/ 17,17)

an unambiguous assignment of the quasi-core orbitals and a direct comparison with the correlation energies obtained from all-electron SCF orbitals.

II. Details of calculations

A. Model core potential method

The detailed derivation of the model core potential method has been published (1, 2). In the following, only the terms that are relevant to the present work are defined.

The one-electron Hamiltonian h_i in the model core potential formalism contains the potential V_i^α and the projection operator P_i^α at the atomic center α:

$$[1] \quad h_i = -\frac{1}{2}\Delta_i + \sum_\alpha \left(-\frac{z_\alpha}{r_{i\alpha}} + V_i^\alpha + P_i^\alpha \right)$$

where z_α is the core charge of atom α (charge of the bare nucleus minus the number of core electrons).

The spherically symmetric local potential V_i^α, which approximates the exact atomic nonlocal core potential, has the form:

$$[2] \quad V_i^\alpha = z_\alpha \left\{ -\sum_I \frac{A_I}{r_{i\alpha}} e^{-\alpha_I r_{i\alpha}^2} - \sum_J A_J e^{-\alpha_J r_{i\alpha}^2} \right\}$$

where I and J refer to the sets of parameters $\{\alpha_I, A_I\}$ and $\{\alpha_J, A_J\}$.

In the projection operator

$$[3] \quad P_i^\alpha = \sum_{c \in \alpha} B_c |\psi_c(i)\rangle\langle\psi_c(i)|$$

the parameter B_c is taken as twice the absolute value of the atomic orbital energy of the core shell c on atom α.

An initial set of the model potential parameters $\{\alpha, A\}$ for a given atom was determined by fitting the potential V_i^α to a numerical core potential consisting of the core electron nuclear attraction, the core Coulomb and core exchange potentials acting on the valence p-type radial function. Further optimization of the parameters was done to maximize the overlap between the atomic model potential orbitals and the all-electron valence functions. The expectation values $\langle r^n \rangle$, with $n = \{-3, -2, -1, 1, 2\}$, of the model potential valence functions are within 1% of those obtained in atomic all-electron calculations using the same well-tempered basis set. The performance of the model potentials was assessed in SCF calculations of P_2, As_2, and Sb_2. The equilibrium distances are within 2% and the harmonic vibrational frequencies are within 10% of the corresponding all-electron results. A detailed description of the parametrization scheme of the model potentials and their performance in molecular calculations will be reported in a forthcoming paper.

B. Basis sets

Basis sets for all atoms were contracted to give the flexibility of five primitive Gaussian-type functions in the outermost valence region. For hydrogen, the well-balanced (12*s*) basis (7) was contracted to (711111) and augmented with a single p-type polarization function ($\zeta_p = 1.0$).

The basis sets for phosphorus, arsenic, and antimony were taken from the compilation of the well-tempered Gaussian basis sets (8–10). The size of the basis and the contraction of the all-electron basis are shown in Table 1. For the valence-electron basis, the s and p valence shells were uncontracted in the outermost region to yield one contracted shell plus five primitive Gaussian functions, e.g., for phosphorus (18,11111/11,11111). All basis sets, except for hydrogen, were augmented with two d-type polarization functions (11). For the electron correlation studies, we implemented the model core potential method into the HONDO (12) program package in order to take advantage of the ability of the HONDO system to remove the spherically symmetric contribution of Cartesian d-type Gaussian functions.

III. Results of calculations

A. Spin-orbit coupling

For the radicals PH, AsH, and SbH, the ground electronic configuration $\sigma^2\pi^2$ gives rise to the states $^3\Sigma^-$, $^1\Delta$, and $^1\Sigma^+$. The zero-field splitting of the $^3\Sigma^-$ state is dominated by the matrix element $\langle ^3\Sigma^- | H_{SO} | ^1\Sigma^+ \rangle$ of the one-electron spin-orbit Hamiltonian H_{SO}. The spin-orbit matrix elements of PH, AsH, and SbH at their experimental bond distances (1.42, 1.53, and 1.72 Å, respectively) were computed using the program package GAMESS (13), enhanced by the addition of the MCP one-electron integral modules. We used a minimal description of the CI wave functions, in which two determinants span the states $^1\Delta$ and $^1\Sigma^+$, and one determinant represents the $^3\Sigma^-$ state. The determinants were generated by the ground state SCF orbitals in a well-tempered basis for the all-electron calculations and in a valence basis for the model core potential calculations. In Table 2, the spin-orbit matrix elements, the energy gaps between the $^1\Sigma^+$ and $^3\Sigma^-$ states, and the second-order spin-orbit couplings of the $^3\Sigma^-$ states, based on the dominant spin-orbit matrix element, are reported. The model potential results agree within 1% with the respective all-electron values and it should be stressed that this excellent agreement was achieved without employing effective core charges different from the actual bare nucleus charges, and without using any other scaling factors.

The purpose of the present work was to establish degree

Table 2. Spin-orbit matrix elements, energy differences, and spin-orbit splitting of 0^+ and 1 states in PH, AsH, and SbH calculated using all-electron (AE) and model core potential (MCP) wave functions (all values are in cm^{-1}).

XH	Method	$\langle ^3\Sigma^-\|H_{so}\|^1\Sigma^+\rangle$	$\Delta E(^3\Sigma^-,^1\Sigma^+)$	Spin-orbit ($0^+ - 1$) splitting
PH	AE	288.2	20 408	4.070
	MCP	288.1	20 400	4.069
AsH	AE	1320	19 470	89.49
	MCP	1318	19 498	89.09
	CAS SCF/SOCI (14)		17 097	
	Experiment (16)			117.6–118
SbH	AE	2775	17 398	442.6
	MCP	2763	17 430	438.0
	Relativistic CI (15)			696
	Experiment (17)			655–660

of agreement between all-electron and MCP results. It is, nevertheless, interesting to compare the present results with both experimental values and results from earlier calculations. The two heavier systems were studied by Balasubramanian and Nannegari, who used CAS SCF followed by the second-order CI method for AsH (14) and relativistic CI for SbH (15). Their results are reported in Table 2, together with experimental values of the spin-orbit splitting between the states 0^+ and 1. The main difference between the present results and those of Balasubramanian is the larger separation between the $^3\Sigma^-$ and $^1\Sigma^+$ states; this difference is expected because of the extremely limited form of the wave function used in the present work. In consequence, the present values of spin-orbit splitting are smaller than the experimental ones.

B. Electron correlation energy

A model core potential and an all-electron SCF calculation of P_2 was performed at its equilibrium distance (1.89 Å) using the same all-electron well-tempered basis in both cases. The model potential valence orbitals reproduce almost exactly the corresponding all-electron orbitals; the deviation of the overlap from 1 is smaller than 4×10^{-4}. As expected, due to the flexibility of the all-electron basis set, all 10 core MOs could be found in the model potential virtual orbital space of P_2. These quasi-core orbitals could be assigned unambiguously, as the overlap with the corresponding all-electron occupied core MOs was larger than 0.999. After reordering the quasi-core VOs, a valence CI-SD calculation with an active virtual orbital space spanned only by the quasi-core orbitals was done. The correlation energy is 0.0009 au, which is less than 0.4% of the all-electron CI-SD correlation energy (0.2409 au) obtained with excitations from the valence space into the full virtual orbital space.

The selection of the quasi-core orbitals based on overlap with the all-electron core molecular orbitals requires that the all-electron calculations be performed. A simpler and more general technique of identifying and shifting the quasi-core orbitals was accomplished by a transformation within the virtual orbital space, using a procedure similar to the method of modified virtual orbitals (18): after the last SCF step, the canonical eigenvector matrix is saved and a new Fock matrix is constructed using model potential one-electron integrals based on scaled B_c parameters (see eq. [3]). The Fock matrix is then transformed into the virtual orbital space, diagonalized, and the resulting eigenvector matrix is transformed back into the AO (basis set) space. This procedure generates transformed virtual orbitals while leaving the occupied orbitals unchanged. Choosing a scaling factor of -100 for all B_c parameters results in a virtual orbital space containing the quasi-core orbitals as the energetically lowest virtual orbitals. The overlap between the canonical model potential SCF VOs and the transformed VOs deviates less than 6×10^{-4} from 1, so that we used this transformation method as a simple substitute for reordering VOs based on their overlaps. It must be stressed that this technique is more general than the one based on calculation of overlaps between the AE and MCP MOs as it does not require the all-electron calculations.

Applying the above transformation procedure, the correlation effects of quasi-core VOs were studied in P_2, As_2, and Sb_2 at their respective equilibrium distances (1.89, 2.10, and 2.34 Å) using model core potential CI-SD wave functions generated by single and double excitations from the valence space into the space spanned by the quasi-core VOs. The resulting correlation energies (Table 3) are smaller than 0.001 au, being less than 1% of the all-electron CI-SD correlation energies. The all-electron CI-SD wave functions were generated by excitations from the valence space of the all-electron SCF wave functions into the full virtual orbital space.

Using the same all-electron well-tempered basis sets, model potential CI-SD calculations were done employing the full virtual orbital space without the quasi-core VOs. This was achieved by using a large positive scaling factor for B (10^4 for P_2 and As_2, 10^7 for Sb_2) in the transformation of the VOs, resulting in the quasi-core VOs as the energetically highest orbitals.

These truncated model potential VO spaces have the same size as the corresponding all-electron full virtual orbital spaces. Consequently, the number of configuration state functions (CSFs) generated in the model potential CI-SD calculations is the same as the number of CSFs in the all-electron calculations. A direct comparison of the model potential correlation energies with the all-electron correlation energies is

Table 3. CI-SD correlation energies of P_2, As_2, and Sb_2 (all values in atomic units).

Method[a]	Active space[b]	P_2	As_2	Sb_2
MCP-AE	Core	0.0010	0.0008	0.0009
AE	Full	0.2409	0.2162	0.1810
MCP-AE	Trunc.	0.2412	0.2167	0.1816
MCP-AE	Full	0.2437	0.2210	0.1886
MCP	Full	0.2429	0.2106	0.1739

[a]All-electron calculation (AE); model core potential calculation using an all-electron basis (MCP-AE) or a valence basis (MCP).

[b]Active space spanned by the quasi-core VOs (core), by all other VOs (trunc.), and the full virtual orbital space (full).

Table 4. Second-, third-, and fourth-order Møller–Plesset correlation energies of P_2, As_2, and Sb_2 in full virtual orbital space (all values in atomic units).

	P_2			As_2			Sb_2		
Method[a]	MP2	MP3	MP4	MP2	MP3	MP4	MP2	MP3	MP4
AE	0.250	0.015	0.021	0.227	0.010	0.020	0.184	0.014	0.014
MCP-AE	0.254	0.013	0.022	0.233	0.009	0.020	0.195	0.013	0.015
MCP	0.253	0.014	0.022	0.224	0.006	0.019	0.181	0.008	0.013

[a]All-electron calculation (AE); model core potential calculation using an all-electron basis (MCP-AE) or a valence basis (MCP).

therefore justified and gives a measure of the quality of the molecular model potential valence and virtual orbitals. The respective correlation energies (Table 3) agree within 0.001 au (a relative error of less than 1%).

In the next set of model potential CI-SD calculations the full virtual orbital space was employed, expanded in the same all-electron basis sets. The correlation energies obtained (Table 3) agree very well with those of the previous calculations, in which the quasi-core VOs were discarded. The deviations, smaller than 5% of the total AE CI-SD correlation energies (0.003 au for P_2, 0.006 au for As_2, and 0.007 au for Sb_2) are larger than the correlation energies resulting from excitations only into the quasi-core orbital space. The difference may be attributed to contributions from CSFs generated via mixed excitations connecting quasi-core orbitals with the remaining virtual orbitals. Furthermore, it is reassuring to see the good agreement between the all-electron and model potential correlation energies obtained in Møller–Plesset calculations up to fourth order (Table 4).

Finally, model potential CI-SD calculations were performed using the valence basis sets and employing the full virtual orbital space. A direct comparison with the all-electron correlation energies is not justified due to the different active spaces. Nevertheless, it can be seen from Table 3 that model potential orbitals, spanned by valence basis functions, are very well suited to recover the valence-electron correlation energy based on AE SCF orbitals. Furthermore, the Møller–Plesset correlation results (Table 4) based on model potential orbitals closely match the corresponding all-electron correlation energies.

IV. Conclusions

By reproducing the AE spin-orbit couplings of PH, AsH, and SbH within 1%, we demonstrated the usefulness of molecular model potential orbitals in the computation of properties that depend on the core region of the wave function.

The model potential correlation energies, calculated employing an all-electron basis, agree very well with the AE correlation energies, and the inclusion of quasi-core orbitals in the active virtual orbital space leads to only slightly (less than 5%) overestimated correlation energies. It should be noted that the all-electron basis sets are capable of generating all core orbitals, whereas the basis sets usually chosen for valence-electron calculations are, at most, flexible enough only to reproduce the core orbitals of the outermost core shell. Contamination of the virtual orbital space by the remaining quasi-core orbitals is expected to have a negligible effect on CI-SD calculations. The occupation numbers of the natural orbitals in the space of the quasi-core orbitals (MCP-AE/core results in Table 3) are smaller than 2×10^{-5}. Furthermore, our results from Møller–Plesset calculations up to fourth order do not indicate any problems in the evaluation of higher terms in the correlation energy expansion. We conclude that the occurrence of quasi-core orbitals in the canonical SCF virtual orbital space does not seem to be a drawback of the model core potential method in the study of valence-electron correlation energies.

Acknowledgments

The calculations were done on SUN 4/370 and RS/6000

workstations purchased with partial assistance from the Natural Sciences and Engineering Research Council of Canada (NSERC). This work was financed partly by a research grant from NSERC, and partly by the University of Alberta.

References

1. S. Huzinaga, M. Klobukowski, and Y. Sakai. J. Phys. Chem. **88**, 4880 (1984).
2. S. Huzinaga. Can. J. Chem. **73**, 619 (1995).
3. M. Krauss and W.J. Stevens. Annu. Rev. Phys. Chem. **35**, 357 (1984).
4. M. Klobukowski. Chem. Phys. Lett. **183**, 417 (1991).
5. M. Klobukowski. Chem. Phys. Lett. **172**, 361 (1990).
6. M. Klobukowski. Theor. Chim. Acta, **83**, 239 (1992).
7. M. Klobukowski. Can. J. Chem. **72**, 1741 (1994).
8. S. Huzinaga and B. Miguel. Chem. Phys. Lett. **175**, 289 (1990).
9. S. Huzinaga and M. Klobukowski. Chem. Phys. Lett. **212**, 260 (1993).
10. S. Huzinaga, B. Miguel, and M. Klobukowski. Well-tempered Gaussian basis sets. Technical Report, University of Alberta. 1993.
11. S. Huzinaga (*Editor*). Gaussian basis sets for molecular calculations. Elsevier, Amsterdam. 1984.
12. M. Dupuis, F. Johnston, and A. Marquez. HONDO 8.5 from CHEM-Station. IBM Corporation, Neighborhood Road, Kingston, N.Y. 1994.
13. M.W. Schmidt, K.K. Baldridge, J.A. Boatz, J.H. Jensen, S. Koseki, M.S. Gordon, K.A. Nguyen, T.L. Windus, and S.T. Elbert. QCPE Bull. **10**, 52 (1990); M.W. Schmidt, K.K. Baldridge, J.A. Boatz, S.T. Elbert, M.S. Gordon, J.H. Jensen, S. Koseki, N. Matsunaga, K.A. Nguyen, S. Su, T.L. Windus, M. Dupuis, and J.A. Montgomery. J. Comput. Chem. **14**, 1347 (1993).
14. K. Balasubramanian and V. Nannegari. J. Mol. Spectrosc. **138**, 482 (1989).
15. K. Balasubramanian. J. Mol. Spectrosc. **124**, 458 (1987).
16. B. Lindgren. Phys. Scr. **12**, 164 (1975); R.N. Dixon and H.M. Lamberton. J. Mol. Spectrosc. **25**, 12 (1968).
17. P. Bollmark and B. Lindgren. Phys. Scr. **10**, 325 (1974).
18. C.W. Bauschlicher, Jr. J. Chem. Phys. **72**, 880 (1980).

Comparative electronic analysis between hydrogen transfers in the CH_4/CH_3^+, $CH_4/CH_3^{\cdot}$, and CH_4/CH_3^- systems: on the electronic nature of the hydrogen (H^-, $H^{\cdot}$, and H^+) being transferred

Jordi Mestres, Miquel Duran, and Juan Bertrán

Abstract: A comparative electronic analysis of the generally termed hydrogen transfers between CH_4 and the CH_3^+, $CH_3^{\cdot}$, and CH_3^- fragments is presented. These systems are taken as simple models of hydride (H^-), hydrogen ($H^{\cdot}$), and proton (H^+) transfers between two carbon fragments (in these simple cases being modelized by two CH_3^+, $CH_3^{\cdot}$, and CH_3^- fragments, respectively). The study is mainly focused on analysis of the electronic nature of the type of hydrogen being transferred in each system, and for this reason a topological analysis of charge density distributions was performed. Computation of Bader atomic charges and construction of the charge density, gradient vector field, and Laplacian of the charge density maps reveal the specific features of the electronic nature of the transferring H^-, $H^{\cdot}$, and H^+. Moreover, characterization of the bond critical points on the charge density surface permits clarification of the differences in atomic interactions between H^-, $H^{\cdot}$, and H^+ and the carbon belonging to each CH_3^+, $CH_3^{\cdot}$, and CH_3^- fragment, respectively. A charge density redistribution analysis is also performed to quantify the reorganization of the electron density when going from the reactant complex to the transition state. Finally, effects of inclusion of the correlation energy at the MP2 and CISD levels are also discussed.

Key words: electron density, hydrogen transfer, topological density analysis, molecular similarity, Bader density analysis.

Résumé : On présente une analyse électronique comparative des transferts dits d'hydrogène entre le CH_4 et les fragments CH_3^+, $CH_3^{\cdot}$ et CH_3^-. On utilise ces systèmes comme des modèles simples pour les transferts d'hydrure (H^-), d'hydrogène ($H^{\cdot}$) et de proton (H^+) entre deux fragments carbonés (qui, dans ces cas simples, sont représentés respectivement par deux fragments CH_3^+, $CH_3^{\cdot}$ et CH_3^-). L'étude est orientée principalement vers l'analyse de la nature électronique du type d'hydrogène qui est transféré dans chaque système et, pour cette raison, on a effectué une analyse topologique des distributions des densités de charge. Des calculs de charges atomiques de Bader et la construction des contours de la densité de charge, du gradient du champ vecteur et du laplacien des contours de la densité de charge permet de mettre en évidence les caractéristiques principales de la nature électronique des H^-, $H^{\cdot}$ et H^+. De plus, la caractérisation des points critiques de liaison sur la surface de la densité de charge permet de clarifier les différences dans les interactions atomiques entre H^-, $H^{\cdot}$ et H^+ et le carbone appartenant à chacun des fragments CH_3^+, $CH_3^{\cdot}$ et CH_3^- respectivement. Une analyse de la redistribution de la densité de charge a aussi été effectuée pour quantifier la réorganisation de la densité électronique lorsqu'on passe du complexe des réactifs vers l'état de transition. Enfin, on discute des effets d'inclusion de l'énergie de corrélation aux niveaux MP2 et CISD.

Mots clés : densité électronique, transfert d'hydrogène, analyse topologique des densités, similarité moléculaire, analyse de densité de Bader.

[Traduit par la rédaction]

Introduction

Hydrogen transfers are one of the most usual processes in general chemistry and biochemistry. Despite having been widely studied, the particular electronic nature of the hydrogen being transferred still remains a matter of controversy. For many years, these kinds of processes were formally differentiated into proton, hydrogen, and hydride transfers. However, few comparative studies analyzing the singular electronic features of each type of transfer have been performed so far. In a pioneering work, Bader and co-workers (1) considered the influence of substituents on isotope effects to distinguish between hydride and proton transfers and established the basic differences between the corresponding transition states in terms of bonding and electron charge density. More recently, Williams et al. (2) discussed, on the basis of qualitative molecular orbital theory, the trends in orbital energy changes for three-center C-H-C systems as a function of decreasing the C—C

Received September 21, 1995.

This paper is dedicated to Professor Richard F.W. Bader on the occasion of his 65th birthday.

J. Mestres[1] **and M. Duran.** Institut de Química Computacional, Universitat de Girona, 17071 Girona, Catalonia, Spain.
J. Bertrán.[2] Grup de Química Teòrica, Departament de Química, Universitat Autònoma de Barcelona, 08193 Bellaterra, Catalonia, Spain.

[1] J. Mestres. E-mail: jordi@stark.udg.es
[2] Author to whom correspondence may be addressed.

distance and closing the C-H-C angle, for hydride and proton transfers.

One of the main difficulties in performing this kind of comparative study is to find systems having the same atomic composition that differ only in the number of electrons involved in the making and breaking of bonds, i.e., two electrons for the hydride transfer, three electrons for the hydrogen transfer, and four electrons for the proton transfer. Also, the degree of simplicity of the chosen common structural model will ultimately determine the level of theory from which the comparative analysis will be done. In this sense, Pain and Williams (3) performed a theoretical comparison of primary deuterium kinetic isotope effects between hydride and proton transfer processes in the structurally related $HNCH_2/HCNH^+$ and $HNCH_2/HCNH^-$ systems at the HF/3-21G level of theory.

Considering all the above-mentioned aspects, we present a comparative study between hydrogen transfer processes in the CH_4/CH_3^+, $CH_4/CH_3^\bullet$, and CH_4/CH_3^- systems, which are taken as the simplest models where hydride (H^-), hydrogen ($H^\bullet$), and proton (H^+) transfers can take place between two carbon fragments. For the sake of clarity, these three processes are illustrated in eqs. [1]–[3].

[1] $$CH_4 + CH_3^+ \rightarrow [CH_3\text{-}H\text{-}CH_3]^+ \rightarrow CH_3^+ + CH_4$$

[2] $$CH_4 + CH_3^\bullet \rightarrow [CH_3\text{-}H\text{-}CH_3]^\bullet \rightarrow CH_3^\bullet + CH_4$$

[3] $$CH_4 + CH_3^- \rightarrow [CH_3\text{-}H\text{-}CH_3]^- \rightarrow CH_3^- + CH_4$$

Equation [1] formally shows the transfer of a H^- between two CH_3^+ fragments, through a $[CH_3\text{-}H\text{-}CH_3]^+$ transition state. Accordingly, eq. [2] illustrates the transfer of a formal $H^\bullet$ between two $CH_3^\bullet$ fragments, through the $[CH_3\text{-}H\text{-}CH_3]^\bullet$ transition state. Finally, eq. [3] represents the formal transfer of a H^+ between two CH_3^- fragments, through a $[CH_3\text{-}H\text{-}CH_3]^-$ transition state. Several studies can be found in the literature dealing with these simple H-transfer models between carbons, although the extent of the treatment differs substantially from one system to another due to the particular electronic characteristics of each system.

Proton transfer between CH_4 and CH_3^- has been theoretically investigated from different viewpoints (4–6). In this system, the transition state is characterized by a symmetric linear structure, with an optimized distance between the two carbons involved in the H^+-transfer event of ca. 2.9 Å.

The potential hypersurface of the hydrogen transfer between CH_4 and $CH_3^\bullet$ has also been experimentally investigated (7) and a number of theoretical studies have tried to reproduce the experimental hydrogen abstraction barrier and provide some structural information about the different stationary points along the potential energy surface (8–13). In this case, the $H^\bullet$ transfer is found to evolve again through a symmetric linear transition state structure, where an average 2.7 Å optimized distance between the two carbons can be encountered.

On the other hand, computation of the unrestricted potential energy surface for the interaction between CH_4 and CH_3^+ does not permit one to naturally study the hydride transfer in this system (14). This is because the structure having the H^- in a position midway between the two CH_3^+ fragments is not a transition state but a minimum in this potential energy surface. For this minimum to exist, the possibility of different isomers has been widely investigated experimentally (15–18) and has been well characterized theoretically (19–23). In particular, evidence for the existence of a C_s symmetry isomer has been presented, this isomer having a distance between the two carbons of about 1.96 Å. Also, a D_{3d} symmetry isomer can be located at different levels of theory although it is not a minimum at correlated levels (22*d*). In this isomer the two carbon atoms come within 2.42 Å of one another. Because these species are minima, the study of the hydride transfer process in this system can only be achieved if the potential energy surface is constrained to a given C—C distance larger than the 2.42 Å found for the D_{3d} isomer, as has recently been reported (14).

From the collection of results discussed above it is evident that these systems show wide structural diversity due to the singular electronic features of each system. Thus, enforced by the fact that hydride transfer in the CH_4/CH_3^+ system can only take place under constrained C—C distance conditions, all three systems under study will be constrained to a given distance between the two carbons throughout the work. The final aim of this contribution is to gain a deeper insight into the characterization of the electronic nature of the transferring H and to try to contribute to the elucidation of the particular conditions under which it can be formally termed as hydride, hydrogen, or proton.

Computational details

The present work has been performed by means of ab initio molecular orbital calculations at the Hartree–Fock (HF) level, and electronic correlation effects have been introduced at the MP2 and CISD levels of theory. The restricted HF method was employed for closed-shell systems while the unrestricted HF method was used for the open-shell system. To minimize basis set effects, the 6-311++G** basis set (24) was used throughout. Restricted geometry optimizations were carried out using Schlegel's method (25), by means of the Gaussian 92 program (26). For MP2 and CISD calculations, generalized densities (27) were always used.

The topological Bader analysis (28) (including construction of charge density maps, location and characterization of bond critical points, gradient vector fields, Laplacian maps, and charge density difference maps between different levels of theory) was carried out through the use of the Electra program (29). In addition, Bader atomic charges were calculated using the Proaim package (30).

A charge density redistribution analysis was performed by computing the quantum molecular similarity measures (QMSMs) of the systems at the different stationary points. The QMSM is defined as the overlap integral between two electron density distributions

[4] $$S_{AB} = \int \rho_A(\boldsymbol{r})\rho_B(\boldsymbol{r})d\boldsymbol{r}$$

where ρ_A and ρ_B are, respectively, the electron density distributions of two molecules A and B (31). The similarity of density distributions ρ_A and ρ_B at a given relative orientation of molecules A and B can then be evaluated by computing the Euclidean distance between QMSMs as

Scheme 1

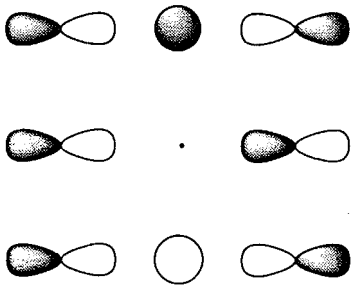

[5] $d_{AB} = (S_{AA} + S_{BB} - 2\,S_{AB})^{1/2}$

This methodology has recently emerged as a very useful tool for tackling all kinds of charge density redistribution problems (32). QMSM calculations were performed by means of the Messem program (33).

Structural analysis

As initially noted by Bader and co-workers (1), the number of electrons involved in the forming and breaking of bonds directly affects the strength of the interaction among the three reacting moieties along the reaction coordinate. These electrons systematically occupy the three molecular orbitals that result from the interaction of those three fragments implicated in the transfer process, namely, the H donor (a CH_3 fragment), the transferring H, and the H acceptor (the other CH_3 fragment). These three orbitals are depicted in Scheme 1.

In hydride transfer (where only two electrons are involved in the bond breaking and forming) the HOMO is the labelled bonding orbital in Scheme 1, while in proton transfer (where four electrons are involved in the forming and breaking bonds) the two additional electrons are accommodated in the labelled nonbonding orbital. The consequences of this electronic disposition on the structure of the transition states for the different processes have already been derived by Bader and co-workers (1): in hydride transfer, the three fragments cement together in a strong, short, highly covalent, and relatively nonpolarizable bond; in contrast, the resulting repulsion of the two additional electrons in proton transfer will lead to a weaker, longer, more ionic, and more polarizable three-center bond.

As mentioned above, Williams et al. (2) derived the same conclusions from a simplified Walsh diagram on the basis of qualitative molecular orbital theory. Quantitative results were also provided by Pain and Williams (3) in their theoretical comparison of structurally related hydride and proton transfers in the $HNCH_2/CHNH^+$ and $HNCH_2/CHNH^-$ systems. In that study, they found that the transition states for hydride and proton transfers are very similar, the main difference lying in the shorter C—C distance for hydride transfer (2.68 Å) as compared to that for proton transfer (2.91 Å).

This trend is also followed by the hydrogen and proton transfer systems considered in this study, but in this particular structural series a comparative study from complete relaxation of all systems is not possible because no transition state exists for the hydride transfer between CH_4 and CH_3^+. Thus, at this stage, in order to include hydride transfer in the comparative analysis, all transfer processes were constrained to evolve within a fixed C—C distance of 3.2 Å. The selection of this value comes from our previous experience in the constrained hydride transfer model system (14), to obtain a hydride transfer with a significant barrier at the three levels of theory employed. Under this constraint, the concept of stationary point is lost and thus, throughout this work, it will be referred to as the reactant complex at the point on the reaction coordinate where the hydrogen to be transferred begins to "notice" the polarization effect of the H-acceptor CH_3 fragment, and as the transition state at the point on the reaction coordinate where the hydrogen being transferred is midway between the two CH_3 fragments. Moreover, the use of a uniform structural constraint for the three types of transfer under study appears to have an additional advantage in that this will permit analyzing the processes from the same structural reference and performing the comparative study from equal structural conditions. In this sense, the three simple models chosen as being representative of hydride, hydrogen, and proton transfers between two carbons become structural artifacts in an attempt to understand the particular electronic characteristics of each H transfer under the same structural environment.

On this basis, the main structural parameters of all reactant complexes and transition states, at the three different levels of theory used, have been collected in Table 1. The nomenclature C^l and C^r stands for the two carbons at the left and right side of the H being transferred (H_t), respectively, under the convention that H_t is initially attached to C^l, so the transfer process proceeds from left to right.

For reactant complexes, the most interesting structural parameter turns out to be the distance between C^l and H_t, denoted as $R(C^l—H_t)$. This distance reveals clearly the strength of the polarization effect on the $C^l—H_t$ bond of the CH_4 fragment in reactant complexes due to the presence of a CH_3^+, $CH_3^\bullet$, or CH_3^- fragment at the constrained C—C distance of 3.2 Å. This polarization effect will strongly influence the transfer process because the larger the polarization effect, the smaller the distance that must be covered by the migrating H_t atom. Taking HF as the reference level of theory, an ordering of the strength of the polarization effect due to the presence of the three different CH_3 fragments can be established, $CH_3^+ > CH_3^- > CH_3^\bullet$, which in turn translates into an ordering of the travelling distance for the H_t being transferred, 0.9510 (H^-) < 1.0166 (H^+) < 1.0568 ($H^\bullet$). Inclusion of the correlation energy tends to enhance the above-mentioned polarization effect on the $C^l—H_t$ bond in reactant complexes, giving rise to a reduction of the distance to be covered for the transferring H_t. In essence, the ordering obtained at the HF level is maintained qualitatively when electron correlation is included to some extent, although MP2 seems to exaggerate the polarization effect with respect to the trend observed at the CISD level of theory.

Among the other structural parameters reported, the main differences are found in the $H\text{-}C^r\text{-}H_t$ angle for reactant complexes, where for proton transfer in the CH_4/CH_3^- system it gives the largest value in comparison with those values found for reactant complexes for the other two processes, due to the presence of a repulsive interaction induced by the two additional electrons furnished by the CH_3^- fragment. Another important difference evident from this table is the progressive opening of the $H\text{-}C\text{-}H_t$ angle for transition states, due to the different amount of electron charge density being accumu-

Table 1. Structural parameters (distances in Å and angles in degrees) for the reactant complexes and the transition states at the HF, MP2, and CISD levels using the 6-311++G** basis set.

	Reactant complex					Transition state	
System	$R(C^l—H_t)$	$R(C^l—H)$	$R(C^r—H)$	$\angle H\text{-}C^l\text{-}H_t$	$\angle H\text{-}C^r\text{-}H_t$	$R(C—H)$	$\angle H\text{-}C\text{-}H_t$
			HF				
CH_4/CH_3^+	1.1245	1.0807	1.0797	107.42	91.18	1.0756	97.56
$CH_4/CH_3\cdot$	1.0716	1.0854	1.0736	109.81	91.93	1.0782	103.25
CH_4/CH_3^-	1.0917	1.0916	1.1048	110.42	112.15	1.0965	110.38
			MP2				
CH_4/CH_3^+	1.1624	1.0879	1.0886	106.14	91.73	1.0866	97.42
$CH_4/CH_3\cdot$	1.0829	1.0909	1.0794	109.75	91.91	1.0855	103.15
CH_4/CH_3^-	1.1124	1.0963	1.1076	110.13	111.40	1.1010	109.70
			CISD				
CH_4/CH_3^+	1.1482	1.0858	1.0871	106.62	91.48	1.0832	97.47
$CH_4/CH_3\cdot$	1.0793	1.0893	1.0784	109.74	91.91	1.0834	103.20
CH_4/CH_3^-	1.1033	1.0947	1.1078	110.35	112.47	1.0995	110.37

Table 2. Characterization of the bond critical points (BCP) of the charge density surface for the transition state at the HF, MP2, and CISD levels using the 6-311++G** basis set. Locations of the BCP from the corresponding H atom (r_c) are in au, charge density at the BCP ($\rho(r_c)$) in e/au^3, and Laplacian of the charge density at the BCP ($\nabla^2\rho(r_c)$) in e/au^5. Also given are the resulting eigenvalues of the Hessian matrix (λ_1, λ_2, and λ_3).

Bond	System	r_c	$\rho(r_c)$	$\nabla^2\rho(r_c)$	λ_1	λ_2	λ_3	$\lvert\lambda_1\rvert/\lambda_3$
				HF				
$C—H_t$	$[CH_3\text{-}H_t\text{-}CH_3]^+$	1.3661	0.0717	−0.0123	−0.0879	−0.0879	0.1636	0.5373
	$[CH_3\text{-}H_t\text{-}CH_3]\cdot$	1.0925	0.0877	−0.0715	−0.1432	−0.1432	0.2148	0.6667
	$[CH_3\text{-}H_t\text{-}CH_3]^-$	0.9054	0.0927	−0.1121	−0.1665	−0.1665	0.2209	0.7537
C—H	$[CH_3\text{-}H_t\text{-}CH_3]^+$	0.6680	0.3027	−1.2014	−0.8847	−0.8532	0.5365	1.6490
	$[CH_3\text{-}H_t\text{-}CH_3]\cdot$	0.7471	0.2869	−1.0440	−0.7396	−0.7290	0.4247	1.7415
	$[CH_3\text{-}H_t\text{-}CH_3]^-$	0.8178	0.2637	−0.8877	−0.6285	−0.5914	0.3322	1.8919
				MP2				
$C—H_t$	$[CH_3\text{-}H_t\text{-}CH_3]^+$	1.2810	0.0741	−0.0291	−0.1027	−0.1027	0.1763	0.5825
	$[CH_3\text{-}H_t\text{-}CH_3]\cdot$	1.0877	0.0873	−0.0775	−0.1425	−0.1425	0.2075	0.6867
	$[CH_3\text{-}H_t\text{-}CH_3]^-$	0.9685	0.0913	−0.0916	−0.1579	−0.1579	0.2241	0.7046
C—H	$[CH_3\text{-}H_t\text{-}CH_3]^+$	0.6732	0.2873	−1.0586	−0.8227	−0.7999	0.5640	1.4587
	$[CH_3\text{-}H_t\text{-}CH_3]\cdot$	0.7305	0.2768	−0.9442	−0.7193	−0.7110	0.4862	1.4794
	$[CH_3\text{-}H_t\text{-}CH_3]^-$	0.7791	0.2573	−0.8058	−0.6277	−0.5986	0.4206	1.4924
				CISD				
$C—H_t$	$[CH_3\text{-}H_t\text{-}CH_3]^+$	1.3089	0.0738	−0.0244	−0.0994	−0.0994	0.1744	0.5700
	$[CH_3\text{-}H_t\text{-}CH_3]\cdot$	1.0936	0.0875	−0.0710	−0.1433	−0.1433	0.2156	0.6647
	$[CH_3\text{-}H_t\text{-}CH_3]^-$	0.9443	0.0924	−0.1007	−0.1627	−0.1627	0.2247	0.7241
C—H	$[CH_3\text{-}H_t\text{-}CH_3]^+$	0.6754	0.2916	−1.0868	−0.8378	−0.8122	0.5632	1.4876
	$[CH_3\text{-}H_t\text{-}CH_3]\cdot$	0.7395	0.2794	−0.9615	−0.7215	−0.7120	0.4720	1.5286
	$[CH_3\text{-}H_t\text{-}CH_3]^-$	0.7983	0.2590	−0.8231	−0.6231	−0.5905	0.3905	1.5956

lated along the C-H_t-C region of space depending on each individual process. Interestingly, geometrical parameters obtained at the CISD level are intermediate between HF and MP2 structures regardless of the process, which reflects the well-known fact that MP2 calculations usually exaggerate the contribution of correlation energy to the electronic energy of molecules and complexes (32*c*).

Electronic analysis

In performing the comparative electronic analysis, more atten-

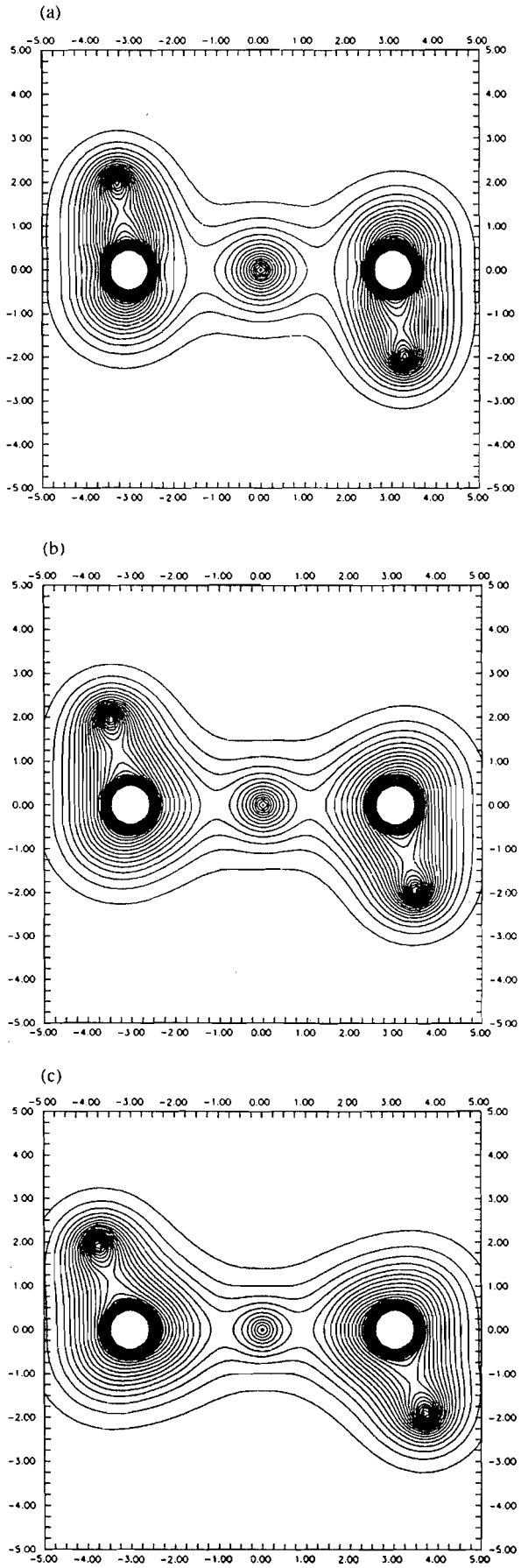

Fig. 1. Electron density maps for the (*a*) $[CH_3\text{-}H_t\text{-}CH_3]^+$, (*b*) $[CH_3\text{-}H_t\text{-}CH_3]^{\bullet}$, and (*c*) $[CH_3\text{-}H_t\text{-}CH_3]^-$ transition states of the corresponding systems at the HF level.

tion will be paid to transition states, because it is at the transition state point of the reaction coordinate where the migrating H_t reaches the midpoint between the two carbons in all three systems, and thus it is more suitable for comparative purposes. References to the results obtained at reactant complexes will be made in those cases where significant information can be extracted. To seek such a goal, electron density contour maps for the three midpoint H transfers of the systems under study have been gathered in Fig. 1, in a plane containing the maximum number of atoms. These maps clearly offer an attractive visual way of distinguishing among what are commonly termed hydride (Fig. 1*a*), hydrogen (Fig. 1*b*), or proton (Fig. 1*c*) transfers, depending on the accumulation of charge isodensity lines around the H_t being transferred.

The influence of correlation energy on the charge density map of each particular H-transfer has been estimated by depicting electron density difference maps. The fact that the three systems are constrained to a common C—C distance is found especially useful in this kind of analysis. Figure 2 shows this effect when correlation energy has been included at the MP2 level. Similar maps are obtained from the CISD electron densities but, as mentioned above, the MP2 level appears to be more suitable for visual purposes as the effect of correlation energy is found to be more exaggerated. The general trend shown by this figure is that inclusion of the correlation energy generally corrects the well-known exaggeration of the weight of ionic structures at the HF level. In valence bond language, HF exaggerates the contribution of the $C^+\ H^-\ C^+$ structure in the hydride transfer (14*a*), while it overestimates that of the $C^-\ H^+\ C^-$ structure in the proton transfer. This can be observed in Fig. 2: at the $[CH_3\text{-}H_t\text{-}CH_3]^+$ transition state (Fig. 2*a*), a diminution of the charge density around H_t is found when correlation energy is added, and it is in turn accumulated in those regions around the carbons; on the contrary, correlation energy concentrates charge density around H_t for the $[CH_3\text{-}H_t\text{-}CH_3]^-$ system (Fig. 2*c*) while it is depleted in the central regions of the C—H_t interaction. Moreover, it turns out that correlation energy has a smaller effect on the overall charge density distribution of the $[CH_3\text{-}H_t\text{-}CH_3]^{\bullet}$ system (Fig. 2*b*).

More precise quantitative information on the topological features of electron density maps can be extracted by locating and characterizing the bond critical points (BCPs) among the different C—H bonds of the three systems under consideration. The results of this analysis are collected in Table 2. Focusing our attention first on results obtained for the C—H_t bond in the three systems, several general trends are exhibited: (*i*) the location of the C—H_t BCP from H_t provides information on the spatial coverage of the particular H_t electronic domain, being found to obey the following order $r_c(C—H^-) > r_c(C—H^{\bullet}) > r_c(C—H^+)$, where a formal electronic character has been assigned to each H_t; (*ii*) the value of the charge density at the C—H_t BCP increases in the order $\rho(r_c)(C—H^-) < \rho(r_c)(C—H^{\bullet}) < \rho(r_c)(C—H^+)$; (*iii*) the values of the Laplacian of the charge density at this C—H_t BCP follow the order $\nabla^2\rho(r_c)(C—H^-) > \nabla^2\rho(r_c)(C—H^{\bullet}) > \nabla^2\rho(r_c)(C—H^+)$, indicat-

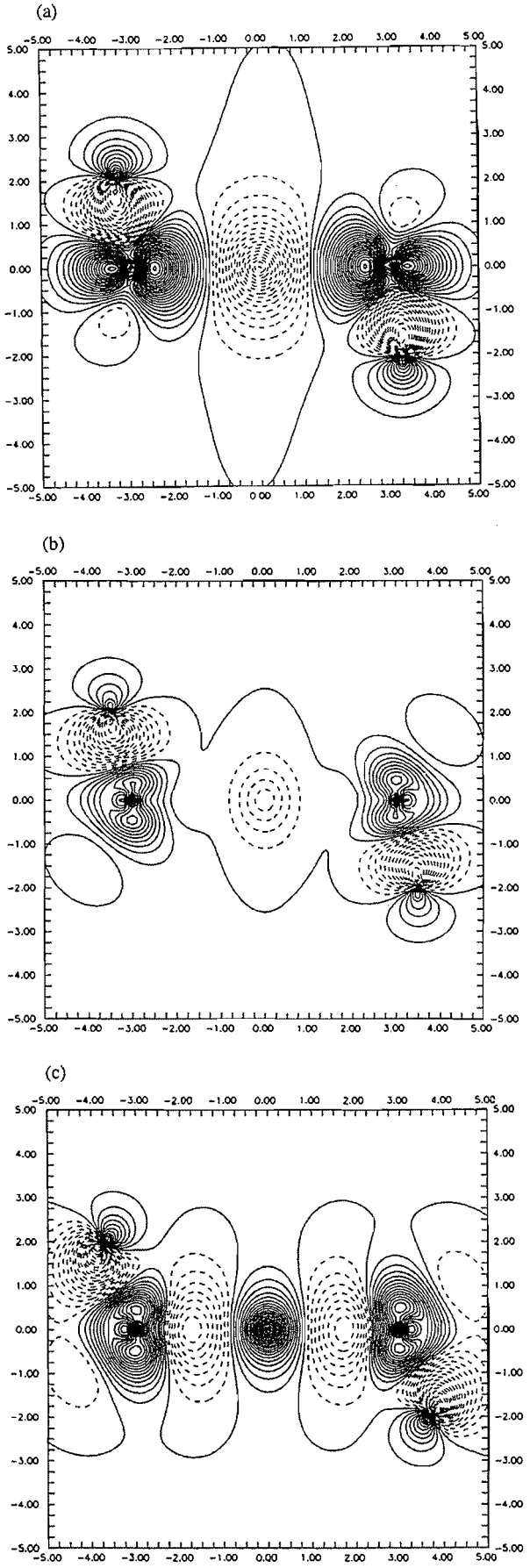

Fig. 2. Electron density difference maps between MP2 and HF ($\rho_{MP2} - \rho_{HF}$) for the (*a*) $[CH_3\text{-}H_t\text{-}CH_3]^+$, (*b*) $[CH_3\text{-}H_t\text{-}CH_3]^{\bullet}$, and (*c*) $[CH_3\text{-}H_t\text{-}CH_3]^-$ transition states of the corresponding systems. Positive values are represented by solid lines and negative values by broken lines.

ing an increasing local concentration of the charge density in this direction; and (*iv*) the $|\lambda_1|/\lambda_3$ values also follow the same trend found for electron densities of the BCPs. The whole ensemble of these results indicates that some amount of electron density tends to be accumulated in regions closer to H_t when going from H^-, $H^{\bullet}$, and H^+, and that the class of atomic interaction between H_t and the two carbon atoms is representative of so-called intermediate interactions (28*a*).

The same analysis can be performed for the six equivalent lateral C—H bonds and, interestingly, a completely opposite trend is observed: (*i*) location of the C—H BCP is closer to the H atom for hydride transfer in the $[CH_3\text{-}H_t\text{-}CH_3]^+$ transition state, and it progressively moves further away in the systems representative of hydrogen and proton transfers. (*ii*) At the same time the value of the charge density at the C—H BCP decreases in the same direction, and (*iii*) the Laplacian value becomes less negative, both factors being evidence of a progressive local depletion of electron density, which is also related to the fact that the C—H bond distance is increased in the same direction (Table 1). (*iv*) Finally, in this case $|\lambda_1|/\lambda_3$ gives values that are larger than unity, which, together with the relatively large values of the charge density and Laplacian, are clearly representative of the formation of typical C—H covalent bonds (28*a*).

The effect of correlation energy on the localization and characterization of BCPs can also be extracted from Table 2. Thus, what was qualitatively observed from the electron density difference maps discussed above (Fig. 2) can now be quantitatively evaluated. In general, all the differences among the topological features of the three types of H_t are now reduced. With respect to the HF level, (*i*) the most remarkable effect is that the location of the C—H_t BCP is found to be clearly closer to the H^-, while it moves apart from H^+. In a wider sense, this indicates that the formal H^-, atomic basin is significantly contracted, that of the formal H^+ is clearly expanded, and that of the formal $H^{\bullet}$ suffers only small differences; (*ii*) while an increment of the electron density is encountered at the C—H^- BCP, smaller electron density values are found at the C—H^+ BCP and no significant differences appear at the C—$H^{\bullet}$ BCP; (*iii*) values of the Laplacian of the charge density become more negative at the C—H^- BCP and less negative at the C—H^+ BCP; finally (*iv*) $|\lambda_1|/\lambda_3$ values at the C—H_t BCPs follow the same trend found for the electron densities. In summary, introduction of the effect of correlation energy makes the differences in the electronic nature of the three types of H_t being transferred even more diffuse than they were at the HF level.

From the above results it turns out that the larger the hydride character of the transferring H, the larger the proton character of the lateral Hs. This statement is clearly reflected in Table 3, where a Bader atomic charge population analysis at the reactant complexes and transition states is presented. Among other population analyses, Bader atomic charges have

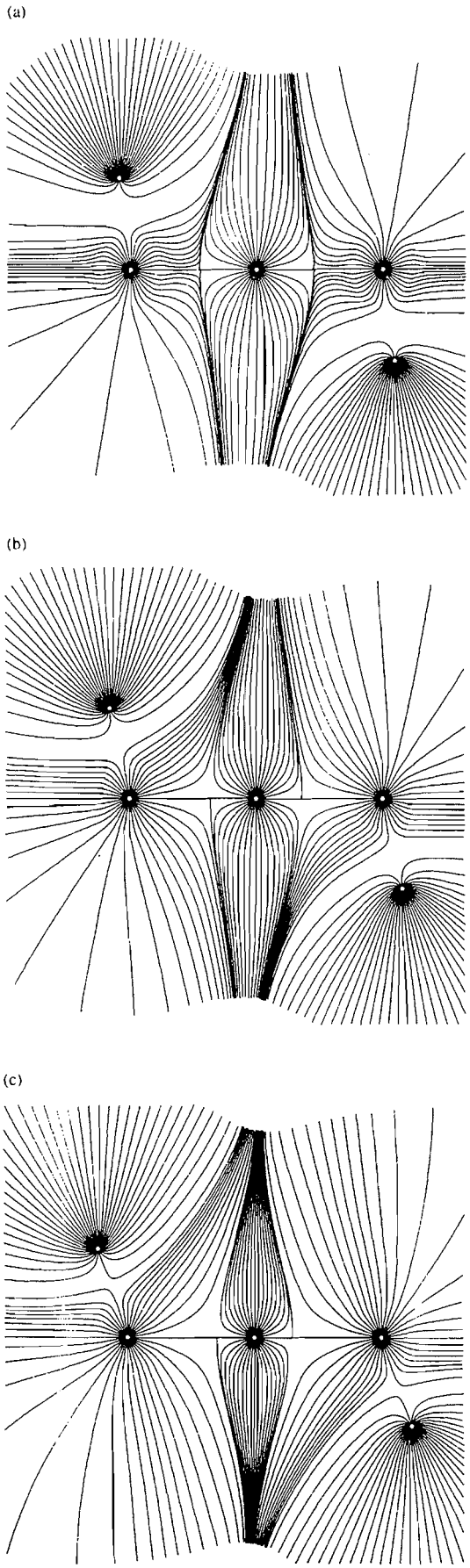

Fig. 3. Gradient vector fields for the (*a*) $[CH_3\text{-}H_t\text{-}CH_3]^+$, (*b*) $[CH_3\text{-}H_t\text{-}CH_3]^{\bullet}$, and (*c*) $[CH_3\text{-}H_t\text{-}CH_3]^-$ transition states of the corresponding systems at the HF level.

the advantage of being consistent with the topological description of the particular electron density distribution.

Comparing first the charges on H_t (q_{Ht}) at the transition states for the three systems, a gradual gain of positive charge is observed in going from the hydride, to the hydrogen, and finally to the proton transfer. However, neither does the hydride acquire an atomic charge of -1 nor does the proton acquire a charge of $+1$. On the contrary, it is found that differences in the electronic nature of the formally transferring H^-, $H^{\bullet}$, and H^+, despite being evident, are very subtle. As deduced from the topological analysis of Table 2, computation of Bader atomic charges on correlated electron density distributions would still lead to a more electronically similar H_t.

On the other hand, comparison of the atomic charges of the six equivalent lateral Hs (q_H) in the transition state leads to the same trend observed in the BCP analysis of Table 2: q_H changes to a less positive value when going from the system representative of hydride transfer to that of proton transfer. As a result, an interesting crossed relationship between each H_t and its lateral H partner is found: while q_H in the $[CH_3\text{-}H_t\text{-}CH_3]^+$ transition state has a value close to q_{Ht} in the $[CH_3\text{-}H_t\text{-}CH_3]^-$ transition state, q_H in the $[CH_3\text{-}H_t\text{-}CH_3]^-$ transition state approaches q_{Ht} in the $[CH_3\text{-}H_t\text{-}CH_3]^+$ transition state.

The atomic charges of H_t, H^l (lateral Hs attached to C^l), and H^r (lateral Hs attached to C^r) at reactant complexes (Table 3) provide a means of characterizing the evolution of each individual atomic charge along the reaction coordinate. This evolution can be visually reproduced by constructing what are called charge migration diagrams, as recently done in an electronic analysis of the hydride transfer in the CH_4/CH_3^+ system (14*b*). Focusing our attention on the transferring H_t, for the H^- in the CH_4/CH_3^+ system, a net gain of negative charge is observed at the HF level when going from the reactant complex to the transition state. For the $H^{\bullet}$ being transferred in the $CH_4/CH_3^{\bullet}$ system a clear accumulation of negative charge is also observed. Finally, a completely opposite evolution is observed for the transferring H^+ in the CH_4/CH_3^- system. In this case, an increase in positive charge is evident.

In Fig. 3 are presented the gradient vector fields for the three systems under study. The diagrams again provide a nice visual means of distinguishing between the hydride (left), hydrogen (center), and proton (right) transfers based upon the spatial extent of each particular H_t atomic basin. This figure clearly exhibits the limits of integration for computing the Bader atomic charges presented in Table 3. These limits were actually revealed when the location of BCPs was described (Table 2). Obviously, the relative size of the atomic basins is directly related to the atomic charges obtained from the Bader atomic charge population analysis (Table 3): the H_t atomic basin is reduced from the formal H^- to H^+ (which translates into a progressive loss of electron density), while the lateral H atomic basins are expanded (which gives a gradual gain of negative charge). Finally, although not reported, the effect of the electron-correlation energy on these maps tends to reduce the perceptible differences between the three H_t atomic basins

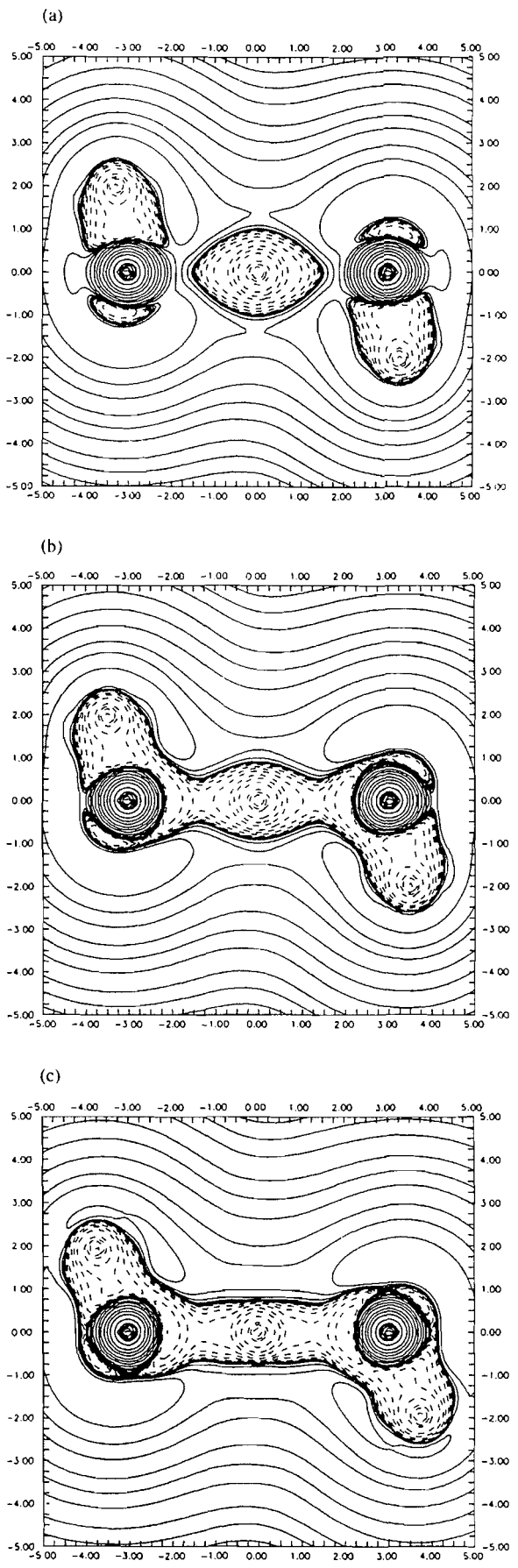

Fig. 4. Laplacian maps for the (*a*) $[CH_3\text{-}H_t\text{-}CH_3]^+$, (*b*) $[CH_3\text{-}H_t\text{-}CH_3]^{\bullet}$, and (*c*) $[CH_3\text{-}H_t\text{-}CH_3]^-$ transition states of the corresponding systems at the HF level. Positive values are represented by solid lines and negative values by broken lines.

(as was already extracted from the topological analysis of Table 2), which merely reflects the widely discussed fact that HF exaggerates the contribution of ionic structures.

A last stage in the topological electronic analysis is accomplished here by presenting the Laplacian maps for the three systems studied (Fig. 4). The usefulness of the Laplacian of the charge density lies in the fact that it exhibits the atomic shell structure and thus can be used as a visual tool to recognize distortions of these shells due to interactions with the neighbouring atomic nuclei. Moreover, its sign also reveals important information on where a local concentration of charge (negative values) or a local depletion of charge (positive values) occurs. On this basis, it is interesting to observe the polarization effect on the *s* shell of formal H^- (left), which appears clearly distorted from its original spherical symmetry, by adopting a football shape due to the interaction with the formal CH_3^+ fragments. The presence of positive Laplacian values between the lines connecting the carbons and the central H^- also gives a hint of the kind of long-range interaction that takes place at the $[CH_3\text{-}H_t\text{-}CH_3]^+$ transition state. Furthermore, the successive addition of one electron into the last system to yield the $[CH_3\text{-}H_t\text{-}CH_3]^{\bullet}$ and $[CH_3\text{-}H_t\text{-}CH_3]^-$ transition states produces an accumulation of charge density on the $C\text{-}H_t\text{-}C$ region that is manifested by the presence of negative Laplacian values all along this region and by the progressively stronger overlapping of the H_t *s* shell with the adjacent carbon shells. Thus, the subtle electronic differences between the three systems become evident from this point of view.

Charge density redistribution analysis

To complete the Bader electronic analysis, which is in widespread use at present, a charge density redistribution analysis is proposed using the methodology developed by Carbó and co-workers (31), briefly outlined in the methodology section.

Table 4 collects the values of the quantum molecular similarity measures (QMSMs) for reactant complexes and transition states together with the Euclidean distances between the two electron density distributions. A recent detailed study on the interpretation of QMSM reveals that this is actually a quantitative measure of the concentration of the electron density (32*e*): the larger the value of the QMSM, the more globally concentrated is the charge density in the molecule. Therefore, comparing QMSM values between reactant complexes and transition states, a general trend is found showing that the electron density is slightly more concentrated for reactant complexes than in transition states, regardless of the level of theory employed to obtain the particular electron densities. This is what, in principle, could be expected from a qualitative point of view, as the H_t migrates from the reactant complex to the transition state.

The result that QMSM values decrease only slightly when going from reactant complexes to transition states is due to the

Table 3. Bader atomic charge populations (q_{Ht}, q_{Hl} and q_{Hr}) for reactant complexes and (q_{Ht} and q_H) transition states at the HF level using the 6-311++G** basis set.

	Reactant complex			Transition state	
System	q_{Ht}	q_{Hl}	q_{Hr}	q_{Ht}	q_H
CH_4/CH_3^+	−0.2152	0.0443	0.2553	−0.2320	0.1672
$CH_4/CH_3^\cdot$	−0.0049	−0.0438	0.0114	0.0449	−0.0043
CH_4/CH_3^-	0.2217	−0.1147	−0.2064	0.3479	−0.1589

Table 4. Quantum molecular similarity measures (QMSM) for reactant complexes and transition states, together with the Euclidean distance between these points at the HF, MP2, and CISD levels using the 6-311++G** basis set.

System	$QMSM_{RC}$	$QMSM_{TS}$	$d_{RC,TS}$
	HF		
CH_4/CH_3^+	63.73463	63.68738	0.3666
$CH_4/CH_3^\cdot$	63.64183	63.54851	0.3563
CH_4/CH_3^-	63.62667	63.52637	0.2001
	MP2		
CH_4/CH_3^+	63.75098	63.69595	0.3158
$CH_4/CH_3^\cdot$	63.68821	63.59139	0.3449
CH_4/CH_3^-	63.68960	63.60923	0.1982
	CISD		
CH_4/CH_3^+	63.75761	63.70567	0.3355
$CH_4/CH_3^\cdot$	63.68628	63.59179	0.3508
CH_4/CH_3^-	63.68534	63.59494	0.2005

fact that the main contribution to the global charge redistribution arises from those few electrons involved in the breaking and forming bonds, i.e., two for H^-, three for $H^\cdot$, and four for H^+ transfer processes. The Euclidean distances provide a quantitative measure of the change undergone by the electron density along the reaction coordinate. The most interesting result is that hydride and hydrogen transfers experience about the same amount of charge density redistribution, while in the proton transfer process this redistribution is noticeably smaller. This is perfectly related to the changes in atomic charges observed from Table 3 and provides a quantitative measure of the fact that the formal hydride and the hydrogen are somehow travelling with a reasonable amount of charge density around them, while the proton leaves part of its initial charge density when moving from the reactant complex to the transition state.

Concluding remarks

This comparative electronic analysis between hydrogen transfers in the CH_4/CH_3^+, $CH_4/CH_3^\cdot$, and CH_4/CH_3^- systems, constrained to a fixed carbon–carbon distance, has clarified, from both qualitative (visual) and quantitative points of view, the subtle differences existing among the electronic natures of the formally termed hydride, hydrogen, and proton entities being transferred. Due to the fact that the chosen distance between carbons is not the natural distance at which the different processes occur, direct extrapolation of the present quantitative results has to be done with some care. However, the overall trends observed in this study are not likely to change qualitatively.

The particular features of each transfer have been revealed by a topological electronic analysis. It has been shown that, from a qualitative point of view, this kind of analysis is able to provide clear visual information by building up the electron density, gradient vector field, and Laplacian maps. Quantitative data can also be obtained by locating and characterizing the bond critical points on the three-dimensional electron density surface and calculating the atomic charges by integration of the electron density inside each atomic basin as delimited by its zero-flux surface. Finally, a charge density redistribution analysis is proposed as a natural extension of the widely established classical Bader electronic analysis.

All analyses have revealed that, although electronic singularities can be identified, differences between the electronic nature of the transferring hydride, hydrogen, and proton appear to be very subtle and rather diffuse in this aspect. In the end, what ultimately determines the formal kind of hydrogen transfer taking place is the a priori knowledge of the number of electrons involved in the breaking and forming bonds. On this basis, a hydrogen transfer involving the rearrangement of two, three, or four electrons can be formally called hydride, hydrogen, or proton transfer, respectively, without the assumption that what is really being transferred is a true hydride, hydrogen, or proton.

Acknowledgements

We are indebted to Professor Richard F.W. Bader for kindly providing us with a copy of his Proaim package. Many helpful comments from Professor Gerry M. Maggiora are gratefully acknowledged.

References

1. C.G. Swain, R.A. Wiles, and R.F.W. Bader. J. Am. Chem. Soc. **83**, 1945 (1961).
2. I.H. Williams, A.B. Miller, and G.M. Maggiora. J. Am. Chem. Soc. **112**, 530 (1990).
3. A.E. Pain and I.H. Williams. J. Chem. Soc. Chem. Commun. 1417 (1991).

4. *(a)* Z. Latajka and S. Scheiner. Int. J. Quantum Chem. **29**, 285 (1986); *(b)* S. Scheiner and Z. Latajka. J. Phys. Chem. **91**, 724 (1987); *(c)* A.D. Isaacson, L. Wang, and S. Scheiner. J. Phys. Chem. **97**, 1765 (1993).
5. R.V. Stanton and K.M. Merz, Jr. J. Chem. Phys. **101**, 6658 (1994).
6. B. Kallies and R. Mitzner. J. Mol. Model. (Electronic Publication), **1**, 68 (1995).
7. J.M. Tedder. Angew. Chem. Int. Ed. Engl. **21**, 401 (1982).
8. M.J.S. Dewar and E. Haselbach. J. Am. Chem. Soc. **92**, 590 (1970).
9. M.T. Rayez-Meaume, J.J. Dannenberg, and J.L. Whitten. J. Am. Chem. Soc. **100**, 747 (1978).
10. M. Sana, G. Leroy, and J.L. Villaveces. Theor. Chim. Acta, **65**, 109 (1984).
11. E. Wünsch, J.M. Lluch, A. Oliva, and J. Bertrán. J. Chem. Soc. Perkin Trans. 2, 211 (1987).
12. C. Musgrave, J.K. Perry, R.C. Merkle, and W.A. Goddard III. Nanotechnology, **2**, 187 (1991).
13. *(a)* M.R. Pederson. Chem. Phys. Lett. **230**, 54 (1994); *(b)* D. Porezag and M.R. Pederson. J. Chem. Phys. **102**, 9345 (1995).
14. *(a)* J. Mestres, A. Lledós, M. Duran, and J. Bertrán. J. Mol. Struct. (Theochem), **260**, 259 (1992); *(b)* J. Mestres, M. Duran, and J. Bertrán. Theor. Chim. Acta, **88**, 325 (1994).
15. *(a)* G.A. Olah, G. Klopman, and R.H. Schlosberg. J. Am. Chem. Soc. **91**, 3261 (1969); *(b)* G.A. Olah, Y. Halpern, J. Shen, and Y.K. Mo. J. Am. Chem. Soc. **93**, 1251 (1971).
16. *(a)* K. Hiraoka and P. Kebarle. J. Am. Chem. Soc. **98**, 6119 (1976); *(b)* Adv. Mass Spectrom. **7b**, 1408 (1978).
17. J. Weiner, G.P.K. Smith, M. Saunders, and R.J. Cross, Jr. J. Am. Chem. Soc. **95**, 4115 (1973).
18. L.I. Yeh, J.M. Price, and Y.T. Lee. J. Am. Chem. Soc. **111**, 5597 (1989).
19. L. Radom, D. Poppinger, and R.C. Haddon. Carbonium ions. *Edited by*, G.A. Olah and P.v.R. Schleyer. Wiley–Interscience, New York. 1976.
20. H.-J. Köhler and H. Lischka. Chem. Phys. Lett. **58**, 175 (1978).
21. R.A. Poirier, E. Constantin, J.C. Abbé, M.R. Peterson, and I.G. Csizmadia. J. Mol. Struct. (Theochem), **88**, 343 (1982).
22. *(a)* K. Raghavachari, R.A. Whiteside, J.A. Pople, and P.v.R. Schleyer. J. Am. Chem. Soc. **103**, 5649 (1981); *(b)* P.v.R. Schleyer and J.W. de M. Carneiro. J. Comput. Chem. **13**, 997 (1992); *(c)* P.R. Schreiner, S.-J. Kim, P.v.R. Schleyer, and H.F. Schaefer III. J. Chem. Phys. **99**, 3716 (1993); *(d)* J.W. de M. Carneiro, P.v.R. Schleyer, M. Saunders, R. Remington, H.F. Schaefer III, A. Rauk, and T.S. Sorensen. J. Am. Chem. Soc. **116**, 3483 (1994).
23. J. Wilkie and I.H. Williams. J. Chem. Soc. Perkin Trans. 2, 1559 (1995).
24. *(a)* R. Krishnan, J.S. Binkley, R. Seeger, and J.A. Pople. J. Chem. Phys. **72**, 650 (1980); *(b)* T. Clark, J. Chandrasekhar, G.W. Spitznagel, and P.v.R. Schleyer. J. Comput. Chem. **4**, 294 (1983); *(c)* M.J. Frisch, J.A. Pople, and J.S. Binkley. J. Chem. Phys. **80**, 3265 (1984).
25. *(a)* H.B. Schlegel. J. Comput. Chem. **3**, 214 (1982); *(b)* Theor. Chim. Acta, **66**, 333 (1984).
26. M.J. Frisch, G.W. Trucks, M. Head-Gordon, P.M.W. Gill, M.W. Wong, J.B. Foresman, B.G. Johnson, H.B. Schlegel, M.A. Robb, E.S. Replogle, R. Gomperts, J.L. Andres, K. Raghavachari, J.S. Binkley, C. Gonzalez, R.L. Martin, D.J. Fox, D.J. Defrees, J. Baker, J.J.P. Stewart, and J.A. Pople. Gaussian 92, Revision A. Gaussian, Inc., Pittsburgh, Pa. 1992.
27. *(a)* N.C. Handy and H.F. Schaefer III. J. Chem. Phys. **81**, 5031 (1984); *(b)* K.B. Wiberg, C.M. Hadad, T.J. LePage, C.M. Breneman, and M.J. Frisch. J. Phys. Chem. **96**, 671 (1992).
28. *(a)* R.F.W. Bader. Atoms in molecules: a quantum theory. Oxford University Press, Oxford, U.K. 1990; *(b)* Chem. Rev. **91**, 893 (1991).
29. J. Mestres. Electra. Institut de Química Computacional, Universitat de Girona, Girona, Spain. 1994.
30. F.W. Biegler, R.F.W Bader, and T. Tang. J. Comput. Chem. **3**, 317 (1982).
31. *(a)* R. Carbó, L. Leyda, and M. Arnau. Int. J. Quantum Chem. **17**, 1185 (1980); *(b)* J. Mestres, M. Solà, M. Duran, and R. Carbó. J. Comput. Chem. **15**, 1113 (1994); *(c)* E. Besalú, R. Carbó, J. Mestres, and M. Solà. *In* Topics in current chemistry: molecular similarity I. Vol. 173. *Edited by* K. Sen. Springer-Verlag, Berlin. 1995.
32. *(a)* M. Solà, J. Mestres, R. Carbó, and M. Duran. J. Am. Chem. Soc. **116**, 5909 (1994); *(b)* M. Solà, J. Mestres, M. Duran, and R. Carbó. J. Chem. Inf. Comput. Sci. **34**, 1047 (1994); *(c)* M. Solà, J. Mestres, R. Carbó, and M. Duran. J. Chem. Phys. **104**, 636 (1996); *(d)* J. Mestres, M. Solà, R. Carbó, F.J. Luque, and M. Orozco. J. Phys. Chem. **100**, 606 (1996); *(e)* M. Solà, J. Mestres, J.M. Oliva, M. Duran, and R. Carbó. Int. J. Quantum Chem. **58**, 361 (1996); *(f)* J.M. Oliva, R. Carbó, and J. Mestres. Adv. Mol. Sim. In press.
33. J. Mestres, M. Solà, E. Besalú, M. Duran, and R. Carbó. Messem. Institut de Química Computacional, Universitat de Girona, Girona, Spain. 1993.

Variability of shapes and properties of atoms in molecules: a case study of the carbonyl oxygen

Boris B. Stefanov and Jerzy Cioslowski

Abstract: A comparative study of carbonyl oxygen atoms in diverse molecular environments is presented. The variability of shapes of oxygen atoms is quantified with a newly developed similarity measure that confirms the qualitative conclusions of visual assessment. Electronic properties of these atoms, such as charges, energies, and dipole moments, are computed and their possible correlations with the atomic shapes are studied. Factors that affect atomic shapes are investigated and found to be distinct from those influencing electronic properties of atoms in molecules. The kinetic energies of the atoms under study correlate poorly with the atomic charges. The second-neighbor effects on the atomic energies and charges are approximately additive. Both the theoretical considerations and the numerical results definitively rule out the possibility of the shapes of atomic basins unambiguously determining the properties of atoms in molecules. The consequences of this observation for the recently contemplated approaches to the prediction of electronic properties of large molecules are discussed.

Key words: atoms in molecules, properties of —; similarity of —; transferability of —.

Résumé : On présente les résultats d'une étude comparative des atomes d'oxygène de carbonyles dans divers environnements moléculaires. On a quantifié la variabilité des formes des atomes d'oxygène à l'aide d'une mesure de similarité développée récemment qui confirme les conclusions qualitatives de l'attribution visuelle. On a calculé les propriétés électroniques de ces atomes, telles que les charges, les énergies et les moments dipolaires et on a étudié leurs corrélations possibles avec les formes atomiques et on a trouvé qu'elles sont différentes de celles qui influencent les propriétés électroniques des atomes dans les molécules. La relation entre les énergies cinétiques des atomes examinés et leurs charges atomiques n'est pas bonne. Les effets du deuxième voisin sur les énergies et les charges atomiques sont approximativement additifs. Les considérations théoriques ainsi que les résultats numériques permettent d'éliminer définitivement la possibilité d'utiliser les formes des bassins atomiques pour déterminer sans ambiguïté les propriétés des atomes dans les molécules. On discute des conséquences de cette observation sur les approches contemplées récemment pour prédire les propriétés électroniques de grosses molécules.

Mots clés : atomes dans les molécules, propriétés des; similarités des; transférabilité des.

[Traduit par la rédaction]

Introduction

The introduction of the theory of atoms in molecules (AIM) by Richard W.F. Bader (1) has marked the advent of a new era in modern chemistry. The ability to discern atoms and functional groups within molecules has paved the way for quantitative understanding of chemical concepts. Consequently, properties such as charges and energies of atoms (1, 2), covalent bond orders (3), and electronegativities in situ (4) have been defined in a rigorous manner. Even more importantly, the meaning of fundamental concepts such as chemical bonds (1) and steric crowding (5) has been elucidated.

The process of identifying atoms in molecules commences with topological analysis of the electron density $\rho(\boldsymbol{r})$. In the course of this analysis all critical points at which the electron density gradient $\nabla\rho(\boldsymbol{r})$ vanishes are identified. Local maxima in $\rho(\boldsymbol{r})$ are called attractors, as they constitute the termini to most gradient paths, i.e., lines that are tangent at each point to $\nabla\rho(\boldsymbol{r})$. The attractors usually coincide with the nuclei present in a given molecule, although nonnuclear attractors are occasionally seen (6). The gradient paths that extend between attractors are known as bond paths or, more generally, attractor interaction lines. Each attractor interaction line passes through a bond critical point at which $\nabla\rho(\boldsymbol{r})$ vanishes and the electron density Hessian has two negative eigenvalues.

The Cartesian space $\mathscr{R}^3$ can be divided into disjoint atomic basins ($\{\Omega_A\}$, each containing an attractor and all the gradient paths that terminate at it. An atom in a molecule is defined as the union of a nuclear attractor and its basin (1). The atomic zero-flux surface, which is a boundary of an atom, encompasses all the bond critical points associated with the respective attractor, together with all the gradient paths for

Received October 26, 1995.

This paper is dedicated to Professor Richard F.W. Bader on the occasion of his 65th birthday.

B.B. Stefanov and J. Cioslowski.[1] Department of Chemistry and Supercomputer Computations Research Institute, Florida State University, Tallahassee, FL 32306-3006, U.S.A.

[1] Author to whom correspondence may be addressed. Telephone: (904) 644-8274. Fax: (904) 644-8281. E-mail: jerzy@kyoko.chem.fsu.edu

which those bond critical points serve as the termini. In other words, the atomic zero-flux surface Π_A is tangent everywhere to $\nabla\rho(\boldsymbol{r})$. One should note that each sheet of a given zero-flux surface is shared by two atoms. This sharing indicates the presence of either chemical bonding (1) or a strong steric repulsion (5) between these atoms.

A one-electron property P_A of an atom A in a molecule is given by the integral of the corresponding property density $\rho_P(\boldsymbol{r})$ over the atomic basin Ω_A

$$[1] \qquad P_A = \int_{\Omega_A} \rho_P(\boldsymbol{r})d\boldsymbol{r}$$

Since $\mathscr{R}^3 \equiv \cup_A \Omega_A$, the sum rule

$$[2] \qquad P = \int \rho_P(\boldsymbol{r})d\boldsymbol{r} = \sum_A P_A$$

is satisfied. The zero-flux property of the atomic boundaries $\{\Pi_A\}$ is a necessary and sufficient condition for the atoms in molecules to satisfy all theorems of quantum mechanics (1). In particular, the atomic virial theorem relates the energy E_A of an atom in a molecule to its kinetic energy T_A by

$$[3] \qquad E_A = -T_A$$

Like their intuitively defined counterparts, functional groups obtained by combining the atoms of Bader's theory are approximately transferable among sufficiently similar molecules. This important property has been empirically verified in a series of recent computational studies. In particular, the approximate transferability of charges and dipole moments (7), molar volumes (8), heats of formation (9), polarizabilities (10), and magnetic susceptibilities (11) of the methyl and methylene groups in normal hydrocarbons has been demonstrated. A method for a theoretical construction of polypeptide molecules from groups of atoms clipped from smaller systems has been proposed (12) on the basis of the observation that electronic properties of the glycil group are approximately transferable among several di- and tripeptides (12). An even bolder approach to the prediction of electronic properties of large systems has been put forward recently.[2] In that approach, large molecules are assembled from atomic fragments taken from a relatively small library of prototype atomic basins (which are extracted from calculations on small chemical species). After docking, the zero-flux surfaces of these prototype, almost-transferable atoms are adjusted to assure their perfect matching. Electronic properties of the adjusted atoms are obtained through semiempirical correlations that, for each prototype atomic basin, relate quantities such as the charge, the multipole moments, and the total energy to the extent of surface adjustment. In turn, electronic properties of the entire molecules are computed by summations over their constituent atoms, eq. [2].

Using the intuitively desirable "building blocks of chemistry" and thus appealing in its simplicity and elegance, the aforementioned method is nevertheless theoretically flawed, as it invokes the assumption that the shape of an atom (or, more precisely, the atomic zero-flux surface Π_A) uniquely determines the electron density within its basin Ω_A and consequently all of its electronic properties (see ref. 1, p. 3). The fallacy of this assumption is readily exposed by the following argument: Let $\rho(\boldsymbol{r})$ be the electron density within a given atomic basin Ω_A, and $\nabla\rho(\boldsymbol{r})$ be the corresponding electron density gradient. $\rho(\boldsymbol{r})$ uniquely determines the atomic zero-flux surface Π_A. Let α be an arbitrary positive constant different from one and $\tilde{\rho}(\boldsymbol{r}) = \alpha\rho(\boldsymbol{r})$ be the electron density within the basin $\Omega_{\tilde{A}}$ of a hypothetical atom $\tilde{A}$. Since the field of $\nabla\tilde{\rho}(\boldsymbol{r})$ is collinear with that of $\nabla\rho(\boldsymbol{r})$,

$$[4] \qquad \Pi_{\tilde{A}} \equiv \Pi_A$$

and

$$\Omega_{\tilde{A}} \equiv \Omega_A$$

At the same time, any one-electron property $P_{\tilde{A}}$ of the hypothetical atom $\tilde{A}$ is related to that of A by

$$[5] \qquad P_{\tilde{A}} = \int_{\Omega_{\tilde{A}}} \tilde{\rho}_P(\boldsymbol{r})d\boldsymbol{r} = \alpha \int_{\Omega_A} \rho_P(\boldsymbol{r})d\boldsymbol{r} = \alpha P_A$$

meaning that atoms with identical zero-flux surfaces and basins can differ in electronic properties. The above result is not surprising considering that the relationship between $\rho(\boldsymbol{r})$ with Ω_A and Π_A corresponds to a noninvertible $\mathscr{R}^3 \rightarrow \mathscr{R}^2$ mapping and therefore is not bijective. One could argue, however, for the possibility of statistically significant correlations between Π_A and P_A of *chemically realizable* atoms A. In this paper, using the example of oxygen atoms in carbonyl compounds, we dispel this notion as well.

Details of calculation

Electronic properties of 21 molecules with the general structure R_1COR_2, where R_1, R_2=H, CH_3, NH_2, Cl, CN, or OH, were calculated at the MP2/6-311G** level of theory with the GAUSSIAN92 (13) suite of programs. All geometries were fully optimized. In cases where several conformers were possible for a given system, the conformer with the lowest energy was selected for the present study. The newly developed variational approach (14) to the determination of atomic surfaces were used, producing properties of atoms in molecules with accuracy exceeding 10^{-4} (au). Calculations of the atomic similarity index (15) were carried out with the recently proposed algorithm (16).

Shapes of oxygen atoms in carbonyl compounds

The difference between the shapes of two atoms A and B that are parts of molecules X and Y, respectively, can be readily assessed with the similarity measures $S_{A(X),B(Y)}$ obtained by maximizing the similarity index (15)

$$[6] \qquad S_{A(X),B(Y)} = \left[\frac{\int_{\Omega_{AB}} \rho_X(\boldsymbol{r})d\boldsymbol{r}}{\int_{\Omega_A} \rho_X(\boldsymbol{r})d\boldsymbol{r}}\right]\left[\frac{\int_{\Omega_{AB}} \rho_Y(\boldsymbol{r})d\boldsymbol{r}}{\int_{\Omega_B} \rho_Y(\boldsymbol{r})d\boldsymbol{r}}\right]$$

over all possible angular orientations of A with respect to B. In eq. [6], $\rho_X(\boldsymbol{r})$ and $\rho Y(\boldsymbol{r})$ are the electron densities in X and Y, respectively, and $\Omega_{AB} = \Omega_{BA} = \Omega_A \cap \Omega_B$ is the common

[2] C. Breneman, personal communication.

Fig. 1. Similarities between the carbonyl oxygen atoms in the systems under study. The notation R_1/R_2 is used to represent the molecule R_1COR_2.

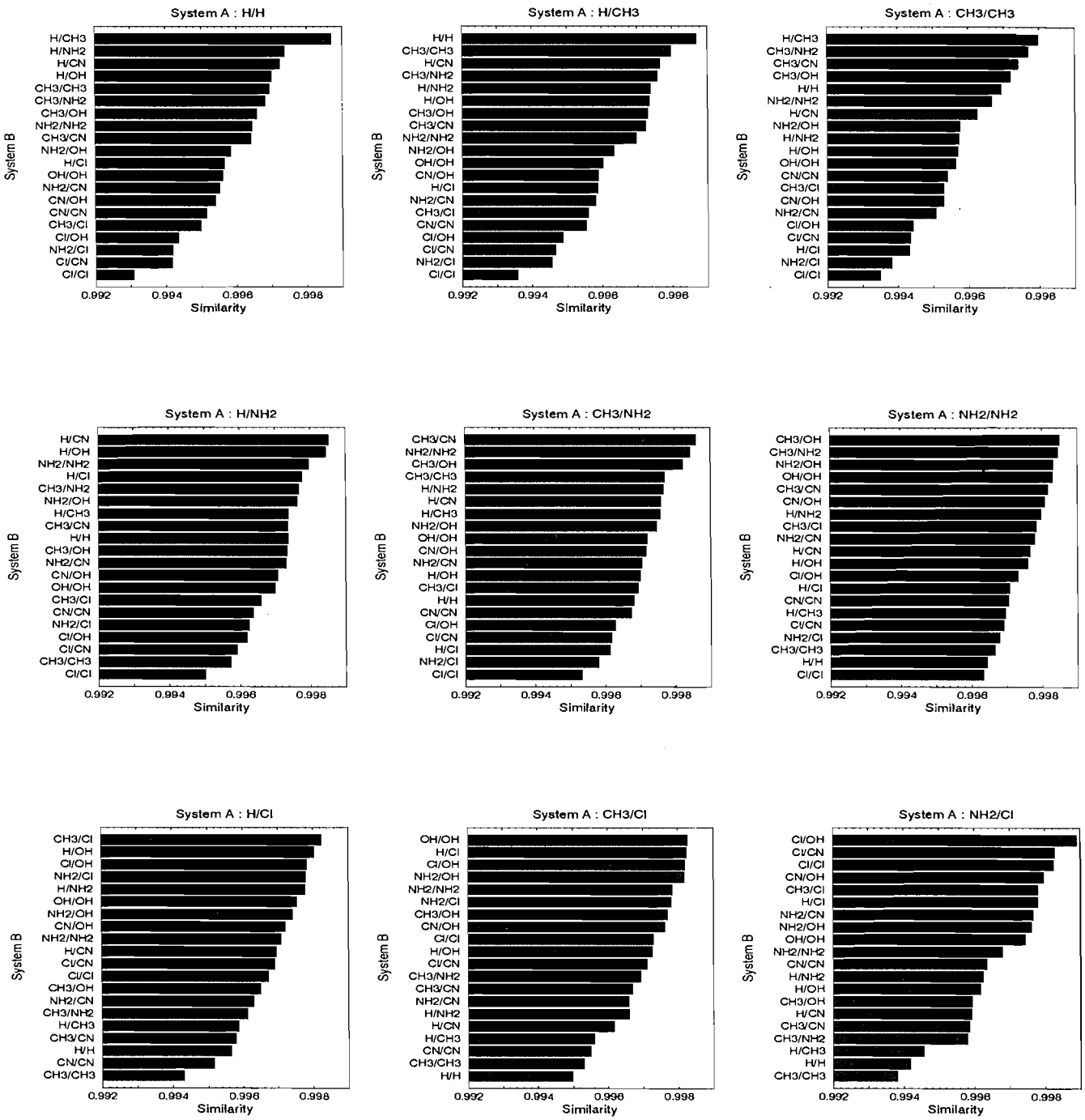

part of the atomic basins Ω_A and Ω_B. Such a similarity measure satisfies the inequality

$$[7] \qquad 0 < S_{A(X),B(Y)} \leq 1$$

with the RHS equality attained only for A and B possessing identical shape. The fact that $S_{A(X),B(Y)}$ measures similarity of atomic shapes (rather than similarity of electron densities within atomic basins) is clearly demonstrated by its invariance with respect to linear scaling of $\rho(\boldsymbol{r})$.

It has been shown that the similarities $S_{A(X),B(Y)}$ of formally identical atoms connected to different first neighbors can be as low as 0.6 (15). On the other hand, similarities in excess of 0.99 are often found for pairs of atoms with identical first but different second neighbors. Although the oxygens of the present study represent the latter case, the second-neighbor effects are clearly discernible in the computed values of similarity measure thanks to the excellent numerical accuracy of our calculations.

Inspection of Fig. 1 reveals the lack of sensitivity of the atomic shapes to electronic effects due to substituents on the carbonyl carbon. In other words, these shapes are almost en-

Fig. 1 (*continued*).

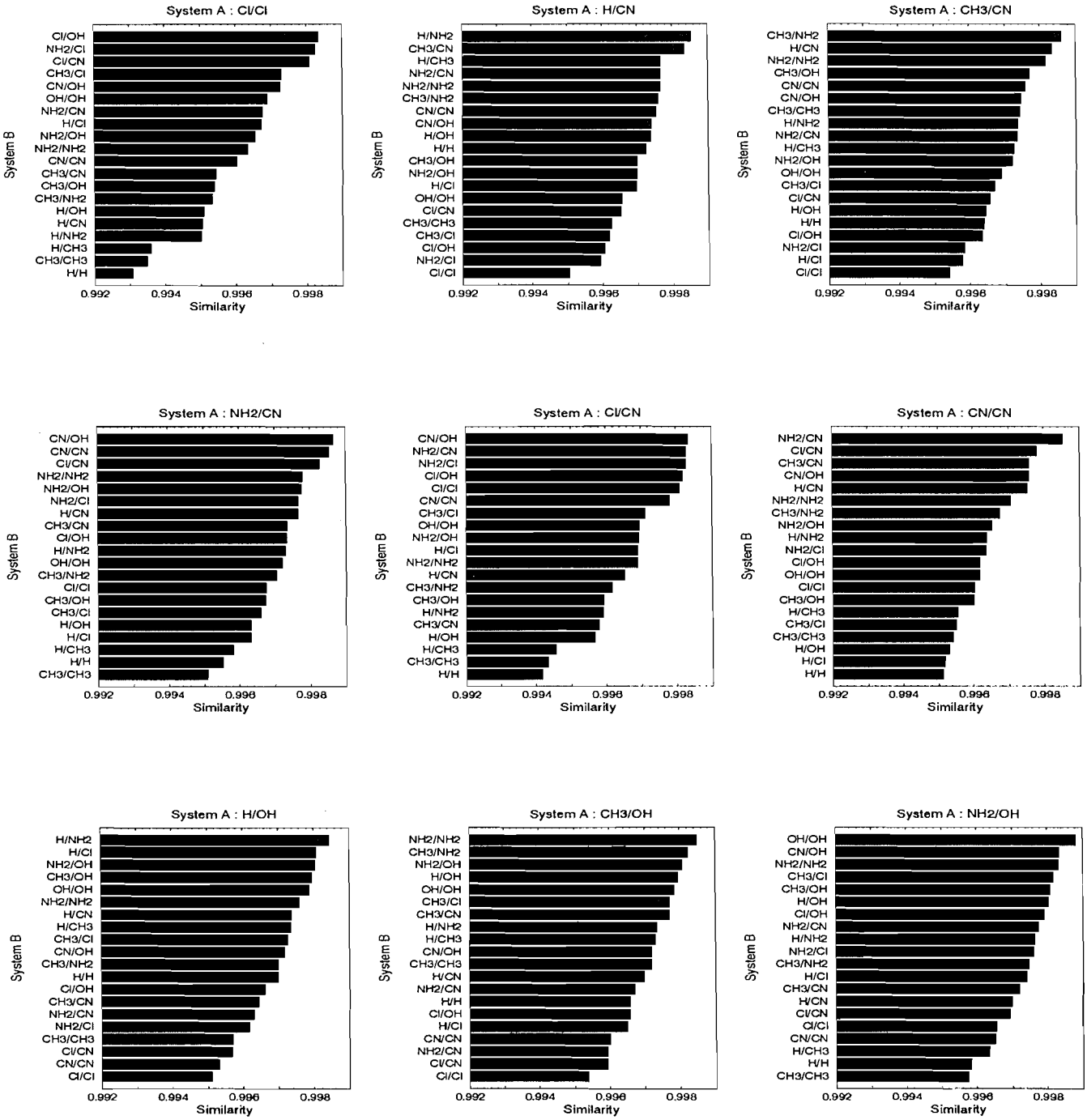

tirely determined by steric effects. This phenomenon is well illustrated by the fact that the magnitudes of $S_{A(X),B(Y)}$ are almost identical for the HCHO vs. NH_2CONH_2 and HCHO vs. CH_3COCN pairs (Fig. 1) despite the presence of two electron-donating groups in NH_2CONH_2 and the combination of one weakly donating and one strongly withdrawing group in CH_3COCN. Consequently, in all cases displayed in Fig. 1, the most similar oxygens are found in systems with substituents of comparable sizes (see HCOCN vs. $HCONH_2$, OHCOOH vs. NH_2COOH, ClCOOH vs. NH_2COCl, etc.)

The aforedescribed trends are also observed in the similarity graph (Fig. 2), in which the relation X ← Y denotes the fact that, from among all systems under study other than X itself, Y possesses the carbonyl oxygen most similar to that in X. In the present case, the similarity graph consists of seven disjoint subgraphs. The compatibility of substituents within each of the three classes, namely "small" (H and CH3), "mid-size" (NH_2, CN, and OH), and "large" (Cl), is evident. Visual inspection of the computed zero-flux surfaces leads to the same conclusion. Therefore, one can unequivocally state

Fig. 1 (*concluded*).

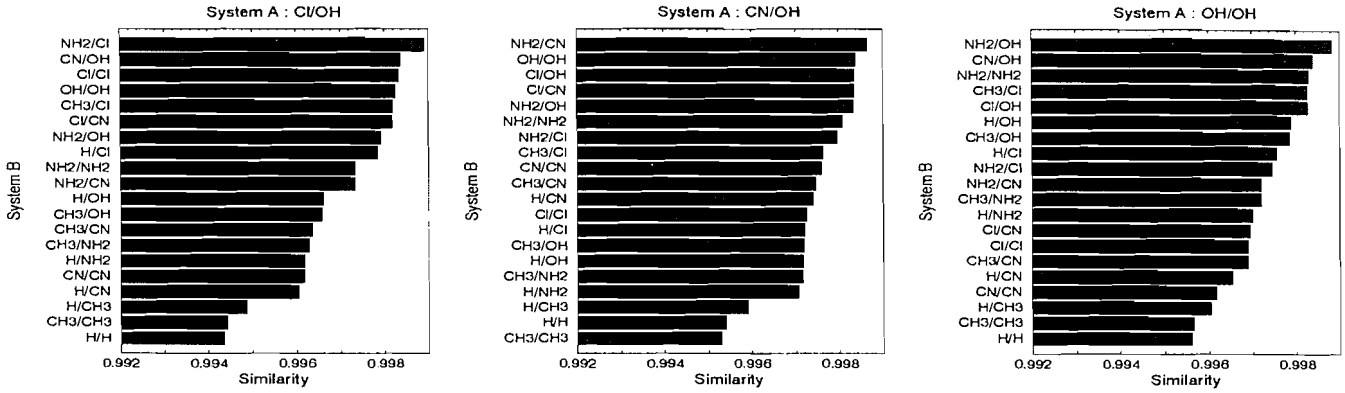

Fig. 2. Relations of maximal similarity between the carbonyl oxygen atoms in the molecules under study. See the text for an explanation of the notation X ← Y.

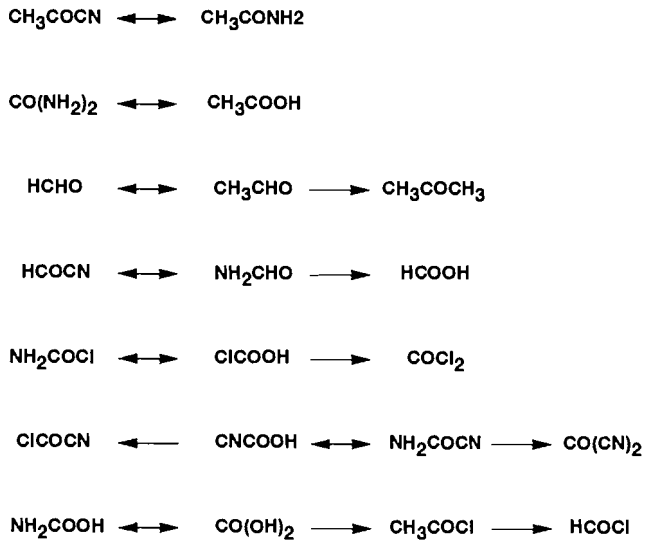

that the shapes of oxygen atoms in carbonyl compounds are determined almost exclusively by the combined bulkiness of their second neighbors, the bulkiness of a given substituent being determined by the magnitude and the spatial extent of its electron density.

Charges, kinetic energies, and dipole moments of the carbonyl oxygens

The calculated charges Q of oxygen atoms span the broad range of -1.18 – -0.94 (Table 1), in agreement with the large variation in Q that has been found in a recent study on carbonyl compounds (17). The electronic effects of the substituents on Q are conspicuous. Compared to hydrogen, OH, NH_2, and, to a lesser extent, CH_3 are electron donating to the oxygen, Cl has almost no effect on the oxygen charge, and CN is strongly electron withdrawing. These trends are in agreement with the commonly accepted signs and magnitudes of the inductive effects elicited by these substituents. The energies of the carbonyl oxygens (equal to the negative kinetic energies T, Table 1) are also markedly influenced by the electronic properties of the substituents. In general, the oxygen atom is destabilized by electron withdrawal. However, the correlation between T and Q is quite poor (Fig. 3).

Fig. 3. The kinetic energy T vs. the charge Q of the carbonyl oxygens in the molecules under study.

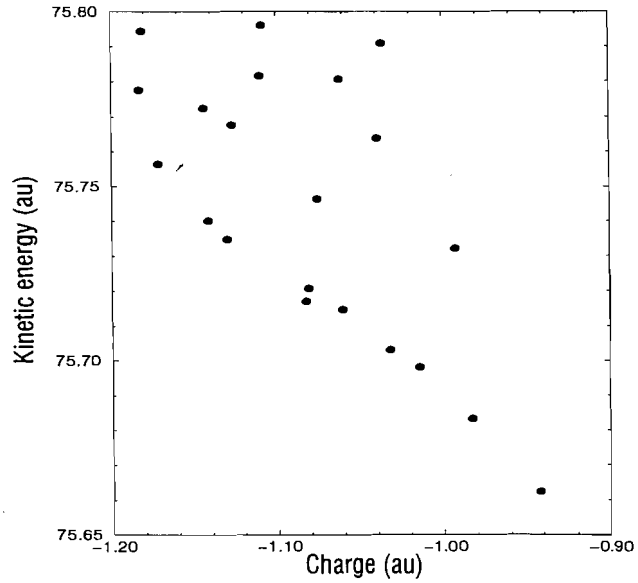

The formation of the carbonyl group is accompanied by a longitudinal polarization of the oxygen atom that lifts its spherical symmetry. The resulting atomic dipole moment is dominated by the component μ_z parallel to the CO bond. This component varies by as much as 20% in the series of molecules under study (Table 1). Inspection of Figure 4 reveals the absence of any correlation between the atomic charge and μ_z.

Although the charges and kinetic energies of the oxygen atoms in the R_1COR_2 systems fall between those of the oxygens in R_1COR_1 and R_2COR_2 in almost all instances (the only exceptions being the cases of R_1 = H or OH and R_2 = Cl), they often deviate significantly from the arithmetic averages of the properties pertinent to the symmetrically substituted compounds (Fig. 5). The slopes of the T vs. Q plots for the individual R_1COR_2, R_1COR_1, R_2COR_2 triads are highly variable. In other words, the effects of the second neighbors on the properties of the carbonyl oxygen atom are approximately additive, but the individual contributions of the substituents to Q and T appear to be totally uncorrelated.

Table 1. The calculated MP2/6-311G** properties of the carbonyl oxygen atoms in R_1COR_2 molecules ($S_{ij,kl}$ is a shorthand for $S_{O(R_iCOR_j),O(R_kCOR_l)}$).

R_1	R_2	$S_{11,12}$	$S_{12,22}$	$S_{11,22}$	Q	T	μ_z
H	H	1.0000	1.0000	1.0000	−1.0324	75.7031	−0.4929
H	CH_3	0.9987	0.9980	0.9969	−1.0608	75.7146	−0.4834
CH_3	CH_3	1.0000	1.0000	1.0000	−1.0813	75.7206	−0.4662
H	NH_2	0.9974	0.9980	0.9964	−1.1303	75.7348	−0.4629
CH_3	NH_2	0.9977	0.9984	0.9967	−1.1418	75.7401	−0.4510
NH_2	NH_2	1.0000	1.0000	1.0000	−1.1720	75.7564	−0.4530
H	Cl	0.9957	0.9967	0.9931	−1.0398	75.7639	−0.5559
CH_3	Cl	0.9953	0.9973	0.9935	−1.0624	75.7806	−0.5530
NH_2	Cl	0.9968	0.9982	0.9963	−1.1106	75.7816	−0.5151
Cl	Cl	1.0000	1.0000	1.0000	−1.0367	75.7909	−0.5594
H	CN	0.9972	0.9975	0.9951	−0.9833	75.6833	−0.4882
CH_3	CN	0.9974	0.9976	0.9954	−1.0147	75.6982	−0.4826
NH_2	CN	0.9978	0.9986	0.9971	−1.0827	75.7170	−0.4627
Cl	CN	0.9981	0.9978	0.9960	−0.9930	75.7321	−0.5259
CN	CN	1.0000	1.0000	1.0000	−0.9423	75.6623	−0.4810
H	OH	0.9970	0.9979	0.9956	−1.1271	75.7675	−0.5081
CH_3	OH	0.9972	0.9979	0.9957	−1.1444	75.7723	−0.4903
NH_2	OH	0.9983	0.9988	0.9983	−1.1834	75.7776	−0.4717
Cl	OH	0.9983	0.9983	0.9969	−1.1092	75.7960	−0.5293
CN	OH	0.9976	0.9984	0.9962	−1.0758	75.7465	−0.5024
OH	OH	1.0000	1.0000	1.0000	−1.1815	75.7943	−0.4888

Fig. 4. The longitudinal component μ_z of the dipole moment vs. the charge Q of the carbonyl oxygens in the molecules under study.

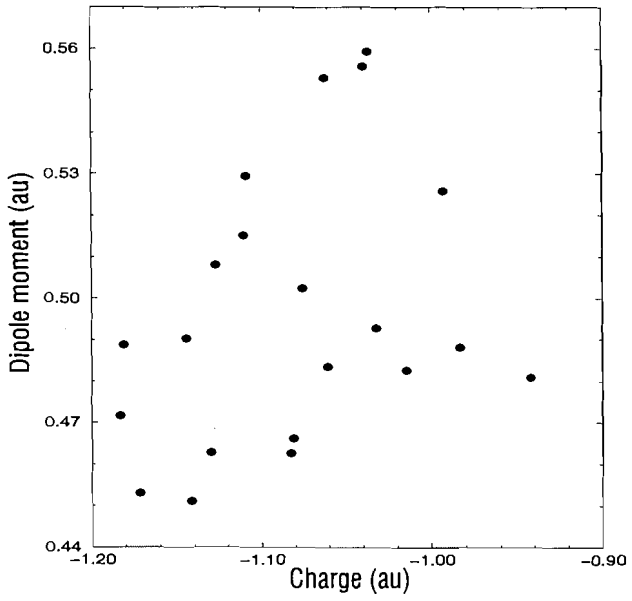

Conclusions

The main conclusion of the present study is that the factors that influence shapes of atoms in molecules are distinct from those that determine their electronic properties. The shapes of atoms in molecules (as quantified by the atomic similarity measure) are affected predominantly by the sizes of their neighbors. The electronic properties of the second neighbors, such as their propensity toward electron donation or withdrawal, appear to be irrelevant in this case. Conversely, charges of atoms in molecules correlate well with the ability of the second neighbors to withdraw or donate electrons.

Several of the trends observed for the carbonyl oxygen are expected to carry over to other atoms. In general, atoms with more negative charges tend to possess lower energies, but the correlation is rather poor. *There is no correlation whatsoever between the shapes and the electronic properties of atoms in molecules.* Although the influences of the second neighbors on the electronic properties of a given type of atom are approximately additive, the additivity is far from being quantitative. There appears to be no correlation between the individual contributions of the second neighbors to the atomic charge and the respective contributions to the atomic kinetic energy.

Our study unequivocally demonstrates that any approach to the calculation of electronic properties of molecules that is based solely on docking of atoms or molecular fragments followed by the adjustment of their zero-flux surfaces is bound to fail. This is so because the knowledge of these surfaces alone is *insufficient* for the determination of properties of atoms (or fragments) in molecules. On the other hand, one can envision formalisms that would successfully predict electronic properties of molecules by employing approximately transferable electron densities taken from a limited number of standard types of atomic basins. However, in such approaches the atomic surfaces would be derived from the adjusted electron densities and thus would play only a secondary role. To reiterate, the electron densities within atomic basins unambiguously determine the shapes of atoms in molecules. The converse is not true from both theoretical and practical standpoints.

Fig. 5. The kinetic energy T vs. the charge Q of the carbonyl oxygens in the triads R_1COR_1 (●), R_2COR_2, (●), and R_1COR_2 (○). See Fig. 1 for the notation used for the individual systems. The points corresponding to the arithmetic average of the properties of the symmetric species are denoted by asterisks.

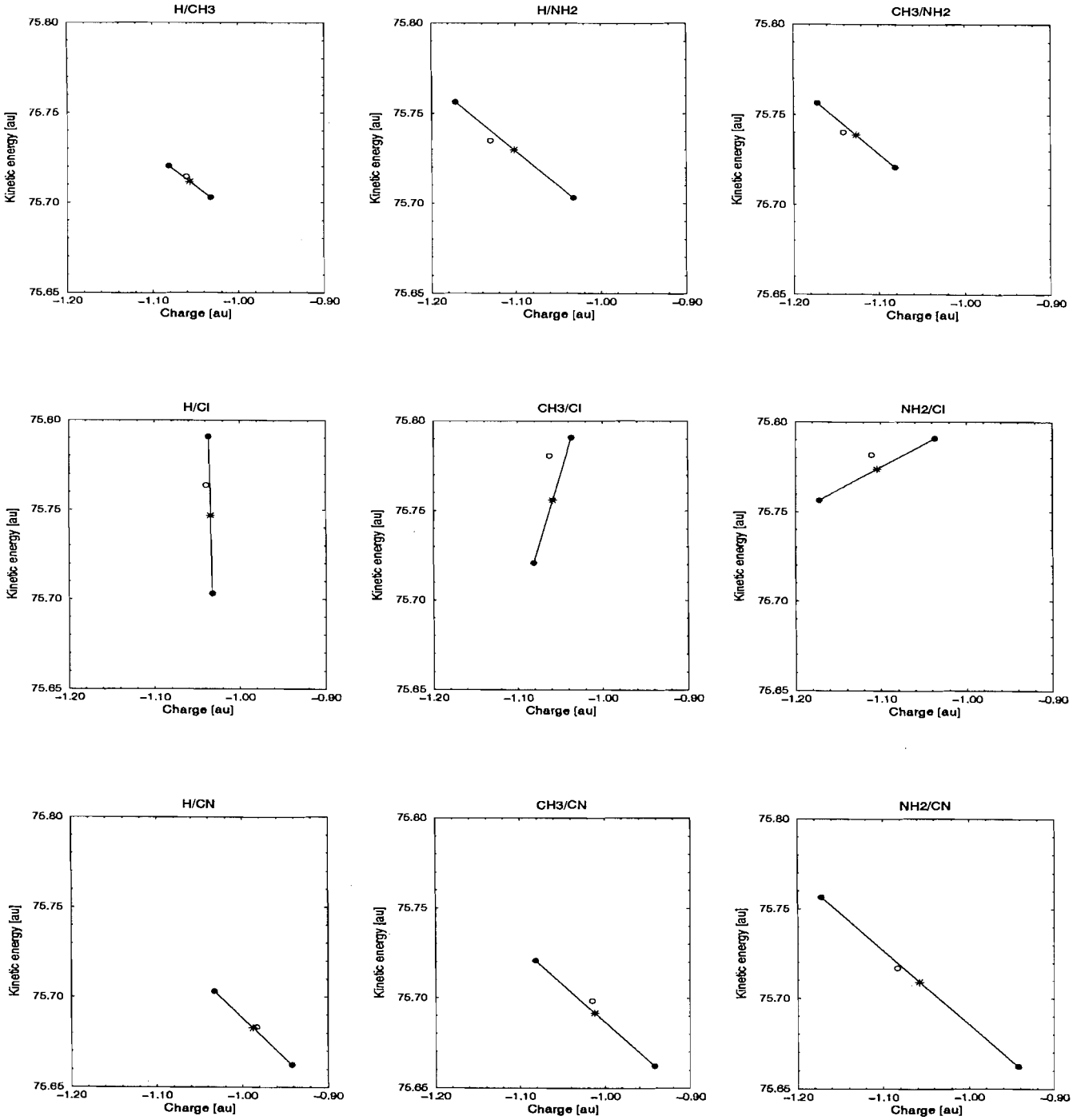

Fig. 5 (*concluded*).

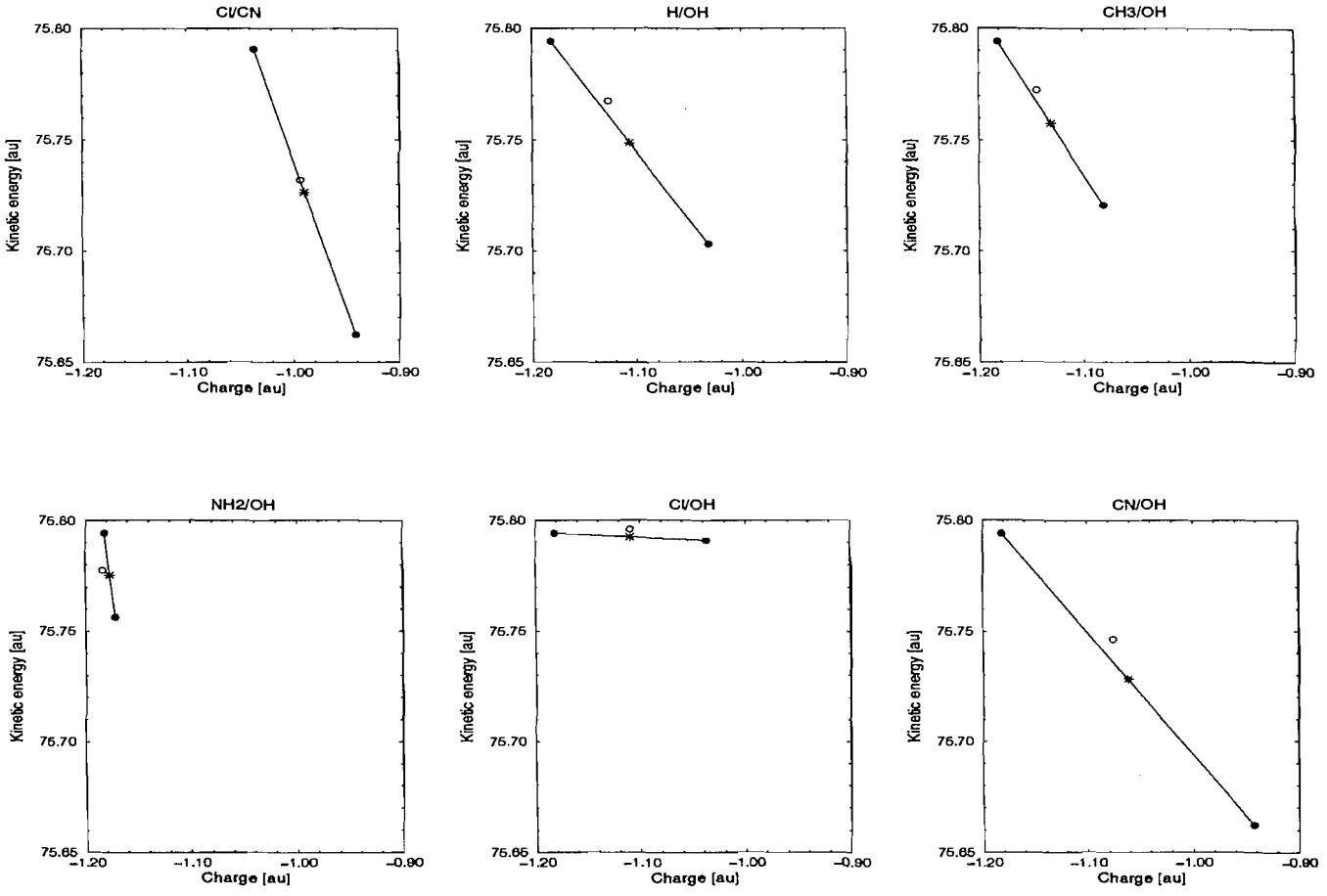

Acknowledgments

This work was partially supported by the National Science Foundation under grant CHE-9224806, by Gaussian Inc. under a software development contract, and by the US DOE through its Supercomputer Computations Research Institute. This research was also sponsored in part by the Phillips Laboratory, Air Force Materiel Command, USAF, under cooperative agreement number F29601-93-0001. The views and conclusions contained in this document are those of the authors and should not be interpreted as necessarily representing the official policies or endorsements, either expressed or implied, of Phillips Laboratory or the US Government.

References

1. R.W.F. Bader. Atoms in molecules: a quantum theory. Clarendon Press, Oxford. 1990.
2. F.W. Biegler-König, R.F.W. Bader, and T.-H. Tang. J. Comput. Chem. **3**, 317 (1992).
3. J. Cioslowski and S.T. Mixon. J. Am. Chem. Soc. **113**, 4142 (1991).
4. J. Cioslowski and S.T. Mixon. J. Am. Chem. Soc. **115**, 1084 (1993).
5. J. Cioslowski and S.T. Mixon. J. Am. Chem. Soc. **114**, 4382 (1992).
6. C. Gatti, P. Fantucci, and G. Pacchioni. Theor. Chim. Acta, **72**, 433 (1987); W.L. Cao, C. Gatti, P.J. MacDougall, and R.W.F. Bader. Chem. Phys. Lett. **141**, 380 (1987); J. Cioslowski. J. Phys. Chem. **94**, 5497 (1990).
7. R.W.F. Bader, A. Larouche, C. Gatti, M.T. Carroll, P.J. MacDougall, and K.B. Wiberg. J. Chem. Phys. **87**, 1142 (1987).
8. R.W.F. Bader, M.T. Carroll, J.R. Cheeseman, and C. Chang. J. Am. Chem. Soc. **109**, 7968 (1987).
9. R.W.F. Bader. Can. J. Chem. **64**, 1036 (1986).
10. R.W.F. Bader, T.A. Keith, K.M. Gough, and K.E. Laidig. Mol. Phys. **75**, 1167 (1992).
11. R.W.F. Bader and T.A. Keith. J. Chem. Phys. **99**, 3693 (1993).
12. C. Chang and R.W.F. Bader. J. Phys. Chem. **96**, 1654 (1992).
13. M.J. Frisch, G.W. Trucks, M. Head-Gordon, P.M.W. Gill, M.W. Wong, J.B. Foresman, B.G. Johnson, H.B. Schlegel, M.A. Robb, E.S. Replogle, R. Gomperts, J.L. Andres, K. Raghavachari, J.S. Binkley, C. Gonzalez, R.L. Martin, D.J. Fox, D.J. Defrees, J. Baker, J.J.P. Stewart, and J.A. Pople. GAUSSIAN 92, Revision B. Gaussian, Inc., Pittsburgh, Pa. 1992.
14. J. Cioslowski and B.B. Stefanov. Mol. Phys. **84**, 707 (1995); B.B. Stefanov and J. Cioslowski. J. Comput. Chem. **16**; 1394 (1995).
15. J. Cioslowski and A. Nanayakkara. J. Am. Chem. Soc. **115**, 11213 (1993).
16. J. Cioslowski, B.B. Stefanov, and P. Constans. J. Comput. Chem. In press.
17. R.E. Rosenberg. J. Am. Chem. Soc. **117**, 10358 (1995).

Charge and energy redistribution in sulfonamides undergoing conformational changes. Hybridization as a controlling influence over conformer stability

Curt M. Breneman and Lawrence W. Weber

Abstract: The redistribution of charge and electronic kinetic energy was studied during rotation about the S—N bonds of sulfonamide and fluorosulfonamide. The rotational potentials and electronic topological features of both compounds were evaluated at the HF/6-31G* level of theory and their electron densities partitioned into atomic contributions using FASTINT, an updated version of the PROAIM program. The results indicate that the stability of each rotamer is strongly dependent upon the hybridization of the sulfonamide nitrogen. The hybridization of the nitrogen was determined by examination of the positions and magnitudes of the electrostatic and Laplacian minima in the nonbonded region of the sulfonamide nitrogen atom. Independent assessments of hybridization were made using nitrogen pyramidalization altitudes. The rotational barriers in these compounds were found to arise mainly from energetic penalties resulting from adding electrons to already electron-rich sulfonyl oxygens while removing electron density from other more electronegative atoms. The fluorine-substituted analogue provided an example in which the sulfur and oxygen atoms were much less electron rich, causing an enhancement of the nitrogen rehybridization effects. The extent of covalent bonding between pertinent pairs of atoms in sulfonamide and fluorosulfonamide was assessed throughout the rotational pathway using the BONDER program. In contrast with much existing dogma, all of these findings were consistent with the same general model of charge and energy flow that has been shown to determine the internal rotational barriers in amides.

Key words: sulfonamide, electron density analysis, rotational barrier, hybridization, atoms-in-molecules calculations.

Résumé : On a examiné la redistribution de charge et d'énergie cinétique électronique accompagnant les rotations autour de liaisons S—N des sulfonamide et fluorosulfonamide. On a évalué les potentiels rotationnels et les caractéristiques topologiques électroniques des deux composés au niveau HF/6-31G* de la théorie et on a effectué une répartition des densités électroniques en contributions atomiques, en utilisant FASTINT, une version améliorée du programme PROAIM. Les résultats indiquent que la stabilité de chaque rotamère dépend beaucoup de l'hybridation de l'azote du sulfonamide. L'hybridation de l'azote a été déterminée par l'examen des positions et des amplitudes des minima électrostatiques et des laplaciens dans la région non liée de l'atome d'azote du sulfonamide. Des évaluations indépendantes de l'hybridation ont été faites en faisant appel aux altitudes de la pyramidalisation de l'azote. On a trouvé que les barrières rotationnelles de ces composés proviennent principalement des pénalités énergétiques qui résultent d'additions d'électrons aux atomes d'oxygènes du sulfonyle déjà riche en électrons accompagnées d'une diminution de la densité électronique d'autres atomes plus électronégatifs. L'analogue portant un atome de fluor est un exemple dans lequel les atomes de soufre et d'oxygène sont beaucoup moins riches en électrons; ceci provoque une augmentation des effets de réhybridation de l'azote. Le degré de liaison covalente entre les paires appropriées d'atomes du sulfonamide et du fluorosulfonamide a été évalué sur l'ensemble de la voie réactionnelle en faisant appel au programme BONDER. Malgré tous les dogmes existants, toutes ces observations sont en accord avec le modèle général d'écoulement de la charge et de l'énergie qui prévaut dans la détermination des barrières rotationnelles internes dans les amides.

Mots clés : sulfonamide, analyse de la densité électronique, barrière rotationnelle, hybridation, calculs d'atomes dans les molécules.

[Traduit par la rédaction]

Received November 1, 1995.

This paper is dedicated to Professor Richard F.W. Bader on the occasion of his 65th birthday.

C.M. Breneman[1] **and L.W. Weber.** Department of Chemistry, Cogswell Laboratory, Rensselaer Polytechnic Institute, Troy, NY 12180, U.S.A.

[1] Author to whom correspondence may be addressed. Telephone: (518) 276-2678. Fax: (518) 276-4045.
E-mail: breneman@xray.chem.rpi.edu

Until the advent of the Atoms in Molecules (AIM) electron density partitioning technique (1), it had been difficult to identify and separate the underlying factors responsible for the relative stabilities of different molecular conformations. Most current models of molecular stability are based either upon stereoelectronic factors, as in the anomeric effect, or on a mixture of steric effects, field effects, inductive effects, and "resonance" effects. Work in our laboratory and those of others has shown that it is often more useful to observe changes in the ab initio molecular electron density distributions of molecules undergoing conformational changes. The results of such electron density analyses have even more predictive power when the torsionally induced electron density flow is examined on an atom by atom basis. The interatomic kinetic energy density flow that governs the conformational preferences of amides has been elucidated in this manner (2). Since it is often difficult and sometimes impossible to get good experimental electron density distribution data for a desired set of molecular conformations, such data are often obtained through HF/6-31G* ab initio calculations. Direct analysis of intramolecular molecular electron density flow is one technique in which it matters little whether the electron density information came from high-quality X-ray results[2] or from good ab initio quantum mechanical calculations. This progress is indicative of the large changes that have taken place in the field of molecular modeling in the past few years. Until recently, molecular orbital models were mostly used to formulate qualitative interpretations of experimental results, and often found their greatest uses as conceptual tools (4). The current computational environment has made it possible to determine ab initio accurate electron densities for medium-sized molecules in a reasonable amount of time. This flexibility has allowed chemists to make the necessary improvements to go beyond the orbital picture, providing in many cases reliable and comprehensive chemical information independent of experiment.

One application in which modern theoretical methods excel is that of reexamining unusual bonding situations. One such bond type that has received a considerable amount of recent attention is that of hypervalent bonding in oxidized sulfur-containing compounds (5). As a result of this interest, several groups have attempted to probe the phenomenon of hypervalent bonding and its sensitivity to structural perturbations. One fundamental question that was addressed by Reed and Schleyer (5) concerns whether *d*-orbital participation involves dsp^3 or d^2sp^3 hybridization, or if "negative hyperconjugation" is a better description of the bonding situation. From the results of that work, Schleyer was able to conclude that the "negative hyperconjugation" model provided the superior description of hypervalent bonding. An even more satisfying explanation is available through the use of AIM charge and energy flow analysis. The basis of this model of stability is that charge will flow from one atomic basin and into another in response to geometric changes that provide a means for rehybridization of the atoms involved and an energetic motivation for such charge flow. This means that in any conformation, atomic electron populations and their associated kinetic energies shift from one atom to another in such a way that the energy of the whole molecule is lowered. This is actually restatement of the Variational Principle, but it is usually not applied with respect to individual atoms in molecules. In the case of a simple amide, alignment of the nitrogen "lone pair" region with the carbonyl π-system allows a small amount of high-energy electron density to be passed from the nitrogen to the carbonyl group; this shift of <0.1 electron is enough to lower the electron repulsion within the nitrogen lone pair sufficiently to allow sp^2 rehybridization to take place. The consequent nitrogen hybridization causes a much larger electron withdrawal through the C—N σ-bond. For this reason, the amide nitrogen has a greater electron population (and integrated electronic kinetic energy) in the planar conformation than in either of the rotational transition states. The electron density gained by the nitrogen originates principally from the carbonyl carbon. In that investigation, it was determined that the electron density transferred to the nitrogen resulted in a 150 kcal/mol stabilization of that atom at the cost of 132 kcal/mol of destabilization of the rest of the molecule, 120 kcal of which came at the expense of the carbonyl carbon. The difference between 150 and 132 (18 kcal/mol) corresponds to the rotational barrier of formamide. Within the AIM paradigm, atomic volume definition is unique and discrete boundaries can be identified between atoms. When this interatomic surface moves in response to changes in the charge density distribution of the molecule, individual atomic populations and energies change (2). This accounts for the fact that while the charge distributions implied by examining the various canonical forms from resonance theory have come under serious scrutiny (6), many predictions made using that model are still sound. Indeed, if only electrostatic potential-derived monopoles are considered to represent "atomic charges," the resonance model for charge distributions generally holds true. This so-called external view of a molecular charge distribution (2) remains a beneficial educational tool that is still useful for describing qualitative effects. To get a full description of the electron density and electronic kinetic energy distribution throughout a molecule, however, an electronic topological approach such as Bader's Theory of Atoms in Molecules (7) must be applied.

Methods

SCF (8) calculations were performed either on a Vaxcluster running an early VMS version of the GAUSSIAN-90 (9) package or on a SUN 4/330 workstation running a later UNIX version of GAUSSIAN-90 (10). Numerical integrations were performed on either the SUN 4/330 workstation or an IBM RS/6000 320h workstation. In this work, a set of rotationally constrained structures were optimized by the Berny method at the HF/6-31G* (11) level of theory.[3] Checkpoint files generated by GAUSSIAN-90 were then used by the psichk90[4] program to obtain wave function files compatible with PROAIM and FASTINT.

The PROAIM program developed by Bader and co-workers (7) formed the basis for our locally developed code FASTINT.[5] The FASTINT program has more realistic distance and integral

[2] Experimental electron densities can be observed by low-temperature wide-angle scattering X-ray analysis, a rather tedious procedure; also, for an electron diffraction investigation, see ref. 3.

[3] The choice of contracted Gaussian basis sets for molecular calculations has been reviewed by Ahlrichs and Taylor (12).

[4] T. Lepage. Yale University, 1988. Unpublished.

[5] C.M. Breneman and M. Rhem. FASTINT. 1992.

cutoffs than the original PROAIM program and calculates fewer properties, but this combination of modifications allows the calculation of numerous atomic properties of the electron density within atomic basins up to 40 times faster than the original PROAIM code. Since both PROAIM and FASTINT utilize the same basic theory, which has been extensively treated in the literature, only an overview of the method is presented here.

It is important to emphasize that the key to molecular partitioning lies in the requirement that the resulting atomic pieces be valid quantum subsystems. A valid quantum subsystem is defined as a fragment of a larger system that behaves as a separate entity, and gives unique values for all of the operators associated with the larger system. In an atomic quantum subsystem, these values would be quantities like electronic kinetic energy, electron population, electric multipole moments, and electrostatic potentials. Quantum subsystems are said to be valid if the electron density within each separate atomic volume independently obeys the Virial Theorem ($-V/T = 2$, where V is potential energy and T is kinetic energy). For this condition to be met, the atomic fragments must be bound by surfaces of zero net flux in electron density (ρ), and contain an attractor (a nucleus). In the general sense, a zero-flux surface defines a region of space where the net flux of electron density normal to the surface is zero. A more practical definition states that the flux of electron density normal to such a surface is zero at all points on that surface. This can be summarized by the expression $\nabla\rho \cdot N = 0$, where N is the surface normal vector.

Determination of an atomic zero-flux surface begins with mapping the electronic topology of the molecule. Electronic topology mapping involves finding all of the stationary (critical) points in ρ, and identifying them according to their signatures. A critical point[6] signature is defined as the number of negative curvatures minus the number of positive curvatures in ρ at that stationary point. For generality, a prefix of "3" designates the dimensionality of the problem. Consequently, atomic nuclei are (3, 3) critical points, bond critical points have (3, −1) signatures, ring critical points have (3,1) signatures, and cage critical points have (3,−3) signatures. With the exception of (3,3) nuclear critical points, all of the other critical points exist on interatomic zero-flux surfaces. Interatomic surface definition routines make use of the fact that (3,−1) (bond) critical points represent local maxima of electron density on each interatomic surface. Consequently, all points on the path followed by a steepest descent walk originating in any direction perpendicular to the bond path are on an interatomic zero-flux surface. Both Bader's original PROAIM program (7) and our later FASTINT program[5] make use of this kind of surface definition. Once defined, the zero-flux surfaces provide boundaries for integration of the electron density properties of each separate atom within a molecule.

After partitioning of a particular molecular electron density distribution has taken place, the atomic overlap matrices for each atom could be used to calculate covalent bond orders using the recently introduced BONDER (13) program. Calculation of these covalent bond orders involves the following steps:

1. Evaluation of the atomic overlap matrices

$$[1] \quad \langle\phi_i|\phi_j\rangle_A = \int_{\xi_A} \phi_i^*(\boldsymbol{r})\phi_j(\boldsymbol{r})\, d\boldsymbol{r}, \qquad 1 \le i,j \le N$$

where $\{\phi_i,\ 1 \le i \le N\}$ are the occupied Hartree–Fock spin-orbitals, N is the number of electrons, and ξ_A is the atomic basin of the atom A.

2. Determination of localized spin-orbitals, $\{\phi_i,\ 1 \le i \le N\}$, which are related to the Hartree–Fock spin-orbitals through a unitary transformation C.

$$[2] \quad \varphi_i = \sum_{j=1}^{N} C_{ij}\phi_j, \qquad 1 \le i \le N$$

and maximization of the localization sum, eq. [3]

$$[3] \quad L = \sum_{i=1}^{N}\sum_{A} \langle\varphi_i|\varphi_i\rangle_A^2$$

3. Calculation of the covalent bond orders, eq. [4]

$$[4] \quad P_{AB} = 2\sum_{i=1}^{N} \langle\varphi_i|\varphi_i\rangle_A\langle\varphi_i|\varphi_i\rangle_B$$

A combination of FASTINT and BONDER techniques can be used to give atomic populations and energies, as well as the covalent bond order between two atoms. Taken together with the values of ρ, $\nabla^2\rho$, and electrostatic potentials in crucial regions of space, we are able to arrive at a set of conclusions concerning the factors that control rotational preferences in conformationally flexible molecules.

Results and discussion

Exhaustive examination of the electron density distributions around the sulfur and amino groups of sulfonamide and fluorosulfonamide were performed at 10° increments of rotation about each S—N bond, as defined by the H6-N5-S2-H1(F1) dihedral angle as well as at each minimum and at both nitrogen inversion and N-H rotational transition states.

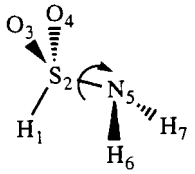

Sulfonamide

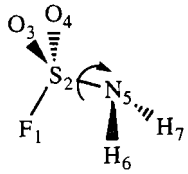

Fluorosulfonamide

The results show that the mechanism of conformer stabilization in sulfonamides is very similar to that reported earlier for amides (6), in which stabilization of the amide nitrogen was found to occur through σ withdrawal of electron density from an adjacent polarized atom. In the case of an amide, this atom is the carbonyl carbon. Such a result is not without controversy, however. Catalan and co-workers (14) reported that there is no similarity between amide and sulfonamide bonding. Catalan has also stated that the hybridization of the amino nitrogen in sulfonamide should have very little effect on the total energy of the sulfonamide system. In an effort to address

[6] As defined by the two negative curvatures and the single positive curvature, which is aligned along the bond path.

Fig. 1. Sulfonamide rotational potential vs. torsional angle.

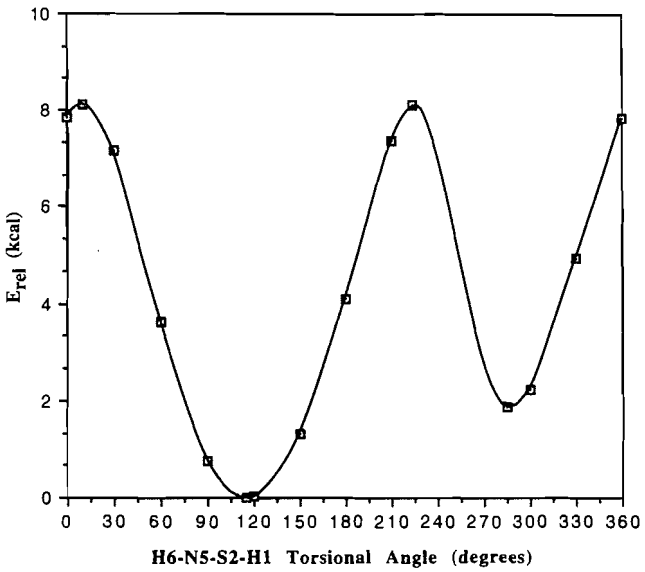

Fig. 2. Fluorosulfonamide rotational potential vs. torsional angle.

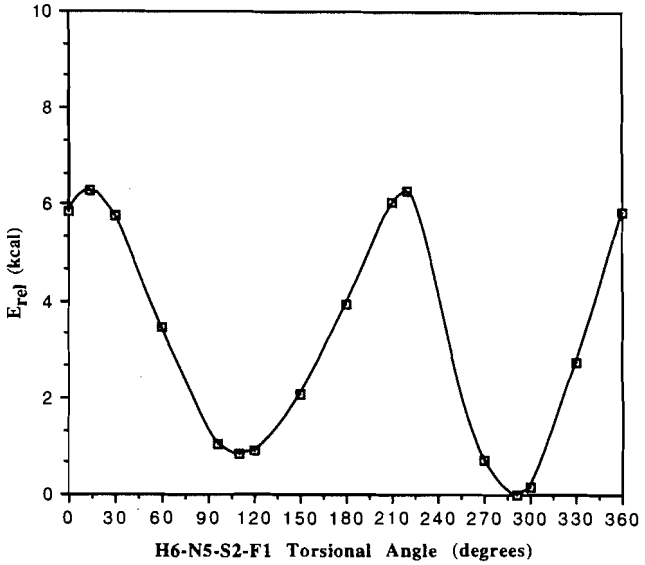

these points, ab initio calculations and electron density distribution analyses (2) were performed on both sulfonamide and fluorosulfonamide. The introduction of fluorine into the system allowed us to alter the normal electron populations of the sulfur and oxygens and to observe the effects on each atom during sulfur–nitrogen bond rotation. Prior to evaluating the interatomic charge flow data, the relative energies of each conformer were examined and the geometric stationary points were characterized. The rotational potentials shown in Figs. 1 and 2 were found to be quite similar in shape for sulfonamide and fluorosulfonamide. The important difference between the two curves is that the geometries at which the molecules reach their global and relative minima are reversed. The relative minimum of sulfonamide occurs at an H-N-S-H dihedral angle 285° while the global minimum occurs at 115°. In fluorosulfonamide, the relative minimum occurs at the corresponding H-N-S-F dihedral of 110° while the global minimum occurs at 291°. This means that sulfonamide is most stable when its

Fig. 3. Sulfonamide relative population by atom vs. torsional angle.

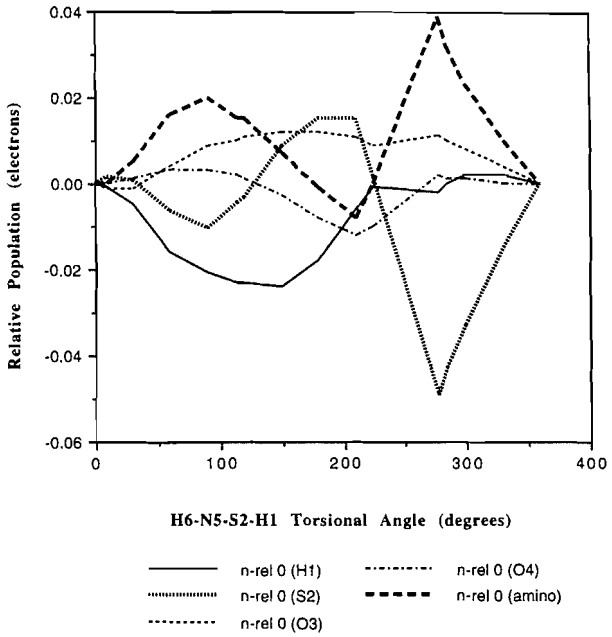

Fig. 4. Fluorosulfonamide relative population by atom vs. torsional angle.

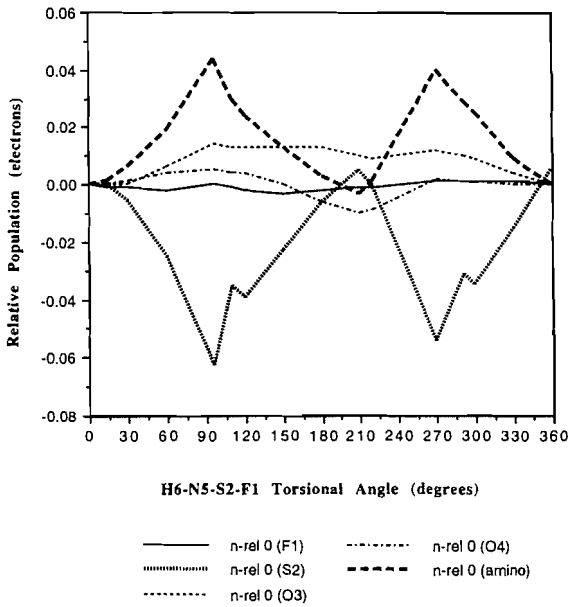

nitrogen lone pair is *syn* to the sulfur–hydrogen bond. The substitution of a fluorine atom for the hydrogen in fluorosulfonamide causes the global and relative minima to reverse in energy ordering. In this case, the molecule is most stable when the nitrogen lone pair is *trans* to the sulfur–fluorine bond. It is also important to note that the minima in both sulfonamide and fluorosulfonamide are very near their respective amino nitrogen inversion transition states, indicating a propensity for planarization of the nitrogen.

Upon examination of the FASTINT atomic integration results, an obvious intramolecular charge shift trend was observed. The data shown in Figs. 3 and 4 show a charge shift taking place between the sulfur and the amino group at geometries corresponding to both minima in fluorosulfonamide and the

Fig. 5. Sulfonamide relative energy by atom vs. torsional angle.

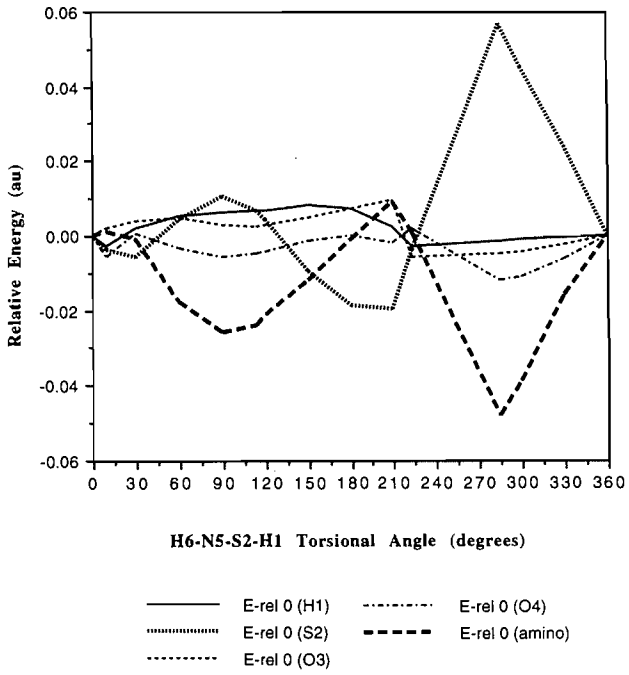

Fig. 6. Fluorosulfonamide relative energy by atom vs. torsional angle.

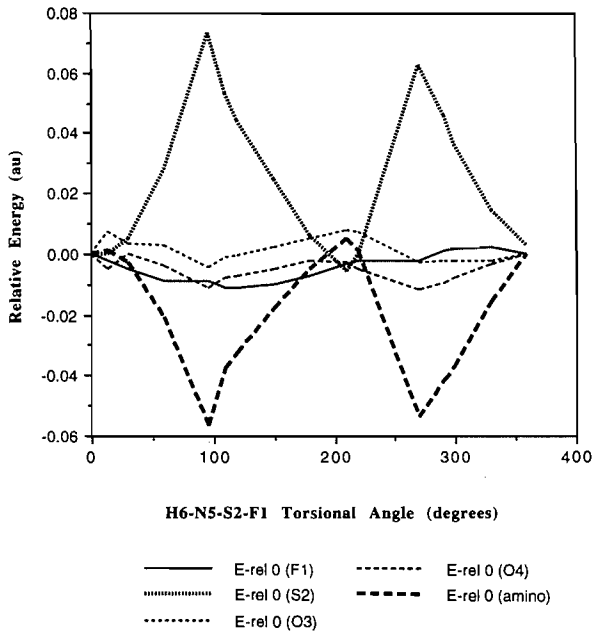

relative minimum in sulfonamide. At these geometries, the amino group is observed to gain electron population, while the sulfur population is depleted by a similar amount. The other atoms within the molecules show little change when compared to the sulfur and nitrogen. A less clear charge redistribution occurs at the conformer that corresponds to the sulfonamide global minimum conformation.

The relative energy by atom curves shown in Figs. 5 and 6 illustrates the electronic kinetic energy flow that comes about as a result of charge redistribution in Figs. 3 and 4. It is important to note that the kinetic energy flow closely follows the

Fig. 7. Sulfonamide total energy and amino group energy vs. torsional angle.

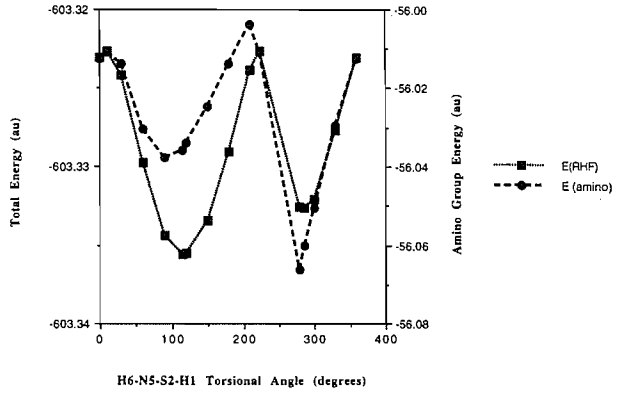

Fig. 8. Fluorosulfonamide total energy and group energy vs. torsional angle.

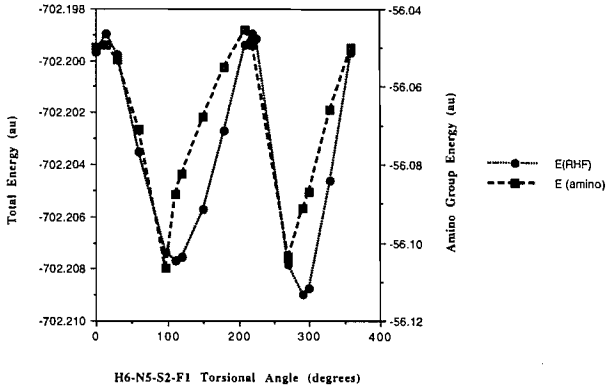

charge flow from atom to atom during S—N bond rotation. The charge and energy transfer interactions are mainly taking place between the sulfur and amino groups, with the amino group reaching a minimum in energy while the sulfur is reaching a maximum in energy. The maximum charge and energy transfer is observed near the minimum energy structures of both molecules. This is to be expected, because motion of electrons from a less electronegative atom (S) to a more electronegative atom (N) is favorable for the whole molecule as the amino group approaches planarity.

The pronounced sulfur–nitrogen interactions shown in Figs. 3–6 led us to focus our attention directly on the sulfur atoms and the amino groups. The data in Table 1 were used to directly compare the relative electronegativities of the sulfur atom and the amino group within sulfonamide and fluorosulfonamide during sulfur–nitrogen bond rotation. Since this definition of electronegativity describes how efficiently an atom or an atomic fragment stabilizes electron density, the slope of a line on an energy vs. electron population plot should give a relative electronegativity of the atom or atomic fragment. When the relative sulfur and amino group energies were analyzed with respect to their relative electron populations, the best-fit least-squares slopes showed that the amino group was 1.08 and 1.16 times more electronegative than the sulfur atom in sulfonamide and fluorosulfonamide, respectively (R^2 > 0.999 in each case). Therefore, for a given amount of electron density transferred, the amino group would gain 8–16% more stability than was lost by the sulfur.

Table 1. Charge properties.

	Torsion	Total energy	Population (e)	Population (e)	Population (e)	Population (e)	Population (e)	Population (e)
Sulfonamide								
	H6-N5-S2-H1	E_{rel} (kcal)	*n* (H1)	*n* (S2)	*n* (O3)	*n* (O4)	*n* (N5)	*n* (H6)
	0	0.00	1.018	12.382	9.503	9.512	8.493	0.558
	30	−0.70	1.013	12.382	9.502	9.513	8.495	0.558
	60	−4.23	1.002	12.375	9.507	9.515	8.522	0.551
	90	−7.09	0.997	12.371	9.512	9.515	8.546	0.538
	120	−7.83	0.995	12.379	9.514	9.513	8.539	0.529
	150	−6.53	0.994	12.391	9.515	9.509	8.505	0.535
	180	−3.75	1.000	12.397	9.515	9.504	8.468	0.547
	210	−0.47	1.012	12.397	9.514	9.500	8.460	0.546
	300	−5.65	1.020	12.349	9.511	9.513	8.533	0.541
	330	−2.92	1.020	12.367	9.507	9.512	8.504	0.556
Relative min	284.7	−5.99	1.018	12.339	9.513	9.513	8.565	0.526
Global min	114.7	−7.86	0.995	12.377	9.513	9.514	8.542	0.529
TS1	223.8	0.26	1.017	12.383	9.512	9.502	8.492	0.535
TS2	277.9	−5.97	1.016	12.332	9.514	9.514	8.589	0.518
Fluorosulfonamide								
	H6-N5-S2-F1	E_{rel} (kcal)	*n* (F1)	*n* (S2)	*n* (O3)	*n* (O4)	*n* (N5)	*n* (H6)
	0	5.86	9.783	11.661	9.491	9.500	8.511	0.527
	30	5.79	9.782	11.656	9.491	9.501	8.513	0.530
	60	3.45	9.781	11.636	9.497	9.504	8.535	0.519
	120	0.93	9.781	11.622	9.504	9.504	8.562	0.515
	150	2.07	9.780	11.638	9.504	9.500	8.523	0.533
	180	3.95	9.781	11.655	9.504	9.494	8.489	0.542
	210	6.04	9.782	11.667	9.501	9.390	8.491	0.533
	270	0.73	9.784	11.607	9.503	9.502	8.593	0.508
	300	0.18	9.784	11.627	9.500	9.501	8.541	0.523
	330	2.75	9.784	11.647	9.495	9.500	8.517	0.526
Global min	290.8	0.00	9.784	11.630	9.501	9.501	8.553	0.520
Relative min	110.4	0.83	9.782	11.626	9.504	9.504	8.574	0.510
TS1	96.2	1.05	9.783	11.599	9.505	9.505	8.612	0.498
TS2	219.7	6.31	9.782	11.662	9.500	9.491	8.511	0.524

This electronegativity difference suggests that the rotationally induced changes in the amino group and sulfur energies in sulfonamide and fluorosulfonamide should be examined in greater detail. Figures 7 and 8 show that the amino groups become more stable at those geometries where both sulfonamide and fluorosulfonamide are most stable. Additionally, the data in Table 1 show that the sulfur energy varies in the opposite way at those same conformations. Thus, there is evidence that sulfur destabilization is occurring in unison with the stabilization of the amino group. If relative electronegativity changes are affecting the stabilization of the amino group and the destabilization of the sulfur, then the bond connecting them is the most likely place to look for changes.

The data in Tables 2 and 5 clearly show that the sulfur–nitrogen bond gets shorter when both sulfonamide and fluorosulfonamide are in their most stable geometries. This bond length contraction implies that the bond is increasing in *s* character as the amino group becomes sp^2 hybridized. It is also important to note that for all conformers, the nitrogen–sulfur bond length in fluorosulfonamide is shorter than in sulfonamide. Additional geometric data are shown in Tables 3, 4, and 6.

The last column in Table 1 shows that the amino group altitude decreases as the group approaches planarity at the most stable geometries of both sulfonamide and fluorosulfonamide. At these geometries, (*i*) the amino group gains electron population while the sulfur atom loses electron population; (*ii*) the amino group becomes more stable while the sulfur atom becomes less stable; (*iii*) the sulfur-nitrogen bond shortens, and (*iv*) the amino group is most planar. These observations point to the conclusion that nitrogen rehybridization to a more nearly sp^2 structure increases its electronegativity and gains overall stability for the molecule.

Further study of the amino nitrogens revealed additional important information. The local minima in the Laplacian ($\nabla^2\rho$) and electrostatic potential were located in the "lone pair region" of space of the nitrogen by using a gradient search procedure. It can be seen in Table 1 that the nitrogen lone pair Laplacian and electrostatic potential minima approach a maximum value (least negative) at geometries where both sulfona-

Table 1. (*continued*).

	Population (e)	Atom energy (au)	Atom energy (au)	Atom energy (au)	Atom energy (au)	Atom energy (au)	Atom energy (au)	Atom energy (au)
Sulfonamide								
	n (H7)	*E* (H1)	*E* (S2)	*E* (O3)	*E* (O4)	*E* (N5)	*E* (H6)	*E* (H7)
	0.534	−0.6277	−395.3672	−75.6615	−75.6542	−55.1658	−0.4292	−0.4174
	0.537	−0.6258	−395.3731	−75.6678	−75.6537	−55.1681	−0.4293	−0.4166
	0.528	−0.6224	−395.3628	−75.6565	−75.6576	−55.1928	−0.4262	−0.4114
	0.521	−0.6217	−395.3566	−75.6584	−75.6598	−55.2088	−0.4197	−0.4093
	0.532	−0.6211	−395.3631	−75.6588	−75.6586	−55.2028	−0.4144	−0.4167
	0.552	−0.6196	−395.3771	−75.6569	−75.6556	−55.1805	−0.4162	−0.4278
	0.569	−0.6207	−395.3861	−75.6543	−75.6541	−55.1559	−0.4216	−0.4362
	0.571	−0.6251	−395.3868	−75.6521	−75.6559	−55.1446	−0.4224	−0.4368
	0.534	−0.6288	−395.3221	−75.6657	−75.6651	−55.2124	−0.4208	−0.4174
	0.535	−0.6283	−395.3431	−75.6641	−75.6605	−55.1822	−0.4284	−0.4189
Relative min	0.526	−0.6291	−395.3107	−75.6663	−75.6662	−55.2347	−0.4128	−0.4128
Global min	0.529	−0.6211	−395.3605	−75.6589	−75.6591	−55.2062	−0.4149	−0.4149
TS1	0.558	−0.6274	−395.3711	−75.6532	−75.6601	−55.1644	−0.4173	−0.4292
TS2	0.517	−0.6288	−395.3037	−75.6671	−75.6675	−55.2505	−0.4078	−0.4078
Fluorosulfonamide								
	n (H7)	*E* (F1)	*E* (S2)	*E* (O3)	*E* (O4)	*E* (N5)	*E* (H6)	*E* (H7)
	0.525	−99.8941	−395.8094	−75.7264	−75.7196	−55.2207	−0.4153	−0.4141
	0.527	−99.8992	−395.8043	−75.7233	−75.7199	−55.2230	−0.4155	−0.4145
	0.529	−99.9034	−395.7816	−75.7238	−75.7237	−55.2472	−0.4089	−0.4148
	0.511	−99.9055	−395.7654	−75.7269	−75.7272	−55.2691	−0.4081	−0.4053
	0.521	−99.9041	−395.7848	−75.7242	−75.7247	−55.2394	−0.4178	−0.4107
	0.536	−99.9013	−395.8033	−75.7214	−75.7219	−55.2140	−0.4224	−0.4185
	0.537	−99.8975	−395.8153	−75.7189	−75.7224	−55.2076	−0.4183	−0.4194
	0.503	−99.8966	−395.7467	−75.7291	−75.7316	−55.3003	−0.4031	−0.4004
	0.525	−99.8923	−395.7729	−75.7288	−75.7278	−55.2621	−0.4119	−0.4129
	0.530	−99.8917	−395.7948	−75.7289	−75.7230	−55.2350	−0.41148	−0.4162
Global min	0.520	−99.8932	−395.7634	−75.7288	−75.7293	−55.2712	−0.4101	−0.4101
Relative min	0.510	−99.9056	−395.7564	−75.7277	−75.7276	−55.2784	−0.4046	−0.4046
TS1	0.498	−99.9029	−395.7362	−75.7307	−75.7307	−55.3123	−0.3972	−0.3972
TS2	0.530	−99.8964	−395.8097	−75.7191	−75.7246	−55.2197	−0.4136	−0.4159

mide and fluorosulfonamide are most stable. The positions of these maxima imply that nitrogen lone pairs exhibit the least "amine" character and thus are least basic at those geometries. These results also imply that the nitrogen lone pair has become more "*p*"-like and very slightly delocalized. One interpretation of these observations is that the delocalization of a small amount of π electron density allows the more electronegative amino group to withdraw a large amount of σ electron density from the less electronegative sulfur thereby increasing the amino group's overall electron population. This results in rehybridization of the amino nitrogen from sp^3 to nearly sp^2, thus increasing the *s* character of the sulfur–nitrogen bond. The amino group therefore becomes more planar and consequently more stable. The sulfur, having lost electron population, would be destabilized to a lesser degree, causing the molecule to become more stable overall.

This leaves but one question: Where did the small amount of delocalized nitrogen lone pair density go? The S—F bond length data given in Table 5 show that in fluorosulfonamide, the nitrogen lone pair could possibly have been partially donated into the sulfur–fluorine bond. This hypothesis is supported by the fact that in the global minimum structure, the sulfur–fluorine bond is favorably oriented with respect to the nitrogen lone pair to allow delocalization of the lone pair into the S—F antibonding orbital. This donation of nonbonded electron density would account for the observed increase of the S—F bond length. In sulfonamide, however, we do not see the corresponding S—H bond-elongation effect to such a large extent. Sulfonamide is most stable when its nitrogen lone pair is *syn* to the sulfur–hydrogen bond but *anti* to the vector sum of the sulfonamide S—O bonds. It is reasonable to postulate that the global minimum in sulfonamide may be controlled by the best electron sink available for the amino lone pair electrons. Since fluorine is more electronegative than oxygen, we can conclude that the fluorine is acting as a more efficient electron sink in fluorosulfonamide than the two oxygens are in sulfonamide. The effect of this sink is also revealed in the barrier to rotation in fluorosulfonamide. Figures 1 and 2 show that the fluorine substitution in fluorosulfonamide causes the nitrogen to undergo greater changes in hybridization and

Table 1. (*concluded*).

	LP EP torsion	LP Laplacian	LP EP minimum	LP Laplacian angle	LP Laplacian distance	LP EP distance	LP EP angle	Pyramidal
Sulfonamide								
	E_{stat} LP-N-S-H1	Del^2(rho) min	LP E_{stat} (kcal)	Del^2 LP-N-S	Del^2 LP-N	E_{stat} LP-N	E_{stat} LP-N-S	Nitrogen altitude (au)
	−118.61	−3.06	−41.43	102.19	0.3887	1.3309	100.17	1.1523
	−88.95	−3.09	−38.39	100.75	0.3886	1.3230	106.21	1.1082
	−57.69	−3.03	−31.39	97.86	0.3895	1.3141	107.41	0.9989
	−25.81	−2.92	−26.48	98.41	0.3907	1.3117	109.97	0.9798
	5.38	−2.91	−27.56	100.47	0.3907	1.3080	111.97	1.0804
	35.28	−3.01	−32.45	101.85	0.3897	1.3029	112.14	1.2044
	63.08	−3.10	−37.56	103.35	0.3887	1.3057	111.18	1.2997
	91.72	−3.13	−41.59	104.49	0.3881	1.3158	109.16	1.3048
	107.44	−2.90	−34.06	94.78	0.3907	1.3522	103.83	0.8721
	213.97	−2.98	−39.48	99.60	0.3896	1.3378	105.82	1.0849
Relative min	180.00	−2.80	−27.90	90.84	0.3918	1.3757	101.19	0.6202
Global min	0.04	−2.90	−26.91	100.10	0.3908	1.3092	111.72	1.0567
TS1	108.75	−3.08	−41.03	102.23	0.3885	1.3285	106.17	1.1504
TS2	179.96	−2.66	−20.07	86.90	0.3932	1.4150	98.36	0.3342
Fluorosulfonamide								
	E_{stat} LP-N-S-F	Del^2(rho) min	LP E_{stat} (kcal)	Del^2 LP-N-S	Del^2 LP-N	E_{stat} LP-N	E_{stat} LP-N-S	Nitrogen altitude (au)
	−117.7	−3.10	−31.40	101.70	0.3882	1.3481	107.1	1.1598
	−87.1	−3.14	−30.70	100.30	0.3880	1.3429	106.7	1.1008
	−54.1	−3.08	−25.40	97.70	0.3887	1.3482	106.8	0.9807
	8.1	−2.89	−20.40	98.40	0.3903	1.3704	107.3	0.9395
	35	−3.05	−26.30	100.40	0.3889	1.3455	109.2	1.1178
	62.7	−3.15	−30.70	101.80	0.3879	1.3346	109.6	1.2258
	92	−3.17	−32.90	102.60	0.3877	1.3378	108.3	1.2249
	167.4	−2.79	−11.00	89.20	0.3919	1.4241	100.8	1.4856
	187.5	−2.98	−22.50	95.80	0.3898	1.3683	106	0.9541
	213.5	−3.05	−27.90	99.70	0.3890	1.3555	107.4	1.1241
Global min	180.2	−2.95	−20.50	94.40	0.3902	1.3757	105	0.8672
Relative min	−0.2	−2.85	−18.00	97.20	0.3908	1.3810	106.3	0.8547
TS1	0.0131017	−2.51	−0.66	89.31	0.3944	1.4993	99.5669	0.2608
TS2	103.504718	−3.13	−31.75	102.46	0.3880	1.3452	106.828565	1.1408

energy than sulfonamide. The cause of this phenomenon is also seen in the sulfur–nitrogen bond lengths in Tables 2 and 5. The fact that the sulfur–nitrogen bond lengths are shorter for all conformers when compared to sulfonamide suggests that the more electronegative nitrogen underwent a greater degree of rehybridization in fluorosulfonamide than in similar geometries for sulfonamide. In sulfonamide, the two S—O bonds are not a good electron acceptor since the energy of its σ* nonbonding orbital is higher than that of the S—O and S—F bonds in fluorosulfonamide. Consequently, in fluorosulfonamide, donation of electron density into the sulfur–fluorine bond is more favorable, thus allowing the nitrogen to rehybridize more than the nitrogen in sulfonamide.

For this new model of sulfonamide stability to be valid, it must be able to reconcile Catalan's (14) recent results, which state that the hybridization of the amino nitrogen does not appear to be important to the total energy of the system. He reported testing this idea by looking at the extreme examples of totally sp^2 hybridized vs. totally sp^3 hybridized nitrogen atoms during the rotation about the S—N bond in sulfonamide. We must conclude that by not allowing his nitrogen atoms to change hybridization during rotation, Catalan inadvertently biased the results of his analysis.

To further address these points, the nitrogen rehybridization scenario proposed in this work was further tested by comparing the values of ρ and $\nabla^2\rho$ at the sulfur–nitrogen bond critical points in each conformer. Covalent bond orders were also calculated using the BONDER (13) method. On the basis of these data, it was possible to assess the degree and type of bonding between each pair of atoms. The results of the critical point electron density analyses are shown in Figs. 9 and 10. Both of these plots show increases of electron density (ρ) at the sulfur–nitrogen bond critical points for both sulfonamide and fluorosulfonamide when the torsional angles approached those of

Table 2. Bond lengths in sulfonamide during N-S rotation (6-31G*).

	Bond distances (angstroms)					
Geometry	H1—S2	O3—S2	O4—S2	N5—S2	N5—H6	N5—H7
Global min	1.3207	1.4243	1.4243	1.6364	1.0004	1.0004
Relative min	1.3259	1.4218	1.4218	1.6182	0.9974	0.9974
Rotational TS	1.3261	1.4272	1.4203	1.6528	1.0024	1.0013
Inversion TS	1.3243	1.4222	1.4224	1.6118	0.9961	0.9958
0°	1.3266	1.4202	1.4264	1.6520	1.0013	1.0021
30°	1.3250	1.4208	1.4278	1.6496	1.0015	1.0026
60°	1.3230	1.4223	1.4267	1.6385	1.0009	1.0012
90°	1.3212	1.4236	1.4250	1.6341	0.9999	1.0000
120°	1.3205	1.4245	1.4241	1.6376	1.0007	1.0006
150°	1.3216	1.4259	1.4231	1.6446	1.0032	1.0028
180°	1.3236	1.4275	1.4213	1.6517	1.0056	1.0052
210°	1.3254	1.4281	1.4200	1.6582	1.0053	1.0044
300°	1.3270	1.4212	1.4217	1.6263	0.9993	0.9992
330°	1.3276	1.4204	1.4234	1.6411	1.0012	1.0011

Fig. 9. Sulfonamide S—N bond critical point electron density vs. torsional angle.

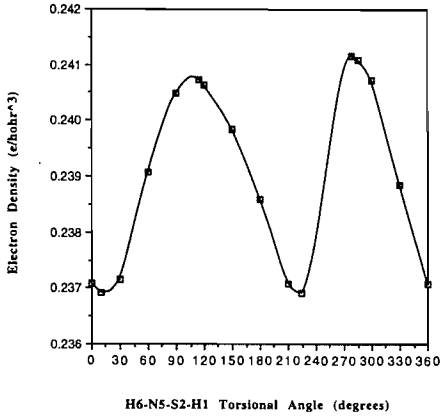

Fig. 10. Fluorosulfonamide S—N bond critical point electron density vs. torsional angle.

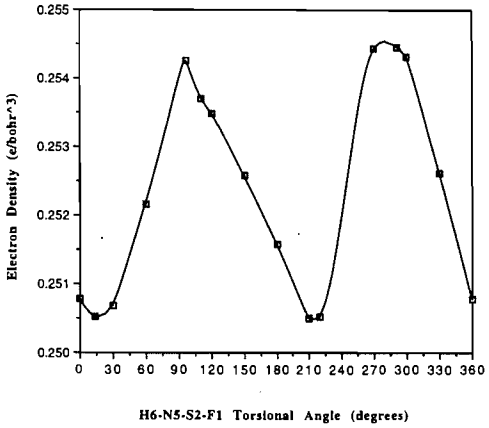

the minimum energy geometries. These increases in ρ indicate an increase in the total bond order of the sulfur–nitrogen bond at those minimum energy geometries. This observation is consistent with the hypothesis that donation of a small amount of

Fig. 11. Relative covalent bond order of S—N bond of sulfonamide vs. torsional angle.

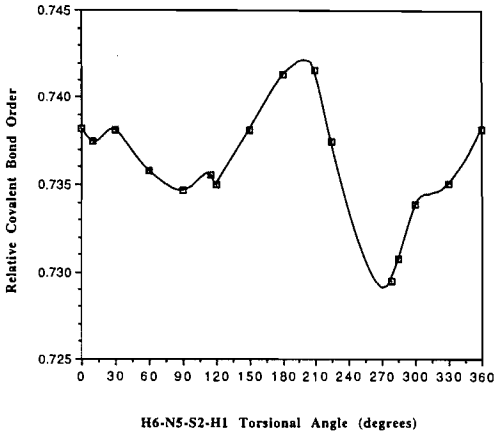

nonbonded electron density from the nitrogen lone pair into the antibonding orbital of the sulfur–oxygen, sulfur–fluorine, or sulfur–hydrogen bonds is required to enable a comparatively larger withdrawal of σ density from the sulfur by the amino group. The withdrawal of this σ density along the sulfur–nitrogen bond would be expected to increase the *s* character of the bond, resulting in its growing shorter (Table 2).

The value of $\nabla^2\rho$ at a bond critical point can be interpreted as describing the relative nature (ionic or covalent) of a bond. The Laplacian data in Table 1 show that in sulfonamide and fluorosulfonamide, the $\nabla^2\rho$ at the bond critical point is at its most positive value where geometric evidence shows that nitrogen rehybridization to nearly sp^2 is taking place. These data imply that the covalent sulfur–nitrogen bond order is decreasing and the bond is becoming more ionic at these geometries. This observation further supports the hypothesis that suggests that electron withdrawal along the sulfur–nitrogen bond takes place during nitrogen rehybridization.

The BONDER results in Figs. 11 and 12 are consistent with the Laplacian results, and reveal that the S—N covalent bond order decreases dramatically at the most stable geometries of both sulfonamide and fluorosulfonamide. This implies that

Table 3. Bond angles in sulfonamide during N-S rotation (6-31G*).

	Bond angles							
Geometry	H1-S2-O3	H1-S2-O4	H1-S2-N5	O3-S2-N5	O4-S2-N5	S2-N5-H6	S2-N5-H7	H6-N5-H7
Global min	107.2625	107.2164	138.7084	108.1543	108.1467	112.8353	112.8409	113.6814
Relative min	106.4403	106.4406	135.1238	107.1126	107.1098	117.6558	117.6460	117.9125
Rotational TS	108.9867	107.6809	141.2491	108.6071	110.1951	110.8348	113.5170	111.1937
Inversion TS	106.4368	106.4187	134.8232	107.2320	107.2563	119.1724	119.1675	119.7170
0°	106.6121	109.4601	140.0959	110.3062	107.6977	114.0681	110.3337	110.9839
30°	109.8551	107.6339	142.8706	109.1595	110.6100	113.0085	112.3978	112.1481
60°	110.9461	106.0131	142.0518	106.8794	112.0350	114.2582	113.4907	114.1964
90°	108.9050	106.1137	139.3604	106.6512	110.2180	114.4809	113.1614	114.8667
120°	107.0104	107.5580	138.7458	108.5520	107.7818	112.3821	112.7109	113.2451
150°	106.3548	109.5485	140.3223	110.7167	106.7001	110.4395	111.6621	110.4292
180°	106.5993	110.6817	142.2799	111.2571	107.5352	109.8074	109.9459	107.6990
210°	107.6449	109.5416	142.2477	109.9454	109.3251	109.4911	110.2548	107.6136
300°	105.8167	107.3269	134.6510	107.6296	106.6005	116.1894	114.9180	115.1761
330°	105.0892	109.2073	136.7822	109.3016	106.2876	115.2876	111.1892	111.7551

Table 4. Dihedral angles in sulfonamide during N-S rotation (6-31G*).

	Torsion angle
Conformer	H7-N5-S2-H1
Global min	−114.6879
Relative min	75.2939
Rotational TS	125.7100
Inversion TS	82.0000
0°	−234.2825
30°	−201.8287
60°	−166.6825
90°	−135.786
120°	−110.5765
150°	−86.7131
180°	−61.7000
210°	−31.7860
300°	78.6960
330°	98.5199

Fig. 12. Relative covalent bond order of S—N bond of fluorosulfonamide vs. torsional angle.

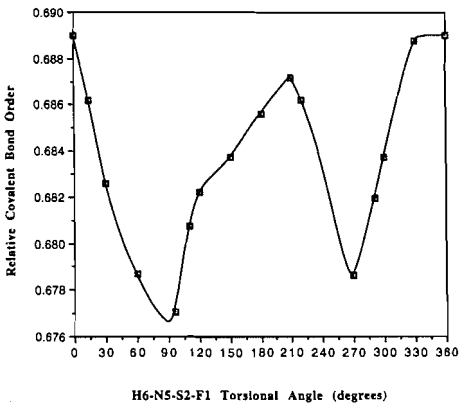

less electron density is being shared between the two nuclei at these geometries and is therefore being more tightly held by the sulfur and the nitrogen. In the cases of sulfonamide and fluorosulfonamide, it is the more electronegative amino group which is becoming the anionic partner of the ionic portion of the bond, and is therefore acting as an electron sink. This σ polarization is manifest by increases of the electron density (ρ) at the sulfur–nitrogen bond critical points and by the more ionic sulfur–nitrogen bond apparent in Figs. 9 and 10. The increased ionic character of the sulfur–nitrogen bond was established by comparing the ρ and $\nabla^2\rho$ results with the BONDER covalent bond orders. The observed relationship between the *total* bond order and the value of ρ at the bond critical point allows separation of the total bonding scheme into variable ionic and covalent parts.

Thus, the results of ρ, $\nabla^2\rho$, and BONDER analysis all support the hypothesis that when a nitrogen is allowed to rehybridize by donating a small amount of its lone pair electron density into the σ^* orbital of another bond, the resulting increase of amino group electronegativity causes a large flux of σ electron density towards the nitrogen. This, in turn, results in the stabilization of the entire molecule, since the more electronegative amino group becomes stabilized at the expense of the sulfur.

Conclusions

Upon examination of charge density flow during rotational isomerism of sulfonamide and fluorosulfonamide, the redistribution of electron density and electronic kinetic energy between the sulfur and nitrogen atoms was found to be the controlling factor over conformational stability. The results showed that, in sulfonamide, at least one minimum was strongly dependent upon the hybridization of the amino nitrogen atom, whereas in fluorosulfonamide, both minima were clearly hybridization controlled. These results lead to the first conclusion: *the total stabilization of both molecules is directly related to the redistribution of charge density between the sulfur and amino nitrogens in a manner analogous to formamide stabilization.*

Table 5. Bond lengths in fluorosulfonamide during N–S rotation (6–31G*).

	Bond distances (angstroms)					
Geometry	F1—S2	O3—S2	O4—S2	N5—S2	N5—H6	N5—H7
Global Min	1.5631	1.4073	1.4073	1.6083	0.9995	0.9995
Relative Min	1.5508	1.4099	1.4100	1.6116	0.9982	0.9982
Rotational TS	1.5564	1.4121	1.4060	1.6386	1.0006	1.0015
Inversion TS	1.5563	1.4092	1.4089	1.5956	0.9959	0.9959
0°	1.5592	1.4059	1.4112	1.6376	1.0016	1.0009
30°	1.5533	1.4062	1.4126	1.6359	1.0014	1.0007
60°	1.5496	1.4074	1.4123	1.6238	1.0000	1.0004
120°	1.5499	1.4104	1.4096	1.6155	0.9971	0.9989
150°	1.5480	1.4118	1.4082	1.6265	1.0016	1.0012
180°	1.5492	1.4128	1.4066	1.6357	1.0035	1.0034
210°	1.5542	1.4127	1.4058	1.6418	1.0022	1.0030
270°	1.5612	1.4083	1.4080	1.5985	0.9971	0.9969
300°	1.5635	1.4070	1.4074	1.6120	1.0003	1.0003
330°	1.5629	1.4061	1.4089	1.6262	1.0017	1.0016

Table 6. Bond angles in fluorosulfonamide during N–S rotation (6–31G*).

	Bond angles							
Geometry	F1-S2-O3	F1-S2-O4	F1-S2-N5	O3-S2-N5	O4-S2-N5	S2-N5-H6	S2-N5-H7	H6-N5-H7
Global min	105.3390	105.3445	102.0686	108.8294	108.7670	115.2503	115.2578	115.6342
Relative min	105.5034	105.4950	100.6731	109.3658	109.4078	115.0048	114.9249	116.6204
Rotational TS	107.4636	106.6376	96.4913	110.7827	111.3556	112.7769	110.8865	111.7904
Inversion TS	105.1520	105.1539	101.8123	109.0820	109.0797	118.9904	118.9891	120.8147
0°	105.5500	107.9144	97.7265	111.6055	109.6244	110.1539	113.1514	111.1268
30°	108.0014	106.6089	95.5999	110.4929	112.1468	111.9703	112.6973	112.6942
60°	108.8953	105.0258	96.7249	108.3736	113.2202	113.2053	114.2465	114.7939
120°	105.2307	106.0787	100.3923	110.0562	108.8460	114.3017	113.8000	115.4913
150°	104.9737	107.8846	98.3918	112.0950	108.0930	112.6582	111.2907	112.2912
180°	105.5373	108.7714	96.1766	112.7973	108.9835	110.9247	110.2989	109.7607
210°	106.7978	107.6025	95.9335	111.5867	110.7408	111.1419	110.1536	109.8904
270°	106.0541	104.4728	102.1399	108.2136	109.6061	118.8548	117.4963	119.4352
300°	105.0041	105.8675	101.8478	109.2092	108.4819	113.9081	114.8017	114.3354
330°	104.4744	107.4360	100.3003	110.7176	108.3169	110.6904	113.9716	111.2559

Table 7. Dihedral angles in fluorosulfonamide during N-S rotation (6-31G*).

	Torsion angle
Conformer	H7-N5-S2-F1
Global min	69.5344
Relative min	109.9781
Rotational TS	345.9644
Inversion TS	263.7938
0°	125.0649
30°	158.2929
60°	193.9077
120°	255.6649
150°	277.1443
180°	301.8274
210°	332.0387
270°	66.8302
300°	74.5399
330°	96.3018

The sulfur–nitrogen bonds were found to be shortest at those geometries where both sulfonamide and fluorosulfonamide became most stable. This implied that in both molecules, the sulfur–nitrogen bond increased in *s* character, with the more stable conformers having the most *s* character.

The positions and magnitudes of electrostatic and Laplacian ($\nabla^2\rho$) minima in the vicinity of the nitrogen "lone pair" region, as well as the amino group pyramidalization altitudes were found to be reliable indicators of nitrogen hybridization. The fluorosulfonamide results demonstrated that the donation of a small amount of electron density from nitrogen's lone pair into the antibonding orbital of the sulfur–fluorine bond allowed for a comparatively larger withdrawal of σ density away from the sulfur atom to the more electronegative amino group. This, in turn, allowed the rotating nitrogen atom in fluorosulfonamide to undergo larger changes in hybridization at the minimum energy geometries.

All of the results presented in this work indicate that nitrogen rehybridization controls the torsional preferences in sul-

fonamide and fluorosulfonamide. The concept of *dynamic relative electronegativity* was found to rationalize the geometry of one minimum of sulfonamide and both minima of fluorosulfonamide. Within this interpretation, individual atomic stabilities are rearranged to serve the "greater good" of the total molecule. In this case, providing the more electronegative amino group with more electron density transferred from the less electronegative sulfur atom allows the nitrogen to rehybridize and stabilize the entire molecule.

The fact that fluorosulfonamide has a greater rotation barrier than sulfonamide is a direct result of the fluorine substitution in fluorosulfonamide. *The fluorine acts as an excellent lone pair electron sink* thereby allowing the amino nitrogen to rehybridize to a larger degree than is possible in sulfonamide. This result is seen in Tables 2 and 5 where the sulfur–nitrogen bonds in fluorosulfonamide are shown to be consistently shorter than those in sulfonamide at all geometries.

Through the implementation of these theoretical–computational methods, the dissimilar views of amide and sulfonyl stability control (resonance, negative hyperconjugation, *p-d* back bonding (3), etc.) have been replaced by one mechanism. Amide and sulfonyl stability were found to be controlled by the redistribution of electron density and its associated kinetic energy, thereby satisfying the intermolecular needs of the most *relatively electronegative* fragment. The result is the overall stabilization of the entire molecule.

Full PROAIM integration data for all rotamers have been deposited as supplementary material.[7]

Acknowledgments

The authors would like to thank Professor Jerzy Cioslowski of Florida State University for performing the BONDER calculations and for helpful discussions. Professor Cioslowski's efforts were supported in part by the Petroleum Research Fund. Thanks also go to Professor Richard Bader for inspirational conversations, and to Professor Kenneth Wiberg for years of good advice.

References

1. F.W. Biegler-Konig, R.F.W. Bader, and T.-H. Tang. J. Comput. Chem. **3**, 317 (1982); R.F.W. Bader, T. Tang, and F.W. Biegler-Konig. J. Am. Chem. Soc. **104**, 946 (1982).
2. (*a*) K.B. Wiberg and K.E. Laidig. J. Am. Chem. Soc. **109**, 5935 (1987); (*b*) R.F.W. Bader, J.R. Cheeseman, K.B. Wiberg, and C.M. Breneman. J. Am. Chem. Soc. **109**, 6530 (1990).
3. J. Brunvoll, M. Kolonits, C. Bliefert, K. Seppelt, and I. Hargittai. J. Mol. Struct. **78**, 307 (1982).
4. (*a*) F. Hund. Z. Phys. **51**, 759 (1928); (*b*) R.S. Mulliken. Phys. Rev. **32**, 186 (1928).
5. A.E. Reed and P.v.R. Schleyer. J. Am. Chem. Soc. **112**, 1434 (1990).
6. K.B. Wiberg, C.M. Hadad, C.M. Breneman, K.E. Laidig, M.A. Murcko, and T.J. LePage. Science, **252**, 1266 (1991).
7. R.F.W. Bader. Acc. Chem. Res. **18**, 9 (1985); Atoms in molecules: a quantum theory. Oxford Univ. Press, Oxford. 1990.
8. P.W. Payne and L.C. Allen. Applications of electronic structure theory. *Edited by* H.H.F. Schaefer. Plenum, New York. 1977. pp. 29–108.
9. M.J. Frisch, J.S. Binkley, H.B. Schlegel, C. Gonzalez, K. Raghavachari, C.F. Melius, R.L. Martin, J.J.P. Stewart, M. Head-Gordon, C.M. Rohling, L.R. Kahn, D.J. DeFrees, R. Seeger, R.A. Whiteside, D.J. Fox, E.M. Fleuder, and J.A. Pople. GAUSSIAN90, Developmental version, revision G. Carnegie-Mellon Quantum Chemistry Publishing Unit, Pittsburgh, Pa. 1988.
10. M.J. Frisch, J.S. Binkley, H.B. Schlegel, C. Gonzalez, K. Raghavachari, C.F. Melius, R.L. Martin, J.J.P. Stewart, M. Head-Gordon, C.M. Rohling, L.R. Kahn, D.J. DeFrees, R. Seeger, R.A. Whiteside, D.J. Fox, E.M. Fleuder, and J.A. Pople. GAUSSIAN90, Developmental version, revision G. Carnegie-Mellon Quantum Chemistry Publishing Unit, Pittsburgh, Pa. 1990.
11. W.H. Hehre, L. Radom, P.v.R. Schleyer, and J.A. Pople. *Ab Initio* molelcular orbital calculations. Wiley, New York. 1986.
12. R. Ahlrichs and P.R. Taylor. J. Chem. Phys. **78**, 315 (1981).
13. J. Cioslowski. The BONDER program. Supercomputer Computations Research Institute, Florida State University, Tallahassee, Fla. 1990.
14. J. Elguero, P. Goya, I. Rozas, J. Catalan, and J.L.G. De Paz. Theochem, **184**, 115 (1989).

[7] The supplementary material referred to above can be purchased from: The Depository of Unpublished Data, Document Delivery, CISTI, National Research Council Canada, Ottawa, Canada K1A 0S2.

1995 Syntex Award Lecture
Correlation and prediction of rate constants for organic reactions[1]

J. Peter Guthrie

Abstract: Marcus theory provides a framework for correlating rate and equilibrium constants, and thus the possibility of predicting rate from structure. This had been successful for a number of simple reactions, including the addition of hydroxide to carbonyl compounds, enolate formation from carbonyl compounds, and aldol addition and elimination reactions. The theory can be extended, as Multidimensional Marcus Theory, to cover concerted reactions such as E2 eliminations, the water-mediated proton switch, or the breakdown of the tetrahedral intermediate in amide hydrolysis. We have now found that Marcus theory can be applied not only to inter-molecular reactions but also to intra-molecular reactions. This is illustrated for aldol condensation and ester/lactone formation.

Key words: Marcus theory, concerted reactions, intramolecular reactions, aldol condensation, ester formation, proton transfer.

Résumé : La théorie de Marcus offre un système pour établir des corrélations entre les constantes de vitesse et d'équilibre et, de ce fait, la possibilité de faire des prédictions relatives aux vitesses à partir des structures. Cette approche a été couronnée de succès pour un certain nombre de réactions simples, y compris l'addition de l'ion hydroxyde à des composés carbonylés, la formation d'énolates à partir de composés carbonylés et les réactions d'addition et d'élimination aldoliques. On a étendue la théorie, sous la forme de la théorie multidimensionnelle de Marcus, pour couvrir les réactions concertées, comme les éliminations E2, l'échange de protons avec l'eau comme médiateur ou la dépyramidalisation de l'intermédiaire tétraédrique lors de l'hydrolyse des amides. On a trouvé que la théorie de Marcus peut être appliquée, non seulement aux réactions intermoléculaires mais aussi aux réactions intramoléculaires. On illustre ce point par la condensation aldolique et le formation d'ester/lactone.

Mots clés : théorie de Marcus, réactions concertées, réactions intramoléculaires, condensation aldolique, formation d'ester, transfert de proton.

[Traduit par la rédaction]

Introduction

There are two aspects to the problem of explaining the chemical origins of enzymic catalysis, as may be seen by examining the simple Michaelis Menton mechanism (1) for enzyme action, eq. [1]. This is despite the fact that, as written, this simple mechanism is so oversimplified that it is necessarily wrong for any real enzyme. An enzyme must bind its substrate using non-covalent interactions (hydrophobicity, electrostatics, hydrogen bonding, etc.) and then cause reaction within an enzyme substrate complex to occur much faster than reaction would occur for the same mechanism with the same reacting groups in an intermolecular reaction (2). It is generally believed that this rate enhancement is achieved by using more elaborate, more concerted mechanisms in the enzymic reaction than are observed in the non-enzymic process. Mechanisms involving simultaneous participation of two or three catalytic groups are often proposed (3). Since enzymes involve rate phenomena, they are part of the larger problem of predicting the rates of organic reactions from the structures of the reactants. Since concerted reactions with several groups simultaneously involved are often suggested, the question of what controls when a reaction is stepwise and when it is concerted is clearly relevant. Finally, the question of how much faster an intramolecular reaction is than is the corresponding intermolecular reaction is clearly at the heart of the problem of explaining enzymic catalysis (4).

$$[1] \quad E + S \underset{K_m}{\rightleftharpoons} ES \xrightarrow{k_{cat}} E + P$$

This paper will be focused on three conjectures that drive my current research. These are to varying degrees still unproven and even controversial, but, I will argue, worthy of exploration and rigorous test. They are part of the general problem of understanding the chemical origins of enzymic catalysis. The conjectures are:

1. **Marcus Theory is generally applicable to organic chemistry, and intrinsic barriers are transferable.** Marcus Theory permits prediction of a rate constant given the corresponding equilibrium constant and the intrinsic barrier evaluated for a similar reaction. Equilibrium constants are in

Received January 4, 1996.

J.P. Guthrie.[2] Department of Chemistry, University of Western Ontario, London, ON N6A 5B7, Canada.

[1] This Syntex Award Lecture was presented by Professor Guthrie at the Annual Conference of the Canadian Society for Chemistry, Guelph, Ontario, May 1995.

[2] Telephone: (519) 679-2111, ext. 6352. Fax: (519) 661-3022.

principle predictable from the structures of the species involved.

2. **Multidimensional Marcus Theory allows the concertedness or otherwise of a process to be predicted as well as the rate of the process.** By generalizing Marcus Theory to more than one potentially concerted bond-making/breaking process it is possible to calculate the nature and rate of the observable reaction.

3. **The effective molarity of an intramolecular reaction can be predicted given the equilibrium constant if data for intermolecular analogs are available. Intra- and intermolecular reactions are governed by the same Marcus intrinsic barrier.** Suitable extensions to the concept of the work term allow Marcus Theory to be applied to intramolecular reactions.

These conjectures, and the evidence supporting them, will now be discussed in turn.

Conjecture 1: Marcus Theory is generally applicable to organic chemistry, and intrinsic barriers are transferable

Marcus developed a theory relating rate and equilibrium for chemical reactions (5–7). In its simplest form this is expressed in eq. [2]

$$\Delta G^{\ddagger}_{corr} = \tilde{G}(1 + \Delta G^{\circ}_{corr}/4\tilde{G})^2$$

[2] $$\Delta G^{\ddagger}_{corr} = \Delta G^{\ddagger}_{obs} - w_R$$

$$\Delta G^{\circ}_{corr} = \Delta G^{\circ}_{obs} - w_R + w_P$$

This equation can be interpreted in terms of Fig. 1, which illustrates the situation for a reaction with two reactants and two products. The reactants must diffuse together, and the cost of bringing them together in an encounter complex is called the work term, w_R. This includes the entropic cost of bringing the two species together, as well as any electrostatic or other interactions between them, any partial desolvation required to get them close enough to react, and any conformational changes needed to achieve the reactive conformation. Similarly, the products are initially formed in an encounter complex, which differs from the products free in solution by another work term, w_P. Reaction occurs within the encounter complex and converts the encounter complex of reactants to the encounter complex of products. Marcus Theory applies to this reaction within an encounter complex, and thus involves a free energy change, ΔG°_{corr}, and a free energy of activation, $\Delta G^{\ddagger}_{corr}$, which need not be the same as the observable values, ΔG°_{obs} and $\Delta G^{\ddagger}_{obs}$.

Marcus Theory involves a parameter, the intrinsic barrier, which I symbolize $\tilde{G}$. This can be interpreted as the kinetic barrier that would result if there were no thermodynamic barrier, Fig. 2. Now it is simple algebra to calculate $\tilde{G}$ given ΔG°_{corr} and $\Delta G^{\ddagger}_{corr}$, or to calculate any of the three quantities given the other two. The problem is to obtain $\tilde{G}$ for a new reaction where one does not know both ΔG°_{corr} and $\Delta G^{\ddagger}_{corr}$. The approximation I have used is that for a class of "similar" reactions, where variation is "far enough" from the reaction center, and the intrinsic barrier is "approximately" constant and thus transferable. The weasel words in quotes are strikingly reminiscent of those used for the Hammett or Taft equations and, analogously to those cases, we have found that the assumption of transferable intrinsic barriers is good enough to permit the use of Marcus Theory for a wide range of organic reactions.

Fig. 1. Model for a reaction, A + B ⇌ A,B ⇌ C,D ⇌ C + D used in applying Marcus Theory. The reactants come together in an encounter complex (A,B) at a free energy cost w_R, and react within this complex to form (C,D), the encounter complex of products, which then separate, releasing free energy w_p. Marcus Theory applies to reactions within the encounter complex where $\Delta G^{\ddagger}_{corr}$ is determined by ΔG°_{corr} and the intrinsic barrier, $\tilde{G}$.

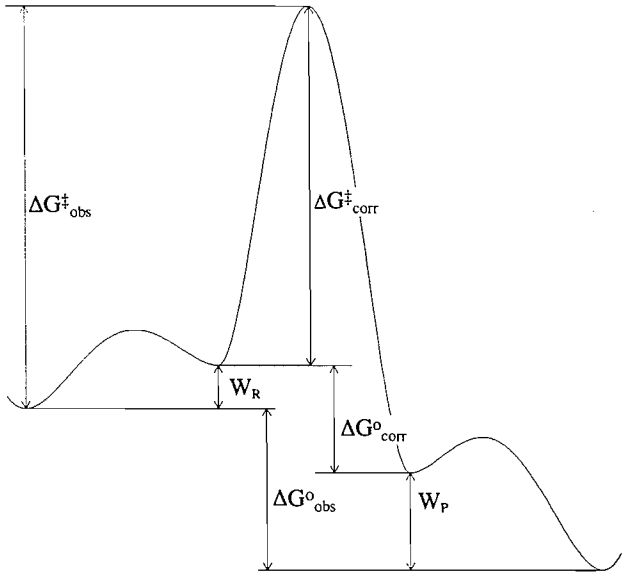

Fig. 2. Interpretation of the intrinsic barrier as the free energy of activation when $\Delta G^{\circ}_{corr} = 0$, even though ΔG°_{obs} is not zero in the case illustrated.

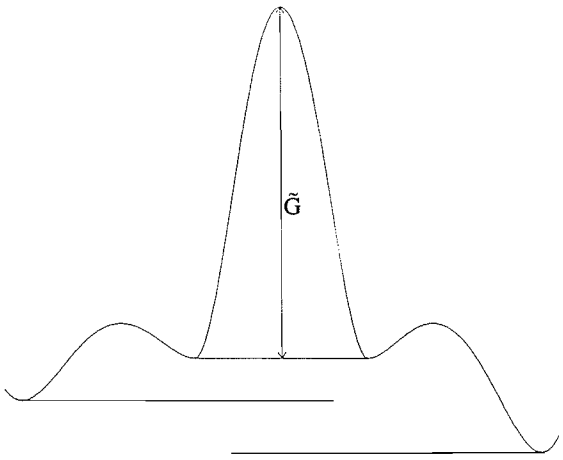

There have been numerous treatments of relations between rate and equilibrium, summarized in Jencks' acronym (8) BEMA HAPOTHLE (9–16). Marcus provided an equation that, if one knew the intrinsic barrier, allowed prediction of rate from equilibrium. He also provided a way, at least for systems where there was an identity reaction, to predict the intrin-

sic barrier. His equation has proven to be more general than the derivation seemed to justify.

It turns out that the work term and the intrinsic barrier are generally subject to covariance, so that if both are allowed to vary, many pairs of values will give very similar fits to the data. I calculated the work term for the most realistic practical model, and then varied only the intrinsic barrier. This means that the intrinsic barriers I report do depend on the model used for the work term, and this must be kept in mind whenever intrinsic barriers from different studies are compared.

To go the next step and apply the theory to concerted reactions we will need equations for the free energy at each point along the reaction coordinate. Several models have been used to provide such equations. One of the commonest is the inverted parabola model (10, 17–20) illustrated in Fig. 3 and eq. [3]. This model has the shape dictated by chemical intuition at the transition state, but looks unrealistic at the reactant and product ends. A model that is equivalent as far as the expression for transition state energy is concerned involves two intersecting parabolas with the same curvature (20), as illustrated in Fig. 4 and eq. [4]. This model seems intuitively more satisfying at the reactant and product ends, but seems too cusplike at the transition state. A third model, which seems likely to be more realistic at the three places where we think we know something, is based on a quartic equation (21–23), Fig. 5 and eq. [5].

$$G = (\Delta G^\circ + 4\tilde{G})x - 4\tilde{G}x^2$$

[3]

$$\Delta G^\ddagger = \tilde{G}\left(1 + \frac{\Delta G^\circ}{4\tilde{G}}\right)^2$$

$$G_1 = 4\tilde{G}x^2$$

[4] $$G_2 = \Delta G^\circ + 4\tilde{G}(1 - x)^2$$

$$\Delta G^\ddagger = \tilde{G}\left(1 + \frac{\Delta G^\circ}{4\tilde{G}}\right)^2 = \tilde{G}\left(1 + 8\left(\frac{\Delta G^\circ}{16\tilde{G}}\right) + 16\left(\frac{\Delta G^\circ}{16\tilde{G}}\right)^2\right)$$

$$G = (3\Delta G^\circ + 16\tilde{G})x^2 - (2\Delta G^\circ + 32\tilde{G})x^3 + 16\tilde{G}x^4$$

[5]

$$\Delta G^\ddagger = \tilde{G}\left(1 + 8\left(\frac{\Delta G^\circ}{16\tilde{G}}\right) + 18\left(\frac{\Delta G^\circ}{16\tilde{G}}\right)^2 - 27\left(\frac{\Delta G^\circ}{16\tilde{G}}\right)^3\right)$$

The first general examination of the applicability of Marcus Theory to organic chemistry was by Hine (24), who showed that for a wide range of organic reactions, the available data seemed to fit quite well to the Marcus model, with transferable intrinsic barriers. In his examination of the reaction of hydroxide with carbonyl compounds, he was limited at that time to data for additions to aldehydes and ketones, since these were the only compounds available. We were able to determine equilibrium constants for addition to esters (25, 26), thioesters (27), and amides (28), by an indirect method based on thermochemistry and thermodynamics (29). With additional data we were able to show that the Marcus correlation extended over 20 powers of 10 in equilibrium and 10

Fig. 3. Inverted parabola model for energy as a function of reaction coordinate. The reaction coordinate is a bond order coordinate, defined to be 0.0 at the reactants and 1.0 at the products.

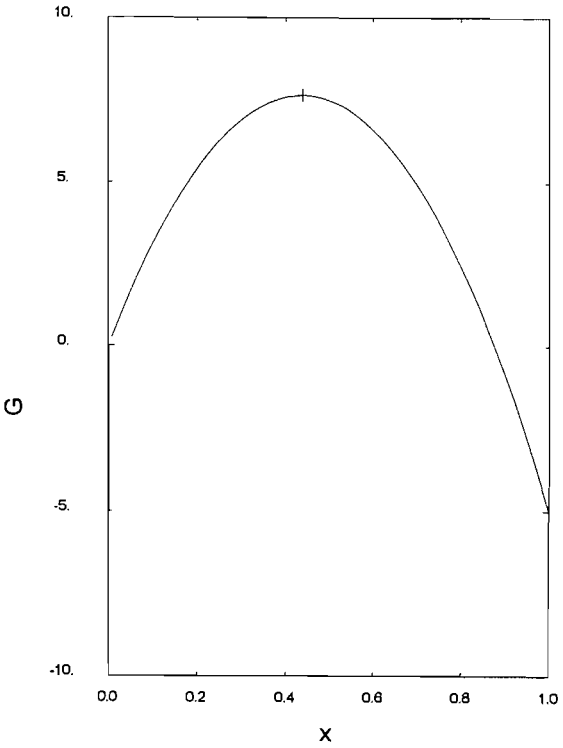

Fig. 4. Two intersecting parabola model for energy as a function of reaction coordinate. Both parabolas have the same curvature.

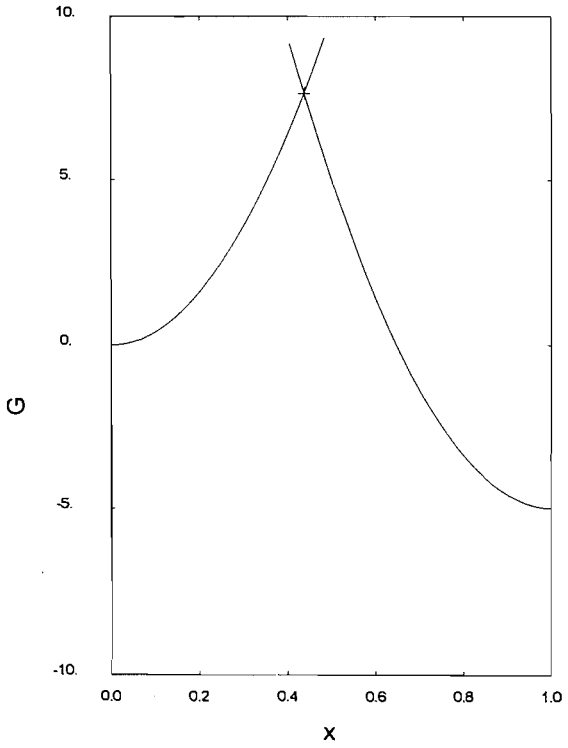

Fig. 5. Quartic model for the energy as a function of the reaction coordinate.

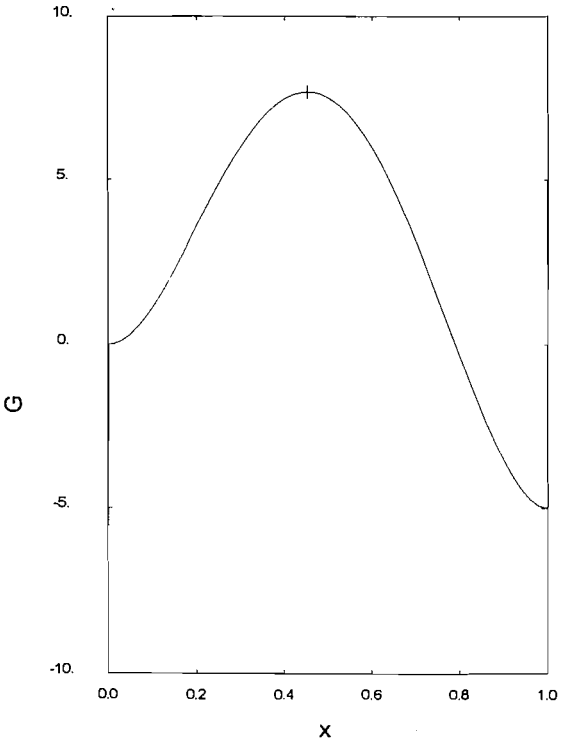

powers of 10 in rate (27); admittedly there were signs of dispersion into slightly different correlations for different groups of compounds. A more recent version of this correlation is shown in Fig. 6. The model for the encounter complex used in this plot involves partially desolvated hydroxide ion in contact with one of the two faces of the carbonyl group. The hydroxide ion must have lost one of its hydrogen-bonded waters in order to be ready to react with the carbonyl. The energy of this hydrogen bond is estimated from the difference in pK_a for water between water and DMSO (30). pK_a values for small, nonpolarizable acids are expected to be about the same in the two solvents: 1 pK_a unit higher because of the lower dielectric constant of DMSO (31); and 1 pK_a unit lower because of the greater basicity of DMSO (31). The source of the difference, which is commonly observed, is that DMSO cannot donate hydrogen bonds. In this way we can estimate that the energy of one of the three hydrogen bonds to hydroxide ion is 7.13 kcal/mol (32). Using this model, which we believe is more realistic, we find that the most reactive compounds deviate from the curve defined by less reactive species. I will argue (33) that this is because the reaction is in fact hydroxide as general-base-catalyzing attack by water, and that only for very reactive aldehydes is there evidence that the intrinsic barrier is smaller. Direct attack will give way to general base catalyzed attack when direct attack of hydroxide on the carbonyl becomes so fast that the main barrier would be formation of the complex with partial desolvation of the hydroxide. Under these circumstances, general-base catalysis provides a way to avoid this encounter complex, which would be a high-energy intermediate

The Marcus relation can also be used to correlate rate and equilibrium constants for enolate formation (32), as shown in

Fig. 6. Rate–equilibrium correlation for hydroxide addition to carbonyl compounds. Calculated for reaction within an encounter complex, with partially desolvated hydroxide. (□) amides, esters, and thioesters; (Δ) aldehydes. For the more reactive esters and aldehydes, the reaction is actually hydroxide-catalyzed attack of water with the hydroxide acting as general base. Only for the very most reactive aldehydes is the intrinsic barrier actually lower. The line is drawn using the average intrinsic barrier.

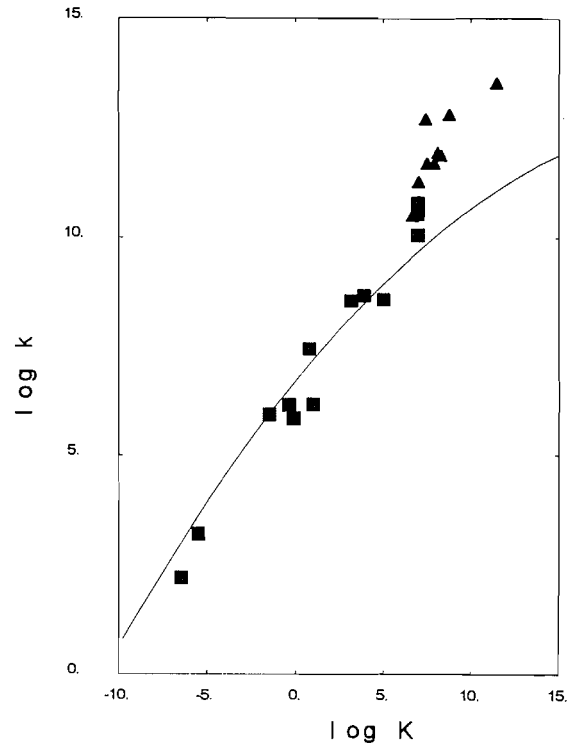

Fig. 7. The model used for the work term in these calculations is that hydroxide ion must be in one of two locations above or below the plane of the carbonyl group (24) and must have lost one of its waters of hydration. The intrinsic barrier for this process is 7.83 ± 0.11 kcal/mol.

We next examine a carbon–carbon bond-forming reaction, the aldol condensation. The detailed mechanism that we use for this analysis is shown in Scheme 1. For the intermolecular aldol addition, the step to which Marcus analysis should be applied involves reaction of the enolate of one component with the other component in an encounter complex, to give the anion of the aldol/ketol. The pK_a of the ketol can be estimated from linear free energy relations (27); the pK_a's of the carbon acids have been determined by Keefe and Kresge (34). For the aldol elimination, the step to which Marcus analysis should be applied involves expulsion of hydroxide from the reactive conformation of the ketol enolate to give the encounter complex of enone with partially desolvated hydroxide; see Scheme 2. The reactive conformation of the ketol enolate has the C—O bond that is to cleave perpendicular to the plane of the enolate. The pK_a's of the ketols as carbon acids were estimated by linear free energy relations starting from the pK_a of 4-methoxybutanone, which was determined from the rate of exchange (35) by means of the Marcus relation for enolate formation described above (27).

Fig. 7. Rate–equilibrium correlation for hydroxide-catalyzed enolate formation from aldehydes and ketones. The reaction was within an encounter complex with partially desolvated hydroxide ion. The line is calculated using an average value for the intrinsic barrier.

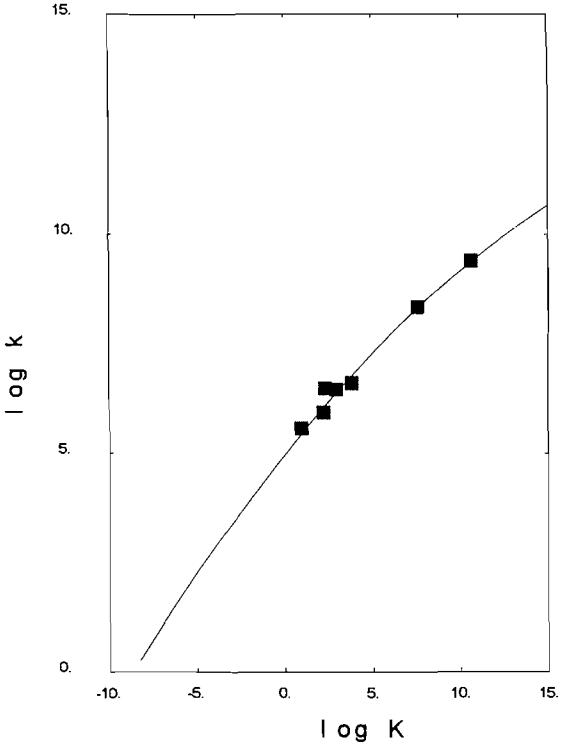

Scheme 1. Detailed mechanism for the aldol addition: horizontal arrows represent the C—C bond-forming process, while vertical arrows represent successive approximations to the microscopic bond-forming process, shown in the lowest line of the scheme.

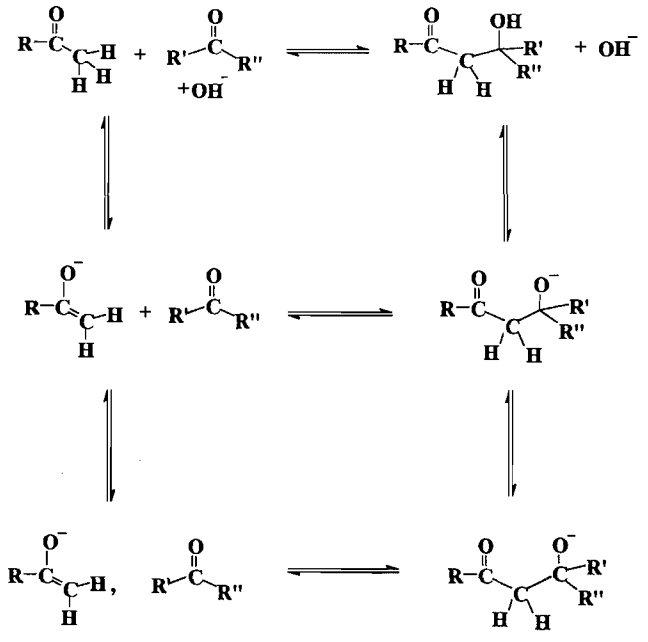

Scheme 2. Detailed mechanism for the aldol elimination step: horizontal arrows represent the dehydration process, while vertical arrows represent successive approximations to the microscopic bond-breaking process, shown in the lowest line of the scheme.

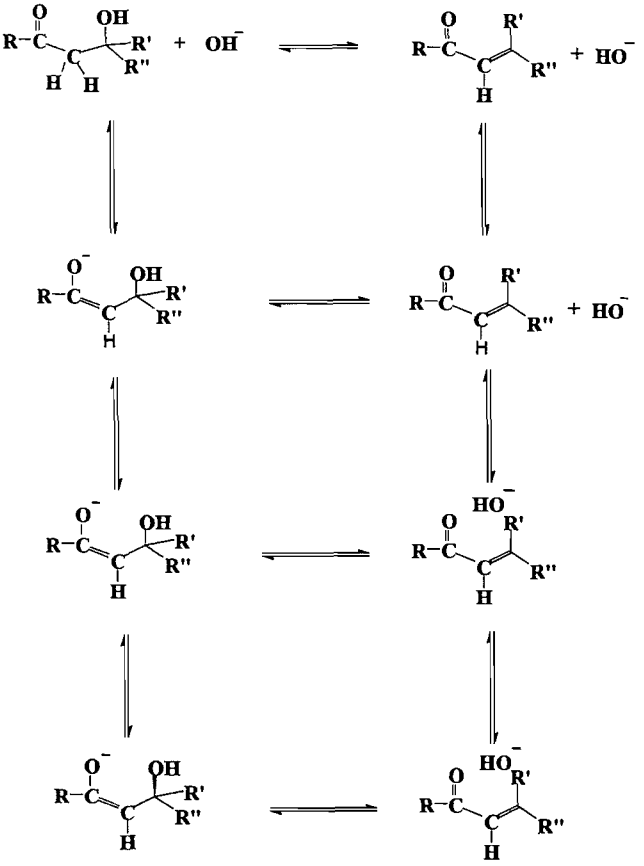

When the rate and equilibrium constants for the microscopic rate-determining step for aldol addition are plotted, Fig. 8, we find that they are in reasonable accord with the Marcus Theory. The intrinsic barrier in free energy terms is 13.89 ± 0.80 kcal/mole (32). The scatter reflects either the inadequacy of our assumption of constant intrinsic barrier, or that there are effects that we have not yet allowed for.

Similarly, when rate and equilibrium constants for the microscopic rate-determining step in the aldol elimination reaction are plotted, Fig. 9, we find that these too are in good accord with Marcus Theory. The intrinsic barrier, in free energy terms, is 14.13 ± 0.49 kcal/mol (32).

One of the attractive potentials of Marcus Theory is the possibility of predicting rates of reactions that have not yet been carried out. Based on equilibrium data for addition of other nucleophiles to trifluoroacetophenone (36), and information about the properties of acetone as a carbon nucleophile (37), I predicted the equilibrium constant for the aldol reaction of acetone with trifluoroacetophenone and, from this, the rate constant for the microscopic step (32). This step was predicted to be 9×10^3 times faster than the analogous rate constant for acetone plus acetophenone, for which we have measured the overall rate constant (38).

Testing this prediction proved to be a challenge because of the high reactivity of trifluoroacetophenone towards all

Fig. 8. Rate–equilibrium correlation for aldol addition. The reaction occurs within an encounter complex of enolate and carbonyl addend, and leads to the aldolate or ketolate anion. The line is based on the average value of the intrinsic barrier.

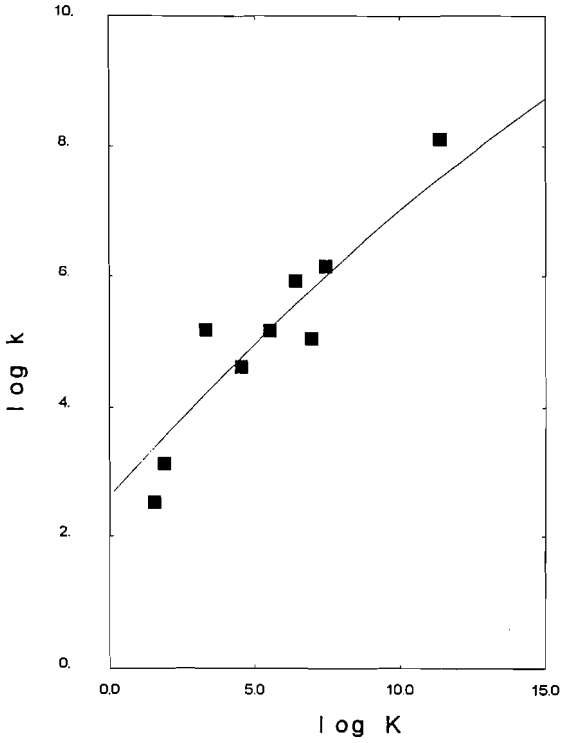

nucleophiles including hydroxide ion. The detailed kinetics have been worked out, and the rate constant for the reaction of acetone enolate with α,α,α-trifluoroacetophenone can be calculated; as predicted it is much faster than the corresponding rate constant for acetone plus acetophenone (38). The actual rate ratio is 7.5×10^3. The magnitude of the problem posed by this system is illustrated in Scheme 3, which shows the species that had to be considered in the analysis. Although trifluoroacetophenone is far more reactive in terms of the microscopic rate constant, it is actually less reactive in terms of the observable behavior under normal synthetic conditions because so much of the total trifluoroacetophenone is tied up as the carbonyl hydrate anion.

The successful prediction of a large rate enhancement means that application of Marcus Theory to aldol reactions has passed a stringent test. It suggests quite strongly that we have a general way to make approximate predictions of the rate constants for new reactions.

This conformity to Marcus Theory can be shown to apply to other carbon–carbon bond-forming reactions. We have determined rate and equilibrium constants for a set of Claisen condensations in methanol, which we believe is the first such study to have been carried out (39). Although the range of equilibrium and rate constants available so far is limited, the data are consistent with a single value of the intrinsic barrier, $\tilde{G} = 15.4 \pm 1.1$ (in methanol). Thus it seems as if a wide range of reactions of carbonyl compounds will fit the Marcus pattern, with transferable intrinsic barriers, although the barriers may differ somewhat from one class of reaction to another.

Fig. 9. Rate–equilibrium correlation for the aldol elimination reaction. The reaction starts with the conformation of the aldol or ketol enolate that has the OH group, which is to depart orthogonal to the plane of the enolate and leads to partially desolvated hydroxide ion in an encounter complex with the enone. The line is based on the average value of the intrinsic barrier.

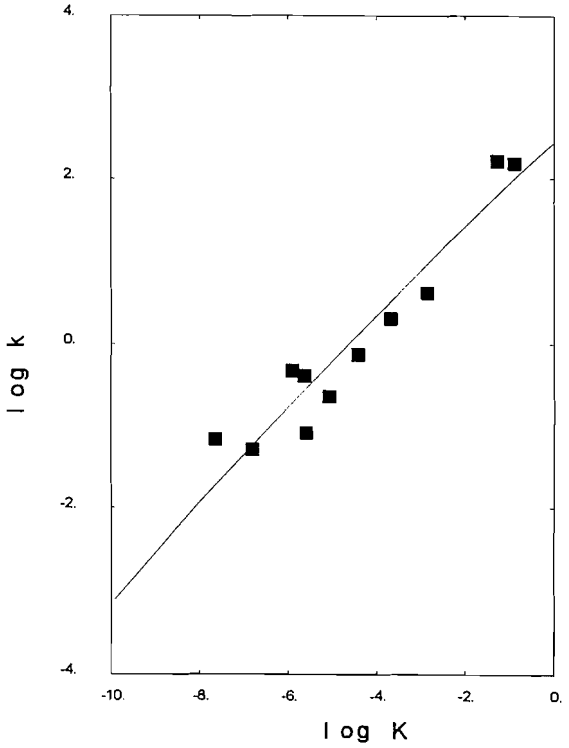

When the intrinsic barrier is large, as in the examples above, then curvature in the line relating rate and equilibrium is slight. Nonetheless, the Marcus curve involves only one adjustable parameter, where a simple linear correlation requires two. Marcus theory directs one to look at the microscopic rate-determining step within an encounter complex if one is to find a rate–equilibrium correlation. This gives a guide to improved predictability.

This has been a brief summary of our contributions to the application of Marcus Theory to organic reactions, which in combination with studies from other laboratories (5, 18, 24, 40–87), provides the basis for carrying on with the first conjecture. Although the application of Marcus theory is still not universally accepted, and has been vigorously challenged (88), there seems at the very least to be enough evidence to support a strong effort to test it further by examining additional reactions.

Conjecture 2: Multidimensional Marcus Theory allows the concertedness or otherwise of a process to be predicted as well as the rate of the process

We now turn to an examination of the requirements for a reaction to be concerted as opposed to stepwise, and of a method

Scheme 3. Acetone plus trifluoroacetophenone.

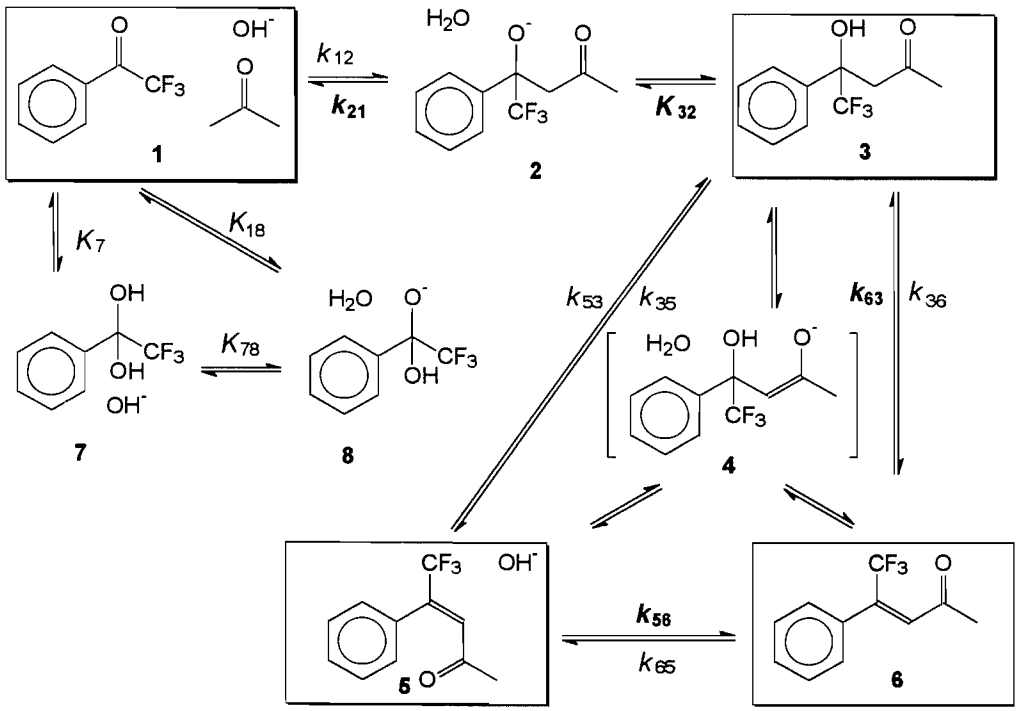

for predicting both concertedness and the rate constant for the concerted reaction. The method that I have developed for this purpose is Multidimensional Marcus Theory, a generalization of the theory to two, three, or even four reaction coordinate dimensions, as well as an energy dimension. Other approaches to handling concerted reactions in terms of multidimensional reaction coordinates have been reported in the literature (55, 63, 69, 89, 90).

The theory is based on four postulates:

1. Reactants are in equilibrium with starting material or product at each point along each reaction coordinate. This is the essential assumption in transition state theory.
2. At each section through the reaction hypersurface for which only one reaction coordinate changes, Marcus Theory will apply. This follows directly if Marcus Theory is applicable to simple organic reactions and postulate 1 is obeyed.
3. The intrinsic barrier for any reaction coordinate is independent of the values of the other reaction coordinates. This postulate is necessary to reduce the amount of empirical information needed to a manageable level. It seems to be justified by experience.
4. For any reaction coordinate chosen as progress variable, at fixed values of the other coordinates, the free energy will be a quartic function of the progress variable. This is a generalization of the quartic function assumption used for simple reactions.

If a reaction can be described by two reaction coordinates, then the position of the transition state can be presented in terms of a reaction square, as illustrated in Fig. 10. These have become familiar as Albery (91) – More O'Ferrall (92) – Jencks (93) diagrams. The position of the transition state on such a diagram shows whether the transition state is central (a highly concerted reaction) or on an edge (a fully stepwise reaction) or has an intermediate character. Energy is of course a third dimension at right angles to the two shown.

Fig. 10. Two-dimensional reaction coordinate diagram. x and y are the two edge coordinates. [0,0] is the starting point, [1,1] is the product, and [1,0] and [0,1] are the corner intermediates corresponding to reaction along only one edge coordinate.

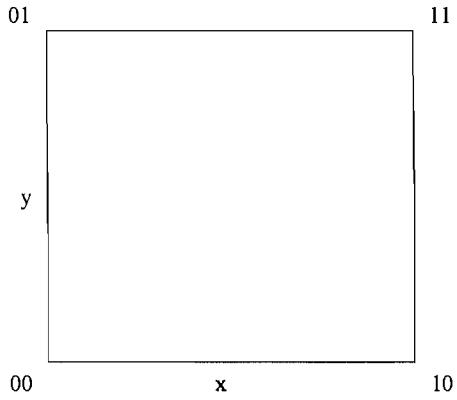

If a reaction requires three reaction coordinates for a satisfactory description, then one needs a reaction cube (89, 94–96), as illustrated in Fig. 11. Although energy is again an additional dimension at right angles to the other three, there is no simple way to show the energy for every point, although it is possible to show the contour for a particular value of the energy. The position of a transition state within the cube shows the nature of the transition state as we saw for the square. There are now three possibilities; a fully concerted reaction will have a transition state near the center of the cube;

Fig. 11. Three-dimensional reaction coordinate diagram. *x*, *y*, and *z* are the three edge coordinates. [0,0,0] is the starting point, [1,1,1] is the product, [1,0,0], [0,1,0], and [0,0,1] are the corner intermediates corresponding to reaction along only one edge coordinate, and [1,1,0], [1,0,1], and [0,1,1] are the corner intermediates corresponding to reaction along two edge coordinates.

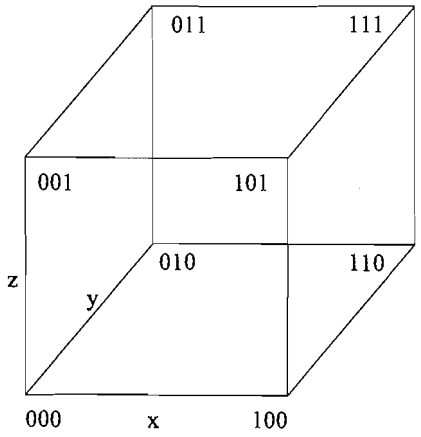

a reaction that is concerted in only two dimensions will have a transition state near the center of one of the 6 faces of the cube; a fully stepwise reaction will have a transition state located on one of the 12 edges of the cube.

Finally, if a reaction requires four reaction coordinates for a satisfactory description, and numerous reactions seem to need this many, then one needs a reaction hypercube. It is difficult to draw a four-dimensional figure on two-dimensional paper. To do so (97) we project one of the dimensions to a vanishing point in the center of the cube involving the other three dimensions. This leads to the diagram shown in Fig. 12. Fortunately we have found that one will essentially never encounter an actual reaction for which the transition state involves concerted change in four reaction coordinates at once. At least for a very symmetrical case it is possible to prove that the requirements for such a concerted reaction are so severe that they are unlikely ever to be met (98). It may still be very useful to use the four-dimensional version of Multidimensional Marcus Theory to find out which reduced dimensional region of the full reaction coordinate space is relevant to the nature of the transition state.

Fig. 12. Four-dimensional reaction coordinate diagram. *w*, *x*, *y*, and *z* are the four edge coordinates. [0,0,0,0] is the starting point, [1,1,1,1] is the product, [1,0,0,0], [0,1,0,0,], [0,0,1,0], and [0,0,0,1] are the corner intermediates corresponding to reaction along only one edge coordinate, [1,1,0,0], [1,0,1,0], [1,0,0,1], [0,1,1,0], [0,1,0,1], and [0,0,1,1] are the corner intermediates corresponding to reaction along two edge coordinates, and [1,1,1,0], [1,1,0,1], [1,0,1,1], and [0,1,1,1] are the corner intermediates corresponding to reaction along three edge coordinates.

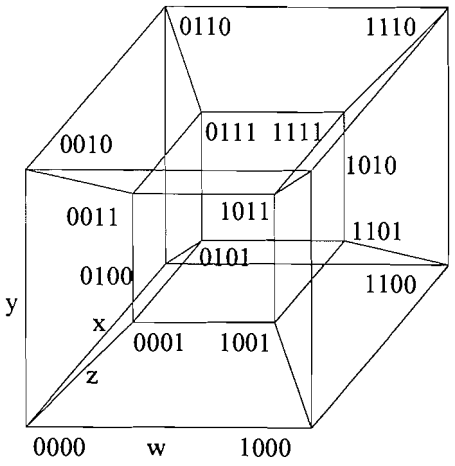

Qualitatively, what one observes is that concerted reactions occur when a concerted path permits the reaction to avoid unstable intermediates. If the corner intermediates are not high energy relative to both starting material and product, then there is little advantage to be gained by avoiding them, and reaction is likely to be stepwise. If one intermediate is much higher energy than the others, then it will be avoided, and a lower dimensional or stepwise path will be followed.

The equations needed to prescribe the energy at each place in the reaction hyperspace can be deduced from the four postulates, but become increasingly complex as the number of dimensions rises. These equations, in their full mathematical beauty, are shown in eq. [6].

$$[6]\quad G = \sum_{i=1}^{N} \{(16\tilde{G}_i + 3\Gamma_i)u_i^2 + (-32\tilde{G}_i - 2\Gamma_i)u_i^3 + 16\tilde{G}_i u_i^4\} + \sum_{j=1}^{N-1}\sum_{k>j}^{N} \left\{9\Gamma_{jk}u_j^2u_k^2 + \sum_{h=1}^{h=2}(-6\Gamma_{jk})u_j^{2+\delta_{1h}}u_k^{2+\delta_{2h}} + 4\Gamma_{jk}u_j^3u_k^3\right\}$$

$$+ \sum_{j=1}^{N-2}\sum_{k>j}^{N-1}\sum_{l>k}^{N} \left\{27\Gamma_{jkl}u_j^2u_k^2u_l^2 + \sum_{h=1}^{h=3}(-18\Gamma_{jkl})u_j^{2+\delta_{1h}}u_k^{2+\delta_{2h}}u_l^{2+\delta_{3h}} + \sum_{h=1}^{h=3}12\Gamma_{jkl}u_j^{3-\delta_{1h}}u_k^{3-\delta_{2h}}u_l^{3-\delta_{3h}} + (-8\Gamma_{jkl})u_j^3u_k^3u_l^3\right\}$$

$$+ \sum_{j=1}^{N-3}\sum_{k>j}^{N-2}\sum_{l>k}^{N-1}\sum_{m>l}^{N} \left\{81\Gamma_{jklm}u_j^2u_k^2u_l^2u_m^2 + \sum_{h=1}^{h=4}(-54\Gamma_{jklm})u_j^{2+\delta_{1h}}u_k^{2+\delta_{2h}}u_l^{2+\delta_{3h}}u_m^{2+\delta_{4h}}\right.$$

$$\left. + \sum_{h=1}^{h=4}\sum_{\substack{g=2,\\ g>h}}^{g=4} 36\Gamma_{jklm}u_j^{2+\delta_{1h}+\delta_{1g}}u_k^{2+\delta_{2h}+\delta_{2g}}u_l^{2+\delta_{3h}+\delta_{3g}}u_m^{2+\delta_{4h}+\delta_{4g}} + \sum_{h=1}^{h=4}(-24\Gamma_{jklm})u_j^{3-\delta_{1h}}u_k^{3-\delta_{2h}}u_l^{3-\delta_{3h}}u_m^{3-\delta_{4h}} + 16\Gamma_{jklm}u_j^3u_k^3u_l^3u_m^3\right\} + \text{etc.}$$

where

$$\Gamma_i = G_{\delta_{i1}\delta_{i2}\delta_{i3}\delta_{i4}\ldots} - G_{0000\ldots}$$

$$\Gamma_{jk} = \sum_{h=0}^{h=1}\sum_{g=0}^{g=1}(-1)^{h+g}G_{\varepsilon_1\varepsilon_2\ldots\varepsilon_i\ldots\varepsilon_N}$$

$$\varepsilon_i = h\delta_{ij} + g\delta_{ik}$$

$$\Gamma_{jkl} = \sum_{h=0}^{h=1}\sum_{g=0}^{g=1}\sum_{f=0}^{f=1} -(-1)^{h+g+f}G_{\varepsilon_1\varepsilon_2\ldots\varepsilon_i\ldots\varepsilon_N}$$

$$\varepsilon_i = h\delta_{ij} + g\delta_{ik} + f\delta_{il}$$

$$\Gamma_{jklm} = \sum_{h=0}^{h=1}\sum_{g=0}^{g=1}\sum_{f=0}^{f=1}\sum_{e=0}^{e=1}(-1)^{h+g+f+e}G_{\varepsilon_1\varepsilon_2\ldots\varepsilon_i\ldots\varepsilon_N}$$

$$\varepsilon_i = h\delta_{ij} + g\delta_{ik} + f\delta_{il} + e\delta_{im}$$

with δ_{ij} being the Kronecker delta.

I have published several examples of the use of this approach to describe organic reactions. The first attempt at a two-dimensional version of Multidimensional Marcus Theory was used to describe the E2 elimination of ethyl, isopropyl, and *tert*-butyl bromides (23). This work led to a qualitative and semi-quantitative prediction of the nature and energy of the transition state, using only information from solvolysis reactions and estimated energies of the carbocation and carbanion "corner intermediates." One disturbing feature of this work is that to obtain sensible free energies of activation the intrinsic barrier for removal of a proton from carbon to give a localized carbanion had to be small, ca. 1 kcal/mol. This was disturbing because increasingly it was being suggested in the literature that the intrinsic barrier for proton transfer between oxygen and oxygen or oxygen and nitrogen was 5 kcal/mol (99–102), which would lead to free energies of activation for elimination reactions that were too high. I will return to this point.

Two-dimensional Multidimensional Marcus Theory was also applied to ester interchange reactions where an aryl ester reacts with an aryloxide ion (103). This analysis showed that the interchange reactions with anions of acidic phenols were concerted displacements, even though the hydrolysis reactions of the analogous aryl acetates followed the standard tetrahedral intermediate mechanism. pK_a values that would give the limiting stepwise mechanisms, either via a tetrahedral intermediate or via an acylium ion, could be deduced as well (103).

More recently I have applied Multidimensional Marcus Theory to proton transfer reactions involving oxygen or nitrogen species, and to water-mediated proton switch reactions in which a proton migrates from one atom of a molecule to another without ever escaping into solution (104). Such mechanisms have been shown to be important in exchange reactions that can be followed by nmr, and in carbinolamine forming processes. As I stated above, my examination of the E2 reaction, combined with a common organic prejudice that proton transfer along a preformed hydrogen bond should be very easy (24, 42, 43, 102, 105–107), led me to expect a small intrinsic barrier for "fast" proton transfers. However examination of the classic data from Eigen (108) on such proton transfers, interpreted in terms of the classic Eigen mechanism, with a chemical step preceded and followed by diffusional steps, showed that application of Marcus theory to the chemical step required a barrier of 4–5 kcal/mol. The way in which this apparent intrinsic barrier fits the data is shown in Fig. 13. This was a serious problem. The resolution came when I read a paper by Berg and Jencks (109). In this paper it was shown that the rate of proton exchange in amines was limited by the energy cost of moving a water out of contact with the amine, leaving a water-sized hole, into which a different water could diffuse. The activation energy for moving the water out was determined by the cavitation energy, the hydrogen bond energy, and the dispersion forces between amine and water. This gives a total very similar to the observed free energy of activation for exchange and also to the activation energy for diffusion. Suddenly the answer to the conundrum was clear. The Eigen mechanism could not lead to a contact hydrogen-bonded pair, because loss of the last water molecule separating the acid and base would be too slow, leading to a rate constant of about 10^7 M^{-1} s^{-1}, while the observed process has a rate constant greater than 10^9 M^{-1} s^{-1}. This water would be held by two hydrogen bonds, each worth just over 3 kcal/mol, and both would have to be lost in order for the last water to move out of contact with the acid and base. This meant that the proton transfer was a two-dimensional process involving motion of one proton to the bridging water and one from it. Analysis in terms of the appropriate square diagram permitted calculation of the activation energy for the proton transfer, giving results within 1 kcal of the true value, with an intrinsic barrier of 1 kcal/mol. A similar model, but with two bridging water molecules, permitted calculation of the rates of water-mediated proton switch reactions (104).

[7] $$AH + B \rightleftharpoons AH,B \rightleftharpoons AH,B \rightleftharpoons A + HB$$

An examination of amide hydrolysis (110, 111), in collaboration with R.S. Brown and co-workers, led to a successful description of the alkaline hydrolysis in terms of a proton switch to give an anionic zwitterion that could then expel amine. The analysis suggested that the rate-limiting step was the proton switch, with breakdown of the anionic zwitterion being a very fast process (110, 112). This mechanism is shown in Scheme 4.

The application of Multidimensional Marcus Theory is much less advanced than the application of Marcus Theory. I hope that the mathematical and computational tools that I have developed will facilitate this approach. Thus far the results are very promising, and further testing on other reactions is an important goal for research in my laboratory.

Conjecture 3: The effective molarity of an intramolecular reaction can be predicted given the equilibrium constant if data for intermolecular analogs are available. Intra- and intermolecular reactions are governed by the same Marcus intrinsic barrier

Now I will turn to the final conjecture, concerning intramolecular reactions. It is commonly found that intramolecular reactions are fast relative to their intermolecular analogs (4). The

Fig. 13. Rate–equilibrium correlation for proton transfer reactions involving acetic acid with (left to right) hydrazine, imidazole, aniline, and *m*-chloroaniline. The line is calculated for the mechanism AH + B ⇌ AH,B ⇌ A,HB ⇌ A + HB with Marcus Theory applied to the second step and the first and third processes being diffusion controlled. The line is calculated with an average intrinsic barrier of 5.23 kcal/mol.

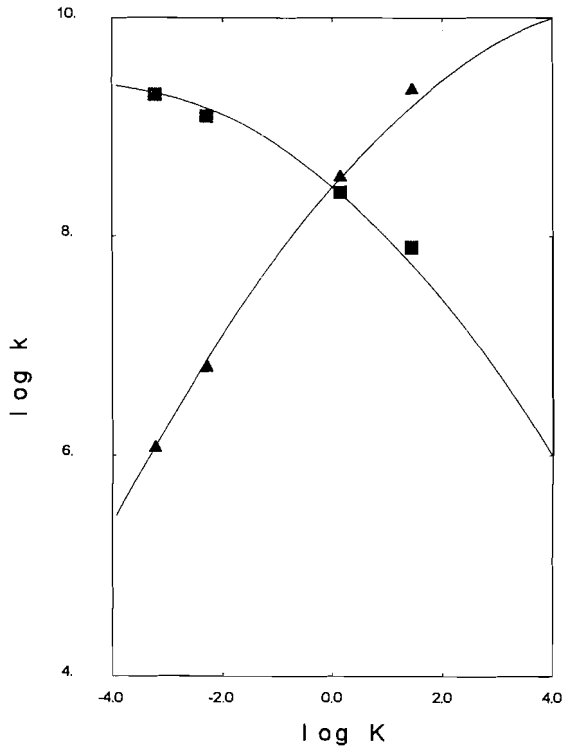

Scheme 4. Mechanism for breakdown of the tetrahedral intermediate in the base-catalyzed amide hydrolysis.

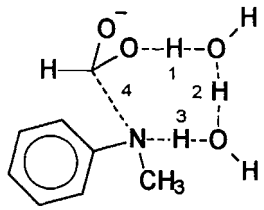

size of the rate enhancement is measured by the "effective molarity," which is the ratio of the first-order rate constant for the intramolecular reaction to the second-order rate constant for the analogous intermolecular reaction. Effective molarities can range from quite small, 10^{-3}, to very large, 10^{8} or even larger (4).

We have studied a series of intramolecular aldol reactions (113, 114), illustrated in Scheme 5. The striking phenomenon is that cyclization of 2,5-hexanedione to form a five membered ring ketol is very similar thermodynamically to cyclization of 2,6-heptanedione to form a six-membered ring ketol, yet is 1000 times slower. There is clearly not a simple rate–equilibrium correlation in terms of overall rates and equilibria. This is a situation governed by Baldwin's rules (115–118): the problem is that it is difficult to get the stereoelectronically required alignment of the planar carbonyl and planar enolate in order to form a five-membered ring, and much easier to get such an alignment to form a six-membered ring. In terms of Baldwin's rules, a 5-(enol *endo*)-*exo*-trig reaction is forbidden while a 6-(enol *endo*)-*exo*-trig reaction is allowed (118). We analyze these reactions in terms of a mechanism analogous to that used for the intermolecular aldols but, in place of encounter complex formation of enolate and carbonyl component, we have rotation to a conformation with the reacting atoms in van der Waals contact and able to react by a simple conrotatory motion, as shown in Scheme 6. The energies of the reactive conformations, with the reacting groups eclipsed for hexanedione, or in what is equivalent to a 1,3-diaxial arrangement for heptanedione, were calculated by MM3[3] (119–121) for the neutral enols. When Marcus Theory is applied to the microscopic rate and equilibrium process defined above, we find that the intrinsic barrier so calculated is the same as for the intermolecular aldol reaction.

Scheme 5. Inter- and intra-molecular aldol condensations.

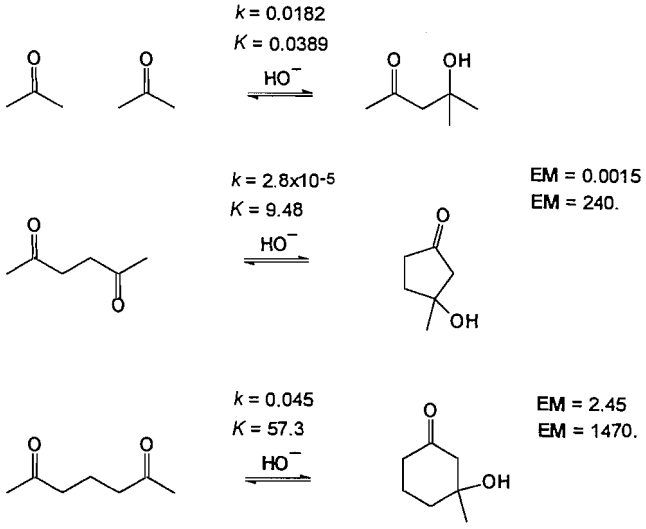

In work that is still in progress we are examining lactone formation. The classic study of this process was by Storm and Koshland (122), who reported the series shown in Scheme 7; to the data reported by Storm and Koshland we have added the rate and equilibrium constants (123) for δ-hydroxyvaleric acid/δ-valerolactone. The rate enhancements became quite dramatic as they moved along the series. The challenge was to see if these reactions also could be explained in terms of Marcus Theory with the same intrinsic barriers as for intermolecular reactions. We interpret these reactions in terms of the detailed reaction mechanism shown in Scheme 8. To apply Marcus Theory we must know the energies of the tetrahedral intermediates, and estimate pK_a values for all the protonated species encountered on the reaction path.

We are in the course of determining the energies of the tetrahedral intermediates for a series of lactonizations by our indirect thermodynamic method (25, 26, 29, 124) We start with the heats of formation for the corresponding orthoesters, determined by reaction calorimetry using the process in eq.

[3] As contained in MM3(89) as obtained from QCPE.

Scheme 6. Detailed mechanism for an intramolecular aldol condensation.

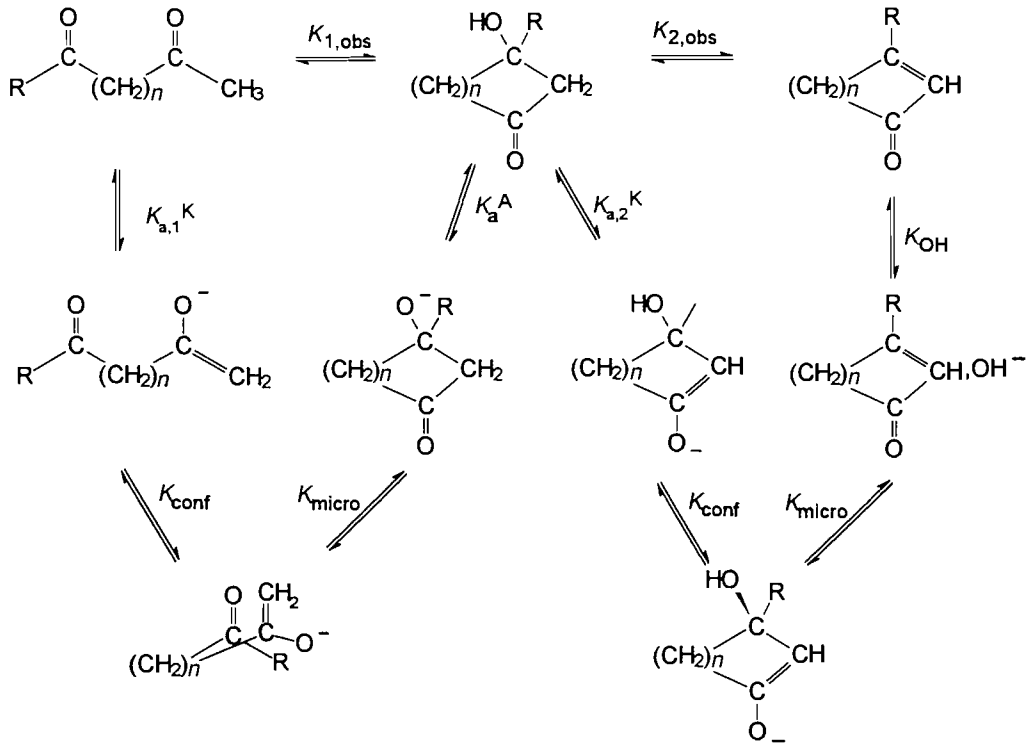

Scheme 7. Intramolecular esterification.

	k_{H+}	EM
CH_3—COOH + $HOCH_2CH_3$	1.8×10^{-5}	
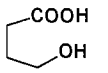	1.43×10^{-3}	79.
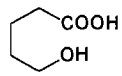	2.21×10^{-3}	122.
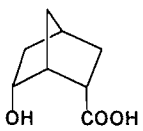	18.7	1.04×10^{6}

[8]. Then, by methods we used before, we could calculate the heats of formation for the liquids, heats of vaporization (125), entropies, free energies of transfer (126), and thus free energies of formation in aqueous solution. Then we could calculate the (small) free energy changes for the hypothetical hydrolysis reactions replacing OCH_3 by OH (29), eq. [9] and arrive at the free energies of formation of the tetrahedral intermediates.

pK_a values were estimated by linear free energy relations, as we have previously described (27). pK_{BH^+} values for the lactones are less well defined because there are no equilibrium studies of protonation of which I am aware. There are studies of methyl transfer equilibria relating cations, which show that the lactones are more basic than simple esters (127). Values of

Fig. 14. Calculated reaction coordinate diagram for the acid-catalyzed formation of ethyl acetate from ethanol and acetic acid. The mechanism assumed is the same as in Scheme 8. Activation barriers for proton transfers assume diffusion control in the favorable direction. Encounter complex formation is assumed to be diffusion controlled, and the equilibrium constant for encounter complex formation is estimated following Hine. The free energies of activation for the addition of alcohol and the expulsion of water were based on previously determined intrinsic barriers. The observed free energy of activation is shown and is within 2 kcal of the calculated value. Note that for this process expulsion of water is the rate-limiting step.

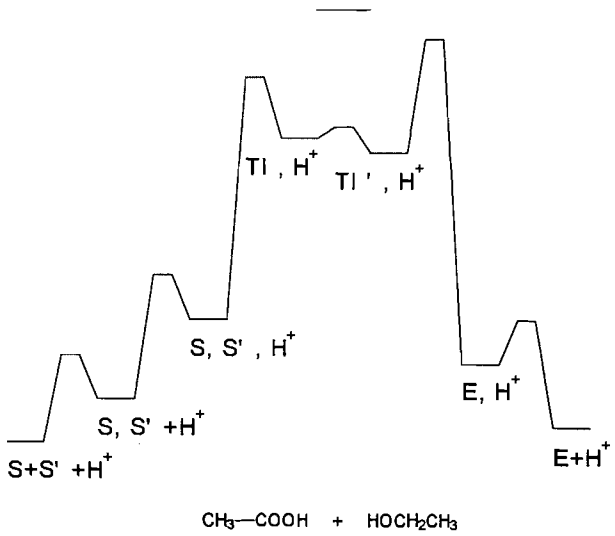

Scheme 8. Mechanism for intramolecular esterification.

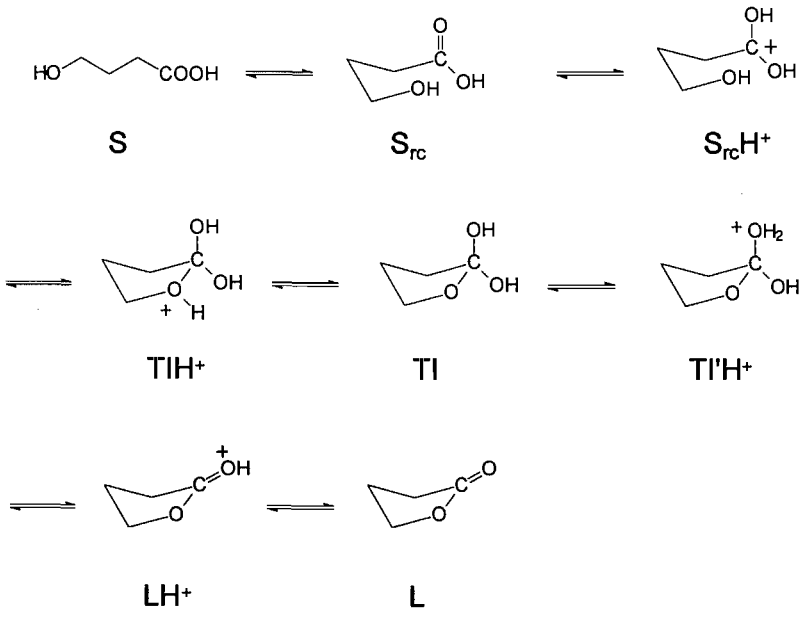

pK_{BH^+} for the lactones were estimated, but are unavoidably uncertain.

The intrinsic barriers for addition of water (33, 103) or methanol (103) (or hydroxide or methoxide) to carbonyl groups are known, and so we have all the information to calculate the full reaction coordinate diagram. We will focus on the cases of ethyl acetate and 2-*endo*-hydroxy[2.2.1]bicycloheptane-6-endocarboxylic acid. Figs. 14 and 15 show the calculated free energy levels for intermediates and transition states, as well as the experimentally observed transition state level. The model used for the carbon–oxygen bond-making/breaking processes was as shown in eq. [10]; by using Multidimensional Marcus Theory we could allow for either general or specific acid catalysis and either simple attack by water or hydroxyl or general-base-catalyzed attack, with water as general base. Clearly we are able to come quite close to the observed value. An additional complication is that the rate-determining steps are expected to be different in these two reactions; because of the lower intrinsic barrier for methoxide expulsion, attack of the alcohol is only rate limiting when lactone formation is strongly favored thermodynamically.

[8] 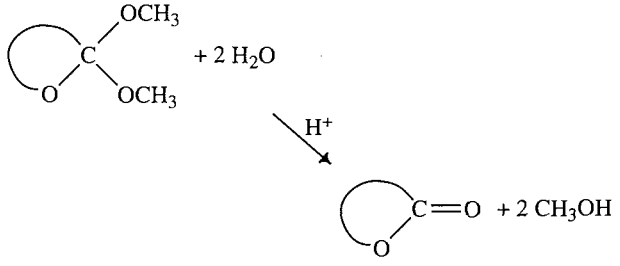

[9] 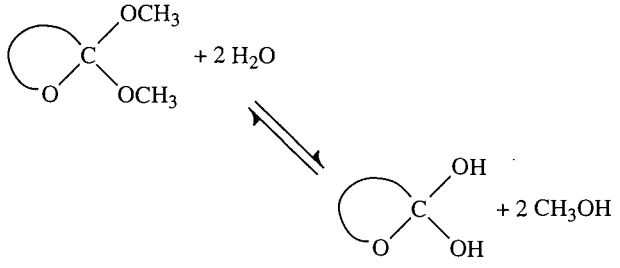

[10] 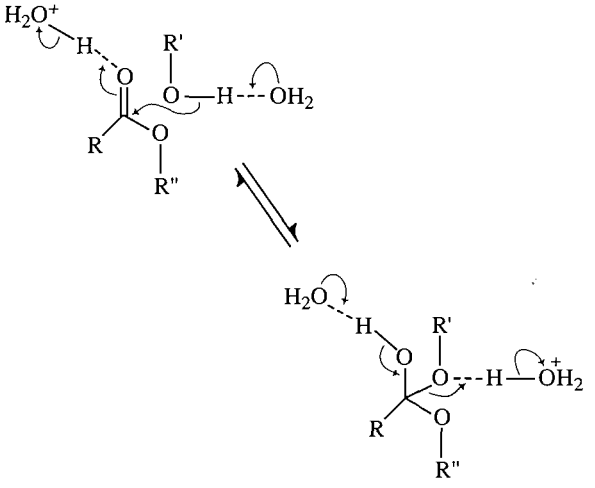

Two examples do not constitute general proof but it is very encouraging that the first two cases to have been examined fit a pattern involving intrinsic barriers for intramolecular reactions that are the same as for the intermolecular analogs. If the intrinsic barrier is in general the same for an intramolecular reaction as for the analogous intermolecular reaction, then once we have the energies of the intermediates and products for the two reactions, and know the intrinsic barrier for the type of reaction involved, we can calculate the effective molarity for the kinetic process. In principle, and increasingly readily in practice, it will be possible to calculate the energies of stable species from structure, so our results hold out the

Fig. 15. Calculated reaction coordinate diagram for the acid-catalyzed formation of lactone from 6-*endo*-hydroxy-[2.2.1]bicycloheptane-2-endocarboxylic acid. The mechanism assumed is the same as in Scheme 8, and the calculations were as described in the legend to Fig. 14. The observed free energy of activation is shown and is within 1 kcal of the calculated value. Note that for this process addition of the alcohol is the rate-limiting step.

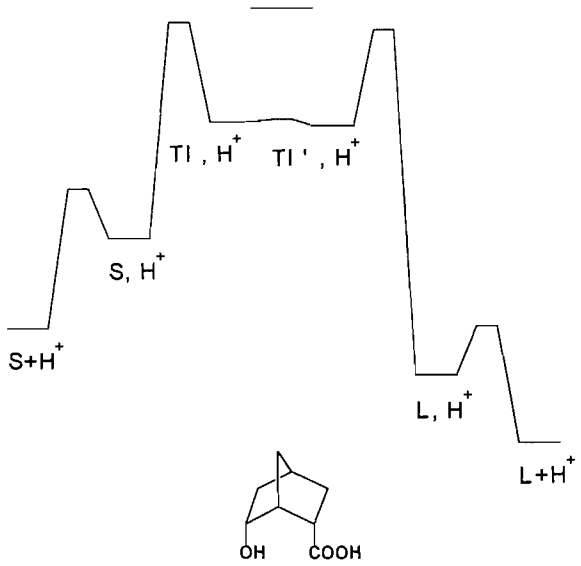

prospect of a complete explanation for intramolecular rate enhancements.

Although the conjectures that currently drive my research are still incompletely proven and controversial, the evidence to date is encouraging and will guide further research as I seek additional tests of these ideas.

Acknowledgments

The experimental studies that provided the data required to develop and test the ideas discussed in this paper have been carried out by a number of co-workers over the years, and I would like to acknowledge them here: J.A. Barker, J. Cossar, P.A. Cullimore, B.A. Dawson, J. Guo, A.P. Huntington, Y-C. Lee, J. Lu, D.C. Pike, K.F. Taylor, and X.P. Wang. I thank the Natural Sciences and Engineering Research Council of Canada for financial support of this work.

References

1. L. Michaelis and M.L. Menton. Biochem. Z. **49**, 333 (1913).
2. W.P. Jencks. Catalysis in chemistry and enzymology. McGraw–Hill, New York. 1969.
3. R.H. Abeles, P.A. Frey, and W.P. Jencks. Biochemistry. Jones and Bartlett, Boston. 1992.
4. A.J. Kirby. Adv. Phys. Org. Chem. **17**, 183 (1980).
5. A.O. Cohen and R.A. Marcus. J. Phys. Chem. **72**, 4249 (1968).
6. R.A. Marcus. J. Am. Chem. Soc. **91**, 7224 (1969).
7. R.A. Marcus. Annu. Rev. Phys. Chem. **15**, 155 (1964).
8. W.P. Jencks. Chem. Rev. **85**, 511 (1985).
9. G.S. Hammond. J. Am. Chem. Soc. **77**, 334 (1955).
10. R.A. Marcus. J. Phys. Chem. **72**, 891 (1968).
11. R.P. Bell. Proc. R. Soc. London, Ser. A: **154**, 414 (1936).
12. M.G. Evans and M. Polanyi. Trans. Faraday Soc. **34**, 11 (1938).
13. J.E. Leffler. Science, **117**, 340 (1953).
14. J.E. Leffler and E. Grunwald. Rates and equilibria of organic reactions. Wiley, New York. 1963.
15. E.R. Thornton. J. Am. Chem. Soc. **89**, 2915 (1967).
16. E.K. Thornton and E.R. Thornton. *In* Transition states of biochemical processes. *Edited by* R.D. Gandour and R.L. Schowen. Plenum, New York. 1978. p. 3.
17. R.A. Marcus. Discuss. Faraday Soc. **29**, 21 (1960).
18. G.W. Koeppl and A.J. Kresge. J. Chem. Soc. Chem. Commun. 371 (1973).
19. W.J. Albery and M.M. Kreevoy. Adv. Phys. Org. Chem. **16**, 87 (1978).
20. J. Kurz. Chem. Phys. Lett. **57**, 243 (1978).
21. B.M. Dunn. Int. J. Chem. Kinet. **6**, 143 (1974).
22. W.J. LeNoble, A.R. Miller, and S.D. Hammann. J. Org. Chem. **42**, 338 (1977).
23. J.P. Guthrie. Can. J. Chem. **68**, 1643 (1990).
24. J. Hine. J. Am. Chem. Soc. **93**, 3701 (1971).
25. J.P. Guthrie. J. Am. Chem. Soc. **95**, 6999 (1973).
26. J.P. Guthrie. Can. J. Chem. **54**, 202 (1976).
27. J.P. Guthrie. J. Am. Chem. Soc. **100**, 5892 (1978).
28. J.P. Guthrie. J. Am. Chem. Soc. **96**, 3608 (1974).
29. J.P. Guthrie. Can. J. Chem. **53**, 898 (1975).
30. W.N. Olmstead, Z. Margolin, and F.G. Bordwell. J. Org. Chem. **45**, 3295 (1980).
31. C.D. Ritchie. *In* Solute-solvent interactions. Vol. 1. *Edited by* J.F. Coetzee and C.D. Ritchie. Marcel Dekker, New York. 1969. p. 219ff.
32. J.P. Guthrie. J. Am. Chem. Soc. **113**, 7249 (1991).
33. J.P. Guthrie. Manuscript in preparation (1996).
34. J.R. Keefe and A.J. Kresge. *In* The chemistry of enols. *Edited by* Z. Rappoport. Wiley, Chichester. 1990. p. 399ff.
35. L.R. Fedor. J. Am. Chem. Soc. **91**, 908 (1969).
36. C.D. Ritchie. J. Am. Chem. Soc. **106**, 7087 (1984).
37. J.P. Guthrie. Can. J. Chem. **56**, 962 (1978).
38. J.P. Guthrie and X.P. Wang. Can. J. Chem. **70**, 1055 (1992).
39. J. Lu. Ph.D. Thesis, University of Western Ontario (1994).
40. M.M. Kreevoy and D.E. Konasewich. Adv. Chem. Phys. **21**, 243 (1972).
41. W.J. Albery, A.N. Campbell-Crawford, and J.S. Curran. J. Chem. Soc. Perkin Trans 2, 2206 (1972).
42. A.J. Kresge. Chem. Soc. Rev. **2**, 475 (1973).
43. A.J. Kresge. Acc. Chem. Res. **8**, 354 (1975).
44. W.J. Albery. Annu. Rev. Phys. Chem. **31**, 227 (1980).
45. M.J. Pellerite and J.I. Brauman. J. Am. Chem. Soc. **105**, 2672 (1983).
46. J.R. Murdoch. J. Am. Chem. Soc. **105**, 2159 (1983).
47. J.R. Murdoch. J. Am. Chem. Soc. **105**, 2660 (1983).
48. M.M. Kreevoy and I.-S.H. Lee. J. Am. Chem. Soc. **106**, 2550 (1984).
49. C.J. Schlesener, C. Amatore, and J.K. Kochi. J. Am. Chem. Soc. **106**, 3567 (1984).
50. D.L. Leussing and M. Emly. J. Am. Chem. Soc. **106**, 443 (1984).
51. M.Y. Chen and J.R. Murdoch. J. Am. Chem. Soc. **106**, 4735 (1984).
52. L. Eberson. Acta Chem. Scand. Ser. B: **B38**, 439 (1984).
53. B.A. Miller and D.L. Leussing. J. Am. Chem. Soc. **107**, 7146 (1985).
54. C.J. Schlesener, C. Amatore, and J.K. Kochi. J. Phys. Chem. **90**, 3747 (1986).
55. W.J. Albery. J. Chem. Soc. Faraday Trans. **78**, 1579 (1982).
56. C.F. Bernasconi. Acc. Chem. Res. **20**, 301 (1987).
57. M.M. Kreevoy, D. Ostovic, I.-S.H. Lee, D.A. Binder, and G.W. King. J. Am. Chem. Soc. **110**, 524 (1988).

58. J.W. Bunting and D. Stefanidis. J. Am. Chem. Soc. **111**, 5834 (1989).
59. E.S. Lewis. Bull. Soc. Chim. Fr. 259 (1988).
60. K. Yates. J. Phys. Org. Chem. **2**, 300 (1989).
61. J. Kurz. J. Am. Chem. Soc. **111**, 8631 (1989).
62. D. Kim, I.H. Lee, and M.M. Kreevoy. J. Am. Chem. Soc. **112**, 1889 (1990).
63. D.L. Leussing. J. Org. Chem. **55**, 666 (1990).
64. S.S. Kristjansdottir and J.R. Norton. J. Am. Chem. Soc. **113**, 4366 (1991).
65. L. Eberson. Adv. Phys. Org. Chem. **18**, 79 (1982).
66. Y. Kim, D.G. Truhlar, and M.M. Kreevoy. J. Am. Chem. Soc. **113**, 7837 (1991).
67. J. Suhnel. Prog. Phys. Org. Chem. **6**, 281 (1993).
68. E.S. Lewis, S. Kukes, and C.D. Slater. J. Am. Chem. Soc. **102**, 1619 (1980).
69. M. Cheong and D.M. Leussing. J. Am. Chem. Soc. **111**, 2541 (1989).
70. E.S. Lewis and D.D. Hu. J. Am. Chem. Soc. **106**, 3292 (1984).
71. E.S. Lewis, M. McLauglin, and T.A. Douglas. J. Am. Chem. Soc. **107**, 6668 (1985).
72. E.S. Lewis. J. Phys. Chem. **90**, 3756 (1986).
73. E. Lewis, T. Douglas, and M. McLaughlan. Isr. J. Chem. **26**, 331 (1985).
74. E. Lewis, T. Douglas, and M. McLaughlin. Adv. Chem. Ser. **215** (1987).
75. W.J. Albery, A.N. Campbell-Crawford, and J.S. Curran. J. Chem. Soc. Perkin Trans. 2, 2206 (1972).
76. J. Bunting and D. Stefanidis. J. Am. Chem. Soc. **110**, 4008 (1988).
77. D.S.J. Bunting. J. Am. Chem. Soc. **112**, 3163 (1990).
78. D. Stefanidis and J. Bunting. J. Am. Chem. Soc. **113**, 991 (1991).
79. S. Wodzinski and J. Bunting. J. Am. Chem. Soc. **116**, 6910 (1994).
80. C. Bernasconi, J.P. Fox, and S. Fornarini. J. Am. Chem. Soc. **102**, 2810 (1980).
81. C.F. Bernasconi, D.J. Carre, and A. Kanavarioti. J. Am. Chem. Soc. **103**, 4850 (1981).
82. C. Bernasconi and G. Leonarduzzi. J. Am. Chem. Soc. **104**, 5133 (1982).
83. C. Bernasconi, C.J. Murray, and J.P. Fox. J. Am. Chem. Soc. **105**, 4349 (1983).
84. C. Bernasconi and R. Killion. J. Am. Chem. Soc. **119**, 7506 (1988).
85. J. Richard. Tetrahedron, **51**, 1535 (1995).
86. J. Kurz and L. Kurz. Isr. J. Chem. **26**, 339 (1985).
87. P. Pruszynski, Y. Chiang, A.J. Kresge, N.P. Schepp, and P.A. Walsh. J. Phys. Chem. **90**, 3760 (1986).
88. C.D. Ritchie, C. Kubisty, and G.Y. Ting. J. Am. Chem. Soc. **105**, 279 (1983).
89. E. Grunwald. J. Am. Chem. Soc. **107**, 4715 (1985).
90. J.E. Critchlow. J. Chem. Soc. Faraday Trans. **68**, 1774 (1972).
91. W.J. Albery. Prog. React. Kinet. **4**, 353 (1967).
92. R.A. More O'Ferrall. J. Chem. Soc. (B) , 274 (1970).
93. W.P. Jencks. Chem. Rev. **72**, 705 (1972).
94. E. Grunwald. J. Am. Chem. Soc. **107**, 4710 (1985).
95. P.H. Scudder. J. Org. Chem. **55**, 4238 (1990).
96. I.V. Trushkov, V.V. Zhdankin, A.S. Kozmin, and N.S. Zefirov. Tetrahedron Lett. **31**, 3199 (1990).
97. G. Gamow. One, two, three ... infinity: facts and speculations of science. Viking Press, New York. 1961.
98. J.P. Guthrie. Submitted (1996).
99. H. Fischer, F.X. DeCandis, S.D. Ogden, and W.P. Jencks. J. Am. Chem. Soc. **102**, 1340 (1980).
100. H.F. Gilbert and W.P. Jencks. J. Am. Chem. Soc. **99**, 7931 (1977).
101. R.A. Bednar and W.P. Jencks. J. Am. Chem. Soc. **107**, 7117 (1985).
102. F. Hibbert. Adv. Phys. Org. Chem. **22**, 113 (1986).
103. J.P. Guthrie. J. Am. Chem. Soc. **113**, 3941 (1991).
104. J.P. Guthrie. Submitted (1996).
105. J. Hine. J. Am. Chem. Soc. **94**, 5766 (1972).
106. E. Grunwald. Prog. Phys. Org. Chem. **3**, 317 (1966).
107. H. Strehlow and P. Hildebrandt. Ber. Bunsen-Ges. Phys. Chem. **94**, 173 (1990).
108. M. Eigen. Angew. Chem. Int. Ed. Engl. **3**, 1 (1964).
109. U. Berg, W.P. Jencks. J. Am. Chem. Soc. **113**, 6997 (1991).
110. H. Slebocka-Tilk, A.J. Bennet, J.W. Keillor, R.S. Brown, J.P. Guthrie, and A. Jodhan. J. Am. Chem. Soc. **112**, 8507 (1990).
111. A.J. Bennet, H. Slebocka-Tilk, R.S. Brown, J.P. Guthrie, and A. Jodhan. J. Am. Chem. Soc. **112**, 8497 (1990).
112. J.P. Guthrie, J. Barker, P.A. Cullimore, J. Lu, and D.C. Pike. Can. J. Chem. **71**, 2109 (1993).
113. J.P. Guthrie and J. Guo. Submitted (1996).
114. J. Guo. Ph.D. Thesis, University of Western Ontario (1995).
115. J.E. Baldwin. J. Chem. Soc. Chem. Commun. 734 (1976).
116. J.E. Baldwin and L.I. Kruse. J. Chem. Soc. Chem. Commun. 233 (1977).
117. J.E. Baldwin, R.C. Thomas, L.J. Kruse, and L. Silberman. J. Org. Chem. **42**, 3846 (1977).
118. J.E. Baldwin and M.J. Lusch. Tetrahedron, **38**, 2939 (1982).
119. N.L. Allinger, Y.H. Yuh, and J.H. Lii. J. Am. Chem. Soc. **111**, 8551 (1989).
120. J.-H. Lii and N.L. Allinger. J. Am. Chem. Soc. **111**, 8566 (1989).
121. N.L. Allinger, K. Chen, M. Rahman, and A. Pathiaseril. J. Am. Chem. Soc. **113**, 4503 (1991).
122. D.R. Storm and D.E. Koshland. J. Am. Chem. Soc. **94**, 5805 (1972).
123. O.H. Wheeler and E.E. Granell de Rodriguez. J. Org. Chem. **29**, 1227 (1964).
124. J.P. Guthrie. Can. J. Chem. **55**, 3562 (1977).
125. J.P. Guthrie. Can. J. Chem. **64**, 635 (1986).
126. J.P. Guthrie. Can. J. Chem. **69**, 1893 (1991).
127. K.B. Wiberg and R.F. Waldron. J. Am. Chem. Soc. **113**, 705 (1991).

1995 McBryde Medal Award Lecture Solid phase microextraction — a unique tool for chemical measurements[1]

Tadeusz Górecki, Anna Boyd-Boland, Zhouyao Zhang, and Janusz Pawliszyn

Abstract: The paper presents recent advances in solid phase microextraction (SPME). The method utilizes a small fused silica fibre coated with a suitable polymeric stationary phase for analyte extraction from various matrices. The fibre is mounted in a syringe-like holder for protection. SPME has been used for the characterization of polymeric coating properties. Infinite-dilution weight-fraction activity coefficients have been determined for five solutes in two different stationary phases. Their values correlate well with the structure of the analytes and the coating. Other SPME uses include simultaneous determination of 60 pesticides in liquid matrices. A comparison between SPME, liquid extraction, and Soxhlet extraction for the analysis of Atrazine, Simazine, and Metolachlor in well water, as well as Metolachlor in soil samples, produced similar results for all three methods. The solvent-free character of SPME enables its use as sample introduction technique for fast GC analysis. Separations of BTEX in less than 9 s, and of volatile compounds described in EPA method 624 in 2.5 min, are described. SPME has also been used for the analysis of tetraethyllead and Pb(II) in water. Before the analysis, lead is derivatized with sodium tetraethylborate, and the tetraethyllead formed is extracted from sample headspace. Sub-ppb detection limits have been achieved with FID. Finally, SPME has been coupled to HPLC with the use of a specially designed interface. The combination has been tested on samples of polyaromatic hydrocarbons and surfactants in water. Very good precision of retention times and peak areas has been achieved.

Key words: solid phase microextraction, coating characterization, pesticide analysis, fast GC, lead and organolead compounds, SPME/HPLC.

Résumé : Dans ce travail, on présente les résultats récents obtenus en microextraction en phase solide (MEPS). La méthode fait appel à une petite fibre de silice fondue recouverte d'une phase stationnaire polymérique appropriée permettant de faire l'extraction de l'analyse à partir de diverses matrices. Pour sa protection, la fibre est montée dans un récipient en forme de seringue. La MEPS a été utilisée pour la caractérisation de propriétés de recouvrements polymériques. On a déterminé les coefficients d'activité à dilution infinie de la fraction massique pour cinq solutés, dans deux phases stationnaires différentes. Les valeurs présentent une bonne corrélation avec la structure des analytes et du recouvrement. La détermination de 60 pesticides dans des matrices liquides est une autre utilisation des MEPS. Une comparaison de la MEPS avec l'extraction liquide et l'extraction au Soxhlet pour l'analyse de l'Atrazine, de la Simazine et du Métolachlore dans l'eau de puits, ainsi que du Métolachlore dans des échantillons de sols, ont conduit à des résultats semblables pour les trois méthodes. Compte tenu du fait que les MEPS n'impliquent aucun solvant, cette méthode peut être utilisée comme technique d'introduction des échantillons pour des analyses en CG rapides. On décrit la séparation du BTEX en moins de 9 s et celle des composés volatils décrits dans la méthode de l'« EPA 624 » en 2,5 min. On a aussi utilisé la MEPS pour l'analyse du tétraéthylplomb et du Pb(II) dans l'eau. Avant l'analyse, le plomb est transformé en dérivé à l'aide de tétraéthylborate de sodium et le tétraéthylplomb formé est extrait de l'échantillon. On a atteint des limites de détection inférieures au ppb avec le «FID». Enfin, on a couplé la MEPS à la CLHP à l'aide d'une interface dessinée à cette fin. On a évalué la combinaison sur des échantillons d'hydrocarbures polyaromatiques et d'agents de surface dans l'eau. On a obtenu de très bonnes précisions pour les temps de rétention et pour les surfaces sous les pics.

Mots clés : microextraction en phase solide, caractérisation du revêtement, analyse des pesticides, CG rapide, composés du plomb et organoplombés, MEPS/CLHP.

[Traduit par la rédaction]

Received October 16, 1995.

T. Górecki,[2] A. Boyd-Boland, Z. Zhang, and J. Pawliszyn.[3] Department of Chemistry and Waterloo Centre for Groundwater Research, University of Waterloo, Waterloo, ON N2L 3G1, Canada.

[1] This is an invited review article based on the 1995 McBryde Medal Award lecture presented by Professor Pawliszyn at the Annual Conference of the Canadian Society for Chemistry in Guelph, Ontario, May 1995.

[2] On leave from Faculty of Chemistry, Technical University of Gdańsk, Poland.
[3] Author to whom correspondence may be addressed. Telephone: (519) 888-4641. Fax: (519) 746-0435. E-mail: Janusz@uwaterloo.ca

Fig. 1. Schematic diagram of the commercial SPME device.

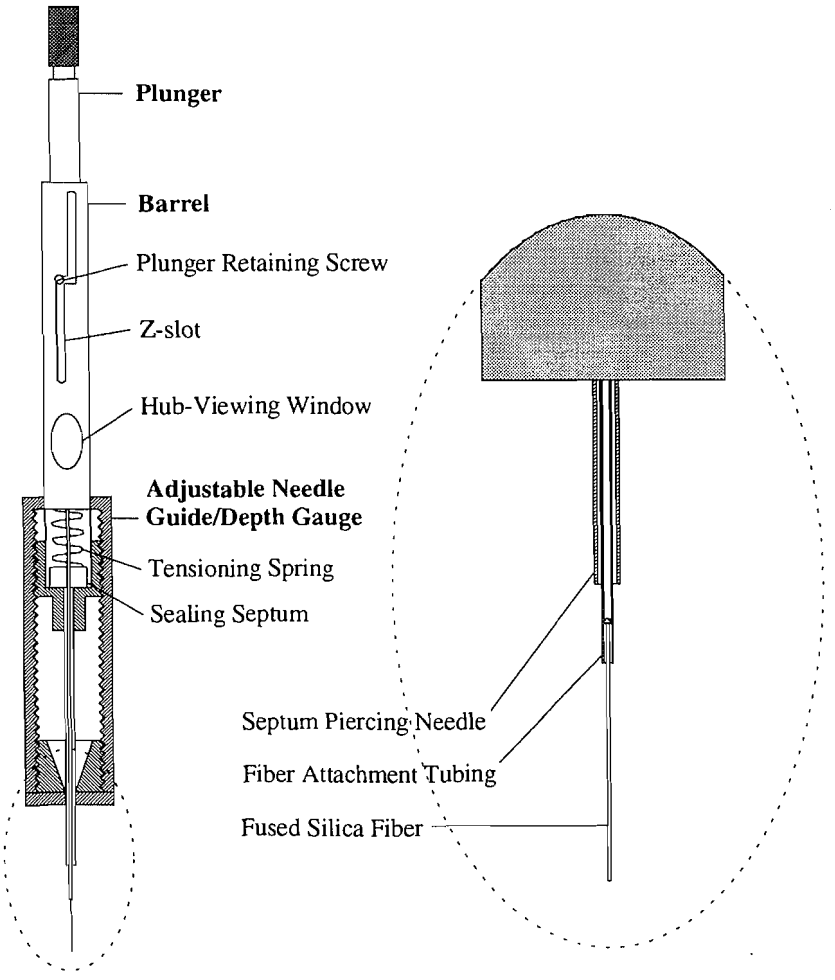

Introduction

Analysis of trace components in natural liquid samples requires, in most cases, isolation and preconcentration of the analyte from the matrix. In the case of organic compounds, this is usually done by liquid–liquid extraction (including Soxhlet extraction), solid phase extraction, or headspace extraction (1). All these methods suffer from numerous drawbacks. Liquid–liquid extraction (LLE) requires large quantities of high-purity solvents, which are expensive to purchase and dispose of, and pose health and environmental hazards. Methods based on LLE are very laborious and time consuming. Their multistage character increases the potential risk of errors.

Solid phase extraction (SPE) is a much more modern approach. In this method analytes are isolated from the liquid matrix by adsorption onto a specially formulated material, usually packed in a cartridge or immobilized in a disk-shaped support. Application of SPE allows the time required for sample preparation to be significantly cut compared to LLE. However, the method is not completely solvent free, as a certain amount of solvent is necessary to liberate the trapped analytes prior to their chromatographic analysis. In many cases the eluate must be further concentrated by controlled evaporation of the solvent, which can pollute the atmosphere. Analyte losses may also occur at this stage. Suspended solids may cause plugging of the cartridges. The biggest SPE drawback, however, is the strong dependence of the breakthrough volumes on matrix composition.

Headspace extraction is, by its nature, limited to volatile and semivolatile analytes. Except static headspace, the method is difficult to automate. Dynamic headspace techniques are multistage, thus potentially error prone. Foaming can be a significant problem when analyzing natural samples. In some variations (closed-loop stripping analysis) small amounts of solvent have to be used for analyte desorption.

Solid phase microextraction

Solid phase microextraction (SPME) is a new approach, introduced about 6 years ago (2). It addresses most of the disadvantages of the methods mentioned above. SPME utilizes a small fused silica fibre, usually coated with a suitable polymeric stationary phase, for analyte extraction from a matrix. The fibre is mounted for protection in a syringe-like device. As the stationary phase is a liquid, analytes are absorbed by it until an equilibrium is reached in the system. The amount extracted

under such conditions is dependent on the partition coefficient between the sample and the coating. No total extraction occurs, thus problems related to breakthrough or limited sample capacity are virtually nonexistent.

Figure 1 presents the commercial SPME device, produced by Supelco, Inc. (Bellefonte, Pa.). The fibre, glued into a piece of stainless steel tubing, is mounted in a special holder. For protection during storage or piercing of a septum the fibre is withdrawn into the needle. During extraction the fibre is exposed to the sample by depressing the plunger. The analytes are allowed to partition into the coating for a predetermined time, and the fibre is then retracted into the needle. The whole device is next transferred to a GC, and the fibre is inserted into a hot injector, where thermal desorption of the trapped analytes takes place. The entire process is very simple and straightforward. It can be easily automated by using a properly modified syringe autosampler, commercially available from Varian (Varian Associates, Sunnyvale, Calif.).

SPME combines sample isolation and preconcentration into a single step, eliminating many potential sources of error. The technique is completely solvent free. Handling of the sample is minimal. Owing to the simple, cylindrical geometry of the sorbent, no plugging can occur. The potential matrix effects can be accounted for by standard addition. The technique requires no instrumental modifications, as regular GC injectors are used for analyte desorption. SPME has been used for many applications, including the determination of substituted benzene compounds (3, 4), caffeine in beverages (5), volatile organic compounds in water (6), polyaromatic hydrocarbons and polychlorinated biphenyls (7), chlorinated hydrocarbons (8), and phenols (9, 10). Sampling can be carried out directly from liquid samples, from their headspace, or from headspace over solid samples (11). Another promising field is application of SPME for the analysis of organic air pollutants (12).

The heart of SPME is the coating. Its physicochemical characteristics determine the suitability of the technique for the analysis of various classes of compounds. Six different coatings are currently available from Supelco: 7 μm, 30 μm, and 100 μm thick poly(dimethylsiloxane), 85 μm thick poly(acrylate), 65 μm thick poly(dimethylsiloxane)/divinylbenzene, and 65 μm thick Carbowax/divinylbenzene. Fibres coated with poly(dimethylsiloxane) are suitable for the analysis of nonpolar and moderately polar analytes. Poly(acrylate) coated fibres work best for analytes of intermediate to high polarity. Fibres containing divinylbenzene are best suited for the extraction of volatile polar and nonpolar compounds. New coatings are still being developed. Finding ones that are suitable for specific groups of analytes among the many possible polymers is not a trivial task. It requires a simple, cost-effective, and time-efficient method for characterization of partition and (or) adsorption properties of these materials. Interestingly, SPME offers new ways to characterize the properties of polymers used not only as coatings, but also as stationary phases in chromatography.

Application of SPME for physicochemical measurements (ref. 13)

Sorbent materials, used as stationary phases or coatings, are essential in the development of SPME, GC, and HPLC. The GC stationary phases are usually characterized by Kovats Indexes and Rohrschneider–McReynolds constants (14). These parameters are obtained by using standardized probe solutes, each representing a group of organic compounds. A similar concept is used for the characterization of coating materials for SPME. However, instead of conventional parameters, infinite-dilution activity coefficients of probe solutes are used to study the absorption or adsorption properties of selected coating materials.

The measurements of infinite-dilution activity coefficients of solutes in a stationary phase are usually made by a static gravimetric method or by a dynamic GC method. Both of these methods suffer from many disadvantages, including the large quantity of the phase required in the static method or the need to prepare a chromatographic column coated with the phase under examination in the GC method. Nowadays, the latter method is normally used for the determination of infinite-dilution activity coefficients.

SPME can be another tool for studying the properties of stationary phases. It has some advantages of both the static and the GC methods, while minimizing their drawbacks. The stationary phases of interest can be coated on fibres made of suitable materials (fused silica, stainless steel, etc.). The process of making fibres is much easier than that of columns. It requires very little material. The SPME device with a selected fibre coating can be used to extract a group of probe compounds, which are then separated on a standard commercially available column and quantified by a GC–MS. No extrapolation is necessary, as very low analyte amounts can be accurately determined.

The probe solutes used are McReynolds test solutes for GC stationary phases: benzene, butanol, 2-pentanone, nitropropane, and pyridine. The measurements consist of two steps. The first step is to measure the partition coefficients of the probe solutes between the stationary phase and the gas phase at near-infinite-dilution concentration levels. Then, from the partition coefficients, the corresponding activity coefficients are determined using the following equation:

$$[1]\quad \ln {}^{w}\gamma_1^{\infty} = \ln {}^{w}\gamma_p^{\infty} - \frac{p_1^0(B_{11} - v_1^0)}{RT} = \ln \frac{\rho_L RT}{K_R p_1{}^0 M_1} - \frac{p_1^0(B_{11} - v_1^0)}{RT}$$

where ${}^{w}\gamma_1{}^{\infty}$ is the virial corrected weight fraction infinite dilution activity coefficient of the solute; ${}^{w}\gamma_p{}^{\infty}$ is the weight fraction infinite dilution activity coefficient; p_1^0 is the solute saturated vapor pressure at temperature T; B_{11} is the second virial coefficient of the solute; v_1^0 is the bulk solute molar volume used to correct the second virial coefficient, R is the gas constant; ρ_L and M_L are the density and the molecular weight of the stationary phase, and K_R is the partition coefficient of the solute.

The measurement of K_R by SPME is straightforward. A gas sample is prepared by spiking n_0 mass of a solute into a capped vial of a volume V_g. SPME sampling is then performed until equilibrium is reached between the coating and the gas phase. If the volume of the vial is sufficiently large, the concentration change of the solute in the vial before and after SPME is negligible. The partition coefficient of the solute between the

Table 1. The weight-fraction infinite-dilute activity coefficients of five probe compounds ($^{w}\gamma_p^{\infty}$) and their virial corrected counterparts ($^{w}\gamma_p^{\infty}$) in two coatings at four different temperatures.

Analyte	Temperature (°C)	SPB-1		SPB-50	
		ln $^{w}\gamma_p^{\infty}$	ln $^{w}\gamma_1^{\infty}$	ln $^{w}\gamma_p^{\infty}$	ln $^{w}\gamma_1^{\infty}$
Benzene	25.00	1.71	1.72	0.56	0.57
	40.00	1.69	1.71	0.81	0.82
	80.00	1.57	1.60	0.46	0.50
	100.00	1.53	1.58	0.55	0.61
1-Butanol	25.00	3.66	3.66	3.07	3.07
	50.00	3.20	3.20	2.79	2.80
	80.00	2.59	2.60	1.93	1.94
	100.00	2.48	2.50	1.72	1.74
2-Pentanone	25.00	2.19	2.20	0.99	1.00
	50.00	2.03	2.05	1.04	1.05
	80.00	1.85	1.88	1.02	1.04
	100.00	1.74	1.78	1.03	1.07
Nitropropane	25.00	2.66	[a]	1.08	[a]
	50.00	2.55	[a]	1.22	[a]
	80.00	2.00	[a]	0.89	[a]
	100.00	1.96	[a]	0.86	[a]
Pyridine	25.00	1.29	1.29	0.34	0.34
	50.00	1.21	1.21	0.60	0.61
	80.00	1.91	1.92	0.32	0.33
	100.00	1.64	1.66	0.39	0.41

[a]Not calculated because v_1^0 and B_{11} values are unavailable.

coating and the gas phase can be calculated from the following equation:

$$[2] \quad K_R = \frac{C_f}{C_g} = \frac{n_f}{V_f} \cdot \frac{V_g}{n_0}$$

where C_f and C_g are the solute concentrations in the coating and the gas phase at equilibrium, respectively; n_f and n_0 are the mass extracted by the fibre coating and the mass spiked into the vial, and V_f and V_g are the volumes of the coating and the vial. To ensure that the concentration of the solute in the vial does not change during the measurement, the vial that contains the gas mixture has a volume about 10^6 times larger than the volume of the fibre coating. During the SPME measurements, the concentration of the solute in the fibre coating must be very low to ensure the validity of the assumption of infinite dilution.

Table 1 summarizes the infinite-dilution weight-fraction activity coefficients (ln $^{w}\gamma_p^{\infty}$) and their virial corrected counterparts (ln $^{w}\gamma_1^{\infty}$) of the five McReynolds solutes measured by SPME in two polymeric coating materials: one is 7 μm poly(dimethylsiloxane) bonded phase (equivalent to SPB-1), the other is 15 μm 50% phenyl-substituted poly(dimethylsiloxane) (equivalent to SPB-50). The weight-fraction infinite-dilution activity coefficients of the five probe compounds are indicators of how these compounds interact with the coating materials, thus can be used to characterize the properties of the coating. The $^{w}\gamma_p^{\infty}$ values of the five compounds in the 50% phenyl poly(dimethylsiloxane) are quite different from those in poly(dimethylsiloxane). The most obvious change is the substantial decrease of ln $^{w}\gamma_p^{\infty}$ values for benzene and pyridine. Compared to the poly(dimethylsiloxane) coating, the 50% phenyl coating provides a physicochemical "environment" more similar to their own molecular structure because of a large number of phenyl groups. Since the structural differences between the solutes and the solvent become smaller, the ln $^{w}\gamma_p^{\infty}$ values also become smaller.

Similar phenomena, although on a smaller scale, are also observed for nitropropane and 2-pentanone. In this case, the π-electrons of both compounds are interacting with phenyl groups and their delocalized π-electrons. The only compound with little change in ln $^{w}\gamma_p^{\infty}$ values is 1-butanol, which is the least polar among the compounds without a ring structure, and also the only compound without π-electrons. It is interesting to point out that for the four compounds (benzene, 2-pentanone, nitropropane, and pyridine) whose ln $^{w}\gamma_p^{\infty}$ values are reduced substantially in the 50% phenyl poly(dimethylsiloxane) coating, the temperature dependence of ln $^{w}\gamma_p^{\infty}$ is also less apparent. This is another indication that these solutes in the 50% phenyl poly(dimethylsiloxane) coating are in an environment more similar to their own molecular structure than in the other coating.

The above empirical discussion is not intended to explain in detail why and how the ln $^{w}\gamma_p^{\infty}$ values change. It indicates, however, that solution properties of the coating materials can be characterized by the ln $^{w}\gamma_p^{\infty}$ values of the five probe com-

Fig. 2. Structures of pepticides analyzed in the combined method.

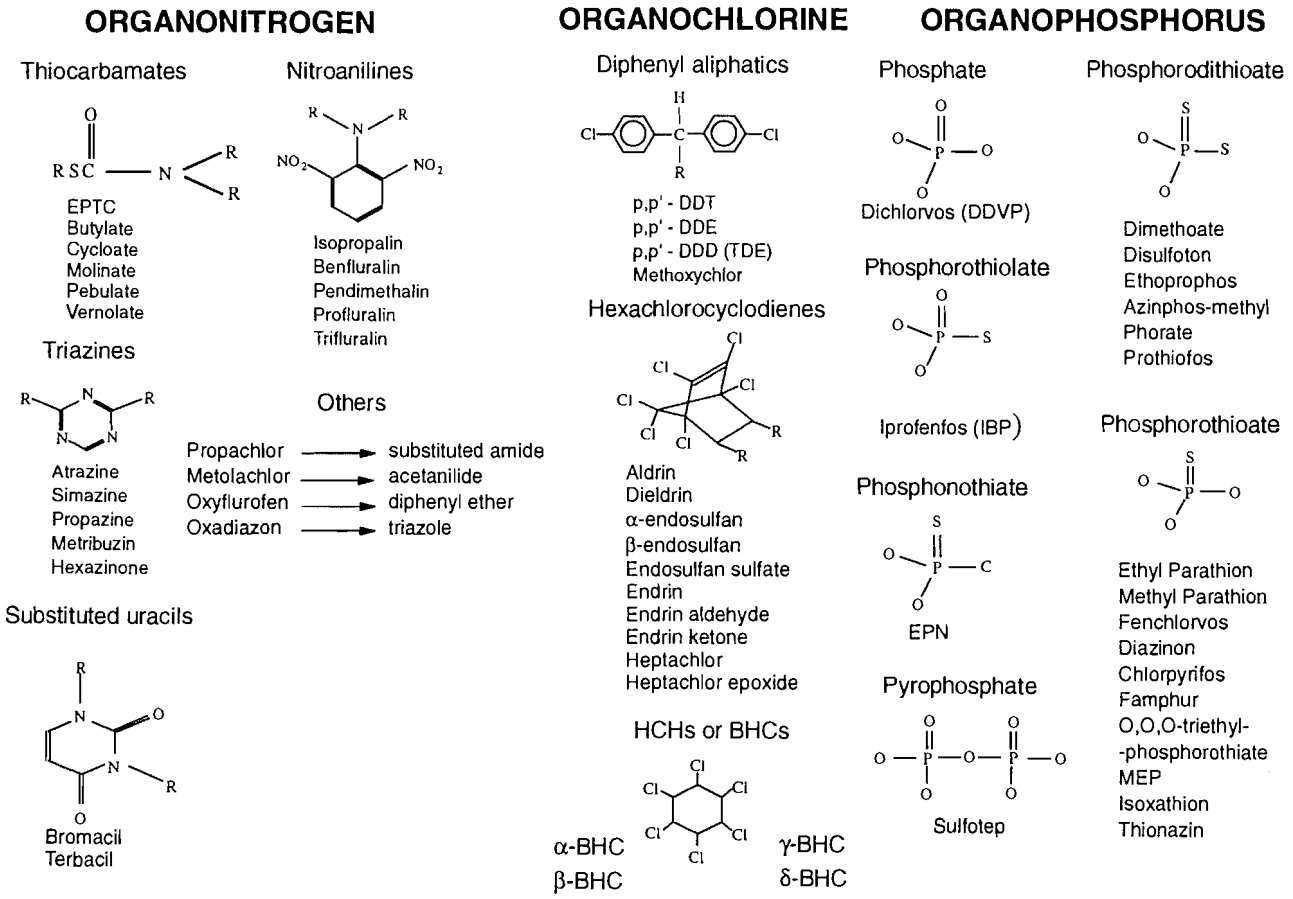

pounds. SPME, while based on the coatings for extraction of analytes, provides at the same time a new, simpler way for evaluating the properties of coating materials.

Once the suitability of the given coating is confirmed, SPME can be used for the analysis of many different types of compounds. The scope of the technique can be broadened by new, nonconventional approaches to the analysis. Following is a brief presentation of some of the latest achievements in practical applications of SPME.

Application of SPME to pesticides analysis

In the United States alone over 100 million hectares of agricultural land is treated with pesticides annually to prevent crop damage from a variety of insects, fungi, and noxious weeds (15). Pesticides are also frequently used for industrial and domestic purposes. The extensive use of pesticides has led to environmental concern because of their persistence and consequent presence in air, soil, and water. Typical concentration levels of pesticides in contaminated waters range from low ppt to low ppb (16–21) Pesticides are classified as either herbicides, insecticides, or fungicides. SPME has been successfully applied to the analysis of pesticides falling mainly into the first two groups.

In total 60 different pesticides have been analyzed by SPME methods developed in our laboratory. The target analytes can be broadly classified into three groups: organophosphorus, organochlorine, and organonitrogen. Within each of these groups, several classes of analytes were examined. Figure 2 shows the structures of the classes and lists the target pesticides that have been analyzed. These pesticides represent a broad range of organic compounds with widely different solubilities in water and polarities.

The development of SPME methods for different pesticides must thus be a carefully optimized process that considers the affinity of different classes of analytes for different coatings. It was observed that nitrogen-containing herbicides and organophosphorus pesticides were generally better extracted by the poly(acrylate) coated fibre (22, 23), whereas the organochlorine pesticides were generally better extracted by the poly(dimethylsiloxane) coated fibre (24). A wide linear range, typically over several orders of magnitude, is achievable for the organochlorine, organophosphorus, and organonitrogen pesticides. The methods developed have detection limits within the range required by the US EPA for most analytes when an FID detector is used. The use of a more selective detector, such as an ECD, NPD, or ion trap MS, enables detection limits that are considerably better than conventional EPA methods can achieve (i.e., low ppt levels). The precision of the methods is good, with RSDs of less than 20% for all analytes with all detectors.

In spite of the fact that some pesticides are better extracted by the poly(dimethylsiloxane) coating, and others by the

Fig. 3. Total ion chromatogram (TIC) of orange juice spiked with 60 pesticides, analyzed by SPME. 1, *o,o,o*-TEP; 2, Dichlorovos; 3, EPTC; 4, Butylate; 5, Vernolate; 6, Pebulate; 7, Molinate; 8, Thionazin; 9, Propachlor; 10, Ethoprofos; 11, Cycloate; 12, Trifluralin; 13, Benfluralin; 14, Sulfotep; 15, Phorate; 16, α-BHC; 17, Dimethoate; 18, Simazine; 19, Atrazine; 20, β-BHC; 21, Propazine; 22, Lindane; 23, Profluralin; 24, Diazinon; 25, δ-BHC; 26, Disulfoton; 27, Terbacil; 28, Iprofenfos; 29, Metribuzin; 30, Methyl Parathion; 31, Heptachlor; 32, Fenchlorovos; 33, Fenitrothion; 34, Bromacil; 35, Isoxathion; 36, Aldrin; 37, Metolachlor; 38, Chloropyrifos; 39, Ethyl Parathion; 40, Isopropalin; 41, Pendimethalin; 42, Heptachlor epoxide; 43, Endosulfan I; 44, Prothiofos; 45, *p,p'*-DDE; 46, Dieldrin; 47, Oxadiazon; 48, Oxyfluorofen; 49, Endrin; 50, Endosulfan II; 51, *p,p'*-DDD; 52, Endrin aldehyde; 53, Famphur; 54, Endosulfan sulfate; 55, *p,p'*-DDT; 56, Hexazinone; 57, Endrin ketone; 58, EPN; 59, Methoxychlor; 60, Azinphos-methyl.

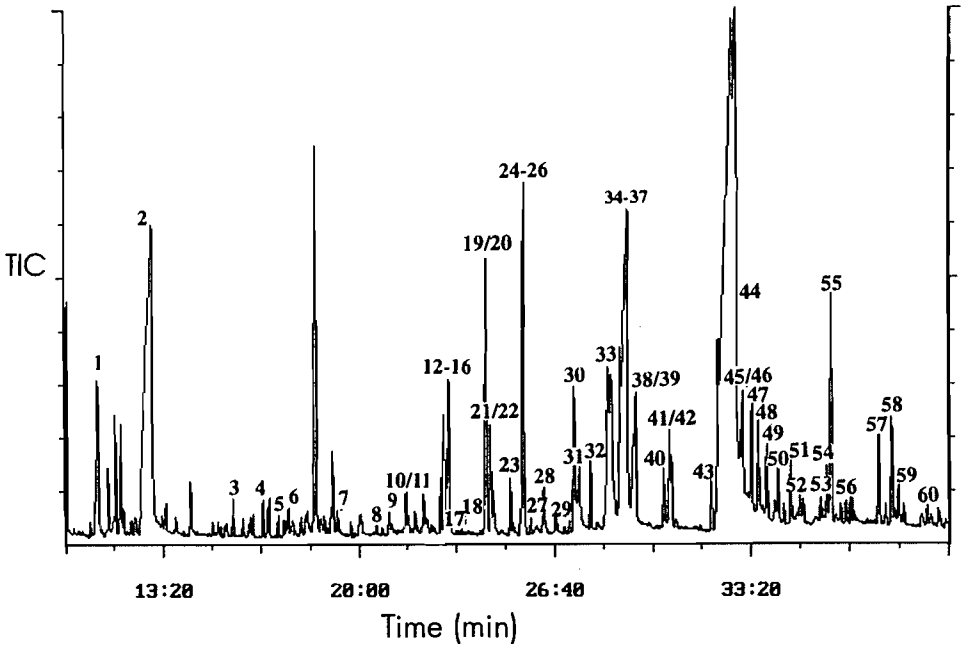

poly(acrylate) coating, all the analytes can be extracted with both of the phases, so the choice of coating need not prohibit successful screening of all the target analytes by either of the commercially available fibres. This last fact enabled development of a method for the combined analysis of 60 pesticides in one mixture (25). Although it is not possible to achieve baseline separation of all the compounds with a relatively short chromatographic analysis, the use of MS detection enables resolution of all the analytes by selecting appropriate masses for quantitation. For some analytes the detection limits with one coating are substantially lower than for the other coating, but generally they are similar, and in all cases better than those required by the US EPA.

Environmental samples can be modified by altering the ionic strength or adjusting the pH of the sample in order to increase the amount extracted by the fibre coating. It was found that for many analytes, the addition of sodium chloride to the sample increased the amount extracted (18–21). This often allows the analyst to improve the extraction of analytes of particular interest whilst still allowing for detection of the other analytes present in the sample (ones for which salt addition does not affect the amount extracted, or reduce it). In general, there was no significant effect on the extraction efficiency at any pH in the range 2–11. The advantage of the SPME method over many other methods is that samples with any pH in the above range can be analyzed with confidence, and if pH modification of a matrix is required for other reasons, the method will not be affected.

The combined method has been applied for quantitative analysis of the 60 pesticides from water and as a screening procedure for the detection of low ppb levels of the target analytes in soil and other matrices. Figure 3 illustrates a chromatogram of the 60 target pesticides spiked into an orange juice sample and detected by SPME and GC–MS. Analyzing such a wide variety of analytes at once allows for rapid screening of environmental samples as well as an accurate determination of the pollutants that may be present. Quantitation of analytes in complex matrices can generally be performed by the use of the standard addition procedure.

Recently a comparison of LLE, immunoassay methods, and the SPME method for the analysis of Atrazine, Simazine, and Metolachlor was undertaken with the Canadian Ministry of Agriculture. Over 100 well-water samples were analyzed by the methods and the results were generally found to agree for the three techniques.[4] A comparison was also made between

[4] A.A. Boyd-Boland, S. Clegg, and J. Pawliszyn. Unpublished results.

Fig. 4. Schematic diagram of the injector 1, injector body; 2, washer; 3, septum; 4, nut; 5, needle guide; 6, 0.53 mm i.d. fused silica capillary; 7, nut; 8, ferrule; 9, heater (0.057 mm o.d. resistive wire); 10, butt connector; 11, relay; 12, capacitor; 13, switch.

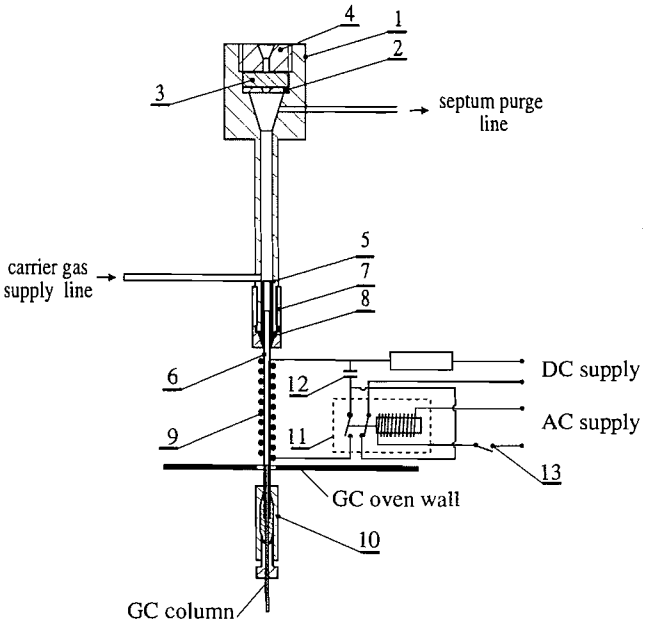

SPME, liquid extraction (using hexane), and Soxhlet extraction for the analysis of Metolachlor in a contaminated core sample. The SPME extraction simply involved suspending the sample in water, stirring the slurry and exposing the SPME fibre directly to the slurry. The results obtained by all three methods were the same: 1.8 mg (Metolachlor)/kg (soil). This indicates that for relatively water-soluble analytes, such as Metolachlor, the SPME method can be used for quantitative analysis of soil samples by simply suspending the soil in water. Obviously this represents a considerably easier analysis procedure for pesticides in soil than those currently used.

Apart from vastly simplifying sample preparation, SPME can offer other advantages over existing techniques. Of great importance is the solventless injection. It allows, among others, a significant reduction of the analysis time, as discussed in the following paragraph.

SPME as a sample introduction technique for fast GC (refs. 26, 27)

Theoretical considerations (28) indicate that desorption of the analytes from the fibre can be very fast (<1 s). It is therefore possible to produce a very narrow injection band, compatible with the requirements of fast GC. To achieve fast desorption, the fibre must be heated very rapidly. Regular GC injectors (split/splitless, programmed-temperature vaporization injector (PTV), septum programmable injector (SPI)) are not capable of doing this, even when the fibre is rapidly introduced to a hot injector. A dedicated injector, presented schematically in Fig. 4 (25), was therefore designed and built. A segment of a fused silica capillary, 6, connected to the injector base and equipped with a heater, 9, coiled along the fused silica capillary constitutes the low-volume part where desorption takes place. The GC column is inserted through a butt connector, 10, into the capillary, 6. The injector is rapidly heated by discharging the capacitor, 12. The switch, 13, is mounted in such a way that the capacitor is discharged simultaneously with fibre withdrawal from the needle. Very low mass and heat capacity of the heated part of the injector assure heating rates better than 1000°C/s. Under optimized conditions, the injector enabled isothermal separation of a BTEX mixture (benzene, toluene, ethylbenzene, *o*, *m*, *p*-xylene) in less than 9 s using a 15 μm PDMS coated fibre and a 4 m × 0.25 mm × 0.25 μm SPB-5 column (27).

Fast separation of more complex mixtures requires columns of higher efficiency, therefore 2.5 m × 0.1 mm × 0.6 μm Vocol and SPB-1 columns were used for the separation of volatile organic compounds listed in EPA method 624: purgeables A (trichlorofluoromethane, 1,1-dichloroethene, dichloromethane, 1,1-dichloroethane, trichloromethane, tetrachloromethane, trichloroethene, 1,2-dichloropropane, 2-chloroethyl vinyl ether, 1,1,2-trichloroethane, tetrachloroethene, dibromochloromethane, chlorobenzene), purgeables B (1,2-dichloroethene, 1,2-dichloroethane, 1,1,1-trichloroethane, benzene, bromodichloromethane, *cis*-1,3-dichloropropene, toluene, *trans*-1,3-dichloropropene, ethylbenzene, tribromomethane, 1,1,2,2-tetrachloroethane), and purgeables C (chloromethane, vinyl chloride, bromomethane, chloroethane). Both isothermal and temperature-programmed separations were performed. Ion traps MS and FID were used for detection. In isothermal runs, purgeables A and B were separated in slightly above 4 min. Purgeables C, which are gases at room temperature, could not be efficiently separated in isothermal runs.

Figure 5 presents temperature-programmed separation of all 28 compounds on the Vocol column. The analysis is completed in ca. 2.5 min, compared to about 20 min required for regular separation (6). Together with cooling down and equilibration, this time is comparable to the sampling time required (4–5 min). It is therefore potentially possible to analyze 10–12 samples per hour. In the regulatory purge-and-trap method the analysis of one sample requires at least half an hour, hence the analytical throughput can be considerably improved by the application of SPME coupled with fast GC.

The repeatability of retention times is excellent. All compounds can be easily quantified when using ion trap MS for detection, even though one pair of compounds (benzene and 1,2-dichloroethane) coelutes on the Vocol column. Precision of peak area determination is generally good (much below 10% RSD), except for the early eluting peaks, in which case the number of data points acquired by the ion trap MS system per peak (3–4) is insufficient for accurate determination. When using FID, precision is directly related to peak area: it is very good for larger peaks, and worse for small peaks. Compared to ion trap MS, FID provides considerably worse sensitivity, as most of the components of the purgeables mix are organohalogen compounds. It should be possible to obtain much better results, without the need to use ion trap mass spectrometry, by the application of selective detectors (ECD or ELCD for organohalogens, PID for aromatics).

Fast desorption of the analytes from the fibre can be achieved not only by rapidly heating the injector, but also by heating the fibre directly. This can be accomplished by using a hollow fibre equipped with an internal microheater. Figure 6

Fig. 5. Separation of purgeables A, B, and C on a VOCOL column. Conditions: 0°C–30°/min–70°C; 2.1 atm, dedicated injector, capacitor voltage 24 V, MS detector, mass range 45–250. 1, chloromethane; 2, vinyl chloride; 3, bromomethane; 4, chloroethane; 5, trichlorofluoromethane; 6, 1,1-dichloroethene; 7, dichloromethane; 8, 1,2-dichloroethene; 9, 1,1-dichloroethane; 10, trichloromethane; 11, 1,1,1-trichloroethane, 12, tetrachloromethane; 13, benzene; 14, 1,2-dichloroethane; 15, trichloroethene; 16, 1,2-dichloropropane; 17, bromodichloromethane; 18, 2-chloroethyl vinyl ether; 19, *cis*-1,3-dichloropropene; 20, toluene; 21, *trans*-1,3-dichloropropene; 22, 1,1,2-trichloroethane; 23, tetrachloroethylene; 24, dibromochloromethane; 25, chlorobenzene; 26, ethylbenzene; 27, tribromomethane; 28, 1,1,2,2-tetrachloroethane.

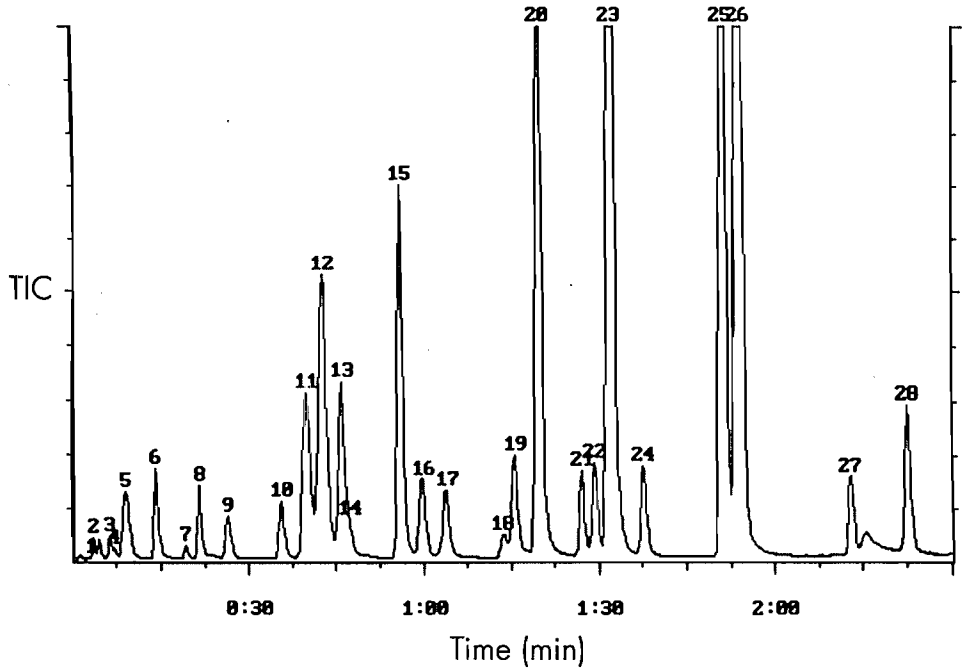

presents the design of such an internally heated fibre, based on a commercial SPME holder (Supelco, Inc.). A 0.32 mm i.d. fused silica capillary, flame sealed at one end, is used as the fibre. The microheater, made of a 0.05 mm o.d. Ag wire, is coiled around another fused silica microcapillary (0.075 mm i.d., 0.15 mm o.d.). One end of the heating wire is passed inside the microcapillary, and the other is outside, which yields excellent electrical insulation between the two leads. The entire heating assembly is inserted inside the 0.32 mm fused silica capillary.

An internally heated fibre prepared in this way was custom coated with poly(dimethylsiloxane) stationary phase and tested on a BTEX mixture in air. Very good repeatability of retention times was achieved. The analysis time, equal to ~10 s, is comparable to the best results obtained with the dedicated injector. Repeatability of peak areas was worse than for the regular fibre used with the dedicated injector, probably because of inferior properties of the custom-made coating. The biggest advantage of the internally heated fibre is that no carryover is observed when using this device.

SPME coupled to GC is mainly suited for the analysis of volatile and semivolatile organic compounds of low to intermediate polarity. However, the scope of applications can be significantly broadened by using different approaches either to the extraction step, or to the final determination. One such possibility is derivatization of otherwise nonvolatile analytes, presented below.

Determination of tetraethyllead and inorganic lead in water by SPME/GC (ref. 29)

Alkylleads and inorganic lead are extremely dangerous environmental pollutants. In the environment alkyllead compounds are mostly of anthropogenic origin, but they may also be produced from biological transformation of Pb^{2+}. Tetraethyllead is still used in many parts of the world as an additive to gasoline. Inorganic lead is ubiquitous and can be found in air, water, and soils. Speciation of alkyllead compounds at low levels found in the environment is not a trivial problem. SPME seems very attractive for this task, as it requires virtually no sample preparation and is capable of achieving very high sensitivity and low detection limits. There are many established methods of Pb^{2+} determination, yet at trace levels they usually require very expensive instrumentation. None of the spectrometric methods of use (GFAAS, ICP–MS) can be adopted for field measurements. Electrochemical methods, especially anodic stripping volatammetry, are known for their high sensitivity and relatively low price, but they require clean, organic-free samples. Environmental samples usually require

Fig. 6. Schematic diagram of the Supelco SPME device modified to accommodate the internally heated fibre.

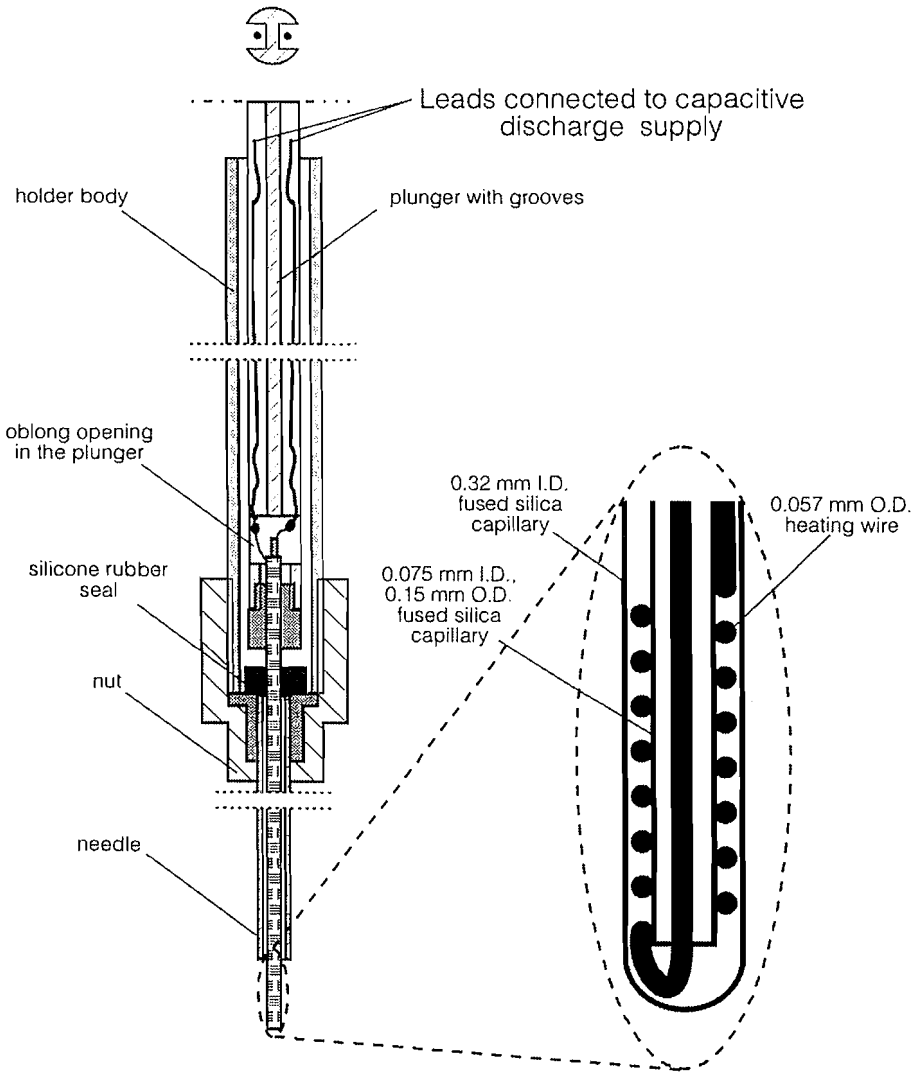

mineralization prior to the analysis, a task that is not easily accomplished in the field.

Rapsomanikis (30) pioneered the use of sodium tetraethylborate (STEB) for ethylation of ionic alkyllead, alkylmercury, as well as inorganic lead and mercury in the aqueous phase. The resultant organometallic compounds are poorly soluble in water and have relatively high vapour pressure, hence they should be easily extracted by SPME. Headspace extraction is favourable, since it avoids problems related to extraction of unwanted large molecular weight compounds that can be present in the sample. Tetraethyllead was chosen as a representative of alkyllead compounds, as its use is the most widespread, and it is the product of inorganic lead ethylation.

Experiments were performed using GC–FID and GC – ion trap MS. It has been found that tetraethyllead is easily extracted from the headspace over aqueous samples. With vigorous stirring, equilibrium is reached after ~7.5 min. The response for FID was found to be linear in the entire range examined, from 0.1 to 100 μg/L, as evidenced by the value of the correlation coefficient $R > 0.998$. The precision of tetraethyllead determination at the 50 ppb level was very good, RSD being equal to 2.4%. Ion trap MS offered excellent detection limits (below 5 ppt), yet its response to tetraethyllead was nonlinear due to secondary fragmentation of unstable ions stored in the trap.

Derivatization of Pb^{2+} was performed by adding STEB solution to a pH buffered sample. The evolved tetraethyllead was extracted by SPME from the headspace over the sample. The system reached equilibrium after ~15 min. The FID response was linear in the entire range examined, from 0.2 to 1000 ppb. The detection limit was found to be ~200 ppt Pb^{2+}. It was slightly adversely affected by the non-zero blank value, most probably related to the reagent used. Precision of the determination at a 50 ppb level, as estimated by the value of the RSD = 5.04%, was very good.

Ion trap MS confirmed the identity of the derivatization product. Figure 7 presents the mass spectrum of the product found after SPME extraction of a pH buffered sample contain-

Fig. 7. Comparison of the mass spectrum of the derivation product (*a*) with library spectrum of tetraethyllead (*b*).

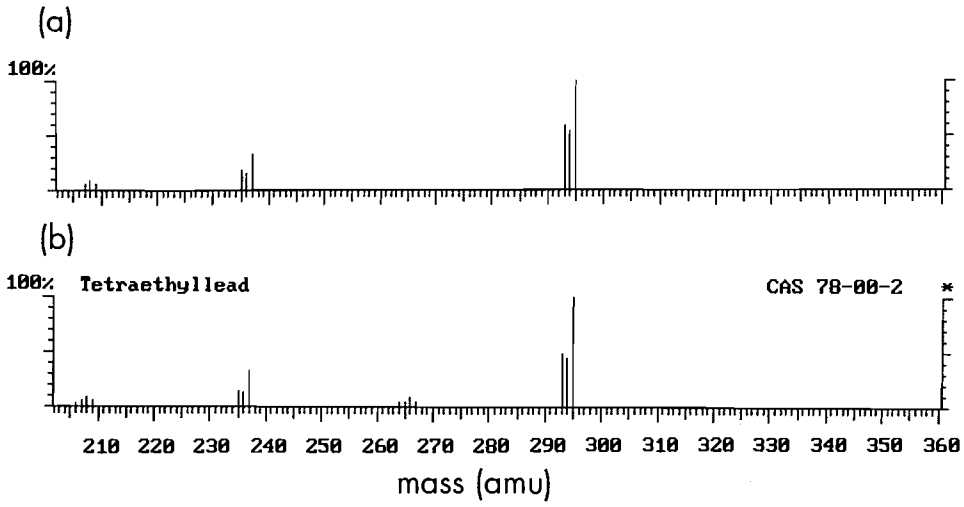

ing 20 ppb Pb^{2+} and the derivatization reagent, and the library spectrum of tetraethyllead. The agreement is excellent. Ion trap MS response in the 5–100 ppb range was nonlinear for the reasons described above.

The results obtained indicate that SPME can be an invaluable tool for alkyllead and inorganic lead speciation in water. Native non-ionic alkyllead compounds can be analyzed first, followed by addition of the derivatizing reagent and determination of ionic alkyllead compounds and inorganic lead. According to the literature, it should be possible to use a similar procedure for the determination of other organometallic compounds, including those of mercury and tin (31). The whole procedure can be easily performed in the field with the use of a portable GC.

Determination of inorganic lead in water by SPME illustrates how the technique can be used for analytes that normally would not be amenable to extraction from water into an organic phase. Derivatization to a form that can be extracted by an SPME device can also be performed in other ways. For example, Hg^{2+} can be electrochemically reduced to Hg^0 using a thin, gold-plated wire in place of the regular SPME fibre. The metallic mercury formed dissolves in the gold layer forming an amalgam. Mercury can then be liberated from the gold layer by rapidly heating the wire to a high temperature. Experiments of this kind were performed using an ion trap MS as the detector. Rapid heating of the wire was achieved by discharging a capacitor directly through the wire, using a modified version of the injector presented in Fig. 4. Initial experiments demonstrated that the method is feasible and very sensitive. At the same time it allows speciation of mercury by choosing a proper potential during the reduction step.

Derivatization broadens the scope of SPME to compounds that cannot be extracted by regular SPME procedures. However, there are a number of compounds that can be easily extracted, but cannot be analyzed by GC due to nonvolatility or thermal instability. These compounds include pharmaceutical products, peptides, proteins, etc. Obviously, other separation and determination techniques should be used in such cases, including SFC, CE, and HPLC.

Coupling to HPLC

Coupling of SPME to HPLC (32) is a natural extension of the method, enabling new, exciting applications. However, in contrast to GC, the existing instrumentation cannot be used for this purpose without modification of the sample introduction system.

Thermal desorption is not feasible in conjunction with HPLC. The alternative is solvent desorption. To accomplish this, a special interface was designed and built. Schematic diagram of this interface is presented in Fig. 8. The heart of the device is a custom-made desorption chamber with three ports in a T-configuration, connected to a six-port valve in place of the sampling loop. With the valve in the "load" position, the desorption chamber is at atmospheric pressure. This enables the fibre assembly to be safely inserted to the chamber via the finger-tight PEEK union (c). The union seals the steel tubing in which the fibre is mounted strongly enough to withstand pressures up to 4500 psi (1 psi = 6.9 kPa). After switching the valve to the "injection" position, the mobile phase flows along the fibre upwards to avoid air bubbles being introduced to the system. The analytes present in the sample partition from the coating to the mobile phase and are swept away to the column.

Theoretical considerations (32) indicate that with properly selected solvent (one for which the affinity of the analytes is high) the desorption process can be very fast, the time required being less than 1 s. This has been proven in an experiment in which the desorption chamber was connected directly to the HPLC detector. For benzo[*a*]pyrene and CH_3CN/H_2O 90/10 used as the mobile phase, the desorption volume was 0.2 μL. This volume increased rapidly with increasing water content in the mobile phase due to poor solubility of benzo[*a*]pyrene in water.

The applicability of the method for real-life analysis was verified on a sample of 13 polycyclic aromatic hydrocarbons (PAH) listed in the EPA method 525. A 100 ppb standard solution of the PAHs in water was sampled with a 7 μm thick PDMS fibre for 30 min, followed by the HPLC analysis. The results were compared to those obtained for loop injection.

Fig. 8. Design of the SPME–HPLC system: (a) stainless steel (SS) T-joint; (b) SS tubing; (c) poly(ether ether ketone) (PEEK) tubing; (d) two-piece finger-tight PEEK union; (e) PEEK union with tubing.

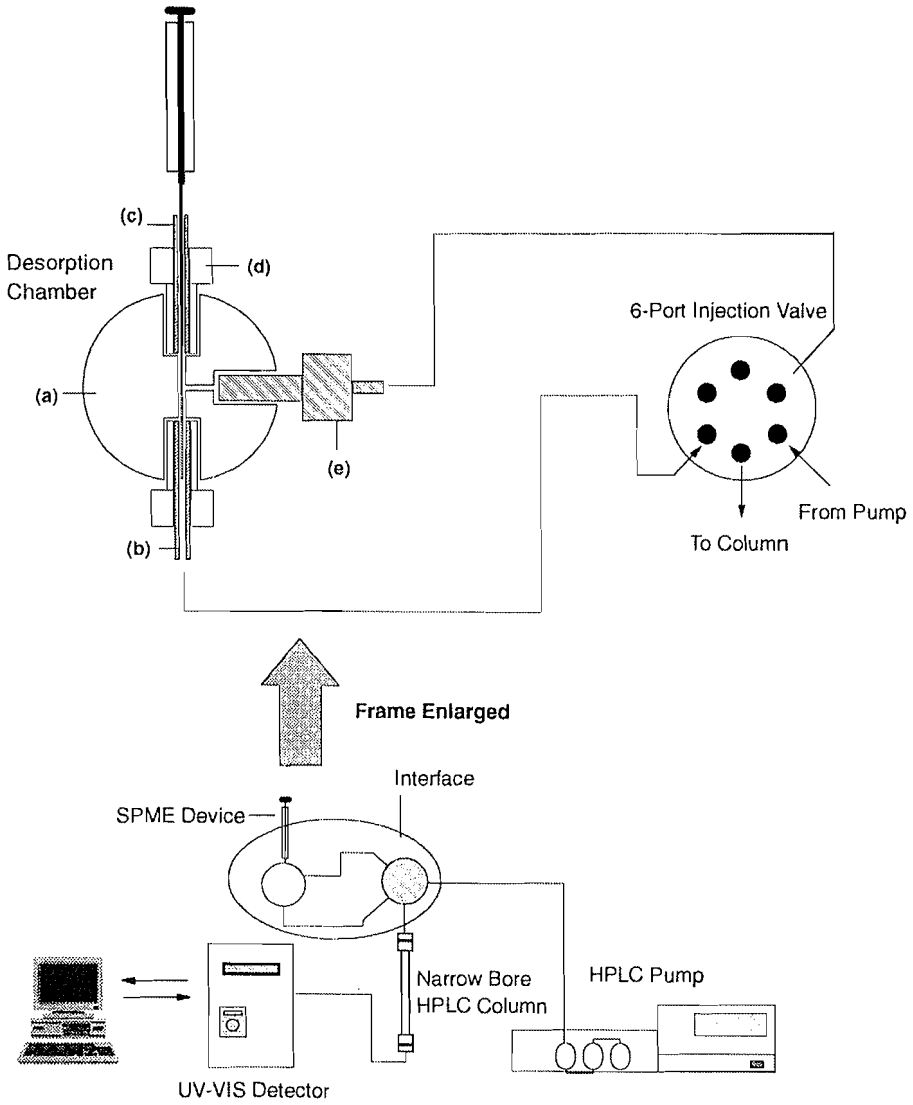

Figure 9 illustrates the chromatograms obtained for both samples. The agreement between the retention times of the analytes is excellent, which indicates that the interface does not contribute significantly to extracolumn effects. The differences in the relative peak areas for some of the analytes are related to the differing affinity of the analytes towards the coating.

The repeatability of retention times and peak areas was examined for a sample of four PAHs (fluoranthene, pyrene, benz[*a*]anthracene, and benzo[*a*]pyrene). Relative standard deviations were very good, below 5% for retention times and below 7% for peak areas. This indicates that SPME coupled to HPLC can be used for both qualitative and quantitative analysis. Additionally, it has been found that there is no carryover when using solvent desorption for liberation of PAHs from the fibre coating. Small carryover was usually observed when thermal desorption was used for the liberation of PAHs from the coating in the GC analysis.

Coupling of SPME to HPLC is still a new technique, in the initial stage of development. A commercially available interface has been introduced by Supelco only recently. The results obtained so far indicate that it has a great potential. The applicability of the technique for samples not amenable to GC analysis has been verified in our laboratory using the example of surfactants in water (33). Very good sensitivity was obtained without complicated sample pretreatment. Work is under way on new, exciting applications.

Conclusions

Although still a young technique, SPME has proven its suitability for many analytical tasks. Since the commercialization of the technique in 1993, the number of papers published, utilizing this technique, has been growing very rapidly. This does not mean, however, that all its potential has already been explored. This paper presents some of the many new possibil-

Fig. 9. Separation of PAH mixture 525 with solvent gradient by (a) 1 μL loop injection of a 100 ppm solution, and (b) fibre injection; 7 μm PDMS fibre, 30 min extraction from a solution containing 100 ppb of each compound spiked into water. Chromatographic conditions: ODS column, 25 cm × 2.1 mm i.d., 5 μm particle diameter, flow rate 0.2 mL/min, detection UV, 254 nm, solvent program, CH_3CN/H_2P (80/20, v/v), linear gradient to 100% CH_3CN in 15 min. Peak identification: 1, acenaphthylene; 2, fluorene; 3, phenathrene; 4, anthracene; 5, pyrene; 6, benz[*a*]anthracene; 7, chrysene; 8, benzo[*b*]fluoranthene; 9, benzo[*k*]fluoranthene; 10, benzo[*a*]pyrene; 11, dibenzo[*ah*]anthracene; 12, indeno[1,2,3-*cd*]pyrene; 13, benzo[*g,h,i*]perylene.

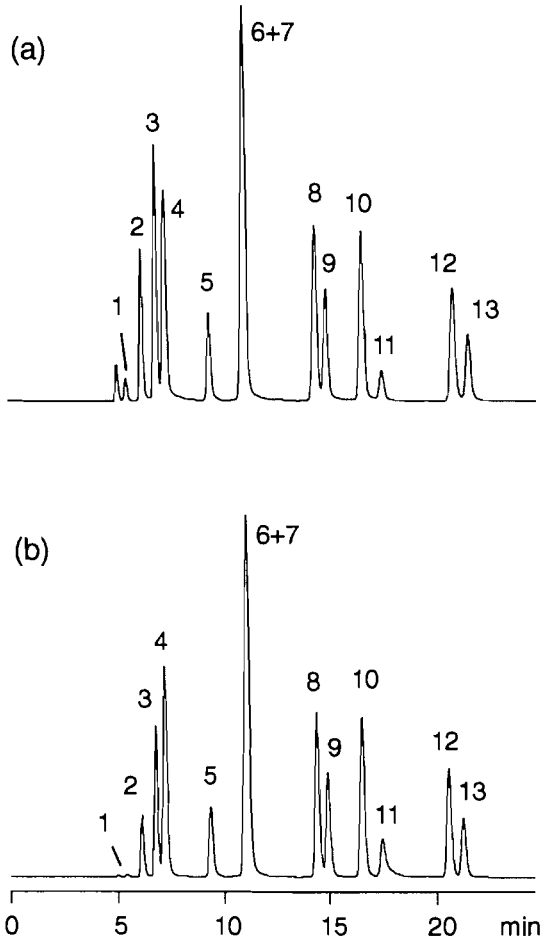

ities offered by SPME. They include basic physicochemical research permitting easy characterization of the properties of stationary phases, simultaneous determination of 60 pesticides representing all the groups currently in use, fast separations made possible without complicated and expensive instrumentation, and analysis of entirely new types of analytes, normally not amenable to GC analysis, by utilization of derivatization in the aqueous phase, or coupling of SPME with HPLC. In our laboratory we are still developing new applications and approaches to SPME. Some of the possibilities include in situ derivatization SPME/electrochemistry and direct coupling of SPME with a mass spectrometer. We expect the scope of applications to be significantly broadened when new coatings are introduced to the market. SPME still remains a fascinating and promising new technology.

Acknowledgments

The financial support of Supelco, Varian, the Natural Sciences and Engineering Research Council of Canada, and the U.S. Environmental Protection Agency, Office of Exploratory Research, is gratefully acknowledged.

References

1. J. Namieśnik, T. Górecki, M. Biziuk, and L. Torres. Anal. Chim. Acta, **237**, 1 (1990).
2. R.P. Belardi and J. Pawliszyn. Water Pollut. Res. J. Can. **24**, 179 (1989).
3. C.L. Arthur, L.M. Killam, S. Motlagh, M. Lim, D.W. Potter, and J. Pawliszyn. Environ. Sci. Technol. **26**, 979 (1992).
4. D.W. Potter and J. Pawliszyn. J. Chromatogr. **625**, 247 (1992).
5. S.B. Hawthorne, D.J. Miller, J. Pawliszyn, and C.L. Arthur. J. Chromatogr. **603**, 185 (1992).
6. C.L. Arthur, K. Pratt, S. Motlagh, J. Pawliszyn, and R.P. Belardi. J. High Resolut. Chromatogr. **15**, 741 (1992).
7. D. Potter and J. Pawliszyn. Environ. Sci. Technol. **27**, 298 (1994).
8. M. Chai, C.L. Arthur, J. Pawliszyn, R.P. Belardi, and K.F. Pratt. Analyst, **118**, 1501 (1993).
9. K. Buchholz and J. Pawliszyn. Environ. Sci. Technol. **27**, 2844 (1993).
10. K. Buchholz and J. Pawliszyn. Anal. Chem. **66**, 160 (1994).
11. Z. Zhang and J. Pawliszyn. Anal. Chem. **65**, 1843 (1993).
12. M. Chai and J. Pawliszyn. Environ. Sci. Technol. **29**, 693 (1995).
13. Z. Zhang and J. Pawliszyn. J. Phys. Chem. Submitted.
14. H. Rotzsche. Stationary phases in gas chromatography. Elsevier Science Pub. Amsterdam, New York. 1991.
15. R. Grover. Environmental chemistry of herbicides, CRC Press Inc., Boca Raton, Fla. 1988.
16. J. Tronczynski, C. Munschy, G. Durand, and D. Barcelo. Sci. Total Environ. **132**, 327 (1993).
17. W.E. Periera and C.E. Rostad. Environ. Sci. Technol. **24**, 1400 (1990).
18. K.A. Caldwell, V.M.S. Ramanujan, Z. Cai, and M.L. Gross. Anal. Chem. **65**, 2372 (1993).
19. J.E. Patrick. Pesticides in Ontario drinking water from surface sources, 1988. Ontario Ministry of Agriculture and Food, September 1990.
20. R.S. Kookana and L.A.G. Aylmore. Aust. J. Soil Res. **32**, 1141 (1994).
21. H. Jobst. Fresenius J. Anal. Chem. **349**, 298 (1994).
22. A.A. Boyd-Boland and J. Pawliszyn. J. Chromatogr. **704**, 163 (1995).
23. S. Magdic and J. Pawliszyn. J. Chromatogr. In press.
24. S. Magdic and J. Pawliszyn. J. Chromatogr. **723**, 111 (1996).
25. A.A. Boyd-Boland and J. Pawliszyn. Analyst. In press.
26. T. Górecki and J. Pawliszyn. J. High Resolut. Chromatogr. **18**, 161 (1995).
27. T. Górecki and J. Pawliszyn. Anal. Chem. **67**, 3265 (1995).
28. D. Louch, S. Motlagh, and J. Pawliszyn. Anal. Chem. **64**, 1187 (1992).
29. T. Górecki and J. Pawliszyn. Anal. Chem. In press.
30. S. Rapsomanikis, O.F.X. Donard, and J.H. Weber. Anal. Chem. **58**, 35 (1986).
31. S. Rapsomanikis. Analyst, **119**, 1429 (1994).
32. J. Chen and J. Pawliszyn. Anal. Chem. **67**, 2530 (1995).
33. A.A. Boyd-Boland and J. Pawliszyn. Anal. Chem. **68**, 1521 (1996).

Bis(pyridine)difluoroboron, tris(pyridine)fluoroboron, and other (pyridine)haloboron cations. A systematic NMR study

Melvin J. Farquharson and J. Stephen Hartman

Abstract: The adducts pyr·BF_2Br and pyr·$BFBr_2$ (pyr = pyridine) form fluoroboron cations by displacement of Br^- by excess pyridine, the ease of cation formation being $pyr_2BF_2^+ \gg pyr_2BFBr^+ \gg pyr_3BF^{2+}$. Cl^- can be displaced from pyr·BF_2Cl and pyr·$BFCl_2$, but much less readily, to form $pyr_2BF_2^+$, pyr_2BFCl^+, and, under forcing conditions, a few percent of pyr_3BF^{2+}. Non-fluorine-containing mixed boron trihalide adducts of pyridine also form haloboron cations by heaviest-halide-ion displacement, for example pyr·$BClI_2$ giving pyr_2BClI^+, the ease of displacement always being $I^- > Br^- > Cl^-$, and displacement always occurring more readily from mixed boron trihalide adducts than from unmixed-halogen adducts. The mechanistic implications of this are discussed. *ortho* Substituents greatly reduce the ability of pyridine to displace heavy halide ion, so 2-methylpyridine gives 2-$Mepyr_2BF_2^+$ and 2-$Mepyr_2BFBr^+$ but not 2-$Mepyr_2BFCl^+$ or 2-$Mepyr_3BF^{2+}$, while 2,6-dimethylpyridine does not form any haloboron cations. ^{19}F spin-lattice relaxation times of the fluoroboron cations are much shorter than those of neutral boron trihalide adducts in the same solution, and provide a further diagnostic test for their presence.

Key words: fluoroboron cations, pyridines, mixed boron trihalide adducts, fluorine-19 NMR, boron-11 NMR.

Résumé : Les adduits pyr·BF_2Br et pyr·$BFBr_2$ (pyr = pyridine) forment des cations du fluorobore par déplacement de Br^- par l'excès de pyridine; la facilité de formation du cation est la suivante : $pyr_2BF_2^+ \gg pyr_2BFBr^+ \gg pyr_3BF^{2+}$. Il est possible de déplacer le Cl^- des adduits pyr·BF_2Cl et pyr·$BFCl_2$, pour former les $pyr_2BF_2^+$, pyr_2BFCl^+, et en forçant les conditions quelques pour cents du pyr_3BF^{2+}, mais la réaction est beaucoup plus lente. Les adduits de la pyridine avec des trihalogénures mixtes du bore ne contenant pas de fluor forment aussi des cations halobores par le déplacement de l'halogène le plus lourd; par exemple, le pyr·$BClI_2$ conduit au pyr_2BClI^+, la facilité de déplacement est $I^- > Br^- > Cl^-$ et le déplacement se fait toujours plus facilement à partir d'adduits trihalogénures mixtes du bore qu'à partir d'adduits non mélanges d'halogénures de bore. On discute des implications mécanistiques de ces résultats. Les substituants *ortho* ralentissent beaucoup la facilité de la pyridine à déplacer les ions halogénures lourds; ainsi, la 2-méthylpyridine conduit aux 2-$Mepyr_2BF_2^+$ et 2-$Mepyr_2BFBr^+$, mais pas aux 2-$Mepyr_2BFCl^+$ ou 2-$Mepyr_3BF^{2+}$ alors que la 2,6-diméthylpyridine ne forme aucun cations halobore. Les temps de relaxation spin-réseau du ^{19}F dans les cations du fluorobore sont beaucoup plus courts que ceux des adduits trihalogénures de bore neutres dans la même solution et ils fournissent une méthode supplémentaire pour diagnostiquer leur présence.

Mots clés : cations du fluorobore, pyridines, adduits des trihalogénures mixtes du bore, RMN du ^{19}F, RMN du ^{11}B.

[Traduit par la rédaction]

Introduction

In previous work (1, 2) we have shown that $R_3N{\cdot}BF_2Br$ adducts selectively and readily undergo bromide ion displacement by neutral (D′) and anionic (Z) donors of low steric hindrance to give difluoroboron cations $D_2BF_2^+$ and $DD'BF_2^+$ and neutral adducts $R_3N{\cdot}BF_2Z$ (eq. [1]).

Received February 29, 1996.

M.J. Farquharson[1] and J.S. Hartman.[2] Department of Chemistry, Brock University, St. Catharines, ON L2S 3A1, Canada.

[1] Deceased, June 1991.
[2] Author to whom correspondence may be addressed. Telephone: (905) 688-5550, ext. 3849. Fax: (905) 682-9020. E-mail: shartman@chemiris.labs.brocku.ca

[1] $D{\cdot}BF_2Br + D' \longrightarrow DD'BF_2^+ + Br^-$

We noted the contrast of the high reactivity of $R_3N{\cdot}BF_2Br$ with the lack of reactivity of the $R_3N{\cdot}BFBr_2$ and $R_3N{\cdot}BBr_3$ adducts present in the same solutions, and the extremely slow chloride ion displacement from $R_3N{\cdot}BF_2Cl$. In our preliminary communication (1) we noted that pyridine was particularly effective as a displacing ligand (D′ in eq. [1]), reacting much faster than any trialkylamine to displace bromide ion, consistent with steric hindrance rather than base strength of the attacking species being the decisive factor in the reaction. Many (R_3N)(substituted pyridine)BF_2^+ ions form readily in this way from $R_3N{\cdot}BF_2Br$ (2). We now report studies of heavy halide ion displacement from pyridine·BF_nX_{3-n} adduct systems that demonstrate even greater acceleration of heavy halide ion displacement when a low steric hindrance pyridine is the donor molecule in $D{\cdot}BF_2Br$ as well as the attacking

ligand D′. We also report formation of the less easily formed cations D_2BFBr^+, D_2BFCl^+, and D_3BF^{2+} from pyr·BFX_2 (X = Cl, Br) according to eq. [2].

$$D{\cdot}BFX_2 + D' \longrightarrow DD'BFX^+ + X^- \quad [2]$$

$$DD'BFX^+ + D' \longrightarrow DD'_2BF^{2+} + X^-$$

Pyridine-fluoroboron cations had not been reported until our work (1), although speculation about their formation has appeared (3). Systematic formation of these cations, by a halide ion displacement process analogous to that used by Ryschkewitsch and co-workers for the formation of hydroboron cations and heavier-halogen haloboron cations (4), requires mixed boron trihalide adducts (5) as starting materials. Unmixed-halogen boron trihalide adducts of pyridine and substituted pyridines have been known for a long time (6), and much has been known about tetrahedral boron-nitrogen compounds including various cations (7). The mixed boron trihalide adducts of 4-methylpyridine (4-Mepyr) were reported in 1972 from this laboratory (8), and are formed in a manner similar to aliphatic tertiary amine – mixed boron trihalide adducts (5, 9). Despite reports of a much wider range of boron cations in recent years, including many cations with three- and even two-coordination at boron (10), and extensive use of ^{11}B NMR to study such species (11), there were only a few scattered reports of four-coordinate fluoroboron cations and little was known about them until our method of synthesis starting from mixed boron trihalide adducts (1, 2, 9).

Experimental section

General

Pyridine, 2-methylpyridine, and 4-methylpyridine (BDH) were purified by fractional distillation and stored over KOH. The other substituted pyridines and other Lewis bases (BDH and Aldrich) were used as supplied. Moisture-sensitive materials were handled under dry nitrogen in a glove bag and (or) on a Schlenk line. Mixed boron trihalide adducts of the pyridines, precursors of the haloboron cations, were formed in solution as described for the corresponding adducts of aliphatic tertiary amines (2, 9). Difluoroboron cation salts containing these pyridines were isolated in a similar manner to the corresponding quinuclidine-containing $(R_3N)_2BF_2^+$ salts (2), and are moderately stable in water and ethanol. The only major difference was the use of the BF_nCl_{3-n} rather than the BF_nBr_{3-n} adduct system because pyr·$BFBr_2$, unlike $R_3N{\cdot}BFBr_2$, reacts with pyridine to form pyr_2BFBr^+ along with $pyr_2BF_2^+$. Use of the less reactive pyr·BF_nCl_{3-n} system and keeping the reaction time short gave $pyr_2BF_2^+$ with negligible pyr_2BFCl^+. When isolation of salts of the cations was not being undertaken, the entire cation formation procedure could be carried out in 5 mm NMR tubes, using 1 mL and 50 μL syringes to inject various reagents.

Halogen exchange and fluoroboron cation formation reactions were monitored in $CDCl_3$ solution by ^{19}F and ^{11}B NMR, supplemented by positive ion fast atom bombardment mass spectrometry (FAB). Elemental analyses for carbon, hydrogen, and nitrogen were consistently satisfactory but those for fluorine were erratic, some being in error by several percent, perhaps due to interference by boron.

Isolation of $D_2BF_2^+$ salts

Typically, water was added to a chloroform solution containing cations and neutral adducts, and extracted the ionic species preferentially. Evaporating the water extract under vacuum, followed by redissolving the residue in chloroform, eliminated all $D{\cdot}BF_nX_{3-n}$ species and any excess amine. Direct addition of hexane or petroleum ether to the new chloroform solution gave immediate precipitation of the cation salt, but of low purity. Higher purity material was obtained by slow evaporation of solvent, or by two-layer exchange: careful addition of a hexane or petroleum ether layer over the $CDCl_3$ layer and allowing the system to stand. The material was then recrystallized from acetone. Closed ground-glass vessels were used past the stage of redissolving in chloroform, to avoid hydrolysis. The pyridine-containing $D_2BF_2^+$ cations have a shorter lifetime in water than the tertiary-amine cations (2), so the time in contact with water was minimized. (This method is not successful if B—Cl or B—Br bonds are present, since cations containing Cl or Br are much more susceptible to hydrolysis.) The isolation of doubly charged cations and mixed-donor cations will be reported elsewhere (12). Elemental analyses (performed by Guelph Chemical Laboratories Ltd.) are as follows: $pyr_2BF_2{\cdot}BPh_4$: found: C 77.55, H 6.18, N 5.42, F 7.50; calcd.: C 77.60, H 5.75, N 5.32, F 7.22. $pyr_2BF_2{\cdot}PF_6$: found: C 34.53, H 2.92, N 7.93, F 43.44, calcd.: C 34.13, H 2.86, N 7.96, F 43.18. $(4\text{-Mepyr})_2BF_2{\cdot}BPh_4$: found: C 77.76, H 6.46, N 4.98, F 3.76; calcd.: C 78.01, H 6.18, N 5.05, F 6.85.

Instrumentation

Most ^{19}F spectra were obtained at 56.4 MHz on a Bruker WP-60 multinuclear Fourier Transform NMR spectrometer as described previously (2). Some were obtained at 188.29 MHz on a Bruker CXP-200 instrument in order to resolve overlapping multiplets. Typically, 8K FIDs were obtained with 100–500 30° pulses covering a 10 000 Hz spectral width; 0.5 Hz of line broadening was applied and 8K of zero filling was added before transforming into 8K spectra. ^{19}F chemical shifts are accurate to ±0.1 ppm and were internally referenced to C_6F_6 as a secondary standard (–162.7 ppm from $CFCl_3$), and are reported in ppm from $CFCl_3$.

^{19}F spin-lattice relaxation time studies were performed at ambient temperature on the WP-60 spectrometer at 56.4 MHz using the Nicolet T_1 Program II (developed by J.W. Cooper) with a $(180° - \tau - 90°\text{–}D_2\text{–})_n$ pulse sequence; 150–250 scans were obtained for each of 10–15 τ values, with a 12 s relaxation delay (D_2) between each sequence. Typical runs were 6–10 h in length. Auto shimming was applied, and τ values were sequenced in a random order. Errors in T_1 values vary with concentration of the various species, and are generally less than 10%. Solution viscosity measurements were carried out on the NMR samples after the T_1 determinations were completed, using a small-scale (0.5 mL volume) home-built Ostwald viscometer.

^{11}B NMR spectra were obtained on a Bruker WH-400 multinuclear Fourier Transform NMR spectrometer operating at 128.38 MHz. A spectral width of 10 000 Hz was used to obtain an 8K FID. The FIDs with 8K of zero filling were trans-

formed with 0.5 Hz of line broadening into 8K spectra. ^{11}B chemical shifts are accurate to ±0.1 ppm and were referenced to external $Et_2O{\cdot}BF_3$, which was prepared by reaction of BF_3 with diethyl ether and fractional distillation of the liquid adduct.

Calculations of ^{19}F and ^{11}B chemical shifts and ^{11}B–^{19}F coupling constants were carried out using empirical "pairwise interaction" parameters (13, 14) as described previously (2). Calculated values agreed well with experimental values and were helpful in assigning haloboron cation resonances.

Positive ion fast atom bombardment mass spectra (FAB spectra) were obtained on an AEI MS-30 mass spectrometer as described previously (2), with glycerol or tetramethylenesulfone as matrix liquid. The FAB spectrum of $pyr_2BF_2^+{\cdot}PF_6^-$ has been reported elsewhere as part of a study of gas phase displacement reactions in FAB (Fig. 2*a* of ref. 15). There are major peaks at *m/z* 207 ($pyr_2BF_2^+$) and 128 ($pyrBF_2^+$) as well as a cluster peak of two cations and an anion at *m/z* 559 ($[pyr_2BF_2^+]_2{\cdot}PF_6^-$). Most FAB spectra had peaks due to glycerol (e.g., *m/z* 93, 85, and 277) removed by spectral subtraction. Verification of the isotope cluster patterns was carried out by the BMASROS scheme in some cases to further confirm the identity of the assigned species. In the later stages of this work we obtained FAB spectra directly on the adduct/cation $CDCl_3$ solutions themselves. The spectra are highly selective for the cations over the neutral adducts, despite the neutral adducts usually being present in higher concentrations. This direct use of FAB is very useful in monitoring these systems and complements solution NMR, although FAB spectra can be complicated by reactions occurring in the gas phase (15, 16). Our FAB studies will be reported in detail elsewhere.

Results

Reactions of $pyr{\cdot}BF_nX_{3-n}$ (X = Cl, Br)

$Pyr{\cdot}BF_2Br$ in $CDCl_3$ solvent undergoes extremely rapid displacement of bromide ion by pyridine at ambient temperature to give $pyr_2BF_2^+$ (eq. [1]). Interestingly, a well-resolved $pyr_2BF_2^+$ ^{19}F 1:1:1:1 quartet can be observed even before all of the uncomplexed BF_nBr_{3-n} (present since the mixed boron trihalide adducts form only under excess-Lewis-acid conditions (2, 9)) is quenched by reaction with pyridine, at a stage when rapid halogen exchange is occurring among most species and usually only broad and exchanging ^{19}F NMR signals can be observed at ambient temperature. This shows that $pyr_2BF_2^+$ is less susceptible to fluorine exchange than the other species present, and also indicates that the reaction to form $pyr_2BF_2^+$ is competitive with donor–acceptor bond formation, normally considered to be diffusion controlled. This is striking and unusual behaviour compared to boron trihalide adduct systems that we have studied previously.

The reaction to give $pyr_2BF_2^+$ is far too fast for ambient temperature ^{19}F NMR monitoring of the changes in a solution containing excess pyridine, as could be done in corresponding aliphatic amine systems (2). Instead, the reaction was monitored by the addition of successive increments of pyridine, followed by equilibration each time before obtaining the ^{19}F spectrum (Fig. 1). Equilibration of most species, including pyr_2BFBr^+ from $pyr{\cdot}BFBr_2$, is achieved within 10 min to 1 h at ambient temperature, depending on the concentration of uncomplexed pyridine. Figure 1*a* shows large 1:1:1:1 quartets (arising from ^{11}B–^{19}F coupling) for all of the fluorine-containing mixed boron trihalide adducts $pyr{\cdot}BF_nBr_{3-n}$ (n = 1–3), all of which along with $pyr{\cdot}BBr_3$ are formed in situ by halogen redistribution when $pyr{\cdot}BF_3$ is reacted with uncomplexed BBr_3 (2, 5, 9). Just enough pyridine had been added to complex with all of the uncomplexed Lewis acid. The large 1:1:1:1 quartet of $pyr{\cdot}BF_2Br$ persists indefinitely under these conditions. A small 1:1:1:1 quartet of $pyr{\cdot}BF_2Cl$ is also present in Fig. 1*a*, showing that some Cl,Br exchange occurs between $pyr{\cdot}BF_2Br$ and the $CDCl_3$ solvent. NMR parameters of the $D_2BF_2^+$ cations are given in Table 1, and those of the boron trihalide adducts $D{\cdot}BX_nY_{3-n}$ (n = 0–3) in Table 2.

Addition of successive increments of pyridine initially

Table 1. NMR parameters of $pyr_2BF_2^+$ and $pyrD'BF_2^+$ cations.[a]

Donors		Chemical shifts[b]		
D	D′	^{19}F	^{11}B	$J(^{11}B–^{19}F)$ (Hz)
pyr	pyr	−155.6	1.7	22.9
	2-Mepyr	−147.5	2.1	25.4
	2-Etpyr	−146.1	2.2	25.7
	2,4-Me_2pyr	−147.7	2.0	25.8
	Quinoline	−146.4	2.6	25.1
	3-Mepyr	−155.8	1.7	23.8
	3,5-Me_2pyr	−155.5	1.6	22.9
	4-Mepyr	−155.7	1.7	21.6
	4-Phpyr	−155.9	1.7	22.7
	HMPA	−147.3		18.9
	TMU	−148.8		17.6
	DMSO	−149.6		21.3
	t-BuNC	−150.7	−2.5	35.0
	MeBenzoate	−153.4		15.4
	DMAC	−147.7	1.0	23.3
	NO_3^-	−163.3		27.3
2-Mepyr	2-Mepyr	−142.3	2.4	28.8
	2-Etpyr	−141.1	2.6	28.0
	2,4-Me_2pyr	−142.7	2.3	28.1
	3-Mepyr	−147.4	2.1	26.6
	3,5-Me_2pyr	−147.3	2.0	25.8
	4-Mepyr	−147.8	2.0	25.3
	DMSO	−144.8	1.2	23.4
	TMU	−144.1		21.6
	t-BuNC		−2.8	34.7
2-Etpyr	2-Etpyr	−139.2	2.7	28.2
	3-Mepyr	−146.1	2.2	26.7
	4-Mepyr	−146.2		25.1
2,4-Me_2pyr	2,4-Me_2pyr	−142.8	2.2	28.4
	3,5-Me_2pyr	−147.4	1.9	26.0
	4-Mepyr	−148.1	1.9	25.1
3-Mepyr	3-Mepyr	−155.5	1.7	22.5
	4-Mepyr	−155.9		22.9
3,5-Me_2pyr	3,5-Me_2pyr	−155.1	1.6	22.3
	4-Mepyr	−155.9	1.5	22.9
4-Mepyr	4-Mepyr	−156.2	1.7	23.5

[a] In $CDCl_3$ or $CHCl_3$.

[b] ^{19}F, ppm to high frequency of $CFCl_3$; ^{11}B, ppm to high frequency of external $Et_2O{\cdot}BF_3$.

Fig. 1. 56.4 MHz ^{19}F NMR spectra of the pyr·BF_nBr_{3-n} system (0.8 M in total adduct species; $CDCl_3$ solvent) following the addition of successive amounts of pyridine to the NMR tube and at least 1 h of equilibration at ambient temperature (D = pyridine). (*a*) Sufficient pyridine to complex all of the uncomplexed boron trihalide; (*b*) – (*f*): further pyridine added to a total amount of (*b*) 10 μL; (*c*) 20 μL; (*d*) 30 μL; (*e*) 50 μL; (*f*) total of 100 μL of pyridine added, followed by equilibration for 8 h at 40°C.

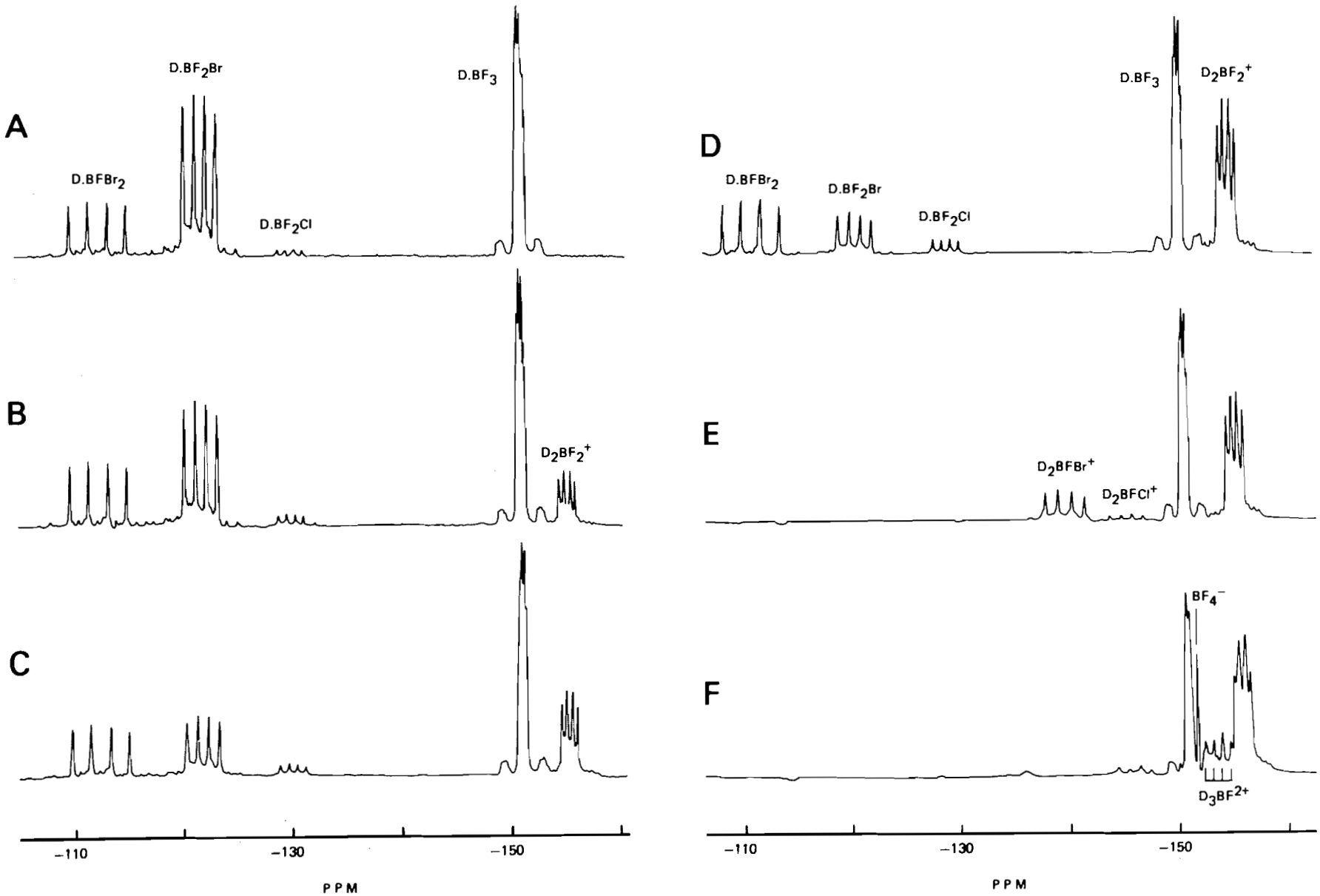

Table 2. NMR parameters of pyridine – boron trihalide adducts[a]

Adduct	pyr	2-Mepyr	3-Mepyr	4-Mepyr[b]	2-Etpyr	4-Phpyr	2,4-Me_2pyr	3,5-Me_2pyr
(i) ^{19}F chemical shifts[c]								
D.BF_3	−151.6	−148.7	−151.5	−152.1	−145.9	−152.1	−147.8	−152.1
D.BF_2Br	−126.5	−120.2	−126.4	−126.7	−120.4	−126.9		−126.6
D.BF_2Cl	−133.5	−128.2	−132.7	−134.5	−127.2	−133.9	−128.5	−133.6
D.$BFBr_2$	−118.5	−106.1	−117.7	−117.7	−105.8		−106.1	−118.2
D.$BFCl_2$	−126.6	−116.8	−126.7	−126.9	−115.6	−126.9	−116.5	−126.5
(ii) ^{11}B chemical shifts[d]								
D.BF_3	0.1	0.0	−0.2	0.1	0.3		0.0	−0.3
D.BF_2Br	2.0	1.6	1.9	1.9	1.6			1.7
D.BF_2Cl	3.8	3.6	3.7	3.7	3.5			
D.$BFBr_2$	0.0	−0.4	−0.1	−0.3	−0.5			
D.$BFCl_2$	6.7	6.6	6.7	6.6				
D.BCl_3	8.0	7.7	8.0	7.8				
D.BCl_2Br	3.5	3.3						
D.BCl_2I	−8.2	−9.6						
D.$BClBr_2$	−1.8	−2.5						
D.$BClI_2$	−29.9	−34.8						
D.BBr_3	−7.8	−9.0	−7.6	−7.8	−9.0		−9.1	−7.8
D.BI_3	−62.2	−67.7						
(iii) ^{11}B–^{19}F coupling constants (Hz)								
D.BF_3	10.2	11.8	10.3	10.5	10.5	10.5	12.1	
D.BF_2Br	48.4	48.0	47.7	47.8	48.1		47.9	
D.BF_2Cl	38.9	39.2	38.8	38.7	39.4	38.2	39.1	38.7
D.$BFBr_2$	82.6	85.9		82.9	85.4		85.0	82.7
D.$BFCl_2$	63.3	65.4	63.1	62.8	64.7	63.9	65.5	63.5
(iv) pK_b values for the pyridine bases[e]	8.79	8.06	8.37	7.98	8.11		7.23	7.85

[a]$CDCl_3$ solution, ambient temperature.
[b]^{19}F chemical shifts were incorrectly recorded in ref. 8.
[c]In ppm to high frequency of $CFCl_3$.
[d]In ppm to high frequency of external $Et_2O{\cdot}BF_3$.
[e]From ref. 33.

affects only the pyr·BF_2Br adduct; its ^{19}F NMR signal shrinks while that of $pyr_2BF_2^+$ grows, in accord with eq. [1] (Figs. 1*b*–1*d*). There is also a slight gain in intensity of the pyr·BF_2Cl resonance as Cl,Br exchange between pyr·BF_2Br and solvent proceeds. After the pyr·BF_2Br adduct is consumed, further pyridine reacts with the $BFBr_2$ adduct, giving initially pyr_2BFBr^+ (Fig. 1*e*) and eventually under stronger reaction conditions $pyr_3BF_2^+$ (Fig. 1*f*), consistent with eq. [2]. At the same time a trace of pyr_2BFCl^+ is formed (Fig. 1*e*), apparently from pyr·$BFBr_2$ by Cl,Br exchange with solvent to give pyr·BFClBr, followed by displacement of the remaining Br by pyridine.

^{11}B NMR spectra confirm the above peak assignments since the characteristic ^{11}B splitting patterns and ^{11}B–^{19}F coupling constants allow unambiguous matching of ^{11}B resonances to the corresponding ^{19}F resonances. An ^{11}B 1:2:1 triplet at 2.0 ppm, $J(^{11}B–^{19}F)$ = 48.4 Hz, assigned to pyr·BF_2Br, is replaced by another 1:2:1 triplet at 1.7 ppm, $J(^{11}B–^{19}F)$ = 22.9 Hz, assigned to $pyr_2BF_2^+$, in the early stages of the reaction sequence of Fig. 1. In the later stages, the 1:1 doublet of pyr·$BFBr_2$ and the 1:2:1 triplet of pyr·BF_2Cl disappear and new 1:1 doublets appear that are assigned to pyr_2BFBr^+, pyr_2BFCl^+, and pyr_3BF^{2+} (Fig. 2 and Table 3). Considerable $pyr_2BBr_2^+$ is also formed in the later stages. The $pyr_2BBr_2^+$ peak was assigned, and the others confirmed, by chemical shift calculations using pairwise interaction NMR parameters as described below.

The pyr·BF_nCl_{3-n} system reacts much more slowly with excess pyridine than the pyr·BF_nBr_{3-n} system. Again the most reactive species is the one with a single heavy halogen, pyr·BF_2Cl, giving $pyr_2BF_2^+$. Stepwise displacement of Cl^- from pyr·$BFCl_2$ is possible, first giving pyr_2BFCl^+. Initial attempts to get conversion of pyr·$BFCl_2$, first to pyr_2BFCl^+ and then to pyr_3BF^{2+}, were carried out by heating samples in capped NMR tubes at 40°C for several days. ^{19}F NMR monitoring showed that reaction of pyr·BF_2Cl to give $pyr_2BF_2^+$ is complete before any appreciable reaction of pyr·$BFCl_2$ occurs. Several days at 40°C give appreciable conversion of

Fig. 2. 128.4 MHz ^{11}B NMR spectrum of the solution of pyr·BF_nBr_{3-n} plus excess pyridine that gave rise to the ^{19}F NMR spectrum of Fig. 1*f* (D = pyridine).

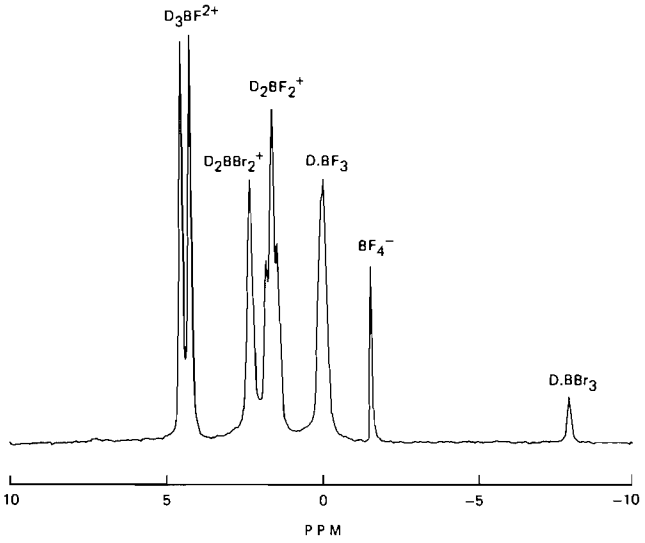

Fig. 3. Positive ion fast atom bombardment (FAB) mass spectrum of pyr_2BFCl^+, obtained directly from a solution of adducts and cations. Peaks at *m/z* greater than 82 are enhanced by a factor of 4 (D = pyridine).

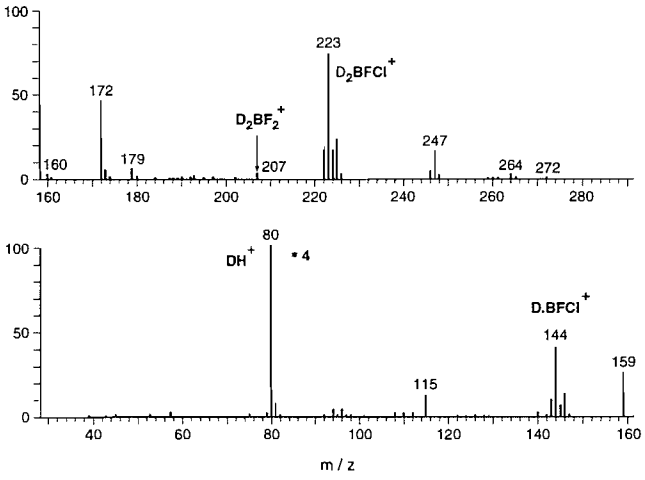

pyr·$BFCl_2$ to pyr_2BFCl^+, but also reversion of $pyr_2BF_2^+$ to pyr·BF_2Cl. It is of interest that the $pyr_2BF_2^+$ formation reaction (eq. [1]) is reversible, and that the reverse as well as the forward reaction is faster for $pyr_2BF_2^+$ than for pyr_2BFCl^+. Complete conversion of pyr·$BFCl_2$ to pyr_2BFCl^+ was achieved by carrying out the reaction in a sealed tube at 110°C, but only a few percent conversion to pyr_3BF^{2+} by further chloride displacement was possible even under these forcing conditions. The FAB spectrum of pyr_2BFCl^+, obtained directly from $CDCl_3$ solution following heating in a sealed tube, is shown in Fig. 3.

Attempted isomerization of pyr·BF_3 to $pyr_2BF_2^+·BF_4^-$

BF_3 complexes of a few Lewis bases, including HMPA·BF_3 (17) and TMU·BF_3 (18), can undergo reaction to form small amounts of their ionization isomers $D_2BF_2^+·BF_4^-$ in solution. Preliminary attempts to form $pyr_2BF_2^+·BF_4^-$ by disproportionation of pyr·BF_3 in the absence of a heavier boron trihalide, by analogy with these cases, were unsuccessful. The ^{19}F NMR spectra of pyr·BF_3 and 2-Mepyr·BF_3 did not change following (*i*) refluxing in toluene or (*ii*) refluxing in toluene with the addition of 1,1,1,3,3,3-hexamethyldisilazane, which has a high affinity for fluoride ion (19) and which we hoped would act as an irreversible extractant for F^- from pyr·BF_3, giving three-coordinate pyr·BF_2^+ that further pyridine could attack. With 1,1,1,3,3,3-hexamethyldisilazane present, 15 min of reflux in toluene did remove some fluorine from the adducts as shown by the presence of a small ^{19}F NMR peak assigned to Me_3SiF (larger in the 2-Mepyr case than with pyr itself), and the pyr·BF_3 resonances were broadened, suggesting some chemical exchange, but no ^{19}F signals arising from boron cations or BF_4^- could be observed.

^{19}F spin-lattice relaxation

Figure 4 shows variations in ^{19}F NMR spin-lattice relaxation

Fig. 4. Changes in the ^{19}F spin-lattice relaxation times of the species present in the pyr·BF_nBr_{3-n} system (0.8 M in total adduct species; $CDCl_3$ solvent; D = pyridine) following additions of pyridine. Some species are formed and consumed as shown in Fig. 1, so T_1 values of these could be obtained only at certain stages of the pyridine titration process.

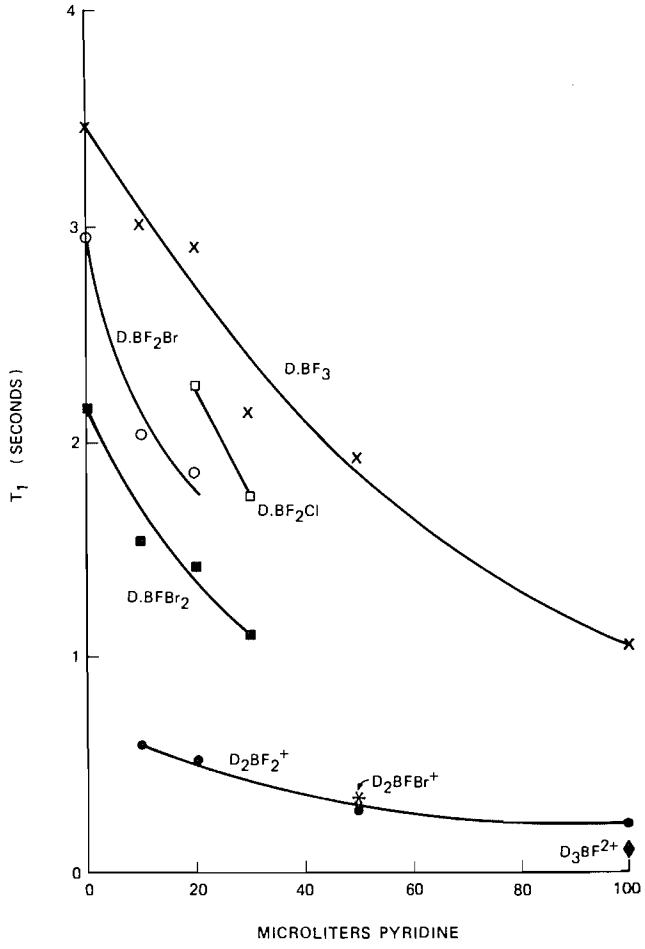

Table 3. NMR parameters of pyridine-containing monofluoroboron cations.[a]

Donors		Chemical shifts (ppm)[b]		$J(^{11}B-^{19}F)$
D	D′	^{19}F	^{11}B	(Hz)
(a) **DD′BFBr⁺**				
pyr	pyr	−142.4	4.9	58.1
	2-Mepyr	−129.4	5.2	62.1
	2-Etpyr	−128.3		62.1
	2,4-Me_2pyr		5.2	61.5
	3-Mepyr	−141.8	5.0	55.6
	3,5-Me_2pyr	−140.0	4.8	59.3
	Quinoline	−128.4		61.6
	N-Mepiperidine	−148.3	6.7	62.4
	Me_2NEt	−145.7	6.4	64.2
	Quinuclidine	−147.3	6.0	60.3
	Me_3N	−147.8	6.2	62.3
2-Mepyr	2-Mepyr	−125.0	5.9	63.6
	3-Mepyr	−129.8	5.3	61.7
	4-Mepyr	−129.9	5.1	61.9
	2,4-Me_2pyr	−126.2	5.8	62.5
	3,5-Me_2pyr	−129.9	5.2	61.8
	Quinuclidine		7.3	61.1
2,4-Me_2pyr	4-Mepyr		5.0	61.3
	2,4-Me_2pyr		5.7	66.0
	3,5-Me_2pyr	−130.2	5.4	62.2
3-Mepyr	3-Mepyr	−141.3	5.0	56.2
	4-Mepyr	−142.1		58.8
	Quinuclidine		6.0	61.1
3,5-Me_2pyr	4-Mepyr	−141.8	4.7	56.5
	3,5-Me_2pyr	−140.0	4.9	58.3
4-Mepyr	2-Etpyr	−128.3	5.2	62.9
	4-Mepyr	−142.4	4.8	57.2
	Me_3N	−148.5	6.1	62.2
	Quinuclidine	−148.0		59.2
	Me_2NEt	−146.1		63.5
(b) **DD′BFCl⁺**				
pyr	pyr	−146.9	6.2	47.8
	Quinuclidine	−152.9		52.0
3-Mepyr	3-Mepyr	−146.4	6.1	47.9
4-Mepyr	4-Mepyr	−147.4	5.9	48.0
	Me_3N	−155.1	6.6	50.6
	Quinuclidine	−153.5	6.3	51.8
(c) **DD′$_2$BF²⁺**				
pyr	pyr	−152.7	4.6	37.6
	3-Mepyr	−153.6	4.6	36.9
2-Mepyr[c]	pyr	−137.5		33.7
3-Mepyr	3-Mepyr	−153.8	4.5	36.9
4-Mepyr	4-Mepyr	−155.1	4.4	36.9

[a]Formed from D·BFX_2 in $CDCl_3$ or $CHCl_3$.

[b]^{19}F, ppm to high frequency of $CFCl_3$; ^{11}B, ppm to high frequency of external $Et_2O·BF_3$.

[c]Will form only when 2-Mepyr is part of the original D·$BFBr_2$. 2-Mepyr as a free base cannot displace bromide to give DD′$_2BF^{2+}$.

times of the various fluorine-containing species present at various stages of the titration of the pyr·BF_nBr_{3-n} adduct system with excess pyridine, as described above and shown in Fig. 1. Some species disappear while others appear after further aliquots of pyridine are added and the solution is reequilibrated. T_1 values of individual species change greatly as solution viscosity changes with the addition of more pyridine, but the signals assigned to all three of the fluoroboron cations consistently have by far the shortest T_1 values. Moreover $pyr_2BF_2^+$, the only one of these cations that can be detected throughout the titration, shows far less variation in T_1 than the neutral adducts. T_1 values depend on molecular tumbling, which is very dependent on solution viscosity, which in turn is dependent on solute concentration and on the amount of pyridine added. Therefore relative T_1 values of different species present in the same solution should be compared rather than absolute values (i.e., compare points lined up vertically in Fig. 4, corresponding to different species present in the same solution). Viscosity, determined using a small-scale (0.5 mL) Ostwald viscometer, increases as the more viscous pyridine is added to the $CDCl_3$ solution. This is consistent with the decreases in T_1 of the same species as successive portions of pyridine are added (Fig. 4). Note that pyr_3BF^{2+} has by far the smallest T_1 value, while $D_2BF_2^+$ and D_2BFBr^+ species have intermediate values and the pyr·BF_nBr_{3-n} adducts have the largest values.

Substituted-pyridine and mixed-donor fluoroboron cations

Various mixed- and unmixed-donor $D_2BF_2^+$ cations such as (pyr)(4-Mepyr)BF_2^+ can be readily formed by titrating one pyr·BF_nX_{3-n} system with another (or the same) pyridine base. Non-*ortho*-substituted pyridines including 3-Mepyr, 4-Mepyr, and 4-Phpyr give very similar chemistry, and ^{19}F and ^{11}B NMR parameters, to pyridine itself when incorporated into BF_nX_{3-n} adducts and $D_2BF_2^+$ cations. Table 1 includes NMR parameters for many such ions. As with the pyridine system itself, Cl^- displacement from D·BF_2Cl occurs much less readily than Br^- displacement from D·BF_2Br. Rates of Cl^- displacement vary in the order 3-Mepyr ≥ pyr > 4-Mepyr > 4-Phpyr but the differences are not large.

Reaction is much slower when the pyridine has an *ortho* substituent. Thus reaction of 2-Mepyr·BF_2Br with 2-Mepyr requires 1–2 h at ambient temperature for complete formation of $(2\text{-Mepyr})_2BF_2^+$, similar to bromide displacement from tertiary-amine (quinuclidine and trimethylamine) BF_2Br adducts (2). We could form 2-Mepyr_2BFBr^+ but not 2-Mepyr_3BF^{2+} from 2-Mepyr·$BFBr_2$, and we could not form 2-MePyr_2BFCl^+ from 2-Mepyr·$BFCl_2$. The 2-ethylpyridine (2-Etpyr) BF_nBr_{3-n} system reacts somewhat more slowly than the 2-Mepyr system.

Although 2,6-dimethylpyridine and 2,4,6-trimethylpyridine readily form mixed boron trihalide adducts D·BF_nX_{3-n} (X = Cl, Br), we have not been able to detect any NMR signals consistent with their incorporation into difluoroboron cations, either as the only donor ($D_2BF_2^+$) or with another less sterically hindered donor (DD′BF_2^+). The presence of a second, less sterically hindered, pyridine in solution with adducts of 2,6-Me_2pyr or 2,4,6-Me_3pyr merely replaces the more hindered pyridine from its adducts, without any cation formation. Adducts of these highly hindered pyridines are

highly reactive, and frequently coagulation of the solvent occurs in the presence of excess base, under heating conditions that are successful in forming fluoroboron cations from less hindered pyridine adduct systems. All of the above is consistent with the greater ease of dissociation of highly sterically hindered adducts compared to unhindered ones. ΔH_f values for formation of BF_3 adducts with highly hindered pyridines are much lower than with less hindered ones: pyr·BF_3, 25.0 kcal/mol; 2-Mepyr·BF_3, 23.2 kcal/mol, 2,6-Me_2pyr·BF_3, 17.5 kcal/mol (20). Catalysis of side reactions at elevated temperatures, by the traces of uncomplexed boron trihalide formed by dissociation of the 2,6-Me_2pyr and 2,4,6-Me_3pyr adducts, likely causes the coagulation of solvent.

Various Lewis bases of low steric hindrance other than pyridines, such as dimethyl sulfoxide and tetramethylurea, can also displace halide ion from pyr·BF_2X. Table 1 includes NMR parameters of various (pyr)D′BF_2^+ ions formed in this way. We previously reported NMR parameters of similar mixed-base cations $(R_3N)(pyr)BF_2^+$ and $(R_3N)(D')BF_2^+$, formed by attack of pyridines and other donors on $R_3N{\cdot}BF_2Br$ (2).

Non-fluorine containing haloboron cations from pyr·BX_nY_{3-n}(X, Y = Cl, Br, I)

The adduct systems pyr·BCl_nI_{3-n} and pyr·BCl_nBr_{3-n} readily form haloboron cations via selective displacement of the heaviest halogen, and we have observed these ions by ^{11}B NMR, supplemented by FAB. ^{11}B chemical shifts are given in Table 4, along with values calculated from pairwise interaction parameters (13, 14) which support our assignments.

Figure 5 shows ^{11}B NMR spectra of the enormously reactive pyr·BCl_nI_{3-n} system. Initially a large amount of uncomplexed BCl_nI_{3-n} ($n = 0 - 3$) is present, as well as pyr·BI_3 and pyr·$BClI_2$ (Fig. 5*a*). BI_3 is the strongest Lewis acid of the boron trihalides and complexes preferentially with the limited amount of pyridine, followed by the next strongest Lewis acid of this series, $BClI_2$. Negligible BCl_2I or BCl_3 seems to be complexed, illustrating the pronounced changes in Lewis acid strength across the series. Minor peaks are present as well. Addition of enough pyridine to complex practically all of the boron trihalide gives a simple spectrum with all of the pyr·BCl_nI_{3-n} adducts as the only major boron-containing species (Fig. 5*b*). The spectrum looks much like the ^{11}B spectrum of any D·BCl_nI_{3-n} adduct system, since chemical shifts depend more on the number and type of halogens than on the specific donor molecule (5, 9, 14). A small amount of uncomplexed BCl_3 remains.

Addition of further pyridine leads to disappearance of the pyr·BCl_2I and pyr·$BClI_2$ signals (Figs. 5*c* and 5*d*), and considerable precipitate formation. It appears that haloboron cations are forming but are largely being precipitated so that their NMR signals do not become large. Small peaks are present that can be assigned to $pyr_2BCl_2^+$, pyr_2BClI^+, and $pyr_2BI_2^+$, consistent with calculated chemical shift values. The only adducts still present at the end of the process are the unmixed-halogen ones pyr·BI_3 and pyr·BCl_3 (Fig. 5*d*). This high selectivity, favouring reaction of the BCl_2I and $BClI_2$ adducts to give the BCl_2^+ and $BClI^+$ cations, was also observed in the much less reactive quinuclidine. BCl_nI_{3-n} system (Fig. 7 of ref. 2). Thus iodide displacement occurs as in eq. [3].

Table 4. Observed and calculated ^{11}B chemical shifts of some pyridine–haloboron cations.

	Observed[a]	Calculated[b]
$pyr_2BF_2^+$	1.7	2.1
pyr_2BFCl^+	6.2	5.5
pyr_2BFBr^+	4.9	4.9
$pyr_2BCl_2^+$	8.4	7.7
pyr_2BClBr^+	5.9	5.9
pyr_2BClI^+	−2.1	−1.6
$pyr_2BBr_2^+$	2.6	2.5
$pyr_2BI_2^+$	−20.2	−19.1
pyr_3BF^{2+}	4.6	4.6
pyr_3BCl^{2+}		7.6
pyr_3BBr^{2+}		7.3
pyr_3BI^{2+}		4.4
pyr_4BF^{3+}	[c]	7.4
(pyr)(2-Mepyr)BF_2^+	2.2	2.4
(pyr)(2-Mepyr)$BFBr^+$	5.2	5.0
2-$Mepyr_2BF_2^+$	2.4	2.8
2-$Mepyr_2BFCl^+$	2.4	2.9
2-$Mepyr_2BFBr^+$	5.9	5.4
(pyr)(3-Mepyr)BBr_2^+	2.6	[d]
(pyr)(quinuclidine)$BClI^+$	1.7	1.8
(2-Mepyr)$(Me_3N)BCl_2^+$	9.9	10.0
(2-Mepyr)(quinuclidine)BCl_2^+	9.7	9.7
3-$Mepyr_2BBr_2^+$	2.6	[d]
4-$Mepyr_2BBr_2^+$	2.4	[d]
(4-Mepyr)(3-Mepyr)BBr_2^+	2.3	[d]

[a]$CDCl_3$ solution; ppm to high frequency of external $Et_2O{\cdot}BF_3$.

[b]By pairwise interaction calculations.

[c]Not observed. However, the 4-Mepyr analogue (as the bromide) has an ^{11}B shift of 6.2 ppm.

[d]Insufficient data to determine meaningful $\eta_{donor,\ donor}$ pairwise terms involving 3-Mepyr and 4-Mepyr.

Again the heaviest halide ion is preferentially displaced. We

[3] pyr·BCl_nI_{3-n} ($n = 0 - 2$) + pyr ⟶ $pyr_2BCl_nI_{2-n}^+ + I^-$

cannot exclude some Cl^- displacement from pyr·BCl_3.

Of the minor peaks present in Fig. 5*a*, three unidentified peaks disappear as pyridine is added. These apparently arise from three-coordinate boron species, possibly pyr·BCl_2^+, pyr·$BClI^+$, and pyr·BI_2^+. Another peak at about 5.2 ppm increases in size as pyridine is added but never becomes major. This peak is tentatively identified as BCl_4^- in Fig. 4*a* on the basis of its chemical shift (21), but as the system becomes pyridine-rich (Figs. 5*c* and 5*d*) it is more likely to arise from a pyridine-rich species such as pyr_3BI^{2+}, pyr_3BCl^{2+}, or even pyr_4B^{3+}, all of which are predicted to absorb in this range (Table 4). We synthesized 4-$Mepyr_4B^{3+}$ as its bromide salt (22) and found its ^{11}B chemical shift in $CDCl_3$ to be 6.2 ppm. Since 4-Mepyr cations have similar ^{11}B NMR parameters to the corresponding cations of pyr itself this is a reasonable estimate for pyr_4B^{3+}, but does not exclude pyr_3BI^{2+} or pyr_3BCl^{2+}.

In contrast to the pyr·BCl_nI_{3-n} system, the pyr·BCl_nBr_{3-n} system reacts slowly with excess pyridine. The rate of cation formation is comparable to the formation of $pyr_2BF_2^+$ from pyr·BF_2Cl, and both $pyr_2BCl_2^+$ and pyr_2BClBr^+ are formed, consistent with Br^- displacement from both pyr·BCl_2Br and

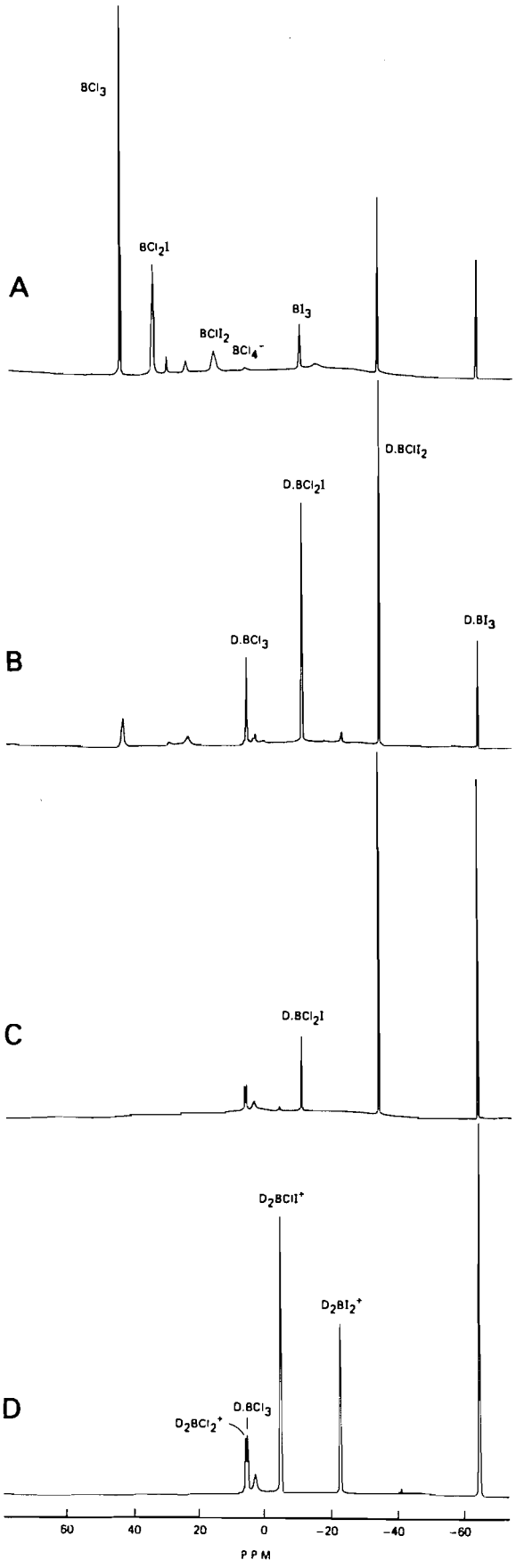

Fig. 5. 128.4 MHz ^{11}B NMR spectra of the pyr·BCl_nI_{3-n} system (0.8 M in total boron species; $CDCl_3$ solvent; D = pyridine). (*A*) Insufficient pyridine to complex all of the Lewis acid; (*B*) approximately equimolar pyridine and Lewis acid; (*C*) and (*D*), increasing excess of pyridine over total boron trihalide.

pyr·$BClBr_2$. Again it is the mixed boron trihalides that react preferentially and the heavier halide ion that is selectively displaced. Because of precipitate formation we do not have as complete a picture of these systems as of the fluorine-containing systems.

Discussion

General

With pyridine as the Lewis base, $D_2BF_2^+$ formation is strikingly accelerated compared to the R_3N-donor systems (1, 2), and additional reactions occur to give pyr_2BFBr^+, pyr_2BFCl^+, and pyr_3BF^{2+}. Low donor steric hindrance is critical, as confirmed by the pronounced drop in efficiency of halide ion displacement when the attacking pyridine has a 2-substituent, and by the absence of any displacement when either the attacking or the already-bonded pyridine is 2,6-disubstituted. This is consistent with earlier work by Ryschkewitsch and co-workers showing the importance of steric hindrance on formation of hydroboron and heavy-halogen haloboron cations by halide ion displacement (4). With 4-methylpyridine as donor they were able to displace all bromines from a BBr_3 adduct in refluxing toluene, giving the D_4B^{3+} ion (22). The effects of steric hindrance on other substitution reactions about boron (23), and similar effects with pyridine ligands about other central atoms (24), have been well documented. Pronounced steric effects on reactivity and equilibrium constants are well established in a wide range of coordination complexes (25, 26). The only previously reported D_2BFCl^+ cation was prepared by the reaction of elemental fluorine with $(Me_3N)_2BH_2^+·Cl^-$ (27).

Many species might exist as both ionic and covalent isomers, such as $CH_3CN·SbCl_5$, which is reported to be present as the ionic $(CH_3CN)_2SbCl_4^+·SbCl_6^-$ in nitrobenzene (28) but as the covalent adduct in nitromethane (29). The possibility of ionization isomers of Lewis acid–base complexes is easily overlooked. NMR, supplemented by FAB, is powerful in identifying haloboron cations and is useful in clarifying situations in which either ionic or covalent isomers (or both together) may be present. It should be kept in mind that unexpected ionic structures can be generated from neutral precursors (30). There have recently been several reports of replacement of a halide ion by a neutral ligand to give a cationic complex (31).

NMR parameters

Steric hindrance affects NMR parameters (25, 32), as observed in our ^{19}F and ^{11}B NMR studies of the mixed boron trihalide adducts (9). More pronounced effects occur in the fluoroboron cations (Table 1) than in the neutral adducts (Table 2). Thus successive methyl substitution in the pyridine 2-position causes high-frequency (low-field) shifts of 8.1 and 5.2 ppm (^{19}F) and 0.4 and 0.3 ppm (^{11}B) in the series $pyr_2BF_2^+$, $(pyr)(2\text{-}Mepyr)BF_2^+$, $2\text{-}Mepyr_2BF_2^+$, compared to shifts of

only 2.9 ppm (^{19}F) and –0.1 ppm (^{11}B) on going from pyr·BF_3 to 2-Mepyr·BF_3. (Other BF_nX_{3-n} adducts do show greater ^{19}F shifts as the donor changes from pyr to 2-Mepyr, however (Table 2), perhaps reflecting greater steric requirements of the heavier halogens compared to fluorine.) *meta* and *para* substitution on pyridine has very little effect on chemical shift. ^{11}B–^{19}F coupling constants are not as large as those of the corresponding more hindered tertiary-amine cations, and they increase appreciably as the pyridine steric hindrance increases, e.g., $pyr_2BF_2^+$, 22.9 Hz; (pyr)(2-Mepyr)BF_2^+, 25.4 Hz; 2-$Mepyr_2BF_2^+$, 28.8 Hz (cf. $(quinuclidine)_2BF_2^+$, 39.5 Hz (2)). There is no correlation of NMR parameters or of reactivity with the pK_b values of the pyridines (33), which are listed in Table 2.

Chemical shifts of many nuclei are not linearly additive with respect to the substituent groups, but nevertheless may be "pairwise additive," i.e., the chemical shift can be expressed as a sum of pairwise terms $\eta_{i,j}$, associated with substituents *i* and *j* and independent of all other substituents. The sum is taken over all possible pairs of substituents about the central atom, excluding the nucleus being observed in the NMR experiment (13). We showed that pairwise additivity applies to ^{19}F and ^{11}B chemical shifts and also to ^{11}B–^{19}F coupling constants in the mixed tetrahaloborate anions (21), and extended this to a wide range of boron trihalide adducts (14) and more recently to trialkylamine-haloboron cations (2). The halogen–halogen $\eta_{i,j}$ terms that apply to the tetrahaloborate anions are also applicable to the neutral adducts and the haloboron cations, with addition of donor–halogen $\eta_{i,j}$ terms for the adducts, and also donor–donor $\eta_{i,j}$ terms for the cations. Chemical shifts for trialkylamine-haloboron cations (2) and pyridine-haloboron cations, calculated using our $\eta_{i,j}$ terms (Table 5), agree well with experiment, the average deviation from the observed value being less than 0.5 ppm, although there are greater discrepancies with a few heavy-halogen-containing species. For the typical haloboron cation pyr_2BClI^+, all possible pairwise combinations of boron substituents are: 1 pyr,pyr; 2 pyr,Cl, 2 pyr,I and 1 Cl,I. Using values from Table 5, this gives $\eta_{pyr,pyr} + 2\eta_{pyr,Cl} + 2\eta_{pyr,I} + \eta_{Cl,I} = -1.6$ ppm for the ^{11}B chemical shift, as listed in Table 4. Pairwise interaction parameters have been used as a purely empirical method for identifying new boron (34) and other element (35) species. When there is a wide chemical shift range, assignments are unambiguous. Since the range of ^{11}B chemical shifts of the haloboron cations (excluding $pyr_2BI_2^+$) is only 12 ppm and overlaps the range of neutral adducts and tetrahaloborate anions, a few peak assignments remain ambiguous.

Table 5. Pairwise substituent NMR parameters η_{ij} for four-coordinate boron species.[a]

η_{ij}	^{19}F chemical shift	^{11}B chemical shift	^{11}B–^{19}F coupling constant
F, F	–50.5	–0.33	–1.0
F, Cl	–36.4	–1.04	14.0
F, Br	–31.1	0.46	19.2
Cl, Cl	–31.4	1.27	26.5
Cl, Br	–28.2	–0.60	32.2
Cl, I		–5.85	
Br, Br	–26.3	–4.00	37.3
Br, I		–12.04	
I, I		–21.23	
pyr, F	–51.3	0.31	5.8
pyr, Cl	–47.5	1.29	18.2
pyr, Br	–45.5	1.31	23.0
pyr, I		0.23	
pyr, pyr	–51.2	1.23	12.2
Me_3N, F	–56.6	0.24	8.5
Me_3N, Cl	–50.6	2.20	21.4
Me_3N, Br	–47.1	2.82	25.7
Me_3N, I		3.05	
Me_3N, pyr	–55.2	1.15	13.8
Me_3N, Me_3N	–52.3[b]	1.09	19.2[b]
Q, F	–55.9	0.17	8.7
Q, Cl	–50.1	1.84	21.0
Q, Br	–47.0	2.68	25.7
Q, I		3.38	
Q, pyr	–54.6	0.96	13.1
Q, Me_3N	–51.3[b]	1.16	20.8[b]
Q, Q	–49.8[b]	1.51	22.0[b]
2-Mepyr, F	–49.1	0.20	6.5
2-Mepyr, Cl	–42.7	1.23	19.3
2-Mepyr, Br	–40.0	1.09	24.0
2-Mepyr, I		–1.42	
2-Mepyr, pyr	–45.8	1.66	11.5
2-Mepyr, Me_3N	–47.5	1.83	15.6
2-Mepyr, Q	–48.9	2.31	13.3
2-Mepyr, 2-Mepyr	–44.5	2.38	15.9

[a]Based on data for tetrahaloborate anions, neutral adducts, and haloboron cations. ^{19}F values refer to chemical shifts in ppm to high frequency of $CFCl_3$; ^{11}B, values refer to chemical shifts in ppm to high frequency of external $Et_2O{\cdot}BF_3$. pyr = pyridine, Q = quinuclidine, 2-Mepyr = 2-methylpyridine.

[b]Only one example of this interaction was available to calculate this η_{ij} value.

Spin-lattice relaxation

The distinctive short ^{19}F spin-lattice relaxation times (T_1's) of the fluoroboron cations (Fig. 3) support our structures, since fluorine in any $D_2BF_2^+$ or D_2BFX^+ ion is in the middle of a chain and can move much less freely than fluorine on the terminal boron of any D·BF_nX_{3-n} adduct. T_1's are frequently proportional to $1/\tau_c$, where τ_c is the correlation time for molecular reorientation. τ_c is proportional to r^3, r being the effective molecular size. Rapid rotation is possible about the D—B bond of D·BF_nX_{3-n} adducts, i.e., the effective molecular size of the BF_nX_{3-n} portion of the adduct is small, and hence T_1 should be relatively long. Substitution of fluorine with successive chlorines or bromines increases the moment of inertia of the rotating group and slows the rotation, so that these adducts have successively shorter T_1's as the number of heavy halogens increases. Rotation is far more restricted when a BF_2 group is between two large adduct molecules. Such fluorines are not free to rotate rapidly about either D—B bond because rotation is restricted by the second donor, which extends far out into the surrounding solvent. Hence the fluoroboron cations should have shorter T_1's than the neutral adducts, as observed. The even shorter T_1, by another factor of 2, of pyr_3BF^{2+} compared to $pyr_2BF_2^+$ and pyr_2BFX^+, is consistent

with **three** large groups anchoring the boron in place, further restricting the motion of the lone fluorine. The slower fluorine motion in the cations results in more efficient spin-lattice relaxation via a more favourable distribution of motional frequencies (36). This T_1 method is of general applicability in confirming the presence of any fluoroboron cation containing at least two donor molecules. While a number of factors including ion pairing (37) could affect T_1 values in these systems, a T_1 much shorter than all others in the same solution should be valuable in identifying fluoroboron cation resonances, especially in the many oxygen-donor systems in which splittings due to ^{11}B–^{19}F couplings are not resolved so assignments cannot be based on such splittings.

Mechanistic implications

The striking ability of one heavy and two light halogens on boron to maximize the ease of displacement of the heavy halogen can be attributed to stabilization of the transition state or reactive intermediate by π bonding from halogen to boron (2). Such π bonding is far more important with fluorine than with the heavier halogens, which makes BF_3 the weakest Lewis acid of the BX_3 series (6). We tentatively excluded a dissociative mechanism and three-coordinate intermediate on several grounds (2), and suggested an S_N2 reaction with a five-coordinate transition state:

[4] $D{\cdot}BF_2Br + D' \longrightarrow$ 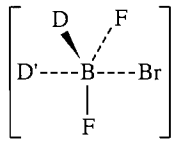 $\longrightarrow DD'BF_2^+ + Br^-$

Lowering of the energy of the transition state, by maximization of halogen-to-boron π bonding when the $D{\cdot}BF_2$ unit becomes planar, is crucial to high selectivity. As in a three-coordinate intermediate, the stabilization by π bonding should become greater as the number of fluorines increases, and can account for the high selectivity.

The far greater reactivity of pyr·BF_2Br with pyridine, compared to quinuclidine·BF_2Br with quinuclidine, will to some extent arise from the decreased steric hindrance of pyridine compared to quinuclidine, but the proposed transition state also predicts far greater reactivity of pyr·BF_2Br, independent of steric effects. Pyridine already attached to boron should be able to stabilize the transition state of eq. [4] due to the additional π bonding that is possible from pyridine to boron:

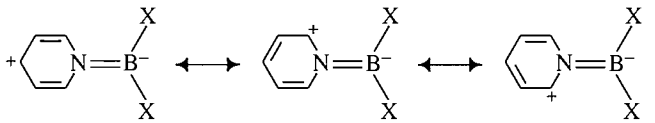

Thus pyridine acts much like fluorine in providing π bonding to stabilize the transition state, whereas a trialkylamine nitrogen cannot participate in π bonding, so that already bonded pyridine accelerates the reaction. This can also explain the observation that the mixed-donor cation (pyr)(Q)BF_2^+ (Q = quinuclidine) forms much more readily when the tertiary amine Q reacts with pyr·BF_2Br, than when pyridine reacts with Q·BF_2Br, despite steric effects in the transition state being essentially the same (2). The proposed five-coordinate transition state can also help to account for the readiness of pyr_3BF^{2+} and pyr_2BFX^+ (X = Cl, Br) to form, while the corresponding trialkylamine species do not. As the number of fluorines available to stabilize the transition state by π bonding decreases, the number of pyridines increases to compensate. One fluorine and one pyridine in the trigonal planar part of the transition state may be almost as effective as two fluorines in providing π bonding to boron. (The lower steric hindrance of pyridine compared to quinuclidine is of course also important, and its importance should increase as the number of Lewis base molecules in the cation increases from two to three.)

Recently the mechanism of reaction of boron trifluoride with pyridine has been analysed in detail by Ou, Wallace, and Janzen (38) on the basis of Janzen's coordination model of reaction mechanisms (39). The analysis, involving a set of plausible dissociation and recombination steps for the case of a 2:1 excess of BF_3 over pyridine, provides insight into why $pyr_2BF_2^+$ should be much slower to undergo chemical exchange than other species including free BF_3, pyr·BF_2^+, BF_4^-, and the fluorine-bridged pyr·BF_2--F--BF_3 that are expected to be present under excess-Lewis-acid conditions. Their analysis is in accord with our observation of a well-defined 1:1:1:1 ^{19}F quartet for $pyr_2BF_2^+$, together with broad ^{19}F signals consistent with rapid chemical exchange among other fluorine-containing species, in the presence of an excess of Lewis acid.

The most important difference between the mixed boron trihalide adducts and BF_3 adducts is that heavy halide ion is a favourable leaving group, while fluoride ion must be transferred among other species and does not exist independently in solvents such as $CDCl_3$. Janzen's coordination model (39), which rationalizes the reactions of a wide range of inorganic fluorides, does not allow displacement of naked F^- but only F^- transfer. The ready formation of pyridine-fluoroboron cations from the mixed boron trihalide adducts, but not from pyr·BF_3, is in accord with displacement of heavy halide ion in a manner that cannot be duplicated by fluoride ion.

Even in non-fluorine-containing $D{\cdot}BX_2Y$ adducts the transitions state would be preferentially stabilized if the lightest available halogens were involved in the planar $D{\cdot}BX_2$ unit, since π bonding from halogen to boron decreases in the order $F \gg Cl > Br > I$ (6). The heaviest halogen, least able to participate in π bonding stabilization of the transition state, would always be preferentially lost, as observed. The relative B—X bond strengths, B—F $\gg$ B—Cl > B—Br > B—I, are also important in favouring the loss of the heaviest halogen but this cannot be the sole effect because the same heavy halogen is lost much less readily from the unmixed rather than the mixed boron trihalide adducts. Because free fluoride is never displaced, halogen redistribution involving fluorine requires the presence of at least traces of uncomplexed Lewis acid so that a transitory B-F-B bridge can form (21, 38–40).

The minor ^{11}B NMR peaks in Fig. 5*a*, which disappear as pyridine is added, may arise from pyr·BCl_2^+, pyr·$BClI^+$, and pyr·BI_2^+. The existence of these species would be favoured by stabilization due to π bonding from pyridine to boron. No similar ^{11}B peaks were observed in the corresponding quinuclidine·BCl_nI_{3-n} system (2) in which π bonding from the donor is not possible. Any such stabilization of pyridine-containing three-coordinate boron cations would be another factor favouring ready formation of the four-coordinate boron cations, since they could easily add another pyridine molecule to

form $pyr_2BX_2^+$. If an analogous $pyr{\cdot}BF_2^+$ species can form readily, as proposed by Janzen and co-workers (38), this would be a factor favouring the observed facile formation of $pyr_2BF_2^+$ even when Lewis acid is present in excess.

Conclusions

Various 4-coordinate fluoroboron and other haloboron cations can be detected in solution under mild conditions by displacement of the heavier halogen as halide ion from pyridine – mixed boron trihalide adducts. Displacement of the heavy halogen is easiest when there are one heavy and two light halogens on boron. It is not yet clear whether kinetic or equilibrium factors are predominant in determining the reactivity patterns in these systems. While many cationic species can be prepared by the reactions described here, firm conclusions on mechanism must await further work.

Acknowledgements

We thank Mr. T.R.B. Jones for technical assistance, Professors J.M. Miller (Brock University), A.F. Janzen (University of Manitoba), and P. Stilbs (Royal Institute of Technology, Stockholm) for helpful discussions, Mr. J. Nye, Ms. C.L. MacLaurin, and Mr. R. Théberge for running FAB spectra, Mr. J. Vandenhoff for construction of a small-scale (0.5 mL volume) Ostwald viscometer, Mr. D.J. Hastings for synthesis of $(4\text{-Mepyr})_4B^{3+}$, the South Western Ontario High Field NMR Centre for providing instrument time, and the Natural Sciences and Engineering Research Council of Canada for financial support.

References

1. M.J. Farquharson and J.S. Hartman. J. Chem. Soc. Chem. Commun. 256 (1984).
2. M.J. Farquharson and J.S. Hartman. Can. J. Chem. **67**, 1711 (1989).
3. D.R. Martin, J.U. Mondal, R.D. Williams, J.B. Iwamoto, N.C. Massey, D.M. Nuss, and P.L. Scott. Inorg. Chim. Acta, **70**, 47 (1983).
4. G.E. Ryschkewitsch. *In* Boron hydride chemistry. *Edited by* E.L. Muetterties. Academic Press, New York. 1975. Chap. 6; H. Nöth. Prog. Boron Chem. **3**, 211 (1970); M.A. Mathur and G.E. Ryschkewitsch. Inorg. Chem. **19**, 3054 (1980).
5. J.S. Hartman and J.M. Miller. Adv. Inorg. Chem. Radiochem. **21**, 147 (1978).
6. A.G. Massey. Adv. Inorg. Chem. Radiochem. **10**, 1 (1967).
7. H. Steinberg and R.J. Brotherton. *In* Organoboron chemistry. Vol. 2. Boron–nitrogen and boron–phosphorus compounds. John Wiley and Sons, New York. 1966. pp. 459–464; B.R. Gragg. *In* Gmelin Handbuch der Anorganischen Chemie. Vol. 37. Borverbindungen, Teil 10, 1976. Chap 3. pp. 32–197.
8. B. Benton-Jones, M.E.A. Davidson, J.S. Hartman, J.J. Klassen, and J.M. Miller. J. Chem. Soc. Dalton Trans. 2603 (1972).
9. A. Fox, J.S. Hartman, and R.E. Humphries. J. Chem. Soc. Dalton Trans. 1275 (1982).
10. P. Kölle and H. Nöth. Chem. Rev. **85**, 399 (1985); H. Nöth and B. Rasthofer. Chem. Ber. **119**, 2075 (1986); W.F. Schneider, C.K. Narula, H. Nöth, and B.E. Bursten. Inorg. Chem. **30**, 3919 (1991).
11. H. Nöth and B. Wrackmeyer. *In* Nuclear magnetic resonance spectroscopy of boron compounds. Vol. 14 of NMR. Basic Principles and Progress. Springer-Verlag, Berlin, Heidelberg, New York. 1978. Table LXXXVIII; B. Wrackmeyer. Annu. Rep. NMR Spectrosc. **20**, 61 (1988); A.R. Siedle. Annu. Rep. NMR Spectrosc. **20**, 205 (1988).
12. J.S. Hartman, Z. Yuan, A. Fox, and A. Nguyen. Can. J. Chem. Accepted (Clark special issue, Nov. 1996); J.S. Hartman and Z. Yuan. Manuscript in preparation.
13. T. Vladimiroff and E.R. Malinowski. J. Chem. Phys. **46**, 1830 (1966); E.R. Malinowski. J. Am. Chem. Soc. **91**, 4701 (1969).
14. J.S. Hartman and J.M. Miller. Inorg. Chem. **13**, 1467 (1974).
15. K. Balasanmugam, J.S. Hartman, J.M. Miller, and Z. Yuan. Can. J. Chem. **67**, 685 (1989).
16. J.M. Miller, Mass. Spectrom. Rev. **9**, 319 (1990).
17. J.S. Hartman and P. Stilbs. J. Chem. Soc. Dalton Trans. 1142 (1980).
18. J.S. Hartman and G.J. Schrobilgen. Inorg. Chem. **13**, 874 (1974).
19. R.K. Marat and A.F. Janzen. Can. J. Chem. **55**, 1167 (1977).
20. H.C. Brown. J. Chem. Soc. 1248 (1956).
21. J.S. Hartman and G.J. Schrobilgen. Inorg. Chem. **11**, 940 (1972).
22. C.W. Makosky, G.L. Galloway, and G.E. Ryschkewitsch. Inorg. Chem. **6**, 1972 (1967); G.E. Ryschkewitsch and G.L. Galloway. Inorg. Synth. **12**, 141 (1970).
23. N.E. Miller and D.L. Rezicek. J. Organomet. Chem. **349**, 11 (1988).
24. K. Sawada, K. Satoh, C. Honda, T. Ishiyama, and T. Suzuki, J. Chem. Soc. Dalton Trans. 377 (1993); R.D. Bach, H.B. Vardha, A.F.M.M. Rahman, and J.P. Oliver. Organometallics, **4**, 846 (1985).
25. C.A. Tolman. Chem. Rev. **77**, 313 (1977).
26. H.C. Clark and M.J. Hampden-Smith. Coord. Chem. Rev. **79**, 229 (1987).
27. N.E. Miller and E.L. Muetterties. J. Am. Chem. Soc. **86**, 1033 (1964).
28. P. Stilbs and G. Olofsson. Acta Chem. Scand. Ser. A: **A28**, 647 (1974).
29. R. Good, D.R. Zbinden, J.E. Kessler, and A. Merbach. Inorg. Chim. Acta, **28**, L155 (1978).
30. W.J. Evans, J.L. Shreeve, J.W. Ziller, and R.J. Doedens. Inorg. Chem. **34**, 586 (1995).
31. D.A. Atwood. J. Am. Chem. Soc. **117**, 6779 (1995); O. Bechstein, B. Zeimer, and D. Hass. Z. Anorg. Allgem. Chem. **582**, 211 (1990); E. Solari, C. Floriani, K. Schenk, A. Chiesi-Villa, C. Rizzoli, M. Rosi, and A. Sgamellotti. Inorg. Chem. **33**, 2018 (1994); P.P.K. Claire, G.R. Willey, and M.G.B. Drew. J. Chem. Soc. Chem. Commun. 1100 (1987); G.R. Willey, M.L. Butcher, M. McPartlin, and I.J. Scowen. J. Chem. Soc. Dalton Trans. 305 (1994); G.R. Willey, M.L. Butcher, T.J. Woodman, and M.G.B. Drew. J. Chem. Soc. Chem. Commun. 2721 (1994).
32. A.R. Barron. J. Chem. Soc. Dalton Trans. 3047 (1988).
33. D.R. Perrin. Dissociation constants of organic bases in aqueous solutions. Butterworths, London. 1965; and Supplement, 1972.
34. J. Atchekzaï, B. Bonnetot, H. Mongeot, S. Boufi, and B. Frange. Can. J. Chem. **70**, 2520 (1992).
35. L.-J Baker and M.J. Taylor. Polyhedron, **13**, 251 (1994); K.B. Dillon and A. Marshall. J. Chem. Soc. Dalton Trans. 315 (1987); S.J. Blunden, P.A. Cusack, and D.G. Gillies. Magn. Reson. Chem. **24**, 921 (1986).
36. E.D. Becker. High resolution NMR: Theory and chemical applications. 2nd Ed. Academic Press, New York. 1980. Chap. 8.
37. R.J. Gillespie and J.S. Hartman. J. Chem. Phys. **45**, 2712 (1966); R.J. Gillespie, J.S. Hartman, and M. Parekh. Can. J. Chem. **46**, 1601 (1968).
38. X. Ou, R. Wallace, and A.F. Janzen. Can. J. Chem. **71**, 51 (1993).
39. A.F. Janzen, Coord. Chem. Rev. **130**, 355 (1994).
40. J.S. Hartman and P. Stilbs. J. Chem. Soc. Chem. Commun. 566 (1975).

Halide ion trapping of nitrenium ions formed in the Bamberger rearrangement of *N*-arylhydroxylamines. Lifetime of the parent phenylnitrenium ion in water

James C. Fishbein and Robert A. McClelland

Abstract: The acid reactions of five arylhydroxylamines (Ar = 2,6-$Me_2C_6H_3$, 2,5-$Me_2C_6H_3$, 2-MeC_6H_4, 2-ClC_6H_4, and C_6H_5) have been studied at constant ionic strength ($NaClO_4$) in the presence of varying amounts of NaBr and NaCl. Each system resulted in the corresponding *p*-aminophenol, the product of Bamberger rearrangement, as the only detectable product in the absence of halide. The addition of halide ion reduced the yield of this product, with the appearance of the corresponding *p*-haloaniline, *o*-haloaniline (where appropriate), and the parent aniline (predominantly with bromide). Rate constants for the reaction were measured in the case of the parent and 2,6-dimethyl systems and showed small decreases (chloride) or increases (bromide) with increasing halide concentration. These changes did not correlate with the change in products, implying that the rate variations were caused by specific salt effects. Product data were analyzed by a mechanism involving rate-limiting formation of the appropriate arylnitrenium ion followed by product-determining steps involving trapping by the solvent or by the added halide. The possibility that a portion of the halide-trapped products were derived from a pre-association mechanism was also included. Kinetic analyses then produced k_{Br}:k_w and k_{Cl}:k_w ratios for two limiting cases, one involving pre-association with an equilibrium constant K_{as} = 0.3, and one ignoring pre-association. From an azide:water ratio (k_{Az}:k_w) previously determined for the 2,6-dimethylphenylnitrenium, k_{Br} was concluded to lie in the range (4–5) × 10^9 M^{-1} s^{-1} for all of the nitrenium ions of this study. This range for k_{Br} then led to k_w values of (1–2) × 10^9 s^{-1} (2,5-Me_2), (2–3) × 10^9 s^{-1} (2-Me), and (4–8) × 10^9 s^{-1} (parent and 2-Cl), where the ranges reflect uncertainties in the exact value of k_{Br} and in the contribution from pre-association. The lifetime of the parent phenylnitrenium ion in water at one molar ionic strength is concluded to lie in the range 125–250 ps.

Key words: nitrenium ion lifetime, phenylhydroxylamine, phenylnitrenium ion, Bamberger rearrangement.

Résumé : Opérant à force ionique constante ($NaClO_4$) en présence de quantités variables de NaBr et de NaCl, on a étudié les réactions d'addition de cinq arylhydroxylamines (Ar = 2,6-$Me_2C_6H_3$, 2,5-$Me_2C_6H_3$, 2-MeC_6H_4, 2-ClC_6H_4 et C_6H_5). Pour chaque système, en l'absence d'halogénure, le seul produit détectable est le *p*-aminophénol correspondant, le produit du réarrangement de Bamberger. L'addition d'halogénure diminue le rendement en ce produit et il y a apparition de la *p*-halogénoaniline correspondante, de l'*o*-halogénoaniline (dans les cas appropriés) et de l'aniline parente (en prédominance avec le bromure). On a mesuré les constantes de vitesse dans les cas des systèmes parent et 2,6-diméthylés et celles-ci diminuent (chlorure) ou augmentent (bromure) légèrement avec une augmentation de la concentration de l'halogénure. Il n'y a pas de corrélation entre ces changements et les changements dans les produits; ceci implique que les variations dans le vitesses sont provoquées par des effets de sel spécifiques. Les données relatives aux produits ont été analysées à l'aide d'un mécanisme impliquant la formation de l'ion arylnitrénium approprié dans l'étape déterminant la vitesse, suivie par des étapes déterminant la nature des produits qui impliquent un piégeage par le solvant ou par l'halogénure ajouté. On a aussi inclus la possibilité qu'une partie des produits dérivant d'un piégeage de l'halogénure dérive d'un mécanisme de pré-association. Les analyses cinétiques ont alors conduit aux rapports k_{Br} : k_w k_{Cl} : k_w pour les deux cas limites, l'un impliquant une préassociation avec une constante d'équilibre, K_{as} = 0,3, et l'un ne tenant pas compte d'une pré-association. En se basant sur un rapport azoture : eau (k_{Az} : k_w) déterminé antérieurement pour le 2,6-diméthylphénylnitrénium, on a conclu que la valeur de k_{Br} est d'environ (4–5) × 10^9 M^{-1} s^{-1} pour tous les ions nitrénium examinés au cours de cette étude. Ces valeurs de k_{Br} conduisent alors à des valeurs de k_w de (1–2) × 10^9 s^{-1} (2,5-diméthyle), (2–3) × 10^9 s^{-1} (2-méthyle) et (4–8) × 10^9 s^{-1} (parent et 2-Cl) dans lesquelles les domaines sont un reflet des incertitudes dans la valeur exacte de k_{Br} et de la contribution de la pré-association. Le temps de vie de l'ion phénylnitrénium parent dans l'eau, à une force ionique molaire, est de l'ordre de 125–250 ps.

Mots clés : temps de vie des ions nitrénium, phénylhydroxylamine, ion phénylnitrénium, réarrangement de Bamberger.

[Traduit par la rédaction]

Received January 26, 1996.

J.C. Fishbein and R.A. McClelland.[1] Department of Chemistry, University of Toronto, Toronto, ON M5A 1A1, Canada.

[1] Author to whom correspondence may be addressed. Telephone: 416-978-3592. Fax: 416-978-3592. E-Mail: rmcclell@alchemy.chem.utoronto.ca

Scheme 1.

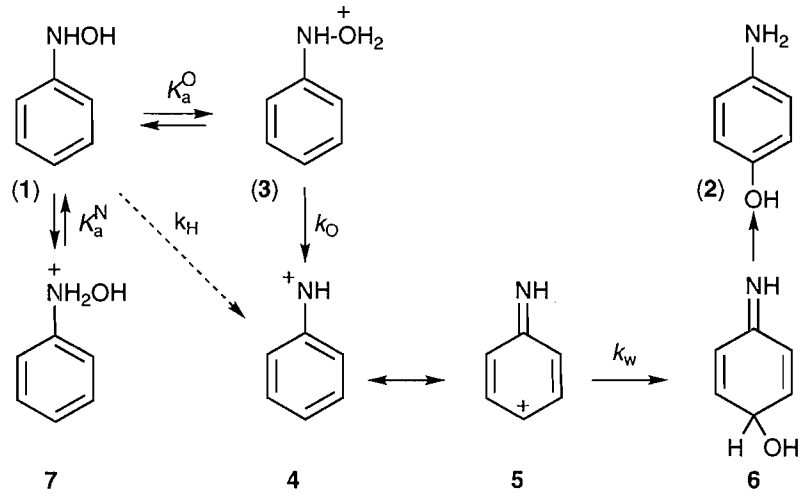

Bamberger reported 100 years ago that *N*-phenylhydroxylamine and its derivatives rearrange in aqueous acid solutions to give 4-aminophenols (1). With the parent compound (**1**) in aqueous sulfuric acid, 4-aminophenol (**2**) was the exclusive product observed, while both 4-chloroaniline and 2-chloroaniline were also formed with HCl as the acid (1, 2). A study by Ingold and co-workers in the 1950s showed that despite the formation of these chloroanilines, the rate was independent of chloride ion concentration (3). This ruled out mechanisms with N—O bond fission concerted with chloride ion attack and was more consistent with an S_N1 type of mechanism. Detailed studies carried out within the last 25 years have elaborated on this suggestion and have lead to the mechanism of Scheme 1. Key features are the activation of the hydroxylamine by O-protonation to form **3**, followed by N—O bond fission with loss of water to form an intermediate nitrenium ion **4**. This cation is trapped at the *para* position (i.e., through a carbenium resonance contributor **5**) to give the intermediate **6**, the tautomer of the ultimate product. In the case where the *para* position is substituted with a methyl group, the iminocyclohexadienol (e.g., 4-hydroxy-4-methyl-2,5-cyclohexadienone imine) can be observed, although this slowly hydrolyzes to the ketone (4).

One important finding was that the reaction occurs in an intermolecular fashion, since rearrangement of **1** in $H_2{}^{18}O$ resulted in full incorporation of solvent oxygen into the product *p*-aminophenol (5). This same study also showed that there was no exchange of ^{18}O into unreacted starting material, establishing that N—O bond fission is not reversible (5) (although a similar study with *N*-1-naphthylhydroxylamine (6) suggests that this is not always the case). Detailed kinetic studies showed that the reaction was first order in phenylhydroxylamine and first order in H^+ to pH 1–2, with the rate then becoming independent of acidity to acids with H_0 of about -1, at which point the rate began to increase again (7–9). Spectral measurements suggested that the initial levelling was associated with protonation to the unreactive N-protonated hydroxylamine **7**, with $pK_a{}^N = 1.90$ for the parent system (7, 9). The acid catalysis at higher acidities was explained by a mechanism involving a diprotonated intermediate $PhN^+H_2O^+H_2$ (7, 10), although a medium or salt effect could not be ruled out (9).

The occurrence of an S_N1-type mechanism leading to an arylnitrenium ion as an intermediate was suggested by several pieces of evidence, including solvent isotope effects (9) and entropies of activation (7, 8) in addition to the previously mentioned experiment in HCl by the Ingold group (3). Substituents in the aromatic ring have a significant effect, with large negative ρ values consistent with the development of considerable positive charge in the ring in the transition state for the reaction. As one example, log k_H for the rearrangement of *meta*-substituted phenylhydroxylamines had a ρ value of -5.8 (7). Arylnitrenium ions have also been proposed as intermediates in the solvolysis of a number of hydroxylamine derivatives — sulfonates $ArNR\text{-}OSO_2CF_3$ (11), sulfates $ArNR\text{-}OSO_3^-$ (12), carboxylates $ArNR\text{-}OOCR'$ (13–15) — as well as *N*-chloroanilines (16). As in the Bamberger rearrangement, these compounds solvolyze in water to products derived from addition of the solvent at the ring carbon *para* to the nitrogen, and large negative ρ values in the range -5 to -9 are observed.

Evidence that arylnitrenium ions can have lifetimes in water that make them viable as intermediates has appeared only recently. The first such experiment involved *N*-(2,6-dimethylphenyl)hydroxylamine (**8**) undergoing its Bamberger rearrangement in the presence of azide ion (17). Two products were observed, the expected *p*-aminophenol **10** and the *p*-azidoaniline **11**. The latter formed in increasing relative amount with increasing concentration of azide, but did so with no increase in the rate of reaction. This is classic evidence for an intermediate, in this case the nitrenium ion **9**, which forms in a rate-determining step and then partitions between the solvent and the added nucleophile in very fast reactions. The product data were fit by the standard equation for such a competition furnishing the partitioning ratio $k_{Az}:k_w$ as 7.5 M^{-1}. With carbenium ions as electrophiles, the assumption has been widely employed that azide ion reacts at the diffusion limit with k_{Az} approximately equal to 5×10^9 M^{-1} s^{-1} (18–20). The same assumption for arylnitrenium ions provided the lifetime of the 2,6-dimethylphenynitrenium ion (**9**) in water ($1/k_w$) as 1.5 ns. This number does indicate that

Scheme 2.

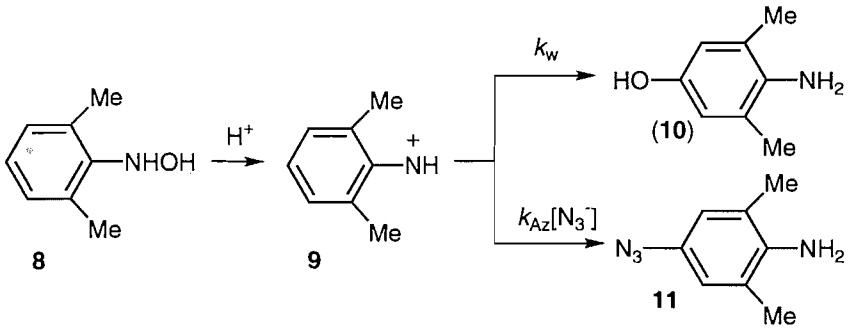

this nitrenium ion can exist as a free cation in water, although its lifetime is very short.

The Novak group has more recently applied the azide-clock approach to a number of arylnitrenium ions formed in the solvolysis of sulfate, pivalate, and *N*-chloro derivatives (21–23). With the above assumption for azide, they found lifetimes varying from the picosecond to the microsecond region. Substituents in the aryl ring exerted significant effects, but the lifetimes did not correlate well with the σ^+ value of the substituent (22). Unlike the case of the Bamberger rearrangement, these experiments form the nitrenium ion initially as an ion pair with the leaving group. With the more reactive nitrenium ions evidence was presented that the solvent and azide reactions were occurring at the ion-pair stage (23). We have also reported such a situation with some *N*-aroyloxy-2,6-dimethylphenylhydroxylamines (24, 25).

Arylnitrenium ions have not been observed under superacid conditions (26–28) although there have been reports of their spectroscopic characterization following the two-electron oxidation/deprotonation of diarylamines (29, 30) and a dimethylamino-stabilized biphenyl derivative (31). Within the last three years several examples have been detected in laser flash photolysis experiments (32–37). These included stabilized examples — the 4-biphenylyl- and 2-fluorenylnitrenium ions and their *N*-acetyl derivatives — that were sufficiently long-lived to be studied in aqueous solution (35, 36). These experiments furnished absolute rate constants for the reaction with water and azide ion, and indeed k_{Az} values of 5×10^9 M^{-1} s^{-1} were obtained, verifying the application of the "azide-clock" approach in competition kinetic experiments. Similar experiments have also verified the applicability of this approach to carbenium ions (38, 39).

In this paper we consider the Bamberger rearrangement of the parent *N*-phenylhydroxylamine (**1**), and the four derivatives **8**, **12–14** in the presence of chloride ion and bromide ion.

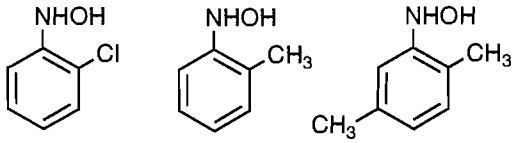

12 **13** **14**

The principal objective of this research was to provide an estimate for the lifetime of the parent phenylnitrenium ion in aqueous solutions. Recent research in our laboratories has established that this nitrenium ion is formed photochemically in aqueous acid solutions following irradiation of phenyl azide by rapid protonation of the so-formed singlet phenylnitrene (40). The phenylnitrenium ion, however, is too short-lived to be detected by laser flash photolysis using excitation sources with nanosecond pulse widths, although the cation might be detectable with faster systems. In principal, the Ingold data (3) from the 1950s should be capable of supplying a chloride:water partitioning ratio $k_{Cl}:k_w$. However, examination of these data shows that there is uncertainty since the amount of trapping by chloride ion is small and there is the possibility that salt effects may be perturbing the data. A second uncertainty is the value for k_{Cl} that would be used to convert the trapping ratio to an absolute rate constant for the solvent. Our approach therefore was to work from the 2,6-dimethyl system (**8**) where the $k_{az}:k_w$ previously measured provides a good estimate of k_w. Ideally we would have liked to have measured $k_{Az}:k_w$ for the parent phenylhydroxylamine. This, however, proved not to be possible since the acidities required for sufficient free azide ion to be present (pH > 4) were too low for the Bamberger rearrangement to occur at a significant rate. In this case, significant quantities of oxidation products are formed even with rigorous dearation (7, 9) and these complicate the analysis. One approach we considered was to move to a phenylhydroxylamine derivative where the phenylnitrenium ion forms by simple ionization, as has been done by the Novak group (21–23). This, however, adds the complication of trapping at the stage of an ion pair (23, 25). The formation of the nitrenium ion from the O-protonated hydroxylamine avoids this problem since the leaving group simply becomes part of the solvent in the solvation shell. Finally, our choice of substrates was dictated by a desire to avoid systems where the *para* position was substituted. In this way we obtained one major product, the *p*-aminophenol, from the reaction with solvent.

Results

Experiments were carried out at 25°C in aqueous solutions containing 0.5% acetonitrile and a mixture of $HClO_4$, $NaClO_4$, and either NaCl or NaBr. The total ionic strength was maintained constant at 1 M. The concentration of the hydroxylamine was 10^{-4} M, and reactions were carried out until there was complete disappearance of this substrate. Products were

analyzed quantitatively by HPLC, by comparison of peak areas with areas obtained for authentic samples. Sets of experiments were conducted with the same concentration of $HClO_4$, and with varying concentrations of NaCl or NaBr starting from 0 M. The acid concentration was chosen to give a rate of reaction sufficient to avoid the formation of oxidation products, and mass balances for the nucleophilic products were in general excellent. The experimental data, product yields as a function of [NaCl] or [NaBr], are provided in Tables S1–S8 as supplementary material.[2] The following provides a brief description of the pertinent results with each hydroxylamine.

N-(2,6-Dimethylphenyl)hydroxylamine (8)

With chloride ion present, two products were observed, 4-amino-3,5-dimethylphenol (**10**) and 4-chloro-2,6-dimethylaniline (**15**). Rate constants were measured in a set of solutions containing 0.000324 M $HClO_4$, ionic strength = 1 M, by following a change in optical density at 280 nm in the UV absorbance spectra. The values of k_{obs} showed a small decrease on increasing chloride concentration, amounting in total to an 8% decrease on proceeding from 0 M to 0.888 M NaCl.

With bromide ion present, three products were observed, 4-amino-3,5-dimethylphenol (**10**), 4-bromo-2,6-dimethylaniline (**16**) and 2,6-dimethylaniline (**17**). As shown in eq. [1], both **16** and **17** are attributed to bromide ion trapping of the nitrenium ion to form the initial adduct **18**, followed by either tautomerization to **16** or reaction with a second bromide ion to give **17** and Br_2. The aniline is the product of formal reduction of the hydroxylamine. The occurrence of such a reaction was first reported by Pelecanou and Novak (41). Evidence for this mechanism in the present case is the increase in the ratio of the reduction product to the adduct ([**17**]:[**16**] with increased concentration of bromide ion.

[1]

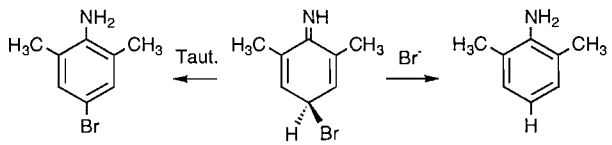

16 18 17

Rate constants were again measured in the set containing 0.000324 M $HClO_4$. In this case there was a small, nonlinear, increase in k_{obs} with increasing bromide concentration. Overall, from 0 M to 0.475 M [Br^-], k_{obs} increased by 25%.

N-Phenylhydroxylamine (1)

With both halides, the only product derived from the solvent was 4-aminophenol (**2**), with 2-aminophenol not detected (<0.5%) in any experiments. With chloride ion present, 4-chloroaniline (**19**) and 2-chloroaniline (**20**) were also obtained, in relative yields that were independent of the concentration of the chloride ion: [**20**]:[**19**] = 0.444 ± 0.016. Similarly, 4-bromoaniline (**21**) and 2-bromoaniline (**22**) were observed with bromide ion, in a relative amount [**22**]:[**21**] = 0.614 ± 0.018. A small amount of the parent aniline (**23**) was also formed. We presume that this is arising from the mechanism of eq. [1], although here it can be noted that the ratio of reduction product to adduct does not change with bromide conentration. This may imply that there is another mechanism in operation for the reduction product.

In the reaction with chloride present, rate constants measured at constant acidity and ionic strength showed a small decrease with increasing chloride concentration. The rate constant at [Cl^-] = 0.93 M was 12% smaller than the one in the absence of chloride. With bromide ion present, small increases in rate constant were observed. The rate constant at [Br^-] = 0.95 M was 13% larger than the one in the absence of bromide.

N-(2-Methylphenyl)hydroxylamine (13)

As with the parent compound, the only product derived from the solvent was the *para* adduct, 4-amino-3-methylaniline (**24**). With chloride ion present, both the *para* adduct 4-chloro-2-methylaniline (**25**) and the *ortho* adduct 6-chloro-2-methylaniline (**26**) were observed, in a ratio [**26**]:[**25**] = 0.089 ± 0.005. The decreased *ortho*:*para* ratio compared to the parent system is undoubtedly associated with the increased steric congestion in this system where *ortho* addition requires three substituents on adjacent carbons of the aromatic ring. A small amount (maximum of 2%) of 2-methylaniline (**27**) was also observed. With bromide ion, the only bromide-containing product formed was the *para* adduct, 4-bromo-2-methylaniline (**28**), no *ortho* adduct (6-bromo-2-methylaniline (**29**) being detectable. In this case, substantial amounts (up to 12%) of the reduction product 2-methylaniline **27** were also formed.

N-(2,5-Dimethylphenyl)hydroxylamine (14)

In this case the only product that was quantitatively analyzed was the solvent adduct, 4-amino-2,5-dimethylphenol (**29**). With chloride ion, the HPLC traces showed the presence of only one other product. Since this could be shown not to be the parent aniline, we presume that it corresponds to the *para* adduct 4-chloro-2,5-dimethylaniline (**30**). The absence of the *ortho* adduct 2-chloro-3,6-dimethylaniline (**31**) makes sense, since this product requires four substituents at adjacent carbons. With bromide, the parent aniline was observed, along with one other product that we assume to be the *para* adduct.

N-(2-Chlorophenyl)hydroxylamine (12)

With this compound, just the reaction in the presence of chloride was studied. Three products were observed, 4-amino-3-chlorophenol (**32**), 2,4-dichloroaniline (**33**), and 2,6-dichloroaniline (**34**). The latter two formed in a ratio [**34**]:[**33**] = 0.27.

Discussion

We start by considering whether the halide-derived products are indeed obtained by trapping at the stage of an arylnitrenium ion. The evidence comes from a comparison of products and kinetics, the combination of these two experiments being carried out in this work with the parent hydroxylamine and the 2,6-dimethyl derivative. In each case, both halides were examined, with the kinetic experiments being performed under the same conditions as the product analyses. A constant acid concentration was employed, to ensure that rate variations could

[2] Supplementary material mentioned in the text can be purchased from: The Depository of Unpublished Data, Document Delivery, CISTI, National Research Council Canada, Ottawa, Canada K1A 0S2.

Scheme 3.

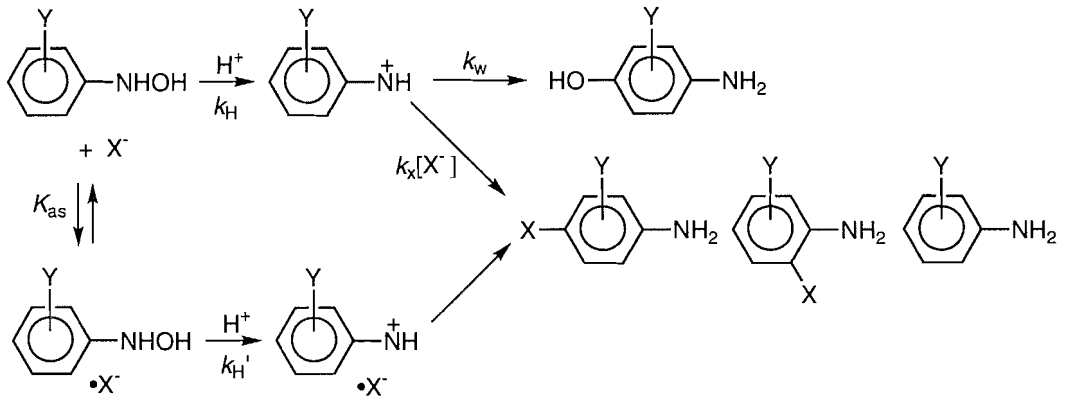

not be attributed to changes in acidity. The ionic strength was also maintained constant, with $NaClO_4$ being replaced with an equivalent amount of NaCl or NaBr. In the case of chloride, the observed rate constants with both hydroxylamines actually decreased slightly with increased chloride content. Thus here there is no correlation with the appearance of chloride products. With bromide, however, increases in k_{obs} were observed. In the 2,6-dimethyl case this amounted to a 25% increase in k_{obs} at the highest concentration of bromide employed. At this concentration, however, 80% of the products are due to bromide trapping, and this requires a 400% or 5-fold increase in k_{obs} if the bromide products are due to some bimolecular mechanism. With the parent compound, a 13% increase was observed in k_{obs} at the highest [Br^-]. Under these conditions 50% of the products are due to the bromide reaction, so a doubling in k_{obs} is required if the reaction is bimolecular. These data therefore exclude the possibility that all of the bromide trapping is due to a bimolecular reaction. The slight rate increase that is observed may be caused by a specific salt effect associated with replacing perchlorate by halide. A slight contribution from a slow bimolecular process is also possible. Whatever the case, the majority of the products must be derived from reaction at the stage of the arylnitrenium ion.

We therefore analyze the product data according to the mechanism of Scheme 3, with rate-limiting formation of the arylnitrenium ion followed by product-determining steps involving trapping by the solvent or by the added halide. A recent paper from the Novak group (23) has demonstrated that pre-association can account for a significant portion of the products from added nucleophiles in the case of nitrenium ions with lifetimes in the region of the ones of this study, and such a possibility has been incorporated in Scheme 3. Pre-association involves the formation of a nucleophile–substrate complex prior to the formation of the nitrenium ion. In Scheme 3 this is shown as occurring at the stage of the neutral hydroxylamine, but a mechanism in which this takes place after protonation would be equivalent. As in the Novak study, Scheme 3 is written such that the nitrenium·halide pair, once formed, only reacts with the halide counterion. To explain the lack of kinetic dependence on halide concentration this mechanism also requires that the halide-substrate complex react to form nitrenium ion at the same rate as the substrate alone. This was also true with the systems involved in the Novak study (23).

In terms of this mechanism, the fractional yield of the *p*-aminophenol is given by eq. [2].

$$[2]\quad F(p\text{-aminophenol}) = \left(\frac{1}{1 + \left(\frac{k_x}{k_w}\right)[X^-]}\right) \times \left(\frac{1}{1 + K_{as}[X^-]}\right)$$

The second term on the right-hand side of this equation represents the decrease in the *p*-aminophenol product due to pre-association with the halide, while the first term represents the decrease associated with trapping of the free nitrenium ion. Equation [2] contains two adjustable parameters, k_x:k_w and K_{as}, and in principle these can be provided by nonlinear least-squares fitting to the experimental data. Our fitting program, however, failed to perform such an operation, since with the scatter in the experimental data the fits to eq. [2] were about equally as good for values of K_{as} ranging upwards from 0 to 0.4–0.6. The problem in the case of systems that show a significant decrease in *p*-aminophenol, such as 2,6-dimethyl with both halides, is that most of this decrease is due to trapping of the free nitrenium ion. Thus, a small contribution from pre-association cannot be distinguished experimentally from the case where there is none. In the case of systems where there is a smaller decrease in *p*-aminophenol, the problem is that the data cannot be extended to high enough halide concentrations to unequivocally define K_{as}.

The association constant K_{as} has been assumed to be 0.3 M^{-1} at 20°C (42, 43). (Novak et al. (23) found that a value of 0.25 provided a better fit to their data at a higher temperature, 50°C.) Accordingly, we took K_{as} as 0.3 and fit to eq. [2] with the trapping ratio as the adjustable parameter. The k_x:k_w ratios so produced are given in Table 1, along with ones obtained assuming no pre-association (i.e., K_{as} = 0). As noted above, the two values of K_{as} in most cases resulted in fits to the experimental data that were indistinguishable. Figure 1 shows the "best" case for pre-association, the parent plus bromide system, where the line produced with K_{as} = 0.3 produces a marginally better fit.

The mechanistic model including pre-association results in lower values for k_x:k_w compared with the one that ignores pre-association. This effect can be quite significant with substrates

Table 1. Trapping ratios for arylnitrenium ions.[a]

Parameter	2,6-Me_2	2,5-Me_2	2-Me	2-Cl	H
With K_{as} = 0					
$k_{Br}:k_w$ (M^{-1})	6.38 ± 0.22	2.95 ± 0.12	2.35 ± 0.12	—	1.05 ± 0.03
$k_{Cl}:k_w$ (M^{-1})	2.67 ± 0.05	1.35 ± 0.03	1.04 ± 0.03	0.65 ± 0.02	0.62 ± 0.02
$k_{Br}:k_{Cl}$	2.4	2.2	2.3		1.7
With K_{as} = 0.3					
$k_{Br}:k_w$ (M^{-1})	5.82 ± 0.17	2.44 ± 0.08	1.85 ± 0.09	—	0.63 ± 0.03
$k_{Cl}:k_w$ (M^{-1})	2.13 ± 0.07	0.91 ± 0.02	0.64 ± 0.02	0.30 ± 0.01	0.27 ± 0.01
$k_{Br}:k_{Cl}$	2.7	2.7	2.9		2.4
$10^{-9}k_w$ (s^{-1})	0.7[b]	1–2[c]	2–3[c]	4–8[d]	4–8[c]

[a]Ionic strength = 1.0 M, 25°C.
[b]From $k_{Az}:k_w$ = 7.5 (K_{as} = 0) to 7.0 (K_{as} = 0.3), with $k_{Az} = 5 \times 10^9\ M^{-1}\ s^{-1}$.
[c]Lower limit uses the value of $k_{Br}:k_w$ obtained with K_{as} = 0, and $k_{Br} = 4 \times 10^9\ M^{-1}\ s^{-1}$. Upper limit uses the value of $k_{Br}:k_w$ obtained with K_{as} = 0.3, and $k_{Br} = 5 \times 10^9\ M^{-1}\ s^{-1}$.
[d]Taken to be same as parent, since $k_{Cl}:k_w$ values are, within experimental error, the same.

Fig. 1. Fractional yields of *p*-aminophenol in the reaction of *N*-phenylhydroxylamine in the presence of bromide ion. The two lines have been drawn according to eq. [2] with K_{as} = 0 and 0.3, with the latter providing the better fit to the experimental data.

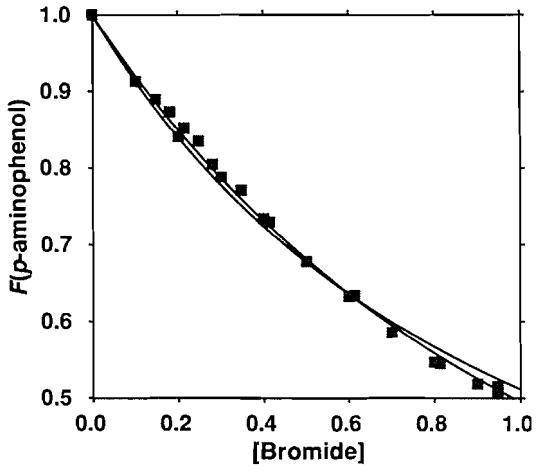

where trapping is relatively inefficient. For example, with the parent system, $k_x:k_w$ values calculated with K_{as} = 0.3 are ~50% of the ones with K_{as} = 0. With systems where there is more efficient trapping, the effect is relatively smaller.

With the 2,6-dimethyl derivative, a value for k_w of 6.8×10^8 s^{-1} is obtained using the previously determined $k_{Az}:k_w$ ratio of 7.5 M^{-1} (17), with the assumption, now supported by direct measurements involving flash photolysis (35, 36), that k_{Az} is 5×10^9 M^{-1} s^{-1}. Inclusion of pre-association with K_{as} = 0.3 reduces $k_{Az}:k_w$ by only 7% to 7.0 M^{-1}, and results in a slightly larger value of k_w of 7.1×10^8 s^{-1}. These k_w values in turn provide rate constants for the two halides, k_{Br} as $(4.1–4.3) \times 10^9$ M^{-1} s^{-1} and k_{Cl} as $(1.5–1.8) \times 10^9$ M^{-1} s^{-1}. The lower value of each pair is the one obtained from the analyses with K_{as} = 0.3, the higher value from models with no pre-association. Thus, even with the 2,6-dimethylphenylnitrenium ion, the rate constants for the two halides exceed 10^9, and the value for bromide approaches the azide limit.

We argue that these two rate constants are likely already very close to their limits. The evidence comes from the observation (Table 1) that, within each mechanistic model, the ratios $k_{Br}:k_{Cl}$ are relatively constant, in spite of a considerable variation in nitrenium ion stability. If the reaction of the 2,6-dimethylphenylnitrenium ion with one or both of the halides was not occurring close to the limit, the further increases in reactivity that accompanied the change to the more reactive nitrenium ions should have appeared experimentally as a narrowing of the difference between the two halides. That the ratio remains constant at ~2 suggests that the situation has been reached with all of the nitrenium ions of this study where the rate constants are at their limit. Limiting rate constants below 5×10^9 M^{-1} s^{-1} have been suggested for cation–anion combination reactions, for cases where the anion component is well hydrated (44, 45). In the present case the order $Cl^- < Br^- \leq N_3^-$ certainly follows the order of diminishing hydration.

In consequence, k_w values have been calculated in two ways, a lower limit based on the higher $k_{Br}:k_w$ ratio obtained with K_{as} = 0 and a value of $k_{Br} = 4 \times 10^9$ M^{-1} s^{-1}, and an upper limit based on the lower $k_{Br}:k_w$ ratio obtained with K_{as} = 0.3, and a value of $k_{Br} = k_{Az} = 5 \times 10^9$ M^{-1} s^{-1}. These values are given in Table 1. Figure 2 shows a plot of log k_w versus log k_H, where k_H is the second-order rate constant for H^+ catalysis of the formation of the nitrenium ion from the neutral hydroxylamine (see Scheme 1). With the uncertainty in k_w, this plot is scattered, although there is a general correlation that increased k_H results in smaller k_w. There is, however, a significantly smaller variation in the latter, a reflection of the very different response of nitrenium ion formation and decay to changing substituents.

Our analysis results in a value of k_w for the parent phenylnitrenium ion in the range $(4–8) \times 10^9$ s^{-1}, corresponding to a lifetime in water of 250–125 ps. Novak et al. previously estimated k_w for the *N*-acetylphenylnitrenium ion as 1.7×10^{11} s^{-1}, based on a correlation of log ($k_{Az}:k_w$) with enthalpies calculated using ab initio methods (22). Considering that there is some uncertainty in the latter number, the $k_w(NCOCH_3):k_w(NH)$ ratio = 20–40 does appear consistent.

Fig. 2. Linear free energy correlation. The constant k_w represents the hydration of arylnitrenium ions. Values are from this work with the exception of 4-Me, which is taken from ref. 23. The constant k_H refers to the H^+-catalyzed formation of the nitrenium ion from the neutral hydroxylamine. Values are taken from ref. 8 with the exception of 4-Me, which is from ref. 9.

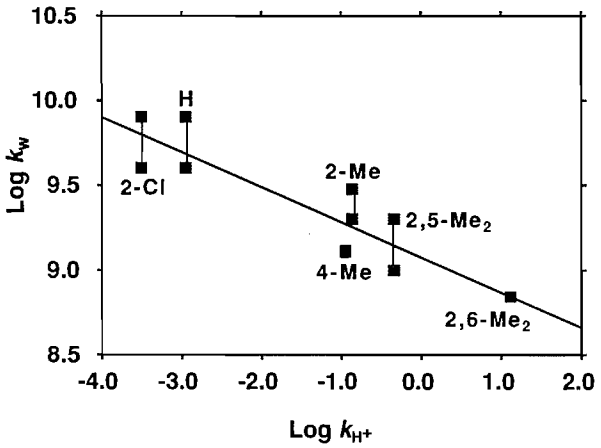

The other systems where this ratio has been obtained (23) are arylnitrenium ions substituted with a π donor at the *para* position: 4-Cl, $k_w(NCOCH_3):k_w(NH)$ = 8; 4-Me, $k_w(NCOCH_3):k_w(NH)$ = 6; and 4-Ph, $k_w(NCOCH_3):k_w(NH)$ = 3. Such substituents localize positive charge at the *para* carbon away from the nitrogen, and should therefore attenuate the effect of the electron-withdrawing acetyl group. This effect is especially important with 4-Ph, which provides an unexpectedly large amount of stabilization and results in relatively small difference in the the lifetimes of the *N*-acetyl and NH ions.

Experimental section

The *N*-arylhydroxylamines were prepared from the corresponding nitroarenes by zinc reduction in methanol:water containing ammonium chloride, followed by recrystallization from benzene:petroleum ether (7, 8). Products were commercially available or were obtained from catalytic hydrogenation of the appropriate nitro compound. Details of the HPLC separations and quantitative determinations of products have been previously published (24). In the present case, analyses were performed on a Waters Microbondapak C18 column, except for *N*(-2-chlorophenyl)hydroxylamine where a Hamilton PRP polyvinylstyrene column was employed. Quantitative measurements were based on standard curves constructed with at least three points. Product identifications were verified by spiking the reaction mixtures with authentic samples. Rate constants were measured as previously described (7–9), by following the change in optical density at an appropriate wavelength in the UV.

Acknowledgements

R.A.M. acknowledges the continued financial support of the Natural Sciences and Engineering Research Council of Canada. J.C.F acknowledges the support in the form of Research Fellowships of the North Atlantic Treaty Organization and the National Institutes of Health.

References

1. E. Bamberger. Ber. Dtsch. Chem. Ges. **27**, 1347 (1894); **27**, 1548 (1984); **33**, 3600 (1900).
2. E. Bamberger and J. Lagutt. Ber. Dtsch. Chem. Ges. **31**, 1500 (1898).
3. H.E. Heller, E.D. Hughes, and C.K. Ingold. Nature (London), **168**, 909 (1951).
4. E. Bamberger. Ber. Dtsch. Chem. Ges. **28**, 245 (1895).
5. I.I. Kukhtenko. Russ. J. Org. Chem. (Engl. Transl.) **7**, 324 (1971).
6. F.F. Kadlubar, J.A. Miller, and E.C. Miller. Cancer Res. **38**, 3628 (1978).
7. T. Sone, Y. Tokuda, T. Sakai, S. Shinkai, and O. Manabe. J. Chem. Soc. Perkin Trans. 2, 298 (1981).
8. T. Sone, K. Hamamoto, Y. Seiji, S. Shinkai, and O. Manabe. J. Chem. Soc. Perkin Trans. 2, 1596 (1981).
9. G. Kohnstam, W.A. Petch, and D.L.H. Williams. J. Chem. Soc. Perkin Trans. 2, 423 (1984).
10. T. Okamoto, K. Shudo, and T. Ohta. J. Am. Chem. Soc. **97**, 7184 (1975).
11. P.G. Gassman and J.E. Granrud. J. Am. Chem. Soc. **106**, 1498 (1972).
12. M. Novak, M. Pelecanou, A.K. Roy, A.F. Andronico, F.M. Plourde, T.M. Olefirowicz, and T.J. Curtin. J. Am. Chem. Soc. **106**, 5623 (1984).
13. M. Novak, M. Pelecanou, and L. Pollack. J. Am. Chem. Soc. **108**, 112 (1986).
14. M. Novak and R.K. Lagerman. J. Org. Chem. **53**, 4762 (1988).
15. G. Galliani and B. Rindone. Nouv. J. Chim. **7**, 151 (1983).
16. P. G. Gassman and G. Hartmann. J. Am. Chem. Soc. **94**, 3891 (1972).
17. J.C. Fishbein and R.A. McClelland. J. Am. Chem. Soc. **109**, 2824 (1987).
18. J.P. Richard and W.P. Jencks. J. Am. Chem. Soc. **104**, 4689 (1982).
19. J.P. Richard, M.E. Rothenburg, and W.P. Jencks. J. Am. Chem. Soc. **106**, 1361 (1984).
20. J.P. Richard. Tetrahedron, **51**, 1535 (1995).
21. M. Novak, M.J. Kahley, E. Eigen, J.S. Helmick, and H.E. Peters. J. Am. Chem. Soc. **115**, 9453 (1993).
22. M. Novak, M.J. Kahley, J. Lin, S.A. Kennedy, and L.A. Swanegan. J. Am. Chem. Soc. **116**, 11626 (1994).
23. M. Novak, M.J. Kahley, J. Lin, S.A. Kennedy, and T.G. James. J. Org. Chem. **60**, 8294 (1995).
24. J.C. Fishbein and R.A. McClelland. J. Chem. Soc. Perkin Trans. 2, 653 (1995).
25. J.C. Fishbein and R.A. McClelland. J. Chem. Soc. Perkin Trans. 2, 663 (1995).
26. G.A. Olah and D.J. Donovan. J. Org. Chem. **43**, 1743 (1978).
27. G.A. Olah, G.K.S. Prakash, and M. Arvanaghi. J. Am. Chem. Soc. **102**, 6640 (1980).
28. G.A. Olah, M. Arvanaghi, and G.K.S. Prakash. J. Am. Chem. Soc. **104**, 1628 (1982).
29. U. Svanholm and V.D. Parker. J. Am. Chem. Soc. **96**, 1234 (1974).
30. D. Serve. J. Am. Chem. Soc. **97**, 432 (1975).
31. A. Riecker and B. Reiser. Tetrahedron Lett. **31**, 5013 (1990).
32. G.B. Anderson and D.E. Falvey. J. Am. Chem. Soc. **115**, 9870 (1993).
33. R.J. Robbins, L.L.-N. Yang, G.B. Anderson, and D.E. Falvey. J. Am. Chem. Soc. **117**, 6544 (1995).
34. S. Srivastava and D.E. Falvey. J. Am. Chem. Soc. **117**, 10186 (1995).

35. P.A. Davidse, M.J. Kahley, R.A. McClelland, and M. Novak. J. Am. Chem. Soc. **116**, 4513 (1994).
36. R.A. McClelland, P.A. Davidse, and G. Hadzialic. J. Am. Chem. Soc. **117**, 4173 (1995).
37. J. Michalak, H.B. Zhai, and M.S. Platz. J. Phys. Chem. In press.
38. R.A. McClelland, V.N. Kanagasabapathy, N. Banait, and S. Steenken. J. Am. Chem. Soc. **113**, 1009 (1991).
39. R.A. McClelland, F.L. Cozens, S. Steenken, T.L. Amyes, and J.P. Richard. J. Chem. Soc. Perkin Trans. 2, 1717 (1993).
40. R.A. McClelland, M.J. Kahley, P.A. Davidse, and G. Hadzialic. J. Am. Chem. Soc. **118**, 4794 (1996).
41. M. Pelecanou and M. Novak. J. Am. Chem. Soc. **107**, 4449 (1985).
42. J.P. Richard and W.P. Jencks. J. Am. Chem. Soc. **106**, 1373 (1984).
43. J.P. Richard, T.L. Amyes, and T. Vontor. J. Am. Chem. Soc. **113**, 5871 (1991).
44. J.P. Richard and W.P. Jencks. J. Am. Chem. Soc. **106**, 1373 (1984).
45. W.P. Jencks. *In* Nucleophilicity. *Edited by* M. Harris and S. McManus. Adv. Chem. Ser., American Chemical Society, Washington, D.C. 1987. pp. 155–167.

Carbon-13 chemical shifts of alkene carbons in 2-acylidene-3,5-diaryl-2,3-dihydro-1,3,4-thiadiazoles and related benzothiazoles and -selenazoles, and their relationship to other push–pull alkenes

Jennifer L. Mueller, Martin S. Gibson, and J. Stephen Hartman

Abstract: Carbon-13 chemical shifts of alkene carbons are observed in the ranges 78–109 ppm (Cα) and 154–164 ppm (Cβ) for a series of 11 2-acylidene-3,5-diaryl-2,3-dihydro-1,3,4-thiadiazoles, 3 2-acylidene-3-alkyl-2,3-dihydrobenzothiazoles, and 2 2-acylidene-3-alkyl-2,3-dihydrobenzoselenazoles of known geometry, indicating appreciable charge polarization in these compounds as in other push–pull olefins. Substitution that promotes more extensive charge delocalization results in the Cα signal shifting to the higher-frequency end of the chemical shift range. The observed shifts are compared with those calculated according to the Pretsch scheme.

Key words: carbon-13 NMR, chemical shifts, push–pull olefins, 1,3,4-thiadiazoles, benzothiazoles, benzoselenazoles.

Résumé : On a observé les déplacements chimiques du ^{13}C des carbones des alcènes dans des régions allant de 78 à 109 ppm (Cα) et 156 à 164 (Cβ), d'une série de 11 2-acylidène-3,5-diaryl-2,3-dihydro-1,3,4-thiadiazoles, de 3 2-acylidène-3-alkyl-2, 3-dihydrobenzothiazoles, et de 2 2-acylidène-3-alkyl-2,3-dihydrobenzosélénazoles de géométries connues; ces résultats indiquent qu'il existe une polarisation importante de la charge dans ces composés, comme dans les autres oléfines « push–pull ». La substitution qui provoque la plus grande délocalisation conduit à un déplacement du signal Cα vers les plus grandes fréquences de la plage des déplacements chimiques. On a comparé les déplacements chimiques observés avec ceux calculés à l'aide du schéma de Pretsch.

Mots clés : RMN du carbone-13, déplacements chimiques, oléfines « push–pull », 1,3,4-thiadiazoles, benzothiazoles, benzosélénazoles.

[Traduit par la rédaction]

Introduction

We have synthesized a number of 2-acylidene-3,5-diaryl-2,3-dihydro-1,3,4-thiadiazoles **1** and thioacyl analogues **2** in which, for the most part, the 3-aryl substituent is either 2,4-dibromophenyl or phenyl (1–5). Recently, from spectroscopic and X-ray crystallographic studies, it has been possible to assign (*Z*) configurations to these compounds and to confirm that they exist in the *s-cis* conformation (shown) as a result of stabilization through an S...O interaction (6). The main features of the four compounds studied (6) are (*a*) short S...O contacts (2.463–2.691 Å), (*b*) C(5)—S...O and S...O=C bond angles of approximately 165° and 100°, respectively, and (*c*) evidence of delocalization within the C(5)-C=C-C=O structural unit, but with C=O bond lengths close to normal. The energy associated with the "nonbonded" or "closed shell" S...O interaction need be no more than a few kcal/mol to account for the overwhelming predominance of the *s-cis* conformer (6–8).

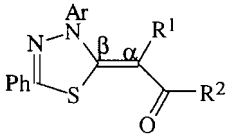

1

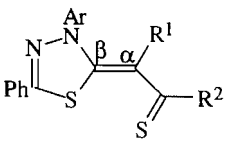

2

Compounds such as **1** and **2** can be viewed as push–pull alkenes (9) in which the heterocyclic ring provides donor substituents and the acyl or the thioacyl substituent provides the acceptor. Push–pull alkenes have polarized charge distributions that arise from electron delocalization through the donor – double bond – acceptor system; the resulting π-electron distributions include large contributions from C—C single bonded formulae in the resonance hybrid such as those shown below for **1**. In this example, the resonance description implies some aromatic character on the heterocyclic ring. In the absence of a generally used notation for the olefinic carbons of push–pull olefins, in this paper we denote the olefinic carbon with acceptor groups Cα and the carbon with donor groups Cβ.

Received October 25, 1995.

J.L. Mueller, M.S. Gibson,[1] and J.S. Hartman.[1] Department of Chemistry, Brock University, St. Catharines, ON L2S 3A1, Canada.

[1] Authors to whom correspondence may be addressed. Telephone: (905) 688-5550, ext. 3849. Fax: (905) 688-2789. E-mail: shartman@chemiris.labs.brocku.ca

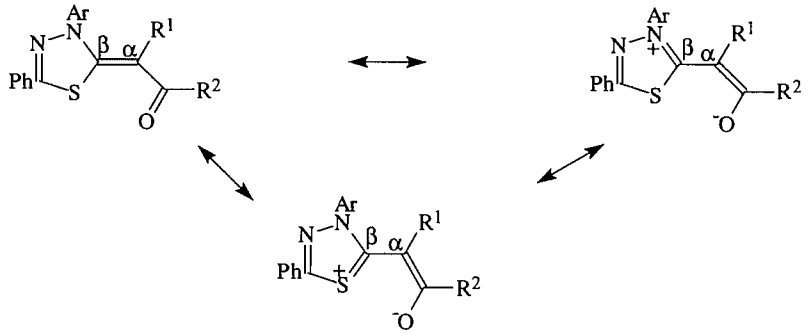

Related conjugated systems (push–pull polyenes) have recently become important in the study of nonlinear optical properties because these properties are enhanced by large changes in dipole moment and hence in charge distribution between the ground and excited states (10).

Push–pull alkenes have been widely studied by ^{1}H NMR spectroscopy since the 1960s (9, 11), and less extensively by ^{13}C NMR spectroscopy (12–19).[2] Of the ^{13}C NMR studies, the results of Kleinpeter and co-workers (12) span a fairly wide variety of compounds, while other workers have contributed data from more restricted ranges of compounds determined by their synthetic or other interests (13–19). In all cases, the alkene carbons of the push–pull system have ^{13}C chemical shifts at the outer limits of the alkene range: significantly more shielded (i.e., to low frequency) for the acceptor-substituted carbon Cα and less shielded (i.e., to high frequency) for the donor-substituted carbon Cβ, relative to the chemical shift range for the corresponding alkene without donor or acceptor substituents. These shifts are readily discernible even when not explicitly assigned (18). The shift difference between the two olefinic carbon atoms has been attributed to the sizable partial positive and negative charges that exist on these atoms, and its numerical value (ΔCβCα in our notation) has been used by some authors as a sensitive, if non-additive, parameter for this charge separation (12). Changes in ΔCβCα can be closely related to changes in charge separation within subsets of similar compounds (12), but ΔCβCα cannot in general be related solely to charge separation because of the many factors that contribute to ^{13}C chemical shifts (20). Quite large chemical shift differences can occur between pairs of olefinic carbons in olefins themselves, in the absence of electron-donating or -accepting substituents, because hydrocarbon substituents can have significant effects on chemical shift (20). Thus the significant part of ΔCβCα in a push–pull olefin, from the point of view of charge separation, must be that part which is over and above what would be observed in the corresponding hydrocarbon of identical structure.

^{13}C NMR spectroscopy thus, within the aforementioned limitations, provides an indication of charge separation within the push–pull systems of **1** and **2**. It was of interest to us in that it may indicate any effects of modification resulting from heteroatom "nonbonded" or "closed shell" interactions, which can result in conformational preference (6–8, 21). We now report ^{13}C NMR data for the series of compounds **1** and **2** and for the related benzothiazoles **3** and benzoselenazoles **4** and **5** (7).

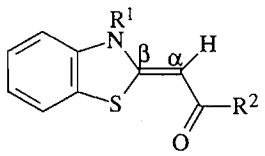

3

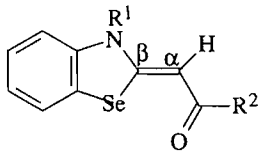

4

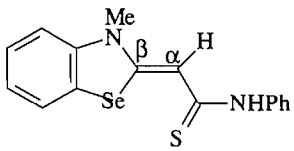

5

Experimental

Compounds were taken from our collection of crystallized samples assembled over the years (1–7) which had been stored at room temperature in the dark. All were in good condition. Two related compounds, where melting point determinations and reference to previous NMR spectra revealed that transformations had occurred, were excluded from the study. A fresh sample of one of these compounds, 2-benzylidene-2,3-dihydro-3,5-diphenyl-1,3,4-thiadiazole, was prepared; this had mp 122–124°C (lit. (5) mp 121–124°C).

All ^{13}C NMR spectra were run on saturated solutions in $CDCl_3$ at 50.3 MHz on a Bruker AC-200 multinuclear Fourier Transform NMR spectrometer at 27°C, with a spectral win-

[2] Also, S.S. Gandhi and M.S. Gibson. Unpublished results.

Table 1. ^{13}C NMR chemical shifts of the push–pull alkenes 1 and 2.[a]

Compound	Ar	R^1	R^2	C=S	C=O	Cα	Cβ (C-2)	C-5	ΔCβCα
1*a*	$C_6H_3Br_2$(2,4)	H	Me		190.6 (196.5)	89.3 (91.2)	158.2 (153.9)	154.2 (154.7)	68.9 (62.7)
1*b*	Ph	H	Me		190.5 (196.5)	88.8 (91.2)	158.3 (153.9)	154.1 (154.7)	69.5 (62.7)
1*c*	Ph	H	Ph		183.8 (187.0)	85.7 (91.2)	160.2 (153.9)	154.8 (154.7)	74.5 (62.7)
1*d*	$C_6H_3Br_2$(2,4)	H	OEt		168.8 (165.0)	78.4 (82.2)	159.4 (156.2)	153.2 (154.7)	81.0 (74.0)
1*e*	$C_6H_3Br_2$(2,4)	Me	Me		192.0 (196.5)	96.6 (100.6)	154.6 (146.5)	154.4 (154.7)	58.0 (45.9)
1*f*	$C_6H_3Br_2$(2,4)	Me	Ph		190.5 (187.0)	95.9 (100.6)	157.5 (146.5)	155.2 (154.7)	61.6 (45.9)
1*g*	Ph	Ph	Me		191.0 (196.5)	105.4 (103.7)	155.5 (142.9)	154.2 (154.7)	50.1 (39.2)
1*h*	Ph	Ph	Ph		187.8 (187.0)	105.3 (103.7)	157.3 (142.9)	154.9 (154.7)	52.0 (39.2)
1*i*	Ph	Ph	$C_6H_4NO_2$(4)		185.1 (187.0)	104.9 (103.7)	158.3 (142.9)	155.6 (154.7)	53.4 (39.2)
1*j*	Ph	COMe	Me		193.5 (196.5)	109.1 (105.5)	162.2 (158.6)	158.8 (154.7)	53.1 (43.1)
1*k*	$C_6H_3Br_2$(2,4)	COOEt	OEt		165.6 (165.0)	88.9 (96.5)	160.3 (160.9)	155.3 (154.7)	71.4 (64.4)
2*a*	$C_6H_3Br_2$(2,4)	H	Ph	202.8 (229.0)		105.9 (76.9)	162.9 (149.2)	151.0 (154.7)	57.0 (72.3)
2*b*	Ph	H	Ph	200.6 (229.0)		106.2 (76.9)	162.9 (149.2)	151.0 (154.7)	56.7 (72.3)

[a]In ppm from TMS; $CDCl_3$ solution. Calculated shifts are in parentheses.

dow of 12 500 Hz and 16 K of data memory, using the J-modulated spin echo sequence, and using the centre peak of the $CDCl_3$ 1:1:1 triplet (77.0 ppm from TMS) as an internal reference. Compound **1b** was also run in $CDCl_3$–DMSO-d_6 (5:1, v/v); this gave upfield shifts of 1.1–1.6 ppm for all signals, resulting in a change in ΔCβCα of only 0.4 ppm from the value in $CDCl_3$. Several of the compounds (**1***c*, **1***f*, **1***h*, **2***a*, **2***b*, **3***b*) fail to display the expected number of CH carbon signals in the aromatic region of the ^{13}C spectrum, and we attribute this to the coincidental superposition of signals.

Carbon-13 chemical shift calculations, using the approach of Pretsch et al. (22), were carried out using the Chemintosh program (Softshell International Ltd., Grand Junction, Colorado, U.S.A.). However, this program as currently set up does not incorporate selenium in its calculations and in fact provides invalid values for selenium-containing compounds.[3]

Results

The pertinent carbon-13 chemical shifts for compounds in the series **1** and **2** are summarized in Table 1, and for those in the series **3**–**5** in Table 2. Calculated chemical shifts (22) are included in parentheses. From Table 1, it is apparent that C-2 and C-5 in the thiadiazole ring have fairly similar chemical shifts. Our assignments are based on the consideration that replacing the acceptor-end olefinic carbon (Cα) by nitrogen as in **6** (Ar = 2,4-dibromophenyl) should have a greater effect on the shift of C-2 than on that of C-5. The spectrum of **6** shows

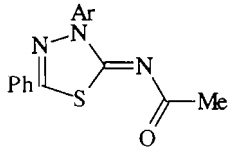

6

the two signals of interest at 156.3 and 165.0 ppm, thus enabling the assignment of C-5 in the related compound **1***a* as the lower-frequency signal at 154.2 and C-2 as the higher-frequency signal at 158.2 ppm. This is consistent with chemical shift calculations.

Replacing the 2,4-dibromophenyl substituent by phenyl, as in **1***a* and **1***b* and in **2***a* and **2***b*, gives no significant change in chemical shifts of the olefinic carbons. Accordingly, we assign C-2 (Cβ) as the signal to high frequency from C-5 for

[3] E. Pretsch, personal communication.

Table 2. ^{13}C NMR chemical shifts of the push–pull alkenes **3–5**.[a]

Compound	R^1	R^2	C=S	C=O	Cα	Cβ (C-2)	ΔCβCα
3*a*	Me	Me		191.1 (196.5)	90.2 (90.1)	160.3 (163.4)	70.1 (73.3)
3*b*	Me	Ph		184.2 (187.0)	86.9 (90.1)	162.0 (163.4)	75.1 (73.3)
3*c*	Et	Me		191.2 (196.5)	89.8 (90.1)	159.8 (163.4)	70.0 (73.3)
4*a*	Me	Me		190.9 (196.5)	93.8 (107.6)	162.0 (144.4)	68.2 (36.8)
4*b*	Me	Ph		184.4 (187.0)	90.6 (107.6)	164.1 (144.4)	73.5 (36.8)
5	Me	NHPh	186.5 (188.2)		95.3 (93.3)	166.2 (139.7)	70.9 (46.4)

[a]In ppm from TMS; $CDCl_3$ solution. Calculated shifts are in parentheses.

the remaining compounds in the series **1***b*–**1***k*. This becomes ambiguous only when the difference between the chemical shifts for C-2 and C-5 is small, e.g., for **1***e* and **1***g*, but here the decision is less crucial as its influence on ΔCβCα is minimal. The same considerations apply to our assignments for **2***a* and **2***b* since it is unlikely that the shift positions of C-2 and C-5 would be reversed by substituting a thioacyl for an acyl group. In fact the shift difference between C-2 and C-5 widens slightly in the thioacyl series. Again, these assignments are consistent with the values calculated using the approach of Pretsch et al.

Discussion

Table 1 shows changes in the chemical shifts of the olefinic carbons within the series of thiadiazoles of general formulae **1** and **2**. The shifts for C=O, Cα, and Cβ are virtually the same for **1***a* and **1***b*, but in **1***c* small shifts to lower frequency are noted for both C=O and Cα. Changes in bond length within the C=C—C portion of the push–pull systems are likely to be involved (6), resulting in a change in the resonance description of **1***c*. The similar but more marked effect seen in **1***d* can be ascribed to resonance of the ester group and the resulting decreased ability of this group to lower electron density at Cα.

The entries for **1***e* and **1***f* show the effect of methyl substitution at Cα. Comparing **1***e* with **1***a*, we note a small higher-frequency shift of C=O, a higher-frequency shift for Cα, and a shift to lower frequency for Cβ, leading to a decrease in ΔCβCα of about 11 ppm. Discounting the change in 3-aryl substituent, we compare **1***f* with **1***c* and observe a higher-frequency shift for C=O, higher-frequency shift for Cα, and lower-frequency shift for Cβ resulting in a decrease in ΔCβCα of 13 ppm. For the effects of phenyl substitution at Cα, we compare **1***g* with **1***b*, and **1***h* with **1***c*. For the former, the C=O shift moves slightly to higher frequency, Cα moves to higher frequency, and Cβ to lower frequency, with a decrease in ΔCβCα of approximately 19 ppm; for the latter, the corresponding changes are a higher-frequency shift of C=O, a higher-frequency shift of Cα, and a lower-frequency shift of Cβ, resulting in a decrease in ΔCβCα of approximately 22 ppm. These effects display a trend towards increasing delocalization of the negative charge as one or more phenyl groups are incorporated in the structure, and are most significant for **1***g* and **1***h*. This is related to the ability of phenyl groups to stabilize a negative charge in the anions of phenylacetone and deoxybenzoin. However, competing steric effects can also arise from α substitution. These lead to some angle widening in the push–pull system to accommodate the α substituent, a shortening of the S...O distance, and some variation in C=C bond lengths, all of which will affect the resonance system (6).

The presence of a nitro group in **1***i* has only a small effect on the corresponding shifts in **1***h* as this group is unable to participate directly in the push–pull system. Thus, the C=O and Cα shifts move slightly to lower frequency and the Cβ shift slightly to higher frequency. A similar effect has been noted elsewhere when comparing 4-nitrobenzoyl with benzoyl as acceptor in other push–pull systems (12, 23), and Kleinpeter and co-workers have correlated Cα and Cβ shift changes to Hammett σ values for nitro and other substituents.

The entries for **1***j* and **1***k* show the effect of further carbonyl substitution at Cα. For **1***j*, we see small higher-frequency shifts for C=O and Cβ and a marked higher-frequency shift for Cα (20.3 ppm) relative to **1***b*, resulting in a drop of approximately 16 ppm in ΔCβCα. This is to be expected given the greater ability of two carbonyl groups to delocalize negative charge (and hence to lower the energy barrier to rotation about the C=C bond: **1***j* shows *one* ^1H signal at δ 2.04 for the six methyl protons at ambient temperature, with evidence of restricted rotation at lower temperatures (6)). Discounting the change in 3-substituent, we next compare **1***k* with **1***d*. Here Cα moves to higher frequency by 10.5 ppm and Cβ moves to higher frequency by only 0.9 ppm, resulting in a decrease in ΔCβCα of 9.6, indicative again of the weaker acceptor ability of carboxylic ester groups than of keto groups; indeed, the effect of the two ester groups is little more in terms of chemical shift than that of one acetyl group, as in **1***a* or **1***b*, as also observed by others (9).

The last two entries in Table 1 show that changing the 3-

aryl substituent from 2,4-dibromophenyl to phenyl does not significantly affect the carbon shifts of interest. The C=S carbon signals appear notably to higher frequency from C=O, as is typical (refs. 13; 20, pp. 233–235; and Table 4.41). The Cα shifts for **2***a* and **2***b* are some 20 ppm to higher frequency of the corresponding shift in **1***c*, while the Cβ shifts are only slightly to higher frequency. This is consistent with other observations (12) that the C=S group is a better electron acceptor than the C=O group and this is thought to be associated with the greater tendency of the thiocarbonyl group to form C—S single bonds, and so assume negative charge despite the lower electronegativity of sulfur relative to oxygen.

One other compound in this series, the thiadiazole **7**, is of interest. In this compound, substitution at Cα is modified by inclusion of the α carbon atom within a rhodanine ring, which features a carbonyl group (acceptor) and sulfur atom (arguably a donor). This compound exhibits signals that we assign as follows: 83.8 ppm (Cα or C-2), 155.3 ppm (Cβ, with C-5 assigned on the same basis as before at 149.9 ppm), and signals at 189.2 and 166.1 ppm, assigned to C=S and C=O, respectively. For this compound, ΔCβCα is 69.5 ppm, indicating appreciable charge separation; this cyclic substitution pattern creates a weak acceptor.

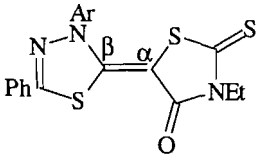

7

Similar effects are noted in Table 2 for analogous benzothiazole and benzoselenazole derivatives **3**–**5**. Comparisons of **3***a* and **3***c* (which exhibits virtually the same shifts as **3***a*) with **3***b*, and of **4***a* with **4***b*, reveal the same small higher-frequency shift of the carbonyl carbon noted in the thiadiazole series, while very small higher-frequency shifts for Cα and Cβ are noted between corresponding pairs when selenium is substituted for sulfur as donor atom in the ring. These lead to slightly smaller values of ΔCβCα for **4***a* and **4***b* than for **3***a* and **3***b*, perhaps because of modification of the resonance system resulting from the larger size of the selenium atom. Finally, the C=S carbon signal for **5** is significantly to lower frequency of the C=S shifts observed for **2***a* and **2***b* as a result of resonance of the thioamide group, mirroring the differences noted in the series **1***a*–**1***d* above. For all compounds listed in the tables, the olefin carbon shift more sensitive to substituent effects in the push–pull system is Cα, as expected since the donor portion of the molecules is substantially unchanged for the compounds within each table.

It has been observed that cyclization in the donor portion of related push–pull alkenes causes an increase in shift differences between Cα and Cβ as well as an increased barrier to rotation about the C=C bond (12). As an example, the five-membered -SCH_2CH_2S- group was compared with two MeS-groups. Abstracting the relevant chemical shifts from that work (12) for comparison with **1***c* (for which ΔCβCα is 74.5), we find comparable shifts for the -SCH_2CH2S- compound of 108.2 (Cα) and 168.0 (Cβ), with an ΔCβCα of 59.8. The larger shift difference for **1***c* (and for **3***b* and **4***b*) would suggest that the five-membered heterocyclic rings explored in our work are less effective donors than the -SCH_2CH_2S- group, and that the barrier to rotation about the C=C bond would be correspondingly increased.

It is of interest to compare the shift differences observed for push–pull alkenes with related compounds lacking the acceptor group. An example is provided by 1,1-dipiperidinoethene, **8** (24), and its 2-benzoyl derivative **9** (23). For the former, the data are Cα 68.2 and Cβ 164.1 (ΔCβCα 95.9), while for the latter the data are Cα 83.8 and Cβ 164.1 (ΔCβCα 84.6), i.e., Cα is the carbon markedly affected by the substitution. Incorporating an acceptor diffuses the charge separation since the negative charge can now be delocalized away from Cα, and the value of ΔCβCα is somewhat decreased.

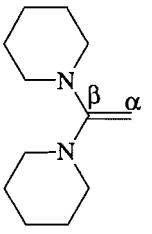

8

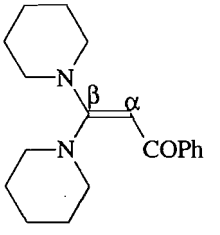

9

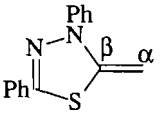

10

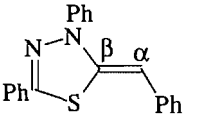

11

The magnitude of the charge separation in the double bond is largely dependent on the donor substituents. The piperidino group is a powerful donor, so **8** and **9** give large ΔCβCα values. The parent methine base **10** (chemical shift data not available due to instability) would have Cα somewhat further to higher frequency. For compound **11**, which contains a phenyl substituent on Cα, the relevant experimental δ values are Cα 90.6, and Cβ 142.8 (ΔCβCα = 52.2). Allowing for the shift to higher frequency associated with this substitution at Cα, estimated δ values for Cα and Cβ of **10** of approximately 75–80 ppm and 150–160 ppm would be of the right order (and are not inconsistent with calculated values: 76.9 and 149.2 ppm). On this basis, the acceptors that most effectively delocalize the negative charge associated with Cα are two acetyls (**1***j*), acyl–phenyl combinations (**1***g*, **1***h*, and **1***i*), and thiobenzoyl (**2***a* and **2***b*), while the least effective are ethoxycarbonyl (**1***d*) and the rhodanine unit (**7**).

The Pretsch–Chemintosh calculation scheme, which is based on additivity rules covering a wide variety of carbon atom types (22), is very convenient but gives at best a semi-quantitative estimate of the olefinic carbon chemical shifts in our compounds. Many calculated values are within 5 ppm but discrepancies can be much greater (Tables 1 and 2). As noted by Pretsch and co-workers themselves, their approach is unable to accommodate the presence of multiple and strongly interacting functional groups with any great accuracy. An obvious example of this in the present work is the calculated chemical shifts of the N-aryl carbons in compounds such as **1***b*

(actual aromatic CH carbon shifts, 125.5–130.7 ppm; calculated values *ortho*, 112.0; *meta*, 129.0, *para*, 118.9). The calculations are based on model compounds in which the nitrogen lone pair is available for delocalization into the benzene ring, whereas in our compounds it is incorporated into the π system of the heterocycle push–pull olefin instead.

The conclusion of Kleinpeter et al. (12), that changes in the parameter ΔCβCα within closely related series of push–pull olefins give a useful qualitative picture of differences in charge separation within the series, is supported by our work. The Pretsch chemical shift calculation scheme is useful but provides no new insights. At the level of accuracy possible with this scheme, no specific "push–pull" term is required. More sophisticated calculations might well require such a term but it would not be large since olefinic carbon shifts and ΔCβCα in push–pull olefins arise primarily as a sum of the individual substituent effects.

Considering that the chemical shift observed in liquids is merely the isotropic average of the three components of the chemical shift tensor, and each component can vary independently with changes in structure (25), it is perhaps surprising that observed chemical shifts agree as well as they do with values from purely empirical calculation schemes. We certainly cannot detect the hoped-for small chemical shift effects arising from nonbonded interactions (6, 7) because of much larger variations due to other factors.

Conclusions

The Pretsch ^{13}C chemical shift calculation scheme, like other correlation schemes, is a useful empirical guide to the assignment of ^{13}C chemical shifts. Despite becoming less accurate in polyfunctional compounds and not taking into account steric effects (22), this scheme predicts the existence of large chemical shift differences between the olefinic carbons of push–pull olefins. The discrepancies between observed and calculated ΔCβCα values are generally less than 15 ppm. Given the inaccuracies inherent in this calculation method, no special term for charge buildup effects in push–pull olefins need be applied.

Acknowledgements

We wish to thank Tim Jones for assistance with the NMR instrumentation, and Imperial Oil Ltd. and the Natural Sciences and Engineering Research Council of Canada for financial support.

References

1. P.D. Callaghan, A.J. Elliott, S.S. Gandhi, M.S. Gibson, H. Mastalerz, and D. Vukov. J. Chem. Soc. Perkin Trans. 1, 2948 (1981).
2. H. Mastalerz and M.S. Gibson. J. Chem. Soc. Perkin Trans. 1, 2952 (1981).
3. H. Mastalerz and M.S. Gibson. J. Chem. Soc. Perkin Trans. I, 245 (1983).
4. H. Mastalerz, T. Mohammad, and M.S. Gibson. Can. J. Chem. **65**, 2713 (1987).
5. T. Mohammad and M.S. Gibson. Phosphorus, Sulfur, Silicon, **70**, 243 (1992).
6. N. Pandya, A.J. Basile, A.K. Gupta, P. Hand, C.L. MacLaurin, T. Mohammad, E.S. Ratemi, M.S. Gibson, and M.F. Richardson. Can. J. Chem. **71**, 561 (1993), and references therein.
7. A.K. Gupta, A. Ben-Mahmud, L.J. Kamphuis, J.L. Mueller, S.S. Rigby, M.S. Gibson, and M.F. Richardson. Can. J. Chem. **73**, 1278 (1995).
8. K.M. Gough and J. Millington. Can. J. Chem. **73**, 1287 (1995).
9. J. Sandström. Topics in stereochemistry. Vol. 14. *Edited by* N. L. Allinger, E. L. Eliel, and S. M. Wilen. Wiley, New York. 1983. Chap. 2.
10. F. Meyers, J. L. Bredas, and J. Zyss. J. Am. Chem. Soc. **114**, 2914 (1992), and references therein; S. R. Marder, J. W. Perry, B. G. Tiemann, C. B. Gorman, S. Gilmore, S. L. Biddle, and G. Bourhill. J. Am. Chem. Soc. **115**, 2524 (1993).
11. I. Wennerbeck and J. Sandström. Org. Magn. Reson. **4**, 783 (1972).
12. (*a*) G. Fischer, W.-D. Rudorf, and E. Kleinpeter. Magn. Reson. Chem. **29**, 212 (1991), and references therein; E. Kleinpeter, St. Thomas, G. Uhlig, and W.-D. Rudorf. Magn. Reson. Chem. **31**, 714 (1993).
13. J. Dabrowski, K. Kamienska-Trela, and L. Kozerski. Org. Magn. Reson. **6**, 499 (1974).
14. D. Tourwé, G. Van Binst, S.A.G. De Graaf, and U.K. Pandit. Org. Magn. Reson. **7**, 433 (1975).
15. V. Milata, D. Ilavsky, I. Golger, and L. Lesko. Collect. Czech. Chem. Commun. **57**, 531 (1992), and references therein; (*b*) V. Milata, D. Ilavsky, and I. Golger. Collect. Czech. Chem. Commun. **54**, 713 (1989); (*c*) I. Golger, V. Milata, and D. Ilavsky. Magn. Reson. Chem. **27**, 138 (1989).
16. N. Namdev and M.S. Gibson. J. Chem. Res. (M), 2301 (1994).
17. U. Kolle, B. Kolb, and A. Mannschreck. Chem. Ber. **113**, 2545 (1980).
18. H. McNab and L.C. Monahan. J. Chem. Soc. Perkin Trans. 1, 863 (1988); A.J. Blake, H. McNab, and L.C. Monahan. J. Chem. Soc. Perkin Trans 2, 2003 (1991); H. McNab and L.C. Monahan. J. Chem. Soc. Perkin Trans. 2, 1459 (1988), and references therein; H. McNab and L.C. Monahan. J. Chem. Soc. Perkin Trans. 1, 3159 (1990).
19. L. Kozerski and A. Krowczynski. Magn. Reson. Chem. **25**, 46 (1987); P.E. Hansen, R. Kawecki, A. Krowczynski, and L. Kozerski. Acta Chem. Scand. **44**, 826 (1990).
20. E. Breitmaier and W. Voelter. Carbon-13 NMR spectroscopy. High-resolution methods and applications in organic chemistry and biochemistry. 3rd ed. VCH Publishers, Weinheim. 1987. Especially pp. 107–133.
21. A. Kucsman and I. Kapovits. Studies in organic chemistry. Vol. 19. Organic sulfur chemistry. *Edited by* F. Bernardi, I.G. Csizmadia, and A. Mangini. Elsevier, Amsterdam. 1985. Chap. 4.
22. E. Pretsch, A. Fürst, M. Badertscher, R. Bürgin, and M.E. Munk. J. Chem. Inf. Comput. Sci. **32**, 291 (1992), and references therein; J.F. Nash. J. Chem. Inf. Comput. Sci. **34**, 1338 (1994).
23. A. Armati, P.D. Ruggieri, E. Rossi, and R. Stradi. Synthesis, 573 (1986).
24. J.S. Hartman and E. Kelusky. Can. J. Chem. **59**, 1284 (1981).
25. J.C. Facelli, D.M. Grant, and J. Michl. Acc. Chem. Res. **20**, 152 (1987); J.C. Facelli and D.M. Grant. Topics in stereochemistry. Vol.19. *Edited by* E.L. Eliel and S.H. Wilen. Wiley, New York. 1989. Chap. 1.

Methoxy-(2-trimethylsilyl)ethoxycarbene. Reactions with Michael acceptors, with hydroxylic compounds, and with miscellaneous functional groups

David L. Pole, Pradeep K. Sharma, and John Warkentin

Abstract: Methoxy-(2-trimethylsilyl)ethoxycarbene reacts with two equivalents of dimethyl acetylene dicarboxylate, methyl propiolate, phenyl acetylene, or phenyl isocyanate without rearrangement of the carbene group. *N*-Phenylmaleimide captures the carbene with 1:1-stoichiometry. The structure of the product implies that a migration of the trimethylsilylethyl group from oxygen to carbon accompanies that reaction. A mechanism for that complex rearrangement is proposed. Phenol and *tert*-butyl alcohol afford the orthoformates expected from overall insertion of the carbene into the OH bond.

Key words: dialkoxycarbene, insertion into O—H, C—H bonds, rearrangement, *N*-phenylmaleimide, dialkoxyoxadiazoline.

Résumé : Le méthoxy-(2-triméthylsilyl)éthoxycarbène réagit avec deux équivalents d'acétylènecarboxylate de diméthyle, de propiolate de méthyle, de phénylacétylène ou d'isocyanate de phényle sans réarrangement du groupe carbène. Le *N*-phénylmaléimide capture le carbène avec une stoechiométrie 1 : 1. La structure du produit implique qu'une migration du groupe triméthylsilyléthyle de l'oxygène au carbone accompagne cette réaction. On propose un mécanisme pour ce réarrangement complexe. Le phénol et l'alcool *tert*-butylique conduisent aux orthoformates attendus pour une insertion globale du carbène dans la liaison OH.

Mots clés : dialkoxycarbène, insertion dans les liaisons OH et CH, réarrangement, *N*-phénylmaléimide, dialkoxyoxadiazoline.

[Traduit par la rédaction]

Introduction

The ready availability of 2,2-dialkoxy oxadiazolines (1), particularly from a precursor such as 2-acetoxy-2-methoxy-5,5-dimethyl-Δ^3-1,3,4-oxadiazoline (**1**) (2) by means of substitution reactions with hydroxylic nucleophiles, prompted us to synthesize (3) 2-methoxy-5,5-dimethyl-2-(2-trimethylsilyl)ethoxy-Δ^3-1,3,4-oxadiazoline (**2**), Scheme 1. Analogous oxadiazolines undergo thermolytic fragmentation to N_2, acetone, and a dialkoxycarbene (2), which, in the case of **2**, would be methoxy(2-trimethylsilyl)ethoxycarbene (**3**, Scheme 1). Dialkoxycarbenes have nucleophilic properties (4) that are the result of conjugative delocalization in the singlet ground state. In the case of **3**, it seemed likely that the β-trimethylsilylethyl group would confer unusual properties onto the carbene itself, and particularly onto adducts of the carbene, if significant charge were to reside on the trimethylsilyl group, as illustrated with the "no bond" contributor **4***b* in terms of a dipolar adduct with a carbonyl compound.

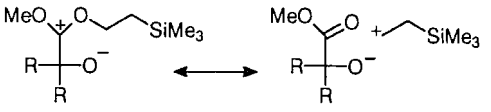

4a **4b**

We now report that the chemistry of **3** includes an unusual feature that appears to reflect the β-effect (5) of the trimethylsilyl group in a ketene acetal intermediate.

Methods, results, and discussion

2-Methoxy-5,5-dimethyl-2-(2-trimethylsilyl)ethoxy-Δ^3-1,3,4-oxadiazoline (**2**) was prepared readily from crude 2-acetoxy-2-methoxy-5,5-dimethyl-Δ^3-1,3,4-oxadiazoline (**1**) (2) by treating it with 2-(trimethylsilyl)ethanol in dichloromethane containing catalytic *p*-toluenesulfonic acid (3).

Thermolysis of **2** in dry benzene at 110°C was complete in 24 h. Carbene trapping reactions were carried out in sealed glass ampoules containing 0.20–0.35 g of **2** (ca. 0.08 M) and excess substrate in dry benzene. The products were separated from excess substrate and (usually) from one another by chromatography. Structures were established by ^{1}H and ^{13}C NMR spectroscopy, infrared spectroscopy, and mass spectrometry, including high-resolution MS.

Thermolysis of **2** in the presence of dimethyl acetylenedicarboxylate (DMAD) afforded the 2:1 adduct **6** as a mixture of diastereomers that could not be separated (Scheme 2). The structure was established from the infrared spectrum as well as

Received February 1, 1996.

D.L. Pole, P.K. Sharma, and J. Warkentin.[1] Department of Chemistry, McMaster University, Hamilton, ON L8S 4M1, Canada.

[1] Author to whom correspondence may be addressed. Telephone: (905) 525-9140, ext. 23478. Fax: (905) 522-2509. E-mail: Warkent@McMaster.ca

Scheme 1.

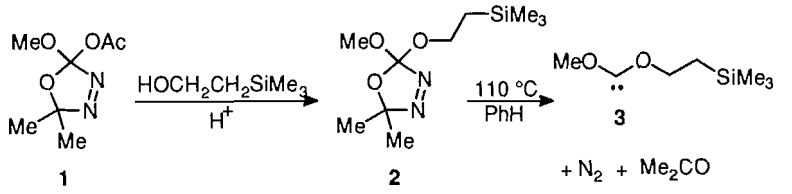

1 2 3

Scheme 2.

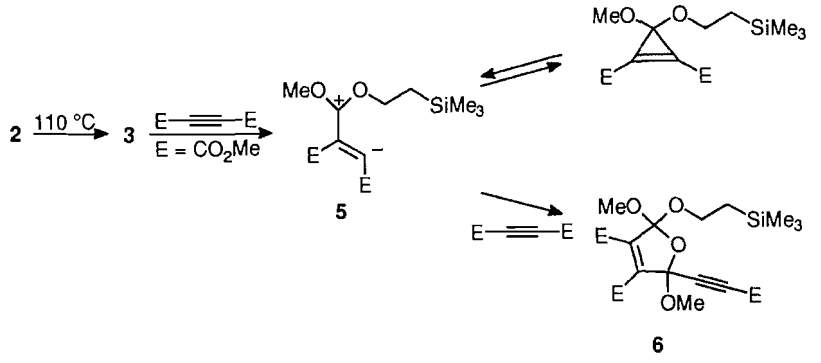

5 6

Scheme 3.

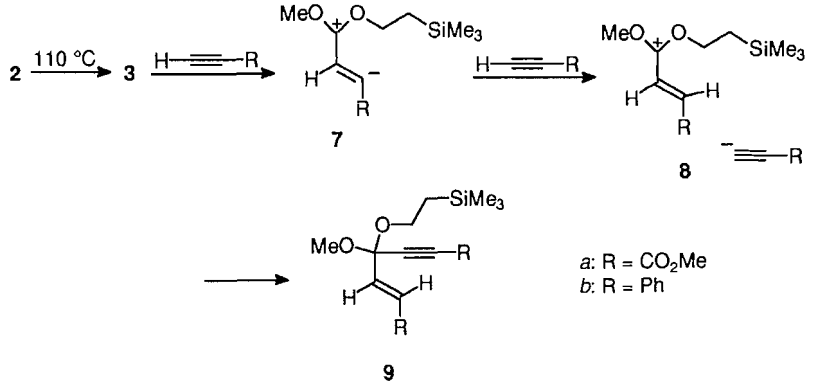

7 8 9

the ^1H and ^{13}C NMR spectra, with reference to the analogous 2:1 adduct from reaction of DMAD with dimethoxycarbene (*6b*). The diastereomer ratio, estimated by averaging the heights of the larger and smaller methoxy signals in the ^1H NMR spectrum, was 1.4. An exact mass determination on the most intense fragment signal ($M^+ - CO_2Me$) was performed, the molecular ion signal being undetectable. Chemical ionization MS, with NH_3, afforded both $M^+ + H$ and $M^+ + NH_4$ signals.

Formation of **6** presumably involves the cycloaddition of 1:1 adduct **5** to a carbonyl double bond of DMAD (6). Adduct **5**, which can also be written as a singlet vinylogous dialkoxycarbene, is presumably equilibrated with the corresponding cyclopropene (7), Scheme 2.

Thermolysis of **2** in the presence of methyl propiolate afforded the ketal of an enynone (*9a*). The E-geometry at the double bond followed from the coupling constant between the vinylic protons (15.7 Hz) and the rest of the structure could be assigned with confidence on the basis of the NMR, IR, and MS evidence. Product *9a* can be accommodated with a mechanism similar to that in Scheme 2, except for a proton transfer step, Scheme 3. Proton transfer from an alkyne to a nucleophilic site, as in **7**, is known (*6b*, 8). Apparently the intermediate dipolar adduct (**7**), which can also be expressed as a vinylcarbene, is more basic than carbene **3** and is protonated by the terminal alkyne to afford a short-lived ion pair (**8**) that collapses to **9**.

Phenyl acetylene reacted with carbene **3** to afford *9b*, a product similar to *9a*. Again, a large coupling constant (16 Hz) between vinylic protons indicated the *E*-geometry at the double bond.

Attack of carbene **3** on *N*-phenylmaleimide involved migration, at some stage, of the trimethylsilylethyl group. This result was immediately evident, for the characteristic signal from OCH_2 of the $OCH_2CH_2SiMe_3$ group was absent in the ^1H NMR spectrum of the product. That product was eventually identified as **13** on the strength of ^1H and ^{13}C NMR spectroscopy, which showed, unambiguously, a CH_2CO group

Scheme 4.

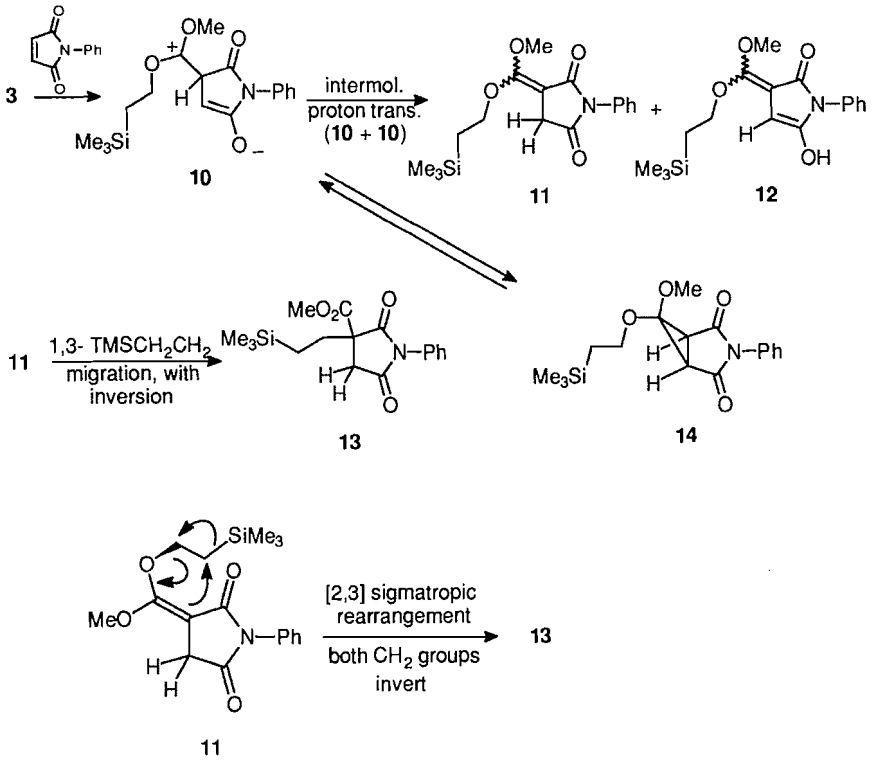

with a large J_{gem} but no other proton couplings. With the vinyl signals of *N*-phenylmaleimide no longer present, it was clear that the CC double bond was the site of attack, rather than carbonyl carbon, as in the case of attack of dimethoxycarbene on anhydrides (9). Analogy to attack at C(sp^2) sites that are electron poor (3, 4*j*, 6*b*) suggests that the first step is formation of a dipolar intermediate **10**, which then undergoes rearrangement to **13**. The mechanism of that rearrangement probably involves intermolecular proton transfer, between two units of **10** to form **11** and (or) its "enol", **12** (Scheme 4). There are many examples of similar intermolecular atom (or group) transfers in the literature (10, 11). While rearrangement of **11** to **13** could also be intermolecular, it is allowed to be a concerted, suprafacial reaction provided that the migrating methylene carbon is inverted in the process (12), Scheme 4. However, the geometry required is hard to attain, and the mechanism does not assign any special function to the TMS group.

There is another mechanistic option, in which the Me_3Si group migrates from one CH_2 group of the ethyl fragment to the other, in concert with migration of the $TMSCH_2CH_2$ moiety from oxygen to carbon. This [2, 3] sigmatropic rearrangement (12, 13), which is also illustrated in Scheme 4, requires inversion of both methylenes of the trimethylsilylethyl group. There is some precedent in the literature for such a complex rearrangement (13*c*) but whether or not it operates in the present case will not be known until one of the CH_2 groups of $TMSCH_2CH_2$ is labelled. Such exchange of labelled methylene groups is known from, for instance, the solvolysis of (2-bromoalkyl)silanes (14). In Scheme 4 it is also assumed that a dipolar intermediate such as **10** is equilibrated with cyclopropanone ketal (**14**) at 110°C.

Phenyl isocyanate captured carbene **3** with 2:1 stoichiometry to afford hydantoin **18**, Scheme 5. It was readily identified with reference to the spectra of the dimethoxy analogue (from dimethoxycarbene) that had been reported by Hoffmann's group (6*c*). For example, the infrared spectrum showed carbonyl absorption (1825 and 1750 cm^{-1}) consistent with the hydantoin ring system and the ^{13}C NMR spectrum showed carbonyl carbons in the expected range of chemical shifts. A molecular ion signal could not be found in the MS, a feature also consistent with the structure that, as the "ketal" of an amide, would be expected to lose an alkoxy group. Formation of **18** is rationalized in terms of Hoffmann's mechanism for formation of the corresponding dimethoxyhydantoin from reaction of dimethoxycarbene with phenyl isocyanate, Scheme 5. Whether or not the dipolar intermediate **15** is equilibrated with the corresponding iminooxirane (**16**) and α-lactam (**17**), Scheme 5, is not known.

As expected, carbene **3** was intercepted with phenol and with *tert*-butyl alcohol by overall OH insertion, Scheme 6. The orthoformates so formed were sensitive to hydrolysis and their purification by chromatography failed. Orthoformate **19**, from phenol, was assigned on the basis of ^1H NMR spectroscopy alone while orthoformate **20**, from *tert*-butyl alcohol, was assigned on the basis of ^1H and ^{13}C NMR spectra.

In summary, thermolysis of oxadiazoline **2** affords carbene **3**. The latter acts as a nucleophile toward α,β-unsaturated carbonyl compounds but it also reacts with phenyl acetylene. During reaction of **3** with *N*-phenylmaleimide, the trimethylsilylethyl group is transferred from oxygen to carbon in a novel [2, 3] type of rearrangement of a ketene acetal. Whether or not the trimethylsilylethyl group will migrate during other reactions of **3** is under investigation.

Evidence for operation of the β-effect of the TMS group on

Scheme 5.

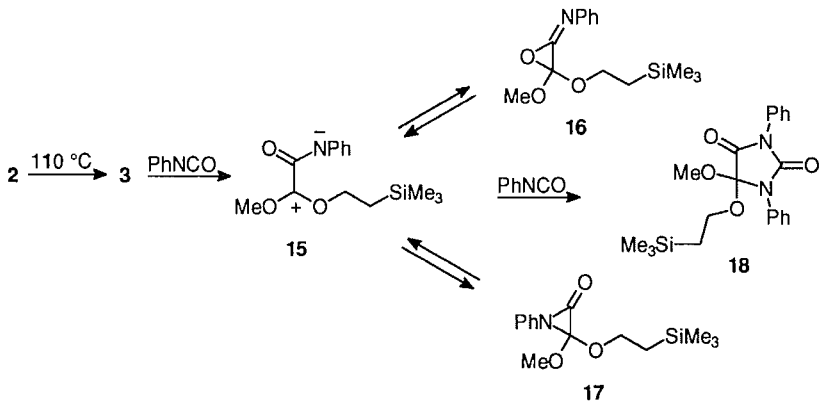

Scheme 6.

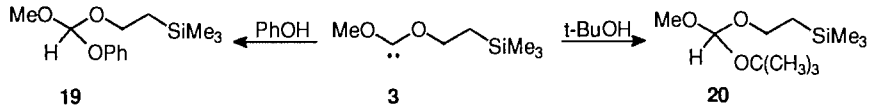

the properties of carbene **3** or on the properties of dipolar intermediates (**5**, **7**, **10**, **15**) was not obtained from studies of the final products but the operation of such an effect on the rate constants and equilibrium constants (e.g., **10** ⇄ **14**) is not excluded.

Experimental

^{1}H NMR and ^{13}C NMR spectra were obtained with solutions in $CDCl_3$ containing TMS. The former were run at 200 MHz and the latter at 50 MHz unless otherwise specified. Infrared spectra of oils were obtained from thin films of neat materials while those of solids were obtained by the KBr pellet method.

2-Methoxy-5,5-dimethyl-2-(2-trimethylsilyl)ethoxy-Δ^3-1,3,4-oxadiazoline (2)

To a solution of crude **1** (7.5 g, 39.9 mmol, 68% pure, containing 1-(1-acetoxy-1-methyl)ethyl-2-methoxycarbonyldiazene (1) in dry CH_2Cl_2 (75 mL) under argon was added 2-(trimethylsilyl)ethanol (3.21 g, 27.1 mmol). Molecular sieves (2 g, 4 Å) and *p*-toluenesulfonic acid (0.516 g, 2.71 mmol) were added and the resulting mixture was stirred for 15 h. After filtration and concentration in vacuo, a viscous yellow oil was obtained. Column chromatography (silica gel, ether:hexane, 1:6) afforded **2** as a colourless oil, 3.2 g, 48%; R_f 0.38 (ether:hexane, 1:6); IR (cm^{-1}): 2989–2840, 1577 (N=N); ^{1}H NMR, δ: 0.27 (s, 9H), 0.97 (t, J = 8.3 Hz, 2H), 1.48 (s, 6H), 3.40 (s, 3H), 3.67–3.86 (m, 2H, diasterotopic OCH_2); ^{13}C NMR, δ: −1.48, 18.10, 24.03, 51.76, 62.48, 118.65, 137.10; MS (EI) *m/z*: 231 ($M^+ - CH_3$, 2), 129 ($M^+ - OCH_2CH_2SiMe_3$, 13), 84 (33), 73 (100); MS (EI, HR): 231.1159; calcd. for $C_{10}H_{22}N_2O_3Si - CH_3$: 231.1165; MS (CI, NH_3) *m/z*: 231 ($M^+ - CH_3$, 2), 194 (8), 166 (14), 149 (16), 106 (5), 90 (100), 60 (8).

Dihydrofuran diastereomers 6

A solution of **2** (0.35 g, 1.42 mmol) and DMAD (0.41 g, 2.89 mmol) in dry benzene (35 mL) was heated at 110°C in a sealed tube for 24 h. Removal of the solvent and chromatography of the residue (Chromatotron, 2 mm plate, 5% EtOAc in hexane) afforded **6** (0.39 g, 62%) as a pale yellow oil. R_f 0.11 (10% EtOAc in hexane); IR (cm^{-1}): 3006–2844, 2110 (C≡C), 1733 (C=O); ^{1}H NMR (major diasteromer) δ: 0.04 (s), 0.8–1.0 (m, overlap with signal from minor isomer), 3.40 (s, 3H), 3.56 (s, 3H), 3.62–3.75 (m), 3.76 (s, 3H), 3.82 (s) and 3.84 (s) overlapping with signals from minor isomer; ^{1}H NMR (minor diastereomer) δ: 0.04 (s), 0.8–1.0 (m), 3.39 (s, 3H), 3.55 (s, 3H), 3.62–3.75 (m), 3.78 (s, 3H), 3.82 (s), 3.84 (s), diastereomer ratio 1.4:1.0, from the three sets of distinct methoxy singlets; ^{13}C NMR (δ): −1.56, 17.71, 17.86, 17.87, 51.50, 51.76, 52.88, 52.99, 62.18, 62.37, 77.44, 78.66, 99.66, 99.71, 123.03, 123.12, 135.18, 140.98, 152.56, 152.57, 153.64, 159.79, 161.66; MS(EI) *m/z*: 413 ($M^+ - OCH_3$, 12), 385 ($M^+ - CO_2Me$, 100), 372 (10), 327 ($M^+ - OCH_2CH_2SiMe_3$, 13), 281 (15), 253 (8), 157 (46), 111 (12), 89 (22), 73 (98), 59 (40); MS (CI, NH_3) *m/z*: 462 ($M^+ + NH_4$, 48), 445 ($M^+ + H$, 63), 413 ($M^+ - OCH_3$, 16), 385 ($M^+ - CO_2Me$, 100).

Ketal 9*a*

A solution of **2** (0.25 g, 1.02 mmol) and methyl propiolate (0.175 g, 2.08 mmol) in dry benzene (10 mL) was heated in a sealed tube at 110°C for 20 h. The oil that remained after removal of the solvent was chromatographed (Chromatotron, 2 mm SiO_2 plate, 10% EtOAc in hexane) to afford 0.21 g (62%) of **9*a*** as a colourless oil. R_f 0.28 (10% EtOAc in hexane); IR (cm^{-1}): 3001–2838, 2238 (C≡C), 1727 (C=O), 1436; ^{1}H NMR (δ): 0.02 (s, 9H), 0.92 (m, 2H), 3.92 (s, 3H), 3.57 – 3.63 (m, 2H, diastereotopic OCH_2), 3.73 (s, 3H), 3.75 (s, 3H), 6.28 (d, J = 15.7 Hz, 1H), 6.74 (d, J = 15.7 Hz, 1H); ^{13}C NMR (δ): −1.45, 17.99, 49.73, 50.85, 51.86, 61.44, 77.12, 80.93, 95.08, 124.81, 142.73, 152.97, 165.85; MS (EI) *m/z*: 269 ($M^+ - CO_2Me$, 11), 217 (9), 211 ($M^+ - OCH_2CH_2SiMe_3$, 100), 183 (9), 151 (9), 113 (10), 89 (15), 73 (72), 59 (12);

MS (EI, HR) *m/z*: 211.0582; calcd. for $C_{10}H_{11}O_5$ (M^+ – $OCH_2CH_2SiMe_3$): 211.0606.

Ketal 9*b*

A procedure like the one described above, with phenylacetylene instead of methylpropiolate and involving elution of a radial chromatography plate with 2% EtOAc in hexane, afforded **9***b* as a colourless oil. R_f 0.53 (10% EtOAc in hexane); IR (cm^{-1}): 3010 – 2835, 2104 (C≡C), 986; ^1H NMR (δ): 0.02 (s, 9H), 0.90–1.10 (m, 2H), 3.39 (s, 3H), 3.80–3.95 (m, 2H), 6.30 (d, J = 16 Hz, 1H), 7.04 (d, J = 16 Hz, 1H), 7.30–7.65 (m, 10H); ^{13}C NMR (δ): −1.60, 17.48, 54.43, 60.73, 85.77, 97.54, 120.97, 127.85, 128.15, 128.24, 128.55, 128.63, 128.74, 129.03, 131.88, 132.92, one expected signal not seen; MS (EI) *m/z*: 349 (M^+ – CH_3, 15), 247 (M^+ – $OCH_2CH_2SiMe_3$, 100), 215 (12), 187 (16), 160 (21), 73 (72); MS (HR) *m/z*: 247.1131; calcd. for $C_{18}H_{15}O$ (M^+ – $OCH_2CH_2SiMe_3$): 247.1123.

Thermolysis of 2 in presence of *N*-phenylmaleimide

A solution of **2** (0.300 g, 1.22 mmol) and *N*-phenylmaleimide (0.234 g, 1.35 mmol) in dry benzene (5 mL) was heated at 110°C in a sealed tube for 24 h. Removal of the solvent and chromatography of the residue (Chromatotron, 1 mm plate, 5% EtOAc in hexane) gave **13** (0.28 g, 69%) as a white solid, mp 127–128°C, from EtOAc–hexane. R_f 0.28 (15% EtOAc in hexane); IR (cm^{-1}): 2955–2840, 1717 (C=O), 1688 (C=O); ^1H NMR (δ): 0.02 (s, 9H), 0.32–0.51 (m, 2H), 2.08 (t, J = 8.5 Hz, 2H), 2.78 (d, J = 18.4 Hz, 1H), 3.32 (d, J = 18.4 Hz, 1H) 3.81 (s, 3H), 7.20–7.55 (m, 5H); ^{13}C NMR (gated, 75 MHz) δ: −1.97 (q, ^1J = 119 Hz, $(CH_3)_3Si$), 10.54 (t, ^1J = 118 Hz, $SiCH_2$), 28.91 (t, ^1J = 132 Hz, CH_2), 37.40 (t, ^1J = 135 Hz, CH_2), 53.38 (q, ^1J = 148 Hz, OCH_3), 56.52 (s, quat), 126.37 (m), 128.82 (m), 131.73 (m), 129.17 (m), 170.09 (t, ^2J = −6.5 Hz ($CH_2\underline{C}O$), 174.15 (s), 174.61 (s); MS (EI) *m/z*: 318 (M^+ – CH_3, 100), 305 (M^+ – CO, 65), 290 (90), 274 (M^+ – CO_2Me, 26), 246 (35), 233 (M^+ – $Me_3SiCHCH_2$, 24), 201 (26), 171 (12), 119 (15), 89 (31), 84 (40), 73 (77); MS (EI, HR) *m/z*: 318.1152; calcd. for $C_{15}H_{20}NO_4Si$ (M^+ – CH_3): 318.1161; MS (CI, NH_3) *m/z*: 351 ($M^+ + NH_4$, 100), 334 (M^+ + H, 100), 318 (M^+ – CH_3, 43), 305 (26), 290 (18)).

Hydantoin 15

A solution of **2** (0.410 g, 1.67 mmol) and phenyl isocyanate (0.460 g, 3.84 mmol) in dry benzene (6 mL) was kept at 110°C for 24 h. Removal of the solvent and chromatography on SiO_2 (Chromatotron, 1 mm plate, 2% EtOAc in hexane) afforded **18** (0.51 g, 77%) as a colourless oil. R_f 0.43 (15% EtOAc in hexane); IR (cm^{-1}): 3030–2840, 1825 (C=O), 1750 (C=O); ^1H NMR (δ): 0.03 (s, 9H), 0.91–0.96 (m, 2H), 3.56 (s, 3H), 3.85–3.90 (m, 2H), 7.20–7.64 (m, 10H); ^{13}C NMR (δ): −1.51, 17.91, 52.32, 62.98, 103.66, 125.20, 126.14, 127.08, 128.50, 128.98, 129.12, 130.66, 133.38, 152.28, 165.66; MS (EI) *m/z*: 339 (15), 281 (M^+ – $OCH_2CH_2SiMe_3$ – OCH_2, 100), 223 (33), 192 (34), 73 (72); MS (HR) *m/z*: 281.0931; calcd. for $C_{16}H_{13}N_2O_3$ (M^+ – $OCH_2CH_2SiMe_3$): 281.0926.

Orthoformate 19

A solution of **2** (0.20 g, 0.81 mmol) and phenol (0.096 g, 1.0 mmol) in dry benzene (10 mL) was kept at 110°C for 24 h. Extraction of excess phenol with cold dilute base, drying of the benzene layer, and removal of the benzene left 0.12 g, ca. 58%, of crude **19** as an oil. R_f 0.50 (10% EtOAc in hexane); ^1H NMR (δ): 0.03 (s, 9H), 0.95 – 0.99 (m, 2H), 3.43 (s, 3H), 3.73 – 3.80 (m, 2H), 5.12 (s, 1H), 7.18–7.32 (m, 5H).

Orthoformate 20

A solution of **2** (0.25 g, 1.02 mmol) and *tert*-butyl alcohol (0.12 g, 1.62 mmol) in dry benzene (10 mL) was kept at 110°C for 20 h. Concentration of the solution in vacuo afforded 0.17 g (83%) of **20** as a colourless oil. R_f 0.62 (10% EtOAc in hexane); IR (cm^{-1}): 2972–2836, 1250, 1093, 1055, 860; ^1H NMR (δ): 0.03 (s, 9H), 0.85–0.95 (m, 2H), 1.23 (s, 9H), 3.23 (s, 3H), 3.52–3.57 (m, 2H), 5.24 (s, 1H); ^{13}C NMR (δ): −1.50, 17.92, 28.67, 49.73, 60.47, 109.12, one expected signal not seen.

Acknowledgements

Financial support for this work was drawn from a Natural Sciences and Engineering Research Council of Canada (NSERC) Operating Grant. The authors gratefully acknowledge the assistance of Drs. Donald Hughes and Richard Smith and of Mssrs. Brian Sayer and Fajar Ramelan with some aspects of the NMR spectroscopy and the mass spectrometry.

References

1. M. El-Saidi, K. Kassam, D. L. Pole, T. Tadey, and J. Warkentin. J. Am. Chem. Soc. **114**, 8751 (1992).
2. K. Kassam, D.L. Pole, M. El-Saidi, and J. Warkentin. J. Am. Chem. Soc. **116**, 1161 (1994).
3. A. de Meijere, S.I. Kozhushkov, D.S. Yufit, R. Boese, T. Haumann, D.L. Pole, P.K. Sharma, and J. Warkentin. Liebigs Ann. 601 (1996).
4. (*a*) K. Kassam and J. Warkentin. J. Org. Chem. **59**, 5071 (1994); (*b*) R.A. Moss, W. Liu, and C.-S. Ge. J. Phys. Org. Chem. **6**, 376 (1993); (*c*) G. Homberger, W. Kirmse, and R. Lelgemann. Chem. Ber. **124**, 1867 (1991); (*d*) X.-M. Du, H. Fan, J.L. Goodman, M.A. Kesselmayer, K. Krogh-Jespersen, J.A. LaVilla, R.A. Moss, S. Shen, and R.S. Sheridan. J. Am. Chem. Soc. **112**, 1920 (1990); (*e*) R.A. Moss, M. Wlostowski, S. Shen, K. Krogh-Jespersen, and A. Matro. J. Am. Chem. Soc. **110**, 4443 (1988); (*f*) R.A. Moss, S. Shen, and M. Wlostowski. Tetrahedron Lett. **29**, 6417 (1988); (*g*) R.A. Moss, M. Wlostowski, J. Terpinski, G. Kmiecik-Lawrynowicz, and K. Krogh-Jespersen. J. Am. Chem. Soc. **109**, 3811 (1987); (*h*) R.A. Moss, C.M. Young, L.A. Perez, and K. Krogh-Jespersen. J. Am. Chem. Soc. **103**, 2413 (1981); (*i*) R.A. Moss and J.K. Husselton. J. Chem. Soc. Chem. Commun. 950 (1976); (*j*) R.W. Hoffmann and M. Reiffen. Chem. Ber. **109**, 2565 (1976).
5. J.B. Lambert. Tetrahedron, **46**, 2677 (1990).
6. (*a*) R.W. Hoffmann, K. Steinbach, and W. Lilienblum. Chem. Ber. **109**, 1759 (1976); (*b*) R.W. Hoffmann, W. Lilienblum, and B. Dittrich. Chem. Ber. **107**, 3395 (1974); (*c*) R.W. Hoffmann, K. Steinbach, and B. Dittrich. Chem. Ber. **106**, 2174 (1973).
7. D.L. Boger and C.E. Brotherton-Pleiss. Advances in cycloaddition. Vol. 2. *Edited by* D.P. Curran. JAI Press, Greenwich, Conn. 1990. p. 147.
8. D.L. Boger and C.E. Brotherton. J. Am. Chem. Soc. **108**, 6695 (1986).
9. D.L. Pole and J. Warkentin. Liebigs Ann. 1907 (1995).
10. (*a*) R. Scarpati, D. Sica, and C. Santacroce. Tetrahedron, **20**, 2735 (1964); (*b*) W.T. Brady and R.D. Watts. J. Org. Chem. **46**, 4047 (1981).

11. (*a*) L. Tenud, S. Farooq, J. Seibl, and A. Eschenmoser. Helv. Chem. Acta, **53**, 2059 (1970); (*b*) J.F. King and M.J. McGarrity. J. Chem. Soc. Chem. Commun. 1140 (1979); (*c*) E. Schaumann, T. Marr, H. Nimmesgern, and S. Sieveking. Chem. Ber. **120**, 335 (1987); (*d*) E. Schaumann, J. Dietz, E. Kausch, and G. C. Schmerse. Chem. Ber. **120**, 339 (1987); (*e*) J.E. Baldwin. J. Chem. Soc. Chem. Commun. 734 (1976).
12. T.L. Gilchrist and R.C. Storr. Organic reactions and orbital symmetry. Cambridge University Press, London. 1972.
13. (*a*) R.W. Hoffmann. Angew. Chem. Int. Ed. Engl. **18**, 563 (1979); (*b*) T. Nakai and K. Mikami. Chem. Rev. **86**, 885 (1986); (*c*) Y.-D. Wu and K.N. Houk. J. Org. Chem. **55**, 1421 (1990).
14. (*a*) M.A. Cook, C. Eaborn, and D.R.M. Walton. J. Organomet. Chem. **24**, 301 (1970); (*b*) A.W.P. Jarvie, A. Holt, and J. Thompson. J. Chem. Soc. (B), 746 (1970).

New investigation of the reaction of 2-amino-2-oxazolines with isocyanates and isothiocyanates. Evidence of a transposition during the second step

Jean-Jacques Bosc, Christian Jarry, Jamal Ouhabi, Michel Laguerre, and Alain Carpy

Abstract: The reaction of some 2-amino-2-oxazolines with isocyanates and arylisothiocyanates yields 3-monosubstituted or 2,3-disubstituted 2-iminooxazolidines depending on the experimental conditions and on the nature of the electrophile reactants. The structures of a mono- and a disubstituted derivative were established by X-ray analysis. The chemical behaviour of the compounds was investigated by molecular and quantum mechanics calculations. An intramolecular transposition during the second step of the reaction was found.

Key words: 2-amino-2-oxazolines, iso(thio)cyanates, transposition, X-ray structure, MOPAC calculations.

Résumé : Par réaction de diverses 2-amino-2-oxazolines avec des isocyanates et des arylisothiocyanates ont été préparées des 2-iminooxazolidines monosubstituées en position 2 et disubstituées en positions 2,3. L'accès à ces composés dépend des conditions expérimentales et de la nature des réactifs électrophiles. Les attributions structurales reposent en particulier sur l'établissement de deux structures cristallines par radiocristallographie. Une étude conformationnelle est rapportée, elle utilise les résultats des calculs énergétiques réalisés en particulier par mécanique quantique. Une transposition intramoléculaire a été mise en évidence lors de la réaction du propylisocyanate sur une 3-phénylcarbamoyl-2-iminooxazolidine.

Mots clés : 2-amino-2-oxazolines, iso(thio)cyanates, transposition, réarrangement, structure cristallines, calculs OM.

Introduction

Alkylation and acylation reactions of ambident nucleophiles with similar sites often result in problems of uncertain regiochemistry. Investigating in detail the reaction of 2-amino-2-thiazoline with phenylisothiocyanate and phenylisocyanate Rasmussen et al. concluded that the addition at low temperature occurred on the endocyclic nitrogen (1). The elucidation of the structure was based on the X-ray structural analysis of one reaction product (2). The resulting 2-imino-*N*-phenylthiazolidinecarboxamide was significantly more stable than the 2-imino-*N*-phenylthiazolidinecarbothioxamide, but nevertheless both compounds underwent an intramolecular N–N′ rearrangement to form thermodynamically stable ureas. The reaction of 2-arylamino-2-thiazolines with phenylisothiocyanate and phenylisocyanate and the structural assignment of the condensation products were recently reported (3).

The reaction of 2-amino-2-oxazolines with iso(thio)cyanates has been less studied. It was first reported by Fromm et al. (4), later by Yamamoto and Reiko (5), and was used to prepare anticonvulsant ureas (6) and anhydronucleosides (7). All results concerned the introduction of a carbamoyl or a thiocarbamoyl substituent on the heterocyclic ring. The structural results agreed with the regioselectivity observed with 2-amino-2-thiazolines: the initial reaction occurred exclusively at the endocyclic sp^2 nitrogen to produce the corresponding 3-carbamoyl- or, 3-thiocarbamoyl-2-iminooxazolidines and these compounds rearranged, on heating, to the corresponding urea isomers.

In the course of our work on 2-amino-2-oxazolines we have investigated the different reactivity of the two nitrogen atoms as nucleophilic centers (8–10). In the present work we report the synthesis of 2,3-diphenylcarbamoyl- and 2,3-dipropylcarbamoyl-2-iminooxazolidines in two ways: (*i*) a one-step reaction of 5-substituted-2-amino-2-oxazolines with two equivalents of isocyanates; (*ii*) a two-step reaction involving the isolation of the mono-substituted intermediates.

Few 2,3-disubstituted-2-iminooxazolidines have been described (11,12). They were synthesized in a one-pot reaction and the corresponding 3-monosubstituted-2-iminooxazolidines were not isolated. We took advantage of our ability to isolate these 3-monosubstituted-2-iminooxazolidines to introduce a different substituent on the *exo* nitrogen atom, which

Received February 8, 1996.

J.-J. Bosc and C. Jarry.[1] Laboratoire de chimie physique, Université de Bordeaux II, 146 rue Léo Saignat, 33076 Bordeaux Cedex, France.
J. Ouhabi,[2] **M. Laguerre,**[3] **and A. Carpy.** Laboratoire de chimie analytique, Université de Bordeaux II, 3 place de la Victoire, 33076 Bordeaux Cedex, France.

[1] Author to whom correspondence may be addressed. Telephone: (33) 57 57 11 76. Fax: (33) 56 24 09 41.
[2] Present address: Département de chimie, Faculté des sciences et techniques, Gueliz, Marrakech, Morocco.
[3] Present address: Centre de recherches Paul Pascap, UPR 8641 CNRS, avenue Albert Schweitzer, 33600 Pessac, France.

Scheme 1. Reaction pathway and list of synthesized compounds.

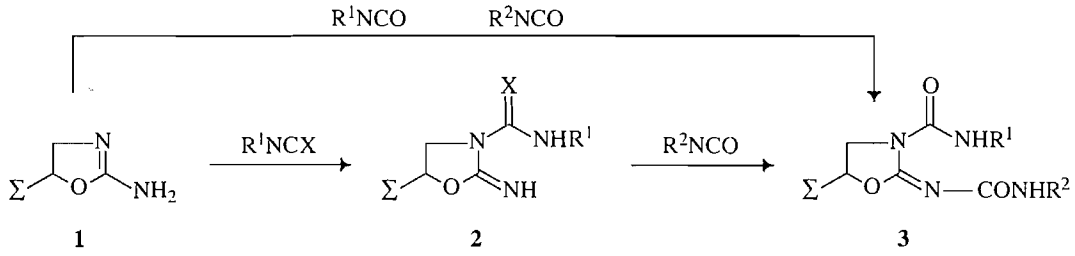

X	R^1		Σ	R^2	
	C_6H_5	2*a*	(1-Phenyl-4-piperazinyl)-CH_2	C_6H_5	3*a*
	C_6H_5	2*b*	C_6H_5-O-CH_2-	C_6H_5	3*b*
	C_6H_5	2*c*	1-Morpholinyl-CH_2	C_6H_5	3*c*
O	$pClC_6H_4$	2*d*	(1-Phenyl-4-piperazinyl)-CH_2		—
	*n*Pr	2*e*	(1-Phenyl-4-piperazinyl)-CH_2	*n*Pr	3*e*
	*n*Pr	—	(1-Phenyl-4-piperazinyl)-CH_2	C_6H_5	3*i*
	*i*Pr	2*f*	(1-Phenyl-4-piperazinyl)-CH_2		
S	C_6H_5	2*g*	(1-Phenyl-4-piperazinyl)-CH_2		
	*p*Me-C_6H_5	2*h*	(1-Phenyl-4-piperazinyl)-CH_2		

permitted us to observe a transposition occurring during the second attack. The assignment of the structures was supported by an X-ray study. The relative stability of the 3-monosubstituted-2-iminooxazolidines vs. their urea isomers was estimated using molecular and quantum mechanics.

Results and discussion

5-Substituted-2-amino-2-oxazolines **1** were allowed to react with an equimolar quantity of aryl- or (iso)propylisocyanates at 0°C in ethanol (Scheme 1). The reaction products were the 5-substituted-3-arylcarbamoyl-2-iminooxazolidines **2**(*a–d*) or the 5-substituted-3-(iso)propylcarbamoyl-2-iminooxazolidines **2**(*e*,*f*). 5-[(1-Phenyl-4-piperazinyl)methyl]-3-arylthiocarbamoyl-2-iminooxazolidines **2**(*g*, *h*) were obtained in the same way from arylisothiocyanates. We noticed that the nature of the C-5 substituent of 2-amino-2-oxazolines had no influence on the advancement of the reaction. In particular we tried to avoid the conversion of 2-iminooxazolidines **2** into ureas by an intramolecular N–N′ rearrangement. As already described, this rearrangement is essentially quantitative after heating (1, 4). We observed that the use of ethanol as a solvent, the choice of anhydrous conditions, and the rigorous control of the temperature increased the yields in compounds **2**. All compounds except **2***e* and **2***f* were insoluble in ethanol, and a rapid separation from the reaction mixture minimized the isomerization.

The structure of **2***a* was established by X-ray crystallography (Fig. 1). The exocyclic C(17)—N(19) bond is 1.251(5) Å. An electron delocalization occurs on bonds N(16)—C(17) = 1.391(5) Å and C(17)—O(18) = 1.344(5) Å (C(15)—N(16) = 1.449(5) Å and C(14)—O(18) = 1.344(5) Å). The five-membered heterocycle is almost planar, C(14) and C(15) being, respectively, a distance of −0.083(4) and 0.013(4) Å from the mean plane defined by N(16), C(17), O(18), and N(19). The *N*-phenylcarbamoyl moiety is coplanar with the heterocycle (C(15)-N(16)-C(20)-O(21) = 1.7(3)°, N(16)-C(20)-N(22)-C(23) = 176.0(3)°, C(20)-N(22)-C(23)-C(24) = 2.0(4)°).

Fig. 1. Stereoscopic view of molecule **2***a* and numbering of atoms.

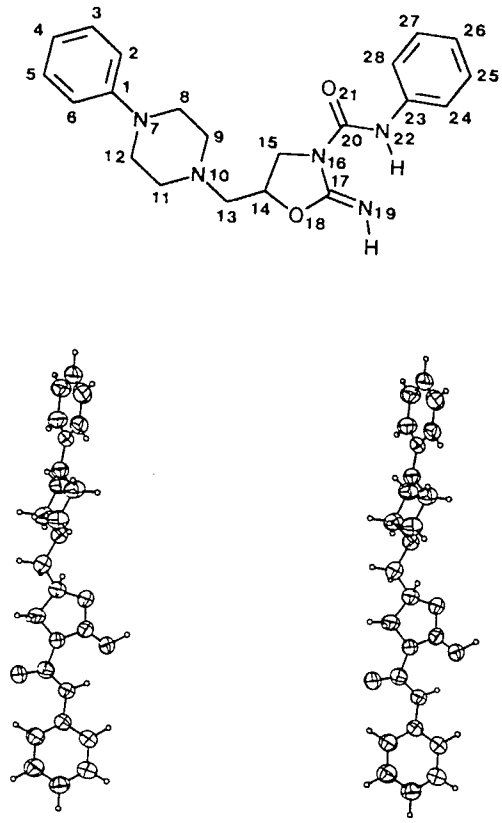

The oxygen atom of the amide group O(21) points away from N(19). The amide group is *trans*. There are two short dis-

Scheme 2. 2/3-Monosubstituted phenylcarbamoyl compounds, H-bonds indicated by dotted lines.

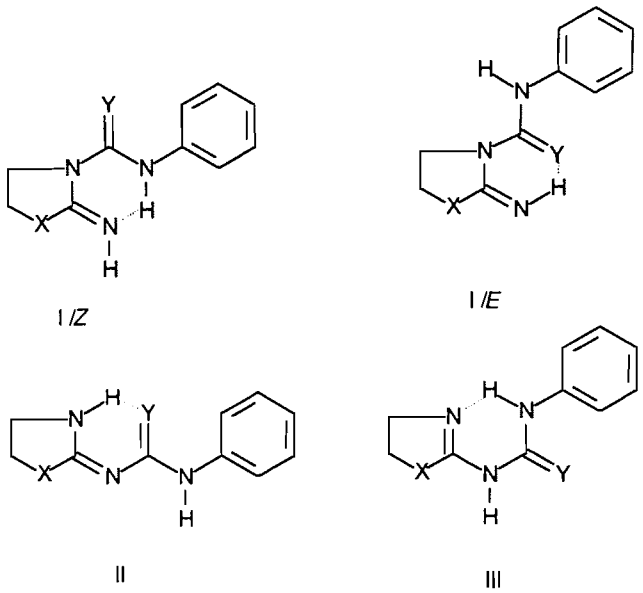

tances N(19)...N(22) = 2.700(4) Å and N(19)...H(122) = 1.900(4) Å with an angle N(19)...H(122)-N(22) = 138(3)° characteristic of an intramolecular H-bond. Consequently there is a pseudo six-membered cycle N(19), C(17), N(16), C(20), N(22), H(122).

The piperazine ring is *chair* with N(7) and N(10) −0.619(3) and 0.685(3) Å away from the mean plane defined by C(8), C(9), C(11), and C(12). The orientation of the phenyl ring vs. the piperazine ring is defined by the torsion angle C(2)-C(1)-N(7)-C(8) = 27.8(3)°. The orientation of the oxazolidine ring vs. the piperazine ring is defined by the two torsion angles C(9)-N(10)-C(13)-C(14) = 173.7(3)° and N(10)-C(13)-C(14)-C(15) = 172.5(3)°.

The C(1)—N(7) bond is 1.406(5) Å. The bond angles around N(7) are 118.6(3)°, 118.6(3)°, and 111.4(3)°. N(10) is hybridized sp^3 with its lone pair *axial*.

To gain information about the relative stability of the 3-monosubstituted-2-iminooxazolidines vs. their urea isomers we performed energy calculations using molecular and quantum mechanics .

The compounds were built and roughly minimized using the MM2* force field implemented in MacroModel and, as the parameters are of poor quality for conjugated systems, the compounds were fully minimized using MOPAC/AM1.

Compounds **I** (X = O) can exist as *Z* or *E* isomers, but only the *Z* isomers were found by X-ray crystallography (Scheme 2). Accordingly, at least for oxazolidines, the *E* isomers appeared less stable than their *Z* counterparts (Table 1). On the other hand, concerning the intramolecular N–N′ rearrangement of **I** into the corresponding ureas **II** / **III**, it appears in all cases that form **I** is the least stable isomer and, except when X = S and Y = O, that form **III** is the most stable one. When X, Y = O, the two tautomeric forms have almost the same energy. This could explain the equilibrium between **II** and **III** evidenced by the X-ray structure.

Table 1. Energy (kJ mol^{-1}) after minimization with MOPAC/MNDO.

Series	X = S Y = S	X = S Y = O	X = O Y = S	X = O Y = O
I / *Z*	375.28	130.50	216.44	−26.29
I / *E*	379.54	125.52	241.85	−9.41
II	345.77	93.46	214.77	−38.58
III	340.08	101.62	199.30	−39.29

When Y = S, the S...H—N_{endo} hydrogen bond in form **II** is avoided from the final minimized structure.

The second part of the work concerns the behaviour of the 5-substituted-3-phenylcarbamoyl- **2**(*a–c*), the 5-[(1-phenyl-4-piperazinyl)methyl]-3-propyl- **2***e*, and the 5-[(1-phenyl-4-piperazinyl)methyl]-3-phenylthiocarbamoyl-2-iminooxazolidine **2***g* towards isocyanates and phenylisothiocyanate (Scheme 1).

The reaction of **2**(*a–c*) with phenylisocyanate and the reaction of **2***e* with propylisocyanate led to the 2,3-diphenylcarbamoyl-2-iminooxazolidines **3**(*a–c*) and to the 2,3-dipropylcarbamoyl-2-iminooxazolidine **3***e*.

The structure of **3***a* was established by X-ray crystallography (Fig. 2). The exocyclic C(17)—N(19) bond is 1,272(3) Å. As in **2***a*, an electron delocalization occurs on bonds N(16)—C(17) = 1.368(3) Å and C(17)—O(18) = 1.333(3) Å (C(15)—N(16) = 1.463(4) Å and C(14)—O(18) = 1.476(4) Å). Contrary to **2***a*, the five-membered heterocycle is not perfectly planar, C(14) and C(15) being, respectively, a distance of −0.256(4) and 0.100(4) Å from the mean plane defined by N(16), C(17), O(18), and N(19). The phenylcarbamoyl moiety at N(16) is in the same plane as these four atoms (C(15)-N(16)-C(29)-O(30) = 0(1)°, N(16)-C(29)-N(31)-C(23) = −172(1)°, and C(29)-N(31)-C(32)-C(33) = −170(1)°). The terminal phenyl ring makes an angle of 161(1)° with this plane. Consequently the electron delocalization observed in the oxazolidine ring expands in the lateral chain up to nitrogen N(31).

The oxygen atom of the amide group O(30) points opposite to N(19). The amide group including C(29) and N(31) is *trans*. There are two short distances N(19)...N(31) = 2.712(4) Å and N(19)...H(131) = 1.91(4) Å with an angle N(19)...H(131)-N(31) = 137(4)° characteristic of an intramolecular H-bond. Consequently, as in **2***a*, there is a pseudo six-membered cycle N(19), C(17), N(16), C(29), N(31), H(131).

The configuration at the imine bond is *Z*. The orientation of the second phenylcarbamoyl moiety at N(19) is defined by the four torsion angles O(18)-C(17)-N(19)-C(20) = −20(1)°, C(17)-N(19)-C(20)-O(21) = −58(1)°, N(19)-C(20)-N(22)-C(23) = −172(1)°, and C(20)-N(22)-C(23)-C(24) = −40(1)°. The mean-plane of atoms N(19), C(20), O(21), and N(22) makes an angle of 122(1)° with that of the heterocycle and an angle of 34(1)° with the terminal phenyl ring.

The piperazine ring is *chair* with N(7) and N(10) −0.543(5) and 0.695(5) Å away from the mean plane defined by C(8), C(9), C(11), and C(12). The orientation of the phenyl ring vs. the piperazine ring is defined by the torsion angle C(2)-C(1)-N(7)-C(8) = −2(1)°. The orientation of the oxazolidine ring

Fig. 2. Stereoscopic view of molecule **3***a* and numbering of atoms.

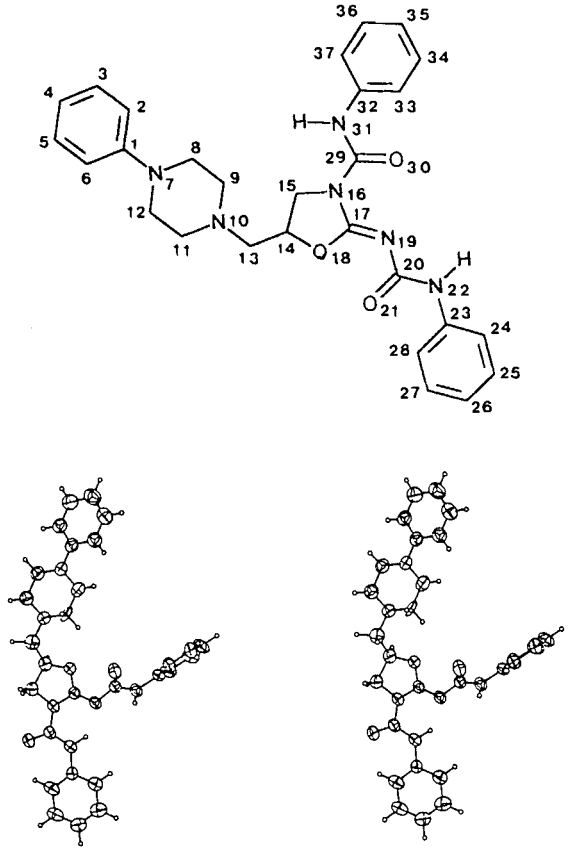

vs. the piperazine ring is defined by the two torsion angles C(9)-N(10)-C(13)-C(14) = 78(1)° and N(10)-C(13)-C(14)-C(15) = 172(1)°. The C(1)—N(7) bond is 1.403(4) Å. The bond angles around N(7) are 115.4(3), 118.3(3), and 113.1(3)°. N(10) is in an intermediate hybridization state between sp^2 and sp^3 with its lone pair *axial*.

Both reactions of **2***a* with propylisocyanate and of **2***e* with phenylisocyanate led to the same 2,3-disubstituted compound **3***i* and showed a transposition during the second attack in one of the reactions of **2**. As suitable crystals could not be obtained, the structural assessment of **3***i* was based on the ^{1}H NMR spectra of the reaction products. For the monosubstituted compounds the ^{1}H δ of the NH-CO groups were the following (Schemes 2 and 3):

formula **I** and a phenyl substituent, δ = 11.6 ± 0.1 ppm (singlet)

formula **I** and a propyl substituent, δ = 9.1 ppm (singlet)

formula **II** and an aryl substituent, δ = 9.3 ppm (triplet, ^3J = 5.4 Hz) (9).

For the symmetrically disubstituted compounds, the ^{1}H δ were as follows:

phenyl substituents, δ NH endo = 10.7 ppm and δ NH *exo* = 7.5 ± 0.1 ppm (all singlets)

Scheme 3. 2,3-Disubstituted-2-iminooxazolidines, H-bonds indicated by dotted lines.

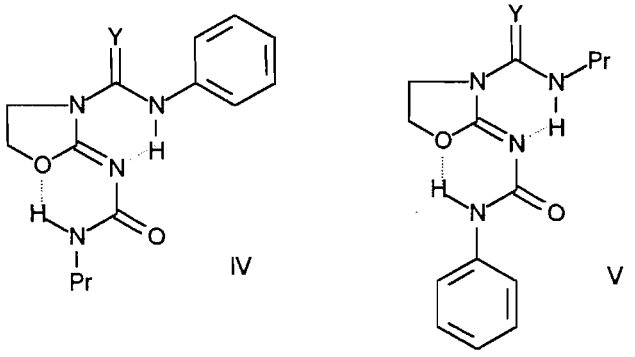

Table 2. Energy (kJ mol^{-1}) after minimization with MOPAC/MNDO and MOPAC/AM1.

Structure	MOPAC/MNDO	MOPAC/AM1
IV	−307.15	−176.60
V	−318.93	−180.00

propyl substituents, δ NH *endo* = 8.5 ppm and δ NH *exo* = 5.1 ppm (all triplets, ^3J = 5.5 and 6.0 Hz).

For the unsymmetrically disubstituted compound **3***i*, we found a triplet at δ = 8.6 ppm (^3J = 5.4 Hz) and an NH singlet at δ = 7.1 ppm, which could be explained by the alkyl substituent on the *endo* nitrogen and by the aryl substituent on the *exo* nitrogen (formula **V**).

To verify this assumption, energy calculations were performed using quantum mechanics (Table 2). Even if molecular mechanics is not adapted to highly conjugated heteroatomic systems, calculations using the MM2* force field (with and without the GB/SA continuum solvation model (13) in chloroform) were performed and showed that form **V** is always more stable than form **IV** (Δ*E* = 30 kJ/mol with chloroform and 10.7 kJ/mol without solvent).

In the particular case of **2***g*, when the second reactant was the phenyl- or the propylisocyanate, only **2***a* or **2***e* was obtained. As an oxidation of the thiocarbonyl function was suspected, we repeated the reaction of **2***g* with 4-chlorophenylisocyanate. Thus **2***d* was isolated and we suppose that, in this case, a transposition followed by an elimination took place. In the case of **2***g*, when the second reactant was phenylisothiocyanate, we isolated only the starting material. We did not know whether a transposition/elimination had occurred, or no reaction at all. However, we proved that the latter (no reaction) had occurred by mixing **2***g* with 4-methylphenylisothiocyanate and isolating the starting oxazolidine **2***g* unchanged.

Conclusion

In this work the reactions of some 2-amino-2-oxazolines with isocyanates and arylisothiocyanate, giving, in a first step, 3-aryl/alkylcarbamoyl- and 3-arylthiocarbamoyl-2-iminooxazo-

lidines, were studied. As 2-iminooxazolidines are more stable than 2-iminothiazolidines (1), the experimental conditions were selected to prevent the classical N–N′ intramolecular rearrangement giving the urea isomers (14). When the reaction was conducted with phenyl/propylisocyanate, two phenyl/propylcarbamoyl substituents were successively introduced, the first on the endocyclic sp^2 nitrogen, the second on the exocyclic nitrogen, giving 2,3-diphenyl/dipropylcarbamoyl-2-iminooxazolidines. Using X-ray crystallography, we confirmed the structures of a 3-phenylcarbamoyl- and of a 2,3-diphenylcarbamoyl-2-iminooxazolidine, and we found that they exist as *Z* isomers. An intramolecular transposition was observed during the reaction of propylisocyanate with the 3-phenylcarbamoyl-2-iminooxazolidine. With phenylisothiocyanate, the first substitution on the *endo* nitrogen occurred, but it was impossible to substitute the *exo* nitrogen atom. Starting from the 3-phenylthiocarbamoyl-2-iminooxazolidine, the reaction with a second phenyl/propylisocyanate resulted in the replacement of the phenylthiocarbamoyl group by a phenyl/propylcarbamoyl one.

Experimental

To prevent secondary hydrolysis reactions all experiments were conducted in an inert, controlled-atmosphere, chamber. Microanalyses were carried out at the Service central d'analyse CNRS, Vernaison, France. Melting points were determined with a Kofler hot stage apparatus and were uncorrected. The IR spectra were obtained with a Bruker IFS 25. NMR spectra were recorded with a Bruker AC-200 and a Brucker AMX-500 spectrometer. All signals were expressed in ppm with respect to TMS. ^{1}H assignments for the piperazine nucleus were obtained by HMBC experiment for **2***a* via the ^3J ^{13}C–^{1}H coupling between N-CH_2 and the piperazine protons.

Crystal structure determinations

Colourless single crystals of **2***a* and **3***a* were obtained by slow evaporation from diisopropyl ether or ethanol solution, respectively. The crystallographic data are the following:

2*a*: $C_{21}H_{25}N_5O_2$, M_r = 379.5, triclinic symmetry; space group P_1, with a = 8.996(3), b = 10.156(3), c = 10.672(3) Å, α = 99.68(2)°, β = 95.50(2)°, γ = 94.75(3)°, V = 951.7(3) Å^3, Z = 2, D_x = 1.32 g cm^{-3}, CuKα, λ = 1.54178 Å, μ = 7.1 cm^{-1}, T = 300 K. Dimensions of the crystal 0.25 × 0.25 × 0.10 mm.

3*a*: $C_{28}H_{30}N_6O_3$, M_r = 498.6, monoclinic symmetry; space group $P2_1/n$, with a = 14.709(7), b = 9.618(2), c = 18.187(8) Å, β = 94.57(4)°, V = 2565.2(2) Å^3, Z = 4, D_x = 1.29 g cm^{-3}, CuKα, λ = 1.54178 Å, μ = 7.1 cm^{-1}, T = 300 K. Dimensions of the crystal 0.50 × 0.37 × 0.20 mm.

In both cases, the unit cell dimensions were determined using the least-squares fit from 25 reflections (θ < 25°). Intensities were collected with an Enraf–Nonius CAD-4 diffractometer using CuKα radiation and a graphite monochromator up to θ = 65° (scan type ω/θ, scan width 2° and 1.6°). With both crystals, no intensity variation of two standard reflections monitored every 90 min was observed. The intensities were corrected for Lorentz and polarization effects but not for absorption. Of 3252 (**2***a*) and 4367 (**3***a*) measured reflections, 1463 (**2***a*) and 2574 (**3***a*) were considered as observed (3σ(*I*) criterion) and included in the refinement. Both structures were determined by direct methods using MULTAN 80 (15). The scattering factors were taken from ref. 16. C, N, and O atoms were refined anisotropically. H atoms were placed in theoretical positions or were located from difference Fourier maps and were refined isotropically. The unweighted agreement factors were R = 0.042 (**2***a*; 853 refined parameters) and R = 0.040 (**3***a*; 454 refined parameters); R_w = 0.053 (**2***a*) and 0.061 (**3***a*). The convergence largest Δ/σ were <1 (on Bs), the highest peaks in final difference maps were 0.3 (**2***a*) and 0.4 (**3***a*) e Å^{-3}. The atomic coordinates have been deposited with the Cambridge Crystallographic Data Centre, University Chemical Laboratory, 12 Union Road, Cambridge CB2 IEZ, U.K.

Theoretical calculations

Calculations were performed on an SGI Indigo R4000 Elan workstation running MacroModel version 4.5 (13) and Biosym softwares version 3.5.[4] Molecules were built *ex nihilo* (without the oxazolidine C-5 substituent) using MacroModel and minimized with a standard method: 1000 cycles, using the TNCG method (Truncated Newton Conjugate Gradient) to a 0.005 kJ Å^{-1} mol^{-1} RMS gradient. Despite some low-quality parameters the MM2* (17) force field was preferred to MM3* (18) which lacks several parameters.

MacroModel files were converted into a CSSR format and exported into Insight[4] where MOPAC/AM1 calculations were made. Energy calculations were performed with minimization of the full *Z*-matrix (default parameters: SCF iterations = 200, energy convergence = 0.00001, gradient norm minimization = NLLSQ, and minimization method = BFGS) (Broyden–Fletcher–Goldfarb–Shanno method).

General procedure for the preparation of 5-substituted-3-phenylcarbamoyl- or 5-substituted-3-phenylthiocarbamoyl-2-iminooxazolidines

To a cold (0°C) stirring solution of 0.1 mol of 2-amino-2-oxazoline in 200 mL of ethanol under argon was slowly added 0.1 mol of isocyanate or phenylisothiocyanate in 20 mL of ethanol. The reaction mixture was stirred for 1 h at room temperature. The precipitate was rapidly collected, washed with anhydrous ether, and recrystallized.

5-[(1-Phenyl-4-piperazinyl)methyl]-3-phenylcarbamoyl-2-iminooxazolidine (**2***a*): mp 146°C (diisopropyl ether); yield: 51%; IR (KBr) cm^{-1}: 3340 (NH), 1700 (C=O), 1680 (C=N), ^{1}H NMR (chloroform-*d*) δ ppm: 11.66 (s, 1H, N*H*), 7.19 (m, 10H, Ar-*H*), 6.01 (s, 1H, N*H*), 4.7 (m, 1H, 5-*H*), 4.26 and 3.82 (2dd, 2H, J = 10.4, 8.2, 7.2 Hz, 4-*H*), 2.97 (m, 10H, NCH_2); ^{13}C NMR (chloroform-*d*) δ ppm: 154.88 (CO), 151.05 (C-2), 150.05, 138.26, 129.09, 128.93, 123.16, 118.84, 115.44 (Ar), 73.16 (C-5), 60.16 (C-5-CH_2), 53.20, 48.18 (CH_2 pip), 46.62 (C-4). Anal. calcd. for $C_{21}H_{25}N_5O_2$: C 66.49, H 6.60, N 18.47; found: C 66.31, H 6.72, N18.49.

5-(1-Phenoxymethyl)-3-phenylcarbamoyl-2-iminooxazolidine (**2***b*): mp 124°C (diisopropyl ether); yield: 75%; IR (KBr) cm^{-1}: 3350 (NH), 1700 (C=O), 1680 (C=N); ^{1}H NMR (chloroform-*d*) δ ppm: 11.54 (s, 1H, N*H*), 7.21 (m, 10H, Ar-*H*), 6.04 (s, 1H, N*H*), 4.89 (m, 1H, 5-*H*), 4.15 (m, 4H, OCH_2

[4] Insight developed and distributed by Biosym Technologies, San Diego, Calif.

and 4-*H*). Anal. calcd. for $C_{17}H_{17}N_3O_3$: C 65.60, H 5.47, N 13.50; found: C 65.43, H 5.51, N 13.38.

5-(1-Morpholinomethyl)-3-phenylcarbamoyl-2-iminooxazolidine (**2***c*): mp 130°C (ethanol); yield: 27%; IR (KBr) cm^{-1}: 3285 (NH), 1700 (C=O), 1680 (C=N); ^1H NMR (chloroform-*d*) δ ppm: 11.56 (s, 1H, N*H*), 7.27 (m, 5H, Ar-*H*), 5.98 (s, 1H, N*H*), 4.66 (m, 1H, 5-*H*), 4.15 and 3.77 (2 dd, 2H, *J* = 10.4, 8.2, 7.4 Hz, 4-*H*), 3.69 (t, 4H, *J* = 4.7 Hz, OCH_2), 2.60 (m, 6H, NCH_2). Anal. calcd. for $C_{15}H_{20}N_4O_3$: C 59.21, H 6.58, N 18.42; found; C 59.12, H 6.62, N 18.30.

5-[(1-Phenyl-4-piperazinyl)methyl]-3-[(4-chloro)phenylcarbamoyl]-2-iminooxazolidine (**2***d*): mp 117°C (diisopropyl ether); yield: 95%; IR (KBr) cm^{-1}: 3320 (NH), 1685 (C=N); ^1H NMR (chloroform-*d*) δ ppm: 11.65 (s, 1H, N*H*), 7.24 (m, 9H, Ar-*H*), 6.01 (s, 1H, N*H*), 4.74 (m, 1H, 5-*H*), 4.65 and 4.15 (2 dd, 2H, *J* = 10.4, 8.2, 6.7 Hz, 4-*H*), 3.22 and 2.71 (2 m, 4H each, NCH_2). Anal. calcd. for $C_{21}H_{24}N_5O_2Cl$: C 60.94, H 5.80, N 16.93, Cl 8.59; found: C 60.82, H 5.87, N 16.71, Cl 8.60.

5-[(1-Phenyl-4-piperazinyl)methyl]-3-propylcarbamoyl-2-iminooxazolidine (**2***e*): To a cold (0°C) stirring solution of 5.2 g (0.02 mol) of 5-[(1-phenyl-4-piperazinyl)methyl]-2-amino-2-oxazoline in 100 mL of anhydrous ethanol under argon was added slowly 1.7 g (0.02 mol) of propylisocyanate. The reaction mixture was stirred for 2 h at room temperature. No precipitate formed during the reaction. After evaporation to dryness the solid was washed with ether and recrystallized from diisopropyl ether; mp 119°C; yield: 86%; IR (KBr) cm^{-1}: 3340 (NH), 1690 (C=O), 1685 (C=N), ^1H NMR (chloroform-*d*) δ ppm: 9.14 (t, 1H, *J* = 5.4 Hz, N*H*), 7.19 (m, 5H, Ar-*H*), 5.77 (s, 1H, N*H*), 4.65 (m, 1H, 5-*H*), 4.12 and 3.70 (2 dd, 2H, *J* = 10.4, 8.2, 7.8 Hz, 4-*H*), 3.21 and 2.68 (2 m, 12H, NCH_2), 1.52 (m, 2H, CH_2), 0.93 (t, 3H, *J* = 7.4 Hz, CH_3); ^{13}C NMR (chloroform-*d*) δ ppm: 156.19 (CO), 153.03 (C-2), 151.15, 129.16, 119.94, 116.18 (Ar), 73.52 (C-5), 61.15 (C-5-CH_2), 53.91, 49.10 (CH_2 pip), 47.64 (C-4), 41.77 (NH-CH_2), 23.02 (CH_2CH_3), 11.50 (CH_2CH_3). Anal. calcd. for $C_{18}H_{27}N_5O_2$: C 62.61, H 7.83, N 20.29; found: C 62.43, H 7.90, N 20.03.

5-[(1-Phenyl-4-piperazinyl)methyl]-3-isopropylcarbamoyl-2-iminooxazolidine (2f): mp 122°C (diisopropyl ether); yield: 86%; IR (KBr) cm^{-1}: 3295 (NH), 1700 (C=O), 1685 (C=N); ^1H NMR (chloroform-*d*) δ ppm: 9.04 (d, 1H, *J* = 7.2 Hz, N*H*), 7.04 (m, 5H, Ar-*H*), 5.79 (s, 1H, N*H*), 4.64 (m, 1H, 5-*H*), 4.11 and 3.72 (2 dd, 2H, *J* = 10.2, 8.4, 7.3 Hz, 4-*H*), 3.98 (m, 1H, C*H*), 3.20 and 2.66 (2 m, 10H, NCH_2), 1.18 (d, 6H, *J* = 6.7 Hz, CH_3); ^{13}C NMR (chloroform-*d*) δ ppm: 153.49 (CO), 149.51 (C-2), 148.51, 126.48, 117.23, 113.49 (Ar), 70.78 (C-5), 58.51 (C-5-CH_2), 51.24, 46.43 (CH_2 pip), 44.91 (C-4), 39.52 (NH-CH), 20.32 (CH_3). Anal. calcd. for $C_{18}H_{27}N_5O_2$: C 62.61, H 7.83, N 20.29; found: C 62.52, H 7.82, N 20.14.

5-[(1-Phenyl-4-piperazinyl)methyl]-3-phenylthiocarbamoyl-2-iminooxazolidine (2g): mp 117°C (diisopropyl ether); yield: 72%; IR (KBr) cm^{-1}: 3320 (NH), 1685 (C=N); ^1H NMR (chloroform-*d*) δ ppm: 13.62 (s, 1H, N*H*), 7.24 (m, 10H, Ar-*H*), 6.41 (s, 1H, N*H*), 4.74 (m, 1H, 5-*H*), 4.65 and 4.15 (2 dd, 2H, *J* = 10.4, 8.2, 6.7 Hz, 4-*H*), 3.22 and 2.71 (2 m, 4H each, NCH_2); ^{13}C NMR (chloroform-*d*) δ ppm: 177.52 (CS), 155.51 (C-2), 151.05, 138.62, 129.10, 128.67, 126.19, 124.40, 119.88, 116.12 (Ar), 73.22 (C-5), 60.97 (C-5-CH_2), 53.88, 49.06 (CH_2 pip), 52.33 (C-4). Anal. calcd. for $C_{21}H_{25}N_5OS$: C 63.80, H 6.33, N 17.72, S 8.11; found: C 63.77, H 6.37, N 17.71, S 8.12.

5-[(1-Phenyl-4-piperazinyl)methyl]-3-[(4-methyl)phenylthiocarbamoyl]-2-iminooxazolidine (2h): mp 135°C (diisopropyl ether); yield: 69%; IR (KBr) cm^{-1}: 3280 (NH), 1680 (C=N); ^1H NMR (chloroform-*d*) δ ppm: 13.44 (s, 1H, N*H*), 7.15 (m, 9H, Ar-*H*), 6.34 (s, 1H, N*H*), 4.69 (m, 2H, 5-*H* and 4-*H*), 4.13 (1 dd, 1H, *J* = 10.0, 6.8 Hz, 4-*H*), 3.21 and 2.70 (2 m, 4H each, NCH_2), 2.33 (s, 3H, CH_3); ^{13}C NMR (chloroform-*d*) δ ppm: 177.70 (CS), 155.51 (C-2), 151.05, 136.07, 136.01, 129.28, 124.55, 119.85, 116.12, 116.03 (Ar), 73.21 (C-5), 60.97 (C-5-CH_2), 53.87, 49.06 (CH_2 pip), 52.36 (C-4), 21.04 (CH_3). Anal. calcd. for $C_{22}H_{27}N_5OS$: C 64.52, H 6.64, N 17.10, S 7.82; found: C 64.86, H 6.58, N 17.27, S 7.69.

General procedure for the preparation of 5-substituted-2,3-diphenylcarbamoyl-2-iminooxazolidines 3(*a–c*) and 5-[(1-phenyl-4-piperazinyl)methyl]-2,3-dipropylcarbamoyl-2-iminooxazolidine 3*e*

From the corresponding 5-substituted-2-amino-2-oxazolines **1**: to a cold (0°C) stirring solution of 0.1 mol of 2-amino-2-oxazoline in 200 mL of dry acetone under argon was slowly added 0.2 mol of phenyl- or propylisocyanate. The reaction mixture was stirred for 24 h at room temperature. The collected solid was recrystallized from a suitable solvent.

From the corresponding 5-substituted-3-phenylcarbamoyl-2-iminooxazolidines **2**: to a cold (0°C) stirred solution of 0.01 mol of 2-iminooxazolidine in 100 mL of dry acetone under argon was slowly added 0.01 mol of phenyl- or propylisocyanate. The reaction mixture was stirred for 3 h at room temperature. The collected solid was recrystallized from a suitable solvent.

5-[(1-Phenyl-4-piperazinyl)methyl]-2,3-diphenylcarbamoyl-2-iminooxazolidine **3***a*: mp 168°C (C_2HCl_3); yield: 67%; IR (KBr) cm^{-1}: 3410, 3250 (NH); 1715, 1660 (C=O); 1640 (C=N); ^1H NMR (chloroform-*d*) δ ppm: 10.76 (s, 1H, N*H*), 7.4 (s, 1H, N*H*), 7.21 (m, 15H, Ar-*H*), 4.82 (m, 1H, 5-*H*), 4.15 and 3.90 (2 dd, 2H, *J* = 10.7, 8.6, 7 Hz, 4-*H*), 3.10 and 2.70 (2 m, 10H, NCH_2); ^{13}C NMR (chloroform-*d*) δ ppm: 155.59 (C-2), 152.74 (N_{exo}-CO), 148.69 (N_{endo}-CO), 150.77, 139.37, 137.34, 128.72, 128.52, 123.70, 122.50, 119.90, 118.63, 118.48, 115.19 (Ar), 76.26 (C-5), 59.28 (C-5-CH_2), 53.21, 48.09 (CH_2-pip), 46.21 (C-4). Anal. calcd. for $C_{28}H_{30}N_6O_3$: C 67.47, H 6.02, N 16.87; found: C 67.47, H 6.02, N 16.82.

5-(1-Phenoxymethyl)-2,3-diphenylcarbamoyl-2-iminooxazolidine **3***b*: mp 156°C (CH_3OH); yield: 84%; IR (KBr) cm^{-1}: 3410, 3280 (NH); 1715, 1645 (C=O); 1620 (C=N); ^1H NMR (chloroform-*d*) δ ppm: 10.71 (s, 1H, N*H*), 7.61 (s, 1H, N*H*), 7.24 (m, 15H, Ar-*H*), 5.02 (m, 1H, 5-*H*), 4.19 (m, 4H, 4-*H*); ^{13}C NMR (chloroform-*d*) δ ppm: 155.60 (C-2), 153.20 (N_{exo}-CO), 148.69 (N_{endo}-CO), 157.77, 138.10, 137.10, 129.62, 128.97, 123.78, 122.96, 121.90, 120.01, 119.06, 114.72 (Ar), 75.42 (C-5), 67.23 (OCH_2), 44.97 (C-4). Anal. calcd. for

$C_{24}H_{22}N_4O_4$: C 66.98, H 5.12, N 13.02; found: C 67.14, H 5.02, N 13.22.

5-(1-Morpholinomethyl)-2,3-diphenylcarbamoyl-2-iminooxazolidine **3***c*: mp 172°C (CH_3OH); yield: 50%; IR (KBr) cm^{-1}: 3410, 3280 (NH); 1715, 1645 (C=O); 1620 (C=N); ^1H NMR (chloroform-*d*) δ ppm: 10.75 (s, 1H, N*H*), 7.54 (s, 1H, N*H*), 7.35 (m, 10H, Ar-*H*), 4.81 (m, 1H, 5-*H*), 4.14 and 3.90 (2 dd, 2H, J = 10.5, 8.6, 7 Hz, 4-*H*), 3.65 (t, J = 4.6 Hz, 4H, OCH_2), 2.59 (m, 6H, NCH_2); ^{13}C NMR (chloroform-*d*) δ ppm: 155.55 (C-2), 152.81 (N_{exo}-CO), 148.88 (N_{endo}-CO), 139.53, 137.53, 128.88, 128.64, 123.80, 122.60, 119.99, 118.60 (Ar), 76.26 (C-5), 66.20 (OCH_2), 59.86 (C-5-CH_2), 53.90 (NCH_2), 46.29 (C-4). Anal. calcd. for $C_{22}H_{25}N_5O_4$: C 62.41, H 5.91, N 16.55; found: C 62.52, H 76.20, N 16.60.

5-[(1-Phenyl-4-piperazinyl)methyl]-2,3-dipropylcarbamoyl-2-iminooxazolidine **3***e*: mp 121°C (heptane); yield: 42%; IR (KBr) cm^{-1}: 3410, 3300 (NH); 1700, 1635 (C=O); 1640 (C=N); ^1H NMR (chloroform-*d*) δ ppm: 8.55 (t, 1H, J = 5.5 Hz, N*H*), 7.17 (m, 5H, Ar-*H*), 5.11 (t, 1H, J = 6 Hz, N*H*), 4.83 (m, 1H, 5-*H*), 4.15 and 3.84 (2 dd, 2H, J = 10.3, 8.2, 7.2 Hz, 4-*H*), 3.19 and 2.68 (2m, 14H, NCH_2), 1.55 (m, 4H, CH_2CH_3), 0.92 (t, 6H, J = 7.3 Hz, CH_2CH_3); ^{13}C NMR (chloroform-*d*) δ ppm: 158.90 (N_{exo}-CO), 152.65 (N_{endo}-CO), 151.09 (C-2), 151.78, 129.08, 119.78, 116.05 (Ar), 75.98 (C-5), 60.18 (C-5-CH_2), 54.07, 49.14 (CH_2 pip), 46.92 (C-4), 42.23, 41.86 (NH-CH_2), 22.99, 22.93 (CH_2CH_3), 11.41, 11.32 (CH_2CH_3). Anal. calcd. for $C_{22}H_{34}N_6O_3$: C 61.40, H 7.91, N 19.53; found: C 61.35, H 8.0, N 19.56.

5-[(1-Phenyl-4-piperazinyl)methyl]-2-propylcarbamoyl-3-phenylcarbamoyl-2-iminooxazolidine **3**i

Preparation of **3***i* was conducted following the same procedure as described above for 2,3-disubstituted-2-iminooxazolidines, either from **2***a* with propylisocyanate or from **2***e* with phenylisocyanate; mp 126°C (CCl_4); yield: 75%; IR (KBr) cm^{-1}: 3410, 3250 (NH); 1700, 1645 (C=O); 1640 (C=N); ^1H NMR (chloroform-*d*) δ ppm: 8.57 (t, 1H, J = 5.4 Hz, N*H*), 7.72 (m, 10H, Ar-*H*), 7.06 (s, 1H, N*H*), 4.72 (m, 1H, 5-*H*), 4.10 and 3.89 (2 dd, 2H, J = 10.3, 8.2, 7.2 Hz, 4-*H*), 3.25 (m, 2H, NH-CH_2), 3.13 (m, 4H, NCH_2), 2.71 (m, 6H, NCH_2), 1.58 (m, 2H, CH_2CH_3), 0.92 (t, 3H, J = 7.4 Hz, CH_2CH_3); ^{13}C NMR (chloroform-*d*) δ ppm: the assessment of ^{13}C NMR chemical shift for quaternary carbons in **3***i* was made using the QUAT non-decoupled technique (observation of ^{13}C–^1H couplings). Thus C(2) was coupled with *H*-C(4) and *H*-C(5) (^3J = 2 Hz in the two cases). Then N_{endo}-CO was coupled with *H*-C(4) (^3J = 4.1 Hz). The quaternary carbons of the phenyl rings were coupled with the corresponding meta protons (^3J = 9.1 and 8.5 Hz). Nevertheless we did not observe any coupling for N_{exo}-CO, which permitted us to assign it as: 156.31 (N_{exo}-CO), 153.98 (N_{endo}-CO), 151.06 (C-2), 151.55, 138.39, 129.04, 128.94, 123.57, 119.73, 118.98, 116.01 (Ar), 76.33 (C-5), 60.03 (C-5-CH_2), 54.05, 49.09 (CH_2 pip), 46.88 (C-4), 41.94 (NH-CH_2), 22.92 (CH_2CH_3), 11.39 (CH_2CH_3). Anal. calcd. for $C_{25}H_{32}N_6O_3$: C 64.66, H 6.90, N 18.10; found: C 64.45, H 7.02, N 17.72.

References

1. C.R. Rasmussen, F.J. Villani, M.S. Mutter, and E.A. Griffin. J. Org. Chem. **51**, 1910 (1986).
2. C.R. Rasmussen, F.J. Villani, and E.A. Griffin. Acta Crystallogr. Sect. C: Cryst. Struct. Commun. **C40**, 2120 (1984).
3. M. Avalos, R. Babiano, P. Cintas, J.L. Jimenez, J.C. Palacios, and C. Valencia. Heterocycles, **35**, 1237 (1993).
4. E. Fromm, R. Kapeller-Adler, L. Pirk, A. Hahn, and T. Leipert. Justus Liebigs Ann. Chem. **447**, 259 (1926).
5. Y. Yamamoto and R. Reiko. Kyoritsu Yakka Daigaku Kenkyu Nempo, **22**, 43 (1977); Chem. Abstr. **90**, 103879 (1979).
6. A. English, K. Koch, and R. Zimmermann. Germ. Pat. 1 302 662 (1960); Chem. Abstr. **74**, 141745 (1971).
7. W. Wierenga and J.A. Woltersom. J. Org. Chem. **43**, 529 (1978).
8. C. Jarry, J.J. Bosc, J. Ouhabi, and A. Carpy. Arch. Pharm. (Weinheim), **323**, 157 (1990).
9. J.J. Bosc, I. Forfar, C. Jarry, J. Ouhabi, J.M. Léger, and A. Carpy. Arch. Pharm. (Weinheim), **323**, 561 (1990).
10. C. Jarry, I. Forfar, J. Thomas, J.M. Léger, and M. Laguerre. Heterocycles, **36**, 2465 (1993).
11. C. Tanaka, I. Ogata, and M. Nishida. Yakugaku Zasshi **97**, 157 (1977); Chem. Abstr. **87**, 39345 (1977).
12. M.R. Harnden and R.R. Rasmussen. J. Med. Chem. **13**, 305 (1970).
13. F. Mohamadi, N.G.J. Richards, W.C. Guida, R. Liskamp, M. Lipton, C. Caufield, G. Chang, T. Hendrikson, and W.C. Still. J. Comput. Chem. **11**, 441 (1990).
14. G. Bourgeois, C. Jarry, J.J. Bosc, G. Deleris, and E. Pays. Org. Mass Spectrom. **26**, 109 (1991).
15. P. Main, S.J. Fiske, S.E. Hull, L. Lessinger, G. Germain, J.P. Declercq, and M.M. Woolfson. MULTAN 80. A system of computer programs for the automatic solution of crystal structures from X-ray diffraction data. Univs. of York, England, and Louvain, Belgium (1980).
16. D.T. Cromer and J.T. Waber. International tables for X-ray crystallography. Vol. IV. 2nd ed. Kynoch Press, Birmingham, U.K. 1974.
17. N.L. Allinger. J. Am. Chem. Soc. **99**, 8127 (1977).
18. N.L. Allinger, Y.H. Yuh, and J.H. Lii. J. Am. Chem. Soc. **111**, 8551 (1989).

Preparation, spectroscopic properties, and ion chemistry of 3-diazo-1,1,1-trifluoro-2-propanone

Paolo Strazzolini, Angelo G. Giumanini, Alberto Gambi, Giancarlo Verardo, and Giovanni Cerioni

Abstract: The title compound (**1**) is prepared in satisfactory yield by reacting CH_2N_2 with trifluoroacetic anhydride in Et_2O; the *d*-analog was obtained by exchange with D_2O. ^1H, ^{13}C, ^{15}N, ^{17}O, and ^{19}F NMR spectra of **1** were studied, as well as its IR spectrum. A single isomer is present corresponding to the more stable *Z* configuration. The structural assignment was made on the basis of quantum mechanical calculations, which revealed that the *Z* form is some 13.4 kJ mol^{-1} more stable than the *E* form and the activation energy for the $E \rightarrow Z$ transition is 64.2 kJ mol^{-1}. Mass spectra under different experimental conditions were recorded and breakdown pathways of the parent ion of **1** charted.

Key words: 3-diazo-1,1,1-trifluoro-2-propanone; 3-*d*-3-diazo-1,1,1-trifluoro-2-propanone; structure; ^1H, ^{13}C, ^{15}N, ^{17}O, and ^{19}F NMR; EI-MS.

Résumé : On a préparé le composé mentionné dans le titre (**1**), avec un rendement satisfaisant, en faisant réagir le CH_2N_2 avec de l'anhydride trifluoroacétique dans l'éther; on a obtenu l'analogue deutéré par échange avec du D_2O. On a étudié les spectres RMN du ^1H, du ^{13}C, du ^{15}N, du ^{17}O et du ^{19}F ainsi que son spectre IR. Il n'existe qu'un seul isomère correspondant à la configuration *Z* la plus stable. On a fait les attributions de structure en se basant sur des calculs de mécanique moléculaire quantique; ils ont mis en évidence que la forme *Z* est environ 13,4 kJ mol^{-1} plus stable que la forme *E* et que l'énergie d'activation pour la transition $E \rightarrow Z$ est égale à 64,2 kJ mol^{-1}. On a enregistré les spectres de masse dans diverses conditions et on présente les voies de décomposition de l'ion parent du composé **1**.

Mots clés : 3-diazo-1,1,1-trifluoropropan-2-one; 3-*d*-3-diazo-1,1,1-trifluoropropan-2-one; structure; RMN du ^1H, du ^{13}C, du ^{15}N, du ^{17}O et du ^{19}F; SM-IE.

[Traduit par la rédaction]

Introduction

One of the simplest diazoketones is 3-diazo-1,1,1-trifluoro-2-propanone (**1**), bp 25°C at 133 Pa (1), which was described in 1953 as being the product (62.5% yield) of the reaction of CF_3COCl with CH_2N_2. Surprisingly, after that distant birth the compound has not received any attention, as can be established by its remarkable absence in the Chemical Abstracts. In view of the synthetic potential of this small building block, we set out to find a convenient synthetic procedure for it, to record and study some of its spectroscopic and mass spectrometric properties, also with the purpose of elucidating its actual structure.

Received February 20, 1996.

P. Strazzolini,[1] A.G. Giumanini, A. Gambi, and G. Verardo. Department of Chemical Sciences and Technologies, University of Udine, I-33100 Udine, Italy.
G. Cerioni. Department of Chemistry, University of Cagliari, I-09100 Cagliari, Italy.

[1] Author to whom correspondence may be addressed. Telephone: +39-432-558 870 and -558 839. Fax: +39-432-558 803. E-mail: G1WUDD32@vm.cineca.it

Results and discussion

Compound **1**, for which *E* and *Z* geometric isomers may be expected, due to a possibly restricted rotation about the (O)C—C(H) bond of the five-center π system, may be described by a suitable mixing of the canonical formulas **1***a–c* (here reported for the *Z* isomer, Scheme 1).

It could be easily obtained from $(CF_3CO)_2O$ and CH_2N_2 in ether solution; careful evaporation of the solvent and the formed methyl trifluoroacetate (**2**), followed by a conventional distillation at slightly reduced pressure, gave **1** in good yield. The yellowish liquid obtained was conveniently ana-

$$(CF_3CO)_2O + 2\,CH_2N_2 \rightarrow \underset{\mathbf{1}}{CF_3COCHN_2} + \underset{\mathbf{2}}{CF_3CO_2CH_3} + N_2$$

lyzed by GC at relatively low injector and column temperatures, using an FID detector, and found to be homogeneous; use of an electron capture detector proved to be suitable, whenever a magnification of the sensitivity is required: the approximate ratio of the responses of the two detectors was found to be close to ca. 50. Under these conditions, the peak for **1** was highly symmetric and the EI-MS spectra at 70 eV recorded along the elution profile showed an absolutely constant pattern. Derivatives of diazoalkanes are expected to yield

Scheme 1.

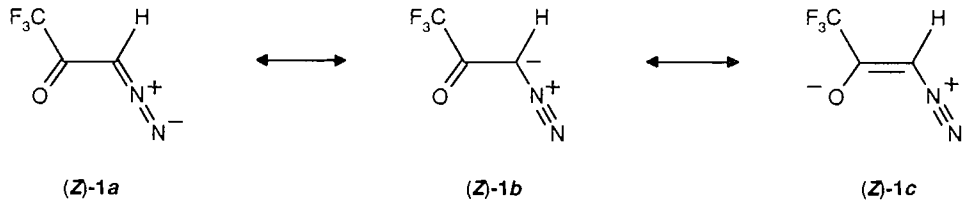

(*Z*)-1*a* (*Z*)-1*b* (*Z*)-1*c*

mixtures of geometric isomers, which may interconvert more or less rapidly (2). The free energy of activation ΔG_{act} is essentially determined by its ΔH_{act} term, which is in turn strictly related to the amount of energy necessary to break the π-component of the relevant C—C bond. Thus a higher ΔG_{act} is an indication of a larger π bond order between these two centers, which in valence bond (VB) descriptive terms corresponds to a larger contribution of the mesomeric form **1***c*. Interconversion of geometric isomers of the respective positive ion, obtained by electron impact, is generally so fast that mass spectrometry is unable to generate different spectra for any two isomers.

Pure **1** appeared to be relatively thermally stable: in fact, a chlorobenzene solution did not show any sign of transformation after 2 h at reflux. Differential scanning calorimetry (DSC) in nitrogen atmosphere revealed that exothermic reactions with traces of molecular oxygen set in at 117.1°C and 148.0°C; the compound underwent a strong exothermic decomposition at 199.0°C. The deuterio analog of **1** (*d*-**1**) could be easily obtained by repeated exchanges with D_2O without any catalyst at room temperature during 15 min. This is a fortunate event because base-catalyzed exchange (3) may induce a haloform reaction (4).

Admission of **1** through a GC column into the electron impact ion source of a mass spectrometer, with the precaution of keeping the temperatures of all sections of the whole system as low as possible and injecting the smallest amount that can generate clean spectra in order to avoid thermal and collision-induced decompositions and material exchanges, produced a simple spectrum at 70 eV, consisting essentially of the parent ion at *m/z* 138, a peak at *m/z* 69, and one at *m/z* 41. Under these conditions the appearance of peaks at *m/z* 110 (loss of N_2) and 91 were minimized and practically negligible, as well as the quasimolecular ion MH^+ at *m/z* 139 (**5**), which appeared related to a peak at *m/z* 70 (Fig. 1). Wulfman and Poling (5) had already found that no loss of N_2 is present in the mass spectra of ethyl diazoacetate and dimethyl diazomalonate recorded in an all-glass system.

The spectrum of **1** obtained at the ionization energy value of 20 eV is reported in Fig. 2: slightly less stringent working conditions produced a richer fragmentation pattern, which is made up of the true spectrum of **1** superimposed with the product(s) of its thermal decomposition in the ion source, a fact which may well affect most of the reported spectra of diazoketones (5). Thus, the ion **4** at *m/z* 110 (**1** − N_2) is most likely the parent ion in the fragmentation process of the Wolff rearrangement product trifluoromethyl ketene (**3**), essentially yielding the cascade at *m/z* 91, 82, and 63 (Scheme 2).

Metastable ion, MIKE, and B^2/E experiments ruled out any appreciable contribution of the observable *m/z* 110 ion (**4**) to an electron impact induced decomposition of the parent ion of

Fig. 1. EI (70 eV) mass spectrum of **1** (GC inlet).

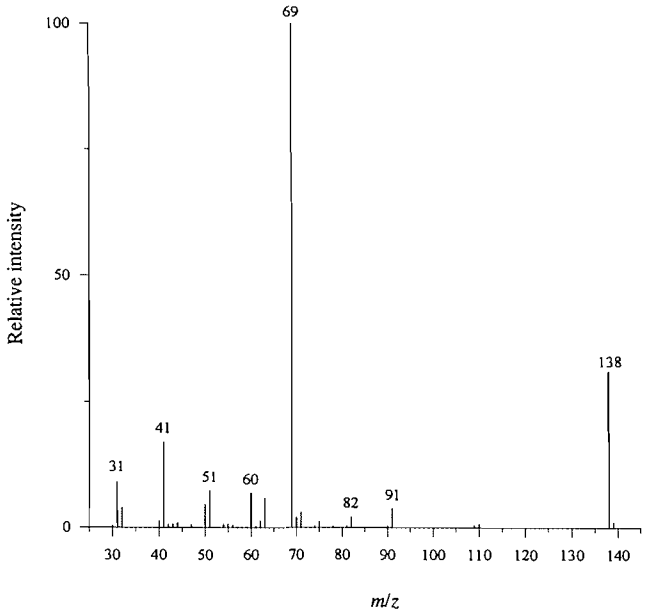

Fig. 2. EI (20 eV) mass spectrum of **1** (GC inlet).

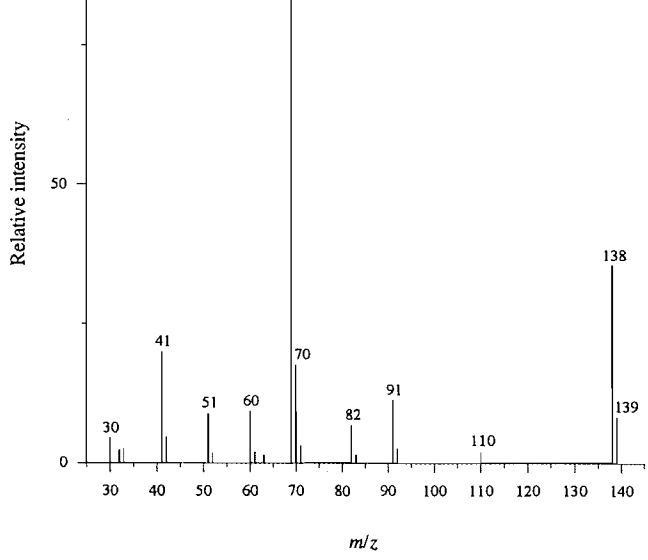

Scheme 2.

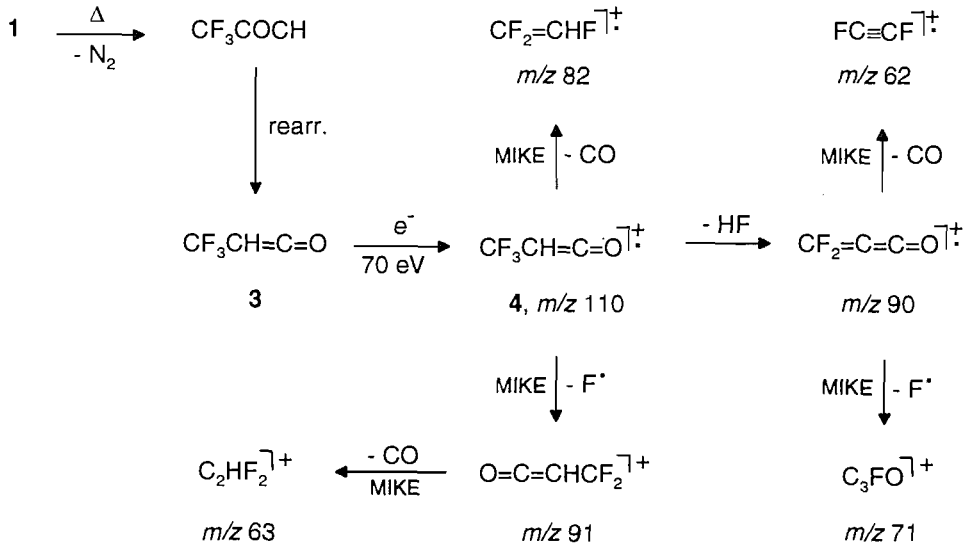

Scheme 3.

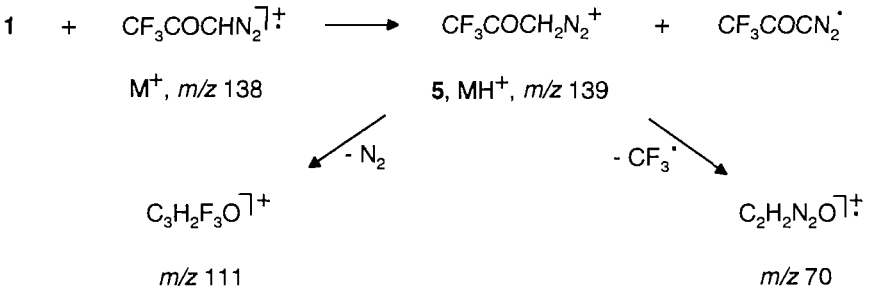

1. A MIKE spectrum correctly related the appearance of the peak at *m/z* 69 to this parent ion. The great efficacy in performing a hydrogen abstraction upon ion–molecule exchange is also borne out by examination of the spectrum of Fig. 2, where the MH^+ ion (**5**) is definitively outstanding, as well as its decomposition product at *m/z* 70 (Scheme 3).

Molecules having the CF_3 group frequently show the corresponding positive ion at *m/z* 69 (**6**) in their mass spectra: confirmation of the ion composition comes from the accompanying presence of the ions at *m/z* 50 (**7**) and 31 (**8**); but the ion at *m/z* 41, whose composition should be C_2HO, indicated as its possible precursor an ion of composition C_2HN_2O (**9**) isobaric with CF_3 (Scheme 4). Confirmation of the hypothesis came from the spectrum of partially deuterated **1**, admitted into the ion source under exactly the same conditions of the spectrum of Fig. 1, showing a doubling of the ion at *m/z* 69, now accompanied by the ion at *m/z* 70; similar splitting was observed for the ion at *m/z* 41 (Fig. 3).

From the ratio of the intensity of the peaks at *m/z* 138 and 139, the relative incidence of the ion decomposition paths **a** and **b** was calculated to be ca. 1.33:1.00. Accurate mass measurements of the ion at *m/z* 69 gave a final confirmation of our observations. The ion at *m/z* 71, whose intensity is strictly related to the appearance of the Wolff product, was found to originate from the ion at *m/z* 91 by loss of HF from the appro-

Fig. 3. EI mass spectrum of *d*-**1** (recorded in the same conditions of the spectrum in Fig. 1).

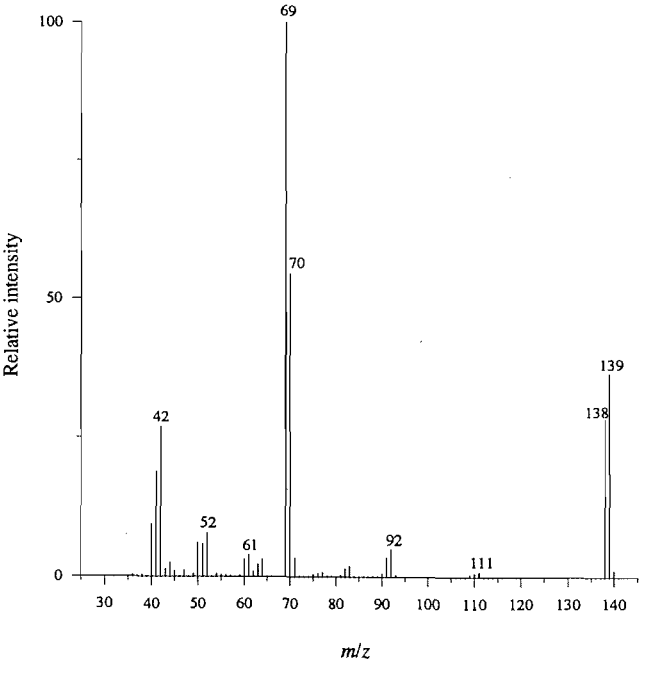

Scheme 4.

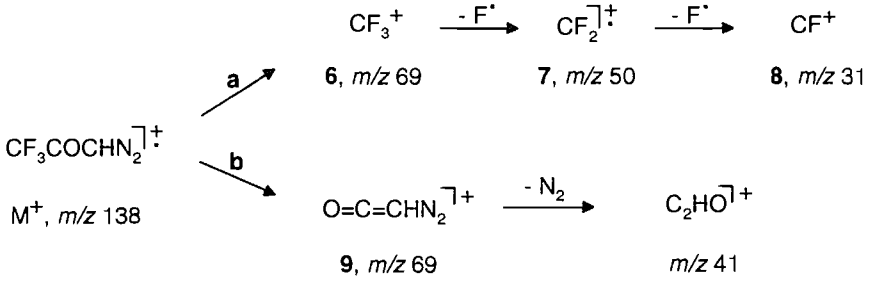

Scheme 5.

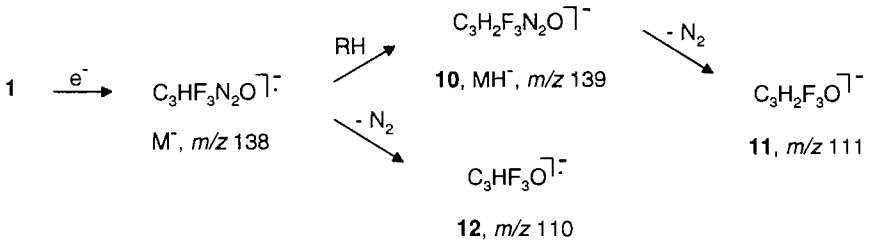

priate MIKE experiment. Incidentally, extensive Wolff rearrangement was correlated (ref. 2, p. 124) with the presence of a *Z* conformer in the mixture actually undergoing decomposition. When neat CF_3COCDN_2 was admitted into the ion source through a nonpolar silicon rubber column in an amount such that ion–molecule collisions were minimized, as can be ascertained by the invariancy of the ion at *m/z* 138 vs. 139 or 69 vs. 70 intensity ratios, these ratios could be considered a good indication of the isotopic composition of the material reaching the ion source. Identical amounts of the protic substance, as determined by the electron multiplier counts, reduced to the purely isotopic content the peaks at *m/z* 139 and 70, a proof of the practical absence of ion–molecule collision with hydrogen donation to the ion. The 70 eV spectrum for the deuterated molecule could therefore realistically be reconstructed. From this spectrum the ratio of the fragmentation ions CF_3 vs. $COCDN_2$ could be determined: this ratio should also hold for the protic ion. Moreover, the ion at *m/z* 41 of the protic material moved to *m/z* 42 for the deuterated molecule. The ratio of intensities of *m/z* 41 vs. *m/z* 138 was very close to the ratio *m/z* 42 vs. *m/z* 139, respectively, for the protic and deuterated molecule: an indication both for the quality of the obtained spectrum of the latter and for the essential correspondence of the two fragmentations even in terms of cleaving propensities.

A chemical ionization positive ion spectrum of **1** was obtained in CH_4 as ionizing gas (Fig. 4). The quasimolecular ion (MH^+, *m/z* 139) was the base peak, with little decomposition taking place. Of interest, some 20% as intense as this was a peak at *m/z* 140 (MH_2^+). The main decomposition pathway leads to the ion at *m/z* 91, with the intermediacy of loss of HF from MH^+, followed by loss of N_2. Interestingly, the direct loss of N_2 from MH^+ was definitively a minor process, perhaps a valuable indication for experiments in condensed phase. A negative ion spectrum (Scheme 5), on the other hand, exhibited only two ions: the base peak being at *m/z* 110 (**12**) with a companion at *m/z* 111 (**11**); an ion of very minor intensity was

Fig. 4. CI-(CH_5^+) mass spectrum of **1**.

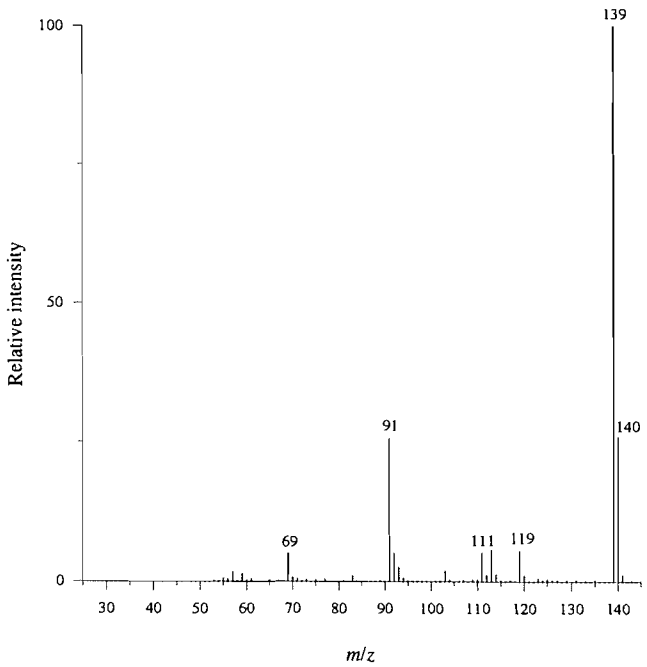

present in the neighbourhood of the parent ion at *m/z* 137. Although **1** is made up of a good cluster of electronegative atoms, it appears unable to accommodate an extra electron in a reasonably stable anion of the same composition. The same and only loss of N_2 occurred both from the parent ion and the negative quasimolecular ion (**10**).

Ions kept in a mass trap may often pick up hydrogen by collision with unionized donors present there, due to the relatively long time of residence, eventually showing decom-

Table 1. NMR data[a] for: $F_3C_{(a)}(C_{(b)}{=}O)C_{(c)}HN_{(a)}{=}N_{(b)}$ (**1**).

^1H		5.86s ($\nu_{1/2}$ = 4.2 Hz)	
^{13}C	$C_{(a)}$	116.0q ($\nu_{1/2}$ = 2.7 Hz)	$^1J(^{13}C{-}^{19}F)$ = 288.6 $^3J(^{13}C{-}^1H)$ undetected
	$C_{(b)}$	176.2qd ($\nu_{1/2}$ = 2.0 Hz)	$^2J(^{13}C{-}^1H)$ = 4.5 $^2J(^{13}C{-}^{19}F)$ = 37.3
	$C_{(c)}$	56.1d ($\nu_{1/2}$ = 12.3 Hz)	$^1J(^{13}C{-}^1H)$ = 207.0 $^3J(^{13}C{-}^{19}F)$ undetected
^{19}F		−77.5s ($\nu_{1/2}$ = 3.3 Hz)	
^{15}N	$N_{(a)}$	−130.7d ($\nu_{1/2}$ = 1.2 Hz)	$^2J(^{15}N{-}^1H)$ = 1.8
	$N_{(b)}$	−26.1d ($\nu_{1/2}$ = 1.6 Hz)	$^3J(^{15}N{-}^1H)$ = 1.4
^{17}O		432.0s ($\nu_{1/2}$ = 224 Hz)	

[a]δ values in ppm (internal references: ^1H, HMDS; ^{13}C, central line of $CDCl_3$ triplet; and ^{19}F, CCl_3F; external references: ^{15}N, neat CH_3NO_2 and ^{17}O, deionized H_2O); s = singlet, d = doublet, q = quartet, and qd = quartet of doublets; *J* values in Hz, $\nu_{1/2}$ = half-height line width.

Fig. 5. EI (70 eV) mass spectrum of **1** obtained from an ion trap mass spectrometer (GC inlet).

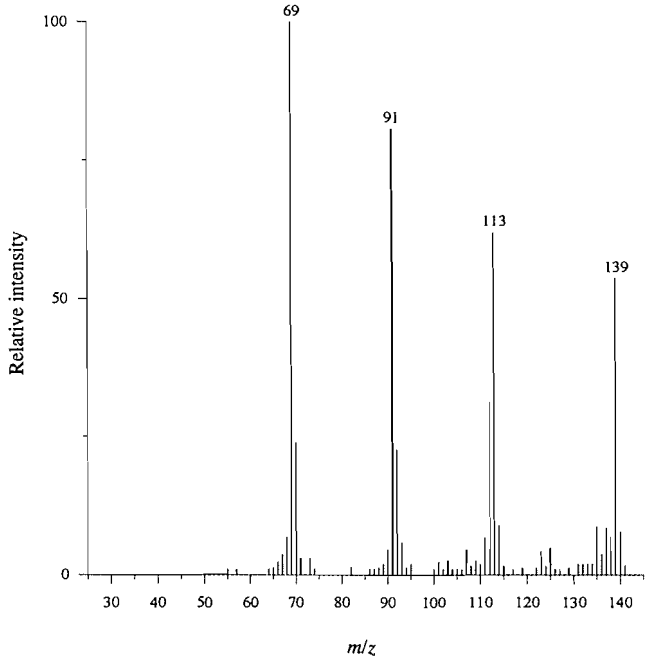

position of the quasimolecular ion MH^+. This process was most efficient when our **1** was admitted to one such spectrometer (Fig. 5): the M^+ disappeared altogether, to be replaced by the MH^+, which decomposed to *m/z* 91 by loss of N_2 followed by fast loss of HF. Beside the base peak at *m/z* 69, the fragmentation of MH^+ showed a peak at *m/z* 70, assumed to have the composition CF_3H^+, and one at *m/z* 113. The latter, for which we assume the composition $C_2F_3O_2$, was possibly generated by the collision of the parent ion of **1** or the ion $C_3H_2F_3N_2O^+$ (MH^+) with neutral CF_3COOH, somehow admitted into the ion trap.

NMR spectroscopy data are collected in Table 1. The ^1H NMR spectrum of **1** at room temperature in $CDCl_3$ exhibited only one peak at 5.86 ppm with a line width at half-height of 4.2 Hz, a location in close agreement with those reported (6) for α-protons of α-diazoketones. ^{13}C NMR signals can be easily assigned from their shifts and ^1H and ^{19}F couplings. The ^{13}C NMR chemical shifts of carbonyl groups in α-diazoketones are shielded compared to *normal* ketones, e.g., acetophenone (196.9 ppm) (7) and ω-diazoacetophenone (186.4 ppm) (8); an analogous shielding is observable also for **1** (176.2 ppm) compared to 1,1,1-trifluoroacetone (187.7 ppm) (7). The same effect, but in a more pronounced fashion, is exhibited by aldehydes, e.g., acetaldehyde (200.5 ppm) (7) vs. diazoacetaldehyde (184.1 and 183.8 ppm for the *E* and *Z* forms, respectively) (8). On the contrary, this shielding is strongly reduced by the contemporary presence of another conjugated group as is the case for, e.g., ethyl acetate (170.3 ppm) (7) vs. ethyl diazoacetate (167.6 ppm) (8). The large upfield shift usually observed (9) for the C_{ipso} is partly relieved by the carbonyl group through the contribution of resonance formulas **1***c*, as discussed below for the ^{17}O NMR results. The value of $^1J_{(^{13}C-^1H)}$ is quite high for an sp^3 hybridized atom and higher than other $^1J_{(^{13}C-^1H)}$ measured for some diazo compounds (8), thus reflecting both a contribution of canonical formula **1***c* as well as the electron-withdrawing effects of the diazo and trifluoroacetyl groups (7). Owing to the lack of literature data, it is difficult to get information from the $^nJ_{(^{13}C-^{19}F)}$ values; nevertheless, we can observe that $^1J_{(^{13}C-^{19}F)}$ is identical for **1** and 1,1,1-trifluoroacetone (10): the large value observed for the latter coupling constant has been attributed to a π-bond contribution between carbon and fluorine. The value of $^2J_{(^{13}C-^{19}F)}$ fits a rough correlation observed (10) between $^1J_{(^{13}C-^{19}F)}$ and $^2J_{(^{13}C-^{19}F)}$. Neither $^3J_{(^{13}C-^{19}F)}$ nor $^3J_{(^{13}C-^1H)}$ has been measurable and we do not have a definite rationale for this observation. The C_{ipso} signal shows a remarkable half-height line width (12.3 Hz), which seems not to be due to slow exchange between *cisoid* and *transoid* rotamers, since on going down to −60°C neither any splitting nor any

Scheme 6.

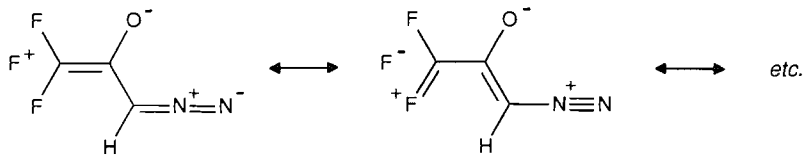

13*a* **13*b***

line sharpening was observed. Kaplan and Meloy (11) experimentally determined a *Z*:*E* ratio of 9:1 for diazoacetone, theoretically confirmed by Csizmadia et al. (12). A further significant increase of this ratio in the case of **1** might prevent observation of the less favoured rotamer by NMR. A possible explanation for the large values observed for the half-height line width of C_{ipso} and for the signal of the ^1H spectrum could thus be that in our system vicinal couplings and $^4J_{(^1H-^{19}F)}$, respectively, have values so small as to prevent their observation but large enough to cause broadening of the respective lines.

The ^{19}F NMR shift is better compared with 1,1,1-trifluoroacetone and CF_3COOEt ($\delta = -83$ and -78 ppm, respectively) (10) or with $CF_3COCF{=}CF_2$ ($\delta = -80.1$ ppm) (13), all reflecting similar situations.

A certain amount of literature data on ^{15}N NMR for diazo groups is available, but only five entries concern diazoketones or diazoesters (8). We observe that both nitrogen atoms are more shielded for these two classes than for diazoalkanes. A full rationalization of variation of shielding in diazo groups resulting from structural variations has not yet been reached, except for the case of the effects observed when a conjugation among diazo and electron-withdrawing groups was present (14). In our case, there is a close similarity of ^{15}N chemical shifts with ethyl diazoacetate ($\delta = -132.6$ and $+3.6$ ppm for $N_{(a)}$ and $N_{(b)}$, respectively) (15). We have also measured, at natural isotopic abundance, $^2J_{(^{15}N-^1H)}$ and $^3J_{(^{15}N-^1H)}$ values. For diazo compounds we are aware of only one other observation (15) of such couplings, i.e., for an ^{15}N enriched sample of ethyl diazoacetate, in which values were found to be 2.8 and 1.0 Hz for $^2J_{(^{15}N-^1H)}$ and $^3J_{(^{15}N-^1H)}$, respectively. The $^2J_{(^{15}N-^1H)}$ value observed for **1** (1.8 Hz, some 64% the value of 2.8 Hz reported in the quoted paper) is in favour of an increased charge on $N_{(a)}$ compared with $N_{(a)}$ of diazoacetate, since an effective removal of the lone pair from the nitrogen atom causes a significant reduction of the values for $^2J_{(^{15}N-^1H)}$ (ref. 11, p. 72).

^{17}O NMR data are in agreement with the previously discussed importance of the resonance structure **1***c*. The strong shielding observed for the carbonyl group of diazoketones, in comparison with ketones lacking the diazo group, has in fact been shown to be due to this reason (16). Moreover, we observe for **1**, compared with 1,1,1-trifluoroacetone (17), a $\Delta\delta^{17}O$ of ca. 160 ppm whilst for α-diazoketones this $\Delta\delta^{17}O$ is usually smaller, ca. 110 ppm (16*b*). In this case, the CF_3 group operates in a direction that is opposite to that observed when comparing acetone (18) and 1,1,1-trifluoroacetone, the latter being actually deshielded by ca. 20 ppm compared to the former. A possible explanation could be found in the not negligible importance of hyperconjugative resonance formulas, such as **13**, which further contribute to diminish the double bond character of the carbonyl group of **1** (Scheme 6). Support for the possibility of a contribution of formulas **13**, particularly **13***b*, to the real structure of **1** can be found also in the high value found for $^1J_{(^{13}C-^{19}F)}$, as previously discussed.

An absorption maximum was found in the UV spectra of **1** recorded in EtOH, $CHCl_3$, and *c*-hexane in the range 273–278 nm; a large increase of the value for the extinction coefficient was observed in *c*-hexane. In addition, a shoulder was quite evident both in EtOH at 247 nm and *c*-hexane (256 nm), but was absent in $CHCl_3$ (Table 2). The location of the maxima and shoulders are those expected from literature data for diazoketones (ref. 2, pp. 115, 116).

The room temperature IR spectra of liquid **1** and its deuterated analog are reported in Figs. 6 and 7, respectively. The spectrum of compound **1** (Fig. 6) exhibits a system of two bands both in the ν_{CH} region and in the ν_{NN} region. The spectra of solid **1** showed only the lower frequency component in the ν_{CH} region, the position of this band being consistent with a hybrid sp^2 carbon. Also the infrared gas-phase spectrum shows only one component with an AB-hybrid type contour, confirming the planar skeleton of the molecule. The disappearance of the higher frequency component can be explained either on the basis of a change in the Fermi resonance, although in this case the total disappearance would be difficult to explain, or, better, by the presence of molecular associates in the liquid phase. The band at lower frequency is definitively broader. Compound *d*-**1** exhibited a ν_{CD} band at 2350 cm^{-1}, which may be compared with a value of 2312 cm^{-1} found for 3-diazo-3-*d*-2-propanone (19).

The IR spectra of diazoketones are characterized by a band around 2100 cm^{-1} (ref. 2, pp. 116, 117) attributed to the ν_{NN} fundamental, and H- and D-α-diazoketones present a band in the range 2104–2114 cm^{-1} (20). The strong band at 2134 cm^{-1} should be assigned to the stretching of the NN bond: the relatively high value of the frequency of this absorption indicates the importance of mesomeric structures with a triple bond between the nitrogen atoms. This result may be ascribed to the effect of the very electronegative nature of the substituent on the neighbouring carbon atom; in fact, the absorption frequency is quite close to that observed for the CN triple bond (21). The relatively high frequency (ca. 1670 cm^{-1}) of the absorption band of the C=O group seems to favour an increased contribution of resonance hybrids with a carbon–oxygen double bond, in comparison with other diazoketones and in contrast with the results of the ^{17}O NMR spectroscopy. However, as discussed by Foffani and co-workers (22), a carbonyl–diazo group field interaction can be of significance and help to overcome the apparent contrast between the results

Table 2. UV properties of **1** in *c*-hexane, $CHCl_3$, and EtOH.

Solvent	Wavelength (nm)	log ε	Concentration (mol L^{-1})
c-Hexane	256	3.59	1.79×10^{-4}
		3.61	1.19×10^{-4}
		3.61	5.96×10^{-5}
	273	3.53	1.79×10^{-4}
		3.56	1.19×10^{-4}
		3.56	5.96×10^{-5}
$CHCl_3$	248	3.69	1.81×10^{-4}
		3.70	1.20×10^{-4}
		3.72	6.02×10^{-5}
	278	3.41	1.81×10^{-4}
		3.42	1.20×10^{-4}
		3.45	6.02×10^{-5}
EtOH	246	3.71	1.72×10^{-4}
		3.73	1.15×10^{-4}
		3.74	5.74×10^{-5}
	278	3.35	1.72×10^{-4}
		3.38	1.15×10^{-4}
		3.39	5.74×10^{-5}

Fig. 6. IR spectrum of neat liquid **1**.

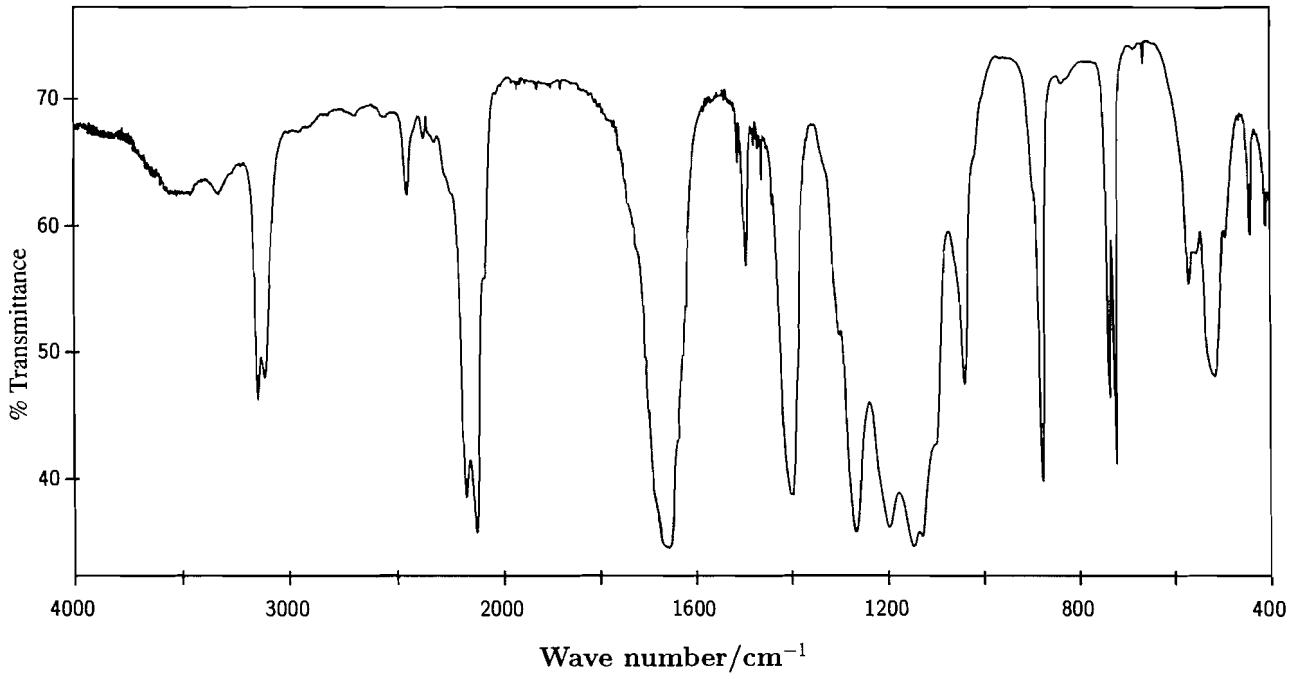

obtained by the two different spectroscopic methods. The higher frequency component of the band system about 2180 cm^{-1} is present also in the solid state and in the gas phase and its intensity does not depend on the temperature; it might be assigned to a Fermi resonance of (1277 + 900) or (1137 + 1043) cm^{-1} combination bands with the near fundamental.

The NMR data and IR spectral features in the CH (CD) stretching, as well as other characteristic absorptions in other regions, induced us to favour the hypothesis of the presence of a single isomer, possibly in the *Z* configuration. Simultaneous presence of two conformers in equilibrium was observed for other diazoketones in a number of studies by several authors

Fig. 7. IR spectrum of neat liquid *d*-**1**, from which background of traces of **1** was subtracted.

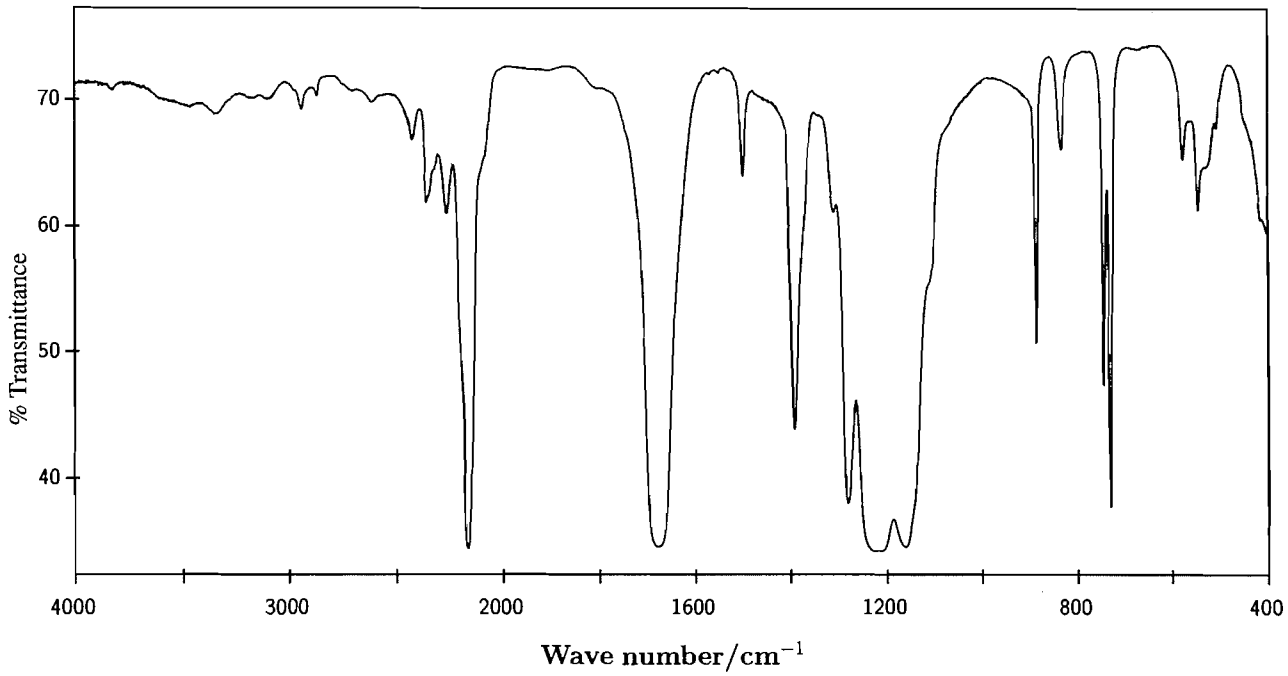

Fig. 8. Geometric structure of the *Z* form of **1**.

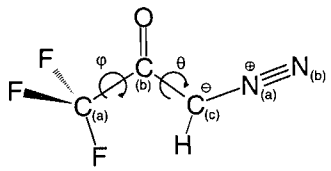

Fig. 9. Interconversion energy barrier of the two conformers (*E* and *Z*) of **1**.

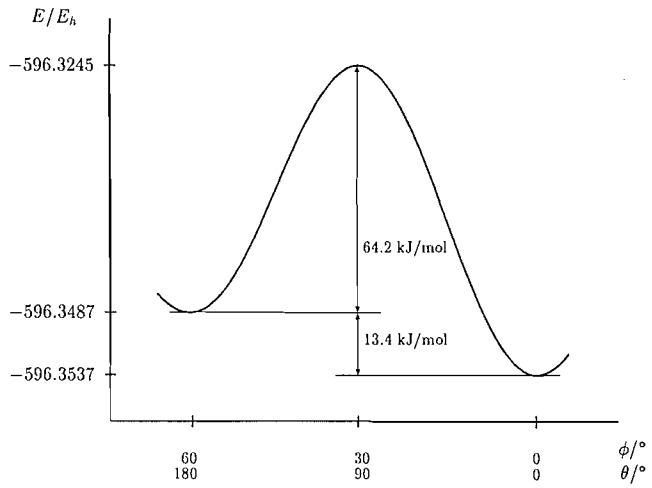

using various physical techniques (11, 23, 24): determination of the dipole moments and theoretical calculations (25) then allowed more precise inferences about the actual structures present at equilibrium. The *Z* form was always more stable than the *E* one. To achieve more certain and detailed information on the actual structure of **1**, we then moved in two different directions. The IR spectrum of **1** in the gas phase was recorded and studied in greater detail. Theoretical calculations, on the other hand, were carried out in order to produce information on the geometry of the *E* and *Z* forms of **1**, their energies, and the activation enthalpy of the $E \rightarrow Z$ transformation. Energy values for the different conformers of **1** are reported in Table 3 and the optimized geometric structures in Table 4.

The theoretical approach was based on Hartree–Fock ab initio calculations aimed at elucidating the conformational and vibrational spectroscopic side of the problem of the structure of **1**, using the GAUSSIAN 92 computer program package (26). The geometric structure of the *Z* form of compound **1** is reported in Fig. 8 and is drawn with $\varphi = \theta = 0°$; the structure of the *E* form is obtained when the dihedral angle θ (defined as H-$C_{(c)}$-$C_{(b)}$-$C_{(a)}$) is 180°. The other dihedral angle φ (defined as F-$C_{(a)}$-$C_{(b)}$-$C_{(c)}$) is relative to the rotation of the CF_3 group and may range from 0° to 60°. The *z*-axis, not shown in the representation of the molecule, points out of the plane of the C-(CO)-CHN_2 core.

The calculations showed that the more stable configuration is a (**Z**)-**1**, having $\varphi = \theta = 0°$; on the other hand, in the case of (***E***)-**1**, the less stable configuration, a minimum of energy is achieved when $\varphi = 60°$ and $\theta = 180°$. From the data collected in Table 3 the enthalpy difference between the two conformations is found to be 13.4 kJ mol^{-1}, a result amply justifying the appearance of only (**Z**)-**1** at equilibrium. The barrier to interconversion of (***E***)-**1** to (**Z**)-**1** is evaluated at 64.2 kJ mol^{-1}, a value that compares well with others previously determined

Table 3. Energy values for the different conformers of **1**.

φ^a	θ^a	E^a
0	0	−596.353 7171
0	90	−596.322 5833
0	180	−596.346 1034
30	0	−596.353 6074
30	90	−596.324 4636
30	180	−596.347 1571
60	0	−596.353 5397
60	90	−596.326 8949
60	180	−596.348 6671

[a]Units are degrees for angles and hartrees for energy.

Table 4. Optimized structures for (*Z*)-**1** and (*E*)-**1**.[a]

	Z: φ = 0°, θ = 0°	*E*: φ = 60°, θ = 180°
F—$C_{(a)}$	1.3134	1.3129
$C_{(a)}$—$C_{(b)}$	1.5377	1.5426
$C_{(b)}$—$C_{(c)}$	1.4332	1.4441
$C_{(c)}$—H	1.0649	1.0680
$C_{(b)}$—O	1.1892	1.1830
$C_{(c)}$—$N_{(a)}$	1.3265	1.3138
$N_{(a)}$—$N_{(b)}$	1.0863	1.0922
∠(F-$C_{(a)}$-$C_{(b)}$)	110.899	110.7907
∠($C_{(a)}$-$C_{(b)}$-$C_{(c)}$)	115.9039	117.5965
∠($C_{(b)}$-$C_{(c)}$-H)	128.6748	121.9559
∠($C_{(c)}$-$C_{(b)}$-O)	125.7204	123.2658
∠($C_{(b)}$-$C_{(c)}$-$N_{(a)}$)	114.9514	121.7421
∠(H-$C_{(c)}$-$N_{(a)}$)	116.0000	116.0000

[a]Bond distances are given in Ångstroms and bond angles in degrees.

(Fig. 9). Interestingly, the angle φ, associated with the conformation of the CF_3 group, showed peculiar and definite preferences: a CF bond invariable lies in the plane of the π-core centers on the less hindered side, i.e., pointing towards the H in (*Z*)-**1** and the O in (*E*)-**1**. These results were obtained thanks to the use of a relatively high theoretical level, employing the 6-311G(d,f) large basis set. Bond lengths (Table 4) appeared to be uninfluenced by configuration, as well as all but two angles showing large variations (∠($C_{(b)}$-$C_{(c)}$-H), ∠($C_{(b)}$-$C_{(c)}$-$N_{(a)}$)), corresponding to rotations of H and the N_2 group about $C_{(c)}$ in the plane of the molecules. Since the (*E*)-**1** shows practically ideal sp^2 orbital alignments of the substituents about the carbon center, the closer approach of N_2 to O in (*Z*)-**1** may well be due to an electrostatic interaction.

Once the geometric optimization was achieved, we resumed computation of vibrational frequencies by determining the second derivatives of the energy with respect to the Cartesian nuclear coordinates and then transforming to mass-weighted coordinates. The intensities of the vibrational modes are evaluated along with the computed fundamentals. To compare the observed IR spectrum of **1** with the calculations relative to the (*E*)-**1** and (*Z*)-**1** forms, we considered the synthetic spectra obtained from the four strongest vibrations of the two forms, the computed wave numbers having also been scaled by ca. 10% in order to compensate for the harmonicity of the calculated values. The intensity patterns of the spectra, reported in Fig. 10, allowed the attribution of the *Z* configuration (*b*) to our product **1**. The band shapes in the gas phase spectrum may be classified as AB-hybrid envelopes and pure C-type profiles, confirming the planarity of the molecule.

Experimental

General methods

All reagents used were commercially available (Aldrich, Milano-I) and were used as received unless otherwise specified. Trifluoroacetic anhydride was freshly distilled prior to use; anhydrous K_2CO_3 was activated by heating at 250°C during 4 h. Careful determinations of bp were made by observing the slow distillation temperature of the center cut of a suitable amount of pure **1**. GC analyses were carried out with a Carlo Erba HRGC gas chromatograph using a 0.32 mm i.d. × 30 m Supelcowax™ 10 (0.25 μm phase film) or a 0.32 mm i.d. × 30 m Supelchem™ SE-54 (0.25 μm phase film) fused silica capillary column (Supelchem, Milano-I); operative conditions were: injection temperature 150°C, isothermal elution at 85°C or 50°C, respectively, detection temperature 200°C. Quantitative analyses for the determination of the concentration of solutions of **1** were performed by the internal standard technique (chlorobenzene), using the Supelcowax™ column: under these conditions, quite suitable in assessing the purity of **1**, complete D/H exchange occurred when *d*-**1** of at least 95% isotopic purity was chromatographed in an isotherm at 85°C. An analogous observation was made with 3-diazo-3-*d*-2-propanone (19). During this experiment we observed that the molecular ion of **1** has a great propensity to pick up a hydrogen atom in the collisions even with unionized molecules of **1**: in isotopic analysis it is therefore mandatory to inject the least amount that can be easily detected in order to avoid mistakes. The phenomenon was also confirmed by the use of an ion trap mass spectrometer. IR spectra were recorded on a Nicolet FTIR Magna 550 spectrophotometer using the KBr technique. In the case of the gas phase IR spectrum, a 5.0 cm path length cell filled with ca. 10 kPa of substance was employed. All calculations were carried out using a CRAY C90 computer system. UV spectra were recorded with a Jasco digital spectrophotometer UV–visible UVIDEC-505 equipped with a derivative scanner model DER-1 and a optical path of 1 cm; spectral data are reported in Table 2. NMR spectra were recorded using a Varian VXR-300 spectrometer equipped with a 10 mm broad-band probe or a 5 mm (^{1}H and ^{19}F) probe, at room temperature (probe temperature = 294 K) and at natural isotopic abundance for all nuclei, or, alternatively, a Bruker AC-200 spectrometer. Solutions of **1** were generally ca. 4.0 M in $CDCl_3$ and spectroscopic parameters for each nucleus examined were as follows. ^{1}H and ^{13}C spectra were obtained under routine conditions, at a nominal frequency of 299.249 and 75.429 MHz, respectively. Proton chemical shifts are reported in ppm on the δ scale relative to TMS as an internal reference (0.00); carbon chemical shifts are reported in ppm relative to the center line of the $CDCl_3$ triplet (77.00). The ^{19}F spectra were recorded at 282.203 MHz, pulse length 5.0 μs (ca. 45°), spectral width 50 kHz, acquisition time 0.3 s, relax-

Fig. 10. Gas phase IR spectrum of **1** (*a*), in comparison with the synthetic spectra of the four strongest calculated fundamentals (see text) for the *Z* (*b*) and *E* (*c*) forms.

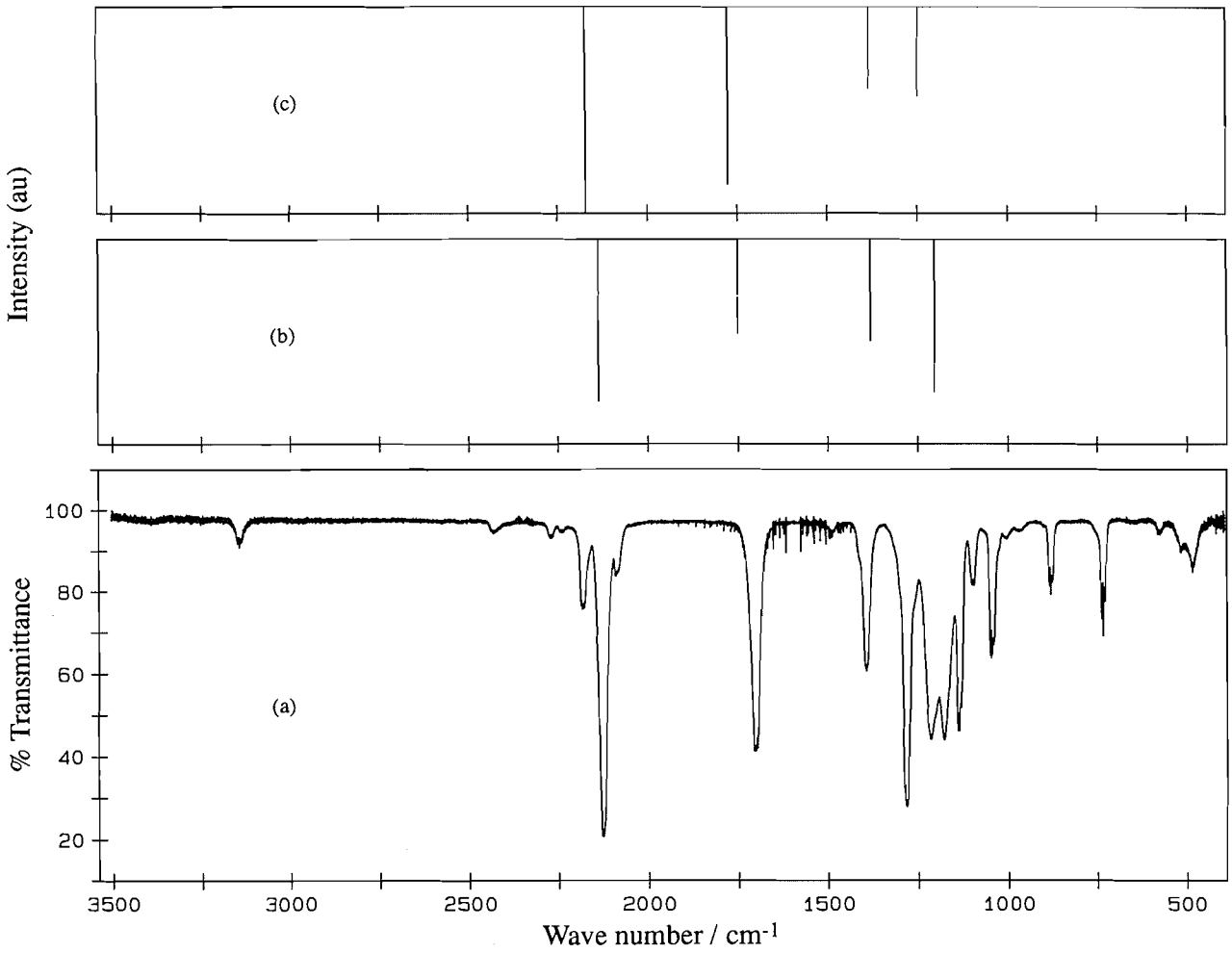

ation delay 4 s, collecting 16 scans; the signal was referenced to internal CCl_3F. ^{15}N spectra were recorded at 30.406 MHz. In the INEPT sequence, pulse length was 24.0 μs (90°), spectral width 15 kHz, acquisition time 2.0 s, relaxation delay 2.0 s, the *J* value used was 1.8 Hz; 3200 and 3840 scans, respectively, for the ^1H decoupled and coupled spectra were collected and the signals were related to external CH_3NO_2. The ^{17}O spectra were recorded at a nominal frequency of 40.662 MHz, pulse length 28 μs (ca. 90°), spectral width 36 kHz, acquisition time 10 ms, preacquisition delay 100 μs, collecting 15 000 scans; the spectra were recorded on a spinning sample without lock and decoupling. The signal-to-noise ratio was improved by applying a 30 Hz exponential broadening factor to the FID prior to transformation; the data point resolution was improved to 0.08 ppm by zero filling to 18 000 data points. The signal was referenced to external deionized water. Coupling constants are reported in hertz (Hz). All NMR data are collected in Table 1. MS spectra in the EI positive and negative ion mode were obtained with a Fisons TRIO-2000 mass spectrometer operating at 70 or 20 eV. CI spectra using CH_4 were obtained from the same instrument. The ion source filament was switched on just before peak elution in order to keep the ion source chamber temperature as low as possible. The actual amount of **1** injected was also kept as low as possible in order to avoid collision-induced decompositions and ion–molecule reactions. Notwithstanding these precautions, we observed that the peak intensities of the ions at *m/z* 138 and 110 differed conspicuously when revealed on different instruments, a fact apparently due to the thermal reactions linked to the geometry and actual temperature of the ion sources. Furthermore, the intensity ratios of peaks related to the fragmentation of the ion at *m/z* 110 also changed drastically. Accurate mass measurements and metastable ion studies were performed on a double focusing, reverse geometry, VG ZAB2F spectrometer (VG, Altrincham, UK): metastable ion transitions were studied by means of mass-analyzed ion kinetic (MIKE) spectra; product and precursor ion spectra were obtained by B/E = const. and B^2/E = const. linked scans, respectively. Metastable scanning MIKE and B^2/E spectra allowed us to rule out formation of the ion at *m/z* 110 from the parent ion, derived from **1**. The ion trap mass spectrometer used for some experiments was a GC–MS Varian Saturn operating with a filament current of 10 μA and a target value set at 20 000. The temperatures of different sections of the instru-

ment were carefully set between 60 and 150°C in order to obtain reproducible results. Tabulated mass spectra report the five most intense peaks with bracketed relative intensities. DSC data were obtained on a Du Pont TA2000 DSC module, operating with a heating rate of 10°C/min in a N_2 atmosphere (N_2 flow: 10°C/min).

Preparation of CH_2N_2

An alcohol-free anhydrous ethereal solution of CH_2N_2 was prepared and titrated essentially according to a described procedure (Method 3) (27), with minor modifications: solid KOH (6.6 g) was dissolved in 2-(2-ethoxyethoxy)ethanol (150 mL) avoiding the addition of H_2O; the required amount of Diazald^R (Aldrich) was dissolved in 225 mL of Et_2O and the ethereal solution of CH_2N_2 obtained was made anhydrous by passing it twice over 10 g anhydrous K_2CO_3.

*3-Diazo-1,1,1-trifluoro-2-propanone (**1**)*

A 0.33 M ether solution of CH_2N_2 (182 mmol) was slowly added from a dropping funnel with all parts made of polished glass and using a PTFE stopcock and cork to a well-stirred ether solution of trifluoroacetic anhydride (85 mmol) of similar molarity kept at ca. 0°C in a dry argon atmosphere in a well-ventilated hood. At the end of the addition, when also gas evolution had subsided, the solvent was gently removed, by heating at 40°C in a stream of argon, through a 50 cm Vigreux column. When the solution was suitably concentrated, it was finally kept at ca. 16 kPa in order to eliminate all the solvent. A final distillation of the residual oil gave a GC homogeneous liquid, 64% yield, bp 70°C at 20 kPa (lit. (1) bp 25°C at 133 Pa), mp (uncorrected) 0°C. Inversion of the order of addition of reactants, as well as the use of one equivalent of Et_3N to neutralize forming acidity, led to much lower conversions. Compound **1** was found to be stable in refluxing chlorobenzene. Differential scanning calorimetry in air showed two transitions before the decomposition curve, likely due to reaction with oxygen, at ca. 117 and 148°C; thermal decomposition of **1** occurred very rapidly in inert atmosphere at ca. 202°C. UV properties of **1** are reported in Table 2; the IR spectrum is reported in Fig. 6; NMR data are collected in Table 1; mass spectra are reported in Figs. 1, 2, 4, and 5. Negative ion MS of **1** (CH_4, 70 eV): *m/z* 137 (M^- − H, 1%), 112 (1), 111 (21), 110 (100), and 69 (2).

*3-d-3-Diazo-1,1,1-trifluoro-2-propanone (d-**1**)*

Suitably anhydrous NaCl and Na_2SO_4 were obtained by storing in vacuo at 200°C for 4 h before use. ^1H and ^{13}C NMR spectra were initially recorded on a solution containing pure **1** (2.03 mmol), CH_2I_2 (1.05 mmol, internal proton standard, δ_H = 3.89 ppm and δ_C = −66.26 ppm), and TMS in $CDCl_3$ (2.0 mL). The integral ratio observed for H singlet peaks was 0.93:1.00 (**1** vs. CH_2I_2). This solution was equilibrated five times at room temperature, for 15 min each time, with D_2O (1.0 mL) containing NaCl (1.0 mmol), then finally dried over Na_2SO_4. ^1H NMR spectrum: ratio H(**1**):H(CH_2I_2) = 0.0028 (indicating a practically complete H/D exchange); ^{13}C NMR spectrum: C(=O), C(F_3), and C(H_2I_2) resonated at the same frequencies with patterns unchanged from the original solution; C-D (triplet, J_{CD} = 30.1 Hz) at 55.70 (central peak) ppm. H-D interchange was equally successful when neat **1** was shaken five times during 15 min at room temperature with the same ratio of D_2O (NaCl) and subsequently dried over Na_2SO_4. The IR spectrum of *d*-**1** is reported in Fig. 7 and the EI mass spectrum in Fig. 3.

Acknowledgements

This work was supported in part by grants to A.G.G. (CNR 92.00391CT03, 93.03024CT03, MURST 1991-93, 40%) and to P.S. (MURST 1991-93, 40%). We express our gratitude to Dr. P. Traldi (CNR, Padova, Italy) for some MS data. Thanks are due to Dr. M. Nebuloni (Lepetit Research Center, Gerenzano, VA, Italy) for the DSC measurements.

References

1. F. Brown and W.K.R. Musgrave. J. Chem. Soc. 2087 (1953).
2. S. Sorriso. *In* The chemistry of diazonium and diazo groups. Part 1. Structural chemistry. *Edited by* S. Patai. John Wiley & Sons, Chichester, U.K. 1978. Chap. 3. pp. 113–126.
3. A. Kamal and A.A. Qureshi. Chem. Ind. 931 (1962).
4. A. Delgado and J. Clardy. Tetrahedron Lett. **33**, 2789 (1992).
5. D.S. Wulfman and B. Poling. *In* Reactive intermediates. Vol. 1. *Edited by* R. A. Abramovitch. Plenum, London. 1980. p. 325.
6. (*a*) M. Regitz, F. Menz, and A. Liedhegener. Liebigs Ann. Chem. **739**, 174 (1970); (*b*) H. Dahn, A. Donzel, A. Merbach, and H. Gold. Helv. Chim. Acta, **46**, 994 (1963).
7. G.C. Levy, R.L. Lichter, and G.L. Nelson. *In* Carbon-13 nuclear magnetic resonance spectroscopy. 2nd ed. John Wiley and Sons, New York. 1980. pp. 137, 140, and 148.
8. M. Regitz and G. Maas. *In* Diazo compounds – properties and synthesis. Academic Press, London. 1986. pp. 48–50, and references cited therein.
9. R.O. Duthaler, H.G. Förster, and J.D. Roberts. J. Am. Chem. Soc. **100**, 4974 (1978).
10. N. Muller and D.T. Carr. J. Phys. Chem. **67**, 112 (1963).
11. F. Kaplan and G.K. Meloy. J. Am. Chem. Soc. **88**, 950 (1966).
12. I.G. Csizmadia, S.A. Houlden, O. Meresz, and P. Yates. Tetrahedron, **25**, 2121 (1969).
13. B.C. Anderson. J. Org. Chem. **33**, 1016 (1968).
14. M. Witanowski, L. Stefaniak, and G.A. Webb. Annu. Rep. NMR Spectrosc. **25**, 64 (1993); **25**, 367 (1993).
15. R.L. Lichter, P.R. Srinivasan, A.B. Smith, III, R.K. Dieter, C.T. Denny, and J.M. Schulman. J. Chem. Soc. Chem. Commun. 366 (1977).
16. (*a*) G. Cerioni, N. Culeddu, and A. Saba. J. Phys. Org. Chem. **5**, 424 (1992); (*b*) Magn. Reson. Chem. **31**, 829 (1993).
17. K.T. Liu, T.R. Wu, and Y.C. Lin. J. Phys. Org. Chem. **2**, 363 (1989).
18. D.W. Boykin and A.L. Baumstark. *In* ^{17}O NMR spectroscopy in organic chemistry. *Edited by* D.W. Boykin. CRC Press, Boca Raton, Fla. 1991. Chap. 8. p. 209.
19. G.T. Knight and B. Saville. J. Chem. Soc. Chem. Commun. 1262 (1969).
20. A. Poletti, G. Paliani, M.G. Giorgini, and R. Cataliotti. Spectrochim. Acta, Part A: **31A**, 1869 (1975).
21. G. Socrates. *In* Infrared characteristic group frequencies. John Wiley & Sons, Chichester, U.K. 1980. p. 39.
22. C. Pecile, A. Foffani, and S. Ghersetti. Tetrahedron, **20**, 823 (1964).
23. G. Paliani, S. Sorriso, and R. Cataliotti. J. Chem. Soc. Perkin Trans. 2, 707 (1976).
24. (*a*) G. Innorta, S. Torroni, A. Foffani, and S. Sorriso. Ann. Chim. (Rome), **66**, 1 (1976); (*b*) H.M. Niemeye. Helv. Chim. Acta, **60**, 1487 (1977); (*c*) S. Sorriso. Z. Naturforsch. B: Anorg. Chem. Org. Chem. **34b**, 1530 (1979); (*d*) F. Kaplan and G. K. Meloy. Tetrahedron Lett. 2427 (1964).

25. S. Sorriso, F. Stefani, A. Flamigni, and E. Semprini. J. Chem. Soc. Faraday Trans. 2, **71**, 682 (1975).
26. M.J. Frisch, G.W. Trucks, M. Head-Gordon, P.M.W. Gill, M.W. Wong, J.B. Foreman, B.G. Johnson, H.B. Schlegel, M.A. Robb, E.S. Replogle, R. Gomperts, J.L. Andres, K. Raghavachari, J.S. Binkley, C. Gonzales, R.L. Martin, D.J. Fox, D.J. DeFrees, J. Baker, J.J.P. Stewart, and J.A. Pople. GAUSSIAN 92. Gaussian Inc., Pittsburgh, Pa. 1992.
27. A.I. Vogel. *In* Vogel's textbook of practical organic chemistry. 5th ed. Longman S. & T., Harlow, Essex, U.K. 1989. pp. 432–433.

Probe of cadmium(II) binding on soil fulvic acid investigated by ^{113}Cd NMR spectroscopy

Kun H. Chung, Seog W. Rhee, Hyun S. Shin, and Christopher H. Moon

Abstract: Binding of cadmium(II) on soil fulvic acid (FA) was investigated over a range of fulvate-to-cadmium concentration ratios (8 – 59 equiv. mol^{-1}) using ^{113}Cd NMR spectroscopy. The ^{113}Cd chemical shift of cadmium bound on fulvate was observed in a more downfield region (δ −20.4 to −15.6) than that bound on synthetic polymers, poly(acrylic acid) (PAA: δ −36.6 to −38.2), poly(methacrylic acid) (PMAA: δ −34.0 to −25.4), and poly(vinyl benzoic acid) (PVBA: δ −34.7 to −31.2). The calculated values of individual chemical shifts for the species CdL^+ and CdL_2 (L: carboxylate) formed in Cd(II)–carboxylate systems (e.g., acetate, benzoate) are δ −22 to −24 and δ −39 to −40, respectively. The relative downfield shift of cadmium(II)–fulvate suggests that functional groups (e.g., hydroxyl and neutral N donor) other than carboxylates may be involved in cadmium coordination. The chemical shifts of cadmium complexes of hydroxycarboxylates (e.g., glycolate) or carboxylates containing neutral N donor (e.g., picolinate) were generally observed in more downfield regions than their carboxylate counterparts.

Key words: fulvic acid, polyfunctionality, binding sites, chemical shift, ^{113}Cd NMR.

Résumé : On a étudié, par spectroscopie de RMN du ^{113}Cd, les sites de liaison du cadmium(II) sur l'acide fulvique (AF) impur en utilisant un intervale de concentration de fulvate : cadmium (8–59 équiv. mol^{-1}). On a observé que les déplacements chimiques du ^{113}Cd, du cadmium lié au fulvate, se situent à champ plus faible (δ −20,4 à −15,6) que les polymères synthétiques, acide polyacrylique (APA : δ −36,6 à −38,2), acide polyméthacrylique (APMA : δ −34,0 à −25,4) et acide polyvinylbenzoique (APVB : δ −34,7 à −31,2). Les valeurs calculées des déplacements chimiques individuels des espèces CdL^+ et CdL_2 (L = carboxylate) formées dans le système Cd(II)–carboxylate (acétate, benzoate par exemple) sont respectivement δ −22 à −24 et δ −39 à −40. Le déplacement chimique relativement faible du complexe cadmium(II)–fulvate suggère que des groupes fonctionnels (par exemple hydroxyle et un donneur neutre d'azote) autres que les carboxylates peuvent être impliqués dans la coordination du cadmium. Les déplacements chimiques des complexes de cadmium des hydrocarboxylates (par exemple le glycolate) ou des carboxylates contenant des donneurs neutres d'azote (par exemple un picolinate) sont généralement observés à des champs plus faibles que leur contrepartie carboxylates.

Mots clés : acide fulvique, polyfonctionnalité, sites de liaison, déplacement chimique, RMN du ^{113}Cd.

[Traduit par la rédaction]

Introduction

Heavy metal contamination of the environment is caused by the wide usage of heavy metals in industries to meet the demands of modern society. In wastewater matrices, the speciation of some heavy metals is dominated by organic complexes, and their characterization is an important aspect of speciation in such matrices (1). In soil matrices, the biological availability of environmental trace metals is influenced strongly by complexes formed with soil organic matters such as humic substances (2). Complexation of trace metals by humic substances is also important in determining their fate in the environment (3).

Studies of the complexation of trace metals (e.g., Cu^{2+}, Cd^{2+}, Pb^{2+}) with humic substances are reported in the literature (4–8). The stability constants of the complexes thus formed have been evaluated using many different modeling techniques, leading to some conflict in the information obtained (9, 10). One cause of uncertainty is in regard to the nature of metal ion binding by humic substances. From the results of base titration, Stevenson et al. indicated the formation of 1:1 and 1:2 complexes (CuL^+ and CuL_2: L are active sites) when Cu^{2+} ions are bound to humic acid (2). Marinsky and Anspach found CuL_2 to be predominant when Cu^{2+} ion is complexed to PMAA gel at a higher neutralization range (11). More recently a joint study with Miyajima was carried out by us on cadmium(II) binding by PAA using potentiometric titration, and the preliminary result shows the formation of 1:1 and 1:2 complexes. By contrast, Perdue and Lytle applied a multiligand model for binding of proton and metal ions by humic acid (12).

In this work, we report the result of our study of the binding of cadmium(II) by a soil fulvic acid as characterized by ^{113}Cd NMR spectroscopy. ^{113}Cd NMR spectroscopy has been used in studies of the structure and dynamics of inorganic and bioinorganic molecules (13–16). The utility of ^{113}Cd NMR as a metallobioprobe is due to the ability of cadmium(II) ion to form complexes over a range of conformation and ligand numbers: ^{113}Cd has a spin of 1/2 with no quadrupolar contri-

Received January 3, 1996

K.H. Chung, S.W. Rhee, H.S. Shin, and C.H. Moon.[1]
Department of Chemistry, Korea Advanced Institute of Science and Technology, 373-1 Kusong-Dong, Yusong-Ku, 305-701 Taejon, Korea.

1 Author to whom correspondence may be addressed. Telephone: 82-42-869-2823. Fax: 82-42-869-2810.

bution to cause NMR relaxation, which broadens the NMR signals. A chemical shift range of over 900 ppm has been observed for ^{113}Cd, depending upon the nature, number, and geometric arrangement of the coordinated ligands (17–22). Fulvic acids possess a variety of functional groups that can bind with metal ions (3). Several types of carboxylic acids, polyfunctional carboxylic acids, and synthetic polymers were used as model ligands in this study.

Experimental

Materials

Fulvic acid used in the experiment was isolated from air-dried soil from the Okchun Basin as described previously (23). Briefly, humic substances were extracted from air-dried soil (1.5 kg) with 15 dm^3 of 0.1 mol dm^{-3} NaOH under N_2 atmosphere. The humic acid fraction was separated by acid precipitation (pH 1) with 6 mol dm^{-3} HCl. The FA fraction remaining in the supernatant was isolated by sorbing it on a column of XAD-8 resins. The sorbed FA fraction was eluted with 0.1 mol dm^{-3} NaOH, and converted to a protonated form using a cation exchange column of Dowex 50X8 (H^+) to remove Na^+. The protonated final product was freeze-dried (C: 51.2 ± 0.5%, H: 4.5 ± 0.2%, O: 41.0 ± 1.0%, N: 2.2 ± 0.1%, and S: 0.2 ± 0.1%). PAA (MW: 5000 daltons) and organic acids were purchased from Aldrich and were used without further purification. PMAA and PVBA were prepared by a radical polymerization technique with AIBN (azobisisobutyronitrile) in ethanol solution and characterized according to procedures given in the literature (24). Cadmium solution was prepared by dissolving $Cd(ClO_4)_2 \cdot 6H_2O$ (Alfa) in doubly deionized water. The isotopically enriched cadmium solution was prepared by dissolving 95.8% ^{113}Cd-enriched metal (Isotec Inc.: Product No. 77-066-01-7; 0.5 g) in an aliquot of hot concentrated $HClO_4$, then diluting with doubly deionized water to 0.10 mol dm^{-3}.

Instrumentation

The ^{113}Cd NMR investigation was performed on a Brucker AM 300 spectrometer operating at 66.576 MHz. All NMR measurements were made with an outer 10 mm NMR tube containing the sample solutions, and a sealed 5 mm inner tube with 0.1 mol dm^{-3} $Cd(ClO_4)_2$ aqueous (D_2O) solution; 0.1 mol dm^{-3} $Cd(ClO_4)_2$ was the reference material and D_2O solvent was used as an external lock to keep the field of homogeneity. The temperature of the samples was kept constant at 24°C by flowing heated air around the tube mounted coaxially in the probe head. Positive chemical sifts are downfield from the reference and indicate decreased shielding. The spectra for Cd(II) – organic acids were obtained using a 30° pulse width (6 μs), acquisition time of 0.885 s, and a relaxation delay of 2.2 s (0.2 s for Cd(II)–polymers and Cd(II)–fulvate). The spectra of Cd(II)–polymers and Cd(II)-fulvate required 50 000–60 000 transients. The solid state ^{113}Cd NMR spectrum was obtained from ca. 0.5 g of a freshly prepared moist precipitate of Cd(II)–fulvate using MAS technique. The delay time was 5 s and the rotor speed was set at 4.0 kHz (collected number of scans, 1500).

Sample preparation

Stock solutions of FA, PMAA, PAA, and PVBA (50.0 cm^3, 0.30 equiv. dm^{-3}) were prepared as follows: 1.990 g of FA was dissolved in 8.0 cm^3 of 1.0 mol dm^{-3} NaOH and diluted with doubly ionized water to a final volume of 50.0 cm^3 and the pH adjusted to 6.0. The total acidity of the acids was measured by pH titration (25) and these values were used to obtain stock solutions with the same concentration given in equiv. dm^{-3}: The measured total acidity of FA, PMAA, PAA, and PVBA is 7.6, 12, 14, 7.0 mequiv. g^{-1}, respectively. An initial sample solution was prepared by mixing 4.0 cm^3 of the stock solution with 1.0 cm^3 of 0.1 mol dm^{-3} cadmium perchlorate solution (95.8% ^{113}Cd-enriched). Subsequently all other sample solutions of a series were prepared by dilution of the initial solution with the stock polymer solution, thereby changing the cadmium concentration in the sample while keeping the polymer concentration constant at 0.24 equiv. dm^{-3}. The sample solutions were kept in darkness over 2 days, with occasional shaking, to equilibrate. Approximately 2 cm^3 of each sample was placed in a 10 mm NMR tube for NMR analysis. A series of sample solutions were also prepared for each organic acid used as model ligand, where $Cd(ClO_4)_2$ was kept constant at 5.56×10^{-2} mol dm^{-3} and the organic acid concentration was varied from 0.025 to 0.6 mol dm^{-3}. All the sample solutions were adjusted to pH 6.0 using $HClO_4$ and NaOH (carbonate free, Baker Co.), and the pH was measured using a glass electrode coupled to a digital pH meter (Metrohm type 632).

Results and discussion

The ^{113}Cd NMR spectra of Cd(II)–fulvate were obtained over a fulvate-to-cadmium ratio of 8–59 equiv. mol^{-1} and they are shown in Fig. 1. At concentration ratios of 8 equiv. mol^{-1} and above (up to 59 equiv. mol^{-1}), Cd(II)–fulvate remained stable in solution, and it was possible to obtain a single averaged chemical shift. A plot of the chemical shift change (δ −20.4 to −15.6) versus fulvate-to-cadmium ratio is shown in Fig. 2. Below 8 equiv. mol^{-1}, the Cd(II)–fulvate formed precipitates. The spectrum of a freshly prepared precipitate of Cd(II)–fulvate is shown in Fig. 3. A freeze-dried precipitate gave a very broad and unresolved spectrum, but moistening the precipitate with a little water (w/w 15%) produced a spectrum of good signal-to-noise ratio with a chemical shift of δ −25 for the solid sample.

Majidi et al. investigated the metal–algae binding site using ^{113}Cd NMR spectroscopy, and observed a chemical shift of δ −10 to −18 for cadmium(II) bound on cell walls, indicative of the metal uptake by carboxylate groups (26). In the characterization of Cd(II) binding sites on *Datura innoxia*, Ke and Rayson obtained chemical shift data indicative of carboxylate–Cd(II) interaction in a 2:1 ratio (27). The observed chemical shift of Cd(II)–fulvate in solution (δ −20.4 to −15.6) and as solid (δ −25) seem to indicate that the bound cadmium ions are coordinated to carboxylate groups. Recently, an investigation of Cd(II)–carboxylate systems (mono- and di-carboxylic acids) in aqueous solution was carried out using ^{113}Cd NMR spectroscopy (28). A single averaged chemical shift was obtained even at reduced temperature (25° to −90°C in ethanol), showing that the species formed in Cd(II)–carboxylate systems are undergoing rapid exchange in solution. Using known stability constants, the individual chemical shifts were calculated to be in the range δ −22 to −24 and δ −39 to −40 for CdL^+ and CdL_2 (L = carboxylate) species. In Cd(II)–car-

Fig. 1. ^{113}Cd NMR spectra of cadmium(II) bound on FA in aqueous solution: $[FA]_t = 0.24$ equiv. mol^{-1} and pH = 6.

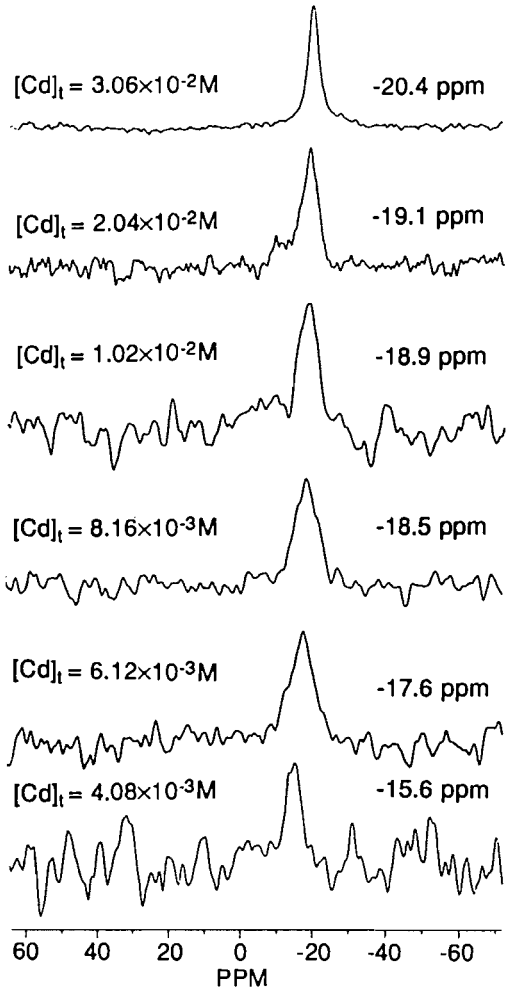

Fig. 2. Plots showing the ^{113}Cd chemical shift changes due to variation of the [polymer]/[Cd(II)] ratio: (*a*) FA, (*b*) PMAA, (*c*) PVBA, and (*d*) PAA.

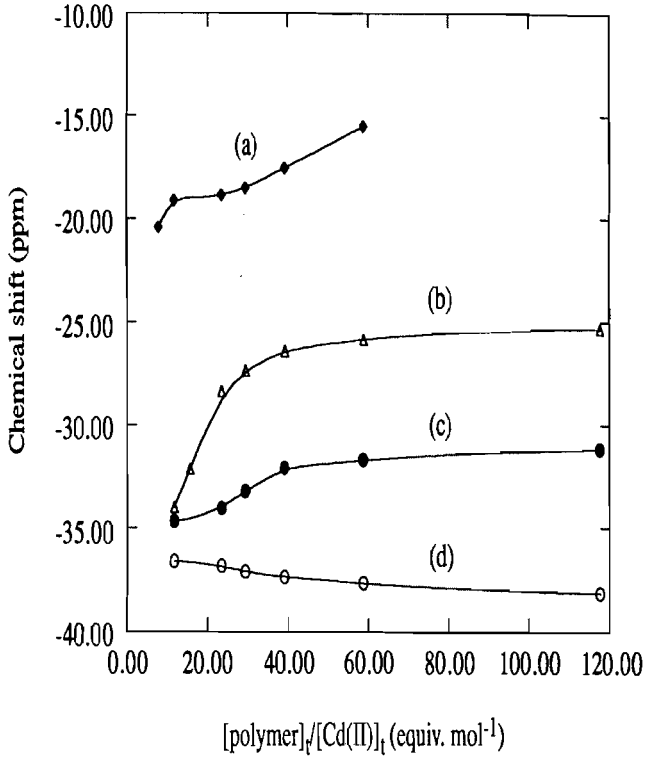

Fig. 3. ^{113}Cd MAS NMR spectrum of Cd(II)–fulvate precipitate.

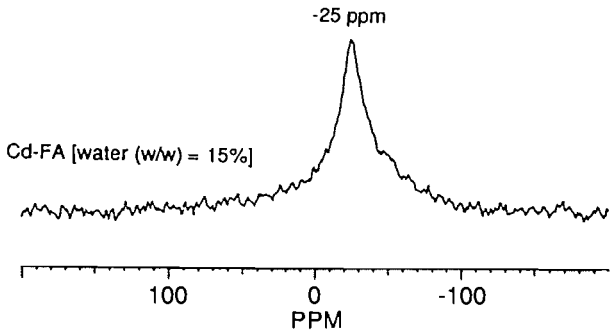

boxylate systems, an increase in the carboxylate-to-cadmium ratio caused the chemical shift to move towards an upfield region: the cadmium ion becomes more shielded when coordinated water molecules are displaced by carboxylates. However, quite the opposite trend was observed for the Cd(II)–fulvate system: an increase of fulvate-to-cadmium ratio caused the chemical shift to move towards a downfield region (less shielding). From surface pressure and viscosity measurements, Ghosh and Schnitzer proposed a model changing humic substances from a flexible "linear molecule" to a rigid "spherocolloid" (29). The ^{113}Cd NMR spectra of cadmium bound on synthetic model polymers PAA, PMAA, and PVBA were obtained at the concentration ratio 12 to 118 equiv. mol^{-1}. The ^{113}Cd NMR spectra of Cd(II)–PAA and –PMAA are shown in Fig. 4 as examples. In the Cd(II)–PAA system, an increase in the PAA-to-cadmium ratio caused the chemical shift towards an upfield region (more shielding) in a manner observed in Cd(II)–carboxylate systems. However, quite different chemical shift changes were observed in the Cd(II)–PMAA and –PVBA systems: an increase of polymer-to-cadmium ratio caused the chemical shift to change to a downfield region (less shielding). The cause for this apparent difference in the chemical shift change behaviour of PMAA and PVBA, and PAA remains unclear. Different chemical shift behavior was also reported for the binding of sodium ion on PMAA and PAA investigated by ^{23}Na NMR, and this was attributed to their structural differences (30).

The ^{113}Cd NMR chemical shift is highly sensitive to the types of donor atoms, coordination number, and geometry (17–22). The results of the ^{113}Cd NMR study with model carboxylate ligands (monomers and polymers) show that when the coordination environment of the cadmium ion is made up solely of carboxylates and water molecules, then the chemical shifts seem to appear at a more upfield region (more shielding) than for Cd(II)–fulvate. This apparent difference in the chem-

Fig. 4. ^{113}Cd NMR spectra of cadmium(II) bound on PAA and PMAA in aqueous solution: $[polymer]_t = 0.24$ equiv. mol^{-1} and pH = 6

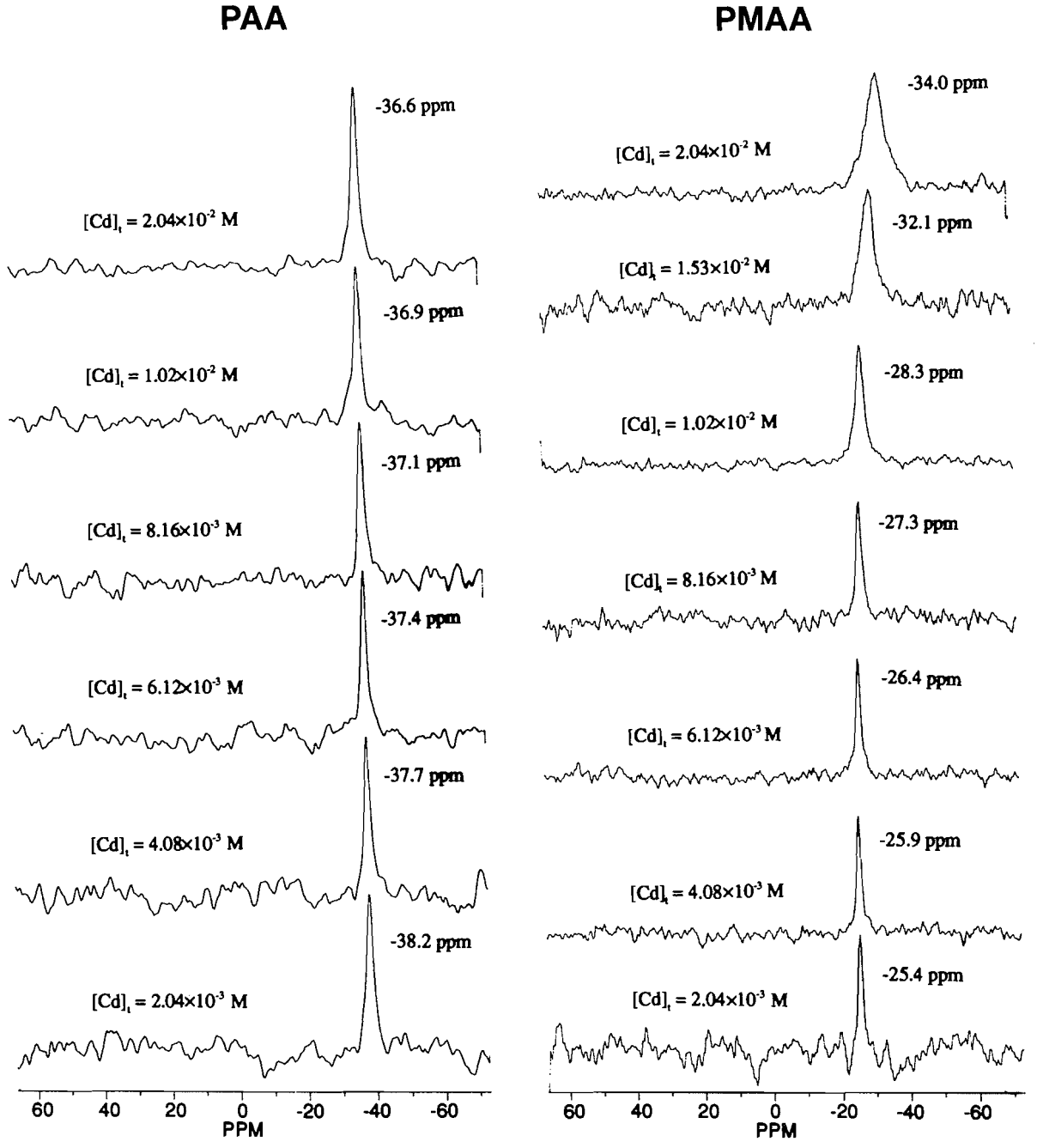

ical shift may be caused by the presence of a diversity of functional groups (carboxylate, phenolic -OH, alcoholic -OH, and minor amounts of N) of fulvic acid, creating a multiligand coordination environment for the cadmium ion. There are several examples of cadmium(II) complexes formed by other model ligands that gave chemical shifts in more downfield regions. One such example may be coordination of cadmium(II) by a malonate-like moiety of fulvic acid. This moiety is shown in one of the average structures proposed for Suwannee River fulvic acid by the U.S. Geological Survey (31). Malonate is capable of forming a six-membered chelate ring (η^5) with cadmium ion. An increase of the malonate-to-cadmium ratio caused the chemical shift to change more gradually towards an upfield region and approached a steady value of δ −19 (28), which lies close to the chemical shift range of Cd(II)–fulvate. The second group of examples may be complexes of cadmium(II) formed by hydroxycarboxylic acids as ligands: specifically those with an -OH attached to the α- and β-carbons (e.g., glycolic, gluconic, 3-hydroxybutanoic, and malic acids) are observed in a more downfield region than

Fig. 5. Plots showing the ^{113}Cd chemical shift change of Cd(II)–hydroxycarboxylate and –carboxylate complexes: (*a*) glycolic acid, (*b*) gluconic acid, (*c*) malic acid, (*d*) 3-hydroxybutanoic acid, (*e*) acetic acid, (*f*) propanoic acid, and (*d*) succinic acid.

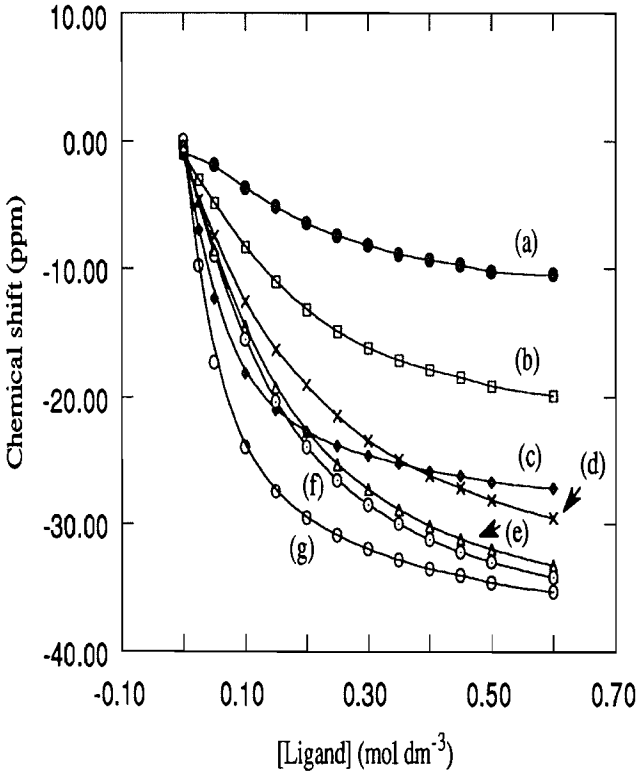

Fig. 6. Plots showing the ^{113}Cd chemical shift change of Cd(II)–carboxylates possessing a neutral N donor: (*a*) picolinic acid, (*b*) methylpicolinic acid, (*c*) dipicolinic acid, and (*d*) nicotinic acid.

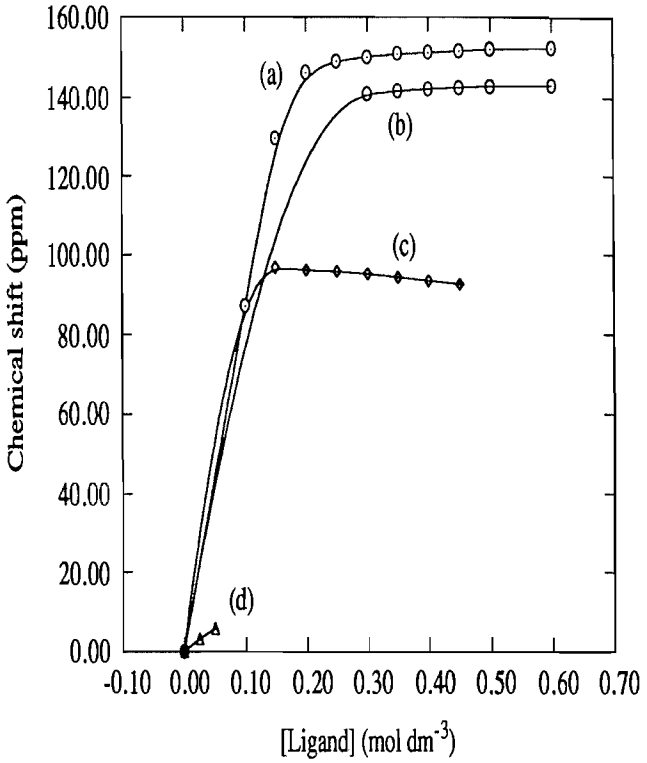

their carboxylic acid counterparts (e.g., acetic, propanoic, and succinic acids). Plots of chemical shift change versus ligand concentration are shown in Fig. 5. The changes for cadmium(II) complexed to those ligands capable of forming five- and six-membered chelate rings (η^4 and η^5) are displayed more downfield. It has been suggested that a probable strong copper(II) binding site may include the phenolic group (4, 5, 32). A salicylate-like moiety may be a possible strong binding site for cadmium ion, but this was not investigated due to precipitate formation. Other possible examples are those complexes of cadmium coordination by a neutral N donor: The minor sites of fulvic acid are said to include neutral N donors. The soil fulvic acid contained approximately 2.2% nitrogen, and the proposed average structure included a neutral N donor (23). The chemical shift changes of complexes of cadmium(II) coordinated to carboxylic acids containing a neutral N donor (e.g., nicotinic, picolinic, and dipicolic acids) are shown in Fig. 6. Much larger downfield shifts are observed in these cadmium(II) complexes: cadmium(II) ion is deshielded by coordinating the neutral N donor group of these ligands (17, 18, 33).

Summary

^{113}Cd NMR spectroscopy has been applied to a study of cadmium(II) binding by a fulvic acid. The chemical shifts of Cd(II)–fulvate seem to reflect the rapidly exchanging conditions in aqueous solution and involve many species that formed by a diversity of functional groups of fulvic acid.

Acknowledgements

This work was supported by the Korea Science and Engineering Foundation Research Grant No. 941-0300-010-2.

References

1. R.M. Sterritt and J.N. Rester. Sci. Total Environ. **34**, 117 (1984).
2. F.J. Stevenson, Alanah Fitch, and M.S. Brar. Soil Sci. **155**, 77 (1993).
3. F.J. Stevenson. *In* Humic substances in soil, sediment, and water. *Edited by* G.R. Aiken, D.M. Mcknight, and R.L. Wershaw. John Wiley & Sons, New York. 1985. pp. 13–52.
4. D.S. Gamble, A.W. Underdown, and C.H. Lanford. Anal. Chem. **52**, 1901 (1980).
5. W.T. Bresnahan, C.L. Grant, and J.H. Weber. Anal. Chem. **50**, 1675 (1978).
6. R.A. Saar and J.H. Weber. Can. J. Chem. **57**, 1263 (1979).
7. E. Tipping and M.A. Hurley. Geochim. Cosmochim. Acta, **56**, 3627 (1992).
8. J.E. Gregor, H.K.J. Powell, and R.M. Town. J. Soil Sci. **40**, 661 (1989).
9. B.M. Bartschat, S.E. Cabaniss, and F.M.M. Morel. Environ. Sci. Technol. **26**, 284 (1992).
10. E. Tipping, M.M. Reddy, and M.A. Hurley. Environ. Sci. Technol. **24**, 1700 (1990).

11. J.A. Marinsky and W.M. Anspach. J. Phys. Chem. **79**, 439 (1975).
12. E.M. Perdue and C.R. Lytle. Environ. Sci. Technol. **17**, 654 (1983).
13. Y. Boulanger, I.M. Armitage, K.-A. Miklossy, and D.R. Winge. J. Biol. Chem. **257**, 13717 (1982).
14. B.R. Bobsein and R.J. Myers. J. Am. Chem. Soc. **102**, 2454 (1980).
15. J.D. Otoves and I.M. Armitage. Biochemistry, **19**, 4031 (1980).
16. J.L. Evelhoch, D.F. Bocian, and J.L. Sudmeier. Biochemistry, **20**, 4951 (1981).
17. P.D. Ellis. Science, **221**, 1141 (1983).
18. M.F. Summers. Coord. Chem. Rev. **86**, 43 (1988).
19. A.D. Cardin, P.D. Ellis, J.D. Odom, and J.W. Howard. J. Am. Chem. Soc. **97**, 1672 (1975).
20. A.R. Harberkorn, L. Que, W.O. gillum, R.H. Holm, C.S. Liu, and R.C. Lord. Inorg. Chem. **15**, 2408 (1976).
21. C.F. Jensen, S. Deshmukh, H.J. Jakobsen, R.R. Inners, and P.D. Ellis. J. Am. Chem. Soc. **103**, 3659 (1981).
22. P.F. Rodesiler and E.L. Amma. J. Chem. Soc. Chem. Commun. 182 (1982).
23. H.S. Shin and H. Moon. Soil Sci. **161**, 250 (1996).
24. M. Philip. *In* Water-soluble synthetic polymers. Vol. 1. CRC Press, Boca Raton, Fla. 1985.
25. J.I. Kim, G. Buckau, G.H. Li, H. Duschner, and N. Psarros. Fresenius J. Anal. Chem. **338**, 245 (1990).
26. V. Majidi, D.A. Laude, Jr., and J.A. Holcombe. Environ. Sci. Technol. **24**, 220 (1990).
27. H.Y.D. Ke and G.D. Rayson. Environ. Sci. Technol. **26**, 1202 (1992).
28. K.H. Chung and C.H. Moon. J. Chem. Soc. Dalton Trans. 75 (1996).
29. K. Ghosh and M. Schnitzer. Soil Sci. **129**, 265 (1980).
30. H. Gustavsson, B. Lindman, and T. Bull. J. Am. Chem. Soc. **100**, 4655 (1978).
31. J.A. Leenheer. *In* Humic substances in the Suwannee river, Georgia: interactions, properties, and proposed structures. *Edited by* R.C. Avertt, J.A. Leenheer, D.M. McKnight, and K.A. Thorn. U.S. Geological Survey: Open-File Report 87-557. 1987.
32. A.W. Underdown, C.H. Lanford, and D.S. Gamble. Environ. Sci. Technol. **19**, 132 (1985).
33. M. Munakata, S. Kitagawa, and F. Yagi. Inorg. Chem. **25**, 964 (1986).

The acid-catalyzed demetalation of 1-(tri-*n*-butylstannyl)-2-phenylethyne. A surprisingly small β-stannyl effect

I. Egle, V. Gabelica, A.J. Kresge, and T.T. Tidwell

Abstract: Rates of conversion of 1-(tri-*n*-butylstannyl)-2-phenylethyne to phenylethyne in H_2O and D_2O solutions of perchloric acid were found to be proportional to acid concentration, giving the hydronium ion rate constant $k_{H^+} = 1.85 \times 10^{-2}$ M^{-1} s^{-1} and the isotope effect $k_{H^+}/k_{D^+} = 3.10$. The magnitude of this isotope effect suggests that the reaction occurs by rate-determining hydron transfer to the substrate, producing a vinyl carbocation; this carbocation then loses its tributylstannyl group, giving phenylacetylene as the only detectable aromatic product. The hydronium ion rate constant, when compared to the rates of protonation of phenylethyne and 1-(trimethylsilyl)-2-phenylethyne, gives a β-stannyl stabilizing effect of $\delta\Delta G^{\ddagger} = 6.6$ kcal mol^{-1} and a differential β-stannyl/β-silyl effect of $\delta\Delta G^{\ddagger} = 3.2$ kcal mol^{-1}. These stabilizations are very much smaller than previously reported β-stannyl effects. Possible reasons for the difference are suggested.

Key words: β-stannyl effect, β-silyl effect, carbocation stabilization, protodemetalation.

Résumé : On a trouvé que les vitesses de conversion du 1-(tri-*n*-butylstannyl)-2-phényléthyne en phényléthyne, en solutions d'acide perchlorique dans du H_2O et dans du D_2O, est proportionnelle à la concentration d'acide; la constante de vitesse de l'ion hydronium $k_{H^+} = 1{,}85 \times 10^{-2}$ M^{-1} s^{-1} et l'effet isotopique $k_{H^+}/k_{D^+} = 3{,}10$. L'amplitude de cet effet isotopique suggère que la réaction se produit par une étape déterminant la vitesse au cours de laquelle il y a transfert d'un hydron au substrat conduisant à la formation d'un carbocation vinylique; ce carbocation perd alors son groupe tributylstannyle ne donnant que du phénylacétylène comme seul produit aromatique pouvant être détecté. Lorsqu'on compare la constante de vitesse de l'ion hydronium aux vitesses de protonation du phényléthyne et du 1-(triméthylsilyl)-2-phényléthyne, on en déduit l'effet stabilisant du groupe β-stannyle, $\delta\Delta G^{\ddagger} = 6{,}6$ kcal mol^{-1}, ainsi que la différence entre les effets β-stannyle et β-silyle, $\delta\Delta G^{\ddagger} = 3{,}2$ kcal mol^{-1}. Ces stabilisations sont beaucoup plus faibles que celles rapportées antérieurement pour les effets β-stannyles. On suggère diverses raisons possibles pour la différence.

Mots clés : effet β-stannyle, effet β-silyle, stabilisation du carbocation, protodémétallation.

[Traduit par la rédaction]

It is well known that silyl substituents in the β-position stabilize carbocations strongly (for reviews, see ref. 1), and other Group IV A metals lying below silicon in the periodic table have even more powerful effects. For example, a stannyl substituent in the β-position was found to accelerate the rate of solvolysis of a cyclohexanol ester over that of the unsubstituted substrate by a factor much in excess of 10^{14} (2), and the remarkably large stannyl/silyl rate ratio of 10^8 was observed in the protonation of metalated acetylenes (3). We were surprised to discover, therefore, that the stannyl group in 1-(tri-*n*-butylstannyl)-2-phenylethyne raises the rate of vinyl cation formation by protonation of this substance, eq. [1]1 (X = $SnBu_3$), over that for phenylacetylene, eq. [1] X = H, by a factor of only 6.5×10^4, and that comparison with the corresponding silyl system, eq. [1] X = $SiMe_3$, gives a stannyl/silyl rate ratio of only 2.1×10^2.

$$[1] \quad PhC{\equiv}CX \xrightarrow{H^+} Ph\overset{+}{C}{=}CHX$$

Received January 11, 1996.

I. Egle, V. Gabelica, A.J. Kresge,[1] and T.T. Tidwell.
Department of Chemistry, University of Toronto, Toronto, ON M5S 3H6, Canada.

[1] Author to whom correspondence may be addressed. Telephone and Fax: (416) 978-7529. E-mail: akresge@alchemy.chem.utoronto.ca

Experimental section

Materials

1-(Tri-*n*-butylstannyl)-2-phenylethyne was prepared by treating lithium phenylacetylide with tributyltin chloride (4). All other materials were best available commercial grades.

Kinetics

Rates of demetalation of 1-(tri-*n*-butylstannyl)-2-phenylethyne were determined by monitoring the decrease in its absorbance at λ = 266 nm. Measurements were made using a Cary 2200 spectrometer whose cell compartment was thermostatted at 25.0 ± 0.05°C. Reactions were initiated by adding 10-μL aliquots of acetonitrile solutions of substrate to 3-mL quantities of perchloric acid solutions contained in quartz cuvettes, which had first been allowed to come to temperature equilibrium with the spectrometer cell compartment. The substrate was poorly soluble in both acetonitrile and aqueous acids, and dissolution was promoted by a few seconds' immersion in an ultrasonic bath. The kinetic data conformed well to the first-order rate law and observed rate constants were eval-

uated by least-squares fitting of an exponential function. Acid concentrations of the reaction mixtures were determined by titrating weighed aliquots.

Results and discussion

Reaction mechanisms

Rates of reaction of 1-(tri-*n*-butylstannyl)-2-phenylethyne were measured in H_2O and D_2O solutions of perchloric acid over the concentration range [Acid] = 0.03 – 0.2 M. The data are summarized in Table S1[2] and are displayed in Fig. 1. It may be seen that observed first-order rate constants are accurately proportional to acid concentration in both solvents. Linear least-squares analysis of the data gave the hydronium ion rate constants $k_{H+} = (1.85 \pm 0.04) \times 10^{-2}$ M^{-1} s^{-1} and $k_{D+} = (5.96 \pm 0.20) \times 10^{-3}$ M^{-1} s^{-1}, whose ratio provides the isotope effect $k_H/k_D = 3.10 \pm 0.12$.

Isotope effects on hydron transfer from the hydronium ion consist of an inverse ($k_H/k_D < 1$) secondary component in addition to the normal ($k_H/k_D > 1$) primary component (5), and overall values consequently tend to be small. The effect determined here is, in fact, close to the maximum expected value, and this provides strong evidence that the process under examination is indeed a rate-determining hydron transfer from the hydronium ion to the substrate, as shown in eq. [1].

The cation formed in this process will then either be captured by water, giving an enol that will subsequently tautomerize to a stannyl-substituted ketone, as shown in eq. [2], or the cation will lose its stannyl group giving phenylacetylene and

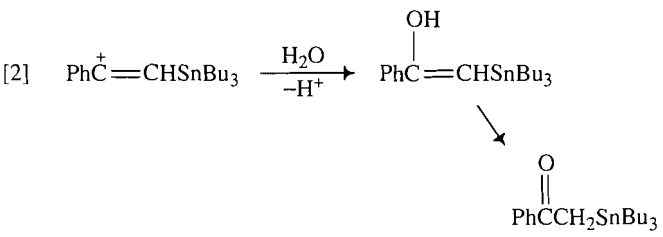

[2] $PhC^{+}{=}CHSnBu_3 \xrightarrow[-H^+]{H_2O} PhC(OH){=}CHSnBu_3 \rightarrow PhCCH_2SnBu_3$ (O)

tributylstannanol, as shown in eq. [3]. HPLC analysis of spent reaction mixtures showed phenylacetylene to be the only aro-

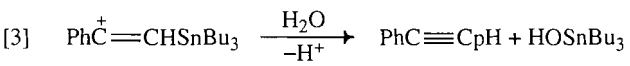

[3] $PhC^{+}{=}CHSnBu_3 \xrightarrow[-H^+]{H_2O} PhC{\equiv}CpH + HOSnBu_3$

matic product formed, indicating that the reaction is indeed a demetalation as shown in eq. [3].

Reactivity

The presently determined rate constant for the protonation of 1-(tri-*n*-butylstannyl)-2-phenylethyne, when compared to the rate of protonation of its unmetalated analog, phenylacetylene (6), shows that the stannyl group accelerates the rate of reaction some 65 000-fold and gives a β-stannyl effect of $\delta\Delta G^{\ddagger} = 6.6$ kcal mol^{-1}. Comparison with the corresponding trimethylsilyl analog, 1-(trimethylsilyl)-2-phenylethyne (7), shows the stannyl substituent to be better than the silyl group by a factor of 210 and gives a differential β-stannyl/β-silyl effect of $\delta\Delta G^{\ddagger} = 3.2$ kcal mol^{-1}.

[2] Table S1 of rate data may be purchased from: The Depository of Unpublished Data, Document Delivery, CISTI, National Research Council Canada, Ottawa, Canada K1A 0S2.

Fig. 1. Relationship between rates of protonation of 1-(tri-*n*-butylstannyl)-2-phenylethyne and acid concentration in aqueous perchloric acid solution at 25°C; ○: H_2O, Δ: D_2O.

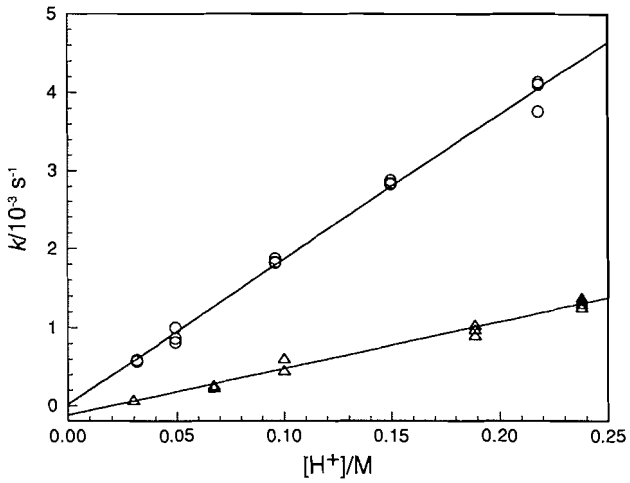

These are substantial effects, but they pale in comparison to the much larger β-stannyl stablizations observed in other systems (2, 3). The difference between the present result and the previously reported stannyl/silyl rate ratio of 5.1×10^7, corresponding to $\delta\Delta G^{\ddagger} = 10.5$ kcal mol^{-1}, is especially striking, for in both cases the reaction examined involved proton addition to a carbon–carbon triple bond.

There are, however, important differences between the present and this previous system. The previous study involved proton addition to a trimethylsilylacetylene with either another trimethylsilyl group or a tributylstannyl group at the other end, eq. [4], while in the present case addition was to a phenylacetylene with the metallic group at the other end, eq. [5]. In the previous system therefore, the vinyl cation formed had its positive charge next to a silyl substituent, whereas in

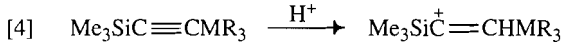

[4] $Me_3SiC{\equiv}CMR_3 \xrightarrow{H^+} Me_3Si\overset{+}{C}{=}CHMR_3$

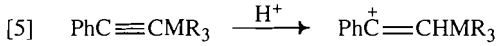

[5] $PhC{\equiv}CMR_3 \xrightarrow{H^+} Ph\overset{+}{C}{=}CHMR_3$

the present case the charge was next to a phenyl group. Since silicon is not very effective at stabilizing an adjacent positive charge (1), while phenyl stabilizes such charge very well, there would be less demand for additional stabilization from the metallic substituent in the phenyl system and the β-metal effect would consequently be reduced. A similar phenyl-induced reduction of the β-silyl effect has been found in the protonation of additionally substituted trimethylsilylacetylenes, eq. [6], where a change from R = Me or *n*-Bu to R = Ph

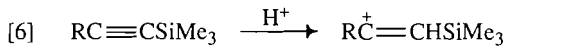

[6] $RC{\equiv}CSiMe_3 \xrightarrow{H^+} R\overset{+}{C}{=}CHSiMe_3$

cut the β-silyl effect in half, from $\delta\Delta G^{\ddagger} = 6.5$ kcal mol^{-1} to $\delta\Delta G^{\ddagger} = 3.4$ kcal mol^{-1} (8).

Another difference between the previous study involving proton addition to acetylenes and the present work is that the previous reactions were carried out in chloroform solution while in the present case the solvent was water. Water is much more polar than chloroform and consequently much better at solvating ions such as the vinyl cations formed in these reac-

tions. The stabilization provided by the better solvation in the present case would once again reduce the demand for additional stabilization from the metal and lead to a smaller β-metal effect.

A reaction mechanism in which proton addition to the acetylene is concerted with metallic group loss would also lead to a reduced β-metal effect, for such a process would lower the amount of positive charge generated on the substrate in the position β to the metal. It is unlikely, however, that the metallic group would leave unassisted as a free cation, and such a process would consequently probably involve nucleophilic displacement at the metal by a water molecule, as shown in eq. [7]. In the transition state of this process, the attacking water

[7] 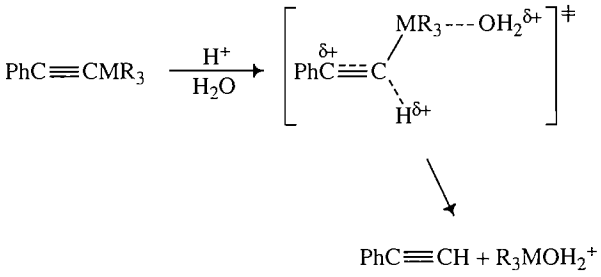

molecule would be taking on positive charge, and that would contribute an additional normal ($k_H/k_D > 1$) component to the solvent isotope effect. The large solvent isotope effect actually observed is consistent with this explanation. On the other hand, it is not clear why such nucleophilic assistance should not have occurred in the previously studied systems, reducing the magnitude of the β-silyl effect there as well. Nucleophilic assistance by the carboxylic acid proton donor was in fact suggested in one of the previous studies (3) as a possible explanation for the observation that the rate of reaction decreased with increasing bulk of the aliphatic ligand attached to the metal,

Table 1. Summary of silyl and stannyl effects.[a]

Substrate	$k_{H^+}/M^{-1}\ s^{-1}$	Relative rate	$\delta\Delta G^{\ddagger}$/kcal mol^{-1}
PhC≡CH[b]	2.86×10^{-7}	1.00	0
PhC≡CSiMe$_3$[c]	8.93×10^{-5}	312	3.4
PhC≡CSnBu$_3$	1.85×10^{-2}	64,700	6.6

[a]Aqueous solution at 25°C.
[b]Reference 6
[c]Reference 7.

i.e., that the tributylstannyl substrate, eq. [4] R = Bu, was less reactive than the trimethylstannyl substrate, eq. [4] R = Me.

Acknowledgement

We are grateful to the Natural Sciences and Engineering Research Council of Canada for financial support of this work.

References

1. J.B. Lambert. Tetrahedron, **46**, 2677 (1988); Y. Apeloig. *In* The chemistry of organic silicon compounds. *Edited by* Z. Rappoport. Wiley, New York. 1989. p. 57.
2. J.B. Lambert, G.-t. Wang, and D.H. Teramura. J. Org. Chem. **53**, 5422 (1988).
3. C. Dallaire and M.A. Brook. Organometallics, **12**, 2332 (1993).
4. M.W. Logue and K. Teng. J. Org. Chem. **47**, 2549 (1982).
5. A.J. Kresge, R.A. More O'Ferrall, and M.F. Powell. *In* Isotopes in organic chemistry. *Edited by* E. Buncel and C.C. Lee. Elsevier, New York. 1987. Chap. 4.
6. N. Banait, M. Hojatti, P. Findlay, and A.J. Kresge. Can. J. Chem. **65**, 441 (1987).
7. A.J. Kresge and J.B. Tobin. Angew. Chem. Int. Ed. Engl. **32**, 721 (1993).
8. V. Gabelica and A.J. Kresge. J. Am. Chem. Soc. **118**, 3838 (1996).

Acid-catalyzed hydrolysis of 4-diazo-3-isochromanone: the effect of coplanarity on the carbon protonation of α-phenyl-α-carbonyldiazo compounds

E.A. Jefferson, A.J. Kresge, and S.W. Paine

Abstract: Hydrolysis of the cyclic α-phenyl-α-carbonyl-diazo compound, 4-diazo-3-isochromanone, in dilute aqueous perchloric acid solutions was found to give the hydronium ion isotope effect $k_{H^+}/k_{D^+} = 2.12$, which shows that this reaction occurs by rate-determining hydronation of the substrate on the carbon atom α to its diazo group. Comparison of the rate constant obtained, $k_{H^+} = 2.48 \times 10^{-3}$ M^{-1} s^{-1}, with that for the corresponding acyclic analog, methyl phenyldiazoacetate, indicates that the cyclic compound is 57 times less reactive. Semi-empirical AM1 molecular orbital calculations suggest that this difference in reactivity is caused by enforced near-coplanarity of the diazo and phenyl groups in the cyclic substrate, as opposed to a staggered arrangement of these groups in the acyclic analog; this coplanarity then enhances delocalization of negative charge from the diazo α-carbon atom into the phenyl group, which reduces the negative charge density on the α-carbon atom and slows the rate of reaction.

Key words: hydrolysis, diazoalkanes, charge delocalization, AM1 calculations.

Résumé : On a trouvé que l'hydrolyse du composé α-phényl-α-carbonyldiazo cyclique, 4-diazo-3-isochromanone, en solutions diluées d'acide perchlorique est accompagnée d'un effet isotopique de l'ion hydronium $k_{H^+}/k_{D^+} = 2{,}12$ qui indique que l'étape déterminant la vitesse de réaction implique une hydronation du substrat au niveau de l'atome de carbone en α du groupe diazo. Une comparaison de la constante de vitesse obtenue, $k_{H^+} = 2{,}48 \times 10^{-3}$ M^{-1} s^{-1}, avec celle de l'analogue acyclique correspondant, le phényldiazoacétate de méthyle, indique que le composé cyclique est 57 fois moins réactif. Des calculs semi-empiriques d'orbitales moléculaires AM1 suggèrent que cette différence de réactivité résulte du fait que, dans le substrat cyclique, les groupes diazo et phényles sont maintenus dans une position pratiquement coplanaire alors que, dans l'analogue acyclique, ils adoptent un arrangement décalé; cette coplanérité augmente la délocalisation de la charge négative de l'atome de carbone en α du diazo vers le groupe phényle, ce qui a pour effet de réduire la densité de la charge négative au niveau de l'atome de carbone en α et de réduire la vitesse de la réaction.

Mots clés : hydrolyse, diazoalcanes, délocalisation de la charge, calculs AM1.

[Traduit par la rédaction]

There is much current interest in the chemistry of ketenes (see, for example, ref. 1), which are a useful class of substances that can be made by the Wolff rearrangement of α-carbonyldiazo compounds (for a brief review, see ref. 2). The utility of α-carbonyldiazo compounds in this respect, however, is limited by the fact that they also undergo facile acid-catalyzed hydrolysis. Information on the nature of this acid-catalyzed reaction, especially how its rate depends on substrate structure, is consequently of some practical value.

In this paper we report the results of an investigation of the hydrolysis of 4-diazo-3-isochromanone, **1**, catalyzed by the hydronium ion in aqueous solution. We have found that this reaction is substantially slower than the corresponding hydrolysis of the acyclic analog, methyl phenyldiazoacetate, **2** (3).

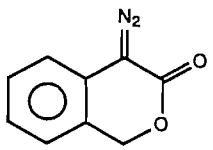

1

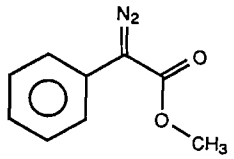

2

Semi-empirical AM1 molecular orbital calculations suggest that this difference in reactivity is due to an enforced near-coplanarity of the diazo and phenyl groups in the cyclic substrate **1**, as opposed to a staggered structure adopted by the acyclic substance **2**.

Experimental section

Materials

4-Diazo-3-isochromanone was prepared by diazo transfer from *p*-acetamidobenzenesulfonyl azide to 3-isochromanone

Received January 11, 1996.

E.A. Jefferson, A.J. Kresge,[1] and S.W. Paine. Department of Chemistry, University of Toronto, Toronto, ON M5S 3H6, Canada.

[1] Author to whom correspondence may be addressed: Telephone and Fax: (416) 978-7259. E-mail: akresge@alchemy.chem.utoronto.ca

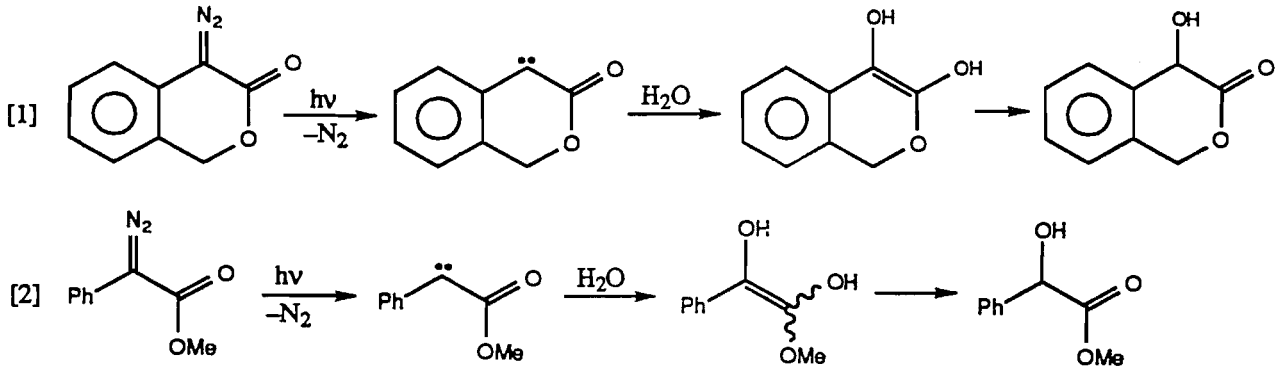

using a literature procedure (4). The product, an orange solid, mp 48–49°C, was obtained in 63% yield. Its spectral properties are: IR, ν/cm^{-1}: 2092 (C=N_2), 1692 (C=O); ^{1}H NMR (200 MHz, $CDCl_3$); δ/ppm: 7.41–6.92 (m, 4H, Ar), 5.32 (s, 2H, CH_2); ^{13}C NMR (50 MHz, $CDCl_3$); δ/ppm: 164.93 (CO), 133.88 (CN_2), 128.98 (Ar), 125.48 (Ar), 125.23 (Ar), 124.59 (Ar), 122.33 (Ar), 118.71 (Ar), 69.81 (CH_2); MS (EI); *m/e*: 174 (58, M^+), 146 (12, $M^+ - CO$), 118 (55, $M^+ - CON_2$), 90 (100, $C_6H_5CH_2$); HRMS: M^+, for $C_9H_6N_2O_2$, *m/e*: 174.0429 (calcd.), 174.0422 (found).

4-Hydroxy-3-isochromanone was obtained by conjugate addition of water to the ketocarbene produced by photodediazotization of 4-diazo-3-isochromanone and subsequent ketonization of the lactone enol so produced, eq. [1], in analogy to a corresponding set of reactions that convert methyl phenyldiazoacetate to methyl mandelate, eq. [2] (5). A solution of 4-diazo-3-isochromanone (100 mg) in acetonitrile (0.3 mL) and water (3.0 mL) was photolyzed for 30 min through a Pyrex filter in a Rayonet apparatus operating at λ = 300 nm. Removal of the solvent by rotary evaporation and recrystallization of the residue from ethanol–pentane gave a colorless solid, mp 82–83°C, in 64% yield. Its spectral properties are: ^{1}H NMR (200 MHz, $CDCl_3$); δ/ppm: 7.67–7.23 (m, 4H, Ph), 5.42–5.16 (m, 3H, CH_2 + CH), 3.51 (s, 1H, OH); ^{13}C NMR (100 MHz, $CDCl_3$); δ/ppm: 173.55 (CO), 133.94 (Ph), 129.25 (Ph), 127.75 (Ph), 124.44 (Ph), 123.66 (Ph), 69.23 (CHOH), 67.86 (CH_2); HRMS: M^+, for $C_9H_8O_3$, *m/e*: 164.0473 (calcd.), 164.0477 (found).

All other materials were best available commercial grades.

Kinetics

Rates of hydrolysis of 4-diazo-3-isochromanone were determined spectroscopically by monitoring the decrease in strong absorbance of the diazo compound at λ = 304 nm. Measurements were made using a Cary 2200 spectrometer whose cell compartment was thermostatted at 25.0 ± 0.05°C. The rate data fit the first-order rate law well, and observed first-order rate constants were calculated by nonlinear least-squares fitting of an exponential function.

Molecular orbital calculations

Semi-empirical AM1 (6) molecular orbital calculations were performed using the program MOPAC 93 (7) in conjunction with a Hewlett Packard 755 computer. The geometries of the singlet ground state for all molecules studied were fully optimized, and energy minima were identified as having all positive eigenvalues and all positive vibrational frequencies.

Results

The hydrolysis of 4-diazo-3-isochromoanone catalyzed by the hydronium ion is expected to occur according to eq. [3], giving

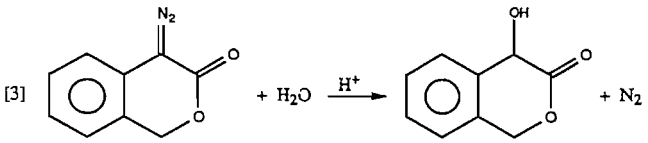

3

4-hydroxy-3-isochromoanone, **3**, as the reaction product. This was confirmed here by subjecting a spent reaction mixture to HPLC analysis. Only one product was found, and spiking with an authentic sample showed it to be **3**.

Rates of this hydrolysis reaction were measured in H_2O and D_2O solutions of perchloric acid over a range of acid concentrations. The data are summarized in Table 1. Observed first-order rate constants proved to be accurately proportional to acid concentration, and linear least-squares analysis gave the hydronium ion catalytic coefficients $k_{H^+} = 2.48 \times 10^{-3}$ M^{-1} s^{-1} and $k_{D^+} = 1.17 \times 10^{-3}$ M^{-1} s^{-1}, whose ratio provides the isotope effect $k_{H^+}/k_{D^+} = 2.12$.

Semi-empirical AM1 molecular orbital calculations were performed to obtain minimum energy structures for 4-diazo-3-isochromanone and methyl phenyldiazoacetate. 4-Diazo-3-isochromanone was found to be a nearly planar molecule with, as Fig. 1 shows, its diazo and carbonyl groups situated only small distances to one side and the other of the benzene ring. The dihedral angles between the diazo group and its benzene ring and carbonyl group substituents produced by these calculations are listed in Table 2, and selected charge distributions obtained from the molecular potential field (8) are given in Table 3.

For methyl phenyldiazoacetate, two minimum energy structures were found, corresponding to *s-cis* and *s-trans* isomerism about the bond connecting the diazoalkane and carbomethoxy groups. The *s-trans* isomer was marginally the more stable, with a difference in heats of formation of $\delta\Delta H_f = 0.94$ kcal/mol^{-1}. As Figs. 2 and 3 show, both isomers had markedly nonplanar structures with diazo and carbonyl groups strongly disposed to opposite sides of the benzene ring. The relevant dihedral angles are listed in Table 2, and selected charge distributions are given in Table 3.

Discussion

The present results show that the hydronium-ion-catalyzed

Table 1. Rates of hydrolysis of 4-diazo-3-isochromanone in aqueous perchloric acid solutions at 25°C.[a]

[Acid]/10^{-2} M	$k_{obs}/10^{-3}$ s^{-1}
H_2O:	
10.0	25.1, 24.9, 25.0
9.20	23.1, 22.9, 23.2
8.00	19.9, 20.3, 20.1
6.80	17.0, 17.0, 17.1
6.00	15.1, 15.3, 15.1
$k_{obs}/s^{-1} = (2.89 \pm 1.79) \times 10^{-6} + (2.48 \pm 0.02) \times 10^{-3}$ [$HClO_4$]	
D_2O:	
10.0	12.0, 12.0, 12.1
9.00	10.9, 10.8, 10.8
8.00	9.85, 9.85, 9.71
7.00	8.39, 8.53, 8.59
6.00	7.35, 7.30, 7.31
$k_{obs}/s^{-1} = (2.93 \pm 1.24) \times 10^{-6} + (1.17 \pm 0.01) \times 10^{-3}$ [$DClO_4$]	
$k_{H^+}/k_{D^+} = 2.12 \pm 0.02$	

[a]Ionic strength = 0.10 M.

Fig. 1. AM1 optimized structure of 4-diazo-3-isochromanone. The black atoms are oxygen; dark gray, nitrogen; light gray, carbon; and white, hydrogen.

hydrolysis of 4-diazo-3-isochromanone occurs with a substantial kinetic isotope effect in the normal direction: k_{H^+}/k_{D^+} = 2.12. This indicates that hydron transfer is rate determining in this reaction and implies that the process occurs by the standard mechanism for diazoalkane hydrolysis, involving rate-determining hydronation on α-carbon followed by rapid displacement of nitrogen by a molecule of water, eq. [4] (9). Another mechanism sometimes found for diazoalkane hydrolysis consists of rapid and reversible α-carbon protonation followed by rate-determining loss of nitrogen, but such a scheme would give an inverse isotope effect, $k_{H^+}/k_{D^+} < 1$ (10), contrary to what has been observed.

It was found previously (3) that the hydronium-ion-catalyzed hydrolysis of the acyclic analog of the presently studied substrate, methyl phenyldiazoacetate, also gives an isotope effect in the normal direction, k_{H^+}/k_{D^+} = 2.72, and that this reaction therefore also occurs by rate-determining hydron transfer to carbon. Comparison of rate constants for the two substrates shows that 4-diazo-3-isochromanone is 57 times less reactive than its acyclic counterpart.

This difference in reactivity can be understood in terms of the structures produced by the AM1 calculations carried out here. Diazoalkanes undergo α-carbon protonation because the diazo group delocalizes negative charge onto the α-carbon

Table 2. Dihedral angles between the diazo group and its phenyl and carbonyl substituents in AM1 optimized structures.

	Dihedral angle/degrees	
Substance	Diazo and phenyl	Diazo and carbonyl
4-Diazo-3-isochromanone	14.9	10.4
Methyl *s-trans*-phenyldiazoacetate	39.5	6.7
Methyl *s-cis*-phenyldiazoacetate	46.3	2.9

Table 3. Charge distributions based on AM1 optimized structures.[a]

	Net charge/electron		
Substance	α-Carbon	Phenyl group	Carbonyl group
4-Diazo-3-isochromanone	−0.419	+0.001	−0.309
Methyl *s-trans*-phenyldiazoacetate	−0.573	+0.195	−0.320
Methyl *s-cis*-phenyldiazoacetate	−0.596	+0.219	−0.351

[a]Calculated by the method of ref. 8.

Fig. 2. AM1 optimized structure of methyl *s-cis* phenyldiazoacetate; atoms as in Fig. 1.

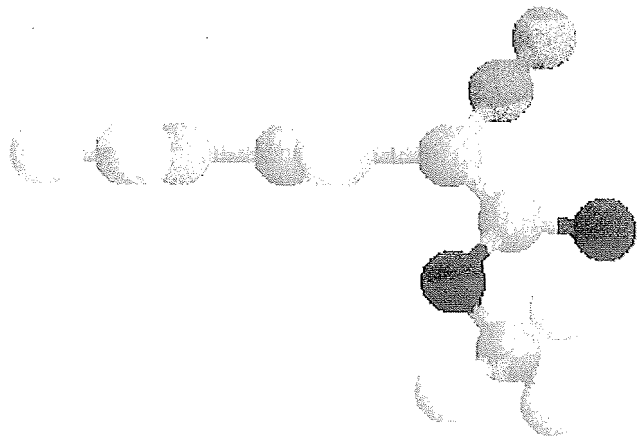

atom, as shown in resonance structure **4**, and it is reasonable to expect that the rate of reaction will be governed by the magnitude of the negative charge on this atom, being greater than the greater charge. This charge, however, can also be delocalized further into an adjacent phenyl group, as shown by resonance structure **5**, and this further delocalization will reduce the reaction rate.

Such further delocalization will be most efficient when the *p*-orbital of the α-carbon atom bearing the negative charge is parallel to the *p*-orbitals of the phenyl group and the dihedral angle between the phenyl and diazo groups is zero. The AM1 structures determined here show a fairly small dihedral angle for the cyclic substrate, 4-diazo-3-isochromanone, but considerably larger ones for its acyclic analog, methyl phenyldiazoacetate (see Table 2). If, as is commonly believed, the strength

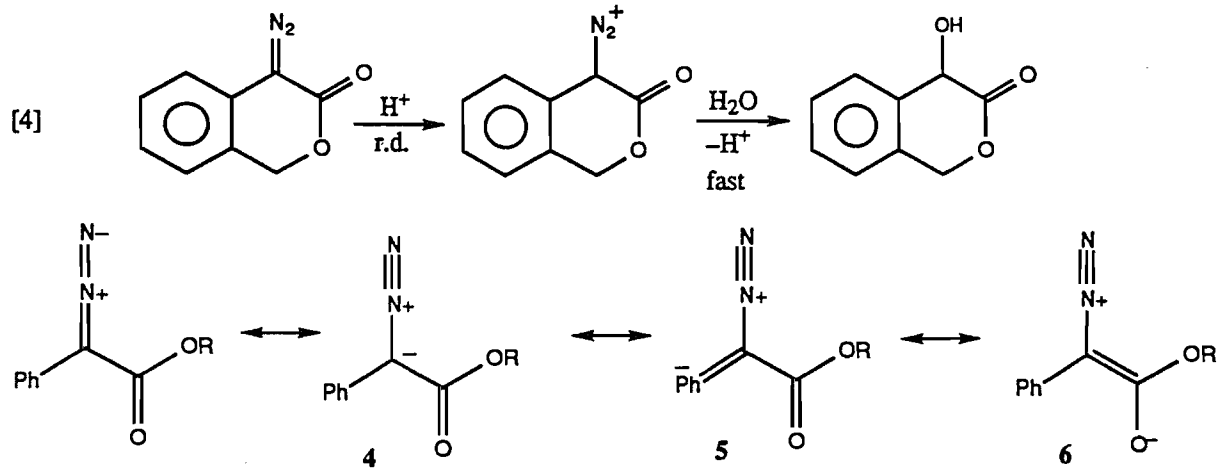

of such conjugative interactions varies as the cosine of the dihedral angle squared, then this interaction will be 93% of its maximum zero-dihedral-angle value for the cyclic substrate but only 60% and 48% of that value for the acyclic *s-trans* and *s-cis* analogs. These expectations are supported by the charge densities listed in Table 3: it may be seen that the negative charge on the α-carbon atom rises from −0.419 electron for the cyclic substrate to −0.573 for the acyclic *s-trans* analog and further to −0.596 for the acyclic *s-cis* substrate. These changes, moreover, occur at the expense of reductions in negative charge in the phenyl group, which becomes progressively more positive along the cyclic to acyclic *s-trans* to acyclic *s-cis* series.

Negative charge can also be delocalized from the α-carbon atom into an adjacent carbonyl group, as shown in resonance structure **6**, and the small dihedral angles between the diazo and carbonyl groups listed in Table 2 indicate that this delocalization is quite efficient. It is interesting that this delocalization becomes stronger in going from the cyclic to the acyclic substrates, in compensation for the weakened delocalization into the phenyl groups. The changes in the carbonyl group interaction are small, however, because the structure of this part of the system is not very different in the cyclic and acyclic substrates, and the extent of delocalization into the phenyl group remains the dominant effect controlling reactivity.

Acknowledgement

We are grateful to the Natural Sciences and Engineering Research Council of Canada and the United States National Institutes of Health for financial support of this research.

Fig. 3. AM1 optimized structure of methyl *s-trans* phenyldiazoacetate; atoms as in Fig. 1.

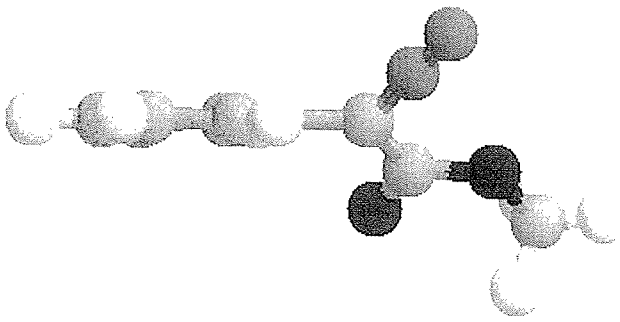

References

1. T.T. Tidwell. Acc. Chem. Res. **23**, 273 (1990); Ketenes. Wiley–Interscience, New York. 1995.
2. M. Regitz and G. Maas. Diazo compounds, properties and synthesis. Academic Press, New York. 1986. pp. 185–195.
3. J. Jones, Jr. and A.J. Kresge. J. Org. Chem. **58**, 2658 (1993).
4. J.S. Baum, D.A. Shook, H.M.L. Davies and D. Smith. Synth. Commun. **17**, 1709 (1987).
5. Y. Chiang, A.J. Kresge, P. Pruszynski, N.P. Schepp, and J. Wirz. Angew. Chem. Int. Ed. Engl. **30**, 1366 (1991).
6. M.J.S. Dewar, E.G. Zoebisch, E.F. Healy, and J.J.P. Stewart. J. Am. Chem. Soc. **107**, 3902 (1985).
7. J.J.P. Stewart. MOPAC 93.00 Manual, Fujitsu Limited, Tokyo, Japan (1993).
8. B.H. Besler, K.M. Merz, Jr., and P.A. Kollman. J. Comput. Chem. **11**, 431 (1990).
9. R.P. Bell. The proton in chemistry. Cornell Univ. Press, Ithaca, N.Y. 1973. pp. 164–171; M. Regitz and G. Maas. Diazo compounds, properties and synthesis. Academic Press, New York. 1986. pp. 122–134.
10. J.R. Keeffe and A.J. Kresge. *In* Techniques of chemistry. Vol. VI. Investigation of rates and mechanisms of reactions. *Edited by* C.F. Bernasconi. Wiley–Interscience, New York. 1986. Chap. XI.

Carbon protonation of some phenylynamines in concentrated aqueous perchloric acid solution. Lowering of the upper limit for the pK_a of phenylynammonium ions

A.J. Kresge and S.W. Paine

Abstract: Rates of carbon protonation of five phenylynamines ($PhC{\equiv}CNH_2$, $PhC{\equiv}CNH^iPr$, $PhC{\equiv}CNHC_6F_5$, $PhC{\equiv}CN(CH_2CH_2CN)_2$, and $PhC{\equiv}CNMeC_6F_5$) were determined in concentrated aqueous perchloric acid solution and the data were analyzed by the Cox–Yates method using the X_0 acidity function. The extrapolated hydronium-ion catalytic coefficients so obtained are consistent with values measured directly in dilute acid solution, and the slopes of the Cox–Yates plots are similar to predictions made with the aid of Marcus rate theory for reactions originating from free ynamine initial states but unlike those predicted for reactions starting from nitrogen-protonated ynammonium ion initial states. This shows that none of these phenylynamines are protonated in even the most acidic solutions used (4 M) and sets new upper limits as low as $pK_a \leq -3.1$ for the conjugate acids of these ynamines. Comparison of the pK_a limit for $PhC{\equiv}CNH_3^+$ with a literature value for the corresponding saturated compound, $PhCH_2CH_2NH_3^+$, gives a base-weakening effect for the phenylethynyl group of at least 12.5 pK units.

Key words: acetylenic amines, concentrated acids, X_0 excess acidity scale, Cox–Yates method, Marcus rate theory.

Résumé : Opérant en solutions concentrées d'acide perchlorique aqueux, on a déterminé les vitesses de protonation des carbones de cinq phénylynamines ($PhC{\equiv}CNH_2$, $PhC{\equiv}CNH^iPr$, $PhC{\equiv}CNHC_6F_5$, $PhC{\equiv}CN(CH_2CH_2CN)_2$ et $PhC{\equiv}CNMeC_6F_5$) et on a analysé les données en faisant appel à la méthode de Cox–Yates de la fonction d'acidité X_0. Les coefficients catalytiques extrapolés de l'ion hydronium ainsi obtenus sont en accord avec les valeurs mesurées directement en solution diluée d'acide et les pentes des courbes de Cox–Yates sont semblables à celles qui sont prédites à l'aide de la théorie des vitesses de Marcus pour des réactions qui ont l'ynamine libre initiale comme origine; elles diffèrent toutefois des valeurs prédites pour des réactions dont les états initiaux sont les ions ynammonium de l'azote protoné. Ce résultat démontre qu'aucune de ces phénylynamines n'est protonée, même dans les solutions les plus acides utilisées (4 M) et fixe de nouvelles limites supérieures pour les pK_a des acides conjugués de ces ynamines qui pourraient ne pas dépasser $-3{,}1$. Une comparaison de la limite du pK_a du $PhC{\equiv}CNH_3^+$ avec une valeur tirée de la littérature pour le composé saturé correspondant, $PhCH_2CH_2NH_3^+$, suggère que le groupe phényléthynyle aurait au effet d'abasissement de la basicité d'au moins 12,5 unités de pK.

Mots clés : amines acétyléniques, acides concentrés, échelle d'acidité en excès X_0, méthode de Cox–Yates, théorie des vitesses de Marcus.

[Traduit par la rédaction]

Previous work performed in our laboratory has shown that the acetylenic group has remarkably strong acid-strengthening (1) and base-weakening (2) effects (for theoretical analyses, see ref. 3). The magnitude of these effects could not be assessed directly by standard methods for determining acid–base dissociation constants because the substances involved, ynols **1** and ynamines **2**, have very short lifetimes in solution. Some information could be obtained, however, from the rate profiles of

$ArC{\equiv}COH$ (**1**) $\quad PhC{\equiv}CNR_2$ (**2**)

Received January 16, 1996.

A.J. Kresge[1] **and S.W. Paine.** Department of Chemistry, University of Toronto, Toronto, ON M5S 3H6, Canada.

[1] Author to whom correspondence may be addressed. Telephone and Fax: (416) 978-7259. e-mail: akresge@alchemy.chem.utoronto.ca

the rapid reactions of these substances in acidic and basic solutions. It was found, for example, that the carbon protonation of ynamines to form keteniminium ions, **3**, eq. [1], was first-order in hydronium ion, and that the direct dependence of rate

[1] $$PhC{\equiv}CNR_2 + H^+ \longrightarrow \underset{\mathbf{3}}{PhCH{=}C{=}NR_2^+}$$

on hydronium ion concentration showed no sign of the saturation expected when nitrogen protonation converts the ynamine to the much less reactive ynammonium ion, **4**, eq. [2]. This set an upper limit on the pK_a of the ynamine conjugate acid equivalent to the highest acid concentration used.

[2] $$PhC{\equiv}CNR_2 + H^+ \rightleftharpoons \underset{\mathbf{4}}{PhC{\equiv}CNHR_2^+}$$

This previous work was done in dilute perchloric acid solutions up to an acid concentration of 0.1 M. We have now

Table 1. Summary of experimental data for the carbon protonation of phenylynamines in aqueous perchloric acid solution at 25°C.

Substrate	m	$k_H^+/M^{-1}\ s^{-1}$ Conc. acid	$k_H^+/M^{-1}\ s^{-1}$ Dilute acid[a]
$PhC{\equiv}CNH_2$	0.27	5.24×10^5	6.70×10^5
$PhC{\equiv}CNH^iPr$	0.43	5.62×10^6	6.42×10^6
$PhC{\equiv}CNHC_6F_5$	1.02	7.93×10^2	8.83×10^2
$PhC{\equiv}CN(CH_2CH_2CN)_2$	1.04	1.49×10^5	1.76×10^5
$PhC{\equiv}CNMeC_6F_5$	1.05	3.76×10^3	4.16×10^3

[a]Reference 2*b*.

extended that study by examining the carbon protonation of some phenylynamines in concentrated perchloric acid solutions up to 4 M. Our results still provide no evidence of nitrogen protonation.

Experimental section

Materials

Phenylynamines were generated as before (2) by flash photolytic photodecarbonylation of the corresponding phenylaminocyclopropenones, eq. [3],

[3] 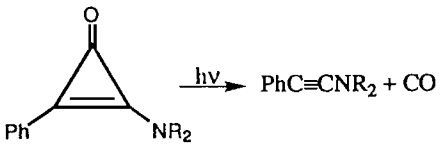

directly in the acid solutions where the rate measurements were made. The phenylcyclopropenones used were samples that had been prepared before (2*b*). All other materials were best available commercial grades.

Kinetics

Rates of reaction of phenylynamines were determined using both conventional (microsecond) (4) and laser (nanosecond) (5) systems that have been described before. For primary and secondary ynamines, the rise in absorbance at λ = 260–270 nm due to ketenimine product formation was monitored, and for tertiary ynamines, which do not give ketenimine products, the drop in ynamine absorbance at λ = 300 nm was monitored. All of the rate data except some for 1-(*N*-isopropylamino)-2-phenylacetylene conformed well to the first-order rate law, and observed first-order rate constants were determined by nonlinear least-squares fitting of single exponential expressions. 1-(*N*-Isopropylamino)-2-phenylacetylene was the most reactive ynamine studied, and its lifetime in the three most concentrated acid solutions used was comparable to the duration of the flash photolysis laser pulse. The data were therefore analyzed by fitting a double exponential function; the faster of the two rate constants so obtained, $k \cong 5 \times 10^7\ s^{-1}$, could be attributed to formation of the ynamine during the laser pulse, and the second, to the carbon protonation reaction of present interest.

The temperature of the reacting solutions was controlled at 25.0 ± 0.05°C.

Fig. 1. Relationship between acid concentration and observed first-order rate constants for the carbon protonation of 1-(*N*-methyl-*N*-pentafluorophenylamino)-2-phenylacetylene in aqueous perchloric acid solutions at 25°C. The line drawn is based on data of ref. 2*b* for the concentration range [acid] = 0.02–0.10 M.

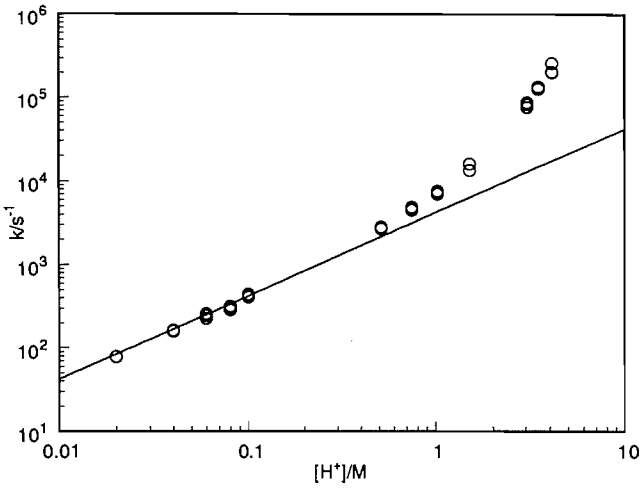

Results

Rates of carbon protonation of the five phenylynamines listed in Table 1 were measured in aqueous perchloric acid solution over the concentration range [acid] = 0.1–4 M.[2] Four to eleven different acid concentrations were used and duplicate or triplicate measurements were made at each concentration. The data are summarized in Table S1.[3]

As Fig. 1 illustrates, rates of reaction in these concentrated acid solutions increased more rapidly than in direct proportion to acid concentration. This is commonly the case for proton transfer to carbon, and acidity functions are therefore generally used to correlate the data. The Cox–Yates X_0 scale (6) appears to be the best function currently available for this purpose (7), and the present data were consequently analyzed using the standard Cox–Yates function, shown in eq. [4],

[4] $$\log(k_{obs}/[H^+]) = k_H^+ + mX_0$$

where k_H^+ is the hydronium-ion catalytic coefficient applicable in dilute solution and m is a slope parameter. Figure 2 shows that the data conform well to this relationship. The parameters determined by these correlations are listed in Table 1; it may be seen that the hydronium-ion catalytic coefficients obtained in this way are consistent with values determined before from rate measurements made in dilute acid solutions (2*b*).

[2] [Acid] = 0.04–1.6 M for 1-(*N*-isopropylamino)-2-phenylacetylene; above 1.6 M, rates of reaction of this substance become too fast to be determined accurately by our laser flash photolysis system.

[3] Table S1 may be purchased from: The Depository of Unpublished Data, Document Delivery, CISTI, National Research Council, Ottawa, Canada K1A 0S2.

Table 2. Predicted Cox–Yates slopes for the carbon protonation of phenylynamines.

Substrate	α	*m*		
		Pre-equilibrium	Rate-determing step	Overall
$PhC{\equiv}CNH_2$	0.34	−1.00	0.41	−0.59
$PhC{\equiv}CNH^iPr$	0.10	−1.20	0.14	−1.06
$PhC{\equiv}CNHC_6F_5$	0.64	−1.20	0.90	−0.30
$PhC{\equiv}CN(CH_2CH_2CN)_2$	0.42	−1.40	0.71	−0.69
$PhC{\equiv}CNMeC_6F_5$	0.59	−1.40	0.99	−0.41

Fig. 2. Cox–Yates correlations for the carbon protonation of phenylynamines in concentrated perchloric acid at 25°C: O, $PhC{\equiv}CNH_2$; Δ, $PhC{\equiv}CNH^iPr$; □, $PhC{\equiv}CNHC_6F_5$; ●, $PhC{\equiv}CN(CH_2CH_2CN)_2$; ▲, $PhC{\equiv}CMeC_6F_5$.

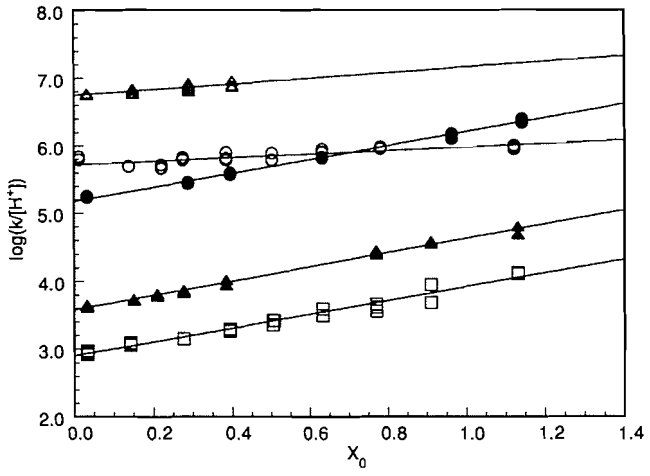

Discussion

Figure 2 shows that rates of reaction for all of the phenylynamines examined here give linear Cox–Yates plots with positive slopes. This is the behavior expected for simple carbon protonation of these substances with free ynamine as the initial state, as opposed to the negative slopes that might be anticipated if significant nitrogen protonation were taking place. In the latter situation, the initial states of the reactions would be phenylynammonium ions, **4**, eq. [5], whose equilibrium ionization to free ynamine prior to the rate-determining

[5] $$\underset{\mathbf{4}}{PhC{\equiv}CNHR_2^+} \rightleftharpoons PhC{\equiv}CNR_2 + H^+ \longrightarrow PhCH{=}C{=}NR_2^+$$

carbon-protonation step would contribute a negative component to the Cox–Yates slope. This negative component would be offset by a positive contribution for the rate-determining step, but it is unlikely that this positive contribution would be strong enough to cancel the negative component completely.

These considerations can be put on a quantitative basis by making numerical estimates of the slopes involved, using our current, fairly good understanding of phenomena in concentrated acids, as outlined, for example, in a recent review (8). It is known that the magnitude of Cox–Yates slopes for the equilibrium protonation of amines increases in inverse proportion to the number of positively charged N—H bonds available for solvolytic stabilization of the amine conjugate acids through hydrogen bonding to water molecules, and that the nominal values $m = 1.00$, $m = 1.20$, and $m = 1.40$ generally apply to primary, secondary, and tertiary amines, respectively. This leads to the negative Cox–Yates slopes $m = -1.00$, -1.20, and -1.40 for the equilibrium ionization of the corresponding phenylynamines in the first step of the reaction scheme of eq. [5]. The subsequent rate-determining carbon-protonation step puts positive charge back on the amine nitrogen atom, but now there is one less N—H bond in the reaction product than there was in the ynammonium ion in the pre-equilibrium step and $m = 1.20$ will consequently apply to primary phenylynamine systems and $m = 1.40$ to secondary systems. For tertiary ynamines, whose carbon-protonation products have no positively charged N—H bonds, we shall use $m = 1.70$, borrowed from the carbon protonation of olefins and aromatics whose cationic products also have no positively charged N—H bonds.

The *m* values for reaching the transition states of the rate-determining steps of the process of eq. [5] will of course be lower than these estimates for full carbon protonation because only a fraction of the positive charge will have been placed on the ynamine at the transition state. This fraction may be identified with the Brønsted exponent α for the process (9), and an estimate of α may be supplied by Marcus rate theory (10). The relevant Marcus relationships are given by eqs. [6] and [7],

[6] $$\Delta G^{\ddagger} = w^r + (1 + \Delta G^0/4\Delta G^{\ddagger}_0)^2 \Delta G^{\ddagger}_0$$

[7] $$\alpha = (1 + \Delta G^0/4\Delta G^{\ddagger}_0)/2$$

in which $\Delta G^{\ddagger}$ is the free energy of activation, w^r is the work required to bring the reactants together to form a reaction complex, ΔG^0 is the free energy of reaction within this reaction complex, and $\Delta G^{\ddagger}_0$ is the intrinsic reaction barrier. Elimination of ΔG^0 between eqs. [6] and [7] leads to eq. [8], and use of $\Delta G^{\ddagger}$ derived from the hydronium ion catalytic coefficients of

[8] $$\alpha = \sqrt{(\Delta G^{\ddagger} - w^r)/4\Delta G^{\ddagger}_0}$$

Table 1 together with $w^r = 8.11$ kcal mol^{-1} and $\Delta G^{\ddagger}_0 = 3.26$ kcal mol^{-1} (*2b*) gives the α values listed in Table 2. These results may then be used to estimate *m* for the rate-determining carbon protonation step as the product of α and *m* for full carbon protonation, and *m* for the overall reaction of eq. [5] may

be evaluated as the sum of m for the pre-equilibrium step plus that for the carbon-protonation step. These results are also listed in Table 2.

It may be seen that all of the values of m predicted in this way are negative, in strong contrast to the positive values actually observed. Values of m predicted for the carbon-protonation step, on the other hand, are much more similar to the observed results and they also provide a similar pattern of dependence on the structure and reactivity of the substrate. The mean difference between observed m values and those predicted for the carbon-protonation step is only $\langle \delta m \rangle = 0.1$, whereas that between observed and predicted overall m values is an order of magnitude greater, $\langle \delta m \rangle = 1.0$. It would appear safe to conclude, therefore, that no significant amount of nitrogen protonation of these phenylynamines had occurred up to the highest acidity used and that the ynamines were in their free unprotonated forms in the initial states of the reactions studied.

This conclusion allows us to set upper limits on the pK_a's of the conjugate acids of these ynamines. On the rather conservative assumption that 10% nitrogen protonation could not have been detected, these limits are p$K_a = -2.7$ for phenylynamine, p$K_a = -1.6$ for the *N*-isopropyl derivative (which unfortunately could not be studied in acids as concentrated as the other ynamines because its rate of carbon protonation became too fast), p$K_a = -2.9$ for the other secondary ynamine, and p$K_a = -3.1$ for the tertiary ynamines.

Comparison of this limit for the pK_a of the conjugate acid of phenylynamine, **5**, with p$K_a = 9.8$ for that of 2-phenylethyl-

$PhC{\equiv}CNH_3^+$ **5** $PhCH_2CH_2NH_3^+$ **6**

amine (11) gives the phenylethynyl group a base-weakening effect of at least 12.5 pK units.

Acknowledgement

We are grateful to the Natural Sciences and Engineering Research Council of Canada for financial support of this work.

References

1. Y. Chiang, A.J. Kresge, R. Hochstrasser, and J. Wirz. J. Am. Chem. Soc. **111**, 2355 (1989); J. Andraos, Y. Chiang, A.S. Grant, H.-X. Guo, and A.J. Kresge. J. Am. Chem. Soc. **116**, 7411 (1994); Y. Chiang, A.J. Kresge, and V.V. Popik. J. Am. Chem. Soc. **117**, 9165 (1995).
2. (*a*) Y. Chiang, A.S. Grant, A.J. Kresge, P. Pruszynski, N.P. Schepp, and J. Wirz. Angew. Chem. Int. Ed. Engl. **30**, 1356 (1991); (*b*) Y. Chiang, A.S. Grant, A.J. Kresge, and S.W. Paine. J. Am. Chem. Soc. **118**, 4366 (1996).
3. B.J. Smith, L. Radom, and A.J. Kresge. J. Am. Chem. Soc. **111**, 8297 (1989); B.J. Smith and L. Radom. J. Am. Chem. Soc. **114**, 36 (1992).
4. Y. Chiang, M. Hojatti, J.R. Keeffe, A.J. Kresge, N.P. Schepp, and J. Wirz. J. Am. Chem. Soc. **109**, 4000 (1987).
5. J. Andraos, Y. Chiang, G.-C. Huang, A.J. Kresge, and J.C. Scaiano. J. Am. Chem. Soc. **115**, 10605 (1993).
6. R.A. Cox and K. Yates. Can. J. Chem. **59**, 2116 (1981).
7. A.J. Kresge, H.J. Chen, G.L. Capen, and M.F. Powell. Can. J. Chem. **61**, 249 (1983).
8. A. Bagno, G. Scorrano, and R.A. More O'Ferrall. Rev. Chem. Intermed. **7**, 313 (1987).
9. A.J. Kresge. *In* Proton transfer reactions. *Edited by* E.F. Caldin and V. Gold. Chapman and Hall, London. 1975. pp. 179–199.
10. R.A. Marcus. J. Phys. Chem. **72**, 891 (1968); A.J. Kresge. Chem. Soc. Rev. **2**, 475 (1993).
11. H.K. Hall. J. Am. Chem. Soc. **79**, 5441 (1957).

Platinum(II) complexes of the tridentate thioether ligands $RS(CH_2)_3S(CH_2)_3SR$ (R = Et, iPr, Ph). Structures of $[PtCl(iPrS(CH_2)_3S(CH_2)_3SiPr)][BF_4]$, $[PtI(PhS(CH_2)_3S(CH_2)_2SPh)][BF_4]$, and $[Pt(PPh_3)(iPrS(CH_2)_3S(CH_2)_3SiPr)][BF_4]_2 \cdot CH_2Cl_2$

Stephen J. Loeb and James R. Mansfield

Abstract: The tridentate thioether ligands $RS(CH_2)_3S(CH_2)_3SR$ (L^1, R = Et; L^2, R = iPr, L^3, R = Ph) were synthesized by nucleophilic addition of thiolate, SR^-, to the ditosylate $TsO(CH_2)_3S(CH_2)_3OTs$. The complexes $[PtX(L^n)][BF_4]$ were prepared by displacement of 1,5-COD from $[PtX_2(1,5\text{-COD})]$ (X = Cl, I) in the presence of one equivalent of $AgBF_4$ and one equivalent of thioether ligand. $[PtCl(L^2)][BF_4]$ crystallized in the monoclinic space group $P2_1/c$ with a = 10.409(6), b = 14.180(4), c = 13.726(8) Å, β = 104.49(4)°, V = 1961(2) Å^3, and Z = 4. The structure refined to R = 5.62% and R_w = 6.86% for 2121 reflections with $F_o^2 > 3\sigma(F_o^2)$. $[PtI(L^3)][BF_4]$ crystallized in the monoclinic space group $P2_1/n$ with a = 13.415(4), b = 12.350(5), c = 14.316(5) Å, β = 107.48(3)°, V = 2262(1) Å^3, and Z = 4. The structure refined to R = 4.85% and R_w = 6.33% for 2168 reflections with $F_o^2 > 3\sigma(F_o^2)$. In both compounds, the thioether ligand acts as a tridentate chelator occupying three of the four sites of the square-planar Pt(II) complex. Variable temperature $^{13}C\{^1H\}$ NMR verified that there are three possible stereoisomers for these complexes resulting from inversion at sulphur: *meso*-A, *meso*-B, and *racemic*. Thermodynamic parameters were calculated for the interconversion among isomers of $[PtCl(L^2)][BF_4]$ by a full line-shape analysis. Removal of chloride ligand from $[PtCl(L^2)][BF_4]$ with Ag^+ in the presence of PPh_3 yielded the phosphine adduct $[Pt(PPh_3)(L^2)][BF_4]_2$, which crystallized in the triclinic space group $P\bar{1}$ with a = 13.266(3), b = 11.315(2), c = 13.970(2) Å, α = 106.04(2)°, β = 84.95(2)°, γ = 86.56(2)°, V = 1999.7(7) Å^3, and Z = 2. The structure refined to R = 4.22% and R_w = 5.38% for 4493 reflections with $F_o^2 > 3\sigma(F_o^2)$. Unlike the two halide complex structures, which crystallized in the *meso*-B form, $[Pt(PPh_3)(L^2)][BF_4]_2$ crystallized in the *racemic* form.

Key words: tridentate thioether ligand, crystal structure, platinum(II) halide, dynamic NMR spectroscopy.

Résumé : On a synthétisé les coordinats thioéthers tridentates $RS(CH_2)_3S(CH)_2)_3SR$ (L^1, R = Et; L^2, R = iPr, L^3, R = Ph) par addition nucléophile de thiolate, SR^-, sur le ditosylate $TsO(CH_2)_3S(CH_2)_3OTs$. On a préparé les complexes $[PtX(L^n)][BF_4]$ par déplacement du 1,5-COD à partir du $[PtX_2(1,5\text{-COD})]$ (X = Cl, I) en présence d'un équivalent de $AgBF_4$ et d'un équivalent de coordinat thioéther. Le composé $[PtCl(L^2)][BF_4]$ appartient au groupe d'espace monoclinique $P2_1/c$ avec a = 10,409(6), b = 14,180(4), c = 13,726(8) Å, β = 104,49(4)°, V = 1961(2) Å^3 et Z = 4. On a affiné la structure jusqu'à des valeurs de R = 5,62% et de R_w = 6,86% pour 2121 réflexions avec $F_o^2 > 3\sigma(F_o^2)$. Le composé $[PtI(L^3)][BF_4]$ appartient au groupe d'espace monoclinique $P2_1/n$ avec a = 13,415(4), b = 12,350(5), c = 14,316(5) Å, β = 107,48(3)°, V = 2262(1) Å^3 et Z = 4. On a affiné la structure jusqu'à des valeurs de R = 4,85% et de R_w = 6,33% pour 2168 réflexions avec $F_o^2 > 3\sigma(F_o^2)$. Dans les deux composés, le coordinat thioéther agit comme un chélatant tridentate occupant trois des quatre sites d'un complexe de Pt(II) carré plan. La RMN du $^{13}C\{^1H\}$ à température variable permet de vérifier que ces complexes ont trois stéréo-isomères possibles : *méso*-A, *méso*-B et *racémique*. On a calculé les paramètres thermodynamiques pour l'interconversion des isomères du $[PtCl(L^2)][BF_4]$ par une analyse de la forme totale. L'enlèvement du chlore du coordinat $[PtCl(L^2)][BF_4]$ par l'ion Ag^+ en présence de PPh_3 conduit à l'adduit phosphine $[Pt(PPh_3)(L^2)][BF_4]_2$ qui cristallise dans le groupe d'espace triclinique $P\bar{1}$ avec a = 13,266(3), b = 11,315(2), c = 13,970(2) Å, α = 106,04(2)°, β = 84,95(2)°, γ = 86,56(2)°, V = 1999,7(7) Å^3 et Z = 2. On a affiné la structure jusqu'à des valeurs de R = 4,22% et de R_w = 5,38% pour 4493 réflexions avec $F_o^2 > 3\sigma(F_o^2)$. Contrairement aux structures des deux complexes halogénés qui cristallisent dans la forme *meso*-B, le complexe $[Pt(PPh_3)(L^2)][BF_4]_2$ cristallise sous la forme *racémique*.

Mots clés : coordinat thioéther tridentate, structure du cristal, halogénure de platine(II), spectroscopie de RMN dynamique.

[Traduit par la rédaction]

Received February 20, 1996.

S.J. Loeb[1] and J.R. Mansfield. Department of Chemistry and Biochemistry, University of Windsor, Windsor, ON N9B 3P4, Canada.

[1] Author to whom correspondence may be addressed. Telephone: (519) 253-4232, ext. 3529. Fax: (519) 973-7098. E-mail: LOEB@UWINDSOR.CA

Scheme 1.

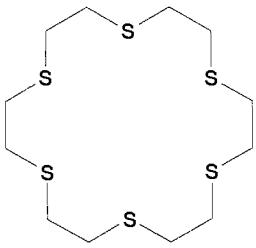

18S6

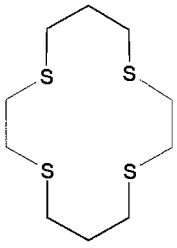

14S4

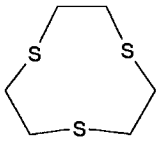

9S3

Scheme 2.

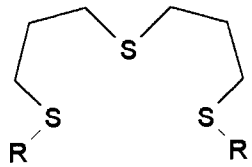

L^1, R = Et; L^2, R = iPr; L^3, R = Ph

Introduction

Macrocyclic thioether ligands such as 1,4,7,10,13,16-hexathiacyclohexadecane, [18]aneS_6, 1,4,8,11-tetrathiatetradecane, [14]aneS_4, and 1,4,7-trithiacyclononane, [9]aneS_3 have been used to enforce a homoleptic MS_x environment at a metal centre and are therefore ideal for studying the electronic effects of coordinated thioethers (1–4).

However, if one wishes to study the effect thioether coordination has on the reaction chemistry of a metal, at least one coordination site must remain unoccupied or contain a labile ancillary ligand (5). To this end, we have prepared a series of simple, open-chain, tridentate thioether ligands designed to coordinate to a metal centre in a *meridional* fashion and hence occupy three of four coordination sites of a four-coordinate, square-planar complex. This paper describes the synthesis of these ligands, preparation of platinum(II) complexes of the type $[PtX(RS(CH_2)_3S(CH_2)_3SR)][BF_4]$ (L^1, R = Et; L^2, R = iPr, L^3, R = Ph; X = Cl, I, PPh_3), and the characterization of these species in the solid state by X-ray diffraction and in solution by variable temperature ^{13}C NMR spectroscopy.

Experimental section

$[PtCl_2(1,5\text{-COD})]$ (6) and $[PtI_2(1,5\text{-COD})]$ (6) were prepared by literature methods. 1-Bromopropanol, sodium sulfide nonahydrate, *p*-toluenesulphonyl chloride, thiophenol, 2-propanethiol, 1,5-cyclooctadiene, K_2PtCl_4, and all deuterated solvents were purchased from Aldrich and used as received. All reactions were carried out under an atmosphere of N_2 using standard Schlenk techniques, and all solvents were dried and degassed prior to use. ^1H, $^{13}C\{^1H\}$, $^{31}P\{^1H\}$, and $^{195}Pt\{^1H\}$ NMR spectra were recorded at 300.1, 75.4, 121.5, and 64.5 MHz on a Brüker AM300 spectrometer locked to the deuterated solvent. Variable temperature ^{13}C NMR line-shape fitting calculations were performed using a locally modified version of DNMR3 (7). Infrared spectra were recorded on a Perkin–Elmer 781 grating spectrometer. GC–MS experiments were performed on a Hewlett–Packard HP 5970 Series MSD coupled to an HP 5890a gas chromatograph. Elemental analyses were performed by Canadian Microanalytical Services, Delta, British Columbia.

Synthesis of 4-thiaheptane-1,7-diol

The following is a modification of the literature preparation (8). 3-Bromopropanol (64.9 g, 476 mmol) and $Na_2S{\cdot}9H_2O$ (54.8 g, 228 mmol) were refluxed in anhydrous ethanol (750 mL) for 18 h. The mixture was cooled, filtered, and the solvent removed in vacuo. The resulting liquid was extracted with CH_2Cl_2, filtered, and the solvent removed in vacuo. The resulting clear, oily liquid was vacuum distilled (bp 134–138°C, 1 Torr (1 Torr = 133.3 Pa)). Yield 23.3 g, 65%. ^1H NMR ($CDCl_3$) δ: 3.64 (s, 2H, OH), 3.61 (t, 4H, OCH_2, $^3J = 6.2$ Hz), 2.54 (t, 4H, SCH_2, $^3J = 7.2$ Hz), 1.74 (q, 4H, CH_2). $^{13}C\{^1H\}$ NMR ($CDCl_3$) δ: 60.91 (CH_2OH), 31.88 (SCH_2), 28.36 (CH_2).

Synthesis of 4-thia-1,7-heptaneditosylate·CH_2Cl_2

4-Thiaheptane-1,7-diol (22.65 g, 151 mmol) was dissolved in freshly distilled, dry pyridine at 0°C and *p*-toluenesulphonyl chloride (57.50 g, 302 mmol) added over a period of 2 h. The reaction mixture was poured over ice (900 g) and set aside until the ice melted. The resulting sticky white solid was filtered and then dissolved in CH_2Cl_2 (300 mL). This solution was washed with 0.1 M HCl(aq) (2 × 160 mL) and distilled water (2 × 100 mL). The aqueous fractions were collected and washed with fresh CH_2Cl_2 (100 mL). The combined organic portions were then dried over anhydrous $MgSO_4$, treated with decolourizing charcoal, filtered, and the solvent removed in vacuo. The resulting liquid was dissolved in an equal volume of diethyl ether and cooled to −10°C for 12 h. The crystallized white solid was collected and washed with anhydrous ethanol (50 mL) and dried in vacuo. Yield 38.42 g (59%). ^1H NMR ($CDCl_3$) δ: 7.78 (d, 4H, aromatic, $^3J = 8.0$ Hz), 7.34 (d, 4H, aromatic), 4.10 (t, 4H, OCH_2, $^3J = 6.0$ Hz), 2.46 (t, 4H, SCH_2, $^3J = 7.1$ Hz), 2.44 (s, 6H, CH_3), 1.86 (q, 4H, CH_2). $^{13}C\{^1H\}$ NMR ($CDCl_3$) δ: 144.83, 132.86, 129.84, 127.81 (aromatic), 68.64 (CH_2O), 28.75 (SCH_2), 27.77 (CH_2), 21.61 (CH_3). Anal. calcd. for $C_{21}H_{28}Cl_2O_4S_3$: C 49.31, H 5.51, S 18.80; found: C 51.59, H 5.58, S 20.14.

Synthesis of 3,7,11-trithiatridecane, L^1

Na metal (1.55 g, 67.4 mmol) was dissolved in anhydrous ethanol (700 mL) and ethanethiol (4.9 mL, 4.11 g, 66.2 mmol) was added to this solution. This mixture was then added dropwise over 2 h to a slurry of 4-thiaheptane-1,7-ditosylate (14.2

g, 33.3 mmol) in anhydrous ethanol (200 mL). The reaction mixture was stirred overnight at 40°C. The solvent was removed in vacuo and the residue redissolved in CH_2Cl_2 (200 mL). The CH_2Cl_2 solution was washed with water (130 mL), dried over anhydrous $MgSO_4$, filtered, and the solvent removed in vacuo. The resulting clear, viscous liquid was vacuum distilled (bp 115–122°C, 1 Torr). Yield 6.16 g (78%). ^1H NMR ($CDCl_3$) δ: 2.47 (t, 4H, $EtSCH_2$, ^3J = 7.2 Hz), 2.47 (t, 4H, CH_2SCH_2), 2.38 (q, 4H, CH_3CH_2, ^3J = 7.4 Hz), 1.70 (q, 4H, SCH_2CH_2), 1.10 (t, 6H, CH_3). $^{13}C\{^1H\}$ NMR ($CDCl_3$) δ: 30.45 ($EtSCH_2$), 29.96 (CH_2SCH_2), 28.90 (SCH_2CH_2), 25.24 (CH_3CH_2), 14.41 (CH_3). MS, *m/e*: 238. Anal. calcd. for $C_{10}H_{22}S_3$: C 50.37, H 9.30, S 40.33; found: C 50.20, H 9.21, S 39.40.

Synthesis of 2,12,-dimethyl-3,7,11-trithiadecane, L^2

Na metal (1.23 g, 53.5 mmol) was dissolved in anhydrous ethanol (550 mL) and 2-propanethiol (4.6 mL, 3.77 g, 49.5 mmol) was added to this solution. This mixture was then added dropwise over 4 h to a slurry of 4-thiaheptane-1,7-ditosylate (10.5 g, 24.5 mmol) in anhydrous ethanol (50 mL). The reaction mixture was stirred overnight at 40°C and then the solvent removed. The residue was redissolved in CH_2Cl_2 (160 mL) and the solution filtered. The filtrate was washed with water (2 × 100 mL), dried over anhydrous $MgSO_4$, treated with activated charcoal, filtered, and the solvent removed in vacuo. The resulting amber viscous liquid was vacuum distilled to give a clear colourless oil (bp 122–129°C, 1 Torr). Yield 4.62 g (71%). ^1H NMR ($CDCl_3$) δ: 2.87 (m, 2H, CH, ^3J = 6.7 Hz), 2.58 (t, 4H, CH_2SCH_2, ^3J = 7.2 Hz), 2.57 (t, 4H, i-$PrSCH_2$), 1.81 (q, 4H, SCH_2CH_2) 1.22 (d, 12H, CH_3). $^{13}C\{^1H\}$ NMR ($CDCl_3$) δ: 34.73 (CH), 30.94 (i-$PrSCH_2$), 29.64 (CH_2SCH_2), 29.24 (SCH_2CH_2), 23.32 (CH_3). MS, *m/e*: 266. Anal. calcd. for $C_{12}H_{26}S_3$: C 54.08, H 9.83, S 36.09; found: C 54.37, H 10.15, S 35.55.

Synthesis of 1,9-diphenyl-1,5,9-trithianonane, L^3

Na metal (1.25 g, 54.4 mmol) was dissolved in anhydrous ethanol (600 mL) and thiophenol (5.4 mL, 5.74 g, 52.1 mmol) was added to this solution. This mixture was then added dropwise over 3 h to a slurry of 4-thiaheptane-1,7-ditosylate (11.1 g, 26.0 mmol) in anhydrous ethanol (100 mL). The reaction mixture was stirred overnight at room temperature and then the solvent removed. The residue was redissolved in CH_2Cl_2 (160 mL) and the solution filtered. The filtrate was washed with water (2 × 100 mL), dried over anhydrous $MgSO_4$, treated with activated charcoal, filtered, and the solvent removed in vacuo. The resulting dark amber oil was vacuum distilled to give a clear colourless oil (bp 209–212°C, 1 Torr). Yield 5.99 g (69%). ^1H NMR ($CDCl_3$) δ: 7.38 (m, 4H, aromatic), 7.23 (m, 6H, aromatic), 3.04 (t, 4H, $PhSCH_2$), 2.63 (t, 4H, CH_2SCH_2, ^3J = 7.1 Hz), 1.92 (q, 4H, SCH_2CH_2). $^{13}C\{^1H\}$ NMR ($CDCl_3$) δ: 135.98, 128.99, 128.67, 125.74 (aromatic), 32.16 ($PhSCH_2$), 30.51 (CH_2SCH_2), 28.55 (SCH_2CH_2). MS, *m/e*: 334. Anal. calcd. for $C_{18}H_{22}S_3$: C 64.62, H 6.63, S 28.75; found: C 64.54, H 6.51, S 27.84.

Synthesis of $[PtCl(L^1)][BF_4]$

L^1 (0.616 g, 2.583 mmol) was dissolved in CH_2Cl_2 (20 mL) and this solution was added to a flask containing $[PtCl_2(1,5\text{-COD})]$ (0.787 g, 2.103 mmol) and $AgBF_4$ (0.419 g, 2.152 mmol). This mixture was stirred for 2 h and then filtered through Celite to remove precipitated AgCl(s). The volume of the solution was reduced to ca. 4 mL and small portions of diethyl ether added until a light yellow precipitate formed. The mixture was then cooled to −10°C for 12 h. The pale yellow microcrystals formed were collected and washed with diethyl ether. Yield 0.919 g (79%). A satisfactory elemental analysis could not be obtained for this material.

Synthesis of $[PtCl(L^2)][BF_4]$

L^2 (1.456 g, 5.463 mmol) was dissolved in CH_2Cl_2 (15 mL) and this solution was added to a flask containing $[PtCl_2(1,5\text{-COD})]$ (2.006 g, 5.361 mmol) and $AgBF_4$ (1.066 g, 5.476 mmol). This mixture was stirred for 1 h and then filtered through Celite to remove precipitated AgCl(s). The solvent was removed and the residue left under vacuum to remove traces of 1,5-COD. The residue was dissolved in CH_2Cl_2 (4 mL) and small portions of diethyl ether were added until a light yellow precipitate formed. The mixture was then cooled to −10°C for 12 h. The yellow microcrystals formed were collected and washed with diethyl ether. Yield 2.856 g (91%). Anal. calcd. for $C_{12}H_{26}BClF_4PtS_3$: C 24.69, H 4.49, S 16.47; found: C 24.69, H 4.61, S 16.60.

Synthesis of $[PtCl(L^3)][BF_4]$

L^3 (0.560 g, 1.67 mmol) was dissolved in CH_2Cl_2 (5 mL) and this solution was added to a flask containing $[PtCl_2(1,5\text{-COD})]$ (0.624 g, 1.67 mmol) and $AgBF_4$ (0.324 g, 1.67 mmol). This mixture was stirred for 1 h and then filtered through Celite to remove precipitated AgCl(s). The solvent was removed and the residue was left under vacuum to remove traces of 1,5-COD. The residue was dissolved in CH_2Cl_2 (2 mL) and small portions of diethyl ether were added until a light yellow precipitate formed. The product was collected and washed with diethyl ether and isolated as the CH_2Cl_2 solvate. Yield 0.724 g (67%). Anal. calcd. for $C_{19}H_{24}BCl_3F_4PtS_3$: C 30.97, H 3.28, S 13.05; found: C 30.85, H 3.32, S 10.29.

Synthesis of $[PtI(L^3)][BF_4]$

L^3 (0.603 g, 1.80 mmol) was dissolved in acetone (6 mL) and this solution was added to a slurry of $[PtI_2(1,5\text{-COD})]$ (1.000 g, 1.80 mmol) in acetone (20 mL). $AgBF_4$ (0.375 g, 1.83 mmol) was added and the solution was stirred for 3 h and then filtered through Celite to remove precipitated AgCl(s). The volume of the solution was reduced to ca. 10 mL and the solution cooled to −10°C for 12 h. The resulting yellow microcrystals were collected and washed with diethyl ether. Yield 0.936 g (70%). Anal. calcd. for $C_{18}H_{22}BF_4IPtS_3$: C 29.08, H 2.98, S 12.94; found: C 29.86, H 3.09, S 12.73.

Synthesis of $[Pt(PPh_3)(L^2)][BF_4]_2$

To a flask containing $[PtCl(L^2)][BF_4]$ (0.297 g, 0.509 mmol) and triphenylphosphine (0.134 g, 0.511 mmol) was added CH_2Cl_2 (15 mL) with stirring. After 1 h, $AgBF_4$ (0.100 g, 0.514 mmol) was added and the mixture was stirred for an additional hour during which time a white precipitate of AgCl(s) formed. The solution was filtered through Celite and the solvent removed in vacuo. The resulting clear colourless oil was redissolved in a minimum volume of CH_2Cl_2 and

Table 1. Crystal data and details of data collection and refinement for $[PtCl(L^2)][BF_4]$, $[PtI(L^3)][BF_4]$, and $[Pt(PPh_3)(L^2)][BF_4]_2 \cdot CH_2Cl_2$.

	$[PtCl(L^2)][BF_4]$	$[PtI(L^3)][BF_4]$	$[Pt(PPh_3)(L^2)][BF_4]_2 \cdot CH_2Cl_2$
Formula	$C_{12}H_{26}ClBF_4PtS_3$	$C_{18}H_{22}BF_4IPtS_3$	$C_{12}H_{26}ClBF_4PtS_3$
Colour and form	Orange-yellow plate	Orange block	Yellow block
Formula weight	583.86	743.35	982.44
Crystal system	Monoclinic	Monoclinic	Triclinic
a (Å)	10.409(6)	13.415(4)	13.266(3)
b (Å)	14.180(4)	12.350(5)	11.315(2)
c (Å)	13.726(8)	14.316(5)	13.970(2)
α (°)	—	—	106.04(2)
β (°)	104.49(4)	107.48(3)	84.95(2)
γ (°)	—	—	86.56(2)
V (Å^3)	1961(2)	2262(1)	1999.7(7)
Space group	$P2_1/c$ (No. 14)	$P2_1/n$ (No. 14)	$P\bar{1}$ (No. 2)
Z	4	4	2
ρ calcd. (g cm^{-3})	1.98	2.18	1.63
Radiation, λ (Å)	0.7107	0.7107	0.7107
μ (cm^{-1})	76.98	78.54	38.83
Temperature (°C)	24	24	24
Data collected	2707	3196	5260
Unique data used	2121	2168	4493
Significance test	$F_o^2 > 3\sigma(F_o^2)$	$F_o^2 > 3\sigma(F_o^2)$	$F_o^2 > 3\sigma(F_o^2)$
No. of variables	166	254	433
Goodness of fit	2.28	1.84	1.75
$R(F_o)$, %	5.62	4.85	4.22
$R_w(F_o)$, %	6.86	6.33	5.38

diethyl ether was added slowly until a white powder precipitated. The solid was collected and washed with diethyl ether. Yield 0.334 g (73%). Anal. calcd. for $C_{30}H_{41}B_2F_8PPtS_3$: C 40.15, H 4.60, S 10.71; found: C 39.95, H 4.70, S 10.23.

General X-ray crystallography

Diffraction experiments were performed on a four-circle Syntex $P2_1$ diffractometer with graphite monochromatized Mo Kα radiation. Initial unit cell constants and orientation matrices were obtained from 15 machine-centred reflections selected from rotation photographs. Partial rotation photographs around each axis were used to determine the crystal system. Following this, 30 high-angle reflections were used to obtain the final lattice parameters and orientation matrices for data collection. Instrument parameters, crystal data, and data collection parameters are summarized in Table 1. The intensities of three standard reflections were recorded every 197 reflections and showed no statistically significant changes over the duration of the data collections. The intensity data were collected in four shells ($2\theta < 30°$, 40°, 45°, and 50°). Empirical absorption coefficients were calculated and absorption corrections applied to the data. The data were processed using the TEXSAN software package running on an SGI Challenge XL computer system.[2] Refinements were carried out by using full-matrix, least-squares techniques on F by minimizing the function $\Sigma w(|F_o| - |F_c|)^2$, where $w = 1/\sigma^2(F_o)$ and F_o and F_c are the observed and calculated structure factors. Atomic scattering factors (9) and anomalous dispersion terms (10, 11) were taken from the usual sources. Fixed H-atom contributions were included with C—H distances of 0.95 Å and thermal parameters 1.2 times the isotropic thermal parameter of the bonded C atoms. No H atoms were refined, but all values were updated as refinement continued.

X-ray structure determination of $[PtCl(L^2)][BF_4]$

Pale yellow crystals of $[PtCl(L^2)][BF_4]$ suitable for X-ray diffraction were grown by vapour diffusion of diethyl ether into a CH_2Cl_2 solution of the complex. Preliminary photography was consistent with a monoclinic crystal system. Observed extinctions were consistent with space group $P2_1/c$. A total of 2707 reflections were collected and 2121 reflections with $F_o^2 > 3\sigma(F_o^2)$ were used in the refinement. The position of the platinum atom was determined using a Patterson synthesis and remaining non-hydrogen atoms were located from successive difference Fourier calculations. In the final cycles of refinement, the BF_4^- anion was input as a rigid group and all non-hydrogen atoms were assigned anisotropic thermal parameters. This resulted in $R = 5.62\%$ and $R_w = 6.86\%$ at convergence. A goodness-of-fit calculation resulted in a value of 2.28, and a final difference Fourier map calculation showed a maximum residual of +2.5 e/Å^3 associated with the Pt atom; largest trough was −2.1 e/Å^3. Atomic positional parameters and selected bonding parameters are summarized in Tables 2 and 3. Thermal parameters and hydrogen atom

[2] TEXSAN-TEXRAY Structure Analysis Package, Molecular Structure Corp., The Woodlands, Tex. 1985.

Table 2. Positional parameters and B(eq) for $[PtCl(L^2)][BF_4]$.

Atom	x	y	z	B(eq)
Pt(1)	0.24625(5)	0.19699(3)	0.08101(4)	3.58(3)
Cl(2)	0.2569(4)	0.0845(3)	0.2062(3)	5.7(2)
S(1)	0.1140(3)	0.0904(3)	−0.0251(3)	4.1(1)
S(2)	0.2424(5)	0.2923(3)	−0.0513(3)	5.2(2)
S(3)	0.3593(4)	0.2974(3)	0.2053(4)	5.5(2)
C(1)	−0.028(2)	0.158(1)	−0.099(1)	6.2(8)
C(2)	−0.003(2)	0.231(2)	−0.168(2)	7(1)
C(3)	0.073(2)	0.318(2)	−0.112(2)	9(1)
C(4)	0.299(4)	0.407(1)	−0.014(2)	14(2)
C(5)	0.358(3)	0.442(2)	0.071(2)	12(2)
C(6)	0.436(3)	0.393(2)	0.155(3)	17(2)
C(7)	0.204(1)	0.0524(10)	−0.117(1)	4.4(6)
C(8)	0.326(2)	0.002(1)	−0.063(1)	6.2(8)
C(9)	0.112(2)	−0.014(1)	−0.197(1)	6.0(8)
C(10)	0.502(2)	0.240(1)	0.286(1)	6.2(8)
C(11)	0.577(3)	0.312(1)	0.362(2)	10(1)
C(12)	0.598(2)	0.193(1)	0.234(2)	8(1)
B(1)	0.8488(9)	0.3432(6)	0.0737(7)	13.1
F(1)	0.800(1)	0.3651(8)	−0.0251(7)	11.1
F(2)	0.775(2)	0.3866(9)	0.130(1)	17.5
F(3)	0.977(1)	0.373(1)	0.105(1)	18.2
F(4)	0.844(1)	0.2482(6)	0.0861(8)	9.5

Table 3. Selected bonding parameters for $[PtCl(L^2)][BF_4]$.

	Distances (Å)		
Pt(1)—Cl(2)	2.327(4)	Pt(1)—S(1)	2.302(3)
Pt(1)—S(2)	2.256(4)	Pt(1)—S(3)	2.306(4)
S(1)—C(1)	1.84(2)	S(1)—C(7)	1.83(2)
S(2)—C(3)	1.79(2)	S(2)—C(4)	1.77(2)
S(3)—C(6)	1.80(3)	S(3)—C(10)	1.81(2)
C(1)—C(2)	1.47(3)	C(2)—C(3)	1.56(3)
C(4)—C(5)	1.26(4)	C(5)—C(6)	1.41(4)
C(7)—C(8)	1.49(2)	C(7)—C(9)	1.58(2)
C(10)—C(11)	1.53(3)	C(10)—C(12)	1.51(3)
	Angles (°)		
Cl(2)-Pt(1)-S(1)	85.8(1)	Cl(2)-Pt(1)-S(2)	173.3(2)
Cl(2)-Pt(1)-S(3)	87.5(1)	S(1)-Pt(1)-S(2)	89.8(1)
S(1)-Pt(1)-S(3)	170.9(2)	S(2)-Pt(1)-S(3)	97.4(2)
Pt(1)-S(1)-C(1)	106.3(6)	Pt(1)-S(1)-C(7)	107.6(5)
Pt(1)-S(2)-C(3)	108.0(8)	Pt(1)-S(2)-C(4)	112.3(8)
C(3)-S(2)-C(4)	100(1)	Pt(1)-S(3)-C(6)	112(1)
Pt(1)-S(3)-C(10)	111.5(6)	C(6)-S(3)-C(10)	101(1)
C(1)-S(1)-C(7)	104.6(8)	S(1)-C(1)-C(2)	118(1)
C(1)-C(2)-C(3)	113(2)	S(2)-C(3)-C(2)	113(2)
S(2)-C(4)-C(5)	132(2)	C(4)-C(5)-C(6)	128(2)
S(3)-C(6)-C(5)	118(2)	S(1)-C(7)-C(8)	109(1)
S(1)-C(7)-C(9)	109(1)	C(8)-C(7)-C(9)	111(1)
S(3)-C(10)-C(11)	109(1)	S(3)-C(10)-C(12)	117(1)
C(11)-C(10)-C(12)	110(2)		

parameters are deposited as supplementary material in Tables S-1 and S-2.[3]

X-ray structure determination of $[PtI(L^3)][BF_4]$

Orange-yellow crystals of $[PtI(L^3)][BF_4]$ suitable for X-ray diffraction were grown by vapour diffusion of diethyl ether into an acetone solution of the complex. Preliminary photography was consistent with a monoclinic crystal system. Observed extinctions were consistent with space group $P2_1/n$. A total of 3196 reflections were collected and 2168 reflections with $F_o^2 > 3\sigma(F_o^2)$ were used in the refinement. The position of the platinum atom was determined using a Patterson synthesis and remaining non-hydrogen atoms were located from successive difference Fourier calculations. In the final cycles of refinement, all non-hydrogen atoms were assigned anisotropic thermal parameters. This resulted in R = 4.85% and R_w = 6.33% at convergence. A goodness-of-fit calculation resulted in a value of 1.84, and a final difference Fourier map calculation showed a maximum residual of 1.5 e/Å^3 associated with the Pt atom; largest trough was −1.9 e/Å^3. Atomic positional parameters and selected bonding parameters are summarized in Tables 4 and 5. Thermal parameters and hydrogen atom parameters are deposited as supplementary material in Tables S-3 and S-4.[3]

X-ray structure determination of $[Pt(PPh_3)(L^2)][BF_4]_2$

Orange-yellow crystals of $[Pt(PPh_3)(L^2)][BF_4]_2$ suitable for X-ray diffraction were grown by vapour diffusion of diethyl ether into a 2:1 CH_2Cl_2–acetone solution of the complex. Preliminary photography was consistent with a triclinic crystal system. Space group $P\bar{1}$ was assumed initially and verified by a successful structure solution and refinement. A total of 5260 reflections were collected and 4493 reflections with $F_o^2 > 3\sigma(F_o^2)$ were used in the refinement. The position of the platinum atom was determined using a Patterson synthesis and remaining non-hydrogen atoms were located from successive difference Fourier calculations. In the final cycles of refinement, all non-hydrogen atoms were assigned anisotropic thermal parameters. This resulted in R = 4.22% and R_w = 5.38% at convergence. A goodness-of-fit calculation resulted in a value of 1.75, and a final difference Fourier map calculation showed a maximum residual of +2.4 e/Å^3 associated with the Pt atom; largest trough was −1.6 e/Å^3. Atomic positional parameters and selected bonding parameters are summarized in Tables 6 and 7. Thermal parameters and hydrogen atom parameters are deposited as supplementary material in Tables S-5 and S-6.[3]

Results and discussion

Synthesis

The three open-chain ligands were easily prepared by a three-step process from commercially available starting materials according to eqs. [1]–[3] (R = Et, iPr, Ph; Ts = tosylate).

Scheme 3.

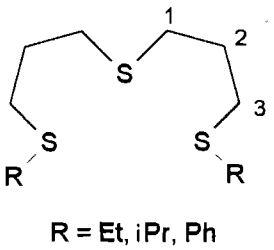

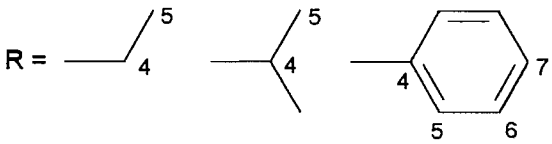

Scheme 4.

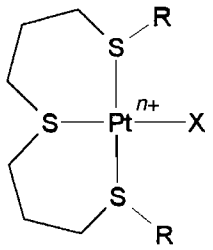

X = Cl, I, PPh_3; R = Et, iPr, Ph

[1] $2\ BrCH_2CH_2CH_2OH + Na_2S \rightarrow S(CH_2CH_2CH_2OH)_2 + 2\ NaBr$

[2] $S(CH_2CH_2CH_2OH)_2 + TsCl \rightarrow S(CH_2CH_2CH_2OTs)_2 + 2\ HCl$

[3] $S(CH_2CH_2CH_2OTs)_2 + 2\ RSH \rightarrow S(CH_2CH_2CH_2SR)_2 + 2\ NaTs$

The ligands L^1, L^2, and L^3 are colourless oils that can be isolated in good yields and are pure by NMR and elemental analysis after one vacuum distillation. The ^1H and ^{13}C NMR spectra of these compounds are first order at the field strength employed and peak assignments were straightforward except for a slight overlap of the H1 and H3 protons for L^1. The $^{13}C\{^1H\}$ NMR spectrum of L^1 exhibits two distinct resonances for the corresponding C1 and C3 nuclei.

The IR spectrum of L^2 showed characteristic peaks attributable to an iPr group at υ = 1370, 1390 cm^{-1}, which were useful for identification purposes in the complexation studies. Mass spectra (EI) of all three ligands showed a parent M^+ ion at the appropriate *m/e* value and observed fragmentation patterns were consistent with the assigned structures. The yellow- to orange-coloured complexes $[PtX(L)][BF_4]$ were easily prepared by reacting an acetone or CH_2Cl_2 suspension of $[PtX_2(1,5\text{-COD})]$ with one equivalent of L and one equivalent

[3] Supplementary Tables S-1 through S-6 may be purchased from: The Depository of Unpublished Data, Document Delivery, CISTI, National Research Council Canada, Ottawa, Canada K1A 0S2. Tables S-2, S-4, and S-6 have also been deposited with the Cambridge Crystallographic Data Centre, and can be obtained on request from The Director, Cambridge Crystallographic Data Centre, University Chemical Laboratory, 12 Union Road, Cambridge, CB2 1EZ, U.K. Structure factor amplitudes are no longer being deposited and may be obtained from the author.

Table 4. Postional parameters and B(eq) for $[PtI(L^3)][BF_4]$.

Atom	x	y	z	B(eq)
Pt(1)	0.42620(5)	0.11231(5)	0.05593(5)	3.71(3)
I(1)	0.62836(10)	0.12902(11)	0.09908(10)	5.98(6)
S(1)	0.4644(4)	−0.0139(4)	0.1791(3)	4.6(2)
S(2)	0.2508(3)	0.1217(4)	0.0333(4)	5.0(2)
S(3)	0.4191(3)	0.2351(4)	−0.0656(3)	4.4(2)
C(1)	0.358(2)	−0.094(1)	0.183(2)	7(1)
C(2)	0.256(2)	−0.041(2)	0.171(2)	7(1)
C(3)	0.196(2)	−0.001(2)	0.068(2)	7(1)
C(4)	0.1816(13)	0.116(2)	−0.096(1)	5.5(8)
C(5)	0.202(1)	0.209(2)	−0.155(1)	7(1)
C(6)	0.306(1)	0.208(2)	−0.1743(12)	5.1(8)
C(7)	0.490(2)	0.058(1)	0.2957(13)	5.1(9)
C(8)	0.438(2)	0.148(2)	0.305(1)	6(1)
C(9)	0.459(2)	0.196(2)	0.393(1)	7(1)
C(10)	0.533(2)	0.157(2)	0.470(2)	8(1)
C(11)	0.592(2)	0.063(2)	0.462(1)	7(1)
C(12)	0.5641(14)	0.016(2)	0.3720(13)	4.8(8)
C(13)	0.3839(13)	0.3632(12)	−0.029(1)	4.6(8)
C(14)	0.364(1)	0.445(2)	−0.0934(14)	5.4(9)
C(15)	0.349(2)	0.546(2)	−0.059(2)	8(1)
C(16)	0.352(2)	0.561(2)	0.033(2)	7(1)
C(17)	0.372(2)	0.481(2)	0.096(2)	7(1)
C(18)	0.393(2)	0.379(1)	0.0715(13)	5(1)
F(1)	0.986(2)	0.127(2)	0.0783(14)	15(1)
F(2)	1.095(1)	0.173(2)	0.2100(13)	13(1)
F(3)	0.936(2)	0.084(2)	0.205(1)	22(2)
F(4)	0.940(2)	0.238(2)	0.166(2)	21(2)
B(1)	0.986(3)	0.152(2)	0.170(2)	9(2)

of $AgBF_4$. After removal of precipitated AgCl, the complexes were isolated by recrystallization from acetone or CH_2Cl_2 and diethyl ether. Dicationic complexes of the type $[Pt(PPh_3)(L)][BF_4]_2$ were prepared by treating the complexes $[PtX(L)][BF_4]$ with a further equivalent of $AgBF_4$ in CH_2Cl_2 solution in the presence of one equivalent of PPh_3.

Stereochemical considerations

A system containing three chiral centres can have a maximum of 8 (2^3) stereoisomers. For a system containing three chiral centres and a potential internal plane of symmetry, this maximum is reduced to three pairs of possible diastereomers (see Scheme 5). All three are possible in this system, although they need not be present in equal proportions. When coordinated to Pt the two terminal sulfur atoms, S(1) and S(3), are chiral centres and, depending upon which lone pair is coordinated to the metal centre, can be of either *R* or *S* absolute configuration. The central S(2) sulfur atom will also be a chiral centre *if* the two terminal S-atoms are of opposite configuration and the absolute configuration at S(2) can be designated noting that *R* chiral groups have precedence over *S* chiral groups. If this is the case, that S(1) and S(3) are of opposite configuration, a plane of symmetry exists through the Pt—S(2) bond perpendicular to the square plane and these are *meso* diastereomers. Since there are two possible sets of *meso* diastereomers, we have arbitrarily designated the isomers with all three lone pairs on the same side of the metal square plane as *meso*-A (*SSR/RRS*) and the isomers with two terminal S-atoms on the same side of the square plane and the central lone pair on the opposite side as the *meso*-B isomer (*SSR/RRS*). The third possibility is that the terminal S-atoms have the same absolute configuration, which orients the *R*-groups and necessarily the lone pairs on opposite sides of the square plane. In this situation, S(2) is *not* a chiral centre and the two possible conformations are enantiomers (*RR* and *SS*) and are therefore referred to as *racemic*.

X-ray structures of $[PtCl(L^2)][BF_4]$, $[PtI(L^3)][BF_4]$, and $[Pt(PPh_3)(L^2)][BF_4]_2$

An ORTEP drawing of the cation $[PtCl(L^2)]^+$ is shown in Fig. 1 with the atom numbering scheme. The geometry at the Pt(II) centre is a slightly distorted square planar with the S-atoms of L^2 occupying three of the sites and a chlorine atom filling the fourth site opposite the central S(2) atom of the thioether ligand. The ligand is in the *meso*-B conformation in this structure which positions the *S*-isopropyl groups on the same side of the square plane, a *syn* arrangement. The terminal S-atoms are chemically equivalent and the Pt—S(1) and Pt—S(3) distances are equal within experimental error: Pt—S(1), 2.302(3) Å; Pt—S(3), 2.306(4) Å. The Pt—S(2) distance of 2.256(4) Å is significantly shorter than the two terminal Pt—S bonds, presumably due to the *trans* influence of the chloride ligand.

Table 5. Selected bonding parameters for $[PtI(L^3)][BF_4]$.

	Distances (Å)		
Pt(1)—I(1)	2.602(2)	Pt(1)—S(1)	2.293(4)
Pt(1)—S(3)	2.289(4)	Pt(1)—S(2)	2.280(5)
S(1)—C(1)	1.76(2)	S(1)—C(7)	1.83(2)
S(3)—C(6)	1.85(2)	S(3)—C(13)	1.78(2)
S(2)—C(3)	1.82(2)	S(2)—C(4)	1.80(2)
C(1)—C(2)	1.48(3)	C(2)—C(3)	1.54(3)
C(4)—C(5)	1.50(3)	C(5)—C(6)	1.51(3)
C(7)—C(8)	1.35(2)	C(7)—C(12)	1.34(2)
C(8)—C(9)	1.34(3)	C(9)—C(10)	1.34(3)
C(10)—C(11)	1.42(3)	C(11)—C(12)	1.36(3)
C(13)—C(14)	1.35(2)	C(13)—C(18)	1.41(2)
C(14)—C(15)	1.38(3)	C(15)—C(16)	1.33(3)
C(16)—C(17)	1.30(3)	C(17)—C(18)	1.36(3)
	Angles (°)		
I(1)-Pt(1)-S(1)	84.0(1)	I(1)-Pt(1)-S(3)	86.0(1)
I(1)-Pt(1)-S(2)	170.8(2)	S(1)-Pt(1)-S(3)	169.6(2)
S(1)-Pt(1)-S(2)	97.3(2)	S(2)-Pt(1)-S(3)	93.0(2)
Pt(1)-S(1)-C(1)	114.4(7)	Pt(1)-S(1)-C(7)	108.2(6)
C(1)-S(1)-C(7)	100.1(9)	Pt(1)-S(3)-C(6)	111.0(6)
Pt(1)-S(3)-C(13)	108.5(7)	C(6)-S(3)-C(13)	100.8(8)
Pt(1)-S(2)-C(3)	113.9(7)	Pt(1)-S(2)-C(4)	109.6(6)
C(3)-S(2)-C(4)	97(1)	S(1)-C(1)-C(2)	119(1)
C(1)-C(2)-C(3)	117(2)	S(2)-C(3)-C(2)	113(1)
S(2)-C(4)-C(5)	115(1)	C(4)-C(5)-C(6)	116(2)
S(3)-C(6)-C(5)	115(1)	S(1)-C(7)-C(12)	117(1)
S(1)-C(7)-C(8)	122(2)	C(8)-C(7)-C(12)	121(2)
C(7)-C(8)-C(9)	119(2)	C(8)-C(9)-C(10)	120(2)
C(9)-C(10)-C(11)	121(2)	C(10)-C(11)-C(12)	116(2)
C(7)-C(12)-C(11)	122(2)	S(3)-C(13)-C(14)	119(2)
S(3)-C(13)-C(18)	118(1)	C(14)-C(13)-C(18)	122(2)
C(13)-C(14)-C(15)	117(2)	C(14)-C(15)-C(16)	121(2)
C(15)-C(16)-C(17)	121(2)	C(16)-C(17)-C(18)	123(2)
C(13)-C(18)-C(17)	115(2)		

There is a very slight tetrahedral distortion evident in the *trans* angles of 173.3(2)° for Cl(1)-Pt(1)-S(2) and 170.9(2)° for S(1)-Pt(1)-S(3).

An ORTEP drawing of the cation $[PtI(L^3)]^+$ is shown in Fig. 2 with the atom numbering scheme. The geometry at the Pt(II) centre is a slightly distorted square planar with the S-atoms of L^3 occupying three of the sites and an iodine atom filling the fourth site opposite the central S(2) atom of the thioether ligand. The ligand is in the *meso*-B conformation in this structure which positions the S-phenyl groups on the same side of the square plane, a *syn* arrangement. The terminal S-atom distances, Pt—S(1) 2.293(4) Å and Pt—S(3) 2.289(4) Å, are equivalent within experimental error and the Pt—S(2) distance is significantly shorter at 2.280(5) Å due to the *trans* influence of the iodide ligand. The Pt—I(1) distance is 2.602(2) Å. There is a very slight tetrahedral distortion evident in the *trans* angles of 170.8(2)° for I(1)-Pt(1)-S(2) and 169.6(2)° for S(1)-Pt(1)-S(3).

An ORTEP drawing of the dication $[Pt(PPh_3)(L^2)]^{2+}$ is shown in Fig. 3 with the atom numbering scheme. The geometry at the Pt(II) centre is a slightly distorted square planar with the S-atoms of L^2 occupying three of the sites and the triphenylphosphine P(1) atom filling the fourth site opposite the central S(2) atom of the thioether ligand. The ligand is in the *racemic* conformation in this structure, which positions the *S*-isopropyl groups on opposite sides of the square plane, an *anti* arrangement. In this conformation, the chemically equivalent, terminal Pt—S bonds, although very similar, are significantly different: Pt—S(1), 2.343(2) Å, Pt—S(3), 2.328(2) Å. The Pt—S(2) distance of 2.339(2) Å is also similar to but still significantly different from the terminal Pt—S bond distances. There is a very slight tetrahedral distortion evident in the *trans* angles of 170.98(9)° for P(1)-Pt(1)-S(2) and 176.31(7)° for S(1)-Pt(1)-S(3).

A number of bonding parameters change systematically as the ancillary ligand changes from Cl to I to PPh_3. The most obvious is the bond distance for the central S-atom *trans* to the ancillary ligand in which the Pt—S(2) distance lengthens from 2.256(4) to 2.289(4) to 2.339(2) Å on changing the *trans* ligand from Cl to I to PPh_3. This simply follows from the variation in *trans* effect; P > I > Cl. The terminal Pt—S bond distances also lengthen but to a lesser degree due to this change in

Scheme 5.

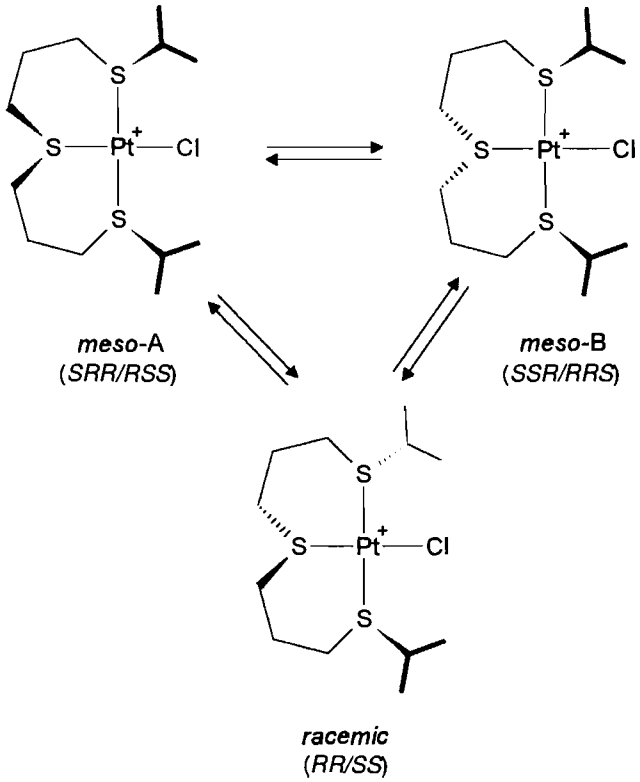

Fig. 1. ORTEP drawing of the $PtCl(L^2)]^+$ cation, showing the atom-numbering scheme. Thermal ellipsoids of 30% probability are shown.

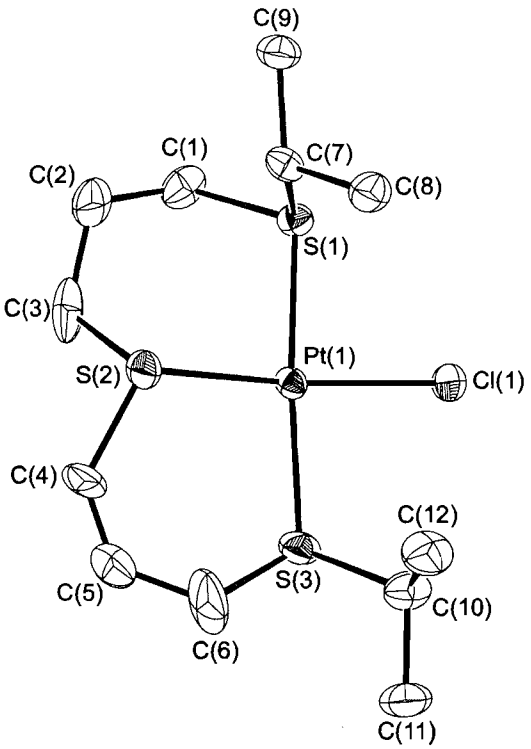

Fig. 2. ORTEP drawing of $[PtI(PhS(CH_2)_3S(CH_2)_2SPh)]^+$ cation showing the atom-numbering scheme. Thermal ellipsoids of 30% probability are shown.

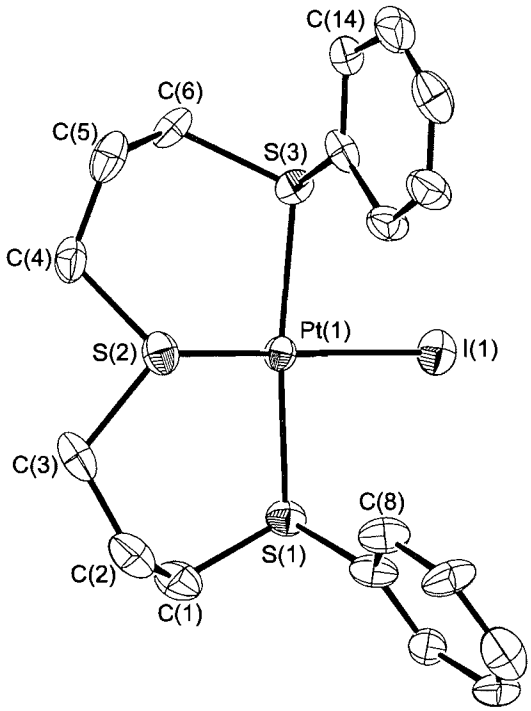

Fig. 3. ORTEP drawing of $[Pt(PPh_3)(L^2)]^{2+}$ cation showing the atom-numbering scheme. Thermal ellipsoids of 30% probability are shown.

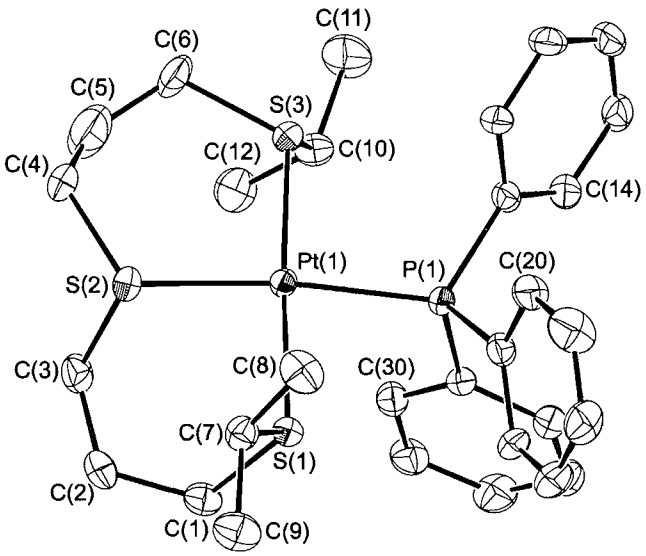

trans effect for the ancillary group. There appear to be only small structural differences due to a change in *S-R* substituent and only a slight variation in terminal Pt—S distances for the two observed ligand conformations, *meso*-B and *racemic*.

Table 6. Positional parameters for $[Pt(PPh_3)(L^2)][BF_4]_2$.

Atom	*x*	*y*	*z*	*B*(eq)
Pt(1)	0.33950(2)	0.27977(3)	0.20596(2)	3.07(2)
S(1)	0.4177(2)	0.2599(2)	0.3454(2)	3.6(1)
S(2)	0.4946(2)	0.1922(2)	0.1132(2)	4.5(1)
S(3)	0.2542(2)	0.3090(2)	0.0745(2)	4.0(1)
P(1)	0.1940(2)	0.3546(2)	0.3181(2)	3.20(9)
C(1)	0.5303(7)	0.3479(9)	0.3503(7)	4.7(5)
C(2)	0.6138(7)	0.303(1)	0.2618(8)	5.4(5)
C(3)	0.5842(7)	0.306(1)	0.1593(8)	5.3(5)
C(4)	0.501(1)	0.188(2)	−0.0187(8)	8.3(8)
C(5)	0.444(2)	0.252(2)	−0.051(1)	15(1)
C(6)	0.332(1)	0.261(1)	−0.0487(7)	6.5(6)
C(7)	0.4712(7)	0.0990(8)	0.3249(7)	4.3(4)
C(8)	0.3856(9)	0.016(1)	0.310(1)	6.2(6)
C(9)	0.530(1)	0.092(1)	0.411(1)	6.6(6)
C(10)	0.2271(8)	0.4762(8)	0.0955(7)	4.7(5)
C(11)	0.144(1)	0.497(1)	0.030(1)	8.2(8)
C(12)	0.320(1)	0.546(1)	0.081(1)	6.9(7)
C(13)	0.0751(6)	0.3685(8)	0.2621(6)	3.7(4)
C(14)	0.0101(7)	0.4753(9)	0.2899(7)	4.4(4)
C(15)	−0.0829(8)	0.479(1)	0.2502(8)	5.5(5)
C(16)	−0.1089(8)	0.377(1)	0.1819(8)	5.9(6)
C(17)	−0.0435(8)	0.270(1)	0.1506(7)	5.3(5)
C(18)	0.0481(7)	0.2659(9)	0.1907(6)	4.3(4)
C(19)	0.1690(6)	0.2593(8)	0.4032(7)	4.0(4)
C(20)	0.1158(8)	0.155(1)	0.3735(7)	5.1(5)
C(21)	0.101(1)	0.080(1)	0.437(1)	7.4(7)
C(22)	0.139(1)	0.107(1)	0.5272(9)	6.6(7)
C(23)	0.1927(9)	0.208(1)	0.5567(7)	5.6(5)
C(24)	0.2072(7)	0.285(1)	0.4961(6)	4.5(4)
C(25)	0.2103(6)	0.5087(7)	0.3972(6)	3.5(4)
C(26)	0.1455(7)	0.5612(9)	0.4874(7)	4.6(4)
C(27)	0.1528(8)	0.680(1)	0.5437(7)	5.4(5)
C(28)	0.226(1)	0.749(1)	0.5106(9)	6.3(6)
C(29)	0.2912(8)	0.6986(9)	0.4254(8)	5.2(5)
C(30)	0.2829(7)	0.5758(8)	0.3671(7)	4.4(4)
B(1)	0.411(1)	0.346(1)	0.710(1)	5.4(6)
F(1)	0.4106(8)	0.2222(6)	0.6996(6)	9.9(5)
F(2)	0.3271(6)	0.4062(8)	0.7654(7)	10.0(5)
F(3)	0.418(1)	0.3709(8)	0.6214(6)	11.9(7)
F(4)	0.4920(6)	0.3908(9)	0.7586(8)	10.8(6)
F(5)	0.710(1)	0.014(1)	1.001(2)	26(2)
F(6)	0.7705(7)	0.1776(7)	0.9822(8)	11.0(6)
F(7)	0.771(2)	0.001(2)	0.870(1)	26(2)
F(8)	0.8712(8)	0.008(1)	0.969(1)	13.9(7)
B(2)	0.782(1)	0.058(2)	0.955(1)	7.9(9)
Cl(1)	0.837(1)	0.007(1)	0.2407(8)	19(1)
Cl(2)	0.957(2)	−0.216(1)	0.180(1)	26(2)
C(31)	0.915(3)	−0.089(3)	0.168(3)	11(2)

Evaluation of the fluxional behaviour of $[PtCl(L^2)][BF_4]$ by NMR spectroscopy

The room temperature ^1H and $^{13}C\{^1H\}$ NMR spectra of the $[PtX(L)]^{n+}$ complexes are characteristic of a system that is exchanging on the NMR time scale. Each coordinated sulfur atom is in a tetrahedral environment as seen from the X-ray analysis and as such has two lone pairs with which to bind to the metal centre. Exchange between the lone pair bound to the metal and the uncoordinated lone pair amounts to inversion at sulfur and interconverts absolute configurations at sulfur. The three possible isomers, *meso*-A, *meso*-B, and *racemic*, can be interconverted by inversion at sulfur as outlined in Scheme 5.

Table 7. Selected bonding parameters for $[Pt(PPh_3)(L^2)][BF_4]_2$.

	Distances (Å)		
Pt(1)—S(1)	2.343(2)	Pt(1)—S(2)	2.339(2)
Pt(1)—S(3)	2.328(2)	Pt(1)—P(1)	2.332(2)
S(1)—C(1)	1.840(9)	S(1)—C(7)	1.849(9)
S(2)—C(3)	1.83(1)	S(2)—C(4)	1.82(1)
S(3)—C(6)	1.85(1)	S(3)—C(10)	1.840(9)
P(1)—C(13)	1.838(9)	P(1)—C(19)	1.835(9)
P(1)—C(25)	1.826(8)	C(1)—C(2)	1.54(1)
C(2)—C(3)	1.53(2)	C(4)—C(5)	1.22(2)
C(5)—C(6)	1.47(2)	C(7)—C(8)	1.51(1)
C(7)—C(9)	1.51(1)	C(10)—C(11)	1.54(2)
C(10)—C(12)	1.54(2)	C(13)—C(14)	1.38(1)
C(13)—C(18)	1.39(1)	C(14)—C(15)	1.40(1)
C(15)—C(16)	1.36(2)	C(16)—C(17)	1.39(2)
C(17)—C(18)	1.39(1)	C(19)—C(20)	1.39(1)
C(19)—C(24)	1.40(1)	C(20)—C(21)	1.39(1)
C(21)—C(22)	1.36(2)	C(22)—C(23)	1.37(2)
C(23)—C(24)	1.38(1)	C(25)—C(26)	1.42(1)
C(25)—C(30)	1.37(1)	C(26)—C(27)	1.37(1)
C(27)—C(28)	1.40(2)	C(28)—C(29)	1.37(2)
C(29)—C(30)	1.42(1)		
	Angles (°)		
S(1)-Pt(1)-S(2)	85.50(8)	S(1)-Pt(1)-S(3)	176.31(7)
S(1)-Pt(1)-P(1)	85.91(8)	S(2)-Pt(1)-S(3)	97.97(8)
S(2)-Pt(1)-P(1)	170.98(9)	S(3)-Pt(1)-P(1)	90.68(8)
Pt(1)-S(1)-C(1)	106.6(4)	Pt(1)-S(1)-C(7)	110.6(3)
C(1)-S(1)-C(7)	103.8(4)	Pt(1)-S(2)-C(3)	104.1(3)
Pt(1)-S(2)-C(4)	114.1(4)	C(3)-S(2)-C(4)	101.6(6)
Pt(1)-S(3)-C(6)	113.9(4)	Pt(1)-S(3)-C(10)	107.9(3)
C(6)-S(3)-C(10)	102.7(5)	Pt(1)-P(1)-C(13)	116.1(3)
Pt(1)-P(1)-C(19)	112.5(3)	Pt(1)-P(1)-C(25)	109.6(3)
C(13)-P(1)-C(19)	105.6(4)	C(13)-P(1)-C(25)	106.2(4)
C(19)-P(1)-C(25)	106.3(4)	S(1)-C(1)-C(2)	116.9(6)
C(1)-C(2)-C(3)	116.6(8)	S(2)-C(3)-C(2)	112.0(8)
S(2)-C(4)-C(5)	123(1)	C(4)-C(5)-C(6)	131(2)
S(3)-C(6)-C(5)	118.5(9)	S(1)-C(7)-C(8)	108.3(7)
S(1)-C(7)-C(9)	109.1(6)	C(8)-C(7)-C(9)	114(1)
S(3)-C(10)-C(11)	108.4(7)	S(3)-C(10)-C(12)	115.1(7)
C(11)-C(10)-C(12)	112(1)	P(1)-C(13)-C(14)	122.7(6)
P(1)-C(13)-C(18)	118.5(6)	C(14)-C(13)-C(18)	118.7(8)
C(13)-C(14)-C(15)	120.7(8)	C(14)-C(15)-C(16)	120(1)
C(15)-C(16)-C(17)	121(1)	C(16)-C(17)-C(18)	119.5(9)
C(13)-C(18)-C(17)	120.6(8)	P(1)-C(19)-C(20)	120.1(7)
P(1)-C(19)-C(24)	121.1(7)	C(20)-C(19)-C(24)	119(1)
C(19)-C(20)-C(21)	120(1)	C(20)-C(21)-C(22)	121(1)
C(21)-C(22)-C(23)	120(1)	C(22)-C(23)-C(24)	120(1)
C(19)-C(24)-C(23)	120.2(9)	P(1)-C(25)-C(30)	119.6(6)
P(1)-C(25)-C(26)	120.5(7)	C(26)-C(25)-C(30)	119.9(7)
C(25)-C(26)-C(27)	120.7(9)	C(26)-C(27)-C(28)	118.8(9)
C(27)-C(28)-C(29)	121.3(9)	C(28)-C(29)-C(30)	120(1)
C(25)-C(30)-C(29)	119.6(8)		

At elevated temperatures (380 K), the ^1H and ^{13}C NMR spectra of the complex $[PtCl(L^2)][BF_4]$ are simple and first order. For example, a simple doublet due to the methyl protons is observed at δ 1.53 ppm in the ^1H NMR spectrum while the same methyl groups exhibit single resonance at δ 21.14 in the ^{13}C NMR spectrum.

In Fig. 4, it can be seen that the high-temperature ^{13}C NMR spectrum contains five resonances, some of which show ^{195}Pt satellites, and at this temperature the sulfur atoms can be considered to be in an "averaged planar" conformation as a result of rapid inversion at the coordinated S centres on the NMR time scale. As the temperature is lowered, these five reso-

Fig. 4. Variable temperature $^{13}C\{^1H\}$ NMR spectra of $[PtCl(L^2)][BF_4]$. Spectra from 240 to 340 K were recorded in CD_3CN. Spectra at 360 and 380 K were recorded in DMSO-d_6 and the septet at δ 39.5 is due to residual solvent.

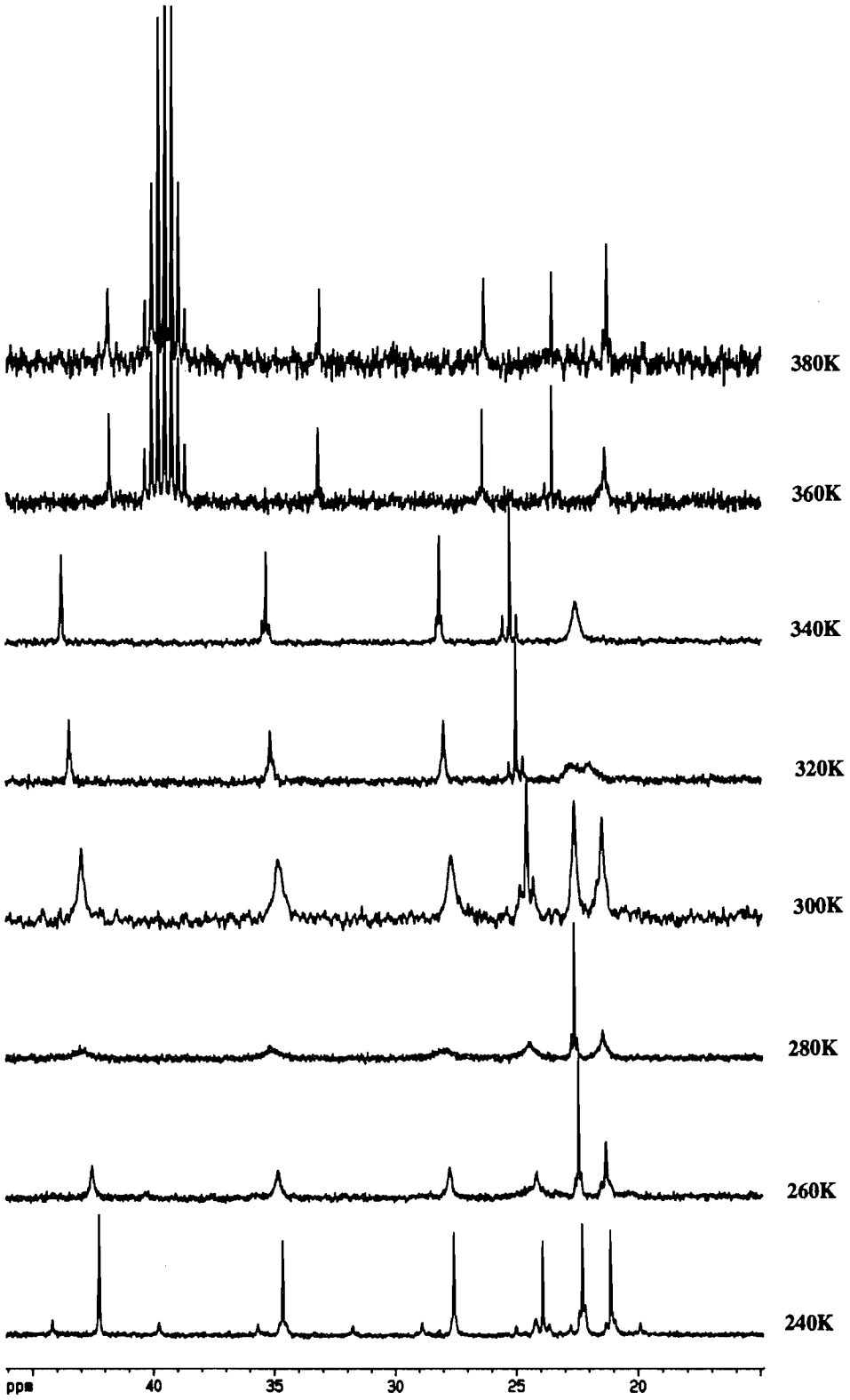

nances broaden and collapse in turn. At lower temperatures, the single peak for the methyl groups has become a six-line system and all the other resonances have split into three separate resonances. The three sets of resonances observed for each of the ligand backbone, methylene carbons, and the isopropyl methine carbons can be assigned to separate reso-

Table 8. $^{13}C\{^1H\}$ NMR spectroscopic data for platinum(II) complexes at 230 K (CD_3CN).

Complex[a]	Population (%)	C(1)	C(2)	C(3)	C(4)	C(5)[b]
$[PtCl(L^1)][BF_4]$	77	33.76	23.02	31.99	28.94	
	14	34.92	23.02	32.45	30.59	
	9	33.32	23.02	31.05	28.28	
$[PtCl(L^2)][BF_4]$	77	34.54	23.78	27.47	42.09	22.18, 21.00
	12	35.58	23.78	28.84	44.13	24.06, 22.59
	11	31.64	23.78	24.90	39.53	21.09, 19.75
$[PtCl(L^3)][BF_4]$[c]	79	36.10	31.05	33.86		
	21	34.78	32.39	34.40		
$[PtI(L^3)][BF_4]$[c]	72	35.57	22.85	34.24		
	15	36.02	23.27	34.52		
	13	35.00	21.60	33.86		
$[Pt(PPh_3(L^2)][BF_4]$	100	35.14	25.51	29.18	44.77	22.05, 20.91

[a]Isomers are listed in order of population from highest to lowest.
[b]Two values are listed for prochiral methyls of the iso-propyl groups.
[c]Aromatic carbon resonances for complexes of L^3 could not be resolved and are not listed.

nances from each of the three possible isomers, *meso*-A, *meso*-B, and *racemic* (Scheme 5). The observation of six methyl resonances is due to the prochiral nature of the isopropyl groups. Since prochiral groups attached to a chiral centre are inequivalent and, barring chance overlap, anisochronous, the methyl groups of *each isomer* are inequivalent, giving rise to the observed six-line pattern.

A full line-shape fitting calculation was performed on the methine carbon resonance of $[PtCl(L^2)][BF_4]$. Spectra at nine temperatures from 230 to 340 K were fitted and the corresponding exchange coefficients used in an Arrhenius-type plot to calculate thermodynamic parameters for the interconversions shown in Scheme 5. The methine carbon resonance was used since it had the smallest $^2J_{Pt,C}$ coupling. The populations used in the calculations were 0.107, 0.775, and 0.118 for the resonances at δ 39.35, 42.09, and 44.13, respectively, and the relaxation (T_2) was calculated from the peak width at half-height of the largest methine peak at 230 K. A plot of $\ln(k/T)$ versus $1/T$ yielded a straight line of the form $y = mx + b$, where $\Delta H^{\ddagger} = -mR$ and $\Delta S^{\ddagger} = R[b - \ln(k_B/h)]$. Values of $\Delta G^{\ddagger}_{300} = 56.6 \pm 4.2$ kJ/mol, $\Delta H = 56.2 \pm 3.6$ kJ/mol, and $\Delta S = -1.3 \pm 8.3$ kJ/mol were obtained. These results are in general agreement with those obtained for bidentate thioether ligands on Pt(II); for example, a $\Delta G^{\ddagger}$ value of 65.6 kJ/mol has been reported (12) for $[PtCl_2(MeS(CH_2)_3SMe)]$.

All the Pt(II) complexes in this series exhibit the type of fluxional behaviour diagrammed for $[PtCl(L^2)][BF_4]$ in Scheme 5. Once the nature of the fluxional process was understood, peak assignments in the $^{13}C\{^1H\}$ NMR spectra of the other complexes were relatively straightforward and are summarized in Table 8. All three isomers were not always observed. For the complex $[Pt(PPh_3)(L^2)][BF_4]_2$ only one isomer was observed while for $[PtI(L^3)][BF_4]$ and $[PtCl(L^3)][BF_4]$ only two isomers were observed at low temperature. There are two possible explanations for this: first, the populations of the unobserved isomers are much smaller than those of the observed isomers at the low-temperature limit; secondly, the peaks due to the minor isomers are still too broad for observation at low temperature. The former is more likely since the barrier to inversion at sulfur is likely very similar for all isomers. Attempts to observe these isomer distributions using ^{195}Pt or ^{31}P NMR spectroscopy were unsuccessful. The ^{195}Pt NMR spectrum (300 K) of $[PtCl(L^2)][BF_4]$ showed a single resonance at −3981 ppm with a width at half-height of 30 Hz. At lower temperatures, this peak broadened but could not be resolved. The ^{31}P NMR spectrum (300 K) of $[Pt(PPh_3)(L^2)][BF_4]_2$ exhibited a single resonance at 13.8 ppm with coupling to ^{195}Pt of 2971 Hz, but again only a single peak was observed even at low temperature.

Conclusions

The thioether ligands $RS(CH_2)_3S(CH_2)_3SR$ (R = Et, iPr, Ph) are easily synthesized by nucleophilic addition of thiolate, SR^- (R = Et, iPr, Ph), to the ditosylate $TsO(CH_2)_3S(CH_2)_3OTs$. Complexes of the type $[PtX(RS(CH_2)_3S(CH_2)_3SR)][BF_4]$ can be readily prepared by displacement of 1,5-COD from $[PtX_2(1,5\text{-COD})]$ (X = Cl, I) in the presence of one equivalent of $AgBF_4$ and the thioether ligand. As designed, these ligands act as tridentate chelators occupying three coordination sites of a square-planar Pt(II) complex. The dynamic behaviour of these complexes, produced by the presence of rapidly inverting chiral thioether centres bound to platinum, can be rationalized in terms of a simple model describing a maximum of three pairs of diastereomers. The thermodynamic parameters obtained for this process are in good agreement with other simpler systems involving Pt(II)-bound thioether ligands.

Finally, preliminary synthetic experiments have shown that these simple halide complexes can act as starting materials for the preparation of square-planar complexes with three sites occupied by thioether donors and the fourth site available for ancillary two-electron donors. This basic coordination geometry should be applicable to more reactive square-planar sys-

tems such as Rh(I) and Ir(I) and offers the opportunity to study the effect of a thioether coordination sphere on bound substrates in an "open coordination site." In this regard, preliminary results show that $[Rh(L)(CO)][BF_4]$ can be prepared fairly easily and the chemistry of this and other Group 9 complexes will be reported in the future.

Acknowledgements

We thank the Natural Sciences and Engineering Research Council of Canada and the University of Winnipeg for financial support of this research and the Faculty of Graduate Studies at the University of Manitoba for allowing J.R.M. to participate in graduate research at the University of Winnipeg.

References

1. S.G. Murray and F.R. Hartley. Chem. Rev. **81**, 365 (1981).
2. S.R. Cooper. Chem. Res. **21**, 141 (1988).
3. S.R. Cooper and S.C. Rawle. Struct. Bonding (Berlin), **72**, 1 (1990).
4. A.J. Blake and M. Schröder. Adv. Inorg. Chem. **35**, 1 (1990).
5. J.P. Collman and L.S. Hegedus. Principles and applications of organotransition metal chemistry. University Science Books, Mill Valley, Calif. 1988.
6. H.C. Clark and L.E. Manzer. J. Organomet. Chem. **59**, 411 (1973).
7. G. Binsch and D.A. Klier. J. Magn. Reson. **3**, 146 (1970).
8. W. Rosen and D.H. Busch. Inorg. Chem. **9**, 262 (1970).
9. D.T. Cromer and J.T. Waber. International tables for X-ray crystallography. Vol. IV. Kynoch Press, Birmingham. 1974. Table 2.2A.
10. J.A. Ibers and W.C. Hamilton. Acta Crystallogr. **17**, 781 (1974).
11. D.T. Cromer and J.T. Waber. International tables for X-ray crystallography. Vol. IV. Kynoch Press, Birmingham. 1974. Table 2.3.1.
12. E.W. Abel, S.K. Bhargava, and K.G. Orrell. Prog. Inorg. Chem. **32**, 1 (1984).

Études des réactions d'oxydation du *n*-heptane et de l'isooctane

Yves Simon, Gérard Scacchi et François Baronnet

Résumé : Dans le but d'aboutir à une meilleure compréhension du mécanisme des phénomènes d'autoinflammation et afin d'améliorer l'adéquation moteur-carburant, nous avons étudié les mécanismes d'oxydation de deux hydrocarbures d'indices d'octane très différents : le *n*-heptane (indice : 0) et l'isooctane (indice : 100). L'étude expérimentale a été menée, à 923 K, en utilisant un montage comprenant un réacteur continu auto-agité par jets gazeux. Les mécanismes d'oxydation du *n*-heptane et de l'isooctane ont été simplifiés en utilisant en premier lieu des considérations purement cinétiques, puis grâce à un logiciel de simulation de mécanismes réactionnels. Le comportement très différent de ces deux hydrocarbures a finalement été attribué à la présence, dans les produits de réactions d'oxydation de l'isooctane, d'alcènes qui agiraient comme des composés antidétonants en formant des radicaux stabilisés par résonance.

Mots clés : réaction d'oxydation, *n*-heptane, isooctane, auto-inflammation, modélisation.

Abstract: The oxidation mechanisms of two alkanes that have quite different octane numbers: *n*-heptane (0) and isooctane (100), were investigated to obtain a better understanding of the chemical mechanism of autoignition phenomena and to improve the compatibility of the available fuels with the engines. The experimental study was performed at 923 K in a setup equipped with a jet-stirred reactor. The oxidation mechanisms of *n*-heptane and isooctane were simplified first by a purely kinetic analysis based on the product formation and then by using a software of simulation of reaction mechanisms. The very different behaviour of these two hydrocarbons was explained by the presence, in the products of isooctane oxidation, of alkenes, which would have an antiknock effect due to the formation of resonance-stabilized radicals.

Key words: oxidation reaction, *n*-heptane, isooctane, autoignition, modelling.

[Traduit par la rédaction]

Introduction

Une meilleure compréhension de l'auto-inflammation spontanée des mélanges air–hydrocarbure en fin de cycle de compression, à l'origine du phénomène de «cliquetis», devrait permettre l'amélioration de l'adéquation moteur-carburants dans le cas des moteurs à allumage commandé. Si les problèmes liés à l'approvisionnement énergétique avaient déjà suscité des recherches dans les années 70 (1, 2), le développement des carburants sans plomb, nécessaires lors de l'utilisation de pots catalytiques, a donné depuis quelques années une nouvelle impulsion à ces recherches (3, 4).

Par ailleurs, la modélisation des phénomènes complexes dans les chambres de combustion des moteurs, incluant les phénomènes d'échange de chaleur, de transfert de matière, de turbulence..., fait appel à des codes de calcul particulièrement complexes. Si un modèle cinétique suffisamment complet est nécessaire de manière à être prédictif, il doit rester d'une dimension limitée (au maximum quelques dizaines de processus élémentaires) pour pourvoir être inséré dans les codes de calcul. Ceci nécessite donc une compréhension fondamentale des phénomènes et paramètres gouvernant les délais d'auto-inflammation et en aucun cas un modèle empirique ne peut suffire.

Dans cette optique, il nous a semblé intéressant d'étudier les mécanismes d'oxydation de deux hydrocarbures d'indices d'octane très différentes : le *n*-heptane (indice : 0) et l'isooctane (indice : 100) qui sont les références des échelles d'indice d'octane des essences.

Le mécanisme d'oxydation des hydrocarbures est très largement dépendant de la température de la phase gazeuse au moment de l'auto-inflammation. Malheureusement, les mesures de température effectuées in situ dans les chambres de combustion sont très imprécises, comme le montrent les études de J.J. Marie et M.J. Cottereau (5). Cette température varie selon les auteurs de 800 K à 1100 K. Nous avons donc choisi, pour cette étude, une température moyenne de 923 K.

Pour conserver, à cette température relativement élevée, des avancements de réaction raisonnables, nous avons opté pour l'utilisation de la technique du réacteur continu auto-agité par jets gazeux.

Conditions expérimentales

L'oxydation du *n*-heptane et de l'isooctane a été étudiée à 923 K dans un réacteur continu auto-agité par jets gazeux. Ce réac-

Reçu le 30 juin 1995.[1]

Y. Simon,[2] G. Scacchi et F. Baronnet. Département de chimie-physique des réactions, Unité de recherche associée n° 328 du Centre national de la recherche scientifique, Institut national polytechnique de Lorraine, École nationale supérieure des industries chimiques, 1, rue Grandville, BP 451, 54001 Nancy Cedex, France.

1. Révision reçue le 29 mars 1996.
2. Auteur à qui adresser toute correspondance. Teléphone: 83 17 51 22. Fax: 83 37 81 20.

Fig. 1. Schéma de l'appareillage expérimental. A.1, A.2 : Ampoules d'échantillonnage B : Ballon de réserve d'air C.1, C.2 : Capteurs de pression V.1 : Vanne de régulation V.2, V.3 : Vannes d'arrêt VP : Vanne pointeau S : Volume tampon.

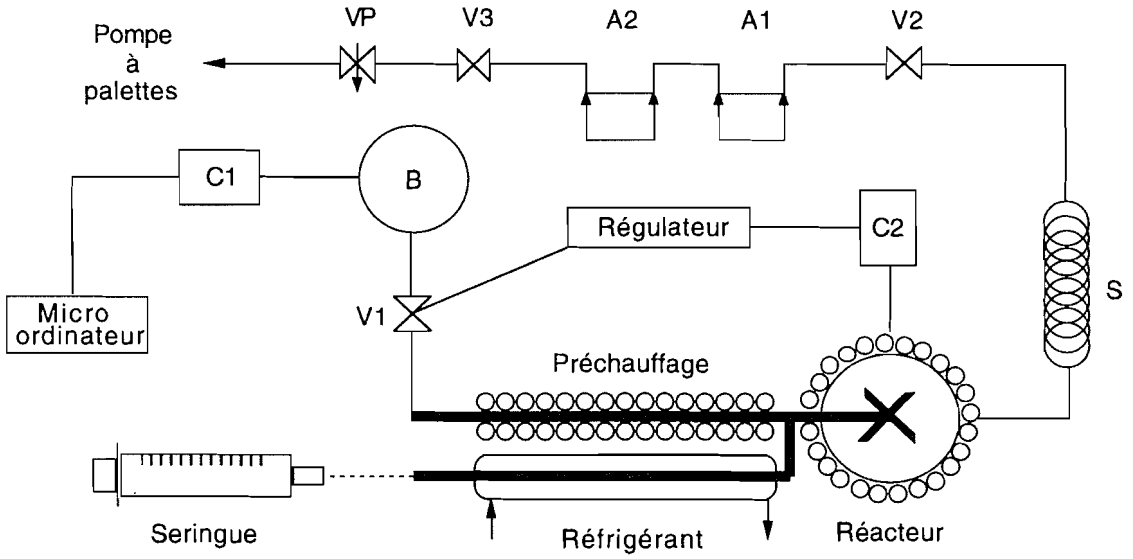

teur sphérique, en silice, a un volume de 23 cm^3 et possède huit injecteurs. Le chauffage du réacteur est assuré par deux coquilles demi-sphériques réalisées avec des résistances électriques isolées de marque «Thermocoax».

Le réacteur est alimenté par deux circuits d'alimentation en réactifs distincts: l'un en hydrocarbure et l'autre en air (voir Fig. 1.).

L'air est stocké dans un ballon de réserve B et débite dans le réacteur en passant par la vanne de régulation V1 dont l'ouverture et la fermeture sont commandées par un régulateur électronique de manière à conserver une pression totale constante dans le réacteur (mesurée par le capteur C2). La pression dans le ballon de stockage B est mesurée par le capteur C1. On détermine alors le flux molaire d'air entrant dans le réacteur en mesurant la variation de pression dans le ballon de réserve, lorsque celui-ci est isolé.

L'hydrocarbure est, par contre, injecté sous forme liquide entre le réacteur et le préchauffage d'air grâce à un pousse-seringue. Au contact de l'air préchauffé, l'hydrocarbure liquide s'évapore et est entraîné, sous forme gazeuse, à l'intérieur du réacteur, où le mélangeage est assuré par les huit injecteurs.

Les composés étudiés, *n*-heptane et isooctane, sont liquides à température ambiante. Pour éviter la condensation de ces réactifs dans les canalisations en verre de l'appareillage expérimental, il convient de travailler avec des pressions partielles de *n*-heptane et d'isooctane inférieures à leurs tensions de vapeur à température ambiante qui sont de l'ordre de 40 Torr (1 Torr = 133,3 Pa). En conséquence, nous avons choisi de fixer la pression partielle de ces deux hydrocarbures à 20 Torr dans le réacteur.

La pression partielle de l'oxygène a été choisie de façon à obtenir un rapport HC/O_2 de 1/2; soit une pression partielle d'air de 200 Torr.

La prise d'échantillon s'effectue dans deux ampoules de chromatographie A1 et A2 montées en série à la sortie du réacteur. Nous avons utilisé, pour l'étude des produits de réaction condensables, une ampoule métallique à quatre voies dont l'étanchéité est assurée par un joint en Téflon. Cette ampoule, réalisée au Laboratoire, permet de supprimer la dissolution de ces composés dans les graisses utilisées sur les robinets des ampoules de verre.

Ces ampoules sont encadrées par deux vannes éléctromagnétiques V2 et V3 qui se ferment successivement afin d'isoler le flux gazeux sortant du réacteur. Le contenu des ampoules d'échantillonnage est analysé par chromatograhie en phase gazeuse.

Enfin, le circuit se termine par une vanne pointeau VP qui permet de modifier le débit total des gaz dans le réacteur.

Résultats expérimentaux

Les produits de réaction ont été dosés par chromatographie en phase gazeuse pour des temps de passage dans le réacteur variant de 0,1 à 0,9 s dans le cas de l'étude de l'oxydation du *n*-heptane et de 0,1 à 1,1 s pour celle de l'isooctane. L'avancement de la réaction varie de 5% à 45% pour les deux hydrocarbures étudiés.

Cas de l'oxydation du *n*-heptane

Cette étude a permis d'identifier et de doser 16 produits d'oxydation différents : hydrogène, méthane, éthylène, éthane, propène, butène-1, pentène-1, hexène-1, heptène-1, heptène-3 *cis* et *trans*, eau, monoxyde et dioxyde de carbone, éthanal, propanal. Les courbes de formation des produits de réaction (à l'exception de H_2 dont la formation, quoique notable, est très irreproductible) sont représentées sur les figures 2, 3 et 4. Il faut noter que l'éthylène n'a été dosé que pour des temps de passage inférieurs à 0,5 s car, au-delà, la quantité d'éthylène formée est trop importante et sature le détecteur du chromatographe.

Fig. 2. Oxydation du *n*-heptane à 923 K. Courbes de formation de CH_4, C_2H_4, C_2H_6, C_3H_6, 1-C_4H_8 et 1-C_5H_{10}.

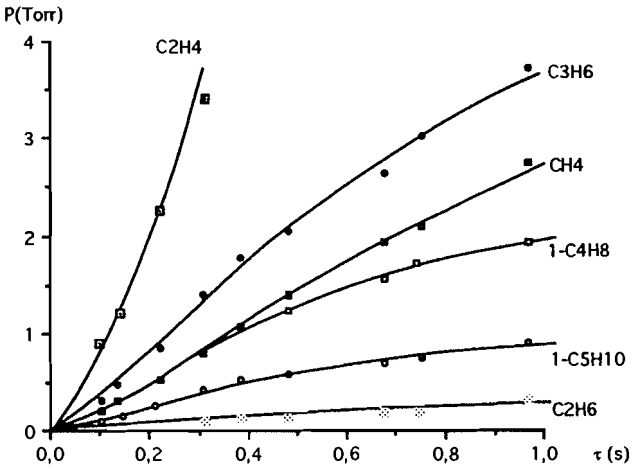

Fig. 3. Oxydation du *n*-heptane à 923 K. Courbes de formation de H_2O, CO, CO_2 et 1-C_6H_{12}.

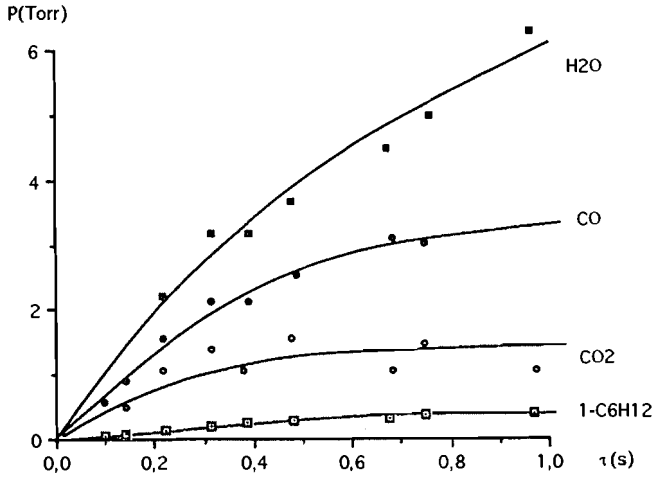

Fig. 4. Oxydation du *n*-heptane à 923 K. Courbes de formation de CH_3CHO, C_2H_5CHO, 1-C_7H_{14}, 3-C_7H_{14} *cis* et *trans*.

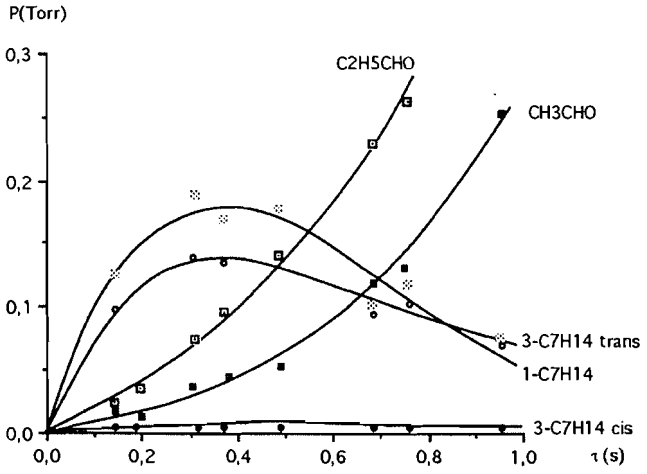

Fig. 5. Oxydation du *n*-heptane à 923 K. Répartition des produits de réaction les plus importants en fonction du temps de passage.

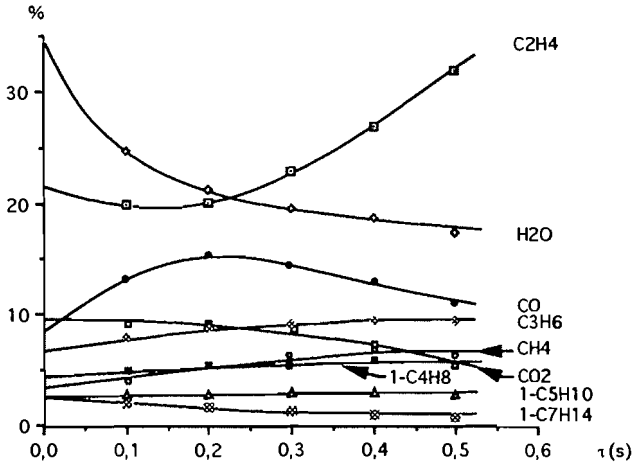

Fig. 6. Oxydation du *n*-heptane à 923 K. Répartition des produits de réaction mineurs en fonction du temps de passage.

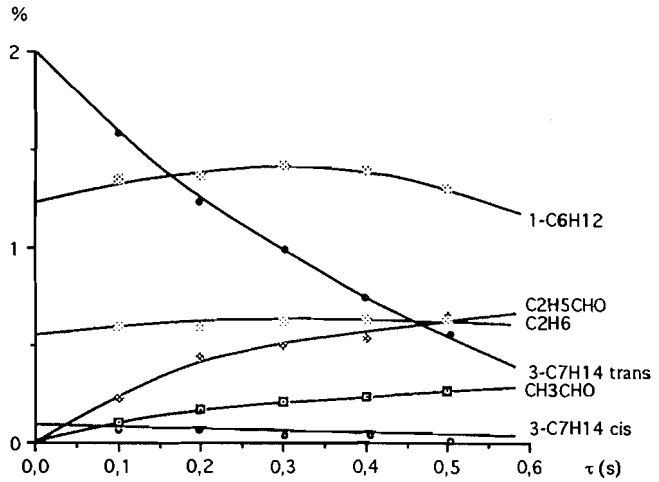

Les «diagrammes horizontaux» correspondant aux produits de réaction sont représentés sur les figures 5 et 6. Ces diagrammes sont tracés en portant le pourcentage molaire du produit considéré par rapport à l'ensemble des produits dosés (réactifs non compris) en fonction du temps de passage. Sur ces diagrammes, le caractère primaire de la formation d'un composé est caractérisé par une courbe ne passant pas par l'origine, alors que, au contraire, le caractère secondaire se distingue par une courbe passant par l'origine. Ces figures montrent que seuls deux produits de réaction sont secondaires : l'éthanal et le propanal.[3]

3. Un produit de réaction est dit «primaire» lorsqu'il est formé à partir des réactifs ou radicaux libres uniquement. Il est dit «secondaire» lorsqu'il est formé à partir des produits primaires. Un produit primaire se caractérise par une vitesse de formation initiale non nulle, alors qu'un produit secondaire possède une vitesse de formation initiale nulle.

Cas de l'oxydation de l'isooctane

Dans cette étude, nous avons identifié et dosé également 16 produits de réaction différents : hydrogène, méthane, éthylène, éthane, propène, propane, isobutène, isobutane, diméthyl-2,4 pentène-1, diméthyl-2,4 pentène-2, diméthyl-4,4 pentène-2, triméthyl-2,4,4 pentène-1, triméthyl-2,4,4 pentène-2, eau, monoxyde et dioxyde de carbone. Les courbes de formation de ces composés (à l'exception de H_2, pour la raison déja invoquée) sont représentées sur les figures 7, 8 et 9 et les «diagrammes horizontaux» correspondant sur les figures 10 et 11. Ces figures montrent que seuls deux produits de réaction sont secondaires : l'éthylène et le propane. Contrairement à l'étude de la réaction d'oxydation du *n*-heptane, aucun aldéhyde n'a pu être identifié ici.

Exploitation des résultats expérimentaux

Les réactions d'oxydation des hydrocarbures dépendent fortement de la température et l'analyse de la littérature fait apparaître deux types de mécanismes fondamentalement différents en fonction du domaine de température exploré :

(*i*) un mécanisme dit de «*haute température*», valable audessus de 1000 K, proposé par Westbrook, Pitz et coll. (6–15) et Warnatz (16–18).

(*ii*) un mécanisme dit de «*basse température*», valable audessous de 800 K et qui constitue l'aboutissement des travaux de Fish (19–22) dans les années 60 puis repris par Quinn et Halstead (2) dans les années 70 et enfin Cox et Cole (23) en 1985.

Fig. 7. Oxydation de l'isooctane à 923 K. Courbes de formation de iso-C_4H_8, CH_4, C_3H_6, C_2H_4, C_2H_6 et diméthyl-4,4 pentène-2.

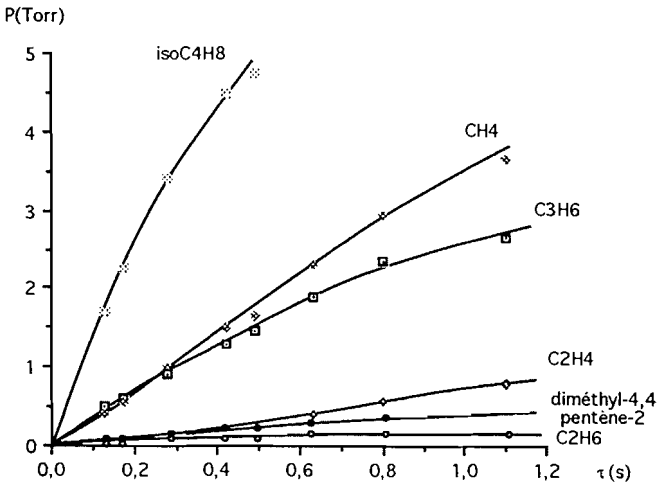

La présence de ces 2 mécanismes résulte de la réversibilité du processus:

$$R^{\cdot} + O_2 \rightleftharpoons RO_2^{\cdot}$$

Ces mécanismes peuvent être schématisés de la façon suivante (Schéma 1) :

Schéma 1. Mécanisme général de l'oxydation des alcanes.

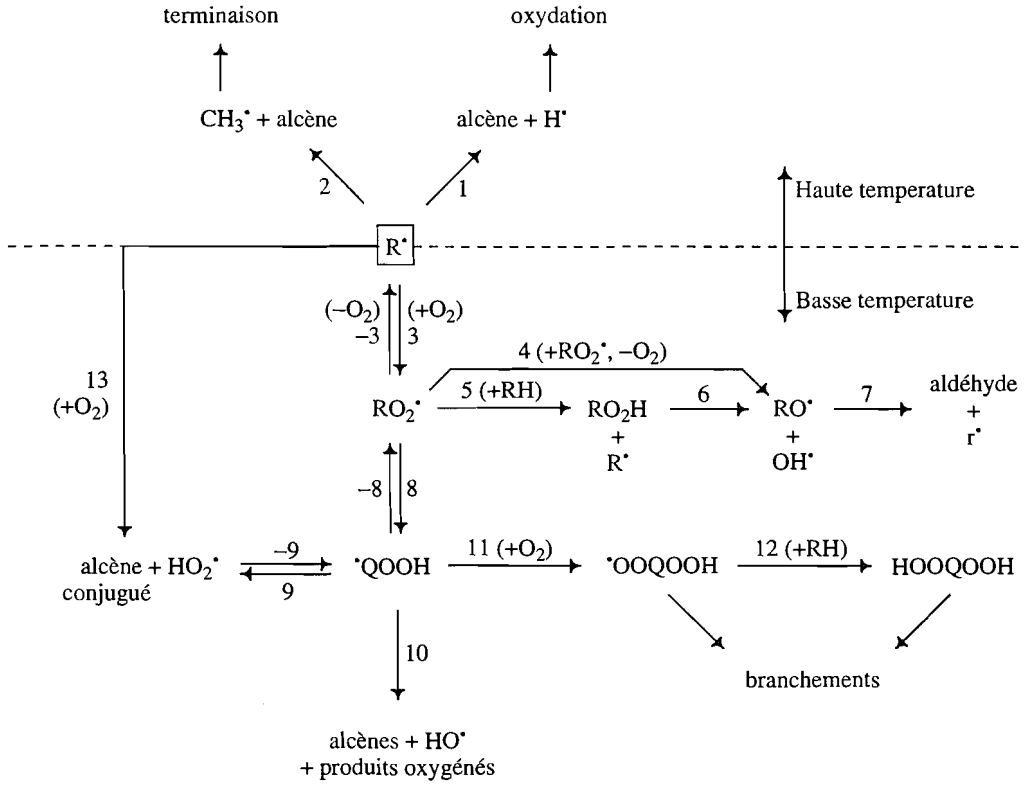

Fig. 8. Oxydation de l'isooctane à 923 K. Courbes de formation de CO, CO_2, H_2O et diméthyl-2,4 pentène-1 + diméthyl-2,4 pentène-2.

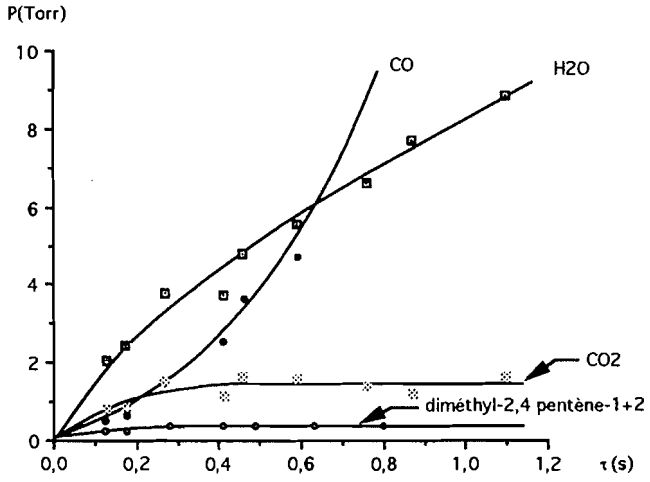

Fig. 9. Oxydation de l'isooctane à 923 K. Courbes de formation de C_3H_8, iso-C_4H_{10}, triméthyl-2,4,4 pentène-1 et triméthyl-2,4,4 pentène-2.

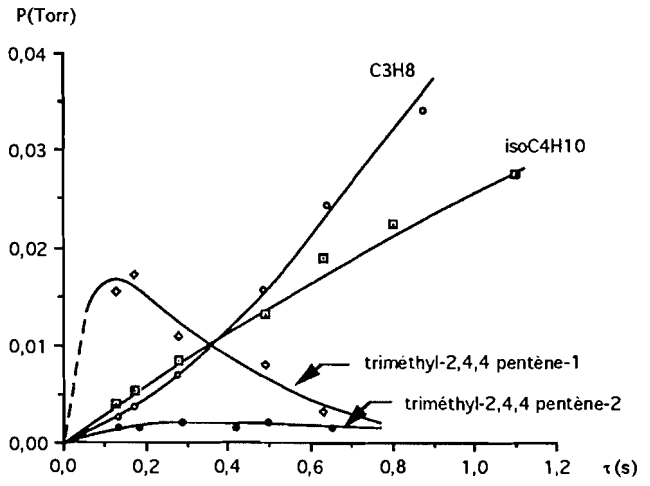

Fig. 10. Oxydation de l'isooctane à 923 K. Répartition des produits de réaction les plus importants en fonction du temps de passage.

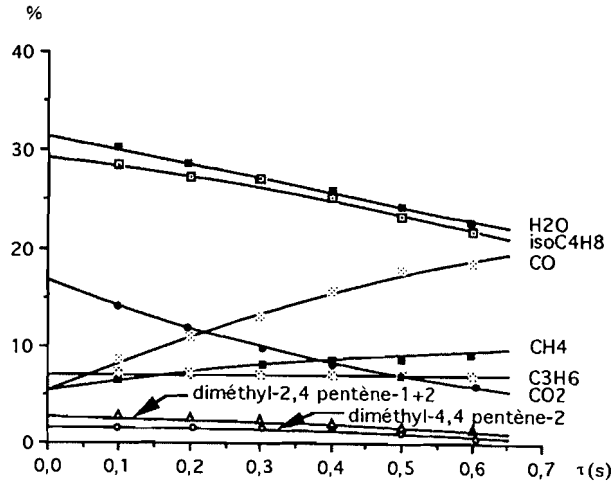

Fig. 11. Oxydation de l'isooctane à 923 K. Répartition des produits de réaction mineurs en fonction du temps de passage.

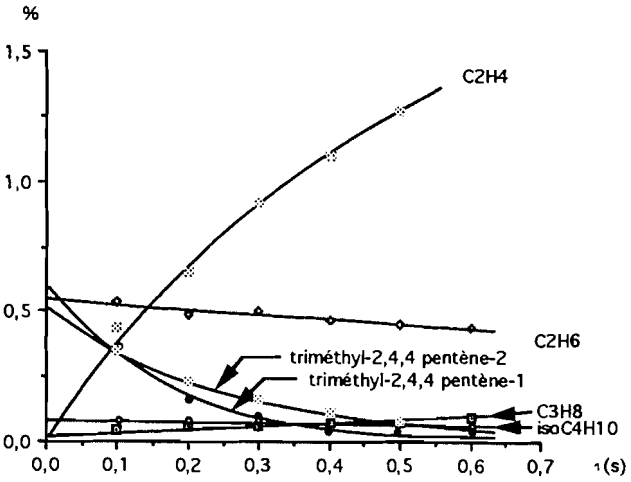

Le radical alcoyle R˙ est formé par le processus d'amorçage à partir de la molécule d'hydrocarbure RH. Ce radical de départ R˙ peut être, dans le cas du *n*-heptane : 1-C_7H_{15}˙, 2-C_7H_{15}˙, 3-C_7H_{15}˙ ou 4-C_7H_{15}˙ et dans le cas de l'isooctane : ˙CH_2-$C(CH_3)_2CH_2$-$CH(CH_3)_2$, $(CH_3)_3C$-CH˙-$CH(CH_3)_2$, $(CH_3)_3C$-CH_2-C˙$(CH_3)_2$ ou $(CH_3)_3C$-CH_2-CH-(CH_3)(CH_2˙).

Nous avons donc tenté d'établir, à partir de considération purement cinétiques puis en utilisant les résultats expérimentaux, quels sont les processus importants dans les mécanismes d'oxydation des deux hydrocarbures étudiés : le *n*-heptane et l'isooctane. Plus particulièrement, nous avons essayé de déterminer l'importance relative des deux mécanismes d'oxydation de *haute et basse température*.

Cas de l'oxydation du *n*-heptane

En considérant le mécanisme d'oxydation de chaque radical alcoyle formé par l'initiation, nous avons calculé le rapport entre la vitesse de réaction V_B suivant le mécanisme de *basse température* et la vitesse de réaction V_H suivant le mécanisme de *haute température*. Les calculs ont été menés en écrivant l'AEQS pour les différents radicaux libres, et en utilisant des constantes de vitesse, soit tirées de la littérature, soit estimées par les méthodes de la cinétique thermochimique (24). Ce calcul fournit, dans le cas du *n*-heptane, une valeur du rapport V_B/V_H variant entre 0,4 et 1,8 suivant le radical R˙ de départ considéré. Ces résultats semi-quantitatifs montrent que les calculs cinétiques ne permettent pas de privilégier l'un des deux mécanismes.

Cependant, ce mécanisme d'oxydation peut être simplifié en analysant les résultats fournis par l'expérience et plus particulièrement, le caractère primaire ou secondaire des produits formés. Prenons le cas de la décomposition du radical alcoyloxy RO˙ (Schéma 2) :

Schéma 2. Formation et décomposition des radicaux RO˙.

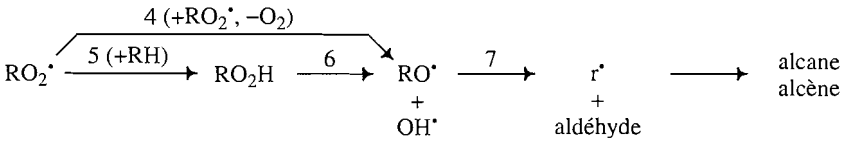

Les radicaux alcoyles r˙ se décomposent essentiellement par rupture d'une liaison C—C pour former, entre autres, du méthane, de l'éthane, et surtout de l'éthylène. Tous les produits formés par la séquence réactionnelle regroupant les processus 5, 6 et 7 sont secondaires puisque provenant de la décomposition d'un produit primaire : l'hydroperoxyde RO_2H. Or, les diagrammes horizontaux (Figs. 5 et 6) montrent sans ambiguïté que l'éthylène est primaire, alors que l'éthanal et le propanal sont secondaires. Cette séquence de processus semble donc minoritaire. La production d'éthylène est due, pour la plus grande part, au mécanisme de haute température et seule la formation des aldéhydes, présents en faible quantité, pourrait provenir essentiellement de cette voie.

Dans le cas de la voie réactionnelle représentée par les processus 4 et 7 tous les produits formés sont primaires, ce qui est en désaccord avec l'allure des diagrammes horizontaux relatifs aux aldéhydes (Fig. 6.). De plus l'éthanal et le propanal ne sont formés expérimentalement qu'un faible quantité, alors que la formation d'éthylène est bien plus importante. Cette séquence réactionnelle peut donc être également considérée comme minoritaire.

Considérons, maintenant, la formation de produits de réaction à partir des processus 8, 9 et 10 (Schéma 1) et prenons l'exemple du radical heptényl-2, noté R(2)˙ (Schéma 3) :

Schéma 3. Décomposition d'un des radicaux RO_2˙ dans l'oxydation du *n*-heptane.

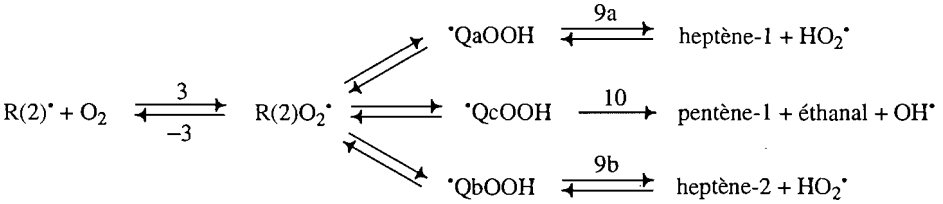

La comparaison des constantes de vitesse des processus d'isomérisation des radicaux $R(2)O_2$˙ montre que les valeurs de ces constantes sont similaires. En considérant que chaque radical ˙QO_2H ne possède qu'une seule voie de décomposition possible, les vitesses d'isomérisation et de décomposition sont égales. La vitesse de formation de l'heptène conjugué (processus 9a ou 9b) par décomposition d'un radical ˙QO_2H, ainsi que celles du pentène-1 ou encore de l'éthanal (processus 10) sont du même ordre de grandeur.

La formation de l'éthanal est secondaire et ne peut pas être interprètée par cette séquence de processus. De plus, la vitesse de formation de pentène-1 par cette voie est théoriquement identique à celle de l'éthanal, alors qu'expérimentalement, la production de pentène-1 est 17 fois plus grande que celle de l'éthanal. Ces deux produits de réaction ne sont donc manifestement pas formés par cette voie.

De même, les vitesses de formation d'éthanal, d'heptène-1 et d'heptène-2 sont théoriquement voisines. La part de production d'éthanal par cette voie est, comme nous l'avons vu, très faible dans la production totale d'éthanal qui ne représente pas plus de 2% des produits formés par la réaction. L'heptène-1 et l'heptène-2 ne sont donc produits, par cette voie, qu'à l'état de traces dans le milieu réactionnel et leur mécanisme de formation, n'ayant aucune influence cinétique, pourra être négligé.

Les réactions d'isomérisation des radicaux $R(2)O_2$˙ pourront donc être négligées dans le mécanisme final. Des raisonnements similaires peuvent être faits dans le cas des trois autres radicaux alcoyles formés par l'amorçage. En résumé, ces simplifications portent exclusivement sur le mécanisme de *basse température* qui se révèle être presqu'entièrement minoritaire. Le mécanisme d'oxydation du ***n*-heptane** peut alors être représenté par le schéma général suivant (Schéma 4).

Cas de l'oxydation de l'isooctane

De façon à déterminer l'importance relative des deux mécanismes de *haute et basse température*, nous avons déterminé, en utilisant la même méthodologie que pour le *n*-heptane, le rapport V_B/V_H pour chacun des 4 radicaux alcoyles formés par l'amorçage. Le rapport obtenu pour les différents radicaux R˙ varie de 0,2 à 2,6. Ces résultats, trop proches de 1, ne permettent donc pas de conclure à une prédominance d'un des deux mécanismes par rapport à l'autre.

Nous avons, alors, comme celà a été fait pour l'oxydation du *n*-heptane, tenté de simplifier le mécanisme réactionnel en utilisant les résultats expérimentaux. Nous avons vu, lors de l'interprétation des résultats expérimentaux de l'oxydation du *n*-heptane, que les courbes de formation des aldéhydes apportaient de précieux renseignements sur l'importance d'un grand nombre de processus de ce mécanisme d'oxydation. Par contre, l'étude expérimentale de la réaction d'oxydation de l'isooctane n'a pas permis de révéler la présence d'aldéhydes. Nous avons alors tenté de déterminer les processus négligeables, par la seule comparaison des courbes de formation des hydrocarbures.

Reprenons le cas de la décomposition du radical RO˙ présentée sur le schéma 2. Les radicaux r˙ se décomposent ici pour former : CH_4, C_3H_6, C_3H_8, $isoC_4H_8$ et $isoC_4H_{10}$.

La voie réactionnelle représentée par la série de processus 5, 6 et 7 conduit à la formation de produits de réaction secondaires. Or, les diagrammes horizontaux (Figs. 10 et 11) mon-

Schéma 4. Mécanisme d'oxydation du *n*-heptane, simplifié en tenant compte des résultats expérimentaux.

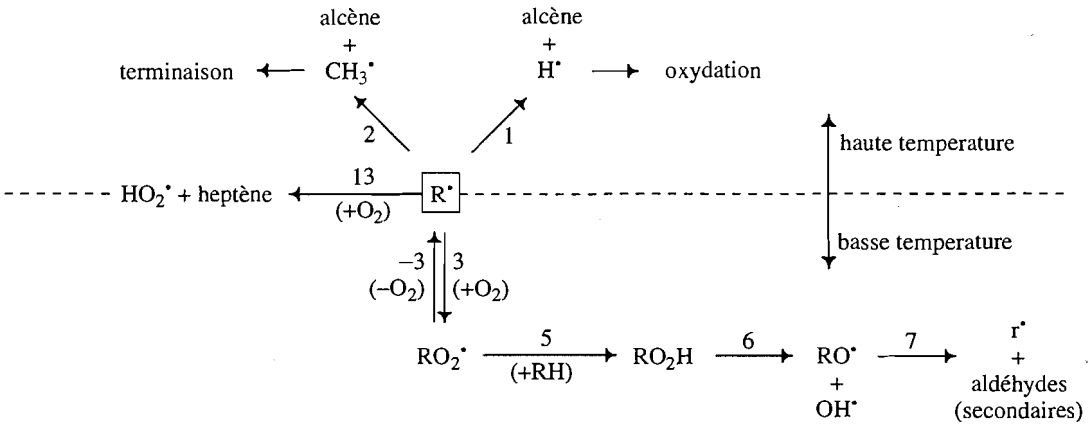

trent que CH_4, C_3H_6, $isoC_4H_8$ et $isoC_4H_{10}$ sont de caractère primaire et que seul C_3H_8 pourrait être formé par un mécanisme secondaire. Cette voie réactionnelle semble donc prendre une part négligeable dans la formation de la plupart des hydrocarbures, mais peut cependant expliquer la formation de propane secondaire. La proportion de propane formé étant inférieure à 0,1%, nous pourrons globalement négliger la séquence de processus précédente.

Par contre, la voie passant par les processus 4 et 7 conduit uniquement à la formation de produits primaires et rien ne permet donc de conclure sur l'importance relative de cette séquence de processus.

Analysons, maintenant, le cas des processus 8, 9 et 10 (Schéma 1). Par similitude avec le raisonnement établi dans le cas de l'oxydation du *n*-heptane, nous pouvons supposer que les vitesses de formation de produits issus de la décomposition d'un même radical $^\bullet QO_2H$ sont approximativement égales (les constantes de vitesse des processus d'isomérisation d'un radical $RO_2^\bullet$ sont voisines). Prenons le cas du radical $RO_2^\bullet$ formé à partir du radical $(CH_3)_3C\text{-}CH^\bullet\text{-}CH(CH_3)_2$ (Schéma 5) :

Schéma 5. Décomposition d'un des radicaux $RO_2^\bullet$ dans l'oxydation de l'isooctane.

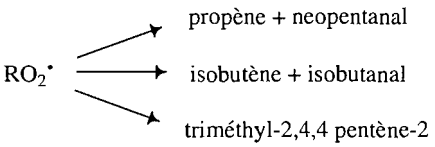

Si ces réactions sont majoritaires dans la formation du propène, de l'isobutène et du triméthyl-2,4,4 pentène-2, nous devrions obtenir expérimentalement des pressions partielles voisines pour ces 3 alcènes; ce qui n'est pas le cas. En effet, pour un temps de passage de l'ordre de 0,2 s on observe : 2,5 Torr d'isobutène, 0,7 Torr de propène et 2×10^{-3} Torr de triméthyl-2,4,4 pentène-2.

Nous pouvons donc supposer que, dans la formation d'isobutène et de propène, la plus grande part est fournie par le mécanisme de *haute température* et considérer la voie précédente comme minoritaire. Des raisonnements identiques peuvent être faits pour les voies utilisant les trois autres radicaux $R^\bullet$ possibles.

L'étude des résultats expérimentaux a ainsi montré que le mécanisme *haute température* était prépondérant dans le mécanisme d'oxydation de **l'isooctane**. Ce mécanisme peut être schématisé de la façon suivante (Schéma 6).

Modélisation des réactions d'oxydation du *n*-heptane et de l'isooctane

L'approche précédente a permis un certain nombre de simplifications concernant particulièrement le mécanisme de *basse température*. Cependant, nous n'avons pas pu conclure sur l'importance de certaines voies réactionnelles par un raisonnement basé uniquement sur les résultats expérimentaux directs. Afin d'aller au-delà dans la simplification de ces mécanismes, nous avons simulé ces résultats expérimentaux.

Les mécanismes d'oxydation simplifiés représentés sur les schémas 4 et 6 ont servi à modéliser les résultats expérimentaux grâce au logiciel de simulation MORSE mis au point au DCPR (25, 26). Ce logiciel permet, à partir d'un mécanisme théorique, d'obtenir les concentrations courantes de tous les produits de réaction et donc les courbes de formation de ces produits. Ces courbes peuvent alors être comparées aux courbes de formation expérimentales.

Le mécanisme de départ ayant servi à cette simulation comporte 199 processus élémentaires dans le cas de l'oxydation du *n*-heptane et 152 processus dans le cas de l'oxydation de l'isooctane. Ces mécanismes, non exhaustifs, ne comportent essentiellement que des processus primaires (à l'exception des processus de formation de CO, CO_2 et du processus 6), donnant naissance à des produits de réaction identifiés expérimentalement. Les constantes de vitesse ont été ajustées raisonnablement de façon à obtenir des courbes de formation théoriques aussi proches que possible des courbes expérimentales (Figs. 12 et 13). Il convient, cependant, de remarquer que les courbes de formation expérimentales reflètent l'intervention de processus secondaires dès que l'avancement devient notable (20% d'advancement à 0,3 s), ce qui explique l'éloignement croissant avec le temps de passage, entre les courbes expérimentales et théoriques. Il n'a, par contre, pas été possible de simuler quantitativement les courbes de formation de CO, CO_2, et dans une moindre mesure H_2O, en utilisant un mécanisme primaire réaliste.

L'analyse de sensibilité, effectuée sur les constantes de vitesse a alors permis de simplifier considérablement ces mécanismes, par la recherche de processus négligeables. Ainsi, le mécanisme d'oxydation du ***n*-heptane** ne comporte

Fig. 12. Oxydation du *n*-heptane à 923 K. Courbes de formation simulées.

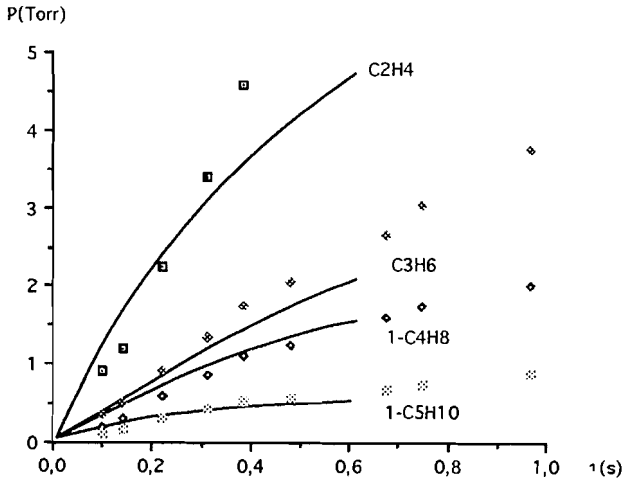

Fig. 13. Oxydation de l'isooctane à 923 K. Courbes de formation simulées.

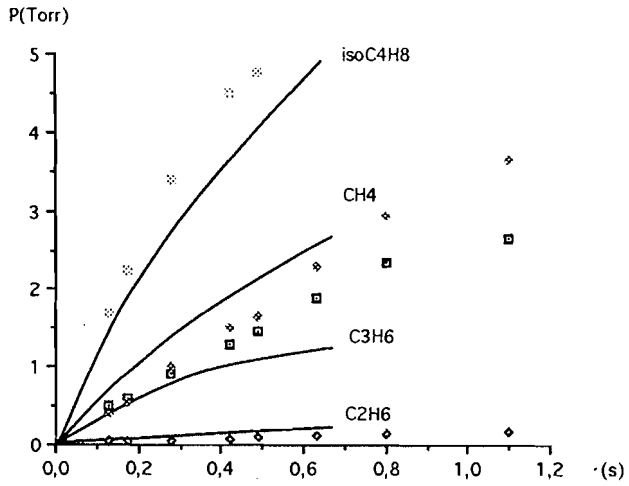

Schéma 6. Mécanisme d'oxydation de l'isooctane, simplifié en tenant compte des résultats expérimentaux.

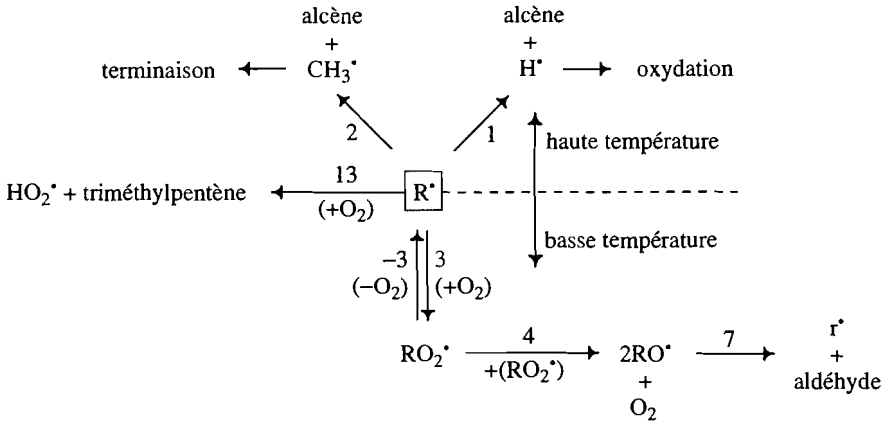

Schéma 7. Mécanisme final d'oxydation du *n*-heptane et de l'isooctane.

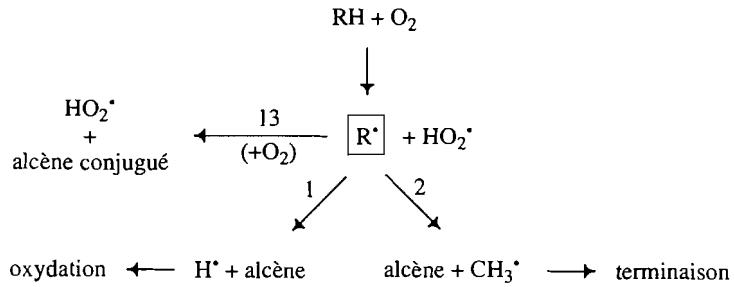

plus finalement que 76 processus élémentaires et celui de **l'isooctane** 71 processus élémentaires (tableaux 1 et 2). Dans les deux cas, les processus d'oxydation du radical R˙ suivant le mécanisme de *basse température* se sont avérés être négligeables. Les deux mécanismes d'oxydation du *n*-heptane et de l'isooctane relèvent donc d'un schéma identique (Schéma 7), correspondant au mécanisme de *haute température*. Ce schéma final correspond, par ailleurs, à celui représentant les mécanismes d'oxydation du *n*-heptane et de l'isooctane dans des conditions de pression plus élevées (27).

Discussion et conclusion

Les mécanismes primaires d'oxydation du ***n*-heptane** et de

Tableau 1. Mécanisme d'oxydation du *n*-heptane à 923 K.

Processus	k (cm^3, mol, s)
$RH + O_2 \rightarrow R1^{\cdot} + HO_2^{\cdot}$	$1,8 \times 10^3$
$RH + O_2 \rightarrow R2^{\cdot} + HO2^{\cdot}$	$4,0 \times 10^3$
$RH + O_2 \rightarrow R3^{\cdot} + HO_2^{\cdot}$	$4,0 \times 10^3$
$RH + O_2 \rightarrow R4^{\cdot} + HO_2^{\cdot}$	$2,0 \times 10^3$
$R1^{\cdot} \rightarrow R2^{\cdot}$	$1,6 \times 10^7$
$R1^{\cdot} \rightarrow R3^{\cdot}$	$2,4 \times 10^9$
$R1^{\cdot} \rightarrow R4^{\cdot}$	$4,4 \times 10^8$
$R2^{\cdot} \rightarrow R3^{\cdot}$	$4,4 \times 10^8$
$R2^{\cdot} \rightarrow R1^{\cdot}$	$3,8 \times 10^6$
$R3^{\cdot} \rightarrow R1^{\cdot}$	$7,0 \times 10^8$
$R4^{\cdot} \rightarrow R1^{\cdot}$	$1,3 \times 10^8$
$R3^{\cdot} \rightarrow R2^{\cdot}$	$4,4 \times 10^8$
$1\text{-}C_5H_{11}^{\cdot} \rightarrow 2\text{-}C_5H_{11}^{\cdot}$	$4,4 \times 10^7$
$2\text{-}C_5H_{11}^{\cdot} \rightarrow 1\text{-}C_5H_{11}^{\cdot}$	$1,3 \times 10^8$
$R1^{\cdot} + O_2 \rightarrow$ heptène-1 $+ HO_2^{\cdot}$	$2,2 \times 10^{11}$
$R2^{\cdot} + O_2 \rightarrow$ heptène-1 $+ HO_2^{\cdot}$	$2,2 \times 10^{11}$
$R2^{\cdot} + O_2 \rightarrow$ heptène-2 $+ HO_2^{\cdot}$	$1,2 \times 10^{11}$
$R3^{\cdot} + O_2 \rightarrow$ heptène-2 $+ HO_2^{\cdot}$	$1,2 \times 10^{11}$
$R3^{\cdot} + O_2 \rightarrow$ heptène-3 $+ HO_2^{\cdot}$	$1,2 \times 10^{11}$
$R4^{\cdot} + O_2 \rightarrow$ heptène-3 $+ HO_2^{\cdot}$	$1,2 \times 10^{11}$
$R1^{\cdot} \rightarrow$ heptène-1 $+ H^{\cdot}$	$1,5 \times 10^5$
$R2^{\cdot} \rightarrow$ heptène-1 $+ H^{\cdot}$	$8,0 \times 10^4$
$R2^{\cdot} \rightarrow$ heptène-2 $+ H^{\cdot}$	$6,0 \times 10^4$
$R3^{\cdot} \rightarrow$ heptène-2 $+ H^{\cdot}$	$1,2 \times 10^5$
$R3^{\cdot} \rightarrow$ heptène-3 $+ H^{\cdot}$	$8,2 \times 10^4$
$R4^{\cdot} \rightarrow$ heptène-3 $+ H^{\cdot}$	$8,2 \times 10^4$
$C_2H_5^{\cdot} \rightarrow C_2H_4 + H^{\cdot}$	$2,4 \times 10^4$
$1\text{-}C_3H_7^{\cdot} \rightarrow$ propène $+ H^{\cdot}$	$1,8 \times 10^5$
$1\text{-}C_4H_9^{\cdot} \rightarrow$ butène-1 $+ H^{\cdot}$	$1,2 \times 10^5$
$1\text{-}C_5H_{11}^{\cdot} \rightarrow$ pentène-1 $+ H^{\cdot}$	$1,0 \times 10^5$
$2\text{-}C_5H_{11}^{\cdot} \rightarrow C_2H_5^{\cdot} +$ propène	$7,1 \times 10^3$
$R1^{\cdot} \rightarrow C_2H_4 + 1\text{-}C_5H_{11}^{\cdot}$	$1,0 \times 10^6$
$R2^{\cdot} \rightarrow$ propène-1 $+ 1\text{-}C_4H_9^{\cdot}$	$1,6 \times 10^6$
$R3^{\cdot} \rightarrow$ butène-1 $+ 1\text{-}C_3H_7^{\cdot}$	$1,7 \times 10^6$
$R4^{\cdot} \rightarrow$ pentène-1 $+ C_2H_5^{\cdot}$	$7,2 \times 10^5$
$R3^{\cdot} \rightarrow$ hexène-1 $+ CH_3^{\cdot}$	$3,4 \times 10^5$
$1\text{-}C_5H_{11}^{\cdot} \rightarrow C_2H_4 + 1\text{-}C_3H_7^{\cdot}$	$7,0 \times 10^5$
$1\text{-}C_4H_9^{\cdot} \rightarrow C_2H_4 + C_2H_5^{\cdot}$	$6,0 \times 10^6$
$1\text{-}C_3H_7^{\cdot} \rightarrow C_2H_4 + CH_3^{\cdot}$	$4,7 \times 10^5$
$RH + H^{\cdot} \rightarrow H_2 + R1^{\cdot}$	$7,4 \times 10^{11}$
$RH + H^{\cdot} \rightarrow H_2 + R2^{\cdot}$	$1,0 \times 10^{12}$
$RH + H^{\cdot} \rightarrow H_2 + R3^{\cdot}$	$1,0 \times 10^{12}$
$RH + H^{\cdot} \rightarrow H_2 + R4^{\cdot}$	$5,1 \times 10^{11}$
$RH + C_2H_5^{\cdot} \rightarrow C_2H_6 + R1^{\cdot}$	$1,1 \times 10^9$
$RH + C_2H_5^{\cdot} \rightarrow C_2H_6 + R2^{\cdot}$	$1,1 \times 10^9$
$RH + C_2H_5^{\cdot} \rightarrow C_2H_6 + R3^{\cdot}$	$1,1 \times 10^9$
$RH + C_2H_5^{\cdot} \rightarrow C_2H_6 + R4^{\cdot}$	$1,1 \times 10^9$
$RH + HO_2^{\cdot} \rightarrow H_2O_2 + R1^{\cdot}$	$3,1 \times 10^8$
$RH + HO_2^{\cdot} \rightarrow H_2O_2 + R2^{\cdot}$	$6,8 \times 10^8$
$RH + HO_2^{\cdot} \rightarrow H_2O_2 + R3^{\cdot}$	$6,8 \times 10^8$
$RH + HO_2^{\cdot} \rightarrow H_2O_2 + R4^{\cdot}$	$3,4 \times 10^8$
$RH + CH_3^{\cdot} \rightarrow CH_4 + R1^{\cdot}$	$7,2 \times 10^9$
$RH + CH_3^{\cdot} \rightarrow CH_4 + R2^{\cdot}$	$1,4 \times 10^{10}$
$RH + CH_3^{\cdot} \rightarrow CH_4 + R3^{\cdot}$	$1,4 \times 10^{10}$
$RH + CH_3^{\cdot} \rightarrow CH_4 + R4^{\cdot}$	$7,0 \times 10^9$
$RH + OH^{\cdot} \rightarrow H_2O + R1^{\cdot}$	$4,2 \times 10^{12}$
$RH + OH^{\cdot} \rightarrow H_2O + R2^{\cdot}$	$9,0 \times 10^{12}$
$RH + OH^{\cdot} \rightarrow H_2O + R3^{\cdot}$	$9,0 \times 10^{12}$
$RH + OH^{\cdot} \rightarrow H_2O + R4^{\cdot}$	$4,5 \times 10^{12}$
$H^{\cdot} + O_2 \rightarrow OH^{\cdot} + O^{\cdot}$	$2,8 \times 10^{10}$
$H^{\cdot} + HO_2^{\cdot} \rightarrow OH^{\cdot} + OH^{\cdot}$	$1,0 \times 10^{14}$
$O^{\cdot} + HO_2^{\cdot} \rightarrow OH^{\cdot} + O_2$	$2,0 \times 10^{13}$
$CH_3^{\cdot} + O^{\cdot} \rightarrow CH_2O + H^{\cdot}$	$7,0 \times 10^{13}$
$CH_2O + O^{\cdot} \rightarrow HCO^{\cdot} + OH^{\cdot}$	$5,2 \times 10^{12}$
$CH_2O + H^{\cdot} \rightarrow HCO^{\cdot} + H_2$	$2,9 \times 10^{12}$
$CH_2O + OH^{\cdot} \rightarrow HCO^{\cdot} + H_2O$	$2,0 \times 10^{12}$
$HCO^{\cdot} + O^{\cdot} \rightarrow CO_2 + H^{\cdot}$	$3,0 \times 10^{13}$
$HCO^{\cdot} + O_2 \rightarrow CO + HO_2$	$1,0 \times 10^{13}$
$C_2H_5^{\cdot} + O^{\cdot} \rightarrow CH_3CHO + H^{\cdot}$	$5,0 \times 10^{13}$
$CH_3CHO + O^{\cdot} \rightarrow CH_3^{\cdot} + CO + OH^{\cdot}$	$4,5 \times 10^{12}$
$CO + OH^{\cdot} \rightarrow CO_2 + H^{\cdot}$	$1,8 \times 10^{11}$
$CO + HO_2^{\cdot} \rightarrow CO_2 + OH^{\cdot}$	$5,0 \times 10^8$
$CH_3^{\cdot} + CH_3^{\cdot} \rightarrow C_2H_6$	$5,0 \times 10^{13}$
$CH_3^{\cdot} + C_2H_5^{\cdot} \rightarrow C_3H_8$	$3,2 \times 10^{13}$
$H^{\cdot} + HO_2^{\cdot} \rightarrow H_2 + O_2$	$2,3 \times 10^{13}$
$HO_2^{\cdot} + HO_2^{\cdot} \rightarrow H_2O_2 + O_2$	$2,0 \times 10^{12}$

Tableau 1 (*suite et fin*).

NOTA : RH représente la molécule de *n*-heptane. R1', R2', R3' sont respectivement les radicaux heptényles 1, 2, 3 et 4.

l'isooctane sont donc tout à fait similaires, y compris les ordres de grandeur des constantes de vitesse des processus élémentaires et ne permettent pas d'expliquer l'écart de comportement entre ces deux hydrocarbures. Il faut noter également que, pour des temps de passages identiques, ces deux réactions possèdent des taux de conversion tout à fait comparables. La seule différence qui peut être observée dans les réactions d'oxydation du *n*-heptane et de l'isooctane se situe au niveau des *produits primaires formés par la réaction* (essentiellement des oléfines). On remarque, en effet, que la réaction d'oxydation du *n*-heptane forme essentiellement des hydrocarbures insaturés en chaîne linéaire (éthylène, propène, butène-1 ...), alors que la réaction d'oxydation de l'isooctane forme aussi des hydrocarbures insaturés ramifiés (isobutène, diméthylpentènes, triméthylpentènes). Les produits oxygénés formés par l'oxydation de ces deux hydrocarbures sont de même nature et produits en quantités équivalentes.

En fait, la vitesse de réaction est étroitement dépendante des constantes de vitesse des processus d'amorçage, de propagation et de terminaison. Les processus d'amorçage ou de branchement des réactions d'oxydation du *n*-heptane et de l'isooctane sont de même nature et ont des constantes de vitesse voisines. Il en est de même des processus de propagation, puisque les réactions d'isomérisation :

$$R^{\cdot} + O_2 \rightleftharpoons RO_2^{\cdot} \rightleftharpoons {}^{\cdot}QO_2H$$

souvent rendues responsables de la différence de comportement des hydrocarbures, ont ici disparu. Seule la nature des processus de *terminaison* semble donc pouvoir expliquer, ici, la différence de comportement entre le *n*-heptane et l'isooctane et plus particulièrement la formation de radicaux libres très peu réactifs (stabilisés par résonance).

Tableau 2. Mécanisme d'oxydation de l'isooctane à 923 K.

Processus	k (cm^3, mol, s)
$RH + O_2 \rightarrow R1^{\cdot} + HO_2^{\cdot}$	$2{,}5 \times 10^4$
$RH + O_2 \rightarrow R2^{\cdot} + HO_2^{\cdot}$	$2{,}5 \times 10^4$
$RH + O_2 \rightarrow R3^{\cdot} + HO_2^{\cdot}$	$8{,}5 \times 10^3$
$RH + O_2 \rightarrow R4^{\cdot} + HO_2^{\cdot}$	$1{,}4 \times 10^4$
$R1^{\cdot} \rightarrow R3^{\cdot}$	$5{,}6 \times 10^9$
$R1^{\cdot} \rightarrow R4^{\cdot}$	$1{,}4 \times 10^9$
$R3^{\cdot} \rightarrow R1^{\cdot}$	$3{,}9 \times 10^8$
$R4^{\cdot} \rightarrow R1^{\cdot}$	$2{,}0 \times 10^9$
$R2^{\cdot} + O_2 \rightarrow$ triméthyl-2,4,4 pentène-2 + $HO_2^{\cdot}$	$6{,}0 \times 10^8$
$R3^{\cdot} + O_2 \rightarrow$ triméthyl-2,4,4 pentène-1 + $HO_2^{\cdot}$	$5{,}2 \times 10^9$
$R3^{\cdot} + O_2 \rightarrow$ triméthyl-2,4,4 pentène-2 + $HO_2^{\cdot}$	$6{,}0 \times 10^8$
$R4^{\cdot} + O_2 \rightarrow$ triméthyl-2,4,4 pentène-1 + $HO_2^{\cdot}$	$5{,}2 \times 10^9$
$R1^{\cdot} \rightarrow$ isobutène + $isoC_4H_9^{\cdot}$	$7{,}0 \times 10^6$
$R1^{\cdot} \rightarrow$ diméthyl-2,4 pentène-1 + $CH_3^{\cdot}$	$2{,}3 \times 10^6$
$R2^{\cdot} \rightarrow$ diméthyl-2,4 pentène-2 + $CH_3^{\cdot}$	$2{,}3 \times 10^5$
$R2^{\cdot} \rightarrow$ diméthyl-4,4 pentène-2 + $CH_3^{\cdot}$	$3{,}6 \times 10^5$
$R3^{\cdot} \rightarrow$ isobutène + $tertC_4H_9^{\cdot}$	$7{,}5 \times 10^5$
$R4^{\cdot} \rightarrow$ propène + $neoC_5H_{11}^{\cdot}$	$1{,}1 \times 10^6$
$R4^{\cdot} \rightarrow$ diméthyl-4,4 pentène-1 + $CH_3^{\cdot}$	$7{,}6 \times 10^6$
$isoC_4H_9^{\cdot} \rightarrow$ propène + $CH_3^{\cdot}$	$1{,}5 \times 10^6$
$neoC_5H_{11}^{\cdot} \rightarrow$ isobutène + CH_3	$1{,}0 \times 10^6$
$R2^{\cdot} \rightarrow$ triméthyl-2,4,4 pentène-2 + $H^{\cdot}$	$3{,}0 \times 10^3$
$R3^{\cdot} \rightarrow$ triméthyl-2,4,4 pentène-2 + $H^{\cdot}$	$6{,}0 \times 10^3$
$R3^{\cdot} \rightarrow$ triméthyl-2,4,4 pentène-1 + $H^{\cdot}$	$1{,}2 \times 10^4$
$R4^{\cdot} \rightarrow$ triméthyl-2,4,4 pentène-1 + $H^{\cdot}$	$3{,}0 \times 10^3$
$isoC_4H_9^{\cdot} \rightarrow H^{\cdot}$ + isobutène	$5{,}0 \times 10^3$
$tertC_4H_9^{\cdot} \rightarrow H^{\cdot}$ + isobutène	$6{,}0 \times 10^3$
$RH + OH^{\cdot} \rightarrow R1^{\cdot} + H_2O$	$2{,}8 \times 10^{12}$
$RH + OH^{\cdot} \rightarrow R2^{\cdot} + H_2O$	$4{,}5 \times 10^{12}$
$RH + OH^{\cdot} \rightarrow R3^{\cdot} + H_2O$	$3{,}1 \times 10^{12}$
$RH + OH^{\cdot} \rightarrow R4^{\cdot} + H_2O$	$1{,}9 \times 10^{12}$
$RH + HO_2^{\cdot} \rightarrow R1^{\cdot} + H_2O_2$	$4{,}6 \times 10^8$
$RH + HO_2^{\cdot} \rightarrow R2^{\cdot} + H_2O_2$	$3{,}4 \times 10^8$
$RH + HO_2^{\cdot} \rightarrow R3^{\cdot} + H_2O_2$	$4{,}1 \times 10^8$
$RH + HO_2^{\cdot} \rightarrow R4^{\cdot} + H_2O_2$	$3{,}1 \times 10^8$
$RH + H^{\cdot} \rightarrow R1^{\cdot} + H2$	$1{,}1 \times 10^{12}$
$RH + H^{\cdot} \rightarrow R2^{\cdot} + H2$	$5{,}0 \times 10^{11}$
$RH + H^{\cdot} \rightarrow R3^{\cdot} + H2$	$2{,}4 \times 10^{12}$
$RH + H^{\cdot} \rightarrow R4^{\cdot} + H2$	$7{,}4 \times 10^{11}$
$RH + CH_3^{\cdot} \rightarrow R1^{\cdot} + CH_4$	$2{,}0 \times 10^9$
$RH + CH_3^{\cdot} \rightarrow R2^{\cdot} + CH_4$	$2{,}0 \times 10^8$
$RH + CH_3^{\cdot} \rightarrow R3^{\cdot} + CH_4$	$3{,}0 \times 10^8$
$RH + CH_3^{\cdot} \rightarrow R4^{\cdot} + CH_4$	$3{,}0 \times 10^8$
$RH + isoC_4H_9^{\cdot} \rightarrow$ isobutane + $R1^{\cdot}$	$6{,}0 \times 10^8$
$RH + isoC_4H_9^{\cdot} \rightarrow$ isobutane + $R2^{\cdot}$	$1{,}2 \times 10^8$
$RH + isoC_4H_9^{\cdot} \rightarrow$ isobutane + $R3^{\cdot}$	$6{,}0 \times 10^7$
$RH + isoC_4H_9^{\cdot} \rightarrow$ isobutane + $R4^{\cdot}$	$4{,}0 \times 10^8$
$RH + tertC_4H_9^{\cdot} \rightarrow$ isobutane + $R1^{\cdot}$	$5{,}0 \times 10^7$
$RH + tertC_4H_9^{\cdot} \rightarrow$ isobutane + $R2^{\cdot}$	$1{,}0 \times 10^7$
$RH + tertC_4H_9^{\cdot} \rightarrow$ isobutane + $R3^{\cdot}$	$1{,}0 \times 10^7$
$RH + tertC_4H_9^{\cdot} \rightarrow$ isobutane + $R4^{\cdot}$	$5{,}0 \times 10^7$
$RH + neoC_5H_{11}^{\cdot} \rightarrow$ neopentane + $R1^{\cdot}$	$6{,}0 \times 10^8$
$RH + neoC_5H_{11}^{\cdot} \rightarrow$ neopentane + $R2^{\cdot}$	$1{,}8 \times 10^8$
$RH + neoC_5H_{11}^{\cdot} \rightarrow$ neopentane + $R3^{\cdot}$	$9{,}0 \times 10^7$
$RH + neoC_5H_{11}^{\cdot} \rightarrow$ neopentane + $R4^{\cdot}$	$4{,}0 \times 10^8$
$H^{\cdot} + O_2 \rightarrow OH^{\cdot} + O^{\cdot}$	$5{,}1 \times 10^{11}$
$H^{\cdot} + HO_2^{\cdot} \rightarrow OH^{\cdot} + OH^{\cdot}$	$7{,}0 \times 10^{13}$
$O^{\cdot} + HO_2^{\cdot} \rightarrow OH^{\cdot} + O_2$	$2{,}0 \times 10^{13}$
$CO + OH^{\cdot} \rightarrow CO_2 + H^{\cdot}$	$1{,}2 \times 10^{11}$
$CO + HO_2^{\cdot} \rightarrow CO_2 + OH^{\cdot}$	$4{,}8 \times 10^8$
$CH_3^{\cdot} + O^{\cdot} \rightarrow CH_2O + H^{\cdot}$	$7{,}0 \times 10^{13}$
$CH_2O + O^{\cdot} \rightarrow HCO^{\cdot} + OH^{\cdot}$	$5{,}2 \times 10^{12}$
$CH_2O + H^{\cdot} \rightarrow HCO^{\cdot} + H_2$	$2{,}9 \times 10^{12}$
$CH_2O + OH^{\cdot} \rightarrow HCO^{\cdot} + H_2O$	$1{,}6 \times 10^{13}$
$HCO^{\cdot} + O_2 \rightarrow CO + HO_2^{\cdot}$	$3{,}0 \times 10^{12}$
$HCO^{\cdot} + O^{\cdot} \rightarrow CO_2 + H^{\cdot}$	$3{,}0 \times 10^{13}$
$CH_3^{\cdot} + CH_3^{\cdot} \rightarrow C_2H_6$	$5{,}0 \times 10^{11}$
$tertC_4H_9^{\cdot} + H^{\cdot} \rightarrow$ isobutane	$1{,}0 \times 10^{14}$
$HO_2^{\cdot} + HO_2^{\cdot} \rightarrow H_2O_2 + O_2$	$2{,}0 \times 10^{12}$
$HCO^{\cdot} + H^{\cdot} \rightarrow CO + H_2$	$2{,}0 \times 10^{14}$
$tertC_4H_9^{\cdot} + CH_3^{\cdot} \rightarrow$ neopentane	$1{,}0 \times 10^{13}$

Tableau 2 (*suite et fin*).

NOTA : RH représente la molécule d'isooctane. R1˙, R2˙, R3˙ et R4˙ sont respectivement les radicaux˙ CH_2-$C(CH_3)_2$-CH_2-$CH(CH3)_2$, $(CH_3)_3$C-CH˙-$CH(CH_3)_2$, $(CH_3)_3$C-CH_2-C˙$(CH_3)_2$ et $(CH_3)_3$C-CH_2-$CH(CH_3)(CH_2˙)$

Tableau 3. Indice d'octane recherche de mélange des produits formés par l'oxydation du *n*-heptane.

Produit	% «Initial»	IORM (réf. 28)
Éthylene	20	—
Propène	8	—
Butène-1	5	144
Pentène-1	3	119
Heptène-1	3	68
Heptène-3	1,7	—
Hexène-1	1,3	97

Les alcènes formés par ces réactions pourraient, par l'intermédiaire de processus secondaires, inhiber ou non la réaction d'oxydation. En effet, la comparaison des tableaux 3 et 4 montre que les produits majoritaires des réactions d'oxydation du *n*-heptane et de l'isooctane sont : l'éthylène, le propène et l'isobutène. Le propène est présent en quantités voisines dans les deux cas (8% pour le *n*-heptane et 7% pour l'isooctane). Sa présence ne peut donc pas expliquer la différence de comportement existant entre le *n*-heptane et l'isooctane. Par contre, le produit majoritaire de l'oxydation de l'isooctane est l'isobutène (31%) qui conduit à la formation du radical isobutènyle stabilisé par résonance, alors que l'oxydation du *n*-heptane forme essentiellement de l'éthylène (20%) qui lui ne forme pas de radicaux stabilisés.

De plus, la comparaison de l'indice d'octane recherche de mélange (IORM) des alcènes produits par les réactions d'oxydation du *n*-heptane et de l'isooctane (Tableaux 3 et 4) montre que les produits formés par la réaction d'oxydation de l'isooctane ont des indices d'octane plus élevés que ceux produits par la réaction d'oxydation du *n*-heptane, en particulier l'isobutène (IORM : 170) formé en très grande quantité.

L'oxydation de l'isobutène est très difficile, car elle conduit

Tableau 4. Indice d'octane recherche de mélange des produits formés par l'oxydation de l'isooctane.

Produit	% «Initial»	IORM (28)
Isobutène	31	170
Propène	7	—
Diméthyl-4,4 pentène-2	2	—
Triméthyl-2,4,4 pentène-1	0,6	164
Triméthyl-2,4,4 pentène-2	0.5	148
Diméthyl-2,4 pentène-1 + Diméthyl-2,4 pentène-2	2	142 135

au radical isobutènyle, stabilisé par résonance. Plusieurs études de réactions de pyrolyse (29) ou d'oxydation (30, 31) ont, en effet, montré le caractère inhibiteur des radicaux allyliques. Le caractère antidétonant de l'éthylterbutyléther et du méthylterbutyléther a, par ailleurs, été expliqué par la formation d'isobutène (32–34).

En dehors de leur participation aux terminaisons, les radicaux allyliques s'oxydent plus difficilement que les radicaux alcoyles. Considérons, par exemple, la réaction d'oxydation de deux alcènes, l'un conduisant à un radical allylique et l'autre à un radical alcoyle. Ces deux radicaux peuvent, soit réagir avec le réactif RH, soit avec l'oxygène, suivant le schéma :

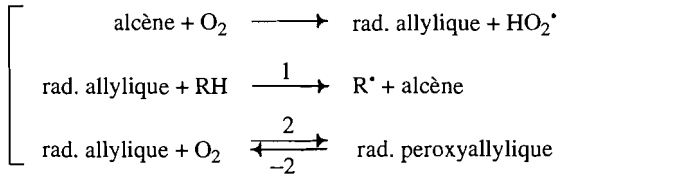

E = 18,8 kcal/mol (35)

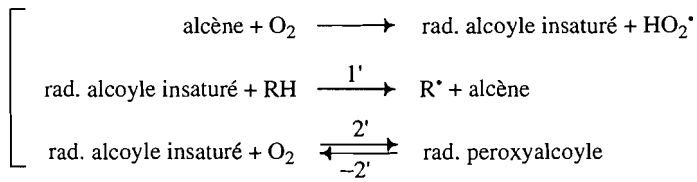

E' = 10,4 kcal/mol (35)

On note, entre les processus 1 et 1′ une différence d'énergie d'activation de 8,4 kcal/mol en faveur du processus 1′ qui est donc plus facile que le processus 1. D'autre part, Benson (36) signale que la constante d'équilibre de la réaction 2′ est supérieure de deux ordres de grandeur par rapport à celle de la réaction 2 à 763 K.

En conclusion, tous les processus de propagation consommant les radicaux formés par décomposition des produits primaires de réaction seront plus rapides si ces radicaux ne sont pas stabilisés par résonance. Au contraire, une concentration élevée de radicaux stabilisés par résonance fera apparaître de nouvelles terminaisons.

La différence d'indice d'octane entre le *n*-heptane et l'isooctane pourrait donc s'expliquer par la présence de radicaux stablisés par résonance formés par décomposition des produits primaires de réaction et plus particulièrement par les alcènes.

Remerciements

Les auteurs remercient Shell Research Ltd pour le soutient financier accordé au cours de ce travail. Ils sont également reconnaissants au Dr. C. Morley (Thornton Research Center) pour des discussions stimulantes et constructives.

Références

1. L.J. Kirsch et C.P. Quinn. Symp. (Int.) Combust. (Proc.) 16th, The Combustion Institute, Pittsburgh, Pa. 1976 p. 233.
2. M.P. Halstead, L.J. Kirsch, A. Prothero et C.P. Quinn. Proc. R. Soc. London, Ser. A: **346**, 515 (1975).
3. P.G. Lignola et E. Reverchon. Oxid. Commun. **14**, 81 (1991).
4. C. Chevalier, W.J. Pitz, J. Warnatz, C.K. Westbrook et H. Melenk. Symp. (Int.) Combust. (Proc.) 24th, The Combustion Institute, Pittsburgh, Pa. 1992. p. 93
5. J.J. Marie et M.J. Cotterreau. SAE Paper, 870 458 (1987).
6. C.K. Westbrook et F.L. Dryer. Symp. (Int.) Cumbust. (Proc.) 18th, The Combustion Institute, Pittsburg, Pa. 1981. p. 749.
7. C.K. Westbrook et W.J. Pitz. Combust. Flame, **63**, 113 (1986).
8. C.K. Westbrook, W.J. Pitz et M.M. Thornton. Combust. Flame, **72**, 45 (1988).
9. N.P. Cernansky, R.M. Green, W.J. Pitz et C.K. Westbrook. Combust. Sci. Technol. **50**, 3 (1986).
10. C.K. Westbrook. A.I.A.A. Aerospace Science Meeting, 24th, Reno, Nev. 1986.
11. W.J. Pitz, C.K. Westbrook, W.M. Proscia et F.L. Dryer. Symp. (Int.) Combust. (Proc.) 20th, The Combustion Institute, Pittsburgh, Pa. 1984. p. 831.
12. C.K. Westbrook et W.J. Pitz. SAE Paper, 872 107 (1987).
13. C.K. Westbrook et W.J. Pitz. Workshop Modell. Chem. React. Syst. (Proc.) 2nd, Heidelberg, Germany. 1986. *Édité par* J. Warnatz et W. Jager. Springer Ser. Chem. Phys. **39**, 1987.
14. E.I. Axelsson, K. Brezinsky, F.L. Dryer, W.J. Pitz et C.K. Westbrook. Symp. (Int.) Combust. (Proc.) 21st, The Combustion Institute, Pittsburgh, Pa. 1986. p. 783.
15. C.K. Westbrook et W.J. Pitz. Communication, ACS Nat. Meeting, Division of Petroleum Chemistry, Miami Beach, Fla. Prepr. 1985. p. 321.
16. J. Warnatz. Symp. (Int.) Combust. (Proc.) 20th, The Combustion Institute, Pittsburg, Pa. 1984. p. 845.
17. C. Esser, U. Maas et J. Warnatz. Int. Colloq. Gas Dynamics of

Explosions and Reactive Systems (ICODERS) 10th, Berkeley, Calif. 1985.
18. L. Warnatz. Ber. Bunsen-Ges. Phys. Chem. **87**, 1008 (1983).
19. W.S. Affleck et A. Fish. Combust. Flame, **12**, 243 (1968).
20. A. Fish. Proc. R. Soc. London, A. **293**, 378 (1966).
21. A. Fish. Proc. R. Soc. London, A, **298**, 204 (1967).
22. A. Fish. Angew. Chem. **7**, 45 (1968).
23. R.A. Cox et J.A. Cole. Combust. Flame, **60**, 109 (1985).
24. S.W. Benson. Thermochemical kinetics. 2nd ed. John Wiley, New York. 1976.
25. G.M. Côme, G. Scacchi, C. Muller et P.M. Marquaire. J. Chim. Phys. **85**, 201 (1988).
26. F. Billaud, K. Elyahyaoui, F. Baronnet, P.M. Marquaire, C. Muller et G.M. Côme. Thermochim. Acta, **164**, 37 (1990).
27. P. Dagaut, M. Revillon et M. Cathonnet. Combust. Sci. Technol. **95**, 233 (1994).
28. A.S.T.M. Knocking characteristics of pure hydrocarbons. Research Project 45. ASTM, Spec. Pub. **225** (1958).
29. F. Baronnet. Thèse d'État, Nancy (1970).
30 I.R. Slagle et D. Gutman. Symp. (Int.) Combust. (Proc.) 21st, The Combustion Institute, Pittsburgh, Pa. 1986. p. 875.
31. Y. Simon, V. Simon, G. Scacchi et F. Baronnet. Oxid. Commun. **17**, 1 (1994).
32. J.C. Brocard, F. Baronnet et H.E. O'Neal. Combust. Flame, **52**, 25 (1983).
33. B. El Kadi. Thèse de Doctorat INPL, Nancy (1990).
34. F. Baronnet et B. El Kadi. J. Chim. Phys. **92**, 706 (1995).
35. M.B. Colket, D.W. Naegeli et I. Glassman. Symp. (Int.) Combust. (Proc.) 16th, The Combustion Institute, Pittsburgh, Pa. 1975. 1023.
36. S.W. Benson, NBS Spec. Pub. (U.S.), **357**, (1970); Mater. Res. Soc. Symp. Proc. 4th, Gaithersburg, Md. 1970.

Determination of the visible spectra of electrode reaction products in strongly absorbing media by diffusion-controlled chronoabsorptometry

David H. Jones and A. Scott Hinman

Abstract: Chronoabsorptometry under diffusion-controlled conditions has been applied to determination of the difference in molar absorptivity between electrode reaction products and reactants. The technique allows complete determination of the ultraviolet–visible spectra of reaction products that are stable on the time scale of a few hundred milliseconds. The technique was implemented with a reflectance cell that employs quartz light pipes to minimize optical absorbance of the bulk solution without obstructing the current path between counter and working electrodes. The spectrum of one-electron oxidized chloro-(5,10,15,20-tetraphenylporphinato)Fe(III) is determined with the new technique and compared with that obtained by conventional thin-layer spectroelectrochemistry.

Key words: spectroelectrochemistry, chronoabsorptometry, thin-layer spectroelectrochemistry.

Résumé : On a appliqué la chronoabsorptométrie sous des contrôles par diffusion à la détermination de la différence d'absorptivité molaire entre les réactifs et les produits de la réaction à l'électrode. La technique permet de faire une détermination complète des spectres UV–visibles des produits réactionnels qui sont stables à l'échelle de temps de quelques centièmes de millisecondes. La technique a été appliquée à l'aide d'une cellule de réflectance qui fait appel à des conduits de lumière en quartz pour minimiser l'absorption optique de l'ensemble de la solution sans interférer avec le champ du courant entre les électrodes de référence et de travail. Faisant appel à cette technique, on a déterminé le spectre du chloro-(5,10,15,20-tétraphénylporphinate)Fe(III) oxydé par un électron et on l'a comparé à celui obtenu par la technique conventionnelle de spectroélectrochimie en couche mince.

Mots clés : spectroélectrochimie, chronoabsorptométrie, spectroélectrochimie en couche mince.

[Traduit par la rédaction]

Determination of the uv–visible spectra of electrochemical reduction or oxidation products of highly coloured species is most frequently accomplished using thin-layer spectroelectrochemical techniques. The short optical pathlength in thin-layer cells facilitates high optical throughput, which is important in maintaining good signal-to-noise ratios. There is, however, a finite time required to achieve complete electrolysis of the thin-layer cavity due to mass transport limitations (1). In practice, even this theoretical minimum time requirement is rarely achieved because of the high solution resistance associated with the thin-layer cavity (2). This delays the onset of electrolysis at points in the thin-layer cavity positioned furthest from the counter electrode with respect to those positioned closer to the counter electrode. The effect is particularly severe in highly resistive nonaqueous media, and increases as the working electrode dimensions increase. Thin-layer techniques are thus not well suited to determining the spectra of electrochemically generated products of limited stability.

Chronoabsorptometry under conditions of semi-infinite linear diffusion has been widely used for the in situ study of redox processes (3, 4), and affords access to much shorter time scales than are feasible with thin-layer techniques. In single potential step chronoabsorptometry, the potential is stepped to a region where the redox reaction under investigation proceeds at a diffusion-controlled rate (Cottrell experiment) and the absorbance of the diffusion layer is monitored as a function of time. In double potential step chronoabsorptometry, the potential is stepped back to the original value after a time, $t = \tau$, and absorbance is similarly monitored. Studies have normally employed a single wavelength, with the object of characterizing the kinetics of the redox process, rather than determining the spectra of products. Wavelengths are usually chosen where the electroactive precursor has negligible absorbance. This condition ensures maximum light throughput and therefore optimum signal-to-noise ratios in the absorbance–time transients (5).

When the starting material limits the optical throughput at the desired wavelength, consideration must be given to either shortening the optical pathlength, or reducing the concentration. Lowering the concentration will improve the optical throughput but will also reduce the absorbance change pro-

Received December 6, 1995.

D.H. Jones and A.S. Hinman.[1] Department of Chemistry, The University of Calgary, Calgary, AB T2N 1N4, Canada.

1 Author to whom correspondence may be addressed. Telephone: (403) 220-6017. Fax: (403) 289-9488. E-mail: ashinman@acs.ucalgary.ca

Fig. 1. Details of the chronoabsorptometric cell.

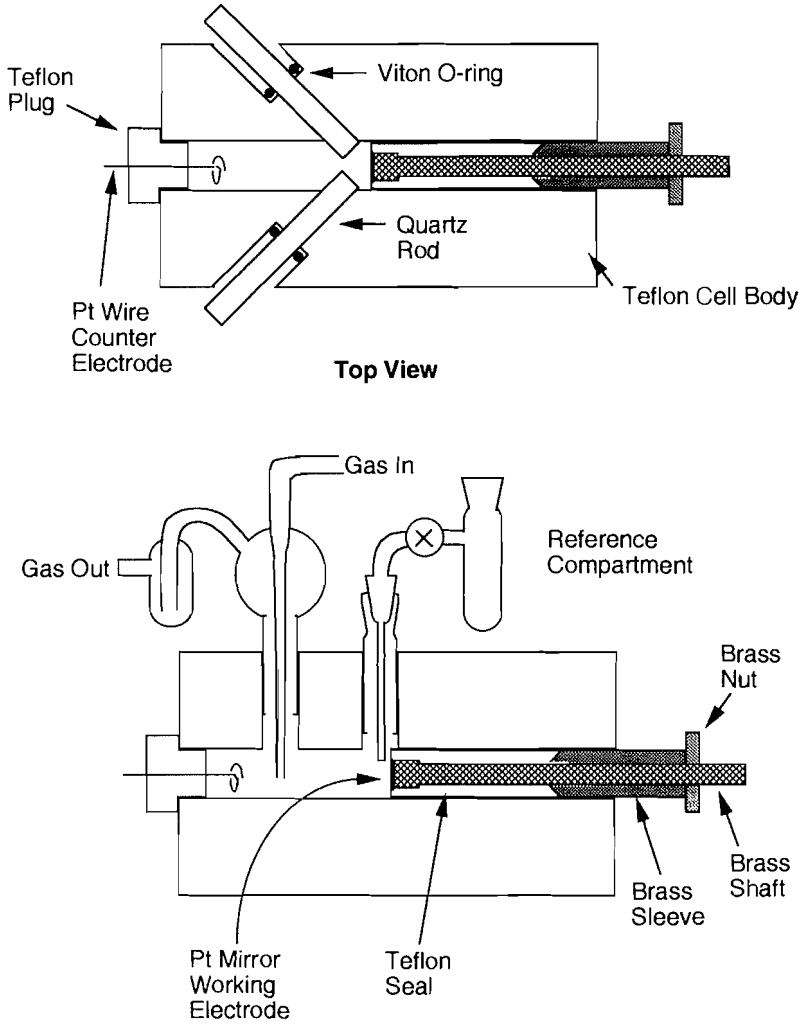

duced on electrolysis. In addition, effects due to impurities or adsorption may become more significant under conditions of high dilution.

Some workers using optically transparent electrodes (OTEs) have reduced the optical pathlength by using a light pipe (e.g., a quartz rod) to transmit light to within a short distance of the OTE surface without loss of throughput (5–7). With a transmission geometry, however, the light pipe obstructs the current path between the working and counter electrodes (5). With highly resistive solutions, or with very short optical pathlengths, this approach can result in uneven potential distribution at the electrode surface and limit the utility of the absorbance–time transients (5–7).

In the present work, we have incorporated the light pipe concept into a spectroelectrochemical cell employing a reflectance, rather than a transmission, geometry. This approach facilitates reduction of the total optical pathlength with little or no obstruction of the current path between the counter and working electrodes. Also, the absorbance change using reflectance is increased over that observed in transmission experiments by a factor of $2/\cos\theta$ (4), where θ is the angle of incidence with respect to the electrode surface normal. When strongly absorbing species necessitate the use of more dilute solutions, the increased sensitivity of the reflectance geometry can help to compensate for the resulting smaller optical changes.

Our objective in this work was to demonstrate for the first time the utility of chronoabsorptometry for determining the complete visible spectrum of an electrochemically generated species on a time scale not normally accessible to thin-layer techniques. Also, we wished to demonstrate the feasibility of this approach to strongly absorbing and highly resistive solutions. The one-electron oxidation of chloro-(5,10,15,20-tetraphenylporphinato)iron(III) (TPPFeCl) in CH_2Cl_2 containing 0.1 M tetra-*n*-butylammonium perchlorate (TBAP) was chosen as the test system. TPPFeCl is strongly absorbing ($\varepsilon_{max} = 1.2 \times 10^5$) and its reversible one-electron oxidation has been well characterized.

Experimental

Cell design

Figure 1 presents a schematic of the spectroelectrochemical

Fig. 2. Schematic of the instrumentation and optics utilized for chronoabsorptometric measurements.

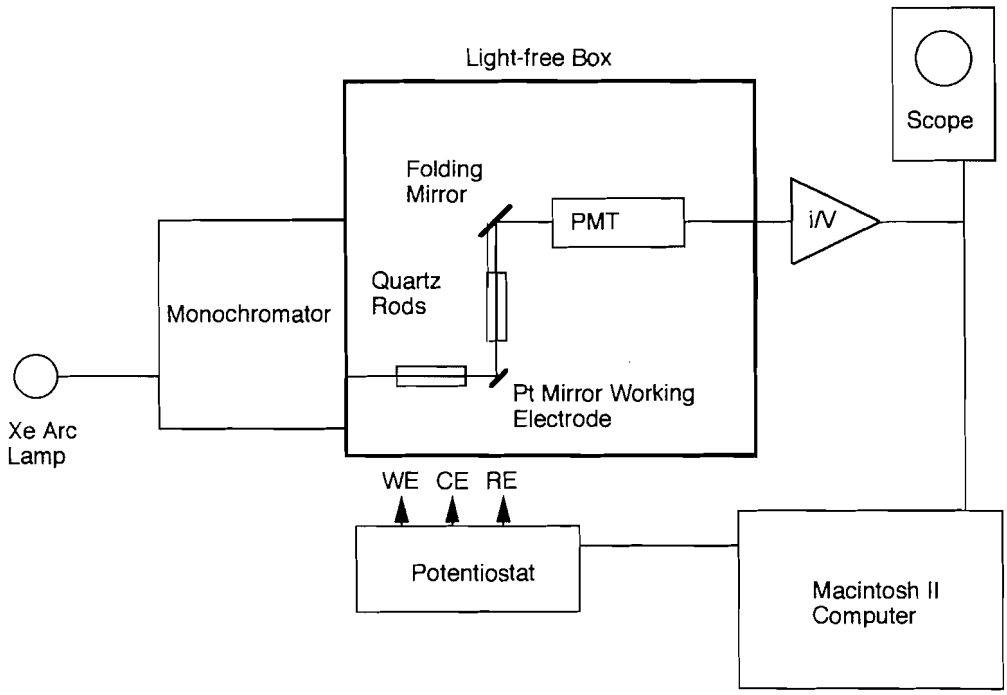

cell used for chronoabsorptometric measurements. The working electrode is a 7 mm diameter Pt disk silver soldered to the end of a brass shaft. This is press fitted into a Teflon seal. The electrode surface is polished to a mirror finish with 0.3 μm alumina polishing powder. The cell body is a Teflon block machined to accept the working electrode and other components illustrated in the figure. Two 5 mm diameter quartz rods, polished flat and clear at their ends, serve to guide incident radiation onto and then away from the Pt mirror electrode. Their longitudinal axes are oriented at 45 degrees with respect to the electrode surface normal. The quartz rods can be positioned to achieve total mean optical pathlengths as small as 3.5 mm, although this smallest optical pathlength maximizes the obstruction to the current path between the counter and working electrodes. In this work, the quartz rods were positioned to achieve a total mean optical pathlength of 1 cm.

Instrumentation and procedure for chronoabsorptometric experiments

Figure 2 illustrates the optical and instrumental configuration employed for chronoabsorptometric experiments. Light from a 75 W Xe arc lamp is focused onto the entrance slit of a GCA-McPherson model EU-701 monochromator. Monochromatic light from the monochromator passes through one of the quartz rod light pipes in the spectroelectrochemical cell and is specularly reflected from the Pt mirror working electrode through the second light pipe. Light emerging from the cell is reflected by a folding mirror onto a Hamamatsu R268 photomultiplier tube (PMT).

The PMT anode current is taken to a Keithley model 427 current amplifier. The output of the current amplifier is monitored with a Macintosh II computer fitted with a G.W. Instruments Macadios II input-output analog-digital interface card. A Think Pascal control program that accessed the Macadios II input-output and data-manipulation libraries was written to allow the generation of successive double potential steps of variable potential and duration with simultaneous collection of up to a 1000 point array at a fixed rate of 5 ms per point with real-time signal averaging. The generated potential step was fed to the adder input of a Hi-Tek model DT2101 potentiostat that controlled the working electrode potential with respect to the reference potential. The data arrays from the experiments could be saved as Microsoft Excel files that could then be further processed with a Microsoft Excel spreadsheet. Absorbance changes are calculated according to $\Delta A = \log(I_1/I_2)$, where I_1 is the light intensity reaching the detector immediately prior to the application of any potential step, and I_2 is the intensity following the potential step.

Other experiments

Conventional time-resolved thin-layer reflectance spectroelectrochemistry was employed to obtain the spectrum of one-electron oxidized TPPFeCl for comparison with that obtained by chronoabsorptometry. The spectroelectrochemical cell, instrumentation, and procedure have been described in detail elsewhere (8, 9).

The diffusion coefficient of TPPFeCl was obtained by chronoamperometry in the same cell as used for the chronoabsorptometry experiments. The electrode area was first calibrated by chronoamperometric oxidation of $K_4Fe(CN)_6$ in 1 M KCl using the well-established diffusion coefficient for the $Fe(CN)_6^{4-}$ species (10).

Reagents and solutions

TPPFeCl (11) was synthesized according to literature procedures. CH_2Cl_2 was shaken with alumina, distilled from P_2O_5

onto CaH_2, and stored over CaH_2 until ready for use. TBAP (Fluka) was recrystallized from isopropanol–water and dried at 80°C in vacuo for several days prior to use. All solutions for spectroelectrochemical experiments employed 0.1 M TBAP, and a home-built aqueous saturated calomel electrode was used throughout. The TPPFeCl concentration was 1.0 mM for the thin-layer spectroelectrochemical measurements. The TPPFeCl concentrations for chronoabsorptometric experiments were 1.06×10^{-5} M for data recorded at 410 and 430 nm, 2.10×10^{-5} M for experiments at 370 and 390 nm, and 9.44×10^{-5} M for all other experiments.

Results and discussion

For a reversible electrode reaction, the absorbance observed on appliation of a potential pulse is proportional to the total charge passed during the experiment (12). Chronoabsorptometry may thus be viewed as the optical analog of chronocoulometry. Winograd et al. (13) have considered transmission geometry where only the product of the electrochemical reaction absorbs and shown that the absorbance–time profile is given by multiplying the chronocoulometric charge–time profile by ε/nFA. Here, ε is the molar absorptivity of the redox product, n is number of electrons, and A is electrode area. Where the potential pulse is sufficient to drive the surface concentration of the reactant to zero, this leads to

$$[1] \quad A(t) = \frac{2\varepsilon C D^{1/2} t^{1/2}}{\pi^{1/2}}$$

In eq. [1], C is the bulk concentration of the reactant, and D is its diffusion coefficient. Where both product and reactant absorb, ε is replaced by the difference in molar absorptivity (14) between product and reactant, $\Delta\varepsilon = \varepsilon_{product} - \varepsilon_{reactant}$, and, if a reflectance geometry is used, the response is multiplied by $2/\cos\theta$ (4) to account for the increased optical pathlength. Equation [1] thus becomes

$$[2] \quad \Delta A(t) = \frac{4\Delta\varepsilon C D^{1/2} t^{1/2}}{\pi^{1/2} \cos\theta}$$

If the concentration and diffusion coefficient of the electrochemical reactant are known, then the slope of a plot of $\Delta A(t)$ vs. $t^{1/2}$ yields $\Delta\varepsilon$. Since the molar absorptivity of the reactant is determinable by conventional methods, the molar absorptivity of the product may be obtained.

For a double potential step experiment, where the potential is returned to its initial value after a time τ, the cumulative absorbance change at times $t > \tau$ may similarly be derived by applying the considerations of refs. 12–14 to the known (15) chronocoulometric response. This leads to

$$[3] \quad \Delta A(t > \tau) = \Delta A(\tau) - \frac{4\Delta\varepsilon C D^{1/2}(\tau^{1/2} - t^{1/2} + (t - \tau)^{1/2})}{\pi^{1/2} \cos\theta}$$

Letting $\tau^{1/2} - t^{1/2} + (t - \tau)^{1/2} = \phi$, a plot of ΔA vs. ϕ for data obtained on the reverse step should have a slope equal in magnitude but opposite in sign to that for the ΔA vs. $t^{1/2}$ plot for the forward step. The plot intercepts the ordinate at $\Delta A = \Delta A(\tau)$, and the abscissa at $\phi = \tau^{1/2}$. This provides criteria for reversibility and lack of complications associated with the electrode reaction. By analogy to chronocoulometric theory, the ratio of the absorbance change at time $t = 2\tau$ to that observed at $t = \tau$ provides a simpler criterion. For a reversible system without complications, this ratio is given by

$$[4] \quad \frac{\Delta A(2\tau)}{\Delta A(\tau)} = 0.414$$

Fig. 3. Absorbance–time transient at 410 nm obtained for double potential step chronoabsorptometry of TPPFeCl in CH_2Cl_2 containing 0.1 M TBAP. The data are an average of 64 experiments.

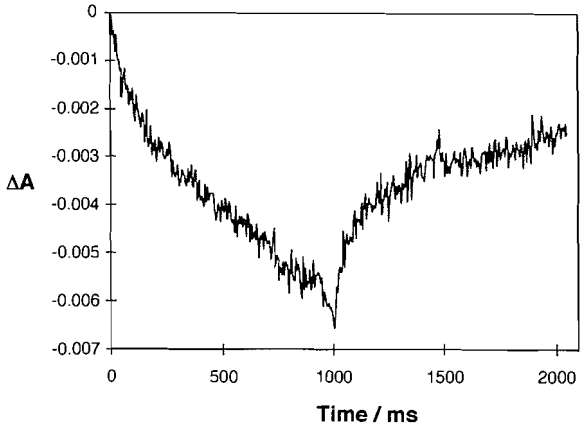

In CH_2Cl_2 containing 0.1 M TBAP, TPPFeCl undergoes a reversible one-electron oxidation with a half-wave potential of 1.13 V vs. SCE. The oxidation product has been formulated as an iron(III) porphyrin π-cation radical (16). Figure 3 illustrates the absorbance–time transient observed for TPPFeCl during a 1 s potential pulse to 1.3 V vs. SCE, followed by a return of the potential to its initial value of 0.9 V. The data were recorded at 410 nm, close to the 415 nm absorbance maximum of TPPFeCl. The solution in the chronoabsorptometric cell had an absorbance of approximately 1.2. Of the wavelengths examined, this represents the worst case in terms of optical throughput, and hence in terms of noise.

Prior to further processing, the data of Fig. 3 were smoothed using an 11 point Savitzky–Golay quadratic smoothing routine (17). After smoothing, the ratio of the absorbance change at time 2τ to that at τ, $\Delta A(2\tau)/\Delta A(\tau)$, was 0.43, in good agreement with the theoretical value of 0.414 for a reversible reaction. Figure 4 presents the smoothed ΔA values plotted against $t^{1/2}$ for times $t < \tau$, and against ϕ for times $t > \tau$. The best-fit lines from linear least-squares regression are also shown in the figure. Good linearity is apparent for both the forward and reverse steps. For the forward step, the slope of the least-squares line was -5.82×10^{-3} absorbance units/$s^{1/2}$. A slope of 5.83×10^{-3} absorbance units/$s^{1/2}$ was obtained for the reverse step. The nearly identical magnitudes of the two slopes are as expected for a reversible electrode process. As is apparent in the figure, the intercepts of the plots are also close to the values expected for a reversible process.

In the present example, we have employed a relatively long duration pulse of 1 s. It is clear, however, that accurate determinations of ΔA transients can be made on a considerably

Fig. 4. Plots of absorbance change versus $t^{1/2}$ or ϕ obtained from the data of Fig. 3. The broken lines represent a linear least-squares fit.

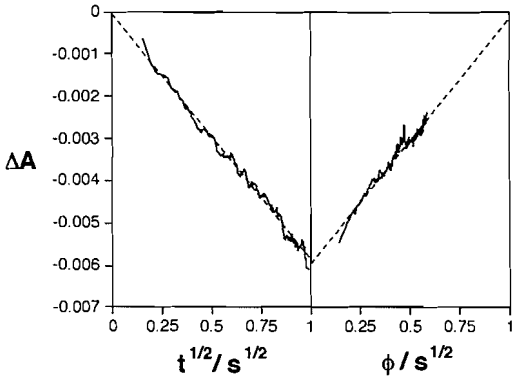

Fig. 5. Ultraviolet–visible spectrum of TPPFeCl (solid line) and its one-electron oxidation product (circles) calculated from chronoabsorptometric data.

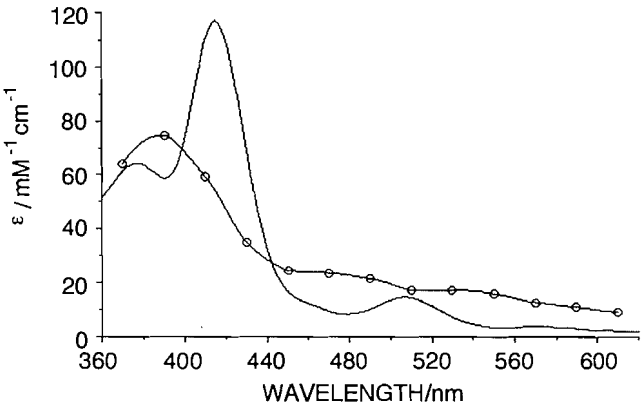

shorter time scale. For instance, the slope of the ΔA vs. $t^{1/2}$ plot obtained using only data from the first 500 ms of the transient of Fig. 3 was 5.84×10^{-3} absorbance units/$s^{1/2}$. This is within 0.4% of that obtained using all of the data recorded during the 1 s pulse. With additional signal averaging and careful attention to uncompensated solution resistance, which can delay the redox reaction during the early portions of the potential pulse, time scales much less than 500 ms should be accessible. Other workers (3, 4), for instance, have obtained accurate absorbance time transients from potential pulses on the order of a few milliseconds or less, although these experiments are normally carried out in more conductive solutions, and at wavelengths where bulk solution absorbance is negligible.

The uv–visible spectrum of TPPFeCl is shown in Fig. 5 together with the spectrum of the corresponding iron(III) porphyrin π-cation radical from the chronoabsorptometric $\Delta\varepsilon$ values and the measured ε values of the unoxidized porphyrin. The relative standard deviations of the molar absorptivities for the π-cation radical were calculated from the standard deviations of the slopes of the ΔA vs. $t^{1/2}$ plots. These were all less than 5%.

Fig. 6. Time-resolved thin-layer spectroelectrochemistry associated with the oxidation of 1 mM TPPFeCl in CH_2Cl_2 containing 0.1 M TBAP. The time between each spectrum is 2.7 s.

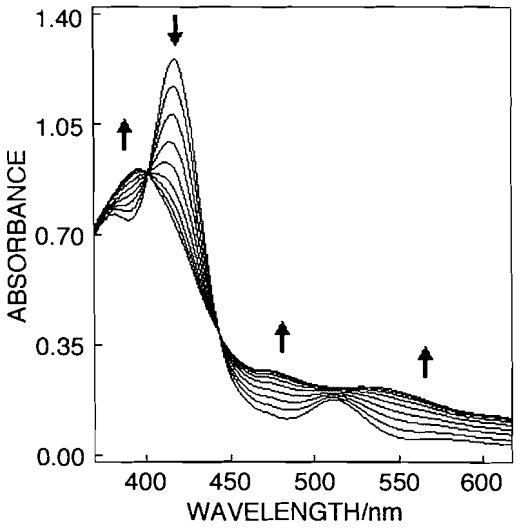

Figure 6 illustrates the time-resolved uv–visible spectral changes associated with electrolysis at 1.3 V vs. SCE of a 1 mM TPPFeCl solution in a thin-layer spectroelectrochemical cell. The oxidation proceeds with isosbestic points to produce a final spectrum of the iron(III) porphyrin π-cation radical. Comparison between the final spectrum of Fig. 6 and the reconstructed spectrum of the iron(III) porphyrin π-cation radical shown in Fig. 5 shows excellent agreement between spectra obtained by the two techniques.

It is clear that the described chronoabsorptometry experiment is capable of determining complete uv–visible spectra of electrochemically generated species that are stable on the time scale of a few hundred milliseconds. To the authors' knowledge, this is the first time chronoabsorptometry has been applied under conditions where the bulk solution possesses significant absorbance, and the first time it has been applied to determine the difference in molar absorptivity between electrochemical reactants and products. We are currently applying the technique to determination of the spectra of several metalloporphyrin oxidation products that have proved too unstable to characterize under thin-layer spectroelectrochemical conditions.

Acknowledgements

The authors are grateful to the Natural Sciences and Engineering Research Council of Canada for financial support.

References

1. A.T. Hubbard. J. Electroanal. Chem. 165 (1969).
2. A.S. Hinman, S. Pons, and J. Cassidy. Electrochim. Acta, **30**, 89 (1985).
3. W.R. Heineman, F.M. Hawkridge, and H.N. Blount. *In* Electroanalytical chemistry. Vol. 13. *Edited by* A.J. Bard. Marcel Dekker, New York. 1983. pp. 1–104.
4. T. Kuwana and N. Winograd. *In* Electroanalytical chemistry. Vol. 7. *Edited by* A.J. Bard. Marcel Dekker, New York. 1974. pp. 1–74.

5. F.R. Shu and G.S. Wilson. Anal. Chem. **48**, 1676 (1976).
6. D.L. Langhus and G.S. Wilson. Anal. Chem. **51**, 1139 (1979).
7. E.F. Bowen, F.M. Hawkridge, J.F. Chlebowski, E.E. Bancroft, C. Thorpe, and H.N. Blount. J. Am. Chem. Soc. **104**, 7641 (1982).
8. D.H. Jones and A.S. Hinman. Can. J. Chem. **68**, 2234 (1990).
9. A.S. Hinman and B.J. Pavelich. Can. J. Chem. **65**, 919 (1987).
10. M. von Stackelberg, M. Pilgrim, and W. Toome. Z. Elektrochem. **57**, 342 (1953).
11. A.D. Adler, F.R. Longo, F. Kampas, and J. Kim. J. Inorg. Nucl. Chem. **32**, 2443 (1970).
12. E.E. Bancroft, H.N. Blount, and F.M. Hawkridge. Anal. Chem. **53**, 1862 (1981).
13. N. Winograd, H.N. Blount, and T. Kuwana. J. Phys. Chem. **73**, 3456 (1969).
14. A.S. Hinman, J.F. McAleer, and S. Pons. J. Electroanal. Chem. **154**, 45 (1983).
15. A.J. Bard and L.R. Faulkner. *In* Electrochemical methods. John Wiley, New York. 1980. pp. 201.
16. P. Gans, G. Buisson, E. Duee, J.-C. Marchon, B.S. Erler, W.F. Scholz, and C.A. Reed. J. Am. Chem. Soc. **108**, 1223 (1986).
17. J. Steiner, Y. Termonia, and J. Deltour. Anal. Chem. **44**, 1906 (1972).

Electroréduction de dérivés dinitrés aromatiques. V. Influences du matériau d'électrode et de systèmes rédox sur les réductions du 4,4′-dinitrodibenzyle et de l'acide 4,4′-dinitrostilbène-2,2′-disulfonique

Anne-Marie Martre, Guy Mousset, Veronica Cosoveanu et Virginia Danciu

Résumé : Ce travail concerne les réductions du 4,4′-dinitrodibenzyle et de l'acide 4,4′-dinitrostilbène-2,2′-disulfonique dans différentes conditions expérimentales. D'une part, il a été envisagé, sur plusieurs matériaux d'électrode (étain, monel, mercure), la réduction électrochimique directe ou en présence d'un couple rédox (Ti^{3+}/Ti^{4+} ou Sn^0/Sn^{2+}) ce qui entraîne des changements dans la nature ou les proportions relatives des produits formés et d'autre part, la réduction chimique en solution par le réducteur Sn^0 préalablement électrogénéré. Les meilleures conditions d'obtention de di- et de mono-amines sont précisées, elles correspondent respectivement à des rendements de l'ordre de 90% pour les diamines, de 70% pour le 4-amino-4′-nitrodibenzyle et de 50% pour l'acide 4-amino-4′-nitrostilbène-2,2′-disulfonique. Une étude analytique préliminaire, sur électrode de mercure et dans les milieux des synthèses (H_2SO_4 5 N – EtOH 50/50, H_2SO_4 2,5 N et HCl à 10%), a permis de préciser et de comparer les caractéristiques électrochimiques des dérivés dinitrés et de chacun des composés $TiOSO_4$, $TiCl_4$, $SnCl_2$, promoteurs des couples rédox utilisés.

Mots clés : 4,4′-dinitrodibenzyle, acide 4,4′-dinitrostilbène 2,2′-disulfonique, électrochimie, réduction, systèmes rédox Ti^{3+}/Ti^{4+} et Sn^0/Sn^{2+}.

Abstract: This work concerns the electrochemical and chemical reductions of 4,4′-dinitrodibenzyl and 4,4′-dinitrostilbene 2,2′-disulfonic acid under various experimental conditions. On the one hand, the electrochemical reduction is realized on Sn, monel, and Hg electrodes with or without the presence of a redox couple, and on the other hand, the chemical reduction is performed by mean of an electrochemically generated reducing agent (Sn^0). According to the type of redox couple used (Ti^{3+}/Ti^{4+} or Sn^0/Sn^{2+}), important changes in the nature and the ratio of reaction products are observed. The best conditions for obtaining di- or mono-amines are defined, they correspond to 90% yield for the diamines, 70% and 50%, respectively, for 4-amino-4′-nitrodibenzyl and for 4-amino-4′-nitrostilbene-2,2′-disulfonic acid. The electrochemical behavior of the dinitro derivatives and of $TiOSO_4$, $TiCl_4$, and $SnCl_2$ used as precursors of the redox couples is studied under conditions of macroscale electrolyses (5 N H_2SO_4 – EtOH 50/50, 2.5 N H_2SO_4, and 10% HCl).

Key words: 4,4′-dinitrodibenzyl, 4,4′-dinitrostilbene 2,2′-disulfonic acid, electrochemistry, reduction, Ti^{3+}/Ti^{4+} and Sn^0/Sn^{2+} redox systems.

Introduction

La réduction des dérivés nitrés aromatiques a donné lieu depuis longemps à de multiples travaux et actuellement il en existe de nombreux qui ont encore comme objectif une meilleure connaissance des mécanismes des réactions ou la mise au point de nouvelles synthèses (1–13 et références citées).

Dans le cadre de recherches effectuées depuis quelques années sur la réduction de dérivés dinitrés aromatiques, nous nous sommes déjà intéressés au 4,4′-dinitrodibenzyle (DNDB) et à l'acide 4,4′-dinitrostilbène-2,2′-disulfonique (DNSS). Sur électrode de mercure, nous avons précisé leurs caractéristiques électrochimiques dans plusieurs milieux, l'importance des phénomènes d'adsorption à la surface de l'électrode et l'influence d'additions de molécules tensioactives (14–16). Nous avons également comparé leurs réductions électrochimiques (par transfert direct d'électrons ou en présence d'un couple rédox) et chimiques par un réducteur préalablement électrogénéré (16, 17). Une étude des cinétiques d'électroréduction du DNDB en milieu hydroalcoolique acide (18), sur des électrodes de Sn, Cu et Pb, en conditions potentiostatique et galvanostatique, a permis d'observer des modifications dans les mécanismes de réduc-

Reçu le 1er décembre, 1995.

A.-M. Martre et G. Mousset.[1] Laboratoire d'électrochimie organique, Université Blaise Pascal de Clermont-Ferrand, Unité associée au Centre national de la recherche scientifique N° 434, Thermodynamique et électrochimie en solution, 24 Avenue des Landais, 63177 Aubière, France.
V. Cosoveanu et V. Danciu. Université Babes Bolyai, Faculté de chimie et chimie industrielle, Collectif de Recherches Chimiques, Str. Arany Janos, nr. 11, 3400 Cluj-Napoca, Roumanie.

1. Auteur auquel la correspondance doit être adressée. Téléphone : 73.40.71.60. Télécopie : 73.27.44.43.

tion en fonction de la surtension d'hydrogène. La détermination de la constante de vitesse et celle de l'énergie d'activation indiquent que l'étain semble le meilleur «matériau cathodique».

L'acide 4,4′-diaminostilbène-2,2′-disulfonique (DASS), préparé essentiellement par réduction de l'acide 4,4′-dinitrostilbène-2,2′-disulfonique, le plus souvent par voie chimique (réduction de Béchamp, hydrogénation catalytique par divers réactifs tels que Pd, Pd–Ni, Ni, Pt–Rh, métaux de Raney), a donné lieu à plusieurs brevets et travaux (19–38) en raison de son utilisation comme constituant des colorants et teintures pour textiles. Son intérêt industriel actuel et celui du 4,4′-diaminodibenzyle (DADB) comme intermédiaire important dans la synthèse des polyuréthanes ont orienté nos recherches vers la synthèse de ces composés (16, 17, 39, 40). À la suite de ces travaux, il nous paraît maintenant intéressant de développer une nouvelle étude concernant l'utilisation d'électrodes solides, matériaux mieux adaptés aux technologies industrielles que le mercure. Nous comparons l'effet du couple rédox Sn^0/Sn^{2+} sur la nature et les rendements respectifs des produits de réduction avec celui de Ti^{3+}/Ti^{4+} et nous définissons la sélectivité de la réduction chimique selon le choix du réducteur et du milieu réactionnel. Toutefois, à des fins de comparaison et pour une meilleure connaisance des caractéristiques électrochimiques, des expériences doivent être également réalisées sur l'électrode de mercure.

A. Études analytiques

Des études analytiques préablables, dans les conditions des réductions préparatives (électrochimique à potentiel constant ou chimique), sont nécessaires pour connaître et comparer les caractéristiques électrochimiques de chacun des dérivés dinitrés et des couples rédox utilisés. Les milieux acides choisis sont respectivement H_2SO_4 5 N – EtOH 50/50 à 60°C pour le DNDB en raison de sa très faible solubilité dans l'eau et H_2SO_4 2,5 N ou HCl à 10% à 30°C pour le DNSS plus soluble. Dans ces solutions, seule l'électrode de mercure, pour laquelle la limite cathodique est à environ −1,0 V/ECS, permet une étude satisfaisante. Nous examinons le comportement électrochimique des ions Sn^{2+}, promoteurs du couple Sn^0/Sn^{2+}, pour le comparer à celui des ions Ti^{4+} ainsi qu'à celui des dérivés dinitrés qui ont déjà fait l'objet d'études antérieures (14, 16, 17).

Réduction de Sn^{2+}

En milieux H_2SO_4 5 N – EtOH 50/50 et H_2SO_4 2,5 N, les voltammogrammes de réduction de $SnCl_2$ sont représentés par les courbes (*a*) de la Fig. 1 (A et B). La réduction, qui met en jeu deux électrons par molécule, correspond au mécanisme

$$Sn^{2+} + 2e^- \leftrightarrows Sn^0$$

Dans les deux cas, la réaction est rapide et bien réversible, elle intervient à des potentiels assez voisins, respectivement : Ep_c = −0,40 V et −0,45 V ; Ep_a = −0,34 V et −0,40 V. L'intensité du pic de réoxydation en Sn^{2+} est fonction des limites en potentiel du cycle de balayage en raison de la formation d'un amalgame avec le mercure. Si le cycle est prolongé vers les potentiels positifs, les ions Sn^{2+} sont oxydés en Sn^{4+} à +0,16 V juste avant l'oxydation du mercure.

En milieu HCl, le chlorure d'étain se réduit comme dans l'acide sulfurique en une étape très réversible avec des potentiels de pics Ep_c = −0,53 V et Ep_a = −0,50 V. Les oxydations de l'électrode de mercure et des ions Cl^- ne permettent pas d'observer celle de Sn^{2+}. Une étude sur électrodes d'or et de platine (41) a montré l'influence des phénomènes importants d'adsorption sur l'oxydation du chlorure d'étain.

Réduction de Ti^{4+}

Nous avons montré précédemment (17) l'influence de l'électrolyte et de la concentration en alcool sur le comportement électrochimique de $TiOSO_4$. En milieux H_2SO_4 5 N – EtOH 50/50 et H_2SO_4 2,5 N, les voltammogrammes de réduction sont reproduits à titre de comparaison, courbes (*b*) de la Fig. 1 (A et B). La réduction a lieu en deux étapes lentes aux potentiels respectifs dans chacun des milieux : Ep_c (1) = −0,14 V et −0,45 V; Ep_c (2) = −0,65 V et −0,87 V. Dans les deux cas, au balayage retour, la réoxydation a lieu en une seule étape, respectivement aux potentiels Ep_a = −0,06 V et −0,02 V.

En milieu HCl à 10%, si le couple rédox Ti^{3+}/Ti^{4+} est obtenu à partir soit du sulfate de titanyle $TiOSO_4$ soit du complexe tétrachlorure de titane – tétrahydrofurane ($TiCl_4$, THF), les voltammogrammes de ces deux composés ont la même allure : la réduction est lente, les potentiels de pic sont respectivement −0,35 V pour $TiOSO_4$ et −0,44 V pour $TiCl_4$, THF; la réoxydation de Ti^{3+} apparaît vers −0,15 V et se superpose ensuite avec celle de l'ion Cl^-.

Les acides H_2SO_4 et HCl étant complexants, il y a formation d'espèces en équilibre dans la solution dont la nature et les proportions relatives dépendent, entre autres paramètres, de l'acidité et de la température (17, 42–44). Le mécanisme global de cette réduction met en jeu un électron par molécule

$$TiO^{2+} + 2H^+ + e^- \leftrightarrows Ti^{3+} + H_2O$$

Réduction des dérivés dinitrés

En solution de H_2SO_4 5 N – EtOH 50/50 à 60°C, la réduction du DNDB a lieu en deux étapes : la première est constituée de deux pics très rapprochés dont les potentiels sont compris entre −0,05 V et −0,10 V et la deuxième lente est très étalée en potentiel au voisinage de −0,73 V (Fig. 1A, courbe *c*). La réduction est irréversible. Au balayage retour, on peut constater la présence d'une anomalie vers 0 V qui correspond à la désorption de la molécule comme cela a été montré par les mesures tensammétriques (14). Les mécanismes de réduction déjà donnés (17) sont classiques : la première étape conduit à la formation de dihydroxylamine, la deuxième correspond à sa réduction en diamine. En présence des couples rédox, nous n'avons pas observé d'effets catalytiques. Compte tenu des conditions des voltammétries cycliques (v = 0,1 V s^{-1}), le transfert d'électrons en phase homogène entre Sn^0 ou Ti^{3+} et le dérivé nitré est certainement lent comparé à la réduction hétérogène de ce dernier.

En milieu H_2SO_4 2,5 N, le DNSS se réduit en une étape unique qui met en jeu approximativement 12 électrons par molécule (16). En raison de la forte conjugaison de la molécule, le potentiel de demi-vague polarographique est voisin de 0 V ($E_{1/2}$ = +0,05 V pour c = 10^{-4} M). En voltammétrie cyclique, la forme du pic (Fig. 1B, courbe *c*) et le déplacement de son potentiel avec la concentration sont caractéristiques

Fig. 1. Voltammogrammes de réduction sur électrode de mercure, $v = 0{,}1$ V s^{-1}. A : milieu H_2SO_4 5 N – EtOH à 60°C; (*a*) $SnCl_2$, $c = 5 \times 10^{-3}$ M; (*b*) $TiOSO_4$, $c = 5{,}6 \times 10^{-3}$ M; (*c*) DNDB, $c = 2 \times 10^{-4}$ M. B : milieu H_2SO_4 2,5 N à 30°C; (*a*) $SnCl_2$, $c = 1{,}3 \times 10^{-3}$ M; (*b*) $TiOSO_4$, $c = 9 \times 10^{-3}$ M; (*c*) DNSS, $c = 1 \times 10^{-3}$ M.

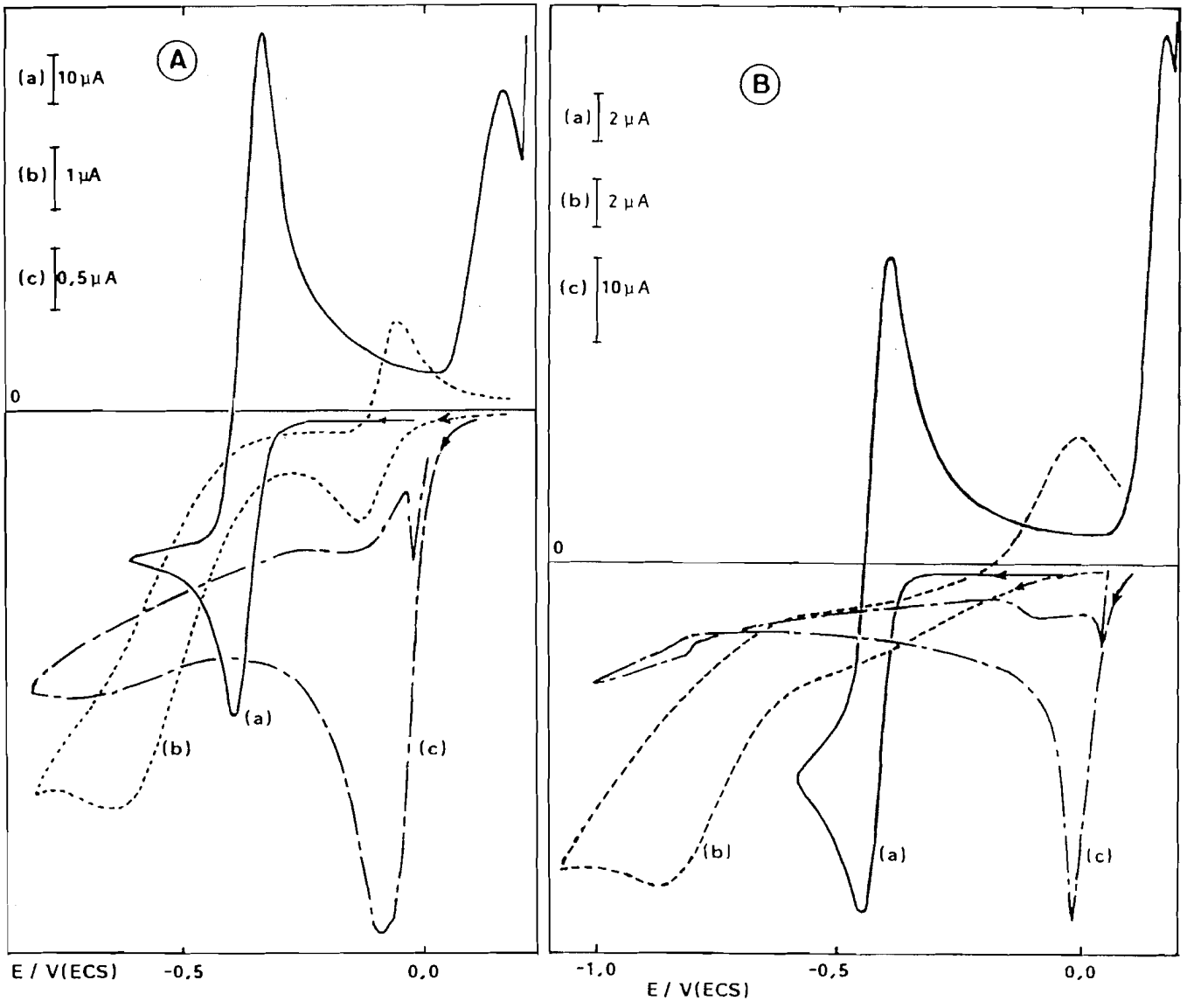

d'une forte adsorption qui a été confirmée par les mesures de capacité différentielle (16). Sur le voltammogramme, les deux pics de faible intensité, à +0,04 V et −0,80 V, sont de nature capacitive et délimitent la zone d'adsorption / désorption du dérivé nitré et (ou) de ses produits de réduction.

En milieu HCl à 10%, le potentiel de la réduction de l'acide dinitrostilbène disulfonique est très proche de celui de l'oxydation des ions Cl^- ce qui empêche la détermination précise de ce potentiel situé vers 0 V.

Les trois courbes des Fig. 1A et 1B permettent de comparer les réductions de chaque dérivé dinitré à celles des couples rédox dans les conditions utilisées. Les écarts relatifs de leurs potentiels, en particulier celui de la réduction des hydroxylamines, laissent prévoir des effets différents sur les mécanismes et par conséquent sur la nature des produits de réduction.

B. Influence des couples rédox et du matériau d'électrode sur la nature des produits formés

Comme dans la partie analytique, les électrolyses à potentiel constant du DNDB sont réalisées en solution H_2SO_4 5N – EtOH 50/50 à 60°C et à une concentration 1×10^{-3} M en raison de sa très faible solubilité et celles du DNSS, à 30°C en milieux H_2SO_4 2,5 N ou HCl à 10%, avec une concentration de 2×10^{-3} M. Elles sont réalisées sur électrodes de mercure, étain et monel. L'influence de la nature de l'électrode sur la réduction de dérivés nitrés a déjà fait l'objet de quelques travaux (45–50). Suivant les matériaux, sur lesquels la réduction des ions H^+ en hydrogène est plus ou moins difficile, on peut s'attendre à des mécanismes dif-

férents d'électronation–protonation ou d'hydrogénation électrocatalytique (51–55).

Électrolyses sur électrode de mercure

Réduction du dinitrodibenzyle

En absence de couple rédox, nous avons montré dans une étude précédente (17), que la réduction électrochimique a un rendement faradique de 90% calculé par rapport à la réduction en diamine et conduit à l'obtention de 75% de DADB, 1% de DNDB, 9% du produit amino-hydroxylé HO-R-R-NH_2 et 2% du produit dihydroxylé HO-R-R-OH avec

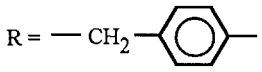

En présence de $TiOSO_4$, nous avons vu dans cette même étude que le pourcentage de DADB peut atteindre 92% tandis qu'il reste 2–5% de composé de départ. L'absence de produits hydroxylés permet d'isoler un DADB très pur.

En présence de $SnCl_2$, le potentiel choisi pour l'électrolyse est celui de la réduction de Sn^{2+}, $E = -0{,}40$ V, et la réaction est effectuée jusqu'à la consommation d'une quantité d'électricité correspondant à celle nécessaire au passage du dérivé dinitré en dérivé diaminé. Après extraction, le produit brut de réaction est analysé par chromatographie en phase vapeur (CPV), RMN et spectrométrie de masse couplée à la CPV. Sa composition comprend une quantité de DADB qui ne dépasse pas 50%, celle du dérivé amino-hydroxylé HO-R-R-NH_2 peut atteindre 38% et le dérivé HO-R-R-OH n'existe qu'à l'état de traces. Ces composés n'ont pu être séparés les uns des autres. Parmi les sous-produits formés, la spectrométrie de masse indique pour quatre d'entre eux (11% au total), des masses molaires respectives $M = 258$, $M = 257$, $M = 257$, $M = 256$ ce qui permet, compte-tenu de la fragmentation, d'écrire les formules

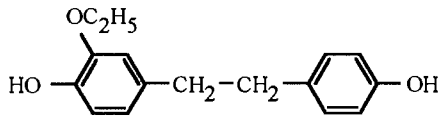

$M = 258$

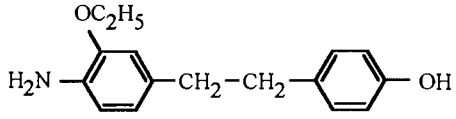

$M = 257$

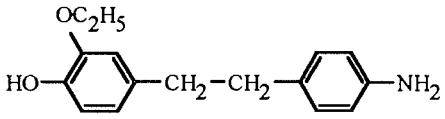

$M = 257$

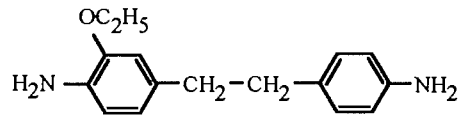

$M = 256$

Pour les molécules de masses $M = 257$ et $M = 256$, on pourrait envisager des structures *N*-éthoxylées. Toutefois, dans la fragmentation du composé de masse $M = 257$, un pic à $m/z = 134$ correspondant à l'ion radical

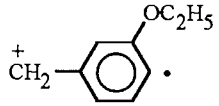

nous fait penser que la position du groupement éthoxy sur l'atome d'azote est peu probable.

La formation des dérivés hydroxylés a été étudiée dans un travail précédent (17). Celle des composés éthoxylés peut être expliquée par l'hypothèse de mécanismes faisant intervenir, en premier lieu, des réactions de protonation compétitives de la fonction hydroxylamine qui conduisent à des structures de type quinone-imine ou à des attaques nucléophiles justifiant la substitution en position 4 ou 4′ par des fonctions hydroxyles :

En présence d'éthanol, nous obtenons des composés qui possèdent un groupement -OC_2H_5 en position 3. Nous n'avons pas mis en évidence le dérivé hydroxylé correspondant qui résulterait d'une transposition de l'hydroxylamine. Une telle fixation préférentielle du groupement éthoxy a déjà été notée dans le cas de la réduction de nitronaphtalènes substitués en milieu H_2SO_4–EtOH 50/50 (56).

Le pourcentage élevé de ces sous-produits formés avec le couple rédox Sn^0/Sn^{2+} alors qu'avec Ti^{3+}/Ti^{4+} ils ne sont observés qu'à l'état de traces, peut être lié au fait que les sels d'étain réduisent très lentement les hydroxylamines en amines (57), ce qui permet aux attaques nucléophiles de se développer.

Réduction de l'acide dinitrostilbène disulfonique

En milieu H_2SO_4 2,5 N, au potentiel de $-0{,}05$ V, la réduction du DNSS en DASS est totale. Le produit de réduction précipite au fur et à mesure de sa formation en cours d'électrolyse ce

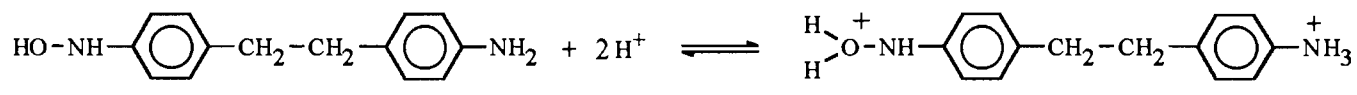

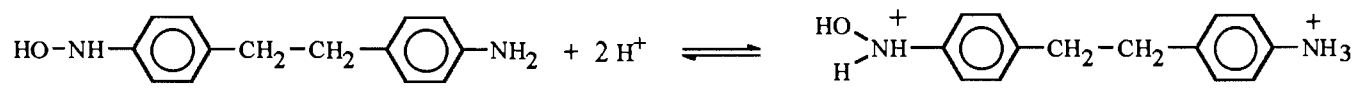

qui permet de l'isoler de manière simple par filtration avec un rendement de l'ordre de 90%. Aucun autre composé n'est détecté en fin d'expérience.

Alors que dans le cas du DNDB, la présence de $TiOSO_4$ améliore le rendement de la réaction en diamine en facilitant les contacts réducteur – dérivé dinitré puisque ce dernier est très peu soluble dans l'eau, sa présence n'a pas d'intérêt pour le DNSS. De même, des essais effectués avec $SnCl_2$ au potentiel $E = -0{,}20$ V, c'est-à-dire avant sa réduction en Sn^0, n'ont pas modifié de manière sensible les résultats. Le DASS est formé avec un rendement similaire à celui obtenu sans couple redox ce qui montre que le cation Sn^{2+} ne réduit pas le dérivé dinitré. Nous avons vérifié par ailleurs que dans les mêmes conditions, un contact prolongé entre le DNSS et $SnCl_2$ n'entraîne pas la formation de DASS. La spectrométrie de RMN permet de détecter, en plus du dérivé diaminé, la présence d'un autre composé de structure symétrique identifié à la dihydroxylamine par spectrométrie de masse ($m/2z = 200$). Lorsque la réduction est réalisée au potentiel de $-0{,}40$ V correspondant à la formation de Sn^0, le dérivé diaminé est obtenu de manière presque exclusive. Il est accompagné seulement de traces de dihydroxylamine.

En milieu HCl, au potentiel de $-0{,}10$ V, il se forme également un précipité dont l'analyse confirme qu'il s'agit de DASS. Une étude par RMN de l'ensemble des produits montre, en plus du DASS, la présence de la dihydroxylamine et parfois du composé amino-nitré mais toujours en très faibles quantités.

Électrolyses sur électrode de monel

L'électrode de monel — alliage de nickel (2/3) et de cuivre (1/3) — est utilisée à l'échelle industrielle à cause de sa bonne résistance à la corrosion en milieu acide et de son coût relativement faible. Nous avons déjà étudié la réduction du nitrobenzène en aminophénol sur cet alliage (résultats non publiés). La surtension de l'hydrogène, peu importante sur ce type de matériau, laisse supposer une compétition entre le mécanisme d'hydrogénation électrocatalytique et celui d'électronation–protonation. Ainsi, au potentiel imposé $E = -0{,}65$ V à 60°C, après une consommation d'électricité égale à quatre fois la valeur théorique, la proportion de DNDB réduite est seulement de 50%. Si le rendement faradique n'est pas très intéressant, le produit de réduction est essentiellement le DADB pur avec un rendement par rapport au DNDB de l'ordre de 45%.

Avec cette électrode comme avec l'électrode de mercure, la présence de $TiOSO_4$ favorise grandement la formation du DADB dont le pourcentage atteint 90% si la concentration en $TiOSO_4$ est supérieure au double de celle en DNDB initial. Aux concentrations moindres en couple rédox, son effet est partiel, ainsi pour 6×10^{-4} M, le rendement en DADB et de 76% et l'on retrouve 6% de DNDB non réduit. Des produits secondaires apparaissent, en particulier les composés hydroxylés.

Dans le cas du DNSS, le potentiel imposé de $-0{,}30$ V, bien que faiblement négatif, ne permet pas non plus d'éviter la réduction du proton ce qui empêche que la réduction soit complète et abaisse le rendement faradique. Le produit obtenu est un mélange de diamine avec en moindres proportions de la dihydroxylamine et des dérivés amino-nitré et dinitré non réduit. La présence de $TiOSO_4$ favorise la formation de diamine qui précipite au cours de l'électrolyse. Le spectre de RMN du solide isolé après sa transformation en sel de sodium confirme ce résultat. Seules des raies supplémentaires correspondant à des traces de dihydroxylamine sont visibles sur le spectre.

Électrolyses sur électrode d'étain

La réduction du DNDB, en milieu H_2SO_4–EtOH 50/50 à 60°C, est effectuée au potentiel de $-0{,}65$ V. La réaction est lente mais l'intensité du courant décroît régulièrement en fonction du temps. La quantité d'électricité nécessaire pour réduire le dérivé dinitré en totalité est supérieure à la valeur théorique de 12 électrons par molécule à cause de la surtension d'hydrogène de l'électrode. Le rendement maximum en DADB n'excède pas 50%. L'analyse chromatographique des produits de réduction indique la formation de nombreux composés, les principaux ont été identifiés grâce à la spectrométrie de masse couplée à cette technique. Le DADB est toujours accompagné des composés mono et dihydroxylés HO-R-R-NH_2 et HO-R-R-OH dans des proportions respectives de l'ordre de 18% et 8%. Les quatre composés éthoxylés sont également formés, leur pourcentage total peut atteindre 15% et l'on peut envisager, à l'état de traces, l'existence des composés HO-R′-R′-NH_2 (M = 301) et HOHN-R-R′-NH_2 (M = 272) avec

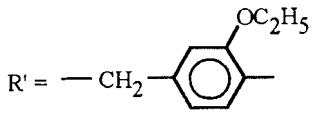

et celle dérivés mono-nitrosés (M = 256). La présence de ces derniers a pu être confirmée par voltammétrie cyclique en milieu DMF. Nous retrouvons dans ces conditions un comportement semblable à celui observé lors de la réduction sur électrode de mercure en présence de $SnCl_2$.

En présence de $TiOSO_4$, à des concentrations supérieures à 2×10^{-3} M et au même potentiel de $-0{,}65$ V, la formation de DADB est favorisée au détriment de tous les produits secondaires qui se forment en son absence. Le rendement en DADB atteint 90%. Il est bien cristallisé et c'est pratiquement le seul produit qui soit extrait.

Au cours des *électrolyses du DNSS*, réalisées en milieu H_2SO_4 2,5 N au potentiel de $-0{,}65$ V, un dépôt se forme sur l'électrode. En fin de réaction, il est facilement détachable et laisse la surface de l'étain très brillante. Les analyses des extraits obtenus soit à partir de ce dépôt soit de l'électrolyte donnent des compositions similaires : la proportion de DASS est toujours majoritaire, les autres produits formés sont des composés di- et mono-nitrés et de la dihydroxylamine.

La présence de $TiOSO_4$ n'apporte pas de modifications : le dépôt sur l'électrode se forme de la même manière et les produits obtenus sont les mêmes.

En milieu HCl, des essais à plusieurs potentiels dans le domaine d'utilisation possible compris entre $-0{,}50$ et $-0{,}90$V n'ont pas mis en évidence d'effets significatifs de ce paramètre sur les produits formés, essentiellement le DASS avec des quantités plus ou moins importantes de dihydroxylamine.

La chromatographie liquide haute performance (HPLC), par analyse de paires d'ions sur silices greffées (58–63), s'est avérée être performante tant au niveau analytique, dans le suivi des réductions par les analyses d'échantillons périodiquement prélevés, qu'au niveau préparatif pour la séparation

Fig. 2. Analyse par HPLC au cours d'une réduction électrochimique du DNSS sur électrode d'étain en milieu HCl à 10% avec enregistrement du gradient de concentration de la phase mobile.

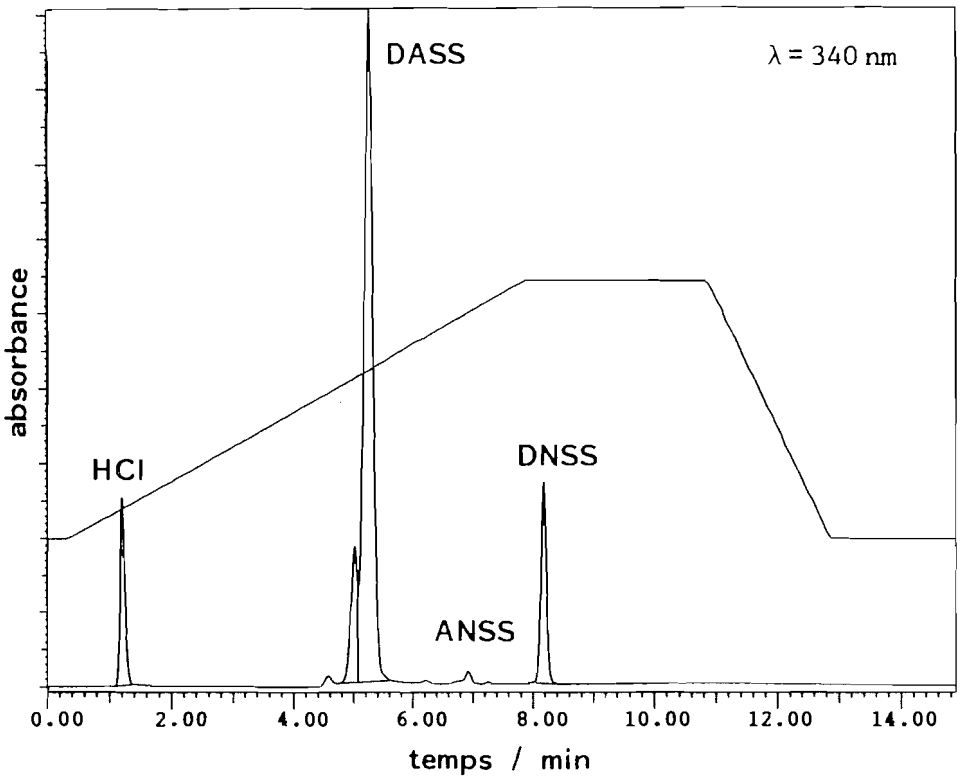

des différents composés de l'extrait. La figure 2 montre un exemple de chromatogramme obtenu au cours d'une réduction en milieu HCl. Elle correspond à l'analyse d'un prélèvement pendant une électrolyse sur électrode d'étain après consommation de 11 électrons par molécule. Les pics correspondant aux différents produits sont nettement caractérisés. Cette méthode nous a permis également de séparer les composés (Fig. 3) et en particulier d'isoler la dihydroxylamine (pic 1) afin de pouvoir l'analyser par spectrométrie de masse par ionisation électrospray. La diamine correspond au pic 3 du chromatogramme. Le pic 2 n'a pas été identifié avec certitude mais comme aucun autre composé n'est détecté sur les spectres de RMN, on peut envisager que ce pic corresponde à une forme de la diamine obtenue par échange de cations Na^+ et Bu_4N^+ par suite de la présence du réactif $Bu_4NH_2PO_4$ dans les éluants. Cet échange intervient en solution avec formation de paires d'ions qui possèdent des temps de rétention différents en HPLC. Cette hypothèse est confortée par le fait que la spectrométrie de masse met en évidence un composé $[DASS + Bu_4N]^-$ ($m/z = 610,5$).

C. Réduction chimique par le réducteur Sn^0 électrogénéré

Les effets très différents des couples rédox Ti^{3+}/Ti^{4+} et Sn^0/Sn^{2+} sur les réductions électrochimiques nous ont incités à les comparer à ceux obtenus en réductions chimiques par les deux réducteurs Ti^{3+} et Sn^0 préalablement électrogénérés.

Réduction chimique du DNDB

Le chlorure stanneux est réduit électrochimiquement sur nappe de mercure au potentiel de −0,50 V à 60°C, dans la solution H_2SO_4 5 N – EtOH. Ensuite, après arrêt de l'électrolyse, le DNDB, solubilisé dans une petite quantité de DMF désoxygéné, est introduit dans cette solution. Après la réduction, l'extrait obtenu est toujours mal cristallisé, de couleur rouge foncé, il est pâteux et adhère aux parois de verre. Les mêmes méthodes d'analyses que précédemment — RMN, CPV et spectrométrie de masse couplée à la CPV — ont également permis de caractériser les produits formés. Le pourcentage de DADB n'est pas supérieur à 50% et l'on retrouve les mêmes sous-produits qu'en réduction électrochimique sur électrode d'étain ou sur électrode de mercure en présence de $SnCl_2$, c'est-à-dire les composés hydroxylés, principalement HO-R-R-NH_2 de l'ordre de 15% et quelques pourcents de HO-R-R-OH. Les composés éthoxylés se forment aussi, leurs pourcentages varient entre 15 et 20%. Plusieurs expériences avec des rapports Sn^0/DNDB différents n'ont pas permis d'obtenir le dérivé amino-nitré (ANDB) même à l'état de traces alors que sa proportion pouvait atteindre 70% avec Ti^{3+} (17); ceci peut être expliqué ici par la lenteur de la réduction de l'hydroxylamine ce qui permet au réducteur de réagir sur les deux groupements NO_2 en priorité. La quantité de DNDB non réduit est fonction de la proportion relative de Sn^0.

Des essais de séparation sur colonne de silice n'ont pas donné de résultats totalement satisfaisants. En effet, l'extrait est difficilement solubilisé dans l'éluant et les produits hydroxylés n'ont pu être séparés du DADB, qui n'est donc pas obtenu aussi pur qu'en réduction chimique par Ti^{3+}.

Fig. 3. Séparation par HPLC des produits formés lors d'une réduction électrochimique du DNSS sur électrode d'étain en milieu HCl. (1) dihydroxylamine; (2) [DASS + Bu_4N]$^+$; (3) DASS; (4) ANSS.

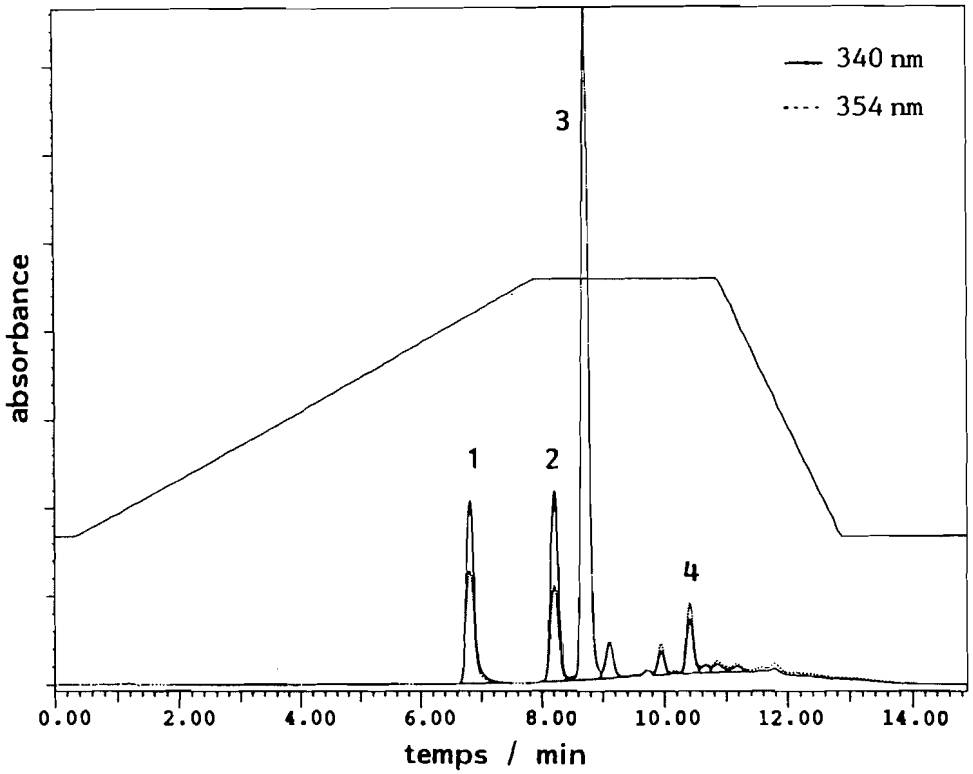

Réduction chimique du DNSS

La réduction chimique du DNSS a été réalisée dans les deux milieux H_2SO_4 2,5 N et HCl à 10%. Le réducteur Sn^0 est préalablement électrogénéré sur électrode de mercure à partir du chlorure stanneux au potentiel de −0,50 V.

Au cours de la réaction, pour des rapports Sn^0/DNSS de l'ordre de 6/1, il se forme un précipité composé principalement de diamine avec une faible quantité de dérivé amino-nitré (ANSS). La solution est traitée après filtration selon le mode opératoire décrit en partie expérimentale et nous identifions les composés mono- et di-aminés dans un rapport 65/35 accompagnés de DNSS non réduit qui peut atteindre 15 à 20%. Au total, la proportion ANSS/DASS est voisine de 60/40 soit légèrement inférieure à celle de 85/15 obtenue pour la réduction par Ti^{3+} dans les mêmes conditions (16). Cette différence peut s'expliquer par le fait que Ti^{3+} est un réducteur beaucoup plus efficace que Sn^0 pour la réduction des hydroxylamines (57).

La comparaison de ces résultats avec ceux de la réduction du dinitrodibenzyle montre d'importantes différences. En effet, la réduction chimique du DNDB par Sn^0 ne conduit pas à la formation du composé mono-aminé mais à celle de composés hydroxylés. Cette constatation peut être interprétée par le fait que la réduction de l'hydroxylamine, toujours lente, intervient dans une zone de potentiel relativement plus négative (entre −0,40 et −0,75 V) dans laquelle se situe celle du système Sn^{2+}/Sn^0, ce qui ne favorise pas le transfert d'électrons et permet à des réactions de substitutions de se développer, rendant la formation du dérivé mono-aminé plus difficile. Au contraire, dans le cas du DNSS, l'étude analytique a montré qu'en raison de sa conjugaison, ce dernier est réduit en milieu acide vers 0 V, en une étape unique mettant en jeu 12 électrons par molécule. De plus, la solubilité du DNSS, beaucoup plus grande que celle du DNDB, permet un meilleur contact avec le réducteur ce qui favorise le transfert d'électrons et par conséquent la formation du dérivé mono-aminé.

Conclusion

Le 4,4′-dinitrodibenzyle étant très peu soluble en milieu aqueux, la présence d'un couple rédox accélère dans tous les cas la réduction électrochimique vraisemblablement en raison d'associations de type donneur–accepteur qui facilitent les échanges électroniques. Chaque type de réducteur garde cependant sa spécificité et conduit à des mécanismes différents qui influent sur la sélectivité des réactions. Ainsi, quel que soit le matériau de l'électrode, $TiOSO_4$ favorise la formation de la diamine et permet de l'obtenir pure avec un rendement supérieur à 90%. L'effet de $SnCl_2$ est différent. La quantité de diamine n'excède pas 50% des produits formés et elle est toujours accompagnée de composés hydroxylés et éthoxylés.

Sur cathode de mercure, la diamine est le seul produit de réduction de l'acide 4,4′-dinitrostilbène 2,2′-disulfonique en milieu H_2SO_4. Elle est obtenue avec un très bon rendement et l'intervention de $TiOSO_4$ ou $SnCl_2$ n'a pas d'effet sur la réaction. L'utilisation d'électrodes solides, mieux adaptées en vue d'applications industrielles, permet également cette synthèse.

Sur l'électrode d'étain, le DASS est formé avec un meilleur rendement que sur l'électrode de monel mais sur cette dernière, les résultats sont améliorés par l'action du couple rédox Ti^{3+}/Ti^{4+} en solution. Les produits secondaires sont identifiés dans chaque cas et des méthodes de dosage et de séparation des produits (photodensitométrie, HPLC), mises au point pour cette étude, se sont avérées bien adaptées et performantes.

La méthode électrochimique permet de générer de manière simple des réducteurs dont le choix oriente la sélectivité de la synthèse. Ainsi, dans le cas du DNDB, le réducteur Sn^0 conduit aux mêmes produits que ceux obtenus par réduction électrochimique sur électrode d'étain ou sur électrode de mercure en présence de chlorure d'étain tandis qu'en choisissant la proportion du réducteur Ti^{3+}, il est possible de préparer le composé amino-nitré résultant de la réduction d'un seul groupement nitré. Les résultats sont différents dans le cas du DNSS pour lequel les deux réducteurs Sn^0 et Ti^{3+} permettent la synthèse de l'acide amino-nitrostilbène disulfonique. Le rendement est légèrement supérieur avec Ti^{3+}. Les résultats ne sont pas modifiés par la nature du milieu acide, H_2SO_4 ou HCl à 10%.

Partie expérimentale

Les principales caractéristiques des produits et des solvants ainsi que les techniques utilisées et les conditions des expériences ont déjà été décrites (14, 16, 17).

Appareils — conditions des expériences — produits

Nous rappelons seulement que les cellules électrochimiques sont thermostatées à 60°C pour la réduction du DNDB et à 30°C pour celle du DNSS. Les dimensions des plaques constituant les cathodes solides sont respectivement 40 × 50 mm pour celle de monel et 50 × 35 mm pour celle d'étain. La cathode de mercure a une diamètre de 72 mm. Les potentiels sont indiqués par rapport à l'électrode de référence au calomel saturé (ECS) et, dans toutes les électrolyses, l'anode est une plaque de plomb.

Le 4,4′-dinitrodibenzyle est un produit industriel recristallisé dans le toluène et le 4,4′-dinitrostilbène-2,2′-disulfonate de sodium est un produit commercial TCI. Les dérivés diaminés, qui ont permis de confirmer l'identification des produits de réduction, sont respectivement d'origines Aldrich et Lancaster. Pour chaque composé, les deux formes, acide et sel de sodium, ont la même abréviation dans le texte, soit DNDB et DNSS pour les dinitrés et DADB et DASS pour les diaminés. Le sulfate de titanyle $TiOSO_4, xH_2SO_4, xH_2O$ est un produit Aldrich. Le complexe tétrachlorure de titane – tétrahydrofurane et le chlorure stanneux dihydraté sont des produits Fluka.

Extraction, séparation et caractérisation des produits de réduction

Après les électrolyses ou les réductions chimiques, des polarographies ou des voltammétries cycliques effectuées sur la solution permettent de détecter la présence des composés réductibles (dérivés amino-nitré et dinitré non réduit).

Les solutions d'électrolyses sont concentrées puis neutralisées par une solution de soude et évaporées. Les produits de réduction du DNDB sont extraits à l'éther tandis que ceux du DNSS le sont avec du DMF. L'identification et la composition des extraits secs sont déterminées par spectrométrie de RMN ^1H ($CDCl_3$), chromatographie en phase vapeur (CPV) et spectrométrie de masse couplée à la CPV pour le DNDB. Dans le cas du DNSS, les caractéristiques de RMN ^1H (DMSO-d_6) des DNSS, DASS et ANSS ont été déterminées dans une étude précédente (16), celles de la dihydroxylamine (déplacements chimiques (en ppm) par rapport au TMS, avec les mêmes conventions que pour les autres dérivés) sont : 7,06 ($2H^{(3 \text{ et } 3')}$, doublet J = 2,4 Hz), 6,16 ($2H^{(5 \text{ et } 5')}$, doublet J = 2,4 Hz et doublet J = 8,2 Hz), 6,75 ($2H^{(6 \text{ et } 6')}$, doublet J = 8,2 Hz), 6,86 ($2H^{(\alpha \text{ et } \alpha')}$, singulet), 5,01 ($4H^{(NHOH)}$, singulet).

Les produits sont séparés par chromatographie sur colonne de silice et analysés par chromatographie sur couche mince sur plaque de silice avec comme éluants le mélange toluène–acétone 80/20 ou toluène–méthanol 90/10 dans le cas du DNDB et le mélange DMF–chloroforme 50/50 dans le cas du DNSS. La mise au point d'une méthode par photodensitométrie associée à cette dernière a permis le dosage des acides mono- et di-aminostilbènes disulfoniques (64). Le DASS, qui est insoluble en milieu acide, peut être isolé de la solution par filtration mais sa purification et sa caractérisation spectroscopique nécessitent sa mise sous la forme de sel de sodium.

La chromatographie liquide à haute performance (HPLC), technique nouvelle dans cette étude, a été effectuée sur un appareil Gilson équipé de deux pompes avec chambre de mélange, d'une vanne d'injection Rheodyne de 20 μL pour les mesures analytiques et de 500 μL pour les séparations de produits. Un détecteur spectrophotométrique UV117 permet deux détections simultanées, les longueurs d'onde choisies correspondent aux maxima d'absorbance du DNSS (λ = 354 nm) et du DASS (λ = 340 nm). Pour les mesures analytiques, la colonne de silice greffée de chaînes octadécyle C18, de granulométrie 5 μm, est de type Spherisorb, sa dimension est 100 × 4,6 mm. Pour les séparations à l'échelle préparative, la colonne est de modèle Rainin Instrument Company DYN FAST PCLC C18, de granulométrie 3 μm, de dimension 50 × 21,4 mm. La phase mobile est un mélange eau–méthanol contenant le contre-ion. L'eau est déionisée, distillée et passée dans une cartouche Millipore. Le méthanol, de qualité RS pour HPLC Carlo Erba, est désaéré aux ultra-sons. Le réactif de paire d'ions est une solution aqueuse d'hydrogénophosphate de tétrabutylammonium ($Bu_4NH_2PO_4$) et les éluants sont préparés suivant la méthode décrite par S.K. Hammond et al. (62). Les analyses chromatographiques sont programmées par le logiciel GILSON 715 GME. Le composé est mis en solution dans l'éluant aqueux et injecté. Les meilleurs résultats sont obtenus en gradient de concentration de 22% à 60% d'éluant méthanolique en 8 min, suivi d'un palier à 60% pendant 3 min et du retour aux conditions initiales en 2 min avec rééquilibrage de la colonne.

Références

1. M. Noel, C. Ravichandran et P.N. Anantharaman. J. Appl. Electrochem. **25**, 690 (1995).
2. E. Laviron, A. Vallat et R. Meunier-Prest. J. Electroanal. Chem. **379**, 427 (1994).
3. R.G. Compton et R.A.W. Dryfe. J. Electroanal. Chem. **375**, 247 (1994).
4. C.A. Ma et Y.Z. Ren. Chin. Chem. Lett. **5**, 81 (1994).
5. C. Ravichandran, M. Noel, S. Thangavelu et P.N. Anantharaman. J. Electroanal. Chem. **369**, 217 (1994).

6. A. Savall. J. Phys. IV, 4(C1, Récents développements en électrochimie), 163 (1994); Actual. Chim. 35 (1992).
7. C. Moinet. J. Phys. IV, 4(C1, Récents développements en électrochimie), 175 (1994).
8. F. Miralles-Roch, A. Tallec et R. Tardivel. Electrochim. Acta, **38**, 2379 (1993).
9. V.P. Gul'tyai et V.N. Leibzon. Russ. J. Electrochem. **32**, 59 (1996).
10. C. Karakus et P. Zuman. J. Electroanal. Chem. **396**, 499 (1995).
11. A. Kalandyk et J. Stroka. J. Electroanal. Chem. **346**, 323 (1993).
12. P. Zuman. Collect. Czech. Chem. Commun. **58**, 41 (1993); Electroanalysis (N.Y.), **4**, 783 (1992).
13. M. Inaba, Z. Ogumi et Z. Takehara. J. Electrochem. Soc. **140**, 19 (1993).
14. V. Danciu, A.M. Martre, P. Pouillen et G. Mousset. Electrochim. Acta, **37**, 1993 (1992).
15. V. Danciu, A.M. Martre, P. Pouillen et G. Mousset. Electrochim. Acta, **37**, 2001 (1992).
16. A.M. Martre, G. Mousset, V. Cosoveanu et V. Danciu. New J. Chem. **18**, 1221 (1994).
17. A.M. Martre, V. Danciu et G. Mousset. Can. J. Chem. **71**, 1136 (1993).
18. L. Oniciu, I.A. Silberg, V. Danciu, M. Olea et S. Bran. 36th Meeting of International Society of Electrochemistry, Salamanca, Spain (1985).
19. B. Noll, D. Raschke, L. Zoclch, G. Bache, G. Wolter, S. Keil, K.L. Kelling, M. Koch et T. Kojtscheff. Ger. (East) DD 242,403 (Cl. C07C143/62), 28 Janv. 1987, Appl. 282,365, 01 Nov. 1985; Chem. Abstr. **107**, 41702b (1987).
20. R.B. Lund et G.W. Brown. Eur. Pat. Appl. EP 221,021 (Cl. C07C143/62) 06 May 1987, US Appl. 787, 883, 16 Oct. 1985.
21. T. Engelhardt, H. Sauter et J. Koppold. Ger. Offen. DE3, 916, 360 (Cl. C07C309/46), 22 Nov. 1990, Appl. 19 May 1989.
22. B.K. Bandlish et R.V. Casciani. Ger. Offen. DE 4, 110, 617 (Cl. C01G23/00) 10 Oct. 1991, US Appl. 504, 492, 04 Apr. 1990.
23. K. Sawaki et M. Kato. Jpn. Kokai Tokkyo Koho JP 04,293,969 (Cl. C09B67/26), 19 Oct 1992, Appl. 91/81, 142, 22 Mar. 1991.
24. Y. Murakami et S. Ooka. Jpn. Kokai Tokkyo Koho JP 04,321,661 (Cl. C07C309/46), 11 Nov 1992, Appl. 91/113,837, 19 Apr. 1991.
25. P.N. Anantharaman, G.S. Subramanian et H.V.K. Udupa. Trans. SAEST, **4**, 38 (1969).
26. F. Wolf et H. Fischer. J. Prakt. Chem. **317**, 103 (1975).
27. J. Barek, A. Berka et K. Jakubec. Microchem. J. **24**, 484 (1979); **25**, 416 (1980).
28. J. Terc. Chem. Prum. **30**, 417 (1980); Chem. Abstr. **94**, 139396t (1981).
29. M. Noel, P.N. Anantharaman et H.V.K. Udupa. Indian J. Technol. **19**, 100 (1981).
30. J. Barek et I. Danhel. Collect. Czech. Chem. Commun. **49**, 2751 (1984); **50**, 1673 (1985).
31. H. Balczewska et T. Paryjczak. Zesz. Nauk.-Politech. Lodz., Chem. N° **41**, 253 (1987).
32. H.V.K. Udupa. Indian Chem. Eng. **30**, 53 (1988).
33. D.M. Lewis et S.M. Smith. Proc. Int. Wool Text. Res. Conf., 8th, **4**, 177 (1990).
34. A. Kazmierczak et T. Parjczak. Zesz. Nauk.-Politech. Lodz., Chem. **616**, 349 (1991).
35. F.B. Bizhanov, B.T. Dosumova et A.T. Masenova. Izv. Nats. Akad. Nauk Resp. Kaz. Ser. Khim. **1**, 30 (1991).
36. S.E. Sadek, J.G. Lee, R.B. Lund et W.W. McConnell. Water Sci. Technol. **26**, 309 (1992).
37. N.V. Mistry et K.R. Desai. J. Inst. Chem. (India), **64**, 157 (1992).
38. National Toxicology Program. Nat. Toxicol. Program Tech. Rep. Ser. **412**, 240 pp. (1992). Chem. Abstr. **118**, 118721u (1993).
39. V. Danciu, I.A. Silberg, O.H. Oprea et L.A. Oniciu. Rom RO 94157 (Cl C 07C87/14) 30/07/88, Appl. 122483, 07/03/86. Chem. Abstr. **114**, 163704u (1991).
40. L. Oniciu, M. Olea et V. Danciu. Rev. Chim. (Bucharest), **41**, 779 (1990).
41. D. Mandler et A.J. Bard. J. Electroanal. Chem. **307**, 217 (1991).
42. G.M. Habashy. Collect. Czech. Chem. Commun. **25**, 3166 (1960); J. Electroanal. Chem. **8**, 237 (1964).
43. L. Kisova, S. Sotkova et I. Komendova. Collect. Czech. Chem. Commun. **59**, 1279 (1994).
44. V.H. Kelsall, D.J. Robbins et W. Wang. Electrochem. Eng. Energy (Proc. Eur. Symp. Electr. Eng.), 3rd, 1994. *Éditeurs* : F. Lapicque, A. Storck et A. Wragg. Plenum Press, New York. 1995. pp. 129–140.
45. J. Chon et W. Paik. Bull. Korean Chem. Soc. **2**, 1 (1981).
46. A.A. Konarev, V. Kh. Katunin, L.S. Pomogaeva, I.A. Avrutskaya et M. Ya. Fioshin. Elektrokhimiya, **20**, 204 (1984).
47. I. Rubinstein. J. Electroanal. Chem. **183**, 379 (1985).
48. A. Davidovic, D. Davidovic et I. Tabakovic. J. Serb. Chem. Soc. **56**, 677 (1991).
49. K. Filipiak, T. Paryjczak et B. Grzelak. Zesz. Nauk.-Politech. Lodz. Chem. **616**, 367 (1991).
50. G. Kokkinidis, A. Papoutsis et G. Papanastasiou. J. Electroanal. Chem. **359**, 253 (1993).
51. J. Chaussard, R. Rouget et M. Tassin. J. Appl. Electrochem. **16**, 803 (1986).
52. J.C. Moutet. Org. Prep. Proced. Int. **24**, 309 (1992).
53. B.J. Coté, D. Despres, R. Labrecque, J. Lamothe, J.M. Chapuzet et J. Lessard. J. Electroanal. Chem. **353**, 219 (1993).
54. J. Lessard, G. Belot, Y. Couture, S. Desjardins et C. Roy. Int. J. Hydrogen Energy, **18**, 681 (1993).
55. R. Menini. Thèse Lyon (1994).
56. M. Jubault et D. Peltier. Bull. Soc. Chim. Fr. n° 4, 1544 (1972); 1551 (1972).
57. M. Noel, P.N. Anantharaman et H.V.K. Udupa. J. Appl. Electrochem. **12**, 291 (1982).
58. R. Rosset, M. Caude et A. Jardy. *Dans* Manuel pratique de chromatographie en phase liquide. Masson, Paris, New York. 1982. pp. 221–234.
59. K. Saag. *Dans* HPLC in food analysis. *Éditeur* : R. Macrae. Academic Press, London. 1988. pp. 268–273.
60. D.E. Linder et M.C. Allen. J. Am. Oil Chem. Soc. **59**, 152 (1982).
61. G.R. Bear. J. Chromatogr. **371**, 387 (1986).
62. S.K. Hammond, T.J. Smith et M.J. Ellenbecker. Am. Ind. Hyg. Assoc. J. **48**, 117 (1987).
63. A. Marcomini, F. Filipuzzi et W. Giger. Chemosphere, **17**, 853 (1988).
64. V. Cosoveanu, V. Danciu, G. Cimpan, A.M. Martre, G. Mousset et S. Gocan. J. Chromatogr. A, **727**, 324 (1996).

Intramolecular Diels–Alder reactions of 2*H*-thiopyran dienes

Dale E. Ward, Thomas E. Nixey, Yuanzhu Gai, Matthew J. Hrapchak, and M. Saeed Abaee

Abstract: A systematic survey of IMDA reactions of 4-[tris(2-methylethyl)silyl]oxy-2*H*-thiopyran derivatives with potential dienophiles tethered at the C-2, C-3, C-5, and C-6 positions is presented. Cycloaddition was not observed with a C_3 or C_4 tether and an unactivated terminal olefin as dienophile. IMDA adducts could be obtained when dienophiles activated by a carbomethoxy group were employed. Compounds having the activated dienophile attached via a C_3 tether to C-2 of the 2*H*-thiopyran gave adducts with high stereoselectivity. Substrates having the dienophile attached to C-3 with a C_3 or C_4 tether cyclized readily. With an (*E*)-enoate as the dienophile, the stereoselectivity was poor (*endo*:*exo* = 1.1–2.5:1) and essentially independent of reaction conditions (i.e., thermal vs. Lewis acid mediated). With the (*Z*)-enoate, a 7:1 mixture of *endo*:*exo* IMDA adducts was obtained under thermal conditions; with Lewis acid catalysis, isomerization of the dienophile was competitive with cycloaddition. Type II IMDA adducts were not observed with C-5 tethered substrates. Compounds having the dienophile attached to C-6 via a C_3 or a five-atom tether also failed to give IMDA adducts. No evidence for isomerization of the 2*H*-thiopyran dienes by [1,5] sigmatropic rearrangement was observed. The *endo* adducts from IMDA reactions of the C-3 tethered substrates can be desulfurized to obtain synthetically useful *trans*-fused hydrindans and decalins with angular methyl groups.

Key words: intramolecular Diels–Alder, 2*H*-thiopyran, *cis*-substituted 1,3-diene surrogate, *trans*-octahydro-3a-methyl-1*H*-indene derivatives, *trans*-decahydro-4a-methylnapthalene derivatives.

Résumé : On présente une étude des réactions DAIM des dérivés du 4-[tris(2-méthyléthyl)silyl]oxy-2*H*-thiopyrane avec des diénophiles potentiels attachés en positions C-2, C-3, C-5 et C-6. On n'observe pas de cycloaddition avec des laisses de 3 ou 4 atomes de carbone et une oléfine terminale désactivée comme diénophile. Les adduits DAIM peuvent être obtenus lorsque l'on utilise des diénophiles activés par un groupe carbométhoxy. Les composés ayant le diénophile attaché par une laisse de 3 carbones attachée au carbone en position 2 du 2*H*-thiopyrane donne des adduits avec une très grande stéréosélectivité. Les substrats ayant un diénophile attaché en C-3 avec une laisse de 3 ou 4 atomes de carbone se cyclisent rapidement. Si on utilise un (*E*)-énoate comme diénophile on obtient une faible stéréosélectivité (*endo* : *exo* = 1,1–2,5 : 1) qui est indépendante des conditions de réaction (c.-à-d., thermique versus une catalyse par acide de Lewis). Avec un (*Z*)-énoate on obtient un mélange d'adduits DAIM *endo* : *exo* dans la proportion de 7 : 1 par voie thermique tandis que la catalyse par un acide de Lewis conduit à une compétition entre l'isomérisation du diénophile et la cycloaddition. On n'a pas observé d'adduits DAIM de type II avec les substrats liés en C-5. Les composés ayant un diénophile attaché en C-6 via une liesse de 3 ou de 5 atomes de carbone ne donnent pas non plus d'adduits DAIM. On n'a pas pu mettre en évidence l'isomérisation des dienes 2*H*-thiopyranes par réarrangement sigmatropique [1,5]. Les adduits *endo* obtenus à partir des réactions DAIM des substrats liés en C-3 peuvent être désulfurisés pour obtenir des hydrindanes condensés en position *trans* et des décalines avec des groupes méthyles angulaires très utiles en synthèse.

Mots clés : Diels–Alder intramoléculaire, 2*H*-thiopyrane, substitut pour les dienes substitués en position *cis*, dérivés *trans*-octahydro-3a-méthyl-1*H*-indène, dérivés *trans*-décahydro-4a-méthylnaphtalène.

[Traduit par la rédaction]

Introduction

Despite its long history (1), the Diels–Alder reaction continues to be of fundamental importance to the theory and practice of organic chemistry (2). The increase in molecular complexity resulting from the simultaneous formation of two σ-bonds and up to four stereogenic centers coupled with the attributes of wide generality, atom economy, and predictable regio- and stereoselectivity contribute to the unrivaled synthetic utility of this reaction. One of the few limitations of the Diels–Alder reaction is the poor reactivity associated with *cis*-substituted dienes (3). As a consequence, certain stereochemical arrays are not readily generated by a Diels–Alder cycloaddition (see Scheme 1).

In an effort to address this problem, we have been investigating a strategy involving the use of 2*H*-thiopyrans as functional equivalents to *cis*-dienes (4–8). Previous work has established that the Diels–Alder adducts from reactions of 2*H*-thiopyrans with dienophiles are, after desulfurization, synthetically equivalent to adducts derived (in principle) from unreactive *cis*-dienes (Scheme 1). We have developed methods for the preparation of a wide variety of substituted 2*H*-thiopyrans

Received January 16, 1996.

D.E. Ward,[1] T.E. Nixey, Y. Gai, M.J. Hrapchak, and M.S. Abaee. Department of Chemistry, University of Saskatchewan, 110 Science Place, Saskatoon, SK S7N 5C9, Canada.

[1] Author to whom correspondence may be addressed. Telephone: (306) 966-4656. Fax: (306) 966-4730. Internet: WardD@sask.usask.ca

Scheme 1.

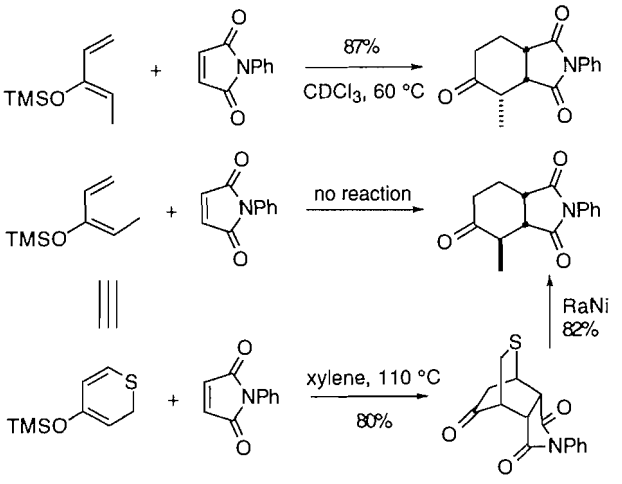

(4–9) and have systematically investigated their Diels–Alder reactivity under a variety of conditions (4–8). The reactions of 2*H*-thiopyrans bearing suitable activating substituent(s) with reactive dienophiles (e.g., maleic anhydride, maleimide) give predominantly *endo* adducts in good yield (4, 5). The reactions are slower using less reactive dienophiles (e.g., acrylate, crotonate) and modest yields are obtained because thermal decomposition of the diene competes effectively with cycloaddition (5). Lewis acid mediated reaction at lower temperatures is often satisfactory in these cases (6, 7).

The intramolecular Diels–Alder (IMDA) reaction has emerged as a powerful synthetic method for the stereoselective construction of polycyclic ring systems in a single step (10). The attenuated reactivity of *cis*-substituted dienes also limits the scope of the IMDA reaction, although not as severely as the intermolecular counterpart (10).[2] Relatively few examples of IMDA reactions involving conformationally mobile (i.e., capable of s-*cis* and s-*trans* conformers) *cis*-dienes (12) or 1,1-disubstituted-1,3-dienes (13) have been reported. Many of these examples involve particular structural elements that favor an s-*cis* conformation of the diene despite the *cis* substitution. Because (*Z*)-dienes often undergo IMDA cyclization with a much higher degree of stereoselectivity than the corresponding (*E*) isomers (10), the incorporation of a (*Z*)-diene moiety to serve as a stereochemical control element in an IMDA reaction can be an attractive tactic (10). However, this approach is limited by the reduced reactivity of (*Z*)-dienes, which can preclude IMDA reaction[3] in favor of competitive pathway(s) including the loss of stereochemical integrity by [1,5] sigmatropic rearrangement and (or) diene isomerization.[4] Preliminary results on the feasibility of using 2*H*-thiopyrans as surrogates for *cis*-dienes in IMDA reactions to address this limitation were reported (8). In this paper we present a full account of our investigations of IMDA reactions of 2*H*-thiopyrans.[5]

Fig. 1. Possible IMDA adducts from 4-(triisopropylsilyl)oxy-2*H*-thiopyran dienes with dienophiles attached at various positions.

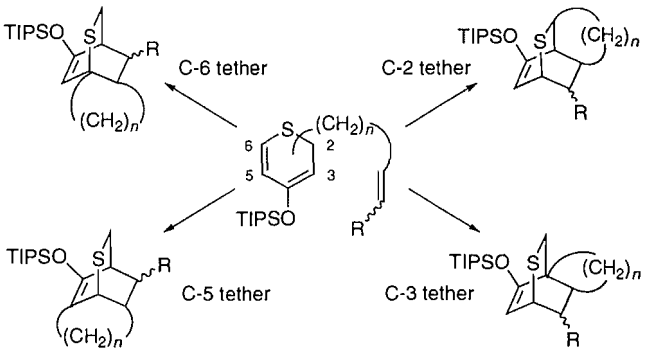

Results and discussion

Our previous work on intermolecular Diels–Alder reactions of 2*H*-thiopyrans had established the 4-(triisopropylsilyl)oxy derivative as a moderately reactive but somewhat unstable diene (4–8). A systematic study of the reactivity of this diene in IMDA reactions was undertaken. A series of substrates with various dienophiles attached to each of the four possible positions of 4-(triisopropylsilyl)oxy-2*H*-thiopyran by a 3- or 4-atom tether were required (Fig. 1). Because our goal was to evaluate IMDA reactivity, we adopted a simple synthetic strategy to produce all of the isomeric compounds from common intermediates.

Unactivated terminal alkene dienophiles were chosen for the first series of substrates. The desired compounds were prepared from the known β-ketoester **1** (15) according to Scheme 2.[6] Alkylation (16) of **1** with 5-bromopentene (17) or 6-bromohexene (17) gave **2a** and **2b**, respectively, in modest yields along with products of *O*-alkylation and ring fragmentation (18). The decarboxylation of compounds such as **2** can be difficult (16*b*), and only a modest yield of **3** was obtained from **2** even using the recommended conditions (16*b*). Dehydrogenation of **3** by reaction with *N*-chlorosuccinimide (NCS) according to the known procedure (19) proceeded with poor regioselectivity, as expected (20), to give inseparable 1.2:1 mixtures of **4** and **5**, respectively. The mixtures of **4a/5a** and **4b/5b** were individually converted into 1.2:1 mixtures of **6a/7a** and **6b/7b** by treatment with triisopropylsilyl trifluoromethanesulfonate (TIPSOTf) and Et_3N (5). Alternatively, CuI mediated conjugate addition (21; see also ref. 16*b*) of the Grignard reagent derived from 5-bromopentene or 6-bromo-

[2] An often cited report (12*o*) claims similar IMDA reactivity for the methyl esters of (2*E*,7*E*)- and (2*E*,7*Z*)-2,7,9-decatrienoic acid. Interpretation of these results in light of those of Roush (11) leads to the conclusion that the 7*E* isomer is considerably more reactive than the 7*Z* isomer.

[3] For examples, see refs. 12*a*, 12*b*, and 13*c*.

[4] For examples, see refs. 12*j*, 12*m*, and 12*n*.

[5] For a recent example involving IMDA reaction of 3*H*-benzofuro[3,2-*c*]thiopyran diene, see ref. 14.

[6] Reactions in Schemes 2–4 were not optimized. Considerable literature precedent suggests that many of these transformations would proceed in high yield if conditions were optimized for the particular substrate. Because our objective was to assess IMDA reactivity, the synthetic scheme was chosen to achieve diversity (as opposed to selectivity) and synthetic reactions were typically performed only once or twice using the published procedures "as is."

Scheme 2.

a: NaH, NaI, RX, acetone, reflux; *b*: LiI, 20% $DMF_{(aq)}$, reflux; *c*: NCS, pyridine, CH_2Cl_2; *d*: TIPSOTf, Et_3N; *e*: MnO_2, CH_2Cl_2; *f*: RMgBr, CuI, DMS.

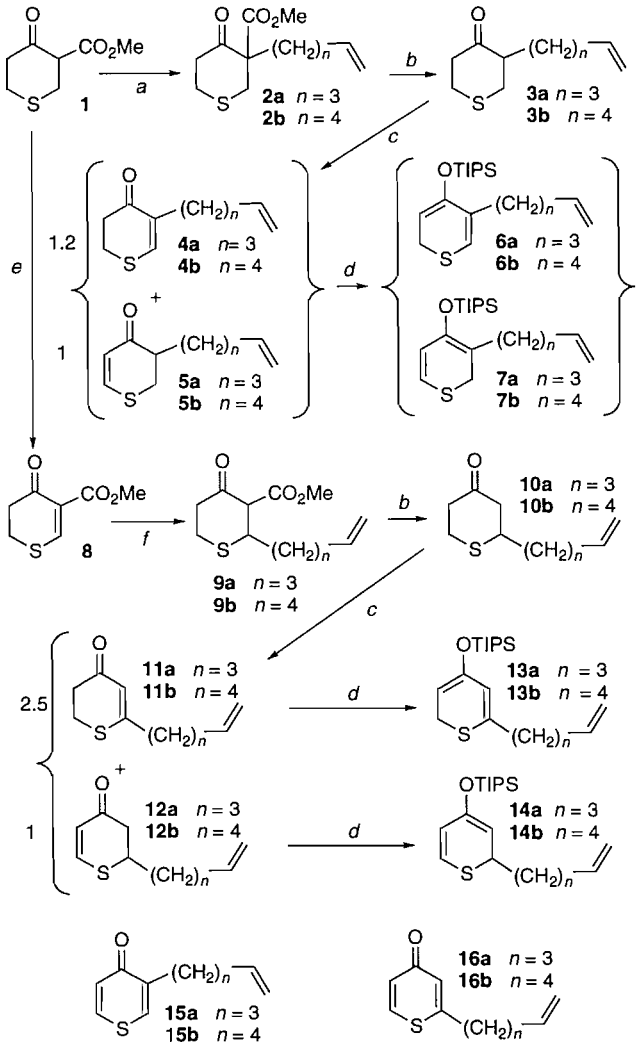

Scheme 3.

a: NaH, NaI, RX, acetone, reflux; *b*: $(Ph_3P)_4Pd(0)$, morpholine, THF; *c*: NCS, pyridine, CH_2Cl_2; *d*: (i) $HClO_4$, acetone, (ii) $Ph_3P{=}CHCO_2Me$, MeOH; *e*: TIPSOTf, Et_3N.

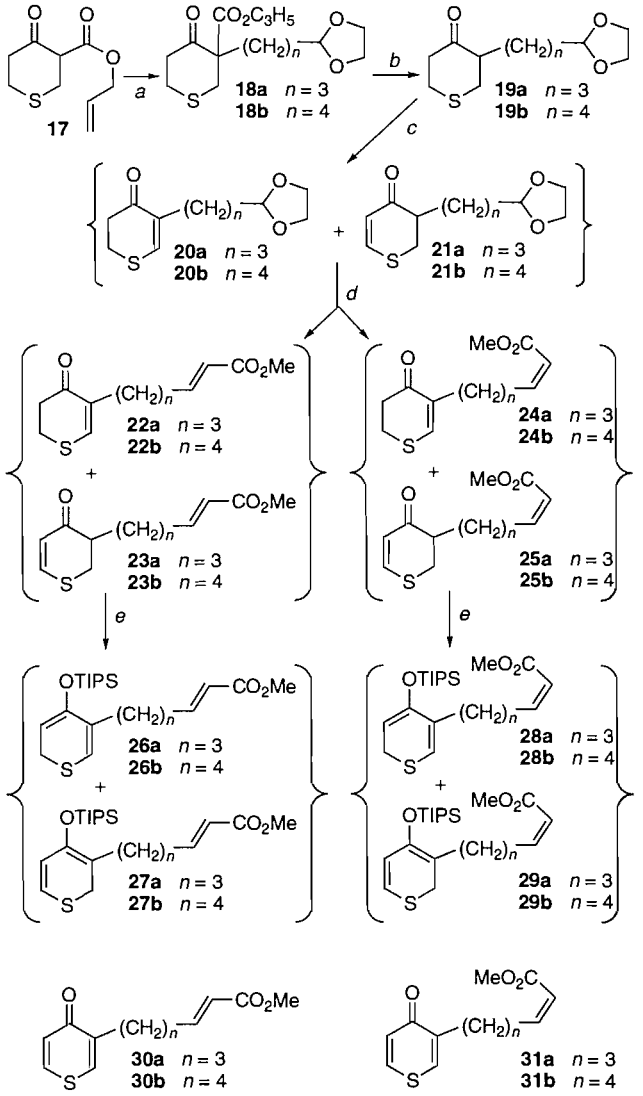

hexene to **8** (21) followed by decarboxylation of the resulting **9** produced **10**. Treatment of **10** with NCS gave separable mixtures of **11** and **12** with the former predominating by a ratio of ca. 2.5:1. The 6- and 2-substituted 2*H*-thiopyrans **13** and **14** were readily derived from **11** and **12**, respectively, by reaction with TIPSOTf. Individual solutions of the IMDA substrates **6a/7a**, **6b/7b**, **13a**, **13b**, **14a**, and **14b** in degassed C_6D_6 or $C_6D_5CD_3$ containing 2,6-di-*tert*-butyl-4-methylphenol (BHT) were heated in sealed NMR tubes at temperatures up to 200°C for several days, resulting in complete decomposition of the substrates. The reactions were monitored by ^1H NMR and, in no case, was the presence of an IMDA adduct indicated. Only products arising from desilylation (i.e., **4**, **5**, **11**, **12**) and oxidation (i.e., **15**, **16**) were detected (4, 5).

In an effort to enhance the IMDA reactivity, substrates with methyl 2-alkenoates as activated dienophiles were investigated. The preparation of compounds with the dienophile tethered at C-3 and C-5 of the 2*H*-thiopyran is outlined in Scheme 3.[6] Because of the low yields previously obtained in the decarboxylation of **2** and **9**, we began with the known allyl β-ketoester **17** (22). The Pd(0) catalyzed decarboxylation of alkylated derivatives of **17** is reported to be much more efficient than LiI–DMF decarboxylation of the analogous methyl esters (22). Alkylation of **17** with 2-(3-bromopropyl)-1,3-dioxolane (23) or 2-(4-bromobutyl)-1,3-dioxolane (24) gave **18a** and **18b**, respectively, in good yields. In each case, decarboxylation of **18** proceeded smoothly to give **19**, which reacted with NCS and pyridine to produce an inseparable mixture of enones **20** and **21** with a slight excess of the former. The individual mixtures of **20a/21a** and **20b/21b** were treated with aqueous acid to provide the corresponding aldehydes, which were immediately olefinated under conditions to maximize the proportion of (*Z*)-enoate formed (25). In both cases, a separable 1.7:1 mixture of (*E*)-enoates and (*Z*)-enoates was obtained. Neither the (*E*)-enoates (**22** and **23**) nor the (*Z*)-enoates (**24** and **25**) could be separated from each other and

Scheme 4.

a: MnO_2, CH_2Cl_2; *b*: (i) RMgBr, CuI, DMS, (ii) $(Ph_3P)_4Pd(0)$, morpholine, THF; *c*: (i) $HClO_4$, acetone, (ii) $Ph_3P{=}CHCO_2Me$, MeOH; *d*: NCS, pyridine, CH_2Cl_2; *e*: TIPSOTf, Et_3N.

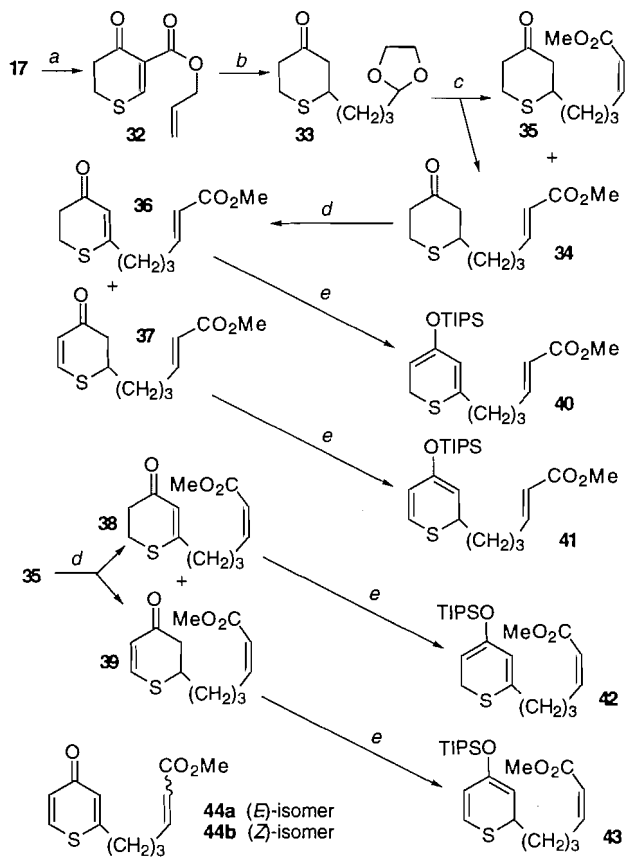

were isolated in the same ratio as that of the precursors **20** and **21** (i.e., **22**:**23** and **24**:**25** = ca. 1.25:1). The individual mixtures of **22a/23a**, **22b/23b**, **24a/25a**, and **24b/25b** were converted in the usual way into the corresponding mixtures of 2*H*-thiopyran isomers **26a/27a**, **26b/27b**, **28a/29a**, and **28b/29b**, respectively.

The preparation of 2*H*-thiopyrans with an activated dienophile attached at C-2 and C-6 is outlined in Scheme 4.[6] Conjugate addition of the Grignard reagent prepared from 2-(3-bromopropyl)-1,3-dioxolane to **32** (22) gave **33** in good yield. Hydrolysis and Wittig reaction of **33**, as described above, gave a separable 1.8:1 mixture of **34** and **35**, respectively. Oxidation of **34** with NCS gave **36** and **37** (2:1); a similar oxidation of **35** provided **38** and **39** (1.5:1). The IMDA substrates **40**–**43** were prepared by reaction of TIPSOTf with **36**–**39**, respectively.

The trienes **26**–**29** and **40**–**43** were produced in near quantitative yield as judged by ^1H NMR immediately after work-up; however, they were used immediately without further purification because of instability. In general, these IMDA substrates were highly prone to oxidation and were readily converted to the corresponding 4*H*-thiopyran-4-ones (i.e., **30**, **31**, **44**) upon heating in solution (or even on standing, especially neat). In the presence of BHT (4, 5), degassed solutions of the trienes at elevated temperatures were relatively stable towards oxidation for several days. The results of attempted IMDA reactions of **26**–**29** and **40**–**43** are presented in Table 1.

A C_6D_6 solution of a 1.2:1 mixture of **26a/27a** containing BHT (0.15 equiv.) was heated at 140°C. After 96 h, the ^1H NMR spectrum of the reaction mixture indicated the absence of **27a** and the presence of two products along with **26a** and a small amount of **30a**. Product isolation was facilitated by treatment of the crude reaction mixture with $HF_{(aq)}$ to hydrolyze the silyl enol ethers. The two IMDA adducts **45** and **46** were obtained in 55% and 43% yields, respectively (based on **23a**). In light of these results, analysis of the ^1H NMR spectrum of the mixture of **26a/27a** obtained by treatment of **22a/23a** with TIPSOTf (1.2 equiv.) in the presence of Et_3N revealed the presence of a small amount (<10%) of the same two products observed above and indicated that TIPSOTf alone could promote the IMDA reaction.[7] Reaction of the mixture of **22a/23a** with TIPSOTf (2 equiv.) for 2 h followed by HF work-up gave **45** (44%) and **46** (42%) in good yield (based on **23a**) in addition to recovered **22a** (81% based on **22a**). Similar results were obtained in a Lewis acid catalyzed reaction. Addition of $EtAlCl_2$ (0.4 equiv.) to a C_6D_6 solution of a 1.2:1 mixture of **26a/27a** resulted in consumption of **26a** within 3 min (^1H NMR) and **45** (38%) and **46** (34%) were isolated in 38% and 34% yields, respectively, after HF work-up and chromatography. Heating a 1.2:1 mixture of **28a/29a** as above (140°C, 96 h) gave the IMDA adducts **47** (70%) and **48** (10%). However, reactions promoted by TIPSOTF or $EtAlCl_2$ gave product mixtures and yields similar to those obtained from **26a/27a**, indicating that isomerization of the dienophile occurs faster than IMDA reaction under these conditions.[8]

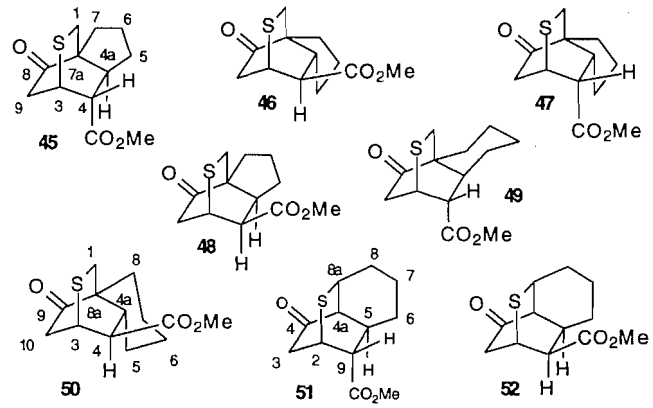

Because of the short tether length and enforced unfavorable regiochemistry, type II IMDA adducts from **26a** (and **28a**) were not expected (27). However, Diels–Alder adducts could, in principle, be derived from **26a** by initial rearrangement to **27a** by a [1,5] sigmatropic H migration (or other mechanism).[9] To test this possibility, isomerically pure **26a** was prepared from **22a** recovered from the TIPSOTf mediated IMDA reaction of the **26a/27a** mixture. No IMDA adducts were detected after heating a C_6D_6 solution of **26a** containing BHT (0.15 equiv.) at 140°C for 4 days. Further heating up to 180°C only resulted in extensive decomposition. Similarly, treatment of **26a** with $EtAlCl_2$ failed to produce any IMDA adduct.

[7] For examples of silyl triflate mediated Diels–Alder reactions see ref. 26.

[8] **47** was shown to be stable to the $EtAlCl_2$ reaction conditions.

[9] For an example of isomerization of 2*H*-thiopyrans under similar conditions, see ref. 5.

Table 1. Attempted IMDA reactions of 4-(triisopropylsilyl)oxy-2*H*-thiopyran dienes.

Entry	Substrate(s)	Conditions[a]	IMDA adduct(s) (% yield)[b]
1.	**6a/7a** or **6b/7b**	Thermal (150–200°C)	None
	13a or **13b**		None
	14a or **14b**		None
2.	**26a/27a** (1.2:1)	Thermal (140°C, 96 h)	**45** (55), **46** (43)
		TIPSOTf (2 h)	**45** (44), **46** (42)
		$EtAlCl_2$ (3 min)	**45** (38), **46** (34)
3.	**26b/27b** (1.3:1)	Thermal (140–180°C)	None[c]
		TIPSOTf (24 h)	None
		$EtAlCl_2$ (30 min)	**49** (40), **50** (15)
4.	**27b**	Thermal (170°C, 60 h)	**49** (37), **50** (14)
		$EtAlCl_2$ (30 min)	**49** (48), **50** (19)
5.	**28a/29a** (1.2:1)	Thermal (140°C, 96 h)	**47** (70), **48** (10)
		TIPSOTf (24 h)	**45** (44), **46** (43)
		$EtAlCl_2$ (3 min)	**45** (34), **46** (27), **47** (30), **48** (trace)[d]
6.	**28b/29b** (1.3:1)	Thermal (140–180°C)	None
		TIPSOTf (24 h)	None
		$EtAlCl_2$ (30 min)	**49** (ca. 25%)[e]
7.	**40**	Thermal (140–180°C)	None
		TIPSOTf (24 h)	None
		$EtAlCl_2$ (30 min)	None
8.	**41**	Thermal (175°C, 17 h)	**51** (86)
		TIPSOTf (13 h)	**51** (17)
		$EtAlCl_2$ (7 h)	**51** (34)
9.	**42**	Thermal (140–180°C)	None
		TIPSOTf (24 h)	None
		$EtAlCl_2$ (30 min)	None
10.	**43**	Thermal (180–210°C, 17 h)	**51** (30), **52** (33)
11.	**62a** or **62b**	Thermal (80–180°C)	None
		$EtAlCl_2$ (30 min)	None
12.	**63a** or **63b**	Thermal (80–180°C)	None
		$EtAlCl_2$ (30 min)	None

[a]See experimental section.
[b]Isolated yield based on the appropriate starting enone.
[c]This result likely due to inefficient deoxygenation (see text).
[d]Detected by ^1H NMR but not isolated.
[e]This compound was not pure; other isomers, if present, were not isolated.

Disappointingly, the expected IMDA adducts were not detected after heating C_6D_6 solutions of 1.3:1 mixtures of **26b/27b** or **28b/29b** at 140–180°C over several days. Only the oxidation products **30b** and **31b** were isolated after the usual HF work-up. Alternatively, $EtAlCl_2$ mediated reaction of a similar mixture of **26b/27b** gave **49** and **50** in 40% and 15% yields, respectively (based on **23b**). Similar treatment of **28b/29b** also produced **49** (ca. 25%) but any isomeric adducts, if present, could not be isolated. No IMDA adducts were detected or isolated after individual treatment of **22b/23b** or **24b/25b** with excess TIPSOTf in the presence of Et_3N even after prolonged reaction times (24 h). To clarify the IMDA reactivity of **27b**, a selective synthesis of **23b** was undertaken using our newly developed protocol (9). Thus, tin hydride mediated addition of **55** (28) to **54** gave **23b** directly in 45% yield (Scheme 5). Heating a degassed C_6D_6 solution of **27b** (prepared from **23b**) in a preheated oil bath at 170°C for 60 h resulted in the completed disappearance of **27b** and the adducts **49** and **50** were isolated in 37% and 14% yield, respectively, after HF work-up. The previous failure of a mixture of **26b/27b** to produce the same adducts under similar conditions is attributed to inefficient deoxygenation of the reaction solution, resulting in an increased rate of oxidation of the trienes at the expense of IMDA reaction. Treatment of **27b** with $EtAlCl_2$ gave **49** (48%) and **50** (19%) in a similar ratio and yield as previously obtained from a mixture of **26b/27b**.

Attempted IMDA reaction of **40** under thermal (140–180°C, several days), $EtAlCl_2$, or TIPSOTf mediated conditions led only to decomposition. Similar results were obtained with **42**. Alternatively, **41** gave **51** as the only product after heating at 175°C for 17 h. The same product was obtained from **41** under Lewis acid mediated conditions. Thermal reaction of **43** is slow at 175°C and heating up to 210°C gave **52** (33%) along with **51** (30%). The formation of **51** in this reaction is due to competitive isomerization of **43** to **41** under the reaction conditions.

Scheme 5.

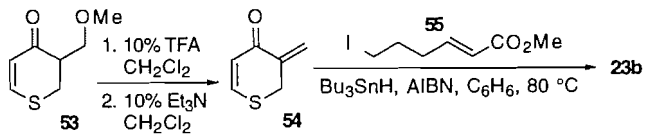

Scheme 6.

a: 2-Mercaptoethanol, NaH, THF; *b*: acryloyl choride or methyl fumaryl chloride, pyridine, CH_2Cl_2; *c*: NCS, CCl_4; *d*: TIPSOTf, Et_3N.

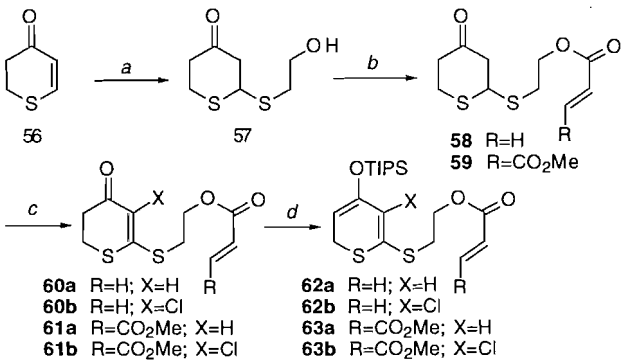

The failure of **40** and **42** to produce adducts (cf. **27**, **29**) is presumably the result of the unfavorable regiochemistry enforced by the short tether, thereby increasing the activation energy for IMDA reaction and precluding cycloaddition in favor of other pathways. To examine the possibility of effecting IMDA reaction of a C-6 tethered substrate that would allow favorable regiochemistry, compounds **62** and **63** were prepared according to Scheme 6. Addition of 2-mercaptoethanol to **56** (19) produced **57**, which was acylated with acryloyl chloride or methyl fumaryl chloride to give the unstable[10] **58** and **59**, respectively. Individual treatment of **58** and **59** with NCS produced a mixture[11] of **60a,b** and **61a,b**, respectively, which were converted into the corresponding 2*H*-thiopyrans by reaction with TIPSOTf. Adducts from IMDA reaction of **62a** and **63a** would be synthetically equivalent (via desulfurization) to adducts from an analogous intermolecular Diels–Alder reaction. Thus 2-mercaptoethanol represents a potential temporary tether of the diene to the dienophile.[12] Unfortunately, all attempts to effect IMDA reaction of **62** and **63** under thermal (in C_6D_6 or $(CD_3)_2SO$)[13] or $EtAlCl_2$ mediated conditions failed to produce any adducts. Presumably the 5-atom tether, the preference for an s-*trans* ester conformation (30),

[10] These compounds were very prone to elimination to give **56** and other by-products.

[11] Chlorination under these conditions is precedented (20).

[12] For a review of the use of silicon-based temporary tethers in IMDA reactions, see ref. 29.

[13] For a review of solvent effects in IMDA reactions see ref. 30.

Fig. 2. Typical $^3J_{(HH)}$ and $^4J_{(HH)}$ coupling constants for 2*H*-thiopyran Diels–Alder adducts.

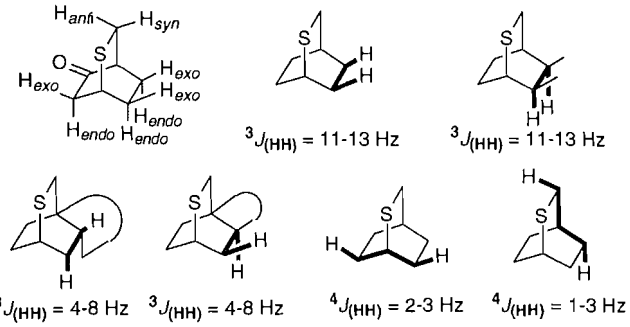

and the instability of **62** and **63** combine to favor other pathways in competition with IMDA reaction.

The IMDA adducts[14] **45–52** were identified on the basis of their spectroscopic properties (IR, MS, ^1H and ^{13}C NMR). In all cases, the spectral data were fully consistent with the proposed structure. In general, spectral features (especially ^1H and ^{13}C NMR) for **45–52** were similar to those from adducts obtained by intermolecular Diels–Alder reactions of 4-(triisopropylsilyl)oxy-2*H*-thiopyran with acrylate and crotonate dienophiles (7). Stereochemical assignments were based on the previously established trends (5, 7) in the $^3J_{HH}$ and $^4J_{HH}$ coupling constants outlined in Fig. 2.

Desulfurization of the IMDA adducts can potentially provide synthetically useful compounds. For example, *trans*-fused angularly methylated hydrindans (**64**) and decalins (**65**) are available by reactions of the *endo* adducts **45** and **49**, respectively, with Raney nickel (see Scheme 7). The synthetic utility of such a process will be dependent on the degree to which the diastereoselectivity (i.e., *endo* vs. *exo*) of the IMDA reaction can be controlled. Interestingly, the *endo* selectivities in the reactions of **27a** (ca. 1.1:1) and **27b** (ca. 2.5:1) are essentially independent of the reaction conditions (i.e., thermal vs. Lewis acid mediated) and are lower than **29a** (7:1).[15] As expected, only a single isomer results from cycloaddition of **41** and **43**.

[14] In principle, the same products could result from sequential Michael reactions (31). We favor a IMDA mechanism at present, because in no case have we detected or isolated the putative products from the "initial" Michael reaction. For a discussion see ref. 7.

[15] For comparison, the uncatalyzed intermolecular Diels–Alder reaction between 4-(triisopropylsilyl)oxy-2*H*-thiopyran and methyl acrylate is slightly *endo* selective (ca. 1.7:1); no adduct was obtained with methyl crotonate (7). Under Lewis acid mediated conditions (7), the reaction is *exo* selective with both methyl acrylate (1–1.6:1) and a crotonate derivative (2.5:1). In comparison to IMDA reactions of related acyclic dienes, thermal IMDA reactions of the methyl esters of (2*Z*,7*E*)- and (2*E*,7*E*)-2,7,9,-decatrienoic acids (i.e., C_3 tether) are unselective and the *endo* stereoselectivity for cycloaddition of the (2*E*,7*E*) isomer (but not the (2*Z*,7*E*) isomer) increases dramatically with Lewis acid catalysis (32*a*). Similarly, the uncatalyzed IMDA reactions (2*Z*,8*E*)- and (2*Z*,8*E*)-2,8,10-undecatrienoates (i.e., C_4 tether) are also unselective but the *endo* stereoselectivity for both isomers increases to ca. 9:1 under $EtAlCl_2$ mediated conditions (32*b*).

Scheme 7.

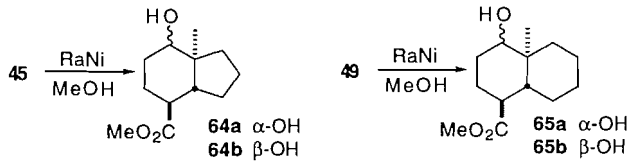

In conclusion, we have systematically investigated the IMDA reactions of derivatives of 4–(triisopropylsilyl)oxy-2*H*-thiopyran with potential dienophiles tethered at the C-2, C-3, C-5, and C-6 positions. Cycloaddition was only observed when dienophiles activated by a carbomethoxy group were employed. Compounds having the dienophile attached to C-2 with a C_3 tether gave adducts with high stereoselectivity. Substrates having the dienophile attached to C-3 via a C_3 or C_4 tether cyclized smoothly. With an (*E*)-enoate as the dienophile, the stereoselectivity was poor (*endo*:*exo* = 1.1–2.5:1) and essentially independent of reaction conditions (i.e., thermal vs. Lewis acid mediated). With the (*Z*)-enoate, a 7:1 mixture of *endo*:*exo* IMDA adducts was obtained under thermal conditions; with Lewis acid catalysis, isomerization of the dienophile was competitive with cycloaddition. Type II IMDA adducts were not observed with C-5 tethered substrates. Compounds having the dienophile attached to C-6 via a C_3 or a 5-atom tether also failed to give IMDA adducts. No evidence for isomerization of the 2*H*-thiopyran derivatives by [1,5] sigmatropic rearrangement was observed. The *endo* adducts obtained from the C-3 tethered substrates can be desulfurized to obtain synthetically useful *trans*-fused angularly methylated hydrindans and decalins.

Experimental

General methods

All solvents were distilled prior to use. Pyridine and Et_3N were distilled from CaH_2 and stored over KOH pellets. Anhydrous solvents were distilled under argon as follows: DMSO and DMF from CaH_2 under reduced pressure (10–15 Torr; 1 Torr = 133.3 Pa) and stored over 3Å molecular sieves; ether and tetrahydrofuran (THF) from benzophenone potassium ketyl; benzene, toluene, and CH_2Cl_2 from P_2O_5 and stored over 3Å molecular sieves; MeOH from $Mg(OMe)_2$. Benzene solutions were degassed by bubbling argon through the solvent (solution) followed by three freeze–thaw cycles under high vacuum (0.01 Torr). Unless otherwise noted, reactions were carried out under an atmosphere of argon and reaction temperatures refer to the bath. Concentration refers to removal of volatiles at water aspirator pressure on a rotary evaporator.

Preparative TLC was carried out on glass plates (20 × 20 cm) precoated (0.25 mm) with silica gel 60 F_{254}. Materials were detected by visualization under an ultraviolet lamp (254 nm) and (or) by treating a 1 cm vertical strip removed from the plate with a solution of phosphomolybdic acid (5%) containing a trace of ceric sulfate in aqueous sulfuric acid (5% v/v), followed by charring on a hot plate. Flash column chromatography (FCC) was performed according to Still et al. (33) with Merck Silica Gel 60 (40–63 μm). Medium pressure chromatography (MPC) was performed with minor modifications of the procedure reported by Taber (34). All mixed solvent eluents are reported as v/v solutions.

Spectral data

High-resolution (HRMS) spectra (exact mass measurement) were obtained on a double focussing VG 70E instument. Low-resolution mass spectra (LRMS) were recorded on a VG-70E or a single sectored, magnetic scanning MS-12. EI ionization was accomplished at 70 eV and CI at 50 eV with ammonia or isobutane as the reagent gas; only partial data are reported. IR spectra were recorded on a Fourier transform interferometer using a diffuse reflectance cell; only diagnostic peaks are reported. Unless otherwise noted, NMR spectra were measured in $CDCl_3$ solution at 300 MHz for ^1H and 75 MHz for ^{13}C. For ^1H NMR, residual $CHCl_3$ in $CDCl_3$ was employed as the internal standard (7.26 δ); for ^{13}C NMR, $CDCl_3$ was employed (77.0 δ). The ^1H NMR chemical shifts and coupling constants were determined assuming first-order behavior. Multiplicity is indicated by one or more of the following: s (singlet), d (doublet), t (triplet), q (quartet), m (multiplet), br (broad), ap (apparent); the list of coupling constants (*J*) corresponds to the order of the multiplicity assignment. ^1H NMR spectra were normally obtained with a digital resolution of 0.244 Hz/pt (sweep width = 4000 Hz, FID = 32 K data points) and coupling constants are reported to the nearest 0.5 Hz. The ^1H NMR assignments were made on the basis of chemical shift and multiplicity and were confirmed, where necessary, by homonuclear decoupling and (or) NOE experiments. The multiplicity of ^{13}C NMR signals refers to the number of attached H's (i.e., s = C, d = CH, t = CH_2, q = CH_3) and was determined by *J*-modulation (35). The ^{13}C assignments were made on the basis of chemical shift, multiplicity, and consistency within a series of similar structures. Assignments for ^{13}C signal of the same multiplicity and similar chemical shift (i.e., $\Delta\delta < 1$ ppm) are tentative. Elemental analyses were performed using a Perkin–Elmer 2400 CHN elemental analyzer.

Materials

Compounds **1** (15), **8** (21), **17** (22), **32** (22), **55** (28), **56** (19), 5-bromopentene (17), 6-bromohexene (17), 2-(3-bromopropyl)-1,3-dioxolane (23), 2-(4-bromobutyl)-1,3-dioxolane (24), 4-[(trimethylsilyl)oxy]-2*H*-thiopyran (5), and methyl fumaryl chloride (36) were prepared as reported. All other reagents were commercially available and, unless otherwise noted, were used as received.

*General procedure for alkylation of **1** and **17** (16)*

NaH (1.2 equiv.) was added to a solution of NaI (1.0 equiv.) and the β-ketoester **1** or **17** in acetone (5 mL/mmol of β-ketoester). After stirring for 5 min at room temperature (rt), the alkyl halide (3 equiv.) was added and the reaction mixture was heated under reflux for 24 h. The resulting mixture was diluted with H_2O, extracted with CH_2Cl_2 (×3), and the combined organic layers were dried over Na_2SO_4, concentrated, and fractionated by FCC to give the products **2** or **18**.

*General procedure for decarboxylation of **2** and **9** (16b)*

LiI (3 equiv.) was added to a solution of the β-ketoester in 20% (v/v) aqueous DMF (6 mL/mmol of β-ketoester) and the reaction mixture was heated under reflux until the starting material was consumed (3–5 days). The cooled (rt) reaction

mixture was diluted with CH_2Cl_2 and washed with water. The aqueous layer was extracted with CH_2Cl_2 (×2) and the combined organic layers were dried over Na_2SO_4, concentrated, and fractionated to give the products.

General procedure for decarboxylation of ***18*** *and the product from conjugate addition to* ***32*** *(22)*

A solution of tetrakis(triphenylphosphine)palladium(0) (0.05 equiv.), morpholine (10 equiv.), and the allyl β-ketoester in THF (8 mL/mmol of β-ketoester) was stirred at rt for 24 h. The reaction mixture was concentrated and fractionated to give the products.

General procedure for dehydrogenation of ***3, 10, 19, 34,*** *and* ***35*** *(19, 20)*

NCS (1.00 equiv.) was added to a stirred solution of the substrate and pyridine (1.05 equiv.) in CH_2Cl_2 (20 mL/mmol of substrate). After stirring for 10–30 min, the reaction mixture was washed with water, dried over Na_2SO_4, concentrated, and fractionated by FCC to give the products.

General procedure for conjugate addition to ***8*** *and* ***32*** *(21)*

A solution of the alkyl bromide (2.0 equiv.) in THF (1 mL/mmol of bromide) was added to a stirred suspension of Mg turnings (2.2 equiv.) in THF (2 mL/mmol of bromide) and the resulting mixture was heated under reflux for 90 min (on occasion I_2 crystals were added to initiate the reaction) and then was allowed to cool to rt.

Dimethyl sulfide (1.3 mL/mmol of CuI) was added dropwise over 5 min to a suspension of CuI (2.1 equiv.) in THF (0.65 mL/mmol of CuI) at −23°C. The resulting mixture was cooled to −78°C, and the Grignard reagent prepared above was added dropwise over 5 min. After 1.5 h, a solution of **8** or **32** in dimethyl sulfide (2 mL/mmol of ketoester) was added dropwise over a 10 min period. The reaction mixture was stirred at −78°C for 1.5 h and then was diluted with ether, warmed to 0°C, washed with $NH_4Cl_{(aq)}$ and with H_2O, dried over Na_2SO_4, concentrated, and fractionated to give the products.

General procedure for Wittig homologation of ***21*** *and* ***33***

A solution of the acetal and $HClO_4$ (0.3 M, 3 equiv.) in acetone (50 mL/mmol of acetal) was stirred at rt for 48 h. Half-saturated $NaHCO_{3(aq)}$ (ca. 1 mL) was added and most of the acetone was evaporated at reduced pressure. The resulting mixture was diluted with H_2O, extracted with CH_2Cl_2 (×2), and the combined organic layers were dried over Na_2SO_4 and concentrated to give a crude aldehyde(s) (^{1}H NMR). Methyl (triphenylphosphoranylidene)acetate (1.2 equiv.) was added to the solution of crude aldehyde(s) in MeOH (20 mL/mmol of acetal). After stirring for 3.5 h, the reaction mixture was concentrated and fractionated to give the *E* and *Z* enoates (ca. 1.5–2:1).

General procedure for preparation of 4-[tris(2-methylethyl)silyl]oxy-2H-thiopyrans

TIPSOTf (1.2 equiv.) was added to a solution of the enone and Et_3N (2.4 equiv.) in CH_2Cl_2 (ca. 10 mL/mmol of enone). The reaction was monitored by TLC and, when the enone was completely consumed (typically 10–20 min), the reaction mixture was diluted with CH_2Cl_2, washed with saturated $NaHCO_{3(aq)}$, dried over Na_2SO_4, concentrated, and placed under high vacuum (ca. 0.1 Torr) for 2 h. The crude products were characterized by ^{1}H NMR, which, in each case, indicated essentially complete conversion of the enone to the silyloxy diene(s). The dienes were unstable (especially neat) and were used directly without further purification.

General procedure for Diels–Alder reactions

Thermal reaction: A solution of the crude silyloxy diene(s) (0.1–0.2 mmol) and BHT (0.15 equiv.) in C_6D_6 or $C_6D_5CD_3$ (1 mL) was degassed by several freeze–thaw cycles and sealed under vacuum in an NMR tube. The mixture was heated in an oil bath and the progress of the reaction was monitored by ^{1}H NMR. When the diene was consumed, the reaction mixture was concentrated and the residue was dissolved in CH_3CN (2 mL) and HF (48–51% aqueous solution; 70 μL) was added. After stirring for 5 min, the reaction mixture was diluted with CH_2Cl_2, washed with saturated $NaHCO_{3(aq)}$, dried over Na_2SO_4, concentrated, and fractionated to give the products.

Lewis acid catalyzed reaction: $EtAlCl_2$ (1 M solution in hexanes, 0.4–1 equiv.) was added to a solution of the silyloxy diene(s) (0.1–0.2 mmol) in C_6D_6 or CH_2Cl_2 (1–2 mL) at rt. After a suitable reaction time, the mixture was diluted with CH_2Cl_2, washed with saturated $NaHCO_{3(aq)}$, dried over Na_2SO_4, and concentrated. The residue was dissolved in CH_3CN (2 mL) and HF (48–51% aqueous solution; 70 μL) was added. After stirring for 5 min, the reaction mixture was diluted with CH_2Cl_2, washed with saturated $NaHCO_{3(aq)}$, dried over Na_2SO_4, concentrated, and fractionated to give the products.

TIPSOTf catalyzed reaction: In this case the general procedure for the preparation of the silyloxy dienes was followed except 1.5–2.0 equiv. of TIPSOTf was used. After stirring for several hours, the reaction mixture was diluted with CH_2Cl_2, washed with saturated $NaHCO_{3(aq)}$, dried over Na_2SO_4, and concentrated. The residue was dissolved in CH_3CN (2 mL) and HF (48–51% aqueous solution; 70 μL) was added. After stirring for 5 min, the reaction mixture was diluted with CH_2Cl_2, washed with saturated $NaHCO_{3(aq)}$, dried over Na_2SO_4, concentrated, and fractionated to give the products.

IMDA reaction of ***26a/27a***

IMDA adducts were obtained after PTLC (0.8% MeOH in CH_2Cl_2). Thermal reaction of a 1.2:1 mixture of **26a** and **27a** (prepared from a 1.2:1 mixture of **22a** and **23a**; 37.8 mg, 0.157 mmol) at 140°C for 96 h gave **45** (9.3 mg, 55%) and **46** (7.4 mg, 43%). Lewis acid catalyzed reaction of a similar mixture of **26a** and **27a** (prepared from a 1.2:1 mixture of **22a** and **23a**; 55 mg, 0.23 mmol) for 10 min gave **45** (9.4 mg, 38%) and **46** (8.5 mg, 34%). TIPSOTf catalyzed reaction (2 h) of a 1.2:1 mixture of **22a** and **23a** (24 mg, 0.1 mmol) gave **45** (4.8 mg, 44%) and **46** (4.5 mg, 42%). In each case a fraction containing a mixture of **22a** and **30a** (^{1}H NMR), which could be further purified, was obtained.

IMDA reaction of ***28a/29a***

IMDA adducts were obtained after PTLC (50% ether in hexane). Thermal reaction of a 1.2:1 mixture of **28a** and **29a** (pre-

pared from a 1.2:1 mixture of **24a** and **25a**; 18 mg, 0.075 mmol) at 140°C for 96 h gave **47** (5.7 mg, 70%) and **48** (0.8 mg, 10%). Lewis acid catalyzed reaction of a similar mixture of **28a** and **29a** (prepared from a 1.2:1 mixture of **24a** and **25a**; 22 mg, 0.092 mmol) for 10 min gave **45** (3.4 mg, 34%), **47** (3.0 mg, 30%), and **46** (2.7 mg, 27%). TIPSOTf catalyzed reaction (24 h) of a 1.2:1 mixture of **24a** and **25a** (14.6 mg, 0.061 mmol) gave **45** (2.9 mg, 44%) and **46** (2.8 mg, 43%). In each case a fraction containing a mixture of **22a** (**24a** in the thermal reaction) and **30a** (**31b** in the thermal reaction) (^{1}H NMR) was obtained but not further purified.

*IMDA reaction of **27b***

IMDA adducts were obtained after FCC (20–75% EtOAc in hexane). Thermal reaction **27b** (prepared from **23b**; 58 mg, 0.23 mmol) at 170°C for 60 h gave **49** (23 mg, 40%) and **50** (8 mg, 14%) along with **23b** (11 mg, 19%) and **30b** (11 mg, 19%). Lewis acid catalyzed reaction of **27b** (prepared from **23b**; 13 mg, 0.041 mmol) for 30 min gave **49** (5 mg, 48%) and **50** (2 mg, 19%) along with **23b** (2 mg, 19%) and **30b** (0.8 mg, 8%). A similar reaction of a 1.3:1 mixture of **26b** and **27b** (prepared from a 1.3:1 mixture of **22b** and **23b**; 46 mg, 0.181 mmol) for 30 min gave **49** (8 mg, 40%) and **50** (3 mg, 15%). No adducts were obtained in TIPSOTf catalyzed reactions.

*IMDA reaction of **28b** and **29b***

No adducts were obtained from attempted thermal or TIPSOTf catalyzed reactions of a 1.3:1 mixture of **28b** and **29b**. A $EtAlCl_2$ mediated reaction of a 1.3:1 mixture of **28b** and **29b** (prepared from a 1.3:1 mixture of **24b** and **25b**; 23 mg, 0.089 mmol) for 30 min gave **49** (3 mg, slightly impure; ca. 25%) after fractionation (PTLC; 50% ether in hexane). Other isomers, if present, could not be isolated. Fractionation (PTLC; 50% ether in hexane) of an attempted thermal reaction of a 1.3:1 mixture of **28b** and **29b** yielded a 1:1 mixture of **30b** and **31b**.

*IMDA reaction of **41***

IMDA adducts were obtained after PTLC (50% ether in hexane). Thermal reaction of **41** (prepared from **37**; 11 mg, 0.046 mmol) at 175°C for 17 h gave **51** (9.5 mg, 86%). Lewis acid catalyzed reaction of **41** (prepared from **37**; 11.8 mg, 0.049 mmol) for 30 min gave **51** (8.1 mg, 68%). TIPSOTf catalyzed reaction (13 h) of **37** (11.8 mg, 0.049 mmol) gave **51** (2 mg, 17%).

*IMDA reaction of **43***

IMDA adducts were obtained after PTLC (1% MeOH in CH_2Cl_2). Thermal reaction of **43** (prepared from **39**; 21.6 mg, 0.090 mmol) at 180°C for 9 h and 210°C for 11 h gave **52** (7.2 mg, 33%) and **51** (6.5 mg, 30%). Due to the previously established propensity for isomerization of the enoates, Lewis acid mediated IMDA reactions were not attempted.

*Methyl tetrahydro-4-oxo-3-(4-pentenyl)-4*H*-thiopyran-3-carboxylate (**2a**)*: 192 mg (48%) from **1** (261 mg, 1.50 mmol) after FCC (25% ether in hexane): IR ν_{max}: 3075, 1729, 1712, 1201 cm^{-1}; ^{1}H NMR δ: 5.75 (1H, dddd, J = 6.5, 6.5, 10.5, 17 Hz, HC-4′), 5.00 (1H, br d, J = 17 Hz, HC-5′), 4.95 (1H, br d, J = 10.5 Hz, HC-5′), 3.77 (3H, s, H_3CO), 3.27 (1H, dd, J = 3, 13.5 Hz, HC-2), 3.00–2.75 (4H, m, HC-5, HC-6), 2.71 (1H, d, J = 13.5 Hz, HC-2), 2.04 (2H, ap dt, J = 6.5, 6.5 Hz, HC-3′), 1.92 (1H, ap dt, J = 4.5, 13.5 Hz, HC-1′), 1.64 (1H, ap dt, J = 4.5, 13.5 Hz, HC-1′), 1.42 (1H, ap dtt, J = 12, 4.5, 7 Hz, HC-2′), 1.21 (1H, ap dtt, J = 12, 4.5, 7 Hz, HC-2′); ^{13}C NMR δ: 205.3 (s, C-4), 171.5 (s, O=CO), 138.0 (d, C-4′), 115.0 (t, C-5′), 63.0 (s, C-3), 52.4 (q, CH_3O), 43.2 (t, C-5), 38.6 (t, C-1′), 33.9 (t, C-2), 33.9 (t, C-3′), 30.8 (t, C-6), 23.8 (t, C-2′); LRMS (CI, NH_3), *m/z* (relative intensity): 260 ([M+18]$^+$, 100), 243 ([M+1]$^+$, 85), 192 (12), 173 (16).

*Methyl 3-(5-hexenyl)-tetrahydro-4-oxo-4*H*-thiopyran-3-carboxylate (**2b**)*: 185 mg (42%) from **1** (300 mg, 1.72 mmol) after FCC (25% ether in hexane): IR ν_{max}: 3074, 1730, 1712, 1201 cm^{-1}; ^{1}H NMR δ: 5.77 (1H, ap ddt, J = 10.5, 17, 6.5 Hz, HC-5′), 4.95 (2H, m, HC-6′), 3.77 (3H, s, H_3CO), 3.28 (1H, dd, J = 2.5, 14 Hz, HC-2), 3.00–2.75 (4H, m, HC-5, HC-6), 2.71 (1H, d, J = 14 Hz, HC-2), 2.08–1.98 (2H, m, HC-4′), 1.98–1.86 (1H, m, HC-1′), 1.70–1.60 (1H, m, HC-1′), 1.45–1.10 (4H, m, HC-2′, HC-3′); ^{13}C NMR δ: 205.4 (s, C-4), 171.5 (s, O=CO), 138.6 (d, C-5′), 114.6 (t, C-6′), 63.0 (s, C-3), 52.4 (q, CH_3O), 43.2 (t, C-5), 38.6 (t, C-1′), 34.2 (t, C-2), 33.4 (t, C-4′), 30.8 (t, C-6), 29.1 (t, C-3′), 24.0 (t, C-2′); LRMS (CI, NH_3), *m/z* (relative intensity): 274 ([M+18]$^+$, 100), 257 ([M+1]$^+$, 84), 173 (24).

*Tetrahydro-3-(4-pentenyl)-4*H*-thiopyran-4-one (**3a**)*: 41 mg (29%) from **2a** (189 mg, 0.78 mmol) after FCC (35% ether in hexane): IR ν_{max}: 3074, 1715, 1424, 914 cm^{-1}; ^{1}H NMR δ: 5.76 (1H, ddt, J = 10, 17, 6.5 Hz, HC-4′), 5.03–4.90 (2H, m, HC-5′), 2.98–2.88 (3H, m, HC-2, H_2C-6), 2.74–2.60 (4H, m, HC-2, HC-3, H_2C-5), 2.04 (2H, ap dt, J = 6.5, 7 Hz, H_2C-3′), 1.90–1.82 (1H, m, HC-1′), 1.42–1.30 (3H, m, HC-1′, H_2C-2′); ^{13}C NMR δ: 210.4 (s, C-4), 138.3 (d, C-4′), 114.8 (t, C-5′), 52.9 (d, C-3), 43.8 (t, C-5), 35.9 (t, C-1′), 33.6 (t, C-3′), 31.0 (t, C-2), 28.9 (t, C-6), 26.2 (t, C-2′); LRMS (CI, NH_3), *m/z* (relative intensity): 202 ([M+18]$^+$, 100), 185 ([M+1]$^+$, 48), 116 (75).

*3-(5-Hexenyl)tetrahydro-4*H*-thiopyran-4-one (**3b**)*: 57 mg (48%) from **2b** (154 mg, 0.60 mmol) after FCC (35% ether in hexane): IR ν_{max}: 3016, 1707, 1464, 965 cm^{-1}; ^{1}H NMR δ: 5.75 (1H, ddt, J = 10, 17, 6.5 Hz, HC-5′), 5.04–4.89 (2H, m, H_2C-6′), 2.98–2.88 (3H, m, H_2C-6, HC-2), 2.76–2.58 (4H, m, HC-2, HC-3, H_2C-5), 2.04 (2H, dt, J = 6.5, 7 Hz, H_2C-4′), 1.93–1.82 (1H, m, HC-1′), 1.44–1.24 (5H, m, HC-1′, H_2C-2′, H_2C-3′); ^{13}C NMR δ: 210.4 (s, C-4), 138.7 (d, C-5′), 114.5 (t, C-6′), 52.9 (d, C-3), 43.8 (t, C-5), 35.9 (t, C-1′), 33.5 (t, C-4′), 31.0 (t, C-2), 29.2 (t, C-6), 28.8 (t, C-3′), 26.4 (t, C-2′); LRMS (EI), *m/z* (relative intensity): 198 ([M]$^+$, 49), 180 (11), 116 (100), 95 (22), 88 (28).

*2,3-Dihydro-5-(4-pentenyl)-4*H*-thiopyran-4-one (**4a**) and 2,3-dihydro-3-(4-pentenyl)-4*H*-thiopyran-4-one (**5a**)*: 9.7 mg (46%; as a 1.2:1 mixture of **4a** and **5a**, respectively) from **3a** (21 mg, 0.12 mmol) after PTLC (50% ether in hexane): ^{1}H NMR δ for **4a**: 7.15 (1H, s, HC-6), 5.79 (1H, ddt, J = 10, 17, 6.5 Hz, HC-4′), 5.07–4.92 (2H, m, H_2C-5′), 3.19–3.13 (1H, m, HC-2), 2.77–2.71 (1H, m, HC-3), 2.29 (1H, ap t, J = 7.5 Hz, HC-1′), 2.14–2.00 (2H, m, HC-3′), 1.64–1.37 (2H, m, HC-2′); δ for **5a**: 7.35 (1H, d, J = 10 Hz, HC-6), 6.11 (1H, d, J = 10 Hz, HC-5), 5.79 (1H, ddt, J = 10, 17, 6.5 Hz, HC-4′), 5.07–4.92

(2H, m, H_2C-5′), 3.31 (1H, dd, J = 4, 13.5 Hz, HC-2), 3.05 (1H, dd, J = 9, 13.5 Hz, HC-2), 2.53 (1H, dddd, J = 4, 5.5, 8, 9 Hz, HC-3), 2.14–2.00 (2H, m, H_2C-3′), 1.86 (1H, dddd, J = 5.5, 5.5, 10.5, 13.5 Hz, HC-1′), 1.64–1.37 (3H, m, HC-1′, H_2C-2′); ^{13}C NMR δ for **4a**: 193.6 (s, C-4), 140.3 (d, C-6), 138.5 (d, C-4′), 134.8 (s, C-5), 114.7 (t, C-5′), 38.4 (t, C-3), 33.6 (t, C-3′), 30.8 (t, C-1′), 28.2 (t, C-2′), 27.3 (t, C-2); δ for **5a**: 196.2 (s, C-4), 145.1 (d, C-6), 138.2 (d, C-4′), 123.2 (d, C-3), 114.9 (t, C-5′), 45.1 (d, C-3), 33.3 (t, C-3′), 31.8 (t, C-1′), 27.6 (t, C-2), 26.3 (t, C-2′).

*5-(5-Hexenyl)-2,3-dihydro-4*H*-thiopyran-4-one (**4b**) and 3-(5′-hexenyl)-2,3-dihydro-4*H*-thiopyran-4-one (**5b**)*: 15.2 mg (71%; as a 1.2:1 mixture of **4b** and **5b**, respectively) from **3b** (22 mg, 0.11 mmol) after PTLC (50% ether in hexane): ^{1}H NMR δ for **4b**: 7.14 (1H, br s, HC-6), 5.79 (1H, ddt, J = 10, 17, 6.5 Hz, HC-5′), 5.04–4.90 (2H, m, H_2C-6′), 3.19–3.13 (2H, m, H_2C-2), 2.77–2.71 (2H, m, H_2C-3), 2.32–2.34 (2H, m, H_2C-1′), 2.11–2.00 (2H, m, H_2C-4′), 1.64–1.30 (4H, m, H_2C-2′, H_2C-3′); δ for **5b**: 7.35 (1H, d, J = 10 Hz, HC-6), 6.11 (1H, d, J = 10 Hz, HC-5), 5.79 (1H, ddt, J = 10, 17, 6.5 Hz, HC-5′), 5.04–4.90 (2H, m, HC-6′), 3.31 (1H, dd, J = 4, 13.5 Hz, HC-2), 3.04 (1H, dd, J = 8.5, 13.5 Hz, HC-2), 2.52 (1H, dddd, J = 4, 5.5, 8.5, 9 Hz, HC-3), 2.11–2.00 (2H, m, H_2C-4′), 1.90–1.80 (1H, m, HC-1′), 1.64–1.30 (5H, m, HC-1′, H_2C-2′, H_2C-3′); ^{13}C NMR δ for **4b**: 193.6 (s, C-4), 140.0 (d, C-6), 138.9 (d, C-5′), 135.0 (s, C-5), 114.4 (t, C-6′), 38.4 (t, C-3), 33.6 (t, C-4′), 31.1 (t, C-1′), 28.6 (t, C-3′), 28.5 (t, C-2′), 27.3 (t, C-2); δ for **5b**: 196.3 (s, C-4), 145.1 (d, C-6), 138.7 (d, C-5′), 123.1 (d, C-5), 114.6 (t, C-6′), 45.2 (d, C-3), 33.6 (t, C-4′), 31.7 (d, C-1′), 28.8 (t, C-3′), 27.9 (t, C-2), 26.4 (t, C-2′).

*4-[[Tris(1-methylethyl)silyl]oxy]-5-(4-pentenyl)-2*H*-thiopyran (**6a**) and 4-[[tris(1-methylethyl)silyl]oxy]-3-(4-pentenyl)-2*H*-thiopyran (**7a**)*

Obtained as a 1.2:1 mixture of **6a** and **7a** from a 1.2:1 mixture of **4a** and **5a**: ^{1}H NMR ($C_6D_5CD_3$) δ for **6a** (partial data): 5.87 (1H, s, HC-6), 5.78–5.68 (1H, m, HC-4′), 5.05–4.91 (2H, m, HC-5′), 4.62 (1H, t, J = 5.5 Hz, HC-3), 2.99 (2H, d, J = 5.5 Hz, HC-2); δ for **7a** (partial data): 5.95 (1H, d, J = 10 Hz, HC-6), 5.87 (1H, d, J = 10 Hz, HC-5), 5.78–5.68 (1H, m, HC-4′), 5.05–4.91 (2H, m, HC-5′), 3.01 (2H, s, HC-2).

*5-(5′-Hexenyl)-4-[[tris(1-methylethyl)silyl]oxy]-2*H*-thiopyran (**6b**) and 3-(5′-hexenyl)-4-[[tris(1-methylethyl)silyl]oxy]-2*H*-thiopyran (**7b**)*

Obtained as a 1.2:1 mixture of **6b** and **7b** from a 1.2:1 mixture of **4b** and **5b**: ^{1}H NMR ($C_6D_5CD_3$) δ for **6b** (partial data): 5.86 (1H, s, HC-6), 5.75–5.65 (1H, m, HC-5′), 5.01–4.87 (2H, m, HC-6′), 4.61 (1H, t, J = 5.5 Hz, HC-3), 2.99 (2H, d, J = 5.5 Hz, HC-2); δ for **7b** (partial data): 5.92 (1H, d, J = 10 Hz, HC-6), 5.84 (1H, d, J = 10 Hz, HC-5), 5.75–5.65 (1H, m, HC-5′), 5.01–4.87 (2H, m, HC-6′), 3.04 (2H, s, HC-2).

*Methyl tetrahydro-4-oxo-2-(4-pentenyl)-4*H*-thiopyran-3-carboxylate (**9a**)*: 310 mg (88%) from **8** (250 mg, 1.45 mmol) after FCC (20% EtOAc in hexane): IR ν_{max}: 3075, 1746, 1714, 1649, 1609 cm^{-1}; ^{1}H NMR (a 1:2 mixture of keto:enol tautomers) δ: 12.69 (0.7H, s, HO[enol]), 5.88–5.68 (1H, m, HC-4′), 5.04–4.91 (2H, m, HC-5′), 3.88 (2H, s, H_3CO[enol]), 3.88 (1H, s, H_3CO[keto]), 3.48–3.41 (1.3H, m, HC-2, HC-3[keto]), 3.02–2.80 (1.7H, m, H_2C-6[enol], HC-6[keto]), 2.70–2.43 (2.3H, m, H_2C-5, HC-6[keto]), 2.17–1.95 (2H, m, H_2C-3′), 1.77–1.39 (4H, m, H_2C-1′, H_2C-2′); ^{13}C NMR δ for keto form: 203.7 (s, C-4), 168.8 (s, OC=O), 137.7 (d, C-4′), 114.8 (t, C-5′), 64.5 (d, C-3), 52.1 (q, CH_3O), 45.7 (d, C-2), 42.4 (t, C-5), 32.8 (t, C-1′ or C-3′), 32.7 (t, C-3′ or C-1′), 26.6 (t, C-6), 25.7 (t, C-2′); δ for enol form: 172.5 (s, C-4), 171.6 (s, OC=O), 138.4 (d, C-4′), 114.3 (t, C-5′), 102.6 (s, C-3), 51.5 (q, CH_3O), 36.1 (d, C-2), 35.0 (t, C-5), 32.8 (t, C-3′), 30.5 (t, C-1′), 27.1 (t, C-2′), 19.8 (t, C-6); LRMS (EI), *m/z* (relative intensity): 242 ([M]$^+$, 21), 173 (73), 141 (77), 83 (100).

*Methyl 2-(5-hexenyl)tetrahydro-4-oxo-4*H*-thiopyran-3-carboxylate (**9b**)*: 190 mg (85%) from **8** (150 mg, 0.871 mmol) after FCC (20% EtOAc in hexane): IR ν_{max}: 3074, 1746, 1714, 1649, 1609 cm^{-1}; ^{1}H NMR (a 1:2 mixture of keto:enol tautomers) δ: 12.64 (0.7H, s, HO[enol]), 5.85–5.67 (1H, m, HC-5′), 5.01–4.88 (2H, m, H_2C-6′), 3.74 (2H, s, H_3CO[enol]), 3.74 (1H, s, H_3CO[keto]), 3.45–3.36 (1.3H, m, HC-2, HC-3[keto]), 3.00–2.77 (1.7H, m, H_2C-6[enol], HC-6[keto]), 2.67–2.41 (2.3H, m, H_2C-5, HC-6[keto]), 2.08–1.97 (2H, m, H_2C-4′), 1.74–1.28 (6H, m, H_2C-1′, H_2C-2′, H_2C-3′); ^{13}C NMR δ for keto form: 203.9 (s, C-4), 169.0 (s, OC=O), 138.5 (d, C-5′), 114.6 (t, C-6′), 64.8 (d, C-3), 52.3 (q, CH_3O), 46.0 (d, C-2), 42.7 (t, C-5), 33.4 (t, C-1′), 33.4 (t, C-4′), 28.3 (t, C-3′), 26.9 (t, C-6), 26.1 (t, C-2′); δ for enol form: 172.7 (s, C-4), 171.9 (s, OC=O), 138.9 (d, C-5′), 114.3 (t, C-6′), 102.9 (s, C-3), 51.7 (q, CH_3O), 36.4 (d, C-2), 35.6 (t, C-5), 33.7 (t, C-4′), 30.8 (t, C-1′), 28.2 (t, C-3′), 27.6 (t, C-2′), 20.0 (t, C-6); LRMS (EI), *m/z* (relative intensity): 256 ([M]$^+$, 12), 197 (24), 173 (62), 141 (62), 84 (100).

*Tetrahydro-2-(4-pentenyl)-4*H*-thiopyran-4-one (**10a**)*: 45 mg (33%) from **9a** (180 mg, 0.743 mmol) after by FCC (30% ether in hexane): IR ν_{max}: 3075, 1712, 1643 cm^{-1}; ^{1}H NMR δ: 5.77 (1H, dddd, J = 6.5, 6.5, 10.5, 17 Hz, HC-4′), 5.00 (1H, br d, J = 17 Hz, HC-5′), 4.96 (1H, br d, J = 10.5 Hz, HC-5′), 3.07 (1H, dddd, J = 3.5, 6.5, 6.5, 10.5 Hz, HC-2), 3.00–2.82 (2H, m, H_2C-6), 2.73 (1H, ddd, J = 1, 3.5, 14 Hz, HC-3), 2.68–2.55 (2H, m, H_2C-5), 2.43 (1H, dd, J = 10.5, 14 Hz, HC-3), 2.10–2.00 (2H, m, H_2C-3′), 1.65–1.45 (4H, m, H_2C-1′, H_2C-2′); ^{13}C NMR δ: 208.7 (s, C-4), 138.1 (d, C-4′), 115.0 (t, C-5′), 50.7 (t, C-3), 44.7 (d, C-2), 43.4 (t, C-5), 35.0 (t, C-1′), 33.3 (t, C-3′), 28.1 (t, C-6), 26.0 (t, C-2′); LRMS (EI), *m/z* (relative intensity): 184 ([M]$^+$, 40), 141 (39), 128 (52), 115 (100).

*2-(5-Hexenyl)tetrahydro-4*H*-thiopyran-4-one (**10b**)*: 87 mg (74%) from **9b** (142 mg, 0.554 mmol) after fractionation by FCC (30% ether in hexane): IR ν_{max}: 3075, 1713, 1640 cm^{-1}; ^{1}H NMR δ: 5.77 (1H, dddd, J = 6.5, 6.5, 10.5, 17.5 Hz, HC-5′), 4.99 (1H, br d, J = 17.5 Hz, HC-6′), 4.94 (1H, br d, J = 10.5 Hz, HC-6′), 3.06 (1H, dddd, J = 3.5, 6.5, 6.5, 10.5 Hz, HC-2), 3.00–2.82 (2H, m, H_2C-6), 2.73 (1H, ddd, J = 1, 3.5, 14 Hz, HC-3), 2.68–2.55 (2H, m, H_2C-5), 2.43 (1H, dd, J = 10.5, 14 Hz, HC-3), 2.10–2.00 (2H, m, H_2C-4′), 1.65–1.35 (6H, m, H_2C-1′, H_2C-2′, H_2C-3′); ^{13}C NMR δ: 208.7 (s, C-4), 138.6 (d, C-5′), 114.6 (t, C-6′), 50.7 (t, C-3), 44.7 (d, C-2), 43.4 (t, C-5), 35.5 (t, C-1′), 33.5 (t, C-4′), 28.5 (t, C-3′), 28.1 (t, C-6), 26.3 (t, C-2′); LRMS (CI, NH_3), *m/z* (relative intensity): 216 ([M + 18]$^+$, 100), 198 (36), 141 (19), 115 (24), 83 (28).

*2,3-Dihydro-6-(4-pentenyl)-4H-thiopyran-4-one (**11a**) and 2,3-dihydro-2-(4-pentenyl)-4H-thiopyran-4-one (**12a**)*

11a (13 mg, 40%) and **12a** (6 mg, 18%) were obtained from **10a** (33 mg, 0.18 mmol) after FCC (50% ether in hexane).

For **11a**: IR ν_{max}: 3075, 1655, 1571 cm^{-1}; ^1H NMR δ: 6.08 (1H, s, HC-5), 5.78 (1H, ap ddt, J = 10.5, 17, 7 Hz, HC-4′), 5.08–5.98 (2H, m, H_2C-5′), 3.19–3.14 (2H, m, H_2C-2), 2.67–2.62 (2H, m, H_2C-3), 2.39 (2H, ap t, J = 7 Hz, H_2C-1′), 2.10 (2H, ap dt, J = 7, 7 Hz, H_2C-3′), 1.70 (2H, ap tt, J = 7, 7 Hz, H_2C-2′); ^{13}C NMR δ: 144.3 (s, C-4), 164.6 (s, C-6), 137.5 (d, C-4′), 121.9 (d, C-5), 115.5 (t, C-5′), 37.6 (t, C-1′), 36.8 (t, C-3), 32.8 (t, C-3′), 27.8 (t, C-2 or C-2′), 27.4 (t, C-2 or C-2′); LRMS (EI), *m/z* (relative intensity): 182 ([M]$^+$, 73), 128 (100), 126 (45), 100 (100), 85 (64).

For **12a**: IR ν_{max}: 3075, 1661, 1548 cm^{-1}; ^1H NMR δ: 7.42 (1H, d, J = 10 Hz, HC-6), 6.16 (1H, d, J = 10 Hz, HC-5), 5.76 (1H, dddd, J = 7, 7, 10.5, 17 Hz, HC-4′), 5.05–4.95 (2H, m, H_2C-5′), 3.53–3.45 (1H, m, HC-2), 2.78 (1H, dd, J = 3.5, 16 Hz, HC-3), 2.58 (1H, dd, J = 11.5, 16 Hz, HC-3), 2.07 (2H, ap dt, J = 7, 7 Hz, H_2C-3′), 1.78–1.68 (2H, m, H_2C-1′), 1.58–1.47 (2H, m, H_2C-2′); ^{13}C NMR δ: 194.6 (s, C-4), 145.6 (d, C-6), 137.7 (d, C-4′), 123.4 (d, C-5), 115.3 (t, C-5′), 44.5 (t, C-3), 43.0 (d, C-2), 33.3 (t, C-1′ or C-3′), 33.2 (t, C-1′ or C-3′), 25.8 (t, C-2′); LRMS (EI), *m/z* (relative intensity): 182 ([M]$^+$, 22), 154 (82), 126 (35), 113 (78), 86 (100).

*6-(5-Hexenyl)-2,3-dihydro-4H-thiopyran-4-one (**11b**) and 2-(5′-hexenyl)-2,3-dihydro-4H-thiopyran-4-one (**12b**)*

11b (45 mg, 60%) and **12b** (15 mg, 20%) were obtained from **10b** (76 mg, 0.38 mmol) after FCC (60% ether in hexane).

For **11b**: IR ν_{max}: 3074, 1653, 1571 cm^{-1}; ^1H NMR δ: 6.08 (1H, s, HC-5), 5.78 (1H, ap ddt, J = 10.5, 17, 7 Hz, HC-5′), 5.06–4.96 (2H, m, H_2C-6′), 3.18–3.13 (2H, m, H_2C-2), 2.67–2.62 (2H, m, H_2C-3), 2.38 (2H, ap t, J = 7 Hz, H_2C-1′), 2.07 (2H, ap dt, J = 7, 7 Hz, H_2C-4′), 1.66–1.55 (2H, m, H_2C-2′), 1.48–1.38 (2H, m, H_2C-3′); ^{13}C NMR δ: 194.4 (s, C-4), 164.9 (s, C-6), 138.3 (d, C-5′), 121.7 (d, C-5), 114.9 (t, C-6′), 38.2 (t, C-1′), 36.8 (t, C-3), 33.3 (t, C-4′), 28.1 (t , C-2′), 28.1 (t, C-3′), 27.4 (t, C-2); LRMS (EI), *m/z* (relative intensity): 196 ([M]$^+$, 24), 167 (22), 141 (46), 128 (100), 100 (99).

For **12b**: IR ν_{max}: 3075, 1663, 1548 cm^{-1}; ^1H NMR δ: 7.42 (1H, d, J = 10 Hz, HC-6), 6.16 (1H, d, J = 10 Hz, HC-5), 5.78 (1H, dddd, J = 7, 7, 10.5, 17 Hz, HC-5′), 5.05–4.95 (2H, m, H_2C-6′), 3.53–3.45 (1H, m, HC-2), 2.78 (1H, dd, J = 3.5, 16 Hz, HC-3), 2.58 (1H, dd, J = 11.5, 16 Hz, HC-3), 2.12–2.01 (2H, m, H_2C-4′), 1.71 (2H, m, H_2C-1′), 1.51–1.35 (4H, m, H_2C-2′, H_2C-3′); ^{13}C NMR δ: 194.7 (s, C-4), 145.7 (d, C-6), 138.4 (d, C-5′), 123.4 (d, C-5), 114.8 (t, C-6′), 44.5 (t, C-3), 43.1 (d, C-2), 33.8 (t, C-1′), 33.4 (t, C-4′), 28.4 (t, C-3′), 26.0 (t, C-2′); LRMS (EI), *m/z* (relative intensity): 196 ([M]$^+$, 11), 168 (9), 139 (10), 113 (52), 86 (100).

*4-[[Tris(1-methylethyl)silyl]oxy]-6-(4′-pentenyl)-2H-thiopy-ran (**13a**)*: ^1H NMR ($C_6D_5CD_3$) (partial data) δ: 5.86 (1H, d, J = 1 Hz, HC-5), 5.64 (1H, ddt, J = 10.5, 17, 7 Hz, HC-4′), 4.98–4.88 (2H, m, HC-5′), 4.52 (1H, dt, J = 1, 6.5 Hz, HC-3), 3.11 (2H, d, J = 5.5 Hz, HC-2).

*6-(5′-Hexenyl)-4-[[tris(1-methylethyl)silyl]oxy]-2H-thi-opyran (**13b**)*: ^1H NMR ($C_6D_5CD_3$) (partial data) δ: 5.87 (1H, d, J = 1 Hz, HC-5), 5.68 (1H, ddt, J = 10.5, 17, 7 Hz, HC-5′), 4.98–4.88 (2H, m, HC-6′), 4.53 (1H, dt, J = 1, 5.5 Hz, HC-3), 3.12 (2H, d, J = 5.5 Hz, HC-2).

*4-[[Tris(1-methylethyl)silyl]oxy]-2-(4′-pentenyl)-2H-thiopy-ran (**14a**)*: ^1H NMR ($C_6D_5CD_3$) (partial data) δ: 5.97 (1H, d, J = 10 Hz, HC-6), 5.87 (1H, dd, J = 1, 10 Hz, HC-5), 5.63 (1H, ddt, J = 10.5, 17, 7 Hz, HC-4′), 4.97–4.87 (2H, m, HC-5′), 4.77 (1H, dd, J = 1, 6.5 Hz, HC-3), 3.17 (1H, br ddd, J = 6.5, 6.5, 6.5 Hz, HC-2).

*2-(5′-Hexenyl)-4-[[tris(1-methylethyl)silyl]oxy]-2H-thiopy-ran (**14b**)*: ^1H NMR ($C_6D_5CD_3$) (partial data) δ: 5.97 (1H, d, J = 10 Hz, HC-6), 5.87 (1H, dd, J = 1, 10 Hz, HC-5), 5.68 (1H, ddt, J = 10.5, 17, 7 Hz, HC-5′) 4.98–4.88 (2H, m, HC-6′), 4.78 (1H, dd, J = 1, 6.5 Hz, HC-3), 3.17 (1H, ddd, J = 6.5, 6.5, 6.5 Hz, HC-2).

*2-Propenyl 3-[3-(1,3-dioxolan-2-yl)propyl]tetrahydro-4-oxo-2H-thiopyran-3-carboxylate (**18a**)*: 591 mg (75%) from **17** (500 mg, 2.50 mmol) after FCC (60% ether in hexane): IR ν_{max}: 1727, 1711, 1129 cm^{-1}; ^1H NMR δ: 5.92 (1H, dddd, J = 5.5, 5.5, 10.5, 17 Hz, HC-2′), 5.35 (1H, br d, J = 17 Hz, HC-3′), 5.26 (1H, br d, J = 10.5 Hz, HC-3′), 4.83 (1H, dd, J = 4.5, 4.5 Hz, HC-2‴), 4.68 (2H, br d, J = 5.5 Hz, H_2C-1′), 3.98–3.79 (4H, m, H_2C-4‴, H_2C-5‴), 3.31 (1H, dd, J = 2.5, 13.5 Hz, HC-2), 2.99–2.74 (4H, m, H_2C-5, H_2C-6), 2.73 (1H, d, J = 13.5 Hz, HC-2), 1.97 (1H, ddd, J = 4.5, 12, 12.5 Hz, HC-1″), 1.74 (1H, ddd, J = 4.5, 12, 12.5 Hz, HC-1″), 1.70–1.62 (2H, m, H_2C-3″), 1.55–1.25 (2H, m, H_2C-2″); ^{13}C NMR δ: 205.1 (s, C-4), 170.6 (s, OC=O), 131.5 (d, C-2′), 119.1 (t, C-3′), 104.2 (d, C-2‴), 66.1 (t, C-1′), 64.9 (t ×2, C-4‴, C-5‴), 63.0 (s, C-3), 43.2 (t, C-5), 38.4 (t, C-1″), 34.2 (t, C-2 or C-3″), 34.0 (t, C-2 or C-3″), 30.8 (t, C-6), 19.1 (t, C-2″); LRMS (EI), *m/z* (relative intensity): 314 ([M]$^+$, 5), 252 (23), 199 (44), 141 (74), 114 (100).

*2-Propenyl 3-[4-(1,3-dioxolan-2-yl)butyl]tetrahydro-4-oxo-2H-thiopyran-3-carboxylate (**18b**)*: 1.35 g (79%) from **17** (1.04 g, 5.20 mmol) after FCC (35% EtOAc in hexane): IR ν_{max}: 1730, 1712, 1129 cm^{-1}; ^1H NMR δ: 5.90 (1H, ap ddt, J = 17, 10, 4.5 Hz, HC-2′), 5.35 (1H, dddd, J = 1.5, 1.5, 1.5, 17 Hz, HC-3′), 5.26 (1H, dddd, J = 1.5, 1.5, 1.5, 10 Hz, HC-3′), 4.82 (1H, dd, J = 4.5, 4.5 Hz, HC-2‴), 4.67 (2H, br d, J = 5.5 Hz, H_2C-1′), 4.00–3.78 (4H, m, H_2C-4‴, H_2C-5‴), 3.29 (1H, dd, J = 2.5, 13.5 Hz, HC-2), 3.01–2.73 (4H, m, H_2C-5, H_2C-6), 2.72 (1H, d, J = 13.5 Hz, HC-2), 1.99–1.88 (1H, m, HC-1″), 1.75–1.12 (7H, m, HC-1″, H_2C-2″, H_2C-3″, H_2C-4″); ^{13}C NMR δ: 205.3 (s, C-4), 170.7 (s, OC=O), 131.5 (d, C-2′), 119.1 (t, C-3′), 104.4 (d, C-2‴), 66.0 (t, C-1′), 64.9 (t ×2, C-4‴, C-5‴), 63.0 (s, C-3), 43.2 (t, C-5), 38.6 (t, C-1″), 34.3 (t, C-2), 33.5 (t, C-4″), 30.9 (t, C-6), 24.4 (t, C-2″ or C-3″), 24.3 (t, C-2″ or C-3″); LRMS (EI), *m/z* (relative intensity): 328 ([M]$^+$, 34), 311 (25), 268 (25), 267 (100), 244 (29), 240 (22).

*3-[3-(1,3-Dioxolan-2-yl)propyl]-tetrahydro-4H-thiopyran-4-one (**19a**)*: 453 mg (74%) from **18a** (835 mg, 2.66 mmol) after FCC (60% ether/hexane): IR ν_{max}: 1707, 1422, 1140 cm^{-1}; ^1H NMR δ: 4.84 (1H, dd, J = 4.5, 4.5 Hz, HC-2″), 3.98–3.80 (4H, m, H_2C-4″, H_2C-5″), 3.00–2.60 (7H, m, H_2C-2, HC-3, H_2C-5, H_2C-6), 1.96–1.85 (1H, m, HC-1′), 1.70–1.62 (2H, m, HC-3′), 1.45–1.35 (3H, m, HC-1′, H_2C-2′); ^{13}C NMR δ: 210.2 (s, C-4),

104.3 (d, C-2″), 64.9 (t ×2, C-4″, C-5″), 53.0 (d, C-3), 43.9 (t, C-5), 35.8 (t, C-3′), 33.8 (t, C-1′), 31.0 (t, C-2), 29.2 (t, C-6), 21.4 (t, C-2′); LRMS (CI, NH_3), *m/z* (relative intensity): 248 ($[M+18]^+$, 54), 231 ($[M+1]^+$, 27), 213 (82), 73 (100).

*3-[4-(1,3-Dioxolan-2-yl)butyl]-4*H*-thiopyran-4-one* (***19b***): 576 mg (61%) from **18b** (1.28 g, 3.90 mmol) after FCC (35% ether in hexane): IR ν_{max}: 2949, 2876, 1708, 1140, 1026 cm^{-1}; ^{1}H NMR δ: 4.83 (1H, dd, J = 4.5, 4.5 Hz, HC-2″), 4.00–3.80 (4H, m, H_2C-4″, H_2C-5″), 3.00–2.91 (3H, m, HC-2, H_2C-6), 2.75–2.62 (4H, m, HC-2, HC-3, H_2C-5), 1.95–1.84 (1H, m, HC-1′), 1.69–1.61 (2H, m, H_2C-4′), 1.49–1.27 (5H, m, HC-1′, H_2C-2′, H_2C-3′); ^{13}C NMR δ: 210.3 (s, C-4), 104.5 (d, C-2″), 64.9 (t ×2, C-4″, C-5″), 52.9 (d, C-3), 43.8 (t, C-5), 35.9 (t, C-1′), 33.7 (t, C-4′), 31.0 (t, C-2), 29.4 (t, C-6), 26.9 (t, C-2′), 24.0 (t, C-3′); LRMS (EI), *m/z* (relative intensity): 244 ($[M]^+$, 55), 182 (100), 154 (30), 126 (45), 116 (73), 99 (88).

*5-[3-(1,3-Dioxolan-2-yl)propyl]-2,3-dihydro-4*H*-thiopyran-4-one* (***20a***) *and 3-[3-(1,3-dioxolan-2-yl)propyl]-2,3-dihydro-4*H*-thiopyran-4-one* (***21a***): 132 mg (55%; as a 1.1:1 mixture of **20a** and **21a**, respectively) from **19a** (242 mg, 1.05 mmol) after FCC (40% EtOAc in hexane): ^{1}H NMR δ for **20a**: 7.16 (1H, br s, HC-6), 4.84 (1H, t, J = 4 Hz, HC-2″), 3.98–3.80 (4H, m, H_2C-4″, H_2C-5″), 3.18–3.12 (1H, m, HC-2), 2.76–2.70 (1H, m, HC-3), 2.32 (1H, t, J = 7.5 Hz, HC-1′), 1.73–1.61 (2H, m, H_2C-3′), 1.60–1.50 (2H, m, H_2C-2′); δ for **21a**: 7.35 (1H, d, J = 10 Hz, HC-6), 6.10 (1H, d, J = 10 Hz, HC-5), 4.85 (1H, t, J = 4 Hz, HC-2″), 3.98–3.80 (4H, m, H_2C-4″, H_2C-5″), 3.30 (1H, dd, J = 3.5, 13.5 Hz, HC-2), 3.04 (1H, br dd, J = 9, 13.5 Hz, HC-2), 2.52 (1H, dddd, J = 3.5, 5.5, 8, 9 Hz, HC-3), 1.88 (1H, dddd, J = 5.5, 5.5, 10, 13 Hz, HC-1′), 1.73–1.61 (2H, m, H_2C-3′), 1.60–1.50 (2H, m, H_2C-2′), 1.48–1.40 (1H, m, HC-1′); ^{13}C NMR δ for **20a**: 193.5 (s, C-4), 140.5 (d, C-6), 134.5 (s, C-5), 104.4 (d, C-2″), 64.9 (t ×2, C-4″, C-5″), 38.3 (t, C-3), 33.3 (t, C-3′), 30.9 (t, C-1′), 27.3 (t, C-2), 23.3 (t, C-2′); δ for **21a**: 74, 196.0 (s, C-4), 145.1 (d, C-6), 123.2 (d, C-5), 104.2 (d, C-2″), 64.9 (t ×2, C-4″, C-5″), 45.2 (d, C-3), 33.7 (t, C-3′), 31.6 (t, C-1′), 27.9 (t, C-2), 21.4 (t, C-2′).

*5-[4-(1,3-Dioxolan-2-yl)butyl]-2,3-dihydro-4*H*-thiopyran-4-one* (***20b***) *and 3-[4-(1,3-dioxolan-2-yl)butyl]-2,3-dihydro-4*H*-thiopyran-4-one* (***21b***): 198 mg (31%; as a 1.3:1 mixture of **20b** and **21b**, respectively) from **19b** (635 mg, 2.60 mmol) after FCC (50% EtOAc in hexane): IR ν_{max}: 2943, 1775, 1713, 1661, 1352, 1176, 1140 cm^{-1}; ^{1}H NMR δ for **20b**: 7.15 (1H, s, HC-6), 4.85 (1H, dd, J = 2.5, 5 Hz, HC-2″), 4.10–3.20 (4H, m, H_2C-4″, H_2C-5″), 3.19–3.13 (2H, m, H_2C-2), 2.77–2.71 (2H, m, H_2C-3), 2.31–2.26 (2H, m, H_2C-1′), 1.75–1.60 (2H, m, H_2C-4′), 1.60–1.40 (4H, m, H_2C-2′, H_2C-3′); δ for **21b**: 7.35 (1H, d, J = 10 Hz, HC-6), 6.10 (1H, d, J = 10 Hz, HC-5), 4.85 (1H, dd, J = 2.5, 5 Hz, HC-2″), 4.10–3.20 (4H, m, H_2C-4″, H_2C-5″), 3.32 (1H, dd, J = 4, 13 Hz, HC-2), 3.04 (1H, dd, J = 9, 13 Hz, HC-2), 2.56–2.48 (1H, m, HC-3), 1.93–1.80 (1H, m, HC-1′), 1.75–1.60 (2H, m, H_2C-4′), 1.60–1.40 (5H, m, HC-1′, H_2C-2′, H_2C-3′); ^{13}C NMR δ for **20b**: 193.5 (s, C-4), 145.1 (d, C-6), 134.8 (s, C-5), 104.5 (d, C-2″), 64.8 (t ×2, C-4″, C-5″), 38.4 (t, C-3), 33.7 (t, C-4′), 31.2 (t, C-1′), 28.9 (t, C-2′), 27.2 (t, C-2), 23.7 (t, C-3′); δ for **21b**: 196.2 (s, C-4), 140.2 (d, C-6), 123.1 (d, C-5), 104.4 (d, C-2″), 64.8 (t ×2, C-4″, C-5″), 45.1 (d, C-3), 33.7 (t, C-4′), 31.7 (t, C-1′), 28.0 (t, C-2), 26.9 (t, C-2′), 23.9 (t, C-3′); LRMS (EI), *m/z* (relative intensity): 242 ($[M]^+$, 3), 197 (3), 114 (9), 99 (28), 73 (100), 56 (19), 45 (15).

Methyl (E)*-6-(3,4-dihydro-4-oxo-2*H*-thiopyran-5-yl)-2-hexenoate* (***22a***)*, methyl* (E)*-6-(3,4-dihydro-4-oxo-2*H*-thiopyran-3-yl)-2-hexenoate* (***23a***)*, methyl* (Z)*-6-(3,4-dihydro-4-oxo-2*H*-thiopyran-5-yl)-2-hexenoate* (***24a***)*, and methyl* (Z)*-6-(3,4-dihydro-4-oxo-2*H*-thiopyran-3-yl)-2-hexenoate* (***25a***)

A 1.2:1 mixture of **22a** and **23a** (31 mg, 35%) and a 1.2:1 mixture of **24a** and **25a** (18 mg, 21%) were obtained from a 1.2:1 mixture of **20a** and **21a** (84 mg, 0.37 mmol) after PTLC (50% ether in hexane, developed ×2)

For **22a/23a**: ^{1}H NMR δ for **22a**: 7.16 (1H, br s, HC-6′), 6.94 (1H, dt, J = 15.5, 7 Hz, HC-3), 5.82 (1H, dt, J = 15.5, 1.5 Hz, HC-2), 3.72 (3H, s, H_3CO), 3.19–3.13 (2H, m, HC-2′), 2.77–2.71 (2H, m, HC-3′), 2.29 (2H, ap t, J = 7.5 Hz, H_2C-6), 2.20 (2H, ap ddt, J = 1.5, 7.5, 7 Hz, H_2C-4), 1.59 (2H, ap tt, J = 7.5, 9 Hz, H_2C-5); δ for **23a**: 7.35 (1H, d, J = 10 Hz, HC-6′), 6.94 (1H, dt, J = 15.5, 7 Hz, HC-3), 6.09 (1H, d, J = 10 Hz, HC-5′), 5.82 (1H, dt, J = 15.5, 1.5 Hz, HC-2), 3.72 (3H, s, H_3CO), 3.29 (1H, dd, J = 4, 13.5 Hz, HC-2′), 3.03 (1H, dd, J = 9, 13.5 Hz, HC-2′), 2.57–2.48 (1H, m, HC-3′), 2.26–2.19 (2H, m, H_2C-4), 1.89–1.81 (1H, m, HC-6), 1.62–1.50 (3H, m, H_2C-5, HC-6); ^{13}C NMR δ for **22a**: 193.4 (s, C-4′), 167.0 (s, C-1), 148.9 (d, C-3), 140.8 (d, C-6′), 134.2 (s, C-5′), 121.2 (d, C-2), 51.4 (q, CH_3O), 38.3 (t, C-3′), 31.8 (t, C-6), 30.9 (t, C-4), 27.4 (t, C-5), 27.2 (t, C-2′); δ for **23a**: 195.8 (s, C-4′), 167.0 (s, C-1), 148.5 (d, C-3), 145.2 (d, C-6′), 123.1 (d, C-5′), 121.4 (d, C-2), 51.3 (q, CH_3O), 45.0 (d, C-3′), 32.0 (t, C-4), 31.7 (t, C-6), 27.8 (t, C-2′), 25.5 (t, C-5).

For **24a/25a**: ^{1}H NMR δ for **24a**: 7.17 (1H, br s, HC-6′), 6.22 (1H, dt, J = 11.5, 7.5 Hz, HC-3), 5.78 (1H, dt, J = 11.5, 1.5 Hz, HC-2), 3.71 (3H, s, H_3CO), 3.19–3.13 (2H, m, H_2C-2′), 2.77–2.71 (2H, m, H_2C-3′), 2.69–2.61 (2H, m, H_2C-4), 2.32 (2H, ap t, J = 7.5 Hz, H_2C-6), 1.63–1.52 (2H, m, H_2C-5); δ for **25a**: 7.35 (1H, d, J = 10 Hz, HC-6′), 6.22 (1H, dt, J = 11.5, 7.5 Hz, HC-3), 6.10 (1H, d, J = 10 Hz, HC-5′), 5.78 (1H, br d, J = 11.5 Hz, HC-2), 3.71 (3H, s, H_3CO), 3.31 (1H, dd, J = 3.5, 13.5 Hz, HC-2′), 3.05 (1H, dd, J = 8.5, 13.5 Hz, HC-2′), 2.69–2.61 (2H, m, H_2C-4), 2.60–2.50 (1H, m, HC-3′), 1.87 (1H, dddd, J = 5.5, 5.5, 10, 13 Hz, HC-6), 1.64–1.48 (3H, m, H_2C-5, HC-6); ^{13}C NMR δ for **24a**: 193.5 (s, C-4′), 166.8 (s, C-1), 150.2 (d, C-3), 140.7 (d, C-6′), 134.4 (s, C-5′), 119.6 (d, C-2), 51.0 (q, CH_3O), 38.4 (t, C-3′), 31.1 (t, C-6), 28.5 (t, C-4), 28.3 (t, C-5), 27.3 (t, C-2′); δ for **25a**: 196.0 (s, C-4′), 166.8 (s, C-1), 149.7 (d, C-3), 145.2 (d, C-6′), 123.1 (d, C-5′), 119.9 (d, C-2), 51.0 (q, CH_3O), 45.0 (d, C-3′), 31.8 (t, C-6), 28.7 (t, C-4), 27.8 (t, C-2′), 26.4 (t, C-5).

Methyl (E)*-7-(3,4-dihydro-4-oxo-2*H*-thiopyran-5-yl)-2-heptenoate* (***22b***)*, methyl* (E)*-7-(3,4-dihydro-4-oxo-2*H*-thiopyran-3-yl)-2-heptenoate* (***23b***)*, methyl* (Z)*-7-(3,4-dihydro-4-oxo-2*H*-thiopyran-5-yl)-2-heptenoate* (***24b***)*, and methyl* (Z)*-7-(3,4-dihydro-4-oxo-2*H*-thiopyran-3-yl)-2-heptenoate* (***25b***)

A 1.3:1 mixture of **22b** and **23b** (64 mg, 31%) and a 1.3:1 mixture of **24b** and **25b** (36 mg, 17%) were obtained from a 1.3:1 mixture of **20b** and **21b** (198 mg, 0.818 mmol) after PTLC (50% ether in hexane).

For **22b/23b**: IR ν_{max}: 2931, 1721, 1658, 1435, 1272, 1202,

1175 cm^{-1}; ^1H NMR δ for **22b**: 7.14 (1H, s, HC-6′), 6.95 (1H, dt, J = 15.5, 7 Hz, HC-3), 5.78 (1H, br d, J = 15.5 Hz, HC-2), 3.70 (3H, s, H_3CO), 3.15–3.09 (2H, m, H_2C-2′), 2.73–2.67 (2H, m, H_2C-3′), 2.26–2.14 (4H, m, H_2C-4, H_2C-7), 1.56–1.30 (4H, m, H_2C-5, H_2C-6); δ for **23b**: 7.36 (1H, d, J = 10 Hz, HC-6′), 6.95 (1H, dt, J = 15.5, 7 Hz, HC-3), 6.07 (1H, d, J = 10 Hz, HC-5′), 5.78 (1H, br d, J = 15.5 Hz, HC-2), 3.70 (3H, s, H_3CO), 3.26 (1H, dd, J = 4, 13 Hz, HC-2′), 3.01 (1H, dd, J = 8.5, 13 Hz, HC-2′), 2.52–2.44 (1H, m, HC-3′), 2.26–2.14 (2H, m, HC-4), 1.88–2.75 (1H, m, HC-7), 1.56–1.30 (5H, m, H_2C-5′, H_2C-6, HC-7); ^{13}C NMR δ for **22b**: 193.5 (s, C-4′), 167.0 (s, C-1), 149.3 (d, C-3), 140.4 (d, C-6′), 134.6 (s, C-5′), 121.0 (d, C-2), 51.4 (q, CH_3O), 38.3 (t, C-3′), 31.7 (t, C-4), 31.0 (t, C-7), 28.5 (t, C-6), 27.7 (t, C-5), 27.2 (t, C-2′); δ for **23b**: 196.1 (s, C-4′), 167.0 (s, C-1), 149.1 (d, C-3), 145.1 (d, C-6′), 123.1 (d, C-5′), 121.1 (d, C-3), 51.4 (q, CH_3O), 45.1 (d, C-3′), 31.9 (t, C-4), 31.7 (t, C-7), 27.9 (t, C-2′ or C-5), 27.8 (t, C-2′ or C-5), 26.4 (t, C-6); LRMS (EI), *m/z* (relative intensity): 254 ($[M]^+$, 11), 194 (27), 155 (20), 139 (13), 127 (33), 114 (100).

For **24b/25b**: IR ν_{max}: 2927, 1720, 1658, 1437, 1199, 1174 cm^{-1}; ^1H NMR δ for **24b**: 7.13 (1H, br s, HC-6′), 6.18 (1H, dt, J = 12, 8 Hz, HC-3), 5.74 (1H, br d, J = 12 Hz, HC-2), 3.66 (3H, s, H_3CO), 3.16–3.10 (2H, m, H_2C-2′), 2.73–2.66 (2H, m, H_2C-3′), 2.65–2.58 (2H, m, H_2-C4), 2.31–2.20 (2H, m, H_2C-7), 1.60–1.30 (4H, m, H_2C-5, H_2C-6); δ for **25b**: 7.33 (1H, d, J = 10 Hz, HC-6′), 6.18 (1H, dt, J = 11.5, 8 Hz, HC-3), 6.07 (1H, d, J = 10 Hz, HC-5′), 5.74 (1H, br d, J = 11.5 Hz, HC-2), 3.66 (3H, s, H_3CO), 3.28 (1H, dd, J = 4, 13 Hz, HC-2′), 3.01 (1H, dd, J = 9, 13 Hz, HC-2′), 2.65–2.58 (2H, m, H_2C-4), 2.53–2.44 (1H, m, HC-3′), 1.87–1.78 (1H, m, HC-7), 1.60–1.30 (5H, m, H_2C-5, H_2C-6, HC-7); ^{13}C NMR δ for **24b**: 193.5 (s, C-4′), 166.8 (s, C-1), 150.5 (d, C-3), 145.1 (d, C-6′), 134.8 (s, C-5′), 119.5 (d, C-2), 51.0 (q, CH_3O), 38.4 (t, C-3′), 31.0 (t, C-7), 28.8, 28.7, and 28.6 (t ×3, C-4, C-5, C-6), 27.2 (t, C-2′); δ for **25b**: 196.1 (s, C-4′), 166.8 (s, C-1), 150.3 (d, C-3), 140.2 (d, C-6′), 123.1 (d, C-5′), 119.4 (d, C-2), 51.0 (q, CH_3O), 45.1 (d, C-3′), 31.7 (t, C-7), 28.7 (t, C-4 or C-5), 28.6 (t, C-4 or C-5), 27.8 (t, C-2′), 26.6 (t, C-6); LRMS (EI), *m/z* (relative intensity): 254 ($[M]^+$, 7), 194 (40), 155 (10), 127 (22), 114 (100), 113 (32).

*Methyl (*E*)-7-(3,4-dihydro-4-oxo-*2H*-thiopyran-3-yl)-2-heptenoate (**23b**)*

From **54**: A solution of Bu_3SnH (0.3 mL, 1.1 mmol) and AIBN (10 mg, 0.06 mmol) in dry deoxygenated benzene (5 mL) was added over 30 min to a solution of **54** (126 mg, 1 mmol) and **55** (382 mg, 1.5 mmol) in dry deoxygenated benzene (15 mL) heated under reflux in an oil bath preheated to 90°C. After 8 h, the reaction mixture was concentrated and fractionated by MPC (25% ethyl acetate in hexane) to give **23b** (116 mg, 45%) and **54** (23.5 mg, 19%). IR ν_{max}: 2930, 1721, 1658, 1554, 1272, 1202 cm^{-1}; ^1H NMR δ: 7.33 (1H, d, J = 10 Hz, HC-6′), 6.91 (1H, dt, J = 15.5, 7 Hz, HC-3), 6.07 (1H, d, J = 10 Hz, HC-5′), 5.78 (1H, dt, J = 15.5, 1.5 Hz, HC-2), 3.68 (1H, s, H_3CO), 3.27 (1H, dd, J = 3.5, 13.5 Hz, HC-2′), 3.00 (1H, ddd, J = 0.5, 9, 13.5 Hz, HC-2′), 2.52–2.44 (1H, m, HC-3′), 2.18 (2H, ap ddt, J = 1.5, 7, 7 Hz, HC-4), 1.88–1.76 (1H, m, HC-7), 1.56–1.30 (5H, m, H_2C-5, H_2C-6, HC-7); ^{13}C NMR δ: 196.0 (s, C-4′), 167.0 (s, C-1), 149.1 (d, C-3), 145.1 (d, C-6′), 123.1 (d, C-5′), 121.1 (d, C-2), 51.4 (q, CH_3O), 45.1 (d, C3), 31.9 (t, C-4), 31.7 (t, C-7), 27.9 (t, C-2′ or C-5), 27.8 (t, C-2′ or C-5), 26.4 (t, C-6); LRMS (EI), *m/z* (relative intensity): 254 ($[M]^+$, 20), 223 (9), 195 (12), 114 (100), 86 (91).

*Methyl (*E*)-6-[4-[[tris(1-methylethyl)silyl]oxy]-2*H*-thiopyran-5-yl]-2-heptenoate (**26b**) and methyl (*E*)-6-[4-[[tris(1-methylethyl)silyl]oxy]-2*H*-thiopyran-3-yl]-2-heptenoate (**27b**)*

Obtained as a 1.3:1 mixture from a similar mixture of **22b** and **23b**: ^1H NMR δ for **26b**: 6.96 (1H, dt, J = 15.5, 7 Hz, H-3), 6.05 (1H, s, H-6′), 5.80 (1H, d, J = 15.5 Hz, H-2), 4.76 (1H, t, J = 7 Hz, H-3′), 3.70 (3H, s, H_3CO), 3.19 (2H, d, J = 7 Hz, H_2C-2′), 2.25–2.15 (4H, m, H_2C-4, H_2C-7), 1.52–1.38 (4H, m, H_2C-5, H_2C-6), 1.30–0.90 (21H, m, $(H_3C)_2CHSi$); δ for **27b**: 6.96 (1H, dt, J = 15.5, 7 Hz, H-3), 6.18 (1H, d, J = 10 Hz, H-6′), 5.94 (1H, d, J = 10 Hz, H-5′), 5.80 (1H, d, J = 15.5 Hz, H-2), 3.70 (3H, s, H_3CO), 3.25 (2H, s, H_2C-2′), 2.25–2.15 (4H, m, H_2C-4, H_2C-7), 1.52–1.38 (4H, m, H_2C-5, H_2C-6), 1.30–0.90 (21H, m, $(H_3C)_2CHSi$).

*Methyl (*E*)-6-[4-[[tris(1-methylethyl)silyl]oxy]-2*H*-thiopyran-3-yl]-2-heptenoate (**27b**)*: ^1H NMR δ: 6.97 (1H, ddd, J = 7, 7, 15.5 Hz, HC-3), 6.18 (1H, d, J = 10 Hz, HC-6′), 5.95 (1H, d, J = 10 Hz, HC-5′), 5.82 (1H, dt, J = 15.5, 1.5 Hz, HC-2), 3.73 (3H, s, H_3CO), 3.28 (2H, s, H_2C-2′), 2.26–2.18 (4H, m, H_2C-7, H_2C-4), 1.50–1.38 (4H, m, H_2C-5, H_2C-6), 1.30–0.90 (21H, m, $(H_3C)_2CHSi$).

*Methyl (*Z*)-6-[4-[[tris(1-methylethyl)silyl]oxy]-2*H*-thiopyran-5-yl]-2-heptenoate (**28b**) and methyl (*Z*)-6-[4-[[tris(1-methylethyl)silyl]oxy]-2*H*-thiopyran-3-yl]-2-heptenoate (**29b**)*

Obtained as a 1.3:1 mixture from a similar mixture of **24b** and **25b**: ^1H NMR δ for **28b**: 6.21 (1H, dt, J = 15.5, 7 Hz, H-3), 6.05 (1H, s, H-6′), 5.78 (1H, d, J = 15.5 Hz, H-2), 4.76 (1H, t, J = 7 Hz, H-3′), 3.70 (3H, s, H_3CO), 3.19 (2H, d, J = 7 Hz, H_2C-2′), 2.78–2.60 (2H, m, H_2C-4), 2.23–2.13 (2H, m, H_2C-7), 1.52–1.38 (4H, m, H_2C-5, H_2C-6), 1.30–0.90 (21H, m, $(H_3C)_2CHSi$); δ for **29b**: 6.21 (1H, dt, J = 11.5, 7 Hz, H-3), 6.18 (1H, d, J = 10 Hz, H-6′), 5.94 (1H, d, J = 10 Hz, H-5′), 5.78 (1H, d, J = 11.5 Hz, H-2), 3.70 (3H, s, H_3CO), 3.25 (2H, s, H_2C-2′), 2.69 (2H, m, H_2C-4), 2.23–2.13 (2H, m, H_2C-7), 1.52–1.38 (4H, m, H_2C-5, H_2C-6), 1.30–0.90 (21H, m, $(H_3C)_2CHSi$).

*Methyl (*E*)-6-(4-oxo-4*H*-thiopyran-3-yl)-2-hexenoate (**30a**)*

A solution of a 1.2:1 mixture of **26a** and **27a** (8.3 mg, 0.021 mmol) in $C_6D_5CD_3$ (0.5 mL) was heated at 75°C for 24 h. ^1H NMR of the reaction solution showed essentially complete conversion to **30a**. The mixture was concentrated and fractionated by PTLC to give **30a** (4 mg, 75%). IR ν_{max}: 3024, 1718, 1605, 1272 cm^{-1}; ^1H NMR δ: 7.74 (1H, dd, J = 4, 10 Hz, HC-6′), 7.54 (1H, d, J = 4 Hz, HC-2′), 7.05 (1H, d, J = 10 Hz, HC-5′), 6.98 (1H, dt, J = 15.5, 7 Hz, HC-3), 5.86 (1H, dt, J = 15.5, 1.5 Hz, HC-2), 3.72 (3H, s, H_3CO), 2.64–2.58 (2H, m, H_2C-6), 2.28 (2H, ap ddt, J = 1.5, 7, 7 Hz, H_2C-4), 1.80–1.70 (2H, m, H_2C-5); LRMS (CI, NH_3), *m/z* (relative intensity): 256 ($[M+18]^+$, 25), 239 ($[M+1]^+$, 100), 83 (25).

*Methyl (*E*)-7-(4-oxo-4*H*-thiopyran-3-yl)-2-heptenoate (**30b**)*

Obtained as a minor by-product (<20% yield) from thermal

reaction of a mixture of **26b** and **27b**: IR ν_{max}: 3023, 2945, 1731, 1716, 1653, 1614, 1601, 1271 cm^{-1}; ^1H NMR δ: 7.74 (1H, dd, J = 4, 10 Hz, HC-6′), 7.53 (1H, d, J = 10 Hz, HC-2′), 7.04 (1H, d, J = 10 Hz, HC-5′), 6.94 (1H, dt, J = 15.5, 7 Hz, HC-3), 5.81 (1H, dt, J = 15.5, 1.5 Hz, HC-2), 3.69 (3H, s, H_3CO), 2.61–2.55 (2H, m, H_2C-7), 2.23 (2H, ap dt, J = 6.5, 6.5, 6.5 Hz, H_2C-4), 1.64–1.48 (4H, m, H_2C-5, H_2C-6); ^{13}C NMR δ: 179.3 (s, C-4′), 167.0 (s, C-1), 149.1 (d, C-3), 143.6 (s, C-3′), 136.8 (d, C-6′), 132.4 (d, C-2′), 130.4 (d, C-5′), 121.1 (d, C-2), 51.3 (q, CH_3O), 31.9 (t, C-4), 31.6 (t, C-7), 27.7 (t, C-5), 27.4 (t, C-6); LRMS (EI), *m/z* (relative intensity): 252 ($[M]^+$, 12), 221 (12), 193 (12), 154 (15), 153 (100).

*Methyl (*E*)-7-(4-oxo-4*H*-thiopyran-3-yl)-2-heptenoate (**30b**) and methyl (*Z*)-7-(4-oxo-4*H*-thiopyran-3-yl)-2-heptenoate (**31b**)*

Obtained as an ca. 1:1 mixture (<20% yield) from thermal reaction of a mixture of **28b** and **29b**: IR ν_{max}: 3043, 2929, 2858, 1720, 1656, 1608, 1271, 1200 cm^{-1}; ^1H NMR δ for **30b**: 7.73 (1H, dd, J = 6, 10.5 Hz, HC-6′), 7.54 (1H, d, J = 6 Hz, HC-2′), 7.04 (1H, d, J = 10.5 Hz, HC-5′), 6.95 (1H, dt, J = 15, 8 Hz, HC-3), 5.81 (1H, d, J = 15 Hz, HC-2), 3.72 (3H, s, H_3CO), 2.65–2.57 (2H, m, H_2C-7), 2.40–2.30 (2H, m, H_2C-4), 1.65–1.35 (4H, m, H_2C-5, H_2C-6); δ for **31b**: 7.73 (1H, dd, J = 10.5, 6 Hz, HC-6′), 7.53 (1H, d, J = 6 Hz, HC-2′), 7.04 (1H, d, J = 10.5 Hz, HC-5′), 6.22 (1H, dt, J = 11.5, 8 Hz, HC-3), 5.77 (1H, d, J = 11.5 Hz, HC-2), 3.72 (3H, s, H_3CO), 2.73–2.65 (2H, m, H_2C-4), 2.65–2.57 (2H, m, H_2C-7), 1.65–1.35 (4H, m, H_2C-5, H_2C-6).

*2-[3-(1,3-Dioxolan-2-yl)propyl]-tetrahydro-4*H*-thiopyran-4-one (**33**)*

In this case, the product obtained from addition of the cuprate derived from 2-(4-bromobutyl)-1,3-dioxolane to **32** (750 mg, 769 mmol) according to the general procedure was contaminated with 2-propyl-1,3-dioxolane. This crude product was directly subjected to decarboxylation according to the general procedure to obtain **33** (355 mg, 41%) after FCC (80% ether in hexane): IR ν_{max}: 1711, 1410, 1139 cm^{-1}; ^1H NMR δ: 4.84 (1H, dd, J = 4, 4.5 Hz, HC-2″), 4.00–3.80 (4H, m, H_2C-4″, H_2C-5″), 3.11–3.02 (1H, m, HC-2), 3.00–2.82 (2H, m, HC-6), 2.74 (1H, br dd, J = 3.5, 13.5 Hz, HC-3), 2.70–2.53 (2H, m, H_2C-5), 2.44 (1H, dd, J = 10.5, 13.5 Hz, HC-3), 1.70–1.50 (6H, m, H_2C-1′, H_2C-2′, H_2C-3′); ^{13}C NMR δ: 208.4 (s, C-4), 104.1 (d, C-2″), 64.8 (t ×2, C-4″, C-5″), 50.5 (t, C-3), 44.5 (d, C-2), 43.3 (t, C-5), 35.3 (t, C-1′), 33.3 (t, C-3′), 27.9 (t, C-6), 21.2 (t, C-2′); LRMS (EI), *m/z* (relative intensity): 230 ($[M]^+$, 11), 168 (32), 112 (21), 99 (23), 73 (100).

*Methyl (*E*)-6-(tetrahydro-4-oxo-2*H*-thiopyran-2-yl)-2-hexenoate (**34**) and methyl (*Z*)-6-(tetrahydro-4-oxo-2*H*-thiopyran-2-yl)-2-hexenoate (**35**)*

34 (48 mg, 47%) and **35** (27 mg, 26%) were obtained from **33** (125 mg, 0.534 mmol) after PTLC (50% ether in hexane, developed ×2).

For **34**: IR ν_{max}: 3031, 1715, 1656, 1272 cm^{-1}; ^1H NMR δ: 6.93 (1H, ap dt, J = 15.5, 7 Hz, HC-3), 5.84 (1H, ap dt, J = 15.5, 1.5 Hz, HC-2), 3.72 (3H, s, H_3CO), 3.11–3.01 (1H, m, HC-2′), 2.99–2.83 (2H, m, HC-6′), 2.73 (1H, dd, J = 3.5, 13.5 Hz, HC-3′), 2.72–2.55 (2H, m, HC-5′), 2.44 (1H, dd, J = 10.5, 13.5 Hz, HC-3′), 2.26–2.18 (2H, m, HC-4), 1.66–1.54 (4H, m, H_2C-5, H_2C-6); ^{13}C NMR δ: 208.4 (s, C-4′), 166.9 (s, C-1), 148.4 (d, C-3), 121.5 (d, C-2), 51.4 (q, CH_3O), 50.6 (t, C-3′), 44.5 (d, C-2′), 43.4 (t, C-5′), 34.9 (t, C-6), 31.7 (t, C-4), 28.0 (t, C-6′), 25.3 (t, C-5); LRMS (CI, NH_3), *m/z* (relative intensity): 260 ($[M+18]^+$, 100), 243 ($[M+1]^+$, 84), 211 (26).

For **35**: IR ν_{max}: 3032, 1717, 1644, 1197 cm^{-1}; ^1H NMR δ: 6.19 (1H, dt, J = 11.5, 7.5 Hz, HC-3), 5.79 (1H, dt, J = 11.5, 1.5 Hz, HC-2), 3.70 (3H, s, H_3CO), 3.15–3.05 (1H, m, HC-2′), 3.01–2.82 (2H, m, HC-6′), 2.73 (1H, br dd, J = 3.5, 13.5 Hz, HC-3′), 2.70–2.55 (4H, m, H_2C-4, H_2C-5′), 2.43 (1H, dd, J = 10.5, 13.5 Hz, HC-3′), 1.66–1.54 (4H, m, H_2C-5, H_2C-6); ^{13}C NMR δ: 208.5 (s, C-4′), 166.7 (s, C-1), 149.6 (d, C-3), 120.0 (d, C-2), 51.1 (q, CH_3O), 50.6 (t, C-3′), 44.5 (d, C-2′), 43.4 (t, C-5′), 35.0 (t, C-6), 28.4 (t, C-4), 28.1 (t, C-6′), 26.2 (t, C-5); LRMS (CI, NH_3), *m/z* (relative intensity): 260 ($[M+18]^+$, 100), 243 ($[M+1]^+$, 63), 211 (20), 199 (16).

*Methyl (*E*)-6-(3,4-dihydro-4-oxo-2*H*-thiopyran-6-yl)-2-hexenoate (**36**) and methyl (*E*)-6-(3,4-dihydro-4-oxo-2*H*-thiopyran-2-yl)-2-hexenoate (**37**)*

36 (22 mg, 63%) and **37** (10 mg, 29%) were obtained from **34** (35 mg, 0.14 mmol) after PTLC (50% EtOAc in hexane).

For **36**: IR ν_{max}: 3016, 1720, 1654, 1180 cm^{-1}; ^1H NMR δ: 6.92 (1H, dt, J = 15.5, 7 Hz, HC-3), 5.84 (1H, dt, J = 15.5, 1.5 Hz, HC-2), 6.06 (1H, s, HC-5′), 3.71 (3H, s, H_3CO), 3.19–3.13 (2H, m, H_2C-2′), 2.67–2.61 (2H, m, H_2C-3′), 2.39 (2H, ap t, J = 7.5 Hz, H_2C-6), 2.24 (2H, ap ddt, J = 1.5, 7, 7.5 Hz, H_2C-4), 1.77 (2H, ap tt, J = 7.5, 7.5 Hz, H_2C-5); ^{13}C NMR δ: 194.2 (s, C-4′), 166.8 (s, C-1), 163.8 (s, C-6′), 147.8 (d, C-3), 122.1 (d, C-5′), 121.9 (d, C-2), 51.5 (q, CH_3O), 37.6 (t, C-6), 36.8 (t, C-3′), 31.2 (t, C-4), 27.4 (t, C-2′), 26.9 (t, C-5); LRMS (CI, NH_3), *m/z* (relative intensity): 241 ($[M+18]^+$, 100), 180 (12).

For **37**: IR ν_{max}: 3031, 1720, 1659, 1271 cm^{-1}; ^1H NMR δ: 7.41 (1H, d, J = 10 Hz, HC-6′), 6.92 (1H, dt, J = 15.5, 7 Hz, HC-3), 6.17 (1H, d, J = 10 Hz, HC-5′), 5.84 (1H, dt, J = 15.5, 1.5 Hz, HC-2), 3.74 (3H, s, H_3CO), 3.53–3.42 (1H, m, HC-2′), 2.78 (1H, dd, J = 3.5, 16.5 Hz, HC-3′), 2.59 (1H, dd, J = 11.5, 16.5 Hz, HC-3′), 2.24 (2H, ap ddt, J = 1.5, 7, 7.5 Hz, H_2C-4), 1.80–1.55 (4H, m, H_2C-5, H_2C-6); ^{13}C NMR δ: 194.3 (s, C-4′), 166.9 (s, C-1), 148.0 (d, C-3), 145.3 (d, C-6′), 123.5 (d, C-5′), 121.8 (d, C-2), 51.5 (q, CH_3O), 44.4 (t, C-3′), 42.8 (d, C-2′), 33.3 (t, C-6), 31.6 (t, C-4), 25.1 (t, C-5); LRMS (CI, NH_3), *m/z* (relative intensity): 258 ($[M+18]^+$, 14), 241 ($[M+1]^+$, 100), 113 (20).

*Methyl (*Z*)-6-(3,4-dihydro-4-oxo-2*H*-thiopyran-6-yl)-2-hexenoate (**38**) and methyl (*Z*)-6-(3,4-dihydro-4-oxo-2*H*-thiopyran-2-yl)-2-hexenoate (**39**)*

38 (39 mg, 48%) and **39** (24 mg, 30%) were obtained from **35** (81 mg, 0.33 mmol) after PTLC (50% EtOAc in hexane).

For **38**: IR ν_{max}: 3032, 1718, 1649, 1198 cm^{-1}; ^1H NMR δ: 6.17 (1H, dt, J = 11.5, 7.5 Hz, HC-3), 6.04 (1H, br s, HC-5′), 5.79 (1H, dt, J = 11.5, 1.5 Hz, HC-2), 3.67 (3H, s, H_3CO), 3.18–3.12 (2H, m, HC-2′), 2.68 (2H, ap ddt, J = 1.5, 7.5, 7.5 Hz, H_2C-4), 2.64–2.58 (2H, m, H_2C-3′), 2.39 (2H, ap t, J = 7.5 Hz, H_2C-6), 1.73 (2H, ap tt, J = 7.5, 7.5 Hz, H_2C-5); ^{13}C NMR δ: 194.3 (s, C-4′), 166.6 (s, C-1), 164.2 (s, C-6′), 148.9 (d, C-3), 121.9 (d, C-5′), 120.3 (d, C-2), 51.1 (q, CH_3O), 37.8 (t, C-6), 36.8 (t, C-3′), 28.1 (t, C-4 or 5), 28.0 (t, C-4 or 5), 27.4 (t,

C-2′); LRMS (EI), *m/z* (relative intensity): 240 ([M]$^+$, 6), 208 (18), 180 (100), 141 (69), 128 (88).

For **39**: IR ν_{max}: 3032, 1719, 1660, 1199 cm^{-1}; ^{1}H NMR δ: 7.41 (1H, d, *J* = 10 Hz, HC-6′), 6.19 (1H, ap dt, *J* = 11.5, 7.5 Hz, HC-3), 6.16 (1H, d, *J* = 10 Hz, HC-5′), 5.81 (1H, ap dt, *J* = 11.5, 1.5 Hz, HC-2), 3.70 (3H, s, OCH_3), 3.57–3.46 (1H, m, HC-2′), 2.79 (1H, dd, *J* = 3.5, 16 Hz, HC-3′), 2.69 (2H, ap ddt, *J* = 1.5, 7.5, 7.5 Hz, H_2C-4), 2.59 (1H, dd, *J* = 11.5, 16 Hz, HC-3′), 1.81–1.69 (2H, m, H_2C-6), 1.68–1.53 (2H, m, H_2C-5); ^{13}C NMR δ: 194.4 (s, C-4′), 166.7 (s, C-1), 149.1 (d, C-3), 145.5 (d, C-6′), 123.5 (d, C-5′), 120.2 (d, C-2), 51.1 (q, CH_3O), 44.4 (t, C-3′), 42.8 (d, C-2′), 33.4 (t, C-6), 28.3 (t, C-4), 25.9 (t, C-5); LRMS (EI), *m/z* (relative intensity): 240 ([M]$^+$, 12), 139 (24), 113 (100).

Methyl (E)*-6-[4-[[tris(1-methylethyl)silyl]oxy]-2*H*-thiopyran-6-yl]-2-hexenoate* (***40***): ^{1}H NMR ($C_6D_5CD_3$) (partial data) δ: 6.84 (1H, dt, *J* = 16, 6.5 Hz, HC-3), 5.80 (1H, d, *J* = 1 Hz, HC-5′), 5.72 (1H, br d, *J* = 16 Hz, HC-2), 4.52 (1H, dt, *J* = 1, 5.5 Hz, HC-3′), 3.10 (2H, d, *J* = 5.5 Hz, HC-2′).

Methyl (E)*-6-[4-[[tris(1-methylethyl)silyl]oxy]-2*H*-thiopyran-2-yl]-2-hexenoate* (***41***): ^{1}H NMR ($C_6D_5CD_3$) (partial data) δ: 6.85 (1H, dt, *J* = 16, 6.5 Hz, H-4′), 5.92 (1H, d, *J* = 10 Hz, H-6), 5.84 (1H, dd, *J* = 1, 10 Hz, H-5), 5.71 (1H, br d, *J* = 16 Hz, H-5′), 4.72 (1H, dd, *J* = 1, 6.5 Hz, H-3), 3.04 (1H, br dt, *J* = 6.5, 6.5 Hz, H-2).

Methyl (Z)*-6-[4-[[tris(1-methylethyl)silyl]oxy]-2*H*-thiopyran-6-yl]-2-hexenoate* (***42***): ^{1}H NMR ($C_6D_5CD_3$) (partial data): δ 5.84 (1H, d, *J* = 1 Hz, HC-5′), 5.81–5.74 (1H, m, HC-3), 5.67 (1H, br d, *J* = 12 Hz, HC-2), 4.52 (1H, dt, *J* = 1, 5.5 Hz, HC-3′), 3.12 (2H, d, *J* = 5.5 Hz, HC-2′).

Methyl (Z)*-6-[4-[[tris(1-methylethyl)silyl]oxy]-2*H*-thiopyran-2-yl]-2-hexenoate* (***43***): ^{1}H NMR ($C_6D_5CD_3$) (partial data) δ: 5.94 (1H, d, *J* = 10 Hz, H-6′), 5.85 (1H, dd, *J* = 1, 10 Hz, H-5′), 5.81–5.74 (1H, m, H-3), 5.67 (1H, br d, *J* = 12 Hz, H-2), 4.76 (1H, dd, *J* = 1, 6.5 Hz, H-3′), 3.17 (1H, br dt, *J* = 6.5, 6.5 Hz, H-2′).

*Methyl (3*S**,4*R**,4a*S**,7a*S**)-hexahydro-8-oxo-1*H*-3,7a-ethanocyclopenta[c]thiopyran-4-carboxylate* (***45***): IR ν_{max}: 1726, 1435, 1236 cm^{-1}; ^{1}H NMR δ: 3.73 (3H, s, H_3CO), 3.38 (1H, ddd, *J* = 1, 2.5, 3.5 Hz, HC-3), 3.13 (1H, ddd, *J* = 1, 1.5, 8.5 Hz, HC-4), 3.10 (1H, d, *J* = 11.5 Hz, HC-1), 2.91 (1H, dd, *J* = 2.5, 18.5 Hz, H_{endo}C-9), 2.70 (1H, ddd, *J* = 1.5, 3.5, 18.5 Hz, H_{exo}C-9), 2.64 (1H, d, *J* = 11.5 Hz, HC-1), 2.30–2.09 (3H, m, HC-4a, HC-5, HC-7), 1.86–1.67 (3H, m, HC-5, H_2C-6), 1.42 (1H, ddd, *J* = 4, 10, 14.5 Hz, HC-7); ^{13}C NMR δ: 211.6 (s, C-8), 173.6 (s, OC═O), 54.1 (s, C-7a), 52.3 (q, CH_3O), 51.0 (d, C-4), 45.3 (t, C-9), 42.4 (d, C-4a), 36.6 (d, C-3), 28.1 (t, C-1 or 5 or 7), 28.1 (t, C-1 or 5 or 7), 27.1 (t, C-1 or 5 or 7), 21.7 (t, C-6); LRMS (EI), *m/z* (relative intensity): 240 ([M]$^+$, 87), 212 (19), 127 (61), 113 (77), 105 (100).

*Methyl (3*S**,4*S**,4a*R**,7a*S**)-hexahydro-8-oxo-1*H*-3,7a-ethanocyclopenta[c]thiopyran-4-carboxylate* (***46***): IR ν_{max}: 1722, 1232, 1181 cm^{-1}; ^{1}H NMR δ: 3.77 (3H, s, H_3CO), 3.58 (1H, m, HC-3), 3.03 (1H, d, *J* = 11 Hz, HC-1), 2.88 (1H, dd, *J* = 2.5, 19.5 Hz, HC-9), 2.84 (1H, d, *J* = 11 Hz, HC-1), 2.68 (1H, dd, *J* = 4, 19.5 Hz, HC-9), 2.68–2.61 (2H, m, HC-4, HC-4a), 2.56 (1H, ddd, *J* = 5.5, 9, 13 Hz, HC-7), 2.18–2.08 (1H, m, HC-5), 1.81–1.62 (2H, m, H_2C-6), 1.19 (1H, ddd, *J* = 6.5, 10.5, 13 Hz, HC-7), 1.03–0.87 (1H, m, HC-5); δ in $CDCl_3$/C_6D_6: 2.49 (1H, ddd, *J* = 7, 7, 12.5 Hz, HC-4a), 2.39–2.35 (1H, m, HC-4; on irradiation of HC-3, this signal becomes a 7 Hz doublet); ^{13}C NMR δ: 211.2 (s, C-8), 172.7 (s, OC═O), 52.8 (s, C-7a), 52.4 (q, CH_3O), 51.7 (d, C-3), 48.2 (t, C-9), 45.2 (d, C-4a), 38.3 (d, C-3), 32.9 (t, C-4 or 9), 32.8 (t, C-4 or 9), 28.5 (t, C-7), 22.0 (t, C-6); LRMS (EI), *m/z* (relative intensity): 240 ([M]$^+$, 83), 212 (21), 149 (56), 119 (70), 113 (100)

*Methyl (3*S**,4*R**,4a*R**,7a*S**)-hexahydro-8-oxo-1*H*-3,7a-ethanocyclopenta[c]thiopyran-4-carboxylate* (***47***): IR ν_{max}: 1725, 1435, 1174, 956 cm^{-1}; ^{1}H NMR δ: 3.67 (3H, s, H_3CO), 3.61 (1H, ddd, *J* = 2, 2.5, 11.5 Hz, HC-4), 3.41 (1H, dd, *J* = 3, 19.5 Hz, H_{endo}C-9), 3.32 (1H, ddd, *J* = 2.5, 2.5, 3 Hz, HC-3), 3.02 (1H, d, *J* = 11 Hz, HC-1), 2.92 (1H, d, *J* = 11 Hz, HC-1), 2.77 (1H, ddd, *J* = 2, 2.5, 19.5 Hz, H_{exo}C-9), 2.54 (1H, ddd, *J* = 4, 9.5, 13 Hz, HC-7), 2.51 (1H, ddd, *J* = 7, 11.5, 13 Hz, HC-4a), 1.90 (1H, dddd, *J* = 2.5, 7, 7.5, 13 Hz, HC-5), 1.77–1.53 (2H, m, H_2C-6), 1.14 (1H, ddd, *J* = 7, 11, 13 Hz, HC-7), 0.97 (1H, ap tt, *J* = 9.5, 13 Hz, HC-5); ^{13}C NMR δ: 211.4 (s, C-8), 172.4 (s, OC═O), 53.9 (s, C-7a), 51.5 (q, CH_3O), 47.5 (d, C-4), 44.7 (d, C-4a), 44.5 (t, C-9), 36.7 (d, C-3), 32.4 (t, C-1), 28.9 (t, C-5), 28.5 (t, C-7), 20.9 (t, C-6); LRMS (EI), *m/z* (relative intensity): 240 ([M]$^+$, 100), 212 (46), 193 (87), 127 (88), 113 (88).

*Methyl (3*S**,4*S**,4a*S**,7a*S**)-hexahydro-8-oxo-1*H*-3,7a-ethanocyclopenta[c]thiopyran-4-carboxylate* (***48***): IR ν_{max}: 1725, 1435, 1171 cm^{-1}; ^{1}H NMR δ: 3.46 (1H, ddd, *J* = 3, 3.5, 4 Hz, HC-3), 3.36 (1H, dd, *J* = 4, 11.5 Hz, HC-4), 3.20 (1H, br d, *J* = 11.5 Hz, HC-1), 2.89 (1H, dd, *J* = 3.5, 18.5 Hz, HC-9), 2.81 (1H, br d, *J* = 18.5 Hz, HC-9), 2.58 (1H, br d, *J* = 11.5 Hz, HC-1), 2.48 (1H, dddd, *J* = 9, 10.5, 13, 13 Hz, HC-5), 2.22 (1H, ddd, *J* = 5, 11.5, 14 Hz, HC-7), 2.22–2.11 (1H, m, HC-4a), 1.99–2.89 (1H, m, HC-5), 1.82 (1H, ddddd, *J* = 1.5, 5, 9.5, 9.5, 14, Hz, HC-6), 1.63.1–53 (1H, m, HC-6), 1.27 (1H, ddd, *J* = 6, 9.5, 14 Hz, HC-7); LRMS (EI), *m/z* (relative intensity): 240 ([M]$^+$, 100), 153 (20), 113 (96), 91 (35), 81 (56).

*Methyl (3*S**,4*R**,4a*S**,8a*S**)-hexahydro-9-oxo-3*H*-3,8a-ethano-1*H*-2-benzothiopyran-4-carboxylate* (***49***): IR ν_{max}: 2930, 1724, 1446, 1237, 1197 cm^{-1}; ^{1}H NMR δ: 3.72 (3H, s, CH_3O), 3.44 (1H, d, *J* = 11.5 Hz, H_{syn}C-1), 3.32 (1H, ddd, *J* = 2, 2.5, 3.5 Hz, HC-3), 2.87 (1H, dd, *J* = 2.5, 19 Hz, H_{endo}C-10), 2.86 (1H, ddd, *J* = 2, 2, 7.5 Hz, HC-4), 2.72 (1H, ddd, *J* = 2, 3.5, 19 Hz, H_{exo}C-10), 2.47 (1H, dd, *J* = 1.5, 11.5 Hz, H_{anti}C-1), 2.06 (1H, dddd, *J* = 1.5, 4, 7.5, 12 Hz, HC-4a), 2.01–1.91 (1H, m, HC-8), 1.80–1.50 (5H, m, HC-5, H_2C-6, H_2C-7), 1.44–1.18 (2H, m, HC-5, HC-8); ^{13}C NMR δ: 212.5 (s, C-9), 173.3 (s, OC═O), 52.8 (d, C-4), 52.3 (q, CH_3O), 45.1 (s, C-3), 44.4 (t, C-10), 36.9 (d), 34.8 (d), 30.3 (t), 29.0 (t), 25.3 (t), 25.2 (t), 20.9 (t); LRMS (EI), *m/z* (relative intensity): 254 ([M+]$^+$, 85), 227 (27), 195 (26), 151 (22), 127 (100).

*Methyl (3*S**,4*S**,4a*R**,8a*S**)-hexahydro-9-oxo-3*H*-3,8a-ethano-1*H*-2-benzothiopyran-4-carboxylate* (***50***): IR ν_{max}: 2933, 1735, 1721, 1435, 1223, 1203 cm^{-1}; ^{1}H NMR δ: 3.79 (3H, s, H_3CO), 3.49 (1H, ddd, *J* = 3, 3, 3 Hz, HC-3), 2.84 (1H, dd,

J = 3, 19 Hz, HC-10), 2.77 (1H, d, J = 11 Hz, HC-1), 2.65 (1H, d, J = 11 Hz, HC-1), 2.62 (1H, br dd, J = 3, 19 Hz, HC-10) 2.61–2.55 (2H, m, HC-4, HC-4a), 2.21–2.12 (1H, m, HC-8), 1.85–1.77 (1H, m, HC-5), 1.70–1.40 (3H, m, HC-6, H_2C-7), 1.36–1.23 (1H, m, HC-6), 1.10–0.85 (2H, m, HC-5, HC-8); ^{13}C NMR δ: 212.2 (s, C-9), 172.6 (s, OC=O), 52.7 (d, C-4), 52.3 (q, CH_3O), 47.9 (t, C-10), 46.5 (s, C-8a), 39.4 (d), 37.0 (d), 34.8 (t), 34.5 (t), 31.8 (t), 25.6 (t), 22.8 (t); LRMS (CI, NH_3), *m/z* (relative intensity): 272 ($[M+18]^+$, 20), 255 ($[M+1]^+$, 100), 226 (21), 209 (33).

Methyl (2S,4aS*,5R*,8aS*,9R*)-octahydro-4-oxo-2,5-methano-2H-1-benzothiopyran-9-carboxylate (**51**)*: IR ν_{max}: 1730, 1442, 1289, 1202 cm^{-1}; ^1H NMR δ: 3.71 (3H, s, H_3CO), 3.56–3.49 (2H, m, HC-2, HC-8a), 3.14–3.10 (1H, m, HC-9), 2.71–2.56 (3H, m, H_2C-3, HC-5), 2.44 (1H, dd, J = 3.5, 3.5 Hz, HC-4a), 2.13–1.45 (6H, m, H_2C-6, H_2C-7, H_2C-8); δ in $CDCl_3/C_6D_6$: 2.85 (1H, ddd, J = 2, 3, 5 Hz, HC-9), 2.45 (1H, ddd, J = 2, 3.5, 19.5 Hz, $H_{exo}C$-3), [irradiation of HC-2 reveals $^4J_{HexoC\text{-}3,HC\text{-}9}$ = 2 Hz and $^3J_{HC\text{-}5,HC\text{-}9}$ = 5 Hz]; ^{13}C NMR δ: 212.2 (s, C-4), 173.3 (s, OC=O), 52.3 (q, CH_3O), 50.8 (d, C-4a), 49.2 (d, C-9), 43.3 (t, C-3), 35.7 (d, C-2 or 8a), 35.3 (d, C-2 or 8a), 30.7 (t, C-8), 29.1 (d, C-5), 28.5 (t, C-6), 13.9 (t, C-7); LRMS (EI), *m/z* (relative intensity): 240 ($[M]^+$, 100), 208 (19), 181 (67), 113 (62), 81 (61).

Methyl (2S,4aS*,5R*,8aS*,9S*)-octahydro-4-oxo-2,5-methano-2H-1-benzothiopyran-9-carboxylate (**52**)*: IR ν_{max}: 1730, 1712, 1436, 1177 cm^{-1}; ^1H NMR δ: 3.79 (3H, s, H_3CO), 3.52–3.48 (1H, m, HC-8a), 3.49–3.44 (1H, m, HC-2), 3.13 (1H, dd, J = 2, 12 Hz, HC-9), 2.81 (1H, dd, J = 3, 19.5 Hz, HC-3), 2.56 (1H, dd, J = 3.5, 19.5 Hz, HC-3), 2.58–2.49 (2H, m, HC-4a, HC-5), 2.28–2.18 (1H, m, HC-7), 2.04–1.86 (1H, m, HC-7), 1.76–1.67 (1H, m, HC-8), 1.66–1.53 (1H, m, HC-8), 1.48–1.38 (1H, m, HC-6), 1.32 (1H, ddd, J = 4, 4, 14 Hz, HC-6), [irradiation of HC-2 reveals $^3J_{HC\text{-}5,HC\text{-}9}$ = 12.5 Hz]; ^{13}C NMR δ: 212.8 (s, C-4), 172.0 (s, OC=O), 51.8 (q, CH_3O), 51.5 (d, C-4a), 48.8 (t, C-3), 46.7 (d, C-9), 35.3 (d, C-2), 34.1 (d, C-8a), 30.8 (t, C-8), 27.6 (d, C-5), 26.0 (t, C-6), 15.4 (t, C-7); LRMS (EI), *m/z* (relative intensity): 240 ($[M]^+$, 90), 161 (22), 127 (87), 113 (47), 80 (100).

*2,3-Dihydro-3-(methoxymethyl)-4H-thiopyran-4-one (**53**)*
A solution of anhydrous $ZnBr_2$ in ether (0.25 M, 0.16 mL, 0.040 mmol) was added to a solution of chloromethyl methyl ether (91 μL, 96 mg, 1.2 mmol) and 4-trimethylsilyloxy-2*H*-thiopyran (186 mg, 1.00 mmol) in dry CH_2Cl_2 (5 mL) at rt. After stirring for 30 min, the mixture was poured onto saturated $NaHCO_3$ and extracted with CH_2Cl_2. The combined organic layers were washed with H_2O, dried over Na_2SO_4, concentrated, and fractionated by MPC (30% EtOAc in hexane) to give **56** (10 mg, 9%) and **53** as a clear oil (110 mg, 70%): IR ν_{max}: 3029, 1657, 1555, 1204, 1118 cm^{-1}; ^1H NMR δ: 7.42 (1H, dd, J = 1.5, 10 Hz, HC-6), 6.15 (1H, d, J = 10 Hz, HC-5), 3.74 (1H, dd, J = 4.5, 9.5 Hz, HC-1′), 3.59 (1H, dd, J = 9, 9.5 Hz, HC-1′), 3.37 (3H, s, H_3CO), 3.33 (1H, ddd, J = 1.5, 4.5, 13.5 Hz, HC-2), 3.26 (1H, dd, J = 11, 13.5 Hz, HC-2), 2.87 (1H, dddd, J = 4.5, 4.5, 9, 11 Hz, HC-3); ^{13}C NMR δ: 193.8 (s, C-4), 146.3 (d, C-6), 123.7 (d, C-5), 69.6 (t, C-1′), 59.0 (q, CH_3O), 45.8 (d, C-3), 29.7 (t, C-2); LRMS (EI), *m/z* (relative intensity): 158 ($[M]^+$, 81), 126 (22), 125 (15), 113 (72), 86 (100), 58 (37).

*2,3-Dihydro-3-methlyene-4H-thiopyran-4-one (**54**)*
TFA (0.25 mL) was added to a solution of **53** (100 mg, 0.63 mmol) in CH_2Cl_2 (2 mL) at rt. After stirring for 5 days, the reaction mixture was concentrated and filtered through a short column of silica gel eluting with C_6H_6. The filtrate was concentrated and the residue dissolved in CH_2Cl_2 (2 mL). Et_3N (0.25 mL) was added and after stirring for 1–3 days, the reaction mixture was concentrated and fractionated by FCC (20% ether in hexane) to yield **54** as an oil (60 mg, 75%): IR ν_{max}: 3033, 2900, 1786, 1729, 1658, 1611, 1540, 1167 cm^{-1}; ^1H NMR δ: 7.48 (1H, br d, J = 10 Hz, HC-6), 6.25 (1H, br d, J = 10 Hz, HC-5), 6.06 (1H, br s, HC-1′), 5.51 (1H, br s, HC-1′), 3.87 (2H, br s, H_2C-2); ^{13}C NMR δ: 185.2 (s, C-4), 146.3 (d, C-6), 139.0 (s, C-3), 124.5 (d, C-5), 123.4 (t, C-1′), 34.2 (t, C-2); LRMS (CI, NH_3), *m/z* (relative intensity): 144 ($[M+18]^+$, 4), 127 ($[M+1]^+$, 100), 126 (14), 97 (4).

*2-(2-Hydroxyethylthio)-tetrahydro-4H-thiopyran-4-one (**57**)*
2-Mercaptoethanol (0.13 mL, 1.8 mmol) was added to a suspension of NaH (3 mg, 0.1 mmol) in THF (5 mL). Compound **56** (100 mg, 0.80 mmol) was added and the mixture was stirred at rt for 10 h. The reaction mixture was concentrated and the residue dissolved in CH_2Cl_2; the solution was washed with H_2O (×3), dried over Na_2SO_4, concentrated, and fractionated by FCC (35% EtOAc in hexane) to give **57** (92 mg, 55%): ^1H NMR δ: 4.27 (1H, br t, J = 4.5 Hz, HC-2), 3.64 (1H, s, HO), 3.52 (2H, ap t, J = 6 Hz, H_2C-2′), 3.04 (1H, ddd, J = 6.5, 7, 14 Hz, HC-6), 2.85 (1H, dd, J = 4.5, 14.5 Hz, HC-3), 2.72–2.55 (2H, m, HC-6, HC-1′,), 2.55–2.38 (4H, m, HC-3, H_2C-5, HC-1′); ^{13}C NMR δ: 206.4 (s, C-4), 61.1 (t, C-2′), 49.5 (d, C-2), 48.1 (t, C-3), 42.9 (t, C-5), 34.4 (t, C-1′), 26.0 (t, C-6); LRMS (EI), *m/z* (relative intensity): 192 ($[M]^+$, 10), 115 (100), 87 (41), 73 (35). HRMS *m/z* calcd. for $C_7H_{12}O_2S_2$: 192.0279; found: 192.0278. Anal. calcd. for $C_7H_{12}O_2S_2$: C 43.72, H 6.29; found: C 42.92, H 6.34.

*2-[(Tetrahydro-4-oxo-2H-thiopyran-2-yl)thio]ethyl propenoate (**58**)*
Compound **57** (75 mg, 0.39 mmol) was added to a stirred solution of acryloyl chloride (70 mg, 0.77 mmol) and pyridine (0.6 mL, 0.8 mmol) in CH_2Cl_2 (3 mL) at rt. After 5 h, the reaction mixture was washed with H_2O (5 mL), dried over Na_2SO_4, concentrated, and fractionated by FCC (25% EtOAc in hexane) to give **58** (43 mg, 45%; note: higher yields are obtained if the reaction is conducted at 0°C): ^1H NMR δ: 6.45 (1H, dd, J = 1.5, 17.5 Hz, HC-3), 6.15 (1H, dd, J = 10.5, 17.5 Hz, HC-2), 5.85 (1H, dd, J = 1.5, 10.5 Hz, HC-3), 4.55–4.20 (3H, m, H_2C-1′, HC-2″), 3.28–3.14 (2H, m), 3.13–2.95 (2H, m), 3.10–2.95 (2H, m), 2.90–2.55 (4H, m).

*2-[(Tetrahydro-4-oxo-2H-thiopyran-2-yl)thio]ethyl methyl (E)-butendioate (**59**)*
Methyl fumaryl chloride (535 mg, 4 mmol) was added dropwise to a solution of **57** (517 mg, 2.7 mmol) and pyridine (0.3 mL, 4 mmol) in CH_2Cl_2 at 0°C and the mixture was stirred at rt for 4 h. The mixture was diluted with CH_2Cl_2, washed with water, dried over Na_2SO_4, concentrated, and fractionated by FCC (30% EtOAc in hexane) to give **59** (1.02 g, 89%): ^1H

NMR δ: 6.77 (2H, ap s, HC-2, HC-3), 4.42–4.38 (1H, m, HC-2″), 4.37–4.18 (2H, m, H_2C-1′), 3.73 (3H, s, H_3CO), 3.21 (1H, ddd, J = 5, 9, 14 Hz, HC-6″), 3.01 (1H, dd, J = 5, 14.5 Hz, HC-3″), 3.00–2.92 (1H, m, HC-2′), 2.82–2.76 (1H, m, HC-2′), 2.78–2.69 (1H, m, HC-6″), 2.70–2.55 (3H, m, J = 5.5, 14.5 Hz, HC-3″, H_2C-5″); ^{13}C NMR δ: 205.0 (s, C-4″), 164.9 (s, C-1 or C-4), 164.3 (s, C-1 or C-4), 133.6 (d, C-2 or C-3), 133.0 (d, C-2 or C-3), 63.7 (t, C-1′), 51.3 (q, CH_3O), 49.1 (d, C-2″), 48.2 (t, C-3″), 42.8 (t, C-5″), 30.3 (t, C-2′), 25.8 (t, C-6″); LRMS (CI, NH_3), *m/z* (relative intensity): 322 ([M+18]$^+$, 52), 132 (9), 115 (100), 87 (9). HRMS *m/z* calcd. for $C_{12}H_{16}O_5S_2$: 304.0439; found: 304.0430. Anal. calcd. for $C_{12}H_{16}O_5S_2$: C 47.35, H 5.30; found: C 46.84, H 5.33.

*2-[(3,4-Dihydro-4-oxo-2*H*-thiopyran-6-yl)thio]ethyl propenoate (**60a**), 2-[(5-chloro-3,4-dihydro-4-oxo-2*H*-thiopyran-6-yl)thio]ethyl propenoate (**60b**), 2-[(3,4-dihydro-4-oxo-2*H*-thiopyran-6-yl)thio]ethyl methyl* (E)*-butendioate (**61a**), and 2-[(5-chloro-3,4-dihydro-4-oxo-2*H*-thiopyran-6-yl)thio]ethyl methyl* (E)*-butendioate (**61b**)*

NCS (1.0–1.2 equiv.) was added in portions to a stirred solution of **58** (30 mg, 0.12 mmol) or **59** (255 mg, 0.84 mmol) in CCl_4 (ca. 10 mL/mmol of **58** or **59**) at 0°C. After 15–20 h, the reaction mixture was diluted with CH_2Cl_2, washed with water, dried over Na_2SO_4, concentrated, and fractionated by PTLC (30% EtOAc in hexane) to give a mixture of **60a,b** or **61a,b**. Further fractionated by PTLC (%1 MeOH in CH_2Cl_2) gave the pure components **60a** (7 mg, 24%), **60b** (8 mg, 24%), **61a** (57 mg, 22%), and **61b** (63 mg, 22%).

For **60a**: ^{1}H NMR δ: 6.45 (1H, dd, J = 1.5, 17.5 Hz, HC-3), 6.29 (1H, s, HC-5″), 6.13 (1H, dd, J = 10.5, 17.5 Hz, HC-2), 5.89 (1H, dd, J = 1.5, 10.5 Hz, HC-3), 4.38 (2H, ap t, J = 6.5 Hz, H_2-C1′), 3.26 (2H, ap t, J = 6.5 Hz, H_2C-2′), 3.27–3.15 (2H, m, H_2C-2″), 2.77–2.69 (2H, m, H_2C-3″); ^{13}C NMR δ: 191.4 (s, C-4″), 165.6 (s, C-1), 161.4 (s, C-6″), 131.6 (t, C-3), 127.8 (d, C-2), 119.8 (d, C-5″), 62.1 (t, C-1′), 37.5 (t, C-3″), 32.6 (t, C-2′), 28.6 (t, C-2″); LRMS (CI, NH_3), *m/z* (relative intensity): 245 ([M+1]$^+$, 100), 172 (8.6), 147 (11), 115 (11). HRMS *m/z* calcd. for $C_{10}H_{12}O_3S_2$: 244.0228; found: 244.0231.

For **60b**: ^{1}H NMR δ: 6.47 (1H, dd, J = 1.5, 17.5 Hz, HC-3), 6.15 (1H, dd, J = 10.5, 17.5 Hz, HC-2), 5.90 (1H, dd, J = 1.5, 10.5 Hz, HC-3), 4.43 (2H, ap t, J = 6.5 Hz, HC-1′), 3.35 (2H, ap t, J = 6.5 Hz, HC-2′), 3.31–3.25 (2H, m, HC-2″), 2.98–2.92 (2H, m, H_2C-3″); ^{13}C NMR δ: LRMS (CI, NH_3), *m/z* (relative intensity): 281 ([M+1]$^+$, 50), 279 ([M+1]$^+$, 100), 206 (15), 147 (13), 99 (15). HRMS *m/z* calcd. for $C_{10}H_{11}{}^{35}ClO_3S_2$: 277.9838; found: 277.9836.

For **61a**: ^{1}H NMR δ: 6.87 (2H, ap s, HC-2, HC-3), 6.27 (1H, s, HC-5″), 4.41 (2H, ap t, J = 6.5 Hz, HC-2′), 3.82 (3H, s, H_3CO), 3.27 (2H, ap t, J = 6.5 Hz, H_2C-1′), 3.24–3.18 (2H, m, H_2C-2″), 2.77–2.71 (2H, m, HC-3″); ^{13}C NMR δ: 191.4 (s, C-4″), 165.1 (s, C-1 or C-4), 164.4 (s, C-1 or C-4), 161.1 (s, C-6″), 134.1 (d, C-2 or C-3), 132.8 (d, C-2 or C-3), 119.9 (d, C-5″), 62.8 (t, C-1′), 52.4 (q, CH_3O), 37.5 (t, C-3″), 31.1 (t, C-2′), 28.6 (t, C-2″); LRMS (EI), *m/z* (relative intensity): 302 ([M]$^+$, 30), 172 (36), 139 (50), 113 (60), 85 (100). HRMS *m/z* calcd. for $C_{12}H_{14}O_5S_2$: 302.0283; found: 302.283. Anal. calcd. for $C_{12}H_{14}O_5S_2$: C 47.67, H 4.67; found: C 47.87, H 4.41.

For **61b**: ^{1}H NMR δ: 6.87 (2H, ap s, HC-2, HC-3), 4.45 (2H, ap t, J = 6.5 Hz, H_2C-1′), 3.80 (3H, s, H_3CO), 3.34 (2H, ap t, J = 6.5 Hz, H_2C-2′), 3.31–3.25 (2H, m, H_2C-2″), 2.96–2.90 (2H, m, H_2C-3″); ^{13}C NMR δ: 183.5 (s, C-4″), 165.1 (s, C-1 or C-4), 164.4 (s, C-1 or C-4), 156.2 (s, C-6″), 134.2 (d, C-2 or C-3), 132.8 (d, C-2 or C-3), 119.9 (s, C-5″), 63.1 (t, C-1′), 52.4 (q, CH_3O), 38.4 (t, C-3″), 31.0 (t, C-2′), 28.1 (t, C-2″); LRMS (CI, NH_3), *m/z* (relative intensity): 338 ([M]$^+$, 20), 336 ([M]$^+$, 44), 208 (42), 206 (100), 157 (97), 113 (97). HRMS *m/z* calcd. for $C_{12}H_{13}{}^{35}ClO_5S_2$: 335.9893; found: 335.9892. Anal. calcd. for $C_{12}H_{13}ClO_5S_2$: C 42.79, H 3.89; found: C 43.03, H 4.05.

*2-[4-[[Tris(1-methylethyl)silyl]oxy]-2*H*-thiopyran-6-yl]thio]ethyl propenoate (**62a**)*: ^{1}H NMR δ: 6.42 (1H, dd, J = 1.5, 17.5 Hz, HC-3), 6.24 (1H, d, J = 1.5 Hz, HC-5″), 6.12 (1H, dd, J = 10.5, 17.5 Hz, HC-2), 5.84 (1H, dd, J = 1.5, 10.5 Hz, HC-3), 4.76 (1H, dt, J = 1.5, 5.5 Hz, HC-3″), 4.34 (2H, ap t, J = 7 Hz, H_2C-1′), 3.34 (2H, d, J = 5.5 Hz, H_2C-2″), 3.14 (2H, ap t, J = 7 Hz, H_2C-2′), 1.15–1.04 (21H, m, $(H_3C)_2$CHSi).

*2-[5-Chloro-4-[[tris(1-methylethyl)silyl]oxy]-2*H*-thiopyran-6-yl]thio]ethyl propenoate (**62b**)*: ^{1}H NMR δ: 6.40 (1H, dd, J = 1.5, 17.5 Hz, HC-3), 6.25 (1H, d, J = 1.5 Hz, HC-5″), 6.10 (1H, dd, J = 10.5, 17.5 Hz, HC-2), 5.85 (1H, dd, J = 1.5, 10.5 Hz, HC-3), 4.95 (1H, dt, J = 1.5, 5.5 Hz, HC-3″), 4.35 (2H, ap t, J = 7 Hz, H_2C-1′), 3.30 (2H, d, J = 5.5 Hz, H_2C-2″), 3.20 (2H, ap t, J = 7 Hz, H_2C-2′), 1.15–1.04 (21H, m, $(H_3C)_2$CHSi).

*2-[[4-[[Tris(1-methylethyl)silyl]oxy]-2*H*-thiopyran-6-yl]thio]ethyl methyl* (E)*-butendioate (**63a**)*: ^{1}H NMR δ: 6.86 (2H, ap s, HC-2, HC-3), 6.23 (1H, d, J = 1.5 Hz, HC-5″), 4.76 (1H, dt, J = 1.5, 5.5 Hz, HC-3″), 4.36 (2H, ap t, J = 6.5 Hz, H_2C-1′), 3.80 (3H, s, H_3CO), 3.33 (2H, d, J = 5.5 Hz, H_2C-2″), 3.13 (2H, ap t, J = 6.5 Hz, H_2C-1′), 1.15–1.04 (21H, m, $(CH_3)_2$CHSi).

*2-[[5-Chloro-4-[[tris(1-methylethyl)silyl]oxy]-2*H*-thiopyran-6-yl]thio]ethyl methyl* (E)*-butendioate (**63b**)*: ^{1}H NMR δ: 6.88 (2H, ap s, HC-2, HC-3), 4.98 (1H, dt, J = 1.5, 5.5 Hz, HC-3″), 4.38 (2H, ap t, J = 6.5 Hz, H_2C-1′), 3.80 (3H, s, H_3CO), 3.31 (2H, d, J = 5.5 Hz, H_2C-2″), 3.25 (2H, ap t, J = 6.5 Hz, H_2C-1′), 1.15–1.04 (21H, m, $(CH_3)_2$CHSi).

*Methyl (3a*S**,4*S**,7*R**,7a*R**)-octahydro-7-hydroxy-7a-methyl-1*H*-indene-4-carboxylate (**64a**) and methyl (3a*S**,4*S**,7*S**,7a*R**)-octahydro-7-hydroxy-7a-methyl-1*H*-indene-4-carboxylate (**64b**)*

Raney Ni (0.30 mL) was added to a stirred solution of **45** (5.7 mg, 0.024 mmol) in MeOH (1 mL) and the resuling suspension was heated under reflux for 1 h. The reaction mixture was filtered through Celite with the aid of MeOH. The combined filtrate and washings were concentrated and fractionated by MPC (28% ethyl acetate in hexane) to give **64a** (1.9 mg, 38%) and **64b** (3.1 mg, 62%).

For **64a**: IR ν_{max}: 3468, 2950, 2871, 1735, 1450, 1155 cm^{-1}; ^{1}H NMR δ: 3.67 (3H, s, H_3CO), 3.46 (1H, dd, J = 4.5, 11 Hz, HC-7), 2.28–2.21 (1H, m, HC-4), 1.93–1.25 (11H, m), 0.75 (3H, s, H_3CC-7a); ^{13}C NMR (125 MHz) δ: 176.3, 78.7, 51.4, 49.3, 46.1, 42.2, 37.8, 29.7, 28.5, 25.7, 19.6, 11.2; LRMS (CI, NH_3), *m/z* (relative intensity): 230 ([M+18]$^+$, 67), 227 ([M+1]$^+$, 59), 195 (82), 180 (100), 135 (88), 130 (92).

For **64b**: IR ν_{max}: 3515, 2950, 2874, 1735, 1165 cm^{-1}; ^{1}H NMR δ: 3.80–3.76 (1H, m, HC-7), 3.66 (3H, s, H_3CO), 2.34 (1H, ddd, J = 4, 10, 10 Hz, HC-4), 1.92–1.61 (9H, m), 1.40–

1.22 (2H, m), 0.77 (3H, s, H_3CC-7a); ^{13}C NMR δ: 176.1, 71.6, 51.3, 45.3, 43.4, 41.6, 32.6, 28.3, 25.4, 23.8, 19.2, 18.0; LRMS (CI, NH_3), *m/z* (relative intensity): 2230 ($[M+18]^+$, 61), 227 ($[M+1]^+$, 24), 195 (100), 135 (56), 130 (67).

Methyl (1S,R*,4aR*,8aS*)-decahydro-4-hydroxy-4a-methylnaphthalene-1-carboxylate (**65a**) and methyl (1S*,4S*,4aR*,8aS*)-decahydro-4-hydroxy-4a-methylnaphthalene-1-carboxylate, (**65b**)*

Raney Ni (0.15 mL) was added to a stirred solution of **49** (12.5 mg, 0.049 mmol) in MeOH (2 mL) and the resulting suspension heated under reflux for 1 h. The reaction mixture was filtered through Celite with the aid of MeOH. The combined filtrate and washings were concentrated and fractionated by MPC (20% ethyl acetate in hexane) to give **65a** (5.3 mg, 48%) and **65b** (5.3 mg, 48%).

For **65a**: IR ν_{max}: 3480, 2927, 2862, 1735, 1436, 1171 cm^{-1}; ^1H NMR δ: 3.65 (3H, s, H_3CO), 3.32 (1H, dd, J = 4.5, 11 Hz, HC-4), 2.23 (1H, dt, J = 4, 11 Hz, HC-1), 2.02–1.09 (13H, m), 0.85 (3H, s, H_3C); ^{13}C NMR δ: 176.6, 78.5, 51.4, 45.7, 44.4, 38.8, 37.1, 29.0, 28.0, 26.2, 25.2, 21.2, 10.3; LRMS (CI, NH_3), *m/z* (relative intensity): 244 ($[M+18]^+$, 100), 227 ($[M+1]^+$, 45), 209 (50), 194 (26).

For **65b**: IR ν_{max}: 3513, 2926, 2859, 1735, 1443, 1153 cm^{-1}; ^1H NMR δ: 3.65 (3H, s, H_3CO), 3.36 (1H, br s, HC-4), 2.30 (1H, ddd, J = 4, 4, 12 Hz, HC-1), 1.92–1.00 (13H, m), 0.87 (3H, s, H_3C); ^{13}C NMR δ: 176.4, 74.4, 51.2, 45.0, 39.1, 37.8, 34.8, 27.6, 26.3, 25.7, 23.9, 21.4, 16.7; LRMS (CI, NH_3), *m/z* (relative intensity): 244 ($[M+18]^+$, 37), 227 ($[M+1]^+$, 31), 209 (100).

Acknowledgements

Financial support from the Natural Sciences and Engineering Research Council of Canada and the University of Saskatchewan is gratefully acknowledged.

References

1. O. Diels and K. Alder. Justus Liebigs Ann. Chem. **460**, 98 (1928).
2. (*a*) F. Fringuelli and A. Taticchi. *In* Dienes in the Diels–Alder reaction. Wiley, New York. 1990; (*b*) W. Carruthers. *In* Cycloaddition reactions in organic synthesis. Pergamon, Oxford. 1990; (*c*) G. Desimoni, G. Tacconi, A. Barcoa, and G.P. Pollini. *In* Natural product synthesis through pericyclic reactions. ACS Monograph 180. American Chemical Society, Washington. 1983; (*d*) B.M. Trost and I. Flemming (*Editors*). Comprehensive organic synthesis. Vol. 5. Pergamon Press, Oxford. 1991. Chap. 4.
3. (*a*) J.G. Martin and R.K. Hill. Chem. Rev. **61**, 537 (1961); (*b*) J. Sauer. Angew. Chem. Int. Ed. Engl. **6**, 16 (1967).
4. D.E. Ward, W.M. Zoghaib, C.K. Rhee, and Y. Gai. Tetrahedron Lett. **31**, 845 (1990).
5. D.E. Ward, Y. Gai, and W.M. Zoghaib. Can. J. Chem. **69**, 1487 (1991).
6. D.E. Ward and Y. Gai. Tetrahedron Lett. **33**, 1851 (1992).
7. D.E. Ward and Y. Gai. Can. J. Chem. **70**, 2627 (1992).
8. D.E. Ward and T.E. Nixey. Tetrahedron Lett. **34**, 947 (1993).
9. D.E. Ward, Y. Gai, and Y. Lai. Synlett, 261 (1996).
10. (*a*) W.R. Roush. *In* Comprehensive organic synthesis. Vol. 5. *Edited by* B.M. Trost and I. Flemming. Pergamon, Oxford. 1991. Chap. 4.4; (*b*) W.R. Roush. *In* Advances in cycloaddition. Vol. 2. *Edited by* D.P. Curran. JAI Press, Greenwich, Conn. 1990. p. 91; (*c*) M.J. Taschner. *In* Organic synthesis: theory and application. Vol. 1. *Edited by* T. Hudlicky. JAI Press, Greenwich, Conn. 1989. p. 79; (*d*) D. Craig. Chem. Soc. Rev. **16**, 187 (1987); (*e*) A. Fallis. Can. J. Chem. **62**, 183 (1984); (*f*) E. Ciganek. Org. React. **32**, 1 (1984); (*g*) D.F. Taber. *In* Intramolecular Diels–Alder and ene reactions. Springer–Verlag, Berlin. 1984; (*h*) L.A. Paquette. *In* Asymmetric synthesis. Vol. 3. *Edited by* J.D. Morrison. Academic Press, New York. 1984. Chap. 7; (*i*) G. Brieger and J.N. Bennett. Chem. Rev. **80**, 63 (1980); (*j*) R. Funk, and K.P.C. Vollhardt. Chem. Soc. Rev. **9**, 41 (1980); (*k*) W. Oppolzer. Synthesis, 793 (1978); (*l*) Angew. Chem. Int. Ed. Engl. **16**, 10 (1977); (*m*) G. Mehta. J. Chem. Educ. **53**, 551 (1976); (*n*) R.G. Carlson. Annu. Rep. Med. Chem. **9**, 270 (1974).
11. W.R. Roush, A.I. Ko, and H.R. Gillis. J. Org. Chem. **45**, 4264 (1980).
12. (*a*) K.R. Buszek. Tetrahedron Lett. **36**, 9125 (1995); (*b*) P.A. Wender and T.E. Smith. J. Org. Chem. **60**, 2962 (1994); (*c*) S.F. Martin, Y. Liao, Y. Wong, and T. Rein. Tetrahedron Lett. **35**, 691 (1995); (*d*) M. Sodeoka, H. Yamada, and M. Shibasaki. J. Am. Chem. Soc. **112**, 4906 (1990); (*e*) S.-S.P. Chou and S.-J. Wey. J. Org. Chem. **55**, 1270 (1990); (*f*) S. Wattanasin, F.G. Kathawala, and R.K. Boeckman. J. Org. Chem. **50**, 3810 (1985); (*g*) M. Yoshida, H. Nakai, and M. Ohno. J. Am. Chem. Soc. **106**, 1133 (1984); (*h*) M. Koreeda and J.I. Luengo. J. Org. Chem. **49**, 2079 (1984); (*i*) S.F. Martin, S.A. Williamson, R.P. Gist, and K.M. Smith. J. Org. Chem. **48**, 5170 (1983); (*j*) R.K. Boeckman, and T.R. Alessi. J. Am. Chem. Soc. **104**, 3216 (1982); (*k*) S.G. Pyne, M.J. Hensel, and P.J. Fuchs. J. Am. Chem. Soc. **104**, 5719 (1982); (*l*) M.E. Kuehne, T.H. Matsko, J.C. Bohnert, L. Motyka, and D. Oliver-Smith. J. Org. Chem. **46**, 2002 (1981); (*m*) W. Oppolzer, C. Fehr, and J. Warneke. Helv. Chim. Acta, **60**, 48 (1977); (*n*) R.F. Borch, A.J. Evans, and J.J. Wade. J. Am. Chem. Soc. **99**, 1612 (1977); (*o*) H.O. House and T.H. Cronin. J. Org. Chem. **30**, 1061 (1965).
13. (*a*) T.K. Park, I.J. Kim, S.J. Danishefsky, and S. de Gala. Tetrahedron Lett. **36**, 1019 (1995); (*b*) J.D. Winkler, H.S. Kim, and S. Kim. Tetrahedron Lett. **36**, 687 (1995); (*c*) M.Y. Chu-Moyer, S.J. Danishefsky, and G.K. Schulte. J. Am. Chem. Soc. **116**, 11213 (1994); (*d*) R.W. Jackson and K.J. Shea. Tetrahedron Lett. **35**, 1317 (1994); (*e*) I. Hanna, J.-Y. Lallemand, and P. Wlodyka. Tetrahedron Lett. **35**, 6685 (1994); (*f*) A. Tahri, D. Uguen, A. De Cain, and J. Fischer. Tetrahedron Lett. **35**, 3945 (1994); (*g*) R.V. Bonnert and P.R. Jenkins. J. Chem. Soc. Perkin Trans. 1, 413 (1989); (*h*) K.J. Shea and C.D. Haffner. Tetrahedron Lett. **29**, 1367 (1988); (*i*) E.J. Corey, P.D.S. Jardine, and J.C. Rohloff. J. Am. Chem. Soc. **110**, 3672 (1988); (*j*) J.-F. He and Y.-L. Wu. Tetrahedron, **44**, 1933 (1988); (*k*) F.E. Ziegler, B.H. Jaynes, and M.T. Saindane. J. Am. Chem. Soc. **109**, 8115 (1987); (*l*) P. Magnus, C. Walker, P.R. Jenkins, and K.A. Meanar. Tetrahedron Lett. **27**, 651 (1986); (*m*) K.C. Nicolaou and W.S. Li. J. Chem. Soc. Chem. Commun. 421 (1985); (*n*) P.R. Jenkins, K.A. Menear, P. Barraclough, and M.S. Nobbs. J. Chem. Soc. Chem. Commun. 1423 (1984); (*o*) K.J. Shea and P.D. Davis. Angew. Chem. Int. Ed. Engl. **22**, 419 (1983).
14. T. Saito, T. Shizuta, H. Kikuchi, J. Nakagawa, K. Hirotsu, H. Ohmura, and S. Motoki. Synthesis, 727 (1994).
15. (*a*) E.A. Fehnel and M. Carmack. J. Am. Chem. Soc. **70**, 1813 (1948); (*b*) N.G. Rule, M.R. Detty, J.E. Kaeding, and J.A. Sinicropi. J. Org. Chem. **60**, 1665 (1995); (*c*) S. Tamai, H. Ushirogochi, S. Sano, and Y. Nagao. Chem. Lett. 295 (1995).
16. (*a*) T. Takemura and J.B. Jones. J. Org. Chem. **48**, 791 (1983); (*b*) S. Lane, S.J. Quick, and R.J.K. Taylor. J. Chem. Soc. Perkin Trans. 1, 893 (1985); (*c*) H. Matsuyama, Y. Takei, and M. Kobayashi. Bull. Chem. Soc. Jpn. **59**, 2657 (1986); (*d*) H. Matsuyama, Y. Miyazawa, Y. Takei, and M. Kobayashi. J. Org. Chem. **52**, 1703 (1987); (*e*) T. Fujisawa, B.I. Mobele, and M. Shimizu. Tetrahedron Lett. **32**, 7055 (1991).

17. G.A. Krause and K. Landgrebe. Synthesis, 885 (1984).
18. R.J. Batten, J.D. Coyle, R.J.K. Taylor, and S. Vassiliou. J. Chem. Soc. Perkin Trans. 1, 1177 (1982).
19. C.H. Chen, G.A. Reynolds, and J.H. Van Allan. J. Org. Chem. **42**, 2777 (1977).
20. V.K. Kansal and R.J.K. Taylor. J. Chem. Soc. Perkin Trans. 1, 703 (1984).
21. S. Lane, S.J. Quick, and R.J.K. Taylor. J. Chem. Soc. Perkin Trans. 1, 2549 (1984).
22. G. Casy, A.G. Sutherland, R.J.K. Taylor, and P.G. Urben. Synthesis, 767 (1989).
23. E. Vedejs, M.J. Arnost, and J.P. Hagen. J. Org. Chem. **44**, 3230 (1979).
24. (*a*) S.U. Kulkarni and V.D. Patil. Heterocycles 18, 163 (1982); (*b*) J.K. Baker and T.L. Little. J. Med. Chem. **28**, 46 (1985).
25. H.O. House, V.K. Jones, and G.A. Frank. J. Org. Chem. **29**, 3327 (1964).
26. (*a*) H. Lamy-Schelkens and L. Ghosez. Tetrahedron Lett. **30**, 5891 (1989); (*b*) H. Lamy-Schelkens, D. Giomi, and L. Ghosez. Tetrahedron Lett. **30**, 5887 (1989).
27. K.J. Shea, S. Wise, L.D. Burke, P.D. Davis, J.W. Gilman, and A.C. Greeley. J. Am. Chem. Soc. **104**, 5708 (1982).
28. D.T. Witiak, K. Tomita, and R.J. Patch. J. Med. Chem. **24**, 788 (1981).
29. M. Bols and T. Skrydstrup. Chem. Rev. **95**, 1253 (1995).
30. (*a*) M.E. Jung. Synlett, 186 (1990); (*b*) M.E. Jung and J. Gervay. J. Am. Chem. Soc. **113**, 224 (1991).
31. R.D. Little, M.R. Masjedizadeh, O. Wallquist, and J.I. McLaughlin. Org. React. **47**, 315 (1995).
32. (*a*) W.R. Roush, H.R. Gillis, and A.I. Ko. J. Am. Chem. Soc. **104**, 2269 (1982); (*b*) W.R. Roush and H.R. Gillis. J. Org. Chem. **47**, 4825 (1982).
33. W.C. Still, M. Kahn, and A. Mitra. J. Org. Chem. **43**, 2923 (1978).
34. D.F. Taber. J. Org. Chem. **47**, 1351 (1982).
35. D.W. Brown, T.T. Nakashima, and D.L. Rabenstein. J. Magn. Reson. **45**, 302 (1981).
36. K.A. Walker, M.R. Boots, J.F. Stubbins, M.E. Rogers, and C.W. Davis. J. Med. Chem. **26**, 174 (1983).

Molecular motion in crown ethers. Application of ^{13}C and ^{2}H NMR to the study of 4-carboxybenzo-24-crown-8 ether and its KNCS complex in solution and in the solid phase[1]

G.W. Buchanan, A. Moghimi, and C.I. Ratcliffe

Abstract: Large-amplitude solid phase molecular motion has been detected in the macrocyclic ring of the title crown either via ^{13}C CPMAS NMR. To study the details of the dynamic processes, two selectively deuterated d_4 derivatives have been prepared and examined via ^{2}H NMR as a function of temperature. A phase change occurring around 277 K has been verified by differential scanning calorimetry (DSC) and a model for the motional processes has been developed involving equivalent two-site flips of the CD_2 groups. The amplitude of the CD_2 motions apparently decreases the closer the group is to the aromatic ring. The influence of KNCS complexation on the ^{13}C CPMAS spectrum and on ^{13}C spin lattice relaxation times in solution has been explored.

Key words: macrocyclic ethers, solid phase dynamics.

Résumé : La spectroscopie de RMN et de CPMAS du ^{13}C a permis de déceler un mouvement moléculaire de grande amplitude dans la phase solide du macrocycle de l'éther couronne mentionné dans le titre. Dans le but d'étudier le détail du processus dynamique, on a choisi de préparer deux dérivés deutérés d_4 et on les a étudiés par RMN du ^{2}H en fonction de la température. Il se produit un changement de phase vers 277 K que l'on a pu vérifier par calorimétrie à balayage différentiel (CBD) et on a mis au point, pour ce mouvement, un modèle impliquant deux sites équivalents de pliage des groupes CD_2. L'amplitude des mouvements des groupes CD_2 décroît apparemment lorsque le groupe est très près du cycle aromatique. On a étudié l'influence de la complexation par le KNCS sur le spectre CPMAS du ^{13}C et sur les temps de relaxation spin-réseau en solution du ^{13}C.

Mots clés : éthers macrocycliques, dynamique dans la phase solide.

[Traduit par la rédaction]

Introduction

Complexes of macrocyclic polyethers (crown ethers) are widely recognized as models for molecular recognition. Typically, these free macrocycles have highly flexible geometries in solution, and thus can adapt their conformations for optimum complexation of guest species.

Recent work from these laboratories has shown that a substantial degree of motional freedom also exists in the solid state for several complexes of 18-crown-6 (1–6) and 12-crown-4 (7) ether systems.

Received January 3, 1996.

G.W. Buchanan[2] **and A. Moghimi.**[3] Ottawa–Carleton Chemistry Institute, Department of Chemistry, Carleton University, 1125 Colonel By Drive, Ottawa, ON K1S 5B6, Canada.

C.I. Ratcliffe. Molecular Structures and Dynamics Group, Steacie Institute of Molecular Sciences, National Research Council of Canada, Ottawa, ON K1A 0R6, Canada.

1 Taken in part from the Ph.D. thesis of A. Moghimi, Carleton University, May 1994.

2 Author to whom correspondence may be addressed. Telephone: (613) 788-3841. Fax: (613) 788-3749. E-mail: gwbuchan@ccs.carleton.ca

3 Present address: Department of Chemistry, University of Imam Hosein, Tehran, Iran.

The first indication that motion might be taking place in the 24-crown-8 ether macrocycle in the solid phase came from a comparison of the normal and dipolar dephased (8) ^{13}C CPMAS NMR spectra of a copolymer of styrene and 4-vinylbenzo-24-crown-8 (below).

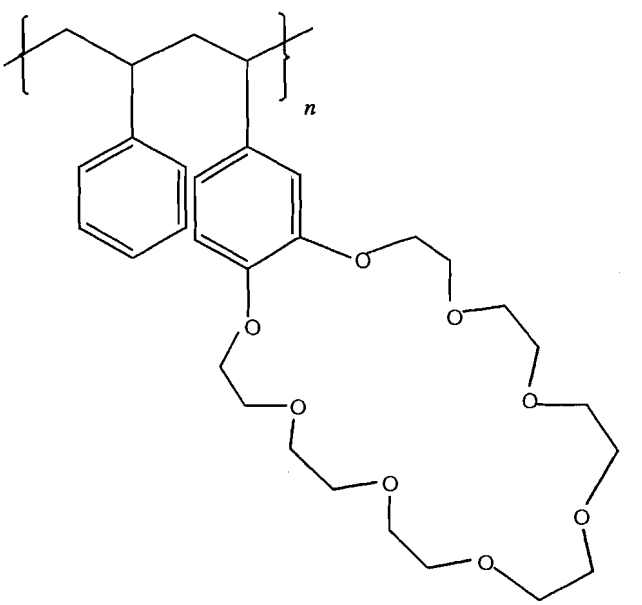

Normally, resonances for protonated carbons are lost in the dipolar dephased experiment. The dipolar dephased spectrum

of this material, however, showed a substantial residual intensity for some of the CH_2-O resonances indicative of some large-amplitude motion in the polyether macrocyle.

To examine the details of such motion in the 24-crown-8 macrocycle, a simpler molecular network that is solid over a wide range of temperatures is required. The 4-carboxybenzo-24-crown-8 molecule, **1**, meets these criteria.

Experimental

Materials

The synthesis of **1** was carried out starting with commercially available 3,4-dihydroxybenzaldehyde (Aldrich), which was condensed with 1,20-dichloro-3,6,9,12,15,18-hexaoxatetradecane. The resulting aldehyde was oxidized to **1**. Details follow. Initially, heptaethylene glycol was prepared according to the procedure outlined below.

A 1 L round-bottom three-necked flask, equipped with a condenser and a dropping funnel, was charged with diethylene glycol (Aldrich) (660.0 g, 6.2 mol) and crushed NaOH pellets (80.0 g, 2 mol), and was heated to 100°C while stirring under a nitrogen atmosphere for 2 h until most of the base had dissolved. Then 1,2-bis(2-chloroethoxy)ethane (Aldrich) (187.1 g, 1.0 mol) was added dropwise to the mixture over a period of 2 h while keeping the temperature at about 120°C. After refluxing for 4 h, the reaction mixture was cooled to room temperature and the water produced in the reaction was removed at reduced pressure. The resulting concentrate was diluted with CH_2Cl_2 (200 mL) and the NaCl was removed by filtration. The solution was dried over anhydrous Na_2SO_4 and, after removal of the drying agent, the solvent was removed by rotoevaporation. Fractional distillation at reduced pressure (0.7 Torr; 1 Torr = 133.3 Pa) yielded 135.0 g (41.4%) of heptaethylene glycol, bp 240–250°C. ^{13}C NMR ($CDCl_3$), δ_C: 72.4, 70.3, 70.1, 61.3. CIMS: M + 1 at 327 (100%).

Heptaethylene glycol was converted to 1,20-dichloro-3,6,9,12,15,18-hexaoxatetradecane according to the following method. Thionyl chloride (52.5 mL, 0.72 mol) was added dropwise with stirring to cooled heptaethylene glycol (108.6 g, 0.33 mol) under nitrogen. The mixture was stirred at room temperature for 14 h, then refluxed for 26 h. The excess thionyl chloride was removed at reduced pressure; the residue was poured onto ice (50 g) and then washed with CH_2Cl_2 (3 × 100 mL). The combined extracts were washed with saturated $NaHCO_3$ (3 × 20 mL), saturated NaCl (30 mL), and water (2 × 20 mL) and were dried over Na_2SO_4. Following solvent removal at reduced pressure, fractional distillation yielded 60.0 g (50.0%) of 1,20-dichloro-3,6,9,12,15,18-hexaoxatetradecane, bp 190–200°C (0.4 Torr). ^{13}C NMR ($CDCl_3$), δ_C: 71.3, 70.6, 70.5, 42.7. CIMS: M + 1 at 363 (62%).

4-Formylbenzo-24-crown-8 ether was prepared as follows: 3,4-dihydroxybenzaldehyde (2.35 g, 0.017 mol) and 18-crown-6 (0.1 g, 0.0003 mol) were dissolved in 500 mL of dry acetonitrile in a 1 L round-bottom two-necked flask equipped with a condenser, under N_2 atmosphere. To this was added K_2CO_3 (7.05 g, 0.051 mol) and 1,20-dichloro-3,6,9,12,15,18-hexaoxatetradecane (6.20 g, 0.017 mol) and the reaction mixture was refluxed for 5 days. Upon cooling, the mixture was filtered and the solvent was removed by rotoevaporation. Subsequent column chromatography on silica gel (grade 60, 230–400 mesh) eluting with ethyl acetate yielded 4-formylbenzo-24-crown-8 ether (3.6 g, 50.0%) as a pale yellow oil. ^{13}C NMR ($CDCl_3$), δ_C: 191.2, 154.9, 149.6, 130.6, 127.1, 112.7, 111.9, 71.7, 71.5, 71.3, 71.2, 71.1, 69.9, 69.8, 69.6. CIMS: M + 1 at 429 (100%).

Oxidation to **1** was carried out starting with Ag_2O (5.0 g, 0.022 mol) dissolved in 500 mL of 0.73 M NH_4OH in a 1 L Erlenmeyer flask covered by aluminum foil and stirred for 5 min. To this was added, dropwise, 4-formylbenzo-24-crown-8 ether (5.0 g, 0.012 mol) dissolved in 10 mL of absolute ethanol. After 30 min, the mirror started to form. The mixture was stirred for 16 h at room temperature, then filtered and washed with CH_2Cl_2 (6 × 50 mL). Evaporation of the solvent from the organic phase gave 1.5 g of mostly unreacted aldehyde. The aqueous phase was then acidified to pH 2 and washed with CH_2Cl_2 (4 × 100 mL). The solvent was removed by rotoevaporation, and the solid residue was kept under vacuum with occasional gentle warming to yield 3.0 g (56.3%) of **1**, mp 87–89°C. ^{13}C NMR ($CDCl_3$), δ_C: 170.6, 153.7, 148.6, 124.9, 122.6, 115.3, 112.6, 71.9, 71.5, 71.4, 71.1, 71.0, 70.9, 70.4, 69.9, 69.8, 69.6, 69.4. High-resolution MS: *m/z* calcd. for $C_{21}H_{32}O_{10}$ (M^+): 444.1996; found: 444.1967 (12.9%).

Preparation of ***1****-11,11′-*d_4

Initially, it was necessary to prepare the 7,7,14,14-d_4 derivative of 1,20-dichloro-3,6,9,12,15,18-hexaoxatetradecane. This was prepared as outlined schematically in Fig. 5 (*a*) and described below.

Ethylene glycol (3.1 g, 0.05 mol) and ethyldiazoacetate (10.5 mL, 0.10 mol) were dissolved in CH_2Cl_2 (100 mL), and the stirred solution was cooled in an ice bath. After addition of 3 drops of the catalyst $BF_3{\cdot}O(Et)_2$, an exothermic reaction occurred and the evolving N_2 gas was allowed to escape. Stirring was continued for another 30 min until no further gas had evolved. The solvent was then removed by rotary evaporation and the oily residue (11.5 g) was subjected to column chromatography on silica gel (grade 60, 230–400 mesh) using 1:1 hexane:diethyl ether as eluant. This gave 8.0 g (68.4 %) of 1,2-bis(ethylacetoxy)ethane. ^{13}C NMR ($CDCl_3$), δ_C: 170.3, 70.9, 68.6, 14.2. CIMS: M + 1 at 235 (100%).

Triethylene glycol-1,8-d_4 was then prepared as follows. All glassware for this reaction was dried in an oven overnight at 110°C. A 1 L round-bottom three-necked flask equipped with a strong magnetic stirrer, condenser, and a dropping funnel was charged with 500 mL anhydrous THF. Lithium aluminum deuteride (2.0 g, 0.048 mol) was added to the flask while the THF was being vigorously stirred under an N_2 atmosphere. The flask was then cooled in an ice–salt bath and 1,2-bis-(ethylacetoxy)ethane (11.8 g, 0.050 mol) dissolved in 20 mL of anhydrous THF was added over a period of 45 min. Two additional aliquots of 50 mL of dry THF were added to the reaction mixture to reduce the viscosity. The ice bath was removed and the temperature of the stirred reaction mixture was allowed to rise to 40°C over a period of 1 h. The excess $LiAlD_4$ was decomposed via slow addition of 1 mL of H_2O to the cooled reaction mixture. Subsequently, dilute (20%) H_2SO_4 (18 mL) was added dropwise to decompose the lithium alkoxide complex. The clear upper organic layer was separated and combined with the organic layers resulting from washing the lower viscous aqueous slurry with 3 × 50 mL of fresh THF. The solvent was removed by rotoevaporation and the resulting crude product was dissolved in 50 mL of H_2O

Fig. 1. Structures and numbering schemes for **1** and deuterated derivatives.

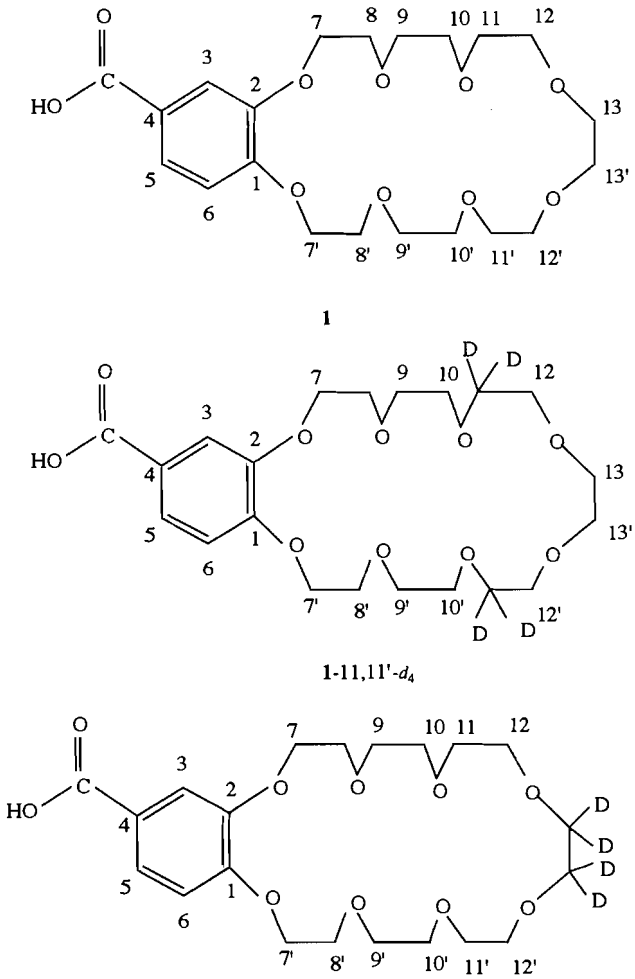

Fig. 2. (*a*): 400 MHz ^{1}H solution NMR spectrum of alphatic region of **1**. (*b*): 100 MHz ^{13}C solution NMR spectrum of alphatic region of **1**.

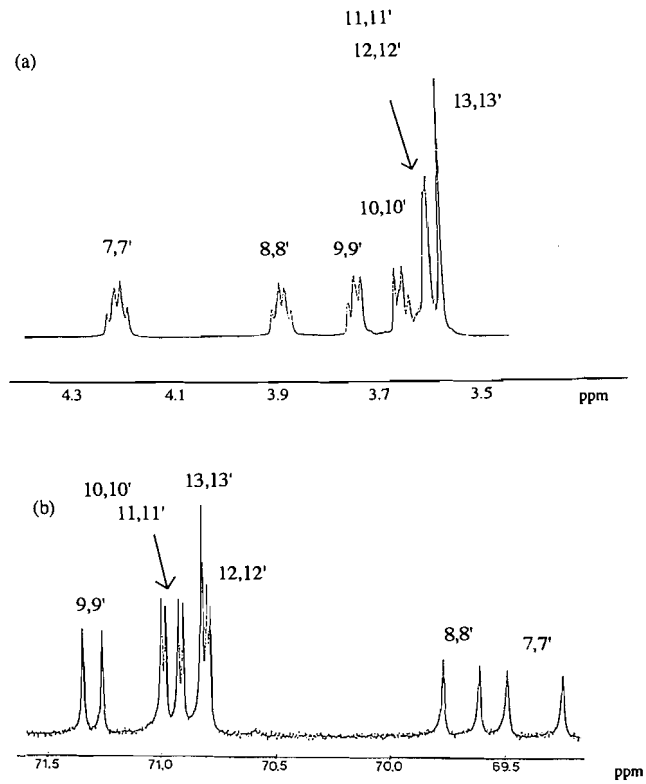

and washed with CH_2Cl_2 (20 mL). The water was removed by evaporation at reduced pressure and the residue was left under vacuum for 3 h, to yield 6.2 g of crude triethylene glycol-1,8-d_4.

This glycol was then converted to 1,8-dichloro-3,6-dioxaoctane-1,8-d_4, via reaction with thionyl chloride by standard methods to yield 5.92 g (80%) of product as a pale yellow liquid. ^{13}C NMR ($CDCl_3$), δ_C: 71.2. 50.6, 40.3 (quintet due to ^{13}C–^2H coupling). This dichloride was then condensed with diethylene glycol as described previously to yield heptaethylene glycol-7,7-14,14-d_4. Subsequent conversion to the 7,7,14,14-d_4 derivative of 1,20-dichloro-3,6,9,12,15,18-hexaoxatetradecane was carried out with $SOCl_2$. This material was then reacted with 3,4-dihydroxybenzaldehyde and oxidized using the same methods as for the nondeuterated compounds to yield **1**-11,11'-d_4. High-resolution MS: *m/z* calcd. for $C_{21}H_{28}O_{10}D_4$: 448.2247; found: 448.2260 (7.7%).

Preparation of ***1****-13,13'*-d_4

In this case it was necessary to synthesize the 10,10,11,11-d_4 derivative of 1,20-dichloro-3,6,9,12,15,18-hexaoxatetradecane as described below.

tert-Butanol (250 mL) was placed in a 500 mL round-bottom three-necked flask equipped with a condenser and a dropping funnel. To this was added a 57% suspension of NaH in mineral oil (4.88 g, 0.116 mol) and the mixture was stirred at room temperature under an N_2 atmosphere for 20 min. A mixture of ethylene glycol-d_6 (Cambridge Isotope Laboratories Inc.) (4.0 g, 0.058 mol) and 1,2-bis(2-chloroethoxy)ethane (Aldrich) (112.24 g, 0.600 mol) was added dropwise to the reaction flask over 1 min and the reaction mixture was refluxed for 5 days. After cooling, 200 mL H_2O was added and the mixture was extracted with CH_2Cl_2 (3 × 100 mL). The organic phase was then dried over anhydrous Na_2SO_4. Subsequent removal of the drying agent and solvent evaporation were followed by fractional distillation at reduced pressure to give a crude product, bp 180–210°C (0.5–0.7 Torr). This material was then subjected to column chromatography on silica gel (grade 60, 230–400 mesh) using 1:1 hexane:diethyl ether as eluent, to give 2.57 g (12.7%) of the 10,10,11,11-d_4 derivative of 1,20-dichloro-3,6,9,12,15,18-hexaoxatetradecane. ^{13}C NMR ($CDCl_3$), δ_C: 71.4, 70.8, 70.7, 70.6, 70.5, 69.7 (quintet), and 42.7. CIMS: M + 1 at 367 (42%).

Subsequently **1**-13.13'-d_4 was prepared in analogous fashion to that described previously. High-resolution MS: *m/z* calcd. for $C_{21}H_{28}O_{10}D_4$ (M^+): 448.2247; found: 448.2244 (4.6%).

Fig. 3. Normal (upper) and dipolar dephased (lower) ^{13}C CPMAS NMR spectra of the CH_2-O region of **1**, **1**-11,11′-d_4, and **1**-13,13′-d_4.

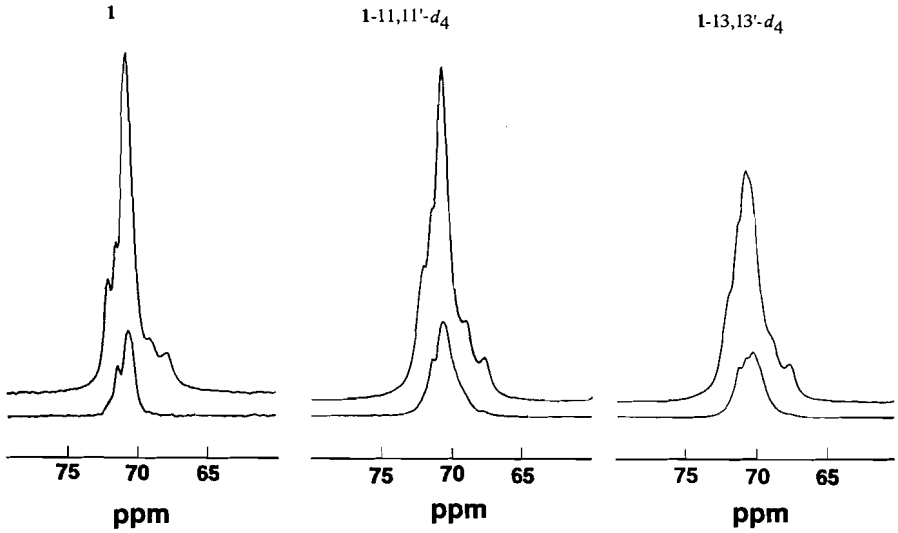

Table 1. ^{13}C NMR chemical shifts for **1** (δ_C from TMS).

	Solution (±0.01)[a]	Solid phase (±0.1)
C1	153.91	154.5
C2	148.72	148.4
C3	115.35	112.0
C4	122.43	118.9
C5	125.17	125.6
C6	112.64	111.1
C7	69.25	67.5
C7′	69.48	69.0
C8	69.61	69.0
C8′	69.78	69.0
C9	71.26[b]	72.0[b]
C9′	71.35[b]	71.9[b]
C10	71.00[b]	71.9[b]
C10′	70.98[b]	71.9[b]
C11	70.90	70.8
C11′	70.92	70.8
C12	70.68	70.8
C12′	70.70	70.8
C13,13′	70.74	70.7
Carboxyl	171.38	173.8

[a]0.1 M in $CDCl_3$.
[b]Assignments may be interchanged.

Table 2. ^{13}C NMR spin lattice relaxation times[a] (T_1(s) for **1** and **1**·KNCS.

	1	**1**·KNCS	ΔT_1
C7,7′	0.20±0.01	0.14±0.01	0.06
C8,8′	0.21±0.01	0.14±0.01	0.07
C10–C13′	0.40±0.01	0.25±0.01	0.15

[a]At 100 MHz for 0.1 M solutions in DMSO-d_6.

Spectra

(a) Solution NMR spectra

These spectra were obtained using a Bruker AMX-400 spectrometer equipped with a 5 mm inverse probe and an Aspect X32 computer. An Aspect 3000 processing controller was employed and all standard microprograms used are in the Bruker Software Library.

^1H–^1H COSY experiments were run using N-type phase cycling with a 45° mixing pulse. Free induction decays were acquired over 1024 data points for each of the 256 values of the evolution time, with a digital resolution of 5 Hz/point. The raw data were zero filled in $F1$ prior to transformation using the qsine window function for both $F1$ and $F2$. The matrix was symmetrized about the diagonal.

For the ^1H–^{13}C HETCOR experiments, the free induction decays were typically acquired over 1024 data points for each of the 512 values of the evolution time, with a digital resolution of ca. 8 Hz/point in $F2$ and 4 Hz/point in $F1$. The raw data were zero filled in $F1$ prior to transformation using the sine window function for both $F1$ and $F2$. The proton relaxation delays were set to 1 s. For one-bond couplings, delays were set to emphasize couplings of 140 Hz, while for the long-range HETCOR experiments, delays were set to correspond to couplings of 5 Hz.

^{13}C T_1's were measured at 100.6 MHz using the inversion–recovery method (9). In the NOESY experiments, the mixing times were selected to be consistent with the $1/T_1$ criterion (10) and, for **1**, this time was set at 0.3 s.

(b) ^{13}C CPMAS spectra

Solid state ^{13}C CPMAS (cross-polarization – magic angle spinning) NMR spectra were obtained at 45.3 MHz on a Bruker CXP-180 spectrometer with a 4.24 T cryomagnet, using a Doty Scientific Inc. 7 mm MAS probe (spin rate ca. 4.1 kHz) *or* at 50.29 MHz on a Bruker MSL-200 spectrometer with a 4.71 T cryomagnet, using a Chemagnetics 7 mm pencil probe (spin rate ca. 3.3 kHz). ^1H 90° pulse lengths were typi-

Fig. 4. (*a*) Normal and (*b*) dipolar dephased 45.3 MHz ^{13}C CPMAS NMR spectra of **1**·KNCS

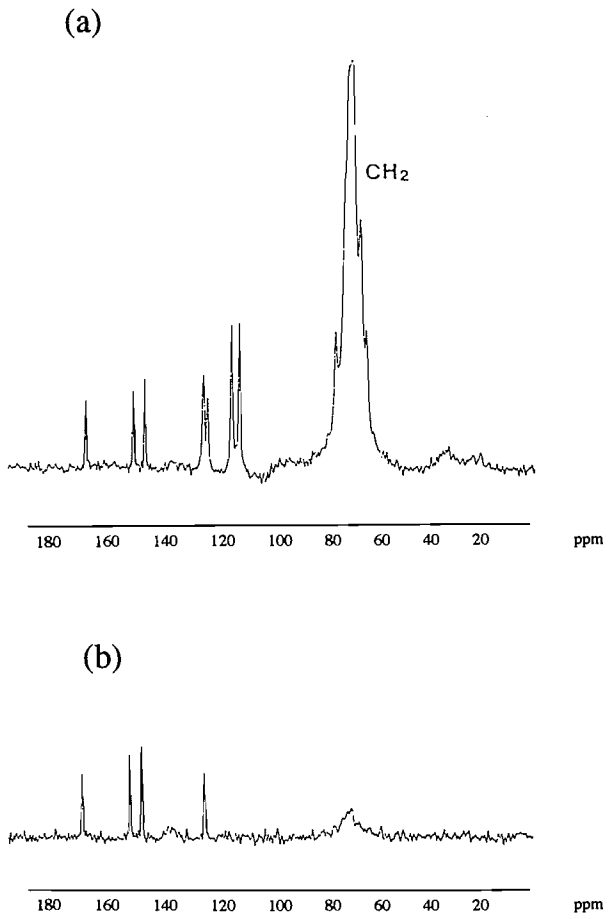

cally 4.5 μs, cross-polarization times were 1–3 ms, and recycle times were 1–4 s. Dipolar dephased spectra (8) were obtained by interrupting the ^1H decoupling for 40 μs immediately after the cross-polarization sequence and before starting the data acquisition. Chemical shifts were measured relative to external solid hexamethylbenzene (HMB) and then corrected to the TMS scale (HMB methyl resonance at 16.9 ppm).

(c) ^2H powder spectra

These spectra were obtained at 46.05 MHz as a function of temperature using a Bruker AMX-300 spectrometer, equipped with a high-power transmitter, using a variable temperature N_2 gas flow probe (5 mm coil) and a Eurotherm temperature controller. A phase-alternated quadrupole echo pulse sequence (11) was employed, with a delay time of 30 μs between X and Y pulses of 2–2.2 μs.

(d) Differential scanning calorimetry (DSC)

A Seiko SSC5200 instrument was used for the DSC studies. The heating rate was 10°C per minute from −50°C to +110°C, with a nitrogen flow rate of 50 mL per minute. The cooling rate was 5°C per minute. Samples were analyzed in a crimped aluminum sample pan, and were heated gently for 1 h under vacuum to remove any trace of solvent before the DSC measurements were performed.

Results and discussion

The structures and numbering schemes for **1** and two selectively deuterated d_4 derivatives are shown in Fig. 1.

Solution ^{13}C NMR spectrum of 1

To aid in the analysis of the solid phase ^{13}C spectrum of this material, it is useful to examine the features of the solution counterpart. The ^1H solution spectrum can in turn be employed to aid in the analysis of the ^{13}C spectrum via HETCOR connectivities.

The aromatic region of the 400 MHz ^1H spectrum appears as an AMX pattern for protons 3, 5, and 6. H5 is coupled vicinally with H6 and then via a ^4J pathway to H3, giving a doublet of doublets centered at 7.88 ppm. H3 is centered at 7.61 ppm while H6 is at 6.91 ppm. The C3, C5, and C6 resonances can then be assigned directly via the ^1J HECTOR experiment. The quaternary carbons can be readily assigned via long-range HETCOR and the result are consistent with expectations based on well-documented effects of carboxyl and ether functions on ^{13}C shieldings (12).

In the aliphatic region, for each O-CH_2-CH_2-O network, the four protons represent an AA′BB′ spin system (13) and hence the patterns are rather complex. The solution ^1H and ^{13}C spectra of the aliphatic regions of **1** are presented in Fig. 2. For assignment of the methylene carbon resonances, a partial analysis can be obtained by starting with results of a ^1H–^1H NOESY experiment. In this experiment, there are connections between the H3 and H6 aromatic resonances and the aliphatic multiplet (4H integration) centered at 4.22 ppm. Thus it appears that the most deshielded aliphatic CH_2-O resonances correspond to those at C7 and C7′, which are closest to the aromatic ring, a result in accord with several earlier investigations (13–15). Subsequent ^1H–^1H COSY can be used to assign protons at the 8 and 8′ sites, and ^1J HETCOR establishes the resonances for the directly bonded carbons. Selective deuteration at the 11,11′ and 13,13′ sites permitted assignments for these protons and carbons as well as those on C12,12′. The solution ^{13}C NMR data are summarized in Table 1. The only resonances that cannot be unambiguously attributed are those for the 9,9′ and 10,10′ sites.

A comparison of the spin lattice relaxation times (T_1) for **1** and the KNCS complex in DMSO-d_6 solution at 298 K is presented in Table 2. The reduction of the observed T_1's for the CH_2O sites of the KNCS complex is consistent with a decrease in the mobility of the macrocycle upon complexation with the cation, assuming that we are in the motional narrowing region and that dipole–dipole relaxation is dominant (9, 16) for these carbons. Likewise, in both free **1** and its KNCS complex there is more mobility at sites 10–13′ than at sites 7–9′.

Solid phase ^{13}C spectra

The normal and dipolar dephased ^{13}C CPMAS NMR spectra of the aliphatic region of **1** and its selectively deuterated derivatives are shown in Fig. 3. Carbons with attached protons disappear from the spectrum, unless the C—H bonds involved are undergoing reorientations that reduce the dipolar coupling, in which case the lines are still present but with reduced intensity.

For **1**, the most notable feature of the dipolar dephased spectrum is the residual intensity observed in the CH_2O carbon region, resonating at values exceeding 70 ppm. There is a

Fig. 5. Synthetic routes to selectively deuterated derivatives of **1**.

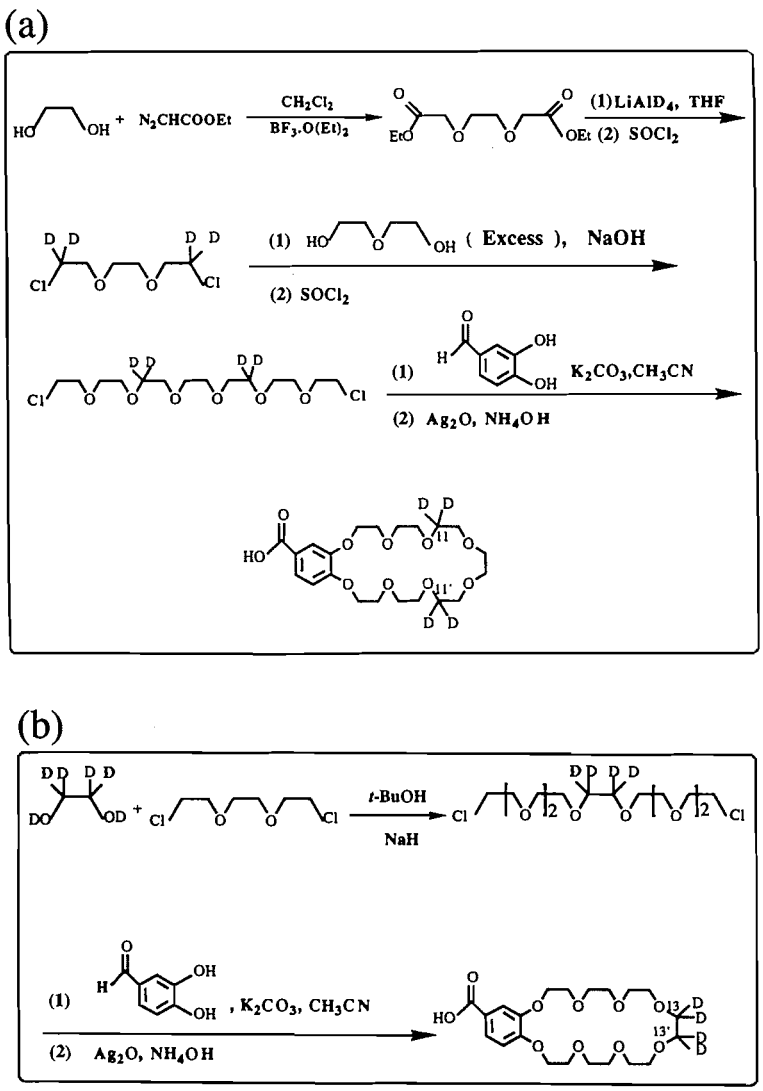

disappearance of the most shielded resonances in the region 67.5–69.0 ppm, indicating that there is no large-amplitude motion present for these most shielded carbons. Using the solution assignments as a guide, we attribute the most shielded CH_2O lines to sites 7,7′ and 8,8′, which are in the closest proximity to the aromatic ring of **1**. It is intuitively reasonable that the least amount of motion in the 24-membered ring of **1** would be in the region of the macrocycle that is most closely bonded to the rigid aromatic moiety.

The spectra of the deuterated molecules show some subtle changes in relative intensities of the features. The CD_2 carbon lines should be affected by spin–spin coupling and residual dipolar coupling (17) and thus have intensity spread over a broader range (as a quintet) than the protonated species, though this is not resolved here. Furthermore, the spectra of the CD_2 carbons should remain unchanged in intensity in the dephased spectrum. Recall that only 2 out of the 14 CH_2O carbons are affected in this way.

It is of interest to contrast these results with those obtained for the KNCS complex of **1** (Fig. 4) where almost all of the CH_2O intensity in the dipolar dephased spectrum has disappeared, indicating that complexation of the macrocycle with the K^+ ion has now also reduced the mobility of the methylene carbons at sites 9,9′ to 13,13′ in the solid phase.

The 11,11′-d_4 and 13,13′-d_4 derivatives of **1** were synthesized specifically to further explore the details of the motion of the macrocycle in the solid state by ^2H NMR. The synthetic scheme for their synthesis is depicted in Fig. 5.

Solid state ^2H NMR results

^2H (I = 1) NMR in solids is dominated by a perturbation in the Zeeman interaction by the quadrupole coupling tensor that arises from the interaction of the nuclear quadrupole moment with the electric field gradient (efg) tensor (18, 19). With a nuclear spin of 1 there are three energy levels and hence two transitions, displaced equally on either side of the Zeeman frequency by the quadrupolar interaction. The ^2H powder lineshape has either two or three pairs of characteristic features (edges, shoulders, and peaks) separated by frequencies

Fig. 6. ^{2}H NMR quadrupole echo spectra of (*a*) **1**-11,11′-d_4 and (*b*) **1**-13,13′-d_4 as a function of temperature (the sharp isotropic liquid line has been truncated in most of the spectra).

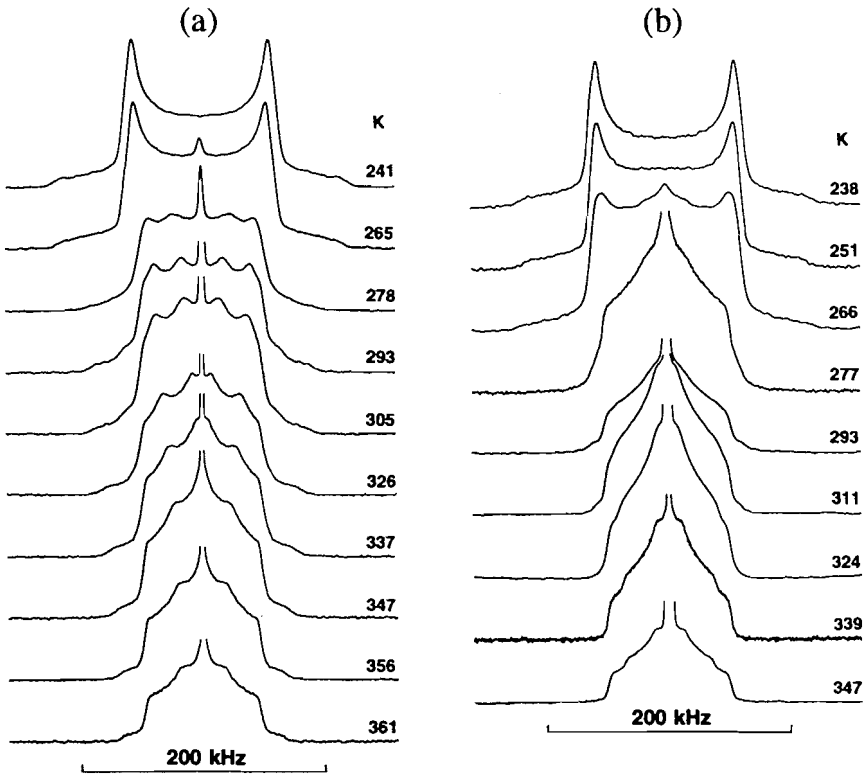

$$\begin{aligned} \Delta\nu_{zz} &= 3\chi/2 \\ \Delta\nu_{yy} &= 3\chi(1+\eta)/4 \\ \Delta\nu_{xx} &= 3\chi(1-\eta)/4 \end{aligned} \quad [1]$$

where χ is the quadrupolar coupling constant in Hz and the asymmetry parameter

$$\eta = (\Delta\nu_{yy} - \Delta\nu_{xx})/\Delta\nu_{zz}$$

The $\Delta\nu_{ii}$ are proportional to the absolute magnitudes of the principal axis components of the effective quadupole coupling tensor.

The dynamics of the molecule can cause narrowing of the ^{2}H NMR lineshape in a manner that is dependent on the specifics of the motion, such as the rate and the axis of reorientation (19–24). In the fast-motion limit (rates about 10^7 jumps/s) the line takes on a shape characteristic of an averaged effective tensor. We have given rather more detailed descriptions of the theory, as applied to crown ethers, before (6, 7).

In our previous papers (6, 7) it was possible to analyze the ^{2}H NMR data in terms of very specific dynamical models, largely because the systems studied were chosen for their apparent simplicity, symmetry, and known crystal structures. In the present compound we have neither symmetry nor a crystal structure, and in any case the benzoic acid group incorporated into the ring is expected to prevent overall rotation of the macrocycle. Thus from the outset it was anticipated that there could be difficulty in defining an exact dynamic model.

Nevertheless the results show conclusively that there is a large-amplitude motion of the CD_2 groups, and several other useful conclusions can be drawn. Inspection of the spectra (Fig. 6) of d_4 derivatives of **1** immediately shows several things.

(*a*) At low temperatures (<270 K) the lines have the characteristic parameters corresponding to CD_2 groups that are virtually static except for a small amount of narrowing due to small-amplitude librational motions. Within experimental error the quadrupole coupling tensors for **1**-11,11′-d_4 and **1**-13,13′-d_4 are identical with $\chi = 16.3 \pm 1.0$ kHz and $\eta = 0.065 \pm 0.009$. These values compare favourably with the values determined previously for 18-crown-6 and 12-crown-4 ether complexes (6, 7).

(*b*) In both cases there is a fairly sudden change from a nearly static lineshape to a dynamically averaged one between 265 and 277 K. This is strongly indicative of a solid–solid phase transition and indeed such a transition was later confirmed by Differential Scanning Calorimetry (DSC) for the undeuterated material (vide infra).

(*c*) Slight distortions of the static lineshape just below the phase transition also indicate the onset of a slow motion even in the low-temperature phase.

(*d*) Above the phase transition all the spectra show an isotropic central line whose intensity grows with increasing temperature. This is distinctly liquid-like behaviour and we strongly suspect that, although the crystals appeared to be dry, they contained small pockets of occluded solution. This should not cause any change in the lineshapes from the solid material, but any narrow features of the solid spectrum could be obscured by the presence of this isotropic line.

Fig. 7. Temperature dependence of the widths of pairs of features of the lineshapes of (*a*) **1**-11,11′-d_4 and (*b*) **1**-13,13′-d_4. The solid lines and their broken extrapolations do not represent rigorous mathematical fits.

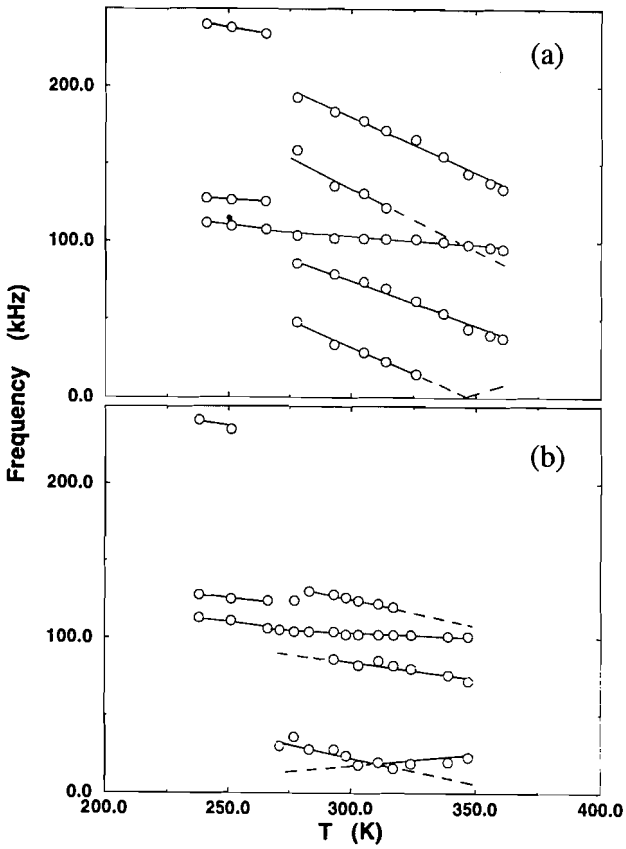

Fig. 8. Calculated lineshapes of (*a*) **1**-11,11′-d_4 and (*b*) **1**-13,13′-d_4 derived from the summation of the two tensors determined at various temperatures.

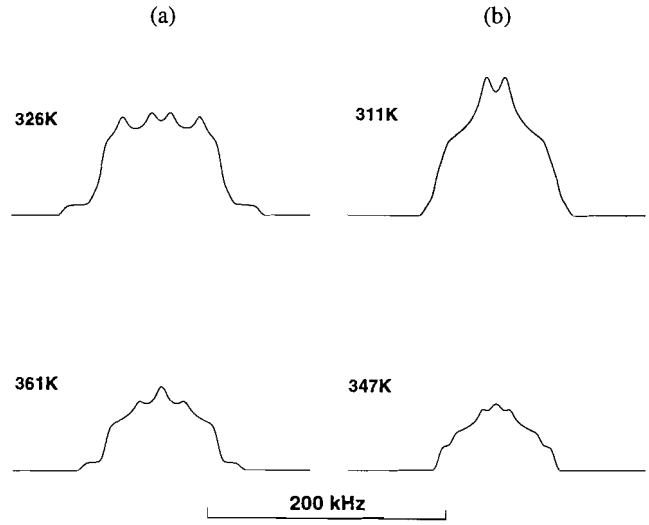

(*e*) Neglecting the isotropic line, we see that above the phase transition the solid spectra all show the effects of rapid dynamic averaging. However, the various features of the lineshapes show continuous variation with increasing temperature. The spectra are fairly complicated, with more than one tensor lineshape superimposed, and in many cases it is not immediately apparent which components are associated with a particular tensor. This is particularly so for the **1**-13,13′-d_4 case, where at 347 K, for example, three pairs of features can be discerned but these do not conform to a single tensor pattern. Note that in each case there are potentially four different tensors, since the lack of symmetry makes the four deuteriums inequivalent.

Fortunately, things become much clearer with the aid of plots of the approximate widths of the pairs of discernable features (peaks, shoulders, edges) of the ^{2}H spectra as a function of temperature (Fig. 7). These plots show the phase transition very clearly, since all the components except $\Delta\nu_{xx}$ are discontinuous. The continuity of $\Delta\nu_{xx}$, its identical value in both cases, and the fact that it shows the least variation over the whole temperature range is particularly informative. From previous work (6) we know the orientation of the eft tensor in the CD_2 group, viz. the *zz* component along the C—D bonds and the *xx* component perpendicular to the CD_2 plane. Consequently the fact that $\Delta\nu_{xx}$ shows little variation suggests that the principal mode of motion causing line narrowing is about an axis parallel to the *xx* component. This also means that the two deuteriums on a CD_2 group behave identically, i.e., their dynamically averaged tensors will be identical. Thus we should see no more than two overlapping tensors in each lineshape, corresponding to each of the two CD_2 pairs at the primed and unprimed sites. Furthermore this *xx* component will be common to *all* the averaged tensors. With this in mind it is easy to pick out two sets of parameters corresponding to two tensors for the **1**-11,11′-d_4 case, where five components are visible between 278 and 315 K. Also it is relatively easy to determine where the less obvious components should be by extrapolation (broken lines in Fig. 7). Similarly, extrapolations help to find the five components needed to define the two tensors **1**-13,13′-d_4.

We can now also see the reason for the initial difficulty in assignment of components for the **1**-13,13′-d_4 case; various components cross at particular temperatures and in these regions the features arising from the two components coalesce. The very narrow components are also obscured by the isotropic "liquid" line.

Figure 8 shows simulated spectra based on the sums of two tensor lineshapes. The comparison with experiment is remarkably good.

Considering the fact that the aromatic ring fixes the molecule so that overall molecular rotation is highly unlikely, the most probable motion of the CD_2 groups about an axis parallel to the direction of the *xx* component would be an up/down two-site flip, as part of a conformational change in the macrocycle. This implies a dynamic disorder in the room temperature phase that would likely show up as partial occupancy of two sites for each C atom in an X-ray crystal structure. This type of flip was found to be involved in the dynamics of 18-crown-6·2$CH_2(CN)_2$ and 12-crown-4·LiNCS (6, 7). Since no crystal structure is available in the present case, we do not know if the two sites are symmetry equivalent, so a unique model cannot be developed.

Two possibilities exist. (*i*) If the molecule has two inequivalent conformations with an energy separation ΔE, they will

Fig. 9. Differential scanning calorimetry of **1**.

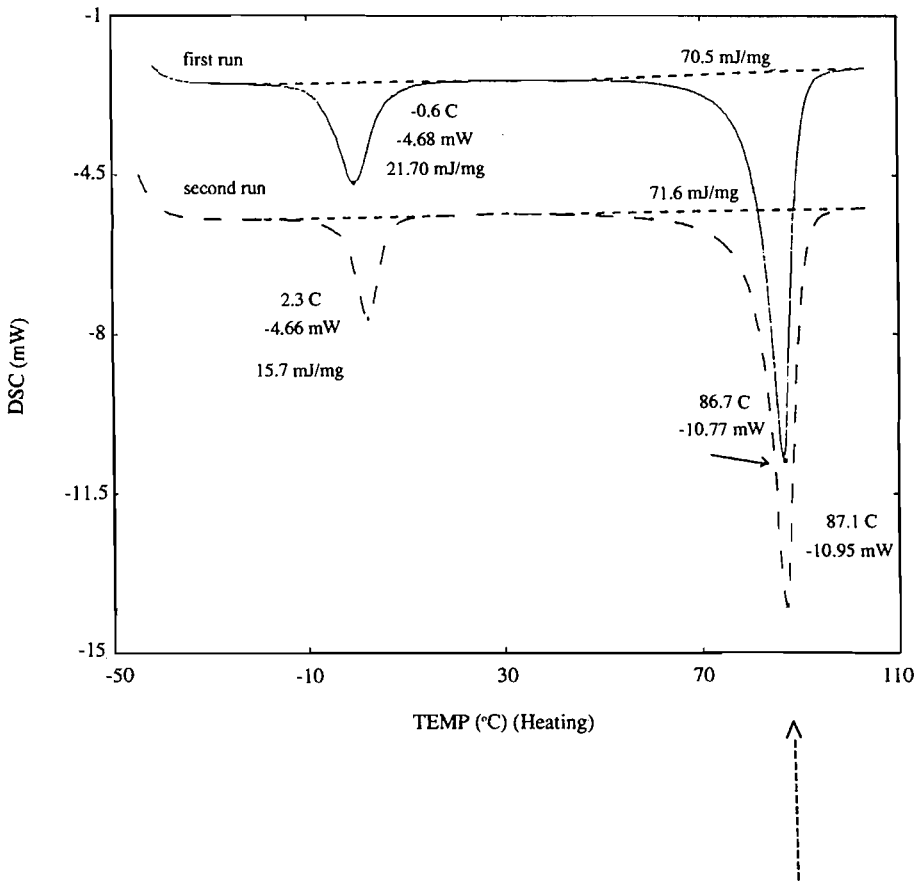

melting point 87-89°C

then have different populations. This could account for the temperature dependence of the averaged lineshape. However, after developing the equations describing the averaging for this kind of situation, we found that no one value of ΔE will simultaneously fit all the data if the flip angle for each CD_2 is kept constant with temperature. If the model is relaxed by allowing the angles to increase with temperature, then a unique fit is no longer possible (though an upper limit to ΔE of about 0.85 kJ/mol can be estimated).

(*ii*) Alternatively, if the two sites were equivalent, one can derive their angular separation using a simple two-site model. Here the temperature dependence arises from an increasing flip angle. A situation in which the two sites are symmetrical could arise if the molecule has a mirror plane in the crystal, perhaps the plane defined by the aromatic ring. Equivalent two-site flips are a simple case to treat and many examples are known (19, 24–26). We will simply give the equations that relate the averaged efg tensor components V_{ii}' to the static tensor components V_{ii} and the half-angle β between the two sites:

$$V_{yy}' = V_{yy} \sin^2\beta + V_{zz} \cos^2\beta$$

$$V_{zz}' = V_{yy} \cos^2\beta + V_{zz} \sin^2\beta$$

The static components themselves have a small temperature dependence due to small-angle librational motions, so "static" values for 300 and 350 K were obtained by extrapolation from low temperatures. The averaged values at these two temperatures were taken from the plots in Fig. 7 and the corresponding values of β were calculated. Two values of β will fit the equations but in all cases the larger value can be discarded as being unrealistic. The calculated values of 2β (below) give an idea of the amplitude of the two-site flip.

	2β (°)	
Sites	300 K	350 K
11/11′	42	54
	61	75
13/13′	65	70
	79	82

If this model is applicable,. three things are evident from these β values. (*i*) The amplitude of motion increases with increasing temperature as expected. (*ii*) The amplitude at sites

13/13′ is greater than at 11/11′, implying greater flexibility the further the CD_2 unit is from the aromatic ring. This also is intuitively reasonable. (*iii*) The significant difference between 11 and 11′ or between 13 and 13′ must reflect crystal packing effects (different environments).

Differential scanning calorimetry (DSC) results

Figure 9 shows the DSC results. The melting point in the vicinity of 87°C is clearly evident along with a phase change at 272.3 K (average of two runs). The phase change is in the temperature range indicated by the ^2H solid state NMR findings.

Acknowledgements

We thank Professor Z.Y. Wang for access to the DSC facility and Pierre Moulinie for technical assistance. The continuing support from the Natural Sciences and Engineering Research Council of Canada to G.W.B. via research grants is gratefully acknowledged. A.M. thanks the Iranian Ministry of Higher Education for a Fellowship.

References

1. G.W. Buchanan, R.A. Kirby, J.A. Ripmeester, and C.I. Ratcliffe. Tetrahedron Lett. **28**, 4783 (1987).
2. G.W. Buchanan, C. Morat, C.I. Ratcliffe, and J.A. Ripmeester. J. Chem. Soc. Chem. Commun. 1306 (1989).
3. G.W. Buchanan, C. Morat, J.P. Charland, C.I. Ratcliffe, and J.A. Ripmeester. Can. J. Chem. **67**, 1212 (1989).
4. K.A. Watson, S. Fortier, M.P. Murchie, J.W. Bovenkamp, A. Rodrigue, G.W. Buchanan, and C.I. Ratcliffe. Can. J. Chem. **68**, 1201 (1990).
5. G.W. Buchanan, A. Rodrigue, C. Bensimon, and C.I. Ratcliffe. Can. J. Chem. **70**, 1033 (1992).
6. C.I. Ratcliffe, J.A. Ripmeester, G.W. Buchanan, and J.K. Denike. J. Am. Chem. Soc. **114**, 3294 (1992).
7. C.I. Ratcliffe, G.W. Buchanan, and J.K. Denike. J. Am. Chem. Soc. **117**, 2900 (1995).
8. S.J. Opella and M.H. Frey. J. Am. Chem. Soc. **101**, 7672 (1979).
9. R.L. Vold, J.S. Waugh, M.P. Klein, and D.E. Phelps. J. Chem. Phys. **48**, 3831 (1968).
10. A.E. Derome. Modern NMR techniques for chemistry research. Pergamon Press, Oxford, U.K. 1987.
11. J.H. Davis, K.R. Jeffrey, M. Bloom, M.I. Valic, and T.P. Higgs. Chem. Phys. Lett. **42**, 390 (1976).
12. J.B. Stothers. Carbon-13 nuclear magnetic resonance spectroscopy. Academic Press, New York. 1972.
13. D. Live and S.I. Chan. J. Am. Chem. Soc. **98**, 3769 (1976).
14. E. Kleinpeter, S. Stoss, M. Gabler, and W. Schroth. Magn. Reson. Chem. **27**, 676 (1989).
15. E. Kleinpeter, M. Gabler, W. Schroth, J. Mahinen, and K. Pihlaja. J. Chem. Soc. Perkin Trans. 2, 1307 (1985).
16. G.W. Buchanan and D.J. Landry. Magn. Reson. Chem. **29**, 127 (1991).
17. A.E. Aliev, K.D.M. Harris, D.C. Apperley, R.K. Harris, and M.M. Sunnetcioglu. J. Chem. Soc. Faraday Trans. **89**, 3791 (1993).
18. M.H. Cohen and F. Rief. Solid State Phys. **5**, 321 (1957).
19. R.G. Barnes. Adv. Nucl. Quadrupole Reson. **1**, 335 (1974).
20. H.W. Speiss and H. Sillescu. J. Magn. Reson. **42**, 381 (1981).
21. A.J. Vega and J. Luz. J. Chem. Phys. **86**, 1803 (1987).
22. R.J. Wittebort, E.T. Olejniczak, and R.G. Griffin. J. Chem. Phys. **86**, 5411 (1987).
23. M.S. Greenfield, A.D. Ronemus, R.L. Vold, R.R. Vold, P.D. Ellis, and T.E. Raidy. J. Magn. Reson. **72**, 89 (1987).
24. C.I. Ratcliffe. J. Phys. Chem. **91**, 6464 (1987).
25. A.E. Aliev, K.D.M. Harris, X. Alcobe, and E. Estop. J. Chem. Soc. Faraday Trans. **89**, 3797 (1993).
26. G.A. Facey, C.I. Ratcliffe, and J.A. Ripmeester. J. Phys. Chem. **99**, 12249 (1995).

Excited state carbon acid dissociation and competing photorearrangements of 5*H*-dibenzo[*a,c*]cycloheptene derivatives

David Budac and Peter Wan

Abstract: The first examples of dissociating excited state carbon acids were reported by our group. A necessary structural feature is the 5*H*-dibenzocycloheptene ring system where the incipient carbanion is formally an antiaromatic system in S_0. In this work, structure–reactivity studies of the excited singlet state carbon acid dissociation and competing formal di-π-methane rearrangement of several 5*H*-dibenzo[*a,c*]cycloheptene derivatives have been carried out in order to gain more insights into the photochemistry displayed by these compounds. Photolysis of 7-deuterio-5*H*-dibenzo[*a,c*]cycloheptene (**9**) in aqueous solution showed that the photogenerated carbanion is allylically delocalized. Derivative **7** was found to be less reactive than **3** with respect to carbon acid dissociation whereas **8** was unreactive. Ethanolamine (in CH_3CN) was found to be an effective base in catalyzing carbon acid dissociation for **3**, **7**, and **9**, as indicated by higher yields of deuterium incorporation and rates of fluorescence quenching. Binaphthyl derivatives **10** and **11** displayed contrasting photobehaviour. Photolysis of binaphthyl **11** resulted in only efficient ($\Phi_p = 0.47$) formal di-π-methane rearrangement under all conditions and no evidence was found for carbon acid dissociation, even in the presence of ethanolamine as base. On the other hand, the formal di-π-methane reaction was very inefficient for binaphthyl **10** ($\Phi_p < 0.001$). Due to the conformational rigidity inherent in **10**, the methylene protons at the 3-position are NMR resolvable as pseudo-axial and pseudo-equatorial protons. Photolysis in the presence of ethanolamine (in D_2O–CH_3CN) resulted in stereoselective deprotonation of the pseudo-axial proton ($\Phi_{ex} \approx 0.02$), as indicated by deuterium exchange studies. The results show that excited state carbon acid dissociation is an observable general reaction of dibenzo and dinaphtho cycloheptenes only if more favourable photochemical pathways are not competing.

Key words: excited state carbon acid, di-π-methane rearrangement, carbanion, stereoelectronic effect, fluorescence quenching.

Résumé : Notre groupe de travail a déjà publié une étude sur les premiers exemples de dissociation acide du carbone dans l'état singulet. Le système cyclique 5*H*-dibenzocycloheptène est une caractéristique structurale nécessaire dans laquelle le carbanion naissant est formellement un système anti-aromatique de type S_0. Dans ce travail nous avons réalisé des études de structure–réactivité sur la dissociation acide du carbone dans l'état singulet excité et le réarrangement di-π-méthane formel compétitif de plusieurs dérivés des 5*H*-dibenzo[*a,c*]cycloheptènes. Cette étude devrait nous permettre d'acquérir de nouvelles connaissances sur la photochimie de ces composés. La photolyse du deutéro-5*H*-dibenzo[*a,c*]cycloheptène (**9**) en solution aqueuse montre que le carbanion généré photochimiquement est délocalisé en position allylique. On a trouvé que le composé **7** est moins réactif que le composé **3** en ce qui a trait à la dissociation acide du carbone tandis que le composé **8** ne montre aucune réactivité. Les vitesses d'extinction de la fluorescence et les rendements élevés obtenus lors de l'incorporation du deutérium montrent que l'éthanolamine est une base efficace pour catalyser la dissociation acide du carbone des composés **3**, **7** et **9**. Les dérivés binaphtyles **10** et **11** exhibent à l'opposé un comportement photochimique. La photolyse du binaphtyle **11** conduit uniquement à un réarrangement di-π-méthane formel efficace ($\Phi_p = 0{,}47$) dans toutes les conditions et on n'a pas pu mettre en évidence la dissociation acide du carbone même en présence d'éthanolamine utilisée comme base. Par ailleurs, la réaction di-π-méthane formelle est inefficace avec le binaphtyle **10** ($\Phi_p < 0{,}001$). En raison de la rigidité conformationelle inhérente du composé **10**, les protons éthyléniques en position 3 sont résolvables, en RMN, comme des protons pseudo axial et pseudo équatorial. Les études réalisées sur l'échange de deutérium indiquent que la photolyse en présence d'éthanolamine (dans le D_2O–CH_3CN) conduit à une déprotonation sélective du proton pseudo axial ($\Phi_{ex} \approx 0{,}02$). Les résultats montrent que la dissociation acide du carbone dans l'état excité est une réaction générale des dibenzo et dinaphto cycloheptènes et n'est observable uniquement qu'en l'absence d'un processus photochimique plus favorable.

Mots clés : acide carbonique dans l'état excité, réarrangement di-π-méthane, carbanion, effet stéréoélectronique, extinction de la fluorescence.

[Traduit par la rédaction]

Received December 6, 1995.

D. Budac and P. Wan.[1] Department of Chemistry, Box 3055, University of Victoria, Victoria, BC V8W 3P6, Canada.

[1] Author to whom correspondence may be addressed. Telephone: (604) 721-7193. Fax: (604) 721-7147. E-mail: pwan@uvic.ca

Scheme 1.

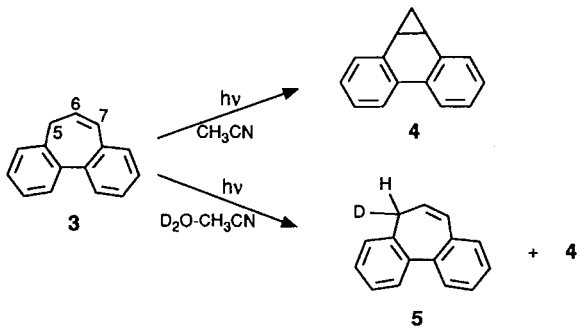

Scheme 2.

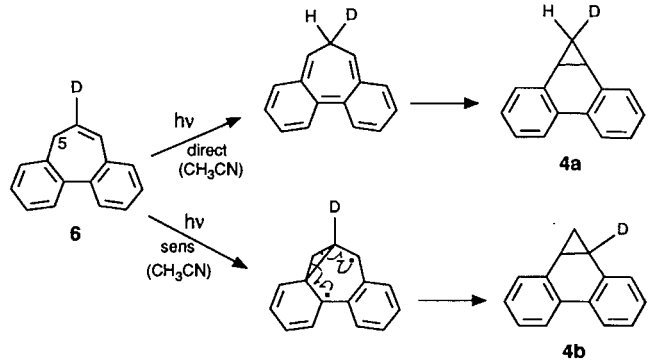

Introduction

Carbanions and their associated carbon acids have been studied extensively in the ground state because of their fundamental importance in organic chemistry (1). Very little experimental data is available for excited state carbon acids although Förster cycle calculations of hydrocarbons related to fluorene (**1**) suggest that the benzylic protons of these systems are very acidic in the excited singlet state ($pK_a(S_1) \approx -6$) (2). However, it is known that fluorene and related compounds do not undergo benzylic C—H bond exchange upon excitation (2) and it has been suggested that this is due to the short lifetimes of excited singlet since C—H bond dissociation is known to be intrinsically slow (1, 2). We published the first examples of dissociating excited state carbon acids (from the 5-position) in *5H*-dibenzo[*a,d*]cycloheptene (**2**) and *5H*-dibenzo[*a,c*]cycloheptene (**3**) (3, 4*a*). We discovered that in order to observe excited state carbon acid dissociation, the incipient carbanion should be formally antiaromatic in the

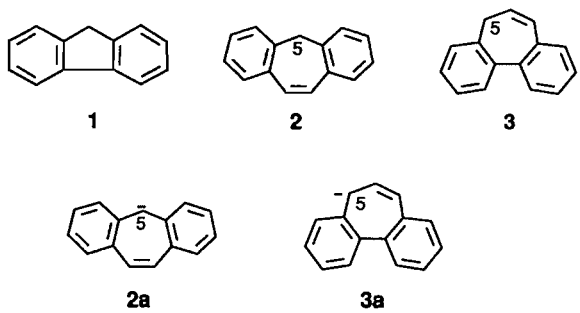

ground state (3, 4*a*). Carbanions generated from **2** and **3** (**2a** and **3a**, respectively) satisfy this requirement whereas the fluorenyl carbanion from **1** does not. We offered a rationalization based on the relative stabilities of $4n$ vs. $4n + 2$ π systems in the excited state in order to explain the difference in carbon acid reactivity observed in these benzannelated systems (3, 4*a*).

Of particular interest was the finding that in addition to excited state proton exchange observed for **3** at the 5-position, a competing formal di-π-methane rearrangement to give dibenzonorcaradiene **4** was also observed (Scheme 1) (4*a*). In 100% CH_3CN, only rearrangement to **4** was observed. Addition of D_2O (acting as the base) resulted in a decrease in the yield of **4** and formation of **5**. Using 6-deutero-*5H*-dibenzo[*a,c*]cycloheptene (**6**), we showed that formation of **4** via S_1 involved an initial 1,7-hydrogen shift followed by electrocyclic ring closure, which gave **4a** (Scheme 2) (4a). Formation of **4** via T_1 involved a true di-π-methane pathway, which gave **4b** (Scheme 2) (4*a*). The general mechanistic problem of competition between a true di-π-methane pathway versus one involving initial sigmatropic shift followed by electrocyclic ring closure was originally delineated by Zimmerman and Pincock (4*b*).

Additional studies of this interesting reaction are warranted. To this end, we have prepared several derivatives of **3**. Compounds **7** and **8** were prepared to study the effect of substitu-

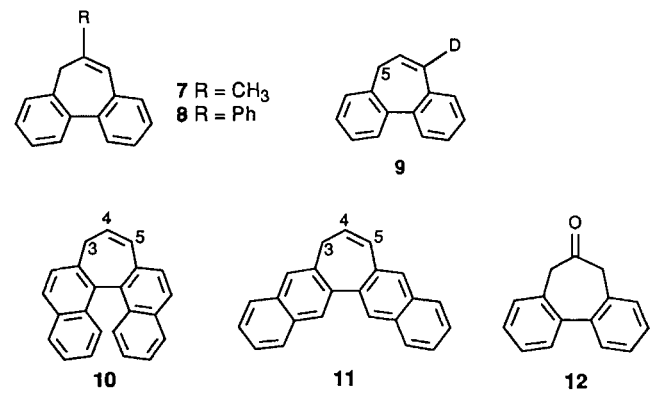

tion at the 6-position on photoreactivity whereas **9** was prepared to probe the degree in which the initially photogenerated carbanion at position 5 (**3a**) is delocalized into the 7-position. Finally, the more unusual binaphthyl systems **10** and **11** were prepared for exploratory studies into the effect of using highly benzannelated chromophores on the photochemistry. The results of this study provide new insights into understanding the reactivity of excited state carbon acids based on the dibenzo[*a,c*]cycloheptene system.

Results and discussion

Syntheses

The parent compound **3** was prepared via a literature method and described in our previous study (4*a*). The 6-methyl and 6-phenyl-*5H*-dibenzo[*a,c*]cycloheptenes (**7** and **8**) were prepared by reaction of MeLi or PhLi with ketone **12** according to the procedure of Tolbert and Ali (5). The synthesis of 7-deuterio-*5H*-dibenzo[*a,c*]cycloheptene (**9**) is outlined in

Scheme 3.

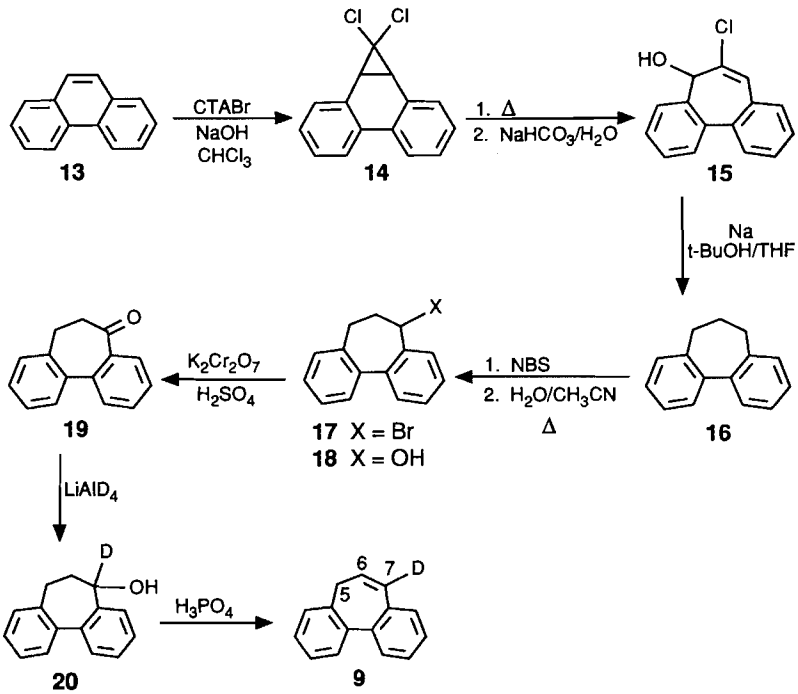

Scheme 3. Conversion of phenanthrene (**13**) to dibenzo[*a*,*c*]cycloheptane (**16**) followed literature methods (6–8). Bromination of **16** with NBS gave **17**, which was hydrolyzed in H_2O–CH_3CN to give **18**. Oxidation of **18** with Jones reagent provided the known ketone **19**. Simple functional group manipulations via alcohol **20** gave the required **9**. ^1H (360 MHz) NMR, ^2H NMR, and MS are consistent with the assigned structure. The ^1H spectrum was identical to the spectrum for **3** except for the lack of the resonance signal at the 7-position (δ 6.7) and associated proton couplings. The ^2H NMR showed one major signal at δ 6.7 along with several minor resonances including a signal at δ 3.05 (≈ 4%) representing deuterium at the 5-position (formation of **5**), indicating some isomerization had taken place during the dehydration step (Fig. 1). The minor amount of **5** present does not interfere with the product studies to be performed for this compound.

Scheme 4 outlines the synthesis of *3H*-cyclohepta[2,1-*a*:3,4-*a*']dinaphthalene (**10**). The initial step involves bromination of 2-methylnaphthalene (**21**), to give **22** (9), followed by formation of the Grignard reagent and subsequent coupling with **22** using $NiCl_2(PPh_3)_2$ catalyst (10) to give **23**. Bromination of **23** with NBS gave dibromide **24**. Bestmann and Both (11) prepared **10** in two steps from **24**. However, numerous attempts by us to duplicate their method were unsuccessful. Therefore, we adapted published methods by Mislow and McGinn (12) for converting **24** to **27**. The key step is the treatment of **24** with KCN, which initially gave the dicyano derivative. Under the action of cyanide ion, a Thorpe–Ziegler condensation of the dicyano groups gave aminonitrile **25**. Standard hydrolysis of **25** gave **26**, which was converted to **27** using standard methods. Treatment of **27** with PBr_3 gave bromide **28**, which was then converted to **10** using potassium *tert*-butoxide.

Fig. 1. ^2H NMR of synthesized **9** showing a small amount (4%) of the deuterium at the 5-position due to **5**.

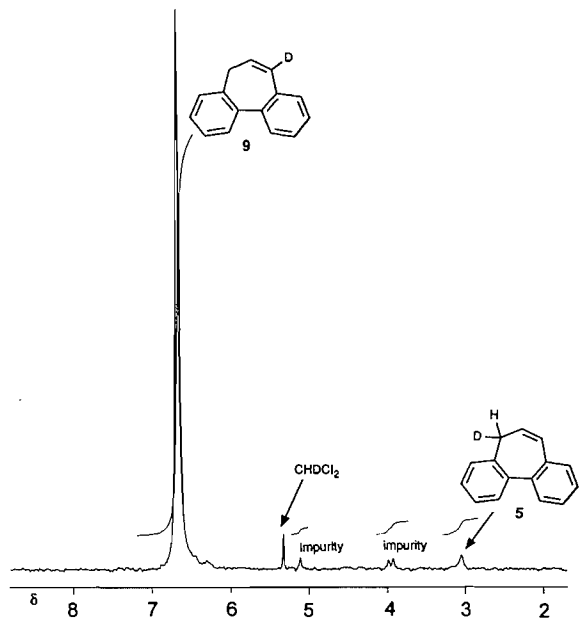

Since we anticipated that the steric requirements of the two naphthalene rings would impart a substantial twist on the cycloheptene ring thereby locking it into a fixed conformation (from analysis of molecular models), we decided to obtain an X-ray crystal structure of **10**. Crystals of **10** were grown in toluene–EtOH and the X-ray parameters of the solved structure are listed in Table 1 with the ORTEP drawing shown in Fig. 2.

Scheme 4.

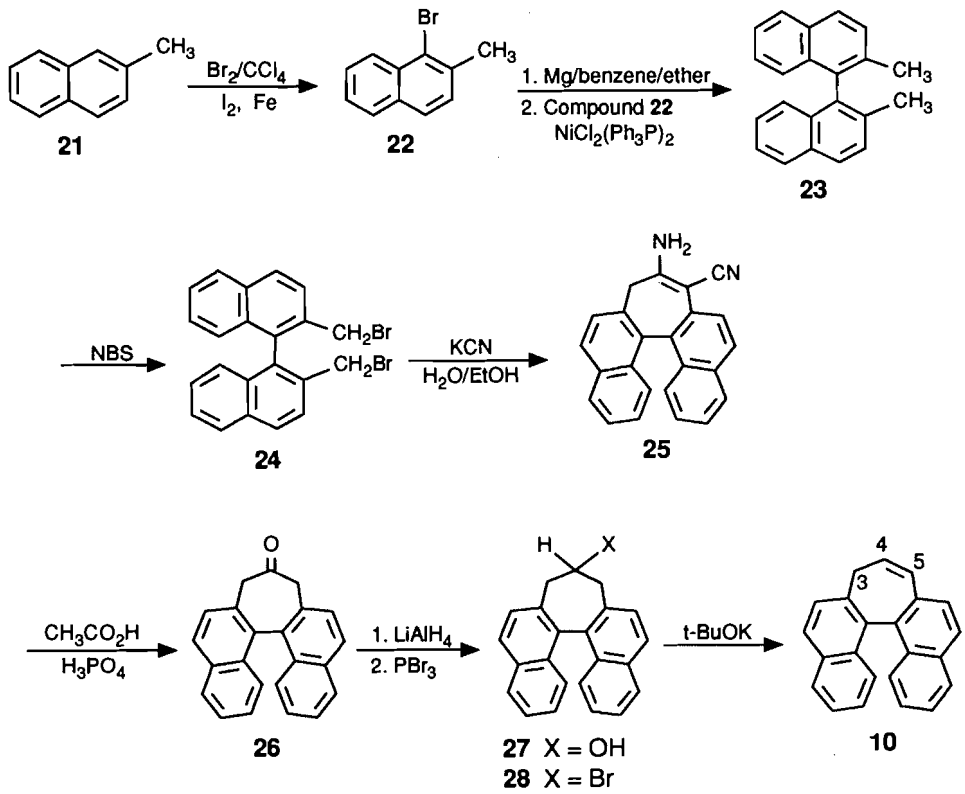

Table 1. Crystallographic data for **10**.

Formula	$C_{16}H_{23}$
Molecular weight	292.38 g/mol
Crystal system	Monoclinic
Space group	$P2_1/n$ (no. 14)
Cell dimensions	
a (Å)	8.5545(6)
b (Å)	18.8395(17)
c (Å)	9.7556(6)
α (deg)	90
β (deg)	94.960(7)
γ (deg)	90
V (Å^3)	1566.347
Z	4
T (°C)	20
λ (Å)	Cu(1.540562)
ρ_{obsd} (g mL^{-1})	1.225
ρ_{obsd} (g mL^{-1})	1.240
μ (cm^{-1})	4.97
$R(F_o)$	0.0508
$R_w(F_o)$	0.0499

Fig. 2. ORTEP diagram of **10** showing the twisted cycloheptene ring giving rise to two ^{1}H NMR differentiable protons at the 3-position, H7B (H_{ax}) and H7A (H_{eq}).

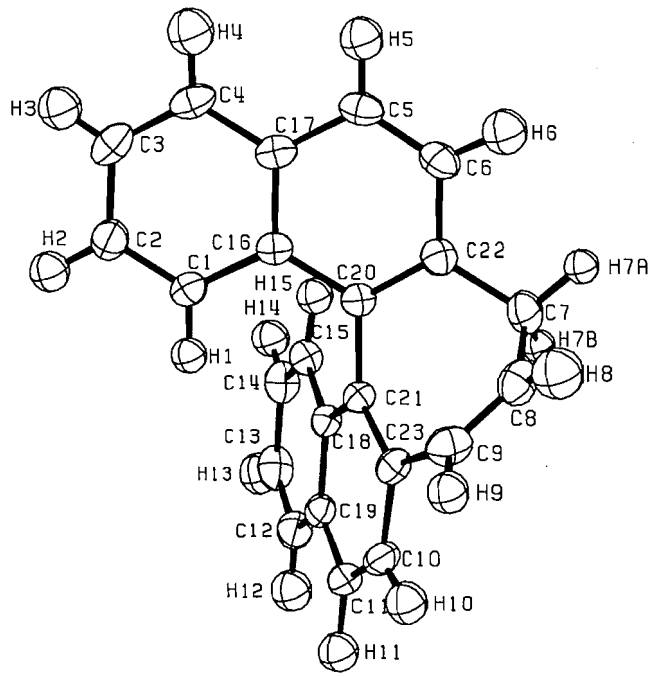

The crystal structure confirms many of the predictions based on simple molecular models. The naphthalene rings have a dihedral angle of 64° and the cycloheptene ring is highly distorted, with the methylene carbon (3-position of **10**) protons taking up pseudo-axial and pseudo-equatorial positions (labelled as H7B and H7A, respectively, on the ORTEP diagram, Fig. 2). The crystal structure also indicates that the axial proton (H7B, Fig. 2) is oriented above the plane of the opposite naphthalene ring, which should result in an upfield shift of this proton relative to the equatorial proton (H7A, Fig. 2).

Fig. 3. ^{1}H (360 MHz) NMR of the aliphatic region of **10** showing the higher field resonance of H_{ax} (δ 2.95) versus H_{eq} (δ 3.32). Note also the larger coupling of H_{ax} (2.2 Hz) to H_5 compared to that of H_{eq} (<1 Hz) to H_5.

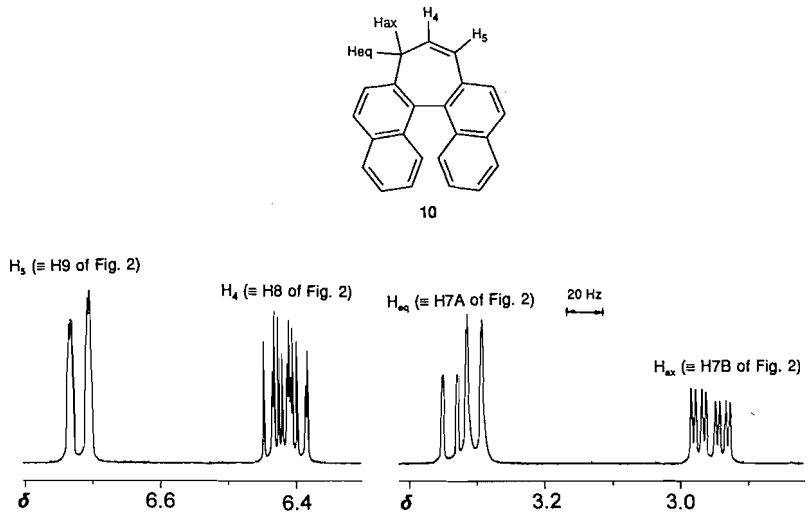

Indeed, two proton signals are observed for the methylene carbon, one for the axial proton (δ 2.95, H7B ≡ H_{ax}), and one for the equatorial proton (δ 3.32, H7A ≡ H_{eq}) (Fig. 3). The larger allylic coupling constant (2.2 Hz) observed in the former suggests that our assignment is correct since the magnitude of 3-carbon allylic couplings (to H9 of Fig. 2) depend on the angle between the allylic protons (H7A and H7B) and the vinyl proton (H9 of Fig. 2) and is largest when they are orthogonal (13).

As far as we are aware, *3H*-cyclohepta[2,1-*b*:3,4-*b'*]dinaphthalene (**11**) has not been reported in the literature. The synthetic route that was used (Scheme 5) is similar to that employed for the synthesis of **10**. The required 2-bromo-3-methylnaphthalene (**31**) was prepared via an established literature method from commercially available **29** (14). Coupling of **31** was then attempted using the procedure employed for **23**. However, only a minor amount of coupling product was observed. The yield was enhanced considerably by concurrent addition of one equivalent of 1,2-dibromoethane with two equivalents of Mg during formation of the Grignard reagent. The remaining steps were identical to those used in Scheme 4. A major undesired product obtained in the last step was the ring-opened isomer **38** (45% yield in last step), which proved difficult to separate from the required **11** via chromatography. However, repeated recrystallization of the mixture in toluene–EtOH provided **11** with >98% yield by GC and NMR. The ^{1}H (360 MHz) NMR showed the expected three signals (δ 3.37, (d) H3; 6.42, (m) H4; and 6.81 (d) H5) outside the aromatic region. Indeed, the splitting patterns observed for these signals resemble the patterns observed for the parent system **3** and is unlike that observed for **10**. Thus, it was not possible to resolve pseudo-axial or pseudo-equatorial protons at the methylene position of **11**, which is consistent with a much more flexible ring system compared to **10**.

Product studies

*7-Deuterio-5*H*-dibenzo[*a,c*]cycloheptene (9)*

In our initial report (4*a*) of the excited state carbon acid behaviour observed for **3**, the question of extent of delocalization of photogenerated **3a** was not addressed. Carbanion **3a** is formally antiaromatic (5) and therefore should be a less delocalized carbanion in the ground state. The extent to which delocalization of photogenerated **3a** is observed would provide insight into the question of whether **3a** is generated initially on the excited state surface or the photoreaction is completely diabatic, in which case little delocalization of the carbanion is expected. Photochemical 1,3-hydrogen shifts of allylic systems catalyzed by amines in dihydronaphthalenes and dihydrophenanthrenes have been reported by Laarhoven and co-workers (15) although, in their examples, it is not well established whether a photogenerated carbanion is a required intermediate. Reaction via initial electron transfer to form radical ion pairs seems to be the likely mechanism.

Direct photolysis (254 nm; 15 min) of **9** in 100% CH_3CN resulted in a complex product mixture consisting of **4a** and **4b** (total of 64%) and minor amounts of 9-deuterophenanthrene (6%) and **6** (6%), as determined by ^{2}H NMR. These products are expected based on initial formation of **4** via formal di-π-methane rearrangement, which on direct photolysis involves initial 1,7-hydrogen shift followed by electrocyclic ring closure (4*a*). Formation of **5** was not observed at all conversions. Direct photolysis of **9** in 50% H_2O–CH_3CN under otherwise identical conditions gave **5** as the major product (30%), **4a** and **4b** (18%), and traces of **6** (4%) and 9-deuterophenanthene, as determined by ^{2}H NMR (Fig. 4). The efficient formation of **5** in 1:1 H_2O–CH_3CN is consistent with reaction via carbanion **3a** in this solvent, which now competes with the formal di-π-methane rearrangement (4*a*). Thus, photogenerated carbanion **3a** is significantly delocalized to position 7 (Scheme 6).

*6-Methyl-5*H*-dibenzo[*a,c*]cycloheptene (7)*

Direct photolysis of **7** in 100% CH_3CN (254 nm, 15 min) gave three products (Scheme 7). The major product observed was cyclopropane **40** (25%), which is the product expected via di-π-methane rearrangement from T_1. Minor products **41** and **42** (3% each) can be thought to arise via secondary photolysis of

Scheme 5.

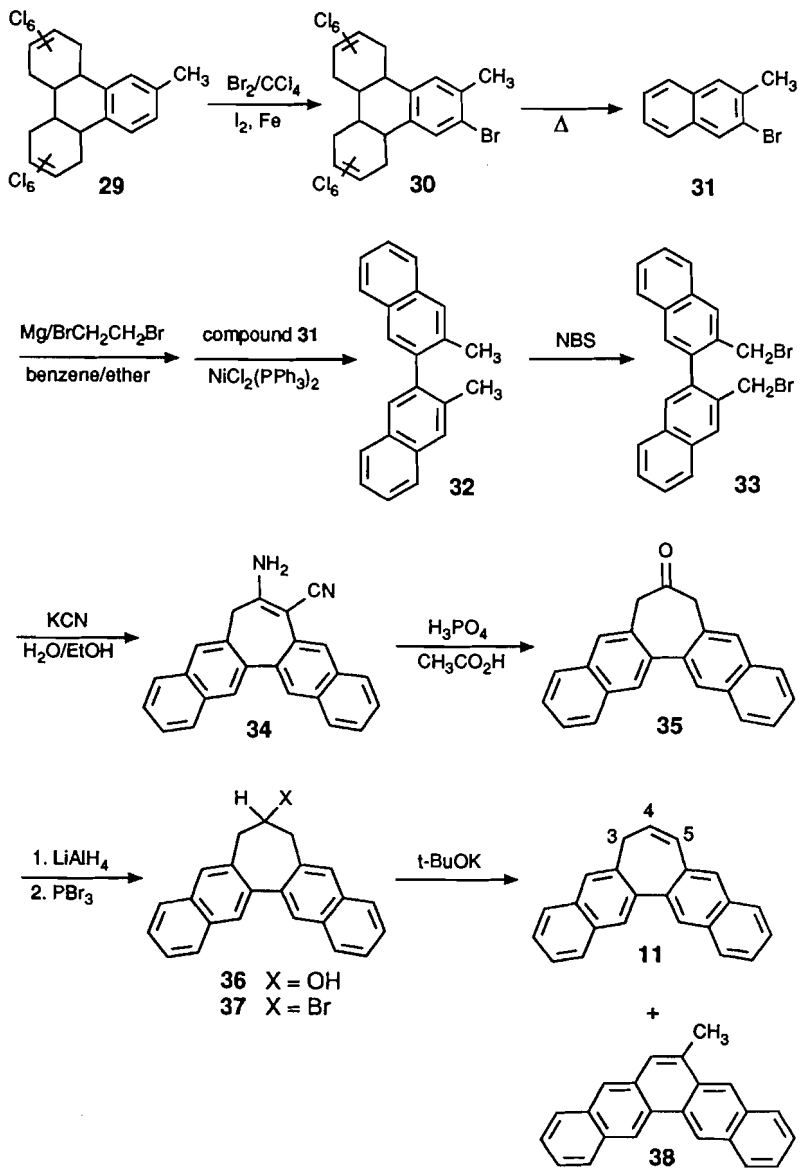

40, the former via carbene extrusion and the latter via initial bond cleavage of the cyclopropane followed by a hydrogen shift. Triplet sensitization of **7** in 100% with 2-benzoylbenzoic acid at 350 nm where **7** does not absorb gave only **40**, consistent with the expectation that this cyclopropane is formed via T_1. The rearrangement product expected from S_1 (viz. **39**), via initial 1,7-hydrogen shift, was not observed in direct photolysis experiments of **7**. One possible reason is the increased steric demand for such a shift when the methyl group is present at the 4-position. Another is an increased rate of intersystem crossing for this compound, which is suggested by a much lower fluorescence quantum yield and lifetime (vide infra).

Photolysis of **7** was carried out in H_2O–CH_3CN to determine if this system exhibited excited state carbon acid behaviour as was observed for **3**. Direct photolysis of **7** in 25% H_2O – CH_3CN (254 nm, 15 min) gave about the same product mixture as observed on photolysis in 100% CH_3CN shown in Scheme 7 (higher % H_2O could not be used due to the low solubility of this compound). In contrast, addition of H_2O (acting as a base) competed for rearrangement products in the photochemistry of **3**, resulting in a lower yield of formal di-π-methane products when water is added to CH_3CN (*4a*). Photolysis of **7** in 25% D_2O – CH_3CN showed ≈10% deuterium incorporation in recovered **7**, significantly less than what was observed for **3** under similar conditions. Thus substitution of a methyl group at the 4-position also results in decreased efficiency with respect to carbon acid dissociation.

6-Phenyl-5H-dibenzo[a,c]cycloheptene (8)

Direct photolysis of **8** in 100% CH_3CN (254 nm, 30 min.) gave only minor products and the substrate could be recovered essentially unchanged. Analysis of the photolysate by ^1H NMR gave no evidence for any trace of cyclopropanes expected from rearrangement of the cycloheptene ring system.

Fig. 4. ^{2}H NMR of product mixture from direct photolysis of **9** in 1:1 H_2O–CH_3CN for 15 min (254 nm).

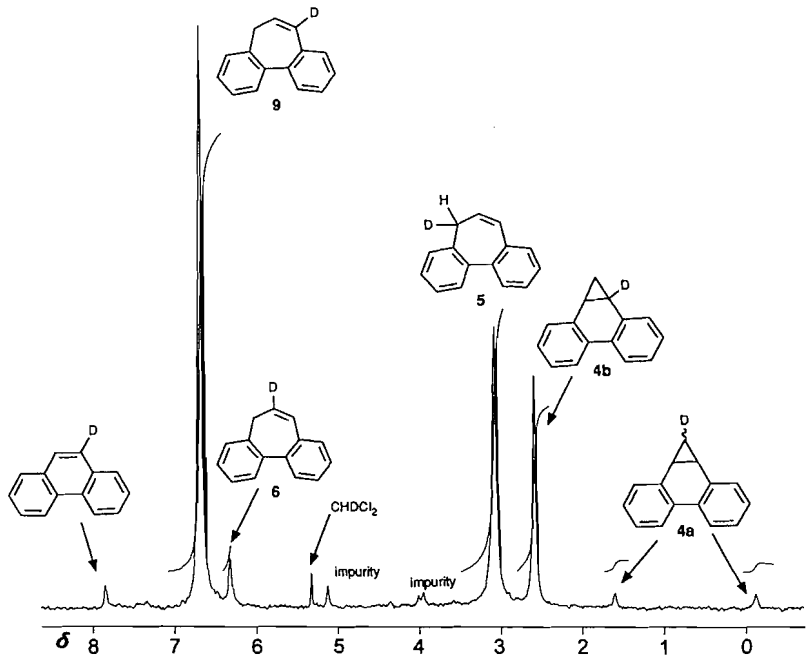

Photolysis in 40% D_2O – CH_3CN gave no measurable deuterium incorporation in substrate. Thus, substitution of a phenyl group at the 4-position not only retards carbon acid dissociation, but also the formal di-π-methane reaction.

3H-Cyclohepta[2,1-a:3,4-a′]dinaphthalene (10)

Photolysis of **10** in 100% CH_3CN (254 nm, 4 h) gave only trace yields (<5%) of the expected formal di-π-methane rearrangement product **43** based on ^{1}H (360 MHz) NMR (eq. [1]). Since extended photolysis failed to result in buildup of **43**, it is likely that **43** is unstable and returns to **10** either thermally or photochemically. Simple molecular models show that **43** is highly strained because the cyclopropyl ring forces the two naphthalenes into a more planar geometry, which is unfavourable due to the interaction of the peri-hydrogens. Photolysis of **10** in 50% D_2O – CH_3CN for 1 h resulted in no observable deuterium incorporation. Under these conditions, **3** exchanged significantly (4*a*). The highly twisted cycloheptene ring system may account for the lack of excited state carbon acid dissociation since the π systems of the naphthalene rings and the alkene moiety are not well disposed for conjugation as in **3**.

Recent studies from our group (16) have shown that primary amines such as ethanolamine (EA) and *n*-propyl amine efficiently catalyze the excited state proton exchange of **2** and related compounds. To determine if **10** exhibited excited state carbon acid dissociation in the presence of a stronger base,

[1]

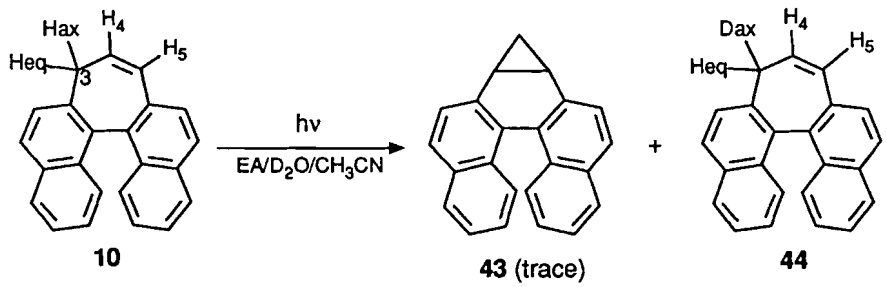

photolyses were carried out in 10% (5.0 M EA – D_2O)–CH_3CN. A series of ^{1}H (360 MHz) NMR spectra of the product mixture showed that the axial proton (H_{ax}) is selectively replaced on photolysis (Fig. 5). The equatorial proton (H_{eq}) and vinyl protons H_4 and H_5 exhibited little change in their relative intensities except at high conversion whereupon the signal due to H_5 and H_{eq} started to show depletion compared to H_4 and H_{ax} (Fig. 5). Analysis of the reaction mixture by ^{2}H NMR showed that deuterium incorporation takes place predominantly at the axial position (H_{ax}), with only minor deuteration at H_{eq} and H_5 at higher conversion (Fig. 6). A plot of relative deuterium incorporation into **10** at the three positions H_{ax}, H_{eq}, and H_5 is shown in Fig. 7. It is clear that deuteration at the axial position occurs much more efficiently. This is consistent with

Scheme 6.

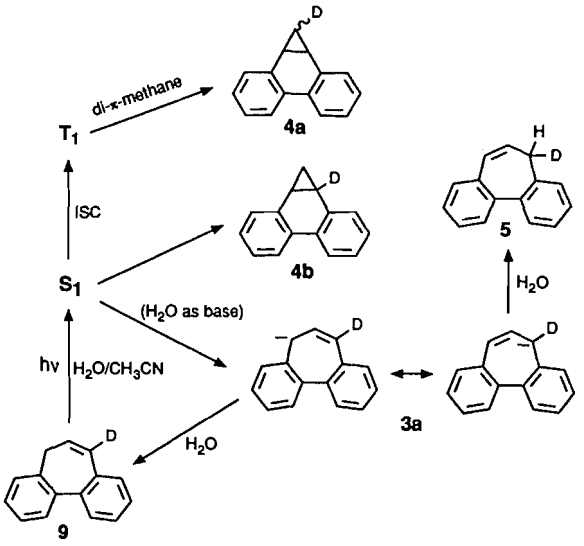

Scheme 7.

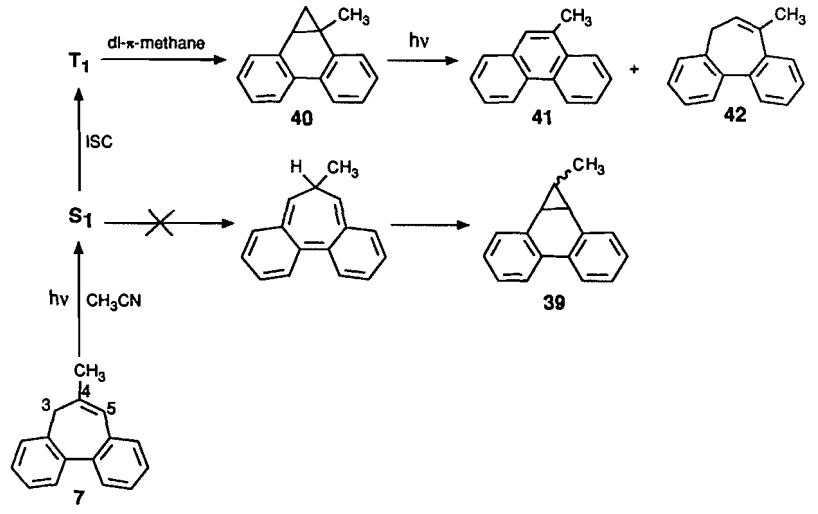

deprotonation at this position as the *primary* photochemical reaction, to generate a carbanion that is hydrogen bonded to the base. Exchange of the departing proton with deuteron in the hydrogen-bonded complex followed by deuteration results in deuterium incorporation exclusively at the axial position. A free carbanion intermediate is unlikely as we have shown that the photochemical exchange of suberene (**2**) involves a high degree of internal return (*4a*). Subsequent deuteration at H_{eq} and H_5 is most likely a *secondary* photochemical reaction.

Shown in Scheme 8 is the proposed mechanism for the deuterations observed in Fig. 7. Stereoelectronic preference for deprotonation of the axial proton (H_{ax}) allows for maximum overlap of the incipient carbanion with the alkene and one of the naphthalene rings (note that delocalization of the negative charge to the other allylic position converts it to its enantiomer and hence would not be distinguishable by NMR). Similar stereoelectronic effects have been noted for ground state reactions involving proton (17) and hydrogen (18) abstractions from carbon. Deuteration at H_{eq} can arise via either a sigmatropic 1,3-shift of D_{ax} or a photoinduced ring flip of the cycloheptene ring system. Deuteration at H_5 can arise via a 1,3-shift of H_{eq}. The greater yield of D_5 is consistent with competition of 1,3-shifts since a primary isotope effect would be expected, resulting in a higher yield of D_5 over D_{eq}. It is not possible to rule out a contribution from a photo-induced ring flip although such a contribution would be very minor considering that D_{eq} is formed in only very small amounts even on prolonged photolysis. In addition, we have not ruled out dideuteration via the carbanion obtained from deprotonation of H_{eq} of **44** or ring opening of deuterated **43** as responsible for the signals at D_5 and D_{eq}.

*3H-Cyclohepta[2,1-b:3,4-b′]dinaphthalene (**11**)*

Photolysis of **11** in 100% CH_3CN efficiently gave the corresponding formal di-π-methane rearrangement product **45** in >90% yield (eq. [2]), according to both ^1H NMR and GC. The ^1H NMR exhibited three new aliphatic proton resonances at δ 0.18 (1H), 1.63 (1H), and 2.77 (2H) with splitting pat-

Fig. 5. ^{1}H (360 MHz) NMR spectra of photolysis of **10** in 10% (5 M EA – D_2O)–CH_3CN as a function of photolysis time. Each spectrum represents about 30 min photolysis at 254 nm.

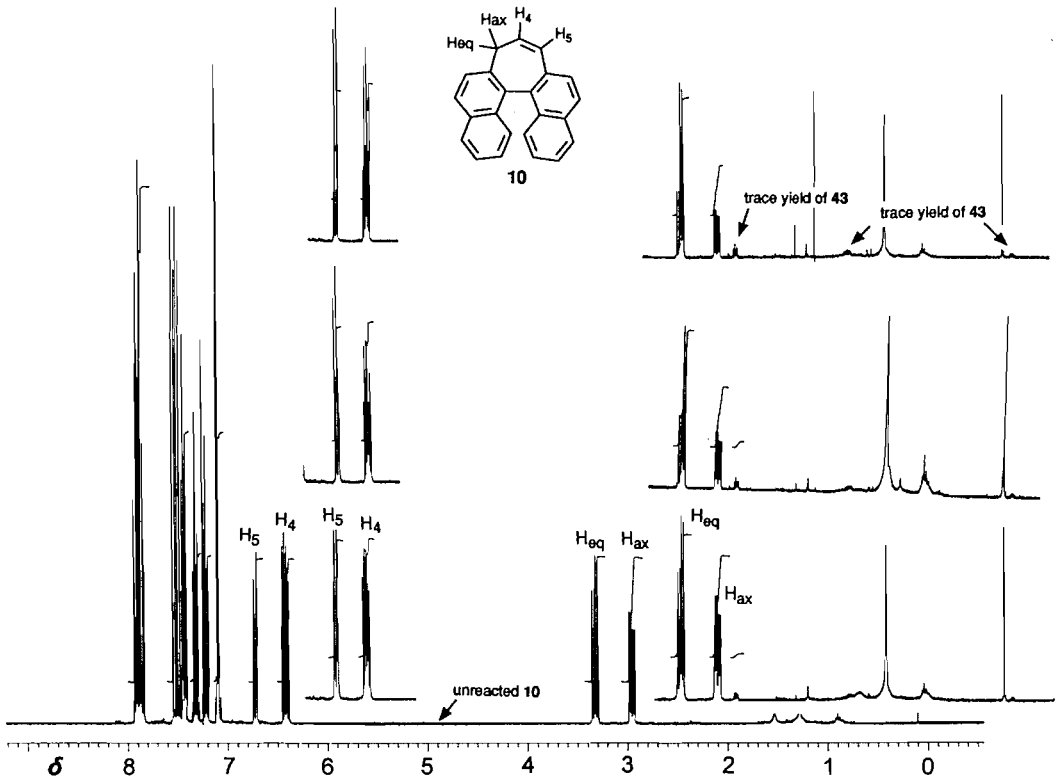

terns that are clearly assignable to **45** (see experimental section). UV–VIS traces of the reaction in 100% CH_3CN also show a clean and efficient reaction with good isosbestic points (Fig. 8). The cyclopropane product **45** has a longer wavelength absorption (330–360 nm) than **11** that is consistent with its more planar structure, allowing for better conjugation of the two naphthalene rings. The much more efficient formal di-π-methane rearrangement observed for **11** compared to **10** is consistent with a less sterically demanding and less strained ring system in **11**; i.e., ring closure to **45** does not lead to the kind of steric interactions as expected for **10** for which the formal di-π-methane product was formed only in trace yield.

Photolysis of **11** in 10% (5 M EA in D_2O) – CH_3CN resulted in no observable deuterium incorporation into substrate by GC–MS; only efficient rearrangement to **45** was observed with no observable change in efficiency compared to a photolysis in 100% CH_3CN. It would appear that binaphthyl cycloheptenes are prone to formal di-π-methane rearrangement unless steric effects prohibit the reaction as in **10**. In such a case, use of an amine base promotes excited state carbon acid dissociation. The above results show that excited state carbon acid dissociation is highly sensitive to structure effects and is observed only in the most favourable cases where competing reactions are absent. This may in part be due to the inherently slow rates of carbon acid dissociation that cannot compete with much faster photochemical pathways when they are feasible.

[2]

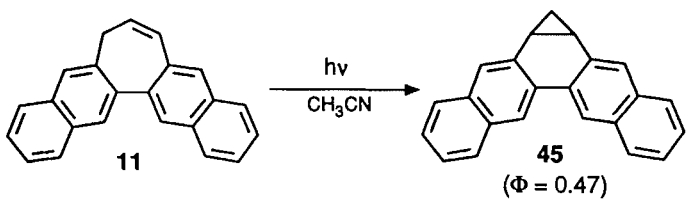

Quantum yield measurements

Quantum yields for deuterium exchange (Φ_{ex}) and for formal di-π-methane rearrangement (Φ_p) were measured in low conversion (<25%) experiments using 254 nm photolysis in a Rayonet RPR 100 photochemical reactor (Table 2). The photochemical exchange reaction of 5,5-dideuterosuberene in 1:1 H_2O–CH_3CN was used as secondary actinometer (Φ = 0.035) (3*b*). Analyses for deuterium incorporation were carried out

Fig. 6. Representative ^2H NMR spectrum taken after photolysis of **10** in 10% (5 M EA – D_2O)–CH_3CN showing formation of three deuterated products, with deuteration of H_{ax} (to give **44**) being the major pathway. Although the peaks assigned for D_{eq} and D_5 are broad and weak, they grow in intensity with prolonged photolysis.

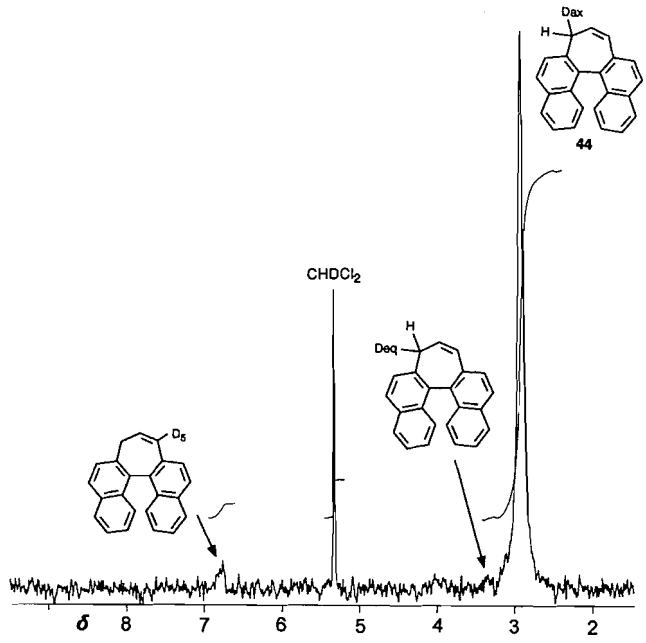

Fig. 7. Plot of relative yield of deuteration at the H_{ax}, H_{eq}, and H_5 positions of **10**.

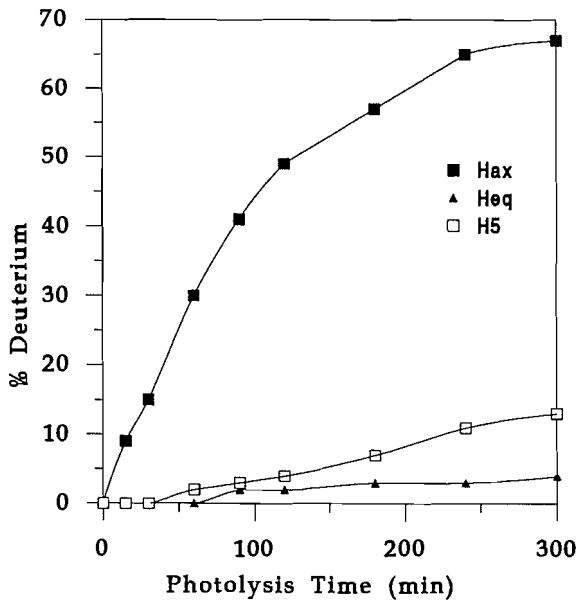

by ^1H (360 MHz) NMR and by GC for formal di-π-methane rearrangement products. For **3**, **7**, and **10**, quantum yields for exchange (Φ_{ex}) increased significantly from using D_2O as base to ethanolamine (EA) without affecting Φ_p to any measurable degree.

Fluorescence measurements

In previous studies (3, 4*a*) of excited state carbon acid dissociation, fluorescence measurements provided a direct method for measuring rates of deprotonation of carbon acids in S_1 since we found that fluorescence quenching by added bases (in CH_3CN) was the direct result of deprotonation of the C—H bond. These fluorescence quenching rate constants (k_q) were equatable to k_H, the bimolecular rate constant for C—H bond deprotonation by the base. Related compounds such as fluorene and diphenylmethane which failed to undergo carbon acid dissociation also had no measurable k_q values (3, 4*a*).

Fluorescence parameters for **3**, **7**, **8**, **10**, and **11** are given in Table 3. Substitution of **3** at the 6-position with methyl or phenyl substituents resulted in a decrease in Φ_f. This is presumably caused by additional internal conversion pathways due to rotations of the 6-substituent. The fluorescence emission spectra of **3** and **7** are structureless and essentially identical with broad λ_{max} = 360–370 nm. However, the fluorescence emission of **8** consists of two bands at 340 nm and 370 nm, each with a different excitation spectrum. This observation along with the fact that biexponential decays were observed in lifetime measurements (Table 3) for this compound is consistent with emission from two distinct chromophores, viz. biphenyl and stilbene moieties (Fig. 9). One of the factors responsible for lack of carbon acid dissociation of **8** may be due to the efficient energy transfer to the stilbene excited state, which is unreactive. However, a detailed photophysical study is required to completely understand the nature of the excited states available for this compound.

The fluorescence excitation and emission spectra of **10** and **11** in CH_3CN are broad and essentially structureless (Fig. 10). Although the fluorescence quantum yields (Φ_f) are the same, their fluorescence lifetimes differ substantially, consistent with the general observation that binaphthyls joined at the 1-position are short-lived (≈2 ns) whereas those joined at the 2-position are much longer lived (≈30 ns) (19). The 15 ns lifetime measured for **11** is consistent with an efficient formal di-π-methane rearrangement occurring for this compound whereas the photoinert **10** (in CH_3CN) has a measured lifetime essentially the same as other nonreactive 1,1′-binaphthyls reported in the literature (19).

The fluorescence quenching rate constants of **3** by primary amines EA and $H_2NCH_2CH_2NH_2$ are more than an order of magnitude larger than for H_2O, consistent with the much higher basicity of the amines (Table 4). The increased quenching efficiency for EA is reflected in the higher quantum yield for deuterium incorporation when EA is used in the exchange studies (Table 2). A similar observation is made for **7** although in this case quenching with H_2O was small and a k_q could not be reliably calculated. No fluorescence quenching was observed using H_2O as base for all of **8**, **10**, and **11**, consistent with the complete lack of deuterium exchange for these compounds when photolyzed in D_2O–CH_3CN. Use of EA as quencher resulted in fluorescence quenching only for **10** ($k_q = 0.86 \times 10^9$ M^{-1} s^{-1}) consistent with deuterium incorporation observed only for this compound in EA–D_2O–CH_3CN. However, its k_q value is an order of magnitude smaller than for **3**, indicating that binaphthyls are intrinsically weaker excited state carbon acids even in favourable cases such as **10**.

Fig. 8. UV–VIS traces for the photolysis of **11** in 100% CH_3CN, showing clean and efficient formation of **45**.

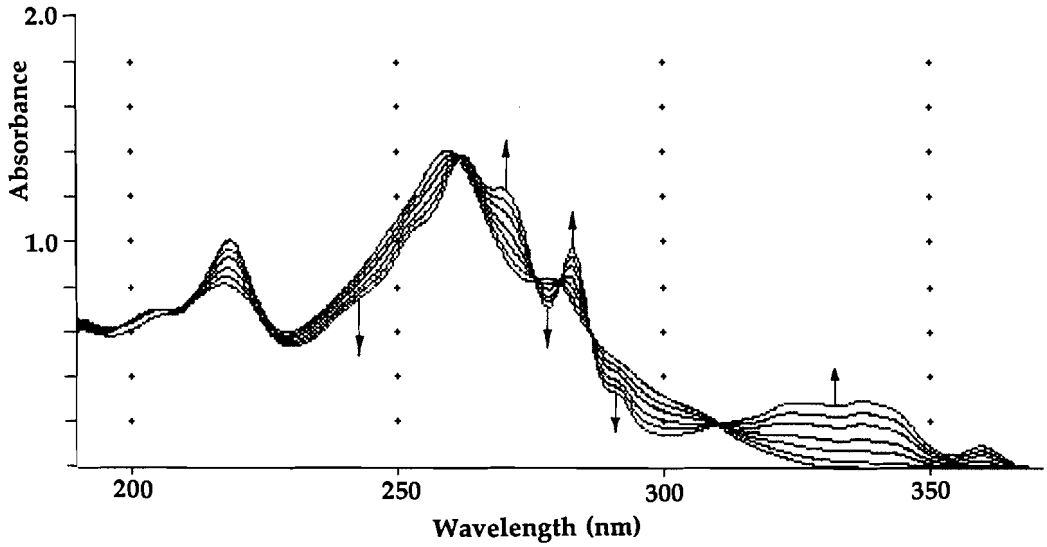

Scheme 8.

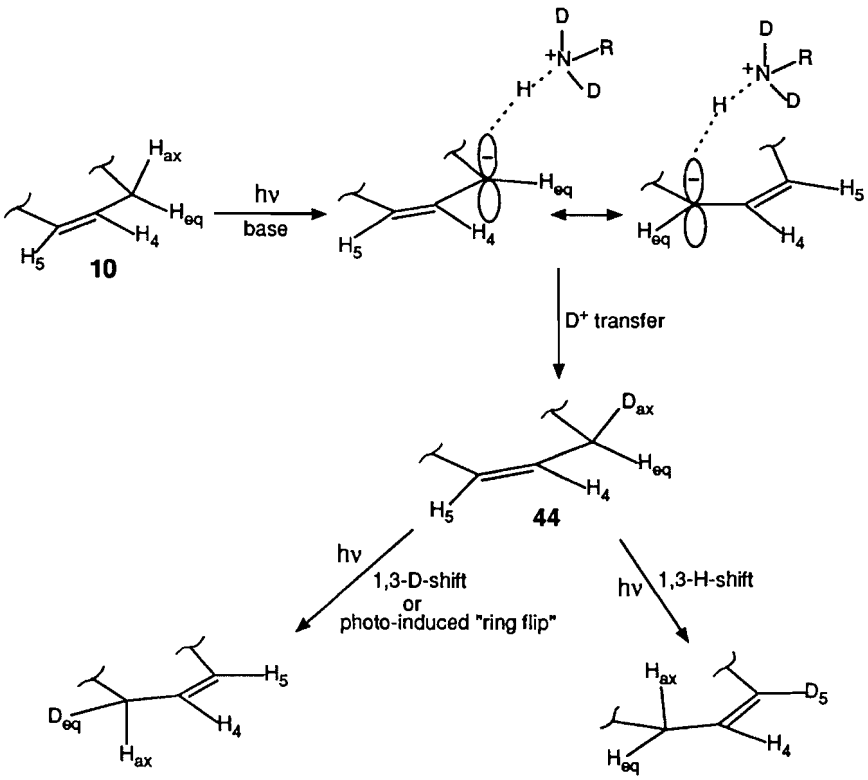

Summary

Study of excited state carbon acid dissociation of **9** has shown that the photochemically generated carbanion **3a** is allylically delocalized. Carbon acid dissociation of **3** was found to be highly sensitive to substituents at the 6-position since **7** was found to be less reactive and **8** completely unreactive with respect to this reaction. Use of EA as base resulted in enhanced rates of carbon acid deprotonation for **3** and **7**. Studies of binaphthyls **10** and **11** have shown that excited state carbon dissociation is observable even in naphthocycloheptene systems if formal di-π-methane rearrangement is retarded and a suitable base such as EA is used. Thus the positive results observed for **10** indicate that excited state carbon acid dissoci-

Table 2. Quantum yields for deuterium incorporation (Φ_{ex}) and product formation (Φ_p) for **3**, **7**, **8**, **10**, and **11**.

Compound	Solvent	Φ_{ex}[a]	Φ_p[a]
3	25% D_2O – CH_3CN[b]	0.03 ± 0.01	0.023 ± 0.006
	10% (5 M EA – D_2O) – CH_3CN	0.08 ± 0.02	0.029 ± 0.008
7	25% D_2O – CH_3CN	0.006 ± 0.002	0.018 ± 0.006
	10% (5 M EA – D_2O) – CH_3CN	0.07 ± 0.02	0.016 ± 0.005
8	40% D_2O – CH_3CN	0.000	< 0.02[c]
10	50% D_2O – CH_3CN	0.000	< 0.001[d]
	10% (5 M EA – D_2O) – CH_3CN	0.02 ± 0.01[d]	< 0.001[d]
11	100% CH_3CN	0.000	0.47 ± 0.05
	10% (5 M EA – D_2O) – CH_3CN	0.000	0.47 ± 0.05

[a]Quantum yields for deuterium incorporation (Φ_{ex}) and for product formation (Φ_p) (formal di-π-methane rearrangement) were measured by photolyzing samples at 254 nm in a Rayonet RPR 100 reactor using the carbon acid exchange reaction of 5,5-dideuterosuberene in 1:1 H_2O – CH_3CN as secondary actinometer (Φ_{ex} = 0.035) (3*b*). Analyses were performed by ^1H (360 MHz) NMR for Φ_{ex} and GC for Φ_p.

[b]Measured in 25% D_2O – CH_3CN for comparison with **7** since **7** was found to be insoluble in more aqueous mixtures.

[c]Estimated based on ^1H (360 MHz) NMR. No formal di-π-methane rearrangement products were observed. Instead, photodecomposition to several minor products was observed as shown by GC.

[d]Estimated based on ^1H (360 MHz) NMR.

Table 3. Fluorescence parameters measured for **3**, **7**, **8**, **10**, and **11**.[a]

Compound	Φ_f[b]	τ[c]
3	0.12 ± 0.02[d]	4.5 ± 0.1[d]
7	0.07 ± 0.01[e]	1.6 ± 0.1
8	0.006 ± 0.002[f]	4.0/20.7[g]
10	0.13 ± 0.02[e]	2.4 ± 0.1
11	0.14 ± 0.02[e]	15.0 ± 0.3

[a]Measured at ambient temperature (20 ± 2°C) in dry CH_3CN (λ_{ex} = 260–280 nm, λ_{em} = 360–370 nm, depending on the substrate).

[b]Fluorescence quantum yields were measured relative to **3** as the secondary standard since the spectra distributions were all similar.

[c]Measured via single photon counting. All decays were good first order unless otherwise indicated.

[d]From ref. 4, for comparison purposes.

[e]Measured using **2** as reference (Φ_f = 0.86 ± 0.05) (3*b*).

[f]Measured using **7** as reference.

[g]Biexponential decays observed. At λ_{ex} = 260 nm and λ_{em} = 370 nm, the short-lived component accounted for 63% of the emission. The percentage of the emission from each component changed with λ_{em} consistent with the presence of two emitting chromophores for this compound, as observed in the steady-state fluorescence spectra.

Table 4. Rates of fluorescence quenching (k_q) measured for **3**, **7**, **8**, **10**, and **11** in CH_3CN from Stern–Volmer analysis.[a]

Compound	Quencher	k_q, 10^9 (M^{-1} s^{-1})
3	H_2O	0.21 ± 0.03[b]
	$H_2NCH_2CH_2OH$ (EA)	6.9 ± 0.2
	$H_2NCH_2CH_2OCH_3$	8.1 ± 0.2
7	H_2O	< 0.05
	EA	3.2 ± 0.1
8	H_2O	< 0.01[c]
	EA	< 0.01[c]
10	H_2O	< 0.01[c]
	EA	0.86 ± 0.04
11	H_2O	< 0.01[c]
	EA	< 0.01[c]

[a]Measured at ambient temperature (20 ± 2°C) in dry CH_3CN.

[b]From ref. 4, for comparison purposes.

[c]Estimate upper limit. No observable quenching up to 0.2 M EA in CH_3CN.

ation is a general reaction for larger benzannelated cycloheptenes but reaction efficiency will be reduced compared to the parent systems **2** and **3**.

Experimental section

General

^1H and ^{13}C NMR spectra were taken on Perkin–Elmer R32 (90 MHz), Bruker WM250 (250 MHz), or AM360 (360 MHz) spectrometers. ^2H NMR spectra were obtained on the Bruker AM360 instrument. MS, GC–MS, and HRMS were taken on a Finnigan 3300 (CI) or Kratos Concept 1H instrument (EI). GC was performed on a Varian 3700 gas chromatograph using a SE-54 capillary column and a Hewlett–Packard 3390A integrator. Preparative thin layer chromatography (TLC) was carried out on 20 × 20 silica gel GF Uniplates (Analtech). IR spectra were obtained on a Perkin–Elmer 283 spectrophotometer using NaCl solution cells. UV spectra were obtained on a Cary 5 spectrophotometer.

Materials

Phenanthrene (**13**), 2-benzoylbenzoic acid, 2-methylnaphthalene (**21**), diphenic anhydride and 2-methylnaphthalene-bis(hexachlorocyclopentadiene) adduct (**29**) were purchased from Aldrich.

Fig. 9. Fluorescence excitation and emission spectra observed for **8** indicative of two emitting chromophores.

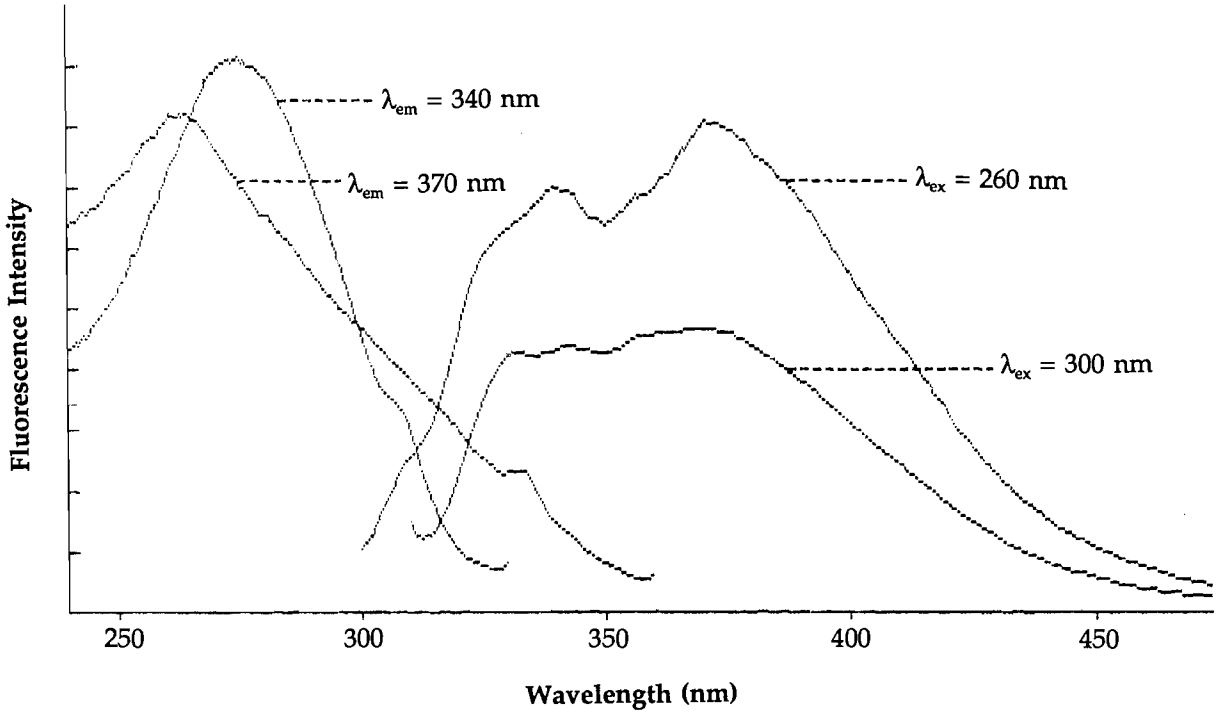

Fig. 10. Fluorescence excitation and emission spectra of **10** and **11** in 100% CH_3CN (λ_{ex} = 280 nm; λ_{em} = 400 nm).

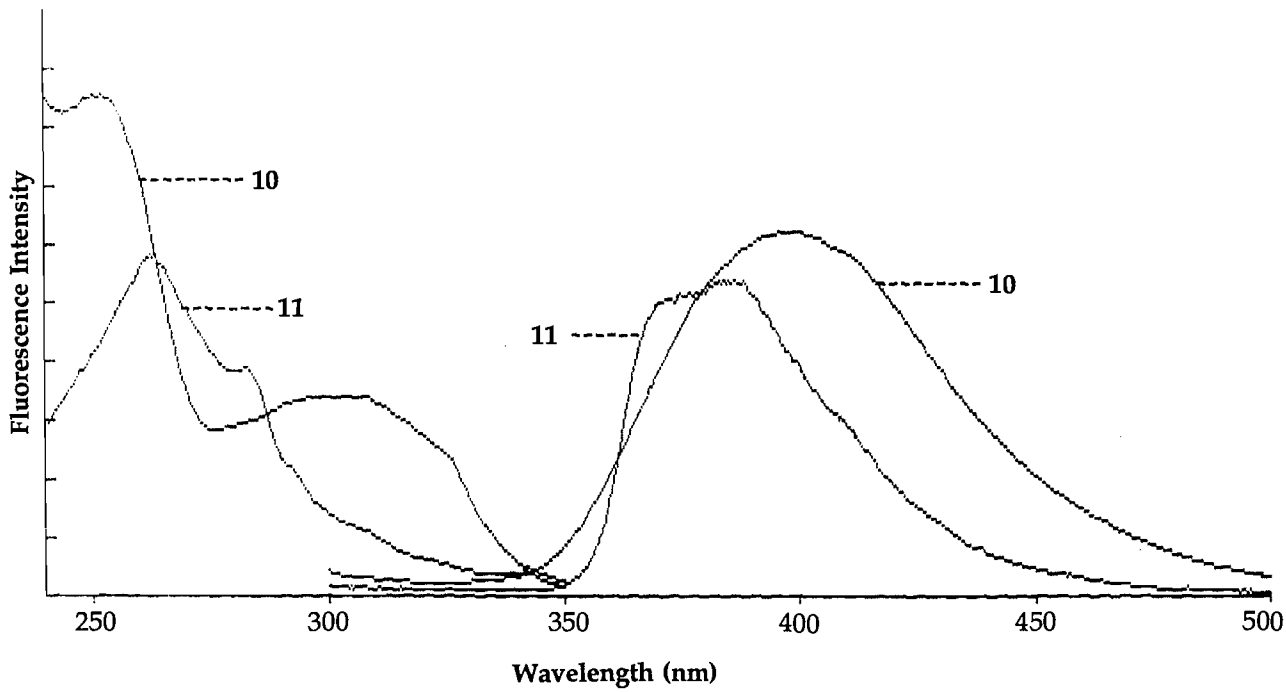

*7,7-Dichlorodibenzo[*a,c*]bicyclo[4,1,0]heptane (**14**)*
The method of Halton and Officer (6) was used for the synthesis of **14** from **13**. The ^{1}H NMR of the material obtained was identical to the literature spectrum (6).

*6-Chloro-5*H*-dibenzo[*a,c*]cyclohepten-5-ol (**15**)*
Alcohol **15** was prepared from **14** following the procedure of Coburn and Jones (7). The ^{1}H NMR of the product was identical to the literature spectrum (7).

*6,7-Dihydro-5H-dibenzo[a,c]cycloheptene (**16**)*
Alcohol **15** (2.4 g, 0.0098 mol) was converted to **16** using the procedure of Griffin and Horn (8). A clear oil (1.5 g, ≈80% yield) with a purity of 99% by GC was obtained, ^{1}H NMR (90 MHz) δ: 1.9–2.6 (m, 6H, $(CH_2)_3$), 7.1–7.4 (m, 8H, arom.); MS (CI) (*m/z*): 195 (M^++1).

*5-Bromo-6,7-dihydro-5H-dibenzo[a,c]cycloheptene (**17**)*
Hydrocarbon **16** (0.5 g, 0.0026 mol) was brominated with NBS in CCl_4 in the presence of benzoyl peroxide (50 mg). The reaction mixture was refluxed overnight. Upon cooling, the solution was filtered and evaporated to give crude **17** (≈50%), as indicated by a new multiplet at δ 5.0 assignable to the benzylic proton substituted with bromine. The crude bromide was used without further treatment in the next step.

*6,7-Dihydro-5H-dibenzo[a,c]cyclohepten-5-ol (**18**)*
All of the bromide **17** from the previous step was dissolved in 1:1 H_2O–CH_3CN (40 mL) and gently refluxed for 1 h. Upon addition of NaCl, the mixture was extracted with CH_2Cl_2, which gave the crude alcohol **18** in 100% conversion by ^{1}H NMR. This material was used in the next step without further treatment. The multiplet at δ 5.0 of **17** moves upfield to δ 4.6 consistent with substitution of bromine by H_2O.

*6,7-Dihydro-5H-dibenzo[a,c]cyclohepten-5-one (**19**)*
The crude alcohol (**18**) (1.0 g, 0.0048 mol) was dissolved in ether (40 mL) and 20 mL of 10% chromic acid added dropwise over a 10 min period. After stirring the solution overnight, the organic layer was separated and the aqueous layer washed with 2 × 50 mL ether. The organic layers were combined and washed with saturated sodium bicarbonate and saturated NaCl solutions. Drying and evaporation of the solvent gave crude ketone **19** (0.60 g, 60%). Purification of **19** was achieved by column chromatography (silica), first eluting with hexanes to wash out nonpolar components of the product mixture and then with 50% CH_2Cl_2–hexanes for the final separation. The material obtained was >95% pure by GC with the ^{1}H NMR identical to the literature spectrum (7), δ: 2.90 (s, 4H, CH_2CH_2), 7.19–7.72 (m, 8H, arom.).

*5-Deuterio-6,7-dihydro-5H-dibenzo[a,c]cyclohepten-5-ol (**20**)*
Ketone **19** (1.5 g, 0.0072 mol) was reduced with $LiAlD_4$ (0.3 g) in ether to give **20** (1.5 g, 100%), whose ^{1}H NMR was identical to that of **18** except for the absence of the methine proton resonance and its associated couplings.

*7-Deuterio-5H-dibenzo[a,c]cycloheptene (**9**)*
Alcohol **25** (200 mg, 0.95 mmol) was dissolved in 50 mL toluene in a round-bottom flask and fitted with a Dean-Stark trap. After addition of 20 mL 85% H_3PO_4 the reaction mixture was refluxed for 3 h, cooled, poured onto ice, and the aqueous fraction extracted with hexanes (2 × 50 mL). The organic fractions were combined and washed with saturated sodium bicarbonate. Drying and evaporation of the solvent provided crude **9** as an oil. Kugelrohr distillation gave a clear oil (110 mg, 60%) with >97% purity by GC (96% deuterium at the 7-position by ^{2}H NMR, see Fig. 1), ^{1}H NMR (360 MHz) δ: 3.08 (br s, 2H, CH_2), 6.27 (t, *J* = 6.9 Hz, 1H, vinyl), 7.22–7.32 (m, 1H, arom.), 7.35–7.44 (m, 5H, arom.), 7.53–7.62 (m, 1H, arom.), 7.71–7.77 (m, 1H, arom.); MS (CI) (*m/z*): 194 (M^++1).

*6-Methyl-5H-dibenzo[a,c]cycloheptene (7) and 6-phenyl-5H-dibenzo[a,c]cycloheptene (**8**)*
Both **7** and **8** were prepared from diphenic anhydride via the procedure used for the synthesis of **8** by Tolbert and Ali (5). Purification of **7** and **8** was achieved using column chromatography (silica) with hexanes as eluent. A clear oil was obtained for **7** with a purity of >97% by GC, UV (CH_3CN) λ_{max} (ε): 238 nm (36 700), 254 (11 600), 292 (1330); ^{1}H NMR (360 MHz) δ: 2.10 (d, *J* = 1.6 Hz, 3H, CH_3), 3.02 (s, 2H, CH_2), 6.36 (q, *J* = 1.6 Hz, 1H, vinyl), 7.23–7.41 (m, 6H, arom.), 7.54–7.59 (m, 1H, arom.), 7.69–7.73 (m, 1H, arom.); MS (CI) (*m/z*): 207 (M^++1). Pure **8** was a white solid, purity >98% by GC, mp 82–83°C (lit. (5) mp 92–94°C); UV (CH_3CN) λ_{max} (ε): 228 nm (21 400), 250 (28 500), 293 (16 300); ^{1}H NMR (250 MHz) δ: 3.28 (br s, 1H, CH), 3.76 (br s, 1H, CH), 6.88 (s, 1H, vinyl), 7.25–7.78 (m, 13H, arom.); MS (CI) (*m/z*): 269 (M^++1).

*1-Bromo-2-methylnaphthalene (**22**)*
Bromination of 2-methylnaphthalene (**21**) (50 g, 0.35 mol) at the 1-position was carried out using the procedure of Adams and Binder (9). Distillation of the crude product mixture gave **22** as a clear oil (71 g, 91%); ^{1}H NMR (90 MHz) δ: 2.56 (s, 3H, CH_3), 7.2–7.8 (m, 5H, arom.), 8.2–8.3 (m, 1H, arom.); MS (CI) (*m/z*): 221 (M^++1, ^{79}Br), 223 (M^++1, ^{81}Br). The spectroscopic data agree with literature values (9, 20).

*2,2′-Dimethyl-1,1′-binaphthyl (**23**)*
Coupling of **22** (178 g, 0.81 mol) via the Grignard reagent was carried out according to the method of Maigrot and Mazaleyrat (10). Unreacted **21** and **22** were removed by Kugelrohr distillation to give crude **23** (86 g, 38%). Further purification was achieved by elution through a silica gel flash column with hexanes to provide **23** with >95% purity by GC. The ^{1}H NMR (90 MHz) agreed with the literature spectrum (20).

*2,2′-Bis(bromomethyl)-1,1′-binaphthyl (**24**)*
Bromination of **23** (86 g, 0.30 mol) with NBS using the procedure for **17** above gave **24** (114 g, 85%). The product was recrystallized in 1:3 benzene–hexanes to give yellowish crystals with a purity of >95%. The ^{1}H NMR (90 MHz) agreed with the literature spectrum (20).

*5-Cyano-4-amino-3H-cyclohepta[2,1-a:3,4-a′]dinaphthalene (**25**)*
To a refluxing solution of KCN (40 g) in 30% H_2O – EtOH (160 mL) was added a 200 mL acetone solution of **29** (24 g, 0.055 mol) via an addition funnel over 2 h period. After addition, most of the acetone was removed by leaving one of the necks of the round-bottom flask open. The solution was then refluxed overnight. The reaction mixture was poured into 2 L of water and the precipitate filtered to give crude **25** (11 g, 60%), IR (CH_2Cl_2) (cm^{-1}): 3495, 3390 (NH_2), 2163 (CN); ^{1}H NMR (90 MHz) δ: 3.11 (d, *J* = 12 Hz, 1H), 3.37 (d, *J* = 12 Hz, 1H), 5.07 (br s, 2H, NH_2), 7.0–8.1 (m, 12H arom.); MS (CI) (*m/z*): 333 (M^++1). This material was used in the next step without further purification.

*3H-Cycloheptan-4-one[2,1-a:3,4-a′]dinaphthalene (**26**)*
Preparation of **26** from **25** (16 g, 0.048 mol) was accomplished using the procedure of Mislow and McGinn (12). Recrystallization of **26** (12 g, 80%) in acetone gave a brown powder (purity >95%) that by ^{1}H NMR (90 MHz) is consistent with

26; IR (CH_2Cl_2) (cm^{-1}): 1710 (s, carbonyl str.); δ: 3.61 (two overlapping doublets, both J = 15 Hz, 4H, $2CH_2$), 7.1–7.6 (m, 8H, arom.), 7.8–8.0 (m, 4H, arom.); MS (CI) (*m/z*): 309 (M^++1).

3H-Cycloheptan-4-ol[2,1-a:3,4-a′]dinaphthalene (27)
Reduction of **26** (2 g, 0.0065 mol) with $LiAlH_4$ in THF gave alcohol **27** (1.8 g, 40%). The product was shown to be sufficiently pure for the next step by ^{1}H NMR (90 MHz), δ: 1.55 (s, 1H, OH), 2.1–3.1 (m, 4H, $2CH_2$), 4.3–4.7 (m, 1H, CH), 7.1–7.6 (m, 8H, arom.), 7.8–8.0 (m, 4H, arom.); MS (CI) (*m/z*): 293 (M^+ − OH).

4-Bromo-3H-cyclohepta[2,1-a:3,4-a′]dinaphthalene (28)
The alcohol **27** (2 g, 0.0065 mol) was dissolved in $CHCl_3$ (100 mL) and PBr_3 (2 g) added dropwise with a pipette. The resulting mixture was refluxed overnight and poured into 200 mL of water. The organic layer was separated and the aqueous portion extracted with CH_2Cl_2. The combined organic extracts were dried over $MgSO_4$ and the solvent evaporated off to obtain crude **28** (2.2 g, 90%), ^{1}H NMR (90 MHz), δ: 2.5–3.4 (m, 4H, $2CH_2$), 4.5–4.8 (m, 1H, CHBr), 6.9–8.1 (m, 12H, arom.). This material was used in the next step without further treatment.

3H-Cyclohepta[2,1-a:3,4-a′]dinaphthalene (10)
Bromide **28** (2.2 g, 0.0059 mol) was dissolved in 150 mL *t*-BuOH with 2 g of t-BuO^-K^+ and refluxed overnight. The reaction mixture was then poured into 100 mL water and the resulting solution extracted with CH_2Cl_2. Evaporation of the solvent gave crude **10** (1.2 g, 70%). The material was recrystallized from toluene–EtOH to give colourless crystals with a purity >99% by GC (mp 166–168°C, (lit. (11) mp 163–164°C)); UV (CH_3CN) λ_{max} (ε): 208 nm (sh, 38 900), 225 (77 600), 251 (35 300), 303 (10 600); ^{1}H NMR (360 MHz), δ: 2.96 (ddd, J = 12.8, 5.6, 2.2 Hz, axial CH), 3.33 (ddd, J = 12.9, 7.9, 0.6 Hz, equatorial H), 6.42 (ddd, J = 9.8, 7.9, 5.6 Hz, 1H, vinyl), 6.72 (dd, J = 9.7, 2.3 Hz, 1H, vinyl), 7.09–7.11 (m, 2H, arom.), 7.19–7.24 (m, 1H, arom.), 7.29–7.35 (m, 1H, arom.), 7.41–7.56 (m, 4H, arom.), 7.84–7.83 (m, 4H, arom.) (the ^{1}H NMR was essential identical to that reported in ref. 11); ^{13}C NMR, δ: 33.9 (CH_2), 124.3, 125.3, 125.4, 125.5, 125.6, 126.5, 127.1, 127.8, 127.9, 128.1, 128.6, 128.8, 129.5, 134.8, 130.3, 131.5, 132.0, 133.0, 135.4, 143.6; MS (EI) (*m/z*): 292 (M^+).

2-Bromo-3-methylnaphthalene-bis(hexachlorocyclopentadiene) adduct (30)
The procedure discussed by Smith et al. (14) was used to make **30** and **31**. Commercially available **29** (200 g) was brominated according to the procedure used for **21**. The product **30** (196 g, 85%) was used in the next step without purification, ^{1}H NMR (90 MHz), δ: 2.39 (s, 3H, CH_3), 3.48 (d, J = 9 Hz, 2H, 2CH), 3.89 (d, J = 9 Hz, 2H, 2CH), 7.58 (s, 1H, arom.), 7.93 (s, 1H, arom.); MS (EI) (*m/z*): 766 (M^+).

2-Bromo-3-methylnaphthalene (31)
The brominated product **30** (100 g, 0.13 mol) was heated using a bulb-to-bulb distillation setup on a rotary evaporator (aspirator vacuum) with a cooled trapping bulb as the receiving flask connected above the flask containing **30**. A heat gun was used to effect distillation, which gave **31** as an oily white solid (23 g, 80%). Recrystallization from hexanes gave pure **31** as white crystals, ^{1}H NMR (90 MHz), δ: 2.49 (s, 3H, CH_3), 7.3–7.8 (m, 5H, arom.), 8.01 (s, 1H, arom.); MS (EI) (*m/z*): 220, 222 (M^+).

3,3′-Dimethyl-2,2′-binaphthyl (32)
As in the synthesis of **23**, the method of Maigrot and Mazaleyrat (10) was used to make **32**, with the modification that during preparation of the Grignard, one equivalent of 1,2-dibromoethane was added and an extra equivalent of Mg was used. Unreacted **31** and 2-methylnaphthalene (**21**) from incomplete bromination were removed from the desired **32** by Kugelrohr distillation. The residue was purified by passing through a silica gel column using hexanes, to give a yellowish brown solid (≈40% yield from **31**), ^{1}H NMR (90 MHz), δ: 2.17 (s, 6H, $2CH_3$), 7.3–7.9 (m, 12H, arom.); MS (CI) (*m/z*): 283 (M^++1).

3,3′-Bis(bromomethyl)-2,2′-binaphthyl (33)
Bromination of **32** (4.5 g, 0.016 mol) with NBS using the same procedure as for **23** gave **33** as an oil (6 g, 85%) that solidified on standing. The product was sufficiently pure to be taken to the next step without further treatment, ^{1}H NMR (90 MHz), δ: 4.2–4.6 (m, 4H, CH_2Br), 7.3–8.1 (m, 12H, arom.).

5-Cyano-4-amino-3H-cyclohepta[2,1-b:3,4-b′]dinaphthalene (34)
Cyclization of **33** (0.5 g, 0.0011 mol) was carried out using the method outlined for **25**. The product **34** (0.15 g, 40%) was obtained as a brown solid (>90% pure); IR (CH_2Cl_2) (cm^{-1}): 3500, 3400 (m, NH_2), 2190 (m, CN); ^{1}H NMR (90 MHz), δ: 2.15 (d, J = 13 Hz, 1H), 2.66 (d, J = 13 Hz, 1H), 5.00 (br s, 2H, NH_2), 7.1 – 8.2 (m, 12H, arom.); MS (CI) (*m/z*): 333 (M^++1).

3H-Cycloheptan-4-one[2,1-b:3:4-b′]dinaphthalene (35)
Ketone **35** (4.5 g, 80%) was prepared from **34** (6 g, 0.018 mol) according to the method described for **26** (6 g, 80%); IR (CH_2Cl_2) (cm^{-1}): 1720 (s); ^{1}H NMR (250 MHz), δ: 3.4–3.9 (m, 4H, overlapping doublets, $2CH_2$), 7.5–7.6 (m, 4H, arom.), 7.74 (s, 2H, arom.), 7.8–8.0 (m, 4H, arom.), 8.13 (s, 2H, arom.); MS (CI) (*m/z*): 309 (M^++1).

3H-Cycloheptan-4-ol[2,1-b:3,4-b′]dinaphthalene (36)
Standard $LiAlH_4$ reduction of ketone **35** (3 g, 9.7 mmol) gave alcohol **36** (2.7 g, 40%), which was purified by passing through a silica gel column with hexanes followed by CH_2Cl_2, to give **36** in >95% purity; ^{1}H NMR (90 MHz), δ: 2.1–3.1 (m, 5H, $2CH_2$ and OH), 4.32 (quintet, J = 6 Hz, 1H), 7.2–8.0 (m, 12H, arom.).

4-Bromo-3H-cyclohepta[2,1-b:3,4-b′]dinaphthalene (37)
Reaction of **36** (2.5 g, 8.1 mmol) with PBr_3 using the method described for **28** gave **37** (2.6 g, 85%). Purification was carried out by passing the material through a silica gel column using hexanes, to give **37** in >95% purity, ^{1}H NMR (90 MHz), δ: 2.8–3.5 (m, 4H, $2CH_2$), 4.6–4.9 (m, 1H, CHBr), 7.3–8.4 (m, 12H, arom.).

3H-Cyclohepta[2,1-b:3,4-b']dinaphthalene (11)
As in the synthesis of **10**, elimination of HBr from **37** (0.5 g, 1.3 mmol) using *t*-BuO^-K^+ gave **11** (0.22 g, 55%). The major by-product (45%) was **38**, as shown by GC and ^{1}H NMR. Purification of **11** was achieved by repeated recrystallization from toluene–EtOH, which gave a purity of >99% (by GC), mp = 169–170°C; UV (CH_3CN) λ_{max} (ε): 209 nm (sh, 24 700), 219 (40 100), 260 (59 500), 280 (sh, 36 100) 303 (sh, 13 600); ^{1}H NMR (360 MHz), δ: 3.37 (d, J = 6.9 Hz, 2H, CH_2), 6.42 (dt, J = 10.2, 6.9 Hz, 1H, vinyl), 6.81 (d, J = 10.3 Hz, 1H, vinyl), 7.47–7.58 (m, 4H, arom.), 7.68 (s, 1H, arom.), 7.81 (s, 1H, arom.), 7.83–8.01 (m, 4H, arom.), 8.09 (s, 1H, arom.), 8.25 (s, 1H, arom.); ^{13}C NMR, δ: 33.4, 124.3, 125.4, 126.1, 126.3, 126.8, 127.4, 127.7, 127.9, 129.1, 129.8, 130.1, 132.3, 132.0, 132.4, 132.7, 134.5, 138.2, 142.0; HRMS (EI) (*m/z*): 292.1254 (calcd. 292.1252). By-product **38** was isolable from the fractional recrystallizations, ^{1}H NMR (90 MHz), δ: 2.63 (s, 3H, CH_3), 7.3–7.7 (m, 5H, arom.), 7.8–8.2 (m, 5H, arom.), 8.30 (s, 1H, arom.), 9.08 (s, 1H, arom.), 9.13 (s, 1H, arom.); MS (CI) (*m/z*): 293 (M^++1).

X-ray crystallography

X-ray diffraction studies involving **10** were performed using a Nonius diffractometer with ω–2Θ scan for collection of data (1613 reflections). Of these reflections 1372 were used to refine the structure. NRC Solver (21) was used to solve the crystal structure and the SHELX least-squares program (22) was used to refine the structure. X-ray crystallographic data are given in Table 1 and an ORTEP drawing in Fig. 2.[2]

Product studies

Preparative photolyses were carried out in a Rayonet RPR 100 photochemical reactor using 254, 300, or 350 nm (for triplet sensitization) lamps and 100 or 200 mL quartz tubes (Pyrex tubes for triplet sensitization). Analytical runs were carried out in 3 mL Suprasil quartz cuvettes on an optical bench using an Oriel 200W Hg arc lamp and an Applied Physics monochromator set at either 254 or 280 nm with 5 nm slits. Solutions for preparative photolyses were cooled with a cold finger (≈15°C) and purged with argon before and during the photolysis. Analytical runs were purged with argon prior to irradiation. In general, any effect of oxygen in the photoreactions was minimal. A number of runs were repeated in the absence of light to check for thermal reaction and none were observed. Representative examples of photolysis experiments are provided below.

*Photolysis of **3** in D_2O–CH_3CN and EA–D_2O–CH_3CN*
Photolysis of **3** (30 mg) in 25% D_2O – CH_3CN solution (254 nm, 15 min) gave **4** (30%), **5** (49%), and phenanthrene (5%), as indicated by ^{1}H NMR (360 MHz). Photolysis of **3** in 10% (5 **M** EA – D_2O) – CH_3CN for 5 min gave **4** (14%), **5** (40%), and phenanthrene (1%), thereby demonstrating base catalysis of deuterium incorporation.

*Photolysis of **9** in 100% CH_3CN and 50% H_2O – CH_3CN*
Photolysis of **9** (50 mg) in 100 mL of 100% CH_3CN with 254 nm lamps (15 min.) gave products shown in or derived from Scheme 6, as indicated by ^{2}H NMR of the photolysate, δ: −0.14, 1.59 (two isomers of **4a**, 6%), 2.57 (**4b**, 58%), 6.31 (**6**, 6%), 7.83 (9-deuterophenanthrene, 6%). Photolysis of **9** in 50% H_2O – CH_3CN under otherwise identical conditions gave a different product mixture, ^{2}H NMR, δ: −0.14, 1.59 (two isomers of **4a**, 2%), 2.57 (**4b**, 16%), 3.08 (**5**, 50%), 6.31 (**6**, 4%), 7.83 (9-deuterophenanthrene, 1%).

*Photolysis of **7** in 100% CH_3CN*
Photolysis of **7** (50 mg) in 100 mL of 100% CH_3CN (254 or 300 nm, 15 min) gave three major products according to GC–MS and ^{1}H NMR: **40** (25% at 254 nm; 4% at 300 nm), **42** (3% at 254 nm; 13% at 300 nm), and **41** (3% at 254 nm; 4% at 300 nm). The products were not separated and the ^{1}H NMR (360 MHz) signals that could be assigned to each compound are listed as follows: **40**, δ: 0.07 (m, 1H, cyclopropyl methylene proton), 1.45 (dd, J = 9.0, 3.8 Hz, cyclopropyl methylene proton), 1.65 (s, 3H of CH_3), 2.34 (dd, J = 9.0, 5.0 Hz, cyclopropyl methine proton); **42**, δ: 2.11 (m, 3H of CH_3), 2.80 (m, axial H of CH_2), 3.05 (dd, J = 13.1, 8.2 Hz, equatorial H of CH_2), 6.08 (m, 1H, vinyl H); **41**, δ: 2.75 (d, J = 1.0 Hz, CH_3), 6.68 (m, aryl H at C10). Additional studies using ^{1}H COSY NMR showed the required correlations in the assigned signals.

*Photolysis of **7** in D_2O–CH_3CN and EA–D_2O–CH_3CN*
Photolysis of **7** (30 mg) in 25% D_2O – CH_3CN (254 nm, 15 min) gave **40** (22%), **42** (3%), and **41** (3%) according to GC and ^{1}H NMR. Integration and comparison of the ^{1}H NMR signals due to the protons at the vinyl and 5-position of **7** in unreacted substrate and in photolyzed material gave ≈10% deuterium incorporation at the 5-position. Photolysis in 10% (5 M EA – D_2O) – CH_3CN (254 nm; 30 min.) gave **40** (29%), **42** (4%), and **41** (12%). GC–MS and ^{2}H NMR analysis of the product mixture indicated extensive deuterium incorporation in the starting material **7** (73% at the 5-position) and in **51** (36% at the cyclopropyl positions). A 5 min photolysis resulted in 36% deuterium incorporation at the 5-position in recovered **7**.

*Photolysis of **8** in 100% CH_3CN and D_2O–CH_3CN*
The product mixture obtained after irradiation of **8** (50 mg) in either CH_3CN or 50% D_2O – CH_3CN was complex (GC and ^{1}H NMR) with no major product (taken up to 20% conversion). Analysis by GC–MS of recovered **8** showed no measurable deuterium incorporation. Due to the complexity of the product mixture and the lack of excited state carbon acid behaviour, no further experiments were carried out to delineate the photochemistry of this compound.

*Photolysis of **10** in EA–D_2O–CH_3CN*
Photolysis of **10** (50 mg) in 10% (5 M EA – D_2O) – CH_3CN (254 nm, 1 h) gave a trace of **43** and deuterium incorporation

[2] Tables of fractional atomic coordinates, interatomic distances, bond angles, and anisotropic temperature parameters are available and can be purchased from: The Depository of Unpublished Data, Document Delivery, CISTI, National Research Council Canada, Ottawa, Canada K1A 0S2. With the exception of the table of anisotropic temperature parameters, these supplementary data have also been deposited with the Cambridge Crystallographic Data Centre, and can be obtained on request from The Director, Cambridge Crystallographic Data Centre, University Chemical Laboratory, 12 Union Road, Cambridge, CB2 1EZ, U.K.

predominantly at H_{ax} of **10** (Fig. 5). Kinetic runs were carried out by photolyzing 300 mg of **10** in 400 mL of 10% (5 M EA – D_2O) – CH_3CN and withdrawing samples at different photolysis times for analysis by ^1H and ^2H NMR. The results are shown in Figs. 5–7.

*Photolysis of **11** in 100% CH_3CN and EA–D_2O–CH_3CN*

Photolysis of **11** (30 mg) in 100 mL 100% CH_3CN (254 nm, 30 min) gave **45** (44%) as the only product by GC and ^1H NMR. Product **45** was not separated from **11** but was characterized based on the characteristic cyclopropyl ring protons in the ^1H NMR of the photolysate, δ: 0.18 (td, J = 5.4, 4.2 Hz, methylene proton of cyclopropyl ring), 1.63 (td, J = 8.9, 4.1 Hz, methylene proton of cyclopropyl ring), 2.77 (dd, J = 8.9, 5.0 Hz, methine protons of cyclopropyl ring), 7.89 (s, 2H, arom.), 8.63 (s, 2H, arom.). The remaining eight aromatic protons were in the same region as those for **11**; GC–MS (CI) (*m/z*): 293 (M^++1). Photolysis of **11** in 10% (5 M EA in D_2O) – CH_3CN using a quartz cuvette showed no deuterium incorporation in recovered **11** by GC–MS when the conversion to **45** was taken to 25%. Photolysis of **11** in 100% CH_3CN under identical conditions also resulted in 25% conversion to **45**.

*Triplet sensitization of **7** in 100% CH_3CN*

A solution of **7** (40 mg) and 2-benzoylbenzoic acid (1 g) in 100 mL 100% CH_3CN was photolyzed at 350 nm in a Pyrex tube for 1 h. After photolysis, CH_3CN was evaporated and the residue taken up in CH_2Cl_2. The sensitizer was removed by extraction of with aqueous NaOH. The major product was **40** (10%), as indicated by GC and ^1H NMR.

Quantum yields for deuterium exchange and di-π-methane rearrangement

Quantum yields for deuterium exchange (Φ_{ex}) and formal di-π-methane rearrangement (Φ_p) were measured using semi-preparative photolyses in a Rayonet reactor using 254 nm lamps. The substrate (10^{-4} mol) dissolved in the appropriate solvent in a 100 mL quartz tube was irradiated to give 5–20% conversion. The amount of deuterium incorporation was calculated by ^1H NMR (360 MHz) and GC was used to monitor for yield of formal di-π-methane products. Light intensities were measured by using the exchange reaction of 5,5-dideuterosuberene in 50% H_2O – CH_3CN (Φ_{ex} = 0.035 ± 0.005) (3). Light intensities varied by less than 5% during the day and were typically 1.57×10^{-4} einsteins–min, which is similar to light intensities measured with potassium ferrioxalate used in previous studies.

Fluorescence measurements

Steady-state fluorescence spectra (uncorrected) were taken on a Perkin–Elmer MPF-66 fluorescence spectrophotometer at ambient temperature (20 ± 2°C). The fluorescence quantum yields of **3**, **7**, **10**, and **11** were measured using **2** (Φ_f = 0.86 ± 0.05 in CH_3CN) (3*b*) as the secondary fluorescence standard. Due to its low fluorescence intensity, the fluorescence quantum yield of **8** was measured relative to **7**. Fluorescence lifetimes (τ) measured were measured using the time-correlated single-photon counting technique on a Photon Technology International (PTI) LS-1 instrument with a hydrogen flash lamp. Analyses were carried out using software supplied by PTI. All decays were good first order except for decays observed for **8** (Table 3).

Acknowledgment

We thank the Natural Sciences and Engineering Research Council (NSERC) of Canada for support of our research program. Additional support was provided by a University of Victoria Faculty Research Grant.

References

1. (*a*) E. Buncel. Carbanions: mechanistic and isotopic aspects. Elsevier, Amsterdam. 1975; (*b*) D.J. Cram. Fundamentals of carbanion chemistry. Academic Press. New York. 1965; (*c*) E. Buncel and T. Durst (*Editors*). Comprehensive carbanion chemistry, Elsevier, Amsterdam. 1980. Part A; (*d*) R. Stewart. The proton: applications to organic chemistry. Academic Press, Orlando, Fla. 1985; (*e*) T.H. Lowry and K.S. Richardson. Mechanism and theory in organic chemistry. Harper and Row, New York. 1987. Chap. 6.
2. (*a*) J.F. Ireland and P.A.H. Wyatt. Adv. Phys. Org. Chem. **12**, 131 (1976); (*b*) L.M. Tolbert. *In* Comprehensive carbanion chemistry. *Edited by* E. Buncel and T. Durst. Elsevier, Amsterdam. 1987. Part C; (*c*) E. Vander Donckt, J. Nasielski, and P. Thiry. J. Chem. Soc. Chem. Commun. 1249 (1969).
3. (*a*) P. Wan, E. Krogh, and B. Chak. J. Am. Chem. Soc. **110**, 4073 (1988); (*b*) D. Budac and P. Wan. J. Org. Chem. **57**, 887 (1992).
4. P. Wan, D. Budac, M. Earle, and D. Shukla. J. Am. Chem. Soc. **112**, 8048 (1990); (*b*) H.E. Zimmerman and J.A. Pincock. J. Am. Chem. Soc. **95**, 2957 (1973).
5. L.M. Tolbert and M.Z. Ali. J. Org. Chem. **47**, 4793 (1982).
6. B. Halton and D.L. Officer. Aust. J. Chem. **36**, 1167 (1983).
7. T.T. Coburn and W.M. Jones. J. Am. Chem. Soc. **96**, 5218 (1974).
8. G.W. Griffen and K.A. Horn. Org. Prep. Proced. Int. **17**, 187 (1985).
9. R. Adams and L.O. Binder. J. Am. Chem. Soc. **63**, 2773 (1941).
10. N. Maigrot and J.-P. Mazaleyrat. Synthesis, 317 (1985).
11. H.J. Bestmann and W. Both. Chem. Ber. **107**, 2926 (1974).
12. K. Mislow and F.A. McGinn. J. Am. Chem. Soc. **80**, 6036 (1958).
13. J.B. Lambert, H.F. Shurvell, D.A. Lightner, and R.G. Cooks. Introduction to organic spectroscopy. Macmillan, New York. 1987.
14. J.G. Smith, P.W. Dibble, and R.E. Sandborn. J. Org. Chem. **51**, 3762 (1986).
15. (*a*) J.B.M. Somers, A. Couture, A. Lablache-Combier, and W.H. Laarhoven. J. Am. Chem. Soc. **107**, 1387 (1985); (*b*) W.H. Laarhoven and N. Berendsen. Recl. Trav. Chim. Pays-Bas, **105**, 367 (1986); (*c*) T.J.H.L. Cuppen, N. Berendsen, and W.H. Laarhoven. Recl. Trav. Chim. Pays-Bas. **109**, 168 (1990); (*d*) J. Woning, P.C.M. Weisenborn, C.A.G.O. Varma, and W.H. Laarhoven. J. Photochem. Photobiol. A: **55**, 169 (1990).
16. D. Budac and P. Wan. J. Photochem. Photobiol. A: In press.
17. (*a*) J. Hine and P.D. Dalsin. J. Am. Chem. Soc. **94**, 6998 (1972); (*b*) F.G. Bordwell, J.E. Bares, J.E. Bartmess, G.J. McCollum, M. Van Der Puy, N. Vanier, and W.S. Matthews. J. Org. Chem. **42**, 321 (1977); (*c*) J.S. Grossert, J. Hoyle, T.S. Cameron, S.P. Roe, and B.R. Vincent. Can. J. Chem. **65**, 1407 (1987); (*d*) C.F. Bernasconi, D.A.A. Ohlberg, and M.W. Stronach. J. Org. Chem. **56**, 3016 (1991); (*e*) F.G. Bordwell, N. R. Vanier, and X. Zhang. J. Am. Chem. Soc. **113**, 9856 (1991).
18. (*a*) K. Hayday and R.D. McKelvey. J. Org. Chem. **41**, 2222 (1976); (*b*) V. Malatesta and K.U. Ingold. J. Am. Chem. Soc.

103, 609 (1981); (*c*) A.L.J. Beckwith and C.J. Easton. J. Am. Chem. Soc. **103**, 615 (1981).
19. S.L. Murov, I. Carmichael, and G.L. Hug. Handbook of photochemistry. 2nd ed. Marcel Dekker, New York. 1993.
20. T. Hayashi, K. Hayashizaki, T. Kiyoi, and Y. Ito. J. Am. Chem. Soc. **110**, 8153 (1988).
21. A. Larson, F. Lee, Y. Page, M. Webster, J. Charland, and E.J. Gabe. NRC Solver: a program for crystal structure determination. Chemistry Division. NRC, Ottawa, Canada. 1985.
22. G.M. Sheldrick. SHELX: a program for crystal structure determination. Anorganish–Chemisches Institut der Universitat Gottingen, Germany. 1976.

Hydrogen isotope fractionation between methanol and diphenylphosphine or dimethylphosphine in the gas phase and in aprotic solvents

Andrzej Wawer and Jerzy Szydłowski

Abstract: D/H fractionation factors between MeOH and Ph_2PH in dilute solutions of tetrachloroethylene, benzene, tetrahydrofuran, pyridine, and acetonitrile and T/H fractionation factors between MeOH and Me_2PH vapors were measured. The experimental results agree very well with values calculated from the statistical theory of isotope effects formulated by Bigeleisen and Mayer. There are correlations between observed fractionation factors and solvent polarity, and the interaction energy of methanol with the given solvent. Another correlation has been found between enthalpy of the exchange reactions and the interaction energy between methanol and the given solvent.

Key words: isotope effects, fractionation factor, diphenylphosphine, methanol.

Résumé : On a mesuré les facteurs de fractionnement D/H entre le MeOH et le PH_2PH, dans des solutions diluées de tétrachloroéthylène, de benzène, de tétrahydrofurane, de pyridine et d'acétonitrile, ainsi que les facteurs de fractionnement T/H entre les vapeurs de MeOH et de Me_2PH. Les résultats expérimentaux sont en bon accord avec les valeurs calculées sur la base de la théorie statistique des effets isotopiques formulée par Bigeleisen et Mayer. Il existe des corrélations entre les facteurs de fractionnement observés et les polarités des solvants ainsi que l'énergie d'interaction du méthanol avec un solvant donné. On a aussi observé une corrélation entre l'enthalpie des réactions d'échange et l'énergie d'interaction entre le méthanol et le solvant donné.

Mots clés : effets isotopiques, facteur de fractionnement, diphénylphosphine, méthanol.

[Traduit par la rédaction]

Introduction

A knowledge of tritium/protium or deuterium/protium fractionation factors in H-exchanging systems is an important aid to understanding the mechanism of chemical and biochemical reactions, and the effects of molecular structure and intermolecular interactions (1–4). A great deal of interest has been devoted to the determination of the D/H fractionation between compounds with exchangeable H-atoms and protic solvents (3, 4). Hydrogen isotope partitioning between chemical species dissolved in aprotic solvents has been less thoroughly studied (4). A cardinal rule in the theory of isotope effects is that isotope substitution does not change the force field (5). On the other hand it is clear that change of aprotic solvents will modify the force field and lead to differences in the zero-point energy (ZPE) of H-isotope exchanging molecules. It is interesting to ask just which physicochemical properties of aprotic solvents determine isotope fractionation.

Phosphines interact very weakly with their environment (6) and this simplifies further discussion. For the present study we chose the alcohol–phosphine system and have studied H/D fractionation between diphenylphosphine (DPP) and methanol (MA) in benzene, tetrachloroethylene, tetrahydrofuran, pyridine, and acetonitrile. Due to the very low vapor pressure of DPP, gas phase exchange reactions with methanol could not be carried out. Instead, the exchange of tritium between dimethylphosphine (DMP) and MA vapors has been studied. The high sensitivity of the radiometric determination of tritium makes such measurements possible even at low vapor pressure. This system forms a convenient reference as well.

Experimental

Hydrogen exchange reaction in the gas phase can be conveniently carried out by using tritium together with appropriate radiometric detection techniques (7). DMP was prepared by a two-step protonation–methylation reaction starting from phosphine (8). Tritium-labelled DMP was synthesized by exchange of Me_2PH with KOH* in $H_2O(T)$ (9).[4] DMP* and MA were dried and degassed. The exchange experiments were

Received September 27, 1995.[1]

A. Wawer[2] and J. Szydłowski.[3] Chemistry Department, Warsaw University, Żwirki i Wigury 101, 02-089 Warsaw, Poland.

[1] Revision received March 29, 1996.

[2] Andrzej Wawer: Telephone: (48-22) 224 881. Fax: (48-22) 225 996.

[3] Author to whom correspondence may be addressed at the Chemistry Department, University of Tennessee, Knoxville, TN 37916, U.S.A. Telephone: (423) 974-2776. Fax: (423) 974-3454. E-mail: szydlowski@novell.chem.utk.edu

[4] The asterisk denotes tritium labelling.

carried out in the same manner as for CH_3OH and H_2S vapors (7). In all experiments the ratio of the partial vapor pressure of DMP to MA was kept equal to 1.5. The total pressure was always smaller than the saturated vapor pressure of any of the components at the given temperature. The radioactivity of DMP was measured in the internal GM gas counter (7) with a standard deviation of ±1.5%.

Most H/D exchange experiments employed an NMR technique. MeOD (product of Isotope Distribution Center, 99.75% of D), Ph_2PH (Aldrich product), and solvents were carefully dried and degassed. The samples were sealed in NMR tubes. Concentrations of the solutions, in which D-exchange between DPP and MA was studied, was about 1 mol/dm^3. All operations were carried out in a glove box in a dry nitrogen atmosphere. The ^1H spectra were recorded by a JEOL Co FX 90Q spectrometer equipped with a temperature probe. The PH (doublet at 5.08 ppm, $^1J_{PH} = 216$ Hz) (10) and OH signals were observed separately. All NMR conditions for quantitative determination of the I^{PH}/I^{OH} ratio were fulfilled[10] ("I" is an integrated intensity of the signal). The reproducibility of the I^{PH}/I^{OH} was better than 1%. Temperature was determined to better than ±0.5°C.

The tritium fractionation factor for the gas phase reaction:

[1] $MeOH(v) + Me_2PH^*(v) = MeOH^*(v) + Me_2PH(v)$

is calculated from the equation:

[2] $\alpha^T_{MA/DMP}(v) = A^{MA}_\infty/A^{DMP}_\infty$

where A_∞ denotes specific tritium radioactivity at isotope equilibrium. Because only A^{DMP}_0 and A^{DMP}_∞ were measured, A^{MA}_∞ was determined from the isotope balance relation (7).

The deuterium fractionation factors for the reaction:

[3] $MeOD(s) + Ph_2PH(s) = MeOH(s) + Ph_2PD(s)$

are defined as

[4] $\alpha^D_{MA/DPP}(s) = (m_D/m_H)/(n_D/n_H)$

where m and n are the numbers of moles of MA and DPP, respectively; subscripts H and D refer to H and D isotopomers at isotope equilibrium. For the exchange process studied we can define the following material and isotope balance relations: (I) $m = m_H + m_D$, (II) $n = n_H + n_D$, (III) $m_H = n_D$, and (IV) $I^{OH}/m_H = I^{PH}/n_H$. Relation (III) is valid in the present case because the exchange reactions are carried out with fully deuterated methanol (CH_3OD). Starting from eq. [4] and using the above relations, in a few successive steps m_D, m_H, n_D, and n_H can be eliminated. At first, n_D is eliminated by using relation (III), then the use of (IV) eliminates m_H, and in the next step using (I) we eliminate m_D. Finally, defining $n_H = nI^{PH}n/(I^{OH} + I^{PH})$ from (II), (III), and (IV), we obtain eq. [5] expressed in the experimentally measured values only:

[5] $$\alpha^D_{MA/DPP}(s) = \left(\frac{I_{PH}}{I_{OH}}\right)\left(\frac{m\,I_{PH}}{n\,I_{OH}} + \frac{m-n}{n}\right)$$

m and n are as defined above and $I^{PH(OH)}$ denotes the integrated intensities of the PH(OH) hydrogen signals. The standard deviation of α^D was ±1%.

Calculations

It is interesting to compare the experimental fractionation factor with the theoretical value expressed in terms of the reduced partition function ratio (RPFR), $(s/s')f$ (5):

[6] $\alpha^D = (s/s')f_{MA}/(s/s')f_{DPP}$

RPFR is given by the equation:

[7] $$(s/s')f = \prod \frac{u_i}{u_i'}\frac{1-\exp(-u_i')}{1-\exp(-u_i)}\exp\frac{u_i'-u_i}{2}$$

where $u_i = hc\omega_i/kT$, and ω_i are the normal mode vibrational frequencies; the prime refers to the light isotopic molecule.

The calculation of the fractionation factor for the exchange between methanol and DPP in solution encounters certain difficulties. To begin with, the vibrational spectra of liquid MA are complex due to strong hydrogen bonding, and spectral data for methanol in the solvents of interest are incomplete. To our best knowledge there are no vibrational data for DPP. On the other hand, gas phase vibrational data for both methanol and DMP are available. The gas phase spectra of MeOH/MeOD reported by Serralah, Mayer, and Gunthard (11) have been used for the calculation of $(s/s')f_{MeOH}(v)$ (7). The gas phase spectra of Me_2PH were studied by Durig and Saunders (12) and those of Me_2PD by Clark and Drake (13). However, the assignments proposed by both sets of authors are doubtful. A better assignment, confirmed by a subsequent force field calculation, was given by McKean and McQuillan (14). Their data were used in our calculation of $(s/s')f_{DMP}(v)$.

Results and discussion

The experimental fractionation factors of deuterium and tritium over the temperature range of 283–330 K are collected in Table 1. Calculated values are also presented in Table 1. The experimental points deviate by 1–1.5% from the calculated ones. The fractionation factor, $\alpha_{MA/DPP}$, was used as the reference point for discussion of isotope fractionation in solution. It is equal to the ratio of $\alpha_{MA/DMP}(v)/\alpha_{DPP/DMP}(v)$ in which experimental values of $\alpha_{MA/DMP}(v)$ and the estimated D/H fractionation factor between DPP and DMP, $\alpha_{DPP/DMP} = 0.98$, at 250–330 K have been used. In addition, for greater completeness, the fractionation factors between liquid MA and DPP determined earlier (9) have also been included.

For all systems studied the fractionation factors are much larger than unity, which means that deuterium(tritium) accumulates in the hydroxyl group of methanol regardless of its solvation character. There is relatively little change between gas phase and solution values. The temperature dependence of the fractionation factors between methanol and diphenylphosphine in gas and in solution is shown in Fig. 1. The fractionation factors decrease regularly on going from gas to acetonitrile. In every case the temperature dependence can be described by a simple linear relation,

Table 1. Experimental fractionation factors of deuterium in exchange reaction between diphenylphosphine and methanol in various solvents.

	Fractionation factor α for MA/DPP system								
T/K	v^*	v^{**}	v^{***}	*III*	TCE	Benzene	THF	Pyr	ACN
250.0	2.42	—	—	2.28	2.48	—	2.35	2.30_5	2.24
273.0	—	—	—	2.16_5	—	—	—	—	—
283.0	2.22	2.23 (3.15)	2.28	—	2.25	2.20_5	2.16	2.12_5	2.07
298.0	2.16	2.16_5(3.03)	2.21_5	2.03	2.18_5	2.14	2.10	2.07	2.01_5
303.0	—	—	—	2.00	—	—	—	—	—
312.0	2.09	2.08_5(2.90)	2.14	—	2.11_5	2.07_5	2.04	2.01	1.96
329.0	2.04	2.03 (2.80)	2.08	—	2.05	2.02_5	1.99	1.96_5	1.92

v^*: calculated values for MA/DMP system using eqs. [6] and [7].

v^{**}: recalculated from the experimental gas phase tritium fractionation factor for the MA/DMP system (in parentheses) using the Swain–Bigeleisen relation (refs. 29, 30) with the exponent 1.42.

v^{***}: gas phase deuterium fractionation factor for the MA/DPP system calculated from tritium fractionation factor.

III: deuterium fractionation factor in pure liquid MA/DPP system (ref. 9).

Fig. 1. Temperature dependence of the experimental fractionation factor in isotope exchange reaction of diphenylphosphine with methanol in various solvents (■ gas phase; ○ tetrachlorethylene; ▲ benzene; ◆ tetrahydrofuran; ▽ pyridine; ● acetonitrile).

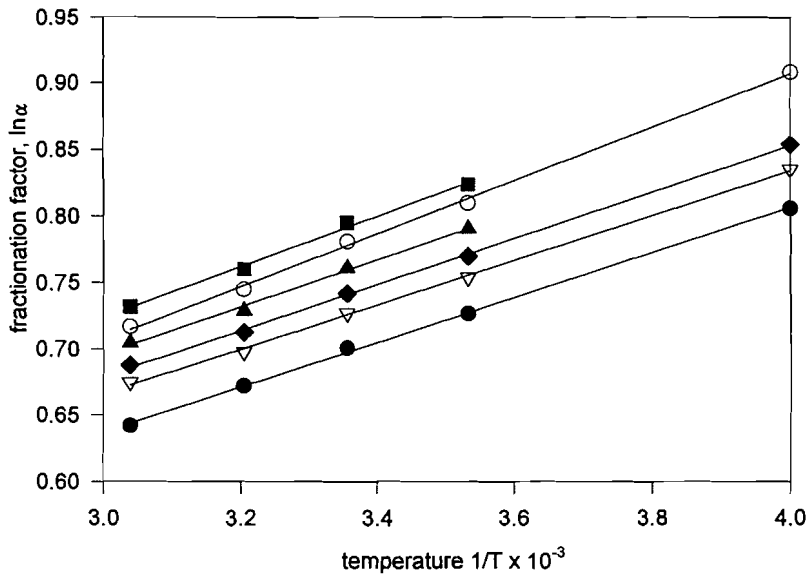

[8] $$\ln \alpha^{D}_{MA/DPP} = \frac{A}{T} + B$$

and *A* and *B* values are collected in Table 2. Equation [8] enables us to calculate isotope effects on the enthalpy changes for reaction [1] or [3]. Values ranging between 1.4 and 1.7 kJ/mol are reported in Table 2. It is worth noting that $\Delta(\Delta H^0)$ for deuterium exchange between methanol and hydrogen sulphide (2.4 kJ/mol) (7) is remarkably larger than that observed for the present solutions. Such a result could have been anticipated from the ZPE differences. There is a much smaller change in ZPE for the Ph_2PH/Ph_2PD pair than for the HSH/HSD one. Another interesting observation is the relatively small change in $\Delta(\Delta H^0)$ that occurs in the series from vapor through the range of solvents, C_2Cl_4 to pyridine (Fig. 1).

Before entering upon the discussion of these effects, let us first consider the experimental conditions. Usually the mole fractions of MA and DPP in C_6H_6, $(CH_2)_4O$, C_5H_5N, and CH_3CN were in the range of 0.04–0.08 and only in C_2Cl_4 solution were they larger (0.10–0.15). In such dilute solutions DPP exists mainly as monomer. It was shown earlier (6) that DPP interacts as a weak proton donor with various electron donors (for example tri-*n*-butylphosphine or diethylphosphide) with an energy of about 3 kJ/mol. It is likely in the present case that the interaction of DPP with the solvents used is also weak, and results in small or negligible differences between individual cases. The same refers to the solutions of deuterated DPP.

Table 2. The values of A and B parameters in the $\ln \alpha^D = A/T + B$ equation for the MA/DPP system and enthalpy changes $\Delta(\Delta H^0)$ in various solvents.

Solvent	A (K)	B	$\Delta(\Delta H^0)$ (kJ/mol)
Vapor*	199 ± 1	0.103 ± 0.002	1.67 ± 0.01
Vapor**	194 ± 7	0.108 ± 0.008	1.63 ± 0.06
Vapor***	196 ± 9	0.133 ± 0.004	1.64 ± 0.07
C_2Cl_4	199 ± 5	0.108 ± 0.007	1.67 ± 0.04
C_6H_6	177 ± 8	0.164 ± 0.06	1.48 ± 0.06
$(CH_2)_4O$	174 ± 2	0.158 ± 0.008	1.42 ± 0.02
CH_3CN	169 ± 3	0.129 ± 0.01	1.39 ± 0.02
C_5H_5N	163 ± 3	0.163 ± 0.01	1.34 ± 0.02

(v)*, (v)**, (v)*** have the same meaning as in Table 1.

Fig. 2. The correlation between the fractionation factor and hydrogen bond energy for the given methanol–solvent system (temperature 298 K).

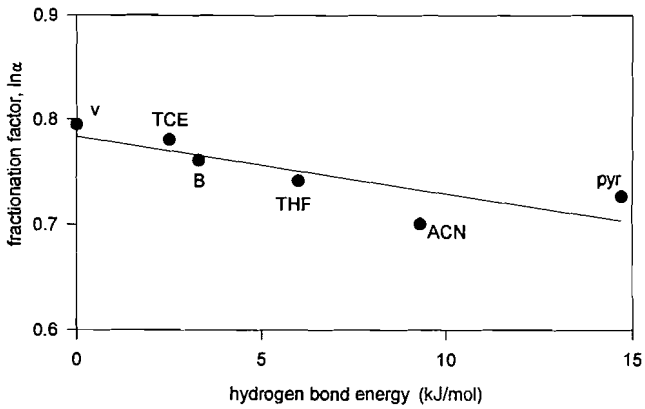

For MA, on the other hand, the OH group interacts with the π-electrons of C_2Cl_4 and C_6H_6 and interacts via O—H...O and O—H...N hydrogen bonds with $(CH_2)_4O$, C_5H_5N, and CH_3CN. These interaction energies (6, 15–19) and, consequently, the solvation energies differ greatly and this should affect the observed fractionation factor. As can be seen from Fig. 2 there is a correlation between the fractionation factor and hydrogen bonding energy (15, 18, 19). An especially good correlation is found between the fractionation factor and the Reichardt E_T parameters (20) (Fig. 3). It is worth noting that an excellent correlation between fractionation factor and hydrogen bond energy was found earlier for $HX_2 + DX$ (X = F, Cl, Br, I) exchange reactions (21). Analysis of the isotope effect calculated from the vibrational data nicely confirms the suggested one-to-one correspondence between isotope effect and force field. The strongest correlation is with the stretching force constant. Even small changes in hydrogen bonding seriously affect the stretching force constant and this is reflected in the isotope effect. Therefore these results clearly show how the given solvent influences the intermolecular force field between methanol and solvent. The second correlation, which is evident between the fractionation factor and E_T, shows that

Fig. 3. The correlation between the fractionation factor and Dimroth–Reichardt parameters of the solvent (temperature: 298 K).

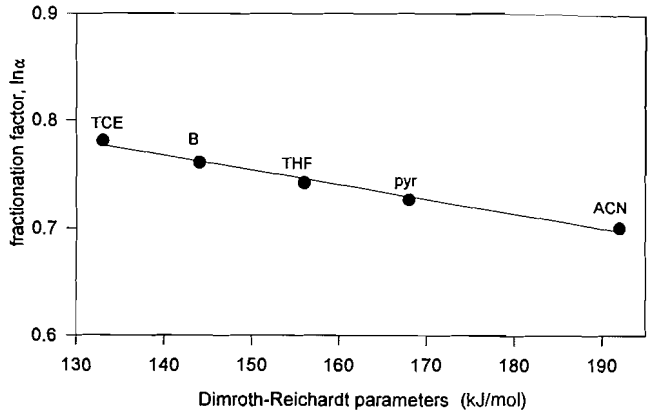

the isotope effect may be a very sensitive indicator of the electron charge distribution. In general, E_T parameters define the electron acceptor properties of the solvent and therefore this correlation is surprising. We would more likely expect a correlation with Gutman DN parameters (22). In this particular case E_T increases from TCE to pyridine; the isotope effects decrease in the same direction. It means, again, that the interaction between solvent and solute molecules seriously affects the solute force field. However, this time it is not the specific interaction centered on the hydrogen atom (more correctly, the OH bond) but the interaction involving oxygen electrons.

As far as the enthalpies of reaction are concerned, we observe some differences over the range of solvents studied. The changes are small but the tendency is clear: more polar solvents lower the enthalpy change. In general $\Delta(\Delta H)$ values correlate poorly with solvent parameters based on electron charge distribution.

It is worth noting that previously determined fractionation factors for the neat liquid MA/DPP system are consistent with the present results. They are placed between acetonitrile and pyridine, in qualitative agreement with the correlations described above (hydrogen bond energy in liquid methanol is reported as 9.3 kcal/mol (23)). It may be of some interest to compare the fractionation factor for the liquid MA/DPP system with those existing in the literature concerning hydrogen exchanges in OH, NH, SH, and PH groups. Most of these reactions were carried out with water; therefore the present result should be recalculated. This can easily be done since the fractionation factor between liquid methanol and water has been accurately determined ($\alpha_{MA/W} = 1.12$ at 298 K (24)). The simple calculation gives $\alpha_{W/DPP} = 1.81$. Since water is used as the reference substance it would be more appropriate to take the reciprocal of the latter, hence $\alpha_{DPP/W} = 0.55$. This is a very low value when compared with exchanges in OH and NH groups where, in most cases, values close to unity have been reported (25). For systems with very strong hydrogen bonding, fractionation factors much smaller than unity have been found (26). Although a small fractionation factor between H_2S and water in the gas phase ($\alpha_{HS/W} = 0.46$ (27)) has been also reported, its low value comes from the low stretching force constant of the SH bond. On the other hand, $\alpha_{DPP/W}$ can be

fairly well compared with the value 0.61 reported for PH_3(gas) + HDO(liquid) exchange (28). It seems, therefore, that the peculiar properties of the PH bond and very weak intermolecular interactions involving this group are responsible for the small value presently reported.

In conclusion, it seems that the most striking feature of the results obtained is the role of the solvent and its effect on the fractionation factor and enthalpy changes. We suggest that it is not the specific interaction between the OH(OD) group of methanol and the solvent but the charge redistribution of each molecule in the solvent shell that determines the force field shifts that result in the final isotope fractionation factor.

Acknowledgement

This work was partially supported by the BST-472/28/94 funds.

References

1. M. Wolfsberg. Acc. Chem. Res. **5**, 225 (1972).
2. W.W. Cleland. *In* Isotopes in organic chemistry. *Edited by* E. Buncel and C.C. Lee. Elsevier, Amsterdam. 1987. Chap. 2. Vol. 7.
3. A.J. Kresge, R.A. More O'Ferrall, and M.F. Powell. *In* Isotopes in organic chemistry. *Edited by* E. Buncel and C.C. Lee. Elsevier, Amsterdam. 1987. Chap. 4. Vol. 7.
4. F.J. Alvarez and R.L. Schowen. *In* Isotopes in organic chemistry. *Edited by* E. Buncel and C.C. Lee. Elsevier, Amsterdam. 1987. Chap. 1. Vol. 7.
5. J. Bigeleisen and M.G. Mayer. J. Chem. Phys. **15**, 261 (1947).
6. A. Wawer, W. Dumkiewicz, and E. Mendyk. Z. Phys. Chem. (Leipzig), **268**, 619 (1987).
7. A. Wawer and J. Szydłowski. Can. J. Chem. **61**, 1060 (1983).
8. W.L. Jolly. Inorg. Synth. **11**, 124 (1968).
9. A. Wawer and I. Wawer. J. Chem. Soc. Perkin Trans. 2, 2045 (1990).
10. T. Kupka, A.Wawer. J. Dzięgielewski, and P.Z. Zacharias. Fresenius J. Anal. Chem. **339**, 253 (1991).
11. A. Serrallach, R. Mayer, and Hs. Gunthard. J. Mol. Spectrosc. **52**, 94 (1974).
12. R. Durig and J.E. Saunders. J. Raman Spectrosc. **4**, 121 (1975).
13. A.J.F. Clark and J.E. Drake. Spectrochim. Acta, Part A: **34A**, 307 (1978).
14. D.C. McKean and G.P. McQuillan. J. Mol. Struct. **63**, 173 (1980).
15. R. Wolf, D. Houlla, and F. Mathis. Spectrochim. Acta, Part A: **23A**, 1641 (1967).
16. A.K. Shurubura, E.V. Rylcev, and I.E. Balbeskul. Teor. Eksp. Khim. **18**, 635 (1982).
17. A.D. Becker. Spectrochim. Acta, **17**, 436 (1961).
18. T. Gramstad. Acta Chem. Scand. **16**, 807 (1962).
19. S.S. Mitra. J. Chem. Phys. **36**, 3286 (1962).
20. C. Reichardt. *In* Molecular interactions. Vol. 3. *Edited by* H. Ratajczak and W.J. Orville-Thomas. John Wiley and Sons, London. 1982. Chap. 5. p. 256.
21. J. Szydłowski. J. Mol. Struct. **127**, 209 (1985).
22. V. Gutman. Spectrochim. Acta, **21**, 661 (1976).
23. J.C. Davis, Jr., K.S. Pitzer, and C.N. Rao. J. Phys. Chem. **64**, 1714 (1960).
24. D.E. Clegg and J.H. Rolston. J. Chem. Soc. Chem. Commun. 1037 (1978).
25. R.M. Jarret and M.J. Saunders. J. Am. Chem. Soc. **107**, 2648 (1985); J. Reuben. J. Am. Chem. Soc. **108**, 1082 (1986).
26. J. Szydłowski. J. Radioanal. Nucl. Chem. **170**, 9 (1993); M.M. Kreevoy and T.M. Liang. J. Am. Chem. Soc. **102**, 3315 (1980); M.M. Kreevoy, T.M. Liang, and K.C. Chiang. J. Am. Chem. Soc. **99**, 5207 (1977); M.R. Ellenberger, E. Farneth, and D.A. Dixon, J. Phys. Chem. **85**, 4 (1981); D.A. Weil and D.A. Dixon. J. Am. Chem. Soc. **107**, 6859 (1985).
27. R.E. Weston. Z. Naturforsch. A: Phys. Phys. Chem. Kosmophys. **28A**, 177 (1973).
28. J. Bigeleisen and R.E. Weston. J. Chem. Phys. **20**, 1400 (1952).
29. C.G. Swain, E.C. Stivers, J.F. Reuwer, Jr., and L.J. Schaad. J. Am. Chem. Soc. **80**, 5885 (1958).
30. J. Bigeleisen. *In* Tritium in the physical and biological sciences. Vol. 1. IAEA, Vienna. 1962. p. 161.

The thermolysis of ε-halodisilanes: a preference for 1,2-Si Si→O rearrangement or Si—O cleavage over Si=O bond formation

Christopher Roos, Graham A. McGibbon, and Michael A. Brook

Abstract: Tris(trimethylsilyl)-2,2,2-trifluoroethoxysilane **6**, tris(trimethylsilyl)-2-fluoroethoxysilane **7**, and tris(trimethylsilyl)-2-chloroethoxysilane **8** were synthesized and characterized by ^{1}H, ^{13}C and ^{29}Si NMR, IR spectroscopy, and EI and CI mass spectrometry. Thermodynamic considerations would suggest that, as a result of the driving force provided by the formation of a Si—F or Si—Cl bond, the thermolyses of these compounds would lead to the formation of bis(trimethylsilyl)silanone **4**. To examine this question, gas chromatography – mass spectrometry was as used a detection technique for products resulting from the high-pressure thermolyses of **6–8**. The elimination of $(Me_3Si)_3SiCl$ appears to be the major thermolytic pathway of decomposition for **8** at ambient or higher pressures, although it is accompanied by the formation of other products, some of which could have arisen from the addition of various halosilanes to a silanone. Neither **6** nor **7** thermolyzed cleanly; the former compound was essentially unreactive under the thermolysis temperatures used (850°C). Of the products produced in the thermolysis of **7**, no evidence for the formation of the silanone was obtained. Independently, mass spectrometry was used to study unimolecular reactions of molecular ions derived from **6–8**. The major route to solitary ions appears to involve a 1,2-trimethylsilyl migration from Si to O (**9→10**) prior to decomposition, for example, of the *m/z* 346 parent ion in the decomposition of **6**. The preparation of the ionized silanone may be a minor pathway. Some of the other fragmentation pathways for **6–8** are discussed.

Key words: gas phase thermolysis, ion rearrangements, silyl group migration, silanone, halosilane.

Résumé : On a synthétisé le tris(triméthylsilyl)-2,2,2-trifluorosilane, **6**, le tris(triméthylsilyl)-2-fluoroéthoxysilane, **7**, et les tris(triméthylsilyl)-2-chloroéthoxysilane, **8**, et on les a caractérisés par la RMN du ^{1}H, du ^{13}C et du ^{29}Si, par la spectoscopie IR et par spectrométrie de masse sous IC et IE. Les considérations thermodynamiques portent à penser que la thermolyse de ces composés pourrait conduire à la formation de bis(triméthylsilyl)silanone, **4**, en raison de la force directrice créé par la formation des liaisons Si—F ou Si—Cl. Pour vérifier cette hypothèse, on a utilisé comme technique de détection, la spectrométrie de masse couplée à la chromatographie en phase gazeuse, pour les produits résultant des thermolyses à haute pression des composés **6–8**. L'élimination du $(Me_3Si)_3SiCl$ semble être le processus thermolytique principal de décomposition du composé **8** à température ambiante ou à de plus hautes pressions, bien qu'il se forme d'autres produits dont quelques uns proviennent de l'addition de divers halosilanes sur la silanone. Ni le composé **6** ni le composé **7** ne subissent nettement la thermolyse; le premier composé ne réagit pas du tout aux températures de thermolyse utilisées (850°C). On n'a pas pu mettre en évidence la présence de silanone parmi les produits résultants de la thermolyse du composé **7**. D'une façon indépendante on a utilisé la spectrométrie de masse pour étudier la réaction unimoléculaire des ions moléculaires produits par les composés **6–8**. La principale voie d'accès aux ions solitaires semble impliquer une migration 1,2-triméthylsilyl à partir de Si à O (**9→10**) avant la décomposition, par exemple, de l'ion parent à *m/z* 346 résultant de la décomposition du composé **6**. La préparation de la silanone ionisée peut être un processus minoritaire. On discute de quelques autres voies de fragmentation.

Mots clés : thermolyse en phase gazeuse, réarrangement des ions, migration du groupe silyle, silanone, halosilane.

[Traduit par la rédaction]

Introduction

Since the turn of the century when Kipping first described materials alleged to contain the Si=O bond (1) (originally named silicones in analogy to ketones, now called silanones), much effort has been expended trying to observe these elusive species. The intermediacy of free silanones has been proposed for many reactions (2–9; however, see ref. 10). Much of the evidence for silanone formation is inferred from the presence of small silicone cyclics in reaction mixtures. Thus, hexamethylcyclotrisiloxane (D_3) and octamethylcyclotetrasiloxane (D_4) have been observed in the thermosylates of silylketenes (Scheme 1A, 11) and silylperoxides (Scheme 1B, 12), in the thermal decomposition of siloxetanes (Scheme 1C, 13), as products of retroene reactions (14), and in other reactions (Scheme 1D, 15, 16). Some of the clearest evidence for silanone formation results from the thermal decomposition of D_4; $Me_2Si{=}O$ formation is inferred from the initial first-order kinetics for the formation of D_3 (17, 18).

Received February 1, 1996.

C. Roos, G.A. McGibbon,[1] and M.A. Brook.[2] Department of Chemistry, McMaster University, 1280 Main St. W., Hamilton, ON L8S 4M1, Canada.

[1] Natural Sciences and Engineering Research Council of Canada Postdoctoral Fellow. Current address: Department of Chemistry, University of Waterloo, Waterloo, ON N2L 3G1, Canada.

[2] Author to whom correspondence may be addressed. Telephone: (905) 525-9140, ext. 23483; Fax: (905) 522-2509; E-mail: mabrook@mcmaster.ca

Scheme 1.

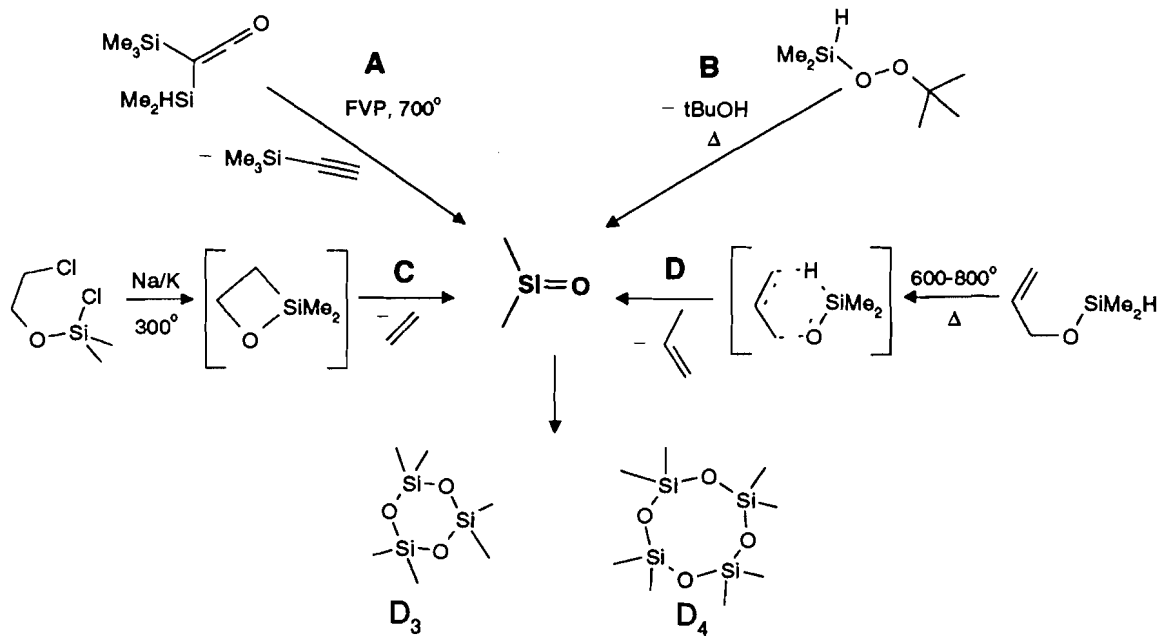

Scheme 2.

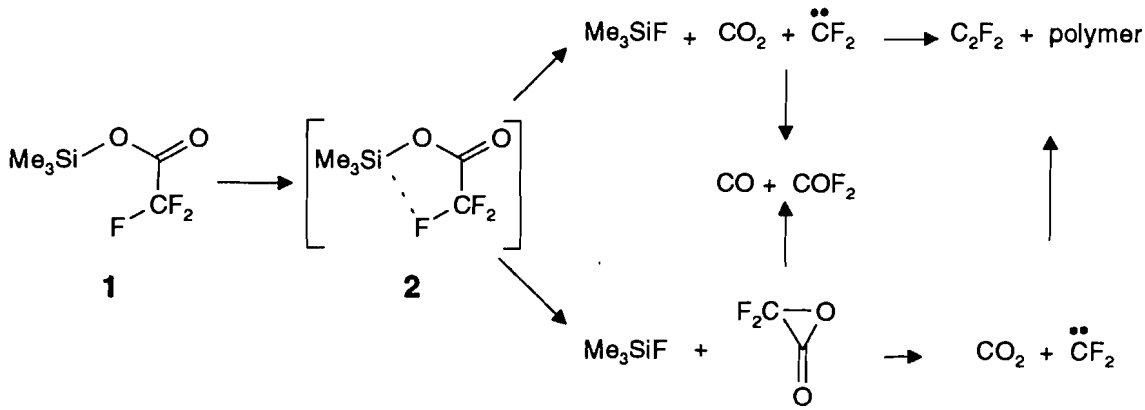

Although a few simple silanones ($R_2Si{=}O$, R = H, Me, Hal) have been characterized by a variety of spectroscopic techniques, including infrared spectroscopy at low temperature (19, 20), the bulk of the present knowledge of silanone properties originates from studies on transients (21, 22); the radical anion of $(t\text{Bu})_2Si{=}O$ has also been reported (23). Thus, unlike other silicon-based reactive intermediates (21), silanones constitute one of the few classes of compounds for which synthetic routes to stable species have yet to be developed.

Fluoride-induced reactions

A variety of silicon-based, reactive intermediates have been generated by the rearrangement of suitable precursor molecules. Rearrangements and other reactions at silicon can be driven by the addition of silylnucleophiles (24). Many cleavage reactions involving Si—X (X = C, O, etc.) (25, 26) are known in silicon chemistry to be promoted by the formation of the very strong Si—F bond (~160 kcal mol^{-1}) (27). For instance, the rate of extrusion of Si—F from fluoroalkylsilanes has been measured (28, 29) and this approach has been used to drive the formation of bis(trimethylsilyl)diphenylsilene from (tris(trimethylsilyl)methyl)diphenylfluorosilane (30) via loss of Me_3SiF.

We have previously demonstrated that the thermal decomposition of esters can be facilitated by the formation of Si—F bonds (31). The decomposition of $F_3CCO_2SiMe_3$ **1** occurs at <725°C to give Me_3SiF whereas the nonfluorinated compound $H_3CCO_2SiMe_3$ was stable to >800°C. Similar results were observed with alkylsulfonic ester derivatives. The observed products from **1** are explained by the mechanisms proposed in Scheme 2. The reactions occur quite cleanly in spite of the fact that several features of these compounds disfavour reaction. For instance, the transition state must be a 5-membered ring **2** with a non-optimal geometry. Moreover, the thermodynamics of the formation of the three-membered ring are not very favourable.

The remarkable lack of side reactions in the examples shown above suggested the use of a similar mechanism to create silanones under comparably mild conditions and with as few by-products as possible. In this respect, compounds of

Scheme 3.

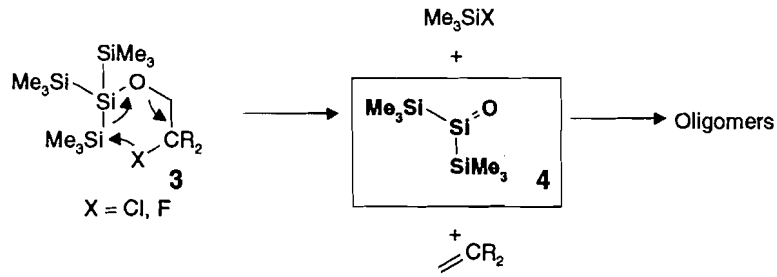

Scheme 4.

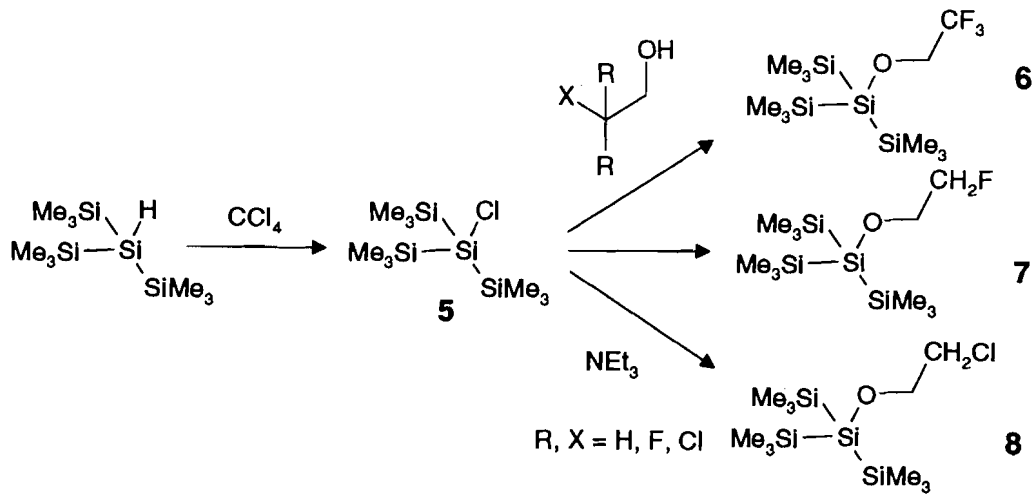

type **3** have several potential advantages (Scheme 3). A significant driving force for the reaction should be the formation of a Si—X bond. Although the absolute value for the Si=O π-bond strength is somewhat controversial (σ+π Si=O 90–190 kcal mol^{-1} estimated (21, 32, 33), 38–63 kcal mol^{-1} π-bond experimental (17, 18, 34)), our estimate of the overall enthapy of the decomposition of **3** (Scheme 3, X = F) is −42 kcal mol^{-1} (Si=O bond strength = 191 kcal mol^{-1} (π 63 + σ 128 kcal mol^{-1})) (21, 27). Secondly, the reaction should occur in a 6-membered ring transition state with a near optimal geometry (Scheme 3). This would yield bis(trimethylsilyl)silanone **4**, which will presumably oligomerize (8, 9). Thirdly, if followed, this reaction mechanism would yield at least two gaseous products (at room pressure). By removing the gaseous products, the probability of reactions between silanone and the by-products would be reduced and, additionally, the reaction would be forced to the product side. Finally, the entropy of the reaction should be very favourable, producing three molecules from one.

Our exploration of the thermal behaviour of compounds of type **3** is presented below. By changing the number and the kind of halides substituted at carbon-2 of the ethoxy group, we have attempted to relate the influence of halide substitution to thermal reactivity at different pressures. In addition to silanone formation, this study allows the exploration of other reaction pathways that could be initiated by Si—X bond formation: silicon compounds are known to undergo rearrangements in the gas phase (35). The reactions were examined using direct thermolysis and, additionally, molecular ions under mass spectrometric conditions.

Results and discussion

Preparation of compounds

The sisyl (tris(trimethylsilyl)silyl) derivatives **6–8** were prepared from the readily available compound $(Me_3Si)_3SiCl$ **5** (Scheme 4). The reaction of the appropriate haloalcohols with **5** in the presence of base led to excellent yields of the compounds **6–8**. These compounds possess the requisite 1,6-halosilane relationship.

Unimolecular reactions of ions derived from 6–8

We initially chose to examine compounds **6–8** under conditions in which decomposition is unimolecular, in a sector field mass spectrometer. Under gas phase conditions, organosilicon ions have a high proclivity to rearrange (35). Therefore, in contrast to carbon-based ions, the reaction mechanisms involving silicon ions are, with some exceptions, poorly understood (36) in spite of the fact that labelling experiments have been utilized.

The mass spectra reported below were obtained on a ZAB-R spectrometer with BE_1E_2 geometry (37). We have examined the spectra of ions from the ion source and, additionally, metastable ion (MI) mass spectra to get more detailed information about the most energetically favourable dissociation pathways of the molecular and daughter ions. Very low vapour pressure

Scheme 5.

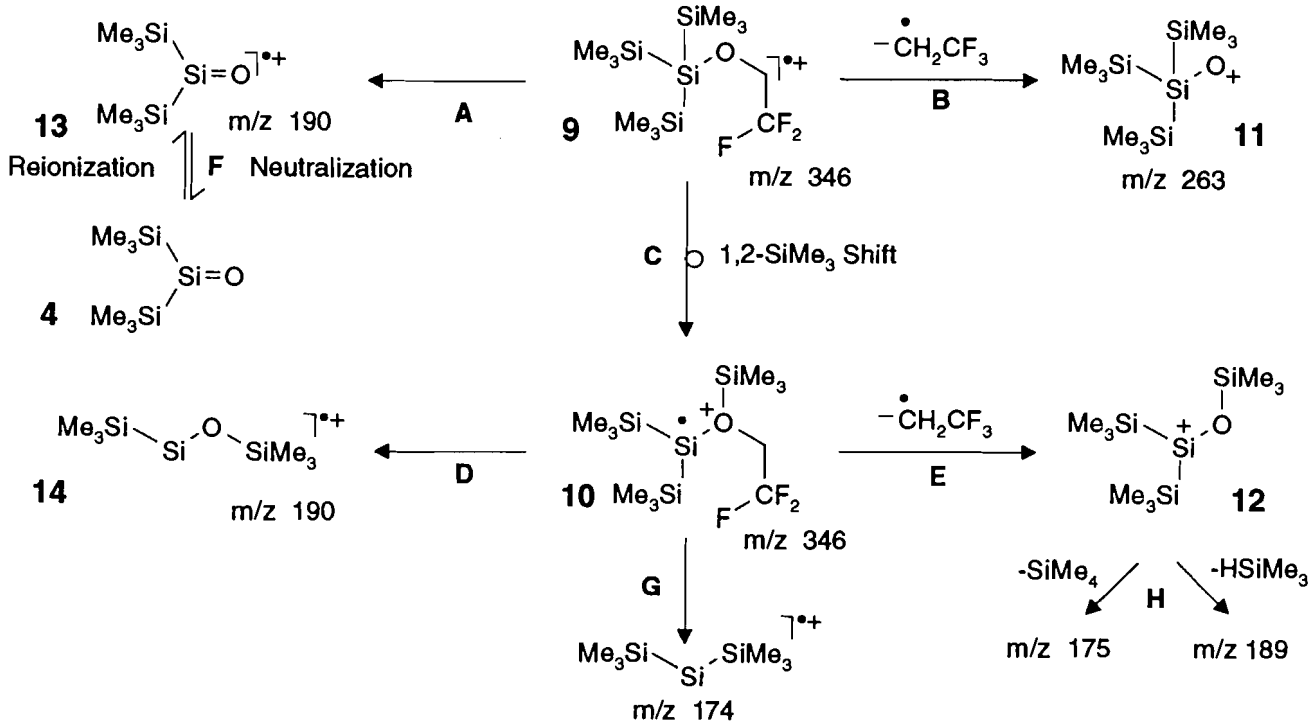

pyrolysis experiments were also performed.[3] The products were analysed by subsequent ionization and MS/MS experiments (metastable ion (MI)/collisionally activated dissociation (CAD), and Neutralization Reionization Mass Spectrometry (NRMS)) (38). The suggested structures for the ions in the various spectra below were based on comparison with examples for decomposition of related organosilicon ions (Scheme 5) (36, 37, 39).

Normal mass spectra of ***6–8***

The electron impact (EI) mass spectrum of **6** showed a molecular ion peak (M^+; *m/z* 346). Although in the EI mass spectra of **7** and **8** only relatively weak molecular ion peaks were observed, the chemical ionization spectra (CI) clearly showed peaks for the protonated molecules (*m/z* 310 and 327, respectively). The fragment ion peaks and corresponding abundances are reported in the experimental section. For **6**, **7**, and **8**, peaks at *m/z* 263, 131, and 117 were observed with similar abundance ratios in the EI spectra; not surprisingly, all spectra showed an abundant *m/z* 73 peak (Me_3Si^+). A high-resolution measurement of *m/z* 263 from **6** indicated the elemental composition $Si_4C_9H_{27}O$, which could correspond to either of the ions **11** and **12** (Scheme 5). We note that these ions are the Si- and O-trimethylsilylated ions of bis(trimethylsilyl)silanone, respectively.

MI and CAD mass spectra

Clearly, the ability to determine and distinguish isomeric ion structures would allow reaction mechanisms to be tested. MI mass spectra provide information about the most favourable (low energy) decomposition pathways. Therefore, MI spectra of *m/z* 346 and 263 from **6** were obtained.

The MI mass spectrum of the *m/z* 346 ion **9** and (or) **10** showed *m/z* 263 as the only intense peak. This decomposition step involving the loss of 83 mass units may be explained by the α-cleavage of the C—O bond and the loss of the radical $^{\bullet}CH_2CF_3$ (Scheme 5B,E) (40) with a prior or concomitant 1,2-$SiMe_3$ shift to yield **11** and (or) **12**. The latter is expected to be more stable than the former since the positive charge is on the silicon, although **11** cannot be excluded; the parent system H_3SiO^+ has been shown to favour the O-protonated silanone structure, $H_2Si{=}OH^+$, analogous to **12** (41).

There was also a very weak peak (5% of base peak *m/z* 263) at *m/z* 190 in the MI spectrum of the molecular ion of **6** (Scheme 5A). This fragment was not observed in the MI spectrum of *m/z* 263. The most optimistic interpretation for the *m/z* 190 peak is that its origin is the ionized silanone $(Me_3Si)_2Si{=}O^{\bullet+}$ **13** formed by a mechanism (Scheme 5A) analogous to that shown in Scheme 3. Based on the ionization potentials of the three proposed products, if formed, the silanone would be expected to be observed as the charged species; the relative ionization potentials are $(Me_3Si)_2Si{=}O$ 8.47 eV,[4] Me_3SiF 10.31 eV (31), and CH_2CF_2 10.29 eV (42). Unfortunately, due to its low intensity, we could not investigate the *m/z* 190 ions produced by metastable dissociation of the molecular ions in the second field free region of the instrument. Instead MI and CAD spectra were obtained from ions *m/z* 190 generated in the ion source.

CAD is commonly employed for ion structure determination (40). For CAD to be reliable, precursors leading to ions of

[3] Attempts to pyrolyze **6** in the mass spectrometer up to 520°C led to no significant change in its EI spectrum, consistent with its behavior in the DSC. Above this temperature minor changes in the intensities appeared but due to instrumental limitations it was not possible to raise the temperature any further than 580°C.

[4] Calculated using MOPAC (AM1), see experimental section.

unambiguous structure are required. Unfortunately, such precursors are not available in this case. Moreover, the propensity for organosilicon ions to rearrange renders CAD a less than definitive probe of structure (35). Perhaps not surprisingly, therefore, the CAD spectrum provided little help in establishing the structure of the *m/z* 190 ion.

NRMS is a technique that can facilitate structure determination and may also be utilized for the preparation of elusive neutrals. In the hope of observing a neutral silanone **4** from ion *m/z* 190, a NRMS experiment (43) was performed (Scheme 5F). Unfortunately, in the experiment on *m/z* 190, no survivor ion was observed. It is therefore impossible to draw a firm conclusion regarding the stability of the neutral (44).

The CAD spectrum of *m/z* 346 from **6** was dominated by *m/z* 263 and 174. Although the direct extrusion of $TMSOCH_2CF_3$ from **9** giving *m/z* 174 is possible, a more likely scenario is that *m/z* 174 arises from the rearranged *m/z* 346 ion **10** by direct bond cleavage yielding $Me_3SiSiSiMe_3^{+\bullet}$ **14**, a silylene radical cation (Scheme 5G).

The base peak in the CAD spectrum of *m/z* 263 is *m/z* 73 $SiMe_3^+$, leaving the structural elements of the silanone as the neutral. The picture is complicated, however, by the observation of abundant peaks at *m/z* 117, 131, 147, 175, and 189. The latter two of these, which correspond to the elimination of Me_3SiH and Me_4Si, respectively, are also observed in the MI spectrum of *m/z* 263 from **6**, indicating that rearrangement takes place prior to dissociation (Scheme 5D).

Fragmentation pathways

Based on the results from **6**, there are two low-energy, decomposition pathways occurring under these conditions. The first, albeit minor pathway, may involve the desired decomposition of the molecular ion **9** to, among other things, the silanone derivative $(Me_3Si)_2Si{=}O^{\bullet+}$ (Scheme 5A). Our results, however, do not permit the distinction between this structure and the isomeric silylene derivative $Me_3SiSiOSiMe_3^{\bullet+}$ (Scheme 5D). Calculations on the parent compounds (H replacing Me groups) suggest that while the two structures are nearly isoenergetic, there is an extremely high energy barrier to interconversion (32).[5] Thus, if the silanone is formed in the rearrangment, it is unlikely to isomerize. The second and major pathway involves initial migration of $SiMe_3$ in the molecular ion to give **10**. Subsequent daughter ions are consistent with this proposal (Scheme 5). We believe the presence of strong *m/z* 263 peaks in the normal mass spectra of **6–8** suggests the Me_3Si Si→O migration is occurring in the decomposition paths of ions derived from all three molecules.

Thermolysis under ambient or elevated pressure: GC–MS characterization

The compounds **6–8** were also thermolysed at higher pressure in a sealed tube for the purposes of comparison with the low-pressure thermolysis results described above. Under such conditions, more complex reactions will clearly occur. While it was impossible under such circumstances to conclusively determine if silanones were present, we report here preliminary results that are consistent with product derived from silanones, arising from the reaction shown in Scheme 3.

Differential scanning calorimetry (DSC)

To determine the decomposition temperatures of the three compounds, DSC measurements (45) of each were taken from 25–600°C. Compound **6**[3] showed essentially no reactivity in this temperature range whereas **7** showed endothermic signals at 297°C and 320°C and an exothermic signal at 322–327°C. The DSC of **8** shows an exothermic signal between 220 and 250°C and a sharp endothermic signal at 264.6°C.

Sealed tube thermolysis

The three compounds were thermolysed in sealed tubes above their decomposition temperatures: **6** was heated at 850°C,[3,6] **7** and **8** at 350°C for a period of 10 min, respectively. The thermolysis of **6** yielded a brown solid, the constituents of which could not be ascertained, **7** a colourless oil, and **8** a yellow oil. The volatile products of the latter two compounds were separated under vacuum and analysed by mass spectrometry; the oils were analysed by GC–MS (45). Only the major products are taken into consideration in the discussion.

Compounds **7** thermolysed to a number of products (Table 1, Table 3) most of which were minor components. There were two primary products in addition to recovered starting material (total yield 75%). In addition to the difficulties in identifying the structure of silicon-containing ions mentioned above, fluorine-containing compounds often have the characteristic of showing a weak molecular ion peak in their mass spectra. The proposed structures of the two species **15** and **16** shown in Table 1 are consistent with the mass spectral data. The formation of **15** and **16** could have arisen from the insertion of $(Me_3Si)_2Si{:}$, analogous to **14** (vide supra), into the starting material and $(Me_3Si)_3SiF$, respectively. No peak at *m/z* 190 was observed in the mass spectra of any of the compounds. The presence of fluorine-containing fragments that do not contain the CH_2CH_2 fragment in **15** suggests that while extrusion of Si-F compounds is occurring, it is the wrong silicon that is undergoing reaction for formation of the silanone (i.e., $FSi(SiMe_3)_3$ versus $FSiMe_3$).

The decomposition of **8** was not nearly as clean as that of **7** as can be seen from Table 4. The major product of the thermolysis of **8** could be clearly identified as tris(trimethylsilyl)chlorosilane **5** by comparison to the GC and MS data of the pure compound. Three other compounds are of particular interest. For instance, the compound obtained at 9.1 min could be an addition product of silanone **4** and chlorotrimethylsilane with *m/z* 298 (M^+) as highest ion mass (**17**, Table 2). The remaining two, the products **18** and **19** at 11.8 and 17.2 min, respectively, have peaks at *m/z* 299 and thus also incorporate the constituents of $(Me_3Si)_2Si{=}O$ and a halosilane. One can envision higher molecular weight products containing these fragments that could have arisen during the thermolysis. Although many pathways could lead to **19**, it is not only tantalizing but reasonable to consider the possibility that it was indeed formed from the addition of **5** to the silanone. Otherwise, its formation would have to involve C—O bond cleavage, a rearrangement, and a bimolecular hydrogen, methyl, or chloride exchange.

[5] The high barrier is present for the neutrals and in this argument we assume that a reasonably high barrier to interconversion will also exist for the analogous ion; the simplest silanone/silylene cations and neutrals do not interconvert in similar MS experiments (41).

[6] It was not possible to establish the threshold decomposition termperature for **6**.

Scheme 6.

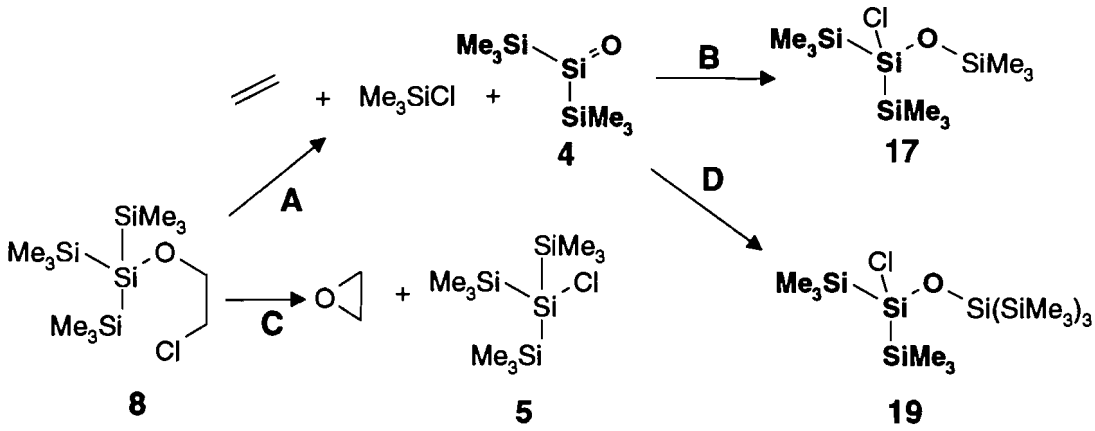

Table 1. Major product distribution of the thermolysis of **7**.

Time (min)	% Composition	Proposed structure
12.7	46.6	**7**
27.0	14.4	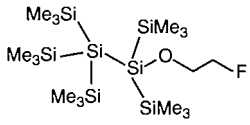 **15**
29.6	23.3	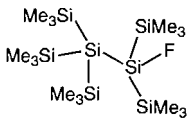 **16**

Table 2. Major product distribution of the thermolysis of **8**.

Time (min)	% Composition	Probable structure
9.1	6.4	**17** $(Me_3Si)_2SiClOSiMe_3$
11.5	28.1	**5** $(Me_3Si)_3SiCl$
11.8	5.8	**18** Cl,[a] 3 × $SiMe_3$, O
17.2	14.8	**19** Cl,[a] 3 × $SiMe_3$, O

[a]The indication Cl, indicates the fragment contains Cl as shown by the isotopic pattern for $^{35}Cl/^{37}Cl$.

Similarly, the other products could arise by addition of a silanone to a halosilane.

The mechanistic proposal outlined above suggested that the formation of a Si=O bond could be driven by the formation of a Si–halogen bond (Scheme 6A). While the migration of a halogen to a $Si(SiMe_3)_3$ group seems to have been the dominant process in the decomposition of **8**, and may also be occurring in the thermolysis of **7**, it was not the desired reaction (Scheme 6C). Nonetheless, the product mixture from **8** contains species that are likely to have arisen from the coupling of silanone **4** with halosilanes (Scheme 6B,D) suggesting that silanone formation is a minor reaction pathway in this thermolysis.

Conclusion

High-pressure thermolysis

There is little experimental evidence to support the involvement of the six-membered transition state as more than a minor decomposition pathway (Scheme 3) for compounds **6–8**. The reaction products of the sealed tube thermolysis of **8** were the most encouraging; many adducts could have arisen from a silanone addition or insertion reaction. The major product of decomposition, however, was $(Me_3Si)_3SiCl$, which would have involved a five-membered transition state if formed in a unimolecular reaction.

In the case of the fluoro compounds **6** and **7**, none of the products of a sealed tube thermolysis showed any indication of involving silanones in their formation. Although low reactivity is often associated with fluoroalkanes (the "Teflon effect"), reflecting the strength of the CF bond, it is somewhat surprising that the even greater bond strength of the SiF bond that would be formed in reactions like that in Scheme 3 was not strongly manifested in the reactions examined. We attribute this observation to a kinetic stability, and believe our original proposal that it should be possible to drive this reaction on enthalpic grounds remains valid: a more reactive intramolecular fluoride delivery system is needed.

Ion decomposition

At low pressures, the unimolecular decomposition of all three compounds followed two major pathways. The most important of these seemed to involve a Si→O $SiMe_3$ migration prior to subsequent decomposition. The minor pathway might involve the desired decomposition to silanone.

Experimental

For preliminary quality checks, ^1H NMR spectra were obtained on a Varian EM-390 (90 MHz) continuous wave spectrometer with $Si(CH_3)_4$ or $CHCl_3$ as an external reference. Otherwise, ^1H and ^{13}C NMR spectra were obtained on Bruker AC-200 (200.1 MHz for ^1H NMR or 50.3 MHz for ^{13}C NMR) spectrometer. Spectra were referenced to the solvent signal of chloroform (contaminant in $CDCl_3$, at 7.24 ppm for ^1H NMR; at 77.0 ppm (t) for ^{13}C NMR) or C_6H_6 in benzene-d_6 (at 7.15 ppm (br) for ^1H NMR). ^{29}Si NMR were performed on a Bruker AC-300 (at 59.63 MHz for silicon) using tetramethylsilane as external standard. NMR data are given in ppm and coupling constants are recorded in hertz. The abbreviations s = singlet, d = doublet, t = triplet, dd = doublet of doublets, dt = doublet of triplets, m = multiplet, and br = broad are used in reporting the spectra. Infrared spectra of a neat film on a KBr window or

of solids as KBr pellets were run on a Perkin–Elmer 283 spectrometer or on a BioRAD FTS 40 spectrometer equipped with a SPC 3200 data station; peaks are noted as strong s, medium m or weak w. The IR data are given in cm^{-1}. Ultraviolet–visible spectra were recorded on a Hewlett Packard HP 8451A Diode Array spectrophotometer.

EI (70 eV), CI (NH_3), and high-resolution mass spectra were obtained on a VG analytical ZAB-E mass spectrometer with a VG11-250 data system. The theoretical mass of the molecular ion was calculated from the masses of the most common isotopes (46). Pyrolysis – mass spectrometric experiments and metastable ion (MI), collisional activated dissociation (CAD), and neutralization–reionization (NRMS) mass spectrometry were performed on a VG Analytical ZAB-R instrument that has BE_1E_2 geometry (B=magnetic, E=electric sector). *N,N*-Dimethylaniline was used for neutralization while O_2 was used as a collision gas (transmission = 70% at each collision) for reionization and CAD.

Gas chromatography – mass spectrometry was performed on a Hewlett Packard 5890 Series II gas chromatograph, using a DB-5, 30 m column, 0.20 mm i.d., attached to a Hewlett Packard 5971A mass selective detector. Gas chromatography was performed on a Hewlett Packard 5890 gas chromatograph with a TCD detector and a Hewlett Packard 3393A integrator using a SPB-1, 30 m, 1.0 μm i.d. column and helium as reference and carrier gas. Melting and decomposition points were measured by a General V4.1C DuPont 2100 differential scanning calorimeter (DSC).

Sources of materials

2-Chloroethanol, 99% $ClCH_2CH_2OH$; triethylamine, 99+% $(CH_3CH_2)_3N$; 2,2,2-trifluoroethanol, 99+% F_3CCH_2OH; and tris(trimethylsilyl)silane, 97% $(Me_3Si)_3SiH$ were obtained from Aldrich and were used from a freshly opened bottle without further purification. The purity was checked by TLC, ^1H NMR, and GC. 1,1,1,3,3,3-Hexamethyldisilazane, 98% $((CH_3)_3)_2SiNH$, was obtained from Aldrich and was distilled before use. $CDCl_3$ (99.8 at.% D), cyclohexane-d_{12} (99.6 at.% D), and benzene-d_6 (99.6 at.% D) were obtained from Isotec Inc. and were used without purification from a new fresh bottle or from freshly opened ampoules.

Purification of solvents

Hexanes and diethyl ether were freshly distilled over sodium–benzophenone under a nitrogen atmosphere. Carbon tetrachloride was stirred hot with 10% by volume of concentrated alcoholic KOH, washed with water, dried over $CaCl_2$, and freshly distilled from P_2O_5 under a nitrogen atmosphere (47).

General experimental procedures for synthesis

Due to the instability of the reagents towards hydrolysis, all syntheses were performed with dry glassware under an atmosphere of anhydrous nitrogen. Addition and transfer of solvents and reagents were done using syringe-septa techniques or using a glove-bag that was dried with anhydrous phosphorus pentoxide (P_2O_5) and continuously purged with anhydrous nitrogen.

The reactions were followed by thin-layer chromatography (TLC) using a closed TLC chamber, hexanes–ether (1:2) as solvent, and Merck plastic-backed aluminum oxide, 60 F254 neutral (type E) precoated, 6.5 × 2.5 mm TLC sheets. For the separation and purification of the products a Chromatotron (model 7924T) of Harrison Research Inc. was used. The plates, 0.1 or 0.4 mm thick, were prepared with silica gel 60 PF254, containing gypsum.

*Synthesis of tris(trimethylsilyl)chlorosilane ($(Me_3Si)_3SiCl$) **5***

The method of Bürger et al. (48) was used to synthesize **5** as follows: In a 50 mL round-bottom flask equipped with reflux condenser, tris(trimethylsilyl)silane (8.63 mL, 0.028 mol) was added dropwise with stirring to dry CCl_4 (11.6 mL, 0.12 mol) and stirred for 20 h. After the evaporation of $HCCl_3$ and excess CCl_4, 6.45 g (0.0228 mol, 76%) of a white solid remained. The product was cleaned by sublimation; mp ~50°C (48); IR (KBr) ν: 2952 s, 2924 s, 1458 w, 1257 m, 1247 s, 839 vs, 746 w, 692 m, 622 cm^{-1}; ^1H NMR ($CDCl_3$, 200 MHz) δ: 0.21 (s); MS (*m/z* reported for the ^{28}Si and ^{35}Cl isotope (%)): EI *m/z*: 282 (8) (M^+), 267 (30), 247 (20), 174 (100), 159 (35), 131 (23), 117 (15), 73 (70), 59 (10); CI *m/z*: 282 (12), 264 (13), 191 (68), 174 (25), 133 (28), 90 (100), 73 (20), 52 (17).

*Synthesis of tris(trimethylsilyl)-2,2,2-trifluoroethoxysilane ($(Me_3Si)_3SiOCH_2CF_3$) (**6**)*

In a 50 mL two-neck round-bottom flask **5** (1.00 g, 3.54 mmol) was dissolved in dry hexanes (3 mL). Slowly 2,2,2-trifluoroethanol (0.51 mL, 7.06 mmol) and triethylamine (0.49 mL, 3.53 mmol) were added dropwise with stirring. The reaction mixture formed two layers. After 24 h of vigorous stirring, the solid was filtered off and the solvent and remaining reagents were removed under vacuum. A white waxy solid (0.873 g, 2.54 mmol, 72%) remained. The product was purified on the Chromatotron using hexanes as solvent; mp 112°C; bp 311°C; IR (KBr) ν: 2952 s, 2855 m, 1454 w, 1397 w 1290 s, 1246 s, 1156 vs, 1130 vs, 964 m, 835 vs, 762 m, 724 m, 688 m, 622 w, 543 w cm^{-1}; ^1H NMR ($CDCl_3$, 200 MHz) δ: 0.18 (s, 27 H), 3.74 (q, 2 H, $^3J_{F-H}$ = 8.6 Hz); ^{13}C NMR ($CDCl_3$, 50.3 MHz) δ: 109.39 (s), 65.61 (q, $^1J_{F-C}$ = 35.6 Hz), 0.02 (s); ^{29}Si NMR ($CDCl_3$, 59.6 MHz) δ: 12.13 (s), −14.76 (s); MS (*m/z* reported for the ^{28}Si isotope (%)): EI *m/z*: 346 (6) (M^+), 331 (10), 263 (33), 251 (32), 247 (19), 193 (32), 174 (100), 159 (23), 131 (29), 73 (48), 59 (4); CI, *m/z*: 364 (9) ($M^+ - NH_4$), 348 (3), 331 (13), 264 (43), 210 (10), 191 (33), 174 (25), 148 (16), 133 (14), 90 (100), 73 (38), 59 (15); HRMS calcd. for $C_{11}H_{29}OSi_4F_3$: 346.1248; found: 346.1261.

*Synthesis of tris(trimethylsilyl)-2-fluoroethoxysilane ($(Me_3Si)_3SiOCH_2CH_2F$) (**7**)*

Synthesis similar to **6**: **5** (1.646 g, 5.83 mmol), with dry hexanes (5 mL), 2-fluoroethanol (0.68 mL, 0.012 mol), triethylamine (0.81 mL, 5.81 mmol), with 1.644 g (5.3 mmol, 91%) of a white waxy solid remaining; mp 122°C; bp 296°C; IR (KBr) ν: 2951 s, 2895 m, 2857 w, 1449 w, 1397 w, 1368, w, 1246 vs, 1123 vs, 1104 s, 1055 m, 937 m, 866 vs, 838 vs, br, 711 m, 688 s, 623 m, 469 w cm^{-1}; ^1H NMR ($CDCl_3$, 200 MHz) δ: 0.18 (s, 27 H), 3.67 (dt, $^3J_{F-H}$ = 27.43, $^3J_{H-H}$ = 4.4 Hz), 4.38 (dt, $^2J_{F-H}$ = 47.6, $^3J_{H-H}$ = 4.3 Hz); ^{13}C NMR ($CDCl_3$, 50.3 MHz) δ: 83.09 (s), 66.94 (d, $^1J_{F-C}$ = 21.0 Hz), 0.20 (s); ^{29}Si NMR ($CDCl_3$, 59.6 MHz) δ: 5.70 (s), −15.61 (s); MS (*m/z* reported for the ^{28}Si isotope (%)): EI, *m/z*: 263 (23), 251 (6), 193 (7), 175 (9), 131 (44), 117 (11), 73 (100); CI, *m/z*: 328 (48), 311 (100), 264 (98), 251 (30), 192 (11), 148 (13), 128 (13), 90 (45), 73 (17); HRMS (no molecular ion was visible (in EI)) calcd. for $C_9H_{27}OSi_4$: 263.1139; found: 263.1142.

Table 3. Product distribution of the thermolysis of **7**.[a]

Time (min)	% Composition	Probable structure	Mass spectral fragments
8.7	2.1	$(Me_3Si)_3SiH$	248 (7), 233 (7), 174 (36), 154 (31), 131 (19), 129 (17), 117 (18), 101 (10), 99 (11), 73 (100)
12.7	46.6	**7**	263 (33), 193 (7), 189 (13), 175 (19), 159 (10), 131 (64), 117 (32), 73 (100)
13.6	5.6		306 (1), 291 (3), 232 (67), 217 (4), 187 (3), 173 (15), 159 (24), 158 (24), 157 (23), 144 (22), 129 (17), 113 (15), 99 (19), 73 (100)
18.0	3.5		290 (73), 275 (6), 217 (24), 216 (13), 215 (12), 202 (13), 201 (16), 199 (9) 187 (7), 186 (7), 173 (13), 171 (20), 159 (11), 157 (34), 143 (17), 141 (11), 131 (6), 129 (12), 127 (7), 125 (10), 99 (11), 73 (100)
24.8	2.6		348 (28), 333 (4), 290 (11), 275 (11), 260 (6), 259 (6), 217 (9), 215 (19), 213 (8), 201 (31), 199 (21) 187 (6), 186 (5), 185 (12), 173 (10), 171 (15), 157 (22), 143 (10), 141 (9), 131 (11), 129 (11), 127 (8), 125 (8), 115 (7), 113 (7), 99 (6), 73 (100)
26.4	1.5		348 (65), 333 (5), 275 (11), 260 (12), 259 (11), 215 (22), 213 (12), 201 (33), 199 (29) 187 (9), 186 (8), 185 (15), 173 (9), 171 (13), 157 (21), 143 (9), 141 (8), 131 (6), 129 (9), 127 (9), 125 (11), 99 (8), 73 (100)
27.0	14.4	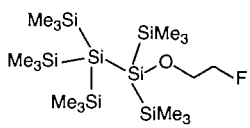 **15**	411 (10) (M^+-$SiMe_3$), 363 (6), 215 (22), 173 (13), 157 (16), 131 (19), 115 (9), 73 (100)
29.6	23.3	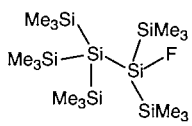 **16**	309 (47) (M^+-$SiMe_3$-Me_2Si), 215 (7), 193 (23), 173 (19), 159 (9), 157 (13), 131 (40), 73 (100)
35.9	1.0		522 (13), 449 (2, 522-$SiMe_3$), 375 (6), 361 (3), 317 (6), 301 (29), 259 (8), 243 (16), 241 (13), 239 (11), 227 (19), 197 (13), 185 (9), 171 (7), 157 (8), 155 (9), 131 (13), 73 (13)

[a]Peaks at *m/z* 131, 117, 99, and 101 are indicative of a $(Me_3Si)_3Si$ group.

*Synthesis of tris(trimethylsilyl)2-chloroethoxysilane ($(Me_3Si)_3SiOCH_2CH_2Cl$) (**8**)*

Synthesis similar to **6**: **5** (1.00 g, 3.54 mmol), dry hexanes (3 mL), 2-chloroethanol (0.47 mL, 7.01 mmol), triethylamine (0.49 mL, 3.53 mmol), 24 h reaction, 0.8982 g (0.0028 mol, 80%) of a white waxy solid remained; mp 87°C; bp 264°C; IR (KBr) ν: 2951 s, 2893 m, 2850 w, 1395 w, 1377 w, 1298 w, 1245 s, 1193 w, 1112 s, 1084 s, 1045 m, 836 vs, 789 w, 744 w, 709 m, 688 m, 622 w cm^{-1}; ^1H NMR ($CDCl_3$, 200 MHz) δ: 0.18 (s, 27 H), 3.51 (t, 2H, $^3J_{H-H}$ = 5.8 Hz), 3.78 (t, 2H, $^3J_{H-H}$ = 5.6 Hz); ^{13}C NMR ($CDCl_3$, 50.3 MHz) δ: 0.23 (s), 44.99 (s), 68.01 (s); ^{29}Si NMR ($CDCl_3$, 59.6 MHz) δ: 5.70 (s), −15.61 (s); MS (*m/z* reported for the ^{28}Si and ^{35}Cl isotope (%); *ions containing ^{37}Cl isotope): EI, *m/z*: 311* (2), 263 (24), 209* (43), 190 (8), 189 (10), 175 (15), 159 (7), 147 (6), 131 (49), 117 (15), 93 (11), 73 (80), 59 (20); CI, *m/z*: 327* (100), 311* (25), 264 (80), 226 (12), 209* (14), 148 (10), 90 (27), 73 (12).

*Synthesis of trimethylsilyl-2-chloroethoxysilane ($Me_3SiOCH_2CH_2Cl$) (**20**)*

This compound was prepared for purposes of comparison with the thermosylate of **8**. In a 50 mL two-neck round-bottom flask with nitrogen inlet and nitrogen outlet with bubble counter, hexamethyldisilazane (4 mL, 3.06 g, 18.9 mmol) was

Table 4. Product distribution of the thermolysis of **8**.

Time (min)	% Composition	Probable structure[a]	Mass spectral fragments[b]
7.2	2.5		281 (5), 265 (Cl, 2), 244 (Cl_2, 7), 229 (Cl_2, 5), 209 (2), 193 (2), 165 (Cl, 1), 136 (Cl, 21), 131 (10), 93 (Cl, 28), 73 (100)
7.4	3.4		299 (5, Cl), 279 (Cl_2, 2), 211 (Cl, 18), 191 (100), 167 (16), 147 (13), 131 (Cl_2, 7), 117 (Cl, 21), 93 (Cl, 12), 73 (80)
9.1	6.4	**17** $(Me_3Si)_2SiClOSiMe_3$	298 (Cl, 2), 283 (Cl, 8), 263 (Cl, 2), 207 (13), 190 (33), 175 (49), 147 (26), 117 (66), 73 (100)
11.5	28.1	$(Me_3Si)_3SiCl$	282 (Cl, 6), 267 (Cl, 15), 174 (57), 159 (41), 131 (24), 129 (21), 115 (13), 99 (9), 73 (100)
11.8	5.8	**18**	299 (1), 281 (Cl, 3), 211 (Cl, 13), 191 (59), 168 (Cl, 12), 147 (13), 133 (6), 117 (8), 101 (Cl, 5), 93 (Cl, 6), 73 (100)
12.6	5.1		279 (3), 265 (11), 253 (6), 207 (43), 191 (10), 175 (6), 147 (12), 131 (15), 117 (23), 101 (3), 73 (100)
13.3	15.8		313 (2), 283 (3), 253 (3), 225 (5), 217 (6), **190** (10), **189** (10), 175 (21), 147 (18), 117 (42), 93 (9), 73 (100)
17.2	14.8	**19** $(Me_3Si)_2SiClOSi(SiMe_3)_3$	299 (Cl, 5), 297 (Cl, 11), 267 (2), 247 (11), 209 (Cl, 10), 189 (83), 173 (5), 165 (Cl, 7), 145 (Cl, 9), 131 (8), 117 (5), 101 (5), 73 100)
17.4	5.2		399 (Cl, 3), 306 (Cl, 3), 291 (2), 233 (4), 221 (7), 217 (8), 203 (Cl, 18), **191** (6), **189** (6), 147 (9), 133 (7), 73 (100), 101 (5)
18.5	3.6		431 (Cl_2, 2), 326 (Cl, 10), 311 (2), 267 (Cl_2, 3), 263 (Cl_2, 3), 253 (Cl, 10), 233 (12), 218 (18), 209 (Cl, 16), 189 (12), 175 (24), 131 (31), 117 (17), 73 (100)
23.0	3.4		403 (Cl, 9), 345 (Cl, 2), 310 (Cl, 31), 267 (Cl, 5), 202 (24), 173 (16), 157 (Cl, 19), 131 (11), 117 (9), 99 (11), 73 (100)

[a] **20** ($Me_3SiOCH_2CH_2Cl$) was not observed.
[b] The designation Cl indicates the fragment contains chlorine; there is a corresponding peak 2 amu higher with an abundance in the correct ratio for $^{35}Cl/^{37}Cl$.

added dropwise under stirring into 2-chloroethanol (2.54 mL, 3.052 g, 37.8 mmol). The evolution of a gas (basic on pH paper) and the formation of a white solid was observed. After no more evolution of gas (NH_3) was observed, a cooling trap (acetone – Dry Ice) was added to the gas outlet and a smooth stream of nitrogen was passed through the system for 24 h. Every 6 h the trap was emptied. The first fraction had to be cleaned by distillation due to contamination by starting material; the last three fractions were pure product: 4.962 g (3.25 mmol, 86%) of a colourless liquid were obtained; ^1H NMR ($CDCl_3$, 200 MHz) δ: 0.11 (s, 9H), 3.78 (t, 2 H, $^3J_{H-H}$ = 6.1 Hz), 3.51 (t, 2 H, $^3J_{H-H}$ = 6.1 Hz).

Reactions

MI/CAD and NRMS experiments
These experiments were performed as previously reported (37).

Thermolysis at ambient pressure
DSC experiments of **6**, **7**, and **8** were performed in a temperature range from 25 to 600°C. **6** showed no reactivity in this temperature range, whereas **7** showed an endothermic signal at 320°C that changed to exothermic. The DSC of **8** showed an exothermic signal between 220 and 250°C and a sharp endothermic signal at 265°C.

Thermolysis at elevated pressure
6 (0.066 g, 0.19 mmol), **7** (0.062 g, 0.20 mmol), or **8** (0.06 g, 0.18 mmol) was independently sealed in a quartz tube with a volume of 25.5 cm^3 under pressure of 10^{-6} Torr (1 Torr = 133.3 Pa). **6** was heated at 850°C, **7** and **8** at 350°C for 10 min. **6** yielded a dark brown solid, **7** a colourless oil, and **8** a yellow oil. The tubes were cooled with liquid nitrogen, opened, and connected to a distillation apparatus. The volatile products were separated under vacuum. The remaining oils were analyzed by GC–MS. The chromatogram of **7** and **8** showed 39

and 57 compounds, respectively, most of them with less than 3 area%. The MS fragment patterns of the major products are shown in Table 3 and Table 4, respectively, with spectral assignments when these are clear; only the major products were taken into consideration in the discussion.

AM1 calculations of 4

Semi-empirical calculations of **4** were carried out on a Comptech 88486/33 MHz computer system with DOS 6.2 as operating system using Hyperchem™ (AM1) under MS Windows. The initial geometries were obtained by molecular mechanics calculations using PC-Model (version 3.1; Serena Software; Bloomington, Ind.) under DOS 6.2.

Acknowledgements

We gratefully acknowledge the financial support of this research by the Natural Sciences and Engineering Research Council of Canada. We also wish to thank the Deutscher Akademischer Austauschdienst for providing McMaster University:Universität Duisburg Exchange Fellowships to C.R. We thank Prof. N.H. Werstiuk for helpful discussions.

References

1. R. Robison and F.S. Kipping. J. Chem. Soc. **93**, 439 (1908); F.S. Kipping and L.L. Lloyd. J. Chem. Soc. **79**, 449 (1901).
2. T.J. Barton and W.D. Wulff. J. Am. Chem. Soc. **101**, 2735 (1979).
3. D. Tzeng and W.P. Weber. J. Am. Chem. Soc. **102**, 1451 (1980).
4. W.F. Goure and T.J. Barton. J. Organomet. Chem. **199**, 33 (1980).
5. I.M.T. Davidson and I.T.J. Wood. J. Chem. Soc. Chem. Commun. 550 (1982).
6. N. Wiberg. J. Organomet. Chem. **273**, 141 (1984).
7. G. Manuel, G. Bertrand, W.P. Weber, and S.A. Kazoura. Organometallics, **3**, 1340 (1984).
8. M. Trommer, W. Sander, and A. Patyk. J. Am. Chem. Soc. **115**, 11775 (1993).
9. A.G. Brook, S.C. Nyburg, F. Abdesaken, B. Gutekunst, G. Gutekunst, R. Krishan, R.K.M.R. Kallury, Y.C. Poon, Y.-M. Chang, and W. Wong-Ng. J. Am. Chem. Soc. **104**, 5667 (1982).
10. T.J. Barton, S.K. Hoekman, and S.A. Burns. Organometallics, **1**, 721 (1982).
11. T.J. Barton and B.L. Groh. J. Am. Chem. Soc. **107**, 7221 (1985).
12. A.V. Tomadze, N.V. Yablokova, V.A. Yablokov, and G.A. Razuvaev. J. Organomet. Chem. **212**, 43 (1981).
13. L.E. Gusel'nikov, Z.A. Kerzina, Yu.P. Polyakov, and N.S. Nametkin. Zh. Obshch. Chim. **52**, 457 (1982).
14. T.H. Lane and C.L. Frye. J. Organomet. Chem. **172**, 213 (1979); T.J. Barton and S. Bain. Organometallics, **7**, 528 (1988).
15. N. Wiberg, G. Preiner, and O. Schieda. Chem. Ber. **114**, 3518 (1981); G. Märkl and M. Horn. Tetrahedron Lett. 1477 (1983); A.G. Brook, W.J. Chatterton, J.F. Sawyer, D.W. Hughes, and K. Vorspohl. Organometallics, **6**, 1246 (1987).
16. G. Hussmann, W.D. Wulff, and T.J. Barton. J. Am. Chem. Soc. **105**, 1263 (1983).
17. I.M. Davidson and J.F. Thompson. J. Chem. Soc. Chem. Commun. 251 (1971).
18. I.M. Davidson and J.F. Thompson. J. Chem. Soc. Faraday Trans. 1, 2260 (1975).
19. R. Withnall and L. Andrews. J. Am. Chem. Soc. **108**, 8118 (1986).
20. C.A. Arrington, R. West, and J. Michl. J. Am. Chem. Soc. **105**, 6176 (1983).
21. G. Raabe and J. Michl. Chem. Rev. **85**, 419 (1985).
22. L.E. Gusel'nikov and N.S. Nametkin. Chem. Rev. **79**, 529 (1979).
23. A.G. Davies and A.G. Neville. J. Organomet. Chem. **436**, 255 (1992).
24. A.G. Brook and A.R. Bassindale. Org. Chem. (N.Y.), **42** (Rearrangements Ground Excited States, pt. 2), 149 (1980); A.G. Brook. Acc. Chem. Res. **7**, 77 (1974).
25. M. Lalonde and T.H. Chan. Synthesis, 817 (1985).
26. E.W. Colvin. Silicon in organic synthesis. Butterworths, London. 1981.
27. R. Walsh. Acc. Chem. Res. **14**, 246 (1981).
28. G. Fishwick, R.N. Hazeldine, C. Parkinson, P.J. Robinson, and R.F. Simmons. J. Chem. Soc. Chem. Commun. **16**, 382 (1965).
29. T.N. Bell, R. Berkley, A.E. Platt, and A.G. Sherwood. Can. J. Chem. **52**, 3158 (1974).
30. C. Eaborn, D.A.R. Happer, P.B. Hitchcock, S.P. Hopper, K.D. Safa, S.S. Washburne, and D.R.M. Walton. J. Organomet. Chem. **186**, 309 (1980).
31. N.H. Werstiuk, M.A. Brook, and P. Hülser. Can. J. Chem. **66**, 1430 (1988).
32. T. Kudo and S. Nagase. J. Phys. Chem. **88**, 2833 (1984).
33. R. Jaquet, W. Kutzelnigg, and V. Stemmler. Theor. Chim. Acta, **54**, 205 (1980).
34. W. Tumas, K.E. Salomon, and J.I. Brauman. J. Am. Chem. Soc. **108**, 2541 (1986).
35. H. Schwarz. *In* The chemistry of organic silicon compounds. Part 2. *Edited by* S. Patai and Z. Rappoport. Wiley, Chichester, U.K. 1989. Chap. 7.
36. C.M. Holznagel, R. Bakhitiar, and D.B. Jacobson. J. Am. Soc. Mass Spectrom. **2**, 287 (1991).
37. H.F. Van Garderen, P.J.A. Ruttink, P.C. Burgers, G.A. McGibbon, and J.K. Terlouw. Int. J. Mass Spectrom. Ion Processes, **121**, 159 (1992).
38. K.L. Busch, G.L. Glish, and S.A. McLuckey. Mass spectrometry. VCH, New York. 1988.
39. R.G. Cooks (*Editor*). Collision spectroscopy. Plenum Press, New York. 1979.
40. D.A. Herold and J.H. Futrell. Org. Mass Spectrom. **24**, 984 (1989).
41. R. Srinivas, D.K. Böhme, D. Sülzle, and H. Schwarz. J. Phys. Chem. **95**, 9836 (1991).
42. S.G. Lias, J.E. Bartmess, J.F. Liebman, J.L. Holmers, R.D. Levin, and W.G. Mallard. J. Phys. Chem. Ref. Data (Suppl. 1), 17 (1988).
43. J.K. Terlouw and H. Schwarz. Angew. Chem. Int. Ed. Engl. **26**, 805 (1987).
44. T. Wong, J. Warkentin, and J.K. Terlouw. Int. J. Mass Spectrom. Ion Processes, **115**, 33 (1992).
45. D.A. Skoog. Principles of instrumental analysis. 3rd ed. Holt, Rinehart and Winston, New York. 1985.
46. R.C. Weast (*Editor*). Handbook of chemistry and physics. 49th ed. CRC Press, Boca Raton, Fla. 1969.
47. A.J. Gordon and R.A. Ford. The chemist's companion. Wiley, 1972.
48. H. Bürger, W. Kilian, and K. Burczyk. J. Organomet. Chem. **21**, 291 (1970); J. Dickhaut and B. Giese. Org. Synth. **70**, 164 (1992).

(Alkylthio)- and (phenylthio)methoxycarbenes from oxadiazolines

Hui-Teng Er, David L. Pole, and John Warkentin

Abstract: Four 2-methoxy-5,5-dimethyl-Δ^3-1,3,4-oxadiazolines bearing an alkylthio or arylthio group at C2 were prepared. The oxadiazolines undergo thermolysis at 60–80°C in solution to afford the corresponding oxythiocarbene intermediates. In the absence of carbene traps, dimers of the carbenes were formed. The carbenes were trapped with ethyl crotonate, with dichloromaleic anhydride, with dimethyl acetylenedicarboxylate, and with phenyl isocyanate. Phenyl isocyanate traps methoxy(methylthio)carbene to form two types of adducts, both fundamentally different from the product obtained from reaction of dimethoxycarbene with phenyl isocyanate. All of the adducts have structures consistent with nucleophilic behaviour of the carbenes.

Key words: oxythiocarbene, oxadiazoline, thermolysis, nucleophilic.

Résumé : On a préparé quatre 2-méthoxy-5,5-diméthyl-Δ^3-1,3,4-oxadiazolines portant un groupe alkylthio ou arylthio en C2. Les oxadiazolines subissent une thermolyse vers 60 à 80°C, en solution, pour conduire aux oxythiocarbènes intermédiaires correspondants. En présence de pièges à carbène, il y a formation des dimères des carbènes. Les carbènes peuvent être piégés par le crotonate d'éthyle, l'anhydride dichloromaléique, l'acétylènedicarboxylate de diméthyle et l'isocyanate de phényle. L'isocyanate de phényle piège le méthoxy(méthylthio)carbène pour former deux nouveaux types d'adduits qui sont tous deux fondamentalement différents du produit obtenu par réaction du diméthoxycarbène avec l'isocyanate de phényle. Tous les adduits ont des structures qui sont en accord avec le comportement nucléophile des carbènes.

Mots clés : oxythiocarbène, oxadiazoline, thermolyse, nucléophile.

[Traduit par la rédaction]

Introduction

Singlet carbenes bearing donor substituents can have ambiphilic or nucleophilic properties (1). These properties result from conjugative donation of electron density into the formally vacant *p*-orbital of the singlet, Scheme 1. The importance of the dipolar contributor is a factor that determines the philicity of the carbene carbon. Dimethoxycarbene, for example, attacks phenyl isocyanate (2) as depicted in Scheme 2, and it reacts with maleic anhydrides (3) as shown in Scheme 3. The products are readily accounted for in terms of initial carbonyl addition to form a dipolar intermediate.

The availability of the exchange method (Scheme 4) for synthesis of various dioxy oxadiazolines from 2-acetoxy-2-methoxy-Δ^3-1,3,4-oxadiazolines (**1**) (4) suggested that it might be possible to prepare 2-alkylthio- and 2-arylthio-2-methoxy-Δ^3-1,3,4-oxadiazoline analogues of **2**, Scheme 4. Their thermolysis would be expected to take the cycloreversion – ylide fragmentation sequence that 2,2-dialkoxy oxadiazolines appear to follow (2*a*, 3–5), leading to (alkylthio)methoxycarbene analogues of **3***a* and corresponding

Scheme 1.

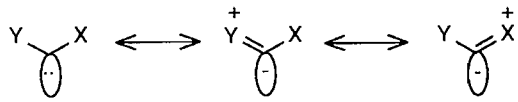

(arylthio)methoxycarbene analogues of **3***b*, Scheme 4, for convenient study of their chemical reactions. Such carbenes have not been reported, to the best of our knowledge.

Methods, results, and discussion

2-Acetoxy-2-methoxy-5,5-dimethyl-Δ^3-1,3,4-oxadiazoline (**1**) containing ca. 30% of acyclic by-product **4** was prepared by oxidation of the methoxycarbonyl hydrazone of acetone with Pb^{IV} acetate in CH_2Cl_2 as previously described (4), Scheme 5.

Treatment of the mixture of **1** and **4** with the appropriate thiol (Scheme 6) afforded **5** contaminated with **4**. Destruction of **4** with aqueous base and chromatography of the residue afforded pure **5** in yields ranging from 44 to 80% for the exchange step of Scheme 6. Their spectroscopic properties are given in the experimental section.

Thermolysis of compounds **5***a–c* in benzene was followed by ^1H NMR spectroscopy. Disappearance of **5** was first order in each case and the first-order rate constants were the same within experimental error: $k(60°C) = 2.07(\pm 0.09) \times 10^{-5}$ s^{-1}. While the effect of the sulfur-bound group (R) at C2 on the thermolysis rate constant is very small, the sulfur atom itself has a significant rate-enhancing effect, for 2,2-dimethoxy-5,5-

Received February 12, 1996.

H.-T. Er, D.L. Pole, and J. Warkentin.[1] Department of Chemistry, McMaster University, Hamilton, ON L8S 4M1, Canada.

[1] Author to whom correspondence may be addressed. Telephone: (905) 525-9140, ext. 23478. Fax: (905) 522-2509. E-mail: Warkent@McMaster.ca

Scheme 2.

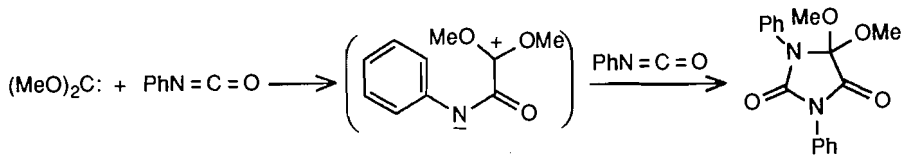

Scheme 3.

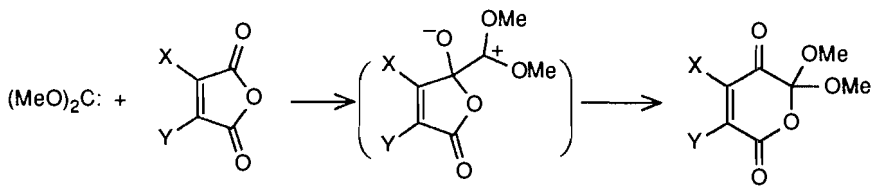

X,Y= H, Me, Cl, Br, for example, in various combinations

Scheme 4.

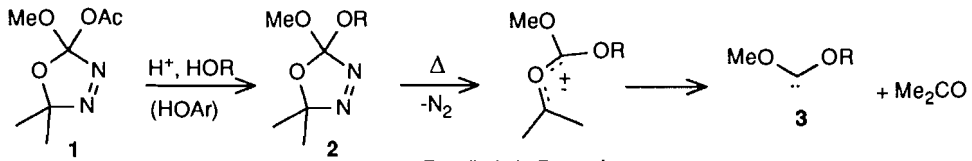

a: R= alkyl *b*: R= aryl

Scheme 5.

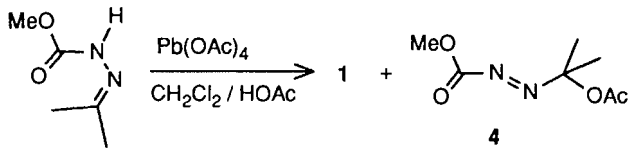

Scheme 6.

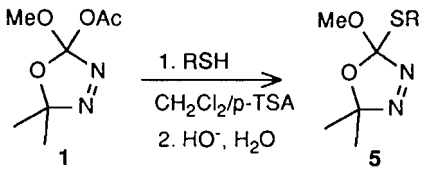

a: R= Ph, *b*: R= CH_2Ph, *c*: R= Et, *d*: R= Me

dimethyl-Δ^3-1,3,4-oxadiazoline undergoes thermal cycloreversion with a comparable rate constant at a temperature 40° higher, i.e., 100°C (2*a*). One potential source of the rate enhancement by a thio substituent is the polarizability of sulfur. Most likely, negative charge develops at positions 2 and 5 of the oxadiazoline as the ylide-like transition state (**6**) develops. Sulfur substitutents exert an anion-stabilizing role, as in anion equivalents generated from 1,3-dithiane. A second source of the rate enhancement could be a ground state energy difference between thio and oxy analogues. The 2,2-dimethoxy oxadiazoline has four electronegative moieties attached to C2, compared to three plus a sulfur-bound group for **5***a*–**5***c*. Clumping electronegative groups on the same carbon atom has the surprising effect of increasing thermodynamic stability (6).

Thermolysis of **5** in benzene afforded the corresponding carbene dimers **7** and **8** (Scheme 7), in yields ranging from 55 to 65%. The *E*:*Z* ratios ranged from 1.2 to 1.8, Table 1.

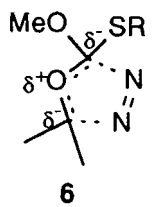

6

Table 1. Yields and isomer ratios.

Oxadiazoline	Thermolysis product		*E* : *Z*
5*a*: R = Ph	**7***a*: 35%	**8***a*: 20%	1.8
b: R = CH_2Ph	*b*: 32%	*b*: 27%	1.2
c: R = Et	*c*: 38%	*c*: 27%	1.4
d: R = Me	*d*: 32%	*d*: 27%	1.2

Preliminary assignment was based on the observation that the major product was eluted first during chromatography and that it ought to be the *E* isomer, in which all dipole vectors should cancel. That assignment was subsequently confirmed by means of the single crystal X-ray structure of **7***b*.[2] The fact that carbene dimers and acetone were major products suggests that all four oxadiazolines (**5**) fragment thermally to form N_2 and a carbonyl ylide, and that the latter fragments efficiently to afford the appropriate carbene and acetone (Scheme 7). A competitive 1,3-dipolar cycloreversion of **5***a* afforded methyl phenylthio carbonate (**9**) and, presumably, 2-diazopropane, Scheme 8.

In the ^{13}C NMR spectra of the carbene dimers, the vinyl

[2] Publication of the crystal and molecular structures will be delayed in the expectation that the data could be made more meaningful by inclusion of the structure of a *Z* isomer.

Scheme 7.

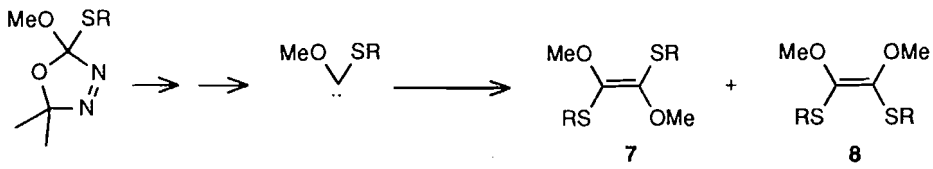

a: R= Ph, *b*: R=CH_2Ph, *c*: R= Et, *d*: R=Me

Scheme 8.

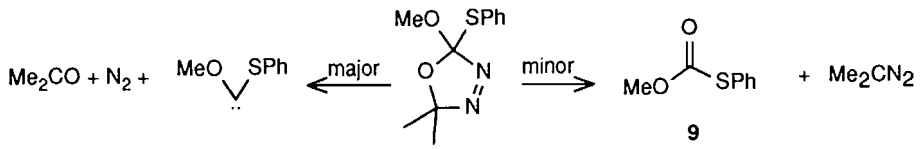

Scheme 9.

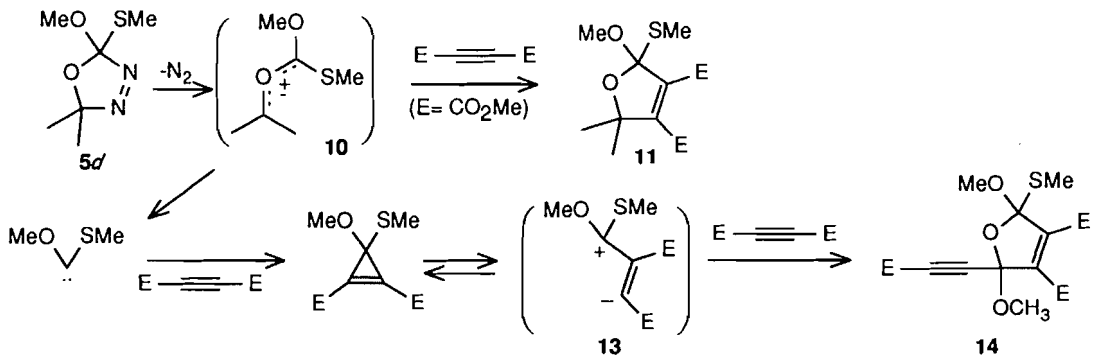

carbon signals are near δ = 143 in **7**(*a–d*) and **8**(*a–d*). For comparison, the vinylic signals of 1,2-dimethoxy-1,2-diphenoxyethenes occur near δ = 138, and those of tetraalkoxyethenes near δ = 141 (7).

Experiments designed to intercept reactive intermediates were revealing. Initial cycloreversion to N_2 and a carbonyl ylide (**10**) was inferred for the case of **5***d* from a reaction with dimethyl acetylenedicarboxylate (DMAD). The reaction mixture was complex, but it was possible to isolate what is formally the ylide–DMAD adduct (**11**), Scheme 9, along with some carbene–DMAD adduct (**14**). This result indicates that a concerted mechanism recently proposed by Smith (8), leading from a 2,2-dialkoxyoxadiazoline analogue of **5** *directly* to carbene, N_2, and acetone, may not be general. However, there is an alternative mechanism for formation of **11**, involving cycloaddition of a carbene–DMAD dipolar adduct to acetone. The fact that the acetone concentration started at zero, and remained below the final DMAD concentration throughout, makes that mechanism less likely. Nevertheless, additional experiments are needed to secure the origin of **11**.

Cycloadducts from an ylide intermediate were not obtained with the other trapping agents, ethyl crotonate, dichloromaleic anhydride, or phenyl isocyanate. Possibly the fragmentation of the ylide to carbene and acetone is fast and only very reactive dipolarophiles can compete at relatively low concentrations (ca. 0.1 M). The overall 1:2 stoichiometry leading to **14** (Scheme 9) for reaction of (methoxy)methylthiocarbene with DMAD has been reported for the case of dimethoxycarbene by Hoffmann et al. (9). A dipolar adduct similar to **13**, with vinyl carbene character, was proposed (9), Scheme 9. The reason for addition to a carbonyl group of DMAD in the second step, rather than to the triple bond, is not well understood. Steric hindrance may be responsible, in part.

Ethyl crotonate intercepted carbene intermediates although not their carbonyl ylide precursors. Thus, thermolysis of **5***a* in the presence of ethyl crotonate afforded four diastereomeric ethyl cyclopropanecarboxylates (**15**), Scheme 10, in 26% total yield. The diastereomers could not be separated but the relative yields (1:2:1.6:3.2) could be obtained from the ^{1}H NMR spectrum of the mixture by integration of the four methoxy signals. The EI and the CI mass spectra gave the appropriate $[M]^+$ and $[M + H]^+$ signals. Both carbene dimers (**7***c*, **8***c*) were detectable as minor coproducts, indicating that reaction of (ethylthio)methoxycarbene with ethyl crotonate is relatively slow. Formation of all four diastereomers of **15** is in keeping with a stepwise mechanism of cyclopropanation, as proposed by Hoffmann (9) to account for the observation that dimethoxycarbene reacts with diethyl maleate to afford only the *trans* product of cyclopropanation.

Thermolysis of **5***a* in dry benzene containing ethyl crotonate gave two diasteromeric cyclopropanes (**16***a*, **16***b*) in yields of 35 and 7%. Again, separation of those diastereomers was not achieved and the spectra of the individual isomers were gleaned from the spectra of the mixture. Assignment of structure **16***a* to the major diastereomer is tentative (Scheme 10).

An important feature that determines the different outcomes of trapping with DMAD and trapping with ethyl crotonate is

Scheme 10.

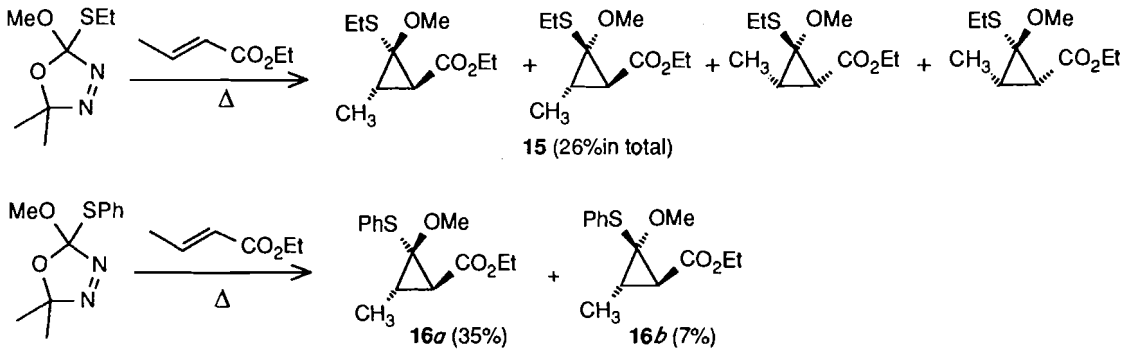

Scheme 11.

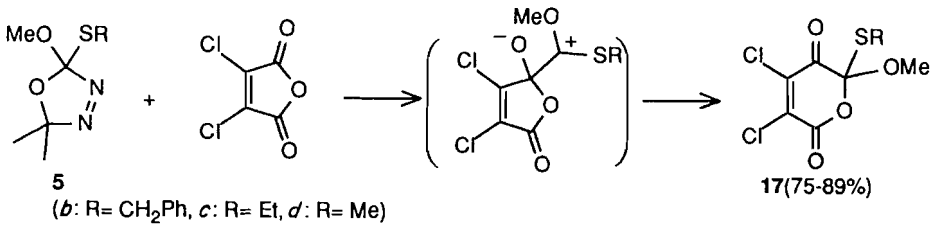

Scheme 12.

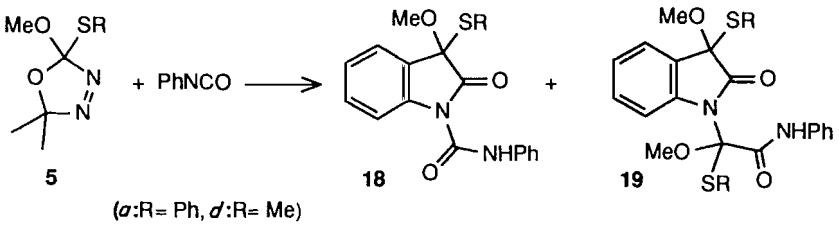

the thermal instability of cyclopropenes. Thus, whereas both reactions presumably result initially in formation of a three-membered ring, cyclopropenes with ester groups at C1 and C2 are thermally labile (10), Scheme 9, whereas cyclopropanes are relatively robust. The former therefore undergo eventual irreversible reaction through a dipolar intermediate (Scheme 9), to afford 1:2 adducts.

Reactions of the carbenes with dichloromaleic anhydride do not mimick the ones with ethyl crotonate. Overall insertion into the ring C—O bond occurs, presumably by nucleophilic addition to carbonyl carbon (3) followed by 1,2-acyloxy migration, Scheme 11. The structure of **17***d* was secured by means of single crystal X-ray diffraction.[3] Possible reasons for the failure of ethyl crotonate to undergo analogous attack include the lower reactivity of esters compared to anhydrides and a slower follow-up step that might not compete well with reversal.

Thermolysis of **5***a* and of **5***d* in benzene containing excess phenyl isocyanate afforded three products in each case. Centrifugal chromatography led to ready separation of a rapidly eluting minor product identified as 2:1 adduct **18***a* from **5***a*, and **18***d* from **5***d*, Scheme 12. *N*-Phenylcarbamoyl oxindoles such as **18** are readily recognized, having NH absorption and an intense broad carbonyl band in the infrared spectrum. The ^{1}H NMR spectrum included, in each case, a low-field doublet ($\delta \simeq 8.3, J \simeq 8$ Hz) corresponding to the oxindolyl aryl hydrogen nearest to the phenylcarbamoyl group. *N*-Acyl indoles also have an especially deshielded aryl hydrogen for the same reason: the proximity of the amide carbonyl oxygen to an aryl hydrogen separated from it by five bonds (11). An analogous product (**20**) had already been observed, from reaction of 2-diazopropane with phenyl isocyanate (12). The fact that the 2:1 adduct was a minor product was surprising, Hoffmann's group (2*b*) having identified *only* a 2:1 adduct from reaction of dimethoxycarbene with phenyl isocyanate. Also surprising was the fact that Hoffmann's product was apparently a hydantoin (Scheme 2) whereas ours, from methoxy(methylthio)carbene, was clearly an oxindole. Thermolysis of 2,2-dimethoxy-5,5-dimethyl-Δ^3-1,3,4-oxadiazoline in benzene containing phenyl isocyanate afforded the Hoffmann hydantoin (65% yield), confirming that dimethoxycarbene and methoxy(methylthio)carbene, each generated thermally from an oxadiazoline precursor, afford quite different 2:1 adducts with phenyl isocyanate.

Equally surprising was the finding that the major products from thermolysis of **5***d* (or **5***a*) in the presence of phenyl isocyanate were 2:2 adducts (**19**) obtained as mixtures of diastereomers. In the case of **19***a* the diastereomers were separable by chromatography but **19***b* could not be separated. Attempts to grow a single crystal from either diastereomer of **19***a*, for single crystal X-ray diffraction, were not successful.

[3] Publication of the details will be delayed in the expectation that an analogous structure, from either a bis(alkylthio)carbene or an alkoxyaminocarbene, will become available for comparisons.

The spectra fit the oxindole structure (**19**) well, for diastereomeric products would be expected in each case, **19***a*, **19***d*. In both cases, the ^{13}C NMR spectra and the IR spectra suggested carbonyl groups in different environments. Those features rule out the 1,4-piperazine-2,5-diones (**21**) and their isomers **22**. The ring carbonyl group and the other amide carbonyl group are in quite different environments and the ^1H NMR spectra rule out the isomeric **23**. Structures such as **23** should also show the characteristic low-field doublet (ca. 8.3 ppm, *J* ca. 8 Hz) of carbamoyl oxindoles, outlined above. Moreover, compounds **19** showed a broad singlet (δ = 7.6 and 8.3 for **19***a* and **19***d*, respectively) in the ^1H NMR spectra, as expected for NH of an amide. Finally, the mass spectra included peaks at *m/z* = 119 and *m/z* = 120, for **19***a* and **19***d*, respectively, attributable to PhNCO and PhNHCO fragments expected from **19**, but not from **23**, as well as the appropriate molecular ions.

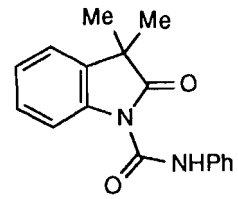

20

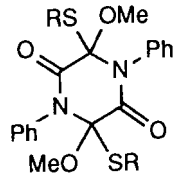

21

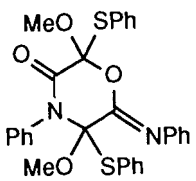

22

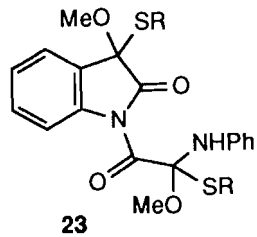

23

What structural features and mechanisms might account for the very different behaviours of dimethoxycarbene and methoxy(methylthio)carbene toward phenyl isocyanate? The connectivities of the products suggest a common first step: nucleophilic addition of the carbene to carbonyl carbon of the isocyanate to form a dipolar intermediate, as suggested by Hoffmann et al. (2*b*), Scheme 13. Presumably such an intermediate is equilibrated with the corresponding α-lactam and iminooxirane (not illustrated). We postulate that the dipolar intermediate of Scheme 2 is more stable than its analogue **24**, because the resonance contributors in the cationic portion of the former are equivalent and because the carbonyl double bond is much stronger than the thiocarbonyl double bond. As a consequence, the rate constant for intramolecular ring closure, to form the dialkoxy analogue of **25**, could be small enough to permit it to undergo intermolecular reaction (Scheme 2) with phenyl isocyanate to afford the hydantoin. On the other hand, **24** cyclizes rapidly to **25**, which cannot aromatize to **26** intramolecularly because a concerted 1,3-H shift would have to be antarafacial (13). It can accumulate, therefore, to react with **25** in an acid–base reaction, generating ion pair **27**. Collapse of the latter would generate the observed diastereomeric 2:2 adducts, **19**, Scheme 13. While this explanation is attractively simple, it is not unique and must be regarded as tentative.

Experimental

^1H NMR spectra were run with $CDCl_3$ or C_6D_6 solutions, with a 200 or a 300 MHz Bruker spectrometer, and ^{13}C spectra were acquired at 50 MHz with a Bruker AC200 spectrometer. Infrared spectra were taken from solutions in CCl_4, in a cell of 0.5 mm path length, with a Biorad FTS-40 spectrophotometer. Solvent absorptions were subtracted. The IR bands are labelled qualitatively with the symbols s and m for strong and medium intensities, respectively. Weaker bands are not labelled and very weak bands are not included. Raman spectra were obtained from neat samples, with a Jobin Yvon/ISA Mole S-3000 spectrometer.

2-Methoxy-5,5-dimethyl-2-phenylthio-Δ^3-1,3,4-oxadiazoline (5*a*)

A solution of *p*-toluenesulfonic acid (pTSA, 0.40 g) in benzene (15 mL) was refluxed for about 1 h in a flask fitted with a Dean and Stark trap containing molecular sieves in the water trapping arm. After the solution had cooled, a solution of 2-acetoxy-2-methoxy-5,5-dimethyl-Δ^3-oxadiazoline (**1**) containing **4** (total weight 5.0 g, 64% **1** by ^1H NMR assay) and thiophenol (2.0 mL) in dichloromethane (10 mL) was added. More dichloromethane (30 mL) was used to rinse traces of thiophenol solution into the flask containing pTSA and the reaction solution so obtained was refluxed under N_2 for 16 h. The solution was cooled, KOH pellets were added, and the heterogeneous mixture was stirred rapidly for 2 h. Water was added and the mixture was shaken vigorously before the organic layer was separated and extracted several times with

Scheme 13.

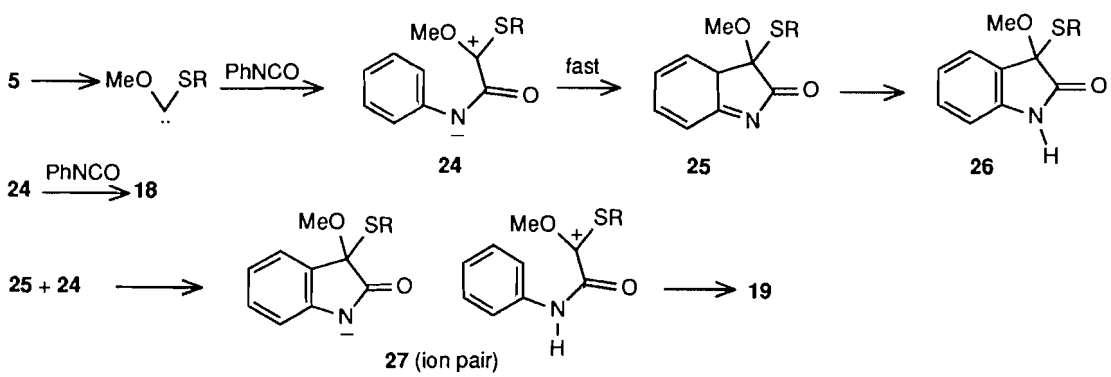

water. Drying over $MgSO_4$ and evaporation of the solvents left a residue that was chromatographed (Chromatotron, 4 mm plate, hexane) to afford the title compound as a white solid (69%), mp 38–39°C. IR (CCl_4) cm^{-1}: 3064, 2993, 2943, 2895, 2838, 1477, 1441, 1366, 1264, 1238, 1204, 1128s, 1064s, 1025, 976m, 959m, 911, 826, 692, 628, 581, 516, 479. ^1H NMR (200 MHz, $CDCl_3$) δ: 1.14 (s, 3H), 1.50 (s, 3H), 3.52 (s, 3H), 7.28–7.34 (m, 3H), 7.57–7.63 (m, 2H). ^{13}C NMR (50 MHz, $CDCl_3$) δ: 22.6, 25.0, 52.2, 122.8 (C5), 128.8, 129.0, 129.2, 135.7, 137.2. MS (EI) *m/z*: 207 ($M^+ - OCH_3$, 5), 153 ($MeOCHSPh^+$, 24), 129 ($M^+ - SPh$, 69), 109 ($C_6H_5S^+$, 100).

2-Benzylthio-2-methoxy-5,5-dimethyl-Δ^3-1,3,4-oxadiazoline (*5b*)

The procedure described above was followed. From 15 g of **1** plus **4** (63% **1**), benzyl mercaptan (5.9 mL), pTSA (1.0 g), and CH_2Cl_2 (120 mL) there was obtained, after refluxing overnight, a liquid product that was chromatographed (Chromatotron, 4 mm plate, 5% EtOAc in hexane) to afford 5.58 g (44%) of **5***b* as a clear liquid. IR (CCl_4) cm^{-1}: 3087, 3031, 2992, 2941, 2839, 1731, 1603, 1496, 1457, 1368, 1237, 1203, 1124s, 1069s, 979m, 910, 828, 703m, 625, 583, 465. ^1H NMR (200 MHz, $CDCl_3$) δ: 1.53 (s, 3H), 1.57 (s, 3H), 3.40 (s, 3H), 4.09 (d, $^2J = -12.7$ Hz, 1H), 4.20 (d, $^2J = -12.7$ Hz, 1H), 7.24–7.36 (m, 5H). ^{13}C NMR (50 MHz, $CDCl_3$) δ: 23.1, 24.8, 34.8, 51.5, 122.6 (C5), 127.1, 128.4, 128.9, 136.6, 137.1. MS (EI) *m/z*: 221 ($M^+ - OCH_3$, 2), 183 ($M^+ - N_2 - C_3H_5$, 5), 167 ($MeOCHSCH_2Ph^+$, 14), 135 ($PhCH_2CS^+$, 17), 133 ($M^+ - N_2 - PhCH_2$, 37), 129 ($M^+ - SCH_2Ph$, 62), 91 (100), 73 (70). MS (CI, NH_3) *m/z*: 270 ($M^+ + NH_4$).

2-Ethylthio-2-methoxy-5,5-dimethyl-Δ^3-1,3,4-oxadiazoline (*5c*)

The exchange method described above was used, with impure oxadiazoline **1** (15.0 g of **1** + **4**, containing 10.5 g, 0.056 mol of **1**), ethanethiol (4.69 mL, 0.062 mol, 97% pure), and pTSA (1.06 g, 5.6 mmol, dried by azeotropic distillation of a benzene solution) in CH_2Cl_2 (120 mL). Heating at reflux for 17 h, cooling, addition of KOH pellets (ca. 2 g), and stirring for several hours caused a change in colour to pale yellow. Addition of water, shaking, separation, and drying of the organic phase and evaporation of the solvent left a residual oil that was chromatographed on silica gel (5% EtOAc in hexane) to afford **5***c* as a clear liquid (6.05 g, 57%). IR (CCl_4) cm^{-1}: 2991, 2938, 2874, 2837, 1456m, 1371, 1268, 1237, 1203m, 1180, 1124s, 1070s, 977m, 910m, 827, 685, 580, 486. ^1H NMR (200 MHz, $CDCl_3$) δ: 1.35 (t, $J = 7.5$ Hz, 3H), 1.54 (s, 3H), 1.57 (s, 3H), 2.81 (dq, $J = 7.5$ and -12.9 Hz, 1H), 2.95 (dq, $J = 7.5$ and -12.9 Hz, 1H), 3.44 (s, 3H). ^1H NMR (200 MHz, C_6D_6) δ: 1.17 (t, $J = 7.4$ Hz, 3H), 1.20 (s, 3H), 1.27 (s, 3H), 2.66 (dq, $J = 7.4$ and -13.0 Hz, 1H), 2.88 (dq, $J = 7.4$ and -13.0 Hz, 1H), 3.20 (s, 3H). ^{13}C NMR (50 MHz, $CDCl_3$) δ: 15.2, 23.0, 24.5, 24.7, 51.3, 122.0 (C5), 136.9 (C2). MS (EI) *m/z*: 129 ($M^+ - SEt$, 8), 105 (10), 84 (28). MS (CI, NH_3): 189 ($M^+ - H$).

2-Methoxy-2-methylthio-5,5-dimethyl-Δ^3-1,3,4-oxadiazoline (*5d*)

A solution of *p*-toluenesulfonic acid (1.0 g, 0.005 mol) in benzene (30 mL) was refluxed in a Dean and Stark apparatus. The dried portion was added to a solution of **2** (15 g of **1** (63%) containing **4**) in dry CH_2Cl_2 (120 mL). Cold methyl mercaptan, collected in a Dry Ice trap after passage of the gas through a tube packed with anhydrous $MgSO_4$, was added from a syringe. The reaction vessel was sealed and maintained at 45°C overnight in an oil bath. Its contents were then transferred to a 250 mL flask containing ca. 2 g of KOH pellets. Vigorous stirring for a few hours, followed by addition of water, shaking, separation, extraction of the organic phase with water, drying, and removal of the solvent, left a residue that was subjected to column chromatography to afford pure **5***d* as a clear liquid, 7.08 g (80%). IR (CCl_4) cm^{-1}: 2993, 2940, 2893, 1561, 1459, 1437, 1367, 1237, 1203, 1124, 1072s, 999, 980, 910, 827, 702, 682, 626, 581. ^1H NMR (200 MHz, $CDCl_3$) δ: 1.55 (s, 3H) 1.57 (s, 3H), 2.33 (s, 3H), 3.46 (s, 3H). ^1H NMR (200 MHz, C_6D_6) δ: 1.20 (s, 3H), 1.25 (s, 3H), 2.09 (s, 3H), 3.20 (s, 3H). ^{13}C NMR (50 MHz, $CDCl_3$) δ: 12.9, 23.2, 24.9, 51.4, 122.6 (C5), 136.6 (C2). MS (EI) *m/z*: 176 (M^+, 1), 145 ($M^+ - OCH_3$, 3), 129 ($M^+ - SCH_3$, 24), 90 (34), 75 (100). MS (CI, NH_3) 177 ($M^+ + H$).

Thermolysis of 2-methoxy-5,5-dimethyl-2-phenylthio-Δ^3-1,3,4-oxadiazoline in benzene

A solution of **5***a* (0.209 g, 0.878 mmol) in benzene (10 mL) was refluxed overnight under N_2 in a Dean and Stark apparatus. The residue left after evaporation of the solvent consisted of methyl phenylthio carbonate **9** (0.0103 g, 7%), *E*-1,2-dimethoxy-1,2-di(phenylthio)ethene **7***a* (0.0467 g, 35%), and the corresponding *Z* isomer **7***b* (0.0267 g, 20%), as determined by chromatographic separation (Chromatotron, 1 mm plate).

A similar thermolysis, in which *p*-xylene served as ^1H NMR standard for integration, gave $k(60°C) = 2.04 \times 10^{-5}$ s^{-1} and yields (not isolated) of 8, 48, 40, and 62% for **9**, **7***a*, **7***b*, and acetone, respectively. Methyl phenylthio carbonate was a clear liquid. IR (CCl_4) cm^{-1}: 3066, 3008, 2954, 2888, 2836, 1730s, 1584, 1480, 1435, 1189m, 1143s, 1093, 1025, 689, 673, 556, 532. ^1H NMR (200 MHz, $CDCl_3$) δ: 3.84 (s, 3H), 7.39–7.42 (m, 3H), 7.51–7.55 (m, 2H). ^{13}C NMR (50 MHz, $CDCl_3$) δ: 54.5, 127.6, 129.2, 129.6, 134.8, 170.2. MS (EI, GC/MS) *m/z*: 168 (M^+, 38), 137 ($M^+ - OCH_3$, 3), 124 (16), 109 (100), 91 (32), 78 (22), 69 (23), 65 (37). An authentic sample, synthesized by treating methyl chloroformate with thiophenol in the presence of pyridine, had matching spectral characteristics.

E *Dimer of (methoxy)phenylthiocarbene, 7*a

The *E* dimer was a white solid, mp 53–55°C. IR (CCl_4) cm^{-1}: 3065, 3007, 2963, 2932, 2892, 2830, 1796, 1718, 1657, 1583m, 1479m, 1442m, 1265, 1206s, 1146s, 1121, 1081, 1023, 1003, 954, 909, 870, 832, 692s, 520. ^1H NMR (200 MHz, $CDCl_3$) δ: 3.55 (6H), 7.17–7.42 (m, 10H). ^{13}C NMR (50 MHz, $CDCl_3$) δ: 58.5, 126.7, 129.0, 129.5, 133.6, 142.8. MS (EI) *m/z*: 304 (M^+, 100), 261 [$(PhS)_2COMe^+$, 91], 218 (32), 195 (13), 153 (28), 109 (PhS^+, 75).

Z *Dimer of (methoxy)phenylthiocarbene, 8*a

Clear liquid. IR (CCl_4) cm^{-1}: 3066, 3004, 2965, 2935, 2894, 2832, 1774, 1725, 1581m, 1479m, 1442, 1264, 1198s, 1122 br, 1085, 1025m, 1006, 959, 880, 692m, 566. ^1H NMR (200 MHz, $CDCl_3$) δ: 3.67 (s, 6H), 7.15–7.36 (m, 10H). ^{13}C NMR (50 MHz, $CDCl_3$) δ: 58.6, 126.4, 128.3, 129.1, 134.2, 143.2. MS (EI) *m/z*: 304 (M^+, 100), 261 (90), 195 (14), 109 (75).

Thermolysis of 5*a* in presence of ethyl crotonate

A solution of **5***a* (0.1201 g, 0.504 mmol) and ethyl crotonate (Aldrich, 96%, predominantly *E* isomer, 0.08 mL, 0.60 mmol) in benzene (10 mL) was sealed into a 100 mL glass tube that was then heated in an oil bath (70°C) overnight. The solvent was removed and the residue was chromatographed (Chromatotron, 1 mm plate, washed with Et_3N in hexane, elution with hexane). Five products were isolated: a pair of ethyl cyclopropane carboxylates, **16***a* and **16***b*, **9**, and the carbene dimers **7***a* and **8***a*.

E,Z-*Ethyl 2-methoxy-3-methyl-2-phenylthiocyclopropanecarboxylate (**16**a)*: Major product, 0.0469 g, 35% yield, clear oil. IR (CCl_4) cm^{-1}: 3064, 2981m, 2965m, 2934m, 2903, 2878, 2829, 1735s, 1584, 1480m, 1444m, 1416, 1367, 1318s, 1265m, 1228m, 1201m, 1170 br, 1117m, 1098m, 1049m, 1024, 998m, 911, 864, 692. ^1H NMR (200 MHz, $CDCl_3$) δ: 1.25 (d, J = 6.4 Hz) overlapping δ 1.27 (t, J = 7.1 Hz), sum 6H, 1.83 (d, J = 6.8 Hz, 1H), 2.27 (5 lines, 1H), 3.37 (s, 3H), 4.181 (q, J = 7.1 Hz) overlapping 4.188 (q, J = 7.1 Hz), sum 2H, 7.15–7.28 (m, 3H), 7.44–7.48 (m, 2H). ^{13}C NMR (50 MHz, $CDCl_3$) δ: 14.2, 28.9, 36.5, 54.9, 60.9, 78.2, 110.7, 126.1, 128.6, 128.8, 134.7, 168.7. MS (EI) *m/z*: 266 (M^+, 3), 235 ($M^+ - OCH_3$, 18), 220 (100), 205 (25), 193 (85), 157 (89), 129 (45), 109 (50), 69 (47). MS (CI, NH_3) *m/z*: 284 ($M^+ + NH_4$, 74), 267 ($M^+ + H$, 39).

Z,E-*Ethyl 2-methoxy-3-methyl-2-phenylthiocyclopropanecarboxylate (**16**b)*: Minor diastereomer, ca. 7%. This product was obtained as a mixture with **16***a* and only a part of the ^1H NMR spectrum was assignable. ^1H NMR (200 MHz, $CDCl_3$) δ: 1.15 (t, J = 7.1 Hz, 3H), 1.27 (m), 1.87 (d, J = 7.2 Hz, 1H), 2.03 (5 lines, 1H), 3.48 (s, 3H), 4.02 (m, 2H), 7.17–7.58 (m).

Thermolysis of 5*a* in presence of phenyl isocyanate

A solution of **5***a* (0.204 g, 0.858 mmol) and phenyl isocyanate (0.19 mL, 1.7 mmol) in benzene (8 mL) was sealed into a glass tube that was then immersed overnight in an oil bath kept at 70°C. Evaporation of the solvent left a residue that was chromatographed (Chromatotron, 1 mm plate) on SiO_2 with hexane. After the first product (**18***a*) had been eluted the solvent was gradually changed to 5% EtOAc in hexane. Two additional products, diastereomers **19***a*, were eluted slowly. Yields of isolated materials were 10, 39, and 28%, respectively.

*3-Methoxy-1-phenylcarbamoyl-3-phenylthio-oxindole, (**18**a)*: White solid, 0.0335 g, mp 139–140°C, 10%. IR (CCl_4) cm^{-1}: 3260, 3064, 2948, 2891, 2832, 1748s, 1600m, 1552s, 1503, 1470m, 1448, 1340, 1310, 1277, 1243, 1204, 1163m, 1112, 1088, 1022, 970, 913, 693m, 574, 505. ^1H NMR (200 MHz, $CDCl_3$) δ: 3.56 (s, 3H), 7.03–7.15 (m, 3H), 7.33–7.58 (m, 9H), 8.32 (d, J = 8.3 Hz, 1H), 10.36 (s, br, 1H). ^{13}C NMR (50 MHz, $CDCl_3$) δ: 53.8, 87.9, 116.8, 120.7, 124.2, 124.5, 124.7, 124.8, 128.8, 129.1, 130.0, 130.9, 136.6, 136.8, 138.5, 149.0, 173.6. MS (EI) *m/z*: 314 (3), 281 (15), 162 (100), 119 (52), 91 (18). MS (CI, NH_3) *m/z*: 391 ($M^+ + H$).

*Major diastereomer of oxindole **19**a*: White solid, mp 169–171°C, 39% (isolated). IR (CCl_4) cm^{-1}: 3411, 3362, 3063, 3034, 2962, 2943, 2891, 2833, 1746s, 1718m, 1604m, 1527s, 1468, 1442m, 1336, 1311, 1279, 1243, 1183, 1158, 1086 br, 1075m, 986, 909s, 692m, 660, 503. ^1H NMR (200 MHz, $CDCl_3$) δ: 3.52 (s, 3H), 3.58 (s, 3H), 6.86–7.54 (m, 20H). ^{13}C NMR (50 MHz, $CDCl_3$) δ: 51.2, 54.2, 87.7, 99.0, 111.7, 119.6, 119.9, 123.5, 124.6, 124.8, 125.1, 128.6, 128.7, 128.8, 129.0, 129.6, 129.9, 130.3, 136.1, 136.8, 137.4, 139.7, 162.2, 172.2. MS (EI) *m/z*: 447 (18), 433 (26), 405 (55), 272 (13), 162 (100), 146 (37), 120 (65), 110 (81), 109 (67), 77 (40). MS (CI, NH_3) *m/z*: 560 ($M^+ + NH_4$).

*Minor diastereomer of oxindole **19**a*: White solid, mp 171–173°C, 28% (isolated). IR (CCl_4) cm^{-1}: 3413, 3396, 3061, 2961, 2891, 2830, 1744s, 1719m, 1604m, 1525s, 1468, 1442m, 1337, 1312m, 1281, 1243, 1193, 1117, 1087, 1087, 1066 br, 986, 947, 909, 824, 691m, 504. ^1H NMR (200 MHz, $CDCl_3$) δ: 3.62 (s, 3H), 3.68 (s, 3H), 6.80 (m), 7.01–7.38 (m, 13H), 7.51–7.55 (m, 4H), 7.62 (s, br, 1H). ^{13}C NMR (50 MHz, $CDCl_3$) δ: 51.4, 53.6, 87.7, 99.6, 112.1, 119.6, 123.2, 124.2, 124.6, 125.0, 128.5, 128.7, 128.8, 129.0, 129.4, 129.6, 129.8, 130.0, 136.4, 137.0, 137.3, 139.5, 161.9, 171.9. MS (EI) *m/z* (rel. intensity): 433 ($M^+ - SPh$, 22), 405 (34), 272 (13), 162 (100), 110 (26), 109 (31), 77 (32). MS (CI, NH_3) *m/z*: 560 ($M^+ + NH_4$).

Thermolysis of 2-benzylthio-2-methoxy-5,5-dimethyl-Δ^3-1,3,4-oxadiazoline in benzene

A solution of **5***b* (0.1553 g, 0.615 mmol) in benzene (10 mL) was refluxed overnight under N_2 in a Dean and Stark apparatus. The final solution contained acetone and the *E* and *Z* isomers of 1,2-bis(benzylthio)-1,2-dimethoxyethene. Chromatography of the latter (Chromatotron, 1 mm plate, hexane) afforded the *E* isomer **7***b* followed by the *Z* isomer **8***b*. The ratio *E*:*Z* ranged from 1.38 to 1.19 from three runs.

E-*1,2-Bis(benzylthio)-1,2-dimethoxyethene (**7**b)*: White solid, mp 82–84°C, 0.0205 g, 32% yield. IR (CCl_4) cm^{-1}: 3086, 3064, 3031, 3003, 2962, 2933, 2894, 2827, 1716, 1601, 1496, 1454, 1427, 1263, 1238, 1203s, 1136s, 1112, 1071, 954m, 915, 871, 700, 672, 561, 472. ^1H NMR (200 MHz, $CDCl_3$) δ: 3.21 (s, 6H), 3.75 (s, 4H), 7.15–7.30 (m, 10H). ^{13}C NMR (50 MHz, $CDCl_3$) δ: 35.9, 57.9, 126.9, 128.3, 128.8, 138.6, 143.5. MS (EI) *m/z*: 332 (M^+, 4), 241 ($M^+ - CH_2Ph$, 45), 91 ($PhCH_2^+$, 100). MS (CI, NH_3) *m/z*: 333 ($M^+ + H$).

Z-*1,2-Bis(benzylthio)-1,2-dimethoxyethene (**8**b)*: Yellow oil, 0.0173 g, 27% yield. ^1H NMR (200 MHz, $CDCl_3$) δ: 3.54 (s, 6H), 3.63 (s, 4H), 7.19–7.31 (m, 10H). ^{13}C NMR (50 MHz, $CDCl_3$) δ: 37.1, 58.6, 127.0, 128.3, 129.0, 137.9, 144.1. MS (EI) *m/z*: 332 (M^+, 6), 241 ($M^+ - CH_2Ph$, 68), 91 ($PhCH_2^+$, 100). MS (CI, NH_3) *m/z*: 333 ($M^+ + H$, 100).

Thermolysis of 5*b* in presence of dichloromaleic anhydride

A solution of **5***b* (0.2046 g, 0.8106 mmol) and dichloromaleic anhydride (0.150 g, 0.898 mmol) in benzene (10 mL) was heated overnight at 80°C in a sealed tube. Removal of the solvent and Kugelrohr distillation of the residue gave a yellow crystalline product, 3,4-dichloro-6-benzylthio-6-methoxy-2*H*-pyran-2,5-(6*H*)-dione (**17***b*), mp 69–70°C, 75%. The product did not survive an attempt at chromatography on silica gel. IR (CCl_4) cm^{-1}: 3087, 3032, 2949, 2894, 2840, 1762s, 1721s, 1583s, 1497, 1457, 1414, 1273m, 1234m, 1196m, 1163s,

1040, 982m, 908, 885, 701s, 666m. ^{1}H NMR (200 MHz, $CDCl_3$) δ: 3.54 (s, 3H), 3.75 (s, 2H), 7.29 (s, br, 5H). ^{13}C NMR (50 MHz, $CDCl_3$) δ: 35.0, 52.5, 108.9, 127.7, 128.7, 129.1, 135.0, 136.8, 141.3, 152.6, 173.5. MS (EI) *m/z*: 337 (3), 335 (7), 333 (10) (M^+ + H), 259 (18), 214 (11), 212 (65), 210 (94), 185 (13), 183 (70), 181 (100), 123 (23), 91 (20). MS (CI, NH_3) *m/z*: 354 (16), 352 (65), 350 (100) ($M^+ + NH_4$), 337 (8), 335 (25), 333 (35), (M^+ + H).

Thermolysis of 5*c* in benzene

A solution of **5***c* (0.1629 g, 0.856 mmol) in benzene (ca. 1 mL) was sealed into an NMR tube. Thermolysis at 60°C, followed by ^{1}H NMR spectroscopy, gave $k(60°C) = 2.1 \times 10^{-5}$ s^{-1}. Acetone and the diastereomeric 1,2-bis(ethylthio)-1,2-dimethoxyethenes were predominant products. Separation of the latter (Chromatotron, hexane) gave *E*-1,2-bis(ethylthio)-1,2-dimethoxyethene (**7***c*, 0.0304 g, 38%) and the *Z* isomer (**8***c*, 0.0250 g, 27%) as clear liquids.

E-*1,2-Bis(ethylthio)-1,2-dimethoxyethene* (**7**c): IR (GC/FTIR) cm^{-1}: 2976m, 2940s, 2887, 2832, 1457 br, 1383, 1310, 1267, 1188, 1079 br, 975, 937, 904, 825, 762, 712. Raman (neat) cm^{-1}: 1581.4, 653.4. ^{1}H NMR (200 MHz, $CDCl_3$) δ: 1.25 (t, *J* = 7.3 Hz, 6H), 2.66 (q, *J* = 7.3 Hz, 4H), 3.61 (s, 6H). ^{13}C NMR (50 MHz, $CDCl_3$) δ: 15.1, 25.4, 58.0, 143.1. MS (EI) *m/z*: 208 (M^+, 15), 193 ($M^+ - CH_3$, 4), 179 ($M^+ - CH_2CH_3$, 29), 165 (13), 135 (3), 49 (100). MS (CI, NH_3) *m/z*: 209 (M^+ + H).

Z-*1,2-Bis(ethylthio)-1,2-dimethoxyethene* (**8**c): IR (GC/FTIR) cm^{-1}: 2972, 2939m, 2887, 2836, 1579, 1457, 1381, 1265, 1194s, 1114 br, 1026, 967, 863, 764. Raman (neat) cm^{-1}: 1596, 655.7. ^{1}H NMR (200 MHz, $CDCl_3$) δ: 1.27 (t, *J* = 7.3 Hz, 6H), 2.65 (q, *J* = 7.3 Hz, 4H), 3.68 (s, 6H). ^{13}C NMR (50 MHz, $CDCl_3$) δ: 14.7, 26.4, 58.8, 143.4. MS (EI) *m/z*: 208 (M^+, 83), 193 ($M^+ - CH_3$, 15), 179 ($M^+ - CH_2CH_3$, 100), 165 (44), 135 (2). MS (CI, NH_3) *m/z*: 209 (M^+ + H).

Thermolysis of 5*c* in the presence of dichloromaleic anhydride

A solution of **5***c* (0.197 g, 1.03 mmol) in benzene (10 mL) containing dichloromaleic anhydride (0.190 g, 1.14 mmol) was heated at 70°C overnight. Kugelrohr distillation of the residue left after removal of the solvent afforded **17***c*, mp 71–74°C. IR (CCl_4) cm^{-1}: 2950, 2881, 1807, 1761s, 1722m, 1583, 1458, 1266, 1236, 1196, 1160m, 1102, 1040s, 982, 909, 886, 827, 667, 527, 478. ^{1}H NMR (200 MHz, $CDCl_3$) δ: 1.24 (t, *J* = 7.5 Hz, 3H), 2.52 (dq, *J* = −12.8 Hz, 7.5 Hz, 1H), 2.60 (dq, *J* = −12.8, 7.5 Hz, 1H), 3.69 (s, 3H). ^{13}C NMR (50 MHz, $CDCl_3$) δ: 13.6, 24.7, 52.5, 109.0, 136.6, 141.2, 152.7, 173.6. MS (EI) *m/z*: 275 (M^+ + H, 2), 273 (M^+ + H, 4), 271 (M^+ + H, 6), 235 ($M^+ - {}^{35}Cl$, 6), 213 (13), 211 (28), 209 (19), 185 (20), 183 (73), 181 (100). MS (CI, NH_3) *m/z*: 292 (4), 290 (13), 288 (20), ($M^+ + NH_4$), 275 (20), 273 (95), 271 (100), (M^+ + H).

Thermolysis of 5*d* in benzene

A solution of **5***d* (0.37 g, 2.1 mmol) in benzene (15 mL) was refluxed overnight. Chromographic separation of the products (Chromatotron, 2 mm plate, hexane) gave the *E* and *Z* dimers of (methoxy)methylthiocarbene, 0.1225 g (32%) and 0.1005 g (27%), respectively, both oils.

E-*1,2-Bis(methylthio)-1,2-dimethoxyethene* (**7**d): IR (GC/FTIR) cm^{-1}: 3005, 2963, 2938m, 2909, 2839, 1445, 1319, 1203s, 1143s, 1023s, 960, 807. ^{1}H NMR (200 MHz, $CDCl_3$) δ: 2.20 (s, 6H), 3.63 (s, 6H). ^{13}C NMR (50 MHz, $CDCl_3$) δ: 14.5, 58.2, 142.8. MS (EI, GC/MS) *m/z*: 180 (M^+, 10), 165 ($M^+ - CH_3$, 22), 137 ($M^+ - CH_3CO$, 74), 75 (100). MS (CI, NH_3) *m/z*: 181 (M^+ + H).

Z-*1,2-Bis(methylthio)-1,2-dimethoxyethene* (**8**d): IR (GC/FTIR) cm^{-1}: 3002, 2938m, 2838, 1584, 1445, 1315, 1194s, 1115 br, 1030, 964, 866. ^{1}H NMR (200 MHz, $CDCl_3$) δ: 2.21 (s, 6H), 3.68 (s, 6H). ^{13}C NMR (50 MHz, $CDCl_3$) δ: 15.3, 58.8, 143.0. MS (EI, GC/MS) *m/z*: 180 (M^+, 10), 165 ($M^+ - CH_3$, 23), 137 ($M^+ - CH_3CO$, 79), 75 (100). MS (CI, NH_3) *m/z*: 181 (M^+ + H).

Thermolysis of 5*d* in the presence of dichloromaleic anhydride

A solution of **5***d* (0.2077 g, 1.18 mmol) and dichloromaleic anhydride (0.22 g, 1.3 mmol) in benzene (10 mL) was kept at 80°C, overnight, in a sealed tube. Evaporation of the solvent and Kugelrohr distillation of the residue gave 0.2575 g of **17***d* (85%) as a yellow solid, mp 89–91°C. IR (CCl_4) cm^{-1}: 3502, 2995, 2948, 2839, 1805m, 1762s, 1721s, 1631, 1584s, 1460, 1436, 1271s, 1236s, 1196s, 1162 br, 1042 br, 962, 909, 887, 826, 670m, 596, 526. ^{1}H NMR (200 MHz, $CDCl_3$) δ: 2.06 (s, 3H), 3.70 (s, 3H). ^{13}C NMR (50 MHz, $CDCl_3$) δ: 12.9, 52.2, 108.6, 136.5, 141.2, 152.6, 172.7. MS (EI) *m/z*: 256 (M^+, 2), 225 ($M^+ - OCH_3$, 2), 223 (5), 221 ($M^+ - {}^{35}Cl$, 15), 213 (3), 211 (13), 209 ($M^+ - SCH_3$, 18), 199 (13), 197 (18), 185 (9), 183 (45), 181 (71). MS (CI, NH_3) *m/z*: 278 (6), 276 (20), 274 (28), 261 (15), 259 (56), 257 (100). Structure **17***d* was confirmed by single crystal X-ray diffraction.

Thermolysis of 2,2-dimethoxy-5,5-dimethyl-Δ^3-1,3,4-oxadiazoline in the presence of phenyl isocyanate

A solution of the oxadiazoline (4) (0.010 g, 0.063 mmol) and phenyl isocyanate (0.051 g, 0.43 mmol) in benzene (0.5 mL) was degassed by means of freeze–pump–thaw cycles and sealed under vacuum into a glass tube. The tube was immersed in an oil bath, kept at 100°C, for 4 days. It was then opened, and the volatiles were distilled off under vacuum, with the maximum pot temperature limited to 100°C. The residue was chromatographed (Chromatotron, silica, hexanes) on a plate that had been pretreated with triethylamine in hexanes (1:20). The yield of the Hoffmann hydantoin (2) was 65% (by ^{1}H NMR), mp 131–132°C (lit. (2) mp 129–130°C).

5,5-Dimethoxy-1,3-diphenyl-2,4-imidazolidinedione (hydantoin): ^{1}H NMR (200 MHz, $CDCl_3$) δ: 3.56 (s, 6H), 7.24–7.57 (m, 8H), 7.61 (d, *J* = 1.5 Hz, 2H). ^{13}C NMR (50 MHz, $CDCl_3$) δ: 52.5, 103.9, 125.3, 126.1, 127.2, 128.6, 129.0, 129.1, 130.5, 133.2, 152.3, 165.3. MS (EI) *m/z*: 281 (M^+ − OMe), 193, 165, 116. The ^{13}C NMR spectrum is in excellent agreement with that reported by Hoffmann et al. (*2b*) for the analogue from *p*-tolyl isocyanate.

Thermolysis of 5*d* in the presence of phenyl isocyanate

A solution of **5***d* (0.50 g, 2.4 mmol) and phenyl isocyanate (0.63 mL, 5.8 mmol) in benzene (25 mL) was refluxed under N_2 for 16 h. The benzene was evaporated and methanol was

added (stirring for 1 h) to destroy excess isocyanate. Excess methanol was evaporated and the residue was chromatographed. Three products, a 2:1 adduct (**18***d*, 8%) and diastereomeric 2:2 adducts (**19***d*, 34%, mp 181–182°C (MeOH), diastereomer ratio 2:1) were found.

*3-Methoxy-3-methylthio-1-phenylcarbamoyloxindole (**18**d)*: Melting point 106–108°C. IR (CCl_4) cm^{-1}: 3298 br, 3259 br, 3145, 3082, 2959, 2931, 1748s, 1601s, 1553s, 1501, 1466m, 1448m, 1339m, 1311, 1277m, 1242m, 1209, 1166m, 1154, 1108m, 1087, 1024, 691, 677, 575, 506. ^1H NMR (300 MHz, $CDCl_3$) δ: 2.38 (s, 3H), 3.43 (s, 3H), 7.14–7.61 (m, 9H), 8.37 (d, J = 8.0 Hz, 1H), 10.48 (br, 1H). ^{13}C NMR (50 MHz, $CDCl_3$) δ: 10.9, 53.1, 117.0, 120.6, 124.4, 124.7, 125.1, 129.1, 131.2, 136.9, 138.8, 149.1, 174.1. MS (EI) *m/z*: 328 (M^+, 6), 281 ($M^+ - SCH_3$, 48), 207 (4), 162 (100), 146 (6), 119 (24). MS (CI, NH_3): 346 ($M^+ + NH_4$, 14), 329 ($M^+ + H$, 17).

Major diastereomer of oxindole **19**d: IR (CCl_4, υ_{max}) cm^{-1}: 3414 br, 3061, 2931, 2832, 1746s, 1604m, 1525s, 1465, 1442m, 1338, 1309, 1279, 1243, 1196, 1180, 1117, 1095 br, 1073, 690. ^1H NMR (200 MHz, $CDCl_3$) δ: 2.12 (s, 3H), 2.39 (s, 3H), 3.33 (s, 3H) 3.54 (s, 3H). Minor diastereomer: 2.13 (s, 3H), 2.36 (s, 3H), 3.40 (s, 3H), 3.53 (s, 3H); composite signals: 7.08–7.61 (m), 8.23 (s, br), 8.41 (s, br). ^{13}C NMR of 2:1 mixture (50 MHz, $CDCl_3$) δ: 10.8, 12.5, 51.2, 51.3, 53.4, 53.9, 82.6, 83.1, 96.6, 96.7, 109.0, 110.0, 111.0, 112.4, 112.8, 119.8, 119.9, 123.9, 124.6, 124.7, 124.9, 125.1, 129.1, 129.2, 130.8, 136.4, 136.6, 140.1, 162.9, 163.1, 172.9. MS (EI) *m/z*: 387 (M^+ − OMe, 4), 371 (M^+ − SMe, 85), 343 (100), 298 (10), 270 (40), 210 (45), 208 (99), 162 (94), 119 (19), 77 (20). MS (CI, NH_3) *m/z*: 436 ($M^+ + NH_4$).

Thermolysis of 5*d* in the presence of dimethyl acetylenedicarboxylate

A solution of **5***d* (0.329 g, 1.87 mmol) and DMAD (0.46 mL, 3.7 mmol) in benzene (20 mL) was heated at 70°C for 16 h in a sealed tube. Thin-layer chromatography of the residue left after removal of the benzene showed five compounds. Only three of them were characterized, a minor compound that had the NMR properties expected for dihydrofuran **11**, and an inseparable mixture of diastereomers **14**.

*2-Methoxy-5,5-dimethyl-2-methylthio-3,4-bis(methoxycarbonyl)-2,5-dihydrofuran (**23**)*: Clear liquid, 6% yield. ^1H NMR (300 MHz, $CDCl_3$) δ: 1.54 (s, 3H), 1.57 (s, 3H), 2.11 (s, 3H), 3.48 (s, 3H), 3.81 (s, 3H), 3.86 (s, 3H). ^{13}C NMR (50 MHz, $CDCl_3$) δ: 13.1, 26.0, 27.3, 51.3, 52.5, 52.7, 88.5, 116.7, 137.7, 141.8, 162.2, 163.0.

cis- *and* trans-*2,5-Dimethoxy-3,4-bis(methoxycarbonyl)-5-[methyl(3-propiolato)]-2-methylthio-2,5-dihydrofuran (**14**, 10%)*: Isomer ratio 1.7:1.0; spectroscopic properties those of the mixture. IR (CCl_4) cm^{-1}: 3008, 2952, 2894, 2839, 1730 br, 1681, 1458, 1436, 1328, 1266 s, 1235 m, 1183, 1116, 1098, 1077, 1038, 1020, 988, 956, 918, 873, 692, 578. ^1H NMR (300 MHz, $CDCl_3$) δ: 2.12 (s), 2.13 (s), 3.49 (s), 3.62 (s), 3.63 (s), 3.81 (s), 3.85 (s), 3.91 (s). ^{13}C NMR (75 MHz, $CDCl_3$) δ: 12.4, 12.6, 52.8, 52.9, 53.0, 53.1, 77.9, 78.1, 78.3, 78.6, 102.1, 118.8, 132.9, 133.0, 143.1, 143.3, 152.8, 159.5, 159.6, 161.7. MS (EI) *m/z*: 374 (M^+, 2), 343 (9), 327 (100), 315 (7), 157 (61), 59 (22). MS (CI, NH_3): 392 ($M^+ + NH_4$, 7), 375 ($M^+ + H$, 8).

Acknowledgements

This work was supported by the Natural Sciences and Engineering Research Council of Canada. The authors are grateful to Mr. Fajar Ramelan and to Dr. Richard Smith for the mass spectrometric data. The assistance of Mr. George Timmins with Raman spectroscopy and the X-ray crystallography by Dr. Jim Britten are also gratefully acknowledged.

References

1. (*a*) C. Gerninghaus, A. Kummell, and G. Seitz. Chem. Ber. **126**, 733 (1993); (*b*) C.-S. Ge, E.A. Jefferson, and R.A. Moss. Tetrahedron Lett. **34**, 7549 (1993); (*c*) R.A. Moss, W. Liu, and C.-S. Ge. J. Phys. Org. Chem. **6**, 376 (1993); (*d*) R.A. Moss, E.G. Jang, H. Fan, M. Włostowski, and K. Krogh-Jespersen. J. Phys. Org. Chem. **5**, 104 (1992); (*e*) A.J. Arduengo III, H.V. Rasika Dias, R.L. Harlow, and M. Kline. J. Am. Chem. Soc. **114**, 5530, 1992; (*f*) G. Homberger, W. Kirmse, and R. Lelgemann. Chem. Ber. **124**, 1867 (1991); (*g*) X.-M. Du, H. Fan, J.L. Goodman, M.A. Kesselmayer, K. Krogh-Jespersen, J.A. LaVilla, R.A. Moss, S. Shen, and R.S. Sheridan. J. Am. Chem. Soc. **112**, 1920 (1990); (*h*) R.A. Moss. Acc. Chem. Res. **22**, 15 (1989); (*i*) R. Bonneau, M.T.H. Liu, and R.V. Suresh. J. Phys. Chem. **93**, 4802 (1989); (*j*) R.A. Moss, M. Włostowski, S. Shen, K. Krogh-Jespersen, and A. Matro. J. Am. Chem. Soc. **110**, 4443 (1988); (*k*) R.A. Moss, S. Shen, and M. Włostowski. Tetrahedron Lett. **29**, 6417 (1988); (*l*) R.S. Sheridan, R.A. Moss, B.K. Wilk, S. Shen, M. Włostowski, M.A. Kesselmayer, R. Subramanian, G. Kmiecik-Lawrynowicz, and K. Krogh-Jespersen. J. Am. Chem. Soc. **110**, 7563 (1988); (*m*) R.A. Moss and J. Włostowska. Tetrahedron Lett. **29**, 2559 (1988); (*n*) R.A. Moss, S. Shen, L.M. Hadel, G. Kmiecik-Lawrynowicz, J. Włostoska, and K. Krogh-Jespersen. J. Am. Chem. Soc. **109**, 4341 (1987); (*o*) R.A. Moss, M. Włostowski, J. Terpinski, G. Kmiecik-Lawrynowicz, and K. Krogh-Jespersen. J. Am. Chem. Soc. **109**, 3811 (1987); (*p*) R.A. Moss, C.M. Young, L.A. Perez, and K. Krogh-Jespersen. J. Am. Chem. Soc. **103**, 2413 (1981); (*q*) R.A. Moss. Acc. Chem. Res. **13**, 58 (1980); (*r*) W.W. Schoeller. Tetrahedron Lett. **21**, 1505 (1980); (*s*) N.P. Smith and I.D.R. Stevens. J. Chem. Soc. Perkin Trans. 2, 1298 (1979); (*t*) R.A. Moss, M. Fedorynski, and W.-C. Shieh. J. Am. Chem. Soc. **101**, 4736 (1979); (*u*) R.A. Moss, C.B. Mallon, and C.-T. Ho. J. Am. Chem. Soc. **99**, 4105 (1977); (*v*) M. Reiffen and R.W. Hoffman. Chem. Ber. **110**, 37 (1977); (*w*) R.A. Moss and J.K. Huselton. J. Chem. Soc. Chem. Commun. 950 (1976); (*x*) R.W. Hoffmann. Angew. Chem. Int. Ed. Engl. **10**, 529 (1971).
2. (*a*) M. El-Saidi, K. Kassam, D.L. Pole, T. Tadey, and J. Warkentin. J. Am. Chem. Soc. **114**, 8751 (1992); (*b*) R.W. Hoffmann, K. Steinbach, and B. Dittrich. Chem. Ber. **106**, 2174 (1973); (*c*) R.W. Hoffmann and M. Reiffen. Chem. Ber. **109**, 2565 (1976).
3. D.L. Pole and J. Warkentin. Liebigs Ann. 1907 (1995).
4. (*a*) K. Kassam, D.L. Pole, M. El-Saidi, and J. Warkentin. J. Am. Chem. Soc. **116**, 1161 (1994); (*b*) A. de Meijere, S.I. Kozhushkov, D.S. Yufit, R. Boese, T. Haumann, D.L. Pole, P.K. Sharma, and J. Warkentin. Liebigs Ann. 601 (1996).
5. (*a*) K. Kassam and J. Warkentin. J. Org. Chem. **59**, 5071 (1994); (*b*) W.W. Win, M. Kao, M. Eiermann, J.J. McNamara, F. Wudl, D.L. Pole, K. Kassam, and J. Warkentin. J. Org. Chem. **59**, 5871 (1994).
6. J. Hine and A.W. Klueppel. J. Am. Chem. Soc. **96**, 2924 (1974).
7. H.-T. Er, D.L. Pole, M. El-Saidi, and J. Warkentin. International Chemical Congress of Pacific Basin Societies, Honolulu, Dec. 1995. Paper no. 1224.
8. W.B. Smith. J. Org. Chem. **60**, 7456 (1995).
9. R.W. Hoffmann, W. Lilienblum, and B. Dittrich. Chem. Ber. **107**, 3395 (1974).

10. (*a*) D.L. Boger and C.E. Brotherton-Pleiss. *In* Advances in cycloaddition. Vol. 2. *Edited by* D.P. Curran. JAI Press, Greenwich, Conn. 1990. pp. 147–216; (*b*) D.L. Boger and J. Wysocki, Jr. J. Org. Chem. **53**, 3408 (1988); (*c*) D.L. Boger, C.E. Brotherton, and G.I. Georg. Org. Synth. **65**, 32 (1987); (*d*) D.L. Boger and C.E. Brotherton. J. Am. Chem. Soc. **108**, 6713 (1986); (*e*) J. Am. Chem. Soc. **108**, 6695 (1986); (*f*) J. Org. Chem. **50**, 3425 (1985); (*g*) J. Am. Chem. Soc. **106**, 805 (1984); (*h*) D.L. Boger, C.E. Brotherton, and C.E. Georg. Tetrahedron Lett. **25**, 5615 (1984).
11. F.G. Bordwell and H.E. Fried. J. Org. Chem. **56**, 4218 (1991).
12. J.B. Fulton and J. Warkentin. Can. J. Chem. **65**, 1177 (1987).
13. I. Fleming. Frontier orbitals and organic chemical reactions. Wiley–Interscience, New York. 1977.

Structural diversity in thallium chemistry: structures of four chlorothallate(III) salts including a novel compound containing three geometrically different anions

Margaret Ann James, Jason A.C. Clyburne, Anthony Linden, Bruce D. James, John Liesegang, and Vilma Zuzich

Abstract: Four new thallium-containing salts with different alkyl ammonium cations have been prepared and characterized by X-ray crystallography: **1**: bis(*p*-toluidinium) pentachlorothallate(III), $[CH_3C_6H_4NH_3]_2$ $[TlCl_5]$, $M = 597.9$, monoclinic, $P2_1/c$, $a = 7.515(2)$, $b = 21.376(6)$, $c = 12.769(2)$ Å, $\beta = 92.13(2)°$, $V = 2050(1)$ Å^3, $Z = 4$, $D_{calc} = 1.937$ Mg m^{-3}, $\mu = 8.512$ mm^{-1}, $T = 293(1)$ K, $R = 0.046$; **2**: 1,5-pentanediammonium pentachlorothallate(III), $[NH_3(CH_2)_5NH_3]$ $[TlCl_5]$, $M = 485.83$, orthorhombic, $P2_12_12_1$, $a = 13.226(2)$, $b = 13.595(2)$, $c = 7.628(2)$ Å, $V = 1371.6(3)$ Å^3, $Z = 4$, $D_{calc} = 2.352$ Mg m^{-3}, $\mu = 12.84$ mm^{-1}, $T = 173(1)$ K, $R = 0.025$; **3**: pentakis(2-adamantaneammonium) bistetrachlorothallate(III) hexachlorothallate(III), $[C_{10}H_{18}N]_5$ $[TlCl_4]_2$-$[TlCl_6]$, $M = 1870.75$, monoclinic, $P2_1$, $a = 16.466(5)$, $b = 25.985(2)$, $c = 7.724(3)$ Å, $\beta = 90.14(3)°$, $V = 3305(2)$ Å^3, $Z = 2$, $D_{calc} = 1.880$ Mg m^{-3}, $\mu = 7.978$ mm^{-1}, $T = 173(1)$ K, $R = 0.056$; **4**: bis(piperazinium) decachlorodithallate(III) trihydrate, $[NH_2C_4H_8NH_2]_2$ $[Tl_2Cl_{10}]\cdot 3H_2O$, $M = 993.62$, monoclinic, $C2/c$, $a = 14.154(3)$, $b = 15.445(3)$, $c = 13.228(3)$ Å, $\beta = 114.44(1)°$, $V = 2632.7(9)$ Å^3, $Z = 4$, $D_{calc} = 2.506$ Mg m^{-3}, $\mu = 13.39$ mm^{-1}, $T = 173(1)$ K, $R = 0.026$. For most of the salts examined, formation of $[TlCl_5]^{2-}$ is possible; however, no isolated $[TlCl_5]^{2-}$ anions were observed. In most cases, high coordination numbers at thallium were observed (CN = 6), and these can be achieved *via* formation of anionic chains or through dimerization, giving $[Tl_2Cl_{10}]^{4-}$. Of particular interest is the solid state structure of salt **3** in which there are three geometrically different chlorothallate ions. Extensive hydrogen-bonding networks are observed in each structure.

Key words: thallium, thallium(III) chlorides, chlorothallate, hydrogen bonding, alkyl ammonium cations.

Résumé : On a préparé quatre nouveaux sels contenant du thallium et différents cations alkylammonium et on les a caractérisés par diffraction des rayons X: **1**, pentachlorothallate(III) de bis(*p*-toluidinium), $[CH_3C_6H_4NH_3]_2$ $[TlCl_5]$, $M = 597{,}9$, monoclinique, $P2_1/c$, $a = 7{,}515(2)$, $b = 21{,}376(6)$, $c = 12{,}769(2)$ Å, $\beta = 92{,}13(2)°$, $V = 2050(1)$ Å^3, $Z = 4$, $D_{calc} = 1{,}937$ Mg m^{-3}, $\mu = 8{,}512$ mm^{-1}, $T = 293(1)$ K, $R = 0{,}046$; **2**, pentachlorothallate(III) de pentane-1,5-diammonium, $[NH_3(CH_2)_5NH_3]$ $[TlCl_5]$, $M = 485{,}83$, orthorhombique, $P2_12_12_1$, $a = 13{,}226(2)$, $b = 13{,}595(2)$, $c = 7{,}628(2)$ Å, $V = 1371{,}6(3)$ Å^3, $Z = 4$, $D_{calc} = 2{,}352$ Mg m^{-3}, $\mu = 12{,}84$ mm^{-1}, $T = 173(1)$ K, $R = 0{,}025$; **3**, bistétrachlorothallate(III) hexachlorothallate(III) de pentakis(adamantane-2-ammonium), $[C_{10}H_{18}N]_5$ $[TlCl_4]_2$ $[TlCl_6]$, $M = 1870{,}75$, monoclinique, $P2_1$, $a = 16{,}466(5)$, $b = 25{,}985(2)$, $c = 7{,}724(3)$ Å, $\beta = 90{,}14(3)°$, $V = 3305(2)$ Å^3, $Z = 2$, $D_{calc} = 1{,}880$ Mg m^{-3}, $\mu = 7{,}978$ mm^{-1}, $T = 173(1)$ K, $R = 0{,}056$; **4**, trihydrate du décachlorodithallate(III) de bis(pipérazinium), $[NH_2C_4H_8NH_2]_2$ $[Tl_2Cl_{10}]\cdot 3H_2O$, $M = 993{,}62$, monoclinique, $C2/c$, $a = 14{,}154(3)$, $b = 15{,}445(3)$, $c = 13{,}228(3)$ Å, $\beta = 114{,}44(1)°$, $V = 2632{,}7(9)$ Å^3, $Z = 4$, $D_{calc} = 2{,}506$ Mg m^{-3}, $\mu = 13{,}39$ mm^{-1}, $T = 173(1)$ K, $R = 0{,}026$. Pour la plupart des sels examinés, la formation de $[TlCl_5]^{2-}$ est possible; toutefois, aucun anion $[TlCl_5]^{2-}$ n'a été isolé. Dans la plupart des cas, on a observé des nombres de coordination élevés pour le thallium (NC = 6) et on peut arriver à ceux-ci par le biais de la formation de chaînes anioniques ou par une dimérisation conduisant à du $[Tl_2Cl_{10}]^{4-}$. La structure du sel **3** à l'état solide est particulièrement intéressante parce qu'elle comporte trois ions chlorothallates géométriquement différents. Dans chacune des structures, on a observé des réseaux étendus de liaisons hydrogènes.

Mots clés : thallium, chlorures de thallium(III), chlorothallate, liaison hydrogène, cations alkylammoniums.

[Traduit par la rédaction]

Received January 1, 1996.

M.A. James[1] and J.A.C. Clyburne. Department of Chemistry, Mount Saint Vincent University, Halifax, NS B3M 2J6, Canada.
A. Linden. Institute for Organic Chemistry, University of Zürich, CH-8057 Zürich, Switzerland.
B.D. James, J. Liesegang, and V. Zuzich. Faculty of Science and Technology, La Trobe University, Bundoora, Vic. 3083, Australia.

[1] Author to whom correspondence may be addressed. Phone: (902) 457-6141. Fax: (902) 457-0579. E-mail: Margaret.James@MSVU.ca

Introduction

Thallium, like most other main group metals and metalloids, can form a variety of polychlorinated anions (1), including $[TlCl_4]^-$, $[TlCl_5]^{2-}$, and $[TlCl_6]^{3-}$, all three species occurring in solutions of thallium(III) chloride in the presence of excess chloride ion (2). Perhaps the most interesting observation concerning the polychlorinated anions of thallium involves those with the $TlCl_5$ stoichiometry, which, when it is observed in solid samples isolated from donor solvents, might be expected to have the sixth coordination site of the metal occupied by a solvent molecule. Thus, discrete $[TlCl_5]^{2-}$ anions are rarely observed in the relatively small number of these compounds that have been characterized by X-ray crystallography. For example, DMSO (3) and water (4) have been shown to coordinate to $[TlCl_5]^{2-}$ fragments, giving six-coordinate species; however, in the calcium salt, $Ca[TlCl_5](H_2O)_7$, it is the calcium(II) ion, rather than the thallium centre, which engages the base (water), high coordination at thallium being realized via dimerization of two $[TlCl_5]^{2-}$ fragments to give the $[Tl_2Cl_{10}]^{4-}$ anion (5). An alternative mode of achieving high coordination at thallium is illustrated in the solid state structure of the salt Cs_2TlCl_5, where the sixth coordination site around thallium is occupied by a chloride ion from a neighbouring pentachlorothallate group, thus forming a chain of $[TlCl_5]^{2-}$ units (6). To date, the only complete report of a discrete $[TlCl_5]^{2-}$ ion is in the structure of the 4-chloropyridinium derivative (7). In addition, the tetraethylammonium salt $[Et_4N]_2[TlCl_5]$ is reported to be isomorphous (and presumably isostructural) with its indium analogue, which contains an isolated pentacoordinate $[InCl_5]^{2-}$ ion (8).

Investigations into the hydrogen-bonding arrangements that might be generated in solids arising from the interaction of thallium(III) chloride with other large organic base cations yielded some crystalline materials having apparent $TlCl_5$ stoichiometry. This paper reports the structures of four of these materials.

Experimental

Compounds **1**–**4** were synthesized by mixing solutions (molar ratio indicated) of the appropriate amine hydrochloride salts (ca. 5% excess) with thallium(III) chloride in a minimum volume of concentrated hydrochloric acid, warming as necessary. Solid materials that precipitated immediately were removed by filtration and the filtrates were allowed to evaporate slowly in an air stream. Generally, several crops of crystals were obtained, and these were isolated by filtration and dried in a vacuum desiccator. Elemental analyses were performed by Atlantic Microlabs Inc., Norcross, Ga.

1: *Bis(*p*-toluidinium) pentachlorothallate(III)*, (1:1, 2nd crop, mp 190–192°C, yellow prisms). Anal. calcd.: C 28.12, H 3.37, N 4.69, Cl 29.64%; found: C 28.23, H 2.99, N 4.46, Cl 29.93%.

2: *1,5-Pentanediammonium pentachlorothallate(III)*, (1:1, 3rd crop, mp 266–268°C, colourless prisms). Anal. calcd.: C 12.36, H 3.32, N 5.77, Cl 36.49%; found: C 12.33, H 3.30, N 5.73, Cl 36.58%.

3: *Pentakis(2-adamantaneammonium) bis[tetrachlorothallate(III)] hexachlorothallate(III)*, (2:1, 2nd crop, mp 262–263°C, slightly yellow prisms). Anal. calcd.: C 32.10, H 4.85, N 3.74, Cl 26.53%; found: C 34.03, H 5.19, N 3.86, Cl 27.18%.

4: *Bis(piperazinium) decachlorodithallate(III)*, (1:1, 2nd crop, mp 250–251°C, colourless prisms). Anal. calcd.: C 9.67, H 3.04, N 5.64, Cl 35.68%; found: C 9.64, H 3.04, N 5.52, Cl 35.75%.

Crystallography

Data for compound **1** were collected using a CAD-4 four-circle diffractometer and a Rigaku AFC5R system for **2**–**4**. Cell constants and orientation matrices for data collection were obtained from least-squares refinements using a number of carefully centred reflections (**1**, 25; **2**–**4**, 24) in the 2θ ranges **1**, 24°–30°; **3**, 38°–40°; and **2** and **4**, 39°–40°. For compound **1**, an empirical absorption correction (DIFABS) (9) was used; for compounds **2**–**4**, semi-empirical absorption corrections based on azimuthal scans of several reflections (10) were applied. Lorentz and polarization corrections were also applied. The intensities of three representative reflections were measured after every 150 reflections. Significant decay was observed only for **3** (ca. 15%) and a linear correction factor was calculated to account for this. Equivalent reflections were merged, apart from those from Friedel pairs for the non-centrosymmetric structures **2** and **3**.

The structures were solved by Patterson methods (11), which revealed the positions of the thallium atoms. All remaining non-hydrogen atoms were located in Fourier expansions of the Patterson solution (12). Except for **3**, described below, all of the non-hydrogen atoms were refined anisotropically. All hydrogen atoms bonded to carbon and nitrogen were fixed in geometrically calculated positions with a C–H or N–H distance of 0.95 Å. Hydrogen atoms bonded to oxygen in compound **4** were fixed in positions indicated by difference electron density maps. Each hydrogen atom was assigned an isotropic temperature factor having a value $1.2 \times U_{eq}$ of the atom to which it was bonded. Hydrogen atoms were not included for the disordered cation of compound **3** (see below). Extinction corrections were applied for **2** and **4** only. The final cycles of full-matrix least-squares refinements (13) were based on the observed reflections and variable parameters listed in Table 1 and converged with unweighted and weighted factors defined by:

$$[1] \quad R = \Sigma||F_o| - |F_c|| / \Sigma|F_o|$$

and

$$[2] \quad R_w = [(\Sigma w(|F_o| - |F_c|)^2 / \Sigma w F_o^2)]^{1/2}$$

All calculations were performed using the TEXSAN crystallographic software package (14). Figures are presented as ORTEP plots (50% probability ellipsoids) (15).

Structures **2** and **3** crystallized in non-centrosymmetric space groups. For **2**, the data collection included the measurement of the Friedel opposites of all reflections in the unique octant, but for **3**, severe decomposition of the crystal precluded the measurement of any Friedel opposites. The correct choice for the direction of the polar axis was confirmed in each case by an additional refinement of the completed structures

Table 1. Crystallographic data.

	1	2	3	4
Formula	$C_{14}H_{20}Cl_5N_2Tl$	$C_5H_{16}Cl_5N_2Tl$	$C_{50}H_{90}Cl_{14}N_5Tl_3$	$C_8H_{24}Cl_{10}N_4Tl_2 \cdot 3H_2O$
M	597.89	485.83	1870.54	993.48
Crystal size/mm^3	—	0.22 × 0.27 × 0.27	0.20 × 0.25 × 0.32	0.25 × 0.30 × 0.38
T/K	293(1)	173(1)	173(1)	173(1)
Radiation	Mo K_α λ = 0.71069 Å	Mo K_α λ = 0.71069 Å	Mo K_α λ = 0.71069 Å	Mo K_α λ = 0.71069 Å
Scan type	$\omega/2\theta$	$\omega/2\theta$	ω	$\omega/2\theta$
System	Monoclinic	Orthorhombic	Monoclinic	Monoclinic
Space group	$P2_1/c$	$P2_12_12_1$	$P2_1$	C_2/c
a/Å	7.515(2)	13.226(2)	16.466(5)	14.154(3)
b/Å	21.376(6)	13.595(2)	25.985(2)	15.445(3)
c/Å	12.769(2)	7.628(2)	7.724(3)	13.228(3)
β/°	92.13(2)		90.14(3)	114.44(1)
V/Å^3	2050(1)	1371.6(3)	3305(2)	2632.7(9)
Z	4	4	2	4
D_c/Mg m^{-3}	1.937	2.352	1.880	2.507
Transmission coefficients	0.813–1.222	0.706–1.000	0.759–1.000	0.525–1.000
$2\theta_{max}$(°)	46	60	60	60
F(000)	1136	904	1812	1848
μ/mm^{-1}	8.508	12.84	7.978	13.39
Measured reflections	3564	5556	10096	4107
Unique reflections	2834	3992	9785	3834
Observed reflections ($I > 3\sigma(I)$)	2181	3738	7453	3092
Parameters refined	202	119	363	124
Weighting scheme	$\sum w(\lvert F_o\rvert - \lvert F_c\rvert)^2$ $w = [\sigma^2(F_o) + (pF_o/2)^2]^{-1}$	$\sum w(\lvert F_o\rvert - \lvert F_c\rvert)^2$ $w = [\sigma^2(F_o) + (pF_o/2)^2]^{-1}$	$\sum w(\lvert F_o\rvert - \lvert F_c\rvert)^2$ $w = [\sigma^2(F_o) + (pF_o/2)^2]^{-1}$	$\sum w(\lvert F_o\rvert - \lvert F_c\rvert)^2$ $w = [\sigma^2(F_o) + (pF_o/2)^2]^{-1}$
p-factor	0.005	0.01	0.01	0.01
$100R$	3.88	2.53	5.59	2.62
$100R_w$	4.60	2.67	4.98	2.81
Goodness of fit	2.081	1.641	2.263	1.816
Max, min peak in difference map/e Å^{-3}	1.01, −1.23	2.51, −2.18	2.21, −3.12	1.94, −1.74

using the program CRYSTALS (16) in which it is possible to refine the enantiopole, or Flack's x, parameter (17, 18). This parameter converged to −0.011(6) for **2** and 0.24(4) for **3**. The reliability of this parameter for **3** is poor, but the correct direction of the polar axis was further confirmed by the refinement of the inverse structure, which resulted in significantly higher R-factors (R = 0.063, R_w = 0.059).

The refinement of compound **3** presented special difficulties. One of the cations exhibited disorder over two sites having a common centroid. It was not possible to successfully build the disordered cation from the electron density peaks alone; therefore a rigid group was constructed to represent the idealized cation by combining several cyclohexane templates from the database of the TEXSAN program. Two of these adamantane rigid groups were then oriented to two sets of three electron density peaks that could be identified as belonging to the two disordered orientations of the cation. The result agreed well with the original peaks observed in this region, and it was possible to refine the individual isotropic temperature factors of the atoms within the rigid groups, but attempts to relax the rigid group constraints led to unsatisfactory results.

The atoms of the anions of **3** were refined anisotropically, while the atoms of all cations were refined isotropically. Attempts to refine the ordered cations anisotropically did not reduce the R-factor significantly and led to several of these atoms having non-positive definite displacement parameters. It is possible that all of the cations, and not just one, are disordered to some extent.

Differential scanning calorimetry curves for compound **2** were obtained using a Mettler-Toledo TA 8000 instrument after sealing a crystalline sample (ca. 10 mg) in a standard aluminum pan. Several heating–cooling cycles (10°C min^{-1}) were carried out that showed that the phase change profiles were reversible. Integration of the 45°C endotherm was performed with the instrument software.

Discussion

Four new salts containing polychlorothallate anions have been isolated and characterized by X-ray crystallography. In general, the products are easily prepared and isolated from acidic solution. Crystal data are presented in Table 1, and fractional atomic coordinates for each of the chlorothallate(III) compounds **1–4** are presented in Tables 2–5, respectively. Perti-

Table 2. Fractional atomic coordinates and equivalent isotropic temperature factors (Å^2) for compound **1**. U_{eq} is defined as one third of the trace of the orthogonalized U_{ij} tensor.

Atom	x	y	z	U_{eq}
Tl	0.25819(5)	0.04607(2)	0.14358(3)	0.0397(1)
Cl(1)	0.0049(4)	0.0808(2)	0.2492(3)	0.067(1)
Cl(2)	0.2521(5)	0.1366(1)	0.0235(3)	0.071(1)
Cl(3)	0.0	0.0	0.0	0.055(1)
Cl(4)	0.5	0.0	0.0	0.058(1)
Cl(5)	0.5254(4)	0.0801(2)	0.2494(2)	0.056(1)
Cl(6)	0.2602(6)	−0.0643(2)	0.2025(3)	0.078(1)
N(1)	0.234(1)	0.0525(4)	−0.2022(8)	0.063(4)
N(2)	0.750(1)	0.1280(4)	0.0405(7)	0.059(4)
C(1)	0.245(1)	0.0891(5)	−0.2984(9)	0.044(4)
C(2)	0.274(2)	0.0616(5)	−0.3916(8)	0.052(4)
C(3)	0.286(2)	0.0995(6)	−0.4780(9)	0.058(5)
C(4)	0.272(1)	0.1620(5)	−0.4753(9)	0.048(4)
C(5)	0.244(2)	0.1897(6)	−0.379(1)	0.060(5)
C(6)	0.230(2)	0.1543(5)	−0.2901(9)	0.058(4)
C(7)	0.291(2)	0.2027(6)	−0.572(1)	0.062(5)
C(21)	0.755(1)	0.1965(5)	0.0303(9)	0.042(4)
C(22)	0.800(2)	0.2236(5)	−0.0590(9)	0.056(4)
C(23)	0.805(2)	0.2879(6)	−0.065(1)	0.063(5)
C(24)	0.770(1)	0.3250(5)	0.0202(9)	0.046(4)
C(25)	0.725(2)	0.2967(5)	0.1087(9)	0.056(4)
C(26)	0.715(2)	0.2313(6)	0.1165(9)	0.062(5)
C(27)	0.778(2)	0.3952(5)	0.013(1)	0.059(4)

Table 3. Fractional atomic coordinates and equivalent isotropic temperature factors (Å^2) for compound **2**. U_{eq} is defined as one third of the trace of the orthogonalized U_{ij} tensor.

Atom	x	y	z	U_{eq}
Tl	0.37273(2)	0.39384(1)	0.03976(3)	0.01321(5)
Cl(1)	0.4619(1)	0.5538(1)	0.0659(2)	0.0216(4)
Cl(2)	0.4779(1)	0.3319(1)	−0.2103(2)	0.0232(4)
Cl(3)	0.2290(1)	0.4772(1)	0.2318(2)	0.0195(4)
Cl(4)	0.4510(1)	0.2929(1)	0.2763(2)	0.0215(4)
Cl(5)	0.2360(1)	0.2719(1)	−0.0407(2)	0.0173(3)
N(1)	0.2553(3)	0.3075(3)	0.5388(7)	0.018(1)
N(2)	−0.0322(3)	−0.1115(4)	0.4924(7)	0.026(2)
C(1)	0.2032(4)	0.2218(4)	0.4621(8)	0.017(1)
C(2)	0.2588(4)	0.1279(4)	0.5103(8)	0.018(2)
C(3)	0.2115(4)	0.0364(4)	0.4266(9)	0.023(2)
C(4)	0.1097(4)	0.0078(4)	0.5112(7)	0.017(1)
C(5)	0.0666(4)	−0.0800(4)	0.4140(8)	0.020(2)

nent bond lengths and angles for the chlorothallate anions of each salt are presented in Table 6. Hydrogen bonds (N—H---Cl) are evident in each structure, and these are summarized in Table 7. The following information has been deposited for compounds **1**–**4**:[2] complete experimental details; positional parameters for all atoms including hydrogens; anisotropic thermal parameters of nonhydrogen atoms where applicable; isotropic temperature factors of hydrogen atoms and other atoms where applicable; bond lengths, bond angles, and torsion angles.

[2] Copies of material on deposit may be purchased from: The Depository of Unpublished Data, Document Delivery, CISTI, National Research Council Canada, Ottawa, Canada K1A 0S2. With the exception of anisotropic thermal parameters and torsion angles, these data have also been deposited with the Cambridge Crystallographic Data Centre, and can be obtained on request from The Director, Cambridge Crystallographic Data Centre, University Chemical Laboratory, 12 Union Road, Cambridge, CB2 1EZ, U.K.

Table 4. Fractional atomic coordinates and equivalent isotropic temperature factors (Å^2) for compound **3**. U_{eq} is defined as one third of the trace of the orthogonalized U_{ij} tensor.

Atom	x	y	z	U_{eq}
Tl(1)	0.03950(5)	0.00213[a]	0.00974(9)	0.0393(2)
Tl(2)	0.57612(4)	0.25201(4)	−0.00213(8)	0.0290(2)
Tl(3)	0.20748(4)	0.12616(4)	0.51026(7)	0.0224(2)
Cl(11)	−0.0128(3)	−0.0434(2)	0.2663(6)	0.049(2)
Cl(12)	−0.0417(3)	0.0807(2)	0.0440(5)	0.035(1)
Cl(13)	0.1752(3)	−0.0329(2)	−0.0188(6)	0.045(2)
Cl(14)	−0.0194(3)	−0.0371(2)	−0.2542(6)	0.044(2)
Cl(21)	0.5308(4)	0.3406(2)	−0.0221(7)	0.057(2)
Cl(22)	0.7205(3)	0.2428(2)	0.0229(6)	0.047(2)
Cl(23)	0.5311(3)	0.2090(2)	−0.2631(6)	0.053(2)
Cl(24)	0.5170(4)	0.2120(2)	0.2485(6)	0.055(2)
Cl(31)	0.3139(3)	0.0577(2)	0.5573(6)	0.041(2)
Cl(32)	0.0828(3)	0.1813(2)	0.4669(5)	0.037(1)
Cl(33)	0.2688(3)	0.1815(2)	0.7565(5)	0.032(1)
Cl(34)	0.1186(3)	0.0782(2)	0.7491(6)	0.045(2)
Cl(35)	0.2823(3)	0.1726(2)	0.2651(6)	0.038(1)
Cl(36)	0.1463(3)	0.0633(2)	0.2720(6)	0.045(2)
N(1)	0.9566(9)	0.0689(5)	0.477(2)	0.035(3)
N(2)	0.832(1)	0.4631(6)	0.461(2)	0.049(4)
N(3)	0.1082(8)	0.1796(5)	0.034(2)	0.033(3)
N(4)	0.3127(9)	0.0740(6)	−0.012(2)	0.042(4)
N(41)[b]	0.380(2)	0.2541(6)	0.510(3)	0.03(2)
N(51)[b]	0.376(1)	0.2540(5)	0.516(3)	0.04(2)
C(1)	0.884(1)	0.0821(7)	0.586(2)	0.037(4)
C(2)	0.811(1)	0.0490(7)	0.542(2)	0.039(4)
C(3)	0.747(1)	0.0605(8)	0.679(3)	0.055(6)
C(4)	0.725(1)	0.1164(7)	0.685(2)	0.044(5)
C(5)	0.800(1)	0.1495(8)	0.708(3)	0.050(5)
C(6)	0.866(1)	0.1398(7)	0.577(2)	0.043(5)
C(7)	0.775(1)	0.0639(8)	0.360(3)	0.051(5)
C(8)	0.693(1)	0.129(1)	0.524(3)	0.059(5)
C(9)	0.833(1)	0.1522(9)	0.402(3)	0.062(6)
C(10)	0.750(1)	0.121(1)	0.357(3)	0.066(6)
C(11)	0.813(1)	0.4108(9)	0.524(3)	0.054(6)
C(12)	0.805(1)	0.3726(8)	0.364(3)	0.048(5)
C(13)	0.725(1)	0.3759(9)	0.275(3)	0.057(6)
C(14)	0.656(1)	0.3740(9)	0.409(3)	0.063(6)
C(15)	0.660(2)	0.414(1)	0.544(3)	0.085(8)
C(16)	0.741(2)	0.409(1)	0.646(3)	0.071(7)
C(17)	0.807(1)	0.3210(9)	0.455(3)	0.069(7)
C(18)	0.739(2)	0.310(1)	0.577(4)	0.095(9)
C(19)	0.660(1)	0.3191(9)	0.472(3)	0.061(6)
C(20)	0.740(1)	0.3546(9)	0.719(3)	0.064(6)
C(21)	0.073(1)	0.2191(7)	−0.073(2)	0.043(5)
C(22)	0.106(1)	0.2731(6)	−0.033(2)	0.027(4)
C(23)	0.073(1)	0.3114(8)	−0.179(3)	0.054(6)
C(24)	−0.018(1)	0.3125(7)	−0.165(2)	0.037(4)
C(25)	−0.051(1)	0.2574(8)	−0.206(2)	0.043(4)
C(26)	−0.021(1)	0.2206(7)	−0.059(2)	0.039(4)
C(27)	−0.045(1)	0.2405(8)	0.114(3)	0.049(5)
C(28)	−0.014(1)	0.2961(9)	0.154(3)	0.064(6)
C(29)	−0.044(1)	0.3321(7)	0.010(2)	0.041(5)
C(30)	0.079(1)	0.2932(8)	0.151(3)	0.048(5)
C(31)	0.389(1)	0.0592(8)	0.101(2)	0.048(5)
C(32)	0.461(1)	0.0890(7)	0.040(2)	0.040(4)

Table 4 (*concluded*).

Atom	x	y	z	U_{eq}
C(33)	0.524(2)	0.079(1)	0.168(4)	0.094(9)
C(34)	0.546(1)	0.0198(8)	0.166(3)	0.053(6)
C(35)	0.471(1)	−0.0097(9)	0.217(3)	0.059(6)
C(36)	0.409(1)	0.0001(8)	0.075(3)	0.047(5)
C(37)	0.434(1)	−0.0161(8)	−0.095(3)	0.048(5)
C(38)	0.493(1)	0.0742(8)	−0.142(3)	0.054(6)
C(39)	0.513(1)	0.0159(8)	−0.143(3)	0.052(6)
C(40)[b]	0.581(1)	0.002(1)	0.029(3)	0.067(7)
C(41)[b]	0.381(1)	0.3050(6)	0.424(2)	0.05(1)
C(42)[b]	0.4099(9)	0.3461(7)	0.554(2)	0.04(1)
C(43)[b]	0.352(1)	0.3478(7)	0.709(2)	0.06(1)
C(44)[b]	0.265(1)	0.3613(7)	0.646(2)	0.06(1)
C(45)[b]	0.2363(9)	0.3202(8)	0.516(3)	0.09(2)
C(46)[b]	0.295(1)	0.3185(7)	0.360(2)	0.04(1)
C(47)[b]	0.411(1)	0.3991(7)	0.465(3)	0.08(2)
C(48)[b]	0.325(1)	0.4127(6)	0.401(3)	0.08(1)
C(49)[b]	0.267(1)	0.4143(7)	0.556(3)	0.05(1)
C(50)[b]	0.296(1)	0.3716(8)	0.271(2)	0.06(1)
C(51)[b]	0.381(1)	0.3090(6)	0.565(2)	0.035(8)
C(52)[b]	0.296(1)	0.3287(7)	0.616(2)	0.05(1)
C(53)[b]	0.2378(8)	0.3227(8)	0.461(3)	0.034(9)
C(54)[b]	0.270(1)	0.3542(7)	0.307(2)	0.05(1)
C(55)[b]	0.355(1)	0.3346(7)	0.256(2)	0.040(9)
C(56)[b]	0.4131(8)	0.3405(7)	0.410(2)	0.034(8)
C(57)[b]	0.301(1)	0.3858(7)	0.667(2)	0.05(1)
C(58)[b]	0.334(1)	0.4174(5)	0.513(3)	0.08(1)
C(59)[b]	0.275(1)	0.4114(7)	0.358(3)	0.10(2)
C(60)[b]	0.419(1)	0.3977(7)	0.462(3)	0.05(2)

[a]Origin defined by fixing the y coordinate of Tl(1).
[b]Disordered atom with site occupation factor of 0.5.

Table 5. Fractional atomic coordinates and equivalent isotropic temperature factors (Å^2) for compound **4**. U_{eq} is defined as one third of the trace of the orthogonalized U_{ij} tensor.

Atom	x	y	z	U_{eq}
Tl	0.06037(1)	0.24618(1)	0.12933(2)	0.01154(7)
Cl(1)	0.25158(9)	0.23607(8)	0.1919(1)	0.0183(4)
Cl(2)	0.03437(9)	0.08415(8)	0.1025(1)	0.0161(4)
Cl(3)	0.07339(9)	0.41455(7)	0.1614(1)	0.0120(4)
Cl(4)	0.0065(1)	0.27350(8)	−0.0746(1)	0.0208(5)
Cl(5)	−0.11889(8)	0.24906(8)	0.1336(1)	0.0130(4)
O(1)	0.3278(3)	0.3950(2)	0.3728(3)	0.019(1)
O(2)[a]	0.0	−0.1275(3)	0.25	0.019(2)
N(1)	0.2902(3)	0.5554(3)	0.6311(3)	0.014(2)
N(4)	0.1745(3)	0.4526(3)	0.4375(4)	0.013(2)
C(2)	0.2858(4)	0.4594(3)	0.6381(4)	0.017(2)
C(3)	0.1870(4)	0.4240(3)	0.5496(4)	0.014(2)
C(5)	0.1765(5)	0.5492(3)	0.4310(5)	0.019(2)
C(6)	0.2761(4)	0.5854(4)	0.5184(4)	0.020(2)

[a]Atom O(2) lies on a 2-fold axis.

Table 6. Important bond lengths (Å) and angles (°) for the chlorothallium fragments.

Compound 1

Tl—Cl(1)	2.487(3)
Tl—Cl(2)	2.469(3)
Tl—Cl(3)	2.7986(7)
Tl—Cl(4)	2.8073(7)
Tl—Cl(5)	2.487(3)
Tl—Cl(6)	2.476(3)
Cl(1)-Tl-Cl(2)	96.1(1)
Cl(1)-Tl-Cl(3)	86.23(7)
Cl(1)-Tl-Cl(4)	170.41(7)
Cl(1)-Tl-Cl(5)	103.7(1)
Cl(1)-Tl-Cl(6)	96.6(1)
Cl(2)-Tl-Cl(3)	82.68(8)
Cl(2)-Tl-Cl(4)	82.36(8)
Cl(2)-Tl-Cl(5)	96.0(1)
Cl(2)-Tl-Cl(6)	159.3(1)
Cl(3)-Tl-Cl(4)	84.18(2)
Cl(3)-Tl-Cl(5)	170.07(7)
Cl(3)-Tl-Cl(6)	81.96(9)
Cl(4)-Tl-Cl(5)	85.89(7)
Cl(4)-Tl-Cl(6)	82.40(9)
Cl(5)-Tl-Cl(6)	96.8(1)
Tl-Cl(3)-Tl^{i}	180.0
Tl-Cl(4)-Tl^{ii}	180.0

Symmetry operators:
(i) $-x, -y, -z$, (ii) $1-x, -y, -z$

Compound 2

Tl—Cl(1)	2.482(1)
Tl—Cl(2)	2.506(2)
Tl—Cl(3)	2.655(1)
Tl—Cl(3^{i})	3.225(2)
Tl—Cl(4)	2.493(2)
Tl—Cl(5)	2.530(1)
Cl(1)-Tl-Cl(2)	95.27(5)
Cl(1)-Tl-Cl(3)	85.52(5)
Cl(1)-Tl-Cl(3^{i})	77.31(4)
Cl(1)-Tl-Cl(4)	103.12(5)
Cl(1)-Tl-Cl(5)	159.02(5)
Cl(2)-Tl-Cl(3)	163.93(5)
Cl(2)-Tl-Cl(3^{i})	81.92(4)
Cl(2)-Tl-Cl(4)	97.79(5)
Cl(2)-Tl-Cl(5)	89.54(5)
Cl(3)-Tl-Cl(3^{i})	82.60(2)
Cl(3)-Tl-Cl(4)	97.65(5)
Cl(3)-Tl-Cl(5)	84.35(5)
Cl(3^{i})-Tl-Cl(4)	179.52(4)
Cl(3^{i})-Tl-Cl(5)	83.19(4)
Cl(4)-Tl-Cl(5)	96.42(5)
Tl-Cl(3)-Tl^{ii}	158.89(6)

Symmetry operators:
(i) $1/2-x, 1-y, -1/2+z$ (ii) $1/2-x, 1-y, 1/2+x$

Table 6 (*continued*).

Compound 3

Tl(1)—Cl(11)	2.465(5)
Tl(1)—Cl(12)	2.456(5)
Tl(1)—Cl(13)	2.423(5)
Tl(1)—Cl(14)	2.475(5)
Tl(1)—Cl(34^{i})	3.109(5)
Tl(1)—Cl(36)	3.116(5)
Tl(2)—Cl(21)	2.425(5)
Tl(2)—Cl(22)	2.397(5)
Tl(2)—Cl(23)	2.419(5)
Tl(2)—Cl(24)	2.405(5)
Tl(3)—Cl(31)	2.523(5)
Tl(3)—Cl(32)	2.525(5)
Tl(3)—Cl(33)	2.588(4)
Tl(3)—Cl(34)	2.667(5)
Tl(3)—Cl(35)	2.563(5)
Tl(3)—Cl(36)	2.657(5)
Cl(11)-Tl(1)-Cl(12)	97.0(2)
Cl(11)-Tl(1)-Cl(13)	102.5(2)
Cl(11)-Tl(1)-Cl(14)	109.1(2)
Cl(11)-Tl(1)-Cl(34^{i})	166.7(1)
Cl(11)-Tl(1)-Cl(36)	85.4(2)
Cl(12)-Tl(1)-Cl(13)	145.5(2)
Cl(12)-Tl(1)-Cl(14)	102.6(2)
Cl(12)-Tl(1)-Cl(34^{i})	76.7(1)
Cl(12)-Tl(1)-Cl(36)	79.2(1)
Cl(13)-Tl(1)-Cl(14)	97.5(2)
Cl(13)-Tl(1)-Cl(34^{i})	78.0(2)
Cl(13)-Tl(1)-Cl(36)	74.4(1)
Cl(14)-Tl(1)-Cl(34^{i})	83.8(1)
Cl(14)-Tl(1)-Cl(36)	164.8(1)
Cl(34^{i})Tl(1)-Cl(36)	81.9(1)
Cl(21)-Tl(2)-Cl(22)	113.9(2)
Cl(21)-Tl(2)-Cl(23)	107.0(2)
Cl(21)-Tl(2)-Cl(24)	109.7(2)
Cl(22)-Tl(2)-Cl(23)	108.8(2)
Cl(22)-Tl(2)-Cl(24)	107.2(2)
Cl(23)-Tl(2)-Cl(24)	110.3(2)
Cl(31)-Tl(3)-Cl(32)	169.6(2)
Cl(31)-Tl(3)-Cl(33)	90.9(1)
Cl(31)-Tl(3)-Cl(34)	87.3(2)
Cl(31)-Tl(3)-Cl(35)	96.0(2)
Cl(31)-Tl(3)-Cl(36)	85.9(2)
Cl(32)-Tl(3)-Cl(33)	95.6(1)
Cl(32)-Tl(3)-Cl(34)	84.8(2)
Cl(32)-Tl(3)-Cl(35)	91.5(1)
Cl(32)-Tl(3)-Cl(36)	87.1(2)
Cl(33)-Tl(3)-Cl(34)	88.0(1)
Cl(33)-Tl(3)-Cl(35)	95.4(1)
Cl(33)-Tl(3)-Cl(36)	175.8(1)
Cl(34)-Tl(3)-Cl(35)	175.2(2)
Cl(34)-Tl(3)-Cl(36)	89.1(2)
Cl(35)-Tl(3)-Cl(36)	87.7(1)
Tl(1^{ii})-Cl(34)-Tl(3)	167.5(2)
Tl(1)-Cl(36)-Tl(3)	167.6(2)

Symmetry operators:
(i) $x, y, -1+z$ (ii) $x, y, 1+z$

Table 6 (*concluded*).

Compound 4	
Tl—Cl(1)	2.486(1)
Tl—Cl(2)	2.533(1)
Tl—Cl(3)	2.629(1)
Tl—Cl(4)	2.517(2)
Tl—Cl(5)	2.562(1)
Tl—Cl(5^{i})	2.894(1)
Cl(1)-Tl-Cl(2)	93.42(4)
Cl(1)-Tl-Cl(3)	90.83(4)
Cl(1)-Tl-Cl(4)	99.96(5)
Cl(1)-Tl-Cl(5)	161.01(4)
Cl(1)-Tl-Cl(5)^{i}	81.72(4)
Cl(2)-Tl-Cl(3)	175.05(4)
Cl(2)-Tl-Cl(4)	93.07(4)
Cl(2)-Tl-Cl(5)	86.12(4)
Cl(2)-Tl-Cl(5)^{i}	97.28(4)
Cl(3)-Tl-Cl(4)	88.70(4)
Cl(3)-Tl-Cl(5)	89.04(4)
Cl(3)-Tl-Cl(5)^{i}	80.81(4)
Cl(4)-Tl-Cl(5)	99.02(5)
Cl(4)-Tl-Cl(5)^{i}	169.41(4)
Cl(5)-Tl-Cl(5)^{i}	79.51(4)
Tl-Cl(5)-Tl^{i}	100.46(4)

Symmetry operators: (i) $-x$, y, $1/2 - z$

Table 7. Hydrogen-bond geometry (Å,°) for the four thallium-containing salts.

D—H···A	D···A	H···A	D—H···A
Compound 1			
N(1)—H(101)···Cl(5)^{i}	3.43(1)	2.52	159
N(1)—H(102)···Cl(1)^{ii}	3.41(1)	2.70	132
N(1)—H(102)···Cl(3)	3.37(1)	2.82	118
N(1)—H(103)···Cl(2)	3.40(1)	2.46	168
N(2)—H(201)···Cl(4)	3.349(9)	2.72	124
N(2)—H(201)···Cl(5)	3.37(1)	2.77	122
N(2)—H(202)···Cl(6)^{i}	3.39(1)	2.51	153
N(2)—H(203)···Cl(1)^{iii}	3.38(1)	2.43	177

Symmetry code: (i) $1-x$, $-y$, $-z$; (ii) $-x$, $-y$, $-z$; (iii) $1 + x$, y, z

Compound 2			
N(1)—H(101)···Cl(4)	3.279(5)	2.44	148
N(1)—H(102)···Cl(1)^{i}	3.442(5)	2.76	129
N(1)—H(102)···Cl(3)	3.306(5)	2.51	141
N(1)—H(102)···Cl(3)^{i}	3.283(5)	2.86	109
N(1)—H(103)···Cl(5)^{ii}	3.254(5)	2.31	170
N(2)—H(201)···Cl(3)^{iii}	3.340(5)	2.48	152
N(2)—H(202)···Cl(2)^{iv}	3.448(6)	2.63	144
N(2)—H(202)···Cl(5)^{iii}	3.148(5)	2.67	112
N(2)—H(203)···Cl(1)^{v}	3.460(5)	2.55	161
N(2)—H(203)···Cl(4)^{iv}	3.452(5)	2.93	116

Symmetry code: (i) $1/2 - x$, $1 - y$, $-1/2 + z$; (ii) x, y, $-1 + z$; (iii) $-x$, $1/2 + y$, $1/2 - z$; (iv) $1/2 - x$, $-y$, $-1/2 + z$; (v) $1/2 + x$, $1/2 - y$, $1 - z$.

Table 7 (*concluded*).

D—H···A	D···A	H···A	D—H···A
Compound 3			
N(1)—H(61)···Cl(32)^{i}	3.58(1)	2.69	157
N(1)—H(61)···Cl(34)^{i}	3.40(1)	2.78	124
N(1)—H(62)···Cl(11)^{i}	3.38(1)	2.76	124
N(1)—H(62)···Cl(14)^{ii}	3.47(1)	2.64	146
N(1)—H(63)···Cl(12)^{i}	3.36(1)	2.46	159
N(2)—H(64)···Cl(14)^{iii}	3.48(2)	2.56	166
N(2)—H(65)···Cl(31)^{iv}	3.43(2)	2.70	134
N(2)—H(66)···Cl(36)^{iv}	3.34(2)	2.44	159
N(3)—H(67)···Cl(32)	3.37(1)	2.53	148
N(3)—H(68)···Cl(34)^{v}	3.44(1)	2.52	163
N(3)—H(69)···Cl(35)	3.38(1)	2.56	144
N(4)—H(70)···Cl(33)^{v}	3.40(2)	2.70	131
N(4)—H(70)···Cl(35)	3.37(2)	2.65	134
N(4)—H(71)···Cl(31)^{v}	3.36(2)	2.43	164
N(4)—H(72)···Cl(13)	3.59(2)	2.77	145
N(4)—H(72)···Cl(36)	3.52(2)	2.75	139

For the disordered cation:

D···A	D···A	Tl—Cl···N
N(41)^{v}···Cl(23)	3.26(2)	121
N(51)^{v}···Cl(23)	3.29(2)	120
N(41)···Cl(24)	3.23(2)	130
N(51)···Cl(24)	3.30(2)	130
N(41)···Cl(33)	3.24(2)	96
N(51)···Cl(33)	3.18(2)	97
N(41)···Cl(35)	3.26(2)	97
N(51)···Cl(35)	3.25(2)	95

Symmetry code: (i) $1 + x$, y, z; (ii) $1 + x$, y, $1 + z$; (iii) $1 - x$, $1/2 + y$, $-z$; (iv) $1 - x$, $1/2 + y$, $1 - z$; (v) x, y, $-1 + z$.

Compound 4			
N(1)—H(12)···Cl(3)^{i}	3.288(4)	2.39	157
N(4)—H(41)···Cl(3)	3.377(4)	2.78	122
N(4)—H(41)···Cl(3)^{ii}	3.251(4)	2.43	145
N(4)—H(41)···Cl(5)^{ii}	3.282(4)	2.84	110
N(1)—H(11)···O(2)^{iii}	2.945(5)	2.03	161
N(4)—H(42)···O(1)	2.787(6)	1.85	171
O(1)—H(101)···Cl(2)^{iii}	3.246(4)	2.37	167
O(1)—H(102)···Cl(1)	3.283(4)	2.55	148
O(2)—H(201)···Cl(4)^{iv}	3.209(4)	2.34	174

Symmetry code: (i) x, $1 - y$, $-1/2 + z$; (ii) $-x$, y, $-1/2 - z$; (iii) $-1/2 + x$, $1/2 - y$, $-1/2 + z$; (iv) x, $-y$, $1/2 - z$.

To make a comparison of the structural features of the four salts, it is first useful to consider the structure of 4-chloropyridinium pentachlorothallate(III), which has a discrete pentacoordinated $[TlCl_5]^{2-}$ anion (7). This anion exhibits a slightly distorted square pyramidal geometry with Tl—Cl distances that range from 2.443(4) to 2.551(5) Å, the shortest distance being the apical Tl—Cl bond. The two longest basal Tl—Cl bonds are involved in hydrogen bonds to the cation, giving cation-anion-cation units.

Fig. 1. Formula unit of salt **1** (ORTEP) highlighting the octahedral coordination environment around the thallium centre (Cl(3) and Cl(4) are on inversion centres, and are shared as bridging atoms). Hydrogen atoms on carbon centres have been removed for clarity.

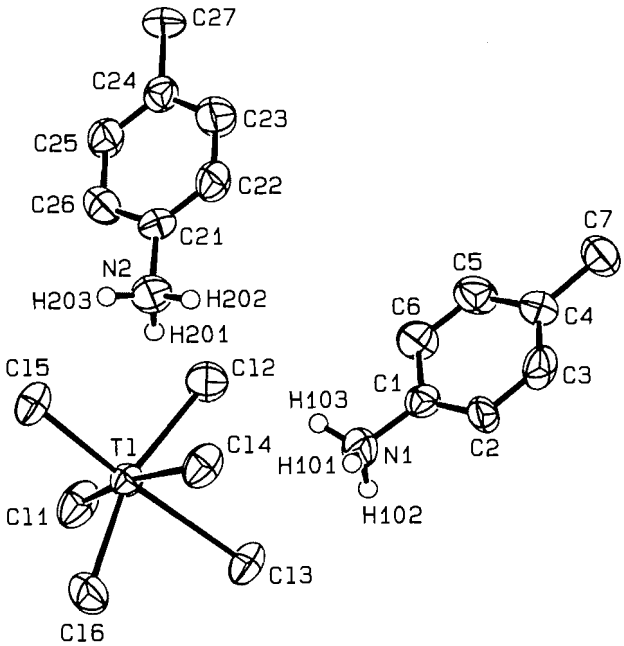

Fig. 2. Packing diagram of salt **1** (projection on (001) plane) showing the anionic *cis* chains.

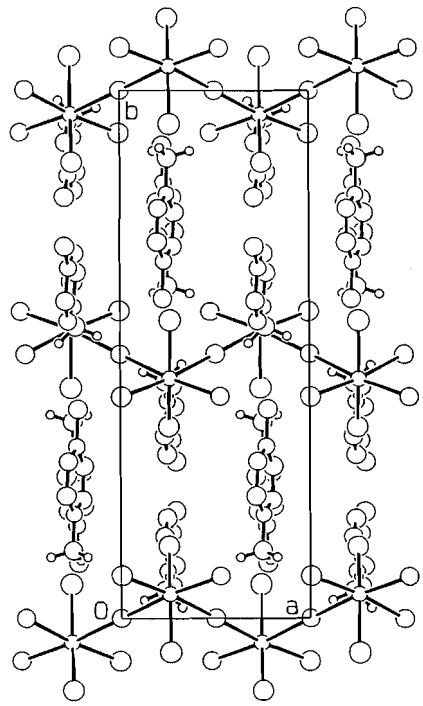

The asymmetric unit of salt **1** (Fig. 1) contains two symmetry-independent *p*-toluidinium cations and a $[TlCl_5]^{2-}$ fragment. In the structure, two chlorine atoms lie on crystallographic inversion centres, and therefore each forms a bridge between two thallium centres. In this way, the chlorine atoms form a distorted octahedron about each thallium tom, giving the overall stoichiometry for the anions of $[TlCl_4Cl_{1/2}Cl_{1/2}]^{2-}$. The two bridging Tl—Cl distances are long (2.8073(7) and 2.7986(7) Å)) while the terminal Tl—Cl distances are close to 2.5 Å, which is typical of six-coordinated Tl(III) (19). A projection of the structure on the (001) plane (Fig. 2) shows that the chlorothallate(III) anions form infinite, one-dimensional *cis*-linked (zigzag) chains (i.e., a Wells type (ii) chain) (20) that run parallel to the *a* axis (Fig. 2). Structural features for the cation are consistent with previous studies (21). The cations lie approximately parallel to the (100) planes, and they are linked via hydrogen bonds to the anionic chain such that all chlorine atoms act as hydrogen-bond acceptors. The anionic chains are not cross-linked by any hydrogen bonds.

Compound **2** contains a $[TlCl_5]^{2-}$ anion and a pentanediammonium dication in its asymmetric unit (Fig. 3). The anions are distorted square pyramidal, with four terminal Tl—Cl distances varying from 2.482(1) to 2.530(1) Å, while the Tl—Cl(3) distance is longer (2.655(1) Å). The angles made

Fig. 3. Asymmetric unit (ORTEP) of salt **2**. Hydrogen atoms on carbon centres have been removed for clarity.

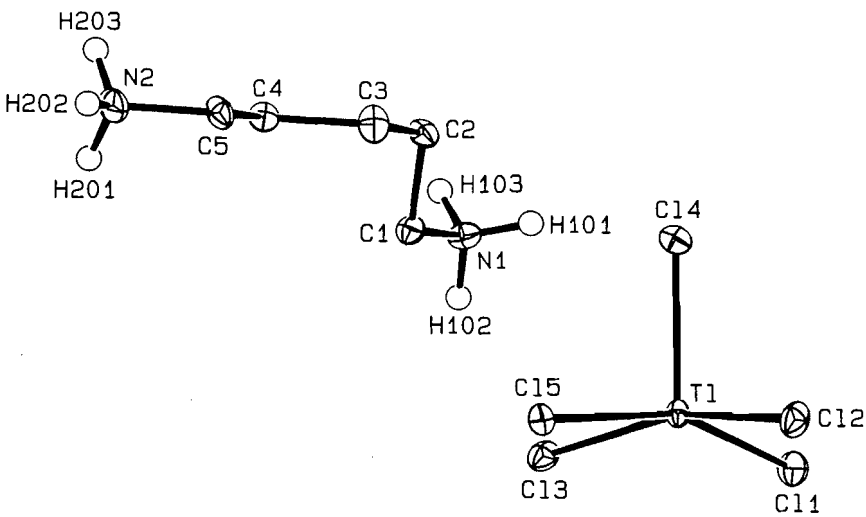

Fig. 4. Packing diagram of salt **2** (projection on (100) plane) illustrating the formation of the anionic chains through bridging Cl(3) sites. Hydrogen atoms on carbon centres have been removed for clarity.

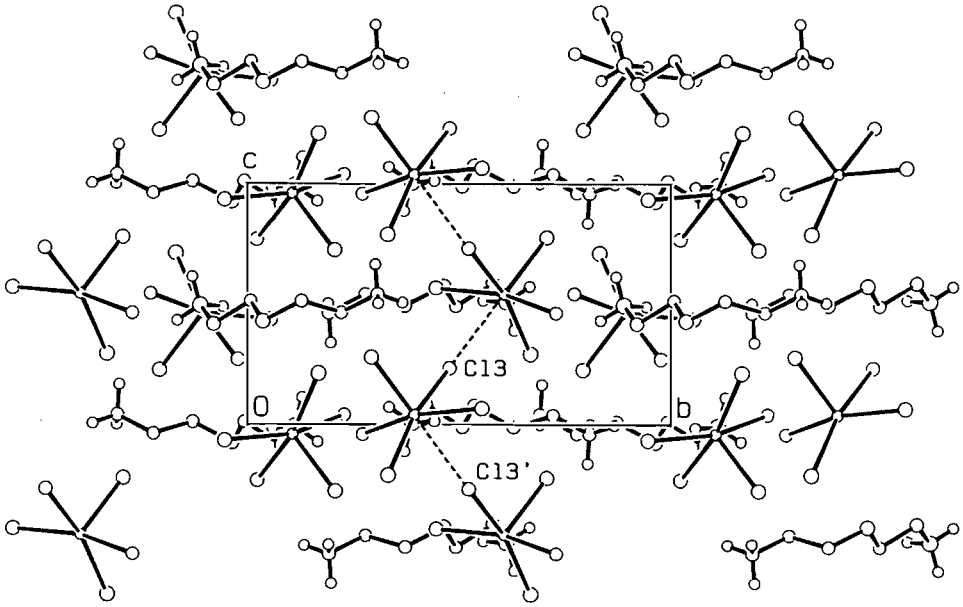

between the apical Tl—Cl(4) bond and those bonds in the basal plane vary from 85.52(5) to 103.12(5)°. The calculated distance of the Tl atom from the basal plane is 0.388(1) Å, while the mean deviation of the four basal Cl atoms from the plane is 0.037 (2) Å.

Each $[TlCl_5]^{2-}$ anion is related to another by a twofold screw axis along the *c* axis, giving a Tl---Cl(3′) contact distance of 3.225(5) Å. Thus Cl(3) forms a lopsided bridge between two thallium centres, and the longer Tl—Cl(3) distance 2.655(1) Å is typical for a TlCl asymmetric bridging bond (5). A helical or zigzag anionic chain extending along the *c* axis is formed (Fig. 4), but the contact distances suggest considerably weaker $[TlCl_5]^{2-}$---$[TlCl_5]^{2-}$ interactions than those in both **1** and Cs_2TlCl_5. Each chain of poly $[TlCl_5]^{2-}$ cross links via hydrogen bonding from N(1)—H to Cl(3) (N(1)---Cl(3) = 3.306(5) Å) in one chain to Cl(3′) (N(1)---(Cl3′) = 3.283(5) Å) in a neighbouring chain, thus forming a planar hydrogen-bonded network parallel to the *ab* plane. There are no Tl---Cl–Tl interactions between the anionic chains. The N(1) hydrogen atoms are also involved in hydrogen bonding to Cl(1), Cl(4), and Cl(5) (Table 7). All five chlorine atoms are hydrogen-bond acceptors from the N(2) hydrogen atoms, although not from the same asymmetric unit. The overall result is a complex three-dimensional network of hydrogen bonding connecting anions and cations within the *ab* layers and between the layers (Fig. 4). An alternative way of describing this system would be as an anion---cation---anion linkage where the anion is poly $[TlCl_5]^{2-}$.

Compound **2** crystallizes in a non-centrosymmetric space group (the absolute structure has been determined) with two cell dimensions of comparable length. Such compounds may display piezoelectric effects. Several halogenometallate compounds have been shown to undergo order–disorder phase transitions (such as K_2SnCl_6) (22) and hydrogen-bonded materials constitute a significant group of piezoelectric compounds. For example, in methylammonium trichloromer-

Table 8. Cell Constants for compound **2** at different temperatures.

Temperature, °C	*a*, Å	*b*, Å	*c*, Å
−100	13.226(2)	13.595(2)	7.628(2)
10	13.313(2)	13.555(3)	7.695(1)
30	13.332(3)	13.526(3)	7.7192(8)

Fig. 5. Differential scanning calorimetry curve for salt **2**.

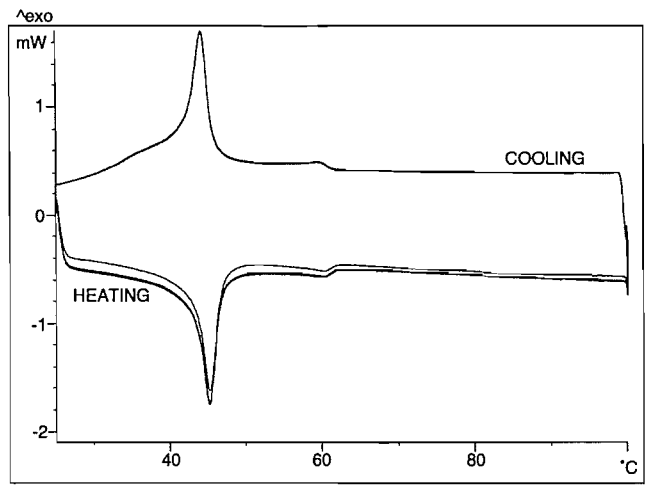

curate(II), N—H---Cl hydrogen bonding appears to be the ordering mechanism by which ferroelectricity is established (23). Although piezoelectricity has not been confirmed for salt **2**, measurements of the cell constants at three different temperatures (Table 8) suggest that the parameters *a* and *b* might, at some point, become equal and thus convert the unit cell to a tetragonal system, especially since the *b* axis contracts with increasing temperature. A phase transition was not observed in the differential scanning calorimetry data (Fig. 5) between

Fig. 6. Asymmetric unit (ORTEP) of salt **3**. Hydrogen atoms on carbon centres have been removed for clarity.

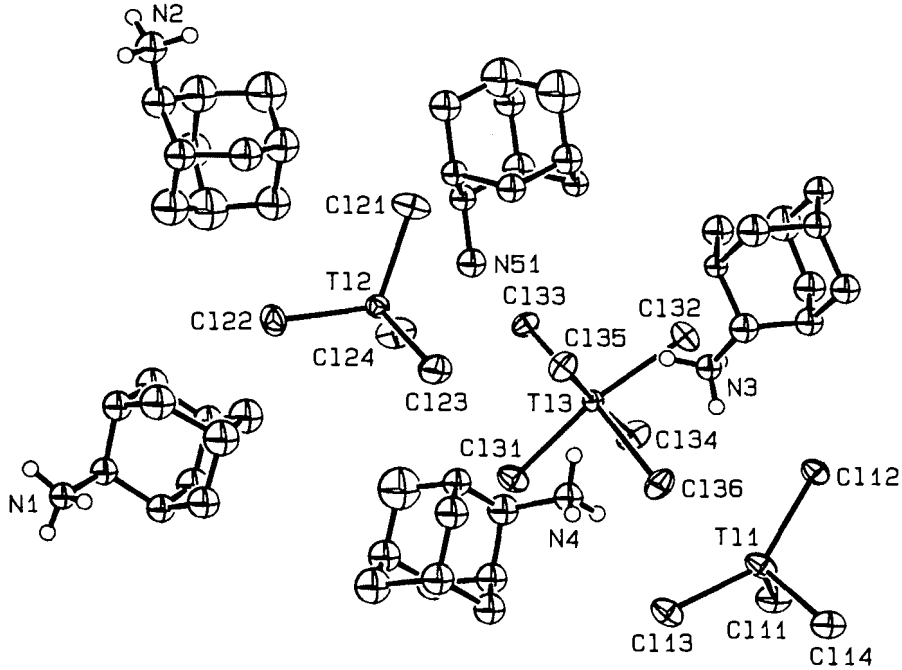

room temperature and −180°C, but a significant endothermic event (ca. 2.2 kJ mol^{-1}), which might be associated with ion reorientation, was observed at 45°C. A marked "shoulder" observed on this peak near 35°C suggests that there may be a gradual approach to the transition, similar to that proposed by Strømme for sodium perchlorate (24). This, together with a smaller (possibly second-order) transition at ca. 58°C, indicates that the thermal behaviour of the material is complex. In view of its high melting point (266°C) this compound is worthy of further investigation as a phase change material.

The asymmetric unit of salt **3** (Fig. 6) contains two structurally different $[TlCl_4]^-$ groups and one $[TlCl_6]^{3-}$ fragment, together with five 2-adamantaneammonium groups, one of which is disordered. The tetrahedral geometry of one of the $[TlCl_4]^-$ groups is regular, whereas the other (Tl(1)) is severely distorted (Table 6). The distorted tetrahedral $[TlCl_4]^-$ anion weakly bridges two regular $[TlCl_6]^{3-}$ octahedra via two long Tl---Cl contacts. This allows the distorted tetrahedral species to adopt a pseudo-octahedral geometry. In turn, each $[TlCl_6]^{3-}$ fragment bridges two distorted $[TlCl_4]^-$ fragments. The bridging Tl—Cl bond lengths of the $[TlCl_6]^{3-}$ ions are 2.657(5) and 2.667(5) Å, and the bridging Tl(1)---Cl contacts are 3.115(5) and 3.109(5) Å. The bridges therefore have the same asymmetric nature as those observed in compound **2**. The $[TlCl_6]^{3-}$ and $[TlCl_4]^-$ ions thus form a chain parallel to the *c* axis by vertex sharing such that the linkages are *cis* related in both the $[TlCl_4]^-$ and $[TlCl_6]^{3-}$ species (Fig. 7). To our knowledge, this type of chain has not been described previously for chlorothallate anions.

The hydrogen-bonding network in compound **3** is complex. Two of the chlorine atoms in the regular tetrahedral $[TlCl_4]^-$ anion are not involved in N—H---Cl hydrogen bonding (Table 7). The disordered cation (N(51)) is hydrogen bonded to two of the regular $[TlCl_4]^-$ fragments as well as to two of the chlorine atoms in the $[TlCl_6]^{3-}$ species. In addition, this latter anion receives hydrogen bonds from the cations containing N(3) and

Fig. 7. Packing diagram of salt **3** (projection on (001) plane). All hydrogen atoms have been removed for clarity. Thin lines between anions and cations represent hydrogen bonding. An additional set of cations has been added in the lower left side of the figure, as well as an extra $[TlCl_4]^{1-}$ in the middle of the figure to illustrate the anionic columns and cation---anion---cation chains which run parallel to the *c* axis.

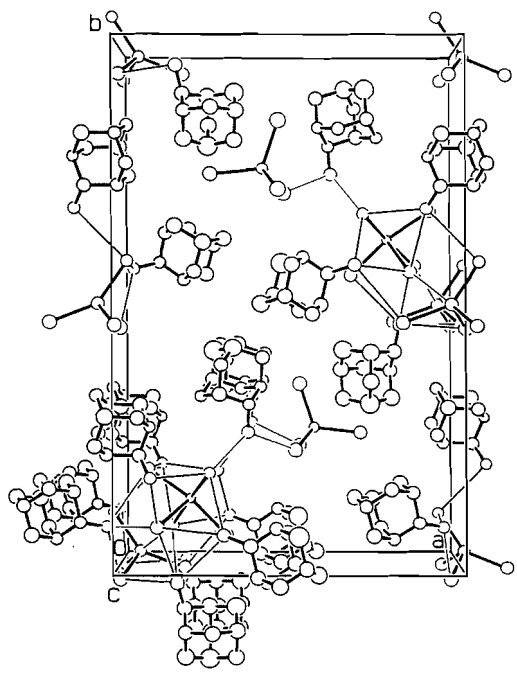

N(4). The N(3) and N(4) containing cations are also involved with hydrogen bonding to the distorted $[TlCl_4]^-$ anion. The N(1) and N(2) containing cations are hydrogen bonded to the distorted $[TlCl_4]^-$ groups as well as to the $[TlCl_6]^{3-}$ moiety. As a result, there is a chain of anionic $--[TlCl_6]^{3-}---[TlCl_4]^-$---

Fig. 8. Formula unit (ORTEP) of salt **4**. Hydrogen atoms on the carbon centres have been removed for clarity.

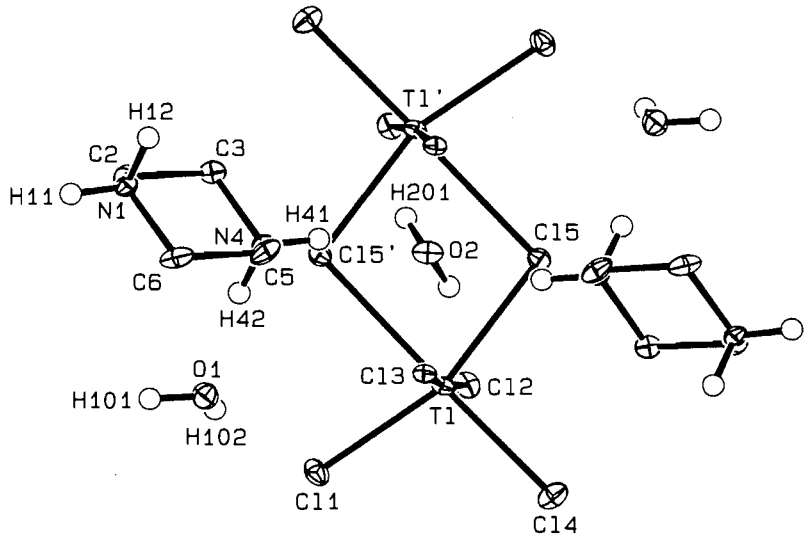

$[TlCl_6]^{3-}$-- units hydrogen bonded to four of the five surrounding adamantaneammonium cations that thus forms a thick column running along the *c* axis. The regular tetrahedral $[TlCl_4]^-$ ion and the disordered cation (Fig. 7) form another chain via hydrogen bonding, giving a cation---anion---cation linkage. The two chains run parallel to each other, and these are cross-linked through hydrogen bonding via the disordered cation. The regular tetrahedral $[TlCl_4]^-$ ion engages in hydrogen bonding with only the disordered cation.

The asymmetric unit of salt **4** contains the $[TlCl_5]$ fragment, one piperazinium cation, and 1.5 water molecules. The formula unit is related to the asymmetric unit by a twofold axis: the anion has twofold symmetry and one of the water molecules lies on a twofold axis. The resulting solid state structure (Fig. 8) is thus composed of piperazinium cations, H_2O molecules, and $[Tl_2Cl_{10}]^{4-}$ anions, the dimeric alternative to $[TlCl_5]^{2-}$. The dimerization results in the thallium centres having distorted octahedral coordination, and the bridging Tl—Cl distances are 2.562(1) and 2.894(1) Å. Alternating layers of cations and anions are clearly visible (Fig. 9) in the projection on the (001) plane. The cations are involved in hydrogen bonding to water molecules and to the chlorine atoms of the anion. The dimeric anion in salt **4** is similar to those observed previously in $CaTlCl_5(H_2O)_7$ and in "pyridinium enneachlorodithallate(III)" (25). The piperazinium dication adopts the "chair" conformation and displays structural parameters comparable to those in previous reports (see for example, ref. 26). The unique water molecule plays a central role in the hydrogen-bonding array. Its hydrogen atoms interact with the terminal Cl atoms of different $[Tl_2Cl_{10}]^{4-}$ units, while the oxygen atom interacts with the piperazinium N-H group. In addition, the symmetrical water molecule (O(2)) links the anion chains in the *c*-direction.

Conclusion

Three of the compounds (**1**, **2**, and **4**) possess the $TlCl_5$ stoichiometry, but none contains the isolated $[TlCl_5]^{2-}$ anion. In addition, three of the structures reported here (**1**, **2**, and **3**) possess

Fig. 9. Packing diagram of salt **4** (projection on 001 plane). Hydrogen atoms on the carbon centres have been removed for clarity.

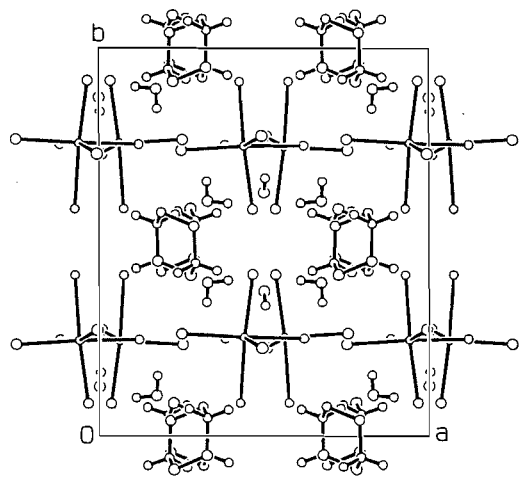

anions that are linked into chains, all of the "vertex-sharing" type. In general, the factors that govern the formation of any particular chain in these anionic coordination complexes are not known. In the case of the chlorothallates, however, it is clear that entry of a chloride ion into the metal's coordination sphere is often favoured over that of water, but this trend is cation dependent, as shown by the contrasting structures of the potassium and rubidium salts that have the $[TlCl_5(H_2O)]$ formula (4). As a result, catenation of some type so as to produce a polynuclear system is more often observed than the mononuclear $[TlCl_5{:}OH_2]^{2-}$ anion. In the context of the structures for compounds having the $TlCl_5$ stoichiometry, the non-chain arrangement in the 4-chloropyridinium salt (7) now appears to be the exception rather than the rule, although the chain observed in compound **2** is probably rather weak. The steric requirements of the cation may also have a significant influence on the structure adopted around the thallium centre. Recently, a series of arene$[SbCl_3]_2$ complexes has been

examined, and the steric demands of the arene as well as the formation of Cl_3Sb---Cl–$SbCl_2$ contacts were identified as key factors affecting the observed solid state structural features (27). Hydrogen-bonding arrangements observed in all four chlorothallate structures reported here also have an unpredictable effect on the structure of the resulting thallium anion, but it is likely that a subtle balance exists between Tl---Cl and N—H---Cl contact formation. In view of these diverse effects, a careful crystallographic reexamination of other salts containing weakly coordinating anions including the tetraethylammonium pentachlorothallate(III) salt would be of interest (8).

Acknowledgments

We would like to thank the Australian Research Council for their support of this work (B.D.J., J.L.), Mount Saint Vincent University for a research grant (M.A.J.), and Mr. G. Egan (FSE Pty. Ltd.) for the loan of a Mettler-Toledo TA 8000 DSC instrument. Special thanks to Professor T. Stanley Cameron (Dalhousie University, Halifax, Nova Scotia) for collecting the data for salt **1**.

References

1. M.A. James, O. Knop, and T.S. Cameron. Can. J. Chem. **70**, 1795 (1992).
2. J. Glaser. Acta Chem. Scand. Ser. A: **A36**, 451 (1982).
3. B.D. James, M.B. Millikan, and M.F. Mackay. Inorg. Chim. Acta, **77**, L251 (1983).
4. G. Thiele and B. Grunwald. Z. Anorg. Allgem. Chem. **498**, 105 (1983).
5. G. Thiele, H.W. Rotter, and M. Faller. Z. Anorg. Allgem. Chem. **508**, 129 (1984).
6. G. Thiele and R. Richter. Z. Kristallogr. **205**, 131 (1993).
7. M.A. James, M.B. Millikan, and B.D. James. Main Group Met. Chem. **14**, 1 (1991).
8. G. Joy, A.P. Gaughan, Jr., I. Wharf, D.F. Shriver, and J.P. Dougherty. Inorg. Chem. **14**, 1795 (1975).
9. N. Walker and D. Stuart. Acta Crystallogr. Sect. A: Found. Crystallogr. **A39**, 158 (1983).
10. A.C.T. North, D.C. Phillips, and F.S. Mathews. Acta Crystallogr. Sect. A: Cryst. Phys. Diffr. Theor. Gen. Crystallogr. **A24**, 351 (1968).
11. G.M. Sheldrick. Acta Crystallogr. Sect. A: Found. Crystallogr. **A46**, 467 (1990).
12. P.T. Buerskens, G. Admiraal, G. Buerskens, W.P. Bosman, S. García-Granda, J.M.M. Smits, and C. Smykalla. DIRDIF-92. The DIRDIF program system. Technical Report of the Crystallography Laboratory, University of Nijmegen, The Netherlands. 1992.
13. W.R. Busing, K.O. Martin, and H.A. Levy, ORFLS. A FORTRAN crystallographic least-squares program. Report ORNL-TM-305, Oak Ridge National Laboratory, Oak Ridge, Tenn. 1962.
14. TEXSAN Single Crystal Structure Analysis Package, Version 5.0. Molecular Structure Corporation, The Woodlands, Tex. 1989.
15. C.K. Johnson ORTEPII. Report ORNL-5138. Oak Ridge National Laboratory, Oak Ridge, Tenn. 1976.
16. J.R. Carruthers and D.L. Watkin. CRYSTALS, Issue 9, Chemical Crystallography Laboratory, Oxford, U.K. 1986.
17. H.D. Flack. Acta Crystallogr. Sect. A: Found. Crystallogr. **A39**, 875 (1983).
18. G. Bernardinelli and H.D. Flack. Acta Crystallogr. Sect. A: Found. Crystallogr. **A41**, 500 (1985).
19. J. Glaser. Acta Chem. Scand. Ser. A: **A34**, 141 (1980).
20. A.F. Wells. *In* Structural inorganic chemistry. 5th ed. Clarendon Press, Oxford. 1975. pp. 98–101.
21. M. Colapietro, A. Domenicano, and G. Portalone. Acta Crystallogr. Sect. B: Struct. Crystallogr. Cryst. Chem. **B38**, 2825 (1982).
22. N.G. Parsonage and L.A.K. Staveley. *In* Disorder in crystals. Clarendon Press, Oxford. 1978. pp. 394–405.
23. (*a*) A. Ben Salah, J.W. Bats, R. Kalus, H. Fuess, and A. Daoud. Z. Anorg. Allgem. Chem. **493**, 178 (1982); (*b*) M. Körfer and H. Fuess. Z. Kristallogr. **183**, 27 (1988); (*c*) Z.-T. Jiang, B.D. James, J. Liesegang, K.L. Tan, R. Gopalakrishnan, and I. Novak. J. Phys. Chem. Solids, **56**, 277 (1995).
24. K.O. Strømme. Acta Chem. Scand. **A28**, 515 (1974).
25. B.D. James, M.B. Millikan, B.W. Skelton, and A.H. White. Main Group Met. Chem. **16**, 335 (1993).
26. (*a*) C. Rérat. Acta Crystallogr. **13**, 459 (1960); (*b*) F. Brisse and J.-P. Sangin. Acta Crystallogr. Sect. B: Struct. Crystallogr. Cryst. Chem. **B38**, 215 (1982).
27. N. Burford, J.A.C. Clyburne, J.A. Wiles, T.S. Cameron, K.N. Robertson. Organometallics, **15**, 361 (1996).

The synthesis and high-resolution NMR spectroscopy of ethyl *N*-(2-triphenylmethylthio)ethanoyl-*O*-{4′-[4″-(1″-bis(2‴-chloroethyl)amino)phenyl]butanoyl}-L-seryl-*S*-benzyl-L-cysteine: a chelate–chlorambucil complex for use as a ligand for ^{99m}Tc radio-imaging

Russell A. Bell, Donald W. Hughes, Colin J.L. Lock, and John F. Valliant

Abstract: A potential agent for the imaging of tumours has been synthesized from the antineoplastic agent chlorambucil. Standard peptide coupling techniques were used to synthesize a tripeptide covalently coupled to chlorambucil in 10 steps. The final product was characterized by high-resolution NMR spectroscopy.

Key words: ethyl *N*-triphenylmethylthioethanoyl-*O*-{4′-[4″-(1″-bis(2‴-chloroethyl)amino)phenyl]butanoyl}-L-seryl-*S*-benzyl-L-cysteine, NMR spectroscopy, synthesis, radio-imaging agent.

Résumé : Utilisant l'agent antinéoplasique, on a synthétisé un agent pouvant éventuellement servir dans l'imagerie des tumeurs. On a utilisé les techniques standard de couplage des peptides pour synthétiser, en 10 étapes, un tripeptide lié d'une façon covalente à du chlorambucil. On a caractérisé le produit final à l'aide de la spectroscopie RMN à haute résolution.

Mots clés : *N*-triphénylméthylthioéthanoyl-*O*-{4′-[4″-(1″-bis(2‴-chloroéthyl)amino)phényl}butanoyl]}-L-séryl-*S*-benzyl-L-cystéine d'éthyle, spectroscopie RMN, synthèse, agent pour radio-imagerie.

[Traduit par la rédaction]

Introduction

There are a number of approaches to the synthesis of technetium complexes that may act as radio-imaging agents. Of these, one of the most important is the synthesis of relatively small molecules that can chelate the technetium atom and that, typically, have three, four, or five coordinating atoms (1, 2). Examples are the ligands based on the *N*,*N*′-bis(mercaptoethyl) ethylenediamine framework, which has two nitrogen and two sulphur coordinating atoms (3). A second, important method is to bind one of these small chelating groups to a biologically significant molecule, often through a spacer chain. The biological molecule should have a well-defined receptor in the human body and, preferably, the nature of the binding site in the biological molecule should be known. The chelant group is bound to the biological molecule at a position distant from the binding site, and one hopes that the chelated metal is sufficiently far away that it does not interfere markedly with binding of the combined molecule to the receptor. Radio-imaging agents based on monoclonal antibodies, naturally occurring biological molecules, and drugs have all been prepared (4). An increasingly popular, third alternative is to synthesize relatively small polypeptides, with one end providing the site that binds to the receptor and the other end providing the chelant groups. In this paper we describe a combination of the two last procedures where we have used a tripeptide to provide the chelant group and the anti-cancer drug chlorambucil (5, 6) as the biological molecule.

Results and discussion

The first method used to try to synthesize **1** (see Fig. 1) was to make the tripeptide fragment and attach chlorambucil subsequently. This led, however, to an inseparable mixture, despite the coupling method used.[3] In the successful approach the pro-

Received February 19, 1996.

R.A. Bell,[1] C.J.L. Lock,[2] and J.F. Valliant. Laboratories for Inorganic Medicine, Departments of Chemistry, Biochemistry, and Pathology, McMaster University, ABB-266A, Hamilton, ON L8S 4M1, Canada.
D.W. Hughes. McMaster University N.M.R. Facility, McMaster University, Hamilton, ON L8S 4M1, Canada.

[1] Author to whom correspondence may be addressed. Telephone: (905) 525-9140, ext. 23479. Fax: (905) 522-2509. E-mail: Bell@mcmaster.ca
[2] Deceased May 1, 1996.

[3] The methods used the following combinations of coupling reagents: oxalyl chloride – dimethylformamide , DCC–DMAP, EDAC-HCl–DMAP.

Fig. 1. Ethyl *N*-(2-triphenylmethylthio)ethanoyl-*O*-{4′-[4″-(1″-bis(2‴-chloroethyl)amino)phenyl]butanoyl}-L-seryl-*S*-benzyl-L-cysteine, **1**.

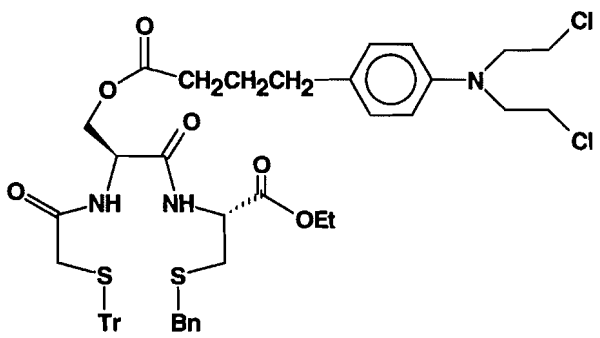

tected dipeptide L-Ser-L-Cys[4] was coupled to chlorambucil before the addition of the mercaptoethanoic acid fragment.

The synthesis of the dipeptide–chlorambucil molecule is outlined in Fig. 2. The ethyl ester of *S*-benzyl-L-cysteine, **3**, was produced as the tosylate salt. The free amine of the cysteine derivative was subsequently coupled to *N-tert*-butoxycarbonyl-L-serine, in 80% yield, with ethyl-3-(3-dimethyl-amino)propylcarbodiimide hydrochloride (EDAC-HCl). The use of the water-soluble carbodiimide resulted in a product that could be isolated by recrystallization. This was in contrast to reactions in which the coupling reagent was dicyclohexylcarbodiimide (DCC), where repeated chromatography was required in order to remove residual dicyclohexylurea. The protected dipeptide **5** contained a free hydroxyl group and was now ready for formation of the chlorambucil ester **6**. The initial approach, which had limited success, was the preparation of the ester through the acid chloride (8). The improved procedure used EDAC-HCl and 4-dimethylaminopyridine (DMAP) as coupling reagents and gave **6** in 71% yield.

N-Hydroxysuccinimido-2-(triphenylmethylthio)ethanoate, **8**, has been reported to be a useful material with which to introduce protected mercaptoethanoic acid into a molecule (9). The literature procedures for the protection and activation of mercaptoethanoic acid are low-yield reactions that leave the final product contaminated with starting material and (or) dicyclohexylurea. In our approach to the protection of mercaptoethanoic acid (Fig. 3), the acid and triphenylcarbinol were dissolved in a mixture of acetic acid and dichloromethane, followed by the addition of boron trifluoride etherate. The use of dichloromethane as a cosolvent allowed reaction to occur at ambient temperatures rather than at 80°C, as the literature suggested, and resulted in a very pure product that was obtained in high yield. Compound **8** was produced by coupling **7** and *N*-hydroxysuccinimide in acetronitrile with EDAC-HCl: the product precipitated in high yield and purity in a short reaction time.

The addition of the final fragment, **8**, required the removal of the carbamate on the dipeptide–chlorambucil adduct (Fig. 4) and this was accomplished with trifluoroacetic acid and triethylsilane (9). The product, **9**, after extraction with acqueous sodium carbonate solution, was coupled to **8** and gave the tripeptide–chlorambucil adduct, **1**. The overall yield from *S*-benzyl-L-cysteine was 30%. Compound **1** was subjected to high-resolution NMR analysis.

NMR spectroscopy

The Bruker DRX-500 spectrometer, with its gradient capability, allowed the acquisition of two-dimensional spectra in remarkably short time periods. The gradient-COSY (10–13) and HSQC (14–16) spectra for compound **1** were each acquired in 5.5 min on approximately 15 mg of sample. The majority of the aliphatic ^{1}H and ^{13}C signals of **1** were assigned (Tables 1 and 2) by the aforementioned two-dimensional techniques and these were consistent with assignments made for the synthetic precursors. There remained several assignments in both the proton and carbon atom spectra of **1** that could not be made unambiguously. Consequently, a Heteronuclear Multiple Bond Correlation (HMBC) (17) experiment and a Heteronuclear Multiple Quantum Coherence – Total Correlation Spectroscopy (HMQC–TOCSY) (18) experiment were performed (Figs. 5 and 6).

The use of the HMBC pulse sequence with a low-pass *J* filter allowed proton resonances to be correlated with neighbouring carbon atom resonances through spin coupling interactions of $^{2}J_{H-C}$ and $^{3}J_{H-C}$ (Fig. 5). The initial use of the HMBC experiment was to assign the four carbonyl signals that corresponded to the two amide and two ester groups. The ethyl ester carbonyl peak (C-24) was assigned by correlation of the quartet of the methylene group of the ester (4.146 ppm) and the carbon atom signal at 169.9 ppm. The amide carbonyl signals were assigned by the observation of a two-bond correlation with the adjacent α proton signal. The α proton chemical shifts had been assigned previously to the appropriate amino acid by use of the COSY experiment. The remaining carbonyl signal belonged to the ester between the chlorambucil unit and the serine hydroxyl group. The HMBC experiment also facilitated the assignment of all the carbon atom signals in the aromatic systems as well as confirming the assignments of H-6, H-12, and H-19.

The HMQC–TOCSY experiment (Fig. 6) was used to corroborate the ^{1}H and ^{13}C assignments. For example, the proton resonance at 4.382 ppm was assigned as the α proton of serine (H-9). In the HMQC–TOCSY experiment, H-9 exhibited a HMQC correlation to C-9, the carbon to which it is directly bound. As a result of the TOCSY portion of the pulse sequence, H-9 also showed correlation with H-8 and H-10, the amide and β protons of serine, respectively. The proton signal assigned as H-10 also correlated to its directly bound carbon

[4] In this paper we have used a number of abbreviations. These are: AcOH, acetic acid; ACQ, acquire; BIRD, bi-linear rotation decoupling; Bn, benzyl; Boc, *tert*-butoxycarbonyl; COSY, correlation spectroscopy; DCC, dicyclohexylcarbodiimide; DCI, direct injection chemical ionization; DMAP, dimethylaminopyridine; EDAC, ethyl-3-(3-dimethylamino)propylcarbodiimide; Et, ethyl; FID, free induction decay; HMBC, heteronuclear multiple bond correlation; HMQC, heteronuclear multiple quantum coherence; HRDEI, high-resolution direct injection electron impact; HSQC, heteronuclear single quantum coherence; NMR, nuclear magnetic resonance; NOESY, nuclear Overhauser effect spectroscopy; TFA, trifluoroacetic acid; TLC, thin–layer chromatography; TOCSY, total correlation spectroscopy; Tr, triphenylmethyl; TsOH, *p*-toluenesulphonic acid. In addition, the standard three-letter abbreviations for amino acids are used (7).

Fig. 2. The synthetic pathway to ethyl *N-tert*-butoxycarbonyl-*O*-{4′-[4″-(1″-bis(2‴-chloroethyl)amino)phenyl]butanoyl}-L-seryl-*S*-benzyl-L-cysteine, **6**.

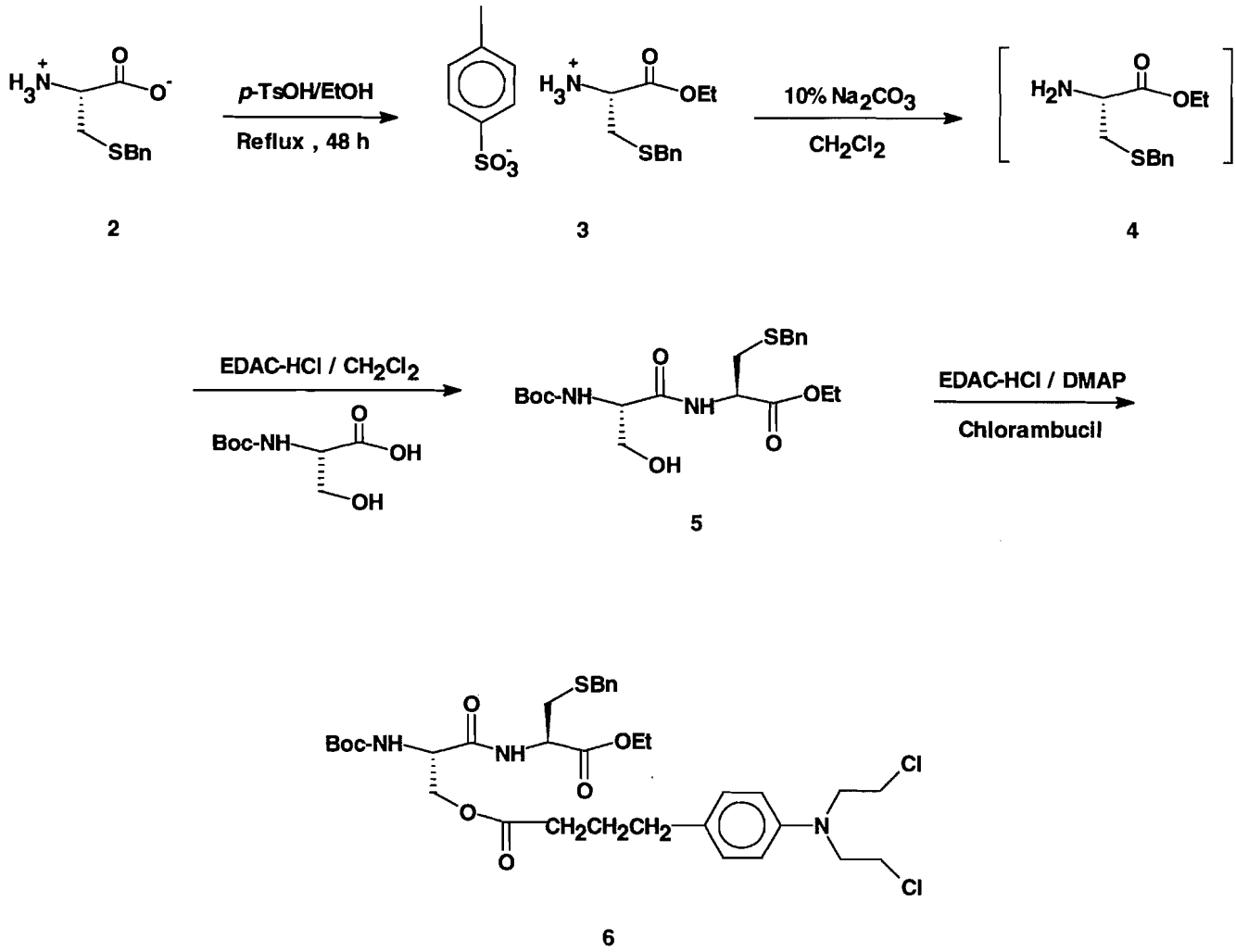

Fig. 3. Synthesis of *O*-(*N*-hydroxysuccinimido)-2-(triphenylmethylthio)ethanoate, **8**.

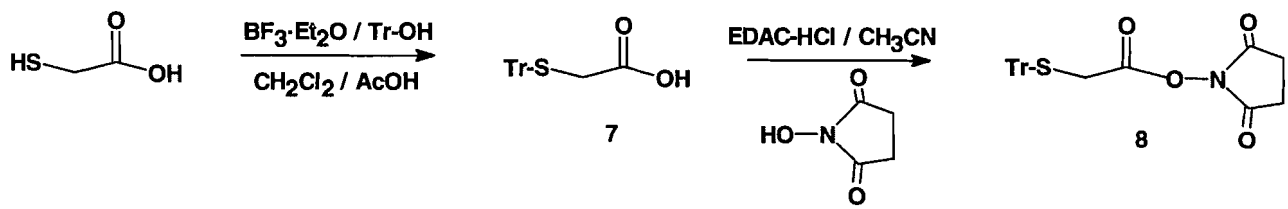

atom. As a result, all the proton and carbon atom signals within the serine portion of the molecule could be assigned. The results of the HMQC–TOCSY experiment were consistent with the assignment made in Tables 1 and 2.

The one-dimensional NOE difference spectra and the two-dimensional NOESY (19) spectra of **1** in $CDCl_3$ were entirely consistent with the assignments presented above. The presence of strong NOEs between H-9 and H-22, and between H-8 and H-6 and the complete absence of NOEs between H-9 and H-6, and H-9 and H-23, showed the anticipated preponderance of the *Z* geometric isomers of the two amide groups. Otherwise the molecule appeared to be relatively flexible with no particularly demanding conformational preferences. Thus the *ortho* protons on each of the aromatic rings showed NOEs to side-chain protons that were on carbon atoms one, two, and three bonds removed from the ring but there was no evidence for NOEs over longer distances. Likewise there were no observable NOEs between one set of aromatic protons and another that might have arisen from any possible stacking of the aromatic rings.

Fig. 4. The deprotection of **6** to yield **9** and subsequent coupling to **8** to yield ethyl *N*-(2-triphenylmethylthio)ethanoyl-*O*-{4′-[4″-(1″-bis(2‴-chloroethyl)amino)phenyl]butanoyl}-L-seryl-*S*-benzyl-L-cysteine, **1**.

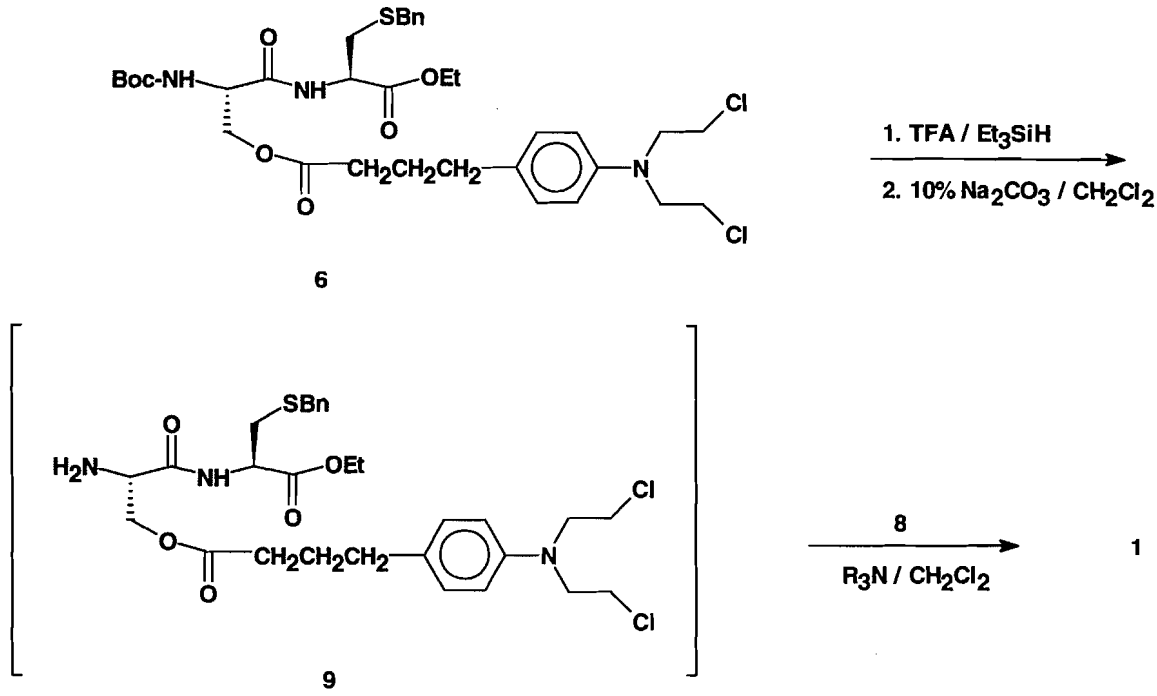

Fig. 5. The gradient HMBC spectrum of **1**.

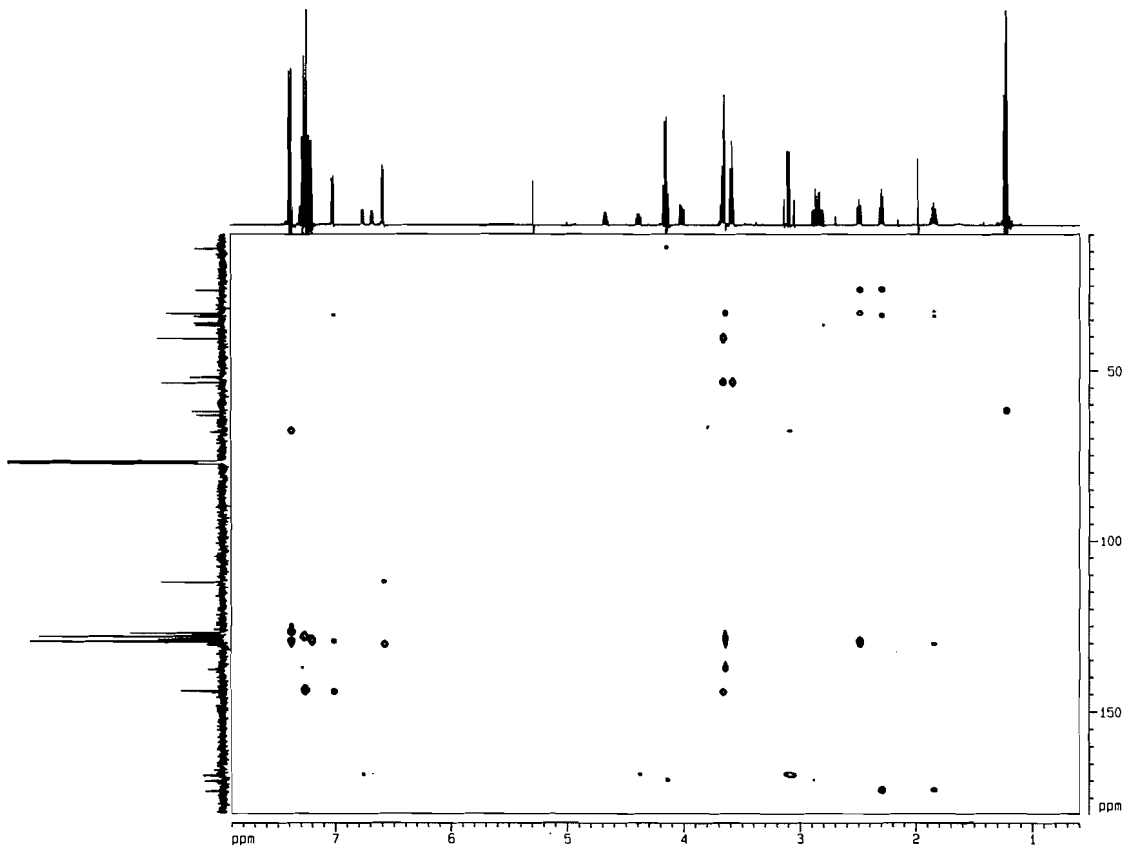

Fig. 6. The HMQC–TOCSY spectrum of compound **1**.

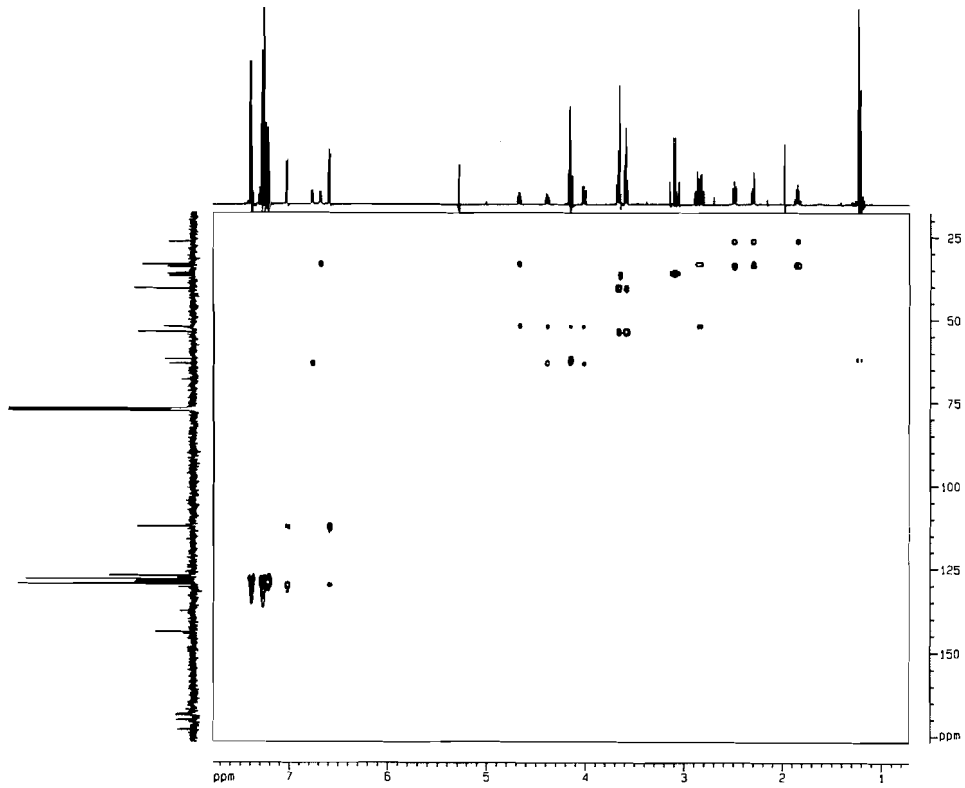

Thus, the synthesis of **1** was completed in 10 steps with 30% overall yield. A combination of two-dimensional NMR techniques was used to assign completely the proton and carbon atom spectra. As a result of the spectrometer's gradient capability the entire collection of spectra, ^{1}H, ^{13}C, COSY, HMQC, HMBC, HMQC–TOCSY, were collected within 6 h on a moderately dilute sample (15 mg/mL). The use of this compound as a reagent for the early detection of breast cancer is currently being investigated.

Experimental section

Analytical TLC was performed on silica gel 60-F_{254} (Merck) with detection by long-wavelength ultraviolet light. Chromatography was performed with a chromatotron (Harrison Research model 7924T) that used a 4 mm plate (EM Science silica gel 60 PF_{254} that contained gypsum). All commercial reagents were used as supplied. Solvents were distilled, under nitrogen, from calcium hydride. Nitrogen was dried by passing it through calcium sulphate. All reactions were protected from light and carried out under a slow flow of nitrogen. Solvents were evaporated with a rotary evaporator (20 Torr; 1 Torr = 133.3 Pa) at elevated temperatures (30–50°C).

The NMR spectra of **1** were recorded on a Bruker Avance DRX-500 spectrometer. Proton spectra were acquired at 500.130 MHz with a 5 mm broadband inverse probe with triple axis gradient capability. Spectra were obtained in eight scans in 32K data points over a 4.006 kHz spectral width (4.096 s acquisition time). Sample temperature was maintained at 30°C by a Bruker Eurotherm variable temperature unit. Gaussian multiplication (line broadening: −1.5 Hz, Gaussian broadening: 0.2) was used to process the free induction decay (FID), which was zero-filled to 64K before Fourier transformation.

Proton COSY two-dimensional NMR spectra were recorded in the absolute value mode with the pulse sequence 90°–t_1–45°–ACQ and included pulsed field gradients for coherence selection. Spectra were acquired in one scan for each of the 256 FIDs that contained 2K data points in $F2$ over the previously mentioned spectral width. The ^{1}H 90° pulse width was 6.6 μs. A 1.0 s relaxation delay was employed between acquisitions. Zero-filling in $F1$ produced a 1K × 1K data matrix with a digital resolution of 3.91 Hz/point in both dimensions. During two-dimensional Fourier transformation a sine-bell squared window function was applied to both dimensions. The transformed data were then symmetrized.

Carbon-13 NMR spectra were recorded at 125.758 MHz with a 5 mm broadband inverse probe with triple axis gradient capability. The spectra were acquired over a 28.986 kHz spectral width in 32K data points (0.577 s acquisition time). The ^{13}C pulse width was 4.0 μs (30° flip angle). A relaxation delay of 0.5 s was used. Exponential multiplication (line broadening: 4.0 Hz) was used to process the FID, which was zero-filled to 64K before Fourier transformation.

Inverse detected ^{1}H–^{13}C two-dimensional chemical shift correlation spectra were acquired in the phase-sensitive mode and used the pulsed field gradient version of the HSQC pulse sequence. The FIDs in the $F2$ (^{1}H) dimension were recorded over a 3.655 kHz spectral width in 1K data points. The 128 FIDs in the $F1$ (^{13}C) dimension were obtained over a 21.368 kHz spectral width. Each FID was acquired in two scans. The fixed delays during the pulse sequence were a 1.0 s relaxation

Table 1. The proton NMR assignments for ethyl *N*-(2-triphenylmethyl-thio)ethanoyl-*O*-{4′-[4″-(1″-bis(2‴-chloroethyl)amino)phenyl]butanoyl}-L-seryl-*S*-benzyl-L-cysteine, **1**.

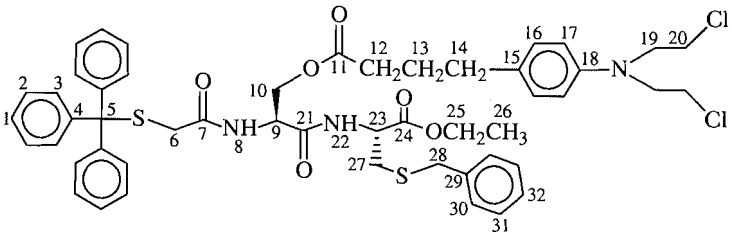

Chemical shift, δ	Proton	*J*(Hz)
7.390–7.180	H-aryl	
7.016	H-16	$^3J_{16,17} = 8.8$
6.761	H-8	$^3J_{8,9} = 7.0$
6.679	H-22	$^3J_{22,23} = 7.6$
6.581	H-17	
4.663	H-23	
4.382	H-9	
4.146	H-25	
4.151	$H\text{-}10_A$[a]	
4.009	$H\text{-}10_B$	$^3J_{AX} = 4.9$ $^3J_{BX} = 6.4$ $^2J_{AB} = -11.2$
3.646	H-28	
3.678–3.563	H-19, H-20	
3.117	$H\text{-}6_A$	$^2J_{6A,6B} = -15.9$
3.065	$H\text{-}6_B$	
2.872	$H\text{-}27_A$	
2.814	$H\text{-}27_B$	$^3J_{AX} = 4.9$ $^3J_{BX} = 5.7$ $^2J_{AB} = -13.9$
2.491	H-14	$^3J_{13,14} = 7.8$
2.299	H-12	$^3J_{12,13} = 7.5$
1.848	H-13	
1.225	H-26	$^3J_{25,26} = 7.1$

[a]In the case of diastereotopic pairs of protons, the symbols A and B refer to the downfield and upfield signals, respectively, where these could be resolved.

delay and a polarization transfer delay of 1.786 ms. The 90° ^{1}H pulse was 6.6 μs while the ^{13}C 90° pulse was 11.6 μs. The data were processed with a sine-bell squared window function shifted by π/2 in both dimensions and linear prediction to 256 data points in *F*1 followed by zero-filling to 1K.

The pulsed field gradient version of the HMBC pulse sequence was used to acquire the inverse detected ^{1}H–^{13}C two-dimensional chemical shift correlation spectra through two- and three-bond coupling interactions in the absolute value mode. The FIDs in the *F*2 (^{1}H) dimension were recorded over a 3.655 kHz spectral width in 1K data points. The 128 FIDs in the *F*1 (^{13}C) dimension were obtained over a 21.368 kHz spectral width. Each FID was acquired in two scans. The fixed delays during the pulse sequence were a 1.0 s relaxation delay, a 3.3 ms delay for the low-pass *J*-filter, and 0.08 s delay to allow evolution of the long-range coupling. The 90° ^{1}H pulse was 6.6 μs while the ^{13}C 90° pulse was 11.6 μs. The data were processed with a sine-bell window function in both dimensions and linear prediction to 256 data points in *F*1 followed by zero-filling to 1K.

The HMQC–TOCSY spectra were acquired in the phase-sensitive mode. The FIDs in the *F*2 (^{1}H) dimension were recorded over a 4.006 kHz spectral width in 1K data points. The 128 FIDs in the *F*1 (^{13}C) dimension were obtained over a 21.368 kHz spectral width. Each FID was acquired in 32 scans. The fixed delays during the pulse sequence were a 1.0 s relaxation delay, a 0.3 s delay between the BIRD pulse and HMQC pulse sequence, and 3.571 ms for polarization transfer. The TOCSY spin lock was 100 ms. The 90° ^{1}H pulse was 6.6 μs while the ^{13}C 90° pulse was 11.6 μs. The ^{1}H spin lock 90° pulse width was 27.0 μs. The data were processed with a sine-bell squared window function shifted by π/2 in both dimensions and linear prediction to 256 data points in *F*1 followed by zero-filling to 1K.

Proton–proton NOE difference spectra were obtained by subtraction of a control FID from an on-resonance FID. The decoupler in the control FID irradiated a position in the spectrum where there was no proton signal. The on-resonance FID was obtained while the proton of interest was selectively saturated. In both cases the same decoupler power and duration of saturation (5.0 s) were used. This saturation period also served as the relaxation delay for both the control and on-resonance

Table 2. The carbon-13 NMR assignments for ethyl *N*-triphenylmethylthioethanoyl-*O*-{4′-[4″-(1″-bis(2‴-chloroethyl)amino)phenyl]butanoyl}-L-seryl-*S*-benzyl-L-cysteine, **1**.

Chemical shift (ppm)	Carbon atom	Chemical shift (ppm)	Carbon atom
173.0	C-11	170.0	C-24
168.5	C-7	168.2	C-21
144.4	C-18	143.9	C-4
137.5	C-29	130.5	C-15
129.6	C-16	129.5	C-3
128.9	C-30	128.6	C-31
128.2	C-2	127.3	C-32
127.1	C-1	112.2	C-17
67.9	C-5	63.1	C-10
61.9	C-25	53.6	C-20
52.0	C-9	51.9	C-23
40.5	C-19	36.6	C-28
36.0	C-6	33.9	C-14
33.2	C-27, C-12	26.4	C-13
14.1	C-26		

FIDs. The decoupler was gated off during acquisition. Eight scans were acquired for both the control and on-resonance FIDs and were repeated four times for a total of 32 scans for the final difference spectrum. A 90° ^{1}H pulse width of 6.6 μs was used. The FIDs were processed with exponential multiplication (line broadening: 4.0 Hz) and were zero-filled to 64K during Fourier transformation. The sample was not degassed.

Two-dimensional NOESY spectra were acquired in the phase-sensitive mode with use of the pulse sequence: 90°–t_1–90°–τ–90°–ACQ. Phase-sensitive data were obtained with time proportional phase incrementation (TPPI) (20, 21). The mixing time τ was 0.8 s. In the *F*2: dimension 2K data points were used during the acquisition of the 256 FIDs. Each FID was acquired in 32 scans over 4.006 kHz spectral width using a 1.0 s relaxation delay. Zero-filling in the *F*1 dimension produced a 1K × 1K data matrix after 2-D Fourier transformation of the phase-sensitive data. This resulted in an *F*2 digital resolution of 3.91 Hz/point. During the 2-D Fourier transform a sine-bell window function shifted by π/2 was applied to both dimensions. The transformed data were not symmetrized.

The compounds used in this study were dissolved in $CDCl_3$ (Isotec, Inc.) to a concentration of approximately 15.0 mg/mL. Chemical shifts are reported in ppm relative to TMS. The residual solvent signals at 7.24 and 77.0 ppm were used as internal references for the ^{1}H and ^{13}C spectra, respectively.

All other NMR spectra were recorded on a Bruker AC-200 spectrometer. Proton spectra were acquired at 200.133 MHz with a 5 mm dual frequency probe. Spectra were obtained in eight scans in 16K data points over a 2.403 kHz spectral width (3.408 s acquisition time). Spectra were acquired at ambient probe temperature. The free induction decay (FID) was processed with exponential multiplication (line broadening: 0.1 Hz) and was zero-filled to 32K before Fourier transformation.

Carbon-13 NMR spectra were recorded at 50.323 MHz with the 5 mm dual frequency probe. The spectra were acquired over a 12.195 kHz spectral width in 16K data points (0.672 s acquisition time). The ^{13}C pulse width was 1.5 μs (42° flip angle). A 0.5 s relaxation delay was used. The FIDs were processed with exponential multiplication (line broadening: 3.0 Hz) and zero-filled to 32K before Fourier transformation.

Synthetic procedures

2-(Triphenylmethylthio)ethanoic acid, 7

Triphenylcarbinol (24 g, 92.3 mmol) and mercaptoethanoic acid (8.5 g, 92.4 mmol) were dissolved in dichloromethane (50 mL) and glacial acetic acid (50 mL). A deep red solution was formed when boron trifluoride etherate (16 mL, 130 mmol) was added. The solution was allowed to stir at room temperature for 1 h, during which a precipitate formed. The dichloromethane was removed in vacuo and water (100 mL) was added to the residue. The product was collected by filtration and washed with water (3 × 100 mL), acetonitrile (50 mL), and cold diethyl ether (20 mL). The product was recrystallized from benzene. Yield: 26.68 g, 87%; mp 155–157°C (lit. (9) mp 158.5–160.0°C); TLC: R_f = 0.33 (10:90 v:v CH_3OH/CH_2Cl_2); ^{1}H NMR (200 MHz) ($CDCl_3$, δ: 7.25 (m, 15H, aryl), 2.90(s, 2H, S-CH_2); ^{13}C NMR (50 MHz) ($CDCl_3$), δ: 175.77 (COOH), 144.09–128.05 (C-aryl), 67.44 (CPh_3), 34.67 (S-CH_2).

O-*(N-Hydroxysuccinimido)-2-(triphenylmethylthio)-ethanoate, 8*

N-Hydroxysuccinimide (1.72 g, 15 mmol) was added to 2-(triphenylmethylthio)ethanoic acid (5.01 g, 15 mmol) in acetonitrile (20 mL). Solid ethyl-3-(3-dimethylamino)propylcarbodiimide hydrochloride (EDAC-HCl) (3.16 g, 16.5 mmol) was added to the mixture and the solution became transparent after 5 min. Shortly thereafter a precipitate was seen. After the suspension was allowed to stir for 2 h the precipitate was collected by filtration. The colourless solid (3.88 g, 60%) was washed with cold acetonitrile (15 mL). After cooling the filtrate to 4°C overnight an additional crop of product was collected by filtration (1.62 g, 25%); mp 183–185°C; TLC: R_f = 0.46 (2:98 v:v CH_3OH/CH_2Cl_2); ^{1}H NMR (200 MHz) ($CDCl_3$, δ: 7.17 (m, 15H, H-aryl), 3.08 (s, 2H, S-CH_2) 2.47 (s, 4H, CH_2-C=O)$_2$); ^{13}C NMR (50 MHz) ($CDCl_3$), δ: 165.0 ((CH_2-*C*=O)$_2$), 163.00 (SCH_2*C*OON), 143.49 (C-ipso), 129.42 (C-*ortho*), 128.17) C-*meta*), 127.08 (C-*para*), 67.98 (*C*Ph_3), 31.35 (S-CH_2), 25.45 ((CH_2-C=O)$_2$).

Ethyl S*-benzyl-*L*-cysteine* p*-toluenesulphonate, 3*

p-Toluenesulphonic acid (10.8 g, 56.8 mmol) was added to *S*-benzyl-L-cysteine (3.0 g, 4.2 mmol) in absolute ethanol (100 mL). The mixture was heated to reflux for 48 h. The solution was then evaporated to dryness and diethyl ether (100 mL) was added. The resulting white precipitate was collected by filtration and washed with ether (200 mL). Yield: 4.67 g, 80%; mp 131–134°C: ^{1}H NMR (200 MHz) (CD_3OD), δ: 7.299 (m, 9H, H-aryl), 4.155 (q, 2H, O*C*$H_2$$CH_3$), 4.102 (m, 1H, H_2N-*C*H), 3.752 (s, 2H, S*C*H_2Ph), 2.886 (m, 2H, CH-*C*H_2S), 2.319 (s, 3H, CH_3-Ph), 1.232 (t, 3H, OCH_2*C*H_3); ^{13}C NMR (50.3 MHz) (CD_3OD), δ: 169.12 (*C*O_2Et), 143.15 (C-SO_3H (*p*TsOH-*para* C) 141.90 (Bn-ipso C), 138.61 (*p*TsOH-ipso C), 130.16 (pTsOH-*meta* C), 129.85 (Bn-*ortho* C), 129.66 (*p*TsOH-*ortho*), 128.42 (Bn-*para* C), 126.95 (Bn-*meta* C),

63.86 (OCH_2CH_3), 53.29 (H_2N-*C*H), 36.79 (SCH_2Ph), 32.06 ($CHCH_2S$), 21.31 (*p*TsOH-CH_3), 14.30 (OCH_2CH_3).

Ethyl N-tert-*butoxycarbonyl-L-seryl*-S-*benzyl-L-cysteine, 5*

Aqueous sodium carbonate (40 mL of 10%) was added to a suspension of **3** (5.0 g, 12.2 mmol) in dichloromethane (80 mL). The mixture was shaken until everything dissolved. The aqueous layer was back-extracted with dichloromethane (2 × 40 mL) and the organic layers combined and dried over anhydrous sodium sulphate. The organic layers were combined and evaporated to dryness. The resulting yellow oil was then diluted with dichloromethane (50 mL). *N-tert*-Butoxycarbonyl-L-serine (2.27 g, 11.1 mmol) and EDAC-HCl (2.33 g, 12.2. mmol) were added to this solution. The solution was stirred under nitrogen and protected from light for 16 h. The solution was extracted with 1 N HCl (2 × 20 mL), 1 N $NaHCO_3$ (2 × 20 mL), and distilled water (2 × 20 mL). The organic layer was evaporated to dryness and the resulting solid recrystallized from acetonitrile. Yield: 3.7 g, 80%; mp 78–79°C; TLC: R_f = 0.58 (10:90 v:v CH_3OH/CH_2Cl_2); ^1H NMR (200 MHz) ($CDCl_3$), δ: 7.308 (s, 5H, H-aryl), 5.485 (d, ^3J = 7.15, 1H, amide NH), 4.740 (m, 1H, $CHCH_2S$), 4.155 (q, 2H, OCH_2CH_3), 4.066 (m, 1H, $CHCH_2OH$), 3.688 (s, 2H, SCH_2Ph), 3.650 (m, 2H, $CHCH_2OH$), 2.851 (m, 2H, $CHCH_2S$), 1.751 (bs, OH), 1.436 (s, 9H, $C(CH_3)_3$), 1.243 (t, $^3J_{18,19}$ = 7.12, 3H, OCH_2CH_3); ^{13}C NMR (50 MHz) ($CDCl_3$), δ: 171.18 (*C*OOEt), 170.54 (amide C=O), 155.78 (carbamate C=O), 137.42 (C-ipso), 128.86 (C-*ortho*), 128.03 (C-*meta*), 127.17 (C-*para*), 80.36 (*Ct*Bu), 62.89 (OCH_2CH_3), 61.91 (CH_2OH), 55.34 ($CHCH_2S$), 51.74 ($CHCH_2OH$), 36.27 (SCH_2Ph), 32.97 ($CHCH_2S$), 28.19 ($C(CH_3)_3$), 13.95 (OCH_2CH_3); MS (NH_3-DCI), *m/z* (RI%): 444 (15, M+1+ NH_3), 427 (100, M+1), 327 (30, M+1−Boc).

Ethyl N-tert-*butoxycarbonyl*-O-*{4'-[4''-(1''-bis(2'''-chloroethyl)amino)phenyl]butanoyl}-L-seryl*-S-*benzyl-L-cysteine, 6*

A solution of EDAC (100 mg, 0.52 mmol) and DMAP (6 mg, 10 mol%) in dichloromethane (5 mL) was added to **5** (200 mg, 0.47 mmol) and chlorambucil (136 mg, 0.45 mmol) in dry dichloromethane (15 mL). The reaction was stirred under a nitrogen atmosphere and protected from the light for 6 h. The solution was then extracted with 1 N HCl (2 × 10 mL), 1 N $NaHCO_3$ (2 × 10 mL), and distilled water (2 × 10 mL). The organic layer was concentrated and the product purified by chromatography (1% CH_3OH in CH_2Cl_2) to yield a colourless oil. Yield: 237 mg, 71%; TLC: R_f = 0.80 (5:200 v:v CH_3OH/CH_2Cl_2); ^1H NMR (200 MHz) ($CDCl_3$), δ: 7.269 (s, 5H, H-aryl), 6.997 (d, 2H, aniline-*meta*), 6.997 (d, 1H, amide NH), 6.584 (d, ^3J = 8.77, 2H, aniline-*ortho*), 5.210 (m, ^3J = 7.18, 1H, Boc-NH), 4.710 (m, 1H, $CHCH_2O$), 4.431 (m, 3H, CH-CH_2O and $CHCH_2S$), 4.154 (q, 2H, OCH_2CH_3), 3.659 (s, 2H, SCH_2Ph), 3.609 (m, 8H, CH_2CH_2Cl), 2.893 (m, 2H, $^3J_{AX}$ = 4.90, $^3J_{BX}$ = 5.71, $^2J_{AB}$ = −19.6, CH_2S), 2.497 (t, 2H, ^3J = 7.77, CH_2Ph), 2.307 (t, ^3J = 7.68, 2H, $C(O)CH_2$), 1.852 (m, 2H, $CH_2CH_2CH_2$), 1.434 (s, 9H, $C(CH_3)_3$), 1.233 (t, ^3J = 7.16, 3H, OCH_2CH_3); ^{13}C NMR (50 MHz), δ: 173.18 ($C(O)CH_2CH_2CH_2$), 170.12 ($C(O)OCH_2CH_3$), 168.96 (amide-C(O)), 154.37 (Boc-C(O)), 144.26 (aniline-ipso), 137.52 (aniline-*para*), 130.33 (benzyl-ipso), 129.60 (benzyl-*ortho*), 128.85 (benzyl-*meta*), 128.52 (aniline-*meta*), 127.21 (benzyl-*para*), 112.08 (aniline-*ortho*), 80.60 ($C(CH_3)_3$), 63.79 ($CH_2OC(O)$), 61.85 (OCH_2CH_3), 53.49 (CH_2Cl), 51.79 ($CHCH_2S$ and $CHCH_2O$), 40.43 (NCH_2), 36.47 (SCH_2Ph), 33.80 (CH_2Ph), 33.21 ($C(O)CH_2$ and $CHCH_2S$), 28.18 ($C(CH_3)_3$), 26.41 ($CH_2CH_2CH_2$), 14.00 (OCH_2CH_3); MS (HRDEI), calcd.: 711.2540; found: 711.2526.

Ethyl N-*(2-triphenylmethylthio)ethanoyl*-O-*{4'-[4''-(1''-bis(2'''-chloroethyl)amino)phenyl]butanoyl}-L-seryl*-S-*benzyl-L-cysteine, 1*

Triethylsilane was added dropwise to a solution of **6** (50 mg, 0.070 mmol) in trifluoroacetic acid, TFA (5 mL), until the yellow solution became colourless. The reaction mixture, which was protected from light, was allowed to stir for 2 h before the TFA was removed in vacuo. The resulting oil was diluted with dry dichloromethane (20 mL) and the reaction mixture extracted with aqueous Na_2CO_3 (10 mL, 10%). The aqueous layer was back-extracted with dichloromethane (2 × 10 mL) and the organic layers combined and evaporated to dryness. The resulting oil was diluted to 10 mL with dichloromethane and compound **8** (28 mg, 0.064 mmol) was added together with freshly distilled diisopropylethylamine (9.1 mg, 0.070 mmol). The reaction was stirred under nitrogen and protected from light for 24 h. The product was isolated by chromatography (1% CH_3OH in CH_2Cl_2). Yield: 33 mg, 50%; TLC: R_f = 0.71 (2:98 v:v CH_3OH/CH_2Cl_2). Anal. calcd.: C 64.7, H 5.9, N 4.5%; found: C 65.2, H 6.1, N 4.6%. For NMR data see Tables 1 and 2.

Acknowledgements

We acknowledge, with thanks, financial support of this work by the Natural Sciences and Engineering Research Council of Canada and the grant of an NSERC postgraduate fellowship to J.F.V.

References

1. E. Deutsch, M. Nicolini, and H.N. Wagner. Technetium in chemistry and nuclear medicine. Raven Press, New York. 1983.
2. F. Tisato, F. Refosco, and G. Bandolini. Coord. Chem. Rev. **135/136**, 325 (1994).
3. S. Lever, K. Baidoo, and A. Mahmood. Inorg. Chim. Acta, **176**, 183 (1990).
4. M. Nicolini, G. Bandoli, and U. Mazzi. Technetium in chemistry and nuclear medicine-3. Raven Press, New York. 1990.
5. J.L. Everett, J.J. Roberts, and W.C.J. Ross. J. Chem. Soc. 2386 (1953).
6. L.M. van Putten and P. Lelieveld. Eur. J. Cancer, **7**, 11 (1971).
7. L. Stryer. Biochemistry. W.H. Freeman and Co., San Francisco. 1975. p. 17.
8. G. Mehta, T. Sambaiah, B.G. Maiya, M. Sirish, and A. Dattagupta. Tetrahedron Lett. **35**, 4201 (1994).
9. D. Brenner, A. Davison, J. Lister-James, and A.G. Jones. Inorg. Chem. **23**, 3793 (1984).
10. P.B. Barker and R. Freeman. J. Magn. Reson. **64**, 334 (1985).
11. I.M. Bereton, S. Crozier, J. Field, and D.M. Dodrell. J. Magn. Reson. **93**, 54 (1991).
12. M. von Kienlin, C.T.W. Moonen, A. van der Toorn, and P.C.M. van Zijl. J. Magn. Reson. **93**, 423 (1991).
13. T.A. Carpenter, L.D. Colebrook, L.D. Hall, and G.K. Pierens. Magn. Reson. Chem. **30**, 768 (1992).
14. A.L. Davies, J. Keeler, E.D. Laue, and D. Moskau. J. Magn. Reson. **98**, 207 (1992).

15. J.R. Tolman, J. Chung, and J.H. Prestegard. J. Magn. Reson. **98**, 462 (1992).
16. J. Boyd, N. Soffe, B. John, D. Plant, and R.E. Hurd. J. Magn. Reson. **98**, 660 (1992).
17. R.E. Hurd and B.K. John. J. Magn. Reson. **91**, 648 (1991).
18. L. Lerner and A. Bax. J. Magn. Reson. **69**, 375 (1986).
19. J. Jeener, B.H. Meier, P. Bachmann, and R.R. Ernst. J. Chem. Phys. **71**, 546 (1979).
20. D. Marion and K. Wuthrich. Biochem. Biophys. Res. Commun. **113**, 967 (1983).
21. G. Bodenhausen, H. Kogler, and R.R. Ernst. J. Magn. Reson. **58**, 370 (1984).

A gas-to-solid phase methanolysis method for the analysis of small amounts of oligosaccharides

Daniel Derbie Asres and Hélène Perreault

Abstract: A gas-to-solid phase methanolysis method for the analysis of oligosaccharides is presented. The advantages of using this new gas-to-solid phase method, as opposed to conventional bulk phase techniques, are described, along with comparisons of results obtained from both techniques. The reliable bulk phase methanolysis methods are used as benchmarks for assessing the extent of completion of the gas-to-solid reactions. Gas chromatographic – mass spectrometric (GC–MS) data show that, in general, higher temperatures and longer reaction times are required for completion of the gas-to-solid methanolysis process than for completion of the bulk phase reaction. On the other hand, the gas-to-solid procedure requires only minimal amounts of substrate that would be difficult to characterize using bulk phase methanolysis due to losses during clean-up procedures. Gas-to-solid methanolysis reactions of permethylated di- and trisaccharides were investigated (GC–FID and GC–MS), following initial experiments performed in order to characterize the GC retention times and mass spectra of permethylated standard monosaccharides. Conversion of neutral disaccharides, as well as neutral and acidic trisaccharides, to their respective monosaccharides was successful using the gas-to-solid method. The GC–FID and GC–MS traces show that the gas-to-solid method gives a cleaner reaction than the bulk phase method.

Key words: oligosaccharides, methanolysis, permethylation, gas chromatography – mass spectrometry, mass spectrometry.

Résumé : Le développement et l'optimization d'une méthode phase gazeuse – phase solide pour la méthanolyse d'oligosaccharides sont décrits. En se basant sur un méthode de méthanolyse conventionnelle pour fins de comparaison, le degré de complétion des réactions phase gazeuse – phase solide a pu être étudié en fonction du temps et de la température. Les résultats d'analyses par chromatographie à phase gazeuse couplée à la spectrométrie de masse (GC–MS) montrent qu'en général, la méthanolyse complète en phase gazeuse – phase solide requiert plus de temps et des températures plus élevées que la méthanolyse conventionnelle en phase liquide. La méthode phase gazeuse – phase solide a été appliquée à des di- et trisaccharides perméthylés, après que des standards de monosaccharides perméthylés ait été étudiés relativement à leurs temps de rétention en chromatographie gazeuse couplée à un détecteur à ionisation par flamme (GC–FID) et en GC–MS. La méthode de méthanolyse phase gazeuse – phase solide permet de briser les liens glycosiques au sein d'oligosaccharides neutres et à caractère acide. De plus, cette méthode permet d'utiliser des quantités de substrat moindres qu'avec la méthode de méthanolyse conventionnelle en phase liquide grâce à l'omission des procédures d'extraction nécéssaires en phase liquide.

Mots clés : oligosaccharides, méthanolyse, perméthylation, chromatographie gazeuse – spectrométrie de masse, spectrométrie de masse.

Introduction

Structural analysis of oligosaccharides by mass spectrometry (MS) and tandem mass spectrometry (MS–MS) is useful for providing information on the total molecular weight and sequence of monosaccharides, but with limited ability in the latter case for distinguishing between different hexose or pentose isomers. In some cases (1–3), MS–MS allows for precise determination of the sequence of monosacharides by comparison with compounds of known structure, although this procedure becomes impossible in the absence of standards. Tandem MS experiments can also be used to indicate branching patterns in oligosaccharides (4, 5).

The important and characteristic carbohydrate features left uncertain after direct mass spectrometric analysis of an oligosaccharide are the position and anomericity of glycosidic bonds and, most often, the exact nature of the monosaccharides involved in the sequence. Some differentiation between different types of hexoses (e.g., mannose vs. glucose vs. galactose, etc.) by methods using mass spectrometry can be achieved, provided that chemical modification such as periodic acid oxidation (6) is performed prior to mass spectral analysis.

Sugar composition of a given oligosaccharide molecule may also be determined by means of methanolysis (7, 8) or acetolysis (9) followed by chromatographic analysis. These methods break the glycosidic bonds between sugar units (monosaccharides) and the products obtained can then be separated by chromatography and identified according to their GC retention times and mass spectra using GC–MS. In general, native (underivatized) monosaccharides present a prob-

Received January 20, 1996.

D.D. Asres and H. Perreault.[1] Department of Chemistry, University of Manitoba, Winnipeg, MB R3T 2N2, Canada.

[1] Author to whom correspondence may be addressed. Telephone: (204) 474-7418. Fax: (204) 275-0905. E-mail: Perreau@cc.umanitoba.ca

lem in routine chromatographic analysis since they decompose at the high temperatures used in GC. Moreover, they contain no chromophores for ultraviolet (UV) detection in high-performance liquid chromatography (HPLC). It is therefore necessary to perform derivatization following methanolysis or acetolysis. Trimethylsilylation (10) has so far been the most popular method used to derivatize monosaccharides for GC with flame ionization detection (FID), and for GC–MS analysis, although methylation (11), acetylation (12), and other methods have also been used. For HPLC–UV analysis, it is preferable to label the monosaccharides obtained from glycosidic cleavage with chromophores. Examples of reagents that have been used for this purpose include benzoyl chloride (13), benzoyl anhydride (14), 4-nitrobenzoyl chloride (15), and benzyl chloride.

This paper reports a new gas-to-solid phase methanolysis procedure that minimizes the amount of substrate required for determination of sugar content. The method was used to cleave oligosaccharides that were permethylated prior to methanolysis. A very thin layer of solid substrate, containing a few nanomoles of the material, was deposited on the walls of an open capillary tube and exposed to the gas phase reagents. The products remained as solids on the surface of the tube and pumping at high vacuum was used to remove excess reagents and by-products. For this technique to be successful the reagents used must boil at much lower temperatures than those at which the substrates melt or decompose. Cleavage of the disaccharide lactose (α and β) was studied in order to determine the conditions necessary for complete reaction. Permethylated lactoses were sufficiently volatile to be analyzed by GC and could be observed in the chromatograms in cases where methanolysis remained incomplete. Permethylated trisaccharides and higher order carbohydrates did not elute at temperatures up to 275°C. Conditions that yielded complete methanolysis of lactose (gas-to-solid, 80°C, 18 h) also seemed to break all glycosidic bonds in trisaccharides, judging from the absence of disaccharide peaks in the corresponding chromatograms.

The compounds of interest for this study were investigated by fast atom bombardment (FAB) MS, GC–FID, and GC–MS. FAB-MS experiments were useful for the determination of the molecular weights of permethylated substrates. The FID and total ion current (TIC) chromatograms provided retention times, whereas the mass spectra obtained from GC–MS analyses were useful for elucidation of some structural features.

Experimental

Chemicals

Monosaccharides L(−)fucose, D(+)galactose, D(+)glucose, and *N*-acetyl neuraminic acid (sialic acid) were obtained from Sigma Chemicals (St. Louis, Mo.). Lactoses (α and β) were also purchased from Sigma. Trisaccharides 2′-fucosyllactose and 6′-sialyllactose were obtained from Oxford Glycosystems (Rosedale, N.Y.). Methyl iodide was obtained from Aldrich Chemicals (St. Louis, Mo.) and 0.5 M methanolic HCl was purchased from Supelco Inc. (Bellafonte, Pa.). Solvents were glass distilled or HPLC grade and were obtained from Pierce Chemicals (Rockfort, Ill.; dimethyl sulfoxide) and Mallinckrodt (Paris, Ky.; chloroform, dichloromethane, acetonitrile, and methanol).

Permethylation of mono-, di-, and trisaccharides

The method employed was derived from that of Larsson et al. (11). Briefly, the saccharides (10–25 nmol) were dissolved in dimethyl sulfoxide (200 μL), and NaOH powder (10 mg) was added. The mixture was sonicated for 10 min and methyl iodide (50 μL) added, followed by sonication at room temperature for 2.5 h. Water (1.5 mL) chloroform (1.5 mL) were added to the reaction mixture and the chloroform layer, containing the permethylated compounds, was extracted 3 times with water (1.5 mL). The solvent was then evaporated in vacuo, and the residue redissolved in acetonitrile or dichloromethane to give a concentration of ca. 0.2 nmol/μL.

Conventional bulk phase methanolysis

The method used in this study is a modification of the technique introduced by Fournet et al. (7) and reviewed by Dell et al. (9). The permethylated di- and trisaccharides (10–25 nmol) in acetonitrile (ca. 100 mL) were placed in screw-cap culture tubes and the solvent evaporated *in vacuo*. Methanolic HCl (0.5 M, ca. 20 μL) was added to the substrate and the mixtures heated at 65°C for 3 h. Methanol and hydrochloric acid were removed under vacuum and the methanolysis products were redissolved in dichloromethane for GC–MS analysis.

Gas-to-solid reactions

These reactions were conducted with an adapted model of the apparatus developed by Vath for microderivatization of peptides and proteins (16) and later used by Domon, Vath, and Costello (17) and Perreault and Costello (5) for derivatization of glycosphingolipids. The use of this apparatus has been described elsewhere (18). Briefly, the apparatus is built based on a hydrolysis tube (Pierce Chemicals, Rockford, Ill.) modified by the addition of a reagent well in its middle section. A model of the apparatus is shown in Diagram 1. A few microlitres of solution of the substrate are placed in a melting-point capillary and the solvent is evaporated under vacuum. The reagent is deposited in the well and the capillary tube is inserted in the main cavity of the apparatus. The reagent is frozen with liquid nitrogen, and the apparatus evacuated and sealed. The reagent is then allowed to thaw and degas under vacuum, and the freeze–pump–thaw cycle is repeated. The apparatus is then placed in an oven and the reaction allowed to take place at a pre-chosen temperature. At the end of the reaction time, the reagent well is frozen again and any condensation on the walls of the apparatus removed by evacuation. The capillary tube containing the product is removed, and the product transferred to a 10 cm^3 screw-cap culture tube with solvent. The solvent, remaining reagent, and any by-products are removed under vacuum. The sample is then redissolved in either acetonitrile for FAB analysis, or dichloromethane for GC–MS analysis.

Gas-to-solid method for methanolysis

The permethylated di- and trisaccharides (10–15 nmol) were deposited on the walls of a melting point capillary tube open at one end by evaporation from a solution. Methanolic HCl (0.5 M, 250 μL) was pipeted into the reagent well of the reaction apparatus. The reaction was completed following the general procedure described above (18) by heating at 80°C for periods of time varying from 6 to 22 h.

Diagram 1. Apparatus used for gas-to-solid phase methanolysis (16–18).

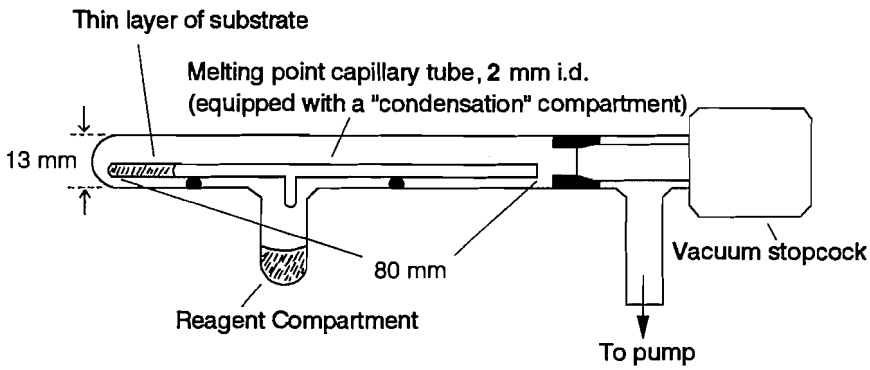

GC–FID analyses

Aliquots of solution (1 μL) of permethylated/methanolyzed compounds in dichloromethane (ca. 0.2 nmol/μL) were injected into a Varian 3400CX gas chromatograph equipped with a megabore (530 μm film thickness, 3 m long DB-1 column (100% methyl-silicone); J&W Scientific), a flame ionization detector, and a Varian Star 4.0 Windows-based data system.

GC–MS analyses

Two different GC–MS systems were used in this study. Chromatographs in both systems were equipped with DB-5 columns (95% methyl-, 5% phenyl silicone; J&W Scientific) with 250 mm i.d. and 0.25 μm film thickness. The first GC–MS system consisted of a Varian 3400 chromatograph and Finnigan Mat Ion Trap Detector 800. The DB-5 column described above was 60 m long and the data system used was Finnigan Mat ITDS, version 4.10. The second GC–MS apparatus used consisted of a Hewlett Packard (HP) 5890 chromatograph (30 min long DB-5 column) linked to a HP 5988A quadrupole mass analyzer. For both GC–MS instruments, repetitive 1 s scans were effected on a range of 50–650 Da. Electron impact (EI) ionization sources were kept at 260°C and electron energy was set at 70 eV.

For all three of the chromatographs used, oven temperatures were programmed as follows: Initial temperature of 80°C kept constant for 10 min, followed y a linear temperature ramp to 280°C at the rate of 7°C/min, and temperature held constant at 280°C for 10 min.

Fast atom bombardment (FAB) analyses

FAB experiments were performed with a VG Analytical 7070E mass spectrometer of E-B geometry. The matrix used was 3-nitrobenzyl alcohol (Sigma, St. Louis, Mo.). The FAB gun (Xe^0) was operated at 8 kV with a current of 1 mA. Conventional scans were at the rate of 2s/decade and the *m/z* range convered was from 50 to 1000 Da. The data system used was PDP11-based 11-250J from VG Analytical.

Results and discussion

Four different monosaccharides were investigated in order to lay the groundwork for the methanolysis of larger species. Permethylation of D(+)-galactose, D(+)-glucose, L(−)-fucose, and *N*-acetylneuraminic acid was carried out and the products analyzed by gas chromatography and mass spectrometry. Electron impact mass spectral data on these compounds have been reported in the MS libraries of the National Institute for Science and Technology (NIST) (19). These reference spectra were used for comparison purposes with the data obtained in this study. GC–MS retention times of the permethylated monosaccharides were measured for further comparison with those of methanolysis products.

Permethylated monosaccharides

Permethylation of D(+)galactose and D(+)glucose was expected to produce anomeric compounds in each case, due to the formation of α and β methyl glycosides. Determination of molecular weights by FAB-MS showed that both glucose and galactose had been pentamethylated, possibly suggesting a closed ring with an a or b methoxy group on C1. The anomericity of the C1—OCH_3 bonds was not differentiable by either EI or FAB when samples were introduced as a mixture of anomers. In fact, permethylated D(+)galactose and D(+)glucose produced very similar FAB fragmentation patterns GC–MS analysis provided more details on these aspects and will be discussed later.

The permethylation and (or) methanolysis products were analysed by GC–FID prior to GC–MS since this technique was much more rapid owing to the use of a shorter column (3 m) than that used for GC–MS (30 and 60 m).

The GC–FID chromatograms obtained for permethylated D(+)galactose and D(+)glucose each showed the presence of two major compounds, possibly the α and β glycosides of each species. The data are reported in Table 1, columns B and C. Permethylation of galactose yielded products eluting over the 12.8–13.5 min time range. The major peak at 13.30 min in fact covers two peaks (resolved on a longer column as will be shown later) and corresponds to the two principal forms of the products while minor peaks at 13.02 and 13.48 min possibly correspond to isomers of the main products. The two major forms of permethylated glucose elute earlier than galactose. The main products from permethylated galactose are observed at 12.54 and 12.97 min, respectively, whereas a less important product elutes at 12.70 min. Three injections were performed for each sample and there is a corresponding ±0.05 min error on retention time values reported.

The GC–MS results obtained for the permethylated monosaccharide standards galactose and glucose showed the same general trends in both total ion current (TIC) and FID

Table 1. Retention times of peaks observed in the GC–FID chromatograms of permethylated standards and methanolysis products (system used: Varian 3400CX GC). Error: ±0.05 min. Abbreviations: Gal = galactose, Fuc = fucose, Glc = glucose, PME = permethylated, Met = methanolyzed, Lact. = lactose (α and (or) β), FL = fucosyllactose, SL = sialyllactose, C = conventional method, G = gas-to-solid method, rt = retention time.

A PME Fuc (rt, min)	B PME Glc (rt, min)	C PME Gal (rt, min)	D PME S.A. (rt, min)	E PME Lact., Met. CG (rt, min)	F PME 2′-FL Met. C (rt, min)	G PME 2′-FL Met. G (rt, min)	H PME 6′-SL Met. G (rt, min)
						10.55	
10.90					11.01	11.04	
11.25							
	12.54						
	12.70				12.62		
	(minor)						
	12.97				12.96	12.93	
				13.03		13.06	13.04
		13.30		13.16	13.14	13.20	
		13.48		13.38	13.37		13.44
		(minor)					
					13.53		13.66
						13.78	13.80
			22.01				21.98

Table 2. Retention times observed in the GC–MS TIC chromatograms of permethylated standards and methanolysis products (system used: Varian 3400 GC/Finnigan Mat ITD-800). Error: ±0.05 min. Abbreviations: See Table 1 caption.

A PME Fuc (rt, min)	B PME Glc (rt, min)	C PME Gal (rt, min)	D PME S.A. (rt, min)	E PME Lact. Met. G (rt, min)	F PME 2′-FL Met. G (rt, min)	G PME 6′-SL Met. G (rt, min)
24.13						
24.30					24.43	
24.55					24.55	
	26.18					
	26.82			26.97	26.76	26.75
		27.13		27.18	26.94	27.30
		27.35		27.35	27.50	27.61
						27.80
			38.49			38.34

traces. The capillary columns used for GC–MS in this study were longer (30 min and 60 m instead of 3 m for GC–FID) and had a narrower bore, such that longer retention times were observed and better resolution and efficiency were achieved. Also, inversions of relative peak intensities from FID to TIC chromatograms were observed due to the difference in relative detection efficiencies (FID current vs. TIC). The data are reported in Table 2, columns B and C.

Interestingly, permethylated galactose (chromatogram shown in Fig. 1*a*) yielded two major peaks instead of the one peak observed in GC–FID owing to the increase in resolution. The electron impact spectra taken at the apex of both peaks are somewhat different (Fig. 2) and could be interpreted as making up two components of the spectrum found in the literature (19*a*, *b*) for methyl 2,3,4,6-tetra-*O*-methyl (β and α) D-galactopyranoside. The main difference between the spectra of Fig. 2 is the occurrence of abundant ions at *m/z* 88 (Fig. 2*a*, corresponding to 27.13 min retention time) while these ions do not appear significantly in the other spectrum (Fig. 2*b*). Also, ions at *m/z* 111 are present only in the spectrum of Fig. 2*a*. Library spectra of tetramethylated D-galactose, non-methylated in position 1, were searched and indeed contain abundant *m/z* 111 ions (19*c*). However, significant higher mass ions of these library spectra could not be found in the spectrum of Fig. 2*a* and therefore the possibility of undermethylation was rejected. In support of this, an undermethylated product would have a

Diagram 2. Suggested structures for the *m/z* 101 ions observed in the case of permethylated (*a*) D(+)galactose (Fig. 1*b*) and (*b*) L(−)fucose (Fig. 4*b*).

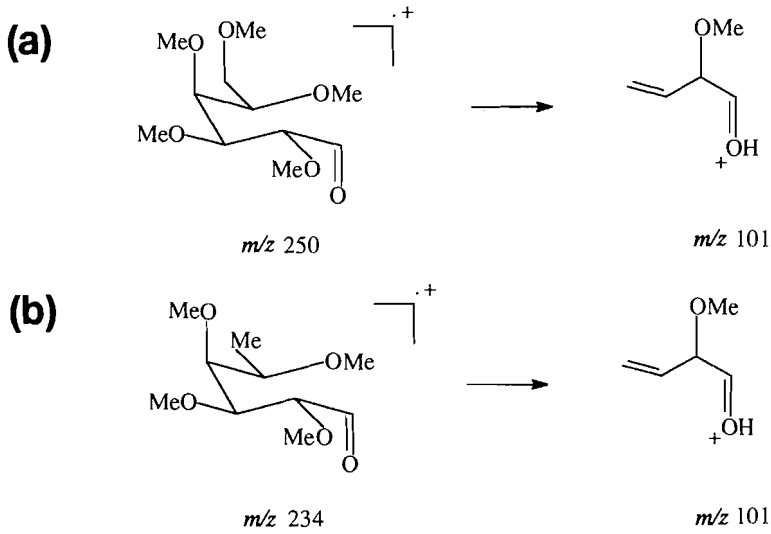

Fig. 1. Portions of the GC–MS total ions chromatograms obtained for permethylated (*a*) D(+)galactose and (*b*) D(+)glucose. Data obtained with the Varian 3400 GC/Finnigan Mat ITD-800 MS system.

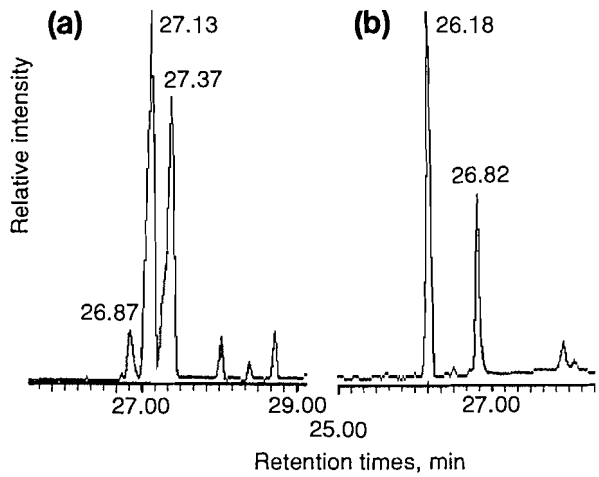

Fig. 2. Electron impact mass spectra recorded at the apex of the GC/TIC peaks observed in Fig. 1*a* (*a*) Peak at 27.13 min; (*b*) peak at 27.37 min.

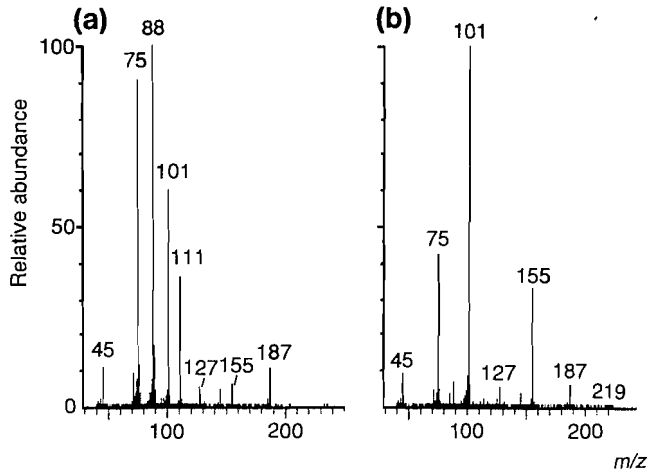

higher boiling point than its permethylated analog, and therefore elute later, which is the reverse of what is observed here. Ions with *m/z* 111 have been observed in the FAB spectra of permethylated oligosaccharides and glycolipids (3, 5) and interpreted as cyclic aromatic ions. The *m/z* 88 ions, also observed in Fig. 2*a*, are found as the major ions in the library spectra of permethylated galactose (19*a*, *b*). The spectrum of Fig. 2*b*, which features predominant *m/z* 101 and 155 ions and corresponds to the apex of the second peak of Fig. 1*a*, could not be matched with any spectrum of the NIST library (19). Diagram 2*a* suggests a possible structure for the ions at *m/z* 101 observed in Fig. 2*b*, whose precursor would be non-cyclic. Globally, permethylation of D-galactose according to these results would yield two unresolved anomers, pyranosides according to the reference spectra (19*a*, *b*) (peak at 27.13 min in Fig. 1*a*), and another product, possibly acyclic but not yet characterized (peak at 27.37 min in the same figure).

As for GC–MS analysis of permethylated glucose, two intense and well-separated peaks were found in the TIC trace (Fig. 1*b*), which was very similar to that obtained by GC–FIB. The mass spectrum at the maxima of the first peak of importance (26.18 min) corresponded well with the library spectra of methyl 2,3,4,6-tetra-*O*-methyl (α- and β) glucopyranose (19*d*, *e*). The second peak, at 26.82 min, showed absence of *m/z* 88 ions and predominance of *m/z* 101 species, suggesting again the formation of a permethylated product that is different from the pyranosidyl anomers, as suggested in the case of galactose.

In the case of fucose, two major peaks were also obtained in the FID (Fig. 3) and TIC traces. The spectrum of the first

Fig. 3. Portion of the GC–FID chromatogram obtained for permethylated L(−)fucose.

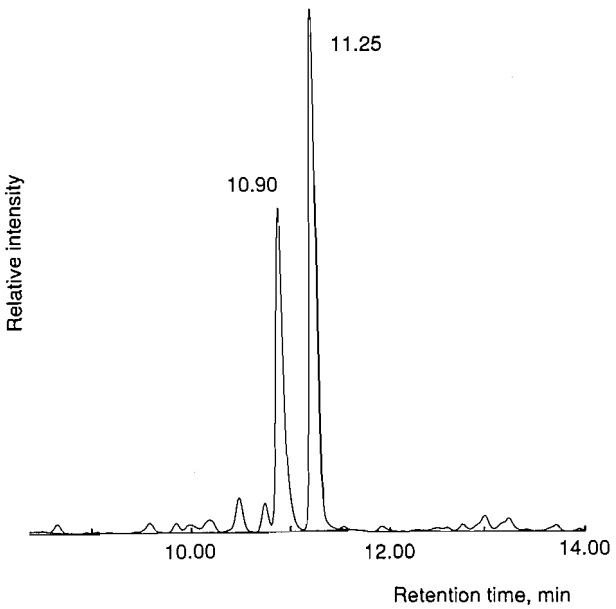

Fig. 4. Electron impact mass spectra obtained from GC–MS of permethylated L(−)fucose. (*a*) Peak at 24.07 min; (*b*) peak at 24.47 min.

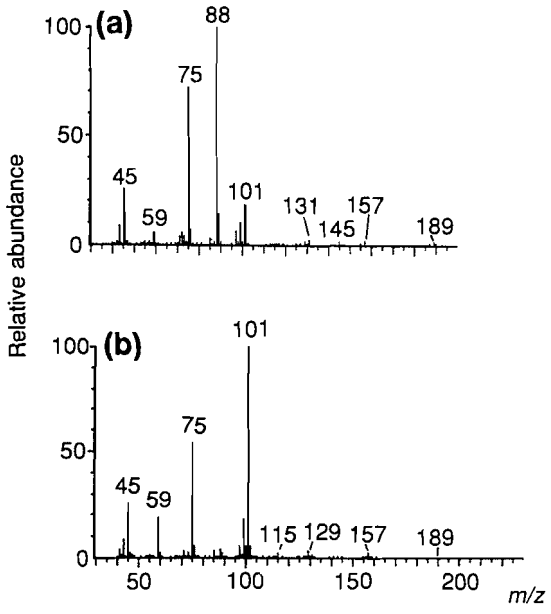

eluted compound (Fig. 4*a*) features the rearrangement ion peak at *m/z* 88 and corresponds with the library spectra of methyl 2,3,4-tri-*O*-methyl-6-deoxy-α- and -β-mannopyranoside (19*f*,*g*). The spectrum of the other product (Fig. 4*b*) again showed predominant ions at *m/z* 101 and no significant ions at *m/z* 88. Diagram 2*b* shows how the ionic species at *m/z* 101 could be formed from acyclic permethylated fucose. As in the case of galactose and glucose, this product has not yet been further characterized. Retention times obtained by GC–FID and GC–MS for permethylation of fucose are shown in column A of Tables 1 and 2.

Permethylation of sialic acid yielded a more complicated chromatographic picture than the other monosaccharides. The most abundant peak in the GC–FID chromatogram had its centroid at 22.01 min (see Table 1, column D) and was almost 0.73 min wide at half height (in comparison, fucose peaks have a half-height width of 0.09 min). The GC–MS results obtained for the permethylation of sialic acid (Table 2, column D) resemble those obtained by GC–FID and show that the main peak occurs at around 39 min, and is almost 1 min wide at half height. The mass spectra taken from one end (38:53 min) and the other (39:09 min) are shown in Fig. 5, (*a*) and (*b*). They are similar to each other in spite of variations in the relative ionic abundances. No major structural differences can be deduced from comparison of these spectra; however, they can be used qualitatively to verify the presence of a sialic acid related residue upon methanolysis of an unknown oligosaccharide. The main component of permethylated sialic acid has a predicted molecular weight of 407 (see structure in Fig. 5), and there are molecular ions at *m/z* 407 in both spectra of Fig. 5. Ions at *m/z* 422 are possibly formed from opening of the ring upon methylation as illustrated by the proposed structures, also in Fig. 5. No ions indicating undermethylation (*m/z* 392) are observed and therefore the large GC peak widths presumably arise form the presence of two compounds (MW 407 and MW 422).

Permethylated disaccharides and methanolysis

This second section of the study was aimed at clarifying two general points, (*i*) the ability to identify the products according to their retention times, elution patterns, and mass spectra and (*ii*) the degree of completion and success of the gas-to-solid phase methanolysis. It was important to first establish retention times for permethylated α- and β-lactose, the dimers under investigation, on the GC–FID and GC–MS systems. It was also important to determine the molecular weight of the permethylation and methanolysis products by FAB-MS. The FAB spectra of permethylated α- and β-lactose were very similar and exhibited $[M + H - CH_3OH]^+$ (*m/z* 423) ions as well as "B_1" ions resulting from glycosidic breakage (16).

In GC–FID, permethylated α- and β-lactose produced almost identical chromatograms, each with two peaks at the same retention times (see Table 1, column E, and Fig. 6*a*). As there was no difference between the results obtained for the two lactose isomers, only the data for β-lactose have been reported. The two peaks possibly arise from anomeric methyl glycosides on the glucose ring. If this is the case the α- and β-methylated anomeric products have the same retention times for both α- and β-lactoses.

With the use of a longer GC column (30 m), two well-resolved major peaks were obtained for each of the permethylated lactoses. Although the spectra of permethylated lactose species were not found in NIST library, the spectrum of a similar compound 2,3,4,6-tetra-*O*-methyl α-D-glucopyranosyl 2,3,4,6-tetra-*O*-methyl α-D-glucopyranoside (19*h*), closely matched the spectra observed here. Since identical products were obtained whether the substrate was α- or β-lactose, it appears that the permethylation process isomerizes the glycosidic bonds.

GC–MS results obtained with the 60 m column showed the

Fig. 5. Electron impact mass spectra obtained from GC–MS analysis of permethylated sialic acid; (*a*) peak at 38.53 min; (*b*) peak at 39.09 min. Data obtained with the Varian 3400 GC/Finnigan Mat ITD-800 MS system.

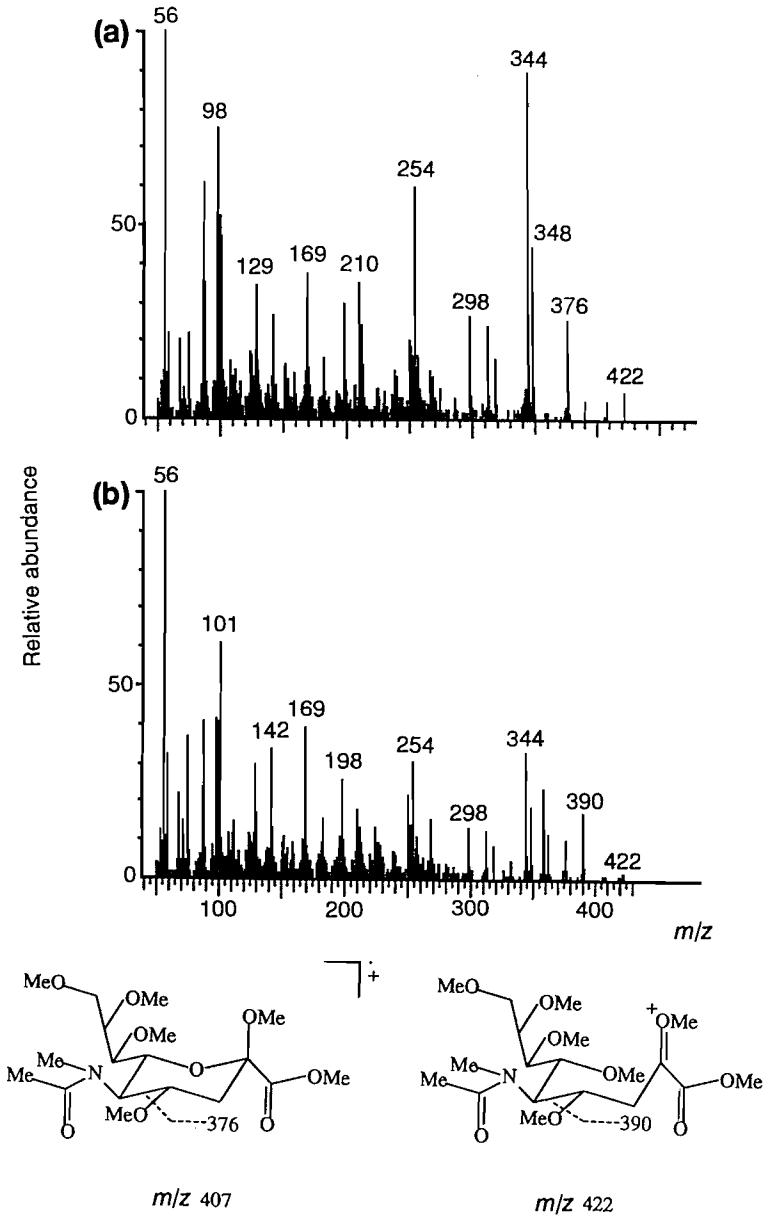

presence of four peaks instead of two (Fig. 7); the four peaks appeared in two pairs. For each pair of peaks, the mass spectra at the maxima showed different fragment ions from one spectrum to the other. The first spectrum of each pair (identical) resembled that of that of the permethylated disaccharide found in the library (19*h*); the second spectrum of each pair (also identical) could not be matched with library data; the combination of the two spectra in each pair gave rise to a spectrum much better matched to the library data (19*h*) than that taken from the first peak only. The permethylation products giving rise to the second peaks in each pair have not yet been further characterized.

Bulk-phase methanolysis, performed according to a well-established method (7), yielded 100% glycosidic bond cleavage in both α- and β-lactoses. GC–FID analysis of methanolyzed α- and β-lactose gave rise to three main peaks at retention times 13.04, 13.17, and 13.38 min and no peaks at around 22 min, the average retention time of permethylated lactoses with this GC–FID system. According to Table 1, column C, the first peak corresponds to a form of permethylated glucose, the second to one of permethylated galactose, and the third to a minor form observed in the chromatogram of permethylated galactose.

Gas-to-solid phase methanolysis required longer reaction times and slightly higher temperatures than the conventional method (see experimental section), but gave rise to a complete reaction. The GC–FID chromatograms of Fig. 6 show the results at the beginning (*a*), at an intermediate stage (*b*), and at

Fig. 6. Portions of the GC–FID traces obtained for methanolysis of β-lactose (permethylated); (*a*) before reaction, permethylated β-lactose; (*b*) after 2 h of gas-to-solid phase reaction; (*c*) after 6 h of gas-to-solid reaction; and (*d*) completed reaction after 18 h of gas-to-solid reaction.

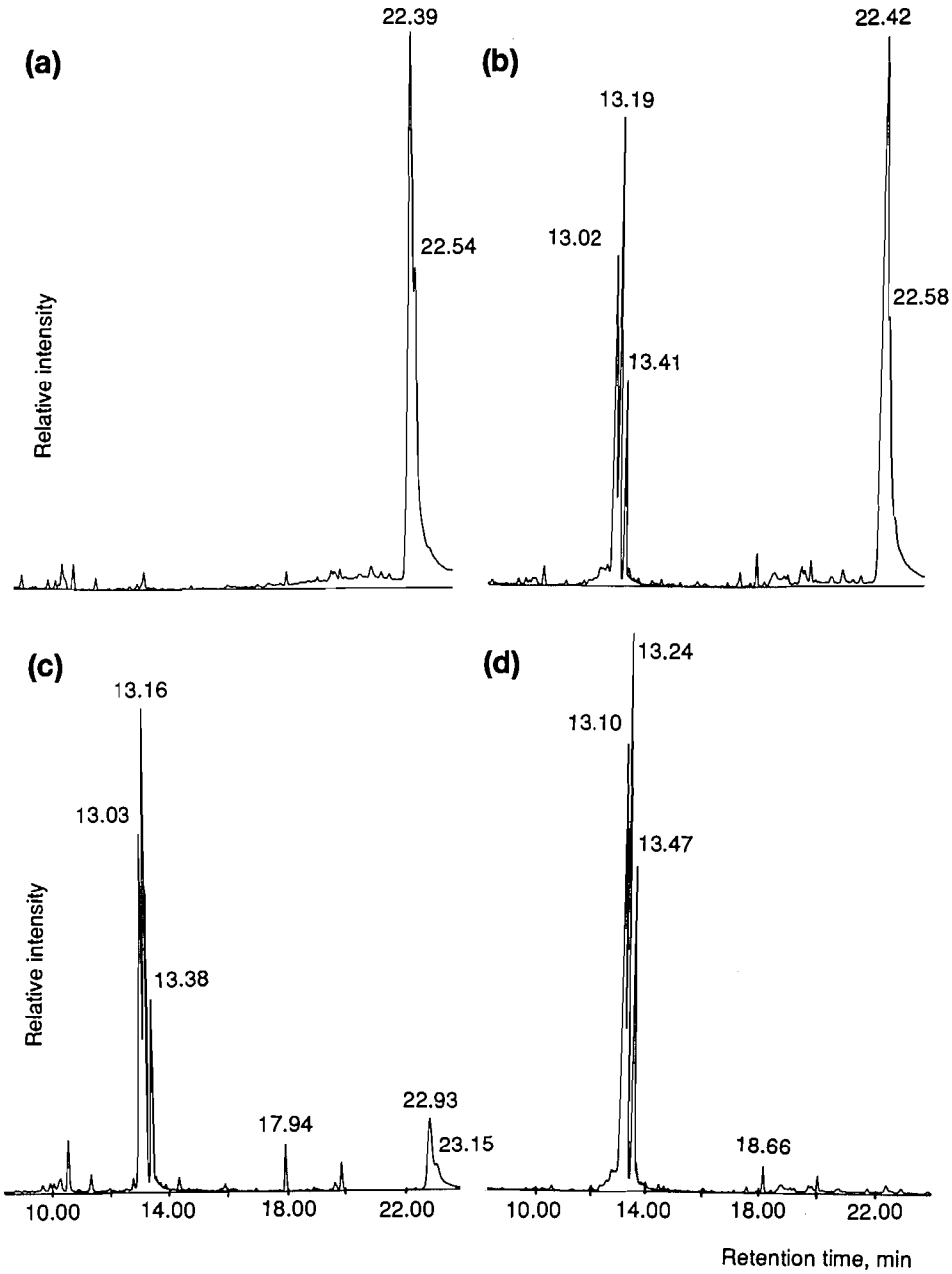

the end of the reaction (*c*). The peaks obtained from breakage of the glycosidic bonds in both α- and β-lactose correspond to those observed for products from the conventional methanolysis method. For either the α or β disaccharide, the three peaks obtained in the chromatograms of the reaction products appear at the same retention times and with similar relative intensities, meaning that the products from one isomer are possibly identical to products from the other isomer. The important fact here is that products obtained from both bulk and gas-to-solid phase methanolysis are the same, and although the reaction completion time was longer with gas-to-solid conditions, the substrate never went into solution and no work-up procedure was required for recovery of the methanolysis products. Moreover, the FID trace of the gas-to-solid reaction products exhibited less background noise and showed that products were cleaner than when performing methanolysis using the conventional method, with the same amount of substrate.

The GC–MS TIC trace of bulk phase methanolysis products from either permethylated α-lactose or β-lactose (Fig. 8*a*) again shows three peaks, whose corresponding mass spectra

Fig. 7. GC–MS total ion chromatogram of permethylated β-lactose, performed on the Varian 3400 GC/Finnigan Mat ITD-800 MS system.

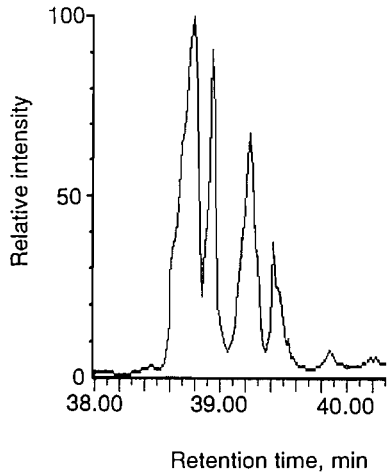

are shown in Fig. 8*b*, *c*, and *d*. The peaks obtained appear at the same retention times and with the same relative intensities (identical chromatograms) whether the products originate from methanolysis of permethylated α-lactose, β-lactose, or methanolysis of a permethylated mixture of the two isomers. The mass spectrum corresponding to the earliest of the three peaks (Fig. 8*b*) and corresponding to a retention time of 26.73 matched the library spectra of permethylated α- and β-glucose (19*d*, *e*). The second peak to appear in the chromatogram (27.18 min) has a mass spectrum (Fig. 8*c*) that is qualitatively similar to the first one and matches the library spectrum of permethylated α- and β-galactose (19*a*, *b*). The third peak (27.35 min) is wider than both first ones and produces a mass spectrum (Fig. 8*d*) that contains ions at *m/z* 173 and 205, suggesting the presence of undermethylated species formed during methanolysis. Given the large peak width, and given also the presence of ions at *m/z* 187 and 219 in the spectrum, it is reasonable to suggest that two compounds coelute and produce the third peak: an undermethylated form of galactose, and another uncharacterized form of permethylated galactose. The spectrum of Fig. 8*d* indeed resembles a combination of the spectrum of Fig. 2*b* (one of the forms of permethylated galactose) and the spectrum of undermethylated galactose (19*c*).

Trisaccharides

Permethylated fucosyllactoses and sialyllactoses were not sufficiently volatile as intact compounds for GC–FID or GC–MS analysis under the operating conditions used in this study. Therefore, gas-to-solid phase methanolysis was effected using the optimal conditions found for the complete breakage of the permethylated lactoses, i.e., 18 h at 80°C.

2′-Fucosyllactose

In Table 1, columns A, F, and G, a comparison has been attempted between the GC–FID retention times observed for permethylated fucose, galactose, and glucose as well as methanolysis products of permethylated 2′-fucosyllactose. An important point is raised by comparing the cleanliness of the chromatograms between that of the conventional bulk phase methanolysis method (Fig. 9*a*) and the trace of the gas-to-solid-phase products (Fig. 9*b* and *c*). The chromatogram of Fig. 9*c*, showing almost complete methanolysis, is less ambiguous, contains fewer products, and is thus easier to characterize than that of Fig. 9*a*. Bulk phase methanolysis gives rise to a hexose/fucose ratio that is higher than that of the gas-to-solid method. However, peaks observed at ca. 19.5 min in the chromatograms and interpreted as arising from fuc-hex moieties (from incomplete methanolysis) are present in the chromatogram of the bulk phase products (Fig. 9*a*) whereas they are absent from the other chromatogram (Fig. 9*c*). The contribution of fucosyl units to these disaccharide products explains the lower fucose/hexose abundance ratio for bulk phase products. Lactose-related products, occurring at 22.3–22.4 min, are observed in Fig. 9*a* and *b*, whereas in the third chromatogram they are in very low abundance, suggesting again that the 18 h gas-to-solid reaction yielded almost complete methanolysis.

Data in Table 1 show that the number of possible products formed increases with the number of glycosidic bonds broken around a given monosaccharide residue. In 2′-fucosyllactose (Diagram 3*a*), the galactose moiety is originally attached to two sugar rings, whereas the glucose is bonded only to one residue. Table 1 shows a larger spreading of galactose-related peaks than peaks derived from glucose-related species. This spreading of products could possibly be attributed to distribution of anomericity upon glycosidic breakage.

The GC–MS analysis of gas-to-solid phase methanolysis products of 2′-fucosyllactose was performed on the Varian 3400 GC/Finnigam Mat ITD-800 system. The TIC trace (Fig. 10*a*) was very similar to that of Fig. 9*c*, in that two major pairs of peaks were obtained, the first for fucose-related residues at around 24 min, and the second at ca. 26–27 min for glucose- and galactose-related residues. The large fucose peak appearing at 11.01 min in Fig. 9*c* is now separated on the longer GC column, producing two peaks 8 s apart. The pattern of hexose compounds is similar to that of the FID trace. Column F in Table 2 lists the peaks observed with this particular GC–MS system for permethylated fucosyllactose. The mass spectra of the fucosyl entities from methanolysis of 2′-fucosyllactose (Fig. 10, *b* and *c*) both exhibit characteristics of the library spectra of α- and β-fucose (19*f*, *g*).

6′-Sialyllactose

The last compound investigated in this study was 6′-sialyllactose (structure given in Diagram 3*b*). GC–FID results for the methanolysis products (gas-to-solid phase method) show that four peaks appear in the hexose retention time zone, i.e., from 13.0 to 13.8 min. Their respective retention times are 13.04, 13.44, 13.66, and 13.80 min, as presented in Table 1, column H. The four peaks do not coincide entirely with respect to retention times (rt) with those of methanolyzed lactose and fucosyllactose, and it appears that three galactose species are formed whereas only one glucose species is observed at rt = 13.04. The peaks corresponding to sialic acid arises at rt = 21.98 min, while the permethylated sialic acid standard showed its major peak at rt = 22.01 min (Table 1, column D).

The GC–MS analysis of the methanolysis products of permethylated sialyllactose showed the same pattern for both the TIC and FID traces. Mass spectra were obtained for each of the major peaks in the trace. The glucose- and galactose-

Fig. 8. GC–MS (*a*) total ion chromatogram, and (*b*), (*c*), (*d*) mass spectra obtained for methanolyzed β-lactose. Varian 3400 GC/Finnigan Mat ITD-800 MS system.

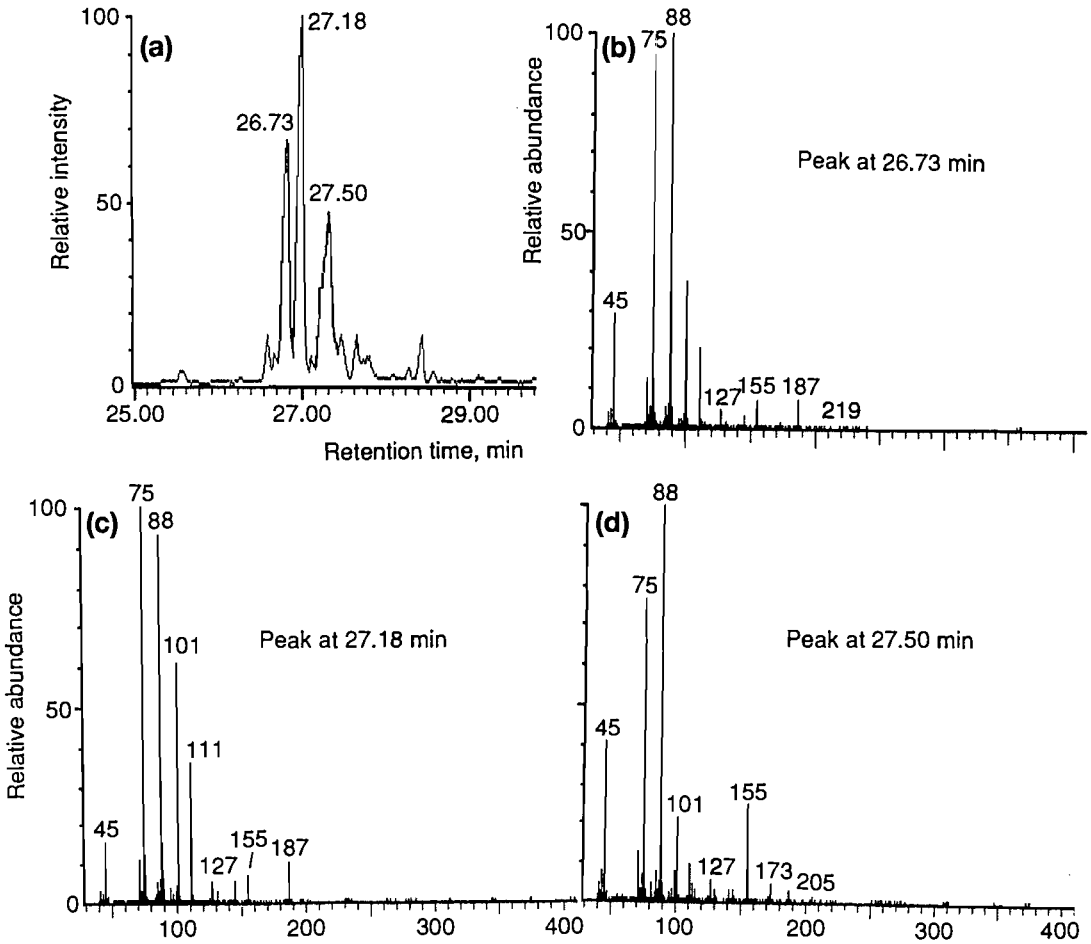

Fig. 9. Portions of the GC–FID chromatograms obtained for methanolysis products of 2′-fucosyllactose. (*a*) Conventional bulk phase methanolysis method; (*b*) gas-to-solid-phase method (6 h); and (*c*) gas-to-solid, 18 h.

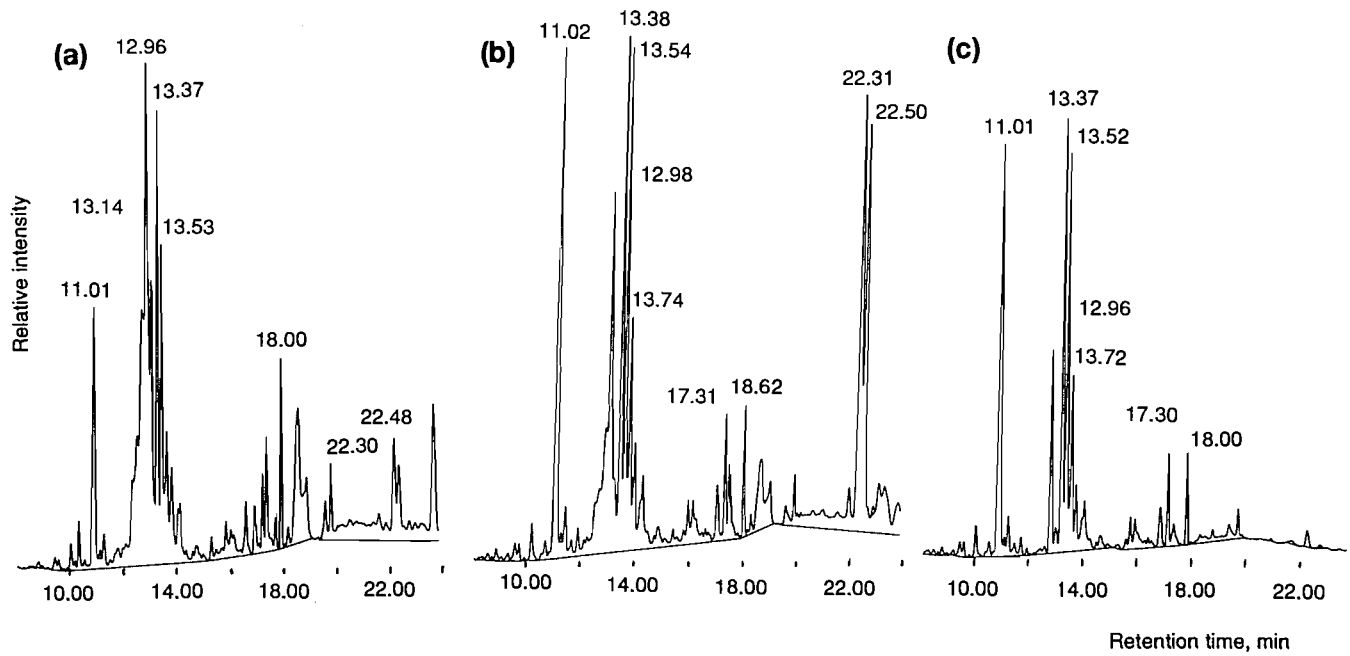

Diagram 3. Structures of (*a*) 2′-fucosyllactose and (*b*) 6′-sialyllactose.

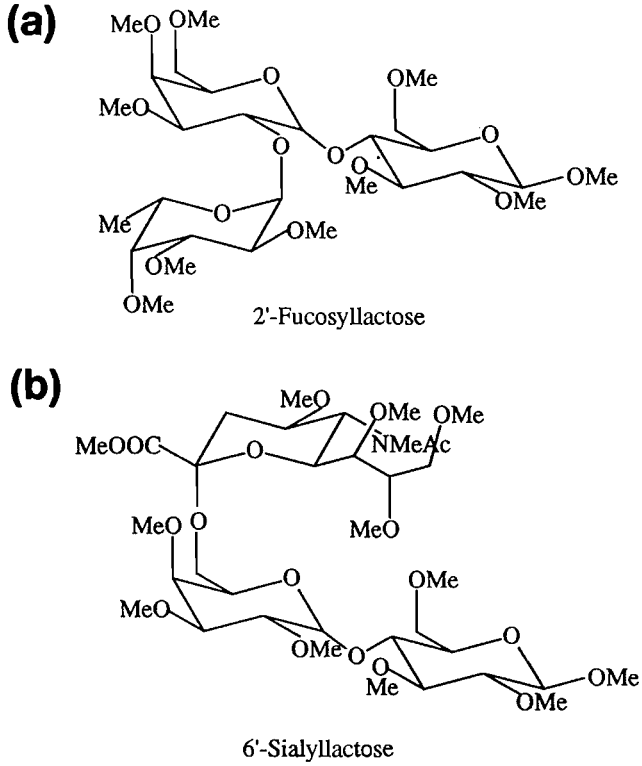

Fig. 10. GC–MS (*a*) total ion chromatogram, and (*b*), (*c*) mass spectra obtained for the methanolysis products of 2′-fucosyllactose, using the gas-to-solid reaction method. Varian 3400 GC/Finnigan Mat ITD-800 MS system.

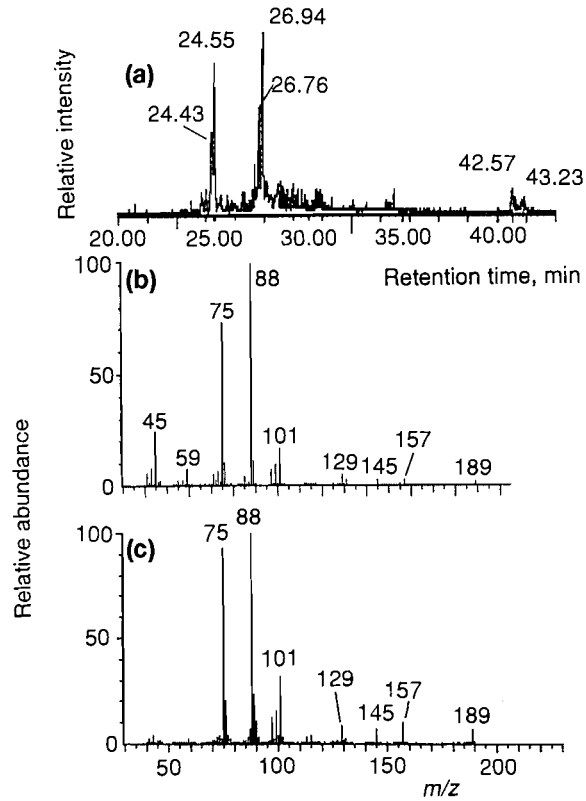

related species produced spectra similar to the corresponding library data (19*a*, *b*; 19*d*, *e*); also, minor peaks indicated the presence of small amounts of undermethylated products.

The spectrum assigned to the sialic acid moiety was also very similar to that of the permethylated sialic acid standard discussed above. Results obtained for methanolysis of 6′-sialyllactose using the conventional bulk phase reaction method yielded the same FID/TIC pattern as products from the gas-to-solid method; however, the reaction was never as complete since low amounts of permethylated lactose and what are believed to be sialyl-hexoses appeared in the chromatograms. The gas-to-solid method, on the other hand, yielded clearer traces, exempt from these residual dimeric compounds. As for fucosyllactose, the optimal conditions found for lactoses were used in order to complete methanolysis.

The FAB mass spectra obtained for permethylated monosaccharides, disaccharides, and trisaccharides all exhibited $[M + H]^+$ and $[M + H - CH_3OH]^+$ ions, as well as fragment ions arising from cleavage of the glycosidic bonds (B_1 and B_2 ions) (3, 17). Interestingly, permethylated compounds that produced more than one chromatographic peak in GC–FIC or GC–MS produced spectra that seemed to reflect the presence of individual compounds in FAB. In other words, the isomeric forms were indistinguishable by FAB. The nonseparated products obtained from methanolysis of α- or β-lactose, 2′-fucosyllactose, and 6′-sialyllactose were also characterized by FAB. The spectra obtained showed sets of $[M + H]^+$ and $[M + H - CH_3OH]^+$ ions that corresponded in the proper proportions to the monosaccharides contained in the substrates. The lower *m/z* portions of the spectra were obscured by the presence of matrix-related peaks that often coincided with fragment ions associated with the analytes.

Conclusion

It has been demonstrated that it is possible and useful to perform gas-to-solid phase methanolysis of small oligosaccharides. In general, the gas-to-solid methanolysis method described here produces cleaner chromatographic traces than bulk phase techniques, although longer reaction times and higher temperatures are required for complete reaction. One of the most important features of using the gas-to-solid apparatus, as already point out for other derivatization methods previously developed (5, 16–18), is that less starting material is required than for a bulk phase reaction in order to produce equally clear and informative mass spectra and (or) chromatographic traces. Owing to avoidance of bulk-phase work-up procedures and direct contact with the reagent(s), the loss of reacted material is minimized, its purity maximized, and products can be analyzed by GC or MS by sampling them directly out of the reaction capillary after addition of solvent. In our hands, the amount of substrate needed for successful methanolysis/analysis has been estimated to be 10 times less than the quantity required for conventional bulk phase methods.

The chromatographic and mass spectral behavior of the substrates and methanolysis products has been closely examined since the use of higher resolution GC techniques often led to separation of a peak, previously thought to be single component, into two peaks with different mass spectra. In some cases the spectra of the separated components could not be reasonably matched to spectra in the NIST library. Electron impact and fast atom bombardment mass spectra of permethylated monosaccharides and methanolysis products have conventionally been interpreted as arising from single components. High-resolution gas chromatography now indicates that some of these products exist in forms other than the cyclic anomers to which library spectra are assigned (19). It is also noted that, for a given type of hexose contained in an oligosaccharide, methanolysis yields products whose diversity and retention times vary with the position and number of substituent(s) on the ring.

The scope of this study was to evaluate the performance of gas-to-solid phase methanolysis and to use the method to summarily characterize the sugar contents of small oligosaccharides. At this point in our study, only FAB-MS and GC–MS (electron impact) have been used to characterize the methanolysis products, whose exact chemical nature remains uncertain. However, at this stage and from a bioanalytical viewpoint, comparison of retention times, peak patterns, and mass spectra gives rise to sufficient information to provide a good estimate of the sugar contents. Further characterization of the methanolysis products is underway by means of insolating individual components using HPLC and capillary electrophoresis (CE) and analyzing their structures by FAB-MS–MS and nuclear magnetic resonance (NMR). These studies should help to clarity structural uncertainties highlighted above. Future work will also be directed toward application of this gas-to-solid phase methanolysis method to the determination of sugar contents of oligosaccharides originating from glycoproteins and glycosphingolipids.

Acknowledgements

The authors wish to acknowledge the technical assistance of W. Buchannon of the University of Manitoba, Chemistry Department, Mass Spectrometry Facility. The partial funding of this research by the Natural Sciences and Engineering Research Council of Canada (NSERC) is sincerely acknowledged. The authors also wish to gratefully thank J.L. Charlton for his helpful comments regarding the manuscript.

References

1. W.J. Richter, D.T. Müller, and B. Domon. Methods Enzymol. **193**, 607 (1990).
2. H. Perreault, O. Koul, J. Street, R.H. McCluer, and C.E. Costello. Proc. 43rd Conf. Mass Spectrom. Allied Topics, May 21–26, 1995, Atlanta, Ga. p. 1179.
3. H. Perreault and C.E. Costello. Can. J. Chem. In press.
4. V.N. Reinhold, B.B. Reinhold, and C.E. Costello. Anal. Chem. **67**, 1772 (1995).
5. H. Perreault and C.E. Costello. Org. Mass Spectrom. **29**, 720 (1994).
6. A.S. Angel and B. Nilsson. Biomed. Environ. Mass Spectrom. **21**, 202 (1992).
7. B. Fournet, G. Strecker, Y. Leroy, and J. Montreuil. Anal. Biochem. **116**, 489 (1981).
8. A. Dell, N.H. Carman, P.R. Tiller, and J.E. Thomas-Oates. Biomed. Environ. Mass Spectrom. **16**, 19 (1988).
9. A. Dell. Methods Enzymol. **193**, 647 (1990).
10. C.C. Sweeley, R. Bentley, M. Makita, and W.W. Wells. J. Am. Chem. Soc. **85**, 2497 (1963).
11. G. Larsson, H. Karlsson, G.C. Hansson, and W. Pimlott. Carbohydr. Res. **161**, 281 (1987).
12. B. Domon, D.R. Müller, and W.J. Richter. Org. Mass Spectrom. **29**, 715 (1994).
13. M.D. Ullman and R.H. McCluer. J. Lipid Res. **26**, 501 (1985).
14. S.K. Gross and R.H. McCluer. Anal. Biochem. **102**, 429 (1980).
15. K. Nishimura and K. Nakamura. J. Biochem. **98**, 1247 (1985).
16. J.E. Vath. Ph.D. Thesis, Massachusetts Institute of Technology, 1990.
17. B. Domon, J.E. Vath, and C.E. Costello. Anal. Biochem. **184**, 151 (1990).
18. C.E. Costello and J.E. Vath. Methods Enzymol. **193**, 738 (1990).
19. NIST Standard Reference Database, Series 1a, NIST/EPA/NIH Database Version 4.5, February 1994, U.S. Department of Commerce. (*a*) α-D-Galactopyranoside, methyl 2,3,4,6-tetra-*O*-methyl-. CAS no.: 3149-64-2, EPA no.: 22952, DB no.: 21122. (*b*) β-D-Galactopyranoside, methyl 2,3,4,6-tetra-*O*-methyl-. CAS no.: 2296-47-1, EPA no.: 31190, DB no. 21127. (*c*) D-Galactopyranose, 2,3,4,6-tetra-*O*-methyl-. CAS no.: 3353-52-4, EPA no.: 31194, DB no.: 7138. (*d*) α-D-Glucopyranoside, methyl 2,3,4,6-tetra-*O*-methyl-. CAS no.: 605-81-2, EPA no.: 101817, DB no.: 22124. (*e*) β-D-Glucopyranoside, methyl 2,3,4,6-tetra-tetra-*O*-methyl-. CAS no.: 3149-65-3, EPA no.: 33672, DB no.: 21248. (*f*) α-D-Mannopyranoside, methyl 2,3,4-tri-*O*-methyl-6-deoxy. CAS no.: 72983-16-5, EPA no.: 101806, DB no.: 21125. (*g*) β-D-Mannopyranoside, methyl 2,3,4-tri-*O*-methyl-6-deoxy. CAS no.: 35939-74-3, EPA no.: 101807, DB no.: 21113. (*h*) α-D-Glucopyranoside, 2,3,4,6-tetra-*O*-methyl-α-D-glucopyranosyl 2,3,4,6-tetra-*O*-methyl. CAS no.: 25018-29-5, EPA no.: 17735, DB no.: 25394. (*i*) D-Glucopyranose, 2,3,4,6-tetra-*O*-methyl-. CAS no.: 7506-68-5, EPA no.: 31193, DB no.: 7137.

An estimate of the spin–spin coupling constant, $^1J(^1H,^{13}C)$, in gaseous benzene

Ted Schaefer, Guy M. Bernard, and Frank E. Hruska

Abstract: An excellent linear correlation ($r = 0.9999$) exists between the spin–spin coupling constants $^1J(^1H,^{13}C)$, in benzene dissolved in four solvents (R. Laatikainen et al. J. Am. Chem. Soc. **117**, 11006 (1995)) and Ando's solvation dielectric function, $\varepsilon/(\varepsilon - 1)$. The solvents are cyclohexane, carbon disulfide, pyridine, and acetone. $^1J(^1H,^{13}C)$ for gaseous benzene is predicted to be 156.99(2) Hz at 300 K.

Key words: spin–spin coupling constants, $^1J(^1H,^{13}C)$ for benzene in the vapor phase; spin–spin coupling constants, solvent dielectric constant dependence of $^1J(^1H,^{13}C)$ in benzene; benzene, estimate of $^1J(^1H,^{13}C)$ in the vapor; nuclear magnetic resonance, estimate of $^1J(^1H,^{13}C)$ in gaseous benzene.

Résumé : Il existe une excellente corrélation linéaire ($r = 0,9999$) entre les constantes de couplage spin–spin $^1J(^1H,^{13}C)$ du benzène dissous dans quatre solvants (R. Laatikainen et al., J. Am. Chem. Soc. **117**, 11006 (1995)) et la fonction de solvatation diélectrique d'Ando, $\varepsilon(\varepsilon - 1)$. Les solvants sont le cyclohexane, le disulfure de carbone, la pyridine et l'acétone. On prédit que $^1J(^1H,^{13}C)$ pour le benzène à l'état gazeux sera 156,99(2) Hz, à 300 K.

Mots clés : constantes de couplage spin–spin, $^1J(^1H,^{13}C)$; dépendance des constantes de couplage de benzène sur la constante diélectrique du solvant; benzène, évaluation de $^1J(^1H,^{13}C)$ en phase vapeur; résonance magnétique nucléaire.

[Traduit par la rédaction]

Introduction

Since the time of its estimate as 159 ± 5 Hz (1), the precision of the measurement of $^1J(^1H,^{13}C) = {}^1J$ in benzene has steadily improved. In 1983 it was remarked that the precision had now improved by three orders of magnitude: the value of ^1J in neat benzene was given as 158.354(1) Hz (2). More recently, ^1J was measured for a number of solutions of benzene (3). The root-mean-square error in the spectral peak assignments was an order of magnitude lower than that of 1983.

Progress in the computation of spin–spin coupling constants has also been made, as described in a recent review (4). However, it appears that ^nJ is rather more difficult to compute accurately from first principles (5) than is the nuclear shielding constant (6). Nevertheless, for first-row elements, values of increasing are being calculated. In particular, reasonably good numbers for $^nJ(H,C)$ and $^nJ(H,H)$ have appeared (4) for the isolated ethylene molecule, judging by the coupling constants measured for solutions in CCl_4 (7).

It is well known (8) that many coupling constants are solvent dependent. Perturbations by the surrounding medium vitiate any stringent comparisons between theory and experiment unless the former can include perturbations or the latter can measure them. Benzene, of course, is an important molecule in chemistry and therefore accurate computations of $^nJ(^1H,^{13}C)$, $^nJ(^1H,^1H)$, and $^nJ(^{13}C,^{13}C)$ may well appear in the near future. While the medium dependence of $^nJ(H,H)$ is small (3), that of ^1J is significant. It is shown below that a good number for ^1J in isolated benzene can be deduced, a number probably difficult to measure with high precision in the vapor phase.

Received April 2, 1996.

T. Schaefer,[1] G.M. Bernard, and F.E. Hruska. Department of Chemistry, University of Manitoba, Winnipeg, MB R3T 2N2, Canada.

[1] Author to whom correspondence may be addressed. Telephone: (204) 474-9321. Fax: (204) 275-0905. E-mail: schaefe@cc.umanitoba.ca

Results and discussion

Table 1 displays ^1J in four solvents (3) of various dielectric constants, ε, and the function $(\varepsilon - 1)/\varepsilon = x$ for the pure solvent; also as corrected for the presence of the benzene solute molecules. The quantity x comes from the solvation model of Ando and Webb (8), which also allows for a minor quadratic dependence of ^1J on x. A linear dependence of ^1J on x is found, as in eqs. [1] and [2]. The correlation coefficient is

$$[1] \quad {}^1J = 1.792x + 157.013(15), \qquad r = 0.9993$$

$$[2] \quad {}^1J = 1.833x + 156.992(6), \qquad r = 0.9999$$

somewhat higher for eq. [2], which uses the x values adjusted for the presence of the solute. The standard deviation for eq. [1] is 0.015 Hz, that for eq. [2] is 0.006 Hz. The second equation yields ^1J as 156.99 Hz for the vibrating molecule at 300 K and $x = 0$, that is, for $\varepsilon = 1$. Note that $0 \leq x \leq 1$ for media of $1 \leq \varepsilon \leq 100$ and that a relatively nonpolar dielectric such as cyclohexane has an $x \sim 0.5$.

^1J for neat benzene is not included; it is known that, in dielectric continuum models of the solvent, benzene behaves as if it had a varying ε, sometimes as high as 7.5 (9): the ^1J of 158.380 Hz in neat benzene implies an effective dielectric constant of 4.1. The satisfactory inclusion of the pyridine solu-

Table 1. $^1J(^1H, ^{13}C)$ in benzene at 300 K in a number of solvents, and some dielectric functions.

Solvent	^1J/Hz[a]	ε[b]	$(\varepsilon - 1)/\varepsilon$	ε[c]	$(\varepsilon - 1)/\varepsilon$
C_6D_{12}	157.917	2.02	0.505	2.03	0.507
CS_2	158.132	2.64	0.621	2.62	0.618
Pyridine-d_5	158.642	12.3	0.919	10.29	0.903
Acetone-d_6	158.735	20.6	0.951	19.68	0.949

[a]From ref. 3.
[b]Dielectric constant of the solvent.
[c]Dielectric constant of the solution, 5 mol% in benzene, whose dielectric constant is taken as 2.27.

tion in the correlation suggests that any complex formation between benzene and pyridine molecules favors the one in which the pyridine C—H bonds interact with the benzene π electrons and not vice versa (3).

The hybridization model (10) of one-bond coupling constants between protons and carbon-13 nuclei, in which ^1J is proportional to the fractional *s* character of the carbon hybrid orbital used in the C—H bond, must be modified to accommodate the increase ^1J caused by electronegative substituents as, for example, in methane derivatives. One explanation (11, 12) of the increase in ^1J attributes it to an increase in the effective nuclear charge of the carbon atom, corresponding to an increase in *s* electron density at the nucleus, presumably also to an increased polarity of the C—H bond. It is therefore interesting, yet perhaps coincidental, that our self-consistent isodensity – polarizable continuum model or SCI–PCM (13, 14) computations (15) yield increasing polarity of the $^-C—H^+$ bonds of benzene as the dielectric constant of the medium rises. As an example, for single point MP2/6-31G* computations (on correlation gradient geometries of the isolated molecule) a linear relationship exists between ^1J and the total Mulliken charge on the carbon atom ($r = 0.995$) if the dielectric constants in Table 1 are employed in the computations.

Another possibility, that the solvent dependence of ^1J is dominated by changes in the C—H bond length, likely can be discounted because it appears that, in methane at least, an increase of 0.1 Å in the length would augment ^1J by only 1.2 Hz (16). A change of more than 1% in the benzene geometry in solution is probably an upper limit (17, 18). Qualitatively, however, one might expect an increase in the C—H bond length as its polarity increases.

Acknowledgements

Support from the Natural Sciences and Engineering Research Council of Canada is gratefully acknowledged. We thank Professor R. Laatikainen for very helpful discussions.

References

1. P.C. Lauterbur. J. Chem. Phys. **26**, 217 (1957).
2. V.A. Chertkov and N.M. Sergeyev. J. Magn. Reson. **52**, 400 (1983).
3. R. Laatikainen, J. Ratilainen, R. Sebastian, and H. Santa. J. Am. Chem. Soc. **117**, 11006 (1995).
4. R.H. Contreras and J.C. Facelli. Annu. Rep. NMR Spectrosc. **27**, 255 (1993).
5. S.A. Perera, M. Nooijen, and R.J. Bartlett. J. Chem. Phys. **104**, 3290 (1996).
6. D.B. Chesnut. Chem. Phys. Lett. **246**, 235 (1995).
7. R.M. Lynden-Bell and N. Sheppard. Proc. R. Soc. London Ser. A: **269**: 385 (1962).
8. I. Ando and G.A. Webb. Org. Magn. Reson. **15**, 111 (1981), and references therein.
9. R.J. Abraham and E. Bretschneider. *In* International rotation in molecules. *Edited by* W.J. Orville-Thomas. Wiley, New York. 1974. Chap. 13. pp. 505–506.
10. N. Muller and D.E. Pritchard. J. Chem. Phys. **31**, 768 (1959).
11. J.N. Shoolery. J. Chem. Phys. **31**, 1427 (1959).
12. D.M. Grant and W.M. Litchman. J. Am. Chem. Soc. **87**, 3994 (1965).
13. J. Tomasi and M. Persico. Chem. Rev. **94**, 2027 (1994).
14. K.B. Wiberg, T.A. Keith, M.J. Frisch, and M. Murcko. J. Phys. Chem. **99**, 9072 (1995).
15. M.J. Frisch, G.W. Trucks, H.B. Schlegel, P.M.W. Gill, B.G. Johnson, M.A. Robb, J.R. Cheesesman, T. Keith, G.A. Petersson, J.A. Montgomery, K. Raghavachari, M.a. Al-Laham, V.G. Zakrzewski, J.V. Ortiz, J.B. Foresman, C.Y. Peng, P.Y. Ayala, W. Chen, M.W. Wong, J.L. Andres, E.S. Replogle, R. Gomperts, R.L. Martin, D.J. Fox, J.S. Binkley, D.J. Defrees, J. Baker, and J.P. Stewart. Gaussian 94, Revision B.2. Gaussian, Inc., Pittsburg, Pa. 1995.
16. W.T. Raynes, J. Geertsen, and J. Oddershede. Chem. Phys. Lett. **197**, 516 (1992).
17. P. Diehl, H. Bösiger, and H. Zimmerman. J. Magn. Reson. **33**, 113 (1979).
18. M.R. Zakin and D.R. Herschbach. J. Chem. Phys. **85**, 2376 (1986).

Gaussian- and Slater-type bases for ground and certain low-lying excited states of positive and negative ions of the atoms H through Xe based on the generator coordinate Hartree–Fock method

A.B.F. da Silva and M. Trsic

Abstract: We applied a discretized version of the generator coordinate Hartree–Fock (GCHF) method to generate Gaussian- and Slater-type functions for mono positive and mono negative ions of the atoms H through Xe. The basis sizes for Slater-type functions are (12*s*, 10*p*, 10*d*) for positive ions, and (13*s*, 11*p*, 10*d*) for negative ions. In the case of Gaussian-type functions the bases are (18*s*, 12*p*, 11*d*) for both positive and negative species. Ground and excited state Hartree–Fock energies are calculated with these bases and the results compared with the best atom-optimized calculations and numerical HF results available. A discussion on the role of weight functions in the evaluation of electronic energies emphasizes the integral character of the GCHF method.

Key words: Slater-type bases, Gaussian-type bases, generator coordinate Hartree–Fock, atomic ions.

Résumé : On a appliqué une version numérique de la méthode de la coordonnée génératrice Hartree–Fock (GCHF) pour générer des fonctions des types de Gauss et de Slater des mono-ions tant positifs que négatifs des atomes allant de H à Xe. Les tailles des ensembles de base pour les fonctions de type Slater sont (12*s*, 10*p*, 10*d*) pour les ions positifs et (13*s*, 11*p*, 10*d*) pour les ions négatifs. Dans le cas des fonctions de type de Gauss, les bases sont (18*s*, 12*p*, 11*d*) tant pour les espèces positives que négatives. Utilisant ces bases, on a calculé les énergies Hartree–Fock de états tant fondamentaux qu'excités et on a comparé les résultats avec les meilleurs résultats disponibles de calculs optimisés des atomes et de résultats numériques de HF. Une discussion sur le rôle des fonctions de pois dans l'évaluation des énergies électroniques met en relief le caractère intégral de la méthode du GCHF.

Mots clés : fonctions du type de Slater, fonctions du type de Gauss, coordonnée génératrice Hartree–Fock, ions atomiques.

[Traduit par la rédaction]

1. Introduction

The generator coordinate (GC) method for the nuclear bound state was introduced in 1957 by Griffin and Wheeler (1). In this method the variational trial function is an integral transform over a nucleonic wave function and a weight function depending on a parameter (generator coordinate), i.e., $f(\alpha)$. In such a manner, the common variational principle, $\delta E/\delta\alpha = 0$, was, a priori, made more powerful with the requirement $\delta E/\delta f(\alpha) = 0$, leading to an integral equation. Most applications in nuclear physics (for a review see, for instance, Wong (2)) relied on the Gaussian overlap approximation (GOA), although there were some attempts at numerical solution (3), and later Lathouwers discussed the GC method against the background of the Fredholm theory of linear integral equations (4).

Perhaps the earliest application of GC to electrons in a molecular (hydrogen molecule) system was due to Laskowski (5). In 1978 Chattopadhyay et al. (6) applied the method to several model problems, including the He atom, with special emphasis on various aspects of the discretization technique. Further developments in discretization techniques were made by Broeckhove, Deumens and co-workers (7).

On the other hand, as early as 1968, Somorjai (8) had introduced the integral transform method, closely related to GC, for atomic and molecular systems. In the applications, Somorjai chose explicit forms for $f(\alpha)$ (such as the delta function), which led to a variational treatment for the integration limits. An extensive bibliography on the method may be found in ref. 9. In the context of this method, accurate correlated functions for two- and three-electron atomic systems were obtained by Thakkar et al. (10).

The generator coordinate Hartree–Fock (GCHF) method was introduced in 1986 (11), and one of the first applications was in the generation of Gaussian- and Slater-type orbital

Received June 27, 1995.[1]

A.B.F. da Silva[2] and M. Trsic. Departamento de Química e Física Molecular, Instituto de Química de São Carlos, Universidade de São Paulo, P.O. Box 780, 13560-970, São Carlos, SP, Brazil.

[1] Revision received April 15, 1996.

[2] Author to whom correspondence may be addressed. Telephone: (55)(16)2749171. Fax: (55)(16)2749163. E-mail: ALBERICO@IQSC.SC.USP.BR

(GTF and STF) universal basis sets for the first and second rows of the periodic table (12, 13). Later, da Silva and Trsic presented GTF and STF universal basis sets encompassing the atoms from H through Xe for atomic and molecular nonrelativistic calculations (14, 15). Also, the GCHF method was recently tested successfully in the generation of universal Gaussian basis sets for relativistic calculations (16–19). Here it is important to mention that the concept of the universal basis set was first introduced by Silver, Wilson, and Nieuwpoort (20).

In this work we are extending the bases of ref. 4 to embrace the positive and negative ions of the atoms H through Xe. The total HF energies of the ground and some excited states are calculated and compared with the best HF values available. We also present a further discussion on the importance of the weight functions in evaluating atomic energies.

2. Results and discussion

2.1. Total energies

The total energies reported in this section were calculated by using Slater-type functions (STF) and Gaussian-type functions (GTF) generated with the GCHF method. In this methodology, the one-electron functions are chosen as integral transforms, i.e.,

$$[1] \quad \psi_i(1) = \int d\alpha\, \phi_i(1,\alpha) f_i(\alpha), \qquad i = 1, \ldots, n$$

where the ϕ_i are the generator functions (they may be STF, GTF, or other types of functions), the f_i are the weight functions, and α is the generator coordinate. Using eq. [1] to build a Slater determinant for the multi-electronic wave function, and minimizing the total energy E with respect to f_i, one obtains the Griffin–Wheeler–HF (GWHF) equations or integral HF equations (11, 14).

The GWHF equations are solved by discretization through a technique called integral discretization (21), which preserves the continuous representation (integral character) of the Generator Coordinate Method (GCM) (1, 22). This technique is implemented through a relabelling of the generator coordinate space, i.e.,

$$[2] \quad \Omega = \frac{\ln \alpha}{A}, \qquad A > 1$$

Here, an equally spaced N-point mesh $\{\Omega_i\}$ is selected for each s, p, and d symmetry. The integration range is then characterized by an initial point, Ω_{min}, an increment, $\Delta\Omega$, and N (discretization point number). The scaling factor A is the same (A = 6.0) for all calculations. We also note from eq. [2] that the numerical integration of the GWHF equations provides a set $\{\Omega_i\}$ and simultaneously an exponent set $\{\alpha_i\}$ for the basis functions.

Since eq. [1] represents a continuous and infinite superposition, we do not need, in the GWHF equations, to specify the principal quantum numbers, n, for the various symmetries of the generator functions, ϕ_i, as the weight functions, f_i, distinguish the n states. Thus, our bases in this work consist of the simplest 1s, 2p, and 3d STF or GTF.

The basis size for STF positive ions is (12s, 10p, 10d) with the following discretization parameters (i.e., orbital exponents):

Symmetry	Ω_{min}	$\Delta\Omega$	N
s	−0.11	0.07	12
p	0.00	0.07	10
d	−0.11	0.07	10

The GTF (18s, 12p, 11d) basis for positive ions is generated with:

Symmetry	Ω_{min}	$\Delta\Omega$	N
s	−0.55	0.16	18
p	−0.40	0.16	12
d	−0.55	0.16	11

The basis size for STF negative ions is (13s, 11p, 10d) with discretization parameters as follows:

Symmetry	Ω_{min}	$\Delta\Omega$	N
s	−0.21	0.07	13
p	−0.10	0.07	11
d	−0.05	0.07	10

The GTF (18s, 12p, 11d) basis for negative ions is generated with:

Symmetry	Ω_{min}	$\Delta\Omega$	N
s	−0.75	0.16	18
p	−0.55	0.16	12
d	−0.75	0.16	11

The basis sets (discretization parameters) for STF and GTF positive ions are the same as those we previously employed for neutral atoms (14). This coincidence was to be expected, as the ionization produces orbital contraction, and thus the bases for the neutral atoms were adequate for describing the total energies for ground and low-lying excited states of positive ions. For negative ions, therefore, it was not possible to describe the total energies by employing the same basis sets as for neutral atoms. This is a consequence of the entrance of one electron in the frontier atomic orbital, making it more diffuse; thus, lower values for Ω_{min} are required for STF and GTF bases.

In Tables 1–4 we present the total STF and GTF HF energies for ground and low-lying excited states of positive and negative ions. Our results are compared with the numerical results of Koga et al. (23) and, only when numerical results are not available, with the atom-optimized values of Clementi and Roetti (24). One can see from Tables 1–4 that our STF energy values (ground and low-lying excited states) compare very favorably with the numerical results and with the atom-optimized results of Clementi and Roetti, often being lower than

Table 1. Total ground state energies (au) of the STF and GTF bases for positive ions.

Ion	Configuration	State	STF energy (12*s*, 10*p*, 10*d*)[a]	Virial theorem STF[b]	GTF energy (18*s*, 12*p*, 11*d*)[a]	Virial theorem GTF[b]	Numerical-HF energy (23) (NHF)
He^+	$1s^1$	^2S	3.9 (−7)	3.3 (−6)	7.0 (−6)	1.6 (−6)	−2
Li^+	$1s^2$	^1S	9.0 (−7)	1.4 (−6)	2.0 (−5)	1.9 (−6)	−7.236 415 2
Be^+	[He] $2s^1$	^2S	1.9 (−5)	8.5 (−6)	7.0 (−5)	2.9 (−6)	−14.277 395
B^+	[He] $2s^2$	^1S	1.0 (−6)	6.2 (−8)	1.1 (−4)	1.4 (−5)	−24.237 575
C^+	[He] $2s^2\ 2p^1$	^2P	1.4 (−5)	1.2 (−6)	1.5 (−4)	5.2 (−6)	−37.292 224
N^+	[He] $2s^2\ 2p^2$	^3P	1.1 (−5)	6.2 (−7)	2.7 (−4)	9.8 (−7)	−53.888 005
O^+	[He] $2s^2\ 2p^3$	^4S	2.1 (−5)	3.0 (−8)	3.4 (−4)	5.6 (−6)	−74.372 606
F^+	[He] $2s^2\ 2p^4$	^3P	2.0 (−5)	1.3 (−6)	4.1 (−4)	3.3 (−7)	−98.831 720
Ne^+	[He] $2s^2\ 2p^5$	^2P	1.0 (−5)	7.5 (−6)	5.8 (−4)	4.3 (−6)	−127.817 81
Na^+	[He] $2s^2\ 2p^6$	^1S	1.3 (−5)	7.2 (−7)	7.9 (−4)	5.8 (−8)	−161.676 963
Mg^+	[Ne] $3s^1$	^2S	6.3 (−5)	1.6 (−6)	1.1 (−3)	3.2 (−6)	−199.371 810
Al^+	[Ne] $3s^2$	^1S	8.3 (−5)	1.0 (−6)	1.4 (−3)	1.1 (−6)	−241.674 670
Si^+	[Ne] $3s^2\ 3p^1$	^2P	1.2 (−4)	5.7 (−7)	1.9 (−3)	2.9 (−6)	−288.573 131
P^+	[Ne] $3s^2\ 3p^2$	^3P	1.5 (−4)	3.3 (−6)	2.6 (−3)	5.9 (−7)	−340.349 776
S^+	[Ne] $3s^2\ 3p^3$	^4S	7.9 (−5)	6.2 (−7)	3.3 (−3)	2.4 (−6)	−397.173 183
Cl^+	[Ne] $3s^2\ 3p^4$	^3P	1.5 (−4)	2.7 (−6)	4.0 (−3)	2.2 (−6)	−459.048 591
Ar^+	[Ne] $3s^2\ 3p^5$	^2P	3.1 (−4)	2.9 (−6)	5.2 (−3)	7.6 (−6)	−526.274 534
K^+	[Ne] $3s^2\ 3p^6$	^1S	4.3 (−4)	6.6 (−8)	6.7 (−3)	9.2 (−6)	−599.017 58
Ca^+	[Ar] $4s^1$	^2S	4.2 (−4)	5.4 (−6)	8.7 (−3)	2.5 (−6)	−676.570 01
Sc^+	[Ar] $4s^1\ 3d^1$	^3D	2.4 (−4)	3.8 (−6)	1.0 (−2)	4.5 (−6)	−759.539 14
Ti^+	[Ar] $4s^1\ 3d^2$	^4F	1.7 (−4)	4.3 (−7)	1.2 (−2)	8.2 (−6)	−848.203 40
V^+	[Ar] $4s^0\ 3d^4$	^5D	2.7 (−4)	2.4 (−6)	1.3 (−2)	5.1 (−6)	−942.670 78
Cr^+	[Ar] $4s^0\ 3d^5$	^6S	5.0 (−4)	4.7 (−6)	1.5 (−2)	2.5 (−6)	−1043.139 4
Mn^+	[Ar] $4s^1\ 3d^5$	^7S	9.0 (−4)	5.3 (−6)	1.7 (−2)	1.3 (−5)	−1149.649 4
Fe^+	[Ar] $4s^1\ 3d^6$	^6D	1.2 (−3)	4.1 (−6)	2.0 (−2)	2.0 (−5)	−1262.213 0
Co^+	[Ar] $4s^0\ 3d^8$	^3F	1.5 (−3)	2.4 (−6)	2.4 (−2)	2.3 (−5)	−1381.128 8
Ni^+	[Ar] $4s^0\ 3d^9$	^2D	1.6 (−3)	6.7 (−7)	2.8 (−2)	2.1 (−5)	−1506.591 1
Cu^+	[Ar] $4s^0\ 3d^{10}$	^1S	1.7 (−3)	8.3 (−7)	3.2 (−2)	1.6 (−5)	−1638.728 2
Zn^+	[Ar] $4s^1\ 3d^{10}$	^2S	1.7 (−3)	2.0 (−6)	3.7 (−2)	8.4 (−6)	−1777.567 5
Ga^+	[Ar] $4s^2\ 3d^{10}$	^1S	1.8 (−3)	2.4 (−6)	4.1 (−2)	2.4 (−6)	−1923.059 7
Ge^+	[Ar] $4s^2\ 3d^{10}\ 4p^1$	^2P	1.9 (−3)	1.9 (−6)	4.5 (−2)	1.7 (−6)	−2075.086 5
As^+	[Ar] $4s^2\ 3d^{10}\ 4p^2$	^3P	2.0 (−3)	1.6 (−6)	5.0 (−2)	3.5 (−6)	−2233.888 3
Se^+	[Ar] $4s^2\ 3d^{10}\ 4p^3$	^4S	2.3 (−3)	3.1 (−7)	5.5 (−2)	2.3 (−6)	−2399.558 6
Br^+	[Ar] $4s^2\ 3d^{10}\ 4p^4$	^3P	2.6 (−3)	2.4 (−6)	6.1 (−2)	9.8 (−6)	−2572.045 2
Kr^+	[Ar] $4s^2\ 3d^{10}\ 4p^5$	^2P	3.2 (−3)	6.2 (−6)	6.9 (−2)	2.1 (−5)	−2751.567 4
Rb^+	[Ar] $4s^2\ 3d^{10}\ 4p^6$	^1S	4.2 (−3)	1.1 (−5)	7.8 (−2)	3.3 (−5)	−2938.219 9
Sr^+	[Kr] $5s^1$	^2S	5.8 (−3)	1.5 (−5)	9.0 (−2)	4.6 (−5)	−3131.373 8
Y^+	[Kr] $5s^2$	^1S	7.6 (−3)	2.1 (−5)	1.1 (−1)	5.7 (−5)	−3331.472 9
Zr^+	[Kr] $5s^1\ 4d^2$	^4F	1.0 (−2)	2.5 (−5)	1.2 (−1)	6.4 (−5)	−3538.809 3
Nd^+	[Kr] $5s^0\ 4d^4$	^5D	1.3 (−2)	2.8 (−5)	1.4 (−1)	6.7 (−5)	−3753.389 5
Mo^+	[Kr] $5s^0\ 4d^5$	^6S	1.7 (−2)	2.8 (−5)	1.6 (−1)	6.6 (−5)	−3975.333 7
Te^+	[Kr] $5s^1\ 4d^5$	^7S	2.0 (−2)	2.5 (−5)	1.8 (−1)	6.1 (−5)	−4204.594 4
Ru^+	[Kr] $5s^0\ 4d^7$	^4F	2.4 (−2)	1.7 (−5)	2.0 (−1)	5.6 (−5)	−4441.322 0
Rh^+	[Kr] $5s^0\ 4d^8$	^3F	2.7 (−2)	6.4 (−6)	2.3 (−1)	5.1 (−5)	−4685.664 2
Pd^+	[Kr] $5s^0\ 4d^9$	^2D	2.9 (−2)	7.2 (−6)	2.5 (−1)	4.7 (−5)	−4937.675 9
Ag^+	[Kr] $5s^0\ 4d^{10}$	^1S	3.0 (−2)	2.1 (−5)	2.8 (−1)	4.7 (−5)	−5197.481 3
Cd^+	[Kr] $5s^1\ 4d^{10}$	^2S	3.0 (−2)	3.3 (−5)	3.1 (−1)	5.2 (−5)	−5464.878 6
In^+	[Kr] $5s^2\ 4d^{10}$	^1S	2.8 (−2)	3.8 (−5)	3.3 (−1)	6.5 (−5)	−5739.978 4
Sn^+	[Kr] $5s^2\ 4d^{10}\ 5p^1$	^2P	2.6 (−2)	2.5 (−4)	3.7 (−1)	8.2 (−5)	−6022.678 3
Sb^+	[Kr] $5s^2\ 4d^{10}\ 5p^2$	^3P	2.5 (−2)	8.7 (−6)	4.1 (−1)	1.1 (−4)	−6313.165 9
Te^+	[Kr] $5s^2\ 4d^{10}\ 5p^3$	^4S	2.9 (−2)	3.6 (−5)	4.6 (−1)	1.3 (−4)	−6611.503 4
I^+	[Kr] $5s^2\ 4d^{10}\ 5p^4$	^3P	4.0 (−2)	1.1 (−4)	5.1 (−1)	1.6 (−4)	−6917.627 3
Xe^+	[Kr] $5s^2\ 4d^{10}\ 5p^5$	^2P	6.4 (−2)	2.2 (−4)	5.8 (−1)	1.8 (−4)	−7231.709 0

[a]This column shows $\Delta E = |E(\text{NHF}) - E(\text{calculated})|$.

[b]This column shows the values of $\Delta = |2 + \text{virial ratio}|$.

Table 2. Low-lying excited state energies (au) of the STF and GTF bases for positive ions.

Ion	Configuration	State	STF energy (12s, 10p, 10d)[a]	Virial theorem STF[b]	GTF energy (18s, 12p, 11d)[a]	Virial theorem GTF[b]	Clementi–Roetti energy (24) (CR)
Sc^+	[Ar] $4s^0\ 3d^2$	^3F	1.7 (−4)	3.8 (−6)	1.0 (−2)	4.1 (−6)	−759.509 74
Sc^+	[Ar] $4s^2$	^1S	1.1 (−4)	2.7 (−6)	1.1 (−2)	3.9 (−6)	−759.461 97
Ti^+	[Ar] $4s^0\ 3d^3$	^4F	3.6 (−4)[c]	1.0 (−6)	1.1 (−2)	7.6 (−6)	−848.186 39
Ti^+	[Ar] $4s^2\ 3d^1$	^2D	5.0 (−5)	3.6 (−7)	1.2 (−2)	8.6 (−6)	−848.056 22
V^+	[Ar] $4s^2\ 3d^2$	^3F	1.8 (−4)	3.5 (−6)	1.3 (−2)	6.2 (−6)	−942.498 22
Cr^+	[Ar] $4s^1\ 3d^4$	^6D	2.0 (−4)[c]	5.2 (−6)	1.4 (−2)	2.6 (−6)	−1043.096 3
Cr^+	[Ar] $4s^2\ 3d^3$	^4F	0.0	5.1 (−6)	1.5 (−2)	2.4 (−6)	−1042.889 7
Mn^+	[Ar] $4s^0\ 3d^6$	^5D	1.0 (−4)[c]	5.1 (−6)	1.6 (−2)	1.3 (−5)	−1149.520 5
Mn^+	[Ar] $4s^2\ 3d^4$	^5D	3.0 (−4)	5.1 (−6)	1.7 (−2)	1.3 (−5)	−1149.368 7
Fe^+	[Ar] $4s^2\ 3d^5$	^6S	4.0 (−4)	3.8 (−6)	2.0 (−2)	2.1 (−5)	−1262.125 2
Co^+	[Ar] $4s^2\ 3d^6$	^5D	9.0 (−4)	1.9 (−6)	2.4 (−2)	2.4 (−5)	−1381.008 9
Ni^+	[Ar] $4s^2\ 3d^7$	^4F	7.0 (−4)	2.2 (−7)	2.8 (−2)	2.2 (−5)	−1506.431 7
Cu^+	[Ar] $4s^2\ 3d^8$	^3F	1.1 (−3)	1.1 (−6)	3.2 (−2)	1.6 (−5)	−1638.479 1
As^+	[Ar] $4s^2\ 3d^{10}\ 4p^2$	^1D	1.5 (−3)	1.2 (−6)	5.0 (−2)	1.5 (−6)	−2233.839 0
As^+	[Ar] $4s^2\ 3d^{10}\ 4p^2$	^1S	1.5 (−3)	9.9 (−7)	5.0 (−2)	2.1 (−6)	−2233.767 7
Se^+	[Ar] $4s^2\ 3d^{10}\ 4p^3$	^2D	1.8 (−3)	2.4 (−7)	5.5 (−2)	2.4 (−6)	−2399.477 4
Se^+	[Ar] $4s^2\ 3d^{10}\ 4p^3$	^2P	1.9 (−3)	8.4 (−8)	5.5 (−2)	2.5 (−6)	−2399.424 5
Br^+	[Ar] $4s^2\ 3d^{10}\ 4p^4$	^1D	2.2 (−3)	2.3 (−6)	6.1 (−2)	9.9 (−6)	−2571.987 1
Br^+	[Ar] $4s^2\ 3d^{10}\ 4p^4$	^1S	2.1 (−3)	2.4 (−6)	6.1 (−2)	1.0 (−5)	−2571.901 4
Zr^+	[Kr] $5s^0\ 4d^3$	^4F	3.5 (−2)[c]	2.5 (−5)	7.6 (−2)	6.4 (−5)	−3538.766 3
Zr^+	[Kr] $5s^2\ 4d^1$	^2D	4.6 (−3)[c]	2.5 (−5)	1.1 (−1)	6.5 (−5)	−3538.694 8
Nb^+	[Kr] $5s^1\ 4d^3$	^5F	9.0 (−4)	2.8 (−5)	1.3 (−1)	6.7 (−5)	−3753.350 5
Nb^+	[Kr] $5s^2\ 4d^2$	^3F	1.9 (−3)[c]	2.8 (−5)	1.3 (−1)	6.7 (−5)	−3753.202 8
Mo^+	[Kr] $5s^1\ 4d^4$	^6D	1.7 (−3)	2.8 (−5)	1.5 (−1)	6.5 (−5)	−3975.236 2
Mo^+	[Kr] $5s^2\ 4d^3$	^4F	1.9 (−3)	2.8 (−5)	1.5 (−1)	6.4 (−5)	−3975.045 9
Tc^+	[Kr] $5s^0\ 4d^6$	^5D	2.1 (−2)[c]	2.5 (−5)	1.4 (−1)	6.1 (−5)	−4204.522 8
Tc^+	[Kr] $5s^2\ 4d^4$	^5D	9.1 (−3)	2.5 (−5)	1.7 (−1)	6.0 (−5)	−4204.312 9
Ru^+	[Kr] $5s^1\ 4d^6$	^6D	1.3 (−2)	1.8 (5)	1.9 (−1)	5.5 (−5)	−4441.267 8
Ru^+	[Kr] $5s^2\ 4d^5$	^6S	1.4 (−2)	1.7 (−5)	2.0 (−1)	5.4 (−5)	−4441.121 6
Rh^+	[Kr] $5s^1\ 4d^7$	^5F	1.5 (−2)	6.6 (−6)	2.2 (−1)	5.0 (−5)	−4685.567 2
Rh^+	[Kr] $5s^2\ 4d^6$	^5D	1.5 (−2)	6.6 (−6)	2.2 (−1)	5.0 (−5)	−4685.345 0
Pd^+	[Kr] $5s^1\ 4d^8$	^4F	3.1 (−2)	7.0 (−6)	2.5 (−1)	4.7 (−5)	−4937.551 0
Pd^+	[Kr] $5s^2\ 4d^7$	^4F	1.6 (−2)	6.9 (−6)	2.4 (−1)	4.7 (−5)	−4937.273 7
Ag^+	[Kr] $5s^1\ 4d^9$	^3D	1.8 (−2)	2.1 (−5)	2.7 (−1)	4.7 (−5)	−5197.261 2
Ag^+	[Kr] $5s^2\ 4d^8$	^3F	1.8 (−2)	2.1 (−5)	2.7 (−1)	4.8 (−5)	−5196.957 9
Cd^+	[Kr] $5s^2\ 4d^9$	^2D	1.6 (−2)	3.3 (−5)	2.9 (−1)	5.4 (−5)	−5464.476 7

[a]This column shows $\Delta E = |E(\text{NHF}) - E(\text{calculated})|$.
[b]This column shows the values of $\Delta = |2 + \text{virial ratio}|$.
[c]Calculated energy is lower than CR energy.

those obtained with the latter. Our GTF energies are only slightly above the STF values in spite of a rather modest increase in the number of basis functions.

For the case of positive ions (Tables 1 and 2), we notice a better performance for both STF and GTF bases for excited states than for ground states when compared with the Clementi and Roetti results. Also for positive and negative ions, the STF energy values are close to the numerical results and competitive with the excited state values of Clementi and Roetti. This capacity to describe excited states with the GCM was commented on in previous papers (6, 14, 21).

We would also like to make a comparison between the STF energy results obtained in this work for the ground state of cations and anions and the STF energy results obtained recently by Koga et al. (25) using doubly even-tempered basis sets for the same ionic species. Here it is important to pay attention to the fact that we are working with universal STF basis sets, and thus the sizes of our basis sets are always the same, namely, (12s, 10p, 10d) for the cations and (13s, 11p, 10d) for the anions. In his work, Koga is working with atom-adapted basis sets, and thus his STF basis set size increases with increase in Z (atomic nuclear charge).

For the cations with s and p orbitals, Koga's basis set size varies from (7s, 5p) to (11s, 7p) for C^+ through Ca^+. For the cations with s, p, and d orbitals, Koga's basis size varies from (11s, 7p, 5d) to (13s, 12p, 8d) for Sc^+ through Xe^+. In general, for the cations, our STF energy results are on average one decimal figure more accurate than Koga's results but, although

Table 3. Total ground state energies (au) of the STF and GTF bases for negative ions.

Ion	Configuration	State	STF energy (13s, 11p, 10d)[a]	Virial theorem STF[b]	GTF energy (18s, 12p, 11d)[a]	Virial theorem GTF[b]	Numerical-HF energy (23) (NHF)
H^-	$1s^2$	^1S	6.0 (−8)	7.1 (−7)	6.8 (−7)	1.7 (−5)	−0.487 929 73
Li^-	[He] $2s^2$	^1S	4.1 (−5)	6.4 (−5)	3.5 (−4)	3.8 (−4)	−7.428 232 1
B^-	[He] $2s^2\ 2p^2$	^3P	2.1 (−4)	7.4 (−5)	1.1 (−3)	3.0 (−4)	−24.519 221
C^-	[He] $2s^2\ 2p^3$	^4S	1.0 (−6)	4.2 (−8)	1.9 (−4)	1.4 (−5)	−37.708 844
N^-	[He] $2s^2\ 2p^4$	^3P	7.0 (−6)	1.3 (−7)	2.2 (−4)	6.8 (−6)	−54.321 959
O^-	[He] $2s^2\ 2p^5$	^2P	3.0 (−6)	8.7 (−7)	2.8 (−4)	1.6 (−6)	−74.789 746
F^-	[He] $2s^2\ 2p^6$	^1S	2.0 (−6)	6.7 (−7)	4.3 (−4)	4.8 (−6)	−99.459 454
Na^-	[Ne] $3s^2$	^1S	8.9 (−5)	5.0 (−6)	1.3 (−3)	2.4 (−5)	−161.855 126
Al^-	[Ne] $3s^2\ 3p^2$	^3P	8.7 (−4)	2.6 (−5)	5.1 (−3)	8.3 (−5)	−241.878 27
Si^-	[Ne] $3s^2\ 3p^3$	^4S	6.0 (−5)	8.0 (−7)	2.7 (−3)	3.5 (−6)	−288.889 66
P^-	[Ne] $3s^2\ 3p^4$	^3P	9.1 (−3)	2.3 (−6)	3.3 (−3)	6.8 (−7)	−340.698 874
S^-	[Ne] $3s^2\ 3p^5$	^2P	2.0 (−4)	7.0 (−7)	4.1 (−3)	3.1 (−6)	−397.538 430
Cl^-	[Ne] $3s^2\ 3p^6$	^1S	2.2 (−4)	2.4 (−6)	5.2 (−3)	1.1 (−5)	−459.576 925
K^-	[Ar] $4s^2$	^1S	3.1 (−4)	4.1 (−6)	1.0 (−2)	7.3 (−6)	−599.161 92
Sc^-	[Ar] $4s^2\ 3d^2$	^3F	5.4 (−4)	5.2 (−6)	1.4 (−2)	9.8 (−6)	−759.688 77
Ti^-	[Ar] $4s^2\ 3d^3$	^4F	7.8 (−4)	5.4 (−6)	1.7 (−2)	1.3 (−5)	−848.372 55
V^-	[Ar] $4s^2\ 3d^4$	^5D	1.1 (−3)	2.7 (−6)	2.0 (−2)	2.4 (−5)	−942.863 13
Cr^-	[Ar] $4s^2\ 3d^5$	^6S	1.2 (−3)	2.9 (−7)	2.4 (−2)	3.8 (−5)	−1043.337 1
Mn^-	[Ar] $4s^2\ 3d^6$	^5D	1.2 (−3)	3.8 (−6)	2.9 (−2)	5.2 (−5)	−1149.729 1
Fe^-	[Ar] $4s^2\ 3d^7$	^4F	1.1 (−3)	5.1 (−6)	3.5 (−2)	6.3 (−5)	−1262.367 1
Co^-	[Ar] $4s^2\ 3d^8$	^3F	9.0 (−4)	4.4 (−6)	4.3 (−2)	6.8 (−5)	−1381.351 8
Ni^-	[Ar] $4s^2\ 3d^9$	^2D	8.0 (−4)	1.9 (−6)	5.1 (−2)	7.1 (−5)	−1506.821 1
Cu^-	[Ar] $4s^2\ 3d^{10}$	^1S	1.0 (−3)	2.1 (−6)	6.1 (−2)	7.2 (−5)	−1638.964 1
Ga^-	[Ar] $4s^2\ 3d^{10}\ 4p^2$	^3P	3.4 (−3)	1.0 (−5)	8.7 (−2)	7.3 (−5)	−1923.260 4
Ge^-	[Ar] $4s^2\ 3d^{10}\ 4p^3$	^4S	3.7 (−3)	1.9 (−5)	9.7 (−2)	9.8 (−5)	−2075.394 7
As^-	[Ar] $4s^2\ 3d^{10}\ 4p^4$	^3P	5.4 (−3)	2.3 (−5)	1.1 (−1)	1.2 (−4)	−2234.222 9
Se^-	[Ar] $4s^2\ 3d^{10}\ 4p^5$	^2P	7.6 (−3)	2.5 (−5)	1.3 (−1)	1.5 (−4)	−2399.904 7
Br^-	[Ar] $4s^2\ 3d^{10}\ 4p^6$	^1S	1.0 (−2)	2.3 (−5)	1.6 (−1)	1.8 (−4)	−2572.536 3
Rb^-	[Kr] $5s^2$	^1S	1.5 (−2)	4.5 (−6)	2.2 (−1)	2.5 (−4)	−2938.354 9
Y^-	[Kr] $5s^2\ 4d^2$	^3F	1.6 (−2)	2.3 (−5)	3.1 (−1)	3.3 (−4)	−3331.659 2
Zr^-	[Kr] $5s^2\ 4d^3$	^4F	1.4 (−2)	1.5 (−4)	3.7 (−1)	3.7 (−4)	−3538.994 5
Nb^-	[Kr] $5s^2\ 4d^4$	^5D	1.2 (−2)	3.4 (−5)	4.4 (−1)	4.0 (−4)	−3753.578 2
Mo^-	[Kr] $5s^2\ 4d^5$	^6S	1.1 (−2)	1.7 (−5)	5.1 (−1)	4.4 (−4)	−3975.526 3
Tc^-	[Kr] $5s^2\ 4d^6$	^5D	8.6 (−2)	2.5 (−5)	6.0 (−1)	4.8 (−4)	−4204.764 6
Ru^-	[Kr] $5s^2\ 4d^7$	^4F	2.0 (−2)	1.1 (−4)	6.9 (−1)	5.3 (−4)	−4441.528 5
Rh^-	[Kr] $5s^2\ 4d^8$	^3F	3.8 (−2)	2.2 (−4)	8.0 (−1)	5.8 (−4)	−4685.875 6
Pd^-	[Kr] $5s^2\ 4d^9$	^2D	7.4 (−2)	4.2 (−4)	9.2 (−1)	6.5 (−4)	−4937.891 5
Ag^-	[Kr] $5s^2\ 4d^{10}$	^1S	1.4 (−1)	6.8 (−4)	1.1	7.3 (−4)	−5197.700 1
In^-	[Kr] $5s^2\ 4d^{10}\ 5p^2$	^3P	4.0 (−1)	1.5 (−3)	1.4	9.2 (−4)	−5740.175 1
Sn^-	[Kr] $5s^2\ 4d^{10}\ 5p^3$	^4S	6.2 (−1)	2.0 (−3)	1.6	1.0 (−3)	−6022.972 7
Sb^-	[Kr] $5s^2\ 4d^{10}\ 5p^4$	^3P	9.3 (−1)	2.7 (−3)	1.9	1.2 (−3)	−6313.481 5
Te^-	[Kr] $5s^2\ 4d^{10}\ 5p^5$	^2P	1.4	3.4 (−3)	2.1	1.3 (−3)	−6611.828 0
I^-	[Kr] $5s^2\ 4d^{10}\ 5p^6$	^1P	1.9	4.3 (−3)	2.4	1.5 (−3)	−6918.075 9

[a]This column shows $\Delta E = |E(\text{NHF}) - E(\text{calculated})|$.

[b]This column shows the values of $\Delta = |2 + \text{virial ratio}|$.

our results are better for the cations lighter than Zr^+, one has to recognize that Koga used smaller basis sets. From Zr^+ on, Koga's basis set size becomes more similar to our universal basis size (12s, 10p, 10d).

The average errors in our STF energies with respect to the numerical HF energies for the cations are, respectively, 0.000 012, 0.000 121, 0.001 36, and 0.023 87 millihartrees for the first, second, third, and fourth rows. The average errors in the energies found by Koga are 0.0004, 0.0063, 0.061, and 0.113 millihartrees for the respective first-, second-, third-, and fourth-row cations.

For the anions, Koga's basis set size varies from (8s, 6p) to (11s, 9p) for B^- through Cl^-, and for K^- it is (12s, 8p). For Sc^- through I^-, it varies from (12s, 8p, 6d) to (14s, 13p, 9d). When we compare our STF energy results with Koga's results for the anions, we notice that our results are on average one decimal

Table 4. Low-lying excited state energies (au) of the STF and GTF bases for negative ions.

Ion	Configuration	State	STF energy (13s, 11p, 10d)[a]	Virial theorem STF[b]	GTF energy (18s, 12p, 11d)[a]	Virial theorem GTF[b]	Clementi–Roette energy (24) (CR)
B^-	[He] $2s^2\ 2p^2$	^1D	9.6 (−4)	2.4 (−4)	3.1 (−3)	6.3 (−4)	−24.490 501
B^-	[He] $2s^2\ 2p^2$	^1S	6.3 (−3)[c]	7.3 (−4)	1.3 (−3)[c]	1.4 (−3)	−24.444 257
C^-	[He] $2s^2\ 2p^3$	^2D	4.7 (−5)[c]	6.8 (−6)	3.2 (−4)	5.6 (−5)	−37.642 523
C^-	[He] $2s^2\ 2p^3$	^2P	2.6 (−5)	2.3 (−5)	6.4 (−4)	1.1 (−4)	−37.600 849
N^-	[He] $2s^2\ 2p^4$	^1D	5.6 (−5)[c]	1.8 (−8)	1.8 (−4)	1.1 (−5)	−54.266 877
N^-	[He] $2s^2\ 2p^4$	^1S	7.0 (−5)[c]	1.8 (−6)	2.4 (−4)	2.6 (−5)	−54.186 826
Al^-	[Ne] $3s^2\ 3p^2$	^1D	2.2 (−3)	5.7 (−5)	8.4 (−3)	1.3 (−4)	−241.856 45
Al^-	[Ne] $3s^2\ 3p^2$	^1S	7.8 (−3)	1.2 (−4)	1.8 (−2)	2.3 (−4)	−241.830 01
Si^-	[Ne] $3s^2\ 3p^3$	^2D	6.0 (−5)[c]	3.2 (−6)	3.2 (−3)	2.0 (−5)	−288.841 43
Si^-	[Ne] $3s^2\ 3p^3$	^2P	1.5 (−4)	9.0 (−6)	4.0 (−3)	3.7 (−5)	−288.811 09
P^-	[Ne] $3s^2\ 3p^4$	^1D	1.4 (−4)[c]	2.0 (−6)	3.2 (−3)	2.2 (−6)	−340.659 80
P^-	[Ne] $3s^2\ 3p^4$	^1S	1.7 (−4)[c]	6.3 (−7)	3.4 (−3)	8.9 (−6)	−340.603 16
Sc^-	[Ar] $4s^1\ 3d^3$	^5F	5.9 (−3)	3.3 (−5)	1.2 (−2)	9.6 (−6)	−759.594 16
Ti^-	[Ar] $4s^1\ 3d^4$	^6D	1.1 (−3)[c]	5.6 (−6)	1.3 (−2)	1.6 (−5)	−848.256 08
V^-	[Ar] $4s^1\ 3d^5$	^7S	5.8 (−4)	8.7 (−7)	3.2 (−2)	1.2 (−3)	−942.766 11
Cr^-	[Ar] $4s^1\ 3d^6$	^6D	1.0 (−3)[c]	1.3 (−5)	2.2 (−2)	3.5 (−5)	−1043.095 6
Ni^-	[Ar] $4s^1\ 3d^{10}$	^2S	9.0 (−3)[c]	7.0 (−5)	4.2 (−1)	1.1 (−2)	−1506.653 3
Ge^-	[Ar] $4s^2\ 3d^{10}\ 4p^3$	^2D	3.2 (−3)	3.4 (−6)	9.7 (−2)	9.5 (−5)	−2075.347 0
As^-	[Ar] $4s^2\ 3d^{10}\ 4p^4$	^1D	5.0 (−3)	2.4 (−5)	1.1 (−1)	1.2 (−4)	−2234.185 4
As^-	[Ar] $4s^2\ 3d^{10}\ 4p^4$	^1S	5.1 (−3)	2.7 (−6)	1.1 (−1)	1.2 (−4)	−2234.131 3
Y^-	[Kr] $5s^1\ 4d^3$	^5F	9.6 (−3)[c]	3.1 (−5)	2.8 (−1)	3.3 (−4)	−3331.578 2
Nb^-	[Kr] $5s^1\ 4d^5$	^7S	1.2 (−2)[c]	3.4 (−5)	4.1 (−1)	4.0 (−4)	−3753.538 5
Mo^-	[Kr] $5s^1\ 4d^6$	^6D	2.2 (−1)	5.5 (−3)	4.9 (−1)	4.4 (−4)	−3975.387 7
Te^-	[Kr] $5s^1\ 4d^7$	^5F	8.0 (−2)[c]	3.0 (−5)	5.8 (−1)	4.8 (−4)	−4204.671 9

[a]This column shows $\Delta E = |E(\text{NHF}) - E(\text{calculated})|$.
[b]This column shows the values of $\Delta = |2 + \text{virial ratio}|$.
[c]Calculated energy is lower than CR energy.

figure more accurate than Koga's results from H^- to Se^-. From Br^- to Ag^-, both STF basis set sizes become more similar and, in general, our results have the same accuracy as Koga's results. From In^- on, Koga's results become more accurate than our results, but he is working with a slightly larger basis set (14s, 13p, 9d) than our universal basis set (13s, 11p, 10d).

The average errors in our STF energies with respect to the numerical HF limits for the anions are, respectively, 0.000 044, 0.001 757, 0.0026, and 0.3784 millihartrees for the first, second, third, and fourth rows. Koga found, for the respective first-, second-, third-, and fourth-row anions, the following average errors in the energies: 0.000 68, 0.0063, 0.087, and 0.112 millihartrees.

In conclusion, we would like to say that comparison of our results with Koga's results brings to attention the fact that when we are developing a universal basis set instead of a fully optimized basis set, we face the penalty of using, mainly for lighter atomic systems (from H through Ca), a larger number of basis functions than a fully optimized basis set needs to obtain the same degree of accuracy. Indeed, our experience in developing universal basis sets always showed that this penalty is reduced when we work with atomic systems from the third row on (14, 16–19).

2.2. The role of the weight functions in the evaluation of the total electronic energies

Since the GWHF equations are obtained from the minimization of the functional E with respect to the weight functions, f_i, the description of f_i governs the quest for the total energies for any atomic system. Achieving the best HF energy for an atomic system means obtaining the best description of f_i through the numerical approximation outlined in Sect. 2.1.

The quest for the best weight function associated with any atomic orbital is implemented by the integral discretization described previously, and the discretization parameters Ω_{min}, $\Delta\Omega$, and N are responsible for attaining the best weight function. When the GCHF method is employed to generate basis sets, the number of points N determines the size of the basis and, certainly, the larger the value of N, the lower is the ground state energy obtained. But the chosen value of N is a compromise between accuracy and size of the basis set.

In ref. 14 we presented a series of weight functions generated by the integration mesh of the neutral atoms, H through Xe, and discussed some practical aspects and properties of the weight functions. All the observations of that paper are valid with respect to the weight functions of the positive and negative ions studied here but, at this time, we add a few relevant

Fig. 1. The 2*s* Gaussian weight functions for Be^+, Be, Li, and Li^-. The point $\Omega_{min} = -0.55$ for *s* functions is indicated.

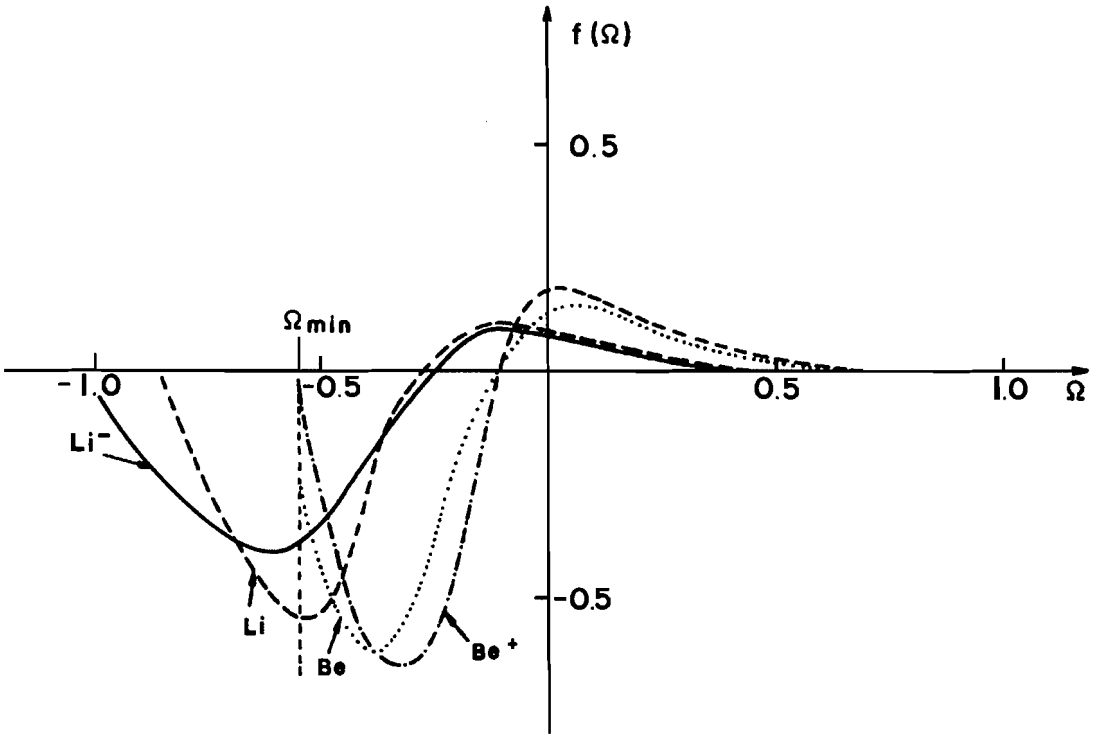

remarks especially related to the ionic species, and we will focus our remarks on the Gaussian weight functions.

In Fig. 1 we have plotted the Gaussian 2*s* weight functions for the isoelectronic species Be^+ and Li and Be and Li^-. It appears that the integration interval with $\Omega_{min} = -0.55$ is satisfactory for the Be^+ and Be species, but it is not adequate for the alkaline atom, and it is particularly insufficient for the negative ion of Li. This is a feature that also appears for the highest occupied orbital of the other alkaline atoms considered, i.e., Na through Cs. For this reason, it was necessary to shift Ω_{min} for the GTF basis set of the negative ions to $\Omega_{min} = -0.75$ for *s* symmetry (Ω_{min} for *s* symmetry STF weight functions was shifted to -0.21). The *p* and *d* symmetry weight functions also required a revision of the integration limits for the negative ions (see discretization parameters in Sect. 2.1).

In Fig. 2 we show how the Gaussian 2*s* weight functions obtained in this work for the species Li and Li^- compare with the corresponding fully integrated weight functions. Both for Li (this work) and Li^- (this work) there appears the need for higher values of the weight functions to compensate the truncation of the integration range. In view of our goal of generating "universal" (a unique set of exponents to be used for all atoms under consideration) bases of tractable size, we opted to retain Ω_{min} values that, in a few cases, did not accomplish a complete numerical integration. It is relevant to point out that this limitation of the Ω_{min} values has little effect on the total HF energy, even for the alkaline atoms and negative ions. Of course, the present selection of lower limits for the numerical integration range should be reconsidered with caution if properties demanding very diffuse orbitals were of interest (26). Otherwise, for most of the atoms and ions considered, the numerical integration ranges were adequate. This is illustrated in Fig. 3 with the example of the Gaussian 2*p* weight functions for neutral and charged fluorine atoms.

3. Concluding remarks

We have obtained STF and GTF basis sets for mono-charged positive and negative atomic species from H through Xe. Our bases stand comparison with numerical results and the best atom-optimized bases available, both for ground and low-lying excited states.

The bases for the positive ions are the same as those that we generated in ref. 14 for neutral atoms. In the case of the negative ions, the numerical integration range, which defines a basis set, was shifted to lower values of the Ω generator coordinate to accommodate the need for very diffuse orbitals.

The weight functions play a very important role in evaluating the total electronic energies. In fact, plots of the weight functions will provide adequate ranges for the numerical integration of the GWHF equations, and consequently we will have accurate basis sets for atomic species.

A penalty is faced when we are developing universal instead of fully optimized basis sets, mainly when we are working with atoms of the first and second rows. The penalty is characterized by the number of extra basis functions needed in the universal basis set to obtain the same degree of accuracy as in a fully optimized basis set.

Acknowledgements

We would like to acknowledge the financial support of CNPq, FAPESP, and FINEP (Brazilian Agencies).

Fig. 2. Comparison of the Gaussian 2*s* weight function for Li and Li^- for the universal bases (this work) and the complete integration range.

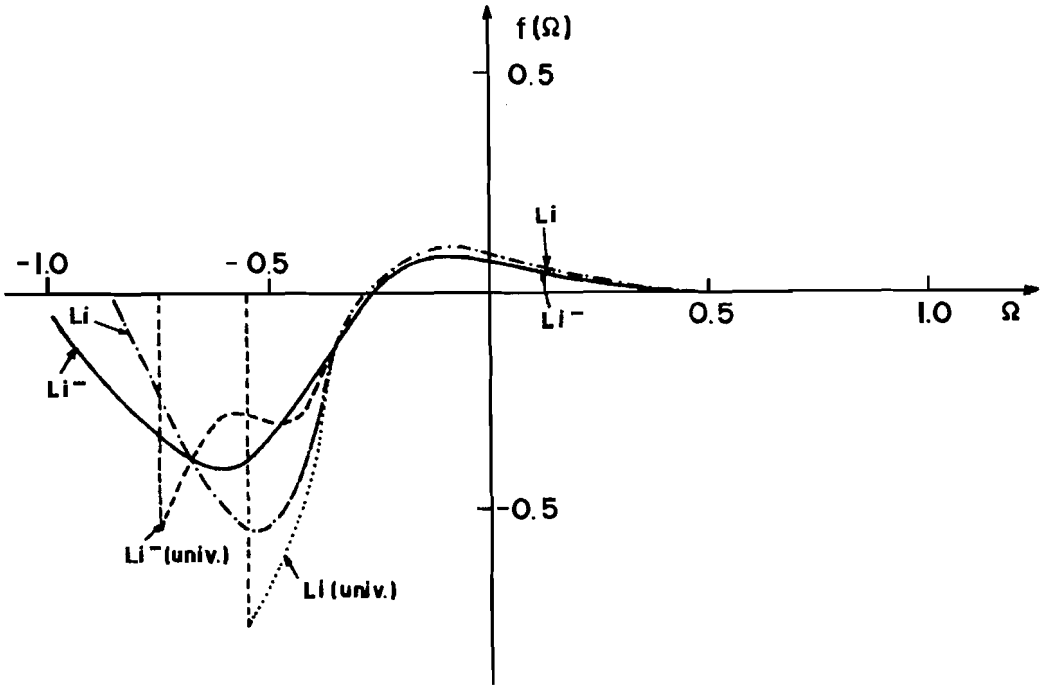

Fig. 3. Plot of the 2*p* Gaussian weight functions for F^+, F, and F^-.

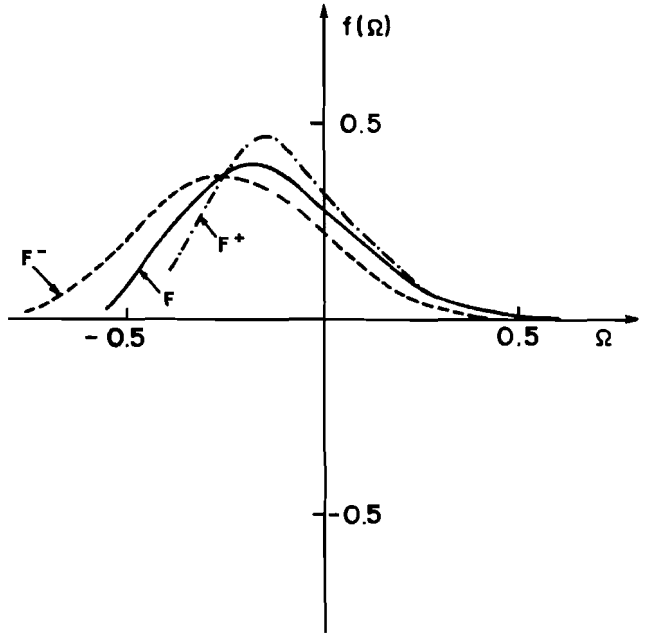

References

1. J.J. Griffin and J.A. Wheeler. Phys. Rev. **108**, 311 (1957).
2. C.W. Wong. Phys. Rev. **15**, 283 (1975).
3. J.D. Justin, M.V. Mihailovic, and M. Rosina. Nucl. Phys. *A*, **182**, 54 (1971).
4. L. Lathouwers. Ann. Phys. **102**, 347 (1976); L. Lathouwers, P. Van Leuven, and M. Bouten. Chem. Phys. Lett. **52**, 439 (1977).
5. B. Laskowski. *In* Quantum science methods and structure, a tribute to Per-Olov Löwdin. *Edited by* J.L. Calais, O. Goscinski, J. Linderberg, and Y. Öhrn. Plenum, New York. 1976. p. 479.
6. P. Chattopadhyay, R.M. Dreizler, M. Trsic, and M. Fink. Z. Phys. A: At. Nucl. **285**, 7 (1978).
7. J. Broeckhove and E. Deumens. Z. Phys. A: At. Nucl. **292**, 243 (1979); F. Arickx, J. Broeckhove, E. Deumens, and P. Van Leuven. J. Comput. Phys. **39**, 272 (1981).
8. R.L. Somorjai. Chem. Phys. Lett. **2**, 399 (1968); Phys. Rev. Lett. **23**, 329 (1969); J. Math. Phys. **12**, 206 (1971).
9. D.M. Bishop and B.E. Schneider. Int. J. Quantum Chem. **9**, 67 (1975).
10. A.J. Thakkar and V.H. Smith, Jr. Phys. Rev. A: Gen. Phys. **15**, 1 (1977); **15**, 16 (1977); **15**, 2143 (1977); A.J. Thakkar. J. Chem. Phys. **75**, 4496 (1981).
11. J.R. Mohallem, R.M. Dreizler, and M. Trsic. Int. J. Quantum. Chem. Symp. **20**, 45 (1986).
12. J. R. Mohallem and M. Trsic. J. Chem. Phys. **86**, 5043 (1986).
13. H.F.M. da Costa, M. Trsic, and J.R. Mohallem. Mol. Phys. **62**, 91 (1987).
14. A.B.F. da Silva and M. Trsic. Mol. Phys. **68**, 433 (1989).
15. A.B.F. da Silva and M. Trsic. Mol. Phys. **78**, 1301 (1993).
16. G.L. Malli, A.B.F. da Silva, and Y. Ishikawa. Chem. Phys. Lett. **201**, 37 (1993).
17. A.B.F. da Silva, G.L. Malli, and Y. Ishikawa. Chem. Phys. Lett. **203**, 201 (1993).
18. G.L. Malli, A.B.F. da Silva, and Y. Ishikawa. Phys. Rev. A: At. Mol. Opt. Phys. **47**, 143 (1993).
19. A.B.F. da Silva, G.L. Malli, and Y. Ishikawa. Can J. Chem. **71**, 1713 (1993).
20. D.M. Silver and W.G. Nieuwpoort. Chem. Phys. Lett. **57**, 421 (1978); D.M. Silver, S. Wilson, and W.G. Nieuwpoort. Int. J. Quantum Chem. **14**, 635 (1978); S. Wilson and D.M. Silver. Chem. Phys. Lett. **63**, 367 (1979).
21. J.R. Mohallem. Z. Phys. D: At. Mol. Clusters, **3**, 339 (1986).

22. D.L. Hill and J.A. Wheeler. Phys. Rev. **89**, 1102 (1953).
23. T. Koga, H. Tatewaki, and A.J. Thakkar. J. Chem. Phys. **100**, 8140 (1994).
24. E. Clementi and C. Roetti. At. Data Nucl. Data Tables, **14**, 177 (1974).
25. T. Koga, E. Shibata, and A.J. Thakkar. Theor. Chim. Acta, **91**, 47 (1995).
26. J.R. Mohallem and M. Trsic. Int. J. Quantum Chem. **33**, 555 (1988).

Spectroscopic and crystallographic studies of phosphino adducts of indium(III) iodide

Martyn A. Brown, Dennis G. Tuck, and Edward J. Wells

Abstract: Indium(III) iodide forms both 1:1 and 1:2 adducts with triphenylphosphine, depending on the reaction conditions, and especially on the solvent used. The complex $InI_3 \cdot PPh_3$ involves four-coordination at indium; the structure is trigonal, with a = 15.105(4) Å, c = 16.769(7) Å, V = 3313(2) Å^3, Z = 6, and space group $R\bar{3}$. Crystals were also obtained in which $InI_3 \cdot PPh_3$ and $InI_3(PPh_3)_2$ are present in a 1:1 ratio; these are also trigonal, a = 15.473(4) Å, c = 41.701(7) Å, V = 8646.1(1.8) Å^3, Z = 3 + 3 and space group $R\bar{3}$. The 1:2 adduct has approximately D_{3h} symmetry in the InI_3P_2 kernel. The bond distances and angles are discussed; in particular, the In—P bonds are extremely weak in the 1:2 adduct. This compound has been shown by ^{31}P NMR to undergo complete dissociation in solution to $InI_3 \cdot PPh_3$ and PPh_3. The addition of R_4NI (R = n-C_3H_7, n-C_4H_9) causes quantitative conversion to InI_4^- and free Ph_3P. Similar experiments are reported for the compound InI_3(dppe) (dppe = 1,2-bis(diphenylphosphino)ethane), whose structure is an infinite chain of InI_3 units linked through In-P-C_2H_4-P-In coordination. The crystal structure showed that InI_3(dppe) cocrystallizes with an equimolar quantity of dppe; these crystals are cubic, a = 41.445(14) Å, b = 15.944(8) Å, c = 16.533(11) Å, β = 102.02(4)°, V = 10 685(9) Å^3, Z = 4 + 4, space group C_2/c. Solid state and solution phase results are discussed in terms of the coordination chemistry of indium(III).

Key words: indium, phosphorus, coordination chemistry, multinuclear NMR, X-ray crystallography.

Résumé : L'iodure d'indium(III) réagit avec la triphénylphosphine pour former, suivant les conditions expérimentales et particulièrement du solvant utilisé, des adduits 1 : 1 ou 1 : 2. Le complexe $InI_3 \cdot PPh_3$ implique un tétracoordination au niveau de l'indium; la structure est trigonale, groupe d'espace $R\bar{3}$, avec a = 15,104(4) et c = 16,769(7) Å, V = 3313(2) Å^3 et Z = 6. On a aussi obtenu des cristaux dans lesquels $InI_3 \cdot PPh_3$ et $InI_3(PPh_3)_2$ sont présents dans un rapport de 1 : 1; ces cristaux sont trigonaux, groupe d'espace $R\bar{3}$, avec a = 15,473(4) et c = 41,701(7) Å, V = 8646.1(1,8) Å^3 et Z = 3 + 3. La symétrie de l'adduit 1 : 2 est approximativement D_{3h} et elle comporte un noyau InI_3P_2. On discute des longueurs et des angles des liaisons; dans l'adduit 1 : 2, on note, en particulier, que les liaisons In—P sont extrêmement faibles. Faisant appel à la RMN du ^{31}P, il a été démontré que, en solution, ce composé subit une dissociation complète en $InI_3 \cdot PPh_3$ et en PPh_3. L'addition de R_4NI (R = n-C_3H_7, n-C_4H_9) provoque une conversion quantitative en InI_4^- et de PPh_3 libre. Des expériences semblables ont été effectuées avec le composé InI_3(dppe) (dppe = 1,2-bis(diphénylphosphino)éthane) dont la strcture correspond à une chaîne infinie d'unités InI_3 liées par une coordination P-C_2H_4-P-In. La structure cristalline montre que le InI_3(dppe) cocristallise avec une quantité équimolaire de dppe; ces cristaux sont cubiques, groupe d'espace C_2/c, avec a = 41,445(14), b = 15,944(8) et c = 16,533(11) Å, β = 102,02(4)°, V = 10 685(9) Å^3 et Z = 4 + 4. On discute des résultats obtenus à l'état solide et en solution en termes de la chimie de coordination de l'indium.

Mots clés : indium, phosphore, chimie de coordiantion, RMN multinoyaux, cristallographie, rayons X.

[Traduit par la rédaction]

Introduction

The formation of adducts with neutral or anionic donor ligands is an important feature of the chemistry of the elements of Group III (or 13), with both applied and fundamental implications (1). The behaviour of derivatives of indium(III) halides and pseudo-halides has been of especial interest in this laboratory. The features of the problem which are most closely relevant to this paper are the range of coordination numbers that is possible, and the dissociation which can occur in nonaqueous solvents, involving loss of either halide or neutral ligand (2). Each of these processes is strongly affected by the nature of both halide and neutral donor atom, and by the solvent. Halide effects are also clearly seen in both the solid state and solution chemistry of anionic indium(III) complexes (1).

The present paper reexamines some of the early work (2) on triphenylphosphine and bis(diphenylphosphino)ethane (dppe) adducts of indium(III) iodide, using the experimental techniques of X-ray crystallography and multinuclear magnetic resonance which were not previously available. The new information on the solution phase behaviour of these substances is relevant to other work in this laboratory on adduct formation and dissociation of the derivatives of Group III and IV halides with ortho- and paraquinones.[3]

Received September 29, 1995.[1]

M.A. Brown and D.G. Tuck.[2] Department of Chemistry and Biochemistry, University of Windsor, Windsor, ON N9B 3P4, Canada.
E.J. Wells. Department of Chemistry, Simon Fraser University, Burnaby, BC V5A 1S6, Canada.

[1] Revision received April 29, 1996.
[2] Author to whom correspondence may be addressed. Telephone: (519) 253-4232, ext. 3541. Fax: (519) 973-7098. E-mail: dgtuck@uwindsor.ca

[3] M.A. Brown, D. Boucher, and D.G. Tuck. Unpublished results.

Experimental section

General techniques

Indium(III) iodide was prepared by reacting gram quantities of the elements in refluxing xylene (3). Triphenylphosphine and bis(diphenylphospino)ethane (Aldrich) were recrystallized before use. Solvents were distilled from suitable drying agents, and stored over molecular sieves.

Microanalysis was by Guelph Chemical Laboratories Ltd. Phosphorus-31 and indium-115 NMR spectra were recorded on Bruker AC 200L and 300L instruments, operating at 81.0 and 43.8 MHz, respectively. The reference standards for these nuclei were, for ^{31}P, 85% $H_3PO_4 = 0$ and, for ^{115}In, $InCl_4^- = 0$ (4). Infrared spectra were run on a Nicolet 4DX instrument. Raman spectra of finely ground solids were recorded with a Jobin Yvon S3000 spectrometer. Mass spectrometry involved heated samples in a Shimadzu 14-B spectrometer operating in the EI mode, with Sun Sparc software.

Conductivity measurements were made on a YSI 3400 model 31 conductivity bridge, using a YSI cell with Pt-Ir alloy electrodes coated with platinum black. Solutions were approximately 1 mmol L^{-1}. The cell constant was checked with a 1 mM aqueous solution of KCl after conditioning the electrodes for ca. 5 min.

Preparative

(i) Triphenylphosphine adducts

A solution of InI_3 (0.99 g, 2 mmol) in ethyl acetate (50 mL) was added dropwise to a stirred solution of Ph_3P (1.20 g, 4.6 mmol) in the same solvent. The yellow solid which precipitated was collected after 1 h, washed with ethyl acetate, and dried in vacuo. This solid is $InI_3(PPh_3)_2$, yield 1.56 g, 77%. Anal. calcd. for $C_{36}H_{30}P_2InI_3$ C 42.4, H 2.96; found: C 42.2, H 2.80. The mass spectrum of this compound (sample temp. 100°C) showed important ions based on *m/e* 262 (Ph_3P^+), 183 (Ph_2P^+-2), and 108 (PhP^+), but no peaks attributable to InI_3 or its derivative ions were observed.

When this product was recrystallized from cyclohexane, colourless crystals of the 1:1 adduct $InI_3 \cdot PPh_3$ were obtained. Anal. calcd. for $C_{18}H_{15}PInI_3$: C 28.5, H 2.00; found: C 28.5, H 1.90. The mass spectrum again has significant peaks at *m/e* 262, 183, and 108, but no ions derived from InI_3.

Recrystallization from ethyl acetate gave yellow crystals, whose analysis corresponded to an equimolar mixture of $InI_3 \cdot PPh_3$ and $InI_3(PPh_3)_2$. Anal. calcd. for $C_{54}H_{45}P_3In_2I_6$ C 36.5, H 2.55: found: C 37.5, H 2.61. The composition of these crystals was confirmed by X-ray crystallography (see below).

(ii) Bis(diphenylphosphino)ethane adduct

The procedure followed that for triphenylphosphine, using ethyl acetate as solvent; the white powdery product was InI_3(dppe), yield 1.05 g, 59%. Anal. calcd. for $C_{26}H_{24}P_2InI_3$: C 34.9, H 2.71; found: C 34.7, H 2.80. The mass spectrum had important features at *m/e* 398 (diphos$^+$), 262, 183, and 108 (Ph_3P^+ and derivatives). The molar conductivity of this compound in dichloromethane was 3.8 $ohm^{-1}\ mol^{-1}\ cm^2$.

Recrystallization from a mixture of ethyl acetate and toluene (50:50, v/v) gave, on cooling, crystals suitable for X-ray study. This study, and the results of elemental analysis, showed that these crystals contained equimolar quantities of InI_3(dppe) and dppe. Anal. calcd. for $C_{52}H_{48}P_4InI_3$, C 48.3, H 3.74; found: C 48.8, H 3.83.

Crystallographic analysis

(i) In the study of $InI_3 \cdot PPh_3$, 1, a colourless crystal mounted on a glass fibre was sited in a Rigaku AFC6S diffractometer, equipped with graphite monochromated Mo-Kα radiation (λ = 0.71069 Å) and a rotating anode generator. Cell constants, and orientation matrices for data collection, were obtained from least-squares refinements, using 20 carefully centred reflections in the range $8.59 < 2\theta < 16.07°$. Based on the systematic absences hkl: $-h + k + l \neq 3n$, the space group was uniquely identified as $R\bar{3}$ (No. 148), and this was confirmed by subsequent solution and refinement of the structure. Details of the intensity collection for all substances studied are given in Table 1.

The intensities of three representative reflections were measured after every 150 reflections. Over the course of data collection, the standards increased 1%, and a linear correction factor was applied to the results. The linear absorption coefficient (53.3 cm^{-1}) was such that an absorption correction using PSI Scan was applied, with transmission factors ranging from 0.80 to 1.00. The results were also corrected for Lorentz and polarization effects. The structure was solved by direct methods, and expanded using Fourier techniques. The non-hydrogen atoms were refined anisotropically; hydrogen atoms on carbon were included in ideal positions but were not refined. The final cycle of full-matrix least-squares refinement was based on 555 observed reflections ($I > 3\sigma(I)$) and 71 variable parameters, and the solution converged at $R = 0.034$ and $R_w = 0.029$. A final Fourier difference map calculation showed no peaks of chemical significance; the maximum and minimum peaks corresponded to 0.68 and −0.45 e $Å^{-3}$, respectively.

(ii) The structural study of crystals of $InI_3 \cdot PPh_3 + InI_3(PPh_3)_2$, **2**, followed essentially the same procedure. The space groups are identical. No decay correction was applied, since the intensities of three representative reflections remained constant throughout the data collection, indicating crystal and electronic stability. The data were corrected for absorption, Lorentz, and polarization effects. The structure was solved by direct methods. The indium, iodine, and phosphorus atoms were refined anisotropically, and carbon atoms were refined isotropically; hydrogen atoms on carbon were initially included in ideal positions, and subsequently refined isotropically. After several cycles of refinement, the structure converged to $R = 0.047$ and $R_w = 0.036$. A final Fourier difference map calculation showed no peaks of chemical significance.

(iii) Similar methods were used in the characterization of InI_3(dppe) + dppe, **3**. Corrections were made for decay (−0.4%), Lorentz and polarization effects, and for absorption (range 0.747–1.000). Indium, iodine, and phosphorus atoms were refined anisotropically, and carbon atoms isotropically. The structural refinement converged at $R = 0.060$, $R_w = 0.060$. The maximum and minimum peaks in the final Fourier map were +0.43 and −0.72 e $Å^{-3}$, and there were no peaks of chemical significance.

In each set of calculations, neutral-atom scattering factors were taken from Cromer and Waber (5). Anomalous dispersion effects were included in the calculations (6); the values for $\Delta f'$ and $\Delta f''$ were those published by Cromer (7). All calculations were performed using the TEXSAN (8) crystallo-

Table 1. Summary of crystal data, intensity collection, and structural refinement.

	1	2	3
Chemical formula	$C_{18}H_{12}I_3PIn$	$C_{18}H_{15}I_3PIn + C_{30}H_{30}I_3P_2In$	$C_{26}H_{24}P_2 + C_{26}H_{24}I_3P_2In$
M	757.82	757.82 + 1020.13	398.43 + 893.96
Crystal system	Trigonal	Trigonal	Cubic
Space group	$R\bar{3}$(No. 148)	$R\bar{3}$(No. 148)	C_2/c
a/Å	15.105(4)	15.473(4)	41.445(14)
b/Å	—	—	15.944(8)
c/Å	16.769(7)	41.701(7)	16.533(11)
β/°	—	—	102.02(4)
V/Å^3	3313(2)	8646.1(1.8)	10685.3(9.5)
Z	6	3 + 3	4 + 4
F(000)	2076	4980	4992
D_{calc}/g cm^{-3}	2.28	2.05	1.60
Crystal dimensions/mm	0.1 × 0.1 × 0.1	0.1 × 0.1 × 0.1	0.1 × 0.1 × 0.1
Abs. coeff./cm^{-1}	53.3	41.3	23.3
2θ° (max)	50	50	50
Total reflections measured	1428	3661	8704
Unique data used	1297	3408	8536
T/°C	23	23	23
No. of parameters	71	131	282
R	0.034	0.047	0.060
R_w	0.029	0.036	0.060
Max. shift/error in final cycle	0.03	4.7	0.02
Max., min. peaks in final difference map /e Å^{-3}	0.68, −0.45	1.05, −1.41	0.43, −0.72

Table 2. Positional parameters and isotropic thermal parameters for non-hydrogen atoms in $InI_3 \cdot PPh_3$ (**1**).

Atom	*x*	*y*	*z*	*B*(eq)
I(1)	0.14273(8)	−0.04921(8)	0.38241(7)	5.71(3)
I(1*)	0.04921(8)	0.19194(8)	0.38241(7)	5.71(3)
I(1*)	−0.19194(8)	−0.14273(8)	0.38241(7)	5.71(3)
In(1)	0.0000	0.0000	0.3465(1)	3.66(3)
P(1)	0.0000	0.0000	0.1913(4)	3.31(9)
C(1)	0.0206(9)	−0.1006(10)	0.1508(8)	3.5(4)
C(2)	0.091(1)	−0.080(1)	0.0922(9)	4.5(4)
C(3)	0.105(1)	−0.157(1)	0.0651(9)	5.9(5)
C(4)	0.052(1)	−0.255(1)	0.098(1)	6.6(6)
C(5)	−0.018(1)	−0.273(1)	0.156(1)	5.5
C(6)	−0.032(1)	−0.196(1)	0.1829(9)	4.6(4)
C(1*)	0.1006(9)	0.1212(10)	0.1508(8)	3.5(4)
C(1*)	−0.1212(9)	−0.0206(10)	0.1508(8)	3.5(4)
C(2*)	0.080(1)	0.170(1)	0.0922(9)	4.5(4)
C(6*)	−0.0164(1)	0.032(1)	0.1829(9)	4.6(4)
C(3*)	0.157(1)	0.263(1)	0.0651(9)	5.9(5)
C(5*)	0.273(1)	0.256(1)	0.156(1)	5.5(5)
C(3*)	−0.263(1)	−0.105(1)	0.0651(9)	5.9(5)
C(5*)	−0.256(1)	0.018(1)	0.156(1)	5.5(5)
C(4*)	0.255(1)	0.306(1)	0.098(1)	6.6(6)
C(4*)	−0.306(1)	−0.052(1)	0.098(1)	6.6(6)

Table 3. (*a*) Bond distance (Å) and (*b*) angles (deg) in $InI_3 \cdot PPh_3$ (**1**).

(*a*)

Atom	Atom	Distance	Atom	Atom	Distance
I(1)	In(1)	2.677(1)	C(1)	C(6)	1.36(2)
In(1)	P(1)	2.603(7)	C(2)	C(3)	1.38(2)
P(1)	C(1)	1.83(1)	C(3)	C(4)	1.37(2)
P(1)	C(1)*	1.83(1)	C(4)	C(5)	1.36(2)
P(1)	C(1)*	1.83(1)	C(5)	C(6)	1.37(2)
C(1)	C(2)	1.36(2)			

(*b*)

Atom	Atom	Atom	Angle	Atom	Atom	Atom	Angle
I(1)	In(1)	I(1)*	115.11(3)	C(1)*	P(1)	C(1)*	107.0(5)
I(1)	In(1)	I(1)*	115.11(4)	C(1)	P(1)	C(1)	107.0(5)
I(1)*	In(1)	P(1)	102.98(5)	P(1)	C(1)	C(2)	120(1)
I(1)*	In(1)	I(1)*	115.11(3)	P(1)	C(1)	C(6)	118(1)
I(1)*	In(1)	P(1)	102.98(5)	C(2)	C(1)	C(6)	120(1)
I(1)*	In(1)	P(1)	102.98(5)	C(1)	C(2)	C(3)	118(1)
In(1)	P(1)	C(1)	111.8(5)	C(2)	C(3)	C(4)	121(1)
In(1)	P(1)	C(1)*	111.8(5)	C(3)	C(4)	C(5)	119(1)
In(1)	P(1)	C(1)*	111.8(5)	C(4)	C(5)	C(6)	119(1)
C(1)	P(1)	C(1)*	106.6(5)	C(1)	C(6)	C(5)	119(1)

Table 4. Positional parameters and isotropic thermal parameters for non-hydrogen atoms in $InI_3 \cdot PPh_3 + InI_3(PPh_3)_2$ (**2**).

Atom	*x*	*y*	*z*	*B*(eq)
I(1)	0.1946(1)	0.1443(1)	0.14870(4)	4.08(6)
I(2)	0.1423(1)	0.6020(1)	0.01395(4)	4.66(7)
In(1)	0	0	0.14793(7)	4.1(1)
In(2)	1/3	2/3	0.03016(6)	3.03(8)
P(1)	0	0	0.2164(2)	4.1(3)
P(2)	0	0	0.0763(2)	2.6(3)
P(3)	1/3	2/3	0.0929(2)	2.5(3)
C(1)	0.112(1)	0.009(1)	0.2337(5)	3.5(4)
C(2)	0.161(2)	0.064(2)	0.2610(6)	5.4(6)
C(3)	0.243(2)	0.065(2)	0.2741(6)	6.1(6)
C(4)	0.275(2)	0.009(2)	0.2600(6)	5.4(6)
C(5)	0.232(2)	−0.046(2)	0.2336(6)	7.5(7)
C(6)	0.147(2)	−0.052(2)	0.2209(5)	6.0(6)
C(7)	0.037(1)	0.123(1)	0.0583(4)	2.6(4)
C(8)	−0.022(1)	0.167(1)	0.0669(4)	3.5(4)
C(9)	0.003(1)	0.259(1)	0.0538(5)	3.8(5)
C(10)	0.078(1)	0.303(1)	0.0332(5)	3.9(5)
C(11)	0.137(1)	0.263(1)	0.0235(4)	3.0(4)
C(12)	0.113(1)	0.173(1)	0.0366(4)	3.5(4)
C(13)	0.457(1)	0.695(1)	0.1082(4)	2.4(4)
C(14)	0.541(1)	0.777(1)	0.0982(4)	3.3(4)
C(15)	0.633(1)	0.799(1)	0.1107(5)	3.6(4)
C(16)	0.639(1)	0.736(1)	0.1315(5)	3.9(5)
C(17)	0.557(2)	0.651(1)	0.1420(5)	4.4(5)
C(18)	0.460(1)	0.626(1)	0.1312(4)	3.2(4)

Table 5. (*a*) Bond distances (Å) and (*b*) angles (deg) in $InI_3 \cdot PPh_3$ + $InI_3(PPh_3)_2$ (**2**).

(*a*)

Atom	Atom	Distance	Atom	Atom	Distance
I(1)	In(1)	2.707(1)	C(2)	C(3)	1.38(3)
I(2)	In(2)	2.691(2)	C(3)	C(4)	1.33(3)
In(1)	P(1)	2.86(1)	C(4)	C(5)	1.35(3)
In(1)	P(2)	2.99(1)	C(5)	C(6)	1.37(3)
In(2)	P(3)	2.616(9)	C(7)	C(8)	1.45(2)
P(1)	C(1)	1.82(2)	C(7)	C(12)	1.37(2)
P(1)	C(1)	1.82(2)	C(8)	C(9)	1.39(2)
P(1)	C(1)	1.82(2)	C(9)	C(10)	1.33(2)
P(2)	C(7)	1.85(2)	C(10)	C(11)	1.40(2)
P(2)	C(7)	1.85(2)	C(11)	C(12)	1.36(2)
P(2)	C(7)	1.85(2)	C(13)	C(14)	1.36(2)
P(3)	C(13)	1.85(2)	C(13)	C(18)	1.45(2)
P(3)	C(13)	1.85(2)	C(14)	C(15)	1.38(2)
P(3)	C(13)	1.85(2)	C(15)	C(16)	1.34(2)
C(1)	C(2)	1.40(2)	C(16)	C(17)	1.37(2)
C(1)	C(6)	1.40(3)	C(17)	C(18)	1.42(2)

(*b*)

Atom	Atom	Atom	Angle	Atom	Atom	Atom	Angle
I(1)	In(1)	I(1)*	119.99(1)	C(7)	P(2)	C(7)	105(2)
I(1)	In(1)	I(1)*	119.986(7)	C(7)	P(2)	C(7)	105(2)
I(1)	In(1)	P(1)	89.31(3)	In(2)	P(3)	C(13)	110.184(5)
I(1)	In(1)	P(2)	90.69(3)	In(2)	P(3)	C(13)	110.184(1)
I(1)*	In(1)	I(1)*	119.986(7)	In(2)	P(3)	C(13)	110.1838(7)
I(1)	In(1)	P(1)	89.31(3)	C(13)	P(3)	C(13)	108.749(9)
I(1)*	In(1)	P(2)	90.69(3)	C(13)	P(3)	C(13)	108.750(8)
I(1)	In(1)	P(1)	89.31(3)	C(13)	P(3)	C(13)	108.75(1)
I(1)*	In(1)	P(2)	90.69(3)	P(1)	C(1)	C(2)	124.62(5)
P(1)	In(1)	P(2)	180.00	P(1)	C(1)	C(6)	117(1)
I(2)	In(2)	I(2)*	113.89(8)	C(2)	C(1)	C(6)	118(1)
I(2)	In(2)	I(2)*	113.89(8)	C(1)	C(2)	C(3)	123.08
I(2)*	In(2)	P(3)	104.6(1)	C(2)	C(3)	C(4)	116.44
I(2)*	In(2)	I(2)*	113.89(8)	C(3)	C(4)	C(5)	123.08
I(2)	In(2)	P(3)	104.6(1)	C(4)	C(5)	C(6)	121.96
I(2)	In(2)	P(3)	104.6(1)	C(1)	C(6)	C(5)	116.96
In(1)	P(1)	C(1)	113.18(1)	P(2)	C(7)	C(8)	116(3)
In(1)	P(1)	C(1)	113.18(1)	P(2)	C(7)	C(12)	126(2)
In(1)	P(1)	C(1)	113.18(1)	C(8)	C(7)	C(12)	118(3)
C(1)	P(1)	C(1)	105.52(1)	C(7)	C(8)	C(9)	117(3)
C(1)	P(1)	C(1)	105.52(2)	C(8)	C(9)	C(10)	120(1)
C(1)	P(1)	C(1)	105.52(2)	C(9)	C(10)	C(11)	124.602(9)
In(1)	P(2)	C(7)	114(2)	C(10)	C(11)	C(12)	115.848(5)
In(1)	P(2)	C(7)	114(2)	C(7)	C(12)	C(11)	124(1)
In(1)	P(2)	C(7)	114(2)	C(13)	C(14)	C(15)	119(13)
C(7)	P(2)	C(7)	105(2)	C(14)	C(13)	C(18)	122.1(7)
C(14)	C(15)	C(16)	120.25	C(15)	C(16)	C(17)	124.09
C(16)	C(17)	C(18)	119.26	P(3)	C(13)	C(14)	120.05(1)
C(13)	C(18)	C(17)	115.37	P(3)	C(13)	C(18)	117.9(7)

graphic software package. The structure of the molecules are shown in Figs. 1, 2, and 3; the positional parameters are in Tables 2, 4, and 6 and important bond distances and angles in Tables 3, 5, and 7.

Tables of hydrogen-atom coordinates and thermal parameters, and anisotropic thermal parameters for other atoms, are available as supplementary data.[4]

[4] These data can be purchased from: The Depository of Unpublished Data, Document Delivery, CISTI, National Research Council Canada, Ottawa, Canada K1A 0S2. The data fro H-atom coordinates have also been deposited with the Cambridge Crystallographic Data Centre, and can be obtained on request from The Director, Cambridge Crystallographic data Centre, University Chemical Laboratory, 12 Union Road, Cambridge, CB2 1EZ, U.K.

Table 6. Positional parameters and isotropic thermal parameters for non-hydrogen atoms in InI_3(dppe) + dppe (**3**).

Atom	*x*	*y*	*z*	*B*(eq)
I(1)	0.09986(6)	0.2821(1)	0.7034(1)	4.9(1)
I(2)	0.05413(5)	0.0080(1)	0.6535(1)	4.9(1)
I(3)	0.16547(5)	0.0223(1)	0.7242(1)	4.1(1)
In(1)	0.10715(5)	0.1123(1)	0.6969(1)	2.85(8)
P(1)	0.1096(2)	0.1259(4)	0.5314(4)	3.0(3)
P(2)	0.1098(2)	0.1026(4)	0.8647(4)	2.9(3)
P(3)	0.6173(2)	0.0217(5)	0.6591(4)	4.2(4)
P(4)	0.7235(2)	−0.0048(5)	0.7861(4)	4.5(4)
C(1)	0.1128(5)	0.020(1)	0.492(1)	2.5(5)
C(2)	0.0744(6)	0.171(2)	0.467(1)	3.3(6)
C(3)	0.0705(7)	0.257(2)	0.459(2)	4.6(7)
C(4)	0.0425(8)	0.297(2)	0.410(2)	5.4(7)
C(5)	0.0179(7)	0.247(2)	0.370(2)	4.9(7)
C(6)	0.0204(7)	0.163(2)	0.377(2)	4.0(6)
C(7)	0.0466(7)	0.123(2)	0.428(2)	4.6(7)
C(8)	0.1436(6)	0.188(1)	0.508(1)	3.1(5)
C(9)	0.1669(6)	0.222(1)	0.571(1)	3.2(5)
C(10)	0.1918(7)	0.272(2)	0.555(2)	5.0(7)
C(11)	0.1945(7)	0.289(2)	0.476(2)	4.5(6)
C(12)	0.1690(7)	0.260(2)	0.413(2)	4.6(7)
C(13)	0.1445(6)	0.210(1)	0.427(1)	2.7(5)
C(14)	0.1132(6)	−0.007(1)	0.901(1)	3.1(5)
C(15)	0.0740(6)	0.146(1)	0.898(1)	3.0(5)
C(16)	0.0418(8)	0.151(2)	0.844(2)	6.1(8)
C(17)	0.0158(8)	0.186(2)	0.866(2)	7.1(9)
C(18)	0.0188(7)	0.206(2)	0.948(2)	5.4(7)
C(19)	0.0472(6)	0.200(1)	1.003(1)	3.2(5)
C(20)	0.0769(6)	0.171(1)	0.980(1)	2.6(5)
C(21)	0.1435(6)	0.159(2)	0.924(1)	3.2(6)
C(22)	0.1745(7)	0.119(2)	0.959(2)	4.2(6)
C(23)	0.2016(8)	0.162(2)	1.000(2)	5.8(8)
C(24)	0.1970(8)	0.248(2)	1.009(2)	5.6(8)
C(25)	0.1694(6)	0.290(1)	0.977(1)	2.8(5)
C(26)	0.1415(7)	0.244(2)	0.932(2)	3.8(6)
C(27)	0.6069(6)	0.023(2)	0.544(1)	3.3(5)
C(28)	0.5881(7)	0.085(2)	0.503(2)	5.3(7)
C(29)	0.5803(7)	0.080(2)	0.416(2)	4.7(7)
C(30)	0.5922(8)	0.024(2)	0.374(2)	5.6(7)
C(31)	0.6111(8)	−0.033(2)	0.413(2)	5.5(8)
C(32)	0.6215(7)	−0.032(2)	0.500(2)	5.2(7)
C(33)	0.6172(6)	0.134(1)	0.680(2)	3.7(6)
C(34)	0.5891(7)	0.163(2)	0.714(2)	4.9(7)
C(35)	0.5880(7)	0.254(2)	0.727(2)	5.0(7)
C(36)	0.6132(7)	0.303(2)	0.709(2)	5.2(7)
C(37)	0.6393(7)	0.276(2)	0.674(1)	4.1(6)
C(38)	0.6408(6)	0.194(2)	0.662(1)	3.6(6)
C(39)	0.6598(7)	−0.001(2)	0.679(2)	5.3(7)
C(40)	0.6803(7)	0.012(2)	0.771(2)	5.7(7)
C(41)	0.7271(6)	−0.119(1)	0.783(1)	3.1(5)
C(42)	0.7040(6)	−0.174(1)	0.793(1)	2.9(5)
C(43)	0.7095(7)	−0.259(2)	0.793(2)	5.1(7)

Table 6 (*concluded*).

Atom	*x*	*y*	*z*	*B*(eq)
C(44)	0.7381(7)	−0.292(2)	0.783(2)	5.6(7)
C(45)	0.7613(7)	−0.235(2)	0.767(2)	5.2(7)
C(46)	0.7575(7)	−0.148(2)	0.769(2)	4.1(6)
C(47)	0.7369(6)	0.011(2)	0.898(1)	3.9(6)
C(48)	0.7194(8)	−0.025(2)	0.957(2)	6.2(8)
C(49)	0.7308(8)	−0.011(2)	1.042(2)	5.8(7)
C(50)	0.7594(8)	0.036(2)	1.065(2)	5.7(7)
C(51)	0.7755(9)	0.074(2)	1.010(2)	8(1)
C(52)	0.7631(8)	0.062(2)	0.927(2)	5.2(7)

Table 7. (*a*) Bond distances (Å) and (*b*) angles (deg) in InI_3(dppe) + dppe (**3**).
(*a*)

Atom	Atom	Distance	Atom	Atom	Distance
I(1)	In(1)	2.729(2)	C(9)	C(10)	1.37(3)
I(2)	In(1)	2.730(3)	C(10)	C(11)	1.35(3)
I(3)	In(1)	2.766(3)	C(11)	C(12)	1.40(3)
In(1)	P(1)	2.769(7)	C(12)	C(13)	1.35(3)
In(1)	P(2)	2.758(6)	C(15)	C(16)	1.45(4)
P(1)	C(1)	1.82(2)	C(15)	C(20)	1.39(3)
P(1)	C(2)	1.77(3)	C(16)	C(17)	1.33(4)
P(1)	C(8)	1.83(2)	C(17)	C(18)	1.37(3)
P(2)	C(14)	1.85(2)	C(18)	C(19)	1.33(3)
P(2)	C(15)	1.83(2)	C(19)	C(20)	1.43(3)
P(2)	C(21)	1.77(3)	C(21)	C(22)	1.44(3)
P(3)	C(27)	1.86(2)	C(21)	C(26)	1.37(3)
P(3)	C(33)	1.83(2)	C(22)	C(23)	1.37(3)
P(3)	C(39)	1.76(3)	C(23)	C(24)	1.40(3)
P(4)	C(40)	1.78(3)	C(24)	C(25)	1.34(3)
P(4)	C(41)	1.83(2)	C(25)	C(26)	1.44(3)
P(4)	C(47)	1.84(2)	C(27)	C(28)	1.34(3)
C(1)	C(14)	1.52(3)	C(27)	C(32)	1.37(3)
C(2)	C(3)	1.38(3)	C(28)	C(29)	1.41(3)
C(2)	C(7)	1.42(3)	C(29)	C(30)	1.30(3)
C(3)	C(4)	1.43(3)	C(30)	C(31)	1.28(4)
C(4)	C(5)	1.36(3)	C(31)	C(32)	1.42(3)
C(5)	C(6)	1.34(3)	C(33)	C(34)	1.46(3)
C(6)	C(7)	1.38(3)	C(33)	C(38)	1.45(3)
C(8)	C(9)	1.38(3)	C(34)	C(35)	1.47(3)
C(8)	C(13)	1.38(3)	C(35)	C(36)	1.38(3)
C(36)	C(37)	1.39(3)	C(37)	C(38)	1.33(3)
C(39)	C(40)	1.60(3)	C(41)	C(42)	1.33(3)
C(41)	C(46)	1.40(3)	C(42)	C(43)	1.36(3)
C(43)	C(44)	1.34(3)	C(44)	C(45)	1.39(3)
C(45)	C(46)	1.40(3)	C(47)	C(48)	1.45(3)
C(47)	C(52)	1.35(3)	C(48)	C(49)	1.40(3)
C(49)	C(50)	1.39(4)	C(50)	C(51)	1.37(4)
C(51)	C(52)	1.38(4)			

Table 7 (*concluded*).

(*b*)

Atom	Atom	Atom	Angle	Atom	Atom	Atom	Angle
I(1)	In(1)	I(3)	127.5(1)	I(1)	In(1)	I(2)	121.7(1)
I(1)	In(1)	P(1)	89.3(1)	P(1)	C(1)	C(14)	120(2)
I(1)	In(1)	P(2)	89.9(2)	P(1)	C(2)	C(3)	122(2)
I(2)	In(1)	I(3)	110.80(8)	P(1)	C(2)	C(7)	123(2)
I(2)	In(1)	P(1)	88.9(2)	C(3)	C(2)	C(7)	115(3)
I(2)	In(1)	P(2)	95.3(2)	C(2)	C(3)	C(4)	125(3)
I(3)	In(1)	P(1)	89.5(2)	C(3)	C(4)	C(5)	117(3)
I(3)	In(1)	P(2)	87.5(2)	C(4)	C(5)	C(6)	121(3)
P(1)	In(1)	P(2)	175.5(2)	C(5)	C(6)	C(7)	124(3)
In(1)	P(1)	C(1)	107.7(7)	C(2)	C(7)	C(6)	119(3)
In(1)	P(1)	C(2)	115.5(8)	P(1)	C(8)	C(9)	120(2)
In(1)	P(1)	C(8)	116.3(8)	P(1)	C(8)	C(13)	121(2)
C(1)	P(1)	C(2)	106(1)	C(9)	C(8)	C(13)	118(2)
C(1)	P(1)	C(8)	108(1)	C(8)	C(9)	C(10)	121(2)
C(2)	P(1)	C(8)	103(1)	C(9)	C(10)	C(11)	122(3)
In(1)	P(2)	C(14)	111.1(7)	C(10)	C(11)	C(12)	116(3)
In(1)	P(2)	C(15)	114.9(8)	C(11)	C(12)	C(13)	123(2)
In(1)	P(2)	C(21)	113.2(8)	C(8)	C(13)	C(12)	119(2)
C(14)	P(2)	C(15)	106(1)	P(2)	C(14)	C(1)	115(2)
C(14)	P(2)	C(21)	108(1)	P(2)	C(15)	C(16)	122(2)
C(15)	P(2)	C(21)	104(1)	P(2)	C(15)	C(20)	119(2)
C(16)	C(17)	C(18)	117(3)	C(16)	C(15)	C(20)	118(2)
C(17)	C(18)	C(19)	123(3)	C(15)	C(16)	C(17)	123(3)
C(18)	C(19)	C(20)	122(2)	C(15)	C(20)	C(19)	116(2)
P(2)	C(21)	C(22)	122(2)	P(2)	C(21)	C(26)	120(2)
C(22)	C(21)	C(26)	118(3)	C(21)	C(22)	C(23)	124(3)
C(22)	C(23)	C(24)	115(3)	C(23)	C(24)	C(25)	125(3)
C(24)	C(25)	C(26)	118(2)	C(21)	C(26)	C(25)	120(3)
C(28)	C(27)	C(32)	118(2)	C(48)	C(47)	C(52)	119(3)
C(27)	C(28)	C(29)	118(3)	C(47)	C(48)	C(49)	120(3)
C(28)	C(29)	C(30)	124(3)	C(48)	C(49)	C(50)	117(3)
C(29)	C(30)	C(31)	119(3)	C(49)	C(50)	C(51)	124(3)
C(30)	C(31)	C(32)	122(3)	C(50)	C(51)	C(52)	118(3)
C(27)	C(32)	C(31)	118(3)	C(47)	C(52)	C(51)	123(3)
P(3)	C(33)	C(34)	115(2)	C(33)	C(38)	C(37)	124(2)
P(3)	C(33)	C(38)	125(2)	C(36)	C(37)	C(38)	115(3)
C(34)	C(33)	C(38)	120(2)	C(35)	C(36)	C(37)	128(3)
C(33)	C(34)	C(35)	115(2)	C(34)	C(35)	C(36)	118(3)
P(3)	C(27)	C(28)	121(2)	P(4)	C(47)	C(48)	122(2)
P(3)	C(27)	C(32)	120(2)	P(4)	C(47)	C(52)	119(2)
C(27)	P(3)	C(33)	100(1)	C(40)	P(4)	C(41)	103(1)
C(33)	P(3)	C(39)	102(1)	C(40)	P(4)	C(47)	101(1)
C(27)	P(3)	C(39)	102(1)	C(41)	P(4)	C(47)	99(1)
P(3)	C(39)	C(40)	118(2)	P(4)	C(40)	C(39)	116(2)
P(4)	C(41)	C(42)	126(2)	P(4)	C(41)	C(46)	124(2)
C(42)	C(41)	C(46)	120(2)	C(41)	C(42)	C(43)	123(3)
C(42)	C(43)	C(44)	123(3)	C(43)	C(44)	C(45)	116(3)
C(44)	C(45)	C(46)	124(3)	C(41)	C(46)	C(45)	116(3)

Results and discussion

Crystallographic studies

The structure of $InI_3 \cdot PPh_3$, **1** (Fig. 1), shows that the stereochemistry at both indium and phosphorus is close to tetrahedral. The indium(III)–iodine bond distance (2.677(1) Å) is in keeping with the values in the literature for other four-coordinate derivatives, for which the range is 2.68 ± 0.04 Å (9). More particularly, the results reported for $InI_3 \cdot PHPh_2$ (r(In–I) (avg.) = 2.673(5) Å, *r*(In-P) (avg.) = 2.599(9) Å), and for

Fig. 1. The molecular structure of $InI_3 \cdot PPh_3$, showing the numbering system; ORTEP diagram, with 30% probability ellipsoids.

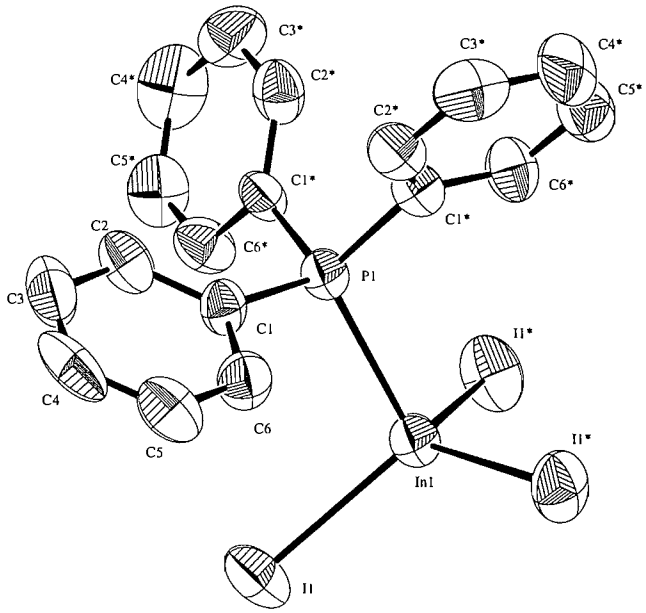

$InI_3 \cdot PHBu^t_2$ (r(In–I) (avg.) = 2.674(5) Å, r(In–P) = 2.586(6) Å)(10) are in good agreement with the values in Table 3.

The substance **2** is unusual, in that the lattice contains equal proportions of $InI_3 \cdot PPh_3$ and $InI_3(PPh_3)_2$. There are some important differences between the results for the $InI_3 \cdot PPh_3$ moiety (Table 5) and those for the pure compound given in Table 3. The In–I bond distance of 2.691(2) Å is significantly longer than in **1**, as is In—P (2.616(9) compared with 2.603(7) Å). There are also interesting changes in the bond angles; I-In-I, which is 115.11(3)° in the isolated molecule in **1** changes to 113.92(5)° in the mixed lattice, while the corresponding values for In-P-C are 111.8(5)° and 110.18(1)°, so that the molecule is slightly flattened at both pseudo-tetrahedral sites in this mixed lattice, relative to the pure substance.

The 1:2 complex is directly comparable with the compound $InI_3(PMePh_2)_2$, for which r(In—I) = 2.736(4), 2.762(2), 2.776(2) Å, and r(In-P) (avg.) = 2.716(4) Å (11). Both show a significant lengthening of the In—I bond relative to the values for the various 1:1 adducts, in keeping with the increased coordination number at indium (cf. ref. 9). Surprisingly, the two In—P bonds are of quite different lengths (2.86(1) and 2.99(1) Å), and these values are both much larger than the average of 2.65 Å derived from work on $InI_3(PMePh_2)_2$, $InBr_3(PMe_2Ph)_2$ (11), $InCl_3(PMe_3)_2$ (12), and $InCl_3(PPh_3)_2$ (13). We return to these results below.

The structure of compound **3** reveals the presence of an infinite chain in which planar InI_3 units are linked by bridging dppe bidentate donors. The presence of isolated dppe molecules allows a comparison between the coordinated and the free state. Apart from a slight contraction of the P—C_6H_5 bonds, there are in fact no significant differences; the total P–P distance is essentially constant at ~5.2 Å in the two molecules. It is also interesting to compare the structure of $[InI_3(dppe)]_\infty$ with that of $(InI_3)_3(dppe)_2$ (12), which represents a sub-unit of the infinite chain structure. The stereochemistry at indium and phosphorus is almost identical in both cases, and the average bond distances in $(InI_3)_3(dppe)_2$ (r(In–I) = 2.731(15) Å, r(In–P) = 2.809(10) Å and r(P–C_6H_5) = 1.83(1) Å are very close to those in Table 7.

The values for In—P bond length in these adducts call for some comment. We first note that the P—C bond distances in all the present structures give an average value of 1.84 Å, which is close to the sum of the covalent radii (0.77 + 1.10 = 1.87 Å), in keeping with the expected formation of single bonds. The covalent radius of indium in tetrahedral InX_4^- species (X = Cl, Br, I) can be calculated from the known average In—X bond lengths (2.350(2), 2.479(2), 2.71(1) for X = Cl, Br, and I, respectively (14)) as 1.36(2) Å, in which case r(In–P) in a tetrahedral environment should be ca. 2.46 Å, which is significantly smaller than the values found in the present work for $InI_3 \cdot PPh_3$ in **1** and **2** (2.603(7), 2.616(9) Å) (Tables 3 and 5). For the five-coordinate species, r(In–P)(avg.) = 2.92(5) in **2** and 2.76(1) in **3** , again substantially greater than that calculated. An alternative approach uses the conventional single bond covalent radii for these elements (15), from which r(In–I) = 1.50 + 1.33 = 2.83 Å, and r(In–P) = 1.50 + 1.09 = 2.59 Å. These values therefore substantially underestimate r(In–I) in both four- and five- coordinate species, while the calculated r(In–P) is slightly lower than the experimental value in $InI_3 \cdot PPh_3$, and significantly so in the other adducts. The large bond distance in the five-coordinate molecules implies the presence of very weak In–P interactions in these species in the crystalline state, which has important implications for the solution studies reported below.

NMR studies on $InI_3(PPh_3)_2$

The ^{31}P resonance of a solution of $InI_3(PPh_3)_2$ in $CDCl_3$ at 293 K is a broad singlet, half width approximately 33 Hz, −16.85 ppm from the reference solution of 85% H_3PO_4 = 0; the comparable values for PPh_3 under the same conditions are δ = −5.44 ppm and $\omega_{1/2}$ = 7.5 Hz. Both the chemical shift (Fig. 4*A*) and the line width (Fig. 4*B*) of a solution of the 1:2 complex change with temperature until, at 213 K, the half width is ca. 100 Hz, and the chemical shift is −15.5 ppm. Below this temperature, the precipitation of crystalline material, identified as the 1:1 complex $InI_3 \cdot PPh_3$, was observed, and the slight maximum observed in Fig. 4*A* at 223 K may have been caused by the presence of small quantities of solid in the solution phase at this temperature.

The significant line width, the increase of this with decreasing temperature, the precipitation of $InI_3 \cdot PPh_3$, and the change in the average chemical shift towards the value for free PPh_3, are all in keeping with the existence in solution of the equilibria

[1] $InI_3(PPh_3)_2 \leftrightarrows InI_3 \cdot PPh_3 + PPh_3$

[2] $InI_3 \cdot PPh \leftrightarrows InI_3 + PPh_3$

The change in the line width with decreasing temperature indicates that the rapid exchange observed at room temperature is being slowed, but clearly we were not able to achieve conditions under which the signals of the individual species could be observed.

The effect of adding PPh_3 to a solution of $InI_3(PPh_3)_2$ in $CDCl_3$ (0.1 M, room temp.) is illustrated in Fig. 5. For reasons

Fig. 2. The structure of **2** showing the numbering system for (*A*) $InI_3 \cdot PPh_3$ and (*B*) $InI_3(PPh_3)_2$; ORTEP diagram, with 30% probability ellipsoids.

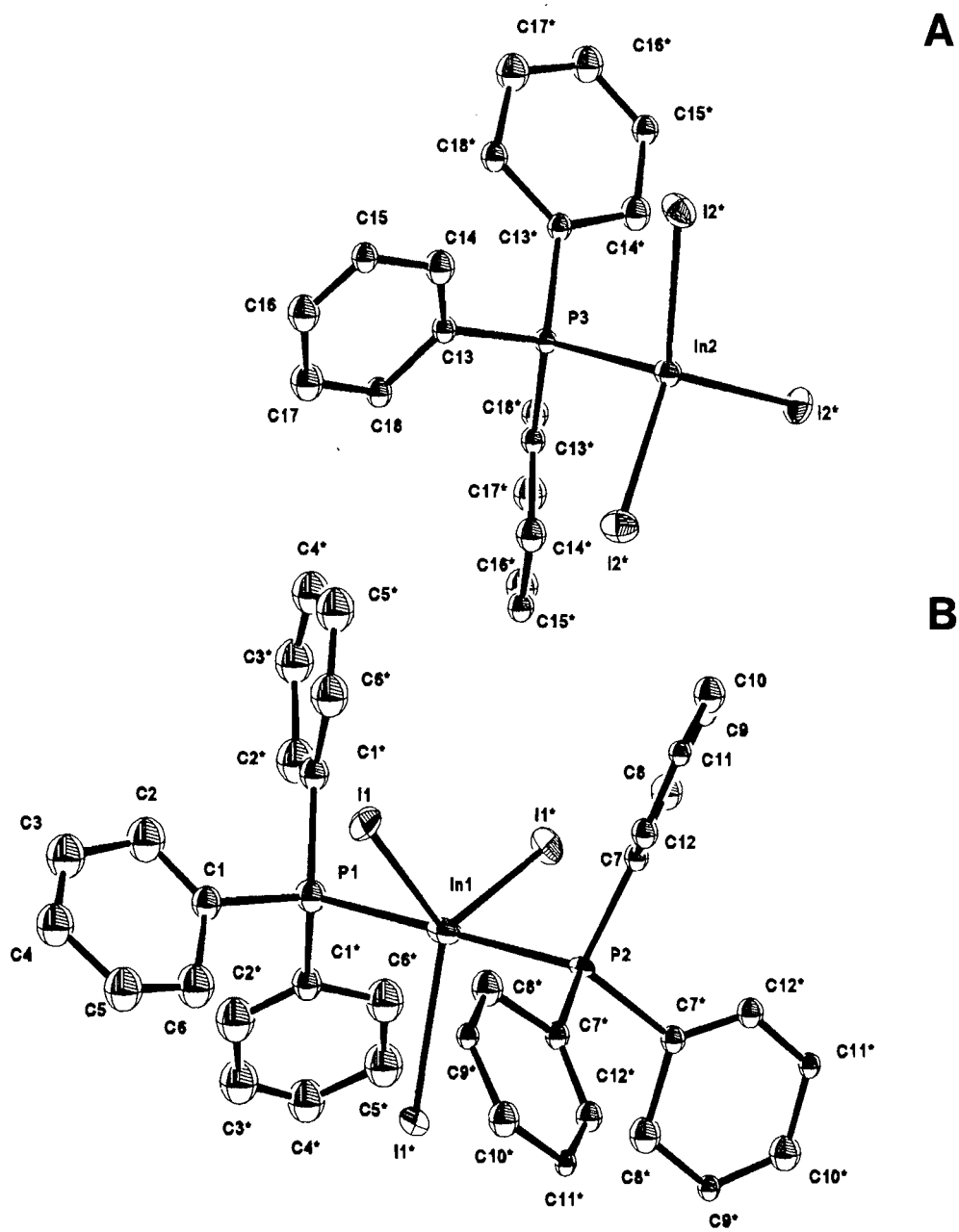

that will be discussed below, this diagram shows both the average ^{31}P chemical shift (5*A*) and the width at half-height (5*B*) as a function of the mole ratio of Ph_3P to the 1:1 complex $InI_3 \cdot PPh_3$, and both parameters move monotonically as a function of this ratio. The limiting chemical shift (−5.4 ppm) is identical to that for free PPh_3. The changes in $T_{1/2}$ show that the exchange processes in solution persist over the range studied, while the sharpening at high ligand: complex ratios indicates that the overall exchange is enhanced under these conditions.

When iodide ion, in the form of either *n*-Pr_4NI or *n*-Bu_4NI, is added to a solution of $InI_3(PPh_3)_2$ in $CDCl_3$, two important phenomena are observed. The ^{31}P chemical shift (Fig. 6*A*) changes linearly as I^- is added, to a point of inflexion at which the quantities of iodide and complex are equal. The ^{31}P resonance at this point, and subsequently, is at −5.2 ppm, indicating the presence of free PPh_3 in the solution. The line width also changes during the addition of iodide, with the results shown in Fig. 6*B*. The point of inflexion again occurs when equimolar quantities of I^- and $InI_3(PPh_3)_2$ are present. The line width beyond that point ($\omega_{1/2}$ = 23 Hz) is similar to that for free PPh_3 under the same conditions.

Studies of the ^{115}In resonance of these solutions showed that no signal could be detected with a solution of $InI_3(PPh_3)_2$

Fig. 3. The structure of **3** showing the numbering system for (*A*) InI_3(dppe) and (*B*) dppe; ORTEP diagram, with 30% probability ellipsoids.

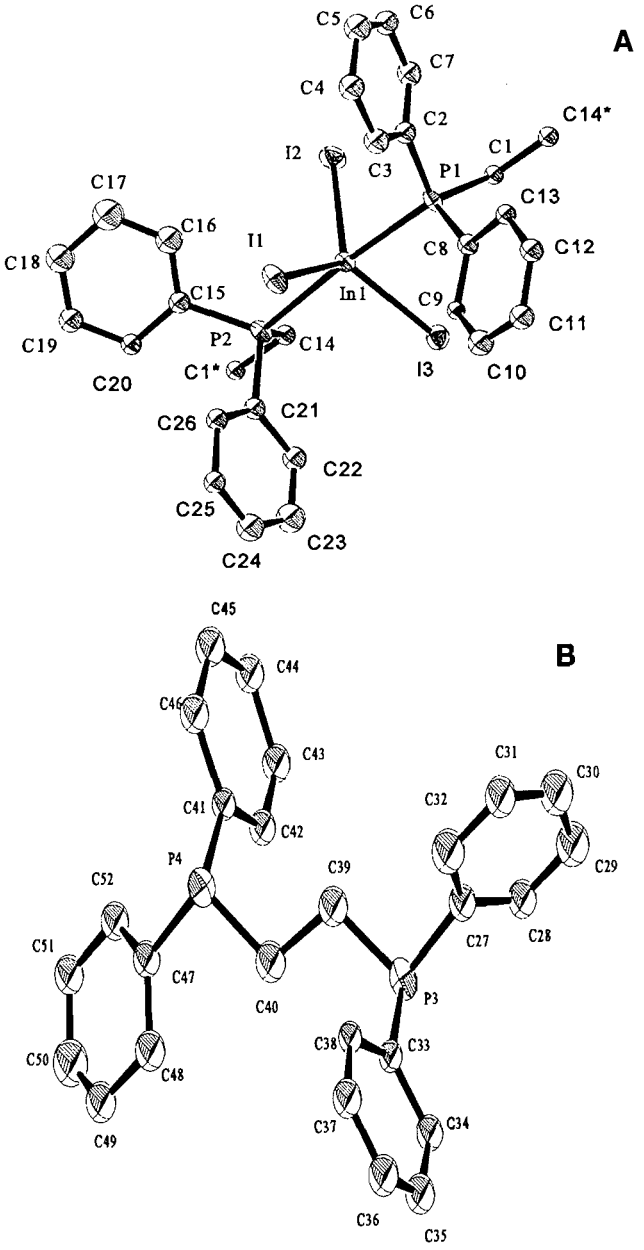

Fig. 4. Effect of temperature on ^{31}P NMR spectrum of a solution of $InI_3(PPh_3)_2$, 0.1 M in $CDCl_3$; (*A*) change in chemical shift, (*B*) change in line width at half-height.

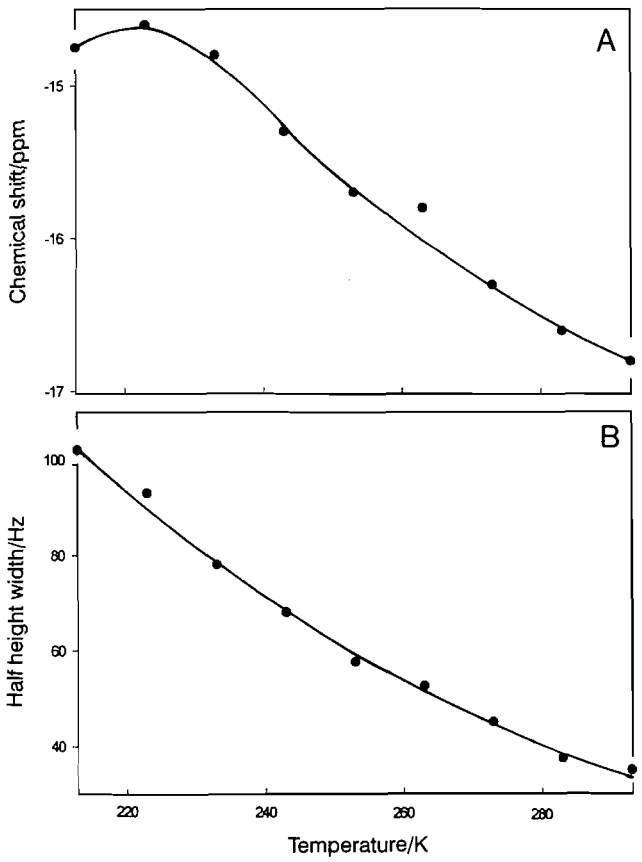

in $CDCl_3$, which is in keeping with earlier observations by many workers that this resonance is only detectable in species of high symmetry because of the high nuclear spin ($I = 9/2$). As I^- was added, however, a signal was detected at −980 ppm relative to $InCl_4^- = 0$ (see ref. (14), indicating the formation of InI_4^- in the solution. The intensity of this signal increased with further addition of R_4NI, and again reached a maximum when the concentration of $InI_3(PPh_3)_2$ and R_4NI were equal. Further addition of R_4NI caused the precipitation of $R_4N[InI_4]$, identified by the characteristic Raman spectrum (139 s, 186 w cm^{-1}; cf. lit. values $\nu_1 = 139$, $\nu_3 = 186$ cm^{-1} (16)), and in the case of *n*-$Pr_4N[InI_4]$ by indium analysis (calcd. In 14.2%; found: In 14.0). These results all show that the process [3] takes place,

[3] $InI_3(PPh_3)_2 + I^- \rightarrow InI_4^- + 2\ PPh_3$

apparently quantitatively, under the conditions used.

The 1:1 complex $InI_3 \cdot PPh_3$ is insufficiently soluble in $CDCl_3$ for ^{31}P investigations, but results were obtained with solutions in acetone. The 1:1 adduct in this solvent shows a sharp resonance at room temperature at −28.8 ppm, $\omega_{1/2}$ = 16.5 Hz. This is significantly sharper than the 1:2 species ($\omega_{1/2}$ = 105 Hz), and we conclude that the dissociation and ligand exchange are absent in this solution, so that eq. [2] lies to the left. The effect of adding PPh_3 to this solution is shown in Fig. 7. As with the 1:2 adduct, there are changes in both δ and $\omega_{1/2}$. The chemical shift of a mixture containing equimolar quantities of $InI_3 \cdot PPh_3$ and PPh_3 is −23.5 ppm, to be compared with the value for a solution of the 1:2 complex in $CDCl_3$ of −16.85 ppm. Given the effect of solvent on the equilibria involved, there is little to be gained by discussing this difference; the more important point is that addition of PPh_3 to $InI_3 \cdot PPh_3$ shifts the resonance towards that of the 1:2 complex. The increasing half width (Fig. 7B) with addition of ligand is evidence of ligand exchange, in keeping with eq. [1].

Dissociative equilibria involving $InI_3(PPh_3)_2$

The present results, and those from the earlier investigations (2), show clearly that eqs. [1], [2], and [3] describe partially

Fig. 5. Effect of adding PPh_3 to a solution of $InI_3(PPh_3)_2$ (0.1 M in $CDCl_3$) at room temperature; (*A*) change in ^{31}P chemical shift, and (*B*) change in line width.

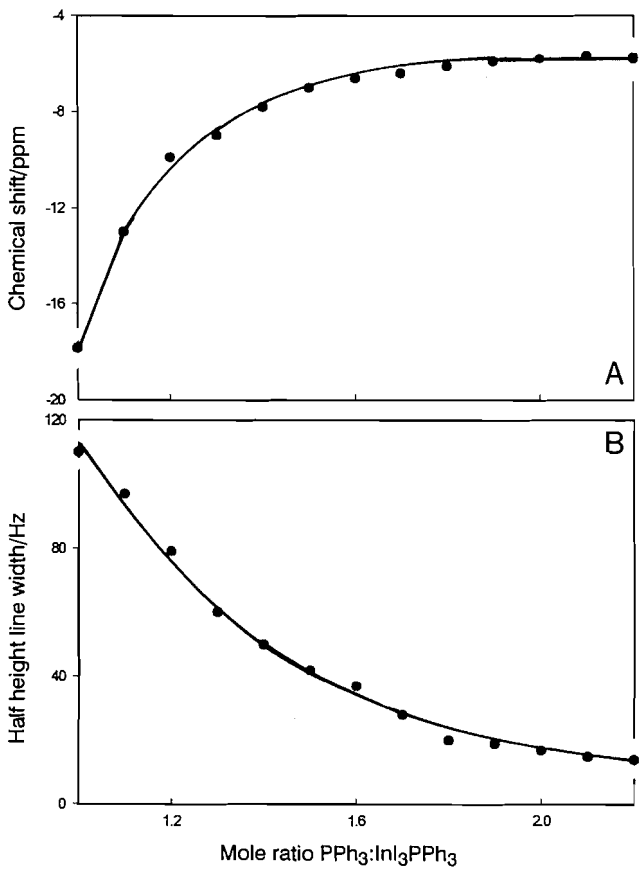

Fig. 6. Effect of adding *n*-Bu_4NI to a solution of $InI_3(PPh_3)_2$ (0.1 M in $CDCl_3$) at room temperature; (*A*) change in ^{31}P chemical shift, (*B*) change in line width.

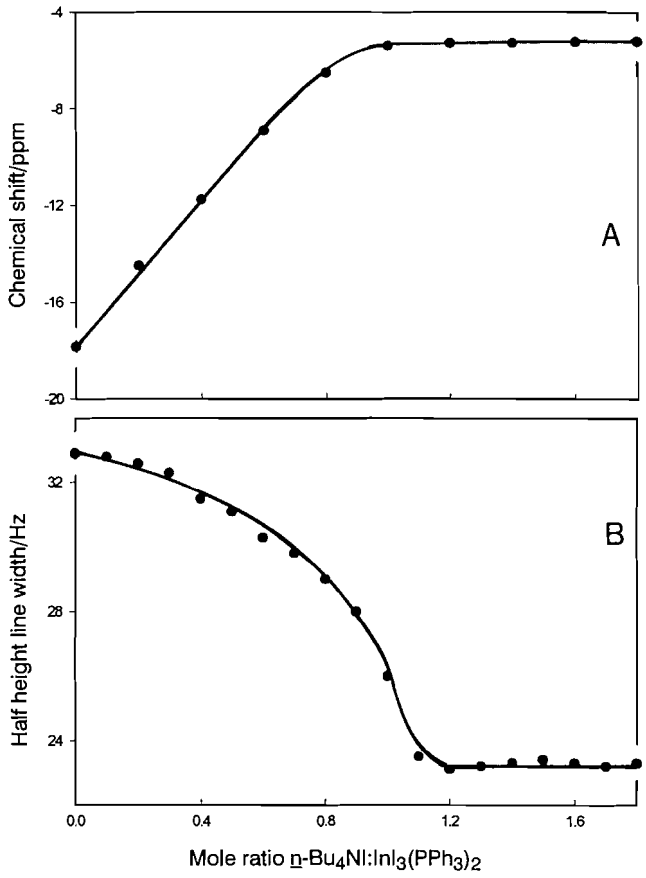

the solution chemistry of $InI_3(PPh_3)_2$. For this system, the possible equilibria can be summarized as

$$[4] \quad InX_3L_{n-1} + L \leftrightarrows InX_3L_n \leftrightarrows InX_2L_n + X^-$$

We note first that the dissociation into ionic species is established by the small but significant electrical conductivity in nitromethane and nitrobenzene (2). Such dissociation is germane to the present discussion only to the extent that free or associated charged species can be assumed to be present in the solvents used in the NMR investigations.

The preparative scale work on the InI_3/PPh_3 system showed that the reaction between these substances in ethyl acetate gives the 1:2 complex, which on recrystallization from the same solvent yields an equimolar solid lattice of 1:2 and 1:1 adducts that is also in keeping with the existence of this same equilibrium in ethyl acetate. Recrystallization of a solution of the 1:2 complex from cyclohexane gives only the 1:1 adduct. These effects, which have been discussed elsewhere (1), are a general feature of the adducts of indium trihalides and related compounds, and serve to emphasize the difficulty of identifying the "most stable" species in a series of possible adducts and (or) coordination numbers.

A quantitative analysis of the various results is hindered by the different solvents which were necessarily used in the various aspects of the work, and by the different concentration ranges involved ($\sim 10^{-3}$ M for conductivity measurements, $<10^{-2}$ for molecular weight determination, $>10^{-1}$ M for NMR studies, and >1 M in the preparative work). We take as a starting point the molecular weight determinations reported earlier (2) for two different sets of conditions. In chloroform at room temperature, the observed value is 614, and in benzene at the freezing point (5.5°C), $M_{obs} = 526$. If the only significant equilibrium is that of eq. [1], then

$$[5] \quad M_{obs} = \frac{(1-x)M_2 + M_1 + xL}{1+x}$$

where M_2, M_1, and M_L are the molecular weights of $InI_3(PPh_3)_2$, $InI_3 \cdot PPh_3$ and PPh_3 respectively, and x is the degree of dissociation of $InI_3(PPh_3)_2$. A value of $M_{obs} = 526$ corresponds to $x \rightarrow 1$ ($M_2 = 1020$, $M_1 = 758$, $M_L = 262$ to the nearest integer), and the result for chloroform is rather similar, so that the conclusion is that, at such dilutions, $InI_3(PPh_3)_2$ undergoes essentially complete dissociation to the 1:1 complex and free triphenylphosphine. This interesting result correlates nicely with the weak In—P bonding in the 1:2 complex (see above).

The ^{31}P NMR results show that the various phosphorus-containing species are undergoing rapid exchange under all

Fig. 7. Effect of adding PPh_3 to a solution of $InI_3 \cdot PPh_3$ (0.1 M) in acetone at room temperature; (*A*) change in ^{31}P chemical shift, (*B*) change in line width.

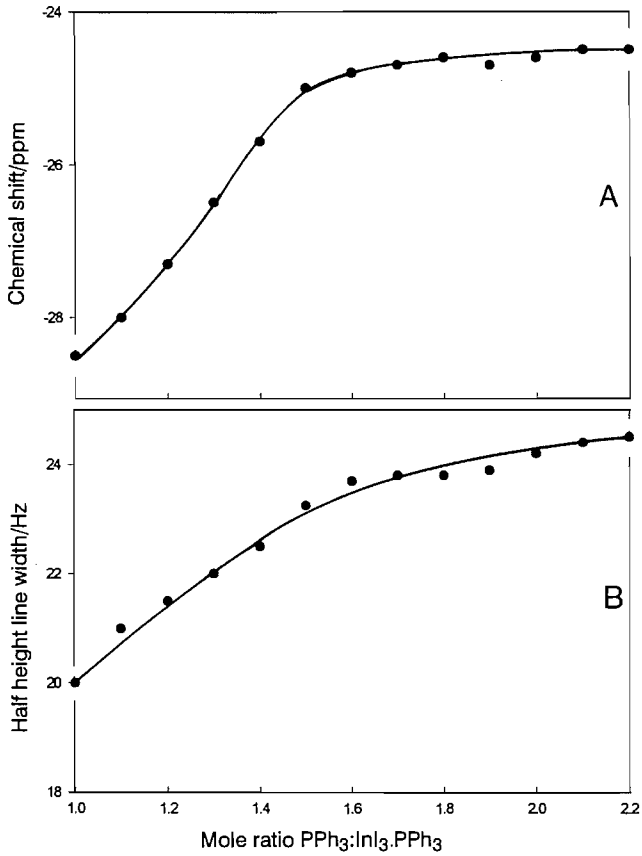

the conditions studied. The presence of substantial quantities of free PPh_3 as the result of the dissociation discussed above provides an obvious mechanism for this exchange. The observed chemical shift in any of these solutions is the weighted average of the individual shifts of the contributing species

$$[6] \qquad \delta_{obs} = \sum_i p_i \delta_i$$

where p_i is the fractional population of the ^{31}P spins present as the *i*th species with characteristic chemical shift δ_i, and one should therefore be able to calculate p_i or δ_i, depending on the assumptions made. If we assume that this solution is completely dissociated into InI_3PPh_3 and PPh_3, following the results just discussed, then from

$$[7] \qquad \delta_{obs} = p_2\delta_2 + p_1\delta_1 + p_L\delta_L$$

where the subscripts refer to the 1:2 and 1:1 complexes and the free ligand, we have $p_2 = 0$, and $p_1 = p_L = 0.5$, so that

$$[8] \qquad \delta_{obs} = 0.5\delta_1 + 0.5\,(-5.44) = -16.85 \text{ ppm}$$

from which $\delta_1 = -28.2$ ppm in $CDCl_3$. The value in acetone is -29.0 ppm (see above), and the agreement is satisfying (assuming no large solvent effect), so that the ^{31}P NMR results are in keeping with the molecular weight determinations in that both imply complete dissociation via eq. [1].

The addition of Ph_3P to a solution of $InI_3(PPh_3)_2$ can then be treated as increasing the concentration of PPh_3 in a solution initially containing equimolar quantities of $InI_3 \cdot PPh_3$ and PPh_3. For this reason, Fig. 5 deals with the results in terms of the mole ratio of these two components. A quantitative analysis of the chemical shift results in Fig. 5 appears impossible in the absence of a value for δ_2, but the curve cannot be reproduced by assuming that PPh_3 is being added to $InI_3 \cdot PPh_3$ without formation of the 1:2 complex. The more acceptable model assumes the formation of the 1:2 complex by the reverse of eq. [1], which then leads to the conclusion that δ_2 must be close to δ_L, and, given the weak long-range nature of this In–P interaction in the solid state, this seems reasonable. It was not possible to further analyze the NMR results to derive the equilibrium constant for eq. [1].

The addition of R_4NI to a solution of $InI_3(PPh_3)_2$ causes δ_{obs} to move in a linear fashion, reaching a constant value when the quantity of I^- added is equal to the initial quantity of $InI_3(PPh_3)_2$ (Fig. 6). Given the complete dissociation of the latter at $[I^-]_{ad} = 0$, we can write

$$[9] \qquad InI_3L + L + I^- \rightarrow InI_4^- + 2L$$

for the limit at $[I^-]_{ad} = [InI_3L_2]_0$. For intermediate conditions, where the quantity of added $I^- = x$, for complete conversion, one has

$$[10] \qquad \delta_{obs} = (1 - x)\delta_1 + (1 + x)\delta_L$$

which leads to a linear plot, as is observed in Fig. 6. This quantitative formation of InI_4^- is in keeping with the known behaviour of indium(III)–iodide systems, in which this tetrahedral anion is observed as an extremely stable species (1), and in the present situation much favored over the $InI_3 \cdot PPh_3$ adduct.

NMR studies of InI_3(dppe)

In view of the differing crystalline forms of this substance, it is important to note that all NMR studies discussed below refer to solutions of the compound InI_3(dppe), as initially prepared (see Experimental). The ^{31}P spectrum of a 0.1 M solution of this compound in $CDCl_3$ at room temperature is a sharp singlet, with $\delta = -15.9$ ppm and $\omega_{1/2} = 5$ Hz. The corresponding shift for dppe in the same solvent is -13.0 ppm, and the small change caused by coordination is in keeping with the structural similarities between free and bound ligand in the solid state (see above). The effect of lowering the temperature is illustrated in Fig. 8; the signal broadens gradually, with a sharp change at 223 K corresponding to the appearance of solid material, while the chemical shift changes by about 2 ppm over the same range. The studies of triphenylphosphine adducts of InI_3 discussed above clearly demonstrate that the four-coordinate species is thermodynamically more stable than the five-coordinate derivative, and the spectrum of InI_3(dppe) can be interpreted in this light. A non-fluxional four-coordinate mononuclear complex would show two ^{31}P resonances, as would a five-coordinate species with apical and equatorial phosphorus atoms; the observation of a single sharp resonance at room temperature and the relatively small tem-

Fig. 8. Effect of temperature on ^{31}P NMR spectrum of a solution of $InI_3(dppe)$ (0.1 M in $CDCl_3$); (A) change in chemical shift, (*B*) change in line width.

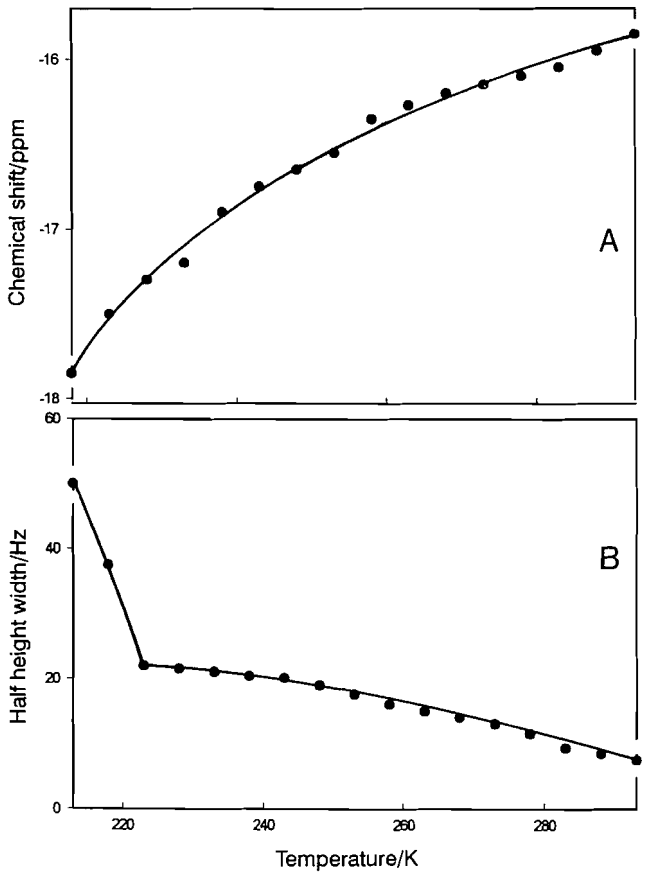

Scheme 1.

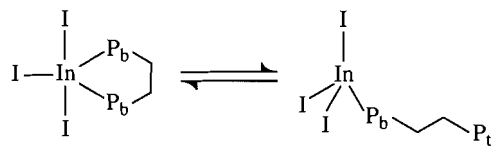

IA **IB**

perature effect in the spectra of $InI_3(dppe)$ itself are taken as evidence of the presence of the rapidly interconverting species (Scheme 1).

Ring-opening processes of this type have been shown to be a feature of the solution chemistry of other indium(III) compounds, and reflect the changes in coordination numbers associated with different ligand environments (17–19). The chemical shift observed is then the appropriately weighted average of the individual shifts of I*A* and I*B* and there will be two values for P_b and P_t in I*A*. The broadening of the signal with decreasing temperature (Fig. 8B) indicates the expected slowing of the exchange process, but it was not possible to identify these as separate resonances in the temperature range available to us. The addition of dppe (Fig. 9) produces a small change in δ, and the curve approaches asymptotically a value

Fig. 9. Effect of adding dppe to a solution of $InI_3(dppe)$ (0.1 M in $CDCl_3$) at room temperature; change in ^{31}P chemical shift.

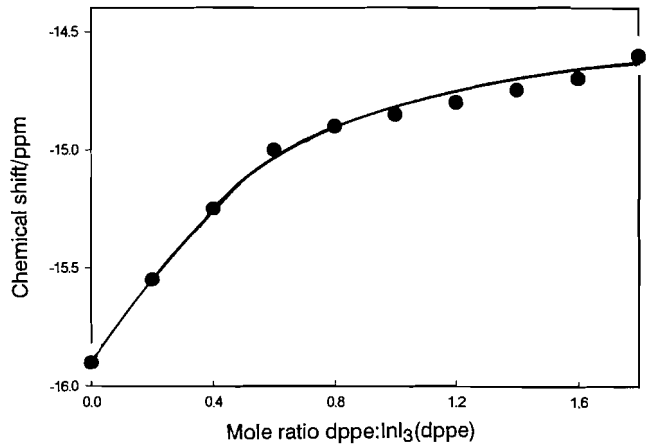

Scheme 2.

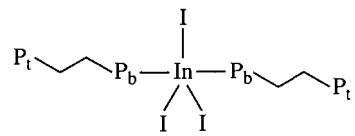

II

of ca. −14.5 ppm. In the absence of a bonding interaction leading to higher complexes between $InI_3(dppe)$ and free ligand, one would expect the linear relationship seen at low dppe concentrations in Fig. 9. There is an obvious deviation from this as the quantity of dppe is increased, but it is clear that an extrapolation to the chemical shift for free dppe would require the addition of large excess of this ligand. The addition of dppe (Fig. 9) also causes line broadening, and a shift in δ_{obs} that is almost linear with the dppe: complex ratio and corresponds to an averaging of δ_L and δ_C, the chemical shifts of the free ligand and the complex at low [dppe]. But at high ligand: complex mole ratios, δ_{obs} falls away from this linearity, which may be due to the formation in solution of species in which InI_3 is coordinated by two dppe ligands. In view of the preparative and crystallographic results, which show that $InI_3(dppe)$, $(InI_3)_3(dppe)_2$, and $[InI_3(dppe)]_\infty$ are readily interconverted, and that indium is five-coordinate in at least two of these systems, such a complex would likely involve two monodentate ligands present in small but not insignificant proportions (Scheme 2). The average ^{31}P chemical shift in such a species would presumably lie between the values for dppe (−13.0) and $InI_3(dppe)$ (−15.9 ppm).

The addition of strong σ-donor ligands, such as dimethyl sulphoxide, dimethylformamide, pyridine, or γ-picoline, to a solution of $InI_3(dppe)$ in $CDCl_3$ leads to the quantitative release of free dppe, as shown by the ^{31}P chemical shift changes. As in the InI_3–PPh_3 system, addition of iodide ion, as *n*-Bu_4NI, also results in the release of dppe and the formation of InI_4^-, by the ^{115}In resonance at −980 ppm. There is a quantitative difference from the InI_3/PPh_3 case, in that the dependence of δ on the complex: iodide mole ratio is not linear (Fig. 10). Extrapolation of the initial and final linear portions of this

Fig. 10. Effect of adding *n*-Bu_4NI to a solution of InI_3(dppe) (0.5 M in $CDCl_3$) at room temperature; change in ^{31}P chemical shift.

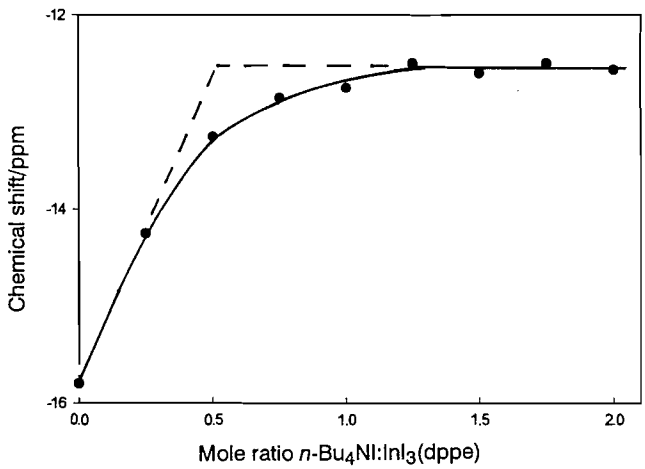

graph gives a point of inflexion at a mole ratio of I^-: complex = 0.5, which can be interpreted in the following way. Firstly, we note that direct nucleophilic attack by I^- on a five-coordinate InI_3(dppe) (structure **IB**) would involve the formation of a six-coordinate InI_4P_2 intermediate, which seems most unlikely in the context of the known coordination chemistry of indium(III). An interaction between I^- and four-coordinate InI_3(dppe) (i.e., structure **IA**) might appear more favorable, but this would not give the reaction stoichiometry observed, and it may well be that steric blocking by dppe at the indium(III) centre would prevent this reaction pathway. We therefore propose that the first step is the weak dissociation of the complex.

[11] $InI_3(dppe) \leftrightarrows InI_3 + dppe$

It is known that in non-coordinating solvents, the dimerization

[12] $2\ InI_3 \rightarrow In_2I_6$

lies completely to the right. Two spectroscopic studies (20, 21) have shown that adduct formation by Ga_2X_6 (X = Cl, Br) involves as a first step the coordination of the donor at one of the metal atoms of the dimer, and that dissociation of the latter (i.e., the reverse of eq. [12]) is not a prerequisite. For the present system, one then has

[13] $In_2I_6 + I^- \rightarrow InI_3 + InI_4^-$

as the final step, so that the overall stoichiometry is

[14] $2\ InI_3(dppe) + I^- \rightarrow InI_4^- + 2\ dppe + 1/2\ In_2I_6$

in keeping with the results shown in Fig. 10. The differences in the behaviour of $InI_3(PPh_3)$ and InI_3(dppe) in this respect are therefore a consequence of the different initial interactions, which are themselves a function of the coordination chemistry of indium(III).

General conclusions

The preparative studies on $InI_3 - PPh_3$ adducts demonstrate that here, as in other related systems, the influences of both solvent and ligand on apparently simple equilibria are complex, and not readily predictable with our present knowledge. The detailed information obtained from the NMR investigations for both PPh_3 and dppe derivatives emphasizes the difficulty of interpreting such matters in a quantitative manner. The most important general conclusion is that the interactions of such seemingly simple molecules are much more complicated than is apparent from a superficial examination, and that further studies of related systems would be profitable.

Acknowledgments

The present NMR work on $InI_3 - PPh_3$ systems is an extension of earlier studies carried out at Simon Fraser University; we wish to thank Mr. Victor Verigin for carrying out these experiments. Dr. S.J. Loeb (University of Windsor) is thanked for his help in the crystallographic studies. The research was supported in part by Research Grants (to D.G.T.) from the Natural Sciences and Engineering Research Council of Canada.

References

1. D.G. Tuck. *In* The chemistry of aluminium, gallium, indium and thallium. *Edited by* A.J. Downs. Blackie, London. 1993. Chap. 8, p. 430.
2. A.J. Carty and D. G. Tuck. J. Chem. Soc. (A), 1081 (1966).
3. B.H. Freeland and D.G. Tuck. Inorg. Chem. **15**, 476 (1976).
4. B.R. McGarvey, C.O. Trudell, D.G. Tuck, and L. Victoriano. Inorg. Chem. **19**, 3432 (1980).
5. D.T. Cromer and J.T. Waber. International tables for X-ray crystallography. Vol. IV. Kynoch Press, Birmingham, U.K. 1974. Table 2.2A.
6. J.A. Ibers and W.C. Hamilton. Acta Crystallogr. **17**, 781 (1974).
7. D.T. Cromer. International tables for X-ray crystallography. Vol. IV. Kynoch Press, Birmingham, U.K. 1974. Table 23.1.
8. TEXSAN-TEXRAY Structure analysis package, Molecular Structure Corporation, The Woodlands, Tex. 1985.
9. M.A. Brown and D.G. Tuck. Inorg. Chem. Acta, **247**, 135 (1996).
10. N.W. Alcock, J.A. Degnan, O.W. Howarth, and M.G.H. Wallbridge. J. Chem. Soc. Dalton Trans. 2775 (1992).
11. W. Clegg, N.C. Norman, and N.L. Pickett. Acta Crystallogr. Ser. C: Cryst. Struct. Commun. **C50**, 36 (1994).
12. I.A. Degnan, N.W. Alcock, S.M. Roe, and M.G.H. Wallbridge. Acta Crystallogr. Ser. C: Cryst. Struct. Commun. **C48**, 995 (1992).
13. M.V. Veidis and G.J. Palenik. Chem. Commun., 586 (1969).
14. M.A. Khan and D.G. Tuck. Acta Crystallogr. Ser. B: Struct. Crystallogr. Cryst. Chem. **B38**, 803 (1982).
15. M.J. Taylor and P.J. Brothers. *In* The chemistry of gallium, indium and thallium. *Edited by* A.J. Downs. Blackie, London. 1993. Chap. 3, p. 116.
16. L.A. Woodward and G.H. Singer. J. Chem. Soc. 716 (1958).
17. G.T. Tanner, D.G. Tuck, and E.J. Wells. Can. J. Chem. **50**, 3950 (1972).
18. H.L. Chung and D.G. Tuck. Can. J. Chem. **52**, 3944 (1974).
19. J.T.B.H. Jastrzebski, G. van Koten, D.G. Tuck, H.A. Meinema, and J.G. Noltes. Organometallics, **1**, 1492 (1982).
20. C. Hambly and J.B. Raynor. J. Chem. Soc. Dalton Trans. 604 (1974).
21. Z. Černý, J. Macháček, J. Jusek, B. Čásenský, O. Kříz, and D.G. Tuck. Inorg. Chem. Acta, **247**, 119 (1996).

Synthesis of glycosylated cationic porphyrins as potential agents in photodynamic therapy

Khalid Driaf, Robert Granet, Pierre Krausz, Mourad Kaouadji, François Thomasson, Albert José Chulia, Bernard Verneuil, Marenglen Spiro, Jean-Claude Blais, and Gérard Bolbach

Abstract: Trisalkylpyridinium porphyrins substituted by one glycosyl (glucosyl, maltosyl, and lactosyl) moiety have been prepared in acceptable yields. These glycosylated cationic porphyrins have been synthesized from pyrrole condensed with 4-pyridinecarboxaldehyde, and suitable *ortho*- or *para* peracetylglycosyloxybenzaldehyde derivatives in refluxing propionic acid – Ac_2O followed by action of alkyliodide in DMF. Deprotection of the glycosylated moieties led to a new class of representative glycosylated porphyrins.

Key words: porphyrins, cationic, glycosylated; phototherapy, cancer.

Résumé : On a préparé des tris(alkylpyridinium)porphyrines substituées par une portion glycosyle (glucosyle, maltosyle et lactosyle) avec des rendements acceptables. On a synthétisé ces porphyrines cationiques glycosylées à partir de pyrrole condensé avec un pyridine-4-carboxyaldéhyde et des dérivés *ortho*- ou *para*-peracétylglycosyloxybenzaldéhydes appropriés, par reflux dans de l'acide propanoïque – Ac_2O, suivi par l'action d'un iodure d'alkyle dans le DMF. La déprotection des portions glycosylées conduit à une nouvelle classe de porphyrines glycosylées représentatives.

Mots clés : porphyrines, cationique, glycosylé; photothérapie, cancer.

[Traduit par la rédaction]

Introduction

Tetrapyrrolic macrocycles and their metallic complexes have been long investigated largely on account of their thermo- or photocatalytic properties. The continuing progress in porphyrin chemistry in recent years has caused a growing interest for such compounds. Porphyrins and their analogs have attracted much attention as phototherapeutic (1) and anti-HIV agents (2).

Photosensitizing porphyrins are a potential treatment in tumor therapy. Photodynamic therapy is based on the principle that these porphyrins become concentrated in tumor cells and, upon subsequent irradiation with visible light in the presence of oxygen, specifically destroy the cells (3). To have an efficient photosensitizing effect, porphyrins must exhibit excellent hydrophilic properties (4). Thus it is of great interest to synthesize new water-soluble molecules.

Cationic porphyrins are highly soluble and the presence of a carbohydrate moiety improves specific receptor targeting (5) and increases plasmatic life time (6). The presence of hydrophilic and hydrophobic parts in the compounds facilitates membrane penetration. In addition, cationic porphyrins have different binding modes with nucleic acids than have neutral porphyrins due to their enhanced affinity for DNA (7). These porphyrin–DNA interactions are of great importance in photodynamic therapy (PDT) (8), anticancer therapy (9), selective cleavage of nucleic acids (10), and as antiviral agents (HIV-1) (11). Since the first work of Mironov et al. (12), a vast and ever-increasing literature on glycosylated porphyrins has been reported (13), although, until now, no work has been devoted to unsymmetrical *O*-glycosylated cationic porphyrins. In a preliminary paper we reported the first synthesis of alkyl pyridinium 4-yl porphyrins bearing a carbohydrate moiety (14). In connection with our research program on glycosylated porphyrins we have extended the range of structures of glycosyl and alkyl substituents. In the present paper we report full experimental data concerning the synthesis and characterization of a series of free base cationic glycosylated porphyrins based on tris 4-(alkyl pyridiniumyl) porphyrin. These unsymmetrical molecules contain one *meso*-phenyl group bearing a mono- or disaccharide in the *ortho* or *para* position and three *meso*-alkyl pyridinium groups with a linear or branched alkyl chain.

Received September 26, 1995.[1]

K. Driaf, R. Granet, P. Krausz,[2] M. Kaouadji, and B. Verneuil. Université de Limoges, Laboratoire de chimie des substances naturelles, 123, Avenue Albert Thomas, F-87060 Limoges-Cedex, France.
F. Thomasson. Université Joseph Fourier-Grenoble I, Service commun de RMN, Domaine de la Merci, F-38706 La Tronche-Cedex, France.
A.J. Chulia. Université de Limoges, Laboratoire de pharmacognosie et phytochimie, 2, rue Docteur Marcland, F-87025 Limoges-Cedex, France.
M. Spiro, J.-C. Blais, and G. Bolbach. Université Pierre et Marie Curie, Laboratoire de chimie structurale organique et biologique, Centre national de la recherche scientifique EP 103, 4 place Jussieu, F-75252 Paris-Cedex 05, France.

[1] Revision received April 24, 1996.
[2] Author to whom correspondence may be addressed. Telephone: 55.45.74.75. Fax: (33) 55.45.72.02.

Results and discussion

Synthesis

The different porphyrins were prepared according to the gen-

Scheme 1.

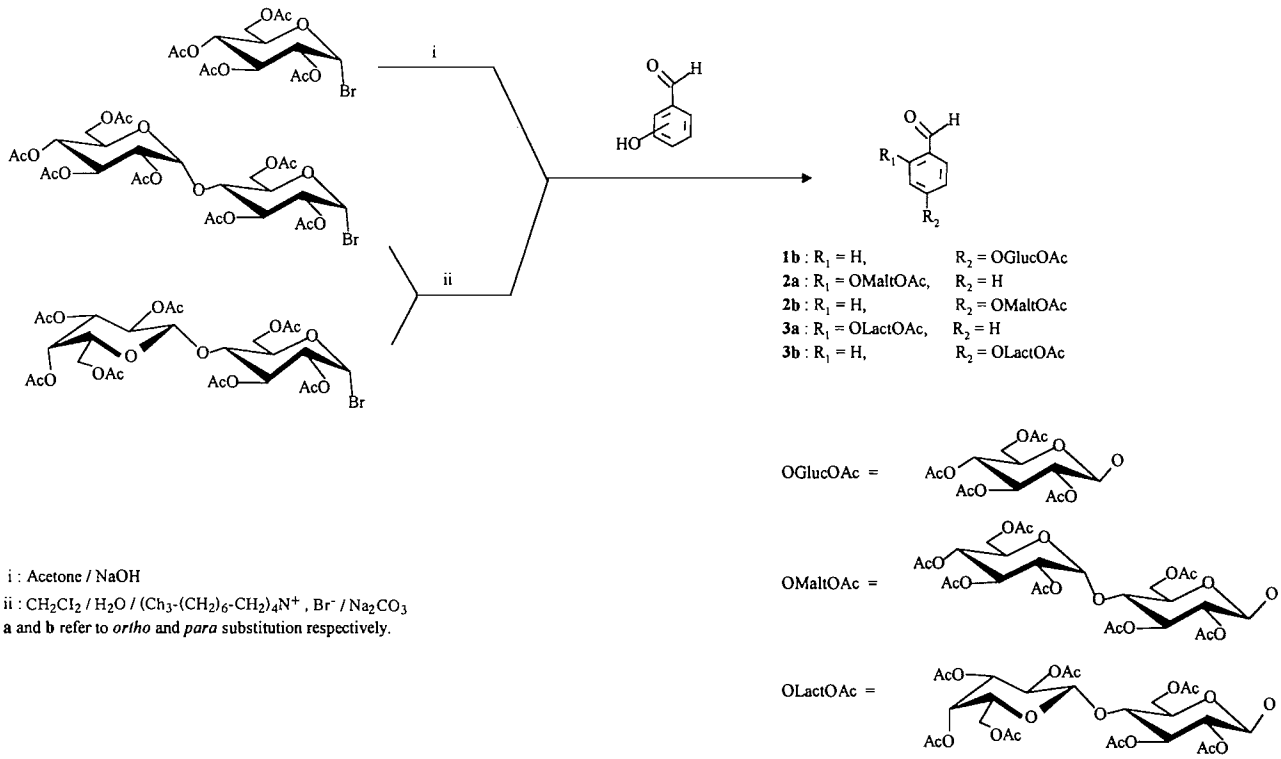

eral route outlined in Schemes 1 and 2. The suitably glycosylated benzaldehydes **1–3** were synthesized following different pathways (Scheme 1). Aldehyde **1a** was prepared from commercially available helicin (2-(β-D-glucopyranosyloxy)benzaldehyde) by acetylation at 0°C during 1.5 h with acetic anhydride in dry pyridine (yield 90%). 4-(2,3,4,6-Tetra-*O*-acetyl-β-D-glucopyranosyloxy)benzaldehyde **1b** was synthesized from 2,3,4,6-tetra-*O*-acetyl-α-D-glucopyranosyl bromide and 4-hydroxybenzaldehyde (2.5 equiv.) in acetone in the presence of 7% aqueous NaOH. After 24 h, the expected compound was obtained in 40% yield. Treatment of hydroxybenzaldehyde with bromoacetylated maltosyl or lactosyl in the same manner gave products **2a,b** and **3a,b** in low yields; therefore, another route to prepare these compounds was selected. 2,3,6,2′,3′,4′,6′-Hepta-*O*-acetyl-β-D-maltosyl or lactosyl benzaldehydes were produced by reaction of *ortho* or *para* hydroxybenzaldehyde with bromoacetylated maltosyl or lactosyl in phase transfer catalysis. This reaction was carried out in a biphasic system of water–chloroform (1:1) in the presence of 1 M aqueous Na_2CO_3 and tetraoctylammonium bromide as catalyst. After the usual work-up, glycosylated benzaldehydes **2a,b** and **3a,b** were obtained with an improved yield for the *para* compounds. Compounds with the disaccharidic substituent in the *ortho* position did not have a similar result probably due to steric hindrance.

With the suitably glycosylated benzaldehydes, pyridyl porphyrin derivatives were then synthesized (Scheme 2). Unsymmetrical porphyrin derivatives **4a,b, 5a,b**, and **6a,b** with three pyridyls and a protected mono- or disaccharide glycosylated group were prepared following the method of Little et al. (15). These syntheses were carried out by condensation of **1a,b–3a,b** (1 equiv.) with 4-pyridinecarboxaldehyde (2 equiv.) and pyrrole (2.6 equiv.) in propionic acid with 10% acetic anhydride, which served to prevent deacetylation of the glycosylated moiety. The yields of chromatographically pure porphyrins were about 6–7%. Such yields are acceptable in comparison to other similar preparations (10*a*). Attempts to use Lindsey's method (16) (condensation of aldehydes and pyrrole in the presence of BF_3–Et_2O in CH_2Cl_2 followed by addition of DDQ) did not lead to the expected compounds **4a,b–6a,b**.

Treatment of glycosylated pyridylporphyrins **4a,b–6a,b** with a large excess of methyl iodide in dry DMF gave the expected cationic glycosylated *N*-methylpyridinium porphyrins **7a,b–9a,b**. These compounds were purified by precipitation in diethyl ether. In a second series of experiments, the alkyl substituents of pyridyl porphyrins **4a,b** were modified. Thus, when treated with a large excess of either isopropyl iodide or *n*-octyl iodide, **4a** and **4b** yielded the corresponding cationic porphyrins **10a,b** as well as **11a,b** in about 70% yield. *N*-Isopropyl derivatives **10a** and **10b** were purified as described for **7a,b–9a,b**; however, *n*-octyl porphyrins were extracted with the mixture *n*-BuOH–AcOH–H_2O (4:1:5) (upper phase) due to their lower polarity with respect to the *N*-methyl and *N*-isopropyl homologues.

Finally, compounds **4–11** were deprotected with Et_3N–MeOH–H_2O (10:10:1) at 0°C, which after purification, led to the unprotected porphyrins **12–19** in nearly quantitative yields.

Acetylated cationic porphyrins were soluble in water with the exception of the *n*-octyl derivatives (**11a,b**), which were soluble in organic solvents such as chloroform, methylene

Scheme 2.

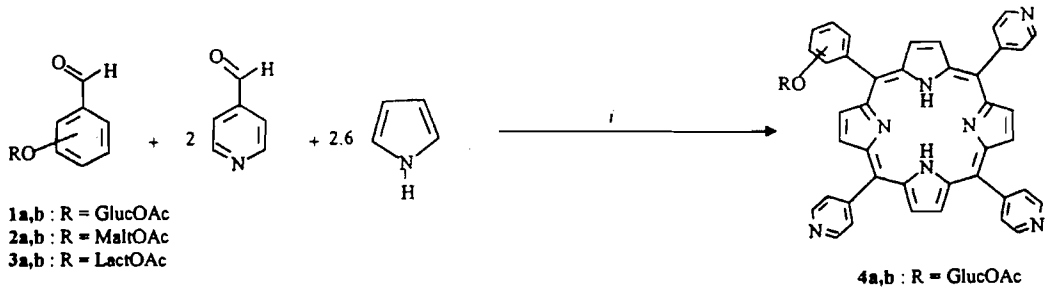

1a,b : R = GlucOAc
2a,b : R = MaltOAc
3a,b : R = LactOAc

4a,b : R = GlucOAc
5a,b : R = MaltOAc
6a,b : R = LactOAc

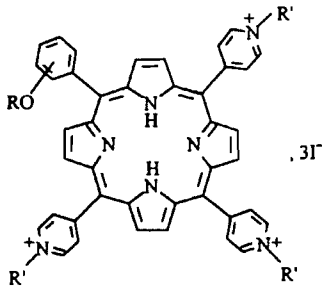

7a,b : R = GlucOAc ; R' = Me
8a,b : R = MaltOAc ; R' = Me
9a,b : R = LactOAc ; R' = Me
10a,b : R = GlucOAc ; R' = *i*-Pr
11a,b : R = GlucOAc ; R' = *n*-Oct

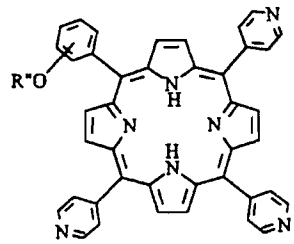

12a,b : R" = GlucOH
13a,b : R" = MaltOH
14a,b : R" = LactOH

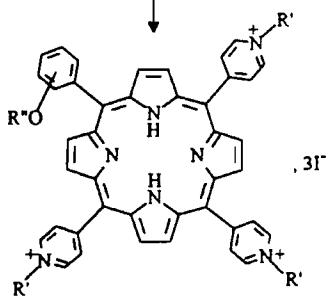

15a,b : R' = Me ; R" = GlucOH
16a,b : R' = Me ; R" = MaltOH
17a,b : R' = Me ; R" = LactOH
18a,b : R' = *i*-Pr ; R" = GlucOH
19a,b : R' = *n*-Oct ; R" = GlucOH

i : EtCOOH / $(AcO)_2O$, reflux, 1.5 h
ii : R'-I / DMF.
iii and *iv* : Et_3N-MeOH-H_2O (10: 10: 1).
a and **b** refer to *ortho* and *para* substitution respectively.

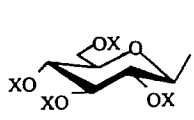

X = OAc : GlucOAc
X = H : GlucOH

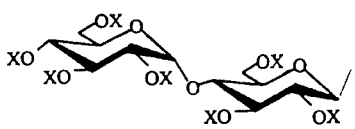

X = OAc : MaltOAc
X = H : MaltOH

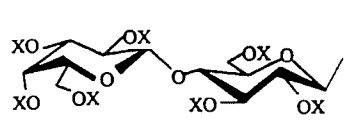

X = OAc : LactOAc
X = H : LactOH

chloride, and ether. The disaccharide acetylated cationic porphyrins **8a,b** and **9a,b** were slightly soluble in methylene chloride. All deacetylated neutral and cationic porphyrins were water soluble.

Mass analysis

Conventional mass spectral analysis (EI and CI) of relatively nonvolatile compounds such as porphyrins requires considerable heating of the sample, which can lead to its degradation. Consequently, ionization modes such as SIMS, FAB, and MALDI (Matrix Assisted Laser Desorption Ionization) were used for characterization of the porphyrins.

Acetylglycosylated neutral porphyrins were analyzed in the SIMS mode (positive and negative). Acetylglycosylated cationic porphyrins were characterized by FAB mass spectrometry. The mass spectra of the deacetylated porphyrins, both neutral and cationic, were obtained in the MALDI mode, the FAB mode being ineffective. In addition to the protonated (positive mode) or deprotonated (negative mode) molecules, an ion corresponding to elimination of an acetylated sugar unit was observed in the SIMS spectrum of acetyl glycosylated porphyrins (**4a,b–6a,b**). Acetylated cationic porphyrins (**7a,b–11a,b**) were characterized by FAB MS in positive mode. In all cases, a protonated quasi molecular ion $(M + H)^+$ was detected. In addition, peaks corresponding to an elimination of one, two, and three alkyl groups (Me, i-Pr, or *n*-Oct) were observed.

In the MALDI mass spectra of deacetylated porphyrins (**12a,b–19a,b**) the molecular peak $(M - 3I^-)^+$ was always observed; no fragment ions were observed.

^{1}H NMR analysis

The ^{1}H NMR data of pyridyl and alkylpyridinium porphyrins were recently published (4) but to the best of our knowledge there exists no information about the ^{1}H NMR of glycosylated pyridylporphyrins.

The ^{1}H NMR of porphyrins **4a,b**, **7a,b**, **10a,b**, and **11a,b** were measured at 200 MHz in DMSO-d_6. The detailed resonance assignments are based on integration, selective homonuclear decoupling, as well as NOE and 2D homonuclear COSY experiments. According to the two substituted phenyl ring groups of *ortho*-tetra-*O*-acetylglucosyl or *para*-tetra-*O*-acetylglucosyl, significative shifts occur for the phenyl substituent as well as for the carbohydrate moiety, the pyridinyl units, and the macrocycle. Such differences in the NMR spectra are consequent to the orientation of the osidic unit with respect to the tetrapyrrolic ring. In the series of related compounds characterized by *p*-tetra-*O*-acetylglucosyl substitution (**4b**, **7b**, **10b**, and **11b**), the ^{1}H NMR spectrum is readily assigned because of the relative high symmetry (C_{2v} group) of each molecule (Tables 1 and 2). This is well illustrated in the ^{1}H NMR of **4b**, taken in $CDCl_3$, by the occurrence of only two sets of protons appearing as doublets ($J = 5.3$ Hz) at δ 9.04 (H-2,6) and δ 8.15 (H-3,5) of the pyridinyl moieties and at δ 8.10 (H-2,6) and δ 7.36 (H-3,5) with $J_{ortho} = 8.7$ Hz for the *p*-disubstituted phenyl ring. Due to their proximity, the pyrrole protons are divided into 2 × 4H exhibiting either a doublet or a singlet. Pyrrole rings in which one proton is near the *p*-(tetra-*O*-acetylglucosyloxy)phenyl and the other is close to a pyridine have their proton resonances split into two doublets ($J =$ 4.5 Hz) at δ 8.91 (H-3,7) and δ 8.81 (H-2,8); in parallel and due to symmetry, pyrrole rings surrounded by two pyridinyl substituents display uncoupled protons appearing as a singlet at δ 8.83 (H-12,13,17,18). Finally, as for *p*-(tetra-*O*-acetylglucosyloxy)benzaldehyde **1b**, the carbohydrate exhibits the expected well-resolved resonances at δ 4.05 (H-5), 4.30 (H-6_A), and 4.41 (H-6_B). The remaining sugar protons are responsible for the overlapped multiplet centered at δ 5.35 (H-1,2 and H-3 or H-4) near to the triplet at δ 5.30 (H-3 or H-4). Change in the substitution of the phenyl ring, by the sugar from the *para* to the *ortho* position with respect to the porphyrin, results in considerable changes in the ^{1}H NMR chemical shifts and (or) in patterns relative to most of the nuclei. This phenomenon reflects a diminished symmetry induced by the orientation of the sugar that in turn leads to an unsymmetrical folded structure because of steric hindrance. Such magnetic perturbations are encountered in the ^{1}H NMR spectra of the related series of compounds, **4a**, **7a**, **10a**, and **11a**, containing *ortho*-tetra-*O*-acetylglucosyloxyphenyl substituent. In comparison with the ^{1}H NMR data of the above-mentioned **4b**, those relative to the homologue **4a** show striking differences in connection with each part of the molecule (Table 2). The pyridinyl protons (H-3,5) close to the macrocycle are shifted downfield by 0.67 ppm, in contrast to the unaffected H-2,6 (δ 9.06). The β-pyrrole proton signals are converted into three doublets ($J =$ 4.9 Hz) at δ 8.94 (H-3), 8.90 (H-7), 8.84 (H-2,8) as well as two singlets at δ 8.83 and 8.78 for H-12,13,17,18. All the sugar protons experience a particularly pronounced shielding from −0.28 ppm (H-6_A) to −1.19 ppm (H-2). These nuclei are obviously located well within the range of the shielding current above the porphyrin macrocycle. Two acetyl groups that would otherwise show a larger shift towards 2.0 ppm are also influenced by the ring current (δ 1.26 and δ −0.97). It is worthwhile noting that the latter group, exhibiting a negative chemical shift value like the typical inner NH protons (δ −2.88), can be unambiguously identified as AcO-2 as predicted by the space-filling model. The ^{1}H NMR spectra of *ortho*- and *para*-protected monoglucosides **4a** and **4b** taken in DMSO-d_6 (Table 1) exhibit chemical shift variations generally entitled solvent effects. This behavior seems to be due to the binding of the polar solvent in the hindered cavity of the macrocycle as indicated by the significative upfield shift (Δδ −0.10 to −0.14 ppm) experienced by the NH groups in both compounds. As a consequence, all the pyrrolic protons are shifted downfield by +0.10 to +0.13 ppm in the *para* isomer. Conversely, only one β-proton of the macrocycle, H-2, displays a significative upfield shift (Δδ −0.11 ppm) in the *ortho* derivative. This phenomenon probably results from the change in the geometry of the macrocycle, whose deformation in the presence of DMSO is more pronounced in **4b** than in **4a** because the orientation of the sugar moiety close to the porphyrin ring in the *ortho* isomer prevents the solvent effect to be clearly expressed on the β-protons. In both compounds, however, the most significant chemical shift variations recorded in the polar solvent are those relative to the pyridinyl and the osidic protons as well as to two particular acetyl groups in **4a** only. Such variations may be partially understood in terms of some combination of steric effect and anisotropy. A consideration of the anisotropy of the sulfoxide function, which acts to cause shielding or deshielding of the protons lying in or out of the cone, seems to be more probable. Regardless of the nature of the effect, the pyridinyls H-3,5 undergo an

Table 1. ^{1}H NMR spectra of glycosylated porphyrins **4a,b**, **5a,b**, and **6a,b** (δ, ppm(*J*,Hz)).

H	4a[a]	4b[a]	4a[b]	4b[b]	5a[b]	5b[b]	6a[b]	6b[b]
Pyrrols								
2	8.84 d (4.9)	8.81 d (4.5)	8.73 d (4.9)	8.94 s[c]	8.73 d (4.8)	8.87 d (4.9)	8.72 d (4.9)	8.86 d (4.9)
3	8.94 d (4.9)	8.91 d (4.5)	8.86 d (4.9)	8.94 s	8.84 d (4.8)	8.92 d (4.9)	8.84 d (5.1)	8.91 d (4.9)
7	8.90 d (4.9)	8.91 d (4.5)	8.84 d (4.9)	8.94 s	8.83 d (4.8)	8.92 d (4.9)	8.82 d (4.9)	8.91 d (4.9)
8	8.84 d (4.9)	8.81 d (4.5)	8.80 d (4.9)	8.94 s	8.78 d (4.8)	8.87 d (4.9)	8.78 d (5.1)	8.86 d (4.9)
12,13	8.83 s[c]	8.83 br s	8.88 s[c]	8.96 s[c]	8.88 s[c]	8.88 s	8.88 s[c]	8.88 s
17,18	8.78 s[c]	8.83 br s	8.87 s[c]	8.96 s	8.87 s[c]	8.88 s	8.87 s[c]	8.88 s
N-H	−3.88 s	−2.90 s	−3.02	−3.00 s	−3.04 s	−3.01 s	−2.89 s	−3.01 s
Pyridin 4-yls								
2,6	9.06 br d (5.6)	9.04 d (5.3)	9.04 d (5.5)	9.16 d (5.7)	9.03 d (5.5)	9.04 d (5.6)	9.04 br d (4.5)	9.03 d (4.8)
								8.24 d (4.8)
3,5	8.17 d (5.6)	8.15 d (5.3)	8.26 d (5.5)[×2H]	8.44 d (5.7)	8.25 d (5.9) [×2H]	8.25 d (5.7)	8.26 d (5.7) [×2H]	
			8.18 d (5.5)[×4H]		8.19 br d (5.9) [×4H]		8.19 m [×4H]	
Aryl								
2		8.10 d (8.7)		8.19 d (8.5)		8.18 d (8.5)		8.17 d (8.3)
3	7.70 br d (7.5)	7.36 d (8.7)	7.69 br d (7.5)	7.50 d (8.5)	7.66 br d (7.5)	7.44 d (8.5)	7.66 br d (7.5)	7.43 d (8.3)
4	7.80 dt (7.5, 1.6)		7.89 dt (7.5, 1.5)		7.89 dd (7.5, 1.4)		7.87 dt (7.5, 1.4)	
5	7.52 dt (7.5, 1.6)	7.36 d (8.7)	7.52 br t (7.5)	7.50 d (8.5)	7.51 br t (7.5)	7.44 d (8.5)	7.51 br t (7.5)	7.43 d (8.3)
6	8.02 dd (7.5, 1.6)	8.10 d (8.7)	8.03 dd (7.5, 1.5)	8.19 d (8.5)	8.02 dd (7.5, 1.4)	8.18 d (8.5)	8.01 dd (7.5, 1.4)	8.17 d (8.3)
***O*-Glycosyl**								
1	4.84 d (7.8)	5.35 m	5.56 d (8.0)	5.96 d (7.9)	5.52 d (7.8)	5.93 d (7.8)	5.49 d (8.0)	5.88 d (7.8)
2	4.16 br t (8.6)	5.35 m	3.84 dd (9.6, 8.0)	5.27 dd (9.5, 7.9)	3.72 dd (9.2, 8.0)	5.16 dd (9.4, 8.1)	4.32 br t (10.2)	5.18 t (8.5)
3	4.62 br t (9.1)	5.35 m[c]	4.96 t (9.6)	5.55 t (9.5)	4.95 t (9.2)	5.59 t (9.2)	4.83 t (9.4)	5.43 t (9.4)
4	4.70 br t (10.2)	5.30 t (9.9)[c]	4.57 t (9.5)	5.13 d (9.5)	3.61 t (9.1)	4.00–4.49 m	Under H_2O peak	4.02 br t (9.1)
5	3.66 ddd (8.6, 5.0, 2.4)	4.05 ddd (9.7, 4.9, 2.3)	4.18–4.21 m	4.40–4.48 m	4.14–4.21 m	4.00–4.49 m	3.68–4.10 m	4.05–4.35 m
6_A	4.02 dd (12.2, 2.4)	4.30 dd (12.1, 2.3)	4.01 dd (11.6, 2.2)	4.19 dd (12.3, 1.7)	4.07 dd (12.3, 4.7)	4.00–4.49 m	3.68–4.10 m	4.05–4.35 m
6_B	4.11 dd (12.2, 5.2)	4.41 dd (12.1, 4.9)	4.14 dd (11.6, 5.2)	4.33 dd (12.3, 5.1)	4.36 br d (12.3)	4.55 br d (10.4)	4.29 br d (11.2)	4.46 br d (9.9)
1′					4.96 d (3.8)	5.38 d (3.8)	4.53 d (7.9)	4.84 d (8.0)
2′					4.69 d (10.4, 3.8)	4.94 dd (10.5, 3.8)	4.71 dd (10.0, 7.9)	4.91 br t (7.8)
3′					5.11 t (9.8)	5.29 br t (9.8)	5.02 dd (10.1, 3.8)	5.20 dd (8.3, 4.2)
4′					4.87 t (9.7)	5.02 t (9.8)	5.09 br d (3.7)	5.27 br d (4.2)
5′					3.80–3.95 m	4.00–4.49 m	3.68–4.10 m	4.05–4.35 m
$6'_A$					4.14–4.21 m	4.00–4.49 m	3.68–4.10 m	4.05–4.35 m
$6'_B$					3.80–3.95 m	4.00–4.49 m	3.68–4.10 m	4.05–4.35 m
***O*-Acetyls**								
	1.97 s	2.20 s	1.96 s	2.16 s	2.06 s	2.12 s	2.09 s	2.14 s
	1.85 s	2.11 s	1.84 s	2.05 s[×2]	1.95 s	2.10 s	1.99 s	2.12 s
	1.26 s	2.10 s	1.39 s	2.03 s	1.94 s	2.04 s [×3]	1.98 s	2.10 s
	−0.97 s	2.09 s	−0.38 s		1.88 s	1.99 s	1.84 s	2.05 s [×3]
					1.76 s	1.97 s	1.75 s	1.91 s
					1.23 s		1.39 s	
					−0.38 s		−0.41 s	

[a]$CDCl_3$.
[b]DMSO-d_6.
[c]Assignments with the same superscript in one column may be interchanged.

Table 2. ^{1}H NMR spectra of glucosides **7a,b**, **10a,b**, and **11a,b** in DMSO-d_6 (δ, ppm (*J*, Hz)).

H	7a	7b	10a	10b	11a	11b
Pyrrols						
2	8.82 d (5.0)	8.98 d (5.6)	8.70–8.79 m	8.95–9.25 m	8.83 d (4.9)	9.01 d (4.9)
3	9.04 d (5.0)	8.99 d (5.6)	8.80–8.90 m	8.95–9.25 m	9.07 d (4.9)	9.11 d (4.9)
7	9.01 d (4.9)	8.99 d (5.6)	8.80–8.90	8.95–9.25 m	9.04 d (4.9)	9.11 d (4.9)
8	8.90 d (4.8)	8.98 d (5.6)	8.70–8.79 m	8.95–9.25 m	8.92 d (4.9)	9.01 d (4.9)
12,13	9.16 br s[a]	9.14 br s	9.00–9.22 m	8.95–9.25 m	9.19 br s[a]	9.17 s
17,18	9.13 br s[a]	9.14 br s	9.00–9.22 m	8.95–9.25 m	9.16 br s[a]	9.17 s
N-H	–3.06 s	–3.05 s	–3.07 s	–2.96 s	–3.03 s	–3.00
***N*-Alkylpyridinium 4-yls**						
2,6	9.48 d (6.3)[×4H] 9.44 d (6.3)[×2H]	9.46 d (6.8)	9.60 d (6.6)[×4H] 9.57 d (6.6)[×2H]	9.65 br s	9.56 br d (6.3)[×4H] 9.54 d (6.3)[×2H]	9.56 d (6.5)
3,5	8.98 br d (6.3)[×6H]	9.02 d (6.8)	8.97 br d (6.6)[×6H]	8.95–9.25 m	9.02 br d (6.3)[×6H]	9.02 d (6.7)
N-Methyls	4.70 s	4.70 s				
N-Isopropyls			1.90 br d (6.2)[×18H] 5.37 m[×3H]	1.96 br d (6.2)[×18H] 5.41 m[×3H]		
N-Octyls					4.95 br t (7.3)[×6H] 1.20–1.43 m[×36H] 0.92 br t (6.4)[×9H]	4.94 br t (7.0)[×6H] 1.20–1.40 m[×36H] 0.93 br t (6.5)[×9H]
Aryl						
2		8.18 d (8.8)		8.25 d (8.1)		8.20 d (8.6)
3	7.70 d (8.4)	7.47 d (8.8)	7.66 d (8.6)	7.50 d (8.1)	7.72 br d (8.6)	7.50 d (8.6)
4	7.94 dt (8.4, 2.2)		7.89 dd (8.6, 7.1)		7.95 dt (8.6, 1.3)	
5	7.56 br t (8.4)	7.47 d (8.8)	7.52 dt (7.1, 2.3)	7.50 d (8.1)	7.58 t (7.54)	7.50 d (8.6)
6	8.02 dd (8.4, 2.2)	8.18 d (8.8)	8.00 dd (7.1, 2.3)	8.25 d (8.1)	8.03 dd (7.4, 1.3)	8.20 d (8.6)
***O*-Glucosyl**						
1	5.56 d (7.6)	5.95 d (7.8)	5.52 d (7.5)	5.97 br d (7.5)	5.56 d (7.9)	5.96 d (7.9)
2	3.79 dd (9.1, 7.6)	5.26 dd (9.5, 7.8)	3.75 dd (9.1, 7.5)	5.29 dd (9.3, 7.5)	3.80 dd (9.4, 7.9)	5.28 dd (9.5, 7.9)
3	4.94 t (9.1)	5.55 t (9.5)	4.84 t (9.1)	5.58 br t (9.3)	4.94 br t (9.4)	5.57 t (9.5)
4	4.53 t (9.1)	5.12 t (9.5)	4.43 t (9.1)	5.16 br t (9.3)	4.53 t (9.4)	5.15 t (9.6)
5	4.08–4.21 m	4.38–4.49 m	4.00–4.18 m	4.42–4.48 m	4.18–4.22 m	4.42–4.48 m
6_A	3.95 br d (11.3)	4.15 dd (12.4, 2.0)	3.85–3.98 m	4.21 dd (12.3, 3.3)	4.12 dd (11.6, 3.2)	4.19 dd (12.6, 2.3)
6_B	4.10 dd (11.3, 5.6)	4.33 dd (12.4, 4.8)	4.00–4.18 m	4.33 dd (12.3, 5.3)	3.96 dd (11.6, 5.2)	4.33 dd (12.2, 5.1)
***O*-Acetyls**						
	1.93 s	2.16 s	1.78 s	2.18 s	1.93 s	2.16 s
	1.83 s	2.05 s	1.41 s	2.07 s[×2]	1.84 s	2.06 s[×2]
	1.38 s	2.04 s	1.33 s	2.05 s	1.38 s	2.03 s
	–0.34 s	2.02 s	–0.40 s		–0.34 s	

[a]Assignments with the same superscript in one column may be interchanged.

upfield shift by −0.56 ppm in **4a** in contrast with those in **4b**, which occur at lower field by +0.29 ppm along with the 2,6-protons, displaced by only +0.12 ppm. Finally, the paramagnetic shifts associated with several osidic protons are more striking than those related to the above-mentioned nuclei. This is well illustrated by the marked dependence of H-1 and H-5, which are shifted downfield by +0.72 and +0.54 ppm, respectively, for **4a** and +0.61 and +0.40 ppm respectively for **4b**.

Replacement of the protected monoglucosyl substituent by a protected diglycosyl group has no significative consequence on the chemical shift values relative to the other parts of the glycosides. In comparison with monoglucosides **4a,b**, the behavior of the β-D-glucosyl protons of the (1→4) diglycoside-protected maltosides **5a,b** and lactosides **6a,b**, is similar except for the H-4 upfield shift due to the loss of the corresponding acetyl group replaced by the interglycosidic linkage (Table 2). As expected, the β-D-glucosyl protons are more shielded in the *ortho* compounds **5a** and **6a** than in the *para* homologues **5b** and **6b** because of the above-mentioned macrocycle ring current (Table 1). They are shifted upfield by ca. 0.2–1.4 ppm for maltoside **5a** and by ca. 0.1–0.9 ppm for lactoside **6a**, the highest Δδ values obviously corresponding to H-2. Shielding of the latter proton in maltoside **5a** (δ 3.72) and in lactoside **6a** (δ 4.32) seems also to be related to the orientation of the second sugar unit: α-glucose for maltoside **5a** and β-galactose for lactoside **6a**. Such a difference for the related proton in the two bioses is cancelled when there is no steric hindrance between the osidic part and the porphyrin core as indicated by the H-2 δ values of 5.16 ppm in maltoside **5b** and 5.18 ppm in lactoside **6b**.

In comparison with the spectra of the non-cationic series run in DMSO-d_6 (Table 1), only two sets of protons moved in the cationic group (Tables 2 and 3). Besides the expected lowfield displacement for the pyridinium nuclei H-2,6 (Δδ 0.30–0.45) and H-3,5 (Δδ 0.58–0.77) (See Experimental), all the β-pyrrolic protons generally exhibited a significative deshielding falling between 0.10 and 0.28 ppm. The most affected nuclei (H-12,13,17,18) were obviously those surrounded by two pyridiniumyl rings and, consequently, by the electron-withdrawing pyridinium nitrogens, which thus were prevented from increasing the electron density in the porphyrin macrocycle.

UV–visible

The data in Table 4 show that the visible absorption bands have positions that in a first approximation are identical to the corresponding non-glycosylated porphyrins even when the substituent is a disaccharidyl group. For the *para*-glycosylated porphyrins in the pyridyl series as well as in the alkylpyridinium series, the relative intensities of the Q(III) and Q(II) bands show an *etio* type ($\varepsilon_{III}/\varepsilon_{II} > 1$). These observations are in interesting contrast to *ortho*-glycosylated porphyrins for which normal pure *etio* spectra were not always observed. For neutral *ortho* peracetyl glycosylated porphyrins **4a**, **5a**, and **6a**, the ratio of $\varepsilon_{III}/\varepsilon_{II} < 1$ corresponds to pure *phyllo* type. For the other *ortho*-glycosylated porphyrins **7a–19a**, the ratio of $\varepsilon_{III}/\varepsilon_{II}$ is always lower than that of the corresponding *para* compound measured in the same solvent. Thus the spectra of *ortho*-glycosylated porphyrins tend toward *phyllo*-type porphyrins.

This phenomenon could result from steric interaction between the glycosyl substituents and the macrocycle, which would affect the solvation (17). However, a significant macrocyclic distortion (18) caused by the steric hindrance of the glycosylated substituents is strongly supported by these results.

Conclusions

In this paper we describe the synthesis and characterization of a new class of water-soluble porphyrins that can be considered as potential agents in cancer phototherapy. These cationic tetrapyrrolic macrocycles are *O*-glycosylated in order to increase cell membrane interactions. Substitutions in the *ortho* or *para* positions lead to further insights into cell membrane interaction. The various lipophilic substituents, such as methyl, isopropyl, and *n*-octyl, allow for increased penetrability of the porphyrins across the cell membrane.

The present strategy may be easily used for preparation of other cationic glycosylated porphyrins, which could interact more specifically with the cellular glycans. The PDT activity of these novel porphyrins is currently under investigation.

Experimental section

General methods

The UV–visible spectra were recorded on a Hewlett Packard 8452A spectrophotometer using 1 or 0.1 cm quartz cells. The rotatory dispersions were measured in chloroform at 22°C in a 10 cm cell with a Jasco (DIP-370) polarimeter. Melting points were determined by capillary tube apparatus and were not corrected. Proton NMR spectra were recorded on a Bruker AC 200 (200 MHz) or on Bruker 300 WM FT (300 MHz) instrument with tetramethylsilane as internal standard. The chemical shifts are given in ppm and coupling constants in Hz in the indicated solvent.

SIMS mass spectra were recorded on a time-of-flight instrument as reported previously (19). MALDI mass spectra were performed with a home-built linear time-of-flight instrument using a nitrogen laser (20). Samples were prepared by mixing equal volumes of the porphyrin solution (ca. 10^{-4} M in THF or H_2O) and a matrix solution (ca. 10^{-1} M 2,5-dihydroxybenzoic or cyano-4 hydroxycinnamic acid in THF or H_2O–acetonitrile 1:4 V/V). One microlitre of the final solution was deposited onto a stainless steel probe and introduced in the mass spectrometer.

FAB^+ mass spectra were performed on ZAB 2 -BEQ at the "Service Central d'Analyse" CNRS Solaize using *meta*-nitrobenzyl alcohol as matrix, and E.I mass spectra at the "Laboratoire Départemental d'Analyse" Limoges on a Shimadzu QP 1000 apparatus.

Elemental analyses were carried out by the "Service Régional de Microanalyse" Université Pierre et Marie Curie, Paris.

Chemicals

All solvents and reagents were purchased from Aldrich, Prolabo, or Janssen. Pyrrole was distilled under reduced pressure immediately before use. Acetic anhydride was distilled and kept over calcium chloride. DMF was distilled over CaH_2 under reduced pressure and kept over 4Å molecular sieves.

Chromatography

Analytical thin-layer chromatography (TLC) was performed on silica gel (Merck, $60F_{254}$) or PEI-Cellulose F (Merck). Col-

Table 3. ^{1}H NMR spectra of maltosides **8a,b** and **9a,b** in DMSO-d_6 (δ, ppm (*J*, Hz)).

H	8a	8b	9a	9b
Pyrrols				
2	8.77 d (4.8)	9.01 d (4.8)	8.82 d (4.8)	9.02 d (4.8)
3	9.00 d (4.8)	9.06 d (4.8)	9.03 d (4.8)	9.06 d (4.8)
7	8.97 d (4.8)	9.06 d (4.8)	9.02 d (4.8)	9.06 d (4.8)
8	8.83 d (4.8)	9.01 d (4.8)	8.90 d (4.8)	9.02 d (4.8)
12,13	9.14 s[a]	9.15 s	9.16 s[a]	9.15 s
17,18	9.12 s[a]	9.15 s	9.14 s[a]	9.15 s
NH	−3.02 s	−3.02 s	−3.05 s	−3.01 s
***N*-Alkyl pyridinium 4-yls**				
2,6	9.46 br d (4.8) [×4H] 9.43 br d (4.8) [×2H]	9.45 br d (6.1)	9.49 br d (5.9) [×4H] 9.46 br d (5.9) [×2H]	9.48 d (6.5)
3,5	8.97 br d (4.8)	8.99 br d (6.1)	8.99 br d (5.9)	8.99 d (6.5)
N-methyls	4.71 s	4.71 s	4.72 s	4.72 s
Aryl				
2		8.19 d (8.5)		8.19 d (8.5)
3	7.68 br d (8.0)	7.48 d (8.5)	7.69 br d (7.6)	7.47 d (8.5)
4	7.94 br t (7.7)		7.92 br t (7.6)	
5	7.56 br t (7.7)	7.48 d (8.5)	7.56 br t (7.6)	7.47 d (8.5)
6	8.02 br d (7.7)	8.19 d (8.5)	8.02 br d (7.6)	8.19 d (8.5)
***O*-glycosyl**				
1	5.52 d (7.9)	5.93 d (8.0)	5.49 d (8.0)	5.90 d (8.0)
2	3.70 br t (8.8)	5.16 br t (8.1)	4.29 br t (9.9)	5.22 dd (10.2, 7.9)
3	5.00 br t (9.7)	5.57 t (9.01)	4.81 t (9.2)	5.42 d (9.2)
4	3.57 br t (9.2)	3.98–4.48 m	3.46 br t (9.4)	3.98–4.25 m
5	3.80–4.40 m	3.98–4.48 m	3.65–4.10 m	3.98–4.25 m
6_A	3.80–4.40 m	4.54 br d (11.2)	3.65–4.10 m	4.46 br d (10.1)
6_B	4.06 dd (12.1, 4.6)	3.98–4.48 m	3.65–4.10 m	3.98–4.25 m
1′	4.99 br d (4.0)	5.38 d (3.5)	4.53 br d (8.0)	4.85 d (7.9)
2′	Under Me peak	4.93 dd (10.5, 3.5)	Under Me peak	4.92 br t (9.0)
3′	5.09 t (10.1)	5.27 t (9.9)	5.02 dd (10.1, 3.5)	5.21 dd (10.4, 2.5)
4′	4.87 t (9.6)	5.02 t (9.8)	5.09 br d (3.5)	5.28 br d (2.5)
5′	3.80–4.40 m	3.98–4.48 m	3.65–4.10 m	3.98–4.25 m
6′	3.80–4.40 m	3.98–4.48 m	3.65–4.10 m	3.98–4.25 m
***O*-Acetyls**				
	2.03 s	2.12 s	2.08 s	2.15 s
	1.95 s	2.10 s	1.99 s	2.13 s
	1.94 s	2.04 s [×3]	1.98 s	2.11 s
	1.89 s	1.99 s	1.84 s	2.06 s
	1.75 s	1.96 s	1.76 s	2.05 s
	1.22 s		1.39 s	2.04 s
	−0.37 s		−0.45 s	1.91 s

[a]Assignments with the same superscript in one column may be interchanged.

umn chromatography was carried out with silica gel 60ACC (15–40 μm) (Merck), or with Sephadex LH20 (Pharmacia) as stationary phase, preparative HPLC on reverse phase (Lichroprep RP18: 15–40 μm) (Merck). The following solvent systems were used as eluents: A: ethyl acetate – petroleum ether (1:1); B: ethyl acetate – petroleum ether (1:1) + 1% of 2-propanol; C: ethyl acetate – petroleum ether (2:1); D: chloroform–ethanol (95:5); E: methylene chloride – ethanol (95:5); F: acetic acid – pyridine (1:1); G: acetic acid – methanol–water (3:2:1); H: *n*-butanol – acetic acid – water (4:1:5) (upper phase); I: methanol–water (7:3); J: methanol–water (95:5); and K: acetone–water (9:1).

Table 4. UV–visible spectra of glycosylated porphyrins **4–19**.

Compound	λ_{nm} ($\varepsilon \times 10^{-4}$)					
	Soret bands	*Q*(IV)	*Q*(III)	*Q*(II)	*Q*(I)	ε (III)/ε (II)
4a[a]	418 (19.18)	512 (2.95)	546 (0.85)	588 (0.93)	642 (0.34)	0.91
4b[a]	418 (17.37)	514 (7.24)	548 (0.27)	588 (0.24)	644 (0.13)	1.12
5a[a]	414 (15.89)	514 (1.20)	548 (0.53)	588 (0.54)	644 (0.27)	0.98
5b[a]	418 (10.47)	514 (8.91)	548 (0.40)	588 (0.32)	644 (0.15)	1.23
6a[a]	416 (17.78)	512 (1.20)	546 (0.40)	586 (0.41)	642 (0.16)	0.98
6b[a]	418 (16.98)	514 (1.02)	548 (0.48)	590 (0.41)	644 (0.26)	1.17
7a[b]	426 (12.30)	516 (1.10)	552 (0.43)	590 (0.41)	644 (0.26)	1.02
7b[b]	424 (10.23)	516 (0.79)	554 (0.37)	558 (0.31)	646 (0.13)	1.20
8a[b]	424 (13.18)	516 (1.17)	554 (0.66)	588 (0.52)	644 (0.28)	1.26
8b[b]	426 (19.95)	516 (1.35)	558 (1.07)	590 (0.71)	644 (0.29)	1.51
9a[b]	424 (13.18)	516 (1.07)	554 (0.81)	592 (0.71)	646 (0.48)	1.15
9b[b]	424 (14.79)	516 (1.10)	556 (0.56)	588 (0.42)	646 (0.18)	1.35
10a[b]	426 (20.41)	516 (6.17)	554 (0.62)	590 (0.50)	646 (0.21)	1.24
10b[b]	424 (17.78)	516 (0.48)	550 (0.29)	590 (0.21)	648 (0.12)	1.35
11a[b]	426 (18.20)	516 (1.07)	558 (0.71)	588 (0.56)	644 (0.26)	1.26
11b[b]	426 (16.98)	518 (1.29)	554 (0.69)	592 (0.54)	648 (0.28)	1.29
12a[b]	414 (15.85)	512 (1.23)	544 (0.48)	588 (0.41)	642 (0.22)	1.17
12b[b]	416 (25.70)	512 (1.55)	548 (0.81)	592 (0.63)	644 (0.50)	1.29
13a[b]	414 (10.23)	512 (0.59)	546 (0.19)	586 (0.18)	640 (0.12)	1.05
13b[b]	416 (12.30)	512 (0.54)	546 (0.13)	588 (0.13)	642 (0.10)	1.07
14a[b]	414 (17.78)	512 (2.45)	546 (1.05)	586 (0.83)	642 (0.37)	1.26
14b[b]	416 (10.00)	512 (0.49)	548 (0.25)	588 (0.19)	644 (0.10)	1.35
15a[b]	424 (10.47)	520 (0.76)	560 (0.43)	584 (0.40)	642 (0.14)	1.10
15b[b]	428 (12.02)	518 (1.91)	556 (1.10)	592 (0.74)	650 (0.36)	1.48
16a[b]	426 (12.59)	518 (0.50)	558 (0.38)	586 (0.30)	644 (0.13)	1.26
16b[b]	426 (10.23)	518 (0.47)	550 (0.38)	590 (0.26)	650 (1.48)	1.45
17a[b]	424 (12.02)	516 (1.38)	552 (0.66)	588 (0.66)	648 (0.35)	1.00
17b[b]	426 (14.13)	518 (1.82)	554 (1.20)	592 (0.98)	650 (0.63)	1.23
18a[b]	424 (16.96)	518 (1.53)	556 (0.83)	588 (0.70)	642 (0.36)	1.18
18b[b]	426 (13.18)	518 (1.25)	556 (0.70)	588 (0.58)	646 (0.33)	1.20
19a[b]	424 (17.36)	516 (1.33)	552 (0.80)	592 (0.65)	648 (0.46)	1.19
19b[b]	426 (15.46)	518 (1.10)	554 (0.65)	590 (0.46)	648 (0.23)	1.40

[a]In CH_2Cl_2.
[b]In $(CH_3)_2CO:H_2O$ (1:1).

Synthesis

*2-(2,3,4,6-Tetra-*O*-acetyl-*β*-D-glucopyranosyloxy)-benzaldehyde (**1a**)*

Acetylation of salicylaldehyde β-D-glucoside (helicin) was carried out according to the literature (21). Helicin (500 mg, 1.76 mmol) and 1.34 mL (14.2 mmol) of acetic anhydride in 1 mL of pyridine were stirred at 0°C for 1.5 h. After evaporation of the solvent, the crude product was dissolved in ethyl acetate (40 mL) and washed several times with ice water (3 × 50 mL). The organic extract was then dried on $MgSO_4$, filtered, and concentrated under reduced pressure. The crude product was recrystallized in ethanol to give 720 mg, (90%) of **1a**. R_f 0.41 (SiO_2, eluent: A); mp 142°C (lit.(22) mp 142°C); $[\alpha]_D$ −30 (*c* = 0.5, $CHCl_3$). ^{1}H NMR (C_6D_6) δ: 10.60 (s, 1H, CHO), 7.91 (dd, 1H, *J* = 7.8 and 1.9 Hz, H-6 Ar), 7.08 (dt, 1H, *J* = 7.4 and 1.9 Hz, H-4 Ar), 6.89 (dd, 1H, *J* = 8.3 and 0.6 Hz, H-3 Ar), 6.74 (dt, 1H, *J* = 7.9 and 0.6 Hz, H-5 Ar), 5.46 (dd, 1H, *J* = 9.0 and 7.9 Hz, H-2 ose), 5.37 (t, 1H, *J* = 9.8 Hz, H-3 ose), 5.22 (t, 1H, *J* = 9.8 Hz, H-4 ose), 4.68 (d, 1H, *J* = 7.5, H-1 ose), 4.16 (dd, 1H, *J* = 12.3 and 5.1 Hz, H-6_A ose), 3.97 (dd, 1H, *J* = 12.3 and 2.5 Hz, H-6_B ose), 3.23 (ddd, 1H, *J* = 7.6, 5.1 and 2.5 Hz, H-5 ose), four singlets integrating each for three protons at 1.69, 1.68, 1.66, and 1.65 (4 AcO). MS (EI) *m/z*: 452 M^+, 409 $(M - AcO)^+$, 122 $(M - GlucOAc + H)^+$. Anal. calcd. for $C_{21}H_{24}O_{11}$: C 55.75, H 5.31; found: C 55.66, H 5.42.

*4-(2,3,4,6-Tetra-*O*-acetyl-*β*-D-glucopyranosyloxy)-benzaldehyde (**1b**)*

Glucosylation of *p*-hydroxylbenzaldehyde was carried out according to the literature (23). 2,3,4,6-Tetra-*O*-acetyl-α-D-glucopyranosyl bromide (800 mg, 1.94 mmol, 1 equiv.) and *p*-hydroxybenzaldehyde (610 mg, 5 mmol, 2.6 equiv.) were mixed in 40 mL of acetone and 10 mL of (7%) aqueous NaOH and then stirred at room temperature for 24 h. Afterward, the solution was added to 100 mL of ice water and stirred for 1 h. The precipitated crude product was then recrystallized from MeOH–H_2O (1:1); 350 mg (40%) of **1b** were obtained. R_f 0.31

(SiO_2, eluent: A); mp 144°C (lit.(21) mp 144–145°C); $[\alpha]_D$ −33.5 (c = 0.5, $CHCl_3$). ^1H NMR ($CDCl_3$) δ: 9.90 (s, 1H, CHO), 7.85 (d, 2H, J = 8.5 Hz, H-3,5 Ar), 7.10 (d, 2H, J = 8.5 Hz, H-2,6 Ar), 5.20–5.40 (m, 4H, H-1, H-2, H-3, and H-4 ose), 3.90 (ddd, 1H, J = 10.0, 5.6, and 2.6 Hz, H-5 ose), 4.15 (dd, 1H, J = 12.0 and 5.6 Hz, H-6_A ose), 4.27 (dd, 1H, J = 12.0 and 2.6 Hz, H-6_B ose), three singlets at 2.06 (×3H), 2.05 (×6H), 2.03 (×3H) (AcO). MS (EI) m/z: 452 $(M + H)^+$, 121 $(M - GlucOAc)^+$. Anal. calcd. for $C_{21}H_{24}O_{11}$: C 55.75, H 5.31; found: C 55.61, H 5.38.

General procedure for preparation of maltosyl and lactosyl benzaldehyde

All per-*O*-acetylglycobiosylbromides were prepared from peracetylated compounds according to the standard procedure (24) by using 33% HBr in acetic acid. Reaction times do not exceed 30 min (23). The crude products were used without further purification. To a solution of acetylated α-glycobiosylbromide (3 g, 4.29 mmol, 1 equiv.) and tetraoctylammonium bromide (2.34 g, 4.29 mmol, 1 equiv.) in CH_2Cl_2 (14.5 mL) were added 1 M Na_2CO_3 aqueous solution (14.5 mL) and hydroxybenzaldehyde (1.37 mL, 13 mmol, 3 equiv.). The two-phase reaction mixture was vigorously stirred at room temperature for 2.5 h. The complete conversion was shown by TLC (SiO_2, eluent C). CH_2Cl_2 (50 mL) was then added and the organic phase was successively washed with 1 M NaOH aqueous solution (50 mL), water (2 × 100 mL), and a saturated solution of NaCl (40 mL). The combined organic extracts were then dried on $MgSO_4$, filtered, and concentrated under reduced pressure to afford crude products. The purification of the products was achieved by using column chromatography (SiO_2, eluent B) and then by preparative high-pressure liquid chromatography (HPLC) using I and J as eluents for maltosyl and lactosyl compounds, respectively.

*2-(2,3,6,2′,3′,4′,6′-Hepta-*O*-acetyl-β-D-maltosyloxy)benzaldehyde (**2a**)*: 1.11 g, (35%); R_f 0.40 (SiO_2, eluent B); mp 141–143°C; $[\alpha]_D$ +19.6 (c = 0.35, $CHCl_3$). ^1H NMR ($CDCl_3$) δ: 10.3 (s, 1H, CHO), 7.85 (dd, 1H, J = 7.7 and 1.6 Hz, H-6 Ar), 7.56 (ddd, 1H, J = 8.4, 7.8, and 1.8 Hz, H-4 Ar), 7.24 (dd, 1H, J = 8.4 and 1.0 Hz, H-3 Ar), 7.14 (br t, 1H, J = 7.8 Hz, H-5 Ar), 5.43 (d, 1H, J = 4.0 Hz, H-1′ ose), 5.37 (t, 1H, J = 10.7 Hz, H-3′), 5.35 (t, 1H, J = 8.1 Hz, H-3 ose), 5.24 (d, 1H, J = 7.4 Hz, H-1 ose), 5.17 (d, J = 7.4 Hz, H-2 ose), 5.04 (t, 1H, J = 9.7 Hz, H-4′ ose), 4.86 (dd, 1H, J = 10.5 and 4.0 Hz, H-2′ ose), 4.50 (dd, 1H, J = 12.1 and 2.8 Hz, H-6a ose), 4.25 (ddd, 1H, J = 6.6, 3.9, and 1.4 Hz, H-5 ose), 4.20–4.30 (m, 1H, H-6_B ose), 3.79–4.10 (m, 2H, H-$6'_A$ and H-$6'_B$ ose), 3.84–3.96 (m, 1H, H-5′ ose), four singlets at 2.09 (3H), 2.07 (3H), 2.04 (9H), 2.02 (3H), 2.00 (3H)(CH_3CO). MS (EI) m/z: 741 M^+, 410 $(M - GlucOAc)^+$, 121 $(M - MaltOAc)^+$. Anal. calcd. for $C_{33}H_{40}O_{19}$: C 53.51, H 5.41; found: C 53.55, H 5.49.

*4-(2,3,6,2′,3′,4′,6′-Hepta-*O*-acetyl-β-D-maltosyloxy)benzaldehyde (**2b**)*: 1.58 g, (50%); R_f 0.36 (SiO_2, eluent B); mp 131–132°C; $[\alpha]_D$ +44.27 (c = 0.38, $CHCl_3$). ^1H NMR (C_6D_6) δ: 9.62 (s, 1H, CHO), 7.52 (d, 1H, J = 8.7 Hz, H-2,6 Ar), 6.82 (d, 1H, J = 8.7, H-3,5 Ar), 5.85 (dd, 1H, J = 10.3 and 9.8 Hz, H-3′ ose), 5.48 (d, 1H, J = 3.9 Hz, H-1′ ose), 5.38 (t, 1H, J = 9.1 Hz, H-3), 5.35 (t, 1H, J = 10.0 Hz, H-4′ ose), 5.25 (dd, 1H, J = 9.2 and 7.6 Hz, H-2 ose), 5.04 (dd, 1H, J = 10.6 and 3.9 Hz, H-2′ ose), 4.86 (d, 1H, J = 7.6 Hz, H-1 ose), 4.41 (dd, 1H, J = 12.4 and 3.9 Hz, H-6a ose), 4.32 (d, 1H, J = 12.0 and 2.4 Hz, H-6b ose), 4.26 (d, 1H, J = 12.1 and 2.8 Hz, H-6′b ose), 4.12–4.20 (m, 1H, H-5′ ose), 4.09 (dd, 1H, J = 12.2 and 4.9 Hz, H-6′b ose), 3.83 (dd, 1H, J = 9.4 and 8.7 Hz, H-4 ose), 2.84 (ddd, 1H, J = 7.5, 4.5, and 2.7 Hz, H-5 ose), six singlets at 1.96 (3H), 1.82 (3H), 1.80 (3H), 1.73 (3H), 1.70 (3H), 1.67 (6H) (CH_3CO). MS (EI) m/z: 741 M^+, 410 $(M - GlucOAc)^+$, 121 $(M - MaltOAc)^+$. Anal. calcd. for $C_{33}H_{40}O_{19}$: C 53.51, H 5.41; found: C 53.46, H 5.59.

*2-(2,3,6,2′,3′,4′,6′-Hepta-*O*-acetyl-β-D-lactosyloxy)benzaldehyde (**3a**)*: 1.27 g, (40%); R_f 0.34 (SiO_2, eluent B); mp 125–126°C; $[\alpha]_D$ −20.6 (c = 0.38, $CHCl_3$). ^1H NMR (DMSO-d_6) δ: 10.15 (s, 1H, CHO), 7.71 (br d, 1H, J = 7.4 Hz, H-6 Ar), 7.69 (br t, 1H, J = 7.4, H-4 Ar), 7.23 (br d, 1H, J = 7.4 Hz, H-3 Ar), 7.20 (br t, 1H, J = 7.4 Hz, H-5 Ar), 5.64 (d, 1H, J = 7.9 Hz, H-1 ose), 5.33 (t, 1H, J = 9.1 Hz, H-3), 5.24 (d, 1H, J = 3.4 Hz, H-4′ ose), 5.17 (dd, 1H, J = 9.7 and 3.5 Hz, H-3′ ose), 5.07 (dd, 1H, J = 9.7 and 8.1 Hz, H-1 ose), 4.86 (br t, 1H, J = 9.5 Hz, H-2′ ose), 4.78 (d, 1H, J = 7.9 Hz, H-1′ ose), 4.37 (br d, 1H, J = 10.3 Hz, H-6a ose), 3.98–4.28 (m, 5H, H-5, H-6b, H-5′, H-6′a, and H-6′b oses), five singlets at 2.10 (3H), 2.04 (3H), 2.01 (12H), 1.90 (3H)(CH_3CO). MS (EI) m/z: 741 M^+, 698 $(M - CH_3CO)^+$, 121 $(M - LactOAc)^+$. Anal. calcd. for $C_{33}H_{40}O_{19}$: C 53.51, H 5.41; found: C 53.12, H 5.45.

*4-(2,3,6,2′,3′,4′,6′-Hepta-*O*-acetyl-β-D-lactosyloxy)benzaldehyde (**3b**)*: 1.7 g, (54%); R_f 0.32 (SiO_2, eluent B); mp 86°C; $[\alpha]_D$ −26.55 (c = 0.59, $CHCl_3$). ^1H NMR ($CDCl_3$) δ: 9.93 (s, 1H, CHO), 7.85 (d, 1H, J = 8.5 Hz, H-2,6 Ar), 7.09 (d, 1H, J = 8.5, H-3,5 Ar), 5.37 (d, 1H, J = 3.1 Hz, H-4′ ose), 5.33 (t, 1H, J = 8.4 Hz, H-3 ose), 5.26 (dd, 1H, J = 10.7 and 7.5 Hz, H-2), 5.23 (br d, 1H, J = 8.0 Hz, H-1 ose), 5.14 (dd, 1H, J = 10.0 and 7.7 Hz, H-2′ ose), 4.99 (dd, 1H, J = 10.3 and 3.1 Hz, H-3′ ose), 4.53 (br d, 1H, J = 7.8 Hz, H-1′ ose), 4.52 (br d, 1H, J = 11.6 Hz, H6a ose), 4.17 (dd, 1H, J = 11.0 and 5.9 Hz, H-6′a ose), 4.07 (br d, 1H, J = 11.4 Hz, H-6b ose), 4.17 (m, 1H, H-6′b ose), 3.80–3.95 (m, 3H, H-4, H-5, and H-5′ ose), four singlets at 2.16 (3H), 2.09 (3H), 2.07 (12H), 1.98 (3H) (CH_3CO). MS (EI) m/z: 741 M^+, 698 $(M - CH_3CO)^+$, 121 $(M - LactOAc)^+$. Anal. calcd. for $C_{33}H_{40}O_{19}$: C 53.51, H 5.41; found: C 53.49, H 5.46.

*General procedure for formation of pyridyl porphyrins **4a,b**, **5a,b**, and **6a,b***

In a typical experiment, a mixture of per-*O*-acetyl glycosylated benzaldehyde (3.3 mmol) in propionic acid (30 mL) and acetic anhydride (3 mL) was heated under reflux with vigorous stirring. To this solution was added slowly 4-pyridinecarboxaldehyde (2 equiv.) and freshly distilled pyrrole (2.6 equiv.). After 1.5 h, the solvent was evaporated to dryness and the crude product was purified by chromatography on SiO_2 using $CHCl_3$ and then D as eluents.

*5-[2-(2,3,4,6-Tetra-*O*-acetyl-β-D-glucopyranosyloxy)phenyl]-10,15,20 tris(4-pyridyl)porphyrin (**4a**)*: **1a** (1.5 g, 3.3 mmol), 4-pyridinecarboxaldehyde (0.635 mL, 6.6 mmol), and pyrrole (0.610 mL, 8.8 mmol) afforded pure product **4a** 150 mg, (6%); R_f 0.22 (SiO_2, eluent D). UV–visible (see Table 4). ^1H NMR (see Table 1). MS (SIMS positive) m/z: 965 $(M + H)^+$,

634 (M − GluOAc + H)$^+$ and SIMS (negative) *m/z*: 963 (M − H)$^-$, 632 (M − GlucOAc − H)$^-$. Anal. calcd. for $C_{55}H_{45}N_7O_{10}\cdot 0.5H_2O$: C 67.89, H 4.77, N 10.08; found: C 67.82, H 4.74, N 10.01.

*5-[4-(2,3,4,6-Tetra-*O*-acetyl-*β*-D-glucopyranosyloxy)phenyl]-10,15,20 tris(4-pyridyl)porphyrin (**4b**)*: **1b** (1.5 g, 3.3 mmol), 4-pyridinecarboxaldehyde (0.635 mL, 6.6 mmol), and pyrrole (0.610 mL, 8.8 mmol) gave **4b** 150 mg, (7%); R_f 0.18 (SiO_2, eluent D). UV–visible (see Table 4). ^{1}H NMR (see Table 1). MS (SIMS positive) *m/z*: 965 (M + H)$^+$, 634 (M − GluOAc + H)$^+$ and SIMS (negative) *m/z*: 963 (M − H)$^-$, 632 (M − GlucOAc − H)$^-$. Anal. calcd. for $C_{55}H_{45}N_7O_{10}\cdot H_2O$: C 67.27, H 4.82, N 9.98; found: C 67.19, H 4.80, N 9.95.

*5-[2-(2,3,6,2′,3′,4′,6′-Hepta-*O*-acetyl-*β*-D-maltosyloxy)phenyl]-10,15,20 tris(4-pyridyl)porphyrin (**5a**)*: **2a** (2.45 g, 3.3 mmol), pyridinecarboxaldehyde (0.635 mL, 6.6 mmol), and pyrrole (0.610 mL, 8.8 mmol) gave **5a** 166 mg, (6%); R_f 0.33 (SiO_2, eluent E). UV–visible (see Table 4). ^{1}H NMR (see Table 1). MS (SIMS positive) *m/z*: 1253 (M + H)$^+$, 634 (M − MaltOAc + H)$^+$ and SIMS (negative) *m/z*: 1251 (M − H)$^-$, 632 (M − MaltOAc − H)$^-$. Anal. calcd. for $C_{67}H_{61}N_7O_{18}\cdot H_2O$: C 63.35, H 5.00, N 7.72; found: C 62.85, H 4.93, N 7.22.

*5-[4-(2,3,6,2′,3′,4′,6′-Hepta-*O*-acetyl-*β*-D-maltosyloxy)phenyl]-10,15,20 tris(4-pyridyl)porphyrin (**5b**)*: **2b** (2.45 g, 3.3 mmol), pyridinecarboxaldehyde (0.635 mL, 6.6 mmol), and pyrrole (0.610 mL, 8.8 mmol) gave **5b** 193 mg, (7%); R_f 0.28 (SiO_2, eluent E). UV–visible (see Table 4). ^{1}H NMR (see Table 1). MS (SIMS positive) *m/z*: 1253 (M + H)$^+$, 634 (M − MaltOAc + H)$^+$ and SIMS (negative) *m/z*: 1251 (M − H)$^-$, 632 (M − MaltOAc − H)$^-$. Anal. calcd. for $C_{67}H_{61}N_7O_{18}\cdot 2H_2O$: C 62.47, H 5.09, N 7.61; found: C 61.98, H 4.89, N 7.15.

*5-[2-(2,3,6,2′,3′,4′,6′-Hepta-*O*-acetyl-*β*-D-lactosyloxy)phenyl]-10,15,20 tris(4-pyridyl)porphyrin (**6a**)*: **3a** (2.45 g, 3.3 mmol), pyridinecarboxaldehyde (0.635 mL, 6.6 mmol), and pyrrole (0.610 mL, 8.8 mmol) gave **6a** 193 mg (6%); R_f 0.31 (SiO_2, eluent E). UV–visible (see Table 4). ^{1}H NMR (see Table 1). MS (SIMS positive) *m/z*: 1253 (M + H)$^+$, 634 (M − LactOAc + H)$^+$ and SIMS (negative) *m/z*: 1251 (M − H)$^-$, 632 (M − LactOAc − H)$^-$. Anal. calcd. for $C_{67}H_{61}N_7O_{18}\cdot 2H_2O$: C 62.47, H 5.09, N 7.61; found: C 62.23, H 5.12, N 7.69.

*5-[4-(2,3,6,2′,3′,4′,6′-Hepta-*O*-acetyl-*β*-D-lactosyloxy)phenyl]-10,15,20 tris(4-pyridyl)porphyrin (**6b**)*: (**3b**) (2.45 g, 3.3 mmol), pyridinecarboxaldehyde (0.635 mL, 6.6 mmol), and pyrrole (0.610 mL, 8.8 mmol) gave **6b**, 193 mg (7%); R_f 0.25 (SiO_2, eluent E). UV–visible (see Table 4). ^{1}H NMR (see Table 1). MS (SIMS positive) *m/z*: 1253 (M + H)$^+$, 634 (M − LactOAc + H)$^+$ and SIMS (negative) *m/z*: 1251 (M − H)$^-$, 632 (M − LactOAc − H)$^-$. Anal. calcd. for $C_{67}H_{61}N_7O_{18}\cdot 0.5H_2O$: C 63.80, H 4.95, N 7.77; found: C 63.95, H 4.65, N 7.67.

General method for alkylation of pyridyl porphyrins ***4a,b – 6a,b***

To a stirred solution of porphyrins **4a,b**, **5a,b**, or **6a,b** in freshly distilled DMF was added a large excess of alkyl iodide and the reaction mixture was heated at 40°C for 3 h for methylation and at 100°C for 12 h and 24 h for isopropylation and *n*-octylation, respectively. The reaction progress was monitored using TLC. After the reactions were complete, the trimethyl and triisopropyl pyridinium porphyrins **7a,b**, **8a,b**, **9a,b**, and **10a,b** were precipitated with diethyl ether. After filtration the compounds were dissolved in methanol and precipitated again with diethyl ether. The compounds were then washed several times with diethyl ether and by CH_2Cl_2 for **7a,b** and **10a,b**. All the products were dried under reduced pressure. For trisoctyl derivatives **11a,b**, DMF was removed under reduced pressure, coevapored with dry toluene, and the resulting compound was dissolved in *n*-BuOH–AcOH–H_2O (4:1:5) (upper phase) and then extracted with diethyl ether.

*5-[(2-(2,3,4,6,-Tetra-*O*-acetyl-*β*-D-glucopyranosyloxy)phenyl)-10,15,20 tris(4-*N*-methylpyridiniumyl)]porphyrin, triiodide (**7a**)*: **4a** (20 mg, 0.021 mmol) and 1.3 mL of methyliodide gave 25 mg of **7a** (90%); R_f 0.3 (SiO_2, eluent G). UV–visible (see Table 4). ^{1}H NMR (see Table 2). MS (FAB$^+$) *m/z*: 1010 (M + H)$^+$, 994 (M − CH_3)$^+$, 979 (M − $2CH_3$)$^+$, 964 (M − $3CH_3$)$^+$. Anal. calcd. for $C_{58}H_{54}N_7O_{10}I_3\cdot 3H_2O$: C 48.25, H 4.19, N 6.79; found: C 48.19, H 4.23, N 6.69.

*5-[(4-(2,3,4,6,-Tetra-*O*-acetyl-*β*-D-glucopyranosyloxy)phenyl)-10,15,20 tris(4-*N*-methylpyridiniumyl)]porphyrin, triiodide (**7b**)*: **4b** (20 mg, 0.021 mmol) and 1.3 mL of methyliodide gave 26 mg of **7b** (94%); R_f 0.27 (SiO_2, eluent G). UV–visible (see Table 4). ^{1}H NMR (see Table 2). MS (FAB$^+$) *m/z*: 1010 (M + H)$^+$, 994 (M − CH_3)$^+$, 979 (M − $2CH_3$)$^+$, 964 (M − CH_3)$^+$. Anal. calcd. for $C_{58}H_{54}N_7O_{10}I_3\cdot 4H_2O$: C 47.65, H 4.27, N 6.71; found: C 47.33, H 4.20, N 6.77.

*5-[(2-(2,3,6,2′,3′,4′,6′-Hepta-*O*-acetyl-*β*-D-maltosyloxy)phenyl)-10,15,20 tris(4-*N*-methylpyridiniumyl)]porphyrin, triiodide (**8a**)*: **5a** (20 mg, 0.016 mmol) and 1.5 mL of methyliodide gave 24 mg of **8a** (90%); R_f 0.75 (cellulose, eluent H). UV–visible (see Table 4). ^{1}H NMR (see Table 3). MS (FAB$^+$) *m/z*: 1298 (M + H)$^+$, 1282 (M − CH_3)$^+$, 1267 (M − $2CH_3$)$^+$, 1252 (M − $3CH_3$)$^+$. Anal. calcd. for $C_{70}H_{70}N_7O_{18}I_3\cdot 2.5H_2O$: C 48.79, H 4.39, N 5.69; found: C 48.66, H 4.28, N 5.72.

*5-[(4-(2,3,6,2′,3′,4′,6′-Hepta-*O*-acetyl-*β*-D-maltosyloxy)phenyl)-10,15,20 tris(4-*N*-methylpyridiniumyl)]porphyrin, triiodide (**8b**)*: **5b** (20 mg, 0.016 mmol) and 1.5 mL of methyliodide gave 25 mg of **8b** (93%); R_f 0.70 (cellulose, eluent H). UV–visible (see Table 4). ^{1}H NMR (see Table 3). MS (FAB$^+$) *m/z*: 1298 (M + H)$^+$, 1282 (M − CH_3)$^+$, 1267 (M − $2CH_3$)$^+$, 1252 (M − $3CH_3$)$^+$. Anal. calcd. for $C_{70}H_{70}N_7O_{18}I_3\cdot 4H_2O$: C 48.04, H 4.49, N 5.60; found: C 47.99, H 4.55, N 5.45.

*5-[(2-(2,3,6,2′,3′,4′,6′-Hepta-*O*-acetyl-*β*-D-lactosyloxy)phenyl)-10,15,20 tris(4-*N*-methylpyridiniumyl)]porphyrin, triiodide (**9a**)*: **6a** (20 mg, 0.016 mmol) and 1.5 mL of methyliodide gave 24 mg of **9a** (90%); R_f 0.68 (cellulose, eluent H). UV–visible (see Table 4). ^{1}H NMR (see Table 3). MS (FAB$^+$) *m/z*: 1298 (M + H)$^+$, 1282 (M − CH_3)$^+$, 1267 (M − $2CH_3$)$^+$, 1252 (M − $3CH_3$)$^+$. Anal. calcd. for $C_{70}H_{70}N_7O_{18}I_3\cdot 5H_2O$: C 47.55, H 4.56, N 5.55; found: C 47.68, H 4.72, N 5.45.

*5-[(4-(2,3,6,2',3',4',6'-Hepta-*O*-acetyl-*β*-D-lactosyloxy)phenyl)-10,15,20 tris(4-N-methylpyridiniumyl)]porphyrin, triiodide (**9b**)*: **6b** (20 mg, 0.016 mmol) and 1.5 mL of methyliodide gave 25 mg of **9a** (93%); R_f 0.63 (cellulose, eluent H). UV–visible (see Table 4). ^{1}H NMR (see Table 3). MS (FAB$^+$) *m/z*: 1298 (M + H)$^+$, 1282 (M − CH_3)$^+$, 1267 (M − $2CH_3$)$^+$, 1252 (M − $3CH_3$)$^+$. Anal. calcd. for $C_{70}H_{70}N_7O_{18}I_3 \cdot 3.5H_2O$: C 48.29, H 4.46, N 5.63; found: C 48.09, H 4.33, N 5.80.

*5-[(2-(2,3,4,6-Tetra-*O*-acetyl-*β*-D-glucopyranosyloxy)phenyl)-10,15,20 tris(4-N-isopropylpyridiniumyl)]porphyrin, triiodide (**10a**)*: **4a** (10 mg, 0.01 mmol) and 1 mL of isopropyliodide gave 14 mg of **10a** (93%); R_f 0.80 (cellulose, eluent F). UV–visible (see Table 4). ^{1}H NMR (see Table 2). MS (FAB$^+$) *m/z*: 1094 (M + H)$^+$, 1050 (M − iPr)$^+$, 1007 (M − 2iPr)$^+$, 964 (M − 3iPr)$^+$. Anal. calcd. for $C_{64}H_{66}N_7O_{10}I_3 \cdot 4.5H_2O$: C 49.43, H 4.86, N 6.31; found: C 49.32, H 4.56, N 6.74.

*5-[(4-(2,3,4,6-Tetra-*O*-acetyl-*β*-D-glucopyranosyloxy)phenyl)-10,15,20 tris(4-N-isopropylpyridiniumyl)]porphyrin, triiodide (**10b**)*: **4b** (15 mg, 0.016 mmol) and 1.5 mL of isopropyliodide gave 21 mg of **10b** (93%); R_f 0.75 (cellulose, eluent F). UV–visible (see Table 4). ^{1}H NMR (see Table 2). MS (FAB$^+$) *m/z*: 1094 (M + H)$^+$, 1050 (M − iPr)$^+$, 1007 (M − 2iPr)$^+$, 964 (M − 3iPr)$^+$. Anal. calcd. for $C_{64}H_{66}N_7O_{10}I_3 \cdot 6H_2O$: C 48.59, H 4.97, N 6.20; found: C 48.02, H 4.85, N 6.54.

*5-[(2-(2,3,4,6-Tetra-*O*-acetyl-*β*-D-glucopyranosyloxy)phenyl)-10,15,20 tris(4-N-n-octylpyridiniumyl)]porphyrin, triiodide* (**11a**): **4a** (20 mg, 0.021 mmol) was reacted with 3.8 mL of *n*-octyliodide. The crude compound was dissolved in 10 mL of *n*-BuOH–AcOH–H_2O (4:1:5) and extracted with 40 mL of diethyl ether to give 26 mg of **11a** (76%); R_f 0.27 (SiO_2, eluent H). UV–visible (see Table 4). ^{1}H NMR (see Table 2). MS (FAB$^+$) *m/z*: 1304 (M + H)$^+$, 1190 (M − *n*-oct)$^+$, 1077 (M − 2*n*-oct)$^+$, 964 (M − 3*n*-oct)$^+$. Anal. calcd. for $C_{79}H_{96}N_7O_{10}I_3 \cdot 6H_2O$: C 52.94, H 6.07, N 5.47; found: C 52.88, H 5.98, N 5.44.

*5-[(4-(2,3,4,6-Tetra-*O*-acetyl-*β*-D-glucopyranosyloxy)phenyl)-10,15,20 tris(4-N-n-octylpyridiniumyl)]porphyrin, triiodide (**11b**)*: **4b** (15 mg, 0.016 mmol) and 3 mL of *n*-octyliodide were reacted. The crude compound was dissolved in 8 mL of *n*-BuOH–AcOH–H_2O (4:1:5) and extracted with 30 mL of diethyl ether to give 21 mg of **11b** (80%); R_f 0.20 (SiO_2, eluent H). UV–visible (see Table 4). ^{1}H NMR (see Table 2). MS (FAB$^+$) *m/z*: 1304 (M + H)$^+$, 1190 (M − *n*-oct)$^+$, 1077 (M − 2*n*-oct)$^+$, 964 (M − 3*n*-oct)$^+$. Anal. calcd. for $C_{79}H_{96}N_7O_{10}I_3 \cdot 7H_2O$: C 52.41, H 6.12, N 5.42; found: C 52.36, H 6.09, N 5.14.

*General procedure for deacetylation of compounds **4–11***

Ten milligrams of protected mono (**4**, **7**, **10**, and **11**) or disaccharide (**5**, **6**, **8**, and **9**) compounds were dissolved, respectively, at 0°C in 15 mL or 30 mL of Et_3N–MeOH–H_2O (10:10:1) and the reaction mixtures were stirred vigorously for 24 h. Deacetylations were followed by TLC. After complete deacetylation the solvent was evaporated and passed through a Sephadex column using methanol as eluent. The products were then precipitated from methanol–ether (1:5).

*5-[2-(β-D-Glucopyranosyloxy)phenyl]-10,15,20 tris(4-pyridyl)porphyrin (**12a**)*: 8 mg (96%); R_f 0.75 (SiO_2, eluent F). UV–visible (see Table 4). MS (MALDI) *m/z*: 797 (M + H)$^+$. Anal. calcd. for $C_{47}H_{37}N_7O_6 \cdot 5H_2O$: C 63.72, H 5.35, N 11.06; found: C 63.70, H 5.23, N 11.15.

*5-[4-(β-D-Glucopyranosyloxy)phenyl]-10,15,20 tris(4-pyridyl)porphyrin (**12b**)*: 8 mg (96%); R_f 0.72 (SiO_2, eluent F). UV–visible (see Table 4). MS (MALDI) *m/z*: 797 (M + H)$^+$. Anal. calcd. for $C_{47}H_{37}N_7O_6 \cdot 3.5H_2O$: C 65.72, H 5.16, N 11.42; found: C 65.88, H 5.03, N 11.58.

*5-[2-(β-D-Maltosyloxy)phenyl]-10,15,20 tris(4-pyridyl)porphyrin (**13a**)*: 7 mg (92%); R_f 0.72 (cellulose, eluent H). UV–visible (see Table 4). MS (MALDI) *m/z*: 959 (M + H)$^+$. Anal. calcd. for $C_{53}H_{47}N_7O_{11} \cdot 6H_2O$: C 59.71, H 5.58, N 9.20; found: C 59.50, H 5.82, N 9.05.

*5-[4-(β-D-Maltosyloxy)phenyl]-10,15,20 tris(4-pyridyl)]porphyrin (**13b**)*: 7 mg (92%); R_f 0.67 (cellulose, eluent H). UV–visible (see Table 4). MS (MALDI) *m/z*: 959 (M + H)$^+$. Anal. calcd. for $C_{53}H_{47}N_7O_{11} \cdot 3H_2O$: C 62.90, H 5.28, N 9.69; found: C 63.02, H 5.12, N 9.52.

*5-[2-(β-D-Lactosyloxy)phenyl]-10,15,20 tris(4-pyridyl)]porphyrin (**14a**)*: 7 mg (92%); R_f 0.85 (cellulose, eluent H). UV–visible (see Table 4). MS (MALDI) *m/z*: 959 (M + H)$^+$. Anal. calcd. for $C_{53}H_{47}N_7O_{11} \cdot 8H_2O$: C 57.76, H 5.76, N 8.90; found: C 57.48, H 5.82, N 8.55.

*5-[4-(β-D-Lactosyloxy)phenyl]-10,15,20 tris(4-pyridyl)porphyrin (**14b**)*: 7 mg (92%); R_f 0.30 (SiO_2, eluent H). UV–visible (see Table 4). MS (MALDI) *m/z*: 959 (M + H)$^+$. Anal. calcd. for $C_{53}H_{47}N_7O_{11} \cdot 5H_2O$: C 60.74, H 5.48, N 9.35; found: C 60.15, H 5.24, N 9.56.

*5-[(2-(β-D-Glucopyranosyloxy)phenyl)-10,15,20 tris(4-N-methylpyridiniumyl)]porphyrin, triiodide (**15a**)*: 8 mg (91%); R_f 0.18 (SiO_2, eluent F). UV–visible (see Table 4). MS (MALDI) *m/z*: 841 (M − $3I^-$)$^+$. Anal. calcd. for $C_{50}H_{46}N_7O_6I_3 \cdot 10H_2O$: C 42.84, H 4.75, N 6.99; found: C 42.52, H 4.83, N 6.55.

*5-[(4-(β-D-Glucopyranosyloxy)phenyl)-10,15,20 tris(4-N-methylpyridiniumyl)]porphyrin, triiodide (**15b**)*: 8 mg (91%); R_f 0.14 (SiO_2, eluent F). UV–visible (see Table 4). MS (MALDI) *m/z*: 841 (M − $3I^-$)$^+$. Anal. calcd. for $C_{50}H_{46}N_7O_6I_3 \cdot 7.5H_2O$: C 44.26, H 4.53, N 7.23; found: C 44.35, H 4.42, N 7.50.

*5-[(2-(β-D-Maltosyloxy)phenyl)-10,15,20 tris(4-N-methylpyridiniumyl)]porphyrin, triiodide (**16a**)*: 7 mg (86%); R_f 0.39 (cellulose, eluent H). UV–visible (see Table 4). MS (MALDI) *m/z*: 1003 (M − $3I^-$)$^+$. Anal. calcd. for $C_{56}H_{56}N_7O_{11}I_3 \cdot 8.5H_2O$: C 43.76, H 4.79, N 6.38; found: C 43.82, H 4.66, N 6.59.

5-[(4-(β-D-Maltosyloxy)phenyl)-10,15,20 tris(4-N-methylpy-

*ridiniumyl)]porphyrin, triiodide (**16b**)*: 8 mg (98%); R_f 0.42 (cellulose, eluent H). UV–visible (see Table 4). MS (MALDI) *m/z*: 1003 $(M - 3I^-)^+$. Anal. calcd. for $C_{56}H_{56}N_7O_{11}I_3 \cdot 9H_2O$: C 43.51, H 4.82, N 6.34; found: C 43.55, H 4.95, N 6.20.

*5-[2-(β-D-Lactosyloxy)phenyl)-10,15,20 tris(4-*N*-methylpyridiniumyl)]porphyrin, triiodide (**17a**)*: 7 mg (86%); R_f 0.50 (cellulose, eluent H). UV–visible (see Table 4). MS (MALDI) *m/z*: 1003 $(M - 3I^-)^+$. Anal. calcd. for $C_{56}H_{56}N_7O_{11}I_3 \cdot 12H_2O$: C 42.04, H 4.04, N 6.13; found: C 41.98, H 5.19, N 6.04.

*5-[4-(β-D-Lactosyloxy)phenyl)-10,15,20 tris(4-*N*-methylpyridiniumyl)]porphyrin, triiodide (**17b**)*: 8 mg (98%); R_f 0.28 (cellulose, eluent H). UV–visible (see Table 4). MS (MALDI) *m/z*: 1003 $(M - 3I^-)^+$. Anal. calcd. for $C_{56}H_{56}N_7O_{11}I_3 \cdot 11H_2O$: C 42.52, H 4.97, N 6.20; found: C 42.50, H 4.86, N 6.18.

*5-[(2-(β-D-Glucopyranosyloxy)phenyl)-10,15,20 tris(4-*N*-isopropylpyridiniumyl)]porphyrin, triiodide (**18a**)*: 8 mg (91%); R_f 0.76 (SiO_2, eluent F). UV–visible (see Table 4). MS (MALDI) *m/z*: 925 $(M - 3I^-)^+$. Anal. calcd. for $C_{56}H_{58}N_7O_6I_3 \cdot 9H_2O$: C 45.82, H 5.22, N 6.68; found: C 45.22, H 5.14, N 6.77.

*5-[(4-(β-D-Glucopyranosyloxy)phenyl)-10,15,20 tris(4-*N*-isopropylpyridiniumyl)]porphyrin, triiodide (**18b**)*: 8 mg (91%); R_f 0.70 (SiO_2, eluent F). UV–visible (see Table 4). MS (MALDI) *m/z*: 925 $(M - 3I^-)^+$. Anal. calcd. for $C_{56}H_{58}N_7O_6I_3 \cdot 12H_2O$: C 44.19, H 5.43, N 6.44; found: C 44.70, H 5.55, N 6.29.

*5-[(2-(β-D-Glucopyranosyloxy)phenyl)-10,15,20 tris(4-*N*-n-octylpyridiniumyl)]porphyrin, triiodide (**19a**)*: 8 mg (90%); R_f 0.51 (SiO_2, eluent K). UV–visible (see Table 4). MS (MALDI) *m/z*: 1135 $(M - 3I^-)^+$. Anal. calcd. for $C_{71}H_{88}N_7O_6I_3 \cdot 13.5H_2O$: C 48.47, H 6.59, N 5.57; found: C 48.55, H 6.66, N 5.43.

*5-[(4-(β-D-Glucopyranosyloxy)phenyl)-10,15,20 tris(4-*N*-n-octylpyridiniumyl)]porphyrin, triiodide (**19b**)*: 8 mg (90%); R_f 0.44 (SiO_2, eluent K). UV–visible (see Table 4). MS (MALDI) *m/z*: 1135 $(M - 3I^-)^+$. Anal. calcd. for $C_{71}H_{88}N_7O_6I_3 \cdot 10.5H_2O$: C 50.00, H 6.44, N 5.75; found: C 50.52, H 6.11, N 5.95.

References

1. (*a*) T.J. Dougherty, G. Lawrence, J.H. Kaufman, D. Boyle, K.R. Weishaupt, and A. Goldfarb. J. Natl. Cancer Inst. **62**, 231 (1979); (*b*) D. Kessel. Photochem. Photobiol. **39**, 851 (1984); (*c*) D. Kessel and E. Spikes. Photochem. Photobiol. **40**, 59 (1984); (*d*) J.R. Spears, J. Srub, D. Shropshire, and S.J. Paulin. Clin. Invest. **71**, 395 (1983).
2. (*a*) D.W. Dixon, L.G. Marzilli, and R. Schinazi. Ann. N.Y. Acad. Sci. **616**, 511 (1990); (*b*) M. Asanaka, T. Kurimura, H. Toya, J. Ogaki, and Y. Kato. AIDS (London), **3**, 403 (1989); (*c*) R.D. Levere, Y.F. Gong, A. Kappas, D.J. Bucher, G.P. Wormser, and N.G. Abraham. Proc. Natl. Acad. Sci. U.S.A. **88**, 1756 (1991); (*d*) J.L. Sessler, M.J. Cyr, B.G. Maiya, M. Judy, J.T. Newman, H.L. Skiles, R. Boriak, J.L. Mattews, and T.C. Chanh. Proc. SPIE-Int. Soc. Opt. Eng. **1203**, 233 (1990); (*e*) D.W. Dixon, M.S. Kim, V. Kumar, G. Obara, L.G. Marzilli, and R.F. Schinazi. Antiviral Chem. Chemother. **3**, 279 (1992).
3. (*a*) D. Kessel. Biochem. Pharmacol. **33**, 1389 (1984); (*b*) J. Moan. Photochem. Photobiol. **43**, 681 (1986); (*c*) H. Van der Berg. Chem. Br. 430 (1986); (*d*) J.J. Crute, A.F. Walul, R.A. Bambara, R.S. Murant, S.L. Gibson, and R. Hilf. Cancer Res. **46**, 153 (1986); (*e*) R.M. Bôhmer and G. Morstyn. Cancer Res. **45**, 5328 (1985), and references therein; (*f*) B. Paquette and J.E. Van Lier. *In* Photodynamic therapy of neoplastic disease. Vol. 1. *Edited by* B.W. Henderson and T.J. Dougherty. Marcel Dekker, New York. 1992. p. 145; (*g*) I. Rosenthal. Photochem. Photobiol. **53**, 859 (1991); (*h*) B.W. Henderson and T.J. Dougherty. Photochem. Photobiol. **55**, 145 (1992).
4. G.G. Meng, B.R. James, K.A. Skov, and M. Korbelik. Can. J. Chem. **72**, 1894 (1994).
5. C. Kieda and M. Monsigny. Invasion & Metastasis, **6**, 347 (1986).
6. (*a*) A. Gabizon and D. Papahadjopoulos. Proc. Natl. Acad. Sci. U.S.A. **85**, 6949 (1988); (*b*) A.L. Klibanov, K. Maruyama, V.P. Torchilin, and L. Huang. FEBS Lett. **268**, 235 (1990).
7. (*a*) E.J. Gibbs and R.F. Pasternack. Semin. Hematol. **26**, 77 (1989); (*b*) R.J. Fiel. J. Biomol. Struct. Dyn. **6**, 1259 (1989); (*c*) R.J. Fiel, J.C. Howard, E.H. Mark, and N. Datta-Gupta. Nucleic Acids Res. **6**, 3093 (1979); (*d*) R.J. Fiel and B.R. Munson. Nucleic Acids Res. **8**, 2835 (1980); (*e*) R.J. Fiel, M.J. Carvlin, E.H. Mark, and J.C. Howard. Nucleic Acids Res. **11**, 6141 (1983); (*f*) R.F. Pasternack, E.J. Gibbs, and J.J. Villafranca. Biochemistry, **22**, 2406 (1983); (*g*) R.F. Pasternack, E.J. Gibbs, and J.J. Villafranca. Biochemistry, **22**, 5409 (1983); (*h*) R.J. Fiel. J. Biolmol. Struct. Dyn. **6**, 1259 (1989); (*i*) L.G. Marzilli. New J. Chem. **14**, 409 (1990); (*j*) M. Rodriguez and A. Bard. J. Inorg. Chem. **31**, 1129 (1992).
8. (*a*) J.B. Verlhac, A. Gaudemer, and I. Kraljic. Nouv. J. Chim. **8**, 401 (1984); (*b*) D. Praseuth, A. Gaudemer, J.B. Verlhac, I. Kraljic, I. Sissoëf, and E. Guillé. Photochem. Photobiol. **44**, 717 (1986), and references therein.
9. L. Ding, J. Balzarihi, D. Schols, B. Meunier, and E. De Clercq. Biochem. Pharmacol. **44**, 1675 (1992).
10. (*a*) L. Ding, C. Casas, G. Etemad-Moghadam, and B. Meunier. New J. Chem. **14**, 421 (1990); (*b*) L. Ding, G. Etemad-Moghadam, S. Cros, C. Auclair, and B. Meunier. J. Med. Chem. **34**, 900 (1991).
11. (*a*) J.T. Groves and T.P. Farrell. J. Am. Chem. Soc. **111**, 4998 (1989); (*b*) G. Pratviel, M. Pitié, J. Bernadou, and B. Meunier. Nucleic Acids Res. **19**, 6283 (1991); (*c*) G. Gasmi, M. Pasdeloup, G. Pratviel, M. Pitié, J. Bernadou, and B. Meunier. Nucleic Acids Res. **19**, 2835 (1991); M. Pitié, G. Pratviel, J. Bernadou, and B. Meunier. Proc. Natl. Acad. Sci. U.S.A. **89**, 3967 (1992); (*e*) V.V. Vlassov, E.A. Deeva, and G.V. Ivanova. Nucleosides Nucleotides, **10**, 641 (1991); (*f*) T. Le Doan, D. Praseuth, L. Perrouault, M. Chassignol, N.T. Thuong, and C. Hélène. Bioconjugate Chem. **1**, 108 (1990).
12. A.F. Mironov, G.M. Isaeva, V.I. Chvets, R.P. Evstigneeva, A.N. Stepanov, A.A. Perov, and S.E. Koupriyanov. Bioorg. Khim. **4**, 1410 (1978).
13. (*a*) V.J. Lee, X. Zhang, J.A. Ibers, and J.I. Brauman. J. Am. Chem. Soc. **115**, 3834 (1993); (*b*) J.H. Fuhrhop, C. Demoulin, C. Boettcher, J. Koning, and U. Siggel. J. Am. Chem. Soc. **114**, 4159 (1992); (*c*) N. Ono, M. Bougauchi, and K. Maruyama. Tetrahedron Lett. **33**, 1629 (1992).
14. K. Driaf, P. Krausz, B. Verneuil, M. Spiro, J.C. Blais, and G. Bolbach. Tetrahedron Lett. **34**, 1027 (1993).
15. R.G. Little, J.A. Anton, P.A. Loach, and J.A. Ibers. J. Heterocycl. Chem. **12**, 343 (1975).
16. J.S. Lindsey, H.C. Hsu, and I.C. Scheirman. Tetrahedron Lett. **22**, 931 (1986).

17. P. Maillard, J.L. Guerquin-Ken, C. Huel, and M. Momenteau. J. Org. Chem. **58**, 2774 (1993).
18. K. Anzai and K. Hatano. Chem. Pharm. Bull. **32**, 1273 (1984).
19. M. Spiro, J.C. Blais, G. Bolbach, F. Fournier, J.C. Tabet, K. Driaf, O. Gaud, R. Granet, and P. Krausz. Int. J. Mass Spectrom. Ion Processes, **134**, 229 (1994).
20. G. Bolbach, K. Riahi, M. Spiro, A. Brunot, F. Breton, and J.C. Blais. Analusis, **21**, 383 (1993).
21. R.W. Jeanloz and P.J. Stoffyn. Methods Carbohydr. Chem. **1**, 221 (1962).
22. Y. Tsuzuki, S. Kataoka, M. Funayama, and K. Satsumabayashi. Bull. Chem. Soc. Jpn. **44**, 526 (1971).
23. B. Schuster, M. Winter, and K. Herrmann. Z. Naturforsch. **41**, 511 (1986).
24. D.H. Brauns. J. Am. Chem. Soc. **51**, 1820 (1927).

3,4-Disubstituted derivatives of 1,2,5-thiadiazole 1,1-dioxide. Ethanol addition reactions and electroreduction of 3-methyl-4-phenyl and 3,4-dimethyl derivatives in acetonitrile and ethanol solvents

José Alberto Caram, María Virginia Mirífico, Silvia Lucía Aimone, and Enrique Julio Vasini

Abstract: 3-Methyl-4-phenyl-1,2,5-thiadiazole 1,1-dioxide (**TMP**), as well as 3,4-dimethyl-1,2,5-thiadiazole 1,1-dioxide (**TMM**), react with ethanol (EtOH), which adds to one of their C=N double bonds. The equilibrium constants for the addition reaction are measured in mixed acetonitrile (ACN) – EtOH solvents by means of UV spectroscopy in the case of **TMP**, and by ^{13}C NMR spectroscopy in the case of **TMM**, since **TMM** presents only terminal UV absorption. Both equilibrium constants are also estimated through cyclic voltammetry (CV) experiments. In the case of **TMP**, the ethanol molecule adds to the C=N bond located on the methyl-substituted side of the substrate, according to ^{13}C NMR spectroscopy and CV results. The electroreduction characteristics of the substrates and their ethanol addition products are studied using CV techniques in ACN, EtOH, and ACN–EtOH solvent mixtures. The radical anion formed by the first electron transfer to **TMM** is unstable and decomposes rapidly while that corresponding to **TMP** undergoes a relatively slow homogeneous second-order reaction with the substrate ($k = 3 \times 10^2$ M^{-1} s^{-1}). The equilibrium constant for EtOH addition and the voltammetric properties of the substrates are compared with those of the previously studied 3,4-diphenyl derivative (**TPP**).

Key words: electrochemistry, thiadiazoles, structure–reactivity relations, kinetics.

Résumé : Le 1,1-dioxyde de 3-méthyl-4-phényl-1,2,5,thiadiazole (**TMP**) aussi bien que le 1,1-dioxyde de 3,4-diméthyl-1,2,5-thiadiazole (**TMM**) réagissent avec le méthanol qui s'additionne sur une de leurs doubles liaisons. On a mesuré les constantes d'équilibre de la réaction d'addition dans un mélange d'acétonitrile et d'éthanol comme solvant (ACN)–EtOH, en faisant appel à la spectroscopie UV dans le cas du **TMP** et à la spectroscopie de RMN du ^{13}C dans le cas du **TMM** puisque ce dernier ne présente que des absorptions terminales en UV. On a également évalué les constantes d'équilibre à l'aide d'expériences de voltamétrie cyclique. Dans le cas du **TMP**, la molécule d'éthanol s'additionne sur la double liaison C=N située du côté du méthyle substitué sur le substrat en accord avec les résultats obtenus par spectroscopie de RMN du ^{13}C. Faisant appel aux techniques de CV dans du ACN, EtOH et du ACN–EtOH comme solvants, on a étudié les caractéristiques de l'électroréduction des substrats et de leurs produits résultant de l'addition de l'éthanol. L'anion radicalaire formé lors du premier transfert d'électron vers le **TMM** est instable et se décompose rapidement tandis que le **TMP** correspondant donne avec le substrat, une réaction d'ordre deux homogène relativement lente ($k = 3 \times 10^2$ M^{-1} s^{-1}). On a comparé les constantes d'équilibre de l'addition d'éthanol et les propriétés voltamétriques des substrats avec celles dérivés 3,4-diphényles (**TPP**) étudiés précédemment.

Mots clés : électrochimie, thiadiazoles, relations structure–réactivité, cinétiques.

[Traduit par la rédaction]

Introduction

The 1,1-dioxides of 1,2,5-thiadiazoles belong to a group of heterocycles containing the sulfamide moiety that present interesting chemical properties and a variety of applications as biologically active compounds and as fine chemicals. A detailed review has been written by Aran et al. (1). Several pharmacological uses have been suggested and patented for 1,2,5-thiadiazole 1,1-dioxides, but their chemical properties are largely unexplored and "only a heterogeneous series of generally unrelated reactions are known" (1).

Our previous work has shown, through UV and ^1H and ^{13}C NMR spectroscopy (2), that 3,4-diphenyl-1,2,5-thiadiazole 1,1-dioxide (**TPP**) in acetonitrile (ACN) – ethanol (EtOH) solvent mixtures is in equilibrium with the thiadiazoline (3-ethoxy-3,4-diphenyl-1,2,5-thiadiazoline 1,1-dioxide: **TPPH·OEt**) formed through the addition of ethanol to one of its C=N double bonds. The formation equilibrium constant at

Received January 29, 1996.

J.A. Caram, M.V. Mirífico, S.L. Aimone, and E.J. Vasini.[1]
Instituto de Investigaciones Fisicoquímicas Teóricas y Aplicadas (INIFTA), Facultad de Ciencias Exactas, Departamento de Química, Universidad Nacional de La Plata, Casilla de Correo 16, Sucursal 4, (1900) La Plata, Argentina.

[1] Author to whom correspondence may be addressed. Telephone: 5.4-21-25-7430 / 7291. Fax: 54-21-25-4642. E-mail: vasini@isis.unlp.edu.ar

25.0°C is 3.3 M^{-1}.[2] Thus **TPP** exists in EtOH solution as the thiadiazoline **TPPH·OEt**.

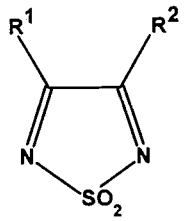

$R^1 = R^2 = Ph$: **TPP**
$R^1 = Me$; $R^2 = Ph$: **TMP**
$R^1 = R^2 = Me$: **TMM**

TPP (3, 4) is voltametrically reduced in ACN solution, in two successive peaks, to a radical anion and to a dianion at ca. −0.8 V (vs. Ag^+ (0.1 M ACN) / Ag), while **TPPH·OEt** in EtOH presents two reduction peaks at ca. −1.7 and −1.9 V.

In this work, the EtOH addition reactions and the electroreduction properties of the related compounds 3-methyl-4-phenyl-1,2,5-thiadiazole 1,1-dioxide (**TMP**) and 3,4-dimethyl-1,2,5-thiadiazole 1,1-dioxide (**TMM**) are studied in ACN and in EtOH solution and compared with those of **TPP**. Interesting differences related to the presence of a methyl group bonded to a very electron-deficient carbon atom are observed.

Experimental

TMP and **TMM** were synthesized, purified, and characterized according to published procedures (5). Standard methods of purification were used for ACN and EtOH solvents.

^1H and ^{13}C NMR spectra were measured with a Bruker 200 MHz instrument.

Conventional cyclic voltammetry techniques were employed. A L.Y.P. M2 potentiostat, a 3-module L.Y.P. sweep generator, and a Houston Omnigraphic 2000 pen recorder were used.

Voltammetric experiments were performed in an undivided, gas-tight, glass cell swept by purified nitrogen. The cell was kept in a dry glove box, where all solution preparation and other experimental manipulations were made. The reference electrode (r.e.) was Ag^+ (0.1 M ACN)/Ag. It was separated from the cell solution by a porous-glass plug. A 2 cm^2 Pt foil was the counter electrode and the working electrode (w.e.) was a Teflon encapsulated vitreous carbon disk of 0.074 cm^2.

Bulk electrolysis experiments were performed in a divided cell. The anodic and cathodic compartments were separated by a sintered glass plate. The cathode was a vitreous carbon rod (0.3 cm diameter and 1.5 cm length) and the anode was a 8 cm^2 Pt foil. The reference and the working electrode described above for cyclic voltammetry were included in the cathodic compartment and were used to measure the concentration of the substrate at convenient intervals during the electrolysis.

Results and discussion

(a) TMP

Voltammetric and bulk electrolysis results in ACN solution

The results of typical voltammetric experiments performed with solutions of **TMP** in ACN are shown in Fig. 1*a* and *b*. Published results corresponding **TPP** are also included in Fig. 1*c* for comparison. As can be observed, under the experimental conditions of Fig. 1*a*, **TMP** presents two redox couples

Fig. 1. Cyclic voltammograms, current function vs. potential, for **TMP** (at selected low and high experimental concentration) and for **TPP**. ACN solvent; 0.25 M $NaClO_4$ supporting electrolyte; vitreous carbon disk w.e.; Ag^+(0.1 M ACN)/Ag r.e.; $v = 0.2$ V s^{-1}. (*a*) **TMP**: 1.06 mM; (*b*) **TMP**: 13.7 mM; (*c*) (····) **TPP**: 1.51 mM.

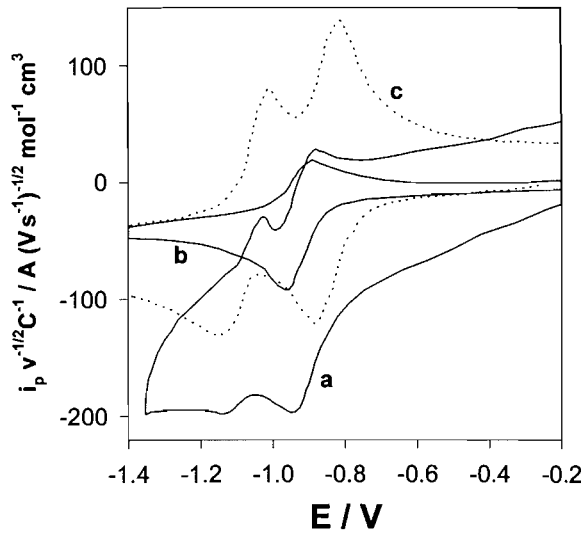

(Ic/Ia; IIc/IIa), which, as in the case of **TPP**, can be assigned to the charge transfers:

$$\mathbf{TMP} + e = \mathbf{TMP}^{\cdot-} \quad \text{Ic/Ia} \qquad E_1$$

$$\mathbf{TMP}^{\cdot-} + e = \mathbf{TMP}^{2-} \quad \text{IIc/IIa} \qquad E_2$$

The first couple is clearly observed under all experimental conditions. The second couple (IIc/IIa) is always less intense and less well defined than the first. It is distinctly observed at low concentrations and high sweep rates, but its current intensity decreases at the higher experimental concentrations. Under the conditions of Fig. 1*b* it is no longer observable. This behavior, although less pronounced, was also observed with **TPP** and was related to interactions of the dianion of **TPP** with the cations of the supporting electrolyte and to adsorption processes (4). Only the processes related to the first couple will be studied in this work.

The current function of the cathodic peak (Ic) of the first couple does not change appreciably with concentration (in the range 1.06–37.7 mM, i_p(Ic) $v^{-1/2}$ C^{-1}/A (V s^{-1})$^{-1/2}$ (mol cm^{-3})$^{-1}$ = 83 ± 6). The diffusion coefficient, calculated with the equation for a reversible voltammetric wave, is 1.7×10^{-5} cm^2 s^{-1}, which is similar to that found for **TPP** (1.2×10^{-5} cm^2 s^{-1}).

Controlled potential electrolysis experiments at −0.9 V in ACN solvent were run with **TMP** initial concentrations ([**TMP**]$_0$) of 21 and 2.2 mM. A duplicate electrolysis experiment with 2.2 mM **TMP** in which water (1.55 M) was added to the ACN solvent was also performed. All three experiments were coincident, within the experimental error (Fig. 2), indicating that *ca.* 0.4 electrons/mol **TMP** are consumed in the bulk electrolysis.

Fig. 2. Bulk electrolysis of **TMP** in ACN solution. Number of moles of electrons vs. relative concentration of **TMP** as measured through the voltammetric current intensity of peak Ic at several intervals during the electrolysis. $[\mathbf{TMP}]_0$: ∇:21 mM; ○:2.2 mM; ●:2.2 mM + 1.55 M water.

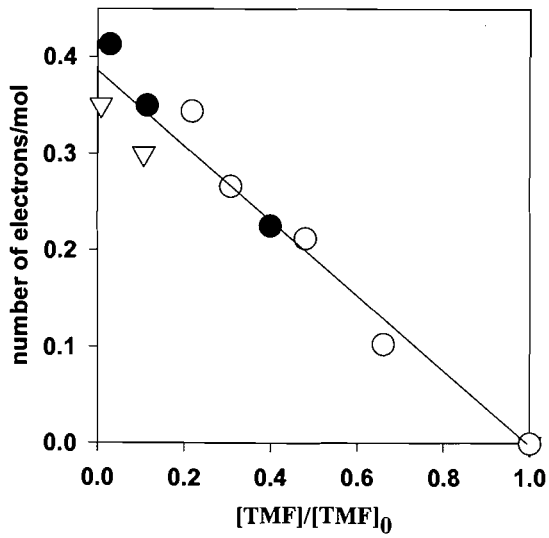

From the very beginning of the electrolysis experiments, the catholyte solution develops a dark red-brown color that originates near the cathode and increases in intensity as the electrolysis progresses. The color intensity decreases and turns yellowish on exposure of the electrolyzed solution to air. Thin-layer chromatographic analysis of the solution at the end of the experiments reveals a complex mixture. Initial efforts to isolate the components have been unsuccessful, but our work in this direction continues in connection with additional studies on the homogeneous reaction kinetics of **TMP**.

The first charge transfer for **TMP** takes place at a more negative potential than that of **TPP** ($E_{pIc[TPP]} - E_{pIc[TMP]} \cong 0.16$ V). This can be related to structural characteristics of the substrates and the radical anions formed.

van der Waals molecular models and X-ray crystal studies of both compounds (6) show that the two phenyl rings of **TPP** cannot be accommodated in the plane of the heterocycle (**TPP** dihedral angles: phenyl–phenyl = 51.9°; phenyl–heterocycle = 34.2 and 41.4°), and that the methyl group in **TMP** hinders the planar disposition of the phenyl ring and the heterocycle to a very similar extent (**TMP** dihedral angle: phenyl–heterocycle = 40.9°). It is reasonable to suppose that the electron transferred to the substrates to form the radical anions should favor a location associated with an electron-deficient heterocyclic carbon atom bonded to a phenyl group (because of charge dispersal reasons). Since more stabilization energy will be gained by delocalizing the additional electron, the phenyl ring involved should be more in the plane of the thiadiazole ring than in that of the parent neutral compound. This can be achieved in **TPP** by the concerted rotation of both rings, but it is not possible in **TMP**.

The peak current intensity ratio ($R_i = i_{pIa}/i_{pIc}$) of the first couple is always smaller than unity and decreases when the cathodic switching potential is made increasingly negative. R_i is also a function of **TMP** concentration and sweep rate as

Fig. 3. Influence of sweep rate and concentration in the ratio of anodic to cathodic peak current intensity (R_i) of the first voltammetric couple of **TMP** for a constant switching potential $E_s = -1.04$ V; ACN solvent; 0.25 M $NaClO_4$ supporting electrolyte; vitreous carbon disk w.e.; Ag^+(0.1 M ACN)/Ag r.e. [**TMP**]: ○:37.7; □:13.7; Δ:9.13; ∇:3.61; ◇:1.06 mM. The dotted line represents the result of a digital simulation for a radical–substrate reaction mechanism with rate constant $k = 3 \times 10^2$ M^{-1} s^{-1} (see also Fig. 6).

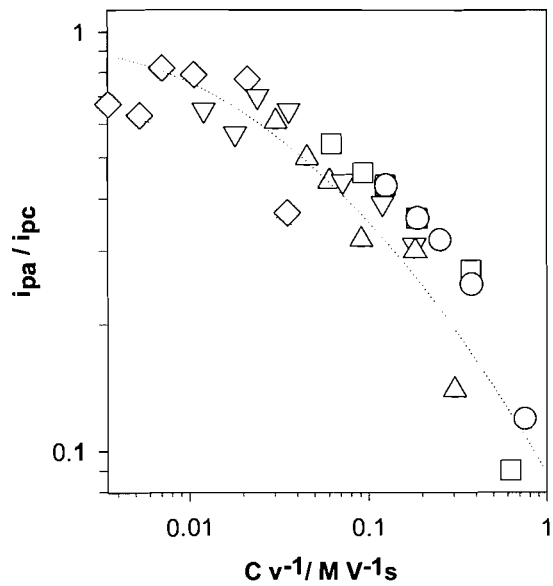

shown in Fig. 3 for a constant switching potential (−1.04 V) that does not include the second couple.

The data shown in Fig. 3 suggest the consumption of $\mathbf{TMP}^{\cdot-}$ by a second-order reaction that, at a constant sweep rate; causes the decrease of R_i with increasing concentration, reflecting the increase in reaction rate; conversely, R_i tends to increase up to unity when the time window is decreased through an increase of the sweep rate. The dotted line in Fig. 3 represents the results of a digital simulation for a radical–substrate second-order reaction, which is justified in the following:

The mechanism of the reaction can be further characterized through the slopes $\delta E_p/\delta \log (v)$ and $\delta E_p/\delta \log [\mathbf{TMP}]$. Figure 4 shows the dependence of the potential of peak Ic with sweep rate at several **TMP** concentrations. A 28.5 mV/dec (r = 0.986; 9 points) $\delta E_p/\delta \log (v)$ slope is observed for [**TMP**] = 37.7 mM for the whole range of experimental sweep rates. At lower concentrations the slope is similar for the lower sweep rates, but $\delta E_p/\delta \log (v)$ tends to zero when the sweep rate is increased. Finally, for [**TMP**] = 1.06 mM, the peak potential does not change with sweep rate.

The $\delta E_p/\delta \log[\mathbf{TMP}]$ slope is shown in Fig. 5 for sweep rates of 0.005, 0.01, and 0.02 V s^{-1}, in the concentration range in which irreversible voltammetric signals are observed. The observed slopes are 43, 34, and 29 mV/dec, respectively. Given the observed $\delta E_p/\delta \log(v)$ slope, the expected $\delta E_p/\delta \log[\mathbf{TMP}]$ slopes for the well-known simple second-order reaction mechanisms are either 19.7 or 29.6 mV/dec (7).

Obviously the slopes are closer to 29.6 mV/dec, which corresponds to a radical–substrate reaction. The discrepancy

might be due to a more complex mechanism or it may be an artifact due to the complex reaction observed in the controlled potential electrolysis experiments. This seems reasonable since the slope departs increasingly from the expected value at decreasing sweep rates.

If the radical–substrate reaction is accepted as the dominant mechanism, a rate constant, k_1, for the reaction:

[1] **TMP**$^{\cdot-}$ + **TMP** = products

can be calculated from the sweep rate (v_i) at which the E_p vs. log ($C\,v^{-1}$) slope changes (7), or, as is shown in Fig. 6, a more detailed view of the fitness of the radical–substrate mechanism can be furnished by a digital simulation that takes into account the electron transfer E_1, followed by reaction [1] and a fast electroreduction of the product (i.e., $E^0_{(product)} \gg E_1$). The simulation results, indicated in Fig. 6 with a solid line, correspond to $k_1 = 3 \times 10^2\ M^{-1}\ s^{-1}$.

The methyl protons of **TMP**, being bonded to a very electron-deficient carbon atom, are weakly acidic. Thus, the radical–substrate reaction might consist of a proton transfer (reaction [1]). The reaction will also be driven forward by the fast electroreduction of the radical **TMPH**$^{\cdot}$ at $E_3 > E_1$.

Anions of the 3-oxo derivatives of 1,2,5-thiadiazole 1,1-dioxides are well known (1). Anion **I**$^-$ has a similar structure although it must be much less stable. Follow-up reactions involving anion **I**$^-$ such as an aldolic-type condensation (reaction [2]), are also possible and have been observed in related compounds (8). The consumption of the substrate by the follow-up reactions can account for the reduced number of electrons per mole observed in the electrolysis experiments.

Voltammetric results in EtOH and ACN/EtOH solutions

The voltammetric results in EtOH solvent are presented in Fig. 7*a* (solid line). The results obtained with **TPP** (4), which have already been discussed, are included for comparison (Fig. 7*a*; dotted line). As was the case for **TPP**, the EtOH molecule adds to one of the C=N double bonds of **TMP** to form a thiadiazoline:

[3] **TMP** + EtOH = **TMPH·OEt**

which is voltammetrically reduced in two peaks (IIIc and IVc) that are very similar to those found with the **TPP** substrate.

When EtOH is added to ACN solutions of **TMP**, the voltammograms evolve in time in essentially the same way as was

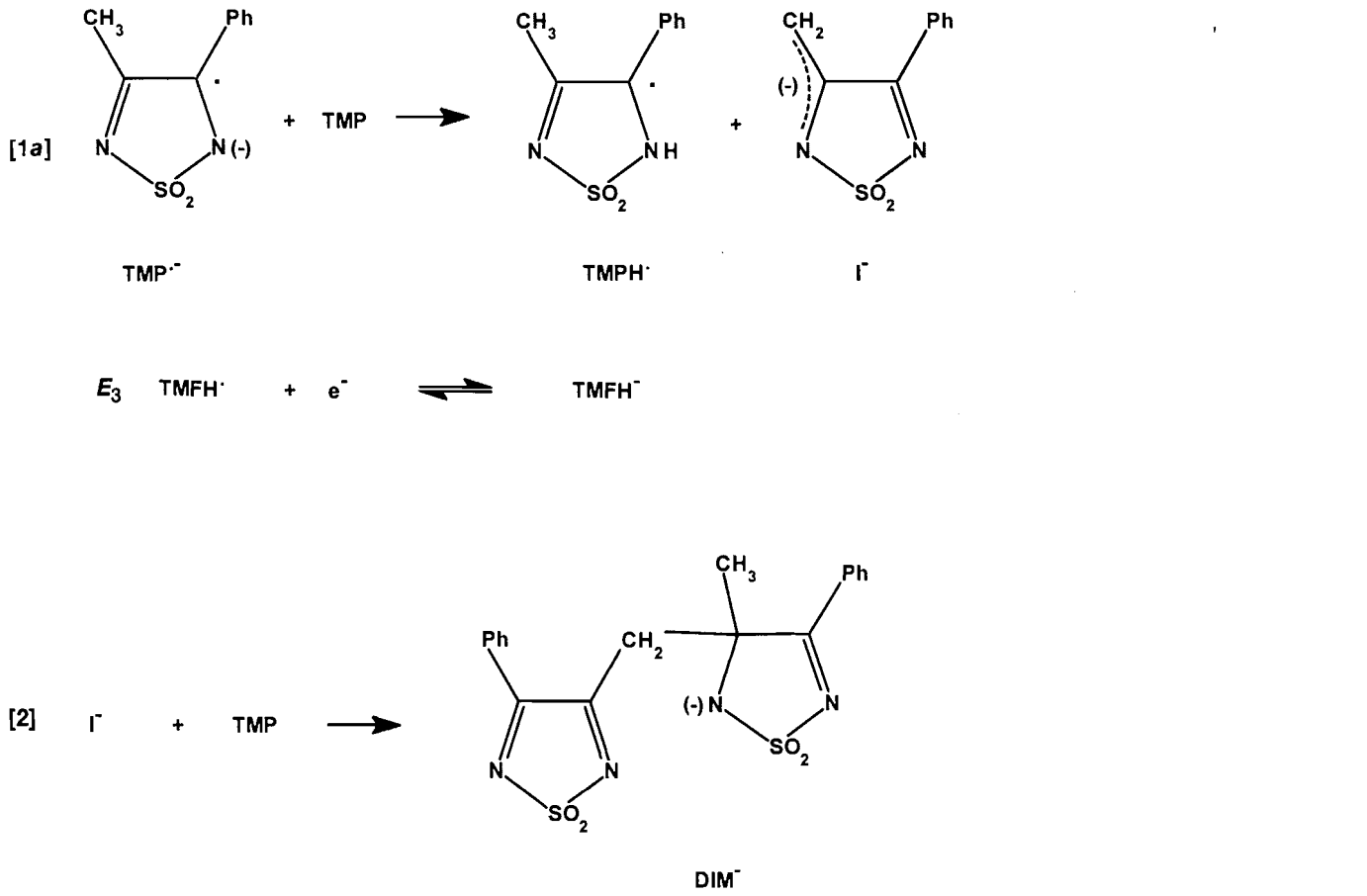

observed for **TPP** (4), that is, the **TMP** voltammetric peaks are observed initially and peak IVc at −1.94 V starts to develop (Fig. 7*b*, solid line). This is followed by the decrease and disappearance of peak IIc, while peak IVc increases. After the disappearance of peak IIc, peak IIIc appears at ca. −1.65 V and grows while the current intensity of peak Ic decreases

Fig. 4. Peak potential for the first couple of **TMP** (E_pIc), vs. Ag^+ (0.1 M ACN)/Ag, as a function of sweep rate for several concentrations of **TMP** in ACN solution; 0.25 M $NaClO_4$ supporting electrolyte; vitreous carbon disk w.e. [**TMP**]: ○:37.7; □:13.7; Δ:9.13; ∇:3.61; ◇:1.06 mM. Solid line through ○ is a least-squares regression (r: 0.986; slope: 28.5 mV/dec); solid line through ◇ is the average of peak potentials for [**TMP**] = 1.06 mM (E_p (mean) = −0.933 V).

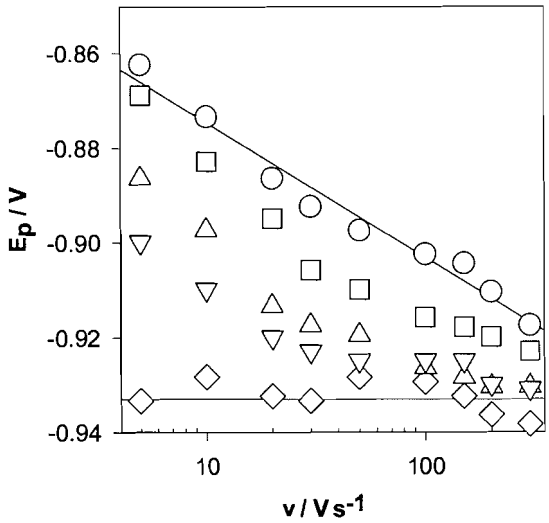

Fig. 5. Peak potential for the first couple of **TMP** (E_pIc), vs. Ag^+(0.1 M ACN)/Ag, as a function of the concentration of **TMP** for several sweep rates in ACN solution; 0.25 M $NaClO_4$ supporting electrolyte; vitreous carbon disk w.e. Sweep rates: ○:0.005; ●:0.010; Δ:0.020 V s^{-1}. The concentration ranges from the highest experimentally used to the lowest in which irreversible peaks are still observed at each sweep rate. Solid lines are least-squares regressions with the following slopes and regression coefficients: 43 mV/dec; r = 0.975 (8 points); 34 mV/dec, r = 0.941 (7 points); Δ:29 mV/dec, r = 0.943 (5 points).

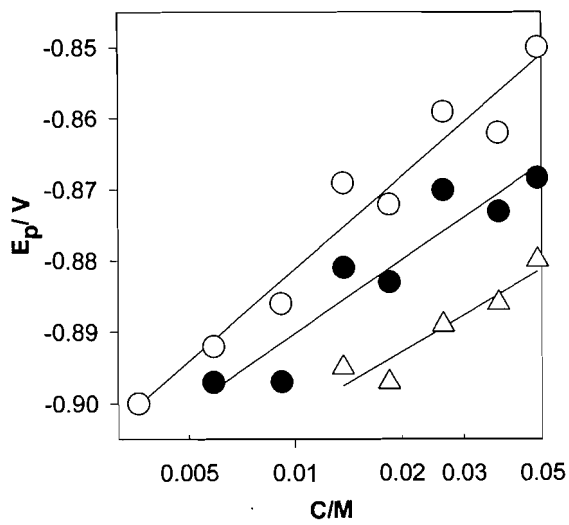

slightly. Finally an equilibrium voltammogram is obtained (Fig. 7*b*, dotted line).

The time evolution described can be interpreted by a reaction mechanism essentially identical to that proposed for **TPP** in ACN–EtOH solvent mixtures. Thus at peak I (Fig. 7*b*) **TMP** is reduced and the radical anion formed reacts

Fig. 6. Peak potential for the first couple of **TMP** (E_pIc), vs. Ag^+ (0.1 M ACN)/Ag as a function of the ratio of **TMP** concentration to sweep rate in ACN solution. [**TMP**]: ○:37.7; □:13.7; Δ:9.13; ∇:3.61; ◇:1.06 mM; (—): digital simulation with k = 3×10^2 M^{-1} s^{-1}.

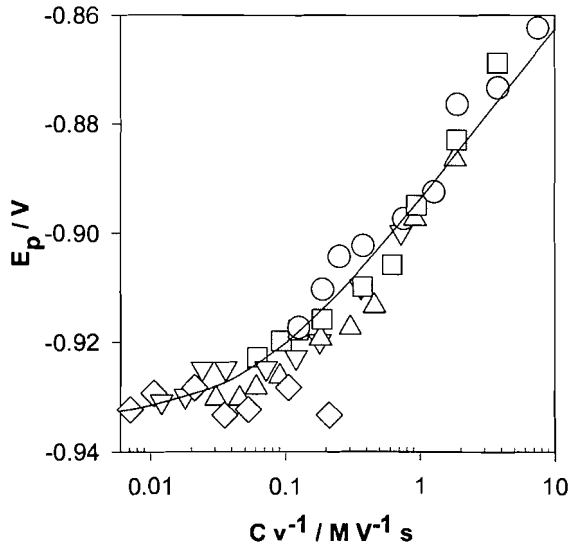

Fig. 7. Cyclic voltammograms at 0.1 V s^{-1} of: (*a*) **TMP** in ethanol; (*b*) in ACN–EtOH, 7.5 wt.% EtOH. (*a*) (—): 5.05 mM **TMP** in EtOH; (····): 3.16 mM **TPP** in EtOH, included for comparison. (*b*) Voltammograms of 3.65 mM **TMP** in ACN–EtOH, 7.5 wt.% EtOH. (—): 15 min after solution preparation; (····): equilibrium voltammogram, 10 days after solution preparation.

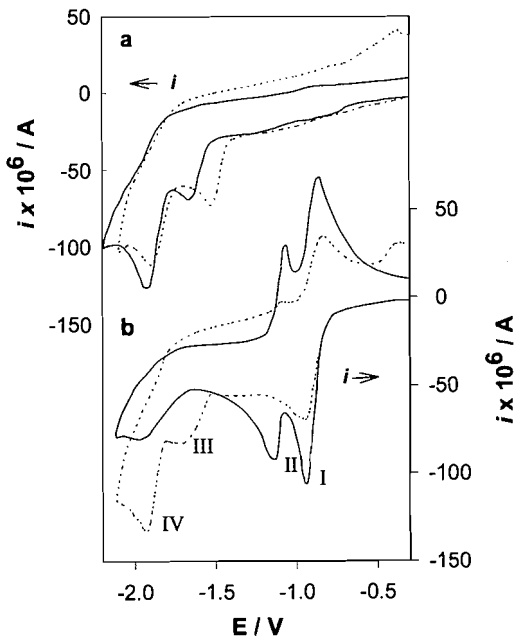

Table 1. Experimental voltammetric results and calculated values of the equilibrium constant K_{TMP} (uncontrolled room temperature, ca. 20°C) for the reaction: **TMP** + EtOH = **TMPH·OEt**.

$[EtOH]_0$/M	$[TMP]_0$/mM	v/(V s^{-1})	i_p(Ic)/(μA)	i_p(IIIc)/(μA)	K_{TMP}/M^{-1}
2.96	3.60	0.10	27.0	27.5	1.03
1.30	3.65	0.10	56.0	25.0	1.46
2.83	3.75	0.10	18.0	25.0	1.33

with EtOH. The product is further reduced at a potential $E_3 > E_1$.

$$\mathbf{TMP}^{\cdot-} + \text{EtOH} = \mathbf{TMPH}^{\cdot} + \text{EtO}^- \qquad C_4$$

$$\mathbf{TMPH}^{\cdot} + e^- = \mathbf{TMPH}^- \qquad E_3$$

If some **TMPH·OEt** has been formed through reaction [3], it reacts with the strong EtO^- base:

$$\text{EtO}^- + \mathbf{TMPH{\cdot}OEt} = \text{EtOH} + \mathbf{TMP{\cdot}OEt}^- \qquad C_5$$

The remaining $\mathbf{TMP}^{\cdot-}$ is further reduced at E_2 (peak IIc). The anions produced at E_3 and C_5 ($\mathbf{TMPH}^-$ and $\mathbf{TMP{\cdot}OEt}^-$) are further reduced at peak IVc. If some **TMPH·OEt** remains it will be reduced at peak IIIc:

$$\mathbf{TMPH{\cdot}OEt} + e^- = \mathbf{TMPH{\cdot}OEt}^{\cdot-} \qquad E_4$$

$$\mathbf{TMPH{\cdot}OEt}^{\cdot-} = \mathbf{TMPH}^{\cdot} + \text{EtO}^- \qquad C_6$$

The $\mathbf{TMPH}^{\cdot}$ formed in C_6 will be immediately reduced to $\mathbf{TMPH}^-$ (E_3).

Thus, once peak IIc is no longer observed, peak Ic will be a two-electron $E_1C_4E_3$ peak, and its intensity will depend on the **TMP** concentration. Likewise, peak IIIc will be a two-electron $E_4C_6E_3$ peak and its current intensity will depend on the actual **TMPH·OEt** interfacial concentration, i.e., its bulk concentration minus the depletion caused by reaction C_5.

The equilibrium constant of reaction [3], k_{TMP}, can be calculated using the same relation of peak intensities used for **TPP** (4), specifically:

$$K_{TMP} = \frac{[\mathbf{TMPH{\cdot}OEt}]}{[\text{EtOH}][\mathbf{TMP}]}$$

$$= (2 \times \{i(\text{IIIc}) + i(\text{Ic})/2\}/[\text{EtOH}]_0 \times i(\text{Ic}))$$

The experimental peak intensities and calculated K_{TMP} for several EtOH concentrations are shown in Table 1.

The equilibrium constant K_{TMP} was also calculated using UV spectral measurements and a Hildebrand-type equation, as has been done with **TPP**. The details will be reported elsewhere, but the spectroscopically measured value, 1.4 M^{-1} at 25.0°C, agrees with the voltammetric value of Table 1.

The resonance of the heteronuclear methyl substituent in ^{13}C NMR measurements of **TMP** is, in benzene-d_6 solution, observed at δ = 17.6 ppm, and in methanol-d_4 solution at δ = 26.5 ppm. The direction and magnitude of the observed shift (Δδ = 8.9 ppm) is in agreement, according to the additivity rules for ^{13}C chemical shifts (9), with the addition of MeOH to the C=N double bond on the methyl "side" of the molecule. Thus the thiadiazoline **TMPH·OEt** has the structure:

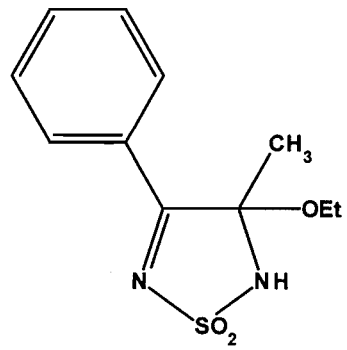

TMP.EtOH

It can be observed that the π-system of **TMPH·OEt** is very similar to that of **TPPH·OEt**, This rationalizes the above-mentioned similarities between the voltammetric responses of both thiadiazolines. The similarity of the delocalization energy increment in going from the thiadiazoles to the thiadiazolines is also shown in the values of the equilibrium constants of the EtOH addition reactions. Thus, k_{TPP} is approximately two times larger than K_{TMP}, as can be expected if only symmetry factors are important.

(b) TMM

Voltammetric results for TMM in ACN solutions

The cyclic voltammetry of **TMM** in ACN solutions results in a single, diffusional, totally irreversible voltammetric peak at ca. −1.00 V under all experimental conditions. The peak shifts cathodically 30 mV/dec of sweep rate and its potential does not depend on the substrate concentration. Its current function ($i_p\, v^{-1/2}\, C^{-1}$) decreases slightly but steadily with the increase in concentration from 71 A V^{-1} $s^{1/2}$ mol^{-1} cm^3 at 1.01 mM, to 66 at 11.2 mM, and then drastically to 40 A V^{-1} $s^{1/2}$ mol^{-1} cm^3 at the highest concentration used (17.1 mM). This is apparently related to an increase in the rate of fouling of the electrode with increasing concentration. In effect, the second voltammetric cycle at all concentrations shows a decrease in current intensity that increases in magnitude when the concentration is increased. The current is restored to its first-cycle value when the electrode surface is cleaned.

These results suggest a one-electron charge transfer followed by a fast chemical reaction and allow the calculation of

a diffusion coefficient, $D_{(TMM)} = 1.2 \times 10^{-5}$ cm^2 s^{-1}, which is similar to those of **TPP** and **TMP**. Thus, as seems reasonable because of the lack of delocalization possibilities, the radical anion of **TMM** is unstable.

Voltammetric results for TMM in EtOH solutions

As found for **TPP** and **TMP**, the current intensity of the voltammetric peak of **TMM** in ACN–EtOH solvent mixtures decreases initially with time and reaches a stable equilibrium value that is lower the higher the EtOH concentration. No new peaks are observed and, since a thiadiazoline is formed according to the NMR evidence given below, it must be concluded that the 3,4-dimethyl thiadiazoline can not be reduced at potentials more anodic than the solvent cutoff.

The ^{1}H NMR spectrum of **TMM** provides evidence of an addition reaction of EtOH to one of the C=N double bonds of **TMM**. A single methyl signal at $\delta = 2.63$ ppm is observed in ACN-d_3, while two methyl signals are present in ethanol-d_6, at $\delta = 2.35$ ppm (assigned to the methyl on the unsubstituted side) and 1.68 ppm (assigned to the methyl on the ethoxyl-substituted side). In ACN-d_3–ethanol-d_6 solvent mixtures the original substrate methyl signal is also observed at 2.62 ppm. A study (at an uncontrolled room temperature of *ca.* 20°C) of the relative intensities of these three signals in ACN-d_3–ethanol-d_6 solvent mixtures with 13.3, 30.0, and 60.0 wt.% ethanol-d_6 allowed an evaluation of $K_{TMM} = 0.3$ M^{-1} (individual measurements were 0.26, 0.30, and 0.32 M^{-1}, respectively).

UV–VIS spectroscopic techniques cannot be used to study the addition reaction, since **TMM** presents only terminal absorption at $\lambda < 300$ nm, but an equilibrium constant can be estimated from voltammetric experiments if the equilibrium peak current intensity (corrected for the viscosity change of the solvent by means of independent measurements of the intensity of the ferrocene couple in the same solvent mixtures, as already described (4)) of the **TMM** peak in ACN–EtOH solvent mixtures is taken as a measure of its equilibrium concentration.

Four voltammetric experiments in ACN–EtOH solvent mixtures with 9.9, 21, 42, and 75.6 wt.% EtOH were performed. The K_{TMM} values (uncontrolled room temperature, ca. 20°C) calculated were 0.16, 0.15, 0.18, and 0.20 M^{-1}. Due to the assumptions involved, this estimate of K_{TMM} can be considered to be in reasonable agreement with the more direct NMR experiments.

Influence of the addition of acids in the voltammetry of TMP and TMM in ACN, EtOH, and mixed ACN–EtOH solvents

TMP or TMM in ACN + acid: Experiments in which several concentrations of dry trifluoracetic acid (TFAcH) were added to ACN solutions of **TMP** or **TMM** were performed. In both cases a kinetic prepeak (ppIc), anodic to the first charge transfer, developed when less than equimolecular quantities of acid were added. The prepeak current intensity increased with increasing relative concentrations of acid and finally replaced the original peaks of the substrate when the relative concentration of acid ([TFAcH]/[**TMP**] or [TFAcH]/[**TMM**]) was 2 or greater. The current intensity of the prepeak under these conditions is twice that of the original peak Ic of the substrate.

At low ratios of acid to substrate concentration, the prepeak can be interpreted as the reduction of the substrate, followed by protonation of the radical anion, i.e., for **TMP**:

$$\mathbf{TMP} + e^- = \mathbf{TMP}^{\cdot-} \qquad E_1$$

$$\mathbf{TMP}^{\cdot-} + 2\,\mathrm{TFAcH} = \mathbf{TMPH}^{\cdot} + (\mathrm{TFAc})_2\mathrm{H}^- \qquad C_7$$

The **TMPH**$^{\cdot}$ radical can be further reduced to the anion and protonated to the thiadiazoline (**TMPH$_2$**) or it can disproportionate to form **TMPH$_2$** and regenerate the substrate, which will be reduced at E_1.

Reaction C_7 includes the well-known homoconjugation reaction of anions in ACN (10).

TMP, TPP, or TMM in ETOH + acid: Similar results are obtained if TFAcH is added to solutions of **TPP** or **TMP** in EtOH solvent. A prepeak (ppIIIc) develops and its associated current intensity increases on increasing the acid concentration. The original peaks (IIIc and VIc, Fig 7*a*) are completely replaced by the prepeaks (which double the current intensity of each original peak) when the acid concentration is more than twice that of the substrate. The prepeaks are interpreted as above by equations similar to E_1 and C_7, in which **TMP** is replaced by **TMPH·OEt**.

As already discussed, the voltammetric electroreduction of **TMMH·OEt** takes place beyond the solvent potential cutoff. The addition of TFAcH to solutions of **TMM** in EtOH solvent does not cause the appearance of new voltammetric peaks.

TMP or TPP in mixed ACN–EtOH + acid: In mixed ACN–EtOH solvents to which TFAcH (with ratios [TFAcH]/[**TMP**] or [TFAcH]/[**TPP**] ca. 4) has been added, it is possible to record voltammograms in which only both prepeaks, ppIc and ppIIIc, are observed.

Since ppIc responds to the concentration of the thiadiazole ([**TPP**] or [**TMP**]) and ppIIIc to the concentration of thiadiazoline ([**TPPH·OEt**] or [**TMPH·OEt**]), it follows that equilibrium constants for the EtOH addition reactions to **TPP** and **TMP** (K_{TPP} and K_{TMP}) can be measured voltammetrically in these mixed solvent solutions. K_{TMP}, for example, can be expressed as:

$$K_{TMP} = \frac{[\mathbf{TMPH{\cdot}OEt}]}{[\mathrm{EtOH}][\mathbf{TMP}]} = \frac{i(\mathrm{ppIIIc})/v^{1/2}}{\{i(\mathrm{ppIc})/v^{1/2}\} \times [\mathrm{EtOH}]}$$

The experimental results are given in Table 2. The calculated equilibrium constants for **TMP** and **TPP** agree with those calculated from the complex mechanism in mixed ACN–EtOH solvents for **TMP** (above) and **TPP** (4).

Acknowledgments

This work was financially supported by the Consejo Nacional de Investigaciones Científicas y Técnicas (CONICET), the Comisión de Investigaciones Científicas de la Provincia de Buenos Aires (CIC Pcia. Bs.As.), and the University of La Plata (UNLP), Facultad de Ciencias Exactas, Departamento de Química. M.V.M and J.A.C. are researchers of CONICET and UNLP, E.J.V. is researcher of CIC Pcia. Bs.As and UNLP. The authors acknowledge the assistance of Prof. Dr. E.G. Gros (UMyMFOR, Universidad de Buenos Aires, CONICET) for the NMR spectral measurements.

Table 2. Experimental voltammetric results for (*a*) **TMP** and (*b*) **TPP** in mixed ACN–EtOH solvents with added trifluoroacetic acid (TFAcH). Calculated values for the equilibrium constants of the EtOH addition reactions (uncontrolled room temperature, ca. 20°C). $i_p/v^{1/2}$ values are the mean of seven values measured at sweep rates between 0.01 and 0.5 V s^{-1}.

[**TMP**]/mM	[TFAcH]/mM	[EtOH]/M	i(ppIc)/$v^{1/2}$	i(ppIIIc)/$v^{1/2}$	K_{TMP}
3.88	9.10	0.59	294	243	1.40
3.93	9.10	1.63	157	397	1.55
3.85	9.10	3.30	95.9	484	1.53

[**TPP**]/mM	[TFAcH]/mM	[EtOH]/M	i(ppIc)/$v^{1/2}$	i(ppIIIc)/$v^{1/2}$	K_{TPP}
4.23	10.4	1.66	76.6	403	3.16
4.24	10.4	2.57	63.3	618	3.80
4.19	10.4	3.32	48.9	546	3.36
4.23	10.4	3.40	42.7	439	3.02
4.20	10.4	4.17	50.0	621	2.98

References

1. V.J. Aran, P. Goya, and C. Ochoa. Adv. Heterocycl. Chem. **44**, 81 (1988)
2. M.V. Mirífico, J.A. Caram, E.J. Vasini, and J.E. Sicre. J. Phys. Org. Chem. **6**; 341 (1993).
3. M.V. Mirífico, J.A. Caram, and E.J. Vasini. Electrochim. Acta, **36**, 167 (1991).
4. J.A. Caram, M.V. Mirífico, and E.J. Vasini. Electrochim. Acta, **39**, 939 (1994).
5. J.B. Wright. J. Org. Chem. **29**, 1905 (1964).
6. E.E. Castellano, O.E. Piro, M.D. Glossman, J.A. Caram, and E.J. Vasini. Proceedings of the XVIII Encontro Nacional de Física da Materia Condensada. Caxambú (MG), Brazil, June 1995.
7. C.P. Andrieux, L. Nadjo, and J.M. Saveant. J. Electroanal. Chem. **42**, 223 (1973).
8. P. Goya, A. Martinez, C. Ochoa, M. Stud, and M. L. Jimeno. Tetrahedron, **41**, 3105 (1985).
9. E. Pretsch, T. Clerc, J. Seibl, and W. Simon. Tabellen zur strukuraufklärung organischer verbindungen mit spektroscopishen methoden. Springer Verlag, Berlin. 1976.
10. J.F. Coetzee and G.R. Padmanabhan with G.P. Cunningham. Talanta, **11**, 93 (1964).

Polyhalide anions in crystals. Part 2. I_3^- asymmetry and N—H...I bonding: triiodides of the $Me_2NH_2^+$, Ph_2I^+, tropanium, *N,N,N′,N′*-Me_4-1,2-ethanediammonium, *N,N,N′,N′*-Me_4-1,3-propanediammonium, *N*-Me-piperazinium(2+), and *N,N′*-Me_2-piperazinium(2+) cations, and Me_2NH_2I[1]

Katherine N. Robertson, T. Stanley Cameron, and Osvald Knop

Abstract: Crystal-structure determinations are reported for $Me_2NH_2I_3$, $(Ph_2I)I_3$, tropanium·I_3, $[Me_2HN(CH_2)_2NHMe_2](I_3)_2$, $[Me_2HN(CH_2)_3NHMe_2](I_3)_2$, (*N*-Me-piperazinium) $(I_3)_2·H_2O$, (*N,N′*-Me_2-piperazinium)$(I_3)_2$, and Me_2NH_2I. The features of these and relevant literature structures are used to (1) classify triiodide structures by their ion-packing types; (2) analyze the relationship between the two I—I bond lengths *d* and *d** in the I_3^- anion; and (3) examine the effect of N—H(N)...I hydrogen bonding on the symmetry of the I_3^- anion. It is found that the *d,d** relationship can be represented to a high degree of correlation by the power function $d^* - d_0 = K(d - d_0)^{-c}$ ($d^* \geq d$, $d_0 = d$(I—I) in I_2(g)) based on the 3c4e model of the anion. An empirical correlation is shown to exist between the H(N)...I and N...I distances both for unbranched and branched N—H(N)...I bonds. Comparison of the degree of asymmetry of I_3^- in two samples, one containing H-bonded I_3^- anions, the other with H-bonding absent, leads to the conclusion that while H-bonding *is* a factor affecting I_3^- symmetry, it is not a *preferential* factor. The four 1:2 title triiodides have structures of, or related to, the CdI_2 type, in which the anions form infinite pseudo-hexagonal channels. The positioning of the divalent cations on the axes of these channels gives rise to an interesting "vernier" effect governed by the cation length and H-bonding ability. Bonding in centrosymmetric I_4 rings in $(Ph_2I)I_3$ and $(Ph_2I)I$ is examined.

Key words: crystal structures, hydrogen bond, iodine–iodine bonds, polyhalide anions, triiodides.

Résumé : On a déterminé les structures de $Me_2NH_2I_3$, $(Ph_2I)I_3$, tropanium·I_3, $[Me_2HN(CH_2)_2NHMe_2](I_3)_2$, $[Me_2HN(CH_2)_3NHMe_2](I_3)_2$, (*N*-Me-pipérazinium)$(I_3)_2·H_2O$, (*N,N′*-$Me_2$-pipérazinium)$(I_3)_2$ et Me_2NH_2I. On a utilisé les caractéristiques de ces structures et d'autres apparentées tirées de la littérature pour (1) classifier les structures des triiodures selon l'empilement de leurs ions; (2) analyser la relation entre les deux longueurs des liaisons I—I, *d* et *d** de l'anion I_3^- et (3) examiner l'effet des liaisons hydrogène N—H(N)...I sur la symétrie de l'anion I_3^-. On a trouvé que, en se basant sur le modèle 3c4e de l'anion, la relation *d,d** peut être représentée, avec un degré élevé de corrélation, par une fonction de puissance $d^* - d_0 = K(d - d_0)^{-c}$ ($d^* \geq d$, $d_0 = d$(I—I), pour I_2(g)). On a montré qu'il existe une corrélation empirique entre les longueurs des liaisons H(N)...I et N...I, pour les liaisons N—H(N)...I tant linéaires que ramifiées. Une comparaison du degré d'asymétrie du I_3^- dans deux échantillons, l'un contenant des anions I_3^- avec des liaisons hydrogène et l'autre dans lequel elles sont absentes, permet de conclure que, même si les liaisons hydrogène *affectent* la symétrie de I_3^-, il ne s'agit pas du facteur *préférentiel*. Les quatre triiodures 1 : 2 mentionnés dans le titre ont tous des structures du type (ou d'un type apparenté) CdI_2 dans lesquelles les anions forment des canaux pseudo-hexagonaux infinis. Le positionnement des cations divalents sur les axes de ces canaux donne lieu à un effet intéressant de vernier qui est gouverné par la longueur du cation et par la possibilité de former des liaisons hydrogène. On a examiné la formation des liaisons dans les cycles I_4 centrosymétriques du $(Ph_2I)I_3$ et du $(Ph_2I)I$.

Mots clés : structures cristallines, liaison hydrogène, liaisons iode–iode, anions polyhalogénés, triiodures.

[Traduit par la rédaction]

Received March 29, 1996.

K.N. Robertson, T.S. Cameron, and O. Knop.[2] Department of Chemistry, Dalhousie University, Halifax, NS, B3H 4J3, Canada.

[1] For Part 1 see ref. 1.

[2] Author to whom correspondence may be addressed. Telephone: (902) 494-3317 or 494-3305. Fax: (902) 494-1310.

In Part 1 (1) we showed that the type of ion packing in triiodides of compact, quasi-spherical cations generally depends on the volume V_I that is occupied in the crystal structure by one formula unit. Given the relative constancy of the amount of space occupied by the I_3^- anion, V_I represents a global measure, largely independent of the details of the cation shape, that can be used for classification and prediction of ion coordination in such structures. This is analogous to the use of the cation/anion size ratio for classifying structures consisting of spherical or quasi-spherical ions, e.g., alkali and similar halides. Although the ion-packing trend in the triiodide set in Part 1 was unmistakable, more detailed conclusions were precluded by the limited number and selection of suitable structures that were available; in particular, only cation/anion = 1 compounds were considered. Since the dependence of the ion-packing type on V_I was not the only interesting aspect of the triiodides studied in Part 1 that suffered from lack of structural information, we now supply, as a partial remedy, a number of crystal-structure determinations of both 1:1 and 1:2 organocation triiodides and of Me_2NH_2I (Table 1).

These determinations provide a significant and varied addition to the meagre body of information on hydrogen bonding to iodine. Based on these and literature results we examine, in the Discussion, the relationship of the two I...I bond lengths in I_3^- anions; the effect of N—H...I bonding on the symmetry of I_3^-; the effect of hydration on ion packing in $KIX_2 \cdot H_2O$ (X = I, Br, Cl); and the geometry of, and bonding in, the diphenyliodonium cation.

Crystal data of the title compounds are assembled in Tables 2 and 3, the positional parameters of nonhydrogen atoms in Table 4, and interatomic distances and bond angles in Table 5. Positional parameters and isotropic temperature factors of hydrogen atoms (Table A), anisotropic thermal parameters of nonhydrogen atoms (Table B), and the I...I bond lengths in a number of relevant triiodide structures (Table C) have been deposited.[3]

Individual structures

2MI

In this simple structure the ion packing is of a distorted CsCl type (Fig. 1). The cations (of symmetry C_2) are H-bonded to I^- anions to form discrete centrosymmetric ring dimers $[...I...H(N) - N - H(N)...]_2^0$ of symmetry C_{2h}. The structure may in fact be regarded as a molecular crystal consisting of these neutral ring dimers located at points of a primitive lattice defined by $\mathbf{a'} = \frac{1}{2}(\mathbf{a} + \mathbf{b})$, $\mathbf{b'} = \frac{1}{2}(-\mathbf{a} + \mathbf{b})$, $\mathbf{c'} = \mathbf{c}$.

The H(N)...I bonds are short, 2.51 Å; H(N)-I-H(N) ~ 75°. The difference between the H-bond system in 2MI and that in the other known Me_2NH_2X halide structure, 2MCl, is represented schematically in Fig. 2. In the ordered, orthorhombic low-temperature β-2MCl a C_2 rotation of alternate cations about one of their N—H...Cl bonds will convert the infinite H-bonded chain into a set of discrete ring dimers such as are found in 2MI. In the high-temperature tetragonal α-2MCl the orientational disorder of the cations gives rise to a variety of local situations, some of which will correspond to ring dimers and others that may be viewed as short segments of the β-2MCl chain. The H-bond connectivity in α-2MCl is thus statistically intermediate between those of 2MI and β-2MCl.[4]

Table 1. Compounds discussed in this paper.[a]

Code	Compound	Reference
This work		
2MI	Me_2NH_2I	
2MI3	$Me_2NH_2I_3$	
TrI3	Tropanium I_3[b]	
2PhII3	$(Ph_2I)I_3$	
Mpip2I3w	*N*-Me-piperazinium(2+) $(I_3)_2 \cdot H_2O$	
2Mpip2I3	*trans-N,N'*-Me_2-piperazinium(2+) $(I_3)_2$	
4Men2I3	$[Me_2HN(CH_2)_2NHMe_2]$ $(I_3)_2$	
4Mpr2I3	$[Me_2HN(CH_2)_3NHMe_2]$ $(I_3)_2$	
Literature		
AI3	NH_4I_3	2
MCI3	1-Me-cytosinium I_3 (MCYTRI)	3
4MI3	Me_4NI_3	1
QI3	Quinuclidinium I_3	1
Da2I3	Dabco(2+) $(I_3)_2$[c]	1
α-2MCl	α-Me_2NH_2Cl (DMEACL01)	4
β-2MCl	β-Me_2NH_2Cl (DMEACL)	5
2PhICl	$(Ph_2I)Cl$ (DPIOCL)	6
2PhIBr	$(Ph_2I)Br$ (DPIODB10, DPIODB01)	6, 7
2PhII	$(Ph_2I)I$ (DIRZOT, DIRZOT01)	6, 8
2PhITB	(Ph_2I) tetraphenylborate (HEYZUG)	9
2PhIN	$(Ph_2I)NO_3$ (PIODON)	11
2PhIX	(Ph_2I) $EtOCS_2$[d] (VATRAJ)	12
pip2IC12	Piperazinium(2+) $(ICl_2)_2$ (PIPCLI)	10
	$KI_3 \cdot H_2O$	13
	$KIBr_2 \cdot H_2O$	14
	$KICl_2 \cdot H_2O$	15

[a] In parentheses, structure code in the Cambridge Crystallographic Data Base.
[b] 8-Me-8-azoniabicyclo[3.2.1]octane I_3.
[c] 1,4-Diazoniabicyclo[2.2.2]octane $(I_3)_2$.
[d] Diphenyliodonium xanthate, Ph_2-ethylxanthogenate iodane.

[3] This material can be purchased from: The Depository of Unpublished Data, Document Delivery, CISTI, National Research Council Canada, Ottawa, Canada K1A 0S2. Tables A and C have also been deposited with the Cambridge Crystallographic Data Centre, and can be obtained on request from The Director, CCDC, University Chemical Laboratory, 12 Union Road, Cambridge CB2 1EZ, U.K.

[4] For H-bonding in other $Me_2NH_2^+$ salts see, for example, the MeCN and Et_2CO solvates of $Me_2NH_2BPh_4$ (16), $(Me_2NH_2)_2SnCl_6$ (17, 18), and $(Me_2NH_2)_4[InCl_6]Cl$ (19).

Table 2. Crystal data of the univalent-cation triiodides.[a]

Parameter	2MI	2MI3	TrI3	2PhII3
Formula	C_2H_8IN	$C_2H_8I_3N$	$C_8H_{16}I_3N$	$C_{12}H_{10}I_4$
fw	173.0	426.8	506.9	661.8
Crystal size, mm^3	0.4 × 0.4 × 0.3	0.4 × 0.3 × 0.25	0.8 × 0.2 × 0.2	0.5 × 0.2 × 0.25
θ-range, deg[b]	2–23/20	2–23/21	2–23/25	2–23/20
μ_{Mo}, cm^{-1}	54.5	100.3	68.3	76.6
Max/min[c]	1.00–0.59	0.94–0.68	1.00–0.81	1.00–0.60
a, Å	11.026(4)	6.423(1)	12.835(2)	14.987(3)
b, Å	9.993(3)	9.946(2)	13.531(2)	17.785(2)
c, Å	5.514(2)	14.512(2)	7.864(1)	6.029(1)
β, deg	110.08(3)	90	90	90.07 (2)
V, $Å^3$	571(1)	927(1)	1366(1)	1607(1)
ρ_c, g/cm^3	2.014(4)	3.058(3)	2.465(2)	2.735(2)
Space group	*C2/m* (no. 12)	*Pccn* (no. 56)	$P2_12_12_1$ (no. 19)	$P2_1/a$ (no. 14)
F(000), e	320	744	920	1176
h, k, l ranges[d]	0/12, 0/10, –6/6	0/7, 0/10, 0/15	0/14, 0/14, 0/8	0/16, 0/19, –6/6
Reflections:				
total measured	446	793	1139	2433
unique total	422	793	1139	2338
$100R_{merg}$	3.59	—	—	1.85
d/r/p[e]	404/0/22	457/0/30	992/0/110	1789/0/146
$100R$; $100R_w$	3.2; 3.7	3.0; 3.5	1.9; 2.2	2.0; 2.4
G.O.F.	3.70	1.15	0.77	0.88
Residual e.d.[f]	–0.92/1.44	–0.92/0.84	–0.45/0.58	–0.41/0.42

[a] $Z = 4$ for all four compounds. For further details see Experimental.

[b] $\theta_{min} \leq \theta \leq \theta_{max}/n$. The lattice parameters and orientation matrices were obtained by least squares from the setting angles θ of suitable *n* reflections.

[c] Maximum and minimum transmission factors applied.

[d] 0/12 stands for $h = 0$ through $h = 12$ etc.

[e] Data/restraints/parameters; $I > 3\sigma(I)$.

[f] Residual electron density ($e/Å^3$) in final difference map.

Fig. 1. 2MI: projection on (001).

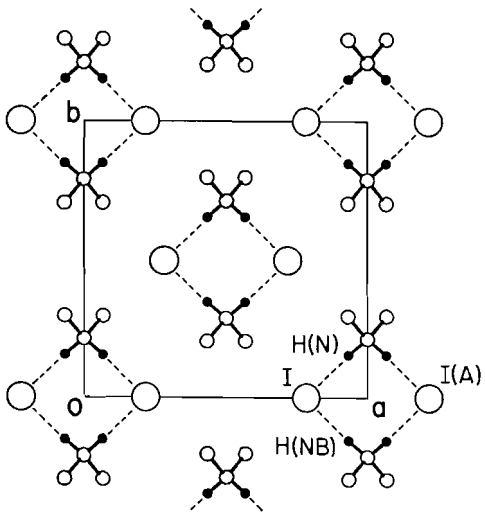

2MI3

The ion packing in this orthorhombic structure is of the NaCl type (Fig. 3). Interestingly, the NaCl arrangement is obtained directly from the corresponding undifferentiated atom arrangement in $Fm\bar{3}m$ by subgroup descent and splitting the undifferentiated atoms positions into two fourfold sets: $Fm\bar{3}m$,

Fig. 2. (*A*) $[...I...H—N—H...]_2$ ring dimers in 2MI, in a plane approximately $\parallel(20\bar{1})$. (*B*) Portion of the planar zigzag $[...Cl...H—N—H...]_\infty$ chain in β-2MCl, in the (001) plane. Breaking the H...Cl bonds at the marked points followed by rotation about the fictitious C_2 axes converts the chain into a sequence (*C*) of $[...Cl...H—N—H...]_2$ ring dimers analogous to those in 2MI. Large circles, halogen atoms; small circles, N and C atoms, the latter eclipsed in the projection. H atoms not shown.

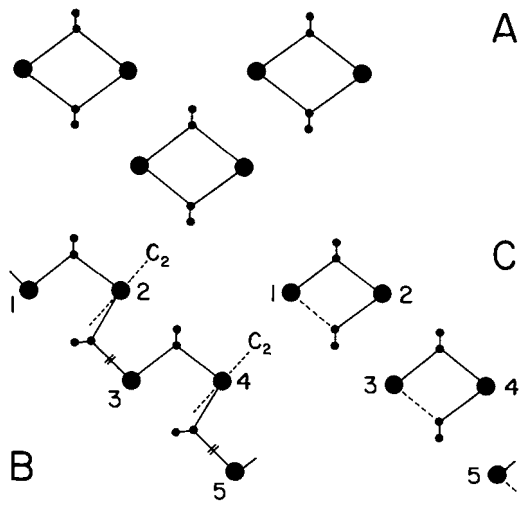

Table 3. Crystal data of the divalent-cation triiodides.[a]

Parameter	Mpip2I3w	2Mpip2I3	4Men2I3	4Mpr2I3
Formula	$C_5H_{16}I_6N_2O$	$C_6H_{16}I_6N_2$	$C_6H_{18}I_6N_2$	$C_7H_{20}I_6N_2$
fw	881.6	877.6	879.6	893.7
Crystal size, mm^3	0.7 × 0.3 × 0.25	1.50 × 0.15 × 0.1	0.3 × 0.25 × 0.09	0.8 × 0.2 × 0.2
θ-range, deg[b]	2–25/23	2–23/23	2–23/25	2–25/22
μ_{Mo}, cm^{-1}	99.1	100.8	96.1	92.0
Max/min[c]	1.00–0.42	1.00–0.52	1.00–0.43	1.00–0.44
a, Å	14.091(3)	8.451(1)	8.642(1)	9.989(1)
b, Å	7.351(4)	12.196(2)	12.044(1)	26.516(2)
c, Å	18.725(3)	9.454(1)	9.537(1)	7.755(1)
α, deg	90	90	90	95.37(1)
β, deg	106.62(1)	108.78(1)	102.96(1)	96.85(1)
γ, deg	90	90	90	84.75(1)
V, $Å^3$	1858(1)	923(1)	967(1)	2024(1)
Z	4	2	2	4
ρ_c, g/cm^3	3.151(2)	3.159(1)	3.019(1)	2.933(1)
Space group	$P2_1/n$ (no. 14)	$P2_1/a$ (no. 14)	$P2_1/a$ (no. 14)	$P\bar{1}$ (no. 2)
F(000), e	1544	768	772	1576
h, k, l ranges[d]	0/16, 0/8, 0/22	0/9, 0/13, −10/10	0/9, 0/13, −10/10	0/10, −29/29, −8/8
Reflections:				
total measured	3713	1465	1538	6012
unique total	3559	1364	1454	5627
$100R_{merg}$	2.1	1.6	1.4	1.8
d/r/p[e]	2124/0/128	968/0/65	1349/7/65[g]	4166/0/272
$100R$; $100R_w$	3.2; 3.8	2.4; 3.0	3.2;[g]	3.1; 4.6
G.O.F.	1.30	1.08	1.10[g]	1.76
Residual e.d.[f]	−1.08/0.77	−0.64/0.72	−1.10/0.74	−1.02/1.23

[a]For footnotes *b–f* see Table 2.
[g]Full matrix on F^2, SHELXL-93 (cf. Experimental). For $I > 2\sigma(I)$, $R1 = 0.032$, $wR2 = 0.091$; all data, $R1 = 0.058$, $wR2 = 0.105$; G.O.F. on F^2, 1.10.

Fig. 3. 2MI3: projection on (100). Black circles, H(N) atoms. Broken lines indicate H(N)...I(2) bonds.

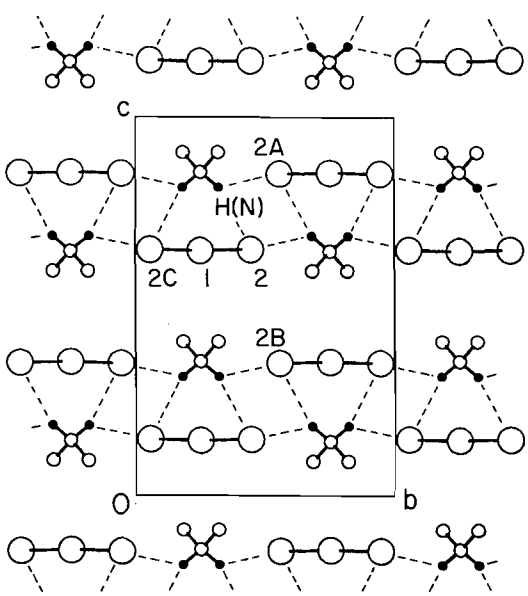

8(*c*) ⊃ *Fmmm*, 8(*f*) ⊃ *Cmca*, 8(*e*) [*abc* → *cab*] → *Abma*, 8(*e*) ⊃ *Pccn*, 4(*c*) + 4(*d*), with I(1) in 4(*c*) and N in 4(*d*), i.e., $(\frac{1}{4}, \frac{1}{4}, \frac{1}{4}) \rightarrow (\frac{1}{4}, \frac{1}{4}, y)$ and $(\frac{1}{4}, \frac{3}{4}, \frac{1}{4}) \rightarrow (\frac{1}{4}, \frac{3}{4}, y)$. Both the cation and the anion have C_2 symmetry. The discrete anion is slightly bent.

Each of the two H(N) atoms is involved in a bifurcated H(N)...I(2),I(2A) bond. This results in the formation of [...I...H(N)...I...] helices ∥*a* and, in turn, of H-bonded twisted double chains ∥*b*. The chains are separated from one another by layers of CH_3 groups. Each terminal atom of an anion participates in an H-bond to the H(N) atoms of different cations, and the two terminal atoms of each anion are H-bonded to the two H(N) atoms of the same associated cation. The H(N)...I bonds are appreciably longer than the unbranched H(N)...I bonds in 2MI, 2.96 and 3.08 Å, respectively, as against 2.51 Å.[4]

TrI3

The ion packing in this chiral orthorhombic structure is of the *anti*-NiAs type, similar to that in 4MI3 and QI3 (Table 1 of ref. 1): $\frac{1}{2}(\mathbf{a_O} + \mathbf{c_O}) \rightarrow \mathbf{a_{H,1}}$, $\frac{1}{2}(-\mathbf{a_O} + \mathbf{c_O}) \rightarrow \mathbf{a_{H,2}}$, $\mathbf{b_O} \rightarrow \mathbf{c_H}$; $2b_O/(a_O^2 + c_O^2)^{1/2} = 1.798 \rightarrow a_H/c_H = 1.633$ (ideal), $a_O/c_O = 1.632 \rightarrow \sqrt{3} = 1.732$ (ideal). The smaller internal angle in the base of the pseudohexagonal cell is 63.0° instead of the ideal 60°.

The anions are arranged in homogeneous layers ∥(010), and ditto for the cation centroids (Fig. 4). Unlike the arrangement in 4MI3 and QI3, the I_3 units are inclined to *all three* crystal-

Table 4. Positional parameters ($\times 10^4$) and isotropic temperature factors ($Å^2$) of nonhydrogen atoms.[a]

Atom	x	y	z	B_{eq}	Atom	x	y	z	B_{eq}
2MI									
I	7827.4(8)	0	0421(2)	3.84(4)	C	9318(9)	2945(10)	6347(16)	4.7(4)
N	1	2121(10)	1/2	4.5(4)					
2M13									
I(1)	1/4	1/4	6466(1)	3.59(6)	N	1/4	1/4	6444(13)	4.9(9)
I(2)	−0915(2)	4442(1)	6493(1)	4.58(5)	C	0891(28)	8177(17)	5920(11)	5.6(9)
Tr13									
I(1)	5273.7(5)	5128.7(5)	2295.0(8)	3.54(3)	C(3)	10564(9)	3131(9)	3429(18)	4.7(6)
I(2)	7444.8(6)	5848.5(6)	1678(1)	4.56(4)	C(4)	9842(10)	2389(9)	4351(13)	4.1(6)
I(3)	3145.7(6)	4569.3(6)	2789(1)	4.79(4)	C(5)	8993(8)	2019(8)	3201(14)	3.8(5)
N	8370(6)	2915(5)	2613(12)	3.5(4)	C(6)	9408(9)	1626(8)	1483(17)	4.3(6)
C(1)	9125(8)	3393(8)	1360(14)	3.6(5)	C(7)	9495(11)	2522(9)	0278(15)	4.4(6)
C(2)	9967(8)	3891(7)	2383(15)	3.8(4)	C(N)	7330(8)	2653(8)	1872(18)	4.9(6)
2PhII3									
I(1)	2492.8(4)	4404.7(3)	0906.0(8)	3.47(2)	C(15)	2184(5)	7710(4)	−5682(15)	4.0(4)
I(2)	3829.8(4)	4672.2(3)	4097(1)	4.67(3)	C(16)	1608(5)	7443(4)	−4068(13)	3.4(4)
I(3)	0993.1(4)	4277.8(3)	−2583.2(9)	3.58(2)	C(21)	−0161(5)	7331(4)	−1222(12)	3.0(3)
I(4)	0412.3(3)	6262.4(3)	−1791.5(8)	2.89(2)	C(22)	0108(5)	7721(5)	0639(12)	3.6(4)
C(11)	1333(5)	6694(4)	−4207(12)	2.7(3)	C(23)	−0215(6)	8463(5)	0867(14)	4.0(4)
C(12)	1614(5)	6213(4)	−5884(13)	3.1(3)	C(24)	−0804(6)	8749(4)	−0676(16)	4.2(4)
C(13)	2210(5)	6498(5)	−7426(12)	3.7(4)	C(25)	−1055(6)	8339(5)	−2516(15)	4.2(4)
C(14)	2489(5)	7251(4)	−7334(13)	3.4(4)	C(26)	−0737(5)	7613(4)	−2783(13)	3.6(4)
Mpip2I3w									
I(10)	1556.4(7)	−0550.7(14)	4988.7(5)	3.24(4)	N(2)	0072(8)	3216(18)	1819(7)	3.3(5)
I(11)	1462.0(7)	0266.5(15)	6445.9(5)	3.59(4)	C(1)	−0859(10)	4674(22)	2610(8)	3.5(6)
I(12)	1665.9(7)	−1546.0(14)	3410.8(5)	3.38(4)	C(2)	−0613(11)	4748(23)	1874(8)	3.9(7)
I(20)	1565.2(7)	−0597.3(14)	−0067.7(5)	3.16(4)	C(3)	1003(10)	3289(20)	2453(9)	3.3(6)
I(21)	1325.6(7)	−1393.7(14)	1372.0(6)	3.82(4)	C(4)	0765(10)	3224(20)	3187(8)	3.1(6)
I(22)	1717.0(8)	0338.9(15)	−1597.7(6)	3.77(4)	C(N)	−0127(12)	4712(24)	3981(9)	4.2(7)
N(1)	0092(8)	4764(17)	3244(8)	3.1(5)	O	0678(8)	3805(16)	0542(6)	4.6(5)
2Mpip2I3									
I(1)	4978(1)	3227.7(8)	4658.9(8)	3.27(3)	C(1)	3446(14)	−0206(10)	0330(14)	3.5(5)
I(2)	5405(1)	3144.3(6)	1533.7(8)	3.33(3)	C(2)	3474(14)	0053(10)	−1252(13)	3.5(5)
I(3)	4567(1)	3277.2(7)	7515.0(9)	3.86(4)	C(N)	4915(19)	0083(11)	3013(14)	4.5(6)
N	4918(12)	0291(8)	1478(10)	3.3(4)					
4Men2I3									
I(1)	4956(1)	3206(1)	7467(1)	3.55(8)	C	5481(16)	−0163(11)	4460(10)	8.3(5)
I(2)	5407(1)	3250(1)	4380(1)	4.18(8)	C(1)	6380(13)	0241(13)	2327(13)	6.0(3)
I(3)	4574(1)	3168(1)	10344(1)	4.74(8)	C(2)	3546(11)	0231(12)	2153(14)	6.3(3)
N	5104(11)	0483(7)	3102(8)	4.4(2)					
4Mpr2I3									
I(10)	10205(1)	4255.3(4)	3090(1)	3.73(5)	C(12)	8746(15)	3764(6)	7792(20)	3.9(7)
I(11)	12278(1)	3506.7(5)	4636(2)	4.70(5)	C(13)	7258(6)	3839(6)	7306(19)	3.8(7)
I(12)	8253(1)	5017.2(5)	1549(2)	4.62(5)	C(14)	10892(18)	2485(6)	7985(24)	5.1(9)
I(20)	7203(1)	1923.7(4)	8234(1)	3.91(5)	C(15)	11530(18)	3339(7)	9317(26)	6.0(10)
I(21)	9440(1)	1218.4(5)	9582(2)	4.62(5)	C(16)	7448(17)	4706(7)	6340(27)	5.5(10)

Table 4 (*concluded*).

Atom	x	y	z	B_{eq}	Atom	x	y	z	B_{eq}
I(22)	5036(1)	2653.2(4)	6877(2)	4.57(5)	C(17)	5215(17)	4402(7)	6560(23)	5.0(9)
I(30)	6663(1)	3395.1(4)	2132(1)	4.38(5)	N(21)	8139(13)	0668(5)	3006(16)	4.2(6)
I(31)	8778(1)	2602.5(6)	3234(2)	6.14(7)	N(22)	4002(13)	1916(5)	2901(16)	4.2(6)
I(32)	4545(1)	4155.3(5)	1012(2)	5.65(6)	C(21)	6655(16)	0786(7)	3003(21)	4.4(8)
I(40)	5399(1)	0486.0(5)	7652(2)	4.85(6)	C(22)	6172(17)	1333(6)	2918(23)	4.5(8)
I(41)	7693(1)	−0274.5(5)	8063(2)	6.75(8)	C(23)	4654(18)	1388(6)	2637(22)	4.5(8)
I(42)	3080(1)	1237.5(5)	7247(2)	6.16(7)	C(24)	8489(18)	0100(7)	2998(25)	5.3(10)
N(11)	10607(12)	3056(4)	7980(15)	3.7(6)	C(25)	8935(19)	0960(8)	4472(28)	6.7(12)
N(12)	6680(12)	4377(5)	7277(16)	3.6(6)	C(26)	4455(20)	2278(7)	1774(28)	6.2(10)
C(11)	9155(16)	3208(6)	8098(22)	4.4(8)	C(27)	2506(17)	1926(8)	2710(25)	5.5(10)

[a]Parameter values of atoms in special positions are not multiplied by 10^4.

Fig. 4. TrI3: projection on (100). Black circles, H(N) atoms. Broken lines indicate H(N)...I(2) bonds.

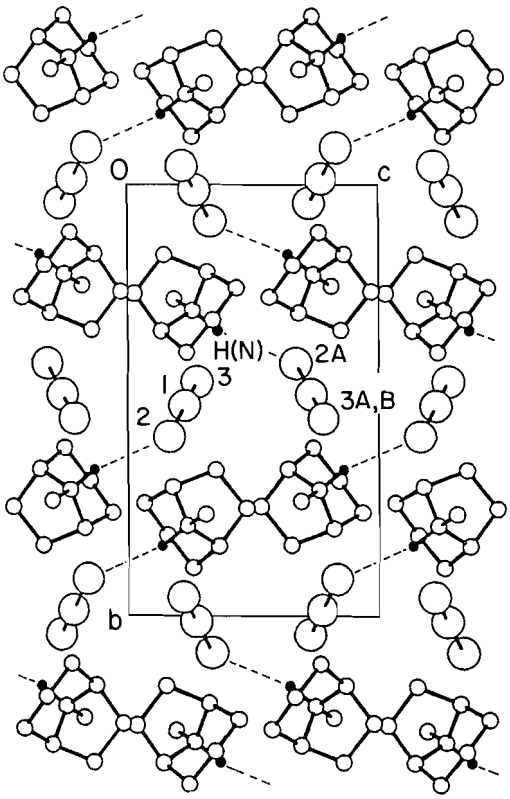

lographic axes. The anion is bent, I(2)-I(1)-I(3) = 176.0°, and discrete, the inter-anion I...I separations being all greater than 4.4 Å.

In the cation (of symmetry C_1), the H(N) atom is in axial position on the N atom of the 6-membered ring. The H-bond between H(N) and I(2A), 2.77 Å, is bent, N-H(N)-I(2A) = 162°. The H-bonding is restricted to cat/an pairs.

2PhII3

In this monoclinic structure layers of cations ||(010) alternate with layers of anions, the mean perpendicular separation of like layers being $\frac{1}{2}b$ = 8.89 Å (Fig. 5*A*). An interesting feature of the structure is the occurrence of four-membered centrosymmetric rings of I atoms formed by the terminal I(3) atoms of the anions and the I(4) atoms of the cations (Fig. 5*B*).[5] The I...I distances in these $[...I(3)...I(4)...]_2$ rings, 3.511 and 3.667 Å, respectively, qualify for weak I...I bonding interactions; they and the almost right I(3)-I(4)-I(3A) and I(4)-I(3)-I(4A) angles, 88.7° and 91.3°, respectively, are strongly reminiscent of similar distances and bond angles in higher organoammonium polyiodides (20). The rings are dimensionally closely similar to the corresponding $Ph_2I(\mu\text{-}I)_2IPh_2$ ring dimers in 2PhII (Figs. 5*C* and 6), except that the simple I^- ions in 2PhII are now replaced by the somewhat bent I_3^- anions approximately perpendicular to the ring plane (Fig. 5*B*; angle between ring plane and I(3)—I(2), 87°). The implications of the dimensional changes that are observed on replacing I^- by I_3^- are discussed below. The shortest *inter-anion* I...I distance is I(2)...I(2B) = 3.852 Å, across an inversion centre; I(1)-I(2)-I(2B) = 153°.

The cation symmetry is C_1. The I(4)—C(11) and I(4)—C(21) bond lengths, and the C(11)-I(4)-C(21) and C(β)-C(α)-C(β′) bond angles, are compared to those in other Ph_2I^+ salts in Table 6. The phenyl rings R1 and R2 are satisfactorily planar, the respective mean deviations of the C atoms from the best planes through the R1 and R2 skeletons being 0.007[4] and 0.008[4] Å; the deviations of the I(4) atom from these planes are −0.026 and 0.168 Å, respectively. The R2/R1 angle is 77.8° compared to 93.5° in 2PhII.

Mpip2I3w, 2Mpip2I3, and 4Men2I3

The structures of these 1:2 triiodides show striking similarities (Table 7, Fig. 7). The anions, which are roughly ||*c*, project on (001) into honeycombs of pseudohexagonal cells the centres of which are occupied by the projected cations. In turn, the projected cations divide the projections on (001) into triangular tilings. The structures can thus be viewed as monoclinic variants of the CdI_2 structure, with the cation centroids exactly or close to coplanar and at the corners of the pseudohexagonal cells.[6] The anions in these cells are in positions corresponding to $\pm(\frac{1}{3}, \frac{2}{3}, z)$ in the CdI_2 aristotype, but the z coordinate is not

[5] The geometry of these rings is analogous to that of the $[...N—H(N)...I...]_2$ rings in 2MI (cf. above).

[6] In Fig. 7 the pseudohexagonal cells are defined by the $(\frac{1}{2}, 0, 0)$ and $(0, \frac{1}{2}, 0)$ points of the corresponding pseudo-orthohexagonal cells shown.

Table 5. Interatomic distances (Å) and bond angles (deg) in the title compounds.

Atoms	Distance	Atoms	Angle
2MI			
N...I	3.529(6)	I-N-I(A)	106.2(3)
H(N)...I	2.51	N-I-N(B)	73.8(3)
I...I(C)	4.970(2)	N-H(N)-I	177
I...I(D)	5.047(2)	H(N)-I-H(NB)	75
I...I(A)	5.643(2)	C-N-C(A)	112.2(10)
A $2-x$ $-y$ $1-z$		C $2-x$ $-y$ $-z$	
B x $-y$ z		D $\frac{3}{2}-x$ $\frac{1}{2}-y$ $-z$	
2MI3			
I(1)—I(2)	2.923(1)	I(2)-I(1)-I(2C)	178.44(8)
I(2)...I(2D)	4.367(2)	N-H(N)-I(2)	135
I(2)...I(2A)	4.481(2)	N-H(N)-I(2A)	121
I(2)...I(2B)	4.626(2)	1(2)-H(N)-I(2A)	96
N...1(2A)	3.705(15)	H(N)-I(2)-H(NE)	118
H(N)...I(2A)	3.08	C $\frac{1}{2}-x$ $\frac{1}{2}-y$ z	
N...I(2)	3.751(10)	D $-\frac{1}{2}-x$ $\frac{1}{2}-y$ z	
H(N)...I(2)	2.96		
H(N)...H(NE)	5.16	E $x-\frac{1}{2}$ $1-y$ $\frac{3}{2}-z$	
A $\frac{1}{2}+x$ $1-y$ $\frac{3}{2}-z$			
B $-x$ $1-y$ $1-z$			
TrI3			
I(1)—I(3)	2.861(1)	I(2)-I(1)-I(3)	175.97(3)
I(1)—I(2)	2.991(1)	N-H(N)-I(2A)	162
I(3)...I(3B)	4.423(1)	H(N)-I(2A)-I(1A)	88
I(2)...I(2A)	4.555(1)	I(2)-H(N)-I(2A)	86
N...I(2A)	3.757(9)	A $\frac{3}{2}-x$ $1-y$ $\frac{1}{2}+z$	
H(N)...I(2A)	2.78	B $\frac{1}{2}-x$ $1-y$ $\frac{1}{2}+z$	
2PhII3			
I(1)—I(2)	2.817(1)	I(2)-I(1)-I(3)	174.43(3)
I(1)—I(3)	3.085(1)	I(1)-I(2)-I(2B)	152.99(3)
I(3)...I(4A)	3.511(1)	I(1)-I(3)-I(4)	90.78(2)
I(3)...I(4)	3.667(1)	I(1)-I(3)-I(4A)	86.84(2)
I(2)...I(2B)	3.852(1)	I(3)-I(4)-I(3A)	88.69(2)
I(3)...I(4C)	4.104(1)	I(4)-I(3)-I(4A)	91.31(2)
I(3)...I(3A)	5.018(1)	C(11)-I(4)-C(21)	92.9(3)
I(4)...I(4A)	5.135(1)	C(11)-I(4)-I(3)	95.9(2)
I(4)—C(11)	2.149(7)	C(11)-I(4)-I(3A)	173.2(2)
I(4)—C(21)	2.114(7)	C(21)-I(4)-I(3)	169.5(2)
A $-x$ $1-y$ $-z$		C(21)-I(4)-I(3A)	83.1(2)
B $1-x$ $1-y$ $1-z$		C(12)-C(11)-C(16)	122.7(7)
C $-x$ $1-y$ $-1-z$		C(22)-C(21)-C(26)	123.9(7)
Mpip2I3w			
I(10)—I(11)	2.834(2)	I(11)-I(10)-I(12)	178.53(5)
I(20)—I(21)	2.871(2)	I(21)-I(20)-I(22)	177.08(5)
I(20)—I(22)	3.013(2)	I(20)-I(21)-I(12)	163.09(4)
I(10)—I(12)	3.090(2)	I(21)-I(12)-I(10)	161.70(4)
I(11)—I(22D)	3.578(2)	I(10)-I(11)-I(22D)	166.03(5)
I(12)...I(21)	3.711(2)	I(11)-I(22D)-I(20D)	163.06(5)

Table 5 (*concluded*).

Atoms	Distance	Atoms	Angle
I(10)...I(11G)	4.338(2)	N(1)-H(N1)-I(12E)	163
I(21)...I(12B)	4.496(2)	N(2)-H(N22)-I(22A)	158
I(20)...I(10B)	4.535(2)	N(2)-H(N21)-O	171
N(1)...I(12E)	3.46(1)	A $-x$ $-y$ $-z$	
H(N1)...I(12E)	2.47		
N(2)...I(22A)	3.57(1)	B $\frac{1}{2}-x$ $\frac{1}{2}+y$ $\frac{1}{2}-z$	
H(N22)...I(22A)	2.60		
H(N22F)...I(22E)	2.60	C $\frac{1}{2}+x$ $\frac{1}{2}-y$ $\frac{1}{2}+z$	
N(2)...O	2.79(2)		
H(N21)...O	1.78	D x y $1+z$	
O...O(F)	2.94(2)	E x $1+y$ z	
O...I(12B)	3.70(1)	F $-x$ $1-y$ $-z$	
O...I(21A)	4.26(1)	G $-x$ $-y$ $1-z$	
2Mpip2I3			
I(1)—I(3)	2.832(1)	I(2)-I(1)-I(3)	179.27(4)
I(1)—I(2)	3.091(1)	I(1)-I(2)-I(3A)	162.44(3)
I(2)...I(3A)	3.637(1)	N-H(N)-I(2)	163
N...I(2)	3.50(1)	H(N)-I(2)-I(1)	92
H(N)...I(2)	2.51	A x y $z-1$	
4Men2I3			
I(1)—I(3)	2.837(1)	I(2)-I(1)-I(3)	179.35(4)
I(1)—I(2)	2.056(1)	I(1)-I(2)-I(3A)	161.90(3)
I(2)...I(3A)	3.755(1)	N-H(N)-I(2)	171
N...I(2)	3.538(8)	H(N)-I(2)-I(1)	110
H(N)...I(2)	2.53	A x y $z-1$	
4Mpr2I3			
I(30)—I(32)	2.899(2)	I(11)-I(10)-I(12)	177.67(5)
I(10)—I(12)	2.913(2)	I(21)-I(20)-I(22)	178.03(5)
I(40)—I(41)	2.919(2)	I(31)-I(30)-I(32)	178.65(6)
I(40)—I(42)	2.921(2)	I(41)-I(40)-I(42)	179.29(6)
I(20)—I(22)	2.934(2)	I(30G)-I(32G)-I(12C)	166.25(5)
I(20)—I(21)	2.937(2)	I(32G)-I(12C)-I(10C)	170.59(5)
I(30)—I(31)	2.950(2)	I(10C)-I(11C)-I(22)	174.79(5)
I(10)—I(11)	2.961(2)	I(11C)-I(22)-I(20)	173.48(5)
I(22)...I(11C)	3.766(2)	I(20)-I(21)-I(41B)	173.45(5)
I(12)...I(32A)	3.865(2)	I(21)-I(41B)-I(40B)	159.23(6)
I(21)...I(41B)	4.012(2)	I(30)-I(31)-I(42D)	166.15(5)
I(42)...I(21C)	4.257(2)	I(31)-I(42D)-I(40D)	155.66(5)
I(32)...I(11C)	4.372(2)	N(11)-H(11)-I(11)	155
I(11)...I(31)	4.392(2)	N(12)-H(12)-I(12E)	149
I(31)...I(42D)	6.110(2)	N(21)-H(21)-I(21F)	164
N(11)...I(11)	3.59(1)	N(22)-H(22)-I(22)	161
H(11)...I(11)	2.65	H(11)-I(11)-I(10)	98
N(12)...I(12E)	3.81(1)	H(12)-I(12E)-I(10E)	108
H(12)...I(12E)	2.90	H(21)-I(21F)-I(20F)	103
N(21)...I(21F)	3.57(1)	H(22)-I(22)-I(20)	94
H(21)...I(21F)	2.58	C $x-1$ y z	
N(22)...I(22)	3.59(1)	D $x+1$ y z	
H(22)...I(22)	2.61	E x y $1+z$	
A $1-x$ $1-y$ $-z$		F x y $z-1$	
B $2-x$ $-y$ $2-z$		G $-x$ $1-y$ $-z$	

well defined (i.e., not close to $\frac{1}{4}$) because the rod-like anions, aligned roughly $\perp(001)$, extend vertically into the adjacent cells. This results in the formation of anion strings with inter-anion I...I separations between ~3.58 and ~3.76 Å (Table 5) and thus qualifying for weak I...I bonding interactions such as are observed in linear polyiodide chains (e.g., refs. 20–23). The structures may therefore also be regarded as consisting of anion channels $\parallel c$ containing the cations.

Fig. 5. (*A*) 2PhII3: projection on (001). (*B*) the centrosymmetric [...I(3)...I(4)...]$_2$ ring dimer in 2PhII3. (*C*) The corresponding [...I(1)...I(2)...]$_2$ ring dimer in 2PhII. The I—I bond lengths are in Å.

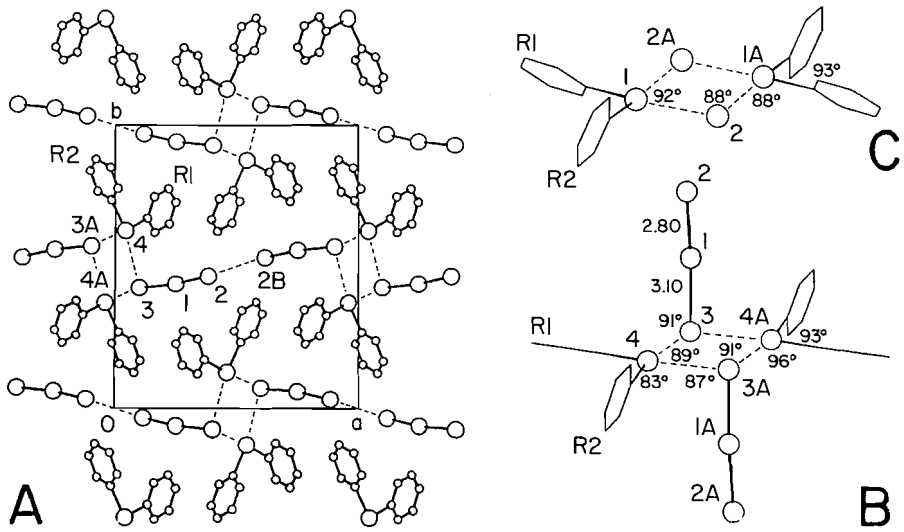

Fig. 6. I_4 ring dimers in 2PhII (top) and 2PhII3 (bottom): comparison of bond lengths and angles. Atom numbering in 2PhII as in ref. 6; in 2PhII3, as in Table 4.

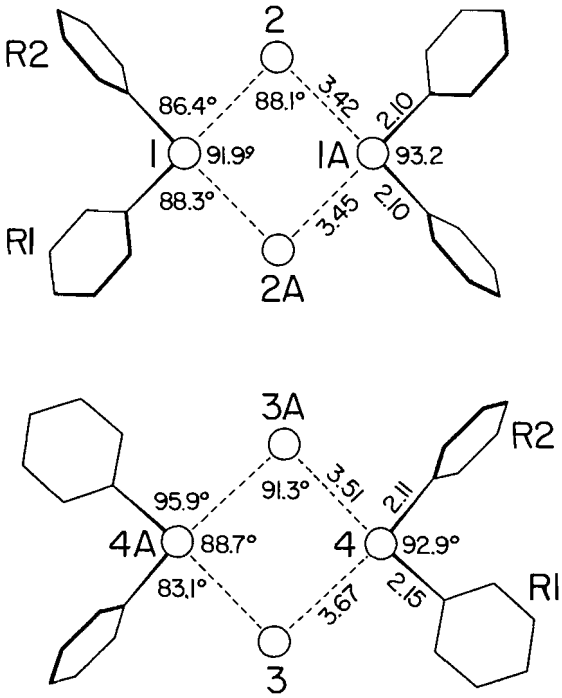

The above three structures are closely related to the structure of the unsubstituted piperazinium salt pip2IC12 reported almost 40 years ago (10). Its triclinic $P\bar{1}$ unit cell *T*, which contains the heteroatomic trihalide anion $IC1_2^-$, can be transformed into the "orthohexagonal" $C\bar{1}$ cell *O* shown in Fig. 7*D* by

$$\begin{pmatrix} a_O \\ b_O \\ c_O \end{pmatrix} = \begin{pmatrix} 0 & 0 & 1 \\ 2 & 0 & 1 \\ 0 & 1 & 0 \end{pmatrix} \begin{pmatrix} a_T \\ b_T \\ c_T \end{pmatrix},$$

$$\begin{pmatrix} x_O \\ y_O \\ z_O \end{pmatrix} = \begin{pmatrix} -\frac{1}{2} & 0 & 1 \\ \frac{1}{2} & 0 & 0 \\ 0 & 1 & 0 \end{pmatrix} \begin{pmatrix} x_T \\ y_T \\ z_T \end{pmatrix} + \begin{pmatrix} \frac{1}{4} \\ \frac{1}{4} \\ 0 \end{pmatrix}$$

The inter-anion C1...C1 separation in the $IC1_2^-$ strings $\| c_O$ is ~3.3 Å.

While the above three triiodide structures are of the same ion-packing type, their particular features differ. The simplest of the three, 2Mpip2I3, can be derived from the CdI_2 aristotype by $P\bar{3}m1 \supset C2/m \supset P2_1/a$; the alternating orientations of the cations and the anions are most directly described in terms of the dichromatic space group P_C2_1/a–$C2/m|P2_1/a$. The anions, almost $\| c$, form hexagonal channels which enclose the cations lengthwise. The centrosymmetric *trans* cations are attached to the walls of the channels by short N—H(N)...I(2) bonds (N...I(2) = 3.50 Å, H(N)...I(2) = 2.51 Å, N-H(N)-I(2) = 163°) roughly perpendicular to the channel axis (Fig. 8*A*). The asymmetric, practically linear anions are arranged in strings $\| c$, in which the end-to-end I(2)...I(3A) separation is 3.637 Å; this is the shortest inter-anion I...I distance in the structure. The anion strings are not completely straight, I(1)-I(2)-I(3A) = 162.4°.

The $P2_1/a$ unit cell of 4Men2I3 is dimensionally closely similar to that of 2Mpip2I3. The overall organization of the two structures is the same (Figs. 7*A*, *B* and 8), and the H-bond geometries are comparable: in 4Men2I3, N...I(2) = 3.54 Å, H(N)...I(2) = 2.53 Å, N-H(N)-I(2) = 171°. The inter-anion I...I distance in the anion chains is slightly longer in 4Men2I3, I(2)...I(3A) = 3.780 Å, but the chains are not straighter than in

Table 6. Bond lengths (Å) and angles (deg) in diphenyliodonium cations.[a]

Compound	d(I—C)	C(α)-I-C(α′)	C(β)-C(α)-C(β′)
2PhII3	2.149(7)	92.9(3)	122.7(7)
	2.114(7)		123.9(7)
2PhIN	2.114(7)	92.0(4)	122.3(8)
	2.114(9)		122.5(8)
2PhII	2.095(9)	93.2(5)	
	2.103(9)		
2PhIBr	2.071(10)	91.8(6)	
	2.095(13)		
2PhIC1	2.078(6)	92.6(3)	
	2.096(7)		
2PhITB	2.069(11)	95.1(4)	120.4(12)
2PhIX	2.152(7)	90.6(3)	123.0(8)
	2.106(8)		123.1(8)
Weighted mean	2.105[24]	92.5[13]	122.8[8]

[a]See Table 1 for codes and references. The cation in all the above compounds is of C_1 symmetry, with the exception of 2PhITB, in which the cation symmetry is C_s.

2Mpip2I3. The I—I bond lengths in the asymmetric but practically linear anion are almost the same as in 2Mpip2I3. The H-bond to the I(2) atom in the two structures would be expected to weaken the I(1)—I(2) bond (cf. ref. 1), and this is in fact observed: I(1)—I(2) = 3.05–3.09 Å, I(1)—I(3) = 2.83–2.84 Å.

The one important difference between the two structures is in the positioning of the cation in the hexagonal channels ||c relative to the anions. While the arrangements of the anion strings are almost identical, the presence of the extra *N*-Me groups in 4Men2I3 displaces the cation along the channel axis in such a way that the Me groups are at the same vertical height ||c as the gaps in the anion chains. More precisely, the cation centre on the channel axis is shifted with respect to the midpoint of the nearest I(1) positions in the associated anion string by $\delta z = -0.034 \sim 0.32$ Å in 2Mpip2I3 but by $\delta z = -0.253 \sim 2.41$ Å in 4Men2I3. This "vernier" effect in the more or less rigid anion framework depends on the length of the cation as well as on the number and positions of the *N*-methyls and thus on the opportunity for H-bond formation. It is present also in Mpip2I3w (Fig. 9, see below), where the offset $\delta z = -0.026 \sim 0.49$ Å accommodates the piperazinium ring (rather than the single terminal *N*-Me group or the H_2O molecule) in the gap between successive anions in the associated chain. The effect is also evident, though in a more complicated way because of the approximate match of the cation and anion lengths, in the 4Mpr2I3 structure (Fig. 10, see below).

In Mpip2I3w the *c* edge is doubled,[7] but the gross features of the structure strongly resemble those of 2Mpip2I3. The

[7] This doubling corresponds to a doubling of the CdI_2 cell: $P\bar{3}m1 \rightarrow P_c\bar{3}m1 \supset C_c2/m$.

Fig. 7. Four CdI_2-type structures projected on (001). (*A*) 2Mpip2I3, $P2_1/a$. (*B*) 4Men2I3, $P2_1/a$. (*C*) Mpip2I3w, $P2_1/n$; H_2O molecules omitted for clarity. (*D*) pip2IC12, $C\bar{1}$ (see text). Black circles, H(N) atoms; dotted lines, H(N)...I bonds. Broken lines indicate the hexagonal tesselations.

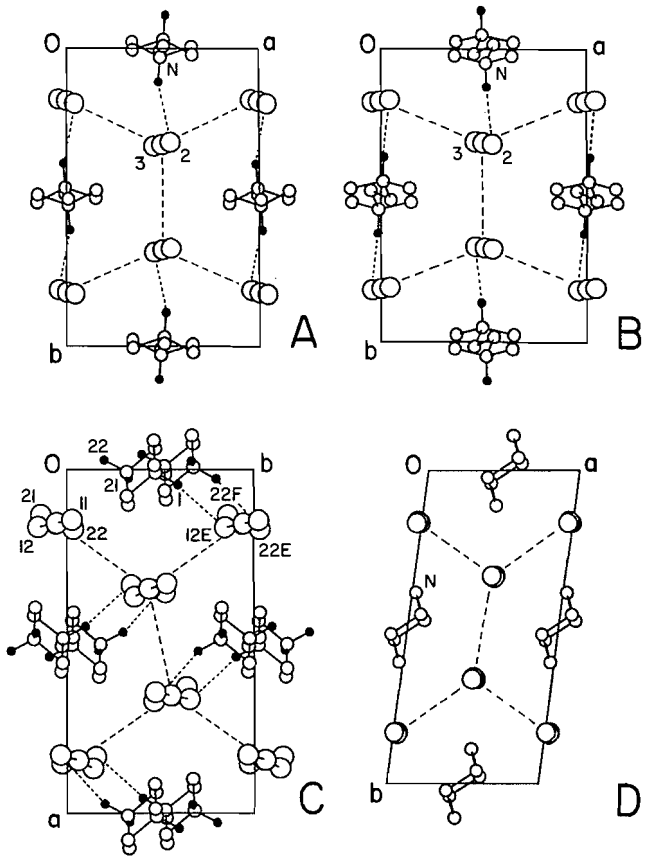

anions again form hexagonal channels ||c, but the cations enclosed in these channels are now joined by the water molecules to form centrosymmetric cat...$(H_2O)_2$...cat dimers (Fig. 9). The H(N1) and H(N22) atoms are bonded to the anions, while H(N21) is bonded to the water molecule. The structure contains two anions, a1 = I(11)-I(10)-I(12) and a2 = I(21)-I(20)-I(22), both asymmetric and slightly bent. In the anion strings ||c (Fig. 9), the end-to-end inter-anion I...I separations are I(11)...I(22D) = 3.578 Å and I(21)...I(12) = 3.711 Å. All the other inter-anion I...I distances are >4.3 Å.

The N—H(N)...I bonds are short and bent; the N—H(N)...O bond is almost straight (Table 5). The O...O distance in the centrosymmetric H_2O pair is 2.94 Å. Since the H(O) atoms were not seen in the difference map, the H-bonding at the water molecules is not established. However, it is plausible to assume that the observed O...O separation corresponds to an O—H...O bond with the H(O) atom disordered across the inversion centre. Thus, with the O...H(N21)—N(21) bond fixed (H(N21)-O-O(F) = 113°) and an O—H(O) bond pointed at O(F), the electron-density maxima expected at ~1 Å at O in the directions of the remaining two "tetrahedral" bond angles should correspond to $\frac{3}{4}$ H each and that between the two oxygen atoms to $\frac{1}{2}$ H (totalling 2 H on each oxygen), not easily discernible in a room-temperature hydrate structure.

Table 7. Title compounds with CdI_2-type structures.[a]

Parameter	Mpip2I3w	2Mpip2I3	4Men2I3	pip2IC12[b]
a (or b), Å	7.35 (= b)	8.45	8.64	6.25
b (or a), Å	14.09 (= a)	12.19	12.04	12.95
c, Å	9.37 × 2	9.45	9.54	8.45
β	106.6°	108.8°	103.0°	97.6°
V_1, Å^3	465	462	484	335
b/a (or a/b)[c]	1.917 (= a/b)	1.443	1.394	(2.07)
$2b(a^2 + c^2)^{-1/2}$[d]	1.178	1.274	1.287	(1.18)
Cation centroid at	[e]	0, ½, 0	0, ½, 0	0, ½, 0

[a]For accurate values see Tables 2 and 3.
[b]Transformed cell, see text. Parameter ratios are for the triclinic axes.
[c]Ideally, $\sqrt{3} = 1.732$.
[d]Ideally, 1.633; the value for Mpip2I3w is for $\frac{1}{2}c$.
[e]0.005, 0.409, 0.274; corresponds to ~0, ~½, ~0 in the $\frac{1}{2}c$ = 9.37 Å cell.

Fig. 8. (*A*) 2Mpip2I3. (*B*) 4Men2I3. Projections on (100). Filled circles, H(N) atoms. H-bonds are indicated by dotted, I_3^- chain connectivity by broken lines.

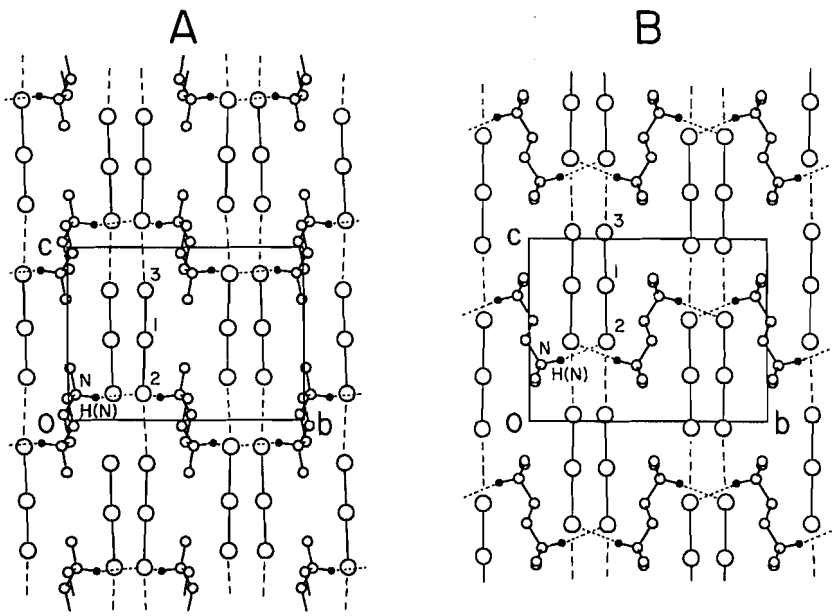

4Mpr2I3

The coincidence, in 2Mpip2I3, 4Men2I3, and pip2IC12, of the cation centre of symmetry with a crystallographic inversion centre results in a simple CdI_2-type structure. In 2Mpip2I3 the cation is noncentrosymmetric, but two of its H(N) atoms are in a *trans* conformation, rendering the cation quasi-centrosymmetric. Although the cation noncentrosymmetry leads to a doubling of c, the packing arrangement still retains the CdI_2 character. In 4Mpr2I3, however, centrosymmetry of the cation is precluded by the odd number of CH_2 groups in the cation skeleton and the cation can adopt not even a *quasi* centrosymmetric conformation. As a consequence the structural arrangement in 4Mpr2I3 (Fig. 10) differs significantly from those in the other three structures, even though there are similarities in the gross features (compare Figs. 8 and 10).

The structure consists of two cations, c1 and c2, and four anions, a1–a4. The anions are only slightly distorted (Table 5). Two of them, a1 and a2, are H-bonded to the cations; a3 and a4 do not participate in H-bonding. The anions form infinite quasi-linear strings approximately ‖(130) (Fig. 10). Each string consists of four-anion segments, ...[a3...a1...a2...a4]..., in which the inter-anion I...I separations range from 3.77 to 4.01 Å (Table 5, Fig. 11). The anion sequences in adjacent strings are antiparallel by virtue of the crystallographic inversion centres. The terminal anions a3 and a4 in the four-segment are kinked with respect to the central anions a1 and a2. The inter-anion separation *between* successive four-segments, I(31C)...I(42B), is 6.11 Å, i.e., the four-segments in the chains are discrete. The shortest I...I distance between the chains is I(42)...I(21C) = 4.26 Å.

The cation N-C-C-C-N skeleton is planar to 0.097[55] Å in c1 and to 0.062[17] Å in c2. Cation c1 is H-bonded exclu-

Fig. 9. Mpip2I3w: projection on (010). Filled circles: large, O atoms; small, H(N) atoms. Hydrogen bonds are indicated by dotted lines, anion connectivity in the chains by broken lines. For codes see Table 5.

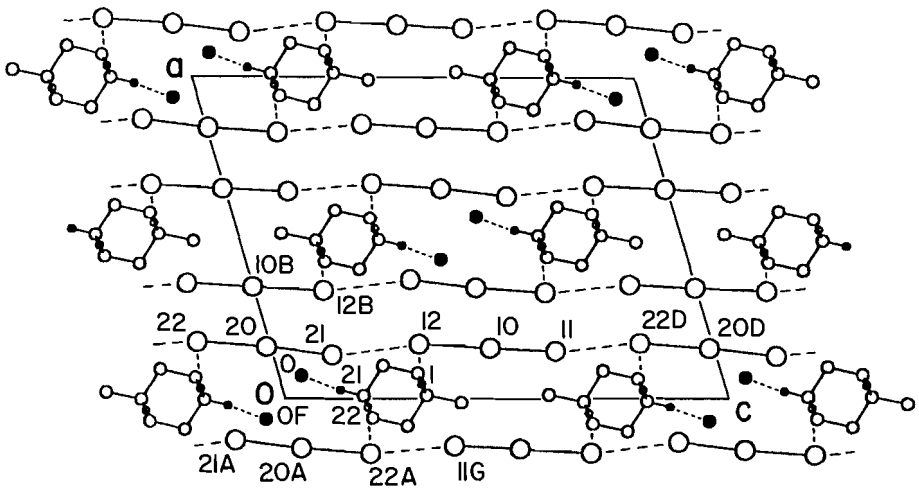

Fig. 10. 4Mpr2I3: projection on (001). For atom code see Table 5. The centre atoms of the anions, I(n0) (n = 0–4), are not numbered. Broken lines connect anions in the four-anion segments (see text).

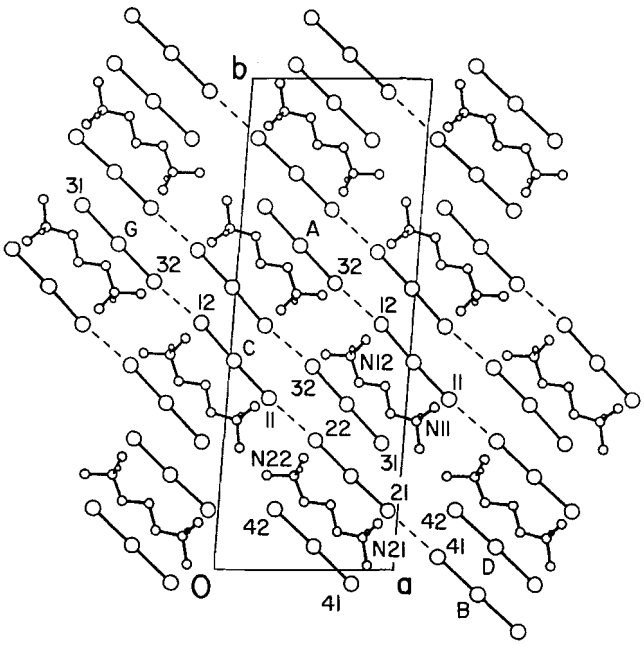

sively to a1, and c2 exclusively to a2 (Figs. 11 and 12). Anions of the same type are H-bonded in stacks ||c, so that all the cross-stapled anions are located in sheets approximately ||(130). These sheets occur in pairs, with the cations sandwiched inside a pair (cf. projection on (001), Fig. 10). The H-bonds in each cation are ipsolateral, but the cation orientations vis-à-vis their associate anions in a sandwich alternate as a result of the displacement, along the string, of the anion sequences in the sandwich-forming strings by half the four-segment period. Three of the H(N)...I bonds are short, ~2.6 Å, N-H(N)-I ~ 155–164°. The fourth bond, H(12)...I(12E), is longer, ~2.90 Å, N-H(N)-I = 149°.

Discussion

I_3^- asymmetry revisited

In reports of crystal structures containing I_3^- the observed asymmetry of the anion is often duly noted but accepted without further comment as an experimental fact. The approximate constancy of the sum of the two I—I bond lengths d(I—I) and d^*(I—I) ($d^* \geq d$) in weakly asymmetric anions has been commented upon by various authors, as has the regularity of the variation of d^* with d, but otherwise little effort appears to have been made to investigate, systematically, the specific causes of the asymmetry beyond referring to the easy polarizability of the iodine atom. While it is possible that in practice detailed attributions cannot be made, it still seems worthwhile to see what *can* be said about the effect of *particular* factors influencing the geometry of the I_3^- anion in crystals. Since large departures from centrosymmetry are sometimes associated with the presence of X—H(X)...I hydrogen bonds in the triiodide structures (cf. ref. 1), it is natural to ask, can H-bonding be singled out as preferentially responsible for such distortions in the simultaneous presence of other factors (distribution and magnitude of Coulombic and dipolar interactions in the crystal, inter-anion I...I bonding interactions)?

Given the variety of anion environments in triiodides, an answer at present can be attempted only in statistical terms. To this end we have assembled (Table C) a d,d^* sample from 25 discrete (see below) I_3^- anions with demonstrated or probable N—H(N)...I bonds (sample HB) and a corresponding sample from 21 discrete anions in structures in which H-bonding is absent (sample NHB). The HB set covers reasonably completely the reported H-bonded anions, while the NHB set represents a more or less random selection of I_3^- anions with statistically significant (in terms of the stated esd's) asymmetry. Neither set contains anions with crystallographic symme-

Fig. 11. 4MPr2I3: a four-anion segment and N—H(N)...I motif, viewed approximately perpendicular to (130), the *c* axis vertical in the page. The code letters correspond to those in Fig. 10. The separation between successive four-anion segments in a chain (i.e., beyond I(31G) and I(42B), respectively) is 4.11 Å.

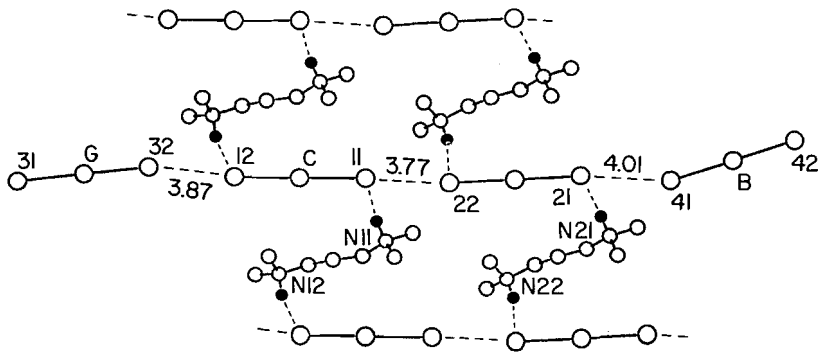

try other than C_1 or C_s (anion in *m*).[8] The two sets are presented in the d^* vs. d plots of Figs. 13*A*, *B* and again in Fig. 13*C*, where the bond-length *difference* $\Delta = d^* - d$ is plotted against the mean bond length $\Sigma = \frac{1}{2}(d + d^*)$.

The two samples contain appreciable scatter, but both a visual examination and a nonparametric test statistic $Z = r_s(n - 1)^{1/2}$ based on Spearman's rank correlation coefficient r_s show[9] unmistakable correlation of d and d^*, as does in a different way the Δ vs. Σ plot. To show whether or not HB and NHB come from the same population, i.e., whether or not H-bonding is a *preferential* factor affecting the symmetry of the anion, we shall assume that I_3^- is a 3c4e system in which *p–p* bonding dominates (24, 25) and in which the two bond lengths can be related by

$$[1] \quad d^* - d_0 = K(d - d_0)^{-c}$$

(the difference power fit DPF of ref. 26). Here d_0 is the asymptotic lower limit of the I—I bond length, taken as the d(I—I) in the free I_2 molecule, 2.667 Å.[10] Regressing $d^* - d_0$ on $d - d_0$ we obtain

Sample	*n*	r^2	*K*, Å	*c*	σ, Å	d_e, Å
HB	24*	0.918	0.09182	0.80219	0.018[11] ~ 7% range	2.933
HB**	24*	0.918	0.05652	1.14433	0.011[6] ~ 8% range	2.930
NHB	21	0.726	0.09304	0.77715	0.017[14] ~ 11% range	2.930
HB + NHB	45*	0.873	0.08906	0.81410	0.017[14] ~ 7% range	2.931

*No. 15 of Table C not included in the regression.

**Reverse regression, $d - d_0$ on $d^* - d_0$. The HB and NHB sets are replotted in a rectified form in Fig. 14.

Two conclusions can be immediately drawn from these results. Both samples conform to the model function, HB closely, NHB adequately (the lower correlation for NHB stems from the scatter, not from inadequacy of the DPF function), hence the 3c4e hypothesis is not contradicted. Secondly, the difference between the HB and the HB + NHB regressions amounts to only the thickness of the HB regression line in Fig. 14, and the difference between NHB and HB + NHB, over the observed range, is very small. Thus, HB and NHB sample the same $d,d,^*$ population and the effect of H-bonding on the I_3^- symmetry cannot, *statistically*, be claimed to be a preferential factor, i.e., the variation of d^* with d follows eq. [1] regardless of the nature of the factor(s) responsible for the I_3^- asymmetry. A large asymmetry may appear for a variety of reasons, not only because of H-bonding, even though in the *present* HB and NHB samples the asymmetry in the H-bonded anions exceeds that in the non-bonded anions ($d^*(\mathrm{HB})_{max} - d^*(\mathrm{NHB})_{max} \sim 0.08$ Å, $\Delta(\mathrm{HB})_{max} - \Delta(\mathrm{NHB})_{max} \sim 0.1$ Å).

[8] Deviations of the anion from nonlinearity have not been taken into account. However, in HB and NHB the difference between $d + d^*$ and the distance between the terminal atoms of the anion does not exceed ~0.014 Å ~ 0.3% of $d + d^*$ (for no. 1) and in most cases is much smaller.

[9] r_s(HB) = 0.906, r_s(NHB) = 0.791; *Z* is approximately a standardized normal variable.

[10] The 3-parameter CSBO (constant sum of bond orders, eq. [4] of ref. 26) function would be theoretically more appropriate but, as explained in ref. 26, in practice the DPF and CSBO fits are statistically indistinguishable. Besides, the ground-state I—I bond length in I_2(g) is unlikely to be reduced by laboratory intervention: application of external pressure appears to have negligible effect on d(I—I) in I_2(s) (27–29). A more encompassing discussion of comprehensive d,d^* sets in *trans* bonds of polyiodide ions is planned for a sequel in this series.

Fig. 12. Hydrogen bonding and cation geometry in 4Mpr2I3 (50% probability thermal ellipsoids, bond lengths in Å). For code letters see Table 5.

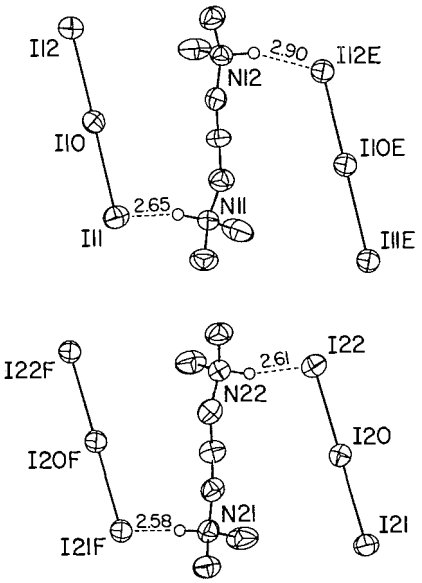

Conformity of HB and NHB to eq. [1] makes it possible to estimate the bond length $d_e = d = d^*$ in the *centrosymmetric* I_3^- in crystals. The best estimate from the above regressions is 2.931[11] Å.[11] Adding to the 3σ of this value an assumed representative correction of 0.02 Å for the effect of thermal motion raises this estimate to an upper limit of 2.98 Å, which still falls ~0.06 Å short of the ab initio (effective core potential) value of 3.044 Å (25), making the latter an overestimate.[12]

In principle, an estimate of d_e should be obtainable directly from the experimental d(I—I) values for I_3^- anions of crystallographic symmetry (or subsymmetry) C_i, and also C_2 and C_s (anion halved by m), provided the I-I-I angle deviates only slightly from 180°.[13] In practice, however, the centre atom of the anion may be positionally disordered about the inversion centre (cf. for example refs. 31 and 32). Unless this possibility has been specifically ruled out, an asymmetric I_3^- anion may be incorrectly included in a sample of genuinely centrosymmetric anions. Secondly, uncorrected d_e values as low as 2.89 Å and as high as 2.95 Å have been reported for anions of crystallographic C_i symmetry, so the validity of a $\bar{d}_e$ estimate may depend critically on the adequacy of sampling. These problems are circumvented by using eq. [1] and asymmetric anions only, although the uncertainty in estimating the thermal correction may well wipe out whatever difference there may exist between the two estimates, d_e(PDF) and $\bar{d}_e(C_i)$.[14] In any event, a comprehensive sample of asymmetric anions will always be larger than a comprehensive sample of symmetric anions.

The bond order s of the d(I—I) = $d(s)$ bond can be estimated from eq. [1] in the form (cf. ref. 26)

$$[2]\quad (\ln s)/\ln s^* = [d(s) - d_0]/[d^*(s^*) - d_0] = K^{-1}[d(s) - d_0]^{c+1} = 11.228[d(s) - 2.667]^{1.8141}$$

$s^* = 1 - s$. Conversely,

$$[3]\quad d(s) = d_0 + K^{1/(c+1)}(\ln s)/\ln s^* = 2.667 + 0.2639(\ln s)/\ln s^*$$

The total range of d(I—I) in the I_3^- anions is thus $d_e - d_0$ = 0.264 Å. The bond order over the observed d range is indicated in Fig. 14.

Is the I_3^- anion discrete?

We now return to the question, are the I_3^- anions in the HB and NHB samples discrete? Increasing asymmetry of the anion depends on an increased interaction of the anion with its surroundings in the crystal. Since such interaction is always present and the anion cannot be asymmetric without it, the question of when an anion may be regarded as discrete, i.e., minimally affected by its neighbours in the crystal, is inextricably linked to the degree and nature of this interaction and to the presence of features in the crystal structure that would indicate directional bonding interaction, such as bonding to another I_3^- at admissible I...I distances and I-I-I bond angles (i.e., close to 180° or 90°). The limit below which an I...I distance may be regarded as bonding (and the anion as no longer discrete) is difficult to preassign unambiguously. For linear or quasi-linear I − I − I...I configurations it will be in the vicinity of 4 Å, while for right-angle configurations this limit may be appreciably shorter. In either case the limit will depend on the particulars of the structure and a discrete/nondiscrete assignment will at times be arbitrary.

With decreasing inter-anion I...I contacts the I_3^- ions may merge into anion polyiodide oligomers, chains or networks, with an attendant redistribution of the atom charges, e.g., with the formation of asymmetric local I...I − I − I aggregates in which the three-atom groups may no longer conform to the above regression function for "discrete" (i.e., 3c4e) I_3^- anions. The applicability of an (adjusted) extension of this function beyond the present d,d^* range is a matter for another investigation.

Hydrogen bonding

Since the range of N—H(N)...I geometries is not well established, it is useful to collect the results of this and previous

[11] A previous (30) estimate is 5.85[5] Å for $2\Sigma = 2d_e$.

[12] The lack of correction for thermal motion is responsible for some of the scatter in Fig. 14 and for some of the d values falling appreciably below d_e in Fig. 13, well below the experimental esd's of the respective I—I bond lengths. However, barring a transcription error in ref. 33, we are unable to explain the gross misfit of point Z in the plots of Figs. 13*A* and 14. This d,d^* pair, 2.868(6), 2.902(6) Å, pertains to an I_3^- anion in a zigzag "polyiodide" chain, which is inside a maltohexaoside antiparallel double helix and in which the inter-anion I...I separations are *long*, ~4.05 Å. The d,d^* in the other I_3^- anion of the chain in what otherwise appears to be a well-determined (p-nitrophenyl α-maltohexaoside)$_2$·Ba$(I_3)_2$·27 H_2O structure, are unexceptionable.

[13] Conversely, anions of C_2 and C_s (anion halved by m) symmetry with I-I-I angles appreciably smaller than 180° can be used to evaluate the angle dependence of d_e.

[14] For a general discussion of equivalence of the d_e obtained from a $d \neq d^*$ sample, the $\bar{d}_e$ from a $d = d^*$ sample, and the d_e obtained from the combined sample, see ref. 26.

Fig. 13. Correlation of d(I—I) and d^*(I—I) bond lengths in I_3^- anions. Structures with (*A*) and without (*B*) N—H(N)...I bonds. (*C*) HB + NHB points replotted as Δ vs. Σ. The 45° line in *A* and *B* corresponds to $d = d^*$. For number code see Table C.

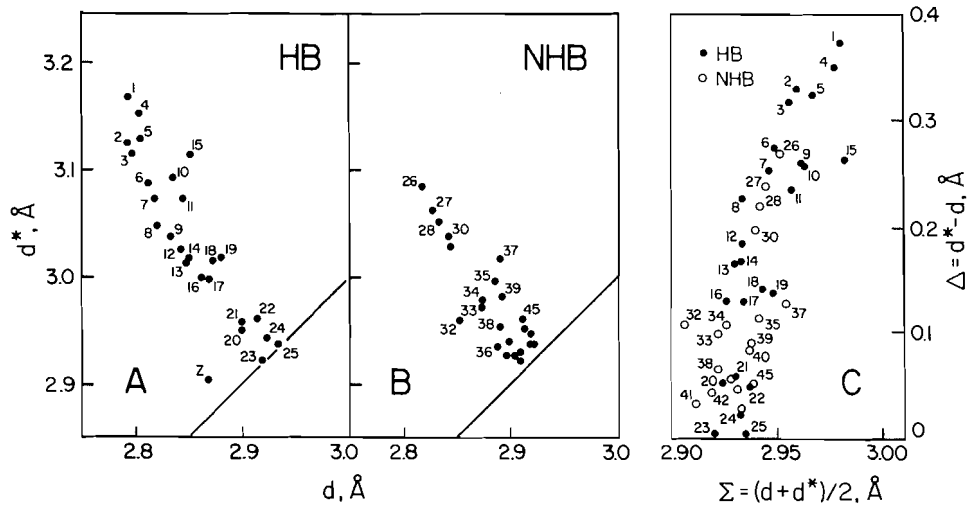

Fig. 14. Rectified correlation of d(I—I) and d^*(I—I) in I_3^-. Regression lines, eq. [1]. HB set: I_3^- in structures containing N—H(N)...I bonds. NHB set: I_3^- in structures without N—H(N)...I bonds. Broken lines, bond order $s(d)$ corresponding to the d(I—I) bond length, cf. eq. [3]. For point Z see text.

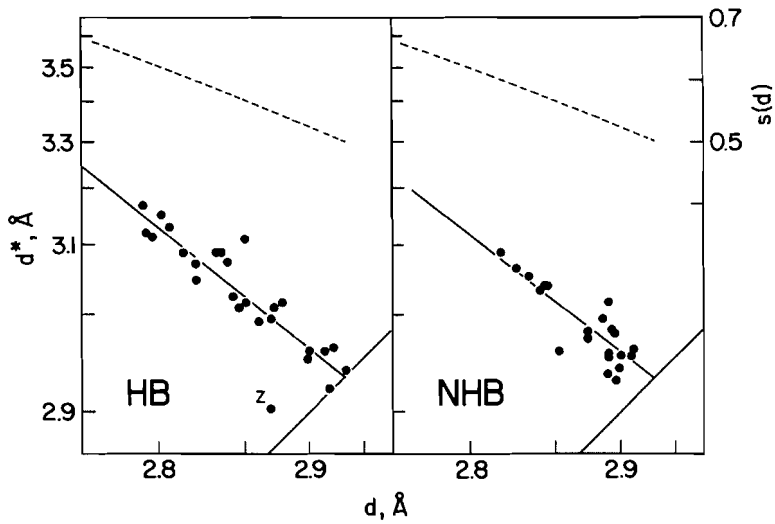

investigations (1–3) in Fig. 15. The H(N) atom has been located only in a few cases and then not too accurately, a typical esd on the H(N)...I bond length being 0.02–0.04 Å and 3° on the N-H(N)-I angle; where the H(N) atom was placed geometrically, the N—H(N) distance was taken to be mostly 1.02 Å. On the assumption that, with increasing d(N...I), the H(N)...I interaction weakens and d(N—H(N)) converges to its free value, a synthetic d(N...I) = 4.50 Å, d(H(N)...I) = 3.48 Å point was added to the set of Fig. 15, in order to ensure monotonic behaviour, and the augmented set was fitted parabolically: $r^2 = 0.97$, d(H(N)...I) = $-9.25 + 5.22d$(N...I) $- 0.5314$ $(d$(N...I))^2. The σ of this convenience fit, 0.03 Å ~ 7% of the actual d(H(N)...I) range, is comparable to the experimental esd's of the individual d(H(N)...I) values. In the present sample, d(N...I) in unbranched N—H(N)...I bonds extends over ~0.35 Å, and over ~0.43 Å for d(H(N)...I).

The locus of the points for the *bifurcated* N—H(N)...2I bonds in Fig. 15 appears to be shifted by 0.15–0.2 Å toward shorter N...I distances. The scatter here is appreciable and, if these few points were the only evidence, the existence of a correlation might well be questioned. However, support comes from the branched O—H(O)...I bonds in $KI_3 \cdot H_2O$, the structure of which was determined by single-crystal neutron diffraction (13). The asymmetrically trifurcated O—H(O)...3I and the asymmetrically bifurcated O—H(O)...2I bonds furnish five accurate d(O...I), d[H(O)...I] pairs, with d(O...I) ranging from ~3.66 to ~3.88 Å and d[H(O)...I] from 2.915 to 3.287 Å. Unconstrained quadratic regression yields

Fig. 15. Correlation of the H(N)...I and N...I distances in N—H(N)...I bonds in triiodide structures, and of H(O)...I and O...I in $KI_3 \cdot H_2O$ (neutron diffraction). For regression lines see text. Large filled circles, unbranched N—H(N)...I bonds; open circles, branched N—H(N)...I bonds; small filled circles, branched O—H(O)...I bonds (read O...I for N...I on the horizontal axis). Some of the N-H-I angles in the unbranched bonds deviate appreciably from 180°.

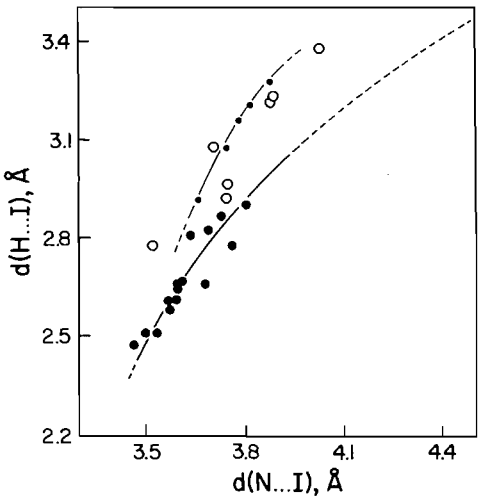

$d(\mathrm{H(O)...I}) = -41.48 + 21.95d(\mathrm{O...I}) - 2.6825(d(\mathrm{O...I}))^2$, $r^2 = 0.996$, $\sigma = 0.007[4]$ Å ~ 2% of range. This is a highly significant correlation and one based on a fully internally consistent set of interatomic distances from *the same structure* and involving the same oxygen atom. The corresponding correlation curve (Fig. 15) is compatible with the d(N...I), d(H(N)...I) points for the branched bonds; given the scatter of that set, the difference between d(N...I) and d(O...I) is inconsequential, and ditto for d(H(N)...I) and d(H(O)...I).

Ion packing in triiodide structures

As pointed out previously (1), the ion-packing type of an (unsolvated) 1:1 triiodide of a compact, symmetric cation can be related to the volume V_1 per formula unit: at small V_1 the NaCl type (at times strongly distorted) prevails, with the *anti*-NiAs type at intermediate V_1, and the CsCl type at large V_1 values. This rough scheme (now enlarged, Table 8) appears to hold up to $V_1 \sim 400$ Å^3, though with the inclusion of additional structures the lack of a clear-cut classification in the intermediate, $V_1 \sim 300$ Å, region becomes increasingly apparent. A closer analysis of factors other than cation volume at play in the transition region will have to await further accumulation of structural information. This is true a fortiori of the few 1:2 triiodide structures with cations suitable for our purpose that have been reported to date (Table 8). As would be expected, CdI_2 and CaF_2 are the principal aristotypes of the 1:2 compounds.

With cations smaller than Rb^+, hydration of the 1:1 triiodides is favoured under ordinary conditions, strongly for Li^+ and Na^+, less so for K^+; $KI_3 \cdot H_2O$ appears to be at the dividing line between the anhydrous and the hydrated salts. The structures of the mixed-anion monohydrates $KIBr_2 \cdot H_2O$ and $KICl_2 \cdot H_2O$ are also known (Table 1), but the effect of the single H_2O molecule on the packing type is not discussed in the original papers. We therefore take advantage of this serendipity to examine these trihalides in the light of the above concerns.

Table 8. Ion packing in simple triiodide structures.[a]

Compound	V_1, Å^3	Type	cat/an
1:1 Triiodides			
MI_3 (M = Tl, NH_4, Rb, Cs) (2, 34)	160–190	[NaCl]	1/1
2MI3	232	NaCl	1/1
4MI3	295	*anti*-NiAs	1/2
MCI3	310	[wurtzite]	1/1
N-Et-pyridinium I_3 (35)	310	not clear	1/1
Me_4PI_3 (1)	314	CsCl	2/3
$HMTI_3$ (36)	317	CsCl	1/1
QI3	318	*anti*-NiAs	1/2
TrI3	341	*anti*-NiAs	1/1
1,2,4-Me_3-pyridinium I_3 (35)	353	CsCl	1/1
$MHMTI_3$ (32)	354	CsCl	1/2
Et_4NI_3(*I*) (37)	380	CsCl	1/2
Et_4NI_3(*II*) (37)	383	CsCl	1/2
1-Azoniapropellane I_3 (1)	389	CsCl	6/7
$MeEt_2PhNI_3$ (38)	410	CsCl	1/2
1:2 Triiodides			
$[Zn(NH_3)_4](I_3)_2$ (39)	429	[b]	1/1
Da2I3	435	$[CaF_2]$	1/2
2Mpip2I3	462	CdI_2	1/1
Mpip2I3w	465	CdI_2	1/1
4Men2I3	484	CdI_2	1/1
4Mpr2I3	506	Not clear	2/4
[Ni(*N*-Me-imidazole)$_6$]$(I_3)_2$ (40)	1013	CaF_2	1/1

[a]See Table 1 for codes and references; cat/an, number of nonequivalent cations to number of nonequivalent anions. HMT, hexamethylenetetrammonium(1+); MHMT, 1-Me-hexamethylenetetrammonium(1+). Brackets indicate strong distortion of ideal packing type.

[b]Arrangement of cation and anion centroids strongly reminiscent of that in α-quartz (low-temperature, same space group).

The three structures are compared, in matching projections, in Fig. 16. In $KI_3 \cdot H_2O$ (neutron diffraction) the packing is of the CsCl type, with the anions in sheets ||(100) and the H_2O molecules and the K^+ ions alternating in infinite zigzag $[...K...OH_2...]_\infty$ chains ||*a*. The two O—H bonds and two K atoms at a mean K...O distance of 2.76[1] Å coordinate the O atom tetrahedrally, so that the structure can be formulated as a distorted CsCl arrangement of $[H_2O(K_{1/2})_2]^+$ cations and I_3^- anions. The shortest inter-anion I...I separation is 3.960(3) Å, between mutually perpendicular anions, i.e., the anions are discrete. The H(1) atom is involved in an asymmetrically trifurcated O—H(1)...I(3A), I(3B), I(2B) bond and H(2) in an asymmetrically bifurcated O—H(2)...I(1), I(1C) bond (see under Hydrogen bonding).[15]

The $KIBr_2 \cdot H_2O$ structure is of the *anti*-NiAs type. Its *Pnnm* unit cell *O*, like those of the isostructural 4MI3 and QI3, can

[15] Atom numbering as in the original reference. A, x, $1 - y$, $\frac{1}{2} + z$; B, $1 + x$, $1 - y$, $\frac{1}{2} + z$; C, $1 + x$, y, z.

Fig. 16. $KIX_2 \cdot H_2O$ structures (Table 1). (*A*) $KICl_2 \cdot H_2O$, $P2_1/m$, projection on (010), *anti*-NiAs type. (*B*) $KIBr_2 \cdot H_2O$, *Pnnm*, projection on (010), *anti*-NiAs type. (*C*) $KI_3 \cdot H_2O$, *Pc*, projection on (100), CsCl type; in the projection, atom I(2B) coincides with I(2A), and I(3B) with I(3A). Circles: large, halogen atoms; stippled, K; small open, O; small filled, H. Lines: solid, reported unit cells; broken, ion-packing cells; dotted, O—H(O)...X bonds (established or putative) and shortest K...O contacts. In the *A* and *B* ion-packing cells the anions at the cell corners represent two vertically superposed anions each, with their centre I atoms at $y = 0$ and $\frac{1}{2}$. Atom numbering as in the original references.

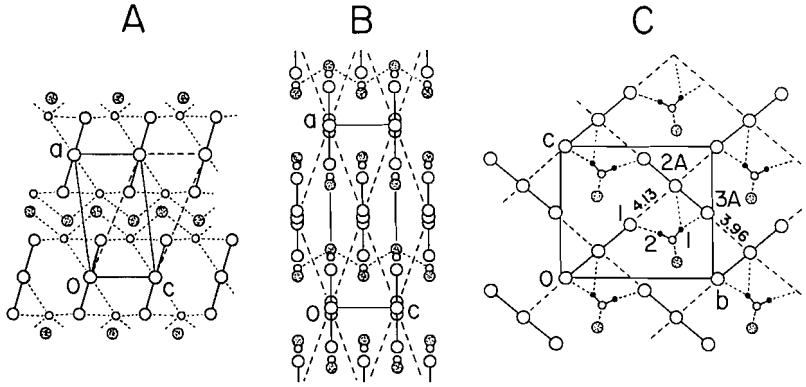

be converted into a pseudohexagonal cell *H* by the transformation described in ref. 1 (a_{OH}/c_{OH} = 2.775, ideal $\sqrt{3}$ = 1.732; $2b_O/(a_O^2 + c_O^2)^{1/2}$ = 2.015). All the atoms are located in 002 mirror planes at $z = 0, \frac{1}{2}$. Half the anions are ~||*b* and half are ~||(010). The oxygen atom is coordinated by two K atoms (O...K, 2.75(2) Å), two Br(1) atoms (O...Br(1), 3.64(2) Å), and two Br(2) atoms (O...Br(2), 3.60(2) Å).[16] The two H atoms, though not located, unless positionally disordered must also be in the mirror planes and involved in a symmetrically bifurcated bond each, H(1)...Br(1),Br(1′), H(2)...Br(2),Br(2′). The near coordination of the oxygen atom is thus tetrahedral. The ...O...K...sequences form zigzag chains ||*c*, and the ...an...O...an...O... sequences form folded chains ||*b*.

The monoclinic $P2_1/m$ unit cell of the simple $KICl_2 \cdot H_2O$ structure itself constitutes a distorted quasi-hexagonal *anti*-NiAs cell. The similarity with the aristotype is even more evident in the transformed cell of Fig. 16*A* (a/c = 1.842, $2b/(a^2 + c^2)^{1/2}$ = 2.106). The anions are approximately in 010 planes. The coordination of the O atom again is tetrahedral, with the two K atoms at 2.77 and 2.84 Å, respectively.[16] The two mirror-related H atoms were not located, but from geometric considerations they are almost certain to engage in trifurcated H-bonds: O...Cl = 3.41 and 3.68 Å, O...I = 3.86 Å. The K and O atoms form planar zigzag chains in 020 planes at $y = \pm\frac{1}{4}$.

The shortest K...O distance is almost the same in the three structures, 2.75–2.77 Å. The hydrated K^+ ion can thus be regarded as a composite cation and the structures can be reformulated as $[K(OH_2)]^+IX_2^-$. This is consistent with the ion packing types found for the three monohydrates: the *anti*-NiAs type corresponds to the smaller V_1 values, 167 and 174 Å^3 (for X = Cl and Br, respectively), and the CsCl type to V_1 = 201 Å^3 for X = I. A direct comparison of the mixed-halide salts with triiodides cannot be made because of the anion size mismatch, but it should be noted that $CsBr_3$, $CsIBr_2$, $CsBrI_2$, and CsI_3 (V_1 = 156, 164, 174, and 190 Å^3, respectively; refs. 34, 41–45) have all been reported as having the strongly distorted NaCl-type *Pnma* structures, while $CsICl_2$ (V_1 = 141 Å^3, refs. 46 and 47) is rhombohedral, $R\bar{3}m$, i.e., of a packing type characteristic of ABX_3 (X = O, S, Se, Te) compounds with small cations and considered to represent a transition type between NaCl and CsCl. This is in agreement with the general observation that the *anti*-NiAs triiodides have larger V_1 values than the distorted-NaCl triiodides (1). However, the V_1 = 201 Å^3 of $KI_3 \cdot H_2O$, which can be compared with the other triiodides in Table 8, is too small to be expected, on the V_1 criterion, to correspond to a CsCl-type packing. The reason for this discrepancy is not clear at present.

Bonding in 2PhII3

It is instructive to examine in some detail the changes that occur in the centrosymmetric $[...I(cat)...I(an)...]_2$ ring dimer when the simple I^- anion in 2PhII is replaced by the terminal I(3) atom of the I_3^- anion perpendicular to the ring plane in 2PhII3 (Figs. 5*B*, *C* and 6). The mean I(cat)...I(an) distance in 2PhII, 3.44 Å, is lengthened in 2PhII3 to 3.59 Å, i.e., by 0.15 Å ~ 4.5%. This increase is attributable to the weakening of the I(cat)...I(an) bonding interaction attendant on the decrease of the full anionic charge of −1 e on I^- to a partial charge on I(3). The net (Mulliken) charge ϵ on a terminal atom of a free, linear symmetric I_3^- anion has been estimated from ab initio calculations (25) to be −0.54 e. However, on I(3) it must be less, owing to the strong asymmetry of the anion. The asymmetry arises (though probably not exclusively) from a weakening of the I(3)—I(1) bond in consequence of an I(2)...I(2B) bonding interaction at the other end

[16] The interatomic distances and angles were calculated, or recalculated, from the atom coordinates in the original references. They do not always agree exactly with the distances and angles tabulated there.

of the anion in the 2PhII3 crystal (Fig. 5*A*; this point is discussed in ref. 1).

On the assumption that the bonding in I_3^- is of the 3c4e type, i.e., through p_z–p_z overlap (25), the interaction of I(3) with I(4) and I(4A) would be through the p_x, p_y orbitals on I(3) perpendicular to the I(3)—I(1) bond. This is supported by the closeness of the I(4)-I(3)-I(4A) angle to 90°. Some electron density might thus be diverted from the p_z orbital on I(3) to p_x and p_y, further weakening the I(3)...I(4) and I(3)...I(4A) bonding interactions.[17]

A conspicuous feature of the 2PhII3 and 2PhII structures is the coplanarity of the I—C(α) bond with the centrosymmetric ring dimer. Similar planarity is observed in 2PhICl and 2PhIBr, isostructural with 2PhII, and also in 2PhIN.[18] In the latter, the cation is part of an infinite, ipsolateral (*cis*) zigzag...O(2″)...I[C(α),C*(α)]...O(2)...I′[C(α′),C*(α′)]... chain; C(α)-I-C(α′) = 92.03(3)°, O(2)-I-O(2″) = 110.6(4)°, with the asymmetric IC(α)C(α′)O(2)O(2″) unit almost planar (mean deviation from the best plane, 0.07[5] Å).

The planarity of the I^+ coordination and the closeness of the C(α)-I-C(α′) angle to 90° suggest that the bonding at the I^+ atom, too, utilizes principally the *p* orbitals, so that the I^+—C(α) bond will be of the $p(I) - sp^3(C)$ type. When the X atoms completing the ring dimer are replaced by more diffuse ligands, e.g., in 2PhITB, the C(α)-I-C(α′) angle appears to increase, i.e., the bond character begins to change from $p(I)$ to $sp^3(I)$. While this interpretation is consistent with the observed coordination geometry at the I^+ atom, the geometric evidence that can be adduced at present in support of the above interpretation leaves something to be desired. This is due in part to the difficulty of locating, with sufficient accuracy, a C atom next to an I atom. Not only are the bond-length and bond-angle comparisons involving the C atoms tenuous, but, more generally, reliable means for I—C bond lengths of different orders do not exist as yet, thus preventing calibration of the observed I—C distances in the Ph_2I^+ structures.

The weighted means of *d*[I—C(α)] and C(β)-C(α)-C(β′), 2.105[24] Å and 122.8[8]°, respectively (Table 6), appear to fit in well with the findings of Domenicano et al. (48, 49) on the effects of exocyclic substitution on the benzene ring.

Information from ^{127}I NQR spectra

A number of triiodides (as well as heteroatomic trihalides) have been studied by ^{127}I NQR spectroscopy (50–53). By a fortunate coincidence they include 2MI3 and the previously (1) reported 4MI3.

Only two resonances were detected in the room-temperature spectrum of 2MI3 in the 70–600 MHz frequency region (52, 53). These were assigned as the ν_1 resonance frequencies of the centre and the terminal atoms, respectively, of a symmetric I_3^- anion, consistent with the result of our structure determination (Table 4). The two resonances persisted down to dry ice and liquid-nitrogen temperatures, pointing to the absence of a structural transition in the observed temperature range.

The 4MI3 structure at room temperature contains two nonequivalent centrosymmetric I_3^- anions. These would be expected to give rise to six resonances in the above frequency region, analogous to $Et_4NI_3(I)$ (37, 52, 53). However, *fifteen* resonance lines were observed in the 140–400 MHz region of the 4MI3 spectrum at liquid-nitrogen temperature, six of which were present also in the −77°C spectrum but disappeared at ca. −60°C; between ca. −196°C and −60°C their frequencies varied smoothly with temperature (52, 53). In contrast, only the six lines were reported in the 77 K spectrum of ref. 50. The presence of the 15 lines was interpreted as arising from 3 nonequivalent asymmetric I_3^- anions in the 4MI3 crystal. The apparent discrepancy between the two sets of spectra and the expectation from the room-temperature crystal structure can be reconciled if one recalls that in the room-temperature structure the cations are positionally disordered and the U_{ii} values of some of the I atoms are unusually high. It is therefore reasonable to assume that on cooling the structure will progressively order until somewhere below −77°C an order–disorder transition temperature is reached. The inability to observe more than six lines in the liquid-nitrogen spectrum of ref. 50 might have been due to instrumental factors or to rapid cooling of the sample that may have quenched the ordering process.

Conclusions

The results of the structure determinations of the title compounds have been used to consolidate the body of structural information on triiodides of small compact monovalent and, in particular, divalent cations. The *general* conclusions arising from the present and the preceding (1) investigations are as follows.

1. The ion-packing type of a triiodide of a small, compact cation can be related to the volume V_1 per formula unit. This permits a rough classification (Table 8): in 1:1 triiodides, small V_1 values correspond to the (distorted) NaCl type, intermediate V_1 values to the *anti*-NiAs type, and large V_1 values (up to $V_1 \sim 400$ Å^3) to the CsCl type. In the intermediate range the classification is not clear-cut and at present only provisional.

A comparable classification of 1:2 triiodide structures is tenuous owing to the paucity of data. Of the four 1:2 title compounds, three are clearly of the CdI_2 type, with strings of I_3^- anions forming hexagonal channels, which accommodate the cations. The cation centroids are positioned on the channel axes in a way that minimizes steric interference with the channel framework, i.e., the cation position relative to the gaps between successive anions in the strings varies with the cation geometry (the "vernier" effect). The fourth 1:2 structure, though more complex, is related to the other three.

2. The information on N—H(N)...I bonds provided by the structures of the title compounds has made it possible to demonstrate an unmistakable correlation between the H(N)...I and N...I distances, both in unbranched and branched H-bonds (Fig. 15).

3. On the supportable assumption that the I_3^- anion is a 3c4e system we have established the validity of the functional relationship between the two I—I bond lengths, *d*(I—I) and

[17] The question of how the presence of I...I bonding interactions perpendicular to the I_3^- axis affects the strength of the I—I bond in the anion, of crucial importance for bonding in the higher polyiodide anions, will be discussed in a later paper in this series.

[18] The mean deviations of the C(α) atoms from the halogen-ring planes are 0.06[2], 0.12[1], 0.13[5], and 0.21[3] Å for 2PhICl, 2PhIBr, 2PhII, and 2PhII3, respectively. In 2PhIN the mean deviation of the C(α) atoms from the I-O(2)-O(2″) plane is 0.16[4] Å.

d^*(I—I), in the ion: $d^* - d_0 = K(d - d_0)^{-c}$, where $d^* \geq d$ and d_0 is the bond length in the free I_2 molecule. Analysis of the available data for discrete I_3^- ions in crystals shows that the asymmetry of the anion can arise from various factors resident in the crystal, of which H-bonding is one but not a *preferential* one (Figs. 13 and 14).

4. An insight into the bonding in the centrosymmetric I_4 ring in the $(Ph_2I)I_3$ structure can be gained from a comparison with the structures of $(Ph_2I)I$ and other Ph_2I^+ salts.

Experimental

The title compounds were prepared by combining a solution of the appropriate iodide in a suitable solvent (mostly MeOH) with a stoichiometric amount of an MeOH solution of iodine, and allowing the resulting solution to crystallize by controlled evaporation at room temperature. The triiodides were recrystallized if required. However, controlling the size and quality of the crystals was not without problems, as large crystals had to be sectioned, not always with entirely gratifying results.

A Rigaku AFC5R system (2.4 kW sealed Mo-anode tube, λ(Mo Kα) = 0.710 690 Å, graphite monochromator; T = 21(2)°C) was used in the data acquisition. All intensities were corrected for Lorentz, polarization, absorption (ψ-scans), and secondary extinction as well as for time-decay effects when appropriate. The anisotropic temperature factor is defined as $\exp[-2\pi^2(U_{11}h^2a^{*2} + ... + 2U_{23}klb^*c^* + ...)]$. The structures were solved by direct methods (54) and refined by full-matrix least squares using the TEXSAN-TEXRAY software package (55) except for 4Men2I3, where the SHELXL-93 system (56) was used to model cation disorder (see below). The function minimized was $\Sigma w(|F_o| - |F_c|)^2$, with unit weights. Since the H atoms were placed geometrically (C—H, 1.08 Å, N—H, 1.02 Å) and not refined (U_{iso}(H) = $1.2U_{eq}$(C, N) of the attached atom), no esd's are quoted on distances and angles involving H atoms. The residual electron-density maxima were all close to the iodine atoms.

Tables of structure factors are available from the Editorial Office.

TrI3

The absolute structure parameter for the reported structure was −0.02(2). The thermal motion of the cation conforms moderately well to the rigid-body-motion model: rms(U_{ij}) = 0.0045 Å^2, rms[esd(U_{ij})] = 0.0064 Å^2 with all C atoms included; with the *N*-methyl carbon omitted, rms(U_{ij}) = 0.0037 Å^2, rms[esd(U_{ij})] = 0.0063 Å^2. The largest mean amplitude about a principal axis of libration was 5.5°. The mean librational correction to the bond lengths in the cation skeleton was 0.008[2] Å; that to the bond angles did not exceed |0.15|°.

4Men2I3

Straightforward refinement without constraints in $p2_1/a$ gave an acceptable structure, but some of the U_{ii} of the cation atoms, in particular U_{11}(C), were large and the C—N and C—C distances not reasonably close to expectation. Various attempts to resolve the difficulty by modelling positional disorder in the cation were made, none of them satisfactory. In the end the C—N and C—C distances were constrained and the structure refined in SHELXL-93, with the results as reported in Tables 4, A, and B. In this instance the function minimized was $wR2 = \{\Sigma[w(F_o^2 - F_c^2)^2]/\Sigma[w(F_o^2)^2]\}^{1/2}$ and the weighting scheme was $w^{-1} = \sigma^2(F_o^2) + (0.0427p)^2 + 7.74p$, $p = [(F_o^2)_{max} + 2F_c^2]/3$.

Acknowledgment

This investigation was supported by research grants from the Natural Sciences and Engineering Research Council of Canada to O.K. and T.S.C.

References

1. P.K. Bakshi. M.A. James, T.S. Cameron, and O. Knop. Can. J. Chem. **74**, 559 (1996).
2. K.-F. Tebbe, B. Freckmann, M. Hörner, W. Hiller, and J. Strähle. Acta Crystallogr. Sect. C: Cryst. Struct. Commun. **C41**, 660 (1985).
3. M. Rossi, L.G. Marzilli, and T. Kistenmacher. Acta Crystallogr. Sect. B: Struct. Crystallogr. Cryst. Chem. **B34**, 2030 (1978).
4. J. Lindgren and N. Arran. Acta Chem. Scand. **26**, 3043 (1972).
5. J. Lindgren and I. Olovsson. Acta Crystallogr. Sect. B: Struct. Crystallogr. Cryst. Chem. **B24**, 549 (1968).
6. N.W. Alcock and R.M. Countryman. J. Chem. Soc. Dalton Trans. 217 (1977).
7. T.L. Khotsyanova, T.A. Babushkina, V.V. Saatsazov, T.P. Tolstaya, I.N. Lisichkina, and G.K. Semin. Koord. Khim. **2**, 1567 (1976).
8. T.L. Khotsyanova, T.A. Babushkina, V.V. Saatsazov, T.P. Tolstaya, and G.K. Semin. Dokl. Akad. Nauk SSSR, **222**, 403 (1975).
9. O. Knop, T.S. Cameron, P.K. Bakshi, A. Linden, and S.P. Roe. Can. J. Chem. **72**, 1870 (1994).
10. C. Rømming. Acta Chem. Scand. **12**, 668 (1958).
11. W.B. Wright and E.A. Meyers. Cryst. Struct. Commun. **1**, 95 (1972).
12. A.P. Bozopoulos, C.A. Kavounis, G.S. Stergioadis, and P.J. Rentzeperis. Z. Kristallogr. **187**, 97 (1989).
13. R. Thomas and F.H. Moore. Acta Crystallogr. Sect. B: Struct. Crystallogr. Cryst. Chem. **B36**, 2869 (1980).
14. S. Soled and G.B. Carpenter. Acta Crystallogr. Sect. B: Struct. Crystallogr. Cryst. Chem. **B29**, 2556 (1973).
15. S. Soled and G.B. Carpenter. Acta Crystallogr. Sect. B: Struct. Crystallogr. Cryst. Chem. **B29**, 2104 (1973).
16. P.K. Bakshi, A. Linden, B.R. Vincent, S.P. Roe, D. Adhikesavalu, T.S. Cameron, and O. Knop. Can. J. Chem. **72**, 1273 (1994).
17. O. Knop, T.S. Cameron, M.A. James, and M. Falk. Can. J. Chem. **61**, 1620 (1983).
18. M.H. Ben Ghozlen, A. Daoud, and J.W. Bats. Acta Crystallogr. Sect. B: Struct. Crystallogr. Cryst. Chem. **B37**, 1415 (1981).
19. O. Knop, T.S. Cameron, D. Adhikesavalu, B.R. Vincent, and J.A. Jenkins. Can. J. Chem. **65**, 1527 (1987).
20. K.-F. Tebbe. *In* Homoatomic rings, chains and macromolecules of main-group elements. *Edited by* A.L. Rheingold. Elsevier, Amsterdam. 1977. pp. 551–606.
21. T.J. Marks and D. Kalina. *In* Extended linear chain compounds. Vol. 1. *Edited by* J.S. Miller. Plenum Press, New York and London. 1982. pp. 197–331.
22. F. Bigoli, M.A. Pellinghelli, G. Crisponi, P. Deplano, and E.F. Trogu. J. Chem. Soc. Dalton Trans. 1349 (1985).
23. T.-Y. Dong, H.-M. Liu, M.-Y. Hwang, T.-Y. Lee, L.-H. Tseng, S.-M. Peng, and G.-H. Lee. J. Organomet. Chem. **414**, 227 (1991).
24. G.A. Bowmaker, P.D.W. Boyd, and R.J. Sorrenson. J. Chem. Soc. Faraday Trans. 2, **80**, 1125 (1984).
25. L.J. Saethre, O. Gropen, and J. Sletten. Acta Chem. Scand. Ser. A: **A42**, 16 (1988).

26. O. Knop, S.C. Choi, and D.C. Hamilton. Can. J. Chem. **70**, 2574 (1992).
27. K. Takemura, S. Minomura, O. Shimomura, Y. Fujii, and J.D. Axe. Phys. Rev. B: Condens. Matter, **26**, 998 (1982).
28. R. Reichlin, A.K. McMahan, M. Ross, S. Martin, Jingzhu Hu, R.J. Hemley, H.-K. Mao, and Yan Wu. Phys. Rev. B: Condens. Matter, **49**, 3725 (1994).
29. Y. Fujii. Abstract 4m.4.D. Book of abstracts, Annual Meeting of the American Crystallographic Association, Montreal, Que., July 23–28, 1995.
30. K.-F. Tebbe and B. Freckmann. Z. Naturforsch. B: Anorg. Chem. Org. Chem. **37b**, 542 (1982).
31. J.W. Bats, J.J. de Boer, and D. Bright. Inorg. Chim. Acta, **5**, 605 (1971).
32. P.K. Hon, T.C.W. Mak, and J. Trotter. Z. Kristallogr. **158**, 213 (1982).
33. W. Hinrichs and W. Saenger. J. Am. Chem. Soc. **112**, 2789 (1990).
34. J. Runsink, S. Swen-Walstra, and T. Migchelsen. Acta Crystallogr. Sect. B: Struct. Crystallogr. Cryst. Chem. **B28**, 1331 (1972).
35. S. Christie, R.H. Dubois, R.D. Rogers, P.S. White, and M.J. Zaworotko. J. Inclusion Phenom. **11**, 103 (1991).
36. K.-F. Tebbe and K. Nagel. Z. Anorg. Allg. Chem. **621**, 225 (1995).
37. T. Migchelsen and A. Vos. Acta Crystallogr. **23**, 796 (1967).
38. K.-F. Tebbe and W. Lindenthal. Z. Anorg. Allg. Chem. **619**, 1483 (1993).
39. K.-F. Tebbe. Z. Kristallogr. **153**, 297 (1980).
40. K.-F. Tebbe and S. Nafepour. Acta Crystallogr. Sect. C: Cryst. Struct. Commun. **C50**, 1566 (1994).
41. M.C. Morris, H.F. McMurdie, E.H. Evans, B. Paretzkin, H.S. Parker, N.P. Pyrros, and C.R. Hubbard. Standard X-ray powder diffraction patterns. NBS Monograph 25, **19**, 33. National Bureau of Standards, Washington, D.C. 1982.
42. G.L. Breneman and R.D. Willett. Acta Crystallogr. Sect. B: Struct. Crystallogr. Cryst. Chem. **B25**, 1073 (1969).
43. J.E. Davies and E.K. Nunn. J. Chem. Soc. Chem. Commun. 1374 (1969).
44. G.B. Carpenter. Acta Crystallogr. **20**, 330 (1966).
45. H.E. Swanson, H.F. McMurdie, M.C. Morris, and E.H. Evans. Standard X-ray powder diffraction patterns. NBS Monograph 25, **7**, 103. National Bureau of Standards, Washington, D.C. 1969.
46. H.E. Swanson, R.K. Fuyat, and G.M. Ugrinic. Standard X-ray powder diffraction patterns. NBS Circular 539, **3**, 50. National Bureau of Standards, Washington, D.C. 1954.
47. F. van Bolhuis and P.A. Tucker. Acta Crystallogr. Sect. B: Struct. Crystallogr. Cryst. Chem. **B29**, 2613 (1973).
48. A. Domenicano, A. Vaciago, and C.A. Coulson. Acta Crystallogr. Sect. B: Struct. Crystallogr. Cryst. Chem. **B31**, 1630 (1975).
49. A. Domenicano, P. Mazzeo, and A. Vaciago. Tetrahedron Lett. 1029 (1976).
50. G.A. Bowmaker and S. Hakobian. Aust. J. Chem. **21**, 551 (1968).
51. W. Gabes, D.J. Stufkens, and H. Gerding. J. Mol. Struct. **20**, 343 (1974).
52. H. Harada, D. Nakamura, and M. Kubo. J. Magn. Reson. **13**, 56 (1974).
53. D. Nakamura and M. Kubo. Adv. Nucl. Quadrupole Reson. **2**, 117 (1975).
54. G.M. Sheldrick. SHELXS-86. *In* Crystallographic computing 3. *Edited by* G.M. Sheldrick, C. Kruger, and R. Goddard. Oxford University Press, Oxford. 1985. pp. 175–189.
55. TEXSAN-TEXRAY single-crystal structure analysis package. Molecular Structure Corporation, The Woodlands, Tex. 1993.
56. G.M. Sheldrick. SHELXL-93 crystal structure refinement program. Institute of Inorganic Chemistry, University of Göttingen, Göttingen. 1993.

Synthesis of 1-alkoxy-1,2,3,4-tetrahydrocarbazoles by mercury(II) mediated heterocyclization of 2-cyclohex-2′-enyl-*N*-alkylanilines[1]

K.C. Majumdar and U. Das

Abstract: The title compounds **3**(*a–i*) were synthesized in high yields by the mercury(II) mediated heterocyclization of 2-cyclohex-2′-enyl-*N*-alkylanilines **2**(*a–g*), which in turn were obtained by the acid-catalyzed amino Claisen rearrangement of 3-*N*-alkylanilinocyclohexenes **1**(*a–g*). Additional supporting evidence for the structure of product **3** was obtained from chemical transformations.

Key words: 1-alkoxy tetrahydrocarbazole, mercury(II) mediated heterocyclization, amino Claisen rearrangement, 3-*N*-methylanilinocyclohexene.

Résumé : On a synthétisé les composés mentionnés dans le titre, **3***a–i*, avec des rendements élevés par le biais de l'hétérocyclisation catalysée par le mercure(II) de (2-cyclohex-2′-ényl)(*N*-alkyl)anilines, **2***a–g*, qui ont été par ailleurs obtenues par un réarrangement amino de Claisen, catalysé par les acides, des 3-*N*-alkylanilinocyclohexènes, **1***a–g*. Des transformations chimiques ont permis d'obtenir des données additionnelles relatives à la structure du produit **3**.

Mots clés : 1-alkoxytétrahydrocarbazole, hétérocyclisation catalysée par le mercure(II), réarrangement amino de Claisen, 3-*N*-méthylanilinocyclohexène.

[Traduit par la rédaction]

Introduction

Organomercurials (2) have been known since 1852 and many synthetic routes to these compounds presently exist. The ability of these compounds to accommodate a wide variety of functional groups and to tolerate quite diverse reaction conditions is well documented (3). Of the various processes involving organomercurials, solvomercuration–demercuration is the most widely used in organic synthesis (4). Aminomercuration–demercuration has been utilized for the synthesis of nitrogen heterocycles by employing unsaturated amine compounds (5). In the case of solvomercuration and aminomercuration, reduction is essential to get rid of mercury from the initial product (6).

During our work on sigmatropic rearrangements (7) we became interested in the cyclization of 2-(2′-cyclohexenyl)-*N*-methylaniline **2**; however, our attempt failed (8) although such a scheme had worked fairly well with oxygen analogues (9). We then considered mediation of mercury(II) for this heterocyclization. Herein we report the results of this investigation.

The starting materials 2-(2′-cyclohexenyl)-*N*-alkylanilines **2**(*a–g*) were prepared by the acid-catalyzed aza-Claisen rearrangement of 3-*N*-alkylanilinocyclohexenes **1**(*a–g*), by refluxing in ethanolic hydrochloric acid (10). The tertiary amines **1** were prepared from 3-bromocyclohexene and the appropriate amines by refluxing in acetone in the presence of anhydrous potassium carbonate (Scheme 1).

Results and discussion

It has been reported (6*a*, 11) that aminomercuration reactions can be performed in aqueous THF as well as under anhydrous conditions with no detectable formation of oxymercurated products. Our attempt to react substrate **2***a* with mercury(II)acetate in aqueous tetrahydrofuran or under anhydrous conditions resulted in the formation of only an amine complex. Barluenga et al. (12) established that aminomercuration of olefins with mercury(II) acetate is an irreversible process that only leads to kinetically controlled products, whereas oxymercuration leads to thermodynamically controlled products. Hence for the problem under consideration, our attention has been to divert the reaction by reducing the lone pair availability on the nitrogen of substrate **2***a*. To achieve this a small amount of acetic acid was added to the reaction mixture. Reaction was monitored by thin-layer chromatography (tlc); starting material was consumed in 48 h with precipitation of metallic mercury. Workup and chromatographic separation furnished **3***a*, mp 51°C in 80% yield, along with 10% of another product, mp 180°C, which is considered to be an N-

Received November 28, 1995.

This paper is dedicated to Professor B.S. Thyagarajan of the University of Texas at San Antonio on the occasion of his 65th birthday.

K.C. Majumdar[2] and U. Das. Department of Chemistry, University of Kalyani, Kalyani-741 235, West Bengal, India.

[1] For a preliminary communication, see ref. 1.
[2] Author to whom correspondence may be addressed.

Scheme 1.

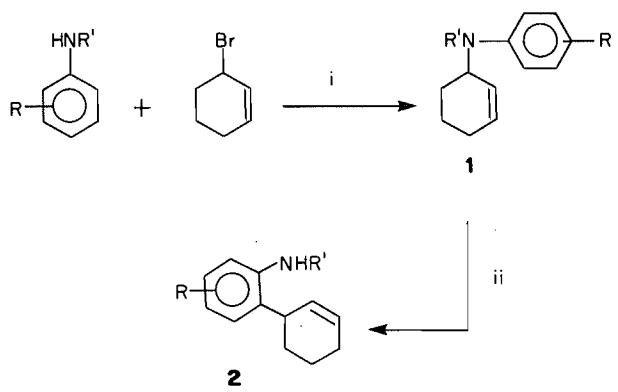

R	R′	R	R′
a, H	CH_3	*e*, H	CH_2CH_3
b, 4-CH_3	CH_3	*f*, 4-CH_3	CH_2CH_3
c, 4-Br	CH_3	*g*, 4-CH_3	$(CH_2)_3CH_3$
d, 2-CH_3	CH_3		

Reagents: i. CH_3COCH_3–K_2CO_3/△; ii. EtOH–HCl/△

mercurated complex from its ^{1}H NMR and IR data. When an excess of acetic acid is added to the reaction mixture, compound **3***a* is exclusively obtained.

The product **3***a* showed absence of N-H (free) and indicated the presence of an ether linkage at 1050 and 1250 cm^{-1}. The ^{1}H NMR spectrum of **3***a* exhibited two singlets at δ 3.45(3H) and δ 3.72(3H) indicating the presence of -OCH_3 and -NCH_3, respectively. The triplet at δ 4.5(1H) is very characteristic and is assignable to the hydrogen at C-1 of the tetrahydrocarbazole derivative **3***a*. The mass spectrum of compound **3***a* showed a molecular ion at *m/e* 215 and a base peak *m/e* 184 (M−31), among others. The ^{13}C spectrum of compound **3***a* shows the presence of all 14 carbons in the molecule. From the DEPT experiment the presence of five C-H signals as well as one -OCH_3 and one -NCH_3 signal can be established. In addition it also reveals the presence of three -CH_2 signals. All these data are accommodated in terms of the following ^{13}C assignments: δ: 18.790 (C3), 20.930 (C4), 26.996 (C2), 28.874 (-NCH_3), 55.241 (-OCH_3), 70.214 (C1), 108.563 (C8), 112.042 (C4a), 118.285 (C6), 118.472 (C5), 126.136 (C4b), 127.467 (C7), 133.655 (C1a), 137.166 (C8a). These assignments were further supported by HETCOR experiment. Protonated carbon resonance assignments were established by direct correlation with proton resonances by HETCOR with normal one-bond C–H coupling, and nonprotonated resonances (C4a, C4b, C8a, and C9a) were assigned convincingly by comparison with literature chemical shifts of the indole alkaloid, indoloquinolizideine (13). The above spectral data and elemental analysis suggested this to be 1-methoxy-9-methyl-1,2,3,4-tetrahydrocarbazole **3***a* (Scheme 2). The following transformations were carried out to get further supporting evidence in favour of structure **3***a*. Dehydrogenation of product **3***a* with DDQ in refluxing xylene for 12 h afforded 1-methoxy-9-methyl carbazole, **4**, a viscous oil, in 83% yield. The same reaction when conducted for a longer period (20 h) with excess of DDQ furnished *N*-methyl carbazole (14), **5**, mp 85°C, yield 30%, and carbazole, **6**, mp 242°C, yield 60%. Dehydrogenation of product **3***a* with palladized charcoal in refluxing diphenyl ether gave only carbazole **6** in 20% yield (Scheme 3).

The reaction was repeated in ethanol and *n*-propanol to give products **3***b* and **3***c* as viscous oils in 85% and 75% yields, respectively. The reaction was generalized by using various substrates **2**(*b–g*) to give products **3**(*d–i*) in 70–82% yields (Scheme 2).

Mercuric acetate is a well-known oxidizing and dehydrogenating agent (15). The formation of **3** from **2** is easily explicable by "pathway a" through species **7**, **8**, **9**, **10**, and **11**. Intermediate **11**, being very unstable under the reaction conditions, becomes dehydrogenated by mercury(II) acetate to product **3**. An alternative "pathway b," where oxidation of **2** by mercury(II) acetate may give an imine **12** followed by cyclization to intermediate hexahydrocarbazole **11**, may also be considered.

The reaction of substrate **2***a* with mercuric acetate in methanol at room temperature without the addition of acetic acid (48 h) furnished product **3***a* in 30% yield. This reaction also gave oxidized product **5** (30%, mp 85°C) along with another inseparable mixture of products (Scheme 2). An attempt to cyclize **2** in a stronger acid, viz. trifluoroacetic acid, also gave the same product **3** but at a much faster rate (16 h instead of 24 h). We were also unsuccessful in our attempt on a similar cyclization of the N-acetyl derivative of **2**, in which there is no hydrogen on the nitrogen, to form the imine **12**.

Several alkoxycarbazoles, including 1-methoxycarbazole, are natural alkaloids (16) and their syntheses involve longer routes. It may be noted here that the simple heterocyclization reported here affords 1-alkoxytetrahydrocarbazoles in a single step and high yields. By using different alcohols as solvent, the reaction gives different 1-alkoxytetrahydrocarbazoles. The reaction has been found to be regioselective and a general one for the synthesis 1-alkoxytetrahydrocarbazoles.

Experimental

Melting points were determined in a sulphuric acid bath and are uncorrected. IR spectra were run on a Perkin–Elmer 1330 apparatus using KBr discs, and UV absorptions were recorded on a Hitachi 200-20 spectrometer for solutions in absolute ethanol. ^{1}H NMR spectra were determined for deuteriochloroform solutions with $SiMe_4$ as internal standard on Bruker WH-400 (400 MHz) or Jeol Fx-100 (100 MHz) instruments at the Indian Institute of Chemical Biology, Calcutta, and on a Bruker AC-250 (250 MHz) spectrometer at the Universität Konstanz, Germany. Elemental analyses and recording of mass spectra were carried out by R.S.I.C.(CDRI), Lucknow. Silica gel (60–120 mesh) and neutral alumina were obtained from SRL, India. Extracts were dried over anhydrous sodium sulphate. Petroleum ether refers to the fractions of bp 60–80°C. Compound **1***a* was prepared according to a published procedure (10).

General procedure for the preparation of 3-*N*-alkylanilinocyclohexenes 1(*b–g*)

A mixture of *N*-alkylaniline (0.1 mol) and 3-bromocyclohexene (0.1 mol) in dry acetone (150 mL) was refluxed in the presence of anhydrous potassium carbonate (10.0 g, excess) for 5 h. The reaction mixture was then cooled, filtered, and

Scheme 2.

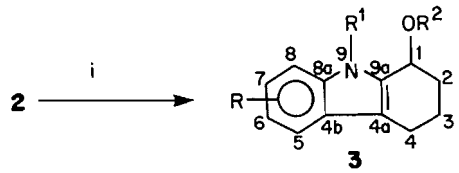

R	R^1	R^2	R	R^1	R^2
a, H	CH_3	CH_3	*f*, 8-CH_3	CH_3	CH_3
b, H	CH_3	CH_2CH_3	*g*, H	CH_2CH_3	CH_3
c, H	CH_3	$CH_2CH_2CH_3$	*h*, 6-CH_3	CH_2CH_3	CH_3
d, 6-CH_3	CH_3	CH_3	*i*, 6-CH_3	$(CH_2)_3CH_3$	CH_3
e, 6-Br	CH_3	CH_3			

Reagents: i. $Hg(OAc)_2$–R^2OH, AcOH

Scheme 3.

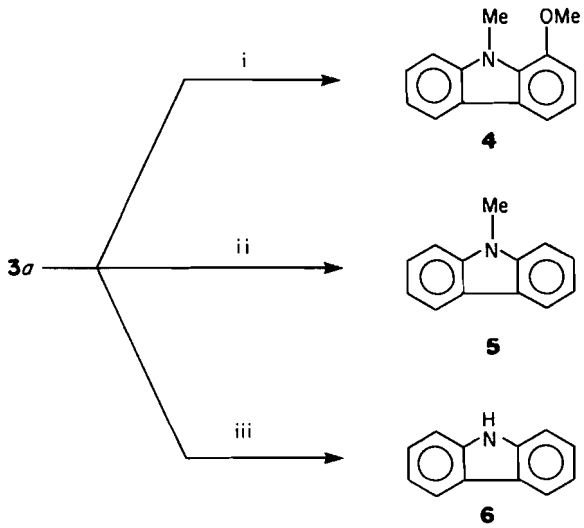

Reagents and conditions:

i. DDQ/xylene, △, 12 h
ii. DDQ(excess)/xylene, △, 20 h
iii. Pd–C, Ph_2O, △

Scheme 4.

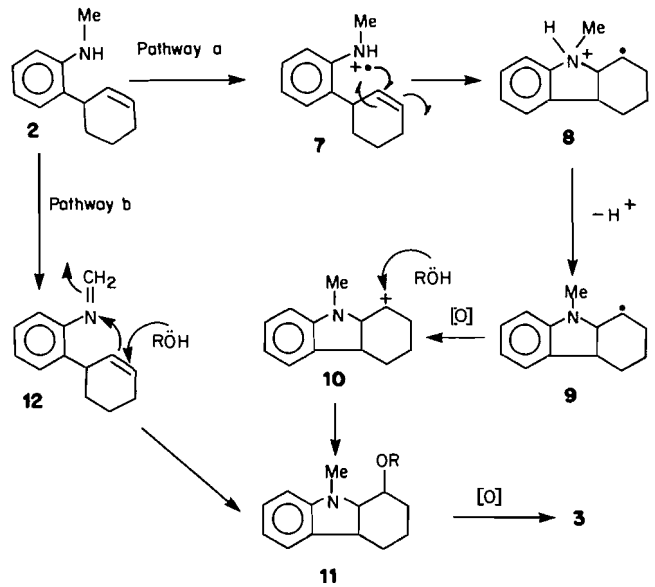

evaporated. The residue was extracted with chloroform and the extract washed with brine, dried, concentrated, and subjected to column chromatography over silica gel using petroleum ether as eluant.

Compound **1**b: yield 90%, viscous liquid; λ_{max}: 210 (log ε 3.20), 238 (2.60), 281 (2.00) nm; ν_{max}: 3020, 2920, 1620, 1520, 1400, 1110, 810 cm^{-1}; ^1H NMR (100 MHz) δ: 1.48–1.84 (m, 4H), 1.96–2.08 (m, 2H), 2.24 (s, 3H), 2.76 (s, 3H), 4.20–4.60 (br s, 1H), 5.52–5.80 (m, 1H), 5.80–6.08 (m, 1H), 6.60–7.24 (m, 4H). Anal. calcd. for $C_{14}H_{19}N$: C 83.53, H 9.51, N 6.96%; found: C 83.32, H 9.22, N 6.75%.

Compound **1**c: yield 92%, mp 50°C; λ_{max}: 207 (log ε 3.20), 264 (3.30), 312 (2.10) nm; ν_{max}: 3020, 2920, 1520, 1340, 1250, 720 cm^{-1}; ^1H NMR (100 MHz) δ: 1.52–1.84 (m, 4H), 1.84–2.12 (m, 2H), 2.76 (s, 3H), 4.20–4.52 (br s, 1H), 5.52–5.76 (m, 1H), 5.80–6.08 (m, 1H), 6.60–7.40 (m, 4H). Anal. calcd. for $C_{13}H_{16}BrN$: C 58.66, H 6.06, N 5.26%; found: C 58.88, H 5.81, N 5.55%.

Compound **1**d: yield 89%, viscous liquid; λ_{max}: 209 (log ε 3.20), 253 (2.80) nm; ν_{max}: 3020, 2920, 1590, 1310, 1250, 720 cm^{-1}; ^1H NMR (100 MHz) δ: 1.52–1.84 (m, 4H), 1.92–2.08 (m, 2H), 2.30 (s, 3H), 2.66 (s, 3H), 3.52–3.76 (br s, 1H), 5.64–6.00 (m, 2H), 6.88–7.32 (m, 4H). Anal. calcd. for $C_{14}H_{19}N$: C 83.53, H 9.51, N 6.96%; found: C 83.31, H 9.72, N 7.19%.

Compound **1**e: yield 89%, viscous liquid; λ_{max}: 207 (log ε 3.00), 260 (3.00) nm; ν_{max}: 3020, 2920, 1380, 1320, 800 cm^{-1}; ^1H NMR (100 MHz) δ: 1.14 (t, 3H, J = 7 Hz), 1.48–1.84 (m, 4H), 1.96–2.12 (m, 2H), 3.28 (q, 2H, J = 7 Hz), 4.24–4.52 (br s, 1H), 5.52–5.72 (m, 1H), 5.80–6.00 (m, 1H), 6.64–7.24 (m,

5H). Anal. calcd. for $C_{14}H_{19}N$: C 83.53, H 9.51, N 6.96%; found: C 83.83, H 9.66, N 6.72%.

Compound **1**f: yield 92%, viscous liquid; λ_{max}: 209 (log ε 3.00), 261 (3.00), 308 (2.20) nm; ν_{max}: 3020, 2920, 1590, 1490, 1390, 740 cm^{-1}; ^1H NMR (100 MHz) δ: 1.12 (t, 3H, J = 7 Hz), 1.44–1.84 (m, 4H), 1.96–2.12 (m, 2H), 2.22 (s, 3H), 3.22 (q, 2H, J = 7 Hz), 4.12–4.44 (br s, 1H), 5.56–5.66 (m, 1H), 5.66–6.00 (m, 1H), 6.60–7.16 (m, 4H). Anal. calcd. for $C_{15}H_{21}N$: C 83.67, H 9.83, N 6.50%; found: C 83.96, H 9.51, N 6.79%.

Compound **1**g: yield 88%, viscous liquid; λ_{max}: 208 (log ε 3.00), 261 (2.90) nm; ν_{max}: 3010, 2920, 1390, 790 cm^{-1}; ^1H NMR (100 MHz) δ: 0.78–1.02 (t, 3H), 1.16–1.80 (m, 8H), 1.96–2.08 (m, 2H), 2.26 (s, 3H), 3.08–3.48 (t, 2H), 4.18–4.46 (br s, 1H), 5.62–6.06 (m, 2H), 6.64–7.18 (m, 4H). Anal. calcd. for $C_{17}H_{25}N$: C 83.89, H 10.35, N 5.75%; found: C 83.69, H 10.50, N 6.04%.

General procedure for the preparation of 2-(2′-cyclohexenyl)-*N*-alkylanilines 2(*a–g*)

Compound **2***a* was prepared according to a published procedure (10). A mixture of compound **1**(*b–g*) (0.1 mol), concentrated HCl (0.8 mL), and ethanol (10 mL) was refluxed for 15 h. After neutralization and extraction with $CHCl_3$, the solvent was evaporated and the rearranged amines were isolated by column chromatography over silica gel using petroleum ether as eluant.

Compound **2**b: yield 88%, viscous liquid; λ_{max}: 211 (log ε 3.20), 248 (2.70), 300 (2.10) nm; ν_{max}: 3400, 3010, 2920, 1500, 1390, 800 cm^{-1}; ^1H NMR (100 MHz) δ: 1.56–1.88 (m, 4H), 2.04–2.16 (m, 2H), 2.24 (s, 3H), 2.84 (s, 3H), 3.04–3.72 (br s, 2H), 5.60–5.84 (m, 1H), 5.88–6.08 (m, 1H), 6.56 (d, 1H, J = 8 Hz), 6.80–7.08 (m, 2H); *m/z*: 201 (M^+). Anal. calcd. for $C_{14}H_{19}N$: C 83.53, H 9.51, N 6.96%; found: C 83.79, H 9.70, N 7.22%.

Compound **2**c: yield 50%, viscous liquid; λ_{max}: 209 (log ε 3.20), 256 (3.00), 309 (2.10) nm; ν_{max}: 3400, 3020, 2900, 1390, 1120, 790 cm^{-1}; ^1H NMR (100 MHz) δ: 1.60–2.00 (m, 4H), 2.04–2.20 (m, 2H), 2.84 (s, 3H), 3.12–3.40 (br s, 1H), 3.40–4.08 (br s, 1H), 5.56–5.88 (m, 1H), 5.88–6.12 (m, 1H), 6.50 (d, 1H, J = 8 Hz), 7.12–7.36 (m, 2H). Anal. calcd. for $C_{13}H_{16}BrN$: C 58.66, H 6.06, N 5.26%; found: C 58.92, H 5.79, N 4.98%.

Compound **2**d: yield 50%, viscous liquid; λ_{max}: 211 (log ε 3.20), 248 (2.70), 300 (2.10) nm; ν_{max}: 3380, 3020, 2920, 1400, 750 cm^{-1}; ^1H NMR (100 MHz) δ: 1.32–1.96 (m, 4H), 2.00–2.12 (m, 2H), 2.34 (s, 3H), 2.78 (s, 3H), 2.92–3.02 (m, 1H), 3.48–3.92 (br s, 1H), 5.60–5.84 (m, 1H), 5.84–6.08 (m, 1H), 6.80–7.16 (m, 3H); *m/z*: 201 (M^+). Anal. calcd. for $C_{14}H_{19}N$: C 83.53, H 9.51, N 6.96%; found: C 83.78, H 9.20, N 6.70%.

Compound **2**e: yield 90%, viscous liquid; λ_{max}: 209 (log ε 3.20), 247 (2.80), 293 (2.20) nm; ν_{max}: 3400, 3020, 2920, 1580, 1400, 740 cm^{-1}; ^1H NMR (100 MHz) δ: 1.24 (t, 3H, J = 7 Hz), 1.60–1.88 (m, 4H), 2.00–2.16 (m, 2H), 3.16 (q, 2H, J = 7 Hz), 3.32–3.56 (m, 1H), 3.56–3.96 (br s, 1H), 5.56–5.80 (m, 1H), 5.84–6.08 (m, 1H), 6.56–6.76 (m, 2H), 7.00–7.24 (m, 2H); *m/z*: 201 (M^+). Anal. calcd. for $C_{14}H_{19}N$: C 83.53, H 9.51, N 6.96%; found: C 83.85, H 9.22, N 7.22%.

Compound **2**f: yield 90%, viscous liquid; λ_{max}: 210 (log ε 3.20), 247 (2.80), 299 (2.20) nm; ν_{max}: 3380, 3020, 2920, 1400, 1260, 800 cm^{-1}; ^1H NMR (100 MHz) δ: 1.24 (t, 3H, J = 7 Hz), 1.60–1.88 (m, 4H), 2.00–2.12 (m, 2H), 2.22 (s, 3H), 3.14 (q, 2H, J = 7 Hz), 3.28–3.64 (br s, 2H), 5.60–5.80 (m, 1H), 5.88–6.08 (m, 1H), 6.56 (d, 1H, J = 8 Hz), 6.80–7.00 (m, 2H); *m/z*: 215 (M^+). Anal. calcd. for $C_{15}H_{21}N$: C 83.67, H 9.83, N 6.50%; found: C 83.48, H 10.01, N 6.75%.

Compound **2**g: yield 66%, viscous liquid; λ_{max}: 210 (log ε 3.30), 233 (3.10), 296 (2.50) nm; ν_{max}: 3400, 3040, 1600, 1400, 1320, 750 cm^{-1}; ^1H NMR (100 MHz) δ: 0.84–1.08 (t, 3H), 1.40–1.88 (m, 8H), 2.00–2.16 (m, 2H), 2.24 (s, 3H), 3.12 (t, 2H, J = 7 Hz) 3.15–3.64 (br s, 2H), 5.64–6.04 (m, 2H), 6.58 (d, 1H, J = 8 Hz), 6.84–7.04 (m, 2H); *m/z*: 243 (M^+). Anal. calcd. for $C_{17}H_{25}N$: C 83.90, H 10.35, N 5.75%; found: C 84.20, H 10.55, N 5.96%.

General procedure for the preparation of 1-alkoxy-9-alkyl-1,2,3,4-tetrahydrocarbazoles 3(*a–i*)

A solution of Hg(II) acetate (1.60 g, 5 mmol) in alcohol (50 mL) was added to a stirred solution of compound **2**(*a–g*) (5 mmol) and glacial acetic acid (0.3 mL) in the same alcohol (10 mL) at room temperature. Stirring was continued for 24 h during which time a black precipitate of mercury separated out. This was filtered off and the solvent was removed. The residue was extracted with chloroform. The chloroform extract was washed successively with sodium bicarbonate solution and brine, and dried (Na_2SO_4). Solvent was removed and the viscous oil obtained was subjected to column chromatography over silica gel using petroleum ether as eluant.

Compound **3**a: yield 80%, mp 50°C; λ_{max}: 242, 295 nm; ν_{max}: 2930, 1611, 1470, 1383, 1310, 1080 cm^{-1}; ^1H NMR (400 MHz) δ: 1.70–2.10 (m, 3H), 2.22–2.30 (m, 1H), 2.50–2.72 (m, 1H), 2.78–2.90 (m, 1H), 3.45 (s, 3H), 3.72 (s, 3H), 4.50 (t, 1H, J = 2.9 Hz, J = 3.6 Hz), 7.03–7.55 (m, 4H); ^{13}C NMR (vide supra); *m/z*: 215 (M^+). Anal. calcd. for $C_{14}H_{17}NO$: C 78.10, H 7.96, N 6.51%; found: C 78.41, H 8.16, N 6.73%.

Compound **3**b: yield 85%, viscous liquid; ν_{max}: 2950, 1660, 1600, 1472, 1385, 1320, 1090 cm^{-1}; ^1H NMR (100 MHz) δ: 1.20–1.35 (t, 3H), 1.75–3.10 (m, 6H), 3.70 (s, 3H), 3.44–3.82 (m, 2H), 4.60 (t, 1H), 7.00–7.60 (m, 4H); *m/z*: 229 (M^+). Anal. calcd. for $C_{15}H_{19}NO$: C 78.56, H 8.35, N 6.11%; found: C 78.88, H 8.01, N 6.36%.

Compound **3**c: yield 75%, viscous liquid; ν_{max}: 2950, 1470, 1380, 1315, 1085 cm^{-1}; ^1H NMR (100 MHz) δ: 0.92–1.05 (t, 3H), 1.64–2.84 (m, 8H), 3.72 (s, 3H), 3.40–3.84 (m, 2H), 4.60 (t, 1H) 6.96–7.56 (m, 4H); *m/z*: 243 (M^+). Anal. calcd. for $C_{16}H_{21}NO$: C 78.97, H 8.70, N 5.76%; found: C 79.26, H 8.40, N 5.99%.

Compound **3**d: yield 80%, mp 58°C; λ_{max}: 208 (log ε 2.70), 216 (3.00), 282 (2.20) nm; ν_{max}: 3000, 2960, 2840, 1500,

1100, 800 cm^{-1}; ^1H NMR (250 MHz) δ: 1.76–2.24 (m, 4H), 2.42 (s, 3H), 2.56–2.76 (m, 2H), 3.42 (s, 3H), 3.68 (s, 3H), 4.48 (t, 1H, J = 2.9 Hz, J = 3.6 Hz), 7.04 (d, 1H), J = 2 Hz), 7.20–7.36 (m, 2H); *m/z*: 229 (M^+). Anal. calcd. for $C_{15}H_{19}NO$: C 78.56, H 8.35, N 6.11%; found: C 78.36, H 8.55, N 6.40%.

Compound **3**e: yield 78%, mp 80°C; λ_{max}: 206 (log ε 3.00), 235 (3.20), 291 (2.20) nm; ν_{max}: 3000, 2960, 1480, 1100, 800 cm^{-1}; ^1H NMR (100 MHz) δ: 1.76–2.28 (m, 4H), 2.48–2.84 (m, 2H), 3.48 (s, 3H), 3.68 (s, 3H), 4.40–4.64 (br s, 1H), 7.12 (d, 1H, J = 8 Hz), 7.24–7.36 (dd, 1H, J = 2 Hz, J = 8 Hz), 7.60 (d, 1H, J = 2 Hz); *m/z*: 293, 295 (M^+). Anal. calcd. for $C_{14}H_{16}BrNO$: C 57.16, H 5.48, N 4.76%; found: C 57.41, H 5.19, N 5.02%.

Compound **3**f: yield 70%, mp 96°C; λ_{max}: 208 (log ε 2.70), 216 (3.00), 282 (2.30) nm; ν_{max}: 3010, 2960, 2880, 1460, 1080, 780 cm^{-1}; ^1H NMR (100 MHz) δ: 1.76–2.24 (m, 4H), 2.48–2.84 (m, 5H), 3.24 (s, 3H), 3.94 (s, 3H), 4.36–4.56 (br s, 1H), 6.84–7.00 (m, 2H), 7.32 (dd, 1H, J = 2 Hz, J = 8 Hz); *m/z*: 229 (M^+). Anal. calcd. for $C_{15}H_{19}NO$: C 78.56, H 8.35, N 6.11%; found: C 78.83, H 8.56, N 5.86%.

Compound **3**g: yield 75%, viscous liquid; λ_{max}: 209 (log ε 3.00), 229 (3.30), 288 (2.60) nm; ν_{max}: 2920, 1440, 1380, 1080, 780 cm^{-1}; ^1H NMR (100 MHz) δ: 1.28–1.44 (m, 3H), 1.84–2.24 (m, 4H), 2.56–2.88 (m, 2H), 3.44 (s, 3H), 4.00–4.28 (m, 2H), 4.44–4.60 (br s, 1H), 7.12–7.60 (m, 4H); *m/z*: 229(M^+). Anal. calcd. for $C_{15}H_{19}NO$: C 78.56, H 8.35, N 6.11%; found: C 78.33, H 8.12, N 6.24%.

Compound **3**h: yield 80%, viscous liquid; λ_{max}: 209 (log ε 2.80), 231 (3.00), 293 (2.30) nm; ν_{max}: 2920, 1400, 1080, 790 cm^{-1}; ^1H NMR (100 MHz) δ: 1.24–1.44 (m, 3H), 1.80–2.16 (m, 4H), 2.40 (s, 3H), 2.56–2.80 (m, 2H), 3.44 (s, 3H), 3.96–4.32 (m, 2H), 4.40–4.56 (br s, 1H), 7.04 (d, 1H, J = 2 Hz), 7.20–7.36 (m, 2H); *m/z*: 243 (M^+). Anal. calcd. for $C_{16}H_{21}NO$: C 78.97, H 8.70, N 5.76%; found: C 78.76, H 8.85, N 6.01%.

Compound **3**i: yield 82%, mp 82°C; λ_{max}: 209 (log ε 3.00), 216 (2.70), 234 (2.80) nm; ν_{max}: 3000, 2960, 2840, 1100, 780 cm^{-1}; ^1H NMR (250 MHz) δ: 0.97 (t, 3H, J = 7.3 Hz), 1.31–1.46 (m, 2H), 1.55–2.28 (m, 6H), 2.43 (s, 3H), 2.55–2.86 (m, 2H), 3.45 (s, 3H), 3.94–4.17 (m, 2H), 4.47 (t, 1H, J = 3.3 Hz, J = 3.6 Hz), 6.98 (d, 1H, J = 2 Hz), 7.01 (d, 1H, J = 2 Hz), 7.13 (d, 1H, J = 8 Hz). Anal. calcd. for $C_{18}H_{25}NO$: C 79.66, H 9.28, N 5.16%; found: C 79.96, H 8.96, N 5.44%.

Aromatization of 3*a* with DDQ, 4

The compound **3***a* (0.43 g, 2 mmol) was refluxed with DDQ (1.12 g, 4 mmol) in dry xylene (20 mL) for 12 h. The reaction mixture was cooled and filtered, and the residue was washed with chloroform (100 mL). The filtrate was washed with 10% potassium hydroxide solution and water, and dried (Na_2SO_4). The solution was then passed through a column of basic alumina and was eluted with chloroform to give a viscous oil.

Compound ***4***: yield 83%, viscous liquid; ν_{max}: 2950, 1610, 1315 cm^{-1}; ^1H NMR (100 MHz) δ: 3.96 (s, 3H), 4.12 (s, 3H), 7.20–7.84 (m, 7H); *m/z*: 211 (M^+). Anal. calcd. for $C_{14}H_{13}NO$: C 79.59, H 6.20, N 6.63%; found: C 79.36, H 5.94, N 6.88%.

Treatment of 3*a* with Pd–C in diphenyl ether, 6

To a solution of **3***a* (0.43 g, 2 mmol) in diphenyl ether (10 mL) was added 1 g of palladium charcoal (10%) and the mixture was heated at reflux for 4 h. The reaction mixture was filtered, diphenyl ether was removed, and the remaining mass was purified by column chromatography over basic alumina. Elution with petroleum ether furnished **6**.

Compound ***6***: yield 20%, mp 242°C; mixture mp and co-ir with authentic sample showed this to be carbazole.

Acknowledgement

We thank the Council of Scientific and Industrial Research (New Delhi) for financial assistance and Dr. A.J. Boulton of the School of Chemical Sciences, University of East Anglia, for helpful discussion.

References

1. K.C. Majumdar, R.N. De, and S. Saha. Tetrahedron Lett. **31**, 1207 (1990).
2. E. Frankland. Philos. Trans. R. Soc. London, **142**, 417 (1852).
3. R.C. Larock. Tetrahedron, **38**, 1713 (1982); Angew. Chem. Int. Ed. Engl. **17**, 27 (1978).
4. D. Seyferth. Pure Appl. Chem. **23**, 391 (1970); Acc. Chem. Res. **5**, 65 (1972).
5. J. Perie, J.P. Laval, J. Roussel, and A. Lattes. Tetrahedron Lett. 4399 (1971); V.G. Aranda, J. Barluenga Mur, G. Asensio, and M. Yus. Tetrahedron Lett. 3621 (1972).
6. (*a*) M.B. Gasc, J.J. Perie, and A. Lattes. Tetrahedron, **34**, 1943 (1978); (*b*) H.C. Brown and P.J. Geopheagan, Jr. J. Org. Chem. **35**, 1844 (1970).
7. K.C. Majumdar and S.K. Chattopadhyay. J. Chem. Soc. Chem. Commun. 524 (1987); K.C. Majumdar, R.N. De, A.T. Khan, S.K. Chattopadhyay, K. Dey, and A. Patra. J. Chem. Soc. Chem. Commun. 777 (1988); K.C. Majumdar, A.T. Khan, and S.K. Chattopadhyay. J. Chem. Soc. Chem. Commun. 654 (1989); K.C. Majumdar and S.K. Ghosh. J. Chem. Soc. Perkin Trans. 1, 2889 (1994).
8. K.C. Majumdar, S.K. Chattopadhyay, and R.N. De. Indian J. Chem. **26B**, 480 (1987).
9. B.K. Sen and K.C. Majumdar. Indian J. Chem. **22B**, 1184 (1983), S.K. Chattopadhyay, B.K. Sen, and K.C. Majumdar. Indian J. Chem. **25**, 56 (1986).
10. G. De. Saqui-Sannes, M. Riviera, and A. Lattes. Tetrahedron Lett. 2073 (1974).
11. R.C. Griffith, R.J. Gentile, T. Davidson, and F.L. Scott. J. Org. Chem. **44**, 3580 (1979).
12. J. Barluenga, J. Perez-Prieto, A.M. Bayon, and A. Sensio. Tetrahedron, **40**, 1199 (1984).
13. G.W. Gribbe, R.B. Nelson, J.L. Johnson, and G.C. Levy. J. Org. Chem. **40**, 3720 (1975).
14. J. Buckingham (*Editor*). Dictionary of organic compounds. Vol. 4. Chapman and Hall, London. 1982. p. 3784. M-01252.
15. M.F. Grundon and B.E. Reynold. J. Chem. Soc. 2445 (1964); N.J. Leonard, L.A. Miller, and P.D. Thomas. J. Am. Chem. Soc. **78**, 3463 (1956).
16. R.S. Kapil. *In* The alkaloids. Chemistry and physiology. Vol. 13. *Edited by* R.H.F. Manske. Academic Press, London. 1971. p. 273.

The chemistry of cyclohexenediones produced by the blackleg fungus

M. Soledade C. Pedras

Abstract: Several oxidation products of metabolites produced by avirulent isolates of *Phoma lingam*, the blackleg fungus, are reported; in addition, the profile of metabolites common to *P. lingam* and *P. wasabiae* is clarified.

Key words: cyclohexenedione, *Phoma lingam, P. wasabiae*.

Résumé : On a étudié plusieurs produits d'oxydation tirés des métabolites produits par des isolats avirulents du *Phoman lingam*, un champignon; de plus, on a clarifié le profil des métabolites communs au *P. lingam* et au *P. wasabiae*.

Mots clés : cyclohexènedione, *Phoma lingam, P. wasabiae*.

[Traduit par la rédaction]

Recent work on the so-called weakly virulent, avirulent, or nonaggressive isolates of the blackleg fungus (*Leptosphaeria maculans* (Desm.) Ces. et de Not., asexual stage *Phoma lingam* (Tode ex Fr.) Desm.) led to the isolation of several metabolites having a cyclohexenone ring as a common structural feature (1–3). Most importantly, this work revealed an unknown relationship between *P. lingam* and *P. wasabiae*. This unforeseen relationship[2] was also supported by analysis of particular DNA sequences of isolates of both species (3). As a consequence of that work, it was proposed that the avirulent isolates of *P. lingam* be formally reclassified (4).

As part of our continuing studies of the chemistry of the blackleg fungus,[3] it was important to determine the phytotoxicity of the cyclohexenones **1**, **2**, **5–8** produced by avirulent isolates. During the purification of these metabolites, unexpected products resulting from the slow oxidation of **5a/5b** and **6** were identified. Here is reported the transformation of phomaligadiones **5** and **6** and phomaligin A (**7**) to phomaligols **1** and **2**, and the intermediates of these oxidative transformations, as well as the products of reaction of phomaligadiones **5** and **6** with diazomethane. These results allow an important clarification regarding the structures of metabolites common to *P. wasabiae* and *P. lingam*. In addition, the implications of these findings on the biogenesis of the cyclohexenone-containing metabolites is discussed and the structures of metabolites common to *P. wasabiae* and *P. lingam* are noted.

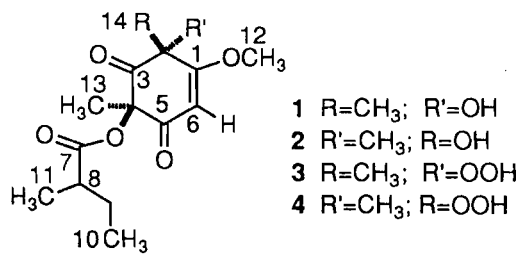

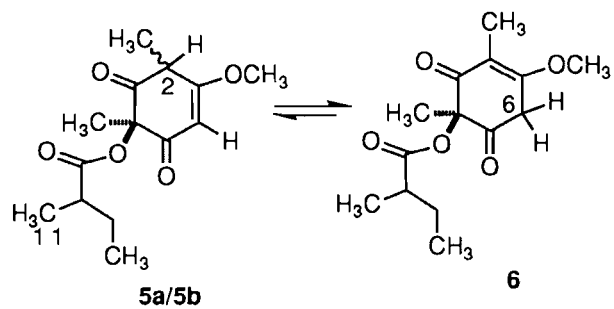

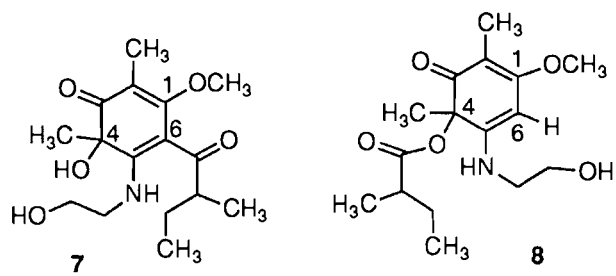

Results and discussion

Phomaligols A (**1**) and A_1 (**2**), phomaligadiones A (**5a/5b**) and B (**6**), and phomaligin A (**7**) were obtained from culture extracts of *P. lingam*, as previously described (1, 3). Phomaligadiones constituted an inseparable yellowish mixture (**5a**:**5b**:**6**, ca. 3:1:2), homogeneous by TLC and HPLC, which

Received April 11, 1996.

M.S.C. Pedras.[1] Department of Chemistry, University of Saskatchewan, 110 Science Place, Saskatoon, SK S7N 5C9, Canada.

[1] Telephone: (306) 966-4772. Fax: (306) 966-4730. Internet: pedras@sask.usask.ca

[2] There are more than 2000 species in the genus *Phoma*.

[3] For a recent review of blackleg chemistry see ref. 4; for a recent review of blackleg biology see ref. 5.

Table 1. NMR data[a] for hydroperoxides **3** and **4** in $CDCl_3$.

Position no.	3			4		
	δ_H	δ_C	HMBC	δ_H	δ_C	HMBC
1	—	172.4		—	171.7	
2	—	84.6		—	85.0	
3	—	202.8		—	206.0	
4	—	81.0		—	83.3	
5	—	192.0		—	190.8	
6	5.67, s	102.0	C-1, C-4, C-5	5.71, s	102.6	C-1, C-4, C-5
7	—	176.2		—	175.6	
8	2.46, ddq (6.8, 7.0, 7.0)	39.90	C-7, C-9, C-10, C-11	2.48, ddq (6.8, 7.0, 7.0)	39.95	C-7, C-9, C-10, C-11
9	1.68, m 1.47, m	26.6	C-7, C-8, C-10, C-11	1.71, m 1.48, m	26.6	C-7, C-8, C-10, C-11
10	0.94, t (7.5)	11.4	C-7, C-8, C-9, C-11	0.94, t (7.5)	11.4	C-7, C-8, C-9, C-11
11	1.13, d	16.2	C-7, C-8, C-9, C-10	1.17, d	16.4	C-7, C-8, C-9, C-10
12	3.89, s	56.9	C-1	3.90, s	57.1	C-1
13	1.60, s	21.7[b]	C-3, C-4, C-5	1.61, s	21.7	C-3, C-4, C-5
14	1.59, s	21.9[b]	C-1, C-2, C-3	1.57, s	23.1	C-1, C-2, C-3
OH	8.60, br s	—		8.70, br s	—	

[a]Data recorded at 500 (^{1}H NMR) and 125.8 (^{13}C NMR) MHz, respectively. Values in parentheses refer to J_{HH} in Hz.
[b]May be interchanged.

decomposed to a rather complex reddish mixture on standing. To determine the products resulting from decomposition of phomaligadiones, a solution of the mixture was left standing for 4 weeks at room temperature. Preparative TLC (CH_2Cl_2–MeOH, 97:3) of this mixture recovered 40% of phomaligadiones and four additional compounds. Analysis of the ^{1}H and ^{13}C NMR spectra of each compound revealed the structures of these components: phomaligols A (**1**) **and** $\mathbf{A_1}$ (**2**), and the corresponding hydroperoxides **3** and **4**. The structures of phomaligols A (**1**) and A_1 (**2**) were readily assigned by comparison of the ^{1}H and ^{13}C NMR spectra, and the optical rotation of each compound with data obtained previously (1). The structures of the hydroperoxides **3** and **4** were assigned from analysis of the spectroscopic data (NMR in Table 1) and reduction of the hydroperoxide groups to the corresponding alcohols, as described below.

The ^{1}H NMR spectra of compounds **3** and **4** were similar (within 0.05 ppm) to those of the corresponding alcohols **1** and **2** (1), except for H-6 at 5.67 ppm in **3** (5.53 ppm in **1**) vs. 5.71 ppm in **4** (5.53 ppm in **2**), and the D_2O exchangeable signals at 8.60 ppm in **3** (2.62 ppm in **1**) vs. 8.70 ppm in **4** (3.44 ppm in **2**). The molecular formula ($C_{14}H_{20}O_7$, obtained by HRCIMS) of each new compound, together with ^{1}H and ^{13}C NMR data, indicated that they might be hydroperoxides. Structures **3** and **4** were elucidated by analysis of the HMBC (6) and HMQC (7) spectra of each compound and by reduction of the hydroperoxide groups to the corresponding alcohols. Analysis of the HMBC and HMQC spectra of **3** and **4** indicated key correlations (Table 1) similar to those previously observed for **1** and **2** (1). For example, in compound **3** the methyl groups at δ_H 1.60 (H_3-13) and 1.59 (H_3-14) showed correlations with the carbonyl carbon at δ_C 202.8 (C-3); the methyl group at δ_H 1.59 displayed additional correlations with carbons at δ_C 84.6 (C-2) and δ_C 172.4 (C-1). The latter carbon (C-1) showed further correlations with an OMe group at δ_H 3.89 (H_3-12) and a methine proton at δ_H 5.67. The methine proton (H-6) was attached to a carbon at δ_C 102.0 (C-6) and displayed further correlations with carbons at δ_C 192.0 (C-5) and 81.0 (C-4) ppm. The methyl group at δ_H 1.60 (H_3-13) displayed an additional long-range correlation with the latter carbon (C-4). Similar correlations indicated in Table 1 were observed in compound **4**.

Finally the relative configurations of the C-2 and C-4 stereogenic centers of compounds **3** and **4** were assigned after reduction of the respective hydroperoxide groups with $P(OMe)_3$ and comparison of the spectroscopic data and optical rotation of each reaction product with those of **1** and **2**, respectively. Based on these results the relative configuration of compound **3** is *trans*, like that of **1**, and the relative configuration of compound **4** is *cis*, as is that of **2**. Similarly to phomaligadiones, phomaligin A (**7**) oxidized on standing. In attempting to purify a sample of **7**, which had been previously purified and stored at 0°C for several months, only 30% was recovered; alcohols **1** and **2**, (10%) and **8** (30%) were isolated, along with several minor unidentified products. A rearrangement of **7** to **8**, followed by oxidation and hydrolysis of the $NHCH_2CH_2OH$ group, would explain the spontaneous transformation of **7** to **1** and **2**.

Following the characterization of the oxidation products of phomaligadiones **5** and **6**, their reaction with diazomethane was examined. The reaction products were identified as the methyl ethers **9** and **10** and the adduct **11**. Methyl ethers **9** and **10** were initially characterized by ^{1}H NMR spectroscopy as a mixture (**9**/**10**, 3:1). The ^{1}H NMR spectrum of this mixture showed the expected resonances for two isomeric methyl ethers; however, the position of the newly introduced (O)Me

Table 2. NMR data[a] for compounds **9** and **11** in $CDCl_3$.

Position no.	9			11		
	δ_H	δ_C	HMBC	δ_H	δ_C	HMBC
1	—	172.7	—	166.1		
2	—	112.8	—	116.8		
3	—	163.3	—	194.0		
4	—	79.2	—	82.6		
5	—	195.4	—	191.5		
6	5.42, s	96.1	C-1, C-4, C-5	—	123.5	
7	—	175.6	—	175.8		
8	2.45, ddq (6.8, 6.8, 7.0)	40.1	C-7, C-9, C-10, C-11	2.50, ddq (6.8, 6.8, 7.0)	40.0	C-7, C-9, C-10, C-11
9	1.72, m 1.47, m	26.6	C-7, C-8, C-10, C-11	1.70, m 1.49, m	26.7	C-7, C-8, C-10, C-11
10	0.96, t (7.5)	11.3	C-7, C-8, C-9, C-11	0.96, t (7.5)	11.4	C-7, C-8, C-9, C-11
11	1.14, d (7.0)	16.3	C-7, C-8, C-9, C-10	1.16, d (7.)	16.4	C-7, C-8, C-9, C-10
12	3.77, s	56.2	C-1	3.90, s	61.9	C-1
13	1.84, s	24.0	C-3, C-4, C-5	1.50, s	23.7	C-3, C-4, C-5
14	1.59, s	9.5	C-1, C-2, C-3	1.90, s	9.0	C-1, C-2, C-3
15	3.74, s	61.2	C-3	3.41, d (4.1)	40.1	
Others	—	—		12.6, br s	—	

[a]Data recorded at 500 (^{1}H NMR) and 125.8 (^{13}C NMR) MHz, respectively. Values in parenthesis refer to J_{HH} in Hz.

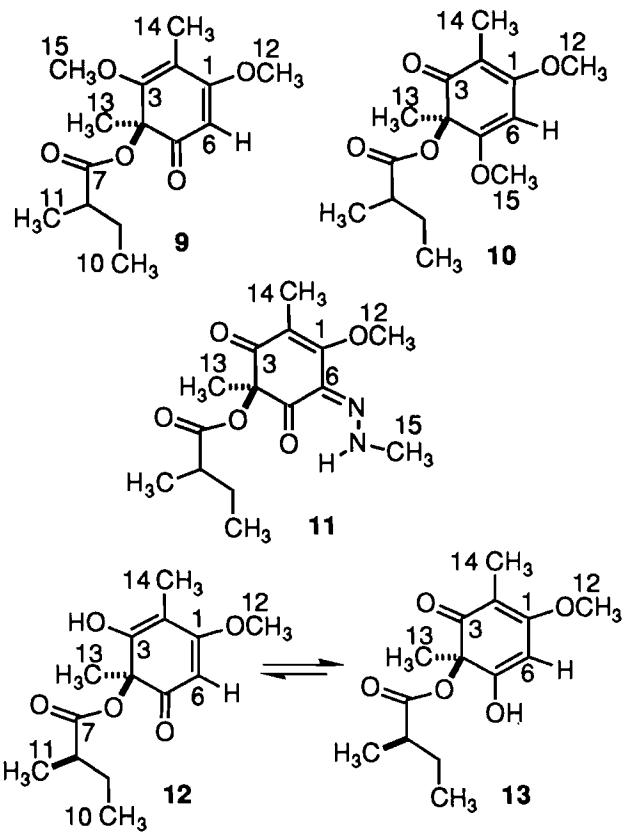

group in each isomer could not be determined unambiguously (i.e., C-3 or C-5). Further separation of the mixture of **9** and **10** yielded sufficient amounts of **9** to allow the unambiguous assignment of this structure. Firstly, the ^{1}H NMR spectrum of **9** (Table 2) displayed the resonances seen for the major product present in the initial mixture of **9** and **10**, that is, a *sec*-butyl group (9 hydrogens) in addition to two Me groups (δ_H 1.84 and 1.59), two Me(O) groups (δ_H 3.74 and 3.77), and a vinylic proton at δ_H 5.42. The proton decoupled ^{13}C NMR spectrum (Table 2) of compound **9** showed the expected 15 resonances, which corroborated the presence of 2 × Me, 2 × Me(O), and a *sec*-butyl group, as indicated in the ^{1}H NMR spectrum. In addition, signals attributable to four carbonyl groups or equivalents (δ_C 195.4, 175.6, 172.7, and 163.3), two sp^2 carbons (δ_C 112.8 and 96.1), and one oxygenated quaternary carbon (δ_C 79.2) confirmed that **9** was a methylated derivative of **5/6**. The EIMS of compound **9** revealed the molecular ion expected for $C_{15}H_{22}O_5$ at *m/z* 282. Finally, the structure of compound **9** was unambiguously assigned on the basis of its HMBC spectral data (Table 2). The location of the Me(O) at C-3 and not at C-5 was deduced from the long-range correlations of C- 3 (δ_C 163.3) with the methyl groups at δ_H 3.74 (H_3-15), δ_H 1.84 (H_3-13), and δ_H 1.59 (H_3-14), as well as the correlation of the lowest field carbonyl carbon (δ_C 195.4, C-5) with the methyl group at δ_H 1.84 (H_3-13). Although insufficient sample was recovered to obtain complete spectroscopic data for **10**, the ^{1}H NMR data attributable to the minor isomer of the methylation product mixture indicated the proposed structure.

The major product of the reaction of phomaligadiones **5/6** with diazomethane was a bright yellow oil (**11**). The HREIMS of product **11** suggested the molecular formula $C_{15}H_{22}N_2O_5$, consistent with the formation of an adduct of **5/6** ($C_{14}H_{20}O_5$) with CH_2N_2. Analysis of the ^1H NMR spectrum of **11** showed the expected resonances for the cyclohexenedione substituents also present in the starting material (**5/6**): one *sec*-butyl group (9 hydrogens), two Me groups (δ_H 1.90 and 1.50), and one Me(O) group (δ_H 3.90). Two new signals at δ_H 3.41 (d, 3H) and 12.6 (bs, 1H, D_2O exchangeable) were attributed to the addition of CH_2N_2 to cyclohexenediones **5/6**, resulting in a =N-NH-Me substituent. The locations of the 2 × Me, MeO, *sec*-butyl-C(=O)O, and 2 × C=O groups on the cyclohexenedione were determined to be identical to those observed in **5/6**, by analysis of the proton decoupled ^{13}C NMR and HMBC spectral data (Table 2). Consequently, the *N*-methylhydrazone (=N-NH-Me) could only be located at C-6 (δ_C 123.5). In this way the structure of the major product was established as adduct **11**.[4]

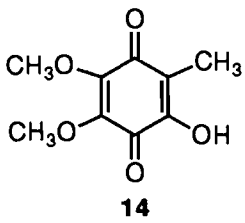

14

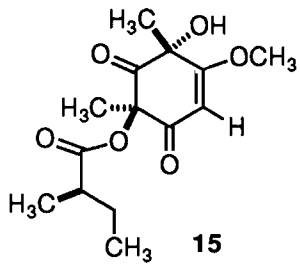

15

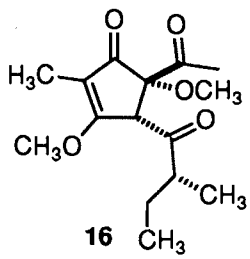

16 CH_3

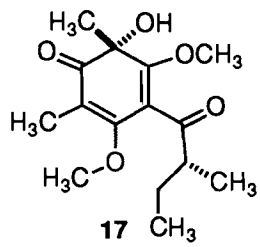

17 CH_3

The products of the reaction of phomaligadiones **5/6** with diazomethane allowed further conclusions with respect to metabolites produced by *P. wasabiae*. It was reported that a compound named wasabidienone A, on treatment with diazomethane, yielded two Me ethers (1:1) having structures **9** and **10** (8). Later on, analysis of the p-nitrobenzoate derivative of wasabidienone A by X-ray crystallography allowed the assignment of its stereogenic centers (9). Based on these results (8, 9) the tautomeric forms **12** and **13** were assigned to wasabidienone A. Furthermore, it was reported that wasabidienone A on standing on a TLC plate decomposed to a brownish material, which was identified as a mixture of compounds **14** (purple) and **15** (colorless) (10). The structure of compound **15**, including absolute configuration, was determined by X-ray crystallography (10). The purple compound **14** had been previously reported as a metabolite of *P. wasabiae* (11[5] but, interestingly, **15** was never reported to be present in cultures of *P. wasabiae*. The NMR, IR, and optical rotation data reported for compound **15** are in close agreement with data obtained for phomaligol A (**1**) (1). In conclusion, wasabidienone A and phomaligadiones appear to be the same compound, existing, at least in $CDCl_3$, as a tautomeric mixture, described more accurately as **5** and **6**, since the resonances corresponding to C-2 in the former, and C-6 in the latter, are clearly due to sp^3 carbons (1), and not sp^2 carbons as in **12** and **13**. The data obtained for methyl ether derivatives **9** and **10** are in complete agreement with data reported previously (8); however, Soga et al. did not report adduct **11** (8). Because the conditions used to prepare these methyl ethers were not specified in that report (8), it is not possible to comment on those results. Our previous work (3) indicated that some of the compounds isolated from cultures of *P. lingam* were also present in cultures of *P. wasabiae*. Now it is clear that the profile of metabolites common to *P. wasabiae* and *P. lingam* is much broader; not only phomaligols (**1**, **2**) and phomaligadiones (**5**, **6**) are present in liquid cultures of both species, but also wasabidienones B_0 (**16**) and B_1 (**17**) (12) were present in similar liquid cultures.

Biogenetically, metabolites **1**, **2**, **5–8** may derive from a pentaketide that is further methylated and oxidized; however, the results reported here indicate that metabolites **1** and **2** can also result from non-enzymatic oxidation of **5–7**.[6] Furthermore, this work has uncovered a relationship for metabolites **1**, **2**, **7**, and **8**; that is, **8** could result from a non-enzymatic rearrangement of **7**, and could then be further oxidized to **1** and **2** (**7** → **8** → **1** + **2**). In fact, it is likely that the reddish pigments characteristic in liquid cultures of avirulent blackleg isolates (13) are most likely oxidation products of the metabolites **1–8** and (or) related ones such as **14**. The phytotoxicity of these metabolites to canola susceptible to blackleg was evaluated; phomaligols **1** and **2** did not cause obvious lesions even at relatively high concentrations (10^{-3} M), whereas **7** and **8** caused only slight lesions at similar concentrations.

Experimental

General

All chemicals were purchased from Aldrich Chemical Company, Inc., Madison, Wis. All solvents were HPLC grade and used as such. Preparative TLC: Merck Kieselgel 60 F_{254}, 20 × 20 cm × 0.25 mm; analytical TLC (Merck Kieselgel 60 F_{254}, aluminum sheets) 5 × 2 cm × 0.2 mm; compounds were visualized by exposure to UV and by dipping the plates in a 5% aqueous (w/v) phosphomolybdic acid solution containing a trace of ceric sulfate and 4% (v/v) H_2SO_4, followed by heating at 200°C. Flash column chromatography: Merck silica gel, grade 60, mesh size 230–400, 60 Å. NMR spectra were recorded on a Bruker AMX 500 or AM 300 spectrometer; δ

[4] No literature precedent was found for this mode of reaction of diazomethane (T. H. Black, Aldrichimica Acta, **16**, 3 (1983)). It may be a simple protonation of diazomethane, followed by enolate attack on the electrophilic terminal nitrogen.

[5] In the course of this work a reddish polar material was isolated, but due to further decomposition, its structure could not be assigned.

[6] The only indication that enzymatic oxidation might occur arises from detection of **1** and **2** in 2–3-day-old cultures, while **5/6** accumulated in 7–9-day-old cultures.

values were referenced to $CHCl_3$ (7.24 ppm) for ^1H (500 MHz), and referenced to $CDCl_3$ (77.0 ppm) for ^{13}C (125.8 MHz). Mass spectra (MS) were obtained on a VG 70-250 SEQ hybrid mass spectrometer or on a Finnigan Mat model 4500 mass spectrometer (high resolution (HR), electron impact (EI), fast atom bombardment (FAB), or chemical ionization (CI) with ammonia as carrier gas), employing a solid probe in both cases.

Air oxidation of phomaligadiones A (5a/5b) and B (6)

A solution of phomaligadiones A (**5a/5b**) and B (**6**) (28 mg in $CHCl_3$–MeOH, 1:1, 1 mL) was left standing for 4 weeks at room temperature. Preparative TLC (CH_2Cl_2–MeOH, 97:3, multiple development) of that mixture gave phomaligols **1** (2 mg; R_f 0.42, hexane–EtOAc, 1:1) and **2**(1 mg; R_f 0.28, hexane –EtOAc, 1:1), hydroperoxides **3** (3 mg; R_f 0.46, hexane–EtOAc, 1:1) and **4** (1 mg; R_f 0.34, hexane–EtOAc, 1:1), and a mixture of phomaligadiones **5a/5b** and **6** (12 mg; R_f 0.60, hexane–EtOAc, 1:1).

Reaction of phomaligadiones A (5a/5b) and B (6) with diazomethane

Diazomethane in ether was added (excess) to a stirred solution of phomaligadiones A (**5a/5b**) and B (**6**) (8 mg in CH_2Cl_2, 1 mL) at room temperature. After 30 min the solvents were removed with a stream of nitrogen and the reaction products were separated by preparative TLC (CH_2Cl_2–MeOH, 97:3, developed twice) to give a mixture of compounds **9** and **10** in one band (2 mg, 3:1) and adduct **11** (3.2 mg). Compounds **9** and **11** were further purified separately by preparative TLC (hexane–EtOAc, 7:3, multiple elution) to yield pure **9** (1.7 mg; R_f 0.75, hexane–EtOAc, 1:1), **10** (0.5 mg; R_f 0.5, hexane–EtOAc, 1:1), and **11** (2.1 mg; R_f 0.75, hexane–EtOAc, 1:1).

Reduction of hydroperoxides 3 and 4

$P(OMe)_3$ (2 mg in CH_2Cl_2, 1 mL) was added to a solution of the hydroperoxide **3** (2.4 mg in CH_2Cl_2, 1 mL) at room temperature. The solvent was immediately evaporated and the reaction product was purified by preparative TLC (hexane–EtOAc, 1:1, multiple elution) to give a pure compound (1.5 mg), identical to phomaligol A (**1**) in all respects, including optical rotation. Similar reaction with hydroperoxide **4** yielded a pure compound (1.1 mg), identical to phomaligol A_1 (**2**).

Phomaligol A hydroperoxide (3): colorless oil; HRCIMS *m/z* (relative intensity) measured: 301.1282 (301.1287 calcd. for $C_{14}H_{21}O_7$); FABMS *m/z* (relative intensity): 301 ($[M+1]^+$ 100; ^1H and ^{13}C NMR, see Table 1.

Phomaligol A_1 hydroperoxide (4): colorless oil; HRCIMS *m/z* (relative intensity) measured: 301.1283 (301.1287 calcd. for $C_{14}H_{21}O_7$); FABMS *m/z* (relative intensity): 301 ($[M+1]^+$ 100; ^1H and ^{13}C NMR, see Table 1.

Compound 9: light yellow film; ^1H NMR ($CDCl_3$) δ:5.44(s), 3.88(s), 3.72(s), 2.45 (ddq, J = 6.8, 7.0, 7.0 Hz), 1.84(s) 1.72(m), 1.59(s), 1.47(m), 1.13(d, J = 7.0 Hz), 0.90 (t, J = 7.5).

Compound 10: light yellow oil; EIMS *m/z* (relative intensity): 282 ($[M]^+$, 9%), 198 (20%), 155 (30%); ^1H and ^{13}C NMR, see Table 2.

Adduct 11: yellow oil; HREIMS *m/z* (relative intensity) measured: 310.1529 (310.1526 calcd. for $C_{15}H_{22}N_2O_5$); EIMS *m/z* (relative intensity): 310 ($[M]^+$, 15%), 209 (40%), 154 (28%); ^1H and ^{13}C NMR, see Table 2.

Acknowledgments

I gratefully acknowledge the financial support of the Natural Sciences and Engineering Research Council of Canada and the University of Saskatchewan. I would like to thank Mr. B. Chatson, Plant Biotechnology Institute, Saskatoon, for NMR spectral determinations.

References

1. M.S.C. Pedras, V.M. Morales, and J.L. Taylor. Tetrahedron, **49**, 8317 (1993).
2. M.S.C. Pedras, V.M. Morales, and J.L. Taylor. Phytochemistry, **36**, 1315 (1994).
3. M.S.C. Pedras, J.L. Taylor, and V.M. Morales. Phytochemistry, **37**, 1215 (1995).
4. M.S.C. Pedras. Rev. Latinoam. de Quim. In press.
5. R.K. Gugel and G.A. Petrie. Can. J. Plant Pathol. **14**, 36 (1992).
6. A. Bax and M.F. Summers. J. Am. Chem. Soc. **108**, 2093, (1986).
7. A. Bax and S. Subramanian. J. Magn. Reson. **67**, 565 (1986).
8. O. Soga, H. Iwamoto, S. Date, T. Watanabe, K. Tanaka, K. Hate, A. Takuwa, and M. Nakayama. Chem. Lett. 339 (1984).
9. O. Soga, H. Iwamoto, A. Takuwa, H. Nozaki, J. Kuramoto, and M. Nakayama. Agric. Biol. Chem. **51**, 283 (1987).
10. O. Soga, H. Iwamoto, K. Hata, R. Maeba, A. Takuwa, T. Fujiwara, Y. Hsu, and M. Nakayama. Agric. Biol. Chem. **52**, 865 (1988).
11. O. Soga. Z. Naturforsch. B: Anorg. Chem. Org. Chem. **35B**, 1497 (1980).
12. O. Soga, H. Iwamoto, A. Takuwa, T. Takata, Y. Tsugiyama, K. Hamada, T. Fujiwara, and M. Nakayama. Chem. Lett. 1535 (1988).
13. R.L. Gabrielson. Seed Sci. Technol. **11**, 749 (1983).

Interaction between tetracyanoethylene and naphthalene in reverse micelles of AOT in *n*-hexane. The electron-donor properties of AOT

M.A. Biasutti and Juana J. Silber

Abstract: The electron donor–acceptor (EDA) interaction between TCNE and naphthalene (Naph) in *n*-hexane and reverse micelles of AOT in n-hexane was studied by UV–visible spectroscopy with the aim of determining the influence of the micellar media on the EDA interaction. The spectra of the mixtures of TCNE–Naph in *n*-hexane show two typical maxima at 418 and 534 nm, assigned to the formation of a π–π EDA complex. In the micellar media a new band is observed at 398 nm. When the spectra of TCNE in *n*-hexane are studied in the presence of AOT two new bands at 398 and 418 nm are detected. These bands are consistent with an EDA interaction between TCNE and AOT as *n*-donor. The stability constants of this interaction were calculated for AOT concentrations below the CMC and in the micellar media at different W ($W = [H_2O]/[AOT]$). The results give evidence of the tendency of AOT to interact very strongly with electron acceptors. Moreover, in the system TCNE–Naph in the micellar media it is shown that Naph and AOT compete to form a complex with TCNE. The formation constants of the complexes of AOT–Naph in the micelle system were determined at $W = 0$ and 5. Despite the competition of AOT for TCNE the stability constant for the complex TCNE–Naph is higher than in homogeneous media, probably due to the high local concentration of the acceptor in the micelle.

Key words : reverse micelles, aerosol-OT, tetracyanoethylene, naphthalene, electron donor–acceptor complexes.

Résumé : Afin de déterminer l'influence du milieu micellaire sur l'interaction donneur d'électron–accepteur (DEA) et faisant appel à la spectroscopie UV–visible, on a étudié l'interaction DEA entre le TCNE et le naphtalène (Naph) dans l'hexane et des micelles inverses d'aérosol-OT (AOT) dans l'hexane. Les spectres des mélanges de TCNE–Naph dans l'hexane présentent deux maximums typiques à 418 et 534 nm, attribuées à la formation d'un complexe π–π DEA. Dans le milieu micellaire, on observe une nouvelle bande à 398 nm. Lorsqu'on a étudié les spectres du TCNE dans l'hexane en présence d'AOT, on a détecté deux nouvelles bandes à 398 et 418 nm. Ces bandes sont en accord avec une interaction DEA entre TCNE et AOT comme donneur *n*. On a calculé les constantes de stabilité de cette interaction pour des concentrations d'AOT inférieures à la CMC et, dans le milieu micellaire à différentes valeurs de W ($W = [H_2O]/[AOT]$). Les résultats fournissent des indications sur la tendance de AOT à interagir très fortement avec les accepteurs d'électrons. De plus, on a montré que, dans le système TCNE–Naph en milieu micellaire, Naph et AOT sont en compétition pour former un complexe avec TCNE. On a déterminé les constantes de formation des complexes AOT–Naph à $W = 0$ et 5. Malgré la compétition de AOT pour TCNE, la constante de stabilité pour le complexe TCNE–Naph est plus élevée dans le milieu homogène, probablement en raison de la concentration locale plus élevée de l'accepteur dans la micelle.

Most clés : micelles inverses, aérosol-OT, tétracyanoéthène, naphtalène, complexes d'électron donneur–accepteur.

[Traduit par la rédaction]

Introduction

Tetracyanoethylene (TCNE) is a well-known π acceptor that forms intensely colored complexes with alkenes and aromatic hydrocarbons. The color arises from electron donor–acceptor (EDA) complexes (1). For weak donors such as alkylbenzenes it has been shown that the complexes have only partial transfer of a π electron from the aromatic hydrocarbon to TCNE. On the other hand, with strong donors such as nickel carbonyl or iodide ion complete electron transfer occurs and the stable TCNE anion is formed (2). The acceptor properties of TCNE as well as its multiple applications in organic chemistry have been comprehensively reviewed (3). As in the case of other polycyano compounds, TCNE is used in the preparation of novel materials with unusual electrical and (or) magnetic properties (4). Some of the most studied EDA complexes of TCNE are with aromatic hydrocarbon donors such as alkylbenzene (5–7) and naphthalenes (4, 8, 9).

Multiple charge transfer bands are observed for alkylbenzene–TCNE complexes (5–7) as well as for polynuclear aromatic TCNE complexes (5, 8, 9). The presence of two charge transfer bands for alkyl-substituted benzenes with TCNE has been rationalized as due to the interactions with the π (b_1) and π (b_2) orbitals of the benzene ring (4, 7) or to isomeric complexes (10). In the case of naphthalenes the two bands are attributed to charge transfer transitions $^*\pi \leftarrow \pi_u$ and $^*\pi \leftarrow \pi_{bu}$ of the naphthalene ring with TCNE (1, 9).

Received January 30, 1996.

M.A. Biasutti and J.J. Silber.[1] Departamento de Química y Física, Universidad Nacional de Río Cuarto-Estafeta, 9, Río Cuarto-5800, Argentina.

[1] Author to whom correspondence may be addressed. Telephone: 54-58-676157. Fax: 54-58-680280. E-mail: nitas@unrccc.edu.ar

The aim of the present contribution is to study the influence of the reverse micelles of AOT in *n*-hexane on the interaction between TCNE and naphthalene (Naph) by UV–visible spectroscopy. The complex of TCNE–Naph has been recognized as a model system for studying and understanding the interaction between TCNE and other donors (9). Moreover, since this EDA complex has well-characterized properties and spectra in several media, its behavior in a micellar system could give information about its microenvironment.

Reversed micelles have received considerable attention in recent years, mainly because of the possibility of performing chemical reactions essentially in an organic phase, but hosting the reactive species in the water pool, e.g. enzymatic reactions, photoelectron transfer reactions, proton transfer, singlet oxygen photosensitization, or inverse microemulsion polymerization (11). In previous work we studied the micropolarity of reversed micelles of AOT in *n*-hexane by following the solvatochromic behavior of chromophores of betaines (12). We showed that in these systems the polarity, as well as the hydrogen bond donor ability, of the AOT polar heads are the determining factors for inclusion of betaine probes in the micelle interface.

It is widely recognized that such properties of a solute as the electronic spectra, capability of forming EDA complexes, and chemical reactivity are dependent on the polarity of the solvent (13). In this sense, the main objective of this work was to examine what effect the AOT reverse micelle microenvironment may have on the stability constant of the TCNE–Naph EDA complex. In the course of this investigation a strong interaction between TCNE and AOT was also found. The spectral properties of this interaction were examined. They show that AOT is a strong electron-donor compound in homogeneous and micellar media.

Experimental

Sodium 1,4-bis(2-ethylhexyl)sulfosuccinate (AOT) was obtained from Fluka A. G. and further purified by the procedure described in ref. 14. Tetracyanoethylene (TCNE), 98%, and naphthalene (Naph) from Aldrich were purified by sublimation under vacuum. 8-Hydroxy-1,3,6-pyrenesulfonic acid trisodium salt (Pyranine) from Kodak was used as received. *n*-Hexane (Sintorgan, HPLC quality) was dried by distillation over metallic sodium just before use.

Water was first distilled over potassium permanganate and then bidistilled until a conductivity of 0.3–0.5 μmho cm^{-1} at 298 K was reached.

The solutions were prepared by weighing and dilution. Water was added to the appropriate solution by a calibrated microsyringe. The micelle solutions were completely stable for at least a day.

The absorption spectra were measured by using a Cary 17 spectrophotometer or HP 8452A and 1 cm path length cells. The working temperature was 25 ± 0.5°C. Fluorescence measurements were carried out with an Aminco Bowman spectrofluorometer.

Results and discussion

1. Absorption spectra of TCNE–Naph in *n*-hexane

Since the absorption spectrum of TCNE in *n*-hexane shows one band at 260 nm while Naph exhibits bands only below 310 nm, the region between 350 and 650 nm constitutes an excellent region for the study of the mixture.

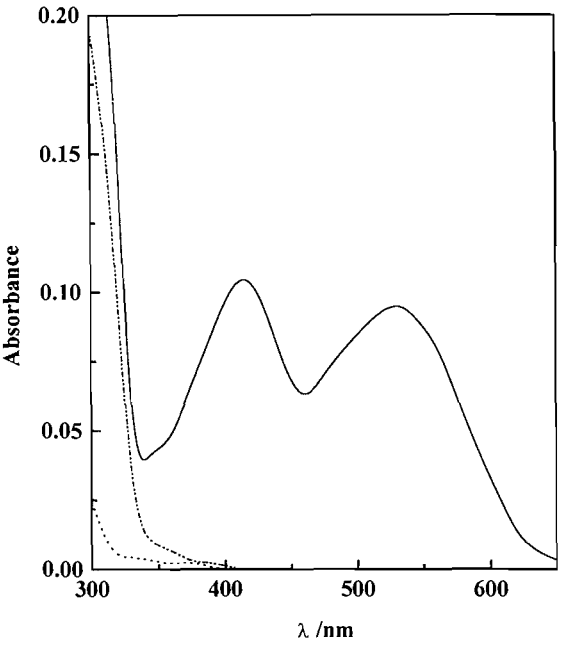

Fig. 1. Absorption spectra of (—·—) 1×10^{-4} M TCNE, (-----) 0.3 M Naph, and (———) mixture of 1×10^{-4} M TCNE and 0.3 M Naph in *n*-hexane.

Table 1. Stability constants, $K_s(1)$, and ε values for the complex 1:1 TCNE–Naph in different solvents, T = 298 K.

Solvent	λ (nm)	$K_s(1)$ (M^{-1})	ε (M^{-1} cm^{-1})
n-Hexane	418	3.70 ± 0.20	1963 ± 67
	534	3.80 ± 0.26	1831 ± 82
$CHCl_3$[a]	432	1.07	
	558	0.97	
CCl_4[a]	430	3.79	
	560	4.23	

[a]From ref. 5.

The absorption spectrum of TCNE–Naph in *n*-hexane is shown in Fig. 1. The spectrum exhibits two maxima, one at 418 nm and the other at 534 nm. Similar bands were observed for this complex using $CHCl_3$ and CCl_4 as solvents (5) and they have been assigned to the π–π* electron donor–acceptor complex between TCNE and Naph.

Assuming a 1:1 complex, the stability constant, $K_s(1)$, was determined spectrophotometrically by following the change of absorbance of these new bands, working at constant $[TCNE]_0 = 2 \times 10^{-4}$ M and varying $[Naph]_0$ from 3×10^{-2} to 20×10^{-2} M. The value of $K_s(1)$ was calculated by an iterative procedure previously described (15). The results are shown in Table 1 where the values of the stability constants reported in other solvents are included for comparison.

It is seen that the K_s values obtained at both wavelengths are similar and consistent with the formation of the 1:1 complex

Fig. 2. Absorption spectra of TCNE– Naph complex in reverse micelles of AOT–*n*-hexane at $[AOT]_0$; (———) 0.029; (----) 0.036; (.....) 0.054; (—·—·—) 0.076; (—··—) 0.092 M. $[TCNE]_0 = 2 \times 10^{-4}$ M, $[Naph]_0 = 0.32$ M, $W = 0$.

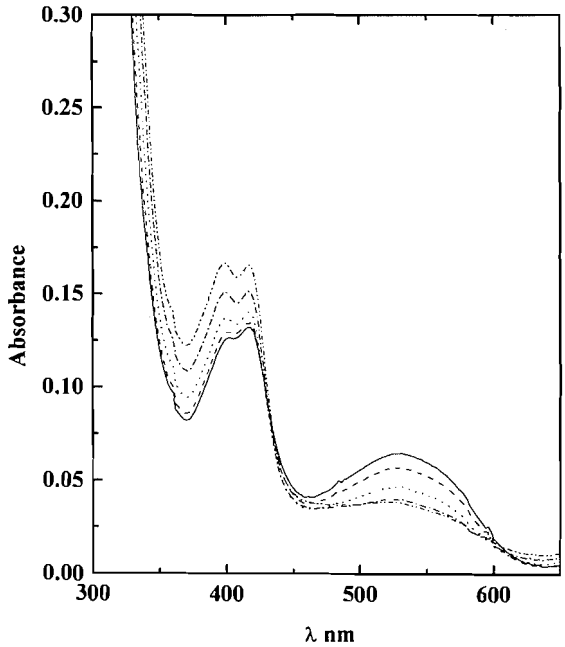

Fig. 3. Absorption spectra of TCNE in AOT–n-hexane at $[AOT]_0$: (*a*1) 0.0; (*a*2) 0.002; (*a*3) 0.003; (*a*4) 0.066; (*a*5) 0.132; (*a*6) 0.198; (*a*7) 0.200 M; $[TCNE]_0 = 2 \times 10^{-4}$ M, $W = 10$. (*b*) Spectrum of TCNE-free AOT–*n*-hexane; $[AOT]_0 = 0.200$ M.

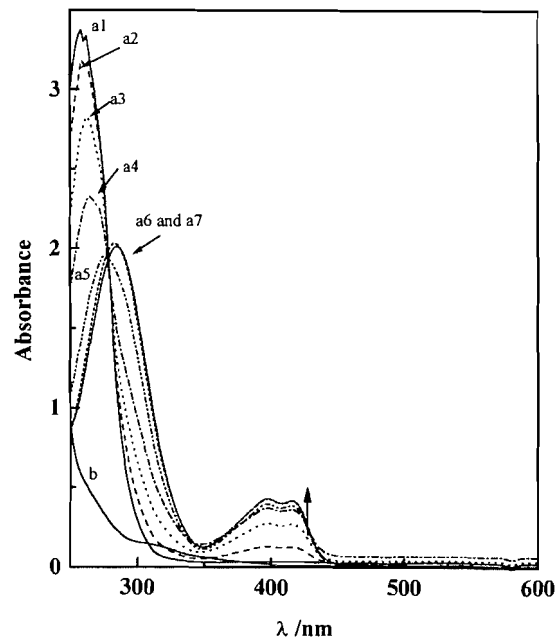

with the two characteristic charge tranfer bands (1, 9). Also, the magnitude of $K_s(1)$ in *n*-hexane is similar to that in CCl_4 but is greater than in the more polar $CHCl_3$, as expected for weak EDA complexes (16).

2. Effects of the AOT addition on TCNE–Naph interaction in the micellar region

The typical spectral changes obtained upon addition of AOT to TCNE–Naph solution in *n*-hexane are shown in Fig. 2.

A band at about 534 nm is still observed although its intensity decreases when the surfactant concentration increases. At concentrations higher than 0.06 M in AOT this band practically disappears. On the other hand, the band present originally at 418 nm for the TCNE–Naph system is seen to split into two with maxima at 416 and 398 nm. An isosbestic point is detected at 435 nm.

The observed decrease in intensity of the 534 nm band with increase in AOT concentration may be due to a competitive interaction of AOT with TCNE. It is well known that TCNE can interact with *n* donors such as alcohols, ethers (17), and amines (8a), giving *n*–π* type EDA complexes (16). As well, in the previously studied I_2-AOT system (18) we found that AOT may act as a "*n*" donor, probably through the free electron pair on carbonyl groups present in the ester functions. Also, an *n*–π* EDA interaction have been proposed between AOT and 7,7,8,8-Tetracyanoquinodimethane (TCNQ) in several organic solvents (19). Thus, it may be that AOT competes with Naph in the association with TCNE. Certainly, the spectra of TCNE in AOT–*n*-hexane systems (Fig. 3) show two bands at 398 and 416 nm that increase in intensity with increasing AOT concentration. Moreover, the 261 nm band of TCNE in hexane decreases in intensity as a new band at 283 nm develops, and an isosbestic point is observed at 278 nm. The spectrum of AOT in *n*-hexane at the highest concentration used is also shown in Fig. 3. New bands appear in the mixture at higher wavelength that those of the donor or the acceptor. Thus, the system TCNE–AOT in *n*-hexane shows the characteristic features that can be expected on formation of an EDA complex (16).

When the bands in the visible region for TCNE–AOT in *n*-hexane are compared with the absorption maxima positions for the system of TCNE with *n*-donors such as methanol,[2] aminopyridines (20), and diethyl ether (17) (Table 2), they all show similar spectra. Furthermore, it can also be concluded

Table 2. Position of the maximum UV–visible absorption band of TCNE with different "*n*" donors.

Solvent	System	λ_{max}/(nm)	λ_{max}/(nm)
CH_3OH[a]	TCNE–CH_3OH	412	394
$C_2H_2Cl_2$[b]	TCNE–2-BzNHPy	417	390
$(C_2H_5)O$[c]	TCNE – $(C_2H_5)O$		347
W = 0[d]	TCNE – AOT	416	398
W = 5[d]	TCNE – AOT	416	398
W = 10[d]	TCNE – AOT	416	398
W = 20[d]	TCNE – AOT	416	398

[a]See footnote 2.
[b]Reference 20.
[c]Reference 17.
[d]$[TCNE]_0 = 2 \times 10^{-4}$ M, [AOT] = 0.02 M in *n*-hexane.

[2] M.A. Biasutti and J.J. Silber, unpublished results.

that the absorption band at 398 nm, which appears in the spectra of TCNE–Naph in AOT–hexane (Fig. 2), is due to interaction between TCNE and AOT. This interaction competes with TCNE–Naph complex formation in the reversed micelle medium. On the other hand, the band at 418 nm is probably due to the contribution of both interactions, TCNE – Naph and TCNE – AOT.

From the position of the absorption bands of the TCNE–AOT complex in *n*-hexane and using the empirical correlations found by Frey (21) for π or *n*-donor–TCNE complexes, (eq. [1]), the value of the molecular ionization energy (I_D) of AOT can be estimated.

$$[1] \quad \lambda_{CT}\,(\text{nm}) = 1240\,(\text{nm/eV}) / 0.810 I_D - 4.28$$

Values of 9.2 and 8.9 eV, which are quite typical for *n*-donors (21), are obtained. However, these values are much lower than the gas-phase I_D expected for the lone pair of a typical carboxylate ester (i.e., 10.10 eV for ethyl acetate) or even of a ketone (i.e., 9.69 eV for acetone) (22). On the other hand, AOT shows other properties such as its vibrational spectra (23) that are not those of a typical carboxylate, due to the asymmetric attachment of the sulfonate group to the succinate backbone and interactions with the Na^+ counterion. Also, even in "dry" hydrocarbon solution the polar head of AOT is expected to be partially hydrated (24). The combination of all these factors may account for the unusual donor behavior of AOT as compared with common esters.

On the other hand, this condition may arise from through-space oxygen–oxygen interactions when the succinate moiety is in an appropriate conformation (25). This may also explain the fact that the peaks in the 398–418 doublet are much narrower than a typical charge transfer band and resemble an intramolecular electronic–vibronic transition.[3] This would require a preferred and a rather fixed *gauche* conformation of the carboxylate groups, as has actually been observed (26, 27), particularly in nonpolar solvents.

It is noteworthy that the position of the maxima in the spectrum of TCNE in the system AOT–hexane is independent of W(= [H_2O/AOT]) as shown in Table 2. This indicates that TCNE is anchored in a similar microenvironment regardless of the amount of water in the micellar core. This is an important fact in considering where TCNE is located in the micelle, as discussed below.

3. Interaction TCNE–AOT in hexane

To obtain a quantitative description of the interactions between TCNE and AOT, studies were performed at different AOT concentrations in *n*-hexane, below the CMC concentration (i.e., 0.4×10^{-3} M) (27, 28).

In solutions of TCNE and AOT where the initial AOT concentration is below the CMC and consequently of the order of the initial $[TCNE]_0$, it can be assumed that a 1:1 complex between AOT and TCNE (eq. [2]) is formed.

$$[2] \quad \text{TCNE} + \text{AOT} \underset{}{\overset{K_s(2)}{\Longleftrightarrow}} \underset{\text{EDA complex}}{(\text{TCNE..AOT})}$$

[3] We thank a referee for suggesting this possibility.

Table 3. Stability constants, $K_s(2)$, and ε values for the complex 1:1 TCNE–AOT in *n*-hexane, T = 298 K.

W	$K_s(2)$ (M^{-1})	ε (M^{-1} cm^{-1})
5	700 ± 130	2090 ± 70
10	500 ± 100	2260 ± 145

The stability constant, $K_s(2)$, was determined spectrophotometrically by following the changes of absorbance of the band at 398 nm working at constant $[TCNE]_0 = 2 \times 10^{-4}$ M and varying $[AOT]_0$ in the range 1×10^{-6} to 2.5×10^{-4} M. Value of $K_s(2) = 2530$ M^{-1} amd $\varepsilon = 416$ cm^{-1} M^{-1} were obtained. The high value of $K_s(2)$ indicates a very strong interaction. These high values for the association constant of the complex are also unusual when comparing complexes formed between TCNE and donors such as ethers or alcohols (17). However, we have found a very high constant for the complex between AOT and I_2 (13). Moreover, although no $K_s(2)$ values were calculated, it has been shown that AOT interacts so strongly with TCNQ (19) that the spectra of the anion radical of this acceptor is detected in reverse micelle systems.

On the other hand, the results obtained at AOT concentrations higher than the CMC, ($[AOT]_0 = 1 \times 10^{-3}$ to 5×10^{-2} M and $[TCNE]_0 = 2 \times 10^{-4}$ M) at W 5 and 10 are shown in Table 3. As can be observed, $K_s(2)$ in the micellar system is somewhat smaller than in the homogeneous solution of AOT in hexane below the CMC. It should be noted that variations in $K_s(2)$ are observed up to $W = 10$. Thereafter, this stability constant is independent of water concentration. This behavior is characteristic of solutes that are located at the interface or for a process that occurs in the interfacial region of AOT reverse micelles. Previous studies performed by other authors (29) with 2-naphthol, located in the interfacial region of AOT reversed micelles, have shown how a substrate residing in the interface experiences environment changes induced by addition of water, due to the competition between the hydroxy group of the naphthol and water regarding localization in the vicinity of AOT ester groups. In this case, the changes were also more significant at $W < 10$. Recently, we found that the properties probed by 1-methyl-8-oxyquinolinium (12) and I_2 (18) in AOT reverse micelles in *n*-hexane are more significant in the micelle domain at $W < 10$ than at higher values of W.

Below $W \leq 10$ hydration of the AOT polar heads can be considered as the key process involving AOT. Thus, hydrogen bonds between water and AOT species could compete with the specific interaction between TCNE and AOT species and this may be the reason for the observed magnitude and variation in the $K_s(2)$ values. At values of W higher than 10, water forms "pools" with normal water properties (30) and no additional changes are observed.

4. Possible localization of TCNE in the reverse micelles of AOT

From the high stability constant calculated for the TCNE–AOT complex it can be assumed that most of the TCNE is in the micelle interior. As well, from the evolution of the band at 283 nm in the presence of increasing concentrations of AOT (Fig. 3) and the concomitant decrease in the typical band of TCNE in hexane at 261 nm it can be inferred that TCNE is

moving to a more polar environment that is near the interface.

Positron annihilation techniques in reversed AOT micelles in benzene (31) have shown that 63.7% of the TCNE is localized in the interfacial region but on the organic side of the micelle. Also, TCNE seems to show much less affinity with AOT in benzene than in hexane. This can be easily rationalized on the basis of the well-known π–π interaction between TCNE and benzene (32). On the other hand, since *n*-hexane can be considered as a relatively inert solvent, the conclusion that TCNE will be in the micelle interior toward the interface seems quite reasonable.

An independent means of estimating the location of TCNE in the AOT– *n*-hexane micelle was attempted using fluorescence quenching studies. Pyranine was used as a fluorescent probe and TCNE as a quencher. This probe has a negative charge and is expected to reside in the water pool. The measurements were performed by excitation at 375 nm and observing the emission at 425 nm. A large decrease in the fluorescence intensity was found, which indicates that TCNE can locate close the water pool. Unfortunately, no quantification of this effect could be performed because of the intense absorption of the TCNE–AOT band (≈398 nm) at the emission and excitation wavelengths that overlap with the observed fluorescence.

It can be concluded that the main driving force for the residence of TCNE in the micelle interior is formation of a strong complex between TCNE and AOT.

5. TCNE–Naph interaction in AOT–hexane reversed micellar system

In light of the results hitherto presented, the decrease in the absorption of the 534 band of the TCNE–Naph complex (Fig. 2) can be ascribed to the competition from the TCNE–AOT complex formation.

As can be observed in Fig. 4, by increasing the Naph concentration at constant AOT and TCNE concentrations, the band at 534 nm increases, its intensity while the band at 392 nm decreases, showing again the competition between Naph and AOT for TCNE.

When water is added to TCNE–Naph in AOT–hexane solution in the range of W from 0 to 10 (Fig. 5), the intensity of the band at 534 nm decreases. Its λ_{max} shifts bathochromically (about 6–8 nm) as expected for a π–π^* type transition. On the other hand, for $W \approx 10 - 20$ the changes are negligible. An isosbestic point is observed at ≈430 nm. Moreover, the intensity of bands at 418 and 398 nm increases and, whereas the first one remains in the same position, the second shifts hypsochromically as would be expected for an n–π^* type transition. The changes are much more significant in the micellar domain (at $W < 10$) than in the microemulsion domain.

Since for $W > 5$ the intensity of the band at 534 nm is quite small, the quantitative study of the TCNE–Naph interaction was performed at $W \leq 5$. The $K_s(1)$ values calculated in the micellar medium were 20 ± 2 M^{-1} (ε = 212 ± 17 M^{-1} cm^{-1}) and 13 ± 2 M^{-1} (ε = 229 ± 15 M^{-1} cm^{-1}) for W = 0 and 5, respectively. To understand the observed magnitude of $K_s(1)$ in the micelle medium there are two effects that should be taken into account. One is the partition process of the solute and the other is the polarity of the medium.

Thus, the increment found for $K_s(1)$ values in the micellar phase with respect to the homogeneous medium (Table 1) may be due to a variation in the local concentration of the reactants in the micellar phase. Actually a solute in this kind of system is distributed essentially among three environments or three sol-

Fig. 4. Effect of variable concentration of Naph on the absorption spectra of TCNE– Naph complex in reverse micelles of AOT–*n*-hexane. $[Naph]_0$ = (———) 0.043; (– – –) 0.069; (—·—·—) 0.143; (–·–·–) 0.178; (-----) 0.309 M; $[TCNE]_0 = 2 \times 10^{-4}$ M, W = 0, [AOT] = 0.02 M.

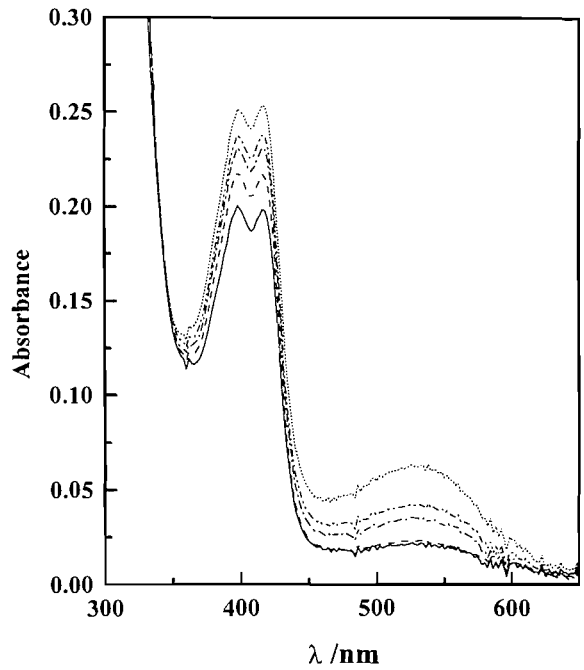

Fig. 5. Absorption spectra of TCNE– Naph complex in reverse micelles of AOT–*n*-hexane at W (1) 5; (2) 10; (3) 20. $[TCNE]_0 = 2 \times 10^{-4}$ M; $[Naph]_0$ = 0.29 M; [AOT] = 0.02 M.

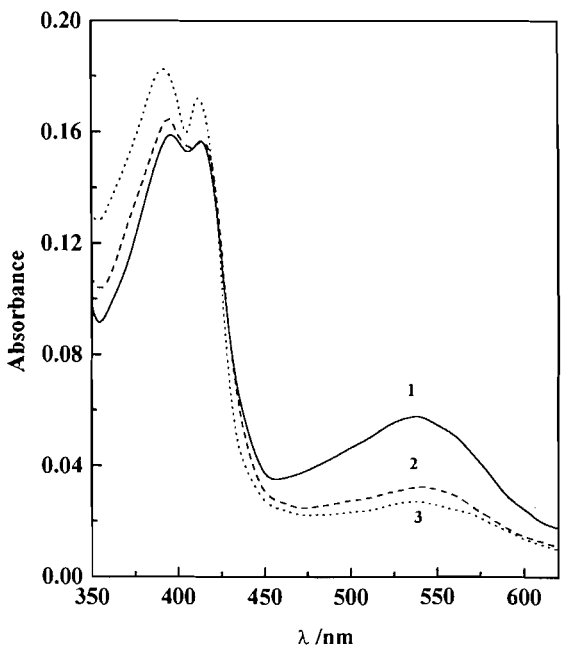

ubilization sites (33). These are (*i*) the micellar water pools, (*ii*) the reversed micellar interface, and (*iii*) the organic continuum. While Naph will be partitioned between the micellar interface and the organic medium, TCNE may be mostly in the micellar interface, as discussed before. The TCNE–Naph complex formation should be produced in the micelle interior and near the interface, where the local concentration of TCNE is greater than in the bulk.

On the other hand, as has already been determined (12), the micropolarity of these micelles increases on water addition. Thus, if the complex is formed in the micelle interior a decrease in $K_s(1)$ values is expected, as is actually observed. The same polarity effect on the stability constants was found by other authors (6) for the TCNE - hexamethylbenzene complex in CH_2Cl_2 and CCl_4.

Conclusions

The observed decrease in intensity of the band assigned to the TCNE–Naph complex at 534 nm by increasing the AOT concentration has been shown to be due to the competitive interaction between TCNE and AOT. The λ_{max} of absorption bands for the TCNE–AOT complex are consistent with the formation of an EDA complex where AOT may act as an *n*-donor. However, the ionization potential inferred from this interaction is lower than that expected for a common ester function and the association constants are much higher than for common oxygen donors. This gives the AOT–*n*-hexane systems quite unique behavior. AOT was also previously found to act as a good electron donor for a σ acceptor such as I_2 (18). Therefore any studies referring to the reverse micelle of AOT–hexane must take into account the possibility of AOT competing with a probe or a solute for a given acceptor. This effect may not be at all important for reverse micelles of AOT–benzene (31). The stability of the TCNE–AOT complex is higher in homogeneous media (at $[AOT]_0 < CMC$) than in the micellar domain. This shows that TCNE resides in a more polar environment, namely, the micelle interface. The effect of water addition is only noticeable until $W \cong 10$, that is, while the polar heads of AOT are involved in the hydration process.

Despite the competition of AOT for TCNE, the apparent stability constant of the TCNE–Naph complex is greater in the micellar media than in *n*-hexane. This is mostly attributed to an increase in the local concentration of AOT in the micelle.

Acknowledgments

Financial support from the Consejo Nacional de Investigaciones Científicas y Técnicas (CONICET), the Consejo de Investigaciones Científicas y Tecnológicas de la Provincia de Córdoba (CONICOR), and the Secretaría de Ciencia y Técnica de la Universidad Nacional de Río Cuarto is gratefully acknowledged.

References

1. R.E. Merrifield and W.D. Phillips. J. Am. Chem. Soc. **80**, 2778 (1958).
2. O.W. Webster, W. Mahler, and R.E. Benson. J. Am. Chem. Soc. **73**, 545 (1962).
3. A.J. Fatiadi. Synthesis, 249 (1986).
4. M. Bonamico, V. Fares, A. Flamini, and P. Imperatori. J. Chem. Soc. Perkin Trans. **2**, 121 (1990), and refs. therein.
5. M.J.S. Dewar and C.C. Thompson. Tetrahedron **7**, 97 (1965).
6. B.M. Britt, L. McHale, and D.M. Friedrich. J. Phys. Chem. **99**, 6347 (1995).
7. J.E. Frey, A.M. Andrews, D.G. Ankoviac, D.N. Beaman, L.E. Du Pont, T.E. Elsner, S.R. Lang, M.A. Oosterbaan Zwart, R.E. Seagle, and L.A. Torreano. J. Org. Chem. **55**, 606 (1990).
8. (*a*) J.R. Gott and W.G. Maisch. J. Chem. Phys. **39**, 2229 (1963); (*b*) A.R. Lepley. J. Am. Chem. Soc. **88**, 2545 (1964).
9. J.E. Frey, A.M. Andrews, S.D. Combs, S.P. Edens, J.J. Puckett, R.E. Seagle, and L.A. Torreano. J. Org. Chem. **57**, 6460 (1992).
10. C.J. Eckhardt, and R.J. Hood. J. Am. Chem. Soc. **101**, 6170 (1979).
11. N. Wittouk, M.R. Negri, M. Amellot, and F.C. De Schryver. J. Am. Chem. Soc. **116**, 10601, (1994).
12. N.M. Correa, M.A. Biasutti, and J.J. Silber. J. Colloid Interface Sci. **172**, 71 (1995).
13. C. Reichardt. Solvent and solvent effects in organic chemistry. 2nd ed. V.C.H., Weiheim. 1990.
14. A.N. Maitra and H.F. Eicke. J. Phys. Chem. **85**, 2687 (1981).
15. (*a*) J. Anunziata, J.O. Singh, and J.J. Silber. Can. J. Chem. **59**, 1291 (1981); (*b*) M.A. Biasutti, J.D. Anunziata, and J.J. Silber. Spectrochim. Acta, Part A: **48**, 169 (1992).
16. (*a*) R. Foster. Organic charge transfer complexes. Academic Press, London. 1969; (*b*) R. Foster (*Editor*). Molecular association. Vol. 1. Academic Press, London. 1975; (*c*) Molecular association. Vol. 2. Academic Press, London. 1979.
17. J.E. Frey, T. Aiello, D.N. Beaman, S.D. Combs, S. Fu, and J.J. Puckett. J. Org. Chem. **59**, 1817 (1994).
18. M.A. Biasutti, L. Sereno, and J.J. Silber. J. Colloid Interface Sci. **164**, 410 (1994).
19. S. Muto and K. Meguro. Bull. Chem. Soc Jpn. **46**, 1316 (1973).
20. G. Tosi, P. Bruni, L. Cardellini, and F. Mari. Gazz. Chim. Ital. **113**, 231 (1983).
21. J.E. Frey. Appl. Spectrosc. Rev. **23**, 247 (1987)
22. H.M. Rosenstock, K. Draxl, B.W. Steiner, and J.T. Herrn. J. Phys. Chem. Ref. Data, **6**, Suppl. No 1 (1977).
23. P.D. Moran, G.A. Bowmaker, R.P. Cooney, J.R. Bartlett, and J.L. Woolfrey. J. Mater. Chem. **5**, 295 (1995).
24. K. Mukherjee, S.P. Moulik, and D.C. Mukherjee. Langmuir, **9**, 1727 (1993).
25. H-D. Martin and B. Mayer, Angew. Chem. Int. Ed. Engl. **95**, 281 (1983).
26. T.K. Jain, M. Varshney, and A. Maitra. J. Phys. Chem. **93**, 7409 (1989).
27. F. Heatley. J. Chem. Soc. Faraday Trans. 1, **83**, 517 (1987);
28. M. Ueno, H. Kishimoto, and Y. Kyogoku. Chem. Lett. 599 (1977).
29. E. Bardez, E. Monnier, and B. Valeur. J. Colloid Interface Sci. **112**, 200 (1986).
30. H. Kondo, I. Miwua, and J. Sumanoto. J. Phys. Chem. **86**, 4826 (1982).
31. J. Jean and H.J. Ache. J. Am. Chem. Soc. **100**, 6320 (1978).
32. M.J.S. Dewar and H. Rodgers. J. Am. Chem. Soc. **84**, 395 (1962)
33. E.B. Leodidis and T.A. Hatton. J. Phys. Chem. **94**, 6400 (1990).

Synthesis of 5-(1-azidovinyl) and 5-[2-(1-azirinyl)] analogs of 2′-deoxyuridine

Rakesh Kumar, Leonard I. Wiebe, and Edward E. Knaus

Abstract: The regiospecific addition of bromine azide to the vinyl substituent of 5-vinyl-3′,5′-di-*O*-acetyl- (or *tert*-butyldimethylsilyl)-2′-deoxyuridines (**2**) yielded the corresponding 5-(1-azido-2-bromoethyl)-3′,5′-di-*O*-protected-2′-deoxyuridines (**3**). Treatment of the 5-(1-azido-2-bromoethyl) compounds **3** with *t*-BuOK, to effect the base-catalyzed elimination of HBr, afforded the corresponding 5-(1-azidovinyl)-2′-deoxyuridines (**4**, **7**). Thermal decomposition of 5-(1-azidovinyl)-2′-deoxyuridine (**7**) at 110°C in dioxane yielded 5-[2-(1-azirinyl)]-2′-deoxyuridine (**9**). 5-(1-Azidovinyl)-2′-deoxyuridine (**7**) exhibited appreciable in vitro antiviral activities against herpes simplex virus type 1 (HSV-1) and varizella zoster virus (VZV). Athough **7** increased the length of survival of HSV-1 brain-infected mice, it did not decrease the mortality rate relative to placebo. 5-[2-(1-Azirinyl)]-2′-deoxyuridine (**9**) was an inactive antiviral agent.

Key words: azidovinyl, azirinyl, 2′-deoxyuridine, antiviral activity.

Résumé : L'addition régiospécifique de l'azoture de brome sur le substituant vinylique des 5-vinyl-3′-di-*O*-acétyl- (ou *tert*-butyldiméthylsilyl)-2′-désoxyuridines (**2**) conduit aux 5-(1-azido-2-bromoéthyl)-3′,5′-protégé-2′-désoxyuridines (**3**). Le traitement des composés **3** par le *t*-BuOK provoque une élimination basocatalysée de HBr qui conduit aux 5-(1-azidovinyl)-2′-désoxyuridines (**4**, **7**). La décomposition thermique de la 5-(azidovinyl)-2′-désoxyuridine (**7**), à 110°C, dans le dioxane, fournit de la 5-[2-(1-azirinyl)]-2′-désoxyuridine (**9**). La 5-(1-azidovinyl)-2′-désoxyuridine (**7**) présente des activités antiviral in vitro appréciables contre le virus de l'herpès simplex de type I (HSV-1) et le virus zoster varizella (VZV). Même si le composé **7** augmente le temps de survie des souris dont le cerveau a été infecté au HSV-1, il ne diminue pas le taux de mortalité par rapport au placebo. Le 5-[2-(1-azirinyl)]-2′-désoxyuridine (**9**) n'est pas actif comme agent antiviral.

Mots clés : azidovinyle, azirinyle, 2′-désoxyuridine, activité antivirale.

[Traduit par la rédaction]

The development of new methods for the synthesis of 2′-deoxyuridines that possess novel vinyl moieties at the C-5 position and exhibit potent antiviral activity represents an important area of drug design. 5-Vinyl-2′-deoxyuridine (**1***a*) has been shown to exhibit potent antiviral activity against herpes simplex virus type-1 (HSV-1), type-2 (HSV-2), and vaccinia virus (1). Among the many 5-substituted pyrimidine nucleosides that have been studied, (*E*)-5-(2-halovinyl)-2′-deoxyuridines (**1***b*; X = I (IVDU); X = Br (BVDU); X = Cl (CVDU)) are among the most active and selective in their action against HSV-1 (2). Incorporation of a methyl substituent at the 1-position of the 5-(2-bromovinyl) moiety of BVDU (**1***c*) (3), or a chloro substituent at the 1-position of the 5-vinyl moiety of VDU (**1***d*) (4), reduced activity against HSV-1. Structure–activity correlations for a group of 5-substituted-2′-deoxyuridines indicated that optimum antiviral activity against HSV-1 occurs when the C-5 substituent is unsaturated and conjugated with the uracil ring, is not larger than four atoms in length, has the (*E*) stererochemisty, and possesses a hydrophobic electronegative atom (3).

As part of an investigation to design broad-spectrum antiviral agents, an azido substituent located at the 1-position of a 5-vinyl moiety attracted our attention. The azido substituent possesses desirable physicochemical properties, relative to other substituents used routinely in structure–activity correlation studies, such as electronic (inductive effect *F* value), steric size (molar refractivity value), and lipophilic (π-value) effects, respectively (5), viz: N_3, 0.30, 10.2, 0.46; H, 0.00, 1.03, 0.00; Me, −0.04, 5.65, 0.56; F, 0.43, 0.92, 0.14; Cl, 0.41, 6.03, 0.71; Br, 0.44, 8.88, 0.86; I, 0.40, 13.94, 1.12; OH, 0.29, 2.85, −0.67. Thus, the electronic effect of azido is between that of OH and I, the steric effect is between that of Br, and I, and the lipophilic effect is between that of F and Me. These physical data suggest an azido group is a good isostere of I, Br, and Cl. Furthermore, the azido group maybe capable of electrostatic binding to an enzyme, such as thymidine kinase, that is not possible with a halogen such as I, Br, or Cl. In a previous study, it was reported that short exposure (<5 min) of 5-(1-azidovinyl)-2′-deoxyuridine treated FM3A thymidine positive (TK^+) cells to irradiation at λ = 254 nm enhanced the cytostatic effect 5-fold due to inhibition of thymidine synthase (TS). This photoaffinity approach may open new perspectives for the treatment of cutaneous disorders such as malignant melanoma with respect to azido-based chemotherapeutic agents that show increased cytostatic activity against HSV TK gene-transfected tumor cells upon short (1–5 min) UV light exposure (6). It was also envisaged that the 1-azidovinyl sub-

Received April 4, 1996.

R. Kumar[1], **L.I. Wiebe and E.E. Knaus.**[2] Faculty of Pharmacy and Pharmaceutical Sciences, University of Alberta, Edmonton, AB T6G 2N8, Canada.

[1] Current address: Department of Medical Microbiology and Immunology, Faculty of Medicine, University of Alberta, Edmonton, Alberta T6G 2H7.

[2] Author to whom correspondence may be addressed. Telephone: (403) 492-5993. Fax: (403) 492-1217. E-mail: eknaus@pharmacy.ualberta.ca

stituent should undergo intramolecular cyclization to yield 2′-deoxyuridine compounds possessing novel C-5 heterocyclic ring systems. We now report the synthesis of the novel 5-(1-azidovinyl)-2′-deoxyuridine (**7**) and the related 5-[2-(1-azirinyl)] (**9**) analog.

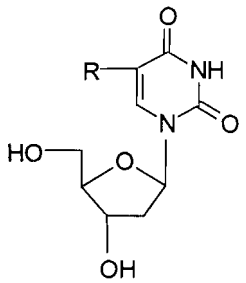

1*a*, R = -CH=CH$_2$
1*b*, R = (*E*)-CH=CHX
1*c*, R = (*E*)-C(Me)=CHBr
1*d*, R = -C(Cl)=CH$_2$

Our initial attempts to synthesize 5-(1-azidovinyl)-2′-deoxyuridine (**7**, Scheme 1) by treatment of 5-(1-azido-2-bromoethyl)-2′-deoxyuridine (**3***d*) with either *t*-BuOK or NaOH using DMSO or DME as solvent gave a low yield of **7** (11%) and the bicyclic compound **10** (66%), which could not be separated by silica gel column chromatography. 3′,5′-Di-*O*-acetyl- (**3***a*) and 3′,5′-di-*O*-*tert*-butyldimethylsilyl-5-(1-azido-2-bromoethyl)-2′-deoxyuridine (**3***b*) were therefore prepared to protect the sugar hydroxyl groups, which decreases the number of equivalents of base required to effect the base-catalyzed elimination of HBr from the 5-(1-azido-2-bromoethyl) moiety. The regiospecific addition of bromine azide to the 5-vinyl substituent of the 2′-deoxyuridine derivative (**2***a* and **2***b*) afforded the corresponding 5-(1-azido-2-bromoethyl)-2′-deoxyuridine analog (**3***a*, 88%) and **3***b* (82%), respectively. The ^{13}C NMR (*J* modulation) spectrum of **3***a* provided conclusive evidence for the regiospecific addition of bromine azide across the 5-vinyl substituent of **2***a*. Compound **3***a* is a mixture of two diastereomers, which differ in configuration (*R* and *S*) at the C-1 carbon atom of the 5-(1-azido-2-bromoethyl) moiety. For example, the bromine atom present in **3***a* is attached to a methylene carbon that showed dual resonances at δ: 33.97 and 34.46, whereas the azido substituent is attached to a methine chiral carbon that exhibited dual resonances at δ: 58.21 and 58.33. This regiospecific addition is consistent with reports that unsymmetrical olefins, capable of halonium ion formation, were found to favor an unsymmetrical bridged intermediate even in solvents having a high dipole moment (7, 8). Reaction of the 3′,5′-di-O-acetyl derivative **3***a* with *t*-BuOK in THF gave rise to three products. Thus, the direct elimination of HBr afforded 5-(1-azidovinyl)-3′,5′-di-*O*-acetyl-2′-deoxyuridine (**4***a*, 27%, Path A) whereas, intramolecular cyclization reactions gave rise to the bicyclic products 5-(3′,5′-di-*O*-acetyl-2′-deoxy-β-D-ribofuranosyl)-furano[2,3-*d*]pyrimidin-6(5*H*)-one (**5**, 13%, Path B) and 3-azido-2,3-dihydro-5-(3′,5′-di-*O*-acetyl-2′-deoxy-β-D-ribofuranosyl)furano[2,3-*d*]pyrimidin-6(5*H*)-one (**6**, 2.8%, Path C), respectively.

The base-catalyzed intramolecular cyclization reaction of **3***a* to **6**, as illustrated in Scheme 2, is analogous to the reported conversion of 5-[2-[(methylsufonyl)oxy]ethyl]uracil to 2,3-dihydrofurano[2,3-*d*]-pyrimidin-6(5*H*)-one using *t*-BuOK in DMSO (9). The mechanism responsible for the formation of the bicyclic compound **5** proceeds via an elimination reaction involving expulsion of HN$_3$ from **6** as illustrated in Scheme 3 since treatment of **6** with a saturated solution of NH$_3$ in MeOH gave the bicylic derivative **10**, rather than the azido compound **11** (see Scheme 1). To prevent the formation of the bicyclic products **5** and **6**, the N-3 position of 5-(1-azido-2-bromoethyl)-3′,5′-di-*O*-acetyl-2′-deoxyuridine (**3***a*) was protected by reaction of **3***a* with benzoyl chloride in dry pyridine, which gave the N-3 benzoyl derivative (**3***c*) in 93% yield. Reaction of **3***c* with *t*-BuOK in THF yielded the 5-(1-azidovinyl) analog **4***c* in higher yield (39%) than that obtained using **3***a* (27%). A similar reaction of the 5-(1-azido-2-bromoethyl)-3′,5′-di-*O*-*tert*-butyldimethylsilyl analog **3***b* gave the 5-(1-azidovinyl) product **4***b* (45%). Deprotection of **4***a* (NH$_3$–MeOH) and **4***b* (*n*-Bu$_4$N$^+$F$^-$–THF) yielded 5-(1-azidovinyl)-2′-deoxyuridine (**7**) in 76 and 86% yield, respectively. Thermal decomposition, using a procedure similar to that reported by Jordan (10) for the conversion of α-azidostyrene to phenylazirine, of the 5-(1-azidovinyl) compounds **4***a–c* in dry toluene at 110°C afforded the corresponding 5-[2-(1-azirinyl)] analogs **8***a–c* in 24, 84, and 54% yield, respectively. The possibility that the 5-[2-(1-azirinyl)] compounds (**8**, **9**) may undergo a [2 + 2] cycloaddition reaction to produce dimeric products **12** was ruled out since the fast atom bombardment (FAB) spectrum of **8***a* and **9** did not exhibit a molecular ion or mass fragmentation pattern indicating a dimeric structure **12**. The FAB spectra (**8***a*, **9**) exhibited the expected M + 1, 5-[2-(1-azirinyl)]uracil and sugar fragment, ions. Attempts to remove the 3′,5′-protecting groups present in compounds **8***a–c* using NH$_3$ in MeOH (**8***a*, **8***c*), NaHCO$_3$ in dry MeOH (**8***a*, **8***b*), or *p*-toluenesulfonic acid (**8***c*) were unsuccessful. In contrast, reaction of **8***b* with *n*-Bu$_4$N$^+$F$^-$ in THF afforded 5-[2-(1-azirinyl)]-2′-deoxyuridine (**9**) in 25% yield. The optimum yield of **9** was obtained by thermal decomposition of 5-(1-azidovinyl)-2′-deoxyuridine (**7**) in dioxane (37% yield).

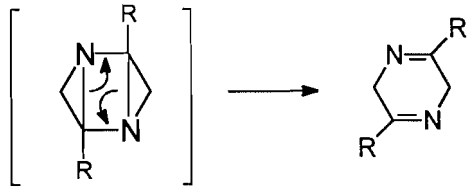

12

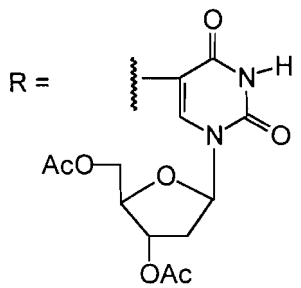

The in vitro antiviral activities of 5-(1-azidovinyl)- (**7**), 5-[2-(1-azirinyl)]-2′-deoxyuridine (**9**), and the related bicyclic analog 5-(2′-deoxy-β-D-ribofuranosyl)furano[2,3-*d*]pyrimidin-6(5*H*)-one (**10**) were determined against four viruses (herpes simplex virus type 1 (HSV-1), type 2 (HSV-2),

Scheme 1.

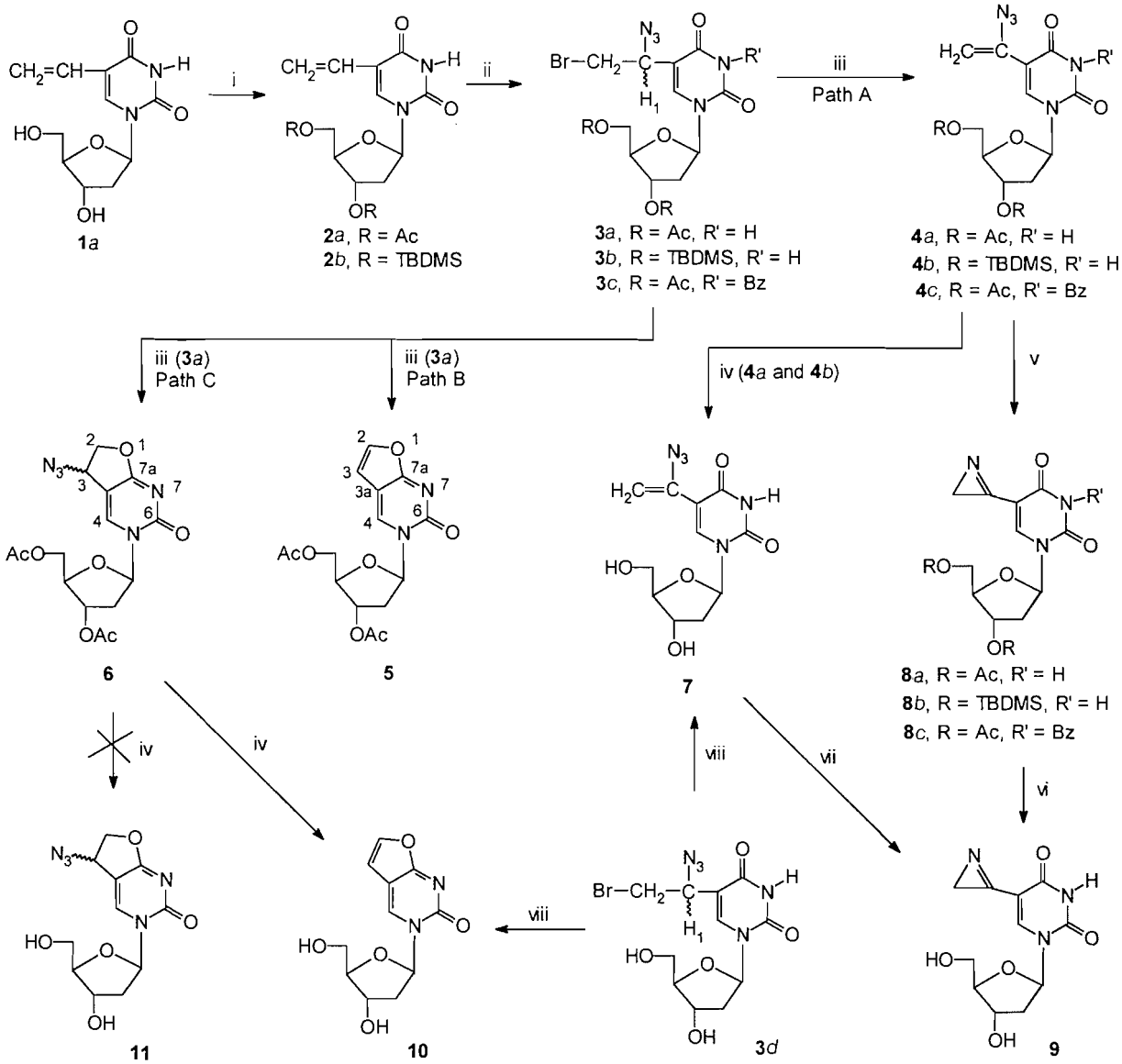

Reagents: i, *tert*-Butyldimethylsilyl chloride, imidazole, DMF, 25°C; ii, *N*-bromosuccinimide, sodium azide, DME, −5°C; iii, *t*-BuOK, THF, 0°C; iv, NH_3, MeOH, 25°C (**4***a*), *n*-$Bu_4N^+ F^-$, THF (**4***b*); v, toluene, 110°C; vi, NH_3, MeOH, 25°C (**8***a*, **8***c*); $NaHCO_3$, MeOH, 4°C (**8***a*, **8***c*); *p*-toluenesulfonic acid, MeOH, 25°C (**8***b*), *n*-$Bu_4N^+ F^-$, THF (**8***b*); vii, dioxane, 110°C; viii, NaOH, or *t*-BuOK, DMSO, 25°C.

Scheme 2.

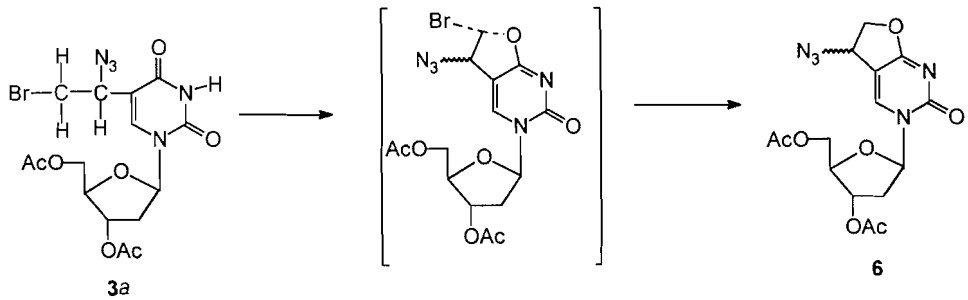

Scheme 3.

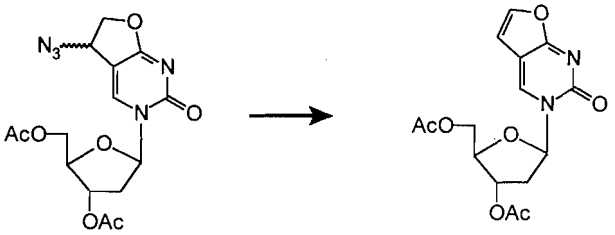

6 5

cytomegalo virus (CMV), and varizella zoster virus (VZV)). The 5-(1-azidovinyl) compound (**7**) exhibited appreciable in vitro activity against HSV-1 (IC_{50} = 0.4 μM) and VZV (IC_{50} = 0.1 μM), but was inactive against HSV-2 (IC_{50} = 150 μM) and CMV (IC_{50} > 20 μM), relative to the reference drug IVDU (HSV-1, IC_{50} = 0.02 μM; HSV-2, IC_{50} = 70 μM; VZV, IC_{50} = 0.001–0.002 μM; CMV, IC_{50} > 20 μM (6). Elaboration of 5-(1-azidovinyl)-2′-deoxyuridine (**7**) and 5-vinyl-2′-deoxyuridine (**1a**) to the corresponding 5-[2-(1-azirinyl)] (**9**) and bicyclic analog (**10**) provided compounds that were inactive in the in vitro assays against HSV-1, HSV-2, VZV, and CMV. These results suggest that an acyclic C-5 substituent may be essential for broad spectrum antiviral activity. The observation that the 5-[2-(1-azirinyl)] compound (**9**) was an inactive antiviral agent was unexpected since the 1-azirinyl ring system is conjugated with the 5,6-olefinic bond and it is an electronegative hydrophobic moiety. The finding that the 5-[2-(1-azirinyl)] compound (**9**) is inactive is consistent with earlier studies that showed that 5-(2,2-dihalocyclopropyl)- and 5-(2-halocyclopropyl)-2′-deoxyuridines exhibit either weak antiviral activity against HSV-1 and HSV-2, or that they are inactive (11, 12).

The in vivo effect of 5-(1-azidovinyl)-2′-deoxyuridine (**7**), acyclovir as a reference drug, and a placebo upon the mortality of mice inoculated intraperitoneally with HSV-1 was determined. Treatment was initiated at 24 h post-inoculation using a twice daily 50 mg/kg ip dose of the test compound (**7** or acyclovir), or placebo, for 7 days. The percent mortality and mean day of death (MDD) were determined. Although, the 5-(1-azidovinyl) compound (**7**) did not protect the mice (93% mortality), the MDD was increased to 8.1 days ($p < 0.001$) relative to placebo (MDD = 6.1 days). In contrast, acyclovir administration as described above resulted in a decreased mortality (27%, $P < 0.1$) with a MDD of 6.8 days, which was not statistically different from placebo. The in vivo ability of 5-(1-azidovinyl)-2′-deoxyuridine (**7**) to increase the length of survival (MDD), but not mortality, could be due to its rapid catabolism (13) and (or) its limited ability to cross the blood brain barrier. The in vivo metabolism, biodistribution, and pharmacokinetics of **7** have not been investigated to date.

Experimental

Melting points were determined with a Buchi capillary apparatus and are uncorrected. Nuclear magnetic resonance spectra (^{1}H NMR, ^{13}C NMR) were determined on a Bruker AM-300 spectrometer using Me_4Si as an internal standard (^{1}H NMR). The assignment of all exchangeable protons (OH, NH) was confirmed by the addition of D_2O. ^{13}C NMR spectra were acquired using the *J* modulated spin echo technique where methyl and methine carbon resonances appear as positive peaks and methylene and quaternary carbons appear as negative peaks. Fast atom bombardment (FAB) and high-resolution electron impact (EI) mass spectra were determined on an AEI-MS-12 and AEI-MS-50 spectrometer, respectively. Preparative thin-layer chromatography (PTLC) was performed using Whatman PLK5F plates, 1.0 mm in thickness, and silica gel column chromatography was carried out using Merck 7734 silica gel (60–200 mesh). 5-Vinyl-3′,5′-di-*O*-acetyl-2′-deoxyuridine (**2*a***) (1) and 5-(1-azido-2-bromoethyl)-2′-deoxyuridine (**3*d***) (14) were prepared using literature procedures.

5-Vinyl-3′,5′-di-*O*-*tert*-butyldimethylsilyl-2′-deoxyuridine (**2*b***)

Imidazole (0.55 g, 8.0 mmol) and *tert*-butyldimethylsilyl chloride (TBDMSCl) (0.60 g, 4.0 mmol) were added to a solution of **1*a*** (0.5 g, 2.0 mmol) in DMF (20 mL) and the reaction was allowed to proceed at 25°C with stirring for 36 h. Removal of the solvent in vacuo and purification of the product by elution from a silica gel column using chloroform–methanol (99:1, v/v) as eluent gave **2*b*** as a viscous oil (0.80 g, 82.5%); ^{1}H NMR ($CDCl_3$) δ: 0.09, 0.10 and 0.11 (three s, 12H total, Si*Me*$_2$), 0.90 and 0.92 (two s, 9H each, C*Me*$_3$), 2.00–2.08 and 2.28–2.36 (two m, 1H each, H-2′), 3.75–3.91 (m, 2H, H-5′), 3.96–4.02 (m, 1H, H-4′), 4.38–4.42 (m, 1H, H-3′), 5.24 (d, J_{cis} = 11 Hz of d, J_{gem} = 2.1 Hz, 1H, CH=C*H*H′), 6.0 (d, J_{trans} = 18 Hz of d, J_{gem} = 2.1 Hz, 1H, CH=CH*H*′), 6.28–6.32 (m, 1H, H-1′), 6.35 (d, J_{trans} = 18 Hz of d, J_{cis} = 11 Hz, 1H, C*H*=CHH′), 7.66 (s, 1H, H-6), 8.32 (s, 1H, NH).

5-(1-Azido-2-bromoethyl)-3′,5′-di-*O*-acetyl-2′-deoxyuridine (**3*a***)

N-Bromosuccinimide (15 mg, 0.084 mmol) was added in small aliquots to a precooled suspension at −5°C, prepared by mixing a solution of **2*a*** (25 mg, 0.074 mmol) in DME (4 mL) with a solution of sodium azide (18.2 mg, 0.28 mmol) in water (100 μL). The initial yellow color observed faded away after each addition. After all of the 5-vinyl compound **2*a*** had been consumed, the reaction mixture was allowed to stand at 0°C for 30 min, prior to pouring onto ice-water (5 mL) and extraction with dichloromethane (3 × 25 mL). The dichloromethane extract was washed with cold water (5 mL), dried (Na_2SO_4), and the solvent was removed in vacuo to yield a residue that was purified by elution from a silica gel column using chloroform–methanol (99:1, v/v) as eluent to yield **3*a*** as a viscous oil (22 mg, 88%); ^{1}H NMR ($CDCl_3$) (mixture of two diastereomers in a ratio of 1:1) δ: 2.06–2.22 (m, 7H, H-2′, *Me*CO), 2.45–2.57 (m, 1H, H-2″), 3.52–3.62 and 3.62–3.72 (1:1 ratio) (two m, 1H total, C*H*H′Br), 3.75–3.88 (m, 1H, CH*H*′Br), 4.24–4.45 (complex m, 3H, H-4′, H-5′), 4.84–4.96 (m, 1H, C*H*(N_3)CH_2Br), 5.20–5.24 (m, 1H, H-3′), 6.28–6.40 (m, 1H, H-1′), 7.64 (s, 1H, H-6), 9.48 (s, 1H, NH); ^{13}C NMR ($CDCl_3$) δ: 20.59, 20.71 and 20.84 (CH_3CO), 33.97 and 34.46 (CH(N_3)CH_2Br), 37.91 (C-2′), 58.21 and 58.33 (*C*H(N_3)-CH_2Br), 63.86 and 63.90 (C-5′), 74.29 (C-3′), 82.63 and 82.68 (C-1′), 85.14 and 85.42 (C-4′), 111.01 and 111.17 (C-5), 137.86 (C-6), 149.57 and 149.66 (C-2 *C*=O), 161.49 (C-4 *C*=O), 170.33 and 170.41 (CH_3*C*O).

5-(1-Azido-2-bromoethyl)-3′,5′-di-*O*-*tert*-butyldimethylsilyl-2′-deoxyuridine (**3*b***)

Reaction of **2*b*** with *N*-bromosuccinimide, using the procedure

outlined for the preparation of **3***a*, and purification of the product by silica gel column chromatography using chloroform-methanol (98:2, v/v) as eluent afforded **3***b* as a viscous oil (0.8 g, 82.5%). Anal. calcd. for $C_{23}H_{42}BrN_5O_5Si_2 \cdot 3/2H_2O$: C 43.73, H 7.17, N 11.08; found: C 43.55, H 6.98, N 10.81.

5-(1-Azido-2-bromoethyl)-3-benzoyl-3′,5′-di-*O*-acetyl-2′-deoxyuridine (3*c*)

Benzoyl chloride (0.17 g, 1.21 mmol) and diisopropylethylamine (74 mg, 0.6 mmol) were added to a solution of **3***a* (0.2 g, 0.43 mmol) in dry pyridine (10 mL) at 0–5°C with stirring. The reaction mixture was allowed to warm to 25°C, the reaction was allowed to proceed at 25°C for 6 h, ice-water (5 mL) was added, and the solvent was removed in vacuo. The residue obtained was purified by silica gel column chromatography using hexane – ethyl acetate (70:30, v/v) as eluent to yield **3***c* (0.225 g, 93%) as a viscous oil; ^{1}H NMR ($CDCl_3$) δ: 2.15–2.32 (m, 7H, H-2′, CO*Me*), 2.50–2.62 (m, 1H, H-2″), 3.60–3.73 (m, 1H, C*H*H′Br), 3.80–3.88 (m, 1H, CH*H*′Br), 4.30–4.34 (m, 1H, H-4′), 4.36–4.50 (m, 2H, H-5′), 4.91–4.98 (m, 1H, C*H*N_3), 5.23–5.28 (m, 1H, H-3′), 6.28–6.38 (m, 1H, H-1′), 7.46–8.14 (m, 6H, benzoyl hydrogens, H-6). Anal. calcd. for $C_{22}H_{22}BrN_5O_8$: C 46.81, H 3.93; found: C 46.59, H 4.00.

5-(1-Azidovinyl)-3′,5′-di-*O*-acetyl-2′-deoxyuridine (4*a*), 5-(3′,5′-di-*O*-acetyl-2′-deoxy-β-D-ribofuranosyl)furano-[2,3-*d*]pyrimidin-6-(5*H*)-one (5), and 3-azido-2,3-dihydro-5-(3′,5′-di-*O*-acetyl-2′-deoxy-β-D-ribofuranosyl)furano[2,3-*d*]pyrimidin-6(5*H*)-one (6)

Potassium *tert*-butoxide (0.21 g, 1.87 mmol) was added to a suspension of **3***a* (0.42 g, 0.913 mmol) in dry THF (60 mL) at −5°C with stirring. The cooling bath was removed and the reaction mixture was stirred at 5°C for 24 h. Removal of the solvent in vacuo gave a residue that was dissolved in dichloromethane (25 mL), washed with cold water (10 mL), the dichloromethane fraction was dried (Na_2SO_4), and the solvent was removed in vacuo. The reaction mixture was separated by silica gel column chromatography using chloroform–methanol (99:1, v/v) as eluent to give three products as viscous oils that eluted in the following order:

*Fraction 1 (**4**a)*: (93 mg, 27%); ^{1}H NMR ($CDCl_3$) δ: 2.12 and 2.14 (two s, 3H each, CO*Me*), 2.15–2.28 (m, 1H, H-2′), 2.5–2.57 (m, 1H, H-2″), 4.28–4.30 (m, 1H, H-4′), 4.36–4.42 (m, 2H, H-5′), 5.10 (d, J_{gem} = 2 Hz, 1H, C(N_3)=C*H*H″), 5.26–5.30 (m, 1H, H-3′), 6.31–6.36 (m, 1H, H-1′), 6.40 (d, J_{gem} = 2 Hz, 1H, C(N_3)=CH*H*′), 7.9 (s, 1H, H-6), 9.88 (s, 1H, NH); ^{13}C NMR ($CDCl_3$) δ: 20.45 (*C*H_3CO), 20.86 (*C*H_3CO), 38.06 (C-2′), 63.96 (C-5′), 74.35 (C-3′), 82.63 (C-1′), 85.44 (C-4′), 102.0 (C(N_3)=*C*H_2), 108.84 (C-5), 135.97 (*C*(N_3)=CH_2), 136.84 (C-6), 148.89 (C-2 *C*=O), 159.97 (C-4 *C*=O), 170.18 and 170.33 (CH_3*C*O). Anal. calcd. for $C_{15}H_{17}N_5O_7 \cdot 3/4H_2O$: C 45.85, H 4.74, N 17.82; found: C 46.09, H 4.71, N 18.19.

*Fraction 2 (**5**)*: (40 mg, 13%); ^{1}H NMR ($CDCl_3$) δ: 2.06–2.22 (m, 7H, C*H*$_3$CO, H-2′), 2.97–3.06 (m, 1H, H-2″), 4.30–4.52 (m, 3H, H-4′, H-5′), 5.23–5.28 (m, 1H, H-3′), 6.35 (dd, *J* = 6 Hz, 1H, H-1′), 6.60 (d, *J* = 2.5 Hz, 1H, OC*H*=CH), 7.42 (d, *J* = 2.5 Hz, 1H, OCH=C*H*), 8.43 (s, 1H, H-6); ^{13}C NMR ($CDCl_3$) δ: 20.74 (*C*H_3CO), 20.83 (*C*H_3CO), 39.31 (C-2′), 63.61 (C-5′), 73.97 (C-3′), 83.31 (C-1′), 88.61 (C-4′), 104.37 and 105.90 (C-2, C-3a), 136.12 (C-4), 144.88 (C-2), 154.37 (C-6), 170.21 (CH_3*C*O), 170.36 (CH_3*C*O), 171.95 (C-7a). Anal. calcd. for $C_{15}H_{16}N_2O_7 \cdot 1H_2O$: C 50.84, H 5.11, N 7.90; found: C 50.81, H 4.84, N 8.21.

*Fraction 3 (**6**)*: (10 mg, 2.8%); ^{1}H NMR ($CDCl_3$) δ: 2.02–2.18 (m, 7H, C*H*$_3$CO, H-2′), 2.86–2.94 (m, 1H, H-2″), 4.32–4.52 (complex m, 3H, H-4′, H-5′), 4.64 (d, J_{gem} = 11 of d, J_{vic} = 2.7 Hz, 1H, furanyl CHCH*H*″), 4.8 (d, J_{gem} = 11 Hz of d, J_{vic} = 6.4 Hz, 1H, furanyl CHC*H*H″), 5.12 (dd, J_{vic} = 6.4 of d, J_{vic} = 2.7 Hz, 1H, furanyl C*H*N_3), 5.20–5.24 (m, 1H, H-3′), 6.26 (dd, *J* = 6 Hz, 1H, H-1′), 8.23 (s, 1H, H-6); ^{13}C NMR ($CDCl_3$) δ: 20.81 (*C*H_3CO), 29.67 (C-2), 39.05 (C-2′), 57.40 (C-3), 63.54 (C-5′), 73.82 (C-3′), 83.08 (C-1′), 88.02 (C-4′), 102.52 (C-3a), 139.20 (C-4), 155.62 (C-6), 170.39 (CH_3*C*O), 176.86 (C-7a). Anal. calcd. for $C_{15}H_{17}N_5O_7 \cdot 1/4H_2O$: C 46.93, H 4.59; found: C 46.72, H 4.80.

5-(1-Azidovinyl)-3′,5′-di-*O*-*tert*-butyldimethylsilyl-2′-deoxyuridine (4*b*)

Potassium *tert*-butoxide (0.29 g, 2.6 mmol) was added as a suspension of **3***b* (0.78 g, 1.32 mmol) in dry THF (350 mL) at −5°C with stirring. The cooling bath was removed and the reaction mixture was stirred at 5°C for 2 h. Removal of the solvent in vacuo gave a residue that was dissolved in chloroform and washed with water (20 mL), the chloroform fraction was dried (Na_2SO_4), and the solvent was removed in vacuo. Purification of the residue by elution from a silica gel column using chloroform–methanol (99:1, v/v) as eluent yielded **4***b* as a viscous oil (0.305 g, 45%); ^{1}H NMR ($CDCl_3$) δ: 0.098, 0.10, and 0.12 (three s, 12H total, *Me*$_2$Si), 0.90 and 0.91 (two s, 9H each, *Me*$_3$C), 2.00–2.10 and 2.32–2.40 (two m, 1H each, H-2′), 3.80–3.84 (m, 2H, H-5′), 4.00–4.04 (m, 1H, H-4′), 4.40–4.44 (m, 1H, H-3′), 5.08 (d, J_{gem} = 2 Hz, 1H, C(N_3)=C*H*H′), 6.25 (d, J_{gem} = 2 Hz, 1H, C(N_3)=CH*H*′), 6.28 (dd, *J* = 6 Hz, 1H, H-1′), 7.92 (s, 1H, H-6), 8.90 (s, 1H, NH). Anal. calcd. for $C_{23}H_{41}N_5O_5Si_2$: C 52.73, H 7.89, N 13.37; found: C 52.72, H 8.30, N 13.57.

5-(1-Azidovinyl)-3-benzoyl-3′,5′-di-*O*-acetyl-2′-deoxyuridine (4*c*)

Reaction of potassium *tert*-butoxide (90 mg, 0.8 mmol) with **3***c* (0.225 g, 0.4 mmol), using the procedure described for the preparation of **4***b*, and purification of the product using chloroform–methanol (98:2, v/v) as eluent afforded **4***c* as a viscous oil (75 mg, 39%). Anal. calcd. for $C_{22}H_{21}N_5O_8 \cdot 1/2H_2O$: C 53.65, H 4.49, N 14.22; found: C 53.64, H 4.39, N 13.89.

5-(1-Azidovinyl)-2′-deoxyuridine (7)

Method A

A solution of **4***a* (50 mg, 0.131 mmol) in a saturated solution of ammonia in methanol (5 mL) was stirred at 25°C for 6 h. Removal of the solvent in vacuo yielded a residue that was purified by silica gel column chromatography using chloroform–methanol (90:10, v/v) as eluent to yield **7** (30 mg, 76%) as a solid; mp 153–155°C (dec.); ^{1}H NMR (CD_3OD) δ: 2.20–2.40 (m, 2H, H-2′), 3.70–3.90 (m, 2H, H-5′), 3.94–4.00 (m, 1H, H-4′), 4.38–4.45 (m, 1H, H-3′), 5.03 (d, *J* = 2 Hz, 1H, C(N_3)=C*H*H′), 6.08 (d, *J* = 2 Hz, 1H, C(N_3)=CH*H*′), 6.30

(dd, J = 6 Hz, 1H, H-1′), 8.36 (s, 1H, H-6); ^{13}C NMR (CD_3OD) δ: 41.62 (C-2′), 62.71 (C-5′), 72.21 (C-3′), 87.01 (C-1′), 89.10 (C-4′), 101.54 ($C(N_3)=CH_2$), 109.38 (C-5), 139.03 ($C(N_3)=CH_2$), 140.65 (C-6), 151.32 (C-2 $C=O$), 163.03 (C-4 $C=O$). Anal. calcd. for $C_{11}H_{13}N_5O_5 \cdot 3/4H_2O$: C 42.79, H 4.72, N 22.68; found: C 43.09, H 4.41, N 22.47.

Method B

A solution of n-$Bu_4N^+F^-$ (0.5 mL of a 1 M solution) in THF was added to a solution of **4***b* (0.17 g, 0.33 mmol) in THF (60 mL) and the reaction was allowed to proceed with stirring for 6 h at 25°C. Removal of the solvent in vacuo and purification of the product as described in Method A gave **7** (90 mg, 86%). The mp and ^{1}H NMR spectrum for **7** were identical to that of **7** prepared according to Method A above.

5-[2-(1-Azirinyl)]-3′,5′-di-*O*-acetyl-2′-deoxyuridine (8*a*)

A solution of 4*a* (90 mg, 0.237 mmol) in dry toluene (25 mL) was heated at 110°C for 3 h. Removal of the solvent in vacuo gave a viscous oil that was purified by silica gel column chromatography. Elution with chloroform–methanol (97:3, v/v) gave impure 8*a*, which was further purified by PTLC using chloroform–methanol (95:5, v/v) as development solvent. Extraction of the ultraviolet visible spot yielded 8*a* as a pale yellow foam (23 mg, 28%); ^{1}H NMR ($CDCl_3$) δ: 1.56 and 1.62 (two d, J_{gem} = 8.4 Hz, 1H each, azirinyl hydrogens), 2.10 and 2.12 (two s, 3H each, CO*Me*), 2.22–2.32 and 2.64–2.74 (two m, 1H each, H-2′), 4.30–4.50 (m, 3H, H-4′, H-5′), 5.25–5.29 (m, 1H, H-3′), 6.32 (dd, J = 6 Hz, 1H, H-1′), 8.25 (s, 1H, H-6), 9.45 (br s, 1H, NH); ^{13}C NMR ($CDCl_3$) δ: 17.25 (azirinyl CH_2), 20.75 and 20.80 (CH_3CO), 38.58 (C-2′), 63.58 (C-5′), 74.03 (C-3′), 83.19 (C-1′), 86.40 (C-4′), 103.08 (C-5), 144.66 (C-6), 148.91 (C-2 $C=O$), 158.89 (azirinyl C-2), 159.16 (C-4 $C=O$), 170.12 and 170.30 (CH_3CO); MS (FAB) *m/z*: 352 (M + 1), 201 (3′,5′-di-*O*-acetyl-2′-deoxyribosyl), 151 (5-[2-(1-azirinyl)]uracil); MS (HRMS), calcd. for $C_9H_{13}O_5$ (3′,5′-di-*O*-acetyl-2′-deoxyribosyl): 201.0762; found: 201.0751; calcd. for $C_6H_5N_3O_2$ (5-(2-(1-azirinyl)]uracil): 151.0381; found: 151.0382. Anal. calcd. for $C_{15}H_{17}N_3O_7$: C 51.28, H 4.87; found: C 50.98, H 4.92.

5-[2-(1-Azirinyl)]-3′,5′-di-*O*-*tert*-butyldimethylsilyl-2′-deoxyuridine (8*b*)

A solution of **4***a* (0.1 g, 1.9 mmol) in dry toluene (25 mL) was heated at 110°C for 2 h. Isolation of the product, as described for the preparation of **8***a*, gave a residue. Purification of this residue by silica gel column chromatography using chloroform–methanol (98:2, v/v) as eluent afforded **8***b* (80 mg, 84%) as a viscous oil; ^{1}H NMR ($CDCl_3$) δ: 0.09, 0.10, and 0.11 (three s, 12H total, Me_2Si), 0.82–0.98 (m, 20H, Me_3C, azirinyl hydrogens), 2.02–2.14 and 2.42–2.50 (two m, 1H each, H-2′), 3.76–3.92 and 3.94–4.02 (two m, 1H each, H-5′), 4.04–4.08 (m, 1H, H-4′), 4.37–4.43 (m, 1H, H-3′), 6.26 (dd, J = 6 Hz, 1H, H-1′), 8.27 (s, 1H, H-6), 9.50 (s, 1H, NH). Anal. calcd. for $C_{23}H_{41}N_3O_5Si_2 \cdot 5/4H_2O$: C 53.30, H 8.26, N 8.10; found: C 53.72, H 8.71, N 7.78.

5-[2-(1-Azirinyl)]-3-benzoyl-3′,5′-di-*O*-acetyl-2′-deoxyuridine (8*c*)

A solution of **4***c* (40 mg, 0.082 mmol) in dry toluene (10 mL) was heated at 110°C for 2 h. Isolation and purification of the product, as described for the preparation of **8***a*, yielded **8***c* as a foam (20 mg, 54%); ^{1}H NMR ($CDCl_3$) δ: 1.62 and 1.68 (two d, J_{gem} = 8.4 Hz, 1H each, azirinyl hydrogens), 2.08 and 2.16 (two s, 3H each, *Me*CO), 2.25–2.36 and 2.63–2.73 (two m, 1H each, H-2′), 4.32–4.52 (m, 3H, H-4′, H-5′), 5.23–5.27 (m, 1H, H-3′), 6.30 (dd, J = 6 Hz, 1H, H-1′), 7.46–7.95 (m, 5H, benzoyl hydrogens), 8.32 (s, 1H, H-6). Anal. calcd. for $C_{22}H_{21}N_3O_8 \cdot 1/2H_2O$: C 56.89, H 4.76, N 9.04; found: C 56.49, H 4.75, N 8.87.

5-[2-(1-Azirinyl)]-2′-deoxyuridine (9)

Method A

A solution of **7** (80 mg, 0.27 mmol) in dry dioxane (50 mL) was heated at 110°C for 2 h. Removal of the solvent in vacuo gave a residue that was purified by silica gel column chromatography using chloroform–methanol (90:10, v/v) as eluent to give **9** (27 mg, 37%) as a light yellow hygroscopic solid; ^{1}H NMR (CD_3OD) δ: 1.46 and 1.50 (two d, J_{gem} = 8.4 Hz, 1H each, azirinyl hydrogens), 2.28–2.48 (m, 2H, H-2′), 3.74–3.80 and 3.84–4.02 (two m, 1H each, H-5′), 3.96–4.00 (m, 1H, H-4′), 4.40–4.44 (m, 1H, H-3′), 6.26 (dd, J = 6 Hz, 1H, H-1′), 8.94 (s, 1H, H-6); ^{13}C NMR (CD_3OD) δ: 16.35 (azirinyl C-3), 42.23 (C-2′), 62.06 (C-5′), 71.31 (C-3′), 87.89 (C-1′), 89.37 (C-4′), 102.67 (C-5), 150.09 (C-6), 151.13 (C-2 $C=O$), 160.33 (C-4 $C=O$), 161.75 (azirinyl C-2); MS (FAB) *m/z*: 267 (M^+), 117 (deoxyribosyl), 151 (5-[2-(1-azirinyl)]uracil). Anal. calcd. for $C_{11}H_{13}N_3O_5 \cdot 1/2H_2O$: C 47.82, H 5.10, N 15.21; found: C 47.96, H 4.92, N 14.83.

Method B (9)

A solution of n-$Bu_4N^+F^-$ (0.1 mL of a 1 M solution) in THF was added to a solution of **8***b* (40 mg, 0.08 mmol) in THF (20 mL) and the reaction was allowed to proceed with stirring for 6 h at 25°C. Removal of the solvent in vacuo and elution of the product from a silica gel column using chloroform–methanol (90:10, v/v) as eluent afforded **9** as a pale yellow solid (8 mg, 25%). The ^{1}H NMR spectrum for **9** was identical to that of **9** prepared using Method A.

Reaction of 5-(1-azido-2-bromoethyl)-2′-deoxyuridine with sodium hydroxide

A solution of NaOH (5 mg, 0.12 mmol) in water (12 μL) was added to a solution of **3***d* (34 mg, 0.09 mmol) in DMSO (5 mL) at ice-bath temperature with stirring. The reaction mixture was then stirred for 1 h at 25°C. Removal of the solvent under high vacuum gave a residue that was purified by silica gel column chromatography using chloroform–methanol (95:5, v/v) as eluent to yield a mixture of **7** (3 mg, 11%) and **10** (15 mg, 66%). The ^{1}H NMR spectrum for this mixture of **7** and **10** was identical to that of **7** and **10** prepared by other methods described in this study.

Reaction of 3-azido-2,3-dihydro-5-(3′,5′-di-*O*-acetyl-2′-deoxy-β-D-ribofuranosyl)furano[2,3-*d*]pyrimidin-6(5*H*)-one (6) with methanolic ammonia

A solution of **6** (0.379 g, 1.0 mmol) in a saturated solution of ammonia in methanol (10 mL) was stirred at 25°C for 5 h. Removal of the solvent in vacuo and purification of the residue obtained by elution from a silica gel column using chloro-

form–methanol (88:12, v/v) as eluent afforded **10** (0.202 g, 80%), which was identical (^{1}H NMR) to the spectral data reported previously (15).

Acknowledgments

We are grateful to the Medical Research Council of Canada (Grant No. MT-12304) for financial support of this research, and to the Pharmaceutical Manufacturers Association of Canada for a PMAC/MRC Fellowship to one of us (R.K.). We also thank the United States National Institutes of Health Antiviral Research Branch, which provided the antiviral test results.

References

1. S.G. Rahim, M.J.H. Duggan, R.T. Walker, A.S. Jones, R.L. Dyer, J. Balzarini, and E. De Clercq. Nucleic Acids Res. **10**, 5285 (1982).
2. E. De Clercq. Pure Appl. Chem. **55**, 623 (1983).
3. J. Goodchild, R.A. Porter, R.H. Raper, I.S. Sim, R.M. Upton, J. Viney, and H.J. Wadsworth. J. Med. Chem. **26**, 1252 (1983).
4. E. De Clercq, J. Descamps, P. De Somer, P.J. Barr, A.S. Jones, and R.T. Walker. Proc. Natl. Acad. Sci. U.S.A. **76**, 2947 (1979).
5. C. Hansch, A. Leo, S.H. Unger, K.H. Kim, D. Nikaitani, and E.J. Lien. J. Med. Chem. **16**, 1207 (1973).
6. J. Balzarini, G. Andrei, R. Kumar, E.E. Knaus, L.I. Wiebe, and E. De Clercq. FEBS Lett. **373**, 41 (1995).
7. D.R. Dalton, V.P. Dutta, and D.C. Jones. J. Am. Chem. Soc. **90**, 5498 (1968).
8. A. Hassner, F.P. Boerwinkle, and A.B. Levy. J. Am. Chem. Soc. **92**, 4879 (1970).
9. J.D. Fissekis and F. Sweet. J. Org. Chem. **38**, 264 (1973).
10. D. Jordan. J. Org. Chem. **54**, 3584 (1989).
11. M. Tandon, S. Singh, L.I. Wiebe, E.E. Knaus, W.P. Gati, and M.L. Tempest. Drug Des. Delivery, **7**, 295 (1991).
12. M. Tandon, S. Singh, L. Xu, P. Kumar, L.I. Wiebe, E.E. Knaus, W.P. Gati, and M.L. Tempest. Drug Des. Discovery, **9**, 79 (1992).
13. J. Samuel, J.M. Gill, T. Iwashina, D.R. Tovell, D.L. Tyrrell, E.E. Knaus, and L.I. Wiebe. Antimicrob. Agents Chemother. **29**, 320 (1986).
14. R. Kumar, L.I. Wiebe, and E.E. Knaus. J. Med. Chem. **36**, 2470 (1993).
15. R. Kumar, E.E. Knaus, and L.I. Wiebe. J. Heterocycl. Chem. **28**, 1917 (1991).

Thermodynamic properties of micellization of sodium dodecyl sulfate in binary mixtures of ethylene glycol with water

Kim Gracie, Dale Turner, and R. Palepu

Abstract: Micellar properties of sodium dodecyl sulfate (SDS) in aqueous mixtures of ethylene glycol (EG) were determined using techniques such as conductivity, density, EMF, surface tension, viscosity, ultrasonic velocity, and spectroscopy (fluorescence). The effective degree of disssociation of micelles (α) was determined using three different methods. Thermodynamics of micellization were obtained from the temperature dependence of critical micelle concentrations (cmc) values. The difference in Gibbs energies of micellization (ΔG_M^0) of SDS, between water and mixed solvent systems, was calculated to evaluate the influence of cosolvent on the micellization process. Surfactant aggregation numbers (N_s) obtained from static fluorescence quenching methods indicated a decrease in the aggregation numbers with increasing concentration of ethylene glycol in the binary solvent mixtures. In addition, the micropolarity of the micellar interior was determined from the pyrene I_1/I_3 ratios. These values were consistent with a decrease in the micropolarity surrounding the probe molecule as the EG content in the solvent mixture was increased.

Key words: thermodynamics, micellization, aggregation numbers, ultrasonic velocity, degree of dissociation.

Résumé : Faisant appel à des techniques telles que conductivité, densité, FEM, tension superficielle, viscosité, vitesse ultrasonique et spectroscopie (fluorescence), on a déterminé les propriétés micellaires du dodécylsulfate de sodium (DSS) en solutions aqueuses d'éthylèneglycol (EG). On a déterminé le degré effectif de dissociation des micelles (α) en faisant appel à trois méthodes différentes. On a obtenue les données thermodynamiques relatives à la micellisation à partir de la dépendance des valeurs «cmc» sur la température. Afin d'évaluer l'influence du cosolvant sur le processus de micellisation, on a calculé la différence des énergies de Gibbs de micellisation (ΔG_M^0) du DSS, entre l'eau et des systèmes de solvants mixtes. Les nombres d'agrégation des agents de surface (N_s) ont été obtenus par des méthodes de piégeage statique de la fluorescence; ils indiquent que les nombres d'agrégation diminuent avec une augmentation de la concentration de l'éthylèneglycol dans les mélanges binaires de solvant. On a de plus déterminé la micropolarité de l'intérieur micellaire à l'aide des valeurs des rapports I_1/I_3 du pyrène. Ces valeurs sont en accord avec une diminution de la micropolarité aux environs de la molécule sonde lorsque la quantité d'EG dans le mélange de solvant augmente.

Mots clés : thermodynamique, micellisation, nombres d'agrégation, vitesse ultrasonique, degré de dissociation.

[Traduit par la rédaction]

Introduction

It is well known that the micellar properties of both anionic or cationic surfactants are significantly influenced by the presence of various nonelectrolytes in solution (1, 2). There has recently been much research dealing with the effects of non-aqueous polar solvents on the formation of cationic micelles (3–22). Micelle or liquid crystal formation has been reported to occur in such solvents as hydrazine (3, 4), glycerol (5, 6), ethylene glycol (7, 8), and formamide (9–18), where all of the aforementioned solvents have high cohesive energy, dielectric constant, and a high degree of hydrogen bonding. Evans and co-workers (19) have indicated that the ability of a solvent to form hydrogen bonds is a necessary condition of micelle formation. However, it has been shown in the literature that the unique structure of water (H-bonding) is not a necessary condition for the aggregation process (23–26). Micelle formation has been reported in solvents such as acetone, acetonitrile, and dimethyl sulfoxide (18, 27, 28) where there is very little or no hydrogen bonding.

We recently investigated (29) the micellar properties of a cationic surfactant, hexadecylpyridium bromide (CPBr), in binary mixtures of water and ethylene glycol (EG) as a function of increasing percentage of EG in the solvent system. The present study deals with the effects of ethylene glycol on the micellar properties of sodium dodecyl sulfate (SDS) in water employing such techniques as conductivity, EMF, fluorescence spectroscopy, surface tension, density, ultrasonic velocity, and viscosity. Measurements were performed up to 60 wt.% of EG in the binary mixtures. Our results are consistent with the formation of aggregate in solvent mixtures containing less than 60% EG; beyond this concentration no aggregate for-

Received March 20, 1996.

K. Gracie, D. Turner, and R. Palepu.[1] Department of Chemistry, University College of Cape Breton, P.O. Box 5300, Sydney, NS B1P 6L2, Canada.

[1] Author to whom correspondence may be addressed. Present address: Chemistry Department, St. Francis Xavier University, Antigonish, NS B2G 2W5, Canada. Telephone: (902) 867-3886. E-mail: rpalepu@juliet.stfx.ca

Table 1. Micellar properties of SDS in ethylene glycol + water mixtures.

		α		
Wt.%	cmc/cmc_0	Method 1	Method 2	Method 3
0	1.00	0.40	0.38	0.41
10 EG	1.01	0.43	0.45	0.45
20 EG	1.07	0.47	0.54	0.54
30 EG	1.32	0.50	0.56	0.63
40 EG	1.54	0.65	0.58	0.65
50 EG	2.31	0.66		

mation was observed. In the present study EG was regarded as a cosolvent rather than a cosurfactant forming mixed micelles.

Experimental section

Sodium dodecyl sulfate (BDH) was crystallized several times from hot methanol, further purified through Soxhlet extraction using diethyl ether for 72–100 h, and dried under vacuum. Freshly opened bottles of ethylene glycol (Aldrich 99%) were used. Water was nanopure.

Equilibrium surface tension (γ) measurements were performed on a Cahn Dynamic Contact angle analyzer model no. 312 using the Wilhelmy plate technique. The solutions were placed in a thermostated beaker to maintain a constant temperature of 298–318 K. Viscosities of SDS in EG–H_2O mixtures at various concentrations were determined using modified Ostwald or Cannon–Fenske viscometers and a viscosity bath (Koehler Instrument). Conductivity measurements were made in a thermostated jacketed beaker with a dip cell having a cell constant of 0.978 cm^{-1} and an automatic conductivity CDM83 bridge operating at 1000 Hz. The conductivity titrations contained at least 20–25 different concentrations of surfactant at a fixed solvent composition and were measured at different temperatures. Density measurements were obtained using an Anton–Parr digital densimeter DMA45 operating in the static mode. The instrument was calibrated with nanopure water and dry nitrogen.

The sodium-ion activities were measured using a Fisher Na^+ ion electrode coupled with a double junction reference electrode (Fisher Scientific 13-620-47). Ammonium nitrate solution was used in the outer chamber of the double junction reference electrode to prevent the precipitation of potassium dodecyl sulfate. The solutions of surfactant were prepared, in the mixed solvent system, on a molal basis and converted to other units using the density data.

Luminescence quenching measurements were carried out on a Shimadzu specrtrofluorophotometer RF-1501. The probe used was pyrene (Aldrich 99%) and it was held at a constant concentration of $\cong 2 \times 10^{-5}$ M. The quencher used was 1-hexadecylpyridinium bromide (CPBr) and the concentration was held low enough so as not to interfere with the assembly of the micelles. Ratios of the intensities of the first and third peaks were measured using a Perkin Elmer MPF-66 fluorescence spectrophotometer to determine the micropolarity of the micellar interior.

Ultrasonic velocities were measured with a Nusonics (model 6080) concentration analyzer using the sing-around method.

Fig. 1. Specific conductance (K) vs. concentration of SDS in aqueous mixtures of ethylene glycol.

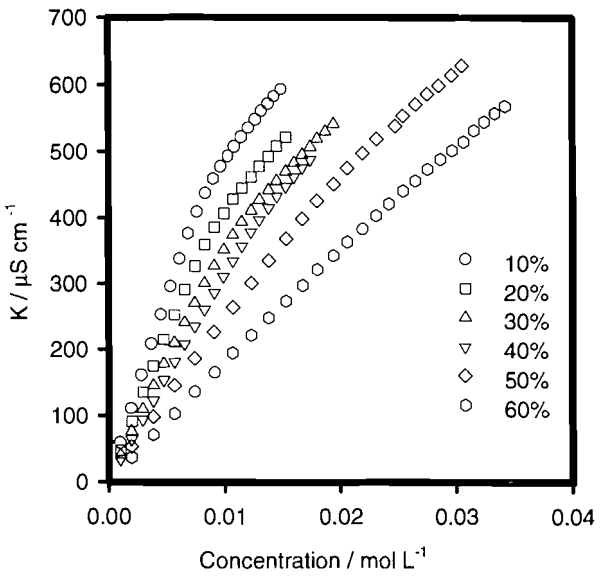

Results

Conductivity

The critical micellar concentration (cmc) values were estimated from the break points in the plots of specific conductance (K) versus the concentration of surfactant (Fig. 1), and are presented in Table 1. The effective degree of dissociation of the counterion (α) was calculated from the ratio of the slopes before and after the cmc in the plots of K and versus C. To distinguish between a proper or cooperative micelle formation and a more gradual association (premicellar aggregation) prior to the cmc, the differential equivalent conductance ($\Delta\Lambda_{eq}$):

$$[1] \quad \Delta\Lambda_{eq} = 10^{-3} \frac{K_1 - K_1^i}{C_1 - C_1^i}$$

(where $K_1 - K_1^i$ and $C_1 - C_1^i$ represent the increment in conductivity and the increment in concentration, respectively) was plotted against the mean concentration. For a normal micellization process the plot of $\Delta\Lambda_{eq}$ vs. mean concentration $(C_1 + C_1^i)/2$ decreases vertically over a narrow concentration

Fig. 2. Differential equivalent conductance vs. mean concentration.

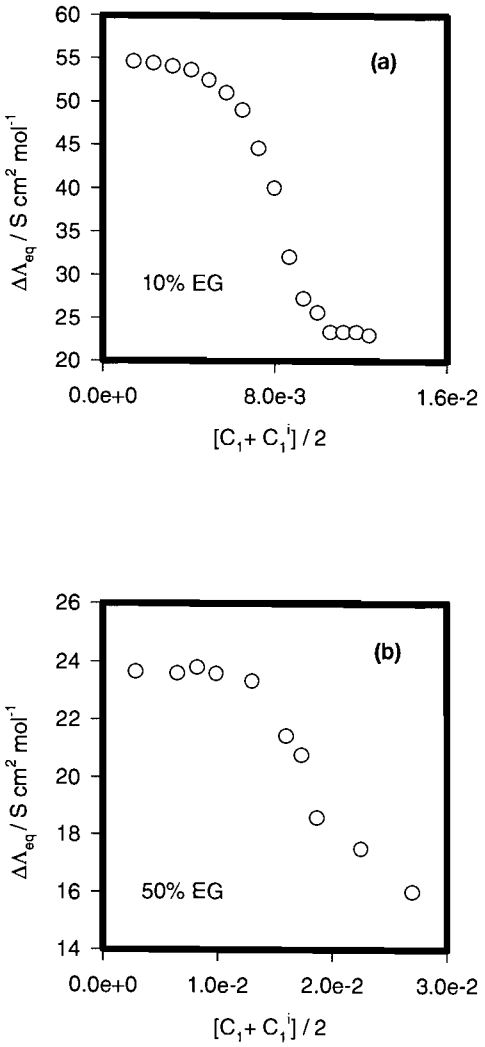

range (Fig. 2*a*), while for a more gradual aggregation the decrease occurs over a wider concentration range (30, 31), as observed at higher concentrations of EG (Fig. 2*b*).

The equivalent conductivity of SDS at infinite dilution (Λ_0) was calculated using the Onsager equation (32).

$$[2] \quad \Lambda = \Lambda_0 - (B\,\Lambda_0 + A)C^{1/2}$$

The values of Λ_0, obtained using eq. [2], are presented in Table 2.

Activation energy of conduction (E_a)

The electrical conductance, as a function of temperature, may be expressed as an Arrhenius-type equation (33).

$$[3] \quad \sigma = \sigma_0 \exp(-E_a/RT)$$

where σ is the electrical conductivity, σ_0 is constant for a given surfactant, R is the gas constant, and E_a is the activation energy of conduction.

Fig. 3. EMF plots of the Na^+/DJ reference electrode system for SDS in EG + H_2O mixtures.

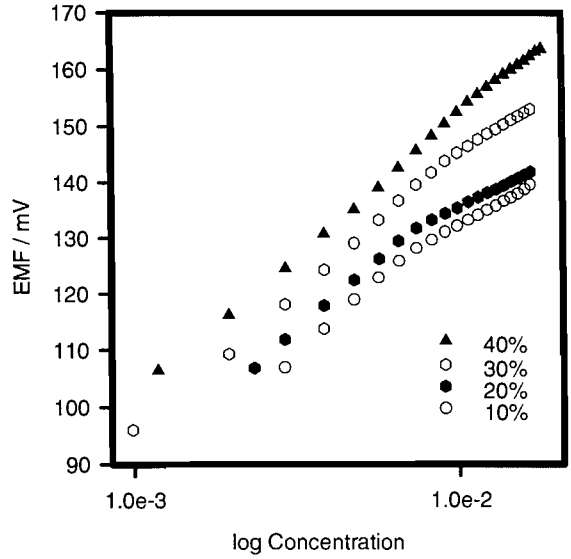

The values of E_a before and after the cmc were obtained from the plots of ln σ vs. $1/T$ and are presented in Table 2.

Electrochemical studies

Plots of EMF (mV) data as a function of log C of the surfactant at various compositions of EG (Fig. 3) show that at the higher weight percentage of EG there is a slight deviation from Nernstian behavior over a narrow concentration range, just before the cmc, indicating that the micellization process is not cooperative. The breakpoint in the plot of EMF vs. log C is indicative of micellar formation. At lower surfactant concentrations, i.e., below the cmc, the slopes of EMF vs. log C were close to Nernstian (56–59 mV/decade).

Effective degree of dissociation

The effective degree of dissociation of the counterion Na^+ as a function of surfactant concentration was determined by three different procedures. Method 1 refers to the conductometric method in which α was taken as the ratio of the slope of the conductivity vs. concentration plot above the cmc to the slope below the cmc (values listed in Table 1).

Method 2 (34) refers to the potentiometric determination of α. Plots of EMF vs. log SDS concentration below the cmc obeyed the Nernst equation:

$$[4] \quad E = E^0 + Y \log a = E^0 + Y \log (\gamma C)$$

where Y is the Nernstian slope, and a, γ, and C are the activity, activity coefficient, and concentration of Na^+, respectively. The values of γ were calculated using Davies equation (32):

$$[5] \quad \log \gamma = \frac{-AC^{1/2}}{1 + C^{1/2}}$$

where

$$[6] \quad A = \frac{1.8246 \times 10^6}{(\varepsilon_r T)^{3/2}}$$

Table 2. Apparent molar quantities and activation energies.

Wt.% EG	Λ_0 (S cm^2 mol^{-1})	E_a before cmc (kJ mol^{-1})	E_a after cmc (kJ mol^{-1})	ΔV_m (cm^3 mol^{-1})	ΔK_m (bar^{-1} cm^3 mol^{-1})
0	73.4	9.0	23.4	10.8	4.7
10	60.4	12.9	20.2	6.9	5.0
20	49.7	19.2	23.1	1.0	5.4
30	40.9	18.7	26.6	0.7	5.7
40	33.8	19.5	23.6	0.5	6.1
50	27.5				
60	19.1				

where ε_r is the dielectric constant of the mixed solvent system (EG + H_2O) and T is the absolute temperature. The values of ε_r were obtained from the literature (35). Once γ was found, the plots of E vs. log a were analysed by linear regression to calculate the values of Y and E^0 in different solvent mixtures. Rearranging the Nernst equation gives

$$[7] \quad a = 10^{(E - E^0)/Y}$$

which enables the calculation of Na^+ activity at all concentrations studied above the cmc. In this range, Na^+ activity is given by:

$$[8] \quad a = \gamma[C_{cmc} + \alpha(C - C_{cmc})]$$

where C_{cmc} is the concentration at the cmc and C is the bulk concentration of SDS. By differentiating the above equation with respect to C and assuming γ to be constant above the cmc, it can be shown that:

$$[9] \quad \alpha = \frac{1}{\gamma}\frac{da}{dC}$$

where da/dC is the slope of log a vs. concentration after the cmc and γ was calculated using the Davies equation with concentration equal to the critical micellar concentration.

In method 3 (34), the α value was determined by studying the effects of an increasing electrolyte concentration on the cmc. The cmc values, in the presence of an electrolyte, were determined using visible and fluorescence spectroscopic methods. The α values were obtained from the following equation:

$$[10] \quad \log\frac{cmc}{cmc_0} = -(1 - \alpha)\log\left[\frac{cmc + C_1}{cmc_0}\right]$$

where cmc_0 is the cmc in the absence of salt and C_1 is the salt concentration. The slope of a plot of log (cmc/cmc_0) vs. log [(cmc + C_1)/cmc_0] is equal to $-(1 - \alpha)$, from which the values of α were obtained (Fig. 4).

Fig. 4. Log (cmc/cmc_0) vs. log [(cmc + C_1)/cmc_0) plot for SDS in 10% EG + 90% H_2O mixtures.

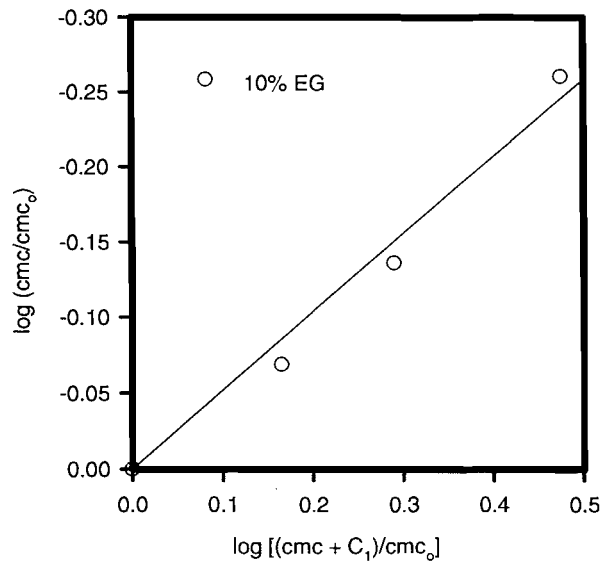

Luminescent quenching

The static fluorescence quenching method originally proposed by Turro and Yekta (36) was used in determining the aggregation numbers of the micelles in the presence of additives. The authors derived a relationship between the bulk quencher concentration and the intensities as a function of the quencher concentration:

$$[11] \quad I = I_0 \exp(-[Q]/[M])$$

where I_0 is the intensity in the absence of quencher, I is the intensity at bulk quencher concentration [Q], and [M] is the micellar concentration and is inversely proportional to the slope of a plot ln (I_0/I) vs. quencher concentration (Fig. 5). Therefore the aggregation number (N_s) can be defined as follows:

$$[12] \quad N_s = \frac{C_{SDS} - cmc}{[M]}$$

The application of the Turro–Yekta method depends on agreement with two experimental criteria (37, 38); firstly, the luminescent probe and quencher must be solubilized in the micelle and be immobile, i.e., they must remain in the micelle

Table 3. Aggregation numbers (N_s), size of SDS micelles, and I_1/I_3 pyrene ratios.

% EG	N_s (±3)	R (Å^3)	a_0 (Å^2)	V/a_0l_c	I_1/I_3 EG	I_1/I_3 0.05 M SDS in EG
0	62	17.3	60.7	0.34	1.82	1.24
6	56	16.7	62.8	0.33	1.80	1.24
10	51	16.2	64.8	0.32	1.80	1.24
20	46	15.7	67.1	0.31	1.78	1.25
30	40	15.0	70.2	0.30	1.75	1.26
40	35	14.3	73.4	0.29	1.78	1.26
50	30	13.6	77.3	0.27	1.68	1.31

Fig. 5. In (I_0/I) vs. quencher concentration in binary mixtures of EG + H_2O containing 50 mM SDS.

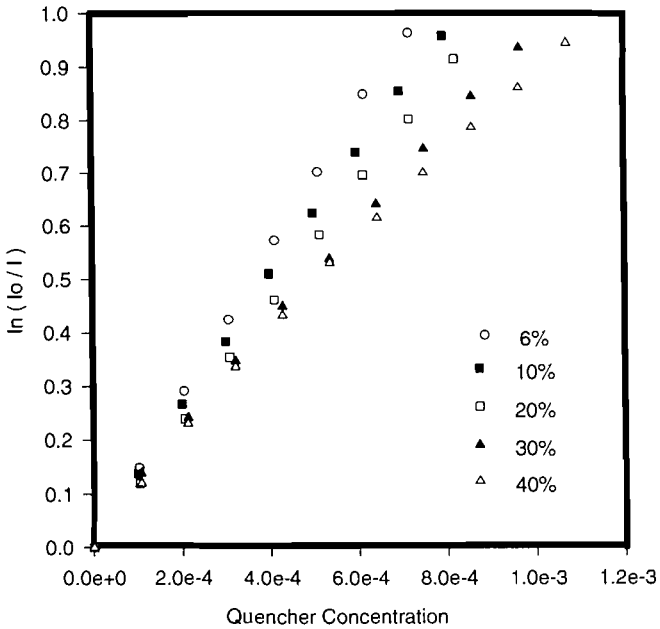

Fig. 6. Surface tension of SDS in 10% EG + H_2O mixtures at 298 K.

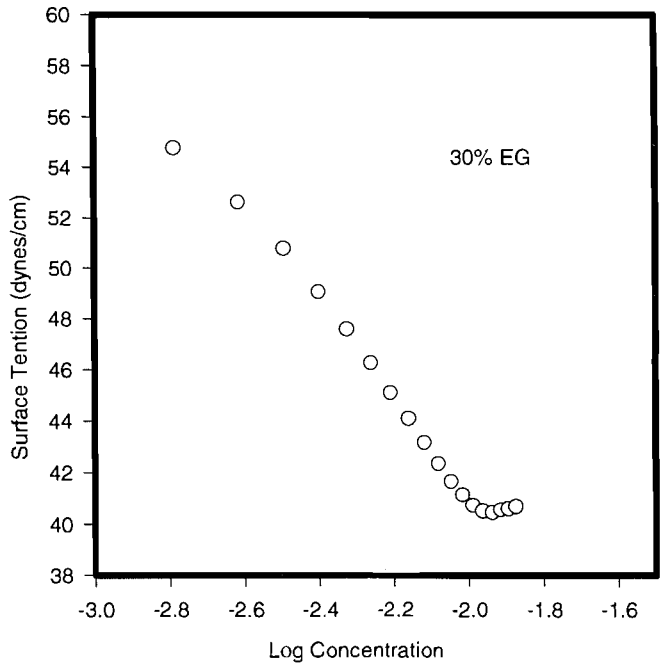

during the lifetime of the probe, and, secondly, quenching must be much faster than the decay of the liminescence intensity so that liminescence is observed only from those micelles that contain a probe and no quencher.

Generally, the application of the Turro–Yekta equation to the determination of micellar aggregation numbers is valid for probe–quencher pairs such as ruthenium tris(biphenyl) chloride – 9-methylanthracene (9-MA) and pyrene – cetylpyridinium ion (CP^+) in micellar systems whose aggregation numbers are less than 80. Aggregation numbers (N_s) of SDS, determined at various EG + H_2O binary mixtures by the static fluorescence quenching method, and the pyrene I_1/I_3 ratios are presented in Table 3. The hydrophobic chain volume of the micelle (v) and the critical chain length (l_c) were obtained using Tanford's equations (39)

[13] $v = 27.4 + 26.9\ n$ (Å^3)

[14] $l_c = 1.5 + 1.265\ n$ (Å)

where n is the number of carbon atoms of the chain. The micellar radius (R) and the surface area per head group (a_0) were obtained assuming spherical shape. The values of R and a_0 along with the values of critical packing parameter ($v/(a_0l_c)$), a parameter known to control the micellar shape (40), are presented in Table 3.

Surface tension

A representative plot of the surface tension (γ), at 298 K, of solution of SDS in a binary mixture of EG + H_2O versus the log of the bulk phase concentration of surfactant is shown in Fig. 6.

The maximum surface excess concentration, T_{max}, the minimum area per surfactant molecule, A_{min} (m^2), at the surfactant–solvent interface, and the value of the surface pressure at cmc, Π_{cmc}, were obtained using the surface tension data and the following equations:

Table 4. Surface excess concentrations (T_{max}), minimum area per molecule (A_{min}), and surface pressure at the cmc (Π_{cmc}) for sodium dodecyl sulfate in aqueous mixtures of ethylene glycol.

Composition (wt.% of EG)	T (K)	$T_{max}X$ (10^6/(mol m^{-2}))	$A_{min}X$ (10^{20}/m^2)	Π_{cmc} (mN m^{-1})
5	298	2.412	68.8	35.24
	308	2.004	82.8	31.37
	318	1.788	92.8	26.40
10	298	2.137	77.6	32.01
	308	1.820	91.2	27.90
	318	1.641	101.2	23.38
30	298	1.299	127.8	18.49
	308	1.125	147.6	14.58
	318	1.037	160.2	8.13

[15] $$T_{max} = -\frac{1}{\nu RT}\left[\frac{\delta\gamma}{\delta \ln C_{T,P}}\right]$$

[16] $$A_{min} = 1/N_a T_{max}$$

and

[17] $$\Pi_{cmc} = \gamma_0 - \gamma_{cmc}$$

where ν is the number of ions per surfactant molecule, R is the gas constant, N_a is Avogadro's number, and γ_0 is the surface tension of the pure solvent. In eq. [15] the term C is used in place of activity because it is assumed that for dilute solution the value of the mean activity coefficient of SDS is approximately equal to 1. The values of Π_{cmc}, A_{min}, and T_{max} are presented in Table 4.

Viscosity

Plots of the solution viscosity (η) vs. SDS concentration in various mixtures of EG and H_2O (Fig. 7) indicate that the cmc is the point of intersection of the two linear portions of the plots.

Information on the hydrodynamic volume of the micelle can be obtained from values of intrinsic viscosity, where the intrinsic viscosity of the micelle is defined by:

[18] $$[\eta]_{mic} = \lim_{C\to cmc}\left(\frac{\eta/\eta_0 - 1}{C - cmc}\right)$$

where η_0 is the viscosity of the media at the cmc and C is the total bulk surfactant concentration. By expressing the viscosity above the cmc as a power series and limiting it to the quadratic term the following equation is obtained:

[19] $$\eta = \eta_0 + a_1(C - C_{cmc}) + a_2(C - C_{cmc})^2$$

where a_1 and a_2 are constants. The intrinsic viscosities of the micelle, equal to a_1/η_0, were obtained by fitting experimental data to eq. [19] and are presented in Table 5.

Fig. 7. Plots of viscosity of SDS solution in EG + H_2O mixtures as a function of SDS concentration.

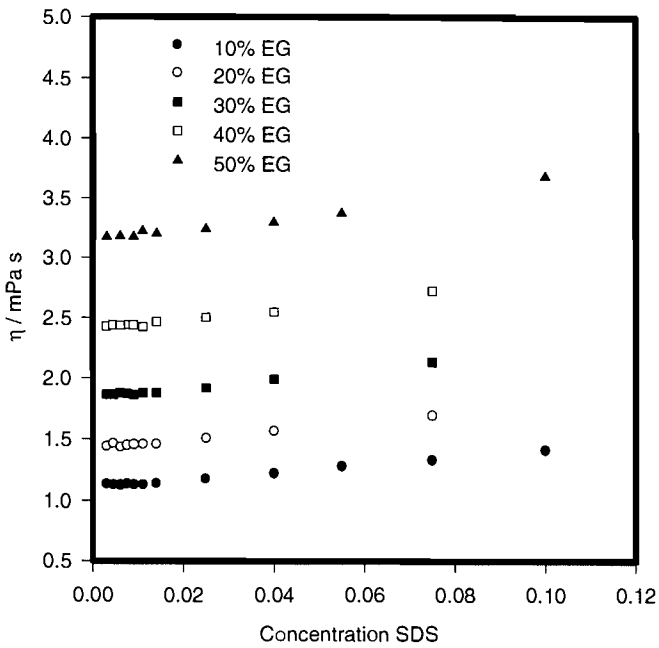

Table 5. Intrinsic viscosities as a function of ethylene glycol content.

Solvent system	$[\eta]$ (mL g^{-1})
H_2O	4.30
10% EG	3.01
20% EG	2.96
30% EG	2.28
40% EG	1.05
50% EG	0.90

Apparent molar volumes

Apparent molar volumes, ϕ_v, were determined from density data using:

$$[20] \quad \phi_v = \frac{M}{d} - \frac{10^3 (d - d_0)}{mdd_0}$$

where M is the molecular weight, d and d_0 are the densities of the solution and the solvent, and m is the molality. When ϕ_v is plotted against $C^{1/2}$, the gradient approaches zero at higher surfactant concentration and this limiting value is subjectively chosen as the apparent molar volume of the micelles (ϕ_v^{mic}) (41).

An alternative method (42) is to fit the data to the following function:

$$[21] \quad \frac{\phi_v}{\phi_v^{mic}} = \frac{m}{(a + m)}$$

where a is an empirical constant. Rearrangement of eq. [21] in the following form:

$$[22] \quad \phi_v = -a(\phi_v/m) + \phi_v^{mic}$$

allows ϕ_v^{mic} to be extrapolated from plots of ϕ_v vs. ϕ_v/m.

The apparent molar volumes at infinite dilution, ϕ_v^0, were determined numerically or graphically using the following equation:

$$[23] \quad \phi_v = \phi_v^0 + A_v C^{1/2} + B_v C$$

where A_v is the Debye–Hückel constant for a 1:1 electrolyte at 298 K, and B_v is an adjustable parameter.

The volume change, $\Delta V_m = \phi_v^{mic} - \phi_v^0$, associated with the formation of aggregates decreases with increasing EG content (Table 2).

Ultrasonic velocity

Ultrasonic velocity (U) data were fitted to the following equation:

$$[24] \quad U = U_0 + GC$$

where U_0 is the ultrasonic velocity in the pure solvent, G is Garnsey's constant, and C is the surfactant concentration. In the plots of U vs. C the intersection point of two straight lines at a definite surfactant concentration is taken as the cmc (Fig. 8*a*).

Adiabatic compressibility coefficients (β) were calculated employing the equation

$$[25] \quad \beta = 1/(U^2 d)$$

where U is the sound speed and d is the solution density (Fig. 8*b*).

Ultrasonic measurements of micellar solutions have been shown to be sensitive to the shape of the aggregate. In the present study, a definite break occurring at the cmc is indicated. The plot of adiabatic compressibility coefficient vs. concentration also shows a small but definite change in slopes at the cmc.

Apparent molar compressibilities

Apparent molar compressibilities, ϕ_k, were determined using the following equation:

Fig. 8. Plots of ultrasonic velocity (U) and adiabatic compressibilities (β) of SDS solutions in 10% EG + 90% H_2O mixture.

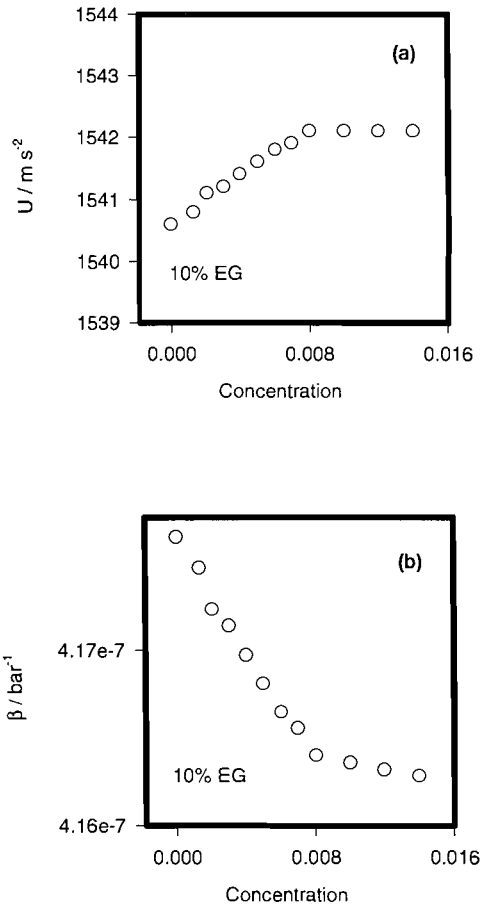

$$[26] \quad \phi_k = 1000\, C^{-1} (\beta - \beta_0) + \beta_0 \phi_v$$

where β and β_0 are the compressibility coefficients of the solution and the solvent. The apparent molar compressibility at infinite dilution (ϕ_k^0) and the micellar compressibility (ϕ_k^{mic}) (42, 43) values were obtained form the plots of ϕ_k as a function of concentration to calculate the compressibility change on micellization, ΔK_{mic} (Table 2).

Thermodynamics of micellization

The Gibbs free energy of micellization was calculated using the equation

$$[27] \quad \Delta G^0_{mic} = (2 - \alpha) RT \ln a\pm_{cmc}$$

where α is the effective degree of dissociation of the counterion (Na^+), R is the gas constant, T is the absolute temperature, and $a\pm$ is the mean activity of the counterion at the cmc. However, in this study, $a\pm_{cmc}$ was replaced by X_{cmc}. When calculating ΔG^0_{mic} at various temperatures, the temperature dependency of α was taken into account. The enthalpy and entropy of micellization (ΔH^0_{mic} and ΔS^0_{mic}) were calculated from the following equations:

Table 6. Thermodynamics of micellization of SDS in various ethylene glycol + water mixtures.

Wt.%	cmc (10^{-3})	ΔG^0 (kJ mol^{-1})	ΔH^0 (kJ mol^{-1})	ΔS^0 (J K^{-1} mol^{-1})	ΔG^0_M (kJ mol^{-1})
10 EG	8.2	−33.3	−11.5	73.1	3.35
20 EG	8.7	−31.0	−11.7	64.1	5.65
30 EG	10.7	−28.3	−13.0	53.4	8.35
40 EG	12.5	−26.1	−13.5	42.3	10.55
50 EG	18.7	−23.7	−13.9	32.9	12.95
60 EG	24.0	−20.1	−16.2	13.1	16.55

[28] $$\Delta H^0_{mic} = (2 - \alpha)R\left(\frac{\delta \ln X_{cmc}}{\delta(1/T)}\right)$$

[29] $$\Delta S^0_{mic} = (\Delta H^0_{mic} - \Delta G^0_{mic})/T$$

The effect of a cosolvent or additive on the micellization process, given by ΔG^0M, was calculated using the following equation:

[30] $$\Delta G^0_M = \Delta G^0_{mic(EG+H_2O)} - \Delta G^0_{mic(H_2O)}$$

The values of the aforementioned parameters are listed in Table 6.

Discussion

The values of the effective degree of dissociation (α) obtained by different methods are in good agreement (Table 1). The EG in the present study is acting as a cosolvent and a structure-breaking solute. Structure-breaking solutes are known to decrease the hydrophobic effect (considered to be the driving force for micellization). Structure breakers in the aqueous phase may disturb the dissolved hydrophobic group, causing a decrease in the entropy increase on micellization, resulting in larger cmc values as the content of EG increases. Another factor that causes the cmc to increase with EG content is a decrease in the cohesive energy or the solubility parameter of water with the addition of EG. Also, a decrease in the dielectric constant of the aqueous phase would result in an increase in the repulsion between the ionic head groups, leading to a delayed micellization. The formation of pre-aggregates before the cmc would also increase the cmc. This is substantiated in the plot of $\Delta\Lambda$ vs. the mean concentration (Fig. 2*a*). The gradual association of monomers before the formation of micelles is well established in pure EG from electrochemical studies (44). The values of Λ_0 (Table 2) show a decrease with increasing concentration of EG, indicating an association of the surfactant monomer with the EG cosolvent. The increase in the E_a after the cmc is due to the counterion binding with the micelle. Other factors involved in the E_a of conduction are the effective degree of dissociation of the counterion (α), the radius of the micelle, and the viscosity of the solvent system. At higher EG concentrations the effective degree of micellar dissociation (α) increases, resulting in more free Na^+ ions to carry the current, and also the aggregation numbers decrease with an increase in EG content, which allows for the lower value of E_a.

As the content of EG increases, the micellization process is less spontaneous, as indicated in the values of the Gibbs energies of micellization (Table 6). The equation used in the calculation of ΔG^0_{cmc} applies normally when the mean aggregation number is large but may not be valid at the higher EG content (9). Therefore, the values of ΔH^0_{mic} and ΔS^0_{mic}, obtained in the present study, should only be viewed as an approximation. From analysis of the present data some generalizations can be drawn. As the EG content increases, the values of ΔS^0_{mic} become less positive, whereas the values of ΔH^0_{mic} become increasingly negative, showing that at the higher EG contents ΔH^0_{mic} becomes a more dominating factor.

The positive values of ΔG^0_M indicate that the micellization process is less favorable in the EG + water mixtures. This is due to the hydrocarbon part of the surfactant being solvated by the hydrophobic part of the cosolvent and the hydrophilic part being solvated by water, so the ability of the cosolvent to associate is decreased. Also, as the amount of EG increases, the values of both Π_{cmc} and T_{max} decrease (Table 4), which is indicative of the hydrocarbon chain of the surfactant interacting with the EG, producing a shift of the surfactant molecules from the interface to the bulk of the solution.

For a spherical, rigid, uncharged, and unhydrated micelle the intrinsic viscosity value would be equal to 2.5 mL/g. However, in reality the micelle is often highly charged and strongly hydrated, ranging in shape from spherical to rodlike (45). The properties that affect the intrinsic viscosity are non-sphericity, flexibility of the micelle, micellar charge, and micellar hydration.

From the values of [η] (Table 5) obtained in the present study, the degree of hydration of the micelles in pure H_2O compared to hydration in the mixed solvent system (EG + H_2O) decreases as the EG content increases, and above 30% EG the micelles are very small and highly charged.

The decreasing values of ΔV_{mic} as the EG content increases (Table 2) suggest that there is less free space in the interior of the aggregates in the presence of EG than with water.

The compressibility charge on micellization, ΔK_{mic}, is positive and increases with EG content (Table 2); this indicates that in the presence of EG the interior of the micelle is more representative of a liquid hydrocarbon.

The decrease in the critical pacing parameter (Table 3) indicates that the addition of EG favors the formation of smaller spherical micelles. The surface area per headgroup increases linearly with EG content, as shown in Fig. 9, and this may be attributed to the replacement of some water molecules in the

Fig. 9. Surface area per head groups (a_0) of SDS micelles vs. EG composition.

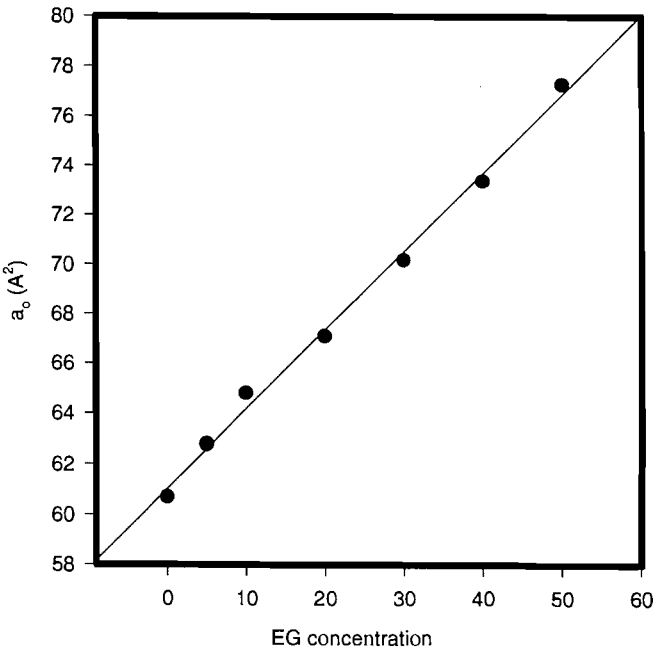

solvation layers of the micelle headgroups by the ethylene glycol molecules, which are approximately 3.1 times larger than a water molecule. Analysis of the pyrene I_1/I_3 ratios (Table 3) gives information about the micropolarity of the environment surrounding the solubilized probe in the micelle. In the EG–H_2O binary system the I_1/I_3 ratios of the pyrene decrease with increasing EG content, indicating a lower polarity as sensed by the pyrene probe. At a given concentration of EG, in the presence of micelles, the polarity decreases as compared to the solvent system, indicating the pyrene is solubilized in the hydrophobic core of the micelle. However, in the ternary mixtures of SDS + EG + H_2O the I_1/I_3 ratios increase slightly with increasing EG content. This may be attributed to the inability of the pyrene to penetrate deep into the micelle, thereby sensing an increase in the polarity due to the location of the pyrene near the micelle–water interface or in the distribution of pyrene in the continuous phase.

In conclusion, the addition of ethylene glycol produces (*i*) an increase in cmc, which is mainly due to an increase in solubility of hydrocarbon tails of the surfactant; (*ii*) a decrease in the solvophobic effect (the difference in free energy for a hydrocarbon chain in oil and in the solvent in question) thereby decreasing the size of the SDS micelles; (*iii*) finally, a decrease in the micellar aggregation numbers, which may be attributed to the increase in the surface area per headgroup.

Acknowledgements

We would like to acknowledge the financial support of the Natural Sciences and Engineering Research Council of Canada (NSERC). K.G. would like to thank the N.S. Department of Economic Development for partial funding in the form of a salary supplement. D.T. wishes to acknowledge award of an Undergraduate student research award (1994) provided by NSERC. We are also grateful to Dr. D.G. Marangoni of the Chemistry Department, St. Francis Xavier University, for his valuable comments on the manuscript.

References

1. M.F. Emerson and A. Holtzer. J. Phys. Chem. **71**, 3320 (1967).
2. K. Shirahama and R. Matsura. Bull. Chem. Soc. Jpn. **38**, 373 (1965).
3. M. Ramadan, D.F. Evans, and R.J. Lumry. J. Phys. Chem. **87**, 4583 (1983).
4. M. Ramadan, D.F. Evans, R. Lumry, and S. Philion. J. Phys. Chem. **89**, 3405 (1985).
5. S.E. Friberg, and Y.C. Liang. Colloid Surf. **24**, 325 (1987).
6. D.F. Evans, A. Yamaguchi, G.J. Wei, and V.A. Bloomfield. J. Phys. Chem. **87**, 3537 (1987).
7. A. Ray. Nature, **231**, 313 (1971).
8. A. Ray. J. Am. Chem. Soc. **91**, 6511 (1969).
9. M. Sjoberg, U. Henriksson, and T. Warnheim. Langmuir, **6**, 1205 (1990).
10. A. Lattes and I. Rico. Colloid Surf. **35**, 221 (1989).
11. K.P. Das, A. Ceglie, M. Monduzzi, O. Soderman, and B. Lindman. Prog. Colloid Polym. Sci. **73**, 167 (1987).
12. I. Rico and A. Lattes. J. Phys. Chem. **90**, 5870 (1986).
13. A. Belmajdoub, A.P. Marchal, D. Canet, I. Rico, and A. Lattes. Nouv. J. Chim. **415**, 11 (1987).
14. X. Auvray, R. Anthore, C. Petipas, I. Rico, and A. Lattes. C.R. Acad. Sci. Ser. 2, **306**, 695 (1988).
15. X. Auvray, C. Petipas, R. Anthore, I. Rico, A. Lattes, S. Ahmah-Zedeh, and A. de Savignac. Colloid Polym. Sci. **265**, 925 (1987).
16. W. Binana-Limbele and R. Zana. Colloid Polym. Sci. **267**, 440 (1989).
17. M. Almgren, S. Swarup, and J. Lofroth. J. Phys. Chem. **89**, 4621 (1985).
18. R. Gopal and J.R. Singh. J. Phys. Chem. **77**, 554 (1973).
19. A. Beesley, D.F. Evans, and R.G. Laughlin. J. Phys. Chem. **92**, 791 (1988).
20. M.S. Bakshi. J. Chem. Soc. Faraday Trans. **89**, 4323 (1993).
21. M. Sjoberg, U. Henriksson, and T. Warnheim. Langmuir, **6**, 1205 (1990).
22. G. Olofsson. J. Chem. Soc. Faraday Trans. **87**, 3037 (1991).
23. M. El Nokaly, L.D. Ford, S.E. Friberg, and D.W. Larsen. J. Colloid Interface Sci. **84**, 228 (1981).
24. D.W. Larsen, S.E. Friberg, and H. Christenson. J. Am. Chem. Soc. **102**, 6565 (1980).
25. B. Bergenstahl and P. Stenius. J. Phys. Chem. **91**, 5944 (1987).
26. D.F. Evans, E.W. Kaler, and W.J. Benton. J. Phys. Chem. **87**, 533 (1987).
27. R. Gopal and J.R. Singh. Kolloid, Z.Z. Polym. **239**, 699 (1970).
28. R. Gopal and J.R. Singh. J. Indian Chem. Soc. **49**, 4 (1972).
29. A. Callaghan, R. Doyle, E. Alexander, and R. Palepu. Langmuir, **9**, 3422 (1993).
30. S. Backlund, B. Bergenstahl, O. Molander, and T. Warnheim. J. Colloid Interface Sci. **39**, 393 (1989).
31. D. Guveli. Colloid Surf. **39**, 349 (1989).
32. R.G. Mortimer. Physical chemistry. The Benjamin/Cumming Publishing Co., New York. 1993.
33. E. Rasch and F.W. Hinrichsen. Electrochemistry, **14**, 41 (1908).
34. M.L. Corrin and W.D. Harkins. J. Am. Chem. Soc. **69**, 684 (1976).
35. G. Douheret and M. Morenas. Can. J. Chem. **57**, 608 (1979).
36. N.J. Turro and A.J. Yekta. J. Am. Chem. Soc. **100**, 5951 (1978).
37. J.M. Denton, D.C. Duecker, and E.D. Sprague. J. Phys. Chem. **97**, 756 (1993).
38. D.G. Marangoni. Ph.D. Thesis, Dalhousie University. 1991.

39. C. Tanford. The hydrophobic effect. Wiley, New York. 1980. pp. 42–59.
40. J.N. Israelachvili. *In* Physics of amphiphiles, micelles, vesicles and microemulsions. *Edited by* V. Degiorgio and M. Corti. North Holland, Amsterdam. 1985. pp. 24–58.
41. T.S. Brun, H. Hoiland, and E. Vikingstad. J. Colloid Interface Sci. **63**, 89 (1978).
42. D. Attwood, R. Blundell, V. Mosquera, M. Garcia, and J. Rodriguez. Colloid Polym. Sci. **272**, 108 (1994).
43. R. Zielinski, S. Ikeda, and H. Nomura. J. Colloid Interface Sci. **119**, 398 (1986).
44. H. Gharibi, R. Palepu, D.M. Bloor, D.G. Hall, and E. Wyn-Jones. Langmuir, **8**, 782 (1992).
45. D.E. Clarke and D.G. Hall. Colloid Polym. Sci. **255**, 153 (1974).

Theoretical and experimental approaches to the effects of solvation on the small internal rotational potential of benzal fluoride

Ted Schaefer, Guy M. Bernard, Younes Bekkali, and David M. McKinnon

Abstract: The internal rotational potential for benzal fluoride is computed at various levels of molecular orbital theory, including correlation-gradient, MP2 (frozen core) methods. The perturbations of the potential caused by solvents are calculated with the Onsager model (ellipsoidal cavity with $l = 6$ in the multipole expansion) as well as with the self-consistent isodensity – polarizable continuum model (SCI–PCM). Analysis of the ^{1}H and ^{19}F nuclear magnetic resonance spectra in cyclohexane-d_{12} and acetone-d_6 solutions yields long-range spin–spin coupling constants from which the expectation values of $\sin^2\phi$ can be derived. These expectation values can be compared with those calculated from the theoretical internal rotational potential. Reasonable agreement is found for potentials obtained from MP2/6-31G* approaches in both solvent models. Long-range coupling constants between ^{19}F and ^{13}C nuclei are also reported and provide very rough checks of the $\langle\sin^2\phi\rangle$ values. For the isolated molecule an additivity scheme based on the potential for benzyl fluoride reproduces much of the potential for benzal fluoride except for a deviation caused by the rather larger relative magnitude of the fourfold component in the latter. The minimum in the potential for benzal fluoride occurs for a torsional angle, ϕ, of 90°, corresponding to a conformation in which the C—H bond of the side chain lies in a plane perpendicular to the phenyl plane and is rationalized on the basis of electrostatic forces. The conformations of minimum energy for the benzyl and benzal fluorides and chlorides are compared and contrasted. The magnitudes of the internal potentials of the fluorides are only a little larger than thermal energies at 300 K and can become smaller than the latter in solution.

Key words: NMR spectroscopy, of benzal fluoride; spin–spin coupling constants, long range in benzal fluoride; solvent effects, on internal rotational potential in benzal fluoride; molecular orbital computations, structure, internal rotational potential, and its solvent perturbations in benzal fluoride; benzal fluoride, ^{1}H, ^{19}F, and ^{13}C NMR on, internal rotational potential, MO computations.

Résumé : On a estimé le potentiel de rotation interne du fluorure de benzal à divers degrés de la théorie des orbitales moléculaires, incluant les méthodes de corrélation-gradient, de MP2 (noyau gelé). On a calculé les perturbations du potentiel, provoquées par le solvant, avec le modèle de Onsager (cavité ellipsoïdale avec $l = 6$ dans l'expansion multipolaire) aussi bien qu'avec le modèle harmonisable du continuum isodensité – polarisable. L'analyse des spectres de RMN du ^{1}H et du ^{19}F, en solution dans le cyclohexane-d_{12} et dans l'acétone-d_6 donne les constantes de couplage spin–spin à longue distance à partir desquelles on a déduit les valeurs attendues de $\sin^2\phi$. On peut comparer ces valeurs attendues avec celles obtenues à partir du potentiel de rotation interne théorique. On a obtenu un accord raisonnable pour les potentiels calculés à partir de MP2/6-31G* dans les deux solvants modèles. On rapporte également les constantes de couplage à longue distance entre les noyaux de ^{19}F et de ^{13}C et ces constantes constituent une vérification grossière des valeurs de $\langle\sin^2\phi\rangle$. Pour la molécule isolée un schéma d'additivité, basé sur le potentiel du fluorure de benzyle, reproduit à peu près le potentiel du fluorure de benzal excepté la déviation provoquée par l'amplitude assez grande des quatre composés dans le dernier. Le minimum du potentiel du fluorure de benzal se produit pour un angle de torsion, ϕ, de 90° ce qui correspond à une conformation dans laquelle la liaison C—H de la chaîne latérale est dans un plan perpendiculaire au phényle et on rationalise ceci sur la base des forces électrostatiques. Les conformations du minimum d'énergie du benzyle et des fluorures et chlorures de benzal sont comparées et opposées. Les intensités des potentiels internes des fluorures sont seulement un petit plus élevées que les énergies thermiques à 300 K et peuvent devenir plus petites que ces dernières en solution.

Mots clés : spectroscopie de RMN, fluorure de benzal; constantes de couplage spin–spin, longue distance dans le fluorure de benzal; effets de solvant, sur le potentiel de rotation interne dans le fluorure de benzal; calculs d'orbitales moléculaires, structure, potentiel de rotation interne et ses perturbations par le solvant dans le fluorure de benzal; fluorure de benzal, sur la RMN du ^{1}H, du ^{19}F et du ^{13}C, potentiel de rotation interne, calculs MO.

[Traduit par la rédaction]

Received April 17, 1996.

T. Schaefer,[1] G.M. Bernard, Y. Bekkali, and D.M. McKinnon. Department of Chemistry, University of Manitoba, Winnipeg, MB R3T 2N2, Canada.

[1] Author to whom correspondence may be addressed. Telephone: (204) 474-9321. Fax: (204) 275-0905. E-mail: schaefe@cc.umanitoba.ca

Table 1. ^{1}H and ^{19}F nmr spectral parameters for benzal fluoride in C_6D_{12} and acetone-d_6 solutions at 300 K.

Parameter	Solvent		Parameter	Solvent	
	C_6D_{12}[a]	Acetone-d_6[b]		C_6D_{12}[a]	Acetone-d_6[b]
ν(CH)[c]	1932.565[e]	2065.588	^4J(H, CH)	−0.488	−0.450
$\nu_2 = \nu_6$[c]	2216.659	2276.567	^5J(H, CH)	0.276	0.270
$\nu_3 = \nu_5$[c]	2191.413	2255.179	^6J(H, CH)	−0.256	−0.222(2)
ν_4[c]	2196.720	2261.339	^4J(F, CH)	−1.125	−1.226
ν(F)[d]	14 525.794	15 123.628	^5J(F, CH)	0.896	0.932
^2J(H, F)	56.600	56.190	^6J(F, CH)	−1.100	−1.208
$^3J_{23} = {}^3J_{56}$	7.797	7.796(2)	Calcd. transitions	795	797
$^3J_{34} = {}^3J_{45}$	7.522	7.523	Assigned	694	649
$^4J_{24} = {}^4J_{46}$	1.262	1.261	Peaks observed	160	330
$^4J_{26}$	1.875	1.894	Largest difference	0.016	0.019
$^4J_{35}$	1.296	1.310	Root-mean-square		
$^5J_{25} = {}^5J_{36}$	0.629	0.623	deviation	0.007	0.009

[a]For a 5.0 mol% solution in C_6D_{12} containing also 0.5 mol% TMS and 0.25 mol% C_6F_6.
[b]For a 2.5 mol% solution in acetone-d_6 with TMS and C_6F_6 as above.
[c]In Hz at 300.135 14 MHz to high frequency of internal TMS.
[d]In Hz at 282.362 62 MHz to high frequency of internal C_6F_6.
[e]The standard deviations, unless otherwise indicated, were ≤0.001 Hz.

Introduction

The primary purpose of this report is the characterization of the small (comparable to ambient thermal energies) internal rotational potential of benzal fluoride and its perturbation by polar and nonpolar media. To this end, molecular orbital computations on the isolated molecule, as well as those on the molecule embedded in a dielectric continuum, are performed. An experimental approach to the solutions of benzal fluoride depends on the measurements of long-range nuclear spin–spin coupling constants, sensitive to the internal rotational potential; these are described.

A secondary purpose is the comparison of the theoretical and experimental data for benzal fluoride with those known for benzyl fluoride, benzyl chloride, and benzal chloride.

That **2** should represent the stable conformer of benzal chloride is an intuitive prediction from the known behaviour of benzyl chloride. A single C—Cl bond entails a low-energy conformer in which this bond sits in a plane perpendicular to that of the phenyl group (1–4). In sharp contrast, the C—F bond in benzyl fluoride seeks a region near the phenyl plane in order to minimize the molecular energy (5, 6). Further (5–7), a sufficiently polar environment shifts the phase of the internal rotational potential of benzyl fluoride so as to produce a minimum at the perpendicular orientation of the C—F bond. Such an environment merely serves to further stabilize the perpendicular conformer of the chloride (1, 2).

The description of benzyl fluoride rests on the conformational dependence of the long-range spin–spin coupling constants between ^{1}H and ^{19}F nuclei in the side chain and ^{1}H or ^{13}C nuclei in the phenyl group. It is confirmed by molecular orbital computations of the internal barrier in the free molecule, as well as by computations of its alteration by solvents of low and high polarity. A similar approach is here described for benzal fluoride, a molecule not as yet characterized by any other physical methods.

Experimental

Benzal fluoride was prepared from benzyl alcohol and morpholinosulfur trifluoride (morph-DAST) by the standard procedure (8). Dilute solutions of this compound in six solvents of varying polarities (see Tables 1 and 2 for details) were filtered into 5 mm o.d. nmr sample tubes. The tubes were degassed by a minimum of five freeze–pump–thaw cycles on a vacuum line and were then flame-sealed to provide reasonably symmetrical tops.

^{1}H, ^{19}F, and proton-decoupled ^{13}C nmr spectra were obtained on a Bruker AM 300 spectrometer at 300 K. Shimming procedures employed the TMS or C_6F_6 free induction decays and yielded peak widths of about 0.04 Hz in the final ^{1}H nmr spectra; the ^{19}F peaks were generally somewhat wider. For ^{1}H and ^{19}F spectra, 32 decays, each acquired for 41 s, were coadded and followed by zero-filling to twice or four times the original data table. Digital resolution was 0.012 Hz/point. Resolution enhancements, often 0.6 LB and −0.1 GB, were applied to the final data. The ^{13}C nmr spectra came from the Fourier transformation of between 200 and 2500 decays, employing acquisition times of 10–12 s and digital resolution between 0.012 and 0.54 Hz per point.

The ^{1}H and ^{19}F nmr spectra corresponded to a AA'BB'CR X_2 spin system and were analyzed with the computer program NUMARIT (9), as modified for partial self-assignment by R. Sebastian and K. Marat (10). An attempted analysis of such spectra for the CS_2 solution proved unsatisfactory, most likely

Table 2. $^{13}C\{^1H\}$ nuclear magnetic resonance parameters for benzal fluoride at 300 K.[a]

Parameter	C_6D_{12}	CCl_4	CS_2	CD_2Cl_2	$(CD_3)_2C{=}O$	CD_3CN
$\delta(CHF_2)$[b]	115.08	114.18	114.38	115.43	115.83	116.20
δ_1	135.82	134.66	134.63	134.83	135.55	135.40
$\delta_2 = \delta_6$	125.92	125.34	125.38	125.88	126.42	126.51
$\delta_3 = \delta_5$	128.87	128.31	128.50	129.11	129.59	129.79
δ_4	130.73	130.22	130.40	131.18	131.65	131.89
$-^1J$(C, F)	239.41	239.2	239.5	237.9	236.2	235.88
^2J	22.45	22.40	22.35	22.22	22.18	22.18
^3J	6.04	6.05	6.01	6.12	6.12	6.16
^4J[c]	0.36	0.39	0.40	0.45	0.49	0.49
^5J	1.96	1.97	1.97	2.01	2.02	2.03

[a]All solutions were 5.0 mol% in benzal fluoride except for the acetone-d_6 solution, which was 2.5 mol%. In addition, each solution contained 0.5 mol% TMS and 0.25 mol% C_6F_6. The CCl_4 and CS_2 solutions also contained 10 mol% of C_6D_{12} as a lock material.

[b]At 75.4869 MHz, TMS at zero.

[c]It is likely that ^4J is negative (5, 6).

because of a near identity of some chemical shifts in the proton region. The $^{13}C\{^1H\}$ spectra consisted of simple first-order triplets.

Molecular orbital computations on benzal fluoride employed the programs GAUSSIAN 92 (11) nd GAUSSIAN 94 (12). Various basis sets[2] were employed in the HF SCF procedures. Internal rotational potentials were found by fixing the torsional angle ϕ in **1** at values between 0° and 90° in steps of 15°, and optimizing the values of other angles and bond lengths, with the constraint, however, that the phenyl moiety remain planar. Correlation-gradient computations, MP2/6-31G* and MP2/6-31G**, frozen core, were also performed on the isolated molecule. Two types of computations of solvent perturbations of the conformational energies were used. The first used the program SCRF PAC (15), interfaced to our copy of GAUSSIAN 92 by R. Sebastian. This approach (16, 17) is based on an elliptical solvent cavity in a dielectric continuum and allows electric moments higher than dipole (up to $l = 6$). The SCI–PCM (self-consistent isodensity – polarizable continuum model) is apparently equivalent to a multipole moment expansion of infinite order (18, 19). It was implemented[3] as given in our copy of GAUSSIAN 94. In these calculations the gas phase Hamiltonian is modified by the interaction of the electrons and nuclei of the solute with the reaction field of the solvent. It was of interest whether the two approaches to the energetic perturbations due to solvent are in approximate congruence.

Some INDO MO FPT (20, 21) computations of coupling constants, particularly of ^6J(H, H), ^6J(H, F), and ^5J(C, F), used the optimized 6-31G* geometries. Such calculations are not quantitatively reliable, yet are useful in assessing the qualitative dependence of long-range coupling constants on conformational angles (22).

Results and discussion

Spectroscopic results

Tables 1 and 2 present the ^1H, ^{19}F, and ^{13}C nmr spectral data obtained for benzal fluoride. Figure 1 displays the experimental and simulated spectra of the ring protons for the acetone solution, while the detail of the central band of the methine proton is shown in Fig. 2, illustrating the spectral fit obtainable in the analysis.

Internal motion and long-range coupling constants

A number of long-range coupling constants between nuclei in the side chain and those in the phenyl moiety of benzene derivatives are strongly dependent, sometimes exclusively, on a σ–π, or hyperconjugative, mechanism (23). These coupling constants are maximal in magnitude when the bonds in the side chain, carrying the nuclei, are situated in a plane perpendicular to that of the phenyl group. An example (23–25) is ^6J(H, H) for the methyl protons in toluene, which can be written as $^6J = {}^6J_{90}\sin^2\phi$, where $^6J_{90}$ corresponds to $\phi = 90°$ (see **1** for the definition of ϕ). Another is ^6J(H, F) in benzyl fluoride and some of its derivatives (6, 26), as is ^5J(C, F). The measured value of such a coupling constant is then determined by $^nJ_{90}$ and $\langle\sin^2\phi\rangle$, the expectation value of $\sin^2\phi$, which, in turn, depends on the potential governing how the bond in question samples the various angles ϕ at a given temperature. If the potential has a simple ϕ dependence, for example, is twofold in nature, then a knowledge of ^6J and its extremum yields the height of the potential directly (27). If, however, the potential contains a number of terms in ϕ, an ambiguity arises in that a range of combinations of these terms will yield the same ^nJ. Nevertheless, useful information about solvent perturbations of the potential can be gleaned from ^nJ, as follows.

[2] Descriptions of the various split-valence basis functions, their notation, references to them and to the MP2 method of assessing electron correlation are given in ref. 13. The semiempirical AM1 algorithm (14) was also used.

[3] An extensive review of methods based on solvent continua is available (18).

Fig. 1. The nmr spectrum at 300 K and 300 MHz of the ring protons of benzal fluoride, as a 2.5 mol% solution in acetone-d_6, is compared with the simulation based on the spectral parameters in Table 1.

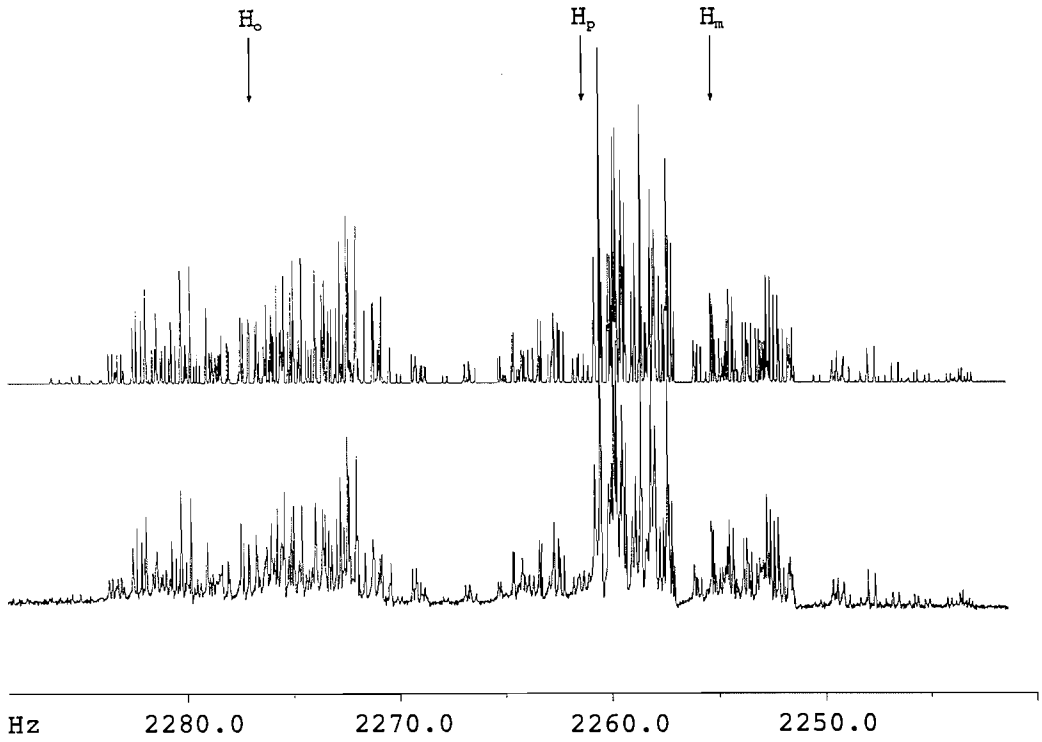

Fig. 2. The central band of the methine proton "triplet" for benzal fluoride in acetone-d_6 solution is shown at 300 MHz and 300 K. The linewidth at half height is ca. 0.04 Hz. There occur some small discrepancies in peak positions between experiment and simulation amounting to as much as 0.01 Hz in one instance.

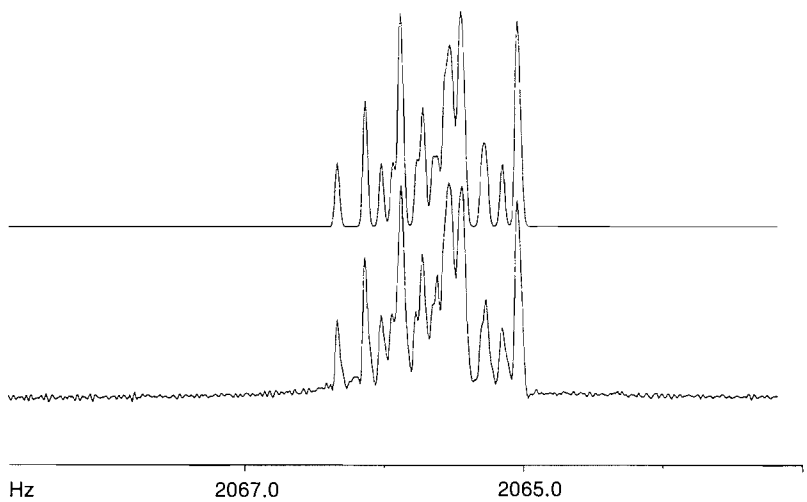

With reference to the data in Table 1, note that both ^4J(H, CH) and ^6J(H, CH) decrease in magnitude in passing from the nonpolar C_6D_{12} solution to that of the polar acetone-d_6. At the simplest level, this means that a polar environment shifts the internal potential such that conformers, in which the C—H bond lies in the ring plane, are more populated than they are in the nonpolar medium. In consequence, the C—F bonds, on average, now spend more time at larger torsional angles, ψ (see **1** and **2**). Hence the ^nJ(H,F) values must increase in magnitude in the more polar solution, given that they contain large components proportional to $\sin^2\psi$. This increase occurs.

Derivation of $\langle\sin^2\phi\rangle$ from ^nJ

The assumption of a tetrahedral geometry at the side chain car-

Table 3. Theoretical internal rotational potentials (in kJ/mol) for benzal fluoride.

Basis[a]	V_2	V_4	V_6	V_8	$-E(\phi = 0)^{b,bc}$	$\langle\sin^2\phi\rangle^d$	μ_o^e	μ_{90}
AM1	−0.89	0.21	−0.17	−0.01	0.130 942	0.545	0.97	0.98
STO-3G	−0.59	0.19	−0.05	−0.00	461.384 000	0.470	1.60	1.56
6-31G*	−2.06	1.22	0.14	−0.03	467.450 894	0.612	2.49	2.40
6-31G**	−2.20	1.12	0.15	−0.02	467.461 512	0.618	2.48	2.40
6-311G*	−1.37	0.82	0.21	0.05	467.554 849	0.572	2.62	2.52
MP2/6-31G*	−2.88	1.47	0.04	−0.05	468.672 088	0.657	2.66	2.58
MP2/6-31G**	−2.51	1.42	0.03	−0.03	468.719 491	0.638	2.65	2.57

[a]Geometry-optimized at intervals of 15° in ϕ (ϕ = 0 corresponds to the conformer in which the C—H bond of the side chain lies in the phenyl plane) with the proviso that the atoms of the phenyl moiety remain in a plane.

[b]The total computed energy at ϕ = 0 in au, that for AM1 being heat of formation.

[c]The fits to $V(\phi) = \Sigma_n V_n \sin^2(n\phi/2)$ had residuals of less than 0.01 kJ/mol.

[d]Expectation values at 300 K.

[e]Dipole moment in debye units, C—H bond in plane, conformer **2**.

bon atom implies $\langle\sin^2\phi\rangle = 1.5 - 2\langle\sin^2\psi\rangle$. Furthermore, write ^6J(H, CH) = $^6J_{90}\langle\sin^2\phi\rangle$ and ^6J(F, CH) = $^6J_{90}\langle\sin^2\psi\rangle$. Finally, on the assumption that $^6J_{90}$ values are invariant to solvent, an assumption borne out for benzyl fluoride, for example (6), one has four values of ^6J in two solvents. These are sufficient to determine $^6J_{90}$ (H,CH) as −0.402(2) Hz, $^6J_{90}$ (F,CH) as −2.551(3) Hz, and that $\langle\sin^2\phi\rangle$ is 0.638(3) in C_6D_{12} and 0.553(2) in acetone-d_6 solutions (the errors are formal, based simply on the standard deviations of the measured coupling constants.[4]

From Table 2, one may then deduce[5] that $^5J_{90}$ (F,C-4) is 4.40(14) Hz. Unfortunately, the range of ^5J(C, F) in the various solvents is very small, as compared to that (5) for ^5J(C, F) in benzyl fluoride, a consequence of the different potentials for the two molecules. It was intended to obtain a good value for $\langle\sin^2\phi\rangle = 1.5 - \langle\sin^2\psi\rangle$ in CS_2 solution from ^5J(C, F) because the ^{1}H and ^{19}F nmr spectra did not yield to analysis — many of the lengthy solvent calculations had already been done for a dielectric constant of 2.64, close to that of the CS_2 solution. Nevertheless, if the ^5J(C, F) value for this solution is used, one finds $\langle\sin^2\phi\rangle = 0.60 \pm 0.03$.

A check of this value is available from ^4J(C, F). For benzyl fluoride it is very likely (5) that ^4J(C, F) is proportional to $A\sin^2\psi + B\sin^2(\psi/2)$, corresponding to a σ,π term in $\sin^2\psi$ and a σ term in $\sin^2(\psi/2)$. On the assumption that a similar proportionality holds for benzal fluoride, the values of ^4J(C, F) in the C_6D_{12} and acetone-d_6 solutions yield ^4J(C, F) = $3.07\sin^2\psi - 1.92\sin^2(\psi/2)$. Here ^4J(C, F) is taken as positive. If it is negative the signs of the coefficients change but do not alter the value of $\langle\sin^2\psi\rangle$, namely, 0.443, obtained for the CS_2 solution. Hence $\langle\sin^2\phi\rangle$ is 0.614, within the range deduced from ^5J(C, F) above. Again, it happens that ^4J(C,F) has a small range, in contrast to ^4J(C, F) in benzyl fluoride.

A vanishing internal rotational potential would entail a $\langle\sin^2\phi\rangle$ of 0.5. A very large potential, with a minimum at ϕ = 0°, as in **2**, would push $\langle\sin^2\phi\rangle$ towards zero. For a purely twofold potential, the experimental values of $\langle\sin^2\phi\rangle$ correspond to a barrier of 2.9 kJ/mol in C_6D_{12} solution with **1** as the minimum, **2** as the maximum in the potential.[6] In the polar acetone-d_6 environment, the apparent twofold barrier drops to 1.0 kJ/mol, with **1** still at the minimum.

The experimental data indicate a small barrier to internal rotation and, most likely, that **1** is the conformation of lowest energy. Of course, a fourfold component in the potential does not contribute to the energy at ϕ = 90°. Nevertheless, although not expected to be larger in magnitude than the leading twofold component, a fourfold component will alter $\langle\sin^2\phi\rangle$. In the section below, recourse is had to theoretical potentials for the isolated molecule as well as for the molecule embedded in a dielectric continuum. Comparison with experiment then arrives at a reasonable description of the internal rotation of the molecule in a vacuum and in solution.

Theoretical internal rotational potentials

(a) The isolated molecule

Table 3 presents the computed internal rotational potentials, V, for various molecular orbital models, including first approximations to electron correlation. Geometries were optimized for each torsion angle, ϕ. Figure 3 plots the potentials.

Except for the minimal basis set, all other potentials have a minimum at ϕ = 90°, as in **1**. The opposite signs of twofold, V_2, and fourfold, V_4, terms produce a global maximum in V not far from ϕ = 45° when $|V_2/V_4|$ is small enough; in consequence, **2**, with ϕ = 0°, represents a local minimum for the larger ab initio basis sets. The values of $\langle\sin^2\phi\rangle$ at 300 K range from 0.470 for the STO-3G potential to 0.638 for that from the

[4] The INDO MO FPT computations agree that ^6J(H, CH) goes as $\sin^2\phi$. For ^6J(F, CH) such calculations yield numbers closely met by $-2.73\sin^2\psi - 0.40\sin 2\psi$, that is, the presence of the second, strongly polar, C—F bond is calculated to perturb the $\sigma-\pi$ interaction of the first. However, for the MP2/6-31G* internal rotational potential (see below), $\langle\sin 2\psi\rangle$ is only 0.26, introducing an error of less than 4% into the approximation used here, if INDO is correct.

[5] The nine values of $^6J_{90}$(H, CH, $^6J_{90}$(F, CH), and $^5J_{50}$(F, C) now a available for toluene, benzyl fluoride, and benzotrifluoride are discussed below.

[6] These numbers come from a hindered rotor model or a classical averaging procedure (27–29); the two methods give the same $\langle\sin^2\phi\rangle$ values for barriers of this magnitude at 300 K, as expected.

Table 4. Theoretical internal rotational potentials (in kJ/mol) for benzal fluoride as a function of basis set and dielectric constant with the Onsager model (SCRF PAC).

	6-31G*/20.7[b]	6-31G*/2.64	6-311G*/20.7	6-311G*/2.64	MP2/6-31G*/20.7	MP2/6-31G*/2.64
V_2[a]	0.51	−0.49	1.70	0.45	−1.21	−1.81
V_4	1.24	1.24	0.80	0.80	1.48	1.50
V_6	−0.11	0.12	0.06	0.14	−0.11	0.02
V_8	−0.10	0.00	0.10	0.03	−0.09	−0.04
$\langle\sin^2\phi\rangle$[c]	0.471	0.527	0.409	0.475	0.570	0.602
$-E(\phi = 0)$[d]	467.457 184	467.454 057	467.562 206	467.558 550	468.676 941	468.674 552
μ_0[e]	3.08	2.80	3.25	2.95	3.42	3.11
μ_{90}[e]	2.78	2.60	2.92	2.73	2.94	2.77

[a]Geometry optimizations were stopped after five iterations.
[b]Dielectric constants of 20.7 and 2.64 were used.
[c]Expectation values at 300 K.
[d]Total energy at $\phi = 0°$, α C—H bond in the phenyl plane.
[e]Dipole moment in debye units at ϕ values of 0° and 90°.

Fig. 3. The internal rotational potentials of benzal fluoride at various levels of molecular orbital theory are plotted as a function of the angle by which the C—H bond of the side chain twists out of the phenyl plane. Geometries were optimized at each torsion angle, which was increased in steps of 15°. The potentials are given in Table 3.

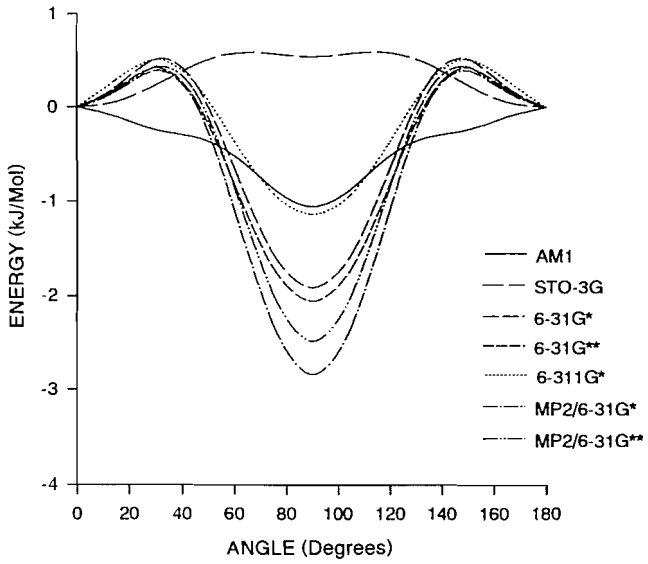

correlation-gradient, MP2/6-31G**, computations. The last number is coincidentally identical to that derived from the coupling constants in the nonpolar C_6D_{12} solution. In the absence of the following computations of solvent effects on the internal potential, the agreement might well have been taken as excellent.

(b) The molecule in solution

Table 4 presents the Onsager or SCRF (15–17) computations of the internal rotational potential for dielectric constants of 2.64 and 20.7, using a number of basis sets. Table 5 gives a somewhat larger data set for such computations, employing the more recent SCI–PCM approach (18, 19). The tables also contain expectation values of $\sin^2\phi$ at 300 K corresponding to the computed potentials, as well as dipole moments for conformers **1** and **2**. Figures 4 and 5 make comparisons of the potentials computed by the two solvent models for low and high dielectric constants, respectively, whereas Fig. 6 collates them for the SCI–PCM model using post-Hartree–Fock computations and four dielectric constants.

The results mainly have the following pattern. For the isolated molecule, the internal rotational potential is dominated by V_2, yielding a relatively deep minimum at $\phi = 90°$ (conformer **1**). V_4 is rather smaller than V_2 in magnitude, but of opposite sign, causing a maximum in the potential near $\phi = 40°$ (V_4 itself, of course, is largest at 45°). In the presence of solvent, $|V_4/V_2|$ increases and becomes larger than unity for a dielectric constant of 20.7 (acetone). Even at this solvent polarity, however, the minimum in the potential occurs at $\phi = 90°$, but only just, in some instances. At low dielectric constants the two models yield nearly coincident potentials (Fig. 4); at high, the SCI–PCM method predicts a larger $|V_4/V_2|$ than does the Onsager model (Fig. 5). In terms of **1** and **2**, with **2** having the higher theoretical dipole moment (Tables 3–5), a zero-order reaction field model entails the increasing energy of **1**. That is, a conformer of higher dipole is increasingly stabilized as the dielectric constant of the surrounding continuum rises. Yet, an attempt to simulate this situation with the Onsager model, using $l = 1$ in the SCRF computations (dipole moment only), was unsuccessful. We have no explanation of this negative result.

Table 6 presents a comparison of some $\langle\sin^2\phi\rangle$ values as derived from the theoretical potentials obtained from various levels of molecular orbital theory in the absence or presence of various dielectric continua. Both solvent models are represented, as are the $\langle\sin^2\phi\rangle$ numbers inferred from long-range coupling constants. Best agreement between experiment and theory is found for the post-Hartree–Fock potentials. It appears unnecessary to go beyond MP2/6-31G*. The two solvent models give closely similar $\langle\sin^2\phi\rangle$ values at this level (use of the Onsager model with the GAUSSIAN suite of programs requires an extra link to the SCRF PAC algorithm,

Table 5. Theoretical internal rotational potentials (in kJ/mol) for benzal fluoride as a function of basis set and dielectric constant using the SCI–PCM (18, 19).

Basis/ε[a]	V_2	V_4	V_6	V_8	$\langle\sin^2\phi\rangle$[b]	$-E(\phi = 0)$[c]	μ_0[d](2)	μ_{90}[d](1)
6-31G*/1.0	−2.06	1.22	0.14	−0.03	0.612	467.450 894	2.49	2.40
6-31G*/2.64	0.88	1.27	0.08	0.07	0.549	467.454 128	2.80	2.65
6-31G*/20.7	−0.14	1.31	0.50	0.16	0.504	467.457 134	2.98	2.86
6-31G*/1.0	−1.37	0.82	0.21	0.05	0.572	467.554 849	2.48	2.40
6-31G*/2.64	−0.05	0.77	0.21	0.00	0.502	467.558 434	2.94	2.78
6-31G*/20.7	0.78	0.81	0.49	0.23	0.455	467.561 689	3.22	3.00
MP2/6-31G*/1.0	−2.88	1.47	0.04	−0.05	0.657	468.672 088	2.66	2.58
MP2/6-31G*/2.10	−2.04	1.53	0.12	0.01	0.619	468.674 155	2.89	2.76
MP2/6-31G*/2.64	−1.85	1.55	0.14	0.02	0.603	468.574 671	2.96	2.81
MP2/6-31G*/20.7	−1.10	1.66	0.24	0.10	0.560	468.676 970	3.21	3.01
MP2/6-31G**/1.0	−2.51	1.42	0.03	−0.03	0.638	468.719 491	2.65	2.57
MP2/6-31G**/2.64	−1.57	1.48	0.11	0.00	0.588	468.721 852	2.94	2.80
MP2/6-31G**/20.7	−0.89	1.26	0.17	0.34	0.549	468.723 945	3.19	2.99

[a]ε is the dielectric constant; the Hartree–Fock calculations used geometry optimization while the MP2 computations were single point on the correlation-gradient geometry of the isolated molecule.
[b]Expectation values at 300 K.
[c]The total energy at $\phi = 0°$; the α C—H bond lies in the phenyl plane.
[d]The dipole moment in debye units at $\phi = 0°$ and $\phi = 90°$.

Table 6. Experimental and theoretical values of $\langle\sin^2\phi\rangle$ at 300 K.

	Basis/model					
	6-31G*		MP2/6-31G*		MP2/6-31G**	
ε[a]	Onsager	SCI–PCM	Onsager	SCI–PCM	SCI–PCM	Experiment
1.00	0.612		0.657		0.638	
2.10				0.619		0.638[b]
2.64	0.527	0.549	0.602	0.603	0.588	0.60(3)[c]
20.7	0.471	0.504	0.570	0.560	0.549	0.553[b]

[a]Dielectric constant.
[b]Deduced from ^6J(H, CH_2) and ^6J(H, F).
[c]From ^5J(C, F).

whereas the SCI–PCM computations form part of GAUSSIAN 94 and are easier to implement).

Qualitative discussion of the internal rotational potential

(a) The isolated molecule

As a preliminary, Fig. 7 shows the correlation-gradient, MP2/6-31G**, structures of two conformations of benzal fluoride. These may well be of interest to molecular spectroscopists. The figure caption gives further information.

A rationalization of the stability of the conformer of lowest energy in benzal fluoride goes as follows. It is convenient to begin with benzyl fluoride, whose most stable conformer has the C—F bond in the phenyl plane (5, 6). In terms of perturbational molecular orbital theory, it is expected that a benzylic anomeric effect will stabilize the perpendicular conformer (the C—F bond in a plane perpendicular to the phenyl plane) because the π system of the ring then interacts best with the antibonding σ orbital of the C—F bond (4). An analogous interaction contributes to the stabilization of the perpendicular conformer of benzyl chloride (4), although it has recently been shown (3) that other donor–acceptor interactions between the σ and π orbitals of the ring and the σ orbitals of the CH_2Cl group make significant contributions to its stabilization.[7]

Whatever the merits of such dissections of the energetic interactions between computed orbitals, a simple model based on electrostatics and on repulsive overlap of nonbonded atoms can also predict the conformer of lowest energy in benzyl fluoride, benzyl chloride, and benzal fluoride. The stability of the in-plane conformer of benzyl fluoride has been attributed (4)

[7] These other interactions are based on a natural bond orbital approach (33) in which appropriate orbitals of the ring and side chain are removed from the Fock matrix during a recalculation of the molecular energy.

Fig. 4. The solvent-perturbed MP2/6-31G* potentials from Tables 4 and 5 are plotted for a dielectric constant of 2.64. The Onsager model used geometry optimization while the self-consistent isodensity – polarizable continuum model (18, 19) did not (not an option at this level in GAUSSIAN 94). At a low polarity the two models nearly coincide in their predictions (compare Fig. 6). The abscissa gives the angle by which the α C—H bond twists out of the phenyl plane.

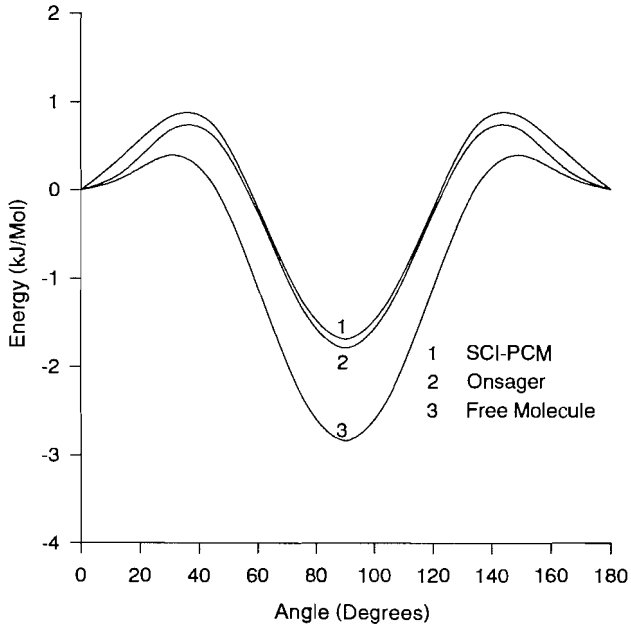

Fig. 5. As in Fig. 4 but for a dielectric constant of 20.7. Here the SCI–PCM approach perturbs the potential more than does the Onsager approach (compare with Fig. 4). Both models lower the magnitude of the negative twofold component and somewhat increase that of the positive fourfold component with respect to the isolated molecule.

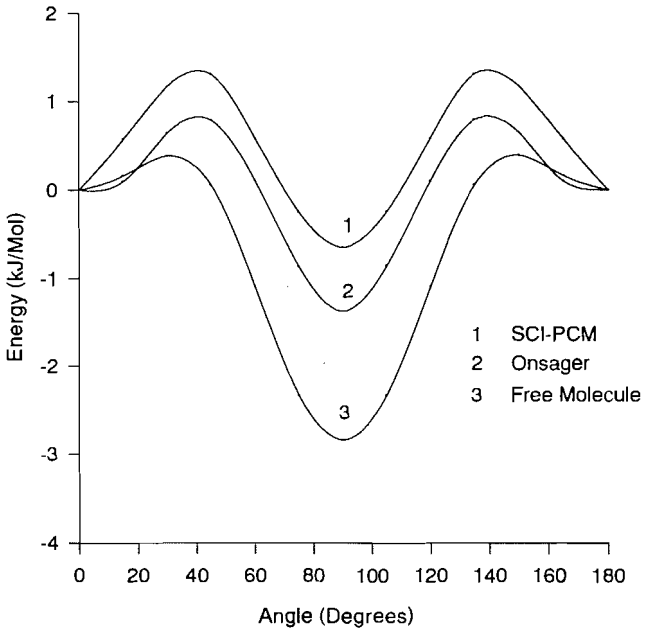

Fig. 6. As in Fig. 4 but, from bottom to top, for dielectric constants of 1.0, 2.0 (cyclohexane-d_{12}), 2.64 (CS_2), and 20.7 (acetone-d_6). The potentials come from SCI–PCM using single-point calculations with the correlation-gradient, MP2/6-31G*, geometries for the isolated molecule.

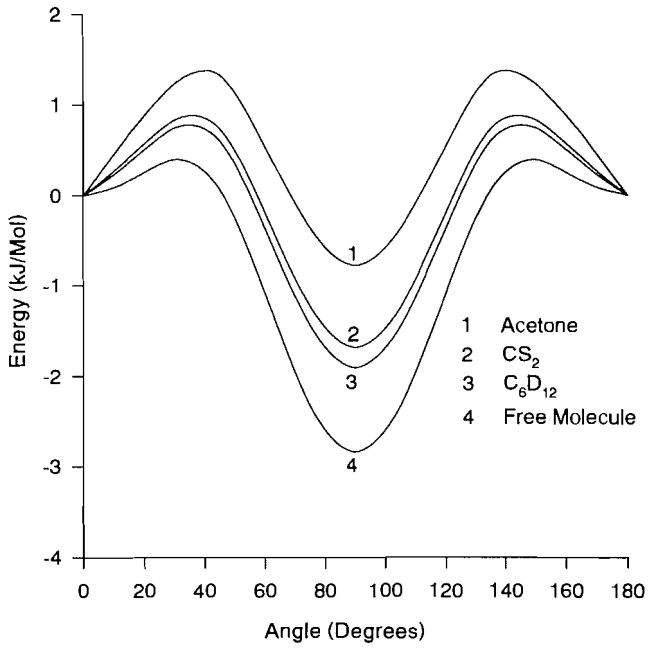

to the dominance of the attractive forces between the $^{+}C–F^{-}$ and the *ortho* $C^{-}–H^{+}$ dipoles in this conformer. In terms of the simple model, these forces dominate the repulsive nonbonded forces: the sum of the van der Waals radii of hydrogen and fluorine is 2.55 Å whereas the interatomic distance would be 2.4 Å for a regular geometry. For benzyl chloride, however, the interatomic distance is again very near 2.4 Å in the in-plane form, yet the sum of the van der Waals radii is 3.0 Å, so that repulsive overlap is now dominant leading to the perpendicular conformer as most stable.[8]

Returning to benzal fluoride, the simple model predicts **1** as the least energetic because it brings both C—F bonds very close to the *ortho* C—H bonds, maximizing electrostatic attractions. By way of contrast, the conformer analogous to **2** should be most stable for benzal chloride, as it is (3, 34), because it reduces the H, Cl distances to 3.0 Å, very near the sum of the nonbonded radii.

The requisite polarities of the C—H and C—F bonds in benzal fluoride are supported by molecular orbital computa-

[8] The simple model is not meant to *replace* the more elaborate one based on molecular orbitals, of course. Thus, the perturbational model might account for the somewhat lower preference for the in-plane conformers of 4-fluorobenzyl fluoride, compared to the parent molecule (6), via an enhanced benzylic anomeric effect in the perpendicular form, fluorine being a π donor. A valence bond model could attribute this to an enhanced contribution from a hyperconjugative bond, no-bond structure, whereas qualitative molecular orbital terminology would attribute the slight stabilization of the perpendicular form to a σ–π interaction aided by the π donor.

Fig. 7. The correlation-gradient, MP2/6-31G**, geometries (planar phenyl groups) are shown for two conformers for benzal fluoride. The hexagonal structure (internal angles) of the benzene moiety is less severely perturbed than by a methyl group; in toluene, the bond angle at the ipso position is 118.1° (30). The C—F bond lengths are 0.02 Å smaller than for benzyl fluoride (6), in the MP2/6-31G* structure as well. The C—H and C—C bond lengths of the phenyl group are rather close to those claimed to be the best (corrected) theoretical values for benzene itself (31). The exocyclic C—C bond is somewhat shorter in the conformer in which the C—H bond lies in the phenyl plane, consistent with stronger σ,π withdrawal in this conformer. As a matter of interest, the substitution structure of CH_2F_2 (32) has a FCF angle of 108.2°, a C—H length of 1.093(3) Å, and a C—F length of 1.357(1) Å. As to solvent effects on computed molecular structures, MP2/6-31G* calculations with the Onsager model for ε = 20.7 (for which geometry optimizations were possible) gave negligible changes in the geometry of the phenyl ring but angle changes at the α carbon atom of up to 2° and a 0.006 Å lengthening of the C—F bond; the latter is perhaps just within the level of significance.

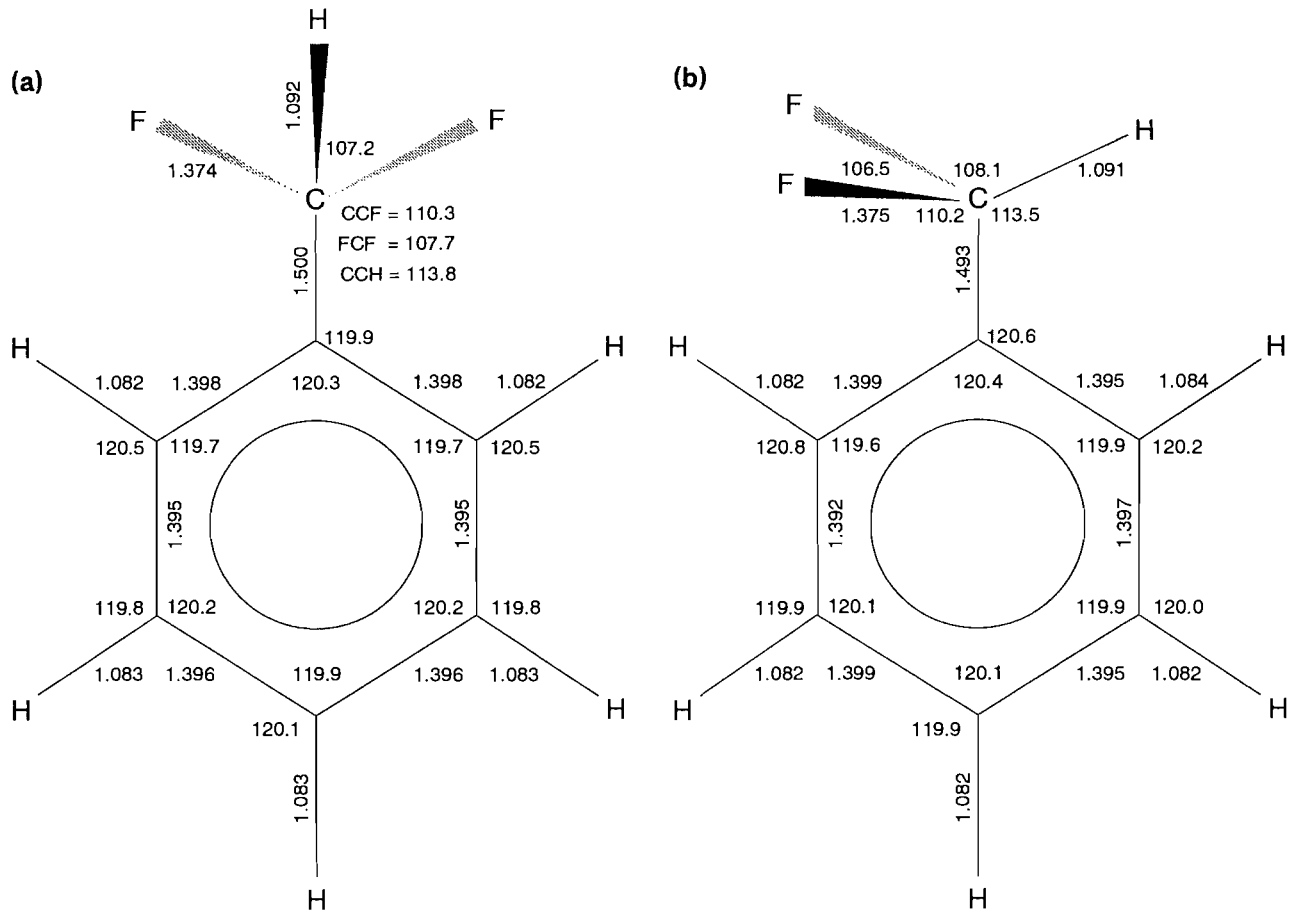

tions. Figure 8 displays Mulliken charges on the atoms derived from the MP2/6-31G* computations for conformers **1** and **2**. The magnitudes are dependent on the basis set, as expected, and would also change somewhat if alternative methods were used to allocate electron probabilities. Nevertheless, it is most unlikely that the signs of the charges would change. The positive charge on the hydrogen of the methine C—H bond would then be an additional cause of the stability of **1** relative to **2** for benzal fluoride.

Notice also that in conformer **2**, in which the C—F bonds are closer to the perpendicular than in **1**, more charge is withdrawn from the phenyl group (particularly at the ipso site) in line with σ, π acceptance by the side chain. The Csp^2—Csp^3 bond also shortens somewhat in **1** (Fig. 7). The prediction is then that a π donor at the *para* position would tend to stabilize **2** relative to **1** and therefore to lower the internal rotational potential. On the other hand, electronegative substituents in the *meta* position could cause further polarization of the bonds *ortho* to the CHF_2 group and, on the electrostatic model, stabilize **1** relative to **2**. Such polarization apparently stabilizes the in-plane conformers of the 3,5-dichloro and 3,5-difluoro derivatives of benzyl fluoride (6, 26).

Whatever the merits of these adumbrations, it is interesting to note that addition of two potentials for benzyl fluoride, one being 120° out of phase with the other, yields a potential (curve (*a*) in Fig. 9) that approximates that of benzal fluoride (curve (*b*) in Fig. 9). However, the maximum near ϕ = 40° in the latter, arising from a relatively large fourfold component, is a nonadditive component.

(b) The molecule in solution

The computed dipole moments, many of which are found in Table 5, show, first, that the unstable conformer, **2**, is some 5% more polar than **1** and, second, that the solvent causes an

Fig. 8. The Mulliken total atomic charges are given for the isolated molecule in (*a*), for a dielectric constant of 2.10 in (*b*), and 20.7 in (*c*). The computations used the correlation-gradient optimized MP2/6-31G* structure for the free molecule and the SCI–PCM procedure. The absolute charges will depend on the basis set. The *changes* induced by solvent are of interest and are very similar for different bases and solvent models.

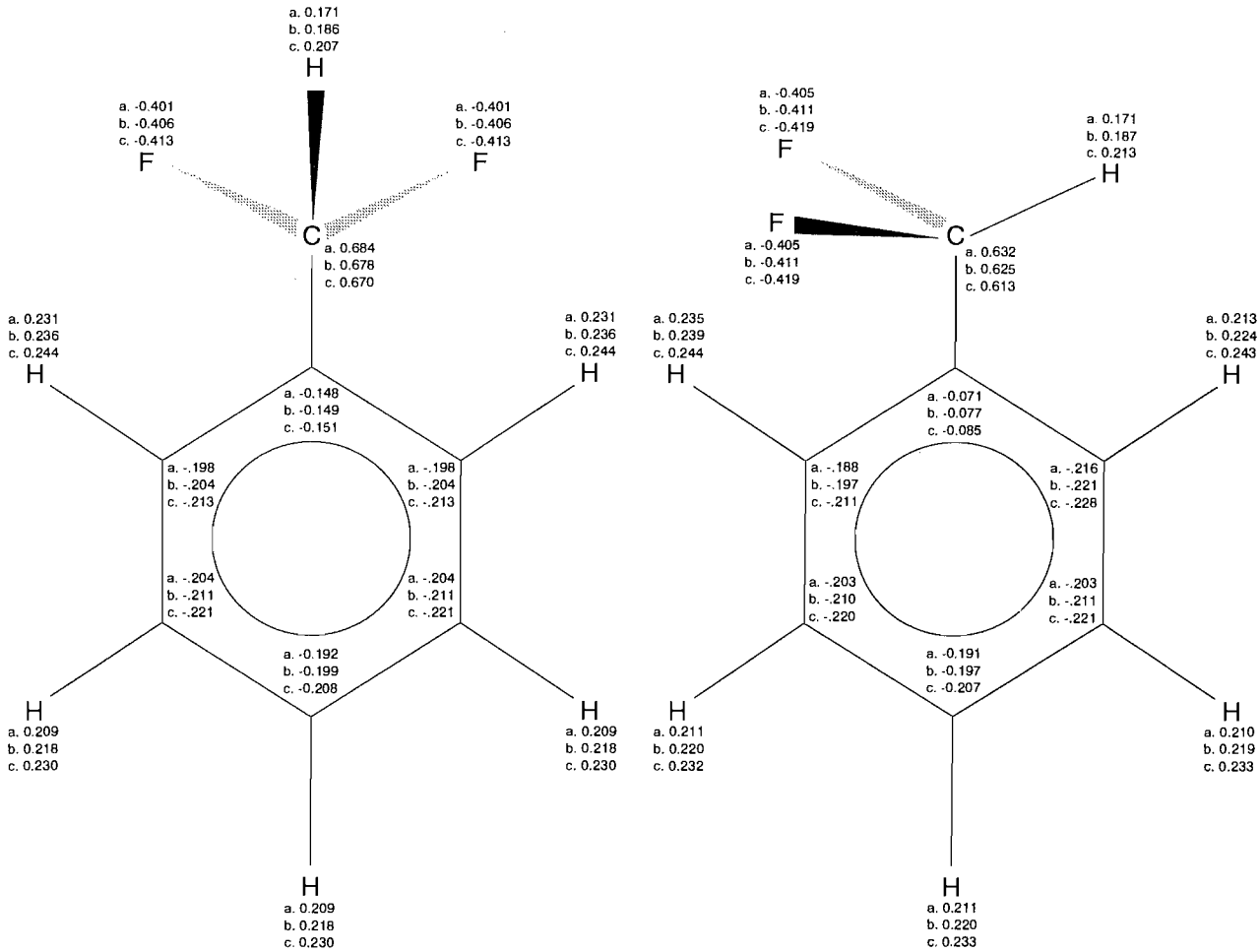

increase in charge separation (see also Fig. 8). A simple reaction field model (35), in which only the dipole of the solute molecule is considered ($l = 1$ in the Onsager model), has $\Delta E^V - \Delta E^S = (\mu^2 B - \mu^2 A)(\varepsilon - 1)/a^3(2\varepsilon + 1)$. Here, ΔE^V is the energy difference between conformers B and A, ΔE^S is the energy difference in the presence of a solvent of dielectric constant, ϵ, and a^3 is the cube of the molecular radius. The dipole moment of benzyl fluoride (36) is reasonably well reproduced by the 6-31G* basis (6). On the assumption that the dipole moment of benzal fluoride is also calculated reliably (Table 5), and taking is radius as 3.6 Å (slightly larger than deduced for benzyl fluoride from its liquid density), one finds that, relative to the vapor and **2**, the energy of **1** is raised by 0.7 kJ/mol in acetone-d_6 solution and by 0.3 kJ/mol in CS_2 solution. In this deduction, the enhanced dipole moments in the solvents are employed (Table 5). Comparison with, for example, the computed pontentials in Fig. 7 or the twofold MP2/6-31G* terms in Table 5 implies that these dipole energies are too low by about a factor of three. Higher order terms in the multipole moment expansion appear to play an important role in the solvent effect, not surprising for a noncompact molecule in which charge is not localized in a few proximate bonds.

In terms of an electrostatic model, the extent of the reduction in the field between the charges on the peripheral atoms (Fig. 8), caused by the dielectric, is problematical. Intuitively, the reduction occurs and destabilizes **1** relative to **2**. The conformation of the latter aids hyperconjugative electron withdrawal from the phenyl group because the C—F bonds lie nearer the perpendicular (Fig. 8) and cause additional charge separation in the more polar media.

The chemical shifts

A considerable literature (37, 38) exists relating ^{13}C and ^1H chemical shifts to computed atomic charges in benzene derivatives. The computations are done on the isolated molecules, the shifts are measured in solution. The *para* proton shielding in monosubstituted benzenes is well correlated with the σ electron density at the *para* hydrogen atom (37). With reference to the proton chemical shifts in C_6D_{12} and acetone-d_6 solutions in Table 1 and the computed σ electron densities in

Fig. 9. In (*b*) the correlation-gradient, MP2/6-31G*, internal rotational potential of benzal fluoride is plotted as a function of the angle by which the α C—H bond twists out of the phenyl plane. In (*a*) the potential, obtained by adding two benzyl fluoride potentials (6), one shifted by 120° from the other in torsional angle, agrees quite well with (*b*), except in the region near 40°; the larger $|V_4/V_2|$ ratio for benzal fluoride produces this divergence.

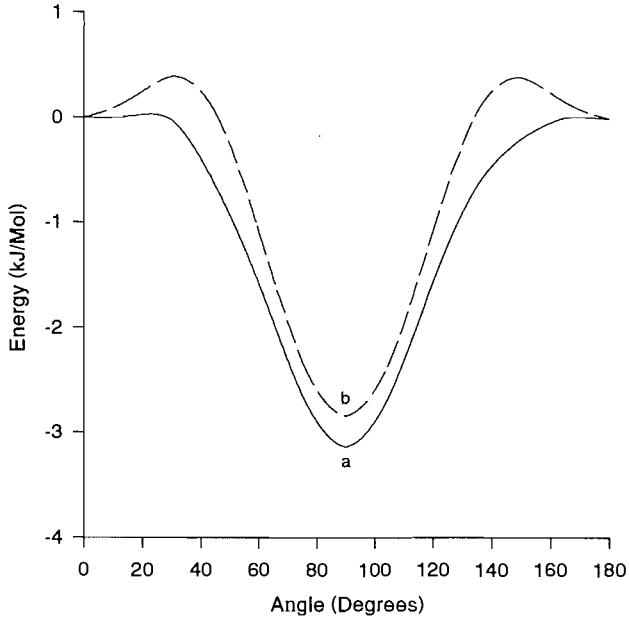

Fig. 8, one has the *para* ring proton less screened in acetone-d_6 solution by 0.215 ppm and the positive charge increased by 0.012_5 electron units. The ratio of these numbers is reasonable in that the screening of the proton in the hydrogen atom is 17.8 ppm. It is interesting that the methine proton is descreened by 0.443 ppm in passing from C_6D_{12} to acetone-d_6 solution, while the positive charge increases by 0.023 units. The two shift/charge ratios, *para* and methine protons, are 17.2 and 19.3 ppm/electron.[9] Of course, a rigorous procedure would average the charges over the computed potential.

Such comparisons might encourage an extrapolation of the shifts to the vapor using the charges computed for the isolated molecule (Fig. 8); gaseous shift values would be of interest to modern approaches to chemical shift calculations (40), rare though they still are for protons (40, 41), but see ref. 39. However, if computations on benzene itself are done, just as for those in Fig. 8, one finds again an increased charge of 0.012 on the protons. But the shift of benzene in C_6H_{12} is 7.211 ppm, is 7.352 ppm in acetone-d_6, and thus the decrease in screening is only 0.141 ppm. Hence the rough proportionality between increased positive charge and decreased screening noticed for the protons in benzal fluoride is likely a coincidence.

[9] There is no theoretical basis for a correlation of the shielding of a nucleus with the electron population of the atom carrying the nucleus in a molecule, but there may occur instances in which such a correlation occurs for protons (39) — perhaps in restricted cases as for the *para* proton in benzene derivatives.

It is conceivable that another basis set and a different method of deriving charges (42) from the density matrix could result in a consistent treatment of charge/shift ratios in benzene and its derivatives in solutions of various polarities; leading to reliable shifts in the vapor phase.

Turning to ^{13}C shifts, that of benzene in solution is usually given as 128.5 ppm (δ value, relative to TMS). The screening of the *para* ^{13}C nucleus is given as proportional to the π electron charge in monosubstituted benzenes as well as to the total electron density (37). The π and total charges are linearly related (37). The chemical shifts of C-4 in Table 2 therefore mean that the CHF_2 group is an electron-accepting substituent, similar, in fact, to the $CH_3S{=}O$ group (43). As the polarity of the solvent increases, C-4 is deshielded, yet the computed total negative charge (Fig. 9) increases. Unfortunately, we do not have the π electron densities because of our parsimony in print-outs of the computer output.

Other long-range coupling constants

(a) $^4J(H, CH)$

In toluene, $^4J(H, CH_3)$ can be written (25, 44) as $-1.08\langle\sin^2\phi\rangle - 0.32\langle\cos^2\phi\rangle$, the second term representing a σ electron contribution, the first the σ,π mechanism. Both of the coefficients in this relationship will be altered by the electronegative fluorine substituents in benzal fluoride. The values of $\langle\sin^2\phi\rangle$ are known for the latter compound in C_6D_{12} and in acetone-d_6, with the result that $^4J(H, CH) = -0.649\langle\sin^2\phi\rangle - 0.20\langle\cos^2\phi\rangle$. It is likely that the internal rotational potential in benzal fluoride is sensitive to *para* substituents, as it is in benzyl fluoride (6), so that $^4J(H, CH_2)$ in such derivatives may well be an alternative to $^6J(H, CH)$ in assessing changes in the potential, as it is for benzyl fluoride derivatives (6, 26).

(b) $^4J(F, CH)$

The magnitudes of $\langle\sin^2\phi\rangle$ (see **2**) in C_6D_{12} and acetone-d_6 solutions are 0.432 and 0.474, respectively. Combined with the corresponding $^4J(F, CH)$ numbers of −1.125(1) and −1.226(1) Hz, one has $^4J_{90}(F, CH)$ as −2.599 or −2.609 Hz. The implication, that $^4J(F, CH) = {}^4J_{90}\langle\sin^2\psi\rangle$, calls to mind a similar functional relationship established for $^4J(F, CH)$ in 3,5-dichlorobenzyl fluoride (26), in which, however, an additional, small, term in $\langle\sin^2\psi\rangle$ also occurs.

$^nJ_{90}$ values in toluene through benzotrifluoride

From the numbers given here (5, 6, 25, 45) it appears that the second fluorine substituent causes a rather larger perturbation of $^{5,6}J_{90}$ than does the first. Thus, $^6J_{90}(H, H)$ decreases in magnitude only from 1.20 Hz in toluene to 0.94 Hz in benzyl fluoride but to 0.40 Hz in benzal fluoride; similar statements apply to $^6J_{90}(H, F)$ and $^5J_{90}(C, F)$. In terms of a hyperconjuga-

	$^5J_{90}$(C, F)	$-^6J_{60}$(H, F)		$-^6J$(H, H)	
CH_2F	5.03(10)	2.85(1)		1.20(1)	CH_3
CHF_2	4.39(15)	2.55(1)		0.94(1)	CH_2F
CF_2	2.78(6)	1.31(3)		0.40(2)	CHF_2

tive model, the $\sigma-\pi$ overlap of the C—H or C—F bond orbitals with those of the phenyl group is reduced as the electronegative fluorine substituent polarizes the C—H or C—F bonds. A second fluorine substituent (changing CF_2F to CHF_2 for ^6J(H, H) and CHF_2 to CF_3 for ^6J(H, F) and ^5J(C, F)) is hence much more effective in reducing the $\sigma-\pi$ interaction, perhaps because a C—H bond responds more easily than a C—F bond to the perturbation. Reasonably linear correlations exist between the numbers in different columns above; their significance, if any, escapes us.

Suggested experiments

The internal rotational potential in benzal fluoride, small and sensitive to solvent, is most likely sensitive also to substituents, including those in *meta* and *para* positions. Such is the case with benzyl fluoride, in which electronegative *meta* substituents stabilize the in-plane conformer (6, 26), whereas a weak π donor in the *para* position favors the perpendicular form of the molecule (6). The prediction is then that electronegative substituents in the *meta* position will lower the energy of **1** relative to **2** for benzal fluoride; the opposite will occur in the presence of a *para* π electron donor. Of course, the presence of a solvent will alter the magnitudes of these relative energies. Useful contributions from molecular spectroscopists would entail the measurements of these potentials for the gaseous molecules, for comparison with the theoretical potentials and with the results of measurements in solution, as illustrated in this report.

Acknowledgements

We thank the Natural Sciences and Engineering Research Council of Canada for financial assistance.

References

1. T. Schaefer, R. Sebastian, and G.H. Penner. Can. J. Chem. **64**, 1372 (1986).
2. G. Celebre, G. DeLuca, M. Longeri, and A. Ferrarini. Mol. Phys. **83**, 309 (1994).
3. R. Bennassi, C. Bertarini, and F. Taddei. J. Mol. Struct. (Theochem), **339**, 103 (1995).
4. G.H. Penner, T. Schaefer, R. Sebastian, and S. Wolfe. Can. J. Chem. **65**, 1845 (1987).
5. T. Schaefer, C. Beaulieu, R. Sebastian, and G.H. Penner. Can. J. Chem. **68**, 581 (1990).
6. T. Schaefer, R.W. Schurko, R. Sebastian, and F.E. Hruska. Can. J. Chem. **73**, 816 (1995).
7. G. Celebre, G. DeLuca, M. Longeri, and J.W. Emsley. Mol. Phys. **67**, 239 (1989).
8. P. Messina, K. Mange, and W.J. Middleton. J. Fluorine Chem. **42**, 137 (1989).
9. J.S. Martin, A.R. Quirt, and K.E. Worvill. The NMR program library. Daresbury Laboratory, Daresbury, U.K.
10. K. Marat and R. Sebastian. Bruker Report, 42 (1993).
11. M.J. Frisch, G.W. Trucks, M. Head-Gordon, P.M.W. Gill, M.W. Wong, J.B. Foresman, B.G. Johnson, H.B. Schlegel, M.A. Robb, E.A. Replogle, R. Gomperts, J.L. Andres, K. Raghavachari, J.S. Binkley, C. Gonzalez, R.L. Martin, D.J. Fox, D.J. Defrees, J. Baker, J.J.P. Stewart, and J.A. Pople. GAUSSIAN 92, Revision C. Gaussian, Inc., Pittsburgh, Pa. 1992.
12. M.J. Frisch, G.W. Trucks, H.B. Schlegel, P.M.W. Gill, B.G. Johnson, M.A. Robb, J.R. Cheeseman, T. Keith, G.A. Petersson, J.A. Montgomery, K. Raghavachari, M.A. Al-Laham, V.G. Zakrzewski, J.V. Ortiz, J.B. Foresman, E.S. Replogile, R. Gomperts, R.L. Martin, D.J. Fox, J.S. Binkley, D.J. Defrees, J. Baker, J.P. Stewart, M. Head-Gordon, C. Gonzalez, and J.A. Pople. GAUSSIAN 94, Revision B.2. Gaussian, Inc., Pittsburgh Pa. 1995.
13. W.J. Hehre, L. Radom, P.v.R. Schleyer, and J.A. Pople. Ab initio molecular orbital theory. Wiley, New York. 1986.
14. M.J.S. Dewar, E.J. Zoebisch, E.F. Healy, and J.J.P. Steward. J. Am. Chem. Soc. **107**, 3902 (1985).
15. D. Rinaldi and R.R. Pappalardo. SCRF PAC. A self-consistent reaction field package. Quantum Chemistry Program Exchange 622. QCPE Bull. **12**, 69 (1992).
16. D. Rinaldi, J.L. Rivail, and N. Rguini. J. Comput. Chem. **13**, 675 (1992).
17. M.F. Ruiz-López, X Assfeld, J.L. Garcia, J.A. Mayoral, and L. Salvatella. J. Am. Chem. Soc. **115**, 8780 (1993).
18. J. Tomasi and M. Persico. Chem. Rev. **94**, 2027 (1994).
19. K.B. Wiberg, T.A. Keith, M.J. Frisch, and M. Murcko. J. Phys. Chem. **99**, 9072 (1995).
20. J.A. Pople, J.W. McIver, Jr., and N.S. Ostlund. J. Chem. Phys. **49**, 2960 (1968); **49**, 2965 (1968).
21. P.A. Dobush and N.S. Ostlund. QCPE, **11**, 281 (1975).
22. R.H. Contreras, M.A. Natiello, and G.E. Scuseria. Magn. Reson. Rev. **9**, 239 (1985).
23. T. Schaefer, W.K. Chan, R. Sebastian, R. Schurko, and F.E. Hruska. Can. J. Chem. **72**, 1972 (1994), and references therein.
24. R. Wasylishen and T. Schaefer. Can. J. Chem. **50**, 1852 (1972).
25. T. Schaefer, R. Sebastian, and G.H. Penner. Can. J. Chem. **63**, 2597 (1985).
26. T. Schaefer, J.R. Mansfield, F.E. Hruska, and R. Sebastian. Can. J. Chem. **70**, 1750 (1992).
27. W.J.E. Parr and T. Schaefer. Acc. Chem. Res. **13**, 400 (1980).
28. P.B. Ayscough, M.S. Brice, and R.E.D. McClung. Mol. Phys. **20**, 41 (1971).
29. G.H. Penner. Can. J. Chem. **65**, 538 (1987).
30. A. Domenicano, P. Mazzeo, and A. Vaciago. Tetrahedron Lett. 1029 (1976).
31. J.M.L. Martin, J. El-Yazal, and J.-P. François. Mol. Phys. **86**, 1437 (1995).
32. E. Hirota, T. Tanaka, A. Sakakibara, Y. Ohashi, and Y. Morino. J. Mol. Spectrosc. **34**, 222 (1970).
33. A.E. Reed, L.A. Curtiss, and F. Weinhold. Chem. Rev. **88**, 899 (1988).
34. T. Schaefer and R. Sebastian. Can. J. Chem. **67**, 2053 (1989).
35. R.J. Abraham and E. Bretschneider. *In* Internal rotation in molecules. *Edited by* W.J. Orville Thomas. Wiley, New York. 1974. Chap. 13.
36. M.T. Rogers. J. Am. Chem. Soc. **69**, 457 (1947).
37. W.J. Hehre, R.W. Taft, and R.D. Topsom. Prog. Phys. Org. Chem. **12**, 159 (1976).
38. D.J. Craik and R.T.C. Brownlee. Prog. Phys. Org. Chem. **14**, 1 (1983).
39. T.A. Keith and R.F.W. Bader. Can. J. Chem. **74**, 185 (1996).
40. D.B. Chesnut. Chem. Phys. Lett. **246**, 235 (1995).
41. R.A. Kirby and A.E. Hansen. Int. J. Quantum Chem. **57**, 199 (1996).
42. R.J. Abraham, M. Edgar, R.P. Glover, M.A. Warne, and L. Griffiths. J. Chem. Soc. Perkin Trans. 2, 333 (1996).
43. D.E. Ewing. Org. Magn. Reson. **12**, 499 (1979).
44. M. Barfield, C.J. Fallick, K. Hata, S. Sternhell, and P.W. Westerman. J. Am. Chem. Soc. **105**, 2178 (1983).
45. T. Schaefer, K. Mart, J. Peeling, and R.P. Veregin. Can. J. Chem. **61**, 2779 (1983).

Sulfonyl esters 7. The second and third sequences in the Trithioorthoformate Reaction

Kashyapa Ananda Ginige, John Edward Goehl, and Richard Francis Langler

Abstract: A previous report has established the intermediacy of a sulfide-sulfonate ester in the one-pot conversion of an aryl mercaptan and a sulfonate ester into the corresponding trithioorthoformate. This report describes evidence for the sequential intermediacy of a bissulfide-sulfonate ester and a dithiosulfene in the conversion of the sulfide-sulfonate ester into the trithioorthoformate. A new sulfonate ester is shown to give the highest yield of trithioorthoformate.

Key words: single electron transfer, sulfonate esters, sulfenes.

Résumé : Une publication antérieure a établi la participation d'un ester sulfure-sulfonate comme produit intermédiaire dans la conversion dans un seul récipient d'un mercaptan arylique et d'un ester sulfonate en trithioorthoformate correspondant. Cette publication décrit la preuve de la participation intermédiaire séquentielle d'un ester bisulfure-bisulfonate et d'un dithiosulfène dans la préparation du trithioorthoformate. On montre qu'un nouvel ester sulfonate donne les rendements les plus élevés de trithioorthoformate.

Mots clés : transfert d'électron unique, esters sulfonates, sulfènes.

[Traduit par la rédaction]

Introduction

In the course of exploratory work on reactions of mercaptans with sulfonic acid esters (1), we discovered the Trithioorthoformate Reaction (see eq. [1]). Scheme 1 outlines the pathway for the first sequence of the Trithioorthoformate Reaction, which produces the intermediate sulfide-sulfonate ester **2** as described earlier (2). We now disclose our findings and conclusions about the processes that transform the sulfide-sulfonate ester **2** into the trithioorthoformate **1**.

Results and discussion

To support our view that sodium hydride serves as an electron-transfer agent, the eq. [1] reaction was successfully rerun with sodium metal[2] (vide eq. [2]), which, presumably, must react as such an agent.

A. The second sequence of the trithioorthoformate reaction

The intermediacy of sulfide-sulfonate ester **2** (Scheme 1) was established after it was isolated cleanly by means of column chromatography (2). We were unable to isolate any other intermediates in this way. However, we repeatedly observed the presence of *p*-tolyl thiolformate in column fractions from routine reactions (vide eq. [3]).

Given the pathway of the first sequence (Scheme 1), it seemed very likely that the Trithioorthoformate Reaction proceeds through sequential sulfide-sulfonate esters as shown in eq. [4].

The failure to isolate **3**, coupled with the isolation of *p*-tolyl thiolformate would be explained by assuming the hydrolysis of **3** during column chromatography as shown in Scheme 2. Note that unimolecular dissociation of sulfonic acid esters with CS bond rupture has some experimental precedent (3).

Due to the apparent instability of **3** to column chromatography, we decided to gather evidence for the intervention of bissulfide-sulfonate esters like **3** by examining model sulfenylations with selected sulfones. Sulfone sulfenylations were selected in the hope that (*i*) $-SO_2R$ would facilitate α-sulfenylation nearly as well as $-SO_2OAr$ but that (*ii*) $-SO_2R$ would be a significantly poorer nucleofuge than $-SO_2OAr$ so that, in contrast to bissulfide sulfonate esters like **3**, product bissulfide sulfones might withstand column chromatography. A series of experiments on phenyl methyl sulfone was initiated (vide eq. [5]). The low consumption of phenyl methyl sulfone (eq.[5]) demonstrates the importance of the SO_2—O linkage for the redox steps that produce disulfide in the Trithioorthoformate Reaction (Scheme 1). Subsequent exploration of sulfenylations employed disulfide as portrayed in eq. [6]. To avoid reaction that might accompany column chromatography, **4** was routinely purified using double recrystallization, which permitted the preparation of clean product in 30% yield. Addition of authentic trithioorthoformate **1** to the crude product of eq. [6] confirmed that **1** *does not form* in detectable amounts (60 MHz nmr) in that reaction. Scheme 3 presents the result when that reaction was worked-up using column chromatography.

The trithioorthoformate **1** is a reaction product in reactions of sulfonic acid esters (eq. [1]) but an artifact produced by column chromatography in reactions of sulfones (Schemes 3 and 4). In addition to the evidence cited above, chromatography

Received December 19, 1995.

K.A. Ginige, J.E. Goehl, and R.F. Langler.[1] Department of Chemistry, Mount Allison University, Sackville, NB E0A 3C0, Canada.

[1] Author to whom correspondence may be addressed. Telephone and Fax: (506) 364-2361.

[2] In early experiments ethanol was present. It was shown to be a spectator species (2).

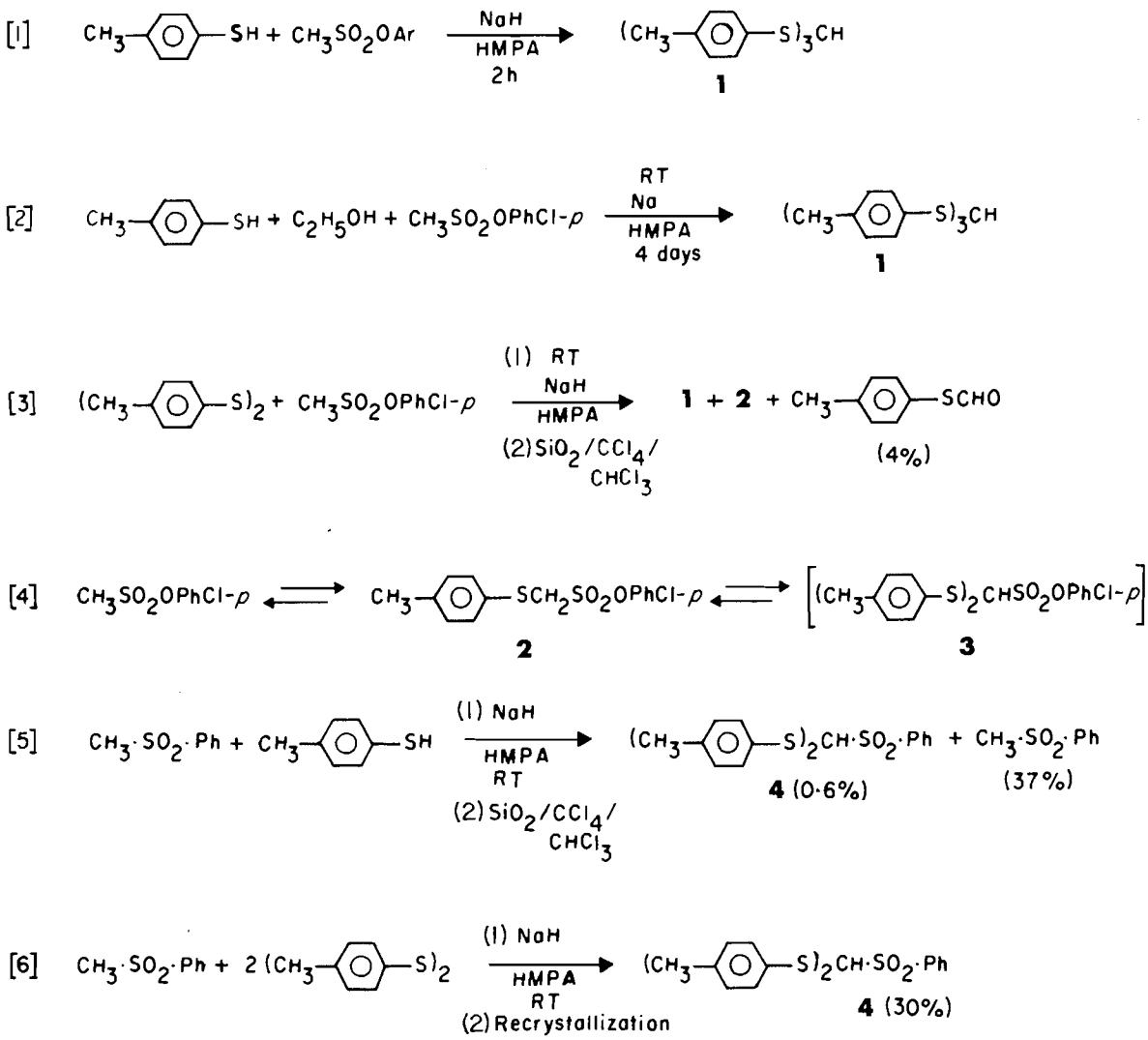

Scheme 1. The first sequence of the Trithioorthoformate Reaction.

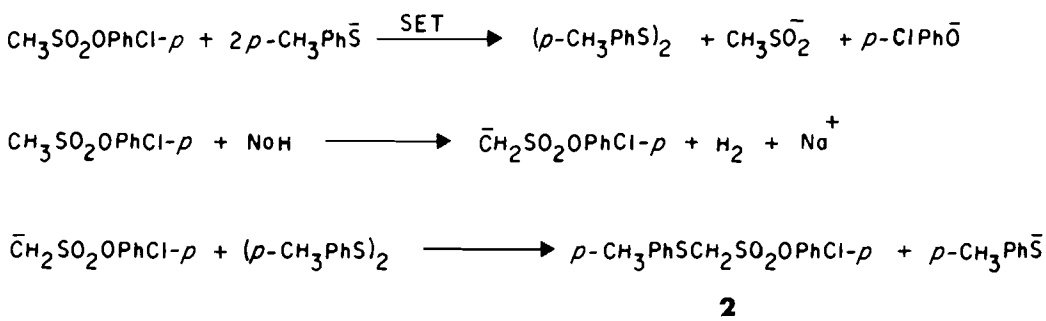

itself provides an indication that **1** is an artifact in reactions producing **4**. Typically, our reactions on sulfonates furnish both *p*-tolyl disulfide and the trithioorthoformate **1**, which are eluted in immediately adjacent fractions using low-polarity solvents (e.g., see "Reaction of **2** with sodium *p*-tolyl mercaptide in the presence of *p*-chlorophenol" in ref. 2). However, elution of the products from the reaction depicted in Scheme 3 provided the disulfide and **1** separated by about 30 fractions. Furthermore, elution of **1** was intermittent, as was elution of *p*-tolyl thiolformate, clearly suggesting reaction during column chromatography. In accord with this evidence, tertiary sulfone sulfides **5** are known to hydrolyse in aqueous acid (4) or in the presence of moist silica gel (5).

One might have expected the reactions given in eq. [6] and Scheme 3 to produce significant amounts of the trissulfide sulfone **6***a* by base-induced sulfenylation of the carbanion

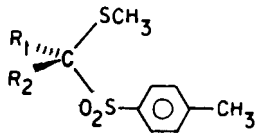

5

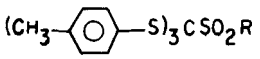

6a R=Ph
6b R=CH$_3$

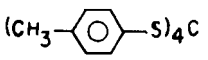

7

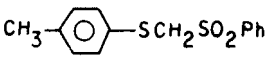

8

Scheme 2.

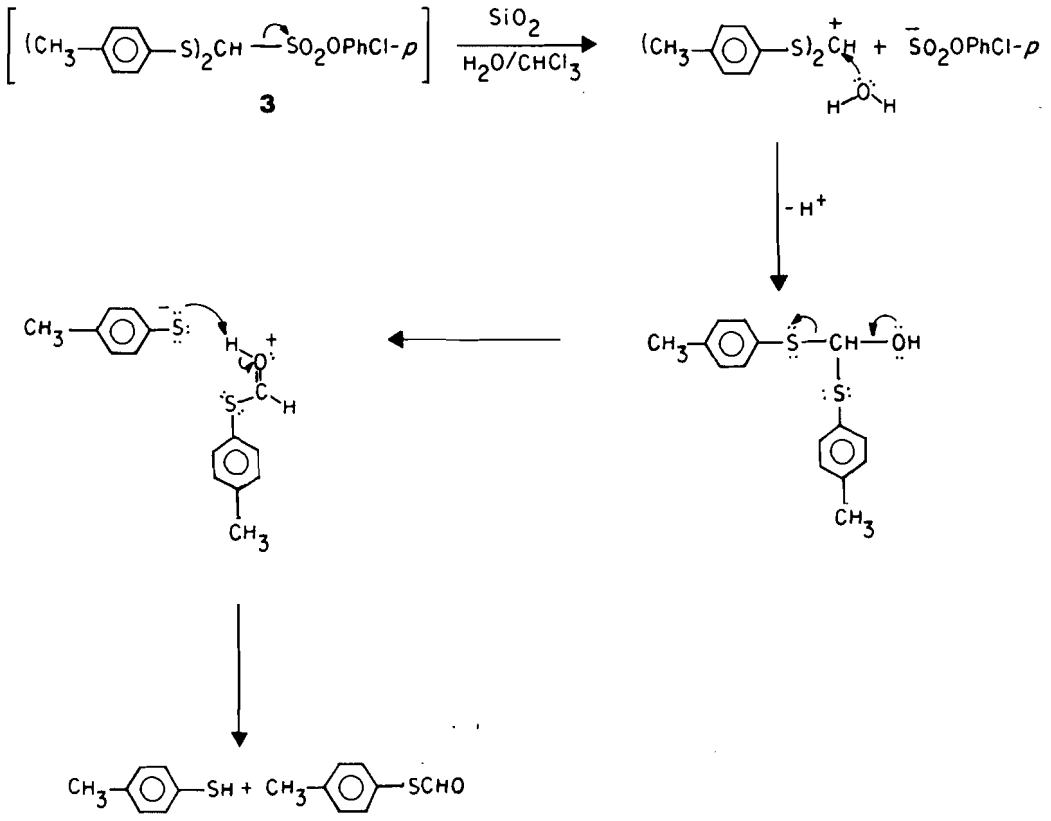

derived from **4**. No such compound was observed. Moreover, purification by column chromatography (Scheme 3) failed to furnish any known tetrathiomethane **7** (6), which would be expected to form from **6***a* by hydrolysis during column chromatography.

The failure of the carbanion derived from the bissulfide sulfone **4** to sulfenylate under conditions which sulfenylate the carbanion derived from **8**[3] can be rationalized on the grounds that the carbanion derived from **4** would enjoy stronger inductive stabilization and would be more hindered, thus making it less reactive.

An earlier result (8) provides evidence for the detrimental effect of anion stability on sulfenylation (see eq. [7]). Despite the much smaller size of the nitro group (relative to sulfonyl) only monosulfenylation of nitromethane was observed. Consistent with both anion stability and steric arguments, sulfenylation of the sulfone-sulfonate ester **9** (eq. [8]) introduces only one thio-*p*-tolyl group. The viability of our proposed unimolecular dissociation of bissulfide sulfonates (Scheme 2) and bissulfide sulfones (Schemes 3 and 4) on moist silica gel rests, in large measure, on the stability of the cationic intermediates $(ArS)_2{}^+CH$. The sulfide-sulfonic acid ester **2** would hydrolyse on moist silica gel to form ArS^+CH_2, which is less stable than $(ArS)_2{}^+CH$. While **2** is moderatlely stable to column chromatography, there is no doubt that some of it

[3] Authentic **8** was available to us (7).

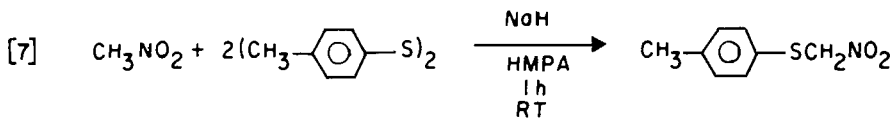

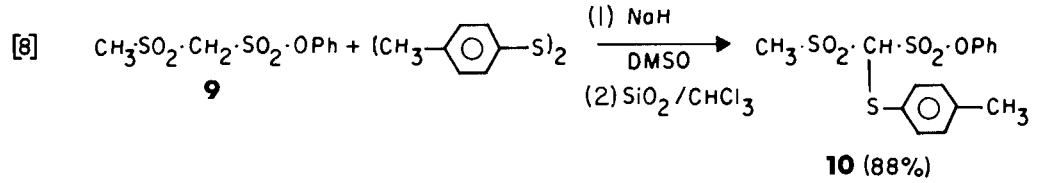

Scheme 3.

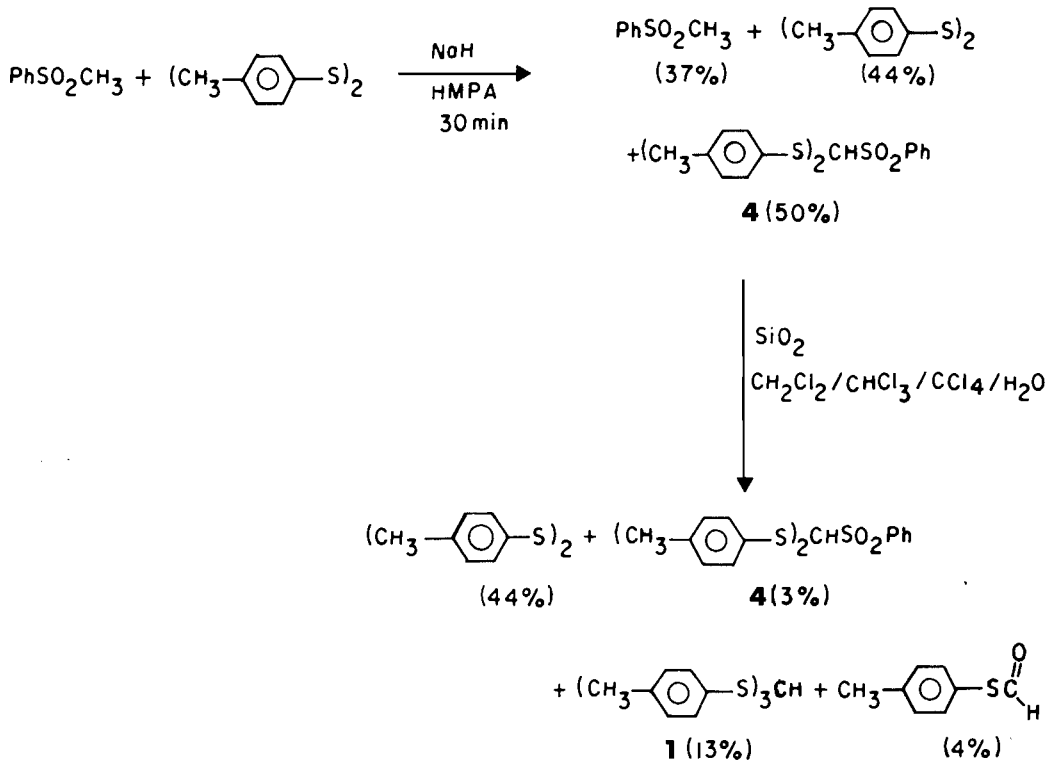

Scheme 4.

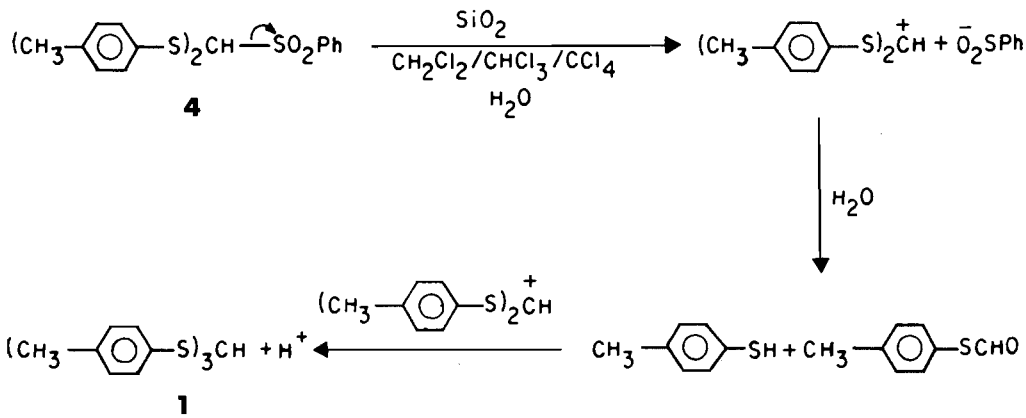

Scheme 5. The second sequence of the Triorthoformate Reaction.

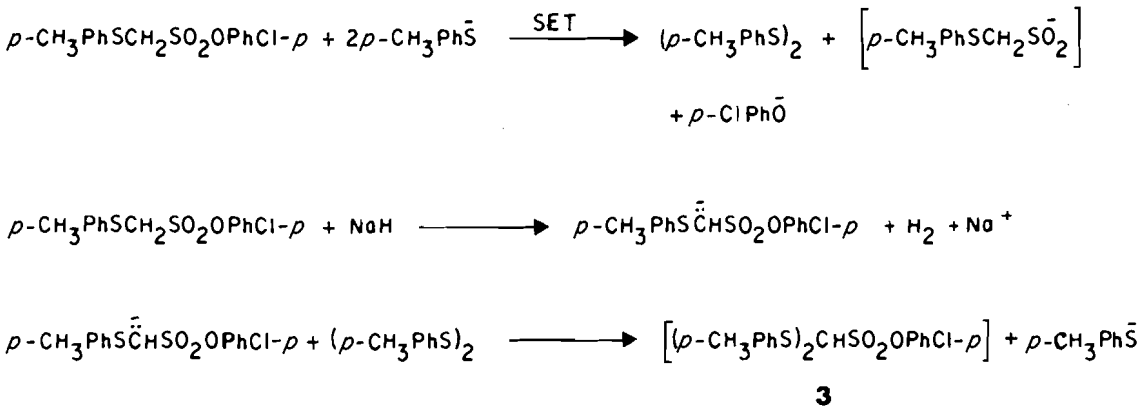

hydrolyses during chromatographic purification, explaining, in part, the modest yields (ca. 30%) routinely obtained from optimized reactions (2). Corresponding behaviour would transform the sulfone-sulfide-sulfonate ester **10** into $ArSO_2^+CHSAr$. The presence of the powerfully destabilizing SO_2 group would make that cation much less stable than ArS^+CH_2. In harmony with this view, **10** is stable to column chromatography.

Given our experience with the Trithioorthoformate Reaction, in conjunction with the pK_a's of butanesulfinic acid and benzenesulfinic acid (2.1 and 1.2, respectively (9)), it seemed reasonable to presume the following order of nucleofugalities for bissulfide sulfonyl compound hydrolyses: $-SO_2OPhCl$-*p* > $-SO_2Ph$ > $-SO_2CH_3$. In an attempt to examine a sulfenylation that would give products with enhanced stability to column chromatography, the following reactions were conducted on dimethyl sulfone (eq. [9]). In the event, **11** and **12** were more stable to column chromatography. Reversibility for sulfone sulfenylations, under our reaction conditions, was established by the reaction shown in eq. [10].

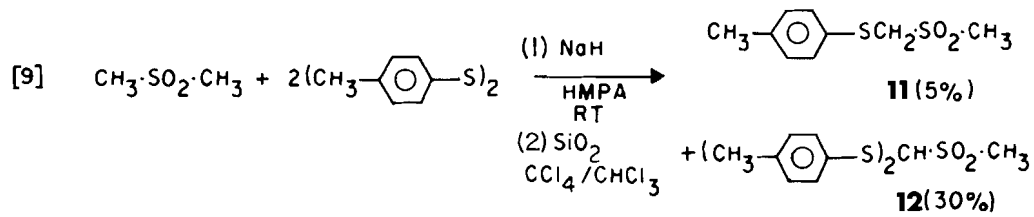

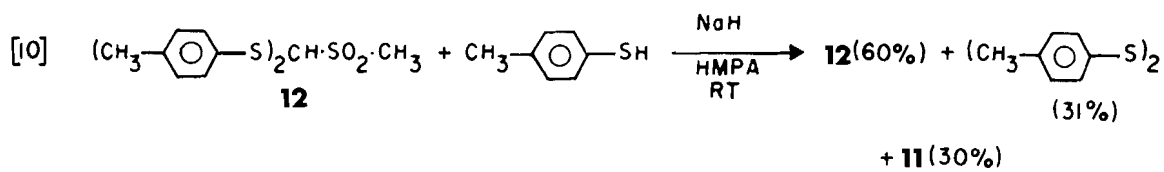

Because the methyl sulfones (eqs. [6] and [9]) and the methanesulfonates (Scheme 1) are similar in acidity[4] and reactions at the α-carbon atoms are subject to similar steric congestion, the sulfones serve as good models for the methanesulfonates. It is now clear that (*i*) reversible sulfenylation, shown as **2**⇆**3** in eq. [4], is almost certainly the second sequence of the Trithioorthoformate Reaction. Additionally, the absence of trissulfide sulfones **6***a* and **6***b* in product mixtures from reactions [6] and [9] along with the absence of hydrolysis products (including $(ArS)_4C$) expected from reaction during column chromatography *strongly militates against the intervention of the trissulfide-sulfonate ester* **13** *in the Trithioorthoformate Reaction (eq. [1]).*

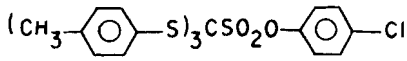

13

The second sequence is presented as Scheme 5.

B. The third sequence of the trithioorthoformate reaction

A priori, there are four reasonable intermediates through which the bissulfide sulfonate ester **3** might be transformed into the trithioorthoformate **1**, viz. (*i*) the trissulfide sulfonate **13**, which has already been dismissed from consideration, (*ii*)

[4] Dimethyl sulfone has a pK_a of 31.1 and phenyl methanesulfonate has a pK_a of 25.2 (10).

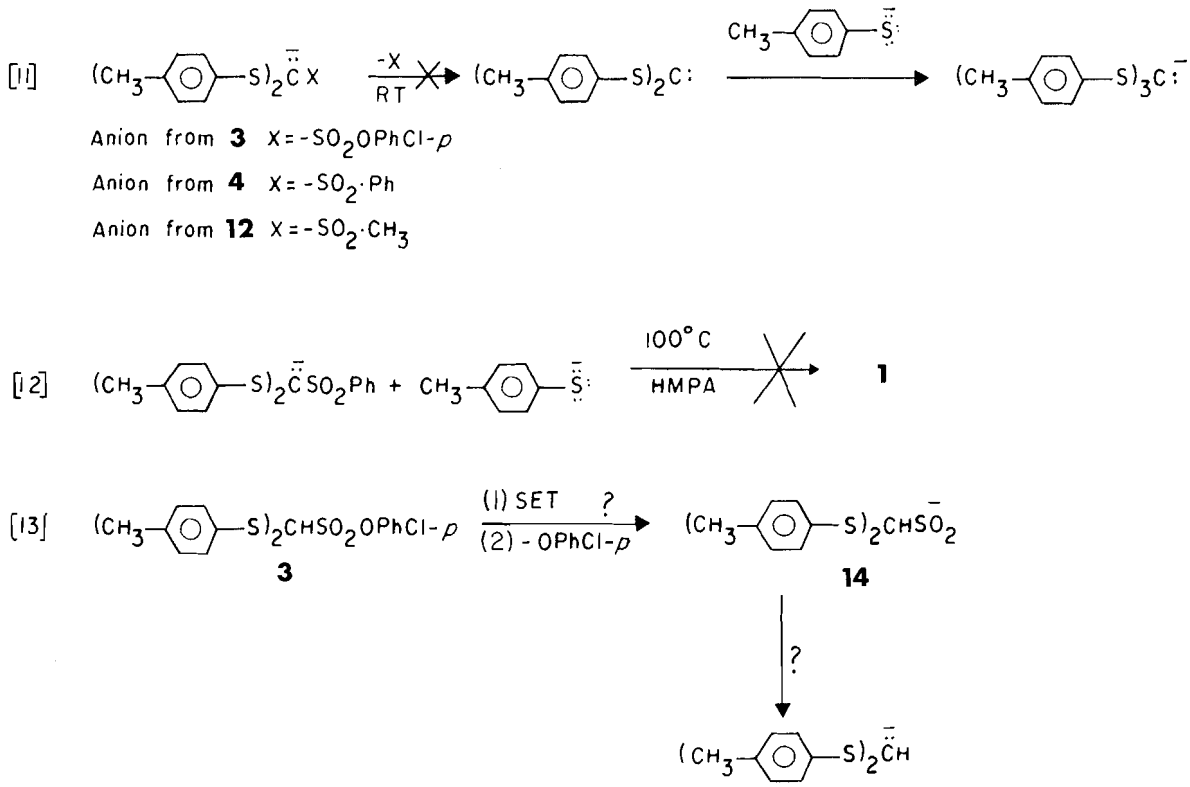

a dithiocarbene, (*iii*) a dithiomethyl carbanion, and (*iv*) a dithiosulfene.

The intermediacy of a dithiocarbene would follow from possible expulsion of a sulfonyl leaving group from a dithiosulfonyl carbanion as in eq. [11].

Based upon the chromatographic instabilities of **3** and **4** (rationalized in Schemes 2 and 4), it seems likely that $-SO_2OPhCl$-*p* and $-SO_2Ph$ have similar nucleofugalities. It follows that the carbanions derived from **3** and **4** should be similarly reactive with respect to dissociation as shown in step 1 of eq. [11]. Since no sulfone reaction conducted at room temperature furnished any trithioorthoformate **1** prior to column chromatography, we have treated the anion from the bissulfide sulfone **4** with *p*-tolyl mercaptide anions in hot HMPA (eq. [12]).

A similar reaction on the carbanion derived from the bissulfide sulfone **12** also failed to produce any trithioorthoformate **1**. We conclude that the carbanions derived from **4** and **12** have no effective way to reach **1** and that the Trithioorthoformate Reaction is unlikely to proceed through a dithiocarbene. In sharp contrast to these sulfone experiments, phenyl methanesulfonate produces no **1** at room temperature but converts *p*-tolyl mercaptide anions into **1** in 40% yield at 100°C (2).

The intermediacy of a dithiomethyl carbanion might be expected following single-electron transfer (SET) to the bissulfide sulfonate **3** (eq. [13]). However, the Trithioorthoformate Reaction completely consumes added NaH to produce carbanions and sulfenylated sulfonate esters. The bissulfide sulfonate **3** would be the strongest acid produced in the reaction and should be essentially quantitatively converted to the corresponding carbanion under the reaction conditions. This anion is an improbable one-electron acceptor. Desulfonylation of **14** would produce a very unstable carbanion[5] and is an unlikely process at ambient temperature. The dithiomethyl carbanion will not be considered further as an intermediate for the third sequence of the Trithioorthoformate Reaction.

A reasonable pathway involving dithiosulfene intermediacy is presented in Scheme 6. The chemistry of sulfenes has been the subject of a recent review (11). Sulfonic acid esters are well-established presursors for the formation of sulfenes (1, 12). Attack by mercaptide anions at the sulfene carbon (Scheme 6) is known as "carbophilic" attack (11) and has ample precedent (13). PM3 computations on CH_2SO_2 show it to have a near-degenerate pair of vacant frontier orbitals (Fig. 1). The coefficients shown in Fig. 1, along with the calculated atomic charge at sulfur (+2.33), lead to the view that sulfur may serve as the hard-acid site in sulfene while carbon serves as the soft-acid site. Optimized PM3 results for $(PhS)_2CSO_2$ are very similar to those just presented for sulfene itself. Note that the third sequence of the Trithioorthoformate Reaction is only the second example of nucleophile-induced CS rupture in a sulfonate ester reaction (see ref. 14 for the first example).

With a complete pathway proposal in hand, we turned our attention to the design and construction of a superior sulfonate. The Trithioorthoformate Reaction requires that the sulfonate ester serve as (*i*) an effective oxidizing agent for mercaptide anions and (*ii*) the source of the methine carbon. The first molecule selected for synthesis was the bissulfonate **15***a*, which has a tribromophenyl-sulfonate linkage for oxidation (15) and a methanesulfonate group for methine carbon.

[5] The following pK_a's come from ref. 10: $(PhS)_3CH$, 22.8; 2-phenyl-1,3-dithiocyclohexane, 30.6; $PhSCH_3$, 42.

Scheme 6. Proposed third sequence of the Trithioorthoformate Reaction.

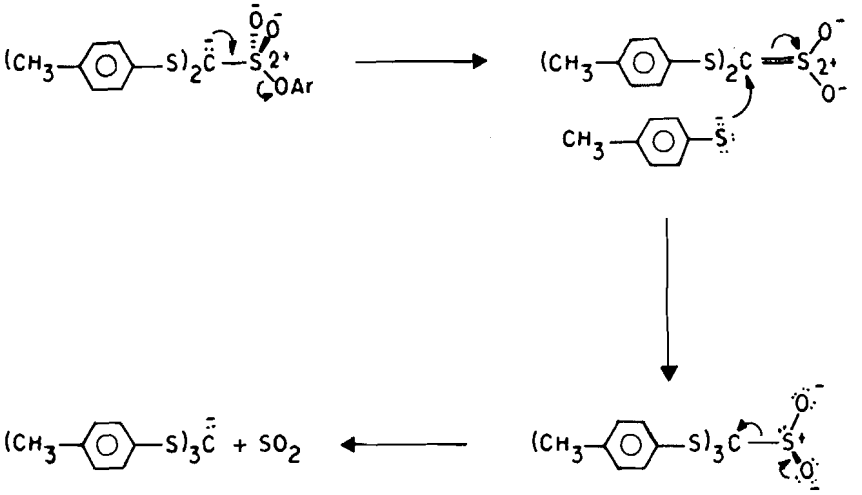

Fig. 1. PM3 vacant frontier and near-frontier orbitals for sulfene.

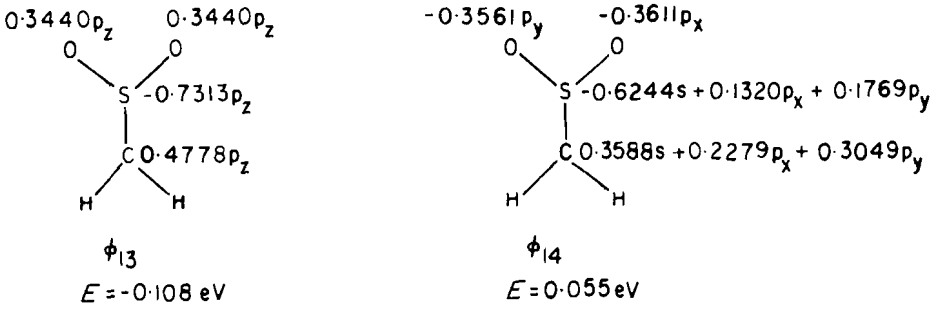

The sulfone sulfonate **15***b* was also targeted for synthesis. It should be a good oxidizing agent but should be unable to deliver methine carbon because it cannot form a dithiosulfene (see Scheme 6). Our approach to the synthesis of **15***b* is presented in eq. [14].

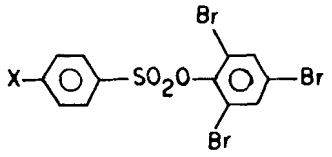

15a X = $CH_3SO_3^-$

15b X = $CH_3SO_2^-$

Earlier work (2) demonstrated that 2,4,6-tribromophenyl methanesulfonate was smoothly reduced by sodium hydride in HMPA. Both **15***a* and **15***b* were reacted with sodium hydride to confirm that these tribromophenyl sulfonates were effective oxidizing agents (eq. [15]). Prior to the experiment on **15***a*, the highest yield[6] of trithioorthoformate **1** (at room temperature) was 10.8 mol%, obtained with *p*-methylsulfonylphenyl methanesulfonate (2). The final experiments employed mixtures of *p*-tolyl mercaptan and *p*-tolyl disulfide in order to avoid exhausting the capacities of the sulfonate-esters to oxidize mercaptide anions (see first step, Scheme 5).

In consonance with our results on sulfones, **15***b* furnished **1** in very low yield[6] (eq. [16]). Trithioorthoformate isolated from this reaction was undoubtedly an artifact resulting from column chromatography.

Reaction with the bissulfonate ester **15***a* furnished the trithioorthoformate **1** in a yield[6] that was twice the magnitude of that obtained with *p*-methylsulfonylphenyl methanesulfonate (2) (eq. [17]). A complete detailed proposal for the pathway of the Trithioorthoformate Reaction has been advanced. Insights arising from the proposal have permitted the design of the best-known reagent, **15***a*, for the oxidative conversion of *p*-tolyl mercaptan into the trithioorthoformate **1**.

Methods

PM3 computations (16) on the two sulfene structures were fully optimized.

Experimental

General

The ir spectra were recorded on a Perkin–Elmer 237B grating spectrophotometer. The nmr spectra were obtained on a Varian EM360A instrument using TMS as the internal standard. Mass spectra were obtained on a Kratos MS 80 gc–ms system. Melting points were determined on a Gallenkamp MFB-595 capillary melting point apparatus and are uncor-

[6] Yields for this discussion are based on consumed sulfonic acid ester.

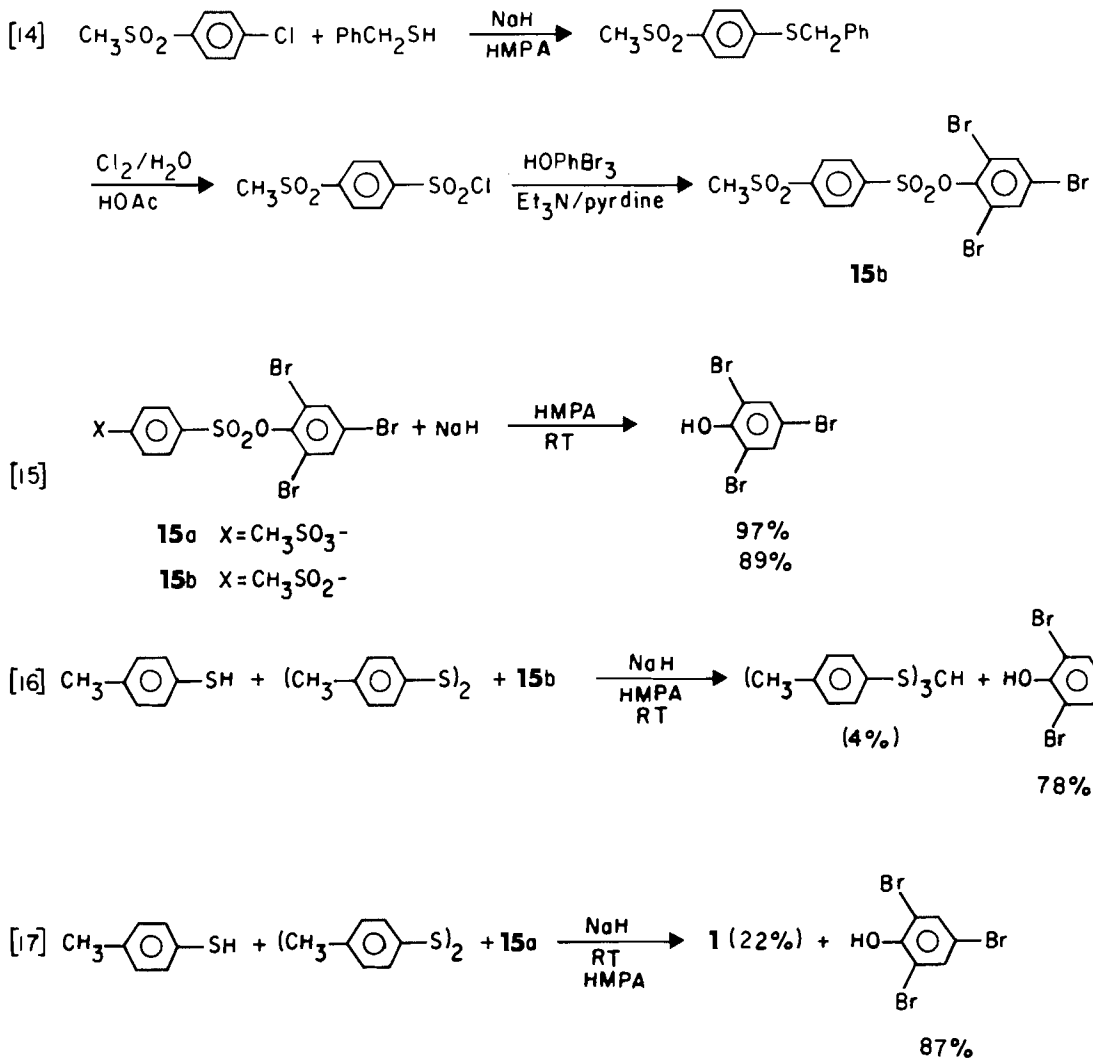

rected. Quantitative analysis of mixtures was accomplished as described elsewhere (17).

Standard work-up

The crude reaction mixture was poured into water (100 mL) and 10% HCl (10 mL). The resultant mixture was washed with diethyl ether (three 100-mL aliquots). The combined ether layers were concentrated and the residue poured into water (100 mL). The resultant mixture was extracted with diethyl ether (three 100 mL aliquots). The combined ether layers were washed with 2.5% NaOH (100 mL), dried ($MgSO_4$), and concentrated.

Trithioorthoformate reaction with Na metal

Sodium metal (0.693 g, 30.1 mmol) was suspended in HMPA (hexamethylphosphoramide) (2) (30 mL). A solution of absolute ethanol (0.638 g, 13.8 mmol) in HMPA (10 mL) was added dropwise over 10 min. A solution of *p*-tolyl mercaptan (1.698 g, 13.6 mmol) was added dropwise over 10 min. Upon completion of the addition the reaction mixture was stirred at ambient temperature for 5 min. *p*-Chlorophenyl methanesulfonate (2.802 g, 13.6 mmol) was added and the reaction mixture stirred at room temperature for 4 days, by which time the sodium was completely consumed.

Standard work-up furnished crude product (1.783 g), which was recrystallized from methanol (40 mL). Clean trithioorthoformate **1** (0.537 g, 1.4 mmol, 30.8%) was obtained and shown to be identical to authentic material by mp, nmr, and double-spotted tlc. The mother-liquor concentrate was chromatographed on silica gel (120 g) employing chloroform elution (100-mL fractions). Fractions **4** and **5** were combined and concentrated affording *p*-chlorophenyl methanesulfonate (0.416 g).

Preparation of p-*tolyl thiolformate*

Authentic *p*-tolyl thiolformate was prepared as described elsewhere (18).

Isolation of p-*tolyl thiolformate from the trithioorthoformate reaction*

Sodium hydride (0.679 g, 28.3 mmol) was suspended in HMPA (100 mL). *p*-Tolyl disulfide (3.375 g, 13.7 mmol) and then *p*-chlorophenyl methanesulfonate (2.828 g, 13.7 mmol) were added. The reaction mixture was stirred at ambient temperature for 1 h 10 min and subjected to standard work-up affording crude product mixture (3.633 g).

Crude product was chromatographed on silica gel (370 g) employing carbon tetrachloride elution (40 100-mL fractions)

and then chloroform (20 100-mL fractions). Fractions 9–22 were combined and concentrated, affording the trithioorthoformate **1** (1.591 g, 4.2 mmol). Recrystallized **1** was identical to authentic material by nmr, tlc, mp, and mixture mp. Fractions 23–25 were combined and concentrated, furnishing *p*-tolyl thiolformate (0.032 g, 0.2 mmol) that was identical to authentic material by ir and nmr. Fractions 26–28 were combined and concentrated, giving *p*-tolyl disulfide (0.143 g, 0.6 mmol). Fractions 47–50 were combined and concentrated, furnishing the sulfide-sulfonate ester **2** (0.264 g, 0.8 mmol). Recrystallized **2** had mp 74.6–75.2°C; ir ($CHCl_3$): 1360, 1150 cm^{-1}; nmr ($CDCl_3$) δ: 7.52 (2H, d, J = 8 Hz), 7.20 (4H, br s), 7.12 (2H, d, J = 8 Hz), 4.40 (2H, s), and 2.32 (3H, s); ms *m/e*, $M^{\cdot+}$ + 2: 330 (0.4%), 328 (1.2%), 137 (100%), and 91 (8.3%). Anal. calcd. for $C_{14}H_{13}ClO_3S_2$: C 51.13, H 3.98; found: C 51.03, H 4.00. Fractions 51 and 52 were combined and concentrated, providing an equimolar mixture (0.238 g) of **2** and *p*-chlorophenyl methanesulfonate. Fractions 53–57 gave *p*-chlorophenyl methanesulfonate (0.456 g).

Reaction of phenyl methyl sulfone with p-*tolyl mercaptan*

Sodium hydride (1.636 g, 68 mmol) was suspended in HMPA (75 mL) (2). A solution of *p*-tolyl mercaptan (4.267 g, 34.4 mmol) in HMPA (25 mL) was added dropwise over a period of 5 min. Phenyl methyl sulfone (2.136 g, 13.6 mmol) was added and the reaction mixture stirred at ambient temperature for 1 h 10 min.

Standard work-up yielded crude product (1.047 g) that was chromatographed on silica gel (100 g), first employing 1:3 methylene chloride – carbon tetrachloride elution (30 100-mL fractions) and then chloroform elution (100-mL fractions). Fractions 2–4 were combined and concentrated, affording *p*-tolyl disulfide (0.087 g). Fractions 12–20 furnished the bissulfide sulfone **4** (0.037 g, 0.092 mmol, 0.6%). Recrystallized **4** had mp 117.4–118.5°C; ir ($CHCl_3$): 1360 and 1155 cm^{-1}; nmr ($CDCl_3$) δ: 8.00 (2H), 7.60 (3H), 7.31 (4H, d), 7.06 (4H, d), 5.00 (1H, s), 2.33 (6H, s). Anal. calcd. for $C_{21}H_{20}O_2S_3$: C 62.96, H 5.03; found: C 63.09, H 5.20. Unchanged phenyl methyl sulfone (0.786 g) was recovered from fractions 21–41.

Routine preparation of bissulfide sulfone 4

Phenyl methyl sulfone (1.506 g, 9.6 mmol) in HMPA (20 mL) (2) was added to a slurry of sodium hydride (0.470 g, 19.5 mmol) in HMPA (10 mL) and the mixture stirred for 5 min. *p*-Tolyl disulfide (4.725 g, 19.2 mmol) was added and the reaction mixture stirred for 1 h 10 min.

Standard work-up furnished crude product (4.624 g) that was recrystallized from methanol (41 mL) and carbon tetrachloride (5 mL), affording off-white crystals (1.886 g). Recrystallized **4** was again recrystallized from methanol (16 mL) and carbon tetrachloride (2 mL), affording clean sulfone bissulfide **4** (1.158 g, 2.8 mmol, 30%).

Reaction of phenyl methyl sulfone with p-*tolyl disulfide employing chromatographic work-up*

A solution of *p*-tolyl disulfide (3.149 g, 12.8 mmol) in HMPA (10 mL) (2) was added to a slurry of sodium hydride (0.310 g, 12.9 mmol) in HMPA (10 mL). Phenyl methyl sulfone (1.000 g, 6.4 mmol) in HMPA (10 mL) was added dropwise over 5 min. The reaction mixture was stirred at ambient temperature for 30 min.

Standard work-up yielded a yellow solid that contained the sulfone bissulfide **4** (50%), phenyl methyl sulfone (0.368 g, 37%), and *p*-tolyl disulfide (1.392 g, 44%). The yellow solid was chromatographed on silica gel (300 g) employing 1:3 methylene chloride – carbon tetrachloride (45 100-mL fractions) followed by chloroform (100-mL fractions). Fractions 4–8 furnished *p*-tolyl disulfide (1.392 g). Fractions 35–38, 49–51, and 66–67 were combined and concentrated, providing the trithioorthoformate **1** (0.325 g, 0.8 mmol, 13%). Fractions 54–57 and 69–71 were combined, giving *p*-tolyl thiolformate (0.038 g, 0.3 mmol, 4%). Fractions 75–79 gave the bissulfide sulfone **4** (0.083 g, 0.2 mmol, 3%). Fractions 81–87 were combined and concentrated, yielding phenyl methyl sulfone (0.368 g).

Reaction of sulfone-sulfonic acid ester 9 with p-*tolyl disulfide*

A solution of the sulfone-sulfonic acid ester **9** (1) (1.021 g, 4.0 mmol) in dimethyl sulfoxide (DMSO, 10 mL) was added dropwise to a slurry of sodium hydride (0.188 g, 7.8 mmol) in DMSO (20 mL). Upon completion of that addition, *p*-tolyl disulfide (0.971 g, 3.9 mmol) was added and the reaction mixture stirred at ambient temperature for 3 days.

Standard work-up *without base extraction* furnished crude sulfone-sulfide-sulfonic acid ester **10** (1.922 g). The crude product was chromatographed on silica gel (170 g) employing chloroform elution (100 mL fractions). Fractions 7–13 gave clean **10** (1.344 g, 3.6 mmol, 88%). Recrystallized **10** had mp 87.9–88.7°C; ir ($CHCl_3$): 1390, 1345, and 1150 cm^{-1}; nmr ($CDCl_3$) δ: 7.65 (2H, d), 7.36 (5H, s), 7.16 (2H, d), 5.26 (1H, s), 3.26 (3H, s), and 2.30 (3H, s); ms *m/e*, $M^{\cdot+}$ − 1: 371 (6%), 228 (70%), 135 (76%), 123 (100%). Anal. calcd. for $C_{15}H_{16}O_5S_3$: C 48.36, H 4.32; found: C 48.08, H 4.27.

Reaction of dimethyl sulfone with p-*tolyl disulfide*

A solution of *p*-tolyl disulfide (3.141 g, 12.7 mmol) in HMPA (10 mL) (2) was added to a slurry of sodium hydride (0.309 g, 12.8 mmol) in HMPA (10 mL). Dimethyl sulfone (0.604 g, 6.4 mmol) in HMPA (10 mL) was added and the reaction mixture stirred at ambient temperature for 1 h 10 min. Standard work-up furnished a crude yellow oil (3.006 g).

Crude product was chromatographed on silica gel (300 g) employing carbon tetrachloride (60 100-mL fractions), then chloroform (100-mL fractions), for elution. Fractions 9–17 were combined and concentrated, giving *p*-tolyl disulfide (1.176 g). Fractions 65–67 yielded trithioorthoformate **1** (0.042 g). Fractions 88–91 afforded the bissulfide sulfone **12** (0.442 g, 1.3 mmol). Recrystallized **12** had mp 85.3–86.5°C; ir ($CHCl_3$): 1320 and 1150 cm^{-1}; nmr ($CDCl_3$) δ: 7.55 (4H, d), 7.20 (4H, d), 5.00 (1H, s), 3.10 (3H, s), and 2.40 (6H, s); ms *m/e* 259 (36%), 137 (63%), and 91 (100%). Anal. calcd. for $C_{16}H_{18}O_2S_3$: C 56.77, H 5.35; found: C 56.71, H 5.39. Fractions 92–97 furnished a mixture of **12** (0.209 g, 0.6 mmol) and the sulfide-sulfone **11** (0.073 g, 0.3 mmol, 5%). The identity of **11** was established by adding authentic material (7), which enhanced the appropriate signals in the nmr spectrum of the mixture.

Reaction of bissulfide sulfone 12 with p-*tolyl mercaptan*

A solution of *p*-tolyl mercaptan (0.138 g, 1.1 mmol) in HMPA (5 mL) (2) was added dropwise to a slurry of sodium hydride (0.035 g, 1.4 mmol) in HMPA (10 mL). After stirring for 5

min, the bissulfide sulfone **12** (0.499 g, 1.4 mmol) was added. The reaction mixture was stirred for 1 h 10 min and subjected to standard work-up, which provided a yellow oil (0.588 g).

The crude product was chromatographed on silica gel (120 g) employing carbon tetrachloride elution (15 100-mL fractions) followed by chloroform elution (100 mL fractions). Fractions 3–7 were combined and concentrated, furnishing impure *p*-tolyl disulfide. Recrystallization gave clean *p*-tolyl disulfide (0.113 g, 0.4 mmol, 31%). Fractions 27–35 were combined and concentrated, affording a mixture of the bissulfide sulfone **12** (0.303 g, 60%) and the sulfone sulfide **11** (0.098 g, 0.4 mmol, 30%) (7).

Preparation of p-*chlorosulfonylphenyl methanesulfonate*

4-(Methylmercapto)phenyl methanesulfonate (2.030 g, 9.3 mmol) (1) was suspended in glacial acetic acid (25 mL) and water (3 mL). Cl_2 (ca. 200 mL/min) was bubbled through the reaction mixture for 10 h. Ice/water cooling was used as necessary to maintain the reaction temperature below 30°C.

Water (50 mL) was added and the resultant mixture washed with chloroform (three 50-mL aliquots). The combined organic layers were washed with 2.5% W/V sodium hydroxide (two 50-mL aliquots). The organic layer was dried and concentrated.

The residue was chromatographed on silica gel (200 g) employing 1:1 methylene chloride – carbon tetrachloride (100-mL fractions) for elution. Fractions 9–11 were combined and concentrated, affording *p*-chlorophenyl methanesulfonate (0.128 g, 0.6 mmol, 7%). Upon recrystallization it was shown to be identical to authentic material by nmr, ir, mp, and mixture mp. Fractions 12–19 were combined, yielding *p*-chlorosulfonylphenyl methanesulfonate (0.923 g, 3.4 mmol, 37%). Recrystallized sulfonyl chloride sulfonate ester had mp 83–84.5°C; ir ($CHCl_3$): 1382, 1365, 1182, and 1152 cm^{-1}; nmr ($CDCl_3$) δ: 8.35 (2H, d), 7.70 (2H, d), and 3.33 (3H, s).

Preparation of p-*(2,4,6-tribromophenoxysulfonylphenyl) methanesulfonate* ***15****a*

Unchromatographed *p*-chlorosulfonylphenyl methanesulfonate (2.161 g) was added in small portions to a cooled solution of 2,4,6-tribromophenol (1.993 g) and dry triethylamine (0.602 g) in dry pyridine (50 mL). The reaction mixture was stirred at ambient temperature for 5 days.

Chloroform (100 mL) was added and the resultant mixture washed with 2.5% HCl (100-mL aliquots) until the aqueous pH remained acidic. The organic layer was washed with 2.5% NaOH (100 mL), dried ($MgSO_4$), and concentrated. Crude product was dissolved in hot methanol (90 mL) and half of the methanol distilled off. The concentrated solution was stored at room temperature overnight. Bissulfonate **15***a* (2.413 g) had mp 121.1–121.7°C; ir ($CHCl_3$): 1380 (br), 1190, 1180, and 1155 cm^{-1}; nmr ($CDCl_3$) δ: 8.20 (2H, d), 7.80 (2H, s), 7.60 (2H, d), and 3.30 (3H, s); ms *m/e*, $M^{\cdot+}$ + 4: 568 (56%), 566 (65%), 564 (65%), 562 (52%), 333 (53%), 331 (64%), 329 (64%), 327 (54%), 235 (84%), 171 (81%), 141 (100%), and 79 (76%). Anal. calcd. for $C_{13}H_9Br_3O_6S_2$: C 27.63, H 1.60; found: C 27.64, H 1.51.

Preparation of p-*methylsulfonylphenyl benzyl sulfide*

Benzyl mercaptan (3.3 mL, 26 mmol) in HMPA (10 mL) (2) was added dropwise to a slurry of sodium hydride (0.639 g, 26.6 mmol) in HMPA (30 mL). Upon completion of the addition, *p*-chlorophenyl methyl sulfone (4.797 g, 25.2 mmol) was added and the reaction mixture stirred at ambient temperature for 1 h 10 min.

Standard work-up furnished crude *p*-methylsulfonylphenyl benzyl sulfide, which was recrystallized from methanol, affording clean sulfone sulfide (6.134 g, 22.0 mmol, 87%). *p*-Methylsulfonylphenyl benzyl sulfide had mp 128–130°C; ir ($CHCl_3$): 1320 and 1155 cm^{-1}; nmr ($CDCl_3$) δ: 7.76 (2H, d), 7.30 (2H, d), 7.28 (5H, s), 4.16 (2H, s), and 3.00 (3H, s); ms *m/e*, $M^{\cdot+}$: 278 (14%) and 91 (100%). Anal. calcd. for $C_{14}H_{14}O_2S_2$: C 60.40, H 5.06; found: C 60.21, H 5.15.

Preparation of p-*chlorosulfonylphenyl methyl sulfone*

p-Methylsulfonylphenyl benzyl sulfide (0.965 g, 3.4 mmol) was suspended in glacial acetic acid (35 mL) and water (3 mL). Cl_2 (ca. 200 mL/min) was bubbled into the reaction mixture for 45 min. Ice/ water cooling was employed as necessary, to maintain the temperature below 30°C.

Chloroform (100 mL) was added and the reaction mixture washed with 2.5% W/V sodium hydroxide (two 50-mL aliquots). The organic layer was dried ($MgSO_4$) and concentrated. The residue was dissolved in dry refluxing carbon tetrachloride (150 mL) and 50 mL of solvent distilled off. Clean crystals of the sulfone-sulfonyl chloride (0.650 g, 2.5 mmol, 74%) were obtained. The sulfone-sulfonyl chloride had mp 166.5–167.3°C; ir ($CHCl_3$): 1360, 1175, and 1158 cm^{-1}; nmr ($CDCl_3$) δ: 8.06 (4H, s) and 2.83 (3H, s); ms *m/e*, $M^{\cdot+}$ + 2: 256 (8%), 254 (18%), and 219 (100%). Anal. calcd. for $C_7H_7ClO_4S_2$: C 33.00, H 2.77; found: C 32.73, H 2.71.

Preparation of p-*(2,4,6-tribromophenoxysulfonylphenyl) methyl sulfone* ***15****b*

A solution of 2,4,6-tribromophenol (1.296 g, 3.9 mmol) and triethylamine (0.405 g, 4.0 mmol) in pyridine (50 mL) was cooled with an ice/water bath. *p*-Chlorosulfonylphenyl methyl sulfone (0.998 g, 3.9 mmol) was added in small portions over 5 min. The reaction mixture was allowed to return to ambient temperature and stirred for 7 days.

Chloroform (100 mL) was added and the resultant mixture washed with 2.5% HCl (100-mL portions) until the aqueous pH remained acidic. The organic layer was extracted with 2.5% sodium hydroxide (100 mL), dried ($MgSO_4$), and concentrated.

Crude sulfone sulfonate **15***b* was recrystallized from methanol (1100 mL), affording clean product (1.238 g, 2.2 mmol, 56%). Recrystallized **15***b* had mp 228.0–228.4°C; ir (KBr): 1400, 1310, 1195, 1180, and 1155 cm^{-1}; nmr ($CDCl_3$) δ: 8.16 (4H, s), 7.66 (2H, s), and 3.10 (3H, s); ms *m/e*, $M^{\cdot+}$ + 6: 552 (0.7%), 550 (1.3%), 548 (1.5%), 546 (0.4%), 219 (50%), 155 (77%), and 76 (100%). Anal. calcd. for $C_{13}H_9Br_3O_5S_2$: C 28.43, H 1.65; found: C 28.52, H 1.51.

Reaction of ***15****a or* ***15****b with NaH–HMPA*

15*a* and **15***b* were each reacted with sodium hydride as described below for the bissulfonate **15***a*.

The bissulfonate ester 15*a* (1.008 g, 1.78 mmol) in HMPA (2) (10 mL) was added dropwise to a slurry of sodium hydride (0.172 g, 7.1 mmol) in HMPA (20 mL). The reaction mixture was stirred at ambient temperature for 2 h 10 min.

The reaction mixture was poured into water (50 mL) and

10% HCl (10 mL). The resultant mixture was extracted with diethyl ether (three 50-mL aliquots). This extractive procedure was repeated twice, affording 2,4,6-tribromophenol (0.547 g, 1.73 mmol, 97%).

The trithioorthoformate reaction with ***15****a or* ***15****b*

15*a* and **15***b* were each reacted with *p*-tolyl mercaptan and *p*-tolyl disulfide as described below for the bissulfonate **15***a*.

p-Tolyl mercaptan (0.229 g, 1.8 mmol) in HMPA (2) (10 mL) was added dropwise to a slurry of sodium hydride (0.169 g, 7.0 mmol) in HMPA (20 mL). Five minutes after completion of the addition, *p*-tolyl disulfide (0.439 g, 1.8 mmol) was added. The bissulfonate ester **15***a* (1.000 g, 1.8 mmol) was added and the reaction mixture stirred for 2 h 10 min.

Standard work-up provided crude product (1.466 g). Crude product was chromatographed on silica gel (150 g) employing carbon tetrachloride elution (100-mL aliquots). Fractions 4–7 were combined and concentrated, furnishing *p*-tolyl disulfide (0.191 g). Fractions 13–19 were combined and concentrated, yielding 2,4,6-tribromophenol (0.506 g, 1.5 mmol). Fractions 23–37 were combined and concentrated affording the trithioorthoformate **1** (0.151 g, 0.4 mmol).

Acknowledgements

The authors acknowledge technical assistance from L. Precedo and C. Hurst. Mass spectra were run by D. Drummond at the University of New Brunswick. We are grateful to Mount Allison University for financial support.

References

1. J.C. Baum, K.A. Durkin, L. Precedo, S.B. O'Blenes, J.E. Goehl, R.F. Langler, G.K. MacCormack, and L.L. Smith. Can. J. Chem. **69**, 2127 (1991), and references therein.
2. J.C. Baum, B.E. Black, L. Precedo, J.E. Goehl, and R.F. Langler. Can. J. Chem. **73**, 444 (1995).
3. J.F. King and M. Aslam. Can. J. Chem. **57**, 3278 (1979).
4. (*a*) K. Ogura, K. Ohtsuki, M. Nakamura, N. Yahata, K. Takahashi, and H. Iida. Tetrahedron Lett. **26**, 2455 (1985); (*b*) Y. Murata, K. Inomata, H. Kinoshita, and H. Kotake. Bull. Chem. Soc. Jpn. **56**, 2539 (1983).
5. K.Ogura, T. Tsuruda, K. Takahashi, and H. Iida. Tetrahedron Lett. **27**, 3665 (1986).
6. G.L. Roof and W.P. Tucker. J. Org. Chem. **33**, 3333 (1968).
7. D.G. Kay, R.F. Langler, and J.E. Trenholm. Can. J. Chem. **57**, 2185 (1979).
8. R.F. Langler and J.L. Steeves. Aust. J. Chem. **47**, 1641 (1994).
9. (*a*) P. Rumpf and J. Sadet. Bull. Soc. Chim. Fr. 447 (1958); (*b*) R.R. Coats and D.T. Gibson. J. Chem. Soc. 442 (1940).
10. F.G. Bordwell. Acc. Chem. Res. **21**, 456 (1988).
11. J.F. King and R. Rathore. *In* The chemistry of sulphonic acids, esters and their derivatives. *Edited by* S. Patai and Z. Rappoport. Wiley, Chichester. 1991. pp. 697–766.
12. (*a*) J.F. King and R.P. Beatson. Tetrahedron Lett. 973 (1975); (*b*) M.B. Davy, K.T. Douglas, J.S. Loran, A. Steltner, and A. Williams. J. Am. Chem. Soc. **99**, 1196 (1977); (*c*) C.J.M. Stirling. Acc. Chem. Res. **12**, 198 (1979); (*d*) M.J. Pregel and E. Buncel. J. Chem. Soc. Perkin Trans. 2, 307 (1991).
13. (*a*) H. Pritzkow, K. Rall, S. Reimann-Andersen, and W. Sundermeyer. Angew. Chem. Int. Ed. Engl. **29**, 60 (1990); (*b*) T. Kempe and T. Norin. Acta Chem. Scand. Ser B: **28**, 609 (1974); (*c*) U. Rheude and W. Sundermeyer. Chem. Ber. **118**, 2208 (1985); (*d*) R. Allmann, W. Hanefeld, M. Krestel, and B. Spangenberg. Angew. Chem. Int. Ed. Engl. **26**, 1133 (1987); (*e*) J.F. King and T. Durst. Can. J. Chem. **44**, 819 (1966); (*f*) J.F. King, E.G. Lewars, and L.T. Danks. Can. J. Chem. **50**, 866 (1972).
14. J.C. Baum, J. Bolhassan, R.F. Langler, P.J. Pujol, and R.K. Raheja. Can. J. Chem. **68**, 1450 (1990).
15. K.A. Durkin, R.F. Langler, and N.A. Morrison. Can. J. Chem. **66**, 3070 (1988).
16. J.J.P. Stewart. J. Comput. Chem. **10**, 209 (1989).
17. J.S. Grossert and R.F. Langler. Can. J. Chem. **55**, 407 (1977).
18. (*a*) W. Stevens and A. van Es. Recl. Trav. Chim. Pays-Bas, **83**, 863 (1964); (*b*) P.C. Bax and W. Stevens. Recl. Trav. Chim. Pays-Bas, **89**, 265 (1970); (*c*) P. Strazzolini, A.G. Giumanini, and S. Cauci. Tetrahedron, **46**, 1081 (1990).

Furo-fused 2*H*-chromenes: synthesis and photochromic properties

Jean-Luc Pozzo, André Samat, Robert Guglielmetti, Vladimir Lokshin, and Vladimir Minkin

Abstract: New photochromic chromenes annulated with a furan ring have been synthesized. Thus, suitable heterocyclic phenols react with different propargylic alcohols in acidic medium to give the corresponding ethers, which cyclize into benzopyrans by thermal Claisen rearrangement. This synthetic approach was found to lead to a mixture of linear and angular chromenes that is strictly related to the nature of the phenol. However, regiospecificity could be obtained by reacting β-phenylcinnamaldehyde, in refluxing aprotic nonpolar solvents, with titanium(IV) salts of the former phenols. Electrocyclization of intermediately generated *o*-quinoid structures occurs on the α position towards the heterocyclic junction. All compounds exhibit photochromic behavior at room temperature. Furo-fused benzopyrans are particularly interesting with respect to naphthopyran parents in view of the bathochromically shifted and broadened absorption spectra of photoinduced forms. This trend is confirmed by the spectral data of several heterocyclospiro(7*H*-furo[3,2-*f*] chromenes). The achievable color depends significantly on the relative position of annulation on the chromenic moiety and substitution on the sp^3 carbon atom.

Key words: photochromism, heterocycle, regiospecificity, 2*H*-chromene, furan.

Résumé : De nouveaux chromènes photochromiques annélés par un noyau furanique, ont été synthétisés. Ils sont obtenus par réaction de phénols hétérocycliques et d'alcools propargyliques en milieu acide. Les éthers correspondants intermédiairement formés se cyclisent en composés benzopyraniques selon un réarrangement thermique de Claisen. Cette approche synthétique conduit à l'obtention d'un mélange de régioisomères angulaires et linéaires. La régiospécificité est obtenue, en faisant réagir les sels de titane(IV) de ces phénols avec le β-phénylcinnamaldéhyde au reflux de solvants aprotiques apolaires. L'électrocyclisation des *o*-quinoneallides n'est réalisée que sur la position en α de la jonction hétérocyclique. Tous les composés obtenus manifestent à température ambiante des propriétés photochromiques qui dépendent significativement du type de régioisomère et de la substitution sur le carbone sp^3. L'annelation du motif benzopyranique par un noyau furanique conduit à un élargissement significatif et à un déplacement bathochromique important du spectre visible par rapport aux naphtopyranes correspondants. L'allure des spectres d'absorption dans le visible des formes ouvertes photoinduites de plusieurs hétérocyclospiro(7*H*-furo[3,2-*f*]chromènes) confirme cette observation.

Mots clés : photochromisme, hétérocycle, régiospécificité, 2*H*-chromène, furane.

Introduction

2*H*-1Benzopyrans (or 2*H*-chromenes) are an important family of oxygenated heterocycles (1) particularly attractive because of their photochromic properties. Indeed, 2*H*-chromenes undergo a reversible ring opening of the pyran cycle (2). The Csp^3—O bond is cleaved by UV irradiation leading to opened coloured forms ("photomerocyanines"). The molecule reverts to its original form via a thermal pathway (Scheme 1).

Over several years 2*H*-chromenes were not considered to be interesting photochromic compounds for applications, and intensive research studies were preferably devoted to their spiroheteroanalogs (spiropyrans) (3). Indeed, the first described chromenes, 2,2-dimethyl-[2*H*]-chromenes and their benzoannulated derivatives (naphthopyrans), showed photochromic behavior only at low temperature (2) and, moreover, led to undesirable by- products (4). In fact, interest in research in this field developed only recently with the demand for industrial applications of materials that undergo variable optical absorption. For this purpose, the desirable properties could be summarized as follows: high efficiency for coloring in the near-ultraviolet region, low quantum yield for bleaching with visible light, and fast thermal fading at ambient temperatures. These kinds of requirements have led to several structural modifications in the chromene series. Particularly, improvement of photochromic properties was obtained by the annulation of the chromenic ring in the 7,8-positions (5), by appropriate substitutions of the naphthopyran cycle (6, 7), replacing the alkyl groups on the Csp^3 carbon atom by cyclopropyl groups (8), spiroadamantyl groups (9), and, overall, by aryl groups (10, 11). This last kind of substitution is nearly indispensable for observing good photochromic properties.

Our interest in benzopyran chemistry has been focused on the design and study of heterocyclo-fused analogues, in order

Received February 6, 1996.

J.-L. Pozzo, A. Samat, and R. Guglielmetti.[1] Équipe de Recherche N° 158 du Centre national de la recherche scientifique, Faculté des Sciences de Luminy, 13288 Marseille Cédex 9, France.
V. Lokshin and V. Minkin. Institute of Physical and Organic Chemistry, av. Stachky 194/3, Rostov-on-Don, 344104 Russia.

[1] Author to whom correspondence may be addressed.

Scheme 1.

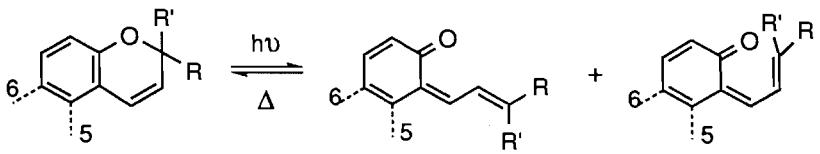

Scheme 2.

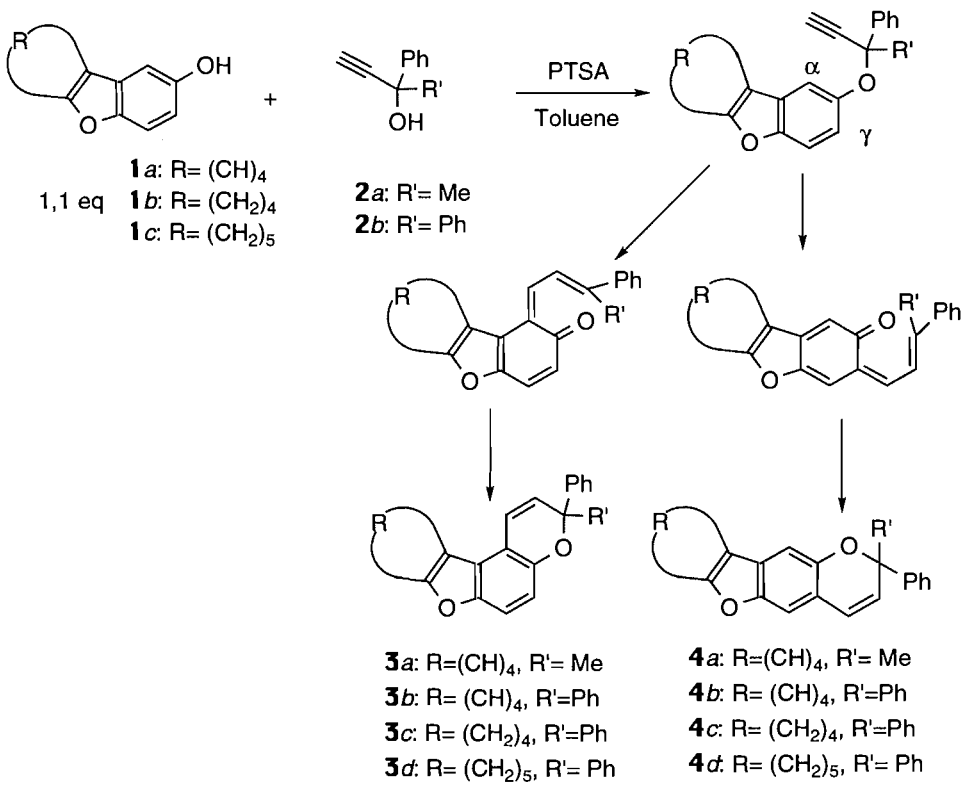

to modify the photochromic parameters (12, 13). Thus, the purpose of the present work was to introduce a furan ring in the C5-C6 position and to investigate its role with respect to photochromic properties and especially to the shape of absorption spectra in the visible region, for useful industrial applications.

Results and discussion

There has long been an interest in the chemistry of 2,2-disubstituted-[2*H*]-chromenes as a consequence of their widespread natural occurrence. These compounds can be obtained through a multistep sequence from chromanones, involving the Kabbe synthesis (14, 15). This method is not readily applicable to 2,2-diaryl analogues (10) and, alternatively, a thermal cyclization of propargylaryl ethers can be considered (16–18). This approach (method A), which appears particularly attractive because of availability of the starting phenols and chloro- or hydroxyalkynes, has been useful in synthesizing diaryl-naphthopyrans (9). The reaction is considered to proceed via a Claisen-like [3,3]-sigmatropic rearrangement which is followed by enolization and a [1,5]-sigmatropic shift. An electrocylization completes the process (19).

The benzopyran derivatives were prepared by heating the appropriate hydroxy-benzofuran with 1,1-diphenylpropyn-1-ol or 3-phenylbutyn-3-ol in an apolar organic solvent, such as toluene or xylene, in the presence of an acid catalyst under mild reaction conditions (Scheme 2). Sufficient time to complete the reaction varies between 2 and 6 h. Mixtures of the desired compounds were initially purified by flash chromatography. Nevertheless the "chromenylation" from furo-fused phenols is not markedly regiospecific since the two possible chromenes were obtained as outlined in Scheme 2. The difference of polarity being very weak, the chromenes were eluted in the same fraction by flash chromatography. The mixtures were recrystallized several times with appropriate solvents so that we were able to isolate pure samples of all angular chromenes (**3***a–d*), which were then fully characterized by electronic spectroscopy and ^{1}H and ^{13}C NMR. Some minor linear regioisomeric chromenes obtained from 2-hydroxydibenzofuran **1***a*, i.e., compounds **4***a*, *b*, were isolated after such specific recrystallization because of a sufficient amount in the starting mixture.

Regioisomer distribution varies from 60/40 to 90/10 as listed in Table 1. The ratio between both isomers, **3** and **4**, was

Table 1. Reaction conditions for the preparation of furofused 2*H*-chromenes.

Phenolic substrate[a]	Method[b]	Reagents	Yield[c](%)	Regioisomer distribution[c](%)	Compound	Melting point (°C)
1*a*: R = $(CH)_4$	**A**	**2***a*	46[c]	61	**3***a*	155
				39	**4***a*	154
	A	**2***b*	62[c]	64	**3***b*	151
				36	**4***b*	158
	B	**5**	39[d]	100	**3***b*	151
1*b*: R = $(CH_2)_4$	**A**	**2***b*	26[c]	88	**3***c*	183
				12	**4***c*[f]	—
	B	**5**	17[d]	100	**3***c*	183
1*c*: R = $(CH_2)_5$	**A**	**2***b*	42[c]	90	**3***d*	152
				10	**4***d*[f]	—
	B	**5**	31[d]	100	**3***d*	152

[a]See scheme 2.
[b]Method **A**: phenolic substrate and propargylic alcohol; Method **B**: phenolic substrate/ Ti^{IV} / β-phenylcinnamaldehyde.
[c]Calculated on mixture of regioisomers purified by flash chromatography and based on propargylic alcohol.
[d]Calculated on pure isolated compound based on β-phenylcinnamaldehyde.
[e]Determined by HPLC.
[f]Not isolated as a pure fraction.

Fig. 1. ^1H NMR spectrum (250 MHz, $CDCl_3$) of the mixture **3***a* + **4***a*.

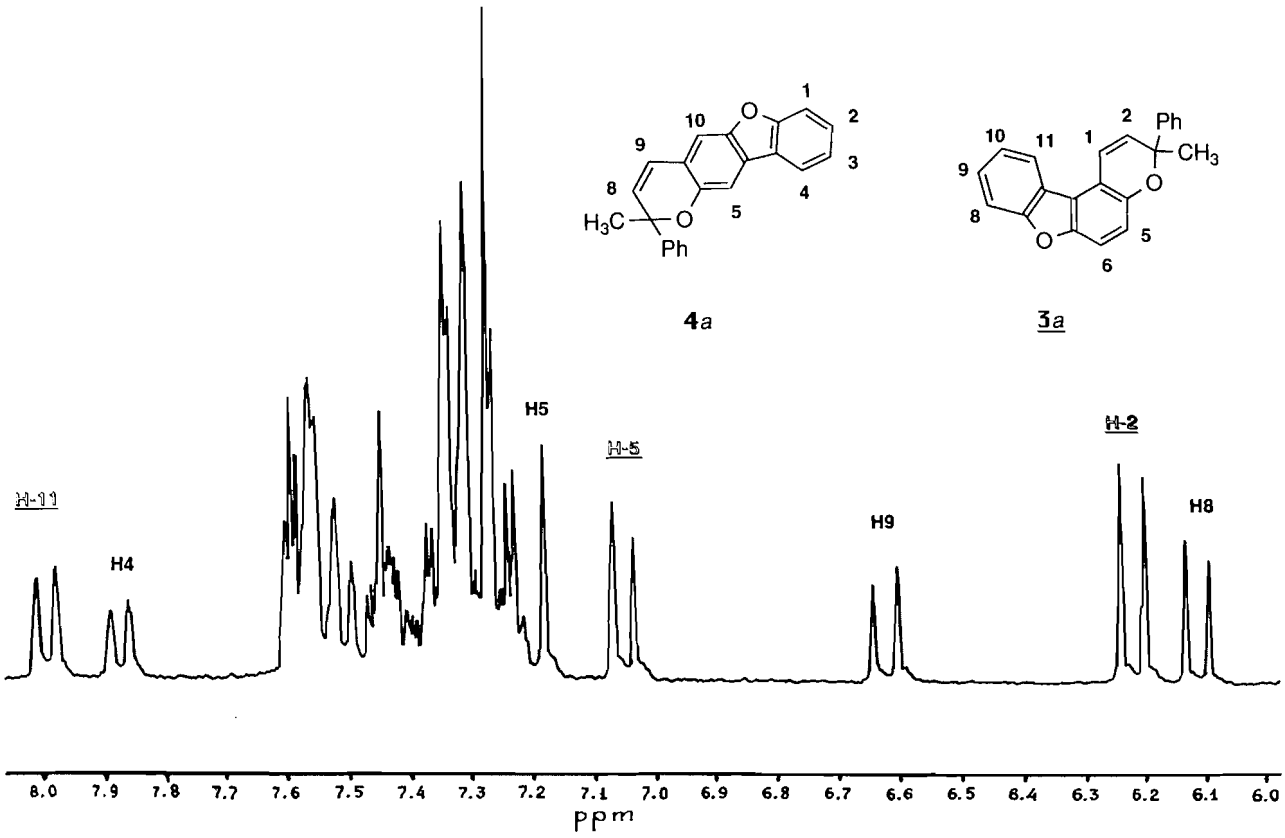

determined by HPLC using a reverse-phase C18 column and electron spectroscopy. Their structures were elucidated by NMR spectroscopy and allow us to conclude that angular chromene predominates in all cases. Indeed, both regioisomers, angular and linear chromenes, are readily distinguishable in the mixture, using ^1H NMR, by comparison with pure regioisomers. For example, the spectrum of the angular isomer (**3***a*) displayed two doublets centred, respectively, at δ 7.03 and 7.28 with a coupling constant of 8.6 Hz, each integrating for one proton and assigned to the protons H-5 and H-6 (see Fig. 1) of the ring directly linked to the pyran moiety, whereas the spectra of the other possible chromene (**4***a*) displayed two

Fig. 2. ^{1}H NMR spectrum (250 MHz, $CDCl_3$) of **4***a*.

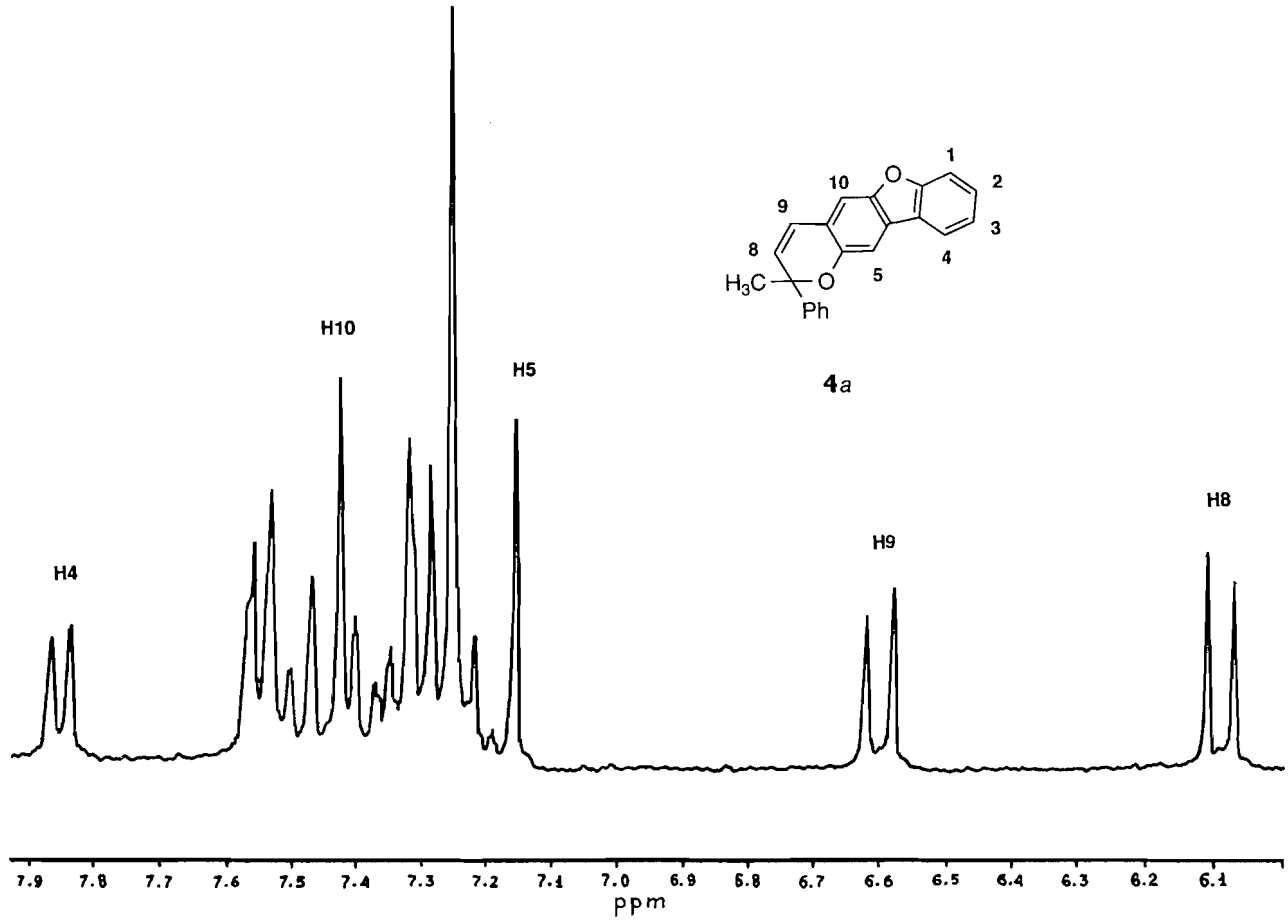

singlets centered at 7.16 and 7.43 that were assigned to H-5 and H-10, respectively (see Figs. 1 and 2). Furthermore, the chemical shift of the protons localized on the pyran ring are also characteristic and could easily be detected, being shielded with respect to the whole aromatic region. For the angular chromene, the ^{1}H NMR spectrum displayed a doublet accounting for one proton, at δ 6.19, with a coupling constant of 9.85 Hz, which is typical for the proton α (H-2) to the quaternary carbon of the pyran ring. An upfield shift, in comparison, is observed for the linear chromene as shown by the chemical shift of the proton H-8 (6.08 ppm). The same effects and trends are observed for the other compounds **3***b–d* and **4***b–d*, with a downfield shift due to the presence of a second phenyl group.

When starting from the naphthol derivatives, the synthetic route used has been reported to proceed in a regiospecific manner, leading to angular chromenes (10). With benzofuranic phenols, the lack of regiospecificity could be a consequence of the less marked difference of electron density at the aromatic termini of the [3,3] rearrangement. In fact, the ratio between angular and linear isomers varies as a function of starting phenolic substrates rather than of the propargylic compound. To understand these results, molecular modelling using semiempirical calculations was performed using the PM3 method. This showed, with no discrepancy, that there is no dramatic change of steric hindrance between the two possible cyclizations. Whatever the starting furo-fused phenol, the formation of one isomer could not be favoured by steric considerations.

Scheme 3.

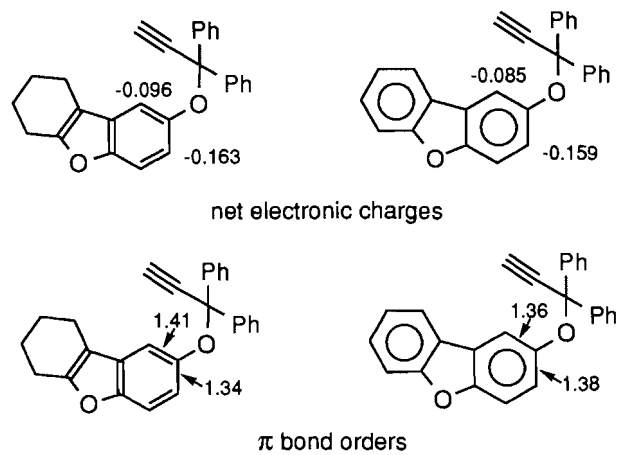

The stability of the transition state could play a significant role in determining the orientation of the final product. The different reactivities observed between the phenols could not be totally explained by charge repartition calculations on phenols or on their corresponding propargylic ethers. On the other hand, the calculated π-bond orders show a marked π-bond character between the C-4 and C-5 atoms rather than between the C-5 and C-6 atoms (Scheme 3) in the case of the cycloalkyl compound, whereas no difference was found for the corre-

Scheme 4. Mechanistic pathway for method B.

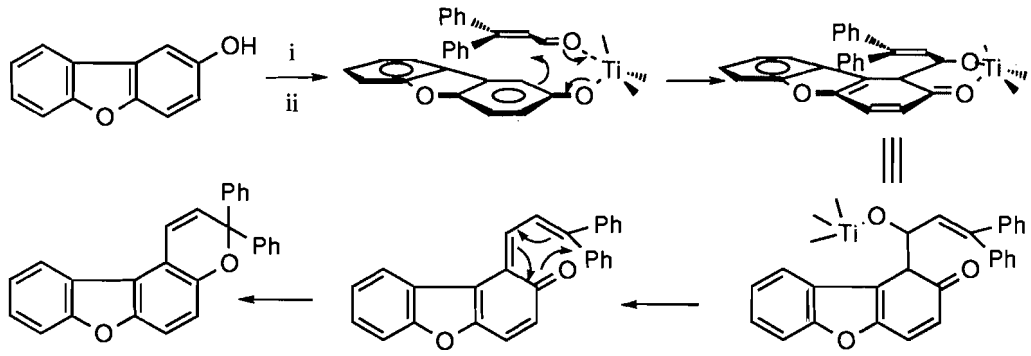

Scheme 5.

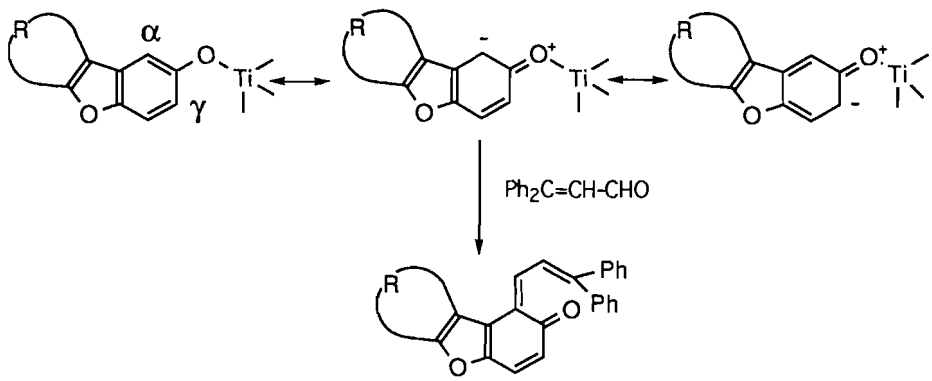

sponding bonds of the 2-propargylicdibenzofuran derivative. According to the proposed reaction mechanism of this intramolecular cyclization, this could lead to the observed mixtures of linear and angular chromenes.

Despite the report that this synthetic approach A is broadly applicable, it suffers, in our case, from the disadvantage of difficult and lengthy purifications of both isomers. Alternatively, the condensation of α,β-unsaturated carbonyl compounds with phenols has received much attention as a route to chromenes (1, 20). Another approach to obtain the desired compounds is to react α,β-unsaturated aldehydes with titanium(IV) salts of phenols (method B), as previously described for 2,2-dialkyl chromenes (21). However, the examples cited therein do not ensure the generality of this route, particularly concerning the furo-fused 2,2-diaryl-[2*H*]-chromenes.

The reaction (Scheme 4) involves the formation of the titanium(IV) salt of the heterocyclic phenol by azeotropic distillation of the ethanol formed. Then β-phenyl cinnamaldehyde is added and the reaction mixture is refluxed for ca. 3 h in toluene. *o*-Quinoid intermediates are generated in situ but are never directly observed, presumably due to their easy cyclization to benzopyran products. In our case, better yields were found using a stoichiometric amount of β-phenylcinnamaldehyde **5**, hydroxybenzofurans, and titanium tetraethoxide (22, 23). New compounds were initially purified by flash chromatography. The remaining solids were recrystallized from appropriate solvents and fully characterized by ^{1}H and ^{13}C NMR and electron spectroscopy. Corresponding yields are listed in Table 1. With this synthetic pathway, no trace of linear chromene was detected. An HPLC chromatogram of the crude reaction product and an ^{1}H NMR study show without doubt that this method affords only the angular chromene. This regioselectivity could be explained by the less carbanionic character at C-γ relative to C-α, arising from resonance stabilization (Scheme 5). The α,β-unsaturated carbonyl compound and heteroannulated phenolic substrate are each coordinated by the transition metal, which leads to univocal intramolecular reaction within the complex.

The approach B to pyran ring formation, despite more difficult work-up than with method A, appears to be the preferred means of preparing the title compounds regiospecifically.

Photochromic properties

All the described chromenes **3***a–d* and **4***a*, *b* exhibit photochromic behavior at room temperature in toluene. The maxima of absorption in the visible spectra of the "photomerocyanines," with an accuracy of 2 nm, and the rate constants of thermal bleaching (ring closure) k_Δ were determined using flash photolysis coupled to a spectrometer. The "colorability" is a function of quantum yield of coloration and the molar absorptivity of the colored species (24) and is evaluated by monitoring the absorbance A_0 at λ_{max} and λ_{sh} immediately after the flash. The experimental conditions are reported in the corresponding section. The photochromic properties for compounds **3***a–d* and **4***a*, *b* are listed in Table 2 and are compared with naphtho[2,1-b]pyrans **6***a*, *b* (10, 25) previously synthesized (Scheme 6).

Scheme 1 gives a very simple picture of photochromic equi-

Table 2. Spectrokinetic parameters of chromenes determined at 25°C in toluene (10^{-5} mol L^{-1}).

Compound[a]	λ_{max}[b]	A_0 Colorability	λ_{sh}[c]	A_0 Colorability[c]	$k_\Delta(s^{-1})$ (25°C)
3*a*	401	0.44	500	0.23	34
3*b*	424[d]	0.63	518[d]	0.29	0.21
3*c*	421	0.57	532	0.18	0.05
3*d*	420	0.55	530	0.19	0.05
4*a*	405	0.58	532	0.13	54/5[e]
4*b*	427[f]	0.91	549	0.32	0.58/0.03[e]
6*a*	399	0.29			2.3
6*b*	432	0.52			0.09
7	427	0.95			0.32

[a]See Schemes 2 and 6.
[b]Maximum absorption wavelength (nm).
[c]Shoulder (nm).
[d]There is a bathochromic shift of about 25 nm if a mixture isopentane/isopropanol is used as solvent (cf. Fig. 4).
[e]Two kinetic constants were observed, the most important being underlined.
[f]The most intense absorption band presents two maxima.

Scheme 6.

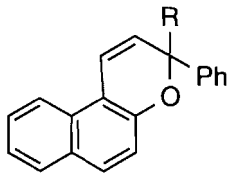

6*a* R= Me
6*b* R= Ph

Scheme 7.

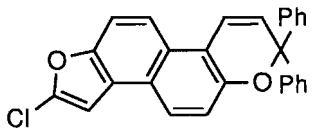

7

librium but the real phenomenon is more complex. For a complete understanding, it is necessary to take into account the electronic structures of open forms as well as their geometries. We are dealing here with different stereoisomers of *cisoid* configuration after the breaking of the C—O bond and of *transoid* configuration after isomerization. The *trans* isomer appears to be more stable because it minimizes the nonbonding interactions. The electronic distribution for photomerocyanines in chromenic series is believed to have mainly a quinoidal character (25). For furo-fused benzopyran, the photomerocyanines obtained by UV irradiation are characterized by a visible absorption spectrum consisting of two maxima. One is observed near 420 nm and the other near 520 nm. Based on the spectral data given in Table 2, such heteroannulation induces important changes in comparison with the corresponding 3,3-diphenyl-[3*H*]-naphtho[2,1-*b*]pyran **6***b*, which exhibits one absorption band centered at 432 nm (Fig. 3). The synthesized

Fig. 3. Electronic absorption spectra of the colored forms of chromenes **6***b* (*a*) and **3***b* (*b*) (isopentane/isopropanol 4:1, $c = 10^{-5}$mol L^{-1}, 77 K).

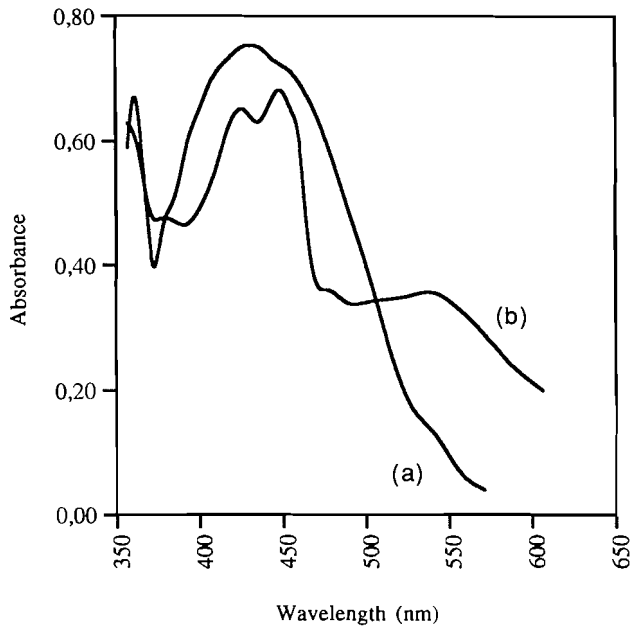

compounds cover a much larger range of wavelengths, as shown in Fig. 3. Because the effects observed for compounds that are benzoannulated or possess a cycloalkyl moiety are very similar, the broadening of the visible absorption spectra is believed to be strictly related to the furan ring annulated directly to the benzopyran part of the molecule, rather than being an extension of the chromophoric system. This assumption is substantiated by spectral data of the furo-fused naphthopyran derivative **7** (Scheme 7), for which the photochromic parameters are very close to those of parent compound **6***b*. For this latter compound, the furan ring induces a slight effect, so it acts as a substituent. Introduction of a second phenyl group on Csp^3 causes a deeper color and a bathochromic shift in the

Scheme 8.

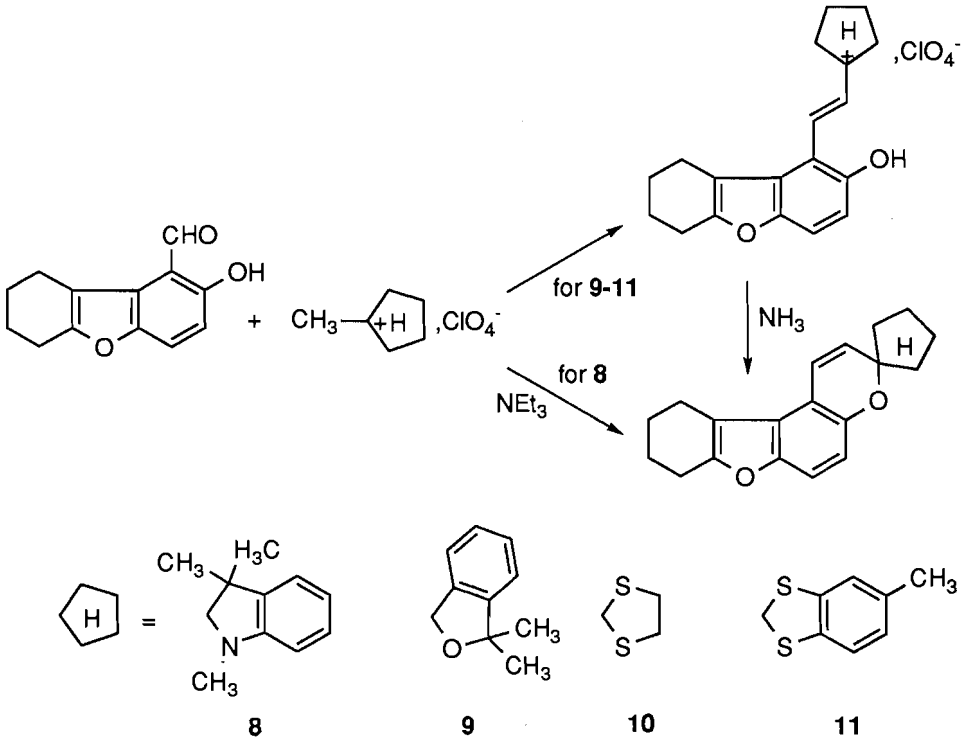

Scheme 9.

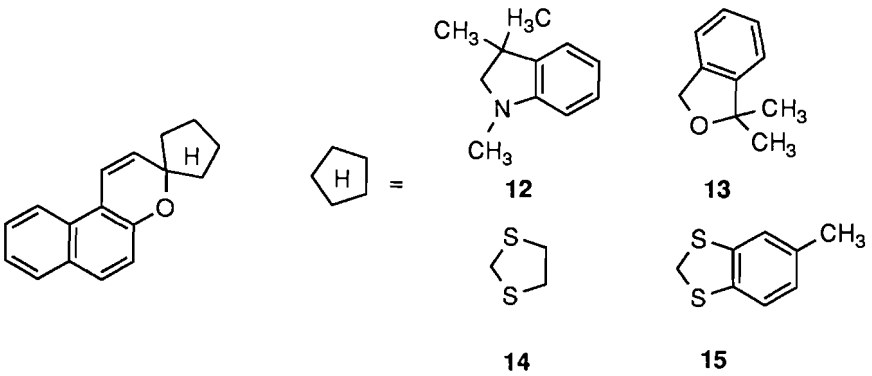

visible spectra of their corresponding activated forms compared to the monoaryl substituted parents. This tends to cause an increase in the quantum yield for coloring in the ultraviolet light region, while providing a much slower thermal fade at ambient temperatures. Interestingly, Table 2 shows that visible absorption of **4***a* and **4***b* undergoes a bathochromic shift compared to that of **3***a* and **3***b*, respectively. The effect on thermal bleaching rates is also important: a significant destabilization of the opened form is observed which could be explained by their electronic structures having a pronounced 2,3-benzoquinoid character. Sometimes two kinetics are observed, attributed to different stereoisomers of the open form, the slower corresponding to the more thermally stable. The properties of this series of 2*H*-chromenes make furo-fused compounds useful in photochromic applications such as lenses.

To evaluate in a more general manner the influence of the annulation by a furan ring on the photoequilibrium parameters, we have prepared and studied some spiro(heterocyclo-furo-fused benzopyran)s (**8–11**) having a five-membered heterocycle as the left moiety. These compounds were obtained through condensation of the corresponding heterocyclic salts with 4-formyl-5-hydroxy-2,3-tetramethylenebenzofuran (26) (Scheme 8) under previously described conditions (27–30). The spiropyrans present two heterocyclic parts linked together by a common tetrahedral sp_3 carbon atom. After irradiation, both halves of the molecule give rise to a conjugated system responsible for a shift of the absorption towards the visible region. Although the structure of the "left" heterocycle has a major influence on the photochromic properties of spiropyrans, the phototransformation takes place on the chromene cycle and we could expect spectral changes for the furo-annulated derivatives similar to those observed in the case of the 2,2-diphenyl-[2*H*]-chromenes. The measured λ_{max} of the colored forms of spiropyrans **8–11**, compared to those of the benzoannelated compounds **12–15** (Scheme 9), are reported in Table 3. We observe that, effectively, whatever the structure

Table 3. Absorption wavelengths (nm) of the colored forms of furo-fused spiropyrans and the corresponding spironaphthopyrans determined in a isopentane/isopropanol mixture (4:1) at 77 K.

Compound[a]	**8**	**12**	**9**	**13**	**10**	**14**	**11**	**15**
λ_{max} at 298 K in toluene	479, 589sh	531[b]	451, 568sh	490[c]	440[d], 570sh[b]	480[c,d]	508, 590sh	545[c]

[a]See Schemes 8 and 9.
[b]From ref. 31.
[c]From ref. 32.
[d]The shift (about 30 nm) compared to the spectrum given in Fig. 4. is due to the solvent change.

Fig. 4. Electronic absorption spectra of the colored forms of spiropyrans **14** (*a*) and **10** (*b*) (isopentane/isopropanol 4:1, $c = 10^{-5}$mol L^{-1}, 77 K).

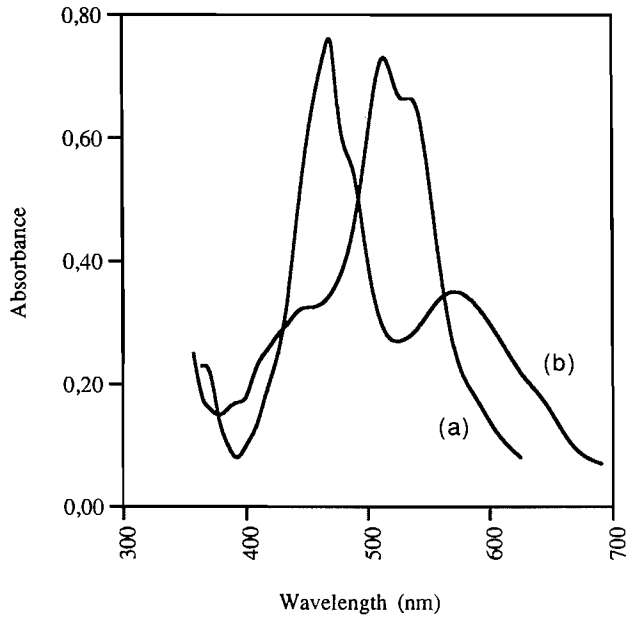

of the "left" heterocycle, the furo-annulation of the spiropyrans leads to the splitting into two bands of the electronic spectra with a significant bathochromic shift (Fig. 4).

Experimental

General experimental procedures

Melting points were determined in capillary tubes on a Buchi 510 apparatus and are uncorrected. ^1H and ^{13}C NMR spectra were recorded in deuterochloroform solution on a Bruker BM 250 or AMX 400 apparatus. UV–visible spectra were recorded on a Beckman DU 7500 on solutions in spectrophotometric grade ethanol (Carlo Erba, ACS quality). Photochromic measurements for chromenes compounds were performed on solutions in spectrophotometric grade toluene (UCB) at 25°C (± 0,2°C), monitored by a thermostat (Huber-ministat) using cylindrical cells having a 5 cm pathlength and a 10 mm section. The fading rate constants were measured at the λ_{max} of absorption of the colored form generated by flash photolysis (xenon tube, 50 μs, 150 J). The initial absorbances (A_0) were given for a standard concentration of 10^{-5} mol L^{-1}.The electronic spectra of colored forms of the chromenes were monitored on a Beckmann DU 7500 diode array spectrometer after irradiation by a Hg lamp (Arquantiel, 500 W). The electronic absorption spectra of spiropyrans at low temperatures were monitored on a Specord UV-visible spectrometer equipped with a thermostated cell. The irradiation source was a Hg DRS-250 lamp with a filter (λ = 313 nm).

The different solvents used were dried on molecular sieve (4Å). Flash chromatographic separations were performed on Merck 60H silica gel (5–40 m). Elemental analyses were performed by Microanalytical Services, University of Aix-Marseille III.

The starting 2-hydroxydibenzofuran was purchased from Aldrich. 5-Hydroxy-2,3-tetramethylenebenzofuran and 5-hydroxy-2,3-pentamethylenebenzofuran were prepared as described earlier (33). 2-Chloro-7-hydroxynaphtho[2,1-*b*]furan was obtained by demethylation, using boron tribromide, of the corresponding methoxy derivative, which was prepared according to the literature procedure (34).

*General procedure for furo-fused 2,2-disubstituted-2*H*-1-benzopyrans*

Method A: Propargylic alcohol (30 mmol) and phenol in slight excess (33–36 mmol) were dissolved in dry toluene (60 mL). Under an atmosphere of nitrogen, a catalytic amount of *p*-toluenesulfonic acid was added to the toluene solution, which was boiled under reflux for 3 h. The reaction solution was cooled and then washed sequentially with dilute (10%) sodium hydroxide and water. The organic layer was separated. The aqueous layer was extracted continuously with methylene chloride. The organic layers were combined, dried over anhydrous magnesium sulfate, and then filtered. The solvent was removed under reduced pressure. The crude product was purified by flash chromatography on silica gel using a 95:5 mixture of pentane and diethyl ether as eluent. The photochromic fractions were collected and the solvent was removed under reduced pressure. The crystalline residue was recrystallized twice from an appropriate solvent (the first time with decolorization by charcoal).

Method B: Under an atmosphere of nitrogen, titanium tetraethoxide (2.4 g, 10.4 mmol) in dry toluene (10 mL) was added over 10 min to the heterocyclic phenol (10.4 mmol) in dry toluene (40 mL). When the addition was complete the reaction mixture was boiled (15 min) and then slowly distilled to remove ethanol. Solvent (20 mL) was collected. The reaction

mixture was allowed to cool to room temperature and β-phenylcinnamaldehyde (2.17 g, 10.4 mmol) in dry toluene (50 mL) was added dropwise. When the addition was complete, the reaction mixture was boiled under reflux (2–5 h), allowed to cool, and poured into 2 M aqueous ammonium chloride solution (100 mL). The organic layer was separated, dried over anhydrous magnesium sulfate, and then filtered. The solvent was removed under reduced pressure. Further purification was done by flash chromatography on silica gel using pentane – diethyl ether (95:5) as eluent. The photochromic fraction was evaporated in vacuo to yield crystalline residue, which was recrystallized from an appropriate solvent.

*3-Methyl-3-phenyl-[3*H*]-benzofuro[3,2-*f*]chromene* **3**a: mp 155°C (from heptane); UV (EtOH) λ_{max} (ε/dm^3 mol^{-1} cm^{-1}): 204(30 540), 231(24 350), 251(15 880), 278(8350), 300(19 880), 312(21 320), 344(6790), and 361(4540) nm; ^{1}H NMR (400 MHz) δ: 1.80 (3H, s, CH_3), 6.19 (1H, d, J = 9.85 Hz, H-2), 7.03 (1H, d, J = 8.7 Hz, H-5), 7.24 (1H, m, H-10), 7.27 (2H, m, H-4′), 7.28 (1H, m, H-6), 7.31 (4H, m, H-3′), 7.36 (1H, d, J = 9.85 Hz, H-1), 7.40 (1H, td, $J_{8,9}$= 7.45 Hz, $J_{9,11}$= 0.9 Hz, H-9), 7.49 (4H, m, H-2′), 7.53 (1H, d, J = 7.5 Hz, H-8), and 7.93 (1H, dd, $J_{10,11}$= 7.45 Hz, $J_{9,11}$= 0.9 Hz, H-11); ^{13}C NMR (100 MHz) δ: 29.9 (CH_3), 79.8 (C-3), 110.9 (C-10), 111.2 (C-8), 116.1 (C-5), 115.8 (C-1a), 119.5 (C-1), 120.3 (C-11b), 121.7 (C-11), 122.1 (C-6), 124.5 (C-11a), 125.3 (C-9), 126.7 (C-2′), 127.4 (C-4′), 127.9 (C-2) 128.0 (C-3′), 147.9 (C-1′), 151.7 (C-4a), and 157.3 (C-7a). Anal. calcd. for $C_{22}H_{16}O_2$: C 84.59, H 5.16; found: C 84.53, H 5.11.

*3,3-Diphenyl-[3*H*]-benzofuro[3,2-*f*]chromene* **3**b: mp 151°C (from hexane–benzene); UV (EtOH) λ_{max} (ε/dm^3 mol^{-1} cm^{-1}): 213(26 600), 228(23 520), 248(16 240), 257(13 410), 280(8680), 301(19 480), 311(20 240), 346(4240), 360(3330), and 369(1920) nm; ^{1}H NMR (400 MHz) δ: 6.39 (1H, d, J = 9.9 Hz, H-2), 7.06 (1H, d, J = 8.8 Hz, H-5), 7.23 (1H, m, H-10), 7.25 (2H, m, H-4′), 7.30 (1H, d, J = 8.8 Hz, H-6), 7.32 (4H, m, H-3′), 7.37 (1H, d, J = 9.9 Hz, H-1), 7.41 (1H, td, $J_{8,9}$= 7.8 Hz, $J_{9,11}$= 1.1 Hz, H-9), 7.49 (4H, m, H-2′), 7.51 (1H, d, J = 7.85 Hz, H-8), and 7.99 (1H, dd, $J_{10,11}$= 7.8 Hz, $J_{9,11}$= 1.1 Hz, H-11); ^{13}C NMR (100 MHz) δ: 82.4 (C-3), 111.7 (C-10), 111.9 (C-8), 115.8 (C-1a), 116.3 (C-5), 120.0 (C-11b), 120.6 (C-1), 122.2 (C-11), 122.6 (C-6), 124.4 (C-11a), 127.0 (C-9), 127.2 (C-2′), 127.7 (C-4′), 128.2 (C-3′), 130.6 (C-2), 144.7 (C-1′), 148.2 (C-6a), 151.3 (C-4a), and 157.0 (C-7a). Anal. calcd. for $C_{27}H_{18}O_2$: C 86.61, H 4.85; found: C 86.60, H 4.78.

*3,3-Diphenyl-8,9-tetramethylene-[3*H*]-benzofuro[3,2-*f*]chromene* **3**c: mp 183°C (from hexane); UV (EtOH) λ_{max} (ε/dm^3 mol^{-1} cm^{-1}): 210(26 990), 255(12 720), 303(16 880), 337(3130), and 347(1700) nm; ^{1}H NMR (400 MHz) δ: 1.86 (4H, m, H-2″, 3″), 2.67 (2H, m, H-1″), 2.77 (2H, m, H-4″), 6.19 (1H, d, J = 9.85 Hz, H-2), 6.79 (1H, d, J = 8.6 Hz, H-5), 7.02 (1H, d, J = 9.85 Hz, H-1), 7.11 (1H, d, J = 8.6 Hz, H-6), 7.26 (2H, m, H4′), 7.30 (4H, m, H-3′), and 7.46 (4H, m, H-2′); ^{13}C NMR (100 MHz) δ: 22.6 (C-2″, 3″), 23.0 (C-1″), 23.7 (C-4″), 81.4 (C-3), 110.9 (C-6), 112.3 (C-5), 113.4 (C-9), 116.2 (C-1a), 120.8 (C-1), 125.4 (C-9a), 127.1 (C-2′), 127.5 (C-4′), 128.1 (C-3′), 128.5 (C-2), 145.2 (C-1′), 147.2 (C-6a), 148.3 (C-4a), and 157.62 (C-8a). Anal. calcd. for $C_{27}H_{22}O_2$: C 85.69, H 5.86; found: C 85.60, H 5.81.

*3,3-Diphenyl-8,9-pentamethylene-[3*H*]-benzofuro[3,2-*f*]chromene* **3**d: mp 152°C (from toluene); ^{1}H NMR (250 MHz) δ: 1.75 (6H, m, H-2″, 3″, 4″), 2.79 (4H, m, H-1″, 5″), 6.13 (1H, d, J = 9.85 Hz, H-2), 6.74 (1H, d, J = 8.65 Hz, H-5), 7.02 (1H, d, J = 8.65 Hz, H-6), 7.12 (1H, d, J = 9.85 Hz, H-1), 7.22 (2H, m, H-4′), 7.30 (4H, m, H-3′), and 7.42 (4H, m, H-2′); ^{13}C NMR (62.5 MHz) δ: 25.1, 28.6, 25.8, 27.9, 29.7 (CH_2), 81.6 (C-3), 110.8 (C-6), 112.5 (C-5), 113.6 (C-9), 116.6 (C-1a), 120.8 (C-1), 125.8 (C-9a), 127.1 (C-2′), 127.3 (C-4′), 128.0 (C-3′), 128.2(C-2), 145.0 (C-1′), 148.0 (C-6a), 148.8 (C-4a), and 157.81 (C-8a). UV (EtOH) λ_{max} (ε/dm^3 mol^{-1} cm^{-1}): 209(35 000), 224sh(20 050), 255(13 440), and 304(15 560) nm. Anal. calcd. for $C_{28}H_{24}O_2$: C 85.68, H 6.16; found: C 85.49, H 6.07.

*7-Methyl-7-phenyl-[7*H*]-benzofuro[2,3-*g*]chromene* **4**a: mp 154°C (from heptane–toluene); UV (EtOH) λ_{max} (ε/dm^3 mol^{-1} cm^{-1}): 205(39 800), 226(30 160), 244(19 590), 253(19 580), 268sh(10 220), 300(20 870), 312(20 870), 342(9950), and 356sh(8500) nm. ^{1}H NMR (250 MHz) δ: 1.78 (3H, s, 3H, CH_3), 6.08 (1H, d, J = 9.7 Hz, H-8), 6.59 (1H, d, J = 9.7 Hz, H-9), 7.16 (1H, s, H-5), 7.25 (2H, m, H-4′), 7.27 (1H, m, H-3), 7.32 (4H, m, H-3′), 7.40 (1H, td, $J_{1,2}$= 8.2 Hz, $J_{2,4}$= 1.1 Hz, H-2), 7.43 (1H, s, H-10), 7.48 (1H, d, J = 8 Hz, H-1), 7.54 (4H, m, H-2′), and 7.85 (1H, d, J = 7.95 Hz, H-4); ^{13}C NMR (62.5 MHz) δ: 29.4 (CH_3), 80.5 (C-7), 107.6 (C-5), 108.9 (C-10), 116.1 (C-1), 120.7 (C-4), 122.6 (C-3), 123.6 (C-9), 125.3 (C-2′), 126.9 (C-2), 127.1 (C-4′), 128.3 (C-3′), and 131.0 (C-8). Anal. calcd. for $C_{22}H_{16}O_2$: C 84.59, H 5.16; found: C 84.53, H 5.11.

*7,7-Diphenyl-[7*H*]-benzofuro[2,3-*g*]chromene* **4**b: mp 158°C (from hexane–benzene); UV (EtOH) λ_{max} (ε/dm^3 mol^{-1} cm^{-1}): 212(37 540), 225(28 745), 250(27 410), 272(22 640), 307(11 980), 320(13 540), 345(6520), and 354(2890) nm; ^{1}H NMR (250 MHz) δ: 6.27 (1H, d, J = 9.8 Hz, H-8), 6.73 (1H, d, J = 9.8 Hz, H-9), 7.17 (1H, s, H-5), 7.22 (1H, s, H-10), 7.23 (1H, t, J = 7.9Hz, H-3), 7.26 (2H, m, H-4′), 7.30 (4H, m, H-3′), 7.38–7.40 (2H, m, H-1, 2), 7.46 (4H, m, H-2′), and 7.81 (1H, d, J = 7.85 Hz, H-4); ^{13}C NMR (62.5 MHz) δ: 85,7 (C-7), 108.5 (C-10), 109.6 (C-5), 111.8 (C-1), 120.9 (C-4), 122.7 (C-3), 124.3 (C-9), 127.3 (C-2′), 127.3 (C-2), 127.8 (C-4′), 128.4 (C-3′), and 130.5 (C-8). Anal. calcd. for $C_{27}H_{18}O_2$: C 86.61, H 4.85; found: C 86.54, H 4.73.

*4-Chloro-9,9-diphenyl-[9*H*]furo[2′,1′:5,6]naphtho[2,1-*b*]-pyran* **7**

This compound was prepared according to method A in 84% yield: mp 259°C (from toluene); UV (EtOH) λ_{max} (ε/dm^{-3} mol^{-1} cm^{-1}): 222(28 770), 287(9660), 310(6930), 323(7510), 355(7260), and 371(7740) nm; ^{1}H NMR (250 MHz) δ: 6.33 (1H, d, J = 10 Hz, H-10), 6.95 (1H, d, J = 0.7 Hz, H-5), 7.26 (2H, m, H-4′), 7.28–7.32 (5H,m, H-7, 3′), 7.35 (1H, d, J = 10 Hz, H-11), 7.49 (4H, m, H-2′), 7.56 (1H, dd, $J_{1,2}$= 8.8 Hz, $J_{2,5}$ = 0.7 Hz, H-2), and 7.83 (2H, m, H-1, 6); ^{13}C NMR (62.5 MHz) δ: 83.1 (C-9), 102.9 (C-5), 112.0 (C-1), 118.4 (C-7), 118.6 (C-11), 119.8 (C-2), 124.8 (C-6), 127.0 (C-2′), 127.6 (C-4′), 128.1 (C-3′), and 128.7 (C-10). Anal. calcd. for $C_{27}H_{17}O_2Cl$: C 79.31, H 4.19, Cl 8.67; found: C 79.35, H 4.18, Cl 8.55.

1′,3′,3′-Trimethyl-1,2-tetramethylenespiro[7H-furo[3,2-f]-2H-1-benzopyran-7,2′-indoline] ***8***

This compound was synthesized according to standard procedure (27), using stoichiometric amount of 1,3,3-trimethyl-2-methyleneindoleninium perchlorate (Fischer's base) and 4-formyl-5-hydroxy-2,3-tetramethylenebenzofuran, in 52% yield: mp 176–178°C (from ethanol); ^{1}H NMR (250 MHz) δ: 1.18, (3H, s, CH_3), 1.32 (3H, s, CH_3), 1.89 (4H, m, H-2″, 3″), 2.72 (2H, m, H-1″), 2.74 (3H, s, NCH_3), 2.84 (2H, m, H-4″), 5.67 (1H, d, J = 10.35 Hz, H-8), 6.52 (1H, d, J = 7.7 Hz, H-7′), 6.56 (1H, d, J = 8.75 Hz, H-5), 6.83 (1H, td, $J_{4',5'}$ = 6.7 Hz, $J_{5',7'}$ = 0.7 Hz, H-5′), 7.07 (1H, dd, $J_{4',5'}$ = 6.6 Hz, $J_{4',6'}$ = 0.8 Hz, H-4′), 7.09 (1H, d, J = 8.8 Hz, H-4), 7.17 (1H, td, $J_{6',7'}$ = 7.6 Hz, $J_{4',6'}$ = 1Hz, H-6′) and 7.27 (1H, d, J = 10.3 Hz, H-9); ^{13}C NMR (62.5 MHz) δ: 20.5-26.1 (*gem*-CH_3), 22.7–22.9 (C-2″, 3″), 23.2 (C-1″), 23.9 (C-4″), 29.2 (NCH_3), 51.8 (C-3′), 103.8 (C-7), 106.9 (C-7′), 110.8 (C-1), 110.9 (C-4), 111.4 (C-5), 112.8 (C-9a), 118.6 (C-5′), 119.2 (C-9), 121.7 (C-6′), 124.8 (C-1a), 126.3 (C-9), 127.3 (C-4′), 137.1 (C-3′a), 148.4 (C-1′a), 149.0 (C-3a), 150.3 (C-5a) and 155.5 (C-2). Anal. calcd. for $C_{25}H_{25}NO_2$: C 80.83, H 6.78, N 3.77; found: C 80.72, H 6.85, N 3.68.

3′,3′-Dimethyl-1,2-tetramethylenespiro[7H-furo[3,2-f]-2H-1-benzopyran-7,1′-[2]oxaindane] ***9***

1,3,3-Trimethyl-3*H*-isobenzofurylium perchlorate (2.61g; 10 mmol) (28) and 4-formyl-5-hydroxy-2,3-tetramethylenebenzofuran (2.38g; 11 mmol) were boiled under reflux for 5 min in 30 mL of acetic acid with 0.03 g of 70% perchloric acid. On cooling, the crude solution gave a precipitate, which was washed with diethyl ether and then dried. The solid was suspended in 30 mL of benzene, and totally dissolved by bubbling in dry ammonia. The solvent was removed under reduced pressure. The residue was chromatographed on alumina using benzene as eluent. The photochromic fraction (R_f =0.9) was recrystallized in heptane, affording the title compound in 75% yield: mp 213–214°C ; ^{1}H NMR (400 MHz) δ: 1.55 (3H, s, CH_3), 1.69 (3H, s, CH_3), 1.9 (4H, m, H-2″,3″), 2.74 (2H, m, H-1″), 2.84 (2H, m, H-4″), 5.88 (1H, d, J = 9.70 Hz, H-8), 6.75 (1H, d, J = 8.75 Hz, H-5), 7.21 (1H, d, J = 8.75 Hz, H-4), 7.29 (1H, d, J = 9.65 Hz, H-9), and 7.38–7.46 (4H, m, H-4′, 5′, 6′, 7′); ^{13}C NMR (100 MHz) δ: 22.5–22.6 (C-2″, 3″), 22.9 (C-1″), 23.7 (C-4″), 28.8–30.5 (*gem*-CH_3), 86.0 (C-7), 105.8 (C-Ar), 111.1 (C-4), 112.1 (C-5), 112.9 (C-Ar), 120.4 (C-4′), 121.1 (C-8), 123.3 (C-7′), 123.78 (C-9), 125.0 (C-Ar), 128.1–129.7 (C-5′, 6′), 140.0, 147.1, 148.0, 149.6, and 155.3 (C-Ar). Anal. calcd. for $C_{24}H_{12}O_3$: C 82.75, H 3.47; found: C 82.69, H 3.51.

1′,2′-Tetramethylenespiro[1,3-dithiolan-2,7′-7H-furo[3,2-f]-2H-1-benzopyran] ***10***

Methyl-1,3-dithiolylanium perchlorate (0.98g; 4,5 mmol) (29) and 4-formyl-5-hydroxy-2,3-tetramethylenebenzofuran (1.08g; 5 mmol) were boiled under reflux for 5 min in 30 mL of acetic acid with a catalytic amount of 70% perchloric acid. On cooling, the crude solution gave a precipitate, which was washed with diethyl ether and then dried. The solid was suspended in 15 mL of benzene, and totally dissolved by bubbling in dry ammonia. The solvent was removed under reduced pressure. The residue was chromatographed on alumina using benzene as eluent. The photochromic fraction (R_f =0.8) was recrystallized in isopropanol (67% yield): mp 193–194°C; ^{1}H NMR (250 MHz) δ: 1.87 (4H, m, H-2″, 3″), 2.71–2.77 (4H, m, H-1″, 4″), 3.46–3.65 (4H, m, H-4, 5), 6.09 (1H, d, J = 9.65 Hz, H-8′), 6.74 (1H, d, J = 8.7 Hz, H-5′), 6.94 (1H, d, J = 9.65 Hz, H-9′), and 7.18 (1H, d, J = 8.7 Hz, H-4′); ^{13}C NMR (62.5 MHz) δ: 22.4–22.5 (C-2″,3″), 22.8 (C-1″), 23.7 (C-4″), 40.0–40.1 (C-4, 5), 106.1 (C-Ar), 111.1-112.3 (C-4′,5′), 112.7, 112.8 (C-Ar), 123.2 (C-8′,9′), 124.9, 147.2, 150.1, and 155.9 (C-Ar). Anal. calcd. for $C_{17}H_{16}O_2S_2$: C 64.55, H 5.1, S 20.25; found: C 64.43, H 5.17, S 20.36.

5-Methyl-1′,2′-tetramethylenespiro[benzo-1,3-dithiol-2,7′-7H-furo[3,2-f]2H-1-benzopyran] ***11***

2,5-Dimethyl-1,3-benzodithiolylium perchlorate (35) and (1.62g; 6 mmol) 4-formyl-5-hydroxy-2,3-tetramethylenebenzofuran (1.41g; 6,5 mmol) were boiled under reflux for 35 min in 20 mL of acetic acid with a catalytic amount of 70% perchloric acid. On cooling, the crude solution gave a brownish precipitate, which was washed with diethyl ether and then dried in vacuum. The solid was suspended in 20 mL of benzene, and totally dissolved by bubbling in dry ammonia. The solvent was removed under reduced pressure. The residue was chromatographed on alumina using benzene as eluent. Further recrystallization from ethanol afforded the spiropyran in 66% yield: mp 191–192°C (from ethanol); ^{1}H NMR (250 MHz) δ: 1.87 (4H, m, H-2″,3″), 2.31 (3H, s, CH_3), 2.71 (1H, m, H-1″), 2.8 (2H, m, H-4″), 6.37 (1H, d, J = 9.65 Hz, H-8′), 6.69 (1H, d, J = 8.7 Hz, H-5′), 6.94 (1H, d, J = 7.95 Hz, H-6), 7.07 (1H, d, J = 9.65 Hz, H-9′), 7.09 (1H, s, H-4), 7.15 (1H, d, J = 8 Hz, H-7), and 7.19 (1H, d, J = 8.7 Hz, H-4′); ^{13}C NMR (62.5 MHz) δ: 20.5 (CH_3), 22.7–22.8 (C-2″, 3″), 23.2 (C-1″), 24.1 (C-4,5), 106.4 (C-Ar), 111.9–112.2 (C-4′,5′), 112.9, 113.1 (C-Ar), 121.6 (C6), 122.3 (C-8′,9′), 125.4 (C-7), 127.1 (C-4), 136.4, 137.7, 139.5, 147.8, 150.6, and 156.3 (C-Ar). Anal. calcd. for $C_{22}H_{18}O_2S_2$: C 69.80, H 4.80, S 16.95; found: C 69.80, H 4.75, S 16.9.

Acknowledgement

We are grateful to Professor Harry G. Heller (University of Wales, Cardiff) and Dr. Barry Van Gemert (PPG Industries, Pittsburgh, Pa) for helpful discussions.

References

1. J.D. Hepworth. *In* Comprehensive heterocyclic chemistry. Vol. 3. *Edited by* A.R. Katritzky and C.W. Rees. Pergamon, Oxford. 1984. p. 737, and relevant references cited therein.
2. R.S. Becker and J. Michl. J. Am. Chem. Soc. **88**, 5931 (1966).
3. R. Guglielmetti. *In* Photochromism: molecules and systems. *Edited by* H. Dürr and H. Bouas-Laurent. Elsevier, Amsterdam. 1990. Chap. 8, p. 314, and relevant references cited therein.
4. A. Padwa, A. Au, G.A. Lee, and W. Owens. J. Org. Chem. **40**, 1142 (1975)
5. H.G. Heller, S.N. Oliver, J. Whittall, J. Brettle, C. Trundle, and M.W. Baskerville. U.S. Patent No. 4 818 096 (1989).
6. B. Van Gemert. WO, 92/09593, (1992).
7. M. Rickwood, K.E. Smith, C.D. Gabbutt, and J.D. Hepworth. WO, 9 422 850 (1994).
8. H.G. Heller. U.S. Patent No. 4 931 221 (1990).
9. H.G. Heller, S.N. Oliver, J. Whitall, and I. Tomlinson. EP, 0 246 114 (1987).
10. B. Van Gemert, M. Bergomi, and D. Knowles. Mol. Cryst. Liq. Cryst. **246**, 67 (1994)

11. B. Van Gemert and M. Bergomi. U.S. Patent No. 5 066 818 (1991).
12. J.L. Pozzo, V.A. Lokshin, and R. Guglielmetti. J. Chem. Soc. Perkin Trans. 1, 2591 (1994).
13. J.L. Pozzo, V.A. Lokshin, and R. Guglielmetti. Mol. Cryst. Liq. Cryst. **24**, 75 (1994).
14. C.D. Gabbutt, D.J. Hartley, J.D. Hepworth, B.M. Heron, M. Kanjia, and M. Rahman. Tetrahedron, **50**, 2507 (1994).
15. H. Kabbe and A. Widdig. Angew. Chem. Int. Ed. Engl. **21**, 247 (1982).
16. I. Iwai and I. Ide. Chem. Pharm. Bull. **11**, 1042 (1963).
17. H.G. Heller, S.N. Oliver, I. Tomlinson, and O. Whittall. U. S. Patent No. 4 826 977 (1989).
18. M. Harfenist and E. Thom. J. Org. Chem. **37**, 841 (1972).
19. J. Zsindely and H. Schmid. Helv. Chim. Acta **51**, 1510 (1968).
20. E.E. Schweizer and D. Meeder-Nycz. *In* Chromenes, chromanones and chromones. *Edited by* G.P. Ellis. Wiley Interscience, New York. 1977. p. 11.
21. G. Sartori, G. Casiraghi, L. Bolzoni, and G. Casnati. J. Org. Chem. **44**, 803 (1979).
22. J.L. Pozzo. Thesis, Université Aix-Marseille II, 1994.
23. J.L. Pozzo, A. Samat, and R. Guglielmetti. Fr. Patent No. 2.718. 447 (1995).
24. P. Appriou, F. Garnier, and R. Guglielmetti. J. Photochem. **8**, 145 (1978).
25. C. Lenoble and R.S. Becker.J. Photochem. **33**, 187 (1986).
26. V.P. Rybalkin, A. Ya. Bushkov, V.A. Bren, and V.I. Minkin. Zh. Org. Khim. **22**, 565 (1986).
27. A. Hinnen, C. Audic, and R. Gautron. Bull. Soc. Chim. Fr. 2066 (1968).
28. S.M. Aldoshin, V.A. Lokshin, A.N. Rezonov, N.V. Volbushko, V.I. Minkin, and L.O. Atovmian. Khim. Geterot. Soedin. **6**, 744 (1987).
29. V.A. Lokshin, N.S. Trofimova, N.A. Voloshin, N.E. Shelepin, and V.I. Minkin. Khim. Geterot. Soedin. **1**, 47 (1980).
30. P. Appriou, J. Guillerez, F. Garnier, and R. Guglielmetti. Helv. Chim. Acta, **58**, 2553 (1975).
31. E. Pottier, R. Dubest, R. Guglielmetti, P. Tardieu, A. Kellmann, P. Tfibel, and J. Aubard, Helv. Chim. Acta, **73**, 303 (1990).
32. T.V. Krasieva, Ya. N. Malkin, V.A. Lokshin, and V.A. Kuz'min. Izv. Akad. Nauk SSSR, Ser. Khim. **11**, 2504 (1989).
33. G. Domschke. J. Prakt. Chem. **32**, 144 (1966).
34. D. Dauzonne and R. Boyer. Synth. Commun. 339 (1988).
35. L. Soder and R. Wizinger. Helv. Chim. Acta, **42**, 1733 (1959).

Shape-similarity analysis of 20 stable conformations of neutral β-alanine

Gerard A. Heal, P. Duane Walker, Michael Ramek, and Paul G. Mezey

Abstract: The family of 20 stable conformations of neutral β-alanine are analyzed in terms of their shape similarities using the topological Shape Group Method, a general molecular shape analysis technique as applied to the three-dimensional electronic density. Molecular electron densities are calculated using the 6-31G** basis set, followed by the determination of the shape groups of local curvature patterns for the entire chemically relevant range of electron density contour surfaces. The results of the shape group analysis are represented by two-dimensional shape maps. Discretized grids of these maps generate numerical shape codes, and comparisons of these numerical codes serve as measures of shape similarity of the various conformers of β-alanine. This technique is based on direct comparisons of the intrinsic shape features of molecules and requires no superposition of molecules for comparisons. Mathematically well-defined and unbiased similarity measures are obtained by this non-visual, computer-based method, useful for the detection, quantification, and analysis of electronic charge distribution similarities. The family of 20 stable conformers of β-alanine serves as a test case for the application of the methodology for a large number of conformers, representing a level of complexity analogous to that of typical conformational problems in computer-aided drug design and the screening of potential drug molecules for shape similarity.

Key words: similarity measures, shape groups, β-alanine, conformation analysis, molecular shape, electron density.

Résumé : On a analysé la famille de 20 conformations stables de la β-alanine neutre en fonction des similitudes de leur forme, en utilisant la Méthode de groupe de forme topologique. On a appliqué la technique d'analyse de la forme moléculaire générale à la densité électronique en trois dimensions. On a calculé les densités moléculaires électroniques en utilisant l'ensemble de base 6-31G**, suivi d'une détermination des groupes de forme du modèle de courbure locale pour tout le domaine chimiquement caractéristique des surfaces de contour de la densité électronique. On représente les résultats de l'analyse des groupes de forme par des diagrammes de forme en deux dimensions. Des grilles discontinues de ces diagrammes génèrent des codes de forme numérique et les comparaisons de ces codes numériques servent de mesure de la similitude de forme des divers conformères de la β-alanine. Cette technique est basée sur la comparaison directe des caractéristiques de formes intrinsèques des molécules et ne requiert pas, pour les comparaisons, la superposition des molécules. On a obtenu des mesures de similitude bien définies mathématiquement et sans influence par cette méthode non visuelle basée sur ordinateur, utile pour la détection, la quantification et l'analyse des similitudes de distribution de la charge électronique. La famille des 20 conformères stables de la β-alanine sert de cas type pour l'application de la méthodologie à un plus grand nombre de conformères, représentant un niveau de complexité analogue à celle des problèmes conformationnels typiques que l'on retrouve dans le dessin des médicaments assisté par ordinateur et dans la protection des molécules ayant un usage pharmaceutique potentiel en raison de la similitude de forme.

Mots clés : mesures de similitude, groupes de forme, β-alanine, analyse conformationnelle, forme moléculaire, densité électronique.

[Traduit par la rédaction]

1. Introduction

Each molecule contains only a set of nuclei and an electron density distribution. The nuclear arrangement is fully reflected in the electron density, consequently, all information about a particular molecular conformation must be contained in the electron density; there is simply no other medium to encode information. Hence, in principle, a detailed enough shape analysis of electronic density clouds should be able to reveal all information about the given conformation of the molecule. The actual relations between electron density shape properties and other physical and chemical properties may be rather complex and not well understood; however, even without a detailed understanding of these relations, correlations between shape and other properties have predictive value, if based on rigorous shape analysis. This fundamental principle of the existence of shape–property relations is the basis of the Shape Group Method introduced earlier for molecular shape analysis (1–4). The Shape Group Method extracts the essential shape information for the whole chemically relevant range of electron density, and can be "tuned" to analyze shape in any detail and at any desired spatial resolution. The technique is rigorous as it has no inherent limitation; the only practical limitations

Received April 15, 1996.

G.A. Heal, P.D. Walker, and P.G. Mezey.[1] Mathematical Chemistry Research Unit, Department of Chemistry, University of Saskatchewan, 110 Science Place Saskatoon, SK S7N 5C9, Canada.
M. Ramek. Institut für Physikalische und Theoretische Chemie, Technische Universität Graz, A-8010 Graz, Austria.

[1] Author to whom correspondence may be addressed. Telephone: (306) 966-4654. Fax: (306) 966-4730. Also at the Department of Mathematics and Statistics, University of Saskatchewan.

are the quality of the electron density used as input, and the spatial and density resolution set by the user (1–4).

Ramek (5) has shown via extensive ab initio SCF-type calculations, using both GAUSSIAN (6) and GAMESS (7–9) quantum mechanical program packages at the RHF/4-31G level, that as many as 38 stable conformers of the neutral species of β-alanine may exist, which include 20 conformational isomers with unique intrinsic geometry, disregarding optical isomers. These conformers involve a number of intramolecular interactions of different chemical nature that have been characterized in detail (5, 10).

In this work, a systematic shape analysis using the Shape Group Method (1–4) has been carried out for the electronic densities of all 20 geometric conformations of β-alanine, excluding mirror images. The geometries were taken from ref. 5, while the energies and electronic density distributions were recalculated using GAUSSIAN 92 (6) employing the 6-31G** basis set, in order to provide a more accurate electron distribution for the various conformations, while still allowing for direct comparison between this and earlier works (5). The Shape Group technique (1–4), as implemented in the computer program GSHAPE 90 (11, 12), has been applied to the computed electron densities of the 20 β-alanine conformers.

Besides being an important test case of the methodology, a rigorous shape classification of the possible conformations of β-alanine is desirable in its own right, since this amino acid is of considerable biological interest. The molecule of β-alanine is found in animal brain and liver tissue, as well as in plants, fruits, and insect cuticle (13–17). Like γ-amino butyric acid (GABA), β-alanine acts as an inhibitor in the nervous system (18–21) binding to the opiod receptors found in the brain. Furthermore, β-alanine can be enzymatically converted (22) into L-α-alanine, an amino acid that can be found in a large number of biologically important peptides.

The next section of this paper contains a brief review of the theory and methodology employed, Sect. 3 contains the results and discussion, and a short summary is given in Sect. 4.

2. A brief review of the Shape Group Method

The Shape Group Method (1–4) is a technique of shape characterization based on local curvature features (geometrical properties) analyzed in terms of the patterns that various curvature domains of the electron density generate (topological properties). The Shape Group algorithm provides a detailed and mathematically rigorous characterization of three-dimensional functions in terms of a family of topological invariants. In the actual case, each three-dimensional contour surface of the electron density is partitioned into domains based on local curvature thresholds. Removal of all domains of a specific curvature classification from the original surface produces a new object that typically shows a new set of topological features. These topological features are described by the shape groups (1–4) of the object, which are the homology groups (23, 24) of the truncated surface. This technique has been used for the shape analysis of many molecular properties described by contour surfaces, including electron density functions or nuclear and electrostatic potential functions (4).

Using the Shape Group Method, shape characterization of electron density is reduced to a two-dimensional (a, b) parameter map where a represents the value of the electron density for the various contour surfaces and b is a threshold for the local curvature of the isodensity surface. The determination of these (a, b) parameter maps is automated through the GSHAPE 90 package of computer programs (11, 12).

Given a fixed nuclear configuration K, and a density threshold value a, a molecular isodensity contour (MIDCO) surface $G(K,a)$ is made up of the collection of all points of the three-dimensional space where the electronic density $\rho(K,\mathbf{r})$ is equal to the constant value a,

$$[1] \quad G(K, a) = \{\mathbf{r}: \rho(K, \mathbf{r}) = a\}$$

By varying the parameter a through a range of relevant electron density values, a set of MIDCO surfaces is generated, each of which can then be classified based on its local shape characteristics.

Specifically, each point on the surface $G(K,a)$ is classified into one of three curvature domains $D_\mu(a,b)$, $\mu = 0,1,2$, depending on how curved the surface is at the particular point with respect to some reference curvature b. Curvature at each point of surface $G(K,a)$ is determined by comparing the eigenvalues of the local Hessian matrix of the surface to the curvature b of a reference tangent sphere with a radius $1/b$, where b is a variable parameter.

A point on the surface $G(K,a)$ is then assigned to a domain $D_2(a,b)$ if both of the eigenvalues of the local Hessian matrix are less than b, to a domain $D_1(a,b)$ if precisely one of the eigenvalues is less than b, and to a domain $D_0(a,b)$ if none of the eigenvalues is less than b. A domain $D_2(a,b)$ is said to be convex relative to reference curvature b. Similarly, a domain $D_1(a,b)$ is of the saddle type relative to reference curvature b, whereas a domain $D_0(a,b)$ is concave relative to reference curvature b.

Truncation of all domains of a given type μ, $\mu = 0, 1, 2$, generates a truncated surface that can be studied by simple topological means, for example, truncation of all domains of the type $D_\mu(a, b)$ generates the truncated surface $G_\mu(a, b)$, where the reference to the nuclear configuration K is omitted from the notation:

$$[2] \quad G_\mu(a, b) = G(a) \setminus \cup D_\mu(a, b)$$

The resulting surface $G_\mu(a, b)$ may consist of a single connected surface with several holes or may form a set of several disjointed surfaces. The surfaces $G_\mu(a, b)$ are in general topologically more distinctive than the original surface $G(a, b)$ and form the basis for evaluating similarities between MIDCO surfaces and, hence, between electron densities. Each surface $G_\mu(a, b)$ is characterized by the corresponding homology groups $H^j\mu(a, b)$ of algebraic topology (22), specifically, by using the one-dimensional Betti number, which is related to the number of holes (n_h) on each surface $G_\mu(a, b)$. The one-dimensional Betti number is the rank of the one-dimensional shape group for each piece of the truncated surface. These Betti numbers are used as numerical shape descriptors for the electron density. The Betti numbers, one for each piece of the surface $G_\mu(a, b)$, are collected into a vector, which is then taken as the shape descriptor for a specified (a, b) pair of parameters.

Although the curvature domain pattern changes as a func-

tion of both parameters a and b, there are invariance domains within a formal (a, b) parameter plane where there is no change in the shape group classification. In fact, for the entire density range and for the entire possible curvature range of each molecule, there are only a finite number of different shape groups. Consequently, it is possible to characterize in detail the shape of the entire electron density, described by a continuum of MIDCO surfaces, using a finite number of Betti numbers as shape descriptors. The parameter plane of electron density thresholds and reference curvature values can be represented by a discretized grid, leading to a finite classification scheme by a numerical shape code (4).

To simplify the task of shape comparison, the vectors representing the sets of Betti numbers are encoded into a single shape integer L. For a given conformation K of a molecule and for a pair of parameters a and b, the unique shape integer $L(K, a, b)$ is defined by the following formula:

$$[3] \quad L(K, a, b) = \prod_{i=0}^{M} (P_i)^{k(i)}$$

where $P_0 = 0$, and for $i > 0$, P_i is the ith prime number in the sequence 1, 2, 3, 5, 7, 11, ... where 1 is taken as an "honorary prime"; each Betti number of value $(i - 2)$ is assigned to the prime number P_i; the exponent $k(i)$ is the number of disconnected surface pieces having their one-dimensional Betti number equal to $(i - 2)$; and where the value of upper limit M is two greater than the largest first Betti number for any of the disconnected pieces of the MIDCO $G(a)$.

If the level of resolution is insufficient to ascertain the presence of one or more of the D_μ curvature domains unambiguously, then a negative sign is assigned to the integer $L(K, a, b)$. Using the Prime Factorization Theorem one can decode this shape integer $L(K, a, b)$, yielding the set of individual Betti numbers for the given pair of parameters a and b.

The (a, b) parameter maps themselves have been standardized using a grid containing 41 threshold values of density and 21 threshold values for curvature (4, 11, 12). The usual density range covered varies from $a_{min} = 0.001$ au to $a_{max} = 0.1$ au. The curvature parameter b covers two ranges, from -1 to -10^{-5} and from 1 to 10^{-5}. The negative region is associated with a reference tangent sphere curving inward against the isodensity surface, while the positive values of b are interpreted as the tangent reference sphere curving away from the isodensity surface.

To accommodate the large variance in scale of both parameters a and b, logarithmic transformations are used for the actual display of the (a, b) parameter maps. Since parameter b can take both positive and negative values, the logarithm of the absolute value of b is used. The value of $\log |b| = -5$, that is, $b = 10^{-5}$ or $b = -10^{-5}$, is taken to represent $b = 0$, so the two ranges of b are regarded as connecting along a single line on the map.

A detailed similarity analysis between molecular electron densities can be carried out by a simple comparison of the (a, b) parameter maps of any two molecular conformations, K and K' (4, 25, 26). By overlaying the two (a, b) parameter maps and assigning a value of 1 to each position (a, b) in the map where the two shape integers $L(K, a, b)$ and $L(K', a, b)$ match, and a value of 0 where the two shape integers are different, a binary map is generated that provides an overview of similarity between the two molecular electron densities. A total similarity measure is then given as

$$[4] \quad S(i, j) = \sum_{k=1}^{N_a} \sum_{k'=1}^{N_b} \Delta(i, j, a_k, b_{k'}) / (N_a N_b)$$

where N_a and N_b are the number of thresholds for the a and b values, respectively, and

$$[5] \quad \Delta(i, j, a, b) = 1 \quad \text{if } \mathbf{L}(i, a, b) = \mathbf{L}(j, a, b)$$
$$= 0 \quad \text{if } \mathbf{L}(i, a, b) \neq \mathbf{L}(j, a, b)$$

Using this procedure, the shape features of the two electron densities can be compared by an algorithmic technique based on detailed shape analysis, providing a method that complements the quantum similarity approaches of Carbó et al. (27–35) and alternative techniques proposed earlier (36–50).

The sensitivity of results obtained by a Shape Group analysis to the quality of electron density and the range of density considered has been studied earlier (12). The quality of basis set used in the computation of ab initio electron densities affects the results of shape analysis; however, for basis sets at and beyond the 4-31G level there is little change in the shape of the electronic density within the chemically relevant molecular density range of density domains (4). Hence, the approach of optimizing geometry at the 4-31G basis level and recalculating energies (as well as densities) at the 6-31G** level is regarded as a practical, as well as sufficiently accurate, approximation for most applications. Shape group analysis of electron densities at the 6-31G** level has been shown to provide excellent shape – toxicological activity correlations for a family of polycyclic aromatic hydrocarbons (51).[2]

Test calculations for a set of small molecules (12) have shown that most of the essential shape features relevant to molecular similarity analysis can be identified by taking the range 0.001–0.1 au (au = atomic unit) for electron density, and some computational savings can be achieved by reducing the wider range of density used in earlier studies. In most of the more recent Shape Group studies (25, 26), the standardized range of 0.001–0.1 au has been used universally for all molecules.

3. Shape characterization and similarity analysis of the stable conformations of β-alanine

Using the geometries of the 20 conformations of β-alanine, which represent local minima on the 4-31G potential energy surface (5), electron density distributions for these conformations have been calculated using the 6-31G** basis set as incorporated in the GAUSSIAN 92 program (6). Table 1 lists the absolute and relative 6-31G** energies of all 20 conformational isomers. For consistency with earlier studies of these conformers, the numbering scheme follows that of ref. 5. Not surprisingly, the change of basis set from 4-31G to 6-31G**

[2] P.G. Mezey, Z. Zimpel, P. Warburton, P.D. Walker, D.G. Irvine, D.G. Dixon, and B. Greenberg. To be published.

Table 1. Calculated 6-31G** energies of geometric isomers of β-alanine (with roman serial indices **I**, **II**, **III**,... indicating the order of the 4-31G energies of an earlier study (5)).

	Hartrees	kJ/mol(relative)
I	−321.883 078	0.00
II	−321.881 434	4.32
V	−321.880 885	5.76
IV	−321.880 742	6.13
VII	−321.879 624	9.07
III	−321.879 315	9.88
XI	−321.879 287	9.95
VIII	−321.878 884	11.01
IX	−321.878 749	11.37
VI	−321.878 340	12.44
XII	−321.877 922	13.54
X	−321.877 868	13.68
XIII	−321.873 165	26.03
XIV	−321.870 884	32.02
XV	−321.870 389	33.32
XVII	−321.867 828	40.04
XVIII	−321.867 620	40.59
XVI	−321.867 505	40.89
XIX	−321.866 198	44.32
XX	−321.865 982	44.89

causes some conformers to change position in the energy-ordered list. Conformer **V**, which contains the N...H—O hydrogen bond, is slightly more stabilized in the 6-31G** description and becomes the third most stable species. Interestingly, the energy difference between the two conformers lowest in energy, both of which contain a weak N—H...O=C interaction, is significantly larger with the 6-31G** basis set than in the 4-31G case. This matches well with the observation that polarization functions sometimes provide higher estimates for nonbonded intramolecular interactions (52).

Figure 1 shows the nuclear positions of all 20 of these conformers along with the molecular isodensity contour (MIDCO) corresponding to a constant electron density value of $a = 0.1$ au. Figures 2 and 3 are the selected examples of the (a, b) parameter maps for conformations **I** and **II**, respectively. Note that the single integer entries within these (a, b) parameter maps follow the order of detection of each shape group type within each conformer, hence the actual comparison between (a, b) parameter maps involves decoding the single integer entries using the respective legend tables shown in the figures. Figure 4 shows the resulting similarity map of the overall similarity between these two conformers, which differ primarily in the orientation of the amino group. The similarity index resulting from this map is 0.824 out of a possible perfect match of 1.00. Whereas the high-density range of the MIDCOs shown in Fig. 1 does not provide many visual clues to shape differences in terms of local curvatures, the more diffuse, lower density contours G(**Y**,0.01) and G(**Y**,0.001), **Y** = **I**,**II**, shown in Fig. 5, reveal many subtle differences in the local curvatures of conformers **I** and **II** of β-alanine.

Table 2 provides the similarity index of all pairwise similarity tests for the 20 conformations of β-alanine. The two most

Table 2. Similarity measures computed for all pairs of the 20 conformers of β-alanine.

	I	**II**	**III**	**IV**	**V**	**VI**	**VII**	**VIII**	**IX**	**X**	**XI**	**XII**	**XIII**	**XIV**	**XV**	**XVI**	**XVII**	**XVIII**	**XIX**	**XX**
I	**1.000**	0.824	0.793	0.788	0.688	0.759	0.812	0.845	0.817	0.788	0.832	0.773	0.832	0.808	0.768	0.758	0.773	0.731	0.719	0.725
II	0.824	**1.000**	0.815	0.770	0.667	0.771	0.815	0.782	0.806	0.784	0.795	0.773	0.806	0.857	0.798	0.778	0.802	0.744	0.765	0.733
III	0.793	0.815	**1.000**	0.723	0.682	0.762	0.751	0.782	0.795	0.782	0.780	0.783	0.780	0.750	0.739	0.716	0.773	0.782	0.747	0.749
IV	0.788	0.770	0.723	**1.000**	0.688	0.715	0.829	0.778	0.838	0.795	0.767	0.835	0.778	0.802	0.872	0.821	0.773	0.785	0.754	0.783
V	0.688	0.667	0.682	0.688	**1.000**	0.644	0.666	0.685	0.693	0.697	0.676	0.699	0.670	0.644	0.680	0.648	0.773	0.660	0.629	0.654
VI	0.759	0.771	0.762	0.715	0.644	**1.000**	0.746	0.767	0.766	0.748	0.775	0.754	0.747	0.751	0.739	0.735	0.773	0.743	0.753	0.730
VII	0.812	0.815	0.751	0.829	0.666	0.746	**1.000**	0.774	0.823	0.831	0.780	0.785	0.793	0.811	0.803	0.852	0.773	0.754	0.772	0.744
VIII	0.845	0.782	0.782	0.778	0.685	0.767	0.774	**1.000**	0.829	0.797	0.860	0.782	0.819	0.769	0.763	0.737	0.773	0.775	0.751	0.744
IX	0.817	0.806	0.795	0.838	0.693	0.766	0.823	0.829	**1.000**	0.850	0.822	0.843	0.797	0.782	0.819	0.784	0.773	0.797	0.767	0.788
X	0.788	0.784	0.782	0.795	0.697	0.748	0.831	0.797	0.850	**1.000**	0.795	0.821	0.767	0.771	0.774	0.794	0.773	0.776	0.769	0.779
XI	0.832	0.795	0.780	0.767	0.676	0.775	0.780	0.860	0.822	0.795	**1.000**	0.801	0.792	0.775	0.754	0.749	0.773	0.745	0.739	0.743
XII	0.773	0.773	0.783	0.835	0.699	0.754	0.785	0.782	0.843	0.821	0.801	**1.000**	0.792	0.790	0.822	0.786	0.773	0.830	0.796	0.826
XIII	0.832	0.806	0.780	0.778	0.670	0.747	0.793	0.819	0.797	0.767	0.792	0.792	**1.000**	0.823	0.795	0.776	0.773	0.758	0.757	0.752
XIV	0.808	0.857	0.750	0.802	0.644	0.751	0.811	0.769	0.782	0.771	0.775	0.790	0.823	**1.000**	0.812	0.819	0.773	0.724	0.753	0.744
XV	0.768	0.798	0.739	0.872	0.680	0.739	0.803	0.763	0.819	0.794	0.754	0.822	0.795	0.812	**1.000**	0.840	0.773	0.809	0.788	0.780
XVI	0.758	0.778	0.716	0.821	0.648	0.735	0.852	0.737	0.784	0.794	0.749	0.786	0.776	0.819	0.840	**1.000**	0.773	0.765	0.814	0.780
XVII	0.773	0.802	0.787	0.736	0.648	0.796	0.789	0.777	0.792	0.820	0.787	0.777	0.779	0.779	0.760	0.753	**1.000**	0.763	0.816	0.799
XVIII	0.731	0.744	0.782	0.785	0.660	0.743	0.754	0.775	0.797	0.776	0.745	0.830	0.758	0.724	0.809	0.765	0.773	**1.000**	0.841	0.850
XIX	0.719	0.765	0.747	0.754	0.629	0.753	0.772	0.751	0.767	0.769	0.739	0.796	0.757	0.753	0.788	0.814	0.773	0.841	**1.000**	0.856
XX	0.725	0.733	0.749	0.783	0.654	0.730	0.744	0.744	0.788	0.779	0.743	0.826	0.752	0.744	0.780	0.780	0.773	0.850	0.856	**1.000**

Fig. 1. The 20 stable conformers of β-alanine: nuclear positions and the 0.1 au MIDCO surfaces.

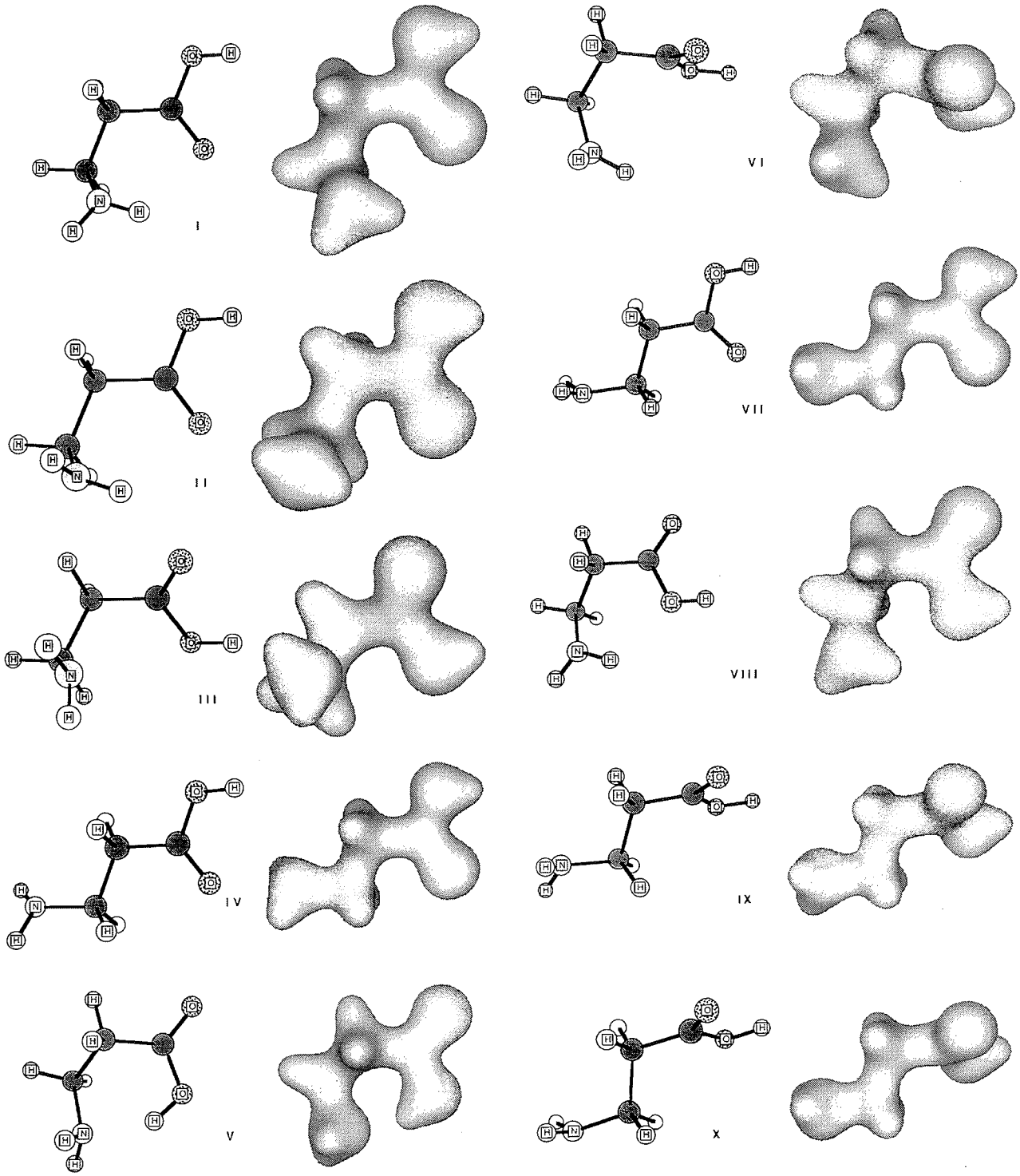

similar conformers based on this similarity criterion are conformers **IV** and **XV** having an overall similarity index of 0.872.

These indices immediately characterize **V** as an exceptional conformer: the similarity indices with all other conformers are below 0.7, whereas all other conformer pairs consistently have indices larger than this value. This characterization is very reasonable, because **V** is the only conformer stabilized by the N...H—O hydrogen bond, which has a major influence on reaction paths, potential barriers, bond lengths, and force constants, as pointed out in ref. 5. In a similar way, **III** and **VI** are also characterized as unusual conformers that show only low sim-

Fig. 1 (*concluded*).

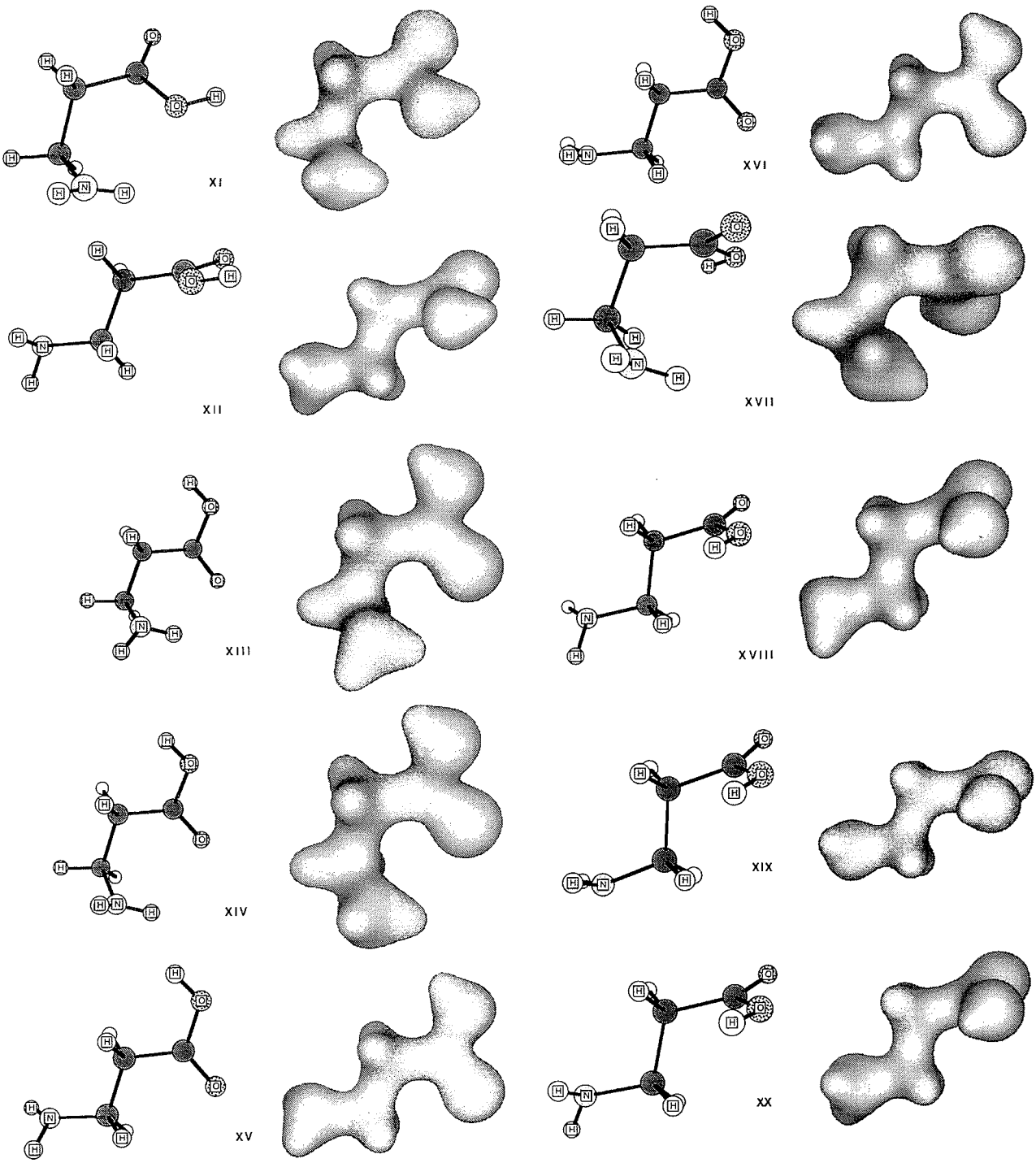

ilarity with any of the other conformers: for **III**, the highest similarity index is 0.815 for the pair **II/III**, all other values are below 0.8; for **VI**, all indices are below 0.8. This classification does make chemical sense: **III** and **V** are the only conformers that cannot be transformed into a good approximation of any other form by a single internal rotation; for example, the conversion of **III** to **II**, which was mentioned above, requires a reorientation of the amino as well as the carboxy group. By contrast, **VI** participates in several conformational equilibria involving internal rotation of a single functional group; some of these equilibria are discussed below. The low similarity indices for **VI** are a manifestation of a peculiarity of a different kind, namely, a considerable degree of local steric interference in the nuclear arrangement, resulting in a peculiar shape of the electron density. This local steric congestion is manifested by the orientation of both the carboxy and the amino groups, and also

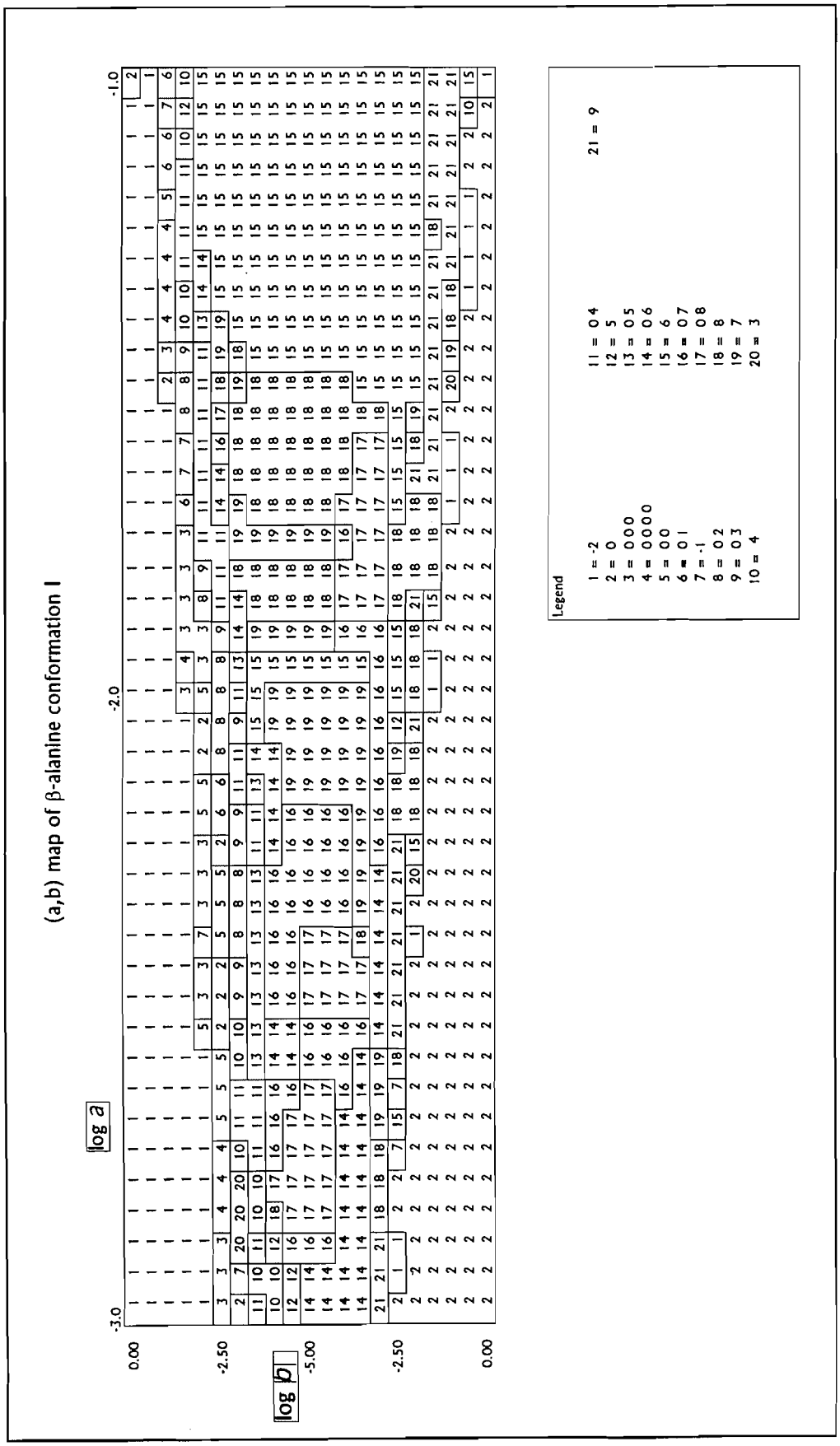

Fig. 2. The (*a*, *b*) parameter map for conformation **I** of β-alanine.

Fig. 3. The (*a*, *b*) parameter map for conformation **II** of β-alanine.

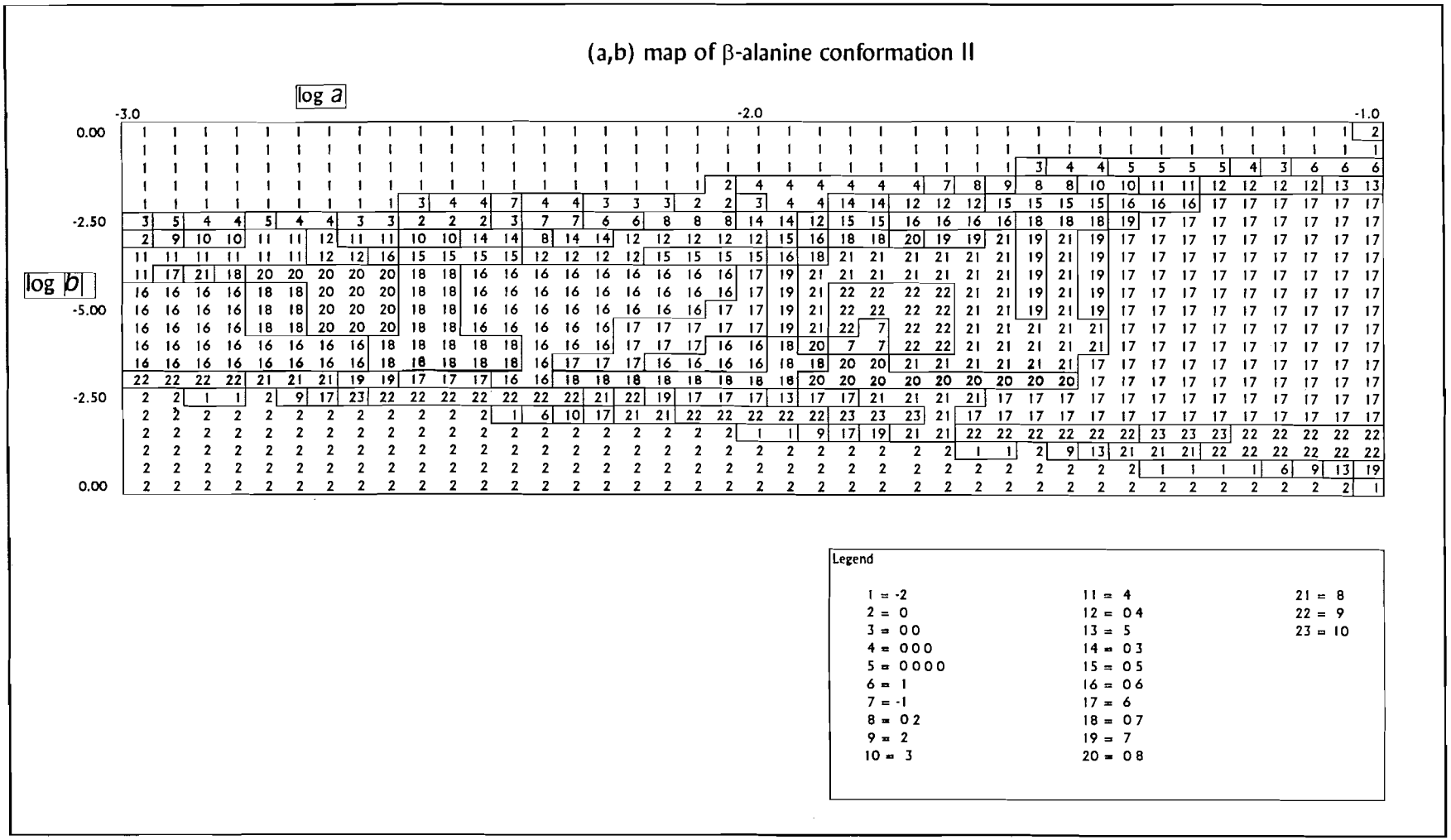

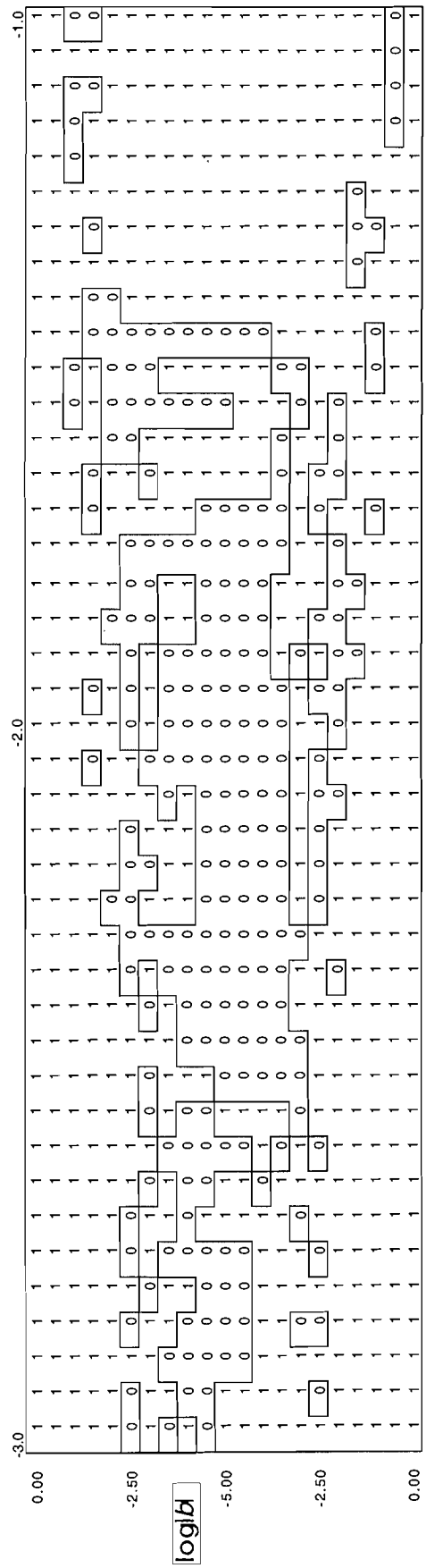

Fig. 4. The binary similarity map between conformations **I** and **II** of β-alanine showing in detail the similarity regions of MIDCO surfaces; "1" indicates a match whereas "0" indicates a mismatch between sets of Betti numbers encoded according to the legend tables in Figs. 2 and 3.

by the 6-31G** energies, as an indication of a formal "strain." In geometrical terms, **VI** shows the largest negative deviation of all β-alanine conformers for the two C-C-C-O torsions from their respective average values and at the same time the largest positive deviation for the H-N-C-C torsions. In terms of energy, **VI** also exhibits the largest increase in relative energy when changing from the 4-31G to the 6-31G** wave function.

As the case of **VI** shows, there is no strict relation between the similarity index values and the number of internal rotations necessary for the interconversion of the conformers involved. The following data strengthen this point: all conformer pairs, which can be transformed into each other by a rotation of the amino group only, are characterized by indices of 0.82 or higher; however, the pair **XII/XVIII** (differing in the amino and hydroxy group orientation) also ranks at 0.83. Rather than being linked to reaction paths, the similarity indices discussed here are obtained from a wide range of electron density values, hence they do reflect changes in intramolecular interactions rather accurately.

This is not only true for the strong intramolecular N...H—O hydrogen bond in **V**, but also true for much more subtle intramolecular interactions, e.g., those introduced by changing the -COOH group from a *syn*- to an *anti*-periplanar orientation. In the *syn* case, which is present in conformers **I–IV** and **VI–XII**, the dipoles of the groups O-H and C=O are in a very favorable orientation, which yields a stabilization of approximately 30 kJ/mol. In the *anti* case, this favorable orientation is no longer present and, except for **V**, the carboxylic hydrogen atom is brought into the vicinity of other hydrogen atoms. If the C-C-COOH arrangement is planar or almost planar, only minor H–H repulsion occurs, since the hydrogen atoms neighboring the carboxylic hydrogen atom point out of the C-C-COOH plane, whereas a rotation of the COOH group out of the C-C-C plane results in considerable H–H repulsion. As a consequence, conformers **XVII–XX**, which represent the latter case, are high in energy and exhibit the largest deviations of the H-O-C-C torsion from planarity. Looking at the similarity indices of those conformers, which form such *syn/anti* pairs, i.e., **I/XIII**, **II/XIV**, **IV/XV**, **VI/XVII**, **VII/XVI**, **IX/XVIII**, **X/XIX**, and **XII/XX**, one finds values of 0.832–0.872 for a planar C-C-COOH arrangement, but values between 0.769 and 0.826 for the nonplanar arrangement.

Other examples demonstrating the sensitivity of these similarity indices in monitoring changes in intramolecular interactions are the reaction cycles involving the conformers **II**, **VI**, and **XI** on the one hand and **IV**, **IX**, and **XII** on the other hand. The conformers in both sets are interconnected by an internal rotation of the carboxy group (in the latter case the mirror image of **IV** has to be considered, which is, however, characterized by the same numerical values as **IV**); in the case of **II**, **VI**, and **XI** significant changes in the interaction between the amino and the carboxy group take place along the reaction path (6), whereas the *trans* orientation of the N-C-C-C skeleton excludes such interactions in the case of **IV**, **IX**, and **XII**. The corresponding similarity indices mirror this difference: in one case they range from 0.771 to 0.795, whereas in the other case they are concentrated between 0.835 and 0.843.

4. Summary

In this work, the Shape Group Method (1–4) has been used to

Fig. 5. Three characteristic MIDCO surfaces, $G(\mathbf{Y},0.1)$, $G(\mathbf{Y},0.01)$, and $G(\mathbf{Y},0.001)$, $\mathbf{Y} = \mathbf{I}, \mathbf{II}$, for conformations **I** and **II** of β-alanine. The more diffuse, low density contours $G(\mathbf{Y},0.01)$ and $G(\mathbf{Y},0.001)$ show the differences in local curvatures resulting from the differences in the interactions between local charge density clouds.

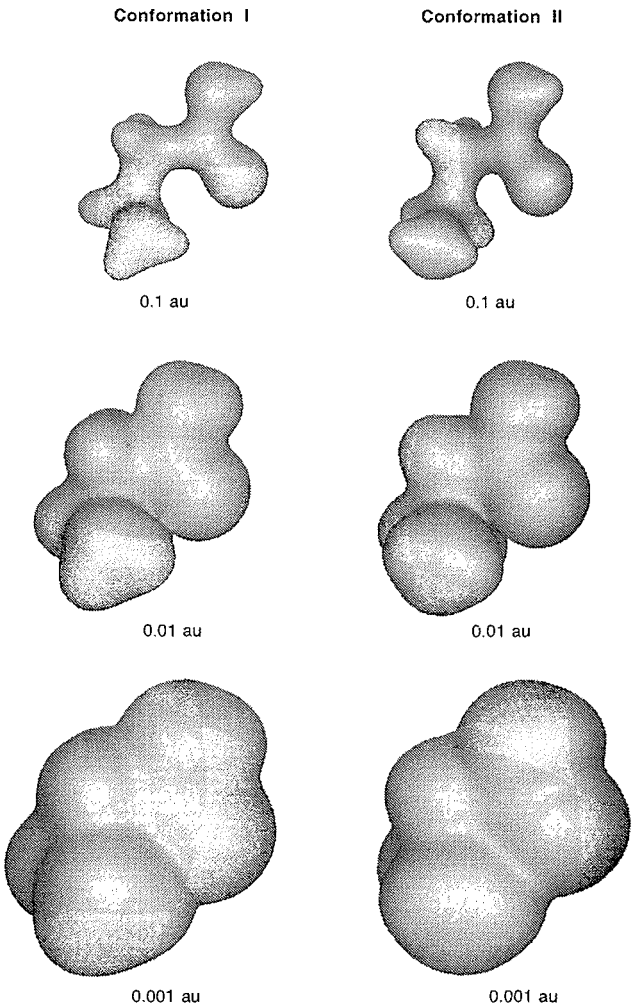

analyze the electron density distributions of 20 symmetry-unique conformers of the neutral form of β-alanine. This particular molecule has a number of well-documented conformers (5) as well as a variety of intramolecular interactions in various conformers (5, 10). In earlier studies, the Shape Group Method was successfully applied for the similarity analysis of various compounds (25) and for conformational changes limited to single rotations (26). This study is the first in which the shape similarities of a large number of conformers are analyzed in a systematic manner.

The similarity indices obtained in the present study proved to be a good measure of similarity and a reliable tool for identifying outstanding conformers using an automated, unbiased algorithm. These similarity measures appear to be very sensitive to changes in nonbonded interactions. Detection of subtle changes in intra- or intermolecular interactions is expected to be of importance in computer-aided drug design, where the quantification of similarities or dissimilarities between differently substituted or differently oriented local groups in various compounds is essential, providing discrimination in their ability to bind to a known receptor.

Acknowledgments

Parts of this work have been supported by the Austrian Fonds zur Förderung der wissenschaftlichen Forschung (Project P6856), and by the Natural Sciences and Engineering Research Council of Canada.

References

1. P.G. Mezey. Int. J. Quantum Chem.: Quantum. Biol. Symp. **12**, 113 (1986).
2. P.G. Mezey. J. Comput. Chem. **8**, 462 (1987).
3. P.G. Mezey. J. Math. Chem. **2**, 325 (1988).
4. P.G. Mezey. Shape in chemistry: an introduction to molecular shape and topology. VCH Publishers, New York. 1993.
5. M. Ramek. J. Mol. Struct. (Theochem), **208**, 301 (1990).
6. M.J. Frisch, M. Head-Gordon, G.W. Trucks, J.B. Foresman, H.B. Schlegel, K. Raghavachari, M.A. Robb, J.S. Binkely, C. Gonzalez, D.J. DeFrees, D.J. Fox, R.A. Whiteside, R. Seeger, C.G. Melius, J. Baker, R.L. Martin, L.R. Kahn, J.J. P. Stewart, S. Topiol, and J.A. Pople. GAUSSIAN 92. Gaussian Inc., Pittsburgh, Pa. 1992.
7. M. Dupuis, D. Spangler, and J.J. Wendoloski. N.R.C.C. Software Catalogue. 1 1980. Program No. QG01. p. 1.
8. M.F. Guest, J. Kendrick, and S.A. Pope. GAMESS Documentation, Daresbury Laboratory, U.K. 1983.
9. M.W. Schmidt, J.A. Boatz, K.K. Baldridge, S. Koeski, M.S. Gordon, S.T. Elbert, and B. Lam. QCPE Bull. **7**, 115 (1987).
10. M. Ramek, M. Flock, A.-M. Kelterer, and V.K.W. Cheng. J. Mol. Struct. (Theochem), **276**, 61 (1992).
11. P.D. Walker, G.A. Arteca, and P.G. Mezey. GSHAPE 90. Mathematical Chemistry Research Unit, University of Saskatchewan, Saskatoon. 1990.
12. P.D. Walker, G.A. Arteca, and P.G. Mezey. J. Comput. Chem. **14**, 1172 (1993).
13. J.P. Greenstein and M. Winitz. Chemistry of amino acids. Wiley, New York. 1961.
14. I.T. Millar and H.D. Springall. Sidgwick's organic chemistry of nitrogen. Clarendon Press, Oxford. 1966.
15. A. Bruun, B. Ehinger, and A. Forsberg. Exp. Brain Res. **19**, 239 (1974).
16. R. Martin del Rio, L.M. Orensanz Muñoz, and F.V. de Feudis. Exp. Brain Res. **28**, 225 (1977).
17. M.R. Kasschau, C.M. Skisak, J.P. Cook, and W.R. Mills. J. Comp. Physiol. B: **154**, 181 (1984).
18. T. Horikoshi, A. Asanuma, K. Yanagisawa, K. Anzai, and S. Goto. Mol. Brain Res. **4**, 97 (1988).
19. D. Choquet and H. Korn. Neurosci. Lett. **84**, 329 (1988).
20. V. Andersen and B.G. Munck. Biochim. Biophys. Acta, **902**, 145 (1987).
21. N. Tamaki, S. Fujimoto, C. Mizota, and M. Kikugawa. Biochim. Biophys. Acta, **925**, 238 (1987).
22. O. Hayashi, Y. Nishuzuka, M. Tatibana, M. Takeshita, and S. Kuno. J. Biol. Chem. **236**, 781 (1961).
23. S. MacLane. Homology. Springer Verlag, Berlin-Göttingen-Heidelberg. 1963.
24. W. Massey. Homology and cohomology theory. Marcel Dekker, New York - Basel. 1978.
25. P.D. Walker, G.M. Maggiora, M.A. Johnson, J.D. Petke, and P.G. Mezey. J. Chem. Inf. Comput. Sci. **35**, 568 (1995).
26. P.D. Walker, P.G. Mezey, G.M. Maggiora, M.A. Johnson, and J.D. Petke. J. Comput. Chem. **16**, 1474 (1995).

27. R. Carbó, L. Leyda, and M. Arnau. Int. J. Quantum Chem. **17**, 1185 (1980).
28. R. Carbó and M. Arnau. Molecular engineering: a general approach to QSAR. *In* Medicinal chemistry advances. *Edited by* F.G. de las Heras and S. Vega. Pergamon Press, Oxford. 1981.
29. R. Carbó, E. Sune, F. Lapena, and BJ. Perez. J. Biol. Phys. **14**, 21 (1986).
30. R. Carbó and Ll. Domingo. Int. J. Quantum Chem. **32**, 517 (1987).
31. R. Carbó and B. Calabuig. Comput. Phys. Commun. **55**, 117 (1989).
32. R. Carbó and B. Calabuig. Int. J. Quantum Chem. **42**, 1681 (1992).
33. R. Carbó and B. Calabuig. Int. J. Quantum Chem. **42**, 1695 (1992).
34. R. Carbó, B. Calabuig, L. Vera, and E. Besalu. *In* Advances in quantum chemistry. Vol. 25. *Edited by* P.-O. Löwdin, J.R. Sabin, and M.C. Zerner. Academic Press, New York. 1994.
35. R. Carbó (*Editor*). Molecular similarity and reactivity: from quantum chemical to phenomenological approaches. Kluwer Academic Publishers, Dordrecht, The Netherlands. 1995.
36. E.E. Hodgkin and W.G. Richards. Int. J. Quantum Chem. Quantum Biol. Symp. **14**, 105 (1987).
37. C. Burt, W.G. Richards, and P. Huxley. J. Comput. Chem. **11**, 1139 (1990).
38. A. Good and W.G. Richards. J. Chem. Inf. Comput. Sci. **32**, 112 (1992).
39. N.L. Allan and D.L. Cooper. J. Chem. Inf. Comput. Sci. **32**, 587 (1992).
40. D.L. Cooper and N.L. Allan. *In* Molecular similarity and reactivity: from quantum chemical to phenomenological approaches. *Edited by* R. Carbó. Kluwer Academic Publishers, Dordrecht, The Netherlands. 1995.
41. S.E. Leicester, J.L. Finney, and R.P. Bywater. J. Mol. Graphics, **6**, 104 (1988).
42. R. Bywater. Communication at the VII Annu. Meet. Molecular Graphics Society, San Francisco, Calif. 1988.
43. R.P. Bywater. *In* Molecular similarity and reactivity: from quantum chemical to phenomenological approaches. *Edited by* R. Carbó. Kluwer Academic Publishers, Dordrecht, The Netherlands. 1995.
44. M.A. Johnson. J. Math. Chem. **3**, 117 (1989).
45. M.A. Johnson and G.M. Maggiora (*Editors*). Concepts and applications of molecular similarity. Wiley, New York. 1990.
46. R. Ponec and M. Strnad. J. Chem. Inf. Comput. Sci. **32**, 693 (1992).
47. B.B. Stefanov and J. Cioslowski. J. Comput. Chem. **16**, 1394 (1995).
48. P.G. Mezey. Top. Curr. Chem. **173**, (1995).
49. P.G. Mezey. *In* Molecular similarity in drug design. *Edited by* P.M. Dean. Chapman & Hall/Blackie Publishers, Glasgow, U.K. 1995.
50. P.G. Mezey. *In* Computational chemistry: reviews and current trends. *Edited by* J. Leszczynski. World Scientific Publishers, Singapore. 1996.
51. P.G. Mezey, Z. Zimpel, P. Warburton, P.D. Walker, D.G. Irvine, D.G. Dixon, and B. Greenberg. J. Chem. Inf. Comput. Sci. **36**, 602 (1996).
52. M. Ramek and V.K.W. Cheng. Int. J. Quantum Chem. Quantum Biol. Symp. **19**, 15 (1992).

The preparation and characterization of $SeCl_3SbF_6$, improved syntheses of $MCl_3(As/Sb)F_6$ (M = S, Se), and the X-ray crystal structure determination of $SeCl_3AsF_6$ and a new phase of SBr_3SbF_6

Jack Passmore, T. Stanley Cameron, Paul D. Boyle, Gabriele Schatte, and Todd Way

Abstract: Alternative and, in some cases, improved syntheses of the salts $MX_3(As/Sb)F_6$ (M = S, Se) and $SCl_3(SbCl_6/AlCl_4)$ are described. In addition, the synthesis of $SeCl_3SbF_6$ is reported. The compounds were characterized by FT–Raman spectroscopy and the X-ray crystal structures of $SeCl_3AsF_6$ (also ^{77}Se NMR)and a new phase of SBr_3SbF_6 were determined. Crystals of $SeCl_3AsF_6$ and SBr_3SbF_6 are monoclinic, space group $P2_1/c$ with [values for SBr_3SbF_6 in brackets] a = 7.678(1) [8.137(1)] Å, b = 9.380(3) [9.583(2)] Å, c = 11.920(3) [12.447(2)] Å, β = 98.19(2)° [97.36(1)]°, V = 849.72(3) [962.6(3)] Å^3, z = 4, D_x = 2.925 [3.502] Mg m^{-3}, R = 0.0525 [0.055], and R_w = 0.0554 [0.060] for 1151 [1472] observed reflections.

Key words: MX_3^+ salts, FT–Raman spectroscopy, X-ray crystal structures of $SeCl_3AsF_6$, SBr_3SbF_6, and preparation of $SeCl_3SbF_6$.

Résumé : On décrit de nouvelles synthèses, quelquefois améliorées, des sels $MX_3(As/Sb)F_6$ (M = S, Se) et $SCl_3(SbCl_6/AlCl_4)$. On rapporte de plus la synthèse du $SeCl_3SbF_6$. On a caractérisé les composés par spectroscopie Raman en transformation de Fourier et par diffraction des rayons X du $SeCl_3AsF_6$ (aussi RMN ^{77}Se) et d'une nouvelle phase du $SeBr_3SbF_6$. Les cristaux du $SeCl_3AsF_6$ et du SBr_3SbF_6 sont monocliniques, groupe d'espace $P2_1/c$ avec [valeurs pour SBr_3SbF_6 entre crochets] a = 7,678(1) [8,137(1)], b = 9,380(3) [9,583(2)] et c = 11,920(3) [12,447(2)] Å, β = 98,19(2)° [97,36(1)]°, V = 849,72(3) [962,6(3)] Å^3, z = 4, D_x = 2,925 [3,502] Mg m^{-3}, R = 0,0525 [0,055], et R_w = 0,0554 [0,060] pour 1151 [1472] réflexions observées.

Mots clés : sels de MX_3^+, spectroscopie Raman–FT, structures cristallines par diffraction des rayons-X de $SeCl_3AsF_6$, SBr_3SbF_6 et préparation de $SeCl_3SbF_6$.

[Traduit par la rédaction]

Introduction

During our work, we required AsF_6^- and SbF_6^- salts of MX_3^+ (M = S, Se; X = Cl, Br) as starting materials for the synthesis of $M_3X_3^+$ salts (1, 2). We report below alternative and, in some cases, improved syntheses of $MCl_3(As/Sb)F_6$ (M = S, Se) and $SCl_3(SbCl_6/AlCl_4)$, the synthesis of $SeCl_3SbF_6$, which was not reported previously, the FT–Raman spectra of MCl_3SbF_6 (M = S, Se), the X-ray crystal structure of $SeCl_3AsF_6$ and of a new phase of SBr_3SbF_6. The MX_3^+ (M = S, Se, Te; X = Cl, Br, I (excluding SI_3^+)) salts have been extensively studied (3–9), and are of interest in terms of the structure of the cations themselves, their solid state architectures, and degree of cation–anion interactions, and are starting reagents for both inorganic and organic reactions (e.g., the chlorination of aromatic systems; see ref. 4).

Received October 5, 1995.[1]

J. Passmore,[2] P.D. Boyle,[3] G. Schatte, and T. Way. Department of Chemistry, University of New Brunswick, Fredericton, NB E3B 6E2, Canada.
T.S. Cameron. Department of Chemistry, Dalhousie University, Halifax, NS B3H 4J3, Canada.

[1] Revision received April 17, 1996.
[2] Author to whom correspondence may be addressed. Telephone: (506) 453-4821. Fax: (506) 453-4981. e-mail: PASSMORE@UNB.CA
[3] Present address: Department of Chemistry, North Carolina State University, Raleigh, NC 27599-3290, U.S.A.

Experimental

General techniques and materials

All reactions were carried out in a one-piece apparatus consisting of two or three thick-walled round-bottom flasks (V = 25 mL) linked by a glass tube (o.d. 10 mm) incorporating a sintered glass filter disk (medium porosity). The three-bulbed vessel consisted of one primary bulb and two secondary bulbs, on the opposite side of the frit to the primary valve. The primary bulb was fitted with a 180° Pyrex glass valve with PTFE piston (diameter, 5 mm; PTT/5, J. Young, London, U.K.), and each secondary bulb with a 90° Pyrex glass valve with PTFE piston (diameter, 5 mm; PTT/5/RA, J.Young, London, U.K.).

Further details regarding general techniques and apparatus are described in refs. 10 and 11. All apparatus were rigorously dried. Moisture-sensitive materials, crystals suitable for X-ray analysis, and all solid products were manipulated in a Vacuum Atmospheres Dri-Lab equipped with a Dri-Train (HE-493) and an internal circulating drying unit containing 1 kg of 3 Å molecular sieves.

Sulfur dioxide (Matheson) and AsF_3 (Ozark-Mahoning) were vacuum distilled and stored over CaH_2 and NaF, respectively. Chlorine (Air Liquid Canada) and bromine (Fisher) were vacuum distilled onto and stored over P_4O_{10}. Selenium (Johnson Matthey, 1–3 mm, amorphous, ground to a powder, 99.999%), $SeCl_4$ (Johnson Matthey, 99.5%), S_2Cl_2 (Fisher Scientific), and AsF_5 (Ozark-Mahoning) were used as received. $AgSbF_6$ (Aldrich, 98%) was used as received, handled in the dark, and used in glass vessels wrapped in aluminum foil. Sulfur (precipitated; Fisher Scientific) was vacuum dried prior to use. Antimony pentafluoride (Ozark-Mahoning) was triple distilled in an all-glass apparatus and stored in a Pyrex glass vessel fitted with a Teflon valve (PTT/5, J. Young, U.K.) (11). Aluminum trichloride (Fisher Scientific) was sublimed under a nitrogen pressure of 40 mbar (1 bar = 100 kPa) through a section of granular Al metal (Fisher Scientific, 8–20 mesh) at a temperature of 175–180°C. The compound $S_3Br_3SbF_6$ was prepared as described in ref. 2.

Preparation of $SeCl_3AsF_6$ from $SeCl_4$, and AsF_5 in SO_2

An excess of AsF_5 (2.497 g, 14.69 mmol) was condensed onto $SeCl_4$ (2.197 g, 5.87 mmol) in SO_2 (8.9 g), producing a yellow solution over a white precipitate on warming to room temperature. The solution was filtered after stirring overnight, leaving 0.110 g of a less soluble product behind ($AsCl_4AsF_6$; FT–Raman). After removal of the volatile materials the resulting white soluble solid product was identified as $SeCl_3AsF_6$ containing small amounts of $AsCl_4AsF_6$ (FT–Raman). Pure $SeCl_3AsF_6$ (2.138 g, 5.71 mmol; 97.3% recovered yield based on $SeCl_4$) was obtained after recrystallization of the crude product (2.671 g) from SO_2 (5.6 g).

Crystals suitable for single-crystal X-ray diffraction were obtained from the reaction of selenium powder (1.007 g, 12.74 mmol) with a mixture of AsF_5 (3.361 g, 19.78 mmol) and Cl_2 (0.871 g, 12.28 mmol) in SO_2 (6.95 g) at −30°C originally designed to give $Se_6(AsF_6)_4$ (cf. $Te_6(AsF_6)_4$ (12)). Within 5 min the color of the solution turned from green into yellow and a light-yellow precipitate, which dissolved upon stirring for 1 h at room temperature. After stirring the light-yellow solution for 24 h at room temperature, slow removal of the solvent into the second bulb (ΔT = 20°C), produced large light-yellow crystals. Several light-yellow crystals were mounted in well-dried capillaries, flame-sealed under nitrogen atmosphere, and stored at −20°C prior to the X-ray analysis. The total product (3.466 g) consisted of 1.955 g (5.22 mmol) of crystalline $SeCl_3AsF_6$ and 1.511 g (2.3 mmol) $Se_4(AsF_6)_2$ (FT–Raman). The material has been stored at −10°C under a dry nitrogen atmosphere for more than 1 year without noticeable decomposition.

The identity of $SeCl_3AsF_6$ was confirmed by single-crystal X-ray diffraction (see below) and its melting point (195°C vs. 196°C reported in ref. 6). The FT–Raman spectrum of crystalline $SeCl_3AsF_6$ is shown in Fig. 1 and the frequencies listed in Table 1. The ^{77}Se FT–NMR spectrum of $SeCl_3AsF_6$ prepared in situ from $SeCl_4$ (0.5261 g, 2.38 mmol) and AsF_5 (1.006 g, 5.92 mmol; 39.7% excess) in SO_2 (4.22 g), at −40°C showed one resonance at δ = 1419 ppm. The NMR spectra were not obtained at lower temperatures since the compound precipitated out of solution and we were unable to obtain a ^{77}Se NMR spectrum of redissolved $SeCl_3AsF_6$ in SO_2.

Preparation of $SeCl_3AsF_6$ from Se, Cl_2, and AsF_5 in AsF_3 or SO_2

Arsenic pentafluoride, AsF_5 (0.719 g, 4.23 mmol, 3.9% excess based on eq. [2]), was condensed onto selenium (0.219 g, 2.71 mmol) in AsF_3 (8.67 g), forming a green solution on warming to room temperature. Chlorine Cl_2 (0.297 g, 4.19 mmol, 2.7% excess based on eq. [2]), was added, the yellow solution stirred overnight, and the volatiles removed, giving a yellow solid with a few orange crystals that turned into a greenish looking powder after removing all of the solvent. The product turned into a white, slightly greenish solid upon grinding. The total product consisted of 0.969 g (cf. expected 1.014 g, 2.71 mmol based on Se) of impure $SeCl_3AsF_6$ (FT–Raman; X-ray powder diffraction). The impurity (reasonably green $Se_8(AsF_6)_2$) was not detected by these methods.

In a similar experiment SO_2 was used as the solvent and in this case a green powder that contained the compound $SeCl_3AsF_6$ (FT–Raman) was obtained.

Preparation of $SeCl_3SbF_6$ from $SeCl_4$, and $AgSbF_6$ in SO_2

$SeCl_4$ (1.318 g, 5.97 mmol) and $AgSbF_6$ (2.061 g, 5.99 mmol) were added in the dark to one bulb of the two-bulb reaction vessel and the Teflon stem of the valve immediately replaced. Addition of SO_2 (5.37 g) gave a yellow solution with a white precipitate, which was stirred for 4 h at room temperature. The solution was filtered through the frit into the second bulb and the insoluble product (AgCl) left behind was washed with SO_2 until the solution became colorless. The volatile products were removed, giving a light-yellow soluble solid product ($SeCl_3SbF_6$, 2.333 g) and a greyish-white insoluble product (AgCl, 0.885 g) (FT–Raman). Pure $SeCl_3SbF_6$ (1.647 g, 5.71 mmol; 65.5% recovered yield based on $SeCl_4$) was obtained after recrystallization of the crude product (2.333 g) from SO_2 (5.8 g). The material was collected and stored at −10°C in a sealed glass tube in a dry nitrogen atmosphere.

Preparation of SCl_3AsF_6 from S_8, Cl_2, and AsF_3

The salt SCl_3AsF_6 was prepared from sulfur, chlorine, and AsF_3 by a modification of the method described in ref. 3. AsF_3 (1.732 g, 13.13 mmol) followed by Cl_2 (2.949 g, 41.6 mmol) were condensed onto the sulfur (0.397 g, 1.55 mmol). A very exothermic reaction occurred upon warming the mixture slowly to room temperature over 1 h, leading to a red solution, likely SCl_3AsF_6 dissolved in liquid $AsCl_3/Cl_2$, over a white precipitate. The mixture was stirred overnight and the volatiles removed, giving a crude product (SCl_3AsF_6 (1.683 g)) that was then dissolved in AsF_3 (7.427 g). Upon cooling this solution to −15°C, a crystalline white solid was formed. The solution was filtered through the frit into the second bulb and the solvent was subsequently removed by evacuation, giving 1.405 g (4.29 mmol; yield: 65.4% based on AsF_3) of pure SCl_3AsF_6 (FT–Raman, Table 1). The material is stable in a dry nitrogen atmosphere at −10°C for at least 6 months.

Fig. 1. FT–Raman spectra of the $SeCl_3AsF_6$ and $SeCl_3SbF_6$ salts measured at room temperature in a melting point tube (resolution: 4 cm^{-1}). The parameters for laser power (mW) and number of scans are: (A) 87 mW, 150; (B) 34 mW, 256.

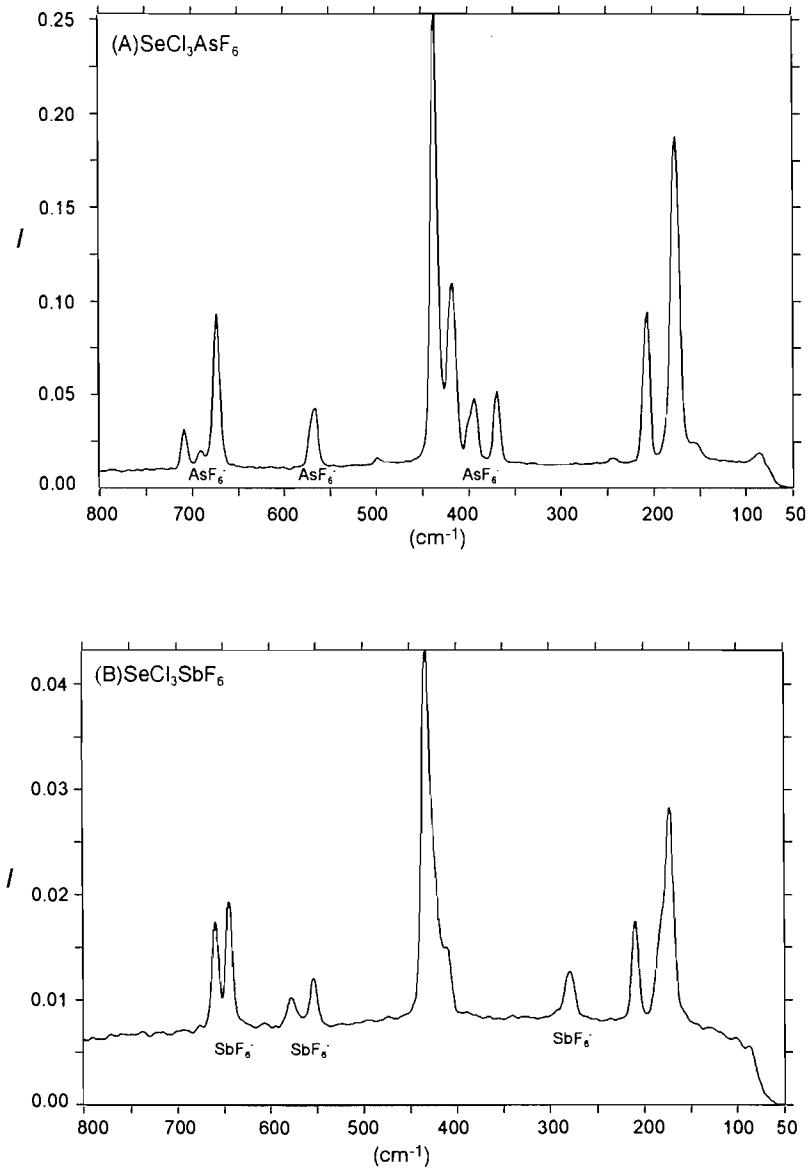

Preparation of SBr_3SbF_6 from S_8, Br_2, and SbF_5 in SO_2

The salt SBr_3SbF_6 (2.714 g, 5.35 mmol; yield: 92% based on sulfur) was prepared by reacting sulfur (1.491 g, 5.81 mmol) with Br_2 (11.74 g, 73.5 mmol, 5.4% excess based on S_8) followed by addition of SbF_5 (18.07 g, 83.4 mmol, 7% excess based on S_8) according to eq. [*5b*] and similar to the reaction in ref. 8. The products SBr_3SbF_6 and the reduced antimony fluoride $(SbF_3)_3{\cdot}SbF_5$ (13) were identified by FT–Raman spectroscopy.

Crystals of SBr_3SbF_6 were obtained from an attempt to grow crystals of $S_3Br_3SbF_6$ (1.35 g, 2.36 mmol) by redissolving the latter in SO_2 (12.5 g). To facilitate crystal growth, the solvent had to be removed very slowly over a period of 18 h with a temperature gradient of 3°C using bulbs cooled to 0°C and −3°C, respectively. The slow removal of the solvent was required by the high solubility of $S_3Br_3SbF_6$, which during the course of the experiment partially decomposed to the crystalline SBr_3SbF_6 (FT–Raman) and S_2Br_2 (visually: red oil). The identity of SBr_3SbF_6 was further established by single-crystal X-ray diffraction. The material has been stored at −10°C in a dry nitrogen atmosphere for at least a year without noticeable decomposition. The stability at room temperature is in the range of a few weeks, as indicated by the presence of bromine.

Preparation of SCl_3SbF_6 from SBr_3SbF_6 and Cl_2 in SO_2 or from $AgSbF_6$, S_2Cl_2, and Cl_2 in SO_2

In one experiment a mixture of SO_2 (10.45 g) and Cl_2 (0.703 g, 9.91 mmol, large excess) was poured onto SBr_3SbF_6 (1.98 g,

Table 1. FT–Raman frequencies (cm^{-1}) of MX_3AF_6 (A = As, Sb; M = Se, S; X = Cl, Br) and $SCl_3AlCl_4/SbCl_6$ with relative peak heights in parentheses.[a]

SCl_3AlCl_4[d,g]	SCl_3SbCl_6[e,h]	SCl_3AsF_6[d,i]	SCl_3SbF_6[d]	SBr_3AsF_6[f,j]	SBr_3SbF_6[d,j]	$SeCl_3AsF_6$[d,i]	$SeCl_3SbF_6$[d]	$SeBr_3AsF_6$[e,k]	$SeBr_3SbF_6$[e,k]	Assignments[a]
				700 (5)		708 (11), 691 (4)		703 (2)	670 (4)	$\nu(AsF_6^-)$, $\nu_3(F_{1u})^b$
531 (42), 518 (22)	535 (58), 522 (46)	545 (24), 529 (22)	542 (30), 526 (27)	436 (11), 417 (21)	429 (11), 414 (18)	418 (23)	410 (19)	292 (100)[c]	312 (18)	$\nu_{as}(MX_3^+)$, $\nu_3(E)$
496 (100)	501 (100)	518 (90)	514 (100)	377 (77)	379 (74)	437 (100)	433 (100)	292 (100)[c]	294 (83)	$\nu_s(MX_3^+)$, $\nu_1(A_1)$
478 (13)	335 (59), 328 (77)	681 (70)	653 (52), 645 (73)	686 (38), 676 (43)	655 (8), 647 (42)	673 (39)	659 (30), 644 (35)	678 (34)	648 (32), 644 (33)	$\nu(As/SbF_6^-; SbCl_6^-)$, $\nu_1(A_{1g})$;[b] $\nu_{as}(AlCl_4^-)$, $\nu_3(F_2)^b$
350 (18)	295 (18)	572 (15)	568 (15)	577 (13), 563 (10)	573 (6), 562 (6)	566 (15)	578 (9), 553 (13)	571 (br,9)	572 (7), 560 (10)	$\nu(As/SbF_6^-)$, $\nu_2(E_g)$;[b] $\nu_s(AlCl_4^-)$, $\nu_1(A_1)^b$
273 (34)	275 (24)	283 (59)	279 (59)	178 (77)	174 (93)	207 (49)	209 (27)	137 (55)	150 (79)	$\delta_s(MX_3^+)$, $\nu_2(A_1)$
214 (26), 205 (38)	217 (12), 208 (26)	215 (100)	217 (97)	131 (100)	129 (100)	176 (82)	172 (58)	110 (85)	112 (100)	$\delta_{as}(MX_3^+)$, $\nu_4(E)$
180 (4)		368 (20)		403 (8), 392 (8)		394 (22)		368 (12)		$\nu(AsF_6^-)$, $\nu_4(F_{1u})$;[b] $\delta_{as}(AlCl_4^-)$, $\nu_4(F_2)^b$
136 (20)	175 (78)		296 (21)	367 (16)	278 (16)	369 (23)	277 (13)		278 (26)	$\nu(SbF_6^-/SbCl_6^-)$, $\nu_5(F_{2g})^b$; $\delta_{as}(AlCl_4^-)$, $\nu_2(E)$

[a]The tentative assignments given were made on the basis of comparison between band positions, relative peak heights, and bond distances observed in related species.
[b]By comparison with $AlCl_4^-$, $SbCl_6^-$, AsF_6^- ($CsAsF_6$), and SbF_6^- ($LiSbF_6$) salts, ref. 28.
[c]No distinction between $\nu_{as}(SeBr_3^+)$ and $\nu_s(SeBr_3^+)$ can be made.
[d]The samples were measured in a melting point tube at room temperature.
[e]Samples were measured in a 5 mm NMR tube at room temperature.
[f]Samples were measured in a 5 mm NMR tube at −100°C.
[g]Previously reported in ref. 4.
[h]Previously reported in ref. 7.
[i]Previously reported in ref. 29.
[j]Previously reported in ref. 8.
[k]Previously reported in ref. 9.

Table 2. Fractional atomic positional parameters for SBr_3SbF_6 and $SeCl_3AsF_6$ with estimated standard deviations (esd's) in parentheses.

Atom	*x*	*y*	*z*	B_{eq}[a]
SBr_3SbF_6				
S(1)	0.19932(32)	0.69885(32)	0.71091(25)	3.15(12)
Br(1)	0.26719(15)	0.56687(14)	0.84882(10)	3.88(6)
Br(2)	0.41322(17)	0.69386(17)	0.62594(12)	4.79(7)
Br(3)	0.20807(16)	0.90566(15)	0.77817(14)	4.93(7)
Sb(1)	0.20409(8)	0.22754(8)	0.06203(6)	2.80(3)
F(1)	0.25940(109)	0.15706(122)	−0.06922(71)	6.9(5)
F(2)	0.14289(101)	0.29738(88)	0.19054(61)	5.2(4)
F(3)	−0.00169(99)	0.28147(99)	−0.01030(78)	6.2(4)
F(4)	0.41075(85)	0.17571(101)	0.13220(82)	6.7(5)
F(5)	0.12230(87)	0.05405(81)	0.09312(63)	4.6(4)
F(6)	0.29284(113)	0.40043(102)	0.03200(72)	6.5(5)
$SeCl_3AsF_6$				
Se(1)	0.18612(9)	0.31995(9)	0.19695(6)	3.16(5)
Cl(1)	0.4021(3)	0.3254(3)	0.1067(2)	3.08(5)
Cl(2)	0.2867(3)	0.4374(2)	0.3405(1)	5.53(14)
Cl(3)	0.2188(3)	0.1116(2)	0.2608(2)	4.96(13)
As(1)	−0.18815(9)	0.26175(9)	−0.07122(6)	5.25(16)
F(1)	−0.2734(9)	0.1013(6)	−0.0445(5)	6.90(35)
F(2)	−0.1233(7)	0.1978(5)	−0.1934(3)	4.94(29)
F(3)	−0.1031(7)	0.4238(5)	−0.1010(4)	5.07(31)
F(4)	−0.2404(9)	0.3273(7)	0.0514(5)	7.39(36)
F(5)	0.0107(7)	0.2140(7)	−0.0012(5)	6.24(33)
F(6)	−0.3832(7)	0.3154(7)	−0.1418(6)	7.20(41)

[a] B_{eq} is the mean of the principal axes of the thermal ellipsoid.

3.90 mmol) cooled to −30°C, yielding an immediate red solution (probably bromine) with a white precipitate (SCl_3SbF_6, 1.46 g, 3.91 mmol, 100.3% yield). The vessel was immersed in a −30°C ethanol bath and gradually allowed to warm to room temperature over a period of 4–6 h. The reaction described here is very temperature and time dependent, and the desired product will not be obtained if the reaction conditions are not met (see preparation of SCl_3SbCl_6).

Alternatively, the compound can be prepared from the reaction of $AgSbF_6$ (4.0389 g, 11.75 mmol, 1.8% excess), S_2Cl_2 (0.7794 g, 5.77 mmol; density: 1.62 g/mL), and Cl_2 (1.2932 g, 18.23 mmol, 5% excess), in a three-bulbed vessel consisting of one primary bulb and two secondary bulbs located on the opposite side of the frit to the primary valve. $AgSbF_6$ was added to one of the secondary bulbs in the dry box and the valve closed. A slight excess of S_2Cl_2 was then added to the unused secondary bulb using a 1 mL syringe with an 18 gauge stainless steel needle in a fumehood. Excess S_2Cl_2 was removed under a dynamic vacuum until the desired amount remained. SO_2 (14.6 g) was then added to the primary bulb, followed by Cl_2. The two solutions were mixed and then poured onto the solid, which had been cooled to −60°C. The resultant mixture was a pale yellow solution over a white precipitate. The reaction was allowed to stir for 1 h, gradually warming from −60°C to 0°C. The soluble compound (3.829 g, 10.28 mmol, 88.6% based on S_2Cl_2) was separated from the insoluble AgCl (1.861 g, 12.98 mmol, 112.5% based on S_2Cl_2) by repeated washing of the solvent through a medium-porosity sintered glass frit followed by solvent removal. The soluble white solid contained SCl_3SbF_6 (FT–Raman, Table 1). The purity of the material may be improved by washing out the more soluble, unreacted excess $AgSb_6F$. The material has been stored under a dry nitrogen atmosphere for 1 week at 30°C, or indefinitely at −10°C.

Preparation of SCl_3SbCl_6 from SBr_3SbF_6 and Cl_2 in SO_2

The compound was prepared by the reaction of SBr_3SbF_6 (2.597 g, 5.12 mmol) with a mixture of Cl_2 (1.287 g, 18 mmol, large excess) and SO_2 (2.425 g) at −20°C. The mixture was warmed to room temperature and allowed to stir for 18 h, giving a white precipitate in a red solution. Removal of the volatiles yielded SCl_3SbCl_6 (2.393 g, 5.06 mmol, 98.85 % yield based on SBr_3SbF_6) as characterized by FT–Raman spectroscopy. Single-crystal X-ray diffraction produced a unit cell that was identical to the one previously reported in ref. 7. The stability of the compound on storage is similar to the SbF_6^- salt reported above.

^{19}F FT–NMR study of the reaction of SBr_3SbF_6 with Cl_2 in SO_2

The reaction was carried out in a 5-mm NMR tube fitted with a 90° J.Young valve. SO_2 (1.299 g, 20.2 mmol) and Freon-11 (0.0184 g, 0.134 mmol), as an internal reference, were condensed onto the solid SBr_3SbF_6 (0.0441 g, 0.086 mmol).

Table 3. Anionic bond distances (Å) and angles (°) and selected interionic angles (°) for SBr_3SbF_6 (esd's in parentheses).[a]

SbF_6^-			
Sb(1)—F(1)	1.875(8)	Sb(1)—F(2)	1.860(7)
Sb(1)—F(3)	1.870(7)	Sb(1)—F(4)	1.860(7)
Sb(1)—F(5)	1.850(8)	Sb(1)—F(6)	1.864(9)
F(1)-Sb(1)-F(3)	88.9(4)	F(1)-Sb(1)-F(4)	90.5(4)
F(1)-Sb(1)-F(5)	89.5(4)	F(1)-Sb(1)-F(6)	90.2(5)
F(2)-Sb(1)-F(3)	89.6(4)	F(2)-Sb(1)-F(4)	91.0(4)
F(2)-Sb(1)-F(5)	90.0(3)	F(2)-Sb(1)-F(6)	90.3(4)
F(3)-Sb(1)-F(5)	91.4(4)	F(3)-Sb(1)-F(6)	90.2(4)
F(4)-Sb(1)-F(5)	89.4(4)	F(4)-Sb(1)-F(6)	88.9(4)
F(1)-Sb(1)-F(2)	178.4(4)	F(3)-Sb(1)-F(4)	179.0(5)
F(5)-Sb(1)-F(6)	178.3(4)		
Interionic angles			
Br(1)-S(1)-F(2a)	81.18(18)	Br(3)-S(1)-F(2a)	80.00(17)
Br(1)-S(1)-F(3b)	155.00(22)	Br(3)-S(1)-F(3b)	94.05(22)
Br(1)-S(1)-F(5c)	85.85(19)	Br(3)-S(1)-F(5c)	167.23(20)
Br(2)-S(1)-F(2a)	173.23(20)	F(2a)-S(1)-F(3b)	85.0(3)
Br(2)-S(1)-F(3b)	88.69(23)	F(2a)-S(1)-F(5c)	93.56(22)
Br(2)-S(1)-F(5c)	82.36(18)	F(3b)-S(1)-F(5c)	74.3(3)

[a]The letters *a, b, c* indicate symmetry-equivalent atoms: *a*, $-x$, $1.0 - y$, $1.0 - z$; *b*, $-x$, $0.5 + y$, $0.5 - z$; *c*, x, $0.5 - y$, $0.5 + z$.

Table 4. Anionic bond distances (Å) and angles (°) and selected interionic angles (°) for $SeCl_3AsF_6$ (esd's in parentheses).[a]

AsF_6^-			
As(1)—F(1)	1.689(7)	As(1)—F(2)	1.713(5)
As(1)—F(3)	1.712(6)	As(1)—F(4)	1.686(7)
As(1)—F(5)	1.693(7)	As(1)—F(6)	1.687(7)
F(1)-As(1)-F(2)	90.9(3)	F(1)-As(1)-F(4)	90.9(3)
F(1)-As(1)-F(5)	91.0(3)	F(1)-As(1)-F(6)	91.1(3)
F(2)-As(1)-F(3)	88.2(3)	F(2)-As(1)-F(5)	88.6(3)
F(2)-As(1)-F(6)	91.4(3)	F(3)-As(1)-F(4)	90.0(3)
F(3)-As(1)-F(5)	89.6(3)	F(3)-As(1)-F(6)	88.3(3)
F(4)-As(1)-F(5)	88.7(3)	F(4)-As(1)-F(6)	91.2(3)
F(1)-As(1)-F(3)	178.9(3)	F(2)-As(1)-F(4)	176.9(3)
F(5)-As(1)-F(6)	177.9(3)		
Interionic angles			
Cl(1)-Se(1)-F(2b)	175.87(14)	Cl(1)-Se(1)-F(3c)	85.26(14)
Cl(1)-Se(1)-F(5)	83.9(2)	Cl(2)-Se(1)-F(2b)	83.74(13)
Cl(2)-Se(1)-F(3c)	85.13(13)	Cl(2)-Se(1)-F(5)	168.2(2)
Cl(3)-Se(1)-F(2b)	81.10(13)	Cl(3)-Se(1)-F(3c)	172.53(14)
Cl(3)-Se(1)-F(5b)	89.6(2)	F(2b)-Se(1)-F(3c)	94.8(2)
F(2b)-Se(1)-F(5)	92.0(2)	F(3c)-Se(1)-F(5)	84.3(2)

[a]The letters *b, c* indicate symmetry-equivalent atoms: *b*, x, $0.500 - y$, $0.500 + z$; *c*, $-x$, $1.000 - y$, $-z$.

Finally, Cl_2 (0.554 g, 7.8 mmol) was added and the NMR tube flame sealed under vacuum with the contents kept at −196°C. A similar sample was prepared, omitting the addition of Cl_2, to determine the effects of Freon-11 on the sample. Both samples were allowed to warm to room temperature for 15 min prior to measurement at both −60°C and −70°C. The control sample showed peaks attributable to Freon-11 (δ = 0 ppm) and the anion, SbF_6^- ($\delta = -110$ ppm, $\Delta\nu_{1/2} = 940$ Hz). The chlorinated sample showed peaks attributable to the internal standard Freon-11, SbF_6^- ($\delta = -110$ ppm), and SOF_2 (δ = +74 ppm; 0.018 mmol). The ^{19}F NMR spectrum of the chlorinated sample recorded again after standing at −10°C for 5 days revealed

Table 5. Average M—X bond distances (Å), X-M-X bond angles (°), and the sum of the M···F bond valencies (valence units, v.u.) in all known $MX_3(As/SbF_6)$ salts (M = S, Se; X = Cl, Br) and the neutral group 15 $M'X_3$ trihalides.

Cation	SCl_3^+		$SeCl_3^+$	$TeCl_3^+$	$TeCl_3^+$
Anion	AsF_6^{-a}		AsF_6^{-b}	AsF_6^{-c}	SbF_6^{-c}
Average d(M—X)	1.970		2.096(2)	2.264(2)	2.258(3)
Average ∠(X-M-X)	102.3		99.77(10)	96.0(1)	95.8(1)
Sum of M···F bond valencies[n]	0.28		0.45	0.88	0.84
Neutral	PCl_3^e		$AsCl_3^f$	$SbCl_3^g$	
Average d(M—X)	2.040(1)[m.w.]		2.162(1)[m.w.]	2.359(1)[X]	
Average ∠(X-M-X)	100.27(9)		98.6(4)	94.13(5)	
Cation	SBr_3^+	SBr_3^+	$SeBr_3^+$	$TeBr_3^+$	
Anion	AsF_6^{-h}	SbF_6^{-b}	SbF_6^{-d}	AsF_6^{-d}	
Average d(M—X)	2.142(8)	2.148(2) [2.143(3)][i,X]	2.269(8)	2.432(3)	
Average ∠(X-M-X)	103.4(2)	103.53(8) [108.2(11)][i,X]	102.73(3)	97.9(1)	
Sum of M···F bond valencies[n]	0.17	0.25	0.44	0.69	
Neutral	PBr_3^j		$AsBr_3^k$	$SbBr_3\alpha^l$	$SbBr_3\beta^m$
Average d(M—X)	2.220(3)[m.w.]		2.324[m.w.]	2.50(5)[X]	2.49(3)[X]
Average ∠(X-M-X)	101.0(4)		99.8	95(1)	95(2)

Abbreviations: [X]X-ray diffraction (crystal); [m.w.] Microwave spectroscopy.
[a]Reference 3.
[b]This work.
[c]Reference 7.
[d]Reference 22.
[e]Reference 30.
[f]Reference 31.
[g]Reference 32.
[h]Reference 10.
[i]Reference 21.
[j]Reference 33.
[k]Reference 34.
[l]Reference 35.
[m]Reference 36.
[n]It has been shown that the strength of the S(IV)···F and Se(IV)···F contacts can be assessed by the relative magnitude of the bond valences (S) in valency units (v.u.) and is directly correlated to the localization of positive charge. An increase of positive charge on an atom leads to an increase in the sum of bond valences around the atom and this is accompanied by the formation of additional bonds and contacts (interionic and (or) intracationic) equal to the charge on the atom. The bond valence S in valence units (v.u.) is given by: $S = (R/R_0)^{-N}$, where R is the observed bond distance (Å), R_0 = 1.73 Å and N = 4 for Se(IV)···F and R_0 = 1.55 Å and N = 3.8 for S(IV)···F (see ref. 27).

peaks at δ = +74 ppm (SOF_2; 0.05 mmol), δ = +120 ppm (SO_2BrF; 0.01 mmol).

Preparation of SCl_3AlCl_4 from S_2Cl_2, Cl_2, and $AlCl_3$

The salt SCl_3AlCl_4 (1.04 g, 3.37 mmol, 90% yield vs. $AlCl_3$) (FT–Raman) was prepared by adding $AlCl_3$ (0.99 g, 7.45 mmol) to a secondary bulb of a three-bulbed vessel in the dry box. S_2Cl_2 (1.01 g, 7.55 mmol, 200% excess) was added to the other secondary bulb as described above, followed by Cl_2 (2.61 g, 36.7 mmol, 300% excess) via condensation. The bulb containing the solution was cooled to −80°C, preparing SCl_4 in situ (green solution over white precipitate). The $AlCl_3$ was then transferred into the cooled bulb containing the "SCl_4", and the solution was allowed gradually to warm to room temperature over 4 h, yielding a green liquid over a white precipitate, followed by filtration and removal of volatiles under dynamic vacuum.

FT–Raman, ^{19}F and ^{77}Se FT–NMR spectroscopy

FT–Raman spectra were obtained from neat samples sealed under nitrogen atmosphere in dried melting point capillaries on an FT–IR spectrometer (Bruker IFS66) equipped with an FT–Raman accessory (Bruker FRA 106) using a Nd-YAG laser (emission wavelength: 1064 nm; maximum laser power: 300 mW). The data were collected in the backscattering mode (180° excitation; resolution: 4 cm^{-1}) at room temperature

Fig. 2. Comparison of the two structures for the SBr_3^+ cation. (A) in the monoclinic unit cell (the letters a, b, c, e, g, h, k, m indicate symmetry-equivalent atoms: a, $-x$, $1.0 - y$, $1.0 - z$; b, $-x$, $0.5 + y$, $0.5 - z$; c, x, $0.5 - y$, $0.5 + z$; e, x, $1.5 - y$, $0.5 + z$; h, $1.0 - x$, $1.0 - y$, $1.0 - z$; k, $1.0 - x$, $0.5 + y$, $0.5 - z$; m, x, $1.00 + y$, $1.00 + z$); (B) in the orthorhombic unit cell (the letters a, b, c, e, j indicate symmetry-equivalent atoms: a, $-1.0 - x$, $0.5 + y$, $-0.5 - z$; b, $-0.5 - x$, $-y$, $-0.5 + z$; c, $-0.5 + x$, $-0.5 - y$, $-1.0 + z$; e, $0.5 + x$, $-0.5 - y$, $-1.0 - z$; j, x, $1.0 + y$, z) (21). Contacts that are less or slightly greater than the sum of the van der Waals radii for S···F ≤ 3.27 Å and for Br···F ≤ 3.32 Å are included (26). The values for the angles Br-S-Br (°) are (the values from ref. 21 are given in brackets): Br(1)-S(1)-Br(2), 103.81(13) (105.5(2)); Br(1)-S(1)-Br(3), 103.86 (15) (101.1(2)); Br(2)-S(1)-Br(3), 102.92(14) (101.6(2)) (additional angles including F atoms are given in the supplementary material). The thermal ellipsoids are scaled to enclose 50% of the probability density (ORTEP, included in the NRCVAX program package, see ref. 16).

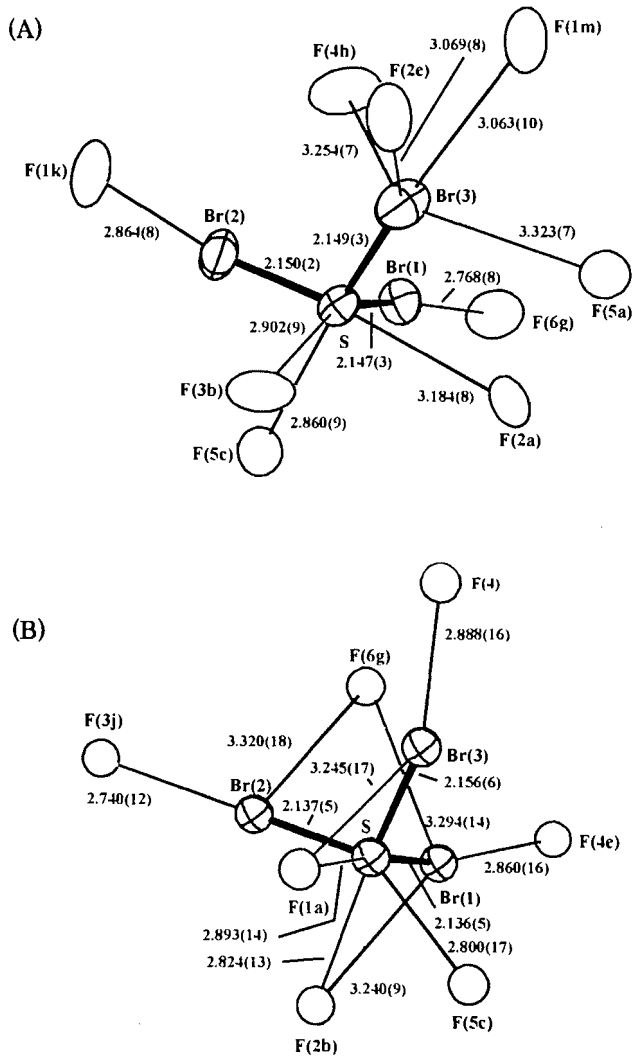

between 4200 and 70 cm^{-1}. The ^{77}Se NMR samples were prepared in situ and measured as outlined in ref. 2. The procedure for measuring ^{19}F FT–NMR spectra is described in ref. 2.

Crystal structure determination

Space group and cell dimensions

The crystals of SBr_3SbF_6 are monoclinic, space group $P2_1/c$ with $a = 8.137(1)$ Å, $b = 9.583(2)$ Å, $c = 12.447(2)$ Å, $\alpha = \gamma = 90.00°$, $\beta = 97.36(1)°$, $V = 962.6(3)$ Å^3, $Z = 4$, $D_x = 3.502$ Mg m^{-3} and $T = 291$ K. Crystal size: $0.56 \times 0.32 \times 0.16$ mm. Empirical formula: Br_3F_6SSb. FW = 507.51. $F(000) = 903.89$. $\lambda(MoK_\alpha) = 0.71069$ Å. $\mu(MoK_\alpha) = 15.46$ mm^{-1}.

The crystals of $SeCl_3AsF_6$ are monoclinic, space group $P2_1/c$ with $a = 7.678(1)$ Å, $b = 9.380(3)$ Å, $c = 11.920(3)$ Å, $\alpha = \gamma = 90.00°$, $\beta = 98.19(2)°$, $V = 849.72(3)$ Å^3, Z (molecules per cell) = 4, $D_x = 2.925$ Mg m^{-3} and $T = 291$ K. Crystal size: $0.1 \times 0.2 \times 0.15$ mm. Empirical formula: $AsCl_3F_6Se$. FW = 374.21. $F(000) = 688$. $\lambda(MoK_\alpha) = 0.71069$ Å. $\mu(MoK_\alpha) = 92.162$ cm^{-1}.

Data collection, structure solution, refinement

Crystals were examined in a dry box using a Wild M3 microscope of long focal length mounted outside the dry box. A number of crystals were flame sealed in rigorously dried capillary tubes.

The data for SBr_3AsF_6 and $SeCl_3AsF_6$ were collected at room temperature on an Enraf–Nonius CAD-4 automated diffractometer operating in the $\omega/2\theta$ ($2\theta_{max}$, 50) scan mode with graphite-monochromated MoK_α radiation.

The data collection (1763 reflections) for SBr_3SbF_6 resulted in 1678 unique reflections, 1472 of which were considered observed ($I \geq 0.5\sigma(I)$). The crystal was indexed using the program DIRAX (14). The structure was solved by automated Patterson interpretation routine (SHELXS 86; PATT instruction) (15) and missing atoms were found by difference Fourier maps. The data were corrected for Lorentz and polarization effects. Refinement by full-matrix least squares led to residuals of $R = 0.055$, $R_w = 0.060$ for 1472 observed reflections and 100 parameters. All atoms were assigned anisotropic displacement parameters. The unit cell constants were obtained by least-squares refinement of the diffractor setting angles for 24 well-centered reflections at $29° < 2\theta < 35°$. Calculations were performed using the PC implementation of the NRCVAX (16) program package.

Cell constants and an orientation matrix for the data collection for $SeCl_3AsF_6$ were obtained from a least-squares refinement using the setting angles of 25 carefully centered reflections in the range $14° < 2\theta < 15°$. Of the 1664 reflections collected, 1484 were unique ($R_{int} = 0.058$). The structure was determined by direct methods (SHELXS 86) and the data were corrected for Lorentz and polarization effects and for absorption using the program DIFABS (17); the maximum and minimum corrections were 1.000 and 0.416, respectively. Refinement by full-matrix least squares with all atoms assigned anisotropic thermal parameters resulted in the final residuals $R = 0.0525$, $R_w = 0.0554$ for 1151 observed reflections ($I \geq 3F(I)$).

Scattering factors for the structure determinations were taken from ref. 18 and effects of anomalous dispersion were included in F_c using the values of Cromer (19).

Fig. 3. Molecular packing of $SeCl_3AsF_6$.

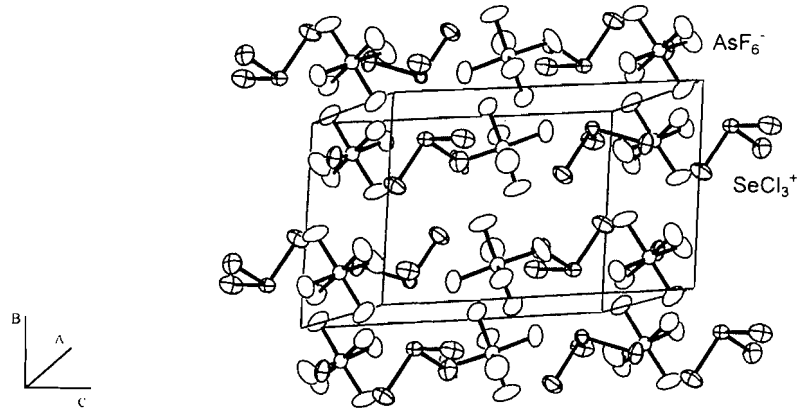

Fig. 4. Structure of the $SeCl_3^+$ cation showing cation–anion contacts (includes contacts that are less or slightly greater than the sum of the van der Waals radii for Se···F ≤ 3.37 Å and for Cl···F ≤ 3.22 Å). The values for the angles Cl-Se-Cl (°) are: Cl(1)-Se(1)-Cl(2), 100.38(10); Cl(1)-Se(1)-Cl(3), 98.39(10); Cl(2)-Se(1)-Cl(3), 100.53(10) (additional angles including F atoms are given in the supplementary material). The thermal ellipsoids are scaled to enclose 50% of the probability density (ORTEP, included in the NRCVAX program package, see ref. 16). The letters b, c, d, l, i indicate symmetry-equivalent atoms: b, x, $0.5 - y, 0.5 + z$; c, $-x$, $1.0 - y$, $-z$; d, $1.0 + x$, $0.5 - y$, $0.5 + z$; l, $-x$, $-y$, $-z$; i, $1.0 + x$, y, $-z$.

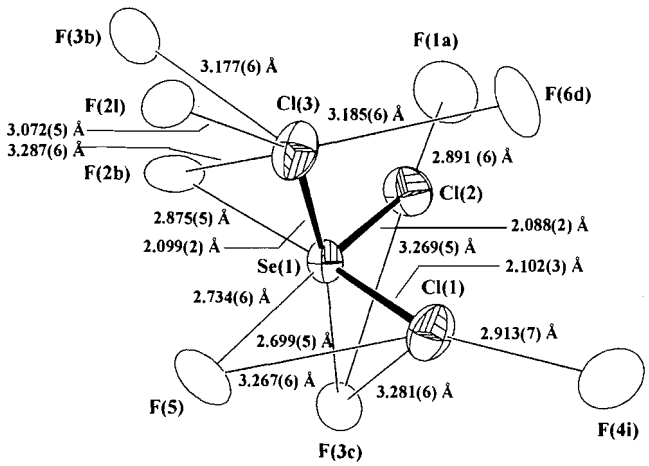

The final atomic coordinates are listed in Table 2. Available as supplementary material is a complete listing of thermal parameters, distances, and angles.[4]

[4] Complete sets of data may be purchased from: The Depository of Unpublished Data, Document Delivery, CISTI, National Research Council Canada, Ottawa, Canada K1A 0S2. The data have been also deposited with the Cambridge Crystallographic Data Centre and can be obtained on request from The Director, Cambridge Crystallographic Data Centre, University Chemical Laboratory, 12 Union Road, Cambridge, CB2 1EZ, U.K.

Discussion

We previously prepared MBr_3AsF_6 (M = S, Se, Te) by the stoichiometric reaction of M, Br_2, and AsF_5 according to eq. [1].

$$[1] \quad 3\,Br_2 + 2\,M + 3\,AsF_5 \xrightarrow{SO_2} 2\,MBr_3AsF_6 + AsF_3$$

The analogous reaction of selenium, chlorine, and arsenic pentafluoride according to eq. [2], leads to $SeCl_3AsF_6$ containing small amounts of green $Se_8(AsF_6)_2$ (11), although both FT–Raman spectroscopy and X-ray powder photography showed only the presence of $SeCl_3AsF_6$.

$$[2] \quad 3\,Cl_2 + 2\,Se + 3\,AsF_5 \xrightarrow{AsF_3} 2\,SeCl_3AsF_6 + AsF_3$$

Pure, white $SeCl_3AsF_6$ (in 97.3% yield) is best prepared by the reaction described in eq. [3].

$$[3] \quad 4\,SeCl_4 + 6\,AsF_5 \xrightarrow{SO_2} 4\,SeCl_3AsF_6 + AsCl_4AsF_6$$

The soluble $SeCl_3AsF_6$ was separated from the less soluble $AsCl_4AsF_6$ by filtration and then recrystallized from SO_2. The previously reported synthesis of $SeCl_3AsF_6$ (6) involved the reaction of $SeCl_4$ (generated in situ from Se and Cl_2) and $AsCl_4AsF_6$ (prepared in situ from AsF_3 and $AsCl_3$) in $AsCl_3$ as solvent; no yields were given.

SCl_3AsF_6 was obtained in 65% yield in a similar reaction as described in ref. 3, but using stoichiometric amounts of reagents, as shown in eq. [4].

$$[4] \quad 1/8\,S_8 + 2\,AsF_3 + 3\,Cl_2 \xrightarrow{SO_2} SCl_3AsF_6 + AsCl_3$$

SBr_3SbF_6 was previously prepared by the reaction of sulfur, bromine, and antimony pentafluoride and described as proceeding according to eq. [5*a*] although the identity of the SbF_3 was not established (8).

$$[5a] \quad 1/8\,S_8 + 3\,SbF_5 + 3\,Br_2 \xrightarrow{SO_2} SBr_3SbF_6 + SbF_3$$

It was later shown that the reduced antimony fluoride product

was in fact $(SbF_3)_3{\cdot}SbF_5$ (10, 13). In this work, the reaction was carried out as described in eq. [5*b*].

$$[5b]\quad 3/4\ S_8 + 9\ Br_2 + 10\ SbF_5 \xrightarrow{SO_2} 6\ SBr_3SbF_6 + (SbF_3)_3{\cdot}SbF_5$$

It was anticipated that the synthesis of SbF_6^- salts of MCl_3^+ (M = S, Se) from the reaction of chalcogen, chlorine, and antimony pentafluoride would be unsuccessful due to chlorine incorporation into the anion. However, SCl_3SbF_6 was prepared under carefully controlled temperature of −30°C, in quantitative yield by the chlorination of SBr_3SbF_6 according to eq. [6]. Warming to room temperature and stirring overnight led to SCl_3SbCl_6.

$$[6]\quad 2\ SBr_3SbF_6 + 3\ Cl_2 \xrightarrow{SO_2} 2\ SCl_3SbF_6 + 3\ Br_2$$

The preferred route to MCl_3SbF_6 (M = S, Se) with yields greater than 90%, is the reaction of $SeCl_4$ or SCl_4 (prepared in situ) with $AgSbF_6$ according to eqs. [7] and [8].

$$[7]\quad SeCl_4 + AgSbF_6 \xrightarrow{SO_2} SeCl_3SbF_6 + AgCl$$

$$[8]\quad 3Cl_2 + S_2Cl_2 + 2\ AgSbF_6 \xrightarrow{SO_2} 2\ SCl_3SbF_6 + 2\ AgCl$$

The SCl_3SbF_6 was previously obtained from the reaction of SH_3SbF_6 (prepared from HF, H_2S and SbF_5) (20) and Cl_2 in a Teflon/FEP vessel in unreported yields (5). The synthesis of $SeCl_3SbF_6$ has not been reported. SCl_3SbCl_6 was previously prepared by the reaction of As_4S_4 and $SbCl_5$ in SO_2 with unreported yields (7). The SCl_3AlCl_4 was prepared as described in ref. 4 according to eq. [9], but was adapted from an open system under a stream of dry nitrogen to a closed leak-tight and moisture-free vacuum system.

$$[9]\quad 3Cl_2 + S_2Cl_2 + 2\ AlCl_3 \xrightarrow{SO_2} 2\ SCl_3AlCl_4$$

In conclusion, reasonable preparative routes have been developed to $SCl_3^+$and $SeCl_3^+$ salts of MF_6^- (M = As, Sb) and to SCl_3SbCl_6 and SCl_3AlCl_4.

A possible reaction pathway for the reaction of SBr_3SbF_6 and Cl_2 leading to SCl_3SbF_6

The reaction described in eq. [6] which occurs at −30°C, may proceed by donation of the π^* electrons from Cl_2 to the empty π^* orbitals of SBr_3^+, leading to BrCl and $SClBr_2^+$ as shown in eq. [10]. The $Br^{\delta+}$—$Cl^{\delta-}$ may then undergo even more favorable reactions with $SBrCl_2^+$ because of the partial negative charge on the chlorine atom leading to the observed products.

[10] 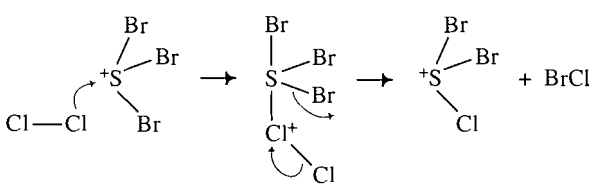

FT–Raman spectra of the MX_3^+ salts

The salts were all characterized by FT–Raman spectroscopy by comparison with previously reported spectra (see Table 1). The spectra of MCl_3SbF_6 (M = S, Se) are reported here for the first time. Overall, our FT–Raman data are better than previously published data, and our spectra include measurements of relative peak intensities (Table 1). The FT–Raman spectrum of $SeCl_3SbF_6$ allowed us to definitively assign the bands attributable to $SeCl_3^+$ in $SeCl_3AsF_6$ previously reported in ref. 6 (see Table 1 and Fig. 1). The symmetric and asymmetric SeCl stretching vibrations are assigned to the bands at 437 and 418 cm^{-1} (AsF_6^- salt) and at 433 and 410 cm^{-1} (SbF_6^- salt), respectively. The asymmetric SeCl stretching vibration was previously assigned to the band at 390 cm^{-1}, which is also observed in our FT–Raman spectrum of $SeCl_3AsF_6$ but in fact belongs to a vibration of the AsF_6^- anion since this band is missing in the FT–Raman spectrum of $SeCl_3SbF_6$. In addition, the presence of the possible impurities $AsCl_4AsF_6$ and $SeCl_4$ have been excluded by comparison with their FT–Raman spectra.[5]

The crystal structures of SBr_3SbF_6 and $SeCl_3AsF_6$

SBr_3SbF_6 is monoclinic, and isomorphous and isostructural with SBr_3AsF_6, and $SeBr_3AsF_6$. The previously reported structure of SBr_3SbF_6 was orthorhombic (21). The SBr_3^+ cation including distances and angles (in the caption of Fig. 2) and cation–anion contacts for both the monoclinic and orthorhombic structure are shown in Fig. 2. Additional bond distances and angles are listed in Table 3. The average S—Br bond distances and Br-S-Br angles in SBr_3AsF_6 and in both phases[6] of SBr_3SbF_6 are identical (see Table 5).

The X-ray crystal structure of $SeCl_3AsF_6$ is isomorphous and isostructural with $TeBr_3AsF_6$ (22). The structure contains alternating sheets of cations and anions tilted slightly out of the *ab* plane (Fig. 3). The $SeCl_3^+$ cation in $SeCl_3AsF_6$ has approximately C_{3v} symmetry. Figure 4 shows the $SeCl_3^+$ cation including distances and angles (in the caption of Fig. 4) and cation–anion contacts. Additional structural data are listed in Table 4. The observed average Se^+—Cl distance and Cl-Se-Cl angle in $SeCl_3AsF_6$ (2.096(2) Å, 99.77(10)°) are similar to those found in $SeCl_3SbCl_6$ (2.10(1) Å, 103.0(4)°) (7), $SeCl_3AlCl_4$ (2.103 Å, 99.2°) (23), and $SeCl_3AuCl_4$ (2.121(3) Å, 98.0(4)°) (24), but the average Se^+—Cl distance is significantly shorter than those found in $SeCl_3(MoOCl_4)$ (2.148(2) Å, no angles given) (25). With the structure of $SeCl_3AsF_6$ determined, the MX_3^+ (M = S, Se; X = Cl, Br) bond distances and angles in very weakly basic AsF_6^- and SbF_6^- salts and the relative strengths of the M···F interactions can now be compared (see Table 5). They now all show the expected trends

[5] FT–Raman data for $AsCl_4AsF_6$ and $SeCl_4$ (cm^{-1}) with relative intensities in parentheses: $AsCl_4AsF_6$: 680 (46) [AsF_6^-], 574 (6) [AsF_6^-], 523 (5), 499, {442 (25), 421 (100)}, {395 (9), 370 (21)} [AsF_6^-], 239 (6), 186 (89), 153 (65); $SeCl_4$: 387 (100), 371 (18), 357 (55), 341 (64), 216 (11), 211 (11), 168 (sh, 17), 161 (18), 128 (38), 98 (42). For detailed assignments see ref. 28.

[6] The two salts are different phases of SBr_3SbF_6. Their reciprocal lattices are not superimposable and the Sb···Sb distances are significantly different (Sb···Sb Å)): monoclinic, 5.578(1), 2 × 6.238(1), 6.275(1), 6.819(1); orthorhombic, 2 × 5.822(6), 2 × 6.326(4), 2 × 6.989(5), (from ref. 21).

discussed in ref. 10. The bond distances of the group 16 cations mirror the trends seen in the neutral group 15 trihalides (see Table 5), and are similar to the M—X distances calculated by the Schomaker–Stevenson equation given in ref. 10. The bond distances in the cations are shorter than the isoelectronic neutral group 15 trihalides, consistent with the smaller size of M^+ (M = elements of group 16) relative to that of M′ (M′ = elements of group 15). The shorter distances in the cation are reflected in the MX_3^+ Raman bands, which are at a higher frequency than the corresponding neutrals, with correspondingly higher force constants (N m^{-1}) for the trihalide cations than the trihalide neutrals (e.g., SBr_3^+ F_r 201.1(2); PBr_3 F_r 170.8(2); $SeBr_3^+$ F_r 168.1(1); $AsBr_3$ F_r 164.2(2) (9)). A comparison of the Raman spectra of the MX_3^+ and $M'X_3$ will be the subject of a future publication.[7] The X-M-X bond angles are conversely larger than those of the isoelectronic X-M′-X neutrals, consistent with the predictions of VSEPR theory (37). The larger effective electronegativity of the M^+ relative to M′ leads to a greater bond–bond repulsion, and a larger angle.

Acknowledgments

We thank the Natural Sciences and Engineering Research Council (NSERC) (Canada) for financial support and for an International Fellowship (Dr. G. Schatte).

References

1. P.D. Boyle, T.S. Cameron, J. Passmore, G. Schatte, and G.W. Sutherland. J. Fluorine Chem. **71**, 217 (1995), and references therein.
2. S. Brownridge, T.S. Cameron, J. Passmore, G. Schatte, and T. Way. J. Chem. Soc. Dalton Trans. 2553 (1996).
3. R. Minkwitz, K. Jänichen, H. Prenzel, and V. Wölfel. Z. Naturforsch. B: Anorg. Chem. Org. Chem. **40B**, 53 (1985).
4. H.E. Doorenbos, J.C. Evans, and R.O. Kagel. J. Phys. Chem. **74**, 3385 (1970).
5. R. Minkwitz and V. Gerhard. Z. Naturforsch. B: Chem. Sci. **44**, 364 (1989).
6. L. Kolditz and W. Schäfer. Z. Anorg. Allg. Chem. **315**, 35 (1962).
7. B.H. Christian, M.J. Collins, R.J. Gillespie, and J.F. Sawyer. Inorg. Chem. **25**, 777 (1986).
8. J. Passmore, E.K. Richardson, and P. Taylor. Inorg. Chem. **17**, 1681 (1978).
9. W.V.F. Brooks, J. Passmore, and E.K. Richardson. Can. J. Chem. **57**, 3230 (1979).
10. J.P. Johnson, M. Murchie, J. Passmore, M. Tajik, P.S. White, and C. Wong. Can. J. Chem. **65**, 2744 (1987).
11. M. Murchie, R. Kapoor, J. Passmore, G. Schatte, and T. Way. Inorg. Synth. **31**, 102 (1996).
12. R.C. Burns, R.J. Gillespie, W. Luk, and D.R. Slim. Inorg. Chem. **18,** 3086 (1979).
13. W.A.S. Nandana, J. Passmore, D.C.N. Swindells, P. Taylor, P.S. White, and J.E. Vekris. J. Chem. Soc. Dalton. Trans. 619 (1983).
14. A.J.M. Duisenberg. J. Appl. Crystallogr. **25**, 92 (1992).
15. G.M. Sheldrick. *In* Crystallographic computing. *Edited by* G.M. Sheldrick, C. Kruger, and R. Goddard. Oxford University Press, Oxford. 1985. p. 175.
16. E.J. Gabe, Y. LePage, J.P. Charland, F.L. Lee, and P.S. White. J. Appl. Crystallogr. **22**, 384 (1989).
17. N. Walker and D. Stuart. Acta Crystallogr. Sect. A: Found. Crystallogr. **A39**, 158 (1993).
18. D.T. Cromer and J.T. Waber. International tables for X-ray crystallography. Vol. IV. Kynoch, Birmingham. 1974. Table 2.2.4.
19. D.T. Cromer. International tables for X-ray crystallography. Vol. IV. Kynoch, Birmingham. 1974. Table 2.3.1.
20. K.O. Christie. Inorg. Chem. **14**, 2230 (1975).
21. R. Minkwitz, R. Lekies, and H. Preut. Z. Naturforsch. B: Chem. Sci. **42**, 1227 (1987).
22. J. Passmore, E.K. Richardson, T.K. Whidden, and P.S. White. Can. J. Chem. **58**, 851 (1980).
23. B.A. Stork-Blaisse and C. Romers. Acta Crystallogr. Sect. B: Struct. Crystallogr. Cryst. Chem. **B27**, 386 (1971).
24. P.G. Jones, R. Schelbach, and E. Schwarzmann. Acta Crystallogr. Sect. C: Cryst. Struct. Commun. **C43**, 607 (1987).
25. A. Gleizes and J.P. Galy. C. R. Seances Acad. Sci. Ser. C: **286**, 29 (1978).
26. A. Bondi. J. Phys. Chem. **68**, 441 (1964).
27. I.D. Brown. *In* Structure and bonding in crystals. Vol. 2. *Edited by* M. O'Keefe and A. Navrotsky. Academic Press, London. 1981.
28. K. Nakamoto. *In* Infrared and Raman spectra of inorganic and coordination compounds. 4th ed. John Wiley & Sons, Inc., New York. 1986.
29. W. Sawodny and K. Dehnicke. Z. Anorg. Allg. Chem. **349**, 169 (1967).
30. K. Hedberg and M. Iwasaki. J. Chem. Phys. **36**, 589 (1962).
31. S. Konaka. Bull. Chem. Soc. Jpn. **43**, 3107 (1970).
32. A. Lipka. Acta Crystallogr. Sect. B: Struct. Crystallogr. Cryst. Chem. **B35**, 3020 (1979).
33. K. Kuchitsu, T. Shibata, A. Yokozeki, and C. Matsumura. Inorg. Chem. **10**, 2584 (1971).
34. A.G. Robiette. J. Mol. Struct. **35**, 81 (1976).
35. D.W. Cushen and R. Hulme. J. Chem Soc. **A**, 4162 (1964).
36. D.W. Cushen and R. Hulme. J. Chem Soc. **A**, 2218 (1962).
37. R.J. Gillespie. *In* Molecular geometry. Van Nostrand Reinhold, London. 1972.

[7] S. Brownridge, J. Passmore, G. Schatte, and T. Way. Manuscript in preparation.

Differentiation of cerebroside isomers and study of fragmentation by liquid secondary ion mass spectrometry and mass spectrometry/mass spectrometry of selected derivatives

Hélène Perreault and Catherine E. Costello

Abstract: The possibility of distinguishing two cerebroside isomers, whose structural variation is in the sugar rings, was investigated by liquid secondary ion mass spectrometry (LSIMS) and tandem mass spectrometry (MS/MS). In addition to the native materials, four types of derivatives of these cerebroside isomers were prepared and studied using these techniques. A first level of comparison between isomers consisted of seeking differences in the conventional LSIMS spectra. Native compounds, galactosyl and glucosyl ceramides, did not yield consistent and meaningful elements of comparison and a few nanomoles of material were required to produce significant spectra. Permethylated cerebrosides gave rise to abundant ceramide ions that do not reveal information about sugar structure; relative abundances of low-mass sugar-related ions allowed isomeric discrimination to a limited extent. Peracetylated and perbenzoylated derivatives of both cerebrosides yielded several sugar-related ions whose relative abundances in the spectra varied systematically between species and allowed distinction of glucosyl- from galacto-cerebrosides. At a second level of comparison, collision-induced dissociation (CID) MS/MS spectra of selected ions containing the hexosyl residues and observed in the LSIMS spectra were recorded to study the extent and pathways of fragmentation for each isomer. Native and permethylated compounds led to disappointing results; on the other hand, peracetylated and perbenzoylated derivatives yielded informative spectra where isomeric differentiation was possible, mostly owing to the production of carbohydrate-related product ions, whereas native and permethylated compounds only produced ceramide-related ions upon CID MS/MS.

Key words: glycosphingolipids, cerebrosides, derivatization, mass spectrometry, MS/MS, LSIMS.

Résumé : La spectrométrie de masse à ionisation par bombardement d'ions (LSIMS) et la spectrométrie de masse en tandem (MS/MS) ont été utilisées dans l'étude de la distinction de deux cérébrosides isomériques. Les composés natifs (non-dérivés) ainsi que quatre types de dérivés de ces cérébrosides ont été charactérisés à l'aide de ces techniques. Une comparaison préliminaire des deux isomères a consisté à chercher les différences apparaissant dans les spectres LSIMS conventionnels. Les composés natifs, aussi désignés sous le nom de glucosyl- et galactosyl-céramide, ne produisent pas d'éléments spectraux intéressants permettant de faire la distinction entre isomères; de plus quelques nanomoles de matériel sont requises pour produire des spectres qualitativement acceptables. Les cérébrosides perméthylés produisent d'abondants ions caractérisant la partie céramide des composés, mais ces ions ne sont pas utiles pour l'étude de la portion hexosyl. Cette dernière produit toutefois des ions à très basse masse dont l'abondance relative aide à caractériser l'hexosyl. Les dérivés peracétylés et perbenzoylés des deux cérébrosides produisent plusieurs ions permettant de caractériser la portion sucre. Les abondances relatives de ces ions varient systématiquement entre les deux différentes espèces et permettent la distinction entre glucosyl- et galactosyl-cérébrosides. Dans une deuxième séries d'expériences, les spectres MS/MS obtenus de la fragmentation par collisions (CID) d'ions LSIMS présélectionnés et contenant la portion sucre des molécules ont été enregistrés dans le but d'étudier les patrons de fragmentation des deux isomères. Les cérébrosides natifs et perméthylés ont produit des résultats non-significatifs; par contre, les composés peracétylés et perbenzoylés produisent des spectres contenant beaucoup d'information et rendant possible la différentiation des isomères.

Mots clés : glycosphingolipides, cérébrosides, dérivé, spectrométrie de masse, MS/MS, LSIMS.

Received April 10, 1996.

H. Perreault[1] and C.E. Costello.[2] Mass Spectrometry Resource, Department of Chemistry, Massachusetts Institute of Technology, 77 Massachusetts Avenue, Cambridge, MA 02139, U.S.A.

[1] Author to whom correspondence may be addressed. Present address: Chemistry Department, University of Manitoba, 144 Dysart Road, Winnipeg, MB R3T 2N2, Canada. Telephone: (204) 474-7418. Fax: (204) 275-0905. E-mail: perreau@cc.umanitoba.ca

[2] Present address: Department of Biophysics, Boston University School of Medicine, 80 E. Concord St., Boston, MA 02118-2394, U.S.A.

Scheme 1. Compounds investigated in this study. **1**: Galactosyl-ceramide (galacto-cerebroside) and **2**: glucosyl-ceramide (gluco-cerebroside).

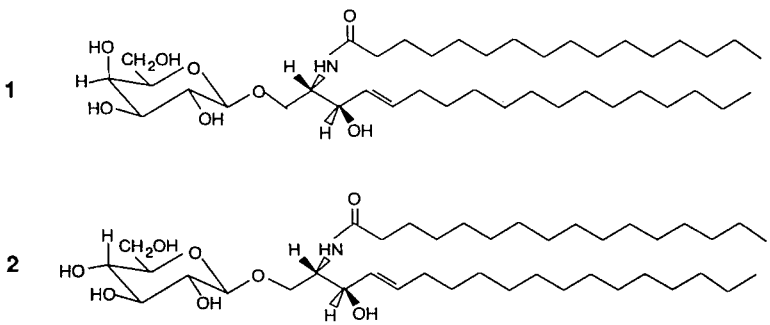

Introduction

Cerebrosides constitute a specific class of glycosphingolipids (GSLs) and are formed by the combination of ceramides and monohexoside residues. Galacto-cerebrosides, which are the basis of formation of another important group of GSLs, the sulfatides, are commonly called "cerebrosides" with no further specification. Glucosyl ceramides, or gluco-cerebrosides, form an essential class of compounds since they precede formation of higher GSLs such as lactosides, globosides, gangliosides, and neolactosides, whose biological functions as receptors and exchangers in cell membranes have been well documented (1–3). Structural features of natural cerebrosides encompass the type of ceramide present in the molecule, and also the type of monohexoside linked to the latter by a glycosidic bond. Variations in ceramides can occur as differences in fatty acyl or sphingosine base chain length, degree of unsaturation, and hydroxylation at former sites of unsaturation, as in 4D-hydroxysphinganine, formerly known as phytosphingosine (4). The structures of isomeric monosaccharides such as glucose and galactose can be determined by ^{1}H nuclear magnetic resonance (NMR) (5), provided that sufficient quantities of sample, in the milligram range (micromoles), are available. Mass spectrometry, owing to the recent advent of sophisticated ionization techniques and derivatization methods, has significantly enhanced structural analysis of glycosphingolipids. In general, lower amounts of materials are required for mass spectral analyses than for NMR characterization; however, detection limits vary, depending on the ionization technique used. So far, matrix-assisted laser desorption/ionization coupled to time-of-flight analyzers (MALDI-TOFMS) and electrospray ionization (ESI) have achieved the highest sensitivity for characterization of derivatized GSLs (6, 7); the amounts of material detected were at the femtomole level. Due to low volatility, thermal lability, and polarity of GSLs, derivatization is often carried out prior to mass spectral analysis by any ionization method. We reported in an earlier study (8) that permethylation, peracetylation, and perbenzoylation enhance sensitivity by two orders of magnitude in liquid secondary ion mass spectrometry (LSIMS) and MALDI-TOFMS; the same observation has also been made in ESI (7) for permethylated GSLs. We also reported on the complementarity of structural information obtained from LSIMS and MS/MS fragmentation of different types of derivatives of the same analyte (8).

This paper focuses on isomeric discrimination of two palmitoyl cerebroside species whose structural difference resides in the monosaccharide moiety. Subnanomole to low nanomole levels of galactosyl and glycosyl ceramides were derivatized using four methods described previously (8) and were studied by positive LSIMS and tandem mass spectrometry (MS/MS) in order to investigate the possibility of isomeric discrimination from mass spectral information. MALDI-TOFMS was used for molecular weight confirmation immediately following derivatization.

Experimental

Chemicals and reagents

Galactosyl palmitoyl cerebroside or galactosyl *N*-palmitoyl (4*E*)-sphingenine (**1** in Scheme 1) was obtained from Sigma Chemicals (St. Louis, Mo.) and used without further purification. Glucosyl palmitoyl cerebroside or glucosyl *N*-palmitoyl (4*E*)-sphingenine (**2**) was graciously provided by R. Duclos and synthesized according to a procedure described elsewhere (9). Reagents methyl iodide, benzoic anhydride, benzoyl chloride, and *N*,*N*-dimethylaminopyridine (DMAP) were purchased from Aldrich (Milwaukee, Wis.), while dimethyl sulfoxide (DMSO) and acetic anhydride were obtained from Pierce Chemicals (Rockford, Ill.). HPLC-grade solvents (pyridine, toluene, hexane, chloroform, acetonitrile, and methanol) were obtained from Mallinckrodt (Paris, Ky). The LSIMS and MALDI matrices used in this study were, respectively, 3-nitrobenzyl alcohol (NBA) and 2,5-dihydroxy benzoic acid (DHB), both purchased from Aldrich.

Derivatization methods

Bulk phase permethylation and gas phase peracetylation and perbenzoylation (using benzoyl chloride) were used as described previously (8). Perbenzoylation with benzoic anhydride and DMAP was performed in the liquid phase (8) due to low volatility of the reagents. Derivatization reactions were conducted using several aliquots of 800 pmol – 1 nmol of material to ascertain reproducibility between samples and consistency of the methods. Derivatized materials were dissolved in acetonitrile to concentrations between 0.1 and 0.2 nmol/μL. Products were verified and characterized using MALDI-TOFMS under the conditions described below.

Mass spectrometry

LSIMS spectra were recorded with a JEOL HX110/HX110

Scheme 2. Fragmentation pathways of cerebrosides according to the nomenclature developed by Domon and Costello (12).

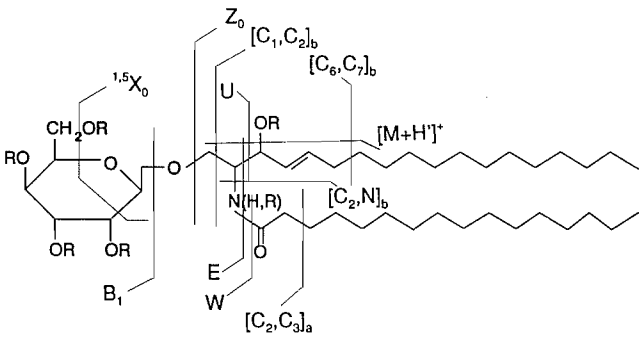

(E1B1-E2B2) tandem instrument operated at +10 kV accelerating voltage with −18 kV postacceleration at the detector. A JEOL cesium gun produced a primary beam of 15 keV Cs^+ ions. For acquisition of conventional mass spectra, the resolution was 1:3000 and the magnetic sector B1 was scanned at a rate of about 25 s/decade. The data system used was a MS-MP7000MD/MT (Complement, JEOL). Sample solutions of derivatized compounds (1 μL, 100–200 pmol) were mixed with 1 μL NBA on an LSIMS chilled probe that has been described in detail elsewhere (10). The use of this probe allowed stability of the signal over longer time ranges than a conventional LSIMS probe and thus the spectra presented here result from integration of at least 3 scans.

For collision-induced dissociation (CID) MS/MS experiments, 7 keV collisions were effected with helium in a cell located between E1B1 (MS1) and E2B2 (MS2). The pressure of helium employed was sufficient to reduce the abundance of the precursor beam to 40% of its original value. MS/MS spectra were obtained by B/E scans of MS2 at the rate of about 40 units/s. Both MS1 and MS2 were tuned for 1:1000 resolution.

MALDI-TOF mass spectra were recorded with a modified Vestec VT2000 (Vestec Corp., Houston, Tex.). A detailed description of this instrument, its optical system, and data processing system has been made elsewhere (6, 11). Desorption/ionization was accomplished using a nitrogen laser (Laser Science Inc., Newton, Mass.) with radiation at 337 nm. The sample (ca. 3 pmol, in 1 μL acetonitrile) was mixed with 1 μL of a 10 g/L solution of DHB matrix in water and applied to a polished metal surface, in order to create a sampling area of about 3 mm diameter. Ions were accelerated to +30 keV.

Results and discussion

The nomenclature system used here to describe fragmentation patterns of compounds **1** and **2** follows that developed by Domon and Costello (12) for GSLs. A few modifications were made to the nomenclature of long-chain cleavages with conservation of the charge on the nitrogen atom of the ceramide moiety (8) and are applied in this study. Scheme 2 summarizes the description of fragmentations according to this system. The prime (′) sign describes ions having lost one ROH molecule (water, methanol, acetic acid, benzoic acid, respectively, for native compounds; permethylated, peracetylated, and perbenzoylated derivatives). The double (″) and triple (‴) primes refer to loss of two and three ROH molecules, respectively. The slash (/) is employed to describe fragmentations occurring at more than one site.

A comparison of conventional LSIMS spectra was accomplished for native isomers and also for each type of derivative investigated in this study; any ion present in the conventional spectra and containing the hexosyl residue was investigated in more detail by CID MS/MS. Molecular ions $[M+H]^+$ were not studied since their $[M+H']^+$ homologs were generally more abundant in the LSIMS spectra and thus easier to characterize by MS/MS. The $[M+H']^+$ ions arise with loss of ROH from the ceramide moiety (8). These ions have fewer degrees of freedom than $[M+H]^+$ and stand a better chance of yielding information on the carbohydrate moieties and their structural differences.

Native isomers **1** and **2** produced very similar mass spectra, exhibiting $[M+H]^+$, $[M+H']^+$, Z_0, Z_0', and W'/C_1 ions. A list of these ions and associated relative abundances is presented in Table 1, Column A. A quantity of sample of 10 nmol was required in order to obtain spectra where, overall, presence of NBA matrix ions did not interfere in the interpretation and molecular weight information could be obtained without ambiguity. With the exception of $[M+H']^+$, fragment ions observed in these spectra did not contain the carbohydrate moieties of the molecules. MS/MS spectra of the latter species at *m/z* 682.5 were recorded (not shown), providing no information on glucosyl and galactosyl residues except ions at *m/z* 548, arising from $^{1,5}X_0$ cross-ring cleavages. Other ions observed are listed with their relative abundances in Table 2, Column A. The two spectra were so similar that they could not lead to any clear differentiation of isomers.

Permethylation of **1** and **2** allowed a sensitivity increase of an average factor of 75 under the same experimental conditions with either LSIMS or MALDI-TOFMS. Thus, for LSIMS analysis, it was possible to obtain informative spectra using 100 pmol of permethylated material; see Table 1, Column B, for more detail on fragmentation. Differences between the conventional spectra of permethylated **1** and **2** reside in the relative abundances of Z_0 and W'/C_1 ions versus the $[M+H]^+$ and $[M+H']^+$ species. However, these differences cannot easily relate to sugar structures since neither Z_0 or W'/C_1 ions contain hexosyl residues. B_1' ions also exhibit different relative abundances. We reported earlier (8) that highly unstable permethylated B_1 ions, which could be studied by MS/MS, decompose mainly by loss of one methanol molecule to form B_1' ions at *m/z* 187. According to Table 1, Column B, this decomposition occurs in the ion source to a greater extent for **2** than for **1**. The CID MS/MS spectrum of the B_1' species from **1** displayed in Fig. 1 is very similar to that obtained for **2** (not shown). Small differences occur, for instance, in the relative abundance of product ions at *m/z* 89 and 155. The similarity between the two spectra suggests that the B_1' precursors may have the same structure. It would be possible to obtain this common structure by elimination of methoxy in position 4 (and H in 5) as illustrated in Scheme 3, center line. Loss of a methanol molecule originating from positions 4 and 5 of the B_1' sugar ring would indicate that, whether *cis* or *trans*, the elimination would proceed preferentially from sites 4 and 5 to form a conjugated double bond system. If this hypothesis holds and B_1' ions of **1** and **2** are identical, then *m/z* 187.1 ions generated from permethylated manno-cerebroside should have a different structure because of the orientation of the methoxy in position 2. As no

Table 1. Relative abundances[a] of ions observed in the LSIMS spectra of native and derivatized **1** and **2**.[b]

	Form of compounds									
	Native		PerMe		PerAc		PerBz (Anh)		PerBz (Cl)	
	1	**2**	**1**	**2**	**1**	**2**	**1**	**2**	**1**	**2**
Ions/Relative abundance	A (calcd. *m/z*)		B (calcd. *m/z*)		C (calcd. *m/z*)		D (calcd. *m/z*)		E (calcd. *m/z*)	
$[M+H]^+$	(700.6)		(784.7)		(910.6)		(1220.7)		(1324.7)	
	45.6	48.0	33.0	22.3	11.1	6.8	10.1	10.8	5.6	5.7
$[M+H']^+$	(682.5)		(752.6)		(850.6)		(1098.7)		(1202.7)	
	54.4	52.0	67.0	77.7	88.9	93.2	89.9	89.2	94.4	94.3
Z_0	(520.5)		(548.5)		(562.5)		(624.5)		(728.6)	
	64.0	56.9	43.2	99.5	10.0	9.5	17.5	15.7	14.2	18.6
Z_0'	(502.5)		(516.5)		(502.5)		(502.5)		(606.5)	
	6.4	6.0	6.8	18.6	8.9	11.6	29.2	28.9	9.4	22.8
Z_0'–R,+H	(502.5)		(502.5)		(502.5)		(502.5)		(502.5)	
	6.4	6.0	2.8	5.2	—		—		30.2	70.0
W/C_1	(282.3)		(310.3)		(324.3)		(386.3)		(490.4)	
	—		—		—		—		34.9	57.1
W'	(444.3)		(514.4)		(580.3)		(860.4)		(964.5)	
	—		—		—		—		94.3	174.3
W'/C_1	(264.3)		(278.3)		(264.5)		(264.5)		(368.5)	
	128.0	119.0	22.7	46.6	52.2	63.2	231.5	231.3	128.3	227.1
W'/C_1–R,+H	(264.3)		(264.3)		(264.5)		(264.5)		(264.5)	
	—		—		—		—		50.0	88.6
U'	(502.4)		(558.5)		(628.5)		(814.5)		(918.6)	
	—		—		3.3	2.8	—		—	
B_1	(163.1)		(219.1)		(331.1)		(579.2)		(579.2)	
	—		—		109.4	25.3	148.3	60.2	143.4	97.1
B_1'	(145.0)		(187.1)		(271.1)		(457.1)		(457.1)	
	—		6.2	20.0	—		—		—	
B_1''	(127.0)		(155.1)		(211.1)		(335.1)		(335.1)	
	—		10.0	30.0	—		—		18.9	17.1
B_1''–R,+H	(127.0)		(141.1)		(169.1)		(231.1)		(231.1)	
	—		—		103.3	100.0	73.0	48.2	73.6	117.1
B_1''–2R,+2H	(127.0)		(127.0)		(127.0)		(127.0)		(127.0)	
	—		—		23.3	18.9	—		—	
B_1'''–R,+H	(109.0)		(109.0)		(109.0)		(109.0)		(109.0)	
	—		—		42.2	52.6	—		—	

[a]Relative abundances vs. $[M+H]^+$ and $[M+H']^+$ added together; ±5%.

[b]The calculated *m/z* appear in parentheses; the experimental *m/z* values were within 0.05% of calculated values.

Abbreviations: perMe = permethylated, PerAc = peracetylated, PerBz (Anh) = perbenzoylated with benzoic anhydride, PerBz(Cl) = perbenzoylated with benzoyl chloride.

manno-cerebroside was available for comparison, B_1'-equivalent (*m/z* 187.1) ions were generated from PME monosaccharides glucose, galactose, and mannose. The $[M+H'']^+$ ions were used as precursors for this purpose. Domon et al. have recently shown that loss of methanol from PME monosaccharides occurs in position 1 (13). This suggests that B_1'' ions from PME **1** and **2**, as well as $[M+H'']^+$ ions from PME galactose and glucose, are formed from similar precursors at *m/z* 219, as illustrated in the top portion of Scheme 3. Unimolecular dissociation MS/MS spectra of the $[M+H'']^+$ ions of PME glucose, galactose, and mannose were recorded. PME glucose and mannose produced very similar spectra while the spectrum of PME galactose showed some minor differences, which were more accentuated than in the case of the B_1' ions of **1** and **2**. These results suggest similar structures for the $[M+H'']^+$ ions of glucose and mannose, which would be possible with elimination of methoxy from position 2 (and H from 3) as shown in the bottom portion of Scheme 3. If the same 2,3-elimination occurred from the $[M+H']^+$ ring of galactose, the resulting $[M+H'']^+$ ion would be structurally different. To summarize, it was difficult to draw structural information from the CID MS/MS spectra of the B_1' ions of PME **1** and **2**. Similar CID MS/

Table 2. Relative abundances[a] of product ions observed in the CID MS/MS spectra of $[M + H']^+$ ions.[b]

	Form of compounds									
	Native		PerMe		PerAc		PerBz (Anh)		PerBz (Cl)	
	1	2	1	2	1	2	1	2	1	2
Ions/Relative abundance	A (calcd. *m/z*)		B (calcd. *m/z*)		C (calcd. *m/z*)		D (calcd. *m/z*)		E (calcd. *m/z*)	
$[M+H'']^+$	(664.5)		(720.6)		(790.6)		(976.6)		(1080.7)	
	6.1	8.0	15.2	28.2	2.0	1.8	2.1	2.1	14.3	4.9
M+H′−2RO	(648.5)		(690.6)		(732.6)		(856.6)		(960.6)	
	—		16.7	35.5	4.0	10.1	1.0	1.3	—	
$^{1,5}X_0'$	(547.5)		(561.5)		(547.5)		(547.5)		(651.5)	
	2.4	2.5	33.3	60.7	3.5	10.1	2.0	1.9	8.1	7.4
$^{1,5}X_0'/[C_5,C_6]_b$	(365.3)		(379.3)		(365.3)		(365.3)		(469.4)	
	—		14.7	17.0	—		—		—	
Y_0'	(518.5)		(532.5)		(518.5)		(518.5)		(622.5)	
	4.9	5.0	—		—		—		—	
Z_0'	(502.5)		(516.5)		(502.5)		(502.5)		(606.5)	
	2.9	2.6	8.3	8.7	2.5	2.0	2.6	1.8	44.6	46.3
$[C_1,C_2]_b'$	(488.5)		(502.5)		(488.5)		(488.5)		(592.5)	
	8.3	6.5	38.2	62.6	12.1	17.2	24.5	11.8	—	
$[C_1,C_2]_b'/[C_5,C_6]_b$	(306.3)		(320.3)		(306.3)		(306.3)		(410.4)	
	6.7	6.0	6.9	8.7	8.9	8.6	7.1	6.3	—	
$[C_5,C_6]_b'$	(400.4)		(570.5)		(668.5)		(916.6)		(1020.6)	
	—		16.0	33.5	1.2	3.2	—		4.0	3.9
$[C_2,C_3]_a'$	(386.3)		(556.5)		(654.5)		(902.6)		(1006.6)	
	—		—		—		1.3	1.0	—	
W/C_1'	(282.3)		(310.3)		(324.3)		(386.3)		(490.4)	
	16.2	16.0	—		—		—		—	
$W'/[C_1,C_2]_b$	(248.2)		(318.2)		(384.3)		(664.4)		(768.5)	
	6.9	8.0	32.8	33.0	8.9	8.1	5.1	5.3	32.4	32.3
W'/B_1	(280.3)		294.3)		(280.3)		(280.3)		(384.3)	
	9.3	10.5	32.7	29.1	7.9	7.6	3.1	2.6	—	
W'/C_1	(264.3)		(278.3)		(264.3)		(264.3)		(368.3)	
	100	100	100	100	100	100	100	100	100	100
W'/C_1−R,+H	(264.3)		(264.3)		(264.3)		(264.3)		(264.3)	
	—		—		—		—		47.3	45.0
B_1	(163.1)		(219.1)		(331.1)		(579.2)		(579.2)	
	—		—		7.9	2.0	6.1	3.1	34.4	22.5
B_1'	(145.0)		(187.1)		(271.1)		(457.1)		(457.1)	
	—		9.0	8.9	—		—		—	
B_1''−R,+H	(127.0)		(141.1)		(169.1)		(231.1)		(231.1)	
	—		—		41.3	36.4	0.5	2.9	11.5	18.6
B_1−2R,+2H	(163.1)		(191.1)		(247.1)		(371.1)		(371.1)	
	—		—		12.4	7.1	—		—	
B_1'''−R,+H	(109.0)		(109.0)		(109.0)		(109.0)		(109.0)	
	—		—		18.8	13.1	—		—	

[a]Relative abundances vs. W'/C_1.

[b]The calculated *m/z* values appear in parentheses; the experimental values were measured as nominal.

Abbreviations: PerMe, PerAc, PerBz (Anh/Cl): see footnote of Table 1.

MS spectra as these could lead to false conclusions since they are easily linked to similar structures. In cases of doubt, unimolecular dissociation MS/MS spectra can yield more accurate information on the nature of a permethylated monosaccharide moiety than can CID MS/MS spectra.

Table 2, Column B enumerates the CID product ions

Fig. 1. CID MS/MS spectrum of B_1' ions generated from permethylated **1**. An almost identical spectrum was obtained for B_1' ions of **2**. The intensities are reported relative to the precursor ions (*m/z* 187.1).

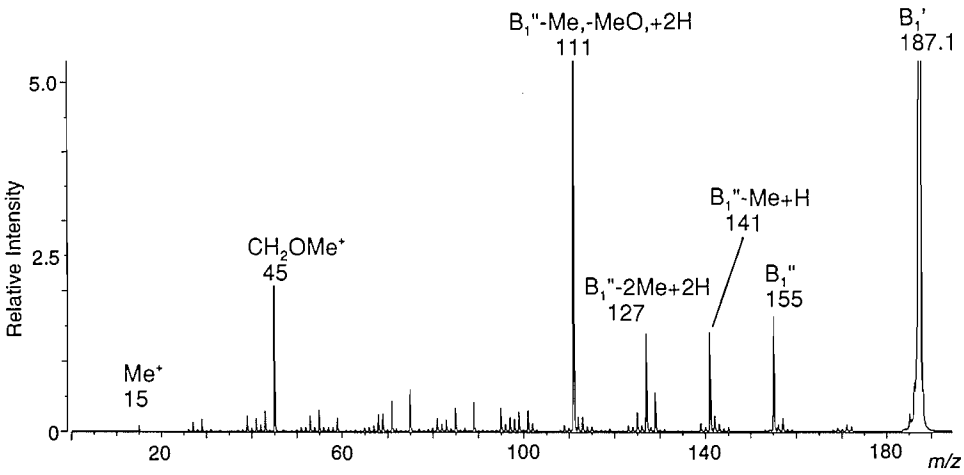

Scheme 3. Speculative model for loss of methanol from B_1 ions of permethylated **1** and **2** and $[M+H']^+$ ions of permethylated galactose, glucose, and mannose. Top line: *m/z* 219 precursors to *m/z* 187 ions. Middle line: unique structure proposed for the B_1' ions of glycosyl- and galactosyl-cerebrosides, suggested by MS/MS CID results; on the right, speculative structure of the B_1' ion of mannosyl-cerebroside. Bottom line: proposed structures for the $[M+H'']^+$ ions of permethylated glucose, galactose, and mannose as suggested by the unimolecular dissociation MS/MS results.

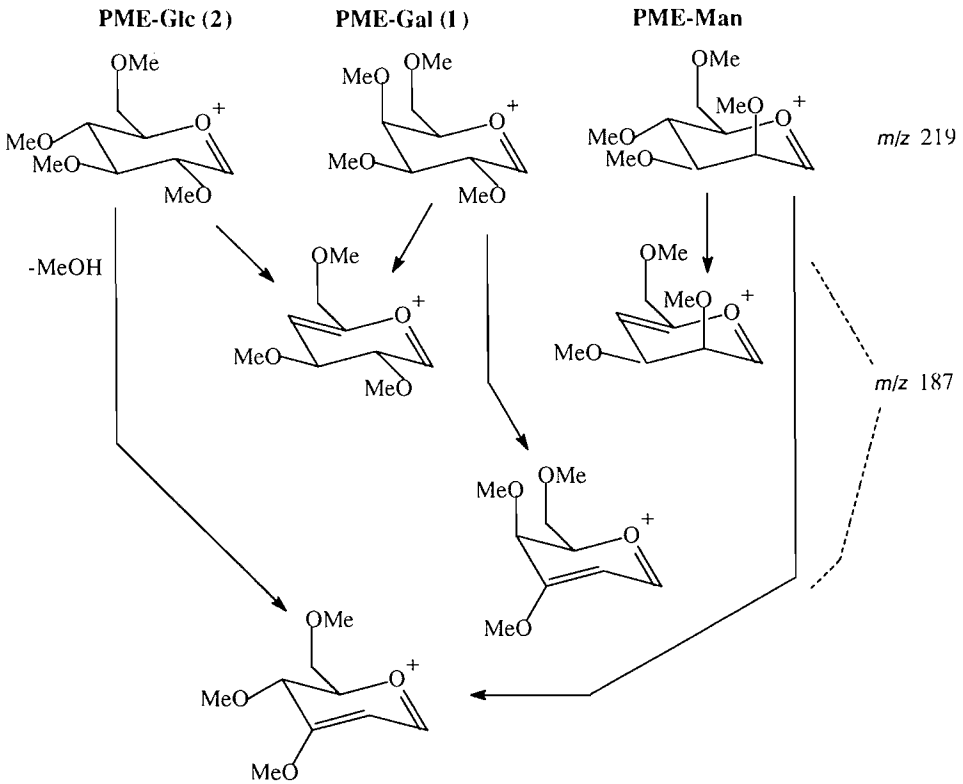

obtained for $[M+H']^+$ precursors of **1** and **2** and their relative abundances in the MS/MS spectra. Most ions observed in these spectra (not shown) were not associated with the isomeric portion of the precursors. Some major differences in relative abundances are observed for $[^{1,5}X_0']$ and $[C_1,C_2]_b'$, which are all produced from cleavages or eliminations in the vicinity of the isomeric center. One interesting species here is $[M+H'-2RO]$, which is more abundant when generated from

Fig. 2. LSIMS spectra of peracetylated (*a*) **1** and (*b*) **2**.

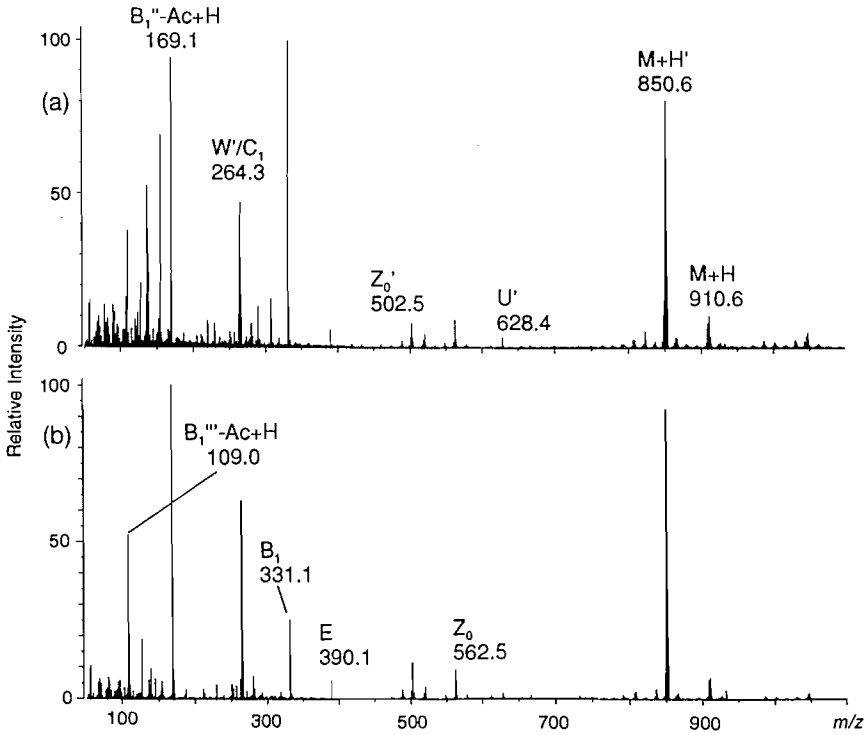

Scheme 4. Speculative model of loss of two RO radicals (R = methyl acetyl, benzoyl) by means of *trans*-elimination.

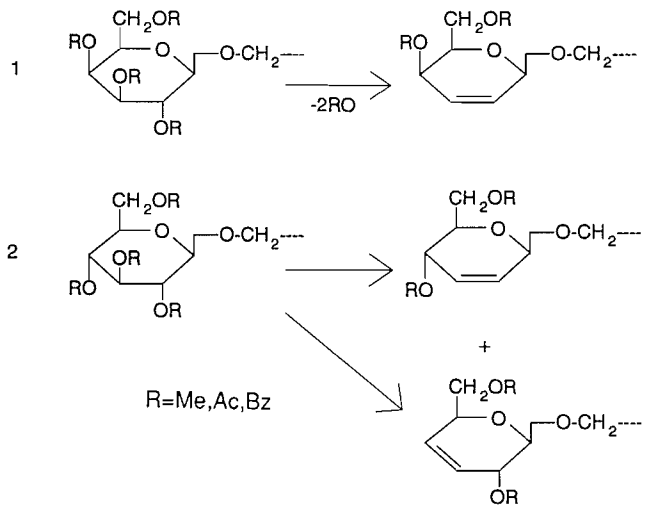

a glucosyl residue. According to Scheme 4, elimination of two RO radicals could be favored for **2**, providing more possible ways of undergoing *trans*-elimination to form a double bond (in either position 2 or 3). On the other hand, compound **1** bears only one possible site for such elimination of the radicals.

To summarize, permethylated cerebrosides yielded, under the experimental conditions employed in this study, restricted information relative to isomer recognition of species that differ in the sugar moieties. In conventional LSIMS spectra, the relative abundance of *m/z* 187 (B_1') ions can be an indicator for isomeric discrimination. However, permethylated GSLs are more useful in yielding molecular weight information on very small quantities of sample, and most abundant fragment ions are related to the ceramide moiety. Hence, permethylated GSLs can play a major role in differentiation of glycosphingolipid species with isomeric ceramides (14).

Peracetylated derivatives were the next investigated for their usefulness toward isomer discrimination. They yielded sensitivity improvement over native species comparable to that of permethylated derivatives. The conventional LSIMS spectra of **1** and **2** are shown in Fig. 2. The most distinct difference between them lies in the relative abundances of B_1 ions at *m/z* 331.1. In addition, $[M+H']^+$ species resulting from loss of acetic acid from the protonated molecular ions are more abundant for **2** than for **1**; production of U and W'/C_1 ions at *m/z* 628.4 and 264.3, respectively, is also observed to different extent for the two isomers. Column C of Table 1 gives an overview of these data. CID MS/MS experiments were conducted on precursors B_1 and $[M+H']^+$ and the corresponding spectra are displayed in Figs. 3 and 4, respectively. Peracetylated B_1 ions formed from oligosaccharides and generated by FAB or LSIMS have been studied in the past, in view of their fragmentation behaviour under CID MS/MS conditions (15, 16). The B_1 ions generated from cerebrosides in this study produced qualitatively the same fragmentation patterns as B_1 from oligosaccharides and Fig. 3 shows that relative abundances in their MS/MS spectra vary from one isomer to the other. The most significant difference is production of more abundant B_1' ions (*m/z* 271) from **2** than from **1**, a trend that was also observed by Guevremont and Wright (15). In that study, the differences between the CID spectra of peracetylated glucose and galactose were attributed to the differ-

Fig. 3. CID MS/MS spectra of B_1 ions generated from peracetylated (*a*) **1** and (*b*) **2**. The intensities are reported relative to the precursor ions (*m/z* 331.1).

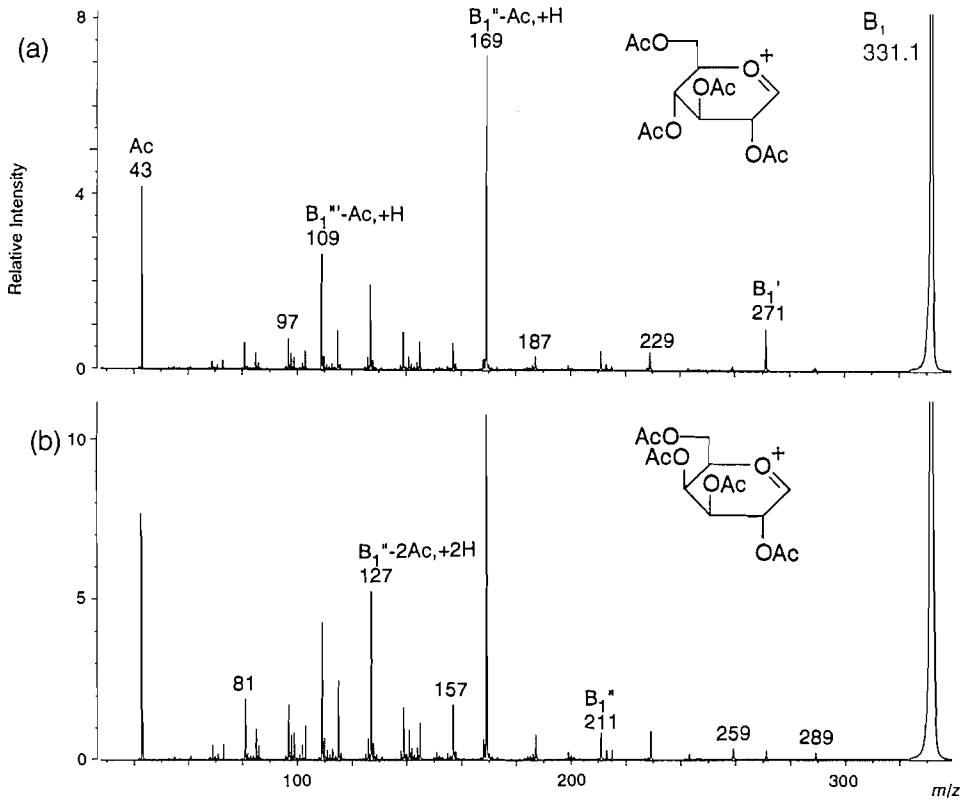

Fig. 4. CID MS/MS spectra of $[M + H']^+$ ions generated from (*a*) **1** and (*b*) **2**. The intensities are reported relative to the precursor ions (*m/z* 850.6).

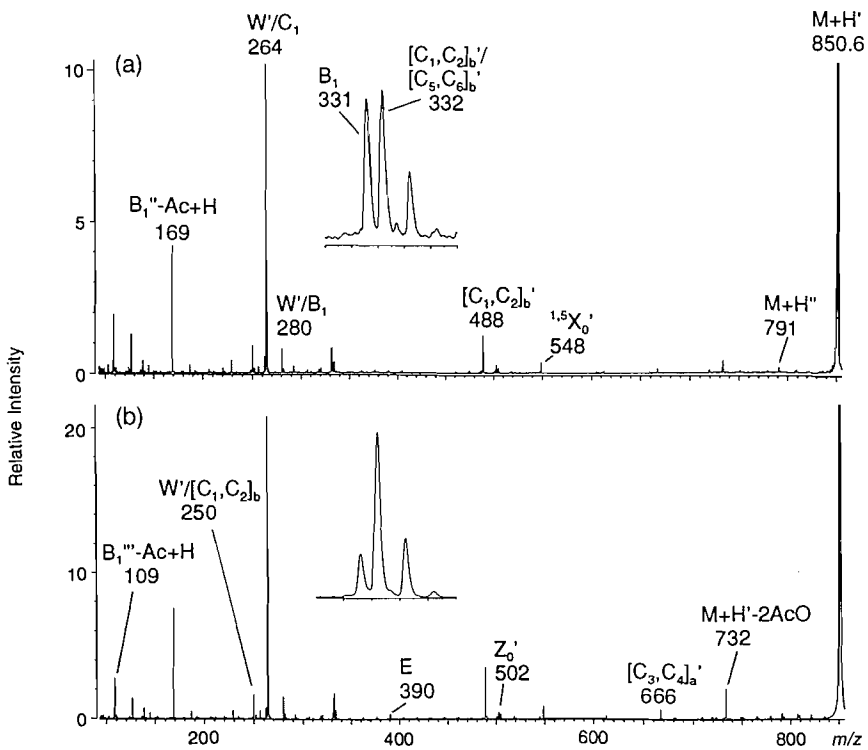

Table 3. Relative abundances[a] of the product ions observed in the CID MS/MS spectra of B_1 ions of peracetylated derivatives[b].

	Form of compounds			
	Peracetylated		Perbenzoylated	
	1	**2**	**1**	**2**
Ions/Relative abundance	A (calcd./*m/z*)		B (calcd./*m/z*)	
B_1–R,+H	(289.1)		(475.1)	
	1.7	1.0	—	
B_1'	(271.1)		(457.1)	
	2.5	13.3	10.4	6.7
B_1–CHOR	(259.1)		(445.1)	
	3.2	1.3	23.4	9.0
B_1–RH	(287.1)		(473.1)	
	—		14.3	16.8
B_1–CHOR,–RH	(215.1)		(339.1)	
	2.5	1.2	11.7	10.1
B_1'–CHOR	(199.1)		(323.1)	
	2.5	1.1	9.1	9.0
B_1'–R,+H	(229.1)		(353.1)	
	8.1	5.6	6.5	5.1
B_1''	(211.1)		(335.1)	
	8.1	5.6	122.7	47.8
B_1'–2R,+2H	(187.1)		(249.1)	
	7.3	4.2	—	
B_1''–R,+H	(169.1)		(231.1)	
	100	100	100	100
B_1'–CHOR,–R,+H	(157.0)		(219.1)	
	16.2	8.9	—	
B_1'–3R,+3H	(145.0)		(145.0)	
	11.1	8.9	—	
B_1''–CHOR	(139.0)		(201.1)	
	15.2	12.2	49.4	20.2
B_1''–2R,+2H	(127.0)		(127.0)	
	48.5	26.7	—	
B_1'–CHOR,–2R,+2H	(115.0)		(115.0)	
	23.2	12.8	—	
B_1'''–R,+H	(109.0)		(109.0)	
	39.4	36.7	6.5	5.6
B_1''–CHOR,–R,+H	(97.0)		(97.0)	
	16.2	10.0	—	
$^{3,5}A_1$	(157.0)		(281.1)	
	—		9.5	9.0
RCO	(71.0)		(133.0)	
	—		7.8	7.9
R^+	(43.0)		(105.0)	
	70.7	58.3	sat'd	77.5

[a]Relative abundances vs. B_1''–R,+H, ±5%.

[b]The *m/z* values in parentheses are the calculated monoisotopic values; the measured values were nominal and matched the values given above.

ence in the tertiary structures of B_1' ions. In the structures proposed (15), acetate is lost in position 3, forming a conjugated system with two double bonds in 1 and 3 instead of 1 and 5 for "identical" species. Reactivity of B_1' ions was attributed to extent of interaction between acetyl groups in concerted loss of ketene plus acetic acid (*m/z* 109, 169), and was different for the two B_1' isomers. Differences in relative abundances are also noticeable for *m/z* 109, 127, 259, and 289 ions. These

ions also appear in the conventional spectra of Fig. 2; however, matrix ions interfere with spectral interpretation with respect to relative ionic abundances, and its is necessary to perform MS/MS experiments in order to eliminate these interferences. Overall MS/MS results for B_1 species are summarized in Column A of Table 3. In Fig. 4, the CID MS/MS spectra of $[M+H']^+$ species of both peracetylated compounds (*m/z* 850.6) appear relatively similar at first observation. For **1** the relative abundance of B_1 ions (*m/z* 331) equals that of *m/z* 332 ions. Compound **2** produces lower abundance B_1 ions, leaving species at *m/z* 332 dominant. The latter ions have been interpreted as $W'/[C_5,C_6]_b$. This region of the spectra is shown with more detail on the figure.

Higher rates of B_1 cleavages for galacto- and than for glucocerebroside cannot be explained by lower extent of hydrogen bonding between the isomeric RO group in position 4 on the sugar ring and portions of the ceramides, since three-dimensional structures of both isomers (see Scheme 1 for reference) show the opposite trend. Relative reactivities of B_1 ions thus have to be invoked and can be related to extent of interaction between acetyl functions substituted on the rings. Other product ions of interest featuring in Fig. 2*b* are $^{1,5}X_0'$, resulting from cross-ring cleavages, and also $[C_1,C_2]_b'$, Z_0', $[C_3,C_4]_a$, and W'/C_1, the dominant species. Aromatic ions related to hexose groups are also observed, however, with similar relative abundances for the two isomers. The loss of two RO radicals from the sugar ring occurs to a larger extent for **2** than for **1**, as observed and discussed above for permethylated $[M+H']^+$ ions. In summary, it is possible to distinguish peracetylated compounds **1** and **2** by MS and MS/MS, owing to more facile production of B_1 ions in one case than the other, differences in the dissociation patterns of these B_1 ions, and other minor differences between the MS/MS spectra of isomeric precursor ions. Perbenzoylated derivatives of **1** and **2** prepared using benzoic anhydride were also investigated in this study. These compounds, like their peracetylated analogs, bear only five acetyl groups since the amide function is not modified upon derivatization. Qualitative aspects of their LSIMS conventional spectra have been discussed elsewhere (8) and fragmentation is summarized in Column D of Table 1. Figure 5 allows a comparison of the spectra obtained for perbenzoylated **1** and **2**. Protonated molecular ions $[M+H]^+$ (M+H on figure) are not clearly defined and form clusters along with other ions, among which they are the most abundant. Identification of the species is possible in light of $[M+H']^+$ species (M+H′ on figure, *m/z* 1098.7). U ions are not present in the spectra and, instead, formation of $[M+H']^+$ and Z_0 ions is observed. It is possible to distinguish one spectrum from another in view of the relative abundances of B_1 ions at *m/z* 579.2. As observed with peracetylated derivatives, their formation is more favored for **1** than for **2**. The CID MS/MS spectra of these isomeric B_1 ions are compared in Fig. 6. Qualitatively, the same ions are observed in both spectra, however, with different relative abundances. The relative abundances of the ions at *m/z* 335 and 231 are reversed from one spectrum to the other. Other more subtle variations are also observed, such as the presence of ions at *m/z* 311 for **1** and not for **2**, which rather produces ions at *m/z* 323. Collision-induced dissociation pathways observed in Fig. 6 are similar to those observed for peracetylated **1** and **2** (Fig. 3), in that they involve losses of ROH, losses of R with proton transfer (−R,+H), and losses of other ester-related species. Product ions from cross-ring cleavages, $^{1,5}X_0$, are observed for both types of derivatives. CID MS/MS experiments were also performed to study $[M + H']^+$ ions (*m/z* 1098.7) of perbenzoylated **1** and **2** since they are the only other species in the conventional spectra (Fig. 5) to contain the sugar moieties. Ions whose relative abundances are above 0.5% are listed in Column D of Table 2. Although the two spectra were almost identical, production of B_1 ions was still more accentuated for **1** than for **2** and interesting structural information could be obtained through W'/C_1, $[C_1,C_2]_b$, Z_0', $^{1,5}X_0'$, B_1, and $[C_2,C_3]_a$ ions among others. Compounds **1** and **2** perbenzoylated in the bulk phase with benzoic anhydride can thus be distinguished, mainly owing to the relative abundances of B_1 ions and the CID MS/MS fragmentation patterns.

Figure 7 shows the LSIMS conventional spectra obtained for **1** and **2**, perbenzoylated in the gas phase using benzoyl chloride. These compounds bear six benzoyl groups instead of five as in the two last types of derivatives discussed. Almost no intact molecular ions are produced and instead $[M + H']^+$ species are observed. The spectra are dominated by abundant W′, B_1, Z_0'−Bz,+H, B_1''−Bz,+H, and Bz+ ions, as listed in Table 1, Column E. Metastable formation of W′ ions, which are unique to spectra of such perbenzoylated GSLs (8), gives rise to a broad ion peak at apparent *m/z* 774, which in fact corresponds to $964.5^2/1202.7$. Obvious differences between the two spectra of Fig. 7 reside in the relative abundances of $[M+H']^+$, W′, and B_1 ions. Formation of B_1 is favored for **1** relative to **2**, following the same trend as observed for peracetylated derivatives and compounds perbenzoylated with benzoic anhydride, while more extensive production of W′ ions is observed for **2** than for **1**. The CID MS/MS spectra of W′ ions (*m/z* 964.5) are shown in Fig. 8. W′ ions constitute the products of the main fragmentation pathway of molecular species $[M+H']^+$, and are also, when collided with helium, precursors of several significant ions, some of which also appear in the conventional spectra of Fig. 7. Relative abundances of W'/C_1 and B_1 ions follow the same tendency as observed in Fig. 7, i.e., the ratio B_1: W'/C_1 decreases from **1** to **2**. Besides Bz^+ species, predominant ions in the spectra feature, among others, for example, $W'/[C_1,C_2]_b$ species, which are formed in preference to W'/C_1 ions. Rupture of the $[C_1,C_2]_b$ bond appears to be favored with benzoylated compounds, as was also observed with the *m/z* 488 product ions in Fig. 4 (peracetylated derivatives). In the proposed structure of W′ shown in Scheme 5, there is a double bond in $[C_2,C_3]_b$ that appears to trigger cleavage of the $[C_1,C_2]_b$ bond with proton transfer to the carbohydrate moiety. A structure for $W'/[C_1,C_2]_b$ is proposed, also in Scheme 4. In Fig. 8, loss of a benzoic acid moiety (W″, *m/z* 842) and of two benzoate groups (W′−2BzO, *m/z* 722) must originate from the sugar ring, since no other benzoate moiety is present on the ceramide portion of W′, and must form a double bond in the ring as illustrated above the Scheme 5. Two ion peaks resulting from cross-ring cleavage are observed. At *m/z* 414, $W'/^{1,5}X_0$ is present in both spectra whereas $W'/^{0,2}X_0$ at *m/z* 410 is relatively more abundant for **1** than for **2**, and carbohydrate-related ions at *m/z* 231 and 335 are relatively more abundant for **2** than **1**. This last trend suggests a greater reactivity in the case of benzoylated glucose, which could be at the origin of the low abundance of B_1 ions in the conventional and MS/MS spectra. Another low

Fig. 5. LSIMS spectra of (*a*) **1** and (*b*) **2**, perbenzoylated in the bulk phase using benzoic anhydride.

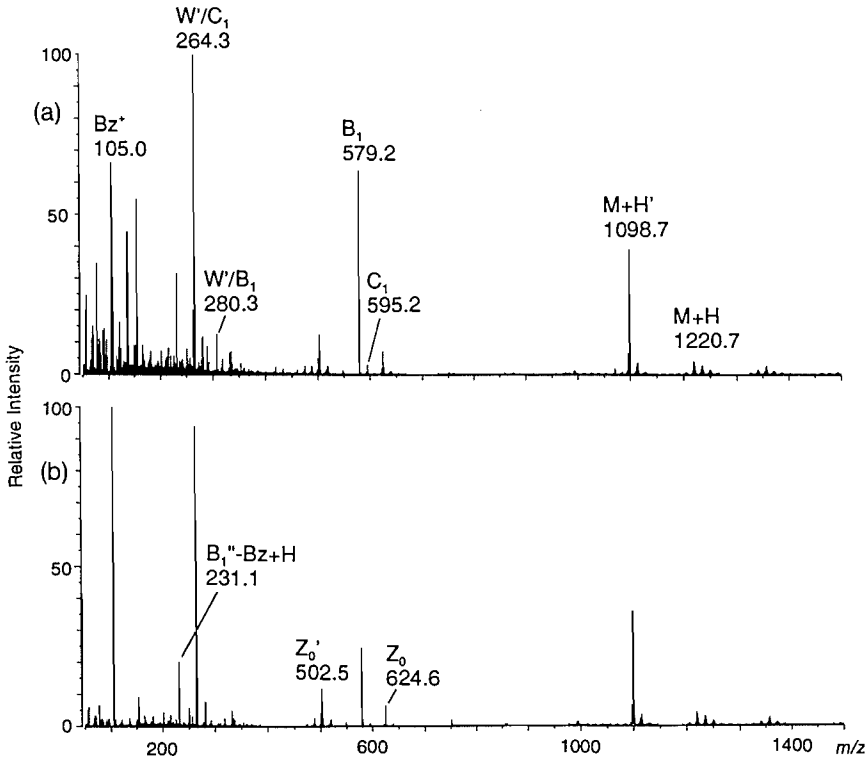

Fig. 6. CID MS/MS spectra of B_1 ions generated from perbenzoylated (*a*) **1** and (*b*) **2**. The intensities are reported relative to the precursor ions (*m/z* 579.2).

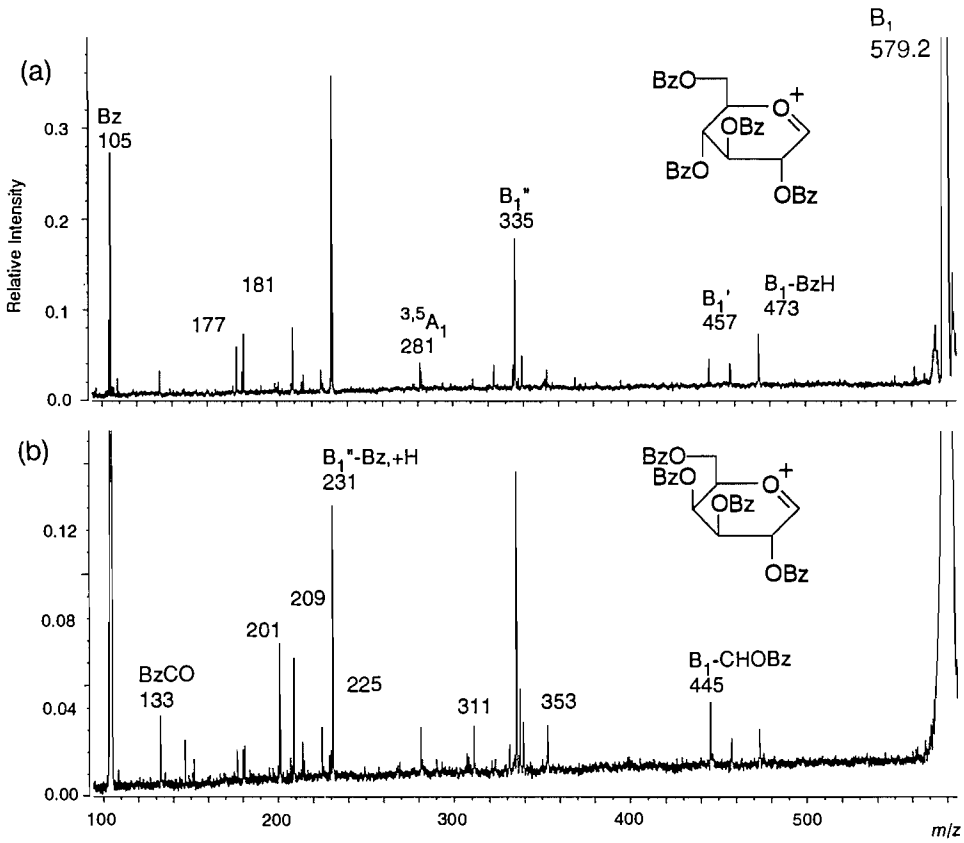

Fig. 7. LSIMS spectra of (*a*) **1** and (*b*) **2**, perbenzoylated in the gas phase using benzoyl chloride.

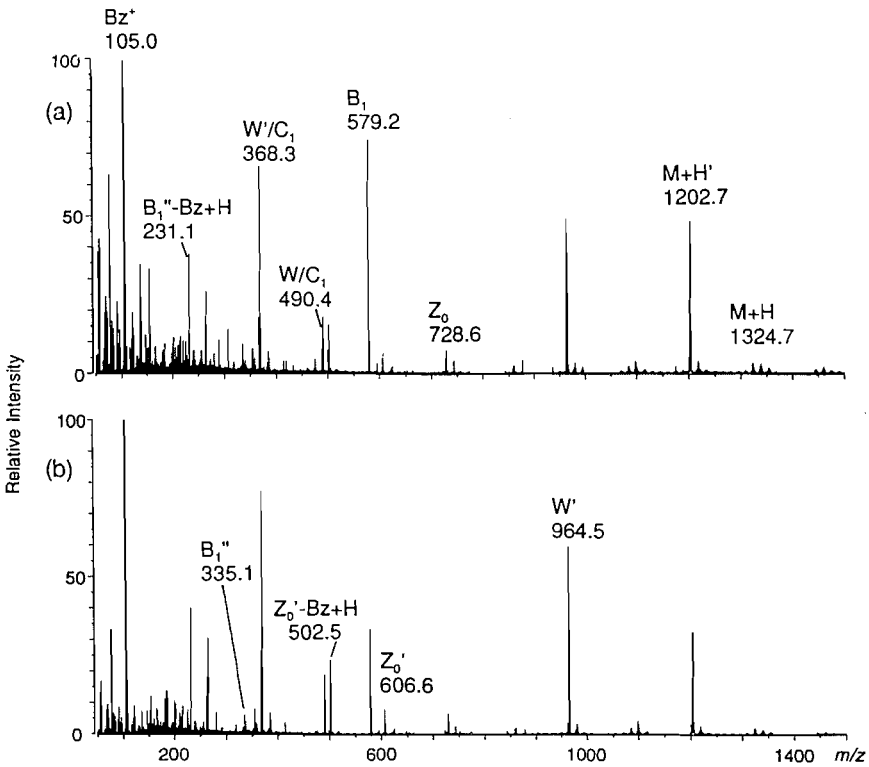

Fig. 8. CID MS/MS spectra of the W′ ions generated by (*a*) **1** and (*b*) **2**, perbenzoylated in the gas phase using benzoyl chloride. The intensities are reported relative to the precursor ions (*m/z* 964.5).

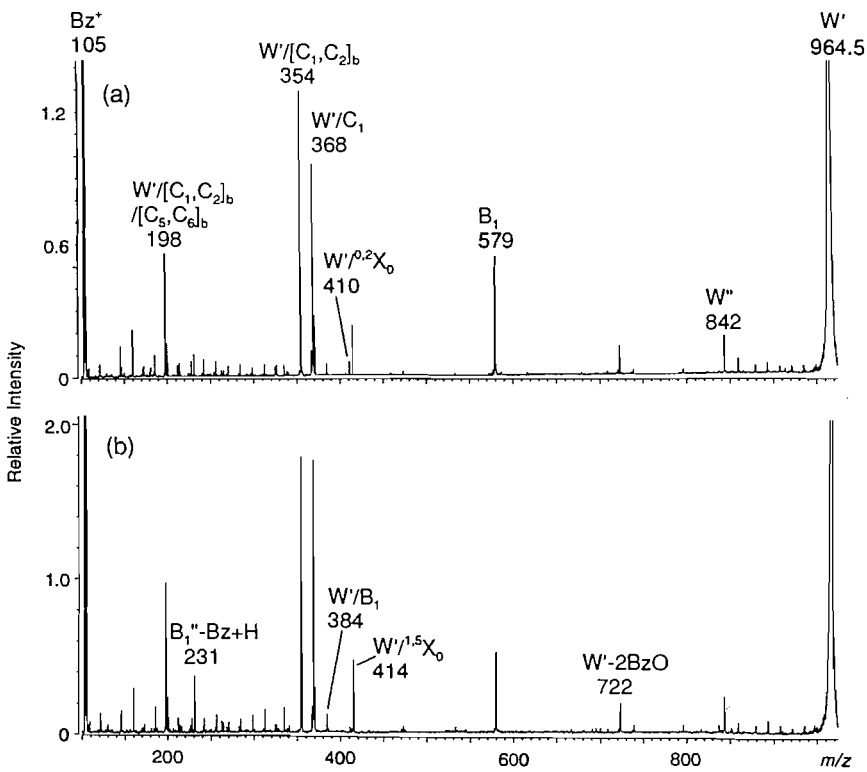

Scheme 5. Proposed structures for $[M+H']^+$, W', W'/C_1, and W'/$[C_1,C_2]_b$ ions generated from **1** and **2**, perbenzoylated using benzoyl chloride.

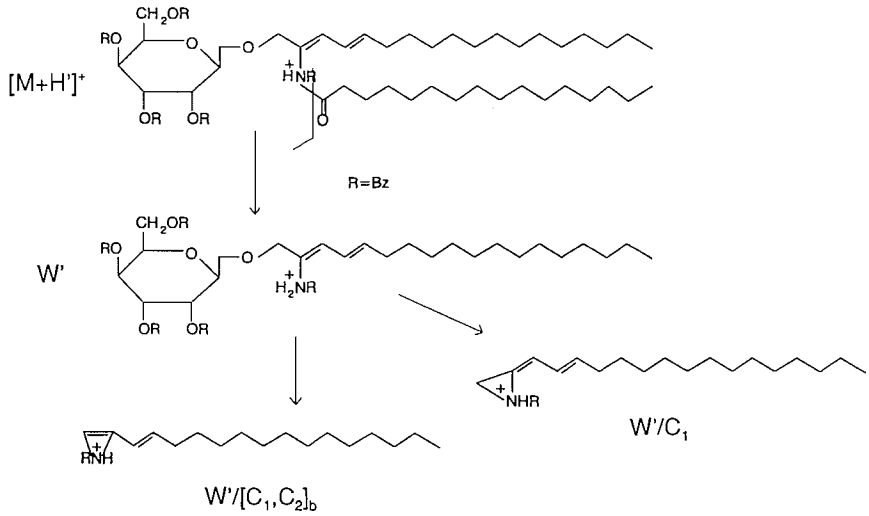

mass ion peak (*m/z* 198) results from Z_0 and $[C_6,C_7]_b$ cleavages, β to the double bond. These spectra are as informative as the CID MS/MS spectra of [M+H'] species (not shown). The latter produced the ions listed in Column E of Table 2. Differences in the relative abundances of B_1 ions still constitute the main insight to isomer recognition. There is an inversion in the abundances of W' and W'/C_1 that could be attributed to relative stabilities of these W-type ions with and without the isomeric hexosyl residue attached. A new type of fragment is observed at *m/z* 500, and can be interpreted by two different structures; the first corresponds to $Z_0'-Bz,-H$ (Z_0 − 106), and the other to Y_0' ions generated by $[M+H']^+$ ions having lost a benzoic acid molecule from the sugar ring instead of from position 2 of sphingosine. However, there is no evidence in the spectra that such precursors exist. The appearance of these unusual *m/z* 500 ions may to be due to a concerted elimination of hexose and benzaldehyde from the [M+H'] species, or to loss of benzaldehyde from Z_0'.

In brief, cerebrosides bearing six benzoyl groups yield interesting and informative fragmentation patterns and also allow a certain extent of isomeric comparison through observation of variations in the relative abundances of B_1 ions in LSIMS spectra and in the CID MS/MS spectra of W' and $[M+H']^+$ ions.

Conclusion

It is possible to make a distinction between galactosyl and glucosyl ceramides by mass spectrometry, provided a judicious choice of derivatization methods and ionization techniques is made. A certain degree of discrimination is obtained with permethylated derivatives; however, peracetylated and perbenzoylated compounds allow the most differences to appear in the mass spectra of cerebroside isomers. Ions whose formation is directly related to the carbohydrate structure are observed with different relative abundances, either in conventional spectra or CID MS/MS spectra of sugar-containing precursor ions. Since cerebrosides most commonly occur as galactosylated or glucosylated species, the study has not been extended to compounds with other types of hexosidyl residues, such as mannose or allose. The relative abundances of ions observed in this study may vary with the type of mass spectrometer used, due amongst other factors to the time frame of the instrument, energy of collisions in CID, and type of detection used. This type of study should be conducted with reference compounds in order to ascertain the relationship between isomeric form and abundance of the ions. It can also be extended to isomeric discrimination of larger GSL, by studying their B_n ions and related species by conventional mass spectrometry and MS/MS (16, 17). For simple GSL molecules such as cerebrosides, this study revealed that derivatization with benzoyl chloride amongst other techniques used yields the most informative MS and MS/MS spectra for general structural information and discrimination between the galactosyl and glucosyl ceramide isomers. Moreover, these derivatives are strongly UV-absorbent, which allows detection of very small amounts of material in chromatographic and electrophoretic separation techniques.

Acknowledgments

The authors would like to acknowledge the contribution of R. DuClos from Boston University School of Medicine for kindly providing the synthetic D-glucosyl ceramide. The MIT Mass Spectrometry Resource was supported by the National Institutes of Health Center for Research Resources, Grant No. RR00317 to K. Biemann. H. Perreault was the recipient of a Post-Doctoral Fellowship from the Natural Sciences and Engineering Council of Canada.

References

1. C.C. Sweeley. *In* Biochemistry of lipids, lipoproteins and membranes. *Edited by* D.E. Vance and J. Vance. Elsevier Science Publishers, Amsterdam. 1991. p. 327.
2. C.E. Costello, P. Juhasz, and H. Perreault. Prog. brain res. **101**, 45 (1994) 1.

3. H. Rahman. Neurochem. Int. **5**, 539 (1983).
4. IUPCA-IUB Commission on Biochemical Nomenclature (CBN). Eur. J. Biochem. **79**, 11 (1977).
5. A. Yoneda, H. Ogawa, I. Matsumoto, I. Ishizuka, S. Hase, and N. Seno. Eur. J. Biochem. **218**, 797 (1993).
6. P. Juhasz and C.E. Costello. J. Am. Soc. Mass Spectrom. **3**, 785 (1992).
7. V.N. Reinhold, B.B. Reinhold, and C.E. Costello. Anal. Chem. **67**, 1772 (1995).
8. H. Perreault and C.E. Costello. Org. Mass Spectrom. **29**, 720 (1994).
9. P. Zimmerman, R. Bommer, T. Bar, and R.R. Schmidt. J. Carbohydr. Chem. **7**, 435 (1988).
10. S.A. Martin, J.A. Hill, and K. Biemann. Proc. 36th ASMS Conf. Mass Spectrom. Allied Topics, San Francisco, Calif. June 5–10, 1988. pp. 795–796.
11. P. Juhasz, J.E. Biller, C.E. Costello, I.A. Papayannopoulos, and K. Biemann. Proc. 39th ASMS Conf. Mass Spectrom. Allied Topics, Nashville, Tenn. May 19–24, 1991. p. 334.
12. B. Domon and C.E. Costello. Glycoconj. J. **5**, 397 (1988).
13. B. Domon, G. Dubreucq, and E. De Hoffmann. Proc. 44th ASMS Conf. Mass Spectrom. Allied Topics, Portland, Oreg. May 12–16, 1996. In press.
14. C.E. Costello, H. Perreault, and L.C. Ngoka. *In* Mass spectrometry in the biological sciences. *Edited by* A.L. Burlingame and S.A. Carr. Humana Press, Totowa, N.J. 1996. pp. 365–384.
15. R. Guevremont and J.L.C. Wright. Rapid Commun. Mass Spectrom. **2**, 47 (1988).
16. B. Domon, D.R. Mueller, and W.J. Richter. Org. Mass Spectrom. **29**, 713 (1994).
17. H. Perreault and C.E. Costello. Proc. 42nd ASMS Conf. Mass Spectrom. Allied Topics, Chicago, Ill. 1994. p. 1154.

Zirconium complexes of a cyclopentadienyl-amido ligand with a pendant amine donor via amine and alkane elimination

Ying Mu, Warren E. Piers, Donald C. MacQuarrie, and Michael J. Zaworotko

Abstract: Zirconium complexes of the multidentate ligand $CpH^{NMe}SiN(H)R$ (SiNR = -$SiMe_2$N-*t*-butyl; NMe = -$CH_2CH_2NMe_2$, **1**) were prepared and characterized via amine and alkane elimination procedures. Reaction of **1** with $Zr(NMe_2)_4$ gave a mixture of bis-amido complexes **2** in which the ligand was 1,2 and 1,3 substituted. This mixture was converted to the analogous dichlorides **3** using $Me_2NH{\cdot}HCl$ and 1,3-**3** was purified at this stage; alternatively, 1,3-**3** was obtained in one pot from **1** and $Zr(NMe_2)_4$ in ≈70% yield. Conversion of 1,3-**3** to dimethyl compound $(Cp^{NMe}SiNR)Zr(CH_3)_2$, 1,3-**4**, was accomplished via reaction of the dichloride with methyllithium; methide abstraction with the Lewis acids $B(C_6F_5)_3$ and $[Ph_3C]^+[B(C_6F_5)_4]^-$ generated the cationic alkyls $[(Cp^{NMe}SiNR)Zr(CH_3)]^+[R'B(C_6F_5)_3]^-$ (R′ = CH_3, **6a**; C_6F_5, **6b**), which were characterized by NMR spectroscopy. Zirconium complexes containing **1** ligated as its 1,2 isomer were obtained from alkane elimination reactions between **1** and in situ prepared R_nZrCl_{4-n} (R = CH_3, n = 3; R = CH_2SiMe_3, n = 2). 1,2-**3** and the methyl chloride complex 1,2-$(Cp^{NMe}SiNR)Zr(CH_3)Cl$, **5**, were obtained in 18 and 30% yield, respectively. Complex **5** was characterized by X-ray crystallography (monoclinic, space group $P2_1/a$, a = 9.6951(10) Å, b = 14.3794(16) Å, c = 14.364(3) Å, V = 1990.3(5) Å^3, Z = 4, R = 0.046, R_w = 0.041.)

Key words: amine elimination, Cp-amido, zirconium complexes.

Résumé : On a préparé les complexes de zirconium du ligand multidentate $CpH^{NMe}SiN(H)R$ (SINR = -$SiMe_2$N-*t*-butyl; NME = -$CH_2CH_2NME_2$, **1**), et on les a caractérisés via les procédés d'élimination d'amine et d'alcane. La réaction du composé **1** avec le $Zr(NMe_2)_4$ donne un mélange de complexes bis-amido dans lequel le ligand est substitué en 1,2 et 1,3. On a transformé le mélange en dichlorures correspondants **3** en utilisant le $Me_2NH{\cdot}HCl$ et on a purifié à ce stade le composé 1,3-**3**. On a obtenu alternativement le composé 1,2-**3** dans un seul récipient à partir du composé **1** et du $Zr(NMe_2)_4$ avec un rendement de 70%. On a transformé le composé 1,3-**3** en composé diméthylé $(Cp^{NMe}SiNR)Zr(CH_3)_2$ via la réaction du dichlorure avec le méthyllithium; l'abstraction d'un méthylure par un acide de Lewis $B(C_6F_5)_3$ et par $[Ph_3C]^+[B(C_6F_5)_4]^-$ a généré les alkyles cationiques $[Cp^{NMe}SiNR)Zr(CH_3]^+[R'B(C_6F_5)_3]^-$ (R′ = CH_3, **6a**; C_6F_5, **6b**) que l'on a caractérisés par la spectroscopie de RMN. Les complexes de zirconium contenant le composé **1** lié comme son isomère 1,2 sont obtenus à partir d'une réaction d'élimination d'alcane entre le composé **1** et le R_nZrCl_{4-n} (R = CH_3, n = 3; R = CH_2SiMe_3, n = 2) préparé in situ. On a obtenu le composé 1,3-**3** et le complexe de chlorure de méthyle 1,2-$(Cp^{NMe}SiNR)Zr(CH_3)Cl$, **5**, avec respectivement des rendements de 18 et 30%. Le complexe **5** est caractérisé par cristallographie de rayons X (groupe d'espace monoclinique $P2_1/a$, a = 9,6951(10) Å, b = 14,3794(16) Å, c = 14,364(3) Å, V = 1990,3(5) Å^3, Z = 4, R = 0,046, R_w = 0,041.)

Mots clés : élimination d'amine, Cp-amido, complexes de zirconium.

[Traduit par la rédaction]

Introduction

The impact of metallocene-based catalyst technology on the polyolefin industry has been substantial in the past five years and continues to expand (1). Deployment of these catalysts on an industrial scale has necessitated the synthesis of complex (and temperamental!) organometallic compounds on a multi-kilogram scale, a non-trivial technological achievement and one that continues to be developed by a number of specialty chemical companies. New methods for ligand attachment are thus of considerable current interest.

Traditional methodology for attaching cyclopentadienyl, *ansa*-type bis-cyclopentadienyl and constrained geometry cyclopentadienyl-amido type ligands, involves generation of a group 1 or 2 metal salt of the ligand, followed by a salt elimination reaction with a suitable group 3 or 4 metal halide. Although this strategy undeniably works for the majority of catalyst targets, it suffers from some disadvantages. In some instances, the dimetal salt of the desired ligand is unstable or formed in low yields. This is particularly the case for Cp-amido type ligands, which may be prone to Si–N bond cleav-

Received April 24, 1996.

Y. Mu and W.E. Piers.[1,2] Department of Chemistry, University of Calgary, 2500 University Dr. N. W., Calgary, AB T2N 1N4, Canada.
D.C. MacQuarrie and M.J. Zaworotko. Department of Chemistry, Saint Mary's University, Halifax, NS B3H 3C3, Canada.

[1] Author to whom correspondence may be addressed. Telephone: (403) 220-5746. Fax: (403) 289-9488. E-mail: wpiers@chem.ucalgary.ca.
[2] Fellow of the Alfred P. Sloan Foundation, 1996–1998.

Scheme 1.

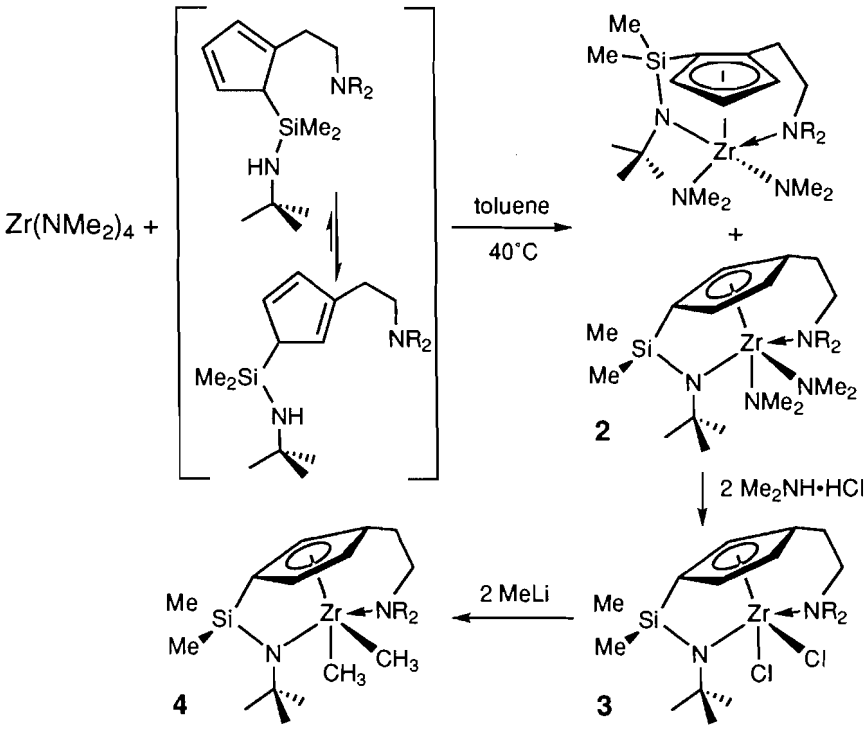

age upon treatment with alkyllithium deprotonating agents. The subsequent reaction with transtion metal halides is sensitive to several variables in reaction conditions, such as temperature, the concentration of donor solvents, and the nature of the group 1 or 2 metal employed. Thus, specific conditions are required for attachment of different ligands where more general procedures would be desirable. Finally, the eliminated salts MX_n are sometimes difficult to remove completely from the products.

To alleviate these problems, alternative strategies for ligand attachment have recently been reported. Taking a cue from some chemistry reported in the 60s by Chandra and Lappert (2), Teuben and co-workers (3) used amine elimination rather than salt elimination as a means to coordinate Cp-amido type ligands to group 4 metals. Other examples (4) of this method of ligand attachment have been reported since then, the most significant being the synthesis by Jordan and co-workers of *rac*-(EBTHI)$Zr(NMe_2)_2$ via reaction between diproteo ethylenebis(tetrahydroindenyl) and $Zr(NMe_2)_4$ (5). In a nice exhibition of synthetic ingenuity, the eliminated amine was allowed to remain in the reaction long enough to convert the kinetic products of the reaction to the thermodynamic (and desired) racemic product thus circumventing the problem of having to separate out the *meso* isomer.

While amine elimination is a promising method, potential problems associated with complete removal of eliminated amine persist. We have thus recently begun to examine alkane elimination as an alternative to the salt or amine elimination strategies described above. Although some examples of alkane elimination have been reported (6), this method has not been widely explored, perhaps because homoleptic alkyl complexes of early transition metals are somewhat unstable (7). We found that attachment of the tridentate Cp-amido ligand 1,3-$CpH^{NMe}SiN(H)R$ (SiNR = -$SiMe_2N$-*t*-butyl; NMe = -$CH_2CH_2NMe_2$, **1**) to scandium via alkane elimination from in situ generated $Sc(CH_2SiMe_3)_3$·2THF was facile (8). In this paper, we describe the synthesis of organozirconium derivatives of **1** via both amine and alkane elimination.

Results and discussion

Ligand attachment via amine elimination

The ligand **1** was prepared as described in detail previously (8). ^1H NMR spectra of these ligands are complex due to the presence of two isomers arising from 1,5-silatropic shifts (9) (Scheme 1) as well as various isomers of both 1,3 and 1,2 substitution arising from 1,2 prototropic shifts (10) (not shown in the scheme). For **1**, the ratio of 1,3:1,2 isomers was determined to be ≈7:3. Ligand **1** was found to be sensitive to heat and moisture, precluding purification by distillation or column chromatography. In addition, attempted deprotonation with the usual reagents (*n*-BuLi, KH, i-PrMgBr) did not lead to pure salts of the ligands, preventing the use of traditional salt elimination reactions for ligand attachment.

The rate of interconversion of the substitutional isomers, as well as the rates of reaction for each of the isomers with deprotonating agents, will dictate which isomer will bind to a metal. In scandium complexes of **1**, the 1,3 isomer attached almost exclusively. In contrast, the 1,2 isomer was active to a degree in amine elimination reactions between **1** and $Zr(NMe_2)_4$; this chemistry is summarized in Scheme 1. The bis-amide derivatives 1,2-**2** and 1,3-**2** were formed in a ≈1:9 ratio as an orange oil and were inseparable. Conversion of the bis-amides to the analogous dichlorides was carried out using Me_2NH·HCl (3). At this stage, the 1,3 isomer of **3** could be purified by recrystallization, since the dichlorides were white crystalline solids.

Scheme 2.

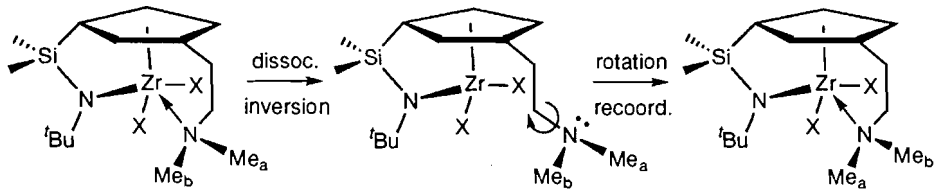

Complete removal of dimethylamine was affected by heating the crude solid product under dynamic vacuum for a brief period. Alkylation of the dichloride 1,3-(Cp^{NMe}SiNR)$ZrCl_2$ with methyllithium proceeded smoothly to yield 1,3-(Cp^{NMe}SiNR)$Zr(CH_3)_2$, 1,3-**4**.

Since the bis-amido complexes **2** were not readily purified, the stepwise procedure from $Zr(NMe_2)_4$ dichloride 1,3-**3** was adapted to a "one-pot" process that dispensed with isolation of the amido intermediates (see Experimental). Yields of 1,3-(Cp^{NMe}SiNR)$ZrCl_2$ from $Zr(NMe_2)_4$ and diproteo ligand **1** were in the 65–75% range and, by ^1H NMR spectroscopy, contained < 2% isomeric 1,2-**3**.

Table 1 gives ^1H and $^{13}C\{^1H\}$ NMR data for new, isolated compounds. The geometry about the zirconium center in these complexes cannot be deduced from this data. We presume, based on models and the solid state structure of the scandium hydride dimer [(Cp^{NMe}SiNR)ScH]$_2$ (8), that an approximately trigonal bypyramidal geometry is present. Because of the planar chirality associated with the unsymmetrical disubstitution of the Cp ring, groups with the same connectivity are diastereotopic in complexes 1,3-**2**, **3**, and **4**, with the exception of the N-methyl groups on the pendant amine arm of the ligand. In each case, a single resonance for these groups was observed in both the ^1H and the $^{13}C\{^1H\}$ NMR spectra at room temperature. This suggests that the amine is either not coordinated to zirconium in these complexes, or undergoes a rapid equilibration process on the NMR time scale. Since the amine arm of the 1,3-substituted ligand does coordinate in related scandium complexes, we favor the latter explanation; a plausible process which exchanges the N-methyl groups (but not the other diastereotopic groups in the molecule) is shown in Scheme 2. Dissociation of the amine, followed by inversion at nitrogen (a low barrier process) (11), bond rotation about C—N, and recoordination of the amine exchanges the N methyl groups.

Since amine dissociation is likely a chemically significant process in these compounds, it is perhaps surprising that dimethyl complex 1,3-**4** reacts rapidly with the Lewis acid activators $B(C_6F_5)_3$ and $[Ph_3C]^+[B(C_6F_5)_4]^-$ to effect methide abstraction (12) and produce the cationic alkyls [(Cp^{NMe}SiNR)$Zr(CH_3)]^+[R'B(C_6F_5)_3]^-$ (R' = CH_3, **6a**; C_6F_5, **6b**) as shown in eq. [1]. Cations **6a** and **6b** are isoelectronic with the neutral scandium alkyl derivative supported by 1,3-**1**, which we

[1]

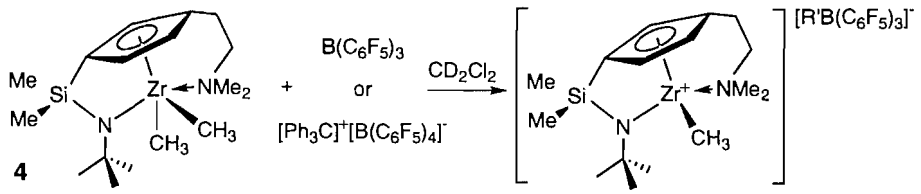

4 **6a, b**

recently reported (8). The chemical shift for the zirconium methyl groups (0.56 and 0.57 ppm for **6a** and **6b**, respectively) are characteristic of cationic zirconium methyl groups (13); other ligand signals also shift downfield relative to those in **4** as a consequence of bonding to the more electropositive zirconium center. Interestingly, only one diastereomeric cation is produced, suggesting that either one of the two diastereotopic methyl groups was abstracted preferentially or that the resulting methyl cation mixture rapidly isomerizes to one diastereomer.

The cations **6a** and **6b** were stable for a few hours in CD_2Cl_2 before decomposition became apparent. The NMR tube scale reactions were quite clean but attempts to isolate these compounds in preparative scale reactions led to oily materials with complex NMR spectra. Since neither **3** nor **4** exhibited significant activity towards propene polymerization upon activation with MAO,[3] the chemistry of these cations was not pursued further.

[3] Y. Mu, I. Munro, and W.E. Piers, unpublished results.

Ligand attachment via alkane elimination

Our success in the use of alkane elimination protocols for generation of organoscandium complexes led us to develop procedures for ligand attachment to zirconium via this strategy. In the reactions we explored, the zirconium-containing products isolated incorporated ligand **1** as its 1,2-substituted isomer. In situ generated R_nZrCl_{4-n} (R = CH_3, n = 3; R = CH_2SiMe_3, n = 2) was allowed to react with the diproteo ligand **1** as a mixture of its 1,2 and 1,3 substituted isomers. Yields of pure products were quite low and 1,3 products were observed only as minor components of the crude product mixture. These poor yields may be a reflection of the thermal instability of the in situ generated zirconium alkyls; for example, when solutions of the methyl reagent were allowed to warm to temperatures above 0°C, discolouration ensued as the reagent decomposed. It is unclear why the 1,2 isomer of the ligand **1** appears to react faster with these zirconium alkyls than the 1,3 substituted species.

Compounds 1,2-**3** and **5** were identified by their distinct

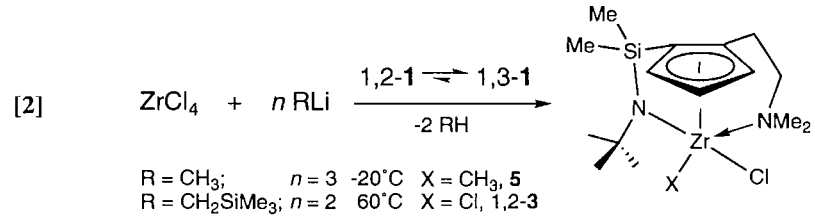

Fig. 1. ORTEP drawing of 1,2-($Cp^{NMe}SiNR$)$Zr(CH_3)Cl$, **5**.

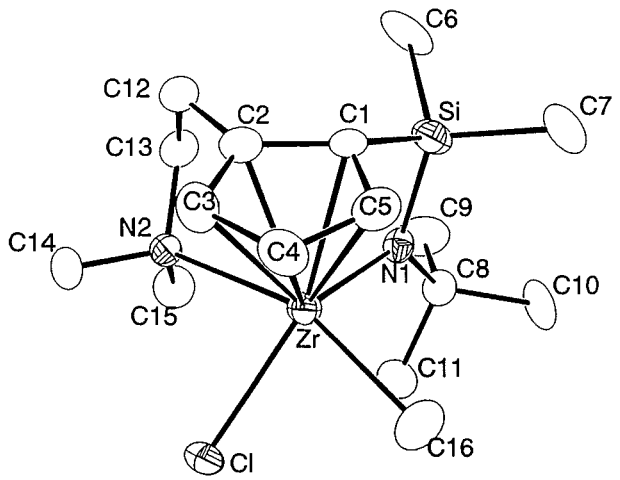

NMR spectra and by an X-ray structural determination of methyl chloride **5**. An ORTEP diagram of the molecular structure of **5** is shown in Fig. 1 and crystal data, atomic coordinates, and selected metrical data are given in Tables 2–4, respectively. If the centroid of the cyclopentadienyl donor is viewed as occupying one coordination site, the geometry about zirconium in this complex is closest to being square pyramidal, although the chlorine ligand tilts ≈25–30° out of the basal plane. This geometry is favoured by the 1,2 substitution on the cyclopentadienyl ring since the N1-Zr-N2 angle is 91.98(23)° compared to N_{amido}-Sc-N_{amine} angles of 111.74(17)° and 116.41(12)° in approximately trigonal-bipyramidal scandium complexes of 1,3-**1**. No disorder between the chloride and the methyl ligands was observed, nor was there any spectroscopic evidence for an isomer of **5** in which these ligands exchange positions.

The zirconium chlorine (14) and zirconium carbon (15) bonds in **5** are comparable to analogous bonds in Cp_2ZrX_2 compounds. The Zr—N_{amide} distance of 2.078(6) Å is much shorter than the Zr—N_{amine} length of 2.603(7) Å. While the former is within the expected range (2.00–2.08 Å) for zirconium amido nitrogen bond lengths (16), the latter is longer than normal (cf. the Zr—N distance of 2.434(3) Å in (η^8-COT)(η^4-COT)$Zr(NH_3)$ (17) and 2.421(9) Å in a zirconium complex containing a pendant pyrrolidine donor (4a)). This is suggestive of a very weak donor bond between zirconium and the amine ligand and is consistent with the observed equilibration of the diastereotopic N-methyl groups via the process given above in Scheme 2.

In conclusion, amine elimination is an effective means of attaching the tridentate ligand $Cp(H)^{NMe}SiN(H)R$ to zirconium, yielding predominately complexes of the 1,3 isomer of the ligand. On the other hand, the products isolated from the alkane elimination reactions are 1,2-isomer ligated complexes. The poor yields of the latter reactions suggest that more well-defined and stable alkane derivatives of zirconium may be required to improve efficiency.

Experimental

General

General techniques, drying of solvents, and analytical tools employed were as described previously (4*a*). All materials were purchased from Aldrich and used as recieved or purified by standard procedures (18). $Zr(NMe_2)_4$ (19), $B(C_6F_5)_3$ (20), and $Ph_3CB(C_6F_5)_4$ (21) were synthesized according to published procedures. Microanalytical data were obtained from Oneida Research Services, Inc., One Halsey Road, Whitesboro, NY 13492; however, like others (22), we found it difficult to obtain satisfactory analysis of carbon in these zirconium complexes due, presumably, to incomplete combustion.

Synthesis of ($Cp^{NMe}SiNR$)$Zr(NMe_2)_2$, 1,3-2

$CpH^{NMe}SiN(H)R$ (2.32 g, 8.7 mmol) in 25 mL of toluene was added to a solution of $Zr(NMe_2)_4$ (2.33 g, 8.7 mmol) in 10 mL of toluene at −78°C. The reaction mixture was allowed to warm to room temperature and then stirred at 40°C for 1 h. Solvent was removed and the residue was heated at 80°C under vacuum for several hours to remove the lower boiling-point impurities. [($Cp^{NMe}SiNR$)$Zr(NMe_2)_2$] (3.66 g, 8.2 mmol, 94%) was obtained as a yellowish oil that was >95% pure by ^1H NMR.

Synthesis of ($Cp^{NMe}SiNR$)$ZrCl_2$, 1,3-3

Method A

($Cp^{NMe}SiNR$)$Zr(NMe_2)_2$ (3.66 g, 8.2 mmol) was dissolved in 40 mL of THF. Anhydrous $Me_2NH{\cdot}HCl$ (1.35 g, 16.5 mmol) was added to the solution at −78°C. The mixture was allowed to warm to room temperature and stirred until the solid $Me_2NH{\cdot}HCl$ disappeared. The volatile materials were removed in vacuo and the residue was extracted with 50 mL of toluene. Insoluble materials were removed by filtration and the toluene was removed to give the crude product as an off-white solid. Pure product (2.74 g, 6.42 mmol, 77.8%) was obtained by recrystallization from hexane.

Method B

$ZrCl_4$ (2.62 g, 11.2 mmol) and $LiNMe_2$ (2.30 g, 45 mmol) were combined in a flask and 50 mL of Et_2O at was added by vacuum transfer at −78°C. The mixture was allowed to warm to room temperature and stirred for 3 h at which time the mixture was cooled again to −78°C. A solution of CpH^{NMe}-SiN(H)R (3.00 g, 11.26 mmol) in 20 mL of toluene was added

Table 1. ^1H and $^{13}C\{^1H\}$ NMR data for isolated new compounds.[a]

Compound	No.	^1H and NMR data			$^{13}C\{^1H\}$ NMR data	
		δ(ppm)	Assignment	*J*(Hz)	δ(ppm)	Assignment
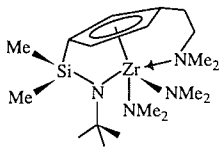	1,3-**2**	6.33, 6.10, 6.00 (m, 3H)	Cp*H*	2.4, 2.0	128.3, 118.3, 118.0,	
		2.84, 2.81 (s, 12H)	$ZrN(CH_3)_2$		115.4, 112.5	Cp*C*
		2.80, 2.70 (m, 2H)	NCH_2		60.9	NCH_2
		2.45, 2.15 (m, 2H)	NCH_2CH_2		56.1	$NC(CH_3)_3$
		2.12 (s, 6H)	CH_3NCH_2		45.3	$(CH_3)_2NCH_2$
		1.28 (s, 9H)	$NC(CH_3)_3$		43.9, 43.6	$ZrN(CH_3)_2$
		0.57, 0.53 (s, 6H)	$SiCH_3$		34.6	$NC(CH_3)_3$
					27.3	NCH_2CH_2
					2.4, 2.1	$Si(CH_3)_2$
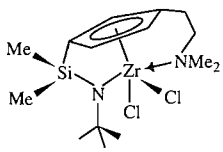	1,3-**3**	6.42, 6.39, 6.13 (m, 3H)	Cp*H*	2.6, 2.2	134.6, 122.1, 121.3,	
		3.48 (ddd, 1H)	NCH_2	12.4, 12.4, 6.4	121.1, 112.2	Cp*C*
		2.11 (ddd, 1H)	NCH_2	6.2, 1.2	61.8	NCH_2
		2.21 (ddd, 1H)	NCH_2CH_2	12.4, 12.4, 6.4	58.8	$NC_2(CH_3)_3$
		1.49 (ddd, 1H)	NCH_2CH_2	6.2, 1.2	47.4	$(CH_3)_2NCH_2$
		2.09 (s, 6H)	CH_3NCH_2		32.6	$NC(CH_3)_3$
		1.55 (s, 9H)	$NC(CH_3)_3$		24.7	NCH_2CH_2
		0.57, 0.45 (s, 6H)	$SiCH_3$		2.5, 0.4	$Si(CH_3)_2$
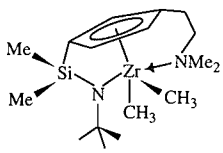	1,3-**4**	6.28, 6.11, 6.10 (m, 3H)	Cp*H*	2.6, 2.2	132.3, 120.2, 117.3,	
		2.99 (ddd, 1H)	NCH_2	12.0, 12.0, 6.4	114.8, 107.2	Cp*C*
		2.22 (ddd, 1H)	NCH_2	6.4, 1.6	62.8	NCH_2
		2.31 (ddd, 1H)	NCH_2CH_2	12.0, 12.0, 6.0	56.5	$NC(CH_3)_3$
		1.57 (ddd, 1H)	NCH_2CH_2	6.0, 1.6	47.1	$(CH_3)_2NCH_2$
		1.86 (s, 6H)	CH_3NCH_2		33.7	$NC(CH_3)_3$
		1.49 (s, 9H)	$NC(CH_3)_3$		31.8, 30.4	$ZrCH_3$
		0.53, 0.52 (s, 6H)	$SiCH_3$		25.4	NCH_2CH_2
		0.00, -0.14 (s, 6H)	$ZrCH_3$		3.2, 1.1	$Si(CH_3)_2$
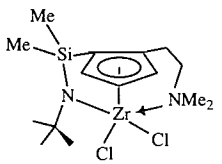	1,2-**3**	6.62, 6.43, 5.95 (m, 3H)	Cp*H*		134.9, 126.8, 120.1,	
		3.02 (ddd, 1H)	NCH_2		118.6, 107.6	Cp*C*
		2.31 (ddd, 1H)	NCH_2		64.0	NCH_2
		2.14 (ddd, 1H)	NCH_2CH_2		58.0	$NC(CH_3)_3$
		1.55 (ddd, 1H)	NCH_2CH_2		49.0	$(CH_3)_2NCH_2$
		2.09 (s, 6H)	CH_3NCH_2		31.8	$NC(CH_3)_3$
		1.34 (s, 9H)	$NC(CH_3)_3$		26.0	NCH_2CH_2
		0.45, 0.27 (s, 6H)	$SiCH_3$		3.7, 2.5	$Si(CH_3)_2$
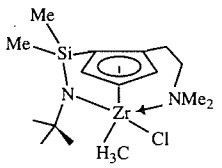	1,2-**5**	6.32, 6.29, 5.81 (m, 3H)	Cp*H*		132.6, 122.7, 117.7	
		2.89 (ddd, 1H)	NCH_2		(2C), 106.6	Cp*C*
		2.41 (ddd, 1H)	NCH_2		62.5	$NC(CH_3)_3$
		2.24 (ddd, 1H)	NCH_2CH_2		56.4	NCH_2
		1.60 (ddd, 1H)	NCH_2CH_2		47.7	$(CH_3)_2NCH_2$
		2.05 (s, 6H)	CH_3NCH_2		35.0	$ZrCH_3$
		1.27 (s, 9H)	$NC(CH_3)_3$		32.9	$NC(CH_3)_3$
		0.37, 0.31 (s, 6H)	$SiCH_3$		26.1	NCH_2CH_2
		0.67 (s, 3H)	$ZrCH_3$		3.8, 2.6	$Si(CH_3)_2$

[a]All spectra recorded in C_6D_6.

via syringe. The mixture was allowed to warm to room temperature and then stirred at 40°C for 1 h. Solvent was removed and the residue was heated at 80°C for several hours to remove volatile materials. The residue was redissolved in THF (50 mL) and anhydrous $Me_2NH{\cdot}HCl$ (1.84 g, 22.5 mmol) was added at −78°C. The mixture was stirred at room temperature until the solid $Me_2NH{\cdot}HCl$ disappeared and was worked up as described above. Yield from $ZrCl_4$, 3.31 g, 7.8 mmol, 69%. Anal. calcd. for $C_{15}H_{28}N_2SiCl_2Zr$: C 42.23, H 6.62, N 6.57; found: C 41.37, H 6.61, N 6.37.

Table 2. Summary of data collection and structure refinement details for 1,2-($Cp^{NMe}SiNR$)$Zr(CH_3)Cl$, **5**.

Empirical formula	$C_{16}H_{31}N_2SiClZr$	d_{calc}, g cm^{-3}	1.36
fw	406.19	μ, cm^{-1}	0.73
Crystal system	Monoclinic	*h, k, l* ranges	−10, 10; 0, 15; 0, 15
Space group	$P\ 2_1/a$	No. unique reflections	2608
Crystal dimensions, mm	0.15 × 0.30 × 0.40	No. observed reflections	1573
Temp, °C	21	($I > 3.0\sigma$)	
a, Å	9.6951(10)	No. of parameters	190
b, Å	14.3794(16)	*k* value	0.000050
c, Å	14.364(3)	Min/Max transmission	0.902/0.998
β, °	96.308(15)	Max residual density, e Å^{-3}	0.410
V, Å^3	1990.3(5)	Min residual density, e Å^{-3}	−0.370
Z	4	*R*, R_w	0.046, 0.041
F(000)	848	Goodness of fit	1.78

Table 3. Atomic parameters *x, y, z* and B_{iso} for 1,2-($Cp^{NMe}SiNR$)$Zr(CH_3)Cl$, **5**.

Atom	*x*	*y*	*z*	B_{iso}[a]
Zr	0.699 94(9)	0.542 58(6)	0.315 80(6)	2.97(4)
Cl	0.746 78(24)	0.581 99(15)	0.487 13(14)	3.89(11)
Si	0.719 5(3)	0.478 66(19)	0.114 63(18)	4.34(14)
N1	0.828 9(6)	0.507 4(4)	0.214 9(4)	3.0(3)
N2	0.726 7(7)	0.378 6(5)	0.392 4(5)	3.3(4)
C1	0.557 2(8)	0.492 6(7)	0.173 6(6)	3.2(4)
C2	0.514 7(8)	0.437 3(7)	0.247 7(6)	3.5(5)
C3	0.446 1(9)	0.492 2(8)	0.307 1(7)	4.3(5)
C4	0.443 5(9)	0.584 7(7)	0.273 1(7)	4.2(5)
C5	0.511 4(9)	0.583 5(7)	0.191 6(7)	4.5(5)
C6	0.710 6(10)	0.568 6(8)	0.017 4(6)	7.2(7)
C7	0.731 3(10)	0.360 7(8)	0.062 0(6)	6.5(6)
C8	0.981 5(9)	0.521 3(6)	0.219 6(6)	3.9(5)
C9	1.017 0(10)	0.598 7(8)	0.153 8(6)	6.2(6)
C10	1.058 6(9)	0.432 1(7)	0.200 5(8)	6.4(6)
C11	1.033 8(8)	0.554 6(7)	0.320 1(6)	4.6(5)
C12	0.539 8(9)	0.334 6(7)	0.264 5(6)	4.3(5)
C13	0.684 0(9)	0.312 9(6)	0.312 7(7)	4.0(5)
C14	0.871 6(9)	0.356 0(6)	0.429 8(6)	4.5(5)
C15	0.638 7(9)	0.360 2(6)	0.469 4(6)	4.1(5)
C16	0.734 9(9)	0.700 8(6)	0.302 7(7)	5.3(5)

[a] B_{iso} is the mean of the principal axes of the thermal ellipsoid.

Synthesis of ($Cp^{NMe}SiNR$)$Zr(CH_3)_2$, 1,3-4

($Cp^{NMe}SiNR$)$ZrCl_2$ (1.2 g, 2.8 mmol) was suspended in Et_2O (60 mL) and MeLi (4.0 mL of a 1.4 M solution in Et_2O, 5.6 mmol) was added via syringe at −78°C. The mixture was stirred at −78°C for 4 h, then warmed slowly to room temperature. The solvent was removed and the product was extracted with hexanes. Insoluble materials were filtered off and the extract was reduced in volume to 2–3 mL and cooled to −40°C for several hours to precipitate the product. The pure product (0.74 g, 1.9 mmol, 69%) was obtained by cold filtration as an off-white crystalline solid. Anal. calcd. for $C_{17}H_{34}N_2SiZr$: C 52.93, H 8.88, N 7.26; found: C 52.32, H 8.74, N 7.23.

In situ generation of [($Cp^{NMe}SiNR$)ZrMe]$^+$[$MeB(C_6F_5)_3$]$^-$, 6a

($Cp^{NMe}SiNR$)$Zr(CH_3)_2$ (25 mg 0.065 mmol) and $B(C_6F_5)_3$ (33 mg, 0.065 mmol) were loaded into a 5 mm NMR tube and dissolved in CD_2Cl_2 (≈0.8 mL). ^1H, ^{13}C, ^{11}B, and ^{19}F NMR spectra were recorded. ^1H NMR (CD_2Cl_2, ppm): 7.03 (m, 1H, ^3J = 2.6 Hz, ^4J = 2.2 Hz, 1H of C_5H_3), 6.42 (m, 1H, C_5H_3), 6.30 (m, 1H, ^4J = 2.2 Hz, C_5H_3), 3.28 (ddd, 1H, ^2J = 13.0 Hz, ^3J = 9.6 Hz, ^3J = 5.2 Hz, NCH_2CH_2), 3.12 (ddd, 1H, ^3J = 5.0 Hz, NCH_2CH_2), 3.01 (ddd, 1H, ^2J = 15.4 Hz, NCH_2CH_2), 2.93 (ddd, 1H, ^2J = 15.4 Hz, NCH_2CH_2), 2.50 (s, 6H, $N(CH_3)_2$), 1.54 (s, 9H, $NC(CH_3)_3$), 0.56 (s, 3H, $ZrCH_3$), 0.47 (br, 3H,

Table 4. Slected bond distances and angles for 1,2-($Cp^{NMe}SiNR$)Zr(CH_3)Cl, **5**.

	Bond lengths (Å)		
Zr—Cl	2.5175(23)	Zr—C16	2.311(9)
Zr—N1	2.078(6)	Zr—N2	2.603(7)
Zr—C1	2.446(8)	C1—C2	1.425(13)
Zr—C2	2.467(8)	C2—C3	1.385(14)
Zr—C3	2.555(9)	C3—C4	1.418(15)
Zr—C4	2.567(9)	C4—C5	1.405(15)
Zr—C5	2.481(9)	C1—C5	1.414(14)
Zr—Cp_{cent}	2.1981(9)		
	Bond angles (°)		
Cl-Zr-N1	132.76(17)	Zr-N1-Si	106.0(3)
Cl-Zr-N2	77.98(16)	Zr-N1-C8	127.4(5)
Cl-Zr-C16	81.1(3)	Si-N1-C8	125.5(5)
N1-Zr-N2	91.98(23)	Zr-N2-C13	103.9(5)
N1-Zr-C16	94.5(3)	Zr-N2-C14	113.5(5)
N2-Zr-C16	156.6(3)	Zr-N2-C15	115.8(5)
N1-Si-C1	93.8(3)	C13-N2-C14	107.9(6)
N1-Si-C6	114.9(4)	C13-N2-C15	108.6(6)
Cp_{cent}-Zr-N1	101.0	Cp_{cent}-Zr-N2	96.3
Cp_{cent}-Zr-C16	104.5	Cp_{cent}-Zr-Cl	125.8

BCH_3), 0.46 (s, 6H, $Si(CH_3)_2$). $^{13}C\{^1H\}$ NMR (CD_2Cl_2, ppm): 137.4, 124.2, 121.7, 120.2, 108.6 (C_5H_3), 70.3 (NCH_2CH_2), 57.9 ($NCMe_3$), 44.7, 44.2 (NMe_2), 39.8 (Zr*Me*), 33.9 (B*Me*), 33.0 ($NCMe_3$), 25.1 (NCH_2CH_2), 1.04, 0.02 ($SiMe_2$). $^{11}B\{^1H\}$ NMR (CD_2Cl_2, ppm, referenced to $BF_3{\cdot}Et_2O$ at 0.0 ppm): −13.4. $^{19}F\{^1H\}$ NMR (CD_2Cl_2, ppm, referenced to at 0.0 ppm): −165.1 (t, ^3J = 23 Hz, *p*-C_6F_5), −167.7 (t, *m*-C_6F_5), −133.1 (d, ^3J = 22 Hz, *o*-C_6F_5).

In situ generation of $[(Cp^{NMe}SiNR)ZrMe]^+[B(C_6F_5)_4]^-$, 6b

($Cp^{NMe}SiNR$)Zr(CH_3)$_2$ (25 mg, 0.065 mmol) and $[Ph_3C]^+[B(C_6F_5)_4]^-$ (63 mg, 0.065 mmol) were loaded into a 5 mm NMR tube and dissolved in CD_2Cl_2 (≈0.8 mL). ^1H NMR (CD_2Cl_2, ppm): δ 7.03 (m, 1H, ^3J = 2.6 Hz, ^4J = 2.2 Hz, C_5H_3), 6.43 (m, 1H, C_5H_3), 6.31 (m, 1H, ^4J = 2.2 Hz, C_5H_3), 3.29 (ddd, 1H, ^2J = 13.0 Hz, ^3J = 9.6 Hz, ^3J = 5.2 Hz, NCH_2CH_2), 3.12 (ddd, 1H, ^3J = 5.2 Hz, ^3J = 5.0 Hz, NCH_2CH_2), 3.01 (ddd, 1H, ^2J = 15.4 Hz, NCH_2CH_2), 2.93 (ddd, 1H, NCH_2CH_2), 2.50 (s, 6H, $N(CH_3)_2$), 1.55 (s, 9H, $NC(CH_3)_3$), 0.57 (s, 3H, $ZrCH_3$), 0.47 (s, 6H, $Si(CH_3)_2$). Partial ^1H NMR (CD_2Cl_2, ppm, −40°C): 2.48, 2.46 (s, 6H, $N(CH_3)_2$), 0.42, 0.40 (s, 6H, $Si(CH_3)_2$). $^{13}C\{^1H\}$ NMR (CD_2Cl_2, ppm): 137.4, 124.2, 121.7, 120.2, 108.6 (C_5H_3), 70.3 (NCH_2CH_2), 57.9 ($NCMe_3$), 44.6, 44.1 (NMe_2), 39.8 (Zr*Me*), 33.0 ($NCMe_3$), 25.0 (NCH_2CH_2), 1.00, −0.07 ($SiMe_2$). $^{11}B\{^1H\}$ NMR (CD_2Cl_2, ppm): −15.1 ($B(C_6F_5)_4^-$). $^{19}F\{^1H\}$ NMR (CD_2Cl_2): −163.2 (t, ^3J = 19.4 Hz, *p*-C_6F_5), −167.2 (t, *m*-C_6F_5), −133.2 (d, ^3J = 19.4 Hz, *o*-C_6F_5).

Synthesis of 1,2-($Cp^{NMe}SiNR$)Zr(CH_3)Cl, 5

$ZrCl_4(THF)_2$ (0.30 g 0.80 mmol) and solid MeLi (0.05 g, 2.4 mmol) were combined in a flask and Et_2O (30 mL) was vacuum transferred in at −78°C. The mixture was warmed to −20°C and stirred for 1 h. A solution of $CpH^{NMe}SiN(H)R$ (0.21 g, 0.80 mmol) in hexanes (10 mL) was added via syringe at −20°C. The mixture was slowly warmed to 0°C and stirred for 30 min, then warmed to room temperature. The solvent was removed and the residue was extracted with hexanes. The extract was reduced in volume to 2–3 mL and cooled to −40°C; the yellowish crystalline product (98 mg, 0.24 mmol, 30%) was collected via filtration and dried in vacuo. Anal. calcd. for $C_{16}H_{31}ClN_2SiZr$: C 47.31, H 7.69, N 6.90; found: C 47.99, H 7.98, N 6.70.

Synthesis of 1,2-($Cp^{NMe}SiNR$)ZrCl_2, 1,2-3

$ZrCl_4(THF)_2$ (0.10 g, 0.27 mmol) and solid $TMSCH_2Li$ (0.05 g, 0.53 mmol) were combined in a flask and Et_2O (20 mL) was vacuum transferred in at −78°C. The mixture was allowed to warm to room temperature and stirred for 1 h. The Et_2O was removed in vacuo and replaced with toluene (20 mL) and the undissolved solids were removed by filtration. A solution of $CpH^{NMe}SiN(H)R$ (71 mg, 0.27 mmol) in 5 mL of toluene was added via syringe. The mixture was stirred at 60°C for 1 h, during which period a white precipitate formed. The solution was concentrated and a few mL of hexanes were added; the white solid was collected on a frit and dried under vacuum (20 mg, 0.05 mmol, 18%). Anal. calcd. for $C_{15}H_{28}Cl_2N_2SiZr$: C 42.23, H 6.62, N 6.57; found: C 41.85, H 6.76, N 6.42.

X-ray crystallographic analysis of 1,2-($Cp^{NMe}SiNR$)Zr(CH_3)Cl, 5

Single crystals were mounted in thin-walled glass capillaries and placed on an Enraf Nonius CAD-4 diffractometer. Unit cell dimensions were determined via least-squares refinement of the setting angles of 24 high-angle reflections and intensity data were collected using the ω-2θ scan mode. Data were corrected for Lorentz, polarization, and absorption effects but not for extinction. Pertinent data collection and structure refinement parameters are presented in Table 2. The structure was solved using direct methods and all non-hydrogen atoms were refined with anisotropic thermal parameters. Aryl and methylene hydrogen atoms were placed in calculated postions (D_{C-H} = 1.00 Å). Methyl hydrogen atoms were located via difference Fourier map inspection. Hydrogen atoms were given isotropic temperature factors based upon the atom to which they are bonded, and fixed during least-squares refinement. A weighting scheme based upon counting statistics was used with the weight modifier k in kF_o^2 being determined via evaluation of variation in the standard reflections that were collected during the course of data collection. Neutral atom scattering factors were taken from *International tables for X-ray crystallography* (23). Values of R and R_w are given by $R = (F_o - F_c)/EF_o$ and $R_w = [E(w(F_o - F_c))^2/E(wF_o^2)]^{1/2}$. All crystallographic calculations were conducted with the PC version of the NRCVAX program package (24) locally implemented on an IBM compatible 80486 computer. Anisotropic thermal parameters and hydrogen atom parameters are available as supplementary material.[4]

[4] Copies of material on deposit may be purchased from: The Depository of Unpublished Data, Document Delivery, CISTI, National Research Council Canada, Ottawa, Canada K1A 0S2. The table of hydrogen atom parameters has also been deposited with the Cambridge Crystallographic Data Centre, and can be obtained on request from The Director, Cambridge Crystallographic Data Centre, University Chemical Laboratory, 12 Union Road, Cambridge, CB2 1EZ, U.K.

Acknowledgments

W.E.P. thanks the Institute for Chemical Science and Technology and the Research Partnerships office (Industrially Oriented Research program) of the Natural Sciences and Engineering Research Council of Canada for financial support of this work.

References

1. (*a*) K.B. Sinclair and R.B. Wilson. Chem. Ind. 857 (1994); (*b*) Chem. Br. **30**, 87 (1994).
2. G. Chandra and M.F. Lappert. J. Chem. Soc. A, 1940 (1968).
3. A.K. Hughes, A. Meetsma, and J.H. Teuben. Organometallics, **12**, 1936 (1993).
4. (*a*) W.E. Piers, Y. Mu, L.R. MacGillivray, and M.J. Zaworotko. Polyhedron, **14**, 1 (1995); (*b*) Y. Mu, W.E. Piers, M.-A. MacDonald, and M.J. Zaworotko. Can. J. Chem. **73**, 2233 (1995).
5. G.M. Diamond, S. Rodewald and R.F. Jordan. Organometallics, **14**, 5 (1995).
6. (*a*) G.B. Deacon and R.H. Newham. Aust. J. Chem. **38**, 1757 (1985); (*b*) M. Booij, N.H. Kiers, H.J. Heeres, and J.H. Teuben. J. Organomet. Chem. **364**, 79 (1989); (*c*) G.B. Deacon, C.M. Forsyth, W.C. Patalinghug, A.H. White, A. Deitrich, and H. Schumann. Aust. J. Chem. **45**, 567 (1992); (*d*) P.N. Nickias, D.D. Devore, and D.R. Wilson. PCT Application, WO 93/08199, 1993 (Dow).
7. D.J. Cardin, M.F. Lappert, C.L. Raston, and P.I. Riley. *In* Comprehensive organometallic chemistry. Vol. 3. *Edited by* G. Wilkinson, F.G.A. Stone, and E.W. Abel. Pergammon Press, New York. 1982. pp. 635–640.
8. Y. Mu, W.E. Piers, D.C. MacQuarrie, M.J. Zaworotko, and V.G. Young, Jr. Organometallics, **15**, 2720 (1996).
9. (*a*) F.A. Cotton and T.J. Marks. Inorg. Chem. **9**, 2802 (1970); (*b*) A. Bonny, R.D. Holmes-Smith, G. Hunter, and S.R. Stobart. J. Am. Chem. Soc. **104**, 1855 (1982); (*c*) A.D. McMaster and S.R. Stobart. J. Am. Chem. Soc. **104**, 2109 (1982).
10. E.W. Abel and M.O. Dunster. J. Organomet. Chem. **33**, 161 (1971).
11. F.A. Cotton and G. Wilkinson. Advanced inorganic chemistry. 5th ed. Wiley, New York. 1988. p. 307.
12. X. Yang, C.L. Stern, and T.J. Marks. J. Am. Chem. Soc. **116**, 10015 (1994).
13. R.F. Jordan, R.E. LaPointe, P.K. Bradley, and N. Baenziger. Organometallics, **12**, 2892 (1989).
14. K. Prout, T.S. Cameron, R.A. Forder, S.R. Critchley, B. Centon, and G.V. Rees. Acta Crystallogr. Ser. B: Struct. Crystallogr. Cryst. Chem. **30**, 2290 (1974).
15. W.E. Hunter, D.C. Hrncir, R.V. Bynum, R.A. Penttila, and J.A. Atwood. Organometallics, **2**, 750 (1983).
16. (*a*) D.C. Bradley, H. Chudzynska, J.D.J. Backer-Dirks, M.B. Hursthouse, A.A. Ibrahim, M. Motevalli, and A.C. Sullivan. Polyhedron, **9**, 1423 (1990); (*b*) Y. Bai, H.W. Roesky, M. Noltemeyer, and M. Witt. Chem. Ber. **125**, 825 (1992); (*c*) C.C. Cummins, G.D. Van Duyne, C.P. Schaller, and P.T. Wolczanski. Organometallics, **10**, 164 (1991).
17. P. Berno, C. Floriani, A. Chiesi-Villa, and C. Rizzoli. J. Chem. Soc. Dalton Trans. 3085 (1991).
18. D.D. Perrin and W.L.F. Armarego. Purification of laboratory chemicals. 3rd ed. Pergamon Press, New York. 1988.
19. D.C. Bradley and I.M. Thomas. J. Chem. Soc. 3857 (1960).
20. A.G. Massey and A.J. Park. J. Organomet. Chem. **2**, 245 (1964).
21. J.C.W. Chien, G.H. Llinas, M.D. Rausch, G.Y. Lin, and H.H. Winter. J. Am. Chem. Soc. **113**, 8569 (1991).
22. M.J. Carney, P.J. Walsh, F.J. Hollander, and R.G. Bergman. Organometallics, **11**, 761 (1992).
23. International tables for X-ray crystallography Vol. IV. Kynoch Press, Birmingham, England. 1974.
24. E.J. Gabe, Y. Le Page, J.-P. Charland, F.L. Lee, and P.S. White. J. Appl. Crystallogr. **22**, 384 (1989).

Synthesis and biological evaluation of carbon-substituted C-4 derivatives of podophyllotoxin

Yvonne Lear and Tony Durst

Abstract: Several C-4 carbon-substituted analogues of podophyllotoxin, **1**, were prepared by treatment of **1** with allyltrimethylsilane or trimethylsilylcyanide in the presence of boron trifluoride etherate. Alternatively, carbon substituents were introduced via additions to the carbobenzyloxy-protected C-4′-dimethylated podophyllotoxone. These 4′-dimethylated derivatives showed promising in vitro antitumour activity and were equally active against human colon cell line HT116 and two multidrug resistant cell lines. The alcohol **6** was evaluated in vivo but was found to be inactive.

Key words: podophyllotoxin analogues, podophyllotox-4-one, C4 carbon substituted podophyllotoxins.

Résumé : On a préparé plusieurs analogues de la podophyllotoxine **1** substitués sur le carbone en position 4, en traitant le composé **1** avec l'allyltriméthylsilane ou le cyanure de triméthylsilane en présence de l'éthérate de trifluorure de bore. Alternativement, on a introduit les substituants sur le carbone via des additions sur la podophyllotoxone déméthylée en C-4′ et protégée par le groupe carbobenzyloxy. Ces dérivés déméthylés en C-4′ exhibent in vitro une activité anti tumorale prometteuse et sont également actifs contre la ligne cellulaire du colon humain HT116 et contre deux lignes cellulaires résistantes a de nombreux médicaments. On a évalué l'alcool **6** in vivo mais elle est inactive.

Mots clés : analogues de la podophyllotoxine, podophyllotox-4-one, podophyllotoxines substituées en C4.

[Traduit par la rédaction]

Introduction

The clinical use of Etoposide **1** as an antitumour agent (1–3) has spurred interest in the modification of its aglycone podophyllotoxin **2** in order to furnish derivatives possessing superior antitumour activity. These efforts have included a number of modifications at the C-4 position of the molecule. New derivatives have included ethers, esters (4), amines (5, 6), sulfides, sulfoxides, and sulfones (7). Except for an isolated example described in 1960 (8), there appear to have been no reports describing the synthesis of derivatives of podophyllotoxin bearing carbon substituents at C-4. Such derivatives should have greater chemical stability than the typical podophyllotoxin derivatives since the C-4 heteroatom bond is susceptible to heterolytic cleavage, which generates a benzylic carbocation intermediate and hence either new substitution or elimination products.

This report describes the synthesis of several derivatives of 4′-demethylpodophyllotoxin in which the OH bond at C-4 has been replaced by a carbon–carbon bond, and the evaluation of their biological activity. These new analogues retain the crucial structural features of the Etoposide aglycone, such as the *trans*-fused lactone (3) and the C-4′ hydroxyl group on the pendant aromatic ring (9). In addition, these derivatives have

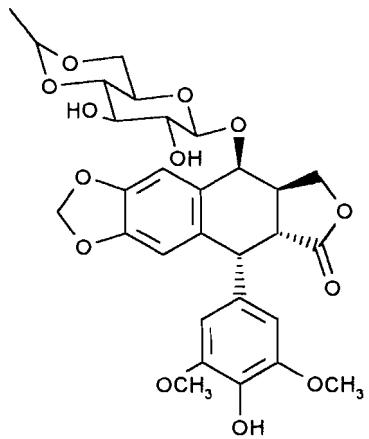

1

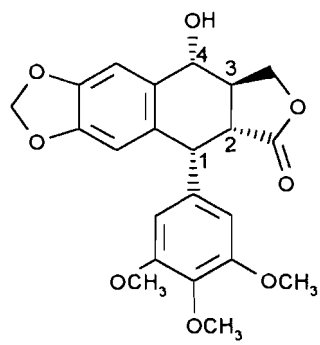

2

Received February 9, 1996.

Y. Lear and T. Durst.[1] Ottawa–Carleton Chemistry Institute, Department of Chemistry, University of Ottawa, Ottawa, ON K1N 6N5, Canada.

[1] Author to whom correspondence may be addressed. Telephone: (613) 562 5800, ext. 6072. Fax: (613) 562 5170. E-mail: tdurst@oreo.chem.uottawa.ca

the preferred β stereochemistry at C-4 for optimal activity (10).

Results and discussion

The desired carbon substituents at C-4 were introduced using either podophyllotoxin or 4′-*O*-carbobenzyloxypodophyllotoxin as starting materials. Thus treatment of podophyllotoxin with allyltrimethylsilane in dichloromethane at 0°C in the presence of boron trifluoride etherate (11, 12), afforded 4-β-allyl-4-deoxypodophyllotoxin, **3**, mp 131°C, in 95% yield. The 4-β-stereochemistry was expected since trapping of the intermediate benzylic cation should occur preferentially from the sterically less hindered β side. This was confirmed by the 5.8 Hz coupling constant between H3 and H4, which is consistent with that observed for similar compounds (13). The coupling constants for the remaining C-ring protons ($J_{1,2}$ = 5.2 Hz and $J_{2,3}$ = 14.3 Hz) show that the podophyllotoxin stereochemistry has been retained.

The intermediate **3** was readily converted to the alcohol **4** in 90% yield by reaction with borane – methyl sulfide followed by $NaOH–H_2O_2$ work-up. Oxidation of **4** with Jones reagent gave the carboxylic acid **5**. Both **4** and **5** were demethylated at C-4′ using anhydrous HBr in dichloromethane to afford **6** and **7**, respectively. The demethylation of **5** to give **7** was highly problematic, giving low yields of the product **7**, which was impossible, due to decomposition, to purify completely either by silica gel chromatography or recrystallization. The spectroscopic properties of these compounds were in agreement with the assigned structures and are reported in the experimental section.

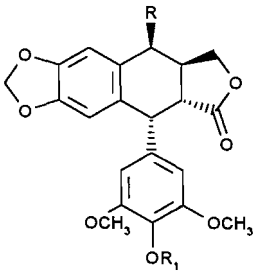

3	R = $CH_2CH{=}CH_2$	$R_1 = CH_3$
4	R = $CH_2CH_2CH_2OH$	$R_1 = CH_3$
5	R = CH_2CH_2COOH	$R_1 = CH_3$
6	R = $CH_2CH_2CH_2OH$	R_1 = H
7	R = CH_2CH_2COOH	R_1 = H
8	R = CN	$R_1 = CH_3$
9	R = $COOCH_2CH_3$	$R_1 = CH_3$
10	R = CN	R_1 = H
11	R = $COOCH_2CH_3$	R_1 = H
12	R = OH	R_1 = Cbz

The preparation of the 4-cyano and 4-carboethoxy derivatives **10** and **11**, respectively, has thus far been unsuccessful. The required 4-cyano-4-deoxypodophyllotoxin, **8**, was obtained in 88% yield from **2** upon treatment with trimethylsilylcyanide and boron trifluoride etherate. Unfortunately, the demethylation of the 4′-methoxy group with HBr under the usual conditions afforded only a small amount of a highly insoluble product, tentatively assigned as **10** on the basis of its MS and ^{1}H NMR data. Hydrolysis of **8** in refluxing ethanolic HCl gave **9** on the basis of MS and ^{1}H NMR data; unfortunately 4′-*O*-demethylation of **9** to provide target compound **11** using HBr or BBr_3 has not been successful.

4′-*O*-Carbobenzyloxypodophyllotoxone, **13**, available by pyridinium dichromate oxidation of the corresponding protected 4′-*O*-carbobenzoxyepipodophyllotoxin **12** (10), was converted into a compound presumed to be **15**, in 80% yield, upon reaction with lithium phenylacetylide. This intermediate was not characterized but was hydrogenated over palladium to remove the Cbz protecting group and reduce the alkyne at C-4 to give **17**, mp 163–164°C, whose structure was verified by NMR and mass spectral data. In a model study, reaction of podophyllotoxone (**8**) with *n*-BuLi gave a mixture of **16** and its C-4 epimer as the major products. A single crystal X-ray diffraction determined that the minor isomer had the α geometry at C-4. Based on this result, it was concluded that the larger phenyl acetylide anion would also give mainly the β geometry, hence products **15** and **17**.

Biological evaluation

The in vitro cytotoxicity of three of the above compounds was evaluated against the human colon cell line HCT 116 and two drug-resistant cell lines HCT116/VM46 and HCT116/VP35 (Table 1). The former exhibits multidrug resistance to lipophilic anticancer drugs such as taxol, Etoposide (VP-16), Teniposide (VM-26), doxorubicin, and vinblastine by overexpressing *p*-glycoprotein, which acts as a cell surface drug efflux pump to limit the accumulation of the above-mentioned drugs in cancer cells. The latter line has reduced levels of topoisomerase II and is resistant to topoisomerase-active drugs such as Etoposide and Teniposide. The results of the tests and comparison to Etoposide and Teniposide are shown in Table 1.

In these in vitro tests, the 4-hydroxypropyl derivative **6** was most active amongst the new structures against all three cell lines. While the alcohol **6** was approximately 4 times less active than Teniposide against the nonresistant strain, it was somewhat more active than Teniposide against the resistant strains. Compound **6** has comparable activity, with an IC_{50} of approximately 0.7 μM, against each of the three cell lines. The in vitro activity of the tertiary alcohol **17** is reduced by a factor of about 3 and that of the acid **7** by more than 10 relative to **6**. Interestingly for **17**, as for **6**, the response of the multidrug-resistant cell lines is similar to that of the nonresistant line HCT 116. This indicates that **6** and **17** are not substrates for the *p*-glycoprotein efflux pump or they inhibit the pump.

Compound **6** was subsequently evaluated in vivo against a distally implanted M109 tumour model in CDF1 mice by administering it interperitoneally as a solution in H_2O – carbomethoxy cellulose at dosages ranging from 50 to 120 mg/kg. Survival times at 50 and 80 mg/kg were identical to that of the control group (test/control, T/C = 100–105). At the highest

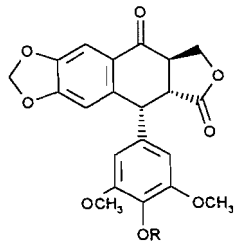

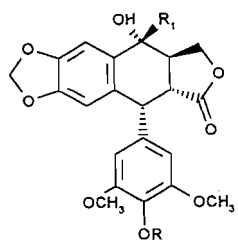

13 R = Cbz

14 R = CH_3

15 R = Cbz R_1 = C≡CPh

16 R = CH_3 R_1 = Bu

17 R = H R_1 = CH_2CH_2Ph

Table 1. In vitro toxicity of podophyllotoxin derivatives in human colon carcinoma cell lines.

Compound tested	IC_{50} (μM)		
	HCT116	HCT116/VM46	HCT116/VP35
6	0.76	0.76	0.66
7	9.5	13	11
17	2.2	2.4	2.2
Etoposide	1.5	8.6	7.4
Teniposide	0.18	0.92	0.76

dosage employed the T/C fell to 87. The other C-4 substituted derivatives were not tested in vivo. Biological testing was carried out by Bristol-Myers Squibb following established protocol.

Experimental

NMR spectra were recorded on either A Varian XL 300 or Bruker AMX 500 spectrometer. Melting points were recorded on a Thomas Scientific melting point apparatus. THF was freshly distilled from sodium and benzophenone prior to use. Chromatography solvents were distilled routinely prior to use. Podophyllotoxin was donated by Bristol-Myers Squibb, Wallingford, Connecticut.

4-β-Allyl-4-deoxypodophyllotoxin 3

Podophyllotoxin, **2** (1 g, 2.4 mmol, 1 equiv.) was stirred with boron trifluoride etherate (750 μL, 2.5 equiv.) and allyltrimethylsilane (80 μL, 2 equiv.) in dry CH_2Cl_2 (1 mL) over 4 Å molecular sieves at 25°C for 4 h. Water (3 mL) was added and the product was extracted with CH_2Cl_2, washed with H_2O, dried ($MgSO_4$), and evaporated to give a white solid. Chromatography on silica gel (1:1 hexane:ethyl acetate) and recrystallization from hexane – ethyl acetate afforded the pure compound (1.05 g, 95% yield); mp 137–138°C. IR: 1775 cm^{-1} (lactone). ^1H NMR ($CDCl_3$): 6.73 (s, 1H), 6.47 (s, 1H), 6.29 (s, 2H), 5.95 (s, 1H), 5.94 (s, 1H), 5.81 (m, 1H), 5.11–5.15 (m, 2H), 4.56 (d, $J_{1,2}$ = 5.2 Hz, 1H), 4.23–4.30 (m, 2H), 3.77 (s, 3H), 3.71 (s, 6H), 3.27–3.40 (m, 1H), 3.05–3.09 (m, 1H), 2.96–3.01 (m, $J_{2,3}$ = 14.3 Hz, $J_{3,4}$ = 5.8 Hz, 1H), 2.57–2.60 (m, 1H), 2.43–2.45 (m, 1H). ^{13}C NMR ($CDCl_3$): 175.1, 152.4, 147.0, 146.9, 137.0, 136.6, 136.1, 133.0, 130.8, 116.9, 110.1, 108.7, 108.4, 101.2, 69.0, 60.7, 56.2, 44.0, 42.2, 38.5, 37.7, 36.1. HRMS calcd. for $C_{25}H_{26}O_7$: 438.1679; found: 438.1681.

4β-(3-Hydroxypropyl)-4-deoxypodophyllotoxin 4

Borane methyl sulfide complex (100 μL 10 M solution) was added dropwise to a solution of **3** (925 mg, 2.1 mmol) in dry CH_2Cl_2 (6 mL) at 0°C. The solution was stirred at 25°C for 4 h, then diluted with 10 mL EtOH. The pH of the solution was maintained at 8 using 3 N aqueous NaOH while H_2O_2 (0.3 mL, 30% in H_2O) was added at 0°C. Water (10 mL) was added and the product extracted with CH_2Cl_2, dried ($MgSO_4$), and the solvent evaporated, leaving a white solid that was recrystallized from hexane – ethyl acetate to give the product (915 mg, 95% yield); mp 118–119°C. IR: 3612, 1775 cm^{-1}. ^1H NMR ($CDCl_3$): 6.69 (s, 1H), 6.43 (s, 1H), 6.25 (s, 2H), 5.92 (s, 1H), 5.90 (s, 1H), 4.53 (d, J = 4.8 Hz, 1H), 4.36 (dd, J = 8.5 Hz, 7.1 Hz, 1H), 4.08–4.13 (m, 1H), 3.77 (s, 3H), 3.72 (s, 6H), 2.95–3.00 (m, 1H), 2.85–2.95 (m, 2H). ^{13}C NMR ($CDCl_3$): 175.1, 152.4, 147.0, 146.8, 137.1, 136.2, 133.8, 130.5, 110.2, 108.8, 108.5, 101.2, 69.0, 62.5, 60.7, 56.2, 44.1, 42.2, 39.3, 36.2, 32.1, 29.7. HRMS calcd. for $C_{25}H_{28}O_8$: 456.1775; found: 456.1773.

4β-(3-Propanoic acid)-4-deoxypodophyllotoxin 5

Jones reagent (2 mL, 0.4 M) was added dropwise to a solution of 160 mg **4** dissolved in acetone until an orange colour persisted. Stirring was continued for 15 min. The reaction mixture was brought to pH 7 using saturated $NaHCO_3$ solution. The mixture was extracted using CH_2Cl_2. The organic layer was washed with H_2O, dried ($MgSO_4$), and the solvent evaporated. The product was isolated by column chromatography on silica gel using 5% MeOH, 63% ethyl acetate, and 32% hexanes as eluent and was recrystallized from hexane – ethyl acetate. Yield: 105 mg (66%); mp 197°C. IR (CH_2Cl_2): 2600–3300 cm^{-1}. ^1H NMR: 6.77 (s, 1H), 6.44 (s, 1H), 6.24 (s, 2H), 5.93 (s, 1H), 5.91 (s, 1H), 4.54 (br, 1H), 4.36 (m, 1H), 4.12 (m, 1H), 3.77 (s, 3H), 3.71 (s, 6H), 3.11 (br, 1H), 2.98 (br, 1H), 2.41–2.49 (m, 2H), 2.02–2.07 (m, 1H), 1.86–1.90 (m, 1H). ^{13}C NMR: 177.2, 174.7, 152.5, 147.1, 137.2, 136.1, 132.7, 130.3, 110.4, 108.8, 108.5, 101.3, 68.6, 60.8, 56.2, 44.1, 41.9, 38.5, 36.1, 32.7, 27.7. HRMS calcd. for $C_{25}H_{26}O_9$: 470.1577; found: 470.1590.

4β-(3-Hydroxypropyl)-4-deoxy-4′-demethylpodophyllotoxin 6

A solution of 10 mL dichloroethane and 3 mL diethyl ether saturated with anhydrous HBr at 0°C was added to 750 mg **4**. The solution was stirred at 0°C for 30 min and at 25°C for 90 min. The solution was neutralized by adding solid K_2CO_3. The organic layer was diluted with CH_2Cl_2 (10 mL) and washed with H_2O (×3), with brine, dried ($MgSO_4$), and the solvent evaporated. The compound was isolated by radial chromatography on silica with ethyl acetate as eluent and was recrystallized from CH_2Cl_2–hexane. Yield: 440 mg (60%); mp 129–130°C. IR: 3000–3500 (br) cm^{-1}. ^1H NMR ($CDCl_3$): 6.69 (s, 1H), 6.43 (s, 1H), 6.27 (s, 2H), 5.92 (s, 1H), 5.90 (s, 1H), 4.52 (d, $J_{1,2}$ = 4.7 Hz, 1H), 4.30–4.33 (m, 1H), 4.11–4.16 (m, 1H), 3.75 (s, 6H), 3.06 (m, 1H), 2.96 (m, 1H), 1.83 (m, 1H), 1.70 (m, 1H), 1.54–1.69 (m, 4H). ^{13}C NMR ($CDCl_3$): 146.3, 131.7,

110.2, 108.8, 108.1, 101.2, 68.9, 62.6, 56.4, 44.0, 42.3, 39.3, 36.1, 21.1, 29.7, 14.6. HRMS calcd. for $C_{24}H_{26}O_8$: 442.1614; found: 442.1630.

4β-(3-Propanoic acid)-4′-demethyl-4-deoxypodophyllotoxin 7

A solvent mixture of 25% ether in dichloroethane was saturated with HBr(g) at 0°C. The solvent mixture (10 mL) was added to 95 mg **5** and stirred at 0°C for 30 min and at 25°C for 2 h. The solution was neutralized with saturated $NaHCO_3$, extracted with CH_2Cl_2, dried ($MgSO_4$), and evaporated. Chromatography on silica gel (5% MeOH, 65% ethyl acetate, 30% hexanes as eluent) by preparative TLC and recrystallization from hexane – ethyl acetate yielded 20 mg (20%) of the impure demethylated compound **7**, which during each attempted purification decomposed considerably; mp 198–200°C, ^{1}H NMR: 6.69 (s, 1H), 6.44 (s, 1H), 6.27 (s, 2H), 5.92 (d, 1H), 5.90 (d, 1H), 4.53 (d, 1H), 4.31–4.33 (m, 1H), 4.12–4.18 (m, 1H), 3.75 (s, 6H), 3.05–3.08 (m, 1H), 2.97 (d, 1H), 2.94 (s, 1H). ^{13}C NMR: 191.0, 175.3, 146.3, 134.2, 133.0, 131.0, 110.2, 108.8, 108.1, 101.2, 68.9, 62.6, 56.4, 44.0, 42.3, 39.3, 36.1, 32.1, 29.7. HRMS calcd. for $C_{24}H_{24}O_9$: 456.1420; found: 456.1440.

4β-Cyano-4-deoxypodophyllotoxin 8

Boron trifluoride etherate (120 μL, 2 equiv.) was added to a solution of podophyllotoxin (200 mg, 1 equiv.) and trimethylsilyl cyanide (70 μL, 1.1 equiv.) in dry CH_2Cl_2 (3 mL) at 0°C. The solution was stirred for 20 min at 0°C and at 25°C for 1.5 h, when TLC showed that no starting material remained. Water was added (10 mL) and extraction carried out with CH_2Cl_2. The organic extracts were dried ($MgSO_4$) and the solvent evaporated to leave a yellow solid that was pure by NMR (180 mg, 88%); mp 158–159°C. IR: 2308, 1784 cm^{-1}. ^{1}H NMR ($CDCl_3$): 6.83 (s, 1H), 6.56 (s, 1H), 6.27 (s, 1H), 6.01 (s, 1H), 5.99 (s, 1H), 4.67 (d, $J_{1,2}$ = 4.6 Hz, 1H), 4.45–4.50 (m, 1H), 4.35 (d, J = 9.4 Hz, 1H), 4.21 (d, $J_{3,4}$ = 5.1 Hz, 1H), 3.80 (s, 3H), 3.74 (s, 6H), 3.05–3.15 (m, 1H), 2.90–3.05 (m, 1H). ^{13}C NMR ($CDCl_3$): 172.6, 152.4, 148.6, 147.7, 137.2, 134.4, 131.1, 122.1, 117.4, 110.7, 108.2, 107.9, 101.7, 68.5, 60.6, 56.0, 43.3, 43.1, 33.5, 33.0. HRMS calcd. for $C_{23}H_{21}O_7N$: 423.1301; found: 423.1314.

4β-Carboethoxy-4-deoxypodophyllotoxin 9

8 150 mg was refluxed in a solution of 3 mL HCl in 6 mL ethanol for 1 h. The solution was brought to pH 7 with saturated aqueous $NaHCO_3$ solution, extracted with CH_2Cl_2, dried ($MgSO_4$), and the solvent was evaporated to yield 95 mg white solid (57% yield); mp 138–139°C. IR: 1776, 1732 cm^{-1}. ^{1}H NMR: 7.11 (s, 1H), 6.47 (s, 1H), 6.07 (s, 1H), 5.94 (s, 1H), 5.92 (s, 1H), 4.44 (d, $J_{1,2}$ = 5.4 Hz, 2H), 4.1–4.2 (m, 1H), 3.83 (d, J = 9.2 Hz, 1H), 3.78 (m, 1H), 3.77 (s, 3H), 3.72 (s, 6H), 3.15–3.20 (m, 1H), 3.00 (dd, $J_{1,2}$ = 5.4 Hz, $J_{2,3}$ = 13.0 Hz, 1H), 1.25 (t, 3H). ^{13}C NMR: 175.6, 171.5, 153.0, 147.7, 147.2, 135.6, 130.5, 121.7. 109.4, 108.9, 106.4, 101.3, 70.2, 61.0, 60.8, 56.2, 46.8, 46.4, 42.2, 32.1, 29.7, 25.7, 14.2. HRMS calcd. for $C_{25}H_{26}O_9$: 470.1577; found: 470.1579.

4′-*O*-Carbobenzyloxypodophyllotoxone 13

A solution of 100 mg 4′-*O*-carbobenzyloxyepipodophyllotoxin **12** (10) and 300 mg pyridinium dichromate in 2 mL dry CH_2Cl_2 was stirred for 26 h at 25°C. Separation by silica gel column chromatography using hexane:ethyl acetate (1:1) and recrystallization from CH_2Cl_2–hexane afforded 82 mg desired product (82% yield); mp 99°C. IR (CH_2Cl_2): 1773, 1733 cm^{-1}. ^{1}H NMR ($CDCl_3$): 7.56 (s, 1H), 7.34–7.44 (m, 5H), 6.70 (s, 1H), 6.42 (s, 2H), 6.11 (s, 1H), 6.09 (s, 1H), 5.27 (s, 2H), 4.87 (d, $J_{1,2}$ = 4.3 Hz, 1H), 4.56–4.57 (m, 1H), 4.34–4.38 (m, 1H), 3.71 (s, 1H), 3.45–3.51 (m, 1H), 3.29 (dd, $J_{1,2}$ = 4.3 Hz, $J_{2,3}$ = 15.6 Hz, 1H). ^{13}C NMR ($CDCl_3$): 191.9, 172.6, 152.8, 151.7, 147.8, 140.7, 134.9, 134.6, 128.1, 127.9, 109.4, 106.7, 105.8, 102.1, 70.1, 66.6, 55.9, 46.3, 44.3, 43.0. FABMS (M + 1) calcd. 533.1369; found: 533.1397.

4′-*O*-Carbobenzoxy-4-(phenylethynyl)-epipodophyllotoxin 15

*n*BuLi (60 μL, 2 N in hexanes, 1 equiv.) was added to a solution of penylacetylene (20 μL, 1 equiv.) in dry THF (2 mL) at −78°C. A solution of 13 (90 mg, 1 equiv.) in dry THF (2 mL) was added and stirring continued at −78°C for 30 min. The reaction was quenched at −78°C with saturated aqueous NH_4Cl. The mixture was allowed to warm to room temperature and was extracted with CH_2Cl_2. The organic layer was washed with H_2O, dried ($MgSO_4$), and the solvent evaporated, leaving 82 mg white solid. The mixture was used for the next step without further purification.

4-Butyl-4-deoxypodophyllotoxin 16

To a solution of podophyllotoxone (6) (250 mg, 0.6 mmol, 1 equiv.) in 3 mL dry THF at −78°C was added 250 μL *n*-BuLi (2.4 M in hexanes, 0.6 mmol, 1 equiv.). The solution was stirred at −78°C for 15 min, then quenched with saturated NH_4Cl. Chromatography on silica gel using hexane:ethyl acetate (1:1) afforded 40 mg of the α-substituted isomer and 70 mg of the β-substituted isomer.

α Isomer: mp 105–106°C. IR: 3425br, 1777 cm^{-1}. ^{1}H NMR: 6.98 (s, 1H), 6.52 (s, 1H), 6.31 (s, 2H), 6.00 (s, 1H), 5.96 (s, 1H), 4.58 (d, $J_{1,2}$ = 4.69 Hz, 1H), 4.27–4.38 (m, 2H), 3.79 (s, 1H), 3.71 (s, 6H), 3.22 (dd, $J_{1,2}$ = 4.9 Hz, $J_{2,3}$ = 14.1 Hz, 1H), 2.88–2.97 (m, 1H), 1.77–1.84 (m, 2H), 1.05–1.4 (m, 4H), 0.89 (t, 3H). ^{13}C NMR: 175.4, 152.5, 147.9, 136.5, 135.1, 134.3, 132.5, 110.5, 107.8, 104.9, 101.5, 72.9, 67.1, 60.7, 55.9, 44.6, 41.7, 39.4, 39.3, 27.8, 23.1, 13.9.

β Isomer: mp 110°C. IR: 3593 br, 1774 cm^{-1}. ^{1}H NMR: 7.05 (s, 1H), 6.45 (s, 1H), 6.29 (s, 2H), 5.96 (s, 2H), 4.56 (d, $J_{1,2}$ = 4.9 Hz, 1H), 4.45 (dd, 1H), 4.27 (s, 1H), 3.78 (s, 3H), 3.73 (s, 6H), 3.08 (dd, $J_{1,2}$ = 4.9 Hz, $J_{2,3}$ = 14.9 Hz, 1H), 2.98 (m, 1H), 1.82–1.88 (m, 2H), 1.2–1.4 (m, 4H), 0.88 (t, 3H). ^{13}C NMR: 174.5, 152.5, 147.7, 147.4, 137.2, 136.3, 135.4, 131.3, 109.6, 108.4, 106.0, 101.4, 74.6, 67.7, 60.7, 56.3, 44.6, 44.5, 44.4, 39.4, 27.2, 23.25, 13.9. HRMS calcd. for $C_{26}H_{30}O_8$: 470.1954; found: 470.1967.

4-(2-Phenylethyl)-4′-demethylepipodophyllotoxin 17

A mixture of **15** (70 mg) and 10% Pd/C (25 mg) in ethyl acetate (5 mL) was stirred under hydrogen atmosphere for 20 min, when TLC showed that no starting material remained. Recrystallization from $CHCl_3$ gave the desired product (25 mg, 45% yield); mp 163–164°C. IR: 3529, 1778 cm^{-1}. ^{1}H NMR (acetone-d_6): 8.00 (s, 1H), 7.28 (s, 1H), 7.18–7.25 (m, 2H), 7.12–7.15 (m, 1H), 6.47 (s, 1H), 6.42 (s, 2H), 5.97 (s, 2H), 4.66 (a,

1H), 4.57 (d, 1H, $J_{1,2}$ = 5.6 Hz), 4.42 (d, 1H, J = 1.5 Hz), 4.40 (s, 1H), 3.70 (s, 6H), 3.36 (dd, 1H, $J_{1,2}$ = 14.9 Hz, $J_{2,3}$ = 5.7 Hz), 3.14–3.21 (m, 1H), 2.75–2.78 (m, 1H), 2.17–2.21 (m, 1H), ^{13}C NMR (acetone-d_6): 175.0, 147.9, 147.6, 147.5, 143.2, 138.1, 135.8, 132.6, 132.2, 128.9, 126.3, 110.0, 107.2, 101.9, 79.0, 74.2, 68.0, 56.5, 45.4, 45.0, 44.4, 41.4, 31.5. HRMS calcd. for $C_{29}H_{28}O_8$: 504.1780; found: 504.1764.

Biological testing

Biological testing was carried out at Bristol-Myers Squibb Laboratories. To determine in vitro cytotoxicity, the cell lines used were human colon carcinoma cell line HCT 116, the VM-26 resistant cell line HCT116/VM46, and the VP-16 resistant cell line HCT116/VP35. Cells were plated and 24 h later drugs were added and serially diluted. After 72 h of continuous drug exposure, the tetrazolium dye XTT was added. Since dehydrogenase enzyme in live cells reduces the XTT to a form that absorbs light at 450 nm, spectrophotometric methods can be used to determine to percentage of live cells. The results in Table 1 reflect drug concentration required to inhibit cell proliferation to 50% of that of untreated control cells.

Acknowledgements

The authors acknowledge the financial support of the Natural Sciences and Engineering Research Council of Canada (NSERC), and are grateful to Dr. D. Vyas of Bristol-Myers Squibb for a gift of podophyllotoxin as well as in vitro test-ing, and to Dr. W.C. Rose, Experimental Therapeutics Dept. Bristol-Myers Squibb Co., Princeton, N.J., for running the in vivo experiment.

References

1. K.R. Hande. Semin. Oncol. **19** (Suppl. 13), 3 (1992).
2. K. Kobayashi and M.J. Ratain. Semin. Oncol. **19** (Suppl. 13), 78 (1992).
3. W. Achterrah, N. Niederle, R. Raettig, and P. Hilgard. Cancer Treat. Rev. **9** (Suppl. A), 3 (1982).
4. L.S. Thurston, Y. Imakura, M. Haruna, D. Li, Z. Liu, S. Liu, Y. Cheng, and K-H. Lee. J. Med. Chem. **32**, 604 (1989).
5. Z. Wang, Y. Kuo, D. Schnur, J.P. Bowen, S. Liu, F. Han, J. Chang, Y. Cheng, and K-H. Lee. J. Med. Chem. **33**, 2660 (1990).
6. P. Allevi, M. Anastasia, and P. Ciuffreda. Tetrahedron Lett. **34**, 7313 (1993).
7. H.D.H. Showalter, R.T. Winters, A.D. Sercel, and A. Michel. Tetrahedron Lett. **32**, 2849 (1991).
8. W.J. Gensler, F. Johnson, and A.D.B., Sloan. J. Am. Chem. Soc. **82**, 6074 (1960).
9. K-H. Lee, S.A. Beers, M. Mori, Z. Wang, Y. Kuo, L. Li, S. Liu, J. Chang, F. Han, and Y. Cheng. J. Med. Chem. **33**, 1364 (1990).
10. K-H. Lee, Y. Imakura, M. Haruna, S.A. Beers, L.S. Thurston, H. Dal, and C. Chen. J. Nat. Prod. **52**, 606 (1989).
11. S. Hashimoto, T. Honda, and S. Ikegami. Tetrahedron Lett. **32**, 1653 (1991).
12. C. Brückner, H. Holzinger, and H. Reissig. J. Org. Chem. **53**, 2440 (1988).
13. J.L. Charlton, S. Maddaford, K. Koh, S. Boulet, and M.H. Saunders. Tetrahedron: Asymmetry, **4**, 645 (1993).

Oxidation pathways of hydroxydopamines and their chloride and bromide salts: an electrochemical study in acidic solutions

Georgios Kokkinidis, Achilleas Papoutsis, and Evdoxia Coutouli-Argyropoulou

Abstract: The anodic oxidation of 6-hydroxydopamine and 5-hydroxydopamine and their chloride and bromide salts was studied in aqueous acidic solutions. The electrodes used were Pt and Pt/M (UPD) (M = Bi, Tl, Pb) modified surfaces. The electrochemical studies revealed that the first two-electron oxidation leads to formation of reactive quinoid intermediates. Reactions of these quinoid intermediates with nucleophiles yield substituted quinones that are not stable in solution. The reactions are initiated by the oxidation of the third hydroxyl group at more positive potentials. Cyclic voltammetry and rotating ring-disc electrode voltammetry were used to elucidate the reaction mechanisms. These techniques provide powerful tools to generate and detect transient intermediates and products and give valuable information regarding the pathways and mechanisms of the redox reactions.

Key words: 6-hydroxydopamine, 5-hydroxydopamine, voltammetry, electrolysis, oxidation mechanism, nucleophilic attack.

Résumé : On a étudié l'oxydation anodique de la 6-hydroxydopamine, de la 5-hydroxydopamine et de leurs chlorures et bromures en solutions aqueuses acides. On a utilisé les électrodes Pt et Pt/M (UPD)(M = Bi,Tl,Pb) à surfaces modifiées. Les études électrochimiques révèlent que la première oxydation à deux électrons conduit à la formation de quinoides intermédiaires. Les réactions de ces quinoides intermédiaires avec des nucléophiles donnent des quinones substituées qui ne sont pas stables en solution. Les réactions sont déclenchées par l'oxydation du troisième groupe hydroxyle à des potentiels plus positifs. On a utilisé la voltamétrie cyclique et la voltamétrie à électrode à disque annulaire rotatif pour élucider ces mécanismes. Ces techniques fournissent des outils puissants pour générer et détecter les intermédiaires transitoires et les produits, et donne des informations valables sur le processus et le mécanisme des réactions redox.

Mots clés : 6-hydroxydopamine, 5-hydroxydopamine, voltamétrie, électrolyse, mécanisme d'oxydation attaque nucléophile.

[Traduit par la rédaction]

Introduction

Increasingly, 6-hydroxydopamine is becoming an interesting compound in neuropharmacology because it is suspected to be the aberrant metabolite of neurotransmitter catecholamines that is highly toxic to the central nervous system (1–3). It has been postulated to be an autooxidation product of dopamine (4, 5). The intermediate dopamine quinone undergoes nucleophilic attack by water at the C(6) position, which leads to 6-hydroxydopamine. This reaction is very slow and may only occur under electrochemical conditions in very acidic solutions (6–9). The high acidity hinders the intramolecular cyclization of dopamine quinone because it prevents the release of the proton from the protonated amino group of the side chain, which, generally, is the first step toward the intramolecular cyclization reaction of catecholamines at pH > 3 to produce indole derivatives (3, 7–11).

6-Hydroxydopamine is more easily oxidized than dopamine. The oxidation leads to the respective *p*-quinone, which is also susceptible to nucleophilic attack (12) and intramolecular cyclization (13, 14). Reactions of the *p*-quinone intermediate with nucleophilic groups of proteins (e.g., thiols) at physiological pH might be related to the neurotoxicity of 6-hydroxydopamine (12).

Previous studies of the electrochemical behaviour of 6-hydroxydopamine are restricted to this first two-electron oxidation and the fate of the *p*-quinoid product in solution (6, 13–15). However, 6-hydroxydopamine-*p*-quinone can undergo further oxidation at more positive potentials at the free phenolic hydroxyl group, which might accelerate secondary reactions with nucleophiles.

The present study was undertaken to give insights into the reactions involved in this potential range that might be of considerable interest for biologically relevant mechanistic information. In addition, 5-hydroxydopamine was also included in this study for the sake of comparison. To the best of our knowledge, 5-hydroxydopamine has not been studied electrochemically so far. The study was carried out in acidic solutions to preclude intramolecular cyclization. The electrodes

Received December 11, 1995.[1]

G. Kokkinidis and A. Papoutsis.[2] Aristotle University of Thessaloniki, Department of Chemistry, Laboratory of Physical Chemistry, 540 06 Thessaloniki, Greece.
E. Coutouli-Argyropoulou. Aristotle University of Thessaloniki, Department of Chemistry, Laboratory of Organic Chemistry, 540 06 Thessaloniki, Greece.

[1] Revision received June 14, 1996.
[2] Author to whom correspondence may be addressed. Telephone: 003031-997755. Fax: 003031-997709.

Fig. 1. Cyclic voltammograms of (*A*) 6-OH-DA (10^{-3} M) and (*B*) 5-OH-DA (10^{-3} M) on Pt in 0.2 M $HClO_4$ in the absence (———) and presence (– – –) of 5×10^{-4} M $Bi(ClO_4)_3$. Scan rate v/mV s^{-1}: (1) 50; (2) 100; (3) 150; (4) 200. Insets: (*C*) Plots of j_p vs. $v^{1/2}$ for 6-OH-DA in the absence (1) and presence (2) of $Bi(ClO_4)_3$. (*D*) Plots of E_p vs. log v for 5-OH-DA in the absence (1) and presence (2) of $Bi(ClO_4)_3$.

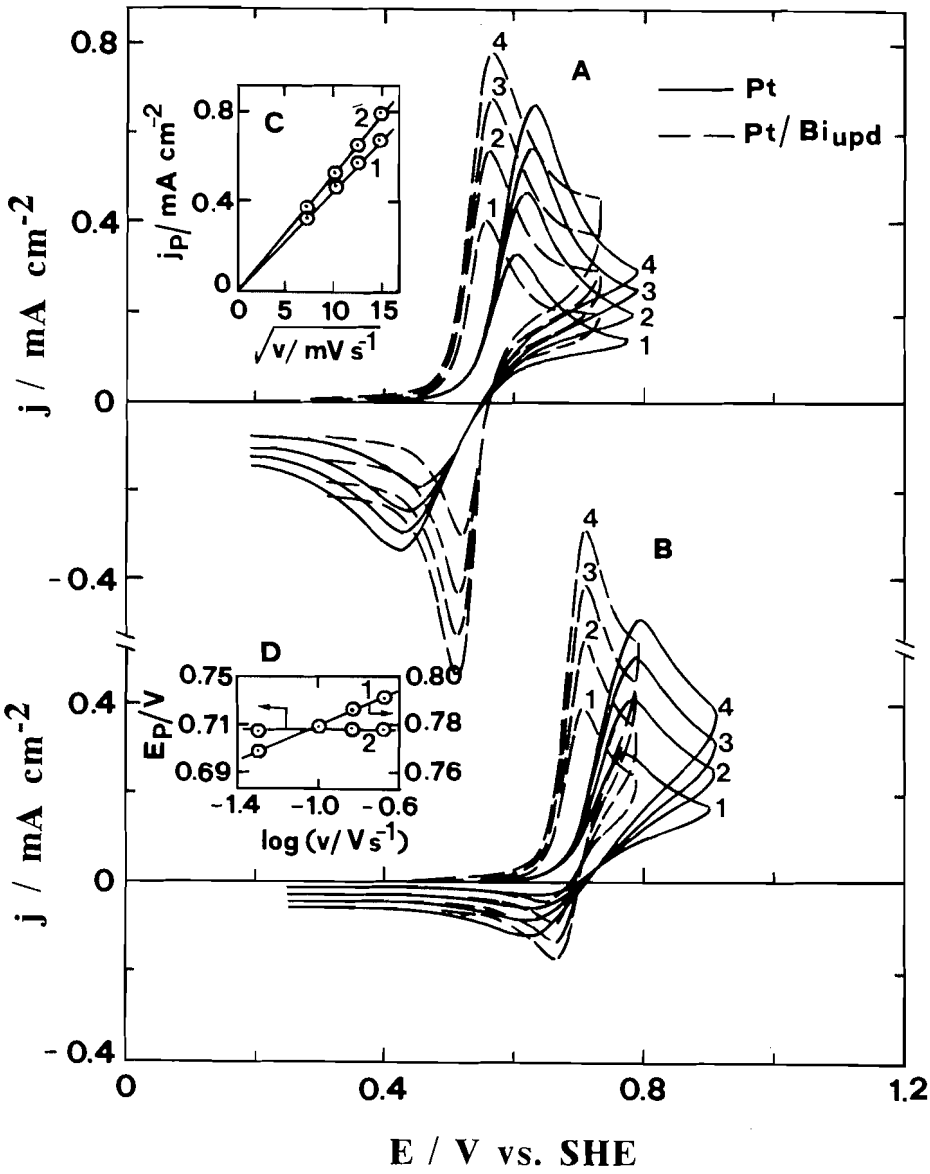

used were Pt and Pt/M(UPD) modified surfaces. It is known that underpotentially deposited (UPD) adlayers of Pb, Tl, and Bi on Pt improve markedly the kinetics of redox reactions (16–20) including the oxidation of catecholamines (20).

Experimental

Potentiostatic disc and ring-disc measurements were performed with a rotating Pt-Pt ring-disc electrode (EAD 10 000 from Tacussel). The electrode was activated by applying a continuous sweep (v = 1 V s^{-1}) between the potentials of hydrogen and oxygen evolution in 0.2 M $HClO_4$. The cell was double walled and thermostated at 25 ± 0.1°C, except where stated otherwise. An $Hg/Hg_2SO_4/Na_2SO_4$ (sat.) electrode, connected to the cell by a Luggin capillary and a Pt sheet served as the reference and the counter electrode, respectively. The solutions were thoroughly deoxygenated by purging the cell system with ultrapure nitrogen. Electrode potentials are given on the standard hydrogen electrode (SHE) scale.

The electronic setup consisted of a Tacussel bipotentiostat (Bi/Pad), with function generators from Bank Electronics (VSG-72) and an HP 7046B X-Y_1, Y_2 recorder.

The supporting electrolyte was prepared from triply distilled water and $HClO_4$ (Merck, suprapure). Stock solutions of perchlorate salts of Pb, Tl, and Bi were prepared from the respective oxides or carbonates (Merck, GR grade) and perchloric acid.

2,4,5-Trihydroxyphenethylamine hydrochloride (6-hydroxy-

Scheme 1.

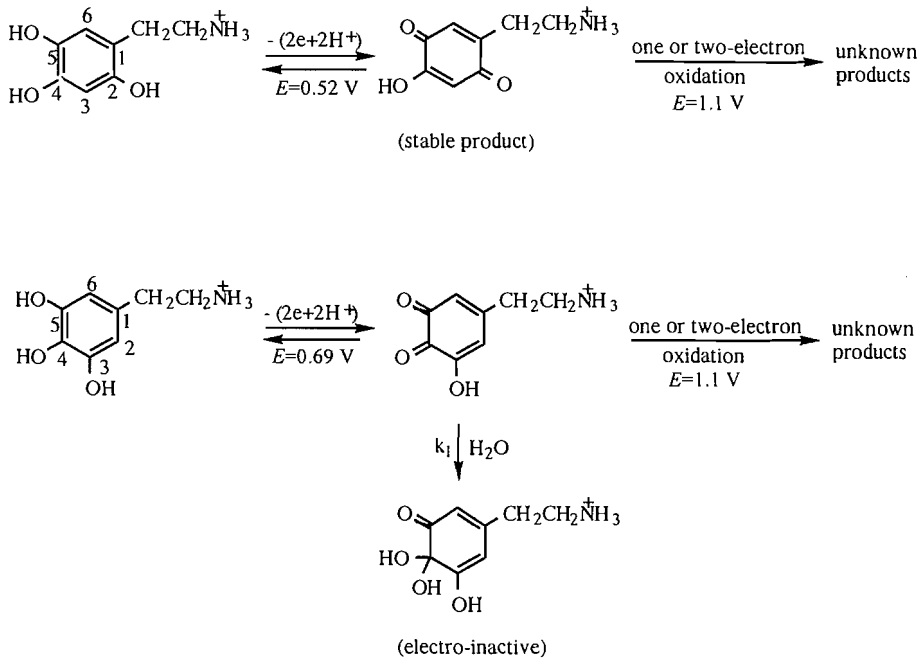

Fig. 2. Ring currents i_R vs. E_R at constant E_D = 1.1 V for DA (10^{-3} M) in 0.2 M $HClO_4$ obtained with a Pt–Pt rotating ring-disc electrode in 0.2 M $HClO_4$ in the absence (———) and presence (– – –) of 5×10^{-4} M $Bi(ClO_4)_3$ ($|dE/dt| = 25$ mV s^{-1}). Rotation frequency *f*/Hz: (1) 12.5; (2) 25; (3) 50.

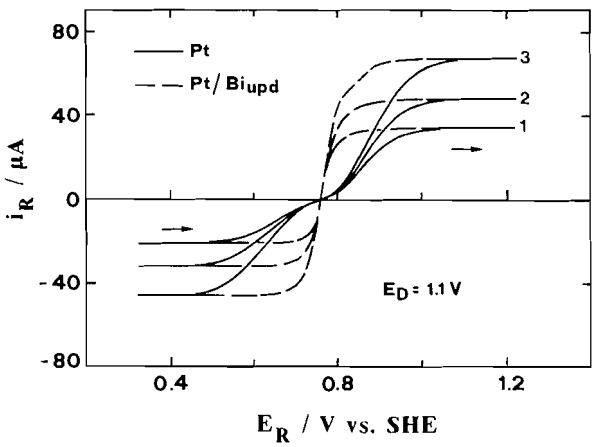

dopamine hydrochloride, 6-OH-DA·HCl), 2,4,5-trihydroxyphenethylamine hydrobromide (6-hydroxydopamine hydrobromide, 6-OH-DA·HBr), 3,4,5-trihydroxyphenethylamine hydrochloride (5-hydroxydopamine hydrochloride, 5-OH-DA·HCl), and 3,4-dihydroxyphenethylamine hydrochloride (dopamine hydrochloride, DA·HCl) were purchased from Sigma Chemical Co. (St. Louis, Mo.). Halide-free solutions of 6-OH-DA, 5-OH-DA, and DA were prepared by replacing Cl^- ions with sulfates. This was achieved by adding the stoichiometric quantity of Hg_2SO_4 to the respective solutions and filtering. It was determined that the residual halide concentration was less than 10^{-6} M.

Table 1. Hydration rate constants of 5-OH-DA-*o*-quinone at different temperatures.

T/K	$(v/D)^{1/3}$	k_1/s^{-1}
288	14.92	2.3 ± 0.2
298	11.75	3.4 ± 0.3
318	8.82	6.3 ± 0.5

Results and discussion

Oxidation of 6-OH-DA and 5-OH-DA on Pt and Pt/M(UPD) electrodes

The electrochemical oxidation of 6-OH-DA and 5-OH-DA was first studied in the absence of halide ions. Since these compounds are purchased as hydrochloride or hydrobromide salts, halide-free solutions were prepared following the procedure described in the experimental section. Figure 1 shows cyclic voltammograms of 6-OH-DA and 5-OH-DA obtained on Pt and Pt/Bi(UPD) electrodes as a function of scan rate. A single oxidation peak, which is diffusion controlled, is obtained. The reaction involved is a simple two-electron oxidation to the respective 6-OH-DA-*p*-quinone and 5-OH-DA-*o*-quinone. A second oxidation peak may appear at more positive potentials (i.e., at around 1.1 V) corresponding to further oxidation of the hydroxy-quinones but this peak is nearly masked by the current due to platinum oxide formation. The oxidation peak of 6-OH-DA is followed on the reverse sweep by a reduction peak of equal height. In the case of 5-OH-DA the reduction peak greatly decreases in height, indicating that the electron-transfer reaction is followed by a rapid chemical reaction, i.e., the process proceeds via an EC mechanism.

The anodic and cathodic processes at bare Pt are irreversible. As can be seen in Fig. 1, the UPD of Bi improves the

Fig. 3. Disc currents j_D vs. E_D and ring currents i_R vs. E_D at constant E_R = 0.2 V for the oxidation of (*A*) 6-OH-DA (10^{-3} M) and (*B*) 5-OH-DA (10^{-3} M) obtained with a Pt-Pt rotating ring-disc electrode in 0.2 M $HClO_4$ in the absence (———) and presence (– – –) of 5×10^{-4} M $Bi(ClO_4)_3$ ($|dE/dt| = 25$ mV s^{-1}). Rotation frequency *f*/Hz: (1) 12.5; (2) 25; (3) 50; (4) 100. Insets: (*C*) Plots of j_L vs. $\omega^{1/2}$ ($\omega = 2\pi f$) for waves (I_a) and (II_a) of 5-OH-DA. (*D*) Plots of $1/N_k$ vs. $1/\omega$ for 5-OH-DA at E_D = 0.95 V at different temperatures *T*/°C: (1) 15: (2) 25: (3) 45.

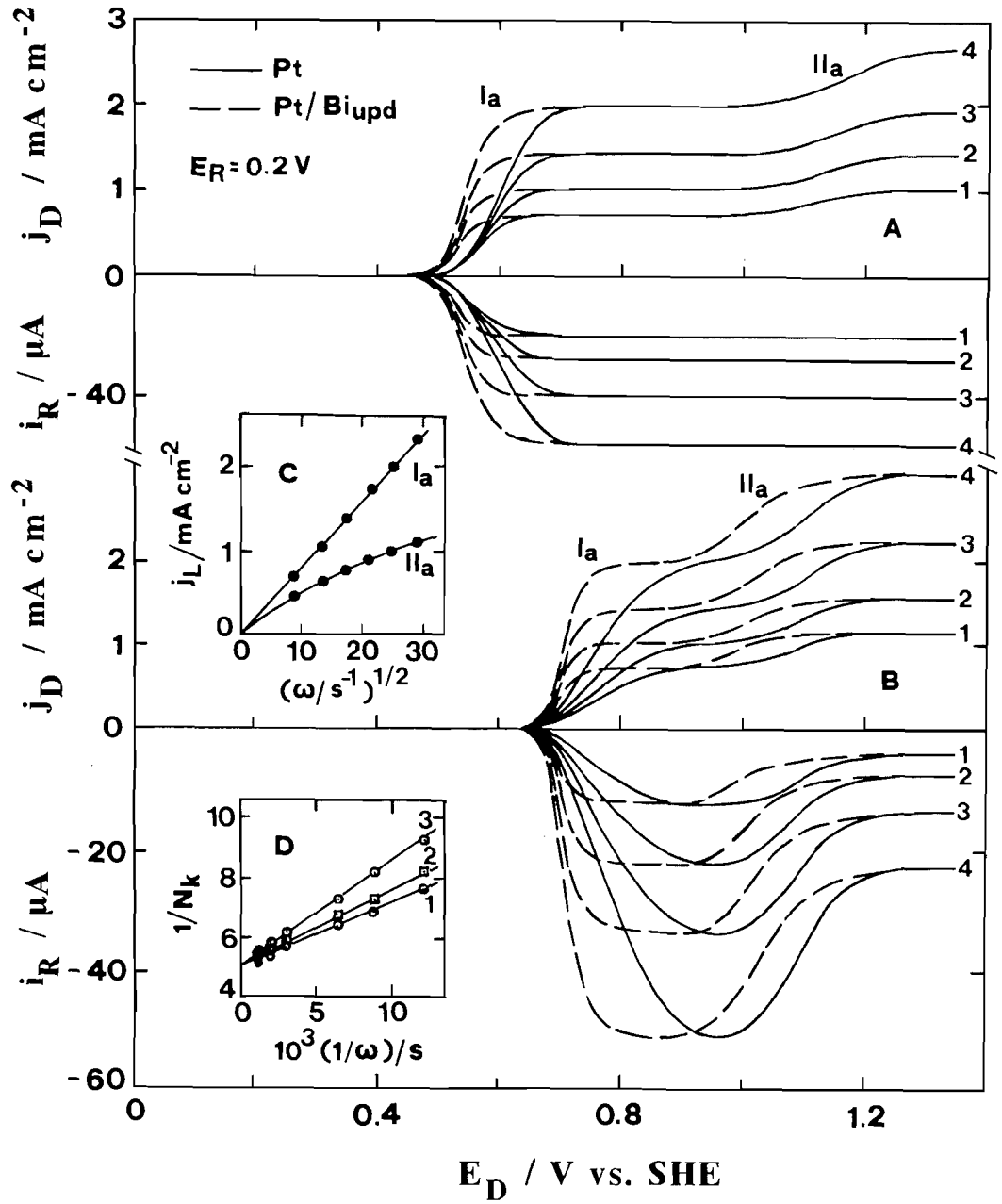

reversibility of the redox reactions. This is readily verified by comparing the peak potentials for Pt/Bi(UPD) with those for bare platinum. Furthermore, although the peak potentials for bare Pt depend linearly on log *v*, for Pt/Bi(UPD) they remain constant at all potential scan rates (see inset *D* of Fig. 1). Also for Pt/Bi(UPD) the difference between the peak potential and half-peak potential for both the anodic and cathodic branches of the cyclic voltammograms is ≈30 mV at all scan rates, which is in good agreement with the theoretical value of 28.2 mV for a two-electron reversible process (21). Similar behaviour was also observed with Tl and Pb UPD adlayers.

As discussed previously (22) for analogous redox systems, the Bi(UPD) layer hinders the adsorption of the reacting molecules, thus leading to the change of the reaction mechanism from an "inner-sphere" mechanism, involving adsorbed intermediates on bare Pt, to an "outer-sphere" one without complications from the adsorption of the reacting molecules, which favours faster electron exchange at the electrode–solution interface. The UPD of Bi also improves the reversibility of the redox reactions of dopamine (DA) itself. This becomes evident from the ring voltammograms of DA, I_R vs. E_R at constant E_D = 1.1 V where DA is oxidized to the open-chain

Fig. 4. Disc voltammograms for the oxidation of (1) 6-OH-DA·HBr (10^{-3} M), (2) 6-OH-DA·HCl (10^{-3} M), and (3) LiBr (10^{-3} M) on Pt in 0.2 M $HClO_4$ ($|dE/dt| = 25$ mV s^{-1}). Rotation frequency $f = 50$ Hz.

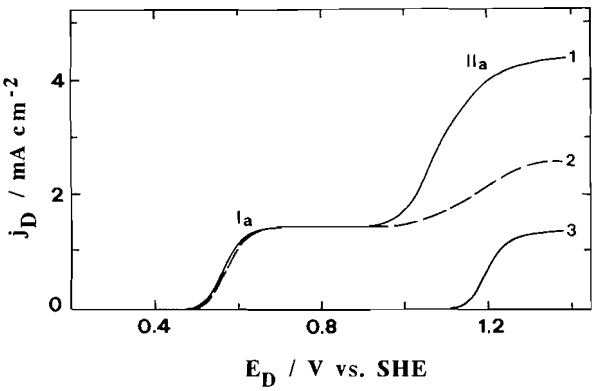

Fig. 5. Cyclic voltammogram of 6-OH-DA·HBr (10^{-3} M) on Pt in 0.2 M $HClO_4$. Scan rate $v = 150$ mV s^{-1}.

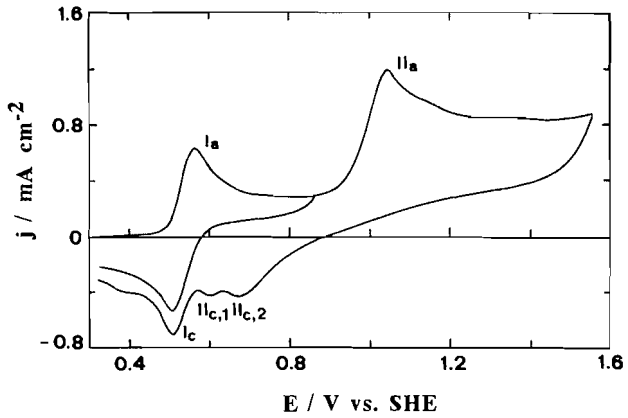

quinone (Fig. 2). Under this condition, both DA and DA-quinone are collected by the ring electrode. A single oxidation–reduction wave is obtained on the Pt/Bi(UPD) ring. The slope of a plot of log $[(i_{L,a} - i)/(i - i_{L,c})]$ vs. E_R at $\omega = 25$ Hz is $\approx$32 mV/decade, which is in good agreement with the theoretical value (29.6 mV/decade) for reversible two-electron-transfer reactions exhibiting Nernstian behaviour.

Figure 3 shows rotating ring-disc electrode (RRDE) voltammograms for 6-OH-DA and 5-OH-DA. The ring potential was kept at $E_R = 0.2$ V where the oxidation of 6-OH-DA-*p*-quinone and 5-OH-DA-*o*-quinone are under diffusion control. The ring current was recorded as a function of the disc potential. Note again the positive catalytic effect of Bi(UPD) on the anodic processes. As can be seen, a second oxidation wave II_a appears in the disc voltammograms of both compounds at around 1.1 V. Its height is about half of that of the first wave I_a and does not depend linearly on the square root of the rotation rate, indicating kinetic character. Obviously, wave II_a corresponds to the oxidation of the third hydroxyl group of 6-OH-DA and 5-OH-DA at C(4) and C(3), respectively. Phenoxy radicals or phenoxonium cations are probably formed by losing one electron or two electrons, respectively, the fate of which is not predictable.

In the case of 6-OH-DA, the ring currents remain constant in the whole disc potential range and the collection efficiency was found to be $N = 0.20$ (disc area = 0.126 cm^2) as well as being independent of the rotation rate. This value is very close to the theoretical value (0.21) calculated according to Albery and Bruckenstein (23) from the geometric data of the electrode ($r_1 = 0.20$, $r_2 = 0.22$, and $r_3 = 0.24$ cm). On the contrary, in the case of 5-OH-DA the collection efficiency is smaller than the theoretical value and depends on both the rotation rate and disc potential.

The voltammetric behaviour of 6-OH-DA and 5-OH-DA described above is consistent with the mechanisms of Scheme 1.

The oxidation of 6-OH-DA yields the corresponding *p*-quinone as the first product of reasonable stability. The solution of 6-OH-DA after exhaustive electrolysis at 0.75 V presents the oxidation wave II_a and a reduction wave of equal height and half-wave potential (of course on Pt/Bi(UPD) with the oxidation wave I_a that is due to the reverse reaction. The oxidation of 5-OH-DA yields the corresponding *o*-quinone, which is not stable in solution. It undergoes fast hydration, most probably at the carbonyl group at position C(4). The hydrated 5-OH-DA-*o*-quinone is electro-inactive, as indicated by CV and rotating-disc electrode voltammetry of the solution after bulk electrolysis at 0.9 V. This behaviour is similar to that observed for ascorbic acid (24, 25), the oxidation of which is followed by a pseudo-first-order chemical reaction due to the hydration of the carbonyl group of the oxidation product. Attempts to identify products of the second oxidation wave II_a were unsuccessful for both compounds. Bulk electrolysis at potentials on the plateau of wave II_a is difficult because of filming of the electrode by products of secondary reactions. However, in the case of 6-OH-DA an assumption could be made based on the results of the RRDE voltammetry. The fact that the currents of the ring electrode are constant, independent of the disc potential, enables us to assume the formation of a dimer by C(3) coupling of the phenoxy radical. Such a dimer should be reduced at the same potential with 6-OH-DA-*p*-quinone and this might explain why the ring currents remain unchanged when the sweep of the disc potential entered the region above 1.1 V.

The rate of the hydration of 5-OH-DA-*o*-quinone was determined from the ring-disc data by using the equation

$$\frac{N}{N_k} = 1 + 1.28\left(\frac{\nu}{D}\right)^{1/3}\frac{k}{\omega}$$

proposed by Albery and Bruckenstein (26) for the EC mechanism. In this equation N_k is the kinetic and N the ordinary collection efficiency and k is the rate constant of the first-order chemical reaction. Values of $N_k = i_R/i_D$ were evaluated from the ring-disc voltammograms of 5-OH-DA at $E_D = 0.95$ V. Plots of $1/N_k$ vs. $1/\omega$ ($\omega = 2\pi f$) at different temperatures are shown in inset *D* of Fig. 3. They are linear with a common intercept corresponding to the collection efficiency of the electrode ($N = 0.20$) and different slopes from which k_1 may be calculated. Values of k_1 are summarized in Table 1. The *D* values needed for this calculation were determined from the Levich plots (j_L vs. $\omega^{1/2}$)of wave I_a by means of the Gregory–Riddiford equation. The analysis taking into account the Arrhenius equation, results in a value of the activation energy E_a of $\approx$6.000 cal mol^{-1}.

Scheme 2.

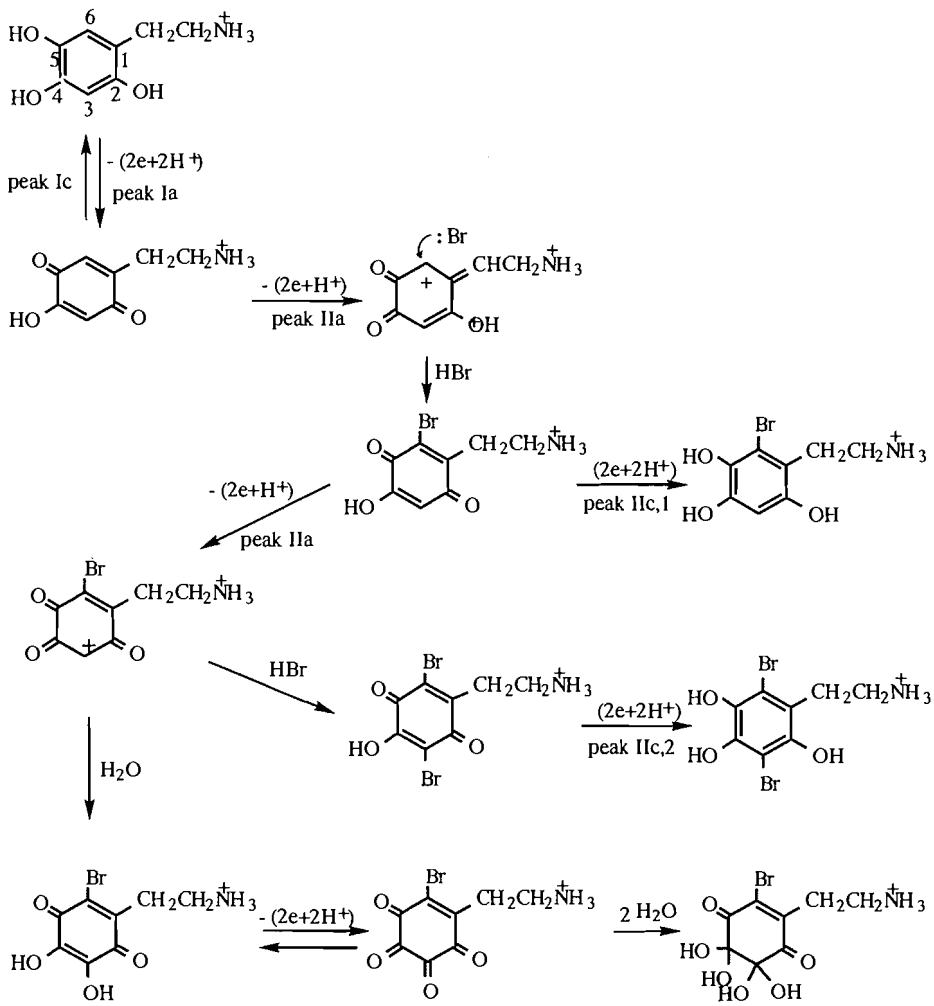

Oxidation of 6-OH-DA·HBr and 6-OH-DA·HCl on Pt

The oxidation of 6-OH-DA·HBr and 6-OH-DA·HCl gives two waves. Typical rotating disc voltammograms in 0.2 M $HClO_4$ are shown in Fig. 4. The height of wave II_a is almost equal to the height of wave I_a for 6-OH-DA·HCl but its height is twice the height of wave I_a for 6-OH-DA·HBr. Wave II_a appears in the potential range where the oxidation of the OH group of 6-OH-DA-*p*-quinone commences in the absence of nucleophiles. It is worth noting that its potential in the presence of Br^- is less positive than the oxidation potential of Br^- itself.

Electrogenerated quinones frequently undergo nucleophilic attack. The nucleophile usually reacts by a Michael 1,4-addition to form a substituted hydroquinone (27, 28). If the substituent is such that the potential for oxidation of the product is lower than the oxidation potential of the hydroquinone from which the quinone is formed, then further oxidation and further addition may occur. In the case of hydroxy-substituted quinones the electrochemical oxidation of the hydroxyl group may accelerate the addition reactions, showing the same general picture of phenolic oxidations (29, 30). The oxidation of the hydroxyl group of electrogenerated 6-OH-DA-*p*-quinone probably enables the addition reactions of HBr and HCl to occur at a significant rate. The voltammetric behaviour indicates that products and kinetics of the reaction depend strongly on the nucleophile species.

Figure 5 shows the cyclic voltammogram of 6-OH-DA·HBr. Peaks I_a and I_c correspond to the first two-electron oxidation–reduction, which in the presence of Br^- form an almost reversible couple. After scanning through oxidation peak II_a, reduction peak I_c decreases in height and new peaks $II_{c,1}$ and $II_{c,2}$ appear at more positive potentials. Similar behaviour was observed with 6-OH-DA·HCl, except that the reduction peak $II_{c,2}$ does not appear in the cyclic voltammogram. The species responsible for reduction peaks $II_{c,1}$ and $II_{c,2}$ are probably the mono- and di-bromo-substituted 6-OH-DA-*p*-quinones. The initial two-electron oxidation of 6-OH-DA is followed by two successive bromination reactions at potentials above 1.0 V (Scheme 2).

The bromination supposedly proceeds through a phenoxonium cation. It is assumed that the first attack of bromide occurs at C(6). Between the two possible phenoxonium cation intermediates, **I** is expected to be more stable than **II** because **I** has a more extented conjugation than **II** in which, furthermore, the formation of a positive charge between two carbon-

Fig. 6. Disc currents j_D vs. E_D and ring currents i_R vs. E_D at constant $E_R = 0.1$ V for the oxidation of 6-OH-DA (10^{-3} M) obtained with a Pt-Pt rotating ring-disc electrode in 0.2 M $HClO_4$ ($|dE/dt| = 25$ mV s^{-1}). Rotation frequency f/Hz: (1) 6.67; (2) 25; (3) 50. The dotted curves shows ring-disc voltammograms for LiBr (10^{-3} M) at $f = 25$ Hz.

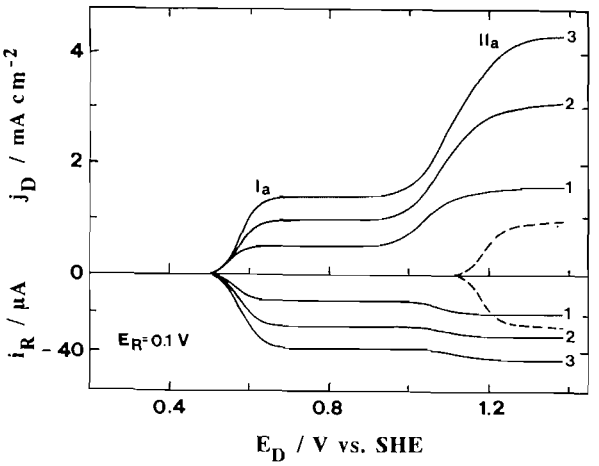

Fig. 7. Disc currents j_D vs. E_D and ring currents i_R vs. E_D at constant $E_R = 0.2$ V for the oxidation of (1) 5-OH-DA·HCl (10^{-3} M), (2) 5-OH-DA·HBr (10^{-3} M), (3) 5-OH-DA·1/2HBr (10^{-3} M), and (4) LiBr (10^{-3} M) obtained with a Pt–Pt rotating ring-disc electrode in 0.2 M $HClO_4$ ($|dE/dt| = 25$ mV s^{-1}). Rotation frequency $f = 50$ Hz.

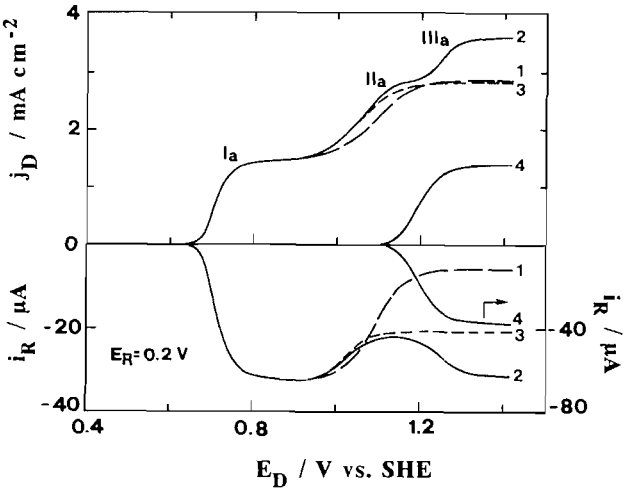

Scheme 3.

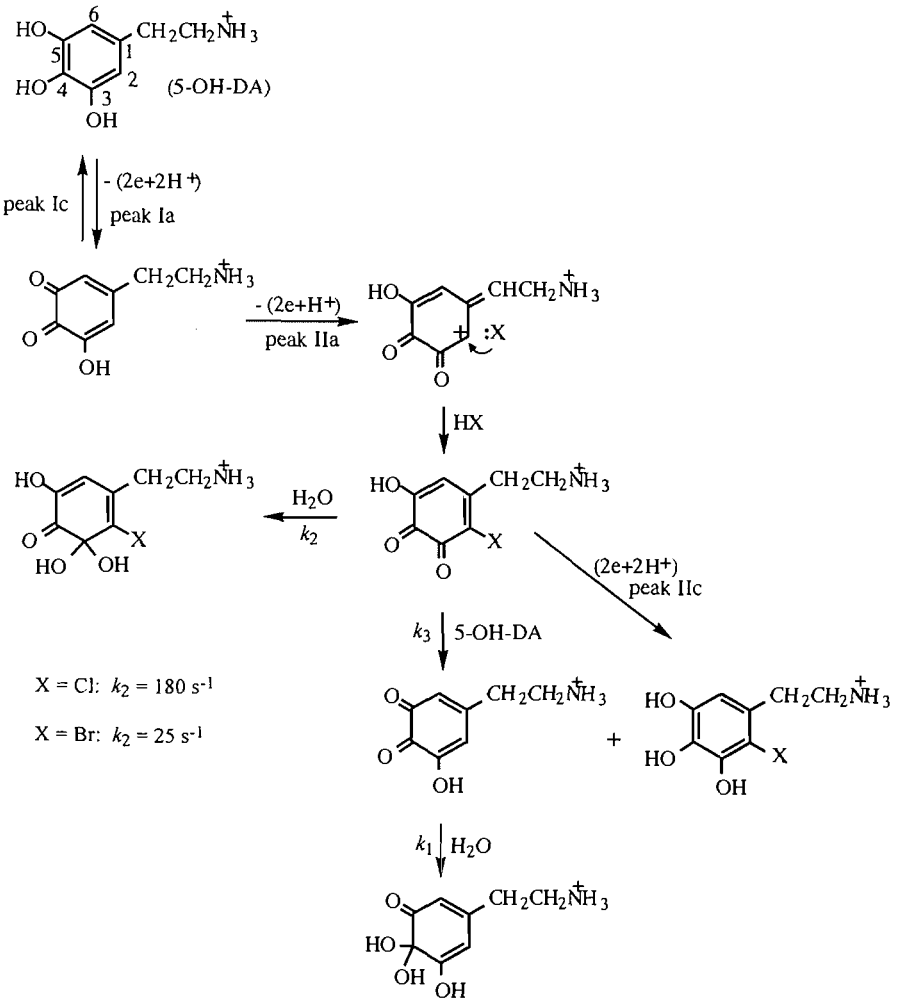

yls is disfavored. This assumption is supported by the fact that nucleophilic attack of glutathione on 6-OH-DA-*p*-quinone occurs at position C(6) (12).

Although diffusion of Br^- ions is faster than diffusion of 6-OH-DA molecules (compare, for instance, the j_L of the two-

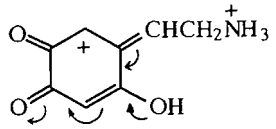

I

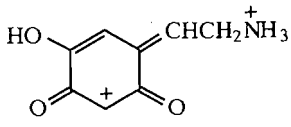

II

electron oxidation wave I_a of 6-OH-DA with the j_L of the one-electron oxidation wave of Br^- ions in Fig. 4), the amount reaching the electrode–solution interface probably is not sufficient for complete bromination at C(3). As a result, partial hydroxylation may take place in parallel with the second bromination reaction. The addition of water is followed by further oxidation, which yields a tetraoxo derivative. This explains why the limiting current on the plateau of wave II_a exceeds slightly the six-electron level at low rotation rates (see the disc voltammograms in Fig. 6) and the ring current exceeds the two-electron level, when the disc potential is on the plateau of wave II_a. On the other hand, this behaviour further supports our initial assumption that the first attack of bromide occurs at C(6) and not at C(3). Otherwise, there is no possible route that could explain the results of the RRDE voltammetry.

In the case of 6-OH-DA·HCl, only the first addition of HCl is fast enough; therefore, the voltammetric behaviour cannot give insights into the subsequent reactions. After electrolyses at the potential of wave II_a, attempts to isolate products from the electrolyzed solutions by common work-up, extraction, and lyophilization of the aqueous solutions were unsuccessful. The halogenated 6-OH-DA-*p*-quinones are probably unstable in solution. They are transformed to electro-inactive species, as indicated by CV of the solutions after electrolyses, which are presumed polymeric in nature.

Oxidation of 5-OH-DA·HCl and 5-OH-DA·HBr on Pt

Figure 7 shows ring-disc voltammograms of 5-OH-DA·HCl and 5-OH-DA·HBr. The ring potential was kept at 0.2 V to collect all oxidation products formed at the disc. The oxidation of 5-OH-DA in the presence of Cl^- and Br^- gives two waves I_a and II_a of equal height. The initial two-electron oxidation at 0.7 V is followed by a further two-electron oxidation-halogenation reaction (Scheme 3) at 1.1 V. The third anodic wave III_a that appears in the disc voltammogram of 5-OH-DA·HBr is due to the electrooxidation of unreacted Br^- ions. As pointed out in the case of 6-OH-DA·HBr, the diffusion of Br^- ions is much faster than the diffusion of hydroxydopamines. Wave III_a matches quite well with that of authentic LiBr, and disappears after the prior removal of the half concentration of bromide from the solution of 5-OH-DA·HBr. It should be noted that the oxidation of Br^- ions to Br_2 clearly occurs at more positive potentials (≈150 mV) than the oxidation–bromination reaction of 5-OH-DA-*o*-quinone.

The nucleophilic attack of Cl^- and Br^- ions occurs at position C(2) or C(6). The halogenated 5-OH-DA-*o*-quinone formed is reduced at less negative potentials than the unsubstituted 5-OH-DA-*o*-quinone. The broad peak II_c in the

Fig. 8. Cyclic voltammograms of 5-OH-DA·HCl (10^{-3} M) on Au in 0.2 M $HClO_4$. Scan rate $v = 400$ mV s^{-1}.

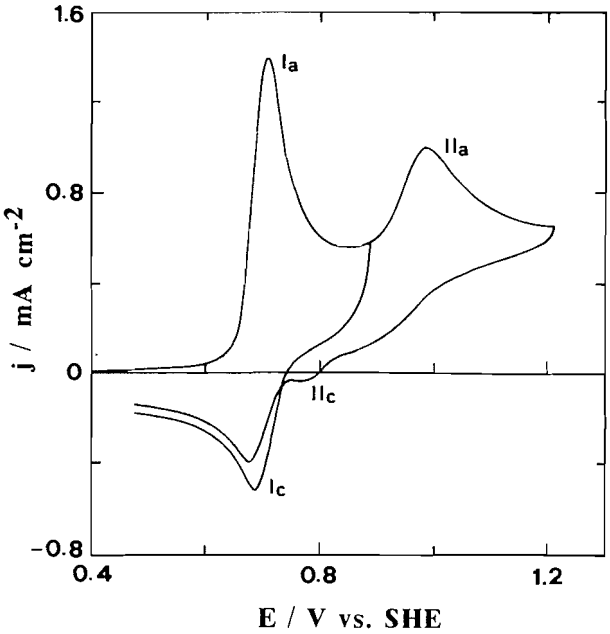

cyclic voltammogram of 5-OH-DA·HCl (Fig. 8) corresponds to this reduction. This peak may only be observed at a Au electrode and at relatively fast scan rates. The halogenated 5-OH-DA-*o*-quinones react with 5-OH-DA or undergo hydration (Scheme 3). The CV and the RRDE voltammetry indicate that the hydration reaction is much faster than the reaction with 5-OH-DA (e.g., $k_2 \gg k_3$). Its rate is even faster than the hydration of 5-OH-DA-*o*-quinone (Scheme 1) as can be concluded by the decrease of the ring currents at disc potentials above 1.0 V (Fig. 7). The rate of the hydration reaction was studied by the rotating ring-disc electrode. Values of N_k as a function of the rotation rate were evaluated at $E_D = 1.30$ V for 5-OH-DA·HCl and $E_D = 1.15$ V for 5-OH-DA·HBr taking into account four-electron oxidation at the disc and two-electron reduction at the ring.

The $1/N_k$ vs. $1/\omega$ plots are reasonably linear. The slopes give the following values of k_2:

For X = Cl: $k_2 = 180 \pm 30$ s^{-1} (25°C)

For X = Br: $k_2 = 25.0 \pm 5.0$ s^{-1} (25°C)

These values are, indeed, greater than the value of $k_1 = 3.4$ s^{-1} (Table 1) determined for the hydration of the unsubstituted 5-OH-DA-*o*-quinone. The hydration rate constant of the bromo derivative is smaller than that of the chloro derivative. This may be attributed to the steric hindrance of the voluminous bromo substituent. On the other hand, this suggests that the hydration occurs at the carbonyl group C(3), which is near to the substituent.

In conclusion, the electrochemical studies of 6-hydroxydopamine and 5-hydroxydopamine revealed that the first two-electron oxidation leads to formation of reactive quinoid intermediates. Reactions of these quinoid intermediates with nucleophiles yield substituted quinones that are not stable in solution. The reactions are initiated by the oxidation of the

third hydroxyl group. Cyclic voltammetry and rotating ring-disc electrode voltammetry were used to elucidate the reaction mechanisms. These techniques provide powerful tools for generating and detecting transient intermediates and products and give valuable information regarding the pathways and mechanisms of the redox reactions.

References

1. H. Thoenen, J.P. Tanzer, and G. Hausler. *In* New aspects of storage and release of catecholamines. *Edited by* H.J. Shuman and G. Kronberg. Springer-Verlag, Berlin. p. 1970. p. 130.
2. J. De Champlain and R. Nadeau. Fed. Proc. **30**, 877 (1971).
3. D.C.S. Ise, R.L. McCreery, and R.N. Adams. J. Med. Chem. **19**, 37 (1976).
4. S. Senoh and B. Witkop. J. Am. Chem. Soc. **81**, 6231 (1959).
5. S. Senoh C.R. Creveling, S. Udenfried, and B. Witkop. J. Am. Chem. Soc. **81**, 6236 (1959).
6. R.N. Adams, E. Murrill, R.L. McCreery, C.L. Blank, and M. Karolczak. Eur. J. Pharmacol. **17**, 287 (1972).
7. A.W. Sternson, R.L. McCreery, B. Feinberg, and R.N. Adams. J. Electroanal. Chem. **46**, 313 (1973).
8. A. Brun and R. Russet. J. Electroanal. Chem. **49**, 287 (1974).
9. J. Li and B.M. Christensen. J. Electroanal. Chem. **375**, 219 (1994).
10. D.M. Hawley, S.V. Tatawawadi, S. Piekarski, and R.N. Adams. J. Am. Chem. Soc. **89**, 447 (1967).
11. G. Dryhurst. *In* Comprehensive treatise of electrochemistry. Vol. 10. *Edited by* Yu.A. Chizmadzhev, J.O'M. Bockris, B.E. Conway, and E. Yeager. Plenum Press, New York and London. 1985. p. 131.
12. Y.O. Liang, R.M. Wightman, P. Plotsky, and R.N. Adams. *In* Chemical tools in catecholamine research. Vol. I. *Edited by* I.G. Jonsson, T. Malmfors, and C. Sachs. North-Holland Publishing Co., Amsterdam. 1975. p. 15.
13. C.L. Bank, P.T. Kissinger, and R.N. Adams. Eur. J. Pharmacol. **19**, 391 (1972).
14. Z. Jiang, J. Wang, and Z. Lian. Stud. Biophys. **136**, 81 (1990).
15. M.R. Deakin, P.M. Kovach, K.J. Stutts, and R.M. Wightman. Anal. Chem. **58**, 1474 (1986).
16. K. Takamura and M. Sakamoto. J. Electroanal. Chem. **113**, 273 (1980).
17. G. Kokkinidis. J. Electroanal. Chem. **172**, 265 (1984).
18. G. Kokkinidis and N. Argyropoulos. Electrochim. Acta, **30**, 1611 (1985).
19. G. Kokkinidis, D. Sazou, and I. Moumtzis. J. Electroanal. Chem. **213**, 135 (1986).
20. K. Takamura and S. Sakamoto. Bioelectrochem. Bioenerg. **10**, 251 (1983)
21. R.S. Nicholson and I. Shain. Anal. Chem. **36**, 706 (1964).
22. G. Kokkinidis. J. Electroanal. Chem. **201**, 217 (1986).
23. W.J. Albery and S. Bruckenstein. Trans. Faraday Soc. **62**, 1920 (1966).
24. J.J. Ruiz, J.M. Rodriguez-Mellado, M. Dominguez, and A.A. Aldaz. J. Chem. Soc. Faraday Trans. **85**, 1567 (1989).
25. P. Karabinas, D. Sazou, and D. Jannakoudakis. Bioelectrochem. Bioenerg. **14**, 469 (1985).
26. W.J. Albery and S. Bruckenstein. Trans. Faraday Soc. **62**, 1946 (1966).
27. H.W. Wanzlick. Angew. Chem. Int. Ed. Engl. **3**, 401 (1964).
28. L. Papouchado, G. Petrie, and R.N. Adams. J. Electroanal. Chem. **38**, 389 (1972).
29. L. Papouchado, R.W. Sandford, G. Petrie, and R.N. Adams. J. Electroanal. Chem. **65**, 275 (1975).
30. N.L. Weinberg (*Editor*). Technique of electroorganic synthesis. Wiley, New York. 1974. Part I, p. 410.

Substituted tetra-2,3-pyrazinoporphyrazines. Part II. Bis(tri-*n*-hexylsiloxy)silicon derivatives

Svetlana V. Kudrevich and Johan E. van Lier

Abstract: Dichlorosilicon complexes of substituted tetra-2,3-pyrazinoporphyrazines were obtained via condensation of 2,3-dicyanopyrazine, 2,3-dicyano-5,6-diphenylpyrazine, 2,3-dicyanoquinoxaline, 2,3-dicyano-benzo[*f*]quinoxaline, and 2,3-dicyano-dibenzo[*f,h*]quinoxaline with silicon tetrachloride in the presence of urea, quinoline, and tri-*n*-butylamine. Hydrolysis of the Si-Cl bond in concentrated H_2SO_4, followed by treatment with 0.01 N NaOH and aqueous NH_3, afforded the corresponding dihydroxides, which were converted to the bis(tri-*n*-hexylsiloxy)silicon derivatives via reaction with tri(*n*-hexyl)silane in 3-picoline (2,4,6-collidine) in the presence of tri-*n*-butylamine. The axial tri-*n*-hexylsiloxy substituents at the central silicon atom prevent aggregation in organic solvents, permitting detailed studies on the effects of structural modifications on the electronic spectra of tetraazaphthalocyanines. Our data show that each benzo ring addition, angularly condensed to the tetra-2,3-quinoxalinoporphyrazine, induces a hypsochromic shift (~10–15 nm) of the main absorption maximum.

Key words: phthalocyanine, aza analog, bis(tri-*n*-hexylsiloxy)silicon complex.

Résumé : Les dérivés substitués des tétra-2,3-pyrazinoporphyrazines du dichlorosilice ont été préparés via la condensation du 2,3-dicyanopyrazine, 2,3-dicyano-5,6-diphenylpyrazine, 2,3-dicyanoquinoxaline, 2,3-dicyano-benzo[*f*]quinoxaline et 2,3-dicyano-dibenzo[*f,h*]quinoxaline avec du tétrachlorure de silice en présence d'urée, de quinoléine et d'amine tri-*n*-butylique. L'hydrolyse de liaison Si–Cl dans du H_2SO_4 concentré, puis dans une solution de 0,01 N de NaOH et d'ammoniac, a produit des dihydroxydes appropriés qui ont été transformés en dérivés substitués de bis(tri-*n*-hexylsiloxy) via la réaction avec le tri-*n*-hexylsilane dans la 3-picoline (2,4,6-collidine) en présence d'amine tri-*n*-butylique. Les substituants axiaux tri-*n*-hexylsiloxy, attachés à l'atome de silicium central, empêchent complètement l'agrégation des molécules d'azaphtalocyanines dans les solvants organiques. Des études détaillées de l'influence de la modification structurelle sur les spectres électroniques du tétraazaphtalocyanine ont été effectuées. Il a été démontré que chaque anneau benzo angulaire, condensé au tétra-2,3-quinoxalinoporphyrazine, produit un déplacement hypsochromique (~10–15 nm) de la bande Q.

Mots clés : phtalocyanine, azaanalogue, complexe du bis(tri-*n*-hexylsiloxy)silice.

Introduction

The potential applications of silicon phthalocyanine (Pc), naphthalocyanine (Nc), and their aza analogs (azaPc's) to the sensitization and stabilization of semiconductor electrodes in photoelectrochemical cells (1), as media for optical data storage with a large capacity memory (2–6) and photosensitizers for photodynamic therapy of cancer (7–15) have been extensively studied over the past decade. These applications require well-defined properties of the substituted Pc's, including the solubility in lipophilic and hydrophilic media and absorbance in the required region of the visible spectrum. It is well known that phenyl substitution (16–18) and linear annelation (19–24) are effective means for *fine tuning* the visible spectra of the Pc and azaPc macrocycles. The effect of angular annelation on the electronic spectra of Pc and its analogs has more recently been addressed through the synthesis of a series of azaPc's differing in the number of angularly condensed benzo rings (16, 25, 26). Studies of the properties of these compounds permitted preliminary conclusions concerning the effect of aza substitution and angular annelation on the electronic spectra of Nc. However, more detailed studies on the spectral properties of the angularly annelated Nc analogs were hampered due to aggregation of the dye molecules in solution. This problem was overcome through *tert*-butyl substitution on the periphery of the macrocycle (26). Although double angular annelation of octaazaNc's was shown to cause a hypsochromic shift of the Q-band of about 25 nm, aggregation of the molecules still interfered, preventing us from estimating the effect of *sequential* annelation on the absorption maxima. Such substitutions appeared to be particularly useful in establishing the effect of phenyl substitution (linear and angular annelation) on the electronic spectra of tetra-2,3-pyrazinoporphyrazine and tetra-2,3-quinoxalinoporphyrazine. It is well known that axial substitution at the central silicon atom prevents the aggregation of Pc molecules in solutions. In this report we address the synthesis of axially substituted silicon complexes of azaPc's. The availability of a series of fully monomerized derivatives of tetraazaPc, containing the same silicon central atom, with good solubility in a single solvent, i.e., chloroform, allowed us to establish the effect of structural modifications about the macrocycle on the spectral properties.

Received March 29, 1996.

S.V. Kudrevich and J.E. van Lier.[1] Medical Research Council Group in the Radiation Sciences, Faculty of Medicine, Université de Sherbrooke, Sherbrooke, QC J1H 5N4, Canada.

[1] Author to whom correspondence may be addressed: Telephone: (819) 563-5555, ext. 4603. Fax: (819) 564-5442. E-mail: jvanlier@courrier.usherb.ca

Scheme 1.

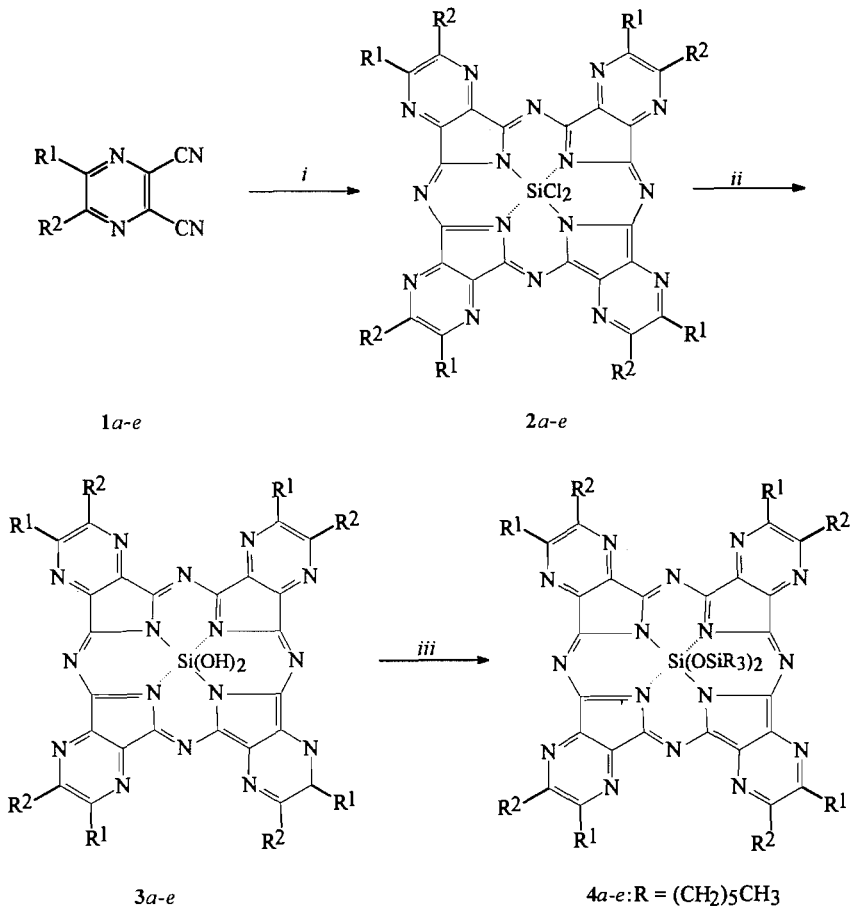

1*a*, 2*a*, 3*a*, 4*a*: $R^1 = R^2 = H$; 1*b*, 2*b*, 3*b*, 4*b*: $R^1 = R^2 = Ph$; 1*c*, 2*c*, 3*c*, 4*c*: $R^1, R^2 =$ 

1*d*, 2*d*, 3*d*, 4*d*: $R^1, R^2 =$  ; 1*e*, 2*e*, 3*e*, 4*e*: $R^1, R^2 =$ 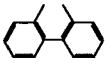

i: $SiCl_4$, quinoline, urea, tri(*n*-butyl)amine; *ii*: (1)H_2SO_4; (2) 0.01 N NaOH, aq. NH_3; *iii*: tri(*n*-hexyl)-chlorosilane, 3-picoline, 2,4,6-collidine.

Results and discussion

The bis(tri-*n*-hexylsiloxy)silicon azaPc's **4***a–e* were prepared via straightforward synthetic routes as outlined in Scheme 1. The precursors of substituted tetra-2,3-pyrazinoporphyrazines, e.g., dinitriles of heterocyclic *o*-dicarboxylic acids, were prepared via dehydration of an appropriate diamide (2,3-dicyanoquinoxaline **1***c* (27)) or via the condensation of *o*-quinones with diaminomaleodinitrile (2,3-dicyano-5,6-diphenylpyrazine **1***b* (28), 2,3-dicyano-benzo[*f*]quinoxaline **1***d* (26), and 2,3-dicyano-dibenzo[*f,h*]quinoxaline **1***e* (28)).

The synthesis of the carbocyclic analogs, e.g., Pc(Nc) dichlorosilicon complexes, starting from the corresponding 1,3-diiminoisoindolines and silicon tetrachloride in tetrahydronaphthalene or quinoline, has previously been reported (1, 13, 29, 30). In our hands, this procedure failed in the case of the heterocyclic diiminoisoindolines. Instead, we found that the corresponding *o*-dinitriles **1***a–e* are good starting materials for the synthesis of dichlorosilicon complexes. Compounds **1***a–e* were condensed with $SiCl_4$ in the presence of urea using quinoline as a solvent and twofold excess of tri-*n*-butylamine as an acceptor of evolving HCl. The products **2***a–e* contain impurities and their thorough purification without modification of the Si—Cl bond was unattainable. Due to their poor solubility in organic solvents, recrystallization of **2***a–e* was impossible and, as we noted before (26), azaPc's cannot be sublimated. IR spectra of **2***a–e* all feature a characteristic band about 480 cm^{-1} (Si–Cl stretch). The products were of sufficient purity to be used as intermediates for the preparation of the dihydroxysilicon complexes **3***a–e*.

The hydrolysis of **2***a–e* was carried out by combining the methodology of Wheeler et al. (1) and Davison and Wynne (31). Heating **2***a–e* in concentrated H_2SO_4 for 2 h did not result in decomposition, suggesting that the aromatic system of silicon octaazaPc's is at least as stable as those of the carbocyclic analogs (1, 32). IR spectra of compounds **3***a–e* feature absorption bands at 3455–3475 cm^{-1} (O-H) and 844–850 cm^{-1} (Si-O). The microanalyses of the dihydroxysilicon azaPc's samples, purified in a Soxhlet extractor, were indicative of contamination with silica. Pure analytical samples of

Table 1. Dichlorosilicon complexes of substituted tetra-2,3-pyrazinoporphyrazines.

No.	Compound	Reaction temperature, °C	λ_{max}, nm (in quinoline)
2*a*	Dichlorosilicon tetra-2,3-pyrazinoporphyrazine	160	638, 575, 378
2*b*	Dichlorosilicon tetra-2,3-(5,6-diphenylpyrazino)porphyrazine	180	664, 370
2*c*	Dichlorosilicon tetra-2,3-quinoxalinoporphyrazine	220	715.5, 680, 379
2*d*	Dichlorosilicon tetra-2,3-benzo[*f*]-quinoxalinoporphyrazine	250	699, 667.5, 378
2*e*	Dichlorosilicon tetra-2,3-dibenzo[*f,h*]-quinoxalinoporphyrazine	250	690, 376

Table 2. Dihydroxysilicon complexes of substituted tetra-2,3-pyrazinoporphyrazines.

		Found[a] (calcd.)				
No.	Formula	% C	% H	% N	% Si	λ_{max}, nm(relative intensity) (in quinoline)
3*a*	$C_{24}H_{10}N_{16}O_2Si \cdot 3H_2O$	44.81 (45.28)	2.85 (2.53)	35.02 (35.20)	4.02 (4.41)	634.5, 376 (1:0.32)
3*b*	$C_{72}H_{42}N_{16}O_2Si \cdot 2H_2O$	71.00 (70.46)	3.80 (3.78)	17.69 (18.26)	2.12 (2.29)	658, 372 (1:0.3)
3*c*	$C_{40}H_{18}N_{16}O_2Si \cdot 4H_2O$	55.34 (56.20)	3.04 (3.07)	25.96 (26.22)	3.37 (3.29)	702, 378 (1:0.44)
3*d*	$C_{56}H_{26}N_{16}O_2Si \cdot 2H_2O$	66.12 (66.00)	3.19 (2.97)	20.85 (21.99)	2.44 (2.76)	698, 378 (1:0.46)
3*e*	$C_{72}H_{34}N_{16}O_2Si$	72.76 (73.09)	3.13 (2.90)	18.91 (18.94)	1.94 (2.37)	680, 376 (1:0.6)

[a]The samples were dried before analysing in vacuo (1 Torr) at 100°C for 4 h.

compounds **3***a–e* were obtained via hydrolysis of chromatographically purified bis(tri-*n*-hexylsiloxy)silicon complexes **4***a–e* (1). Solubility of **3***a–e* in organic solvents is much lower than that of the corresponding dichlorosilicon analogs. The former compounds are barely soluble in quinoline and only micromolar concentrations, suitable for spectral analysis, could be obtained. The visible spectra of dihydroxysilicon complexes **3***a–e* exhibit maxima at somewhat shorter wavelengths than their dichlorosilicon precursors, which is in accordance with literature data for the analogues $SiPcCl_2$ and $SiPc(OH)_2$ (29). The conversion of the dihydroxides **3***a–e* to the bis(tri-*n*-hexylsiloxy)silicon derivatives **4***a–e* was performed following the methodology of Wheeler et al. (1). Compounds **4***a–e* were purified chromatographically on silica gel and characterized by combustion analyses and spectroscopic data.

Comparison of the electronic spectra in the visible region of bis(tri-*n*-hexylsiloxy)SiPc **5** (λ_{max} 668 nm) (1) and its octaaza analog **4***a* (λ_{max} 624 nm), bis(tri-*n*-hexylsiloxy)SiNc **6** (λ_{max} 772 nm) (1) and its octaaza derivative **4***c* (λ_{max} 704 nm), shows that the magnitude of the hypsochromic shift due to the octaaza substitution of the CH groups adjacent to the porphyrazine macro-ring increases from 1080 cm^{-1} for the azaPc to 1250 cm^{-1} for the azaNc. This indicates that linear annelation renders the Pc aromatic system more responsive to aza substitution. Electron donating phenyl substituents, even when oriented out of the plane of the tetra-2,3-pyrazinoporphyrazine molecule, profoundly affect the absorption pattern. Thus, the octaphenyl-substituted compound **4***b* has a principal absorption maximum at 645 nm (bathochromic shift of 21 nm relative to **4***a*). It is interesting to note that the Soret band of **4***b* also undergoes a remarkable bathochromic shift. Addition of linearly condensed benzo rings to **4***a* results in a red shift of the Q-band (corresponding to quinoxaline structure of **4***c* fragments) of 1820 cm^{-1}. The corresponding value for the carbocyclic analogs **5** and **6** is 2015 cm^{-1}. It is evident that the electron-withdrawing character of the exocyclic nitrogen atoms is responsible for the decrease in sensitivity of the Pc aromatic system to the linear annelation.

Fig. 1. Electronic spectra of compounds **4***c* (-----), **4***d* (——), and **4***e* (— —) in chloroform (concentration ~10^{-6} M).

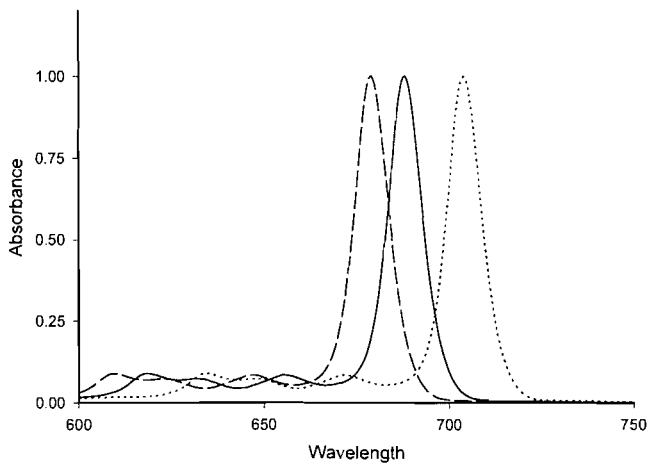

Figure 1 presents the visible region of the electronic spectra of compounds **4***c* (λ_{max} 704 nm), **4***d* (λ_{max} 688 nm), and **4***e* (λ_{max} 679 nm). Comparison of these spectra suggests that each angularly condensed benzo ring causes a *hypsochromic* shift of the main band of 10–15 nm. Compared to known metal complexes of the carbocyclic analogs of **4***c* and **4***e*, we also observe a blue shift of the Q-band of Nc upon double angular annelation: vanadyl Nc absorbs at 817 nm (33), whereas the main absorption maximum of vanadyl tetra-2,3-(dibenzo[*f,h*]naphthalo)porphyrazine is observed at 776 nm

Table 3. Bis(tri-*n*-hexyl siloxy)silicon complexes of substituted tetra-2,3-pyrazinoporphyrazines.

No.	Formula	Yield, %	R_f on silica gel (solvent)	Found (calcd.) %C	%H	%N	FAB MS, *m/z*	λ_{max}, nm (log ε) (in chloroform)	^{1}H NMR, δ (in $CDCl_3$)
4*a*	$C_{60}H_{86}N_{16}O_2Si_3$	25	0.62 ($CHCl_3$)	62.62 (62.79)	8.08 (7.56)	18.98 (19.54)	1148 (72, M^+)	624 (5.44), 597 (4.35), 566 (4.44), 337 (4.88)	9.72 (s, 2H-pyrazino), 0.74 (m, ε-CH_2), 0.64 (t, CH_3), 0.19 (m, δ-CH_2), −0.01 (m, γ-CH_2), −1.38 (m, β-CH_2), −2.42 (m, α-CH_2)
4*b*	$C_{108}H_{118}N_{16}O_2Si_3$	10	0.58 (toluene)	73.42 (73.85)	6.98 (6.77)	12.54 (12.76)	1757 (78, M^+), 1457 (35, M^+ −$C_{18}H_{39}OSi$)	645 (5.42), 617 (4.42), 584 (4.43), 369 (4.95)	8.54 (m, 1,5-Ph), 8.25 (m, 2,4-Ph), 7.88 (m, 3-Ph), 0.82 (m, ε-CH_2), 0.55 (t, CH_3), 0.02 (m, δ-CH_2), −0.02 (m, γ-CH_2), −1.22 (m, β-CH_2), −2.33 (m, α-CH_2)
4*c*	$C_{76}H_{94}N_{16}O_2Si_3$	33	0.44 (toluene]	68.14 (67.72)	7.00 (7.03)	16.28 (16.63)	1348 (58, M^+), 1047 (4, M^+ −$C_{18}H_{39}OSi$)	704 (5.60), 671 (4.53), 646 (4.52), 361 (5.20)	9.14 (m, 5,8-quinoxalino), 8.31 (m, 6,7-quinoxalino), 0.88 (m, ε-CH_2), 0.46 (t, CH_3), 0.21 (m, δ-CH_2), −0.06 (m, γ-CH_2), −1.15 (m, β-CH_2), −2.27 (m, α-CH_3)
4*d*	$C_{92}H_{102}N_{16}O_2Si_3$	28	0.84 ($CHCl_3$)	70.85 (71.37)	6.91 (7.03)	13.89 (14.48)	1549 (51, M^+), 1249 (30, M^+ −$C_{18}H_{39}OSi$)	688 (5.80), 656 (4.74), 618 (4.76), 371 (5.25)	8.93 (m, 5-benzo[*f*]quinoxalino), 8.55 (m, 6-benzo[*f*]quinoxalino), 8.08–8.31 (m, 7,8,9,10-benzo[*f*]quinoxalino), 0.86 (m, ε-CH_2), 0.45 (t, CH_3), 0.17 (m, δ-CH_2), −0.01 (m, γ-CH_2), −1.20 (m,β-CH_2), −2.34 (m, α-CH_2)
4*e*	$C_{108}H_{110}N_{16}O_2Si_3$	14	0.32 (toluene – ethyl acetate 4:1)	73.45 (74.19)	6.42 (6.34)	12.28 (12.82)	1749 (50, M^+), 1449 (14, M^+ −$C_{18}H_{39}OSi$)	679 (5.56), 648 (4.80), 624 (4.77), 375 (5.09)	8.90 (m, dibenzo[*f*, *h*]quinoxalino, 8.05 (m, dibenzo[*f*, *h*]quinoxalino), 0.82 (m. ε-CH_2), 0.45 (t, CH_3), 0.15 (m, δ-CH_2), −0.01 (m, γ-CH_2), −1.17 (m, β-CH_2), −2.40 (m, α-CH_2)

(19) (both spectra in 1-chloronaphthalene). The carbocyclic analog of **4***b*, e.g., unsubstituted tetra-2,3-(benzo[*f*]naphthalo)porphyrazine, is unknown. On the other hand, angular annelation does not have the same effect in the case of Pc's. The Q-band maximum of PcCu is at 678 nm (in 1-chloronaphthalene) (34), 1,2-NcCu absorbs at 690 nm (in *o*-dichlorobenzene) (35), and *tert*-butyl substituted octabenzoPcCu absorbs at 700 nm (in *o*-dichlorobenzene) (36). Therefore, each benzo ring, angularly condensed to the Pc, causes a small shift of the main band, similar but of opposite sign to that observed for the Nc series.

Finally, we prepared a series of silicon complexes of substituted tetra-2,3-pyrazinoporphyrazines, featuring chloro-, hydroxy-, and tri(*n*-hexylsiloxy) axial ligands at the central atom. Tri(*n*-hexylsiloxy)silicon complexes are fully monomerized in chloroform, permitting us to evaluate the effect of angular annelation of tetra-2,3-quinoxalinoporphyrazine on the shift of the Q-band maximum in the electronic spectrum. These data should be particularly useful in the design of new Pc-related structures with *fine tuned* absorption maxima and selected solubility, as substrates for new materials.

Experimental

Materials and methods

FAB-MS were obtained on an LG Autospec Q mass spectrometer from the Department of Chemistry, Université de Montréal. ^{1}H NMR spectra were taken on a Bruker AC-300 (300 MHz) spectrometer using $CDCl_3$ as a solvent. UV–VIS spectra were recorded with a Hitachi U-2000 spectrophotometer. IR spectra were obtained on a Perkin Elmer 1600 spectrometer using KBr plates. Preparative chromatography was conducted on 70–230 mesh silica gel (Aldrich). TLC was performed on 0.25 mm thick Polygram SIL G/UV-254 plates (Macherey-Nagel, Germany). The solvents quinoline, 3-picoline, and 2,4,6-collidine were vacuum distilled from BaO under nitrogen.

2,3-Dicyanopyrazine **1***a* was obtained from a commercial source (Aldrich), 2,3-dicyano-5,6-diphenylpyrazine **1***b* (28), 2,3-dicyanoquinoxaline **1***c* (27), 2,3-dicyano-benzo[*f*]quinoxaline **1***d* (26), and 2,3-dicyano-dibenzo[*f*,*h*]quinoxaline **1***e* (28) were prepared by published methods. All the *o*-dinitriles were dried under high vacuum prior to complexation.

Dichlorosilicon complexes **2**a–e *(Table 1). General procedure*

o-Dinitriles **1***a–e* (7.5 mmol) were triturated with 0.5 g of urea, then dry tri-*n*-butylamine (3.6 mL, 2.78 g, 15 mmol), freshly distilled quinoline (5 mL), and silicon tetrachloride (0.86 mL, 1.28 g, 7.5 mmol) were added and the mixture was heated for 0.5–2 h in a flask protected with a $CaCl_2$ tube. The mixture was allowed to cool, the precipitate was collected, thoroughly washed with hot ethanol, and air dried. Compound **2***a* appears as a dark blue powder, **2***b* as very dark green, **2***c* as greenish-black, and **2***d* and **2***e* as brownish-green powders. The products contained some impurities but were suitable for use as intermediates for the preparation of bis[tri-(*n*-hexylsiloxy)silicon] complexes without further purification. IR spectra of **2***a–e* all contain a band around 480 cm^{-1} (m, Si-Cl).

Dihydroxysilicon complexes **3**a–e *(Table 2). General procedure*

Finely powdered **2***a–e* (1 g) were dissolved in concentrated H_2SO_4 (100 mL) and stirred at 50°C for 2 h. The mixture was filtered over a glass filter without prior cooling, poured over ice, and neutralized with aqueous NH_3. The precipitate was filtered, washed with hot water, acetone, and ethanol, resuspended in a mixture of 0.01 N aqueous NaOH-pyridine 1:1 (v:v), stirred at 50°C for another 2 h, then filtered, thoroughly washed with water, and vacuum dried. An attempt was made to purify analytical samples in a Soxhlet extractor using pyridine and acetone, but microanalysis showed that the samples were still contaminated with silica.

Hydrolysis of chromatographically purified bis[tri(*n*-hexylsiloxy)silicon] complexes **4***a–e* (1) (see below) afforded pure samples of the hydroxides **3***a–e*. IR (KBr): 3455–3475 cm^{-1} (O-H), 844–852 cm^{-1} (Si-O). Compounds **3***a–e* are barely soluble in quinoline (only in spectral concentrations, ~10^{-6} M).

*Bis[tri(*n*-hexylsiloxy)silicon] complexes* **4**a–e *(Table 3). General procedure*

A mixture of dihydroxides **3***a–e* (0.5 g, not Soxhlet-extracted), tri-*n*-hexylchlorosilane (2.5 mL), dry tri-*n*-butylamine (2 mL), and 50 mL of dry, freshly distilled solvent (3-picoline for **3***a–3d*; 2,4,6-collidine for **3***e*) was heated to 120°C for 24 h. The mixture was cooled to room temperature and filtered (the weight of dry residue was taken into account when yields of **4***a–e* were calculated). Methanol (25 mL) was added to the filtrate and the complexes were precipitated upon addition of a few drops of water. Chromatography over silica gel afforded pure compounds **4***a–e*. These complexes are brightly coloured (**4***a*, dichroic blue/red; **4***b*, grass green; **4***c*, dark green; **4***d* and **4***e*, yellow-green) and are highly soluble in toluene, chloroform etc.

Acknowledgements

Financial support by the Medical Research Council of Canada and the Ministère de l'Enseignement Supérieur et de la Science du Gouvernement du Québec (Programme d'Actions Structurantes) is gratefully acknowledged. Authors wish to thank Dr. Jacques Rousseau for his help.

References

1. B.L. Wheeler, G. Nagasubramanian, A.J. Bard, L.A. Schechtman, D.R. Dininny, and M.E. Kenney. J. Am. Chem. Soc. **106**, 7404 (1984) and refs. therein.
2. H. Hagiwara, N. Hayashi, S. Tai, T. Akimoto, and M. Katayose. Jpn. Kokai Tokkyo Koho JP 04,14,486 [92 14, 486] (1992).
3. M. Kuroiwa, T. Yoshitake, S. Miyazaki, and M. Sakamoto. Jpn. Kokai Tokkyo Koho JP 02,106,390 [90 106,390] (1990).
4. S. Tai, N. Hayashi, K. Kamijima, M. Katayose, T. Akimoto, and H. Hagiwara. Eur. Pat. Appl. EP 344,891 (1989).
5. T. Sato and S. Miyazaki. Jpn. Kokai Tokkyo Koho JP 03,173,685 [91 173,685] (1991).
6. S. Miyazaki and T. Sato. Jpn. Kokai Tokkyo Koho JP 03,281,387 [91 281,387] (1991).
7. P.A. Firey and M.A.J. Rodgers. Photochem. Photobiol. **45**, 535 (1987).
8. V. Cuomo, G. Jori, B. Rihter, M.E. Kenney, and M.A.J. Rodgers. Br. J. Cancer **62**, 966 (1990).
9. B.W. Henderson and E. Mayhew. *In* Photodynamic therapy: mechanisms II. Vol. 1203. SPIE – The International Society for Optical Engineering, Bellingham, Wash. 1990. pp. 126–135.
10. C. Bellemo, G. Jori, B.D. Rihter, M.E. Kenney, and M.A.J. Rodgers. Cancer Lett. **65**, 145 (1992).

11. M.M. Zuk, B.D. Rihter, M.E. Kenney, M.A.J. Rodgers, and M. Kreimer-Birnbaum. J. Chromatogr. **568**, 437 (1991).
12. R. Biolo, G. Jori, M. Soncin, R. Pratesi, U. Vanni, B. Rihter, M.E. Kenney, and M.A.J. Rodgers. Photochem. Photobiol. **59**, 362 (1994).
13. N. Brasseur, T.L. Nguyen, R. Langlois, R. Ouellet, S. Marengo, D. Houde, and J.E. van Lier. J. Med. Chem. **37**, 415 (1994).
14. N. Brasseur, R. Ouellet, K. Lewis, W.R. Potter, and J.E. van Lier. Photochem. Photobiol. **62**, 1058 (1995).
15. N. Brasseur, R. Ouellet, S. Marengo, D. Houde, and J.E. van Lier. J. Chim. Phys. **93**, 29 (1996).
16. M.G. Galpern, S.V. Kudrevich, and I.G. Novozhilova. Khim. Geterotsikl. Soedin. **1**, 58 (1992).
17. S.A. Mikhalenko, L.A. Yagodina, and E.A. Luk'yanets. Zh. Obsch. Khim. **46**, 1598 (1976).
18. G.I. Goncharova, M.G. Galpern, and E.A. Luk'yanets. Zh. Obsch. Khim. **52**, 666 (1982).
19. M.G. Galpern and E.A. Luk'yanets. Zh. Obsch. Khim. **39**, 2536 (1969).
20. E.G. Galpern, E.A. Luk'yanets, and M. G. Galpern. Izv. Akad. Nauk SSSR, Ser. Khim. **9**, 1976 (1973).
21. M.G. Galpern and E.A. Luk'yanets. Khim. Geterotsikl. Soedin. **6**, 858 (1972).
22. S.A. Mikhalenko and E.A. Luk'yanets. Zh. Obsch. Khim. **39**, 2554 (1969).
23. V.N. Kopranenkov and E.A. Luk'yanets. Zh. Obsch. Khim. **41**, 2341 (1971).
24. A.B. Korzhenevskii, L.V. Markova, and O.I. Koifman. Khim. Geterotsikl. Soedin. **8**, 1068 (1992).
25. S.V. Kudrevich, M.G. Galpern, and J.E. van Lier. Synthesis, 779 (1994).
26. S.V. Kudrevich, M.G. Galpern, E.A. Luk'yanets, and J.E. van Lier. Can. J. Chem. **74**, 508 (1996).
27. M. Yokote, F. Shibamiya, and H. Hayakawa. Yuki Gosei Kagaku Kyokai Shi, **23**, 151 (1965).
28. H.W. Rothkopff, D. Wöhrle, R. Müller, and G. Koßmell. Chem. Ber. **108**, 875 (1975).
29. C.W. Dirk, T. Inabe, K.F. Schoch, Jr., and T.J. Marks. J. Am. Chem. Soc. **105**, 1539 (1983).
30. E. Ciliberto, K.A. Doris, W.J. Pietro, G.M. Reisner, D.E. Ellis, I. Fragalà, F.H. Herbstein, M.A. Ratner, and T.J. Marks. J. Am. Chem. Soc. **106**, 7748 (1984).
31. J.B. Davison and K.J. Wynne. Macromolecules, **11**, 186 (1978).
32. R.D. Joyner and M.E. Kenney. Inorg. Chem. **1**, 236 (1962).
33. W. Freyer. Z. Chem. **26**, 217 (1986).
34. A.B.P. Lever. Adv. Inorg. Chem. Radiochem. **7**, 27 (1965).
35. Yu. M. Gryaznov, O.L. Lebedev, and A.A. Chastov. Opt. Spectrosc. **20**, 503 (1966).
36. L.E. Marinina, S.A. Mikhalenko, and E.A. Luk'yanets. Zh. Obsch. Khim. **42**, 2025 (1973).

Hydrogen vs. electron transfer mechanisms in the chain decomposition of phenacyl bromides. Use of isotopic labeling as a mechanistic probe

Jocelyn Renaud and J.C. Scaiano

Abstract: Ring-substituted α-bromoacetophenones react with alcohols in a chain reaction leading to the corresponding acetophenone, HBr, and the carbonyl compound from oxidation of the alcohol. Two different mechanisms, involving hydrogen or electron transfer by ketyl radicals, have been proposed in order to accommodate the unusual selectivities of these reactions. By studying the efficiency of isotope incorporation from deuterated alcohols, it has been possible to determine the relative contributions from both mechanisms. For example, electron transfer dominates in the case of 2-propanol, while hydrogen transfer is more important for methanol. The results demonstrate that ring substitution in the starting ketone is not a main contributing factor in the discrimination between the two mechanisms. The only parameter that seems to be playing a major role is the nature (reducing strength) of the ketyl radicals.

Key words: dehydrobromination, charge transfer, isotope effect, ketyl radicals.

Résumé : Les α-bromoacétophénones ayant des substituants sur le cycle réagissent avec les alcools selon une réaction en chaîne pour conduire à l'acétophénone correspondante, au HBr et au composé carbonylé résultant de l'oxydation de l'alcool. Dans le but d'expliquer la sélectivité inhabituelle de ces réactions, on propose deux mécanismes différents, impliquant le transfert d'hydrogène ou d'électron par le radical cétyle. L'étude de l'efficacité de l'incorporation isotopique à partir des alcools deutériés, a rendu possible la détermination des contributions relatives des deux mécanismes. Par exemple, le transfert d'électrons domine dans le cas du 2-propanol, tandis que le transfert d'hydrogène est plus important dans le cas du méthanol. Les résultats démontrent que la présence d'un substituant sur le cycle de la cétone de départ n'est pas le facteur contributif principal dans la discrimination des deux mécanismes. La nature (force réductrice) du radical cétyle semble être, dans ce cas, le seul paramètre important.

Mots clés : déhydrobromination, transfert de charge, radicaux cétyles.

[Traduit par la rédaction]

Introduction

The photodecomposition of α-bromoacetophenone and related phenacyl bromides provides a convenient source of phenacyl radicals, reaction [1] (1–3). These radicals are readily detectable because they have a characteristic absorption band in the 500 nm region (4). Bromine atoms, the other intermediates produced in this photoreaction, are invisible in laser photolysis experiments, but their presence can be confirmed by adding complexing reagents such as benzene or bromide ions (5–7).

[1] 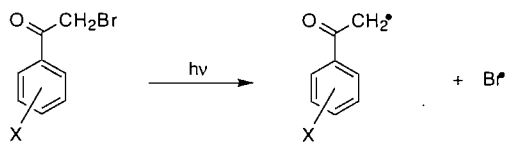

While the phenacyl radical has been written as a carbon-centered species, it can also be written in its canonical form, as an oxygen-centered radical (4), i.e.,

[2] 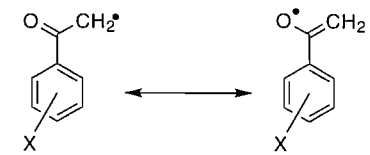

Recent work has suggested that the "oxy" form of this radical may account for its absorption properties (4), which are reminiscent of those recently reported for cumyloxyl radicals (8, 9). While 4-methoxyphenacyl radicals may have a spin density as a high as 0.3 at the carbonyl oxygen, their reactivity is dominated by the radical character at the carbon site (1). Product studies on the addition of phenacyl radicals to olefins show that these reactions lead to C—C bond formation, thus showing typical carbon-centered radical behavior (10, 11). Methoxyphenacyl radicals have modest reactivity; for example, the addition of the *p*-methoxyphenacyl radical to the highly reactive double bond in 1,1-diphenylethylene occurs with a rate constant of 9.4×10^7 M^{-1} s^{-1} (1). In addition, they

Received February 15, 1996.

J. Renaud and J.C. Scaiano.[1] Department of Chemistry, University of Ottawa, Ottawa, ON, K1N 6N5, Canada.

[1] Author to whom correspondence may be addressed. Telephone: (613) 562-5728. Fax: (613) 562-5170.

are also modest hydrogen abstractors: an example showing their low reactivity towards hydrogen abstraction is observed in various alcohol solvents and acetonitrile as solvents. Typical half-lives for the *p*-methoxyphenacyl radical in solvents such as methanol, ethanol, 2-propanol, and acetonitrile are in the neighborhood of 10 μs (1).

Although these carbon-centered radicals seem to be rather unreactive, our work with α-bromoacetophenones shows that steady-state irradiation in alcohol solvents leads to remarkably rapid consumption of the starting material with concomitant formation of the corresponding acetophenone. Typically, irradiation times for significant conversions are 20–50 times shorter in alcohols than in acetonitrile, thus suggesting the involvement of a chain reaction mechanism (3).

It should be noted that other bromo compounds are known to be able to carry similar chains. Chain lengths greater than 10 at temperatures between 30 and 60°C have been measured for systems studying the radical chain reaction of primary and secondary α-bromo esters by 2-propanol and 2-methyldioxolane (12). Also, using vicinal dibromides as starting materials, one can generate two bromine atoms per chain propagation step (13).

Earlier work reporting an exploratory study of this chain reaction mechanism for the dehydrobromination of ring-substituted α-bromoacetophenones in alcohols suggested a more complex mechanism than that originally anticipated (3). What seemed to be a simple electron transfer chain process turned out to be a somewhat more complex mechanism. To rationalize the unusual reactivity/selectivity of these reactions, we suggested a combination of two chain reactions involving hydrogen and electron transfer, taking place concurrently and competing for product formation. This chain reaction is mediated by the ketyl radicals derived by hydrogen abstraction from the alcohols by either the bromine atom or the phenacyl radical. In this article we make use of isotopic labeling in order to establish what fraction of the reaction proceeds by each mechanism; we combine these data with new and earlier results to provide a detailed understanding of these efficient reactions.

Our initial work on phenacyl radicals was stimulated by our interest in the photoinduced yellowing of papers manufactured from ultra-high-yield pulps. The yellowing process results largely from photoinduced reactions involving the chromophores in lignin; among these, mono- and dimethoxyphenols, methoxyacetophenones, and aryloxyanisoles are believed to play an important role (14). The absorption of light leads to various unstable intermediates, such as aromatic ketone singlets and triplets, phenoxyl, phenacyl, and peroxyl radicals, and presumably singlet oxygen. Ultimately, yellow products such as quinones, oligomers, and other degradation products are formed (14, 15). The knowledge of the kinetics and mechanisms of the reactions of unstable intermediates, particularly phenacyl radicals, should advance our understanding of lignin photochemistry in general, and ultimately lead to rational strategies to inhibit the photoyellowing of paper.

Phenacyl radicals can be produced in lignin by several reactions, including the photocleavage of structures containing the α-phenoxyacetophenone moiety. To study the behavior of this radical without the spectral and chemical interferences of the phenoxyl radical, ring-substituted derivatives of α-bromoacetophenones can be used as phenacyl precursors, where the primary photoprocess involves cleavage of the α-C—Br bond to yield the phenacyl radical and a bromine atom, reaction [1]. Ketones **1–5** are the subject of this work.

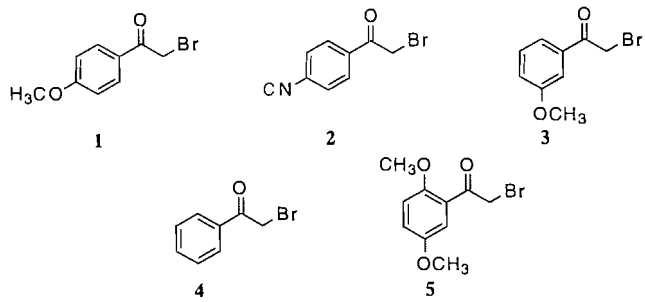

Experimental

Materials

The various substituted α-bromoacetophenones were obtained from either Lancaster or Aldrich and were recrystallized from hexane before use. Bromide ions were added as $(C_4H_9)_4NBr$ from Aldrich, which had suitable solubility in the alcohol solvents used. *n*-Dodecane was a BDH product, valerophenone; *p*-methoxyacetophenone, and *p*-cyanoacetophenone were purchased from Aldrich. Solvents were OmniSolv grade from BDH. Deuterated alcohol solvents were obtained from either Aldrich or Cambridge Isotope Laboratories.

General techniques

Competitive studies

Typical samples were 3 mL, containing 2–10 mM concentration of a ketone (**1–5**) in alcohol solvents. The samples were contained in Pyrex tubes and were deaerated (15 min) by bubbling with oxygen-free nitrogen. The samples were irradiated with two to six RPR-3500 lamps; irradiations were carried out in a "merry-go-round" apparatus to ensure that all samples received the same irradiation dose. Irradiation times varied between 1 and 5 min and were adjusted in order to obtain around 20% conversion of the starting material. Calculations of conversions were done using *n*-dodecane as an internal standard. The temperature of the irradiation chamber was in the 30–35°C range. The product ratios were analyzed by GC and (or) by GC–MS. Product identification was achieved by comparison of GC retention times with authentic samples and (or) GC–MS analysis.

Deuterium labeled product studies

Typical samples were 1 mL, containing 2 mM *para*-substituted α-bromoacetophenones in deuterated alcohol solvent. The samples were contained in Pyrex tubes and were deaerated (15 min) by bubbling with oxygen-free nitrogen. The samples were irradiated as described above. Sodium carbonate was added to each sample to prevent any acid-catalyzed isotopic exchange between the ketone product and the solvent. Substitution patterns were analyzed by GC–MS. Control samples were prepared to ensure that isotopic substitution remained intact throughout the experiment. This was done using a 2 mM solution of *p*-methoxyacetophenone in CH_3OD, CD_3OH, and

$CH_3CHODCH_3$, adding 1 mM HBr, purging for 15 min with oxygen-free nitrogen, and irradiating at 350 nm with two lamps for 2 min. The only system that did show deuterium incorporation was that involving CH_3OD as the solvent. CD_3OH and $CH_3CDOHCH_3$ were considered "clean" systems since any exchange with the solvent would not alter the substitution pattern. Control experiments using $CD_3CHOHCD_3$ were also carried out to verify that no atom transfer involving loss of hydrogen atom from the methyl group of the ketyl radical to form $CD_2{=}C(OH)CD_3$ would interfere in the deuteration pattern of the final ketone. This was done with the compounds **1** and **2** and, for both sytems, the M+1 peak was measured to be ~10%, as expected from the ^{13}C abundance. All calculations of percentage electron transfer took into consideration the natural abundance of ^{13}C, which was measured to be 9.5% (expected: 9.9% for **1**–**3**) using authentic samples of the corresponding acetophenones. Furthermore, no M − 1 contribution were observed for any mass spectra during this analysis.

Quantum yields

These were determined by two different experiments. In a first experiment, compound **1** was used as a starting material and the quantum yields were measured by comparing the acetophenone yields in cyclohexane with those obtained in alcohols. Irradiations were carried out at 350 nm and product concentrations determined as indicated below. The quantum yield for the primary photocleavage of the C—Br bond in cyclohexane was taken as 0.35, the same value determined earlier in methanol solvent (2). The second experiment involved using a reference system as an actinometer. Valerophenone in benzene yields acetophenone with a quantum yield of 0.30 (16). Compound **4** was used as a starting material and the quantum yields were measured in methanol, ethanol, and isopropanol. Both systems had concentrations adjusted to have an absorption of 1.5 at 350 nm. Concentrations of 25 mM for the α-bromoacetophenone system and 100 mM for the reference system were used throughout these experiments. Deaerated samples were irradiated side by side with one to six RPR-3500 lamps as described above. Irradiation times were varied between 10 s and 70 min. Calculations of conversions were done using *n*-dodecane as an internal standard. The ratios between acetophenone formation and internal standard were analyzed by GC and then plotted as a function of time. Comparing slopes between the two systems permitted measurement of chain lengths.

Gas chromatography

The competitive studies of ketone photodecomposition in alcohol solvents and quantum yield experiments using valerophenone as a reference system were quantitatively analyzed on a Perkin Elmer model 8320 capillary gas chromatograph equipped with a flame ionization detector (FID) and a DB-5 bonded-phase column of 15 m length (from J & W Scientific).

GC–MS

Analyses of samples, including those containing Bu_4NBr, were quantitatively performed on a Fisons Instruments 8000 series gas chromatograph with a capillary (DB-5, 15 m, 0.25 mm) column coupled with a MD-800 series mass spectrometer equipped with an EI ion source and a Dynolite detector, and controlled by a DEC/486 PC operating with Masslab software, release 1.12.

Cyclic voltammetry

Cyclic voltammetry measurements were carried out using a standard three-electrode cell with a glassy carbon working electrode 3 mm in diameter, a platinum coil counter electrode, and a platinum wire reference electrode in a Bu_4NBF_4 (0.1 M) – acetonitrile solution. The solvent for all measurements was distilled acetonitrile (EM Science) containing 0.1 M tetrabutylammonium perchlorate (TBAP/Fluka) as the supporting electrolyte, which was recrystallized twice from a CH_2Cl_2–ether mixture. Solutions were deoxygenated with a stream of dry argon. Measurements were made using a PAR model 173 potentiostat equipped with a PAR model 175 universal cell programmer. Voltammograms were recorded on a HP 7045B X–Y recorder. All potentials are reported with respect to the saturated calomel electrode (SCE). The voltammogram obtained for α-bromoacetophenone (**4**) at 200 mV s^{-1} showed two reduction peaks. The first cathodic peak, located at −0.78 V with respect to the saturated calomel electrode, is relevant to the irreversible reduction of compound **4**, and its height (measured with respect to the monoelectronic wave of ferrocene) corresponds to the consumption of one electron per molecule. The second peak that was observed corresponds to the reduction of acetophenone as shown by comparison with an authentic sample. The same cyclic voltammetric behavior was observed with compounds **1** and **2**. The results obtained by these experiments are summarized in Table 4 and were done at the National Research Council under the supervision of Drs. A. Houmam and D.D.M. Wayner.

Bond energy data analysis

Bond energies for the various ketyl radicals were calculated using the NIST Structures and Properties Database and Estimation Program, software version 1.1 (17).

Results and discussion

It is well established that ketones **1**–**5** undergo efficient photodecomposition in alcohol solvents upon broad band irradiation centered at 350 nm. For example, in the case of compound **1**, the relative yields of *p*-methoxyacetophenone in various solvents were determined to be 1:4:97 for cyclohexane, methanol, and 2-propanol (3). Taking the quantum yield for the primary photocleavage of the C—Br bond in cyclohexane as 0.35 (2), the overall quantum yields are 1.4 and 34 for methanol and 2-propanol, respectively, showing a long chain in 2-propanol and a short one in methanol.

To achieve a better understanding of the chain lengths involved in these systems, valerophenone in benzene was chosen as an actinometer (16), since it gave the same photoproduct as our compound **4** in the alcohol systems of interest. Figure 1 shows the results obtained in three alcohol solvents using six UV lamps.

When comparing slopes for any given experiment with that for valerophenone (used as actinometer) one obtains relative chain lengths of 2.5 and 19 for methanol and ethanol, respectively, and a lower limit of $\geq$116 for isopropanol. In isopropanol, the conversion was so high that very short irradiation times had to be employed in order to minimize any interfer-

Fig. 1. Acetophenone yield ratios as a function of time of irradiation for valerophenone as a reference and for compound **4** in methanol, ethanol, and isopropanol irradiated with six RPR-3500 lamps.

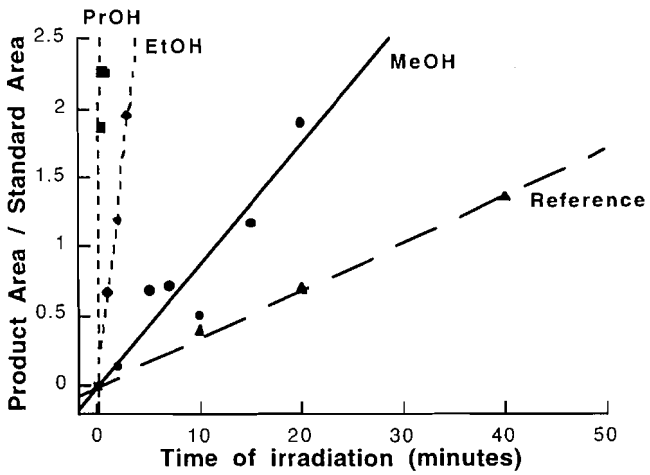

ence from the photoproducts; exposure times were of the order of seconds as opposed to minutes for the other two solvents. Depletion of the starting material led to nonlinear production of acetophenone even after 30 sec. Taking into consideration the quantum yield of acetophenone formation of 0.30 for 100 mM valerophenone in benzene (16), values of 0.75, 5.7, and a lower limit of ≥35 were obtained as overall quantum yields of product formation. Again, short (or nonexistent) chain lengths in methanol and increasing chain lengths for ethanol and isopropanol were shown.

In a chain reaction mechanism involving photochemical initiation, the chain length is inversely proportional to the square root of the light absorbed, i.e.,

$$\text{Rate}_p \propto (\text{Rate}_i/k_t)^{1/2} \times k_p \times (\text{conc. term})$$

where the "concentration term" will usually contain one of the reactants. Rate_i is the rate of initiation. The chain length, λ, is given by:

$$\lambda = (\text{Rate}_p/\text{Rate}_i) = k_p/(\text{Rate}_i \times k_t)^{1/2} \times (\text{conc. term})$$

For a reaction initiated photochemically, the rate of initiation will be directly proportional to the light intensity absorbed (I_a) by the photoinitiator,

$$\text{Rate}_i \propto I_a$$

thus,

$$\lambda \propto 1/I_a^{1/2}$$

In a first, rather rough, approximation, I_a is proportional to the number of lamps used in the photoreactor, leading to:

$$\lambda \propto 1/(\text{no. of lamps})^{1/2}$$

To verify this mathematical relationship, the number of lamps was varied in a series of experiments. Table 1 shows the

Table 1. Chain lengths of compound **4** in various alcohol solvents.

Solvent	UV lamps	Slope ratio	Chain length
MeOH	1	5.3	1.6
i-PrOH	2	263	79
MeOH	6	2.5	0.75
EtOH	6	19	5.7
i-PrOH	6	>116	>35

results obtained in methanol and isopropanol. These results are in agreement with the mathematical relationship derived above, and therefore the chain length increased when fewer lamps were used in the photoreactor. Table 1 also includes results obtained in ethanol using six UV lamps.

It is well established that the primary photoprocess involves cleavage of the C—Br bond, as shown in eq. [1]. The radicals produced in this reaction can abstract hydrogen readily from alcohols and can initiate chain reactions by two distinct mechanisms. Schemes 1 and 2 illustrate the mechanism in the case of methanol.

Since both mechanisms involve the intermediacy of a common radical ($\cdot CH_2OH$), they cannot function as independent chains and we presume one of them will normally dominate. The final products from both reactions should be the same. Scheme 2 represents an electron transfer mechanism, which we anticipated would be favored in the case of electron-deficient molecules such as **2**. At low conversions, the reactions are quite clean, giving only the expected products.

Scheme 1. Bromine atom mechanism (hydrogen transfer).

$$Br^{\cdot} + CH_3OH \xrightarrow{k_2} HBr + \dot{C}H_2OH$$

$$\dot{C}H_2OH + ArCOCH_2Br \xrightarrow{k_3} Ar\dot{C}(OH)CH_2Br + CH_2O$$

$$Ar\dot{C}(OH)CH_2Br \xrightarrow{k_4} ArC(OH)CH_2 + Br^{\cdot}$$

$$\downarrow$$

$$ArCOCH_3$$

Scheme 2. Phenacyl radical mechanism (electron transfer).

$$ArCOCH_2^{\cdot} + CH_3OH \xrightarrow{k_5} ArCOCH_3 + \dot{C}H_2OH$$

$$\dot{C}H_2OH + ArCOCH_2Br \xrightarrow{k_6} CH_2O + H^+ + [ArCOCH_2Br]^{\dot{-}}$$

$$[ArCOCH_2Br]^{\dot{-}} \xrightarrow{k_7} ArCOCH_2^{\cdot} + Br^-$$

To distinguish between the mechanisms of Schemes 1 and 2, experiments were carried out in the presence of 10 mM bromide ions, added as Bu_4NBr. We assumed that the mechanism of Scheme 1 would be heavily influenced, since bromine atoms form the less reactive intermediate $Br_2^{\dot{-}}$ by complexation with bromide, i.e., (6, 13, 18),

$$[3] \quad Br^{\cdot} + Br^- \rightleftharpoons Br_2^{\dot{-}}$$

We found that in methanol solvent, addition of bromide ion caused a 4.5 times decrease in product formation in the case of **1**, but this was reduced to only a factor of 2.0 in the case of **2**.

These results suggest that the bromine atom mechanism must be dominant for **1** and possibly plays a role even in the case of the electron-deficient cyano-substituted compound **2**.

To determine the relative reactivity of ketones **1–5** towards ketyl radicals, we carried out a series of competitive experiments in which ketones **1–5** were irradiated in pairs, and the ratio of products was examined for various ratios of starting materials. The product ratio for ketones **A** and **B** is related to the ratio of precursors according to:

$$[4] \quad \frac{\phi_A}{\phi_B} = \frac{k_r^A}{k_r^B} \frac{[A]}{[B]}$$

where k_r^A and k_r^B represent the values of k_3 and k_6, since these are the only steps in which the two ketones compete for reaction with the ketyl radical, i.e.,

$$[5] \quad k_r^A = k_3^A + k_6^A$$

Clearly, product formation in both reaction schemes is determined by reaction of the ketyl radicals with the α-bromoacetophenones, regardless of which one is the predominant mechanism.

Figure 2 shows plots according to eq. [4] for representative pairs of ketones in methanol, while Fig. 3 shows the corresponding plots for **1** and **2** in methanol, ethanol, and 2-propanol. The values of k_r^A/k_r^B obtained from these studies have been summarized in Table 2. The *para*-substituted ketones follow the anticipated order of reactivity according to their electron-accepting ability, i.e., *p*-CN > *p*-H > *p*-CH_3O.

We were surprised by the results for **1–2** mixtures in the different alcohols. These results (see Table 2) show that the selectivity order is 2-propanol > ethanol > methanol. Assuming that the better reducing agent (2-propanol) will react faster, one would have anticipated the lowest selectivity in this case.

The fact that **1** is less reactive than **2** suggests that the reaction is not in the Marcus inverted region since the kinetics follow the normal dependence on driving force (19, 20), A more likely explanation for the unusual selectivity–structure dependence is that the hydrogen transfer mechanism of Scheme 1 is intrinsically less selective than the electron transfer process of Scheme 2. Further, we anticipate that the mechanism of Scheme 1 will be more likely to be favored over Scheme 2 in the case of methanol than for 2-propanol. This rationale is based on our analysis of bond energy data for the various ketyl radicals, where reaction [6] is not very sensitive to the detailed substitution pattern.

$$[6] \quad R^1R^2\dot{C}OH \longrightarrow R^1R^2CO + H$$

The ΔH_r for reactions is 30.3, 27.7, and 27.2 kcal/mol for the radicals from methanol, ethanol, and 2-propanol, respectively (17).

A quantitative approach to discriminating between these two schemes is to utilize deuterium-labeled alcohols, since both reaction pathways should give a distinct isotopic pattern. Under such isotopic labeling conditions, Schemes 1 and 2 would yield the same product, acetophenone, with one unit mass difference, and Schemes 3 and 4 show the reaction products for the case of compound **1** in CD_3OH.

Fig. 2. Dependence of product ratios following 350 nm irradiation of **1/2** (●) and **4/2** (■) mixtures in methanol.

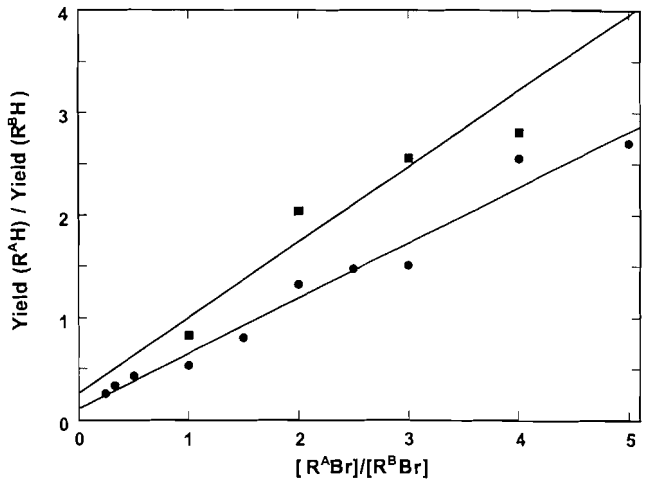

Fig. 3. Dependence of the product ratios following 350 nm irradiation of **1/2** mixtures in methanol, ethanol, and 2-propanol.

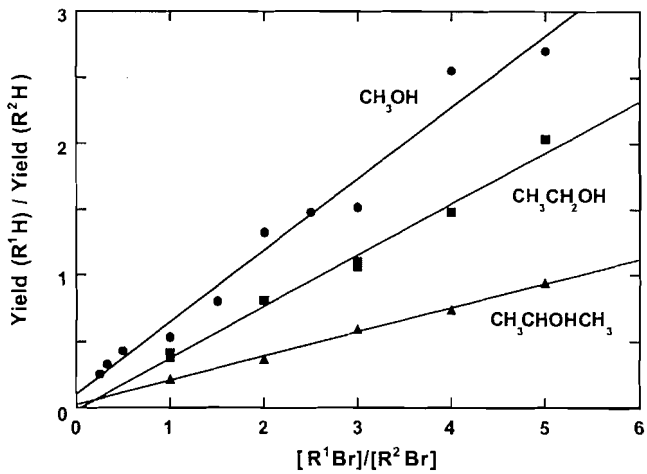

Table 2. Competitive studies of ketone photodecomposition in alcohol solvents at room temperature

Substrates			
A	B	Solvent	k_r^A/k_r^B
1	2	Methanol	0.54
1	3	Methanol	1.68
4	2	Methanol	0.74
3	5	Methanol	0.52
1	2	Ethanol	0.39
1	2	2-Propanol	0.18
4	2	Ethanol	0.67
4	2	2-Propanol	0.35

Scheme 3. Bromine atom mechanism.

$$Br^{\bullet} + CD_3OH \xrightarrow{k_2} DBr + \dot{C}D_2OH$$

$$\dot{C}D_2OH + ArCOCH_2Br \xrightarrow{k_3} Ar\dot{C}(OH)CH_2Br + CD_2O$$

$$Ar\dot{C}(OH)CH_2Br \xrightarrow{k_4} ArC(OH)CH_2 + Br^{\bullet}$$

Ar = 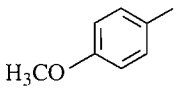

$ArCOCH_3$

$m/z = 150$

Scheme 4. Phenacyl radical mechanism.

$$ArCOCH_2^{\bullet} + CD_3OH \xrightarrow{k_5} ArCOCH_2D + \dot{C}D_2OH$$

$(m/z) = 151$

$$\dot{C}D_2OH + ArCOCH_2Br \xrightarrow{k_6} CD_2O + H^+ + [ArCOCH_2Br]^{\dot{-}}$$

$$[ArCOCH_2Br]^{\dot{-}} \xrightarrow{k_7} ArCOCH_2^{\bullet} + Br^-$$

Table 3 shows the percentage of electron transfer measured for compounds **1** and **2** in *three* different deuterated alcohol solvents. The choice of substrates permitted study of both extremes of the electron-accepting capability of the *para*-substituted family, and the choice of alcohols permitted study of both extremes of the electron-donating capability of the ketyl radicals.

The percentage of electron transfer was determined by measuring and comparing the intensity (%TIC) of the molecular ion peaks corresponding to the parent and the mono-deuterated acetophenones. A measured natural abundance of ^{13}C of 9.5% was taken as the correction factor for adjusting these peaks. For example, the system studying the photochemistry of compound **1** in CD_3OH was analyzed as follows:

Product formation resulting from Scheme 3 gives a molecular ion peak of 150. Correcting for the ^{13}C content, the molecular ion peak now corresponds to:

$$M_{150} = M_{150\,(exp.)}\,(1 + 9.5\%)$$

Product formation resulting from Scheme 4 gives a molecular ion peak of 151. Correction of this peak corresponds to:

$$M_{151} = \{M_{151\,(exp.)}\,(1 - (M_{150\,(exp.)} \times 9.5\%))\} \times (1 + 9.5\%)$$

where the last multiplying factor takes into consideration the ^{13}C abundance present in the mono-deuterated peak.

Therefore the percentage of electron transfer (%et) is given by the following relationship:

$$\%et = M_{151} / (M_{150} + M_{151}) \times 100\%$$

and consequently the percentage of hydrogen transfer (%Ht) is given by:

$$\%Ht = 100\% - \%et$$

Clearly, these results demonstrate that the nature of the starting material is not a main contributing factor in the discrimination between the two schemes. The only parameter that seems to be playing a major role is the nature (reducing strength) of the ketyl radicals.

Table 3. Percent of electron transfer measured for compounds **1** and **2** in various deuterated alcohol solvents (^{13}C corrected).

Compound	CD_3OH	$CH_3CDOHCH_3$	$CH_3CHODCH_3$
1	21	81	96
	23	85	98
	22	77	96
Average	22	81	97
2	23	88	96
		89	94
		87	93
		82	
Average	23	86	94

Table 4. Reduction potentials[a] for compounds **1**, **2**, and **4** in acetonitrile – 0.1 M TBAP at 25°C, reported with respect to the saturated calomel electrode (SCE).

Compound	E (RBr / R·Br$^-$) V vs. SCE
1	−0.78
2	−0.68
4	−0.78

[a]Estimated irreversible reduction potentials, see experimental section.

Because of isotope effects, one can anticipate that the hydrogen transfer step in the overall mechanism (k_3) will be the one that is going to be influenced the most by the nature of the deuterated solvent. This effect will explain the differences in percentage of electron transfer between the two isopropanol solvents. In the case of $CH_3CHODCH_3$, that step is slowed down to the degree of being unable to compete anymore with the electron transfer step (k_6) and therefore we observe near-quantitative electron transfer for that system.

Cyclic voltammetry experiments were performed on the *para*-substituted family in order to verify that the starting material is an unimportant parameter in the overall chain reaction mechanism. Table 4 summarizes the results obtained for the reduction potentials measured in acetonitrile. These results are in agreement with the previous statement that the nature of the substrate is of little consequence in determining the reaction pathway chosen during the photodecomposition.

Conclusion

In conclusion, the photoinitiated reaction of ring-substituted α-bromoacetophenones with alcohols involves an efficient chain reaction leading to the corresponding acetophenone, HBr, and the carbonyl compound from oxidation of the alcohol. Two different mechanisms, involving hydrogen or electron transfer by ketyl radicals, were proposed in order to accommodate the unusual selectivities of these reactions. Studies of isotope incorporation from deuterated alcohols leads to the conclusion that electron transfer (Scheme 2) dominates in the case of 2-propanol, while hydrogen transfer (Scheme 1) is most important for methanol.The results demonstrate that ring substitution in the starting ketone is not a main contributing factor in the discrimination between the two

mechanisms; the observation is further corroborated by the relatively minor variations observed (see Table 4) in the reduction potentials. The only parameter that seems to be playing a major role is the nature (reducing strength) of the ketyl radicals.

Acknowledgments

This work has been supported by the Natural Sciences and Engineering Research Council of Canada (NSERC) and the Canadian Networks of Centres of Excellence, through its program on Mechanical and Chemimechanical Wood Pulps. J.R. is the recipient of an NSERC graduate scholarship and J.C.S. of a Killam Fellowship awarded by the Canada Council. The authors thank Drs. A. Houmam and D.D.M. Wayner for help regarding the cyclic voltammetry measurements.

References

1. S.V. Jovanovic, J. Renaud, A.B. Berinstain, and J.C. Scaiano. Can. J. Chem. **73**, 223 (1995).
2. W.G. McGimpsey and J.C. Scaiano. Can. J. Chem. **66**, 1474 (1988).
3. J. Renaud and J.C. Scaiano. Res. Chem. Intermed. **21**, 457 (1995).
4. J.C. Scaiano, M.K. Whittlesey, A.B. Berinstain, P.R.L. Malenfant, and R.H. Schuler. Chem. Mater. **6**, 836 (1994).
5. G.L. Hug. Optical spectra of nonmetallic inorganic transient species in aqueous solution. National Bureau of Standards, Washington, D.C. 1981.
6. J.C. Scaiano, M. Barra, G. Calabrese, and R. Sinta. J. Chem. Soc. Chem. Commun. 1418 (1992).
7. J.C. Scaiano, M. Barra, M. Krzywinski, R. Sinta, and G. Calabrese. J. Am. Chem. Soc. **115**, 8340 (1993).
8. D.V. Avila, K.U. Ingold, A.A. Di Nardo, F. Zerbetto, M.Z. Zgierski, and J. Lusztyk. J. Am. Chem. Soc. **117**, 2711 (1995).
9. D.V. Avila, J. Lusztyk, and K.U. Ingold. J. Am. Chem. Soc. **114**, 6576 (1992).
10. G.A. Russell and S.V. Kulkarni. J. Org. Chem. **58**, 2678 (1993).
11. G.A. Russell, S.V. Kulkarni, and R.K. Khanna. J. Org. Chem. **55**, 1080 (1990).
12. F. Fontana, R.J. Kolt, Y. Huang, and D.D.M. Wayner. J. Org. Chem. **59**, 4671 (1994).
13. J.C. Scaiano, M. Barra, M. Krzywinski, T. Hancock, G. Calabrese, and R. Sinta. Chem. Mater. **7**, 936 (1995).
14. G.J. Leary. J. Pulp Paper Sci. **20**, J154 (1994).
15. A.B. Berinstain, M.K. Whittlesey, and J.C. Scaiano. *In* Photochemistry of lignocellulosic materials. *Edited by* C. Heitner and J.C. Scaiano. American Chemical Society, Washington, D.C. 1993. p. 111.
16. P.J. Wagner, P.A. Kelso, A.E. Kemppainen, J.M. McGrath, H.N. Schott, and R.G. Zepp. J. Am. Chem. Soc. **94**, 7506 (1972).
17. S.E. Stein, J.M. Rukkers, and R.L. Brown. NIST structures and properties database and estimation program: Version 1.1. NIST, U.S. Department of Commerce, Gaithersburg, Md. 1991.
18. V. Nagarajan and R.W. Fessenden. J. Phys. Chem. **89**, 2330 (1985).
19. R.A. Marcus. Can. J. Chem. **37**, 155 (1959).
20. R.A. Marcus. J. Chem. Phys. **24**, 966 (1956).

Synthesis of chemically and functionally diverse scaffolds from pentaerythritol

Stephen Hanessian, Hubli Prabhanjan, Dongxu Qiu, and Sudhir Nambiar

Abstract: Pentaerythritol (2,2-bis-hydroxymethyl-propane-1,3-diol) was converted into a series of mono-, di-, and trisubstituted derivatives, comprising allyl ethers and amino-alkyl ethers, by systematic chemical manipulation of the hydroxy groups. The remaining hydroxymethyl group in the case of the trisubstituted analog was functionalized with ether groups bearing terminal ω-carboxyl or ω-alkene groups. These derivatives are versatile templates and scaffolds for single, double, or triple substitution with appropriate ligands forming amides and esters, and allowing the attachment of the ω-alkene or ω-carboxyl group to solid support for combinatorial chemistry.

Key words: molecular diversity, scaffolds, templates and tris(2-aminoethyl)-pentaerythritol.

Résumé : Le pentaérythritol (2,2-bis-hydroxymethyl-propane-1,3-diol) a été converti en une série de dérivés mono-, di- et trisubstitués portant des groupes éther allylique et éther aminoalkyle par manipulation systématique des fonctions hydroxy. Le groupe hydroxyméthyle restant dans le cas des dérivés trisubstitués a été fonctionnalisé par un des groupes ethers avec un groupe terminal carboxy ou alcényle. Les dérivés sont utiles comme des sources de branchement des ligands pharmacologiquement actives par des liaisons amides ou ester. Des applications dans la chimie combinatorielle sur phase solide sont aussi envisageables.

Mots clés : diversité moléculaire, tris(2-aminoethyl)-pentaerythritol.

Recent interest in chemical diversity in conjunction with combinatorial methods of lead structure generation has instigated a search for readily available polyfunctional organic molecules that can be manipulated in a systematic manner (for recent reviews, see ref. 1). Such molecules can be utilized as templates or scaffolds onto which one can introduce variable functionality with spatially predetermined dispositions (2). For example, the incorporation of specific pharmacophores or related motifs at the extremities of such scaffolds can lead to binding at different receptor sites with potentially novel therapeutic applications (3). Alternatively, the attachment of the template or scaffold molecule to a polymer support through one of its arms, allows the voluntary elaboration of one or more remaining chains in a parallel or combinatorial mode for the discovery of biologically active sequences on growing chains. In the case of templates capable of replicating outwards from a core unit, it is possible to construct dendritic molecules (for selected examples, see ref. 4) with intriguing shapes and exciting physical properties.

In connection with our interest in the general area of chemical and functional diversity (5), we wished to prepare organic templates capable of accommodating one, or more, bioactive molecules in order to release them in a sustained manner in a chemically or enzymatically induced process. Another objective was to prepare polyfunctional molecules that could allow us to generate clusters of immunologically relevant haptens on a given template. We have previously shown that pentaerythritol can serve as an excellent anchor for clustering potential megacaloric nutrients upon its framework by ester linkages (6).

We report herein our studies in the systematic manipulation of the readily available pentaerythritol (2,2-bis-hydroxymethyl-propane-1,3-diol) **1**, and the introduction of versatile functionality through a series of O-substitution and S_N2 displacement reactions.

In spite of the low cost and versatile structure of pentaerythritol, relatively few differentially functionalized derivatives are known (7). Tetrabromo and tetraamino derivatives of pentaerythritol have been known for many years (8). Recently, Neumann, Woulfe, and co-workers (9) reported the synthesis of a triamino analog of pentaerythritol in conjunction with novel routes to 1,1,1-tris(aminomethyl)ethane (TAME), which is a well-known ligand for metal ions. Newkome et al. (10) recently reported the preparation of tetrakis (ω-bromoalkyl)methanes from pentaerythritol, and their utilization in carbon extension reactions to generate functionalized cascade core molecules. Finally, Kremers and Meijer (11) utilized pentaerythritol for the preparation of chiral dendrimers in their racemic forms.

Scheme 1 illustrates the sequence for the synthesis of monofunctionalized derivatives of tris(2-aminoethyl)pentaerythritol proceeding via the intermediacy of the corresponding tris(2-azidoethyl) ether of pentaerythritol. A variety of ether and ester functions could be introduced on the remaining hydroxymethyl group without affecting the resident azidoethyl groups.

Stoichiometrically controlled silylation of pentaerythritol **1**

Received March 28, 1996.

S. Hanessian,[1] H. Prabhanjan, D. Qiu, and S. Nambiar. Department of Chemistry, Université de Montréal, P.O. Box 6128, Succ. Centre-ville, Montréal, QC, H3C 3J7, Canada.

[1] Author to whom correspondence may be addressed. Telephone: (514) 343-6738, Fax: (514) 343-5728, E-mail: hanessia@ere.umontreal.ca

Scheme 1.

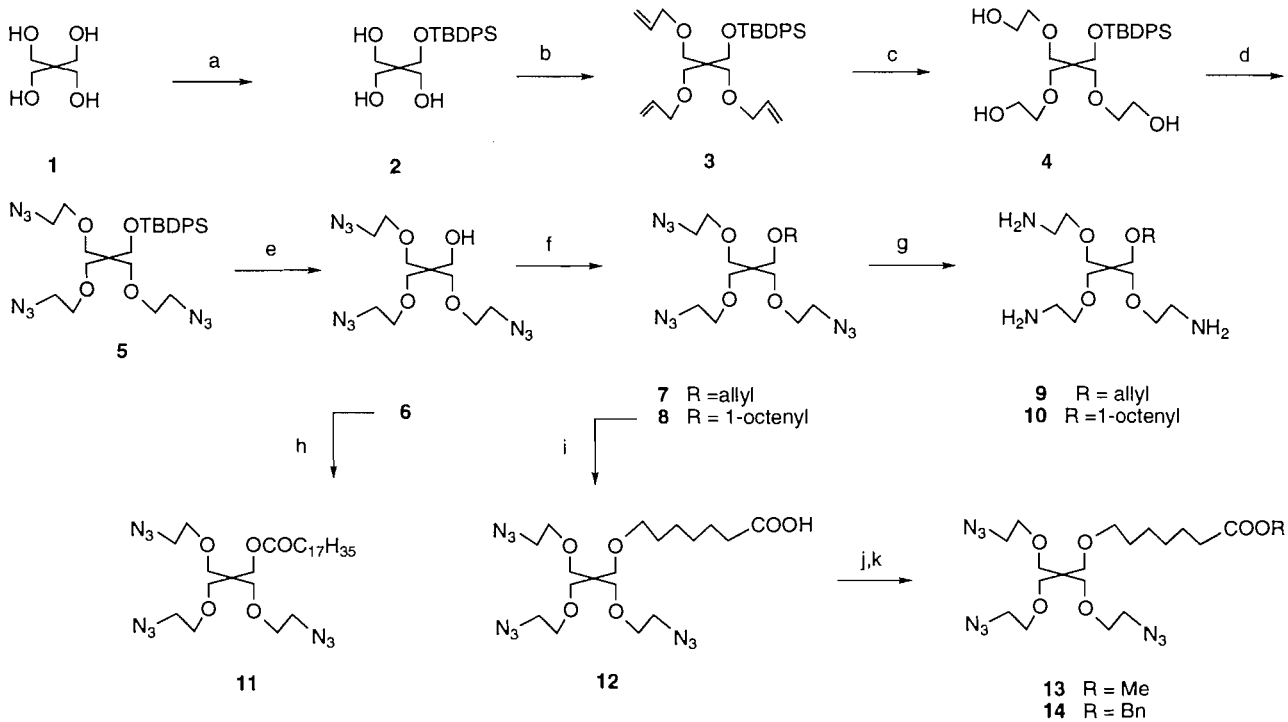

a 0.5 equiv. TBDPSCl, DMF, 0 - 15 °C. b. allyl bromide, DMF, NaH, 0 °C - r.t. c. O_3, CH_2Cl_2, - 78 °C ; $NaBH_4$,EtOH, r.t. d. MsCl, Pyridine, 0 °C - r.t. ; NaN_3, DMF, 130 °C. e. TBAF, THF, -10 °C - r.t. f. for **7** allyl bromide, DMF, NaH, 0°C, r.t ; for **8**, 1- octenyl bromide, DMF, KH, TBAI, 0 °C - r.t g. Ph_3P, THF, r.t. h. $C_{17}H_{35}COOH$, DCC, CH_2Cl_2, r.t. i. O_3 , MeOH, -78 °C ; PDC, DMF, r.t. j. for **13**, BnOH, DCC, DMF, r.t; k for **14**, MeOH, Dowex IR -H^+, r.t.

with *tert*-butylchlorodiphenylsilane in DMF (12) gave the monosilylated derivative **2** in 84% yield, which was transformed into the tri-*O*-allyl derivative **3** under standard conditions. The allyl groups were oxidatively cleaved by ozonolysis and the resulting trialdehyde was reduced with $NaBH_4$ to give the triol **4** in good overall yield.

Conversion to the triazido derivative **5** was accomplished by treating **4** with mesyl chloride in pyridine at 0°C to form the trimesyl ester, followed by displacement by azide ion. After removing the *tert*-butyldiphenylsilyl group in **5** with TBAF, the resulting alcohol **6** was converted to allyl and 1-octenyl derivatives **7** and **8** in high yields, by treating with allyl bromide and 1-octenyl bromide, respectively. Finally, reduction of the azido functions in **7** and **8** with triphenylphosphine in THF (13) afforded the desired scaffold molecules **9** and **10**, respectively, as viscous light yellow syrups that were sufficiently pure to be used in subsequent transformations.

The triazido derivative **6** could be easily esterified with a fatty acid. Thus, treatment with stearic acid in the presence of DCC and DMAP gave the stearoyl derivative **11** in high yield. The terminal double bond in **8** was ozonolyzed, and the resulting aldehyde was oxidized to an acid **12** upon treatment with PDC. Esterification of the acid with methanol and benzyl alcohol individually gave the respective ester derivatives **13** and **14**.

We have used the monofunctional tris(2-aminoethyl) derivatives **9** and **10** as tripodal primary amines for amide bond formation with appropriate glycosylamino acid derivatives (14). Such clustered glycopeptide derivatives are interesting haptens for immunological studies in conjunction with the preparation of artificial vaccines (15) against certain types of tumors.

The preparation of a mono(aminoethyl) ether derivative of pentaerythritol involved a different strategy, which is illustrated in Scheme 2. Controlled allylation of diol **15** (16) with allyl bromide in DMF gave the monoallylated derivative **16** in 60% yield, which was in turn converted into diol **17**, by ozonolysis of the double bond to an aldehyde and subsequent reduction with $NaBH_4$. Treatment of **17** with *tert*-butylchlorodiphenylsilane in DMF led to the monosilylated derivative **18** without any detectable disilylation, undoubtedly due to the neopentylic nature of the other hydroxymethyl group. Hydrogenolytic cleavage of the benzyl groups over Pd–C gave the triol **19** in high yield.

In a parallel sequence of reactions similar to those leading to **18**, the two hydroxyl groups in **15** could be allylated under conditions described for **3** to give **20**. Oxidative cleavage of **20**, followed by reduction, gave a diol **21** that was converted to **22** by selective monosilylation. Mesylation of **22** followed by nucleophilic displacement with azide ion gave the azido ion derivative **23** in high overall yield. Treatment of **23** with thiolacetic acid (17) gave the corresponding N-acetyl derivative **24**, which was subjected to hydrogenolysis to give the diol **25**.

It was also of interest to prepare tris(1,1,1-aminomethyl)

Scheme 2.

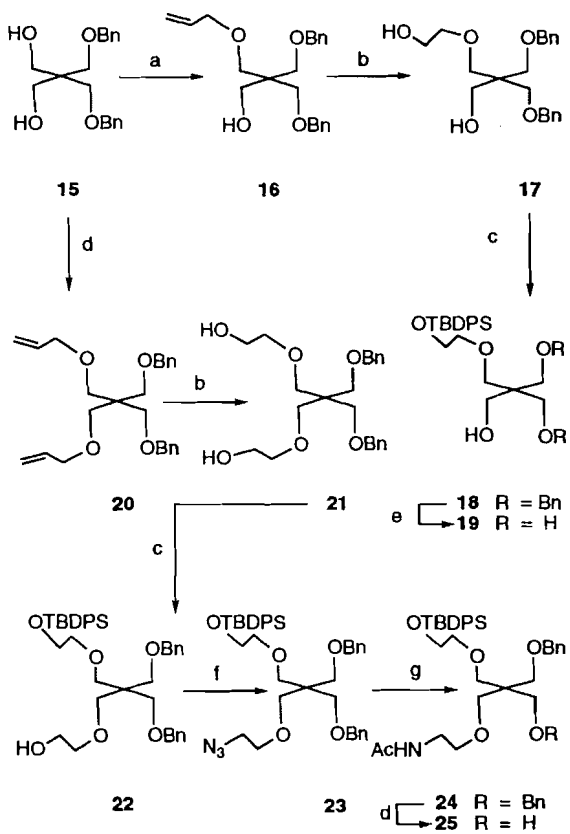

a. Allyl bromide (0.9 equiv.), DMF, NaH, 0 °C b. O_3, CH_2Cl_2, -78 °C; $NaBH_4$, EtOH, r.t. c. TBDPS-Cl, Imidazole, DMF, 0 °C-r.t. d. Allylbromide (5 equiv.), DMF, NaH, 0 °C. e. H_2, Pd-C, MeOH, r.t. f. MsCl, Pyridine, 0 °C; NaN_3, DMF, 130 °C. g. Thiolacetic acid, r.t.

Scheme 3.

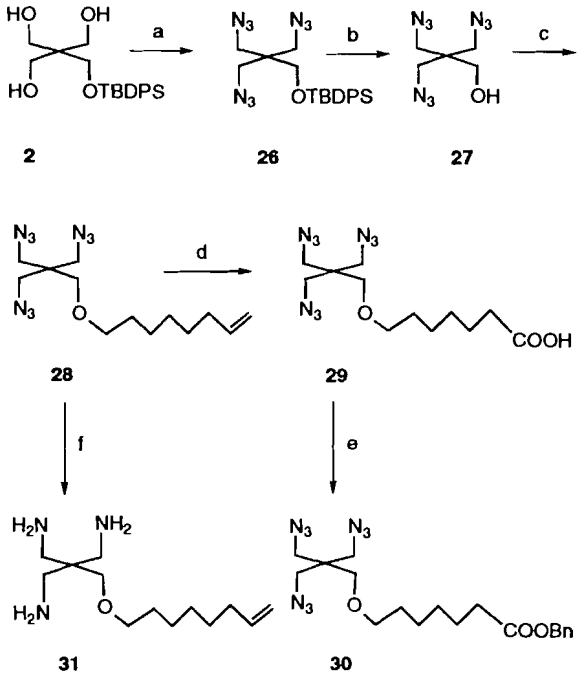

a. MsCl, Pyridine, 0 °C; then NaN_3, DMF, 130 °C. b. TBAF, THF, -10 - 0 °C. c. 1-octenyl bromide, KH, TBAI, DMF, 0 °C - r.t. d. O_3, CH_2Cl_2, -78 °C; then PDC, DMF, r.t. e. BnOH, DCC, CH_2Cl_2, r.t. f. Ph_3P, THF, r.t.

ethanol, a triamino pentaerythritol in which one hydroxymethyl group was free for further elaboration into ether and acid groups with a view of conjugation to appropriate carriers or attachment to solid-phase matrices. The preparation of mono-*O*-benzyl triazido-trideoxy pentaerythritol and its reduction to the corresponding triamino derivative was described by Woulfe and co-workers (9), adopting the method of Fleischer (18) (NaN_3, diethylene glycol, 120°C, followed by Pd/C, H_2 in methanol).

Our protocol started with the tri-mesylation of **2** and subsequent displacement with sodium azide in DMF at 120°C to give **26** in good overall yield (Scheme 3). Treatment with fluoride ion removed the silyl ether group to give the triazido-derivative **27**, which was isolated as a syrup. Working in the mmol scale, we encountered no problems with the azido functions, although caution must be exercised at all times with polyazido compounds, especially with larger runs (8). The 1-octenyl ether **28** was readily prepared by alkylation in the presence of KH and tetrabutylammonium iodide in DMF at 0°C. Presumably, alkylation was accelerated by formation of the tetrabutylammonium alkoxide, which is more reactive than the corresponding potassium alkoxide (19). Ozonolytic cleavage of **28**, followed by oxidation and esterification, gave the corresponding carboxylic acid **29** and the benzyl ester **30**. Finally it was possible to achieve chemoselective reduction of the azido group in **28** by treatment with triphenylphosphine to afford the corresponding triamino derivative **31**.

The functionally differentiated derivatives of pentaerythritol shown in Schemes 1–3 should find utility in a number of areas relating to the expression of chemical diversity on polyfunctional scaffolds and templates. The presence of carboxylic acid, alcohol, and olefinic groups on tethers of appropriate chain lengths should allow the attachment of these pentaerythritol-derived motifs on solid supports and the further exploration of their chemistry.

Experimental

Melting points are uncorrected. ^1H NMR spectra were recorded at 300 MHz in $CDCl_3$ (unless otherwise indicated), with $CHCl_3$ as reference. ^{13}C NMR spectra were recorded at 75 MHz in $CDCl_3$ (unless otherwise indicated), with $CHCl_3$ as reference. Wherever necessary, ^1H NMR assignments were supported by appropriate homonuclear correlation experiments (COSY). IR spectra of samples were recorded as films. Mass spectra were recorded using electron ionization (EI) at 70 eV or by the fast atom bombardment (FAB) technique. Chromatography was performed on 230–400 mesh silica gel by flash technique (20). Thin-layer chromatography (TLC) was performed on glass plates coated with a 0.02 mm layer of silica gel 60 F-254. All solvents were freshly distilled before use.

2,2-Bis-hydroxymethyl-propane-1,3-diol mono *tert*-butyldiphenylsilyl ether (2)

To a solution of pentaerythritol **1** (3.1 g, 22.5 mmol) in 150 mL anhydrous DMF was added recrystallized imidazole (1.56 g, 24 mmol) followed by the dropwise addition of *tert*-butyldiphenylchlorosilane (3.15 mL, 12 mmol). The solution was stirred for 24 h, poured into 600 mL water, and extracted twice with ethyl acetate. The organic phase was washed with brine and water, and the extracts were dried ($MgSO_4$), filtered, concentrated, and purified by silica gel flash column chromatography (EtOAc–hexanes, 1:1) to give **2** as an oil that solidified on standing (3.76 g, 84%, on the basis of the reagent added). ^{1}H NMR ($CDCl_3$) δ: 7.67–7.63 (m, 6H), 7.43–7.40 (m, 6H), 3.71 (d, 2H), 3.63 (s, 2H), 2.75 (bn s, 1H), 1.07 (s, 9H). ^{13}C NMR ($CDCl_3$) δ: 135.5–127.7 (Ph), 65.2, 64.4 (O-CH_2-C), 45.5 (C quat.), 19.3 (-$(CH_3)_3$). HRMS (EI), calcd. for $C_{21}H_{31}O_4Si$ (M+H): 375.1984; found: 375.1960.

3-Allyloxy-2,2-bis-allyloxymethyl-propane-1-ol *tert*-butyldiphenylsilyl ether (3)

To a solution of **2** (3.76 g, 10 mmol) in 150 mL anhydrous DMF was added allyl bromide (4.3 mL, 50 mmol). The reaction mixture was cooled in an ice-water bath, and sodium hydride (60%, 1.76 g, 45 mmol) was added in three portions. The solution was stirred overnight at room temperature, and 2 mL of methanol was added dropwise. The solution was partially concentrated in vacuo, poured into cold water (500 mL), extracted with ethyl acetate, washed with water, dried over $MgSO_4$, and concentrated. The residue was purified by silica gel flash column chromatography (EtOAc–hexanes, 1:20) to give the tri-allylated product **3** as an oil (3.90 g, 66%). ^{1}H NMR ($CDCl_3$) δ: 7.70–7.67 (m, 5H), 7.42–7.37 (m, 5H), 5.86 (m, 1H), 5.28 (m, 6H), 3.97 (m, 6H), 3.7 (s, 2H), 3.49 (s, 2H), 1.04 (s, 9H). HRMS (FAB), calcd. for $C_{26}H_{33}O_4Si$ [M−C$(CH_3)_3$]: 437.2124; found: 437.2148.

3-(2-Hydroxy-ethoxy)-2,2-bis(2-hydroxy-ethoxymethyl)-propane-1-ol *tert*-butyldiphenylsilyl ether (4)

Ozone was bubbled through a solution of 3 (3.90 g, 7.9 mmol) in 150 mL dichloromethane–methanol 1:1 at −78°C until the solution was saturated. Argon was bubbled through the solution for 15 min to remove the residual ozone and an excess of methyl sulfide was added. The solution was allowed to warm to room temperature and concentrated to a syrup that was dissolved in ethanol (30 mL). Sodium borohydride (1.7 g, 45 mmol) was added in four portions to the cooled solution at 0°C. After stirring for 24 h at room temperature, the solution was acidified with 20% HCl to pH 6, then concentrated to a syrup that was partitioned between ethyl acetate and water. After the usual work-up, a syrupy material was obtained that was purified by silica gel flash column chromatography (EtOAc–hexanes, 1:20) to give the title product **4** as a syrup that solidified on standing (2.94 g, 76%). ^{1}H NMR ($CDCl_3$) δ: 7.64–7.64 (m, 10H), 3.67 (m, 6H), 3.64 (s, 2H), 3.55–3.63 (m, 12H), 1.06 (s, 9H). ^{13}C NMR ($CDCl_3$) δ: 135.4–127.5 (Ph), 72.4, 69.8, 61.3 (O-CH_2-C), 43.2 (C quat., *t*-Bu), 19.5 ($(CH_3)_3$). HRMS (FAB), calcd. for $C_{27}H_{43}O_7Si$ (M+H): 507.2773; found: 507.2780.

3-(2-Azido-ethoxy)-2,2-bis(2-azido-ethoxymethyl)-propane-1-ol *tert*-butyldiphenylsilyl ether (5)

To a solution of **4** (506 mg, 1 mmol) in anhydrous pyridine (5 mL) at 0°C was added mesyl chloride (0.248 mL, 3.6 mmol) dropwise. The reaction mixture was stirred for 4 h at 25°C, water (1 mL) was added after recooling the reaction mixture to 0°C, and stirring was continued for 30 min. The mixture was poured into ice-water and extracted twice with ethyl acetate. The combined organic layers were washed successively with 20% HCl and water, dried over $MgSO_4$, concentrated to a syrup, which was dissolved in anhydrous DMF (5 mL), and NaN_3 (390 mg, 6 mmol) was added. The mixture was heated at 130°C in an oil bath for 5 h, then cooled to room temperature. The contents of the flask were poured into ice-cold water, extracted with ethyl acetate, the organic layers were washed with water, dried over $MgSO_4$, concentrated, and the residue was purified by silica gel flash column chromatography (EtOAc–hexanes, 1:25) to give **5** as an oil (501 mg, 86%). ^{1}H NMR ($CDCl_3$) δ: 7.7–7.43 (10H), 3.75 (s, 2H), 3.63 (m, 6H), 3.55 (s, 6H), 3.3 (m, 6H), 1.1 (s, 9H). ^{13}C NMR ($CDCl_3$) δ: 135.4–127.4 (Ph), 70.3, 68.9, 61.7 (O-CH_2-C), 50.6 (-CH_2N_3), 45.9 (C quat.), 26.7 (C quat., *t*-Bu), 19.3 (-$(CH_3)_3$). HRMS (EI), calcd. for $C_{23}H_{30}O_4Si$ [M−C$(CH_3)_3$]: 524.2188; found: 524.2131.

3-(2-Azido-ethoxy)-2,2-bis(2-azido-ethoxymethyl)-propane-1-ol (6)

To a solution of **5** (581 mg, 1 mmol) in anhydrous THF (5 mL) was added tetra-*n*-butylammonium fluoride (2 mL, 1 M in THF) dropwise at 0°C. The solution was stirred overnight and then concentrated. The residue was purified by silica gel flash column chromatography (EtOAc–hexanes, 1:1) to give **6** as a semi-solid (331 mg, 97%) that was used as such in subsequent steps. ^{1}H NMR ($CDCl_3$) δ: 3.7 (s, 2H), 3.6–3.50 (t, 6H), 3.42 (s, 6H), 3.3 (m, 6H). ^{13}C NMR ($CDCl_3$) δ: 70.05 (C-CH_2-CH_2N_3), 69.9 (C-CH_2-O), 64.1 (C-CH_2-OH), 50.2 (CH_2N_3), 42.5 (C quat.). HRMS (FAB), calcd. for $C_{11}H_{22}N_9O_4$ (M+H): 344.1779; found: 344.1794.

3-[3-(2-Azido-ethoxy)-2,2-bis(2-azido-ethoxymethyl)-propoxy]-propene (7)

To a solution of **6** (1.24 g, 7.2 mmol) in anhydrous DMF (10 mL) was added allyl bromide (1 mL, 10 mmol), the solution was cooled to 0°C, and NaH (400 mg, 60% in oil) was added. The reaction mixture was stirred for 24 h at room temperature, methanol (3 mL) was added, and stirring was continued for 30 min. Solvent was removed under vacuum and the residue was partitioned between ethyl acetate and water. The organic layers were washed with water, dried, and concentrated to a syrup that was purified by silica gel flash column chromatography (EtOAc–hexanes, 1:10) to give **7** as an oil (1.93 g, 71%). ^{1}H NMR ($CDCl_3$) δ: 5.80 (m, 1H), 5.15 (m, 2H), 3.95 (m, 2H), 3.62 (t, 6H), 3.52 (s, 6H), 3.47 (s, 2H), 3.33 (s, 6H). This product was used in the next step as such.

3-[3-(2-Azido-ethoxy)-2,2-bis(2-azido-ethoxymethyl)-propoxy]-oct-1-ene (8)

To a solution of **6** (342 mg, 1 mmol) in anhydrous THF (5 mL) was added 5 mg of tetrabutylammonium iodide and 1-octenyl bromide (0.5 mL, 3 mmol) followed by KH (250 mg, 30% in oil) at 0°C. The reaction mixture was stirred for 48 h at room temperature and processed as for **7**. Purification by silica gel flash column chromatography (EtOAc–hexanes, 1:15) gave **8** as an oil (368 mg, 81%). ^{1}H NMR ($CDCl_3$) δ: 5.81 (m, 1H),

4.91 (m, 2H), 3.61 (t, 6H), 3.49 (s, 6H), 3.3–3.41 (s, 10H), 2.04 (m, 2H), 1.34–1.6 (m, 8H). ^{13}C NMR ($CDCl_3$) δ: 138.9 (=CH), 114.0 (=CH_2), 71.3, 70.3, 69.6, 68.7, (O-CH_2-C), 50.6 (CH_2N_3), 44.9 (C quat.), 33.6 (CH_2CH=CH_2), and 28.8, 25.9, 24.3 (alkyl chain CH_2). HRMS (EI), calcd. for $C_{19}H_{36}O_4N_9$ (M+H): 454.2890; found: 454.2920.

3-[3-(2-Amino-ethoxy)-2,2-bis(2-amino-ethoxymethyl)-propoxy]-propene (9)

To a solution of **7** (1.9 g, 4.96 mmol) in 50 mL of anhydrous THF was added PPh_3 (5 g). The mixture was stirred for 24 h at room temperature and 2 mL of water was added. Stirring was continued for another 24 h and the solvents were removed under vacuum. The residue was dissolved in water (20 mL), filtered over Celite, and the insolubles were washed with water. The combined water phase was washed with ethyl acetate and the organic phase was processed as usual to give **9** as a syrup (0.9 g, 60%). ^{1}H NMR (CD_3OD) δ: 5.80 (m, 1H), 5.16 (m, 2H), 3.88 (m, 2H), 3.45 (m, 14H), 2.75 (m, 4H), 1.99 (m, 6H). ^{13}C NMR ($CDCl_3$) δ: 134.8 (=CH), 116.2 (=CH_2), 73.1, 72.1, 69.8, 69.7, 69.6, 69.1 (O-CH_2-CH_2N_3), 45.3 (C quat.), 41.5 (CH_2), HRMS (FAB), calcd. for $C_{14}H_{31}N_3O_4$ (M+Na): 328.2192; found: 328.2212.

3-[3-(2-Amino-ethoxy)-2,2-bis(2-amino-ethoxymethyl)-propoxy]-oct-1-ene (10)

A solution of **8** (80 mg, 0.17 mmol) in 5 mL of anhydrous THF was treated with PPh_3 in a similar fashion as for compound **9** to afford **10** as a syrup (58 mg, 79%). ^{13}C NMR ($CDCl_3$) δ: 140.05 (=CH), 114.86 (=CH_2), 72.60 (O-CH_2-CH_2NH_2), 71.04 (C-O- CH_2), 70.62 (O-CH_2-C), and 70.53 (O-$CH_2(CH_2)_5$). HRMS (FAB), calcd. for $C_{19}H_{36}O_4N_9$ (M+HSCH$_2$CH(OH)CH$_2$OH+H): 485.3600; found: 485.3448.

Heptadecanoic acid 3-(2-azido-ethoxy)-2,2-bis(2-azido-ethoxymethyl)-propyl ester (11)

A solution of **6** (80 mg, 0.2 mmol) in dichloromethane–EtOAc (5 mL, 1:1) was treated with stearic acid (140 mg), DCC (40 mg, 0.2 mmol), and DMAP (5 mg) for 24 h at room temperature. The mixture was diluted with dichloromethane (10 mL), washed with water, dried ($MgSO_4$), and evaporated. The residue was purified by silica gel flash column chromatography (EtOAc–hexanes, 1:9) to give **11** as a semi-solid (106 mg, 81%). ^{13}C NMR ($CDCl_3$) δ: 70.3 (C-CH_2-CH_2N_3), 69.2 (C-CH_2-O), 50.5 (CH_2N_3) and 43.8 (C quat.). HRMS (FAB), calcd. for $C_{29}H_{56}N_9O_5$ (M+H): 610.4376; found: 610.4404.

7-[3-(2-Azido-ethoxy)-2,2-bis(2-azido-ethoxymethyl)-propoxy]-heptanoic acid methyl ester (13)

Ozone was bubbled through a solution of **8** (453 mg, 1.0 mmol) in 10 mL dichloromethane–methanol (1:1) at −78°C until TLC showed completion of the reaction. Argon was bubbled through the solution for 15 min to remove the residual ozone and an excess of methyl sulfide was added. The solution was allowed to warm to room temperature and concentrated to give an aldehyde intermediate. IR cm^{-1} (film): 2100 (N_3), 1740 (CHO). This residue was dissolved in dry DMF (5 mL), and treated with PDC (1.34 g). After being stirred for 24 h, the mixture was partitioned between ethyl acetate and water, and the organic layers were washed with water, dried ($MgSO_4$), and evaporated. Purification of the residue by silica gel flash column chromatography (EtOAc–hexanes, 3:7) gave **12** as a syrup (404 mg, 92%); IR cm^{-1} (film), 2100 (N_3), 1730 (COOH); A solution of **12** (210 mg, 0.42 mmol) in methanol was treated with freshly generated IR–120 (H^+) resin (200 mg) at room temperature for 24 h. The resin was filtered off, washed with methanol, and the filtrate and washings were concentrated. Purification of the residue by silica gel flash column chromatography (EtOAc–hexanes, 1:9) gave **13** an a syrup (171 mg, 70%). IR cm^{-1} (film): 2100 (N_3). ^{1}H NMR ($CDCl_3$) δ: 3.60 (m, 6H), 3.47 (s, 6H), 3.50 (s, 2H), 3.41 (s, 3H), 3.31 (t, 2H), 3.25 (t, 6H), 2.30 (t, 2H), 1.67–1.33 (8H). ^{13}C NMR ($CDCl_3$) δ: 71.0, 69.3, 68.5 ($CH_2CH_2N_3$), 50.5 (CH_2OCH_2 CH_2N_3), 44.7 (C quat.). HRMS (FAB), calcd. for $C_{19}H_{35}O_6N_9$ (M+H): 486.2799; found: 486.2788.

7-[3-(2-Azido-ethoxy)-2,2-bis(2-azido-ethoxymethyl)-propoxy]-heptanoic acid benzyl ester (14)

A solution containing **12** (150 mg, 0.3 mmol), DCC (80 mg, 0.4 mmol), benzyl alcohol (50 mg, 0.4 mmol), and 4-pyrrolidinopyridine (10 mg) in 10 mL of dry dichloromethane was stirred for 24 h. The reaction mixture was diluted with 25 mL of dichloromethane, the organic layers were successively washed with dilute HCl, $NaHCO_3$, and water, dried ($MgSO_4$), and evaporated. Purification of the residue by silica gel flash column chromatography (EtOAc–hexanes, 1:9) gave **14** as a syrup (100 mg, 60%). IR cm^{-1} (film), 2100 (N_3); ^{1}H NMR ($CDCl_3$) δ: 7.35 (s, 5H), 5.12 (s, 2H), 3.62 (m, 6H), 3.49 (s, 6H), 3.41 (s, 2H), 3.38 (t, 2H), 3.13 (t, 6H), 2.36 (t, 2H), 1.60–1.33 (m, 8H). ^{13}C NMR ($CDCl_3$) δ: 70.36 ($CH_2(CH_2)_5COOBn$), 69.7 ($CH_2CH_2N_3$), 68.7 ($CH_2CH_2N_3$), 65.99 (CH_2O-alkyl), 66.0 (CH_2Ph), 50.6 ($CH_2OCH_2CH_2N_3$), 44.5 (C. quat.). HRMS (FAB), calcd. for $C_{25}H_{39}O_6N_7$ (M−N_2): 533.2889; found: 533.2667.

3-Allyloxy-2,2-bis(benzyloxy-methyl)-propane-1-ol (16)

To a cooled (0°C) solution of **15** (7.1 g, 22.4 mmol) in dry DMF (180 mL) was added sodium hydride (4.8 g) and allyl bromide (1.9 mL, 20 mmol), and the mixture was stirred overnight at 0°C. The reaction mixture was quenched by adding 5 mL of methanol and stirring was continued for 1 h. Solvents were removed under vacuum and the residue was purified by flash chromatography on silica gel column (EtOAc–hexanes, 2:8) to afford **16** (4.8 g, 60%) as a syrup. ^{1}H NMR ($CDCl_3$) δ: 7.36–7.25 (m, 10H), 5.85 (m, 1H), 5.16 (m, 2H), 4.49 (s, 4H), 3.92 (m, 2H), 3.76 (s, 2H), 3.55 (s, 4H), 3.52 (s, 2H), 2.8 (br s, 1H). ^{13}C NMR ($CDCl_3$) δ: 140.01 (=CH), 139.8–126.7 (Ph), 115.1 (=CH_2), 44.1 (C quat.). HRMS (FAB), calcd. for $C_{22}H_{28}O_4$ (M+H): 357.2076; found: 357.2065.

2,2-Bis(benzyloxy-methyl)-3-(2-hydroxy-ethoxy)-propane-1-ol (17)

Compound **16** (1.83 g, 5.1 mmol) was subjected to ozonolysis to give an aldehyde that was subsequently reduced with $NaBH_4$, as described above, to give **17** (1.184 g, 64%) as a syrup. ^{1}H NMR ($CDCl_3$) δ: 7.34–7.27 (m, 10H), 4.45 (s, 4H), 3.62 (br s, 4H), 3.54–3.49 (m, 8H), 2.7 (br s, 2H). ^{13}C NMR ($CDCl_3$) δ: 140.01 (=CH), 138.8–126.4 (Ph), 72.9, 71.9, 70.2, 69.9, 64.6, 60.9 (-CH_2O-), 44.5 (C quat.). HRMS (EI), calcd. for $C_{21}H_{28}O_5$ (M+H): 361.2021; found: 361.2015.

2,2-Bis(benzyloxy-methyl)-3-(2-hydroxy-ethoxy)-propane-1-ol mono *tert*-butyldiphenylsilyl ether (18)

To a cooled solution of **17** (2.0 g, 5.5 mmol) in dry DMF (30 mL) was added *tert*-butyldiphenylchlorosilane (2.3 mL) and imidazole (2.8 g). The mixture was stirred at room temperature and monitored by TLC. After 6 h, ether (100 mL) was added, the organic layers were washed with water dried ($MgSO_4$), and evaporated. Purification of the residue by silica gel flash column chromatography (EtOAc–hexanes, 3:7) gave **18** (2.31 g, 69%) as a syrup. ^{1}H NMR ($CDCl_3$) δ: 7.76–7.27 (m, 10H), 4.50 (s, 4H), 3.79 (s, 2H), 3.76 (t, 2H), 3.59 (s, 2H), 3.59 (s, 4H), 3.52 (t, 6H), 2.3–2.5 (br s, 1H), 1.06 (s, 9H). ^{13}C NMR ($CDCl_3$) δ: 140.1–127.0 (Ph), 72.6, 72.4, 68.8, 68.0, 65.7, 62.7 (CH_2), 44.1 (C quat.), 18.1 (C quat., *t*-Bu), 16.18 (-$(CH_3)_3$). HRMS (FAB), calcd. for $C_{37}H_{46}O_5Si$ (M+H): 599.8; found: 599.3.

2-(2-Hydroxy-ethoxymethyl)-2-hydroxymethyl-propane-1,3-diol mono *tert*-butyldiphenylsilyl ether (19)

A methanolic solution of **18** (0.9 g, 1.5 mmol) was hydrogenolyzed in presence of 10% Pd/C (400 mg). Work-up and purification by silica gel flash column chromatography (EtOAc–hexanes, 3:7) gave **19** (0.433 g, 69%) as a syrup. ^{1}H NMR ($CDCl_3$): δ: 7.69–7.20 (m, 10H), 4.12 (dd, 2H), 3.73 (t, 2H), 3.71 (s, 4H), 3.55 (s, 4H), 2.98 (brs, 3H), 1.09 (s, 9H). ^{13}C NMR ($CDCl_3$) δ: 139.1–126.7 (Ph), 44.4 (C quat.), 19.5 (C quat., *t*-Bu), 16.6 (-$(CH_3)_3$). HRMS (FAB), calcd. for $C_{23}H_{34}O_5Si$ (M+Na): 441.5, found: 441.3.

3-(3-Allyloxy-2,2-bis-benzyloxy-methyl-propoxy)-propene (20)

Allylation of the dibenzylated diol **15** (15) (5.1 g, 16.4 mmol) in dry DMF, essentially as described for **2**, gave **20** (5.51 g, 88%) as an oil. ^{1}H NMR ($CDCl_3$) δ: 7.33–7.24 (m, 10H), 5.80 (m, 2H), 5.15 (m, 4H), 4.51 (s, 4H), 3.97 (m, 4H), 3.57 (s, 4H), 3.54 (s, 4H). ^{13}C NMR ($CDCl_3$) δ: 139.8–127.0 (=CH and Ph), 114.7 (=CH_2), 44.1 (C quat.); HRMS (FAB), calcd. for $C_{25}H_{32}O_4$ (M+H): 396.5292; found: 396.5298.

2-[2-(2-Azido-ethoxymethyl)-3-benzyloxy-2-(benzyloxy-methyl)-propoxy]-ethanol *tert*-butyldiphenylsilyl ether (23)

Compound **20** (0.9 g, 2.2 mmol) was ozonolyzed and reduced with $NaBH_4$, as described above, to give the diol **21** (0.68 g, 74%) as a syrup. A solution of **21** (0.2 g, 0.5 mmol) was monosilylated, essentially as described above for **17**, to give **22** (0.280 g, 84%) as a syrup. Compound **22** (1.1 g, 1.7 mmol) was mesylated and the resulting product was subsequently displaced with azide ion, essentially as described for **5**, to give the azido derivative **23** as an oil (0.843 g, 74%). IR cm^{-1} (film): 2100 (N_3). ^{1}H NMR ($CDCl_3$) δ: 7.74–7.23 (m, 10H), 4.49, 4.48 (s, 4H), 3.76 (s, 2H), 3.56 (m, 10H), 3.24 (m, 2H), 1.1 (s, 9H). ^{13}C NMR ($CDCl_3$) δ: 136.7–126.4 (Ph), 44.4 (C quat.), 19.4 (C quat., *t*-Bu), 18.5 (-$(CH_3)_3$). HRMS (FAB), calcd. for $C_{39}H_{49}O_5N_3Si$ (M+H): 668.4; found: 668.5.

***N*-{2-[2,2-B680is(benzyloxy-methyl)-3-(2-hydroxy-ethoxy)-propoxy]-ethyl}-acetamide *tert*-butyldiphenylsilyl ether (24)**

The azido compound **23** (123 mg, 0.19 mmol) was dissolved in a minimum volume of dichloromethane, thiolacetic acid (3 mL) was added at room temperature, and the reaction mixture was stirred for 48 h, then concentrated. Purification of the residue by silica gel flash column chromatography (EtOAc–hexanes, 7:3) gave **24** (102 mg, 78%) as a syrup. ^{1}H NMR ($CDCl_3$) δ: 7.71–7.24 (m, 10H), 5.82 (br s, 1H), 4.49 (s, 4H), 3.77 (s, 2H), 3.30–3.56 (m, 14H), 1.82 (s, 3H), 1.1 (s, 9H). ^{13}C NMR ($CDCl_3$) δ: 137.4–127.0 (Ph), 44.7 (C quat.), 23.5 (CH_3CONH), 20.4 (C quat., *t*-Bu), 17.4 (-$(CH_3)_3$). HRMS (FAB), calcd. for $C_{41}H_{53}O_6NSi$ (M+H): 684.3; found: 684.5.

***N*-{2-[3-(2-680Hydroxy-ethoxy)-2,2-bis-hydroxymethyl-propoxy]-ethyl}-acetamide *tert*-butyldiphenylsilyl ether (25)**

The benzyl groups in **24** (0.4 g, 0.58 mmol) were hydrogenolyzed as described above for **19** to give **25** (0.210 mg, 70%) as a syrup. ^{1}H NMR ($CDCl_3$) δ: 7.69–7.24 (m, Ph), 6.19 (br s, NH), 3.70 (s, -CH_2OTBDPS), 3.73–3.40 (m, CH_2), 2.63 (br s, OH), 1.96 (s, OCOCH_3), 1.1 (s, t-Bu). ^{13}C NMR ($CDCl_3$) δ: 170.8 (*C*=O), 135.8–128.3 (Ph), 45.3 (C quat.), 23.9 (CH_3CONH), 20.4 (C quat., *t*-Bu), 19.4 (-$(CH_3)_3$). HRMS (FAB), calcd. for $C_{27}H_{42}O_6NSi$ (M+H): 504.2781; found: 504.2798.

3-Azido-2,2-bis-azidomethyl-propane-1-ol-*tert*-butyldiphenylsilyl ether (26)

Tri-*O*-mesylation and subsequent azide displacement of the triol **2** (4.4 g, 11.8 mmol), essentially as described for **5**, gave **26** as a syrup (3.01 g, 57%). IR cm^{-1} (film): 2100 (N_3). ^{1}H NMR ($CDCl_3$) δ: 7.65–7.43 (m, 10H), 3.49 (s, 2H), 3.38 (s, 6H), 1.10 (s, 9H). ^{13}C NMR ($CDCl_3$) δ: 135.5–127.7 (Ph), 61.8 (CH_2OTBDPS), 51.0 (CH_2N_3), 45.14 (*C*CH_2N_3). HRMS (FAB), calcd. for $C_{21}H_{28}ON_9Si$ (M+H): 450.2186; found: 450.2238.

3-Azido-2,2-bis-azidomethyl-propane-1-ol (27)

The silyl group in **26** (450 mg, 1.0 mmol) was removed by treating with TBAF in THF, as described above for **6**, to give **27** as a syrup (200 mg, 95%). IR cm^{-1} (film): 2100 (N_3). ^{1}H NMR ($CDCl_3$) δ: 3.54 (m, 2H), 3.38 (s, 6H), 1.75 (m, 1H). ^{13}C NMR ($CDCl_3$) δ: 62.04 (CH_2OH), 51.4 (CH_2N_3), 44.41 (*C*CH_2N_3). HRMS calcd. for $C_5H_{10}ON_9$ (M+H): 212.1008; found: 212.0987.

8-(3-Azido-2,2-bis-azidomethyl-propoxy)-oct-1-ene (28)

]A solution of **27** (356 mg, 1.1 mmol) in 5 mL of THF was alkenylated as described for **8**, to give **28** as a syrup (285 mg, 53%). IR cm^{-1} (film): 2100 (N_3). ^{1}H NMR ($CDCl_3$) δ: 5.82 (m, 1H), 4.97 (m, 2H), 3.41 (t, 2H), 3.33 (s, 6H), 3.25 (s, 2H), 2.04 (dd, 2H), 1.58–1.30 (m, 8H). ^{13}C NMR ($CDCl_3$) δ: 138.9 (CH=), 114.1 (=CH_2), 71.4 (CH_2O-alkyl), 68.7 (OCH_2-$(CH_2)_5$CH=CH_2), 51.4 (CH_2N_3), 44.6 (*C*CH_2N_3). HRMS (FAB), calcd. for $C_{13}H_{24}ON_9$ (M+H): 322.2103; found: 322.2130.

7-(3-Azido-2,2-bis-azidomethyl-propoxy)-heptanoic acid (29)

Compound **27** (150 mg, 0.46 mmol) was subjected to ozonolysis to give an aldehyde that was subsequently oxidized to a carboxylic acid, in a similar fashion as described for **12**, to give **29** as a syrup (73 mg, 72%). IR cm^{-1} (film), 2100 (N_3), 1700 (COOH), ^{1}H NMR ($CDCl_3$) δ: 3.42 (t, 2H), 3.30 (s, 6H),

3.26 (s, 2H), 2.36 (m, 2H), 1.65–1.34 (m, 8H). ^{13}C NMR ($CDCl_3$) δ: 71.32 (CH_2O-alkyl), 68.91 ($OCH_2(CH_2)_5COOH$), 51.6 (CH_2N_3), 44.7 (CCH_2N_3). HRMS (FAB), calcd. for $C_{12}H_{22}O_3N_9$ (M+H): 340.1845; found: 340.1786.

7-(2-Azido-2,2-bis-azidomethyl-propoxy)-heptanoic acid benzyl ester (30)

The carboxylic acid function in **29** (210 mg, 0.6 mmol) was esterified with benzyl alcohol as described for **14**, to give **30** as a syrup (155 mg, 60%). IR cm^{-1} (film): 2100 (N_3). ^1H NMR ($CDCl_3$) δ: 7–7.26 (m, 5H), 5.12 (s, 2H), 3.40 (t, 2H), 3.32 (s, 6H), 3.25 (s, 2H), 2.36 (m, 2H), 1.66–1.25 (m, 8H). ^{13}C NMR ($CDCl_3$) δ: 154.5 (*C*OOBn), 128.42–128.1 (Ph), 71.3 (CH_2O-alkyl), 68.8 ($OCH_2(CH_2)_5COOBn$), 65.9 (CH_2Ph), 51.5 (CH_2N_3), 44.6 (C quat.). HRMS (FAB), calcd. for $C_{19}H_{27}N_9O_3$ (M+H): 430.4824; found: 430.4795.

8-(3-Amino-2,2-bis-aminomethyl-propoxy)-oct-1-ene (31)

Triphenylphosphine (0.4 g) was added to a solution of **28** (850 mg, 2.6 mmol) in dry THF and the reaction mixture was processed as usual to give the triamino compound **31** as a syrup (380 mg, 60%). ^{13}C NMR ($CDCl_3$) δ: 140.1 (CH=), 114.8 ($=CH_2$). HRMS (FAB), calcd. for $C_{16}H_{38}O_3N_3$ ($M+HSCH_2CH(OH)CH_2OH+H$): 352.2633; found: 352.2598.

Summary

The readily available pentaerythritol was systematically functionalized to give a series of azido, azidoalkyl, carboxyalkyl, and ω-alkenyl derivatives either as single substituents or in combination. These derivatives are versatile scaffolds and templates for further elaboration with a variety of ligands to produce chemical and molecular diversity.

Acknowledgments

We thank the Natural Sciences and Engineering Research Council of Canada (NSERC) for generous financial assistance through the Medicinal Chemistry Chair Program. We acknowledge the valuable assistance given by Dr. Gurijala V. Reddy in the preparation of this manuscript, and Heng Wang and Xinxia Cai for verification of correct nomenclature using the Autonom program (Beilstein).

References

1. N.K. Terrett, M. Gardner, D.W. Gordon, R.J. Kobylecki, and J. Steele. Tetrahedron, **51**, 8135 (1995); E.M. Gordon, W.R. Barrett, W.J. Dower, S.P.A. Fodor, and M.A. Gallop. J. Med. Chem. **37**, 1386 (1994); M.A. Gallop, R.W. Barrett, W.J. Dower, S.P.A. Fodor, and W.M. Gordon. J. Med. Chem. **37**, 1233 (1994); W.H. Moos, G.D. Green, and M.R. Pavia. Annu. Rep. Med. Chem. **28**, 315 (1993).
2. M. Patek, B. Drake, and M. Lebl. Tetrahedron Lett. **35**, 9169 (1994).
3. (*a*) R. Hirschmann, K.C. Nicolaou, S. Pietranico, J. Salvino, E.M. Leahy, P.A. Sprengeler, G Furst, A.B. Smith, C.D. Strader, M.A. Cascieri, M.R. Candelore, C. Donaldson, W. Vale, and L. Maechler. J. Am. Chem. Soc. **114**, 9217 (1992); (*b*) B.A. Bunin and J.A. Ellman. J. Am. Chem. Soc. **114**, 10997 (1992); (*c*) J.R. Hanske and S.M. Julin. Tetrahedron Lett. **34**, 4909 (1993).
4. J.M. Frechet. Science, **263l**, 1710 (1994; D.A. Tomalia. Aldrichimica Acta, **26**, 91 (1993); H.-B. Mekelburger, W. Jaworek, and F. Vögtle. Angew. Chem. Int. Ed. Engl. **31**, 1571 (1992); D.A. Tomalia, A.M. Naylor, and W.A. Goddard. Angew. Chem. Int. Ed. Engl. **29**, 138 (1990); G.R. Newkome, C.M. Moorefield, G.R. Baker, A.L. Johnson, and R.K. Behera. Angew. Chem. Int. Ed. Engl. **30**, 1176 (1991).
5. S. Hanessian and P. Devasthale. Tetrahedron Lett. **37**, 987 (1996)
6. S. Hanessian, C. Hoornaert, A.G. Pernet, and A.M. Nadzan. Carbohydr. Res. **137**, C4 (1985).
7. C.H. Issidorides and R. Gulen. Org. Synth. **39**, 2351(1974); K.M. Lynch and W.P. Dailey. J. Org. Chem. **60**, 4666 (1995); E.R. Wilson and M.B. Frankel. J. Org. Chem. **50**, 3211 (1985); G. Bergson. Ark. Kemi, **19**, 195 (1962).
8. (*a*) A. McAuley, S Subramanian, and T.W. Whitcombe. Can. J. Chem. **67**, 1650 (1989); (*b*) A. McAuley, K. Beveridge, S. Subramanian, and T.W. Whitcombe. Can. J. Chem. **67**, 1657 (1989).
9. J.T. Dunn, W.L. Neumann, M.M. Rogic, and S.R. Woulfe. J. Org. Chem. **55**, 6368 (1990).
10. G.R. Newkome, S. Arai, F.R. Fronczek, C.N. Moorefield, X. Lin, and C.D. Weis. J. Org. Chem. **58**, 898 (1993).
11. J.A. Kremers and E.W. Meijer. J. Org. Chem. **59**, 4262 (1994).
12. S. Hanessian and P. Lavallée. Can. J. Chem. **53**, 2975 (1975).
13. M. Vaultier, N. Knouzi, and R. Carrié. Tetrahedron Lett. **24**, 763 (1983).
14. S. Hanessian, D. Qiu, H. Prabhanjan, and B. Lou. Can. J. Chem. **74**, 1738 (1996).
15. N.R. Rabinovitch, D. McInnes, D.L. Klein, and P.F. Hall. Science, **265**, 1401 (1994); J.P. Tam. Proc. Natl. Acad. Sci. U.S.A. **85**, 5409 (1988).
16. E. Weber. J. Org. Chem. **47**, 3478 (1982).
17. T. Rosen, I.M. Lico, and D.T.H. Chu. J. Org. Chem. **53**, 1580 (1988).
18. E.B. Fleischer, A.E. Gembala, A. Levey, and P.A. Tasker. J. Org. Chem. **36**, 3042 (1971).
19 S. Czernecki, C. Georgoulis, and C. Provelenghiou. Tetrahedron Lett. 3535 (1976).
20. W.C. Still, M. Kahn, and A. Mitra. J. Org. Chem. **43**, 2923 (1978).

Synthesis of clustered D-GalNAc (Tn) and D-Galβ(1→3)GalNAc (T) antigenic motifs using a pentaerythritol scaffold

Stephen Hanessian, Dongxu Qiu, Hubli Prabhanjan, Gurijala V. Reddy, and Boliang Lou

Abstract: The tris(aminoethyl) and triamino derivatives of pentaerythritol have been used as scaffolds or templates for the attachment of immunologically relevant carbohydrates such as D-Galβ(1→3)GalNAc (T) and GalNAc (Tn), through amide linkages with the respective α-glycolyl and α-*N*-acetyl-L-serinyl glycosides. These clustered glycosidic motifs are intended as haptens for use in the preparation of tumor specific carbohydrate antigens and vaccines.

Key words: glycoside synthesis, 2-thiopyridyl carbonate, glycosyl donors and glycopeptide motifs

Résumé : Les dérivés du tris(aminométhyl) et triamino du pentaérythritol ont été utilisés comme points d'attachement pour des carbohydrates immunoactifs tel que D-Galβ(1→3)GalNAc (T) et GalNAc (Tn) via des liens peptidiques avec des glycosides α-glycolyl et α-*N*-acetyl-L-serinyl. Ces motifs branchés ont été préparés avec l'intention de les utiliser comme des haptens et ultérieurement comme des vaccins contre des tumeurs portant des marqueurs carbohydrates antigéniques.

Mots clés : Synthèse de glycoside, de carbonate 2-thiopyridyl, donneurs de glycosyles et motifs glycopeptidiques.

The importance of specific carbohydrate antigens in understanding the etiology of cell surface phenomena during the proliferation of various types of cancers has been amply documented (1). Indeed, tumor-associated antigens are expressed to varying degrees on the surface of cancer cells, and their presence can be quantitatively related to tumor progression (2). Such tumor-associated antigens are D-GalNAc (Tn) (3, 4) and Thomsen–Friedenreich antigen D-Galβ(1→3)GalNAc (T) (3, 5), which are present as terminal units in glycoproteins expressed on the cell surface (6). Their presence, either alone or as sialyl glycosides such as sialyl Tn (7), and their overexpression has been demonstrated to be linked with certain types of tumors (see, for example, ref. 8).

In view of the immunological specificity of such tumor-associated antigens, we considered the incorporation of Tn and T glycosidic motifs in bi- and trianternary structures and their use as potential antigens. Administration of such antigens to patients in remission may produce enough circulating tumor-specific antibodies to protect them from recurring tumors. The notion of a "cancer vaccine" has been a subject of great interest over the years, and the prospects for its realization is a much sought after goal (9).

The potential of clustered antigens for cooperative binding to several protein receptors has been previously discussed, principally by Lee et al. (10*a*) and by Peter et al. (10*b*). The attachment of Tn and T glycosides to amino acid backbones has been described by Hakomori and co-workers (11), Ogawa and co-workers (12), Ciommer and Kunz (13), and Paulsen et al. (14). Examples with other backbones have been reported (see, for example, ref. 15).

In this paper, we report the synthesis of novel di- and trihaptenic clusters composed of Tn and T glycosides attached to linker arms derived from pentaerythritol (16). In the preceding paper (16) we described the synthesis of various podands prepared from pentaerythritol by suitable chemical modification. We have now selected two triamino derivatives **1** and **2** to form clusters containing two and three Tn and T carbohydrate residues that are glycosidically attached to serine and glycolic acid spacers **3** and **4** (Scheme 1). The length of the spacer between the cluster and the terminal carboxylic acid may have an influence on the efficacy of its coupling with proteins, and ultimately on its immunogenicity. Thus, we chose allyl and 1-octenyl chains as sources for the terminal carboxylic acids.

Synthesis of Galβ(1→3)GalNAc disaccharides

The synthesis of the disaccharide **7** was done by a classical Koenig–Knorr reaction with 2,3,4,6-tetra-*O*-acetyl-α-D-galactopyranosyl bromide **5** as a glycosyl donor and *tert*-butyldimethylsilyl 2-azido-2-deoxy-4,6-*O*-isopropylidene-α-D-galacto-pyranoside **6** (17*b*) as acceptor (Scheme 2). Glycosidations with Ag_2CO_3–$AgClO_4$ as promoter in dichloromethane afforded 71% of the desired disaccharide **7**, accompanied by about 13% of the (1→6) disaccharide **7a**. The formation of the latter was due to the intramolecular migration of the isopropylidene group of the acceptor molecule, thus exposing the 6-hydroxyl group as a competing nucleophile. With $Hg(CN)_2$ in a mixture of toluene and nitromethane (2:1) the yield was modest and variable amounts of the (1→6) disaccharide were also formed. Stereochemistry and position of

Received March 28, 1996.

S. Hanessian,[1] D. Qiu, H. Prabhanjan, G.V. Reddy, and B. Lou. Department of Chemistry, Université de Montréal, P.O. Box 6128, Succ. Centre Ville, Montréal, QC H3C 3J7, Canada

[1] Author to whom correspondence may be addressed. Telephone: (514) 343-6738. Fax: (514) 343-5728. E-mail: hanessia@ere.umontreal.ca

Scheme 1.

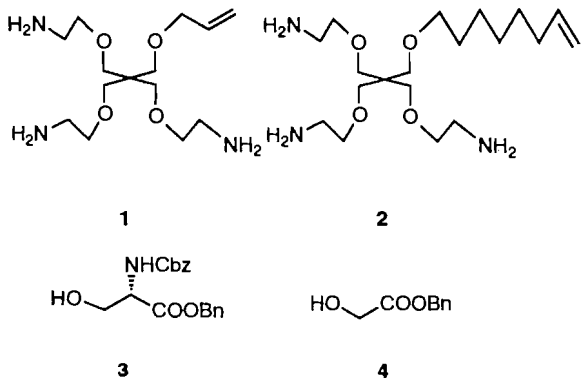

Scheme 2.

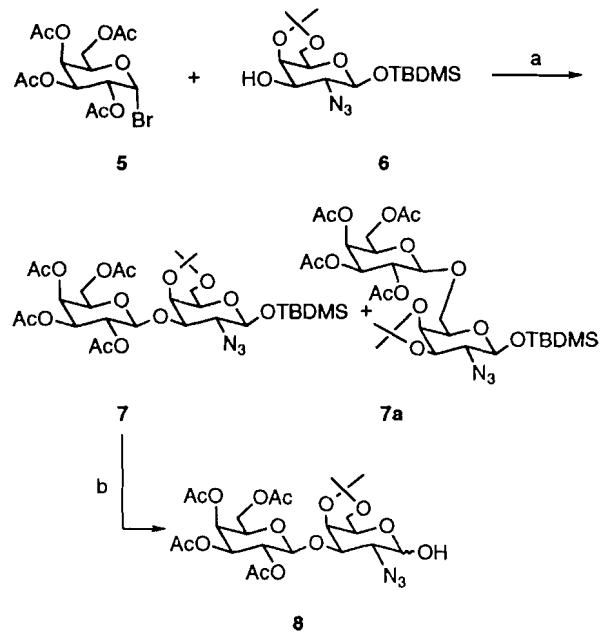

a. Ag_2CO_3, $AgClO_4$, CH_2Cl_2, r.t. b. Bu_4NF, THF, -20 °C

the glycosidic linkage in **7** were ascertained from the chemical shifts of H-1 and H-3 protons in ^{1}H NMR spectrum. A doublet at δ 4.61 ($J_{1,2}$ = 8.0 Hz) and a doublet of doublets at δ 3.21 were confirmative of a β (1→3) linkage in **7**. In addition, the chemical shift of the quaternary carbon in the acetal group was very different in **7** and **7a** (^{13}C δ 98.9 ppm and 110.7 ppm, respectively). After treatment with aqueous acetic acid and subsequent acetylation, the ^{1}H NMR spectrum of the peracetylated compound obtained from **7a** showed a very clear downfield shift (δ 4.56) for the H-3 proton due to the presence of an ester group, while the peracetate of **7** showed a doublet of doublets for H-3 at a relatively high field (δ 3.48) indicating that the C-3 hydroxyl was not esterified but glycosidically linked. Treatment of disaccharide **7** with tetrabutylammonium fluoride in THF at −20°C removed the silyl protection at the anomeric position to give **8** in high yield.

There are several reports on the synthesis of this disaccharide using different glycosylation and protective group strategies (17*a–f*). Generally, 4,6-*O*-benzylidene protected acceptors have given better results, perhaps due to a lesser tendency to undergo intramolecular migration to form a 3,4-*O*-acetal. However, Kinzy and Schmidt (17*b*) used 2-azido-2-deoxy-4,6-*O*-isopropylidene-β-D-galactopyranoside **6** as the glycosyl acceptor and reported disaccharide formation in high yield with 2,3,4,6-tetra-*O*-benzoyl-α-D-galactopyranosyl trichloroacetimidate as a glycosyl donor and BF_3·OEt as the promoter. By contrast, Paulsen and Paal (17*c*) also observed acetal migration.[2]

Stereoselective synthesis of α-serinyl and α-glycolyl glycosides of Tn and T

For the synthesis of Tn and T haptens with N-protected L-serine benzyl ester (18; see also refs. 17*a*, *b*, *e*) we used our recently developed (19)[3] 1,2-*cis*-selective glycosylation reaction in which the new anomeric 2-thiopyridyl carbonates (TOPCAT) were used as glycosyl donors. The 2-thiopyridyl carbonate derivatives **11** and **12** were easily prepared from the respective 1-OH precursors **8** and **10** by treatment with di-(thiopyridyl)carbonate **9** in the presence of triethylamine (Scheme 3).[4] Glycosidations of the N-Cbz protected L-serine derivative **3** with **11** and **12** in dry CH_2Cl_2 in the presence of AgOTf (20) afforded the desired α-glycosides **13** and **16** as major products and in acceptable yields accompanied by the corresponding β-glycosides as minor products. With benzyl glycolate **4** as the glycosyl acceptor, and TOPCAT as the leaving group, the glycolic ester α-D-glycosides **19** and **23** were formed as major products. The anomeric configurations of the above mentioned glycosides were ascertained by ^{1}H NMR studies.

The TOPCAT glycosyl donors offer a number of distinct advantages in stereocontrolled glycoside synthesis (19). They are easily prepared and purified by column chromatography to give stable, often crystalline, products of defined stereochemistry. They can be activated under mild conditions with silver triflate to generate reactive oxonium ion species, which lead to 1,2-*cis* glycosides as major products when in the absence of participating groups as in **11** and **12**. The presence of a chromophore and the generation of pyridine 2-thione as the reaction progresses allows easy monitoring by TLC. The fragmentation of the leaving group into a stable heterocycle and carbon dioxide constitutes an excellent driving force for the reaction.

The azido groups in **13** and **16** were reduced by treatment with hydrogen sulfide in aqueous pyridine (21), and the resulting amine was acetylated in presence of Ac_2O–pyridine to give 2-acetamido derivatives **14** and **17**, respectively. Reactions catalyzed by thiolacetic acid (22) also gave the desired products in similar yields. Hydrogenolytic cleavage of the benzyloxycarbonyl groups in **14** and **17** with Pd/C afforded the glycosyl amino acid derivatives, which were transformed to the N-Boc protected derivatives **15** and **18**. The N-Boc group was found to be compatible with the method of amide

[2] For a recent review on anomeric activation by the trichloroacetimidate method, see ref. 17*g*.

[3] Also, S. Hanessian, B. Lou, and H.K. Hoan, unpublished results.

[4] For other syntheses of glycosides related to **11** and **12**, see, ref. 12*a*. For recent reviews on O-glycosyl amino acids, see ref. 18*b*.

Scheme 3.

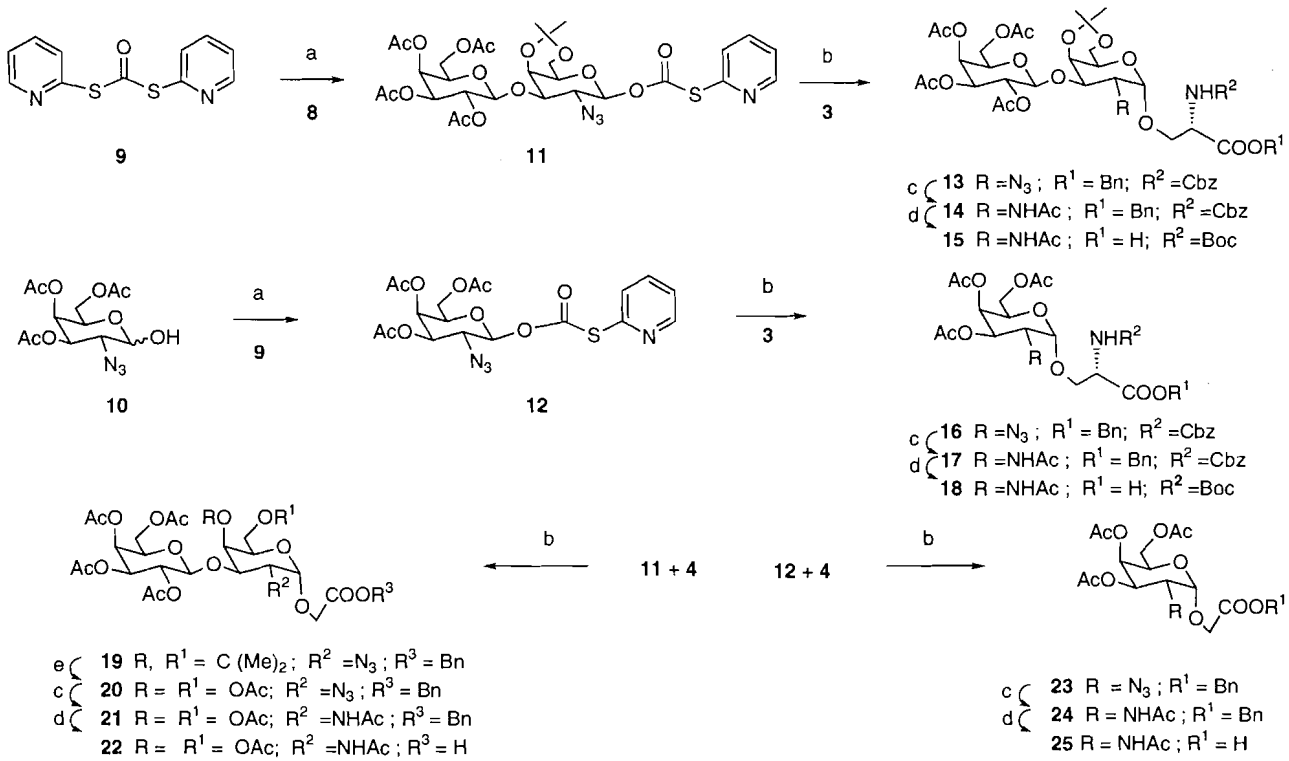

a. Et_3N, CH_2Cl_2, r.t. b. AgOTf, CH_2Cl_2, r.t. c. H_2S, aq. pyridine, Ac_2O, pyridine or CH_3COSH d. Pd/C on activated carbon (for **15** and **18** followed by Boc anhydride, Et_3N, r.t.) e. aq.AcOH, 60°C (for **20** followed by Ac_2O, pyridine, r.t.).

bond formation (vide infra). It was not possible to use the N-acetyl serinyl glycosyl amino acids for coupling to the triamines because of the known propensity of the acetyl group for participation (11*a*).

Treatment of either **11** or **12** with benzyl glycolate in the presence of AgOTf led to the corresponding α-D-glycosides **19** and **23** as the preponderant anomers. Acid hydrolysis of the O-isopropylidene group in **19** followed by treatment of the resulting diol **20** with thiolacetic acid and peracetylation gave **21**. Similar reduction and N-acetylation of the azido functions in **20** and **23** gave the corresponding 2-acetamido-2-deoxy compounds **21** and **24**, respectively, in good yields. Hydrogenolytic cleavage of the benzyl ester groups with Pd–C afforded the free carboxylic acid derivatives **22** and **25**.

Synthesis of Tn and T clusters

Having successfully accomplished the synthesis of haptenic carboxylic acids, we next addressed the amide couplings with **1** and **2**. The initial coupling reactions using EDC and EEDQ as activators were very slow. Variations in the stoichiometry of the reagents and the activators, or variations in the reaction time, did not result in improvement in yield. We, therefore, investigated conditions for amide formation using the mixed anhydride method. The procedure consisted in initial activation of the respective acids with isobutyl chloroformate in the presence of *N*-methylmorpholine to form the mixed anhydride in DMF at 0°C for 30 min followed by addition of the amines. Monitoring the reactions by TLC showed that the desired products were formed in less than 30 min, accompanied with some urethanes arising from unreacted amines.

With a 1:1 solvent mixture of DMF and THF, coupling of triamines **1** and **2** with Tn and T-serinyl derivatives **18** and **15** proceeded smoothly to afford trimeric and dimeric products in each case. Chromatographic purification of products **26**, **32** and **29**, **35** including a Tn-hapten was not possible because of very close R_f values. These products were separated after conversion to N-acetyl derivatives and removal of protecting groups to give trimers **28**, **31**, and their corresponding dimers **34** and **37** (Scheme 4). Similar treatment of the serinyl T motifs with the triamine **2** gave **38** and **41**.

Characterization of the major amide coupling products containing three T and Tn units each showed the expected ^1H and ^{13}C NMR signals for both the linker and hapten moieties. The serine-containing Tn motifs **26**, **29**, **32**, and **35** were treated with TFA to remove the N-Boc groups and the products were acetylated to give fully O- and N-acetylated derivatives (Scheme 4). The isopropylidene groups in the T derivatives **38** and **41** were cleaved with TFA to give **39** and **42**, respectively. Treatment of the Tn clusters NaOMe in methanol and chromatographic purification led to dimeric (**34**, **37**, and **43**) and trimeric (**28**, **31**, and **40**) target compounds in high yields. Similar treatment of **39** and **42** gave the trimeric and dimeric Tn clusters **40** and **43**, respectively (Scheme 4).

Coupling of the glycolyl Tn motif **25** to **2** gave the expected trimeric hapten **44** (Scheme 5). The expected trimeric prod-

Scheme 4.

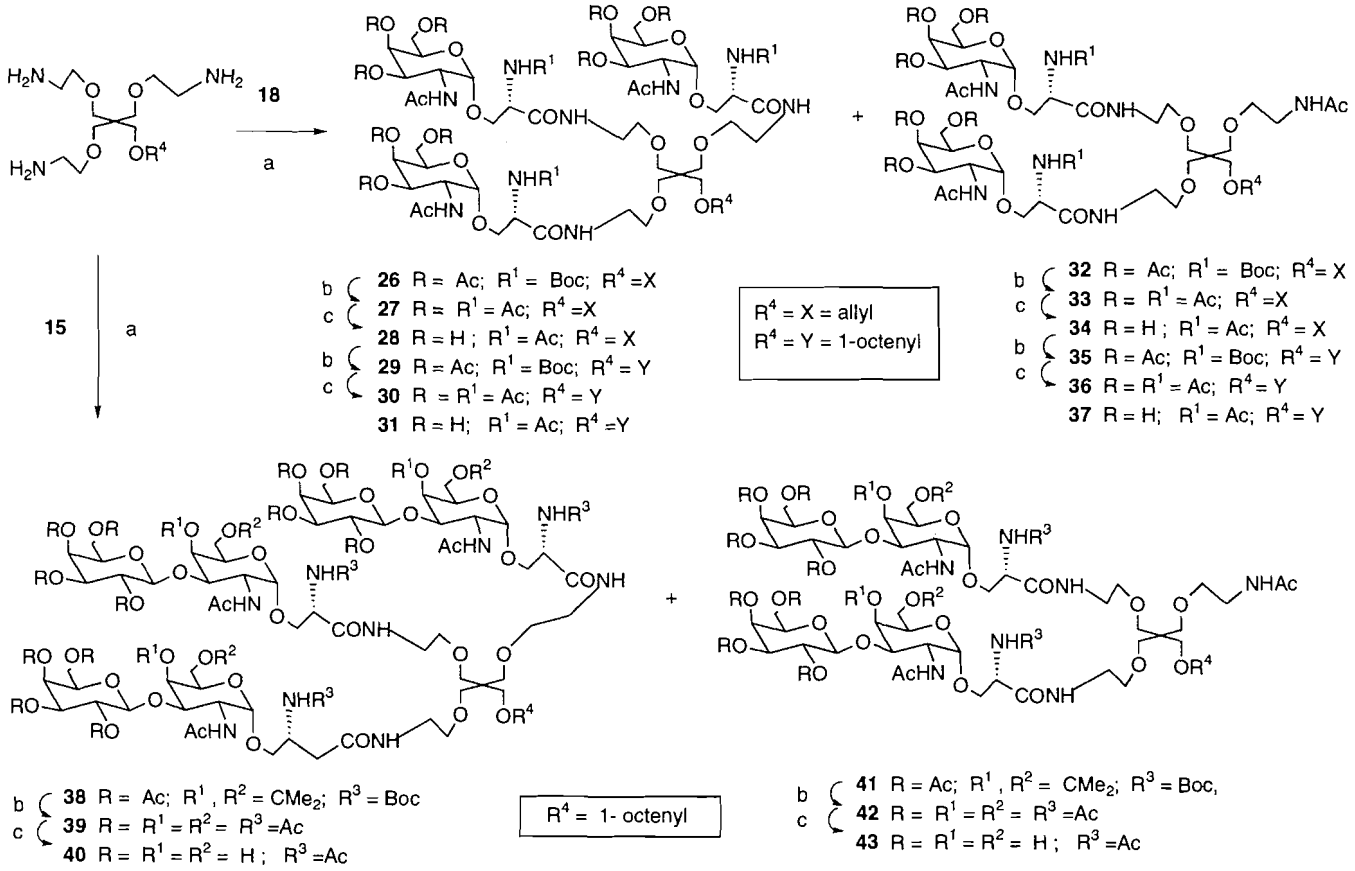

a. i-BuOCOCl, THF, DMF, *N*-methylmorpholine, -20 °C, r.t. b. TFA, then Ac_2O-Pyr. c. MeONa, MeOH

ucts **46** and **48** were formed by coupling of **1** and **2** with **22**, respectively. Variable amounts of coupling products containing two glycolyl T units **50** and **52** and a urethane moiety on the unreacted amino group were also formed. Chromatographic separation in each of the above couplings gave glycolic Tn and T trimeric clusters **44**, **46**, and **48**, and dimers **50** and **52**. Treatment of these products individually with sodium methoxide gave the desired T and Tn clustered motifs **45**, **47**, **49**, **51**, and **53** after chromatographic purification.

In summary, glycoside synthesis using the 2-thiopyridyl carbonate group as a glycosyl activator (19) has been successfully applied to the stereoselective synthesis of α-serinyl and carboxymethyl glycosides of Tn and T. These were clustered on a pentaerythritol template to give di- and tri-haptenic motifs, which have been coupled to KLH and HSA as carrier proteins. Results pertaining to their immunological properties will be reported in due course.

Experimental

Melting points are uncorrected. ^1H NMR spectra were recorded at 300 MHz in $CDCl_3$ (unless otherwise indicated), with $CHCl_3$ as reference. ^{13}C NMR spectra were recorded at 75 MHz in $CDCl_3$ (unless otherwise indicated), with $CHCl_3$ as reference. Wherever necessary, ^1H NMR assignments were supported by appropriate homonuclear correlation experiments (COSY). IR spectra of samples were recorded as films. Mass spectra were recorded by using electron ionization (EI) at 70 eV or fast atom bombardment (FAB) techniques. Optical rotations were measured at 25°C at the sodium line. Flash chromatography was performed on 230–400 mesh silica gel (23). Thin-layer chromatography (TLC) was performed on glass plates coated with a 0.02 mm layer of silica gel 60-F-254. All solvents were freshly distilled before use.

tert-Butyldimethylsilyl *O*-(2,3,4,6-tetra-*O*-acetyl-β-D-galactopyranosyl)-(1→3)-2-azido-2-deoxy-4,6-isopropylidene-β-D-galactopyranoside (7)

A suspension of 5 (16.3 g, 39.7 mmol) and 4 Å molecular sieves (7 g) in dichloromethane (75 mL) was stirred for 6 h at room temperature. A mixture of **6** (9.7 g, 27 mmol), silver carbonate (10.8 g, 39.7 mmol), silver perchlorate (8.25 g, 39.7 mmol), and 4 Å molecular sieves (14 g) in dichloromethane (100 mL) was prepared separately, and was treated with the above mixture containing **5** at 5–10°C. The stirred reaction mixture was permitted to attain room temperature and after 9 h the insolubles were filtered off (Celite), washed with CH_2Cl_2, and the filtrate and washings were concentrated. Flash column chromatography (EtOAc–hexane, 4:6) of the residue over silica gel column gave **7** (13.2 g, 71%); $[\alpha]_D$ +38.4 (*c* 0.68,

Scheme 5.

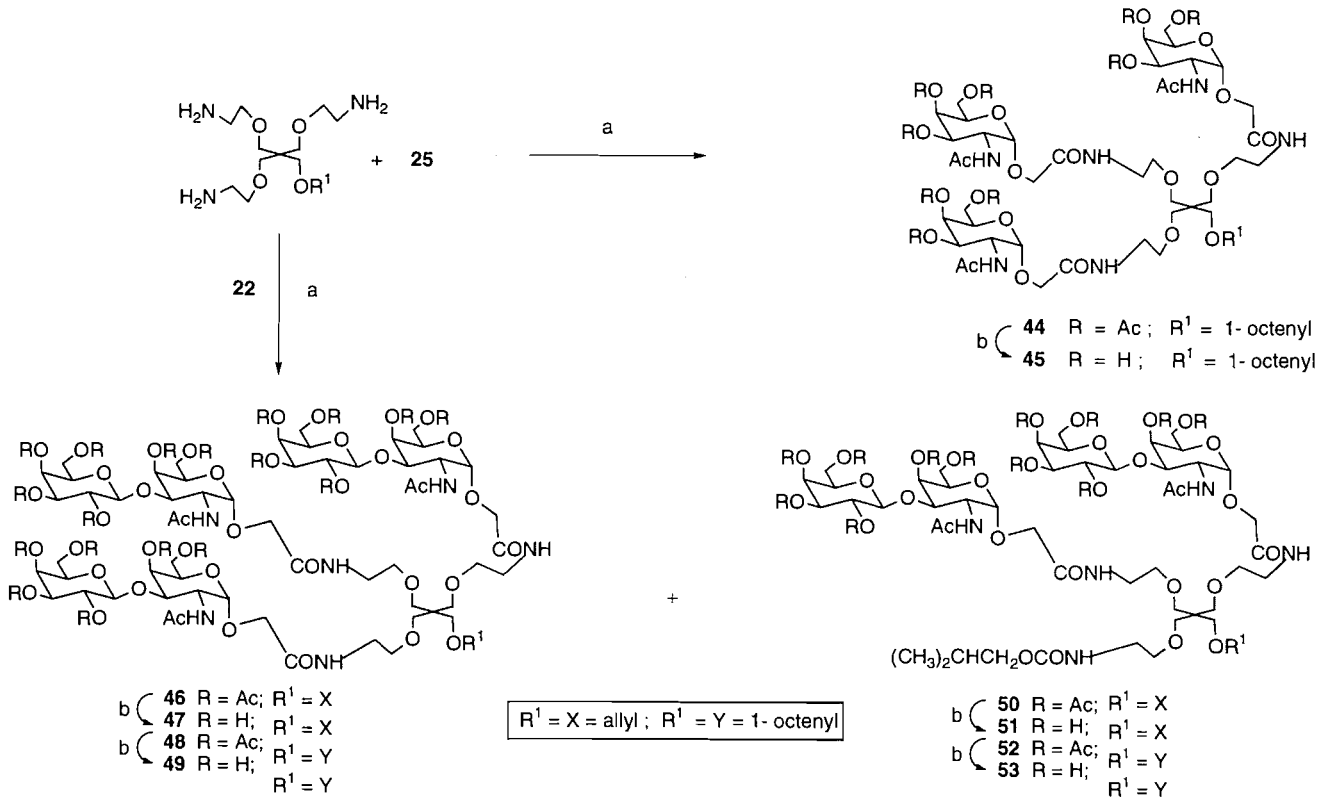

$CHCl_3$). IR cm^{-1} (film): 2130 (N_3), 1725 (C=O), ^1H NMR ($CDCl_3$) δ: 5.36 (d, $J_{4',5'}$ = 2.4 Hz, H-4'), 5.28 (dd, $J_{2',3'}$ = 10.4 Hz, H-2'), 4.98 (dd, $J_{2,3}$ = 10.5 Hz, $J_{3',4'}$ = 3.3 Hz, H-3'), 4.63 (d, $J_{1,2}$ = 8.0 Hz, H-1), 4.46 (d, $J_{1',2'}$ = 7.5 Hz, H-1'), 4.17 (d, $J_{3,4}$ = 3.3 Hz, H-4), 3.64 (dd, $J_{2,3}$ = 10.6 Hz, H-2), 3.25 (dd, $J_{2,3}$ = 10.7 Hz, $J_{3,4}$ = 3.3 Hz, H-3), 3.21 (s, H-5), 2.15, 2.08, 2.03, 1.98 (OAc), 1.47, 1.417 (s, $C(CH_3)_2$), 0.92 (s, *tert*-butyl), 0.12, 0.14 (s, CH_3). ^{13}C ($CDCl_3$) δ: 170.2, 170.0, 169.3 (CO), 102.9 (C-1'), 98.9 ($C(CH_3)_2$), 97.2 (C-1), 80.1, 70.8, 68.5, 67.5, 66,7, 66.3, 64.1, 62.6, 61.2 (ring carbons), 28.8, 25.6, 20.5, 20.4, 18.6, and 17.8 (CH_3). HRMS (FAB), calcd. for $C_{29}H_{48}O_{14}Si$ (M+H): 690.2950; found: 690.2977.

S-2-Pyridyl 3-*O*-(2,3,4,6-tetra-*O*-acetyl)-β-D-galactopyranosyl)-2-azido-2-deoxy-4,6-*O*-isopropylidene-D-β-galactopyranosyl thiocarbonate (11)

A solution of 7 (2.1 g, 3.0 mmol) in dry THF (25 mL) was treated with TBAF (4 mL, 1 M solution in THF) at −20°C for 3 h. The mixture was diluted with ethyl acetate (20 mL), and the organic layer was processed by washing with water, drying over $MgSO_4$, filtering, and concentration. Flash column chromatography (EtOAc–hexane, 1:1) of the residue over silica gel gave an anomeric mixture of 2-azido-2-deoxy-3-*O*-(2,3,4,6-tetra-*O*-acetyl-β-D-galactopyranosyl)-4,6-*O*-isopropylidene-D-galactopyranose **8** as solid (1.3 g, 86%), which was directly used in the next step. Compound **8** (2.0 g, 3.48 mmol), 2.60 g (10.4 mmol) of di-(2-thiopyridyl)carbonate **9**, 1.5 mL of Et_3N, and 50 mL of dichloromethane were stirred at room temperature for 24 h and concentrated. Flash chromatographic purification of the residue over silica gel (EtOAc–hexane, 2:8) gave 2.28 g (92%) of the desired product **11** as crystals, mp 97–99°C; $[\alpha]_D$ +28.0 (*c* 1.3, $CHCl_3$). IR cm^{-1} (film): 2130 (N_3), 1750 (C=O). ^1H NMR ($CDCl_3$) δ: 8.63–8.61 (m, pyr-H-6), 7.76–7.74 (m, pyr-H-3 and H-4), 7.34–7.26 (m, pyr-H-5), 5.47 (d, $J_{1,2}$ = 8.4 Hz, H-1), 5.40 (d, $J_{3',4'}$ = 3.3 Hz, H-4'), 5.31 (dd, $J_{1,2}$ = 7.8 Hz, $J_{2',3'}$ = 10.5 Hz, H-2'), 5.03 (dd, $J_{2,3}$ = 10.5 Hz, $J_{3',4'}$ = 3.3 Hz, H-3'), 4.72 (d, $J_{1',2'}$ = 7.8 Hz, H-1'), 4.28 (d, $J_{3,4}$ = 3.3 Hz, H-4), 3.89–4.18 (m, H-5', H-6', H-6, and H-2), 3.45 (dd, $J_{2,3}$ = 10.5 Hz, $J_{3,4}$ = 3.3 Hz, H-3), 3.40 (br s, H-5), 2.17, 2.09, 2.05, 2.00 (OAc), 1.51, 1.46 (s, $C(CH_3)_2$). ^{13}C NMR ($CHCl_3$) δ: 170.09, 170.04, 169.96, 169.18, and 167.86 (CO), 150.2, 137.2, 129.4, 123.7 (Py), 102.68 (C-1') 99.17 ($C(CH_3)_2$), 95.16 (C-1), 80.1, 70.9, 70.8, 68.6, 67.4, 67.2, 66.8, 62.1, 61.3 (ring carbons), 28.8, 24.2, 20.5, 20.4, 20.3, and 18.5 (CH_3). HRMS (FAB), calcd. for $C_{29}H_{36}O_{15}N_4SNa$ (M+Na): 735.1795; found: 735.1838.

S-2-Pyridyl 3,4,6-tri-*O*-acetyl-2-azido-2-deoxy-β-D-galactopyranosyl thiocarbonate (12)

A mixture of 320 mg (1.04 mmol) of 3,4,6-tri-*O*-acetyl-2-azido-2-deoxy-D-galactopyranose **10**, 777 mg (3.12 mmol) of di-(2-thiopyridyl)carbonate **9**, and 435 μL (3.12 mmol) of Et_3N in 8 mL of CH_2Cl_2 was stirred at room temperature for 30 h. Concentration and flash chromatographic purification of

the residue over a silica gel column (EtOAc–hexane, 1:1) gave 330 mg (72%) of the desired product **12**; $[\alpha]_D$ +27.8 (*c* 1.1, $CHCl_3$); IR cm^{-1} (film): 2130 (N_3), 1750 (C=O). ^1H NMR ($CDCl_3$) δ: 8.64-8.62 (m, pyr-H-6), 7.78–7.76 (m, pyr-H-3 and H-4), 7.36–7.26 (m, pyr-H-5), 5.59 (d, $J_{1,2}$ = 8.4 Hz, H-1), 5.38 (dd, $J_{4,5}$ = 0.9 Hz, $J_{4,3}$ = 3.3 Hz, H-4), 4.90 (dd, $J_{3,2}$ = 10.8 Hz, $J_{3,3}$ = 3.3 Hz, H-3), 4.14 (m, H-6), 4.02 (dt, $J_{5,4}$ = 0.9 Hz, $J_{5,6}$ = 6.8 Hz, H-5), 3.87 (dd, $J_{1,2}$ = 8.4 Hz, $J_{2,3}$ = 10.9 Hz, H-2), 2.18, 2.08, 2.04 (OAc). ^{13}C NMR ($CHCl_3$) δ: 170.03, 169.69, 169.33 (CO), 150.1, 137.3, 128.2, 123.7 (Py), 94.7 (C-1), 71.7, 71.2, 65.9, 60.7 (ring carbons), 59.5 (C-2), and 20.3 (CH_3). HRMS (FAB), calcd. for $C_{18}H_{21}O_9N_4S$ (M+H): 469.1029; found: 469.1039.

Benzyl *N*-carbobenzyloxy-L-serinyl 3-*O*-(2,3,4,6-tetra-*O*-acetyl-β-D-galactopyranosyl)-2-azido-2-deoxy-4,6-*O*-isopropylidene-α-D-galactopyranoside (13)

To a mixture of **11** (480 mg, 0.67 mmol) and 3 (330 mg, 1 mmol) in 20 mL of dichloromethane were added powdered 4Å molecular sieves and 260 mg (1 mmol) of AgOTf. The mixture was stirred at room temperature for 2 h. After addition of 0.5 mL of pyridine, the mixture was concentrated. Flash chromatographic purification of the residue over silica gel (EtOAc–hexane, 1:1) gave **13** and its β anomer (375 mg, 63%, α/β, 5:1). For **13** (300 mg): mp 70–72°C, $[\alpha]_D$ +59.1 (*c* 1.0, $CHCl_3$); IR cm^{-1} (film): 2130 (N_3), 1750 (C=O). ^1H NMR ($CDCl_3$) δ: 7.36 (m, Ph), 5.80 (d, *J* = 8.2 Hz, NH), 5.38 (d, $J_{4',5'}$ = 2.7 Hz, H-4′), 5.30 (dd, $J_{2',1'}$ = 7.9 Hz and $J_{2',3'}$ = 10.4 Hz, H-2′), 5.19 and 5.10 (s, CH_2Ph), 5.0 (dd, $J_{2,3'}$ = 10.5 Hz and $J_{3',4'}$ = 3.3 Hz, H-3′), 4.88 (d, $J_{1,2}$ = 3.3 Hz, H-1), 4.61 (d, $J_{1',2'}$ = 7.9 Hz, H-1′), 4.53 (m, Ser α-H), 3.70–4.30 (m, H-2, H-3, H-4, H-5′, H-6, H-6′ and Ser β-H), 3.40 (m, H-5), 2.14, 2.05, 2.02, 1.97 (OAc), 1.44, 1.37 (s, $C(CH_3)_2$). ^{13}C NMR ($CDCl_3$) δ: 170.0, 169.9, 169.5, 169.2 (CO), 128.5, 128.4, 128.2, 128.1, 127.9 (Ph), 102.7 (C-1′), 99.6 ($C(CH_3)_2$), 98.7 (C-1), 76.7, 70.8, 70.6, 69.3, 68.1, 67.5, 66.9, 66.7, 62.9, 62.3 and 60.1, 57.9 (C-2), 54.4 (*C*NH in Ser), 29.1, 20.8, 20.4, 17.9 (CH_3). HRMS (FAB), calcd. for $C_{41}H_{51}O_{18}N_4$ (M+H): 887.3198; found: 887.3258.

Benzyl *N*-carbobenzyloxy-L-serinyl 3-*O*-(2,3,4,6-tetra-*O*-acetyl-β-D-galactopyranosyl)-2-acetamido-2-deoxy-4,6-*O*-isopropylidene-α-D-galactopyranoside (14)

Hydrogen sulfide gas was passed through a solution of **13** (2.9 g, 3.77 mmol) in pyridine–water (3:1, 30 mL) for 1 h at 0°C. The mixture was stirred for 10 h at room temperature and evaporated. The dry residue was stirred for 5 h in 30 mL of pyridine – acetic anhydride (2:1, 30 mL). Water (10 mL) was added and the mixture was further stirred for 1 h and extracted with ethyl acetate. The organic layers were successively washed with dilute HCl, saturated sodium carbonate, and water, dried over $MgSO_4$, and concentrated. The residue was purified over a silica gel column to afford compound **14** (2.4 g, 81%), which was directly used in the next step.

***N-tert*-Butoxycarbonyl-L-serinyl 3-*O*-(2,3,4,6-tetra-*O*-acetyl-β-D-galactopyranosyl)-2-acetamido-2-deoxy-4,6-*O*-isopropylidene-α-D-galactopyranoside (15)**

A suspension containing **14** (2.2 g, 2.44 mmol) and Pd/C (10%, 500 mg) in dry THF–methanol (20 mL, 1:1) was stirred for 10 h under hydrogen. The catalyst was filtered off and washed with methanol. The combined filtrate and washings were concentrated to a residue that was redissolved in 30 mL of dry methanol and treated with 0.9 g of *tert*-butoxycarbonyl anhydride and 0.5 mL of Et_3N. After 4 h at room temperature, the solvents were removed and the residue was purified by flash chromatography over silica gel (toluene–MeOH–AcOH, 15:1:1) to give **15** (1.6 g, 84%) as a syrup; $[\alpha]_D$ +79.5 (*c* 1.0, MeOH). ^1H NMR (CD_3OD) δ: 7.2 (m, Ph), 5.37 (d, $J_{4',3'}$ = 2.9 Hz, H-4′), 4.80–5.10 (m, H-2′ and H-3′), 4.44 (d, $J_{1,2}$ = 3.6 Hz, H-1), 4.40 (dd, $J_{3,2}$ = 10.8 Hz, and $J_{3,4}$ = 3.6 Hz, H-3), 3.98 (dd, $J_{2,1}$ = 3.1 Hz and $J_{2,3}$ = 11.4 Hz, H-2), 2.13, 2.04, 2.03, 2.00, 1.96 (OAc), 1.46, 1.40 (s, $C(CH_3)_2$). ^{13}C NMR (CD_3OD) δ: 178.5, 172.0, 171.9, 171.5, 171.2, 171.1 (CO), 129.9, 129.2, 126.3 (Ph), 103.8 (C-1′), 100.1 ($C(CH_3)_2$), 99.9 (C-1), 77.3, 72.6, 71.9, 70.3, 70.1, 69.9, 68.8, 64.2, 63.8, 62.6, 29.6, 28.8, 23.3, 21.9, 20.9, 20.6, 20.5, and 18.9. HRMS (FAB), calcd. for $C_{33}H_{50}O_{19}N_2Na$ (M+Na): 801.2905; found: 801.3020.

Benzyl *N*-carbobenzyloxy-L-serinyl 3,4,6-tri-*O*-acetyl-2-azido-2-deoxy-α-D-galactopyranoside (16)

To a mixture of **12** (1.045 g, 2.3 mmol) and *N*-benzyloxycarbonyl-L-serine benzyl ester **3** (0.913 g 2.77 mmol) in 50 mL of dichloromethane were added 3 g of powdered 4Å molecular sieves and 1.25 g (3.46 mmol) of AgOTf at room temperature and the mixture was stirred for 4 h. The mixture was treated with 0.2 mL pyridine, then filtered through a bed of Celite and concentrated. Flash chromatographic purification of the residue over silica gel (EtOAc–hexane, 1:1) gave 0.88 g (69%) of a 5:1 α:β anomeric mixture of the desired product that was easily separable. For the α anomer **16** (0.7g); $[\alpha]_D$ +75.8 (*c* 1.1, $CHCl_3$) (lit. (17*d*) $[\alpha]_D$ +73.5; (11*a*) $[\alpha]_D$ +92.6). IR cm^{-1} (film): 2120 (N_3), 1750 (C=O). ^1H NMR ($CDCl_3$) δ: 7.37–7.26 (m, Ph), 5.85 (d, *J* = 8.0, NH), 5.36 (d, $J_{4,3}$ = 3.1 Hz, H-4), 5.24–5.18 (m, H-3 and CH_2Ph), 4.88 (d, $J_{1,2}$ = 3.7 Hz, H-1), 4.63–4.60 (m, Ser α-H), 4.16–3.98 (m, H-5, H-6 and Ser β-H), 3.56 (dd, J_1 = 3.4 Hz and *J* = 11.2, H-2) 2.12, 2.05, 1.99 (OAc). ^{13}C NMR ($CDCl_3$) δ: 170.3, 169.8, 169.5, 169.2 (CO), 155.7, 135.9, 134.8, 128.5, 128.4, 128.1, 127.9 (Ph), 99.1 (C-1), 69.8, 67.7, 67.2, 67.0, 57.13, 54.13, 54.3, and 20.5. LRMS (FAB), calcd. for $C_{30}H_{35}O_{12}N_4$ (M+H): 643.2; found: 643.2.

Benzyl *N*-carbobenzyloxy-serinyl 3,4,6-tri-*O*-acetyl-2-acetamido-2-deoxy-α-D-galactopyranoside (17)

The azido group in compound **16** (1.5 g) was reduced and the resulting amine was subsequently acetylated, essentially as described for **14**, to give **17** as a syrup (1.16 g, 77%); $[\alpha]_D$ +53.7 (*c* 1.0, $CHCl_3$). ^1H NMR ($CDCl_3$) δ: 7.37–7.34 (m, Ph), 5.85 (d, *J* = 8.0 Hz, NH), 5.62 (d, *J* = 9.1 Hz, NH), 5.37 (d, $J_{4,3}$ = 3.3 Hz, H-4), 5.12–5.19 (m, CH_2Ph), 5.03 (dd, *J* = 2.8 and *J* = 11.4 Hz, H-3), 4.78 (d, $J_{1,2}$ = 3.6 Hz, H-1), 4.45–4.62 (m, Ser α-H), 3.85–4.12 (m, H-5, H-6 and Ser β-H), 4.47 (dd, *J* = 3.52 Hz and *J* = 11.4 Hz, H-2), 2.14, 1.99, 1.98, 1.90 (OAc and NAc). ^{13}C NMR ($CDCl_3$) δ: 171.5–169.5 (CO), 135.3, 134.7, 128.9, 128.7, 128.5 128.1 (Ph), 99.9 (C-1), 70.2, 69.1, 68.9, 68.7, 68.6, 62.6, 54.8, 48.1, 23.5, 20.2, and 20.1. HRMS (FAB), calcd. for $C_{32}H_{39}N_2O_{13}$ (M+H): 659.2477; found: 659.2452.

***N-tert*-Butoxycarbonyl-L-serinyl 3,4,6-tri-*O*-acetyl-2-acetamido-2-deoxy-α-D-galactopyranoside (18)**

Hydrogenation of **17** (3.6 g, 5.6 mmol) using Pd/C (0.8 g) gave

a product that was converted into the *N*-Boc derivative, essentially as described for **15**, to give **18** as an amorphous solid (2.1 g, 73%); $[\alpha]_D$ +73.7 (*c* 1.0, $CHCl_3$). ^1H NMR ($CDCl_3$ + 2 drops of CD_3OD) δ: 5.33 (d, $J_{4,3}$ = 3.0 Hz, H-4), 5.10 (dd, $J_{3,2}$ = 11.4 Hz, $J_{3,4}$ = 3.1 Hz, H-3), 4.93 (d, $J_{1,2}$ = 3.0 Hz, H-1), 4.38 (dd, $J_{2,1}$ = 3.0 Hz and $J_{2,3}$ = 11.6 Hz, H-2), 3.80–4.18 (m, H-5, H-6, Ser α- and β-H), 2.11, 2.02, 1.96, 1.94 (OAc and NAc), 1.42 (s, *tert*-butyl). ^{13}C NMR ($CDCl_3$ + 2 drops CD_3OD) δ: 173.9, 172.2, 172.1, 171.9 (CO), 99.5 (C-1), 80.5, 70.2, 69.7, 69.1, 68.6, 68.5, 67.9, 62.8, 56.8, 28.8, 27.8, 22.7, 20.6, 20.5, and 19.5. HRMS (FAB), calcd. for $C_{22}H_{34}N_2O_{13}Na$ (M+Na): 557.5074; found: 557.5132.

Benzyloxycarbonylmethyl 3-*O*-(2,3,4,6-tetra-*O*-acetyl-β-D-galactopyranosyl)-2-azido-2-deoxy-4,6-*O*-isopropylidene-α-D-galactopyranoside (19)

Glycosylation of benzyl glycolic ester 4 (0.4 g, 2.4 mmol) with **11** (1.4 g, 1.96 mmol), essentially as described for **13**, gave the α anomer **19** (0.60 g, 59%) along with the β anomer (0.12 g, 12%). For the α anomer, $[\alpha]_D$ +47.0 (*c* 0.36, $CHCl_3$). IR cm^{-1} (film): 2100 (N_3), 1750 (C=O). ^1H NMR ($CDCl_3$) δ: 7.33–7.54 (m, Ph), 5.36 (d, $J_{4'3'}$ = 3.4 Hz, H-4′), 5.26 (dd, $J_{2',3'}$ = 10.44 Hz, H-2′), 5.15 (s, CH_2Ph), 5.05 (d, $J_{1,2}$ = 3.6 Hz, H-1), 4.95 (dd, $J_{3',2'}$ = 10.4 Hz, H-3′), 4.68 (d, $J_{1',2'}$ = 8.0 Hz, H-1′), 4.37 (d, $J_{4,3}$ = 3.1 Hz, H-4), 4.1 (dd, *J* = 16.3 Hz, CH_2COOBn), 3.96 (dd, H-2), 3.83 (dd, $J_{3,2}$ = 10.8 Hz, H-3), 2.13, 2.02, 2.00, 1.95 (OAc), 1.38, 1.43 ($C(CH_3)_2$). ^{13}C NMR (CD_3OD) δ: 170.7, 169.9, 169.3, 169.1 (CO), 134.9, 128.4, 128.3 128.2 (Ph), 102.8 (C-1′), 99.0 ($C(CH_3)_2$), 98.9 (C-1), 70.9, 70.7, 68.4, 68.3, 66.8, 66.7, 64.9, 63.2, 62.4, 61.3, 58.2, 29.1, 20.5, 20.4, and 18.0. HRMS (FAB), calcd. for $C_{32}H_{43}O_{16}N_3$ (M+H): 725.7082; found: 725.3496.

Benzyloxycarbonylmethyl 3-*O*-(2,3,4,6-tetra-*O*-acetyl-β-D-galactopyranosyl)-2-acetamido-2-deoxy-4,6-di-*O*-acetyl-α-D-galactopyranoside (21)

Compound **19** (300 mg, 0.4 mmol) was dissolved in acetic acid–water (8:2, 100 mL), and the solution was heated at 60°C for 4 h and concentrated. Acetylation in the presence of Ac_2O and pyridine followed by flash chromatographic purification over silica gel column gave the fully acetylated derivative **20** as an amophous solid (289 mg, 90%); $[\alpha]_D$ +78.4 (*c* 1.1, $CHCl_3$). A mixture of **20** (0.563 g, 0.73 mmol) and thiolacetic acid (6 mL) was stirred for 48 h at room temperature after which time TLC showed that the reaction was complete. Concentration of the reaction mixture and flash column chromatography of the residue over silica gel (EtOAc–hexane, 7:3) gave the product **21** (369 mg, 65%); $[\alpha]_D$ +8.1 (*c* 0.49, $CHCl_3$). ^1H NMR ($CDCl_3$) δ: 7.35–7.26 (m, Ph), 6.21(d, *J* = 9.3 Hz, NH), 5.35 (d, $J_{4,3}$ = 2.7 Hz, H-4), 5.31 (d, $J_{4',3'}$ = 3.3 Hz, H-4′), 5.16 (s, CH_2Ph), 5.04 (dd, H-2′), 4.90 (dd, H-3′), 4.84 (d, $J_{1,2}$ = 3.58 Hz, H-1), 4.57 (d, $J_{1',2'}$ = 7.7 Hz, H-1′), 4.53 (dd, H-2), 3.92 (dd, H-3), 2.12, 2.10, 2.02 (2), 2.01, 1.97, 1.93 (OAc and NAc). HRMS (FAB), calcd. for $C_{35}H_{46}NO_{19}$ (M+H): 784.2688; found: 784.2664.

Carboxymethyl 3-*O*-(2,3,4,6-tetra-*O*-acetyl-β-D-galactopyranosyl)-2-acetamido-2-deoxy-4,6-di-*O*-acetyl-α-D-galactopyranoside (22)

To a cooled (0–10°C) solution of **21** (213 mg, 0.27 mmol) in THF–methanol (1:1, 10 mL) was added Pd/C 10% (100 mg) followed by addition of 100 μL of acetic acid. The mixture was hydrogenated for 2 h, and the catalyst was filtered off and washed with methanol. The combined filtrate and washings were concentrated to a syrup that was purified by flash column chromatography over silica gel (EtOAc–MeOH, 15:1) to yield **22** as an amorphous solid (179 mg, 90%); $[\alpha]_D$ +28.1 (*c* 0.5, $CHCl_3$). ^1H NMR (CD_3OD) δ: 5.40 (d, $J_{4,3}$ = 3.3 Hz, H-4), 5.34 (d, $J_{4'3'}$ = 3.3 Hz, H-4′), 5.04 (dd, $J_{3'2'}$ = 10.5 Hz, H-3′), 4.96 (dd, $J_{2',3'}$ = 10.5 Hz, H-2′), 4.84 (s, CH_2COOH), 4.79 (d, $J_{1,2'}$ = 3.8 Hz, H-1), 4.75 (d, $J_{1',2'}$ = 7.5 Hz, H-1′), 4.42 (dd, H-2), 1.93–2.12 (OAc and NAc). ^{13}C NMR (CD_3OD) δ: 171.2–177.9 ($COCH_3$, and $NHCOCH_3$), 99.1, 102.4 (C-1, C-1′), 75.1, 72.3, 71.8, 71.3, 70.3, 68.8, 68.7, 67.8 (ring carbons), 62.3, 63.9 (C-6, C-6′), 20.4-23.2 (7 $COCH_3$, and $NHCOCH_3$). HRMS (FAB), calcd. for $C_{28}H_{39}NO_{19}Na$ (M+Na): 716.2041; found: 716.2014.

Benzyloxycarbonylmethyl 3,4,6-tri-*O*-acetyl-2-azido-2-deoxy-α-D-galactopyranoside (23) and its β anomer

Glycosylation of benzyl glycolate **4** (0.5 g, 3.0 mmol) with **12** (1.36 g, 2.9 mmol), essentially as described for **13**, gave **23** along with the β anomer (0.972 g, 70%; α:β, >4:1) as an inseparable mixture. ^1H NMR ($CDCl_3$) δ: 7.37–7.26 (m, Ph), 5.15 (d, $J_{1,2}$ = 3.7 Hz, H-1α), 4.54 (d, $J_{1,2}$ = 8.0 Hz, H-1β), 3.73 (dd, $J_{2,1}$ = 3.5 Hz, $J_{2,3}$ = 11.1 Hz, H-2α), 2.13, 2.05, and 2.02 (OAc). ^{13}C NMR $CDCl_3$) δ: 102.2 (C-1β), 98.0 (C-1α). HRMS (FAB), calcd. for $C_{21}H_{26}O_{10}N_3$ (M+H): 480.1616; found: 480.1666.

Benzyloxycarbonylmethyl 3,4,6-tri-*O*-acetyl-2-acetamido-2-deoxy-α-D-galactopyranoside (24)

Treatment of compound **23** (α:β, >4:1; 0.9 g, 1.88 mmol) with thiolacetic acid (16 mL), in a similar fashion as described for compound **21**, afforded **24** as an oil after chromatographic separation (0.64 g, 69%); $[\alpha]_D$ +80.0 (*c* 1.0, $CHCl_3$); ^1H NMR ($CDCl_3$) δ: 7.35–7.34 (m, Ph), 6.18 (d, *J* = 9.5 Hz, NH), 5.38 (d, $J_{4,3}$ = 3.2 Hz, H-4), 5.20 (dd, $J_{2,1}$ = 3.2 Hz, and $J_{2,3}$ = 11.4 Hz, H-2), 5.19 (s, CH_2Ph), 4.91 (d, $J_{1,2}$ = 3.7 Hz, H-1), 4.62 (m, H-2), 4.04–4.25 (m, H-5, H-6, and OCH_2COO-), 2.16, 2.03, 1.99, 1.99 (OAc and NAc). ^{13}C NMR ($CDCl_3$) δ: 170.7, 170.4, 170.2, 169.4 (CO), 128.6, 128.3, 98.6 (C-1), 68.1, 67.3, 67.1, 66.9, 64.6, 61.6, 47.3, 23.1, 20.6, and 20.5. HRMS (EI), calcd. for $C_{23}H_{30}O_{11}N$ (M+H): 495.1725; found: 495.1725.

Carboxylmethyl 3,4,6-tri-*O*-acetyl-2-acetamido-2-deoxy-α-D-galactopyranoside (25)

Hydrogenation of **24** (50 mg, 0.1 mmol), in a similar procedure as described for compound **22**, gave **25** as an amorphous solid (38 mg, 94%); $[\alpha]_D$ +101.0 (*c* 1.0, $CHCl_3$). ^1H NMR ($CDCl_3$ + 2 drops of CD_3OD) δ: 5.33 (d, $J_{4,3}$ = 3.3 Hz, H-4), 5.17 (dd, $J_{3,4}$ = 3.3 Hz and $J_{3,2}$ = 11.4 Hz, H-3), 4.82 (d, $J_{1,2}$ = 3.5 Hz, H-1), 4.49 (dd, $J_{2,1}$ = 3.5 Hz and $J_{2,3}$ = 11.4 Hz, H-2), 3.82–4.17 (m, H-5, H-6, and OCH_2COO-), 2.12, 2.00, 1.94, 1.92 (OAc, NAc). ^{13}C NMR ($CDCl_3$ + 2 drops of CD_3OD) δ: 171.5, 170.7, 170.5 (CO), 97.8 (C-1), 68.3, 67.1, 66.4, 61.5, 47.0, 22.3, 20.4, and 20.3. HRMS (FAB), calcd. for $C_{16}H_{23}O_{11}NNa$ (M+Na): 428.1168; found: 428.1127.

Compounds 28 and 34

To a cooled solution of **18** (320 mg, 0.624 mmol) in dry THF–DMF (1:1, 3 mL) was added *N*-methylmorpholine (63 mg) fol-

lowed by isobutyl chloroformate (196 μL) at −20°C. Stirring was continued at −20°C until a fine precipitate was observed (20 min). After 5 min, a solution of the triamine **1** (48 mg, 0.15 mmol) in dry DMF (1 mL) was added and stirring was continued for 1 h. The reaction mixture was diluted with dichloromethane (20 mL) and washed successively with saturated $NaHCO_3$ solution and water, dried ($MgSO_4$), and evaporated to a syrup. Flash chromatography of the residue on silica gel (CH_2Cl_2–MeOH, 95:5) gave an inseparable 1:1 mixture of **26** and **32** (170 mg, 65%) as an amorphous solid. A solution of this mixture (360 mg) in 5 mL of TFA was stirred for 3 h at room temperature, after which toluene (10 mL) was added and the solvents were removed in vacuo. The residue was acetylated (Ac_2O–pyridine; 5 mL, 1:2) to give **27** and **33** as a mixture of trimer and dimer, respectively (280 mg). A portion of the above mixture (200 mg) was treated with NaOMe in methanol (4 mL) for 12 h at room temperature. The base was neutralized with IR-H^+ resin, filtered, washed with methanol, and concentrated. The residue was chromatographed on silica gel (CH_2Cl_2–MeOH, 1:1) followed by purification on Sephadex-LH-20 (CH_2Cl_2–MeOH, 3:2) to give **28** (15 mg, 80% from **27**) and **34** (100 mg, 65% from **33**) as amorphous solids. For **28**: $[\alpha]_D$ +56.3 (*c* 1.0, MeOH). ^{1}H NMR (CD_3OD) δ: 5.85 (m, CH_2=C*H*), 5.27–5.1 (m, CH_2=C*H*), 4.83 (d, $J_{1,2}$ = 3.3 Hz, H-1), 4.60 (m, Ser α-H), 4.25 (dd, $J_{2,1}$ = 3.7 Hz and $J_{2,3}$ = 10.9 Hz, H-2), 3.93–3.74 (m), 3.45–3.25 (m), 2.04, 2.02, 1.95 (NAc). ^{13}C NMR (CD_3OD) δ: 174.1, 172.0, 172.5 (NH*C*O), 136.2 (*C*H_2=*C*H), 116.6 (*C*H_2=CH), 100.0 (C-1), 73.4, 72.6, 70.9, 70.8, 70.6, 70.2, 69.8, 69.5, 62.9, 51.4, 46.7, 40.5, 22.9, and 22.7. HRMS (FAB), calcd. for $C_{42}H_{73}O_{21}N_7Na$ (M+Na): 1034.4758; found: 1034.4809. For **34**: $[\alpha]_D$ +62.9 (*c* 1.0, MeOH). ^{1}H NMR (CD_3OD) δ: 5.89 (m, CH_2=C*H*), 5.21 (m, C*H*$_2$=CH), 4.81 (d, $J_{1,2}$ = 3.3 Hz, H-1), 4.61 (m, Ser α-H), 4.26 (dd, $J_{2,1}$ = 3.7 Hz and $J_{2,3}$ = 10.9 Hz, H-2), 3.90–3.65 (m), 3.5–3.3 (m), 2.04, 2.02, 1.94 (NAc). ^{13}C NMR (CD_3OD) δ: 173.8, 173.2, 172.0 (CO), 136.5 (CH_2=*C*H), 116.7 (*C*H_2=CH), 100.1 (C-1), 73.4, 72.9, 70.9, 70.8, 70.3, 69.8, 69.6, 62.8, 54.8, 51.5, 49.7, 46.8, 40.6, 40.5, 23.0, 22.9, 22.8, and 22.7.

Compounds 31 and 37

A solution of **18** (561 mg, 1.08 mmol) in dry THF–DMF (3 mL, 1:1) was coupled with triamine **2** (128 mg, 0.34 mmol in dry DMF, 2 mL) as described for compounds **26** and **32**, to afford a mixture of **29** and **35** (380 mg, 76%) as an amorphous solid. A portion (255 mg) was treated with TFA, followed by N-acetylation as described for **27** and **33** to give 205 mg of **30** and **36** as a syrupy mixture which was treated with NaOMe, as described for **28** and **34**, to give **31** (120 mg) and **37** (20 mg). For **31**: $[\alpha]_D$ +73.4 (*c* 0.5, MeOH). ^{1}H NMR (CD_3OD) δ: 5.80 (m, CH_2=C*H*), 4.95 (m, CH=C*H*$_2$), 4.83 (d, $J_{1,2}$ = 3.7 Hz, H-1), 4.60 (m, Ser α-H), 4.20 (dd, $J_{2,1}$ = 3.7 Hz, $J_{2,3}$ = 10.9 Hz, H-2), 4.77–3.28 (m), 2.05, 2.02 (NAc), 1.88–1.31 (m, CH_2). ^{13}C NMR (CD_3OD) δ: 174.5, 174.0, 172.2 (CO), 140.2 (CH_2=*C*H), 114.9 (*C*H_2=CH), 99.5 (C-1), 72.6, 70.7, 69.8, 69.3, 68.9, 62.4, 62.3, 54.7, 51.2, 40.4, 23.1, and 22.8. HRMS (FAB), calcd. for $C_{58}H_{101}O_{28}N_9$ (M+Na): 1394.6653; found: 1394.6628. For **37**: $[\alpha]_D$ +68.0 (*c* 0.25, MeOH). ^{1}H NMR (CD_3OD) δ: 5.80 (m, CH_2=C*H*), 4.95 (m, CH=C*H*$_2$), 4.82 (d, $J_{1,2}$ = 3.6 Hz, H-1), 4.61 (m, Ser α-H), 4.20 (dd, $J_{2,1}$ = 3.6 Hz, $J_{2,3}$ = 11.1 Hz, H-2), 3.91–3.7 (m), 3.48–3.29 (m), 2.05, 2.04, 2.02 (s, NAc), 1.89–1.32 (m, CH_2). ^{13}C NMR (CD_3OD) δ: 174.6, 174.1, 172.1 (CO), 140.2 (CH_2=*C*H), 114.9 (*C*H_2=CH), 99.4 (C-1), 72.7, 72.6, 70.7, 70.6, 69.9, 69.2, 68.9, 62.4, 54.7, 51.1, 40.3, 23.0, and 22.3. HRMS (FAB), calcd. for $C_{47}H_{83}O_{21}N_7Na$ (M+Na): 1104.5538; found: 1104.5463.

Compounds 38 and 41

Compound **15** (850 mg, 1.09 mmol) was coupled with the triamine **2** (102 mg, 0.27 mmol) following the procedure described above, to give compound **38** after chromatographic separation (180 mg, 25%) and **41** (250 mg, 35%) as amorphous solids. For **38**: $[\alpha]_D$ +52.0 (*c* 0.5, $CHCl_3$); IR cm^{-1} (film): 3450 (NH), 1750 (C=O). 1230 (ester), 1670 and 1540 (amide). ^{1}H NMR (CD_3OD) δ: 5.80 (m, CH_2=C*H*), 5.37 (d, $J_{4',3}$ = 2.7 Hz, H-4′), 4.48 (m, Ser α-H), 4.16–3.3 (m), 2.14–2.04, 2.03, 1.99, 1.92 (OAc and NAc), and 1.45–1.34 (m, -CH_2(C*H*$_2$)$_4$ CH-). ^{13}C NMR (CD_3OD) δ: 172.7, 172.0, 171.9, 171.5, 171.1 (CO), 140.1 (CH_2=*C*H), 114.8 (*C*H_2=CH), 103.7 (C-1′), 100.7 (C-1), and 100.1 (*C*Me_2), 77.1, 72.6, 71.9, 71.1, 70.9, 70.5, 70.3, 69.9, 68.8, 67.6, 64.5, 63.8, 62.7, 40.6, 34.8, 30.1, 29.6, 28.8, 23.3, 20.9, 20.7, 20.4, and 19.0. For **41**: $[\alpha]_D$ +51.2 (*c* 0.25, $CHCl_3$); IR cm^{-1} (film): 3450 (NH), 1750 (C=O). 1230 (ester), 1670 and 1540 (amide). ^{1}H NMR (CD_3OD) δ: 5.80 (m, 1H, CH_2=C*H*), 5.37 (d, $J_{4',3}$ = 2.0 Hz, H-4′), 4.82 (m, Ser α-H), 5.1–3.3 (m), 2.14, 2.03, 1.99, 1.97, 1.92 (OAc and NAc), and 1.45–1.34 (m, -CH_2 (C*H*$_2$)$_4$ CH-). ^{13}C NMR ($CHCl_3$ + CD_3OD) δ: 172.8, 172.0, 171.9, 171.5, 171.1 (CO) 140.1 (CH_2=*C*H), 114.8 (*C*H_2=CH), 103.7 (C-1′), 100.6 (C-1), 100.1 (*C*Me_2), 77.1, 72.6, 71.2, 71.0, 70.9, 70.3, 69.9, 68.8, 67.6, 64.5, 63.8, 62.6, 40.6, 30.1, 29.6, 28.8, 23.4, 20.9, 20.7, 20.5, and 19.0.

Compounds 40 and 43

The *N*-*t*-Boc group and O-isopropylidene groups in **38** (130 mg, 0.05 mmol) and **41** (400 mg, 0.21 mmol) were individually removed by treating each compound with TFA followed by N- and O-acetylation, to give **39** (98 mg, 77%), $[\alpha]_D$ +25 (*c* 0.5, MeOH) and **42** (286 mg, 72%), $[\alpha]_D$ +51.2′ (*c* 0.25, MeOH). Treatment of **39** (75 mg, 0.028 mmol) and **42** (120 mg, 0.21 mmol) with NaOMe in MeOH, as described above, gave **40** (42 mg, 79%) and **43** (69 mg, 78%), respectively. For **40**: $[\alpha]_D$ +47.2 (*c* 0.25, H_2O). ^{1}H NMR (CD_3OD +D_2O) δ: 5.84 (m, CH_2=C*H*), 5.39 (d, $J_{4',3}$ = 3.3 Hz, H-4′), 4.90 (m, CH_2=C), 4.86 (d, $J_{1,2}$ = 3.5 Hz, H-1), 4.57 (m, Ser α-H), 4.42 (d, $J_{1',2'}$ = 7.5 Hz, H-1′), 4.33 (dd, $J_{2,1}$ = 3.5 Hz, $J_{2,3}$ = 10.9 Hz, H-2), 3.30–4.00 (m), 2.09, 2.01 (NAc), 1.25–1.60 (m, -CH_2(C*H*$_2$)$_4$ CH-). ^{13}C NMR (CD_3OD+D_2O) δ: 174.7, 173.6 (CO), 140.6 (CH_2=*C*H), 115.0 (*C*H_2=CH), 105.6 (C-1′), 99.9 (C-1). HRMS (FAB), calcd. for $C_{76}H_{131}O_{43}N_9Na$ (M+Na): 1880.8267; found: 1880.8214. For **43**: $[\alpha]_D$ +35.2 (*c* 0.25, H_2O). ^{1}H NMR (CD_3OD +D_2O) δ: 5.85 (m, CH_2=C*H*), 5.03 (d, $J_{4',3'}$ = 3.3 Hz, H-4′), 4.90 (m, CH_2=C), 4.83 (d, $J_{1,2}$ = 3.5 Hz, H-1), 4.57 (m, Ser β-H), 4.42 (d, $J_{1',2'}$ = 7.5 Hz, H-1′), 4.31 (dd, $J_{2,1}$ = 3.5 Hz, $J_{2,3}$ = 10.9 Hz, H-2), 4.28–3.27 (m), 2.04, 1.99–1.96 (NAc), 1.54–1.30 (m, -CH_2(C*H*$_2$)$_4$CH-). ^{13}C NMR (CD_3OD + D_2O) δ: 175.0, 174.6, 172.1 (CO), 140.9 (CH_2=*C*H), 115.0 (*C*H_2=CH), 105.6 (C-1′), 99.2 (C-1), 78.1, 76.0, 73.7, 72.8, 71.9, 71.7, 70.5, 70.4, 69.6, 69.5, 68.6, 62.1, 61.9, 54.7, 40.2, 34.1, 29.5, 29.1, 23.1, and 22.8. HRMS (FAB), calcd. for $C_{59}H_{103}O_{31}NNa$ (M+Na): 1428.6589; found: 1428.6445.

Compound 44

To a solution of **25** (46 mg, 0.107 mmol) in dry DMF (3 mL, 1:1) cooled to −20°C was added *N*-methylmorpholine (10 mg), followed by isobutyl chloroformate (14 μL). Stirring was continued at −20°C until a fine precipitate was observed (20 min). In a separate flask, a solution of the triamine **2** (10 mg, 0.026 mmol) in dry DMF (1 mL) was mixed under anhydrous conditions with *N*-methylmorpholine (5 μL). This solution was gradually added to the above solution of **25** at −20°C under argon during a period of 10 min. Stirring was continued at room temperature for 90 min with occasional monitoring by TLC. The reaction mixture was diluted with dichloromethane (20 mL), washed successively with saturated $NaHCO_3$ solution and water, dried ($MgSO_4$), and evaporated to a syrup. Flash chromatography of the residue on silica gel (CH_2Cl_2–MeOH, 95:5) gave **44** as an amorphous solid (30 mg, 60%); $[\alpha]_D$ +72.3 (*c* 2.0, $CHCl_3$); IR cm^{-1} (film): 3450 (NH), 1750 (C=O). 1230 (ester), 1670 and 1540 (amide). ^1H NMR (CD_3OD) δ: 5.76 (m, CH_2=C*H*), 5.36 (d, $J_{4,3}$ = 2.8 Hz, H-4), 5.16 (dd, $J_{3,2}$ = 11.6 Hz, H-3), 4.95 (m, CH_2=CH), 4.88 (d, $J_{1,2}$ = 3.4 Hz, H-1), 4.58 (m, H-2), 4.2–3.2 (m, H-5, OCH_2 and NCH_2), 2.14–1.95 (OAc, NAc), 1.60–1.20 (m, -CH_2(CH_2)$_4$CH-). ^{13}C NMR (CD_3OD) δ: 170.9, 170.8, 170.6, 170.3, 169.1 (*C*OCH_3, and NH*C*OCH_3), 138.7 (CH_2=*C*H), 114.1 (*C*H_2=CH), 98.2 (C-1), 76.8, 76.3, 69.7, 69.6, 69.5, 67.8, 66.8, 66.7, 61.6, 60.3, 38.8, 33.5, 28.7, 28.6, 25.8, 22.5, 20.5, and 20.4. HRMS (FAB), calcd. for $C_{70}H_{112}O_{36}N_6S$·$HSCH_2CHOHCH_2OH$, (M+$CH_2SHCHOHCH_2OH$): 1644.6838; found: 1644.6869.

Compound 45

The acetyl groups in compound **44** (20 mg, 0.0113 mmol) were removed by treatment with NaOMe in methanol (2 mL) as described for **28** and **34**, to give **45** (15 mg, 96%) as a syrup; $[\alpha]_D$ +32.3 (*c* 1.0, MeOH), ^1H NMR (CD_3OD) δ: 5.80 (m, CH_2=C*H*), 4.90 (m, H-4, and CH_2=CH), 4.37 (dd, $J_{3,4}$ = 3.6 Hz, and $J_{3,2}$ = 11.0 Hz, H-3), 3.91 (d, $J_{1,2}$ = 2.8 Hz, H-1), 3.81 (m, H-2), 3.82–3.28 (m, H-5, H-6, CH_2), 2.02 (NAc), 1.60–1.20 (m, -CH_2(CH_2)$_4$CH-). HRMS (FAB), calcd. for $C_{52}H_{94}O_{27}N_6SNa$·$HSCH_2CHOHCH_2OH$, (M+Na+$CH_2SHCHOHCH_2OH$): 1289.5785; found: 1289.5646.

Compounds 47 and 51

A solution of **22** (200 mg, 0.3 mmol) in DMF was treated with triamine **1** (45 mg, 0.14 mmol) in dry DMF, in a similar fashion as described for compound **44**, to give **46** (93 mg, 41%); $[\alpha]_D$ +50.7 (*c* 1.1, MeOH) and **50** (76 mg, 30%); $[\alpha]_D$ +36.2′ (*c* 0.9, MeOH) each as an amorphous solid. The O-acetyl groups in compounds **46** (190 mg, 0.08 mmol) and **50** (60 mg) were removed by treating separately with NaOMe, as described above for compounds **28** and **34,** to give **47** (118 mg, 92%) and **51** (40 mg, quant.) as syrups after chromatographic separation. For **47**: $[\alpha]_D$ +82.5 (*c* 0.25, H_2O); ^1H NMR (CD_3OD–D_2O, 1:1) δ: 5.90 (m, CH_2=C*H*), 5.25 (m, CH_2=CH), 4.87 (d, $J_{1,2}$ = 3.1 Hz, H-1), 4.50–3.30 (m, H-1′; H-4, H-5, H-5′, H-6, H-6′), and 2.02 (NAc). ^{13}C NMR (D_2O) δ: 175.0, 172.1 (NH*C*OCH_3), 135.4 (CH_2=*C*H), 118.1 (*C*H_2=CH), 105.8 (C-1′), 99.0 (C-1), 78.1, 76.1, 73.8, 73.3, 72.3, 71.8, 70.6, 69.7, 67.3, 62.2, 39.7, and 23.1. HRMS (FAB), calcd. for $C_{62}H_{106}O_{40}N_6Na$ (M+Na): 1597.5569; found: 1597.5498. For **51**: $[\alpha]_D$ +66.0 (*c* 0.5, H_2O). ^1H NMR (CD_3OD–D_2O, 10:1) δ: 5.89 (m, CH_2=C*H*), 5.29 (m, CH_2=CH), 4.87 (d, $J_{1,2}$ = 3.6 Hz, H-1), 4.50–3.30 (m), 2.02 (NAc), 0.90 (d, *J* = 6.8 Hz, $CHCH_3$). ^{13}C NMR (D_2O) δ: 175.0, 172.1 (NH*C*OCH_3), 135.5 (CH_2=*C*H), 117.9 (*C*H_2=CH), 105.9 (C-1′), 99.1 (C-1), 78.2, 76.1, 73.9, 73.3, 72.3, 72.2, 71.9, 71.1, 70.6, 69.9, 69.8, 67.3, 62.2, 62.1, 39.7, 28.8, 23.1, and 19.3. HRMS (FAB), calcd. for $C_{51}H_{89}O_{30}N_5Na$ (M+Na): 1274.5437; found: 1274.5417.

Compounds 49 and 53

A solution of **22** (303 mg, 0.43 mmol) in dry DMF was treated with triamine **2** (58 mg, 0.15 mmol) essentially in the same fashion as described for compound **44**, to give **48** (173 mg, 50 %); $[\alpha]_D$ +40.6 (*c* 1.1, MeOH) and **52** (61 mg, 16%); $[\alpha]_D$ +82.0 (*c* 1.8, MeOH) each as an amorphous solid after chromatographic separation. The O-acetyl groups in **48** (73 mg, 0.03 mmol) and **52** (91 mg, 0.05 mmol) were removed by treating separately with NaOMe, in a similar fashion as described above for compounds **28** and **34**, to give **49** (42 mg, 84%) and **53** (56 mg, 90%) as amorphous solids. For **49**: $[\alpha]_D$ +52.8 (*c* 1.1, H_2O). ^1H NMR (D_2O) δ: 5.87 (m, CH_2=C*H*), 4.98 (m, CH_2=CH), 4.96 (d, $J_{1,2}$ = 3.3 Hz, H-1), 4.53 (d, $J_{1,2}$ = 7.7 Hz, H-1′), 3.94 (d, H-4), 4.4–3.4 (m), 2.13 (NAc), 1.46–1.23 (m, CH_2(CH_2)$_4$CH). ^{13}C NMR (D_2O) δ: 174.3, 171.3 (NH*C*OCH_3), 139.9 (CH_2=*C*H), 114.0 (*C*H_2=CH), 104.3 (C-1′), 97.7 (C-1), 78.9, 77.8, 72.3, 71.7, 71.1, 70.7, 69.8, 68.5, 68.4, 66.1, 60.8, 48.7, 45.0, 38.5, 28.4, 27.9, 25.4, and 22.0. HRMS (FAB), calcd. for $C_{67}H_{116}O_{40}N_6Na$ (M+Na): 1667.7079; found: 1667.7135. For **53**: $[\alpha]_D$ +47.3 (*c* 1.0, H_2O); ^1H NMR (D_2O) δ: 5.7 (m, CH_2=C*H*), 4.98 (m, CH_2=CH), 4.96 (d, $J_{1,2}$ = 3.1 Hz, H-1), 4.43–3.0 (m), 2.09 (NAc), 1.41–1.27 (m, -CH_2(CH_2)$_4$CH), 0.88 (d, $CHMe_3$). ^{13}C NMR (CD_3OD) δ: 173.8, 172.3, 170.7 (O*C*ONH and NH*C*OCH), 139.1 (CH_2=*C*H), 113.7 *C*H_2=CH), 104.2 (C-1′), 97.3 (C-1), 76.4, 74.6, 74.4, 72.1, 70.8, 70.7, 70.6, 69.9, 69.0, 68.9, 68.5, 65.8, 65.7, 60.6, 60.4, 60.3, 47.8, 44.7, 38.1, 32.8, 28.1, 27.9, 27.8, 27.2, 25.0, 21.7, and 17.9. HRMS (FAB), calcd. for $C_{56}H_{99}O_{30}N_5Na$ (M+Na): 1344.6240; found: 1344.6198.

Summary

Immunologically relevant carbohydrates such as D-GalNAc(Tn) and D-Galβ(1→3)GalNAc(T) have been attached to triamino and tris(aminoethyl) pentaerythritol-based scaffolds through amide linkages with the aim of generating clustered haptenic motifs for use as tumor-specific carbohydrate antigens and vaccines.

Acknowledgments

We thank the Natural Sciences and Engineering Research Council of Canada (NSERC) for generous financial assistance through the Medicinal Chemistry Chair program.

References

1. (*a*) S. Sell. Human Patholol. **21**, 1003 (1990); (*b*) J.A. Alhadeff. Crit. Rev. Oncol. Hematol. **9**, 37 (1989); (*c*) S. Hakomori. Adv. Cancer Res. **52**, 257 (1989).
2. (*a*) A.J. Leathem and S.A. Brooks. Lancet, 1054 (1987); (*b*) M.R. Price, A.J. Clarke, J.R. Robertson, C. O'Sullivan, R.W. Baldwin, and R.W. Blamey. Cancer Immunol. Immunother. **31**,

269 (1990); (*c*) H. Kobayashi, T. Terao, and Y. Kawashima. J. Clin. Res. **10**, 95 (1992).
3. G.F. Springer. Science, **224**, 1198 (1984).
4. (*a*) P.R. Desai, H. Tegmeyer, E.V. Chandrasekaran, and G.F. Springer. J. Tumor Marker Oncol. **2**, 233 (1987); (*b*) G.F. Springer, C.R. Taylor, D.R. Howard, E.V. Tegmeyer, P.R. Desai, S.M. Murthy, B. Felder, and E.F. Scalon. Cancer, **55**, 561 (1985).
5. G.D. MacLean and B.L. Longenecker. Semin. Cancer Biol. **2**, 433 (1991).
6. D. Zhuang, S. Yousef, and J.W. Dennis. Cancer Biochem. Biophys. **12**, 185 (1991); J. Samuel, A.A. Noujaim, G.D. MacLean, M.R. Suresh, and B.M. Longenecker. Cancer Res. **250**, 4801 (1990).
7. S.H. Itzkowitz, M. Yuan, C.K. Montgomery, T. Kjedsen, S.K. Takahashi, W.L. Bigbee, and Y.S. Kim. Cancer Res. **49**, 197 (1989).
8. N.R. Rabinovich, P. McInnes, D.L. Klein, and P.F. Hall. Science, **265**, 1401 (1994); J.-C. Byrstryn. Cancer Metastasis Rev. **9**, 81 (1990); P.O. Livingston, G. Ritter, P. Srivastava, M. Padavan, M.J. Calves, H.F. Oettgen, and L.J. Old. Cancer Res. **49**, 7045 (1989); T. Dohi, G. Nores, and S. Hakomori. Cancer Res. **48**, 5680 (1988); P.O. Livingston, M.J. Calves, and E.J. Natoli, Jr. J. Immunol. **138**, 1524 (1987); P.O. Livingston, E.J. Natoli, M.J. Calves, E. Stockert, H.F. Oettgen, and L.J. Old. Prot. Natl. Acad. Sci. U.S.A. **84**, 2911 (1987); T.W. Sher. Proc. Natl. Acad. Sci. U.S.A. **68**, 2078 (1971); see also A Cancer Vaccine. *In* Alberta Report, Oct. 24, 1988. pp. 28–33.
9. G.D. MacLean, M.Reddish, R.R. Koganty, T. Wong, S. Gandhi, M. Smolenski, J. Samuel, J.M. Nabholtz, and B.M. Longenecker. Cancer Immunol. Immunother. **36**, 215 (1993); S.H. Itzkowitz, E.J. Bloom, W.A. Kokal, G. Modin, S. Hakomori, and Y.S. Kim. Cancer, **66**, 1960 (1990); T. Kjeldsen, H. Clausen, and S. Hirihishi. Cancer Res. **48**, 2214 (1988).
10. (*a*) Y.C. Lee and R.T. Lee. Acc. Chem. Res. **28**, 321 (1995); Y.C. Lee. Biochem. Soc. Trans. **21**, 460 (1993); Y.C. Lee, R.T. Lee, K. Rice, Y. Ichikawa, and T. Wong. Pure Appl. Chemistry, **63**, 499 (1991); R.T. Lee, K.G. Rice, N.B.N. Rao, Y. Ichikawa, T. Barthel, V. Diskarev, and Y.C. Lee. Biochemistry, **28**, 8351 (1989); R.T. Lee and Y.C. Lee. Glycoconjugate J. **4**, 317 (1987); Y.C. Lee, R.R. Townsend, M.R. Hardy, J. Lönngren, and K. Black. Biochem. Biophys. Stud. Proteins Nucleic Acids, 349 (1984); Y.C. Lee. Carbohydr. Res. **67**, 509 (1978); (*b*) M.G. Peter, P.C.Boldt, Y. Niederstein, and J. Peter-Katalinic. Liebigs Ann. Chem. 863 (1990).
11. (*a*) T. Toyokuni, B. Dean, and S. Hakomori.Tetrahedron Lett. **31**, 2673 (1990); (*b*) T. Toyokuni, B. Dean, S. Cai, D. Bovin, S. Hakomori, and A.K. Singhal. *J.* Am. Chem. Soc. **116**, 395 (1994).
12. (*a*) Y. Nakahara, H. Iijima, and T. Ogawa. *In* Synthetic oligosaccharides – indispensable probes for the life sciences. *Edited by* P. Kovac. ACS Symp. Ser. **566**, 249 (1994); (*b*) Y. Nakahara, H. Iijima, S. Sibayama, and T. Ogawa. Tetrahedron Lett. **31**, 6897 (1990).
13. M. Ciommer and H. Kunz. Synlett, 593 (1994); H. Kunz, S. Birnbach, and P. Wernig. Carbohydr. Res. **202**, 207 (1990).
14. H. Paulsen and M. Paal. Tetrahedron Lett. **24,** 1759 (1983); H. Paulsen, G. Merz, and I. Brockhausen. Liebigs Ann. Chem. 719 (1990).
15. S. Arawind, W.K.C. Park, S. Brochu, and R. Roy. Tetrahedron Lett. **35**, 7739 (1994); R. Roy, D. Zanini, S.J. Meunier, and A. Romanowska. *In* Synthetic oligosaccharides – indispensable probes for the life sciences. *Edited by* P. Kovac. ACS Symp. Ser. **566**, 104 (1994); S. Sabesan, J.O. Duus, S. Neira, P. Domaille, S. Kelm, J.C. Paulson, and K. Bock. J. Am. Chem. Soc. **114**, 8363 (1992); K. von dem Bruch and H. Kunz. Angew. Chem. Int. Ed. Engl. **33**, 101 (1994).
16. S. Hanessian, H. Prabhanjan, D. Qiu, and S. Nambiar. Can. J. Chem. **74**, 1731 (1994).
17. (*a*) B. Luning, T. Norberg, and J. Tejbrant. Glycoconjugate J. **6**, 5 (1989); (*b*) W. Kinzy and R.R. Schmidt. Carbohydr. Res. **166**, 265 (1987); (*c*) H. Paulsen and M. Paal. Carbohydr. Res. **135**, 53 (1984); (*d*) H. Paulsen and J. Holck. J. Carbohydr. Res. **109**, 89 (1982); (*e*) V.V. Bencomo, J. Jacquinet, and P. Sinay. Carbohydr. Res. **110**, C9 (1982); (*f*) H.M. Flowers and D. Shapiro. J. Org. Chem. **30**, 2041 (1965); (*g*) R.R. Schmidt and W. Kinzy. Adv. Carbohydr. Chem. Biochem. **50**, 21 (1994).
18. (*a*) H. Paulsen, W. Rauwald, and U. Weichert. Liebigs Ann. Chem. 75 (1988); B. Ferrari and A.A. Pavia. Carbohydr. Res. **79**, C1 (1980); H. Kunz and S. Birnbach. Angew. Chem. Int. Ed. Engl. **25**, 360 (1986); H. Paulsen and K. Adermann. Liebigs Ann. Chem. 751 (1989); (*b*) H.G. Garg, K. von dem Bruch, and H. Kunz. Adv. Carbohydr. Chem. Biochem. **50**, 277 (1994).
19. S. Hanessian, J.J. Conde, and B. Lou. Tetrahedron Lett. **36**, 5865 (1995); S. Hanessian. Can. Pat. Appl. July 19 (1993).
20. S. Hanessian and J. Banoub. Carbohydr. Res. **53**, C13 (1977); Methods in Carbohydr. Chem. **8**, 247 (1980).
21. T. Adachi, I. Inoue, and I. Saneyoshi. Synthesis, 45 (1977).
22. T. Rosen, I.M. Lico, and D.T.H. Chu. J. Org. Chem. **53**, 11580 (1988).
23. W.C. Still, M. Kahn, and A. Mitra. J. Org. Chem. **43**, 2923 (1978).

The generator coordinate Dirac–Fock method applied to beryllium-like atomic species

F.E. Jorge and A.B.F. da Silva

Abstract: The recently formulated generator coordinate Dirac–Fock method for relativistic closed-shell atoms is applied to the Be atom and Be-like ions Ne^{6+}, Ar^{14+}, and Sn^{46+} in order to assess its efficacy for light atomic systems. The Dirac–Fock equations are integrated numerically in the generator coordinate Dirac–Fock method so as to generate Gaussian basis sets for the atomic species under study. The results obtained with the application of the generator coordinate Dirac–Fock method in this work for Dirac–Fock–Coulomb and Dirac–Fock–Breit energies for Be-like ions are in excellent agreement with Declaux's benchmark numerical calculations, and are better than the Dirac–Fock–Coulomb and Dirac–Fock–Breit energies obtained with even-tempered Gaussian-type function calculations. For the Be atom, the Dirac–Fock–Coulomb energy result obtained with the generator coordinate Dirac–Fock method is lower than the corresponding value obtained with the Declaux's numerical finite-difference program.

Key words: Dirac–Fock–Coulomb energy, Dirac–Fock–Breit energy, Gaussian basis sets, generator coordinate Dirac–Fock method.

Résumé : La méthode de la coordonnée génératrice Dirac–Fock récemment formulée, pour les atomes ayant une couche électronique relativement complète, est appliquée à l'atome de Be et aux ions ressemblant à l'atome de Be : Ne^{6+}, Ar^{14+} et Sn^{46+} dans le but de vérifier l'efficacité de cette méthode pour les systèmes atomiques légers. Les équations de Dirac–Fock sont intégrés numériquement dans la méthode de la coordonnée génératrice Dirac–Fock de façon à générer l'ensemble de base de Gauss pour les espèces atomiques étudiées. Les résultats obtenus avec la méthode de la coordonnée génératrice Dirac–Fock pour les énergies Dirac–Fock–Coulomb et Dirac–Fock–Breit pour les ions du type Be sont en parfait accord avec les calculs numériques de référence de Declaux et sont meilleurs que les énergies de Dirac–Fock–Coulomb et Dirac–Fock–Breit obtenues avec les calculs avec les fonctions de Gauss également tempérés. Dans le cas de l'atome de Be, l'énergie de Dirac–Fock–Coulomb obtenue avec la méthode de la coordonnée génératrice Dirac–Fock est plus basse que l'énergie correspondante obtenue avec le programme de différences finies numérique de Declaux.

Mots clés : énergie Dirac–Fock–Coulomb, énergie Dirac–Fock–Breit, ensembles de base de Gauss, méthode de la coordonnée génératrice Dirac–Fock.

[Traduit par la rédaction]

1. Introduction

Ab initio Dirac–Fock (DF) self-consistent-field (SCF) calculations for many-electron atoms have been carried out either by using numerical finite-difference or basis set expansion methods (1–4). Slater-type functions (STF) and Gaussian-type functions (GTF) that satisfy the relativistic boundary conditions have been used for ab initio DF calculations on atoms. However, as relativistic atomic and molecular calculations are based on the Dirac equation whose solutions for an electron in a finite nucleus have been shown to be Gaussian (5, 6), the GTF are the natural choice for ab initio relativistic atomic and molecular calculations. Besides, the GTF that satisfy the boundary conditions for the finite nucleus automatically satisfy the condition of the so-called kinetic balance for a finite speed of light (6).

In this letter we apply the generator coordinate Dirac–Fock (GCDF) method developed recently for us (7, 8) to calculate the ground state Dirac–Fock–Coulomb (DFC) and Dirac–Fock–Breit (DFB) energies of Be, Ne^{6+}, Ar^{14+}, and Sn^{46+} in order to evaluate its efficacy for light atomic systems. Our results for the total DFC and DFB energies obtained with the GCDF method surpass previous calculations for Ne^{6+}, Ar^{14+}, and Sn^{46+} using even-tempered GTF (9), and are competitive with the results obtained by using Declaux's numerical finite-difference program (9). For the case of the Be atom, the DFC energy computed with our GTF is lower than the corresponding value obtained by both even-tempered GTF and numerical finite-difference calculations.

The GTF exponents generated here with the GCDF method for Be, Ne^{6+}, Ar^{14+}, and Sn^{46+} represent the first set of GTF exponents for these species obtained directly from a relativistic environment (code), as the usual procedure in relativistic calculations, so far, has been to employ GTF exponents obtained from a nonrelativistic environment by variational optimization or other techniques and carry them over to relativistic calculations (9–16) as suggested primarily by

Received March 11, 1996.

F.E. Jorge[1] and A.B.F. da Silva.[2] Departamento de Quimica e Física Molecular, Instituto de Quimica de São Carlos, Universidade de São Paulo, C.P. 780, 13560-970, São Carlos, SP, Brazil.

[1] Permanent address: Departamento de Física - CCE, Universidade Federal do Espírito Santo, 29060-900, Vitória, ES, Brazil.

[2] Author to whom correspondence may be addressed. Telephone: (55)(16) 2749171. Fax: (55)(16) 2749163. E-mail: ALBERICO@IQSC.SC.USP.BR

Matsuoka and Huzinaga (16). In that pioneer work, Matsuoka and Huzinaga showed that the same set of well-tempered GTF exponents obtained for a nonrelativistic atom could be carried over to the relativistic calculation.

2. Theoretical

In a previous paper we introduced the GCDF method for closed-shell atoms (7), and afterwards we included the Breit interaction term in the GCDF formalism in order to perform DFB calculations (8). This methodology is a result of applying the generator coordinate (GC) formalism (17), originally formulated for applications in nuclear physics, to the DF equations. For this purpose we chose the radial large and small components, $P_{n\kappa}(r)$ and $Q_{n\kappa}(r)$, respectively, as integral transforms, viz.

$$[1] \qquad P_{n\kappa}(r) = \int X_\kappa^{\mathrm{L}}(r, \gamma) f_{n\kappa}^{\mathrm{L}}(\gamma) \mathrm{d}\gamma$$

and

$$[2] \qquad Q_{n\kappa}(r) = \int X_\kappa^{\mathrm{S}}(r, \gamma) f_{n\kappa}^{\mathrm{S}}(\gamma) \mathrm{d}\gamma$$

where X_κ^{L} and X_κ^{S} are, respectively, the large (L) and small (S) generator functions (GTF or STF), $f_{n\kappa}^{\mathrm{L}}$ and $f_{n\kappa}^{\mathrm{S}}$ are, respectively, the large and small weight functions, and γ is the generator coordinate. In the GCDF method, although we resorted to a discretization technique for the solution of the integral DF equations

$$[3a] \qquad \int [F_\kappa^{\mathrm{LL}}(\gamma, \eta) f_{n\kappa}^{\mathrm{L}}(\eta) + F_\kappa^{\mathrm{LS}}(\gamma, \eta) f_{n\kappa}^{\mathrm{S}}(\eta)] \mathrm{d}\eta = \int \varepsilon_{n\kappa} S_\kappa^{\mathrm{LL}}(\gamma, \eta) f_{n\kappa}^{\mathrm{L}}(\eta) \mathrm{d}\eta$$

and

$$[3b] \qquad \int [F_\kappa^{\mathrm{SL}}(\gamma, \eta) f_{n\kappa}^{\mathrm{L}}(\eta) + F_\kappa^{\mathrm{SS}}(\gamma, \eta) f_{n\kappa}^{\mathrm{S}}(\eta)] \mathrm{d}\eta = \int \varepsilon_{n\kappa} S_\kappa^{\mathrm{SS}}(\gamma, \eta) f_{n\kappa}^{\mathrm{S}}(\eta) \mathrm{d}\eta$$

the continuous character of the original GC formalism (17) was retained. This was achieved by simply choosing equally spaced discretization points in an attempt to find an adequate numerical integration of the eqs. [3]. This approach is referred to as integral discretization (ID) (18) in contrast to the procedure of variationally optimizing orbital exponents, common in nonrelativistic calculations. The ID is implemented through a relabelling of the generator coordinate space γ

$$[4] \qquad \Theta = \ln \gamma / A, \qquad A > 1$$

In the new generator coordinate space Θ, an equally spaced N-point mesh $\{\Theta_w\}$ is selected, and the integration range is characterized by a starting point $\Theta_{\min}$, an increment $\Delta\Theta$, and N (number of points).

After the integral discretization, eqs. [3], for symmetry type κ, take the form

$$[5] \qquad \boldsymbol{F}_\kappa \boldsymbol{f}_\kappa = \boldsymbol{S}_\kappa \boldsymbol{f}_\kappa \boldsymbol{E}_\kappa$$

where the overlap matrix is given by

$$[6] \qquad \boldsymbol{S}_\kappa = \begin{pmatrix} \boldsymbol{S}_\kappa^{\mathrm{LL}} & \boldsymbol{0} \\ \boldsymbol{0} & \boldsymbol{S}_\kappa^{\mathrm{SS}} \end{pmatrix}$$

The DFC and the DFB matrices are

$$[7] \qquad \boldsymbol{F}_\kappa = \boldsymbol{o}_\kappa + \boldsymbol{t}_\kappa$$

and

$$[8] \qquad \boldsymbol{F}_\kappa = \boldsymbol{o}_\kappa + \boldsymbol{t}_\kappa + \boldsymbol{b}_\kappa$$

respectively. Where the one-electron part $\boldsymbol{o}_\kappa$ is

$$[9] \qquad \boldsymbol{o}_\kappa = \begin{pmatrix} \boldsymbol{V}_\kappa^{\mathrm{LL}} & c\boldsymbol{\Pi}_\kappa^{\mathrm{LS}} \\ c\boldsymbol{\Pi}_\kappa^{\mathrm{SL}} & \boldsymbol{V}_\kappa^{\mathrm{SS}} - 2c^2 \boldsymbol{S}_\kappa^{\mathrm{SS}} \end{pmatrix}$$

The two-electron part $\boldsymbol{t}_\kappa$, which consists of the matrices of two-electron Coulomb and exchange interactions, is given by

$$[10] \qquad \boldsymbol{t}_\kappa = \begin{pmatrix} \boldsymbol{J}_\kappa^{\mathrm{LL}} - \boldsymbol{K}_\kappa^{\mathrm{LL}} & -\boldsymbol{K}_\kappa^{\mathrm{LS}} \\ -\boldsymbol{K}_\kappa^{\mathrm{SL}} & \boldsymbol{J}_\kappa^{\mathrm{SS}} - \boldsymbol{K}_\kappa^{\mathrm{SS}} \end{pmatrix}$$

The frequency-independent Breit interaction leads to the term $\boldsymbol{b}_\kappa$ in the matrix SCF equation, eq. [5], viz.

$$[11] \qquad \boldsymbol{b}_\kappa = \begin{pmatrix} \boldsymbol{B}_\kappa^{\mathrm{LL}} & \boldsymbol{B}_\kappa^{\mathrm{LS}} \\ \boldsymbol{B}_\kappa^{\mathrm{SL}} & \boldsymbol{B}_\kappa^{\mathrm{SS}} \end{pmatrix}$$

The one- and two-electron matrix elements in eqs. [9]–[11] are expressed in terms of the generator coordinate γ, and have been shown elsewhere (7, 8). In the GCDF method the $\boldsymbol{b}_\kappa$ term is introduced in the SCF procedure according to the previous work of Quiney et al. (19), which showed that there is no necessity for the $\boldsymbol{b}_\kappa$ term to be treated as a first-order perturbation, as was widely believed. Later, Ishikawa et al. (20) developed the DFB SCF method including the $\boldsymbol{b}_\kappa$ term in the SCF procedure, as suggested by Quiney et al. (19), using GTF basis sets.

3. Some considerations about the even-tempered exponents and the ID technique

In this section we would like to draw attention to the similarity between the even-tempered technique and the ID technique used in the GCDF method. The definition for the even-tempered exponents is $\xi = \alpha\beta^{i-1}$, where α and β are constants to be determined, and $i = 1, 2, \ldots, N$. Thus, the increment $\Delta\xi$ is $\Delta\xi = \xi_{i+1} - \xi_i = \alpha\beta^{i-1}(\beta - 1) = \xi_i(\beta - 1)$, i.e., the basis function exponent ξ_i times a constant. In our case, the ID technique was proved to be particularly efficient with a relabelling technique of the generator coordinate space γ (see eq. [4]) with Gaussian generator functions, namely, $\gamma_i = \exp(A\Theta_i)$, and $\Delta\gamma = \gamma_{i+1} - \gamma_i = \exp(A\Theta_i)[\exp(A\Delta\Theta - 1)] = \gamma_i[\exp(A\Delta\Theta) - 1]$, i.e., again a basis function exponent times a constant. Despite the similarity between the two techniques, the even-tempered formula never aimed at the solution of a continuous problem (the parameters α and β are generally determined variationally), whereas our discretization parameters are determined through numerical integration in order to adequately simulate eqs. [3]. Thus, the even-tempered gen-

eration of basis function exponents is unrelated to ours. Indeed, the application of the two techniques to study the same atomic system will lead (for a finite basis set of fixed size) to different energy values, because the basis function exponents generated by each technique would be different.

It is important to mention that through our technique we are always able to generate accurate universal basis sets for a large number of atomic species (12–15, 21). On the other hand, to generate a universal basis set variationally with the even-tempered formula is almost impossible, as trying to do that implies finding variationally a unique set of parameters α and β that can describe the energy of a considerable number of atoms. This is the reason why papers published in the literature in which even-tempered basis sets are determined variationally always have one different set of parameters α and β for each orbital symmetry in each atomic system studied. In a unique case, Silver and Nieuwpoort in 1978 indeed generated a universal even-tempered basis set for 10 atoms using Slater-type functions, but the parameters α and β were chosen quite arbitrarily instead of being determined variationally (22).

4. Results and discussion

The DFC and DFB SCF calculations on Be and Be-like species Ne^{6+}, Ar^{14+}, and Sn^{46+} are performed by using the closed-shell GCDF method presented briefly in Sect. 2. The finite nuclear model of uniform proton charge distribution and kinetic balance constraints (5, 6, 19) are used in our calculations in this work. The atomic masses used for Be, Ne, Ar, and Sn nuclei are, respectively, 9.0, 20.0, 39.948, and 118.69 amu. The speed of light c is in all calculations taken to be 137.0370 au.

The GTF exponents generated here with the GCDF method for Be atom and Be-like ions can easily be reproduced by using eq. [4] and the discretization parameters Θ_{min} (starting exponent), $\Delta\Theta$ (increment), and N (number of exponents) shown in Tables 1–5 for each atomic species studied. The scaling parameter A in eq. [4] is used in all calculations as 6.0. From the discretization parameters shown in Tables 3–5, we notice that the starting exponent can differ from one ion to another, despite having a unique (universal) set of GTF exponents used for Ne^{6+}, Ar^{14+}, and Sn^{46+}. For each atomic species studied, we increased the number of exponents per $s_{1/2}$ symmetry until a total DFC energy value was obtained with an accuracy comparable to (or better than) that obtained with the numerical finite-difference program. Afterwards, we used the same set of exponents to perform the corresponding DFB calculations.

Table 1 shows the convergence pattern for Be, and Tables 2–5 display the results for DFC and DFB energies (E_{DFC} and E_{DFB}, respectively), $1s$ and $2s$ DFC and DFB orbital energies (ε_{1s} and ε_{2s}, respectively), and the Breit interaction energy (E_B) obtained with the GCDF method and other approaches for Be, Ne^{6+}, Ar^{14+}, and Sn^{46+}. $E_{B(SCF)}$ denotes the variational Breit interaction energy computed as the difference between E_{DFB} and E_{DFC}. $E_{B(PT)}$ is the first-order Breit interaction energy evaluated perturbatively (1, 9).

Table 1 displays the convergence pattern of the DFC, DFB, and E_B energies for the Be atom. One can see from Table 1 that the Be DFC and DFB energies converge to the lowest

Table 1. Convergence pattern for the DFC, DFB, and E_B energies of the Be atom (in hartrees).

N^a	$(E_{DFC})^b$	$(E_{DFB})^c$	$(E_B)^d$
11	−14.392 428 47	−14.391 765 97	0.000 662 50
13	−14.550 554 70	−14.549 857 29	0.000 697 41
15	−14.572 705 08	−14.572 002 49	0.000 702 59
19	−14.575 844 96	−14.575 141 77	0.000 703 19
21	−14.575 886 99	−14.575 183 79	0.000 703 20
25	−14.575 892 95	−14.575 189 75	0.000 703 20
26	−14.575 893 02	−14.575 189 82	0.000 703 20
27	−14.575 893 05	−14.575 189 85	0.000 703 20
28	−14.575 893 06	−14.575 189 86	0.000 703 20
29	−14.575 893 06	−14.575 189 86	0.000 703 20
30	−14.575 893 06	−14.575 189 86	0.000 703 20

[a]The discretization parameters used in all calculations are $\Theta_{min} = -0.64$ and $\Delta\Theta = 0.119$.
[b]E_{DFC} represents the Dirac–Fock–Coulomb energy.
[c]E_{DFB} represents the Dirac–Fock–Breit energy.
[d]E_B represents the variational Breit interaction energy.

Table 2. Calculated DF energies for the Be atom (in hartrees).[a]

	GTF (this work) $N = 28$[b]	Even-tempered GTF (9)	Numerical finite-difference calculations[c]
E_{DFB}	−14.575 189 86	−14.575 189 13	−14.575 189 49
ε_{1s}	−4.732 941	−4.732 935	
ε_{2s}	−0.309 310 0	−0.309 308 4	
E_{DFC}	−14.575 893 06	−14.575 891 57	−14.575 891 97
ε_{1s}	−4.733 500	−4.733 493	−4.733 498
ε_{2s}	−0.309 323 0	−0.309 321 1	−0.309 322 1
$E_{B(SCF)}$	+7.032 0(−4)	+7.024 4(−4)	
$E_{B(PT)}$		+7.024 8(−4)	+7.024 8(−4)

[a]Entries of the form $a(b)$ are to be interpreted as $a \times 10^b$.
[b]$\Theta_{min} = -0.64$ and $\Delta\Theta = 0.119$.
[c]Obtained from ref. 9.

limit of −14.575 893 06 and −14.575 189 86 hartrees, respectively, when the basis set size reaches $N = 28$. It is interesting to mention that for $N = 21$ the Breit interaction energy has already converged whereas the DFC and DFB total energies have not yet done so.

Table 2 contains several energy results for the Be atom computed with the GCDF method and other approaches. From Table 2 we can see that the DFC and DFB energy results obtained with the GCDF method are lower, respectively, by 1.49 and 0.73 μhartree than their counterparts obtained with even-tempered basis set (9), and by 1.09 and 0.37 μhartree than those obtained by using the numerical finite-difference method (9). The excellent performance of our GTF basis set in describing the DFC energy for the Be atom is attributed to the proper representation of the wave function inside the nucleus due to the higher numerical accuracy of the Gaussian basis functions generated here with the GCDF method. This evidence is not completely new, as in a previous paper Parpia and Mohanty (23) already verified the possibility of basis set functions being able to better rep-

Table 3. Calculated DF energies for the Ne^{6+} ion (in hartrees).[a]

	GTF (this work) $N = 31$[b]	Even-tempered GTF (9)	Numerical finite-difference calculations[c]
E_{DFB}	−110.242 107 3	−110.242 106 6	−110.242 105 6
ε_{1s}	−40.576 50	−40.576 50	
ε_{2s}	−7.500 461	−7.500 461	
E_{DFC}	−110.255 973 6	−110.255 972 9	−110.255 974 0
ε_{1s}	−40.588 39	−40.588 39	−40.588 39
ε_{2s}	−7.501 338	−7.501 339	−7.501 339
$E_{B(SCF)}$	+1.386 63(−2)	+1.386 63(−2)	
$E_{B(PT)}$			+1.386 84(−2)

[a]Entries of the form *a(b)* are to be interpreted as $a \times 10^b$.
[b]$\Theta_{min} = -0.10$ and $\Delta\Theta = 0.104$.
[c]Obtained from ref. 9.

Table 4. Calculated DF energies for the Ar^{14+} ion (in hartrees).[a]

	GTF (this work) $N = 32$[b]	Even-tempered GTF (9)	Numerical finite-difference calculations[c]
E_{DFB}	−379.111 135 8	−379.111 135 4	−379.111 113 2
ε_{1s}	−144.859 9	−144.859 9	
ε_{2s}	−31.247 57	−31.247 57	
E_{DFC}	−379.198 184 2	−379.198 183 9	−379.198 185 7
ε_{1s}	−144.936 3	−144.936 3	−144.936 3
ε_{2s}	−31.254 40	−31.254 40	−31.254 40
$E_{B(SCF)}$	+8.704 84(−2)	+8.704 85(−2)	
$E_{B(PT)}$			+8.707 25(−2)

[a]Entries of the form *a(b)* are to be interpreted as $a \times 10^b$.
[b]$\Theta_{min} = -0.10$ and $\Delta\Theta = 0.104$.
[c]Obtained from ref. 9.

Table 5. Calculated DF energies for the Sn^{46+} ion (in hartrees).

	GTF (this work) $N = 31$[a]	Even-tempered GTF (9)	Numerical finite-difference calculations[b]
E_{DFB}	−3157.780 377 1	−3157.780 375 4	−3157.778 808 6
ε_{1s}	−1239.498	−1239.498	
ε_{2s}	−297.736 0	−297.736 0	
E_{DFC}	−3159.833 052 0	−3159.833 050 3	−3159.833 054 6
ε_{1s}	−1241.327	−1241.327	−1241.327
ε_{2s}	−297.925 9	−297.926 0	−297.926 0
$E_{B(SCF)}$	+2.052 675	+2.052 675	
$E_{B(PT)}$			+2.054 246

[a]$\Theta_{min} = -0.10$ and $\Delta\Theta = 0.104$.
[b]Obtained from ref. 9.

resent the wave function inside the nucleus than numerical finite-difference calculations. The DFC and DFB orbital energies computed with the GCDF method for Be are slightly lower than the corresponding DFC and DFB orbital energies obtained with the other two approaches. The E_B obtained for Be with the GCDF method is in good agreement with the other values obtained with the even-tempered GTF and the perturbative approach (9).

Tables 3–5 display the results for the Ne^{6+}, Ar^{14+}, and Sn^{46+} ions using our GTF basis set generated with the GCDF method, the even-tempered GTF basis set (9), and the numerical finite-difference method (9). Here, it is interesting to draw attention to the fact that for Ne^{6+}, Ar^{14+}, and Sn^{46+} we have generated, with the GCDF method, a universal Gaussian basis set to describe this set of positive ions, while the even-tempered basis sets have a different set of parameters α and β for each one of the three positive ions studied, and these parameters are obtained variationally in a nonrelativistic environment. One can see from the footnotes of Tables 3–5 that Θ_{min} and $\Delta\Theta$ are always the same for the three ionic species studied here. From these tables, we see that our DFC energies are always better than the even-tempered GTF results and are very close to the results obtained with the numerical finite-difference method. On the other hand, our DFB energies obtained for these ionic species are always lower than the DFB energies obtained with the even-tempered GTF basis set and the numerical finite-difference method. For the three ions studied, the DFC and DFB orbital energies obtained with our GTF are in excellent agreement when compared to the corresponding orbital energies obtained with the numerical finite-difference approach. Besides, the E_B computed with our GTF is in good agreement with the perturbative approach despite the E_B obtained with the perturbative approach being slightly larger in magnitude than the E_B results obtained with the GCDF method. According to Ishikawa (9), the difference between the E_B calculated variationally and that calculated by using the perturbative approach indicates that first-order perturbation calculations overestimate the E_B, and the error is not negligible for a moderately high-Z atom (for Sn^{46+} the difference is 10^{-3} au). Quiney et al. (19) pointed out that this difference may be attributed to the inclusion of higher-order ($\alpha^4 \ldots$) covariant contributions in the SCF treatment of the Breit interaction that are absent in the first-order perturbation treatment.

We attribute the high accuracy of our GTF basis set, presented in this work for Be-like atomic species, to the ID technique of the GCDF method. In the GCDF, the ID technique is implemented inside the DF equations, and thus the GTF exponents are generated directly from a relativistic environment. We believe the reason why our DF energy results, obtained here for Be-like atomic species with the GCDF method, are better than the even-tempered basis set counterparts (9) is related to the fact that the ID technique of the GCDF method is implemented directly inside the DF equations. It is important to mention that the even-tempered GTF exponents used by Ishikawa (9) were originally inside a nonrelativistic environment, and afterwards transferred to the relativistic environment in order to perform DF calculations. Thus we see that the GCDF method is able to provide very accurate Gaussian basis sets for relativistic calculations, as presented here for light atomic systems and previously for heavy atoms (7, 8).

5. Conclusion

The DF energy values reported in this work for Be-like atomic species show that with a careful numerical integration of the DF equations in the GCDF method we are able to generate very accurate GTF to be used in relativistic atomic and

molecular calculations. With the GCDF method, the GTF exponents are generated by the discretization of the integral DF equations with the best numerical integration as a goal. Thus, in the GCDF formalism, the GTF exponents are not parameters to be variationally optimized as usual. The GCDF method represents an algorithm capable of generating GTF exponents directly from a relativistic environment (code).

The DFC and DFB energies obtained in this work with the GCDF method are competitive in accuracy with the corresponding values obtained with the numerical finite-difference method and better than the DFC and DFB energies obtained with an even-tempered GTF basis set. The excellent DFC and DFB energy results obtained here for the Be atom, when compared to the numerical finite-difference counterpart, are attributed to the higher accuracy of our GTF basis set due to the implementation of the ID technique inside the relativistic environment.

Acknowledgments

The financial support by CNPq and FINEP (Brazilian Agencies) is gratefully acknowledged.

References

1. J.P. Desclaux. Comput. Phys. Commun. **9**, 31 (1975).
2. I.P. Grant, B.J. McKenzie, P.H. Norrington, D.F. Mayers, and N.C. Pyper. Comput. Phys. Commun. **21**, 207 (1980).
3. F.A. Parpia, A.K. Mohanty, and E. Clementi. J. Phys. B: At. Mol. Opt. Phys. **25**, 1 (1992).
4. Y.-K. Kim. Phys. Rev. **154**, 17 (1967).
5. Y. Ishikawa, R. Baretty, and R.C. Binning, Jr. Chem. Phys. Lett. **121**, 130 (1985).
6. Y. Ishikawa and H.M. Quiney. Int. J. Quantum Chem. Symp. **21**, 523 (1987).
7. F.E. Jorge and A.B.F. da Silva. J. Chem. Phys. **104**, 6278 (1996).
8. F.E. Jorge and A.B.F. da Silva. J. Chem. Phys. In press.
9. Y. Ishikawa. Chem. Phys. Lett. **166**, 321 (1990).
10. S. Okada and O. Matsuoka. J. Chem. Phys. **91**, 4193 (1989).
11. A.K. Mohanty and E. Clementi. J. Chem. Phys. **93**, 1829 (1990).
12. A.B.F. da Silva, G.L. Malli, and Y. Ishikawa. Chem. Phys. Lett. **203**, 201 (1993); **201**, 37 (1993).
13. A.B.F. da Silva, G.L. Malli, and Y. Ishikawa. Can. J. Chem. **71**, 1713 (1993).
14. G.L. Malli, A.B.F. da Silva, and Y. Ishikawa. Phys. Rev. A: At. Mol. Opt. Phys. **47**, 143 (1993).
15. G.L. Malli, A.B.F. da Silva, and Y. Ishikawa. J. Chem. Phys. **101**, 6829 (1994).
16. O. Matsuoka and S. Huzinaga. Chem. Phys. Lett. **140**, 567 (1987).
17. J.J. Griffin and J.A. Wheeler. Phys. Rev. **108**, 311 (1957).
18. J.R. Mohallem. Z. Phys. D: At. Mol. Clusters, **3**, 339 (1986).
19. H.M. Quiney, I.P. Grant, and S. Wilson. J. Phys. B: At. Mol. Opt. Phys. **20**, 1413 (1987).
20. Y. Ishikawa, H.M. Quiney, and G.L. Malli. Phys. Rev. A, **43**, 3270 (1991).
21. A.B.F. da Silva, H.F.M. da Costa, and M. Trisic. Mol. Phys. **68**, 433 (1989).
22. D.M. Silver and W.C. Nieuwpoort. Chem. Phys. Lett. **57**, 421 (1978).
23. F.A. Parpia and A.K. Mohanty. Phys. Rev. A, **46**, 3735 (1992).

The chemistry of thujone. XIX.[1] Acid-promoted ring cleavage of thujone-derived cyclopropylcarbinols

James P. Kutney, Yong-Huang Chen, and Steven J. Rettig

Abstract: Thujone-derived cyclopropylcarbinols can cleave via three distinct pathways: the *exo* cleavage, the *endo* cleavage, and the interesting cyclopropylcarbinyl rearrangement. Factors determining which pathway is adopted under specific conditions are discussed. A short sequence leading to synthesis of the sesquiterpene (+)-β-cyperone is described.

Key words: thujone, cyclopropylcarbinols, cyclopropylcarbinyl rearrangement, β-cyperone synthesis.

Résumé : Les cyclopropylcarbinols dérivés de la thujone peuvent subir trois clivages distincts : le clivage *exo*, le clivage *endo* et l'intéressant réarrangement cyclopropylcarbinyle. On discute des facteurs qui déterminent le processus suivi dans des conditions spécifiques. On décrit une courte séquence conduisant à la synthèse du sesquiterpène (+)-β-cypérone.

Mots clés : thujone, cyclopropylcarbinols, cyclopropylcarbinyle, réarrangement, synthèse de la β-cypérone.

[Traduit par la rédaction]

In continuing the development of the monoterpene thujone (**1**)[3] as an efficient chiral building block (1), we discovered a novel procedure for functionalizing thujone and its derivatives of general structure (i) by ozonation (Fig. 1) (2). The ozonation procedure provides two valuable intermediates of general structures (ii) and (iii) amenable for synthetic exploitation. The cyclopropylcarbinols have been applied in the synthesis of antifeedant polygodial derivatives (2) and the fragrance compounds damascone and damascenone (2, 3). The cyclopropyl ketone derivatives, on the other hand, have been utilized in the synthesis of ambergris fragrances (2). In this article, we would like to detail our recent studies on acid-promoted ring cleavage of thujone-derived cyclopropylcarbinols.

Cleavage reactions, *exo* and *endo*

It is well known that cyclopropylcarbinols can be readily cleaved in the presence of acids (4). Thujone-derived nonsymmetrically substituted cyclopropylcarbinols of structure (ii) in Fig. 1 are expected to produce two regioisomers. For example, the nucleophilic attack of halide X^- at C5 in (ii) will lead to a homoallylic halide of a cyclohexyl skeleton, through cleavage of the C5—C1 bond (i.e., *endo* cleavage); the nucleophilic attack of halide X^- at C6 will form a homoallylic halide of a cyclopentyl skeleton, through cleavage of the C6—C1 bond (i.e., *exo* cleavage) (Fig. 2).

When the thujone-derived alcohol **2** was treated with concentrated hydrochloric acid in methylene chloride, homoallylic chloride **3** was obtained in 85% yield by the *exo*-cleavage pathway. The putative *endo*-cleavage product **4** was not isolated. In brief, the ^{1}H NMR spectrum of **3** showed two methyl singlets at δ 1.63 and 1.70 ppm, indicating the presence of an isopropylidene group, and a multiplet (2H, octet) at δ 3.55 ppm, characteristic of the A/B portion of an ABX system, corresponding to the chloromethylene group.

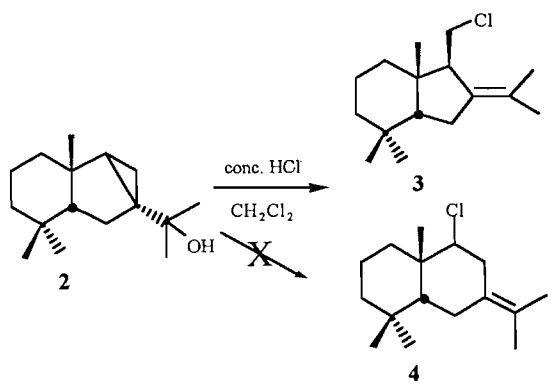

Treatment of another thujone-derived cyclopropylcarbinol **5** with concentrated HCl also gave the *exo*-cleavage product **6** as the major product (75% yield), the *endo*-cleavage product was not isolated.

Stirring of chloride **6** in the presence of silica gel in methylene chloride overnight regenerated the starting ketol **5** exclusively. The β orientation of the chloromethyl group of the *exo*-cleavage products was therefore verified.

Received February 14, 1996.

J.P. Kutney,[2] Y.-H. Chen, and S.J. Rettig. Department of Chemistry, University of British Columbia, 2036 Main Mall, Vancouver, BC V6T 1Z1, Canada.

[1] For the previous publication in this series, see ref. 1.

[2] Author to whom correspondence should be addressed: Telephone and Fax: (604) 822-2710. E-mail: Kutney@unixg.ubc.ca

[3] This natural product is actually a mixture of two epimers, (−)-α-thujone (α-methyl at C-4) and (+)-β-thujone (β-methyl at C-4) in a ratio of 10:1, respectively. However, any base-catalyzed condensation at C-4 leads to only one chiral isomer with the angular methyl group in a β orientation as shown in partial structure (i) (Fig. 1).

Fig. 1.

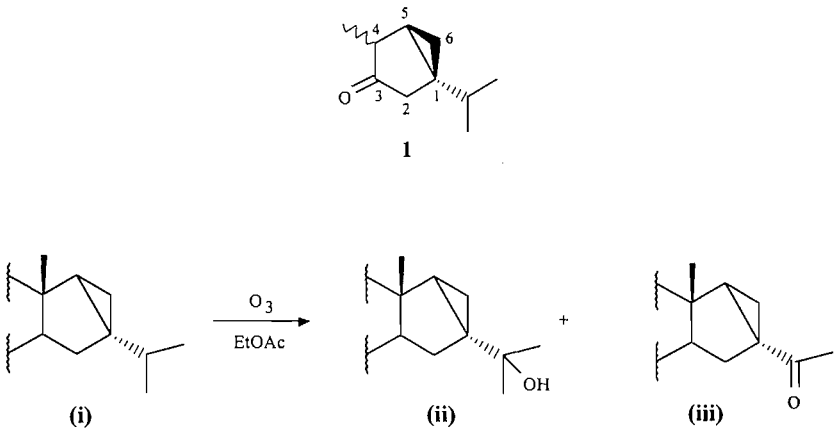

Fig. 2.

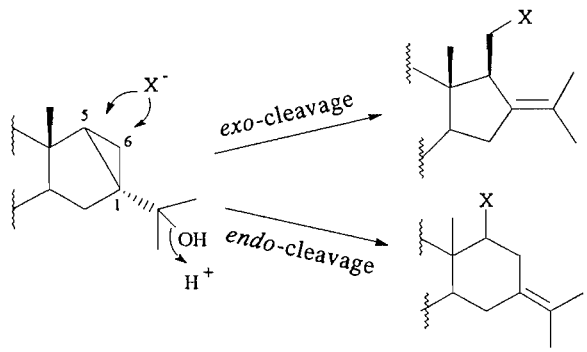

The hydrochloric acid promoted *exo*-cleavage reaction is applicable to other thujone-derived cyclopropylcarbinols with a saturated sp^3-hybridized C3 centre. For example, compound **7** was converted to chloride **8** in the synthesis of drimane antifeedant analogues (2). In a sequence leading to synthesis of the rose oil fragrances, β-damascone and β-damascenone (2, 3), thujone derivative **9** was converted into **10**.

It appears that the nucleophilic attack of chloride is concurrent with the cleavage of the C—C bond. Otherwise, if the C—C bond cleavage preceded the chloride attack, the *endo*-cleavage pathway would generate a more stable secondary carbocation as its intermediate and might become the dominant pathway. This conclusion is consistent with the previous observation with regard to the stereochemistry of the acid-promoted cleavage of 1-alkoxymethyl bicyclo[3.1.0]hexanes (5). Therefore, the preference for this *exo* cleavage is very likely due to the more exposed and accessible nature of the C6 methylene compared to the C5 methine in the cyclopropyl ring.

However, the regioselectivity of ring cleavage is altered under the same experimental conditions, when thujone-derived cyclopropylcarbinols are sp^2-hybridized at C3. Thujonol (**11**), which is a mixture of C4 epimers (**11**α and **11**β in a ratio of 10:1), was treated with concentrated hydrochloric acid at room temperature to give carvacrol (**12**) (6) and the chloro-enone **13** in 40 and 45% yields, respectively.

The chloro-enone **13** was rather unstable and therefore the ^1H NMR spectrum obtained was always contaminated with extra signals due to the presence of carvacrol (**12**). However, a "difference spectrum" between the "contaminated spectrum"and the spectrum of **12** clearly revealed all signals of **13**.

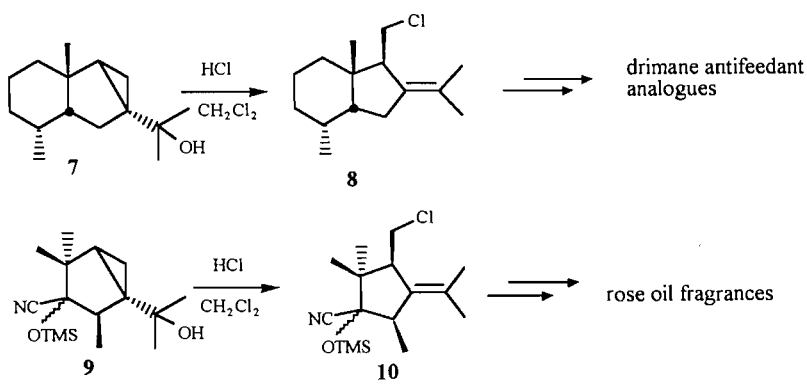

Fig. 3. A formal synthesis of (+)-β-cyperone (**17**).

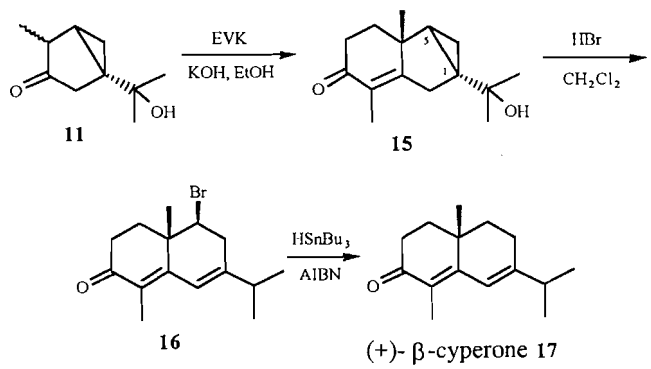

Fig. 4. The ring cleavage reaction of **15** via the *endo*-type cleavage pathway.

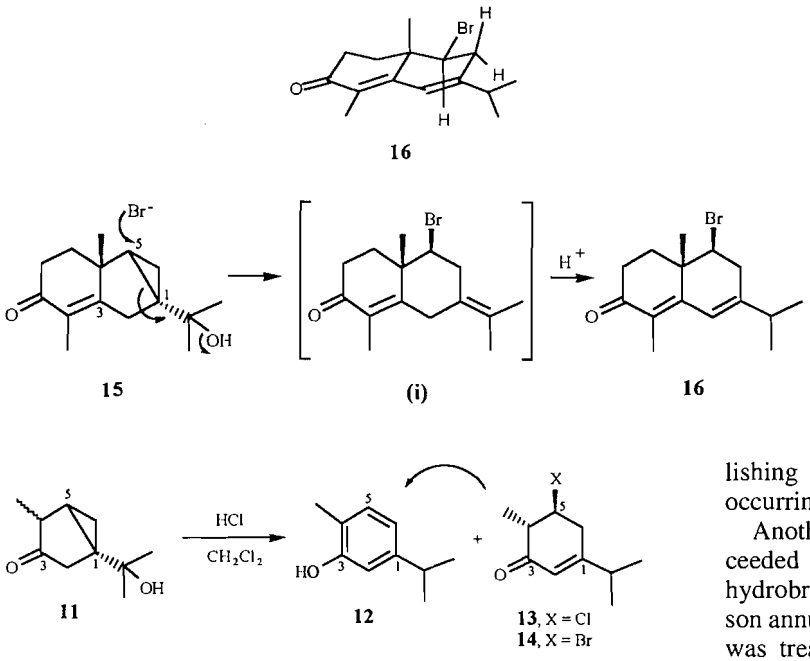

This difference spectrum of **13** showed a multiplet (doublet of triplet) at δ 4.06 ppm (1H, J = 4.4 and 9.8 Hz) corresponding to the methine proton at the chlorine bearing carbon (C5), and a broad singlet at δ 5.95 ppm (1H) due to the olefinic proton at C2. The splitting pattern of the methine at C5 indicated that the methyl group and the chlorine are in the *trans* configuration. The nucleophilic attack of the chloride anion from the back side of the cleaving C1—C5 bond should afford the designated β orientation of the chlorine as shown in **13**.

Thujonol (**11**) was also treated with concentrated hydrobromic acid in methylene chloride. Carvacrol (**12**) and the bromoenone **14** were isolated in 10 and 85% yields, respectively. The latter (**14**) is much more stable than the analogous chloroenone **13**. The ^{1}H NMR spectrum of **14** is very similar to that of **13**. A multiplet (doublet of triplet) signal at δ 4.19 ppm (J = 4.4 and 10.2 Hz) is due to the methine proton at the bromine-bearing carbon (C5) while a broad singlet at δ 5.97 ppm is clearly due to the olefinic proton at C2. The specific rotation of **14** was measured to be +42 (c = 0.29, $CHCl_3$), thereby establishing that a significant amount of racemization was not occurring in the conversion of **11** to **14**.

Another thujone-derived cyclopropylcarbinol also proceeded via the *endo*-cleavage pathway when treated with hydrobromic acid. Hydroxy-enone **15**, obtained from Robinson annulation of thujone (**11**) with ethyl vinyl ketone (EVK), was treated with hydrobromic acid in methylene chloride. Bromo-dienone **16** was isolated in 91% yield (Fig. 3). Compound **16** was previously reduced to (+)-β-cyperone (**17**) by tributyltin hydride in an earlier synthesis of (+)-β-cyperone from thujone (2). Thus, a new sequence to (+)-β-cyperone was completed in four steps using ozonation of thujone, Robinson annulation of thujonol (**11**), acid-promoted ring cleavage of **15**, and radical-mediated reduction of **16**.

The formation of **16** is similar to that of **13** and **14**. The ring cleavage reaction generates an unstable intermediate that then rearranges to the more stable dienone **16** with a fully conjugated dienone system (Fig. 4).

The reason for the *endo*-cleavage selectivity in the thujone-derived intermediates that possess an unsaturated system in ring A, that is, an sp^2-hybridized center at C3, is not well understood. Perhaps the interaction of the double bond *exo* to the bicyclo[3.1.0]hexane and the C1—C5 bond in hydroxy-enone **15** and thujonol (**11**) leads to the weakening of C1—C5 and eventually its facile cleavage under acidic conditions.

The cyclopropylcarbinyl rearrangement

Previous studies have shown that 1-alkyoxymethyl bicy-

clo[3.1.0]hexanes can be cleaved through the *endo*-cleavage pathway by using non-nucleophilic conditions. There are examples in the literature showing the use of other solvolysis conditions (5). The poor nucleophilicity of the attacking groups such as H_2O and HOAc under this set of conditions may allow the ring cleavage reaction to occur in a less synchronized mechanism so that, in the transition state, the C—C bond cleavage to a carbocationic species becomes more predominant than bond formation between the carbon atom and the incoming nucleophile. The *endo*-type cleavage proceeds through a more stable transition state because the tertiary center C5 accommodates the developed partial charge better than the secondary center C6. Therefore, the *endo*-type cleavage prevails.

When the thujone-derived cyclopropylcarbinol **2** was treated with a catalytic amount of *p*-toluenesulfonic acid in dioxane:H_2O (1:1), a novel rearrangement product **18** was obtained in 85% yield. The two expected *exo*- and *endo*-cleavage products **19** and **20** were not isolated. The absence of any signals at δ 3.0–4.0 ppm in the NMR spectrum clearly revealed that the product obtained could not be a primary or secondary alcohol. The ^1H NMR spectrum contained a one-proton broad singlet at δ 5.33 ppm corresponding to the olefinic proton, and five methyl singlets at δ 0.87, 1.01, 1.17, 1.21, and 1.22 ppm. From the chemical shifts, it is obvious that none of the methyl groups is adjacent to the double bond.

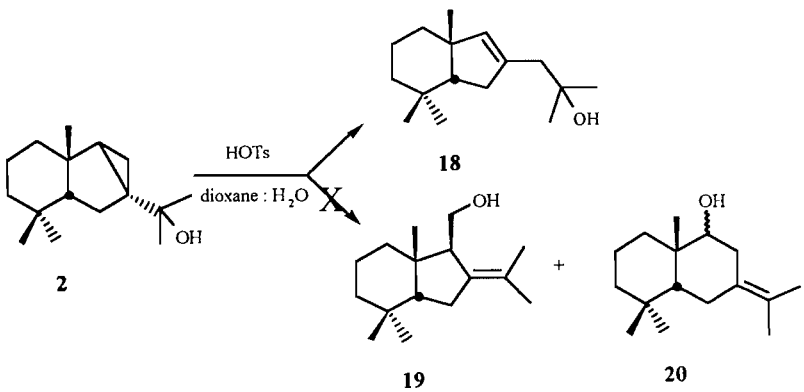

To confirm the structure of **18**, a series of chemical conversions was carried out. Treatment of **18** with *m*-CPBA in methylene chloride produced a crystalline epoxide **21** in 90% yield. The NMR spectrum showed that the singlet olefinic signal at δ 5.33 ppm is replaced by the proton signal of the epoxide ring at δ 2.85 ppm. The orientation of the epoxide in **21** and, in turn, confirmation of the structure **18** were subsequently established by the X-ray crystal analysis of **21** (Fig. 5). The *cis* A/B ring junction in **21** and the β-orientation for the epoxide ring are clearly revealed. Details of the X-ray analysis will be published elsewhere.

When epoxide **21** was further treated with LAH in THF, an unexpected product, the allylic alcohol **22**, was obtained in

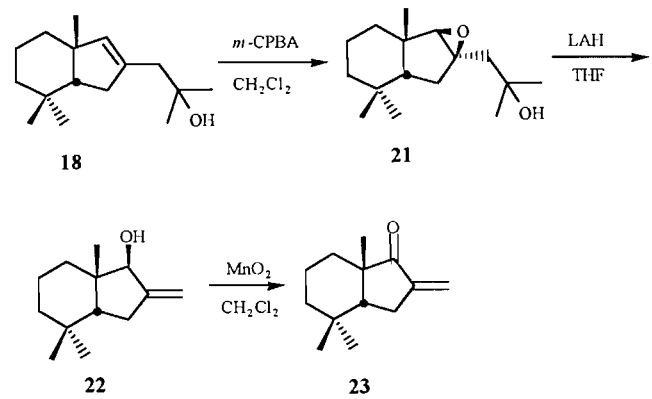

almost quantitative yield. The mass spectrum showed its molecular ion peak at *m/z* 194, corresponding to a loss of an acetone molecule (*m/z* = 58) from **21**. The IR spectrum displayed hydroxyl absorptions at 3100–3650 cm^{-1} while the ^1H NMR spectrum indicated only three methyl singlets at δ 0.82, 1.02, and 1.14 ppm, a one-proton singlet at δ 3.80 ppm corresponding to the allylic tertiary proton α to the hydroxyl group, and two olefinic one-proton singlets at δ 5.06 and 5.21 ppm. The β orientation of the hydroxyl group in **22** is clear from the mechanistic argument shown in Fig. 6.

Allylic alcohol **22** was subjected to allylic oxidation by manganese dioxide (7) in methylene chloride at room temperature to provide enone **23** in 70% yield. The mass spectrum showed the molecular ion peak at *m/z* 192. Its UV spectrum in methanol displayed an intense absorption at 235 nm (log ε = 4.0) and a weaker one at 278 nm (log ε = 2.5). The IR spectrum indicated a conjugated carbonyl absorption at 1710 cm^{-1}. The ^1H NMR spectrum confirmed the disappearance of the allylic tertiary proton signal previously noted in the spectrum of **22**.

To achieve a more conventional hydride-catalyzed opening of the epoxide, the β orientation of the epoxide ring in **21** dictates hydride attack from the very hindered concave α face. Consequently, the fragmentation reaction shown in Fig. 6 becomes the exclusive pathway. The epoxide **21** was treated with "superhydride" (lithium triethylborohydride) in order to see if the reduction rather than the fragmentation would take place. Again, the allylic alcohol **22** was obtained as the only product.

The rearrangement from **2** to **18** is a mechanistically novel process, a stepwise description of which is shown in Fig. 7. Initially the cyclopropylcarbinyl cation (i) is formed by a proton-catalyzed elimination of the hydroxyl group in **2**. The following 1,3-shift of the methylene on the cyclopropane ring would result directly in a spiro-cyclopropylcarbinyl cation (ii). The alternative rearrangement, via the cyclobutyl carbocation indicated, could also afford the cation (ii). This cat-

Fig. 5. Single crystal X-ray structure of epoxide **21** (PLUTO drawing).

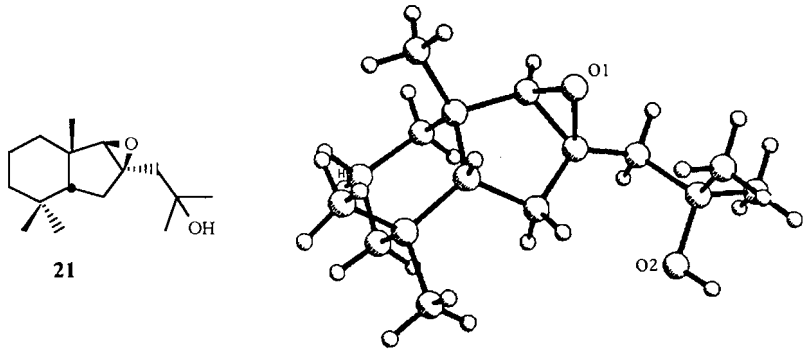

Fig. 6. Mechanism of the fragmentation of epoxide **21**.

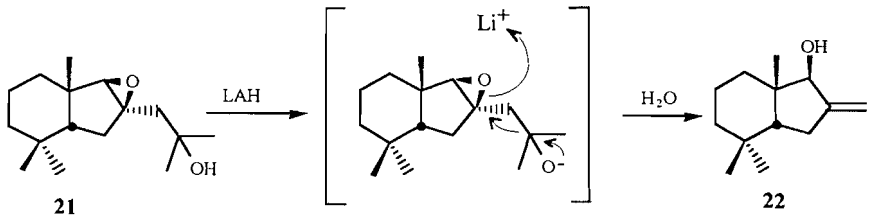

Fig. 7. The mechanism of the cyclopropylcarbinyl rearrangement reaction.

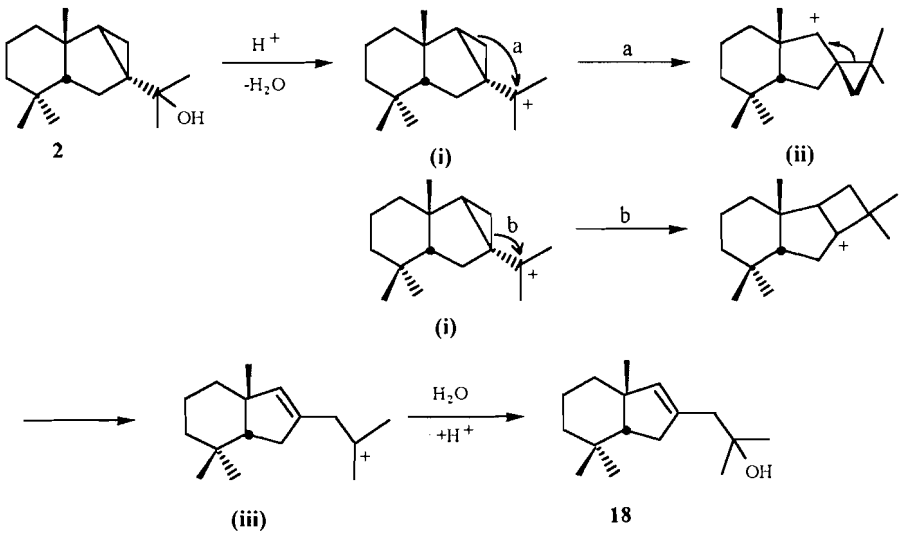

ion (ii) further cleaves regioselectively to form a more stable homoallylic cation (iii) and the latter, upon reaction with water, converts to **18**. The particular transformation between two cyclopropylcarbinyl cations in a manner similar to that between (i) and (ii), normally referred to as the cyclopropylcarbinyl rearrangement, was also termed as the "cyclopropane sliding reaction" by a Japanese group who studied this type of transformation in greater detail with their system (8). Mechanistic proposals involving this interesting reaction are also available in the literature (9) It seems that the thermodynamic stabilities among three carbocations (i), (ii), and (iii) determine the outcome of the solvolysis reaction.

Acetic acid treatment of **2** at 85°C also produced the cyclopropylcarbinol rearrangement product **24** in 60% yield in addition to the *exo*-cleavage product **25** in 6% yield. The competition of *exo* cleavage in this case is likely, because **25** may only slowly convert to the cyclopropylcarbinyl-like cation (i) shown in Fig. 7 once it is formed. The *exo*-cleavage product **19** could not be isolated in the previous reaction. The ^{1}H NMR spectrum of **24** is similar to that of **18**, except that an additional three-proton signal at δ 1.97 ppm due to the acetyl group was noted. For the minor product **25**, a two-proton multiplet (octet) signal at δ 3.92–4.25 ppm, which has a splitting pattern characteristic of the A/B portion of an ABX

system, can be assigned to the methylene attached to the acetate group.

The rearrangement reaction is applicable to other thujone-derived cyclopropylcarbinols but rather specific conditions are required. For example, ketol **26** was converted into product **27** in 87% yield by employing a catalytic amount of *p*-toluenesulfonic acid in a dioxane:water (1:1) mixture. However, rather surprisingly, treatment of **26** with acetic acid gave mainly the *exo*-cleavage product **28** (56%) and the *endo*-cleavage product **29** (14%). Although a very minor peak at δ 5.17 ppm in the ^{1}H NMR spectrum of **28** indicated a possible presence of the rearrangement product **30**, the very minor amount prevented its isolation.

Summary

In summary, acid-promoted ring cleavage reactions of thujone-derived cyclopropylcarbinols proceed through three distinct pathways, including the *exo* cleavage, *endo* cleavage, and the novel cyclopropylcarbinyl rearrangement reaction. Both reaction conditions and substrate structures influence which pathway becomes dominant. The availability of these diverse cleavage patterns allows a more versatile utilization of such thujone-derived cyclopropylcarbinols as chiral synthetic intermediates in subsequent synthetic routes to various natural products and related compounds.

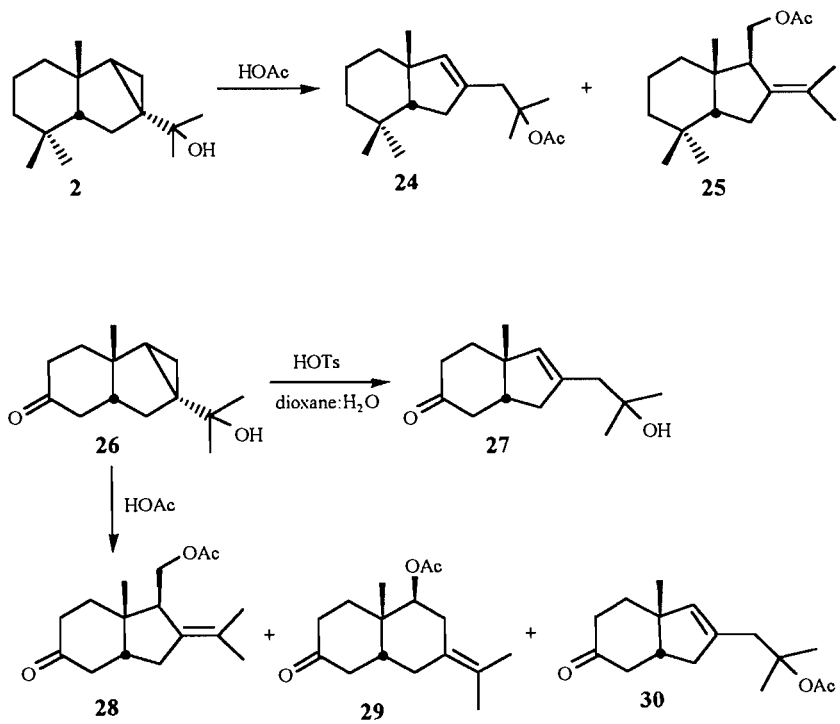

Experimental

Commercially available reagent grade solvents were used for chromatography without further purification. Unless otherwise stated, all reaction products were purified by "flash chromatography" using silica gel (230–400 mesh) supplied by E. Merck Co. with air pressure to obtain a suitable flow (10). Thujone was distilled from Western red cedar leaf oil, which was generously donated by Intrinsic Research and Development Incorporated.

Melting points were measured using a Kofler block melting point apparatus and are uncorrected. Optical rotations were recorded on a Perkin–Elmer 141 automatic polarimeter in chloroform solution using a quartz cell of 10 cm path length with the concentration (in g/100 mL) given in parentheses. The ultraviolet spectra were recorded on Cary 15 or Perkin–Elmer Lambda 4B UV/VIS spectrometers using quartz cells of 1 cm path length. The infrared spectra were recorded on Perkin–Elmer 710, 710B, and 1710 spectrometers in chloroform solution using NaCl cells of 0.1 mm path length or as thin film using NaCl plates. The ^{1}H NMR spectra were obtained from Bruker WH-400 or Varian XL-300 spectrometers with deuteriochloroform as solvent and the chemical shifts are reported in the delta (δ) scale in ppm relative to tetramethylsilane. The low- and high-resolution mass spectra were recorded on AEI-MS-9 and KRATOS-MS-50 spectrometers, respectively, using the electron impact ionization method while the chemical ionization mass spectra were recorded on a Delsi Nermag R10-1 OC spectrometer using ammonia as carrier gas. Elemental analyses were performed by Mr. P. Borda, Microanalytical Laboratory, University of British Columbia.

Chloride 3: the *exo* cleavage

Alcohol **2** (100 mg, 0.420 mmol) in methylene chloride (5.0 mL) was stirred with concentrated hydrochloric acid (5.0 mL) at room temperature for 30 min. Separation and concentration of the methylene layer gave the crude product, which was chromatographed with ethyl acetate:hexanes (1:8, v/v) to afford **3** as a colorless oil (92 mg, 85%).

The physical properties of **3** are as follows: $[\alpha]_D^{25}$ +33.5

(c = 1.00, $CHCl_3$). IR ν_{max} (film): 2910 (C-H stretching) cm^{-1}. ^1H NMR (400 MHz, $CDCl_3$) δ: 0.75–1.85 (22H, m, including 0.84 (3H, s), 1.04 (3H, s), 1.22 (3H, s), 1.63 (3H, s), and 1.70 (3H, s)), 2.04–2.55 (3H, m), 3.40–3.75 (2H, m). MS *m/z*: 256/254 (M^+, 4.8/14.8%), 241 (12.8%), 239 (37.6%), 203 (96.4%), 109 (100%). High-resolution mass measurement: calcd. for $C_{16}H_{27}{}^{37}Cl$: 256.1772; found: 256.1763; calcd. for $C_{16}H_{27}{}^{35}Cl$: 254.1801; found: 254.1801.

Chloroketone 6: the *exo* cleavage

Ketol **5** (78 mg, 0.33 mmol) in methylene chloride (5.0 mL) was stirred with concentrated hydrochloric acid (5.0 mL) at room temperture for 30 min. Water (20 mL) was added to quench the reaction. After methylene chloride extraction (2 × 10 mL), drying over magnesium sulfate, and evaporation of solvent in vacuo, the crude product was chromatographed with ethyl acetate:hexanes mixture (1:8, v/v) to afford the starting ketol **5** (15 mg, 19%) and chloride **6** (51 mg, 74%).

The physical properties of **6** are as follows: $[\alpha]_D^{25}$ +1.4 × 10^2 (c = 0.50, $CHCl_3$). IR ν_{max} (film): 1700, 1641 cm^{-1}. ^1H NMR (400 MHz, $CDCl_3$) δ: 1.00 (3H d, J = 7.0 Hz), 1.05 (1H, m), 1.24 (1H, m), 1.44 (3H, s), 1.58–1.80 (7H, including 1.60 (3H, s) and 1.71 (3H, s)), 2.10 (6H, m), 3.45–3.65 (2H, m). MS *m/z*: 256/254 (M^+, 0.6%/2.2%), 239 (0.5%), 218 (34.6%), 203 (18.4%), 133 (85.0%), 41 (100%). High-resolution mass measurement: calcd. for $C_{15}H_{23}O^{35}Cl$: 254.1437; found: 254.1437; calcd. for $C_{15}H_{23}O^{37}Cl$: 256.1408; found: 256.1412.

Carvacrol (12) and chloroenone 13: the *endo* cleavage

Thujonol (**11**) (500 mg, 2.98 mmol) was treated with concentrated hydrochloric acid (25 mL) in methylene chloride (25 mL) at room temperature for 1.5 h. The methylene chloride solution was separated, dried over magnesium sulfate, and concentrated *in vacuo*. Column chromatography with ethyl acetate:hexanes (1:20, v/v) provide chloro-enone **13** (252 mg, 45%) and carvacrol (**12**) (177 mg, 40%).

The physical properties of **12** are as follows: IR (film) ν_{max}: 3400 (O-H stretching) cm^{-1}. ^1H NMR (400 MHz, $CDCl_3$) δ: 1.22 (6H, d, J = 6.6 Hz), 2.21 (3H, s), 2.82 (1H, septet, J = 6.6 Hz), 3.96 (1H, bs), 6.66 (1H, d, J = 1.8 Hz), 6.72 (1H, dd, J = 1.8 and 7.1), 7.04 (1H, d, J = 7.1 Hz). MS *m/z*: 150 (M^+, 35.5%), 135 (100%), 107 (15.6%). High-resolution mass measurement: calcd. for $C_{10}H_{14}O$: 150.1045; found: 150.1051.

The physical properties of **13** are as follows: IR (film) ν_{max} 1675 (C=O stretching), 1630 (C=C stretching) cm^{-1}. ^1H NMR (400 MHz, $CDCl_3$) δ: 1.09 (6H, d, J = 7.2 Hz), 1.30 (3H, d, J = 7.8 Hz), 2.43 (1H, septet, J = 7.2 Hz), 2.54 (1H, m), 2.78 (2H, m), 4.06 (1H, dt, J = 4.4 and 9.8 Hz), 5.95 (1H, bs) ppm. MS *m/z*: 188/186 (M^+, 5.8%/19.1%), 151 (100%), 135 (15.9%).

Carvacrol (12) and bromoenone 14: the *endo* cleavage

Thujonol (**11**) (600 mg, 3.57 mmol) in methylene chloride (25 mL) was stirred with concentrated (48%) hydrobromic acid (25 mL) for 1.5 h at room temperature. The organic layer was separated, dried over magnesium sulfate, and concentrated in vacuo. The crude product was purified by column chromatography using ethyl acetate:hexanes (1:15, v/v) mixture to provide bromoenone **14** (700 mg, 85%) and carvacrol (**12**) (51 mg, 10%).

The physical properties of **14** are as follows: $[\alpha]_D^{25}$ +42 (c = 0.29, $CHCl_3$). UV (MeOH, c = 20 mg/L) λ_{max}: 234 nm (log ε = 3.95). IR (film) ν_{max}: 1670 (C=O stretching), 1630 (C=C stretching) cm^{-1}. ^1H NMR (400 MHz, $CDCl_3$) δ: 1.11 (6H, d, J = 6.8 Hz), 1.34 (3H, d, J = 7.1 Hz), 2.43 (1H, septet, J = 6.8 Hz), 2.55 (1H, m), 4.19 (1H, dt, J = 4.4 and 10.2 Hz), 5.97 (1H, bs). MS *m/z*: 232/230 (M^+, 1.1%/1.3%), 151 (100%), 135 (33.6%), 123 (60.2%). High-resolution mass measurement: calcd. for $C_{10}H_{15}O^{81}Br$ and $C_{15}H_{15}O^{79}Br$: 232.0287 and 230.0130; found: 232.0280 and 230.0116.

Hydroxyenone 15: Robinson annulation

To 1-dimethylaminopentan-2-one iodomethane salt (2.84 g, 9.44 mmol) in ethanol (80 mL) was added the solution of ketol **11** (1.43 g, 8.51 mmol) in ethanol (20 mL). After potassium hydroxide (0.92 g, 80% pure, 13 mmol) was added, the mixture was refluxed under nitrogen for 3 h. Concentration of the reaction mixture in vacuo gave a yellow oil that was chromatographed using ethyl acetate:hexanes mixture (1:1, v/v) to provide compound **15** as a colorless oil (636 mg, 32%).

The physical properties of **15** are as follows: $[\alpha]_D^{25}$ +90.3 (c = 2.03, $CHCl_3$). UV (MeOH, c = 40.6 mg/L) λ_{max}: 248 nm (log ε = 4.04). IR (film) ν_{max}: 3200–3600 (O-H stretching), 1645 (C=O stretching) cm^{-1}. ^1H NMR (400 MHz, $CDCl_3$) δ: 0.76 (1H, t, J = 4.7 Hz), 1.11 (3H, s), 1.20 (6H, s), 1.67 (3H, s) ppm. MS *m/z*: 234 (M^+, 1.2%), 216 (31.5%), 201 (48.0%), 173 (34.7%), 59 (100%). High-resolution mass measurement: calcd. for $C_{15}H_{22}O_2$: 234.1619; found: 234.1613.

Bromodienone 16: the *endo* cleavage

Hydroxy-enone **15** (39 mg, 0.17 mmol) in methylene chloride (5 mL) was stirred with concentrated (48%) hydrobromic acid (5 mL) at room temperature for 3 h. The methylene chloride layer was separated and the aqueous layer was extracted with methylene chloride (5 mL). The combined methylene chloride solution was dried over magnesium sulfate and concentrated in vacuo. Column chromatography of the crude product afforded bromo-dienone **16** (45 mg, 91%).

The physical properties of **16** are as follows: $[\alpha]_D^{25}$ +420 (c = 1.00, $CHCl_3$). UV (MeOH, c = 20 mg/L) λ_{max}: 293 nm (log ε = 4.40). IR (film) ν_{max}: 1660 (C=O stretching), 1620 (C=C stretching) cm^{-1}. ^1H NMR (400 MHz, $CDCl_3$) δ: 1.12 (6H, d, J = 6.0 Hz), 1.17 (3H, s), 1.86 (3H, s), 2.00–2.90 (7H, m), 4.14 (1H, dd, J = 6.0 and 10.0 Hz), 6.31 (1H, s). MS *m/z*: 298/296 (M^+, 80.0%/88.5%), 217 (100%), 175 (56.3%). High-resolution mass measurement: calcd. for $C_{15}H_{21}O^{79}Br$: 296.0775; found: 296.0768.

Alcohol 18: the cyclopropylcarbinyl rearrangement

To the solution of alcohol **2** (80 mg, 0.34 mmol) in a dioxane:water mixture solvent (4.00 mL, 1:1, v/v) was added *p*-toluenesulfonic acid hydrate (20 mg, 0.10 mmol, 0.30 equiv.). The mixture was heated at 85°C for 1 h and cooled to room temperature. Water (10 mL) was added and methylene chloride (2 × 10 mL) was used to extract the aqueous solution. The methylene solution was washed with brine (10 mL), dried over magnesium sulfate, and concentrated in vacuo. Column chromatography of the crude product with ethyl acetate:hexanes mixture (1:8, v/v) gave homoallylic alcohol **18** (70 mg, 87%).

The physical properties of **18** are as follows: $[\alpha]_D^{25}$ +45.2 (c = 1.00, $CHCl_3$). IR ν_{max} (film): 3100–3650 (OH stretching)

cm^{-1}. ^{1}H NMR (400 MHz, $CDCl_3$) δ: 0.88 (3H, s), 1.02 (3H, s), 1.07–1.70 (18H, m, including 1.18 (3H, s), 1.21 (3H, s) and 1.22 (3H, s)), 2.05–2.45 (4H, m), 5.33 (1H, bs). MS *m/z*: 236 (M^+, 0.1%), 218 (1.6%), 203 (5.0%), 178 (7.1%), 163 (100%), 135 (21.1%). High-resolution mass measurement: calcd. for $C_{16}H_{28}O$: 236.2140; found: 236.2145.

Epoxyalcohol 21: epoxidation

To a solution of alcohol **18** (172 mg, 0.729 mmol) in chloroform (5.0 mL) was added *m*-CPBA (243 mg, 80% pure, 11 mmol, 1.5 equiv.). The mixture was stirred at room temperature for 1 h. After addition of methylene chloride (5.0 mL) and washing with sodium bicarbonate solution (10 mL, 10%), the mixture was dried over magnesium sulfate and concentrated in vacuo. Column chromatography of the crude product with ethyl acetate:hexanes mixture (2:8, v/v) gave epoxide **21** (159 mg, 87%).

The physical properties of **21** are as follows: mp: 82–84°C. $[\alpha]_D^{25}$ +56.7 (*c* = 1.00, $CHCl_3$). IR ν_{max} (film): 3700 (O-H stretching) cm^{-1}. ^{1}H NMR (400 MHz, $CDCl_3$) δ: 0.70–1.70 (24H, m, including 0.80 (3H, s), 0.98 (3H, s), 1.20 (3H, s), 1.24 (3H, s) and 1.31 (3H, s)), 1.75–2.02 (2H, m), 2.04–2.15 (1H, dd, *J* = 7.2 and 13.6 Hz), 2.85 (1H, s). MS *m/z*: 252 (M^+, 0.2%), 234 (4.1%), 219 (6.9%), 194 (17.9%), 179 (19.8%), 161 (19.3%), 123 (100%), 109 (90.4%). High-resolution mass measurement: calcd. for $C_{16}H_{28}O_2$: 252.2089; found: 252.2088. Anal. calcd. for $C_{16}H_{28}O_2$: C 76.14, H 11.18; found: C 76.14, H 1.05.

Allylic alcohol 22: reductive fragmentation by LAH

Epoxide **21** (30.3 mg, 0.583 mmol) in anhydrous THF (1.0 mL) was added in a dropwise manner to a slurry of LAH (18.4 mg) in THF (1.0 mL) under nitrogen. The mixture was then heated at about 70°C (bath temperature) for 2 h. After cooling to room temperature, ethanol (5.0 mL) was added and stirring continued for 10 min. Subsequently, water (15 mL) was added and the resulting mixture was extracted with ethyl acetate (2 × 10 mL). The ethyl acetate solution was dried over magnesium sulfate and concentrated in vacuo. Column chromatography of the crude product with ethyl acetate:hexanes mixture (1:8, v/v) gave allylic alcohol **22** (20 mg, 87%).

The physical properties of **22** are as follows: $[\alpha]_D^{25}$ +5.4 (*c* = 1.00, $CHCl_3$). IR ν_{max} (film): 3100–3650 (O-H stretching), 3060 (C-H stretching, olefinic), 1650 (C=C stretching) cm^{-1}. ^{1}H NMR (400 MHz, $CDCl_3$) δ: 0.82 (3H, s), 1.02 (3H, s), 1.05–1.72 (13H, m, including 1.14 (3H, s)), 1.78 (1H, t, *J* = 8.8), 2.20–2.60 (2H, m). MS *m/z*: 194 (M^+, 13.1%), 179 (21.6%), 161 (13.0%), 123 (100%), 109 (85.5%). High-resolution mass measurement: calcd. for $C_{13}H_{22}O$: 194.1670; found: 194.1661.

Enone 23: allylic oxidation by MnO_2

Allylic alcohol **22** (29 mg, 0.15 mmol) in methylene chloride (2.0 mL) was treated with manganese dioxide (65 mg, 0.75 mmol). The slurry was stirred at room temperature for 72 h. After filtering the slurry and washing with methylene chloride (10 mL), the methylene chloride solution was concentrated in vacuo. Column chromatography of the crude product gave enone **23** (8.0 mg, 67% based on recovery) and starting allylic alcohol **22** (17 mg, 59% recovery).

The physical properties of **23** are as follows: $[\alpha]_D^{25}$ +57 (*c* = 0.58, $CHCl_3$). UV (MeOH), *c* = 23 mg/L) λ_{max}: 235 nm (log ε = 4.0), 278 (log ε = 2.5). IR ν_{max} (film): 1710 (C=O stretching), 1635 (C=C stretching) cm^{-1}. ^{1}H NMR (400 MHz, $CDCl_3$) δ: 0.75–1.70 (16H, m, including 0.85 (3H, s), 1.07 (3H, s), and 1.22 (3H, s)), 2.35–2.65 (2H, m), 5.37 (3H, bs), 6.07 (3H, bs). MS *m/z*: 192 (M^+, 49.9%), 177 (20.3%), 149 (28.9%), 123 (80.7%), 68 (100%). High-resolution mass measurement: calcd. for $C_{13}H_{20}O$: 192.1514; found: 192.1515.

Acetates 24 and 25: the cyclopropylcarbinyl rearrangement

A solution of alcohol **2** (60 mg, 0.26 mmol) in acetic acid (2.5 mL) was heated at 65°C for 2 h. After cooling to room temperature, methylene chloride (10 mL) was added and the mixture was extracted with 10% sodium bicarbonate solution (10 mL). The methylene chloride solution was dried over magnesium sulfate and concentrated in vacuo. Column chromatography of the crude product with ethyl acetate:hexanes mixture (1:25, v/v) yielded acetate **24** (41 mg, 60% based on recovery), acetate **25** (4.0 mg, 6% based on recovery), and the starting alcohol **2** (2.9 mg, 5%).

The physical properties of **24** are as follows: $[\alpha]_D^{25}$ +41.7 (*c* = 1.00, $CHCl_3$). IR ν_{max} (film): 1735 (C=O stretching), 1650 (C=C stretching) cm^{-1}. ^{1}H NMR (400 MHz, $CDCl_3$) δ: 0.85 (3H, s), 1.00 (3H, s), 1.03–1.60 (16H, including 1.15 (3H, s), 1.38 (3H, s), and 1.45 (3H, s)), 1.97 (3H, s), 2.02–2.35 (2H, m), 2.39–2.62 (2H, AB type, *J* = 7.2 Hz), 5.26 (1H, s). MS *m/z*: 218 (M−HOAc, 37.0%), 203 (100%), 175 (16.7%), 147 (21.5%). High-resolution mass measurement: calcd. for $C_{16}H_{26}$ ($C_{18}H_{30}O_2$ − HOAc): 218.2034; found: 218.2030. Chemical ionization (NH_3 as carrier gas): 279 ($M + H^+$), 219, 203.

The physical properties of **25** are as follows: $[\alpha]_D^{25}$ +63 (*c* = 0.20, $CHCl_3$). IR ν_{max} (film): 1730 (C=O stretching) cm^{-1}. ^{1}H NMR (400 MHz, $CDCl_3$) δ: 0.75–1.80 (22H, m, including 0.85 (3H, s), 1.03 (3H, s), 1.14 (3H, s), 1.61 (3H, s) and 1.69 (3H, s)), 2.01 (3H, s), 2.10–2.32 (2H, m), 2.39 (1H, t, *J* = 5.6 Hz). MS *m/z*: 278 (M^+, 0.3%), 218 (26.0%), 203 (100%). High-resolution mass measurement: calcd. for $C_{18}H_{30}O_2$: 278.2246; found: 278.2248.

Ketol 27: the cyclopropylcarbinyl rearrangement

To the solution of ketol **26** (82 mg, 0.37 mmol) in a dioxane:water mixture solvent (4.00 mL, 1:1, v/v) was added *p*-toluenesulfonic acid hydrate (22 mg, 0.11 mmol, 0.30 equiv.). The mixture was heated at 85°C for 3.8 h. After cooling to room temperature, the mixture was diluted with water (10 mL) and extracted with methylene chloride (2 × 10.0 mL). The methylene solution was extracted with brine (10 mL), dried over magnesium sulfate, and concentrated in vacuo. Column chromatography of the crude mixture with ethyl acetate:hexanes mixture (2:17, v/v) gave product **27** (72 mg, 87%).

The physical properties of **27** are as follows: $[\alpha]_D^{25}$ + 111 (*c* = 1.00, $CHCl_3$). IR ν_{max} (film): 3050–3650 (O-H stretching), 1700 (C=O stretching), 1650 (C=C stretching) cm^{-1}. ^{1}H NMR (400 MHz, $CDCl_3$) δ: 1.10–1.90 (13H, m, including 1.20 (3H, s) and 1.23 (6H, two singlets)), 1.95–2.60 (7H, m), 2.75 (1H, dd, *J* = 8.8 and 17 Hz), 5.20 (1H, bs). MS *m/z*: 222 (M^+, 2.8%), 204 (13.6%), 189 (10%), 147 (100%), 133 (34.6%), 106 (47.4%). High-resolution mass measurement: calcd. for $C_{14}H_{22}O_2$: 222.1620; found: 222.1618.

Keto-acetates 28 and 29

A solution of alcohol **26** (65.2 mg, 0.294 mmol) in acetic acid (2.5 mL) was heated at 85°C for 2 h. After cooling to room temperature, methylene chloride (10 mL) was added and the mixture was extracted with 10% sodium bicarbonate solution (10 mL). The methylene chloride solution was dried over magnesium sulfate and concentrated in vacuo. Column chromatography of the crude product with hexanes:ethyl acetate (1:8, v/v) yielded acetate **27** (44 mg, 56%) and acetate **28** (11 mg, 14%).

The physical properties of **28** are as follows: $[\alpha]_D^{25}$ + 63.0 (c = 1.00, $CHCl_3$). IR $\nu_{max.}$ (film): 1735 (C=O stretching of the acetate group), 1705 (C=O stretching) cm^{-1}. ^1H NMR (400 MHz, $CDCl_3$) δ: 1.28 (3H, s), 1.50–1.85 (8H, m, including 1.59 (3H, s) and 1.70 (3H, s)), 1.92 (1H, m), 2.06 (3H, s), 2.10–2.60 (7H, m), 3.95–4.20 (2H, m). MS *m/z*: 264 (M^+, 0.1%), 204 (23.6%), 189 (13.2%), 147 (100%), 134 (85.1%), 119 (44.4%). High-resolution mass measurement: calcd. for $C_{16}H_{24}O_3$: 264.1725; found: 264.1720.

The physical properties of **29** are as follows: $[\alpha]_D^{25}$ = + 30 (c = 0.66, $CHCl_3$). IR $\nu_{max.}$ (film): 1710 (C=O stretching) cm^{-1}. ^1H NMR (400 MHz, $CDCl_3$) δ: 1.17 (3H, s), 1.40–1.80 (8H, m, including 1.65 (3H, s), and 1.72 (3H, s)), 1.90–2.80 (12H, m, including 2.10 (3H, s)), 5.19 (1H, dd, J = 4.2 and 10.2 Hz). MS *m/z*: 204 (M − HOAc, 43.5%), 189 (19.2%), 147 (91.9%), 133 (100%), 119 (54.4%), 105 (51.2%). High-resolution mass measurement calcd. for $C_{14}H_{20}O$ (M − HOAc): 204.1514; found: 204.1508. Chemical ionization (NH_3): 282 ($M + NH_4^+$), 265 ($M + H^+$), 222 ($M - HOAc + NH_4^+$), 205 ($M - HOAc + H^+$).

Acknowledgement

We would like to express our gratitude to the Natural Sciences and Engineering Research Council of Canada for financial support, and to Intrinsic Research and Development Inc. for generous samples of Western red cedar oil.

References

1. J.P. Kutney, Y.H. Chen, and S.J. Rettig. Can. J. Chem. **74**, 666 (1996).
2. J.P. Kutney. *In* Stereoselective Synthesis (part I). Vol. 14. *Edited by* Atta-ur-Rahman. Studies in Natural Products Chemistry Series, Elsevier Science Publishers, Amsterdam. 1994. pp. 389–447.
3. P. Gunning. Ph.D. thesis, University of British Columbia, 1991.
4. (*a*) S. Sarel, J. Yovell, and M. Sarel-Imber. Angew. Chem. Int. Ed. Engl. **7**, 577 (1968); (*b*) H.N.C. Wong, M.-Y. Hon, T. Hudlicky, C.-W. Tse, and Y.-C. Yip. Chem. Rev. **89**, 165 (1989); (*c*) Z. Rappoport, (*Editor*). The chemistry of the cyclopropyl group. John Wiley & Sons, New York. 1987.
5. (*a*) M.S. Paren, W.S. Mellon, H.K. Schnoes, and H.F. DeLuca. Bioorg. Chem. **13**, 62 (1985); (*b*) H.E. Paren, H.F. DeLuca, and H.K. Schnoes. J. Org. Chem. **45**, 3523 (1980).
6. (*a*) M.S. Carpenter and W.M. Easter. J. Chem. Soc. **20**, 401 (1955); (*b*) E. Zavarin and A.B. Anderson. J. Chem. Soc. **20**, 83 (1955).
7. I.M. Goldman. J. Org. Chem. **34**, 1979 (1969).
8. (*a*) K. Hayano, H. Shirahama, and T. Matsumoto. Bull. Chem. Soc. Jpn. **63**, 628 (1990); (*b*) K. Hayasaka, T. Ohshikazu, H. Shirahama, and T. Matsumoto. Tetrahedron Lett. **26**, 873 (1990); (*c*) T. Fujita, T. Ohtsuka, H. Shirahama, and T. Matsumoto. Tetrahedron Lett. **23**, 4091 (1982).
9. (*a*) W.D. Closson and G.T. Kwiatkowski. Tetrahedron, **21**, 2779 (1965); (*b*) W.G. Dauben, L.E. Friderich, P. Obserhanli, and E.I. Aoyagi. J. Org. Chem. **37**, 9 (1972); (*c*) R.W. Thies, and J.E. Billigmerier. J. Org. Chem. **38**, 1758 (1973); (*d*) R.W. Thies and H.J. Shih. J. Org. Chem. **42**, 280 (1977).
10. W.C. Still, M. Kahn, and A. Mitra. J. Org. Chem. **43**, 2923 (1978).

COMMUNICATION

Novel, air-stable, lanthanide catalysts for the hetero Diels–Alder reaction

Claude Spino, Laurel Clouston, and David Berg

Abstract: Novel, air-stable, yttrium and ytterbium complexes were found effective in the catalysis of the typical hetero Diels–Alder reaction of crotonaldehyde and ethylvinyl ether. They represent an attractive solution to the problem of ligand lability in the realm of lanthanide catalysts.

Key words: lanthanide, catalyst, hetero Diels–Alder, yttrium, ytterbium.

Résumé : Deux nouveaux complexes d'yttrium et d'ytterbium, stable à l'air, se sont avérés très efficace comme catalyseurs d'une réaction typique de Diels–Alder hétéro impliquant la crotonaldéhyde et l'éther d'éthylevinyle. Ils représentent une solution attrayante au problème chronique de la labilité des ligands chez les catalyseurs de lanthanide.

Mots clés : lanthanide, catalyseur, Diels–Alder hétéro, yttrium, ytterbium.

Lanthanides are increasingly used in organic synthesis as mild reagents and catalysts that can spare many sensitive functional groups (1 and, for reviews, 2). Catalytic systems based on lanthanide metals have been found for many organic reactions, including the Friedel–Crafts reaction, acetal and ether formation, reduction and oxidation, and the Diels–Alder cycloaddition or, more particularly, the hetero Diels–Alder reaction involving an oxygen on the dienophile or diene (1, 3). Complex and sensitive molecules give high yields of products with few side reactions, testimony to the mildness of these catalysts (1–3). Asymmetric versions of the latter type of Diels–Alder reactions have been limited to only a few isolated examples (4–6) with little success in the cycloaddition of vinyl ethers to α,β-unsaturated aldehydes (3). All of the lanthanide complexes tried as catalysts were in fact either NMR shift reagents or commercially available complexes designed for other uses (1–3). Part of the obstacle to achieving high asymmetric induction with lanthanide catalysts can be attributed to the lability of the ligands around the metal. In reality, this lability confers a degree of uncertainty about the actual structure of the active catalyst. In addition, it may impair induction because of ligand displacement during catalysis.

We felt that a necessary step in designing efficient lanthanide catalysts for that reaction was to find suitable ligands with low lability and to make complexes of a well-defined structure. Only then could we rationally design chiral complexes with the hope of increasing the enantioselectivities so far achieved with lanthanide systems. We describe herein our success in synthesizing two novel, air-stable, and effective yttrium and ytterbium complexes that show low ligand lability and are efficient catalysts for the hetero Diels–Alder reaction. To the best of our knowledge, these are the first examples of well-defined hexadentate[2] ligand–metal complexes of a lanthanide or yttrium that are effective catalysts.[3] Their stability in air is a good indicator of low ligand lability and we believe they are strong forerunners of chiral complexes.

The rationale for using tripodal ligands was to contribute extra stability to the complex, in effect "locking" the ligand in place.[4] Well-defined monomeric tripodal structures would thus provide a solid base from which to design and develop highly effective chiral catalysts. Starting from the observation that lanthanide complexes derived from trifluoromethyl-β-diketone-type ligands are effective catalysts for the hetero Diels–Alder reaction (1, 2, 8), we initially believed that derivatives such as ligand **2** would be well suited for our purpose, being tripodal in nature, easily prepared, and easily altered for the eventuality of chiral design. Ligand **2** was prepared in 80% purified yield by refluxing 1,1,1-trifluoroacetoacetate in a benzene solution of tris(aminoethyl)amine **1** with concurrent

Received April 19, 1996.

Claude Spino.[1] Université de Sherbrooke, Département de Chimie, Sherbrooke, QC J1K 2R1, Canada.
Laurel Clouston and David Berg.[1] University of Victoria, Chemistry Department, P.O. Box 3055, Victoria, BC V8W 3P6, Canada.

[1] Authors to whom correspondence may be addressed.
C.S.: Telephone: (819) 821-7087. Fax: (819) 821-8017.
D.B.: Telephone: (604) 721-7161. Fax: (604) 721-7147.

[2] The complex is hexadentate assuming there is no interaction between the arene ring and the metal. This interaction may exist and would be interesting. It has not yet been examined.

[3] Similar but non-catalytic heptadentate lanthanide complexes can be found in ref. 7.

[4] Even though a "hinging motion" is possible, it is unlikely that more than one arm would do this at any one time. "Hinging" specifically refers to partial dissociation of one arm, i.e., bidentate to monodentate for that arm.

Table 1. Efficiency of the different catalysts on the hetero Diels–Alder of **8** and **9**.

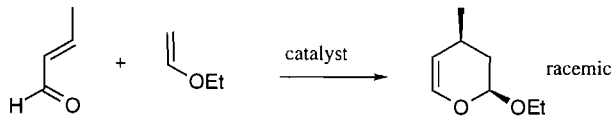

8 **9** **10**

Entry	Catalyst	Conditions[a]	Time (h)	Conversion[b]	Yield[c]
1	**3**	A	96	0	0
2	**7***a*	A	72	98	95
3	**7***b*	A	96	80	80
4	$Yb(fod)_3$	A	96	98	90
5	$ZnCl_2$	A	48	98	46
6	$BF_3 \cdot Et_2O$	A	48	98	12
7	**7***a*	B	96	69	69
8	$Yb(fod)_3$	B	96	69	65
9	**7***a*	C	96	89	89
10	**7***b*	C	96	89	89
11	$Yb(fod)_3$	C	96	0	0

[a]Method A = ethylvinyl ether as solvent, 2 mol% catalyst; Method B = method A + dioxane (0.5 equiv.) (similar results if **7** is prepared in a coordinating solvent); Method C = method A + deliberately exposed to air for 7 days.
[b]Disappearance of starting materials analysed by gas chromatography.
[c]Isolated yield after distillation.

Scheme 1.

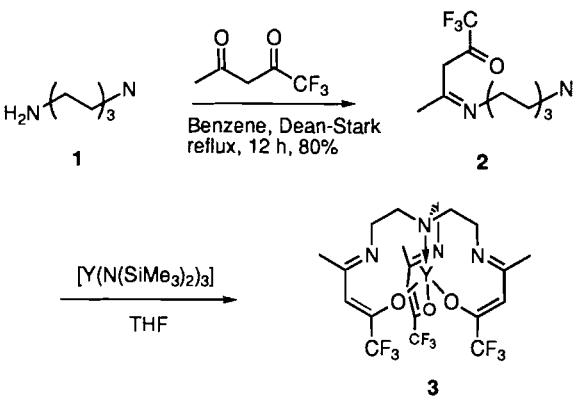

1 **2** **3**

Scheme 2.

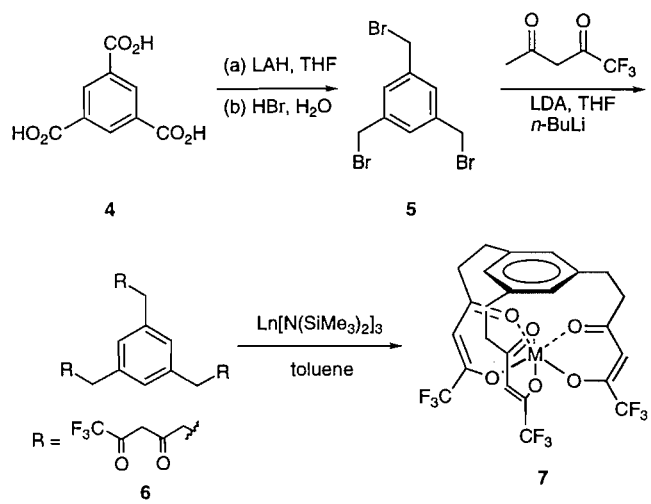

4 **5** **6** **7**

removal of water (Scheme 1). The metal complex **3** was prepared by mixing the ligand with a solution of yttrium tris(bistrimethylsilyl)amide (9) in tetrahydrofuran. It was characterized by single-crystal X-ray diffraction.

We were surprised to find that this complex showed no catalytic behaviour toward the cycloaddition reaction of crotonaldehyde and ethylvinyl ether (see Table 1). Several factors could be responsible for this lack of activity and we suspected that either the imine nitrogen or the coordinating amine nitrogen could electronically saturate the metal and thereby lower its Lewis acidity. Nevertheless, we reasoned that the needed ligand should possess the unaltered trifluoromethyl-β-diketone functionality. Such units could be linked by the end methyl group via a number of linkers, thereby leaving the β-diketone unit intact. 1,3,5-Tribromomesitylene **5** caught our attention as being a useful linker because of its relative ease of preparation and high reactivity toward alkylation.

We looked at several ligands before ultimately settling for the tribenzyltrifluoroacetoacetate ligand **6** (Scheme 2). Ligand **6** was thus prepared starting from 1,3,5-benzenetricarboxylic acid **4**. The aluminium salts resulting from the reduction of **4** with LAH are directly treated with aqueous hydrobromic acid to give an 80% yield of **5**.

The dianion of 1,1,1-trifluoroacetylacetone was generated using slight modifications of a standard procedure (10). Though its reactivity was lower than that of non-fluorinated β-diketones, effective alkylation in THF at room temperature

Fig. 1. Partial NMR spectrum of yttrium complex **7***a* showing a coordinated THF molecule.

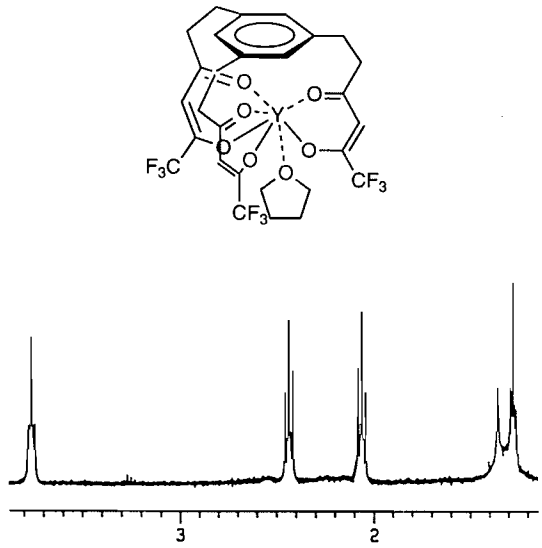

with tribromomesitylene **5** could be achieved. The tripodal ligand **6** was thus obtained in 40% yield after recrystallization and sublimation at 140°C / 10^{-2} Torr (1 Torr = 133.3 Pa).

The metal complexes **7***a* (M = Y) and **7***b* (M = Yb) were prepared by mixing the ligand with a solution of yttrium or ytterbium tris(bistrimethylsilyl)amide in toluene (9). In each case, an instantaneous reaction occurred with concomitant precipitation of the complex, which was washed several times with toluene. Unfortunately, we could not grow crystals of adequate quality to perform a single-crystal X-ray crystallographic analysis on either of the complexes and neither were soluble in non-coordinating solvents. To secure the structure of the yttrium complex **7***a*, we prepared it in THF and isolated the powdery material by simple reduced pressure evaporation of the solvent. Although no X-ray quality crystals could be grown, the proton NMR analysis of the complex in benzene-d_6 was unequivocal and established the coordination of a molecule of THF (Fig. 1). Mass spectral data, Exact Mass measurement, and elemental analysis on this compound were satisfactory. The structure of the ytterbium complex **7***b* was inferred only from mass spectral data and by analogy to **7***a*.

Catalytic activities were tested on the hetero Diels–Alder cycloaddition of crotonaldehyde and ethylvinyl ether, the latter serving as solvent, with 2 mol% of catalyst (Table 1). In each example involving lanthanide or yttrium catalysts, with the exception of **3**, the isolated yields of the respective dihydropyran product **10** were excellent, testimony to their mildness (entries 2–4). In contrast, zinc chloride and BF_3-etherate gave 46 and 12% isolated yield, respectively, of **10** (entries 5 and 6). The thermal reaction proceeds at 175°C to give product **10** in 87% yield (8). The same reaction can also be carried out under high-pressure conditions (15 kbar (1 bar = 100 kPa), 75°C, 24 h) to give 89% of the *endo* adduct (11).

Each reaction was monitored by gas chromatography at specific time intervals. The yttrium catalyst **7***a* was superior to all others, including the commonly used $Yb(fod)_3$ (12), having the fastest conversion rate and giving a good isolated yield of **10** (entry 2). As expected, the product isolated was regiochemically and diastereomerically pure (racemic) and was derived from the *endo* approach of the dienophile as verified by proton NMR (12*a*). If dioxane was utilized as an internal standard for quantitative work, the reaction rate between **8** and **9** dropped (entries 7 and 8), indicating a competition for the active site between the coordinating solvent and crotonaldehyde **8**. We found that when the complexes **7** were prepared in or came in contact with coordinating solvents, the reaction rate dropped also, presumably due to the incorporation of a coordinating solvent molecule. In turn, this coordinating solvent molecule may compete with crotonaldehyde for the active site or simply reduce the Lewis acidity of the complex. More importantly, both catalysts **7** remained active even after several days of exposure to the ambient air (entries 9 and 10), even though the complexes may have picked up water molecules from exposure to air. A 3-month-old sample of complex **7***a* stored in an opened vial still retained complete catalytic activity. In contrast, all other catalysts including $Yb(fod)_3$ had to be kept in a rigorously dry atmosphere to remain active (entry 11). The air and moisture stability of these complexes is undoubtedly linked to the low pK_a coupled with the tripodal nature of the ligand **6**.

In conclusion, we have prepared the first lanthanide complexes that possess a tripodal ligand and are active catalysts. Their high stability, even in air, is not only desirable in terms of handling but is also very promising as a base from which to develop chiral catalysts showing high asymmetric induction.

Acknowledgements

We thank the Natural Sciences and Engineering Research Council of Canada for financial support as well as for a scholarship to L.C., and the University of Victoria for financial support.

References

1. T. Imamoto. *In* Lanthanides in organic synthesis. Academic Press, San Diego, Calif. 1994.
2. (*a*) H.B. Kagan and J.L. Namy. Tetrahedron, **42**, 6573 (1986); (*b*) G.A. Molander. Chem. Rev. **92**, 29 (1992).
3. (*a*) D.L. Boger and S. Weinreb. *In* Hetero Diels–Alder in organic synthesis. Academic Press, San Diego, Calif. 1987; (*b*) T. Kametani and S. Hibino. Adv. Heterocycl. Chem. **42**, 245 (1987).
4. Aluminium catalysts: K. Maruoka, T. Itoh, T. Shirasaka, and H. Yamamoto. J. Am. Chem. Soc. **110**, 310 (1988).
5. Boron catalysts: Q. Gao, T. Maruyama, M. Mouri, and H. Yamamoto. J. Org. Chem. **57**, 1951 (1992).
6. Lanthanide catalysts: M. Bednarski and S. Danishefsky. J. Am. Chem. Soc. **108**, 7060 (1986).
7. D.J. Berg, S.J. Rettig, and C. Orvig. J. Am. Chem. Soc. **113**, 2528 (1991).
8. R.I. Longley, Jr. and W.S. Emerson. J. Am. Chem. Soc. **72**, 3079 (1950).
9. D.C. Bradley, J.G. Ghotra, and F.A. Hart. J. Chem. Soc. Dalton Trans. 1021 (1973).
10. S.N. Huckin and L. Weiler. J. Am. Chem. Soc. **96**, 1082 (1974).
11. W.G. Dauben and H.D. Krabbenhoft. J. Org. Chem. **42**, 282 (1977); B.B. Snider and G.B. Phillips. J. Org. Chem. **48**, 2790 (1983).
12. (*a*) S. Danishefsky and M. Bednarski. Tetrahedron Lett. **25**, 721 (1984); (*b*) M. Bednarski and S. Danishefsky. J. Am. Chem. Soc. **105**, 6968 (1983).

1995 Fisher Scientific Award Lecture Reflections of an atmospheric chemist wondering why he won an analytical chemistry award[1]

H.I. Schiff

Abstract: The author recalls his scientific career starting with electrochemistry and gas phase kinetics and leading, largely by serendipity, to atmospheric chemistry and measurements in the atmosphere using rockets and stratospheric balloons. The scientific problems met along the way required measurements with instruments that were not commercially available and required development of new methods and techniques. These included mass spectrometry, chemiluminescence, and tunable Diode Laser Absorption Spectrometry (TDLAS) to measure trace concentrations of gases in the lower and upper atmosphere. TDLAS is considered to be the method of choice where freedom from interferences, high sensitivity, and fast time response are required. Lead salt laser diodes operate in the near infrared where most molecules of atmospheric interest have strong fundamental absorptions. The research groups at York University and at Unisearch Associates have been pioneers in applying this powerful technique to atmospheric measurements in a variety of environments including the pristine air over the Pacific, at the top of Mauna Loa, at the Grand Canyon, and the polluted air of Los Angeles and other major cities. The results of recent measurements of the emissions of two strong greenhouse gases, CF_4 and C_2F_6, from Quebec aluminium refineries are described. More recently a family of instruments based on near-infrared laser diodes have been developed that can make remote-sensing measurements of a number of pollutants in ambient air and industrial stacks. Examples of passive, on-road, remote-sensing measurements of automobile exhaust emissions of CO and CO_2 and of in-stack emissions of HF are presented. Another remote-sensing instrument that has been developed is an improved visible and UV Differential Optical Absorption Spectrometer (DOAS) capable of measuring, remotely and simultaneously, a number of important pollutants. Examples of measurements of NO, NO_2, O_3, benzene, and toluene are presented.

Key words: air measurements, instruments, remote sensing.

Résumé : L'auteur fait un historique de sa carrière scientifique en partant de l'électrochimie et de la cinétique en phase gazeuse conduisant, en grande partie par un heureux hasard, à la chimie atmosphérique et aux mesures dans l'atmosphère à l'aide de fusées et de ballons lancés dans la stratosphère. Les problèmes scientifiques rencontrés exigeaient des mesures à l'aide d'instruments non disponibles commercialement et requéraient de nouvelles méthodes et de nouvelles techniques. Celles-ci comprennent la spectrométrie de masse, la chimiluminescence et la spectrométrie d'absorption au laser à diode adjustable (SALDA) pour mesurer les très faibles concentrations des gaz présents dans la basse et la haute atmosphère. La SALDA est considéré comme étant une méthode de choix lorsqu'une réponse rapide sans interférence et de grande sensibilité est requise. Les lasers à diodes aux sels de plomb opèrent dans le proche infra-rouge, là où les molécules d'un intérêt atmosphérique ont de fortes absorptions fondamentales. Les groupes de recherche de l'université York et de l'Unisearch Associates ont été les pionniers dans l'application de cette puissante technique aux mesures atmosphériques de divers écosystèmes incluant l'air du Pacifique, non pollué par la civilisation, le sommet du Mauna Loa, le Grand Canyon et l'air pollué de Los Angeles et des grandes villes. On décrit les résultats de mesures récentes des émissions de deux gaz à effet de serre, CF_4 et C_2F_6, produites par les raffineries d'aluminium du Québec. Plus récemment on a mis au point une famille d'instruments basés sur les lasers à diodes opérant dans le proche infra-rouge et qui permettent de mesurer à distance un grand nombre de polluants dans l'air ambiant et dans les cheminées industrielles. On présente des examples de télémesures passives, sur la route, des gaz d'émission des voitures, CO et CO_2, et des émissions de HF à l'intérieur des cheminées. Un autre instrument de télémesure mis au point, est un spectromètre d'absorption optique différentielle (SAOD) opérant dans le visible et dans l'UV et capable de mesurer à distance et simultanément, un nombre important de polluants. On présente des exemples de mesure du NO, du NO_2, du O_3, du benzène et du toluène.

Mots clés : mesures de l'air, instruments télémesure.

[Traduit par la rédaction]

Received May 4, 1996.

H.I. Schiff.[2] York University, 4700 Keele Street, Downsview, ON M3J 1P3, Canada, and Unisearch Associates Inc., 222 Snidercroft Rd, Concord, ON L4K 1B5, Canada.

[1] This is an invited review article based on the 1995 Fisher Scientific Award lecture presented at the Annual Conference of the Canadian Society for Chemistry in Guelph, Ontario, May 1995.

[2] Telephone: (416) 485-2046. Fax: (416) 485-2046. E-mail: hschiff@yorku.ca

Being named the Fisher Scientific Award Lecturer in analytical chemistry came as quite a surprise. Although my scientific career has taken a number of paths since I was awarded a Ph.D. in electrochemistry, many years ago, none of them bore the signpost "Analytical Chemistry." So receiving this award has made me reflect on how this unlikely event could have occurred.

It probably began when Gerhard Herzberg visited my laboratory in 1950 while I was a post-doctorate fellow at NRC with Dr. E.W.R. Steacie. I had been working on the gas phase kinetics of hydrogen atoms, which I made by passing hydrogen gas through an electric discharge. When Herzberg asked me to flow nitrogen through the apparatus I was amazed to find the entire apparatus filled with a bright yellow glow. He told me I was looking at "active nitrogen," which had been discovered around the turn of the century by Lord Rayleigh. Some 2000 papers had been written about active nitrogen but no one had been able to identify the chemically reactive species. N_3, which Kistiakowsky, an eminent Harvard kineticist and one of the pioneers of the atom bomb, had called *nozone*, was one popular suggestion.

A mass spectrometer seemed to me to be a likely analytical method for identifying the reactive species. Commercial mass spectrometers were not available in the 1950s so when I got my first academic appointment at McGill I built a mass spectrometer with help from Fred Lossing of NRC. The chemically reactive species turned out to be atomic nitrogen (1) and the glow was a result of the chemiluminescent reaction:

$$N + N \rightarrow N_2^* \rightarrow N_2 + h\nu$$

Since this was the only mass spectrometer in Quebec I supplemented my meagre assistant professor's salary by analyzing samples for a number of pharmaceutical and chemical companies in the Montreal area.

My research group went on to investigate the chemical kinetics of nitrogen atoms, oxygen atoms, and ozone. The next surprise came when the US Air Force offered to support my research, which I could not imagine would be of any interest to them. It turned out that the Russians had just launched "Sputnik" and the space race was on. This was before NASA had been established, and the three US military services were vying with one another to launch the first USA object into space. One question being asked was what sort of environment that object would encounter. The speculation was that a great deal of the oxygen and nitrogen might be present in the dissociated, atomic state but nobody really knew how these species might react with their hardware. The only research on the reactions of these atomic gases was that of an unknown assistant professor at a Canadian university who had been publishing papers on these reactions. So I suddenly found I was an atmospheric chemist.

One of the reactions we studied was that of O atoms with NO (2, 3), which was also accompanied by chemiluminescence.

$$O + NO \rightarrow NO_2^* \rightarrow NO_2 + h\nu$$

But this time the glow is greenish. The intensity of the light is first order in the concentrations of both O and NO and so, if you know the concentration of NO, you can use the intensity of the glow to determine the concentration of O atoms. We performed the first chemical titration of the upper atmosphere by releasing 25 kg of NO from a rocket at a height of 90 km over the desert at White Sands, New Mexico, and produced a green glow in the night sky about 2 km in diameter. It was bright enough to frighten the natives and produce headlines, of numerous sightings of UFOs, in the papers the next day. This experiment not only provided the first direct evidence for the presence of O atoms in the upper atmosphere but also gave an estimate of their concentration.

A related reaction that we studied (4) was between NO and O_3, which also produces a glow, this time in the red part of the spectrum:

$$O_3 + NO \rightarrow O_2 + NO_2^* \rightarrow NO_2 + h\nu$$

The intensity of the glow was also found to be first order in the concentration of both reactants. We used this property in the laboratory to measure the concentrations of either NO or O_3 by adding an excess of the other reagent and monitoring the light intensity. I was, however, not smart enough to recognize the commercial possibilities of this finding, but Arthur Fontijn, who had been working on this project as a post-doctorate fellow, was, as is usually the case, smarter than his research director. When he went to Aerochem in New Jersey he developed a commercial instrument for measuring NO based on this reaction that has since become the standard method around the world for measuring this important atmospheric pollutant. Arthur won the American Chemical Society award some 15 years ago for this development.

In 1972 the US government appointed me to a panel of 20 so-called experts to advise them on the environmental impacts of a fleet of supersonic aircraft (SSTs), designed to fly in the stratosphere. The chemists on the panel concentrated on the effects of water vapour from the contrails of these aircraft. But Harold Johnston, a prominent kineticist at the University of California, Berkeley, chastised the rest of us for failing to recognize that NO from the exhausts, rather than H_2O, constituted the major threat to the ozone layer. I was particularly guilty for this oversight because I had been studying these reactions in the laboratory. When I pointed out that no one knew how much NO was naturally present in the atmosphere, Johnston maintained that this did not matter. I had difficulty in understanding that there would be any major effects if the natural atmosphere contained hundreds of times as much NO as the SSTs would add. So I returned from this meeting determined that we had to measure the natural amount of NO in the stratosphere.

The commercial instruments based on the chemiluminescence of NO with O_3 were simply not sensitive enough for such measurements and so Brain Ridley, working with me as a post-doctorate fellow, designed and built a highly sensitive version of this instrument (5, 6). With funding from the US government we flew this instrument on a balloon in 1974 and made the first measurement of NO in the stratosphere (5, 6) over the altitude range of 20–40 km. It turned out that the mixing ratio of NO in the stratosphere was indeed very low and the proposed fleet of SSTs, according to our understanding of atmospheric chemistry at that time, did, indeed, pose a threat to the ozone layer.

Of course the fleet of SSTs never materialized, aside from

the few Concordes made by the French and English, and attention switched to chlorofluorocarbons (CFCs), used primarily as propellants in spray cans and as refrigerants, as the major threat to the ozone layer. I had the privilege of chairing the US Academy of Science Panel that reported on this threat (7) and led to the banning of nonessential uses of these chemicals in the USA and Canada.

Our laboratory now extended into the earth's atmosphere and we were looking for better and more universal methods for measuring trace species in the atmosphere. A promising new technique involved the use of tunable diode laser spectroscopy (TDLAS). Tunable diode lasers are small crystals, about 1 mm^2 in area, made of Pb containing small amounts of Group 4 elements such as Se S, Te, Sn. When a current is passed through these crystals at temperatures below 170 K they emit laser radiation in the mid-infrared region between about 3 and 20 μm. Changing the current through these diodes changes the wavelength of the radiation, permitting scanning the spectrum of the absorbing molecule over individual rotational–vibrational lines.

This technique had been used for laboratory high-resolution spectroscopic studies but had not previously been applied to atmospheric measurements although some laboratory work performed at McMaster University had shown its potential for air measurements. Since most molecules of atmospheric interest have strong, fundamental absorption in the 3–20 μm spectral region, it provides a universal method for measuring atmospheric gases. The high spectral resolution provides unequivocal identification of the selected gas free of interferences from other gases. The technique is also capable of making measurements in less than a second with sensitivities in the sub parts per billion concentration levels.

Our first successful use of this method was to make measurements of nitrogen oxides in the stratosphere with a TDLAS instrument carried on a balloon that flew to 35 km above the earth's surface. It then became apparent that this technique had applications for air measurements at ground level and might be of some commercial interest. So in 1980 we started a spin-off R&D company, called Unisearch Associates, and I suddenly found myself in the business world. My atmospheric interests had descended from the upper atmosphere through the stratosphere and troposphere to ground level and now, some of my academic colleagues would maintain, to the nether regions of crass commercialization.

Unisearch received its first contract from the Coordinating Research Council, a funding agency jointly sponsored by the three US auto manufacturers and five major oil companies. With their support we built a TDLAS system (8) and used it to measure a number of pollutants in the Los Angeles area. We were pioneers in the application of TDLAS to atmospheric measurements. Unisearch has sold TDLAS instruments to the Planck and the Fraunhoffer Institutes, to NASA, AES, OME, and the British Meteorological Service as well as a number of universities. We have also used our instruments to make measurements of pristine air over the Pacific from NASA aircraft (9–11) as well as from our mobile laboratory on the top of Mauna Loa, Hawaii, at the Grand Canyon, and in the polluted air of downtown Los Angeles (12).

One example of the use of the mid-infrared TDLAS system was a series of measurements of the emissions of CF_4 and C_2F_6 from aluminium smelting (13). These two perfluorocarbons are potent greenhouse gases, thousands of times stronger than CO_2. But, since the mixing ratios of these gases in the atmosphere are only about 80 pptv for CF_4 and 2–4 pptv for C_2F_6, they were not formerly believed to contribute significantly to global warming until it was recognized that there are no known removal processes for these compounds from the atmosphere. Their atmospheric lifetimes have been estimated to be at least 10 000 years and, as has happened in other cases such as nuclear waste disposal, there is a disproportionate concern about putting potentially harmful substances into the environment that will remain there for thousands of years.

The main source of CF_4 and C_2F_6 in the atmosphere appears to be the aluminium industry. Aluminium is produced by the reduction of alumina, Al_2O_3, in electrolytic cells. The alumina is dissolved in a mixture of molten cryolite (Na_3AlF_6) and AlF_3. Both anodes and cathodes are carbon. Normally, oxygen is released at the anode where it forms CO and CO_2. Periodically, however, when the concentration of alumina in the cell drops below a certain level, the voltage of the cell rises and fluoride ions are also discharged at the anode to form the perfluorocarbons, which are emitted in a sort of a burp, known as an anode event, that lasts anywhere from about 2 to 20 min. The amount of gas emitted depends both on the frequency and the duration of these anode effects.

Determination of the contribution of the PFCs to global warming requires a knowledge of current emissions from aluminium production. Such data were largely lacking in the early 1990s, and in 1992 l'Association de l'Industrie de l'Aluminium de Québec commissioned Unisearch Associates to make measurements of emissions from eight smelter sites in Québec. The TDLAS was the instrument of choice since it allowed unequivocal measurements of the two gases in the presence of a very complex mixture with high precision and time resolution.

Figure 1 gives one example of the measurements (13) during several anode events. A large data base was accumulated with approximately 700 h of measurements and more than 200 000 individual observations.

When the emissions from each of the measured sites were combined with the respective production figures for each of the sites, an estimate could be made of the total annual emissions of these gases from Canadian aluminium production. We were also able to estimate that the contribution of these emissions to global warming from Canadian sources amounts to approximately 0.4% compared to the total contribution of other greenhouse gases.

Recently two new families of remote-sensing instruments have been developed by Unisearch. Most instruments that are currently being used to measure air quality are point-source monitors that sniff the air at a sampling point. Monitoring the emissions from stacks also uses these point-source instruments to sample the emissions by sucking out aliquots of the stack gases in a rather cumbersome extraction process. Remote-sensing instruments using optical techniques are rapidly gaining popularity over these point-source monitors for air quality networks, for area monitoring from landfills to entire cities, and for perimeter monitoring around industrial sites. For stack monitors, optical techniques are continuous, relatively simple, and can be readily adopted to process control functions. Remote-sensing monitors can also be used for passive, on-road monitoring of automobile exhausts.

Fig. 1. The measurements of CF_4 and C_2F_6 emissions from an aluminium smelter showing two "anode events."

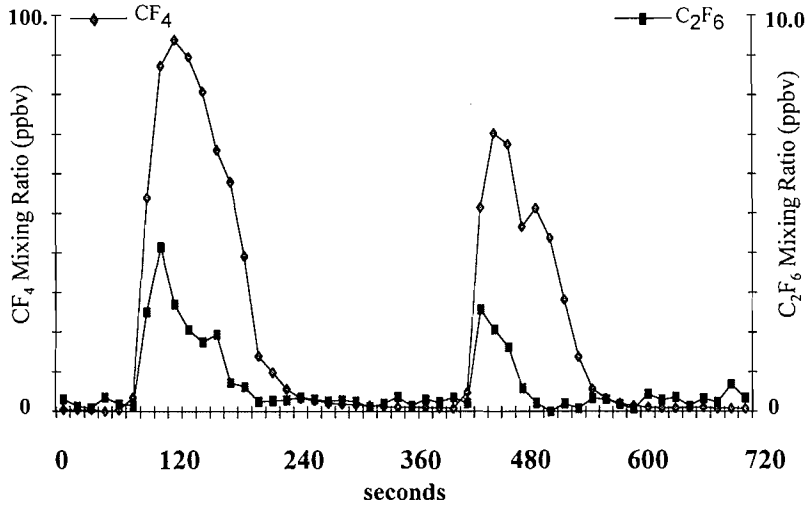

We have developed a remote-sensing system based on tunable diode lasers (14, 15) but of the type used for the fibre optics communication industry and in domestic products such as CD players and laser printers. These laser diodes are based on Group V elements such as GA, As, and P, which emit radiation in the near-infrared (NIR) region between 0.59 and 2.5 μm. Unlike the Pb salt diodes they operate at ambient temperatures that can be controlled by small thermoelectric coolers. Moreover, they are of sufficiently high quality that high-frequency modulation techniques, which can be built with "off-the-shelf" television components, can be used. These features can be exploited to reduce both the size and cost of the instrument and to increase its sensitivity. The response of the system for most gases is in the range of a few parts per million per meter, which is more than adequate for most industrial applications. Another advantage of operating in the near-infrared is that pressure broadening does not present as large a problem as it does at the longer wavelengths, which makes it suitable for remote sensing at atmospheric pressure. Some of the gases that absorb in this spectral region include HF, HCl, CH_4, H_2S, CO, CO_2, CO, NH_3, C_2H_2, C_2H_4, and NO_2.

Three versions of the instrument have been developed — the LASAIR-R for remote sensing, the LASAIR-S for in-stack monitoring, and the LASAIR-P for point-source monitoring. All three versions use a common control unit that contains the diode laser and its temperature and current control circuits; the detector and its circuitry; the connectors to the launching and receiving optical fibres; the interface to the computer for automatic control, and data acquisition and logging; and a reference cell containing a known concentration of the gas.

The laser beam is brought to one or more of the measurement stations by fiber optics. A fiber optic multiplexer can be used to split the beam for operating several sensors at the same time in a time-sharing mode as shown in Fig. 2. A single controller can also contain and control several lasers that can feed the combined light to a single or several sensors simultaneously, providing a great deal of versatility and economy. This controller can be located at any suitable location within the site, such as the control room of a plant, and does not have to be protected from harsh climatic or hazardous environments. Since none of the sensors' heads have electrical parts or components, they can be mounted in an explosive or hazardous location and operated in virtually any climatic or environmental condition.

The point-source version of the instrument draws the measured air continuously through a White or Herriot-type multipass cell. The cell can be located either within the controller itself or at some remote location. A remote location can be chosen for one or more of the multipass cells if desired, and connected to the controller by fiber optics.

A 4 in. Schmidt–Cassgrain telescope is used in the LASAIR-R version to both transmit the beam to a retroreflector and to receive the returned beam. The use of a single telescope to both transmit and receive also provides the advantage of easy alignment as well as providing a very stable configuration that is insensitive to vibrations. An example of measurements made with the LASAIR-R is provided by an on-road intercomparison study of automobile exhausts (16). The intercomparison was made at the Ford Motor Company Dearborn Proving Grounds between the on-board monitoring systems installed in a Ford Aerostar test vehicle and LASAIR-R. The Aerostar contains an on-board, variable path, multi-pass FTIR, able to make continuous emissions of CO and CO_2. Comparisons were made of the concentrations of CO and CO_2. The on-board computer system controls engine air-to-fuel ratios and controls and monitors numerous engine operating parameters. These engine parameters, when combined with the emission data from the FTIR, provide a comprehensive and accurate account of the vehicle emissions and the conditions that produced them. The Aerostar van was operated at speeds in the range 15–35 mph, air/fuel rations (λ) between 0.8 and 1.0, and with the gear set in 1st, 2nd, or 3rd during a pass by. This provided CO emissions in the range 0.05–~8%. Over 120 passes were monitored to provide a comprehensive data set with a minimum of 6 measurements under identical conditions for statistical validation. The LASAIR measurements were made across a 25 ft single traffic lane.

Figure 3 shows some real-time data for two passages of the

Fig. 2. Schematic of LASAIR system showing several possible sensors operating from a common controller.

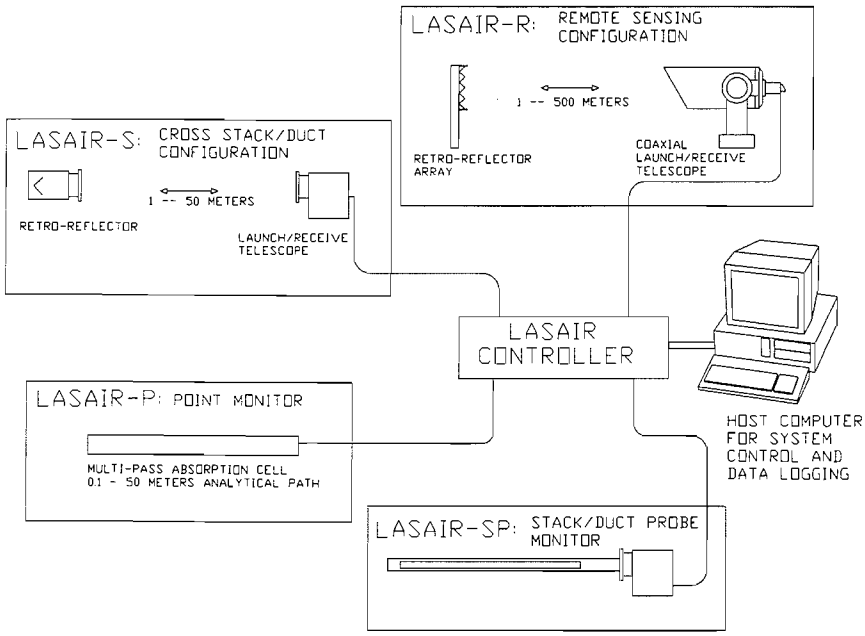

Fig. 3. Real-time remote-sensing measurements of CO and CO_2 in an automobile exhaust made with a LASAIR-R instrument across a 25 ft test track. The upper curve is with the test vehicle operating at an air-to-fuel ratio of 1.0 and the lower curve with the vehicle operating at a fuel-to-air ratio of 0.8.

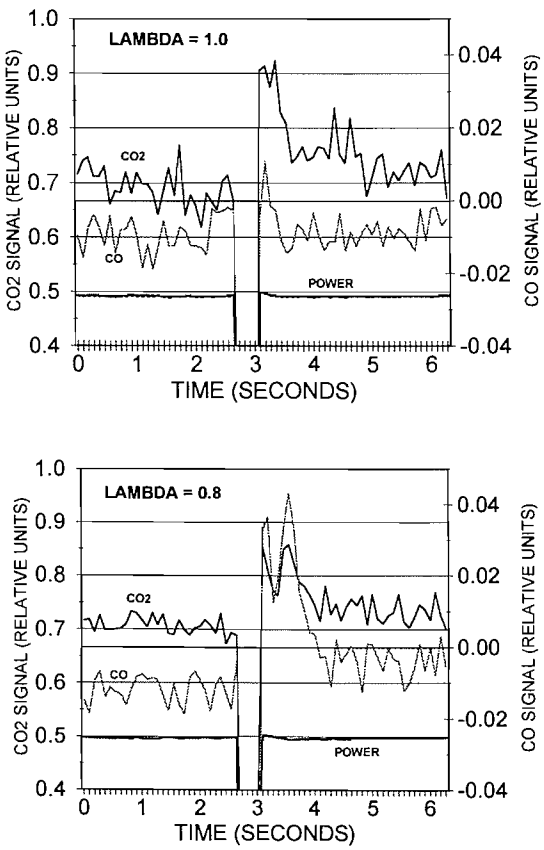

test vehicle, one when the vehicle was operated with an air-to-fuel ratio, λ, of 0.8 and the other with $\lambda = 1$. Measurements were made of CO and of CO_2 along with the power incident on the detectors at a sampling rate of 80 Hz and were averaged into 0.1 data points. The passage of the car was determined by the power dropping to less than 90% of its value. This signalled the data processing to start. To prevent an event being falsely identified if a cat or a person walked across the beam, values of CO_2 before and after the power drop were compared. If CO_2 increased by less than 5% after the beam was interrupted, the interruption was not identified as a motor vehicle event. We presumed that the cat does not give out this much CO_2. Passage of the vehicles is clearly indicated as are the increases in both CO and CO_2. For the case of stoichiometry the CO is very much smaller than for $\lambda = 0.8$. As CO goes down, CO_2 goes up.

Figure 4 shows the comparison between the CO/CO_2 ratio measured by the LASAIR-R and the on-board equipment with a vehicle speed of 35 mph. Each point represents the average of 6 passes of the vehicle under identical conditions. Good agreement is found for all data sets with the slopes of the regression lines indicating that the absolute values of the CO/CO_2 ratios by the two instruments agrees to within $\pm 3\%$, and the linearity was also excellent ($R^2 > 0.95$). The very small offset is probably due to the fact that the two instruments were not intercalibrated.

The LASAIR-S was developed for in-stack monitoring and process control. The diode laser and detector are both mounted in a control unit at some suitable location inside the plant. The laser beam is then transmitted to the stack by fibre optics, launched across the stack, and returned to the detector by fibre optics. Two options are available for transmission across the stack. One is an open path with the launching optics and the retroflector offset from the stack to prevent exposure to the

Fig. 4. Scatter diagram of the comparison between the CO/CO_2 ratios measured with the remote-sensing LASAIR-R and the on-board FTIR instrument taken on the Ford Motor Company Dearborn Proving Grounds. The speed of the vehicle was 35 mph and the air-to-fuel ratio was varied between 0.8 and 1.0. Data obtained at 10 Hz have been averaged over the time (~0.5 s) during which the exhaust plume impacted the measurement path.

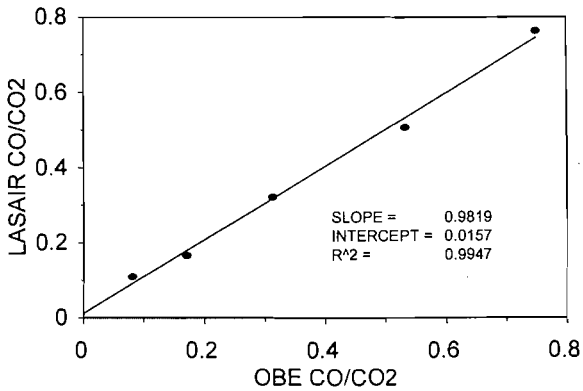

Fig. 5. Observed variation in the HF signal measured by the LASAIR-S in the stack emissions of an aluminium smelter when the number of filters in the stack were reduced from 9 filters at ~15:00, reduced again to 5 filters at 15:40, and subsequently increased back to 9 filters at ~16:00.

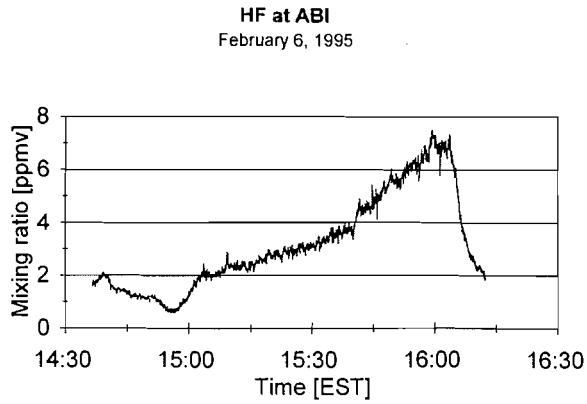

exhaust gases and temperature. An example of measurements made with the cross-stack version of the LASAIR-S is again provided by the aluminium industry. An installation was made in an aluminium smelter in Quebec for monitoring HF emissions from a 4 m stack. The complete installation was made in less than 1 h. The control unit and laser were located more than 1.5 km from the stack installation. In one test, the emissions from 120 pots were passed through up to 9 filter packs before being vented through the stack. The number of filters on line at any one time could be changed and variations due to such changes were monitored. Figure 5 shows the results of this test made in February, 1995. The HF level of about 2 ppmv was the normal operating level. The value decreased between 14:45 and 15:00 as some of the pots were shut off. The HF levels then rose between 15:00 and 16:00 as filters were removed in succession until all nine had been removed to produce an HF level of about 7 ppmv, after which the filters were reinstalled. Figure 6 shows an intercomparison made of HF mixing ratios measured by the LASAIR-S and an EPA-approved, wet chemical technique in the stack emissions from the same aluminium smelter. The agreement is excellent with the LASAIR providing considerably better precision than the wet chemical method.

Another remote-sensing instrument that has been developed by Unisearch, called the SENSAIR, is capable of measuring a number of pollutants simultaneously (17, 18). It is based on optical absorption in the visible and ultraviolet portion of the spectrum and has the generic name of Differential Optical Absorption Spectroscopy (DOAS). The method was originally developed by Professor Uli Platt of Heidelberg University and has been used successfully to make a number of important atmospheric measurements. Of particular interest these days is the ability of DOAS to measure aromatic compounds such as benzene, toluene, and the xylenes, which cannot be monitored adequately by alternative remote-sensing techniques such as Fourier Transform Infrared (FTIR) because of interference from ubiquitous water vapour and carbon dioxide. The conventional DOAS system uses a telescope to transmit a beam of broad-band light through the atmosphere. The transmitted

Fig. 6. Comparison of the HF mixing ratios measured by the LASAIR-S and the EPA-approved wet chemical method in the stack emissions of an aluminium smelter. The changes in the HF mixing ratio were created by removing recycled alumina from several of the stack filter units.

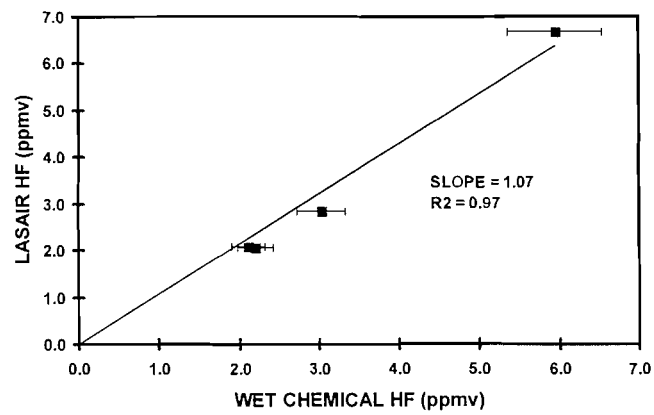

beam is then received by a similar telescope at the other end of a long path and disbursed by a spectrograph. Light paths of 500 m are commonly used for most molecules at concentrations encountered in rural and urban conditions. So we cannot claim to have invented this technique. What we think we have done is to make some very major improvements.

Our instrument has overcome the inconvenience of having to provide power and water cooling for the light source separated by long distances from the receiver, by the use of a retroreflector. The same telescope, shown schematically in Fig. 7, is used to both send the beam to a retroreflector and to receive the reflected light beam. The use of a single telescope has the additional advantage of ensuring that the sending and receiving optics remain coaxial, getting double the optical path for the same distance. We incorporated into this telescope a baffle that can be rotated to block the outgoing beam and that detects the light being emitted by the lamp. This gives, in essence, a zero path length and acts to provide the zero absorp-

Fig. 7. Schematic of the SENSAIR-DOAS remote-sending telescope. The telescope both launches the optical beam to a retroreflector placed at the other end of the optical path and directs the reflected beam to the fibre optic cable connected to the analysing spectrometer. A shutter can be activated to direct the beam directly into the telescope, which provides a zero-path reading. A calibration cell can also be inserted into the optical path.

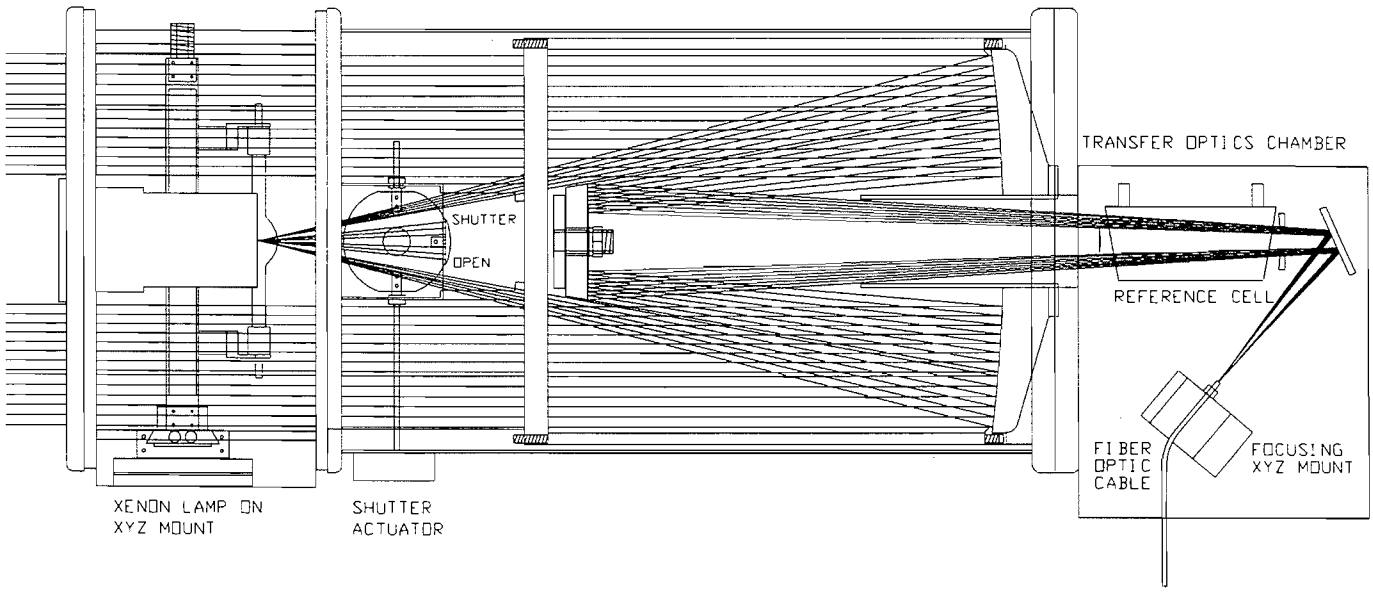

tion in Beer's Law expression. In addition, a reference gas cell can be placed in front of the fiberoptic cable entrance for calibration. Since both outgoing and reflected beams traverse the same path the effect of air turbulences are minimized. In fact, the main problem encountered with any long-path measurement is the turbulence or scintillations of the air along the path that occur at time scales of 0.1–1 Hz.

In the original design, Platt and his group solved this problem by replacing the exit slit of the spectrometer by a rotating disc containing some 20 radial slits. Only one slit at a time is exposed to the spectrometer. Since the rotational speed of the disc is about 300 rpm, successive spectra are obtained at a frequency of about 100 Hz, which is much faster than the frequency of air turbulences. Several tens of thousands of scans are added over 10–15 min to get the desired sensitivity. The problems inherent with the wheel include the need to have all the slits identical in order to co-add successive spectra and, second, the rotational speed of the wheel must be maintained to a very high degree of accuracy for the same reason. These requirements add considerably to the size and cost of the system. Furthermore, the slits do not remain vertical as the wheel rotates, causing distortion of the spectrum. Each instrument must therefore be calibrated for each gas to be measured — not a trivial task.

We have "uninvented" the wheel. We have replaced it by a miniature, electrochemically swept slit, which provides a repetitive, bidirectional sweep of the spectrum in which the change of wavelength is linear with respect to time. The replacement of the wheel by a linear scanner reduces both the size and cost of the instrument. In addition, since the slit is always vertical and its displacement linear it is no longer necessary to calibrate the instrument for each gas; literature spectra can be incorporated into the library of the data-processing computer.

An example of some measurements made with this system is provided by a study we made to determine practical detection limits of the system for a number of important pollutant gases. Determining detection limits of a remote-sensing instrument in a polluted atmosphere can be a controversial issue. At trace levels close to the detection limit, it may be difficult to separate real variations in pollutant levels from the variations due to residual noise sources in the system. The least ambiguous method appears to be simultaneous measurements using two long-path instruments mounted side by side and probing essentially the same air mass.

Two DOAS telescopes and spectrometers were set up side by side on the second floor of the Unisearch facilities, both directed to the same retroreflector located on the roof of a neighboring building, providing a total path length of 314 m. The surrounding area, in suburban Toronto, is a light industrial zone with considerable vehicular traffic, providing a realistic situation where there is considerable variation in the pollutant concentrations. The study was made for a number of gases including NO, NO_2, O_3, benzene, and toluene. Figure 8 is a time plot of some of the toluene data taken with the two instruments. The very variable toluene peaks starting at 07:30 correspond with the start of daily industrial activity in this area and appear quite frequently. Figure 9 is a scatter plot of the same data. From this plot a standard error of 1.88 ppbv and a detection limit of 1.3 ppbv toluene for a single instrument are obtained.

In conclusion, I have tried to show you why I have never considered myself to be an analytical chemist. I have always been interested in trying to solve particular scientific problems — the nature of active nitrogen, the composition of the atmosphere, and the reactions that occur in that large laboratory either naturally or as a result of human activities. To answer these questions I needed to make measurements. In most cases

Fig. 8. Some real-time measurements of toluene made with two SENSAIR-DOAS instruments operating over a 314 m path in suburban Toronto in January. The variable toluene peaks starting at 07:30 correspond to the start of daily industrial activity in this area.

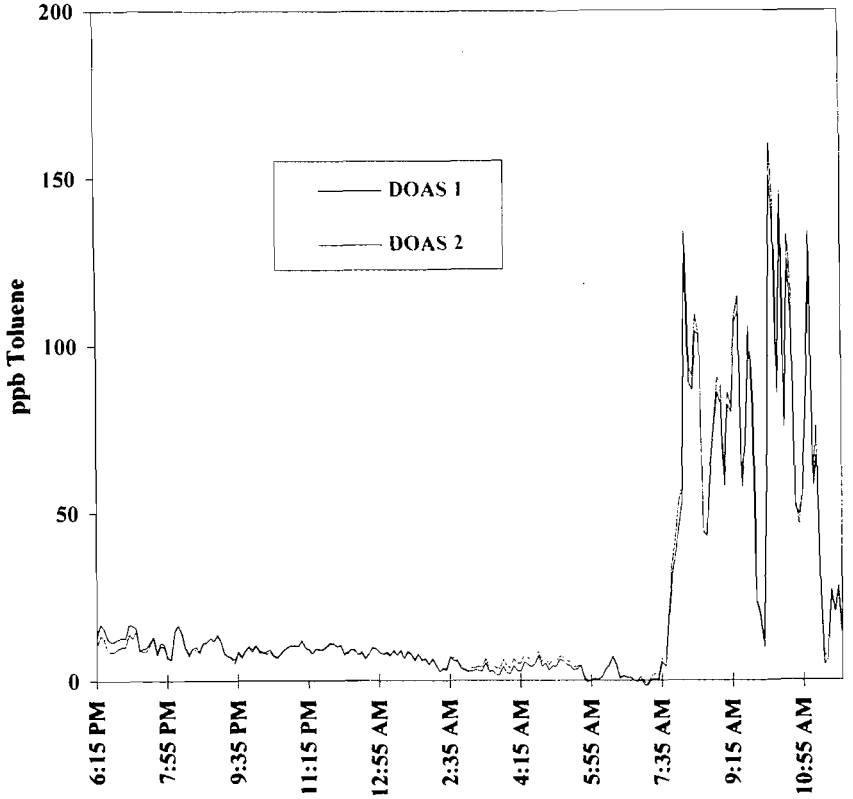

Fig. 9. Scatter diagram for the measurements of toluene made simultaneously over the same air path by two SENSAIR-DOAS instruments.

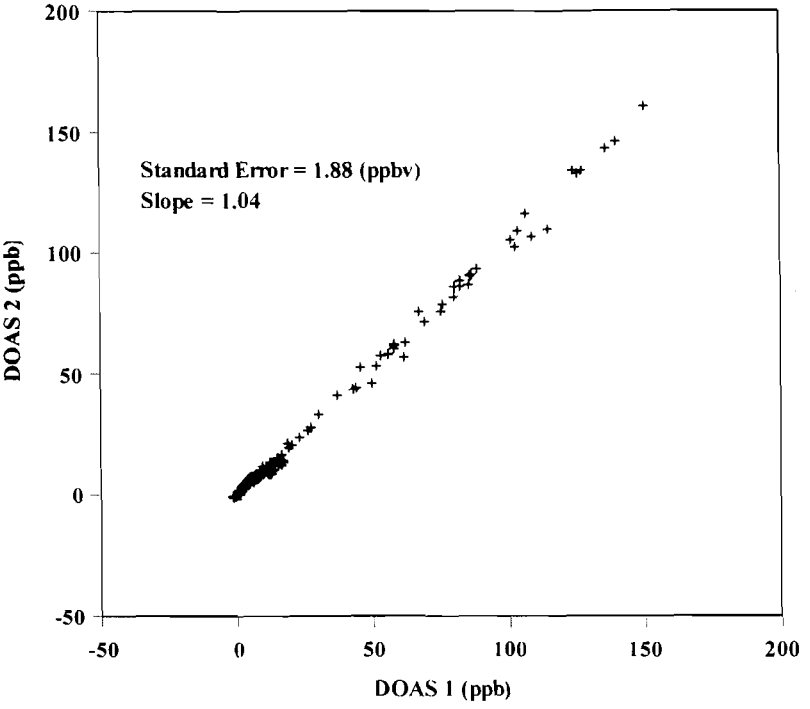

the instruments required to make these measurements simply were not available. So we had to design and build them. Fortunately for me, I always had students and colleagues who were much more skillful at this than I was.

If that makes me eligible for this prestigious award then all I can do is to thank the Society. Life is full of surprises!

References

1. D.S. Jackson and H.I. Schiff. J. Chem. Phys. **23**, 2333 (1955).
2. E.A. Ogryzlo and H.I. Schiff. Can. J. Chem. **37**, 1690 (1959).
3. H.P. Broida, H.I. Schiff, and T.M. Sugden. Trans. Faraday Soc. **57**, 259 (1961).
4. A. Fontijn and H.I. Schiff. *In* Chemical reactions in the lower and upper atmosphere. Interscience, New York. 1961. pp. 239–251.
5. B.A. Ridley, H.I. Schiff, A.W. Shaw, L. Bats, C. Howlett, H. LeVaux, L.R. Megill, and T.E. Ashenfelter. Nature, **245**, 310 (1973).
6. B.A. Ridley, H.I. Schiff, A.W. Shaw, L.R. Megill, L. Bates, C. Howlett, H. LeVaux, and T.E. Ashenfelter. Planet. Space Sci. **22**, 19 (1974).
7. H.I. Schiff (*Editor*). Stratospheric ozone depletion by halocarbons: chemistry and transport national. Academy of Sciences, Washington, D.C. 1979.
8. D.R. Hastie, G.I. Mackay, T. Iguchi, B.A. Ridley, and H.I. Schiff. Environ. Sci. Technol. **17**, 352A (1983).
9. H.I. Schiff, D.R. Karecki, G.W. Harris, D.R. Hastie, and G.I. Mackay. J. Geophys. Res. [atmos.], **95**, 10147 (1990).
10. G.L. Gregory, J.M. Hoell, Jr., B.J. Huebert, S.E. van Bramer, P.J. LeBel, S.A. Vay, R. Marinaro, H.I. Schiff, D.R. Hastie, G.I. Mackay, and D.R. Karecki. J. Geophys. Res. [atmos.] **95**, 10089 (1990).
11. G.L. Gregory, J.M. Hoell, Jr., M.A. Carroll, B.A. Ridley, D.D. Davis, J. Bradshaw, M.O. Rodgers, S.T. Sandholm, H.I. Schiff, D.R. Hastie, D.R. Karecki, G.I. Mackay, G.W. Harris, A.L. Torres, and A. Fried. J. Geophys. Res. [Atmos.], **95**, 10103 (1990).
12. G.I. Mackay, L.K. Mayne, and H.I. Schiff. Aerosol Sci. Technol. **12**, 56 (1990).
13. H.I. Schiff, J. Bechara, J.T. Pissano, and G.I. Mackay. Proc. AWMA 87th Annu. Meet., Cincinnati, Ohio. 1994.
14. H.I. Schiff, S.D. Nadler, and G.I. Mackay. Proc. AWMA Symp. on Optical Sensing for Environmental Monitoring. McLean, Va. 1994. Paper 23661-11.
15. H.I. Schiff, G.I. Mackay, and S.D. Nadler. Infrared Phys. Tech. **37**, 39 (1996).
16. G.I. Mackay, S.D. Nadler, D.R. Kareck, H.I. Schiff, J.W. Butler, C.A. Gierzack, and G. Jesion. Proc. AWMA 88th Annu. Meet. and Exhibition, San Antonio, Tex. 1995.
17. H.I. Schiff, J.C. Robbins, S.D. Nadler, and G.I. Mackay. AWMA Symp. on Optical Sensing for Environmental Monitoring. McLean, Va. 1994. Paper 19.3.
18. H.I. Schiff, J. Robbins, A. Chanda, D. Nadler, G.I. Mackay, D. Kita, and D. Appel. Proc. AWMA Annu. Meet. Nashville, Tenn. 1996. Paper No. 96-TP26B.04.

The decomposition of aliphatic *N*-nitro amines in aqueous sulfuric acid. Bisulfate as a nucleophile[1]

Robin A. Cox

Abstract: In aqueous sulfuric acid, aliphatic *N*-nitro amines decompose to N_2O and alcohols. An excess acidity analysis of the observed rate constants for the reaction shows that free carbocations are not formed. The reaction is an acid-catalyzed S_N2 displacement from the protonated *aci*-nitro tautomer, the nucleophile being a water molecule at acidities below 82–85% H_2SO_4, and a bisulfate ion at higher acidities. Bisulfate is the poorer nucleophile by a factor of about 1000. Twelve compounds were studied, of which results obtained for nine at several different temperatures enabled calculation of activation parameters for both nucleophiles. The reaction appears to be mainly enthalpy controlled. The intercept standard-state rate constants are well correlated by the σ^* values for the alkyl groups; the slopes are negative, with a more negative value for the slower bisulfate reaction. Interestingly the $m^{\ddagger}m^*$ slopes also correlate with σ^*, although the scatter is bad.

Key words: *N*-nitro amines, excess acidity, bisulfate, nucleophiles, acid-catalyzed, kinetics.

Résumé : En solution dans l'acide sulfurique aqueux, les *N*-nitroamines aliphatiques se décomposent en N_2O et en alcools. Une analyse des constantes de vitesse de ces réactions par la méthode de l'excès d'acidité montre qu'il ne se forme pas de carbocations libres. La réaction est une substitution S_N2 acidocatalysée sur le tautomère *aci*-nitro protoné dans laquelle le nucléophile est une molécule d'eau à des acidités inférieures à 82–85% de H_2SO_4 et un ion bisulfate à des acidités supérieures. Comme nucléophile, le bisulfate est mille fois moins efficace. On a étudié 12 composés; les résultats obtenus à diverses températures avec 9 d'entre eux ont permis de calculer les paramètres d'activation pour les deux nucléophiles. Il semble que la réaction est principalement contrôlée par l'enthalpie. Dans les cas des groupes alkyles, les valeurs de σ^* permettent d'établir une bonne corrélation avec l'ordonnée à l'origine des constantes de vitesse de l'état standard; les pentes sont négatives et elles le sont encore plus pour la réaction plus lente du bisulfate. Il est intéressant de noter que les pentes $m^{\ddagger}m^*$ donnent aussi une bonne corrélation avec σ^*, même si l'éparpillement est mauvais.

Mots clés : *N*-nitroamines, excès d'acidité, bisulfate, nucléophiles, acidocatalysé, cinétique.

[Traduit par la rédaction]

Introduction

As part of a continuing interest in the mechanisms of organic reactions in strong acids (1), this paper is concerned with the decomposition of monoalkyl nitramines to alcohols and nitrous oxide that takes place in concentrated aqueous sulfuric acid media.

Little information is available in the open literature concerning this functional group, probably because military explosives are often alkylnitramines, the two best known being RDX and HMX (2). In contrast, the parent molecule nitramide, NH_2NO_2, has been widely studied, and the results

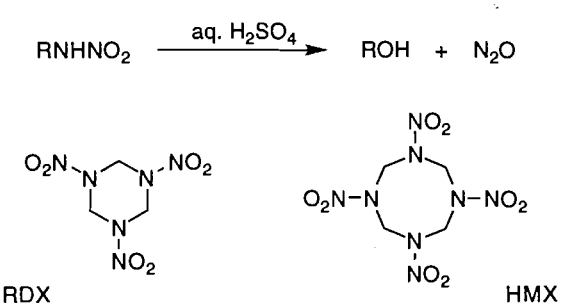

have contributed greatly to the theory of acid–base catalysis (3). Interest in nitramide continues to this day (4–6). The rearrangement of aromatic nitramines to nitroanilines has also received some attention (7).

Apart from one early study (8), all of the information on the acid-catalyzed hydrolysis of alkylnitramines comes from the group of L. L. Kuznetsov (9–11) in what was then the Soviet Union. Kuznetsov's papers were published without an affiliation being given, which probably means that the work was carried out at a military facility; I eventually managed to track him down in Leningrad in 1987 and was able to discuss this work with him, as far as was possible through an interpreter in a hotel lobby with a KGB minder in the middle distance, and I

Received January 5, 1996.

This paper is dedicated, somewhat belatedly, to Professor John T. Edward of McGill University.

R. A. Cox.[2] Department of Chemistry, University of Toronto, 80 St. George St., Toronto, ON M5S 3H6, Canada.

[1] Presented in part at the 69th CIC Chemical Conference, Saskatoon, June 1986, No. OR-C1-3.

[2] Telephone: (416) 978-4581. Fax: (416) 978-8775. E-mail: rcox@alchemy.chem.utoronto.ca

Fig. 1. Excess acidity plot of log log k_ψ − log C_{H^+} vs. X for the reaction of *N*-nitroethylamine in sulfuric acid at 15 and 40°C. For convenient reference a wt.% H_2SO_4 concentration scale is included at the top, and a line of unit slope at the right.

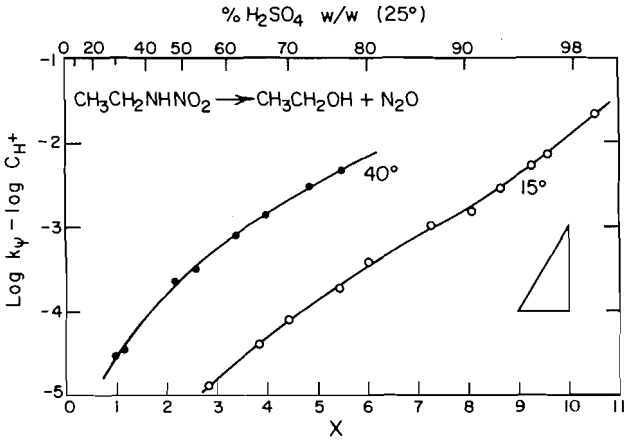

think that he is in substantial agreement with the analysis in this paper.

The results are analyzed using the excess acidity method (1), which has been widely applied to organic reactions in sulfuric acid in recent years, most recently to aromatic hydrogen exchange (12), phenylazo ether cleavage (13), imidazole cyclizations (14), and the hydrations of fluorinated alkyl vinyl ethers (15).

Results

The excess acidity method works by examining plots of of log k_ψ − log C_{H^+} against X, where k_ψ are observed rate constants as a function of acidity for the reaction in question. C_{H^+} is the molar proton concentration and X the excess acidity of the medium (1); values are given in Cox and Yates (16). If these plots are linear the reaction mechanism is A1 or A-S_E2, and if curved, A2 (1). Such a plot for the decomposition of *N*-nitroethylamine in sulfuric acid at two temperatures is shown in Fig. 1. This curves downward up to an acidity of ~85% H_2SO_4, and then starts to curve upward; this means that the reaction mechanism is clearly not A1 or A-S_E2. Once a mechanism is identified in this way as being A2, the species reacting with the protonated substrate at the transition state (Nu) can be positively identified by plotting log k_ψ − log C_{H^+} − log a_{Nu} against X (a = molar activity), trying different Nu until linearity is achieved (1). This is shown for the same *N*-nitroethylamine data in Fig. 2. A preliminary double linear regression using the most plentiful data, that for *N*-nitromethylamine at 25°C (9–11), with X as one variable and log a_{H_2O} as the other, gave the slope in the water activity, r, as being 0.965 ± 0.058, i.e., below ~85% H_2SO_4 Nu is one water molecule. The line deviates upwards after this point but, as shown, the deviant points become linear on the assumption that the Nu changes to one bisulfate ion above this acidity.

The *N*-nitroalkylamines in this study are identified by alkyl group in Table 1. The rate constants as a function of sulfuric acid concentration at 15, 25, 40, and 60°C used were those of Kuznetsov and co-workers (9), together with some additional data from his group for **5** at 25, 35, 45, and 55°C (10, 11), and some values obtained by Lamberton and co-workers for **1**, **3**, **4**, **5**, and **7** in dilute acid at 85°C (8). The data obtained by different groups at different times are in excellent agreement, as can be seen from Fig. 2. The results for the parent compound **9** are taken from the following paper (6). Tables 2 and 3 give the slope ($m^{\ddagger}m^*$) and intercept (log $k_0^{25°}$) data obtained from the Fig. 2 plots for **2**, **4**–**8**, and **10**–**12**. With results at several temperatures available for these compounds, activation parameters can be obtained as described previously (17), and these are also given in Tables 2 and 3. Since temperature-corrected values of X, log C_{H^+}, log a_{H_2O}, and log $C_{HSO_4^-}$ were used, these refer only to the reaction mechanism, medium effects having been eliminated (1, 17).

Fig. 2. Excess acidity plot for the reaction of *N*-nitroethylamine in sulfuric acid at several temperatures, assuming reaction with one water molecule (left axis and lines) or with one bisulfate ion (right axis, two rightmost lines).

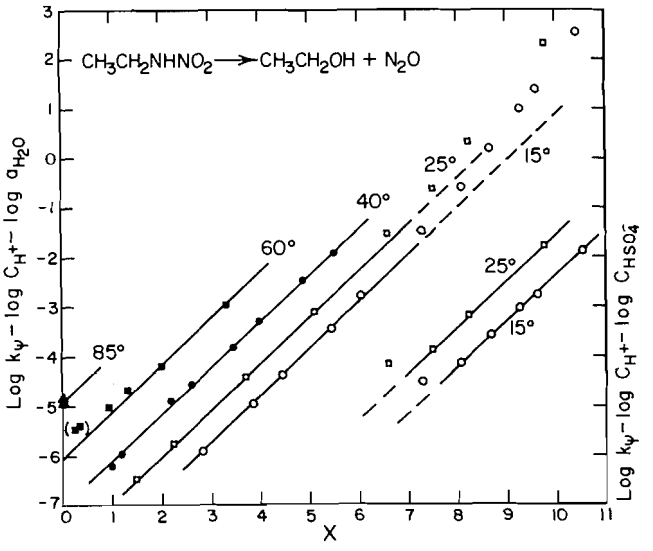

Because data for **1** and **3** were only available at 85°C, the data in Tables 2 and 3 were used to evaluate log $k_0^{85°}$ values for the reaction with H_2O for the other compounds as well, and all of these intercept data are collected in Table 1. Also given there is statistical information regarding the data fit; for greater accuracy the program used rejects any points that have a 95% or greater probability of not being part of the same data set as the other points (points in parentheses in Fig. 2 and Table 1). Included in Table 1 are σ* values for the different alkyl groups obtained from ref. 18*a*; values for the alkyl groups not directly listed there (**8** and **10**) were calculated according to the procedure given in ref. 18*b*.

Linear free energy relationship plots against σ* for the standard-state intercept log k_0 values are given in Fig. 3. The ρ* values (slopes) are −1.71±0.19 for the 25°C intercepts and −1.29 ± 0.11 for the 85°C ones, both for Nu = H_2O and including results obtained for **9** (6), and −2.79 ± 0.35 for the 25°C, Nu = HSO_4^- case.

Discussion

The mechanism proposed for the decomposition of the alkylnitramines is shown below, an A2 reaction with Nu being one water molecule below, and one bisulfate ion above, ~85% H_2SO_4. Initial tautomerization to the *aci*-nitro form, proposed

Table 1. R in $RNHNO_2$, σ^* and log $k_0^{85°}$ values, and statistical data.

Compound	R	σ^{*a}	log $k_0^{85°b}$	$\pm \sigma_y^c$	N^d
1	$(CH_3)_3C$	−0.30	−3.206[e]	0.008	3
2	$CH_3CH_2CH_2CH_2$	−0.25	−2.954	0.049	33(3)
3	$(CH_3)_2CH$	−0.19	−3.073[e]	0.053	7
4	CH_3CH_2	−0.10	−3.185	0.064	39(2)
5	CH_3	0.00	−3.344	0.035	64(3)
6	$H_2C{=}CHCH_2$	0.00	−3.606	0.053	32(2)
7	$HO_2CCH_2CH_2$	0.35	−3.719	0.058	28(1)
8	$CH_3C(NO_2)_2CH_2CH_2$	0.47[f]	−4.148	0.044	23
9[g]	H	0.49	−3.758	0.045	33
10	$(NO_2)_3CCH_2CH_2$	0.65[f]	−4.674	0.047	26
11	$N{\equiv}CCH_2CH_2$	0.87	−4.284	0.050	25(1)
12	HO_2CCH_2	1.08	−4.895	0.093	25(1)

[a]From ref. 18*a*.
[b]For the Nu = H_2O reaction. Measured directly for **1** and **3**, obtained from ref. 6 for **9**, and calculated using the activation data given in Table 2 for the rest.
[c]Root-mean-square error of the fit.
[d]Number of data points. The number rejected by the program, if any, is given in parentheses, see text.
[e]Only 85°C data available.
[f]Estimated, see ref. 18*b*.
[g]Data for the parent compound are from the following paper, ref 6.

Table 2. Intercepts, slopes, and activation parameters for the Nu = H_2O reaction.

Compound	log $k_0^{25°}$	$m^{\ddagger}m^*$	$\Delta H^{\ddagger a}$	$\Delta S^{\ddagger b}$
2	−6.022 ± 0.032	0.9288 ± 0.0079	24.44 ± 0.38	−12.1 ± 1.3
4	−6.149 ± 0.042	0.938 ± 0.010	23.59 ± 0.38	−15.5 ± 1.3
5	−6.447 ± 0.016	0.9586 ± 0.0039	24.72 ± 0.17	−13.10 ± 0.56
6	−6.695 ± 0.041	0.977 ± 0.011	24.61 ± 0.44	−14.6 ± 1.5
7	−6.928 ± 0.041	0.9926 ± 0.0097	25.59 ± 0.39	−12.4 ± 1.3
8	−7.376 ± 0.040	1.0456 ± 0.0092	25.74 ± 0.33	−13.9 ± 1.1
10	−8.053 ± 0.055	1.098 ± 0.011	26.96 ± 0.46	−12.9 ± 1.5
11	−7.535 ± 0.054	1.035 ± 0.011	25.94 ± 0.45	−14.0 ± 1.5
12	−8.30 ± 0.15	1.046 ± 0.028	27.2 ± 1.1	−13.2 ± 3.8

[a]In kcal mol^{-1}.
[b]In cal mol^{-1} K^{-1}.

by analogy with the well-established mechanisms for base-catalyzed nitramide decomposition (4), is followed by protonation and rate-determining S_N2 attack.

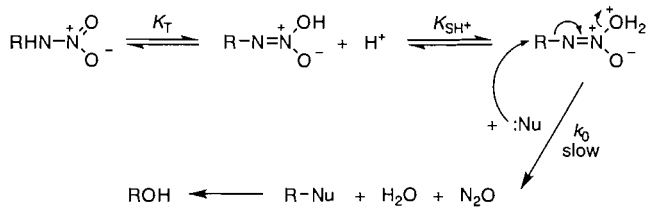

The curvature seen in Fig. 1 immediately eliminates the previously proposed mechanisms for this process. Lamberton thought that fast nitrogen protonation was followed by rate-determining cleavage to a carbocation and NH_2NO_2, which subsequently decomposed to water and N_2O (8). This is an A1 process that would not give the Fig. 1 curvature, and if instead the NH_2NO_2 decomposition was rate determining, the different alkylnitramines would all decompose at the same rate, contrary to observation. Kuznetsov gives a mechanism like the one shown, except that the rate-determining log k_0 step is given as A1 carbocation formation, without nucleophile involvement (9). Apart from the lack of Fig. 1 curvature already mentioned, formation of free carbocations like $^+CH_3$ in these aqueous reaction media seems, on the face of it, highly unlikely.

Derivation of an excess acidity rate equation for the proposed mechanism is not difficult (1, 6), it is log k_ψ − log C_{H^+} − log a_{Nu} = log(k_0K_T/K_{SH^+}) + $m^{\ddagger}m^*$ X, where the term definitions have already been given, except for K_T and K_{SH^+}, which refer to the two equilibria in the reaction scheme above. This is the equation which gives the straight-line Fig. 2 plots. However, the intercepts, referred to for simplicity as log k_0 in the tables, and the $\Delta H^{\ddagger}$ and $\Delta S^{\ddagger}$ values derived from them, are in fact composites of log k_0 and these two equilibrium constants. Further separation is unfortunately not possible, since the two K's are not known. Not a lot is known about the nitro–*aci*-nitro tautomerism of the K_T process in any case (except that the pK_T

Table 3. Intercepts, slopes, and activation parameters for the Nu = HSO_4^- reaction.

Compound	log $k_0^{25°}$	$m^{\ddagger}m^*$	$\Delta H^{\ddagger a}$	$\Delta S^{\ddagger b}$
2	−10.53 ± 0.28	0.896 ± 0.030	29.0 ± 2.0	−9.4 ± 6.7
4	−10.59 ± 0.37	0.900 ± 0.039	30.0 ± 2.6	−6.5 ± 8.7
5	−10.94 ± 0.19	0.920 ± 0.021	27.4 ± 1.4	−16.8 ± 4.7
6	−10.31 ± 0.24	0.883 ± 0.027	24.8 ± 2.3	−22.6 ± 7.7
7	−12.26 ± 0.61	1.107 ± 0.078	25.0 ± 4.3	−31 ± 15
8	−13.05 ± 0.41	1.191 ± 0.048	30.5 ± 2.5	−16.1 ± 8.7
10	−12.80 ± 0.24	1.137 ± 0.028	33.0 ± 1.5	−6.6 ± 5.3
11	−12.69 ± 0.43	1.140 ± 0.052	34.1 ± 2.0	−2.1 ± 7.1
12	−13.94 ± 0.38	1.223 ± 0.043	37.7 ± 2.3	+4.2 ± 7.7

[a,b]See Table 2.

Fig. 3. Linear free-energy correlations with σ* for the intercept data in the tables.

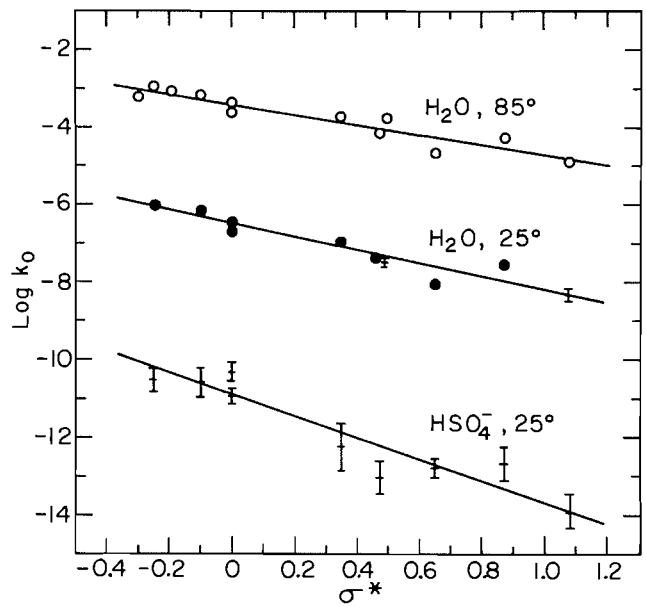

for nitramide itself has recently been estimated to be ~6 (4)). However, it is reasonable to assume that it is fast, since proton transfers to and from nitrogen and oxygen, known to be fast (19), are involved; only proton transfers at carbon (and possibly sulfur (20)) are slow. Protonation constants for alkylnitramines are not known either, beyond the fact that no signs of equilibrium protonation are visible in the acidity range covered by the experiments. In any event the OH group of the *aci*-nitro tautomer, at which protonation leads to further reaction, is unlikely to be the most basic site in the molecule.

Bisulfate ion is not normally thought of as being nucleophilic, and it is clear from Fig. 2 that for this reaction it is in fact some 1000 times worse than water as a nucleophile in the standard state (i.e., at $X = 0$), since the vertical separation of the H_2O and HSO_4^- lines in Fig. 2 is about three log units. (A more detailed calculation, averaging over all the compounds in this work that have data for both, gives the difference in nucleophilicity between 55.34 M water and 1 M bisulfate as being 3.031±0.056 log units in these sulfuric acid media.) Consideration of the concentrations of the various species in aqueous sulfuric acid (21) means that the change in nucleophile occurs at 82–85 wt.% H_2SO_4, a concentration at which mechanistic changes take place for many reactions (1, 21).

The activation parameters in Tables 2 and 3 indicate that the observed differences in reaction rates are primarily due to differences in the enthalpy of activation for the different compounds. In the Nu = H_2O case the entropies of activation are all the same, averaging to −13.39 ± 0.37 cal mol^{-1} K^{-1}. Although it may not look like it, the entropies of activation in the Nu = HSO_4^- case are not statistically different from one another either, when account is taken of the larger errors, and on weighting the numbers with their errors these average to −10.6 ± 2.3 cal mol^{-1} K^{-1}. This is less negative than for the Nu = H_2O case, as would be expected since charge destruction is taking place when Nu = HSO_4^-, freeing up solvating species; in fact I would have expected it to be zero or even positive, as has been found for amide hydrolysis (22). The $m^{\ddagger}m^*$ values in Tables 2 and 3 are near one; m^*, which refers to the equilibrium protonation behavior of the substrate, is unknown but for oxygen protonations a value of less than one would be expected (16). However, since m^* also contains an unknown contribution from the nitro–*aci*-nitro tautomerism, further comment as to the value of $m^{\ddagger}$ (referring to the transition state) seems unjustified, beyond noting that the combined values seem acceptable according to what is known about them (1, 16, 22).

The relative reactivity order given in Tables 1 and 2 and Fig. 3 for compounds **1**, **3**, **4**, **5**, and **12** is in exact agreement with the order found in very recent theoretical calculations (SCF–MO AM1) concerning the reactivity of these molecules under acidic conditions, *t*-Bu > i-Pr > Et > Me > CH_2CO_2H (23).[3] The ρ* values for the LFER plots in Fig. 3 seem about right for this type of reaction (18), and it is apparent that the differences between the different alkyl groups are due to polar rather than steric interaction with the reaction center. Poorer

[3] One of the referees comments that H:Me (and *t*-Bu:Me) rate ratios are very large in many solvolysis reactions, and thus it is quite surprising that the point for the H substituent (nitramide itself) falls on the same line with the other substituents. This is comparison of a base attack with the nucleophilic attack under consideration here (see following paper (6)), and thus too much significance should not be attached to this agreement as it may well be fortuitous (the activation parameters for nitramide (6) are quite different from those in Table 2).

agreement for the i-Pr and *t*-Bu derivatives **3** and **1** might have been expected because of the anticipated steric effect of these groups; it is unfortunate that only very few experimental measurements are available for these two compounds, and only at 85°C (8). The fact that the points for **1** and **3** *do* fall on the line is an argument in favor of an early transition state for the reaction, diminishing the importance of steric effects; the fact that single water molecules (rather than two or three acting in concert) act as nucleophiles is another argument for an early transition state, as discussed previously (1).

The ρ^* for the bisulfate reaction is more negative than that for the water reaction, implying greater influence for the substituents, which probably means that the weaker bisulfate nucleophile is putting more demand on them. The ρ^* for the faster water reaction at 85°C is less negative than the value at 25°C. Interestingly the $m^{\ddagger}m^*$ values in Table 3 are also linearly correlated with σ^*, although with some scatter; for clarity these plots are not included in Fig. 3. For Nu = H_2O the slope is 0.126 ± 0.023 (intercept 0.961 ± 0.008, correlation coefficient 0.89) and for Nu = HSO_4^- it is 0.294 ± 0.039 (intercept 0.931 ± 0.017, correlation coefficient 0.94). Since these $m^{\ddagger}m^*$ values are already LFER slope parameters (1), it is difficult to know what interpretation to put upon this observation, but it is worth noting that behavior like this has been seen before, in σ^+ plots (24), and so there may in fact be one.

Acknowledgments

Valuable discussions with Dr. L. L. Kuznetsov and Professor A. J. Kresge are acknowledged.

References

1. R.A. Cox. Acc. Chem. Res. **20**, 27 (1987).
2. J.T. Edward. J. Chem. Educ. **64**, 599 (1987).
3. R.P. Bell. The proton in chemistry. 2nd ed. Cornell University Press, Ithaca, N.Y. 1973. pp. 160–164.
4. C.H. Arrowsmith, A. Awwal, B.A. Euser, A.J. Kresge, P.P.T. Lau, D.P. Onwood, Y.C. Tang, and E.C. Young. J. Am. Chem. Soc. **113**, 172 (1991); C.H. Arrowsmith, A.J. Kresge, and Y.C. Tang. J. Am. Chem. Soc. **113**, 179 (1991).
5. P. Politzer, N. Sukumar, K. Jayasuriya, and S. Ranganathan. J. Am. Chem. Soc. **110**, 3425 (1988); J. P. Ritchie. J. Am. Chem. Soc. **111**, 2517 (1989).
6. R.A. Cox. Can. J. Chem. **74**, 1779 (1996).
7. H.J. Shine, J. Zygmunt, M.L. Brownawell, and J. San Filippo. J. Am. Chem. Soc. **106**, 3610 (1984), and references cited therein.
8. J. Barrott, I.N. Denton, and A.H. Lamberton. J. Chem. Soc. 1998 (1953).
9. E.N. Vorob'eva, L.L. Kuznetsov, and B.V. Gidaspov. Zh. Org. Khim. **19**, 698 (1983); J. Org. Chem. USSR, **19**, 615 (1983).
10. A.A. Astrat'ev, E.N. Vorob'eva, L.L. Kuznetsov, and B.V. Gidaspov. Zh. Org. Khim. **15**, 1136 (1979); J. Org. Chem. USSR, **15**, 1015 (1979).
11. A.A. Glukhov, L.L. Kuznetsov, and B.V. Gidaspov. Zh. Org. Khim. **19**, 704 (1983); J. Org. Chem. USSR, **19**, 620 (1983).
12. R.A. Cox. J. Phys. Org. Chem. **4**, 233 (1991).
13. R.A. Cox, I. Onyido, and E. Buncel. J. Am. Chem. Soc. **114**, 1358 (1992).
14. R.A. Cox, D. Moore, and R.S. McDonald. Can. J. Chem. **72**, 1910 (1994).
15. J.-P. Bégué, F. Benayoud, D. Bonnet-Delpon, A.D. Allen, R.A. Cox, and T.T. Tidwell. Gazz. Chim. Ital. **125**, 399 (1995).
16. R.A. Cox and K. Yates. J. Am. Chem. Soc. **100**, 3861 (1978).
17. R.A. Cox, M.F. Goldman, and K. Yates. Can. J. Chem. **57**, 2960 (1979).
18. D.D. Perrin, B. Dempsey, and E.P. Serjeant. pK_a prediction for organic acids and bases. Chapman and Hall, London. 1981. (*a*) pp. 109–126; (*b*) pp. 37–38.
19. A.J. Kresge. Acc. Chem. Res. **8**, 354 (1975).
20. R.A. Cox and K. Yates. Can. J. Chem. **60**, 3061 (1982).
21. R.A. Cox. J. Am. Chem. Soc. **96**, 1059 (1974).
22. R.A. Cox and K. Yates. Can. J. Chem. **59**, 2853 (1981).
23. H.-M. Xiao, Y.-M. Li, and Y.-F. Li. Huaxue Xuebao, **53**, 438 (1995); Chem. Abstr. **123**, 313171*v* (1995).
24. R.A. Cox and K. Yates. J. Org. Chem. **51**, 3619 (1986).

The acid-catalyzed decomposition of nitramide

Robin A. Cox

Abstract: Much attention has been paid to the base-catalyzed decomposition of nitramide, but despite this it was not certain that a corresponding acid-catalyzed reaction even existed before the work described in this paper. The excess acidity method has been applied to nitramide decomposition rate constants obtained in aqueous perchloric acid media, and to a lesser extent in aqueous hydrochloric and sulfuric acids. This analysis shows that the decomposition in dilute acid solution is actually a base-catalyzed reaction, with water acting as the base (perhaps in a cyclic process involving two water molecules), with rate constants in good agreement with previous estimates. However, in more concentrated acid media a true acid-catalyzed reaction can be dissected out. Activation parameters are given for both mechanisms, and it is shown that the acid-catalyzed process is similar to the acid-catalyzed decomposition of alkylnitramines. In sulfuric acid the reaction is slightly faster than it is in the other acids, due to the presence of a base-catalyzed process involving sulfate.

Key words: nitramide, excess acidity, acid-catalyzed, base-catalyzed, kinetics.

Résumé : Même si on s'est beaucoup intéressé à la décomposition du nitramide catalysée par les bases, il n'est pas certain qu'une réaction acidocatalysée correspondante ait été rapportée avant celle décrite dans ce travail. On a appliqué la méthode de l'excès d'acidité aux constantes de vitesse de décomposition du nitramide obtenues dans un milieu d'acide perchlorique aqueux et, à un degré moindre, dans des solutions aqueuses d'acides chlorhydrique et sulfurique. Cette analyse démontre que la décomposition en solution acide dilué est, en fait, une réaction catalysée par les bases dans laquelle l'eau agit comme base (possiblement dans un processus cyclique impliquant deux molécules d'eau), pour laquelle les constantes de vitesse sont en bon accord avec les évaluations antérieures. Toutefois, dans des milieux acides plus concentrés, on peut mettre en évidence une vraie réaction acidocatalysée. On rapporte les paramètres d'activation pour les deux mécanismes et on démontre que le vrai processus acidocatalysé est semblable à la décomposition acidocatalysée des alkylnitramines. Dans l'acide sulfurique, la réaction est légèrement plus rapide que dans les autres acides; on attribue cette différence à la présence d'un processus catalysé par les bases impliquant l'ion sulfate.

Mots clés : nitramide, excès d'acidité, acidocatalysé, catalysé par les bases, cinétique.

[Traduit par la rédaction]

Introduction

In connection with a recent study of the decomposition of alkylnitramines to alcohols and nitrous oxide that takes place in aqueous sulfuric acid media (1), it was also of interest to find out what happens to the parent compound nitramide, NH_2NO_2, under similar conditions. Although wholly inorganic, nitramide has the status of an "honorary" organic molecule amongst physical organic chemists, because of the contribution that the study of the base- and buffer-anion-catalyzed decomposition of this molecule has made to our understanding of acid–base catalysis (2). However, in spite of the many studies that have been made of this molecule, there is still new information to be obtained. Quite recently a whole new base-catalyzed decomposition mechanism was discovered for nitramide in strongly basic media (3). Theoretical calculations seem unable to agree on such basic matters as whether or not the molecule is twisted (4). It has only recently been discovered that the oxygens in the molecule are more basic than the NH_2 nitrogen, according to gas-phase protonation and ab initio studies (5).

Only two groups have reported kinetic studies of the decomposition of nitramide in acidic media, Marlies and La Mer (in 1935), and more recently the group of M. N. Hughes. The first group studied the reaction in dilute aqueous hydrochloric acid solutions at 25°C (6), and the second used aqueous perchloric, hydrochloric, and sulfuric acids at several temperatures (7). This paper is concerned with an excess acidity analysis (8) of these results, and represents an extension of the excess acidity kinetic method to perchloric and hydrochloric acid media, from the sulfuric acid solutions used almost exclusively until now.

Received January 5, 1996.

Dedicated to the memory of Professor John W. Bunting, 1943–1995.

R.A. Cox.[1] Department of Chemistry, University of Toronto, 80 St. George St., Toronto, ON M5S 3H6, Canada.

[1] Telephone: (416) 978-4581. Fax: (416) 978-8775. E-mail: rcox@alchemy.chem.utoronto.ca

Results and discussion

The available rate constants, k_ψ, as a function of acid concentration and temperature (6, 7) are plotted against X in the excess acidity format, as $\log k_\psi - \log C_{H^+}$, in Fig. 1. (The data quoted as being measured at a temperature of ?43° in Fig. 1 are said to be 35°C values in the original paper (7), but this almost certainly is in error, since assuming a temperature of 43°C

Fig. 1. Excess acidity plots of log k_ψ − log C_{H^+} vs. X for the decomposition of nitramide in aqueous perchloric acid at several temperatures (lower) (7), and (upper) for the decomposition in aqueous sulfuric and hydrochloric acids at a temperature thought to be 43°C (7), and in aqueous hydrochloric acid at 25°C (6).

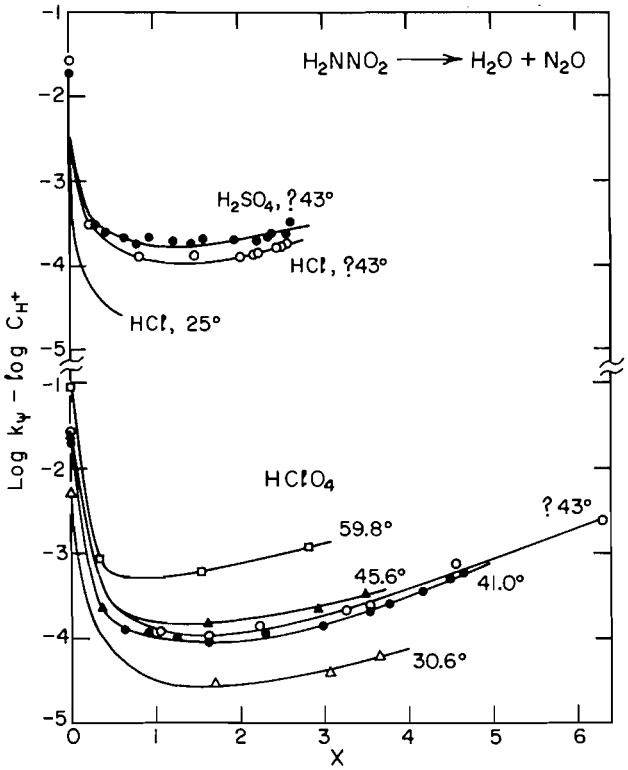

gives excellent agreement for these data with all of the rest; see below.) The excess acidities X for sulfuric and perchloric acid are from Cox and Yates (9), and values for hydrochloric acid are also available (10); all are corrected to the reaction temperature as before (11). Values of C_{H^+} are simply the acid molarities for the monobasic acids (10); quoted values are used for sulfuric acid (9), and all are corrected to temperature via the densities.

It is obvious from Fig. 1 that a sharp initial drop in rate is followed by a shallow increase. Nitramide is known to react with water alone (2, 3); Hughes realized this and subtracted the neutral water values from his data (7). This does not really change the Fig. 1 curvature, except for the initial points. Hughes reports that these corrected rate constants show good linearity with H_0, which he took as evidence for acid catalysis, but the resulting slopes are very shallow at ~0.3 (7). Marlies and La Mer (6) report similar behavior for their data. The picture is evidently more complicated than this, according to the Fig. 1 curvature; Fig. 1 does not represent an acid-catalyzed reaction with water acting as a base, since the plots would curve downwards rather than upwards in that case (1, 8). Consequently it was decided to develop an excess acidity rate equation for neutral water reacting with neutral nitramide in these acid media, to see if this could account for the observed behavior.

The mechanism of Scheme 1 is proposed for the water-cat-

Fig. 2. Excess acidity plots according to eq. [3], assuming reaction with two water molecules only, for the decomposition of nitramide in aqueous perchloric acid at (bottom to top) 30.6, 41.0, (probably) 43, 45.6, and 59.8°C.

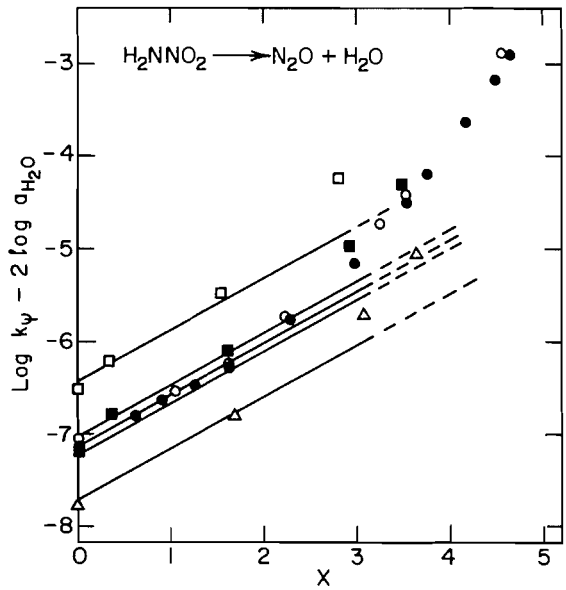

alyzed reaction. Initial tautomerization to the *aci*-nitro form (1, 3) is followed by reaction with water in the rate-determining step. The two-water-molecule cyclic transition state is proposed on the basis of no evidence whatever, beyond the fact that it looks very plausible, involving no charge transfer, and by analogy with other cyclic proton transfers of this type commonly proposed (12, 13). In fact the analysis in this paper is unable to distinguish between one and two water molecules, good agreement with the experimental results being obtained on either assumption.

The rate equation derivation is straightforward (8). Using the terminology of Scheme 1, and with C = molar concentration, a = molar activity, and f = molar activity coefficient:

$$[1] \quad k_\psi C_S = k_0 a_T a_{H_2O}^2 (1/f_\ddagger)$$

where k_ψ are the observed rate constants and $f_\ddagger$ is the activity coefficient of the transition state. Substituting $a_T = K_T a_S$ and $a_S = C_S f_S$ into eq. [1] and taking logs gives

$$[2] \quad \log k_\psi - 2 \log a_{H_2O} = \log(k_0 K_T) + \log(f_S / f_\ddagger)$$

and it is known that all types of log activity coefficient ratio terms such as the rightmost one in eq. [2] are linear in X (8, 9, 14), so this becomes

$$[3] \quad \log k_\psi - 2 \log a_{H_2O} = \log(k_0 K_T) + mX$$

Plots of the perchloric acid data according to eq. [3] are shown in Fig. 2. Water activities at 25°C are available for all three acid systems from several sources (15); the 25°C data were used because as yet only water activities in sulfuric acid can be calculated at other temperatures (16). (This is not a major problem because the water activities in sulfuric acid at differ-

Scheme 1.

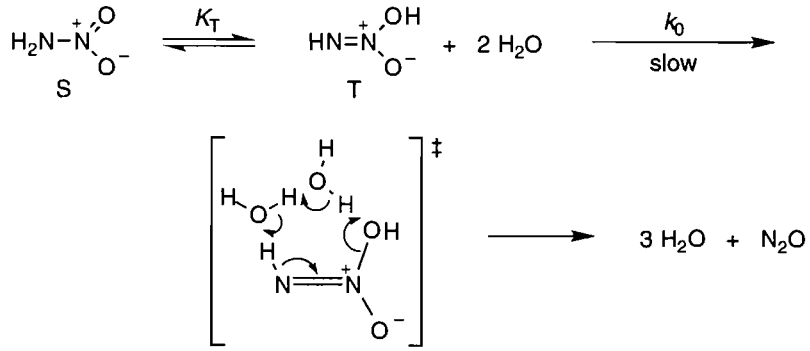

Scheme 2.

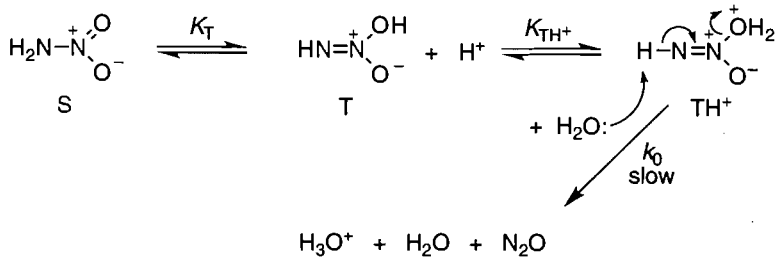

ent temperatures are almost the same as one another at the relatively low acidities used here, and presumably the behavior of perchloric and hydrochloric acids would be similar.) The values of the excess acidity X used are corrected to the reaction temperature (11), which means that the same slope m applies at all temperatures (11), and thus all the lines in Fig. 2 are necessarily parallel.

As can be seen from Fig. 2, the data are linear in eq. [3] but only up to a point, beyond which an upward deviation is apparent. Two water molecules are assumed to be involved; since the variation of water activity with acidity is barely observable in these dilute acid solutions, plots on the basis of one water (or any other number) look just the same. The different intercepts obtained at the different temperatures enable activation parameters for the reaction to be calculated; they are $\Delta H^{\ddagger}$ = 19.67 ± 0.68 kcal mol^{-1} and $\Delta S^{\ddagger} = -29.1 \pm 2.3$ cal mol^{-1} K^{-1}. This large negative $\Delta S^{\ddagger}$ seems quite reasonable for the cyclic transition state proposed. (The ?43° data in Fig. 2 agree very well with the rest if the temperature is assumed to be 43°C, but certainly do not if the quoted temperature of 35°C (7) is used.) The slope m is 0.557 ± 0.017, but the magnitude of this number is not meaningful as there is nothing with which to compare it; this is the first use of eq. [3] in kinetic analysis. Using the activation parameters to calculate a standard-state (i.e., $X = 0$) value for k_{H_2O} gives a value of 3.16×10^{-5} s^{-1} at 25°C (value in 55.34 M water), which compares adequately with listed values, e.g., $(4.632 \pm 0.015) \times 10^{-5}$ s^{-1} (3, 17), and the value of $(4.741 \pm 0.002) \times 10^{-5}$ s^{-1}, which is the intercept of a plot of the data of Marlies and La Mer (6) against [HCl].

Since the values in Fig. 2 deviate upwards at the higher acidities, it is reasonable to assume that an acid-catalyzed process is taking over, and by analogy with the alkylnitramines (1) the mechanism in Scheme 2 is proposed, with one water molecule acting as a base. (This might also be a cyclic process; imagine a proton added to Scheme 1.) A rate equation for this is readily derived (8). Using the terminology of Scheme 2:

$$[4] \quad k_{\psi} C_S = k_0 a_{TH^+} a_{H_2O} (1 / f_{\ddagger})$$

Substituting $a_{TH^+} = a_T a_{H^+} / K_{TH^+}$, $a_T = K_T a_S$, $a_{H^+} = C_{H^+} f_{H^+}$, and $a_S = C_S f_S$ into eq. [4] and taking logs gives

$$[5] \quad \log k_{\psi} - \log C_{H^+} - \log a_{H_2O} = \log(k_0 K_T / K_{TH^+}) + \log(f_S f_{H^+} / f_{\ddagger})$$

It is known (8) that $\log(f_S f_{H^+} / f_{\ddagger}) = m^{\ddagger} \log(f_S f_{H^+} / f_{SH^+}) = m^{\ddagger} m^* X$, so eq. [5] becomes

$$[6] \quad \log k_{\psi} - \log C_{H^+} - \log a_{H_2O} = \log(k_0 K_T / K_{TH^+}) + m^{\ddagger} m^* X$$

The perchloric acid data are plotted according to eq. [6] in Fig. 3. As can be seen, the points that deviate from linearity in Fig. 2 become linear in Fig. 3, so the supposition that the mechanism changes from a water-catalyzed process to an acid-catalyzed one is justified. (All the lines in Fig. 3 are parallel for the same reason as given above for Fig. 2.) As before, standard-state (8) activation parameters can be calculated from the intercepts at different temperatures: $\Delta H^{\ddagger} = 29.7 \pm 1.3$ kcal mol^{-1} and $\Delta S^{\ddagger} = -1.0 \pm 4.3$ cal mol^{-1} K^{-1}. These are different from the alkylnitramine values (1) in that the activation enthalpy is somewhat higher and the activation entropy considerably less negative. A closer correspondence cannot really be expected, since the reaction under consideration here is a base attack rather than a nucleophilic one; perhaps the transition state is later here, thus partaking more of the larger number of species present in the product state (two species

Fig. 3. Excess acidity plot according to eq. [6], assuming an acid-catalyzed reaction with one water molecule, for the decomposition of nitramide in aqueous perchloric acid at (bottom to top) 30.6, 41.0, (probably) 43, 45.6, and 59.8°C.

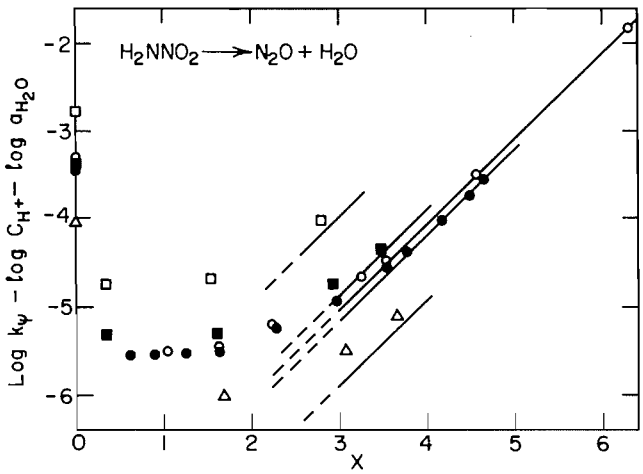

become three), and explaining the much less negative $\Delta S^{\ddagger}$ value. The latter value also rules out any type of cyclic mechanism for the acid-catalyzed process.

From the activation parameters can be calculated log $k_0^{25°} = -7.48 \pm 0.11$ and log $k_0^{85°} = -3.758$. These numbers, with the $m^{\ddagger}m^*$ slope of 0.972 ± 0.018, fall on the same σ^* correlation lines as the 11 alkylnitramines studied in the previous paper (see Fig. 3 of ref. 1). This may be a coincidence, but it is certainly suggestive with respect to the interpretation of this reaction as a true acid-catalyzed decomposition.

The standard curve-fitting computer program used (18) fits all 33 perchloric acid data points simultaneously (none were rejected (1)) using 6 coefficients, 2 being equivalent to the $\Delta H^{\ddagger}$ and $\Delta S^{\ddagger}$ values (intercepts) and 1 to the m value (slope) of eq. [3] and Scheme 1, and 2 to the $\Delta H^{\ddagger}$ and $\Delta S^{\ddagger}$ and 1 to the $m^{\ddagger}m^*$ of eq. [6] and Scheme 2; the overall fit was very good, with a root-mean-square difference of only ± 0.045 between the experimental points and the theoretical fit.

Far fewer data at only one (uncertain) temperature were available for the nitramide decomposition in hydrochloric acid (7); using only three coefficients (Scheme 1 slope and intercept, Scheme 2 intercept, slope assumed to be one) gave the fit to the HCl data indicated by the lines through the squares in Fig. 4. The Scheme 1 slope was 0.496 ± 0.018, not that different from the perchloric acid number given above, and the intercept is equivalent to a log k_0 value of -3.47, again not that different from the value of -3.65 that can be calculated from the perchloric acid data at 43°C. As can be seen from Fig. 4, the data of Marlies and La Mer (6) do not extend to high enough acidities to show an acid-catalyzed process.

Figure 4 also shows that the results obtained in sulfuric acid (7) are consistently above those obtained at the same temperature in hydrochloric acid (and in perchloric acid). Accordingly the hydrochloric acid results were used to calculate values for the overall rate constants at the sulfuric acid X values, on the assumption that the water and acid-catalysis rates should be the same in the two acids, and these were subtracted from the experimental numbers. Assuming that the resulting difference

Fig. 4. Excess acidity plots according to the mechanisms established in perchloric acid for the decomposition of nitramide in aqueous hydrochloric (6, 7) and sulfuric (7) acid media, in the latter case illustrating the reaction with sulfate ion.

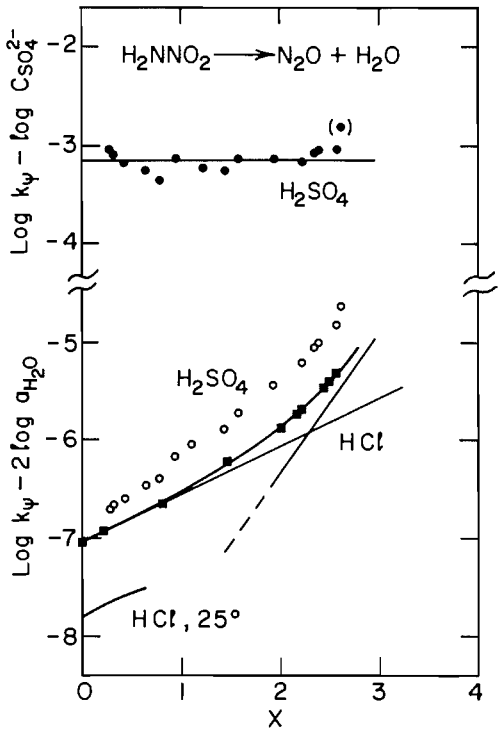

represents a sulfate ion base-catalyzed process, sulfate concentrations (19) were subtracted from these and the resulting corrected log k_ψ − log $C_{SO_4^{2-}}$ values are plotted in the upper part of Fig. 4. The slope of this line is zero, which means that activity coefficient effects are unimportant, and the intercept is -3.157 ± 0.007, which means that sulfate as a base catalyst ($pK_a = 1.99$ (20)) has a catalytic coefficient of 7.0×10^{-4} M^{-1} s^{-1}, rather better than that of water ($pK_a = -1.74$), $k_{H_2O} = 3.16 \times 10^{-5}$ s^{-1} at 25°C in 55.34 M water, see above.

Acknowledgments

Valuable discussions with Professor A.J. Kresge and his group are acknowledged.

References

1. R.A. Cox. Can. J. Chem. **74**, 1774 (1996).
2. R.P. Bell. The proton in chemistry. 2nd ed. Cornell University Press, Ithaca, N.Y. 1973. pp. 160–164, and references cited therein.
3. A.J. Kresge and Y.C. Tang. J. Chem. Soc. Chem. Commun. 309 (1980); A.J. Kresge, Y.C. Tang, A. Awwal, and D.P. Onwood. J. Chem. Soc. Chem. Commun. 310 (1980); C.H. Arrowsmith, A. Awwal, B.A. Euser, A.J. Kresge, P.P.T. Lau, D.P. Onwood, Y.C. Tang, and E.C. Young. J. Am. Chem. Soc. **113**, 172 (1991); C.H. Arrowsmith, A.J. Kresge, and Y.C. Tang. J. Am. Chem. Soc. **113**, 179 (1991).
4. P. Politzer, N. Sukumar, K. Jayasuriya, and S. Ranganathan. J. Am. Chem. Soc. **110**, 3425 (1988); J.P. Ritchie. J. Am. Chem. Soc. **111**, 2517 (1989).

5. M. Attinà, F. Cacace, E. Ciliberto, G. de Petris, F. Grandinetti, F. Pepi, and A. Ricci. J. Am. Chem. Soc. **115**, 12398 (1993).
6. C.A. Marlies and V.K. La Mer. J. Am. Chem. Soc. **57**, 1812 (1935).
7. M.N. Hughes, J.R. Lusty, and H.L. Wallis. J. Chem. Soc. Dalton Trans. 261 (1983).
8. R.A. Cox. Acc. Chem. Res. **20**, 27 (1987).
9. R.A. Cox and K. Yates. J. Am. Chem. Soc. **100**, 3861 (1978).
10. R.A. Cox and K. Yates. Can. J. Chem. **59**, 2116 (1981).
11. R.A. Cox and K. Yates. Can. J. Chem. **62**, 2155 (1984).
12. R.A. Cox, Ü.L. Haldna, K.L. Idler, and K. Yates. Can. J. Chem. **59**, 2591 (1981); R.A. Cox and K. Yates. Can. J. Chem. **59**, 2853 (1981).
13. G. Gopalakrishnan and J.L. Hogg. J. Org. Chem. **49**, 3161 (1984); S. Hoz, K. Yang, and S. Wolfe. J. Am. Chem. Soc. **112**, 1319 (1990); O.J. Muscio, J. Meng, H. Wang, and S. Shi. J. Org. Chem. **57**, 6454 (1992).
14. R.A. Cox and K. Yates. Can. J. Chem. **60**, 3061 (1982).
15. J.F. Bunnett. J. Am. Chem. Soc. **83**, 4956 (1961); C.J. O'Connor. J. Chem. Educ. **46**, 686 (1969).
16. W.F. Giauque, E.W. Hornung, J.E. Kunzler, and T.R. Rubin. J. Am. Chem. Soc. **82**, 62 (1960).
17. Y.C. Tang. M.Sc. Thesis, University of Toronto. 1978.
18. P.R. Bevington. Data reduction and error analysis for the physical sciences. McGraw-Hill, New York. 1969. pp. 232–245.
19. R.A. Cox. J. Am. Chem. Soc. **96**, 1059 (1974).
20. Y.C. Wu and D. Feng. J. Solution Chem. **24**, 133 (1995).

A deuterium NMR study of guest molecular dynamics in tris(5-acetyl-3-thienyl) methane inclusion compounds

Paul S. Sidhu, Jason Bell, Glenn H. Penner, and Kenneth R. Jeffrey

Abstract: Deuterium nuclear magnetic resonance (NMR) spectra and spin-lattice relaxation times (T_1) are used to investigate the guest molecular dynamics of tris(5-acetyl-3-thienyl) methane (TATM) inclusion compounds. The seven guests: acetonitrile, nitromethane, dimethyl sulfoxide, benzene, mesitylene, *ortho*-xylene, and *para*-xylene show a wide variety of motional behaviour. The reorientation of acetonitrile in TATM and nitromethane in TATM were both modelled as precession on a cone, the base of which is more elliptical in shape for nitromethane, as would be expected considering their molecular symmetries. DMSO in TATM does not undergo any reorientation other than methyl rotation at the temperatures investigated. At low temperatures, the ^{2}H lineshape and the deuterium spin-lattice relaxation time both depend on the rate of methyl rotation. Activation barriers of 11.7 (±0.4) kJ/mol and 11.2 (±0.5) kJ/mol were found from the two techniques, respectively. Benzene undergoes sixfold reorientation about the principal molecular axis; however, the rate is still greater than 10^8 Hz down to 113 K. The spin-lattice relaxation time profile does not reach a minimum on decreasing temperature to 112 K, while the slope of this plot provides an activation energy of 4.1 (±0.4) kJ/mol for the sixfold reorientation. The deuterium NMR spectra of mesitylene-d_9 in TATM can be simulated using a model where the guest occupies two different sites in the TATM lattice, with the guest molecules performing in-plane C_3 rotation either very rapidly ($k > 10^8$ Hz) or very slowly ($k < 10^3$ Hz), with the relative populations of each changing with temperature. Another model proposed suggests the possibility that there is a continuous distribution of motional rates, the median of which is increasing with temperature. This second model is more realistic; however, too many parameters are present to consider a detailed fit. Finally, both *o*-xylene and *p*-xylene are rigidly held in the TATM clathrate, while rotation of the methyl groups is rapid.

Key words: inclusion compounds, solid state deuterium NMR spectroscopy, molecular dynamics.

Résumé : On a utilisé les spectres de résonance magnétique nucléaire du deutérium (RMN) et les temps de relaxation spin-réseau (T_1) pour étudier la dynamique de l'invité moléculaire des composés d'inclusion du tris(5-acétyl-3-thiényl)méthane (TATM). Les sept invités (acétonitrile, nitrométhane, diméthylsulfoxyde, benzène, mésitylène, *ortho*-xylène et *para*-xylène) présentent des comportements de mouvement très différents. On a développé un modèle pour la réorientation de l'acétonitrile et du nitrométhane dans le TATM; il implique la précession sur un cône dont la forme de la base est plus ellipsoïdale dans le cas du nitrométhane, comme on pourrait s'y attendre en considérant les symétries moléculaires. Dans le TATM, aux températures étudiées, le DMSO ne subit pas de réorientation autre que la rotation du méthyle. À basses températures, la forme de la raie du ^{2}H et le temps de relaxation spin-réseau du deutérium dépendent tous les deux sur la vitesse de rotation du méthyle. Sur la base de données obtenues à l'aide de chacune de ces deux techniques, on a évalué que les barrières d'activation sont respectivement de 11,7 (±0,4) et de 11,2 (±0,5) kJ mol^{-1}. Le benzène subit une réorientation sextuple autour de l'axe moléculaire principal; toutefois, à des températures allant jusqu'à 113 K, la vitesse est encore supérieure à 10^8 Hz. Le profil du temps de relaxation spin-réseau n'atteint pas de minimum lorsqu'on abaisse la température jusqu'à 112 K; la pente de cette courbe fournit une énergie d'activation de 4,1 (±0,4) kJ mol^{-1} pour la réorientation sextuple. On peut simuler les spectres de RMN du deutérium du mésitylène-d_9 dans le TATM en faisant appel à un modèle dans lequel l'invité occupe deux sites différents dans réseau de TATM et les molécules invitées subissant des rotations C_3 dans le plan qui peuvent être très rapides ($k > 10^8$ Hz) ou très lentes ($k < 10^3$ Hz); les populations relatives de chacune varient avec la température. Un autre modèle a été proposé; il suggère la possibilité d'une distribution continue des vitesses de mouvement dont la médiane augmenterait avec la température. Ce dernier modèle est plus réaliste; toutefois, pour le moment, il manque trop de paramètres pour pouvoir considérer la possibilité d'effectuer un

Received April 15, 1996.

P.S. Sidhu, J. Bell,[1] and G.H. Penner.[2] Guelph–Waterloo Centre for Graduate Work in Chemistry, Department of Chemistry and Biochemistry, University of Guelph, Guelph, ON N1G 2W1, Canada.
K.R. Jeffrey. Guelph–Waterloo Program for Graduate Work in Physics, Department of Physics, University of Guelph, Guelph, ON N1G 2W1, Canada.

[1] NSERC undergraduate research participant.
[2] Author to whom correspondence may be addressed. Telephone: (519) 824-4120. Fax: (519) 766-1499. E-mail: gpenner@uoguelph.ca

ajustement détaillé. Enfin, les xylènes, tant *ortho* que *para*, sont fermement maintenant dans le clathrate de TATM alors que la rotation des groupes méthyles est rapide.

Mots clés : composés d'inclusion, spectroscopie RMN du deutérium à l'état solide, dynamique moléculaire.

[Traduit par la rédaction]

Introduction

Inclusion compounds are structures in which one type of molecule (the "host") forms cages, or cavities, in a regular or repeating pattern, on the molecular scale. In some cases, a "guest" molecule of the right dimensions is able to occupy the cages of the host, and an interaction of appreciable strength can occur (1). In general, there is a larger proportion of host to guest molecules, and the structure is held together by van der Waals forces, or in some cases by hydrogen bonding. Inclusion compounds are generally prepared by dissolving the solid host in a solution of the guest, with subsequent slow evaporation of the excess solvent. The enclathrated guest molecule generally experiences considerable motional freedom in its cage. These dynamics can be investigated through a number of techniques, such as deuterium NMR spectroscopy (2, 3), ^{13}C CP/MAS (magic angle spinning) NMR (4, 5), relaxation time measurements (6, 7), X-ray crystallography (8, 9), and differential scanning calorimetry (10, 11). The study of the dynamics of a guest molecule in a clathrate compound provides insight into the guest–host interaction. For example, when they involve hydrogen bonding, the potential for rotation is undoubtedly hindered. These intermolecular forces are important because they determine the stability (or instability) of the inclusion compound.

In the last decade, deuterium NMR has become a very popular technique for the study of dynamic processes in the solid state (12). This method makes possible the investigation of different motional modes occurring over a wide range of rates of reorientation. Dynamic processes occurring with rates in the range 10^3–10^8 Hz (i.e., when the motional rate is comparable in magnitude to the deuterium quadrupolar coupling constant) can be studied by lineshape analysis of the deuterium NMR spectrum of a polycrystalline powder (13). For motion on the order of, and greater than, 10^8 Hz (when the rate approximates the deuterium Larmor precession frequency), the lineshapes become independent of the exchange rate, and an analysis of the deuterium spin-lattice relaxation time as a function of temperature is used to discriminate among the types and rates of motion (14). With the availability of computer programs (15) capable of simulating ^2H lineshapes as a function of motional rates, molecular geometry, and dynamic models, deuterium NMR spectroscopy has developed into an excellent probe for the study of dynamic processes. In addition, selective deuteration of the deuterium isotopomer at specific sites in the molecule makes this technique even more attractive (16).

In this paper, the molecular motion of seven guest molecules: acetonitrile, nitromethane, dimethyl sulfoxide, mesitylene, benzene, *o*-xylene, and *p*-xylene, in the host tris(5-acetyl-3-thienyl) methane are studied.

Tris(5-acetyl-3-thienyl) methane (TATM), **1**, was first synthesized by Yakubov et al. in 1973, from 2-acetyl thiophene and chloroform, in the presence of excess aluminum chloride. It was also noted that TATM forms inclusion compounds on recrystallization from various solvents (17). In 1977, Bin Din and Meth-Cohn found that TATM forms 2:1 host:guest clathrates with a wide variety of organic compounds (18). The guest molecules reside in cavities formed by the TATM molecules. Furthermore, their study, to that point in time, failed to reveal a solvent that was not incorporated. Although the pure host compound melts at about 55°C, TATM inclusion compounds generally melt at temperatures above 100°C.

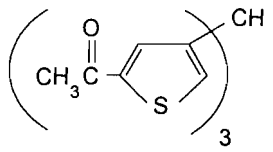

1

Recently, four crystal structures of TATM with various guests have been reported (19–22). In the presence of guest molecules, the TATM molecules generally take up a lattice of triclinic symmetry. In each of the crystal structures, there was only one guest molecule per unit cell. In addition, their inability to precisely identify the positions of the guest atom led them to conclude that the guest molecules are disordered. The TATM molecules form cavities of different sizes and shapes, depending on the guest molecule included. To the best of our knowledge, no further studies on TATM inclusion compounds have been reported.

Theoretical background

Solid state deuterium NMR spectroscopy is one of the principal techniques used to study guest motion in inclusion compounds. Deuterium (nuclear spin $I = 1$) has a nuclear quadrupole moment, and it is the interaction of this moment with the electric field gradient arising from the surrounding charge distribution that gives rise to the quadrupolar coupling.

In a typical deuterium NMR experiment, the external applied magnetic field strength, and therefore the nuclear Zeeman interaction, is sufficiently strong that the quadrupole interaction may be treated as a perturbation. The resulting NMR spectrum is a doublet symmetrically placed about the Larmor frequency with a quadrupole splitting of

$$[1] \quad \Delta\nu_Q = \frac{3e^2qQ}{4h}(3\cos^2\beta - 1 + \eta\sin^2\beta\cos 2\alpha)$$

The electric field gradient (EFG) in the principal axis system (PAS) is described in terms of its principal component eq and the asymmetry parameter η, where

$$[2] \quad eq = \partial^2V/\partial z^2$$

and

$$[3] \quad \eta = (\partial^2V/\partial x^2 - \partial^2V/\partial y^2) / \partial^2V/\partial z^2$$

V is the electric potential at the nucleus, while the quantity eQ

is the magnitude of the nuclear quadrupole moment. The angles α and β describe the orientation of the PAS in the laboratory frame of reference defined by the applied magnetic field. In aliphatic compounds, the electric field gradients are usually axially symmetric ($\eta = 0$) about the bond axis, with coupling constants given by $\chi = e^2qQ/h = 170$ kHz. In aromatics, the EFGs are slightly asymmetric, with $\eta \sim 0.05$ and coupling constants $\chi = e^2qQ/h = 185$ kHz are typical.

In a powder, the C—D bonds are randomly distributed, and the resulting spectrum is a superposition of doublets corresponding to the many possible bond directions. The resulting powder pattern, often referred to as a "Pake doublet," has two 90° orientation spikes that are separated by $3e^2qQ/4h$.

If molecular motion occurs, the angles α and β become time dependent. In an isotropic system, the average quadrupolar interaction is zero, and a single spectral line at the Larmor frequency is observed. To consider the effects of molecular motion in an anisotropic environment, it is convenient to use two transformations of coordinates. The first transforms from the PAS to a conveniently defined time-independent intermediate frame, while the second transforms from the intermediate frame to the lab frame. The intermediate frame is chosen so that its z-axis coincides with an axis of motional symmetry. In a powder sample, the observed spectrum will reveal the influence of both the motion about axes of motional symmetry and the random orientation of these axes in the laboratory frame. Motional narrowing occurs when the rate of motion, k, is greater than the quadrupole coupling constant. When the motional rates are of the order of the QCC, the lineshapes cannot easily be predicted analytically, and are highly sensitive to the reorientation rate and the details of the motional process. Fortunately, elaborate computer programs, such as MXQET (15), have been developed to simulate deuterium quadrupolar split powder patterns in this intermediate regime.

The simplest type of motion involves exchange of a deuterium nucleus between three or more equivalent sites. In the fast rate limit, the asymmetry parameter averages to zero, and the spectrum is compressed by a factor of $\frac{1}{2}(3\cos^2\theta - 1)$, where θ is the angle between the X—D bond and the rotation axis. In between the two extremes, a slow evolution of the spectrum from one form to the other is observed. Examples include three-site exchange of the deuterons in a methyl group (14) ($\theta = 70.5°$), and in-plane six-site exchange of the deuterons on a benzene ring (23) ($\theta = 90°$).

An example of asymmetric motion is exchange of a deuteron between only two equivalent sites. When $k > 10^8$ Hz, a non-zero asymmetry parameter is observed. For instance, consider the two-site exchange of the *ortho* and *meta* deuterons of a monosubstituted benzene ring (24) ($\theta = 60°$). The effective asymmetry parameter η and the quadrupolar coupling constant χ in the averaged spectrum depend on the angle θ for the motion involved (25).

Enclathrated guest molecules often undergo a precessional type of motion. It can be thought of as rotation of the principal symmetry axis on a cone, which may have a circular or elliptical shape. This type of motion usually has a very small activation energy, and is only encountered in the fast rate limit at working temperatures. The motion can most simply be broken down into two components: precession on a circular cone and a two-site libration (26).

A further complicating factor in considering the motion of guest molecules is the possibility of unequal populations of the sites taken up by the exchanging deuterium nucleus (27). Since this leads to more or less preferred orientations for the guest, it introduces asymmetry into the powder spectrum. The justification for unequal populations can be either a non-uniform guest–host interaction, or when a rotation axis is not a symmetry axis.

The quadrupolar interaction and the molecular reorientation also determine the deuterium spin-lattice relaxation rate, which can be written as (in the case where the static EFG is axially symmetric)

$$[4] \quad \frac{1}{T_1} = \frac{3\pi^2}{10}\left(\frac{eqQ}{h}\right)^2 [J_1(\omega_0) + 4J_2(2\omega_0)]$$

The influence of the molecular motion is contained in the spectral density functions, J_1 and J_2, which are defined with respect to the direction of the applied magnetic field. Torchia and Szabo have derived expressions for the spectral density functions encompassing a wide variety of models of molecular reorientation (14). It is often convenient to assume that the correlation function describing the motion is exponential, and to analyze T_1 data using the general BPP (Lorentzian) spectral density functions (28). The resulting equation is

$$[5] \quad \frac{1}{T_1} = K\left[\frac{\tau_c}{1 + \omega_0^2\tau_c^2} + \frac{4\tau_c}{1 + 4\omega_0^2\tau_c^2}\right]$$

K is a constant that depends on the static quadrupolar coupling constant and the mode of molecular reorientation, while ω_0 is the Larmor precession frequency. The use of this equation is really an oversimplification, which averages over any angular dependence of the spin-lattice relaxation. Assuming that the molecular motion is a rate-activated process

$$[6] \quad \tau_c = \tau_\infty \exp(E_a/RT)$$

In this equation, τ_c is interpreted as the correlation time for the motion ($\tau_c \propto k^{-1}$), τ_∞ is the correlation time at infinite temperature, and E_a is the activation energy for the motion causing modulation of T_1.

Experimental

TATM was prepared according to the method of Yakubov et al. (17). 2-Acetyl thiophene and chloroform (6.2 equivalents) were refluxed for 24 h, in the presence of excess aluminum chloride (2.5 equivalents). After refluxing, 10% HCl was added to dissolve the remaining $AlCl_3$. The TATM was then extracted with chloroform, and the organic phase was washed with saturated NaCl aqueous solution. Following this procedure, the organic phase was dried, filtered, and excess $CHCl_3$ was removed by rotary evaporation. The resulting plaque was then recrystallized from ethanol. Finally, heating under vacuum for 12 h at 130°C removed enclathrated ethanol. The resulting amorphous solid was ground to yield an orange powder that had a broad melting point range of 52–58°C. The purity was confirmed by solution NMR.

Mesitylene-d_9 was prepared according to a literature procedure (29), which involved refluxing 10 mL of dry DMSO-d_6 with mesitylene (5 mL), for 24 h at 100°C, in the presence of sodium hydride (0.5 g). The reaction mixture was washed with

D_2O, and then with ordinary water. Finally, the organic layer was dried over sodium. The extent of deuteration of the methyl groups, approximately 67%, was determined by ^1H and ^2H NMR. All other deuterated guest compounds were obtained commercially (Aldrich).

Inclusion compounds were prepared by dissolving approx. 200 mg of the host solid in 2–3 mL of the deuterated guest, followed by slow evaporation. Verification of inclusion was done by ^1H NMR of isotopically normal dissolved inclusion compound. Samples were packed in 5 mm o.d. NMR tubes that had been cut to lengths of 2–3 cm.

The deuterium spectra and spin-lattice relaxation times were determined using a home-built, phase-coherent pulsed NMR spectrometer operating at 44.7 MHz. The spectrometer was used with a 50 mm bore, 6.1 T (Bruker/Nalorac) superconducting magnet. The nuclear signal was digitized in a Nicolet Explorer digital oscilliscope, which was interfaced to an IBM/pc. The computer was programmed to provide automatic temperature regulation for the sample and data acquisition. The sample probe was designed to study powder samples over a temperature range of −160 to 200°C. The sample chamber was surrounded by a thick-walled copper container. Channels had been milled into the copper vessel, and cold N_2 gas was passed through these, to cool the sample chamber. The temperature of the sample was electronically regulated to within ±0.1°C over the course of a measurement by a heater wound nonconductively on the copper vessel and a copper–constantan thermocouple attached to it. A second separate thermocouple located near the sample itself was used to record the actual sample temperature, which was known to within ±0.5°C.

The deuterium NMR spectra were obtained using the quadrupolar echo pulse sequence (30): $(\pi/2)_{\pm x}$–τ_Q–$(\pi/2)_y$–τ_Q–acquire. The length of the $\pi/2$ pulses were approximately 3.5 μs. At each temperature, the echo signals were collected using a τ_Q value of 50 μs, and the echo signals were Fourier transformed, after applying a linebroadening of 100 Hz, to obtain the spectra. To obtain symmetric spectra the signal collected in the imaginary channel was set to zero before Fourier transformation. Between 400 and 1000 scans were acquired and coadded for each spectrum.

The deuterium T_1 data were acquired using an inversion recovery pulse sequence modified for quadrupolar nuclei: $(\pi)_x$–τ–$(\pi/2)_{\pm x}$–τ_Q–$(\pi/2)_y$–τ_Q–acquire. Typically, 12 values of τ were used to determine T_1 at each temperature. The pulse spacing, τ_Q, for the T_1 determination was 50 μs. The time between repetitions of the pulse sequence was always greater than $5T_1$. The amplitude of the signal for each τ value was determined from the integral over the echo peak. These echo integrals were fit using a nonlinear least-squares algorithm employing an exponential fitting function to obtain the relevant relaxation time parameters.

Lineshape simulations of quadrupolar echo spectra were carried out by standard methods using the program MXQET (15). Simulated spectra were visually matched to experimental lineshapes. These simulations took into account the effects of finite pulses and the pulse spacing, τ_Q.

Results and discussion

Acetonitrile–TATM and nitromethane–TATM

Acetonitrile and nitromethane are two guest molecules of TATM somewhat related in that their respective dynamic characteristics are similar. The deuterium NMR powder spectra, along with simulations, for acetonitrile-d_3–TATM and nitromethane-d_3–TATM are presented in Figs. 1 and 2 respectively. It is clearly evident, from the observed spectral averaging, that they both exhibit methyl rotation with rates greater than 10^8 Hz, down to 173 K.

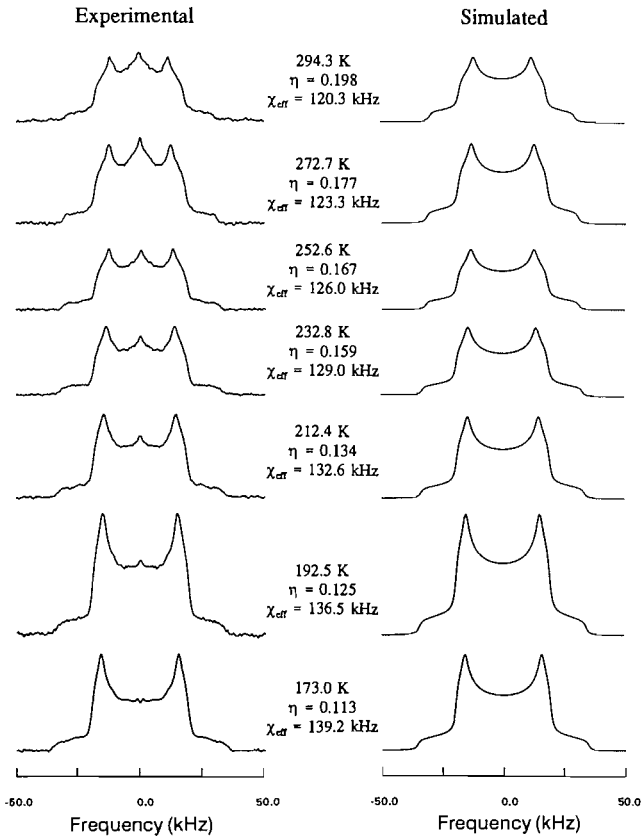

Fig. 1. Deuterium NMR spectra for the acetonitrile-d_3–TATM inclusion compound, at various temperatures, together with simulations.

The other type of common motion is precession of the principal molecular symmetry axis, which affects both χ_{eff} and η_{eff}. Although the precessional motion is best described as diffusion within a cone, where the possible angles, ψ, are governed by a distribution function $g(\psi)$, a simpler model was used, in which the molecule is allowed to precess about a cone of half-angle ψ.

Many guest molecules in inclusion compounds undergo this type of precessional motion. A more realistic description of the reorientation would be a small-amplitude whole-body librational motion, but the model of precession employed here gives a simple analytical model. The precession can be thought of as a rotation of the principal symmetry axis on a cone, the base of which is either circular or elliptical. This type of motion has a very small activation energy, and the rate of reorientation is usually of the same order as the rate of vibrational motion of a molecule inside a potential energy well, about 10^{12} Hz.

The motion can be broken down into two components, precession on a circular cone (corresponding to the angle θ), and a two-site libration (the magnitude of which is proportional to

Fig. 2. Deuterium NMR spectra for the nitromethane-d_3–TATM inclusion compound, at various temperatures, together with simulations.

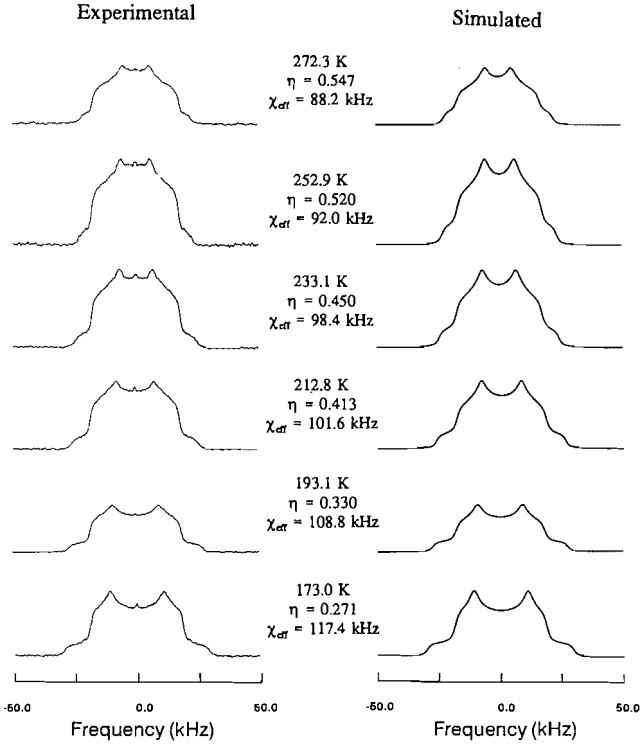

Scheme 1.

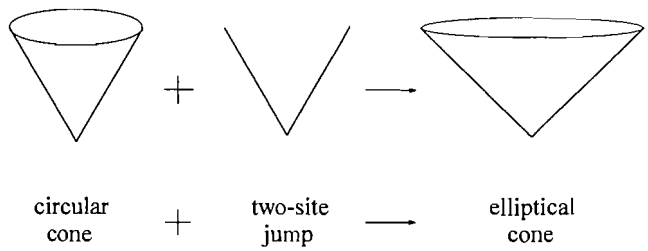

the angle ϕ), which transforms the circular base cone into an elliptical cone (see Scheme 1). In the elliptical case, the precession leads to a non-zero asymmetry parameter, since it is motion in a preferred direction.

We calculated the matching ^{2}H NMR simulations by allowing the guest molecule to reorient between two sites ϕ degrees apart. On top of this, we incorporate the circular cone wobble by simply using a motionally averaged effective quadrupolar coupling constant, and calculating the angle θ from $\chi_{eff}/\chi_{static} = (3\cos^2\theta - 1)/2$. Rather than reporting the angles θ and ϕ at each temperature, we have chosen to present values of the spectral asymmetry η (proportional to ϕ) and the effective quadrupolar coupling constant (inversely proportional to ϕ), as these parameters can be measured easily from the deuterium powder spectrum. From simulations, we were able to extract the angles θ and ϕ, for both guests, at each temperature. As mentioned before, the angle ϕ is directly proportional to the spectral asymmetry observed, while the angles θ and ϕ together determine the averaging of χ_{eff} observed in the experimental ^{2}H powder spectrum. In Fig. 3, we plot the effective asymmetry parameter, η_{eff}, and

Fig. 3. Graph of the effective asymmetry, η_{eff}, and the effective quadrupole coupling constant, χ_{eff}, as a function of temperature, for TATM guests acetonitrile and nitromethane. The lines serve as a guide to the eye. Legend: η(acetonitrile) : open square; η(nitromethane) : open triangle; χ(acetonitrile) : filled square; χ(nitromethane) : filled triangle.

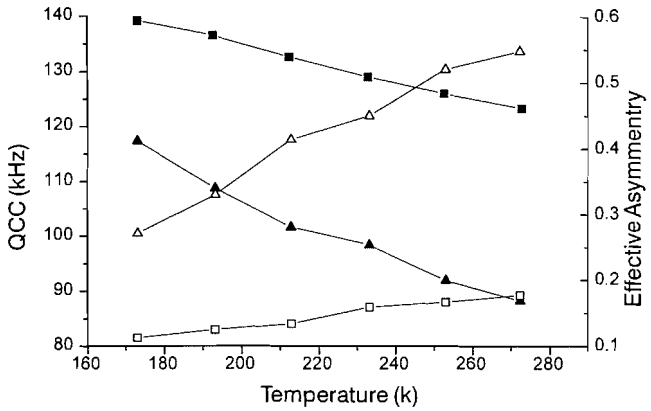

the effective quadrupole coupling constant, χ_{eff}, for each guest, as a function of temperature.

A number of trends are evident from Fig. 3. First, the effective asymmetry parameter observed for nitromethane-d_3–TATM is greater than that for acetonitrile-d_3–TATM, at all temperatures studied. This suggests that the cone on which nitromethane precesses, **2**, is much more elliptical than that for acetonitrile, **3**. This is to be expected, based on a comparison of their molecular symmetries. Nitromethane would prefer to librate parallel to the NO_2 plane, because a parallel libration minimizes the motion of the oxygen atoms, compared to a perpendicular libration. Acetonitrile, with its axial symmetry, should show no preferred precessional direction. The reason that the spectra of acetonitrile show some asymmetry (note that $\eta \propto \phi$), is due to its non-uniform interaction with a TATM cavity of low symmetry.

Nitromethane: Acetonitrile:

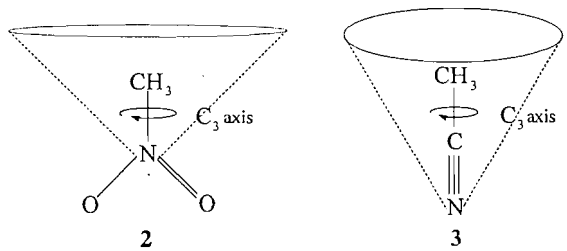

As far as the effective quadrupole coupling constants are concerned, Fig. 3 shows that χ_{eff} is much greater for acetonitrile (than nitromethane) at all temperatures investigated. This is a surprising result, as one would have expected acetonitrile, being a smaller molecule than nitromethane, to show more motional averaging (i.e., a smaller effective quadrupole coupling constant). Therefore, this trend may instead be due to the size, or symmetry, of the host's cavity. In the four determinations of crystal structures from X-ray diffraction available for TATM inclusion compounds, the shape of the host cavity is different for each of the four included guests (19–22). If the TATM cavity formed to enclose nitromethane is larger than

Fig. 4. Simulated and experimental ^2H NMR spectra for dimethyl sulfoxide-d_6 in the TATM inclusion compound, at the temperatures indicated. The threefold flipping rates determined from the simulations are also given.

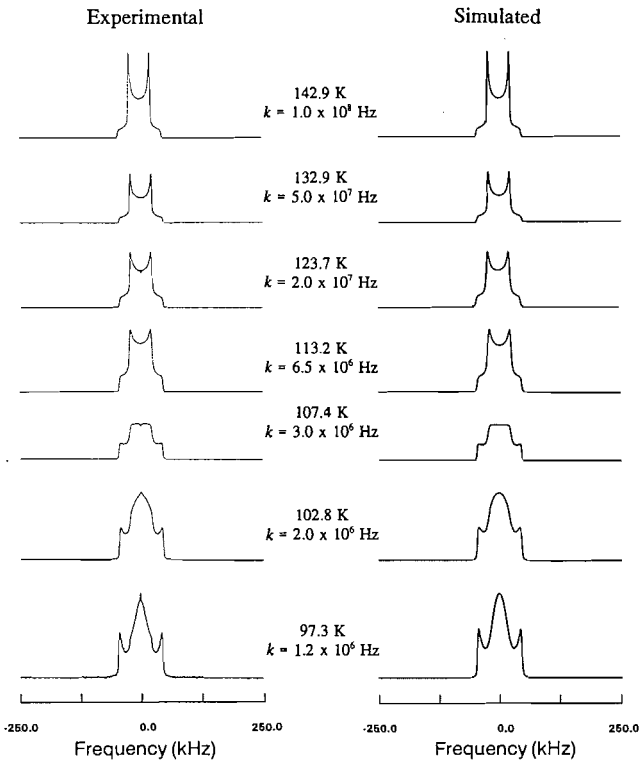

that to enclose acetonitrile, nitro-methane would be more easily able to engage in large-amplitude librational motions. This would spectrally manifest itself as a smaller effective quadrupole coupling constant for nitro-methane, which is observed experimentally. In addition, from X-ray crystallographic data, it was noted that the TATM molecules were unable to completely enclose benzene in the benzene–TATM inclusion compound (20). Thus TATM may not only form a larger host cavity for nitromethane, but it may instead be unable to completely enclose the nitromethane guest, which would again result in greater molecular motion, and consequently a smaller effective quadrupole coupling constant.

Dimethyl sulfoxide – TATM

The deuterium NMR powder spectra of dimethyl sulfoxide-d_6 in the TATM inclusion compound are presented in Fig. 4, along with simulations. The spectrum at room temperature is a Pake doublet with an effective quadrupolar coupling constant $\chi_{eff} = 51.3$ kHz. This implies that the motion giving rise to lineshape changes below 143 K is internal rotation of the methyl groups of DMSO. Indeed, the ^2H NMR spectra were simulated on the basis of this model. The rate of methyl rotation is indicated along with each spectrum in Fig. 4. Note that we were only able to obtain spectra down to a rate of 1.2×10^6 Hz (at 97.3 K). Below this temperature, in the intermediate exchange regime, the intensity of the echo becomes very weak, as the *effective* transverse relaxation time approaches the magnitude of the interpulse spacing (50 μs) in the quadrupole echo pulse sequence. This precluded the acquisition of spectra below 97

Fig. 5. A plot of the rate of internal rotation of the methyl groups of dimethyl sulfoxide in TATM, determined independently from ^2H NMR spectra and deuterium-spin lattice relaxation time data. A best fit solid line for the ^2H NMR spectral data is included. The dotted line joins the T_1 data points. Legend: open square: ^2H NMR spectral data; asterisk: spin-lattice relaxation time data.

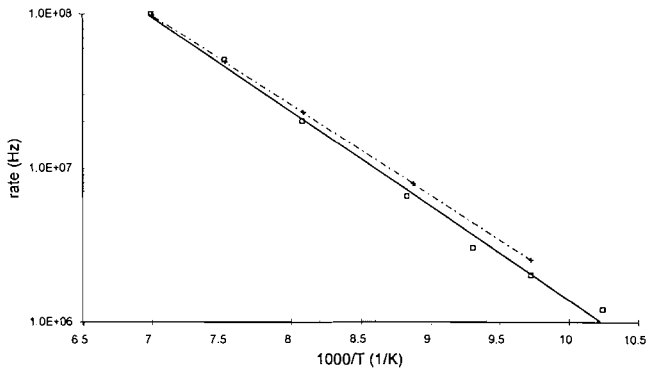

K. By plotting ln k vs. $1000/T$ (Fig. 5), we calculate an activation barrier to methyl rotation of 11.7 (±0.4) kJ/mol. This compares to an activation energy of 12.0 kJ/mol determined for dimethyl sulfoxide in the gas phase (31). In the solid state, the two methyl groups of pure DMSO are crystallographically and dynamically inequivalent (32). It was determined from variable temperature proton spin-lattice relaxation times that the activation energy for the C_3 rotation of one methyl group was 13.3 kJ/mol ($\tau_\infty = 5.6 \times 10^{-13}$ s), while the other methyl group had a significantly higher activation barrier of 21.7 kJ/mol ($\tau_\infty = 6.8 \times 10^{-14}$ s) (33). In the TATM inclusion compound and in the gas phase, the activation energy is determined primarily by intramolecular interactions, whereas in the pure solid the rotation of one of the methyl groups must be significantly hindered by intermolecular forces.

In addition, note that the spectrum at 142.9 K has an effective asymmetry parameter $\eta_{eff} = 0$. This implies that the methyl groups are not distorted from tetrahedral geometry, in contrast to acetone in TATM, where the dihedral angle between two of the deuterons goes from 120° to 124°, giving rise to an asymmetry parameter $\eta = 0.14$, when the methyl rotation rate is in the fast rate limit (34).

From the deuterium NMR spectra, there seems to be no motion other than methyl rotation present that is causing modulation of the lineshape. This again is in contrast to acetone in the same host, where the guest was observed to undergo twofold flips about the carbonyl bond (34). The lack of a similar motion in DMSO may be due to the fact that dimethyl sulfoxide is much larger than acetone. Therefore, DMSO would likely interact more strongly with the TATM host molecules, and be more restricted in its motion.

The spin-lattice relaxation time data for dimethyl sulfoxide-d_6 in TATM appears in Fig. 6. Only one minimum is observed, due to the internal rotation of the methyl groups. Proof of this statement comes from a consideration of the activation energy determined from the best-fit curve, which is 11.2 (±0.5) kJ/mol, as compared to 11.7 (±0.4) kJ/mol determined from ^2H spectral simulations. The correlation time at infinite temperature is 2.7×10^{-13} s, and the constant K (see eq. [5]) is approximately 8×10^{10} s^{-2}.

It is possible to derive explicit expressions for T_1 and the

Fig. 6. Deuterium spin-lattice relaxation times for perdeuterated dimethyl sulfoxide, in TATM, plotted against 1000/*T*. From the best fit curve, a barrier to rotation of 11.2 (±0.5) kJ/mol was determined.

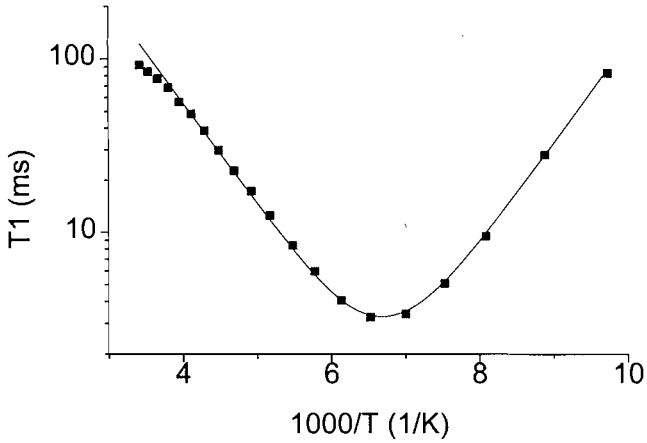

spin-lattice relaxation time minimum value by considering the situation where a C—D bond can jump between three equivalent sites. The expression for T_1 is (14):

$$[7]\quad 1/T_1 = (\omega_Q^2/8)\{g(\tau_c,\omega_0)[A_1B_4 + A_2B_5 - 8A_3B_3\cos 3\phi] + g(\tau_c,2\omega_0)[4A_1B_5 + A_2B_6 + 8A_3B_3\cos 3\phi]\}$$

where $\tau_c = (3k)^{-1}$, ω_0 is the deuterium Larmor precession frequency, and $\omega_Q = 3\chi/4$. The angles θ and ϕ describe the orientation of the static magnetic field in the crystal-fixed axis system. The C–D bond makes an angle Θ with respect to the C_3 rotational axis. The angular functions A_i and B_i depend on θ and Θ, and are given in ref. 14. It is the cos 3ϕ term in eq. [7] that, in principle, leads to non-exponential recovery of the magnetization; however, this effect is small, and it is reasonable to average over the angles θ and ϕ. The angle Θ is set to 109.5°, the tetrahedral angle. This leads to:

$$[8]\quad \frac{1}{T_1} = \frac{\chi^2}{15}\left[\frac{\tau_c}{1+\omega_0^2\tau_c^2} + \frac{4\tau_c}{1+4\omega_0^2\tau_c^2}\right]$$

Thus, the constant K in eq. [5] is given by $\chi^2/15$. Using the value of K from the T_1 fit of 8×10^{10} s^{-2}, we calculate that the static quadrupolar coupling constant should be about 174 kHz (for Θ = 109.5°). If the angle between the C—D bond and the threefold axis is increased to 111.5°, the calculated value for χ would increase to approximately 178 kHz, in good agreement with the experimental value, determined from the splitting of the deuterium NMR spectrum, as 178.2 kHz. This compares with a static deuterium quadrupole coupling constant of 177 kHz determined for DMSO-d_6 in the DMSO–kaolinite intercalation compound, obtained from ^{2}H solid state NMR spectra (35).

In addition, the value of the T_1 minimum is given (36) by:

$$[9]\quad \frac{1}{T_{1\min}} = \frac{1.42}{15}\times\frac{\chi^2}{\omega_0}$$

Fig. 7. Deuterium NMR spectrum of benzene-d_6 in the TATM inclusion compound at 294 K.

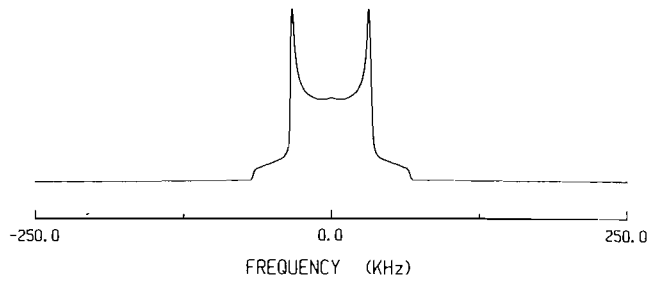

If we use the experimental value of 178.2 kHz for the quadrupolar coupling constant, and the deuterium spectrometer frequency of 44.667 MHz, the value of T_1 at the minimum should be about 2.2 ms. This compares with the experimental value of 3.2 ms at about 148 K. The DMSO-d_6 guest in the kaolinite intercalate was found to go through a T_1 minimum of approximately 7.2 ms, around 205 K (35).

It would be useful to compare the motion of DMSO-d_6 in TATM with that of pure dimethyl sulfone, $SO_2(CH_3)_2$. It is known that dimethyl sulfone, with its tetrahedral geometry, undergoes jumps about its unique C_2 axis to exchange the two methyl groups and the two oxygens, respectively (37). In comparison, DMSO is a molecule of much lower symmetry (C_s). It has no proper axis of symmetry about which to reorient. This is accompanied by a lack of motion, to the best of our knowledge, of the DMSO molecule in TATM, other than methyl rotation, at the temperatures investigated. The activation energy for methyl rotation in dimethyl sulfone was found from ^{1}H spin-lattice relaxation time measurements to be 17.0 kJ/mol ($\tau_\infty = 1.5 \times 10^{-13}$ s) (38).

Benzene–TATM

The room temperature deuterium spectrum of benzene-d_6, in the TATM inclusion compound, is shown in Fig. 7, and it indicates that the benzene molecules are likely performing in-plane 60° jumps about the molecular C_6 axis. This type of reorientation results in a ^{2}H spectrum that is 50% of the width of the static spectrum (i.e., ½(3 cos$^2\theta$ − 1) = 0.50), with no change in lineshape ($\theta \sim 90°$). The appearance of the spectrum does not change from room temperature down to 113 K, suggesting that the sixfold reorientation is proceeding at a rate greater than 10^8 Hz to the lowest temperature measured. The populations of the six sites are equal, as they must be by the symmetry of the guest molecule. However, χ_{eff} is 86.8 kHz at room temperature and 92.9 kHz at the lowest temperature measured (113 K). This suggests that the benzene molecules are engaged in small-amplitude librational motions while in the TATM cavity, to cause further spectral averaging on top of the C_6 reorientation. The experimental value of χ_{static} at 113 K is 185.8 kHz, which is a typical value for a static aromatic deuteron. The value of the static quadrupole coupling constant as a function of inverse temperature is depicted in Fig. 8. At low temperatures, the graph is becoming flat, suggesting that the precessional motion is being frozen out.

The deuterium spin-lattice relaxation times for benzene-d_6–TATM also appear in Fig. 8. Notice that the T_1 curve does not reach a minimum down to the lowest temperature measured. The motion is always in the extreme narrowing limit (i.e., $\omega_0\tau_c$

Fig. 8. Graph of ^2H spin-lattice relaxation time for the benzene-d_6–TATM clathrate, along with the effective quadrupole coupling constant at each temperature.

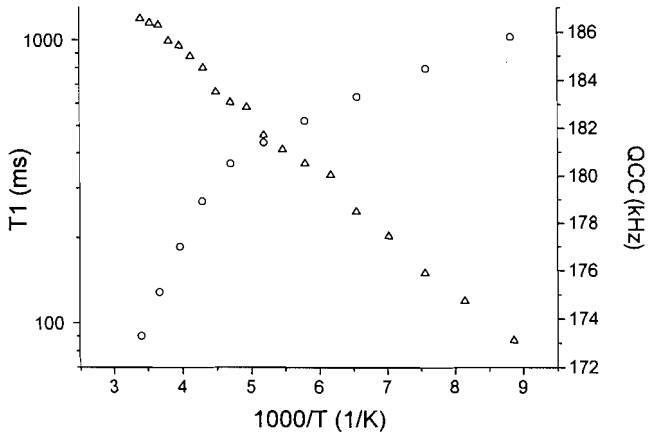

<< 1.) This complements the ^2H spectral data, as it indicates that the rate of sixfold rotation is likely larger than the Larmor precession frequency ($\sim 4 \times 10^7$ Hz) down to 115 K. The lack of a T_1 minimum precluded us from performing a complete T_1 fit; however, the slope of the curve provided us with an activation energy of 4.1 (±0.4) kJ/mol for the C_6 rotation of benzene-d_6 in TATM. This compares with an activation energy of 16.5 kJ/mol (39) and 16.8 kJ/mol (40), for pure, solid benzene, determined from ^2H powder NMR and relaxation time measurements, respectively. When benzene is in an inclusion compound, E_a varies from 4.0 kJ/mol in the tri-*ortho*-thymotide clathrate (41), to 24.9 kJ/mol in 1,3-cyclohexanedione (39). A consequence of the very low activation barrier for the reorientation of benzene in TATM is that we were unable to slow the reorientation rate below even 10^8 Hz down to 113 K.

An X-ray determination of the crystal structure was performed on benzene–TATM (20). This study indicated that the TATM thienyl rings did not completely enclose the benzene molecule, as they do for ethanol, hexane, and ethyl acetate (19, 21, 22), where the thienyl rings form globular cavities in which the guest resides. The inability of TATM to completely surround the benzene guest may give an indication of why the benzene–TATM activation energy is very low compared to most other studies of the dynamics of benzene.

Mesitylene–TATM

The ^2H NMR spectra of mesitylene-d_9 (deuterated on the methyl groups) in TATM appear in Fig. 9. It is expected that mesitylene (1,3,5-trimethyl benzene) would reorient by 120° in plane rotational jumps to exchange the methyl groups about the molecular C_3 axis. However, this type of motion (or 60° jumps for that matter) leads to simulations that do not match the experimental spectra at intermediate rates (10^4–10^6 Hz).

A model that may be considered is that there are two dynamically distinct types of mesitylene molecules. One is performing C_3 rotation at a rate that is fast on the ^2H spectral time scale ($k > 10^8$ Hz), and the other is rotating slowly ($k < 10^3$ Hz). There are no mesitylene molecules in the intermediate exchange region. This model would require the existence of two different sites in the TATM lattice. The proportion of these two sites (and hence the ratio of the two dynamically different types of mesitylene molecules) is changing with temperature. At high temperatures, most of the mesitylene molecules are moving rapidly, while at the lowest temperature the majority are in the rigid lattice limit. The percentage of molecules moving rapidly (P_1), and the percentage moving slowly (P_2), at each temperature, are indicated with the simulations in Fig. 9. Note that this model contradicts information obtained for other TATM inclusion compounds, by X-ray crystallography, which suggests that there is only one guest molecule per unit cell in all four TATM inclusion compounds investigated to this point.

Fig. 9. Simulated and experimental ^2H NMR spectra for mesitylene-d_9 in the TATM inclusion compound, at the temperatures indicated, along with the percent populations of fast moving (P_1) and slow moving (P_2) mesitylene molecules.

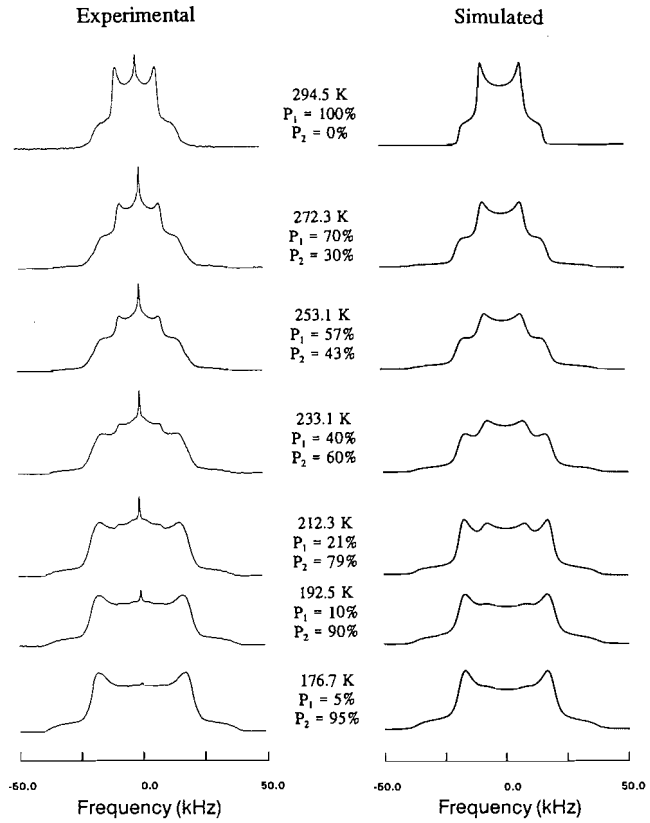

However, it is important to note that this model is the simplest one we could consider. There may be a continuous distribution of jump rates. The molecules that are performing C_3 rotation at rates between approximately 10^4 Hz and 10^6 Hz would contribute very little to the overall spectral intensity, compared to the molecules rotating rapidly or slowly, due to the fact that the echo intensity is attenuated considerably for molecules in the intermediate exchange region. This model is physically more reasonable, because small differences in the guest–host interaction from one cavity to the next could result in a distribution of motional rates. In Fig. 10, the normalized echo intensity is plotted as a function of jump rate, calculated for in-plane 120° jumps of the mesitylene molecule. It can be seen that the echo (and thus spectrum) intensity, at 5×10^4 Hz, falls to only 15% of that at very fast C_3 motional rates. Therefore there would be very little contribution to the spectral

Fig. 10. Plot of normalized echo intensity, as a function of jump rate, calculated for in-plane C_3 rotation of a mesitylene molecule.

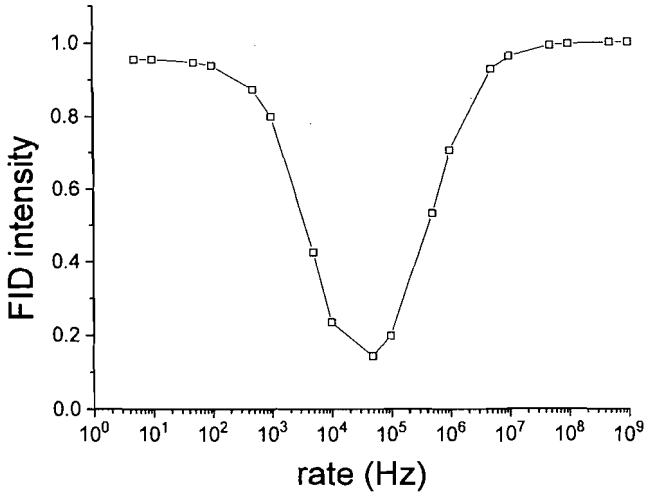

Fig. 11. Simulated ^{2}H spectra for C_3 rotation of a mesitylene molecule, with an equal population distribution over five rates, weighted by the echo attenuation at each rate.

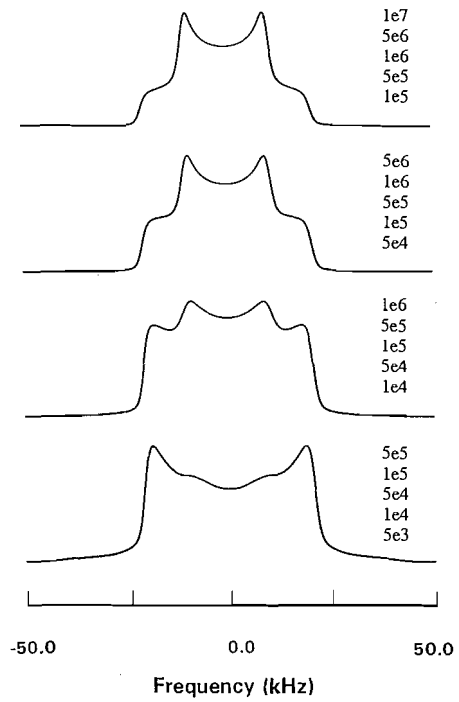

intensity at intermediate rates, where the agreement between simulated and experimental spectra is at its weakest. It would seem instructive to investigate this matter further.

In Fig. 11, we present simulations based on equal populations of mesitylene molecules over five rates, with the distribution slowly changing from faster rates to slower rates (corresponding to a decrease in temperature). Although the populations of the five sites/rates are equal in each spectrum (as indicated in the figure), the contributing spectra have been properly weighted according to the attenuation of the echo intensity at intermediate rates. By comparing these simulations with the experimental spectra in Fig. 9, it can be seen that

Fig. 12. *A*: Experimental ^{2}H NMR spectrum for *o*-xylene-d_{10}–TATM at room temperature. *B*: Experimental ^{2}H NMR spectrum for *p*-xylene-d_{10}–TATM at room temperature.

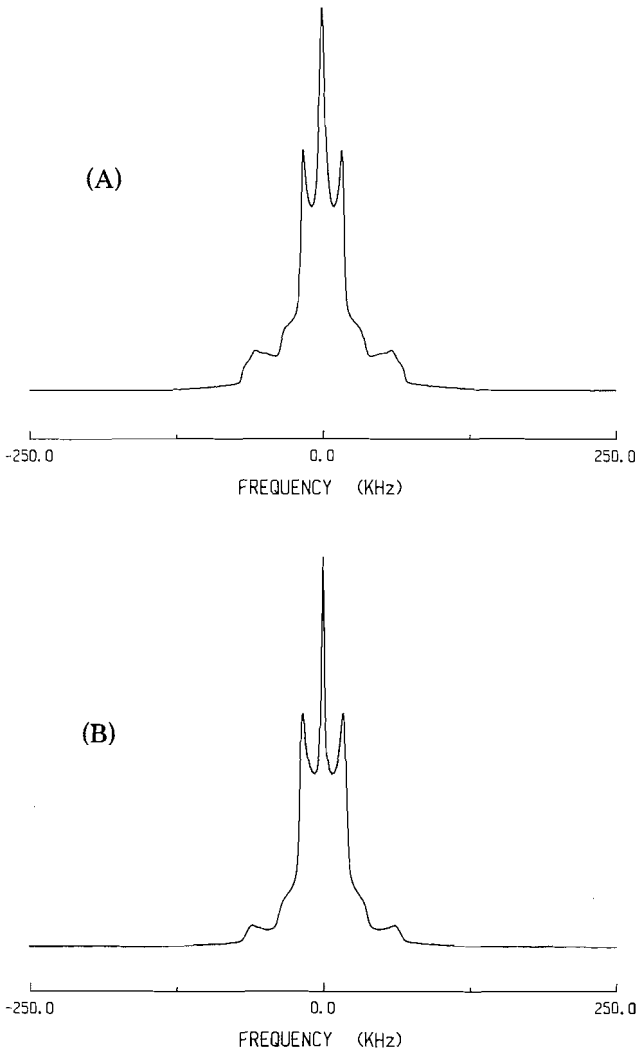

the agreement is quite good. This model is somewhat more elaborate than the one described above, but it is more realistic to consider the population distribution as Gaussian, rather than the rectangular one we have chosen. However, there are simply too many variables to consider a detailed lineshape fit with this scheme.

ortho-Xylene–TATM

The ^{2}H spectrum of *o*-xylene-d_{10} (*o*-dimethylbenzene) in the TATM inclusion compound, at room temperature, is depicted in Fig. 12*A*. Note that there are two spectral components, aside from the isotropic-type line at zero frequency. The inner component (χ_{eff} = 47.4 kHz) is typical of methyl groups that are undergoing fast methyl rotation. Because χ_{eff} is less than 56.7 kHz, the guest molecule is probably undergoing a librational motion, of half angle $\theta = 19.3°$ at room temperature. The outer component corresponds to the four static phenyl deuterons, with a non-zero static asymmetry parameter η = 0.06 commonly observed for aromatic deuterons. Their effective quadrupolar coupling constant was found to be 165 kHz. This is

Table 1. Host–guest ratios for TATM inclusion compounds, determined from ^{1}H NMR solution spectra of isotopically normal clathrates dissolved in $CDCl_3$, along with experimentally observed melting points.

Guest molelcule	Host:guest ratio	Melting point (°C)
Acetone	2:1	99–104
Acetonitrile	2:1	103–106
Benzene	2:1	115–118
1,2-Dichloroethane	2:1	116–119
Dimethylformamide	2:1	105–108
Dimethyl sulfoxide	2:1	113–116
Mesitylene	2:1	79–81
Methylene chloride	2:1	107–114
Methylene bromide	2:1	114–116
Methylene iodide	2:1	111–113
Nitromethane	2:1	106–109
Pyridine	2:1	114–117
Toluene	2:1	116–118
ortho-Xylene	2:1	111–112
meta-Xylene	2:1	84–86
para-Xylene	2:1	94–95

smaller than a typical value of 190 (±5) kHz for aromatic deuterons, also suggesting some motional averaging due to a librational motion (a librational angle of 17.2° is implied).

para-Xylene–TATM

The ^{2}H spectrum of *p*-xylene-d_{10} (*p*-dimethylbenzene)–TATM, at room temperature, is shown in Fig. 12*B*. Note the general similarity to the spectrum of *o*-xylene–TATM. The inner component, again from the six methyl deuterons, is indicative of methyl rotation as the only motion being present. The quadrupolar coupling constant, 50.5 kHz, indicates that the guest is wobbling, about an axis normal to the ring plane, with a half angle $\theta = 15.7°$ at room temperature. The χ_{eff} value for the ring deuterons is 175 kHz (suggesting $\theta = 13.3°$), again indicating a partial averaging due to the wobbling motion.

Summary

In summary, we have investigated the dynamic behaviour of acetonitrile, nitromethane, dimethyl sulfoxide, benzene, mesitylene, *ortho*-xylene, and *para*-xylene, included in a solid TATM host, by deuterium NMR lineshape and T_1 analysis. The reorientational motion of each guest molecule is restricted to some degree, the extent of which is influenced by the guest–host interaction. Acetonitrile, nitromethane, dimethyl sulfoxide, *ortho*-xylene, and *para*-xylene undergo reorientation of the methyl groups, in addition to some degree of overall librational motion of the molecule. Benzene and mesitylene reorient about an axis perpendicular to the phenyl ring plane.

Acknowledgements

We are very grateful to the Natural Sciences and Engineering Research Council of Canada (NSERC), for financial support. In addition, we would like to thank Professor Otto Meth-Cohn for providing us with his procedure for the synthesis of TATM.

References

1. J.F. Brown Jr. Sci. Am. 82 (1962).
2. G.H. Penner, J.M. Polson, C. Stuart, G. Ferguson, and B. Kaitner. J. Phys. Chem. **96**, 5121 (1992).
3. S.J. Heyes. J. Phys. Chem. **95**, 1547 (1991).
4. K. Muller. Magn. Reson. Chem. **30**, 228 (1992).
5. J.A. Ripmeester. J. Inclusion Phenom. **6**, 31 (1988).
6. R.E. Wasylishen and M.L.H. Gruwel. Z. Naturforsch. A: Phys. Sci. **47**, 1073 (1992).
7. M.R. MacIntosh, B. Fraser, M.L.H. Gruwel, R.E. Wasylishen, and T.S. Cameron. J. Phys. Chem. **96**, 8572 (1992).
8. S. Cerrini, G. Pochetti, F. Gallese, and E. Possagno. Acta. Crystallogr. Sect. C. Cryst. Struct. Commun. **C49**, 1087 (1993).
9. A.E. Armah, K. Suzuki, S. Fujii, K. Tomita, Z. Asfori, and J. Vicens. Acta. Crystallogr. Sect. C: Cryst. Struct. Commun. **C48**, 1474 (1992).
10. R. Clement, C. Mazieres, M. Gourdji, and L. Guibe. J. Chem. Phys. **67**, 5381 (1977).
11. Y. Chatani, H. Anraku, and Y. Taki. Mol. Cryst. Liq. Cryst. **48**, 219 (1978).
12 (*a*) L.W. Jelinski. Annu. Rev. Mater Sci. **15**, 359 (1985); (*b*) D.A. Torchia. Annu. Rev. Biophys. Bioeng. **13**, 125 (1984); (*c*) H.W. Spiess. Adv. Polym. Sci. **66**, 23 (1985).
13. R.J. Wittebort, E.T. Olejniczak, and R.G. Griffin. J. Chem. Phys. **86**, 5411 (1978).
14. D.A. Torchia and A. Szabo. J. Magn. Reson. **49**, 107 (1982).
15. J.S. Greenfield, A.D. Ronemus, R.L. Vold, R.R. Vold, P.D. Ellis, and T.R. Raidy. J. Magn. Reson. **72**, 89 (1987).
16. A.F. Thomas. Deuterium labelling in organic chemistry. Meredith Corp., New York. 1971.
17. A.P. Yakubov, Y.K. Sudarushkin, L.I. Belenkii, and Y.L. Goldfarb. J. Org. Chem. (USSR), **9**, 1549 (1973).
18. L. Bin Din and O. Meth-Cohn. J. Chem. Soc. Chem. Commun. **21**, 741 (1977).
19. P.H. Van Rooyen and H.M. Roos. Acta. Crystallogr. Sect. C: Cryst. Struct. Commun. **C47**, 2468 (1991).
20. P.H. Van Rooyen and H.M. Roos. Acta. Crystallogr. Sect. C: Cryst. Struct. Commun. **C47**, 2718 (1991).
21. H.M. Roos and J.L.M. Dillen. Acta. Crystallogr. Sect. C: Cryst. Struct. Commun. **C48**, 1882 (1992).
22. J.L.M. Dillen and H.M. Roos. Acta. Crystallogr. Sect. C: Cryst. Struct. Commun. **C48**, 2229 (1992).
23. A.E. Aliev, K.D.M. Harris, and A. Mahdyafar. J. Chem. Soc. Faraday Trans. **91**, 2017 (1995).
24. M.H. Frey, J.A. DiVerdi, and S.J. Opella. J. Am. Chem. Soc. **107**, 7311 (1985).
25. D.T. Amm, S.L. Segel, and K.R. Jeffrey. Can. J. Phys. **64**, 22 (1986).
26. S.J. Heyes and C.M. Dobson. Magn. Reson. Chem. **28**, S37 (1990).
27. D. Reichert and H. Schneider. Z. Phys. Chem. **190**, 63 (1995).
28. N. Bloembergen, E.M. Purcell, and R.V. Pound. Phys. Rev. **73**, 679 (1948).
29. T.S. Chen, J. Wolinska-Mocydlarz, and L.C. Leitch. J. Labelled Compd. **6**, 285 (1970).
30. J.H. Davis, K.R. Jeffrey, M. Bloom, M.I. Valic, and T.P. Higgs. Chem. Phys. Lett. **42**, 390 (1976).
31. H. Dreizler and G. Dendl. Z. Naturforsch. A: Astrophys. Phys. Phys. Chem. **20A**, 1431 (1965).
32. S. Jurga. Ser. Fiz. (Uniw. Adama Mickiewicza Poznaniu), 41 (1980).
33. T. Hasebe and R. Sato. Fukushima Daigaku Kyoikugakubu Ronshu, Rika Hokoku, **46**, 19 (1990).
34. P.S. Sidhu, J. Bell, G.H. Penner, and K.R. Jeffrey. Can. J. Chem. **73**, 2196 (1995).
35 S. Hayashi. J. Phys. Chem. **99**, 7120 (1995).
36. A. Abragam. The principles of nuclear magnetism. Oxford University Press, London. 1961.

37. C. Schmidt, S. Wefing, B. Blümich, and H.W. Spiess. Chem. Phys. Lett. **130**, 84 (1986).
38. F. Koksal and S. Bahceli. Z. Naturforsch. A: Phys. Phys. Chem. Kosmophys. **39A**, 548 (1984).
39. J.H. Ok, R.R. Vold, R.L. Vold, and M.C. Etter. J. Phys. Chem. **93**, 7618 (1989).
40. E.R. Andrew and R.G. Eades. Proc. R. Soc. London Ser. A: **218**, 537 (1953).
41. A.E. Aliev, K.D.M. Harris, and A. Mahdyarfar. J. Chem. Soc. Faraday Trans. **91**, 2017 (1995).

Conformational behaviour of highly hindered ethanes: *meso*- and racemic-2,2,2′,2′-tetramethyl-1,1′-biindanyl

T. Bruce Grindley, Paula J. MacLeod, James A. Pincock, and T. Stanley Cameron

Abstract: MM3(94), AM1, and STO-3G calculations on racemic 2,2,2′,2′-tetramethyl-1,1′-biindanyl (**1**) show that seven minima are present on its conformational potential energy surface. **1** crystallizes in the space group *Pbcn* (no. 60) with cell parameters $a = 11.190(7)$, $b = 11.679(7)$, $c = 13.19(1)$ Å, $V = 1724(3)$ Å^3, $Z = 4$, $R = 0.0357$, $R_w = 0.0362$ in the conformation predicted to be the global minimum by STO-3G and AM1, but not by MM3(94). Application of the Karplus equation and observation of a deshielded proton signal indicate that the same conformation is the major species present in solution, perhaps along with another conformation. The *meso* isomer **2** shows evidence of slow exchange between conformers in its room temperature NMR spectra. Barriers to exchange were obtained from ^{13}C NMR coalescence experiments and from ^{1}H NMR line shape analysis of the exchanging AB pattern. The potential energy surface for **2** was calculated as for **1** and used to determine the nature of the process observed. The slow exchange was calculated to be between two enantiomeric conformers. The populated conformers for both **1** and **2** had the benzene rings from the two halves of the dimer stacked in an offset manner and the favourable interactions associated with this stacking may be a factor in the relative stabilities of these conformations.

Key words: MM3, molecular mechanics, hindered rotation, dialkyldiphenylethanes, X-ray crystal structure.

Résumé : Des calculs MM3(94), AM1 et STO-3G sur le 2,2,2′,2′-tétraméthyl-1,1′-biindanyle (**1**) mettent en évidence la présence de sept minimums sur sa surface d'énergie potentielle conformationnelle. Le composé **1** cristallise dans le groupe d'espace *Pbcn* (no. 60) avec $a = 11,190(7)$ et $b = 11,679(7)$, $c = 13,19(1)$ Å, $V = 1724(3)$ Å^3, $Z = 4$, $R = 0,0357$, $R_w = 0,0362$, dans la conformation qui est prédite par le minimum global d'énergie par STO-3G et AM1, mais pas par la méthode MM3(94). L'application de l'équation de Karplus et l'observation d'un signal correspondant à un proton déblindé indiquent que la même conformation serait l'espèce majeure présente en solution; il est possible qu'une autre conformation lui soit associée. Dans le cas de l'isomère *méso*, **2**, les spectres RMN à la température ambiante suggèrent qu'il existe un échange lent entre les conformères. On a déterminé les barrières pour l'échange à partir d'expériences de coalescence des spectres RMN du ^{13}C et d'une analyse de la forme des raies des spectres RMN du ^{1}H du patron AB des atomes qui s'échangent. Comme dans le cas du produit **1**, on a déterminé la surface de l'énergie potentielle du composé **2** et on l'a utilisée pour déterminer la nature du processus observé. On a calculé que l'échange lent se fait entre les deux conformères énantiomères. Les conformères les plus populeux des composés **1** ainsi que **2** comportent des noyaux benzéniques des deux parties du dimère empilées de façon décalée; il est possible que les interactions favorables associées à cet empilement soient un facteur dans les stabilités relatives de ces conformations.

Mots clés : MM3, mécanique moléculaire, rotation empêchée, dialkyldiphényléthanes, détermination d'une structure cristalline, diffraction des rayons-X.

[Traduit par la rédaction]

Introduction

The relative importance of aryl–aryl interactions in the aggregation of compounds containing aromatic rings has attracted considerable attention (1, 2). The two molecules discussed in this publication can exist in conformations that have two benzene rings either stacked in an offset face-to-face stack or distant from each other. Calculations on benzene dimers in the gas phase using electrostatic plus nonbonded terms suggested that the offset face-to-face stack was one of the most favourable geometries for these interactions, only slightly less favourable than the best arrangement, the edge-to-face dimer (3, 4). Recently, high-level ab initio calculations with electron correlation have indicated that the parallel-displaced dimer, fairly similar in geometry to the offset stack possible here, is the most stable arrangement, 9.6 kJ mol^{-1} more stable than two monomers (5).

The title compounds **1** and **2**, two of the six products from the photolyses of 2,2-dimethyl-1-indanyl acetate and pivalate, were isolated by column chromatography on silica gel (6). These two compounds are the diastereomeric dimers formed from coupling of 2,2-dimethyl-1-indanyl radicals; the former

Received October 11, 1995.[1]

T.B. Grindley,[2] P.J. MacLeod, J.A. Pincock,[2] and T.S. Cameron.[2] Department of Chemistry, Dalhousie University, Halifax, NS B3H 4J3, Canada.

[1] Revision received July 15, 1996.

[2] Authors to whom correspondence may be addressed. Telephone (T.B.G.): (902) 494-3305. Fax: (902) 494-1310. E-mail: Grindley@chem1.chem.dal.ca or Pincock@chem1.chem.dal.ca

is a racemic mixture of compounds having (*R,R*) or (*S,S*) configurations at the two new stereogenic centres, while the latter is a *meso* (*R,S*) compound. The former mixture will be called the racemic dimer.

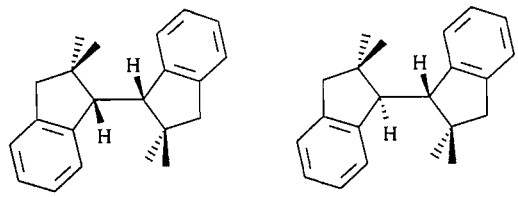

1 **2**

Surprisingly, the ^{1}H NMR spectra of these very similar dimers were very different at room temperature; one contained only sharp lines while the other consisted of broadened signals. It will be demonstrated that the signals were broadened because of slow exchange between conformations arising from barriers to rotation about the C—C bond joining the two halves of the symmetrical dimer. The variable temperature ^{1}H and ^{13}C NMR spectra of both dimers have been investigated and an X-ray diffraction analysis was performed on dimer **1**, establishing its structure unambiguously.

There has also been considerable interest about various properties of compounds having highly congested sp^3—sp^3 single bonds. Large barriers to rotation (>40 kJ mol^{-1}) about this type of single bond have been observed in many compounds (7–12) and a number of compounds, particularly substituted triptycene or dihydroanthracene derivatives, even have high enough barriers that two conformational isomers can be isolated (7). In most of the compounds with high barriers, the two carbon atoms in the bond about which rotation is hindered are quaternary. Barriers about bonds between two tertiary carbons are normally much lower; for instance, the barrier for rotation about the bond between the two isopropyl groups in 2,3-dimethylbutane is about 18 kJ mol^{-1} (10). Where higher barriers were observed about bonds between two tertiary carbons, several very large groups have always been present at both ends of the bond and the barriers observed have often resulted from correlated motion of several groups (8, 11, 13–15). There has also been considerable interest in bond lengths (16, 17), in bond dissociation energies (11, 15), and in the applicability of molecular mechanics calculations (18) to compounds containing sterically congested bonds of this type.

The potential energy surface for rotation around the central carbon–carbon bond in dimers **1** and **2** was evaluated, using both the AM1 semi-empirical method and the MM3(94) molecular mechanics force field. Surprisingly, the results of AM1 calculations were in closer agreement with experimental observations on which conformers were populated and on the size of the barriers between conformers, even though the geometries predicted for the saturated parts of the molecules were much poorer than predicted by MM3. The causes of these surprising observations will be discussed.

Results and discussion

Racemic dimer (1) — crystallography

One of the dimers (**1**) crystallized easily from hexanes, the other resisted all attempts at crystallization and remained an oil. The crystal structure was solved by direct methods and refined to $R = 3.57\%$. Full details of the structure solution have been deposited.[3] The atomic coordinates are given in Table 1 and some structural data are located in Table 2. An ORTEP representation of one of the molecules in the unit cell is given in Fig. 1 where the structure pictured is the *R,R* stereoisomer. The crystalline sample is the racemic compound **1**. In the crys-

Fig. 1. ORTEP representation (50% probability) of an (*R,R*) molecule of 2,2,2′,2′-tetramethyl-1,1′-biindanyl from the X-ray crystal structure of racemic **1**.

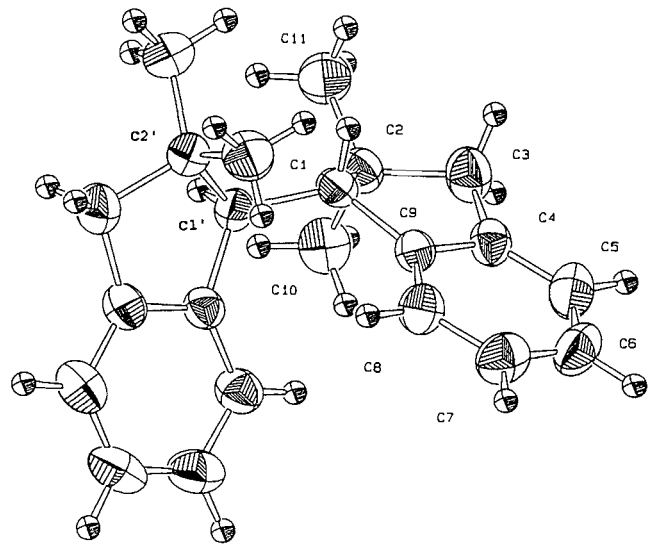

Table 1. Positional parameters and *B*(eq) for 2,2,2′,2′-tetramethyl-1,1′-biindanyl.

Atom	*x*	*y*	*z*	*B*(eq)[a]
C(1)	0.0240(2)	0.4685(2)	0.3053(2)	3.1(1)
C(2)	0.1524(3)	0.5184(3)	0.3208(2)	3.6(2)
C(3)	0.1819(3)	0.4784(3)	0.4292(2)	4.6(2)
C(4)	0.1172(3)	0.3660(3)	0.4393(2)	3.5(2)
C(5)	0.1358(3)	0.2783(3)	0.5079(2)	4.6(2)
C(6)	0.0633(3)	0.1823(3)	0.5048(3)	4.8(2)
C(7)	−0.0267(3)	0.1749(3)	0.4332(3)	4.7(2)
C(8)	−0.0464(3)	0.2633(3)	0.3649(2)	3.9(2)
C(9)	0.0262(2)	0.3591(2)	0.3674(2)	3.1(1)
C(10)	0.2430(3)	0.4658(3)	0.2477(2)	4.6(2)
C(11)	0.1560(3)	0.6482(3)	0.3107(2)	4.8(2)

[a] *B*(eq) is one-third of the trace of the orthogonalized B_{ij} tensor.

[3] Lists of atomic coordinates, bond lengths and angles, torsion angles, and anisotropic thermal parameters may be purchased from: The Depository of Unpublished Data Document Delivery, CISTI, National Research Council Canada, Ottawa, Canada K1A 0S2. The lists of atomic coordinates and bond lengths and angles have also been deposited with the Cambridge Crystallographic Data Centre, and can be obtained on request from The Director, Cambridge Crystallographic Data Centre, University Chemical Laboratory, 12 Union Road, Cambridge, CB2 1EZ, U.K.

Fig. 2. A 400 MHz ^{1}H NMR spectrum of the racemic dimer **1** in chloroform-*d* at 20°C.

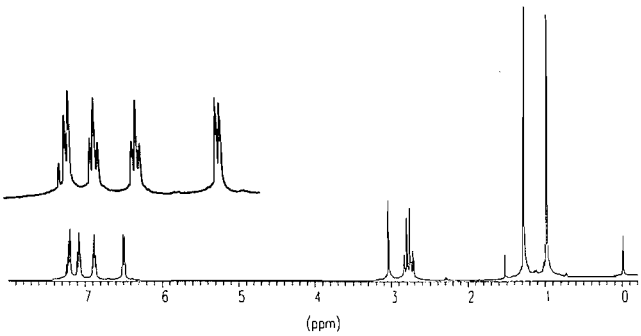

tal, the two halves of the dimer are related by a crystallographic twofold axis through the central C(1)—C(1′) bond. The C(1) — C(1′) bond length is 1.554(5) Å, though the effective esd is larger than the quoted value because of the twofold axis. The five-membered ring is in an envelope conformation. As expected, the four carbon atoms of this ring, C(1), C(3), C(4), and C(9), that are part of, or bonded to, the aromatic ring are coplanar with a mean deviation from the least-squares plane of 0.003(3) Å. The fifth atom is 0.537 Å from the plane. The two halves of the molecule, connected through the C(1)—C(1′) bond, have a C(9)- C(1)- C(1′)- C(9′) torsion angle of −23.0(6)°. The unit cell contains two *S,S* molecules and two *R,R* molecules.

Racemic dimer (1) — NMR results

The ^{1}H NMR spectrum of the racemic dimer at 20°C, shown in Fig. 2, is simple because the two halves of the molecule are equivalent by virtue of its C_2 symmetry. No significant changes in the spectrum were observed upon heating or cooling in the range from −60°C to +45°C. The methyl groups give rise to two singlets at 1.00 and 1.30 ppm. The protons of the CH_2 group appear as an AB quartet (J = −15.0 Hz) centered at 2.80 ppm, very close to the chemical shift of the methylene group hydrogens in 2,2-dimethylindane, 2.75 ppm. The geminal coupling constant is assumed to have a negative sign (19). The CH signal is a singlet at 3.07 ppm, with a ^{13}C satellite 61.0 Hz to higher frequency. The satellite at lower frequency was obscured by the methylene signals. Confirmation that this small peak, having approximately 0.5% of the intensity of the main peak, was indeed a ^{13}C satellite, was obtained by recording the spectra at both 250 and 400 MHz, and also by measuring $^1J_{C,H}$ from the coupled ^{13}C NMR spectra. The value obtained was 122 Hz, twice the separation of the satellite from the main CH signal. The satellite signal was not split, indicating that the H(1)—H(1′) vicinal coupling constant was <1 Hz. The aromatic region consists of two doublets and two triplets as expected for a first-order pattern of a 1,2-disubstituted aromatic ring. The absorption of one pair of *ortho* hydrogens is considerably shielded, appearing as a doublet at 6.52 ppm. In comparison with the chemical shift of the two equivalent *ortho* hydrogens of 2,2-dimethylindane, a very large Δδ of −0.65 is observed. The ^{13}C NMR solution spectrum, shown in Fig. 3*a*, contains 11 signals, consistent with the C_2 molecular symmetry.

A CP/MAS ^{13}C NMR spectrum of this dimer in the solid state is shown in Fig. 3*b*. The spectrum is very similar to the solution spectrum, except that spinning side bands from the

Fig. 3. (*a*) A 62.5 MHz ^{13}C NMR spectrum of the racemic dimer **1** in chloroform-*d* at 20°C. (*b*) A CP/MAS ^{13}C NMR spectrum at 100 MHz of the racemic dimer **1** in the solid state. Spinning side bands are indicated with an X.

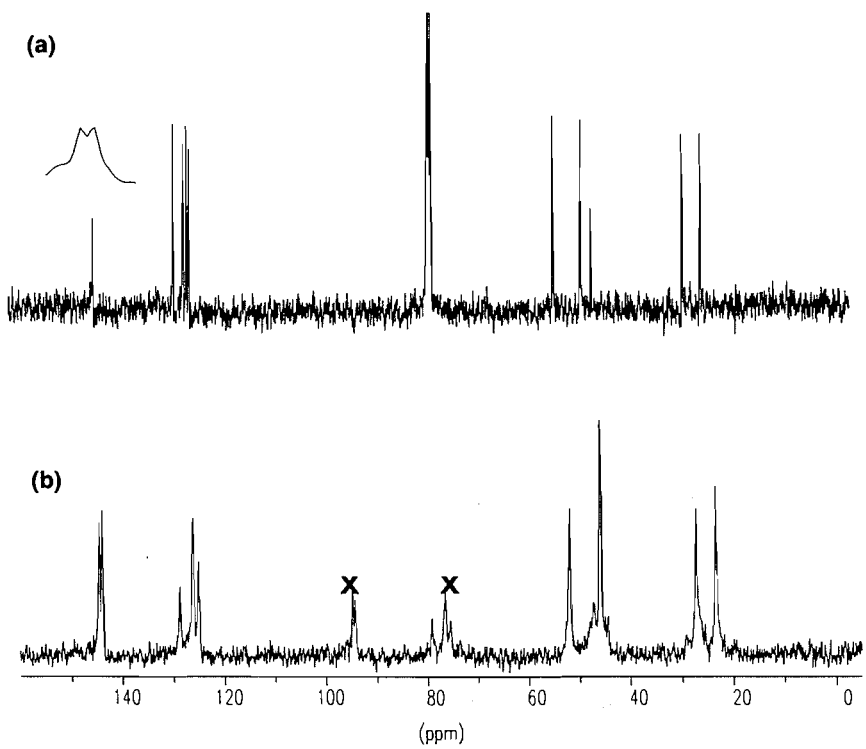

Table 2. Selected data about the conformational minima for the racemic dimer.[a]
(*a*)

	Conformer							
	a1			**a2**			**a3**	
Feature	MM3	AM1	STO-3G	MM3	AM1	STO-3G	MM3	AM1
Relative energy	1.1[b]	5.2[c]	3.5[d]	0.0[b]	0.3[c]	1.2[d]	17.2[b]	12.0[c]
C(2)-C(1)-C(1′)-C(2′)	101.4	97.6	111.6	170.5	142.7	152.2	294.9	286.6
H-C(1)-C(1′)-H	−153.9	−145.1	−132.8	−72.5	−95.1	−86.4	46.1	48.8
C(1)-C(9)-C(4)-C(3)	−2.2	0.4	−0.8	−3.9	2.1	−1.6	0.5	2.0
C(9)-C(4)-C(3)-C(2)	−21.4	−10.5	−18.8	−19.4	−7.8	−15.4	−20.7	−7.5
C(4)-C(3)-C(2)-C(1)	36.0	16.1	29.9	34.2	10.1	25.5	33.1	9.8
C(3)-C(2)-C(1)-C(9)	−36.4	−15.6	−29.8	−35.9	−8.9	−26.0	−33.1	−8.6
C(2)-C(1)-C(9)-C(4)	24.4	9.8	19.6	24.8	4.4	17.5	21.1	4.3
C(2)-C(1)-C(9), sp^3	99.0	103.6	101.3	99.8	104.5	101.9	100.2	104.8
C(1)-C(2)-C(3), sp^3	103.8	106.1	103.9	104.3	106.2	104.9	104.8	106.3
C(2)-C(3)-C(4), sp^3	101.3	105.2	103.1	101.2	105.7	103.5	101.3	105.7
C(3)-C(4)-C(9), sp^2	109.7	110.8	110.2	110.7	111.1	111.0	110.4	110.9
C(1)-C(9)-C(4), sp^2	111.4	111.6	111.4	110.3	111.4	111.3	111.0	111.4
C(1)—C(1′)	1.583	1.529	1.582	1.581	1.527	1.577	1.571	1.527
C(1)—C(2)	1.578	1.571	1.584	1.574	1.571	1.585	1.574	1.563

[a]Note that conformers in the **a** and **c** families have C_2 symmetry while those in the **b** family have no symmetry.
[b]With respect to the global MM3 minimum, conformer **a2**.
[c]With respect to the global AM1 minimum, conformer **c1**.
[d]With respect to the global STO-3G minimum, conformer **c1**.
[e]The signs of the torsional angles for the crystal structure have been reversed in this column to match those from the calculations, which are for the (*S,S*) enantiomer. The crystal structure diagram (Fig. 1) and the coordinates of **1** (Table 1), are of the (*R,R*) enantiomer.

aromatic carbons are present. Chemical shift anisotropies of aromatic carbons are much larger than those of the aliphatic carbons (20), making removal of spinning side bands of aromatic carbons by MAS more difficult.

Theoretical calculations for the racemic dimer (1)

The coordinates for several conformations of the (*S,S*) diastereomer of the racemic dimer (**1**) were initially generated using the molecular mechanics program pcmodel.[4] These coordinates were used as input for calculations using MM3(94) (21) in which the carbons in the benzene rings were treated as conjugated (type 2 carbons). All conformational minima had the five-membered rings in envelope conformations, with one atom, C(2) or C(2′), out of the plane. Thus, in all conformational minima, two torsional angles in each of these rings, C(1)-C(2)-C(3)-C(4) and C(3)-C(2)-C(1)-C(9), were calculated to be large, of approximately equal magnitude between 27° and 40°, and of opposite sign. The potential energy surface was explored by performing dihedral angle driver calculations using the angles C(2)-C(1)-C(1′)-C(2′), C(1)-C(2)-C(3)-C(4), and C(1′)-C(2′)-C(3′)-C(4′). Three unique families of conformations were found, termed families **a**, **b**, and **c**, which for the *S,S* stereoisomer have both C(1)-C(2)-C(3)-C(4) and C(1′)-C(2′)-C(3′)-C(4′) torsional angles positive, one positive and one negative, and both negative, respectively. When this angle is positive in an (*S,S*) diastereomer, the flap of the five-membered ring envelope, that is, C-2 or C-2′, is directed away from the other half of the dimer and the bond joining the two halves of the dimer, C(1)—C(1′), is in a quasi-axial orientation with respect to that five-membered ring. This will be termed an "out" orientation of the five-membered ring. When the angle is negative and the same bond, C(1)—C(1′), is now quasi-equatorial, the envelope is flapped toward the other half of the dimer in what will be termed an "in" orientation.

The **a** or "out,out" family contained three minima with C(2)-C(1)-C(1′)-C(2′) torsional angles of 101.4° (**a1**), 170.5° (**a2**), and 294.9° (**a3**). ATOMS representations of two conformers of the "out,out" family, **a1** and **a2**, are shown in Fig. 4. The **a2** is calculated to be the global minimum, but **a1** is only 1.1 kJ mol^{-1} higher in energy. The third minimum, **a3**, is 17.2 kJ mol^{-1} higher. The second or "out, in" family contains two minima with C(2)-C(1)-C(1′)-C(2′) torsional angles of 136.0° (**b1**) and 295.8° (**b2**) calculated to be 22.6 and 28.1 kJ mol^{-1}, respectively, higher in energy than the global minimum (**a2**). The third or "in,in" family contains two minima with C(2)-C(1)-C(1′)-C(2′) torsional angles of 139.6° (**c1**) and 302.1° (**c2**) calculated to be 15.6 and 58.1 kJ mol^{-1} higher in energy than the global minimum (**a2**). Information about these conformations is shown in Table 2.

The coordinates for the seven MM3 minima were used as input for AM1 (22) calculations and geometry optimizations

[4] PCMODEL Version 4.0. A molecular mechanics package by K.E. Gilbert and J.J. Gajewski, Indiana University. Available from Serena Software, Box 3096, Bloomington, IN 47402-3076, U.S.A.

Table 2 (*concluded*).
(*b*)

	Conformer								
	b1		**b2**		**c1**				**c2**
Feature	MM3	STO-3G	MM3	AM1	MM3	AM1	STO-3G	Crystal structure[e]	MM3
Relative energy	22.6[b]	7.1[d]	28.1[b]	7.7[c]	15.6[b]	0.0[c]	0.0[d]		58.1[b]
C(2)-C(1)-C(1′)-C(2′)	136.0	130.4	295.8	288.7	139.6	129.7	132.6	131.0(4)	302.1
H-C(1)-C(1′)-H	−102.7	−104.3	51.9	48.8	−95.0	−104.5	−98.7	−100	61.3
C(1)-C(9)-C(4)-C(3)	−0.4	0.9	−0.4	1.6	0.1	3.1	1.4	0.7(3)	−0.1
C(9)-C(4)-C(3)-C(2)	23.6	19.7	24.3	3.0	23.0	6.3	19.2	20.4(3)	25.4
C(4)-C(3)-C(2)-C(1)	−36.4	−31.1	−37.4	−6.1	−35.9	−12.6	−30.8	−31.9(3)	−39.5
C(3)-C(2)-C(1)-C(9)	36.2	31.4	37.2	6.9	36.0	14.2	31.5	32.2(3)	39.2
C(2)-C(1)-C(9)-C(4)	−22.7	−20.8	−23.5	−5.4	−22.9	−11.0	−21.1	−21.2(2)	−24.9
C(1′)-C(9′)-C(4′)-C(3′)	0.3	0.9	−1.5	1.7	0.1	3.1	1.4	0.7(3)	−0.1
C(9′)-C(4′)-C(3′)-C(2′)	−22.2	−18.0	−17.3	−3.3	23.0	6.3	19.2	20.4(3)	25.4
C(4′)-C(3′)-C(2′)-C(1′)	34.6	27.2	28.8	3.6	−35.9	−12.6	−30.8	−31.9(3)	−39.5
C(3′)-C(2′)-C(1′)-C(9′)	−34.3	−26.3	−29.2	−2.7	36.0	14.2	31.5	32.3(3)	39.2
C(2′)-C(1′)-C(9′)-C(4′)	21.3	16.3	19.3	0.7	−22.9	−11.0	−21.1	−21.2(2)	−24.9
C(2)-C(1)-C(9), sp^3	101.0	102.7	101.2	105.3	101.4	111.2	102.7	103.2(2)	100.2
C(1)-C(2)-C(3), sp^3	102.9	102.5	102.0	105.9	102.7	105.8	102.5	101.9(2)	101.7
C(2)-C(3)-C(4), sp^3	101.2	103.5	101.4	106.2	101.4	105.4	103.5	104.1(2)	100.9
C(3)-C(4)-C(9), sp^2	110.6	110.7	110.1	111.1	110.6	104.7	110.7	110.0(3)	109.9
C(1)-C(9)-C(4), sp^2	109.3	109.6	109.6	111.1	109.3	110.8	109.6	109.3(3)	109.6
C(1)—C(1′)	1.575	1.575	1.560	1.525	1.555	1.520	1.565	1.554(5)	1.554
C(1)—C(2)	1.572	1.579	1.571	1.564	1.571	1.570	1.579	1.563(4)	1.575

were performed. Results are also shown in Table 2. There are several significant differences from the MM3 results. Most importantly, the conformer stability order is changed. The **c1** is now the global minimum, 0.3 kJ mol^{-1} more stable than the MM3 global minimum **a2**. This conformation (**c1**) has a dihedral angle for C(2)-C(1)-C(1′)-C(2′) similar to that in the solid state (131.0°). However, other geometric features are not reliably reproduced. First, the AM1 five-membered rings were unrealistically flat, as indicated by the small torsional angles through C(2) and C(2′). As a result, two of the higher energy MM3 minima were not AM1 minima but changed during the optimization process to other conformers, **c2** to **b2**, and **b1** to **a2**. In addition, the central C(1)—C(1′) bond length, 1.520 Å, was considerably shorter than the bond length observed by X-ray diffraction (1.554 C). This bond length was, however, well reproduced by the MM3(94) force field (1.555 Å).

STO-3G optimizations were performed on several of the low-energy conformations. These calculations give the same stability order as AM1 but, unlike the AM1 method, also reproduce reasonably well the nonplanar geometry of the five-membered rings observed in the X-ray structure of **1**. For the absolute values of the four largest torsional angles in the five-membered rings, the STO-3G results average 0.7° lower than the X-ray results, AM1 results average 15.4° low, and MM3 results average 3.2° high. Agreement between the calculated and experimental C(1)—C(1′) bond lengths was also reasonably good, 1.565 Å in **c1**, compared to 1.554(5) Å in the X-ray results and 1.555 and 1.520 Å by MM3 and AM1, respectively. In *meso*-1,2-di-*tert*-butyl-1,2-diphenylethane, the central C—C bond length varies from 1.573 to 1.577 Å in different molecules in the unit cell, while it is 1.589 Å in the racemic isomer (15), suggesting that the current molecules are less strained. In addition, the critical C(2)-C(1)-C(1′)-C(2′) angle is only 1.6° larger in the STO-3G results than measured by X-ray diffraction.

Discussion for the racemic dimer (1)

The lowest energy MM3 minimum is not the conformer observed experimentally. The X-ray structure combines a C(2)-C(1)-C(1′)-C(2′) torsional angle of 131.0(4)° with symmetry-related C(1)-C(2)-C(3)-C(4) and C(1′)-C(2′)-C(3′)-C(4′) torsional angles of −31.9(3)°, opposite in sign to that of the C(2)-C(1)-C(1′)-C(2′) torsional angle, and therefore this structure belongs to the "in,in" conformational family. Conformer **c1** fits the X-ray data fairly closely, even though it was calculated to be 15.6 kJ mol^{-1} less stable than **a2** and 14.5 kJ mol^{-1} less stable than **a1**. In contrast, both the AM1 and STO-3G methods calculate that **c1** is the global minimum, if only by a slight amount.

There are two pieces of evidence that indicate that the pop-

Fig. 4. ATOMS representation of MM3 geometries of conformers of the racemic dimer (**1**): from the **a** or "out,out" family: (*a*) the **a1** conformer, (*b*) the **a2** conformer; and from the **c** or "in,in" family: (*c*) the **c1** conformer.

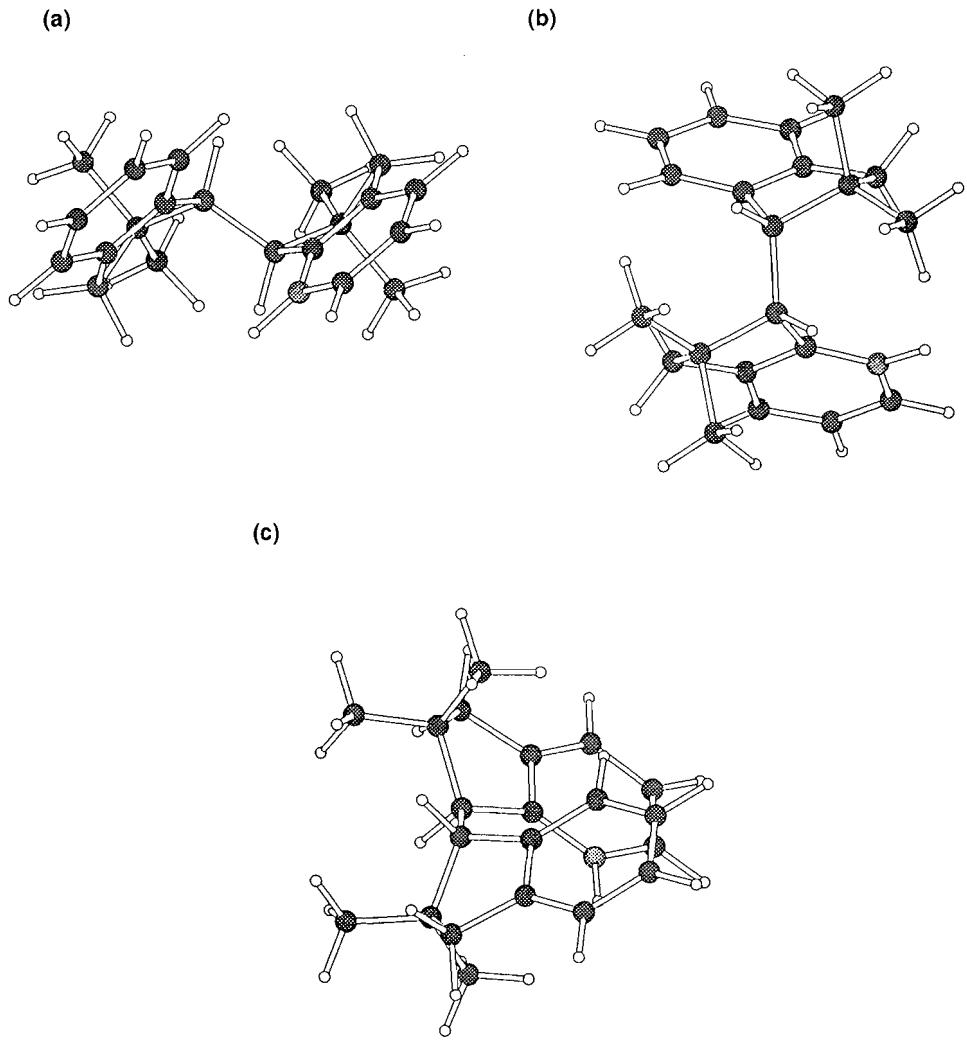

ulated conformations in solution are either **c1** alone or a **c1**–**a2** mixture. The H(1)–H(1′) $^3J_{H,H}$ value, obtained from a ^{13}C satellite of the H(1), H(1′) is <1 Hz, consistent with a dihedral angle close to 90°. By MM3, this angle is calculated to be 95.0° (104.5° by AM1 and 98.7° by STO-3G) in **c1**, but 153.9° (145.1° by AM1 and 132.8° by STO-3G) and 72.5° (95.1° by AM1 and 86.4° by STO-3G) in **a1** and **a2**, respectively. If conformation **a1** is significantly populated, an observable $^3J_{H\text{-}1,H\text{-}1'}$ value would have been obtained. However, conformation **a2** would also give a very small coupling constant, particularly if the STO-3G torsional angle is close to the actual angle. In addition, an *ortho* hydrogen was shielded by 0.65 ppm, consistent with its presence in the shielding cone of a second benzene ring. Models show that this arrangement is only possible in **c1**, not in **a1** or **a2**. Thus, experimental evidence indicates that **c1** is the global minimum, but perhaps only by a small amount. The MM3 energies must be incorrect by at least 16 kJ mol^{-1} in disfavouring the offset π-stacked conformer **c1**. The AM1 and STO-3G energies fit the experimental observations well.

In the global minimum (**c1**), the two phenyl rings are slightly tilted away from being parallel with each other and are offset such that one of the two *ortho* hydrogens from each benzene ring lies over C(8) and C(9) at the end of the other benzene ring. Distances of this hydrogen to these two carbons are 2.86 and 2.81 Å, respectively, from MM3. However, the smaller C(2)-C(1)-C(1′)-C(2′) torsional angle in the X-ray structure brings the two rings slightly closer together. Distances between planes of about 3.5 Å have previously been calculated to be optimal for offset π stacking (3, 4).

NMR results for the *meso* dimer (2)

The NMR spectra of this compound were surprisingly complex. The ^1H NMR spectrum at 25°C is shown in Fig. 5*b*. Broadened signals were observed that can be interpreted only in terms of a conformational barrier to interconversion of S_{axis}-related conformers, largely by rotation about the C(1)—C(1′) bond. The broad signals split, then sharpened as the temperature was lowered. The ^1H NMR spectrum at −40°C is shown in Fig. 5*c*. Assignments for the low-temperature spectrum were made on the basis of integration and a HETCOR experiment. As summarized following, the low-temperature spec-

Fig. 5. 400 MHz ^{1}H NMR spectra of the *meso* dimer **2**: (*a*) at +45°C; (*b*) at +25°C; (*c*) at −40°C.

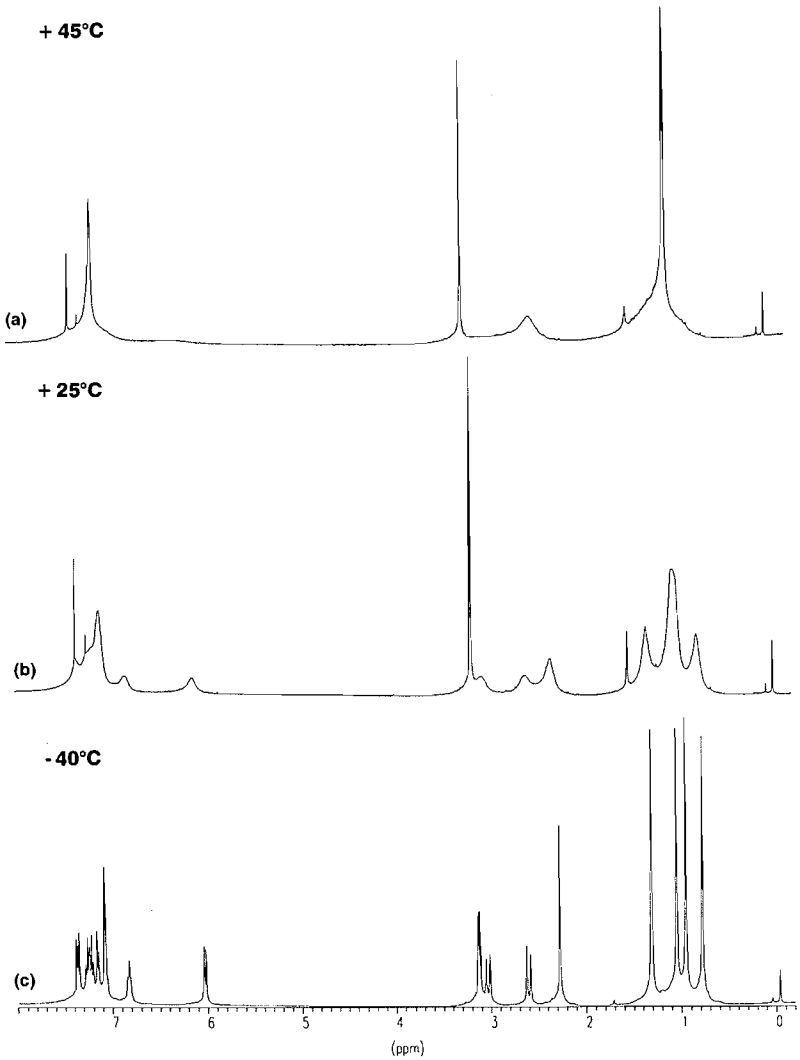

trum was consistent with a structure that had no symmetry. Four signals assigned to methyl groups appeared at 1.35, 1.09, 1.00, and 0.82 ppm. In comparison, the methyl groups in 2,2-dimethylindane absorb at 1.18 ppm. Therefore, one methyl group is significantly shielded and another somewhat deshielded. A singlet at 2.32 ppm integrates for two protons and is assigned to the methylene group in one of the five-membered rings; the methylene groups in 2,2-dimethylindane absorb at 2.75 ppm. The two protons in this methylene group are accidentally isochronous. An AB quartet with absorptions at 3.07 and 2.65 ppm and $J = -16.1$ Hz is assigned to the methylene group in the other five-membered ring. Unlike the other signals, a resonance at 3.17 ppm due to the two methine protons was relatively sharp at room temperature. It decreased in intensity and broadened slightly upon cooling and then split at about −30°C into two distinct bands that sharpened into an AB quartet, with $\Delta\nu = 0.0270$ ppm and $J_{A,B} = 2.0$ Hz at −55°C. The remainder of the signals are assigned to the aromatic protons and it is evident that there are more than four environments for aromatic protons in the populated conformer at −40°C, consistent with lack of symmetry. An interesting feature was a doublet at 6.07 ppm assigned to an *ortho* proton. The $\Delta\delta$ value of −1.10 ppm for this signal with respect to the value for the *ortho* protons of 2,2-dimethylindane is considerably larger than that observed for the corresponding signal from the racemic dimer.

The ^{1}H NMR spectrum recorded at 45°C is shown in Fig. 5*a*. By this temperature, the signals of the aromatic protons have coalescesed. In the methyl group region of the spectrum, a sharp signal due to a pair of methyl groups is now superimposed on the broad hump arising from the coalescence of the signals of the two remaining methyl signals, which had a much larger chemical shift difference at −40°C. The methine signals have not quite reached coalescence at this temperature.

The ^{13}C NMR spectrum of this compound at room temperature also contained broadened signals. In contrast, at −40°C, 22 sharp lines were observed, one for each of the carbon atoms in the molecule. Chemical shifts and assignments have been given previously (6).

The magnitude of the barrier to conformational motion was obtained by two methods in order to give a wide range of rate constants. Rate constants at temperatures from 15 to 47°C

were obtained from the coalescence temperatures of most of the aliphatic ^{13}C NMR (62.5 MHz) signals using equations [1] and [2] (23).

$$[1] \quad k(s^{-1}) = \frac{\pi \Delta \nu}{\sqrt{2}}$$

$$[2] \quad \Delta G^{\ddagger}(\text{kJ/mol}) = RT\left[23.76 + \ln\left(\frac{T}{k}\right)\right]$$

T is the coalescence temperature of the signals. The $\Delta\nu$ values were taken from the −40°C spectra and assumed to be temperature invariant. The ^{13}C NMR spectra were recorded from −40°C to 55°C, increasing the temperature in 5° steps except close to a coalescence point where they were recorded at intervals of 2°C or around 47°C, in 1° intervals.

Rate constants from −30°C to −15°C were obtained by line shape analysis of the coalescence of the AB pattern due to H(1) and H(1′) using the program Quabex (24) modified to run on a PC. The chemical shift differences for this AB pattern were measured from −60°C to −35°C and the linear plot (r = 0.9998) was extrapolated into the exchange region. The results of both treatments are shown in Table 3. The values of $\Delta H^{\ddagger}$ and $\Delta S^{\ddagger}$ for the conformational motion were determined from a plot of $\ln(k/T)$ vs. $1/T$ as outlined in eq. [3]. The values obtained from this analysis are $\Delta H^{\ddagger} = 42.8 \pm 1.8$ kJ mol^{-1} and $\Delta S^{\ddagger} = -61.6 \pm 6.5$ J K^{-1} mol^{-1}. The uncertainties are based on the regression analysis only. These values yield a $\Delta G^{\ddagger}$ of 61.2 kJ mol^{-1} at 298 K.

$$[3] \quad \ln\left(\frac{k}{T}\right) = 23.76 - \frac{\Delta H^{\ddagger}}{8.31\,T} + \frac{\Delta S^{\ddagger}}{8.31}$$

As will be discussed later, the NMR data for the *meso* dimer provided considerable information about the structure of the low-temperature conformer and the kinetics of the hindered rotation.

Table 3. Kinetic data from NMR measurements for the *meso* dimer.

Signal	Δν (Hz)	T (K)	$\Delta G^{\ddagger}$ (kJ mol^{-1})	k_c (s^{-1})
H(1), H(1′)	3.9	243	57.5	2.2[a]
H(1), H(1′)	3.7	245	57.7	2.6[a]
H(1), H(1′)	3.4	247	57.9	3.0[a]
H(1), H(1′)	3.1	249	58.1	3.4[a]
H(1), H(1′)	2.9	251	58.3	3.8[a]
H(1), H(1′)	2.6	253	58.6	4.2[a]
H(1), H(1′)	1.9	258	59.0	6[a]
C(2), C(2′)	14.3	288[b]	62.2	32[c]
C(3), C(3′)	63.9	303[b]	61.8	142[c]
2 CH_3	77.3	307[b]	62.1	172[c]
2 CH_3	124.0	311[b]	61.8	274[c]
C(1), C(1′)	370.1	320[b]	60.7	822[c]

[a]From line shape analysis.
[b]Coalescence temperature.
[c]From the coalescence equation, eq. [1].

Theoretical calculations for the *meso* dimer (2)

As with the racemic dimer, coordinates for a conformer of the *meso* dimer (**2**) from pcmodel[4] were used as initial input for MM3(94) (21) and then minima on the MM3 potential energy surface were found by driving C(2)-C(1)-C(1′)-C(2′), C(1)-C(2)-C(3)-C(4), and C(1′)-C(2′)-C(3′)-C(4′) torsional angles. Again, all conformational minima had the five-membered rings in envelope conformations, with one atom, C(2) or C(2′), out of the plane. In numbering the molecule on which calculations were performed, C(1) and C(1′) are (*S*) and (*R*) stereogenic centres, respectively. Three unique families of conformations were found that can be defined by the sign of the C(1)-C(2)-C(3)-C(4) and C(1′)-C(2′)-C(3′)-C(4′) torsional angles. In one type of family, termed family **d**, these angles were both positive, which results in the flap of one envelope being directed towards the other half of the dimer, while the flap of the other envelope is directed away from the other half of the dimer. Thus, family **d** will be called the "in,out" family. There is also a fourth family of conformations, termed the **d′** or "out,in" family, that is enantiomeric to the "in,out" family (**d**). In the second unique family (**e**), the angle in the ring containing the (*S*) stereogenic centre was positive and the angle in the other ring negative, which results in both envelopes being flapped away from the other half of the dimer. This family is the "out, out" family. The third family (**f**) has "in,in" conformations for the five-membered rings. Saddlepoints on the surface were found by taking the approximate maxima on dihedral angle drives between minima and minimizing those points using full-matrix Newton–Rapson minimization in MM3. Confirmation that these points were indeed saddlepoints was provided by the presence of single imaginary frequencies in the calculated vibrational spectra. In some cases, it was necessary to use dihedral angle intervals as small as 1° in order to find the saddlepoints. Additional grid points for the potential energy surface were generated by first driving C(2)-C(1)-C(1′)-C(2′) from saddlepoints between the **d** and **e** families and between the **d** and **f** families from 0° to 360°, then taking points every 20° along these cuts and driving C(1)-C(2)-C(3)-C(4) and C(1′)-C(2′)-C(3′)-C(4′) slightly beyond the values found in the **d**, **e**, and **f** families. The four-dimensional energy surface was approximated as a three-dimensional surface by representing the changes in the two five-membered rings by means of the average of the difference between the C(1)-C(2)-C(3)-C(4) and C(1′)-C(2′)-C(3′)-C(4′) torsional angles. Using this approximation, conformations in the **d** family have differences close to 0°, those in the **e** family have average differences between 30° and 40°, similar to the actual sizes of the torsional angles, while those in the **f** family have average differences between −30° and −40°. The **d′** family would also have average differences close to 0°, in this case arising from differences between negative values whereas these angles both are positive in the **d** family. The 3D interpolation function in the program Sigmaplot was used to provide data at regular intervals. A contour representation is shown in Fig. 6. Cuts across the 3D potential energy surface are shown in Fig. 7.

There are three unique minima in the **d** family, termed **d1**, **d2**, and **d3**, in order of increasing C(2)-C(1)-C(1′)-C(2′) torsional angle, and two pairs of two unique minima related by centres of symmetry in each of the **e** family and **f** families, termed **e1**, **e2**, **e2′**, and **e1′**, and **f1**, **f2**, **f2′**, and **f1′**, respectively,

in order of increasing C(2)-C(1)-C(1′)-C(2′) torsional angle. Selected information about these minima are given in Table 4. Similar information about the saddlepoints has been deposited.[3]

Two minima, **d2** and **e1**, with C(2)-C(1)-C(1′)-C(2′) torsional angles of 155.1° and 81.7° and H-C(1)-C(1′)-H torsional angles of 158.5° and 72.2°, respectively, are calculated by MM3 to have about the same stability, and to be considerably more stable than the other five minima. The broadening in the NMR spectra arises from slow interconversions of conformers that exchange nonequivalent positions for identical atoms in the two halves of the dimer. In theory, this can occur by interconversion of conformers related by a centre of symmetry, for instance, **e1** and **e1′** or **f2** and **f2′** or by interconversion of conformers from enantiomeric families, for instance, **d1** and **d1′**, or **d2** and **d2′**. Saddlepoints are named by using letters to indicate conformational family, numbers to indicate the order of increasing torsional angle, and with an **s** added to indicate a saddlepoint. For instance, **ds2** is the saddlepoint in the **d** conformational family between **d1** and **d2** and **des1** is the saddlepoint between **d1** and **e1**. The lowest energy pathway on the surface that interconverts **e1** and **e1′** involves passing from **e1** (0.0 kJ mol^{-1}) over a barrier (**es2**) of 17.9 kJ mol^{-1} to reach **e2** (8.9 kJ mol^{-1}), then over another barrier (**es3**), the centre of this conformational family, 11.5 kJ mol^{-1} higher in energy than **e1** to reach **e2′** then over the enantiomer of the first barrier (**es2′**) to **e1′**. To interconvert **d2** and **d2′**, one route proceeds from **d2** (0.10 kJ mol^{-1}) over a barrier (**des2**) of 54.5 kJ mol^{-1}, to **e2** (8.9 kJ mol^{-1}), then to **e2′** as before, and over the **des2′** barrier to **d2′**. An alternative pathway proceeds from **d2** over a barrier (**ds2**) of 28.1 kJ mol^{-1} to **d1** (7.0 kJ mol^{-1}), then over a barrier (**des1**) of 34.2 kJ mol^{-1} to **e1**, then over a barrier (**des3′**) of 32.2 kJ mol^{-1} to **d3′**, and finally over a barrier (**ds3′**) of 57.6 kJ mol^{-1}, to **d2′**.

The seven minima from the MM3 calculations were used as input for AM1 calculations and geometry optimizations were performed. Data on energy minima are listed in Table 4. Three MM3 minima, **d1**, **e2**, and **f1**, were not AM1 minima, all minimizing to **e1**. The global minimum, **e1**, is the same by both methods; however, AM1 suggests that the five-membered rings are virtually planar, which is unlikely. By MM3, the second lowest minimum, **d2**, is almost equal in stability to the lowest; AM1 calculates that this conformation is 24.7 kJ mol^{-1} less stable and makes **d3** the second most stable conformation. Experimental evidence to be discussed following indicates that **d2** is not populated significantly, in contrast to the results of the MM3 calculations.

STO-3G calculations were performed on the lowest energy MM3 conformers and the results are given in Table 4. Again, the STO-3G results were closer to the AM1 results in energy but to the MM3 results in geometry. Conformer **e1** was the global minima.

Discussion for the *meso* dimer (2)

The low-temperature NMR spectra indicate that conformers with smaller C(2)-C(1)-C(1′)-C(2′) dihedral angles, that is, **e1** and (or) **d1**, are significantly more populated than the others. A 2.0 Hz coupling constant was measured between the protons on C(1) and C(1′) that corresponds to an H-C(1)-C(1′)-H angle of 65° or 111° using the Altona version (25) of the Karplus equation with electronegativities of 2.3 for $C(Me)_2CH_2$ and 2.41 for phenyl.[5] Differences between the bond angles and bond lengths along the coupling pathway in this molecule in comparison with those in the unstrained saturated model compounds used to develop the equation causes some uncertainty in the values of the calculated angles. However, the calculated value for the H-C(1)-C(1′)-H torsional angle of 158.5° present in **d2** is 10.7 Hz. The small observed magnitude of $^3J_{H,H}$ is only consistent with populated minima with H-C(1)-C(1′)-H torsional angles close to 65°. On the MM3 potential energy surface, **d1** and **e1**, with H-C(1)-C(1′)-H torsional angles of 68.3° and 72.2°, respectively, are consistent with this observation. The major difference between these two is in the direction of puckering of the five-membered rings; **d1** is an "in,out" structure while **e1** is an "out,out" structure. In these two conformers, which have C(2)-C(1)-C(1′)-C(2′) torsional angles of 74 and 82°, one *ortho* hydrogen lies over the other aromatic ring in its shielding cone. This geometric relationship explains the observation of a very large Δδ value of −1.10 ppm for one *ortho* aromatic proton. This value is much larger than those observed for stacking in the adenine dinucleotide ApA (26) or for adenine-naphthalene stacks (1). Moreover, in these conformers, the benzene ring containing the shielded hydrogen has the correct orientation to shield one methyl group (0.36 ppm shielding observed) and a methylene group (0.43 ppm shielding observed).

Because the *meso* compound shows temperature-dependent NMR spectra, S_{axis}-related conformers must have two substantial barriers separating them on the potential energy surface. The S_{axis}-related conformers have C(2)-C(1)-C(1′)-C(2′) torsional angles that deviate from 180° by equal amounts in opposite directions. Two substantial barriers are necessary to observe rate effects because the conformers can be interconverted by rotation about the central bond through either 180° or 0° and both directions of rotation must be slowed. $\Delta H^{\ddagger}$ is 42.8 kJ mol^{-1} for the smaller of these two barriers as determined by variable temperature NMR experiments. The MM3-calculated potential energy surface is shown in Figs. 6 and 7. Barriers calculated for passing through the C(2)-C(1)-C(1′)-C(2′) torsional angle of 0° were much larger than the observed barrier and it can be assumed that the interconversion process does not follow this route. The MM3-calculated potential energy surface does not contain a barrier for rotation around the C(1)-C(1′) bond through C(2)-C(1)-C(1′)-C(2′) torsional angles of 180° that is nearly as large as the observed barrier. In particular, as outlined in the results section, the largest barrier (**es2**) for interconverting the global minima, **e1** to **e1′**, is 17.9 kJ mol^{-1}. Therefore, the barrier calculated by the MM3(94) program is about 25 kJ mol^{-1} too small. Part of this difference must lie in the fact that MM3 does not account for aryl–aryl interactions. Stabilizing those conformations that have offset π–π stacking will increase the barrier by the amount of the stabilization, which has been calculated to be about 9 kJ mol^{-1} (3).

The NMR results suggest that the barrier to conformational interconversion includes a contribution from a substantial negative value of the entropy of activation ($\Delta S^{\ddagger} = -61.6 \pm 6.5$ J K^{-1} mol^{-1}). Conformer entropies are evaluated by MM3

[5] We thank Dr. J.S. Grossert for a basic computer program that calculates $^3J_{H,H}$ values based on Altona's equation (25).

Fig. 6. A contour diagram of the MM3(94) potential energy surface for the *meso* dimer (**2**). The *Y*-axis is the difference between the C(1)-C(2)-C(3)-C(4) and C(1)′-C(2)′-C(3)′-C(4)′ torsional angles divided by two. The locations of individual conformers on this surface are indicated with the letters used to describe them in the text.

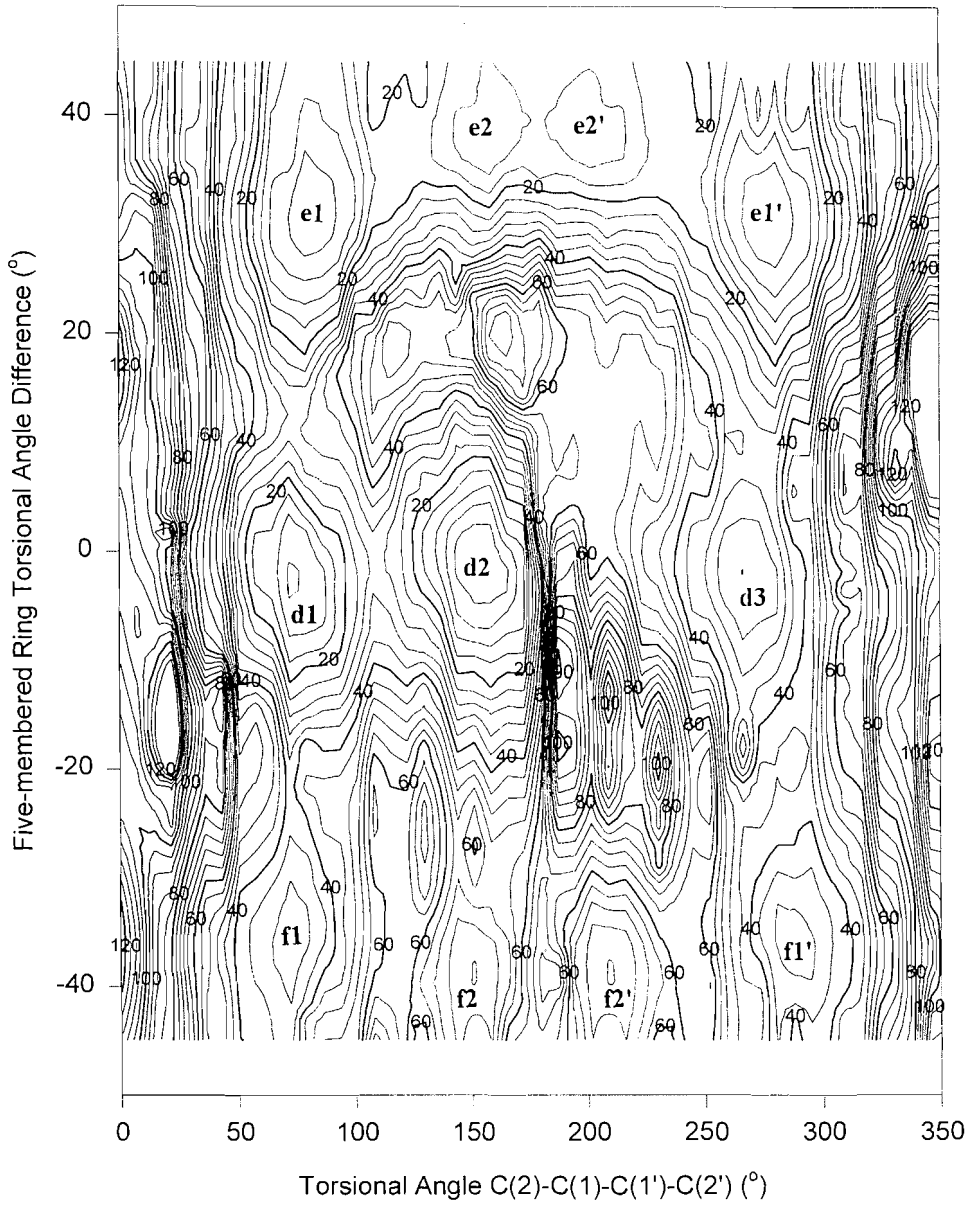

and the saddlepoints for interconversion were found to have substantially less positive entropies than the minima. The $\Delta S^{\ddagger}$ values for the equilibria of the global minima with the two saddlepoints most likely to be barriers are, **e1** ⇄ **es2**, −19.0 J K^{-1} mol^{-1}, and **e1** ⇄ **es3**, −32.2 J K^{-1} mol^{-1}. While these values are considerably less than the value obtained from the NMR data, calculation of these values does indicate that a negative entropy of activation does make a significant contribution to the barrier.

On the AM1 potential energy surface, the global minimum, **e1**, is considerably more stable than the other two minima, consistent with the NMR observations that the most populated conformations have C(2)-C(1)-C(1′)-C(2′) torsional angles that are in the 60°–80° region. The AM1 surface curve shows two significant barriers to interconversion between the +86.0° and −86.0° conformers. There is a very large barrier to rotation through 0° and a smaller barrier of 54.6 kJ mol^{-1} for rotation about 180°. The size of the barrier to rotation through 180° is in reasonable agreement with that obtained by NMR measurements of 42.8 kJ mol^{-1}.

Additional compounds

During the photochemical studies, analogous diastereomeric dimers **3** and **4** were isolated where the aromatic ring was substituted with a methoxy group in the 5-position, and dimers **5** and **6** when a methoxy group was in the 6-position. In each

Fig. 7. Cuts through a 3D representation of the MM3(94) potential energy surface of **2**: (*a*) the **d** conformational family, where C(1)-C(2)-C(3)-C(4) and C(1)′-C(2)′-C(3)′-C(4)′ torsional angles have the same sign, resulting in an average difference close to 0°; (*b*) the **e** conformational family, where the C(1)-C(2)-C(3)-C(4) torsional angles are positive and the C(1)′-C(2)′-C(3)′-C(4)′ torsional angles are negative, resulting in an average difference close to the value in the first ring.

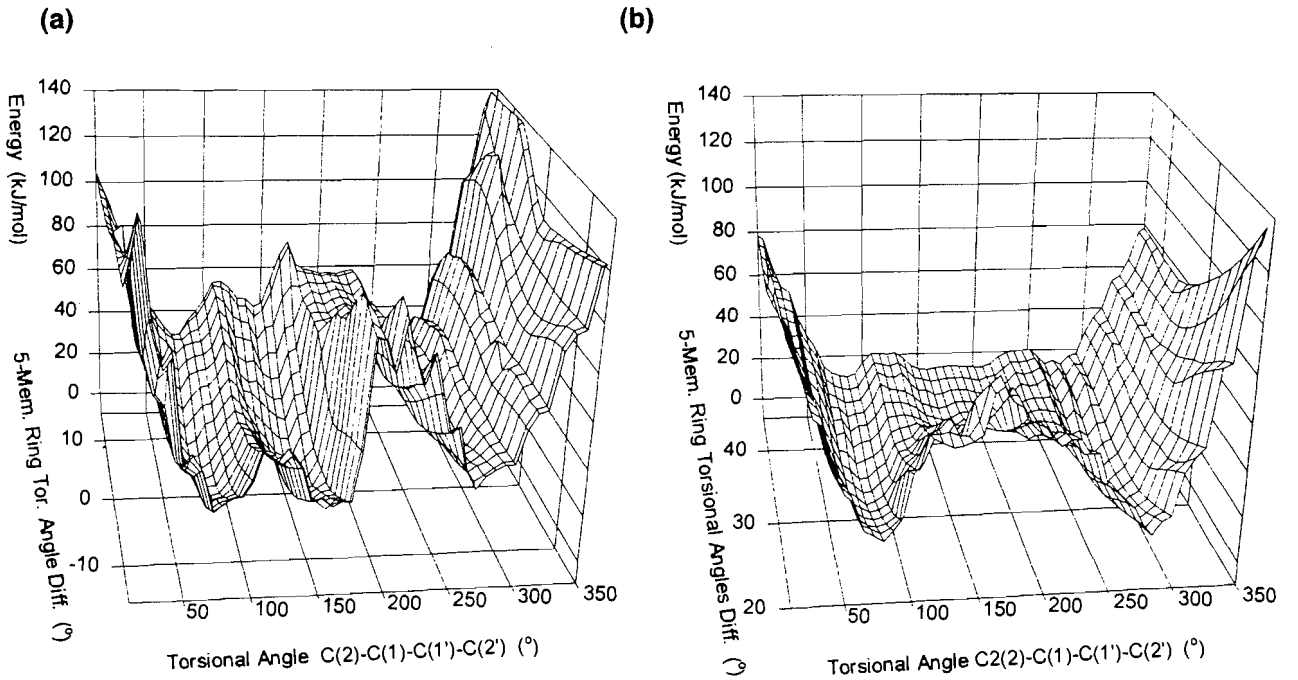

Fig. 8. ATOMS representations of the MM3 geometries of the *meso* dimer (**2**): (*a*) from the **e** or "out,out" family, the **e1** conformer; (*b*) from the **d** or "in,out" family, the **d2** conformer.

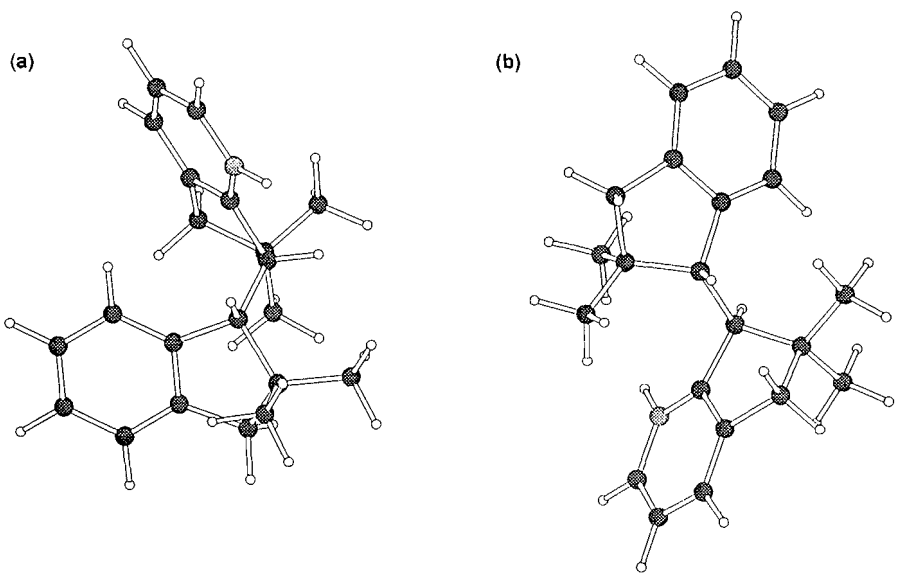

case, one of the dimers was crystalline and gave sharp signals in the NMR at room temperature. The other was an oil and gave broadened NMR signals at room temperature. Low-temperature NMR spectra of the methoxy *meso* dimers **4** and **6** were very similar to those of the unsubstituted *meso* dimer.

Compounds very similar to dimers **1** and **2** have been reported in the literature. Orliac-Le Moing et al. (27) have obtained both the racemic and *meso* forms of bis-1,1′-(2,2-dimethyl-1-indanol) (**7** and **8**, respectively) from the coupling of the radical anions produced by electrochemical reduction of the monomeric ketone. Both dimers were crystalline. The structure of the racemic compound was established by X-ray

Table 4. Selected data about the conformational minima for the *meso* dimer.
(*a*)

	Conformer							
	d1		**d2**			**d3**		
Feature	MM3	STO-3G	MM3	AM1	STO-3G	MM3	AM1	STO-3G
Relative stability (kJ/mol)	7.0[a]	12.4[c]	0.1	24.7[b]	18.0[c]	23.3	7.1	14.9[c]
C(2)-C(1)-C(1′)-C(2′)	73.6	78.6	155.1	141.0	143.0	268.6	270.3	266.9
H-C(1)-C(1′)-H	68.3	74.2	158.5	142.1	146.0	−80.6	−81.4	−83.8
C(1)-C(9)-C(4)-C(3)	−1.2	0.8	4.6	3.9	3.1	−4.7	0.5	−0.6
C(9)-C(4)-C(3)-C(2)	24.0	20.6	22.3	16.5	22.2	23.4	10.9	16.9
C(4)-C(3)-C(2)-C(1)	−36.2	−32.2	−39.4	−29.2	−37.0	−31.8	−17.5	−25.2
C(3)-C(2)-C(1)-C(9)	35.1	32.1	41.5	31.1	38.2	29.4	17.5	24.8
C(2)-C(1)-C(9)-C(4)	−21.6	−21.3	−29.2	−22.5	−26.7	−15.9	−11.5	−15.7
C(1′)-C(9′)-C(4′)-C(3′)	−0.3	−0.4	4.3	4.2	3.9	0.6	2.2	0.3
C(9′)-C(4′)-C(3′)-C(2′)	21.0	18.7	20.8	13.0	19.7	16.9	8.5	13.6
C(4′)-C(3′)-C(2′)-C(1′)	−32.8	−28.7	−36.6	−24.1	−34.2	−27.3	−15.2	−21.4
C(3′)-C(2′)-C(1′)-C(9′)	32.5	28.1	38.2	25.9	35.6	27.1	16.3	21.1
C(2′)-C(1′)-C(9′)-C(4′)	−20.2	−17.7	−26.7	−19.0	−25.1	−17.5	−11.8	−13.8
C(2)-C(1)-C(9), sp^3	100.6	102.0	99.2	102.1		102.8	105.0	103.9
C(1)-C(2)-C(3), sp^3	102.7	101.9	101.8	104.9	102.7	103.6	105.1	103.4
C(2)-C(3)-C(4), sp^3	101.8	103.9	100.9	110.4	102.6	102.2	105.6	104.4
C(3)-C(4)-C(9), sp^2	110.1	110.1	109.8	116.8	109.9	110.7	111.1	111.0
C(1)-C(9)-C(4), sp^2	110.4	110.3	109.4	111.1	111.1	110.0	110.5	110.2
C(1)—C(1′) (Å)	1.567	1.574	1.565	1.525	1.574	1.569	1.526	1.576
C(1)—C(2) (Å)	1.580	1.588	1.568	1.578	1.587	1.574	1.564	1.582

[a]With respect to the global MM3 minimum, conformer **e1**.
[b]With respect to the global AM1 minimum, conformer **e1**.
[c]With respect to the global STO-3G minimum, conformer **e1**.

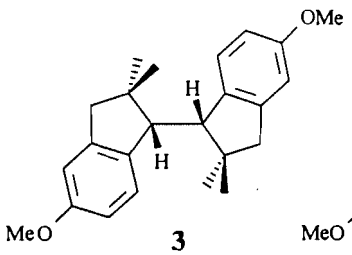

3

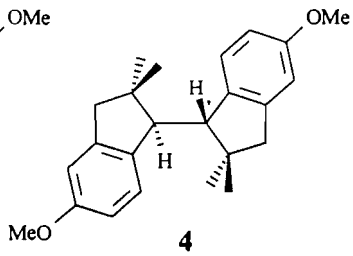

4

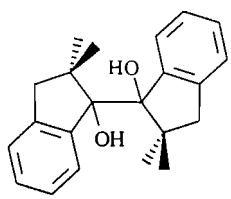

7 and 8

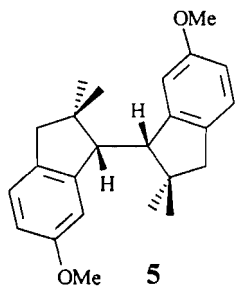

5

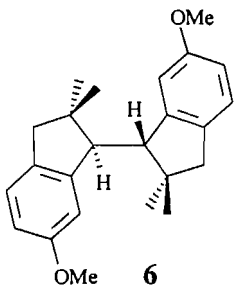

6

crystallography. Although no numerical details were reported, the structure shown has the two OH groups approximately *anti* across the central C—C bond, with the two phenyl rings *gauche* and also the two $C(CH_3)_2$ groups *gauche*. The structure presented suggests that the torsional angle involving the phenyl rings is considerably less than 60° while that involving the $C(CH_3)_2$ groups is considerably more than 60°. This structure is probably similar to conformer **c1**, with a C(2)-C(1)-C(1′)-C(2′) torsional angle of 101.4° (MM3) or 97.6° (AM1).

The authors of this work did not observe broadened lines in the ^1H NMR spectrum of the *meso* dimer (**8**), which contained singlets at 1.04 ppm ($2 \times CH_3$) and 1.38 ppm ($2 \times CH_3$), and at 2.47 ppm ($2 \times CH_2$). This absence of broadening in a spectrum that is consistent with S_1 or S_2 symmetry indicates that the barriers to interconversion of the S_{axis}-related conformers in this compound are reduced in comparison to that in **2**. Two different barriers lie on the potential energy surface shown in Fig. 5, either of which could have been responsible for the broadening observed in the spectra of **2**. The strain energy of the tran-

Table 4 (*concluded*).
(*b*)

	Conformer						
	e1			e2	f1	f2	
Feature	MM3	AM1	STO-3G	MM3	MM3	MM3	AM1
Relative stability (kJ/mol)	0.00	0.0	0.0	8.9[a]	29.7[a]	43.5[a]	51.2
C(2)-C(1)-C(1′)-C(2′)	81.7	86.2	84.0	158.9	72.1	151.0	146.6
H-C(1)-C(1′)-H	72.2	80.7	76.9	155.3	62.7	147.9	143.8
C(1)-C(9)-C(4)-C(3)	−1.3	0.4	−0.3	−6.5	−1.4	−4.9	7.6
C(9)-C(4)-C(3)-C(2)	−20.3	−7.5	−16.8	−20.8	23.6	21.5	17.9
C(4)-C(3)-C(2)-C(1)	33.4	11.4	26.4	39.2	−35.3	−38.6	−35.1
C(3)-C(2)-C(1)-C(9)	−33.5	−11.0	−26.0	−42.2	34.1	40.8	38.8
C(2)-C(1)-C(9)-C(4)	22.0	6.8	16.9	30.3	−21.0	−28.9	−29.5
C(1′)-C(9′)-C(4′)-C(3′)	0.5	−2.6	−1.6	4.5	2.2	0.0	−4.1
C(9′)C(4′)-C(3′)-C(2′)	17.7	7.3	15.0	21.5	−24.5	−24.7	−14.0
C(4′)-C(3′)-C(2′)-C(1′)	−28.2	−9.0	−21.8	−38.2	36.0	38.7	25.5
C(3′)-C(2′)-C(1′)-C(9′)	28.4	7.5	20.8	39.7	−34.9	−38.2	−27.5
C(2′)-C(1′)-C(9′)-C(4′)	−18.2	−3.2	−12.3	−27.8	21.0	23.9	19.9
C(2)-C(1)-C(9), sp^3	99.5	104.9		98.0	100.8	99.1	100.8
C(1)-C(2)-C(3), sp^3	104.7	106.2	105.7	103.0	102.7	102.3	101.7
C(2)-C(3)-C(4), sp^3	101.6	105.7	104.0	100.2	102.1	100.9	102.9
C(3)-C(4)-C(9), sp^2	110.1	111.0	111.9	110.2	110.1	110.0	109.9
C(1)-C(9)-C(4), sp^2	111.6	111.4		109.5	110.6	109.5	108.7
C(1)-C(1′) (C)	1.573	1.528	1.577	1.590	1.557	1.568	1.580
C(1)-C(2) (C)	1.576	1.564	1.585	1.573	1.582	1.565	1.565

sition state (TS) for rotation with a C(2)-C(1)-C(1′)-C(2′) angle of 180° would not be increased as much as that of the minima or the other TS by introduction of additional substituents because in this 180° TS the new substituents are perfectly staggered. Thus, the barrier for going over the 180° TS should become smaller because the strain energies of the minima on the potential energy surface for rotation are greater. This argument suggests that the 180° TS is the barrier that slows rotation in **2**.

The conformational properties of **9** and **10**, the noncyclized analogues of **1** and **2**, have been investigated by means of molecular mechanics calculations, X-ray crystallography, and NMR measurements (15). In contrast to the current observations, in the solid state and solution, the *meso* compound **9** was present in the *anti* conformation, whereas the racemic compound **10** had the phenyl groups *gauche* in the solid state and in solution. For these compounds, the most stable conformations have the *tert*-butyl groups are far apart as possible. In the X-ray structure of **10**, the two phenyl rings adopt the offset π-stacked arrangement with the planes of the phenyl rings close to parallel.

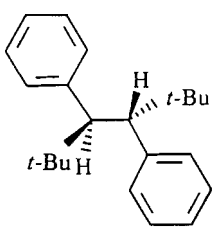

9

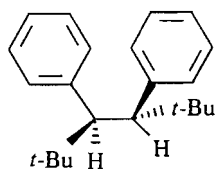

10

Crystallographic studies have been reported for a series of 1,1′-diphenyl-1,1′-bicycloalkyl systems **11** (n = 2–5), which

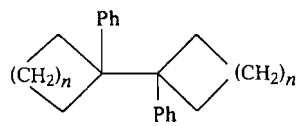

11

included 1,1′-diphenyl-1,1′-bicyclopentyl (17, 28). The major focus of this work was studying bond lengths as a function of steric interactions. The bicyclopentyl compound has a central C—C bond length of 1.575 Å. The energy as a function of the C(2)-C(1)-C(1)′-C(2)′ torsional angle was determined by MM2 (28) and by AM1 calculations (17). The MM2 method correctly predicted that the *gauche* conformation would be more stable than the *trans* conformation for the bicyclopentyl derivative, and the reverse would be true for the other three but the AM1 method gave an incorrect answer for the bicyclohe-

ptyl derivative. The central C—C bond lengths in **9** and **10** were 1.573–1.589 Å (15), considerably longer than those in **1**. Thus, compounds **1** and **2** are probably considerably less strained than their noncyclic analogues.

Conclusions

MM3(94) and STO-3G calculations indicate that the conformational potential energy surface for racemic-2,2,2′,2-tetramethyl-1,1′-biindanyl (**1**) contains seven minima, one of which is present in the solid state and this conformer probably is also the major contributor in solution. These conformers arise from restriction to rotation about the bond joining the two indanyl units and also from restriction to motion in the two hindered five-membered rings.

The potential energy surface for the *meso* diastereomer (**2**) is more complex, containing 14 minima in pairs related by centres or planes of symmetry. Variable temperature NMR spectra show that the S_{axis}-related conformers are undergoing interconversion at a rate that is slow on the NMR time scale at room temperature. NMR arguments based on the Karplus equation and the observation of the signal of a proton that has a large deshielding suggest that a single pair of S_2-related conformers are the major species present in solution.

The STO-3G results reproduce accurately the geometries and energies of the minima for these two compounds. MM3(94) results are in good agreement with the X-ray geometries but the relative stabilities of the conformers are far from those observed experimentally. Apparently, MM3 does not handle this type of mixed aromatic–aliphatic compound well. The AM1 results are in good agreement with observed conformer energies but the geometries are so poor in the saturated portion of the conformers that the energy agreement must be regarded as fortuitous. The global minima for both **1** and **2** have the benzene rings from the two halves of the molecules stacked in an offset manner. This effect may have been a factor in the poor performance by MM3(94).

Experimental

Proton (^{1}H) and carbon (^{13}C) NMR spectra at 250 and 62.8 MHz were obtained in $CDCl_3$ on an Bruker AC 250 F NMR spectrometer in automation mode; proton NMR spectra at 400 MHz were obtained on a Bruker AMX-400. Chemical shifts are reported in parts per million (δ) relative to tetramethylsilane (0.00) as an internal standard. The ^{13}C NMR spectrum of the solid sample was measured on a Bruker AMX-400 NMR spectrometer with magic angle spinning at 5 kHz.

Line shape analysis for the exchange of the H(1) and H(1)′ signals of the *meso* dimer (**2**) was done by means of the program Quabex (24) modified to run on a PC and compiled with Microsoft Fortran Powerstation. The output of this program was a two-dimensional matrix containing chemical shifts and intensities that were plotted using Sigmaplot. Chemical shift differences in the exchange region were obtained by an extrapolation of the very linear ($r = 0.9998$) plot of chemical shift difference against temperature using points every 5°C from −35 to −60°C. $T2$ values in the exchange region were initially obtained by fitting the signals at −35°C, assuming that the rate of exchange was negligible. However, the $T2$ value obtained was too great to fit the peaks from −15 to −26°C. It was found that the peak at −15°C was not very sensitive to the value of the exchange rate but was very dependent on the value of $T2$. Therefore, this peak was fit by adjusting the $T2$ value using an approximately correct k value. Then, this value of $T2$, 0.18 s, was used to fit the other spectra.

Materials

The preparation and characterization of compounds **1–6**, except for the low-temperature data for compound **2** given below, have been described previously (6).

X-ray structure determination

Racemic compound **1** forms white, air-stable needles with approximately square cross sections. The X-ray data were collected with a Rigaku AFC5R four-circle diffractometer attached to a 2.4 kW X-ray generator. *Crystal data:* $C_{22}H_{26}$, fw = 290.45, F(000) = 632, crystal size 0.20 × 0.20 × 0.40 mm; $a = 11.190(7)$, $b = 11.679(7)$, $c = 13.19(1)$ Å, $V = 1724(3)$ Å^3, space group *Pbcn* (no. 60), $Z = 4$, $\rho_C = 1.119$ g cm^{-3}; Mo Kα (graphite monochrometer) $\lambda = 0.71069$ Å, $\mu = 0.582$ cm^{-1}, 1416 unique measured reflections to 22 (max) of 46° with 643 observed ($I > 3\sigma(I)$). The cell dimensions were determined from 20 well-centered reflections with 2θ range 12–26°. The data were corrected for Lorentz and polarization effects but three azimuthal scans each showed less than 2% variation in intensity and no absorption corrections were applied.

The structure was solved by direct methods, which revealed the positions of all non-hydrogen atoms. The non-hydrogen atoms were refined anisotropically. All of the hydrogen atoms were placed in geometrically calculated positions with a C—H distance of 0.95 Å, their positions were not refined, and they were assigned fixed isotropic temperature factors with a value of $1.2 \times B_{eq}$ of the atom to which each was bonded. The final cycle of full-matrix least-squares refinement[6] (29) was based on 634 observed reflections ($I > 3\sigma(I)$) and 101 variable parameters, and converged (largest parameter shift was 0.0002 times its esd) with unweighted and weighted agreement factors of: $R = \Sigma||F_o| - |F_c|| / \Sigma|F_o| = 0.0357$, $R_w = [(\Sigma w(|F_o| - |F_c|)^2 / \Sigma wF_o^2)]^{1/2} = 0.0362$. The standard deviation of an observation of unit weight[7] was 1.731. The weighting scheme was based on counting statistics and included a factor ($p = 0.01$) to downweight the intense reflections. Plots of $w(|F_o| - |F_c|)^2$ versus $|F_o|$, reflection order in data collection, $\sin\theta/\lambda$, and various classes of indices showed no unusual trends. A correction for secondary extinction was applied (coefficient = 6.95×10^{-7}). The maximum and minimum peaks in the final difference Fourier map corresponded to 0.10 and −0.11 e Å^{-3}, respectively.

Neutral atom scattering factors for non-hydrogen atoms were taken from Cromer and Waber (30) and the scattering factors for hydrogen atoms were taken from Stewart, Davidson, and Simpson (31). Anomalous dispersion effects were

[6] Function minimized: $\Sigma w(|F_o| - |F_c|)^2$, where $w = 4F_o^2/s^2(F_o^2) \equiv [\sigma^2(F_o) + (pF_o/2)^2]^{-1}$, $F_o^2 = S(C - RB)/\text{Lp}$ and $\sigma^2(F_o^2) = [S^2(C + R^2B) + (pF_o^2)^2]/\text{Lp}^2$, S = scan rate, C = total integrated peak count, R = ratio of scan time to background counting time, B = total background count, Lp = Lorentz-polarization factor, p = p-factor.

[7] Standard deviation of an observation of unit weight: $[\Sigma w(|F_o| - |F_c|)^2/(N_o - N_v)]^{1/2}$, where N_o = number of observations, N_v = number of variables.

included in F_{calc} (32); the values for $\Delta f'$ and $\Delta f''$ were those of Cromer and Ibers (33). All calculations were performed using the TEXSAN (34) crystallographic software package of Molecular Structure Corporation.

Acknowledgements

P.J.M. thanks the Natural Sciences and Engineering Research Council of Canada (NSERC) and the Killam Trust for graduate scholarships. This work was supported by NSERC grants to J.A.P., T.B.G., and T.S.C. We thank Professor N.L. Allinger for a microcomputer version of MM3(94), Dr. Don Hooper and Mike Lumsden of the Atlantic Regional Medical Research Council (ARMRC) for NMR time and help with variable temperature NMR spectra, and Kate Grindley for technical assistance.

References

1. L.F. Newcomb and S.H. Gellman. J. Am. Chem. Soc. **116**, 4993 (1994).
2. S. Paliwal, S. Geib, and C.S. Wilcox. J. Am. Chem. Soc. **116**, 4497 (1994).
3. W.L. Jorgenson and D.L. Severance. J. Am. Chem. Soc. **112**, 4768 (1990).
4. C.A. Hunter and J.K.M. Sanders. J. Am. Chem. Soc. **112**, 5525 (1990).
5. P. Hobza, H.L. Selzle, and E.W. Schlag. J. Am. Chem. Soc. **116**, 3500 (1994).
6. J.A. Pincock and P.J. Wedge. J. Org. Chem. **60**, 4067 (1995).
7. M. Oki. The chemistry of rotational isomers. Springer-Verlag, Berlin. 1993; U.Berg and J. Sandström. Adv. Phys. Org. Chem. **25**, 1 (1989).
8. M.A. Cremonini, L. Lunazzi, G. Placucci, R. Okazaki, and G. Yamamoto. J. Am. Chem. Soc. **112**, 2915 (1990).
9. W.D. Hounshell, D.A. Dougherty, and K. Mislow. J. Am. Chem. Soc. **100**, 3149 (1978).
10. L. Lunazzi, D. Macciantelli, F. Bernardi, and K.U. Ingold. J. Am. Chem. Soc. **99**, 4573 (1977).
11. H.-D. Beckhaus, C. Rhchardt, and J.E. Anderson. Tetrahedron, **38**, 2299 (1982).
12. A.J.M. Reuvers, A. Sinnema, F. van Rantwijk, J.D. Remijnse, and H. van Bekkum. Tetrahedron, **25**, 4455 (1969).
13. P. Finocchiaro, D. Gust, W.D. Hounshell, J.P. Hummel, P. Maravigna, and K. Mislow. J. Am. Chem. Soc. **98**, 4945 (1976); D.A. Dougherty, K. Mislow, J.F. Blount, J.B. Wooten, and J. Jacobus. J. Am. Chem. Soc. **99**, 6149 (1977).
14. S. Brownstein, J. Dunogues, D. Lindsay, and K.U. Ingold. J. Am. Chem. Soc. **99**, 2073 (1977).
15. H.D. Beckhaus, K.J. McCullough, H. Fritz, C. Rhchardt, B. Kitschhke, H.J. Lindner, D.A. Dougherty, and K. Mislow. Chem. Ber. **113**, 1867 (1980).
16. P. Maslak, J.N. Narvaez, and M. Parvez. J. Org. Chem. **56**, 602 (1991).
17. D. Zhang, Y. Xu, L.L. Koh, Y.L. Lam, and H.H. Huang. Acta Crystallogr. Sect. C: Cryst. Struct. Commun. **C49**, 1002 (1993).
18. H.-D. Beckhaus. Chem. Ber. **116**, 86 (1983).
19. R. Cahill, R.C. Cookson, and T.A. Crabb. Tetrahedron, **25**, 4711 (1969).
20. W.S. Veeman. Prog. NMR Spectrosc. **16**, 193 (1984).
21. N.L. Allinger, Y.H. Yuh, and J.-H. Lii. J. Am. Chem. Soc. **111**, 8551 (1989).
22. Dewar Research Group and J.J.P. Stewart. Austin Method I, Package 1.0. QCPE 506, QCPE Bull. **6**, 2 (1986).
23. M.L. Martin, J.-J. Delpuech, and G.J. Martin. *In* Practical NMR spectroscopy. Heydon, London. 1980. pp. 291–349.
24. G. Binsch. Top. Stereochem. **3**, 97 (1968).
25. C.A.G. Haasnoot, F.A.A.M. DeLeeuw, and C. Altona. Tetrahedron, **36**, 2783 (1980).
26. S.I. Chan and J.H. Nelson. J. Am. Chem. Soc. **91**, 168 (1969).
27. A. Orliac-Le Moing, J. Delaunay, A. LeBouc, and J. Simonet. Tetrahedron, **41**, 4483 (1985).
28. W. Bernlöhr, H.-D. Beckhaus, H.-J. Lindner, and C. Rüchardt. Chem. Ber. **117**, 3303 (1984).
29. W.R. Busing, K.O. Martin, and H.A. Levy. ORFLS. A FORTRAN crystallographic least-squares program. Report ORNL-TM-305, Oak Ridge National Laboratory, Oak Ridge, Tenn. 1962.
30. D.T. Cromer and J.T. Waber. International tables for X-ray crystallography. Vol. IV. The Kynoch Press, Birmingham, England (Present distributor Kluwer Academic Publishers, Dordrecht). 1974. Table 2.2A, pp. 71–98.
31. R.F. Stewart, E.R. Davidson, and W.T. Simpson. J. Chem. Phys. **42**, 3175 (1965).
32. J.A. Ibers and W.C. Hamilton. Acta Crystallogr. **17**, 781 (1964).
33. D.T. Cromer and J.A. Ibers. International tables for X-ray crystallography. Vol. IV, The Kynoch Press, Birmingham, England (Present distributor Kluwer Academic Publishers, Dordrecht). 1974. Table 2.3.1, pp. 149–150.
34. TEXSAN - TEXRAY Single crystal structure analysis package, Version 5.0. Molecular Structure Corporation, The Woodlands, Tex. 1992.

Reflection in the ^{1}H NMR spectrum of $^{37}Cl/^{35}Cl$ isotope effects on the ^{19}F NMR chemical shifts of 1-chloro-2,4-difluorobenzene. An isotope effect over five bonds

Ted Schaefer, Guy M. Bernard, and Frank E. Hruska

Abstract: In an ABX high-resolution NMR spectrum the detection of combination peaks in the X region yields only the chemical shift of X, $J_{AX} + J_{BX}$, and the positive quantities $\{[(\nu_A - \nu_B) \pm \frac{1}{2}(J_{AX} - J_{BX})]^2 + J_{AB}{}^2\}^{1/2} = 2C_{\pm}$. However, the presence of an additional isotopic perturbation on $\nu_A - \nu_B$, the difference between the resonance frequencies of A and B, yields two X spectra; therefore four quantities, C. Hence all quantities in the surd become available from the composite X spectrum. A generalization to ABMRX spin systems, applicable to the ^{1}H and ^{19}F NMR spectra of the two isotopic molecules of 1-chloro-2,4-difluorobenzene, is possible. It turns out that, from the H-5(X) spectrum alone, the following spectral quantities are extractable: the two values of $\nu_A - \nu_B$ where A and B are the ^{19}F nuclei; J_{AB}; J_{AX} and J_{BX} with their relative signs; J_{MX} and J_{RX} where M and R are H-3 and H-6. No $^{37}Cl/^{35}Cl$ isotope effect is detectable on the ^{1}H shielding nor on any coupling constants. F-2 undergoes an isotope shift of $-1.64(3)$ ppb. The isotope shift, over five formal bonds, of F-4 is $-0.54(3)$ ppb (larger shielding in the presence of ^{37}Cl). This magnitude is three times larger than that over four formal bonds in another molecule, 2,6-dichloro-4-fluorophenol.

Key words: ^{1}H NMR, of 1-chloro-2,4-difluorobenzene, isotope effects in NMR, reflection of $^{37}Cl/^{35}Cl$ isotope effects on ^{19}F shielding in the ^{1}H NMR spectrum of 1-chloro-2,4-difluorobenzene; isotope effects in NMR, over three and five bonds by $^{37}Cl/^{35}Cl$ on ^{19}F shielding in 1-chloro-2,4-difluorobenzene; ^{19}F NMR, $^{37}Cl/^{35}Cl$ isotope effects over three and five bonds in 1-chloro-2,4-difluorobenzene.

Résumé : Dans un spectre RMN ABX à haute résolution, la détection des raies de combinaison dans la région de X ne fournit que le déplacement chimique de X, $J_{AX} + J_{BX}$ et les quantités positives $\{[\nu_A - \nu_B) \pm \frac{1}{2}(J_{AX} - J_{BX})]^2 + J_{AB}{}^2\}^{1/2} = 2C_{\pm}$. Toutefois, en présence d'une perturbation isotopique additionnelle sur $\nu_A - \nu_B$, la différence entre les fréquences de résonance de A et de B, il est possible d'obtenir deux spectres de X et donc quatre quantités C. Toutes les quantités deviennent donc disponibles à partir du spectre composé de X. Il est possible de faire une généralisation aux systèmes de spin ABMRX et de l'appliquer aux spectres RMN du ^{1}H et du ^{19}F de deux molécules isotopiques du 1-chloro-2,4-difluorobenzène. En fait, sur la base du spectre de seulement H-5(X), il est possible d'extraire les valeurs spectrales suivantes : les deux valeurs de $\nu_A - \nu_B$ dans lesquelles A et B sont les noyaux ^{19}F; J_{AB}; J_{AX} et J_{BX} et leurs signes relatifs; J_{MX} et J_{RX} pour lesquelles M et R sont H-3 et H-6. Il n'est pas possible de détecter l'effet isotopique $^{37}Cl/^{35}Cl$ sur le blindage du ^{1}H ou sur l'une quelconque des constantes de couplage. Le F-2 subit un déplacement isotopique de $-1,64(3)$ ppb. Le déplacement isotopique, sur cinq liaisons formelles, du F-4 est de $-0,54(3)$ ppb (un blindage plus important en présence de ^{37}Cl). Cette valeur est trois fois plus importante que celle sur quatre liaisons formelles dans une autre molécule, le 2,6-dichloro-4-fluorophénol.

Mots clés : RMN du ^{1}H, 1-chloro-2,4-difluorobenzène; effets isotopiques en RMN, réflexion des effets isotopiques $^{37}Cl/^{35}Cl$ sur le blindage du ^{19}F dans les spectres RMN du 1-chloro-2,4-difluorobenzène; effets isotopiques en RMN, à travers trois et cinq liaisons par $^{37}Cl/^{35}Cl$ sur le blindage du ^{19}F dans le 1-chloro-2,4-difluorobenzène; RMN du ^{19}F, effets isotopiques $^{37}Cl/^{35}Cl$ à travers trois et cinq liaisons dans le 1-chloro-2,4-difluorobenzène.

[Traduit par la rédaction]

Introduction

One aim of this report is to establish the existence of an unprecedented $^{37}Cl/^{35}Cl$ isotope effect, $^{5}\Delta F(^{37/35}Cl)$ over five formal bonds on an ^{19}F nmr chemical shift in a benzene derivative. Examples of $^{4,3}\Delta F(^{37/35}Cl)$ have recently been given from this laboratory (1). A second aim concerns a discussion of the structure of high-resolution nmr spectra arising from a class of spin systems described (2) as ABMRX···. The simplest member of this class, ABX, illustrates most of the basic principles of spectral analysis (2–5). It is true that computer analysis of nmr spectra is now a universal practice; yet an understanding of the fundamental properties of the spectrum, as consequences of the high-resolution Hamiltonian, can even today provide a more rapid or, indeed, correct (7), convergence in the machine analysis of a given spectrum.

Received April 24, 1996.

T. Schaefer,[1] G.M. Bernard, and F.E. Hruska. Department of Chemistry, University of Manitoba, Winnipeg, MB R3T 2N2, Canada.

[1] Author to whom correspondence may be addressed. Telephone: (204) 474-9321. Fax: (204) 275-0905. E-mail: schaefe@cc.umanitoba.ca

Scheme 1.

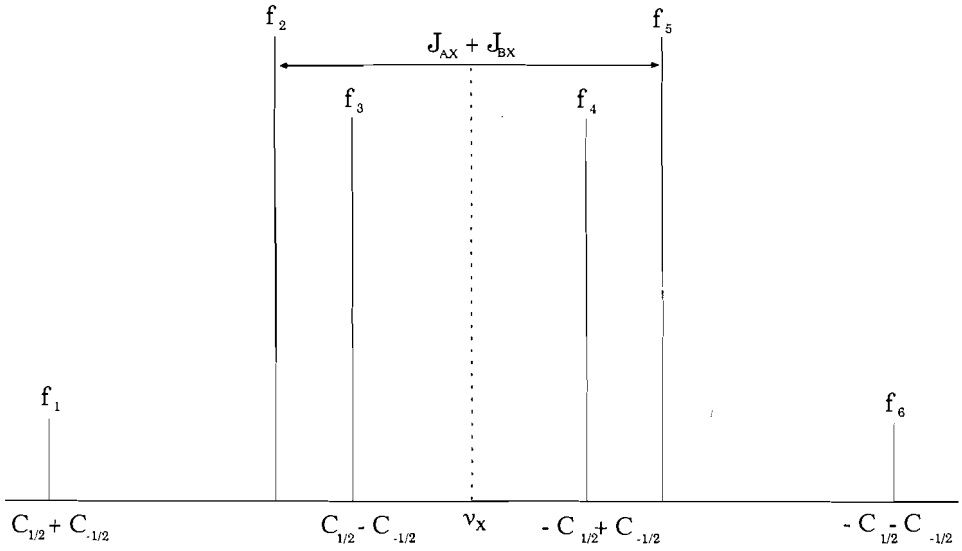

For example, it turns out that the $^{37}Cl/^{35}Cl$ isotope effect on the ^{19}F nmr spectrum of the title molecule can be determined from the ^{1}H nmr spectrum alone. In fact, for an ABX spectrum, in which the chemical shifts, but not the coupling constants, of nuclei A and (or) B undergo a secondary isotope effect, the latter can be determined from the X spectrum under certain circumstances, as discussed further below.

Some properties of ABMRX ··· spectra

(a) The ABX spectrum (refs. 2–6)

Concentrating on the X region, there occur two transitions of equal intensity, separated by $J_{AX} + J_{BX}$, as shown in Scheme 1. These transitions carry half the total intensity of the X spectrum. Four additional transitions can occur. They are also centered on ν_X, the resonance frequency of nucleus X. Their intensities can be deduced from eqs. [1]–[5], where $C > 0$, $0 \leq \theta \leq 180$.

$$[1] \quad 2C(\pm\tfrac{1}{2}) \cos 2\theta(\pm\tfrac{1}{2}) = [(\nu_A - \nu_B) \pm \tfrac{1}{2}(J_{AX} - J_{BX})]$$

$$[2] \quad 2C(\pm\tfrac{1}{2}) \sin 2\theta(\pm\tfrac{1}{2}) = J_{AB}$$

$$[3] \quad 2C(\pm\tfrac{1}{2}) = \{[(\nu_A - \nu_B) \pm \tfrac{1}{2}(J_{AX} - J_{BX})]^2 + J_{AB}{}^2\}^{1/2}$$

$$[4] \quad P(f_1) = P(f_6) = \sin^2 [\theta(\tfrac{1}{2}) - \theta(-\tfrac{1}{2})]$$

$$[5] \quad P(f_3) = P(f_4) = \cos^2 [\theta(\tfrac{1}{2}) - \theta(-\tfrac{1}{2})]$$

In these equations, $\nu_A - \nu_B$ is the positive difference in the resonance frequencies of nuclei A and B and P is a probability of transition. The intensities of peaks f_1 and f_6, the so-called combination lines, depend on the relative magnitudes of J_{AB} and C.

It follows that the X spectrum yields ν_X and $J_{AX} + J_{BX}$. Suppose now that ν_A and (or) ν_B undergo a small secondary isotope shift due, for example, to the presence of chlorine isotopes in the molecules. If the coupling constants do not display a detectable isotope effect (all known isotope effects on coupling constants arise from $^{1}H/^{2}H$ or $^{1}H/^{3}H$ substitution, none being found to date due to "heavier" substitutions (8)), then the sample of these molecules will display an X spectrum for each of the chlorine isotopes. Hence four quantities C are available and are related to four spectral quantities, namely, J_{AB}, $J_{AX} - J_{BX}$, and the two differences in chemical shift. The C values follow from differences in the peak frequencies shown in Scheme 1. The X spectrum now yields most spectral parameters of interest, with the exception, of course, of the individual values, ν_A and ν_B.

(b) The ABMRX ··· spectrum

By an obvious extension of eqs. [1]–[5], one has, for instance, eq. [6], where $m, r, x\cdots$ can each be $\pm\frac{1}{2}$. Suppose, as above, that the X region displays combination lines. The spectrum of nucleus X consists of a superposition of the patterns in Scheme 1, the centres of which are displaced from ν_X by $mJ_{MX} + rJ_{RX}$. The number of positive constants $C(m, r, x\cdots)$ is 2^n, where n is the number of M, R, and X nuclei. The spectral quantities in the surd of eq. [6] increase in number only as $(n + 2)$. Consequently, for an ABMX spectrum, as an example, there exist four C values in the X region. These values yield $\nu_A - \nu_B$ and the coupling constants J_{AB}, J_{AX}, and J_{BX}, together with the relative signs of the latter two.[2]

$$[6] \quad 2C(m, r, x\cdots) = \{[(\nu_A - \nu_B) + m(J_{AM} - J_{BM}) + r(J_{AR} - J_{BR}) + x(J_{AX} - J_{BX}) + \cdots]^2 + J_{AB}{}^2\}^{1/2}$$

If an isotope effect on $\nu_A - \nu_B$ exists, then its magnitude is also available from the X spectrum or from any of the other spectral regions M, R··· displaying combination peaks. This statement follows because now the number of C parameters becomes 2^{n+1}, and the number of quantities within the surd is $(n + 3)$.

[2] Similar generalizations can be made for $ABM_nR_oX_p$ ··· and, indeed, for $AB_2M_nR_oX_p$ ··· spin systems (9).

Table 1. The ^1H and ^{19}F nmr spectral parameters of 1-chloro-2,4-difluorobenzene in acetone-d_6 at 300 K.

Parameter	Value[a]		Parameter	Value[a]	
ν_2	14 712.629(4)[b,d]	14 712.167(5)[c,d]	$^4J_{24}$	6.830[b,g]	6.830[c,g]
ν_3	2166.819(1)[e]	2166.817(2)	$^4J_{26}$	8.523(2)	8.517(3)
ν_4	14 719.985(3)[d,f]	14 719.834(6)[d]	$^4J_{35}$	2.897(2)	2.899(2)
ν_5	2121.979(1)	2121.978(1)	$^4J_{46}$	5.762(2)	5.767(3)
ν_6	2271.078(1)	2271.076(2)	$^5J_{25}$	−1.558(4)	−1.559(5)
$^3J_{23}$	9.579(2)	9.576(3)	$^5J_{36}$	0.320(2)	0.319(2)
$^3J_{34}$	8.763(2)	8.765(3)	Root-mean-square		
$^3J_{45}$	8.081(3)	8.081(4)	error	0.005	0.006
$^3J_{56}$	8.988(1)	8.990(2)	Largest difference	0.009	0.017

[a]For a 5.0 mol% solution in acetone-d_6, containing also 0.5 mol% of TMS and 0.25 mol% of C_6F_6.
[b]This column refers to an analysis of the spectrum from the ^{35}Cl molecules.
[c]This column refers to the molecules containing ^{37}Cl atoms.
[d]In Hz to high frequency of internal C_6F_6 at 282.362 64 MHz.
[e]In Hz to high frequency of internal TMS at 300.134 93 MHz.
[f]Numbers in parentheses are the standard deviations in millihertz.
[g]As determined from the many repeated spacings in the ^{19}F spectral region.

Recognition of patterns of the kind discussed here has three advantages. First, if A and B represent, say, ^{19}F nuclei (see below), then only, say, ^1H spectra are needed for a fairly complete analysis: by no means do all laboratories carry ^{19}F probes. Second, excellent initial magnitudes of spectral parameters for an iterative computer analysis are then available, even when MRX··· are not quite "first-order" spins. Third, this approach has a significant pedagogical value.

Experimental

A dilute solution of 1-chloro-2,4-difluorobenzene (Aldrich) in acetone-d_6 (see Table 1 for details) was filtered into a 5 mm o.d. nmr sample tube. The tube was degassed by five freeze–pump–thaw cycles and was then flame-sealed to yield a reasonably symmetric top. The ^1H and ^{19}F nmr spectra were obtained with a Bruker AM 300 spectrometer at a probe temperature of 300 K. As many as 64 free induction decays were coadded, using 16–32 K data points and acquisition times of 40 s for spectral regions of 200 Hz. Zero-filling and resolution enhancement procedures gave linewidths at half-height of as little as 0.04 Hz.

Results and discussion

Spectral analysis

Spectral analytical procedures employed the program NUMARIT (10) as extensively reworked by R. Sebastian and K. Marat (11). During these procedures it was found that slight inconsistencies existed between ^1H and ^{19}F transitions, originating in very small changes in the chemical shift differences between the ^{19}F nuclei, that is, the difference in chemical shift changed a little between the time of recording the ^1H nmr spectrum and that of acquiring the ^{19}F nmr data. We believe this change was caused by very small temperature variations, with the consequence that the fluorine shielding altered slightly and differentially: slight alteration of solvent effects. However, the spectral parameters in Table 1 are fairly reliable even though their standard deviations are somewhat larger than normal. It may also be noted that, probably because of the complexity introduced by the chlorine isotope effects, a satisfactory iterative fit, using the partially self-assigning computer program, was not easily forthcoming until the underlying spectral structure was ascertained as described below.

The ^{19}F parameters reflected in the spectrum of H-5

If the composite ^1H and ^{19}F nmr spectrum is treated as arising from an ABMRX system, then it is clear from eq. [6] that in the, say, X spectrum for a given chlorine isotope, eight quantities $C(m, r, x)$ are available (compare with the discussion of the ABX system) because m, r, and x can each be $\pm\frac{1}{2}$. This statement assumes that the so-called combination peaks (the weak peaks in Scheme 1, for example, for an ABX system) are detectable. The differences in the surd of eq. [6] can now be found in terms of the quantities C in a number of ways. One direct procedure (one has eight equations with which to work) involves elimination of all but one of these differences and so forth. This straightforward, if tedious, algebra was performed for the X spectrum (H-5) of **1**.

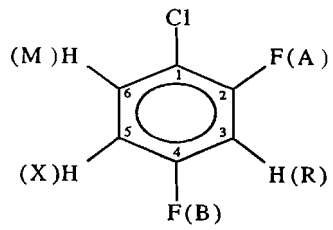

1

The subspectra of H-5 are indicated in Fig. 1. They are easily picked out, as is also illustrated in Fig. 1. Finally, the frequency differences between the centres of the subspectra yield sums and differences of coupling constants of H-5(X) with H-3(R) and H-6(M). Of course, $J_{AX} + J_{BX}$ is repeated four times if no isotopic perturbation of this sum is present, as is strongly

Fig. 1. The nmr spectrum at 300 MHz and 300 K of H-5 of 1-chloro-2,4-difluorobenzene, as a 5 mol% solution in acetone-d_6, is displayed at the top. Beneath it is shown the simulated spectrum using the spectral parameters in Table 1. The subspectra corresponding to various spin states of H-3, nucleus R, and H-6, nucleus M, are indicated by stick spectra. Each subspectrum contains a more intense set, corresponding to ^{35}Cl, of six peaks and a less intense set, corresponding to ^{37}Cl, of *four* peaks. Because no detectable isotope effect on the coupling constants exists, the peaks separated by $J_{AX} + J_{BX}$ (X = H-5) coincide for the molecule containing ^{35}Cl or ^{37}Cl (see Scheme 1). The combined ^1H and ^{19}F nmr spectra do not correspond exactly to a spin system, ABRMX, for a given isotope of chlorine in the sense that the internal proton chemical shifts are not all exceedingly large compared to $^nJ(^1H, ^1H)$; that is, $^nJ(^1H, ^1H)$ on the off-diagonals of the Hamiltonian matrix do somewhat affect the spectrum, the intensities more than the frequencies, as expected from perturbation theory. However, treatment as an ABMRX situation leads to a clear decomposition of the spectrum of H-5 and a set of reasonably accurate constants, C (see text), from which the internal fluorine chemical shifts of the isotopic molecules can be derived, as can all the spin–spin coupling constants involving H-5; also J_{AB}. Note that, in each subspectrum, the C values are $C(r, m, \pm\frac{1}{2})$.

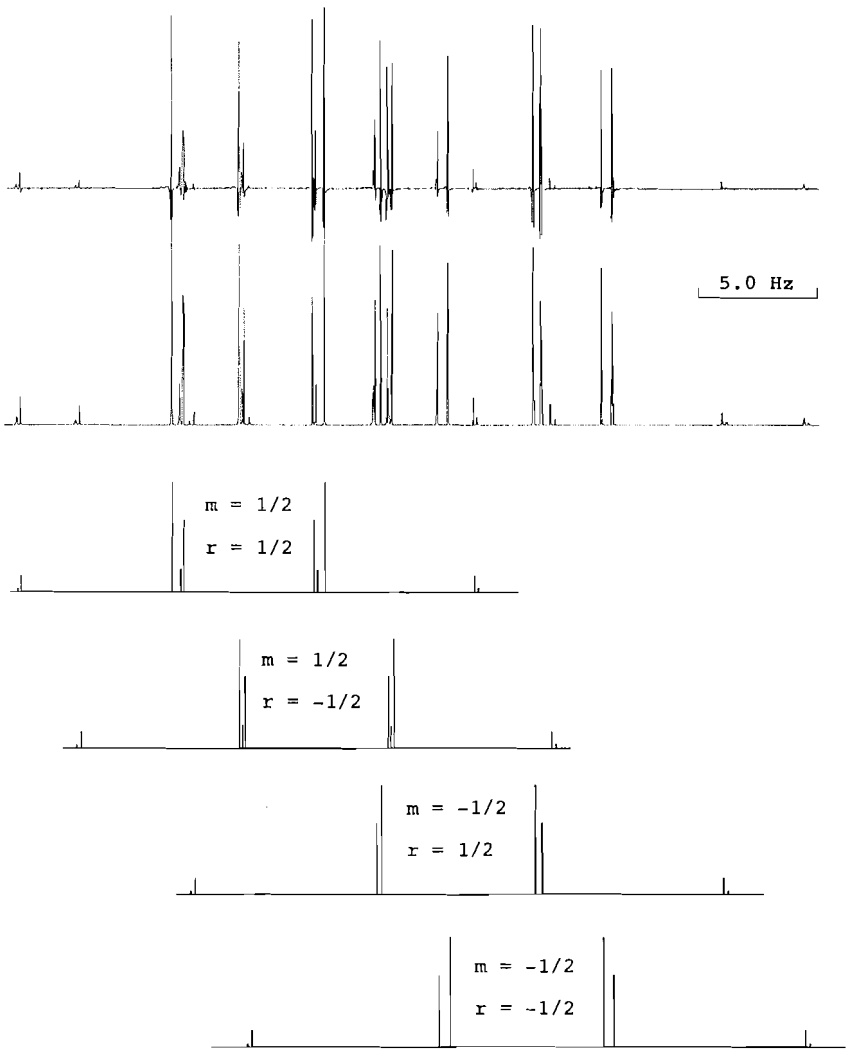

indicated by the spectrum (at a linewidth of about 0.04 Hz no evidence of a doubling of the peaks separated by $J_{AX} + J_{BX}$ was observable). From the H-5 spectrum in Fig. 1, therefore, the following spectral parameters are obtained: J_{AX}, J_{BX} and their relative signs, $J_{AR} - J_{BR}$, $J_{AM} - J_{BM}$, J_{AB}, the two values of $\nu_A - \nu_B$ corresponding to the two kinds of isotopically labelled molecules (16 C values in total), as well as J_{MX} and J_{MR}. From the M and R regions individual values of J_{AM}, J_{BM},

J_{AR}, and J_{BR} follow, together with relative signs. The separations between these peaks and their intensities are determined by the same eight C values extracted from the X region, but by different combinations of them, so that the peak intensities may be undetectable. In fact, the combination peaks vanish in the M(H-6) and R(H-3) spectral regions of the present molecule.

Returning to the X(H-5) spectrum, the spectral parameters extracted from the C values differed by no more than 0.01 Hz from those obtained in the iterative analysis presented in Table 1. The internal chemical shifts of the fluorine nuclei, obtained from the H-5 spectrum, differed by 0.31(2) Hz or 1.1(1) ppb, being larger in the presence of ^{37}Cl. These numbers[3] represent $|^3\Delta F(^{37/35}\text{Cl}) - {}^5\Delta F(^{37/35}\text{Cl})|$. The known range of $^3\Delta F$ in fluorobenzene derivatives is 1.58–1.61 ppb (1) and therefore implies the existence of a finite $^5\Delta F$, about 0.5 ppb, in the molecule under discussion. Of course, the actual shifts of the ^{19}F nuclei are required to establish this number and are obtainable only from the ^{19}F nmr spectrum.

The isotope shifts

The chemical shifts in Table 1 give $^3\Delta F$ as $-1.64(3)$ ppb and $^5\Delta F$ as $-0.54(3)$ ppb, the negative sign meaning, conventionally, that the heavier isotope causes increased shielding. The $^5\Delta F$ is as large as $^4\Delta F$ in 2-chloro-6-fluorocyanobenzene and *three* times larger than $^4\Delta F$ in 2,6-dichloro-4-fluorophenol (1). A variety of fluorobenzene derivatives are to be synthesized in an attempt to establish patterns of $^{4,5}\Delta F$; $^3\Delta F$ appears to be constant within about 0.02 ppb. That $^5\Delta F(^{37/35}\text{Cl})$ can be larger than $^4\Delta F(^{37/35}\text{Cl})$ is reminiscent of an early measurement, yielding $^5\Delta F(^2\text{H}/^1\text{H})$ as -11 ppb in fluorobenzene-4-*d* and $^4\Delta F(^2\text{H}/^1\text{H})$ as -8 ppb in fluorobenzene-3-*d* (12).

[3] Some authors prefer to write the isotope shift for F-2 as $^3\Delta F + {}^7\Delta F$ and that for F-4 as $2(^5\Delta F)$.

Acknowledgments

We thank the Natural Sciences and Engineering Research Council of Canada for financial assistance.

References

1. G.M. Bernard and R.W. Schurko. Magn. Reson. Chem. **33**, 879 (1995).
2. G.A. Williams and H.S. Gutowsky. J. Chem. Phys. **25**, 1288 (1956).
3. J.A. Pople, W.G. Schneider, and H.J. Bernstein. High-resolution nuclear magnetic resonance. McGraw–Hill, New York. 1959. Chap. 6.
4. P.L. Corio. Structure of high-resolution nmr spectra. Academic Press, New York. 1966. Chap. 7.
5. R.J. Abraham. Analysis of high resolution nmr spectra. Elsevier, Amsterdam. 1971. Chap. 6.
6. J.A. Pople and T. Schaefer. Mol. Phys. **3**, 547 (1960).
7. R.K. Harris, M.S. Jones, and A.M. Kenwright. Magn. Reson. Chem. **31**, 1085 (1993).
8. N.M. Sergeyev. NMR Basic Principles and Progress, **22**, 33 (1990).
9. P. Diehl and J.A. Pople. Mol. Phys. **3**, 557 (1960).
10. J.S. Martin, A.R. Quirt, and K.E. Worvill. The NMR program library. Daresbury Laboratory, Daresbury, U.K.
11. K. Marat and R. Sebastian. Bruker Rept. 42 (1993).
12. W.R. Young and C.S. Yannoni. J. Am. Chem. Soc. **91**, 4581 (1969).

DISQUAC characterization of the carbonyl–oxygen interactions in binary liquid organic mixtures containing linear molecules: ketones and a monoether, diether, or triether

J.A. González, J.M. Fernández Martínez, I. García de la Fuente, and J.C. Cobos

Abstract: The available data in the literature on vapor–liquid equilibria, excess Gibbs energies, and excess enthalpies for linear ketones + linear mono- or poly-ether mixtures are examined in terms of the DISQUAC group contribution model. Interaction parameters are reported. The quasichemical interchange coefficients are independent of the compounds in the systems; the dispersive interchange coefficients depend on the intramolecular environment of the carbonyl and (or) oxygen groups. Proximity effects, which seem to lead to an important increase of the interaction parameters, are briefly considered in treating systems including 1-methoxy-2-propanone or dimethyl carbonate molecules. DISQUAC consistently describes the experimental data of the mixtures investigated. The rather good representation obtained for vapor–liquid equilibria at high temperatures is noteworthy. A discussion in terms of effective and reduced dipole moments of binary mixtures containing carbonyl and oxygen groups in the same or different molecules is also presented.

Key words: liquids, mixtures, thermodynamics, dipole moments, group contributions.

Résumé : Faisant appel au modèle de contribution de groupe «DISQUAC», on a examiné les données disponibles dans la littérature relatives aux équilibres vapeur–liquide, aux énergies de Gibbs en excès et aux enthalpies en excès pour des cétones linéaires + des mélanges de mono- ou poly-éthers linéaires. On a déterminé les paramètres d'interaction. Les coefficients d'échange quasichimiques sont indépendants de la nature des composés dans les systèmes; les coefficients d'échange dispersifs dépendent de l'environnement intramoléculaire du groupe carbonyle et (ou) des oxygènes. Dans le traitement des systèmes comportant des molécules de 1-méthoxypropan-2-one ou du carbonate de diméthyle, on a brièvement considéré des effets de proximité qui semblent conduire à une augmentation importante des paramètres d'interaction. La méthode DISQUAC décrit d'une façon consistante les données expérimentales des mélanges étudiés. La représentation relativement bonne obtenue pour les équilibres vapeur–liquide à température élevée mérite d'être notée. On présente aussi une discussion en terme de moments dipolaires effectifs et réduits des mélanges binaires contenant des groupes carbonyles et des oxygènes dans les mêmes molécules ou dans des molécules différentes.

Mots clés : liquides, mélanges, thermodynamique, moments dipolaires, contributions de groupes.

[Traduit par la rédaction]

1. Introduction

DISQUAC (1, 2) is a group contribution method widely and successfully applied to many classes of mixtures using interaction parameters that are assumed to be structure dependent. This assumption improves predictions, mainly in the case of branched and cyclic molecules, and for the first members of homologous series. Moreover, it is remarkable that, for a given system, the same set of interchange coefficients can be used to represent rather accurately the thermodynamic properties: low-pressure fluid phase equilibria; vapor–liquid (VLE), liquid–liquid (LLE), or solid–liquid (SLE), equilibria; excess functions, such as Gibbs energies, G^E, enthalpies, H^E, or heat capacities at constant pressure, C_p^E; as well as the related partial molar excess quantities at infinite dilution.

On the other hand, systems are investigated in order of increasing complexity of molecular structure and intermolecular interactions. Attention is paid to the electronic structure and configuration of the organic molecules. Proximity and other intramolecular effects: steric hindrance, polarity, polarizability, and induction, are more carefully examined than usual.

An example of the philosophy of application of the model is the so-called CO/O project, in which mixtures containing the carbonyl (CO) and (or) the oxygen (O) groups are investigated in order to characterize intra- and inter-molecular effects related to the presence of the CO and O groups in the same or in different molecules. Up to now, the following classes of systems have been treated:

Received March 15, 1996.

J.A. González,[1] **J.M. Fernández Martínez, I. García de la Fuente, and J.C. Cobos.** Departamento de Termodinámica y Física Aplicada, Universidad de Valladolid, 47071, Valladolid, Spain.

[1] Author to whom correspondence may be addressed. Telephone: +34 83 42 31 37. Fax: +34 83 42 31 36 or +34 83 42 30 13. e-mail: jagl@wamba.cpd.uva.es

Fig. 1. Excess functions, G^E (□) and H^E (○), at 398.15 K for the acetic anhydride (1) + *n*-octane (2) system. Points, experimental results (11); solid lines, DISQUAC calculations.

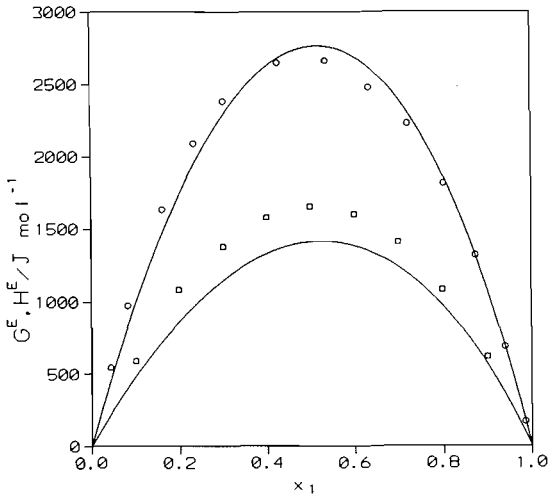

Fig. 2. VLE at 388.30 K for the 2-propanone (1) + diethyl ether (2) system. Points, experimental results (22); solid lines, DISQUAC calculations (x_1 and y_1 are, respectively, the mole fractions in the liquid and vapor phases).

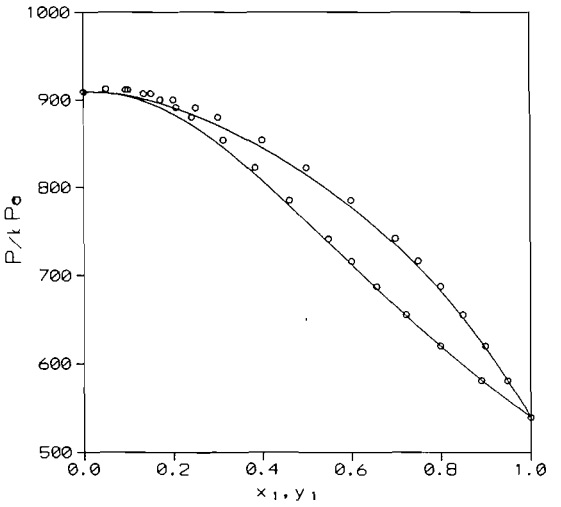

CH_3-$(CH_2)_{n-1}$-O-$(CH_2)_{m-1}$-CH_3 + *n*-alkanes, or + cyclohexane (3)

CH_3-$(CH_2)_{n-1}$-CO-$(CH_2)_{m-1}$-CH_3 + *n*-alkanes, or + cyclohexane (4)

CH_3-$(CH_2)_{n-1}$-COH + *n*-alkanes, or + cyclohexane (5, 6)

$H(CH_2)_{n-1}$-COO-$(CH_2)_m$H + *n*-alkanes, or + cyclohexane (7)

CH_3-$(CH_2)_{n-1}$-OCOO-$(CH_2)_{m-1}$-CH_3+*n*-alkanes,or+ cyclohexane (8, 9)

CH_3-$(CH_2)_{n-1}$-CO-O-CO-$(CH_2)_{m-1}$-CH_3 + *n*-alkanes (10)

Table 1. Relative group increments for molecular volumes, $r_G = V_G/V_{CH_4}$ and areas $q_G = A_G/A_{CH_4}$.[a]

Group	r_G	q_G
CH_3[b]	0.79848	0.73103
CH_2[b]	0.59755	0.46552
O[c]	0.21612	0.20690
CO[d]	0.68344	0.55174

[a] $V_{CH_4} = 17.12 \times 10^{-6}$ m^3 mol^{-1}; $A_{CH_4} = 2.90 \times 10^{-5}$ m^2 mol^{-1}.
[b] Reference 15.
[c] Reference 3.
[d] Reference 13.

Polyethers and cyclic molecules, ethers or ketones, have been also studied in the framework of DISQUAC (3, 4).

Figure 1 is an example of the ability of DISQUAC to represent the recent data on excess functions at very high temperatures by Haan et al. (11) using our interchange coefficients published five years ago (10) (see also Fig. 2). It is noteworthy that the acetic anhydride + *n*-octane mixture shows a miscibility gap at room temperature, and that the same interaction parameters give an excellent description of the LLE coexistence curve of the acetic anhydride + *n*-heptane system (10).

The aim of this work was to develop the DISQUAC treatment of binary liquid organic mixtures containing linear ketones and linear mono- or poly-ethers. Previously, linear ketones + 2,5-dioxahexane systems were treated by assuming structure-dependent interchange coefficients for those contacts involving the carbonyl group (12–14). The zeroth approximation of DISQUAC was used for the carbonyl–oxygen (12) and oxygen–aliphatic contacts (15). The carbonyl–aliphatic contacts were represented by quasichemical interchange coefficients only with coordination number, *z*, equal to 10 (13, 14). DISQUAC interchange coefficients now being available for the interactions between the aliphatic group and the CO or O groups (3, 4), we report in this paper those for the CO–O contacts.

2. The DISQUAC model

2.1 Theory

In the framework of DISQUAC, mixtures of linear ketones with linear ethers are regarded as possessing three types of surface: (*i*) type a, aliphatic (CH_3, CH_2 in ketones and ethers); (*ii*) type e, oxygen (O in ethers); and (*iii*) type k, carbonyl (CO in ketones).

The equations used to calculate G^E and H^E are the same as in other applications (16). The reference value was chosen as coordination number, that is, $z = 4$.

The temperature dependence of the interaction parameters is expressed in terms of the dispersive (DIS) and (or) quasichemical (QUAC) interchange coefficients $C_{st,l}^{DIS}$ and $C_{st,l}^{QUAC}$, where s, t = a, e, or k, and l = 1 (Gibbs energy) or l = 2 (enthalpy). Heat capacity coefficients, l = 3, have not been considered.

2.2 Assessment of geometrical parameters

When DISQUAC is applied, the total relative molecular volumes, r_i, surfaces, q_i, and the molecular surface fractions, α_{si}, of the compounds present in the mixture are usually calculated

Table 2. Interchange coefficients, dispersive $C^{DIS}_{ae,l}$ and quasichemical $C^{QUAC}_{ae,l}$ (l = 1, Gibbs energy; l = 2, enthalpy) for contacts (a, e) (Type a, CH_3, CH_2 in n-alkanes; Type e, O in linear mono- or polyethers) for the ethers considered in this work (3). The coordination number used for the QUAC part is z = 4.

Ether	$C^{DIS}_{ae,1}$	$C^{DIS}_{ae,2}$	$C^{QUAC}_{ae,1}$	$C^{QUAC}_{ae,2}$
Methyl butyl ether	10.60	18.20	3.40	5.60
Diethyl ether	10.60	18.20	3.30	5.00
Dipropyl ether	10.60	18.20	2.80	2.90
Dibutyl ether	10.60	18.20	2.60	1.50
2,5-Dioxahexane	10.60	18.20	3.50	5.90
3,6,9-Trioxaundecane	10.60	18.20	2.90	3.70

Table 3. Interchange coefficients, dispersive $C^{DIS}_{ak,l}$ and quasichemical $C^{QUAC}_{ak,l}$ (l = 1, Gibbs energy; l = 2, enthalpy) for contacts (a, k) (4) (Type a, CH_3, CH_2 in n-alkanes; Type k, CO in linear ketones); n and m represent the number of C atoms of the n-alkyl group attached to the ketone under consideration. The coordination number used for the QUAC part is z = 4.

(n, m)	$C^{DIS}_{ak,1}$	$C^{DIS}_{ak,2}$	$C^{QUAC}_{ak,1}$	$C^{QUAC}_{ak,2}$
(1, 1)	2.90	5.05	6.08	8.25
(1, 2)	3.25	6.16	5.35	6.35
(1, ≥3)	3.31	6.92	5.29	5.94
(2, 2)	3.60	7.27	4.62	4.46
(2, ≥3)	3.65	8.03	4.56	4.04
(≥3, ≥3)	3.71	8.79	4.50	3.63

additively on the basis of the group volumes V_G and surfaces A_G, as recommended by Bondi (1968) (17). As volume and surface units, the volume V_{CH_4} and surface A_{CH_4} of methane are taken arbitrarily (15). The geometrical parameters for the groups referred to in this work are collected in Table 1.

2.3 Estimation of the interaction parameters

The three types of surface generate three pairs of contacts: (a, e); (a, k), and (e, k).

The (a, e) contact has been described in the past using DIS coefficients only, i.e., on the basis of the random mixing approximation ($C^{DIS}_{ae,1}$ = 15.73, $C^{DIS}_{ae,2}$ = 29.04) (15). DISQUAC improves the representation of the experimental data, especially that of H^E. The differences between random mixing and DISQUAC calculations increase with the oxygen surface fraction (3). The DIS and QUAC parameters needed in this work are listed in Table 2.

The (a, k) contacts have been described previously in terms of the quasichemical approximation with z = 10, assuming that the interaction parameters change regularly with the structure of the ketones (13, 14). Application of DIS and QUAC coefficients (Table 3; (4)) improves mainly the coexistence curves of liquid–liquid equilibria for the 2-propanone + n-alkane systems (González et al., unpublished results).

Hence, because the (a, e) and (a, k) parameters are known, only the DIS and QUAC interchange coefficients for the (e, k) contacts need to be fitted.

The general procedure used by us in the fitting of any set of interaction parameters has been described in detail elsewhere (18–20). However, in the present case the adjustment of the interchange coefficients is more complicated due to the lack of experimental data on G^E, as the QUAC enthalpic parameters depend on the first QUAC interchange coefficients. For this reason, we kept constant the $C^{QUAC}_{ek,1}$ coefficients for all the systems investigated. Moreover, in order to keep a lower number of interaction parameters, we also made the $C^{QUAC}_{ek,2}$ coefficients independent of the compounds in the mixture. After several calculations developed to study the change in the symmetry of the G^E and H^E curves with the interaction parameters, we finally took $C^{QUAC}_{ek,l}$ (l = 1, 2) = 0.50 together with the corresponding $C^{DIS}_{ek,l}$ (l = 1, 2) coefficients (Table 4).

For systems containing the longer symmetrical linear monoethers, say from dipropyl ether, calculations show that the main contributions to the excess functions are due to the aliphatic–CO and aliphatic–O contacts. Thus, the $C^{DIS/QUAC}_{ek,l}$ interchange coefficients obtained on the basis of the available data for alkanones + dibutyl ether mixtures can be used. In the case of shorter symmetrical monoethers, dimethyl or diethyl ether, such contributions decrease rather quickly with the size of the alkanone, when, moreover, size effects become very important. So different interaction parameters are needed. The $C^{DIS}_{ek,2}$ coefficients were estimated using the H^E data by Hirobe for the 2-propanone + diethyl ether mixture (21)[2] and taking into account, for such parameters, a variation with the size of the alkanone similar to that encountered previously. On the other hand, for nonsymmetrical linear monoethers (n-O-m) + n-alkane mixtures the interchange coefficients are mainly determined by the shortest group n (n, m are the numbers of aliphatic groups attached to the oxygen atom) (3). For the actual mixtures, this is still valid. So, we consider two groups of different DIS enthalpic parameters depending on the n, m values: $n \leq 2$ and $n, m \geq 3$ (Table 4). In exchange, the $C^{DIS}_{ek,1}$ coefficients can be considered as independent of the monoether. This is possible due to the smooth variation observed for such parameters from the 2-propanone + diethyl ether mixture to the 2-heptanone + dibutyl ether system (the only mixtures under consideration characterized by a set of VLE data (22, 23)). This variation agrees fairly well with the inductive effect observed in the $C^{DIS}_{ek,2}$ coefficients in a

[2] Cf. ref. 34.

Table 4. Interchange coefficients, dispersive $C^{DIS}_{ek,l}$ (l = 1, Gibbs energy; l = 2, enthalpy) for contacts (e, k) (this work) (Type e, O in linear mono- or poly-ethers; Type k, CO in linear ketones). The coordination number used for the QUAC part is z = 4; and $C^{QUAC}_{ek,1} = C^{QUAC}_{ek,2} = 0.50$.

		Ketone[a]									
Ether[a]		1CO1	1CO2	1CO3	1CO4	1CO5	1CO6	1CO7	2CO2	3CO3	4CO4
	$C^{DIS}_{ek,1}$	1.85	2.75	3.60	4.55	4.55	4.55	4.55	3.60	4.55	4.55
n-O-*m* ($n \leq 2$)											
	$C^{DIS}_{ek,2}$	3.50	3.55	3.60	3.70	4.50	4.50	4.50	4.00	5.20	5.20
	$C^{DIS}_{ek,1}$	1.85	2.75	3.60	4.55	4.55	4.55	4.55	3.60	4.55	4.55
n-O-*m* ($n, m \geq 3$)											
	$C^{DIS}_{ek,2}$	0.90	0.96	1.02	1.10	1.70	3.50	3.50	2.01	5.15	9.10
	$C^{DIS}_{ek,1}$[b]	1.85	2.75	3.60	4.55	4.55	4.55	4.55	3.60	4.55	4.55
1-O-2-O-1											
	$C^{DIS}_{ek,2}$	−3.20[b]	−2.35[b]	−2.49	−2.62	−2.66	−2.81	−2.81	−1.87	−0.12	0.14
	$C^{DIS}_{ek,1}$[b]	1.85	2.75	3.60	4.55	4.55	4.55	4.55	3.60	4.55	4.55
2-O-2-O-2-O-2											
	$C^{DIS}_{ek,2}$	−6.50[b]	−3.80[b]	−2.60[b]	−1.50[b]	−1.00	−0.15[b]	−0.15	0.80[b]	2.82	4.16

[a]The figures or letters mean the number of aliphatic groups attached to the CO or O groups (e.g., 1CO4 is 2-hexanone; 1-O-2-O-1 is 2,5-dioxahexane).
[b]Estimated values.

Table 5. Molar excess Gibbs energies G^E (T; x_1 = 0.5) for linear ketones (1) + monoethers (2) systems at various temperatures, T (K), and equimolar composition. Comparison of experimental results (exp) with DISQUAC values calculated (calcd.) using the coefficients from Tables 2–4 (N is the number of experimental data of each system).

			G^E/J mol^{-1}		σ_r (P)[a]	
System	T/K	N	Exp	Calcd.	Exp[b]	Calcd.[c]
2-Propanone + diethyl ether	298.06[d]	13	447	453	0.0006	0.0023
	338.19[d]	13	444	441	0.0007	0.0022
	388.30[d]	13	440	414	0.0009	0.0080
2-Heptanone + dibutyl ether	363.15[e]	15	323	324	0.0029	0.0029
	393.22[e]	14	341	312	0.0140	0.0067
3-Heptanone + dibutyl ether	363.15[e]	15	269	296	0.0007	0.0066
	393.15[e]	14	273	289	0.0010	0.0052
4-Heptanone + dibutyl ether	363.15[e]	13	259	281	0.0026	0.0058
	393.15[e]	13	264	269	0.0012	0.0020

[a]Relative standard deviations in pressure, eq. [1].
[b]Values obtained when data are correlated using an equation of the Redlich–Kister type.
[c]DISQUAC results.
[d]Reference 22.
[e]Reference 23.

series with a given monoether (Table 4). It is noteworthy that while these parameters depend on the position of the CO group in the ketone molecule (values can be obtained by interpolation of those for the 2-ketone and for the corresponding symmetrical molecule), this does not occur for the $C^{DIS}_{ek,1}$ coefficients.

Finally, we remark that polyethers were treated as monoethers; i.e., we made no distinction between the different oxygen atoms present in the polyether. In the case of mixtures of noncyclic monoethers with *n*-alkanes, the interchange coefficients are obtained by ignoring O atoms when ascertaining the n and m values of the *n*-O-*m* groups in polyethers, or as an average of the various types of *n*-O-*m* groups present. For example, both O atoms in 2,5-dioxahexane are of the 1-O-3 type, and the parameters used are those for methyl propyl ether (3). However, such rules cannot be kept for the mixtures under study.

Table 6. Molar excess enthalpies H^E for linear ketones (1) + oxaalkanes (2) systems at 298.15 K and equimolar composition. Comparison of experimental results (exp) (28) with DISQUAC calculations (calcd.) using the coefficients from Tables 2–4. Also listed is a comparison between experimental standard deviations (exp) for H^E, $\sigma(H^E)$, (eq. [2], obtained when data are correlated using a Redlich–Kister equation type) with DISQUAC results (N is the number of data points of each system).

		H^E/J mol^{-1}		$\sigma(H^E)$/J mol^{-1}		
					Calcd.	
System	N	Exp.	Calcd.	Exp.	I[a]	II[b]
2-Propanone + diethyl ether		505[c]	504			
		565[d]				
2-Butanone + dibutyl ether	32	849	859	4.2	16.0	
2-Pentanone + dibutyl ether	24	670	693	4.3	18.0	
2-Hexanone + dibutyl ether	20	562	564	2.8	6.1	
2-Heptanone + dibutyl ether	22	478	479	2.5	4.8	
2-Octanone + dibutyl ether	20	426	435	2.9	8.1	
2-Nonanone + dibutyl ether	26	386	377	2.4	7.7	
3-Pentanone + dibutyl ether	21	599	605	2.4	8.5	
4-Heptanone + dibutyl ether	22	433	435	2.5	13.0	
5-Nonanone + dibutyl ether	20	361	365	1.2	11.0	
2-Pentanone + 2,5-dioxahexane	19	−99	−97	0.6	3.5	34.0
2-Hexanone + 2,5-dioxahexane	23	−46	−43	0.8	3.7	9.7
2-Heptanone + 2,5-dioxahexane	25	21	25	0.9	8.5	3.1
2-Octanone + 2,5-dioxahexane	19	86	92	1.0	12.0	15.0
2-Nonanone + 2,5-dioxahexane	20	160	164	1.4	12.0	18.0
3-Pentanone + 2,5-dioxahexane	20	−91	−90	1.0	2.5	20.0
4-Heptanone + 2,5-dioxahexane	25	110	114	1.0	9.6	8.9
5-Nonanone + 2,5-dioxahexane	19	260	266	1.6	11.0	7.0
2-Heptanone + 3,6,9-trioxaundecane	18	83	77	1.2	11.0	
2-Nonanone + 3,6,9-trioxaundecane	18	197	207	1.5	4.6	
4-Heptanone + 3,6,9-trioxaundecane	21	206	204	1.7	5.4	
5-Nonanone + 3,6,9-trioxaundecane	20	336	342	1.8	6.0	

[a]DISQUAC results using coefficients from Tables 2–4.
[b]Values obtained using the quasichemical approximation for the carbonyl–aliphatic interactions (13, 14); the zeroth approximation for the ether–aliphatic (15) and ether–carbonyl (12) interactions (the carbonyl–aliphatic and ether–carbonyl interactions are assumed to be represented by structure-dependent interchange coefficients; see text and ref. 12).
[c]Reference 21.
[d]Reference 29.

3. Comparison with experiment

A detailed comparison between experimental data and calculated values from the DISQUAC model for the thermodynamic properties VLE, G^E, and H^E is presented in Tables 5 and 6 and in Figs. 2–7.

We note that for the sake of major clarity, Table 5 lists the relative standard deviations in pressure, $\sigma_r(P)$ defined by:

$$[1] \quad \sigma_r(P) = \{1/N[\Sigma (P_{exp} - P_{calc})^2/P_{exp}]^{1/2}\}$$

where N stands for the number of data points for each system. Similarly, Table 6 also lists the standard deviation for H^E, $\sigma(H^E)$ defined by:

$$[2] \quad \sigma(H^E)/\text{J mol}^{-1} = [1/N \Sigma (H^E_{exp} - H^E_{calc})^2]^{1/2}$$

We note the rather good description obtained for the VLE data at very high temperatures. For G^E at equimolar composition, differences between experimental and calculated values do not exceed 10% (Table 5). We also note, as mentioned above, that no distinction is made for homomorphic ketones when calculating G^E for a given ether.

Larger discrepancies are found for H^E of mixtures of ketones with 2,5-dioxahexane. Much better results can be obtained using different QUAC and DIS enthalpic parameters for each system of this type. In this case, the interchange coefficients vary in a rather erratic way, indicating inaccuracies in the experimental data, which may explain some of the observed discrepancies.

Predictions for G^E and H^E at equimolar composition and T = 298.15 K for several alkanones + linear monoethers are shown in Figs. 8 and 9.

Fig. 3. H^E at 298.15 K for CH_3-CO-$(CH_2)_{n-1}$-CH_3 (1) + dibutyl ether (2) systems. Points, experimental results (○, n = 2; □, n = 3; △, n = 4; ●, n = 5; ▲, n = 6 (28)); solid lines, DISQUAC calculations.

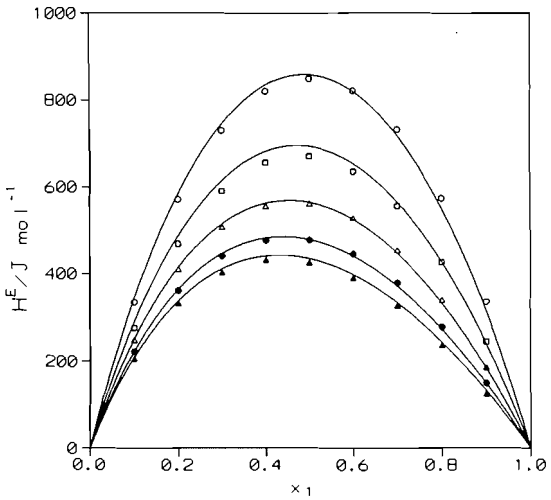

Fig. 4. H^E at 298.15 K for CH_3-$(CH_2)_{n-1}$-CO-$(CH_2)_{n-1}$-CH_3 (1) + dibutyl ether (2) systems. Points, experimental results (○, n = 2; □, n = 3; △, n = 4 (28)); solid lines, DISQUAC calculations.

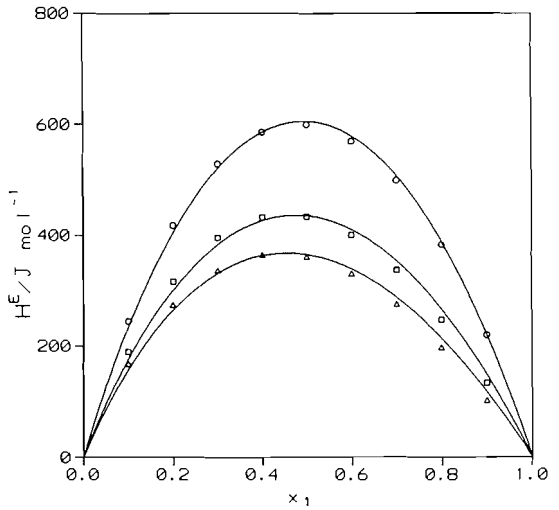

Fig. 5. H^E at 298.15 K for CH_3-CO-$(CH_2)_{n-1}$-CH_3 (1) + 2,5-dioxahexane (2) systems. Points, experimental results (○, n = 3; □, n = 4; △, n = 5; ●, n = 6; ■, n = 7 (28)); solid lines, DISQUAC calculations.

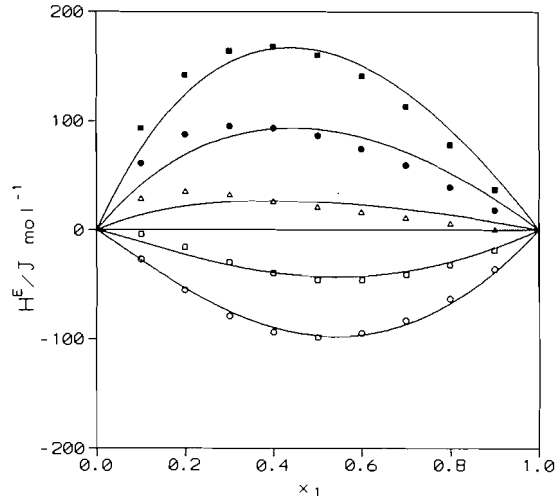

Fig. 6. H^E at 298.15 K for CH_3-$(CH_2)_{n-1}$-CO-$(CH_2)_{n-1}$-CH_3 (1) + 2,5-dioxahexane (2) systems. Points, experimental results (○, n = 2; □, n = 3; △, n = 4 (28)); solid lines, DISQUAC calculations.

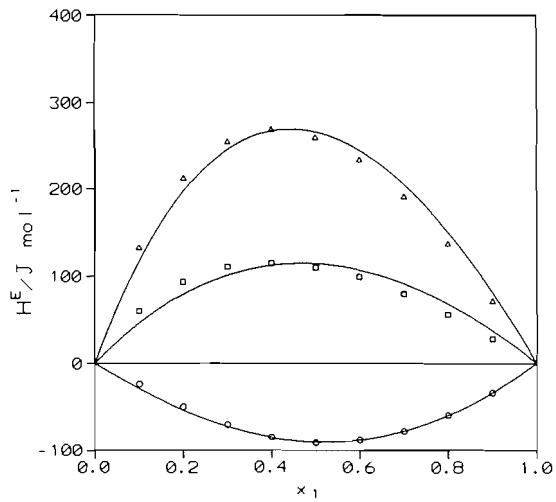

4. Discussion

The linear ketones + dibutyl ether systems behave similarly to mixtures of these ketones with a common *n*-alkane: H^E is rather large and positive, lower than for the latter systems, and falls in the order 2-propanone > 2-butanone > 2-pentanone (Tables 6 and 7). This effect is primarily due to the fact that, although the actual dipole moments of the ketones listed above are approximately constant (Table 8), the effective dipole moment decreases as the length of the aliphatic chain increases (Table 8) and this weakens the ketoxy interactions in the condensed phase. In fact, the effective polarity of a molecule is reasonably well correlated by the dimensionless ratio (24)

$$[3] \quad \bar{\mu} = [\mu^2/4\pi\varepsilon_0\sigma^3 k_B T]^{1/2}$$

or equivalently, by virtue of the corresponding states principle, with

$$[4] \quad \bar{\mu} = [\mu^2 N_A/4\pi\varepsilon_0 V_c k_B T]^{1/2}$$

where $\bar{\mu}$ is the effective dipole moment and μ the permanent electric dipole moment, ε_0 is the permittivity of vacuum, σ is an appropriate molecular size parameter (say, the effective hard sphere diameter), N_A is the Avogadro constant, k_B is the Boltzmann constant, T is the thermodynamic temperature, and V_c the critical molar volume. To characterize the effective

Fig. 7. H^E at 298.15 K for CH_3-$(CH_2)_{n-1}$-CO-$(CH_2)_{m-1}$-CH_3 (1) + 3,6,9-trioxaundecane (2) systems. Points, experimental results (○, $n = 1$, $m = 5$; □, $n = 1$, $m = 7$; △, $n = m = 3$; ▽, $n = m = 4$ (28)); solid lines, DISQUAC calculations.

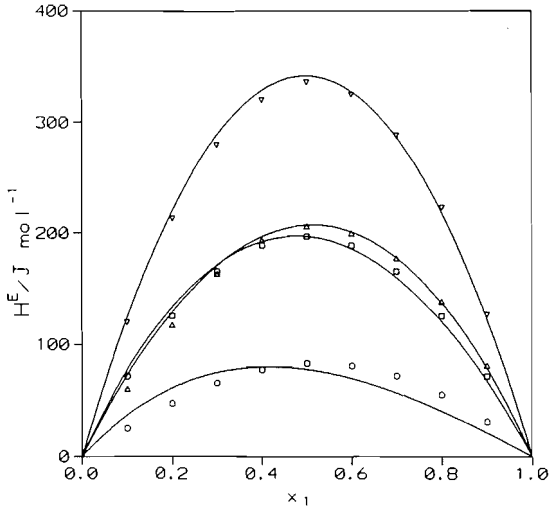

Fig. 8. DISQUAC predictions for G^E at equimolar composition and 298.15 K for linear ketones + linear monoethers vs. n, the number of carbon atoms in the ketone (the ethers are represented by u-O-v, where u and v are the numbers of aliphatic groups attached to the oxygen atom).

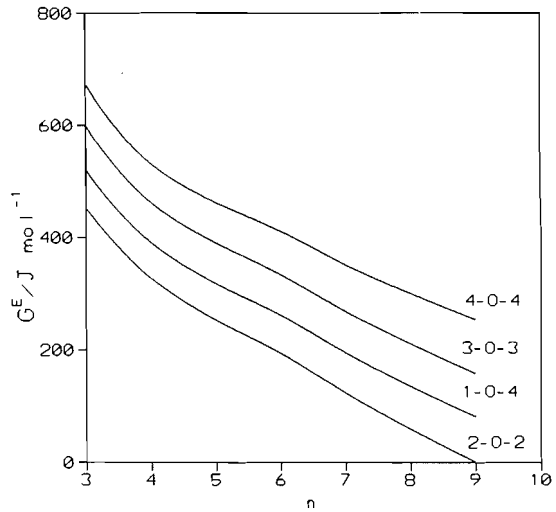

polarity of a molecule with μ, it is also possible to define a reduced dipole moment (25) according to:

$$[5] \quad \mu^* = [\mu^2/4\pi\varepsilon_0\sigma^3\varepsilon]^{1/2}$$

where ε is the interaction potential. This expression may advantageously be transformed, by virtue of the corresponding states principle, to:

$$[6] \quad \mu^* = [\mu^2 N_A/4\pi\varepsilon_0 V_c k_B T_c]^{1/2}$$

where T_c is the critical temperature. Since critical molar volume data are much scarcer than critical pressure data P_c, one may use alternatively:

Fig. 9. H^E at equimolar composition and 298.15 K for linear ketones + linear monoethers vs. n, the number of carbon atoms in the ketone. Points, experimental results (○, ketones + 4-O-4 (28); 2-propanone + 2-O-2: ● (21), ▲ (29)); solid lines DISQUAC predictions (the ethers are represented by u-O-v, where u and v are the numbers of aliphatic groups attached to the oxygen atom).

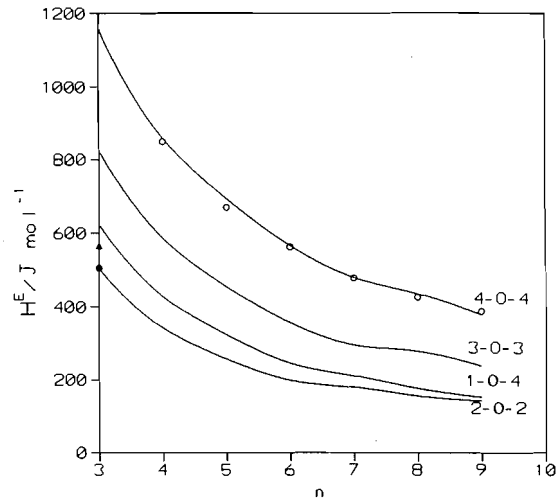

Table 7. Experimental excess enthalpy, H^E, at equimolar composition and 298.15 K for some systems involved in the CO/O project.

System	H^E/J mol^{-1}
Dibutyl ether + n-C_7	119[a]
2,5-Dioxahexane + n-C_7	1285[a]
3,6,9-Trioxaundecane + n-C_7	1179[a]
2-Propanone + n-C_7	1704[b]
2-Butanone + n-C_7	1339[c]
2-Pentanone + n-C_7	1135[c]
3-Pentanone + n-C_7	1078[c]
2-Heptanone + n-C_7	886[c]
4-Heptanone + n-C_7	812[c]
Methyl ethanoate + n-C_7	1782[d]
Ethyl ethanoate + n-C_7	1464[d]
Propyl ethanoate + n-C_7	1199[d]
Dimethyl carbonate + n-C_7	1988[e]
Diethyl carbonate + n-C_7	1328[e]
1-Methoxy-2-propanone + n-C_6	1753[f]

[a]Reference 3.
[b]Reference 13.
[c]Reference 14.
[d]Reference 30.
[e]References 8, 9.
[f]T = 303.15 K, ref. 26.

$$[7] \quad \mu^* = [\mu^2 P_c/4\pi\varepsilon_0 k_B^2 T_c]^{1/2}$$

The above-mentioned lowering of H^E, due to the destruction of dipole–dipole interactions in the pure liquid ketones, is now compensated in part by the creation of new dipole–dipole interactions between the ketones and the ether. For those mix-

Table 8. Critical properties, pressure, P_c, temperature, T_c, volume, V_c, and dipole moments, μ, reduced dipole moments, μ^*, and effective dipole moments, $\bar{\mu}$, for some molecules used in this work.

Compound	P_c[a]/atm	T_c[a]/K	V_c[a]/L mol^{-1}	μ[b]/D	μ^*	$\bar{\mu}$
2-Propanone	46.35	508.10	0.209	2.78	0.56	0.75
2-Butanone	41.52	536.78	0.267	2.79	0.49	0.65
2-Pentanone	36.46	561.08	0.301	2.77	0.44	0.61
3-Pentanone	36.80	561.46	0.336	2.74	0.42	0.57
2-Hexanone	32.80	587.00	0.377[c]	2.69	0.38	0.49
2-Heptanone	29.50	611.15	0.433[c]	2.66	0.34	0.49
Methyl acetate	46.88	506.55	0.228	1.83	0.35	0.46
Ethyl acetate	38.31	523.30	0.286	1.88	0.32	0.42
Propyl acetate	33.20	549.73	0.345	1.81	0.27	0.37
Dimethyl carbonate	43.20[c]	524.20[c]	0.247[c]	0.87	0.16	0.21
Diethyl carbonate	34.20[c]	569.00[c]	0.359[c]	0.90	0.13	0.18
Dibutyl ether	25.63	580.00	0.501[c]	1.13	0.14	0.19
2,5-Dioxahexane	38.20	536.00	0.271	1.71	0.30	0.40
3,6,9-Trioxaundecane	24.42	614.[c]	0.537[c]	1.92	0.22	0.32

[a]Reference 31.
[b]Reference 32.
[c]Value estimated by Joback's method (33).

Fig. 10. Excess functions at temperature T for 1-methoxy-2-propanone (1) + solvents (2) systems. Points, experimental results (□, G^E of the 1-methoxy-2-propanone (1) + methylcyclohexane (2) mixture at 318 K (27); ○, H^E of the 1-methoxy-2-propanone (1) + n-hexane (2) mixture at 303.15 K (26)); solid lines, DISQUAC calculations.

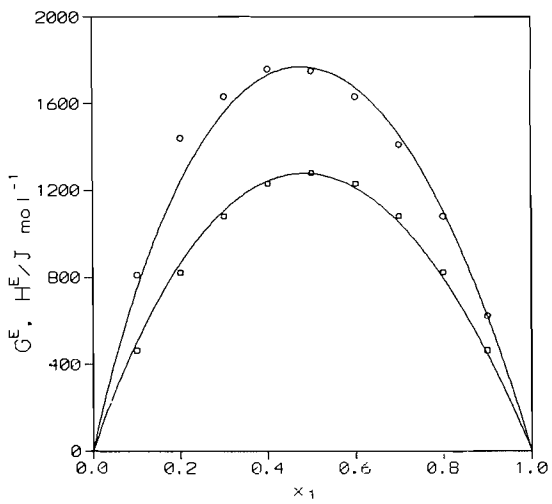

tures containing 2,5-dioxahexane or 3,6,9-trioxaundecane, H^E is eventually negative for the shorter ketones, indicating the presence of strong forces between dissimilar molecules. For a common ketone, we note that the forces are stronger in the case of the diether because H^E (2,5-dioxahexane) < H^E (3,6,9-trioxaundecane) (Table 6). This may be because the effective dipole moment of the diether is larger than that of the triether (Table 8).

On the other hand, comparing H^E of systems containing n-heptane and homomorphic polar molecules (i.e., dimethyl carbonate (-O-CO-O- group), ethyl acetate (-CO-O- group), or 3-pentanone (-CO- group)) (Table 7), we note that each atom attached to the carbonyl group, while decreasing the overall dielectric dipole moment, increases the dissimilarity between the force fields of the polar compounds and the alkane, and hence also H^E.

It is also possible to compare mixtures containing esters or organic carbonates and n-alkanes with those of linear ketones and dibutyl ether (-O- group), or 2,5-dioxahexane (two -O- groups), respectively. In this case, we observe that when the two oxygen atoms and the -CO- group belong to the same molecule (the former directly attached to the latter, or separated by a number of aliphatic groups as in the 1-methoxy-2-propanone + n-hexane mixture (26)), H^E is larger than when the -CO- and -O- groups belong to different molecules (Tables 6, 7).

However, comparison of the interchange coefficients is rather difficult because mixtures containing carbonates or esters with n-alkanes are characterized, in terms of DISQUAC, by only one contact, while those of ketones + oxaalkanes have three contacts.

The natural continuation of the CO/O project is to investigate proximity effects, analyzing systems including two functional groups in the same molecule, namely -CO- and -O- groups (ketoethers), or the -CO- and -CO-O- groups (ketoesters). We expect that the proximity effects may lead to an important increase of the interchange coefficients. In fact, in a previous step we examined the 1-methoxy-2-propanone + n-hexane mixture (26) (Fig. 10) and the limiting case of the dimethyl carbonate + n-alkane systems (8, 9), assuming that the carbonate molecule is composed of two aliphatic groups, two oxygen atoms, and the -CO- group. For the 1-methoxy-2-propanone + n-hexane mixture, we obtained $C^{DIS}_{ek,l}$ = 5.0;

$C^{QUAC}_{ek,1}$ = 2.0 and $C^{DIS}_{ek,2}$ = 12.0; $C^{QUAC}_{ek,2}$ = 10.0 (the Gibbs energy parameters calculated using VLE data for the 1-methoxy-2-propanone + methylcyclohexane system (27) and assuming this molecule as an *n*-alkane (8)). This increase in the interchange coefficients may be due to stronger dipole–dipole interactions in the 1-methoxy-2-propanone molecule than those in the mixtures treated above. For dimethyl carbonate + *n*-alkanes mixtures, the behaviour is similar. The interchange coefficients are $C^{DIS}_{ek,1}$ = 14.2; $C^{QUAC}_{ek,1}$ = 28.2 and $C^{DIS}_{ek,2}$ = 28.5; $C^{QUAC}_{ek,2}$ = 36.5.

5. References

1. H.V. Kehiaian. Fluid Phase Equilib. **13**, 243 (1983).
2. H.V. Kehiaian. Pure Appl. Chem. **57**, 15 (1985).
3. H.V. Kehiaian, M.R. Tiné, L. Lepori, E. Matteoli, and B. Marongiu. Fluid Phase Equilib. **46**, 131 (1989).
4. H.V. Kehiaian, S. Porcedda, B. Marongiu, L. Lepori, and E. Matteoli. Fluid Phase Equilib. **63**, 231 (1991).
5. M.R. Tiné, G. Della Gatta, and H.V. Kehiaian. Fluid Phase Equilib. **54**, 277 (1990).
6. M.R. Tiné and B. Marongiu. Thermochim. Acta, **199**, 63 (1992).
7. G. Avedis, J.-P.E. Grolier, J. Fernández, and H.V. Kehiaian. J. Solution Chem. **23**, 135 (1994).
8. H.V. Kehiaian, J.A. González, I. García, J.C. Cobos, C. Casanova, M.J. Cocero. Fluid Phase Equilib. **64**, 1 (1991).
9. J.A. González, I. García de la Fuente, J.C. Cobos, C. Casanova, and H.V. Kehiaian. Thermochim. Acta, **217**, 57 (1993).
10. H.V. Kehiaian, J.A. González, I. García, R. Escarda, J.C. Cobos, and C. Casanova. Fluid Phase Equilib. **69**, 91 (1991).
11. A.B. de Haan, A. Heine, K. Fischer, and J. Gmehling. J. Chem. Eng. Data, **40**, 1228 (1995).
12. F.J. Rey and J. Martín-Gil. Thermochim. Acta, **144**, 1 (1989).
13. H.V. Kehiaian, J.-P.E. Grolier, M.R. Kechavarz, and G.C. Benson. Fluid Phase Equilib. **5**, 159 (1980).
14. H.V. Kehiaian, J.-P.E. Grolier, M.R. Kechavarz, G.C. Benson, O. Kiyohara, and Y.P. Handa. Fluid Phase Equilib. **7**, 95 (1981).
15. H.V. Kehiaian, J.-P.E. Grolier, and G.C. Benson. J. Chim. Phys. **75**, 1031 (1978).
16. H.V. Kehiaian and B. Marongiu. Fluid Phase Equilib. **40**, 23 (1988).
17. A. Bondi. Physical properties of molecular crystals, liquids and glasses. Wiley, New York. 1968.
18. J.A. González, I. García de la Fuente, J.C. Cobos, and C. Casanova. Ber. Bunsen-ges. Phys. Chem. **95**, 1658 (1991).
19. J.A. González, I. García de la Fuente, J.C. Cobos, and C. Casanova. Fluid Phase Equilib. **78**, 61 (1992).
20. J.A. González, I. García de la Fuente, J.C. Cobos, C. Casanova, and A. Ait-Kaci. Fluid Phase Equilib. **112**, 63 (1995).
21. H. Hirobe. J. Fac. Sci. Imp. Univ. Tokyo, Sect. 1: **1**, 155 (1926).
22. B.D. Smith. Int. DATA Ser., Sel. Data Mixtures, Ser. A: **4**, 252 (1985).
23. H.S. Wu and S.I. Sandler. Int. DATA Ser., Sel. Data Mixtures, Ser. A: **3**, 209 (1988).
24. A.H. Roux, J.-P.E. Grolier, A. Inglese, and E. Wilhem. Ber. Bunsen-ges. Phys. Chem. **88**, 986 (1984).
25. E. Wilhelm, A. Laínez, and J.-P.E. Grolier. Fluid Phase Equilib. **49**, 233 (1989).
26. J.M. Monzón, S. Otín, and C. Gutiérrez Losa. Acta Cient. Compostelana, **22**, 285 (1985).
27. R.V. Orye. Int. DATA Ser., Sel. Data Mixtures, Ser. A: 74 (1973).
28. C. Casanova, J. Rey, and J.C. Cobos. Int. DATA Ser., Sel. Data Mixtures, Ser. A: **2**, 102 (1986).
29. W. Drinkard and D. Kivelson. J. Phys. Chem. **62**, 1494 (1958).
30. H.V. Kehiaian, R. Bravo, M. Pintos Barral, M.-I. Paz Andrade, R. Guieu, and J.-P.E. Grolier. Fluid Phase Equilib. **17**, 187 (1984).
31. J.A. Riddick, W.B. Bunger, and Th.K. Sakano. Organic solvents. Physical properties and methods of purification. Vol. II. 4th ed. J. Wiley & Sons, New York. 1986.
32. A.L. McClellan. Tables of experimental dipole moments. Vols. 2, 3. Rahara Enterprises, El Cerrito, Calif. 1974.
33. R.C. Reid, J.M. Prausnitz, and B.E. Poling. The properties of gases and liquids. 4th ed. McGraw-Hill, New York. 1987.
34. J.J. Christensen, R.W. Hanks, and R.M. Izatt. Handbook of heats of mixing. J. Wiley & Sons, New York. 1982.

On the dissociation energy of $Ti(OH_2)^+$. An MCSCF, CCSD(T), and DFT study

A. Irigoras, J.M. Ugalde, X. Lopez, and C. Sarasola

Abstract: The dissociation energy of the $Ti(OH_2)^+$ ion–molecule complex was calculated by the multiconfigurational self-consistent field theory, coupled cluster theory, and two density functional theory based methods, using both all-electron basis sets and effective core potentials. The calculations show that approximate density functional theory gives results in better agreement with experiment than either the multiconfigurational self-consistent field theory or the coupled cluster theory, with both all-electron basis sets and effective core potentials. Nevertheless, the optimized geometries and harmonic vibration frequencies are very similar, irrespective of the level of theory used. The interconfigurational energy ordering of the two valence electronic configurations $d^{n-1}s$ and $d^{n-2}s^2$ of the ^4F electronic state of the titanium cation were also calculated and are discussed.

Key words: ab initio, dissociation energy, ion–molecule complex, effective core potentials, transition metals.

Résumé : On a calculé l'énergie de dissociation du complexe ion–molécule, $Ti(OH_2)^+$, à l'aide de la théorie de champ autocohérent multiconfigurationnel, de la théorie de l'agrégat couplé et de deux méthodes basées sur la théorie de la densité fonctionnelle, utilisant des ensembles de base de tous les électrons ainsi que tous les potentiels effectifs des noyaux. Les calculs montrent que la théorie approximative de la densité fonctionnelle conduit à des résultats qui sont en meilleur accord avec les données expérimentales que ceux obtenus à l'aide tant de la théorie du champ autocohérent multiconfigurationnel que de la théorie de l'agrégat couplé incorporant les ensembles de base de tous les électrons ainsi que tous les potentiels effectifs des noyaux. Néanmoins, les géométries optimisées et les fréquences de vibration harmonique sont très semblables, quel que soit le niveau de la théorie utilisé. On a aussi calculé l'ordre des énergies interconfigurationnelles des deux configurations électroniques de valence $d^{n-1}s$ et $d^{n-2}s^2$ de l'état électronique ^4F des cations du titane et on en discute.

Mots clés : ab initio, énergie de dissociation, complexe ion–molécule, potentiels effectifs des noyaux, métaux de transition.

[Traduit par la rédaction]

1 Introduction

Solvation of first-row transition metal ions by water has been the subject of much recent research work. Both experimental and theoretical methods have been used to gain insight into the bonding energies of water molecules to transition-metal positive ions. The $Ti(OH_2)^+$ cluster, in particular, was studied earlier by both experimentalists and theoreticians. Thus, the bond dissociation energy of the $Ti(OH_2)^+$ complex was first reported by Magnera et al., obtained by the use of collision-induced dissociation in a triple-quadrupole mass spectrometer (1). They gave a value of 38.0 ± 3 kcal/mol. Later, Dalleska et al. (2) reported the bond dissociation energies of water molecules from first-row transition-metal positive ions as determined by collision-induced dissociation in a guided ion beam mass spectrometer. The threshold energy for the collision-induced reactions is equivalent to the 0 K bond dissociation energy;[2] therefore, their value for the dissociation energy of the $Ti(OH_2)^+$ ion–molecule complex at 0 K is 36.9 ± 1.4 kcal/mol.[3] Simultaneously, ab initio molecular orbital theory was also used to estimate the dissociation of $Ti(OH_2)^+$. Rossi and Bauschlicher (3) reported calculations with the modified coupled pair functional (MCPF) method and a fairly large basis set. They obtained a value of 38.3 kcal/mol, using for the zero-point vibrational energy (ZPVE) correction the corresponding energy correction of the $Cu(OH_2)^+$ system. Magnusson and Moriarty (4) used both Möller–Plesset (MP) perturbation theory and truncated configuration interaction (CI) methods with a variety of basis sets. Their results show, as indeed do those of Rossi and Bauschlicher, that in every case the dissociation energy of the $Ti(OH_2)^+$ is overestimated with respect to the experimental value of Dalleska et al.

During recent years, however, there has been increasing interest in the use of gradient-corrected approximate density functionals (5, 6). In particular, there is growing evidence that approximate functionals yield accurate bonding energies for both the first- (7, 8) and second-row (9) transition metal complexes. Thus, in this work we consider the bonding energy of $Ti(OH_2)^+$. Our goal is to determine the reliability of the approximate density functionals BLYP and B3LYP used in conjunction with effective core potentials and valence basis sets of double- and triple-zeta quality. Comparison of available experimental data, with respect to both BLYP and B3LYP and multiconfigurational self-consistent field

Received May 14, 1996.

A. Irigoras, J.M. Ugalde,[1] X. Lopez, and C. Sarasola. Kimika Fakultatea, Euskal Herriko Unibertsitatea, P.K. 1072, 20080 Donostia, Euskadi, Spain.

[1] Author to whom correspondence may be addressed. Telephone: +34-43-216 600. Fax: +34-43-212 236. E-mail: ugalde@sq.ehu.es

[2] P.B. Armentrout, personal communication.

[3] See Table 3 of ref. 2.

(MCSCF) and coupled cluster (CCSD(T)) calculations with all-electron double-zeta and triple-zeta basis sets and effective core potentials, will be made. Inclusion of corrections due to the zero-point vibrational energy and to the basis set superposition energy, estimated with the counterpoise method (10) will also be explicitly considered.

2 Methods

All calculations reported in this paper have been carried out with the GAMESS (11) and the GAUSSIAN94/DFT (12) suites of programs.

2.1 Level of theory

Both ab initio molecular orbital MCSCF and CCSD(T) methods and BLYP and B3LPY approximate density functional theory (DFT) methods have been used in the present study. For the MCSCF calculations, a full optimization at the Hartree–Fock level of theory was initially carried out to properly select the active space window. In particular, we chose six orbitals, corresponding to the five 3*d* and the one 4*s* valence orbitals of titanium, to allocate three electrons. This active space will be denoted, as usual, (3/6). Both Ti^+ and $Ti(OH_2)^+$ have been fully optimized at this level of theory, while for the H_2O only the Hartree–Fock level was used. These structures were confirmed to be true minima by inspection of the force constants matrix, evaluated at the corresponding level of theory.

The singles and doubles, with a noniterative estimate for the triples, coupled cluster (CCSD(T)) calculations were carried out at the CCD optimized structures. Also, at this level of theory the zero-point vibrational energy corrections (ΔZPVE) were taken from a frequency calculation at the CCD level of theory.

The approximate DFT methods that were used are associated with the well-known Becke (5) and Lee, Yang, and Parr (6*d*) (BLYP) approximate functionals and the three-parameter hybrid approximate functional of Becke (13):

$$[1]\quad (1-a_0)E_x^{\mathrm{LSD}} + a_0E_x^{\mathrm{HF}} + a_xE_x^{\mathrm{B88}} + a_cE_c^{\mathrm{LYP}} + (1-a_c)E_c^{\mathrm{VWN}}$$

where $a_0 = 0.20$, $a_x = 0.72$, and $a_c = 0.81$, and LSD stands for the Slater exchange (14), B88 is the Becke 1988 exchange functional correction (5), LYP stands for the gradient-corrected correlation functional of Lee, Yang, and Parr (6*d*), and VWN for the local correlation functional of Vosko, Wilk, and Nusair (15). The choice of these two approximate DFT methods was largely motivated by their satisfactory performance as reported recently (8, 16) for transition-metal-containing systems.

2.2 Basis sets

2.2.1 All-electron basis sets

As indicated by Hay and co-workers (17), good uncontracted basis sets are normally too large for application to molecules and, so, need to be appropriately contracted. In the present paper three different contracted basis sets (18), two of double-zeta plus polarization quality, namely the DZVP and DZVP2 given by Salahub and co-workers (19), and one of triple-zeta plus polarization quality were used for the calculations. The triple-zeta-quality basis set, TZVP, used in the present paper is, for the titanium, that given by Schäfer, Hubert and Ahlrichs (20), supplemented by the two 4*p* polarization functions optimized by Wachters (21) for the excited states and augmented with a diffuse *s* function (with an exponent 0.30 times that of the most diffuse *s* function on the original set) and one diffuse *d* function (optimized by Hay (22)). For both the oxygen and hydrogen we have taken the standard 6-311++G(d,p) basis set of Pople and co-workers (23).

2.2.2 Effective core potentials (ECP)

The use of atomic effective core potentials (ECP) and model potentials (MP) to eliminate chemically inactive atomic core electrons from quantum mechanical calculations has become routine during the past decade (24). Because of the economic advantage associated with reduced size of the basis sets that can be achieved with the ECP method and corresponding nodeless pseudo-orbitals, the SKBJ relativistic compact effective potentials (24) were used. These consider the first 10 electrons of the titanium and the first 2 electrons of the oxygen to be part of the core, and the rest are described by the SKBJC valence basis set. Three different sets have been built from the standard SKBJC set. The smallest one has one extra heavy atom polarization function on the oxygen (SKBJC(d)); the intermediate one has one extra *d* polarization function on the oxygen and one *p*-type polarization function on the hydrogens (SKBJC(d,p)); finally, the largest one has a *d* polarization function on the oxygen plus two *p* polarization functions on the hydrogens (SKBJC(d,2p)). The contractions for these three sets are as follows:

SKBJC(d)→[4*sp*3*d*/2*sp*1*d*/2*s*]

SKBJC(d,p)→[4*sp*3*d*/2*sp*1*d*/2*s*1*p*]

SKBJC(d,2p)→[4*sp*3*d*/2*sp*1*d*/2*s*2*p*]

Since the importance of relativistic effects decreases steadily from the third-row transition-metal series to the first, it is customarily (3, 4) assumed that these are sufficiently small for titanium not to be considered explicitly in the all-electron basis sets. Therefore, the dissociation energies reported in this paper for all-electron basis sets were calculated as the difference between the energy of the isolated monomers and the complex, without considering relativistic effects, but including both BSSE and ZPVE corrections. All the structures shown in this paper have been confirmed to be true minima by a frequency calculation at the corresponding computational level. Further, these calculations have provided us with the zero-point vibrational energy (ZPVE) corrections.

3 Results

Discussion here is directed at finding out which of the methods used can be selected as a computational strategy that is economical and, at the same time, reliable. Multiconfigurational methods are adequate to describe properly the different configurations that arise from the nonequivalence of *d* orbitals in $d^{n-2}s^2$, $d^{n-1}s$, and d^n states (25). On the other hand, DFT, a monoconfigurational method that includes correlation and that seems to work properly for these kinds of systems (7–9,

Table 1. Total (E) (in au) and relative energy (Δ_{sd}). (in eV) and expectation value of the $\hat{S}^2$ operator for the sd^2 and d^3 electronic configurations of $Ti^+(^4F)$ calculated with the B3LYP and various basis sets and ECPs.

	Electronic configuration	E	$\langle S^2 \rangle$	Δ_{sd}
SKBJC(d)	sd^2	−57.684 00	3.75	−0.06
	d^3	−57.681 93	3.75	
DZVP	sd^2	−848.980 09	3.75	0.54
	d^3	−848.999 86	3.75	
DZVP2	sd^2	−848.986 81	3.75	0.38
	d^3	−849.000 70	3.75	
TZVP	sd^2	−849.115 15	3.75	0.19
	d^3	−849.122 19	3.75	

16), is computationally a less demanding method than the correlated ab initio MCSCF and CCSD(T) methods.

3.1 Ti^+

It was pointed out earlier (26) that the correct prediction of the interconfigurational energy ordering of the two valence electronic configurations, $d^{n-1}s$ and $d^{n-2}s^2$, of transition-metal atoms is crucial for the accurate description of the dissociation energies of the clusters. In particular, the ground state of the Ti^+ cation is the ^4F state, which corresponds to the $3d^24s^1$ electronic configuration, and the first excited state, the $^4F(3d^3)$, lies 0.10 eV above (27). However, it has been demonstrated (28) that subtraction of the relativistic corrections from the energies of both states switches the stability order, rendering a $^4F(3d^3)$ ground state with the $^4F(3d^24s^1)$ being the first excited state, 0.07 eV above.

Inspection of Table 1 reveals that the B3LYP method describes correctly the above-mentioned energy ordering. Thus, for the all-electron basis function sets used in the present research, of which neither accounts for the relativistic effects, the $^4F(3d^3)$ state should be found to be the ground state, as is the case, and $^4F(3d^24s^1)$ the first excited state. But, for the SKBJ(d) effective core potential, which does account for the relativistic effects, the $^4F(3d^24s^1)$ is predicted to be the ground state. Nevertheless, it is particularly worth noting that, for the all-electron basis functions, the relative energy difference is overestimated with respect to the experimental energy corrected for relativistic effects. The best relative energy is obtained at the B3LYP/TZVP level of theory, Δ_{sd} = 0.19 eV, which is to be compared with the relativistic corrected experimental energy of 0.07 eV. However, for the ECP the relative energy difference is only slightly underestimated. Indeed we predict a difference of 0.06 eV, while the experimental value is 0.1 eV. This again raises the question of the legitimacy of employing effective core potentials derived from atomic HF calculations in approximate DFT methods, a question that was addressed recently, and has been given an empirical justification (9, 29).

Results obtained with the MCSCF and CCSD(T) methods, collected in Tables 2 and 3, respectively, also deserve a short comment. It is observed that both, irrespective of whether effective core potentials or all-electron basis sets are used, predict a $^4F(3d^24s^1)$ ground state, with the $^4F(3d^3)$ state lying more than 0.2 eV above. While this energy ordering is qualitatively correct for the ECPs, it should be regarded as incorrect for the all-electron basis, for which the $^4F(3d^3)$ should be the lowest energy state, as stated above. Notice, also, that the qualitatively correct energy level ordering prediction obtained with the ECPs is unsatisfactory from a quantitative point of view, since the experimental energy difference is 0.1 eV while the MCSCF theory predicts 0.24 eV and the CCSD(T) theory 0.72 eV.

Table 2. Total (E) (in au) and relative energy (Δ_{sd}) (in eV) for the sd^2 and d^3 electronic configurations of $Ti^+(^4F)$ calculated at MCSCF(3/6) level with various basis sets and ECPs.

	Electronic configuration	E	Δ_{sd}
SKBJC(d)	sd^2	−57.254 19	−0.24
	d^3	−57.245 49	
DZVP	sd^2	−848.025 48	−0.23
	d^3	−848.017 14	
DZVP2	sd^2	−848.029 04	−0.30
	d^3	−848.018 07	
TZVP	sd^2	−848.187 82	−0.46
	d^3	−848.170 87	

Table 3. Total (E) (in au) and relative energy (Δ_{sd}) (in eV) for the sd^2 and d^3 electronic configurations of $Ti^+(^4F)$ calculated at the CCSD(T) level with various basis sets and ECPs.

	Electronic configuration	E	Δ_{sd}
SKBJC(d)	sd^2	−57.448 71	−0.72
	d^3	−57.422 24	
DZVP	sd^2	−848.023 63	−0.19
	d^3	−848.016 70	
DZVP2	sd^2	−848.027 80	−0.26
	d^3	−848.018 31	
TZVP	sd^2	−848.193 97	−0.21
	d^3	−848.186 45	

Table 4. MCSCF(3/6) optimized relevant geometric data for the $^4B_2$ state of the $Ti(OH_2)^+$ ion–molecule complex with various basis sets. Distances are in angstroms and angles in degrees.

Basis set	R(Ti—O)	r(O—H)	<TiOH
SKBJC(d)	2.200	0.968	127.0
SKBJC(d,p)	2.194	0.963	126.8
SKBJC(d,2p)	2.196	0.962	126.4
DZVP	2.178	0.951	126.4
DZVP2	2.185	0.950	126.6
TZVP	2.196	0.951	126.6

3.2 $Ti(OH_2)^+$

Tables 4, 5, and 6 show the optimized geometry of the

Table 5. B3LYP and BLYP approximate density functional theory optimized geometries for the corresponding $^4B_1$ and $^4B_2$ states of the $Ti(OH_2)^+$ ion–molecule complex with various basis sets. Distances in Å and angles in degrees.

	BLYP			B3LYP		
Basis set	*R*(Ti—O)	*r*(O—H)	<TiOH	*R*(Ti—O)	*r*(O—H)	<TiOH
SKBJ(d)	2.107	0.999	127.0	2.109	0.989	127.0
SKBJ(d,p)	2.104	0.995	126.9	2.107	0.985	126.9
SKBJ(d,2p)	2.097	0.996	126.8	2.108	0.985	127.0
DZVP	2.107	0.984	126.4	2.103	0.973	126.6
DZVP2	2.105	0.985	126.4	2.099	0.974	126.6
TZVP	2.115	0.971	126.4	2.106	0.982	126.2

Table 6. CCD optimized relevant geometric data for the $^4B_1$ state of the Ti(OH2)+ ion–molecule complex with various basis sets. Distances are in angstroms and angles in degrees.

Basis set	*R*(Ti—O)	*r*(O—H)	<TiOH
SKBJC(d)	2.149	0.993	127.3
SKBJC(d,p)	2.148	0.984	127.2
SKBJC(d,2p)	2.150	0.982	127.4
DZVP	2.173	0.970	127.0
DZVP2	2.177	0.970	127.2
TZVP	2.166	0.968	125.6

$Ti(OH_2)^+$ ion–molecule complex at various levels of theory. Data are given only for the $^4B_2$ state; however, it is worth noting that a $^4B^1$ state, nearly degenerate in energy and with a nearly coincident optimum geometry, has also been found in every case. Inspection of the data of Tables 4–6 reveals that both the approximate density functionals BLYP and the hybrid procedure B3LYP yield a shorter Ti—O bond length than the MCSCF(3/6) method, for the basis set investigated. This is a tendency reported recently for hydrogen-bonded complexes (30) and for charge-transfer complexes (31). However, for our ion–molecule complex the discrepancies between the approximate density functional and molecular orbital theories are not as severe as those found for the above-mentioned systems. On the other hand, for the coupled cluster (CCD) theory Ti—O and O—H optimized distances lie in between MCSCF and DFT values, as shown in Table 6. The largest discrepancy with the ECPs is found for the SKBJC(d), for which the B3LYP method predicts a Ti—O bond length 0.091 Å shorter than that of the MCSCF(3/6) method. Nevertheless, it should be pointed out that the O—H bond is predicted to be ~0.035 Å larger by both of the DFT-based methods used in the present paper. The agreement found for the TiOH bond angle for all the methods is also remarkable, see column 4 of Tables 4 and 6 and columns 4 and 7 of Table 5.

In summary, the MCSCF(3/6) method predicts a bond length close to 2.2 Å for the $Ti(OH_2)^+$ ion–molecule complex, the CCD theory prediction lies in the range between 2.18 and 2.15 Å, depending on the basis set used, and both of the DFT-based methods used predict it to be around 2.1 Å, irrespective of whether an all-electron basis function set or an effective core potential is used.

3.3 Dissociation energies

Table 7 shows the electronic energies, zero-point vibrational energy corrections, basis set superposition error energy corrections, and the dissociation energies of the $Ti(OH_2)^+$, calculated at various levels of theory. In every case, the dissociation energy has been calculated as the energy difference between the $^4B_2$ state of the $Ti(OH_2)^+$ and the most stable electronic configuration of the ^4F state of the Ti^+ plus the energy of one water molecule. In addition, both the zero-point vibrational energy correction and the basis set superposition error energy correction have been taken into account.

Inspection of Table 7 reveals that both approximate density functional based methods, BLYP and B3LYP, overestimate slightly the dissociation energy of the $^4B_2$ state of $Ti(OH_2)^+$, with respect to the best experimental value of 36.9 kcal/mol. The best value obtained using DFT with ECPs was obtained using the B3LYP/SKBJC(d,2p) method, i.e., 37.9 kcal/mol, only 1 kcal/mol higher than experiment. However, it should be mentioned that provision of the basis set superposition energy error must be taken into account, in order to arrive at such a good estimate, for it can be as large as 2.3 kcal/mol. When all-electron basis sets are used with our approximate DFT methods, the BSSE error appears to be smaller than for ECPs, and the dissociation energies are even closer to the experimental value. Remarkably, at the B3LYP/TZVP level of theory we obtain D_0 = 36.7 kcal/mol, only 0.2 kcal/mol below the experimental result. Notice that for the all-electron basis set, both the BLYP and B3LYP lead to estimates of D_0 within the error bars of the experimental value, namely 36.9 ± 1.4 kcal/mol. In addition, the B3LYP method also fits the estimate for D_0, using the SKBJC(d,2p), within the error bars. These data contribute to the mounting evidence that B3LYP also performs reliably for open-shell transition-metal-containing compounds (8, 9, 16).

On the other hand both molecular orbital theory methods, MCSCF(3/6) and CCSD(T), with ECPs severely underestimate the dissociation energy of the title compound by 7.7 and 6.7 kcal/mol, at the MCSCF(3/6)/SKBJC(d,2p) and CCSD(T)/SKBJC(d,2p) levels of theory, respectively. Using all-electron basis sets instead of ECPs does not remedy the apparent weakness of the method, although it improves the

Table 7. Total energies E (in hartree/particle), zero-point vibrational energy corrections ΔZPVE (in kcal/mol), basis set superposition error corrections BSSE (in kcal/mol), and dissociation energies D_0 (in kcal/mol), for the $Ti(OH_2)^+$ ion–molecule complex.

Method		E	ΔZPVE	BSSE	D_0
BLYP	SKBJC(d)	−74.827 57	1.5	2.2	39.6
	SKBJC(d,p)	−74.836 40	1.6	2.5	39.5
	SKBJC(d,2p)	−74.838 39	1.5	2.9	38.7
	DZVP	−925.507 60	1.6	1.2	38.1
	DZVP2	−925.516 85	1.6	0.4	37.1
	TZVP	−925.608 12	1.7	0.7	36.5
B3LYP	SKBJC(d)	−74.915 65	1.6	1.7	38.9
	SKBJC(d,p)	−74.925 34	1.6	2.0	38.9
	SKBJC(d,2p)	−74.927 22	1.7	2.3	37.9
	DZVP	−925.511 90	1.8	0.9	37.3
	DZVP2	−925.521 89	1.8	0.4	37.3
	TZVP	−925.620 64	1.8	0.8	36.7
MCSCF(3/6)	SKBJC(d)	−74.154 48	1.5	3.7	30.4
	SKBJC(d,p)	−74.167 08	1.6	3.7	30.6
	SKBJC(d,2p)	−74.168 72	2.2	3.6	29.2
	DZVP	−924.118 55	1.8	2.7	30.0
	DZVP2	−924.127 35	1.8	2.3	28.2
	TZVP	−924.272 08	1.8	1.8	29.7
CCSD(T)	SKBJC(d)	−74.533 49	1.6	3.7	31.6
	SKBJC(d,p)	−74.556 29	1.3	3.6	31.5
	SKBJC(d,2p)	−74.560 32	1.4	3.5	30.2
	DZVP	−924.324 65	1.6	1.9	33.4
	DZVP2	−924.328 23	1.5	2.1	31.2
	TZVP	−924.495 05	1.5	1.0	32.9

estimate. Notice that at the MCSCF(3/6)/TZVP level of theory the dissociation energy is still underestimated by 7.2 kcal/mol, and by 4.0 kcal/mol at the CCSD(T)/TZVP level of theory. This is suggestive of the slower convergence of the CCSD(T) method with the basis set, with respect to the B3LYP. Hence, in the small basis sets used in this work, it yields poorer agreement with experiment. However, this might not be so in the complete basis set. It is worth pointing out that both the MCSCF and CCSD(T) calculations are affected by a noticeably large BSSE error of 3.6 kcal/mol, when ECPs are used (3).

Finally, our calculations highlight one more interesting point. Namely, the approximate ΔZPVE value of 1.7 kcal/mol, used by Rossi and Bauschlicher (3) for the first-row transition-metal positive water clusters is well justified, even for approximate density functional based methods.

4 Conclusions

Our calculations show that the approximate DFT functionals BLYP and B3LYP, with both double-zeta-quality all-electron basis sets and effective core potentials, correctly predict the energy ordering of the two electronic configurations associated with the ground ^4F state of Ti^+. However, the calculated relative energies are overestimated with respect to their corresponding experimental values for every all-electron basis set used in the present study. On the other hand, for the SKBJC(d) effective core potentials of Stevens et al. (24), a good estimate, only 0.04 eV smaller, of the true experimental interconfigurational energy is obtained. Both the MCSCF and CCSD(T) method perform more poorly than the B3LYP procedure, yielding only a qualitative correct estimate for Δ_{sd} with the SKBJC(d) effective core potential. All-electron basis sets are not successful even in predicting the expected energy level ordering.

Optimum molecular geometries of the $^4B_2$ state of the $Ti(OH_2)^+$ ion–molecule complex do not depend appreciably on the basis sets used, but they do depend on the method. Thus, the MCSCF method leads to the largest Ti—O optimum bond distances, namely 2.2 Å, DFT yields the shortest, around 2.1 Å, and CCSD(T) predicts an in-between value, close to 2.15 Å.

Finally, the dissociation energy of the $Ti(OH_2)^+$ ($^4B_2$), is best reproduced at the B3LYP/TZVP level of theory, and reasonable estimates are obtained at both the BLYP/SKBJC(d,2p) and B3LYP/SKBJC(d,2p) levels of theory. On the other hand, both molecular orbital theory methods, MCSCF and CCSD(T), severely underestimate the dissociation energy.

Therefore, it is concluded that the B3LYP method used in conjunction with either the SKBJC effective core potentials or triple-zeta-quality basis sets represents a feasible computa-

tional strategy to deal with the molecular and electronic structures of the first-row transition-metal ligand complexes. In particular, it should be an efficient and accurate method to aid in understanding recent experiments (32) on primary reactions of Ti^+ with small molecules in the gas phase. Such work is in progress in our laboratory.

Acknowledgments

This research was supported by a grant (GV/203.215-49/94) from The University of the Basque Country (Euskal Herriko Unibertsitatea) and the Basque Government (Eusko Jaurlaritza). A.I. wishes to thank the Basque Goverment for a Grant. The authors thank Professors P.B. Armentrout, T.C. Cundari, and L.A. Eriksson for helpful comments.

References

1. T.F. Magnera, D.E. David, and J. Michl. J. Am. Chem. Soc. **111**, 4100 (1989).
2. N.F. Dalleska, K. Honma, L.S. Sunderlin, and P.B Armentrout. J. Am. Chem. Soc. **116**, 3519 (1994).
3. M. Rossi and C.W. Bauschlicher. J. Chem. Phys. **90**, 7264 (1989).
4. E. Magnusson and N.W. Moriarty. J. Comput. Chem. **14**, 961 (1993).
5. A.D. Becke. Phys. Rev. A: Gen. Phys. **38**, 3098 (1988).
6. (*a*) J.P. Perdew and Y. Wang. Phys. Rev. B: Condens. Matter, **33**, 8800 (1986); (*b*) J.P. Perdew. Phys. Rev. B: Condens. Matter, **33**, 8822 (1986); **34**, 7406 (1986); (*c*) J.P. Perdew and Y. Wang. Phys. Rev. B: Condens. Matter, **45**, 13244 (1992); J.P. Perdew. *In* Electronic structure of solids. *Edited by* P. Ziesche and H. Eischering. Akademie, Berlin. 1991; J.P. Perdew, J.A. Chevary, S.H. Vosko, K.A. Jackson, M.R. Pederson, D.J. Singh, and C. Fiolhais. Phys. Rev. B: Condens. Matter, **46**, 6671 (1992); (*d*) C. Lee, W. Yang, and R.G. Parr. Phys. Rev. B: Condens. Matter, **37**, 785 (1988).
7. A. Ricca and C.W. Bauschlicher. J. Phys. Chem. **99**, 9003 (1995).
8. A. Ricca and C.W. Bauschlicher. J. Phys. Chem. **98**, 12899 (1994).
9. L.A. Eriksson, L.G.M. Petterson, P.E.M. Siegbahn, and U. Wahlgren. J. Phys. Chem. **102**, 2 (1995).
10. S.F. Boys and F. Bernardi. Mol Phys. **19**, 553 (1970); D.W. Schwenke and D.B. Truhlar. J. Chem. Phys. **82**, 2418 (1985).
11. (*a*) M. Dupuis, D. Spangler, and J.J. Wendoloski. NRCC software catalog. University of California, Berkeley, Calif. 1980. Program QG01. (*b*) M.W. Schmidt, K.K. Baldridge, J.A. Boatz, J.H. Jensen, S. Koseki, M.S. Gordon, K.A. Nguyen, T.L. Windus, and S.T. Elbert. QCPE Bull. **10**, 42 (1990).
12. M.J. Frisch, G.W. Trucks, M. Head-Gordon, P.M.W. Gill, M.W. Wong, J.B. Forseman, B.G. Johnson, H.B. Schlegel, M.A. Robb, E.S. Repogle, R. Gomperts, J.L. Andres, K. Raghavachari, J.S. Binkley, C. Gonzales, R.L. Martin, D.J. Fox, D.J. Defrees, J. Baker, J.J.P. Steward, and J.A. Pople. Gaussian92/DFT, Revision F.4. Gaussian, Inc., Pittsburgh, Pa. 1992.
13. A.D. Becke. J. Chem. Phys. **98**, 5648 (1993).
14. J.C. Slater. Quantum theory of molecules and solids. Vol. 4. The self-consistent field for molecules and solids. McGraw–Hill, New York. 1974.
15. S.H. Vosko, L. Wilk, and M. Nusair. Can. J. Phys. **58**, 1200 (1980).
16. C.W. Bauschlicher and P. Maitre, J. Phys. Chem. **99**, 3444 (1995).
17. T.V. Russo, R.L. Martin, and P.J. Hay. J. Chem. Phys. **101**, 7729 (1994).
18. T.H. Dunning and P.J. Hay. *In* Methods of electronic structure theory. Vol. 3. *Edited by* H.F. Schaefer III. Plenum Press, Inc., New York. 1997. pp. 1–27.
19. F. Sim, D.R. Salahub, S. Chim, and M. Dupuis. J. Chem. Phys. **95**, 4317 (1991); N. Godbout, D.R. Salahub, J. Andzelm, and E. Wimmer. Can. J. Chem. **70**, 560 (1992).
20. A. Schäfer, C. Hurbert, and R. Ahlrichs. J. Chem. Phys. **100**, 5829 (1994).
21. A.J. Wachters. J. Chem. Phys. **52**, 1033 (1970).
22. P.J. Hay. J. Chem. Phys. **66**, 4377 (1971).
23. J.S. Krishnan, J.S. Binkley, P.v.R. Schleyer, and J.A. Pople. J. Chem. Phys. **72**, 650 (1980).
24. W.J. Stevens, M. Krauss, H. Basch, and P.G. Jasien. Can. J. Chem. **70**, 612 (1992).
25. B.H. Botch, T.H. Dunning, and J.F. Harrison. J. Chem. Phys. **75**, 3466 (1981).
26. R.O. Jones and O. Gunnarson. Rev. Mod. Phys. **61**, 689 (1989).
27. C.E. Moore. Atomic energy levels. National Bureau of Standards, Washington, D.C. 1952; Natl. Bur. Stand. Circ. **2**, **3**, 467 (1959).
28. K. Raghavachari and G.W. Trucks. J. Chem. Phys. **91**, 2457 (1989).
29. V. Jonas and W. Thiel. J. Chem. Phys. **102**, 8474 (1995).
30. J. Belbere, W.B. Person, and K. Szczepaniak. J. Phys. Chem. **99**, 10705 (1995).
31. E. Ruiz, D. Salahub, and A. Vela. J. Am. Chem. Soc. **117**, 1141 (1995).
32. B.C. Guo, K.P. Kerns, and A.W. Castleman, Jr. J. Phys. Chem. **96**, 4879 (1992).

Aqueous nonelectrolyte solutions. Part XIV. D-ice and D-hydrate freezing points of deuterium oxide – ethylene oxide solutions and the formula of congruent ethylene oxide D-hydrate

David N. Glew and Norman S. Rath

Abstract: D-ice freezing temperatures and D-hydrate formation temperatures have been measured by the dynamic cooling method for deuterium oxide – ethylene oxide (EO) solutions containing from 0 to 95.5 mol% EO. The D-ice and the congruent EO D-hydrate freezing temperatures exhibited standard errors (SEs) on a single measurement of 0.004°C and 0.017°C, respectively. The D-ice–D-hydrate eutectic temperature was observed at 1.500°C with standard error (SE) 0.002°C and at composition 2.207 mol% EO with SE 0.010 mol% EO. The congruent EO D-hydrate was found to freeze at 13.242°C with SE 0.007°C and at composition 12.60 mol% EO with SE 0.07 mol% EO. The formula of the congruent EO D-hydrate was EO·6.93D_2O with SE 0.045 mol D_2O/mol EO. Only one type of D-hydrate was found over the whole composition range down to –23°C: the shoulder of the D-hydrate freezing curve above 40 mol% EO resulted from the high activity coefficients of dilute deuterium oxide in concentrated EO solutions. Equations and best values for the D-ice freezing temperatures and the D-hydrate formation temperatures together with their SEs were evaluated by the method of least squares. Properties of EO D-hydrate are compared with those of EO hydrate.

Key words: clathrate D-hydrate of ethylene oxide, freezing of deuterium oxide – ethylene oxide, ethylene oxide D-hydrate, formula of ethylene oxide D-hydrate.

Résumé : Faisant appel à la méthode de refroidissement dynamique, on a mesuré les températures de congélation de la glace-D et de formation d'hydrate-D de solutions d'oxyde d'éthylène (OE), contenant de 0 à 95,5 mol% d'OE, dans l'oxyde de deutérium. Les erreurs standards (ES) sur une mesure unique des températures de congélation de la glace-D et des hydrates-D d'OE apparentés sont respectivement de 0,004°C et de 0,017°C. On a observé la température eutectique de la glace-D–hydrate-D à 1,500°C, avec une erreur standard (ES) de 0,002°C, et à une composition de 2,207 mol% d'OE, avec une erreur standard de 0,010 mol% sur l'OE. On a trouvé que l'hydrate-D de l'OE apparenté gèle à 13,242°C, avec une ES de 0,007°C, et à une composition de 12,60 mol% d'OE, avec une ES de 0,07 mol% sur l'OE. La formule de l'hydrate-D de l'OE apparenté est OE·6,932D_2O, avec une ES de 0,045 mol D_2O/mol OE. En abaissant la température jusqu'à –23°C, on n'a observé qu'un seul type d'hydrate-D sur l'ensemble de la plage de compositions : l'épaulement de la courbe de congélation de l'hydrate-D au-dessus de 40 mol% d'OE résulte de coefficients d'activité élevés de l'oxyde de deutérium dilué dans les solutions concentrées d'OE. On a fait appel à la méthode des moindres carrés pour déterminer les équations et les meilleures valeurs pour les températures de congélation de l'eau-D, les températures de formation de l'hydrate-D ainsi que leurs ES. On a comparé les propriétés de l'hydrate-D de l'OE avec celles de l'hydrate de l'OE.

Mots clés : clathrate hydrate-D d'oxyde d'éthylène, congélation d'oxyde de deuterium – oxyde d'éthylène, formule de l'hydrate-D de l'oxyde d'éthylène.

[Traduit par la rédaction]

Introduction

This work was part of earlier studies on aqueous nonelectrolyte solutions and the gas hydrates (1) and was a direct extension of work on EO hydrate reported recently (2). Deuterium oxide and EO liquids were miscible in all proportions, as in the water–EO system, and the enthalpies of mixing of deuterium oxide or water with EO were quantitatively similar (3). Solid EO D-hydrate was formed on cooling EO – deuterium oxide solutions over a very wide composition range. This study of the freezing behavior of EO – deuterium oxide solutions was made to define the stability of EO D-hydrate relative to that of EO hydrate.

In an earlier comparison of D-hydrates of krypton and xenon (4) with their hydrates (5, 6), the solid gas hydrates were formed only from dilute solutions of the gases in highly aqueous-rich phases. By contrast, in this work the formation

Received May 22, 1996.

D.N. Glew[1] **and N.S. Rath.**[2] Exploratory Research Laboratory, Dow Chemical Canada Inc, Sarnia, ON N7T 7M1, Canada.

[1] Retired; to whom correspondence may be addressed at 536 Highbury Park, Sarnia, ON N7V 2J9, Canada. Telephone: (519) 337-3136.

[2] Lambton College, P.O. Box 969, Sarnia, ON N7T 7K4, Canada.

Table 1D. (ITS-90). Variation of temperature for freezing of D-ice with composition and the eutectic temperature.

Run-RD no.	EO mf (mol%)	T_{FDI} (deg C)	Run-RD no.	EO mf (mol%)	T_{FDI} (deg C)	Eutectic (deg C)
69	0.0000	3.800	122	1.0000	2.770	
70	0.0000	3.800	118	1.2501	2.504	
111	0.0000	3.797	73	1.2527	2.505	
112	0.0000	3.798	126	1.4137	2.330	
113	0.0000	3.798	120	1.5001	2.239	
114	0.0000	3.797	66	1.5010	2.238	
115	0.0000	3.798	65	1.7482	1.981	
121	0.0000	3.803	119	1.7501	1.974	
127	0.0000	3.801	132	1.9402	1.769	
129	0.0466	3.751	131	1.9587	1.748	
130	0.1496	3.644	125	1.9801	1.730	
134	0.2029	3.603	64	1.9986	1.704	
71	0.2486	3.546	117	2.0001	1.700	
116	0.2494	3.544	75	2.0758	1.630	1.502
133	0.2992	3.499	59	2.1494	1.546	
124	0.4984	3.288	62	2.1876	1.504	1.499
68	0.5100	3.280	63	2.2063		1.507
72	0.7480	3.026	61	2.2251		1.498
123	0.7502	3.026	74	2.2610		1.504
67	0.9985	2.772	76	2.7502		1.493

of EO D-hydrate from its solutions was directly comparable with that of EO hydrate over a wide range of liquid composition, extending from highly aqueous-rich phases to highly EO-rich phases.

A recent study (7) of the similar completely miscible aqueous tetrahydrofuran (THF) system has compared the melting temperatures of THF D-hydrate with THF hydrate over a more limited range of liquid composition.

A valuable review of the clathrate hydrates, including work on both EO hydrate and EO D-hydrate up to 1973, has been given by Davidson (8).

Extending our work on the water–EO system (1, 2), we now report measurements of D-ice freezing points and of D-hydrate formation temperatures from deuterium oxide solutions of EO. Just as the EO hydrate data were presented (2) in Tables 1–3 and Fig. 1, similar EO D-hydrate data are presented here in Tables 1D–3D and Fig. 1D; Fig. 2D is the difference of Fig. 1D minus Fig. 1.

Experimental

Materials

All materials were as described earlier (1, 2). EO was selected from the production of Dow Chemical Canada, Limited, and had impurities <80 ppm by wt. Deuterium oxide was obtained from Atomic Energy of Canada, Limited; analysis 99.72 mol% D_2O, 0.28 mol% H_2O; complete isotopic analyses have been given earlier (1).

Apparatus and procedure

The method of use of the freezing point cell has already been described (2). Some D-ice freezing points of EO solutions were earlier reported and analysed in a different manner (1).

Calibration of thermocouple of freezing point cell

The freezing point cell thermocouple was calibrated against a standardized (IPTS-48) platinum resistance thermometer between +15 and –25°C (1, 2). Calibrations were made prior to and at the end of the runs using deuterium oxide solutions. The SE on a single temperature determination, due only to electrical instrumental effects, (*i*) was 0.0035°C between –6.5 and +6.5°C, (*ii*) was 0.0070°C between –13 and –6.5 and between 6.5 and 13.0°C, and (*iii*) was 0.014°C between –26 and –13 and between 13 and 15°C. These estimates are minimum values for the SE for the three recorder ranges.

The original experimental temperatures, measured on the International Practical Temperature Scale of 1948 (IPTS-48), have been converted to the International Temperature Scale of 1990 (ITS-90), using the differences in Table 4 by Goldberg and Weir (9). This conversion has a root-mean-squared bias of less than 0.0004°C over the range –25 to +15°C, about an order of magnitude smaller than our most precise measurements. Temperatures and equations are reported in units of degree Celsius (ITS-90).

Measurement of temperature for freezing of D-ice

As for freezing ice (2), the freezing of D-ice from dilute EO solutions of deuterium oxide generally exhibited larger supercoolings (~0.3–0.6°C) than those shown for the formation of D-hydrate (~0.005–0.15°C) from the same solutions. Table 1D lists the D-ice freezing temperatures corrected for bias, assuming the same bias, –0.0126°C, found for freezing ice from water under the same conditions (2).

Measurement of temperature for formation of eutectic

The eutectic temperature was measured directly on solutions initially freezing D-ice and initially forming D-hydrate, using

Table 2D. (ITS-90). Variation of temperature for formation of D-hydrate with composition.

Run-RD no.	EO mf (mol%)	T_{FDH} (deg C)
62	2.1876	1.366
63	2.2063	1.441
74	2.2610	1.698
57	2.2999	1.913
55	2.4505	2.631
53	2.6004	3.269
51	2.7502	3.869
76	2.7502	3.668
47	2.9004	4.426
49	3.0242	4.857
45	3.1499	5.267
43	3.2502	5.565
41	3.3999	5.990
39	3.6003	6.588
37	3.8000	7.082
1	3.9993	7.593
2	3.9994	7.565
35	4.2511	8.103
5	4.5000	8.595
33	4.7297	8.999
6	4.9488	9.384
31	5.3559	9.957
27	5.7502	10.462
29	6.2503	11.011
10	6.6864	11.423
12	7.7480	12.190
16	9.5004	12.862
14	11.0018	13.168
18	11.5369	13.189
20	11.9993	13.238
22	12.6737	13.252
23	13.0414	13.225
21	13.9984	13.226
24	14.0003	13.175
19	15.0000	13.087
17	15.9983	12.998
15	17.4999	12.797
25	19.5000	12.504
13	20.9993	12.268
26	23.9993	11.779
11	26.9993	11.364
28	30.4971	10.888
9	34.5025	10.416
30	39.5002	9.965
7	43.9996	9.599
32	49.4975	9.179
4	54.9995	8.808
34	59.5001	8.377
3	63.9983	7.879
36	68.9976	7.169
38	71.9999	6.550
40	73.9986	6.044
42	76.0009	5.484
44	77.4993	4.960
46	78.9989	4.348
50	80.4987	3.618
48	80.4994	3.601
52	81.2939	3.207
54	81.9994	2.770
56	82.9989	2.135
60	83.4993	1.705
58	83.9999	1.342
77	84.4993	0.907
78	85.0002	0.483
79	85.4997	0.030
80	86.0006	−0.460
81	86.4995	−1.016
82	86.9999	−1.556
83	87.5001	−2.153
84	88.0004	−2.841
85	88.4981	−3.521
86	88.9996	−4.267
87	89.5001	−5.085
88	89.9993	−5.964
89	90.4998	−6.937
90	90.9998	−7.975
91	91.4992	−9.076
92	91.7495	−9.676
93	91.9998	−10.303
94	92.2502	−11.000
95	92.4997	−11.677
96	92.7501	−12.329
97	92.9995	−13.109
98	93.2494	−13.886
99	93.5002	−14.777
100	93.7502	−15.724
101	94.0001	−16.619
102	94.2498	−17.665
103	94.4995	−18.824
104	94.7502	−19.917
105	94.9997	−20.917
110	94.9998	−20.876
106	95.2497	−21.988
109	95.2500	−22.140
107	95.5000	−23.352

Table 2D (*concluded*).

a final small cooling differential of ~0.1°C. The six observed eutectic temperatures are listed in Table 1D.

Measurement of temperature for formation of D-hydrate

With the developed cooling technique of the freezing point cell, the preselected temperature differential applied for the first formation of D-hydrate was ~0.4°C, and for subsequent formations was reduced to ~0.1°C. EO D-hydrate formation temperatures listed in Table 2D were extrapolated to zero supercooling (2).

In contrast to work on EO hydrate, many fewer runs were made on the formation of EO D-hydrate and very few measurements were repeated. In the congruent region, temperatures for D-hydrate formation were measured on the least sensitive

Fig. 1D. Freezing point curve of EO D-hydrate.

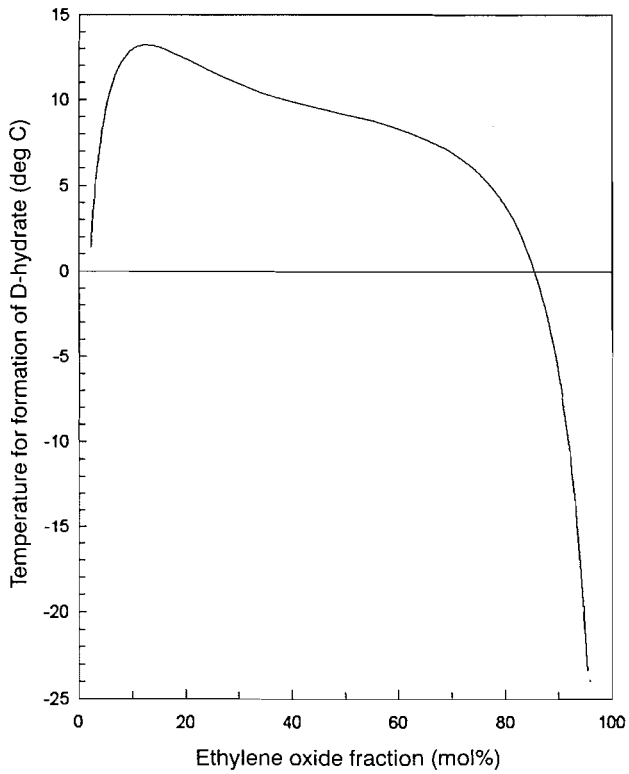

recorder range with largest SE. As a result random errors of measurement for EO D-hydrate are somewhat larger than those for EO hydrate.

Results and Discussion

Measurement of freezing of D-ice

Table 1D lists corrected temperatures for freezing of D-ice from deuterium oxide solutions containing between zero and 2.1876 mol% EO. The first column shows the run RD-number, the second column the solution composition, and the third the corrected temperature for freezing D-ice from the solution. The 36 measurements for freezing D-ice from EO solutions are best represented by the three-parameter equation,

$$[1] \quad T_{FDI} = 3.8000 - 1.0168\,C - 0.01518\,C^2$$
$$(0.0010) \quad (0.0031) \quad (0.00148)$$

where the freezing temperature T_{FDI} is in degree Celsius and C is the solution concentration of EO in mol% EO. Least-squares estimates of the SE on the parameters are shown in parentheses and the estimated SE on a single D-ice freezing point determination is 0.0037°C with 30 degrees of freedom.

The nine freezing points of 99.72 mol% deuterium oxide without EO give a mean temperature of 3.800°C with SE 0.0007°C and with SE on a single measurement 0.0020°C. The perfect agreement between the mean of the replicates and the regression is fortuitous, recognising that the minimum SE estimate from thermocouple calibration was 0.0035°C (1, 2).

Measurement of formation of eutectic

The eutectic temperature 1.500°C, with estimated SE 0.0020°C, is the mean of the six measurements listed in Table 1D, with initial solution compositions between 2.0758 and 2.7502 mol% EO. The SE for a single eutectic temperature measurement is 0.0049°C.

The eutectic composition 2.207 mol% EO, with SE 0.010 mol% EO, is estimated from the directly observed mean eutectic temperature together with the intersections of the curves for freezing of D-ice and for formation of D-hydrate. The D-ice–D-hydrate intersection estimate for the eutectic temperature is 1.477°C, with bias –0.023°C below the best observed mean value: this negative bias arises from the two biases for D-ice freezing and for D-hydrate formation.

Bias of the temperature for formation of D-hydrate at 2.207 mol% EO is at least –0.023°C, identical with that at the EO–water eutectic (2).

Measurement of formation of D-hydrate

Table 2D lists measurements of the formation temperature for EO D-hydrate from deuterium oxide solutions containing between 2.1876 and 95.5000 mol% EO. The first three columns show the RD-number, the solution composition, and the temperature for D-hydrate formation. Measurement precision justifies four decimal places for solution mol% EO, and three places for D-hydrate formation temperature °C. Figure 1D is a plot of these measurements showing the EO D-hydrate "freezing point" curve.

The measurements in Table 2D, shown in Fig. 1D, exhibit a continuous envelope at all compositions, without discontinuities of value or of slope: this confirms EO D-hydrate has a structure I type lattice (2) over the whole range of solution composition.

Regression analysis of data in Table 2D involves taking 13–16 adjacent measurements around a predefined solution composition and making a local analysis of D-hydrate formation temperature as a polynomial function of solution composition. The best-fit residuals are random and reconfirm the continuity of the measurements. Since the number of runs forming D-hydrate are many fewer than those forming hydrate, the number of D-hydrate measurements used in each regression is made to extend over about the same composition range as that used for the hydrate (2).

Estimates of temperature for formation of D-hydrate

Eutectic point data are listed in the first row of Table 3D. Estimates of the EO D-hydrate formation temperature with composition are listed in Table 3D and are defined by the 33 best-fit regression analyses at the compositions shown in column one. Estimates of the temperature for formation of D-hydrate, T_{FDH}; its SE, SE T_{FDH}; the SE on a single D-hydrate measurement, SE T_{obs}; the slope of the T_{FDH} envelope, and its SE are listed in columns two to six, respectively. In column seven the numbers separated by a dash indicate the number of measurements and of parameters used in the best model.

Errors of D-hydrate measurement are greatest at lowest temperatures for the most EO-rich (Deuterium oxide-dilute) solutions, as seen in the final row of Table 3D. Column four shows the progressive change of SE T_{obs} with increase both of D-hydrate formation temperature and of deuterium oxide content of the solution. The lower SE T_{obs} from 40 to 25 mol% EO and below 8 mol% EO derives from the use of more sensitive and accurate recorder ranges. In contrast, the higher SE T_{obs} in the congruent region between 9 and 22 mol% EO mainly

Table 3D. (ITS-90). Estimates of temperature for formation of D-hydrate with composition: value, slope, and errors.

Solution composition (mol% EO)	Temperature for formation of D-hydrate T_{FDH} (deg C)	Standard error on T_{FDH} SE T_{FDH} (deg C)	Standard error on a single measurement SE T_{obs} (deg C)	Slope of T_{FDH} envelope (deg C/mol%)	Standard error of slope (deg C/mol%)	Number of data – number of parameters
2.207	1.500	0.0020	0.005	—	—	6–1
2.50	2.842	0.0058	0.012	4.384	0.0161	15–4
3.00	4.771	0.0050	0.012	3.391	0.0154	15–4
4.00	7.565	0.0050	0.013	2.286	0.0103	15–4
5.00	9.447	0.0067	0.016	1.542	0.0106	13–5
6.00	10.750	0.0050	0.012	1.098	0.0065	13–6
7.00	11.675	0.0062	0.016	0.759	0.0076	14–6
8.00	12.316	0.0054	0.014	0.518	0.0083	15–7
9.00	12.731	0.0066	0.018	0.331	0.0039	16–5
10.00	12.998	0.0066	0.017	0.204	0.0037	15–5
11.00	13.155	0.0067	0.018	0.113	0.0060	16–6
12.50	13.242	0.0072	0.019	0.009	0.0057	15–7
12.604	13.242	0.0065	0.017	0.000	0.0042	14–5
14.00	13.192	0.0074	0.020	–0.064	0.0047	16–7
16.00	12.995	0.0072	0.018	–0.120	0.0037	14–6
18.00	12.729	0.0073	0.017	–0.148	0.0032	13–5
20.00	12.425	0.0075	0.018	–0.158	0.0029	13–5
22.00	12.102	0.0077	0.018	–0.158	0.0025	13–6
25.00	11.641	0.0049	0.012	–0.150	0.0019	13–7
30.00	10.943	0.0051	0.012	–0.127	0.0011	13–6
35.00	10.382	0.0057	0.014	–0.102	0.0015	13–7
40.00	9.910	0.0064	0.015	–0.084	0.0012	13–6
45.00	9.517	0.0077	0.019	–0.074	0.0009	13–5
50.00	9.166	0.0073	0.018	–0.073	0.0015	13–7
55.00	8.779	0.0076	0.018	–0.080	0.0015	13–6
60.00	8.340	0.0076	0.018	–0.100	0.0022	13–7
65.00	7.759	0.0078	0.019	–0.134	0.0025	13–7
70.00	6.971	0.0070	0.017	–0.187	0.0018	13–5
75.00	5.782	0.0067	0.016	–0.295	0.0025	13–6
80.00	3.874	0.0105	0.020	–0.494	0.0055	13–6
85.00	0.482	0.0097	0.019	–0.898	0.0070	13–5
90.00	–5.969	0.0065	0.014	–1.834	0.0060	13–4
92.50	–11.644	0.0121	0.027	–2.815	0.0151	13–4
95.00	–20.938	0.0281	0.079	–4.608	0.0589	13–3

reflects use of the least sensitive recorder range. Over the very wide solution composition range 9–90 mol% EO, the SE on a single D-hydrate temperature determination is 0.018°C, and is sensibly constant.

The congruent temperature 13.242°C, with SE estimate 0.0065°C, is determined at the maximum of the D-hydrate formation curve representing 14 measurements with solution compositions between 7.7480 and 20.9993 mol% EO. The temperature for formation of EO D-hydrate, T_{FDH}, is best represented by the five-parameter equation,

$$[2]\quad T_{FDH} = \underset{(0.0065)}{13.242} + \underset{(0.0042)}{0.0000D} - \underset{(0.00088)}{0.02940D^2} + \underset{(0.000203)}{0.002681D^3} - \underset{(0.000027)}{0.000098D^4}$$

where T_{FDH} is in °C and D = (mol% EO–12.604) = (C–12.604) mol% EO. Least-squares estimates of the SE on the parameters are shown in parentheses and the SE on a single hydrate temperature measurement is 0.017°C with 9 degrees of freedom, in good agreement with estimates from adjacent regressions.

The congruent composition 12.604 mol% EO, with SE 0.071 mol% EO, is determined as the composition for zero slope of eq. [2], and the SE from the error on that slope. Formula for the congruent EO D-hydrate is EO·6.93D_2O with SE 0.045 mol D_2O/mol EO.

Congruent EO D-hydrate comprises 6.63EO·46D_2O per unit cell, with EO molecules occupying mainly the six tetrakaidecahedral sites and filling about one third of the two dodecahedral sites. These estimates for the formula of EO D-hydrate are insignificantly different from those for the EO hydrate (2).

Fig. 2D. Stability difference of EO D-hydrate and EO hydrate.

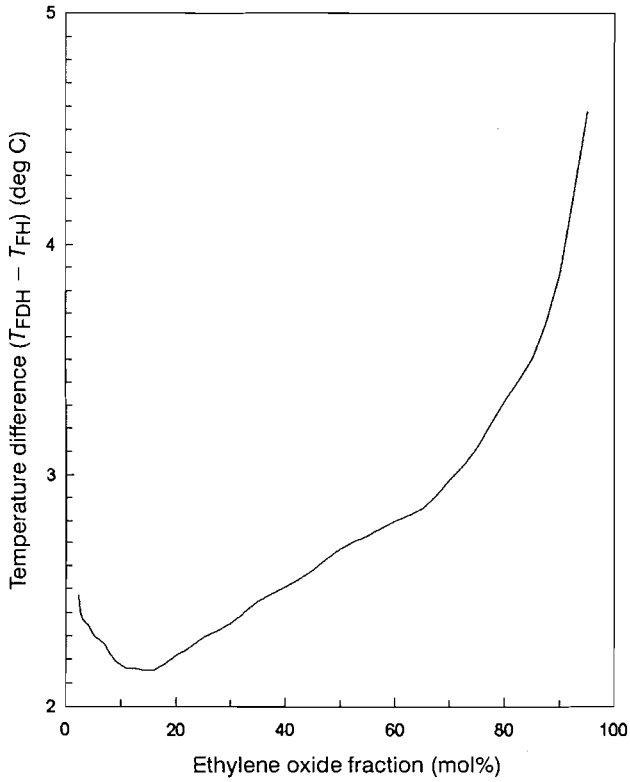

The slope of the D-hydrate formation curve in the EO-rich region is negative and passes through a narrow minimum at 20–22 mol% EO and through a wide maximum at about 50 mol% EO. The small absolute values of the negative slopes between 14 and 65 mol% EO reflect (*i*) a high enthalpy change for crystallization of EO D-hydrate from solution (10), together with (*ii*) positive and high Raoult-law activity coefficients for deuterium oxide in these EO-rich solutions (2).

Comparison of EO D-hydrate with EO hydrate

The congruent solution for EO D-hydrate contains 12.605 mol% EO with SE 0.071 mol% EO, while that for EO hydrate contains 12.644 mol% EO with SE 0.021 mol% EO. The congruent composition difference of –0.039 mol% EO with the combined SE of 0.074 mol% EO shows that the difference is not statistically significant and could arise by pure chance at a probability level of greater than 50%. This clearly shows that the formula EO·6.93D_2O for EO D-hydrate is not significantly different from the better determined formula EO·6.91H_2O for EO hydrate (2).

At any given solution composition the formation temperature of EO D-hydrate is always higher than that of EO hydrate, indicating a greater stability of the D-hydrate relative to its solutions than that of the hydrate relative to its solutions. The temperature difference for formation of D-hydrate minus that for formation of hydrate provides a quantitative measure of the greater stability of the D-hydrate compared with the hydrate.

Figure 2D shows a plot of this temperature difference ($T_{FDH} - T_{FH}$) against solution composition evaluated at 48 EO fractions. The stability difference is 2.47°C at 2.207 mol% EO in the most EO-dilute region, the minimum stability difference is 2.16°C at the congruent point, and the greatest stability difference is 4.58°C at 95.00 mol% EO in the extreme EO-rich region.

We note that the composition dependence of the negative temperature difference curve, $-(T_{FDH} - T_{FH})$, has a geometrically similar shape to that of its constituent formation curves Fig. 1D for D-hydrate and Fig. 1 for hydrate (2). This requires that the envelope of the EO D-hydrate formation curve have a numerically smaller slope than that of the EO hydrate formation curve at all equal EO fractions.

Comparison of Table 3D with Table 3 (2) confirms that the absolute values of the slope for the EO D-hydrate formation curve are invariably slightly smaller than those for the EO hydrate at the same composition: this requires that the enthalpy change for formation of the EO D-hydrate from deuterium oxide solutions of EO be numerically larger than that for formation of the EO hydrate from water solutions of EO (10).

Comparison with THF D-hydrate and THF hydrate

In the study of the aqueous THF system (7) the difference of the melting temperature of THF D-hydrate minus that of THF hydrate is about 2.5°C with SE 0.5°C over the composition range 2.0–37.3 mol% THF. This temperature difference is similar to the values found here for the EO hydrates. The measurements (7) are not of sufficient accuracy to confirm or deny a minimum difference of temperature at the congruent composition, although this would be expected from enthalpy change considerations (10).

Acknowledgment

This work was supported in part by grants under the National Research Council of Canada, Industrial Research Assistance Program, for 1964, 1965, and 1966.

References

1. D.N. Glew, H.D. Mak, and N.S. Rath. Can. J. Chem. **45**, 3059 (1967).
2. D.N. Glew and N.S. Rath. Can. J. Chem. **73**, 788 (1995).
3. D.N. Glew and H. Watts. Can. J. Chem. **49**, 1830 (1971).
4. M. Godchot, G. Cauquil, and R. Calas. C. R. Acad. Sci. **202**, 759 (1936).
5. R. de Forcrand. C. R. Acad. Sci. **176**, 355 (1923).
6. R. de Forcrand. C. R. Acad. Sci. **181**, 15 (1925).
7. H.J.M. Hanley, G.J. Meyers, J.W. White, and E.D. Sloan. Int. J. Thermophys. **10**, 903 (1989).
8. D.W. Davidson. *In* Water: a comprehensive treatise. Vol. 2. *Edited by* F. Franks. Plenum Press, New York. 1973. pp. 115–234.
9. R.N. Goldberg and R.D. Weir. Pure Appl. Chem. **10**, 1545 (1992).
10. D.N. Glew. Trans. Faraday Soc. **61**, 30 (1965).

Chiral synthesis of (+)-8′-demethyl abscisic acid[1]

Patricia A. Rose, Bo Lei, Angela C. Shaw, M. K. Walker-Simmons, Scott Napper, J. Wilson Quail, and Suzanne R. Abrams

Abstract: An enantioselective synthesis of (+)-8′-demethyl ABA (**2**) is described. The chiral intermediate **7** was prepared by yeast reduction of a substituted monoprotected cyclohexa-2,5-dien-1,4-dione (**9**) synthesized through a phenol oxidation. The scope and limitations of the phenol oxidation is described. 8′-Demethyl ABA shows ABA-like activity in wheat embryo germination inhibition, showing that the 8′-methyl group is not essential for biological activity.

Key words: abscisic acid, phenol oxidation, yeast reduction.

Résumé : On décrit une synthèse énantiosélective de l'acide (+)-8′-déméthyl-abscisique (AAB) (**2**). On a préparé l'intermédiaire chiral **7** par réduction, à l'aide de levures, d'une cyclohexa-2,5-diène-1,4-dione substituée monoprotégée (**9**) obtenue par oxydation d'un phénol. On décrit la généralité et les limitations de l'oxydation des phénols. L'acide 8′-déméthyl-abscisique présente une activité semblable à celle de l'AAB comme inhibiteur de la germination des embryons de blé; ce résultat démontre que le groupe 8′-méthyle n'est pas essentiel à l'activité biologique.

Mots clés : acide abscisique (AAB), oxydation des phénols, réduction par des levures.

[Traduit par la rédaction]

Introduction

The plant hormone (+)-(S)-abscisic acid (ABA, **1**) regulates a wide range of processes in plants, including transpiration through controlling stomatal aperture and responses to environmental stress. In developing seeds, ABA affects accumulation of proteins, acquisition of desiccation tolerance, maintenance of dormancy, and inhibition of germination (for reviews on ABA action in plants, see ref. 1). We have used optically active analogs of the hormone to probe the mechanisms by which ABA triggers different physiological effects such as germination inhibition and induction of genes in plants (2, 3). Enantiomerically pure molecules are required for these investigations, as previous studies have shown that the enantiomers of ABA can have different effects in the same tissue, and optically pure analogs can be either ABA agonists or antagonists depending upon the enantiomer tested (4).

Received May 16, 1996.

P.A. Rose, B. Lei, A.C. Shaw, and S.R. Abrams.[2] Plant Biotechnology Institute, National Research Council of Canada, 110 Gymnasium Place, Saskatoon, SK S7N 0W9, Canada.
M.K. Walker-Simmons. Agriculture Research Service, United States Department of Agriculture, 209 Johnston Hall, Washington State University, Pullman, WA 99164-6420, U.S.A.
S. Napper. Department of Biochemistry, University of Saskatchewan, Saskatoon, SK S7N 5E5, Canada.
J.W. Quail. Department of Chemistry, University of Saskatchewan, Saskatoon, SK S7N 5C9, Canada.

[1] NRCC No. 40027.
[2] Author to whom correspondence may be addressed. Fax: (306) 975 4839. E-mail: sabrams@pbi.nrc.ca

In this phase of our research we undertook to synthesize and test the optically pure ABA analog **2**, which lacks one of the geminal methyl groups of ABA, the 8′-carbon atom (following the conventional ABA numbering system). The aim was to provide analogs that could be used for differential screening to relate physiological and molecular effects in plant tissues. Methyl groups on the six-membered ring are important for activity. Racemic 8′-demethyl ABA had earlier been prepared and, in an assay looking at the growth inhibition of rice seedlings, was found to have moderate activity (5). Both enantiomers of the analog missing the 7′-methyl group are completely inactive in germination inhibition of excised wheat embryos, while the optically active analogs missing both of the geminal methyls have some activity (3).

In addition, the analog **2** is a probe for differentiating between the activity conferred by ABA and its oxidized metabolites. The major pathway of ABA metabolism is through oxidation of the 8′-methyl group, transiently affording 8′-hydroxy ABA, **3**, which then cyclizes through an internal Michael addition to phaseic acid (**4**). While **4** is generally considered to be inactive (6), a method for trapping the open form **3** has recently been developed, and it was found to be as active as ABA in increasing very long chain fatty acid production in Brassica embryos (7).

We had previously developed the synthesis of (+)-2′,3′-dihydroABA (**5**) (8), which is oxidized in a plant cell culture at the 8′-carbon to give 8′-hydroxy-2′,3′-dihydroABA, **6**. This metabolite cannot cyclize to form phaseic acid. Analog **5** was found to be as active as ABA in germination inhibition of wheat embryos (2) and in inducing freezing tolerance in plant cells; however, its metabolic product **6** was inactive (9). Compound **6** appeared to exist in equilibrium with the hemi-ketal formed through the 4′-carbonyl. The lack of activity of the metabolite may arise from inactivity of the predominant ring-

closed form. Compound **5** did not conclusively answer the question of whether ABA or 8′-hydroxy ABA was the active plant hormone in the wheat embryo assay. 8′-Demethyl ABA **2** cannot be oxidized to an 8′-hydroxy ABA intermediate, as it is missing the 8′-methyl group, making it a useful tool for differentiating between the activity of ABA and its metabolites.

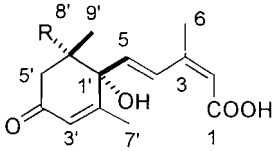

1 R = CH_3
2 R = H
3 R = CH_2OH

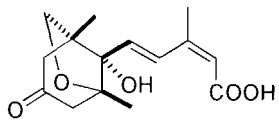

4

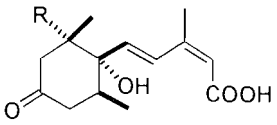

5 R = CH_3
6 R = CH_2OH

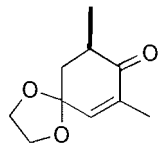

7

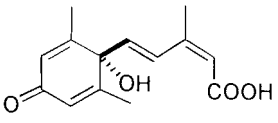

8

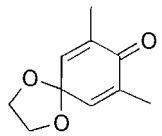

9

We report here an enantioselective synthesis of (+)-8′-demethyl ABA, **2**, its activity in inhibiting wheat embryo germination, and its effect in reducing transpiration in wheat seedlings.

Results and discussion

Abscisic acid type compounds are readily synthesized by reaction of the appropriate cyclohexenone derivatives with side chains containing lithium acetylides. The dienoic side chain is generated by reduction of the propargylic alcohol with RedAl. Standard functional group manipulations afford a wide variety of analogs (10).

For the synthesis of 8′-demethyl ABA **2**, we decided to prepare chiral ring synthon **7** with the intention that the new chiral centre, generated through lithium acetylide addition to the carbonyl, would be formed stereoselectively. The preferred conformation for **7** presumably has the methyl group equatorial, to avoid 1,3-diaxial interactions between an axial methyl group and the ketal (Fig. 1). In the preferred conformation, the less hindered side of attack should be from the same face as the methyl group.

We synthesized the key intermediate **7** from 2,6-dimethylphenol in two steps: the first a phenol oxidation and the second a stereoselective yeast reduction. We had previously modified a phenol oxidation procedure for the synthesis of an achiral cyclohexadienone analog of ABA, **8** (11). The key intermediate for this synthesis, **9**, was prepared directly through an oxidation of 2,6-dimethyl phenol. The oxidation

Fig. 1. Conformations of enone **7**.

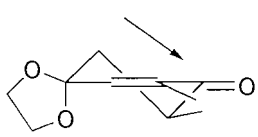

7, equatorial methyl

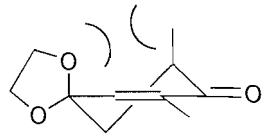

7, axial methyl

was a modification of Pelter's iodobenzene diacetate oxidation of phenols in methanolic solution (12), which affords quinone mono-dimethyl ketals. Replacing methanol with ethylene glycol and adding hexane to form a biphasic reaction mixture directly gave the more stable ethylene ketal in good yield.

As an aside, because the ethylene ketal is more convenient for synthetic purposes, we explored the scope of this reaction. This procedure worked for a number of phenols (entries 1–5, 7, Table I) in moderate yield. Unsubstituted phenol underwent oxidation to give the desired product (as determined by GC–MS), but the product was not stable to the work-up conditions (entry 5). Oxidation of *meta*-substituted phenols showed the steric limitations of this reaction. The introduction of one *meta* substitutent lowered the yield of ketalized product significantly (entry 8), whereas 3,5-dimethyl phenol (entry 9) produced only the quinone. Presumably, steric hinderance of the *meta* substituents hinders the formation of the 1,3-dioxolane ring. Phenols substituted with electron-withdrawing groups at either the *ortho* (difluoromethyl group) or *meta* (trifluoromethyl group) positions were unreactive, with only starting materials being recovered. The introduction of manipulable functional groups to the ring system can be accomplished, however, through an allyl group (entry 4) or a protected hydroxy methyl group (entry 7). Although 2-hydroxymethyl-6-methylphenol decomposed under the reaction conditions (entry 6), oxidation of its *tert*-butyldimethylsilyl ether gave the ketalized product in 67% yield (entry 7). This is a facile reaction that provides highly functionalized molecules in one step, and should prove to be useful in the synthesis of natural products and their analogs.

The second step in the synthesis of 8′-demethyl ABA was an enantioselective yeast reduction of the quinone monoketal **9** to introduce the chiral centre. Yeast reductions have previously been carried out under non-deketalizing conditions, and have been shown to reduce electron-deficient double bonds in reasonable yields and with good stereoselectivity (13). We were able to reduce quinone monoketal **9** in 50% yield (92% ee) to enone **7**, with little epimerization of the newly formed chiral centre, hydrolysis of the ketal, or overreduction of the second double bond.

The remaining steps in the synthesis of 8′-demethyl ABA closely follow those previously reported for the synthesis of ABA (14), with the exception of combining the alkyne addition and subsequent reduction of the triple bond into one step (see Fig. 2). Enone **7** was reacted with the lithium anion of *cis*-(5-*tert*-butyldimethylsiloxy-3-methylpent-3-enyne) (8), **10**, to give one diastereomer and after the alkyne addition was complete, Redal® was added directly to the reaction mixture, reducing the triple bond to a *trans* double bond, as well as cleaving the silyl protecting group, to give dienol **11** in a one-

Table 1. Iodobenzene diacetate oxidation of phenols in ethylene glycol–hexane.

Entry	Phenol	Product	Yield (%)
1	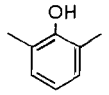	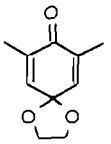	63
2		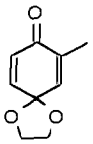	56
3	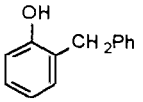	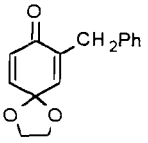	35
4	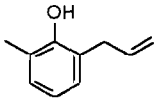	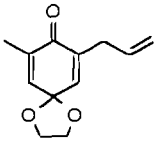	55
5		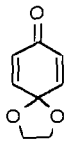	45[a]
6	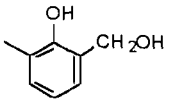	Decomposed	
7	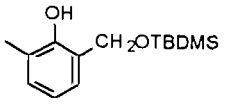	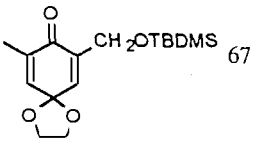	67
8	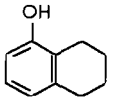	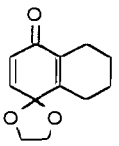	27
9	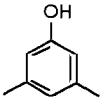	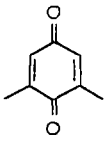	63

[a]Yield based on GC analysis.

pot reaction in 38% yield. Yields for the Redal® reduction of the isolated alkyne were very low when the reaction was carried out independently. The bulky protecting group on the alcohol of the pentenyne chain was found to be necessary for obtaining high diastereoselectivity when reacted with chiral enone **7**. Addition of the lithium dianion of the unprotected alcohol gave a mixture of both *cis* and *trans* addition products. Assuming addition is only occurring at the less hindered face of the ketone (Fig. 1), either the remote bulky protecting group is contributing to the increased diastereoselectivity, or possibly the lithium anion of the unprotected alcohol is chelating with the oxygens on the ketal to facilitate addition from either face.

Dienol **11** was deketalized in 83% yield under standard conditions to give enone **12**, which was then oxidized to the aldehyde with MnO_2, and then to the ester (15) to give the methyl ester of 8′-demethyl ABA, **13**, in 35% yield over the two steps. Other oxidants gave unwanted isomerization of the *cis* double bond. Methyl ester **13** could be analyzed on a Chiralcel OD HPLC column, showing that no racemization of the 6′-methyl group of ketone **7** had occurred during addition of the side chain, and, using preparative HPLC, the compound was purified to greater than 99% ee. The methyl ester was cleaved using porcine liver esterase (to avoid possible aromatization of the ring under alkaline hydrolysis conditions) to give the desired (+)-8′-demethyl abscisic acid, **2**.

The stereoselectivity of the yeast reduction and diastereoselectivity of alkynylation were proven through an X-ray crystal structure of Mosher's ester **14**, made from an intermediate of which we had made quantities while trying to improve reduction of the triple bond. Compound **14** was prepared by reacting enone **7** with the lithium anion of **10** to give one diastereomer, **15**, in 83% yield (see Fig. 3). Alkyne **15** was deprotected in succession with Bu_4NF, to remove the silyl group, and then with pTsOH to remove the ketal, to form acetylenic alcohol **16**. The C1-hydroxy group of **16** was then coupled with *R*-(+)-α-methoxy-α-(trifluoromethyl)phenyl acetic acid using DCC to form the crystalline Mosher's ester. The X-ray structure is displayed in the PLUTON92 (16) drawing in Fig. 4 and shows the chiral center of enone **7** (generated by the yeast reduction) to be *R*, and relationship of the side-chain and 9′-methyl group of **2** to be *cis*, as shown.

Biological results

The effectiveness of compound **2** compared to (+)-ABA (**1**) as a germination inhibitor was determined with isolated wheat (cultivar Brevor) embryos. The compounds were tested over a range of concentrations and the concentrations required to inhibit embryo germination by 50% were 0.05 μM for (+)-ABA and 0.5 μM for (+)-8′-demethyl ABA. In a wheat seedling transpiration assay, 8 h after applying 100 μM (+)-ABA as a root drench, the transpiration rate of the seedlings was reduced by 80%. 8′-Demethyl ABA applied at 100 μM concentration reduced transpiration by 45% under the same conditions. This strong activity of an analog that has no 8′-methyl group available for oxidation suggests that ABA itself is the active hormone in germination inhibition, and transpiration reduction. These results do not preclude 8′-hydroxy ABA from also being biologically active, and investigations are ongoing to determine the biological activity of 8′-hydroxy ABA in wheat.

Experimental

General

Melting points were determined with a microscope hot stage

Fig. 2. Synthesis of (+)-8′-demethyl ABA **2**.

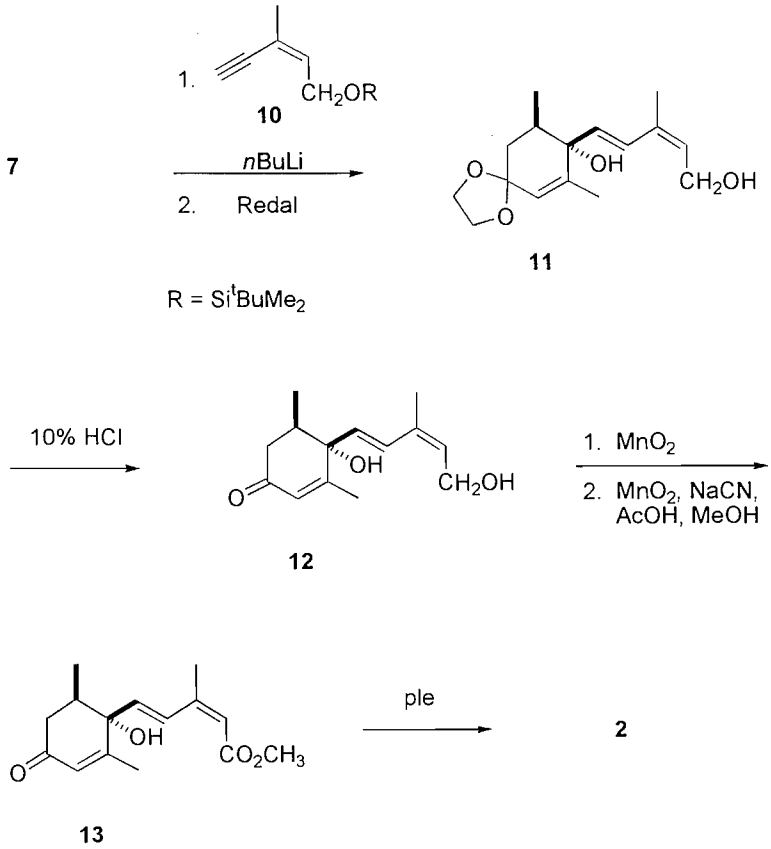

apparatus and are uncorrected. ^{1}H NMR spectra were recorded on a Bruker AMX-500 spectrometer, employing $CDCl_3$ as solvent with $CHCl_3$ as reference, unless otherwise specified. For clarity, the conventional ABA numbering system is employed in assignments of peaks in the ^{1}H NMR spectra. IR spectra were obtained with a Perkin Elmer 237B instrument or a Perkin-Elmer Paragon 1000 FTIR. Optical rotations were obtained from a Perkin–Elmer 141 polarimeter. Flash column chromatography was performed using E. Merck silica gel 60 (230 – 400 mesh). High-resolution electron impact (HREIMS) mass spectra were recorded with a VG 70-250SEQ double-focusing hybrid spectrometer. Elemental analyses were carried out by the Microanalytical Laboratory of the University of Saskatchewan. Commercially available compounds were used in this work without further purification. Tetrahydrofuran was distilled over sodium and benzophenone (indicator). Fleischmann's brand bakers' yeast was used in the yeast reduction reaction. The wheat embryo germination assay was carried out as previously reported (8). The transpiration assay was carried out as previously reported (17).

X-ray analysis of 14

Crystal data: $C_{24}F_3O_5H_{25}$, M_r=450.45, monoclinic, $P2_1$, a = 11.91(2), b = 7.612(3), c = 12.50(1) Å, β=105.71(1)°, V = 1091(2) Å^3, Z = 2, $F(000)$ = 472, D_x = 1.372 Mg m^{-3}, μ = 0.11 mm^{-1}, crystal dimensions 0.68 × 0.12 × 0.09 (mm). Intensity data were measured at 123(2) K on an Enraf–Nonius CAD-4 diffractometer, using graphite monochromatized MoK_α (λ = 0.71073 Å) radiation. Intensity data were collected with ω scans to a maximum 2Θ angle of 49.7°. The unit-cell dimensions were obtained by a least-squares fit of 25 centered reflections in the range 17 ≤ 2Θ ≤ 29°. The scan width, Δω, for each reflection was (1.20 + 0.35 tan Θ)° with a scan speed of 0.40–2.74° min^{-1}. Three standard reflections were monitored every two hours for intensity and two standard reflections were monitored every 200 reflections for orientation. A total of 2130 reflections were measured, of which 2022 were unique (R_{merge} = 0.046) with index range h −14/+13, k 0/+8, l 0/+14, and 1328 were observed (I)2σ(I)). Intensities were corrected for Lorentz and polarization factors, but no correction was made for absorption.

The structure was solved by direct methods and refined using full-matrix least-squares techniques, minimizing the function to R = 0.112 and R_w = 0.103, S = 3.40. Final $(\Delta/\sigma)_{max}$ was 0.000. In the final difference map $\Delta\rho_{max}$ = 0.79 e Å^{-3} and $\Delta\rho_{min}$ = −0.92 e Å^{-3}. The function minimized was Σwith w = 1.0/(σ^2(F) + 0.0001 F^2). Because the crystal was weakly diffracting and the number of observed reflections was too small for anisotropic refinement, isotropic temperature factors were used for all non-hydrogen atoms. Once the non-hydrogen atoms were refined, H-atoms were placed in calculated positions on the corresponding C and O atoms (d(C—H) = 1.00, d(O—H) = 0.80 Å) and not refined. The U_{iso} of each hydrogen atom was assigned as equal to the U_{iso} of the attached atom plus 0.01. The configuration of the molecule was determined from the known configuration of Mosher's acid. All calcula-

Fig. 3. Synthesis of Mosher's ester **14**.

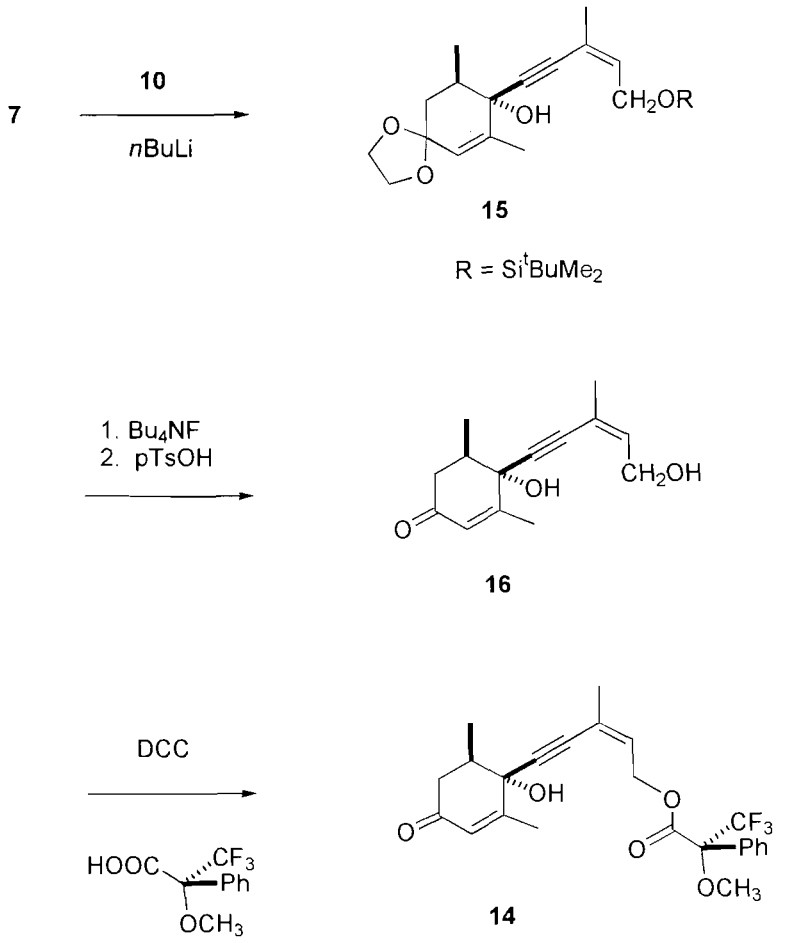

Fig. 4. PLUTON92 drawing of Mosher's ester **14**.

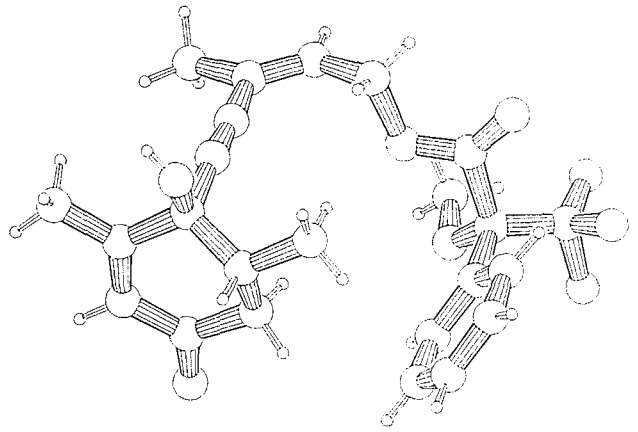

tions were performed with the NRCVAX crystallographic program package (18). The atomic scattering factors were taken from the International Tables for X-ray Crystallography (1974) (19).

Detailed atomic coordinates, bond distances and angles have been deposited at the Cambridge Crystallographic Data Center. These data can be obtained, on request, from the Director, Cambridge Crystallographic Data Centre, 12 Union Road, Cambridge, CB2 1EZ, U.K.

General procedure for the preparation of quinone monoketals

2,6-Dimethyl-4,4-ethylenedioxycyclohexa-2,5-dienone (9) Iodobenzene diacetate (20.29 g, 0.063 mol) was suspended in hexane (250 ml), mechanically stirred, and cooled with an external ice bath. To the suspension was added 2,6-dimethyl phenol (3.66 g, 0.030 mol) in anhydrous ethylene glycol (20 mL). The ice bath was removed and the mixture stirred for 2 h before being quenched with H_2O (200 mL). The two phases were separated and the aqueous layer was extracted with ether (200 mL). The organic layers were combined and washed with 5% $NaHCO_3$ and saturated NaCl solution, dried over $MgSO_4$, and concentrated. Distillation under vacuum removed most of the iodobenzene by-product and the residue was purified by flash chromatography (5% EtOAc – hexane) to give 3.38 g (63%) of product as a solid. Recrystallization from ether–hexane gave a white crystal, mp 47–49°C. IR ($CHCl_3$) ν_{max} cm^{-1}: 1715 (C=O), 1630 (C=C). ^1H NMR, δ: 6.39 (s, 2H, H-3, H-5), 4.18 (s, 4H, OCH_2CH_2O), 1.86 (s, 6H, Me). ^{13}C NMR, δ: 186.4, 138.3 (2C), 135.5 (2C), 98.8, 65.3 (2C), 15.4 (2C). HRE-IMS: (M^+) at *m/z* 180.0786 ($C_{10}H_{12}O_3$ requires 180.0786).

2-Methyl-4,4-ethylenedioxycyclohexa-2,5-dienone (Table 1, entry 2): IR(neat) ν_{max} cm^{-1}: 1720 (C=O), 1680, 1650 (C=C). ^1H NMR, δ: 6.58 (*dd*, 1H, J = 10.0, 3.1 Hz, H-5), 6.38

(m, 1H, H-3), 6.13 (d, 1H, J = 10.0 Hz, H-6), 4.11 (s, 4H, OCH_2CH_2O), 1.85 (d, 3H, J = 1.6 Hz, vinyl Me); ^{13}C NMR, δ: 185.9, 142.9, 138.6, 136.0, 128.9, 99.0, 65.7 (2C), 15.4; HREIMS: [M^+] at m/z 166.0644 ($C_9H_{10}O_3$ requires 166.0630).

4,4-Ethylenedioxycyclohexa-2,5-dienone (entry 5): IR(neat) ν_{max} cm^{-1}: 1680 (C=O). ^1H NMR, δ: 6.60 (d, 2H, J = 10.1 Hz, H-3, H-5), 6.14 (d, 2H, J = 10.1 Hz, H-2, H-6), 4.12 (s, 4H, OCH_2CH_2O); ^{13}C NMR, δ: 185.3, 143.2, 129.0, 98.2, 65.8; HREIMS: [M^+] at m/z 152.0462 ($C_8H_8O_3$ requires 152.0734).

2-Benzyl-4,4-ethylenedioxycyclohexa-2,5-dienone (entry 3): IR(neat) ν_{max} cm^{-1}: 1680 (C=O), 1650 (C=C). ^1H NMR, δ: 7.29–7.17 (m, 5H, phenyl H), 6.58 (dd, 1H, J = 10.0, 3.1 Hz, H-5), 6.16 (d, 1H, J = 10.0 Hz, H-6), 6.12 (m, 1H, H-3), 4.07-4.03 (m, 4H, OCH_2CH_2O), 3.59 (d, 2H, J = 0.8 Hz, CH_2); ^{13}C NMR, δ: 185.2, 142.9, 139.4, 139.2, 137.9, 129.4, 128.9, 128.6, 126.4, 99.1, 65.7, 34.9; HREIMS: [M^+] at m/z 242.0934 ($C_{15}H_{14}O_3$ requires 242.0943.)

2-Allyl-6-Methyl-4,4-ethylenedioxycyclohexa-2,5-dienone (entry 4): IR(neat) ν_{max} cm^{-1}: 1685 (C=O), 1650 (C=C). ^1H NMR, δ: 6.36 (m, 1H, CH=CH*H*), 6.32 (m, 1H, CH=C*H*H), 5.78 (m, 1H, C*H*=CHH), 5.15 (m, 1H, H-3), 5.07 (m, 1H, H-5), 4.08 (s, 4H, OCH_2CH_2O), 3.00 (dd, 2H, J = 6.8, 1.1 Hz, CH_2), 1.85 (d, 3H, J = 1.4 Hz, CH_3); ^{13}C NMR, δ: 185.8, 138.4, 138.3, 138.0, 135.9, 134.4, 117.6, 99.1, 65.6 (2C), 32.9, 15.7; HREIMS: [M^+] at m/z 206.0946 ($C_{12}H_{14}O_3$ requires 206.0943).

*2-(*tert*-Butyldimethylsiloxymethyl)-6 methylphenol*
Hydroxymethyl-6-methylphenol (20) (3.1 g, 0.022 mol) was dissolved in 30 mL CH_2Cl_2 and cooled to 0°C. *tert*-Butyldimethylsilylchloride (1.2 equiv. 4.0 g) and imidazole (1.2 equiv. 1.8 g) were added, and the reaction vessel removed from the ice bath. After 1 h, the mixture was filtered and the filtrate washed with 1 M HCl and brine solution, and then dried over Na_2SO_4. The crude material was purified by flash chromatography (3% ether in hexane) yielding 3.9 g (69% yield) of product. IR ν_{max} cm^{-1}: 3350 (O-H). ^1H NMR, δ: 8.15 (s, 1H, O-H), 7.05 (d, 1H, J = 7.3 Hz, phenyl H), 6.79 (d, 1H, J=7.1 Hz, phenyl H), 6.72 (*t*, 1H, J=7.3 Hz, phenyl H), 4.89 (s, 2H, CH_2OSi), 2.25 (s, 3H, $PhCH_3$), 0.94 (s, 9H, $SiC(CH_3)_3$), 0.15 (s, 6H, $Si(CH_3)_2$). HREIMS: [M^+] at m/z 252.1544 ($C_{14}H_{22}O_2Si$ requires 252.1546).

*2-(*tert*-Butyldimethylsiloxymethyl)-4,4-ethylenedioxy-6-methyl-cyclohexa-2,5-diene-1-one (entry 7):* IR ν_{max} cm^{-1}: 1645 (C=O). ^1H NMR, δ: 6.61 (m, 1H, =CH), 6.40 (m, 1H, =CH), 4.39 (d, 2H, J = 1.6 Hz), 4.12 (m, 4H), 1.84 (d, 3H, J = 1.3 Hz), 0.90 (s, 9H, $SiC(CH_3)_3$), 0.07 (6H, s, $Si(CH_3)_2$). ^{13}C NMR, δ: 185.6 (C=O), 139.36, 138.7, 137.1, 135.7, 99.8, 65.3, 60.0, 26.1, 26.1, 18.5, 15.3, −9.5. HREIMS: [M^+] at m/z 310.1607 ($C_{16}H_{26}O_4Si$ requires 310.1600).

4,4-Ethylenedioxy-5,6,7,8-tetrahydronaphtha-2,5-dienone (entry 8): IR(neat) ν_{max} cm^{-1}: 1675 (C=O), 1645, 1620 (C=C). ^1H NMR, δ: 6.63 (d, 1H, J = 10.0 Hz, H-5), 6.10 (d, 1H, J = 10.0 Hz, H-6), 4.15 (m, 4H, OCH_2CH_2O), 2.28 (m, 4H, CH_2), 1.65 (m, 4H, CH_2). ^{13}C NMR, δ: 185.2, 150.3, 142.4, 134.6, 127.7, 99.8, 66.2 (2C), 22.8, 22.0, 21.4 (2C). HREIMS: [M^+] at m/z 206.0939 ($C_{12}H_{14}O_3$ requires 206.0943).

Synthesis of 8′-demethylABA

*(6*R*)-2,6-Dimethyl-4,4-ethylenedioxycyclohexa-2-enone (**7**)*
Sucrose (25 g) was dissolved in 1.0 L of 0.1 M HEPES buffer (pH 6.5) and warmed to 45°C. Yeast (50 g) was added and the mixture was shaken for 30 min. 2,6-Dimethyl-4,4-ethylenedioxycyclohexa-2,5-dienone (2.13 g) in ethanol (10 mL) was added dropwise. The fermentation mixture was shaken at room temperature and the reduction monitored by GC. After the reaction was completed (typically 3–4 h), 200 mL ether was added and the mixture was filtered through a pad of Celite®. Alternatively, centrifugation for 20 min at 10 000 rpm effectively removed the yeast cells. The filtrate was extracted with large quantities of ether (3 × 400 mL) to avoid emulsions. The combined ether extracts were dried over $MgSO_4$ and concentrated. Column chromatography (5% EtOAc – hexane) gave 1.08 g (50% yield) product as a colorless liquid. $[\alpha]_D^{20}$ +31.8 ($CHCl_3$, *c* 2.0). IR ($CHCl_3$) ν_{max} cm^{-1}: 1682 (C=O). ^1H NMR, δ: 6.32 (m, 1H, H-3), 3.87–4. 08 (m, 4H, OCH_2CH_2O), 2.73 (m, 1H, H-6), 2.15 (ddd, 1H, J = 2.1, 4.8, 13.3 Hz, H-5ax), 1.98 (t, 1H, J = 13.0 Hz, H-5eq), 1.77 (d, 3H, J = 1.5 Hz, $=CCH_3$), 1.14 (d, 3H, J = 7 Hz, CH_3). ^{13}C NMR, δ: 201.37 (C=O), 140.63 (C=), 137.20 (C=), 104.59, 65.06, 64.73, 41.56, 39.50, 15.77, 15.01. HREIMS: (M^+) at m/z 182.0950 ($C_{10}H_{14}O_3$ requires 182.0950).

*(+)-8-(1*E*,3*Z*)-(8*R*,9*R*)-8-(5-Hydroxy-3-methylpent-1,3-dienyl)-7,9-dimethyl-1,4-dioxaspiro[4.5]dec-6-en-8-ol, **11***
A solution of known alkyne **10** (8) (2.1 g, 9.9 mmol) in dry THF (40 mL) was cooled in a Dry Ice – acetone bath under an argon atmosphere. *n*-Butyllithium (Aldrich, 0.63 M in hexane, 5.6 ml, 8.9 mmol) was added dropwise with stirring. A solution of ketal **7** (1.29 g , 7.1 mmol) in dry THF (20 mL) was added dropwise. After the addition was complete, the reaction solution was allowed to warm to room temperature (over 45 min). The reaction mixture was then cooled in an ice bath, and sodium bis(2-methoxyethoxy) aluminium hydride (Redal®, Aldrich, 3.4 M in toluene, 4.1 mL, 14.2 mmol) in THF (20 mL) was added dropwise. The reaction solution was allowed to warm to room temperature. After 1.5 h, the reaction was cooled to 0°C and water was added carefully to destroy the excess reducing agent. The THF was removed and the aqueous layer extracted with ether three times. The pooled organics were dried over Na_2SO_4 and concentrated. Purification by flash chromatography eluting with ether afforded alcohol **11** (760 mg, 38%). IR ($CHCl_3$) ν_{max} cm^{-1}: 3600 (O-H). ^1H NMR (C_6D_6), δ: 6.80 (d, 1H, J = 15.7 Hz, H-5), 5.63 (d, 1H, J = 15.8 Hz, H-4), 5.52 (s 1H, H-3′), 5.41 (*t*, 1 H, J = 5.8 Hz, H-2), 4.1 (*t*, 2H, J = 5.8 Hz, H-1), 3.61–3.46 (m, 4H, OCH_2), 2.20 (m, 1H, H-6′), 1.90 (d, 1H, J = 13.5 Hz, H-5′), 1.80 (dm, 1H, J = 13.7 Hz, H-5′), 1.65 (s, 3H, $=CCH_3$), 1.63 (s, 3H, $=CCH_3$), 0.90 (d, 3H, J = 7.8 Hz, CH_3). ^{13}C NMR (C_6D_6), δ: 144.16, 133.68, 129.79, 127.50, 125.57, 106.15, 77.41, 64.62, 64.34, 58.40, 40.29, 40.18, 20.52, 17.59, 15.58. HREIMS: [M^+] at m/z 280.1693 ($C_{16}H_{24}O_4$ requires 280.1675).

*(+)-(1*E*,3*Z*)-(4*R*,5*S*)-4-Hydroxy-4-(5-hydroxy-3-methylpent-1,3-dienyl)-3,5-dimethylcyclohex-2-enone, **12***
Compound **11** (106 mg), 10% HCl (10 mL), and THF (10 mL) were stirred at room temperature for 1.5 h. The mixture was diluted with water and extracted into ether (3 × 30 ml). The

combined organics were washed with brine, dried over Na_2SO_4, and concentrated. The crude material (74 mg, 83%) was carried through to the next step. $[\alpha]_D^{20}$ +246.4 (MeOH, *c* 0.84). IR (neat) ν_{max} cm^{-1}: 3380 (br O-H), 1705 (C=O). ^1H NMR, δ: 6.69 (d, 1H, *J* = 15.8 Hz, H-5), 5.89 (s, 1H, H-3′), 5.66 (d, 1H, *J* = 15.7 Hz, H-4), 5.62 (t, 1 H, *J* = 6.9 Hz, H-2), 4.28 (d, 2H, *J* = 6.9 Hz, H-1), 2.41 (ddd, 1H, *J* = 0.9, w coupling to H-3′, 4.2, 16.8 Hz, H-5′eq), 2.31–2.38 (m, 1H. H-6′), 2.21 (*dd*, 1H, *J* = 13.2, 16.8 Hz, H-5′ax), 1.92 (d, 3H, *J* = 1.1 Hz, =CCH_3), 1.84 (d, 3H, *J* = 0.8 Hz, =CCH_3), 0.99 (d, 3H, *J* = 6.7 Hz, H-9′). ^{13}C NMR, δ: 198.15, 165.24, 134.13, 129.63, 128.14, 128.05, 127.41, 77.48, 58.34, 43.06, 41.24, 20.61, 18.46, 15.04. HREIMS: [M^+] at *m/z* 236.1393 ($C_{14}H_{20}O_3$ requires 236.1412). Anal. calcd. for $C_{14}H_{20}O_3$: C 71.14, H 8.54; Found: C 71.02, H 8.56.

(+)-(1E,3Z)-(4R,5R)-4-Hydroxy-4-(4-carbomethoxy-3-methylbutyl-1,3-dienyl)-3,5-dimethylcyclohex-2-enone, ***13***

A mixture of MnO_2 (15 equiv. 4.1 mmol, 352 mg) and diene **12** (64 mg, 0.27 mmol) in 15 mL of acetone was stirred at room temperature for 1.5 h. The suspension was filtered and the cake of MnO_2 washed with excess ether. After concentration, 50 mg of aldehyde was recovered and directly reacted in the following manner. To the aldehyde (50 mg, 0.21 mmol) in MeOH (10 mL) was added sequentially MnO_2 (3.2 mmol, 274 mg), NaCN (0.65 mmol, 25 mg), and AcOH (0.21 mmol, 12 mL). The reaction was stirred at room temperature for 1.5 h. The suspension was filtered and washed with MeOH. After concentration, the residue was partitioned between Et_2O and H_2O and the organic layer washed with saturated NaCl solution, dried over Na_2SO_4, and concentrated. The crude product was purified on a Chromatotron eluting with ether, giving 25 mg (35% yield over the two steps) of the desired ester. Analysis on chiral HPLC (semiprep Chiralcel OD column, 10% IPA in hexane, flow rate of 4 mL/min) showed the product to be a 87:13 mixture of enantiomers. Preparative separation of the major enantiomer gave ester **13** with greater than 99% ee. $[\alpha]_D^{20}$ +359.4 (MeOH, *c* 1.38). IR ($CHCl_3$) ν_{max} cm^{-1}: 3450 (br O-H), 3600 (sharp OH), 1660 (C=O, enone), 1705 (C=O, ester). ^1H NMR, δ: 7.81 (d, 1H, *J* = 16.2 Hz, H-5), 6.00 (d, 1H, *J* = 16.2 Hz, H-4), 5.92 (s, 1H, =CH), 5.73 (s, 1H, =CH), 3.68 (s, 3H, $COOCH_3$), 2.35–2.45 (m, 2H), 2.19–2.26 (m, 2H), 1.99 (d, 3H, *J* = 1.0 Hz, =CCH_3), 1.95 (d, 3H, *J* = 1.2 Hz, =CCH_3), 1.00 (d, 3H, *J* = 6.5 Hz, H-9′). ^{13}C NMR, δ: 197.83, 166.39, 164.62, 149.24, 133.72, 129.29, 127.70, 118.42, 77.53, 51.21, 43.01, 41.22, 21.10, 18.40, 15.10. HREIMS: [M^+] at *m/z* 264.1368 ($C_{15}H_{20}O_4$ requires 264.1362).

(+)-(1E,3Z)-(4R,5R)-4-Hydroxy-4-(4-carboxy-3-methylbutyl-1,3-dienyl)-3,5-dimethylcyclohex-2-enone, ***2***

Optically pure ester **13** (28.7 mg, 0.11 mmol) was dissolved in methanol (12 drops) and potassium phosphate buffer (0.1 M, pH 7.5, 2.5 mL), porcine liver esterase (EC 3.1.1.1, Sigma E-3128, 200 mL), and KOH solution (1 M, added dropwise to adjust the pH to 8.0) were added and the solution stirred overnight. 10% HCl was added until the pH was lower than 3 and the mixture was repeatedly extracted with ethyl acetate (6 × 10 mL) to obtain the product from the resultant emulsion. The combined ethyl acetate phases were extracted with saturated aqueous $NaHCO_3$ (3 × 25 mL). The aqueous phases were acidified with HCl and extracted with ethyl acetate (3 × 25 mL). The ethyl acetate extracts were washed with brine and dried over Na_2SO_4. Evaporation gave 24 mg (89% yield) of pure product. $[\alpha]_D^{20}$ +430.3 (MeOH, *c* 2.30). IR ($CHCl_3$) ν_{max} cm^{-1}: 3000–3500 (O-H), 1675 (C=O), 1650 (C=O). ^1H NMR (CD_3OD), δ: 7.72 (d, 1H, *J* = 16.2 Hz, H-5), 6.09 (d, 1H, *J* = 16.2 Hz, H-4), 5.91 (s, 1H. =CH), 5.74 (s, 1H, =CH), 4.86 (*bs*, 1H, -OH), 3.29-2.25 (m, 3H, H5 and H6), 2.02 (d, 3H, *J* = 1.0 Hz, =CCH_3), 1.95 (d, 3H, *J* = 1.2 Hz, =CCH_3), 1.03 (d, 3H, *J* = 6.5 Hz, H-9′); ^{13}C NMR (DMSO-d_6): δ: 201.02, 169.38, 169.19, 150.89, 130.47, 128.13, 121.65, 119.72, 78.37, 43.81, 42.57, 21.17, 19.14, 15.45. HREIMS: [M^+] at *m/z* 250.1198 ($C_{14}H_{18}O_4$ requires 250.1205).

Synthesis of Mosher's ester 14

*(+)-8-(4Z)-(8S,9R)-8-(5-*tert*-Butyldimethylsiloxy-3-methylpent-3-en-1-ynyl)-7,9-dimethyl-1,4-dioxaspiro[4.5]dec-6-en-8-ol,* ***15***

A solution of known alkyne **10** (8) (2.1 g, 10.2 mmol) in dry THF (40 mL) was cooled in a Dry Ice – acetone bath under an argon atmosphere. *n*-Butyllithium (Aldrich, 0.63 M in hexane, 6.4 mL, 10.2 mmol) was added dropwise with stirring. The reaction solution was kept at −78°C for 1 h. A solution of enone **7** (930 mg, 5.1 mmol) in dry THF (20 mL) was added dropwise. After the addition was complete, the reaction solution was allowed to warm to room temperature (over 45 min), quenched with water, and extracted into ether. The pooled organics were washed with brine and dried over Na_2SO_4. Separation by flash chromatography eluting with ether–hexane (30:70) gave alkyne **15** in 83% yield (1.65 g). Alkyne **15** showed the following spectral properties: $[\alpha]_D^{20}$ +122.2 (MeOH, *c* 1.70). IR (neat) ν_{max} cm^{-1}: 3440 (O-H). ^1H NMR (C_6D_6), δ: 5.78 (dt, 1 H, *J* = 1, 6.2 Hz, H-2), 5.42 (s, 1H, H-3′), 4.48 (m, 2H, H-1), 3.42-3.57 (m, 4H, OCH_2), 2.13 (d, 1H, *J* = 13.3 Hz, H-5′ax), 1.89 (s, 3H, =CCH_3), 1.85 (dt, 1H, *J* = 2.1, 13.4 Hz, H-5′eq), 1.69 (s, 1H, OH), 1.64 (s, 3H, =CCH_3), 1.21 (d, 3H, *J* = 6.7 Hz, H-9′), 0.99 (s, 9H, Si^{t}Bu), 0.13 (s, 3H, $SiCH_3$). ^{13}C NMR (C_6D_6), δ: 142.39, 138.11, 125.30, 118.06, 105.94, 93.69, 84.60, 73.73, 64.60, 64.31, 62.61, 40.47, 39.85, 26.13, 22.84, 18.47, 17.72, 16.33, −4.98. HREIMS: [M^+] at *m/z* 392.2402 ($C_{22}H_{36}O_4Si$ requires 392.2383). Anal. calcd. for $C_{22}H_{36}O_4Si$: C 67.31, H 9.25; found: C 67.13, H 9.16.

(+)-4Z-(4S,5R)-4-Hydroxy-4-(5-hydroxy-methylpent-3-en-1-ynyl)-3, 5-dimethylcyclohex-2-enone, ***16***

To an ice-cooled solution of alkyne **15** (900 mg, 0.2.3 mmol) in dry THF (50 mL) under argon was added, dropwise, tetrabutylammonium fluoride (1.0 M in THF, 3.45 m, 3.45 mmol). The reaction solution was allowed to warm to room temperature. After 0.75 h, water was added and the aqueous layer extracted three times with ether. The pooled organics were dried over Na_2SO_4 and concentrated. The crude product was directly treated with 10% aqueous HCl (25 mL) in THF (25 mL), and was stirred at room temperature for 0.5 h. After addition of water, the mixture was extracted three times with ether, and the combined organic extracts were washed with brine, dried over Na_2SO_4, and purified by flash chromatography eluting with ether. Acetylenic alcohol **16** was produced in 87% yield (470 mg) over two steps. IR (neat) ν_{max} cm^{-1}: 3605 (s, OH), 3400 (br, O-H). ^1H NMR, δ: 5.92 (dt, 1 H, *J* = 1.4, 6.8 Hz, H-2), 5.81 (s, 1H, H-3′), 4.26 (dd, 2H, *J* = 0.8, 6.8 Hz, H-

1), 2.74 (bs, 1H, -OH), 2.43 (m, 3H), 2.11 (d, 3H, J = 1.1 Hz, $=CCH_3$), 1.87 (d, 3H, J = 1.0 Hz, $=CCH_3$), 1.20 (d, 3H, J = 6.0 Hz, H-9′). ^{13}C NMR, δ: 198.62, 163.86, 136.91, 126.31, 120.17, 90.62, 85.57, 72.75, 60.85, 43.42, 41.01, 22.96, 18.76, 15.91. HREIMS: [M^+] at m/z 234.1234 ($C_{14}H_{18}O_3$ requires 234.1256).

Mosher's ester, ***14***

Acetyleneic alcohol **16** (0.36 mmol, 84 mg), DCC (0.36 mmol, 74 mg), R-(+) α-methoxy α-(trifluoromethyl)phenyl acetic acid (0.32 mmol, 76 mg), and DMAP (0.04 mmol, 4 mg) were added to 5 mL of CH_2Cl_2 and stirred at room temperature overnight. The CH_2Cl_2 was washed with water and 10% HCl, dried over Na_2SO_4, and concentrated. Purification on a Chromatotron, eluting with 75:25 ether–hexane gave 34 mg recovered starting material and 78 mg of product (81% based on recovered starting material). Analysis of enantiotopic purity by chiral HPLC (Semiprep Chiralpak AS column, 25% IPA in hexane, flow rate 2 ml/min) showed an 85:15 ratio of diastereomers after recrystallization from ether–hexane, which could be purified to >99% ee by preparative chiral HPLC; mp 129–130. $[\alpha]_D^{20}$ +227.3 ($CHCl_3$, c 2.39). IR ($CHCl_3$) ν_{max} cm^{-1}: 3600 (OH), 1750 (C=O, ester), 1665 (C=O, enone). ^1H NMR, δ: 7.48 (m, 2H, aromatic), 7.39 (m, 2H, aromatic), 5.88 (dt, 1H, J = 1.2, 7.3 Hz, H-2), 5.81 (s, 1H, =CH), 4.96 (dd, 1H, J = 7.3, 12.1 Hz, H-1), 4.91 (dd, 1H, J = 7.3, 12.1 Hz, H-1), 3.52 (s, 3H, OCH_3), 2.61 (bs, 2H, OH), 2.33–2.46 (m, 3H), 2.09 (d, 3H, J = 1.0 Hz, $=CCH_3$), 1.89 (s, 3H, $=CCH_3$), 1.19 (d, 3H, J = 5.8 Hz, H-9′). ^{13}C NMR, δ: 198.03, 166.45, 162.74, 132.12, 130.18, 129.99, 129.70, 128.56, 128.45, 127.27, 126.66, 124.52, 122.06, 92.14, 84.98, 72.91, 63.99, 55.47, 43.38, 40.95, 22.93, 18.58, 15.83. HREIMS: [M^+] at m/z 450.1612 ($C_{24}H_{25}O_3F_3$ requires 450.1654).

Acknowledgements

The authors thank Brock Chatson, Lawrence Hogge, and Doug Olson for NMR and mass spectroscopy measurements and Tammy Leriche for carrying out the transpiration assay.

References

1. (*a*) T.L. Thomas. Plant Cell, **5**, 1401 (1993). (*b*) A.S. Hetherington and R. Quatrano. New Phytol. **119**, 10 (1991); (*c*) J. Giraudat, F. Parcy, N. Bertauche, F. Gosti, J. Leung, P-C. Morris, M. Bouvier-Durand, and N. Vartanian. Plant Mol. Biol. **26**, 1557 (1994); (*d*) M. Black. *In* Abscisic acid: physiology and biochemistry. *Edited by* W.J. Davies and H.G. Jones. BIOS Scientific Publishers; Oxford, U.K. 1991. pp. 99–124.
2. M.K. Walker-Simmons, R.J. Anderberg, P.A. Rose, and S.R. Abrams. Plant Physiol. **99**, 501 (1992).
3. M.K. Walker-Simmons, P.A. Rose, A.C. Shaw, and S.R. Abrams. Plant Physiol. **106**, 1279 (1994).
4. R.W. Wilen, D.B. Hays, R.M. Mandel, S.R. Abrams, and M.M. Moloney. Plant Physiol. **101**,469 (1993).
5. M. Nanzyo, T. Oritani, and K. Yamashita. Agric. Biol. Chem. **41**, 1711 (1977).
6. J.A.D. Zeevaart and R.A. Creelman. Annu. Rev. Plant Physiol. Plant Mol. Biol. **39**, 439 (1988).
7. J. Zou, G.D. Abrams, D.L. Barton, D.C. Taylor, M.K. Pomeroy, and S.R. Abrams. Plant Physiol. **108**, 563, (1995).
8. N. Lamb and S.R. Abrams. Can. J. Chem. **68**, 1151 (1990).
9. N. Lamb, A.C. Shaw, S.R. Abrams, M.J. Reaney, B. Ewan, A.J. Robertson, and L.V. Gusta. Phytochemistry, **34**, 905 (1993).
10. (*a*). N. Lamb, N. Wahab, P.A. Rose, A.C. Shaw, S.R. Abrams, A.J. Cutler, P.J. Smith, L.V. Gusta, and B. Ewan. Phytochemistry, **41**, 23 (1996); (*b*) P.A. Rose, S.R. Abrams, and L. V. Gusta. Phytochemistry, **31**, 1105 (1992); (*c*) P.A. Rose, S.R. Abrams, and A. Shaw. Tetrahedron: Asymmetry, **3**, 450 (1992); (*d*) L.A.K. Nelson, A.C. Shaw, and S.R. Abrams. Tetrahedron, **47**, 3259 (1991).
11. B. Lei, S. R. Abrams, B. Ewan, and L. V. Gusta. Phytochemistry, **37**, 289 (1994).
12. A. Pelter and S. Elgendy. Tetrahedron Lett. **29**, 677 (1988).
13. (*a*) S. Servi. Synthesis, 1 (1990); (*b*) H.G.W. Leuenberger. *In* Biocatalysts in organic synthesis. *Edited by* J. Tramper, H.C. Van der Plas, and P. Linko. Elesevier, Amsterdam. 1985. pp. 99–118.
14. H.J. Mayer, N. Rigassi, U. Schwieter, and B.C.L. Weedon. Helv. Chim. Acta, **59**, 1424 (1976).
15. E.J. Corey, N.W. Gilman, and B.E. Ganem. J. Am. Chem. Soc. **90**, 5616 (1968).
16. A.L. Spek. PLUTON92. Program for the display and analysis of crystal and molecular structures. Univ. of Utrecht, The Netherlands. 1992.
17. P. A. Rose, B. Lei, A. Shaw, D. L. Barton, M.K. Walker-Simmons, and S.R. Abrams. Phytochemistry, **41**, 1251 (1996).
18. E.J. Gabe, Y. Le Page, J.-P. Charland, F.L. Lee, and P.S. White. J. Appl. Crystallogr. **22**, 384 (1989).
19. International tables for X-ray crystallography. Vol. IV. Kynoch Press, Birmingham, England. 1974.
20. G. Schiemann. Makromol. Chem. **63**, 162 (1963).

A solid state NMR and X-ray crystallographic investigation of dynamic disorder in solid tetrahydronaphthalene derivatives

Glenn A. Facey, Terrence J. Connolly, Corinne Bensimon, and Tony Durst

Abstract: The solid state disorder of two tetrahydronaphthalene derivatives, *N*-methyl-*N*-methoxy-5,6,7,8-tetrahydro-1-naphthamide and 5,6,7,8-tetrahydro-1-naphthoic acid, was studied by solid state NMR and single crystal X-ray diffraction. The X-ray crystal structure of *N*-methyl-*N*-methoxy-5,6,7,8-tetrahydro-1-naphthamide was obtained at 123 K. It indicated the presence of two distinct molecular conformations. Solid state ^{13}C CP/MAS NMR data using the dipolar dephasing technique revealed that the two conformations of the molecule are dynamically disordered, while solid state ^{2}H NMR data, collected on a specifically deuterated analog, were used to determine the populations of each conformation as well as an apparent activation energy. Solid state NMR experiments were also used to show that 5,6,7,8-tetrahydro-1-naphthoic acid possesses the same type of dynamic disorder.

Key words: deuterium NMR, solid state NMR, dynamic disorder, X-ray, tetrahydronaphthalene derivatives

Résumé : Faisant appel à la RMN à l'état solide et à la diffraction des rayons X sur un cristal unique, on a étudié le désordre à l'état solide de deux dérivés du tétrahydronaphthalène, le *N*-méthyl-*N*-méthoxy-5,6,7,8-tétrahydro-1-naphthamide et de l'acide 5,6,7,8-tétrahydro-1-naphthoïque. On a déterminé la structure cristalline du *N*-méthyl-*N*-méthoxy-5,6,7,8-tétrahydro-1-naphthamide à 123 K. Elle indique la présence de deux conformations moléculaires distinctes. Les données de la RMN CP/MAS du ^{13}C à l'état solide, obtenues en utilisant la technique du déphasage dipolaire, ont révélé que les deux conformations de la molécule sont dynamiquement désordonnées; on a utilisé les données de la RMN du ^{2}H à l'état solide, obtenues à l'aide d'un analogue spécifiquement deutéré, pour déterminer les populations de chacun des conformères ainsi qu'une énergie d'activation apparente. On a aussi utilisé les expériences de RMN à l'état solide pour montrer que l'acide 5,6,7,8-tétrahydro-1-naphtoïque présente le même type de désordre dynamique.

Mots clés : RMN du deutérium, RMN à l'état solide, désordre dynamique, rayons X, dérivés tétrahydronaphtalènes.

[Traduit par la rédaction]

Introduction

The structural characterization of molecules is typically tackled with a broad arsenal of techniques including all forms of spectroscopy, mass spectrometry, and diffraction. Often chemists will put a great deal of effort into the growth of single crystals suitable for X-ray diffraction analysis, as this technique is often the one that will prove, beyond doubt, the structure of the material in question. In this contribution, we would like to illustrate that although often essential, single crystal X-ray diffraction data can be open to interpretation and that in such instances solid state NMR spectroscopy is an essential complementary technique needed to fully characterize the solid state structure. Single crystal X-ray diffraction is a technique sensitive to long-range order. The collection of data takes hours or days. These two facts render the technique unable to distinguish between static disorder and dynamic disorder.

Unlike single crystal diffraction techniques, solid state NMR spectroscopy is a technique sensitive to short-range order. Typical data collection times for a single transient are on the hundreds of microseconds to tens of milliseconds time scale. These two facts make this technique sensitive to molecular motions and, as a result, the distinction between static and dynamic disorder is possible. Also, it has the advantage that polycrystalline powders rather than single crystals can be used. This study involves the structural characterization of the two tetrahydronaphthalene derivatives **5a** and **6a** (Scheme 1). It demonstrates the complementary nature of single crystal X-ray diffraction and solid state NMR spectroscopy.

Background

^{2}H is a spin $I = 1$ nucleus having three Zeeman states. The pure Zeeman states are perturbed by the electric quadrupolar interaction, producing two resonance frequencies for each crystallographically unique deuteron. The difference in frequency between the two resonances is determined by the quadrupolar coupling constant, $\chi = (e^2Qq//h)$, and the orientation of the electric field gradient tensor at the nuclear site with respect to the static magnetic field. For deuterons

Received June 18, 1996.

G.A. Facey,[1] T.J. Connolly, C. Bensimon, and T. Durst. Department of Chemistry, University of Ottawa, Ottawa, ON K1N 6N5, Canada.

[1] Author to whom all correspondence may be addressed. Telephone: (613) 562-5800, ext. 6077. Fax: (613) 562-5170. E-mail: gafacey@oreo.chem.uottawa.ca

Scheme 1. Reagents: (a) K_2CO_3, THF:D_2O, Δ; (b) $LiAlH_4$, THF; (c) (*i*) *n*BuLi, TMEDA, Pentane, Δ, (*ii*) CO_2(s), (*iii*) HCl; (d) H_2, Pd/C, HOAc; (e) (*i*) $SOCl_2$, CH_2Cl_2, Δ, (*ii*) $(MeO(Me)NH_2^+Cl^-$, Et_3N, CH_2Cl_2.

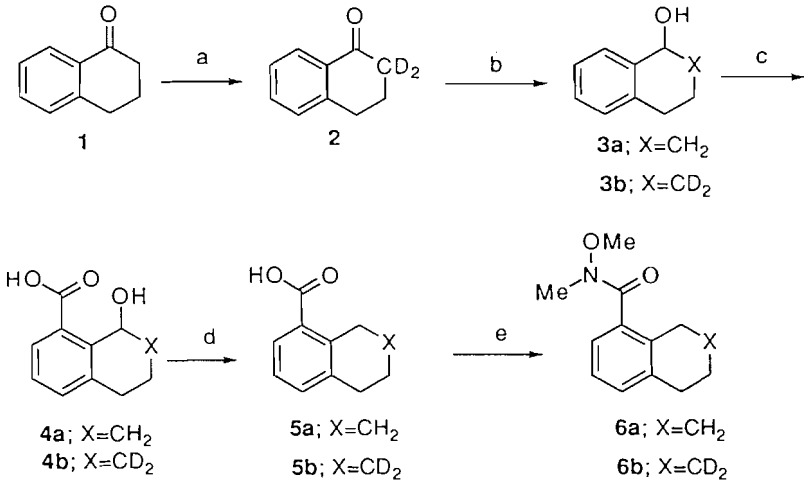

attached to carbon atoms the electric field gradient tensor, V_{ij}, is very often axially symmetric with its largest component, $V_{zz} = eq$, parallel to the C—D bond and, since V_{ij} has a trace of zero, $V_{zz} = (V_{yy} + V_{xx})$ with $V_{yy} = V_{xx}$. In the cases where axial symmetry is not present, it is conventional to assign $V_{zz} > V_{yy} > V_{xx}$. It is useful to define an asymmetry parameter, η, where $\eta = (V_{yy} - V_{xx})/V_{zz}$ where $0 \leq \eta \leq 1$.

The ^2H NMR spectrum of a single crystal consists of a sharp doublet for every crystallographically distinct deuteron whose splitting depends on the orientation of the crystal with respect to the magnetic field. For polycrystalline powders, where all orientations of the crystals are represented equally, the result is an envelope or powder spectrum from the sum of all possible doublets. The lineshape for such spectra can be readily calculated (1). In general, the spectra are symmetric about the centre with three pairs of singularities separated by frequencies, $\Delta\nu_{zz}$, $\Delta\nu_{yy}$, and $\Delta\nu_{xx}$, where $\Delta\nu_{zz} > \Delta\nu_{yy} > \Delta\nu_{xx}$. The frequency separations are proportional to the principal components of V_{ij} and are given by:

$$[1] \qquad -\Delta\nu_{XX} = \frac{-3\chi}{4}(1-\eta)$$

$$[2] \qquad -\Delta\nu_{YY} = \frac{-3\chi}{4}(1+\eta)$$

$$[3] \qquad \Delta\nu_{ZZ} = \frac{3\chi}{2}$$

The negative signs are added to the frequency differences to maintain a trace of zero.

The electric quadrupolar interaction, dominating the lineshapes of solid state ^2H NMR spectra, is exceedingly sensitive to molecular motions (2). The motions give rise to an averaged electric field gradient tensor and modify the shape of the powder spectrum. The effects can be grouped into three categories based on the rates of the molecular motion:

(a) Slow motions: These are motions occurring on a time scale much longer than the reciprocal line width of the static spectrum ($\sim 10^4$ s^{-1}). The effects are negligible on the NMR spectrum as there is essentially no change in the electric field gradient tensor during the course of the quadrupolar echo measurement.

(b) Intermediate rate motions: These are motions that occur on a time scale of the same order as the reciprocal line width of the static spectrum ($\sim 10^4$–10^7 s^{-1}). These motions have a profound effect on the observed lineshape (3–6). The lineshapes are very sensitive to the spacing between the pulses in the quadrupolar echo experiment (7) as well as to the rate and mechanism of the molecular motion. Although reduced significantly in amplitude compared to the rigid spectrum, the intermediate rate spectra can be simulated (8–10) in order to confirm a particular mechanism of a molecular motion or to determine its rate at the temperature of the measurement.

(c) Fast molecular motions: These motions occur on a time scale much shorter than the reciprocal line width of the static spectrum ($>10^7$ s^{-1}). The motion gives rise to an averaged electric field gradient tensor and spectra take on the same type of lineshape as those for rigid systems with the frequency differences between pairs of spectral singularities reduced. Such spectra are insensitive to the rate of the motion but may often be used to confirm the mechanism for the molecular motion. Fast motion limit spectra may be temperature dependent in cases where the population ratio for the sites occupied during the motion changes with temperature (11).

Experimental

All solid state NMR spectra were acquired on a Bruker ASX-200 solid state NMR spectrometer. Solid state ^{13}C CP/MAS spectra were acquired using a Bruker MAS probe with 7 mm o.d. zirconia rotors. The ^1H π/2 pulses were 3.6 μs, and 1 ms contact times were used. The spinning rate was set at 4000 Hz and was stable to within 2 Hz. In some cases the spinning side bands were suppressed (12). The solid state ^2H NMR spectra were acquired using a Bruker wideline probe accepting 5 mm o.d. glass tubes. The quadrupolar echo tech-

nique (13) was used with 3.2 μs $\pi/2$ pulses and an interpulse delay of 35 μs. The receiver was gated on 33 μs after the second pulse and the data were left shifted to the top of the echo before Fourier transformation. Although the temperature was regulated with the variable temperature control unit of the spectrometer, it was measured directly by placing a thermocouple on the rf coil containing the sample immediately after data collection. The reported temperatures are accurate and precise to within 1 degree. ^2H T_1 measurements were made using the inversion–recovery technique with magnetization being sampled with a quadrupolar echo. In all measurements at least 10 recovery times were used and the T_1's were calculated using the three-parameter nonlinear fit provided by the software of the spectrometer.

The single crystal X-ray data for **6a** were collected at 123 K on a Rigaku diffractometer with Cu Kα radiation using the ω–2θ scan technique to a maximum 2θ value of 100°. The cell constants and an orientation matrix for data collection were obtained from least-squares refinement using the setting angles of 25 reflections in the range $80° < 2\theta < 100°$. A total of 1297 reflections was collected. The unique set contained only 1195 reflections. The standards were measured after every 150 reflections. No crystal decay was noticed. The data were corrected for Lorentz and polarization effects, no correction being made for absorption. The structure was solved by direct methods. All non-hydrogen atoms were refined anisotropically. The maximum and minimum peaks in the final difference Fourier map corresponded to 0.460 and −0.440 e/Å^3, respectively.

All materials used for this study were prepared according to Scheme 1 (14) and the details dealing with the synthesis will be published elsewhere.

Results and discussion

The single crystal X-ray diffraction data (deposited as supplementary material)[2] for **6a** taken at 123 K show that the compound crystallizes in the space group $P2_1/a$ with four molecules in the unit cell. The cell constants are as follows: a = 8.6171 Å; b = 12.2350 Å; c = 11.2223 Å, and β = 102.937°. An ORTEP plot of the structure is given in Fig. 1. The structure shows a molecular confirmation where the carbonyl bond is almost normal to the plane of the aromatic ring, thus leaving a great deal of void space around the methylene carbons in the 6 and 7 positions. Another very obvious feature of the crystal structure is that there are two sets of coordinates found for each of the carbons in the 6 and 7 positions of the cyclohexene moiety. This indicates that there are two conformations of the cyclohexene ring present in the crystal. The disorder was refined using fixed thermal parameters and letting the occupancies for the four sites occupied by carbons 6 and 7 refine. The results gave occupancies close to 0.75:0.25. The occupancies were then fixed to these values

[2] Supplementary material can be purchased from: The Depository of Unpublished Data, Document Delivery, CISTI, National Research Council Canada, Ottawa, Canada K1A 0S2. These data have also been deposited with the Cambridge Crystallographic Data Centre, and can be obtained on request from The Director, Cambridge Crystallographic Data Centre, University Chemical Laboratory, 12 Union Road, Cambridge, CB2 1EZ, U.K.

Fig. 1. ORTEP plot of the crystal structure of **6a** at 123 K refined under the assumption that the population ratio is 0.75:0.25.

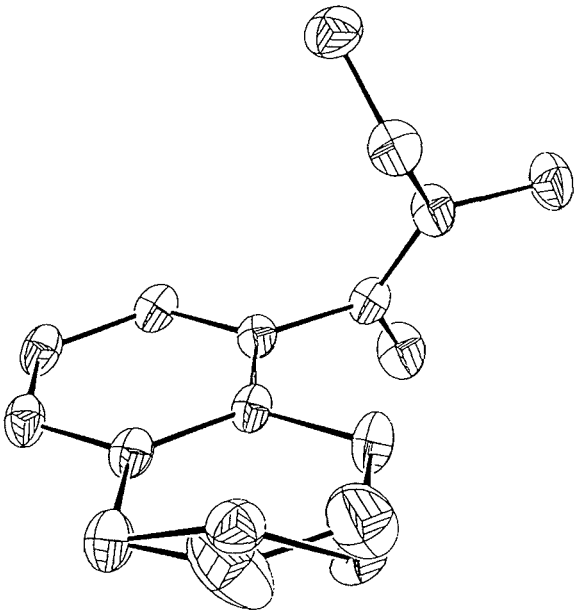

and the thermal parameters refined. It is interesting to note that the thermal parameters are not equal for each of the two conformations, the major conformation having much larger thermal parameters than the minor one. One possible explanation of this may be that the local intermolecular forces for each of the sites may be different, allowing one of the conformations to have slightly more mobility than the other. The X-ray data are unable to confirm whether the structure is rigid with both conformations present (static disorder) or whether the two conformations are exchanging dynamically with one another (dynamic disorder).

The solid state ^{13}C CP/MAS NMR spectrum of **6a** taken at room temperature is shown in Fig. 2*A*. The spectrum is highly resolved, each nonequivalent carbon giving rise to a resonance. The only coincidental overlap occurs for the resonances of the carbons in the 6 and 7 positions on the cyclohexene ring. The carbonyl carbon and the *N*-methyl carbon are broadened from partially unaveraged dipolar interactions between ^{13}C and ^{14}N (15). If there was a static disorder in the structure at room temperature, one might expect to observe two resonances for each carbon atom in the molecule, one set for each of the two nonequivalent conformations (16). Furthermore, the intensities of the lines would approximately represent the population ratio of the conformers present. This does not seem to be the case. The ^{13}C CP/MAS spectrum acquired with dipolar dephasing is given in Fig. 2*B*. In dipolar dephasing experiments (17) a short delay (40 μs in this case) is inserted between the contact pulse and the beginning of the acquisition. During this delay the $^{13}C - {}^1H$ dipolar interactions are only partially averaged by the magic angle spinning. Also, the magnetization due to carbon nuclei having large $^{13}C - {}^1H$ dipolar interactions dephases and the corresponding resonances are absent from the frequency domain spectrum. This is true for fairly rigid carbon atoms directly bound to protons. Carbon atoms not bearing protons or methyl car-

Fig. 2. (*A*) ^{13}C CP/MAS NMR spectrum of **6a** at room temperature. (*B*) Same as *A* with a 40 μs dipolar dephasing delay. In both traces the first-order spinning side bands were suppressed (12).

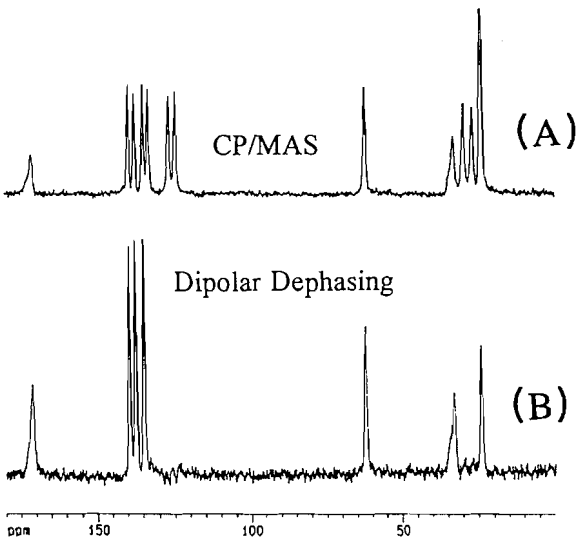

bons whose dipolar interactions with protons are averaged as a result of fast methyl group rotation, will show up in the spectrum, albeit slightly attenuated. The data in Fig. 2*B* show that not only do the carbonyl, methyl, and quaternary aromatic resonances survive the dephasing delay, but the 6 and 7 methylene carbons of the cyclohexene ring do as well. This can be the case only if the ^{13}C – ^{1}H dipolar interactions for these methylene carbons are averaged by some sort of molecular motion. Therefore, we can conclude that the nature of the disorder present in the structure at room temperature is dynamic rather than static. This, however, does not prove whether or not the disorder observed at 123 K in the X-ray data is static or dynamic in nature.

The analogue to **6a** labelled with deuterium on the 7 position, **6b**, was prepared to address the dynamic nature of the structural problem. The wideline solid state ^{2}H NMR spectra of **6b** are given in Fig. 3 as a function of temperature. At all temperatures the width of the powder spectrum is narrower than one would expect for a completely rigid system (18). Furthermore, at all temperatures above 178 K, the ^{2}H NMR spectra are in the fast motion limit. That is, the molecular motion is occurring at a rate much greater than the reciprocal width of the rigid powder spectrum (expected to be ~260 kHz) (18). Spectra collected below 178 K are in the intermediate motion regime. The separation between the spectral singularities at the top, middle, and base of the powder spectra are plotted against temperature in Fig. 4. One can see that one splitting (the separation of the middle shoulders) remains essentially constant throughout the entire temperature range. This indicates that the axis of the molecular motion must lie parallel to one of the two principal components of the electric field gradient tensor perpendicular to the C—D bond. Furthermore, the lineshape observed at 300 K is characteristic of a two-site exchange between equally populated sites with the C—D bond subtending the tetrahedral angle over the course of the motion. (18) These observations

Fig. 3. Broadline solid state ^{2}H NMR spectra of **6b** recorded as a function of temperature. The relaxation delay was greater than the T_1 by at least a factor of 5.

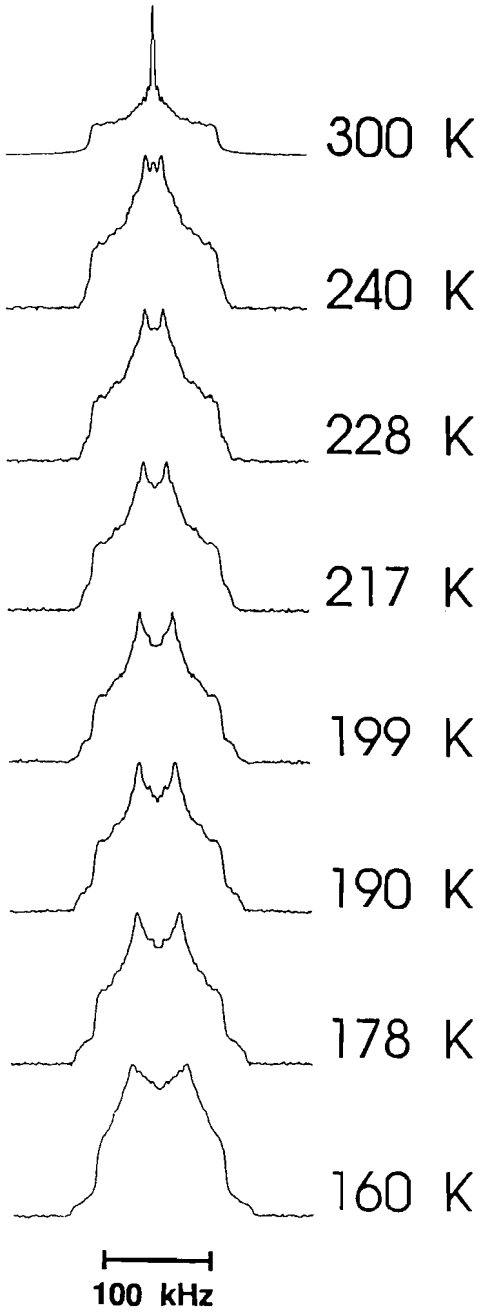

are consistent with the model depicted in figure 5. In this model, the cyclohexene moiety undergoes a transformation akin to the chair to chair inversion of cyclohexane. The sites however must not be equally populated over the entire temperature range as this would leave the spectra invariant with temperature. As the temperature is lowered one site becomes more populated than the other. The frequency differences between the singularities of the fast motion lineshape are determined by the eigenvalues of the averaged electric field gradient tensor. These are calculated by taking the weighted average of the electric field gradient tensors for each of the

Fig. 4. Plot of the frequency differences, $\Delta\nu'_{XX}$, $\Delta\nu'_{YY}$, and $\Delta\nu'_{ZZ}$, between the features of the solid state ^2H spectra of **6b** as a function of temperature.

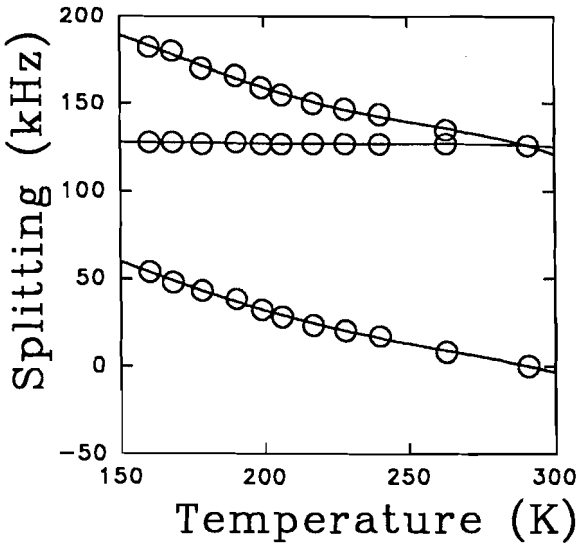

Fig. 5. Model depicting the inversion of the cyclohexene moiety.

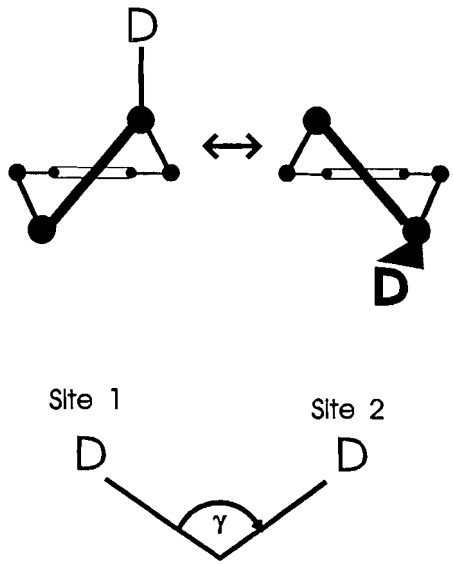

sites occupied over the course of the molecular motion, then diagonalizing the averaged tensor if necessary. To do this calculation we must define all of the electric field gradient tensors in a common axis system. This is most conveniently accomplished by choosing an axis defined by the motion and then redefining each of the tensors with respect to this new axis system in terms of the Euler angles, α, β, and γ (19). The electric field gradient for each of these sites is defined as follows:

$$[4]\qquad V(\alpha,\beta,\gamma)=\begin{bmatrix} a_{11} & a_{12} & a_{13} \\ a_{21} & a_{22} & a_{23} \\ a_{31} & a_{32} & a_{33} \end{bmatrix}$$

where $a_{ij} = a_{ji}$. Each of the matrix elements are defined as follows:

$$[5]\quad a_{11} = (\cos^2\alpha\cos^2\beta\cos^2\gamma+\sin^2\alpha\sin^2\gamma-2\sin\alpha\cos\alpha\cos\beta\sin\gamma\cos\gamma)V_{XX}+(\sin^2\alpha\cos^2\beta\cos^2\gamma+\cos^2\alpha\sin^2\gamma+2\sin\alpha\cos\alpha\cos\beta\sin\gamma\cos\gamma)V_{YY}+(\sin^2\beta\cos^2\gamma)V_{ZZ}$$

$$[6]\quad a_{22} = (\cos^2\alpha\cos^2\beta\sin^2\gamma+\sin^2\alpha\cos^2\gamma+2\sin\alpha\cos\alpha\cos\beta\sin\gamma\cos\gamma)V_{XX}+(\sin^2\alpha\cos^2\beta\sin^2\gamma+\cos^2\alpha\cos^2\gamma-2\sin\alpha\cos\alpha\cos\beta\sin\gamma\cos\gamma)V_{YY}+(\sin^2\beta\sin^2\gamma)V_{ZZ}$$

$$[7]\quad a_{33} = (\cos^2\alpha\sin^2\beta)V_{XX}+(\sin^2\alpha\sin^2\beta)V_{YY}+(\cos^2\beta)V_{ZZ}$$

$$[8]\quad a_{12} = (-\cos^2\alpha\cos^2\beta\sin\gamma\cos\gamma+\sin^2\alpha\sin\gamma\cos\gamma+\sin\alpha\cos\alpha\cos\beta(\sin^2\gamma-\cos^2\gamma))V_{XX}+(-\sin^2\alpha\cos^2\beta\sin\gamma\cos\gamma+\cos^2\alpha\sin\gamma\cos\gamma+\sin\alpha\cos\alpha\cos\beta(\cos^2\gamma-\sin^2\gamma))V_{YY}+(-\sin^2\beta\cos\gamma\sin\gamma)V_{ZZ}$$

$$[9]\quad a_{13} = (\cos^2\alpha\cos\beta\sin\beta\cos\gamma-\sin\alpha\cos\alpha\sin\beta\sin\gamma)V_{XX}+(\sin^2\alpha\sin\beta\cos\beta\cos\gamma+\cos\alpha\sin\alpha\sin\beta\sin\gamma)V_{YY}+(-\sin\beta\cos\beta\cos\gamma)V_{ZZ}$$

$$[10]\quad a_{23} = (-\cos^2\alpha\cos\beta\sin\beta\sin\gamma-\sin\alpha\cos\alpha\sin\beta\cos\gamma)V_{XX}+(-\sin^2\alpha\sin\beta\cos\beta\sin\gamma+\sin\alpha\cos\alpha\sin\beta\cos\gamma)V_{YY}+(\sin\beta\cos\beta\sin\gamma)V_{ZZ}$$

For the two-site model described in Fig. 5, we can define an axis normal to the plane defined by the two-site exchange with the origin on the carbon atom and then define the Euler angles with respect to this axis. We have $\alpha_1 = 0°$, $\beta_1 = 90°$, and $\gamma_1 = -54.75°$ for one site and $\alpha_2 = 0°$, $\beta_2 = 90°$, and $\gamma_2 = 54.75°$ for the second site. Substituting the values of α and β into

eqs. [5]–[10], we get:

$$[11] \quad V_i(\gamma_i) = \begin{bmatrix} \sin^2\gamma_i V_{YY} + \cos^2\gamma_i V_{ZZ} & \sin\gamma_i \cos\gamma_i (V_{YY} - V_{ZZ}) & 0 \\ \sin\gamma_i \cos\gamma_i (V_{YY} - V_{ZZ}) & \cos^2\gamma_i V_{YY} + \sin^2\gamma_i V_{ZZ} & 0 \\ 0 & 0 & V_{XX} \end{bmatrix}$$

Let the populations of the two sites equal P_1 and P_2. The weighted average of $V_i(\gamma_i)$ is given by:

$$[12] \quad \overline{V(\gamma)} = \begin{bmatrix} \sin^2\gamma V_{YY} + \cos^2\gamma V_{ZZ} & \sin\gamma\cos\gamma (V_{YY} - V_{ZZ})(P_2 - P_1) & 0 \\ \sin\gamma\cos\gamma (V_{YY} - V_{ZZ})(P_2 - P_1) & \cos^2\gamma V_{YY} + \sin^2\gamma V_{ZZ} & 0 \\ 0 & 0 & V_{XX} \end{bmatrix}$$

The eigenvalues, λ_i can be obtained by diagonalization.

$$\lambda_1 = \frac{(V_{YY} + V_{ZZ}) + (V_{YY} - V_{ZZ})\sqrt{1 - 4\sin^2\gamma\cos^2\gamma(1 - (P_2 - P_1)^2)}}{2}$$

$$[13] \quad \lambda_2 = \frac{(V_{YY} + V_{ZZ}) + (V_{YY} - V_{ZZ})\sqrt{1 - 4\sin^2\gamma\cos^2\gamma(1 - (P_2 - P_1)^2)}}{2}$$

$$\lambda_3 = V_{XX}$$

We can express the components of the unaveraged electric field gradient tensor, V_{ii}, in terms of χ and η then set γ to one half of the tetrahedral angle. The frequency splittings, $\Delta\nu'_{XX}$, $\Delta\nu'_{YY}$, and $\Delta\nu'_{ZZ}$ in the averaged spectrum can then be expressed as follows:

$$[14] \quad -\Delta\nu'_{XX} = \frac{\chi}{8}(3(1-\eta) - (3+\eta)\sqrt{1 + 8(P_2 - P_1)^2})$$

$$[15] \quad -\Delta\nu'_{YY} = -\frac{3}{4}\chi(1-\eta)$$

$$[16] \quad \Delta\nu'_{ZZ} = \frac{\chi}{8}(3(1-\eta) + (3+\eta)\sqrt{1 + 8(P_2 - P_1)^2})$$

If we know the quadrupolar coupling constant and asymmetry parameter for the rigid spectrum and have measured the splittings in an averaged spectrum, we can directly evaluate the populations of the sites at a given temperature. Unfortunately, χ and η are not available in the literature and our equipment did not allow the measurement of spectra at sufficiently low temperatures for their experimental determination. However, these data have been reported for cyclohexane (20) ($\chi = 173.7 \pm 1.7$ kHz and $\eta \leq 0.01$). If we assume that these parameters are not significantly different for our case, we can take $\chi = 174$ kHz and $\eta = 0$ and obtain the populations from eqs. [14] and [16]. The ratio of populations is expected to follow the Boltzman distribution, hence a plot of $\ln(P_1/P_2)$ vs. $1/T$ should be linear with slope $-\Delta E/R$, where ΔE is the energy difference between the two conformations and R is the gas constant. These data are plotted in Fig. 6*A* and the energy difference obtained is 3.2 ± 0.3 kJ/mol.

^{2}H T_1 relaxation times were measured as a function of temperature. When dominated by the quadrupolar interaction, in the case of a two-site exchange, the rate of relaxation can be described by (21):

$$[17] \quad \frac{1}{T_1} = \frac{3}{16}\chi^2\left(\frac{\tau_c}{1 + (\omega_0\tau_c)^2} + \frac{4\tau_c}{1 + (2\omega_0\tau_c)^2}\right)$$

Fig. 6. (*A*) Plot of the population ratios calculated from eqs. [14] and [16] for **6b** as a function of temperature. (*B*) Same as *A* for **5b**.

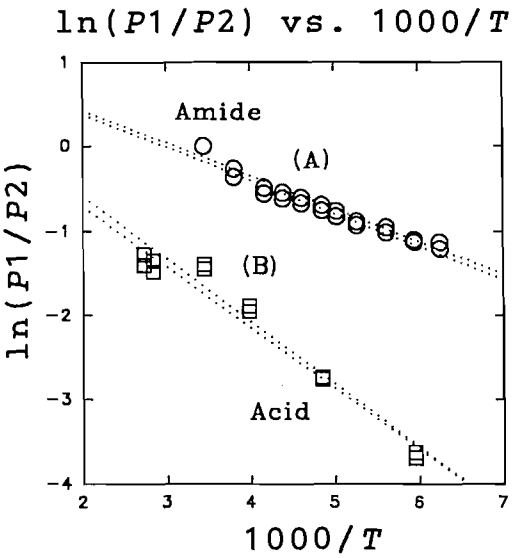

where ω_0 is the angular Larmor frequency and τ_c is the correlation time. The T_1's were calculated from the inner singularities of the powder spectra. A plot of log T_1 vs. reciprocal temperature is presented in Fig. 7. A T_1 minimum is observed at ~196 K. This minimum occurs when $\omega_0\tau_c = 0.6158$ and can be used to determine the correlation time at the temperature of the minimum. The correlation time at 196 K is 3.19 ns. The slope of the line in the high-temperature regime can be used to evaluate an activation barrier from the Arrhenius relation. The activation barrier was evaluated at 12.3 ± 0.2 kJ/mol. We can compare this to that measured for cyclohexene in solution (22.2 kJ/mol) (22). Strictly speaking, activation energies and correlation times evaluated in this way assume that the populations remain equal throughout the entire temperature range, therefore the activation barrier

Fig. 7. Plot of $\ln(T_1)$ vs. $(1000/T)$ for the ^2H data collected for **6b**.

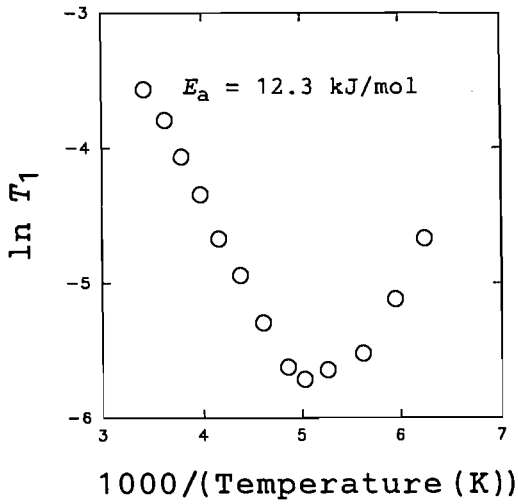

and correlation time presented here are best referred to as "apparent." The relatively low "apparent" activation energy evaluated here may be due to the large amount of void space in the vicinity of the cyclohexene moiety of **6b** in the crystal lattice.

If we make the reasonable assumption that **6b** is structurally identical to **6a**, we can conclude that the disorder observed in the X-ray diffraction data is dynamic in nature. By extrapolation of the data in Fig. 6*B* we can estimate the populations of the two conformations to be approximately 86:14. Based on this information, the initial 0.75:0.25 population ratio used in the X-ray diffraction data was replaced by 86:14 and a further refinement carried out. This modification, however, made very little difference to the atomic coordinates or thermal parameters.

The solid state ^{13}C CP/MAS NMR spectrum of **5a** taken at room temperature is shown in Fig. 8*A* with the corresponding dipolar dephased spectrum in Fig. 8*B*. Unlike the ^{13}C CP/MAS dipolar dephased spectrum of **6a**, the spectrum of **5a** does not show any significant intensity for the methylene carbons in the 6 and 7 positions. This observation can mean one of two things. Either the system is rigid with one or more conformations or there is a similar conformational exchange as observed for **6a** except that the population difference is very close to unity. In either case the net $^{13}C - {}^1H$ dipolar interaction would still be large and the ^{13}C signal for the methylenes would be expected to decay significantly during the 40 μs dipolar dephasing delay.

The wideline solid state ^2H NMR spectra of **5b** are given in Fig. 9 as a function of temperature. As with **6b**, the spectra are narrower than expected for a completely rigid system. Also similar to the ^2H spectra of **6b**, the spectra are temperature dependent and in the fast-motion limit. This eliminates the hypothesis that the system is completely rigid. A plot of the spectral frequency separations as a function of temperature are given in Fig. 10. The data are very similar to those in Fig. 4, indicating that the motion is of the same type as that observed for **6b**. If we assume the same model for dynamic disorder as in **6b** and that the quadrupolar coupling constant for the rigid system is 174 kHz with $\eta = 0$, then the

Fig. 8. (*A*) ^{13}C CP/MAS NMR spectrum of **5a** at room temperature. (*B*) Same as *A* with a 40 μs dipolar dephasing delay. The peaks marked with an asterisk are spinning side bands.

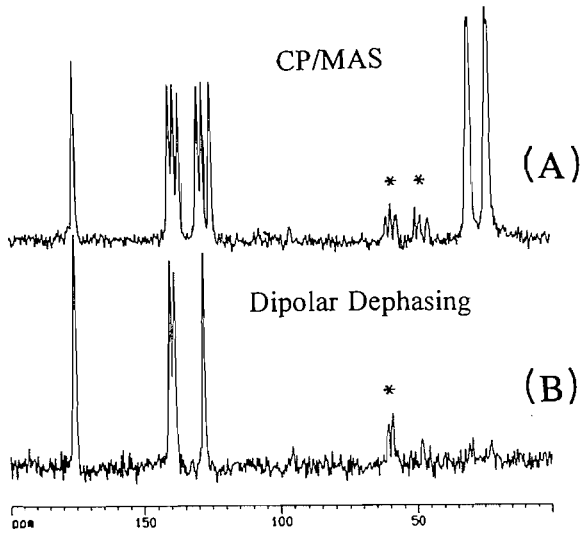

Fig. 9. Broadline solid state ^2H NMR spectra of **5b** recorded as a function of temperature. The relaxation delay was 10 s.

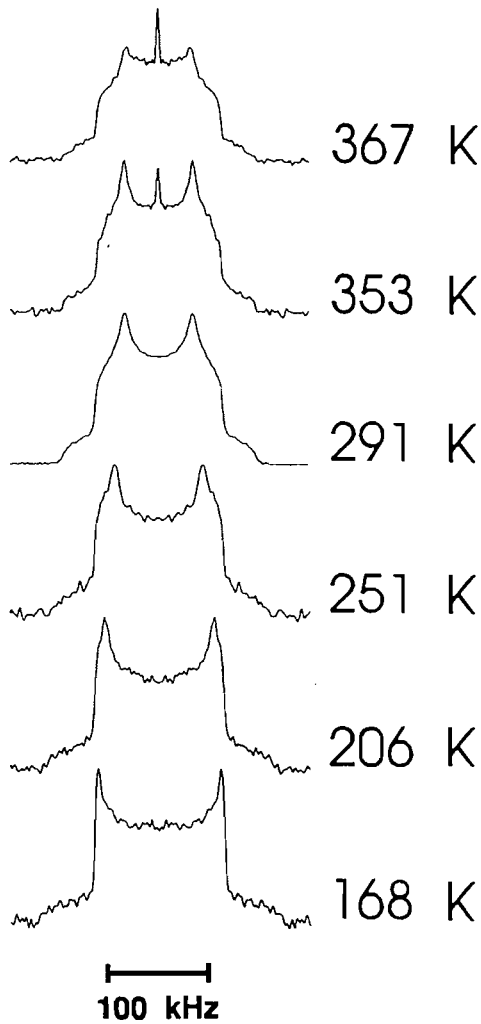

Fig. 10. Plot of the frequency differences, $\Delta\nu'_{XX}$, $\Delta\nu'_{YY}$, and $\Delta\nu'_{ZZ}$, between the features of the solid state ^2H spectra of **5b** as a function of temperature.

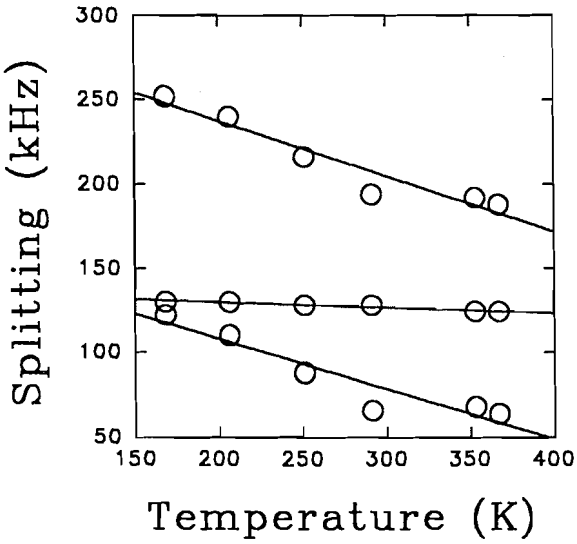

populations can be calculated as before and the energy difference between the two conformations evaluated. The data are plotted in Fig. 6*B* and give $\Delta E = 6.1 \pm 0.2$ kJ/mol. From both the ^{13}C and ^2H solid state NMR data it is apparent that **5b** undergoes an exchange akin to a chair-to-chair inversion of the cyclohexene ring in the solid state where one of the conformations is highly favoured with respect to the other. The fact that the population difference for **5b** is larger than that for **6b** may suggest that for the case of the acid there is less void space around the cyclohexene ring in the crystal lattice.

Conclusion

The X-ray crystal structure obtained for **6a** shows a molecular conformation where the carbonyl bond is almost normal to the plane of the aromatic ring. This conformation leaves a great deal of void space around the cyclohexene moiety, giving it the freedom to undergo molecular motions. The crystal structure shows that there are two distinct conformations present but is unable to confirm whether they are disordered statically or dynamically. Solid state ^{13}C CP/MAS data taken at room temperature reveal that the disorder is dynamic at room temperature, and the ^2H NMR data are able to evaluate the population ratios as a function of temperature as well as determine an apparent activation barrier based on a simple two-site ring inversion. The ^2H NMR data for **5b** support the notion that the same sort of ring inversion occurs in this compound; however, the population differences are much larger. The large population difference is consistent with the absence of methylene signals in the ^{13}C CP/MAS spectrum with dipolar dephasing.

References

1. M. Mehring. *In* NMR basic priciples and progress: High-resolution NMR spectroscopy of solids. *Edited by* P. Diehl, E. Fluck, and R. Kosfeld. Springer-Verlag, New York. 1976.
2. A. Abragam. *In* The principles of nuclear magnetism. *Edited by* R.K. Adair, R.J. Elliot, W.C. Marshal, and D.H. Wilkinson. Clarendon Press, Oxford. 1961. pp. 424–479.
3. K. Beshah and R.G. Griffin. J. Magn. Reson. **84**, 268 (1989).
4. K. Beshah, E.T. Olejniczak, and R.G. Griffin. J. Chem. Phys. **88**, 4730 (1987).
5. M.J. Collins, C.I. Ratcliffe, and J.A. Ripmeester. J. Phys. Chem. **93**, 7495 (1987).
6. E. Meirovitch and J.H. Freed. Chem. Phys. Lett. **64**, 311 (1979).
7. A.J. Vega and Z. Luz. J. Chem. Phys. **86**, 1803 (1986).
8. R.J. Wittebort, E.T. Olejniczak, and R.G. Griffin. J. Chem. Phys. **86**, 5411 (1987).
9. M.S. Greenfield, A.D. Ronemus, R.L. Vold, R.R. Vold, P.D. Ellis, and T.E. Raidy. J. Magn. Reson. **72**, 89 (1987).
10. H.W. Spiess and H.J. Sillescu. J. Magn. Reson. **42**, 381 (1981).
11. J.A. Ripmeester. J. Chem. Phys. **85**, 747 (1986).
12. M.A. Hemminga and P.A. de Jager. J. Magn. Reson. **51**, 339 (1983).
13. J.H. Davis, K.R. Jeffrey, M. Bloom, M.I. Valic, and T.P. Higgs. Chem. Phys. Lett. **42**, 390 (1976).
14. Terrence J. Connolly. Ph.D. Thesis, University of Ottawa (1996).
15. R.K. Harris and A.C. Olivieri. Prog. NMR Spectrosc. **24**, 435 (1992).
16. C.A. McDowell, A. Naito, J.R. Scheffer, and Y-F Wong. Tetrahedron Lett. **22**, 4779 (1981).
17. L.B. Alemany, D.M. Grant, T.D. Alger, and R.J. Pugmire. J. Am. Chem. Soc. **105**, 6697 (1983).
18. R.G. Barnes. Adv. Nucl. Quadrupole Reson. **1**, 335 (1974).
19. J. Mathews and R.L. Walker. *In* Mathematical methods of physics. W.A. Benjamin, New York. 1965. p. 374.
20. R.G. Barnes and J.W. Bloom. J. Chem. Phys. **56**, 1549 (1972).
21. D.A. Torchia and A. Szabo. J. Magn. Reson. **49**, 107 (1982).
22. F.A.L. Anet and M.Z. Haq. J. Am. Chem. Soc. **87**, 3147 (1965).

Fonctionnalisation du δ-pyronène, un nouveau synthon terpénique

Marie Jeanne Quirin, Martine Taran et Bernard Delmond

Résumé : Le δ-pyronène, un synthon terpénique nouvellement accessible à partir du myrcène, composé développé industriellement, a été diversement fonctionnalisé. Il constitue une matière première intéressante pour accéder à des intermédiaires actuellement utilisés dans la synthèse de parfums et de rétinoïdes. De plus, de nouveaux composés terpéniques possédant un squelette cyclogéranyle particulier ont été préparés.

Mots clés : terpènes, pyronènes, dérivés cyclogéranyles, parfums.

Abstract: δ-Pyronene, a terpenic synthon recently made industrially available from myrcene, has been characterized. It is an excellent raw material for the preparation of numerous intermediates used in the synthesis of perfumes and retinoids. Furthermore, new terpenic compounds including the cyclogeranyl skeleton have been prepared.

Key words: terpenes, pyronenes, cyclogeranyl derivatives, perfumes.

[Journal translation]

Introduction

Les pyronènes (Schéma 1) sont des hydrocarbures diéniques, possédant le squelette 1,1,2,3-tétraméthylcyclohexane, obtenus — essentiellement les isomères α **1** et β **2** — lors de la pyrolyse de l'α-pinène (1). Ils résultent alors d'une isomérisation thermique des alloocimènes formés intermédiairement (2).

Schéma 1.

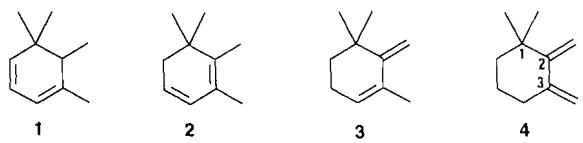

Le γ-pyronène **3** a été préparé (3) avec un bon degré de pureté lors de la dégradation d'Hoffman des sels d'ammonium de l'α-cyclogéranyle amine; cependant ce type de réaction réalisée sur le chlorhydrate de la diméthyl β-cyclogéranyle amine (4) conduit à un mélange de γ-pyronène **3** et de δ-pyronène **4**. Le δ-pyronène **4** (1,1-diméthyl-2,3-diméthylène cyclohexane) peut être cependant obtenu de manière plus spécifique et avec une excellente pureté à partir du mycène (5), matière première préparée industriellement à partir du β-pinène.

Aussi compte tenu de cette disponibilité récente et du peu de travaux (6) réalisés à ce jour concernant la chimie du δ-pyronène **4** nous avons entrepris d'analyser la réactivité de ce composé.

Lors d'un travail précédent (7) nous avons étudié son époxydation et montré que l'époxy-pyronène **5** (Schéma 2) était un synthon (8) permettant d'accéder à des intermédiaires importants (β-cyclocitral **6**, β-ionone **7**) utilisés par les industries des parfums et des cosmétiques.

Schéma 2.

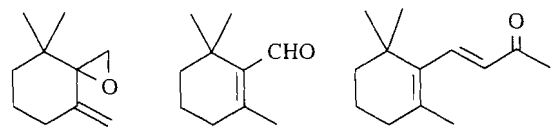

5 **6** **7**

Nous présentons dans ce mémoire différents aspects de la réactivité du δ-pyronène **4**, mettant en jeu le système diénique et conduisant, selon les réactifs, à des produits issus d'une addition-1,2 ou d'une addition-1,4.

Nous montrerons en particulier, que de nouveaux composés terpéniques appartenant à la série "iso" (Schéma 3) et dont le squelette cyclogéranyle diffère de la série normale par une localisation différente de la chaîne latérale fonctionnelle (R), peuvent être préparés à partir de ce composé.

Schéma 3.

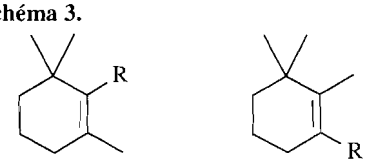

série normale série "iso"

Résultats

Dihydroxylation du δ-pyronène 4

Nous avons réalisé la dihydroxylation du δ-pyronène **4** par le permanganate de potassium en milieu basique aqueux (9).

Reçu le 28 mars 1996.

M.J. Quirin et B. Delmond.[1] Laboratoire de chimie organique et organométallique, Unité de recherche associée n° 35 du Centre national de la recherche scientifique, Institut du Pin, Université Bordeaux 1, 351, cours de la Libération, 33405 Talence Cedex, France.

M. Taran. Unité d'enseignement et de recherche des sciences pharmaceutiques, Université Bordeaux II, 351 cours de la Libération, 33405 Talence Cedex, France.

1. Auteur auquel la correspondance doit être adressée. Téléphone: 56 84 69 95. Télécopie: 56 84 64 22.

Après 15 h d'agitation à température ambiante, on observe la formation exclusive du diol **8** que l'on isole par flash-chromatographie, avec un rendement de 60% (Schéma 4).

Schéma 4.

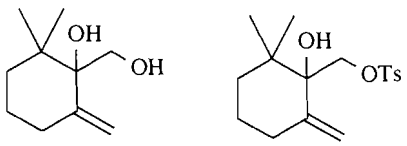

8 **9**

La localisation du système dihydroxylé sur le squelette a pu être déduite d'une expérience de RMN 2D (10) mettant en jeu les corrélations $^{1}H/^{13}C$ à travers des couplages à longue distance (^{2}J et ^{3}J). Nous observons en particulier des corrélations de type ^{3}J entre d'une part le carbone quaternaire hydroxylé à 80,1 ppm et les protons du groupement *gem*-diméthyle à 0,89 ppm et d'autre part le carbone sp^2 de type méthylène à 110,7 ppm avec les protons allyliques appartenant au cycle et résonnant à 2,31 ppm.

Comme lors de l'époxydation par les peracides (7), cette réaction n'est pas stéréosélective, cependant on note une addition sélective sur le méthylène en -2, que l'on peut interpréter par un effet électronique (+I) prépondérant du groupement *gem*-diméthyle sur cette double liaison.

Compte tenu de la haute régiosélectivité de cette réaction, le diol **8**, sans purification ultérieure, a été transformé, via son hydroxy-tosylate **9**, puis traitement de celui-ci à l'alumine en époxy-pyronène **5**, avec un rendement global de 52%. Cela constitue une voie d'accès nouvelle et sélective à l'époxy-pyronène **5** précurseur (6) du β-cyclocitral **6** et de la β-ionone **7**.

Hydroboration du δ-pyronène 4

Kane et Von Genk (11) avaient précédemment réalisé l'hydroboration du δ-pyronène par la diborane généré in situ dans le diglyme. Ils obtiennent avec un rendement médiocre les alcools correspondants à l'hydroboration respectivement des deux doubles liaisons. Nous avons, en ce qui nous concerne, réalisé cette réaction dans le tétrahydrofuranne en utilisant du diborane généré hors du réacteur. Dans ces conditions et après oxydation en milieu basique (H_2O_2/OH^-) on isole avec un rendement de 47% un mélange (24/76) constitué par du cyclohexane méthanol-3,3-diméthyl-2-méthylène **10** ("iso"-γ-cyclogéraniol) et du γ-cyclogéraniol **11** (Schéma 5).

Schéma 5.

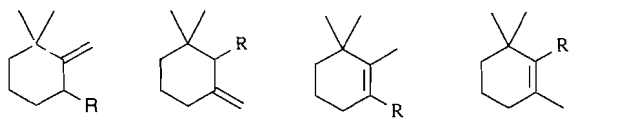

10 R=CH_2OH **11** R=CH_2OH **14** R=CHO **15** R=CHO
12 R=CHO **13** R=CHO **16** R=CH_2Br **17** R=CH_2Br
18 R=CH_2OH

Par contre, lorsque l'on utilise un agent d'hydroboration hautement régiosélectif, le 9-BBN (bora-9-bicyclo[3,3,1]nonane) qui est très sensible à l'encombrement stérique de la double liaison, nous inversons la régiochimie de cette réaction et obtenons les alcools **10** et **11** dans un rapport 67/33 avec un rendement de 42%. L'alcool minoritaire **11** résulte de l'addition sur le méthylène en -2, plus encombré stériquement par le voisinage du groupement *gem*-diméthyle.

Les composés hydroxylés **10** et **11** aisément séparés par chromatographie sur alumine (6% H_2O) sont oxydés par le chlorochromate de pyridinium respectivement en "iso"-γ-cyclocitral **12** (Rdt 81%) et γ-cyclocitral **13** (Rdt 87%). Ces aldéhydes traités en présence d'alumine s'isomérisent quantitativement en "iso"-β-cyclocitral **14** et β-cyclocitral **15**.

L'alcool **10** ainsi que les aldéhydes **12** et **14** sont des composés inédits possédant un squelette cyclogéranyle avec une position différente de la chaîne fonctionnelle ("iso" cyclogéranyle).

Hydrobromation du δ-pyronène 4

Par analogie avec les réactions réalisées sur le myrcène, le δ-pyronène **4** a été traité par une solution d'acide bromhydrique à 48% en présence de bromure cuivreux (12). La réaction est complète au bout de 2 h et nous mettons en évidence sur le brut réactionnel un mélange (70/30) des deux dérivés bromés **16** et **17**; l'addition d'acide bromhydrique sur le complexe δ-pyronène–Cu_2Br_2 a lieu préférentiellement sur la double liaison la plus réactive pour ce type de réaction.

Cependant si on prolonge le temps de réaction nous constatons l'évolution du dérivé bromé **17** qui subit une réaction de débromhydratation en γ-pyronène **3**. Sa disparition est totale au bout de 20 h; seul subsiste le bromure d'"iso"-β-cyclogéranyle **16**, qui sans être isolé est traité successivement par de l'acétate de potassium puis $LiAlH_4$ pour conduire à l'"iso"-β-cyclogéraniol **18** avec un rendement de 33% par rapport au δ-pyronène. Ceci constitue une nouvelle voie d'accès plus spécifique pour cet alcool également inédit.

Addition du chlorure de benzène sulfényle au δ-pyronène 4

La réaction du chlorure de benzène sulfényle (13) à −70°C sur le δ-pyronène **4** en solution dans du dichlorométhane conduit quantitativement à un mélange (56/44) des chlorosulfures **19** (adduit −1,4) et **20** (adduit −1,2) que nous ne pouvons séparer efficacement en raison de leur très faible stabilité (Schéma 6). Lors de cette réaction mettant en jeu un mécanisme ionique via un ion épisulfonium, on note de nouveau l'addition exclusive sur le méthylène -2 plus riche en électrons.

Schéma 6.

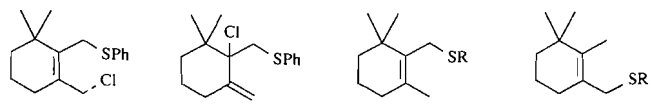

19 **20** **21** R=Ph **22** R=Ph
23 R=Et **24** R=Et

Cependant par un chauffage de 3 h au reflux du dichlorométhane, nous initions une isomérisation totale de l'adduit -1,2 en adduit -1,4 que l'on peut alors isoler par flash-chromatographie. Sa réduction par $AlLiH_4$ à 0°C dans l'éther anhydre conduit avec un rendement de 80% au phénylcyclogéranylsulfure **21**, intermédiaire particulièrement important (14) pour accéder via la sulfone correspondante à la vitamine A et à divers rétinoïdes.

Addition de thiols au δ-pyronène 4

Le δ-pyronène **4** a été traité dans un premier temps par le

thiophénol (4 h à 90°C) en présence d'AIBN. Après purification du brut réactionnel sur colonne d'alumine désactivée, on isole avec un rendement de 90% un mélange (70/30) des sulfures **22** et **21** que l'on ne peut séparer que difficilement par chromatographie sur gel de silice imprégnée de 5% de nitrate d'argent. Une réaction analogue, réalisée sous rayonnement ultra-violet, avait été décrite par Takabe et al. (6).

L'addition de l'éthanediol sur le δ-pyronène **4** réalisée dans des conditions semblables (5 h à 50°C) nous a permis d'obtenir avec un rendement de 95% un mélange (60/40) des sulfures **24** et **23**, dont la séparation sur colonne de gel de silice est beaucoup plus aisée.

Ces réactions réalisées dans des conditions radicalaires on conduit à des mélanges de régioisomères. Cependant on observe pour chacun d'entre eux la formation exclusive de l'adduit -1,4 l'étape de transfert intervenant préférentiellement à partir du radical allylique le moins substitué.

Les deux sulfures **23** et **24** sont ensuite traités par un mélange d'iodure de méthyle et d'iodure de sodium dans l'acétonitrile (15). À partir du sulfure **24** on isole avec un rendement de 80% l'iodure d'"iso"β-cyclogéranyle **26**. Par contre, avec le sulfure **23** il n'est pas possible d'isoler l'iodure de cyclogéranyle **25** correspondant; il subit rapidement une réaction de déhydroiodation pour conduire au γ-pyronène **3** (Rdt 97%) (Schéma 7).

Schéma 7.

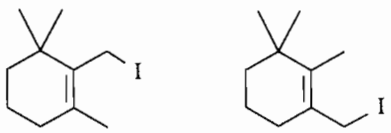

25 **26**

Cette observation nous a permis d'optimiser un procédé d'obtention du dérivé iodé **26**, en traitant directement le mélange des sulfures **23** et **24** par CH_3I–NaI. Après élimination sous pression réduite, de l'hydrocarbure **3**, nous isolons avec un rendement de 51% l'iodure d'"iso"β-cyclogéranyle **26**.

Conclusions

Les réactions d'addition réalisées selon des processus ioniques mettent en évidence une différence de réactivité significative pour les deux insaturations du δ-pyronène.

Ceci peut s'expliquer par la présence du groupement *gem*-diméthyle en -1 qui a un double rôle (électronique et stérique).

La double liaison la plus proche, semble plus réactive vis-à-vis de réactifs électrophiles, en raison de l'effet électronique inductif (+I) de ce groupe, dans la limite des contraintes stériques liées à l'approche du réactif.

Le δ-pyronène **4** constitue donc un synthon terpénique particulièrement efficace (Schéma 8) permettant l'accès direct à des composés de la série cyclogéranyle normale tels que le cyclogéraniol, le cyclocitral ou le cyclogéranylsulfure utilisés pour la synthèse de composés odorants ou de rétinoïdes.

D'autre part il est également le précurseur de terpénoïdes inédits possédant le squelette cyclogéranyle avec une position différente de la chaîne latérale fonctionnelle (série "iso").

Schéma 8.

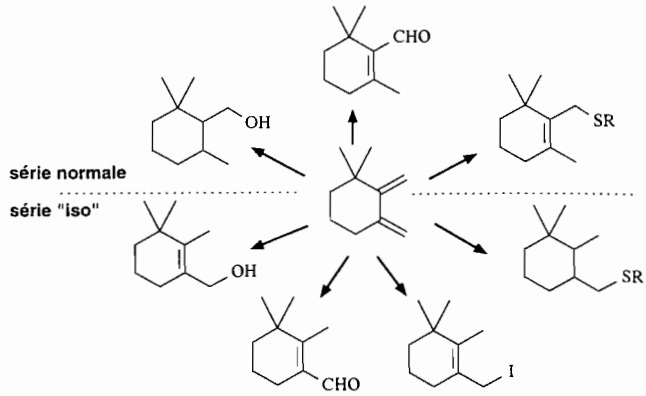

Partie expérimentale

Les analyses de chromatographie en phase gazeuse (CPG) sont effectuées avec un appareil Intersmat IGC 121 FL (colonne capillaire 52 CB, 25 m).

Les spectres infra-rouge ont été enregistrés au moyen d'un spectrographe Unicam SP 200, soit en film, soit en solution dans le tétrachlorure de carbone. Les spectres de RMN ^1H et ^{13}C sont enregistrés en solution dans $CDCl_3$ avec le TMS comme référence interne sur un appareil Bruker AC 250 MHz. Les études par spectrométrie de masse ont été réalisées en basse résolution au moyen d'un appareil VG Micromass 16F.

Dihydroxylation du δ-pyronène 4

À une solution de 696 mg (4,4 mmol) de permanganate de potassium dans 1 L d'eau glacée sont ajoutés 25 mL d'une solution aqueuse de soude à 40%, puis 300 mg (2,2 mmol) de δ-pyronène **4**. Après 15 h d'agitation à température ambiante on ajoute une solution de $NaHSO_3$, puis on acidifie avec H_2SO_4 10%. Après extraction à l'éther, lavage avec une solution saturée de NaCl, puis séchage ($MgSO_4$), on isole après un flash-chromatographie 225 mg (Rdt 60%) du diol **8** pur (liquide incolore).

8 : RMN ^1H (δ) : 0,86 (3H, s), 0,89 (3H, s), 3,58 et 3,85 (AB; J_{AB} = 11 Hz), 4,97 (CH_2=); RMN ^{13}C (δ) : 22,5 (CH_2), 22,7 (CH_3), 24,1 (CH_3), 33,5 (CH_2), 37,9 (CH_2), 38,2 (*C*), 63,4 (CH_2OH), 80,1 (*C*-OH), 110,7 (CH_2=), 148,9 (*C*=). Anal. calc. pour $C_{10}H_{18}O_2$: C 70,59, H 10,59; trouvée : C 70,81, H 10,47.

Obtention de l'époxy-pyronène 5

À une solution de 1,22 g (7,2 mmol) de diol **8** dans 7 mL de pyridine refroidie à 0°C on ajoute 1,78 g (9,3 mmol) de chlorure de tosyle. L'agitation est maintenue pendant 3 h à 0°C, puis le milieu réactionnel est hydrolysé à cette température avec HCl 10%. Après extraction à l'éther le produit brut **9** est dissout dans 45 mL d'éther de pétrole puis agité, pendant 7 h à température ambiante en présence de 45 g d'alumine.

Après filtration et évaporation du solvant on isole 565 mg (Rdt 52%) d'époxy-pyronène (6) pur **5**.

Hydroboration du δ-pyronène 4

Avec le diborane

Le diborane préparé à partir de 1,1 mL (9 mmol) de $BF_3 : OEt_2$ et 172 mg (4,5 mmol) de $NaBH_4$ dans 10 mL de diglyme est envoyé à l'aide d'une canule dans 1,36 g (10 mmol) de δ-pyronène **4** en solution dans 10 mL de THF.

Après 1 h d'agitation à température ambiante la solution est traitée pendant 1 h avec 2 mL d'une solution de NaOH 3 N et 1,4 mL d'H_2O_2 30%.

Après extraction à l'éther, lavage (NaCl saturé) et séchage ($MgSO_4$), les solvants sont évaporés. Le produit brut est purifié par chromatographie sur colonne d'alumine désactivée (6% d'H_2O). On obtient 725 mg (Rdt 47%) d'un mélange (24/76; CPG) constitué par les alcools **10** et **11**.

Avec le 9-BBN

À une solution de 1,36 g (10 mmol) de δ-pyronène **4** dans 3 mL de THF on ajoute 22,7 mL (11,1 mmol) d'une solution 0,5 M de 9-BBN dans du THF, puis on porte au reflux pendant 6 h. Après refroidissement on ajoute 6 mL d'éthanol et 2 mL d'une solution de soude 6 N, puis goutte à goutte 4 mL (35,3 mmol) d'H_2O_2 à 30% et on agite pendant 1 h à 50°C.

Après concentration et extraction au pentane, les phases organiques sont lavées (NaCl saturé), séchées ($Mg SO_4$), puis évaporées sous pression réduite.

On isole 647 mg (Rdt 42%) d'un produit brut constitué par un mélange (67/33; CPG) des alcools **10** et **11** que l'on sépare par chromatographie sur alumine (6% H_2O) en éluant avec le mélange ether de pétrole/éther (8/2 à 6/4).

10 : RMN ^{1}H (δ) : 1,07 (3H, s), 1,10 (3H, s), 3,59 et 3,66 (CH_2OH), 4,59 et 4,81 (CH_2=); RMN ^{13}C (δ) : 21,5 (CH_2), 26,6 (CH_3), 29,5 (CH_3), 31,8 (CH_2), 37,0 (C), 41,6 (CH), 41,9 (CH_2), 65,7 (CH_2OH), 103,1 (CH_2=), 157,0 (C=). Anal. calc. pour $C_{10}H_{18}O$: C 77,92, H 11,69; trouvée : C 78,10, H 11,58.

11 : RMN ^{1}H (δ) : 0,86 (3H, s), 0,95 (3H, s), 3,55 et 3,86 (CH_2OH), 4,75 et 4,94 (CH_2=C); RMN ^{13}C (δ) : 23,1 (CH_2), 26,4 (CH_3), 28,5 (CH_3), 31,9 (CH_2), 33,9 (C), 36,4 (CH_2), 56,3 (CH), 59,5 (CH_2OH), 111,5 (CH_2=), 147,5 (C=).

Oxydation de l'alcool 10

À une solution de 690 mg (3,2 mmol) de chlorochromate de pyridinium dissous dans 6,6 mL de CH_2Cl_2 on ajoute 322 mg (2,1 mmol), d'alcool **10**, puis on agite pendant 45 min à température ambiante.

Le mélange est ensuite "flash" chromatographié sur alumine désactivée. On isole 260 mg (Rdt 81%) d'"iso"-γ-cyclocitral **12** qui s'isomérise quantitativement en "iso"-β-cyclocitral **14** au contact prolongé (1 nuit) avec de l'alumine en suspension dans de l'éther de pétrole.

12 (liquide incolore) : RMN ^{1}H (δ) : 0,92 (3H, s), 1,04 (3H, s), 4,65 et 4,93 (CH_2=), 9,60 (1H, d); RMN ^{13}C (δ) : 20,2 (CH_2), 26,8 (CH_2), 28,0 (CH_3), 28,2 (CH_3), 37,8 (C), 40,9 (CH_2), 54,6 (CH), 109,1 (CH_2=), 152,3 (C=), 203,7 (CHO). Anal. calc. pour $C_{10}H_{16}O$: C 78,94, H 10,53; trouvée : C 78,84, H 10,61.

14 (liquide jaune clair) : RMN ^{1}H (δ) : 1,05 (6H, s), 2,06 (3H, s), 10,09 (1H, s); RMN ^{13}C (δ) : 12,3 (CH_3), 18,0 (CH_2), 23,2 (CH_2), 27,2 (2 × CH_3), 36,4 (C), 38,5 (CH_2), 132,8 (C=), 161,7 (C=), 192,0 (CHO). Anal. calc. pour $C_{10}H_{16}O$: C, 78,94, H 10,53; trouvée : C 79,11, H 10,45.

Oxydation de l'alcool 11

À une solution de 965 mg (4,5 mmol) de chlorochromate de pyridinium dissous dans 10 mL de CH_2Cl_2 on ajoute 440 mg (2,9 mmol) d'alcool **11**, puis on agite pendant 45 min à température ambiante.

Le mélange est ensuite "flash" chromatographié sur alumine désactivée. On isole 377 mg (Rdt 87%) de γ-cyclocitral **13** qui par contact prolongé (1 nuit) avec de l'alumine en suspension dans l'éther de pétrole s'isomérise quantitativement en β-cyclocitral **15**.

13 : RMN ^{1}H (δ) : 0,87 (3H, s), 0,99 (3H, s), 2,60 (1H, m), 4,62 et 4,82 (CH_2=), 9,75 (1H, d); RMN ^{13}C (δ) : 22,7 (CH_2), 25,9 (CH_3), 28,0 (CH_3), 34,8 (C), 33,3 (CH_2), 37,3 (CH_2), 66,4 (CH), 112,3 (CH_2=), 143,3 (C=), 202,7 (CHO).

15 : RMN ^{1}H (δ) : 1,15 (6H, s), 2,04 (3H, s), 2,14 (2H, t), 10,08 (1H, s); RMN ^{13}C (δ) : 18,1 (CH_2), 18,6 (CH_3), 27,2 (2 × CH_3), 32,4 (C), 35,1 (CH_2), 40,1 (CH_2), 139,9 (C=), 155,5 (C=), 191,1 (CHO).

Hydrobromation du δ-pyronène 4

À une solution de 250 mg de CuBr dissout dans 12,5 mL d'HBr 48% sont ajoutés 900 mg (6,6 mmol) de δ-pyronène-**4**. Après 20 h d'agitation, la phase organique est extraite à l'éther. Après évaporation des solvants le mélange dissout dans 10 mL d'acétone est traité avec 2 g d'acétate de potassium pendant 24 h. Après addition d'éther, la solution organique est filtrée, concentrée et additionnée à une suspension de 610 mg d'$AlLiH_4$ dans 50 mL d'éther anhydre à 0°C. Après 3 h d'agitation, le milieu est versé sur de la glace, acidifié et extrait à l'éther. Après évaporation des solvants, on isole 335 mg (Rdt 33%) d'"iso"-β-cyclogéraniol **18** (liquide incolore).

18 : RMN ^{1}H (δ) : 0,93 (6H, s), 1,59 (3H, s), 3,99 (2H, s); RMN ^{13}C (δ) : 12,9 (CH_3), 19,3 (CH_2), 27,8 (2× CH_3), 28,7 (CH_2), 34,6 (C), 39,3 (CH_2), 63,7 (CH_2), 129,6 (C), 137,8 (C). Anal. calc. pour $C_{10}H_{18}O$: C 77,92, H 11,69; trouvée : 77,04, H 12,00.

Addition du chlorure de benzène sulfényle au δ-pyronène 4

δ-pyronène **4** (1,632 mg; 12 mmol) est ajouté à −70°C à une solution de 10 mL de dichlorométhane contenant 10 mmol de chlorure de benzène sulfényle, préparé à partir de thiophénol et de *N*-chlorosuccinimide, puis le mélange est laissé revenir à température ambiante. Après évaporation du solvant, le résidu est repris par CCl_4 puis filtré. Après concentration on obtient 2,8 g (Rdt ~ 100%) d'un mélange (56/44; RMN ^{1}H) constitué par les chlorosulfures **19** et **20**.

Isomérisation de 20 en 19

Le mélange brut des chlorosulfures est repris dans 10 mL de dichlorométhane, puis chauffé au reflux pendant 3 h. Après évaporation du solvant, on obtient 2,6 g (93%) du composé **19** (huile).

19 : RMN ^{1}H (δ) : 1,19 (6H, s), 3,72 (2H, s), 4,23 (2H, s), 7,26–7,36 (5H, Ph); RMN^{13} C (δ) : 19,0 (CH_2), 28,4 (2 × CH_3), 28,8 (CH_2), 31,7 (CH_2), 35,3 (C), 39,1 (CH_2), 45,7 (CH_2), 126,0 (CH, Ph), 128,6 (2 × CH, Ph), 129,0 (2 × CH, Ph), 133,6 (C), 137,9 (C), 138,9 (C).

Réduction du chlorosulfure 19

Chlorosulfure **19** (670 mg; 2,38 mmol) est ensuite ajouté à 0°C à une suspension de 280 mg de $LiAlH_4$ dans 15 mL d'éther anhydre. Après 6 h d'agitation, le milieu est versé sur de la glace, acidifié et extrait à l'éther.

Après évaporation des solvants, on récupère 470 mg (Rdt 80%) de phénylcyclogéranyl sulfure **21**.

21 : RMN ^{1}H (δ) : 1,09 (6H, s), 1,74 (3H, s), 3,61 (CH_2SPh), 7,10–7,33 (5H, Ph); RMN ^{13}C (δ) : 19,3 (CH_2), 20,3 (CH_3),

28,7 (2 × CH_3), 32,6 (CH_2), 33,0 (CH_2SPh), 34,6 (*C*), 39,4 (CH_2), 125,3 (*C*H, Ph), 128,2 (2 × *C*H, Ph), 128,7 (2 × *C*H, Ph), 131,9 (*C*), 133,6 (*C*), 139,0 (*C*).

Addition de thiophénol au δ-pyronène 4

À 4,033 g (29,6 mmol) de δ-pyronène **4** sont ajoutés 500 mg d'AIBN, puis 5 mL (48,7 mmol) de thiophénol. Le mélange réactionnel est ensuite porté à 90°C pendant 4 h, puis dilué à l'éther et lavé successivement avec une solution de NaOH / N et une solution saturée de NaCl. La phase organique après séchage ($MgSO_4$) est concentrée. On récupère 6,6 g (Rdt 90%) d'un mélange (70/30; RMN) des sulfures **22** et **21**.

Leur séparation peut être réalisée par chromatographie sur gel de silice imprégnée de 5% d'$AgNO_3$.

22 (liquide incolore) : RMN ^{1}H (δ) : 0,94 (6H, s), 1,44 (3H, s), 3,47 (CH_2SPh), 7,12–7,36 (5H, Ph); RMN ^{13}C (δ) : 13,3 (CH_3), 19,5 (CH_2), 28,0 (2 × CH_3), 30,0 (CH_2), 35,0 (*C*), 38,7 (CH_2), 39,5 (CH_2), 125,1 (*C*), 126,4 (*C*H, Ph), 128,7 (2 × *C*H, Ph), 131,1 (2 × *C*H, Ph), 136,9 (*C*), 138,9 (*C*). Anal. calc. pour $C_{16}H_{22}S$: C 78,05, H 8,94; trouvée : C 78,20, H 8,57.

Addition de l'éthanethiol au δ-pyronène 4

À 4,040 g (30 mmol) de δ-pyronène **4** sont ajoutés 500 mg d'AIBN, puis 4,4 mL (60 mmol) d'éthanethiol. Ce mélange réactionnel est agité à 50°C pendant 5 h, puis dilué à l'éther et lavé successivement avec une solution de NaOH / N et une solution saturée de NaCl. La phase organique est séchée sur $MgSO_4$, puis concentrée. On récupère 5,65 g (Rdt 95%) d'un mélange (60/40; RMN) des sulfures **24** et **23** que l'on sépare par chromatographie sur colonne de gel de silice.

24 (liquide incolore) : RMN ^{1}H (δ) : 1,00 (6H, s), 1,25 (3H, t), 1,65 (3H, s), 2,47 (2H, q), 3,14 (2H, s); RMN ^{13}C (δ) : 13,4 (CH_3), 15,0 (CH_3), 19,4 (CH_2), 25,6 (CH_2), 28,0 (2× CH_3), 29,7 (CH_2), 34,9 (*C*), 35,1 (CH_2), 39,5 (CH_2), 126,3 (*C*), 137,2 (*C*). Anal. calc. pour $C_{12}H_{22}S$: C 72,73, H 11,11; trouvée : C 72,81, H 11,07.

23 : RMN ^{1}H (δ) : 1,06 (6H, s), 1,28 (3H, t), 1,73 (3H, s), 2,55 (2H, q), 3,20 (2H, s); RMN ^{13}C (δ) : 14,8 (CH_3), 19,0 (CH_2), 20,2 (CH_3), 27,7 (CH_2), 28,7 (2× CH_3), 30,6 (CH_2), 32,8 (CH_2), 34,6 (*C*), 39,5 (*C*), 131.9 (*C*), 133,3 (*C*).

Obtention du dérivé iodé 26

À 530 mg (3,5 mmol) d'iodure de sodium, 4 mL (6,4 mmol) d'iodure de méthyle en solution dans 3 mL d'acétonitrile on ajoute 523 mg (2,6 mmol) de sulfure **24**. Le milieu est agité pendant 15 h à température ambiante et on obtient après chromatographie sur gel de silice (éluant éther de pétrole), 550 mg (Rdt 80%) d'iodure d'"iso"-β-cyclogéranyle **26**.

26 (huile colorée) : RMN ^{1}H (δ) : 1,06 (6H, s), 1,75 (3H, s), 3,50 (2H, s); RMN ^{13}C (δ) : 15,2 (CH_2), 19,6 (CH_2), 28,3 (2× CH_3), 32,5 (CH_2), 35,5 (*C*), 39,5 (CH_2), 58,7 (CH_2), 124,6 (*C*), 142,7 (*C*). Anal. calc. pour $C_{10}H_{17}I$: C 45,45, H 6,44; trouvée : C 46,30, H 7,10.

Remerciements

Nous remercions la Société Rhône Poulenc Nutrition Animale pour la fourniture de matières premières, M. Petraud et B. Barbe pour la réalisation des spectres de RMN et G. Bourgeois pour les spectres de masse (Centre d'Études Structurales et d'Analyse des Molécules Organiques, Université Bordeaux 1).

Bibliographie

1. (*a*) G. Dupont et R. Dulou. C.R. Séances Acad. Sci. **201**, 219 (1985); (*b*) L.A. Goldblatt et S. Palkin. J. Am. Chem. Soc. **63**, 3517 (1941); (*c*) D.V. Banthorpe et D. Whittaker. Q. Rev. **20**, 373 (1966); (*d*) K.J. Crowley et S.G. Traylor. Tetrahedron, **34**, 2783 (1978).
2. (*a*) L.A. Goldblatt et S. Palkin. J. Am. Chem. Soc. **66**, 655 (1944); (*b*) J. Am. Chem. Soc. **72**, 2151 (1960).
3. K. Mori, M. Ohki, A. Kobayashi et M. Matsui. Tetrahedron, **26**, 2815 (1970).
4. B.J. Kane et R.A. Von Gear. Brevet US. 4 179 468 (1978).
5. J.P. Duchesne. Brevet Eur. 446 116 (1991).
6. (*a*) K. Takabe, T. Yamada et T. Katagin. Chem. Ind. 540 (1980); (*b*) T. Yamada et K. Takabe. Chem. Lett. 29 (1993).
7. (*a*) P. Chabardes, D. Serramedan, B. Delmond, C. Filliatre et M. Pereyre. Brevet Fr. 901 3249 (1990) et US. 5 175 373 (1992); (*b*) D. Serramedan, F. Marc, M. Pereyre, C. Filliatre, P. Chabardes et B. Delmond. Tetrahedron Lett. **33**, 4457 (1992).
8. F. Marc, B. Soulet, D. Serramedan et B. Delmond. Tetrahedron, **50**, 3381 (1994).
9. (*a*) V. Bushan, R. Rathore et S. Chandrasekaran. Synthesis, 431 (1984); (*b*) A.J. Fatiadi. Synthesis, 87 (1987).
10. A. Bax. J. Magn. Reson. **53**, 217 (1983).
11. B.J. Kane et R.A. Von Genk. Brevet US. 4 244 890 (1981).
12. A. Brooke. Brevet Br. 896262 (1962).
13. W.H. Mueller et P.E. Butler. J. Org. Chem. **33**, 2642 (1968).
14. (*a*) O. Isler. Pure Appl. Chem. **51**, 447 (1979); (*b*) J. Paust. Pure Appl. Chem. **63**, 45 (1991); O. Isler et F. Klenzle. *Dans* Kirk–Othmer Encyclopedia 3ème édition. Vol. 24. J. Wiley Interscience, New York. 1981. pp. 140–148 et 214–226.
15. E.J. Corey et M. Jantelat. Tetrahedron Lett. 5787 (1968).

Stereoselectivity of directed epoxidations of 22-hydroxy-Δ^{23}-sterol side chains

Thomas G. Back and Denise L. Baron

Abstract: A series of 22-hydroxy-Δ^{23}-sterols comprising (3β,5α,6β,22*S*)-6-methoxy-3,5-cyclo-25,26,27-trinorcholest-23-en-22-ol (**6**), (3β,5α,6β,22*S*,23*E*)-6-methoxy-3,5-cyclo-26,27-dinorcholest-23-en-22-ol (**7**), 3β,5α,6β,22*R*)-6-methoxy-23-methyl-3,5-cyclo-25,26,27-trinorcholest-23-en-22-ol (**10**), 3β,5α,6β,22*S*,23*Z*)-6-methoxy-3,5-cyclo-26,27-dinorcholest-23-en-22-ol (**11**), and 3β,5α,6β,22*R*)-6-methoxy-3,5-cyclo-26,27-dinorergost-23-en-22-ol (**12**) were subjected to epoxidation with *m*-chloroperbenzoic acid and *tert*-butyl hydroperoxide in the presence of either vanadyl acetoacetonate or molybdenum hexacarbonyl, and the *threo*:*erythro* ratios of the products were determined. The results are of relevance for the synthesis of sterols with oxygenated side chains, such as brassinolide (**1**). The oxidations of **6** and **7** were *erythro* selective with all three oxidants, especially with the vanadium-catalyzed system. Peracid oxidation of the 22-*tert*-butyldimethylsilyl ether (**8**) and 22-pivaloate (**9**) of alcohol **7** showed similar *erythro* selectivity to that of the parent compound **7**. Allylic alcohol **10** gave exclusively the *erythro* epoxide with all three oxidants, while **11** and **12** were *threo*-selective under all three conditions. Molecular modeling indicated that *erythro* selectivity in the vanadium-catalyzed epoxidation of **10** was consistent with a destabilizing interaction ($A^{(1,2)}$ strain) between the *gem*-methyl and C(21) methyl groups in the conformation required for formation of the *threo*-isomer. The *threo*-selective peracid oxidations of **11** and **12** were attributed to $A^{(1,3)}$ strain between the *cis*-methyl groups and C(20) in the conformation required for formation of the *erythro*-epoxide. The differences in the calculated energies of conformations leading to the *threo*- and *erythro* epoxide diastereomers of substrates containing no *gem* or *cis* substituents proved too small to permit reliable prediction of diastereoselectivity.

Key words: 22-hydroxy-Δ^{23}-sterols, brassinosteroids, allylic alcohols, epoxidation, diastereoselectivity

Résumé : On a soumis une série de 22-hydroxy-Δ^{23}-stérols, comportant les (3β,5α,6β,22*S*)-6-méthoxy-3,5-cyclo-25,26,27-trinorcholèst-23-én-22-ol (**6**), (3β,5α,6β,22*S*,23*E*)-6-méthoxy-3,5-cyclo-26,27-dinorcholèst-23-en-22-ol (**7**), 3β,5α,6β,22*R*)-6-méthoxy-23-méthyl-3,5-cyclo-25,26,27-trinorcholést-23-én-22-ol (**10**), 3β,5α,6β,22*S*,23*Z*)-6-méthoxy-3,5-cyclo-26,27-dinorcholèst-23-en-22-ol (**11**), et 3β,5α,6β,22*R*)-6-méthoxy-3,5-cyclo-26,27-dinorergost-23-én-22-ol (**12**), à une époxydation par l'acide *m*-chloroperbenzoïque et l'hydroperoxyde de *tert*-butyle, en présence soit d'actoacétonate de vanadyle soit d'hexacarbonyle de molybdène; on a déterminé les rapport *thréo/érythro* des produits obtenus. Les résultats présentent de l'importance pour la synthèse de stérols portant des chaînes latérales oxygénées, comme le brassinolide (**1**). Les oxydations des composés **6** et **7** sont *érythro*-sélectives avec chacun des trois oxydants, particulièrement avec le système catalysé par le vanadium. Les oxydations du 22-*tert*-butyldiméthylsilyloxyde (**8**) et du 22-pivaloate (**9**) de l'alcool **7** par le peracide donnent des *érythro*-sélectivités semblables à celle du composé parent (**7**). L'alcool allylique **10** conduit exclusivement à l'époxyde *érythro* avec chacun des trois oxydants alors que les composés **11** et **12** sont *thréo*-sélectifs dans les trois conditions expérimentales. La modélisation moléculaire indique que l'*érythro*-sélectivité observée lors de l'époxydation du produit **10** catalysée par le vanadium pourrait être le résultat d'une interaction déstabilisante (tension $A^{(1,2)}$) entre le *gem*-diméthyle et les groupes méthyles en C(21) dans la conformation requise pour la formation de l'isomère *thréo*. Les oxydations *thréo*-sélectives des composés **11** et **12** obtenues avec le peracide sont attribuées à une tension $A^{(1,3)}$ entre les groupes *cis*-méthyles et le C(20) dans la conformation requise pour la formation de l'époxyde *érythro*. Les différences des énergies calculées des conformations conduisant aux époxydes *thréo* et *érythro* diastéréomères des substrats ne contenant pas de substituants *gem* ou *cis* sont trop faibles pour permettre de faire des prédictions satisfaisantes de la diastéréosélectivité.

Mots clés : 22-hydroxy-Δ^{23}-stérols, brassinostéroïds, alcools allyliques, époxydation, diastéréosélectivité.

[Traduit par la rédaction]

Introduction

The discovery of numerous biologically active sterols containing oxygenated side chains has prompted interest in the development of new methods for their preparation (1). Among such compounds, brassinolide (**1**) (2) and related brassinosteroids are of particular interest because of their powerful plant growth promoting activity (3). The four contiguous stereocenters at C(20), C(22), C(23), and C(24) and the vicinal diol moiety at C(22) and C(23) in the side chains of these compounds provide the principal challenge in their synthesis. A number of strategies for this purpose have been reported (4), some of which exploit stereoselective epoxidations of appropriate unsaturated substrates (5), usually followed by reduction or reaction with carbanion nucleophiles. The hydroxyl-

Received May 27, 1996.

T.G. Back[1] **and D.L. Baron.** Department of Chemistry, University of Calgary, Calgary, AB T2N 1N4, Canada.

[1] Author to whom correspondence may be addressed. Telephone: (403) 220-6256. Fax: (403) 289-9488. E-mail: tgback@acs.ucalgary.ca

Scheme 1.

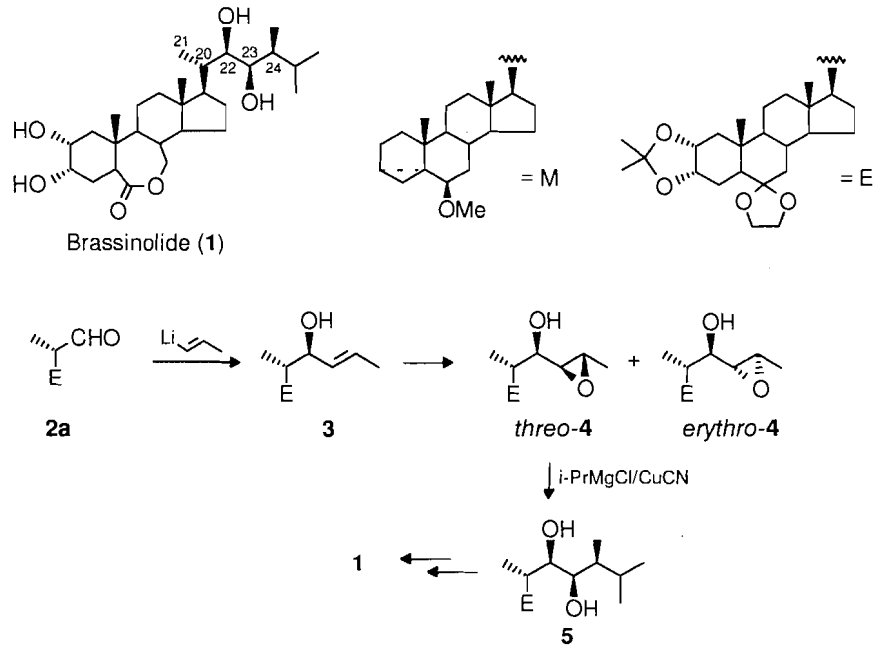

directed epoxidation of allylic alcohol **3**, followed by epoxide opening of **4** with an isopropyl nucleophile (Scheme 1), provides an exceptionally concise synthesis of the brassinolide side chain (6), but results in unfavourable diastereoselectivity in the epoxidation step unless a chiral oxidant is employed. Since this and other epoxide-based methods offer potential access to new brassinolide analogues and to stereoisomers that are of interest in structure–activity studies, as well as to other sterols possessing oxygenated side chains, a more detailed investigation of the stereoselectivity of the key epoxidation step was undertaken. Thus, allylic alcohols **6–12**, prepared as shown in Scheme 2, were subjected to three different epoxidizing conditions, in order to systematically observe the effects of substituents at the *t* (*trans*), *g* (*gem*), and *c* (*cis*) positions, as well as the effect of blocking the alcohol functionality through silyl ether or ester formation.

The directing effect of the hydroxyl group in the epoxidation of allylic alcohols with peracids was first noted by Henbest and Wilson (7). Subsequently, hydroxyl-directed vanadium-catalyzed epoxidations with *tert*-butyl hydroperoxide were reported, as well as those using other transition metal catalysts such as molybdenum and titanium, thereby providing improved diastereoselectivity in many instances (8). The inclusion of chiral, tartrate-based ligands with titanium catalysts gave rise to the widely employed Sharpless method for the enantioselective epoxidation of allylic alcohols (9).

The diastereoselectivity of peracid- and vanadium-catalyzed epoxidations has been studied with both cyclic and acyclic substrates. Several early models for the peracid epoxidation of allylic alcohols were proposed by Sassiver and English (10), Whitham and co-workers (11), and Chautemps and Pierre (12). In most cases, secondary acyclic allylic alcohols afford *threo*-epoxides preferentially, and the stereoselectivity is enhanced by the presence of a *cis* substituent. However, *erythro* selectivity is often observed when a substituent is present in the *gem* position. More recently, Sharpless and co-workers (8*d*, 13) proposed a revised model for peracid

Scheme 2.

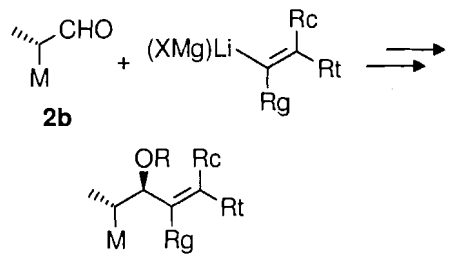

6 R = R_g = R_c = R_t = H
7 R = R_g = R_c = H; R_t = Me
8 R = $OSiMe_2t$-Bu; R_g = R_c = H; R_t = Me
9 R = C(O)t-Bu; R_g = R_c = H; R_t = Me
10 R = R_c = R_t = H; R_g = Me
11 R = R_g = R_t = H; R_c = Me
12 R = R_g = H; R_c = R_t = Me

epoxidations with a preferred dihedral angle (O-C-C-C=) of 120° that accommodates the stereoelectronic requirement for back-side attack by the olefinic π-bond upon the peroxide moiety of the peracid. Thus, the two conformations **13** and **14** lead to *threo* and *erythro* epoxides, respectively, as shown in Scheme 3.

On the other hand, vanadium-catalyzed epoxidations with *tert*-butyl hydroperoxide are generally *erythro* selective, with enhancement or reversal of this stereoselectivity observed with bulky *gem* or *cis* substituents, respectively (8d, 13, 14). A preferred dihedral angle (O-C-C-C=) of 50° has been suggested for these types of oxidations (8d, 13), leading to *threo* and *erythro* epoxides via conformations **15** and **16**, respectively (Scheme 3). Molybdenum-catalyzed epoxidations resemble those of peracids when *trans* alkyl groups are present, and are intermediate in stereoselectivity between per-

Scheme 3.

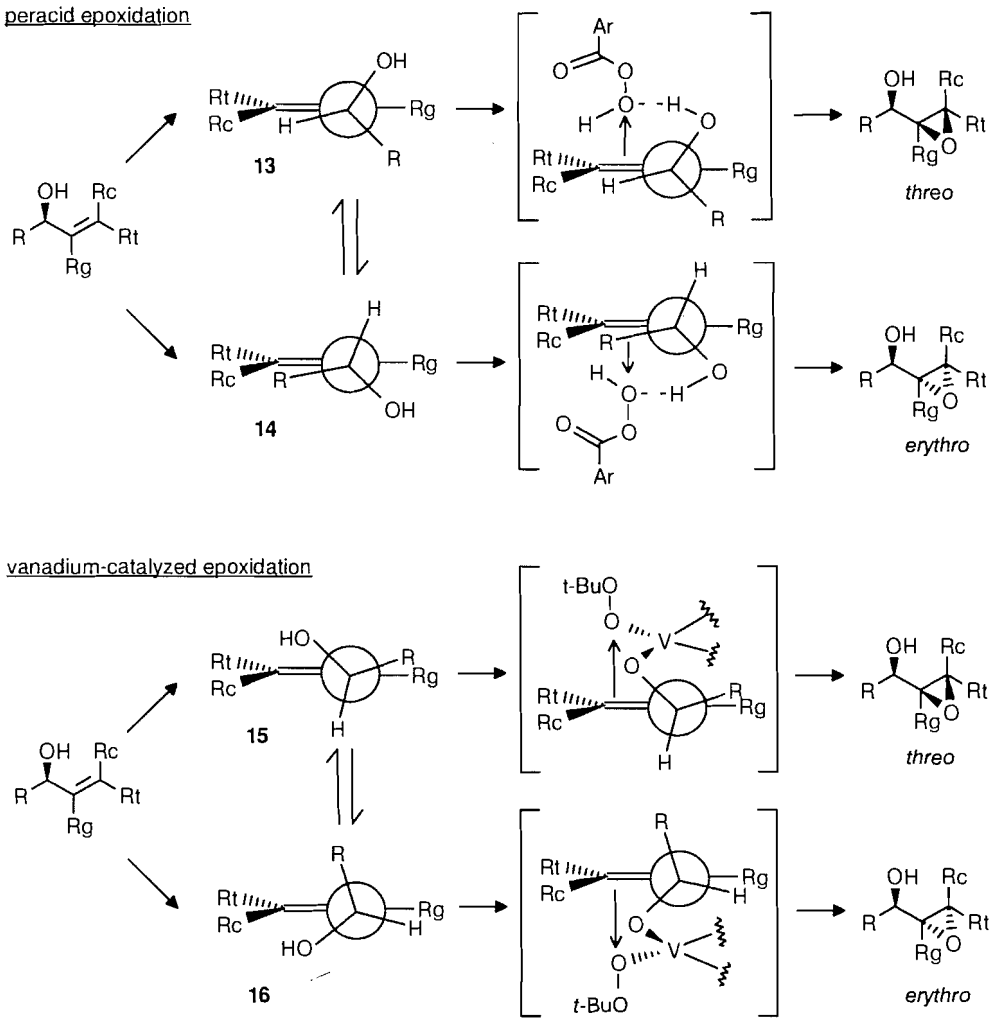

acid- and vanadium-catalyzed epoxidations with many other types of allylic alcohols. The observed stereoselectivity has been rationalized by consideration of allylic strain (A-strain) and other interactions in the transition states derived from conformations corresponding to **13–16** (8d, 13, 14, 15).

Results and discussion

The Cram addition products **6**, **7**, and **10–12**, along with smaller amounts of their anti-Cram epimers, were obtained by the addition of the appropriate Grignard reagent or organolithium compound to aldehyde **2b** (Scheme 2). The silyl ether **8** and pivaloate **9** were prepared by silylation and esterification of **7**. Products **6**, **7**, and **10–12** were then subjected to epoxidation with *m*-chloroperbenzoic acid (MCPBA), and with *tert*-butyl hydroperoxide in the presence of catalytic amounts of either vanadyl acetoacetonate, or molybdenum hexacarbonyl. Compounds **8** and **9** were oxidized only with MCPBA. The results are shown in Table 1.

The configurations of the epoxide products in Table 1 were determined by spectroscopic methods and (or) by their stereospecific conversion to more easily identified products. Thus, *erythro*-**17** was treated with isopropylmagnesium chloride and cuprous cyanide (16) to give diol **24**, which underwent a stereospecific Corey–Winter deoxygenation (17) to the known (*Z*)-olefin **25** (18). The *erythro* epoxide **18** has been reported previously (6), and both it and *erythro*-**22** afforded the same *erythro* diol **26** when reduced with lithium borohydride in the presence of titanium tetraisopropoxide (19), thereby confirming the assignment of stereochemistry to *erythro*-**22**. Similar treatment of *threo*-**22** produced the diastereomeric *threo*-diol **27**. Epoxides **19** and **20**, obtained from epoxidation of silyl ether **8** and pivaloate **9**, respectively, were identified by comparison with the products of silylation and pivaloylation of the known *erythro* epoxide **18** (6). *Erythro*-**21** was subjected to regioselective ring-opening with mesitylene-selenolate (20), followed by Corey–Winter reaction of the resulting diol **28** to afford the olefin **29**, which was shown to be the (*Z*) isomer by NOE experiments. Finally, the *threo*-epoxide **23** was reduced with lithium borohydride – titanium tetraisopropoxide to diol **30**, which was in turn converted into the known sterol **31** (21). These transformations are shown in Scheme 4.

The following results are evident from Table 1. The unsubstituted allylic alcohol **6** and the *trans*-allylic alcohol **7** afforded the corresponding *erythro* epoxides with modest diastereoselectivity using MCPBA or Mo-catalysis, and with very high selectivity with V-catalysis. While *erythro* selectiv-

Scheme 4.

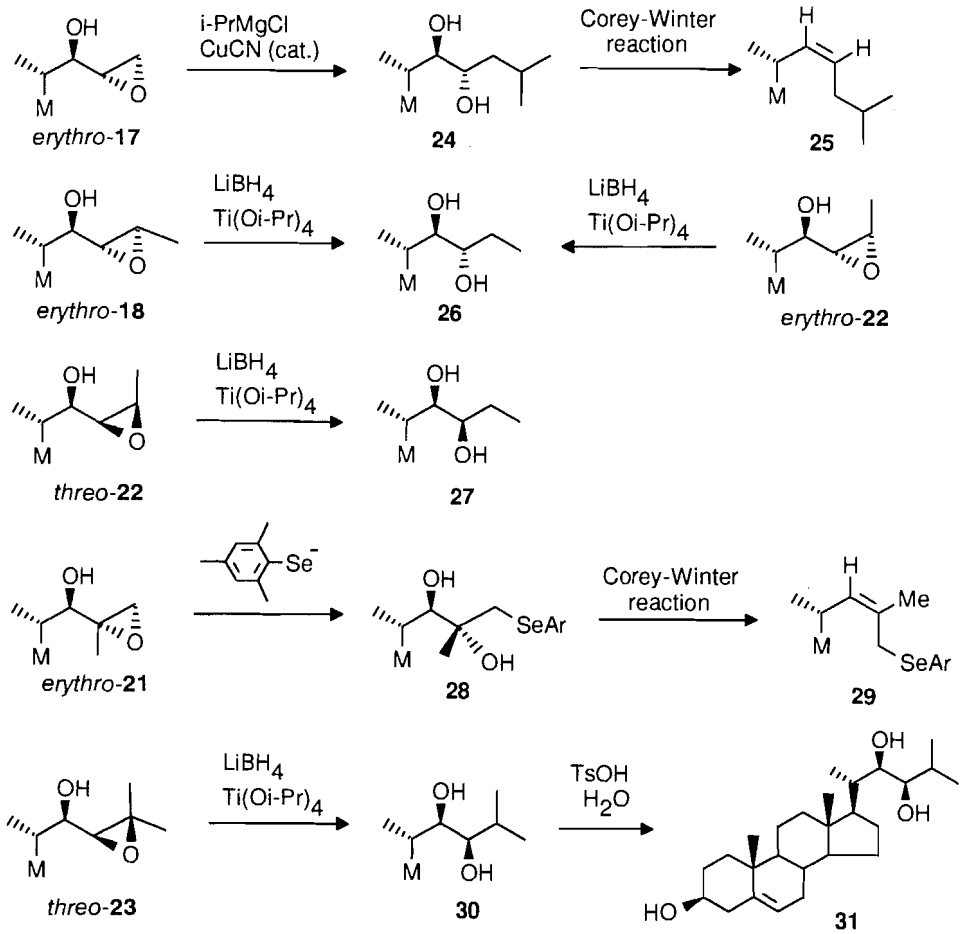

Table 1. Epoxidation of allylic alcohol derivatives **6–12**.

		% Yield[a] (*threo*:*erythro* ratio)[b]		
Substrate	Epoxide	MCPBA	$VO(acac)_2$/*t*-BuOOH	$Mo(CO)_6$/*t*-BuOOH
6	**17**	100 (36:64)	93 (<5:95)	58 (26:74)
7	**18**	87 (40:60)	90 (<5:95)	— (40:60)
8	**19**	67 (26:74)	—	—
9	**20**	77 (34:66)	—	—
10	**21**	98 (<5:95)	85 (<5:95)	57 (<5:95)
11	**22**	88 (>95:5)	93 (65:35)	60 (>95:5)
12	**23**	72 (91:9)	78 (81:19)	82 (93:7)

[a]Isolated yields are reported.
[b]Ratio was obtained by NMR integration.

ity is expected in the V-catalyzed system because of the destabilizing $A^{(1,2)}$ strain between R and R_g in conformation **15** (Scheme 3) that leads to the *threo* epoxide, the effect is usually small when R_g = H. Moreover, the *threo* selectivity that is generally observed in the peracid epoxidations of other allylic alcohols can be attributed to $A^{(1,3)}$ strain between R and R_c in conformation **14**, although it is again small when R_c = H. Thus, the observation of *erythro* selectivity in the peracid oxidations of **6** and **7**, and its magnitude in the V-catalyzed cases, are somewhat atypical.

Furthermore, the alcohol group of the substrate is believed to act as an H-bond donor to the hydroxylic peracid oxygen atom (8*d*), and is thus responsible for the directing effect observed in the peracid epoxidation of allylic alcohols. Protection of the allylic alcohol moiety might therefore be expected to change the diastereoselectivity by disrupting its H-bonding

Table 2. Molecular modeling of allylic alcohol derivatives **6–12.**

	Substrate						
	6	**7**	**8**	**9**	**10**	**11**	**12**
D.A.[a] of E_{min}	8.2	9.1	24.3	21.5	19.2	−158.1	−158.5
Global E_{min}[b]	236.2	235.5	257.0	303.4	240.1	240.2	239.9
E of **13** (D.A. = −120°)	240.6	239.8	—	—	252.0	245.7	246.1
E of **14** (D.A. = 120°)	244.9	244.6	—	—	249.6	266.1	269.4
E of **15** (D.A. = −50°)	239.3	238.3	—	—	254.1	246.0	246.2
E of **16** (D.A. = 50°)	243.1	242.4	—	—	246.8	247.9	248.2
ΔE (**14** − **13**)	4.3	4.8	—	—	−2.4	20.4	23.3
ΔE (**16** − **15**)	3.8	4.1	—	—	−7.3	1.9	2.0

[a]Dihedral angles (D.A.) refer to O-C(22)-C(23)-C= and are given in degrees; the D.A. is positive when C(23) moves clockwise relative to C(22) while sighting from C(22) to C(23).

[b]Energies (E) are given in kJ mol^{-1}.

ability and freeing it from the constraints of the models in Scheme 3. Bulky O-protecting groups could further affect the stereochemistry by altering the preferred conformation through increased steric interactions. Surprisingly, however, neither silylation nor esterification of the hydroxyl group of **7** (i.e., to give **8** and **9**, respectively) had a significant effect upon the stereochemical outcome of the peracid epoxidation. Blocking the hydroxyl group is therefore not a useful strategy for changing the *erythro*:*threo* ratio and does not provide a means for realizing *threo* diastereoselectivity in this reaction.

The *gem*-substituted allylic alcohol **10** afforded the *erythro*-epoxide as essentially a single stereoisomer with all three oxidation methods. The predominant formation of this product is consistent with literature precedents, although the very high diastereoselectivity observed is unusual in the peracid oxidation.

Compounds **11** and **12**, the two substrates investigated that possess *cis* substituents, afforded the corresponding *threo*-epoxides as the major products with all three oxidation methods. This is attributed to destabilization of the *erythro* conformation **14** in the peracid oxidation by $A^{(1,3)}$ strain between R and R_c, but the cause is less obvious in the case of the less stereoselective V-catalyzed process.

In an attempt to gain further understanding of the stereoselectivity of the above oxidations, we subjected compounds **6–12** to molecular modeling with MacroModel (Version 4.5). Energy minimizations in the MM2 mode followed by Monte Carlo searches to determine the conformations corresponding to the global energy minima were performed for each compound. The results are shown in Table 2. It is noteworthy that the dihedral angle O-C(22)-C(23)-C(24) is relatively small for **6–10** (8.2°–24.3°), where R_c = H, indicating a roughly *syn*-coplanar geometry as shown in conformation **32**. In contrast, the dihedral angle in the *cis*-substituted compounds **11** and **12** is −158.1° and −158.5°, respectively, indicating an essentially *anti*-coplanar conformation **33**. Evidently, substantial A-strain between the hydroxyl group and the *cis* substituent results from replacement of H by Me in the *cis* position. This destabilizes the *syn* conformation **32** relative to **33** and leads to rotation about the C(22)—C(23) bond. On the other hand, A-strain is not significantly increased by silylation or esterification of the alcohol moiety in **8** and **9**, where the *syn* conformation **32** persists despite the relatively bulky O-substituents.

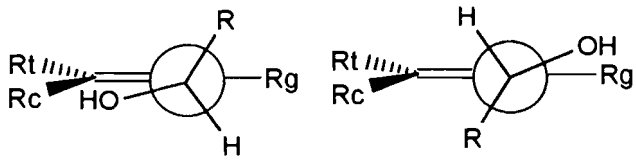

32(*syn*) **33**(*anti*)

We next investigated conformations **13–16** for each of the allylic alcohols **6**, **7**, and **10–12**, in order to identify any A-strain or other strongly destabilizing interactions. We envisaged that appropriately rotationally restricted conformations of the free alcohols could serve as models for their complexes with peracids or vanadium catalysts, and for the ensuing transition states, since the O-C(22)-C(23)-C(24) dihedral angles shown in **13–16** are required for stereoelectronic reasons, as explained earlier. The dihedral angles of compounds **6**, **7**, and **10–12** were therefore constrained to −120°, 120°, −50° and 50°, corresponding to the ideal conformations for *threo* and *erythro* epoxidations with peracids (**13** and **14**, respectively) and V-catalyzed *tert*-butyl hydroperoxide (**15** and **16**, respectively). The resulting energies are shown in Table 2. Compounds **8** and **9** were omitted from consideration because they lack a free hydroxyl group to direct the epoxidation.

The most striking differences in the calculated energies (ΔE) of the *erythro*- and *threo*-forming conformations were observed in the V-catalyzed epoxidation of **10** (−7.3 kJ/mol) and in the peracid oxidations of **11** and **12** (20.4 and 23.3 kJ/mol, respectively). The predicted and observed *erythro* selectivity in the former case is attributed to $A^{(1,2)}$ strain and the associated unfavourable steric interaction between the *gem*-methyl and C(21) methyl groups in the *threo* conformation **15**, where the nearest contact is only 2.242 Å. The strong *threo* selectivity of **11** and **12** is consistent with substantial $A^{(1,3)}$-strain in the *erythro* conformations **14**, where the closest contacts of 2.036 and 2.009 Å, respectively, are between the *cis*-methyl groups and the C(20) hydrogen atoms.

In contrast to the above cases, the differences in energies between the *threo*- and *erythro*-forming conformations in the

other examples in Table 2 are relatively small (ΔE is less than 5 kJ/mol). This suggests that more subtle secondary steric and stereoelectronic effects, as well as factors such as solvation and the possibility of reactions proceeding via higher energy conformations (Curtin–Hammett principle), can play a determining role in deciding the stereochemical outcome. The fact that the other examples in Table 2 predict modest *threo* selectivity, which it will be recalled is generally observed in the peracid oxidations of other allylic alcohols, while the corresponding *erythro* diastereomers were actually favoured with substrates **6–10**, demonstrates that caution must be used in attempts to predict the stereochemistry of these processes in the absence of strongly directing *cis* or *gem* substituents.

In summary, of the steroidal allylic alcohols that were studied, those lacking both *cis* and *gem* substituents (**6** and **7**) displayed strong *erythro* selectivity in vanadium-catalyzed epoxidation and modest *erythro* selectivity with the other oxidants investigated. Silylation or esterification of the hydroxyl group of **7** (to give **8** and **9**) did not significantly alter the course of the peracid epoxidation. The presence of a *gem* substituent in **10** resulted in the essentially exclusive formation of the *erythro* diastereomer with all three oxidants, while *cis*-substituted substrates **11** and **12** provided the only cases of *threo* selective epoxidations. Molecular modeling indicated $A^{(1,3)}$ strain in **14** as the cause of *threo* selectivity in the peracid oxidations of **11** and **12**, and $A^{(1,2)}$ strain between the *gem*-methyl and C(21) methyl groups in **15** as the reason for *erythro* selectivity in the V-catalyzed oxidation of **10**. However, modeling results proved inconclusive in attempts to rationalize the stereoselectivity of the other examples investigated.

Experimental section

Melting points were obtained on an A.H. Thomas hot-stage apparatus and are uncorrected. FT-IR spectra were recorded on a Mattson 4030 spectrometer. Proton (200 MHz) and ^{13}C NMR (50 MHz) spectra were acquired on a Bruker ACE 200 spectrometer, with deuteriochloroform as the solvent and residual chloroform as the internal standard. Other NMR spectra were obtained on a Bruker AM 400 instrument and are so indicated. Only selected signals are reported in ^1H NMR spectra. Low- and high-resolution mass spectra were obtained on a Kratos MS80 or a VG 7070 mass spectrometer. Elemental analyses were carried out by Ms. D. Fox of the Chemical Instrumentation Laboratory. Analytical TLC was carried out with Merck aluminum sheets coated with silica gel 60 F-254, and the spots were visualized with UV light, or by spraying with a 9% ammonium molybdate (VI) tetrahydrate solution in 16% aqueous sulfuric acid followed by heating for a few minutes. Preparative TLC was performed on Analtech 20 × 20 cm glass plates coated with 1 mm of silica gel GF. Flash chromatography was carried out according to the method of Still et al. (22). Radial chromatography was done on a model 7924T Chromatron using glass plates coated with 2 mm of Merck silica gel 60 PF-254.

2-Propenyllithium (23), (*E*)-1-propenylmagnesium bromide (24), and 2-methyl-1-propenyllithium (25) were prepared according to literature methods. Vinylmagnesium bromide was purchased from the Aldrich Chemical Co. 2-Propenyllithium and 2-methyl-1-propenyllithium were titrated with diphenylacetic acid (26), (*E*)-1-propenylmagnesium bromide was titrated using 1,10 phenanthroline and *sec*-butyl alcohol (27), and *n*-butyllithium was titrated with 2,5-dimethoxybenzyl alcohol (28). Aldehyde **2b** (29), allylic alcohol **7** (6), and di-(2,4,6-trimethylphenyl) diselenide (30) were synthesized according to literature methods. All other reagents were obtained from commercial sources and used without further purification. Anhydrous THF was obtained by distillation from lithium aluminum hydride. Anhydrous benzene, pyridine, DMF, and ether were obtained by distillation from calcium hydride.

(3β,5α,6β,22*S*)-6-Methoxy-3,5-cyclo-25,26,27-trinorcholest-23-en-22-ol (6) and its (22*R*) isomer

Vinylmagnesium bromide in THF (10.5 mmol) was added dropwise to a solution of aldehyde **2b** (3.00 g, 8.73 mmol) in 120 mL of dry THF at −78°C. The mixture was stirred for 1 h and then was quenched with aqueous NH_4Cl and diluted with ether. The aqueous layer was extracted with ether and the combined ether extracts were washed with aqueous $NaHCO_3$ and NaCl solutions, dried ($MgSO_4$), and evaporated in vacuo. The products were separated by flash chromatography (elution with 5% ethyl acetate – hexanes) to afford 2.02 g (62%) of **6**; mp 102–103°C (from hexanes) (lit. (31) mp 107–108°C) and 0.46 g (14%) of the 22*R* epimer; mp 122–123°C (from hexanes) (lit. (31) mp 124–125.5°C).

(3β,5α,6β,22*S*,23*E*)-6-Methoxy-3,5-cyclo-26,27-dinorcholest-23-ene 22-*tert*-butyldimethylsilyl ether (8)

Allylic alcohol **7** (6) (152 mg, 0.392 mmol), *tert*-butyldimethylsilyl chloride (154 mg, 1.02 mmol) and imidazole (107 mg, 1.57 mmol), were stirred in 3 mL of dry DMF at 65°C for 5 h. The mixture was diluted with ether, washed several times with water, dried ($MgSO_4$), and purified by flash chromatography (elution with 5% ethyl acetate – hexanes) to give 173 mg (88%) of silyl ether **8**: R_f 0.75 (7% ethyl acetate – hexanes); mp 150–153°C (from ether); IR (Nujol): 1250, 1124, 1096, 1027, 1004, 965, 773 cm^{-1}; ^1H NMR (200 MHz) δ: 5.51 −5.46 (m, 2 H), 4.10–4.08 (m, 1 H), 3.33 (s, 3 H), 2.78 (t, J = 2.8 Hz, 1 H), 1.67 (d, J = 4.2 Hz, 3 H), 1.03 (s, 3 H), 0.90 (s, 9 H), 0.88 (d, J = 5.8 Hz, 3 H), 0.72 (s, 3 H), 0.02 (s, 3 H), −0.02 (s, 3 H); mass spectrum, *m/z* (relative intensity): 500 (0.3, M^+), 499 (0.3), 485 (2), 443 (14), 185 (100). Anal. calcd. for $C_{32}H_{56}O_2Si$: C 76.73, H 11.27; found: C 76.77, H 10.96.

(3β,5α,6β,22*S*,23*E*)-6-Methoxy-3,5-cyclo-26,27-dinorcholest-23-enyl 22-pivaloate (9)

Allylic alcohol **7** (6) (134 mg, 0.347 mmol), trimethylacetyl chloride (213 μL, 1.73 mmol), and 4-dimethylaminopyridine (8.7 mg, 0.071 mmol) were stirred in 4 mL of dry pyridine at room temperature for 2.5 h. The mixture was then diluted with ether and water, washed with 10% HCl and $NaHCO_3$ solution, dried ($MgSO_4$), and purified by flash chromatography (elution with 10% ethyl acetate – hexanes) to afford 87 mg (53%) of ester **9**: R_f 0.50 (7% ethyl acetate – hexanes); mp 159.5–162°C (from ether); IR (KBr): 1726, 1281, 1165, 1097 cm^{-1}; ^1H NMR (200 MHz) δ: 5.64–5.30 (m, 3 H), 3.32 (s, 3 H), 2.77 (t, J = 2.7 Hz, 1 H), 1.69 (d, J = 5.9 Hz, 3 H), 1.23 (s, 9 H), 1.02 (s, 3 H), 0.99 (d, J = 6.8 Hz, 3 H), 0.75 (s, 3 H); mass spectrum, *m/z* (relative intensity): 470 (44, M^+), 455 (12), 438 (17), 415 (23), 283 (63), 57 (100). Anal. calcd. for $C_{31}H_{50}O_3$: C 79.10; H 10.71; found: C 78.86, H 10.63.

3β,5α,6β,22*R*)-6-Methoxy-23-methyl-3,5-cyclo-25,26,27-trinorcholest-23-en-22-ol (10) and its (22*S*) isomer

Aldehyde **2b** (1.5 g, 4.4 mmol) in 15 mL of dry THF was added over 45 min to a solution of 2-propenyllithium (6.5 mL of a 0.87 M solution in ether, 5.6 mmol) at −78°C. The reaction was quenched after 2 h and 15 min with aqueous NH_4Cl. The mixture was diluted with ether and the aqueous layer was extracted once with ether. The combined ether extracts were washed with aqueous $NaHCO_3$, dried (Na_2SO_4), and evaporated under vacuum. The products were separated by flash chromatography (elution with 0–10% ethyl acetate – hexanes) to afford 1.15 g (68%) of the less polar 22*R* allylic alcohol **10** and 486 mg (29%) of the more polar 22*S* epimer. The 22*R* isomer had R_f 0.59 (20% ethyl acetate – hexanes); mp 100–102.5°C (from hexanes); IR (KBr): 3468, 1650, 1642, 1077, 968, 896 cm^{-1}; ^1H NMR (200 MHz) δ: 4.99 (m, 1 H), 4.93 (m, 1 H), 4.11 (m, 1 H), 3.34 (s, 3 H), 2.78 (m, 1 H), 1.67 (s, 3 H), 1.03 (s, 3 H), 0.81 (d, J = 6.2 Hz, 3 H), 0.75 (s, 3 H); mass spectrum, *m/z* (relative intensity): 386 (13, M^+), 371 (10), 354 (12), 331 (22), 283 (100). Anal. calcd. for $C_{26}H_{42}O_2$: C 80.77, H 10.95; found: C 80.93, H 10.90.

The 22*S* isomer had R_f 0.41 (20% ethyl acetate – hexanes); mp 105–107°C (from hexanes); IR (KBr): 3474, 1643, 1098, 1016, 970, 897, 756 cm^{-1}; ^1H NMR (200 MHz) δ: 4.93 (m, 1 H), 4.91 (m, 1 H), 4.13 (d, J = 3.9 Hz, 1 H), 3.33 (s, 3 H), 2.78 (t, J = 2.7 Hz, 1 H), 1.78 (s, 3 H), 1.03 (s, 3 H), 0.96 (d, J = 6.9 Hz, 3 H), 0.77 (s, 3 H); mass spectrum, *m/z* (relative intensity): 386 (14, M^+), 371 (13), 354 (10), 331 (26), 283 (100). Anal. calcd. for $C_{26}H_{42}O_2$: C 80.77, H 10.95; found: C 80.58, H 11.08.

3β,5α,6β,22*S*,23*Z*)-6-Methoxy-3,5-cyclo-26,27-dinorcholest-23-en-22-ol (11) and its (22*R*) isomer

Aldehyde **2b** (200 mg, 0.581 mmol) in 1 mL of dry THF was added to a solution of (*E*)-1-propenylmagnesium bromide (2.0 mL of a 1.2 M solution in THF, 2.3 mmol) at −78°C. The reaction was worked up after 2 h and the product was purified as in the preparation of **6**, to afford 176 mg (78%) of the 22*S* isomer **11** and 36 mg (16%) of the 22*R* isomer. The 22*S* isomer **11** had R_f 0.53 (20% ethyl acetate – hexanes); mp 135–137°C (from acetone-methanol) (lit. (32) mp 136.5–137.5°C). The 22*R* isomer was a solid foam that had: R_f 0.17 (20% ethyl acetate – hexanes). The spectra of both epimers were in good agreement with those reported in the literature (32).

3β,5α,6β,22*R*)-6-Methoxy-3,5-cyclo-26,27-dinorergost-23-en-22-ol (12) and its (22*S*) isomer

Aldehyde **2b** (205 mg, 0.60 mmol) in 3 mL of dry THF was added to a solution of 2-methyl-1-propenyllithium (4.4 mL of a 0.26 M solution in ether, 1.2 mmol) at −78°C over 5 min. The mixture was stirred for 8 h and then was worked up and purified as in the preparation of **6**, providing 46 mg (23%) of starting material **2b**, 136 mg (57%) of the 22*R* isomer **12** and 45 mg (19%) of the 22*S* isomer. The 22*R* isomer **12** was a solid foam that had R_f 0.51 (20% ethyl acetate – hexanes); IR (KBr): 3461, 1098, 968 cm^{-1}; ^1H NMR (200 MHz) δ: 5.33 (br d, J = 8.1 Hz, 1 H), 4.45 (d, J = 8.1 Hz, 1 H), 3.33 (s, 3 H), 2.78 (t, J = 2.5 Hz, 1 H), 1.72 (s, 3 H), 1.66 (d, J = 0.8 Hz, 3 H), 1.02 (s, 3 H), 0.96 (d, J = 6.0 Hz, 3 H), 0.72 (s, 3 H); ^{13}C NMR (50.3 MHz) δ: 133.6 (C), 127.3 (CH), 82.4 (CH), 70.6 (CH), 56.5 (CH), 56.4 (CH_3), 52.7 (CH), 48.0 (CH), 43.4 (C), 42.8 (C), 41.9 (CH), 40.2 (CH_2), 35.3 (C), 35.1 (CH_2), 33.4 (CH_2), 30.6 (CH), 27.9 (CH_2), 25.9 (CH_3), 25.0 (CH_2), 24.2 (CH_2), 22.8 (CH_2), 21.5 (CH), 19.3 (CH_3), 18.2 (CH_3), 13.1 (CH_2), 12.3 (CH_3), 12.1 (CH_3); mass spectrum, *m/z* (relative intensity): 400 (2, M^+), 385 (3), 368 (3), 350 (7), 284 (55), 253 (56), 85 (100). Exact Mass calcd. for $C_{27}H_{44}O_2$: 400.3341; found: 400.3336. The ^1H NMR spectrum was in agreement with a literature spectrum of the 22*R* isomer prepared by a different method (33).

The 22*S* isomer had R_f 0.35 (20% ethyl acetate – hexanes); mp 138–142°C (from hexanes); IR (KBr): 3347, 1673, 1098, 1015, 986, 970 cm^{-1}; ^1H NMR (200 MHz) δ: 5.27 (br d, J = 9.6 Hz, 1 H), 4.41 (dd, J = 9.6, 3.7 Hz, 1 H), 3.33 (s, 3 H), 2.77 (t, J = 2.6 Hz, 1 H), 1.76 (d, J = 1.1 Hz, 3 H), 1.74 (d, J = 1.2 Hz, 3 H), 1.03 (s, 3 H), 1.01 (d, J = 6.3 Hz, 3 H), 0.75 (s, 3 H); mass spectrum, *m/z* (relative intensity): 400 (1, M^+), 382 (11), 367 (8), 350 (24), 335 (14), 327 (15), 253 (100). Anal. calcd. for $C_{27}H_{44}O_2$: C 80.94, H 11.07; found: C 80.71, H 11.11.

Epoxidation of allylic alcohol 6 with MCPBA — typical procedure

Allylic alcohol **6** (61 mg, 0.16 mmol) was treated with MCPBA (169 mg of 50%, 0.49 mmol) in 1 mL of dichloromethane for 2 h. After dilution with dichloromethane, the mixture was washed several times with K_2CO_3 solution and dried ($MgSO_4$). The volatile material was removed in vacuo and the residue was purified by flash chromatography (elution with 10% ether – hexanes) to afford 63 mg (100%) of an unseparated mixture of *threo-* and *erythro* epoxides **17** in the ratio of 36:64 as determined by ^1H NMR integration of their H-22 signals at δ 3.62 and 3.92, respectively. The signal from the *erythro* epoxide **17** was assigned by comparing the spectrum of the above mixture with the spectrum of the pure *erythro* diastereomer prepared by the vanadium-catalyzed procedure (see below). The diastereomers were separated by means of preparative TLC (50% ether – hexanes) of their corresponding benzoates.

The *erythro* benzoate had R_f 0.51 (50% ether – hexanes); mp 80–82°C (from ethyl acetate – methanol); IR (Nujol): 1719, 1268, 1098, 710 cm^{-1}; ^1H NMR (400 MHz) δ: 8.04 (dd, J = 8.3, 1.1 Hz, 2 H), 7.58 (t, J = 7.5 Hz, 1 H), 7.48 (dd, J = 7.7, 7.7 Hz, 2 H), 5.04 (dd, J = 5.7, 1.4 Hz, 1 H), 3.31 (s, 3 H), 3.11 (m, 1 H), 2.87 (dd, J = 5.3, 2.6 Hz, 1 H), 2.83 (dd, J = 5.3, 3.8 Hz, 1 H), 2.75 (t, J = 2.7 Hz, 1 H), 1.26 (d, J = 6.8 Hz, 3 H), 1.02 (s, 3 H), 0.79 (s, 3 H); ^{13}C NMR (50.3 MHz) δ: 165.7 (C═O), 133.1 (CH), 130.1 (C), 129.6 (CH), 128.4 (CH), 82.3 (CH), 75.2 (CH), 56.5 (CH), 56.3 (CH_3), 52.4 (CH), 51.0 (CH), 47.9 (CH), 46.7 (CH_2), 43.3 (C), 42.7 (C), 40.2 (CH_2), 38.1 (CH), 35.3 (C), 34.8 (CH_2), 33.3 (CH_2), 30.5 (CH), 28.0 (CH_2), 24.9 (CH_2), 24.0 (CH_2), 22.8 (CH_2), 21.5 (CH), 19.3 (CH_3), 13.6 (CH_3), 13.0 (CH_2), 12.1 (CH_3); mass spectrum, *m/z* (relative intensity): 492 (12, M^+), 477 (11), 460 (15), 437 (19), 105 (100). Exact Mass calcd. for $C_{32}H_{44}O_4$: 492.3240; found: 492.3226.

The *threo* benzoate had R_f 0.43 (50% ether – hexanes); mp 132–133°C (from hexanes–methanol); IR (Nujol): 1723, 1602, 1584, 1267, 1098, 757, 709 cm^{-1}; ^1H NMR (400 MHz) δ: 8.08 (dd, J = 8.2, 1.1 Hz, 2 H), 7.58 (t, J = 7.5 Hz, 1 H), 7.47 (dd, J = 7.8, 7.6 Hz, 2 H), 5.07 (m, 1 H), 3.32 (s, 3 H), 3.24 (m, 1 H), 2.82 (dd, J = 4.5, 4.5 Hz, 1 H), 2.75 (t, J = 2.6 Hz, 1 H), 2.61 (dd, J = 4.8, 2.7 Hz, 1 H), 1.27 (d, J = 6.8 Hz, 3 H), 1.02

(s, 3 H), 0.78 (s, 3 H); mass spectrum, *m/z* (relative intensity): 492 (6, M^+), 477 (7), 460 (7), 437 (12), 205 (53), 105 (100). Anal. calcd. for $C_{32}H_{44}O_4$: C 78.01, H 9.00; found: C 77.63, H 8.76.

Epoxidation of allylic alcohol 6 with vanadyl acetylacetonate and *tert*-butyl hydroperoxide — typical procedure

Allylic alcohol **6** (48 mg, 0.13 mmol) and $VO(acac)_2$ (0.4 mg, 0.001 mmol) were dissolved in 5 mL of toluene followed by the addition of *tert*-butyl hydroperoxide (0.50 mL of a 90% solution). After 12 h at room temperature the mixture was filtered through Celite and evaporated in vacuo. Flash chromatography (elution with 10% ether – hexanes) of the crude material afforded 47 mg (93%) of **17** with a *threo*:*erythro* ratio of <5:95 as determined by ^{1}H NMR integration. Epoxide **17** was isolated as a pure diastereomer after recrystallization from ether, mp 128–130°C; R_f 0.52 (50% ether-hexanes); IR (KBr): 3474, 1093, 1085 cm^{-1}; ^{1}H NMR (200 MHz) δ: 3.92 (br s, 1 H, 22-H), 3.33 (s, 3 H,), 2.97–2.88 (m, 2 H), 2.83–2.76 (m, 2 H), 1.03 (s, 3 H), 0.98 (d, J = 6.5 Hz, 3 H), 0.75 (s, 3 H); mass spectrum, *m/z* (relative intensity): 388 (44, M^+), 373 (60), 356 (73), 333 (100). Anal. calcd for $C_{25}H_{40}O_3$: C 77.27, H 10.37; found: C 76.87, H 10.34.

Epoxidation of allylic alcohol 6 with molybdenum hexacarbonyl and *tert*-butyl hydroperoxide — typical procedure

tert-Butyl hydroperoxide (0.5 mL of 90%) was added to a mixture of **6** (47.7 mg, 0.13 mmol) and $Mo(CO)_6$ (0.4 mg, 0.001 mmol) in benzene at 60°C. The reaction mixture was filtered through Celite after 8 h and the solvent was removed in vacuo. Purification of the crude product by flash chromatography (elution with 10% ether – hexanes) afforded 29 mg (58%) of the mixture of *threo*- and *erythro* epoxides **17** in the ratio of 26:74, as determined by ^{1}H NMR integration.

Epoxidation of compounds 7–12

These epoxidations were performed by the same procedures as described above for **6**. The yields and ratios of diastereomers are shown in Table 1, and the properties of the products are given below.

Threo *and* erythro *epoxides* ***18***

These compounds were reported previously (6).

Threo *and* erythro *epoxides* ***19***

The mixture of diastereomers had R_f 0.50 (7% ethyl acetate – hexanes); ^{1}H NMR (200 MHz) δ: (*threo* isomer): 3.33 (s, 3 H), 3.14 (br d, J = 6.9 Hz, 1 H), 2.79–2.73 (m, 3 H), 1.32 (d, J = 5.2 Hz, 3 H), 1.03 (s, 3 H), 0.98 (d, J = 6.5 Hz, 3 H), 0.92 (s, 9 H), 0.73 (s, 3 H), 0.051 (s, 3 H), 0.046 (s, 3 H). Signals from the major *erythro* isomer were identified by comparison with those of an authentic sample prepared by silylation of pure *erythro*-**18**. *Erythro*-**19**: R_f 0.50 (7% ethyl acetate – hexanes); mp 175–179°C (from ether–ethanol); IR (KBr): 1248, 1132, 1099, 1084, 836, 773 cm^{-1}; ^{1}H NMR (200 MHz) δ: 3.48 (m, 1 H), 3.33 (s, 3 H), 2.90 (dq, J = 5.2, 2.2 Hz, 1 H), 2.78 (t, J = 2.7 Hz, 1 H), 2.61 (dd, J = 5.4, 2.1 Hz, 1 H), 1.32 (d, J = 5.2 Hz, 3 H), 1.03 (s, 3 H), 0.98 (d, J = 6.5 Hz, 3 H), 0.90 (s, 9 H) 0.75 (s, 3 H), 0.055 (s, 3 H), 0.049 (s, 3 H); mass spectrum, *m/z* (relative intensity): 459 (4, M^+ – *t*-Bu), 427 (11), 335 (12), 283 (25), 253 (60), 73 (100). Anal. calcd. for $C_{32}H_{56}O_3Si$: C 74.36, H 10.92; found: C 74.17, H 11.03.

Threo *and* erythro *epoxides* ***20***

The mixture of diastereomers had R_f 0.43 (50% ether – hexanes); ^{1}H NMR (200 MHz) δ: (*threo* isomer) 4.81–4.78 (m, 1 H), 3.33 (s, 3 H), 2.85–2.79 (m, 3 H), 1.32 (d, J = 4.8 Hz, 3 H), 1.25 (s, 9 H), 1.13 (d, J = 6.9 Hz, 3 H), 1.03 (s, 3 H), 0.75 (s, 3 H). Signals from the major *erythro* isomer in the mixture were identified by comparison with those of an authentic sample prepared by treatment of pure *erythro*-**18** with pivaloyl chloride in refluxing pyridine in the presence of 4-dimethylaminopyridine. *Erythro* epoxide **20**: R_f 0.43 (50% ether – hexanes); mp 166–168°C (from ether); IR (KBr): 1731, 1162, 1154, 1096, 1081 cm^{-1}; ^{1}H NMR (200 MHz) δ: 4.79 (dd, J = 5.3, 1.3 Hz, 1 H), 3.32 (s, 3 H), 3.02 (dq, J = 5.2, 2.1 Hz, 1 H), 2.77 (t, J = 2.6 Hz, 1 H), 2.67 (dd, J = 5.3, 2.1 Hz, 1 H), 1.30 (d, J = 5.2 Hz, 3 H), 1.22 (s, 9 H), 1.10 (d, J = 6.8 Hz, 3 H), 1.03 (s, 3 H), 0.75 (s, 3 H); ^{13}C NMR (100.6 MHz) δ: 177.6 (C=O), 82.3 (CH), 73.8 (CH), 58.2 (CH), 56.5 (CH), 56.5 (CH_3), 53.7 (CH), 52.4 (CH), 47.9 (CH), 43.3 (C), 42.6 (C), 40.3 (CH_2), 39.1 (C), 37.8 (CH), 35.3 (C), 34.8 (CH_2), 33.3 (CH_2), 30.5 (CH), 28.0 (CH_2), 27.2 (CH_3), 24.9 (CH_2), 24.0 (CH_2), 22.7 (CH_2), 21.5 (CH), 19.2 (CH_3), 17.2 (CH_3), 13.4 (CH_3), 13.0 (CH_2), 12.0 (CH_3); mass spectrum, *m/z* (relative intensity): 486 (26, M^+), 471 (35), 454 (33), 431 (100). Exact Mass calcd. for $C_{31}H_{50}O_4$: 486.3709; found: 486.3662.

Erythro *epoxide* ***21***: R_f 0.71 (50% ether – hexanes); mp 118–119.5°C (from acetonitrile); IR (KBr): 3506, 1131, 1101, 793 cm^{-1}; ^{1}H NMR (200 MHz) δ: 3.82 (br s, 1 H), 3.34 (s, 3 H), 3.07 (d, J = 4.8 Hz, 1 H), 2.78 (t, J = 2.8 Hz, 1 H), 2.67 (d, J = 4.8 Hz, 1 H), 1.33 (s, 3 H), 1.03 (s, 3 H), 0.91 (d, J = 6.3 Hz, 3 H), 0.75 (s, 3 H); mass spectrum, *m/z* (relative intensity): 402 (9, M^+), 387 (11), 372 (31), 357 (40), 317 (71), 289 (88), 55 (100). Anal. calcd. for $C_{26}H_{42}O_3$: C 77.56, H 10.51; found: C 77.43, H 10.70.

Threo *epoxide* ***22***: R_f 0.18 (50% ether – hexanes); mp 149–150°C (from ether); IR (KBr): 3410, 1084, 840, 803, 749 cm^{-1}; ^{1}H NMR (200 MHz) δ: 3.61 (dd, J = 6.1, 5.0 Hz, 1H), 3.33 (s, 3 H), 3.13 (dq, J = 5.6, 4.4 Hz, 1 H), 3.02 (dd, J = 4.4, 6.2 Hz, 1 H), 2.78 (t, J = 2.7 Hz, 1 H), 1.34 (d, J = 5.6 Hz, 3 H), 1.05 (d, J = 6.3 Hz, 3 H), 1.03 (s, 3 H), 0.74 (s, 3 H); mass spectrum, *m/z* (relative intensity): 402 (23, M^+), 387 (33), 370 (31), 358 (19), 347 (55), 303 (68), 289 (74), 105 (99), 91 (100). Anal. calcd. for $C_{26}H_{42}O_3$: C 77.56, H 10.51; found: C 77.77, H 10.39.

Erythro *epoxide* ***22***: R_f 0.29 (50% ether – hexanes); mp 124–126°C (from ether); IR (KBr): 3383, 1091, 1075, 966 cm^{-1}; ^{1}H NMR (200 MHz) δ: 3.65–3.58 (m, 1H), 3.33 (s, 3 H), 3.17 (dq, J = 5.6, 4.1 Hz, 1 H), 2.96 (dd, J = 7.7, 4.1 Hz, 1 H), 2.78 (t, J = 2.7 Hz, 1 H), 1.37 (d, J = 5.6 Hz, 3 H), 1.08 (d, J = 6.3 Hz, 3 H), 1.03 (s, 3 H), 0.77 (s, 3 H); mass spectrum, *m/z* (relative intensity): 402 (48, M^+), 387 (71), 370 (63), 347 (81), 149 (100). Anal. calcd. for $C_{26}H_{42}O_3$: C 77.56, H 10.51; found: C 77.53, H 10.27.

Threo *and* erythro *epoxides* ***23***

The mixture of diastereomers was separated after conversion

into their corresponding benzoates. The minor *erythro* benzoate was a solid foam that had R_f 0.61 (50% ether – hexanes); IR (KBr): 1715, 1602, 1270, 1114, 1098, 756, 711 cm^{-1}; ^1H NMR (200 MHz) δ: 8.10–8.05 (m, 2 H), 7.61–7.44 (m, 3 H), 4.94 (dd, J = 7.8, 1.6 Hz, 1 H), 3.31 (s, 3 H), 2.90 (d, J = 7.8 Hz, 1 H), 2.75 (t, J = 2.7 Hz, 1 H), 1.44 (s, 3 H), 1.33 (s, 3 H), 1.28 (d, J = 6.8 Hz, 3 H), 1.02 (s, 3 H), 0.78 (s, 3 H); ^{13}C-NMR (50.3 MHz) δ: 165.5 (C═O), 132.7 (CH), 130.1 (C), 129.4 (CH), 128.2 (CH), 82.1 (CH), 73.2 (CH), 62.2 (CH), 59.9 (C), 56.2 (CH_3), 56.1 (CH), 52.2 (CH), 47.7 (CH), 43.1 (C), 42.5 (C), 40.0 (CH_2), 37.5 (CH), 35.0 (C), 34.6 (CH_2), 33.1 (CH_2), 30.2 (CH), 27.7 (CH_2), 24.6 (CH_2), 24.2 (CH_3), 23.8 (CH_2), 22.5 (CH_2), 21.2 (CH), 19.2 (CH_3), 18.9 (CH_3), 13.1 (CH_3), 12.7 (CH_2), 11.8 (CH_3); mass spectrum, *m/z* (relative intensity): 520 (10, M^+), 505 (12), 488 (10), 465 (16), 343 (20), 253 (37), 105 (100). Exact Mass calcd. for $C_{34}H_{48}O_4$: 520.3553; found: 520.3532. The major *threo* benzoate had R_f 0.46 (50% ether – hexanes); mp 158.5–161°C (from hexanes). It was saponified with 1 M NaOH to afford the free *threo* epoxy alcohol **23**: R_f 0.42 (50% ether – hexanes); mp 117–118°C (from acetonitrile); IR (KBr): 3455, 1097, 754 cm^{-1}; ^1H NMR (200 MHz): 3.33 (s, 3 H), 2.84 (d, J = 6.2 Hz, 1 H), 2.78 (t, J = 2.6 Hz, 1 H), 1.34 (s, 3 H), 1.33 (s, 3 H), 1.04 (d, J = 7.2 Hz, 3 H), 1.03 (s, 3 H), 0.74 (s, 3 H); mass spectrum, *m/z* (relative intensity): 416 (9, M^+), 401 (10), 384 (8), 361 (17), 344 (26), 329 (52), 312 (50), 289 (100). Anal. calcd. for $C_{27}H_{44}O_3$: C 77.84, H 10.64; found: C 77.52, H 10.68.

(3β,5α,6β,22*R*,23*S*)-6-Methoxy-3,5-cyclocholestane-22,23-diol (24)

Isopropylmagnesium chloride (10.2 mmol) in ether was added to a suspension of cuprous cyanide (92 mg, 1.0 mmol) in 10 mL of dry ether at −78°C. After 1 h, the *erythro*-epoxide **17** (794 mg, 2.04 mmol) in 15 mL of dry ether was added dropwise. The mixture was stirred for 15 min at −78°C and 1 h at room temperature. Aqueous NH_4Cl and ether were added and the aqueous layer was extracted once with ether. The combined ether extracts were washed with $NaHCO_3$ and NaCl solutions, dried ($MgSO_4$), and evaporated to dryness under vacuum. The crude product was purified by flash chromatography (elution with 10% ethyl acetate – hexanes) to afford 706 mg (80%) of diol **24**: R_f 0.27 (20% ethyl acetate – hexanes); mp 95–97°C (from hexanes); IR (KBr): 3423, 1099, 966, 759 cm^{-1}; ^1H NMR (200 MHz) δ: 3.72–3.60 (m, 1 H), 3.44–3.38 (m, 1 H), 3.33 (s, 3 H), 2.78 (t, J = 2.7 Hz, 1 H), 1.02 (d, J = 6.7 Hz, 6 H), 0.97 (s, 3 H), 0.94 (d, J = 7.1 Hz, 3 H), 0.77 (s, 3 H); mass spectrum, *m/z* (relative intensity): 432 (18, M^+) 417 (17), 400 (20), 377 (33), 313 (46), 283 (37), 43 (100). Anal. calcd. for $C_{28}H_{48}O_3$: C 77.73, H 11.18; found: C 77.34, H 10.76.

3β,5α,6β,22*Z*)-6-Methoxy-3,5-cyclocholest-22-ene (25)

Diol **24** (154 mg, 0.36 mmol) and 1,1′-thiocarbonyldiimidazole (71 mg, 0.39 mmol) were refluxed in 10 mL of dry toluene for 48 h. The mixture was diluted with ether, washed several times with water, and dried ($MgSO_4$). After removal of the volatile material under vacuum, the residue was flash chromatographed on neutral alumina (elution with 5% ethyl acetate – hexanes) to afford 122 mg (72%) of (3β,5α,6β,22*R*, 23*S*)-6-methoxy-3,5-cyclocholestane-22,23-thionocarbonate as a solid foam: R_f 0.55 (50% ether-hexanes); IR (KBr): 1287, 1098, 947, 933 cm^{-1}; ^1H NMR (400 MHz) δ: 4.92–4.89 (m, 2 H), 3.33 (s, 3 H), 2.79 (t, J = 2.7 Hz, 1 H); 1.07 (d, J = 6.4 Hz, 3 H), 1.03 (s, 3 H), 1.02 (d, J = 7.5 Hz, 3 H), 0.98 (d, J = 6.5 Hz, 3 H), 0.74 (s, 3 H); ^{13}C NMR (100.6 MHz) δ: 192.4 (C═O), 86.7 (CH), 83.6 (CH), 82.3 (CH), 56.6 (CH_3), 56.2 (CH), 52.1 (CH), 47.8 (CH), 43.3 (C), 42.8 (C), 39.9 (CH_2), 37.3 (CH), 36.2 (CH_2), 35.1 (C), 35.0 (CH_2), 33.3 (CH_2), 30.6 (CH), 28.4 (CH_2), 25.6 (CH), 24.9 (CH_2), 24.1 (CH_2), 23.2 (CH_3), 22.7 (CH_2), 21.7 (CH_3), 21.4 (CH), 19.2 (CH_3), 13.8 (CH_3), 13.1 (CH_2), 12.0 (CH_3); mass spectrum, *m/z* (relative intensity): 474 (58, M^+), 459 (53), 442 (74), 419 (96), 253 (81), 55 (100). Exact Mass calcd. for $C_{29}H_{46}O_3S$: 474.3168; found: 474.3149. The thionocarbonate was refluxed in 1.5 mL of trimethylphosphite for 96 h. It was then extracted several times with chloroform and the chloroform extracts were washed several times with 4% NaOCl solution. The remaining volatile material was removed in vacuo and the residue was purified by flash chromatography (elution with 10% benzene – hexanes) to afford 15 mg (54%) of olefin **25**, which furnished an ^1H NMR spectrum in close agreement with that reported in the literature (18).

3β,5α,6β,22*R*,23*S*)-6-Methoxy-3,5-cyclo-26,27-dinorcholestane-22,23-diol (26)

Erythro-epoxide **18** (108 mg, 0.268 mmol) and titanium(IV) isopropoxide (136 μL, 0.457 mmol) were dissolved in 5 mL of dry benzene and after 5 min lithium borohydride (23 mg 1.1 mmol) was added. The mixture stirred for 18 h at 50°C and then 5% H_2SO_4 solution and ether were added. After 20 min, the layers were separated and the aqueous layer was extracted once with ether. The combined ether extracts were washed with aqueous $NaHCO_3$, dried (Na_2SO_4), concentrated in vacuo, and purified by flash chromatography (elution with 5–10% ethyl acetate – hexanes) to give 60 mg (55%) of diol **26**: R_f 0.17 (20% ethyl acetate – hexanes); mp 156.5–161°C (from acetonitrile); IR (KBr): 3417, 1261, 1098, 1082, 969 cm^{-1}; ^1H NMR (400 MHz) δ: 3.52–3.44 (m, 2 H), 3.33 (s, 3 H), 2.78 (t, J = 2.7 Hz, 1 H), 1.03 (s, 3 H), 1.02 (t, J = 5.7 Hz, 3 H), 0.97 (d, J = 6.7 Hz, 3 H), 0.77 (s, 3 H); ^{13}C NMR (100.6 MHz) δ: 82.4 (CH), 75.7 (CH), 73.4 (CH), 56.6 (CH_3), 56.5 (CH), 52.7 (CH), 48.0 (CH), 43.4 (C), 42.8 (C), 40.3 (CH_2), 36.2 (CH), 35.3 (C), 35.0 (CH_2), 33.4 (CH_2), 30.6 (CH), 27.9 (CH_2), 27.0 (CH_2), 25.0 (CH_2), 24.1 (CH_2), 22.8 (CH_2), 21.5 (CH), 19.3 (CH_3), 13.1 (CH_2), 12.2 (CH_3), 12.0 (CH_3), 9.9 (CH_3); mass spectrum, *m/z* (relative intensity): 404 (29, M^+), 389 (34), 372 (32), 349 (62), 312 (66), 289 (100). Exact Mass calcd. for $C_{26}H_{44}O_3$: 404.3290; found: 404.3327.

The same diol **26** was obtained in 84% yield by the similar treatment of *erythro* epoxide **22**.

3β,5α,6β,22*R*,23*R*)-6-Methoxy-3,5-cyclo-26,27-dinorcholestane-22,23-diol (27)

threo Epoxide **22** (101 mg, 0.251 mmol) was treated with titanium(IV) isopropoxide (120 μL, 0.40 mmol) and lithium borohyride (23 mg, 1.1 mmol) as in the preceding procedure, except that the reaction was performed at room temperature for 24 h, to afford 25 mg (25%) of starting material **22** and 51 mg (50%) of diol **27** as a solid foam: R_f 0.12 (20% ethyl acetate – hexanes); IR (KBr): 3392, 1268, 1203, 1099, 1083, 969, 804, 756 cm^{-1}; ^1H NMR (200 MHz) δ: 3.49 (dt, J = 8.0, 2.9 Hz, 1 H), 3.44 (d, J = 8.3 Hz, 1 H), 3.33 (s, 3 H), 2.78 (t, J = 2.7 Hz, 1 H), 1.03 (s, 3 H), 1.00 (t, J = 7.5 Hz, 3 H), 0.91 (d, J = 6.1

Hz, 3 H), 0.73 (s, 3 H); ^{13}C NMR (50.3 MHz) δ: 82.4 (CH), 76.5 (CH), 74.3 (CH), 56.6 (CH_3), 56.4 (CH), 52.5 (CH), 48.0 (CH), 43.3 (C), 42.6 (C), 40.3 (CH_2), 37.3 (CH), 35.2 (C), 35.1 (CH_2), 33.3 (CH_2), 30.6 (CH), 27.9 (CH_2), 25.7 (CH_2), 24.9 (CH_2), 24.0 (CH_2), 22.8 (CH_2), 21.4 (CH), 19.3 (CH_3), 13.1 (CH_2), 12.1 (2 X CH_3), 9.6 (CH_3); mass spectrum *m/z* (relative intensity): 404 (45, M^+), 389 (55), 372 (48), 349 (100). Exact Mass calcd. for $C_{26}H_{44}O_3$: 404.3290; found: 404.3252.

3β,5α,6β,22*R*,23*S*)-6-Methoxy-3,5-cyclo-23-methyl-24-(2,4,6-trimethylphenylseleno)-25,26,27-trinorcholestane-22,23-diol (28)

Sodium borohydride (25 mg, 0.66 mmol) was slowly added to a solution of *erythro* epoxide **21** (88 mg, 0.22 mmol) and di-(2,4,6-trimethylphenyl) diselenide (47 mg, 0.12 mmol) in 8 mL of ethanol. After 6 h, the mixture was diluted with water, extracted several times with ether, and dried (K_2CO_3). The volatile material was removed in vacuo and the residue was purified by flash chromatography (elution with 10% ether – hexanes) to afford 105 mg (80%) of diol **28**: R_f 0.38 (20% ethyl acetate – hexanes); mp 153–155°C (from acetonitrile); IR (KBr): 3575, 3484, 1205, 1095, 1080, 850, 792 cm^{-1}; ^{1}H NMR (400 MHz) δ: 6.94 (s, 2 H), 3.59 (d, *J* = 6.2 Hz, 1 H), 3.34 (s, 3 H), 3.04 (d, *J* = 11.5 Hz, 1 H), 2.85 (d, *J* = 11.5 Hz, 1 H), 2.78 (t, *J* = 2.7 Hz, 1 H), 2.60 (s, 1 H, exchanged with D_2O), 2.56 (s, 6 H), 2.27 (s, 3 H), 2.08 (d, *J* = 6.2 Hz, 1 H), 1.30 (s, 3 H), 1.03 (s, 3 H), 0.99 (d, *J* = 6.7 Hz, 3 H), 0.75 (s, 3 H); mass spectrum, *m/z* (relative intensity): 602 (6, M^+, ^{80}Se), 584 (4), 384 (10), 352 (16), 329 (43), 289 (49), 200 (78), 119 (100). Anal. calcd. for $C_{35}H_{54}O_3Se$: C 69.86, H 9.04; found: C 69.78, H 8.91.

3β,5α,6β,22*E*)-6-Methoxy-3,5-cyclo-23-methyl-24-(2,4,6-trimethylphenylseleno)-25,26,27-trinorcholest-22-ene (29)

n-Butyllithium in hexanes (0.25 mmol) was added dropwise to a solution of **28** (83 mg, 0.14 mmol) in 6 mL of dry THF. After 5 min, 1,1′-thiocarbonyldiimidazole (43 mg, 0.24 mmol) was added and the mixture was refluxed for 4 h. It was quenched with aqueous NH_4Cl and extracted several times with ether. The ether layers were washed with water, dried (Na_2SO_4), concentrated in vacuo, and purified by flash chromatography (elution with 10% ether – hexanes) to give 70 mg (80%) of 3β,5α,6β,22*R*,23*R*)-6-methoxy-3,5-cyclo-23-methyl-24-(2,4,6-trimethylphenylseleno)-25,26,27-trinorcholestane-22,23-thionocarbonate: R_f 0.63 (50% ether – hexanes); mp 164.5–165.5°C (from ethanol); IR (KBr): 1597, 1313, 1272, 1156, 1098, 1086 cm^{-1}; ^{1}H NMR (200 MHz) δ: 6.95 (s, 2 H), 4.64 (s, 1 H), 3.34 (s, 3 H), 3.06 (br s, 2 H), 2.79 (m, 1 H), 2.56 (s, 6 H), 2.28 (s, 3 H), 1.62 (s, 3 H), 1.04 (d, *J* = 7.4 Hz, 3 H), 1.03 (s, 3 H), 0.70 (s, 3 H); ^{13}C-NMR (100.6 MHz) δ: 191.1 (C=O), 142.4 (C), 139.0 (C), 129.0 (CH), 127.2 (C), 91.23 (C), 91.15 (CH), 82.3 (CH), 56.6 (CH_3), 56.3 (CH), 52.5 (CH), 47.7 (CH), 43.3 (C), 42.8 (C), 39.9 (CH_2), 37.9 (CH), 35.1 (CH_2), 35.0 (C), 33.3 (CH_2), 30.5 (CH), 29.4 (CH_2), 28.3 (CH_2), 26.2 (CH_3), 24.9 (CH_2), 24.3 (2 × CH_3), 24.1 (CH_2), 22.7 (CH_2), 21.4 (CH), 20.9 (CH_3), 19.2 (CH_3), 13.5 (CH_3), 13.1 (CH_2), 11.9 (CH_3); mass spectrum, *m/z* (relative intensity): 644 (1, M^+, ^{80}Se), 628 (3), 596 (4), 369 (15), 337 (16), 283 (28), 197 (52), 119 (100). The thionocarbonate (30 mg, 0.046 mmol) was refluxed in 5 mL of trimethylphosphite for 72 h. The mixture was diluted with chloroform and washed several times with water. The chloroform layer was left under a stream of nitrogen for 14 h to remove traces of trimethylphosphite. After evaporation of the remaining solvent in vacuo the residue was purified by flash chromatography (elution with 5% ethyl acetate – hexanes) to afford 16 mg (61%) of olefin **29** as an oil: R_f 0.49 (7% ethyl acetate – hexanes); IR (KBr): 1098, 1016, 849 cm^{-1}; ^{1}H NMR (200 MHz) δ: 6.93 (s, 2 H), 4.97 (d, *J* = 9.8 Hz, 1 H), 3.40 (d, *J* = 10.7 Hz, 1 H), 3.34 (s, 3 H), 3.27 (d, *J* = 10.7 Hz, 1 H), 2.77 (m, 1 H), 2.58 (s, 6 H), 2.26 (s, 3 H) superimposed on 2.26–2.15 (m, 1 H), 1.82 (d, *J* = 1.2 Hz, 3 H), 1.03 (s, 3 H), 0.79 (d, *J* = 6.5 Hz, 3 H), 0.69 (s, 3 H); irradiation of the peak at δ: 4.97 (H-22) produced a 3.3% enhancement of the signal at δ: 1.82 (olefinic CH_3) and vice versa (3.4% enhancement); ^{13}C NMR (100.6 MHz) δ: 143.3 (C), 138.1 (C), 135.5 (CH), 128.5 (C), 128.41 (C), 128.36 (CH), 82.4 (CH), 56.6 (CH_3), 56.5 (CH), 56.4 (CH), 48.1 (CH), 43.4 (C), 42.7 (C), 40.2 (CH_2), 35.4 (C), 35.2 (CH), 34.9 (CH_2), 33.4 (CH_2), 30.5 (CH), 29.8 (CH_2), 28.0 (CH_2), 25.0 (CH_2), 24.5 (CH_3), 24.2 (CH_2), 23.2 (CH_3), 22.8 (CH_2), 21.6 (CH), 20.9 (CH_3), 20.6 (CH_3), 19.3 CH_3), 13.0 (CH_2), 12.5 (CH_3); mass spectrum, *m/z* (relative intensity): 568 (5, M^+, ^{80}Se), 536 (9), 337 (94), 253 (57), 119 (100). Exact Mass calcd. for $C_{35}H_{52}OSe$: 568.3190; found: 568.3228.

3β,5α,6β,22*R*,23*R*)-6-Methoxy-3,5-cyclo-26,27-dinorergostane-22,23-diol (30)

The *threo* epoxide **23** (119 mg, 0.29 mmol) was treated with titanium(IV) isopropoxide (145 μL, 0.486 mmol) and lithium borohydride (25 mg 1.1 mmol) according to the procedure for the conversion of *erythro*-**18** or *erythro*-**22** into diol **26**, except that the crude product was purified using radial chromatography (elution with 30% ether – hexanes) to give 91 mg (76%) of diol **30**: R_f 0.46 (20% ethyl acetate – hexanes); IR (KBr): 3417, 1099, 998, 757 cm^{-1}; ^{1}H NMR (200 MHz) δ: 3.56 (d, *J* = 8.0 Hz, 1 H), 3.49 (s, 1 H, exchanged with D_2O), 3.42 (dd, *J* = 7.8, 2.6 Hz, 1 H), 3.33 (s, 3 H), 2.78 (t, *J* = 2.8 Hz, 1 H), 2.04 (br s, 1 H, exchanged with D_2O), 1.03 (s, 3 H), 1.02 (d, *J* = 5.3 Hz, 3 H), 0.92 (d, *J* = 6.2 Hz, 3 H), 0.87 (d, *J* = 6.8 Hz, 3 H), 0.74 (s, 3 H); ^{13}C NMR (100.6 MHz) δ: 82.4 (CH), 77.0 (CH), 74.3 (CH), 56.6 (CH_3), 56.4 (CH), 52.6 (CH), 48.0 (CH), 43.4 (C), 42.6 (C), 40.3 (CH_2), 37.6 (CH), 35.2 (C), 35.1 (CH_2), 33.4 (CH_2), 30.6 (CH), 29.2 (CH), 27.9 (CH_2), 24.9 (CH_2), 24.1 (CH_2), 22.8 (CH_2), 21.5 (CH), 20.3 (CH_3), 19.3 (CH_3), 14.7 (CH_3), 13.1 (CH_2), 12.2 (2 × CH_3); mass spectrum, *m/z* (relative intensity): 418 (30, M^+), 403 (31), 386 (24), 363 (59), 289 (75), 41 (100). Exact Mass calcd. for $C_{27}H_{46}O_3$: 418.3447; found: 418.3419.

(3β,22*R*,23*R*)-26,27-dinorergost-5-ene-3,22,23-triol (31)

Diol **30** (7.4 mg, 0.018 mmol) and *p*-toluenesulfonic acid (0.283 mL of a 0.0125 M solution in 1,4 dioxane, 0.0354 mmol) were heated in 1 mL of 1,4-dioxane:water (5:1) for 4 h at 70°C. The 1,4 dioxane was removed in vacuo and the residue was diluted with ether, washed several times with water, dried ($MgSO_4$), and evaporated under vacuum. The crude material was purified by flash chromatography (elution with 0–10% methanol – chloroform) to give 5 mg (69%) of **31**, which was recrystallized from methanol – ethyl acetate: R_f 0.10 (25% ethyl acetate – benzene); mp 215–217°C (lit. (21) mp 219–221°C); ^{1}H NMR (200 MHz) δ: 5.36 (m, 1 H), 3.59–3.42 (m, 3 H), 2.30–2.23 (m, 2 H), 1.02 (d, *J* = 6.9 Hz, 3 H),

1.02 (s, 3 H) 0.93 (d, $J = 6.2$ Hz, 3 H), 0.87 (d, $J = 6.8$ Hz, 3 H), 0.71 (s, 3 H).

Acknowledgements

We thank the Natural Sciences and Engineering Research Council of Canada (NSERC) for financial support. D.L.B. gratefully acknowledges receipt of an NSERC Postgraduate Scholarship, a Ralph Steinhauer Award of Distinction, and an Honorary Killam Fellowship. We also thank Dr. R. Yamdagni, Ms. D. Fox, and Ms. Q. Wu for assistance in obtaining certain spectra.

References

1. (*a*) J. Redpath and F.J. Zeelen. Chem. Soc. Rev. **12**, 75 (1983); (*b*) D.M. Piatak and J. Wicha. Chem. Rev. **78**, 199 (1978).
2. M.D. Grove, G.F. Spencer, W.K. Rohwedder, N. Mandava, J.F. Worley, J.D. Warthen, Jr., G.L. Steffens, J.L. Flippen-Anderson, and J.C. Cook, Jr. Nature (London), **281**, 216 (1979).
3. H. G. Cutler, T. Yokota, and G. Adam (*Editors*). Brassinosteroids: chemistry, bioactivity and applications. ACS Symp. Ser. 474, Washington, D.C. 1991.
4. T.G. Back. *In* Studies in natural products chemistry. Vol. 16. *Edited by* Atta-ur-Rahman. Elsevier, Amsterdam. 1995. pp. 321–364, and references cited therein.
5. (*a*) S. Fung and J.B. Siddall. J. Am. Chem. Soc. **102**, 6580 (1980); (*b*) S. Takatsuto, N. Yazawa, M. Ishiguro, M. Morisaki, and N. Ikekawa. J. Chem. Soc. Perkin Trans. 1, 139 (1984); (*c*) S. Takatsuto and N. Ikekawa. J. Chem. Soc. Perkin Trans. 1, 439 (1984); (*d*) J. Chem. Soc. Perkin Trans. 1, 2269 (1986); (*e*) Y. Hirano, S. Takatsuto, and N. Ikekawa. J. Chem. Soc. Perkin Trans. 1, 1775 (1984); (*f*) S. Takatsuto. J. Chem. Soc. Perkin Trans. 1, 1833 (1986); (*g*) K. Mori and T. Takeuchi. Liebigs Ann. Chem. 815 (1988); (*h*) K. Mori, M. Sakakibara, and K. Okada. Tetrahedron, **40**, 1767 (1984); (*i*) K. Mori, M. Sakakibara, Y. Ichikawa, H. Ueda, K. Okada, T. Umemura, G. Yabuta, S. Kuwahara, M. Kondo, M. Minobe, and A. Sogabe. Tetrahedron, **38**, 2099 (1982); (*j*) M. Aburatani, T. Takeuchi, and K. Mori. Agric. Biol. Chem. **50**, 3043 (1986); (*k*) M. Sakakibara and K. Mori. Agric. Biol. Chem. **48**, 745 (1984); (*l*) Agric. Biol. Chem. **47**, 1407 (1983); (*m*) T.G. Back, P.G. Blazecka, and M.V. Krishna. Tetrahedron Lett. **32**, 4817 (1991); (*n*) T.G. Back and M.V. Krishna. J. Org. Chem. **56**, 454 (1991); (*o*) H. Hayami, M. Sato, S. Kanemoto, Y. Morizawa, K. Oshima, and H. Nozaki. J. Am. Chem. Soc. **105**, 4491 (1983); (*p*) V.A. Khripach, V.N. Zhabinskiy, and V.K. Olkhovick. Tetrahedron Lett. **31**, 4937 (1990); (*q*) V.A. Khripach. Pure Appl. Chem. **62**, 1319 (1990); (*r*) W.-S. Zhou and L.-F. Huang. Tetrahedron, **48**, 1837 (1992); (*s*) W.-S. Zhou, B. Jiang, and X. Pan. Tetrahedron, **46**, 3173 (1990); (*t*) S. Zheng-Wu and Z. Wei-Shan. J. Chem. Soc. Perkin Trans. 1, 1765 (1990); (*u*) W.-S. Zhou. Pure Appl. Chem. **61**, 431 (1989); (*v*) B.G. Hazra, P.L. Joshi, B.B. Bahule, N.P. Argade, V.S. Pore, and M.D. Chordia. Tetrahedron, **50**, 2523 (1994); (*w*) B.G. Hazra, N.P. Argade, and P.L. Joshi. Tetrahedron Lett. **33**, 3375 (1992); (*x*) T. Takahasi, A. Ootake, H. Yamada, and J. Tsuji. Tetrahedron Lett. **26**, 69 (1985).
6. T.G. Back, P.G. Blazecka, and M.V. Krishna. Can. J. Chem. **71**, 156 (1993).
7. H.B. Henbest and R.A.L. Wilson. J. Chem. Soc. 1958 (1957).
8. (*a*) A.H. Hoveyda, D.A. Evans, and G.C. Fu. Chem. Rev. **93**, 1307 (1993); (*b*) A.S. Rao. *In* Comprehensive organic synthesis. Vol. 7. *Edited by* B.M. Trost. Pergamon Press, Oxford. 1991. Chap. 3.1; (*c*) A.S. Rao, S.K. Paknikar, and J.G. Kirtane. Tetrahedron, **39**, 2323 (1983); (*d*) K.B. Sharpless and T.R. Verhoeven. Aldrichimica Acta, **12**, 63 (1979).
9. (*a*) R.A. Johnson and K.B. Sharpless. *In* Comprehensive organic synthesis. Vol. 7. *Edited by* B.M. Trost. Pergamon Press, Oxford. 1991. Chap. 3.2; (*b*) B.E. Rossiter. *In* Asymmetric Synthesis. Vol. 5. *Edited by* J.D. Morrison. Academic Press, Orlando, Fla. 1985. Chap. 7; (*c*) M.G. Finn and K.B. Sharpless. *In* Asymmetric Synthesis. Vol. 5. *Edited by* J.D. Morrison. Academic Press, Orlando, Fla. 1985. Chap. 8.
10. M.L. Sassiver and J. English. J. Am. Chem. Soc. **82**, 4891 (1960).
11. P. Chamberlain, M.L. Roberts, and G.H. Whitham. J. Chem. Soc. (B), 1374 (1970).
12. P. Chautemps and J.-L. Pierre. Tetrahedron **32**, 549 (1976).
13. B.E. Rossiter, T.R. Verhoeven, and K.B. Sharpless. Tetrahedron Lett. 4733 (1979).
14. E.D. Mihelich. Tetrahedron Lett. 4729 (1979).
15. A.S. Narula. Tetrahedron Lett. **22**, 2017 (1981).
16. E. Erdik. Tetrahedron, **40**, 641 (1984).
17. E.J. Corey and R.A.E. Winter. J. Am. Chem. Soc. **85**, 2677 (1963).
18. M.P. Zimmerman, H. Li, W.L. Duax, C.M. Weeks, and C. Djerassi. J. Am. Chem. Soc. **106**, 5602 (1984).
19. L. Dai, B. Lou, Y. Zhang, and G. Guo. Tetrahedron Lett. **27**, 4343 (1986).
20. R. Monahan, D. Brown, L. Waykole, and D. Liotta. *In* Organoselenium chemistry. *Edited by* D. Liotta. Wiley, New York. 1987. Chap. 4.
21. S. Takatsuto, N. Yazawa, and N. Ikekawa. Phytochemistry, **23**, 525 (1984).
22. W.C. Still, M. Kahn, and A. Mitra. J. Org. Chem. **43**, 2923 (1978).
23. S.D. Young, and W.T. Borden. J. Org. Chem. **45**, 724 (1980).
24. B. Méchin and N. Naulet. J. Organomet. Chem. **39**, 229 (1972).
25. W.A. Kinney, M.J. Coghlan, and L.A. Paquette. J. Am. Chem. Soc. **107**, 7352 (1985).
26. W.G. Kofron and L.M. Baclawski. J. Org. Chem. **41**, 1879 (1976).
27. S.C. Watson and J.F. Eastham. J. Organomet. Chem. **9**, 165 (1967).
28. M.R. Winkle, J.M. Lansinger, and R.C. Ronald. J. Chem. Soc. Chem. Commun. 87 (1980).
29. (*a*) J.A. Steele and E. Mosettig. J. Org. Chem. **28**, 571 (1963); (*b*) J.J. Pappas, W.P. Keaveney, E. Gancher, and M. Berger. Tetrahedron Lett. 4273 (1966); (*c*) R.F.N. Hutchins, M.J. Thompson, and J.A. Svoboda. Steroids, **15**, 113 (1970); (*d*) W.G. Salmond and M.C. Sobala. Tetrahedron Lett. 1695 (1977); (*e*) J.R. Wiersig, N. Waespe-Sarcevic, and C. Djerassi. J. Org. Chem. **44**, 3374 (1979).
30. K. Hiroi and S. Sato. Synthesis, 635 (1985).
31. R.D. Walkup, G.D. Anderson, and C. Djerassi. Tetrahedron Lett. 767 (1979).
32. Y. Fujimoto, M. Kimura, F.A.M. Khalifa, and N. Ikekawa. Chem. Pharm. Bull. **32**, 4372 (1984).
33. V.A. Khripach, V.N. Zhabinskii, and E.V. Zhernosek. Tetrahedron Lett. **36**, 607 (1995).

5-Perfluoroalkyldipyrromethanes and porphyrins derived therefrom

Tilak P. Wijesekera

Abstract: Acid-catalyzed condensation of pyrrole and perfluoroalkyl aldehydes produced, in a single step, α,β-unsubstituted 5-perfluoroalkyldipyrromethanes, which were isolated and characterized for the first time. These dipyrromethanes were used as the key intermediates in the synthesis of *trans*-perfluroalkylporphyrins as well as *meso*-tetrakis(perfluoroalkyl)porphyrins. The two-step procedure described here provides access to a wide variety of porphyrins with *trans* perfluoroalkyl groups.

Key words: 5-perfluoroalkyldipyrromethanes, perfluoroalkylporphyrins, electron-deficient porphyrins.

Résumé : La condensation acido-catalysée du pyrrole et des aldéhydes perfluoroalkylés produit en une seule étape les 5-perfluoroalkyldipyrrométhanes non substitués en positions α,β que l'on a isolés et caractérisés pour la première fois. Ces dipyrrométhanes sont utilisés comme intermédiaires clés dans la synthèse des *trans* perfluoroalkylporphyrines et des *méso*-tétrakis(perfluoroalkyl)porphyrines. Le procédé en deux étapes que l'on décrit dans cette publication donne accès à une grande variété de porphyrines avec le groupe perfluoroalkyle en position *trans*.

Mots clés : 5-perfluoroalkyldipyrrométhanes, perfluoroalkylporphyrines, porphyrines pauvres en électrons.

[Traduit par la rédaction]

Introduction

Electron deficiency created at the metal center has been shown to increase the catalytic activity of porphyrinatoiron(III) complexes towards hydroxylation of alkanes by oxygen and other oxidants (1). The electron-withdrawing groups most commonly employed at the *meso* positions are the perhalophenyls, because of the ease of accessibility of *meso*-tetraphenylporphyrins by the direct condensation of pyrrole and the corresponding aldehyde (2), and the ease of functionalization of the β positions of a preformed *meso*-tetraphenylporphyrin (3). However, due to the practical implications of the high cost (and the high mass per iron center) of catalysts carrying perfluorophenyl groups, our attention was directed towards the synthesis of metalloporphyrin systems having perfluoroalkyl groups at the *meso* positions. We report here a general synthetic route to *trans*-perhaloalkylporphyrins (**5**), using the key intermediates, 5-perfluoroalkyldipyrromethanes (**3**), which were prepared and isolated for the first time (4) by the direct condensation of pyrrole and the appropriate perfluoroalkyl aldehyde.

Results and discussion

Although acid-catalyzed co-condensation of pyrrole and an aldehyde produces *meso*-aryl or *meso*-alkyl porphyrins in good yields (5, 6), attempts to prepare *meso*-tetrakis(trifluoromethyl)porphyrin, even under harsher reaction conditions, lead only to very small quantities of porphyrin. However, the reaction of 2 equivalents of pyrrole (**1**) and one equivalent of trifluoroacetaldehyde (**2**, $R^1 = CF_3$; as the methyl or ethyl hemiacetal) in refluxing THF and concentrated HCl (50:1) produced the 5-trifluoromethyldipyrromethane **3***a* in yields up to 70% (see Scheme 1). Reaction times greater than 2–3 h and (or) stronger acid conditions generally led to increased quantities of oxidized and (or) polymerized by-products, but no porphyrin could be detected. Substitution of heptafluorobutyraldehyde (**2**, $R^1 = C_3F_7$; as the hydrate) for trifluoroacetaldehyde in the above condensation reaction gave the corresponding 5-heptafluoropropyldipyrromethane **3***b* in up to 50% yield. The purified dipyrromethanes were found to be stable in the refrigerator for several months.

5-Perfluoroalkyldipyrromethanes **3***a* and **3***b* were co-condensed separately with trifluoroacetaldehyde, heptafluorobutyraldehyde, and pentafluorobenzaldehyde, in $CHCl_3$ under acid conditions, to give, after oxidation with 2,3-dichloro-5,6-dicyano-1,4-benzoquinone (DDQ), the electron-deficient porphyrins **5***a–d*. Of the several acid catalysts that were previously employed for such condensations (7), montmorillonite K10 clay (8) not only gave the best isolated yields of the porphyrins, but also facilitated the purification procedure, since most of the polypyrrolic impurities were adsorbed on the clay. Condensation of the dipyrromethanes with perfluoroalkyl aldehydes **4***b* and **4***c* required longer reaction times (15–20 h) at reflux temperature, and the yields of the porphyrins were lower (5–10%), compared with the condensations with pentafluorobenzaldehyde **4***a*.

The two-step procedure described here provides, for the first time, a general method for the synthesis of porphyrins that carry perfluoroalkyl groups at opposite *meso* positions while the other two *meso* positions may have the same or different perhalocarbyl groups. As such, it differs from the recently published syntheses (9) of *meso*-tetrakis(perfluoroalkyl)porphyrins, where 2-(hydroxymethyl)pyrroles are subjected to tetramerization followed by cyclization. This allows

Received May 16, 1996.

T. Wijesekera.[1] Chemicals Technology Division, Research & Development Department, Sun Company Inc., P.O. Box 1135, Marcus Hook, PA 19061, U.S.A.

[1] Telephone: (610) 859-1782. Fax: (610) 859-1645.

Scheme 1.

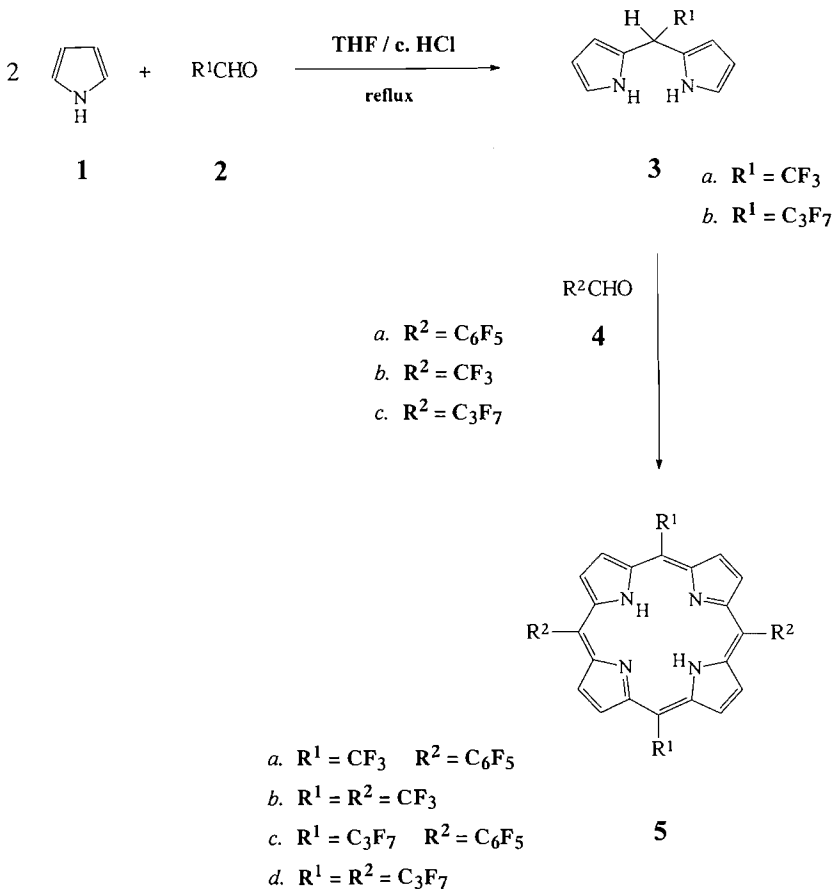

us to compare the effect of perhaloalkyl groups on the catalytic activity of porphyrinatoiron(III) systems with that of other electron-withdrawing groups. Iron insertion and β-halogenation of the *meso*-perfluorocarbylporphyrins **5***a–d* were carried out using modifications of literature procedures (2) and the catalytic studies using such complexes have been reported elsewhere (10).

Experimental

Methods and materials

Tetrahydrofuran chloroform and pyrrole were dried and distilled under argon just prior to use. Trifluoroacetaldehyde, methyl hemiacetal, and heptafluorobutyraldehyde hydrate (both technical grade) were purchased from Lancaster Synthesis Inc. and pentafluorobenzaldehyde was purchased from Aldrich Chemical Co. and used without further purification. Column chromatography was carried out on neutral alumina (Fisher A950/60–325 mesh) using the solvents indicated. Absorption spectra of the porphyrins were obtained using a Hewlett–Packard model 8452A diode array spectrophotometer. ^{1}H and ^{19}F NMR spectra were recorded on a Bruker MSL-300 instrument. Fast Atom Bombardment (FAB) high-resolution mass spectral analyses were carried out at the analytical laboratories of M-SCAN Inc. of West Chester, Pennsylvania, using a VG Analytical ZAB 2SE high-field mass spectrometer. Microanalyses were performed at Oneida Research Services Inc. of Whitesboro, New York. Melting points of the new compounds were obtained using a Fisher–Johns hot-stage melting point apparatus, and are uncorrected.

5-Trifluoromethyldipyrromethane (*3a*)

Pyrrole (3.35 g, 50 mmol), trifluoroacetaldehyde methyl hemiacetal (3.58 g, 27.5 mmol), and concentrated hydrochloric acid (2 mL) were refluxed in degassed tetrahydrofuran (100 mL) in an argon atmosphere for 2 h. The reaction mixture was cooled, then neutralized with $NaHCO_3$; the organic layer was diluted with $CHCl_3$ and washed with saturated $NaHCO_3$ and water. The dark orange-colored oil remaining after removal of the solvent was repeatedly extracted with low-boiling petroleum ether to separate the desired dipyrromethane product from the colored impurities. Petroleum ether was removed and the resulting oil was chromatographed on neutral alumina using CH_2Cl_2–hexane (1:1) for elution. The eluate was evaporated to dryness when the pure dipyrromethane solidified. The isolated yields varied between 50 and 70% depending on the purity of the commercially available technical grade trifluoroacetaldehyde methyl hemiacetal, anaerobic conditions of the reaction, and the method and extent of neutralization of the acid catalyst prior to isolation; mp 63–65°C; ^{1}H NMR ($CDCl_3$, 300 MHz) δ (ppm): 7.96 (bs, 2H), 6.73 (s, 2H), 6.24 (m, 4H), 4.80 (q, 1H); ^{19}F NMR ($CDCl_3$, 282 MHz) δ (ppm): −68.05 (d). Accurate Mass calcd. for $C_{10}H_9N_2F_3$: 214.0718; found by HRMS (FAB): 214.0712 (ΔM = −2.7 ppm). Anal. calcd. for $C_{10}H_9N_2F_3$: C 56.08, H 4.24, N 13.08; found: C 55.88, H 4.20, N 12.95.

5-Heptafluoropropyldipyrromethane (*3b*)
This was prepared in 35–50% yields by reacting pyrrole and heptafluorobutyraldehyde, hydrate under conditions similar to those described above. Due to the high solubility of colored impurities in petroleum ether, prepurification prior to chromatography was avoided. This resulted in product purities of ~95% (GC) after one filtration through neutral alumina (CH_2Cl_2–hexane 1:1 as the eluent) and was used for the porphyrin syntheses without further purification. Analytical samples were prepared by the slow chromatography of the above material on neutral alumina using CH_2Cl_2–hexane 1:2 as the eluent; mp 64–66°C; ^{1}H NMR ($CDCl_3$, 300 MHz), δ (ppm): 8.12 (bs, 2H), 6.75 (s, 2H), 6.23 (s, 2H), 6.19 (q, 2H), 4.92 (t, 1H); ^{19}F NMR ($CDCl_3$, 282 MHz) δ (ppm): −82.86 (m, 3F), −115.21 (m, 2F), −127.11 (t, 2F). Accurate Mass calcd. for $C_{12}H_9N_2F_7$: 314.0654; found by HRMS (FAB): 314.0651 (ΔM = −0.9 ppm). Anal. calcd. for $C_{12}H_9N_2F_7$: C 45.87, H 2.89, N 8.92; found: C 46.10, H 3.02, N 8.70.

5,15-Bis(pentafluorophenyl)-10,20-bis(trifluoromethyl)porphyrin (*5a*)
Trifluoromethyldipyrromethane (**3***a*; 1.07 g, 5 mmol, in 10 mL $CHCl_3$) and pentafluorobenzaldehyde (**4***a*; 989 mg, 5 mmol, in 10 mL $CHCl_3$) were added to degassed $CHCl_3$ (200 mL) containing activated montmorillonite K-10 (7.5 g) and stirred at room temperature under argon for 24 h. A solution of DDQ (1 g) in benzene (60 mL) was added while gently heating the solution, and heating in air was continued for a further 1 h. The clay was removed by filtration (directly into a solution of DDQ (600 mg) in benzene (20 mL)), and was washed thoroughly with hot $CHCl_3$. The filtrate was refluxed for 90 min, solvent removed, and the residue was redissolved in $CHCl_3$ and chromatographed on neutral alumina using $CHCl_3$ as the eluent. The solution was evaporated to dryness, the residue redissolved in CH_2Cl_2, and the porphyrin crystallized from CH_3OH; yield: 478 mg; 24.1%. UV–VIS, λ_{max} nm (log ε): 406 (5.21), 506 (4.12), 538 (3.95), 586 (3.76), 638 (3.83); ^{1}H NMR ($CDCl_3$, 300 MHz) δ (ppm): 9.71 (d, 4H), 8.91 (d, 4H), −2.73 (bs, 2H), ^{19}F NMR ($CDCl_3$, 282 MHz) δ (ppm): −36.12 (s, 6F), −136.17 (dd, 4F), −150.37 (t, 2F), −160.58 (t, 4F). Accurate Mass calcd. for $C_{34}H_{10}N_4F_{16}$: 778.0650; found by HRMS (FAB): 778.0630 (ΔM = −2.6 ppm). Anal. calcd. for $C_{34}H_{10}N_4F_{16}$: C 52.46, H 1.30, N 7.20; found: C 52.23, H 1.43, N 7.12.

5,10,15,20-Tetrakis(trifluoromethyl)porphyrin (*5b*)
Trifluoromethyldipyrromethane (**3***a*; 2.14 g, 10 mmol), trifluoroacetaldehyde methyl hemiacetal (technical grade, 2.2 g, 16.9 mmol), and activated montmorillonite K-10 clay (10 g) were placed in dry degassed $CHCl_3$ (500 mL) and heated at reflux under argon for 20 h. The reaction mixture was allowed to cool, a solution of DDQ (2 g) in benzene (60 mL) was added, and heating at reflux was continued for a further 1 h. The hot solution was filtered to remove the clay, then washed with hot CH_3OH, and more DDQ (1 g in 60 mL benzene) was added and refluxed for a further 12–15 h. The solvents were removed under reduced pressure, the solid was redissolved in a minimum amount of hot $CHCl_3$, and the solution was passed through neutral alumina. The forerunning porphyrin was eluted with $CHCl_3$, the solvent evaporated under reduced pressure, and the product crystallized from CH_2Cl_2–CH_3OH to isolate 165 mg (5.7%). UV–VIS, λ_{max} nm (log ε): 404 (5.08), 510 (3.94), 544 (3.94), 594 (3.63), 648 (3.92); ^{1}H NMR ($CDCl_3$, 300 MHz) δ (ppm): 9.61 (s, 8H), −2.09 (bs, 2H); ^{19}F NMR ($CDCl_3$, 282 MHz)) δ (ppm): −40.86 (s; 12F). Accurate Mass calcd. for $C_{24}H_{10}N_4F_{12}$: 582.0714; found by HRMS (FAB): 582.0735 (ΔM = 3.6 ppm). Anal. calcd. for $C_{24}H_{10}N_4F_{12}$: C 49.50, H 1.73, N 9.62; found: C49.47, H 1.79, N 9.64.

5,15-Bis(heptafluoropropyl)-10,20-bis(pentafluorophenyl)porphyrin (*5c*)
This porphyrin was prepared by reacting 5-heptafluoropropyldipyrromethane (**3***b*; 3.14 g, 10 mmol) and pentafluorobenzaldehyde (1.96 g, 10 mmol) in refluxing $CHCl_3$ (400 mL) using activated montmorillonite K10 clay (10 g) as the catalyst. Reaction times of 8–10 h were sufficient and the yields varied between 10 and 15%. UV–VIS, λ_{max} nm (log ε): 406 (5.26), 506 (4.09), 540 (3.98), 584 (3.73), 638 (3.92); ^{1}H NMR ($CDCl_3$, 300 MHz) δ (ppm): 9.58 (d, 4H), 8.92 (d, 4H), −2.58 (bs, 2H); ^{19}F NMR ($CDCl_3$, 282 MHz) δ (ppm): −81.22 (br t, 6F), −84.27 (m, 4F), −121.97 (br t, 4F), −138.73 (t, 4F), −153.10 (t, 2F), −163.37 (t, 4F). Accurate Mass calcd. for $C_{38}H_{10}N_4F_{24}$: 978.0522; found by HRMS (FAB): 978.0535 (ΔM = 1.3 ppm). Anal. calcd. for $C_{38}H_{10}N_4F_{24}$: C 46.65, H 1.03, N 5.73; found: C 46.40, H 1.20, N 5.89.

5,10,15,20-Tetrakis(heptafluoropropyl)porphyrin (*5d*)
This porphyrin was prepared by reacting 5-heptafluoropropyldipyrromethane (**3***b*; 1.57 g, 5 mmol) and heptafluorobutyraldehyde, hydrate (technical grade, 1.3 g) in refluxing $CHCl_3$ (200 mL) using activated montmorillonite K10 clay (5 g) as the catalyst, under the conditions described for **5***b*. Purification by chromatography on neutral alumina using CH_2Cl_2–hexane (1:2) as the eluent gave 230 mg (9.3%). UV–VIS, λ_{max} nm (log ε): 404 (5.01), 510 (3.98), 544 (3.91), 592 (3.70), 646 (3.89); ^{1}H NMR ($CDCl_3$, 300 MHz) δ (ppm): 9.50 (s, 8H), −2.30 (bs, 2H); ^{19}F NMR ($CDCl_3$, 282 MHz) δ (ppm): −80.4 (t, 12F), −81.3 (br s, 8F); −119.6 (br s, 8F). Accurate Mass calcd. for $C_{32}H_{11}N_4F_{28}$ (M + H): 983.0537; found by HRMS (FAB): 983.0548 (ΔM = 1.2 ppm). Anal. calcd. for $C_{32}H_{10}N_4F_{28}$: C 39.12, H 1.03, N 5.70; found: C 39.40, H 1.18, N 5.53.

Acknowledgements

This work was supported by the U.S. Department of Energy (Morgantown Energy Technology Center), the Gas Research Institute, and Sun Company. The author wishes to thank Dr. R.A. Merrill for providing the NMR spectroscopic data of the new compounds.

References

1. (*a*) J.E. Lyons and P.E. Ellis, Jr. *In* Metalloporphyrins in catalytic oxidations. *Edited by* R. Sheldon. Marcel Dekker, New York. 1994. pp. 297–324; (*b*) D. Mansuy and P. Battioni. *In* Metalloporphyrins in catalytic oxidations. *Edited by* R. Sheldon. Marcel Dekker, New York. 1994. pp. 99–132; (*c*) B. Meunier. Chem. Rev. **92**, 1411 (1992).
2. T.P. Wijesekera and D. Dolphin. *In* Metalloporphyrins in catalytic oxidations. *Edited by* R. Sheldon. Marcel Dekker, New York. 1994. pp. 193–239.
3. (*a*) T.G. Traylor and S. Tsuchia. Inorg. Chem. **26**, 1338 (1987); (*b*) T.P. Wijesekera, A. Matsumoto, D. Dolphin, and D. Lexa. Angew. Chem. Int. Ed. Engl. **29**, 1028 (1990); (*c*) J.E. Lyons and P.E. Ellis, Jr. Catal. Lett. **8**, 45 (1991); (*d*) J.F. Bartoli, P.

Battioni, W.R. De Foor, and D. Mansuy. J. Chem. Soc. Chem. Commun. 23 (1994).
4. T.P. Wijesekera. Eur. Patent Appln. 0 655 438 A2; (1995); U.S. Patent 5,502,211 (1996).
5. A.D. Adler, F.R. Longo, J. Finarelli, J. Goldmacher, J. Assour, and L. Korsakoff. J. Org. Chem. **32**, 476 (1967).
6. J.S. Lindsey, I.C. Schreiman, H.C. Hsu, P.C. Kearney, and A.M. Marguerettaz. J. Org. Chem. **52**, 827 (1987).
7. (*a*) H. Ogoshi, H. Sugimoto, T. Nishiguchi, T. Watanabe, Y. Matsuda, and Z. Yoshida. Chem. Lett. 29 (1978); (*b*) R. Young and C.K. Chang. J. Am. Chem. Soc. **107**, 898 (1985); (*c*) J.S. Manka and D.S. Lawrence. Tetrahedron Lett. **30**, 6989 (1989); (*d*) A. Osuka, T. Nagata, F. Kobayashi, and K. Maruyama. J. Heterocycl. Chem. **27**, 1657 (1990).
8. (*a*) M. Onaka, T. Shinoda, Y. Izumi, and E. Nolen. Chem. Lett. 117 (1993); (*b*) M. Onaka, T. Shinoda, Y. Izumi, and E. Nolen. Tetrahedron Lett. **34**, 2625 (1993).
9. (*a*) T.P. Wijesekera and R.W. Wagner. U.S. Patent 5,241,062 (1993); (*b*) S.G. DiMagno, R.A. Williams, and M.J. Therien. J. Org. Chem. **59**, 6943 (1994).
10. T.P. Wijesekera, J.E. Lyons, and P.E. Ellis, Jr. Catal. Lett. **36**, 69 (1996).

Selection of new Fe(III)/Fe(II) chelating agents as catalysts for the oxidation of hydrogen sulfide to sulfur by air

Arthur E. Martell, Ramunas J. Motekaitis, Dian Chen, Robert D. Hancock, and Derek McManus

Abstract: The removal and oxidation to sulfur of H_2S, contained in a broad range of sour gas streams including natural gas, by a Fe(III)/Fe(II) chelate system imposes several requirements on the iron chelate that is employed as the redox catalyst. The solution of the catalyst must be neutral or mildly alkaline to efficiently absorb H_2S from the gas passed through the solution. The stability of the iron(III) chelate must be high enough that solid $Fe(OH)_3$ not precipitate at the pH employed. Also the stability of the iron(II) chelate must be high enough to prevent the precipitation of FeS from the reaction mixture. The difference in stabilities of the Fe(III) and Fe(II) chelates must be low enough so that the Fe(III) form can be reduced by HS^- and that the Fe(III) chelate can be regenerated by aeration of the solution at alkaline pH. An unexpected result of this study is that chelating agents designed for high stability of iron(III) chelates do not form satisfactory redox catalysts. Ligands that form suitable iron complexes as catalysts have both oxygen and nitrogen donors. All complexes investigated are readily reoxidized from the ferrous to the ferric chelate by air.

Key words: iron chelates, stability constants, redox potentials, hydrogen sulfide, redox catalysts.

Résumé : L'utilisation d'un système de chélate Fe(III)/Fe(II) pour l'enlèvement et l'oxydation du H_2S (en S) contenu dans une grande variété de sources de gaz aigres impose plusieurs limitations sur la nature du chélate de fer à utiliser comme catalyseur rédox. Pour que le H_2S soit absorbé efficacement à partir du gaz qui barbote dans la solution de catalyseur, il faut que celle-ci soit neutre ou légèrement alcaline. La stabilité du chélate de fer(III) doit être suffisamment élevée pour que le $Fe(OH)_3$ ne précipite pas au pH utilisé. Il faut aussi que la stabilité du chélate de fer(II) soit suffisamment élevée pour prévenir la précipitation du FeS à partir du mélange réactionnel. La différence dans les stabilités des chélates Fe(III) et Fe(II) doit être suffisamment basse pour que la forme Fe(III) puisse être réduite par HS^- et que le chélate Fe(III) puisse être régénéré par aération de la solution à un pH alcalin. Cette étude a conduit à un résultat inattendu; les agents chélatants développés pour donner des chélates de Fe(II) de grand stabilité ne donnent pas de catalyseurs rédox satisfaisants. Les coordinats qui forment des complexes de fer appropriés comme catalyseurs comportent à la fois des oxygènes et des azotes comme donneurs. Tous les complexes examinés peuvent facilement être réoxydés en chélate ferrique sous l'action de l'air.

Mots clés : chélates de fer, constantes de stabilité, potentiels rédox, sulfure d'hydrogène, catalyseurs rédox.

[Traduit par la rédaction]

Introduction

Iron(III) chelate systems are used as catalysts for the removal of H_2S from various gas streams including natural gas and for the oxidation of H_2S to S_8 by air. The reaction is usually carried out in two steps. In the absorber, H_2S is absorbed from the gas by a neutral or mildly alkaline solution of the catalyst and is oxidized by the ferric chelate to sulfur, S_8, which is eventually removed by filtration or other means, while the catalyst is converted to the ferrous form of the complex. The reduced catalyst is then oxidized by air in a separate part of the apparatus, called the oxidizer. In most cases the catalyst used commercially is an iron(III)/iron(II) chelate, and the chelating agent is an aminopolycarboxylic acid, such as NTA (nitrilotriacetic acid), EDTA (ethylenediaminetetraacetic acid), or HEDTA (*N*-hydroxyethylethylenediamine-*N*,*N*′,*N*″-triacetic acid), but such information is for the most part proprietary. The use of iron chelates of aminopolycarboxylic acids as catalysts in this process is covered by a number of patents, only a few of which are cited here (1–3).

Significant operating costs are incurred in the process due to the oxidation and eventual loss of the chelating ligand, which then has to be continuously replenished. The oxidation is probably a radical reaction, and two papers describing this problem in detail have been published (4, 5). This paper describes the chelating agents that form iron(III)/iron(II) chelate systems that promise to be effective catalysts for hydrogen sulfide oxidation. The choice of chelating agent is controlled by the conditions required for carrying out an efficient industrial process. The questions involved in the possible oxidative degradation of the chelating agent are not addressed. Such studies would require a separate, in-depth, study of the oxidation of the iron chelates involved.

Received March 12, 1996.
A.E. Martell,[1] **R.J. Motekaitis, D. Chen, and R.D. Hancock.** Department of Chemistry, Texas A&M University, College Station, Texas 77843-3255, U.S.A.
D. McManus. Wheelabrator Clean Air Systems, Inc., Plainfield, Illinois 60544, U.S.A.

[1] Author to whom correspondence may be addressed. Telephone: (409) 845-2011. Fax: (409) 845-4719.

Fig. 1. Plot of log K_1 for complexes of Fe^{2+} against log K_1 for the corresponding complexes of Fe^{3+}. This type of diagram shows the relative preference of Fe^{+3} for the harder ligands containing negative oxygen donors (○) compared to the softer ligands containing a mixture of nitrogen and oxygen donors (●).

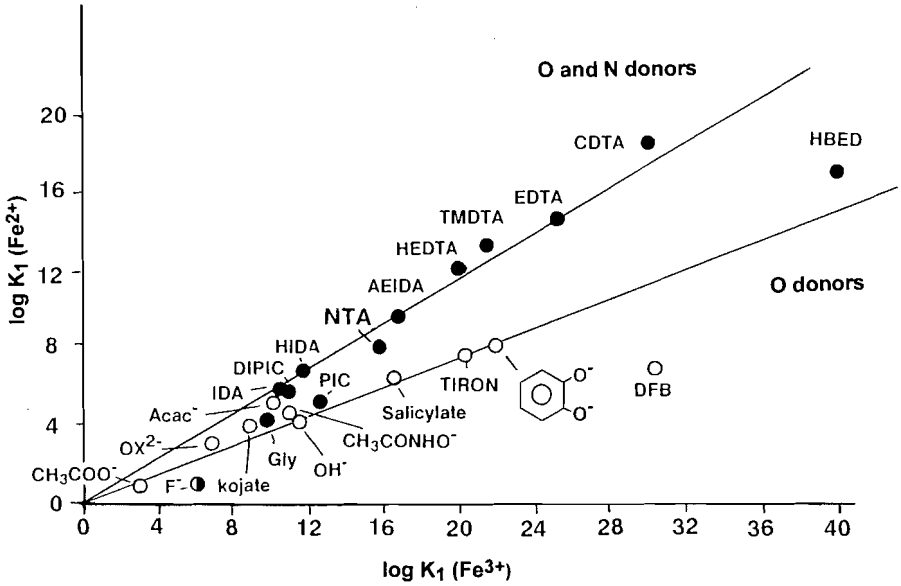

Iron chelating ligands

In Fig. 1 are plotted the log equilibrium constants (formation constants) of 24 ligands with ferric and ferrous ions. The equilibrium constants used are for one mole of ligand per mole of ferric ion or ferrous ion. Since the scales of the ordinate and abscissa are the same, it is seen that a change in the nature and number of donor groups increases the stabilities of the ferric complexes much more than the ferrous complexes. Also, since the Fe^{3+} is a small hard acid (on the HSAB scale) (6, 7) it prefers to coordinate to an oxygen donor ligand with negative oxygen donor groups such as hydroxamate, phenolate, and catecholate donor oxygens. Where the ligand has some of the softer nitrogen donors, the stability of the ferrous chelate increases with basicity, but not as much as that of the ferric chelate. Thus the data in Fig. 1 seem to divide into two groups: those with ligands having only oxygen donors, with a high ratio of Fe(III)/Fe(II) stabilities, and those with both oxygen and nitrogen donors, with a lower ratio of Fe(III)/Fe(II) stability constants. The factors governing the stabilities of metal chelates have been described in detail (8, 9).

An important consideration is the coordination number of the metal ion, since the most stable complexes will be formed when the number of donor atoms of a ligand matches the requirement of the metal ion, provided of course that the donor atoms are sterically available to combine with the metal ion. Most of the complexes of Fe(II) and Fe(III) are octahedral, with a coordination number of six for a metal ion, matched by the coordinating donor groups supplied by a hexadentate ligand. Some complexes of the Fe^{3+} ion, however, are seven-coordinate, probably due in part to steric problems associated with the ligand. To appreciate such steric effects, MM calculations were carried out using the MM program SYBYL (10). The Fe(III) was modeled using the TAFF force field (10), with ideal Fe—O and Fe—N bond lengths of 2.00 and 2.38 Å, respectively, and Fe—O and Fe—N force constants of 100 kcal, mol^{-1} $Å^{-1}$. The angle bending force constants around the Fe, which are the N-Fe-N, N-Fe-O, and O-Fe-O angle bending force constants, were set to zero, and the geometry was generated by van der Waals repulsion between the donor atoms. Trial coordinates for the MM calculations were either taken from crystal structures, or were generated with the model-building facility of SYBYL. The resulting coordinates were plotted with PLUTON (11). Figure 2 shows the results of this molecular mechanics simulation of the Fe(III) chelate of EDTA in aqueous solution. The seven-coordinate structure

Fig. 2. Structure of Fe(II) complex of EDTA generated by Molecular Mechanics calculation and the program SYBYL.

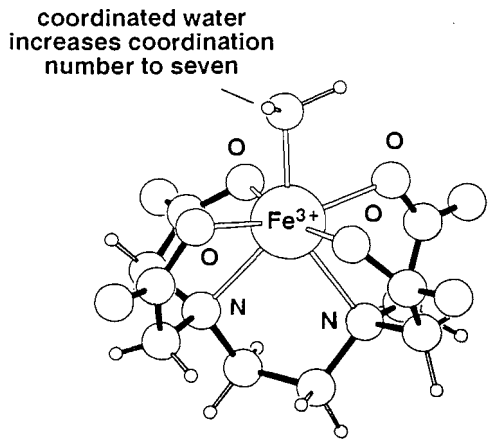

agrees well with the crystal structure described earlier for the Fe(III)–EDTA chelate (12).

Because the absorber solution must be neutral or mildly alkaline, the possible precipitation of FeS and of $Fe(OH)_3$ are important considerations. Since the solubility product of FeS is $10^{-18.1}$ (13), it seems that FeS would precipitate if the concentration of $[Fe^{2+}]$ exceeds $10^{-9.2}$ (assuming $[HS^-]$ to be 10^{-3} M and taking log K_2^a of H_2S as 14.3; the solubility product of FeS is obtained from the displacement equilibrium constant log $[M][H_2S]/[H^+]^2 = 3.0$). This places a lower limit on the stability constant of the ferrous chelate of the chelating agent selected. Similarly, if the solubility product of $Fe(OH)_3$ is $10^{-38.6}$ (14), it can be shown that $Fe(OH)_3$ would precipitate at pH 8.5 if the concentration of ferric ion is greater than $10^{-22.9}$ M. Thus the stability of the Fe(III) chelate must be higher than that which would allow the precipitation of Fe(III) as $Fe(OH)_3$ (in other words the pM ($-\log [M]$) must be higher than 22.9).

In this paper the pM ($-\log [M]$) of a metal ion is calculated for a metal buffer system in which there is an equal amount of the free chelating agent and metal chelate. Most metal chelates described below have 1:1 stoichiometry of metal ion M to chelating agent L; thus the stability constant $K = [ML]/[M][L]$. When $[L] = [ML]$, log $K = -\log [M]$ and the analogy to a hydrogen ion buffer is complete. When the ligand:metal stoichiometry is 2:1 or 3:1, the excess free ligand necessary to form a metal buffer solution is proportionally higher. The excess free ligand used in this paper is an equivalent amount (100%) of that needed to form the metal complex.

The standard reduction potential E_0 of ferric to ferrous ion under standard conditions is +0.770 V (15). Since pM is $-\log [M]$, the half cell for the reduction of iron at pH 8.5 in the presence of 100% excess ligand is

$$[1] \quad \begin{aligned} E &= 0.770 + 0.059\ (\text{pM (Fe(II))} - \text{pM (Fe(III))}) \\ E &= 0.770 - 0.059\ \Delta\ \text{pM} \end{aligned}$$

For the reduction of sulfur, the reaction is

$$S(s) + 2H^+ + 2e^- \rightleftharpoons H_2S$$

and the standard reduction potential is +0.141 V (15).

The above equation is written in terms of HS^- since the latter is virtually the only form at pH 8.5. Since the first dissociation constant of H_2S is $10^{-6.82}$ (14)

$$E = E_0 - 0.0295 \log [H_2S]/[H^+]^2$$

$$[H_2S] = 10^{6.82}[H^+][HS^-]$$

$$E = 0.141 - 0.0295 \log 10^{6.82}\ [HS^-]/10^{-8.5}$$

Assume that $[HS^-]$ is approximately 10^{-3} M, a reasonable concentration.

$$E = 0.141 - 0.0295\ (6.82 - 3 + 8.5)$$

$$E = -0.223$$

For the overall reaction the reduction potential of the iron chelate and the oxidation potential of HS^- are employed:

$$[2] \quad \begin{aligned} E &= 0.770 - 0.059\ \Delta\ \text{pM} + 0.223 \\ E &= 0.993 - 0.059\ \Delta\ \text{pM} \end{aligned}$$

For the two-electron redox reaction at pH 8.5 the conditional equilibrium constant may now be calculated.

$$[3] \quad \log K_c = (0.993 - 0.059\ \Delta\ \text{pM})/0.0295$$

Thus the values of the conditional constants K_c for the equilibrium

$$2Fe^{III}L + HS^- \rightleftharpoons 2Fe^{II}L + H^+ + S(s)$$

were calculated for Tables 1 and 2, for pH 8.5, 100% excess ligand, and assuming the concentration of HS^- to be 10^{-3} M.

The conditions used for Tables 1 and 2, and which apply to the conditional equilibrium constant K_c, specify pH 8.5, which corresponds to the pH used in the Wheelabrator "Low-Cat" process. The use of a much lower pH, such as 7.0, used in the Dow "Sulferox" system, would result in much lower S^{2-} and OH^- concentrations, and therefore the precipitation of FeS and $Fe(OH)_3$ would occur less readily. Thus, chelating agents labeled in Table 1 with (S) and (OH) and in Table 2 as (borderline), would be satisfactory. The rate of absorption of H_2S, however, would be slower, and a larger absorber vessel would be needed.

Another condition that may be employed for this process is the use of a lesser amount of excess ligand. The reduction of 100% excess ligand to 10% excess would reduce the pM value of the catalyst system by an order of magnitude. This change could be tolerated better in the low pH process, where the demands on the chelating agent to keep the iron in solution are not so stringent.

Because certain aminopolycarboxylate chelates are now in use commercially to form the iron chelate catalysts for this process, it seems appropriate to compare these systems with other aminopolycarboxylates. Table 1 compares 10 aminopolycarboxylates for which the stabilities meet the requirements for the oxidation of H_2S to S_8 at pH 8.5 and 10^{-3} M $[HS^-]$. The structures and names of the ligands are indicated in Plate 1. It is seen that the reaction is favorable for all ligands listed in Table 1 with conditional constants that vary between 10^8 and 10^{24}. It is seen that TMDTA and EGTA are unsatisfactory ligands because they do not prevent the precipitation of $Fe(OH)_3$ at pH 8.5. Also, NTA calculates out as a marginal ligand with respect to both FeS and $Fe(OH)_3$ precipitation. The fact that it is being successfully used in industrial applications indicates that the operating conditions are at least a little different from those used in the calculations. In some cases an additive is used to increase the complexation of iron(III).

A larger variety of chelating agents are listed in Table 2, including ligands with very basic oxygen donors designed to form very stable Fe(III) chelates. The structures and names of these ligands are given in Plate 2. It is noted that the stabilities of the Fe(II) complexes of four of these ligands have not been measured. Their values are estimated (extrapolated) from the stability constants of other transition divalent metal complexes with the same ligands. The accuracy of this approximation is considered adequate. It is seen in Table 2 that the stabilities of the Fe(III) chelates of TETA and ACAC are not high enough to prevent precipitation of $Fe(OH)_3$. The most

Plate 1.

Aminopolycarboxylic Acids: Names, Acronyms, Formulas

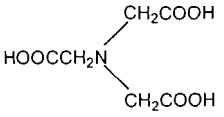

Nitrilotriacetic acid, H_3L (NTA)

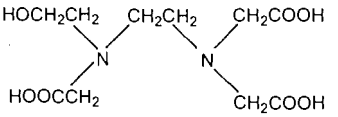

N(-2-hydroxyethyl)ethylenediamine-N,N',N'-triacetic acid, H_3L (HEDTA)

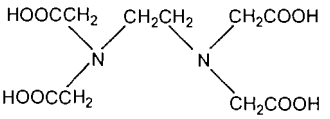

Ethylenedinitrilotetraacetic acid, H_4L (EDTA)

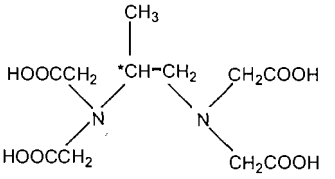

Racemic-propylenediaminetetraacetic acid, H_4L (PDTA)

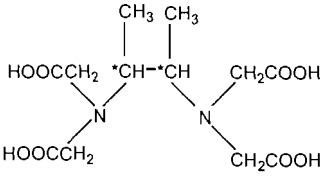

Racemic-1,2-dimethylethylenediamine-tetraacetic acid, H_4L (DMEDTA)

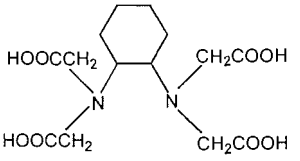

trans-1,2-diaminocyclohexanetetraacetic acid, H_4L (CDTA)

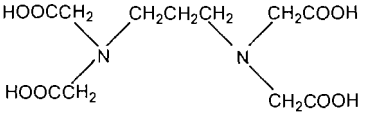

Trimethylenediminetetraacetic acid H_4L (TMDTA)

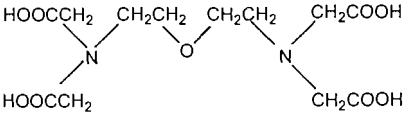

Oxybis(ethylenenitrilo)tetraacetic acid H_4L (EEDTA)

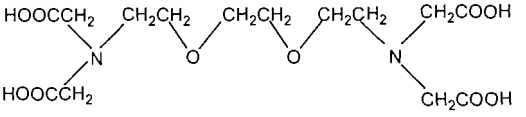

Ethylenebis(oxyethylenenitrilo)tetraacetic acid, H_4L (EGTA)

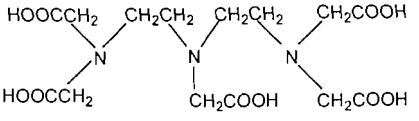

Diethylenetriaminepentaacetic acid, H_5L (DTPA)

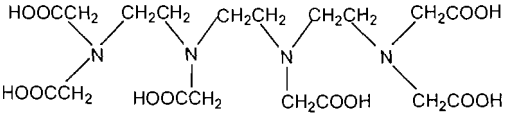

Triethylenetetraminehexaacetic acid, H_6L (TTHA)

Plate 2.

Miscellaneous Chelating Agents: Names, Acronyms, Formulas

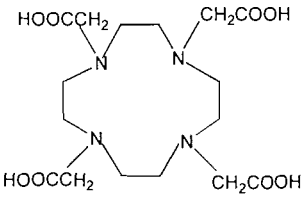

1,4,7,10-tetraazacyclododecane-N,N',N'',N'''-tetraacetic acid, H_4L (DOTA)

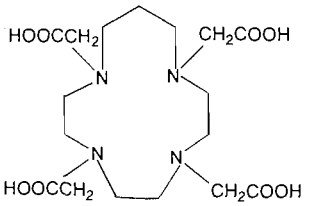

1,4,7,10-tetraazacyclotridecane-N,N',N'',N'''-tetraacetic acid, H_4L (TRITA)

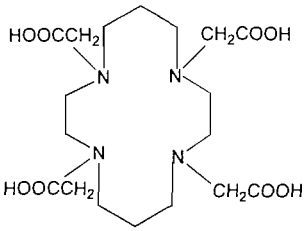

1,4,8,11-tetraazacyclotetradecane-N,N',N'',N'''-tetraacetic acid, H_4L (TETA)

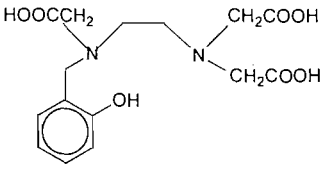

N-(2-hydroxybenzylethylenediamine-N,N',N'-triacetic acid, H_4L (HBET)

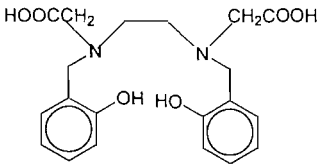

N,N'-bis(20hydroxybenzyl)ethylenediamine-N,N'-diacetic acid, H_4L (HBED)

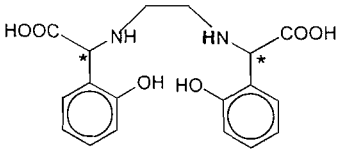

Racemic-ethylene-N,N'-bis(2-hydroxyphenylglycine, H_4L (EHPG)

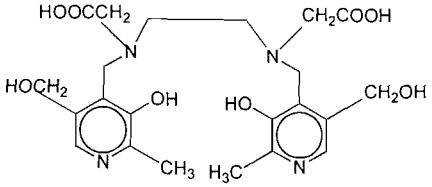

N,N'-bis(2-methyl-3-hydroxy-5-hydroxymethyl 4-pyridylmethyl)ethylenediamine-N,N'-diacetic cid, H_4L (PLED

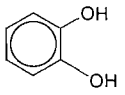

1,2-dihydroxybenzene, catechol H_2L (CAT)

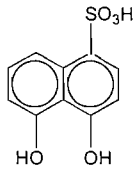

1,8-dihydroxynaphthalene-4-sulfonic acid H_3L (DHNS)

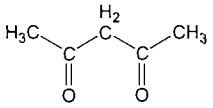

Acetylacetone, 2,4-pentanedione HL (ACAC)

Table 1. Stability constants of Fe(II) and Fe(III) chelates, pM's, and log K_c's[a] for the aminopolycarboxylic acids.

	Log K_{ML}[b]		pM[c]				
	Fe^{2+}	Fe^{3+}	Fe^{2+}	Fe^{3+}	ΔpM	$E(Fe^{3+} \rightarrow Fe^{2+})$[d]	Log K_c[a]
NTA	8.05	15.9	8.0 (S)[e]	20.8 (OH)[e]	12.8	0.013	7.98
HEDTA	12.2	19.8	10.9	23.7	12.8	0.013	7.98
EDTA	14.30	25.10	12.6	25.2	12.6	0.025	8.38
PDTA	15.50	26.0	13.1	23.6	10.5	0.149	12.58
DMEDTA	17.8	28.05	14.0	25.0	11.0	0.119	11.56
CDTA	18.90	30.00	15.0	26.2	11.2	0.107	11.16
TMDTA	13.46	21.61	11.4	19.6 (OH)[e]	8.2	0.285	17.17
EEDTA	14.20	24.7	12.7	23.2	10.5	0.149	12.58
EGTA	11.20	20.50	10.4	19.1 (OH)[e]	8.7	0.255	16.16
DTPA	16.40	28.00	14.2	25.6	11.4	0.096	10.78
TTHA	17.00	26.80	18.9	23.7	4.8	0.486	23.97

[a]K_c are the conditional constants for the reaction 2 $Fe^{III}L + HS^- \rightleftharpoons 2Fe^{II}L + H^+ + S(s)$ at pH 8.5 and HS^- taken as 10^{-3} M.
[b]Log K_{ML} taken from NIST Critical Stability Constant Database No. 46.
[c]For 100% excess ligand, 10^{-2} M metal chelate.
[d]E for reduction of ferric to ferrous ions taken from pM values of the metal ions and the equation $E = 0.770 - 0.059 \log [Fe^{2+}]/[Fe^{3+}]$.
[e](S) and (OH) indicate propensity for FeS and $Fe(OH)_3$ formation, respectively.

Table 2. Stability constants of Fe(II) and Fe(III) chelates, pM's, and log K_c's[a] for other ligands.

	Log K_{ML}[b]		pM[c]				
	Fe^{2+}	Fe^{3+}	Fe^{2+}	Fe^{3+}	ΔpM	$E(Fe^{3+} \rightarrow Fe^{2+})$[d]	log K_c[a]
DOTA	20.22	39.40	16.3	35.4	19.1	−0.360	−4.63 (weak)
TRITA	17.6	27.50	13.5	23.4	9.9	+0.184	13.76
TETA	13.32	26.50	9.5	22.6 (OH)[e]	13.1	−0.005	7.37
HBET	15.0 (est.)	32.02	10.9	27.9	17.0	−0.236	−0.44 (weak)
HBED	22.7 (est.)	39.01	15.7	32.1	16.4	−0.200	0.78 (weak)
EHPG	20.6 (est.)	35.54	14.2	29.1	14.9	−0.111	3.89 (borderline)
PLED	17.9 (est.)	30.80	13.7	26.6	12.9	+0.007	7.78
CAT	8.3	20.4	4.4 (S)[e]	25.3	20.9	−0.466	−8.22 (weak)
DHNS	8.99	19.84	7.0 (S)[e]	25.5	18.5	−0.324	−3.41 (weak)
ACAC	5.07	9.30	6.9 (S)[e]	21.3 (OH)[e]	14.4	−0.082	4.77

[a]K_c are the conditional constants for the reaction 2 $Fe^{III}L + HS^- \rightleftharpoons 2Fe^{II}L + H^+ + S(s)$ at pH 8.5 and HS^- taken as 10^{-3} M.
[b]Log K_{ML} taken from NIST Critical Stability Constant Database No. 46.
[c]For 100% excess ligand, 10^{-2} M metal chelate.
[d]E for reduction of ferric to ferrous ions taken from pM values of the metal ions and the equation $E = 0.770 - 0.059 \log [Fe^{2+}]/[Fe^{3+}]$.
[e](S) and (OH) indicate propensity for FeS and Fe(OH)3 formation, respectively.

remarkable feature of the data in Table 2 is that the chelating agents that form very stable Fe(III) chelates are not suitable for the oxidation of H_2S to S_8. Any ligand that produces a conditional constant lower than 10^4 is considered too weak an oxidizing agent. This behavior may be rationalized on the basis of the fact that the Fe(III) chelate is very stable, compared to the Fe(II) chelate, and the metal ion therefore prefers to remain in the ferric form. A successful ligand is one that stabilizes the Fe(II) form sufficiently so that it is only moderately less stable than the Fe(III) chelate. The best measure of the relative effects of the ligand on these metal ions is the difference in pM values, since pM takes into account environmental considerations such as pH and concentration.

The reoxidation of the ferrous to the ferric chelate by air, which takes place in the oxidizer vessel, involves the following reaction:

$$4Fe^{II}L + O_2 + 4H^+ \rightleftharpoons 4Fe^{III}L + 2H_2O$$

and the equilibrium constant, in the form of a concentration constant, is

$$[4] \quad K' = \frac{[Fe^{III}L]^4}{[Fe^{II}L]^4[H^+]^4 P_{O_2}}$$

where all solution species are expressed as molar concentration, except the concentration of O_2 which is expressed as partial pressure.

If one takes pH 8.5 as the operating pH and employs 0.20 as the partial pressure of oxygen in air, and substitutes these values in eq. [4], one obtains an equation for the corresponding conditional constant.

$$K'([H^+]^4)0.2 = \frac{[Fe^{III}L]}{[Fe^{II}L]}$$

$$K'_c = K'(10^{-34})(0.2) = \frac{[Fe^{III}L]}{[Fe^{II}L]}$$

$$\log K'_c = \log K' - 34.7 = \log \frac{[Fe^{III}L]}{[Fe^{II}L]}$$

The emf corresponding to the overall reaction can be considered as the sum of the emf's of the half reactions for the oxidation of the iron chelate and the reduction of O_2. For the latter,

$$O_2 + 4H^+ + 4e \rightarrow 2H_2O$$

E is +1.229 V for unit molality of H^+ and unit partial pressure of O_2 (15).

$$E = 1.229 - 0.01479 \log 1/(0.2) - 0.059\ (8.5) = 0.727$$

For the whole reaction, E'_c is therefore:

$$[5] \quad E'_c = E(Fe^{II}L \rightarrow Fe^{III}L) + 0.727 \text{ V}$$

Therefore, K'_c can be expressed by the following:

$$[6] \quad \log K'_c = E'_c/0.01479$$

The values of log K'_c are given in Table 3 for oxidation of the ferrous chelates of the 21 systems described in Tables 1 and 2. It seems that, for all the chelate systems considered, whether or not they are satisfactory for the oxidation of H_2S in the absorber, the equilibrium constants for the oxidation reactions are very positive, and the oxidation of all the ferrous chelates to the ferric form is highly favored. The authors have checked the use of several iron chelates as catalysts in the oxidation of H_2S to S by air and have not encountered any difficulties due to slow kinetics. Although all phases of the reaction were adequately rapid, the reoxidation of the ferrous to the ferric chelate seemed to be the slower part of the process. The slowest part of the reoxidation is the dissolution of oxygen from air to the aqueous phase. This part of the process may be maximized by the use of an appropriate gas–liquid contacting device.

Although all the constants listed in Table 3 are highly positive, they do not provide information on the kinetics of reaction, except that the oxidation step is highly favored.

Table 3. Conditional equilibrium constants[a] for the oxidation of ferrous chelates to the ferric form by air in the presence of 100% excess ligand at pH 8.5.

Ligand	$E(Fe^{2+} \rightarrow Fe^{3+})$[b]	E_c (reaction)	log K'_c[a,c]
NTA	−0.013	0.714	48.3
HEDTA	−0.013	0.714	48.3
EDTA	−0.025	0.762	47.5
PDTA	−0.149	0.578	39.1
DMEDTA	−0.119	0.608	41.1
CDTA	−0.107	0.620	41.9
TMDTA	−0.285	0.442	29.9
EEDTA	−0.149	0.578	39.1
EGTA	−0.255	0.472	31.9
DTPA	−0.096	0.631	42.7
TTHA	−0.486	0.241	16.3
DOTA	+0.360	1.087	73.5
TRITA	−0.184	0.543	36.7
TETA	+0.005	0.732	49.5
HBET	+0.236	0.963	65.1
HBED	+0.200	0.927	62.7
EHPG	+0.111	0.838	56.7
PLED	+0.007	0.720	48.7
CAT	+0.466	1.193	80.7
DHNS	+0.324	1.051	71.06
ACAC	+0.082	0.809	54.7

[a]Equilibrium constant for the reaction: $4Fe^{2+} + O_2 + 4H^+ \rightarrow 4Fe^{3+}L + 2H_2O$ at pH 8.5 and P_{O_2} of 0.20 (air) in the presence of 100% excess ligand.

[b]Oxidation potential of the Fe(II)/Fe(III) chelate couple in the presence of 100% excess ligand.

[c]Calculated from the equation $E_c = 0.059/n \log K_c$.

Conclusions

To form Fe(II)/Fe(III) chelates that are useful as catalysts for the oxidation of H_2S to S, a chelating agent must:

1. Function in the neutral or mildly alkaline pH range to rapidly absorb H_2S gas.
2. Form sufficiently stable Fe(III) chelates that are not converted to $Fe(OH)_3$ at alkaline pH.
3. Form sufficiently stable Fe(II) chelates to prevent precipitation of FeS from alkaline solution.
4. The Fe(III) chelates are generally more stable than the Fe(II) chelates, the ΔpM values varying between 5 and 13 for the amino carboxylic acids and up to 21 for the other ligands. If the Fe(III) chelate is too stable relative to the Fe(II) chelate (ΔpM > 16), the catalyst is ineffective. (The chelate prefers to remain in the Fe(III) state.)
5. Favorable redox reactions are associated with conditional constants that vary over a wide range of numerical values. At pH 8.5 and $[HS^-]$ of 10^{-3} M, the conditional constant may vary between 10^4 and 10^{24}.
6. Because all the ligands listed in Tables 1 and 2, and in Fig. 1, have Fe(III) stability constants that are higher than those of Fe(II), oxidation of the Fe(II) chelate to the Fe(III) chelate by air is a highly favored reaction. While there are ligands that stabilize the ferrous form more than the ferric chelates, such ligands are not useful in this process and are not discussed here.

Glossary

ACAC	acetylacetone, 2,4-pentanedione
AEIDA	*N*-(2-aminoethyl)iminodiacetic acid
CAT	1,2-dihydroxybenzene, catechol
CDTA	*trans*-1,2-diaminocyclohexanetetraacetic acid
CH_3CONHO^-	acethydroxamic acid anion
CH_3COO^-	acetic acid anion
DFB	desferriferrioxamine-B
DHNS	1,8-dihydroxynaphthalene-4-sulfonic acid
DIPIC	dipicolinic acid
DMEDTA	*racemic*-1,2-dimethylethylenediaminetetraacetic acid
DOTA	1,4,7,10–tetraazacyclododecane-*N*,*N*′,*N*″,*N*‴-tetraacetic acid
DTPA	diethylenetriaminepentaacetic acid
EDTA	ethylenedinitrilotetraacetic acid, ethylenediaminetetraacetic acid
EEDTA	oxybis(ethylenenitrilo)tetraacetic acid
EGTA	ethylenebis(oxyethylenenitrilo)tetraacetic acid
EHPG	*racemic*-ethylene-*N*,*N*′-bis(2-hydroxyphenylglycine)
Gly	glycine
HBED	*N*,*N*′-bis(2-hydroxybenzyl)ethylenediamine-*N*,*N*′-diacetic acid
HBET	*N*-(2-hydroxybenzyl)ethylenediamine-*N*,*N*′,*N*′-triacetic acid
HEDTA	*N*-(2-hydroxyethyl)ethylenediamine,*N*,*N*′,*N*′-triacetic acid
HIDA	*N*-(2-hydroxyethyl)iminodiacetic acid
IDA	iminodiacetic acid
Kojate	kojic acid anion
NTA	nitrilotriacetic acid
Ox^{2-}	oxalic acid anion
PDTA	*racemic*-propylenediaminetetraacetic acid
PIC	picolinic acid
PLED	*N*,*N*′-bis(2-methyl-3-hydroxy-5-hydroxymethyl-4-pyridylmethyl)ethylenediamine-*N*,*N*′-diacetic acid
TETA	1,4,8,11-tetraazacyclotetradecane-*N*,*N*′,*N*″,*N*‴-tetraacetic acid
Tiron	3,5-disulfocatechol
TMDTA	trimethylenediaminetetraacetic acid
TRITA	1,4,7,10-tetraazacyclotridecane-*N*,*N*′,*N*″,*N*‴-tetraacetic acid
TTHA	triethylenetetraminehexaacetic acid

Acknowledgment

This work was supported by the Texas Advanced Technology Program, Texas A&M University, and by Wheelabrator Clean Air Systems, Inc.

References

1. Z. Diaz. U.S. Patent No. 4,388,239, June 14, 1983.
2. D. McManus and F.R. Kin. U.S. Patent, 4,622,212, November 11, 1986.
3. S.A. Bedell. U.S. Patent No. 4,891,205, January 20, 1990.
4. D. Chen, R.J. Motekaitis, A.E. Martell, and D. McManus. Can. J. Chem. **71**, 1524 (1993).
5. D. Chen, A.E. Martell, and D. McManus. Can. J. Chem. **73**, 264 (1995).
6. A.E. Martell and R.D. Hancock. ACS Symp. Ser. **565**, 240 (1994).
7. R.G. Pearson. Chem. Ber. **3**, 103 (1967).
8. R.D. Hancock and A.E. Martell. Chem. Rev. **89**, 1875 (1989).
9. S. Ahrland, J. Chatt, and N.R. Davies. Q. Rev. Chem. Soc. **12**, 321 (1958).
10. M. Clarke, R.D. Cramer, and N. Vanopdenbosch. J. Comput. Chem. **10**, 982 (1989).
11. A.L. Spek. Byvoet Center for Biomolecular Research, University of Utrecht, The Netherlands.
12. M.J. Hamor, T.A. Hamor, and J.L. Hoard. Inorg. Chem. **3**, 34 (1964).
13. R.M. Smith and A.E. Martell. Critical stability constants. Vol. 4. Plenum Press, New York. 1976.
14. R.M. Smith, A.E. Martell, and R.J. Motekaitis. Critical stability constants database. NIST Standard Reference Data No.46, Version 2, Gaithersburg, Md. 1995.
15. A.E. Martell and L.G. Sillen. Stability constants of metal-ion complexes. The Chemical Society, Special Publication No.17, 1964.

Total synthesis of isodeoxypodophyllotoxin using the Me_3Sn radical initiated carbocyclization

Stephen Hanessian and Sacha Ninkovic

Abstract: The lactone portion of the podophylotoxin framework was assembled from a free-radical carbocyclization reaction, and the target structure was constructed based on intramolecular Friedel–Crafts reaction. In addition to isodeoxypodophyllotoxin, there were formed unusual tri- and tetracyclic compounds.

Key words: free-radical carbocyclization, C—Sn bond cleavage, podophyllotoxin analog.

Résumé : La partie lactone de la structure de la podophyllotoxine a été synthétisée en utilisant une carbocyclisation radicalaire. La structure entière a été construite en applicant une réaction de Friedel et Crafts intramoléculaire. En plus de l'isodéoxypodophyllotoxine, on isole des produits tri- et tétracycliques.

Mots clés : carbocyclisation radicalaire, scission de la liaison C—Sn, analoque de la podophyllotoxine.

[Traduit par la rédaction]

Introduction

Over the years, the lignans (1) have been recognized as challenging targets for organic synthesis, particularly because of their unusual structures and interesting biological properties (2) (Fig. 1). A number of methods have been devised for the construction of this class of molecules (1), and several efforts have culminated in the total synthesis of podophyllotoxin **1** (3), steganacin **2** (4), their derivatives (5), and related compounds (6). These efforts have led to the development of the antitumor drugs (7) etoposide and teniposide which are glucosides of epipodophyllotoxin **4**. These semi-synthetic molecules are currently in use for treatment of a variety of tumors, including small cell lung carcinoma (8), testicular cancer (9), and malignant lymphoma (10).

Ward (3*a*) has recently reviewed the synthesis of molecules having the podophyllotoxin skeleton. To the best of our knowledge only 2,3-dibenzylbutyrolactones (11)[2] have been synthesized using a radical cyclization approach. More recently, a tributyltin hydride mediated carbocyclization provided the aryltetralin unit present in the isopicropodophyllotoxin skeleton (5*a*).

We recently reported that the trimethylstannyl radical adds to terminal olefins of a variety of dienes and trienes, leading to a number of interesting carbocyclic and heterocyclic systems of the tetrahydrofuran and pyrrolidine types (12). We have also reported a novel oxidative cleavage of the C—Sn bond with ceric ammonium nitrate (CAN) resulting in an aldehyde or acetal depending upon the conditions used (temperature, time, solvent, etc). This approach to the construction of 3,4-disubstituted tetrahydrofurans was applied to the total synthesis of the lignan antibiotic burseran (13) and to the kainoids (14).

We describe herein a total synthesis of racemic isodeoxypodophyllotoxin **3** using trimethylstannyl radical addition to a dienic system for the construction of the dibenzylbutyrolactone motif as well as the aryltetralin unit.

Fig. 1. The podophyllotoxin family.

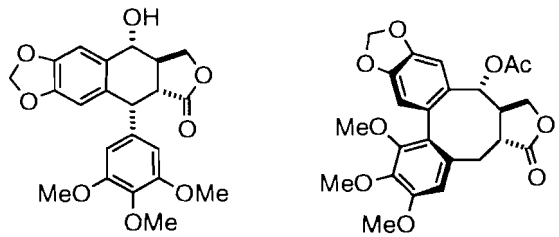

Podophyllotoxin, **1** Steganacin, **2**

Isodeoxypodophyllotoxin, **3** Epipodophyllotoxin, **4**

Results and discussion

A disconnective route to the intended target is shown in Fig. 2 in which one of the two critical steps involves a free radical mediated carbocyclization (bond a) to an acrylate ester. The

Received May 21, 1996.

S. Hanessian[1] and S. Ninkovic. Department of Chemistry, Université de Montréal, P.O. Box 6128, Succ. Centre-ville, Montréal. QC H3C 3J7, Canada.

[1] Author to whom correspondence may be addressed. Telephone: (514) 343-6738. Fax: (514) 343-5728. E-mail: hanessia@ere.umonteal.ca

[2] For a synthesis via C-H insertion reaction, see ref. 11*c*.

Fig. 2. Disconnective analysis.

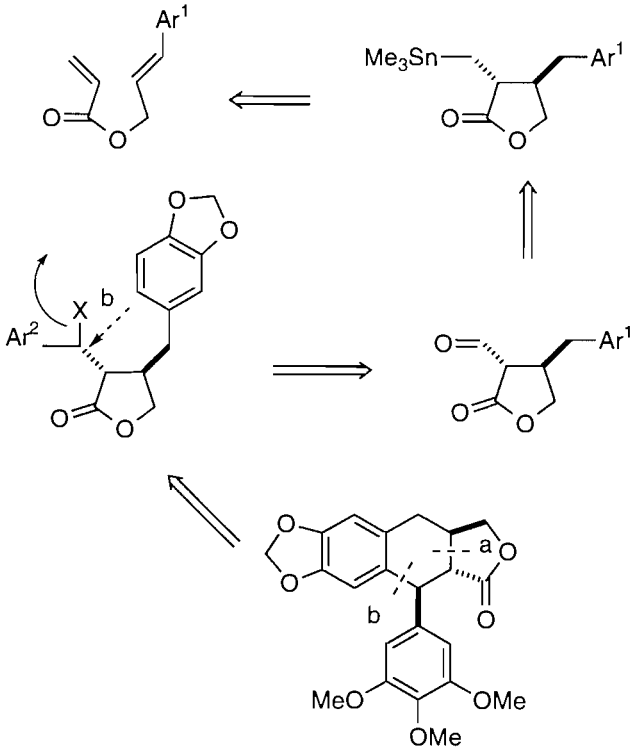

Scheme 1.

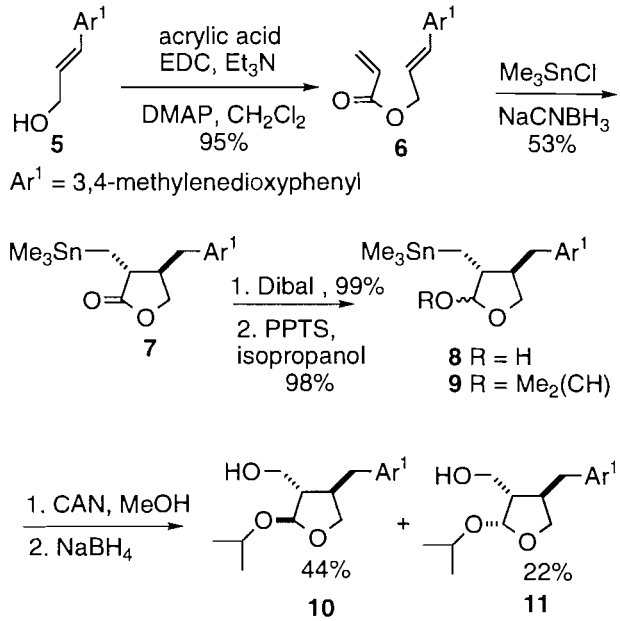

construction of the tetracyclic system involves a reaction of the Friedel–Crafts type as a second step (bond b) where an important stereochemical issue must be addressed.

Our synthesis started with the treatment of diene **6**, obtained from alcohol **5** and acrylic acid, with trimethyltin radical generated according to Stork and Sher (15) (Scheme 1). This gave lactone **7** in 46% yield in a 4:1 *trans/cis* ratio, with the uncyclized reduced compound as a side-product. Although attempts to significantly increase the yield failed, a modest level of improvement resulted when it was found that the proportion of uncyclized by-product could be minimized by a slow addition of sodium cyanoborohydride to a refluxing solution of diene **6** over a period of 9 h. Thus, lactone **7** and its *cis* isomer were formed in an optimized yield of 53%. Separation by recrystallization afforded the major *trans*-lactone **7** in a ratio greater than 50:1. The structure of **7** was unambiguously proved by single crystal X-ray analysis and by nOe experiments. The remaining *cis*-lactone could be epimerized to the *trans*-lactone **7** (>9:1) under basic conditions.

Although the radical carbocyclization proceeds exclusively in a 5-*exo*-trig mode (16), the observed selectivity favoring the *trans* isomer differs from the Me_3Sn-mediated carbocyclization of dienes leading to tetrahydrofurans and pyrrolidines, which give the *cis/trans* products in ratios of 2:1 (12, 13). The classical chairlike and boatlike transition states may probably not apply in the radical carbocyclizations of lactones since they would involve a rather rigid ester moiety.

At this stage of the synthesis, we had to address the problem of selective cleavage of the C—Sn bond with CAN, being cognizant of the fact that aryloxymethyl ethers are oxidized to the corresponding quinones under the same general oxidative conditions at low temperature and in a relatively short time (17). In addition, the problem of oxidative coupling (17*a*) loomed as a major obstacle to the intended sequence. We were encouraged, however, by our previous results (12), since chemoselective oxidative cleavage of the trimethylstannyl group was possible in the presence of an electron-rich aryl group as in our previously published total synthesis of burseran (13).

Attempts to selectively cleave the C—Sn bond in **7** under the CAN conditions led to decomposition. The main difference in comparison to the precursor to burseran (13) is that the γ position to the stannyl group bears a carbonyl group in **7**. Thus, the selective CAN oxidative destannylation of γ-stannyl lactones presented a case that warranted further study. To verify this hypothesis, the lactone was reduced to the hemiacetal **8** and protected as acetal **9** (1.5:1 favoring the β anomer vs. the α anomer) under acidic conditions. To our satisfaction, chemoselective cleavage of the trimethylstannyl group was achieved by slow addition of CAN at 0°C, giving the aldehyde derivative directly and without affecting the aromatic moiety. The alcohols **10** and **11** were obtained in 44 and 22% yield, respectively, after reduction with sodium borohydride. The stereochemical relationships in **10** and **11**, respectively, were confirmed by nOe experiments. It is possible that the presence of the electron-withdrawing carbonyl group reduces the reactivity at the C—Sn center, thus leading to undesired reactions in the attempted oxidative cleavage of **7**. Another possibility could involve the formation of a highly reactive β-dicarbonyl, which under the CAN conditions could further react giving dimerization and oligomerization products (18).

The trimethoxybenzyl group was introduced by treatment of aldehyde **12**, obtained from PCC oxidation of alcohol **10** with 3,4,5-trimethoxyphenyl lithium (19), producing an epimeric mixture of adducts **13** that was acetylated to afford the epimeric benzylic acetates **14** (Scheme 2). Our hope was that under acidic conditions, the Friedel–Crafts cyclization

Scheme 2.

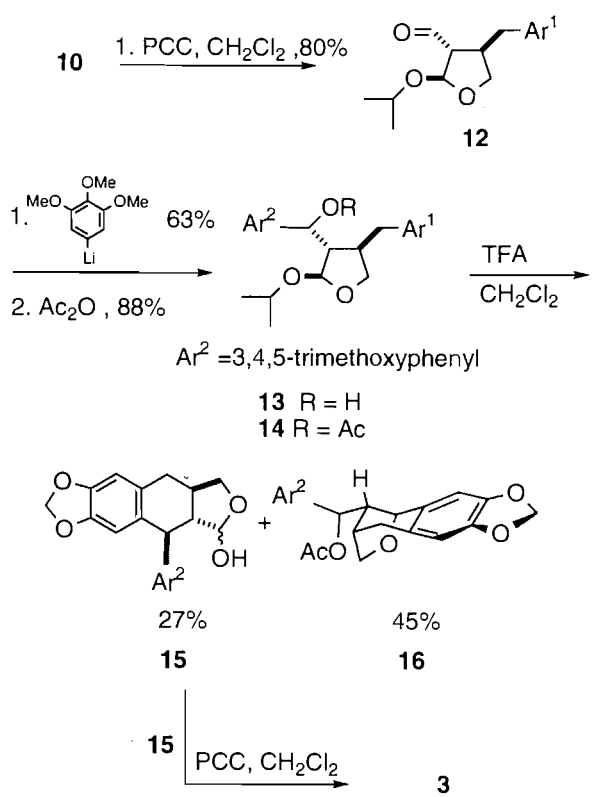

Scheme 3.

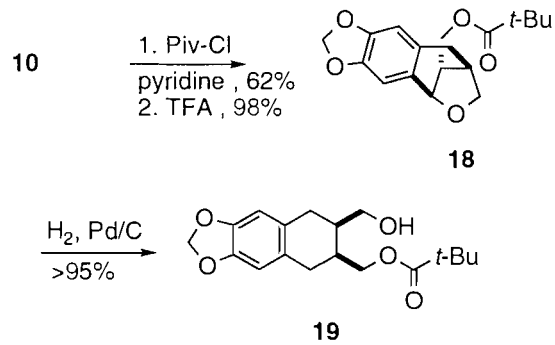

would be directed by the β-isopropoxy group, thus leading to the 1,2-*cis*/2,3-*trans* stereochemistry found in the podophyllotoxin type skeleton (Fig. 1). Treatment of **14** with trifluoroacetic acid gave the hemiacetal **15** in only 27% yield accompanied by a tetracyclic by-product **16** (45%). Extensive NMR studies corroborated the isodeoxypodophyllotoxin-type structure for **15**. Oxidation of **15** with PCC gave isodeoxypodophyllotoxin **3**. The by-product **16** arising in the Friedel–Crafts reaction had been formed as a result of an attack of the aromatic ring on the anomeric carbon, most probably via the intermediate oxocarbenium ion.

To clarify the nature of this cyclization, we attempted the same reaction with a similar substrate (Scheme 3). When alcohol **10** was protected as a pivaloyl ester and treated with TFA, the only result observed was aromatic substitution at the anomeric position leading to the tricyclic compound **18** in quantitative yield. This structure now has an oxygen atom of the tetrahydrofuran directly connected to a benzylic carbon. It was thus possible to cleave this C—O bond by hydrogenolysis to give compound **19** with a *cis* configuration at C3/C4 in which one of the two alcohol functions is protected. Since we were in possession of both anomers **10** and **11**, we decided to verify if the orientation of the isopropoxy group had an influence on the stereochemical outcome of the Friedel–Crafts reaction. Thus, following the identical sequences as for **10**, oxidation of alcohol **11** and subsequent treatment with 3,4,5-trimethoxyphenyl lithium produced one epimer of adduct **21** (Scheme 4). Protection of the alcohol was accomplished with trifluoroacetic anhydride to give **22**. When treated with TFA, adduct **22** underwent Friedel–Crafts ring closure to afford hemiacetal **15** in 41% yield, accompanied by the acetal **23** (15%). It is interesting that in the case of **22** the major products arise from the expected Friedel–Crafts cyclization of the methylenedioxyaryl moiety onto the benzylic cation generated on the other trimethoxyaryl moiety. In the case of **14**, however, the analogous Friedel–Crafts cyclization occurred to the extent of only 27%, the major product being the bridged compound **16** (>8:1 of isomeric acetals). This product may form in part in a competing Friedel–Crafts condensation on an incipient oxocarbenium ion, which may result from the facile trifluoroacetolysis of the 1,2-*trans* glycoside in the medium compared to **22**. It is also possible that one of the epimers of the benzylic acetates (2:1 ratio) in **14** is kinetically more prone to solvolysis to generate a benzylic cation intermediate to give **15**. Compound **16** was found to be a mixture of a major and a minor acetate in a ratio of >8:1, unlike the 2:1 ratio of the original **14**, which corroborates the above-stated hypothesis. The formation of the hemiacetal **15** may be the result of the aqueous work-up wherein the corresponding anomeric isopropoxy (or trifluoroacetate group) is cleaved. Finally, the possibility of neighboring group participation by the *anti*-oriented benzylic acetate in **14** may also play an important role in the predominance of kinetically labile intermediates. Thus, the anomeric configuration in **14** and **22** and the nature of the benzylic ester may have an important kinetic influence in these Friedel–Crafts condensations with regard to their rates of solvolysis and aqueous hydrolysis upon work-up.

The preferential oxidative cleavage of the C—Sn bond in the presence of the electron-rich aromatic ring in compound **9** is intriguing. In an effort to study the influence of the disposition of the aromatic ring vis-a-vis the trimethylstannyl group, we prepared model compounds in which the distance between the aryl group and the site of oxidative cleavage was varied (Scheme 5 and Table 1). There are several interesting observations emerging from this study. First, normal conditions (12, 13) (10 equiv. CAN, RT) cannot be utilized for the destannylation of compounds containing an electron-rich aromatic moiety due to competing reactions. When the substituted aromatic ring is replaced by a phenyl group, cleavage of the C—Sn bond under the above-mentioned conditions is achieved effectively leading, to dimethyl acetals as major products (entries 1 and 5). However, when a slow addition of 2 equivalents of CAN (condition b) over a period of 1.5 h at 0°C was carried out, destannylation occurred without affecting the

Scheme 4.

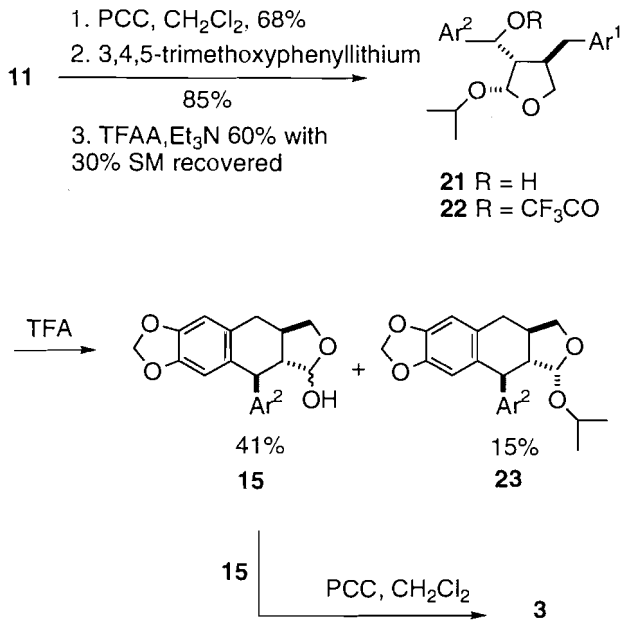

sensitive methylendioxyphenyl group (entries 3 and 4), while starting materials were completely recovered when Ar = Ph using the same conditions (entries 2 and 6). This suggests a probable involvement of a complexation between Ce(IV) of CAN and the electron-rich aromatic moiety in dilute solutions, thus permitting a faster destannylation. When on the other hand, $n > 3$ (entries 7 and 8), the methylenedioxyphenyl ring is preferentially attacked, leading to side reactions. In these cases the Ce(IV) is not effective in selectively cleaving the C—Sn group due to the longer distance separating it from the Me_3Sn function.

We believe that the mechanism of the chemoselective destannylation begins with a homolytic fragmentation of the stannyl radical cation generated by the electron transfer from CAN, producing an alkyl radical and Me_3Sn^+. A cerium (IV)-coordinated nitrate ester intermediate would then be formed after attack of a second molecule of CAN; this intermediate could then fragment in two different ways. The first could lead to the aldehyde and involve an intramolecular β-elimination while the second could produce nitrate esters by a ligand transfer from CAN. The intermediacy of an organocerium intermediate in which a C—Ce bond is involved cannot be ruled out. Nitrate esters and methyl ethers can be isolated in some instances, depending on the nature of the trimethylstannyl compound (12).

We have described a novel route to the podophyllotoxin skeleton that results in the *epi*-isomer as the major product. Friedel–Crafts cyclization in some oxonium ion intermediates leads to intriguing, di-, tri-, and tetracyclic structures.

Scheme 5.

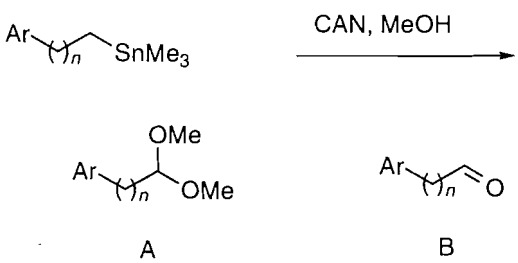

Table 1. Chain extension study.

Entry	Ar	*n*	Conditions	Product, yields
1	Ph	1	[a]	A, 44%
2	Ph	1	[b]	SM
3		1	[b]	A + B
4		2	[b]	A, 8% B, 32%
5	Ph	2	[a]	A
6	Ph	2	[b]	SM
7		4	[b]	Decomp.
8		5	[b]	Decomp.

[a]10 equiv. CAN 10 h, RT.
[b]slow addition, 2 equiv. CAN 1.5 h, 0°C.

Experimental section[3]

Acrylic acid 3-benzo[1,3]dioxol-5-yl-allyl ester 6

Method A

To a solution of methylenedioxy cinnamyl alcohol (2.0 g) and acrylic acid (6 mL, 6 equiv.) in dichloromethane (70 mL) was added, at 0°C, triethylamine (10 mL, 3 equiv.), EDC (7.0 g, 3 equiv.), and DMAP (cat). The reaction mixture was stirred at room temperature for 10 h and then poured into a separatory funnel containing 200 mL of ether and 20 mL of a 10% solution of HCl. The organic phase was washed twice with 20 mL of 10% HCl, four times with 20 mL of saturated sodium bicarbonate, and once with 30 mL of brine. The organic phase was dried ($MgSO_4$) and concentrated. Flash chromatography (10–20% ethyl acetate – hexane) gave 2.63 g (97%) of diene **6**.

Method B

To a solution of methylenedioxy cinnamyl alcohol (2.14 g) in dichloromethane (200 mL) was added at −15°C over a period of 10 min a solution of acryloyl chloride (5 mL, 5 equiv.) in dichloromethane (50 mL). The reaction mixture was brought to 0°C over 1 h and poured into a separatory funnel containing 350 mL of ether and 75 mL of a 10% solution of HCl. The organic phase was washed with 10% HCl, then with saturated sodium bicarbonate (40 mL), and finally with brine (50 mL). The organic phase was dried ($MgSO_4$) and concentrated. Flash

[3] Nomenclature from AUTONOM, Beilstein Institute, Copyright 1990-1991, Frankfurt, Germany.

chromatography (10–20% ethyl acetate – hexane) gave 2.29 g (82%) of diene **6**. ^{1}H NMR ($CDCl_3$) δ: 6.94 (d, 1H, J = 1.6 Hz, *H* arom), 6.83 (dd, 1H, J = 7.9 and 1.6 Hz, *H* arom), 6.76 (d, 1H, J = 7.9 Hz, *H* arom), 6.59 (d, 1H, J = 15.9 Hz, *H* benzyl), 6.45 (dd, 1H, J = 17.3 and 1.6 Hz, $O_2CCH{=}CH_2$), 6.2–6.1 (m, 2H, OCH_2CH and $H_2C{=}CH$), 5.96 (s, 2H, O-CH_2-O), 5.85 (dd, 1H, J = 9.8 and 1.5 Hz, $O_2CCH{=}CH_2$), 4.79 (dd, 2H, J = 6.6 and 1.3 Hz, OCH_2). The compound was used immediately due to its instability.

(3,4-trans)-4-Benzo[1,3]dioxol-5-ylmethyl-3-(trimethylstannylmethyl)-dihydrofuran-2-one (7)

To a refluxing solution of diene **6** (51 mg) and trimethyltin chloride (64 mg, 1.5 equiv.), in *tert*-butanol (25 mL) was added a solution of sodium cyanoborohydride (75 mg) and AIBN (cat. 10%) in a 4:1 methanol/*tert*-butanol (5 mL) solution over a period of 9 h. After completing the addition, the reaction mixture was heated under reflux for 30 min more and then cooled to room temperature. Ammonium hydroxide (10% solution) was added until the solution became clear. The reaction mixture was then poured into a separatory funnel containing 40 mL of ether. The organic phase was next washed with brine (10 mL), dried ($MgSO_4$), and concentrated. Flash chromatography (10–20% ethyl acetate – hexane) gave 46 mg (53%) of compound **7** as a 1:4 *cis/trans* mixture. The isomers were separated by recrystallization in methanol to give compound **7**. The structure of **7** was substantiated by x-ray crystallography. ^{1}H NMR ($CDCl_3$) δ: 6.75 (d, 1H, J = 7.8 Hz, *H* arom), 6.62–6.57 (m, 2H, *H* arom), 5.95 (s, 2H, O-CH_2-O), 4.22 (dd, 1H, J = 9.1 and 7.0 Hz, H_1), 3.83 (dd, 1H, J = 1.6 Hz, H_1'), 2.92 (dd, 1H, J = 13.8 and 4.9 Hz, *H* benzylic), 2.55 (dd, 1H, J = 13.8 and 9.0 Hz, *H* benzylic), 2.45–2.30 (m, 2H, H_1 and H_3), 1.07 (dd, 1H, J = 13.1 and 5.2 Hz, CH_2Sn), 0.87 (dd, 1H, J = 13.1 and 9.5 Hz, CH_2Sn), 0.13 (s, 9H, $(CH_3)_3Sn$); ^{13}C NMR ($CDCl_3$) δ: 180.0 (*C*=O), 147.8, 146.3 (2 *C*-O arom), 131.7 (*C* quat. arom), 121.4, 108.7, 108.3 (*C*-H arom), 100.9 (O-CH_2-O), 70.6 (CH_2O), 47.4, 43.6 (*C*-3 and *C*-4), 37.6 (CH_2 benzylic), 10.9 (CH_2-Sn), −9.0 (CH_3Sn); MS (FAB+) for $C_{16}H_{22}O_4Sn$: 383 (M − Me). Anal. calcd. for $C_{16}H_{22}O_4Sn$: C 48.40, H 5.57; found: C, 48.55, H, 5.63.

Epimerization of 7

A solution of lactone **7** (170 mg, 1:2 *trans/cis*) and DBU (7 equiv., 0.45 mL) in toluene (13 mL) was refluxed for 30 h. After cooling to room temperature, the reaction mixture was poured into a separatory funnel containing 35 mL of ether and 7 mL of a 10% solution of HCl. The organic phase was washed with 6 mL of HCl (10%), then with saturated sodium bicarbonate, and finally with brine, and was dried ($MgSO_4$) and concentrated. Flash chromatography afforded 145 mg (85%) of a 9:1 *trans/cis* mixture of compound **7**, which could be further recrystallized in methanol to afford a white crystalline solid (>50:1 *trans/cis*).

*(3,4-*trans*)-4-Benzo[1,3]dioxol-5-ylmethyl-3-(trimethylstannylmethyl)-tetrahydrofuran-2-ol (8)*

Lactone **7** (2.3 g) was dissolved in toluene (125 mL, 0.04 M) and the solution was cooled to −78°C before adding slowly a solution of DIBAL in toluene (1.0 M solution, 1.2 equiv., 7 mL). The reaction was followed by TLC and, after 15 min, ice cubes were added until gas evolution stopped. A few drops of water were added, after which the reaction mixture was brought to 0°C and stirred for 30 min at the same temperature. After adding ether (150 mL) and stirring for another 90 min at room temperature, magnesium sulfate was added and the mixture was filtered. Flash chromatography (40% ethyl acetate – hexane) afforded 2.3 g (99%) of lactol **8**. ^{1}H NMR ($CDCl_3$) δ: 6.73–6.57 (m, 3H, C*H* arom), 5.92 (s, 2H, OCH_2O), 5.26 and 5.03 (2 d, 1H, J = 4.6 and 3.3 Hz, C*H* anom. α and β), 4.07–3.47 (m, 2H, CH_2O), 2.95–1.86 (m, 5H, $CHCH_2SnMe_3$, $CHCH_2CO_2Me$, CH_2CO_2Me), 0.99–0.72 (m, 2H, CH_2SnMe_3), 0.19–0.01 ($CH_2Sn(CH_3)_3$); MS (FAB+) for $C_{16}H_{24}O_4Sn$: 385 (M−Me).

*(3,4-*trans*)-5-[5-Isopropoxy-4-(trimethylstannylmethyl)-tetrahydrofuran-3-ylmethyl]-benzo[1,3]dioxole (9)*

Hemiacetal **8** (400 mg) and PPTS (30 mg) were dissolved in dry 2-propanol (10 mL, 0.1 M) and the solution was stirred vigorously for 24 h. The solvent was removed under reduced pressure untill 1 mL of 2-propanol was left. Ether (20 mL) was added and the organic phase was washed with saturated sodium bicarbonate and then with brine. The organic phase was dried ($MgSO_4$), filtered, and concentrated. Flash chromatography (20% ethyl acetate – hexane) gave 435 mg (98%) of acetal **9** as an inseparable 1:1.5 α,β mixture of anomers. ^{1}H NMR ($CDCl_3$) δ: 6.72 (d, 1H, J = 7.7 Hz, *H* arom), 6.64–6.58 (m, 2H, *H* arom), 5.92 (s, 2H, O-CH_2-O), 4.98 (d, 1H, J = 4.5 Hz, O-C*H*-O *cis*), 4.77 (d, 1H, J = 2.5 Hz, O-C*H*-O *trans*), 3.96–3.81 (m, 2H, Me_2CHO and CH_2O *cis/trans*), 3.62 (dd, 1H, J = 8.3 and 8.3 Hz, CH_2O *trans*), 3.50 (dd, 1H, J = 8.1 and 8.0 Hz, CH_2O *cis*), 2.86–2.80 (m, 1H, *H* benzyl *cis/trans*), 2.57 (dd, 1H, J = 13.7 and 9.2 Hz, *H* benzyl *trans*), 2.36 (dd, 1H, J = 13.9 and 10.1 Hz, *H* benzyl *cis*), 2.30–1.90 (m, 2H, H_2 and H_3 *cis/trans*), 1.22 and 1.15 (d, 6H, $(CH_3)_2CHO$ *trans*), 1.14–1.1 (m, 6H, $(CH_3)_2CHO$ *cis*), 0.94-0.80 (m, 2H, CH_2Sn *cis/trans*), 0.09 (s, 9H, Me_3Sn *cis/trans*); ^{13}C NMR ($CDCl_3$) δ: 147.5, 145.7, 134.5 and 134.4 (*C* quater. arom *cis/trans*), 121.3, 121.2 (*C* arom *cis/trans*), 109.6, 108.9, 108.2, 108.1 (OCHO *trans*, C arom *cis/trans*, OCH_2O *cis*), 103.2 (OCHO *cis*), 100.7 (OCH_2O *trans*), 71.8, 71.6 (*C*-4 *cis/trans*), 68.9, 68.3 (Me_2CHO *cis/trans*), 50.9, 49.8 (*C*-2, *C*-3 *trans*), 48.3, 47.2 (*C*-2, *C*-3 *cis*), 38.8, 38.5 (*C*-benzyl *cis/trans*), 23.8, 23.8, 21.7 ($(CH_3)_2CHO$ *cis/trans*), 14.8, 8.9 (CH_2Sn *trans/cis*), −9.0, −9.5 ($(CH_3)_3Sn$ *cis/trans*); MS (FAB+) for $C_{19}H_{30}O_4Sn$: 427 (M − Me), 368 (M+H−Me−2-propanol).

*(2,3-*trans*-3,4-*trans*)-4-Benzo[1,3]dioxol-5-ylmethyl-2-isopropoxytetrahydrofuran-3-carbaldehyde **12** and (2,3-*cis*-3,4-*trans*)-4-benzo[1,3]dioxol-5-ylmethyl-2-isopropoxy-tetrahydrofuran-3-carbaldehyde (**20**)*

Acetal **9** (90 mg) was dissolved in 4 mL (0.05 M) of methanol and cooled to 0°C. Slow addition of CAN (cerium ammonium nitrate, 2 equiv., 230 mg in 5 mL of methanol) was done with a syringe pump over a period of 1 h. After the addition was completed, saturated ammonium chloride (2 mL) was added and the mixture was poured into a separatory funnel with 10 mL of ether. Work-up was done by washing with water and then with brine (5 mL). The organic phase was dried ($MgSO_4$) and concentrated. Flash chromatography (20–40% ethyl acetate – hexane) gave 35 mg (59%) of an inseparable mixture of aldehydes **12** and **20** (2:1), 4 mg of alcohol **11** (6%), and 8 mg of alcohol **10** (12%).

*(2,3-*trans*-3,4-*trans*)-(4-Benzo[1,3]dioxol-5-ylmethyl-2-isopropoxytetrahydrofuran-3-yl)-methanol* ***10*** *and (2,3-*cis*-3,4-*trans*)-(4-benzo[1,3]dioxol-5-ylmethyl-2-isopropoxytetrahydrofuran-3-yl)-methanol (**11**)*

The aldehyde (35 mg) was dissolved in methanol (1.2 mL, 0.1 M), the reaction mixture was cooled to 0°C, and sodium borohydride (3 equiv., 14 mg) was added. After 1 h a saturated ammonium chloride solution was added followed by the usual work-up. Flash chromatography (30–40% ethyl acetate – hexane) gave 19 mg of alcohol **10** (53% yield) and 10 mg of alcohol **11** (29% yield).

*For alcohol **10**:* ^{1}H NMR ($CDCl_3$) δ: 6.71 (d, 1H, J = 7.9 Hz, *H* arom), 6.65 (d, 1H, J = 1.6 Hz, *H* arom), 6.71 (dd, 1H, J = 7.9 and 1.6 Hz, *H* arom), 5.91 (s, 2H, OCH_2O), 5.09 (d, 1H, J = 2.2 Hz, OC*H*O), 3.94–3.84 (m, 2H, Me_2CHO and H_4), 3.64 (dd, 1H, J = 8.6 and 8.4 Hz, H_4), 3.53–3.40 (m, 2H, CH_2OH), 2.80–2.64 (m, 2H, *H* benzyl), 2.17–2.10 (m, 1H, H_3), 2.03–1.99 (m, 1H, H_2), 1.21 and1.15 (2 d, 6H, J = 6.1 Hz, $(CH_3)_2CHO$); ^{13}C NMR ($CDCl_3$) δ: 147.6, 145.8 (2 *C*-O arom), 134.1 (*C tert.* arom), 121.3, 108.9, 108.1, and 105.0 (3*C*H arom and O*C*HO), 100.7 (O-*C*H_2-O), 71.5, 69.0, 63.4, 53.8, 42.6, 38.7, 23.6, 21.6 (Me_2CHO, *C*-3, *C*-4, CH_2OH, *C* benzyl, *C*-5 , $(CH_3)_2CHO$); HRMS for $C_{16}H_{22}O_5$ −1, calcd.: 293.1389; found: 293.1398; MS (FAB+) for $C_{16}H_{22}O_5$: 293 (M−1), 233 (M-1−2-propanol).

*for alcohol **11**:* ^{1}H NMR ($CDCl_3$) δ: 6.72 (d, 1H, J = 7.9 Hz, *H* arom), 6.68 (d, 1H, J = 1.6 Hz, *H* arom), 6.62 (dd, 1H, J = 7.8 and 1.6 Hz, *H* arom), 5.92 (s, 2H, OCH_2O), 5.26 (d, 1H, J = 5.2 Hz, OC*H*O), 4.01 (dd, 1H, J = 8.2 and 8.1 Hz, H_4), 3.91 (qq, 1H, J = 6.2 and 6.1 Hz, Me_2CHO), 3.78 (dd, 1H, J = 11.8 and 2.6 Hz, CH_2OH), 3.59–3.52 (m, 2H, CH_2OH and H_4), 2.81–2.69 (m, 2H, *H* benzyl), 2.54–2.45 (m, 1H, H_3), 1.97–1.93 (m, 1H, H_2), 1.18 and 1.15 (2 d, 6H, J = 6.2 Hz, $(CH_3)_2CHO$); ^{13}C NMR ($CDCl_3$) δ: 147.6, 145.9 (2 *C*-O arom), 133.7 (*C tert.* arom), 121.4, 108.9, 108.1, and 104.2 (3 *C*H arom and O*C*HO), 100.7 (O-*C*H_2-O), 69.4, 50.7, and 38.7 (Me_2CHO, *C*-3, and *C*-4), 71.8, 59.6, 39.2 (CH_2OH, *C* benzyl, and *C*-5), 23.5 and 21.7 ($(CH_3)_2CHO$); HRMS (FAB+) for $C_{16}H_{22}O_5$ −H, calcd.: 293.1389; found: 293.1379; MS (FAB+) for $C_{16}H_{22}O_5$: 293 (M − 1).

*(2,3-*trans*-3,4-*trans*)-4-Benzo[1,3]dioxol-5-ylmethyl-2-isopropoxytetrahydrofuran-3-carbaldehyde (**12**)*

Into a solution of alcohol **10** (121 mg) and molecular sieves in dichloromethane (0.1 M, 4.2 mL) was added PCC (2 equiv., 180 mg) at 0°C. The reaction mixture was brought to room temperature, stirred for 2 h, filtered over Celite–silica gel, and concentrated. Flash chromatography (30% ethyl acetate – hexane) gave 96 mg (80%) of aldehyde **12**. ν_{max} : 2960, 2925, 1720, 1495, 1485, 1435, 1370, 1360, 1240, 1090, 1030, 920, 800 cm^{-1}; ^{1}H NMR ($CDCl_3$) δ: 9.46 (d, 1H, J = 1.4 Hz, C*H*O), 6.79–6.59 (m, 3H, *H* arom), 5.93 (s, 2H, OCH_2O), 5.42 (d, 1H, J = 2.1 Hz, OC*H*O), 4.01–3.87 and 3.71 (m and dd, 3H, J = 8.3 and 8.2 Hz, CH_2O, Me_2CHO), 2.81–2.71 (m, 4H, 2 *H* benzyl, C*H*CH_2 benzyl, and C*H*CHO), 1.22 and 1.16 (2 d, 6H, J = 6.2 Hz and 6.1 Hz, $(CH_3)_2CHO$); ^{13}C NMR ($CDCl_3$) δ: 199.2 (*C*HO), 147.8, 146.1, (2 *C*-O arom), 133.4 (*C tert.* arom), 121.5, 109.0, 108.3, and 101.8 (3 *C*H arom and O*C*HO), 100.9 (O-*C*H_2-O), 69.7, 64.1, and 41.9 (Me_2CHO, *C*HCHO, and *C*HCH_2 benzyl), 71.6, 38.3 (CH_2O and CH_2 benzyl), 23.6 and 21.7 ($(CH_3)_2CHO$).

*(2,3-*trans*-3,4-*trans*)-[(4-Benzo[1,3]dioxol-5-ylmethyl-2-isopropoxytetrahydrofuran-3-yl)]-(3,4,5-trimethoxyphenyl)-methanol (**13**)*

BuLi (2.4 M in hexane, 3.9 equiv., 0.45 mL) was added at −78°C to a solution of 3,4,5-trimethoxy-1-bromobenzene (18) (0.27g, 4 equiv.) in THF (6 mL). After stirring for 1 h at the same temperature, a solution of aldehyde **12** (80 mg) in THF (5 mL) was added to the reaction mixture over a period of 5 min. Stirring was continued for another hour at −78°C and the reaction was quenched by the addition of ice cubes. The mixture was then poured in ether (30 mL), washed with water and then with brine, dried over magnesium sulfate, and filtered. Evaporation of the solvent and flash chromatography of the residue afforded 80 mg (63%) of compound **13** as a 1:1 mixture of benzylic alcohols. ν_{max} : 3440, 2930, 1585, 1490, 1450, 1325, 1230, 1180, 1120, 1030, 1000, 920, 800, 730 cm^{-1}; ^{1}H NMR ($CDCl_3$) δ: 6.63–6.27 (m, 5H, *H*arom), 5.91–5.86 (m, 2H, OCH_2O), 5.32, 4.98, 4.69, and 4.27 (4 d, 1H+1H, J = 1.5, 1.7, 6.1, and 8.8 Hz, OC*H*O and C*H*OH benzyl), 4.10–3.60 (m, 12H, 3 $(CH_3)O$, Me_2CHO and CH_2O), 2.72–2.05 (m, 4H, 2 *H* benzyl, C*H*CH_2 benzyl and C*H*CH benzyl) 1.25–0.98 (m, 6H, $(CH_3)_2CHO$); ^{13}C NMR ($CDCl_3$) δ: 153.2, 153.1, 147.5, 145.7, 138.2, 138.1, 137.6, 137.2, 134.4, 134.2 (7 *C* quat. arom), 121.2, 108.7, 108.6, 107.9, 105.0, 104.6, 103.6, 103.1, 92.9 (5 *C*H arom and O*C*HO), 100.8 (O-*C*H_2-O), 75.8, 74.9, 68.9, 68.7 (Me_2CHO, *C*HOH benzyl), 72.3, 71.6 (CH_2O), 60.8, 58.3, 57.9, 56.0, 55.9, 43.1, 41.7 (*C*HCH_2 benzyl, *C*HCHOH benzyl, 3 CH_3O), 39.7 and 38.9 (CH_2 benzyl), 23.7, 23.6, 21.6 and 21.4 ($(CH_3)_2CHO$); MS (FAB+) for $C_{25}H_{32}O_8$: 460 (M).

*(2,3-*trans*-3,4-*trans*)-Acetic acid-[(4-benzo[1,3]dioxol-5-ylmethyl-2-isopropoxytetrahydrofuran-3-yl)-]-(3,4,5-trimethoxyphenyl)-methyl ester (**14**)*

Into a solution of alcohol **13** (80 mg) in dichloromethane (3.5 mL) was added acetic anhydride (2 equiv.), triethylamine (3.5 equiv.), and DMAP (cat) at 0°C. The reaction mixture was brought to room temperature over 1 h and poured into a separatory funnel containing 30 mL of ether. The organic phase was then washed three times with HCl (10%), twice with 7 mL of saturated sodium bicarbonate, and once with 8 mL of brine. The organic phase was dried ($MgSO_4$), filtered, and concentrated. Flash chromatography (20–30% ethyl acetate – hexane) gave 77 mg (88%) of compound **14** as an isomeric mixture of benzylic acetates. ^{1}H NMR ($CDCl_3$) δ: 6.72–6.50, 6.32–6.23 (m, 5H, *H* arom), 5.94–5.90 (m 2H, OCH_2O), 5.73, 5.41, 5.10, and 4.81 (4 d, 2H, J = 8.3, 10.1, 1.5, and 1.7 Hz, OC*H*O and C*H*OAc), 3.94–3.62 (m, 12H, 3 $(CH_3)O$, Me_2CHO, CH_2O), 2.82–1.94 (m, 7H, C*H*CH_2 benzyl, C*H*CHOAc, CH_2 benzyl, and O_2CCH_3), 1.39, 1.22, 1.15, and 0.87 (4 d, 6H, J = 6.1 Hz, $(CH_3)_2CHO$); MS (FAB+) for $C_{27}H_{34}O_9$; 502 (M), 443 (M−2-propanol), 383 (M−2-propanol − O_2CCH_3).

*(trans-trans)-5-(3,4,5-Trimethoxyphenyl)-5,5a,6,8,8a,9-hexahydrofuro[3'-4'-6,7]naphtho[2,3-*d*][1,3]dioxol-6-9l (**15** and **16**)*

Trifluoroacetic acid (50 equiv.) was added to a solution of **14** (65 mg) in dichloromethane (12 mL) at 0°C. The reaction mixture was stirred for 30 min at the same temperature, poured into ether (25 mL), and washed with 5 mL of saturated sodium

bicarbonate and then with 6 mL of brine. The organic phase was dried ($MgSO_4$), filtered, and concentrated. Flash chromatography (30–40% ethyl acetate – hexane) gave 14 mg (27%) of compound **15** and 25 mg of compound **16** (45%) in an isomeric ratio of >8 to 1.

*For compound **15**:* ^{1}H NMR ($CDCl_3$) δ: 6.61 (s, 1H, C*H* arom), 6.41 (s, 2H, C*H* arom), 6.35 (s, 1H, C*H* arom), 5.89 (d, 1H, J = 1.3 Hz, OCH_2O), 5.87 (d, 1H, J = 1.4 Hz, OCH_2O), 5.14 (d, 1H, J = 4.2 Hz, HOC*H*O), 4.35 (dd, 1H, J = 7.8 and 7.7 Hz, CH_2O), 4.06 (d, 1H, J = 11.6 Hz, C*H* benzyl), 3.90 (s, 3H, CH_3O), 3.80 (m, 2H, 2 CH_3O), 3.59 (dd, 1H, J = 9.8 and 8.1 Hz, CH_2O), 3.00 (dd, 1H, J = 15.2 and 4.6 Hz, CH_2 benzyl), 2.73–2.57 (m, 2H, CH_2 benzyl, C*H*CH_2 benzyl), 1.99 (dd, 1H, J = 11.9, 4.2 Hz, C*H*CH benzyl); HRMS for $C_{22}H_{24}O_7$, calcd.: 400.1522; found 400.1525.

*For compound **16**:* ^{1}H NMR ($CDCl_3$) δ: 6.61 and 6.47 (2 s, 4H, C*H* arom), 6.70 and 6.58 (2 s, C*H* arom minor), 5.93–5.90 (m, OCH_2O minor), 5.88 (s, 2H, OCH_2O), 5.64 (d, 1H, J = 10.6 Hz, C*H*OAc), 5.50 (d, 1H, J = 10.7 Hz, C*H*OAc minor), 4.25–4.19 and 3.88–3.62 (m, 12H, 3 (CH_3)O, PhC*H*O, CH_2O), 3.15 (d, 1H, J = 16.9 Hz, CH_2 benzyl), 2.84 (dd, 1H, J = 16.9 and 2.3 Hz, CH_2 benzyl), 2.72 (s, 1H, C*H*CH_2 benzyl), 2.50 (d, 1H, J = 10.6 Hz, C*H*CHOAc), 2.12 (s, 3H, O_2CCH_3); HRMS for $C_{24}H_{26}O_8$, calcd.: 442.1628; found: 442.1602; MS (EI/HR) for $C_{24}H_{26}O_8$; 442 (M), 382 (M+H−OAc).

*Isodeoxypodophyllotoxin (**3**)*

PCC oxidation of the hemiacetal **15** (15 mg) was done following the same procedure as for compound **10**. Isodeoxypodophyllotoxin **3** (12 mg) was purified by chromatography with 30% ethyl acetate – hexane to give an amorphous solid. ^{1}H NMR ($CDCl_3$) δ: 6.60 (s, 1H, C*H* arom), 6.41 (s, 2H, C*H* arom), 6.35 (s, 1H, C*H* arom), 5.90 (d, 1H, J = 1.3 Hz, OCH_2O), 5.89 (d, 1H, J = 1.4 Hz, OCH_2O), 4.52 (dd, 1H, J = 8.6 and 6.2 Hz, CH_2O), 4.06 (d, 1H, J = 10.4, C*H* benzyl), 3.99 (dd, 1H, J = 10.0 and 8.7, CH_2O), 3.85 (s, 3H, CH_3O), 3.82 (s, 6H, 2 CH_3O), 3.01–2.91 and 2.68–2.47 (m, 4H, CH_2 benzyl, C*H*CH_2 benzyl, C*H*CH benzyl); HRMS for $C_{22}H_{22}O_7$, calcd.: 398.1366; found: 398.1378.

*Compound **18***

To a solution of alcohol **10** (15 mg) in pyridine (0.05 M, 1 mL) at 0°C, was added pivaloyl chloride (3 equiv.) and the reaction mixture was stirred overnight at room temperature. Ice cubes were added at 0°C and the reaction mixture was stirred 20 min at the same temperature and 15 min at room temperature before the solvent was removed under reduced presure. Flash chromatography (10% ethyl acetate – hexane) afforded 12 mg (62%) of **17**. ^{1}H NMR ($CDCl_3$) δ: 6.78–6.58 (m, 3H, *H* arom), 5.92, 5.91 (2 s, 2H, OCH_2O), 5.02 (d, 1H, J = 2 Hz, OC*H*O), 4.01–3.83, 3.65 (m, dd, 5H, CH_2O-Piv, 2 H_4, Me_2CHO), 2.84 (dd, 1H, J = 13.8, 6.3 Hz, *H* benzyl), 2.64 (dd, 1H, J = 13.8 and 8.3 Hz, *H* benzyl), 2.19–2.09 (m, 2H, H_2 and H_3), 1.26–1.13 (m, 6H, $(CH_3)_2CHO$), 1.19 (s, 9H, *t*-Bu).

Ester **17** (12 mg) was dissolved in dichloromethane (1 mL) and the trifluoroacetic acid (20 equiv.) was added at room temperature. The reaction mixture was stirred for 10 min, then poured into ether (50 mL), and the organic phase was washed with a saturated sodium bicarbonate solution and then with brine, dried over magnesium sulfate and filtered. The solvent was evaporated and the residue was purified by flash chromatography (20% ethyl acetate – hexane) to give 10 mg (>98%) of compound **18**. ^{1}H NMR ($CDCl_3$) δ: 6.63 (s, 1H, *H* arom), 6.60 (s, 1H, *H* arom), 5.90, 5.89 (2 d, 2H, OCH_2O), 4.61 (s, 1H, OC*H*Ph), 4.16–4.01, 3.65 (m, d, 4H, J = 8.7 Hz, CH_2O-Piv, 2 H_4), 3.13–3.06, (m, 1H, *H* benzyl), 2.78 (dd, 1H, J = 13.9 and 2.3 Hz, *H* benzyl), 2.56–2.51, 2.43 (m, dd, 2H, J = 8.5 and 7.0 Hz, H_2, H_3), 1.22 (s, 9H, *t*-Bu); ^{13}C NMR ($CDCl_3$) δ:178.4 (C=O), 147.6, 145.7 (2 *C*-O*tert.* arom), 132.5, 127.5 (2 *Ctert.* arom), 109.2, 107.8, (2 *C*H arom), 100.9 (O-CH_2-O), 78.1 (PhCHO), 71.1, 63.7 (2 CH_2O), 45.9, 36.1 (2 *C*H aliph.), 38.8 (*Ctert* of *t*-Bu), 37.8 (CH_2 benzyl), 27.2 (*t*-Bu).

*[1,3] (*trans*)-2,2-Dimethylpropionic acid 7-hydroxymethyl-5,6,7,8-tetrahydro-naphtho[2,3-*d*]dioxol-6-ylester (**19**)*

Compound **18** (3.5 mg) was dissolved in ethyl acetate (1 mL), Pd/C (10%) was added, and the mixture was hydrogenated under 45 psi (1 psi = 6.9 kPa) for 3 days. The reaction mixture was filtered over Celite and the filtrate was concentrated to afford compound **19** (98%); ^{1}H NMR ($CDCl_3$) δ: 6.55 (s, 2H, H arom), 5.88 (s, 2H, OCH_2O), 4.26, 3.93, 3.76, 3.64 (dd, dd, dd, dd, 4H, J = 11.0 and 5.8, 11.0 and 7.8, 10.9 and 7.3, 10.9 and 7.2 Hz, CH_2O), 2.80–2.58 (m, 4H, H benzyl), 2.48–2.37, 2.29–2.18 (m, 2H, CH aliph.), 1.21 (s, 9H, *t*-Bu); ^{13}C NMR ($CDCl_3$) δ:178.4 (C=O), 145.8, 127.4, 127.2 (2 C-Otert. arom, 2 Ctert. arom), 108.8, 108.7 (2 CH arom), 100.5 (O-CH_2-O), 64.5, 63.5 (2 CH_2O), 38.7, 37.9, 33.9, 31.3, 29.9 (2 CH aliph., Ctert of t-Bu, 2 CH_2 benzyl), 27.1 (*t*-Bu); HRMS for $C_{18}H_{24}O_5$, calcd.: 319.1545; found: 319.1566; MS (FAB+) for $C_{18}H_{24}O_5$; 319 (M−1).

*(2,3-*cis*-3,4-*trans*)-4-Benzo[1,3]dioxol-5-ylmethyl-2-isopropoxytetrahydrofuran-3-carbaldehyde (**20**)*

To a solution of alcohol **11** (130 mg) in dichloromethane (8 mL, 0.06 M) and molecular sieves, was added PCC (3 equiv., 290 mg). The reaction mixture was stirred for 2 h at room temperature then filtered over Celite and concentrated. Flash chromatography (20% ethyl acetate – hexane) gave 88 mg of aldehyde **20** (68% yield). ν_{max} : 2960, 1715, 1485, 1435, 1240, 1100, 1030, 920 cm^{-1}; ^{1}H NMR ($CDCl_3$) δ: 9.46 (d, 1H, J = 2.7 Hz, C*H*O), 6.70 (d, 1H, J = 7.9 Hz, *H* arom), 6.64–6.59 (m, 2H, 2 *H* arom), 5.90 (s, 2H, OCH_2O), 5.42 (d, 1H, J = 5.3 Hz, OC*H*O), 4.09 (dd, 1H, J = 8.3 and 8.3 Hz, H_4), 3.83 (m, 1H, Me_2CHO), 3.63 (dd, 1H, J = 8.5 and 6.2 Hz, H_4), 3.19–3.06 and 2.81–2.52 (2 m, 4H, 2 *H* benzyl, H_2 and H_3), 1.13 and 1.07 (2 d, 6H, J = 6.2 Hz, $(CH_3)_2CHO$); ^{13}C NMR ($CDCl_3$): 199.3 (*C*HO), 147.7, 146.1, (2 *C*-O arom), 133.0 (*C tert.* arom), 121.6, 109.0, 108.2, and 102.2 (3 *C*H arom and OCHO), 100.8 (O-CH_2-O), 69.8, 61.2, and 39.5 (Me_2*C*HO, *C*-3, and *C*-4), 71.5, 39.5 (*C* benzyl and *C*-5), 23.4 and 21.7 ($(CH_3)_2$CHO).

*[(2,3-*cis*-3,4-*trans*)-(4-Benzo[1,3]dioxol-5-ylmethyl-2-isopropoxytetrahydrofuran-3-yl)-]-(3,4,5-trimethoxyphenyl)-methanol (**21**)*

BuLi (2.4 M in hexane, 3.9 equiv., 0.5 mL) was added at −78°C to a solution of 3,4,5-trimethoxy-1-bromobenzene (18) (0.300 g) in THF (10 mL). After stirring for 1 h at the same temperature, a solution of aldehyde **20** (87 mg) in THF (5 mL) was added to the reaction mixture over a period of 5 min. It was then stirred for another hour at -78°C and the reaction was quenched by the addition of ice cubes. The mixture is then poured into ether (30 mL), washed with water and then

with brine, dried over magnesium sulfate, and filtered. The solvent was evaporated and the residue was purified by flash chromatography to afford 90 mg (70%) of **21**. ν_{max} : 3490, 2945, 1595, 1505, 1495, 1450, 1420, 1360, 1240, 1130, 1040, 930 cm^{-1}; ^1H NMR ($CDCl_3$) δ: 6.63–6.59 and 6.40–6.35 (m, 5H, *H* arom), 5.89 (m, 2H, OCH_2O), 5.35 and 5.06 (2 d, 1H+1H, *J* = 6.1 and 1.8 Hz, OC*H*O and C*H*OH benzyl), 4.09–3.81 (m, 11H, 3 CH_3O, Me_2CHO, and H_4), 3.62 (dd, 1H, *J* = 10.3 and 5.2 Hz, H_4), 2.82–2.70 (m, 1H, H_3), 2.25–2.13 (m, 3H, 2 *H* benzyl and H_2) 1.25 and1.18 (2 d, 6H, *J* = 6.2 Hz, $(CH_3)_2CHO$). ^{13}C NMR ($CDCl_3$) δ:153.1, 147.5, 145.7, 138.3, 136.8, 134.2 (7 *C* quat. arom), 121.3, 108.8, 107.8, 104.6, 103.8, and 102.5 (5 *C*H arom and OCHO), 100.8 (O-CH_2-O), 71.5 (*C*-5), 70.8, 69.6 (Me_2CHO, *C*HOH benzyl), 60.8, 56.1, 56.0, 40.9, 37.9 (*C* benzyl, *C*-2, *C*-3, 3 CH_3O), 23.7 and 21.8 ($(CH_3)_2CHO$); MS (NBA) for $C_{25}H_{32}O_8$; 461 (M + 1).

*(2,3-*cis*-3,4-*trans*)-Trifluoroacetic acid [(4-benzo[1,3]dioxol-5-ylmethyl-2-isopropoxytetrahydrofuran-3-yl)-]-(3,4,5-trimethoxyphenyl)-methyl ester (22)*

Into a solution of alcohol **21** (57 mg) in dichloromethane (0.05 M, 2.5 mL) was added trifluoroacetic anhydride (1.5 equiv., 0.027 mL) and triethylamine (3.5 equiv., 0.061 mL) at 0°C. The reaction mixture was warmed to room temperature over 1 h and poured into a separatory funnel containing 30 mL of ether. The organic phase was washed with HCl (10%), saturated sodium bicarbonate, and then with brine. The organic phase was dried ($MgSO_4$), filtered, and concentrated. Flash chromatography (20–30% ethyl acetate – hexane) gave 43 mg (60%) of compound **22** as well as 17 mg (30%) of starting material. ^1H NMR ($CDCl_3$) δ: 6.72–6.55 (m, 5H, *H* arom), 6.03 (d, 1H, *J* = 9.2 Hz, PhC*H*O), 5.93 and 5.92 (2 s, 2H, OCH_2O), 4.80 (d, 1H, *J* = 4.6 Hz, OC*H*O), 3.99 (dd, 1H, *J* = 8.2 and 8.2 Hz, H_4), 3.87 (s, 6H, 2 (CH_3)O *meta*), 3.85 (s, 3H, MeO *para*) 3.72-3.60 (m, 2H, Me_2CHO, H_4), 3.01 (dd, 1H, *J* = 13.3, 3.7 Hz, *H* benzyl), 2.68–2.46 (m, 3H, *H* benzyl H_3 and H_2) 1.11 and 0.91 (2 d, 6H, *J* = 6.2 Hz, $(CH_3)_2CHO$); ^{13}C NMR ($CDCl_3$) δ: 153.1, 147.7, 146.0, 138.5, 133.6, 132.8 (7 *C*quat. arom, C=O), 121.5, 108.9, 108.1, 104.5, 101.6 (5 *C*H arom and OCHO), 100.8 (OCH_2O), 81.0 (*C*H benzyl), 71.2 (CH_2O), 68.8, 60.8, 56.1, 53.8 (3 CH_3O, Me_2CHO, *C*-2, *C*-3), 40.5 (CH_2 benzyl), 23.5 and 21.4 ($(CH_3)_2CHO$).

*Compound **15** and (*trans-trans*)-6-isopropoxy-5-(3,4,5-trimethoxyphenyl)-5,5a,6,8,8a,9-hexahydrofuro[3′,4′:6,7]naphtho[2,3-*d*][1,3]dioxole (23)*

After dissolving compound **22** (40 mg) in dichloromethane (0.03 M, 2.5 mL), trifluoroacetic acid (6 equiv., 0.033 mL) was added at −15°C. The reaction mixture was stirred overnight at room temperature, poured into ether (25 mL), and washed with saturated sodium bicarbonate, then with brine. The organic phase was dried ($MgSO_4$), filtered, and concentrated. Flash chromatography with 20–40% ethyl acetate – hexane gave 12 mg of compound **15** (41%) and 5 mg of compound **23** (15%). PCC oxidation of **15** gave isodeoxypodophyllotoxin.

For compound 23: ^1H NMR ($CDCl_3$) δ: 6.59 (s, 1H, C*H* arom), 6.37 (s, 2H, C*H* arom), 6.31 (s, 1H, C*H* arom), 5.87 (d, 1H, *J* = 1.3 Hz, OCH_2O), 5.86 (d, 1H, *J* = 1.4 Hz, OCH_2O), 4.81 (d, 1H, *J* = 4.3 Hz, OC*H*O), 4.25 (dd, 1H, *J* = 7.7 and 7.7 Hz, CH_2O), 4.06 (d, 1H, *J* = 11.9, C*H* benzyl), 3.85 (s, 3H, CH_3O), 3.80 (m, 7H, 2 CH_3O, Me_2CHO), 3.57 (dd, 1H, *J* = 9.5 and 8.1 Hz, CH_2O), 2.97 (dd, 1H, *J* = 14.9 and 4.6 Hz, CH_2 benzyl), 2.69 (dd, 1H, *J* = 14.9 and 14.3 Hz, CH_2 benzyl), 2.59–2.50 (m, 1H, C*H*CH_2 benzyl), 1.97 (ddd, 1H, *J* = 16.1, 11.7, 4.2 Hz, C*H*CH benzyl), 1.18 and 1.09 (2 d, 6H, *J* = 6.1 and 6.2 Hz, $(CH_3)_2CHO$); ^{13}C NMR ($CDCl_3$) δ: 153.1, 146.0, 145.9, 140.7, 137, 133.4, 129.2 (8 *C*quat. arom), 109.6, 108.5, 106.1, 101.1 (4 *C*H arom and OCHO), 100.8 (OCH_2O), 72.4 (CH_2O), 77.2, 69.1, 60.9, 56.1, 54.3, 46.5, 37.7 (3 CH_3O, Me_2CHO, *C*HCH_2 benzyl, *C*HCH benzyl, *C*H benzyl), 34.1 (CH_2 benzyl), 23.7 and 22.3 ($(CH_3)_2CHO$); HRMS for $C_{25}H_{30}O_7$, calcd.: 442.1992; found: 442.2002; MS (EI/HR) for $C_{25}H_{30}O_7$: 442 (M), 382 (M−2-propanol), 351 (M−2-propanol − MeO).

Acknowledgments

We acknowledge generous financial assistance given by the Natural Sciences and Engineering Research Council of Canada. (NSERC), through the Medicinal Chemistry Chair program, FCAR, and Merck Frosst. We thank Dr. M. Simard for X-ray crystallographic analysis.

References

1. (*a*) R.S. Ward. Nat. Prod. Rep. **12**, 183 (1995); (*b*) Nat. Prod. Rep. **10**, 1 (1993); (*c*) T. Morimoto and M. Chiba. Heterocycles, **33**, 435 (1992); (*d*) R.S. Ward. Tetrahedron, **46**, 5029 (1990).
2. (*a*) O. Middel, H.J. Woerdenbag, W. van Uden, A. van Oeveren, J.F.G.A. Jansen, B.L. Feringa, A.W.T. Konings, N. Pras, and R.M. Kellogg. J. Med. Chem. **38**, 2112 (1995); (*b*) W.D. MacRae and G.H.N. Towers. Phytochemistry, **23**, 1207 (1984); (*c*) D.C. Ayres and J. D. Loike. *In* Lignans. Chemical, biological and clinical properties. Cambridge University Press, London. 1990. Chaps 3 and 4, and references cited therein.
3. For a review: (*a*) R.S. Ward. Synthesis, 719 (1992), and references cited therein. For total synthesis: (*b*) E.J. Bush and D.W. Jones. J. Chem. Soc. Chem. Commun. 1200 (1993); (*c*) R.V. Speybroeck, H. Guo, J. Van der Eycken, and M. Vandewalle. Tetrahedron, **47**, 4675 (1991); (*d*) N. Rehnberg and G. Magnusson. J. Org. Chem. **55**, 4340 (1990); (*e*) R.C. Andrews, S.J. Teague, and A.I. Meyers. J. Am. Chem. Soc. **110**, 7854 (1988). Formal total synthesis: (*f*) G.A. Kraus and Y. Wu. J. Org. Chem. **57**, 2922 (1992).
4. A.S. Kende and L.S. Liebeskind. J. Am. Chem. Soc. **98**, 267 (1976).
5. (*a*) H. Ishibashi, K. Ito, T. Hirano, M. Tabuchi, and M. Ikeda. Tetrahedron, **49**, 4173 (1993), and references cited therein; (*b*) M.B. Glinski, J.C. Freed, and T. Durst. J. Org. Chem. **52**, 2749 (1987); (*c*) A. Pelter, R.S. Ward, and N.P. Storer. Tetrahedron, **50**, 10829 (1994); (*d*) A. Kamal and M. Daneshtalab. Tetrahedron Lett. **35**, 3879 (1994). Analogs: (*e*) J.L. Charlton, G.L. Plourde, K. Koh, and A.S. Secco. Can. J. Chem. **68**, 2022 (1990).
6. (*a*) A. Pelter, R.S. Ward, L. Qianrong, and J. Pis. Tetrahedron: Asymmetry, **5**, 909 (1994); (*b*) A. van Oeveren, J.F.G.A. Jansen, and B.L. Feringa. J. Org. Chem. **59**, 5999 (1994); (*c*) A. Suárez, F. López, and R.S. Compagnone. Synth. Commun. **23**, 1991 (1993); (*d*) J.A. Gaboury and M.P. Sibi. J. Org. Chem. **58**, 2173 (1993); (*e*) T. Morimoto, M. Chiba, and K. Achiwa. Tetrahedron, **49**, 1793 (1993); (*f*) D.W. Jones and A.M. Thompson. J. Chem. Soc. Perkin Trans 1, 2541 (1993); (*g*) T. Itoh, J.-I. Chika, Y. Takagi, and S. Nishiyama. J. Org. Chem. **58**, 5717 (1993), and references cited therein; (*h*) M.P. Sibi and J.A. Gaboury. Synlett, 83 (1992); (*i*) P. Boissin, R. Dhal, and E. Brown. Tetra-

hedron, **48**, 687 (1992); (*j*) A. Pelter, R.S. Ward, D.M. Jones, and P. Maddocks. Tetrahedron: Asymmetry, **3**, 239 (1992); (*k*) T. Morimoto, M. Chiba, and K. Achiwa. Tetrahedron Lett. **31**, 261 (1990); (*l*) J.-P. Robin, R. Dhal, and E. Brown. Tetrahedron, **38**, 3667 (1982); (*m*) F.E. Ziegler and J.A. Schwartz. J. Org. Chem. **43**, 985 (1978); (*n*) R.E. Damon and R.H. Schlessinger. J. Org. Chem. **41**, 3772 (1976).

7. (*a*) T.W. Doyle, B.F. Issell, F.M. Muggia, S.K. Carter, D. Schaefer, and J. Schuring. *In* Etoposide (VP-16), Current status and new developments. *Edited by* B.F. Issell, F.M. Muggia, and S.K. Carter. Academic Press, New York. 1984; (*b*) I. Jardine. *In* Anticancer agents based on natural product models products. *Edited by* J.M. Cassady and J. Douros Academic Press, New York. 1980. pp. 319–351.
8. J. Aisner, M.Y. Whitacre, D.R. Budman, K. Propert, G. Strauss, D.A. Vanecho, and M. Perry. Cancer Chemother. Pharmacol. **29**, 435 (1992).
9. B.A. Price and N.H. Peters. Eur. J. Cancer, **28**, 615 (1992).
10. (*a*) E.A. Stadtmauer, P.A. Cassileth, and R.P. Gale. Leuk. Res. **13**, 639 (1989); (*b*) B. Bastrom, D.J. Weisdorf, T. Kim, J.H. Kersey, and N.K.C. Ramsay. Bone Marrow Transplant. **5**, 83 (1990).
11. (*a*) J.L. Belletire and N.O. Mahmoodi. J. Nat. Prod. **55**, 194 (1992); (*b*) E. Lee, C.U. Hur, Y.C. Jeong, Y.H. Rhee, and M.H. Chang. J. Chem. Soc. Chem. Commun. 1314 (1991); (*c*) M.P. Doyle, M.N. Protopopova, Q.L. Zhou, and J.W. Bode. J. Org. Chem. **60**, 6654 (1995).
12. S. Hanessian and R. Leger. J. Am. Chem. Soc. **114**, 3115 (1992).
13. S. Hanessian and R. Leger. Synlett, 402 (1992).
14. S. Hanessian and S. Ninkovic. J. Org. Chem. **61**, 5418 (1996).
15. G. Stork and P.M. Sher. J. Am. Chem. Soc. **108**, 303 (1986).
16. J.E. Baldwin. J. Chem. Soc. Chem. Commun. 734 (1976).
17. (*a*) P. Jacob III, P.S. Callery, A.T. Shulgin, and N.Jr. Castagnoli. J. Org. Chem. **41**, 3627 (1976); (*b*) L. Syper, K. Kloc, J. Mlochowski, and Z. Szulc. Synthesis, 521 (1979).
18. T.R. Hoye and P.A. Kease. Synth. Commun. **12**, 49 (1982).
19. (*a*) C.L. Wong and J.K. Kochi. J. Am. Chem. Soc. **101**, 5593 (1979); (*b*) S. Lochynski, B. Boduszek, and H.J. Shine. J. Org. Chem. **56**, 914 (1991).

Studies on the interaction of selenite and selenium with sulphur donors. Part 5. Thiocyanate[1]

Christopher Milne and John Milne

Abstract: The oxidation of thiocyanic acid by selenous acid has been shown to take place in an analogous way to that found for selenous acid oxidation of most thiols and thiolates to give the corresponding selenotrisulfide and disulfide products.

$$H_2SeO_3 + 4\ HSCN = Se(SCN)_2 + NCSSCN + 2\ H_2O$$

The products of this reaction have been studied by IR, Raman, and Se-77, C-13, and N-15 NMR spectroscopy. The vibrational spectra of the solid $Se(SCN)_2$ have been assigned based on S-bonded thiocyanate ligands and, through NMR and vibrational spectroscopy, both this linkage isomer and the isomer with N- and S-bonded thiocyanate have been identified and characterized in solutions of $Se(SCN)_2$. A complex combination of scalar relaxation processes, involving chemical exchange and quadrupolar effects, accounts for the line broadening observed in the carbon-13 NMR spectra.

Key words: selenite, thiocyanate, selenium dithiocyanate, Se-77, N-15, and C-13 NMR; Raman spectroscopy; linkage isomerism.

Résumé : On montre que l'oxydation de l'acide thiocyanique par l'acide sélénieux suit une voie analogue à celle trouvée pour l'oxydation de la plupart des thiols et des thiolates par l'acide sélénieux pour donner les sélénotrisulfures correspondants et des produits disulfurés.

$$H_2SeO_3 + 4\ HSCN = Se(SCN)_2 + NCSSCN + 2\ H_2O$$

On a étudié les produits de cette réaction par la spectroscopie IR, Raman et par la RMN du Se-77, du C-13 et du N-15. On a attribué les spectres de vibration du $Se(SCN)_2$ solide en se basant sur les ligands thiocyantes liés par le soufre, et au moyen de la RMN et de la spectroscopie vibrationnelle dans des solutions de $Se(SCN)_2$, on a identifié et caractérisé cet isomère de liaison et l'isomère où le thiocyanate est lié par l'azote et le soufre. Une combinaison complexe du processus de relaxation scalaire, impliquant un échange chimique et des effets quadrupolaires, est reponsable de l'élargissement de la raie observé dans les spectres de RMN du C-13.

Mots clés : sélénite; thiocyanate; dithiocyanate de sélénium; RMN du Se-77, du N-15 et du C-13; spectroscopie Raman; isomérie de liaison.

[Traduit par la rédaction]

Introduction

Selenium dithiocyanate was first prepared by Ohlberg and van der Meulen (1) from selenous acid and thiocyanic acid. They proposed that the main reaction was represented by

[1] $3\ H_2SeO_3 + 7\ HSCN = 3\ Se(SCN)_2 + 5\ H_2O + HCN + H_2SO_4$

as supported by chemical analysis of the products. Selenous acid usually reacts cleanly with thiolic compounds to give selenotrisulfide and disulfide products (2).

[2] $H_2SeO_3 + 4\ RSH = RSSeSR + RSSR + 2\ H_2O$

although some exceptions are known (3). Selenium dithiocyanate, as the solid and in solution, and the course of reaction [1] have not been studied by vibrational and NMR spectroscopic methods and this was of interest in relation to other thiol oxidations by selenous acid studied in this series (2*d*, 3*a*). Oxygen- and sulphur-bonded selenium (II) species have been observed in the course of the oxidation of sulfite and thiosulfate ions by selenous acid. Such linkage isomerism may arise in selenium dithiocyanate with both N and S bonding to selenium(II) possible, in addition to stereoisomerism arising from the *cis* or *trans* arrangement of the CN groups with respect to the SSeS plane. Stereoisomerism has been observed in solid selenopentathionates (4) but no evidence for it has been found

Received June 4, 1996.

C. Milne and J. Milne.[2] Ottawa–Carleton Chemistry Institute, Department of Chemistry, University of Ottawa, Ottawa, ON K1N 6N5, Canada.

[1] Part 4: See ref. 2*d*.

[2] Author to whom correspondence may be addressed. Telephone: (613) 562-5800, ext. 6054. Fax: (613) 562-5170. E-mail: jmilne@oreo.chem.uottawa.ca

in solution phase (2*d*). Solid selenium dithiocyanate contains isolated $Se(SCN)_2$ molecules with S-bonding to Se(II) and a cis arrangement of the CN groups (5). No spectroscopic characterization of $Se(SCN)_2$ has been done and the reported stoichiometry (1) of the SeO_2/SCN^- reaction is exceptional compared to that of other reactions of SeO_2 with thiolates. This work was undertaken to explore the parallel with other work on SeO_2 oxidation of thiolates and extend our understanding of Se(II) chemistry.

Experimental section.

Materials

Freshly ground vitreous selenium (BDH), selenium dioxide (Aldrich), analyzed by titration (3*a*), trifluoroacetic acid (3 M), ammonium thiocyanate (Mallincrodt), and ^{13}C and ^{15}N enriched potassium thiocyanate (Cambridge Isotope Laboratories) were used directly. Dioxane and THF were treated with cuprous chloride to remove peroxide. These solvents as well as acetonitrile were distilled from phosphorus pentoxide to remove traces of water. Acetic acid was treated with acetic anhydride, then distilled. Dimethyl formamide was distilled from fresh Drierite. All boiling temperatures were within accepted ranges.

Preparations

Selenium dithiocyanate was prepared from solutions of selenium dioxide in dilute hydrochloric acid and aqueous thiocyanate (1), mixed at 0°C. The yellow crystals, which were thoroughly washed with glacial acetic acid and ether, were stable over a period of months at −5°C. The X-ray powder pattern confirmed that the product was identical with that characterized by Ohlberg and Vaughan (5). All solutions decomposed, producing red selenium, over a period of hours. Decomposition was accelerated by the presence of water.

Thiocyanogen, 0.2 M in a 1:20:13 mole ratio acetic anhydride/acetic acid/carbon tetrachloride solution was prepared by a standard method (6).

Methods

Raman spectra were measured as described previously (3). The mass spectrum was measured with a VG 7070E spectrometer. Selenium-77, carbon-13, and nitrogen-15 NMR spectra of solutions were measured on a Bruker AMX 500 spectrometer operating at 95.47, 125.77, and 50.69 MHz respectively. Carbon-13 spectra were also measured on Varian FT300 (75.46 MHz) and Gemini 200 (50.31 MHz) spectrometers. Sample concentrations were generally of the order of tenth molar. Selenium-77 spectra were taken using conditions described previously (2*d*). Normally at least 500 transients were taken, giving a signal-to-noise ratio (S/N) of 10. Nitrogen-15 spectra were measured using a 26 μs pulse width and a 15 s pulse delay. Spectra were made up from 120 transients, giving S/N of 8. At the end of an experiment no decomposition of the sample was observed. Spectral resolution was between 0.4 and 1.2 Hz/data point. The chemical shifts were measured from $CH_3{}^{15}NO_2$. Carbon-13 spectra were taken with a 16 μs pulse width and a 10 s pulse delay. A S/N of 20 was achieved with 32 transients. Spectral resolution was 0.5–1.2 Hz/data point. The MAS Se-77 NMR spectra were measured at 38.16 MHz on a Bruker ASX200 spectrometer using a 120 s pulse delay with a 4 μs pulse width. The spectral resolution was 44 Hz/data point. At 5 kHz spin rate S/N was 6 for 12 transients while at 2 kHz, S/N was 6 for the strongest signal with 57 transients. Although no CP enhancement of the signal was possible via protons, the spectrum was obtained easily.

Results and discussion

Selenothiocyanate, $SeSCN^-$, formation constant

Elemental selenium dissolves to a small extent in solutions of thiocyanate (29 ± 4 mg Se in 100 mL 0.20M NH_4SCN). Gravimetric analysis gives $K = 4 \times 10^{-3}$ for the equilibrium,

[3] $SCN^- + Se = SeSCN^-$

This is comparable to the formation constant for the selenothiosulfate (3.6×10^{-3} (2*d*)) but is much smaller than that observed for 2-hydroxyethanethiolate (0.382 (7)) and sulfite (0.515 (3)). There is an inverse relationship between the seleno-anion formation constant and the proton dissociation constant of parent sulphur acid. Thiocyanic acid (8) and the hydrogen thiosulfate[3] anion are moderately strong acids while 2-mercaptoethanol and the hydrogen sulfite ion, especially the HSO_3^- tautomer, which is the principal species in solution (9), are weak acids.

The reaction of selenous acid with thiocyanic acid

When selenous acid is added to aqueous thiocyanic acid in the molar ratio of 1:4 (1), a yellow coloured solution is formed from which slowly precipitate golden needles of selenium dithiocyanate (1). When this reaction is monitored by Se-77 NMR at 3°C, only the selenous acid signal at 1292 ppm is observed and this decreases in intensity with time. The solubility of $Se(SCN)_2$ in water is insufficient to permit observation of the signal for this product. The C-13 NMR spectrum of the solution exhibits initially a strong broad resonance with a half-height line width ($w_{1/2}$) of 45 Hz at 130.5 ppm that lies close to the chemical shift for aqueous SCN^- at 134 ppm (10), for which we found $w_{1/2}$= 13 Hz. The breadth and shift of this signal shows that thiocyanate is undergoing exchange with species such as the SeO_2SCN^- ion and $SeO(SCN)_2$, which are likely intermediates on the way to $Se(SCN)_2$, judging from the mechanism for reaction of thiols with H_2SeO_3[4]. A very weak signal is also observed at 104.4 ppm ($w_{1/2}$ = 2 Hz), which grows in intensity with time as the broad signal weakens and shifts down field to 132.7 ppm and $Se(SCN)_2$ precipitates. A solution of dithiocyanogen 0.20 M in 1/20/13 acetic anhydride/acetic acid/carbon tetrachloride (6) gave a narrow chemical shift ($w_{1/2}$= 2.2 Hz) at 108.9 ppm and the narrow signal in the aqueous H_2SeO_3–thiocyanate solution is due to this species. The 5.5 ppm difference in chemical shift results from solvent effects. No other signals were observed. The reaction of H_2SeO_3 with thiocyanic acid in 1:4 molar ratio leads to the typical products of H_2SeO_3/thiol reactions (2).

[4] $H_2SeO_3 + 4\ HSCN = NCSSeSCN + NCSSCN + 3\ H_2O$

In as much as no signal at 167.9 ppm, which would indicate the presence of CN^- ion, was observed even after a day of

[3] J. Milne, unpublished.

standing, dithiocyanogen appears to be stable in water under these conditions and no decomposition to cyanide and sulfate ion as reported by Ohlberg and Van der Meulen (1) was observed.

Crystalline selenium dithiocyanate

X-ray powder diffractometry confirms the orthorhombic unit cell found in earlier photographic work (5) with more precise unit cell dimensions (a = 9.908(1) Å; b = 13.047(2) Å; c = 4.417(3) Å). Refinement of the powder intensities under *Pnma* symmetry (Z = 4) gives atomic positions consistent with those reported and shows that the molecule has C_s symmetry, that the CN groups are *cis* with respect to the SSeS plane, and that the SCN groups are linear.[4]

The Raman spectrum of solid $Se(SCN)_2$ is shown in Fig. 1 and the IR and Raman spectra are listed in Table 1 along with a partial assignment of the bands. The crystal structure shows a central Se with S-bonded thiocyanate ligands and C_s symmetry for which 15 vibrational modes are expected (8A′ + 7A″). The three A′ stretching modes, ν(SeS), ν(SC), and ν(CN), are readily assigned by comparison with comparable modes for other selenotrithionate species (2*d*, 3*a*, 7) and for thiocyanate ion (11) and by their ease of observation by Raman spectroscopy where symmetric modes are usually strong, at 359, 678, and 2141 cm^{-1}, respectively. The band at 340 cm^{-1} is assigned to the *A″* SeS stretching mode, which lies below the *A″* stretching mode in bis(2-hydroxyethanethiol)selenium ($\nu(A')$ = 396 cm^{-1}; $\nu(A'')$ = 372 cm^{-1}(7)). Both the *A′* and *A″* SeX_2 stretching frequencies for the related SeX_2 molecules (X = Cl, F) (12) and the relative Raman intensities of these two SeS_2 stretching modes in Fig. 1 support this assignment. The weak IR band at 2068 cm^{-1} is the *A″* CN stretching mode. The in- and out-of-plane symmetric and asymmetric SCN deformation modes are assigned to the four peaks at 409,440,457, and 480 cm^{-1}, which are close to this mode in the SCN^- spectrum (11). The SeSC deformation modes are probably masked by the SeS stretching bands. The strong band at 168 cm^{-1} is assigned to the SSeS deformation mode, which is found in the spectra of the $Se(S_2O_3)_2^{2-}$ ion (2*d*) and $SeCl_2$ (12) at 162 and 165 cm^{-1}, respectively. The peaks at 110 and 131 cm^{-1} are assigned to the *A′* and *A″* torsional modes and the remaining low-frequency bands at 59, 74, and 104 cm^{-1} probably arise from lattice modes.

The electron impact mass spectrum of $Se(SCN)_2$ shows the characteristic isotopic intensity profile of Se (49/24/9/9/8 for isotopes 80/78/82/76/77; respectively) for the parent molecular ion (centred at 196), SeSCN (mass:138), SeS (mass:112), Se (mass:80). Species like SeN, SeN_2, SeNC, and $Se(NC)_2$ are not observed, indicating that N-bonded Se is either of low stability or not present. In addition, fragments such as CN, S, SCN are present in addition to HNCS, resulting from traces of water in the spectrometer itself.

The Se-77 NMR spectrum of crystalline $Se(SCN)_2$ at a MAS spin rate of 5 kHz consists of a single line at 997 ppm, which is the isotropic chemical shift. The single line at this spin rate indicates that only one site exists for the Se atoms in the unit cell, consistent with the reported crystal structure (5), and that the site is highly isotopic. At 2 kHz MAS spin rate, five lines are observed. The line intensities of the side bands

[4] C. Bensimon and J. Milne, unpublished.

Fig. 1. The Raman spectrum of crystalline $Se(SCN)_2$.

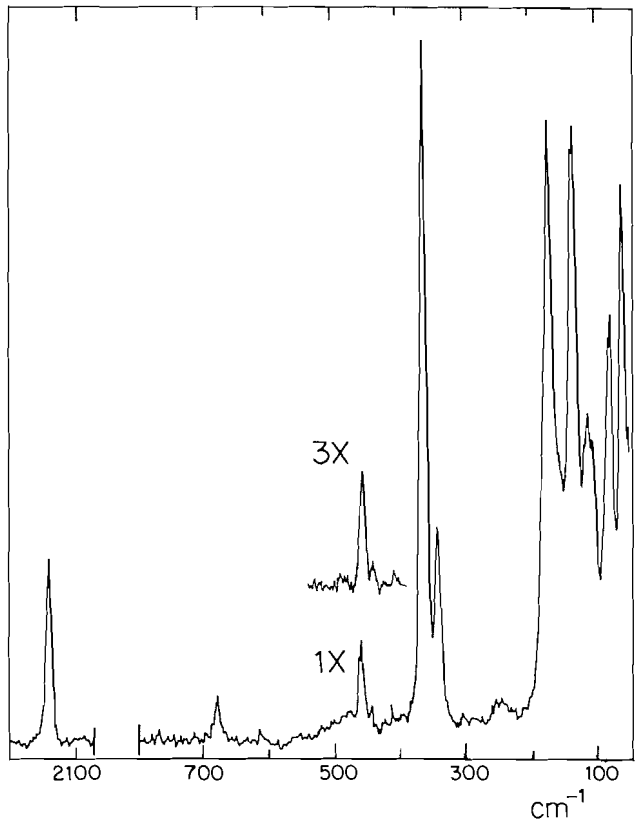

relative to the isotropic line intensity were used to calculate the chemical shift tensors by the Herzfeld–Berger method (13) giving $\sigma_{11} = -124 \pm 4$, $\sigma_{22} = -12 \pm 2$ and $\sigma_{33} = 136 \pm 6$ ppm. These chemical shift tensors are among the smallest observed (14) and are unusual in a compound of such low symmetry. This may be a reflection of the ionic character of the Se(II)—SCN bond. The electronegativity of the thiocyanate group has been reported to be comparable with that of chlorine (15).

Solutions of selenium dithiocyanate

Selenium dithiocyanate exhibits generally low solubility (1) and solutions precipitate red selenium within an hour at laboratory temperatures, especially in the presence of water. Saturation solubilities at 25°C, estimated to be 0.15 ± 0.3 M, are found for acetone, acetonitrile, dioxane, and tetrahydrofuran, which are among the best solvents for the compound. Decomposition was more rapid in acetone. The concentrations were sufficient for the measurement of IR, Raman, and NMR spectra provided that solutions were made up cold and run immediately.

NMR spectroscopy

The Se-77 NMR chemical shifts and intensities of $Se(SCN)_2$ in acetonitrile, acetic acid(HOAc), trifluoroacetic acid, (HOTFA), dimethyl formamide(DMF), dioxane, and tetrahydrofuran(THF) are listed in Table 2. In all cases except for HOTFA, two signals are observed with the least shielded the most intense. The chemical shifts are consistent with those of Se(II) compounds where the ligand has electronegativity

Table 1. IR and Raman spectra of $Se(SCN)_2$, solid and in solution.

$Se(SCN)_2$								
Solid		In THF						
Raman	IR[c]	Raman	IR[c]	In AN Raman	In D Raman	SCN^-[a] Raman	$(SCN)_2$[b] Raman	Assignment ($Se(SCN)_2$)
59(7)	—	—	—	—	—	—	—	Lattice modes
74(4)	—	—	—	—	—	—	—	
104(3)	—	—	—	—	—	—	—	
110(3)	—	—	—	—	—	—	—	τ
131(8)	—	—	—	—	—	—	—	
168(8)	—	160(0)	—	—	—	—	—	δ (SSeS)
—	—	270(1)	—	—	270(1)	—	—	
339(2)	—	348(7)	—	350(10)	350(10)	—	—	ν (SeS_2)
359(10)	—	365(10)	—	368(10)	360(10)	—	—	
409(0)	—	410(0, br)	—	—	—	—	396(10)	δ (SCN)
440(0)	—	450(1)	—	—	—	—	—	
457(1)	—	—	—	460(2)	458(0, sh)	—	—	
480(0)	—	488(1)	—	—	—	485[d]	—	
—	—	—	—	—	—	—	489(6)[e]	
—	—	570(0)	—	580(0)	—	—	—	ν (SC)
—	669(w)	—	—	—	—	—	—	
678(1)	676(w)	670(0)	—	680(0)	670(2, br)	751(8)	[f]	
—	—	—	799(m)	—	—	—	—	ν(S=C)
—	—	[f]	—	[f]	938(2)	—	—	
—	—	—	994(w)	—	—	—	—	
—	—	—	—	—	—	1235(1)[g]	—	ν(N=C)
—	—	—	1778(va)	—	—	—	—	$\nu(C\ N)_a$
—	2068(m)	—	2028(m)	—	—	—	—	$\nu(C\ N)_s$
2141(7)	2145(s)	2148(3)	2149(s)	2150(1)	2150(3, br)	2063(10)	2152(6)	

[a]2 M KSCN.
[b]0.2 M $(SCN)_2$ in 1:20:13 Ac_2O/HOAc/CCl_4.
[c]To 650 cm^{-1}.
[d]Calculated from the overtone at 1235 cm^{-1} and ν(SC).
[e]ν(SS).
[f]Masked by solvent.
[g]Overtone (δ(SCN) + ν(SC)).

Table 2. Se-77 chemical shifts for $Se(SCN)_2$.

Solvent	T(°C)	Chemical shifts[a] (ppm)	$W_{1/2}$[c] (Hz)
Acetronitrile	27	960(1.0), 1002(1.5)	29/36
Dioxane	27	968(1.0), 1018(1.8)	30/30
Dioxane (0.04% HOTFA)	27	967(1.0), 1018(1.23)	69/47
THF	27	987(1.0), 1040(1.7)[b]	45/38
HOAc	27	963(1.0), 1007(1.5)	55/84
DMF	−33	993(1.0), 1041(3.3)	35/80
HOTFA	27	993	
Solid	27	997	

[a]δ referred to $\delta(Me_2Se)$ = 0.0 ppm; intensities in parentheses.
[b]Weak signals developed over 1 h at 960 and 1054 ppm.
[c]Half-height line widths; same respective order as chemical shifts.

above 3.0 (16, 17). Comparison of the Raman spectra of these solutions (vide infra) with that of crystalline $Se(SCN)_2$ show that S-bonded $Se(SCN)_2$ is present. Two types of isomerism, rotational (4) and linkage (2*d*, 3), are expected for thiocyanate bound to Se(II). Rotational isomers with CN groups *cis* or *trans* to the SeS_2 plane have only been observed in solids (4) and are unlikely in solution due to the expected low barrier to rotation about the SeS bond. For the SS bond, this barrier, which is probably higher than or comparable to that for the SeS bond, is estimated to be 25–38 kJ mol^{-1} (18) and restricted rotation about the SS bond in 1,2-dithiane is rapid on the proton NMR time scale at ambient temperatures (19). In solution both the selenotrithionates and selenopentathionates exhibit O- and S-bonded linkage isomerism (2d,3) and selenium dithiocyanate apparently forms N- and S-bonded isomers in a similar fashion. Three isomers are possible, NCSSeSCN(SS), NCSSeNCS(NS), and SCNSeNCS(NN), and in analogous cases (3*a*, 20) all are observed. The observa-

Table 3. N-15 chemical shift (δ), half height line widths ($w_{1/2}$), and peak areas (A) of Lorentzian curve-resolved peaks for solutions of $Se(SCN)_2$.

Solvent	δ_1[a] (ppm)	$w_{1/2}$ (Hz)	A_1[b]	δ_2[a] (ppm)	$w_{1/2}$ (Hz)	A_2[b]	δ_3[a] (ppm)	$w_{1/2}$ (Hz)	A_3[b]
THF	−100.3	740	1.0	−112.5	247	0.86	−117.6	233	1.36
Dioxane	−94.7	997	1.0	−102.5	362	0.85	−106.1	253	1.35

[a]δ_1: N-15 bound to Se; δ_2: N-15 terminal in the NS isomer; δ_3: N-15 terminal in the SS isomer.
[b]Normalized to the area of the δ_1 shift.

tion of just two signals is probably due to the presence of just the SS and NS isomers. It is not possible to assign either signal unequivocally to the SS isomer on the basis of the chemical shift for the solid, which is known to contain the SS isomer, because of the uncertainty in the solid to solution shift, which is usually of the order of 10 ppm (14). The chemical shift for the solid, 997 ppm, lies between the two signals observed in the solution spectra. Since the shift range for Se(II) bonded to nitrogens (1128–1394 ppm (21)) is in general higher than that of Se(II) bonded to sulphurs (430–687 ppm (21)), as expected on the basis of the electronegativity difference between N and S, the more deshielded signal above 1000 ppm is assigned to the NS isomer and the more shielded signal, to the SS isomer. The signal intensities show that more of the NS isomer than the SS isomer is present in all solutions.

The N-15 NMR spectra of $Se(SCN)_2$ in THF and dioxane solutions show two peaks (THF: −100.3, −117.6 ppm; dioxane: −94.7, −106.1 ppm) with a distinct shoulder or skewing to the less screened side of the stronger peak. The spectrum of a 0.2 M solution of $Se(SCN)_2$ in THF is shown in Fig. 2. Curve resolution of the spectral envelope, assuming Lorentzian line shapes, shows three signals. The chemical shifts, half-height line widths, and relative peak areas for the curve-resolved peaks are given in Table 3. The SS isomer will exhibit a single N-15 resonance while the NS isomer is expected to give two N-15 signals, one for terminal N and the other for N bonded to Se. The nitrogen bonded to C and Se is expected to be less shielded than the terminal nitrogen and the signal to low field is therefore assigned to N-15 in the N-bonded thiocyanate moiety of the NS isomer, while the nearly overlapped signals to high field arise from the S-bonded thiocyanates in both the SS and NS isomers. The signal areas of the peaks for the NS and SS isomers are consistent with the areas determined from Se-77 NMR spectra and show that the NS isomer is present in higher concentration than the SS isomer. Upon cooling the THF sample to 223 K, the less shielded signal disappears, the signal at −117.6 ppm shifts to −119.6 ppm, and the half-height line width decreases to 220 Hz. The SS isomer is apparently favoured at lower temperatures.

The C-13 NMR spectrum of $Se(SCN)_2$ (natural abundance nitrogen) in THF consists of a single broad resonance at 115.9 ppm ($w_{1/2}$ = 131 Hz at 11.74 T). The most likely origin of the signal breadth is scalar relaxation due to chemical exchange and spin coupling to the quadrupole of nitrogen-14, with other relaxation processes playing a minor role. Both scalar relaxation processes are important. Spectra taken at lower field strengths give narrower signals ($w_{1/2}$ = 70 Hz at 7.044 T; $w_{1/2}$ = 40 Hz at 4.696 T). This behaviour is characteristic of broadening due to chemical exchange and not coupling to a quadrupolar relaxed nucleus (22). On the other hand, decrease in temperature results in narrowing of the C-13 signal down to T = 207.5 K, as shown in Table 4 and Fig. 3, which is typical of relaxation by coupling to a quadrupolar nucleus (22). Assuming that the half-height line width is inversely related to the correlation time and directly related to the rate of the correlation process, a plot of $\ln(w_{1/2})$ vs. $10^3/T$ should yield a straight line giving the activation energy for the process. The plot in Fig. 3 shows that the line width is governed by several processes and that as the temperature is lowered chemical exchange begins to play a more important role with the line eventually broadening with decrease in temperature. The limiting slope at the highest temperatures measured (decomposition occurred rapidly at elevated temperatures) gives an activation energy of 15 kJ/mol, which is low and consistent

Fig. 2. Nitrogen-15 NMR spectrum of $Se(SCN)_2$ dissolved in THF. Vertical lines indicate the position and maximum intensity of the N-15 bands in the SS and NS isomers. The Lorentzian lineshapes are indicated by dashed lines.

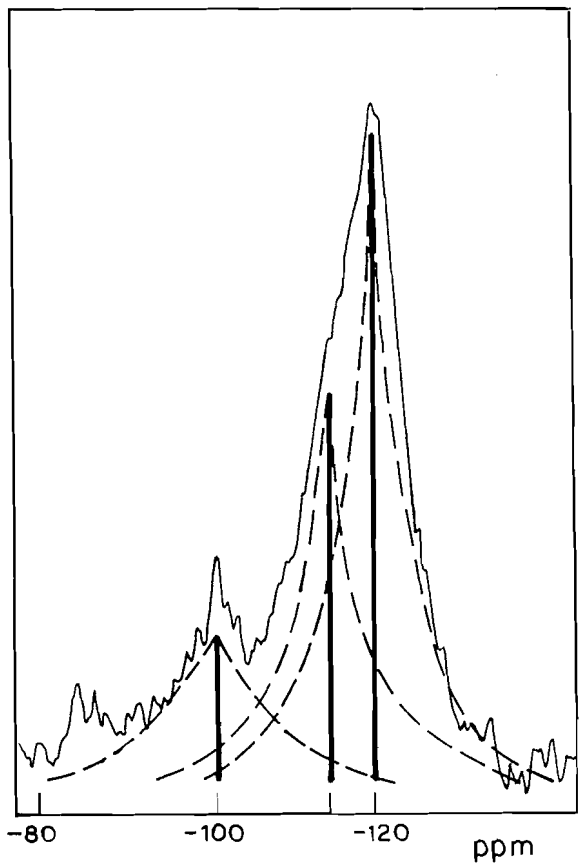

Fig. 3. A plot of the logarithm of the half-height line width vs. temperature (K) showing the transition from the quadrupole relaxation broadening to chemical exchange broadening.

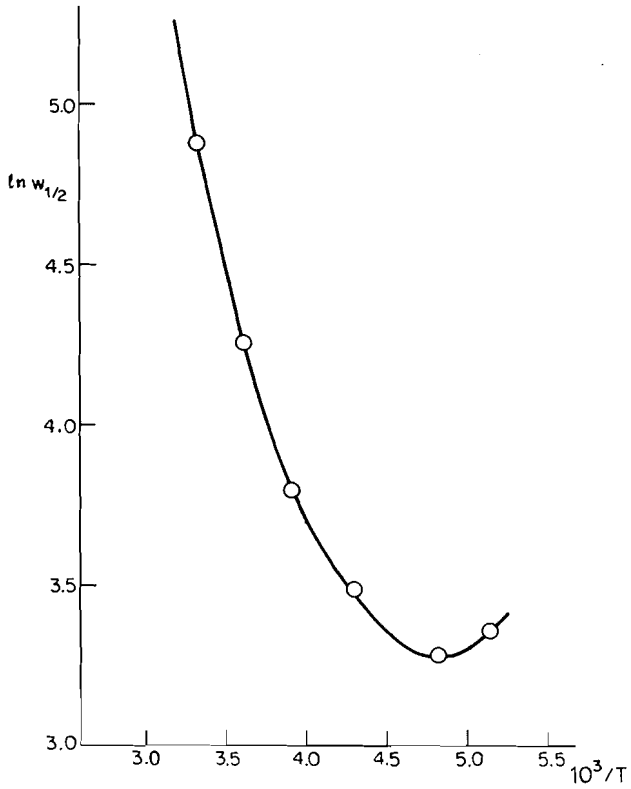

with a facile process such as tumbling of the solute in a weakly solvating solvent. The halfheight line widths for thiocyanogen (see above) and thiocyanate ion (0.2 M $KS^{13}CN$ in H_2O) are 2.2 and 13 Hz, respectively, and, since, in media of comparable viscosity, $Se(SCN)_2$ with its larger size would be expected to tumble more slowly and exhibit an even narrower signal due to quadrupolar relaxation, it is apparent that chemical exchange must contribute significantly to the signal broadening. Thiocyanogen and the thiocyanate ion are not expected to undergo chemical exchange but $Se(SCN)_2$ may undergo intermolecular and intramolecular thiocyanate exchange. No evidence for separate signals due to the SS and NS linkage isomers is observed in the ^{13}C spectrum and, in spite of quadrupole broadening effects, some indication of these isomers would be expected in view of their observation in the ^{15}N NMR spectrum. This indicates that the C-13 signals for the various carbon environments in the isomers of $Se(SCN)_2$ must differ by less than 2 ppm. Reported carbon-13 chemical shifts for ethylthiocyanate and isothiocyanate and the N- and S-bonded thiocyanate ligand in Co(III) complexes differ by 16.7 and 18.2 ppm, respectively (10).

Table 2 shows that the half-height line widths of the Se-77 signals are greater in acetic acid than those measured in THF and dioxane. Addition of trifluoroacetic acid to a dioxane solution of $Se(SCN)_2$ in dioxane leads also to signal broadening. A single narrow signal is observed for $Se(SCN)_2$ dissolved in 100% trifluoroacetic acid, indicating that rapid exchange between linkage isomers is occurring. The exchange is promoted by acid and no doubt occurs via the formation of thiocyanic and isothiocyanic acids, both of which are known (8) and may be readily formed by the protonation of the N-bonded and S-bonded $Se(SCN)_2$ isomers and cleavage of the bond to Se.

Table 4. Variation in the half-height line width of the ^{13}C NMR signal for $Se(SCN)_2$ in THF with temperature.

T(K)	$w_{1/2}$(Hz)
195.0	28.5
207.5	26.5
233.0	32.5
255.4	44.2
276.0	70.0
300.0	131.0

[3] $NCSSeSCN + H^+ = NCSSe^+ + HNCS$

[4] $HNCS = HSCN$

[5] $NCSSe^+ + HSCN = NCSSeNCS + H^+$

While the N-15 NMR spectra for $Se(SCN)_2$ in THF measured at low temperature show an increase in SS isomer concentration, the Se-77 spectra for DMF solutions at −33°C indicate a decrease in SS isomer concentration. A consideration of the relative intensities of the SS and NS isomer Se-77 NMR peaks in Table 2 shows that, in general, the SS isomer concentration falls with decreasing acidity of the solvent. This is consistent with the expected Brønsted and Lewis acidity of $Se(SCN)_2$. The SS isomer with two terminal nitrogens is expected to exhibit stronger basicity towards the proton than the NS isomer with a single terminal nitrogen and a more weakly basic terminal sulphur. Therefore the SS isomer would be favoured in acidic media. In more basic media it might be expected that the Se atom would act as a Lewis acid centre and that the NS isomer would be a stronger Lewis acid than the SS isomer on the basis of the greater electronegativity of nitrogen compared to sulphur. This would result in a higher relative concentration of the NS isomer in DMF due to coordination by the basic solvent at Se(II).

Vibrational spectroscopy

The Raman spectra of $Se(SCN)_2$ in acetonitrile, dioxane and THF, each of which provides a particular vibrational spectral window to observe the isomers present in solution, are listed in Table 1. The IR spectrum of the solution in THF is also given, as well as the spectra for solid $Se(SCN)_2$, the thiocyanate ion, and thiocyanogen. The Raman spectra of the $Se(SCN)_2$ solutions exhibit a strong parallel with that of the solid compound, indicating the presence of the SS isomer. Few additional bands are observed, which might be attributed to the NS isomer, or more correctly the N-bonded NCS group in the NS isomer, since the bands arising from the S-bonded group are probably very similar to related bands in the SS isomer. Additional bands in the Raman spectrum of the solution

compared to that of the solid are observed at 270, 570, and 938 cm^{-1} and the low-frequency member of the SeS stretching bands at 350 cm^{-1} increases in relative intensity when the $Se(SCN)_2$ is in solution. The IR spectrum of the THF solution provides more substantial evidence of the presence of the NS isomer. The strongest band in this spectrum is observed at 1778 cm^{-1}, which is readily attributed to the N-bonded thiocyanate, and a weak peak at 994 cm^{-1}, which may be due to an overtone. Judging from the frequency of the CN stretching mode in the N-bonded isomer, the CN bond adopts considerable double bond character when thiocyanate is N-bonded, consistent with a resonant form having a non-linear SeNC bond angle and doubly bonded terminal sulphur.

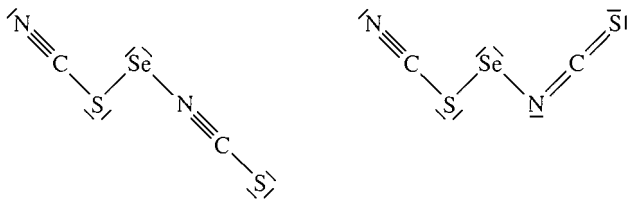

A B

The additional bands in the Raman spectrum are readily assigned on the basis of structure **B**. The band at 270 cm^{-1} is assigned to δ(N=Se-S). The increase in intensity of the peak at 350 cm^{-1}, which coincides with the asymmetric SeS stretching mode, is attributed to δ(Se-N=C). The comparable mode in BrCN, which is the closest isoelectronic species with which comparison can be made, lies at 342 cm^{-1} (23). The weak Raman bands near 570 cm^{-1} are assigned to δ(S=C=N) and that at 938 cm^{-1} to terminal C=S stretching. These latter modes may be compared with those of carbonyl sulfide (OCS), which has a related electronic structure with double bonds to sulphur and oxygen for which the δ(S=C=O) and (C=S) are at 520 and 859 cm^{-1}, respectively.

Conclusion

It is remarkable that, in spite of the complex mechanism involved (2*c*, footnote 4), SeO_2 reacts with thiols and thiolate-derived inorganic species like $S_2O_3^{2-}$ (2*d*) and SO_3^{2-} (3*a*) to give, in apparently 100% yield, the selenotrithionate derivative. and, with few exceptions (3), a disulfide oxidation product. Thiocyanate has now been shown to behave in an entirely analogous way, giving selenium dithiocyanate and thiocyanogen. Like the seleno-pentathionate and -trithionate species, $Se(SCN)_2$, which is S-bonded in the solid state (5), forms NS-bonded and SS bonded linkage isomers in solution. Thiocyanate is well known as an ambidentate ligand in metal coordination chemistry (10) and several covalent thiocyanates and isothiocyanates are known. Se(II) may also bind to the SCN group over sulphur or nitrogen. Unfortunately $Se(SCN)_2$ decomposes slowly in solution and further studies on the chemistry of this interesting Se(II) species will be difficult.

Acknowledgements

Dr. Glen Facey and Raj Capoor are thanked for help with the NMR spectra and Sheila Ball is thanked for some preliminary studies.

References

1. S.M. Ohlberg and P.A. van der Meulen. J. Am. Chem. Soc. **75**, 997 (1953).
2. (*a*) H.E. Ganther. Biochemistry, **7**, 2898 (1968); (*b*) J.L. Kice and H. Slebocka-Tilk. J. Am. Chem. Soc. **104**, 7123 (1982); (*c*) W. Amaratunga and J. Milne. Can. J. Chem. **72**, 2506 (1994); (*d*) S. Rahim and J. Milne. Can. J. Chem. **74**, 753 (1996); (*e*) D.L. Rabenstein and K.-S. Tan. Magn. Reson. Chem. **26**, 1079 (1988).
3. (*a*) S. Ball and J. Milne. Can. J. Chem. **73**, 716 (1995); (*b*) J.L. Kice, T.W.S. Lee, and S. Pan. J. Am. Chem. Soc. **102**, 4448 (1980).
4. O. Foss and O. Tjomsland. Acta Chem. Scand. **8**, 1701, (1954).
5. S.M. Ohlberg and A. Vaughan. J. Am. Chem. Soc. **76**, 2649 (1954).
6. W.H. Gardner and H. Weinberger. in Inorg. Synth. **1**, 84 (1939).
7. W. Amaratunga, O. Chaudry, and J. Milne. Can. J. Chem. **72**, 1165 (1994).
8. M.N. Hughes, *In* The chemistry and biochemistry of thiocyanic acid and Its derivatives. *Edited by* A. A. Newman. Academic Press, London. 1975. chap 1.
9. R.E. Connick, T.M. Tan, and E. von Deuster. Inorg. Chem. **21**, 103 (1982).
10. J.A. Kargol, R.W. Crecely, and J.L. Burmeister. Inorg. Chem. **18**, 2532 (1979).
11. P.O. Kinel and B. Strandberg. Acta Chem. Scand. **13**, 1607 (1959).
12. J. Milne. Polyhedron, **4**, 65 (1985).
13. J. Herzfeld and A.E. Berger. J. Chem. Phys. **73**, 6021 (1980).
14. M.J. Collins, C.I. Ratcliffe, and J.A. Ripneester. J. Magn. Reson. **68**, 172, (1986).
15. D.H. McDaniel and A. Yingst. J. Am. Chem. Soc. **86**, 1334 (1964).
16. W. Gombler. Z. Naturforsch. **36B**, 535 (1981).
17. M. Lamoureux and J. Milne. Polyhedron, **9**, 589 (1990).
18. R.R. Fraser, G. Boussard, J.K. Saunders, J.B. Lambert, and C.E. Mixan. J. Am. Chem. Soc. **93**, 3822 (1971).
19. G. Claeson, B.M. Androes, and M. Calvin. J. Am. Chem. Soc. **82**, 4428 (1960).
20. M. Lamoureux and J. Milne. Can. J. Chem. **67**, 1936 (1989).
21. H. Duddeck. Progr. Nucl Magn. Reson. Spectrosc. **27**, 1 (1995).
22. J.W. Akitt. NMR and chemistry. 2nd ed. Chapman and Hall, London. 1983. pp. 68–75.
23. H. Siebert. Anwendungen de Schwingungsspektroskopie in der Anorganischen Chemie. Springer, Berlin. 1966.

Electrochemical study of the reaction between progressively alkylated thiazine leucodyes and Fe(III) on a glassy carbon electrode

S. Ahmed and S.K. Saha

Abstract:An electrochemical investigation on five progressively alkylated thiazine dyes in the presence of Fe(III) ions is reported. The theory of the catalytic regeneration mechanism involving an electrode reaction followed by a coupled chemical reaction is applied to derive kinetic parameters of homogeneous reaction. The second-order rate constant for the reaction of thiazine leucodyes with Fe(III) ions was found to increase from 0.25×10^4 to 1.6×10^4 dm^3 mol^{-1} s^{-1} upon monomethylation and to vary from 0.7×10^4 for the dimethyl derivative to 1.4×10^4 dm^3 mol^{-1} s^{-1} for the tetramethyl one. The electron-donating nature as well as the hydrophobic characteristics of the methyl group influence the kinetics of the homogeneous reaction.

Key words: cyclic voltammetry, thiazine dyes, ferric ion, catalytic regeneration, kinetics.

Résumé : Opérant en présence d'ions Fe(III), on a effectué une étude électrochimique de cinq colorants de la thiazine de plus en plus alklyés. Afin de déterminer les paramètres cinétiques de la réaction homogène, on a appliqué la théorie du mécanisme de la régénération catalytique impliquant une réaction à l'électrode suivie par une réaction chimique couplée. On a trouvé que la constante de vitesse du deuxième ordre des leucocolorants de la thiazine avec les ions Fe(III) passe de $0{,}25 \times 10^4$ à $1{,}6 \times 10$ dm^3 mol^{-1} s^{-1} par monométhylation et qu'elle passe de $0{,}7 \times 10^4$ pour le dérivé diméthylé à $1{,}4 \times 10$ dm^3 mol^{-1} s^{-1} pour le dérivé tétraméthylé. Le caractère électrodonneur ainsi que les caractéristiques hydrophobiques du groupe méthyle influencent tous les deux la cinétique de la réaction homogène.

Mots clés : voltampérométrie cyclique, colorants de la thiazine, ion ferrique, régénération catalytique, cinétique.

[Traduit par la rédaction]

1. Introduction

The most successful photogalvanic (PG) cell for solar energy conversion is the ferrous/thionine cell, yet this too is far from having ideal conversion efficiency (1, 2). In this PG cell the photoreduction of thionine (Th) by Fe(II) ions produces semithionine (S) and Fe(III) ions. Semithionine rapidly disproportionates to Th and leucothionine (L). The advantage of the

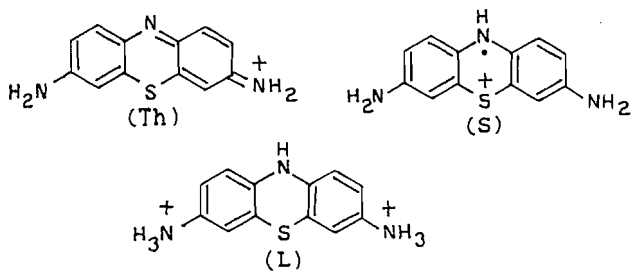

above system lies in achieving partial selectivity of charge carriers for appropriate electrodes. However, greatest efficiency would be obtained with a PG cell in which each electrode is perfectly selective for a different couple. Unfortunately, in homogeneous solution, thermal back reaction of electron transfer also takes place. This dissipation of free energy constitutes a considerable problem in the use of the ferrous/thionine PG cell for any practical purposes (3). The following reaction scheme adequately summarizes the whole process, including the relevant recombination reactions (pH 3) (4):

[1] $\mathrm{Th + Fe(II) + H^+} \xrightarrow{h\nu} \mathrm{S + Fe(III)}$

[2] $\mathrm{2S + H^+} \rightleftharpoons \mathrm{Th + L}$

Back reaction

[3] $\mathrm{S + Fe(III)} \longrightarrow \mathrm{Th + Fe(II) + H^+}$

[4] $\mathrm{L + Fe(III)} \longrightarrow \mathrm{S + Fe(II) + 2H^+}$

However, the homogeneous reaction scheme is very complicated and must be properly characterized. Solubility as well as aggregation characteristics of dyes are important criteria that control PG output. Alkyl substitution in dyes affects both these characteristics, and this prompted us to utilize some progressively alkylated thiazine dyes for a detailed study on homogeneous reactions with Fe(III) ions. In view of this, an electrochemical technique was adopted with the aid of dc voltammetry. An electrode reaction coupled with a chemical reaction is an interesting subject of investigation for electrochemists (5). The electrochemical reduction of progressively alkylated thiazine dyes to the corresponding leucodyes at the stationary electrode in the presence of Fe(III) ions may be described as a so-called "catalytic regeneration mechanism,"

Received April 18, 1996.

S. Ahmed and S.K. Saha.[1] Department of Chemistry, University of North Bengal, Darjeeling 734430, India.

[1] Author to whom correspondence may be addressed. (Telephone: (0353) 450-425. Fax: (0353) 450-546.

according to which an initial electroactive species is regenerated by the homogeneous chemical reaction. This mechanism can be represented by the following scheme (5):

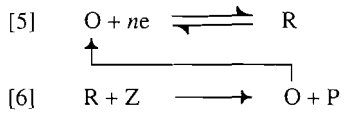

If applied judiciously, this technique yields kinetic parameters of the chemical reaction from a simple electrochemical experiment. Although thermal back reactions have been studied in considerable detail by a flash photolysis technique (4, 6–8), the former technique has been applied only recently for the homogeneous reaction relevant to the ferrous/thionine PG cell. Kinetic parameters were also determined using an indium-doped SnO_2 electrode, assuming a pseudo-first-order reaction condition to prevail even though the experimental result did not always conform with theory (9). The present study was undertaken in view of the pivotal importance of the nature of the electrode surface in such a study and also to examine the role of hydrophobic interaction, if any, on the reaction kinetics. In this paper, we summarize the results of such an electrochemical study on the reaction between various alkyl derivatives of thiazine leucodyes with Fe(III) on a glassy carbon electrode that has been found to behave well in the present set of systems.

2. Experimental

Five progressively alkylated thiazine dyes, viz., thionine, azure C, azure A, azure B, and methylene blue, that are used for the present study were supplied by Aldrich Chemical Co., U.K. All other chemicals were of analytical grade (Aldrich/B.D.H.) and used as received. The structures of the dyes are given below:

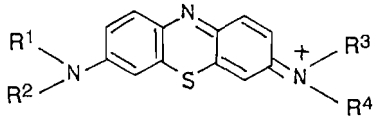

Thionine(Th): $R^1 = R^2 = R^3 = R^4 = H$
Azure C(AzC):$R^1 = R^2 = R^3 = H$; $R^4 = CH_3$
Azure A(AzA):$R^1 = R^2 = H$; $R^3 = R^4 = CH_3$
Azure B(AzB):$R^1 = H$; $R^2 = R^3 = R^4 = CH_3$
Methylene blue (MB):$R^1 = R^2 = R^3 = R^4 = CH_3$

All the dyes were found to contain coloured impurities and were purified over a chromatographic column of silica gel using a chloroform–methanol mixture as eluent. Azure C was extracted efficiently with an 8:2 chloroform–methanol mixture whereas azure A was extracted with a 7:3 solvent mixture. All other dyes were eluted by less polar solvent mixtures than that used for azure A. Finally, the dyes were recrystallized and dried at 50°C under vacuum. Final purities of dye samples were checked by TLC using an 8:2 water – acetic acid mixture as the mobile phase, and the purities of all the dyes except AzC were found to be excellent. The commercial sample of AzC contained a high percentage of insoluble materials in addition to other coloured impurities. Even after repeated chromatographic treatment, the sample gave a faint additional spot on the TLC plate, indicating the presence of a small amount of impurity. Although this dye could not be purified up to the level of other four dyes, various analyses (spectral and analytical) showed that the final purity of the dye was satisfactory.

For electrochemical experiments, the supporting electrolyte was sulphuric acid. All solutions were purged with pure nitrogen before the experiment. Cyclic voltammetric experiments were carried out employing a BAS cyclic voltammograph (CV-27, U.S.A.). The working electrode was a glassy carbon microelectrode (MF-2012, BAS, diam. 3.2 mm) with a platinum wire as auxiliary electrode. Potentials were measured with respect to the saturated calomel electrode. All measurements were done at a constant pH of 2.0 and at room temperature (25 ± 1°C).

3. Results and discussion

A cyclic voltammogram of azure C (5.0×10^{-5} mol dm^{-3} in 0.1 mol dm^{-3} H_2SO_4) is shown in Fig. 1A. Voltammograms of all other dyes are similar and consistent with reversible two-electron transfer systems within the range of potential scan (v) of 5–100 mV s^{-1}. Data pertaining to the position of peak potentials and current ratios, i_{pc}/i_{pa}, for the five thiazine dyes are shown in Table 1. Current vs. (scan rate)$^{1/2}$ plots deviate from linearity above scan rates of 100 mV s^{-1} (plots not shown, see Table 1).

The peak potentials (E_{pa} and E_{pc}) are not sensitive to scan rates and ΔE_p's do not vary up to a scan rate of 300 mV s^{-1} except for AzC. This shows that the electrode processes are very fast and the quasi-reversibility is apparent only in AzC. Previous reports available for Th and MB were, however, consistent with the present observation (9–12). Diffusion coefficient (D_0) values are determined from cyclic voltammetry measurements as 3.05×10^{-6}, 2.66×10^{-6}, 4.40×10^{-6}, 4.90×10^{-6}, and 5.7×10^{-6} cm^2 s^{-1} for Th, AzC, AzA, AzB, and MB, respectively (determined from the slopes of i_{pc} vs. $v^{1/2}$ plots at slow scan rates, employing the Randles–Seveik equation (5)).

Interestingly, the D_0 value increases regularly upon progressive alkylation of the dye molecule, with the only exception being AzC. On the other hand, the Fe(II)/Fe(III) system exhibits irreversible electron transfer at the GC electrode in the potential range of 0.3–0.6 V (Fig. 2). But the couple is no longer electrochemically active in the presence of thiazine dyes, which of course have much higher heterogeneous kinetics (k_s(Th) = 5×10^{-3} cm s^{-1}, k_s (Fe) = 3.1×10^{-5} cm s^{-1} on a gold foil electrode (4)).

On the other hand, voltammograms of thionine and its derivatives in the presence of varying amounts of Fe(III) ions (5.0×10^{-5} – 1.0×10^{-3} mol dm^{-3}) show striking changes from those obtained in the absence of Fe(III) ions. The observed catalytic current results from the regeneration of dyes from the reduced leucodyes by reaction with Fe(III) ions. Representative voltammograms of AzC are shown in Fig. 1*b*,*c*. Along with the catalyltic regeneration of thiazine dyes in the presence of Fe(III) ions, which of course is believed to be the major process occurring in the system, a certain amount of semithiazines may also be present via a dismutation equilibrium (8). These semithiazines were oxidized at the GC electrode to give the small anodic peak current at higher positive potential on the reversed scan (Fig. 1*b*). Although the Fe(II)/Fe(III) couple is electrochemically inactive at the GC elec-

Table 1. Electrochemical data from cyclic voltammetry of thiazine dyes (5×10^{-5} mol dm^{-3} in 0.1 mol dm^{-3} H_2SO_4).

Dye	Scan rate (mV s^{-1})	E_{pa} (V)	E_{pc} (V)	ΔE_p (V)	i_{pa}/i_{pc}	$(E_{pc/2} - E_{pc})$ (V)	$i_{pc}v^{-1/2}$ (μA mV$^{1/2}$s$^{1/2}$)	$0.058/\Delta E_p$
	5	0.225	0.195	0.030	0.870	0.025	5.93	1.93
	10	0.223	0.195	0.028	0.890	0.026	5.50	2.07
	20	0.220	0.193	0.027	0.900	0.027	5.32	2.14
Th	40	0.218	0.190	0.028	0.980	0.030	6.25	2.07
	60	0.215	0.185	0.030	0.930	0.032	6.15	1.93
	100	0.214	0.185	0.029	0.950	0.032	6.65	2.00
	200	0.210	0.182	0.028	0.970	0.033	7.72	2.07
	300	0.210	0.182	0.031	0.980	0.035	8.59	1.93
	5	0.198	0.165	0.033	0.800	0.035	5.00	1.75
	10	0.198	0.163	0.035	0.880	0.035	5.25	1.65
	20	0.196	0.160	0.036	0.800	0.037	4.96	1.61
AzC	40	0.195	0.158	0.037	0.760	0.038	5.50	1.56
	60	0.191	0.150	0.041	0.840	0.040	5.64	1.41
	100	0.185	0.145	0.040	0.830	0.042	6.33	1.45
	200	0.182	0.135	0.047	0.770	0.043	6.04	1.23
	300	0.180	0.130	0.050	0.770	0.045	7.31	1.16
	5	0.229	0.198	0.031	0.890	0.028	6.43	1.87
	10	0.226	0.195	0.031	0.880	0.028	6.25	1.87
	20	0.224	0.192	0.032	0.830	0.030	6.38	1.81
	40	0.222	0.191	0.031	0.790	0.032	6.75	1.87
AzA	60	0.220	0.188	0.032	0.730	0.035	6.97	1.81
	100	0.218	0.186	0.032	0.690	0.038	8.22	1.87
	200	0.214	0.180	0.034	0.610	0.043	8.05	1.70
	300	0.212	0.178	0.034	0.590	0.045	8.40	1.70
	5	0.300	0.270	0.030	0.870	0.028	5.54	1.93
	10	0.300	0.268	0.032	0.850	0.029	6.00	1.81
	20	0.298	0.265	0.033	0.840	0.030	6.17	1.76
AzB	40	0.297	0.262	0.035	0.840	0.035	6.93	1.66
	60	0.295	0.260	0.035	0.770	0.040	7.59	1.66
	100	0.294	0.260	0.034	0.730	0.042	8.01	1.70
	200	0.293	0.258	0.035	0.660	0.042	8.05	1.66
	300	0.293	0.257	0.036	0.580	0.045	8.04	1.61
	5	0.215	0.183	0.032	0.840	0.028	6.78	1.81
	10	0.215	0.182	0.033	0.810	0.030	6.75	1.76
	20	0.214	0.181	0.033	0.750	0.032	7.27	1.76
MB	40	0.212	0.180	0.032	0.610	0.032	7.75	1.81
	60	0.210	0.180	0.030	0.610	0.035	8.20	1.93
	100	0.205	0.175	0.030	0.630	0.036	9.01	1.93
	200	0.197	0.165	0.032	0.660	0.038	10.86	1.81
	300	0.195	0.160	0.035	0.650	0.040	10.97	1.66

trode in the presence of thiazine dyes, its adverse effect on the voltammograms of the latter by increasing the background current cannot be ignored. To confirm that the experimental results conform to the theory of catalytically coupled reactions (EC′) of the type shown in eqs. [5] and [6] as a major process, it is necessary to draw a diagnostic plot of the current function against the potential scan rates.

This correlation can be seen by simply plotting $i_{pc}/v^{1/2}$ as a function of log v (13). A representative diagnostic plot for AzB is shown in Fig. 3. In the absence of any Fe(III) ions, the plots for all the dyes are linear and parallel to the potential scan rate axis up to 100 mV s^{-1} (Fig. 3*a*). This is expected for a diffusion-controlled reversible electrode process. However, at higher scan rates the observed upward shift of the plot is indeed the manifestation of positive deviation from the linear relationship of i_{pc} with $v^{1/2}$ (Table 1) for almost all the dyes. On the other hand, in the presence of Fe(III) ions (5.0×10^{-5} – 1.0×10^{-3} mol dm^{-3}), the diagnostic, the diagnostic plots are similar for all dyes and are indicative of an EC′ type of coupled catalytic chemical reaction. The catalytic regeneration of dyes as a major process is particularly apparent at lower scan rates as the reaction gets sufficient time for generation of dyes

Fig. 1. Cyclic voltammograms of AzC (5×10^{-5} mol dm^{-3}) in the presence of various concentrations of Fe^{3+}: (*a*) 0, (*b*) 8×10^{-4}, (*c*) 1.5×10^{-3} mol dm^{-3}. Supporting electrolyte: 0.1 mol dm^{-3} H_2SO_4.

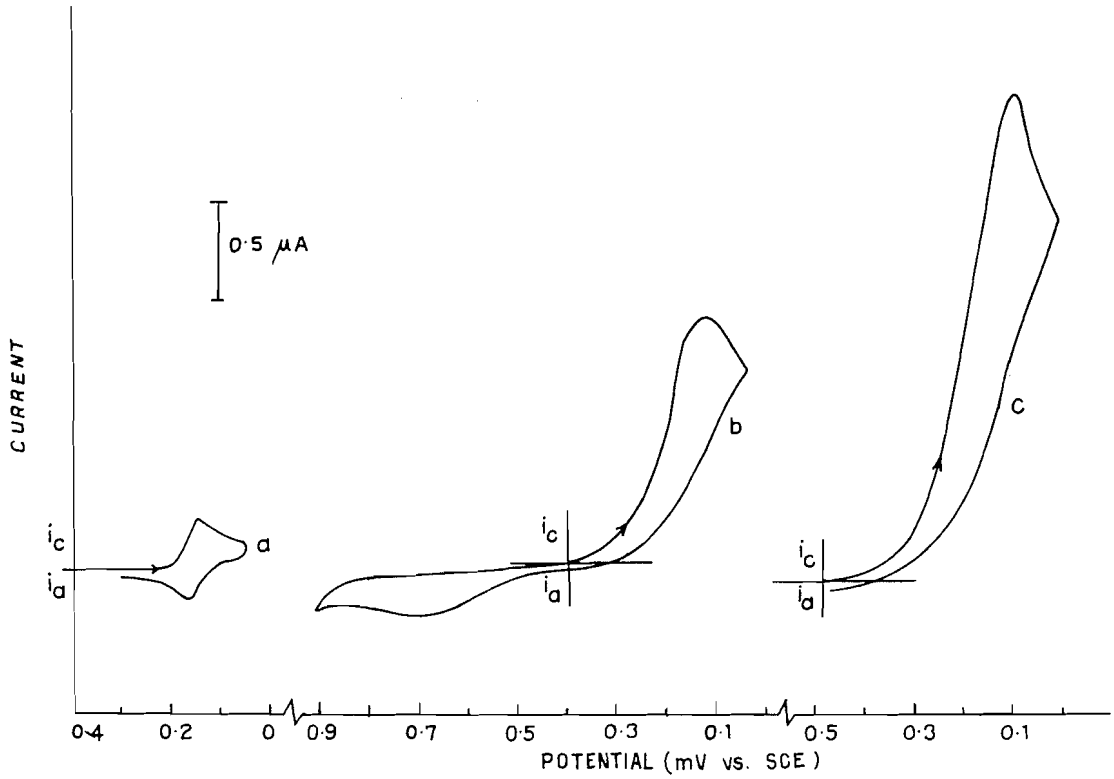

Fig. 2. Cyclic voltammograms of $FeCl_3$ (in the presence of 0.1 mol dm^{-3} H_2SO_4) at a GC electrode. Concentration of Fe(III): (1) 2×10^{-4}, (2) 4×10^{-4}, (3) 6×10^{-4}, (4) 8×10^{-4} mol dm^{-3}. Scan rate: 5 mV s^{-1}.

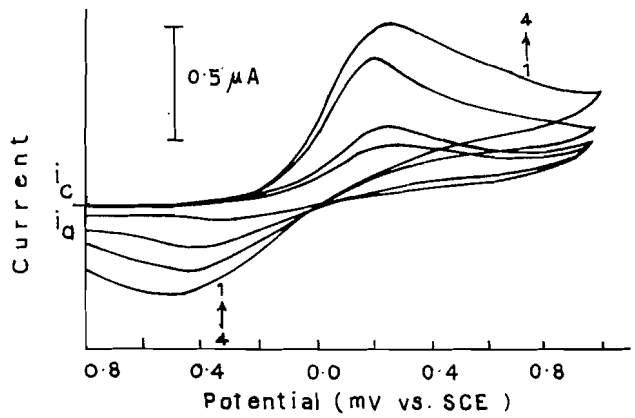

from the reduced leucoforms by reaction with Fe(III) ions, consistent with the theoretical model (14, 15). However, when the scan rate increases, the ratio of kinetic current in the presence of Fe(III) to the cathodic peak current in the absence of Fe(III), i_d/i_{pc}, should tend towards unity. But this situation was not attained in the present study even at a sweep rate of 300 mV s^{-1} (Fig. 3). Similar results were also observed by previous workers for the intermolecular electron transfer of Cytochrome C in presence of *pseudomonas* Cytochrome C551 (13) and for the homogeneous reaction of leucothionine with Fe(III) (9). Whereas we failed to identify any other mechanisms of coupled chemical reactions than EC′ to be operative in the present systems, the exact reason for the above remains uncertain.

Despite the simplified approach in view of the above and the complicated back reaction in the present systems, attempts have been made to derive kinetic information form the observed data. Using a working curve (Fig. 14 of ref. 14) of i_k/i_d vs. the kinetic parameter, $(k_f/a)^{1/2}$, we plotted the data of k_f/a (where $a = nF/RT$) against $1/v$, which should be linear under first-order conditions (Fig. 4). The result shows marked deviation from the predicted linearity at slower scan rates, which is consistent with loss of first-order conditions. The reactant dye is not in sufficiently large excess and so is consumed to a considerable extent in the diffusion layer during the time period of a slower scan rate. Second-order kinetics is probably followed and the situation is identical to one that occurred in the intermolecular electron transfer of cytochrome C(13). Moreover, the initial slope of each curve (Fig. 4) at infinite scan rates is proportional to the true pseudo-first-order rate constant k_f^0,

$$k_f^0 = (nF/RT) \text{ (initial slope)}$$

Drawing tangents to the above curves at $1/v \rightarrow 0$ yields values of k_f^0 for each experiment. An alternative method of finding k_f^0 is to calculate the effective pseudo-first-order rate constant k_f', from each k_f/a value at a given scan rate where,

$$k_f' = (F/RT)\, v\, (k_f/a) \qquad \text{(ref. 13)}$$

Fig. 3. Diagnostic plots of current functions $i_{pc}/v^{1/2}$ vs. log v for AzB (5×10^{-5} mol dm^{-3} in 0.1 mol dm^{-3} H_2SO_4) at various concentrations of Fe^{3+}: (*a*) 0, (*b*) 2×10^{-4}, (*c*) 4×10^{-4}, (*d*) 6×10^{-4}, (*e*) 8×10^{-4}, (*f*) 1×10^{-3} mol dm^{-3}.

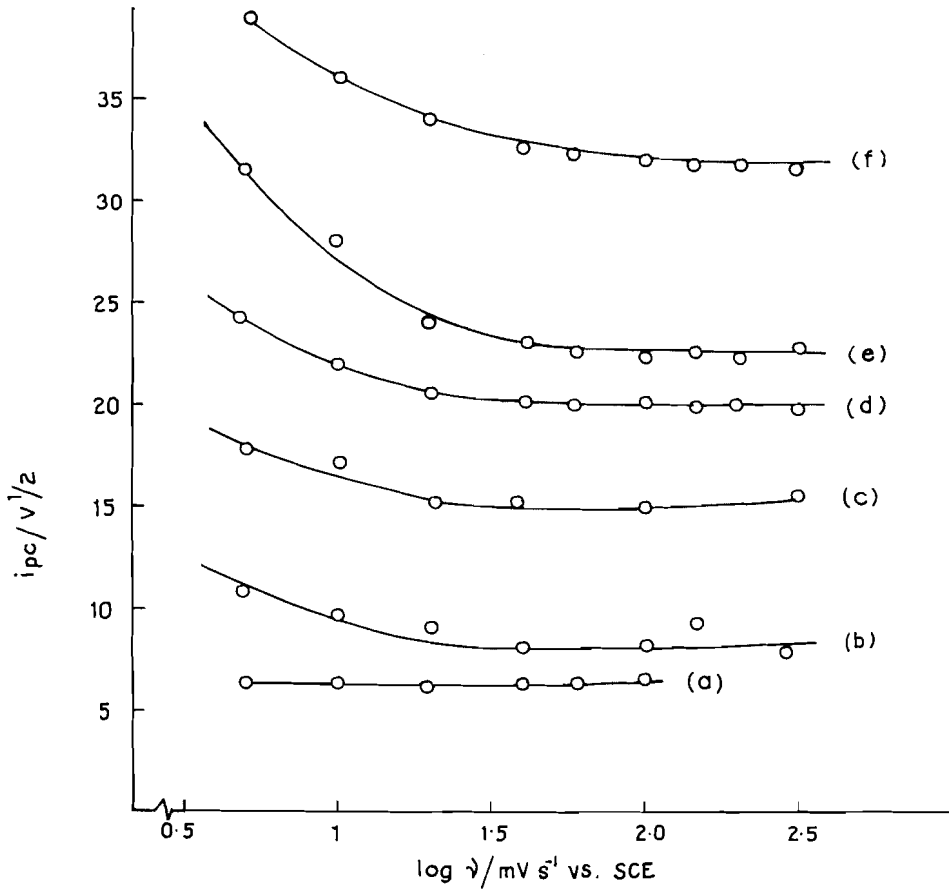

Plotting k_f' as a function of $1/v$ and extrapolating to $1/v \rightarrow 0$, one can evaluate the pseudo-first-order rate constant, k_f^0, at infinite scan rate. This latter method seems to be more convenient, and data for thionine are plotted in Fig. 5. (Similar plots for all other dyes are submitted as supplementary material.)[2] The nature of the plots is again similar for all five dyes and also similar to those observed by Hill and Walton for intermolecular electron transfer in cytochrome C(13). Finally, k_f^0 values at infinite scan rates and for varying concentrations of Fe(III) are plotted against the concentrations of Fe(III) ions in order to examine the second-order rate constants, k_2, for the homogeneous reaction of Fe(III) with various leucodyes. These plots are linear, indicating that the homogeneous reaction is first order with respect to Fe(III) ions and, indeed, the overall reaction is of second order (inset of Fig. 5). However, a striking feature is that, unlike Th, slopes of the plots for all other dyes decrease drastically at low Fe(III) concentrations (at $C_{Fe(III)} < 2.0 \times 10^{-4}$ mol dm^{-3} for AzC, AzA and at $C_{Fe(III)} < 4.0 \times 10^{-4}$ mol dm^{-3} for AzB, MB), resulting in the deviation of the plots from linearity. This result suggests that at low Fe(III) concentrations the actual scheme of reaction should be more complex than the one shown in eqs. [5] and [6] and supports the hypothesis that the return of leucodyes to the corresponding thiazine dyes by Fe(III) ions occurs by a two-step process via the formation of semithiazine as an intermediate species. Conversion of semithiazines to the corresponding thiazine dyes may occur either by Fe(III) or through the dismutation equilibrium (as mentioned before), forming leuco dyes and the original dyes. The latter process is, however, more significant at low Fe(III) concentrations (8). Nevertheless, observed gradients of the straight lines are significant and the second-order rate constants, k_2, derived from these data are depicted in Table 2.

Table 2. Second-order rate constants of the homogeneous reaction between thiazine dyes and Fe^{3+} ions.

Leucodyes	$k_2 \times 10^{-4}$ (dm^3 mol^{-1} s^{-1})
Th	0.25
AzC	1.60
AzA	0.70
AzB	1.00
MB	1.40

The table shows that the k_2 value for thionine is 0.25×10^4 dm^3 mol^{-1} s^{-1}, which is the lowest among all the dyes used.

[2] These figures can be purchased from: The Depository of Unpublished Data, Document Delivery, CISTI, National Research Council Canada, Ottawa, Canada K1A 0S2.

Fig. 4. Plots of kinetic parameter, k_f/a, against $1/v$ for the AzB–Fe(III) system at various concentrations of Fe^{3+}: (*a*) 2×10^{-4}, (*b*) 4×10^{-4}, (*c*) 6×10^{-4}, (*d*) 8×10^{-4}, (*e*) 1×10^{-3} mol dm^{-3} (in presence of 0.1 mol dm^{-3} H_2SO_4).

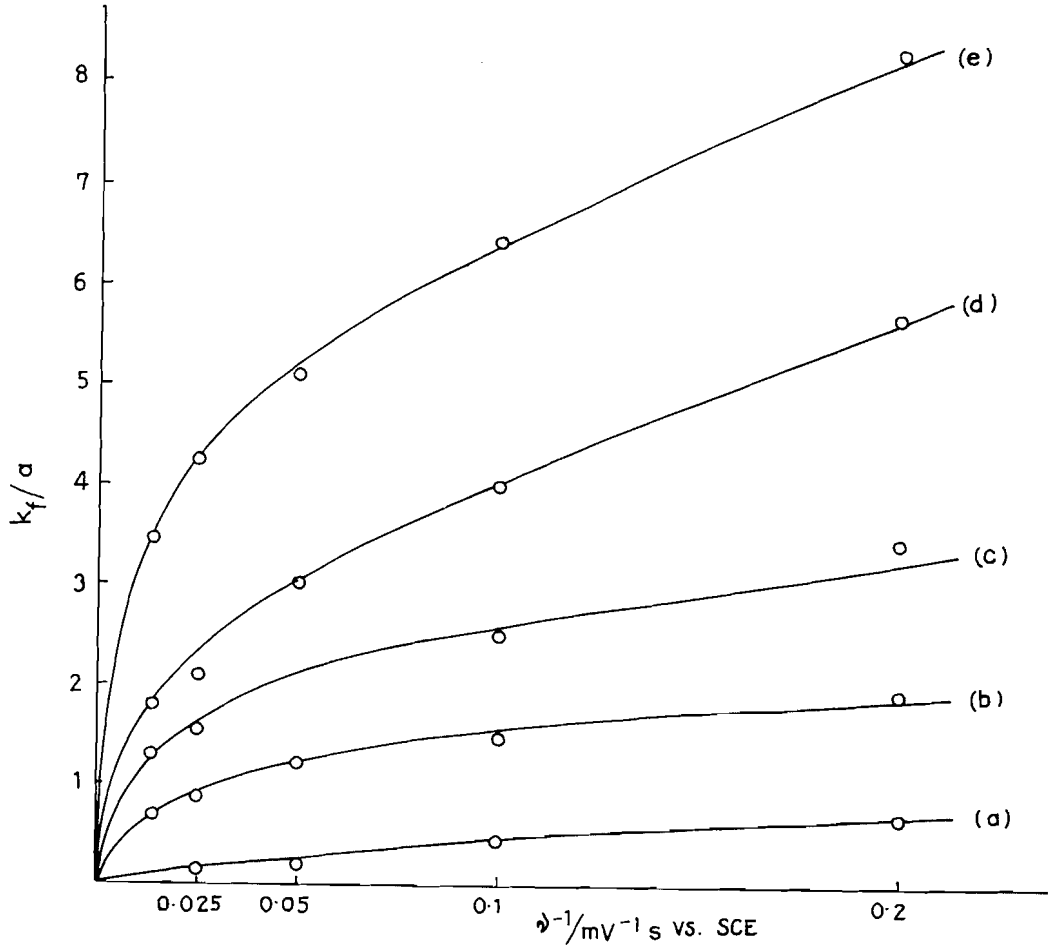

Upon progressive alkylation of the dyes this value increases regularly with an exception only for AzC, which gives the highest value of 1.6×10^4 dm^3 mol^{-1} s^{-1}. Regular increase of k_2 with progressive alkylation of the dye molecule would indeed be expected from the electron-donating nature of a methyl group. However, in the present systems, while the first methyl group brings about a sixfold increase of the rate, the second one causes a twofold decrease, and adding the third and the fourth has only a small effect (1.4-fold increase with each methyl). In fact, the leucodye with four methyl groups is oxidized more slowly than the dye with only one methyl group. It seems apparent that factors other than the electron-donating effect of the methyl group are involved. Substitution of hydrogens on the nitrogen of a dye molecule by methyl groups introduces hydrophobicity in the molecule as well. It has also been shown that a hydrophobic environment in the presence of certain micelles delays back electron transfer in solution (4, 16) while substitution with ionic or polar groups, for example disulfonated thionine, shows faster back electron transfer in PG cells (17, 18). Thus, increased hydrophobicity due to alkylation of the present dyes may in turn slow down the electron transfer reaction with Fe(III) ions in aqueous solution to some extent. These two mutually opposite effects of the methyl group may thus be responsible for the observed variation of rates. It is also important to note in this context that the formal potential values ($E^{0\prime}$) for progressively methylated dyes are 0.205, 0.175, 0.207, 0.281, and 0.196 V (average values for v between 5 and 100 mV s^{-1}, Table 1), respectively, and the observed lowest value of $E^{0\prime}$ for AzC is consistent with the above results. However, one can infer from the foregoing result that, with the exception of AzC, the PG output will decrease continuously with alkyl substitution in the dye molecule. All previous reports showed that PG output for the Fe(II)–MB cell is always less than that for the Fe(II)–thionine cell. An earlier report of second-order rate constants (measured by flash photolysis) ranged from values of 0.47×10^3 to 1.0×10^3 dm^3 mol^{-1} s^{-1} for various modified thiazine dyes (7). Ferreira and Harriman report a value of 9.0×10^4 dm^3 mol^{-1} s^{-1} for the Fe(III)–thionine system by a similar flash photolysis technique (8). On the other hand, with the help of an electrochemical method similar to one applied in the present study, Murthy and Srivastava estimated the value as 4.0×10^5 dm^3 mol^{-1} s^{-1} for the reaction between Fe(III) ions and leucothionine (9). While a close comparison between data reported

Fig. 5. Effective pseudo-first-order rate constant, k_f', as a function of reciprocal scan rate extrapolated to $1/v \rightarrow 0$, for experiments with the Th–Fe(III) system: (1) 2×10^{-4}, (2) 4×10^{-4}, (3) 6×10^{-4}, (4) 8×10^{-4}, (5) 1×10^{-3} mol dm^{-3} Fe^{3+} (in the presence of 0.1 mol dm^{-3} H_2SO_4) (lower figure). Pseudo-first-order rate constant, k_f^0, as a function of the concentrations of Fe^{3+} with the same system (upper figure).

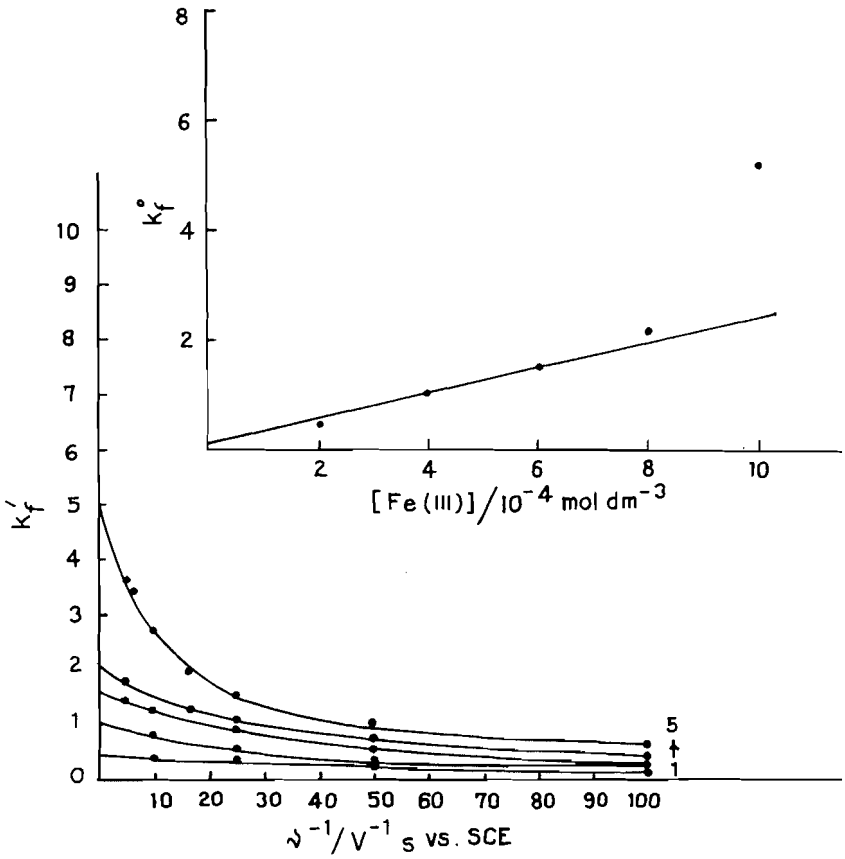

by different methods and under different conditions is not always valid, the general trend of the present result is satisfactory and, especially, the observed variation of k_2 due to progressive alkylation of the dye molecule demonstrates the usefulness of the comparatively simpler electrochemical technique adopted in the present investigation.

Acknowledgement

One of the authors (S.A.) wishes to thank the University Grants Commission, New Delhi, for the award of a teacher fellowship.

References

1. W.J. Albery. *In* Photovoltaic and photoelectrochemical solar energy conversion. *Edited by* F. Cardon, W.P. Gomesand, and W. Dekeyser. Plenum Press, New York 1981. p. 313.
2. S. Lodha, S. Khamesra, B. Sharma, and S.C. Ameta. Int. J. Energy Res. **15**, 431 (1991).
3. W.J. Albery and A.W. Foulds. J. Photochem. **10**, 41 (1979).
4. E.J.J. Groenen, M.S. de Groot, R. de Ruiter, and N. de Wit. J. Phys. Chem. **88**, 1449 (1984).
5. A.J. Bard and L.R. Faulkner. Electrochemical methods — fundamentals and applications. John Wiley & Sons, New York 1980. p. 429.
6. J.C.M. Brokken-Zijp and M.S. de Groot. Chem. Phys. Lett. **76**, 1 (1980).
7. D.W. Hay, S.A. Martin, S. Ray, and N.N. Lichtin. J. Phys. Chem. **85**, 1474 (1981).
8. M.I.C. Ferreira and A. Harriman. J. Chem. Soc. Faraday Trans. 1, **173**, 1085 (1977).
9. A.S.N. Murthy and T. Srivastava. J. Chem. Soc. Faraday Trans. **86**, 105 (1990).
10. T.I. Quickenden and I.R. Harrison. J. Electrochem. Soc. **132**, 81 (1985).
11. P. Joo. Colloids and Surf. **49**, 29 (1990).
12. J.M. Bauldreay and M.D. Archer. Electrochim. Acta; **28**, 1515 (1983).
13. H.A.O. Hill and N.J. Walton. J. Am. Chem. Soc. **104**, 6515 (1982).
14. R.S. Nicholson and I. Shain. Anal. Chem. **36**, 706 (1964).
15. L. Nadjo and J.M. Save'ant. J. Electroanal. Chem. **48**, 113 (1973).
16. M. Gratzel. Proc. Int. Conf. Photochem. Convers. Storage Sol. Energy, 3rd, 1980, Cambridge. 1981. p. 131.
17. W.J. Albery, P.N. Bartlett, J.P. Davies, A.W. Foulds, A.R. Hillman, and F.A. Souto-Bachiller. Faraday Discuss. Chem. Soc. **70**, 341 (1980).
18. W.J. Albery, P.N. Bartlett, A.W. Foulds, F.A. Souto-Bachiller, and R. Whiteside. J. Chem. Soc. Perkin Trans. 2, 794 (1981).

COMMUNICATION

A study of the vacuum pyrolysis of 11-oxatricyclo[6.2.1.$0^{2,7}$]undeca-2,9-diene. The HeI ultraviolet photoelectron spectrum of 1,2-cyclohexadiene

Nick Henry Werstiuk, Chandra Deo Roy, and Jiangong Ma

Abstract: A newly developed ultraviolet photoelectron spectrometer – CO_2 laser apparatus that utilizes a 50-watt CW CO_2 laser as a directed heat source is used to study the vacuum pyrolysis of 11-oxatricyclo[6.2.1.$0^{2,7}$]undeca-2,9-diene (**4**). We report the HeI photoelectron spectrum of the strained cyclic allene 1,2-cyclohexadiene (**1**) that correlates with the HAM/3 ionization energies calculated with the optimized C_2 equilibrium structure obtained with AM1 and the molecular orbital energies of the optimized C_2 equilibrium structure calculated at the ab initio HF/6-31G** level of theory.

Key words: 11-oxatricyclo[6.2.1.$0^{2,7}$]undeca-2,9-diene, vacuum pyrolysis, HeI ultraviolet photoelectron spectrum, 1,2-cyclohexadiene.

Résumé : On a utilisé un spectromètre photoélectronique ultraviolet à laser au CO_2 de 50 watt CW développé récemment comme source de chaleur dirigée pour d'étudier la pyrolyse sous vide du 11-oxatricyclo[6.2.1.$0^{2,7}$]undéca-2,9-diène (**4**). On a déterminé le spectre photoélectronique HeI du cyclohexa-1,2-diène (**1**), un allène cyclique tendu; il existe une bonne corrélation entre ce spectre expérimental et les énergies d'ionisation HAM/3 calculées en utilisant une structure en équilibre C_2 optimisée obtenue avec AM1 ainsi que les énergies d'orbitales moléculaires de la structure en équilibre C_2 optimisée calculée au niveau ab initio HF/6-31G** de la théorie.

Mots clés : 11-oxatricyclo[6.2.1.$0^{2,7}$]undéca-2,9-diène, pyrolyse sous vide, spectre photoélectronique ultraviolet HeI, cyclohexa-1,2-diène.

[Traduit par la rédaction]

Studies that combine ultraviolet photoelectron spectroscopy (pes) and calculations of molecular orbital (MO) energies and orbital coefficients at the semi-empirical or ab initio levels of theory provide fundamental information about the structures and bonding of stable compounds and transient species that is obtained by no other technique. In the past, transient species studied with pes generally were prepared by vacuum pyrolysis of compounds using electrically heated furnaces centimetres in length (1, 2). To facilitate the study of highly reactive transients in the gas phase, we developed a CW CO_2 laser – pes apparatus (the laser is used as a directed heat source to produce a hot zone that is 1–2 mm in length) and used it successfully to study the vacuum pyrolysis of a number of substrates (3–5).

Because of its unique structure and kinetic reactivity, the highly strained cyclic allene, 1,2-cyclohexadiene (**1**), has been the focus of studies by experimentalists and theoreticians for some time (6). When generated from a wide range of precursors in solution it is trapped with reactive dienes and hydroxylic solvents or it dimerizes and tetramerizes. And, there have been two reports of attempts to prepare and study **1** with the matrix isolation technique. Wentrup et al. pyrolyzed bicyclo[3.10]hexane-6-carbonyl chloride (**2**) at 1073 K and obtained infrared spectroscopic data that indicated the successful trapping of **1** in an Ar martix at 11 K (7). Runge and Sander subsequently challenged the conclusions reached in this paper on the basis of the results they obtained by pyrolyzing 6-bromo-6-(trimethylstannyl)bicyclo[3.10]hexane (**3**) at 873 K and trapping the pyrolysate at 10 K (8). Given these findings and the fact that (*a*) there have been no reports of the pe spectrum of **1** and (*b*) we wished to establish the scope and limitations of studying transient species with our newly devel-

Received May 8, 1996.

N.H. Werstiuk,[1] C.D. Roy, and J. Ma. Department of Chemistry, McMaster University, Hamilton, ON L8S 4M1, Canada.

[1] Author to whom correspondence may be addressed. Telephone: (905) 525-9140. Fax: (905) 522-2509. E-mail: werstiuk@mcmaster.ca

Fig. 1. (*a*) HeI photoelectron spectrum of **4** obtained at ambient temperature (the vertical lines mark the HAM/3 IEs calculated with the AM1 optimized equilibrium structure); (*b*) HeI photoelectron spectrum of **4** obtained at a laser power level of 26 W; (*c*) HeI photoelectron spectrum of the pyrolysate of **4** obtained at a laser power level of 46 W; (*d*) spectrum obtained by subtracting (*b*) from (*c*); (*e*) HeI photoelectron spectrum of furan obtained at a laser power level of 47 W; (*f*) HeI photoelectron spectrum of 1,3-cyclohexadiene obtained at a laser power level of 47 W; (*g*) spectrum obtained by subtracting (*f*) from (*d*); (*h*) spectrum obtained by subtracting (*e*) from (*g*) (the solid vertical lines mark the HAM/3 IEs calculated with the AM1 optimized equilibrium structure; the broken lines correspond to the negative of the MO energies calculated for the HF/6-31G** optimized equilibrium structure).

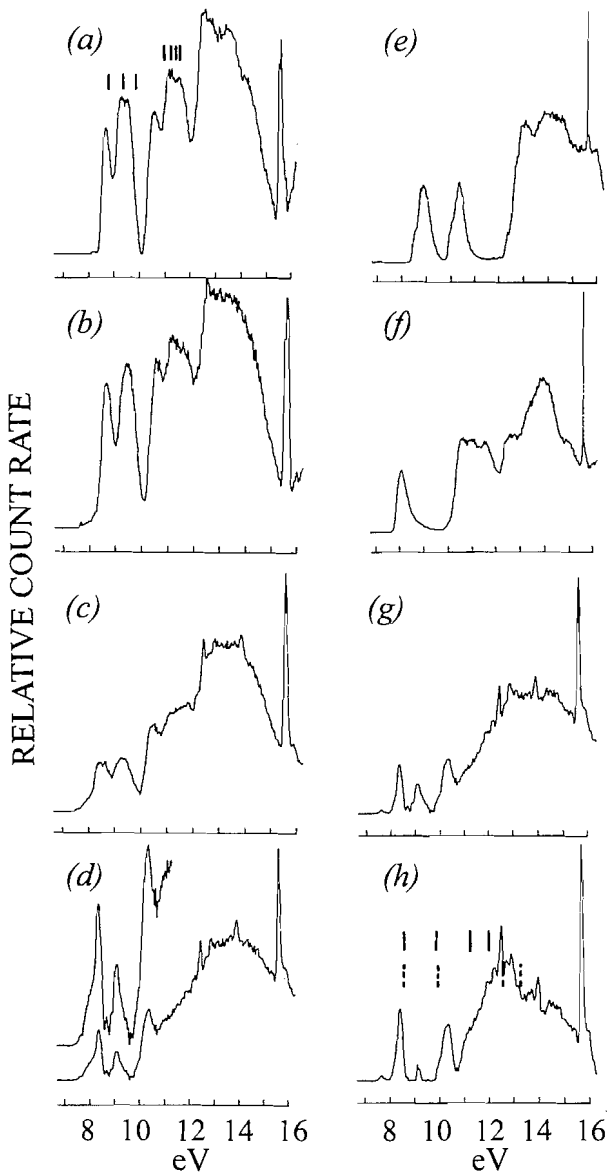

oped pes – CW CO_2 laser apparatus, we undertook to prepare **1** in the gas phase and obtain its pe spectrum. In this communication, we report the results of a study on the pyrolysis of 11-oxatricyclo[6.2.1.$0^{2,7}$]undeca-2,9-diene (**4**).

We chose to prepare and study **4** (9) with the expectation that its pyrolysis in a 1–2 mm hot zone of a quartz nozzle (3–5) would yield **1** and furan, a stable product that would be easily identified by photoelectron spectroscopy. The photoelectron spectra of **4** along with its pyrolysate obtained at two laser power levels are displayed in Fig. 1. Figure 1 (*a*) is the pe spectrum of **4** obtained at ambient temperature. The seven lowest ionization energies (IEs) (8.98, −9.54, 10.02, 11.06, 11.26, 11.53, and 11.69 eV) calculated with HAM/3 (10) — the equilibrium optimized structure of **4** obtained with AM1 (11) was used in this case — are marked on the spectrum as solid lines, indicating that this combination of computational methods yields the IEs with good accuracy and allowing the molecular orbitals of **4** to be characterized. Spectra (*b*) and (*c*) were obtained at laser power levels of 26 W (the tip of the nozzle is 550 ± 50°C) and 47 W(850 ± 50°C), respectively. It is seen that the latter one differs significantly from spectrum (*a*). Spectrum (*b*) (scaled by 0.7), not (*a*), was subtracted from (*c*) to obtain the difference spectrum (*d*)[2]. In this way, the effect of potential changes in the spectrum of **4** induced by the high temperature would be minimized although the signals due to **1** and furan would be reduced to some extent as well. Spectra of authentic samples of furan and 1,3-cyclohexadiene — the latter compound is formed from **1** via a 1,3-hydrogen shift (8) — were also obtained at 47 W and are displayed as spectra (*e*) and (*f*), respectively. Spectrum (*g*) is obtained by subtracting (*f*) (scaled by 0.28) from spectrum (*d*). This operation reduces the shoulder at 8 eV of the lowest IE peak found in (*d*) and brings out the lowest IE bands of furan at 9.00 and 10.38 eV, respectively. Spectrum (*h*) is obtained by subtracting the spectrum of furan (*e*), scaled by 0.4) from (*g*). There are no sharp bands centered at 9.60 eV in spectra (*g*) and (*h*) that are characteristic of the pe spectrum of 1-buten-3-yne (12), indicating that the retro Diels–Alder reaction of **1** observed by Runge and Sander (8) does not occur to a significant extent under the experimental conditions employed in this study. That **1** does not dimerize is indicated by the fact that spectra (*g*) and (*h*) do not exhibit a band at 9.6 eV, a peak seen in the spectrum (not shown; obtained at 47 W) of an authentic sample of **5** (13) that exhibits two low-IE bands of equal intensity at 8.40 and 9.60 eV. That the experimental pe spectrum (the vertical IEs of the two low-lying bands are 8.4 and 10.4 eV) obtained in this study correlates with the HAM/3 IEs (the four lowest ones at 8.60, 9.89, 11.40, and 12.00 eV calculated with the AM1 optimized C_2 structure are indicated with solid lines) and the negative of the energies of the four highest occupied MOs (8.64, 9.96, 12.61, and 13.12 eV, shown as broken lines) of the optimized C_2 structure obtained at the HF/6-31G** level of theory (*a*) indicates that **1** is obtained from **4** and (*b*) provides support

[2] We recognize that care should be exercised when difference spectra are obtained, especially when fairly featureless spectra are involved. Because the spectra acquired in this study differed in intensity, scaling was required to obtain the difference spectra. When spectrum (*d*) was obtained by subtracting (*b*) from (*c*), special attention was paid to the region at 10 eV to ensure that the subtraction did not yield a negative baseline. This criterion was also used in the other cases. That the low-IE band of furan is cleanly recovered in the difference spectrum (*d*) and the two low-IE bands of spectrum (*h*) are roughly equal in area, in our view, validates the process.

Fig. 2. (*a*) Optimized equilibrium structure of **1** obtained at the HF/6-31G** level of theory; (*b*) a display of the HOMO of **1**; (*c*) a display of the HOMO-1 of **1**.

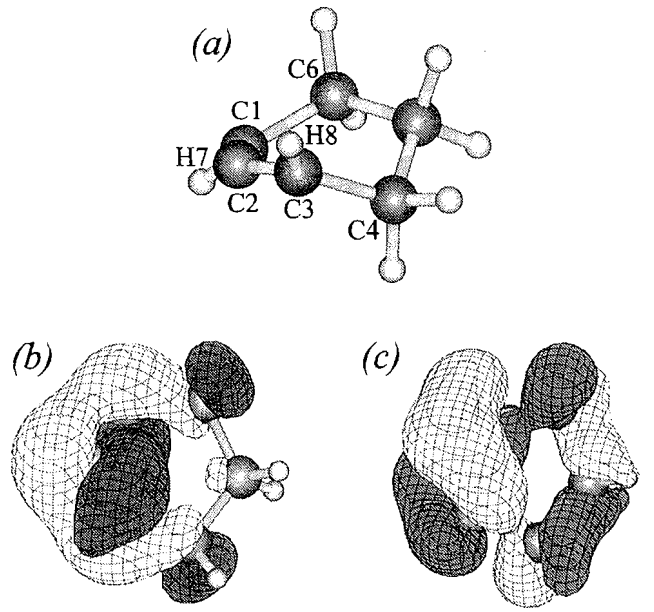

that **1** is a chiral allenic singlet species (6). The optimized equilibrium C_2 structure calculated at the ab initio HF/6-31G** level of theory using Gaussian 94 (14) is displayed as Fig. 2(*a*). As seen from a comparison of several selected geometrical parameters, the ab inito and AM1 optimized C_2 structures of **1** are similar (HF/6-31G**: C1—C2 1.306 Å, C3—C4 1.526 Å, C4—C5 1.572 Å, ∠C1-C2-C3 133.9°, ∠H7-C1-C2-C3 141.4°, ∠C6-C1-C2-C3 −26.0°; *AM1*: C1-C2 *1.320* Å, C1—C6 *1.504* Å, C4—C5 *1.542* Å, ∠C1-C2-C3 *134.8*°, ∠H7-C1-C2-C3 *151.3*°, ∠C6-C1-C2-C3 *−23.4*°) with the largest difference seen in the H7-C1-C2-C3 dihedral angles. The C6-C1-C3-C4 dihedral angles of the structures obtained at the HF/6-31G** and AM1 levels of theory are −47.8° and −43.7°, respectively, approximately half the angle expected for an allene. Thus, the twist angles for the double bonds of the HF/6-31G** and AM1 structures are 20.7° and 22.8°, well within the value required to maintain effective overlap of adjacent *p* orbitals. The HOMO and HOMO-1 of **1** calculated with AM1 and visualized with HyperChem[3] are displayed as Figs. 2(*b*) and 2(*c*), respectively. The HOMO/HOMO-1 gap of **1** is surprisingly large (calculated 1.3 eV, experimental 2 eV) given that 2,3-pentadiene optimized with the C2-C3-C4 angle fixed at 134° exhibits a HOMO/HOMO-1 gap of 0.15 eV. This study also indicates that **4** may be useful for generating **1** in matrix isolation experiments.

[3] HyperChem Version 4.0. Hypercube Inc., 419 Philip St., Waterloo, ON N2L 2X2, Canada.

Acknowledgement

We thank the Natural Sciences and Engineering Research Council of Canada for financial support.

References

1. R. Schulz and A. Schweig. *In* Structure and reactivity. *Edited by* J.F. Liebman and A. Greenberg. VCH Publishers Inc., New York. 1988. Chap. 8.
2. N.P.C. Westwood. Chem. Soc. Rev. **18**, 317 (1989).
3. N.H. Werstiuk, C.D. Roy, and J. Ma. Can. J. Chem. **72**, 2537 (1994).
4. N.H. Werstiuk, C.D. Roy, and J. Ma. Can. J. Chem. **73**, 146 (1995).
5. N.H. Werstiuk, J. Ma, C.D. Roy, A.J. Kresge, and E. Jefferson. Can. J. Chem. **73**, 1738 (1995).
6. R.P. Johnson. Chem. Rev. **89**, 1111 (1989), and references cited therein.
7. C. Wentrup, G. Gross, A. Maquestiau, and R. Flammang. Angew. Chem. Int. Ed. Engl. **22**, 542 (1983).
8. A. Runge and W. Sander. Tetrahedron Lett. **27**, 5835 (1986).
9. A.T. Bottini, L.L. Hilton, and J. Plott. Tetrahedron, **31**, 1997 (1975).
10. L. Asbrink, C. Fridh, and E. Lindholm. HAM/3. Quantum Chemistry Program Exchange (QCPE) Bulletin, **13**, 393 (1981).
11. Dewar Research Group and J.J.P. Stewart. Austin Model 1 Package 1.0(AMPAC). QCPE, 506 (1986).
12. F. Brogli, E. Heilbronner, J. Wirtz, E. Kloster-Jensen, R.G. Bergman, K.P.C. Vollhardt, and A.J. Ashe III. Helv. Chim. Acta, **58**, 2620 (1975).
13. W.R. Moore and W.R. Moser. J. Am. Chem. Soc. **92**, 5469 (1970).
14. M.J. Frisch, G.W. Trucks, H.B. Schlegel, P.M.W. Gill, B.G. Johnson, M.A. Robb, J.R. Cheeseman, T. Keith, G.A. Petersson, J.A. Montgomery, K. Raghavachari, M.A. Al-Laham, V.G. Zakrzewski, J.V. Ortiz, J.B. Foresman, C.Y. Peng, P.Y. Ayala, W. Chen, M.W. Wong, J.L. Andres, E.S. Replogle, R. Gomperts, R.L. Martin, D.J. Fox, J.S. Binkley, D.J. Defrees, J. Baker, J.P. Stewart, M. Head-Gordon, C. Gonzalez, and J. A. Pople. Gaussian 94, Revision B.3. Gaussian, Inc., Pittsburgh, Pa. 1995.

1995 Alcan Award Lecture
New intermediates in the homolytic and heterolytic splitting of dihydrogen[1]

Robert H. Morris

Abstract: Some of the research of the author and his research group into the structure and reactions of dihydrogen complexes of transition metals is reviewed. The characterization of osmium complexes that can be regarded as having intermediate structures on the way to the homolytic splitting and to the heterolytic splitting of dihydrogen is described. The properties of an iridium complex with novel short proton–hydride contacts is also reviewed.

Key words: transition metal, dihydrogen, hydride, complexes, NMR, neutron diffraction, osmium, iridium.

Résumé : On présente une revue des travaux de recherche effectués dans les laboratoires de l'auteur sur la structure et les réactions des complexes dihydrogénés des métaux de transition. On décrit la caractérisation des complexes de l'osmium qui peuvent être considérés comme possédant des structures intermédiaires entre celles conduisant aux ruptures de la liaison H—H du dihydrogène soit homolytiques soit hétérolytiques. On passe aussi en revue les propriétés d'un complexe d'iridium qui comporte de nouveaux contacts courts hydrons–hydrure.

Mots clés : métal de transition, dihydrogène, hydrure, complexes, RMN, diffraction des neutrons, osmium, iridium.

[Traduit par la rédaction]

Introduction

The reaction of dihydrogen gas with soluble transition metal complexes is an important step in many catalytic hydrogenation steps (1). The product of the reaction with H_2 is one of at least three complexes (Scheme 1).

The initial product, intermediate, or transition state contains a dihydrogen ligand coordinated side-on with a short H—H distance (2) (referred to as an η^2-H_2 ligand (3)). This complex might then undergo an oxidative addition reaction where the H—H bond is split homolytically to give, when starting with a six-coordinate dihydrogen complex, a seven-coordinate dihydride product (4).[3] Alternatively, if there is a suitable base present, the dihydrogen bond is split heterolytically to give a six-coordinate metal hydride product and a protonated base. This last reaction is an important feature of dihydrogen chemistry since H_2(g) is not an acid ($pK_a \approx 35$) while dihydrogen complexes can be very acidic with pK_a values of less than 0 (4). This lecture explores the structures and reactions of dihydrogen complexes and intermediates on the way to the dihydride or monohydride products.

Scheme 1. Homolytic splitting (oxidative addition) and heterolytic splitting of the H—H bond in dihydrogen complexes.

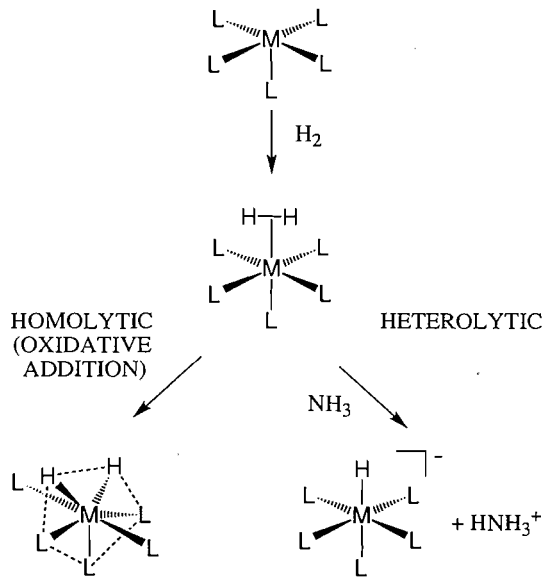

Types of dihydrogen complexes

Several hundred stable dihydrogen complexes have been prepared since the discovery of the first complex $W(H_2)(CO)_3(P^iPr_3)_2$ by Kubas et al. at Los Alamos National Laboratory in 1984 (2). Most have the metal in the d^6 electron configuration, i.e., Cr(0), Mo(0), W(0), Mn(I), Tc(I), Re(I),

Received: February 8, 1996.

This paper is dedicated to Professor Howard C. Clark in recognition of his contributions to Canadian chemistry.

R.H. Morris.[2] Department of Chemistry, University of Toronto, 80 St. George St., Toronto, ON M5S 3H6, Canada.

[1] This is an invited review article based on the 1995 Alcan Award Lecture presented at the 78th Annual Conference of the Canadian Society for Chemistry, Guelph, Ontario, May 26 – June 1, 1995.

[2] Telephone and Fax: (416) 978-6962. E-mail: rmorris@chem.utoronto.ca

[3] There is an intermolecular homolytic splitting reaction as well; see ref. 4.

Fig. 1. Bonding components of the dihydrogen ligand to transition metals.

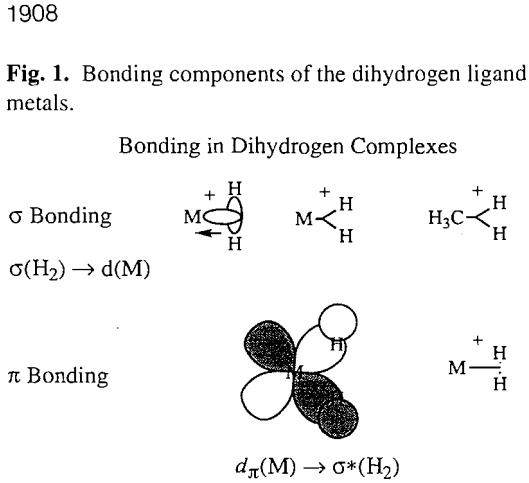

Fe(II), Ru(II), Os(II), Co(III), Rh(III), Ir(III). We reported the determination of the structure of the Fe(II) complex *trans*-$[Fe(H_2)(H)(dppe)_2]BF_4$, dppe = $PPh_2CH_2CH_2PPh_2$, by single crystal X-ray diffraction in 1985 (3). In the same year Crabtree and co-workers reported the existence of iridium dihydrogen complexes including an Ir(III) complex $[Ir(H_2)_2(H)_2(PCy_3)_2]^+$, which is proposed to have two dihydrogen ligands (5). Some unstable dihydrogen complexes with the metal in the d^6 configuration were also reported that year (6–8). A few stable complexes are known with the metal ion in other *d* configurations including the d^4 Re(III) complex $[Re(H_2)(H)_2(CO)(PMe_2Ph)_3]^+$, also reported by Crabtree's group (9).

Bonding

There are two important components to the bonding in dihydrogen complexes (Fig. 1). The first is the donation of σ electrons from H_2 into an empty metal orbital. If this were the only interaction it would be written as a three-centre, two-electron bond as in boron hydride chemistry. However strong main-group Lewis acids do not form stable H_2 complexes; for example the CH_5^+ ion has only transient existence at low temperature. The second crucial component is π-back-donation from a filled *d* orbital into the empty σ* orbital of H_2. The energy of these *d* electrons is an important determinant in the reactivity of the dihydrogen ligand. For example, the higher the energy of these *d* electrons, the more likely it is that the H_2 ligand will undergo homolytic cleavage.

Two methods that we have found to be useful for estimating the energies of the π-bonding *d* orbitals are to determine the infrared spectrum and the redox potentials of the corresponding *dinitrogen* complexes (10, 11). Since the σ and π components in $M(H_2)$ and $M(N_2)$ bonds are similar, the N_2 complexes are indicators of the properties of the H_2 complexes (Fig. 2).

Electrochemical potentials $E_{1/2}(M(N_2)^+)$ of less than 0.5 V (versus NHE) and $\nu(N_2)$ values of less than 2050 cm^{-1} suggest that the complexes are too reducing to make stable H_2 complexes; instead, homolytic splitting occurs to give a dihydride. Redox potentials greater than 2 V and $\nu(N_2)$ greater than 2200 cm^{-1} indicate that there is not enough back-bonding to stabilize the η^2-H_2 ligand with respect to loss of H_2.[4] Therefore we choose metal ions and ligands (guided by Lever's additive electrochemical parameters for ligands as mentioned below) that give properties in the intermediate region. In an attempt to make very acidic dihydrogen complexes we try to work at the 2 V limit.

[4] These guidelines for the stability of dihydrogen complexes do not take into account the relative stabilities of products of dihydrogen loss or oxidative addition of the H—H bond. In certain cases the formation of products is particularly favorable for reasons other than the electronic considerations given here. Then these simple guidelines break down.

Fig. 2. N_2 stretching wave numbers and electrochemical potentials of dinitrogen complexes are indicators of the properties of corresponding dihydrogen complexes.

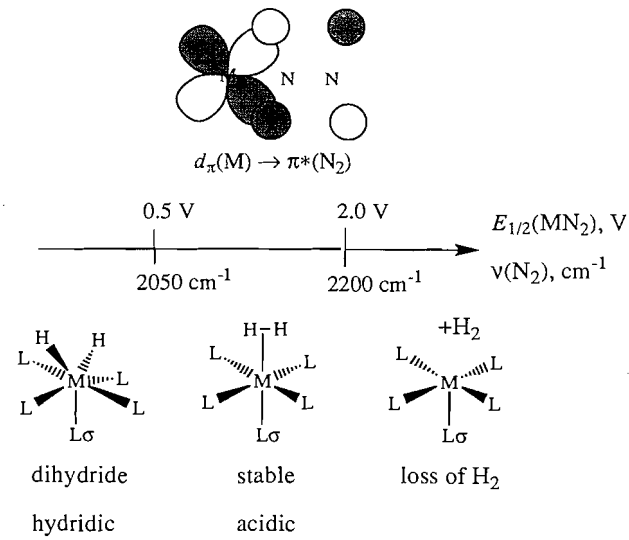

Scheme 2. Synthesis of dihydrogen complexes from H_2 gas (routes i, ii, and iii) or by adding a proton to a hydride complex (routes iv and v).

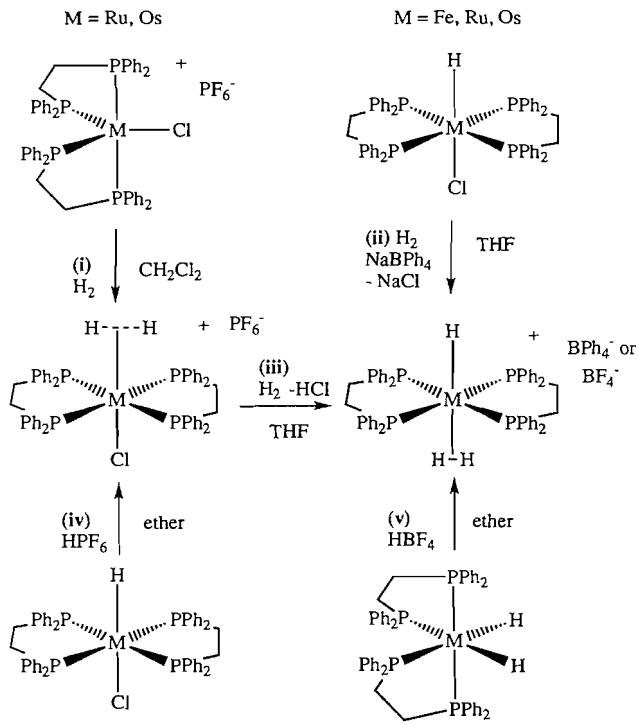

Synthesis of dihydrogen complexes

Scheme 2 illustrates two general methods for generating dihy-

drogen complexes. The first involves the reaction of metal complexes with dihydrogen gas (reactions i, ii, and iii). In the second (routes iv and v) a proton is added to a metal hydride complex to produce the H_2 ligand in the reverse of the heterolytic splitting reaction. The reactant in step i is a coordinatively unsaturated complex $[MCl(dppe)_2]PF_6$, where M is either Ru or Os, with interesting distorted trigonal bipyramidal structures. These react rapidly with 1 atm (101.3 kPa) H_2 to give complexes with dihydrogen *trans* to the chloride ligand in *trans*-$[M(H_2)Cl(dppe)_2]PF_6$, M = Ru, Os (12). The complexes with dihydrogen *trans* to hydride in *trans*-$[M(H_2)H(dppe)_2]^+$ are prepared by reacting *trans*-$MCl(H)(dppe)_2$ with Na^+ under 1 atm H_2, reaction (ii). A third reaction with H_2(g) (reaction iii) converts the chloride complex to the hydride complex in the presence of $NaBPh_4$. This reaction is not well understood.

The reactions of acid with the appropriate metal hydrides (steps iv, v) result in the formation of the same dihydrogen complexes as produced above with H_2. Reaction v involves a rearrangement after the protonation step. In this lecture I will concentrate on the chemistry with M being Os and the chelating phosphine ligand, dppe.

Homolytic splitting of dihydrogen

First I will look at intermediate structures on the way to the homolytic splitting of dihydrogen, reaction [1]. This reaction is favoured by metal ions with high *d*-electron energies and ligands that push electrons onto the metal ion. Both of these effects increase back-donation into the σ^* orbital of the H_2 ligand. Metals that form strong M—H bonds and ligands with the correct bite angles will favour the oxidative addition product while ligands with 90° angles will favour the reactant.

$$[1] \quad M(H_2)L_5 \rightleftarrows M(H)_2L_5$$

It is important to understand these factors since such reactions are found in several industrial catalytic processes. Related chemical reactions such as the homolytic splitting of carbon–hydrogen and silicon–hydrogen bonds follow similar principles. In addition, several fluxional rearrangements of metal hydride complexes involve the reverse of this reaction (4).

Determination of H—H distances in the solid state

How does one know when there is a short H—H distance? The question can be answered most precisely for solid samples. If large crystals are available, a neutron diffraction structure determination is done by the group of T.F. Koetzle at the Brookhaven National Laboratory. Hydrogens are located accurately by use of this method because ^1H nuclei diffract neutrons as well as any other nucleus. Such structure determinations over the last 8 years have revealed that a continuum of H—H distances is possible from short distances of 0.85 Å to long ones of 1.8 Å found in dihydride complexes. The 0.85 Å bond lengths are 0.11 Å longer than that of free H_2 gas. Occasionally the H atoms are located in X-ray diffraction studies of smaller crystals but the H—H distances so obtained are not as accurate due to the difficulty in detecting the two electrons of H_2 buried in the cloud of electrons of the transition metal. Solid state NMR has been applied by Zilm and Millar (13) to

Fig. 3. Structures of four osmium complexes whose structures trace out the oxidative addition of H_2.

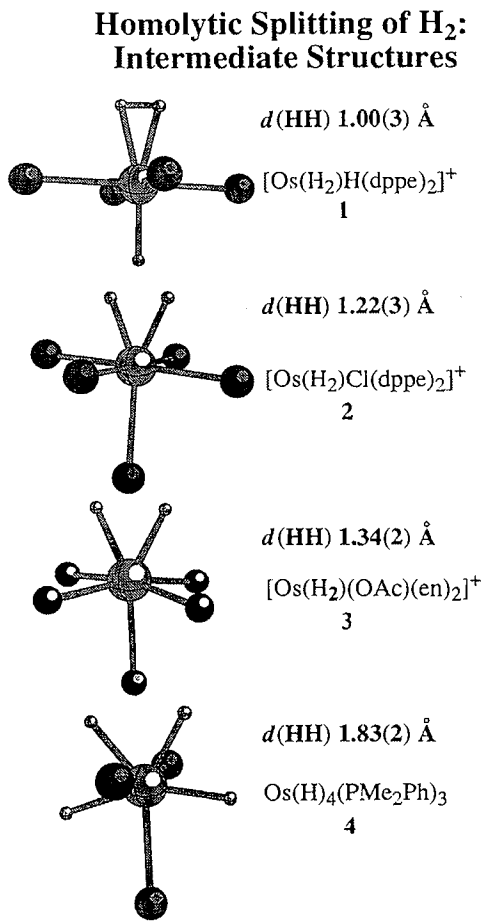

complexes containing H—H distances of less than 1.1 Å. Infrared spectroscopy will occasionally reveal the weak H—H mode found between 3000 and 2400 cm^{-1} in η^2-H_2 complexes (14). However, often ligand vibration overtones obscure these bands. Usually dihydride complexes can be identified by an M–H stretching mode with wave number between 2200 and 1500 cm^{-1}. The method of inelastic neutron scattering provides definitive proof for the existence of a short H—H distance when peaks due to quantum mechanical tunneling of nuclei through H–H librational barriers are observed (15).

Recently structures have become available for osmium complexes that illustrate the continuum of H—H distances possible (Fig. 3). The structures trace out a possible trajectory for the homolytic splitting reaction. All of these complexes have seven atoms coordinated to the central osmium. Complex *trans*-$[Os(H_2)H(dppe)_2]^+$ (**1**) at the top of the figure is octahedral with the dihydrogen ligand occupying one site on Os(II).[5] At the bottom of the figure is an example of an Os(IV) polyhydride complex $Os(H)_4(PMe_2Ph)_3$ (**4**) with no H—H bonding (16). The other two complexes have intermediate structures where the H–H splitting has been arrested. When the *trans* hydride ligand in **1** is replaced by chloride in $[Os(H_2)Cl(dppe)_2]^+$ (**2**) the H—H distance lengthens from 1.0

[5] P.A. Maltby, R.H. Morris, W. Klooster, T.F. Koetzle, J.S. Ricci, and A. Albinati. In progress.

Fig. 4. Plot of d(HH) determined in the solid state versus the J(H,D) coupling constant measured on the corresponding HD complex in solution.

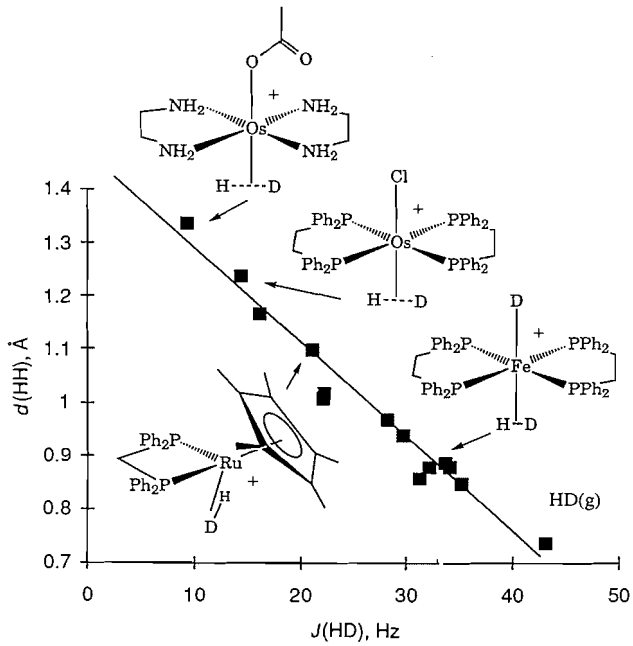

to 1.22(3) Å (17). The origin of this effect is a combination of an increase in σ-Lewis acidity of the osmium and an increase in d–π electron energy. When the dppe ligands are replaced by ethylenediamine (en) ligands in *trans*-$[Os(H_2)(OAc)(en)_2]^+$ (**3**), while retaining a similar π-base ($O_2CCH_3^-$ versus Cl^-) *trans* to the H_2 ligand, the H—H distance lengthens to 1.34 Å (18). As discussed later, the en ligands make the Os centre considerably more reducing than the one containing the dppe ligands.

Determining H–H distances in solution

It is a more challenging problem to estimate H—H distances in solution. Yet this is important if we are to correlate structure with reactivity — for example, acidity, as expressed by the pK_a of the H_2 complex. We have found that the J(H,D) coupling of the HD ligand as observed in the ^1H NMR spectrum of the complex $M(HD)L_n$ correlates smoothly with the H—H distance determined by neutron diffraction studies (Fig. 4). We have good evidence that these complexes maintain the same structure in solution as in the solid state although there might be a small effect in replacing H by D. As indicated on the scale, a short H—H distance of 0.80 Å corresponds to a large J(H,D) of 32 Hz while dihydrides have couplings of less than 5 Hz. A relationship that holds for a large number of complexes is

$$[2] \quad d(\mathrm{HH}) = -0.0167\,(J(\mathrm{H,D})) + 1.42$$

In principle, the minimum T_1 value, T_1^{min}, of the H nuclei of the H_2 ligand should provide an accurate H—H distance in solution since in many cases dipolar relaxation of one H by its close neighbour dominates so that T_1 is proportional to $d(HH)^6$

[6] T_1^{min} must be corrected to account for the contributions to the relaxation rate from other dipolar nuclei.

Fig. 5. Scales relating J(H,D) and T_1(min) NMR parameters with H—H distance.

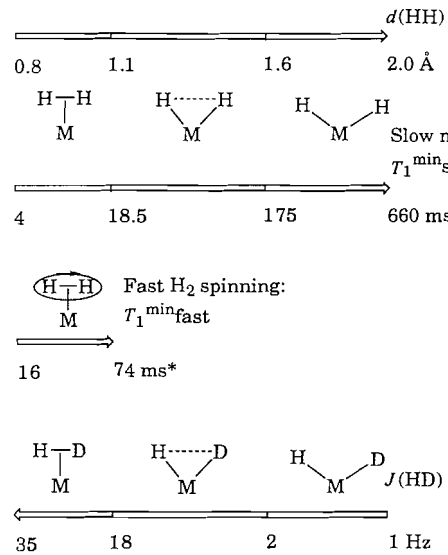

* At 400 MHz, corrected for dipolar contributions from other nuclei

(19). The T_1^{min} value is found by varying the temperature. If the H nuclei of the H_2 ligand have slow motion relative to the correlation frequency of tumbling of the complex in solution (approximately the spectrometer frequency), then the scale in Fig. 5 can be used to relate T_1^{min}(slow) at 400 MHz to d(HH).[6] Note how sensitive T_1^{min}(slow) is to the H—H distance. As the distance elongates from 0.8 to 1.6 Å the T_1^{min} value changes from 4 to 175 ms. Equation [3] is applied if the motion is known to be slow:

$$[3] \quad d(\mathrm{HH}) = 5.81 \sqrt[6]{\frac{T_1^{min}(\mathrm{slow})}{\nu}}$$

where ν is the spectrometer frequency in MHz and T_1^{min} (slow) is in seconds (20).

Unfortunately the dihydrogen ligand often has fast motion relative to 400 MHz and this makes the interpretation of T_1^{min} difficult. If the H_2 is rapidly spinning like a propeller then the scale for T_1^{min}(fast) applies (21). For a given H—H distance, the T_1 values measured are 4 times longer when there is fast spinning and a different equation is used to determine d(HH).

$$[4] \quad d(\mathrm{HH}) = 5.81 \sqrt[6]{\frac{T_1^{min}(\mathrm{fast})}{4\nu}} = 4.61 \sqrt[6]{\frac{T_1^{min}(\mathrm{fast})}{\nu}}$$

If the type of motion is not known, then a measured T_1^{min} value of 16 ms, for example, could correspond to either a 1.08 Å H_2 ligand with no extra motion or a 0.85 Å H_2 ligand with fast spinning relative to 400 MHz. Other types of motion such as hopping between sites could result in the calculation of distances between these two values. Therefore other spectroscopic methods need to be developed to elucidate the nature of the H_2 motion.

I will now illustrate examples of complexes in the fast-spin-

Fig. 6. Dihydride and dihydrogen tautomers of $[Ru(H_2)(C_5Me_5)(dppm)]BF_4$ in equilibrium.

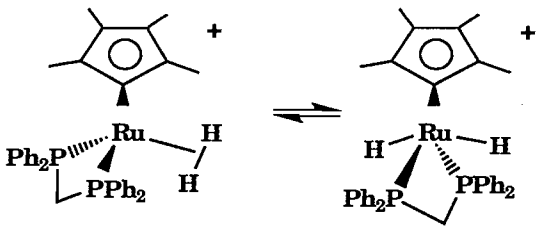

ning and slow-motion regimes. The single crystal neutron diffraction structure of *trans*-$[Fe(H_2)H(dppe)_2]BPh_4$ was reported in 1989 (22). The H—H distance was 0.82(1) Å. Later it was discovered that the librational motion of the H_2 ligand even at 15 K in the solid state results in an underestimation of the H—H distance. This was traced to the crystallographic computer program fitting an ellipsoid to nuclear density smeared out, because of the librational motion, into the shape of a banana. If a "banana correction" is applied the H—H distance lengthens to about 0.85 Å. This value is then in better agreement with the distance of 0.90(1) Å determined by Zilm's group (13) using solid state NMR methods. In solution the large J(H,D) value of 32 Hz in *trans*-$[Fe(HD)(D)(dppe)_2]BF_4$ in acetone-d_6 is consistent with a short H—H distance. When the observed T_1^{min} value of 0.017 s at 400 MHz is substituted, only eq. [4] for fast spinning gives a distance of 0.88 Å, which agrees with the neutron and solid state NMR studies.

The complex $[Ru(H_2)(C_5Me_5)(dppm)]BF_4$ has an elongated H_2 ligand with a high barrier to spinning (23). The neutron structure shows that the dihydrogen ligand has an unusual elongation with a d(HH) of 1.10(1) Å. The H—H vector lies parallel to the C_5Me_5 ligand. In this orientation the H_2 ligand benefits from overlap of its σ^* orbital with the filled $d\pi$-bonding orbital of Ru(II) in the three-legged piano stool. Since there is no similar concentration of π-bonding electrons if the H_2 rotates 90°, a barrier results. In this respect the H_2 ligand is acting as a compass needle (24) to indicate the orientation of π electron density.

The J(H,D) value of 21 Hz for $[Ru(HD)(C_5Me_5)(dppm)]BF_4$ also indicates the presence of an elongated H_2 ligand with d(HH) = 1.05 Å (see eq. [2]). Of the two possible distances (1.10 and 0.90 Å, for slow and fast spinning, respectively) calculated from the T_1^{min} value (18 ms at 400 MHz), the longer distance is the logical one. In fact it was chosen 2 years before (25) the neutron structure was reported (23).

This system provides an interesting example of homolytic H_2 splitting. A dihydride tautomer and dihydrogen tautomer are in equilibrium (Fig. 6). Such tautomers become important when comparing the kinetics of proton transfer (see below).

The heterolytic splitting of dihydrogen

The existence of dihydrogen complexes allows a systematic study of the factors that determine the kinetics and thermodynamics of proton transfer in hydrogenation reactions.

As indicated earlier, acidic dihydrogen complexes have positive electrochemical potentials arising from combinations of electron-withdrawing ligands and a positive charge. Very acidic but stable dihydrogen complexes have $E_{1/2}(MN_2)$ near to 2 V vs. NHE. However, such positive $E_{1/2}$ values mean that there is little $d\pi \rightarrow \sigma^*$ back-bonding to the H_2 ligand and therefore a strong H—H bond. This can lead to a complex that is not as acidic as might be expected on the basis of $E_{1/2}$ values alone (see below).

A better knowledge of the heterolytic splitting of H_2 will serve us in many ways. There are industrial processes that rely on this reaction, including the recovery of nickel from nickel ores and the formation of methanol from synthesis gas. Nature's hydrogenase enzymes allow bacteria to utilize hydrogen as their fuel source. The action of this enzyme relies on a complex of nickel and probably iron and could involve the deprotonation of a dihydrogen complex at nickel (26) or iron. Understanding the heterolytic splitting of the H—H bond helps to unravel the factors involved in the more complex electrophilic cleavage of carbon–hydrogen bonds, a very promising way to functionalize methane gas (27, 28).

To my knowledge I am the "third generation" of chemists working in this area in Canada. The first was Jack Halpern when he was at the University of British Columbia. The second is Brian James, my Ph.D supervisor, also at U.B.C.

Kinetic and thermodynamic aspects of the acidity of dihydrogen complexes

An important kinetic feature of this chemistry is that a dihydrogen complex transfers a proton to a base more rapidly than a related dihydride complex. This is demonstrated by cooling an interconverting mixture of dihydrogen and dihydride forms of $[Ru(C_5H_5)H_2(dppe)]^+$ in CD_2Cl_2 until the rate of exchange is nil (at approx. 240 K). When a strong base, NaOEt, is added to this mixture, only the dihydrogen tautomer is deprotonated (eq. [5]) (25).

$$[5] \quad [Ru(C_5H_5)(\eta^2\text{-}H_2)(dppe)]BF_4 + [Ru(C_5H_5)(H)_2(dppe)]BF_4 + NaOEt \rightarrow Ru(C_5H_5)(H)(dppe) + [Ru(C_5H_5)(H)_2(dppe)]BF_4 + HOEt + NaBF_4$$

There is a small kinetic barrier to deprotonation of the η^2-H_2 tautomer because there is little rearrangement of the complex on going to the monohydride product $Ru(C_5H_5)(H)(dppe)$; both complexes are formally six-coordinate Ru(II), of the class RuX_2L_4 (29). There is a larger barrier to rearrange the dihydride tautomer, formally a seven-coordinate Ru(IV) complex (RuX_4L_3), into the monohydride RuX_2L_4 product.

Heinekey's group and my own have attempted to estimate the pK_a values of dihydrogen complexes in order to gain a semi-quantitative understanding of the heterolytic splitting reaction. In this lecture I will illustrate this approach by a study of the acidity of the complexes *trans*-$[Os(H_2)L(dppe)_2]^{2+}$, where the pK_a varies dramatically as a function of the *trans* ligand, L = Cl^- (**2**) and H^- (**1**) (17). These acidic dihydrogen complexes are titrated with bases PMe_2Ph and $Ru(C_5Me_5)(H)(PPh_3)_2$, respectively. The pK_a of the conjugate acid forms on the extrapolated aqueous scale are known: 6.5 for $HPMe_2Ph^+$ and 11.1 for $[Ru(C_5Me_5)(H)_2(PPh_3)_2]^+$. These are chosen because they do not displace the H_2 ligand and their relative concentrations are

readily determined by NMR spectroscopy. Bulky phosphines are particularly useful in the titration of dihydrogen complex acids (eq. [6]):

[6] *trans*-$[Os(H_2)Cl(dppe)_2]^+ + PMe_2Ph \rightleftarrows$

trans-$Os(H)(Cl)(dppe)_2 + HPMe_2Ph^+$

The equilibrium constant for eq. [6] can be obtained by use of ^1H and ^{31}P NMR spectroscopy. The pK_a of **2** with dihydrogen *trans* to chloride is determined to be 7.4.

There is a large increase in pK_a when H_2 is *trans* to hydride in **1** compared to when it is *trans* to chloride in **2**. Even the most basic phosphine P^{t}Bu$_3$ is not sufficiently basic to deprotonate **1**.[7] Therefore the complex $Ru(C_5Me_5)(H)(PPh_3)_2$ was used as the base (eq. [7]).

[7] *trans*-$[Os(H_2)H(dppe)_2]^+ + Ru(C_5Me_5)(H)(PPh_3)_2 \rightleftarrows$

cis and *trans*-$Os(H)_2(dppe)_2 + [Ru(C_5Me_5)(H)_2(PPh_3)_2]^+$

The pK_a of **1** is thus determined to be approximately 13.6.

An important factor that makes **1** much less acidic than **2** is the stronger H—H bonding in the former complex. We have evidence that the H—H distance is significantly shorter in **1** in solution. The H–D coupling constant of $[Os(HD)(D)(dppe)_2]^+$ (**1**-d_2) is 25.5 Hz and by use of eq. [2] this corresponds to an H—H distance of 1.00 Å. This is in agreement with the 1.00 Å distance from the T_1 method by use of eq. [4] for a fast-spinning H_2 ligand. It is also consistent with the distance in the solid state as measured by neutron diffraction (1.00 Å) when this distance has been corrected for librational motion. The J(H,D) value of **2**-d_1 is 13.9 Hz, which corresponds to a d(HH) in solution of 1.20 Å. This almost coincides with the H—H distance of 1.22(3) Å determined by neutron diffraction. The T_1(min) value gives a distance of 1.35 or 1.08 Å when eqs. [3] and [4] are applied, respectively. Since the other methods give d(HH) values between these limiting values, this suggests that the H_2 ligand has a motional frequency near to 400 MHz. In this case there is independent evidence that the frequency of the motion of the H_2 ligand is similar to that of the tumbling of the molecule from plots of ln T_1 versus $1/T$. These curves do not have the usual "V" shape and so eqs. [3] or [4] do not apply. A spectral density function needs to be determined to describe the as yet undefined motion of the H_2 ligand in the molecule so that the H—H distance can be calculated from the T_1 data. In summary, the best estimates of the H—H distances for **1** and **2** are 1.00 and 1.20 Å, respectively. The shorter H—H distance for **1** results in a less acidic complex.

Very acidic, stable dihydrogen complex

When L is changed to CH_3CN in *trans*-$[Os(H_2)(L)(dppe)_2]^{2+}$ then a very acidic complex *trans*-$[Os(H_2)(CH_3CN)(dppe)_2](BF_4)_2$, **5**, is obtained (30). The complex was found by low-temperature X-ray diffraction to have an H—H distance of 0.9(1) Å. When the isolated dihydrogen complex is dissolved in dry CH_2Cl_2 and treated with dry diethyl ether, it is partially converted into the monohydride complex *trans*-$[Os(H)(CH_3CN)(dppe)_2](BF_4)$ according to eq. [8].

[7] HP^{t}Bu$_3^+$ has a pK_a of 12.1.

Table 1. The properties of three osmium dihydrogen complex with H—H distances increasing from **1** to **5** to **2**.

Complex	**1**	**5**	**2**
Ligand	H^-	CH_3CN	Cl^-
J(H,D), Hz	25.5	21.4	13.9
d(HH), Å	1.0	1.1	1.2
pK_a	13.6	−2	7.4
$E_{1/2}$, V, vs. Fc^+/Fc	−0.20	+0.58	−0.13
$\Delta H_{BDE}\{M(H_2)\}$, kcal mol^{-1}	80	77	73

[8] $[Os(H_2)(CH_3CN)(dppe)_2](BF_4)_2 + Et_2O \rightleftarrows$

$[Os(H)(CH_3CN)(dppe)_2](BF_4) + HOEt_2(BF_4)$

Complex **5** is completely deprotonated by water. Therefore the pK_a of **5** is near to that of protonated ether, which has been estimated to be −2.3 on the aqueous scale.

To determine whether the acidity of dihydrogen complexes depends on the H—H bond length it is necessary to estimate the latter for the complexes in solution. As described above, the coupling constant J(H,D) is the best indicator. The H—H distances increase with L in *trans*-$[Os(H_2)L(dppe)_2]^{2+}$ as: $H^- < CH_3CN < Cl^-$ (Table 1).

The H-atom abstraction energy, $\Delta H_{BDE}\{M(H_2)\}$ as an indicator of H—H bonding

Tilset and Parker have described how metal–hydride bond dissociation energies, ΔH_{BDE}(MH), of complexes MHL_5 can be determined by measuring the pK_a of the hydride complex, p$K_a(MHL_5)$ and the electrochemical potential of the conjugate base hydride, $E_{1/2}(ML_5/ML_5^-)$ (31, 32). We made use of an identical thermochemical cycle to determine the bond dissociation energies (BDE) for dihydrogen complexes, MH_2L_5 (eqs. [9]–[13]) (11, 33).

[9] $M(HH)L_5 \rightarrow [MHL_5]^- + H^+$, $\Delta G = 1.37\ pK_a\{M(H_2)\}$

[10] $[MHL_5]^- \rightarrow MHL_5 + e^-$, $\Delta G = 23.1E_{1/2}(MH/MH^-)$

[11] $H^+ + e^- \rightarrow H^\cdot$, ΔG = constant

[12] $M(HH)L_5 \rightarrow MHL_5 + H^\cdot$, $\Delta G_{BDE} = 1.37\ pK_a\{M(H_2)\} + 23.1E_{1/2}(MH/MH^-) +$ constant

Thus the free energies of deprotonation of the dihydrogen complex (eq. [9]), the oxidation of the deprotonated complex (eq. 10), and the reduction of the proton (eq. [11]) combine to produce the free energy of the H-atom abstraction reaction (eq. [12]). The constant in the corresponding enthalpy expression, $\Delta H_{BDE}\{M(H_2)\}$, has been determined from the $\Delta H_{BDE}\{MH\}$ of known metal hydrides to be 66 as in eq. [13].

[13] $\Delta H_{BDE}\{M(H_2)\} = 1.37\ pK_a\{M(H_2)\} + 23.1\ E_{1/2}(MH/MH^-) + 66$

kcal/mol (pseudo aqueous) V vs. $Cp_2Fe^{+/0}$ in THF

The calculation of $\Delta H_{BDE}\{M(H_2)\}$ values that are larger than those expected for metal hydride bonds (55–75 kcal mol^{-1}) should signal the presence of H—H bonding since not only do M—H but also H—H bonds have to be broken when the H atom is abstracted from the dihydrogen complex (11).

The values required to calculate this energy for the complexes *trans*-$[Os(H_2)L(dppe)_2]^{2+}$ are listed in Table 1. The electrochemical potentials of the complexes *trans*-$[OsH(L)(dppe)_2]^+$ increase with L in the order $H^- < Cl^- < CH_3CN$. The ΔH_{BDE} values decrease as d(HH) increases. The ΔH_{BDE} values for **1** and **5** are large enough to suggest the presence of H—H bonding while that for **2** is of the magnitude typical of an osmium hydride BDE. Therefore there appears to be little H—H bonding in **2**, which has a stretched H—H distance of 1.2 Å. This work and the work on the corresponding ruthenium complexes (12) is the first to illustrate the importance of the *trans* ligand on the acidity of a dihydrogen complex. The general conclusion from this work is that there is little H—H bonding in dihydrogen complexes that have d(HH) $\geq$ 1.1 Å.

The effect on the acidity of changing the *cis* ligand from dppe in **5** to en in *trans*-$[Os(H_2)(CH_3CN)(en)_2]^{2+}$, **6**, en = $NH_2CH_2CH_2NH_2$ (18), can be predicted by use of eq. [13] and Lever's additive electrochemical method (34). The d(HH) in **6** is calculated by use of eq. [2] and J(H,D) of 17.7 Hz to be 1.2 Å. The $E_{1/2}$ value for the conjugate base hydride form of **6** can be predicted to be -0.8 ± 0.2 V vs. Fc^+/Fc. Therefore the pK_a of **6** is estimated to be 17 ± 3. Thus a dramatic decrease in acidity is predicted with the replacement of two dppe ligands with two electron-donating en ligands.

Intermediate structures in proton transfer from dihydrogen complexes

Figure 7 is arranged to show three structures that appear to trace out the trajectory of proton transfer from the dihydrogen ligand to a base. The top two structures show the positions of the anions in the solid state structures of **2** and **5**. These have a fluoride of the anion in proximity to the H_2 ligand, with the more acidic complex, **5**, having the shorter d(HF) of 2.5 Å. The anion is poised, as a stronger base might be, to receive a proton from the dihydrogen ligand in the heterolytic splitting reaction. The complex **1**, with a less acidic H_2 ligand, does not have a close H_2–F interaction.

The third structure of Fig. 7 can be viewed as being produced by transfer of a proton from an unstable iridium dihydrogen complex to the nitrogen of a coordinated mercaptopyridine ligand (35). The novel feature of this structure is that the proton and hydride remain in close proximity (d(HH) 1.75 Å), even in solution.

The complex $[Ir(H\cdots HNC_5H_4S)_2(PCy_3)_2]BF_4$, **7**, is prepared by reacting $Ir(H)_5(PCy_3)_2$ with $[HNC_5H_4SH]BF_4$ in CH_2Cl_2 (35). In a ^1H NMR experiment, irradiation of the hydride resonance of **7** in CD_2Cl_2 produces a large nuclear Overhauser enhancement of 11% in the NH signal. Therefore the proton on nitrogen and the hydride on iridium are in close proximity (Fig. 8). A distance of 1.75 ± 0.05 Å is calculated by use of eq. [3] and the minimum T_1 value of the hydrogens on N and Ir.

When complex **7** in CD_2Cl_2 is treated with D_2 gas at 1 atm, both the NH and IrH positions are rapidly deuterated (eq. [14]).

Fig. 7. Structures that appear to trace out the trajectory of heterolytic splitting of dihydrogen.

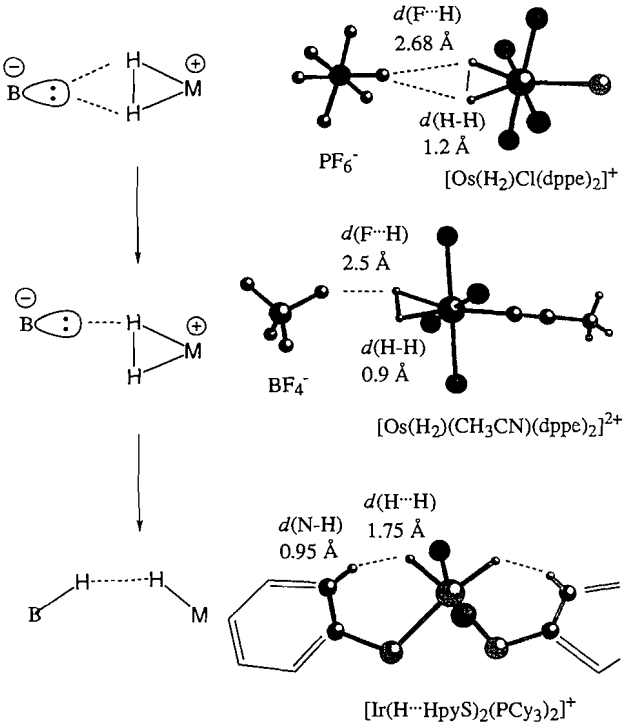

[14] $7 + 2D_2 \rightarrow [Ir(D\cdots DNC_5H_4S)_2(PCy_3)_2]BF_4 + 2H_2$

We propose that this reaction proceeds via the formation of an unobserved tautomeric complex containing a dihydrogen ligand. Such a complex might readily exchange H_2 with D_2. Heterolytic splitting of the D_2 complex produces the deuterated product (Scheme 3).

It appears that the proton–hydride interaction is crucial for fast H_2/D_2 exchange. When complex **7** is dissolved in THF-d_8 under D_2 gas, no exchange is observed under the conditions where exchange is complete with **7** in CD_2Cl_2. Since THF is a better hydrogen-bond acceptor than the iridium hydride, the complex adopts a new conformation where the pyridinium groups have rotated in order to hydrogen bond to the THF (Fig. 8). Now when the hydride resonances are irradiated, there is no nuclear Overhauser enhancement of the NH resonances and instead there is a weak enhancement of the peaks of the C-H groups *ortho* to the sulfur in the mercaptopyridinium ligands.

Both Crabtree's group (36) and our group discovered, independently, this type of proton–hydride interaction. It is turning out to be a common phenomenon in chemistry. We recently described the synthesis of iridium complexes with short proton···hydride···proton contacts. The search is now on for examples of short *intermolecular* proton···hydride interactions.

Conclusions

In the homolytic splitting of dihydrogen, there is a continuum of structures possible, with H—H distances ranging from 0.8

Fig. 8. Structure of **7** in CD_2Cl_2 and THF.

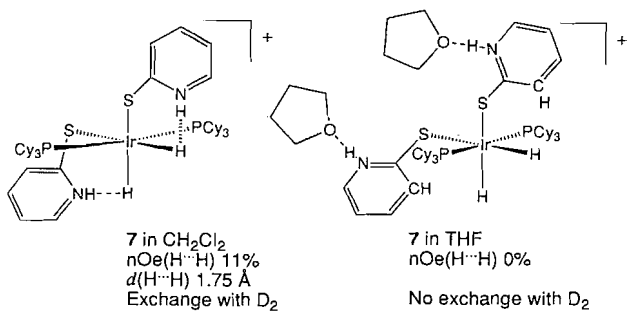

Scheme 3. A mechanism to explain H_2/D_2 exchange in complex **7**.

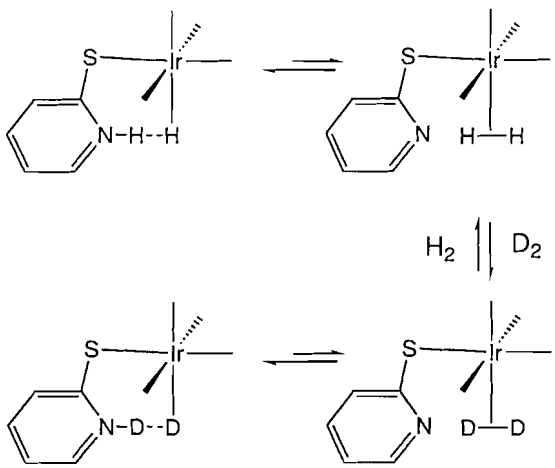

Å (dihydrogen complexes) to 1.1 Å (elongated dihydrogen complexes) to 1.3 Å (compressed dihydrides) to >1.6 Å (dihydrides). The energy of the *d* electrons is an important factor in determining the degree of activation of the H—H bond. The energy barrier to homolytic splitting can be high or low or the splitting can be arrested at structures M(H···H) anywhere between those of dihydrogen and dihydride complexes. The coupling constant *J*(H,D) and eq. [2] appear to be the best way of determining H—H distances in solution. The T_1 method should in principle give accurate H—H distances but the analysis is complicated by the undefined motion of the H_2 ligand. In certain cases the H_2 ligand has been shown to be spinning rapidly like a propeller so that eq. [4] with T_1^{min}(fast spinning) is appropriate for calculating *d*(HH), while in other cases the motion of the ligand is slow relative to the tumbling of the molecule. Other methods are needed to probe the motion of the H_2 ligand in solution.

For the heterolytic splitting of dihydrogen, a wide range of $pK_a\{M(H_2)\}$ values is possible: from −2 to greater than 17. The *trans* ligand has a large effect on the acidity of the H_2 ligand. Stable but very acidic complexes can be prepared and these will be tested as catalysts for new reactions. Hydrogen-atom abstraction enthalpies, $\Delta H_{BDE}\{M(H_2)\}$, which are calculated from $E_{1/2}$ and pK_a, reflect the amount of H—H bonding in dihydrogen complexes. Energies greater than or equal to 80 kcal mol^{-1}, which are observed for dihydrogen complexes with *d*(HH)<1.1 Å, suggest the presence of significant H—H bonding while values of less than 75 kcal mol^{-1}, which are observed for complexes with *d*(HH) greater than 1.1 Å, are more consistent with M—H bonding alone in a "compressed dihydride." If ΔH_{BDE} values can be predicted, then the acidity of dihydrogen complexes can be predicted by use of Lever's parameters.

New principles have been uncovered in the kinetics and mechanisms of proton transfer. Dihydrogen complexes have higher kinetic acidity than dihydrides. Stages of proton transfer from dihydrogen to a base are modeled in crystal structures. The proton transfer can be arrested in new IrH···HN interactions.

It is amazing how such simple complexes can have such a rich chemistry. There is the promise of more to come.

Acknowledgments

I acknowledge the excellent contributions of my current graduate students, Marcel Schlaf, Cameron Forde, Tina Fong, Sunghan Park, and Tanya Bartucz and those of students who have graduated from my lab including Dr Caroline Schweitzer, Dr Patricia Maltby, Dr Tim Burrow, Ms Samantha Drouin, Mr Paul Cappellani, Dr Maria Bautista, Ms Kelly Earl-Luck, Dr Andrea Sella, Dr Natalie Lazarowych, and Dr Rudy Luck. Many postdoctoral fellows have contributed to this work including Dr Wei Xu, Dr Ravi Ramachandran, Dr Bronwyn Greaves, Dr Philip Jessop, Dr Gouchen Jia, Dr Jeff Zubkowski, Dr Joel Ressner, and Dr Hormoz Azizian. Excellent undergraduate students who have contributed to this work include Amanda Chan, Thomas Schleis, Nada Ricciuto, Bain Chin, Adina Petroff, Cinzia D'Agostino, Martin Steinbeck, Suzanne Brinkmann, and Theresa Hoffstede. Crystallographers Dr Alan Lough and Dr Jeffrey Sawyer did key structure determinations by X-ray diffraction and Dr Wim Klooster and Dr Tom Koetzle of Brookhaven National Laboratory and Dr John Ricci of the University of Maine did the crucial neutron structure determinations. I thank Nick Plavac for obtaining NMR spectra and training students in NMR techniques. The work was funded by the Natural Sciences and Engineering Research Council of Canada, the Petroleum Research Fund as administered by the American Chemical Society, and Johnson Matthey, which provided loans of platinum metals.

References

1. B.R. James. Adv. Organomet. Chem. **17**, 319 (1979).
2. G.J. Kubas, R.R. Ryan, B.I. Swanson, P.J. Vergamini, and H.J. Wasserman. J. Am. Chem. Soc. **106**, 451 (1984).
3. R.H. Morris, J.F. Sawyer, M. Shiralian, and J. Zubkowski. J. Am. Chem. Soc. **107**, 5581 (1985).
4. P.G. Jessop and R.H. Morris. Coord. Chem. Rev. **121**, 155 (1992).
5. R.H. Crabtree and M. Lavin. J. Chem. Soc. Chem. Commun. 1661 (1985).
6. S.P. Church, F.-W. Grevels, H. Hermann, and K. Schaffner. J. Chem. Soc. Chem. Commun. 30 (1985).
7. R.L. Sweany. J. Am. Chem. Soc. **107**, 2374 (1985).
8. R.K. Upmacis, G.E. Gadd, M. Poliakoff, M.B. Simpson, J.J. Turner, R. Whyman, and A.F. Simpson. J. Chem. Soc. Chem. Commun. 27 (1985).
9. X.-L. Luo and R.H. Crabtree. J. Am. Chem. Soc. **112**, 6912 (1990).

10. R.H. Morris, K.A. Earl, R.L. Luck, N.J. Lazarowych, and A. Sella. Inorg. Chem. **26**, 2674 (1987).
11. R.H. Morris. Inorg. Chem. **31**, 1471 (1992).
12. B. Chin, A.J. Lough, R.H. Morris, C.T. Schweitzer, and C. D'Agostino. Inorg. Chem. **33**, 6278 (1994).
13. K.W. Zilm and J.M. Millar. Adv. Magn. Opt. Reson. **15**, 163 (1990).
14. G.J. Kubas. Acc. Chem. Res. **21**, 120 (1988).
15. J. Eckert and G.J. Kubas. J. Phys. Chem. **97**, 2378 (1993).
16. D.W. Hart, R. Bau, and T.F. Koetzle. J. Am. Chem. Soc. **99**, 3872 (1977).
17. P.A. Maltby, M. Schlaf, M. Steinbeck, A.J. Lough, R.H. Morris, W.T. Klooster, T.F. Koetzle, and R.C. Srivastava. J. Am. Chem. Soc. **118**, 5396 (1996).
18. T. Hasegawa, Z. Li, S. Parkin, H. Hope, R.K. McMullan, T.F. Koetzle, and H. Taube. J. Am. Chem. Soc. **116**, 4352 (1994).
19. D.G. Hamilton and R.H. Crabtree. J. Am. Chem. Soc. **110**, 4126 (1988).
20. K.A. Earl, G. Jia, P.A. Maltby, and R.H. Morris. J. Am. Chem. Soc. **113**, 3027 (1991).
21. M.T. Bautista, K.A. Earl, P.A. Maltby, R.H. Morris, C.T. Schweitzer, and A. Sella. J. Am. Chem. Soc. **110**, 7031 (1988).
22. J.S. Ricci, T.F. Koetzle, M.T. Bautista, T.M. Hofstede, R.H. Morris, and J.F. Sawyer. J. Am. Chem. Soc. **111**, 8823 (1989).
23. W.T. Klooster, T.F. Koetzle, G. Jia, T.P. Fong, R.H. Morris, and A. Albinati. J. Am. Chem. Soc. **116**, 7677 (1994).
24. V.C. Gibson. Angew. Chem. Int. Ed. Engl. **33**, 1565 (1994).
25. G. Jia, A.J. Lough, and R.H. Morris. Organometallics, **11**, 161 (1992).
26. M. Zimmer, G. Schulte, X.L. Luo, and R.H. Crabtree. Angew. Chem. Int. Ed. Engl. **30**, 193 (1991).
27. M. Lin and A. Sen. Nature, **368**, 613 (1994).
28. A. Sen. Acc. Chem. Res. **21**, 421 (1988).
29. M.L.H. Green. J. Organomet. Chem. **500**, 127 (1995).
30. M. Schlaf, A.J. Lough, P.A. Maltby, and R.H. Morris. Organometallics, **15**, 2270 (1996).
31. M. Tilset and V.D. Parker. J. Am. Chem. Soc. **112**, 2843 (1990).
32. M. Tilset and V.D. Parker. J. Am. Chem. Soc. **111**, 6711 (1989).
33. E.P. Cappellani, S.D. Drouin, G. Jia, P.A. Maltby, R.H. Morris, and C.T. Schweitzer. J. Am. Chem. Soc. **116**, 3375 (1994).
34. A.B.P. Lever. Inorg. Chem. **29**, 1271 (1990).
35. A.J. Lough, S. Park, R. Ramachandran, and R.H. Morris. J. Am. Chem. Soc. **116**, 8356 (1994).
36. J.C. Lee, Jr. A.L. Rheingold, B. Muller, P.S. Pregosin, and R.H. Crabtree. J. Chem. Soc. Chem. Commun. 1021 (1994).

1996 Noranda Award Lecture Thermal properties of solids: Étude in three-part anharmony[1]

Mary Anne White

Abstract: The harmonic oscillator is a useful starting point for understanding many intermolecular interactions, and it successfully predicts many properties. However, anharmonic terms in the interaction potential are responsible for several observed phenomena. This review summarizes our recent experimental investigations of three thermal properties of molecular solids that result from anharmonic intermolecular interactions, viz. thermal expansion, Grüneisen parameters, and thermal conductivity.

Key words: anharmonicity, thermal expansion, Grüneisen parameter, thermal conductivity.

Résumé : L'oscillateur harmonique est un point de départ utile pour la compréhension de plusieurs interactions moléculaires et elle permet de prédire avec succès plusieurs propriétés. Toutefois les termes anharmoniques dans le potentiel d'interaction sont responsables de plusieurs phénomènes observés. Cette revue résume nos récentes recherches expérimentales sur les trois propriétés des solides moléculaires qui résultent des interactions moléculaires anharmoniques à savoir l'expansion thermique, les paramètres de Grüneisen et la conductivité thermique.

Mots clés : anharmonicité, expansion thermique, paramètre de Grüneisen, conductivité thermique.

[Traduit par la rédaction]

Introduction

Advancing understanding of forces is one of the common themes binding physical scientists. In principle, if we knew all intermolecular forces exactly, including their orientational dependence and how to handle many-body interactions, we could calculate virtually all properties of matter. However, we do not know all intermolecular potentials and, even for simple cases like the rare gases, mathematically exact potentials may not be achievable.

All is not lost, however, as we can understand many physical properties with very simple potentials. For example, even a square-well potential explains condensation of gases. However, a square-well has no sensitivity to intermolecular distance at the bottom of the well, and there are much better simple potentials.

One example is the Lennard–Jones "6-12" potential,

$$[1] \quad \phi(r) = -\frac{C_6}{r^6} + \frac{C_{12}}{r^{12}}$$

where the intermolecular potential, ϕ, is expressed in terms of the intermolecular separation, r. A Lennard–Jones potential can satisfactorily fit experimental observables such as sublimation energy, and it has the further advantage of being differentiable.

As useful as the Lennard–Jones potential is, many properties of matter can be considered using an even simpler potential, that of a harmonic oscillator as shown in Fig. 1 for Ar–Ar interactions, in comparison with a more accurate Ar–Ar potential derived from properties of solid and gaseous argon (1). The harmonic potential stems from Hooke's law considerations of intermolecular forces, viz.

$$[2] \quad F(r') = -kr'$$

where $F(r')$ is the restoring force and r' is the deviation from equilibrium intermolecular separation. As can be seen in Fig. 1, the harmonic potential is a good approximation near the minimum in the potential. Since atoms (and molecules) in solids far below their melting points are quite close to their lattice sites, i.e., near their minimum-energy positions, the harmonic approximation can be very useful in the solid state. For example, many of the features of lattice dynamics, including temperature dependence of heat capacity, can be well approximated starting from the harmonic potential.

Despite the great utility of the harmonic oscillator, many important properties arise from anharmonicity. Even rare gas solids are highly anharmonic, due to the presence of hard short-range interactions, as shown in Fig. 1.

Received February 9, 1996.

This paper is dedicated to Professor Howard C. Clark in recognition of his contributions to Canadian chemistry.

M.A. White.[2] Department of Chemistry, Dalhousie University, Halifax, NS B3H 4J3, Canada.

[1] This is an invited review article based on the 1996 Noranda Award Lecture delivered by Mary Anne White at the annual conference of the Canadian Society for Chemistry, St. John's, Newfoundland, June 1996.

[2] Telephone: (902) 494-3894 or -3305. Fax: (902) 494-1310. E-mail: mawhite@chem1.chem.dal.ca

Fig. 1. Intermolecular potentials and thermal expansion for Ar. The solid line represents the Barker–Fisher–Watts potential for Ar–Ar interactions, using parameters from fits to solid and gaseous properties (1), and the broken line is a harmonic potential fit to the bottom of the Barker–Fisher–Watts well. (○) The average intermolecular separation for the harmonic potential, where different positions correspond to different thermal energies for the system. (●) The average intermolecular separation for the anharmonic Barker–Fisher–Watts potential, showing thermal expansion.

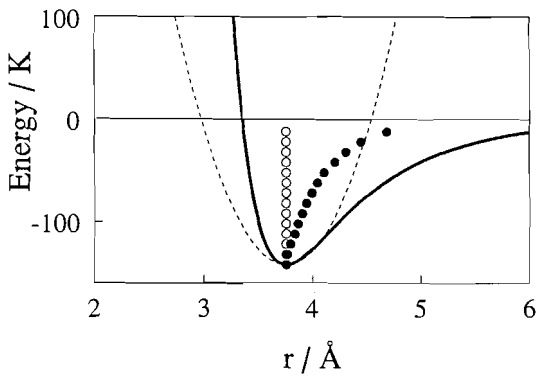

One of several observable consequences of anharmonicity is thermal expansion. As shown schematically in Fig. 1, a harmonic solid maintains the same lattice spacing as the temperature is increased, whereas an anharmonic solid generally shows an increase in lattice spacing with increasing temperature. Thermal expansion, α_j, is defined as

$$[3] \quad \alpha_j = \frac{1}{j}\frac{\mathrm{d}j}{\mathrm{d}T}$$

where j is a dimension in a given direction, a lattice parameter, or the volume, and deviation of α_j from the harmonic value of zero can be a direct measure of anharmonicity in the interaction potential.

Phonon–phonon interactions also result from anharmonicity. As a phonon of wave vector $\boldsymbol{q}$ moves through a lattice, some atoms are closer to each other than at their equilibrium distance while others are farther apart. If another phonon of wave vector $\boldsymbol{q}$ tries to pass through this part of the lattice, it will experience different elasticity and concomitant variation in the refractive index in the compressed region due to anharmonic terms in the intermolecular potential; the phonon $\boldsymbol{q}$ can be reflected from this, as if from a diffraction grating. If the wave vector is conserved, the reflected phonon has wave vector $\boldsymbol{q}''$:

$$[4] \quad \boldsymbol{q}'' = \boldsymbol{q} + \boldsymbol{q}'$$

and this is referred to as an N-process (N stands for "Normal"). If $\boldsymbol{q}$ and $\boldsymbol{q}'$ are so large that the resultant wave vector $\boldsymbol{q}''$ would lie outside the first Brillouin zone, then

$$[5] \quad \boldsymbol{q}'' + \boldsymbol{G} = \boldsymbol{q} + \boldsymbol{q}'$$

where $\boldsymbol{G}$ is a reciprocal lattice vector and this is called a U-process (U stands for Umklapp, indicating that the phonons turn back in this process (3)), which can lead to thermal resistance.

Phonon–phonon interactions lead to several important consequences: phonons have finite lifetimes; phonon energies are not sharply defined; phonon energies can be altered. Furthermore, the phonon–phonon collision probability depends on the number of phonons so the lifetimes of phonons will depend on the temperature. An observable consequence is that thermal conductivity, κ, of a real solid is finite ($\kappa = \infty$ for a harmonic solid) and temperature dependent. Furthermore, phonon–phonon interactions destroy the harmonic solid's dynamical independence of different lattice modes, and this could further affect thermal conductivity.

A useful parameter to consider when discussing anharmonicity is the Grüneisen (4) "constant," γ, which can be defined for mode j in terms of the frequency ω_j and the volume, V:

$$[6] \quad \gamma_j = -\frac{1}{2}\frac{\partial \ln \bar{\omega}^2}{\partial \ln V}$$

For a harmonic solid ω_j is independent of volume and therefore $\gamma = 0$; thus deviations of γ from zero can indicate anharmonic interactions.

Further manifestations of anharmonicity are that elastic constants of real solids depend on temperature and pressure (i.e., adiabatic and isothermal elastic constants are not the same); the heat capacity of a real solid rises above the Dulong–Petit value at high temperatures (5); spin-lattice interactions in a solid depend on anharmonicity (6). A recent review (7) shows the importance of anharmonicity in atomic displacement parameters (Debye–Waller factors) determined by X-ray diffraction.

Complete understanding of anharmonicity is not sufficient to understand all properties of solids; for example, anharmonicity alone is insufficient to explain behaviour near a displacive phase transition. Nevertheless, quantification of anharmonicity can lead to better understanding of many properties of materials, particularly with respect to interactions between phonons. It has been pointed out that molecular dynamics is superior to analytical methods that treat anharmonicity as a perturbation (8). Other methods also can be used: for example, a density functional approach has recently been used to study phononic properties of monatomic solids near the melting point (9).

Several aspects of anharmonicity have been summarized already (10), and the purpose of the present report is to review our experimental studies of properties associated with anharmonic effects in molecular solids.

Although the majority of the more than 14 000 000 chemical substances catalogued to date by Chemical Abstracts contain molecular units, our understanding of structural and dynamical properties of molecular solids is less complete than that of simpler atomic and metallic materials. The major difference between atomic and molecular solids lies in the degrees of freedom. Whereas atomic systems have only translational or lattice vibrational degrees of freedom, molecular systems also can have orientational and internal degrees of freedom. The former can in certain circumstances lead to orientationally disordered phases, and the latter can be associated with optical phonons that can play an important role in several physical properties. One of the purposes of our research has been to study the interplay between physical properties, especially those associated with thermally activated processes, and intermolecular potentials.

Experimental methods

In the work to be described, several physical properties have been determined experimentally. Thermal expansion, α, was determined from variable-temperature X-ray or neutron powder diffraction with Rietveld fitting procedures (11,12). Thermal conductivity, κ, was determined by steady-state determinations of the temperature gradient (dT/dx) of single crystals of cross-sectional area A with a quantified heat flux ($\dot{q}$), according to the definition of κ:

$$[7] \quad \kappa = \frac{\dot{q}}{A}\frac{dx}{dT}$$

Although the Grüneisen parameter, γ, can be determined through eq. [6], it was calculated here from the thermodynamic definition, which for the volume Grüneisen parameter is

$$[8] \quad \gamma_V = \frac{\alpha_V V_m}{\chi_T C_V}$$

where α_V is thermal expansion, V_m is the molar volume, χ_T is the isothermal compressibility ($= -V^{-1}(\partial V/\partial P)_T$), and C_V is the molar heat capacity at constant volume. An expression analogous to eq. [8] gives γ_j, where j is one of the unit cell directions.

Inclusion compounds

Inclusion compounds are materials that are composed of more than one chemical component, with one species forming a host lattice in which one or more other species can reside as guests. For the situation of guest species trapped in the host lattice, Powell (14) coined the term clathrate. Examples include clathrate hydrates (H_2O as the host lattice; see ref. 15 for a review of structures) and several hydrogen-bonded organics. Through slight changes in the structure of the host and (or) guest species, inclusion compounds offer an opportunity to examine the role of guest–host interactions in determining properties associated with anharmonicity, such as thermal conductivity, thermal expansion, and the Grüneisen parameter.

A mystery concerning the thermal conductivity of a clathrate hydrate became apparent in 1981 (16): the thermal conductivity of tetrahydrofuran clathrate hydrate was found to be considerably less than that of ice, but even more puzzling was the temperature dependence, $d\kappa/dT > 0$ for $100\ K < T < 250\ K$. For a simple crystalline solid this temperature range should correspond to phonon–phonon interactions determining the mean phonon free path λ (i.e., phonon–phonon collisions limit the phonon lifetimes and the thermal conductivity), and thermal activation of phonons would be expected to lead to lower thermal conductivity at higher temperatures, i.e., $d\kappa/dT < 0$. Our measurement of the thermal conductivity of tetrahydrofuran (THF) clathrate hydrate down to 15 K showed (13) continuous decrease in thermal conductivity with decrease in temperature, more like what is observed in aperiodic systems such as glasses (17) than what had been the observed behaviour for crystalline solids. The low thermal conductivity of THF clathrate hydrate is consistent with Tse's observations (18) of increased thermal expansion and low-temperature Grüneisen parameter for THF clathrate hydrate relative to ice Ih, both indications of enhanced anharmonicity in the crystal potential. Our understanding of the temperature dependence of the thermal conductivity of clathrate hydrates is that the heat-carrying acoustic phonons have their mean free paths shortened by motions of the guest species (19). The cages within a clathrate hydrate are rather isotropic, such that even polar guests such as THF do not succumb to positional ordering forces except at low temperatures, as shown by dielectric measurements (20) and analysis of the heat capacity of the guests (21). On the basis of a resonance interaction between the acoustic phonons of the host lattice and the optic modes associated with the guest molecules, we have successfully fit the temperature dependence of the thermal conductivity of THF clathrate hydrate (19).

An ideal test of this model would be to remove the guest species from the clathrate hydrate and determine the thermal conductivity of the "empty" clathrate. However, although there are many different phases of "ice" under different conditions, the clathrand (empty clathrate) is not a stable structure. There are only a few inclusion compounds that are known to exist in the same structure both with and without guests. One of these, Dianin's compound (4-(3,4-dihydro-2,2,4-trimethyl-2H-1-benzopyran-4-yl)phenol, **1**), met both this criterion and

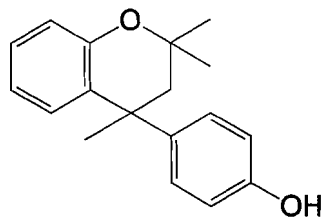

1

our additional requirement, viz. it is possible to grow rather large (mm dimensions in every direction) crystals both with and without guests. A further advantage of Dianin's host lattice became known as we studied various structural and dynamic properties: Dianin's compound can include either mobile guests (ethanol molecules reside two per cage and explore the cages of the host with liquidlike degrees of freedom as evidenced by heat capacity analysis (22) and solid state NMR (23)) or guests that are more rigidly trapped (one carbon tetrachloride molecule can be included per cage, and apparently the fit is rather tight so the CCl_4 molecule just librates at an average frequency of about 35 cm^{-1} (24)). Many of the results of our structural, thermal, and dynamical investigations of Dianin's compound and its clathrates have been summarized previously (25). In light of the present emphasis, we draw attention to the slight increase in thermal expansion with mobile ethanol guests, relative to the clathrand and the clathrate with the less mobile CCl_4 molecules as guests (see Fig. 2) (24, 26). However, the effect of the guest on the volume Grüneisen parameter is that γ_V is enhanced almost equally for ethanol and CCl_4 guests (27); see Fig. 3. (Of course α and γ are both anisotropic, and we have studied their directional dependences (24, 26, 27) but it does not resolve this apparent contradiction.)

Most striking is the effect of the guest on thermal conductivity: there is more thermal resistance (lower κ) when the

Fig. 2. The temperature dependence of the volume thermal expansion, α_V, for: (.....) Dianin's compound; (- - - -) CCl_4 clathrate of Dianin's compound; (_____) ethanol clathrate of Dianin's compound. The curves were derived from fits to the volume as a function of temperature (from refs. 24 and 26), giving an uncertainty in α_V of $\pm 3 \times 10^{-5}$ K^{-1}.

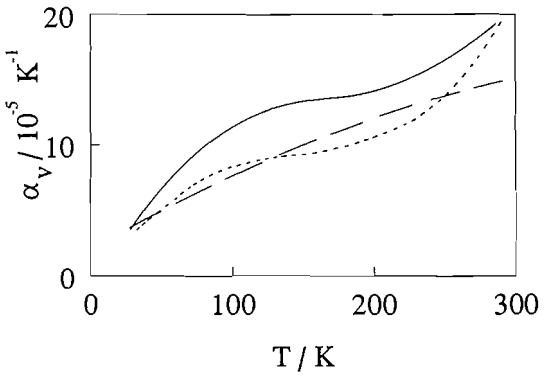

Fig. 3. The temperature dependence of the volume Grüneisen parameter, γ_V, for: (.....) Dianin's compound; (- - - -) CCl_4 clathrate of Dianin's compound; (_____) ethanol clathrate of Dianin's compound. Reproduced from ref. 27 with permission of Institute of Physics Publishing.

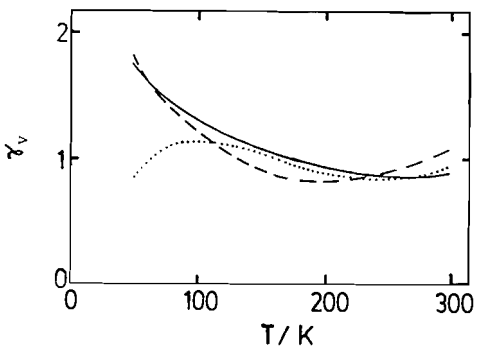

Fig. 4. The temperature dependence of the thermal conductivity, κ, for: (○) Dianin's compound; (▲) CCl_4 clathrate of Dianin's compound; (●) ethanol clathrate of Dianin's compound, with data from refs. 28 and 29; uncertainty in κ is ±10%.

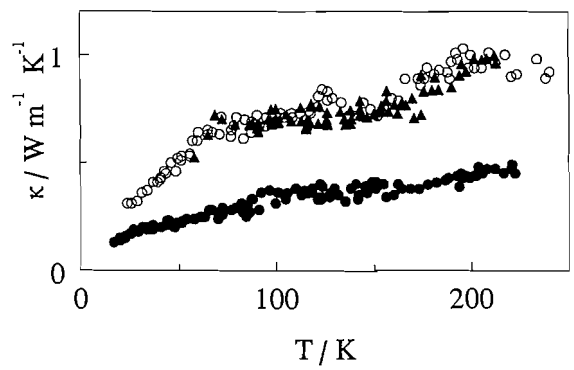

more mobile ethanol guests are present, but the presence of CCl_4 guests leaves κ virtually the same as for the clathrand (28, 29); see Fig. 4. We have interpreted this in terms of shortened lifetimes for the acoustic phonons when a mobile guest is present in the clathrate, i.e., showing that guest mobility enhances the anharmonic interactions in the system (29). Perhaps even more surprising is our finding that the thermal conductivity of the clathrand is low, with a positive temperature coefficient. Given the flexibility of the Dianin molecule, **1**, we interpret this as the effect of the parent molecule's optic phonons in attenuating the transmission of heat-carrying acoustic phonons (28).

We have recently extended our investigations to the more symmetrical host molecule, hexakis(phenylthio)benzene, **2**

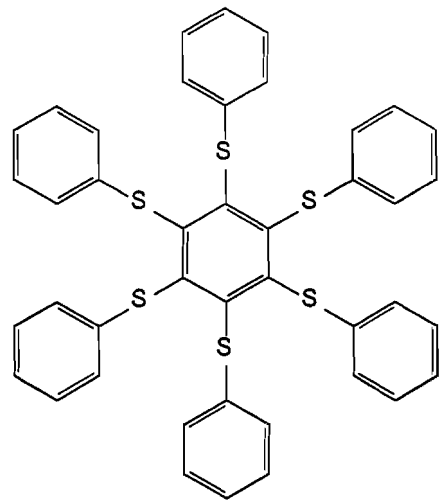

2

(abbreviated HPTB) and its CBr_4 clathrate. In this case the host molecule and clathrate are not isomorphous (space groups $P\bar{1}$ and $R\bar{3}$, respectively (12)), so direct comparisons are more difficult. For example, the higher thermal expansion and Grüneisen parameter of HPTB relative to HPTB·$2CBr_4$ are not necessarily indicative of enhanced anharmonicity, as packing interactions will play an important role here (30). Nevertheless, our recent investigations of the thermal conductivity of HPTB·$2CBr_4$ show it to be similar to THF clathrate hydrate and Dianin's compound, viz. κ small and $(d\kappa/dT) > 0$.[3]

To summarize our conclusions concerning properties of inclusion compounds: we find rather large values of thermal expansion (which is evidence of the softness of the potential at large intermolecular distances), Grüneisen parameters that are considerably greater than zero, and low thermal conductivities with positive temperature coefficients, all indications that the crystal potential in these systems is rather anharmonic. We interpret $d\kappa/dT > 0$ as an indication of coupling between heat-carrying acoustic phonons and optic modes associated with the guests and (or) the host lattice. Although we do not know the physical origins of the coupling, if the lattice was perfectly harmonic such interactions could not take place. There is other evidence showing that this interaction can be "tuned" to some extent: in the urea–hexadecane inclusion compound, Ross has found $(d\kappa/dT) \approx 0$ in the high-temperature phase in which the guests are more disordered, and $(d\kappa/dT) < 0$ in the low-temperature (presumably ordered) phase (31).

[3] D. Michalski and M.A. White. Unpublished work.

Fig. 5. The temperature dependence of the volume Grüneisen parameter, γ_V, for CBr_4. Reproduced with permission from ref. 33.

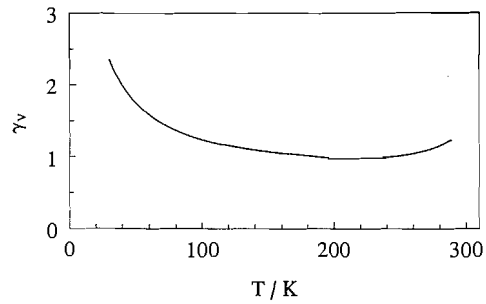

Single-component molecular systems

Although inclusion compounds can be useful in the context of delineating intermolecular interactions, there are a great many single-component molecular systems that also have interesting properties. Brief mention is made here of two systems that we have investigated recently, CBr_4 and C_{60}.

Solid state properties of tetrahedral molecules or molecular ions, especially methane and ammonium salts and their deuterated isotopomers, have been investigated extensively (32), largely because of the possibility of orientational disorder associated with only weak anisotropy in the intermolecular potential. CBr_4 is an interesting system to study because, unlike CH_4 and NH_4^+, it can be treated classically. As part of our analysis of the thermal conductivity of the inclusion compound HPTB·2CBr_4, we required data for the subambient heat capacity of CBr_4. Finding none in the literature, we measured this; details are published elsewhere (33). With that data, we were able to determine the volume Grüneisen parameter, γ_V, for CBr_4, as shown in Fig. 5. The important feature here is the increase in γ_V as $T \rightarrow 0$, in contrast with what one might predict (i.e., $\gamma_V \rightarrow 0$ as $T \rightarrow 0$ due to increased harmonicity). In solid carbon dioxide a similar low-temperature elevation of the Grüneisen parameter has been associated with the presence of low-frequency librational modes (34), and our heat capacity analysis also shows the presence of low-frequency librational modes in CBr_4, corresponding to an Einstein oscillator of characteristic temperature $\leq$60 K (33).

For C_{60} we have a rather different situation with respect to lattice dynamics. Whereas the internal modes and external modes are close in frequency range in CBr_4, the rather rigid C_{60} molecule leads to internal modes that are at much higher frequencies than the external (whole-molecule) modes. C_{60} has other interesting features, namely, a transition at about 260 K from a high-temperature orientationally disordered phase to a low-temperature phase in which there is still appreciable dynamical orientational disorder; the kinetic barrier to orientational order in this phase leads to a glassy phase transition ($T_g \approx 90$ K), and concomitant anomalous behaviour in a number of physical properties, including thermal conductivity (35), heat capacity (36), and thermal expansion (37). Our recent determinations (38) of the Grüneisen parameters of C_{60} are shown in Fig. 6. This figure includes both γ(overall), i.e., as determined from eq. [8] using the total heat capacity, and γ(external), determined from eq. [8] using only the external mode contributions to the heat capacity. γ(external) is small

Fig. 6. The temperature dependence of: (*a*) the overall Grüneisen parameter, γ(overall) and (*b*) the external Grüneisen parameter, γ(external) for C_{60}. Reprinted from ref. (38), Solid State Communications, **94**, M.A. White, C. Meingast, W.I.F. David, and T. Matsuo, "Anharmonic Interactions in C_{60}, as Determined by the Grüneisen Parameter", 481–484, Copyright 1995, with kind permission from Elsevier Science Ltd, The Boulevard, Langford Lane, Kidlington OX5 1GB, U.K.

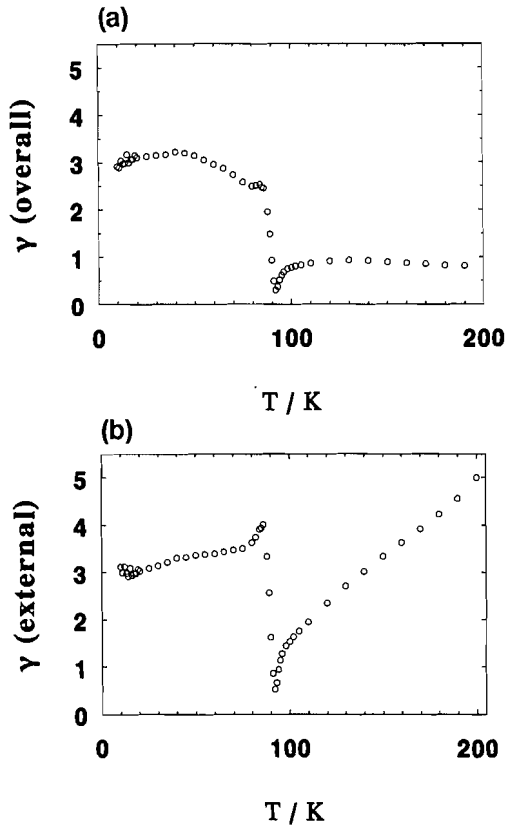

for $T > T_g$, reflecting the anomalously small thermal expansion in this temperature range due to the temperature dependence of the degree of orientational disorder. Below T_g, γ(overall) $\approx$ γ(external) $\approx$ 3, showing C_{60} to be exceptionally anharmonic, especially given the low relative temperature (as low as $\Theta_D/5$, where Θ_D is the Debye characteristic temperature). We attribute this to low compressibility of C_{60} due to its hard core, compared with, for example, a rare gas solid (38). Indeed, γ(overall) for C_{60} is very similar to γ_c for graphite (39), which shows that low-temperature interactions in C_{60} are dominated by the (isotropic) intermolecular potential. Furthermore, intramolecular Grüneisen parameters, determined by IR and Raman spectroscopy through the method of eq. [6], range from -0.04 to 0.09 (40, 41), showing that internal modes do not contribute significantly to anharmonicity in C_{60}.

Conclusions

Our experimental investigations of thermal expansion, Grüneisen parameters, and thermal conductivity show molecular solids to be rather anharmonic in their intermolecular potentials. This is especially the case when there are low-frequency modes, for example, associated with orientational disorder or

libration of molecular units. Of the properties investigated, the most important is thermal conductivity, especially as it changes greatly in both magnitude and temperature dependence from one material to another. On the basis of our experiments, we suspect that coupling between heat-carrying acoustic phonons and low-frequency optic phonons may be responsible for the low thermal conductivities and positive temperature coefficients observed in several molecular systems. Anharmonicity likely plays a role in this coupling; direct investigations of phonon–phonon interactions in molecular systems would be very useful in delineating the mechanism.

Acknowledgements

This work would not have been possible without the contributions of many excellent co-workers. Those involved directly in the work described are W. Abriel, W.I.F. David, T. Matsuo, C. Meingast, D. Michalski, J. Ripmeester, R.G. Ross, I. Swainson, J. Tse, and M. Zakrzewski. P. Bessonette, D. Michalski, and V. Murashov provided helpful comments on this manuscript. Financial support from the Natural Sciences and Engineering Research Council, Dalhousie University, and Energy, Mines and Resources is gratefully acknowledged.

References

1. J.A. Barker, R.A. Fisher, and R.O. Watts. Mol. Phys. **21**, 657 (1971).
2. J.M. Ziman. *In* Electrons and phonons. Clarendon, Oxford. 1960. p. 133.
3. R. Peierls. Ann. Phys. **3**, 1055 (1929).
4. E. Grüneisen. Handb. Phys. **10**, 21 (1926).
5. T.H.K. Barron, J.G. Collins, and G.K. White. Adv. Phys. **29**, 618 (1980).
6. J.H. Van Vleck. Phys. Rev. **59**, 730 (1941).
7. W.F. Kuhs. Acta Crystallogr. Sect. A: Found. Crystallogr. **A48**, 80 (1992).
8. L.J. Lewis and M.L. Klein. *In* Dynamical properties of solids. Vol. 6. *Edited by* G.K. Horton and A.A. Maradudin. Elsevier, Amsterdam. 1990. Chap. 7.
9. M. Ferconi and M.P. Tosi. J. Phys.: Condens. Matter, **3**, 9943 (1991).
10. R.A. Cowley. Rep. Prog. Phys. **31**, 123 (1968).
11. W. Abriel and U. Bismayer. Phase Transitions, **15**, 49 (1989).
12. D. Michalski, M.A. White, P.K. Bakshi, T.S. Cameron, and I. Swainson. Can. J. Chem. **73**, 513 (1995).
13. M.A. White. J. Phys. (Paris), Cl-565 (1987).
14. H.M. Powell. J. Chem. Soc. 61 (1987).
15. J.A. Ripmeester, C.I. Ratcliffe, D.D. Klug, and J.S. Tse. Ann. N.Y. Acad. Sci. **715**, 161 (1994).
16. R.G. Ross, P. Andersson, and G. Bäckstrom. Nature, **290**, 322 (1981).
17. D.G. Cahill and R.O. Pohl. Annu. Rev. Phys. Chem. **39**, 93 (1988).
18. J. Tse. J. Phys. (Paris), Cl-543 (1987).
19. J.S. Tse and M.A. White. J. Phys. Chem. **92**, 5006 (1988).
20. S.R. Gough, R.E. Hawkins, B. Morris, and D.W. Davidson. J. Phys. Chem. **77**, 2969 (1973).
21. M.A. White and M.T. MacLean. J. Phys. Chem. **89**, 1380 (1985).
22. M.A. White and M. Zakrzewski. J. Inclusion Phenom. Mol. Recognit. Chem. **8**, 215 (1990).
23. T. Bernhard, H. Zimmermann, and U. Haeberlen. J. Chem. Phys. **92**, 2178 (1990).
24. W. Abriel, A. du Bois, M. Zakrzewski, and M.A. White. Can. J. Chem. **68**, 1352 (1990).
25. M. Zakrzewski and M.A. White. Condens. Matter News, **2**, 7 (1993).
26. M. Zakrzewski, M.A. White, and W. Abriel. J. Phys. Chem. **94**, 2203 (1990).
27. M. Zakrzewski and M.A. White. J. Phys.: Condens. Matter, **3**, 6703 (1991).
28. M. Zakrzewski and M.A. White. Phys. Rev. B: Condens. Matter, **45**, 2809 (1991).
29. D. Michalski and M.A. White. J. Phys. Chem. **99**, 3774 (1995).
30. D. Michalski, R.T. Perry, and M.A. White. J. Phys.: Condens. Matter, **8**, 1647 (1996).
31. R.G. Ross. J. Inclusion Phenom. Mol. Recognit. Chem. **8**, 227 (1990).
32. N.G. Parsonage and L.A.K. Staveley. Disorder in crystals. Clarendon Press, Oxford. 1978.
33. D. Michalski and M.A. White. J. Chem. Phys. **103**, 6173 (1995).
34. T.H.K. Barron, J.G. Collins, and G.K. White. Adv. Phys. **29**, 609 (1980).
35. R.C. Yu, N.H. Tea, M.B. Salamon, D. Lorents, and R. Malhotra. Phys. Rev. Lett. **68**, 2050 (1992).
36. T. Matsuo, H. Suga, W.I.F. David, R.M. Ibberson, P. Bernier, A. Zahab, C. Fabre, A. Rassat, and A. Dworkin. Solid State Commun. **83**, 711 (1992).
37. F. Gugenberger, R. Heid, C. Meingast, P. Adelmann, M. Braun, H. Wühl, M. Halska, and H. Kuzmany. Phys. Rev. Lett. **69**, 3774 (1992).
38. M.A. White, C. Meingast, W.I.F. David, and T. Matsuo. Solid State Commun. **94**, 481 (1995).
39. A.C. Bailey and B. Yates. J. Appl. Phys. **41**, 5088 (1970).
40. K. Aoki, H. Yamawaki, Y. Fakudata, M. Yoshida, S. Usuba, M. Yokoi, S. Fujiwara, Y. Bae, R. Malhotra, and D. Lorents. J. Phys. Chem. **95**, 9037 (1991).
41. S.H. Tolbert, A.P. Alivisatos, and H.E. Lorenzana. Chem. Phys. Lett. **188**, 163 (1992).

A facile synthesis of metalla-octafluorocyclopentane complexes of ruthenium and nickel

Waltraud Gasafi-Martin, Gabriele Oberendfellner, and Konrad von Werner

Abstract: Reduction of the dihalogeno complexes $RuCl_2(PPh_3)_4$ and $NiBr_2L_2$ (L = tertiary phosphine) with sodium hydride in MeCN in the presence of tetrafluoroethylene gives complexes containing five-membered MC_4F_8 rings. 1,2-Dihydrotetrafluoroethane is a by-product of these syntheses, especially when hydrogen is added. The M—C bonds of the metalla-perfluorocyclopentane complexes are remarkably stable against hydrogenolysis.

Key words: metalla-octafluorocyclopentanes of ruthenium(II) and nickel(II).

Résumé : La réduction des complexes dihalogénés $RuCl_2(PPh_3)_4$ et $NiBr_2L_2$ (L = phosphine tertiaire) avec de l'hydrure de sodium dans MeCN, en présence de tétrafluoroéthène, conduit à des complexes contenant des cycles MC_4F_8 à cinq chaînons. Le 1,1,2,2-tétrafluoroéthane est un sous-produit de ces synthèses, particulièrement lorsqu'on ajoute de l'hydrogène. Les liaisons M—C des complexes du métalla-perfluorocyclopentane sont particulièrement stables vis-à-vis de l'hydrogénolyse.

Mots clés : métalla-octafluorocyclopentanes du ruthénium(II) et du nickel(II).

[Traduit par la rédaction]

Metal(O) complexes of group VIII metals are known to react with tetrafluoroethylene (TFE) to give a variety of different products by means of oxidative additions to the metal center. Typical reactions and products are listed below:

(*i*) Formation of a side-on bonded complex: $(Ph_3P)_2$ Pt(η_2-C_2F_4) (1).

(*ii*) Insertion of TFE into a metal-metal bond: $(OC)_4$ Co-CF_2CF_2-Co $(CO)_4$ (2).

(*iii*) Bridging of two metal centers by two molecules of TFE:

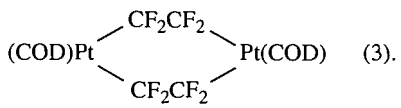

(3).

(*iv*) Coupling of two TFE units at the metal center, resulting in the formation of MC_4F_8 rings: $Fe(C_4F_8)(CO_4)$ (4), $Ru(C_4F_8)(CO)_2(PPh_3)_2$ (5), and $Ni(C_4F_8)$(1.5-COD) (6).

We have shown that sodium hydride in acetonitrile is a very efficient reagent for the reduction of dihalide complexes of group VIII metals, affording metal(O)–carbonylphosphine complexes of nickel, palladium, and ruthenium in high yield when the reaction is performed under CO (7). We now have extended the reduction with NaH to the preparation of metallaoctafluorocyclopentane derivatives of nickel(II) and ruthenium(II) (see Table 1). Starting materials were $RuCl_2(PPh_3)_4$ and $NiBr_2L_2$ (L = tertiary phosphine or diphosphine) and tetrafluoroethylene. In contrast, similar reactions of $PdCl_2(PPh_3)_2$ or $FeBr_2(PPh_3)_2$, with two equivalents of PPh_3 added to the iron compound, did not result in the formation of MC_4F_8 complexes in the presence of TFE. The method also failed to work with the nickel complexes L_2NiBr_2 (L_2: N,N′-chelating ligand). However, NiC_4F_8 (bipy) could be obtained from $NiC_4F_8(PPh_3)_2$ by means of ligand exchange in MeCN in good yield.

We believe that the formation of the metallaoctafluorocyclopentane complexes occurs through the following reaction sequence: (*a*) displacement of halide ions by hydride to give dihydridocomplexes, (*b*) reductive elimination of hydrogen resulting in the formation of metal(O) complexes, (*c*) sequential coupling of two molecules of TFE at the metal(O)center.

It is interesting to note that all of the crude reaction mixtures obtained from the NaH reactions contained some 1,2-dihydrotetrafluoroethane, the hydrogenation product of TFE. A further point of interest concerns the fact that $(Ph_3P)_2NiC_4F_8$ is formed even in the presence of carbon dioxide, acetaldehyde, or hydrogen. When the reaction was run under simultaneous application of TFE and hydrogen (10 bar each; 1 bar = 100 kPa), the yield of the complex rose to 30%.

The observation that 1,2-dihydrotetrafluoroethane is always found can be explained by assuming the following reaction sequence:

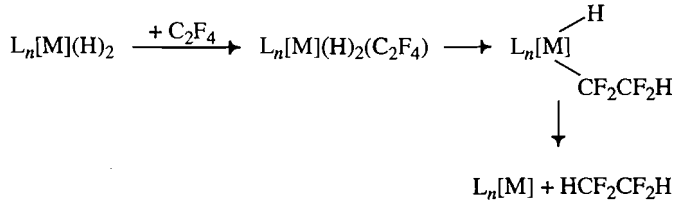

Received November 29, 1995.

This paper is dedicated to Professor Howard C. Clark in recognition of his contributions to Canadian chemistry.

W. Gasafi-Martin, G. Oberendfellner, and K. von Werner.[1]
Hoechst AG, Werk Gendorf, 84504 Burgkirchen, Germany.

[1] Author to whom correspondence may be addressed.
Telephone: (0 86 79) 7 46 55. Fax: (0 86 79) 45 45.

Table 1. Metalla-octafluorocyclopentane complexes of ruthenium(II) and nickel(II).

	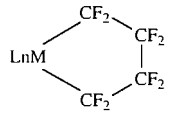	Reaction conditions		Yield		^{19}F NMR[a]		
		T(°C)	t(h)	(%)	Colour	α-CF_2	β-CF_2	Solvent
1	$Ru(C_4F_8)(PPh_3)_4$ $L_2Ni(C_4F_8)$	30	12	33	Pale yellow	−47.6 36.7 Hz, ^3J(PF)*trans* 17.2 Hz, ^3J(PF)*cis*	−60.5 (m)	CD_3CN
2	L = PPh_3	40	12	20	Pale yellow	−28.1 (broadened)[b]	−61.4	$CDCl_3$
3	L_2 = $Ph_2P(CH_2)_2PPh_2$	50	10	30	Yellow	−26.1 t, 28.1 Hz, ^3J(PF)	−60.4	CD_3CN
4	L_2 = $Ph_2P(CH_2)_3PPh_2$	50	7	35	Yellow	−24.5 t, 29.5 Hz, ^3J(PF)	−60.4	$CDCl_3$
5	L_2 = 2.2′-Bipyridine	20	1	75	Yellow	−31.3	−61.6	Acetone-d_6

[a]At 282.4 MHz and 30°C, δ ^{19}F (ppm), upfield from CF_3CO_2H (external reference); δ CF_3CO_2H = −77.5 ppm vs. $CFCl_3$.
[b]Unresolved coupling, ^3J (PF).

Table 2. Elemental analyses.

		Calculated				Found			
Compound	Formula	C	H	F	M	C	H	F	M
1	$C_{76}H_{60}F_8P_4Ru$	67.60	4.48	11.36	7.49	67.4	4.4	11.3	7.6
2	$C_{40}H_{30}F_8P_2Ni$	61.33	3.86	19.40	7.49	61.2	3.8	19.5	7.5
3	$C_{30}H_{24}F_8P_2Ni$	54.83	3.68	23.13	8.93	55.0	3.7	23.2	8.9
4	$C_{14}H_8F_8N_2Ni$	40.53	1.94	36.63	14.15	40.7	1.9	36.5	14.0

The unsaturated species L_n[M] is required for metallacycle formation. A high excess of tetrafluoroethylene will favour the formation of the metallacycle, whereas an addition of hydrogen should be expected to favour the formation 1,2-dihydrotetrafluoroethane.

The metal–carbon bonds of the complexes **1–4** are very stable against hydrogenolysis. Complex **1** did not react with hydrogen (20 bar) in toluene solution even in the presence of a very active hydrogenation catalyst (2% palladium on Al_2O_3) up to 60°C. Hydrogenation of **2** with the same catalyst in MeCN gave a surprising result: hydrogenation of the triphenylphosphine ligands set in at ca. 100°C; however, the NiC_4F_8 group was still intact.

Experimental part

All reactions and work-up procedures were carried out under dry nitrogen or argon, using carefully dried solvents. MeCN was distilled from P_4O_{10} through a column, and the main run was stored over molecular sieve (3 Å).

Typical procedure for the synthesis of 1–4

A stainless steel autoclave (150 mL), equipped with manometer, gas inlet, a thermocouple for temperature control, and a PTFE-coated stirring bar, was charged with a solution of $(Ph_3P)_4RuCl_2$ (or of a nickel complex L_2NiBr_2) in anhydrous MeCN (3.0 mmol of the complex in 50 mL solvent). Sodium hydride (6.6 mmol), as a 20% suspension of NaH in DAB9 mineral oil (obtained from Merck), was added with a syringe. The autoclave was closed, cooled to 0°C, and pressurized with TFE (10 bar), and the reaction was carried out with stirring under the conditions given in Table 1. After cooling to room temperature and releasing the pressure, the contents of the autoclave were transferred to a flask and the solvent was removed in vacuo. The residue was stirred with toluene (50 mL) at 40°C and filtered through a frit that contained 2 g of Celite. In the case of **3** and **4**, a mixture of toluene (40 mL) and CH_2Cl_2 (10 mL) was used. The filtrate was concentrated under vacuum and crystallization was induced by adding ether and (or) *n*-hexane and cooling. The product was collected on a frit, washed with cold *n*-hexane, and dried in vacuo. Recrystallization from CH_2Cl_2 and *n*-hexane and drying at 50°C at 10^{-3} mbar finally gave the pure products.

We did not attempt to fully optimize the yields.

Synthesis of 2,2′-bipyridine-nickelaoctafluorocyclopentane, 5

2,2′-Bipyridine (85.9 mg, 0.55 mmol) was added to a stirred solution of complex **2** (392 mg, 0.5 mmol) in 5 mL of MeCN. The solution soon became cloudy. After 1 h, *n*-hexane (2 mL) was added and the crystalline product was filtered off, washed with 5 mL of cold *n*-hexane, and dried at 10^{-3} mbar (yield: 253 mg). The element analyses of the complexes **1–5** are shown in Table 2.

Spectra

The IR spectra of all products in Nujol were measured with a Perkin Elmer 882 spectrophotometer. The bands observed for

the compounds **2**, **3**, and **5** in the region of 1300–750 cm^{-1} are in good agreement with the data reported in ref. 6 (maximum deviation: 15 cm^{-1}), although the methods of preparation were different. The spectra of **3** and **4** are very similar. The ruthenium complex **1** showed the following bands in the above region: 1306 w, 1261 m, 1210 w, 997 w, 916 w, 852 w, 799 s.

^{19}F NMR spectra were measured with a Bruker AC 300 instrument at 30°C. The couplings reported in Table 1 are based on the following assumptions:

1: $(AMX_2)_2$ spin system, where A is ^{31}P *cis* to α-CF_2, M is ^{31}P *trans* to α-CF_2 and X is ^{19}F of α-CF_2.

2, **3**, and **4**: $(AX_2)_2$ spin system, where A is ^{31}P and X is ^{19}F of α-CF_2.

References

1. M. Green, R.B.L. Osborn, A.J. Rest, and F.G.A. Stone. J. Chem. Soc. (A), 2525 (1968).
2. A.D. Beveridge and H.C. Clark. J. Organomet. Chem. **11**, 601 (1968).
3. M. Green, J.A.K. Howard, A. Laguna, M. Murray, J.L. Spencer, and F.G.A. Stone. J. Chem. Soc. Chem. Commun. 451 (1975).
4. T.A. Manuel, S.L. Stafford, and F.G.A. Stone. J. Chem. Soc. Chem. Commun. 249 (1961).
5. R. Kuwae, K. Kawakami, and T. Tanaka. Inorg. Chim. Acta, **22**, 39 (1977).
6. C.S. Cundy, M. Green, and F.G.A. Stone. J. Chem. Soc. (A), 1647 (1970).
7. K. von Werner. Hoechst AG, DE 42 34 485 A 1, published 1994.

Direct syntheses of pentakis(trifluoromethyl)cyclopentadienide salts and related systems[1]

Richard D. Chambers, Alex J. Roche, and Julian F.S. Vaughan

Abstract: The well-established synthesis of heptafluorobut-2-ene **2** from hexachlorobutadiene **1** and potassium fluoride has been further investigated, and novel dienes **3** and a triene **4** have been observed. Remarkably, the potassium salt of pentakis(trifluoromethyl)cyclopentadienide **7** has been isolated from this system. Salt **7** has also been obtained directly from **2**. Cyclopentadiene **6** has been isolated from salt **7** by distillation from sulphuric acid. Bi- and tri-cyclic analogues of **7** have also been obtained, i.e., **9** and **10**, by reaction of **2** with perfluorocyclopentene.

Key words: heptafluorobut-2-ene, pentakis(trifluoromethyl)cyclopentadienide, 5*H*-pentakis(trifluoromethyl)cyclopentadiene.

Résumé : On a étudié à nouveau la synthèse bien connue de l'heptafluorobut-2-ène **2** à partir de l'hexachlorobutadiène **1** et du fluorure de potassium; on a observé la formation de nouveaux dienes **3** et d'un triène **4**. D'une façon remarquable, on a isolé de ce système le pentakis(trifluorométhyl)cyclopentadiénure de potassium **7**. Par distillation du sel **7** en présence d'acide sulfurique, on a isolé le cyclopentadiène **6** à partir du sel **7**. La réaction du composé **2** avec le perfluorocyclopentène a permis aussi d'obtenir les analogues bi- **9** et tricycliques **10** du composé **7**.

Mots clés : heptafluorobut-2-ene, pentakis(trifluorométhyl)cyclopentadiénure, 5*H*-pentakis(trifluorométhyl)cyclopentadiène.

[Traduit par la rédaction]

There is a wide interest in methodology for the introduction of trifluoromethyl and other perfluoroalkyl groups into organic compounds (2), and we are concerned with the alkene (*Z*)-2*H*-heptafluorobut-2-ene **2** as a potential "building block" for this purpose. This F-alkene is especially significant because it can be obtained directly from hexachloro-1,3-butadiene **1**, by simple displacement using potassium fluoride in an aprotic solvent. This synthesis was described in 1963 by Maynard (3), from the du Pont Co., and has subsequently been used by other workers, including this laboratory (4). However, in recent further investigation of this reaction, we have discovered some remarkable new products.

The overall procedure involves heating hexachloro-1,3-butadiene **1** with anhydrous potassium fluoride in an aprotic solvent; Maynard (3) described *N*-methyl-2-pyrrolidinone and we have found that sulpholan is very satisfactory (4). The products vary significantly with reaction conditions, and we have now identified and separated from **2** two interesting new fluorinated dienes **3a** and **3b**, and even a triene **4**. These compounds were separated by fractional distillation and the stereochemistry of the major diene isomer **3a** follows from ^{19}F NMR coupling constant data, since it is known that ^{5}J(*cis*-CF_3,CF_3) values are greater than 10 Hz, ^{5}J(*trans*-CF_3,CF_3) values are typically less than 2 Hz, and ^{4}J(*trans*-CF_3,F) coupling constants are less than for ^{4}J(*cis*-CF_3,F) (5), as shown in Fig. 1. In contrast, we were unable to deduce the structure of the minor isomer **3b** (see experimental section) because the splitting in the ^{19}F NMR spectrum was insufficiently resolved.

The mechanism of formation of the dienes **3a** and **3b**, and the triene **4** is outlined in Scheme 1, arising from fluoride ion initiated oligomerization of **2**, and other evidence for this process stems from the fact that these compounds may also be obtained directly from **2** by heating with fluoride ion in a sealed system.

We have also examined the filtered sulpholan residue from the preparation of **2**, and, remarkably, the ^{19}F NMR spectrum showed only one sharp resonance at $\delta_F = -50$ ppm! It is unlikely that we would have been able to identify this component from this unusual signal, except for the fact that we had already synthesized various salts of the pentakis(trifluoromethyl)cyclopentadienide (6), and these had given similar ^{19}F NMR signals. FAB mass spectroscopy confirmed the presence of potassium (*m/z* 39 (100%), in the positive ion spectrum), and showed only a *m/z* 405 (100%) peak in the negative ion spectrum, which is consistent with **7**. Thus we had obtained potassium pentakis(trifluoromethyl)cyclopentadienide **7** in one step from hexachloro-1,3-butadiene and potassium fluoride! This is amusing to those of us who were seeking syntheses of **7** because, in our own laboratory, it is clear that we have been disposing of samples of **7** with the residue, following the synthesis of **2**!

5*H*-Pentakis(trifluoromethyl)cyclopentadiene (**6**) has been

Received November 14, 1995.

This paper is dedicated to Professor Howard C. Clark in recognition of his contributions to Canadian chemistry.

R.D. Chambers,[2] A.J. Roche, and J.F.S. Vaughan. Department of Chemistry, University of Durham, South Road, Durham, DH1 3LE, U.K.

[1] For a preliminary publication, see ref. 1.

[2] Author to whom correspondence may be addressed. Telephone: 0191 374 3120. Fax: 0191 384 4737. E-mail: R.D.Chambers@durham.ac.uk

Scheme 1.

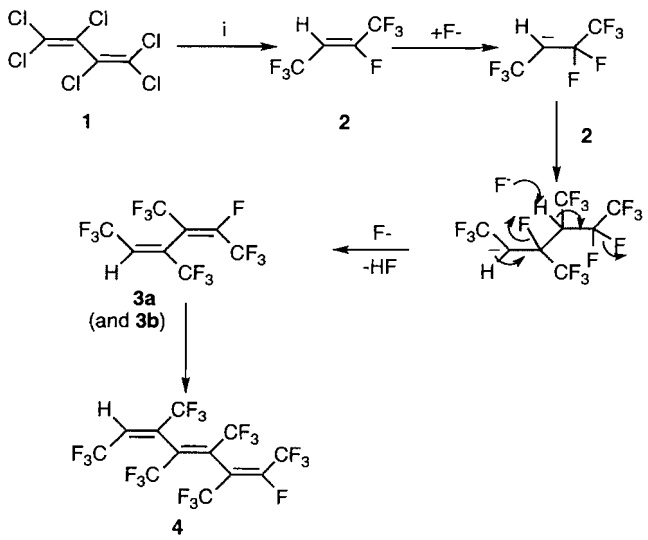

Reagents and conditions: i, KF, sulpholan, 190°C.

Fig. 1. ^{19}F NMR coupling constant data.

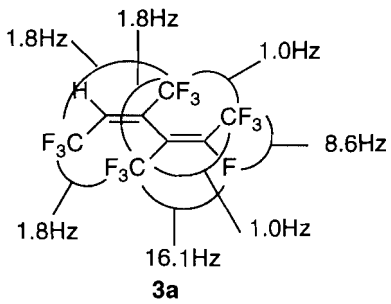

Scheme 2.

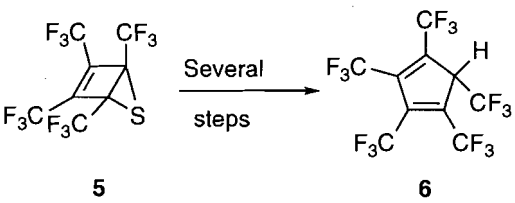

described by Laganis and Lemal (7) in several steps, starting with a valence isomer of tetrakis(trifluoromethyl)thiophene (**5**) (Scheme 2), and they also showed that **6** is a very strong acid ($pK_a \leq -2$). However, we have now been able to isolate and characterize the acidic diene **6** by distillation from the sulpholan residue, after the addition of concentrated sulphuric acid.

The mechanism of formation of **7** is probably that outlined in Scheme 3, essentially derived from **2**. The cyclization step to give **6** is extremely interesting because, as a *5-endo-trig* process, it is formally "disallowed" by the Baldwin rules (8). It seems more appropriate, therefore, to regard the process as an initial electrocyclic ring closure, to give **6**, followed by elimination of the acidic proton by fluoride ion, now acting as a base. In confirmation of this mechanism, we have also shown that **7** can be obtained by reaction of **2** with caesium fluoride in sulpholan in a sealed tube. Again this is a direct route to **7** from easily accessible starting materials.

Furthermore, a variety of salts may be obtained by reaction of an aqueous solution of the appropriate halide with the acidic diene **6** (Scheme 4). Single crystal X-ray structural analyses of tetraalkylammonium salts of **7** confirmed the product structure. However, rotation within the crystal, even at low temperatures, prevents a precise determination of bond lengths and angles.

The results described above pointed the way to a synthesis of a variety of more complex fluorocarbon salts. For example, we have shown that reaction of fluoride ion with **2** in the presence of perfluorocyclopentene **8** gave a mixture of two novel salts **9** and **10**, while the diene **3** in the presence of **8** with fluoride ion gave only **9**. These compounds were characterized by ^{19}F NMR and FAB mass spectrometry, which is a particularly valuable tool with these and related systems. However, attempts to obtain the corresponding dienes from **9** and **10**, by distillation from concentrated sulphuric acid, has, so far, led to products too complex to separate, although GLCMS revealed the presence of the desired dienes, but accompanied by other unidentified products.

Experimental

^1H NMR spectra were recorded on a Bruker AC250 spectrometer operating at 250.13 MHz, a Varian Gemini VXR200 spectrometer operating at 199.98 MHz, or a Varian VXR400S spectrometer operating at 399.96 MHz. ^{19}F NMR spectra were recorded on the Bruker AC250 spectrometer operating at 235.34 MHz or on the Varian VXR400S spectrometer operating at 376.29 MHz. ^{13}C spectra were recorded on the Varian VXR400S spectrometer operating at 100.58 MHz, or the Varian Gemini VXR200 spectrometer operating at 50.29 MHz. All spectra were recorded with TMS and fluorotrichloromethane as internal references. The *J* values are given in Hz. GLCMS mass spectra were recorded on a Fisons Trio 1000 spectrometer linked to a Hewlett Packard 5890 series II gas chromatograph fitted with a 20 m cross-linked methyl silicone capillary column. All GLCMS mass spectra were generated by electron impact. FAB mass spectra were recorded using a VG7070E spectrometer, and glycerol as a solvent. FTIR spectra were recorded on a Perkin Elmer 1600 series FTIR spectrometer. Solid samples were run as KBr discs, liquid samples were run as thin films between KBr plates, and volatile samples were run in a gas cell fitted with KBr plates.

Reaction of 1 with potassium fluoride

The method used was essentially that used by Maynard (3), using hexachlorobuta-1,3-diene **1** (334 g, 1.3 mol), potassium fluoride (600 g, 10.2 mol), and sulpholan (2 L). The volatile products were collected at liquid air temperatures, and fractional distillation gave (Z)-2H-*heptafluorobut-2-ene* **2** (105.1 g, 45%); bp 7–8°C (lit. (3) bp, 7–10°C); ν_{max}/cm^{-1}: 1220, 1310; δ_H(250 MHz; $CDCl_3$): 5.45 (dq, *J* 28.3 and 5.3, C*H*); δ_F(235 MHz; $CDCl_3$): −61.6 (3 F, s, CF_3CH), −76.2 (3 F, s, CF_3CF), −119.9 (1 F, s, C*F*); δ_C(100 MHz; $CDCl_3$):

Scheme 3.

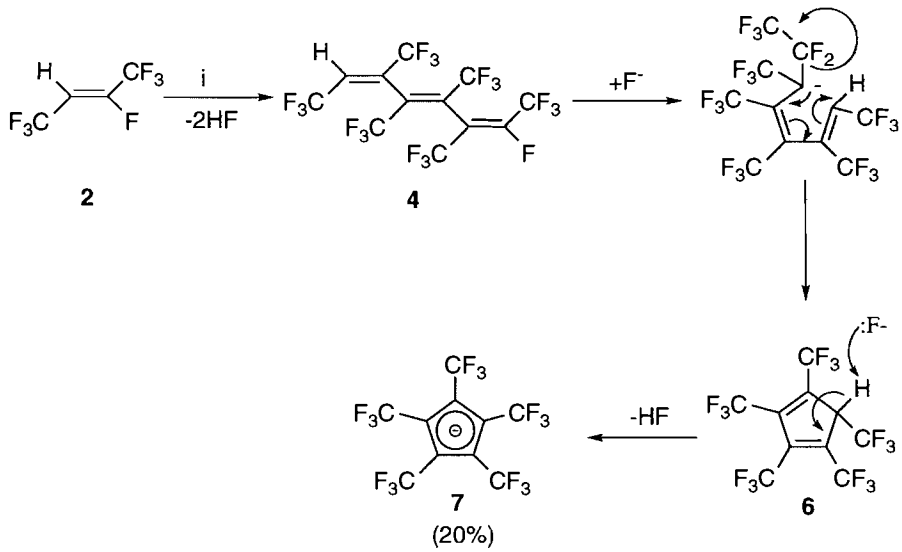

Reagents and conditions: i, CsF, sulpholan, 190 °C.

Scheme 4.

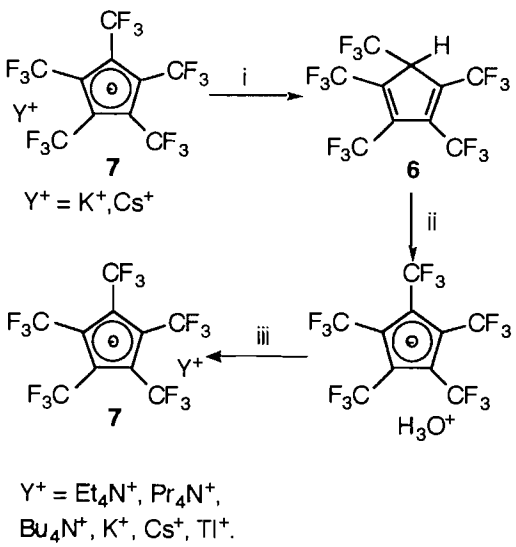

$Y^+ = Et_4N^+$, Pr_4N^+, Bu_4N^+, K^+, Cs^+, Tl^+.

Reagents and conditions: i, 98% H_2SO_4; ii, H_2O; iii, Y-Hal.

101.3 (q, *J* 39.1, *C*H), 116.2 (qd, *J* 272.5 and 38.3, CF_3CF), 119.5 (q, *J* 269.5, CF_3CH), 150.8 (dqq, *J* 283.3, 41.2 and 5.9, $CFCF_3$); *m/z* 182 (M^+, 23%), 163 (54), 113 (90), 69 (100).

A higher boiling fraction (bp 78–80°C) was shown by GLCMS to contain three components, and preparative scale GLC (SE30/40°C) produced a 4:1 mixture of two isomers of *5H-perfluoro-3,4-bis(trifluoromethyl)hexa-2,4-diene* ***3a*** and ***b*** (13.2 g, 6%). For the diene mixture (Anal. calcd. for C_8HF_{13}: C 28.0, H 0.3%; found: C 28.0, H 0.2%); $\lambda_{max}(CH_3CN)$/nm: 295; ε/dm^3 mol^{-1} nm^{-1}: 1148; ν_{max}/cm^{-1}: 1400, 1300–1200. The major isomer was confirmed as the (*Z, E*) isomer (**3a**). δ_H(250 MHz; $CDCl_3$): 6.68 (q, *J* 6.3, C*H*); δ_F(235 MHz; $CDCl_3$): −60.8 (3 F, dqq, *J* 16.1, 1.8, 1.0, CF_3C-3), −62.3 (3 F, sept, *J* 1.8, CF_3C-4), −68.7 (3 F, m, *J* 1.8, 6-CF_3), −70.4 (3 F, dsept, *J* 8.6 and 1.0, 1-CF_3), −105.0 (1 F, qq, *J* 16.1 and 8.6, C*F*); *m/z*: 343 (M^+ − 1, 21%), 293 (100), 243 (98), 69 (50). The stereochemistry of the minor isomer **3b** has not been confirmed as yet; δ_H(250 MHz; $CDCl_3$): 6.41 (q, *J* 6.7, C*H*); δ_F(235 MHz; $CDCl_3$): −56.7 (3 F, s, CF_3C-3), −62.1 (3 F, s, CF_3C-4), −64.6 (3 F, s, 1-CF_3), −68.3 (3 F, s, 6-CF_3), −101.8 (1 F, s, C*F*); *m/z*: 343 (M^+ − 1, 20%), 293 (50), 69 (100). In the original diene distillate there was a component (1% by GLCMS) identified as *7H-perfluoro-3,4,5,6-tetra(trifluoromethyl)octa-2,4,6-triene* ***4***; *m/z*: 505 (M^+ − 1, 2%), 467 (33), 321 (66), 69 (100). The residual sulpholan solution was shown to contain *potassium pentakis(trifluoromethyl)cyclopentadienide* (***7***) (12.9 mmol, 3%) (by ^{19}F NMR integrated against an internal standard of 1,1,1-trifluorotoluene); δ_F(235 MHz; $CDCl_3$): −49.8 (s, CF_3); FAB+ *m/z*: 39 (M^+, 100%), FAB− *m/z*: 405 (M^+, 100%).

The residual sulpholan solution was filtered and 98% sulphuric acid (750 mL, 14.1 mol) was added dropwise under reduced pressure. Volatile products were collected at liquid air temperatures, and were shown by GLCMS to contain one compound identified as *5H-pentakis(trifluoromethyl)cyclopentadiene* (***6***) (4.5 g, 86%); ν_{max}/cm^{-1}: 2977, 1664, 1450–1000; δ_H(250 MHz; $CDCl_3$): 4.80 (q, *J* 5.6, C*H*); δ_F(235 MHz; $CDCl_3$): −57.1 (6 F, s, 2-CCF_3), −60.2 (3 F, s, 5-CCF_3), −60.9 (6 F, s, 1-CCF_3); δ_C(100 MHz; $CDCl_3$): 58.4 (q, *J* 32.1, C-5), 119.2 (q, *J* 275.1, CF_3C-5), 120.2 (q, *J* 272.4, CF_3C-1), 122.6 (q, *J* 284.1, CF_3C-1) 139.7 (q, *J* 40.4, C-1), 139.8 (q, *J* 40.3, C-2); *m/z*: 406 (M^+, 2%), 69 (100).

H_2O (100 mL) was added to **6**, producing *hydronium pentakis(trifluoromethyl)cyclopentadienide* (11.1 mmol, quant.); δ_F(235 MHz; D_2O): −51.4 (s, CF_3). On addition of aqueous tetraethylammonium iodide (15.9 g, 64.4 mmol), a precipitate formed, which was recrystallized (diethyl ether – hexane), giving colourless crystals identified as *tetraethylammonium pentakis(trifluoromethyl)cyclopentadienide* (5.7 g, 83% from

Scheme 5.

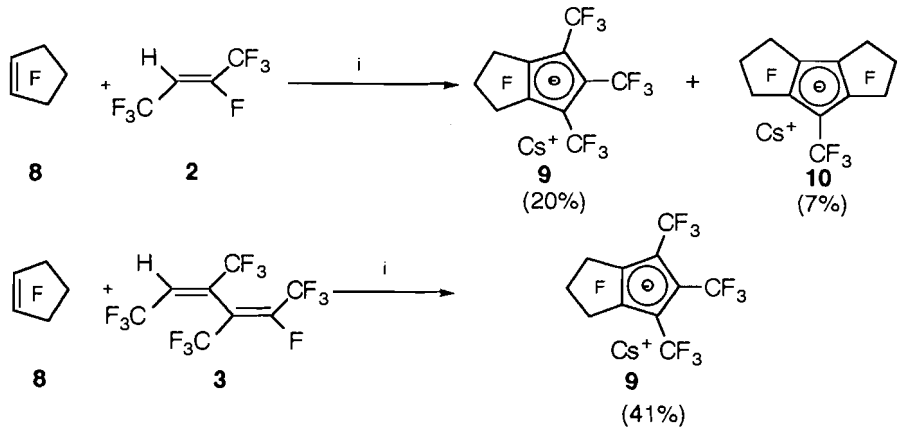

Reagents and conditions: i, sulpholan, CsF, 110°C.

Table 1. Formation of salts of anion **7**.

Salt used	Product	Yield (%)
Et_4NI	Et_4N^+ $C_5(CF_3)_5^-$	83
Et_4NBr	Et_4N^+ $C_5(CF_3)_5^-$	80
Pr_4NI	Pr_4N^+ $C_5(CF_3)_5^-$	80
Bu_4NI	Bu_4N^+ $C_5(CF_3)_5^-$	86
KI	K^+ $C_5(CF_3)_5^-$	15[a]
CsF	Cs^+ $C_5(CF_3)_5^-$	12[a]
$Tl(CH_3CO_2)$	Tl^+ $C_5(CF_3)_5^-$	15[a]

[a]Products were continuously extracted (dichloromethane) due to some solubility of these products in water, and this resulted in lower yields.

potassium pentakis(trifluoromethyl)cyclopentadienide); mp 241°C (dec.); ν_{max}/cm^{-1}: 3050, 1200, 1150; δ_H(250 MHz; $CDCl_3$): 1.42 (3 H, tt, *J* 7.2 and 1.9, CH_3), 3.51 (2 H, q, *J* 7.2, CH_2); δ_C(100 MHz; $CDCl_3$): 15.7 (s, CH_3), 53.1 (t, *J* 2.6, CH_2), 110.2 (q, *J* 19.2, CCF_3), 124.7 (q, *J* 271.3, CF_3); δ_F(235 MHz; $CDCl_3$): −50.9 (s, CF_3); FAB+ *m/z*: 130 (M^+, 100%); FAB− *m/z*: 405 (M^+, 100%). Anal. calcd. for $C_{18}H_{20}F_{15}N$: C 40.4, H 3.7, N 2.6%; found: C 40.1, H 3.9, N 2.9%.

General procedure for salt formation

As above, an aqueous solution of the desired halide salt (typically 500% excess) was added to the aqueous hydronium pentakis(trifluoromethyl)cyclopentadienide solution. This mixture was stirred for 1 h, before extraction (dichloromethane) and recrystallization (ether–hexane).

Tetrapropylammonium pentakis(trifluoromethyl)cyclopentadienide: mp 141–142°C; ν_{max}/cm^{-1}: 3100, 1350, 1225; δ_H(250 MHz; $CDCl_3$): 0.96 (3 H, t, *J* 7.2, CH_3), 1.70 (2 H, sext, *J* 7.2, CH_3CH_2), 3.01 (2 H, m, NCH_2); δ_C(100 MHz; $CDCl_3$): 15.3 (s, CH_3), 31.0 (s, CH_3CH_2), 55.2 (s, NCH_2), 110.1 (q, *J* 19.0, CCF_3), 123.3 (q, *J* 270.5, CF_3); δ_F(235 MHz; $CDCl_3$): −50.9 (s, CF_3); FAB+ *m/z*: 186 (M^+, 100%); FAB− *m/z*: 405 (M^+, 75%), 91 (solvent, 100). Anal. calcd. for $C_{22}H_{28}F_{15}N$: C 44.7, H 4.7, N 2.4%; found: C 44.8, H 4.6, N 2.4%.

Tetrabutylammonium pentakis(trifluoromethyl)cyclopentadienide: mp 118–119°C; ν_{max}/cm^{-1}: 3050, 1500, 1225, 1150; δ_H(250 MHz; $CDCl_3$): 0.95 (3 H, t, *J* 7.2, CH_3), 1.33 (2 H, sext, *J* 7.2, CH_3CH_2), 1.60 (2 H, pent, *J* 7.2, NCH_2CH_2), 3.11 (2 H, m, NCH_2); δ_C(100 MHz; $CDCl_3$): 13.1 (s, CH_3), 19.2 (s, CH_3CH_2), 23.4 (s, NCH_2CH_2), 58.5 (s, NCH_2), 109.6 (q, *J* 18.5, CCF_3), 123.7 (q, *J* 269.9, CF_3); δ_F(235 MHz; $CDCl_3$): −50.1 (s, CF_3); FAB+ *m/z*: 242 (M^+, 100%); FAB− *m/z*: 405 (M^+, 100%). Anal. calcd. for $C_{26}H_{36}F_{15}N$: C 48.2, H 5.6, N 2.2%; found: C 48.2, H 5.7, N 2.0%.

Potassium pentakis(trifluoromethyl)cyclopentadienide: mp >330°C; ν_{max}/cm^{-1}: 1500, 1200, 1050; δ_F(235 MHz; $CDCl_3$): −49.8 (s, CF_3); FAB+ *m/z*: 39 (M^+, 100%); FAB− *m/z*: 405 (M^+, 100%). Anal. calcd. for $KC_{10}F_{15}$: C 27.0%; found: C 27.1%.

Caesium pentakis(trifluoromethyl)cyclopentadienide: mp >330°C; ν_{max}/cm^{-1}: 1500, 1250, 1100; δ_F(235 MHz; $CDCl_3$): −49.9 (s, CF_3); FAB+ *m/z*: 133 (M^+, 100%); FAB− *m/z*: 405 (M^+, 100%). Anal. calcd. for $CsC_{10}F_{15}$: C 22.3%; found: C 22.3%.

Thallium pentakis(trifluoromethyl)cyclopentadienide: mp >330°C; ν_{max}/cm^{-1}: 1450, 1200, 1100; δ_F(235 MHz; $CDCl_3$): −49.8(s, CF_3); FAB+ *m/z*: 93 (solvent, 100%), 205 (M^+, 41%); FAB− *m/z*: 405 (M^+, 100%). Anal. calcd. for $TlC_{10}F_{15}$: C 19.7%; found: C 19.6%.

CsF and ***2*** *in a sealed system*

A Carius tube containing **2** (1.18 g, 4.68 mmol), caesium fluoride (6.00 g, 39.47 mmol), and sulpholan (10 mL) was heated and rotated at 190°C for 3 days. Volatiles were removed under reduced pressure, and the sulpholan residue was shown by ^{19}F NMR (integrated against an internal standard of 1,1,1-trifluorotoluene) and FAB mass spectrometry to contain *caesium pentakis(trifluoromethyl)cyclopentadienide* (0.28 mmol, 13%), as above.

Synthesis of ***9*** *and* ***10***

A Carius tube containing **2** (0.7 g, 3.8 mmol), perfluorocyclohexene **8** (1.04 g, 4.9 mmol), caesium fluoride (2.00 g, 13.2

mmol), and sulpholan (20 mL) was heated and rotated at 110°C for 5 days. Volatiles were removed under reduced pressure, and the sulpholan residue was shown by ^{19}F NMR (integrated against an internal standard of 1,1,1 trifluorotoluene) and FAB mass spectrometry to contain *caesium perfluoro-1,2,3-trihydro-4,5,6-trimethylpentalenide* **9** (0.4 mmol, 20%); δ_F(235 MHz; $CDCl_3$): −49.7 (3 F, s, 5-CCF_3), −52.5 (6 F, s, 4-CCF_3), −97.7 (4 F, s, 1-CF_2), −121.1 (2 F, s, 2-CF_2); FAB+ *m/z*: 133 (M^+, 100%); FAB− *m/z*: 417 (M^+, 100%); and *caesium perfluoro-1-methyl-2,3,4,5,6,7-hexahydrodicyclopenta[*b,d*]cyclopentadienide* **10** (0.2 mmol, 7%); δ_F(235 MHz; $CDCl_3$): −54.4 (3 F, s, CF_3), −98.4 (4 F, s, 2-CF_2), −100.1 (4 F, s, 4-CF_2), −122.2 (4 F, s, 3-CF_2); FAB+ *m/z*: 133 (M^+, 100%), FAB− *m/z*: 429 (M^+, 29%), 395 (100).

Synthesis of ***9***

A Carius tube containing perfluorocyclohexene **8** (1.04 g, 4.9 mmol), caesium fluoride (2.00 g,13.2 mmol), (*Z,E*) and (*Z,Z*)-5*H*-perfluoro-3,4-dimethyl-2,4-diene **3** (1.6 g, 4.7 mmol), and sulpholan (20 mL) was heated and rotated at 110°C for 5 days. The volatiles were removed under reduced pressure, and the sulpholan residue was shown by ^{19}F NMR (integrated against an internal standard of 1,1,1 trifluorotoluene) and FAB mass spectrometry to contain *caesium perfluoro-1-methyl-2,3,4,5,6,7-hexahydrodicyclopenta*[b,d]*cyclo-pentadienide* **9** (1.9 mmol, 41%), as above.

Attempted protonation of ***9*** *and* ***10***

Sulphuric acid (98%, 50 mL) was added dropwise to a sulpholan (20 mL) solution containing caesium perfluoro-1,2,3-trihydro-4,5,6-trimethylpentalenide **9** (0.98 mmol) and caesium perfluoro-1-methyl-2,3,4,5,6,7-hexahydrodicyclopenta-[*b,d*]cyclopentadienide **10** (0.34 mmol) under reduced pressure. Volatile products were collected in a trap maintained at liquid air temperatures, and were shown by GLCMS to contain greater than 10 different compounds, two of which have been proposed on the basis of their GLCMS data as *5H-perfluoro-1,2,3-trihydro-4,5,6-trimethylpentalena-4,6-diene*, *m/z*: 368 ($M^+ - CF_2$, 86%), 349 ($M^+ - CF_3$, 54), 318 ($M^+ - CF_2CF_2$, 100), and *1H-perfluoro-1-methyl-2,3,4,5,6,7-hexahydrodicyclopenta*[b,d]*cyclopenta-8,9-diene*, *m/z*: 380 ($M^+ - CF_2$, 34%), 361 ($M^+ - CF_3$ 16), 330 ($M^+ - CF_2CF_2$, 49).

Acknowledgements

We thank the Engineering and Physical Sciences Research Council (EPSRC) and EA Technology for financial support (to A.J.R. and J.F.S.V.), and J.A.K Howard and A.S. Batsanov for the X-ray structure analyses.

References

1. R.D. Chambers, J.F.S. Vaughan, S.J. Mullins, T. Nakamura, and A.J. Roche. J. Fluorine Chem. **72**, 231 (1995).
2. (*a*) M.A. McClinton and D.A. McClinton. Tetrahedron, **48**, 189 (1992); (*b*) J.P. Begue and D. Bonnet-Delphon. Tetrahedron, **47**, 3207 (1991); (*c*) D.J. Burton and Z.Y. Yang. Tetrahedron, **48**, 189 (1992).
3. J.T. Maynard. J. Org. Chem. **28**, 112 (1963).
4. R.D. Chambers and A.J. Palmer. Tetrahedron, **31**, 3293 (1969).
5. (*a*) R.D. Chambers, S. Partington, and D.B. Speight. J. Chem. Soc. Perkin Trans. 1, 2673 (1974); (*b*) J.W. Emsley, L. Phillips, and V. Wray. Fluorine coupling constants. Pergamon, Oxford. 1977.
6. R.D. Chambers, S.J. Mullins, A.J. Roche, and J.F.S. Vaughan. J. Chem. Soc. Chem. Commun. 841 (1995).
7. E.D. Laganis and D.M. Lemal. J. Am. Chem. Soc. **102**, 6633 (1980).
8. J.E. Baldwin. J. Chem. Soc. Chem. Commun. 734 (1976).

Monomeric and dimeric V(III) complexes supported by organic amides

Pietro Berno, Mark Moore, Ravinder Minhas, and Sandro Gambarotta

Abstract: Reaction of $VCl_3(THF)_3$ with two equivalents of R_2NLi (R = Cy, Me_3Si) yielded the two corresponding complexes $(Cy_2N)_2V(\mu\text{-}Cl)_2Li(THF)_2$ (**1**) and $[(Me_3Si)_2N]_2VCl(THF)$ (**2**). Both complexes decomposed in hot toluene. In the case of complex **1** the reaction led to dimerization and formation of the dimeric $[(Cy_2N)_2V(\mu\text{-}Cl)]_2$ (**3**). Reaction of **2** with $NaBH_4$ yielded the unprecedented borohydride derivative $[(Me_3Si)_2N]_2V(BH_4)(THF)$ (**4**). The structures of all the complexes were elucidated by X-ray analysis.

Key words: vanadium, trivalent, amide, borohydride, dinuclear.

Résumé : La réaction du $VCl_3(THF)_3$ avec deux équivalents de R_2NLi (R = Cy, Me_3Si) conduit aux deux complexes correspondants $(Cy_2N)_2V(\mu\text{-}Cl)_2Li(THF)_2$ (**1**) et $[(Me_3Si)_2N]_2VCl(THF)$ (**2**). Les deux complexes se décomposent dans le toluène bouillant. Dans le cas du complexe **1**, la réaction conduit à une dimérisation et à la formation du dimère $[(Cy_2N)_2V(\mu\text{-}Cl)]_2$, **3**. La réaction du composé **2** avec le $NaBH_4$ conduit au dérivé borohydrure inconnu $[(Me_3Si)_2N]_2V(BH_4)(THF)$, **4**. Les structures de tous les complexes ont été élucidées par diffraction des rayons X.

Mots clés : vanadium, trivalent, amide, borohydrure, dinucléaire.

[Traduit par la rédaction]

Introduction

There has been a steady growth of interest in the recent literature (1) in the chemistry of medium-valent vanadium complexes and, in particular, those containing the metal in the oxidation state +3. This is probably due to the rich and diversified chemical reactivity displayed by these derivatives which includes dinitrogen fixation (2), possible relevance for desulfurization processes (3), and formation of precursors for hydrogenation (4) and of reactive moieties such as nitrides (5), carbenes (6), alkyls (7), and hydrides (5*c*, 8). In fact, this particular oxidation state of vanadium combines a medium Lewis acidity with the presence of available *d* electrons, which together contribute to its fairly high reactivity. Last but not least, trivalent vanadium seems to play an important role in some naturally occurring systems such as vanadium nitrogenase (9) and others (see for example ref. 10), where remarkable transformations are carried out in a catalytic manner and under mild reaction conditions.

Anionic organic amides seem to be particularly versatile supporting ligands with which to study the chemistry of trivalent vanadium. There are several characteristics that make them unique. First of all, there is a virtually unlimited possibility of fine tuning the steric hindrance via the appropriate selection of the substituents attached to the nitrogen atom. Their rather strong reducing power (11) and electronic flexibility allow the stabilization of a rather wide range of oxidation states and, in particular, of the lower states. Finally, these ligands are readily available via simple deprotonation of commercially available primary or secondary amines.

We recently reported the preparation of several V(III) complexes supported by nitrogen-donor-based ligands and described their involvement in dinitrogen activation (2, 12) and hydrogen transfer processes (4, 5*c*). These findings encouraged us to extend further the chemistry of these derivatives toward further functionalization and in particular to attempt the preparation of hydrides and alkyls. In this perspective, complexes such as $(R_2N)_2VCl$, containing a chlorine atom that should be easy to replace, will be the most promising starting materials.

In this paper we describe the convenient and straightforward preparation of monomeric and dimeric V(III) halide complexes supported by organic amides and the transformation of one of them into an unusual borohydride derivative.

Experimental

All operations were performed under the inert atmosphere of a nitrogen-filled dry-box (Vacuum Atmosphere) or by using standard Schlenk techniques. Cy_2NLi (13) and $VCl_3(THF)_3$ (14) were prepared according to published procedures. $NaBH_4$ (Aldrich) was used as received. $(Me_3Si)_2NLi$ (Aldrich) was recrystallized from hexane. Infrared spectra were recorded on a Mattson 9000 FTIR instrument from Nujol mulls prepared in the dry-box. Samples for magnetic susceptibility measurements were weighed inside the dry-box equipped with an analytical balance, and sealed into calibrated tubes. Magnetic measurements were carried out with a Gouy balance (Johnson

Received February 21, 1996.

This paper is dedicated to Professor Howard C. Clark in recognition of his contributions to Canadian chemistry.

P. Berno, M. Moore, R. Minhas, and S. Gambarotta.[1]
Department of Chemistry, University of Ottawa, D'Iorio Hall, 10 M. Curie, Ottawa, ON K1N 6N5, Canada.

[1] Author to whom correspondence may be addressed. Telephone: (613) 824-4859. Fax: (613) 562-5170. E-mail: sgambaro@oreo.chem.uottawa.ca

Matthey) at room temperature. The magnetic moment was calculated following standard methods (15), and corrections for underlying diamagnetism were applied to the data (16). Elemental analyses were carried out with a Perkin Elmer PE 2400 CHN analyzer. Ratios between heavy atoms were determined by X-ray fluorescence by using a Philips XRF 2400 instrument.

Preparation of $(Cy_2N)_2V(\mu\text{-}Cl)_2Li(THF)_2$ (1)

Freshly prepared Cy_2NLi (6.96 g, 37.1 mmol) was added to a red suspension of $VCl_3(THF)_3$ (6.94 g, 18.6 mmol) in THF (100 mL) at −30°C. The color immediately turned green and the resulting suspension was stirred overnight at room temperature. After evaporation to dryness, toluene (120 mL) was added to the solid residue. The resulting suspension was filtered and the solution was concentrated to small volume. The addition of diethyl ether (150 mL) caused the precipitation of a dark microcrystalline solid (3.7 g, 5.8 mmol, 31%). Crystals suitable for X-ray analysis were obtained upon addition of hexane to a concentrated THF solution of **1** and storage at −25°C. IR (Nujol mull, cm^{-1}): 2671(br), 1449(vs), 1365(sh), 1343(m), 1248(br), 1162(s), 1145(s), 1121(br), 1034(vs), 980(w), 955(vs), 890(vs), 842(s), 804(m), 779(m), 728(w), 698(vs), 587(s), 513(s), 451(w). Anal. calcd. (found) for $C_{32}H_{60}O_2N_2Cl_2LiV$: C 60.66(60.11), H 9.54(8.99), N 4.41(4.21). $\mu_{eff} = 2.68\mu_B$.

Preparation of $\{[(CH_3)_3Si]_2N\}_2VCl(THF)$ (2)

A suspension of $VCl_3(THF)_3$ (7.06 g, 18.9 mmol) in THF (80 mL) was treated at room temperature with $(Me_3Si)_2NLi$ (6.3 g, 38 mmol). The color rapidly turned deep blue-green. After stirring for 3 h at room temperature, the solvent was evaporated in vacuo. The residual solid was redissolved in hexane (70 mL) and the resulting solution was filtered and allowed to stand overnight at −30°C. Dark blue-green crystals of **2** separated (7.9 g, 16.4 mmol, 87%). IR (Nujol mull, cm^{-1}): 1462(vs), 1376(m), 1249(s), 1001(w), 906(s), 890(s), 846(s), 784(m), 759(w), 690(m), 665(s). Anal. calcd. (found) for $C_{16}H_{44}N_2ClSi_4OV$: C 40.10(39.91), H 9.25(9.17), N 5.85(5.72). $\mu_{eff} = 2.79\mu_B$.

Preparation of $[(Cy_2N)_2V(\mu\text{-}Cl)]_2$ (3)

Solid Cy_2NLi (24.98 g, 133.4 mmol) was added to a red suspension of $VCl_3(THF)_3$ (24.92 g, 66.7 mmol) in THF (200 mL) at −30°C. The resulting dark green suspension was stirred overnight at room temperature. After evaporation of the solvent in vacuo, the dark brown solid residue was suspended in toluene (250 mL) and the resulting solution was boiled and filtered while hot. Dark brown crystals of **3** (14.98 g, 17 mmol, 51%) separated after allowing the resulting brown solution to stand at −25°C for 2 days. IR (Nujol mull, cm^{-1}): 2667(br), 1449(vs), 1364(sp), 1343(m), 1296(w), 1285(w), 1250(s), 1160(s), 1146(s), 1119(vs), 1067(w), 1037(vs), 980(w), 956(vs), 890(s), 841(s), 803(w), 778(m), 697(s), 612(w), 585(m), 514(s), 495(w), 484(w), 449(w), 424(w). Anal. calcd. (found) for $C_{24}H_{44}N_2ClV$: C 64.48(64.31), H 9.92(9.77), N 6.27(6.22). $\mu_{eff} = 1.79\mu_B$.

Preparation of $\{[(CH_3)_3Si]_2N\}_2V(BH_4)(THF)$ (4)

A solution of **2** (3.0 g, 6.3 mmol) in THF (100 mL) was stirred with $NaBH_4$ (1.9 g, 50.2 mmol) for 24 h at room temperature. The resulting deep blue mixture was filtered and the solvent evaporated in vacuo. The oily residue was dried overnight in vacuo at room temperature and the resulting solid was redissolved in hexane. The mixture was filtered to remove the small amount of insoluble material, concentrated, and allowed to stand at −30°C. Dark blue crystals of **4** (0.160 g, 0.3 mmol, 6%) were obtained. IR (Nujol mull, cm^{-1}): 2434(s), 2396(s), 2240(m), 2134(s), 1463(s), 1373(s), 1351(w), 1243(vs), 1167(w), 1129(m), 1020(w), 999(s), 881(v br), 663(s), 441(s). The extreme air sensitivity prevented elemental analysis determination. $\mu_{eff} = 2.91\mu_B$.

X-ray crystallography

Data were collected in the temperature range −144 to −161°C. The ω–2θ scan technique was used for suitable air-sensitive crystals mounted on glass fibers. Cell constants and orientation matrices were obtained from the least-squares refinement of 25 centered reflections. The intensities of three standard reflections, measured after every 150 reflections, showed no statistically significant decay over the duration of the data collections. Data were corrected for Lorentz and polarization effects, but no absorption corrections were applied to the data except for complex **4**. In this case, absorption corrections (DIFABS) significantly improved the agreement factors. The structures of **1**, **2**, and **3** were solved by direct methods by locating all the non-hydrogen atoms. Their positions were refined anisotropically. Hydrogen atom positions were introduced at their calculated positions except for complex **4** where the positions of the hydrogens connected to the boron atom were located from difference Fourier maps. The data were processed using the TEXSAN software package on a Digital VAX workstation. Refinements were carried out by using full-matrix least-squares techniques on F, minimizing the function $\Sigma w(|F_o| - |F_c|)^2$, where $w = 4F_o2/\sigma2(F_o^2)$ and F_o and F_c are the observed and calculated structure factors. Atomic scattering factors and anomalous dispersion terms were taken from the usual sources (Cromer and Waber) (17). Details on the data collections and structure refinements are listed in Table 1. The final atomic coordinates are given as supplementary material.[2] Selected bond distances and angles are given in Table 2.

Results

According to Scheme 1, the reaction of $VCl_3(THF)_3$ with two equivalents of R_2NLi (R = Cy, $(CH_3)_3Si$) led to the formation of the corresponding derivatives $(Cy_2N)_2V(\mu\text{-}Cl)_2Li(THF)_2$ (**1**) and $\{[(CH_3)_3Si]_2N\}_2VCl(THF)$ (**2**). In both cases, the reactions were instantaneous and were accompanied by a rapid color change to dark green or blue-green. The two complexes were isolated in crystalline form. The formulation of the two species was indicated by the values of the combustion analy-

[2] Copies of material on deposit may be purchased from: The Depository of Unpublished Data, Document Delivery, CISTI, National Research Council Canada, Ottawa, Canada K1A 0S2. Tables of atomic coordinates and bond lengths and angles have also been deposited with the Cambridge Crystallographic Data Centre, and can be obtained on request from The Director, Cambridge Crystallographic Data Centre, University Chemical Laboratory, 12 Union Road, Cambridge, CB2 1EZ, U.K.

Table 1. Crystal data and structure analysis results.

	1	2	3	4
Formula	$C_{32}H_{60}O_2N_2VCl_2Li$	$C_{16}H_{44}N_2OVSi_4Cl$	$C_{24}H_{44}N_2VCl$	$C_{16}H_{48}OBN_2VSi_4$
Formula weight	633.63	479.27	447.02	458.66
Space group	$P2_1/n$ (No. 14)	P-1 (No. 2)	$P2_1/n$ (No. 14)	$P2_1/n$ (No. 14)
a (Å)	14.188(1)	11.636(3)	9.310(1)	11.732(1)
b (Å)	17.113(1)	15.767(4)	21.5129(9)	19.199(1)
c (Å)	14.499(2)	8.561(2)	12.680(2)	12.086(1)
α (deg)		94.08(2)		
β (deg)	97.332(9)	108.98(2)	99.10(1)	97.77(1)
γ (deg)		105.55(2)		
V (Å^3)	3492(1)	1409.2(6)	2507.6(8)	2697.3(8)
Z	4	2	4	4
Radiation (Mo Kα, Å)	0.71069	0.71069	0.71069	1.54178
T (°C)	−161	−150	−144	−162
D_{calcd} (g cm^{-3})	1.205	1.129	1.184	1.129
μ_{calcd} (cm^{-1})	4.56	6.11	5.01	49.02
R, R_w	0.034, 0.047	0.045, 0.045	0.054, 0.068	0.068, 0.078

$R = \Sigma||F_o| - |F_c|| / \Sigma|F_o|$; $R_w = [(\Sigma(|F_o| - |F_c|)^2 / \Sigma w F_o^2)]^{1/2}$.

Table 2. Selected bond distances (Å) and angles (deg).

1	2	3	4
V1—Cl1 = 2.375(1)	V1—Cl1 = 2.276(2)	V1—Cl1 = 2.391(2)	V1—O1 = 2.057(7)
V1—Cl2 = 2.355(1)	V1—O1 = 2.034(3)	V1—Cl1a = 2.347(2)	V1—B1 = 2.38(2)
V1—N1 = 1.902(3)	V1—N1 = 1.918(4)	V1—N1 = 1.856(4)	V1—N1 = 1.876(8)
V1—N2 = 1.864(3)	V1—N3 = 1.953(3)	V1—N2 = 1.875(4)	V1—N2 = 1.940(8)
N1—C9 = 1.459(5)	N1—Si1 = 1.741(4)	Cl1-V1-N1 =105.7(1)	N2—Si1 = 1.737(9)
N1—C15 = 1.474(4)	N1—Si2 = 1.745(4)	Cl1-V1-N2 = 113.3(1)	N1—Si2 = 1.755(8)
Li1—O1 = 1.920(7)	Cl1-V1-O1 = 95.2(1)	Cl1-V1-Cl1a = 92.85(5)	V1—H48 = 1.711(7)
Li1—O2 =1.916(6)	Cl1-V1-N1 = 106.9(1)	V1-Cl1-V1a = 87.15(5)	V1—H47 =1.916(6)
Li1—Cl1 = 2.344(6)	Cl1-V1-N3 = 114.8(1)	C1-N1-C7 =116.0(4)	B1—H47 = 0.943
Li1—Cl2 = 2.400(7)	O1-V1-N1 = 113.2(1)	V1-N1-C1 = 107.0(3)	B1—H48 = 1.43(7)
N1-V1-Cl1 = 106.0(1)	O1-V1-N3 = 100.5(1)	V1-N1-C7 = 137.0(3)	N1-V1-O1 = 119.0(4)
N1-V1-Cl2 = 113.25(9)	N1-V1-N3 = 122.7(1)	V1-N2-C13 = 111.7(3)	N1-V1-N2 = 113.9(4)
N1-V1-N2 = 120.9(1)	Si1-N1-Si2 = 120.5(2)	V1-N2-C18 = 131.2(3)	N2-V1-O1 = 99.3(3)
N2-V1-Cl1 = 105.55(9)	V1-N1-Si1 = 122.2(2)	C13-N2-C18 = 117.0(4)	Si2-N1-Si4 = 117.7(5)
N2-V1-Cl2 = 112.30(9)	V1-N1-Si2 = 114.9(2)	N1-V1-N2 = 120.8(2)	V1-N1-Si4 = 123.4(4)
Cl1-V1-Cl2 = 94.89(4)		V1..V1a = 3.266(2)	V1-N1-Si2 = 117.5(5)
V1-Cl1-Li1 = 85.6(2)			
V1-Cl2-Li1 = 84.8(1)			
Cl1-Li1-Cl2 = 94.5(2)			
V1-N1-C9 = 131.1(2)			

ses. The X-ray fluorescence spectrum confirmed the presence of chlorine in the expected ratio with the metal centers. Both complexes are paramagnetic at room temperature with magnetic moments as expected for the d^2 electronic formulation of V(III) metal centers.

The chemical connectivity of both complexes was elucidated by X-ray analysis. Complex **1** features a vanadium atom residing in the center of a distorted tetrahedron (N1-V1-N2 = 120.9(1)°, N1-V1-Cl1 = 106.0(1)°, Cl1-V1-Cl2 = 94.89(4)°) defined by the two nitrogen atoms of the two amide groups (V1—N1 = 1.902(3) Å, V1—N2 = 1.864(3) Å) and two chlorides (V1—Cl1 = 2.375(1) Å, V1—Cl2 = 2.355(1) Å). Similar to the case of the closely related titanium derivative $[(Cy_2N)_2Ti(\mu\text{-}Cl)_2(Li(TMEDA)]$ (18), the distortion of the coordination geometry is probably due to the large steric bulk of the amide groups since the angle subtended at vanadium by the two amide groups is significantly wider than expected for a normal tetrahedral angle. The two chloride atoms bridge to one lithium cation (Cl1—Li1 = 2.344(6) Å, Cl2—Li1 = 2.400(7) Å) forming an almost planar VCl_2Li core (torsion angle V1-Cl1-Li1-Cl2 = 3.7(2)°). Two molecules of THF complete the tetrahedral coordination geometry of the alkali

Scheme 1.

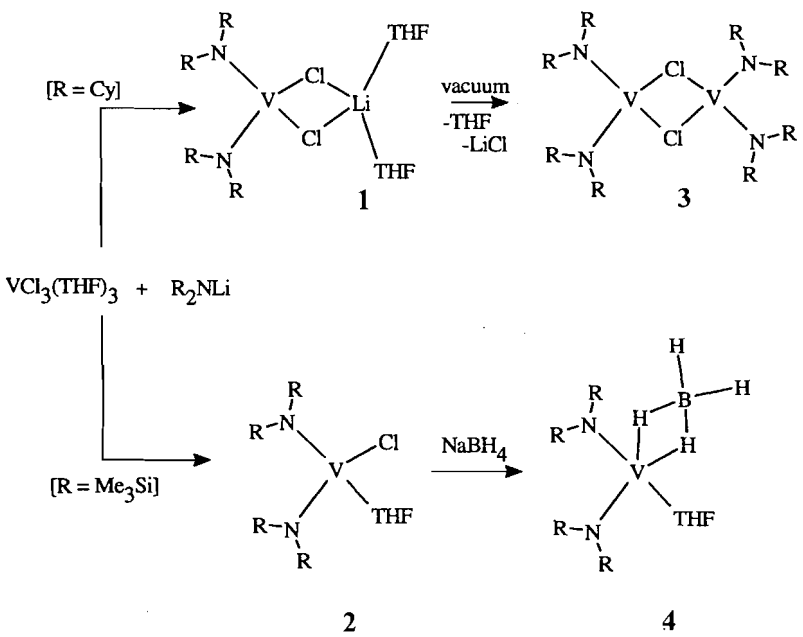

Fig. 1. ORTEP plot of **1**. Thermal ellipsoids are drawn at the 50% probability level.

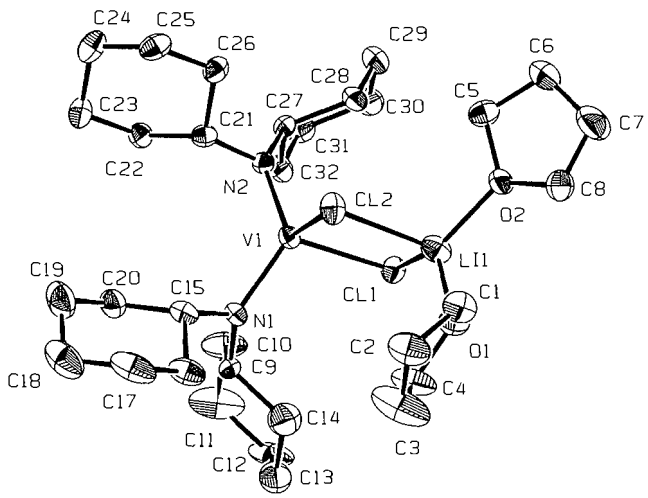

Fig. 2. ORTEP plot of **2**. Thermal ellipsoids are drawn at the 50% probability level.

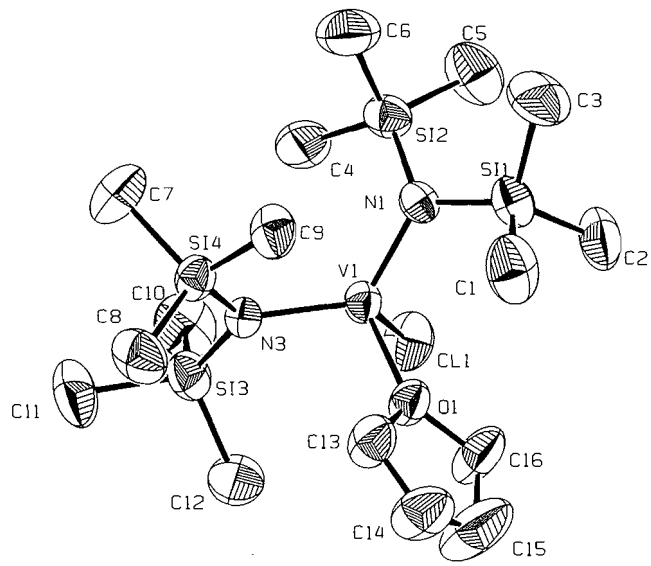

cation (Li1—O1 = 1.920(7) Å, Li1—O2 = 1.916(6) Å). The coordination geometry around each amide nitrogen atom is trigonal planar (C9-N1-C15 = 114.2(3)°, C9-N1-V1 = 131.1(2)°, C15-N1-V1 = 113.6(2)°), possibly suggesting some extent of π-interaction of the amide groups with the metal center.

The structure of complex **2** was more straightforward and predictable, consisting of a tetrahedral vanadium atom also placed in the center of a distorted tetrahedron (N1-V1-N3 = 122.7(1)°, N1-V1-Cl1 = 106.9(1)°, N1-V1-O1 = 113.2(1)°, Cl1-V1-O1 = 95.2(1)°) defined by two nitrogen atoms of two amide ligands (V1—N1 = 1.918(4) Å, V1—N3 = 1.953(3) Å), one chlorine (V1—Cl1 = 2.276(2) Å), and one oxygen atom of one molecule of THF (V1—O1 = 2.034(3) Å). Even in this case the distortion of the coordination geometry around vanadium is probably due to the large steric bulk of the two amide groups. The V—Cl and V—O distances are in the expected range for such bonds. The coordination geometry around each nitrogen atom is trigonal planar, again suggesting the possibility of some extent of π-interaction with the metal center (Si1-N1-V1 = 122.2(2)°, Si2-N1-V1 = 114.9(2)°, Si1-N1-Si2 = 102.5(2)°).

Both complexes were extremely air sensitive but stable at room temperature in both the solid state and solution under inert atmosphere. Nevertheless, a rather rapid color change to

Fig. 3. ORTEP plot of **3**. Thermal ellipsoids are drawn at the 50% probability level.

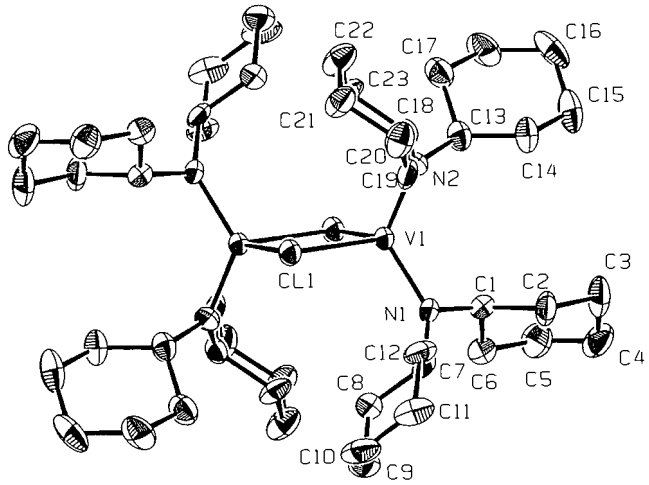

Fig. 4. ORTEP plot of **4**. Thermal ellipsoids are drawn at the 50% probability level.

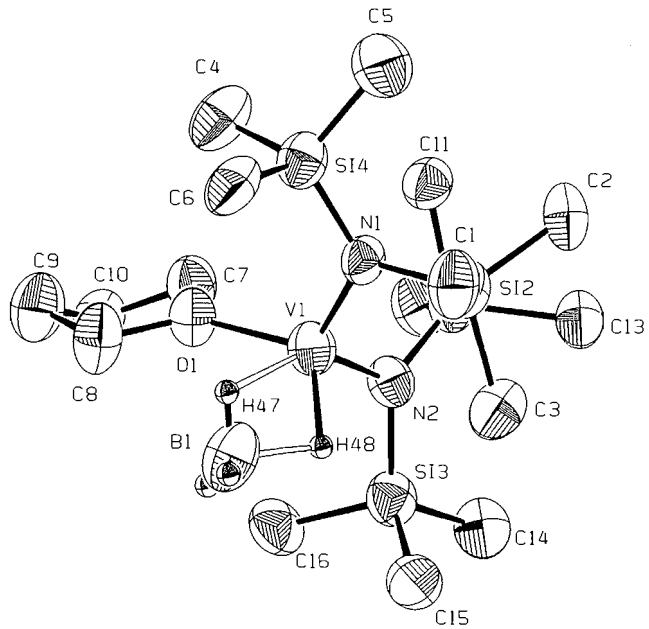

brown was observed upon heating toluene solutions of both complexes. While in the case of complex **2** this behavior may be attributed to the dissociation of THF from the coordination sphere of the metal center, in the case of complex **1** the thermal instability was unexpected since the heating should lead only to desolvation of the lithium cation. Nevertheless, the color change indicated that a reaction involving the vanadium center probably occurred. After suitable work-up, a new brown crystalline material **3** was isolated. Conversely, in the case of complex **2** the thermolysis led only to intractable solutions. The combustion analysis and X-ray fluorescence of **3** clearly indicated the loss of one chlorine atom per vanadium atom with respect to **1**. These data were in agreement with the formulation $[(Cy_2N)_2VCl]_2$. Further, the magnetic moment calculated on the basis of the proposed formula was found to be considerably reduced with respect to the value expected for a d^2 electronic configuration of the V(III) metal center, possibly indicating the presence of a magnetic coupling between the metal centers. To unambiguously characterize the complex, the molecular structure was elucidated by an X-ray analysis.

Complex **3** is dimeric and consists of two distorted tetrahedral vanadium centers linked together by two bridging chlorides, forming a planar V_2Cl_2 core (torsion angle V1-Cl1-V1a-Cl1a = 0.0°). The coordination geometry around each vanadium center is distorted tetrahedral (N1-V1-N2 = 120.8(2)°, N1-V1-Cl1 = 105.7(1)°, Cl1-V1-Cl1a = 92.85(5)°, N2-V1-Cl1 = 113.3(1)°) and is defined by two nitrogens of two amide groups (V1—N1 = 1.856(4) Å, V1—N2 = 1.875(4) Å) and two bridging chlorides. The V—Cl distances (V1—Cl1 = 2.391(2) Å, V1—Cl1a = 2.347(2) Å) are normal although slightly longer than in complexes **1** and **2**. As in the cases of complexes **1** and **2**, the distortion of the tetrahedral geometry around the metal centers can be ascribed to the large steric bulk of the amides. The coordination geometry around each nitrogen atom is also trigonal planar (V1-N1-C1 = 107.0(3)°, V1-N1-C7 = 137.0(3)°, C1-N1-C7 = 116.0(4)°), again suggesting some extent of π-interaction between the nitrogen atoms and the metal center. The intermetallic distance (V1—V1a = 3.266(2) Å) is rather long and excludes the presence of a direct bonding interaction.

Chlorine replacement reactions were attempted with $NaBH_4$. While in the case of **1** and **3** the work-up afforded only intractable materials, a clean reaction was observed with **2**. The reaction proceeded smoothly, resulting in the formation of a deep blue solution from which a new complex $\{[(CH_3)_3Si]_2N\}_2V(BH_4)(THF)$ (**4**) was isolated in low yield as a homogeneous crystalline mass. Unfortunately, the extreme air sensitivity prevented the obtaining of reproducible and meaningful values of the combusion analysis data. The magnetic moment, calculated on the basis of the formula where the chlorine atom of **2** has been replaced by a BH_4^- group, was as expected for the d^2 electronic configuration of a V(III) metal center. The IR spectrum of these species shows a rather unusual pattern with three intense absorptions at 2434, 2396, and 2134 cm^{-1} and a medium-intensity band at 2240 cm^{-1}. This spectrum is not in agreement with any of those commonly observed for the η^1-, η^2-, and η^3-bonded BH_4 groups (19). Since we were unable to understand the spectroscopic data and to obtain meaningful analytical data we have undertaken a crystallographic analysis.

The molecular structure of **4** was elucidated by X-ray analysis. The complex is virtually isostructural with complex **2**, with comparable bond distances (V1—N1 = 1.876(8) Å, V1—N2 = 1.940(8) Å, V1—O1 = 2.057(7) Å) and angles (N1-V1-N2 = 113.9(4)°, N1-V1-O1 = 119.0(4)°, N2-V1-O1 = 99.3(3)°). Even in this case the tetrahedral coordination geometry around the vanadium center is distorted. The V—B distance is rather long (V1—B1 = 2.38(2) Å) and falls in the expected range for a η^2-bonded BH_4 group. The hydrogen atom positions for the BH_4 group were obtained from difference Fourier maps. Although the crystal structure was not of sufficient accuracy to permit drawing definite conclusions about the positions of the hydrogen atoms, it indicates, as an interesting possibility, that the bonding mode of the BH_4^-

group may be regarded as somewhat intermediate between η^2-BH_4 and the limiting case of an aggregation of a V—H complex with BH_3. In fact, the two bridging hydrogens were found to possess significantly different bond distances with the vanadium and boron centers. In particular, one of the two bridging hydrogens was found in the normal bonding range with the boron atom (B1—H47 = 0.943 Å) while the second was significantly closer to the vanadium center (V1—H48 = 1.711(7) Å) and significantly further from the boron atom (B1—H48 = 1.43(7) Å).

Complex **4** represents one of the rare examples of a vanadium borohydride derivative (20) and we are actively investigating its chemical reactivity.

Supplementary information available

A full list of atomic coordinates, anisotropic thermal parameters, bond distances and angles for **1**, **2**, **3**, and **4** has been deposited.[2]

Acknowledgments

This work was supported by the National Science and Engineering Council of Canada (NSERC) through a strategic and operating grant.

References

1. (*a*) A.L. Odom and C.C. Cummins. J. Am. Chem. Soc. **117**, 6613 (1995); (*b*) M.G. Fickes, W.M. Davis, and C.C. Cummins. J. Am. Chem. Soc. **117**, 6384 (1995); (*c*) C.C. Cummins, R.R. Schrock, and W.M. Davis. Inorg. Chem. **33**, 1448 (1994); (*d*) A.R. Wills and P.G. Edwards. J. Chem. Soc. Dalton Trans. 1253 (1989); (*e*) A.A. Danopoulos and P.G. Edwards. Polyhedron, **8**, 1339 (1989). (*f*) A.R. Wills, P.G. Edwards, M. Harman and M.B. Hursthouse. Polyhedron, **8**, 1457 (1989).
2. (*a*) A. Hills, D.L. Hughes, G.J. Leigh, and R. Prieto-Alcon. J. Chem. Soc. Dalton Trans. 3609 (1993); (*b*) S. Gambarotta. J. Organomet. Chem. **500**, 117 (1995), and refs. cited therein; (*c*) J.J.H. Edema, A. Meetsma, and S. Gambarotta. J. Am. Chem. Soc. **111**, 6878 (1989); (*d*) D. Rehder, C. Woitha, W. Priebsch, and H. Gallius. J. Chem. Soc. Chem. Commun. 364 (1992); (*e*) J.K.L. Buijink, A. Meetsma, and J.H. Teuben. Organometallics, **12**, 2004 (1993); (*f*) R. Ferguson, E. Solari, C. Floriani, A. Chiesi-Villa, and C. Rizzoli. Angew. Chem. Int. Ed. Engl. **32**, 396 (1993); (*g*) G.J. Leigh. Acc. Chem. Res. **25**, 177 (1992).
3. (*a*) J.C. Reynolds, S.C. Sendlinger, A.M. Murray, J.C. Huffman, and G. Christou. Angew. Chem. Int. Ed. Engl. **31**, 1253 (1992); (*b*) T.F. Yen. The role of trace metals in petroleum. Ann Arbor Science, Ann Arbor, Mich. 1975; (*c*) P. Psundararman. Anal Chem. **57**, 2204 (1986); (*d*) J.C. Reynolds, E.J. Gallegos, R.H. Fish, and J.J. Komlenic. Energy Fuels. **1**, 36 (1987); (*e*) B.G. Sibernagel. J. Catal. **56**, 315 (1979); (*f*) P.C.H. Mitchell, C.E. Scott, J.P. Bonnelle, and J.C. Grimblot. J. Chem. Soc. Faraday Trans. **81**, 1047 (1985).
4. P. Berno and S. Gambarotta. Organometallics, **14**, 2569 (1995).
5. (*a*) D.B. Sable and W.H. Armstrong. Inorg. Chem. **31**, 163 (1992), and refs. cited therein; (*b*) T.S. Haddad, A. Aistars, J.W. Ziller, and N.M. Doherty. Organometallics, **12**, 2420 (1993), and refs. cited therein; (*c*) P. Berno and S. Gambarotta. Angew. Chem. Int. Ed. Engl. **34**, 822 (1995); (*d*) J. Jubb, L. Scoles, H. Jenkins, and S. Gambarotta. Chemistry, European J. **2**, 767 (1996).
6. B. Hessen, A. Meetsma, and J.H. Teuben. J. Am. Chem. Soc. **111**, 5977 (1989).
7. B. Hessen, J.H. Teuben, T.H. Lemmen, J.C. Huffman, and K.G. Caulton. Organometallics, **4**, 946 (1985).
8. (*a*) B. Hessen, F. van Bolhuis, J.H. Teuben, and J.L. Petersen. J. Am. Chem. Soc. **110**, 295 (1988); (*b*) F. Sussmilch, W. Glockner, and D. Rehder. J. Organomet. Chem. **388**, 95 (1990); (*c*) K. Jonas, V. Wiskamp, Y.H. Tsay, and C. Kruger. J. Am. Chem. Soc. **105**, 5480 (1983).
9. (*a*) B.J. Hales, E.E. Case, J.E. Morningstar, M.F. Dzeba, and M.A. Mautere. Biochemistry, **25**, 7521 (1986); (*b*) R.R. Eady. Biofactors, **1**, 111 (1988); (*c*) G.N. George, C.L. Coyle, B.J. Hales, and S.P. Cramer. J. Am. Chem. Soc. **110**, 4057 (1988); (*d*) J.E. Morningstar and B.J. Hales. J. Am. Chem. Soc. **109**, 6854 (1987).
10. (*a*) D.C. Crans, R.A. Felty, and M.M. Miller. J. Am. Chem. Soc. **113**, 265 (1991), and refs. cited therein; (*b*) D.C. Crans, C.D. Rithner, and L.A. Theisen. J. Am. Chem. Soc. **112**, 2901 (1990), and refs. cited therein.
11. L. Scoles, K. Babu, and S. Gambarotta. J. Am. Chem. Soc. In press.
12. (*a*) J.H. Song, P. Berno, and S. Gambarotta. J. Am. Chem. Soc. **116**, 6927 (1994); (*b*) P. Berno, S. Hao, R. Minhas, and S. Gambarotta. J. Am. Chem. Soc. **116**, 7417 (1994).
13. J. Jubb, S. Hao, and S. Gambarotta. Inorg. Chem **34**, 3563 (1995).
14. L.E. Manzer. Inorg. Synth. **21**, 138 (1982).
15. M.B. Mabbs and D. Machin. Magnetism and transition metal complexes. Chapman and Hall, London. 1973.
16. G. Foese, C.J. Gorter, and L.J. Smits. Constantes Selectionnées Diamagnetisme, Paramagnetisme, Relaxation Paramagnetique. Masson, Paris. 1957.
17. D.T. Cromer and J.T. Waber. International tables for X-ray crystallography. The Kynoch Press, Birmingham, England. 1974.
18. L. Scoles, R. Minhas, R. Duchateau, J. Jubb, and S. Gambarotta. Organometallics, **13**, 4978 (1994)
19. T.J. Marks and J.R. Kolb. Chem. Rev. **77**, 263 (1977).
20. (*a*) R.L. Bansemer, J.C. Huffman, and K.G. Caulton. J. Am. Chem. Soc. **105**, 6163 (1983); (*b*) J.A. Jensen and G.S. Girolami. J. Am. Chem. Soc. **110**, 4450 (1988).

Observation of buttressing effect and hindered rotation about C(sp^2)—C(sp^2) single bond in styrenes coordinated to a ruthenium cation, Cp(diphosphine)Ru$^+$

Kenzo Ohkita, Hideo Asano, Hideo Kurosawa, Toshikazu Hirao, Yohko Miyaji, and Isao Ikeda

Abstract: Complexes of (η^5-cyclopentadienyl)(bis(di-*p*-tolylphosphino)ethane)ruthenium(II) cation with some styrenes containing *meta* or *para* substituents were prepared and their NMR spectra examined in detail. Variable-temperature NMR studies on the unsubstituted and *para*-substituted styrene analogues demonstrated occurrence of a restricted rotation about the C(sp^2)—C(sp^2) single bond of the styrenes where one of the *ortho* hydrogens of the styrene phenyl group receives a very large diamagnetic shielding effect by one of the phosphine tolyl groups. Similar studies on the *meta*-substituted styrene complexes showed existence of two unequally populated conformational isomers arising from the similar restricted rotation where the *meta* substituent in the dominant isomer was placed further away from the C=C group. The origin of such conformational isomerism was deduced to be the buttressing effect of the *meta* substituent transmitted via the *ortho*-hydrogen atom.

Key words: buttressing effect, hindered rotation, Ru–styrene complex.

Résumé : On a préparé un certain nombre de complexes du cation (η^5-cyclopentadiényl)(bis(di-*p*-tolylphosphino)éthane)-ruthénium(II) avec quelques styrènes contenant des substituants en *méta* et en *para* et on a examiné leurs spectres RMN en détail. Les études de RMN à température variable des analogues *para*-substitués et non substitués ont démontré, dans les cas où les hydrogènes en *ortho* du groupe phényle du styrène subissent un important blindage diamagnétique de la part de l'un des groupes tolyles de la phosphine, il existe une rotation restreinte autour de la liaison C(sp^2)—C(sp^2) des styrènes. Des études semblables avec les complexes de styrènes substitués en *méta* mettent en évidence l'existence de deux isomères conformationnels dont les populations sont semblables; cette situation découle de l'existence d'une rotation restreinte qui, dans l'isomère dominant, éloigne le substituant *méta* du groupe C=C. On a déduit que l'origine de cette isomérie conformationnelle est liée à l'effet de compression du substituant en *méta* qui est transmis par le biais de l'atome d'hydrogène en *ortho*.

Mots clés : effet de compression, rotation empêchée, complexe Ru–styrène.

[Traduit par la rédaction]

Introduction

Complexation of organic molecules to a metal center often brings about a unique opportunity to study new conformational and stereodynamic aspects of these molecules (1). Detailed examinations of solution dynamics of such metal complexes by means of NMR spectroscopy are of particular relevance to development of stereoselective, metal-mediated organic transformations (2*a*–*d*) and dynamic supramolecular devices (2*e*). We describe here a clear observation of hindered rotation about the C(sp^2)—C(sp^2) single bond of unsubstituted as well as substituted styrenes that was made possible by their complexation to a (η^5-cyclopentadienyl)(bis(di-*p*-tolylphosphino)ethane)ruthenium(II) cation. The hindered rotation about a C(sp^2)—C(sp^2) single bond has been a subject of some variable-temperature NMR studies on metal-free organic compounds (3), but its extension to metal-coordinated analogues is still limited.

Received January 17, 1996.

This paper is dedicated to Professor Howard C. Clark in recognition of his contributions to Canadian chemistry.

K. Ohkita, H. Asano, H. Kurosawa,[1] T. Hirao, Y. Miyaji, and I. Ikeda.[1] Department of Applied Chemistry, Faculty of Engineering, Osaka University, Suita, Osaka 565, Japan.

[1] Authors to whom correspondence may be addressed. Telephone: 06-879-7392. Fax: 06-879-7394.

Results and discussion

We previously reported (4) generation and stability estimation of a series of substituted styrene complexes [Ru(η^5-C_5H_5)(dtpe)(CH_2=CHC_6H_4Y)]BF_4 (dtpe = bis(di-*p*-tolylphosphino)ethane). In the present work we have examined variable-temperature ^{1}H NMR aspects of complexes **1**–**5**. The bis(di-*p*-tolylphosphino)ethane ligand was employed for the sake of ^{1}H NMR simplicity. Thus, the ^{1}H NMR resonances at room temperature of the unsubstituted and substituted styrene analogues can readily be interpreted as those having four nonequivalent phosphine-tolyl groups as well as four nonequivalent CH_2CH_2 protons arising from the chiral nature of the molecule; for typical room temperature spectra of **1**, **2**, and **3**, see

Scheme 1.

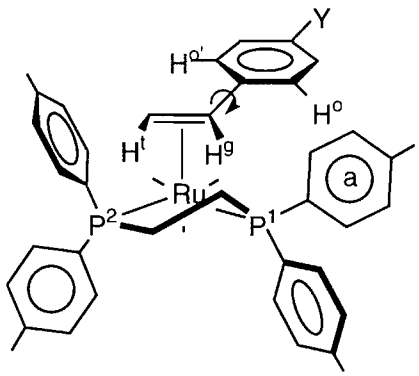

Figs. 1, 2*a*, and 3*a*; detailed assignments are described in the experimental section.

A particularly interesting feature in these spectra at room temperature is that the *ortho*-hydrogen resonance of the styrene ligand occurred at considerably higher field (e.g., δ 6.37 and 6.33 for **1** and **2**, respectively; marked H° in Figs. 1 and 2*a*) than those of the free styrene (upfield shift, Δδ = ca. 1 ppm). The large upfield shift suggests proximity of the *ortho*-hydrogen(s) to some face(s) of the phosphine-tolyl ring. This was confirmed by an analysis of variable-temperature ^{1}H NMR spectra described later. The solid state structure of **4** shown in Fig. 4, albeit with large *R* values (R = 0.102, R_w = 0.143) due to disorders about the BF_4 group, also indicates proximity of one *ortho*-hydrogen atom of the styrene to one phosphine-tolyl. The distance from the *ortho* hydrogen of the *m*-C_6H_4Cl group to the nearest tolyl ring is roughly estimated to be 2.6 Å. Next we show that the coordination geometry of the styrene in Fig. 4 is most likely maintained in **1**–**5** also *in solution*.

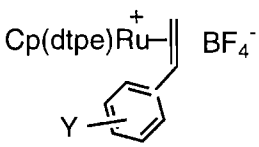

1 Y= H; **2** Y= *p*-OMe;
3 Y= *m*-F; **4** Y= *m*-Cl; **5** Y= *m*-Br
(dtpe= bis(di-*p*-tolylphosphino)ethane)

The first step of the structural determination in solution is unambiguous assignment of the *ortho*-hydrogen resonances of the phosphine-tolyls (δ 6.51, 7.22, 7.46, 7.72) made by a 2D ^{31}P–^{1}H COSY spectrum of **1** (Fig. 1), where it is only these resonances among the aromatic proton signals that show appreciable spin–spin couplings with ^{31}P nuclei. Figure 1 shows that the P^1 nucleus (δ −68.9) correlates with the *ortho* hydrogens at δ 7.22 and 7.46 and the P^2 nucleus (δ −62.6) with those at δ 6.51 and 7.72. Moreover, the ^{31}P–^{1}H COSY spectrum indicates that the vinyl hydrogen H^g (Scheme 1; the Cp ring omitted) at δ 3.45 shows spin–spin coupling with the P^1 nucleus, whereas the vinyl hydrogen H^t at δ 1.54 does so with the other phosphorus nucleus P^2, suggesting spatial proximity between H^g and P^1, and H^t and P^2.

Next we carried out NOE experiments. Thus, selective irradiation of the peak at δ 7.46 due to the *ortho* hydrogens of one particular phosphine-tolyl group (a in Scheme 1) led to 1% increase of the *ortho*-hydrogen peak (δ 6.37) of styrene. The *ortho*-hydrogen resonance of this particular tolyl group (a) also had an NOE correlation (1%) with the resonance due to H^g. We thus presume that the C=C bond is oriented nearly parallel to the P–P vector also in solution, in accordance with the orientation of the C=C bond in analogous series of complexes (5).

All the ^{1}H NMR spectra showed remarkable temperature dependency. Typical variable-temperature spectra of the methoxy analog **2** are shown in Fig. 2. With decrease of the temperature, both the *ortho* (δ 6.33 at 25°C) and the *meta* (δ 6.62 at 25°C; marked H^m) hydrogen resonances of *p*-methoxystyrene became broader with some chemical shift change. Most significantly, the *ortho*-hydrogen resonance disappeared at ca. −45°C (with a 400 MHz instrument) and remained unobservable down to ca. −70°C below which it reappeared as two broad signals with equal intensity (1H each) at quite distant chemical shifts from one another (δ 5.1 and 6.8; Fig. 2*d*, marked H^o and $H^{o'}$). These became two doublets at δ 5.06 and 6.86 at −95°C (Fig. 2*e*). Similarly, the *meta*-hydrogen resonance split into two doublets, albeit with smaller separation (δ 6.32 and 6.67; marked H^m and $H^{m'}$), at −95°C. This smaller separation is in agreement with the coalescence of these *meta*-hydrogen resonances at lower temperature (−66°C) than that of the *ortho*-hydrogen resonances.

These observations can be best attributed to a restricted rotation about the C(sp^2)—C(sp^2) single bond of the styrene ligand (Scheme 1, Y = OMe) at the lower temperature.[2] As shown in Fig. 2, other proton resonances of **2** such as those of the vinylic and the tolyl ring protons also changed their chemical shifts to a smaller extent with decrease of the temperature. A few phosphine-tolyl proton resonances also began to broaden or disappear from ca. −80°C. The observation of small temperature dependency of the chemical shifts of most of the resonances may be attributed to a change of the degree of ion pair contacts and (or) a small change of internal ligand geometries (e.g., twisting about the P—C(tolyl) bond). Disappearance of the phosphine-tolyl proton resonances suggests commencement of a restricted rotation about the P—C bond at the very low temperature. At any rate, the appearance of one *ortho*-hydrogen resonance of the styrene at an extraordinarily high field (δ 5.06) clearly indicates fixation of the *ortho* hydrogen (H^o) in front of the phosphine-tolyl ring a (Scheme 1). Further NOE experiments to confirm this assumption at the low temperatures gave no satisfactory results. Assuming the

[2] One reviewer raised the possibility that the temperature-dependent ^{1}H NMR aspects are attributed to rotation of the olefin molecule about the Ru–Cc axis (Cc is center of C=C bond). This is assumed to be an unlikely path since molecular models suggest extremely severe steric strains during this rotation. Moreover, it is only the styrene *ortho* and *meta* proton resonances that had split into two resonances upon lowering of the temperature. The chemical shifts of the other protons should also have been affected by this rotation and therefore would have undergone splitting. Unfortunately, experiments to confirm spin–spin coupling connectivity between H^o and $H^{o'}$ or H^m and $H^{m'}$ at the low temperature, which is consistent with the path shown in Scheme 1, were unsuccessful owing to extreme broadness of these proton resonances ($^4J_{HH}$ is usually less than 3 Hz).

Fig. 1. $^{31}P-^{1}H$ COSY spectrum of **1** at 25°C in CD_2Cl_2. X denotes solvent signal, and Y H_2O signal. Note that the magnetic field becomes higher to the left of the ^{1}H chemical shift axis.

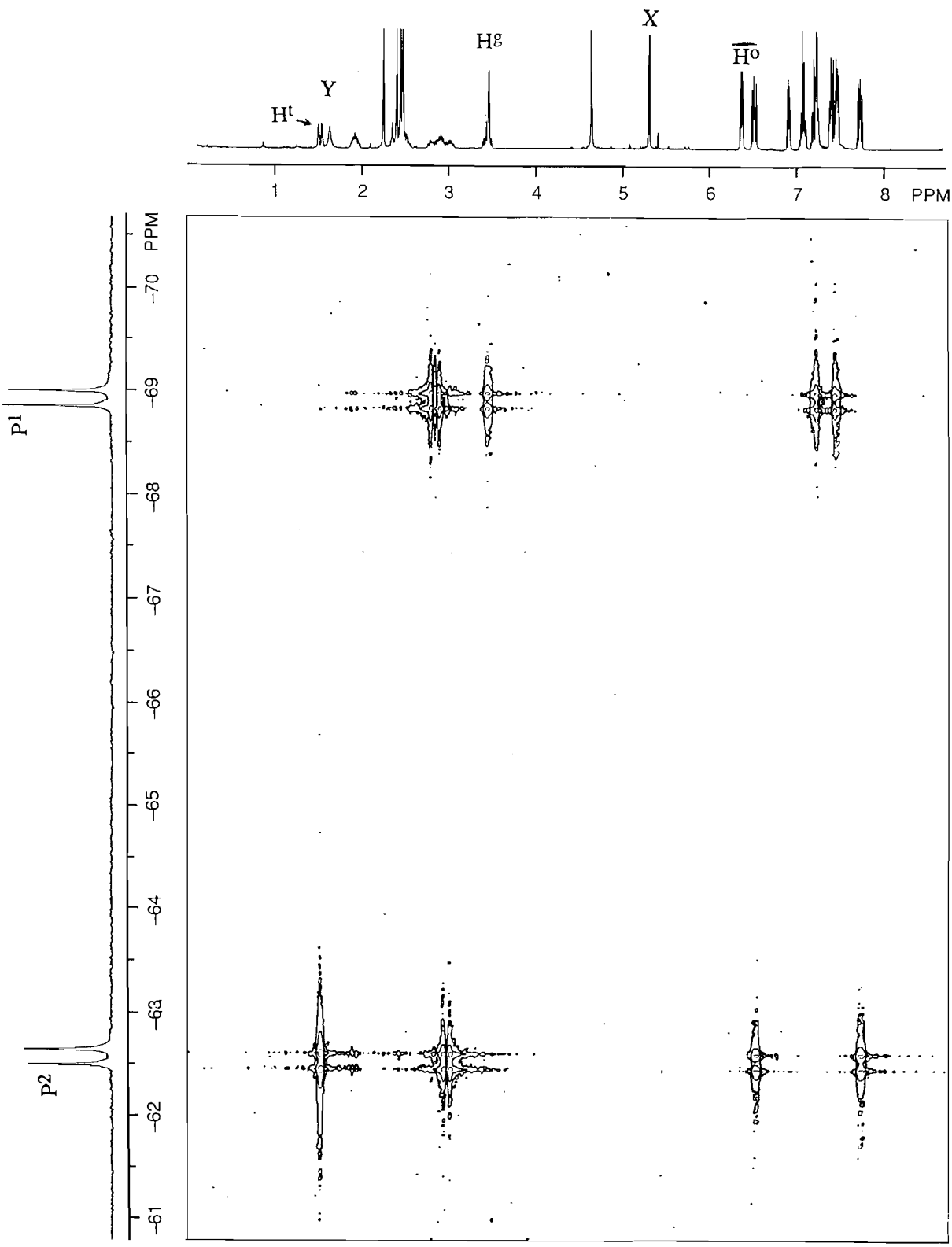

chemical shift difference of the *ortho* and *meta* hydrogens of **2** observed at −95°C to be those corresponding to the frozen state and ignoring chemical shift change with temperature, approximate $\Delta G^{\ddagger}$ values for the rotation at the coalescence temperature (−50°C and −66°C) were calculated (6) as 40.4 and 40.2 kJ/mol, respectively.

Fig. 2. ^{1}H NMR spectra (400 MHz) of **2** in CD_2Cl_2 at 25°C (*a*), −40°C (*b*), −66°C (*c*), −80°C (*d*), and −95°C (*e*). X denotes solvent signal, and Y H_2O signal.

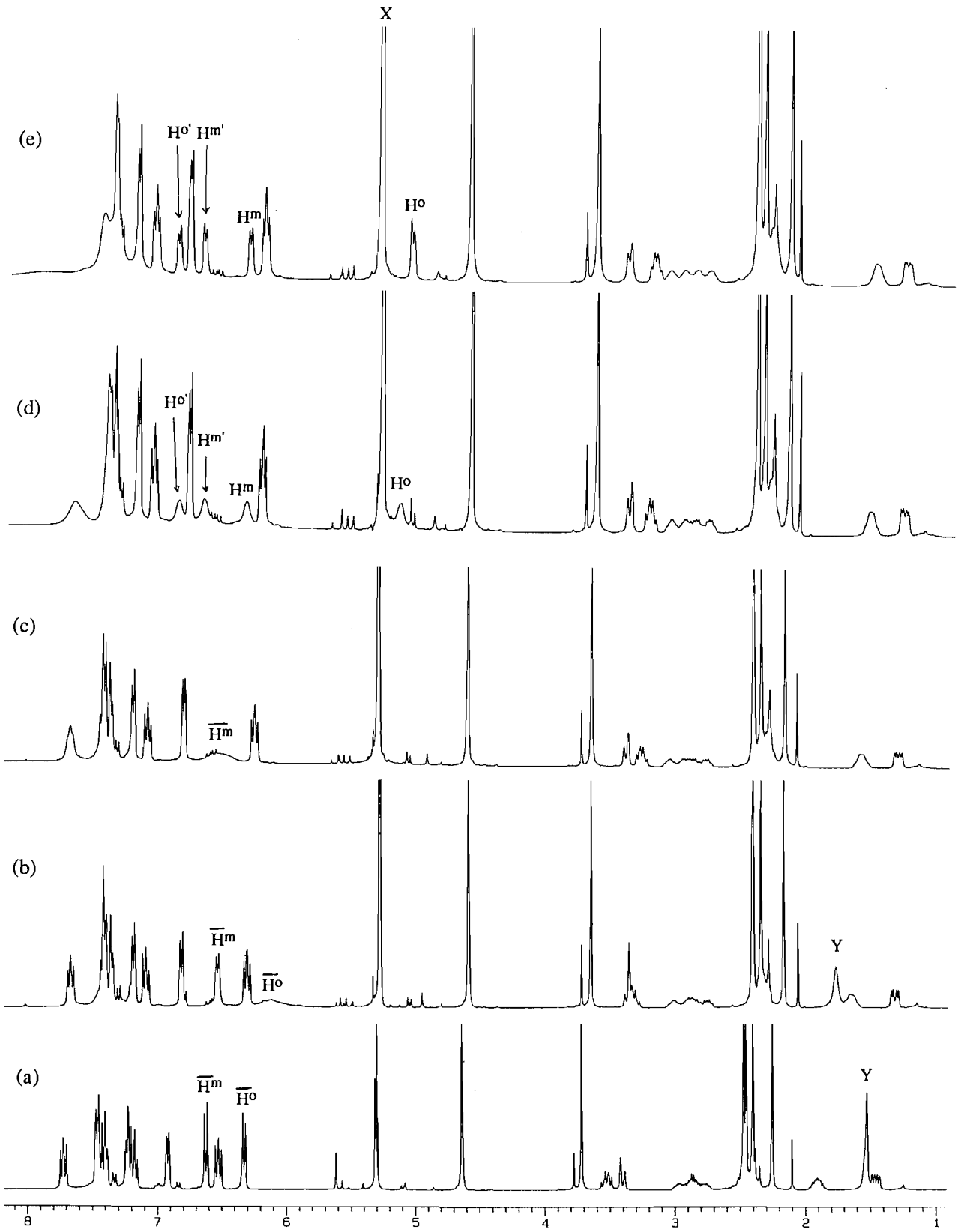

Scheme 2.

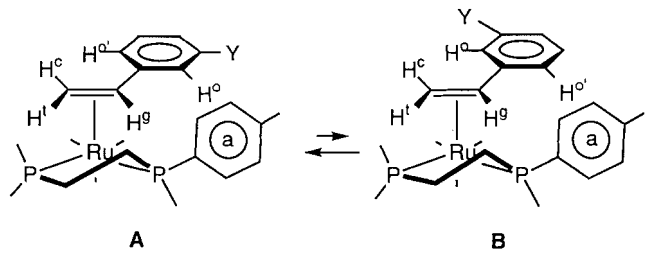

The low-temperature NMR spectra of the unsubstituted styrene analog **1** likewise showed separate resonances at δ 5.09 and 6.92 for the *ortho* hydrogens of styrene, although observation of a consistent variable-temperature behavior of the *meta*-hydrogen resonances was hampered by their overlapping with other aromatic proton resonances. Thus, the hindered rotation about the C—C single bond is also apparent in the unsubstituted styrene.

The *meta*-fluoro- and *meta*-bromostyrene complexes also showed temperature-dependent NMR spectra (see Fig. 3), which are similar to those of the unsubstituted and *para*-substituted styrene complexes in one sense, but different from the latter in the other. The difference arises from occurrence of two rotational isomers with unequal population (Scheme 2).

In the ^{19}F NMR spectra of **3**, a single signal for *meta*-fluorine atom observed at room temperature at δ −50.2 (relative to $PhCF_3$, ddd, J_H = 6.2, 8.3, 10.5 Hz) split into two broad signals at δ −50.6 and −49.5 in a 64:36 ratio at −95°C. In the ^1H NMR spectra, with decrease of the temperature, a doublet for the *ortho* hydrogen vicinal to F (δ 5.74, J_F = 10.5 Hz, Δδ = 1.38, at room temperature; marked $\overline{H^o}$ in Fig. 3*a*) became broader, disappeared (Fig. 3*c*), and then reappeared at δ 4.5 at ca. −70°C (600 MHz instrument; Fig. 3*d*). Significantly, the intensity of the doublet (J = 10 Hz) at δ 4.44 at −95°C (Fig. 3*e*) corresponded to only ca. 0.6 atom H. In addition, a doublet for the other *ortho* hydrogen at δ 6.27 (J_H = 7 Hz; Δδ = 0.91) at room temperature (marked $\overline{H^{o'}}$) reappeared at −95°C as a broad doublet at δ 4.96 (Fig. 3*e*; marked $H^{o'}$) having an integration corresponding to ca. 0.4 atom H. Thus, these results suggest the isomer ratio **A**/**B** = 64/36 where the doublet at δ 4.44 in Figure 3*e* corresponds to H^o in **A** and the doublet at δ 4.96 to $H^{o'}$ in **B**. Unfortunately, it was unable to detect a lower field component of each *ortho*-hydrogen resonance pair, namely H^o in **B** and $H^{o'}$ in **A**, which should possess an integration value of 0.36 H and 0.64 H, respectively, possibly because of overlapping with aromatic signals at normal chemical shifts.

The ^1H NMR spectral aspect of *meta*-bromostyrene complex **5** at −95°C (Fig. 3*f*) was different from that of the *meta*-fluoro analog in that the resonances due to almost only one isomer were discernible. Thus, a singlet at δ 5.88 (Δδ = 1.68) at room temperature due to the *ortho* hydrogen vicinal to Br disappeared on lowering the temperature (from ca. −40°C), and reappeared at ca. −65°C as a very broad signal at ca. δ 4.7. Finally at −95°C this became a singlet at δ 4.48 (H^o in Fig. 3*f*) possessing an integration value corresponding to more than 0.9 atom H. In Fig. 3*f* we were unable to unambiguously define any doublet signal, in the range δ 4.0–6.5, assignable to the other *ortho* hydrogen ($H^{o'}$) that would have received a higher field shift by the phosphine-tolyl ring a relative to the δ 6.59 resonance (25°C). It might have been hidden in other stronger resonances. The ^1H NMR spectrum at −95°C of the *meta*-chlorostyrene analog **4** also showed the existence of almost only one isomer (δ 4.30 for the *ortho*-hydrogen vicinal to Cl; at room temperature, δ 5.73, Δδ = 1.67). Thus, the almost exclusive isomer in **4** and **5** at −95°C is the rotamer **A** in which the halogen atom is placed further away from the C=C bond.[3] This also corresponds to the solid state structure of **4** (Fig. 4). The degree of predominance of this isomer might have been enhanced particularly at the lower temperature judging from the considerable upfield shift of the *ortho*-hydrogen singlet for H^o on lowering the temperature. The cause of the observed isomer distribution in the *meta*-halogen-substituted styrene complexes may be steric in origin. Molecular models based on the structure of **4** suggested that the steric hindrance to the substituent Y by Cp in **B** is less significant than that by the phosphine-tolyl group in **A**. Thus, inter-ligand repulsions would play little significant role, if any, in determining the conformational preference. We explain the trend in the rotamer preference of the complexes in terms of internal steric strain in the styrenes, as follows.

Of two vinylic hydrogens (H^c, H^g) of styrene, H^c is closer to the *ortho* position than is H^g. Therefore, in both **A** and **B** one *ortho* hydrogen close to H^c is thought to receive greater steric constraints than the other *ortho* hydrogen close to H^g. Since in the *meta*-substituted styrenes the *ortho* hydrogen next to the substituent Y (H^o) is expected to be pushed away from Y, this particular *ortho* hydrogen would exert a larger steric hindrance to the vinylic hydrogens than does the other one ($H^{o'}$), resulting in the conformer involved in **A** being more stable than that in **B**. It is then understandable that the complex having the larger substituent (Y = Cl, Br) showed a larger **A**:**B** ratio than that having the smaller substituent (Y = F).

Concluding remarks

The present observation of the hindered rotation about the C—C single bond in styrenes was made possible by the large chemical shift difference of the *ortho*-hydrogen resonances undergoing coalescence, which in turn was brought about by the complexation of styrenes to the arylphosphine-ruthenium center. The close disposition of the styrene-aryl group to the phosphine-tolyl group proposed here may also have its origin, to some extent, in an aromatic edge–face interaction (8).

We also found that the distribution of the two rotamers arising from the *meta*-substituted styrenes depends on the steric bulk of the *meta* substituent. An indirect steric effect of a substituent group on a remote position transmitted over sp^2-carbon frameworks has attracted attention as a buttressing effect, particularly in studies of barriers to racemization of axially dissymmetric aromatic molecules (9). However, transmission of this effect via an intermediary hydrogen atom, which has clearly been confirmed in the present study, has rarely been detected (9*b*), particularly in a ground state event (10).

[3] An X-ray structure determination of a styrene derivative containing two alkoxy substituents at the *meta* and *para* positions (7) revealed the existence of a conformer analogous to **A**.

Fig. 3. ^{1}H NMR spectra in CD_2Cl_2 of **3** at 25°C (*a*), −15°C (*b*), −40°C (*c*), −70°C (*d*), and −95°C (*e*) and of **5** at −95°C (*f*). The spectra (*a*)–(*d*) were taken with a 600 MHz instrument, and (*e*) and (*f*) with a 400 MHz one. X denotes solvent signal, and Y H_2O signal.

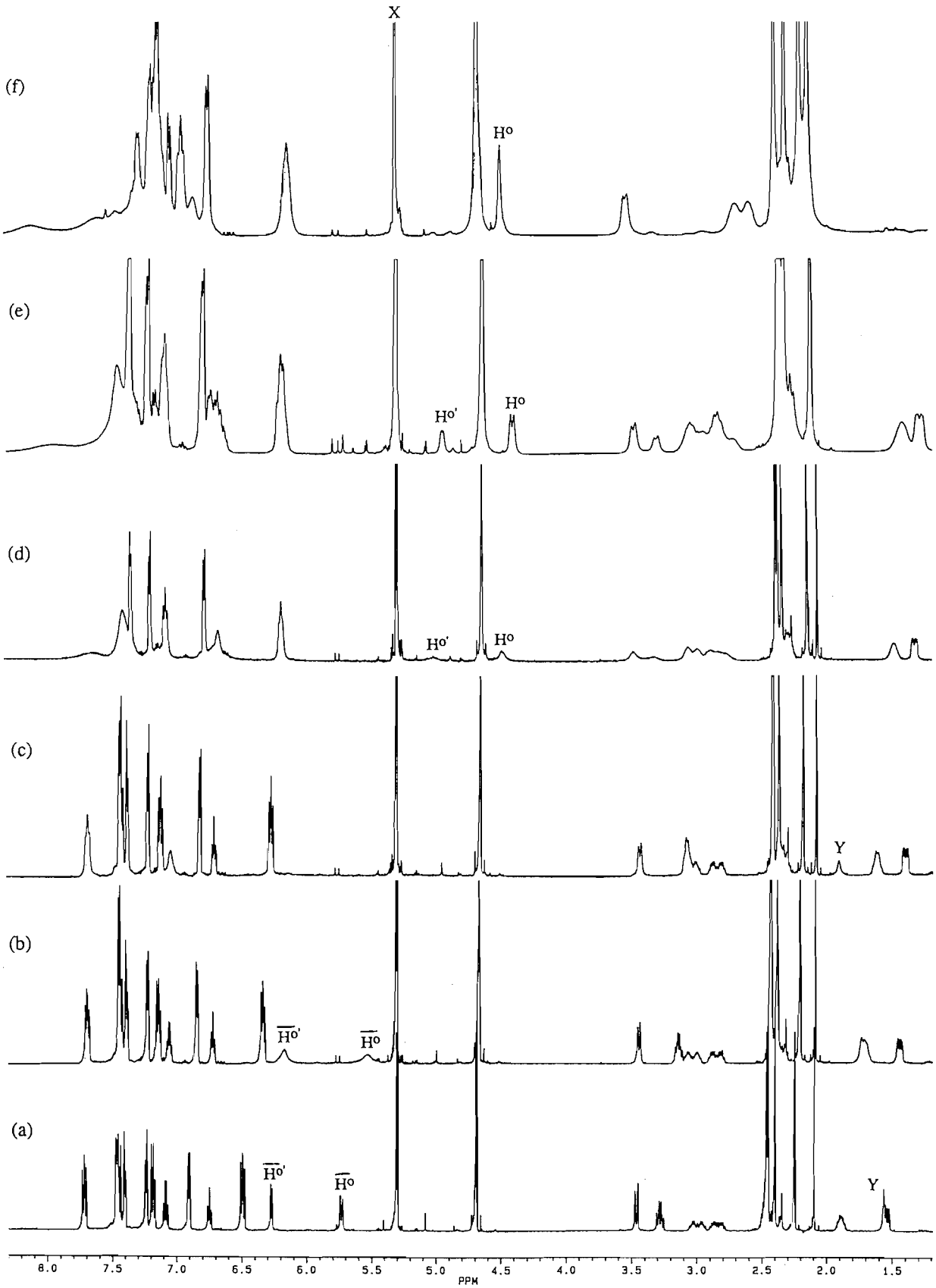

Fig. 4. Molecular structure of [Ru(η^5-C_5H_5)(dtpe)(CH_2=CHC_6H_4Cl-*m*)] BF_4 with thermal ellipsoids at 50% probability levels for non-hydrogen atoms. Relevant hydrogens are shown only for convenience at the idealized positions. The anion and CH_2Cl_2 of crystallization are omitted.

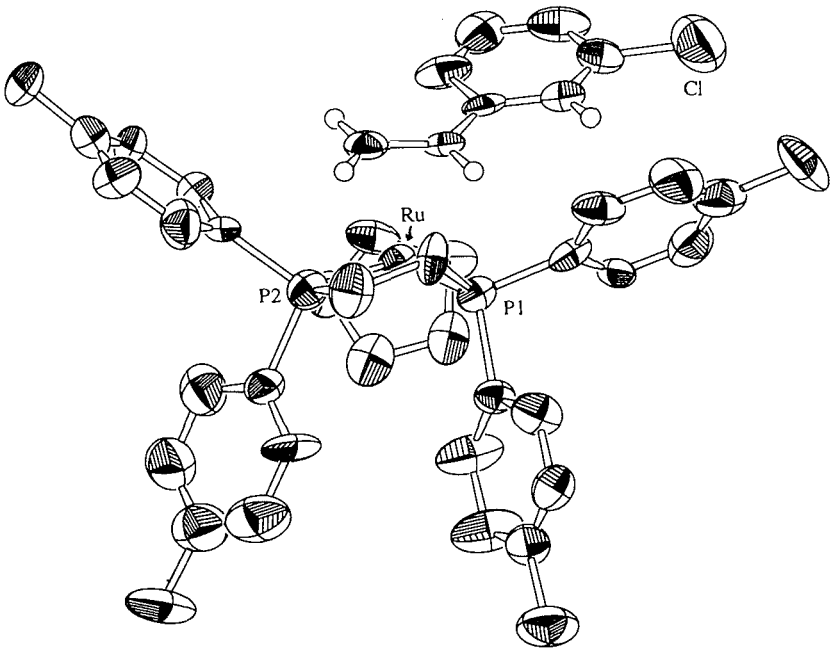

Experimental

Most of commercially available reagents were used without further purification. Silver tetrafluoroborate (purity 90%) was used after drying under vacuum. 1,2-Bis(di-*p*-tolylphosphino)ethane (dtpe) was prepared from tri-*p*-tolylphosphine and sodium metal in liquid ammonia followed by treatment with 1,2-dichloroethane (11). Preparation of Ru(η^5-C_5H_5)(dtpe)Cl was carried out according to the literature (12). ^{1}H NMR spectra were obtained on JEOL GSX-400 and Bruker AM600 spectrometers. Chemical shifts were referenced to $CHCl_3$ (δ 7.27) in $CDCl_3$ and $CHDCl_2$ (δ 5.30) in CD_2Cl_2. ^{31}P NMR spectra were obtained on a GSX-400 spectrometer operating at 162 MHz and chemical shifts were referenced to external $P(OMe)_3$ (δ 0.00). ^{19}F NMR spectra were obtained on a GSX-400 spectrometer operating at 376 MHz and chemical shifts were referenced to $PhCF_3$ (δ 0.00).

Preparation of [(η^5-C_5H_5)Ru(dtpe)(CH_2=CHC_6H_5)]BF_4 (1)

To a solution of 150 mg (0.229 mmol) of Ru(η^5-C_5H_5)(dtpe)Cl and 80 mg (0.77 mmol) of styrene in 5 mL of acetone, 70 mg (0.32 mmol) of silver tetrafluoroborate in 5 mL of acetone was added under inert atmosphere. The resulting dark red solution was stirred until the color turned yellow (ca. 1 h) and filtered. The filtrate was evaporated under reduced pressure. The residue was extracted with 3 mL of CH_2Cl_2 and purified through a short Florisil column. To the eluent was added *n*-hexane to give 160 mg (86%) of pale yellow fine needles. These were washed with ether and *n*-hexane; mp 145°C (dec.). ^{1}H NMR (CD_2Cl_2, 25°C) δ: 1.54 (dd, J_H = 5 Hz, J_P = 16 Hz, 1H, =CH*H* *trans* to Ph), 1.92 (m, 1H, PCH*H*-), 2.25 (s, 3H), 2.41 (s, 3H), 2.55 (s, 3H) and 2.57 (s, 3H) (each CH_3), 2.48 (m, 1H), 2.86 (dm, J_P = 39 Hz, 1H) and 2.95 (dm, J_P = 42 Hz, 1H) (each PCH*HC*H_2P), 3.45 (m, 2H, PhC*H*= and =CH*H* *cis* to Ph), 4.63 (s, 5H, C_p), 6.37 (d, J_H = 7 Hz, 2H, *ortho-H* of Ph), 6.51 (dd, J_H = 7 Hz, J_P = 11 Hz, 2H, *ortho-H* of tolyl), 6.91 (d, J_H = 7 Hz, 2H, *meta-H* of tolyl), 7.1–7.5 (m, 13H), 7.72 (dd, J_H = 7 Hz, J_P = 11 Hz, 2H, *ortho-H* of tolyl). The following *ortho-H* resonances of the other tolyl groups were defined by the ^{31}P–^{1}H COSY spectrum δ: 7.22 and 7.46. ^{31}P NMR (CD_2Cl_2, 25°C) δ: −62.6 (d, J_{PP} = 25 Hz), −68.9 (d). Anal. calcd. for $C_{43}H_{45}P_2BF_4Ru$: C 63.63, H 5.59; found: C 63.11; H 6.00.

[(η^5-C_5H_5)Ru(dtpe)(CH_2=CHC_6H_4OMe-*p*)]BF_4 (2)

This compound was prepared similarly as pale yellow fine needles of **2**·CH_2Cl_2 (59%); mp 150–155°C (dec.). ^{1}H NMR (CD_2Cl_2, 25°C) δ: 1.45 (ddd, J_H = 2.5, 8.0 Hz, J_P = 15 Hz, 1H, =CH*H* *trans* to Ar (Ar = C_6H_4OMe)), 1.91 (m, 1H, PCH*H*-), 2.25 (s, 3H), 2.40 (s, 3H), 2.47 (s, 3H) and 2.49 (s, 3H) (each CH_3), 2.45 (m, 1H), 2.81 (dm, J_P = 37 Hz, 1H) and 2.93 (dm, J_P = 40 Hz, 1H) (each PCH*HC*H_2P), 3.40 (dd, J_H = 2.5, 13 Hz, 1H, =CH*H* *cis* to Ar), 3.53 (ddd, J_H = 8.0, 13 Hz, J_P = 11 Hz, 1H, ArC*H*=), 3.73 (s, 3H, OCH_3), 4.63 (s, 5H, C_p), 6.33 (d, J_H = 8 Hz, 2H, *ortho-H* of Ar), 6.52 (dd, J_H = 7 Hz, J_P = 11 Hz, 2H, *ortho-H* of tolyl), 6.62 (d, J_H = 8 Hz, 2H, *meta-H* of Ar), 6.93 (d, J_H = 7 Hz, 2H, *meta-H* of tolyl), 7.1–7.5 (m, 10H), 7.72 (dd, J_H = 7 Hz, J_P = 11 Hz, 2H, *ortho-H* of tolyl). ^{31}P NMR (CD_2Cl_2, 25°C) δ: −62.5 (d, J_{PP} = 23 Hz), −68.6 (d). Anal. calcd. for $C_{45}H_{49}OP_2BF_4Cl_2Ru$: C 58.33, H, 5.33; found: C, 58.61, H 5.53. The presence of CH_2Cl_2 of crystallization was confirmed by the ^{1}H NMR spectrum in $CDCl_3$.

[(η^5-C_5H_5)Ru(dtpe)(CH_2=CHC_6H_4F-*m*)]BF_4 (3)

3 was prepared similarly as pale yellow fine needles of **3**·1/2

CH_2Cl_2 (78%); mp 133°C (dec.). ^{1}H NMR (CD_2Cl_2, 25°C) δ: 1.54 (ddd, J_H = 3.0, 8.1 Hz, J_P = 17 Hz, 1H, =CH*H trans* to Ar (Ar = C_6H_4F)), 1.89 (m, 1H, PCH*H*-), 2.26 (s, 3H), 2.41(s, 3H), 2.46 (s, 3H) and 2.48 (s, 3H) (each CH_3), 2.48 (m, 1H), 2.85 (dm, J_P = 34 Hz, 1H) and 2.97 (dm, J_P = 38 Hz, 1H) (each PCH*HCH*$_2$P), 3.29 (dt, J_H = 8, 12 Hz, J_P = 12 Hz, 1H, ArC*H*=), 3.46 (dd, J_H = 3, 12 Hz, 1H, =CH*H cis* to Ar), 4.70 (s, 5H, C_p), 5.74 (d, J_F = 10.5 Hz, 1H, *ortho-H* of Ar), 6.26 (d, J_H = 7 Hz, 1H, *ortho-H′* of Ar), 6.50 (dd, J_H = 7 Hz, J_P = 11 Hz, 2H, *ortho-H* of tolyl), 6.76 (dd, J_H = 7 Hz, J_F = 8 Hz, 1H, *para-H* of Ar), 6.91 (d, J_H = 7 Hz, 2H, *meta-H* of tolyl), 7.09 (dt, J_H = 7 Hz, J_F = 6 Hz, 1H, *meta-H* of Ar), 7.18 (dd, J_H = 7 Hz, J_P = 10 Hz, 2H, *ortho-H* of tolyl), 7.4–7.5 (m, 8H), 7.71 (dd, J_H = 7 Hz, J_P = 11 Hz, 2H, *ortho-H* of tolyl). ^{31}P NMR (CD_2Cl_2, 25°C) δ: −62.7 (d, J_{PP} = 23 Hz), −68.9 (d). ^{19}F NMR (CD_2Cl_2, 25°C) δ: −50.22 (ddd, J_H = 6, 8, 11 Hz, 1F, C*F*), −89.78 (q, J_{BF} = 9.5 Hz, 4F, BF_4). Anal. calcd. for $C_{43.5}H_{45}P_2BF_5ClRu$: C 59.91, H 5.20; found: C 60.09, H 5.21. The presence of 1/2 mol of CH_2Cl_2 of crystallization was confirmed by the ^{1}H NMR spectrum in $CDCl_3$.

[(η^5-C_5H_5)Ru(dtpe)(CH_2=CHC_6H_4Cl-*m*)]BF_4 (4)

Compound **4** was prepared similarly as pale yellow fine needles (75%); mp 137–139°C (dec.). ^{1}H NMR (CD_2Cl_2, 25°C) δ: 1.52 (ddd, J_H = 3, 8.1 Hz, J_P = 16 Hz, 1H, =CH*H trans* to Ar (Ar = C_6H_4Cl)), 1.82 (m, 1H, PCH*H*-), 2.25 (s, 3H), 2.40 (s, 3H), 2.46 (s, 3H) and 2.47 (s, 3H) (each CH_3), 2.45 (m, 1H), 2.83 (dm, J_P = 35 Hz, 1H) and 3.01 (dm, J_P = 39 Hz, 1H) (each PCH*HCH*$_2$P), 3.18 (ddd, J_H = 8.3, 13 Hz, J_P = 12 Hz, 1H, ArC*H*=), 3.52 (dd, J_H = 3, 13 Hz, 1H, =CH*H cis* to Ar), 4.71 (s, 5H, C_p), 5.73 (s, 1H, *ortho-H* of Ar), 6.48 (dd, J_H = 7 Hz, J_P = 11 Hz, 2H, *ortho-H* of tolyl), 6.52 (d, J_H = 7 Hz, 1H, *ortho-H′* of Ar), 6.92 (d, J_H = 7 Hz, 2H, *meta-H* of tolyl), 7.0-7.5 (m, 12H), 7.72 (dd, J_H = 7 Hz, J_P = 11 Hz, 2H, *ortho-H* of tolyl). ^{31}P NMR (CD_2Cl_2, 25°C) δ: −62.7 (d, J_{PP} = 23 Hz), −68.6 (d). Anal. calcd. for $C_{43}H_{44}P_2BF_4ClRu$: C 61.04, H 5.24; Found: C 60.57, H 5.31.

[(η^5-C_5H_5)Ru(dtpe)(CH_2=CHC_6H_4Br-*m*)]BF_4 (5)

This compound was prepared similarly as pale yellow fine needles (85%); mp 137°C (dec.). ^{1}H NMR (CD_2Cl_2, 25°C) δ: 1.50 (ddd, J_H = 3, 8.3 Hz, J_P = 17 Hz, 1H, =CH*H trans* to Ar (Ar = C_6H_4Br)), 1.79 (m, 1H, PCH*H*-), 2.25 (s, 3H), 2.40 (s, 3H), 2.48 (s, 3H) and 2.49 (s, 3H) (each CH_3), 2.48 (m, 1H), 2.85 (dm, J_P = 36 Hz, 1H) and 3.01 (dm, J_P = 38 Hz, 1H) (each PCH*HCH*$_2$P), 3.18 (ddd, J_H = 8.3, 13 Hz, J_P = 12 Hz, 1H, ArC*H*=), 3.52 (dd, J_H = 3, 13 Hz, 1H, =CH*H cis* to Ar), 4.72 (s, 5H, C_p), 5.88 (s, 1H, *ortho-H* of Ar), 6.48 (dd, J_H = 7 Hz, J_P = 11 Hz, 2H, *ortho-H* of tolyl), 6.59 (d, J_H = 7 Hz, 1H, *ortho-H′* of Ar), 6.90 (d, J_H = 7 Hz, 2H, *meta-H* of tolyl), 7.03 (t, J_H = 7 Hz, 1H, *meta-H* of Ar), 7.16 (m, 3H), 7.23 (d, J_H = 7 Hz, 2H, *meta-H* of tolyl), 7.4–7.5 (m, 6H), 7.72 (dd, J_H = 7 Hz, J_P = 11 Hz, 2H, *ortho-H* of tolyl). ^{31}P NMR (CD_2Cl_2, 25°C) δ: −62.7 (d, J_{PP} = 24 Hz), −68.7 (d). Anal. calcd. for $C_{43}H_{44}P_2BF_4BrRu$: C 58.00, H 4.98, found: C 57.77, H 5.24.

X-ray structure determination of 4·CH_2Cl_2

A yellow prismatic crystal with approximate dimensions of 0.40 × 0.30 × 0.20 mm was mounted in a glass capillary. All measurements were made on a Rigaku AFC 5R diffractometer with graphite monochromated Mo Kα radiation and a 12 kW rotating anode generator. Cell constants and an orientation matrix for data collection were obtained from a least-squares refinement using the setting angles of 24 centered reflections. Omega (ω) scans of several intense reflections, made prior to data collection, had an average width at half-height of 0.30° with a take-off angle of 6.0°. Scans of (1.21° + 0.35 tan θ)° were made at a speed of 24.0°/min (in ω). Corrections for Lorentz and polarization effects were applied to the intensity data.

Table 1. Crystallographic data for **4** · CH_2Cl_2.

Formula	$C_{44}H_{46}P_2BF_4Cl_3Ru$
Space group	$P2_1/c$
a, Å	17.693(3)
b, Å	17.434(4)
c, Å	18.177(2)
β, deg	115.020(9)
V, Å^3	5080(1)
Z	4
d(calcd.), g cm^{-3}	1.220
F_{000}	1912
Radiation	MoKα
Temperature	Ambient
Scan type	ω–2θ
$2\theta_{max}$, deg	55.2
No. of total reflections	12489
No. of unique reflections	12109
No. of observations	3178($I > 3.0\sigma(I)$)
No. of variables	496
R	0.102
R_w	0.143

All calculations were made with the TEXSAN crystallographic software package of the Molecular Structure Corporation, Woodlands, Tex. The structure was solved by heavy-atom methods and refined by the full-matrix least-squares procedure, the function minimized being $\Sigma w(|F_o|-|F_c|)^2$. Only the non-σ-weighted least-squares procedure was performed, because σ-weighted calculations yielded larger *R* values and more distorted BF_4 geometries. These results may have arisen both from disorder about the BF_4 ion and the low quality of the crystal, as is evident in the fact that only 1/4 of the independent reflections were observed as significant. Experimental data for the X-ray diffraction analysis are shown in Table 1.[4]

Acknowledgement

Partial support of this work through Grants-in-Aid for Scientific Research, Ministry of Education, and the Asahi Glass

[4] Tables of supplementary X-ray data have been deposited. Copies of material on deposit, including tables of atomic coordinates, anisotropic displacement parameters, bond lengths and angles, may be purchased from: The Depository of Unpublished Data, Document Delivery, CISTI, National Research Council Canada, Ottawa, Canada K1A OS2. With the exception of the tables of anisotropic displacement parameters, these tables have also been deposited with the Cambridge Crystallographic Data Centre, and can be obtained on request from the Director, Cambridge Crystallographic Data Centre, University Chemical Laboratory, 12 Union Road, Cambridge, CB2 1EZ, U.K.

Foundation is gratefully acknowledged. We also thank Analytical Centre, Faculty of Engineering, Osaka University, for the use of NMR facilities.

References

1. (*a*) L. Li, A. Decken, B.G. Sayer, M.J. McGlinchey, P. Bregaint, J.Y. Thepot, J.R. Hamon, and C. Lapinte. Organometallics, **13**, 682 (1994); (*b*) A. Restelli and J.S. Siegel. J. Am. Chem. Soc. **114**, 1091 (1992); (*c*) K.V. Kilway and J.S. Siegel. J. Am. Chem. Soc. **114**, 255 (1992); (*d*) M.J. McGlinchey. Adv. Organomet. Chem. **34**, 285 (1992).
2. (*a*) S.E. Garner and A.G. Orpen. J. Chem. Soc. Dalton Trans. 533 (1993); (*b*) S.G. Davies, A.E. Derome, and J.P. McNally. J. Am. Chem. Soc. **113**, 2854 (1991); (*c*) S. Shambayati, W.E. Crowe, and S.L. Schreiber. Angew. Chem. Int. Ed. Engl. **29**, 256 (1990); (*d*) J.M. Brown and P.L. Evans. Tetrahedron, **44**, 1988 (1988); (*e*) T.R. Kelly, M.C. Bowyer, K.V. Bhaskar, D. Bebbington, A. Garcia, F. Lang, M.H. Kim, and M.P. Jette. J. Am. Chem. Soc. **116**, 3657 (1994).
3. S. Sternhell. *In* Dynamic nuclear magnetic resonance spectroscopy. *Edited by* L.M. Jackman and F.A. Cotton. Academic, New York. 1975. Chap. 6.
4. K. Ohkita, H. Kurosawa, T. Hirao, and I. Ikeda. J. Organomet. Chem. **470**, 189 (1994).
5. (*a*) J.R. Lomprey and J.P. Selegue. J. Am. Chem. Soc. **114**, 5518 (1992); (*b*) R. Mynott, H. Lehmkuhl, E.M. Kreuzer, and E. Joussen. Angew. Chem. Int. Ed. Engl. **29**, 289 (1990).
6. H.S. Gutowsky and C.H. Holm. J. Chem. Phys. **25**, 1228 (1956).
7. A.G. Talma, H. van Vossen, E.J.R. Sudholter, J. van Eerden, and D.N. Reinhondt. Synthesis, 680 (1986).
8. (*a*) S.K. Burley and G.A. Petsko. Science, **229**, 23 (1985); (*b*) W.L. Jorgensen and D.L. Severance. J. Am. Chem. Soc. **112**, 4768 (1990); (*c*) J.E. Cochran, T.J. Parrott, and H.W. Whitlock. J. Am. Chem. Soc. **114**, 2269 (1992).
9. (*a*) M. Oki. Application of dynamic NMR spectroscopy to organic chemistry. Verlag Chemie, Berlin. 1985. Chap. 4; (*b*) F.H. Westheimer. *In* Steric effects in organic Chemistry. *Edited by* M.S. Newman. John Wiley, New York. 1956. p. 552; (*c*) G. Bott, L.D. Field, and S. Sternhell. J. Am. Chem. Soc. **102**, 5618 (1980); (*d*) J.E. Anderson and C.J. Hazlehurst. J. Chem. Soc. Chem. Commun. 1188 (1980); (*e*) J.E. Anderson, D.J.D. Barkel, and C.J. Cooksey. Tetrahedron Lett. **24**, 1077 (1983); (*f*) R.N. Armstrong, H.L. Ammon, and J.N. Darnow. J. Am. Chem. Soc. **109**, 2077 (1987).
10. M. Decouzon, P. Ertl, O. Exner, J.F. Gal, and P.C. Maria. J. Am. Chem. Soc. **115**, 12071 (1993).
11. W. Hewertson and H.R. Watson. J. Chem. Soc. 1490 (1962).
12. G.S. Ashby, M.I. Bruce, I.B. Tomkins, and R.C. Wallis. Aust. J. Chem. **32**, 1003 (1979).

Micelle-induced change of mechanism in the reaction of muonium with acetone

John M. Stadlbauer, Krishnan Venkateswaran, Hugh A. Gillis, Gerald B. Porter, and David C. Walker

Abstract: Muonium atoms add to the O atom of the carbonyl group of acetone to give the muonated free radical $(CH_3)_2\dot{C}$-O-Mu when the reaction takes place in water or hydrocarbons, but not when the acetone is localized in micelles. Micelles have no effect on the formation of muonated cyclohexadienyl radicals when muonium reacts with benzene under similar conditions. The addition reaction with acetone appears to have been subsumed by a faster alternative reaction in the micellar environment. Evidence is presented for this interpretation rather than for an inhibition of the radical or for a shift in the muon level-crossing resonance spectrum with hydrogen (muonium) bonding, though major shifts are seen for the spectrum of this radical in pure solvents of widely different dielectric constant. It is suggested that muonium's "abstraction" reaction takes over in micelles because significant micelle-induced enhancement effects were previously observed in that type of reaction. The data are consistent with a rate constant for the abstraction reaction of muonium with acetone in micelles of $>6 \times 10^8$ M^{-1} s^{-1}.

Key words: muonium, kinetic isotope effects, micelle enhancement, H/Mu-addition, H/Mu abstraction.

Résumé : Lorsqu'on opère en solution dans l'eau ou dans les hydrocarbures, les atomes de muonium s'ajoutent à l'atome d'oxygène du groupe carbonyle de l'acétone pour conduire à un radical muoné $(CH_3)_2\dot{C}$-O-Mu; ce n'est toutefois pas le cas lorsque l'acétone est localisée dans des micelles. Les micelles n'ont aucun effet sur la formation de radicaux cyclohexadiényles muonés lorsqu'on fait réagir des atomes de muonium avec le benzène, dans des conditions semblables. Il semble que, dans un environnement micellaire, la réaction d'addition sur l'acétone est dépassé par une autre réaction plus rapide. On présente des résultats confortant cette interprétation plutôt que celle faisant appel à une inhibition du radical ou à un déplacement du spectre de résonance de croisement au niveau du muon avec une liaison hydrogène (muonium); toutefois, on observe des déplacements pour les spectres de ce radical dans des solvants purs de constantes diélectriques fort différentes. On suggère que la réaction d'«enlèvement» des muonium se produit dans des micelles en raison des effets de rehaussement induit par les micelles qui ont été observés antérieurement dans ce type de réaction. Les données sont en accord avec une constante de vitesse, pour la réaction d'enlèvement du muonium avec l'acétone dans les micelles, qui serait supérieure à 6×10^8 M^{-1} s^{-1}.

Mots clés : muonium, effets isotopiques cinétiques, rehaussement par les micelles, addition H/muonium, enlèvement H/muonium.

[Traduit par la rédaction]

Introduction

Muonium (Mu) is the hydrogen isotope with a short-lived positive muon of one-ninth the mass of a proton as its nucleus. In aqueous solution it reacts like H, undergoing a variety of reaction types including reduction, substitution, combination, addition, and abstraction. In the case of ^1H reacting with acetone as a solute in acidified water, both "addition" and "abstraction' reactions occur, the former with $k_H = 0.9 \times 10^6$ M^{-1} s^{-1} and the latter with $k_H = 1.7 \times 10^6$ M^{-1} s^{-1} (1(*a*)). A recent value puts the total k_H some 40% lower, in strongly acid solution (1(*b*)).

The Mu analogues are given by eqs. [1] and [2],

[1] $$Mu + (CH_3)_2CO \longrightarrow (CH_3)_2\dot{C} - O - Mu$$

[2] $$Mu + (CH_3)_2CO \longrightarrow MuH + CH_3CO\dot{C}H_2$$

but with reaction [1] evidently dominant (2–4). Its reaction rate ($k_M = 8.7 \times 10^7$ M^{-1} s^{-1} at pH = 1 (5), and 1.1×10^8 M^{-1} s^{-1} at pH = 7 (6)) corresponds to a kinetic isotope effect (k_M/k_H) of ~45 for the overall rate and ~125 for the addition reaction.

The $(CH_3)_2\dot{C}$-O-Mu radical produced in reaction [1] has been thoroughly characterized by high-field muon spin-

Received December 1, 1995.

This paper is dedicated to Professor Howard C. Clark in recognition of his contributions to Canadian chemistry.

J.M. Stadlbauer,[1] K. Venkateswaran,[2] H.A. Gillis,[3] G.B. Porter and D.C. Walker.[4] Chemistry Department and TRIUMF, University of British Columbia, Vancouver, BC V6T 1Y6, Canada.

[1] Permanent address: Chemistry Dept., Hood College, Frederick, MD 21701, U.S.A.
[2] Permanent address: Hindustan Lever Research Centre, Bombay 400 099, India.
[3] Permanent address: AVP, St Francis Xavier University, Antigonish, NS B2G 2W5, Canada.
[4] Author to whom correspondence may be addressed. Telephone: (604) 822-3187. Fax: (604) 822-2847. E-mail Walker@Triumf.ca

rotation (μSR) studies of pure liquid acetone (2) and concentrated aqueous solutions (3). It has also been well characterized by level-crossing resonance spectroscopy (μLCR) in the neat liquid state (7) and in dilute solutions in hexane and in water (4). It has an isotropic muon hyperfine coupling constant (A_μ) of 26.1 MHz in neat acetone. This is 9 times larger than that of the analogous H-atom adduct (A_p), even after compensation for the 3.18-fold higher nuclear moment of μ^+ compared to p^+ [8]. This is by far the largest hyperfine-coupling isotope effect yet encountered. It has been variously attributed to the much smaller moment of inertia of Mu compared to ^1H in the rotation of O-Mu about the C—O bond axis (2), and to the greater hyperconjugation of the Mu isotope resulting from its higher librational frequency (3).

Another unique trait of the muonated free radicals formed when Mu adds to acetone is the fact that A_μ changes markedly with the molecular dipole of the solvent involved. A_μ is largest in water (3), intermediate in neat liquid acetone (2), and smallest in hydrocarbons (4). The increase from neat acetone to water has been ascribed to "muonium bonding," isotopomeric hydrogen bonding (3). In effect, the electrostatic bonding of $Mu^{\delta+}$ in C-O-Mu to an $O^{\delta-}$ of water reduces the moment of inertia (and the librational frequency) more than in neat acetone. There is also more muonium bonding to the O of acetone in neat liquid acetone than in a hydrocarbon solvent, hence the further decrease in A_μ.[5] This observed solvent effect on the hyperfine coupling of Mu requires that a full range of μLCR fields be covered in the present study, because the $(CH_3)_2\dot{C}$-O-Mu free radical in the micellar phase could have an A_μ intermediate between that in a pure hydrocarbon and that in water.

Surfactants are amphiphilic molecules that aggregate into roughly spherical micelles as their concentration passes through a critical micelle concentration. Organic solutes are invariably solubilized within these micelles, but Mu is not preferentially localized there (9, 10). Thus rate enhancements have been shown not to arise simply from "concentration amplifications." Instead, Mu diffuses indiscriminately in and out of the micellar phase, reacting with solutes according to non confined competitive kinetics.

In a Letter published a few years ago (4) we noted that the μLCR signal at 1840 MHz, corresponding to the Mu radical of eq. [1] from acetone in water, was missing when a large excess of micelles was added to the solution. In the present study we analyse the reason for this by exploring the effect of added surfactants as a function of their concentration up through the critical micelle concentration. We also look to see if, in those earlier experiments, there was merely a shift in the position of the level-crossing resonance due to a change in the polarity of the microenvironment.

Experimental

Muonium atoms form at the end of some muon tracks when water is bombarded by high-energy positive muons. They react as free thermalized Mu atoms with solutes present, but not with the water itself. The muons decay with mean lifetimes of 2.2 μs, so if the chemical lifetime of Mu is of the order of a microsecond, then the μSR technique can be used to watch reactions of Mu and to evaluate its reaction rate constant k_M. The μLCR technique, on the other hand, is used to directly observe only those muons that are already incorporated into free Mu radicals on the μs time scale of muon decay.

The present studies use only μLCR, conducted on the M20B surface muon channel at the TRIUMF cyclotron using the Helios superconducting magnet in longitudinal-field mode. The technique was fully described previously (11). At certain fields (B_R in eq. [3]) a muon–proton spin flip-flop occurs

$$[3] \quad B_R \simeq |\, 0.5(A_\mu - A_H)/(\gamma_\mu - \gamma_p)\,|$$

that results in loss of muon spin polarization due to resonance between the proton (A_H) and muon (A_μ) hyperfine couplings in a free radical, where the γs are the magnetogyric ratios of the muon and the proton. μLCR allows the determination of both the identity (11, 12) and yield (13) of free radicals that contain the muon as a Mu atom bonded in the α, β, or γ positions of a free radical. The μLCR spectrum is determined by measuring the muon's "asymmetry" as a function of applied longitudinal magnetic field. The ordinate ($A^+ - A^-$) is the difference in observed asymmetry when a small flip-field is added or subtracted to the main longitudinal field. This gives the plots a differential appearance with a resonance centered where the difference count rates cross the baseline. A computer fitting program then draws the lines and calculates the best resonance field (B_R), amplitude (Amp), and linewidth (ΔB) (see Fig. 1).

All solutions for these experiments were composed of reagent-grade chemicals (acetone, benzene, hexane, heptane, and decyltrimethylammonium bromide, hereafter DTAB) and triply distilled water. They were thoroughly deoxygenated by bubbling with pure nitrogen immediately before being pumped under nitrogen into the reaction cell. For the major series of experiments, samples of stock solutions of acetone in water at 100, 27, 10 mM were used with various amounts of the micelle-forming surfactant (DTAB) added. The actual concentration of micelles present was calculated, approximately, from the relationship, [micelle] = ([surfactant] – CMC)/A, where A is the aggregation number of the surfactant (48 for DTAB) and CMC the critical micelle concentration (65 mM for DTAB). DTAB was chosen because its solubility is relatively high and it forms large micelles to accommodate many acetone molecules. The concentration of DTAB was increased from 10 to 500 mM, corresponding to micelle concentrations of zero to 9.1 mM.

Results

1. μLCR spectra of Mu-acetone radicals

Figure 1 shows the μLCR spectra obtained for 27 mM solutions of acetone in water, and in solutions of DTAB below and above its CMC. The signal clearly decreases with increasing micelle concentration. These spectra correspond to resonances involving the six equivalent H_β atoms as reported previously for the $(CH_3)_2\dot{C}$-O-Mu radical (4, 7).

[5] A_p also increases (8), actually more than does A_μ, on moving from neat acetone to its solutions in water, so that A_μ/A_p falls from 9.0 to 4.5. Perhaps this suggests Mu bonding is somewhat weaker than H bonding.

Fig. 1. μLCR spectra of 27 mM acetone in: (*i*) water alone (□), (*ii*) with 25 mM DTAB added (△), and (*iii*) with 50 mM DTAB added (×).

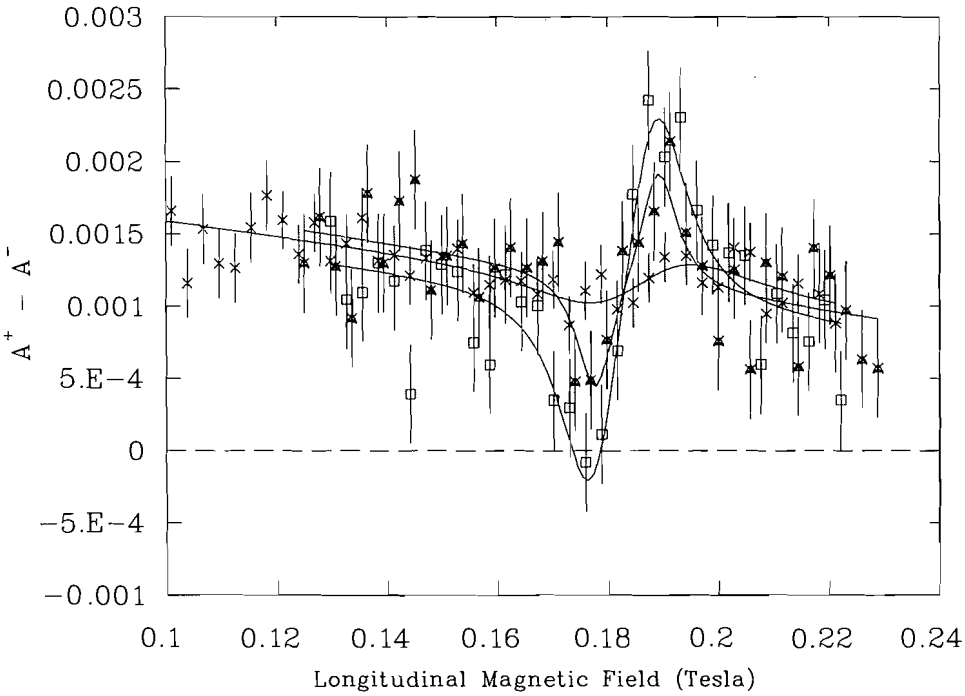

The μLCR spectrum of this Mu radical shifts considerably as a result of changes to its microenvironment. Spectra were obtained for the radical in neat acetone (1540 G) and in various concentrations of water (~1820 G) and hexane (~1425 G). Figure 2(*a*) shows this variation of B_R, displayed as a function of the dielectric constant of the solvent. The latter is not the ideal parameter to use as a measure of the actual degree of hydrogen bonding (muonium bonding here), but the plot shows the strong dependence of hyperfine splittings on solvent polarity. The magnitude of B_R is proportional to the difference between A_μ and A_H, as in eq. [3], but it can, presumably, be almost totally attributed to changes in A_μ, with A_H = 56 MHz (4, 7), as shown in Fig. 2(*b*), because the H-atoms are attached to C and can exhibit no hydrogen bonding. (It should be noted that because Mu is attached to a C atom in Mu radicals from acrylamide, styrene, and most others studied so far, none of them show μLCRs that shift with the nature of the solvent or change when the solute is solubilized by micelles.)

Our data show no evidence for replacement of the Mu radical in water (at ~1820 G) by a buildup at a lower field (corresponding to B_R in a hydrocarbon) as the majority of acetone molecules get localized at micellar phases as surfactant is progressively added to an aqueous solution of acetone. The only resonances found were centered at 1820 G, with nothing at lower fields. Most experiments were scanned from 1200 to 2200 G, and occasionally from 600 to 2200 G.

2. Yields of Mu radical (P_R) from aqueous solutions of acetone as surfactant was added

Radical yields were determined using eq. [4] (13),

$$[4] \quad P_R = \frac{\mathrm{Amp}(\Delta B)^2(\gamma_\mu - \gamma_p)^2}{\mathrm{As}\cdot v_r^2}$$

Fig. 2. Plots of (*a*) B_R and (*b*) A_μ against the dielectric constant of the solvent, for the Mu radical from acetone in water and hexane solutions, and as neat acetone. (A_μ is calculated using eq. [3] with A_{H_β} = 56 MHz.)

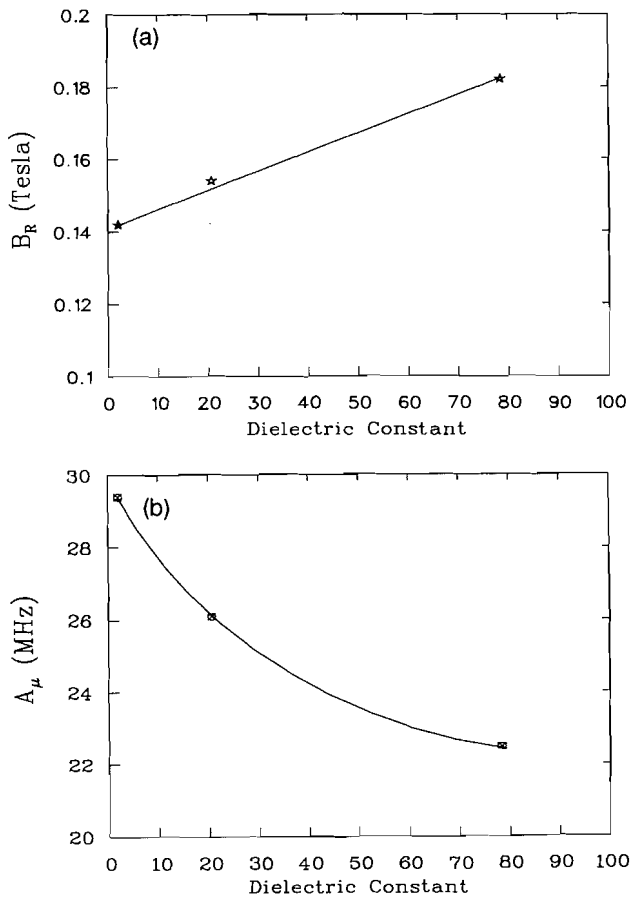

Fig. 3. Data of Table 1, showing the effect of increasing surfactant concentration on the observed yields of the Mu radical from acetone in water at: (*i*) 100 mM (△), (*ii*) 27 mM (◇), and (*iii*) 10 mM (⊗) concentrations.

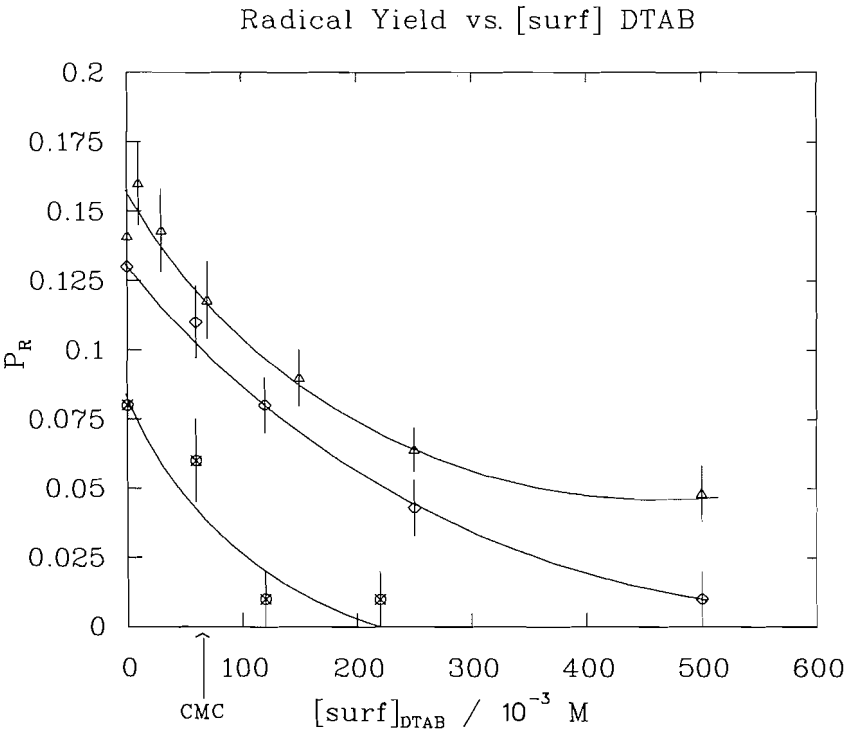

Table 1. Yields of Mu radicals formed in aqueous acetone solutions of 100, 27, and 10 mM concentration to which increasing amounts of the micelle-forming surfactant DTAB was progressively added.

[Ac]/mM	[DTAB]/mM	[mic]/mM	P_R[a]
100	0	0	0.141
100	10	0	0.160
100	30	0	0.143
100	70	~0.08	0.118
100	150	1.8	0.087
100	250	3.9	0.064
100	500	9.1	0.048
27	0	0	0.13
27	60	~0.05	0.11
27	120	1.2	0.075
27	250	3.9	0.04
27	500	9.1	<0.02
10	0	0	0.08
10	60	~0.05	0.06
10	120	1.2	<0.2
10	220	3.2	<0.2

[a] P_R is the radical yield (fraction of incident muons seen as radicals) calculated from Amp$(\Delta B)^2$ of the μLCR spectra at 1820 G using eq. [4].

where As is the intrinsic asymmetry of the apparatus, and v_r is the LCR frequency, proportional to $A_\mu A_p/B_R$. For a given resonance, $P_R \propto$ Amp$(\Delta B)^2$, and all yields for a given resonance can be normalized by comparison with neat acetone using the published yield of 0.41 (4).

Table 1 shows the Mu-radical yields obtained at three concentrations of acetone (100, 27, and 10 mM) for surfactant additions up through the CMC to micelle concentrations of 9 mM. These data are plotted as P_R against the surfactant concentration in Fig. 3.

Errors in P_R range from about 10% when the yields are high, to ~50% as they merge into the background. However, a clear trend is seen for all three acetone concentrations — the yield decreasing markedly as micelles form and solubilize the acetone molecules. At a concentration of 100 mM not all of the acetone is encapsulated in the micelles, even at the highest DTAB concentrations. This can explain why the radical yield drops to only ~25%, because there remains a high concentration of acetone in the water able to react with some Mu to form the observed radical product still in the aqueous phase. At 10 mM, on the other hand, the acetone concentration was so low that many of the muons in Mu decay before Mu reacts chemically, which results in P_R dropping off prematurely. Only at 27 mM is a complete scavenging curve seen.

3. Yields of Mu-benzene radicals (P_{R_b}) obtained in micelle solutions of benzene

μLCR studies of neat liquid benzene have established that the muonated cyclohexadienyl radical, resulting from Mu addition into the benzene ring, has its H_β resonance at $B_R \simeq$ 20 780 G [12]. This can be used to calibrate the asymmetry characteristics of the apparatus, as in the last line of Table 2. Virtually the same μLCR spectrum was obtained here for benzene solubilized in aqueous micelles, as in Fig. 4. This figure also shows the effect of adding 50 mM acetone to the 50 mM benzene in the 9 mM micelle. (All concentrations are moles per litre of total solution.) Only a small decrease in

Fig. 4. μLCR spectra of 50 mM benzene in 0.5 M DTAB solution: (*i*) with no added acetone (□), and (*ii*) with 50 mM acetone added (△).

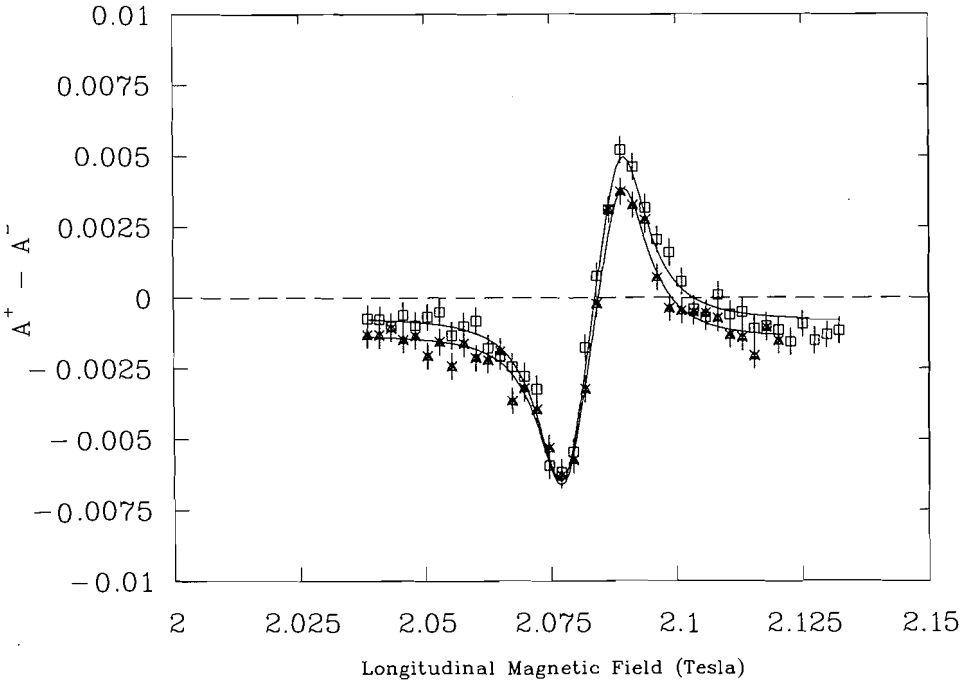

Table 2. Yields of Mu radicals in benzene solutions to which micelles and acetone were added. P_{R_b} is the Mu-cyclohexadienyl radical observed at $B_R \approx 20\,780$ G, whereas B_R (as in Table 1) would correspond to the Mu radical from acetone at 1820 G.

[Ac]/mM	[Bz]/mM	[DTAB]/mM	[mic]/mM	P_{R_b}
0	50	500	9.1	0.161
50	50	500	9.1	0.146
150	50	500	9.1	0.144
0	pure	0	0	[0.82][a]

[a]The value of 0.82 has already been established for the radical yield in neat liquid benzene (14). It was used here to put all P_R values on an absolute basis — as a normalizing factor for the actual asymmetry of the apparatus (As, in eq. [4]).

amplitude is evident. When this latter solution was scanned in the 1200–2200 G range, no resonance was observed corresponding to the $(CH_3)_2\dot{C}$-O-Mu radical.

Table 2 gives the actual yields of the Mu-benzene radicals in solution taking $P_{R_b} = 0.82$ in neat benzene (14). The yield of $P_{R_b} = \sim 0.16$ in the micelles is in reasonable accord with the yield of Mu in water previously established for a solute present at more than three solutes per micelle, on average, when the micelle concentration was ~9 mM (9). It is similar to the Mu-radical yield found for 10 mM acetone in water (Table 1). Evidently there is no significant loss of Mu-benzene radicals by encapsulating the benzene in micelles. This is in sharp contrast to acetone. Furthermore, acetone competes with the benzene for Mu when both solutes are localized in the micelles, but only weakly. (In the case of the 150 mM acetone experiment there was far too much acetone for it to be significantly accommodated by 9 mM micelles, which may account for a negligible further decrease.)

4. Related Mu-radical searches

To check the possibility that localization of acetone in micelles may greatly enhance the fraction of acetone molecules in the "enol" form, μLCR scans were run from 11 000 to 13 000 G, where H_β resonances typically occur when Mu adds to a vinyl group. None was found. The region around 19 000–20 000 G was also studied in the event Mu added to the C of acetone's carbonyl to form an oxyl radical, but, again, no resonances were detected.

μLCR's scans were performed on acetophenone in the 1200–2200 G range looking for carbonyl addition, and around 20 000 G for benzene ring-addition. Resonances were found only for the latter, showing that addition occurs at the benzene ring at least an order of magnitude faster than to a ketone carbonyl group. (These findings removed the possibility of checking whether the carbonyl radical of acetophenone would be curtailed like that of acetone when solubilized by micelles, so at the present time there are no data on other carbonyl compounds to compare with acetone.)

Discussion

The gross suppression by micelles noted earlier (4) is confirmed here by the observation of a gradual decrease of the Mu radical by progressive addition of surfactants to aqueous solutions of acetone. It is also now shown that the radical was not missed previously due to a shift in the μLCR spectrum of this Mu radical as the microenvironment of the acetone changes from water to micelle.

There is, nevertheless, a strong shift in A_μ on switching from water to pure hexane as solvent (as in Fig. 2). But,

even if the acetone radical moves between the aqueous and micellar phases as rapidly as photo-excited acetone seems to do (15), the fluctuation in coupling constant should not wipe out the signals here. This is because, in the μLCR technique, there is involved only the particular state, and thus its coupling constant, of the species that exists at the very moment when the muon decays.

Under almost identical conditions the Mu radical formed by reaction of Mu with benzene as solute was not suppressed by addition of micelles (Table 2), so the inhibition of the radical spectrum of acetone was not caused by spurious effects such as exclusion of Mu from the hydrophobic phase of the micelle, nor from interference by impurities in the surfactants. Also, micelles were found to enhance, not reduce, the overall rate of reaction of muonium with acetone — by a factor of about 250, in fact (4). Consequently, the radicals are not "missing" because of subsequent reactions of Mu radicals with the surfactants or their impurities.

It seems to be a case of an alternative faster reaction taking over when the interaction of Mu with acetone takes place within a micelle (or at its Stern-layer interface). Two other Mu-addition radicals are possible to envisage, though they seem unlikely, under the strained orientated localization of acetone in the Stern layer: first, a greatly enhanced occurrence of the enol tautomer of acetone, $CH_2{=}C(OH)CH_3$, giving the $CH_2(Mu)\text{-}\dot{C}(CH_3)OH$ radical; and second, preferred addition to the C of C=O rather than the O, giving the oxyl radical $(CH_3)_2C(Mu)\dot{O}$. The former might be expected to have a μLCR in the range 11 000–13 000 G, which is where vinyl adducts of Mu generally occur (12, 13, 15), but none was found here. Possible occurrence of the Mu-oxyl radical was also searched for (at ~20 000 G where Mu-thiyl radicals have resonances (16)) but, again, none was detected. μLCR can readily observe oxyl and thiyl radicals where ESR cannot due to rapid electron spin relaxations.

The most likely explanation for the present results seems to be for the abstraction reaction (eq. [2]) to supersede the normal addition reaction (eq. [1]) when the reaction occurs in micelles. This cannot be checked directly because the diamagnetic product of eq. [2] is not observable by μSR techniques (17); but there are good reasons for speculating along these lines — it is specifically abstraction reactions that have previously been seen to show large micelle-induced enhancements (9), and Mu is expected to react to some extent by this mechanism because this is the predominant reaction of its heavy isotope H, even in water (1).

A micelle-controlled mechanism would be given by reactions [5]–[7],

$$[5]\quad Mu_{(aq)} + Ac_{(aq)} \longrightarrow R$$

$$[6]\quad Mu_{(aq)} + mic \rightleftharpoons Mu_{(mic)}$$

$$[7]\quad Mu_{(mic)} + Ac_{(mic)} \longrightarrow D$$

where R represents the observed radicals at 1820 G (eq. [1]), and D the diamagnetic abstraction product (MuH) of eq. [2]. (Ac is acetone and mic the micelles.)

A steady-state treatment for short-lived Mu within the micelles, as in eq. [8],

$$[8]\quad \frac{-dMu_{(mic)}}{dt} = k_6[Mu_{(aq)}][mic] - [Mu_{(mic)}](k_{-6} + k_7[Ac_{(mic)}]) \simeq 0$$

leads to eq. [9] for the ratio R/D of product yields,

$$[9]\quad \frac{R}{D} = \frac{k_5[Ac_{(aq)}](k_7[Ac_{(mic)}] + k_{-6})}{k_6[mic].k_7[Ac_{(mic)}]}$$

and thus to eq. [10],

$$[10]\quad \frac{R_0}{R} = 1 + \frac{k_7[Ac_{(mic)}]k_6[mic]}{(k_5[Ac_{(aq)}](k_{-6} + k_7[Ac_{(mic)}])}$$

as the inverse of the fraction of Mu atoms leading to radicals (R_0 being the value of R with no surfactant added).

A major problem in trying to extract k_7 by "fitting" the data to eq. [10] is the fact that the fraction of acetone in the aqueous phase relative to the micellar phase is a nonlinear function of [mic] because micelles undoubtedly become saturated with acetone (perhaps after 10 or 20 molecules). Some indication of the magnitude of k_7 that is required to explain these data can, nevertheless, be gleaned from the observation that for 100 mM acetone (and 27 mM) the yield of radicals is halved by some 2.5 ± 0.5 mM of micelles (150–250 mM DTAB, as in Fig. 3). Leigh and Scaiano have determined an equilibrium constant of 52 for photochemically excited triplet acetone molecules at low concentrations in sodium dodecyl sulphate micelles, based on an escape rate of 10^8 s^{-1} (in ref. 15). If we take this 52 as an upper limit (because of the saturation effect) for our ground-state acetone in DTAB (similar in size, just of opposite charge), and the 10^8 s^{-1} as a lower limit for k_{-6} for muonium (estimated previously as ~5×10^8 in CTAB [9]), then we can proceed with an "order-of-magnitude" estimation in the following way. We take $[Ac_{(mic)}]/[Ac_{(aq)}][mic] < 52$ and put $k_{-6} > 10^8$ s^{-1}, and use $k_5 = 1 \times 10^8$ M^{-1} s^{-1} (6) and $k_6 \simeq 5 \times 10^{10}$ M^{-1} s^{-1} (9, 10) as published. For the limiting lower case, we also neglect $k_7[Ac_{(mic)}]$ relative to k_{-6} in the denominator of eq. [10], as if Mu generally does not react on encountering an acetone, even within a micelle. This gives a lower limit for k_7 of 6×10^8 M^{-1} s^{-1}.

Despite the obvious uncertainties in this estimate of k_7, all of its assumptions work in the same sense — a lower limit. It implies that Mu and acetone react very much faster within the micelle, consistent with observed micelle-induced rate enhancement of abstraction reactions (4). Also, the value $k_7 > 6 \times 10^8$ M^{-1} s^{-1} is not unreasonably high considering the fact that the abstraction reaction of Mu with 2-propanol undergoes a micelle-induced enhancement to $k > 10^{10}$ M^{-1} s^{-1} (9).

Our basic conclusion is that the "addition" reaction of Mu is subsumed by a faster competitive reaction for acetone in micelles, with "abstraction" a realistic alternative.

Acknowledgements

We gratefully acknowledge assistance with the experiments by Dr. Syd Kreitzman and Curtis Ballard, and financial support from the Natural Sciences and Engineering Research Council of Canada (NSERC). J.M.S. also thanks the Hood College Board of Associates for financial assistance.

References

1. (*a*) R.A. Witter and P. Neta. J. Org. Chem. **38**, 484 (1973). (*b*) S.P. Mezyk and D.M. Bartels. Can. J. Chem. **72**, 2516 (1994).
2. (*a*) E. Roduner, P.W. Percival, D.G. Fleming, J. Hochmann, and

H. Fischer. Chem. Phys. Lett. **57**, 37 (1978); (*b*) E. Roduner. Radiat. Phys. Chem. **28**, 75 (1986).
3. (*a*) A. Hill, M.C.R. Symons, S.F.J. Cox, R. de Renzi, C.A. Scott, C. Bucci, and A. Vecli. J. Chem. Soc. Faraday Trans. 1, **81**, 433 (1985); (*b*) S.F.J. Cox and M.C.R. Symons. Radiat. Phys. Chem. **27**, 53 (1985).
4. K. Venkateswaran, R.F. Kiefl, M.V. Barnabas, J.M. Stadlbauer, B.W. Ng, Z. Wu, and D.C. Walker. Chem. Phys. Lett. **145**, 289 (1988).
5. P.W. Percival, E. Roduner, H. Fischer, M. Camani, F.N. Gygax, and A. Schenck. Chem. Phys. Lett. **47**, 11 (1977).
6. M.V. Barnabas, K. Venkateswaran, and D.C. Walker. Can. J. Chem. **67**, 120 (1989).
7. M. Heming, E. Roduner, B.D. Patterson, W. Odermatt, J. Schneider, Hp. Baumler, H. Keller, and I.M. Savic. Chem. Phys. Lett. **128**, 100 (1986).
8. H. Zeldes and R. Livingston. J. Chem. Phys. **45**, 1946 (1966).
9. (*a*) K. Venkateswaran, M.V. Barnabas, Z. Wu, J.M. Stadlbauer, B.W. Ng, and D.C. Walker. Chem. Phys. Lett. **143**, 313 (1988); (*b*) K. Venkateswaran, M.V. Barnabas, J.M. Stadlbauer, and D.C. Walker. Can. J. Phys. **68**, 952 (1990); (*c*) Hyperfine Interact. **65**, 959 (1990).
10. (*a*) K. Venkateswaran, M.V. Barnabas, B.W. Ng, and D.C. Walker. Can. J. Chem. **66**, 1979 (1988); (*b*) J.M. Stadlbauer, K. Venkateswaran, G.B. Porter, and D.C. Walker. Hyperfine Interact. **87**, 941 (1994).
11. (*a*) R.F. Kiefl, S.R. Kreitzman, M. Celio, R. Keitel, J.H. Brewer, G.M. Luke, D.R. Noakes, P.W. Percival, T. Matsuzaki, and K. Nishiyama. Phys. Rev. A: Gen. Phys. **34**, 681 (1986); (*b*) R.F. Kiefl. Hyperfine Interact. **32**, 707 (1986).
12. P.W. Percival, R.F. Kiefl, S.R. Kreitzman, D.M. Garner, S.F.J. Cox, G.M. Luke, J.H. Brewer, K. Nishiyama, and K. Venkateswaran, Chem. Phys. Lett. **133**, 465 (1987).
13. K. Venkateswaran, M.V. Barnabas, R.F. Kiefl, J.M. Stadlbauer, and D.C. Walker. J. Phys. Chem. **93**, 388 (1989).
14. E. Roduner. The positive muon as a probe of free radical chemistry. Springer, Berlin. 1988.
15. W.J. Leigh and J.C. Scaiano. J. Am. Chem. Soc. **105**, 5652 (1983).
16. (*a*) C.J. Rhodes, M.C.R. Symons, and E. Roduner. J. Chem. Soc. Chem. Commun. 3 (1988); (*b*) M.V. Barnabas and D.C. Walker. Chem. Phys. Lett. **168**, 9 (1990).
17. D.C. Walker. Muon and muonium chemistry. Cambridge University Press, Cambridge. 1983.

Homoleptic carbonyl cations of palladium(I), palladium(II), platinum(II), and gold(I) — simplified synthetic routes to their fluoroantimonate(V) salts

Changqing Wang, Sun Chau Siu, Germaine Hwang, Christian Bach, Bianca Bley, Matthias Bodenbinder, Helge Willner, and Friedhelm Aubke

Abstract: The original synthetic routes to the new noble metal carbonyl cations $[Au(CO)_2]^+$ and $[M(CO)_4]^{2+}$, M = Pd or Pt, as $[Sb_2F_{11}]^-$ salts are multi-step procedures that involve corrosive reagents and require commercially unavailable starting materials. We report here two general simplifications: (*i*) the sole use of liquid antimony(V) fluoride as reaction medium in a single-step carbonylation process, and (*ii*) the use of the commercially available chlorides $AuCl_3$ and MCl_2, M = Pd or Pt, as starting materials, in addition to the binary fluorosulfates $Au(SO_3F)_3$, $Pd[Pd(SO_3F)_6]$, and $Pt(SO_3F)_4$. The simplified routes developed here for $[Au(CO)_2][Sb_2F_{11}]$ and $[M(CO)_4][Sb_2F_{11}]_2$, M = Pd or Pt, should make these new reagents more easily available for wider use in synthesis. In addition, these routes are found suitable for the generation of new carbonyl cations of electron-rich metals.

Key words: metal carbonyl cations of Au(I), Pd(I), Pd(II), and Pt(II); solvolysis reactions in liquid SbF_5, reductive carbonylation in liquid SbF_5; carbonylations in strong acidic media.

Résumé : La première voie de synthèse des nouveaux cations carbonyles de métal $[Au(CO)_2]^+$ et de $[M(CO)_4]^{2+}$, M = Pd ou Pt, sous forme de sels de $[Sb_2F_{11}]^-$ est une synthèse en plusieurs étapes impliquant des agents corrosifs et qui requiert des produits de départ non disponibles commercialement. Nous rapportons deux simplifications générales : (*i*) l'emploi uniquement du fluorure d'antimoine(V) liquide comme milieu réactionnel dans une réaction de carbonylation en une étape et (*ii*) l'utilisation de $AuCl_3$, et de MCl_2, M = Pd ou Pt, comme produits de départ disponibles commercialement en plus des fluorosulfates binaires $Au(SO_3F)_3$, $Pd[Pd(SO_3F)_6]$, et $Pt(SO_3F)_4$. La méthode simplifiée développée ici pour la synthèse du $[Au(CO)_2][Sb_2F_{11}]$ et du $[M(CO)_4][Sb_2F_{11}]_2$, M = Pd ou Pt, devrait rendre ces nouveaux réactifs plus facilement accessibles pour des synthèses de plus grande envergure. De plus on a trouvé que ces nouvelles méthodes sont plus appropriées pour générer les nouveaux cations carbonyles de métaux riches en électrons.

Mots clés : cations de métal carbonyle de Au(I), Pd(I), Pd(II), et Pt(II); réactions de solvolyse dans du SbF_5 liquide; carbonylation réductive dans du SbF_5 liquide; carbonylations dans des milieux fortement acides.

[Traduit par la rédaction]

Introduction

While three carbonyl chlorides of platinum(II), among them *cis*-$Pt(CO)_2Cl_2$, are the very first transition metal carbonyl compounds to be reported (1), thermally stable, uncharged binary (homoleptic) carbonyls of platinum (2, 3) as well as of palladium (2, 4) and gold (5) are still unknown (6). Transient fragments of all three metals containing carbon monoxide have been obtained by co-condensation of CO and the corresponding metal atom vapors (7) and studied by matrix isolation techniques only.

Recently, evidence has been obtained by us for the existence of the thermally stable homoleptic carbonyl cations $[Au(CO)_2]^+$ (8, 9) and $[M(CO)_4]^{2+}$, M = Pd or Pt (10, 11). The cations are generated either in solution of superacids (8, 10) or obtained in the solid state as $[Sb_2F_{11}]^-$ salts, $[Au(CO)_2][Sb_2F_{11}]$ (9) and $[M(CO)_4][Sb_2F_{11}]_2$ (11), M = Pd or Pt. As surprising as are the existence and the relatively high thermal stability of these ennea fluoro diantimonate(V) salts (usually well beyond 100°C), are the structural, spectroscopic, and bonding features of the metal carbonyl cations. Their molecular geometries, linear ($D_{\infty h}$) for $[Au(CO)_2]^+$ (9) and square planar for $[M(CO)_4]^{2+}$, M = Pd or Pt (11), are unprecedented among thermally stable transition metal carbonyls. Their average CO stretching vibrations occur at significantly higher wave numbers, between 2235.5 and 2260 cm^{-1} (8–10), than are found for free CO (2143 cm^{-1}) (12, 13). Likewise, ^{13}C chemical shifts are found at lower frequencies than CO (184

Received February 14, 1996.

This paper is dedicated to Professor Howard C. Clark in recognition of his contributions to Canadian chemistry.

C. Wang, S.C. Siu, G. Hwang, and F. Aubke.[1] Department of Chemistry, The University of British Columbia, Vancouver, B.C., V6T 1Z1, Canada.

C. Bach, B. Bley, M. Bodenbinder, and H. Willner. Institut für Anorganische Chemie der Universität, Callinstr. 9, D-30167 Hannover, Germany.

[1] Author to whom correspondence may be addressed. Telephone: (604) 822-3817. Fax: (604) 822-2847.

ppm) (14) while high-frequency shifts are usually observed for transition metal carbonyls relative to CO (15).

Homoleptic mononuclear carbonyl cations in thermally stable salts are uncommon and prior to our work were limited to the hexacarbonyl cations in group 7 of the type $[M(CO)_6]^+$, M = Mn, Tc, or Re, with $[AlCl_4]^-$ or $[FeCl_4]^-$ as anion (16). The noble gas formalism or the effective atomic number rule, which holds for the above-mentioned cations of the type $[M(CO)_6]^+$, M = Mn, Tc, or Re, is usually valid for binary metal carbonyls (6). However, in $[Au(CO)_2]^+$ there are 14 and in $[M(CO)_4]^{2+}$, M = Pd or Pt, 16 electrons associated with the central metal ion. This departure from the 18 electron count does not seem to cause unusual reactivity, a tendency towards metal–metal bonding resulting in cluster formation, or strong reducing power, as are commonly associated with such low electron counts in organo transition metal compounds (6).

There are, however, strong similarities in structural and spectroscopic features between the carbonyl cations and the isoelectronic cyanide anions $[Au(CN)_2]^-$ and $[M(CN)_4]^{2-}$, M = Pd or Pt (17, 18), which in turn suggest that CO in the homoleptic carbonyl cations acts predominantly as a σ-donor ligand. π-Back donation, the second component of a synergetic M—CO bonding (6), appears to be reduced to insignificance (19), judging by the various criteria cited above.

A consequence of the predominant σ-bonding and the concomitant reduction in π-back-bonding in metal carbonyl cations is the presence of positive partial charges on the carbon atom of the carbonyl group (electrophilic carbon) and the juxtaposition of positive partial charges on both the metal and the adjacent C-atoms (19).

Hence it is expected that homoleptic carbonyl cations will display different reactivities than do neutral carbonyls or the carbonylate anions, including the highly reduced carbonylates (20). Nucleophilic attack either on the metal center, resulting in a displacement of CO by the nucleophile, or on the adjacent C-atom is now possible, which in the latter case should lead to a chemical modification of the coordinated CO ligand.

So far very little is known about the reactivity of metal carbonyl cations. No systematic study has been undertaken. The only reported reaction is the substitution of CO by acetonitrile (9) according to:

[1] $[Au(CO)_2][Sb_2F_{11}] + 3\ CH_3CN \xrightarrow{CH_3CN} [Au(NC_2H_3)_2][SbF_6] + CH_3CNSbF_5$

which leads to the structurally characterized product $[Au(NC_2H_3)_2][SbF_6]$ (9).

A contributing reason for the lack of such systematic reactivity studies are the multi-step synthetic procedures used (8–11) in their synthesis. The highly reactive and corrosive reagents employed, among them SO_3, HSO_3F, and elemental fluorine, as well as the unavailability of many reagents and starting materials from commercial sources, severely limit synthetic work, frequently on account of safety concerns.

The purpose of this publication is to report on simplified procedures for syntheses of salts of the carbonyl cations of Au(I), Pd(I), Pd(II), and Pt(II) with $[Sb_2F_{11}]^-$ as the anion in all instances. The reaction medium chosen is liquid antimony pentafluoride, SbF_5, which is commercially available. The general synthetic procedure, solvolysis in liquid SbF_5 at slightly elevated temperatures (60–80°C) in the presence of gaseous CO at 0.5–2.0 atmospheres of pressure (1 atm = 101.3 kPa), has recently been reviewed by us (21). Two types of metal derivatives are used as starting materials: (*i*) binary metal fluorosulfates, whose syntheses are well known (22), and (*ii*) binary metal chlorides, which are all commercially available. Hence the syntheses of all known carbonyl-cation-containing salts of gold, palladium, and platinum from commercially available starting materials should be possible.

Experimental

(a) Chemicals

Palladium(II) chloride and platinum(II) chloride were donated to us by Prof. B.R. James, University of B.C. Gold(III) chloride was obtained from Johnson and Mathey. All three metal chlorides were manipulated and stored inside a dry box. They were used without further purification. Antimony pentafluoride, SbF_5, was obtained from Atochem North America and purified by distillation methods as described (9, 11). The binary fluorosulfates $Pd[Pd(SO_3F)_6]$ (23), $Pt(SO_3F)_4$ (24), $Au(SO_3F)_3$ (25), and $[Pd_2(\mu\text{-}CO)_2](SO_3F)_2$ (26) were synthesized by oxidation of the metal powders (all obtained from the Ventron Corporation) with bis(fluorosulfuryl)peroxide, $S_2O_6F_2$, in fluorosulfuric acid as reported (23–26). $S_2O_6F_2$ was obtained by the catalytic (AgF_2) fluorination of SO_3 (27) and HSO_3F technical grade (Orange County Chemicals) was purified by distillation as described before (28). Carbon monoxide was obtained from Medi Gas Inc.

(b) Instrumentation

Infrared spectra were recorded with a Bomem M.B–102 F.T.I.R instrument. Raman spectra were recorded with Bruker FRA–106 FT Raman accessory mounted on an optical bench of a Bruker IFS-66v instrument.

Gaseous and volatile reagents and products were manipulated and measured in a vacuum line of known volume. Pressure measurements were made with a Setra capacity manometer type 280E (Setra Instruments, Acton, Mass.). Synthetic reactions were carried out in various glass reactors (10–50 mL volume) fitted with Teflon stem valves (Young, London, U.K.) and Teflon-coated stirring bars. Solid materials were manipulated inside a Vacuum Atmosphere Corp. Drilab filled with dry N_2. Microanalyses were performed by Mr. P. Borda, Department of Chemistry, U.B.C.

(c) Synthetic reactions

The synthetic procedures and the methods of product isolation were adopted from the previously reported solvolytic conversions of $Au(CO)SO_3F$ and *cis*-$M(CO)_2(SO_3F)_2$, M = Pd or Pt (10), to $[Au(CO)_2][Sb_2F_{11}]$ (9) and $[M(CO)_4][Sb_2F_{11}]_2$ (11) in liquid antimony(V) fluoride in a CO atmosphere. The identification of known products was accomplished by the mass balance of the reaction, volumetric CO-uptake measurements, microanalysis for carbon only, the determination of melting or decomposition points, a comparison of the vibrational spectra with the published precedents (9, 11), and the characterization of by-products by their vibrational spectra.

To illustrate the synthetic procedure, the synthesis of $[Au(CO)_2][Sb_2F_{11}]_2$ (9) starting either from $Au(SO_3F)_3$ or from $AuCl_3$ is described below in detail. The solvolytic conversion of $[Pd_2(\mu\text{-}CO)_2](SO_3F)_2$ to the previously unknown $[Pd_2(\mu\text{-}CO)_2][Sb_2F_{11}]_2$ is also described below. The remaining reactions leading to $[M(CO)_4][Sb_2F_{11}]_2$, M = Pd or Pt, are carried out in an identical manner and on a comparable small scale.

(i) The synthesis of $[Au(CO)_2][Sb_2F_{11}]$ from $Au(SO_3F)_3$

About 3 mL SbF_5 was distilled onto 224 mg (0.494 mmol) of $Au(SO_3F)_3$ in vacuo. The 50 mL round-bottom flask was warmed to room temperature. No reaction between the orange $Au(SO_3F)_3$ and clear, colorless SbF_5 was observed. Carbon monoxide (4.85 mmol) was admitted to the reaction vessel. The mixture was warmed to 65°C to facilitate stirring. The solid present changed color from orange to brown after 10 min. White particles were visible in the mixture after 30 min. After 45 min, the solution turned dark yellow. The solid was gradually consumed at this stage. The solution was clear and colorless after 2 h and no solid appeared to be present. Heating was stopped and the solution was left stirring for 20 h.

At ambient temperature the solution separated into a white, cloudy, viscous upper layer and a light brown, oily lower layer. Warming the mixture to 80°C caused the two layers to combine to form a clear, colorless solution, but the brown oil returned upon cooling the reactor to room temperature. Infrared spectra of the volatile materials in the reactor were obtained at −196°C, −78°C, and 20.5°C. The volatiles were found to be CO, CO_2, $S_2O_5F_2$, and possibly $Sb_2F_9SO_3F$, respectively. The excess SbF_5 was removed in vacuo, leaving a white solid. CO (3.18 mmol) was removed from the reactor.

In total, 1.67 mmol CO appeared to react with 0.494 mmol $Au(SO_3F)_3$. The white solid was identified as $[Au(CO)_2][Sb_2F_{11}]$ by comparison of its vibrational spectra to published data (9). The conversion reaction proceeds quantitatively.

(ii) The synthesis of $[Au(CO)_2][Sb_2F_{11}]$ from $AuCl_3$

To 100.3 mg (0.33 mmol) of finely ground, yellow-orange, crystalline $AuCl_3$, contained in a reaction vial of an approximate volume of 100 mL, an excess of about 3 mL of purified SbF_5 was added in vacuo. The CO pressure was adjusted to about 0.6 atm. Upon warming the reaction mixture, first to room temperature and then to 60–70°C, in order to reduce the viscosity of SbF_5, the crystals turned black immediately and then slowly became white in color. After heating for 5 days no further change in color and CO-uptake was noted, and the reaction was judged to be complete. The excess of SbF_5 was removed in vacuo overnight, with the reactor at 55°C. In the highly volatile gaseous fraction only CO and COF_2 could be detected by IR spectroscopy. The white solid residue was identified as $[Au(CO)_2][Sb_2F_{11}]$, which had formed in quantitative yield.

(iii) The synthesis of $[Pd_2(\mu\text{-}CO)_2][Sb_2F_{11}]_2$

An amount of 27.2 mg (0.058 mmol) of orange-colored crystalline $[Pd_2(\mu\text{-}CO)_2](SO_3F)_2$, used previously to obtain samples for the crystal structure determination by X-ray diffraction (26), was finely ground inside the dry box and transferred to a one-part reactor of an approximate volume of 50 mL. After weighing, approximately 2 mL of SbF_5 were added in vacuo. The reactor was kept at room temperature without stirring but with occasional shaking by hand, resulting in a swirling of the mixture. As time went by, the color of the suspension turned lighter, and became uniformly yellow after 6 months. After removal of all volatiles, 67.3 mg (expected were 68.4 mg) of a yellow powder was left behind. On heating in a melting point capillary the compound started to decompose at 115°C and gray spots appeared. At 145°C the material had turned uniformly dark. Carbon analysis: calcd. for $COF_{11}Sb_2Pd$: 2.05%; found: 2.05%. Vibrational spectra: (*a*) IR, $\bar{\nu}$ in cm^{-1}: 2032 vw, 2006 vs, 1970 w, 1349 vw, 1186 vw, 1045 vw, 884 vw, 721 vs, 708 s, 682 vs, 648 s, 569 vs, 492 ms, 390 m. (*b*) Raman, $\Delta\bar{\nu}$ in cm^{-1}: 2048 vs, 734 vw, ~710 vw, sh, 696 vs, 681 s, 643 vs, 571 ms, 409 m, 296 w, b, 248 w, 228 w, 135 vw, 82 w. Abbreviations: $\bar{\nu}$ = wave number, $\Delta\bar{\nu}$ = Raman shift, s = strong, m = medium, w = weak, v = very, b = broad and sh = shoulder.

Results and discussion

There are two general alternative routes of great simplicity found for all three fluoroantimonate(V) salts $[Au(CO)_2][Sb_2F_{11}]$ and $[M(CO)_4][Sb_2F_{11}]_2$, M = Pd or Pt as described below.

As best illustrated by the original synthesis of $[Au(CO)_2][Sb_2F_{11}]$ (8, 9), the original approach is cumbersome and experimentally demanding. Starting with the synthesis of gold(III) fluorosulfate (24) according to:

$$[2] \quad 2\,Au + 3\,S_2O_6F_2 \xrightarrow[60°C]{HSO_3F} 2\,Au(SO_3F)_3$$

both the purification of the solvent, HSO_3F (28), and the synthesis of bis(fluorosulfuryl)peroxide, $S_2O_6F_2$ (27), by the catalytic fluorination of sulfur trioxide with elemental fluorine, are demanding procedures that require specially developed equipment (26, 27). Furthermore, by-products of the catalytic fluorination may be extremely hazardous (27*b*); however, their formation can be avoided according to a recent study (27*c*). The subsequent reductive carbonylation of $Au(SO_3F)_3$ according to:

$$[3] \quad Au(SO_3F)_3 + 3\,CO \xrightarrow[25°C]{HSO_3F} [Au(CO)_2]^+_{(solv)} + SO_3F^- + CO_2 + S_2O_5F_2$$

is straightforward, facile, and completed within a few hours, but nucleophilic displacement of one mole of CO by SO_3F^- on heating or on solvent removal according to:

$$[4] \quad [Au(CO)_2]^+_{(solv)} + SO_3F^- \longrightarrow Au(CO)SO_3F + CO_{(g)}$$

will produce $Au(CO)SO_3F$ in quantitative yield (8) that will, after isolation by sublimation, convert in liquid SbF_5 to the final product $[Au(CO)_2][Sb_2F_{11}]$ in a CO atmosphere of 580 mbar (1 bar = 100 kPa) according to:

$$[5] \quad Au(CO)SO_3F + CO + 4\,SbF_5 \xrightarrow[80°C,\ 10\ h]{SbF_5} [Au(CO)_2][Sb_2F_{11}] + 2\,Sb_2F_9SO_3F$$

Two additional complications are encountered in the reductive carbonylation of $Pt(SO_3F)_4$ (24) and the mixed valency compound $Pd[Pd(SO_3F)_6]$ (23). The rather slow reduction of $Pt(SO_3F)_4$ in HSO_3F by CO produces a solid, yellow intermediate of the composition $[Pt(CO)_4][Pt(SO_3F)_6]$, which has been isolated and characterized (29). This intermediate will convert completely under slightly more forcing conditions to white *cis*-$Pt(CO)_2(SO_3F)_2$. The reductive carbonylation of $Pd[Pd(SO_3F)_6]$ in HSO_3F produces, in addition to *cis*-$Pd(CO)_2(SO_3F)_2$ a second isomer with bridging CO groups according to the IR spectrum (10) which has so far not been isolated in pure form. Both forms of $Pd(CO)_2(SO_3F)_2$ are, however, easily converted in liquid SbF_5 and in the presence of CO to $[Pd(CO)_4][Sb_2F_{11}]_2$ (11).

These complications, the use of HSO_3F as solvent and the necessity to isolate the metal carbonyl fluorosulfates as intermediates, are all avoided when liquid SbF_5 is used as reaction medium. The reductive carbonylation of the binary fluorosulfates of palladium, platinum, and gold proceeds in a straight foward manner as, for example, .

[6] $Au(SO_3F)_3 + 3\ CO + 4\ SbF_5$

$$\xrightarrow[65°C,\ 1\ d]{SbF_5} [Au(CO)_2][Sb_2F_{11}] + CO_2 + S_2O_5F_2 + Sb_2F_9(SO_3F)$$

The rather low volatility of SbF_5 requires prolonged heating of the product mixture to ~65°C in vacuo during the product isolation. This causes no problems, because $[Au(CO)_2][Sb_2F_{11}]$, as well as $[M(CO)_4][Sb_2F_{11}]_2$, M = Pd or Pt, shows sufficient thermal stability well beyond 100°C.

The simplified synthetic procedure, initially developed for the preparation of $[Au(CO)_2][Sb_2F_{11}]$ and $[M(CO)_4][Sb_2F_{11}]_2$, M = Pd or Pt, has found two recent applications, which have significantly expanded the field of homoleptic metal carbonyl cations: (*i*) The solvolysis of $Hg(SO_3F)_2$ (30) in liquid SbF_5 in a CO atmosphere resulted in the isolation (31) and subsequent structural characterization (32) of $[Hg(CO)_2][Sb_2F_{11}]_2$, the first thermally stable carbonyl derivative of a post-transition metal. (*ii*) Reductive carbonylation of $M(SO_3F)_3$, M = Ru (33) or Os (34), in liquid SbF_5 allowed for the first time the isolation of $[M(CO)_6][Sb_2F_{11}]_2$ (35), M = Ru or Os. In the first case, carbonylation of $Hg(SO_3F)_2$ in HSO_3F was unsuccessful while, in the case of ruthenium and osmium, carbonyl fluorosulfates of the divalent metals were obtained as intermediates but they have so far not been isolated and completely characterized (35).

These synthetic reactions (31, 32, 35) as well as the syntheses of $[Au(CO)_2][Sb_2F_{11}]$ and $[M(CO)_4][Sb_2F_{11}]_2$, M = Pd or Pt, described here, still require binary fluorosulfates as starting materials. Their preparation is best accomplished by metal oxidation with $S_2O_6F_2$ in HSO_3F as reaction medium (23–25, 30, 33, 34). Hence neither the use of HSO_3F nor the difficulties involved in the synthesis of $S_2O_6F_2$ are completely avoided. Therefore a further simplification of the synthetic methodology is desirable.

Such a simplification is achieved when the metal chlorides $AuCl_3$ and MCl_2, M = Pd or Pt, are employed instead of the corresponding fluorosulfates. A precedent is seen in the reported solvolytic conversion of ICl_3 into $[ICl_2]$ $[SbF_6]$ (37). The conversion reaction of $AuCl_3$, formulated as:

[7] $AuCl_3 + SbF_5 + 3\ CO$

$$\xrightarrow[65°C]{SbF_5} [Au(CO)_2][Sb_2F_{11}] + COCl_2 + SbF_4Cl$$

is expected and solid $[Au(CO)_2][Sb_2F_{11}]$ is indeed formed and identified by comparison with an authentic sample (9). The mixed fluoride–chloride by-product formulated as SbF_4Cl is, unlike $Sb_2F_9(SO_3F)$ (38), not fully characterized and corresponds in its composition to materials encountered by Ruff and Plato (39) during the original synthesis of SbF_5 from $SbCl_5$ and HF and later described in more detail by Ruff (40).

Somewhat surprising is the observation, by gas phase IR, of COF_2 instead of $COCl_2$, which is usually obtained in the reductive carbonylation of $AuCl_3$ to give Au(CO)Cl (41–43). Since COF_2 can be prepared from $COCl_2$, phosgene, and a mixture of Sb(III) and Sb(V) fluorides (44), it is assumed that initially formed phosgene is quantitatively converted to carbonyl fluoride by reaction with an excess of SbF_5. Alternatively, the initial conversion of the starting material $AuCl_3$ to AuF_3 by SbF_5 may be considered. The synthesis of $[Au(CO)_2][Sb_2F_{11}]$ from AuF_3, CO, and SbF_5 as reaction medium is known (9) and will produce COF_2 as by-product. As in the solvolysis of $AuCl_3$, a black-brown color also develops here (9) immediately after combining the reagents. The nature of this black intermediate is unclear at the moment, but the disappearance of the black color as the reaction progresses provides an indication of when the conversion has gone to completion. Finally, a white solid product, suspended in SbF_5, is formed.

Black-brown intermediates that are similar in appearance are observed in the solvolysis reactions of $PdCl_2$ and $PtCl_2$, which proceed according to:

[8] $MCl_2 + 4\ CO + 6\ SbF_5$

$$\xrightarrow[80°C,\ 10–14\ d]{SbF_5} [M(CO)_4][Sb_2F_{11}]_2 + 2\ SbF_4Cl, \qquad M = Pd\ or\ Pt$$

In this case, the black-brown particles form as soon as the metal halide powders come in contact with SbF_5 even before CO is added, and it will take several days before sizable quantities of the white final products form.

Attempts to characterize the black intermediates by vibrational spectroscopy have been unsuccessful. The opaque powders do not scatter Raman light very well and give very poorly resolved FT-IR. As is in case of the solvolyses of $AuCl_3$ and AuF_3 (9), the slow disappearance of the black intermediates, allows monitoring the course of the reaction. Since all carbonylation reactions of metal halides in liquid SbF_5, appear to be heterogeneous processes, starting materials, intermediates, and final products are suspended rather than completely dissolved in liquid SbF_5. It is advisable to react small amounts at a time, to use a large excess of SbF_5,

and to grind the solid metal chlorides very finely inside a dry box before use. In case of solvolysis reactions in SbF_5 that involve fluorosulfates, it is advisable to reuse SbF_5 after product separation. The by-product formed, $Sb_2F_9(SO_3F)$ (38), is found to reduce the viscosity of antimony(V) fluoride (45) and hence facilitate the reaction. A potential dilutant, $C_4F_9SO_2F$, has so far found use only in the isolation of $[Hg(CO)_2][Sb_2F_{11}]$, where it is used to dissolve some of the excess of SbF_5 in a decanting procedure (32).

It is noticeable that solvolysis reactions in SbF_5 and in a CO atmosphere proceed very slowly, where the oxidation state of the metal does not change as in the conversion of MCl_2, M = Pd or Pt, into $[M(CO)_4]^{2+}$ salts. Since in MCl_2 the divalent metal ion is in a square-planar environment in both the α and β- forms (6), the conversion involves square-planar substitution, seemingly on solids. Hence the long reaction times are not surprising.

The remaining four synthetic reactions discussed here involve reductive carbonylation and solvolysis. All are considerably faster and are suggested to proceed via initially formed "naked" metal ions as intermediates (21). The "naked" metal cations are strong Lewis acids that are stabilized by coordination to CO to produce $[Au(CO)_2][Sb_2F_{11}]$, from either $AuCl_3$ or $Au(SO_3F)_3$ (25), or $[M(CO)_4][Sb_2F_{11}]_2$, M = Pd or Pt, from either $Pd[Pd(SO_3F)_6]$ (23) or from $Pt(SO_3F)_4$ (24). Hence the obvious advantage to produce the $[M(CO)_4][Sb_2F_{11}]_2$, M = Pd or Pt, from commercial reagents is in part offset by rather long reaction times and the necessity to react small quantities at a time as discussed above.

While all reactions discussed so far lead to previously known compounds in a simpler, more direct way, this is not the case in the solvolysis of *c*-$[Pd_2(\mu\text{-}CO)_2](SO_3F)_2$ (26) with an excess of SbF_5, which results in the formation of a new compound *c*-$[Pd_2(\mu\text{-}CO)_2][Sb_2F_{11}]_2$ according to:

[9] *c*-$[Pd_2(\mu\text{-}CO)_2](SO_3F)_2 + SbF_5$ → (25°C, 6 min; SbF_5) *c*-$[Pd_2(\mu\text{-}CO)_2][Sb_2F_{11}]_2 + 2\ Sb_2F_9SO_3F$

To avoid oxidation of palladium, which is in the formal oxidation state +1, by SbF_5, the reaction is allowed to proceed at room temperature and requires reaction times of several months. Only very small quantities are reacted, because only small amounts of *c*-$[Pd_2(\mu\text{-}CO)_2](SO_3F)_2$ had been available and the objective was to obtain IR and Raman spectra of $[Pd_2(\mu\text{-}CO)_2][Sb_2F_{11}]_2$.

We previously reported the molecular structure of $[Pd_2(\mu\text{-}CO)_2](SO_3F)_2$ (26). During attempts to provide a complete vibrational analysis for the cyclic $[Pd_2(\mu\text{-}CO)_2]^{2+}$ cation, which has D_{2h} symmetry, two Raman active fundamentals, ν_5 and ν_6, remained undetected. They are expected to be weak, to occur at ≈600 cm^{-1}, and may perhaps be accidentally degenerate. For $[Pd_2(\mu\text{-}CO)_2][Sb_2F_{11}]_2$ all bands (listed in the experimental section) between 500 and 700 cm^{-1} are best attributed to Sb–F stretching vibrations according to precedents (9, 11, 32).

A clearer picture is found in the CO stretching region where the mutual exclusion principle is followed. In the IR spectrum the asymmetric CO stretch ν_7 (B_{1u}) is shifted from 1977 cm^{-1} with a ^{13}C satellite at ≈1940 cm^{-1} for the fluorosulfate to 2006 cm^{-1} with a ^{13}C satellite band at ≈1970 for the $[Pd_2(\mu\text{-}CO)_2][Sb_2F_{11}]$. The Raman active ν_1 (A_g) stretch shifts from 2027 to 2048 cm^{-1} for the pair of compounds. Hence $\bar{\nu}_{av}(CO)$ has increased from 2002 cm^{-1} for $[Pd_2(\mu\text{-}CO)_2](SO_3F)_2$ to 2027 cm^{-1} for $[Pd_2(\mu\text{-}CO)_2][Sb_2F_{11}]_2$. Both values are well outside the range of $\bar{\nu}$ (CO) between 1700 and 1850 cm^{-1} commonly (6, 13*b*, 46) quoted for bidentate, symmetrically bridging CO groups in neutral molecules.

The noncoincidence of IR and Raman active modes is consistent with the retention of D_{2h} symmetry for the $[Pd_2(\mu\text{-}CO)_2]$-metallo cycle in both compounds. As in $[Pd_2(\mu\text{-}CO)_2](SO_3F)_2$ (26) where, according to the molecular structure, bidentate, weakly bridging fluorosulfate groups are present, no vibrational coupling between individual cations is apparent for $[Pd_2(\mu\text{-}CO)_2][Sb_2F_{11}]_2$ in the $\bar{\nu}$(CO) region. This is in contrast to observations for previously reported acetate derivatives determination (47, 48) where two $[Pd_2(\mu\text{-}CO)_2]^{2+}$ cations are linked by bidentate bridging acetate groups into tetranuclear clusters of the type $[Pd_4(\mu\text{-}CO)_4(\mu\text{-}CH_3CO_2)_4] \cdot 2\ CH_3CO_2H$ according to a crystal structure determination (47, 48). Extensive anion bridging, alternating with CO bridging, is also suggested for the halides of the type $[Pd(\mu\text{-}CO)(\mu\text{-}X)]_n$, X = Cl or Br (49, 50), even though the molecular structures are so far unknown.

In contrast to the clean synthesis of $[Pd_2(\mu\text{-}CO)_2][Sb_2F_{11}]_2$ from the fluorosulfate precursor reported here, the solvolysis in SbF_5 in the presence of CO and at 70°C produces $[Pd(CO)_4][Sb_2F_{11}]_2$ rather easily. But since the starting material $[Pd_2(\mu\text{-}CO)_2](SO_3F)_2$ is difficult to obtain, this is not a recommended synthetic route.

To conclude this report, a few exploratory reactions in liquid antimony(V) fluoride are briefly summarized. While *cis*-$M(CO)_2(SO_3F)_2$, M = Pd or Pt, are converted cleanly in SbF_5 to $[M(CO)_4][Sb_2F_{11}]_2$, M = Pd or Pt, in a CO atmosphere as discussed above, in the absence of CO different reactions occur. *cis*-$Pt(CO)_2(SO_3F)_2$ is solvolyzed cleanly in SbF_5 to give a white, crystalline solid of the composition $Pt(CO)_2(Sb_2F_{11})_2$. Attempts to determine its molecular structure failed, because the crystals did not diffract. Both $\bar{\nu}$ CO stretches are shifted by ~+20 cm^{-1} relative to *cis*-$Pt(CO)_2(SO_3F)_2$ but both remain Raman and IR active, which would be consistent with a bent $Pt(CO)_2$ moiety.

In contrast, *cis*-$Pd(CO)_2(SO_3F)_2$ converts in SbF_5 to a mixture of $[Pd(CO)_4][Sb_2F_{11}]_2$ and c-$[Pd_2(\mu\text{-}CO)_2][Sb_2F_{11}]_2$, according to the vibrational spectra. No attempt is made to separate the mixture because both components are known compounds.

When $Au(CO)(SO_3F)$ (8) is dissolved in SbF_5 in the absence of additional CO, a pale yellow oil results after the removal of the excess of SbF_5 in vacuo (9). The composition of this oil varies from one preparation to the next and the solvated cation $[Au(CO)]^+$ is so far only identified in solution of HSO_3F or of magic acid, HSO_3F–SbF_5 (9), but not in the solid state.

The solvolytic conversion of a halide into a fluoroantimonate salt in the presence of CO allows the generation of the well-known (16*a*, 51) cations $[M(CO)_6]^+$, M = Mn or Re, and their stabilization as $[Sb_2F_{11}]^-$ salts according to:

[10] $M(CO)_5Cl + CO + 3\ SbF_5$

$$\xrightarrow[0.5\text{–}0.8\ \text{atm CO}]{25\text{–}80^\circ C,\ SbF_5} [M(CO)_6][Sb_2F_{11}] + SbF_4Cl, \qquad M = Mn \text{ or } Re$$

The reactions proceed in a more facile manner than in the original syntheses, which employ $AlCl_3$ as Lewis acid and $AlCl_4^-$ as counteranoin at CO pressures of 200 atm, necessitating the use of an autoclave (51).

While the reaction of $Re(CO)_5Cl$ in SbF_5–CO is very straightforward, in the case of $Mn(CO)_5Cl$, a large excess of CO must be admitted to the reactor before slowly warming the reaction mixture from −196°C to 25°C, in order to avoid side reactions and the formation of colored materials. The vibrational spectra obtained for the two $[M(CO)_6][Sb_2F_{11}]$ salts, M = Mn or Re, do not differ significantly in the CO stretching region from previous reports (12, 52).

It is illustrated by the synthesis of $[Ir(CO)_6][Sb_2F_{11}]_3$ that reductive carbonylation of a binary halide in SbF_5 can lead to salts with new homoleptic carbonyl cations according to:

[11] $2\ IrF_6 + 15\ CO + 12\ SbF_5$

$$\xrightarrow[50^\circ C]{SbF_5} 2\ [Ir(CO)_6][Sb_2F_{11}]_3 + 3\ COF_2$$

Details on this reaction and the spectroscopic identification of the $[Ir(CO)_6]^{3+}$ cation will be published shortly (53).

Summary

The simplified synthetic approaches to the noble metal carbonyl salts $[Au(CO)_2][Sb_2F_{11}]$ (9) and $[M(CO)_4][Sb_2F_{11}]_2$ (11), M = Pd or Pt, reported here should facilitate wider use of these salts in synthesis. Their chemistry, which has so far remained largely unexplored, promises to be interesting. It remains to be seen how many more metal carbonyl cations can be generated in liquid SbF_5 in addition to $[Hg(CO)_2]^{2+}$ (31, 32) and $[M(CO)_6]^{2+}$, M = Ru or Os.

Acknowledgment

Financial support by the following agencies is gratefully acknowledged: Deutsche Forschungsgemeinschaft DFG (to H.W.), Fonds der Chemischen Industrie (to. B.B.), the North Atlantic Treaty Organization NATO (to H.W. and F.A.), the Natural Sciences and Engineering Research Council of Canada (NSERC) (to F.A.), and the Alexander von Humboldt-Foundation (to F.A.).

References

1. (*a*) P. Schützenberger. Annales, Paris, 15 (1868). (*b*) Bull. Soc. Chim. Fr. **10**, 188 (1868); (*c*) C.R. Hebd. Seances Acad. Sci. **70**, 1134 (1870); (*d*) Bull. Soc. Chim. Fr. **14**, 97 (1870).
2. S.C. Tripathy, S.C. Srivastava, R.P. Mani, and A.K. Srima. Inorg. Chim. Acta, **17**, 257 (1976).
3. M. Roundhill. *In* Comprehensive coordination chemistry. Vol. 5. Pergamon Press, Oxford. 1987. p. 377.
4. M.N. Vargaftik, T.A. Stromnova, and I.I. Moiseev. Russ. J. Inorg. Chem. (Engl. Transl.), **25**, 127 (1980).
5. (*a*) R.J. Puddephatt. The chemistry of gold. Elsevier, Amsterdam. 1978; (*b*) *In* Comprehensive coordination chemistry. Vol. 7. Pergamon Press, Oxford. 1987. p. 861.
6. (*a*) F.A. Cotton and G. Wilkinson. *In* Advanced inorganic chemistry. 5th ed. J. Wiley, New York. 1988. pp. 58 and 1035; (*b*) F.P. Pruchnick. *In* Organometallic chemistry of transition elements. Plenum Press, New York. 1990. p. 23; (*b*) H. Werner. Angew. Chem. Int. Ed. Engl. **29**, 1109 (1990).
7. M. Moskovits and G.A. Ozin. *In* Cryochemistry. J. Wiley, New York. 1976. p. 261, and ref. therein.
8. H. Willner and F. Aubke. Inorg. Chem. **29**, 2195 (1990).
9. H. Willner, J. Schaebs, G. Hwang, F. Mistry, R. Jones, J. Trotter, and F. Aubke. J. Am. Chem. Soc. **114**, 8972 (1992).
10. G. Hwang, C. Wang, M. Bodenbinder, H. Willner, and F. Aubke. J. Fluorine Chem. **66**, 159 (1994).
11. G. Hwang, C. Wang, M. Bodenbinder, H. Willner, and F. Aubke. Can. J. Chem. **71**, 1532 (1993).
12. K. Nakamoto. *In* Infrared spectra of inorganic and coordination compounds. 3rd ed. J. Wiley, New York. 1978.
13. (*a*) P.S. Braterman. *In* Metal carbonyl spectra. Academic Press, New York. 1975; (*b*) S.F.A. Kettle. Top. Curr. Chem. **71**, 111 (1977).
14. J. Browning, P.L. Goggin, R.J. Goodfellow, M.J. Norton, A.J.M. Rattray, B.F. Taylor, and J. Mink. J. Chem. Soc. Dalton Trans. 2061 (1977).
15. B.E. Mann. Adv. Organomet. Chem. **12**, 133 (1974).
16. (*a*) E.W. Abel and S.P. Tyfield. Adv. Organomet. Chem. **8**, 117 (1970); (*b*) W. Beck and K.-H. Sünkel. Chem. Rev. **88**, 1405 (1988).
17. (*a*) B.M. Chadwick and A.G. Sharpe. Adv. Inorg. Chem. Radiochem. **8**, 83 (1966); (*b*) A.G. Sharpe. *In* The chemistry of cyano complexes of transition metals. Academic Press, New York. 1976.
18. L.H. Jones. *In* Inorganic vibrational spectroscopy. Vol. 1. Macel Dekker, New York. 1971. p. 122, and ref. therein.
19. (*a*) F. Aubke and C. Wang. Coord. Chem. Rev. **137**, 483 (1994); (*b*) F. Aubke. J. Fluorine Chem. **72**, 195 (1995); (*c*) A. Veldkamp and G. Frenking. Organometallics, **12**, 4613 (1993); (*d*) M.A. Lynn and B.E. Bursten. Inorg. Chim. Acta, **229**, 437 (1995).
20. J.E. Ellis. Adv. Organomet. Chem. **31**, 1 (1990).
21. C. Wang, G. Hwang, S.C. Siu, B. Bley, M. Bodenbinder, C. Bach, H. Willner, and F. Aubke. Eur. J. Inorg. Solid State Chem. In press.
22. F. Aubke, M.S.R. Cader, and F. Mistry. *In* Synthetic fluorine chemistry. *Edited by* G.A. Olah, R.D. Chambers, and G.K. Surya Pakash. J. Wiley, New York. 1992. p. 43.
23. (*a*) K.C. Lee and F. Aubke. Can. J. Chem. **55**, 2473 (1977); (*b*) Can. J. Chem. **57**, 2058 (1979).
24. K.C. Lee and F. Aubke. Inorg. Chem. **23**, 2124 (1984).
25. K.C. Lee and F. Aubke. Inorg. Chem. **18**, 389 (1979).
26. C. Wang, M. Bodenbinder, H. Willner, S.J. Rettig, J. Trotter, and F. Aubke. Inorg. Chem. **33**, 779 (1994).
27. (*a*) G.H. Cady and J.M. Shreeve. Inorg. Synth. **7**, 124 (1963); (*b*) G.H. Cady. Inorg. Synth. **11**, 155 (1968); (*c*) D. Zhang, C. Wang, F. Mistry, B. Powell, and F. Aubke. J. Fluorine Chem.**76**, 83 (1996).
28. J. Barr, R.J. Gillespie, and R.C. Thompson. Inorg. Chem. **3**, 1149 (1964).
29. G. Hwang, M. Bodenbinder, H. Willner, and F. Aubke. Inorg. Chem. **32**, 4661 (1993).
30. S.P. Mallela and F. Aubke. Can. J. Chem. **62**, 382 (1984).

31. H. Willner, M. Bodenbinder, C. Wang, and F. Aubke. J. Chem. Soc. Chem. Commun. 1189 (1994).
32. M. Bodenbinder, G. Balzer-Jöllenbeck, H. Willner, R.J. Batchelor, F.B.W. Einstein, C. Wang, and F. Aubke. Inorg. Chem. **35**, 82 (1996).
33. P.C. Leung and F. Aubke. Can. J. Chem. **62**, 2892 (1984).
34. P.C. Leung, G.B. Wong, and F. Aubke. J. Fluorine Chem. **35**, 607 (1987).
35. C. Wang, B. Bley, G. Balzer-Jöllenbeck, A.R. Lewis, S.C. Siu, H. Willner, and F. Aubke. J. Chem. Soc. Chem. Commum. 2071 (1995).
36. R.A. DeMarco and J.M. Shreeve. Adv. Inorg. Chem. Radiochem. **16**, 110 (1974).
37. W.W. Wilson, J.R. Dalziel, and F. Aubke. J. Inorg. Nucl. Chem. **37**, 665 (1975).
38. W.W. Wilson and F. Aubke. J. Fluorine Chem. **13**, 431 (1979).
39. O. Ruff and W. Plato. Ber. Dtsch. Chem. Ges. **37**, 673 (1904).
40. O. Ruff. Ber. Dtsch. Chem. Ges. **42**, 4021 (1909).
41. W. Manchot and H. Gall. Ber. Dtsch. Chem. Ges. **58**, 2175 (1925).
42. M.S. Kharash and H.S. Isbell. J. Am. Chem. Soc. **52**, 2919 (1930).
43. D. Belli Dell'Amico, F. Calderazzo, and G. Dell'Amico. Gazz. Chim. Ital. **107**, 101 (1977).
44. H.J. Emeléus and J.F. Wood. J. Chem. Soc. 2183 (1948).
45. M.S.R. Cader and F. Aubke. Can. J. Chem. **67**, 1700 (1989).
46. P.S. Braterman. Metal carbonyl spectra. Academic Press, New York. 1975.
47. T.A. Stromnova, L.G. Kuz'mina, M.N. Vargaftik, G.Ya. Mazo, Yu.T. Struchkov, and I.I. Moiseev. Izv. Akad. Nauk SSSR Ser. Khim. 720 (1978).
48. I.I. Moiseev, T.A. Stromnova, M.N. Vargaftik, G.Ya. Mazo, L.G. Kuz'mina, and Yu.T. Struchkov. J. Chem. Soc. Chem. Commun. 27 (1978).
49. R.Colton, R.H. Farthing, and M.J. McCormick. Aust. J. Chem. **26**, 2607 (1973).
50. P.L. Goggin and J. Mink. J. Chem. Soc. Dalton Trans. 534 (1974).
51. (*a*) E.O. Fischer and K. Öfele. Angew. Chem. **73**, 581 (1961); (*b*) Chem. Ber. **95**, 249 (1962).
52. E.W. Abel, R.A.N. McLean, S.P. Tyfield, P.S. Braterman, A.P. Walker, and J.P. Hendra. J. Mol. Spectrosc. **30**, 29 (1969).
53. C. Bach, H. Willner, C. Wang, S.J. Rettig, J. Trotter, and F. Aubke. Angew. Chem. In press.

The energetics of the oxidative addition of trisubstituted silanes to photochemically generated $(\eta^5\text{-}C_5R_5)Mn(CO)_2$

Bentley J. Palmer and Ross H. Hill

Abstract: The rates for the oxidative addition reaction of trisubstituted silanes (Et_3SiH, Et_2MeSiH, $EtMe_2SiH$, Et_2SiH_2) to photochemically generated $(\eta^5\text{-}C_5R_5)Mn(CO)_2$ ($R_5 = H_5$, Me_5, H_4Me) species have been measured for the temperature range 70 – 125 K. The reactions were carried out in either neat silane or a 50/50, by volume, mixture of methylcyclohexane and silane. The activation energies, determined using Arrhenius law, varied from 2 to 35 kJ/mol. The kinetic data fit an isokinetic relationship with an isokinetic temperature of 102 ± 6 K. The results are interpreted in terms of a variation in the loss of solvation prior to the oxidative addition. When the solvating molecule is methylcyclohexane, then loss of the solvent molecule precedes oxidative addition. In cases where solvation is by the silane, the incomplete loss of this silane precedes the oxidative addition.

Key words : mechanism, oxidative addition, solvation.

Résumé : Opérant à des températures allant de 70 à 125 K, on a mesuré les vitesses de la réaction d'addition oxydante de silanes trisubstitués (Et_3SiH, Et_2MeSiH, $EtMe_2SiH$ et Et_2SiH_2) à des espèces générées photochimiquement $(\eta^5\text{-}C_5R_5)Mn(CO)_2$ ($R_5 = H_5$, Me_5, H_4Me). Les réactions ont été effectuées soit en présence de silane pur, soit dans un mélange 50/50 par volume de méthylcyclohexane et de silane. Les énergies d'activation, déterminées à l'aide de la loi d'Arrhenius, varient de 2 à 35 kJ mol^{-1}. Les données cinétiques s'ajustent à une relation isocinétique avec une température isocinétique de 102 ± 6 K. On interprète les résultats en termes d'une variation dans la perte de solvatation avant l'addition oxydante. Lorsque la molécule effectuant la solvatation est le méthylcyclohexane, la perte de la molécule de solvant précède alors l'addition oxydante. Dans les cas où la solvatation se fait par le silane, la perte incomplète de ce silane précède l'addition oxydante.

Mots clés : mécanisme, addition oxydante, solvatation.

[Traduit par la rédaction]

Introduction

Oxidative addition by d^6 systems is very important in catalytic (1) and stoichiometric processes including, for example, C-H activation by $(\eta^5\text{-}C_5H_5)Re(CO)PMe_3$ (2). In solution, the oxidative addition of trisubstituted silane to $(\eta^5\text{-}C_5H_5)Mn(CO)_2$ and $(\eta^5\text{-}C_5Me_5)Mn(CO)_2$ has been shown to result from irradiation of the corresponding tricarbonyl (3, 4).

In this paper we report the results of an experimental study of the oxidative addition of trialkyl silanes to d^6, $16e^-$ unsaturated species. The organometallic reagents were generated at low temperature by the irradiation of $(\eta^5\text{-}C_5R_5)Mn(CO)_3$ ($R_5 = H_5$, Me_5, H_4Me) species. The photochemical and thermal reactions are summarized in eqs. [1] and [2], respectively. It is also possible that the $16e^-$ intermediate may react with the photogenerated CO (eq. [3]). The reaction eqs. [1]–[3] neglect the possible involvement of solvation by the glass. In a low-temperature glass it is possible to cause the photochemical reaction, CO dissociation, to occur at a rate substantially faster than the subsequent thermal oxidative addition of the trialkylsilane. Consequently, at low temperatures, reaction [1] can be made to occur faster than reaction [2] thereby accumulating $(\eta^5\text{-}C_5R_5)Mn(CO)_2$. This was demonstrated previously by Wrighton and co-workers (5–7). As long as the back reaction with free CO is too slow to compete for the dicarbonyl, the rate of eq. [2] is directly measurable.

$$[1]\quad (\eta^5\text{-}C_5R_5)Mn(CO)_3 \xrightarrow{h\nu} (\eta^5\text{-}C_5R_5)Mn(CO)_2 + CO$$

$$[2]\quad (\eta^5\text{-}C_5R_5)Mn(CO)_2 + R'_3SiH \xrightarrow{\Delta} (\eta^5\text{-}C_5R_5)MnH(SiR'_3)(CO)_2$$

$$[3]\quad (\eta^5\text{-}C_5R_5)Mn(CO)_2 + CO \xrightarrow{\Delta} (\eta^5\text{-}C_5R_5)Mn(CO)_3$$

Since the above studies were released several significant contributions to our understanding of the oxidative addition reaction have appeared (8–11). Of particular interest have been the contributions to understanding the role of the solvation of the coordinatively unsaturated intermediate in these studies. These studies do prompt one to question the effect of the low-temperature glass in the previous studies. In this study we provide some evidence concerning the effect of solvation in the low-temperature glass environment.

Received February 2, 1996.

This paper is dedicated to Professor Howard C. Clark in recognition of his contributions to Canadian chemistry.

B.J. Palmer and R.H. Hill.[1] Department of Chemistry, Simon Fraser University, Burnaby, BC V5A 1S6, Canada.

[1] Author to whom correspondence may be addressed. Telephone: (604) 291-4871. Fax: (604) 291-3765.

Fig. 1. FTIR spectral changes associated with the photolysis of $(\eta^5\text{-}C_5H_4Me)Mn(CO)_3$ in a 50/50 (v/v) mixture of $SiEt_2H_2$ and methylcyclohexane at 115 K. Spectrum prior to photolysis subtracted from spectrum after photolysis. Bands associated with $(\eta^5\text{-}C_5H_4Me)Mn(CO)_3$ at 2020 and 1935 cm^{-1} appear negative while bands associated with $(\eta^5\text{-}C_5H_4Me)Mn(CO)_2$ at 1949 and 1880 cm^{-1} and $(\eta^5\text{-}C_5H_4Me)\text{-}MnH(SiEt_2H)(CO)_2$ at 1978 and 1914 cm^{-1} appear positive.

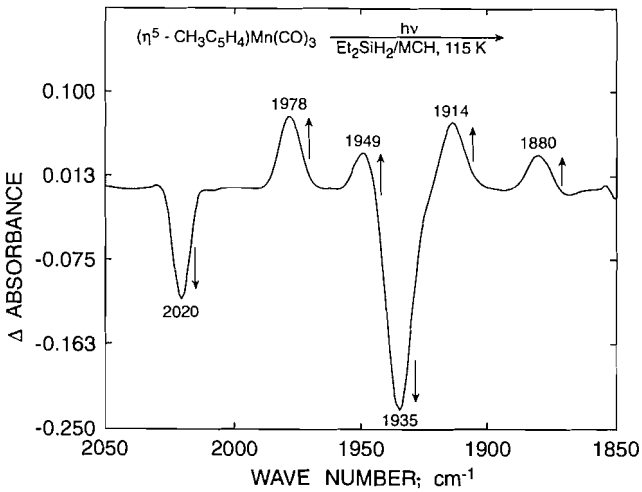

The kinetics of the oxidative addition of R'_3SiH ($R'_3 = Et_3$, Et_2Me, $EtMe_2$, Et_2H) to photogenerated $(\eta^5\text{-}C_5R_5)Mn(CO)_2$ ($R_5 = H_5$, Me_5, H_4Me) have been studied in the temperature range 70–125 K. The results of this study are used to provide insight into the intimate details of the mechanism of the oxidative addition with emphasis on the effect of solvation on the energetics..

Results

A sample consisting of $(\eta^5\text{-}C_5H_4Me)Mn(CO)_3$ in Et_2SiH_2–methylcyclohexane was cooled to 115 K and photolyzed (Fig. 1). Upon photolysis there was a decrease in absorption bands at 2020 and 1935 cm^{-1} due to $(\eta^5\text{-}C_5H_4Me)Mn(CO)_3$ and the appearance of absorption bands due to $(\eta^5\text{-}C_5H_4Me)Mn(CO)_2$ at 1949 and 1880 cm^{-1} and due to $(\eta^5\text{-}C_5H_4Me)\text{-}MnH(SiEt_2H)(CO)_2$ at 1978 and 1914 cm^{-1}. The intermediate was previously identified in a 77 K glass (12). The product was assigned by comparison with similar species (3, 5–7). Subsequently, spectra were obtained as a function of time following the consumption of the $(\eta^5\text{-}C_5H_4Me)Mn(CO)_2$ species and the formation of the oxidative addition product, $(\eta^5\text{-}C_5H_4Me)MnH(SiEt_2H)(CO)_2$. Figure 2 illustrates a typical result obtained for the reaction of $(\eta^5\text{-}C_5H_4Me)Mn(CO)_2$ with Et_2SiH_2 in a Et_2SiH_2–methylcyclohexane glass. In Fig. 2 are the absorbance difference spectra (spectrum after photolysis subtracted from subsequent spectra) showing the consumption of $(\eta^5\text{-}C_5H_4Me)Mn(CO)_2$ (negative peaks) and the formation of $(\eta^5\text{-}C_5H_4Me)MnH(SiEt_2H)(CO)_2$ (positive peaks). A plot of $\ln\{[(\eta^5\text{-}C_5H_4Me)Mn(CO)_2]_{t=0}/[(\eta^5\text{-}C_5H_4Me)Mn(CO)_2]_t\}$ against time (Fig. 3) is linear, and the slope yields the rate constant, k (3.78×10^{-4} s^{-1}), according to eq. [4]. For each of the systems studied, the decrease in absorbance due to $(\eta^5\text{-}C_5R_5)Mn(CO)_2$ species (or increase in absorbance due to $(\eta^5\text{-}C_5R_5)Mn\ H(SiR'_3)(CO)_2$ species) was found to be first order in $(\eta^5\text{-}C_5R_5)Mn(CO)_2$. In both cases the kinetic results were interpreted in terms of the first-order rate law given in eq. [4].

Fig. 2. Changes in absorbance following the monitoring of the sample generated above showing the selected spectral changes following 8, 16, 27, 40, 56, 80, and 107 min.

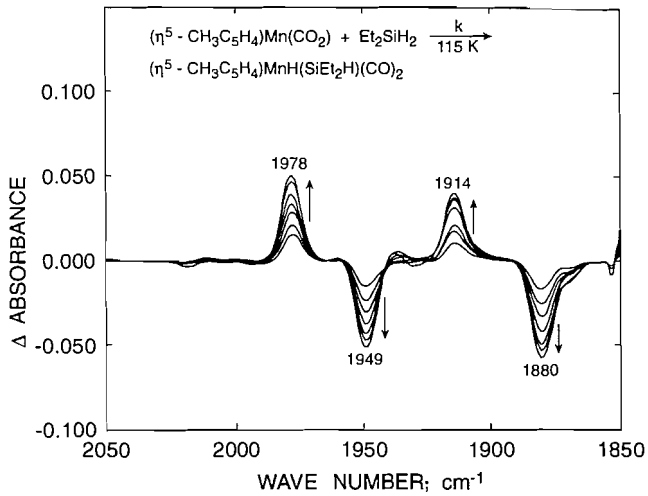

$$[4]\quad \frac{-d\,[(\eta^5\text{-}C_5R_5)Mn(CO)_2]}{dt} = k\,[(\eta^5\text{-}C_5R_5)Mn(CO)_2]$$

The photolysis of $(\eta^5\text{-}C_5H_4Me)Mn(CO)_3$ in a $EtMe_2SiH$ glass at 90 K gave rise to absorption bands in the FTIR due to the $16e^-$ species, $(\eta^5\text{-}C_5H_4Me)Mn(CO)_2$, at 1942 and 1870 cm^{-1}, and an unassigned band at 1845 cm^{-1}. Two bands assigned to the oxidative addition product, $(\eta^5\text{-}C_5H_4Me)MnH(CO)_2(SiEtMe_2)$, appeared at 1968 and 1900 cm^{-1}. In a dilute trialkylsilane glass at 110 K (1:1 methylcyclohexane/$EtMe_2SiH$ mixture by volume at room temperature) photolysis resulted in bands due to $(\eta^5\text{-}C_5H_4Me)Mn(CO)_2$, at 1946 and 1876 cm^{-1}, and an unassigned band at 1847 cm^{-1}. The two CO bands assigned to the oxidative addition product appeared at 1972 and 1905 cm^{-1}.

The photolysis of $(\eta^5\text{-}C_5H_5)Mn(CO)_3$ in a methylcyclohexane–Et_2MeSiH glass at 125 K showed bands due to the $16e^-$ species, $(\eta^5\text{-}C_5H_5)Mn(CO)_2$, at 1954 and 1885 cm^{-1}, and two unassigned bands at 1868 and 1834 cm^{-1}. The origin of the unexplained bands was unclear; however, their intensity did not vary on the time scale of the kinetic run. Therefore, it was concluded that eq. [2] represented the net thermal chemistry of all the $(\eta^5\text{-}C_5R_5)Mn(CO)_2$ ($R_5 = H_5$, Me_5, H_4Me) species studied. Relevant band positions for the compounds studied are summarized in Table 1.

For each of the systems studied, the photolysis of $(\eta^5\text{-}C_5R_5)Mn(CO)_3$ species in a dilute (50/50 v/v (289 K)) trialkylsilane–methylcyclohexane mixture or neat trialkylsilane (R'_3SiH) glass led to the loss of IR absorptions due to the starting complexes and the growth of new bands associated with the $16e^-$ species $(\eta^5\text{-}C_5R_5)Mn(CO)_2$ and the oxidative addition product $(\eta^5\text{-}C_5R_5)Mn\ H(SiR'_3)(CO)_2$. It was not possible

Table 1. Spectroscopic data for relevant compounds in trialkyl silane.

Complex	T, K (±1 K)	(CO) cm^{-1}
$(\eta^5\text{-}C_5H_4Me)Mn(CO)_3$	298	2023, 1940
	113	2020, 1935
	114	2021, 1935[a]
$(\eta^5\text{-}C_5H_4Me)Mn(CO)_2$	113	1946, 1877
	114	1948, 1889[a]
$(\eta^5\text{-}C_5H_4Me)MnH(SiEt_3)(CO)_2$	113	1971, 1906
$(\eta^5\text{-}C_5H_4Me)MnH(SiEt_2Me)(CO)_2$	113	1974, 1907
	114	1974, 1908[a]
$(\eta^5\text{-}C_5H_4Me)MnH(SiEtMe_2)(CO)_2$	90	1968, 1900
	110	1972, 1905[a]
$(\eta^5\text{-}C_5H_4Me)MnH(SiEt_2H)(CO)_2$	105	1976, 1910
	115	1978, 1914[a]
$(\eta^5\text{-}C_5Me_5)Mn(CO)_3$	298	2010, 1926
	110	2006, 1921
	108	2006, 1921[a]
$(\eta^5\text{-}C_5Me_5)Mn(CO)_2$	100	1933, 1864
	108	1933, 1864[a]
$(\eta^5\text{-}C_5Me_5)MnH(SiEt_2Me)(CO)_2$	100	1954, 1895
	108	1954, 1895[a]
$(\eta^5\text{-}C_5Me_5)MnH(SiEtMe_2)(CO)_2$	110	1954, 1893[a]
$(\eta^5\text{-}C_5H_5)Mn(CO)_3$	298	2028, 1945
	90	2024, 1940
	125	2024, 1940[a]
$(\eta^5\text{-}C_5H_5)Mn(CO)_2$	90	1954, 1885
	125	1954, 1885[a]
$(\eta^5\text{-}C_5H_5)Mn\ H(SiEt_2Me)(CO)_2$	90	1977, 1910
	125	1977, 1910[a]

[a]Solvent was a 50/50 mixture (by volume at room temperature) of silane and methylcyclohexane.

to see free CO (2132 cm^{-1}) in trialkylsilane (or a 1:1 trialkylsilane/methylcyclohexane mixture) glasses due to the overwhelming Si-H absorption. However, the stoichiometry of the photochemical loss of CO for the manganese complexes studied has been shown to be one mole of CO produced per mole of $(\eta^5\text{-}C_5R_5)Mn(CO)_3$ consumed (5). Although the direct monitoring of the increase or decrease in the CO absorption was not possible, it should be noted that photoproducts other than $(\eta^5\text{-}C_5R_5)Mn(CO)_2$ were not, in general, detected. The two exceptions were in the monitoring of the $(\eta^5\text{-}C_5H_4Me)Mn(CO)_3$–$EtMe_2SiH$ and the $(\eta^5\text{-}C_5H_5)Mn(CO)_3$–$Et_2MeSiH$ systems. In these cases the intensity of the unassigned bands did not vary during the thermal reaction. It is interesting to note that previous workers (12) assigned bands in similar positions as due to a photogenerated monocarbonyl although it is unlikely that such a species would be stable under the conditions of this reaction. The calculated rate constants for reaction of trialkylsilanes with the $(\eta^5\text{-}C_5R_5)\text{-}Mn(CO)_2$ complexes are presented in Table 2.

Discussion

The photochemical loss of CO from $(\eta^5\text{-}C_5R_5)Mn(CO)_3$ to give coordinatively unsaturated species (eq. [1]) in low-temperature trialkylsilane and methylcyclohexane–trialkylsilane glasses is consistent with previous work (5–7). Unfortunately, the Mn-H stretch was not observed in the IR, consistent with it being much weaker than bands associated with the CO stretching (4). However, the formation of a two-band pattern in the IR (at higher frequency, relative to the unsaturated $16e^-$ species) concurrent with the disappearance of the two bands due to the intermediate was consistent with the oxidative addition of the trialkylsilane. The room temperature photolysis of each tricarbonyl–silane system resulted in the appearance of ^1H NMR peaks in the −14.0 to −12.0 ppm region consistent with the formation of metal hydrides (13). IR absorption spectra of all the oxidative addition products possess two, approximately equal intensity, CO absorption bands indicative of 90° OC-Mn-CO angles (based on arguments similar to those in ref. 14). Therefore, in agreement with earlier studies, each $(\eta^5\text{-}C_5R_5)Mn\ H(SiR'_3)(CO)_2$ complex is formulated as the *cis* isomer. This is consistent with the crystallographically determined structure of $(\eta^5\text{-}C_5H_4Me)MnH(SiMePhNp)(CO)_2$ (Np ≈ 1-$C_{10}H_7$), which has a 91.4° OC-Mn-CO angle, and $(\eta^5\text{-}C_5H_5)MnH(SiPh_3)(CO)_2$ with an 88.7° OC-Mn-CO angle (in the solid state), both prepared by photolysis of the appropriate tricarbonyl in the presence of trialkylsilane (15, 16). It should be noted that the oxidative addition of an Si—H bond to a transition metal center does not always result in complete Si—H bond breakage. The incomplete oxidative addition of an Si—H bond may be viewed as a two-electron three-center (M, Si, H) bond. Such an interaction has been observed, by neutron diffraction, in the complex $(\eta^5\text{-}C_5H_4Me)MnH(SiFPh_2)(CO)_2$ (17). Recent X-ray and neutron diffraction results, and ^{29}Si NMR studies to obtain the coupling constants J(SiMH), show that the extent to which the oxidative addition is complete is greater when there are electron-releasing ligands on M and (or) highly electron-withdrawing substituents (R′) on Si (15).

Fig. 3. A plot of $\ln\{[(\eta^5\text{-}C_5H_4Me)Mn(CO)_2]_{t=0}/[(\eta^5\text{-}C_5H_4Me)Mn(CO)_2]_t\}$ against time for the experiment of Fig. 2.

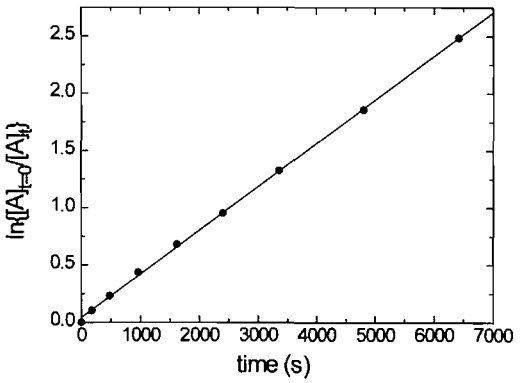

The order of the reaction

The trialkylsilane concentration, for experiments conducted in a neat trialkylsilane glass, was not incorporated into the rate equation. The rate of a bimolecular reaction can be thought of as being dependent on two main factors; (*i*) the frequency of

Table 2. Rate constants for the reaction of $16e^-$ $(\eta^5\text{-}C_5R_5)Mn(CO)_2$ complexes with R'_3SiH and R'_2SiH_2.

Arene	$[R'_3SiH]$, M[a]	T, K ± 1 K	k_{obs}, s^{-1}	k, $M^{-1}\ s^{-1}$	Error (%)[b] k_{obs} and k
$C_5H_4CH_3$	Et_2SiH_2				
	5.1	110	1.55×10^{-4}	3.04×10^{-5}	2
	5.1	115	3.81×10^{-4}	7.47×10^{-5}	1
	5.1	120	1.24×10^{-3}	2.43×10^{-4}	5
	15.6	70	1.43×10^{-6}	9.16×10^{-8}	10
	15.6	80	1.82×10^{-6}	1.16×10^{-7}	8
	15.6	90	3.19×10^{-6}	2.04×10^{-7}	7
	15.6	95	3.41×10^{-6}	2.19×10^{-7}	9
	Et_2MeSiH				
	4.1	105	5.19×10^{-6}	1.26×10^{-6}	9
	4.1	110	4.79×10^{-5}	1.17×10^{-5}	3
	4.1	115	2.64×10^{-4}	6.43×10^{-5}	1
	4.1	120	8.45×10^{-4}	2.06×10^{-4}	7
	4.1	123	2.12×10^{-3}	5.17×10^{-4}	7
	8.5	103	4.10×10^{-5}	4.82×10^{-6}	7
	8.5	105	1.21×10^{-4}	1.42×10^{-6}	5
	8.5	108	2.95×10^{-4}	3.47×10^{-5}	3
	8.5	110	2.18×10^{-4}	2.56×10^{-5}	8
	8.5	113	4.63×10^{-4}	5.45×10^{-5}	2
	8.5	115	1.24×10^{-3}	1.46×10^{-4}	4
	$EtMe_2SiH$				
	4.8	100	3.83×10^{-6}	7.98×10^{-7}	4
	4.8	105	2.96×10^{-5}	5.60×10^{-6}	1
	4.8	115	4.66×10^{-4}	9.71×10^{-5}	4
	4.8	118	8.57×10^{-4}	1.79×10^{-4}	4
	4.8	120	2.80×10^{-3}	5.83×10^{-4}	8
	13.8	90	5.58×10^{-7}	4.04×10^{-8}	10
	13.8	112	2.74×10^{-4}	1.99×10^{-5}	6
	13.8	115	3.16×10^{-4}	2.29×10^{-5}	8
	13.8	118	1.20×10^{-3}	8.69×10^{-5}	8
	Et_3SiH				
	7.0	103	1.15×10^{-5}	1.64×10^{-6}	2
	7.0	108	6.44×10^{-5}	9.20×10^{-6}	3
	7.0	113	2.63×10^{-4}	3.76×10^{-5}	2
	7.0	115	2.65×10^{-4}	3.79×10^{-5}	2
	7.0	118	1.14×10^{-3}	1.63×10^{-4}	2
	7.0	120	1.29×10^{-3}	1.84×10^{-4}	2
C_5H_5	Et_2MeSiH				
	8.2	80	4.19×10^{-6}	5.11×10^{-7}	[c]
	8.2	90	1.29×10^{-5}	1.57×10^{-6}	[c]
C_5H_5	Et_2MeSiH				
	4.1	115	2.54×10^{-4}	6.20×10^{-5}	2
	4.1	120	1.05×10^{-3}	2.56×10^{-4}	4
	4.1	122	2.09×10^{-3}	5.10×10^{-4}	3
	4.1	125	3.39×10^{-3}	8.26×10^{-4}	2
C_5Me_5	Et_2MeSiH				
	4.1	100	8.12×10^{-5}	1.98×10^{-5}	4
	4.1	104	1.36×10^{-4}	3.32×10^{-5}	4
	4.1	108	3.30×10^{-4}	8.05×10^{-5}	5
	4.1	110	1.17×10^{-3}	2.85×10^{-4}	6
	$EtMe_2SiH$				
	4.8	100	1.84×10^{-4}	3.83×10^{-5}	4
	4.8	105	3.62×10^{-4}	7.54×10^{-5}	2
	4.8	110	7.02×10^{-4}	1.46×10^{-4}	3
	4.8	115	1.21×10^{-3}	2.52×10^{-4}	11

[a]Trialkylsilane concentrations corrected for solvent contraction at 77 K.
[b]Obtained from statistical analysis of data.
[c]Insufficient data for statistical analysis.

collision between reacting molecules, and (*ii*) the collision energy (and geometry of the two species) being appropriate to surmount the activation barrier. Generally, for the case of gas phase reactions, the incorporation of reactant concentration is crucial. In gas phase reactions (assuming relatively low concentrations and pressure) there are a limited number of reactants and a great deal of empty space. Therefore, including the concentration of the reactive species is important in determining the rate of the reaction. Analogously, in solution, the inclusion of concentrations is important as a result of diffusional processes. However, in a neat trialkylsilane glass, clearly each $(\eta^5\text{-}C_5R_5)Mn(CO)_2$ species is entirely surrounded by silane molecules. Therefore, the probability of each $(\eta^5\text{-}C_5R_5)Mn(CO)_2$ molecule being surrounded by a sphere of silane molecules is unity. Hence, each collision that a $(\eta^5\text{-}C_5R_5)Mn(CO)_2$ molecule undergoes is with a trialkylsilane molecule.

For kinetic experiments done in a 50/50 mixture of trialkylsilane/methylcyclohexane one cannot simply neglect the trialkylsilane concentration. The probability of a $(\eta^5\text{-}C_5R_5)Mn(CO)_2$ species colliding with a trialkylsilane molecule, in a solvent mixture, cannot be assumed to be unity. In a neat trialkylsilane glass there is no doubt that the probability of the unsaturated species colliding with a trialkylsilane molecule is one. However, in a glass containing a mixture of two solvents the reduced probability of a $(\eta^5\text{-}C_5R_5)Mn(CO)_2$ species colliding with a trialkylsilane molecule must be taken into consideration. In a 50/50 silane/methylcyclohexane mixture it is possible that, during the process of forming a glass, methylcyclohexane preferentially forms a coordination sphere around the $(\eta^5\text{-}C_5R_5)Mn(CO)_3$ molecules. However, this possibility does seem remote. The other extreme, which seems just as unlikely, is that in a 50/50 mixture the trialkylsilane preferentially forms a sphere around the tricarbonyl complex. The only workable assumption, and the one that was made, was that the $(\eta^5\text{-}C_5R_5)Mn(CO)_3$ molecules have a statistical ratio of trialkylsilane and methylcyclohexane surrounding them. The probability of $(\eta^5\text{-}C_5R_5)Mn(CO)_2$ colliding with a trialkylsilane molecule would now be dependent on the concentration of trialkylsilane molecules surrounding the fragment.

Each of the rate constants was determined according to eq. [4]. Each of the rate constants in Table 2 is the result of dividing the observed rate by the silane concentration. The use of the silane concentration in cases where neat silane is utilized is expected to be a source of error. In spite of this limitation the relative correction provided by this procedure is perhaps the most appropriate procedure possible.

Analysis of the reaction energetics

For each $(\eta^5\text{-}C_5R_5)Mn(CO)_3$–$R'_3SiH$ system summarized in Table 2, the activation energy was determined using Arrhenius law. The activation parameters were determined from the slope and intercept of plots of $\ln(k)$ vs. $1/T$. For cases where rate constants were obtained in both neat silane glass and dilute silane–methylcyclohexane glass three sets of activation parameters were obtained. The first set of parameters was obtained from a plot of all the rate data for each silane. The second and third sets of activation parameters were obtained separately from plots of the data collected in neat silane and the dilute silane glass. All of these data are summarized in Table 3.

In a similar fashion, plots of $\ln(k/T)$ vs. $1/T$ were used to obtain the activation enthalpy and entropy from activated complex theory. The parameters obtained from the data collected in both neat and dilute silane, analyzed as above, are presented in Table 3.

The activation energies in Table 3, which include some literature data, cover a range of 44 kJ/mol. In cases where rate constants were determined in both neat and dilute glasses, two general cases were found. In the reaction of Et_2MeSiH with $(\eta^5\text{-}C_5H_4Me)Mn(CO)_2$ no significant variation in the activation parameters was identified between the analysis of the individual data and the combined data. For the remainder of the data a significant variation was found between the activation energy in neat silane glass and in a mixed silane–methylcyclohexane glass. In each case the variation resulted in a lower activation barrier in the neat silane and a smaller preexponential factor. In terms of activated complex theory we have a lower activation enthalpy and a more negative entropy of activation in the neat silane glass.

In Fig. 4 a plot of the enthalpy of activation versus the entropy of activation is presented. When the measurements were made in different glasses the data for silane glass and for the silane–methylcyclohexane glass are given separately. All data points except for the data associated with the strongly electron-withdrawing $(\eta^5\text{-}C_5Cl_5)Mn(CO)_2$ fragment clearly define a free energy relationship. Such a correlation is indicative of an isokinetic relationship (IKR) (18,19). From the slope of the plot the isokinetic temperature is determined to be ca. 102 ± 6 K.

The presence of the free energy relationship is usually taken to indicate that all the reactions follow a similar mechanism, at least to the point of the rate-determining step. Perhaps of most significance within the data presented is that the reactions all fall along the same line. For example, the activation energy for reaction of $(\eta^5\text{-}C_5H_4Me)Mn(CO)_2$ with Et_2SiH_2 increased from 2 to 23 kJ/mol upon changing the media from neat silane to the silane–methylcyclohexane mixture. In spite of this change in glass both these points are in keeping with the free energy relationship. This indicates that a similar step is controlling the energetics of the reaction of these species in the different glasses.

Discussion of the oxidative addition reaction

The initial unsaturated complex formed upon CO extrusion is quickly solvated by the glassy medium. In neat silane, the solvent may coordinate through a C—H bond (eq. [5]). However, in dilute trialkylsilane the coordinating species could be methylcyclohexane (eq. [6]) or the trialkylsilane.

[5] $(\eta^5\text{-}C_5R_5)Mn(CO)_2 + HSiR_3 \longleftrightarrow (\eta^5\text{-}C_5R_5)Mn(CO)_2(HSiR_3)$

[6] $(\eta^5\text{-}C_5R_5)Mn(CO)_2 + MeC_6H_{11} \longleftrightarrow (\eta^5\text{-}C_5R_5)Mn(CO)_2(MeC_6H_{11})$

The reaction that was studied in this paper is the reaction of this solvated species with the silane to yield the oxidative addition product. According to the possible discrete solvated

Table 3. Activation parameters for the reaction of 16e⁻ $(\eta^5\text{-}C_5R_5)Mn(CO)_2$ complexes with R'_3SiH and R'_2SiH_2.

Complex	Solvent	Silane	E_a, kJ mol^{-1}	ln(A)	H, kJ mol^{-1}	S, J mol^{-1} K^{-1}
$(\eta^4\text{-}C_4H_4)Fe(CO)_2$	Silane	Et_3SiH[a]	46 ± 3	36 ± 2	44 ± 2	46 ± 20
$(\eta^5\text{-}C_5Me_5)Mn(CO)_2$		Et_3SiH[a]	36 ± 2	36 ± 2	35 ± 2	51 ± 16
$(\eta^5\text{-}C_5H_5)Mn(CO)_2$		Et_3SiH[a]	34 ± 1	28 ± 1	33 ± 1	−9.6 ± 6
$(\eta^5\text{-}C_5Cl_5)Mn(CO)_2$		Et_3SiH[a]	41 ± 4	15 ± 24	0 ± 4	−129 ± 17
$(\eta^5\text{-}C_5H_4Me)Mn(CO)_2$		Et_3SiH	29 ± 2	20 ± 22	8 ± 2	−74 ± 17
$(\eta^5\text{-}C_5H_4Me)Mn(CO)_2$		$EtMe_2SiH$	26 ± 21	8 ± 3	25 ± 2	−96 ± 19
	Silane	$EtMe_2SiH$	23 ± 2	14 ± 2	22 ± 2	−127 ± 13
	MCH[b]	$EtMe_2SiH$	31 ± 2	23 ± 2	30 ± 2	−53 ± 16
$(\eta^5\text{-}C_5Me_5)Mn(CO)_2$	MCH[b]	$EtMe_2SiH$	12 ± 0.2	4.5 ± 0.2	11 ± 0.3	−205 ± 2.5
$(\eta^5\text{-}C_5H_4Me)Mn(CO)_2$		Et_2SiH_2	12 ± 3	1.8 ± 3.6	11 ± 2	−168 ± 30
	Silane	Et_2SiH_2	2.1 ± 0.4	−12.6 ± 0.6	1.5 ± 0.4	−347 ± 5
	MCH[b]		21.2 ± 3	14.4 ± 2.5	22 ± 2	−124 ± 16
$(\eta^5\text{-}C_5H_5)Mn(CO)_2$		Et_2MeSiH	13.6 ± 2	5.4 ± 1.6	13 ± 1	−199 ± 13
	MCH[b]		32 ± 2.3	23.6 ± 2.3	31 ± 2	−51 ± 17
	MCH[b,c]		6.6	−4.6	6	−280
$(\eta^5\text{-}C_5H_4Me)Mn(CO)_2$		Et_2MeSiH	30 ± 42	2 ± 4.5	29 ± 4	−64 ± 36
	Neat	Et_2MeSiH	32 ± 8	25 ± 9	31 ± 8	−38 ± 73
	MCH[b]	Et_2MeSiH	35 ± 2	27 ± 1.7	34 ± 2	−24 ± 14
$(\eta^5\text{-}C_5Me_5)Mn(CO)_2$	MCH[b]	Et_2MeSiH	22 ± 6	15.9 ± 7	21 ± 6	−114 ± 50

[a]from reference 5,6 and 7 after correcting for solvent contraction.
[b]The solvent in these cases was methylcyclohexane (MCH).
[c]Insufficient data was obtained to provide a statistical estimate of the error.

systems described in eqs. [5] and [6], the oxidative addition reaction should be described according to eqs. [7] and [8].

[7] $(\eta^5\text{-}C_5R_5)Mn(CO)_2(HSiR_3) + HSiR_3 \longrightarrow (\eta^5\text{-}C_5R_5)MnH(SiR_3)(CO)_2 + HSiR_3$

[8] $(\eta^5\text{-}C_5R_5)Mn(CO)_2(MeC_6H_{11}) + HSiR_3 \longrightarrow (\eta^5\text{-}C_5R_5)MnH(SiR_3)(CO)_2 + MeC_6H_{11}$

The reaction energetics suggest that in methylcyclohexane-diluted glasses reaction [8] describes the dominant reaction observed kinetically. For example, the reaction with trialkylsilanes occurred with a ca. 9 kJ mol^{-1} higher barrier when the reaction was carried out in a hydrocarbon solvent. This suggests that the difference between the activation energies of eqs. [7] and [8] is associated with this different solvation (i.e., eqs. [5] and [6]). This allows one to surmise that the difference in solvation energies is on the order of 9 kJ mol^{-1} stronger for the methylcyclohexane than for the silane itself. Further evidence about the chemistry in the dilute glass is found from examination of the rate constants for reaction in the dilute glass. In Fig. 5 a plot of ln(k/T) vs. $1/T$ for the reactions of $(\eta^5\text{-}C_5H_4Me)Mn(CO)_2$ with various silanes in dilute glasses is given. The data fit a single line reasonably well with an activation enthalpy of 30 ± 2 kJ/mol and an activation entropy of −58 ± 2 J mol^{-1} K^{-1}). These activation parameters presumably apply primarily to the dissociation of the methylcyclohexane solvent according to the reverse of eq. [6].

While this simple explanation appears to account for the observations, we believe that it does not explain the data. This result is apparently inconsistent with the report based on photoacoustic calorimetry that indicates that solvation of $(\eta^5\text{-}C_5H_5)Mn(CO)_2$ with hydrocarbon is less stable than the solvation by silane (9).

Following the result of Burkey and co-workers (9), the solvation with hydrocarbon is less stable than the solvation with the silane. The differences in the apparent activation energetics must then be a result of the extent to which solvation must be lost prior to reaction. In the case of methylcyclohexane the limiting case is complete loss of the methylcyclohexane solvation prior to the oxidative addition reaction. This results in the barrier of ca. 30 kJ mol^{-1}. In the case of the silane adducts, while solvation is stronger, as demonstrated by Burkey and co-workers, only incomplete loss of the silane is required for the oxidative addition of the already coordinated silane to occur. In simple terms, eq. [5] is never reversed in the operation of eq. [7]. This indicates that eq. [7] does not require an additional silane and is best written as eq. [9].

[9] $(\eta^5\text{-}C_5R_5)Mn(CO)_2(HSiR_3) \longrightarrow (\eta^5\text{-}C_5R_5)MnH(SiR_3)(CO)_2$

The observation of the IKR is then due to the loss of solvation occurring to different extents in the different systems. In the case of systems with a low activation enthalpy and large negative activation entropy, such as Et_2SiH_2–$(\eta^5\text{-}C_5H_4Me)Mn(CO)_2$, the reaction is an isomerism with a low barrier and a transition state that is highly ordered. This is consistent with an intermolecular isomerism. At the other extreme is the Et_3SiH–$(C_4H_4)Fe(CO)_2$ system, which apparently requires near complete loss of the silane from the coordination sphere.

Fig. 4. A plot of the enthalpy of activation versus the entropy of activation is presented for the reactions of silane with unsaturated metal fragments (data from Table 3).

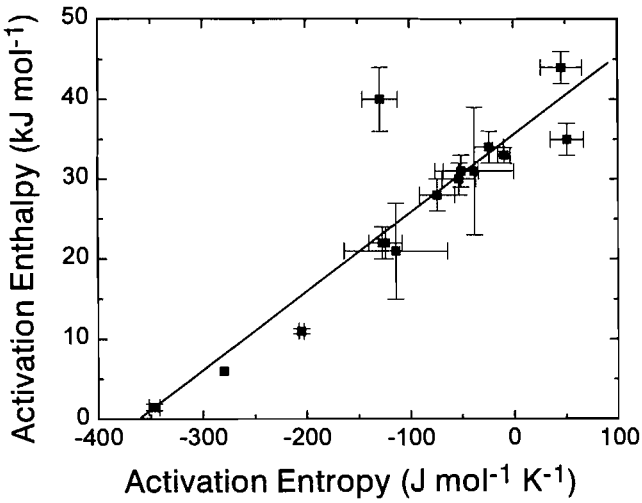

Fig. 5. A plot of $\ln(k/T)$ vs. $1/T$ for reaction of $(\eta^5\text{-}C_5H_4Me)Mn(CO)_2$ with various silanes in dilute glasses.

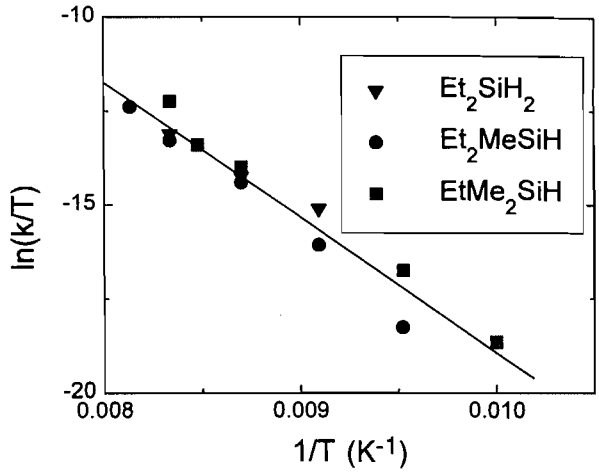

If solvent dissociation is the rate-limiting step, it is not surprising that the $(\eta^5\text{-}C_5Cl_5)Mn(CO)_2$–$Et_3SiH$ results could not be included in the full statistical analysis. The ability of the $(\eta^5\text{-}C_5Cl_5)Mn(CO)_2$ fragments to coordinate a solvent molecule should be much greater as a result of the electron-withdrawing nature of the $(\eta^5\text{-}C_5Cl_5)$ ligand. The $(\eta^5\text{-}C_5Cl_5)$ ligand should also affect the oxidative addition step. The calculated E_a value of 45 kJ mol^{-1} for the $(\eta^5\text{-}C_5Cl_5)Mn(CO)_3$–$Et_3SiH$ system is consistent with the enhanced ability of the $(\eta^5\text{-}C_5Cl_5)Mn(CO)_2$ fragments to strongly coordinate the silane molecule.

This interpretation of the data is also consistent with the general scheme presented by Yang and co-workers (11). The only modification required, and previously suggested by Burkey, is the inclusion of a silane-solvated dicarbonyl as a local minimum on the reaction coordinate. In the case of the $(\eta^5\text{-}C_5H_5)Mn(CO)_2$–$Et_3SiH$ discussed in that paper the difference between the local minimum in silane and in the hydrocarbon is not sufficiently different to be detectable.

Based on the above interpretation two points should be made. The first is that the intermediate dicarbonyl species for which spectroscopic data are presented are most likely solvated. The solvation does not provide a sufficient perturbation to allow us to spectroscopically assign silane or hydrocarbon solvation. The second point that must be considered is the use of a bimolecular rate constant for the interpretation of the reactions that occur according to eq. [9]. Equation [9] is unimolecular and k_{obs} would seem the appropriate rate constant to use for further work. However, to the extent that eq. [7] occurs, a bimolecular rate constant is required. The errors involved in the activation energy determinations are such that the differences imposed by the interpretation from k or k_{obs} are not significant.

Conclusions

The results of this study indicate that the oxidative addition of silane to photogenerated $(\eta^5\text{-}C_5R_5)Mn(CO)_2$ occurs through discrete processes dependent upon the nature of the reaction medium. In the absence of a solvent $(\eta^5\text{-}C_5R_5)Mn(CO)_2(HSiR_3)$ is the first intermediate formed following CO loss. This species undergoes an intramolecular rearrangement with incomplete loss of the silane. Where the reaction medium includes methylcyclohexane, $(\eta^5\text{-}C_5R_5)Mn(CO)_2(MeC_6H_{11})$ is formed. This species must undergo complete loss of the methylcyclohexane molecule in the oxidative addition step, resulting in a higher activation energy being observed for this process.

Experimental section

Instruments

Infrared spectral data were recorded by using a Bruker IFS 85 Fourier transform infrared spectrometer operating at 1 cm^{-1} resolution. ^{1}H NMR spectra were run on room temperature solutions using a Bruker SY100 NMR spectrometer. Chemical shifts are referenced to TMS. Irradiations were carried out by using the H_2O-filtered output (10 cm path length/Pyrex optics) from an Osram 100-W high-pressure Hg lamp. Low-temperature spectra were possible by means of a CTI Cryogenics model 22 cryocooler and a 350R compressor system equipped with a Lake Shore Cryotronics DRC 80C temperature controller. The temperature of the cell was monitored with a Lake Shore Cryotronics silicon diode sensor (DT500 DRC). The IR cell was constructed of high-conductivity copper and contained CaF_2 windows. The sample path length was 0.127 mm.

The trialkylsilane concentrations were corrected for solvent contraction associated with the lowering of the temperature. As a result of the experiments being conducted in the temperature range 70 –125 K, the volume of solvent was reduced considerably. In an effort to correct for the volume change, the percentage contraction was measured at 77 K. Both the neat trialkylsilane and the trialkylsilane–methylcyclohexane mixtures were measured for contraction. Neat trialkylsilane was placed in an NMR tube and the height of the meniscus was

Table 4. Percentage contraction of solvents at 77 K.

Solvent	% Contraction[a]
Et_3SiH	10
$EtMe_2SiH$	45
Et_2SiH_2	50
Et_2MeSiH	20
Et_3SiH/MeC_6H_{11}	14
$EtMe_2SiH/MeC_6H_{11}$	20
Et_2SiH_2/MeC_6H_{11}	24
Et_2MeSiH/MeC_6H_{11}	18

[a]Error in percentage contraction is estimated to be 10%.

Table 5. ^1H NMR of relevant compounds.

Compound	δ(Mn-H[a])
$(\eta^5\text{-}C_5H_4Me)MnH(SiEt_3)(CO)_2$	−13.50
$(\eta^5\text{-}C_5H_4Me)MnH(SiMeEt_2)(CO)_2$	−13.27
$(\eta^5\text{-}C_5H_4Me)MnH(SiMe_2Et)(CO)_2$	−13.09
$(\eta^5\text{-}C_5H_4Me)MnH(SiEt_2H)(CO)_2$	−12.63
$(\eta^5\text{-}C_5H_5)MnH(SiMeEt_2)(CO)_2$	−13.50
$(\eta^5\text{-}C_5Me_5)MnH(SiMeEt_2)(CO)_2$	−13.33
$(\eta^5\text{-}C_5Me_5)MnH(SiMe_2Et)(CO)_2$	−13.01

[a]Chemical shifts quoted, in ppm, relative to TMS.

measured. The NMR tube was then placed in a liquid nitrogen bath and allowed to equilibrate. Once the sample had equilibrated, at 77 K, the height of the meniscus was measured again and the percentage contraction calculated. The percentage contraction of the trialkylsilane–methylcyclohexane equal volume mixtures was measured in the same manner. Even though this method is not the most accurate method of measuring the solvent contraction, it is better than neglecting the volume contraction entirely. The percentage contraction for each solvent is summarized in Table 4, and the estimated error in the values is 10%.

Chemicals

The trialkylsilanes Et_3SiH, Et_2MeSiH, $EtMe_2SiH$, and Et_2SiH_2 were obtained from Petrarch Systems Inc. and used without further purification. The $(\eta^5\text{-}C_5H_4Me)Mn(CO)_3$ was obtained from Alfa Products and used without further purification. The $(\eta^5\text{-}C_5H_5)Mn(CO)_3$ and $(\eta^5\text{-}C_5Me_5)Mn(CO)_3$ were purchased from Strem Chemicals and were recrystallized prior to their use.

Kinetic measurements

All the kinetic measurements were conducted similarly and a typical one will be described in detail. A 50/50 Et_2SiH_2/methylcyclohexane solution containing $(\eta^5\text{-}C_5H_4Me)Mn(CO)_3$ was purged with N_2, and placed in a copper cell. The sample was then loaded into the cold head of the cryocooler, cooled to the appropriate temperature, and allowed to equilibrate. The solutions of $(\eta^5\text{-}C_5R_5)Mn(CO)_3$ (where $R_5 = H_5$, MeH_4, Me_5) were prepared so that the most intense absorption due to the CO ligands was between 0.2 and 1.0 (1×10^{-4} M). Subsequently, the sample was removed from the IR bench and photolyzed, using the Pyrex/water-filtered output (bandpass $\lambda > 313$ nm) of a high-pressure Hg lamp, so that approximately 15–20% of the $(\eta^5\text{-}C_5H_4Me)Mn(CO)_3$ was consumed and $(\eta^5\text{-}C_5H_4Me)Mn(CO)_2$ was detected by FTIR. After photolysis the IR spectrum typically showed a mixture of $(\eta^5\text{-}C_5H_4Me)\text{-}Mn(CO)_3$, $(CH_3C_5H_4)$, and $(\eta^5\text{-}C_5H_4Me)Mn\,H(SiEt_2H)(CO)_2$. It should be pointed out that the relative amounts of these species depended on temperature and photolysis time. Generally, photolysis was conducted in 10 s intervals until the absorbance due to the intermediate was 0.1. After generating the $16e^-$ intermediate, FTIR spectra were then obtained as a function of time, in the dark, to monitor the disappearance of the $(\eta^5\text{-}C_5H_4Me)Mn(CO)_2$ and the formation of the oxidative addition product, $(\eta^5\text{-}C_5H_4Me)Mn\,H(SiEt_2H)(CO)_2$. Care was taken to ensure that the IR beam of the spectrometer did not accelerate the "dark" reactions between the $16e^-$ species and the trialkylsilane. For some of the experiments, the sample was left in the IR beam continuously. Duplicate experiments were conducted, in which the sample was placed in the IR beam only when spectra were collected. No beam-induced chemistry on the time scale of data acquisition was observed.

NMR analysis

A NMR characterization of the starting materials and their photo-generated oxidative addition products was conducted using a Bruker SY100 spectrometer. The typical procedure was as follows: To a 5 mm NMR tube containing approximately 0.5 mL of C_6D_6 was added 0.025 mL of Et_2SiH_2 and 0.003 mL of $(\eta^5\text{-}C_5H_4Me)Mn(CO)_3$. The NMR spectrum of the light yellow solution was obtained. The sample was then photolyzed for 1 min using the water-filtered (10 cm path length, Pyrex optics) output of a 100-W high-pressure Hg lamp. Another NMR spectrum was obtained and the sample was then photolyzed for an additional 5 min, whereupon a final NMR spectrum was obtained. Relevant chemical shifts are quoted in Table 5.

References

1. C. Masters. Homogeneous transition metal catalysis. Chapman Hall, London. 1981.
2. R.G. Bergman, P.F. Seidler, and T. T. Wenzel. J. Am. Chem. Soc. **107**, 4358 (1985).
3. W. Jetz and W.A.G. Graham. Inorg. Chem. **10**, 4 (1971).
4. W.A.G. Graham. J. Organomet. Chem. **300**, 81 (1986).
5. R.H. Hill and M.S. Wrighton. Organometallics, **6**, 632 (1987).
6. R.H. Hill and M.S. Wrighton. Organometallics, **4**, 413 (1985).
7. K.M. Young and M.S. Wrighton. Organometallics, **8**, 1063 (1989).
8. T.J. Burkey. J. Am. Chem. Soc. **112**, 8329 (1990).
9. S. Hu, G.F. Farrell, C. Cook, R. Johnston, and T.J. Burkey. Organometallics, **13**, 4127 (1994).
10. D.L. Lichtenberger and A. Rai-Chaudhuri. J. Am. Chem. Soc. **112**, 2392 (1990).
11. D.M. Hester, J. Sun, A.W. Harper, and G.K. Yang. J. Am. Chem. Soc. **114**, 5234 (1992).
12. J.D. Black, M.J. Boylan, and P.S. Braterman. J. Chem. Soc. Dalton Trans. 673 (1981).
13. J.P. Collman, L.S. Hegedus, J.R. Norton, and R.G. Finke. Principles and applications of organotransition metal chemistry. University Science Books, Mill Valley, Calif. 1987.

14. F.A. Cotton and C.S. Kraihanzel. J. Am. Chem. Soc. **84**, 4432 (1962).
15. F. Carre, E. Colomer, F.J.B. Corriu, and A. Vioux. Organometallics, **3**, 1272 (1984), and references cited therein.
16. W.A.G. Graham. J. Organomet. Chem. **81**, 300 (1986).
17. U. Shubert, K. Ackermann, and B.J. Wörle. J. Am. Chem. Soc. **104**, 7378 (1982).
18. J.E. Leffler and E. Grunwald. Rates and equillibria of organic reactions. Wiley, New York. 1963.
19. O. Exner. Prog. Phys. Org. Chem. **10**, 411 (1973).

Synthesis, spectroscopic and structural studies of *O*-methyl and *O*-isopropyl monothiocarbonate (monoxanthate) derivatives of dimethyl- and diphenyltellurium(IV). Crystal structures of $Me_2Te[SCO_2(i\text{-}Pr)]_2$, $Ph_2Te[SCO_2(i\text{-}Pr)]_2$, $Me_2TeCl[SCO_2Me]$, and $Me_2TeBr[SCO_2(i\text{-}Pr)]$

John E. Drake, Robert J. Drake, Layla N. Khasrou, Anil G. Mislankar, Raju Ratnani, and Jincai Yang

Abstract: Monothiocarbonate derivatives of diorganotellurium(IV), $R_2Te[SCO_2R']_2$, and $R_2TeX[SCO_2R']$, where R = Me, Ph; R′ = Me, i-Pr; X = Cl, Br, and I, have been prepared and characterized by vibrational and ^1H, ^{13}C, and ^{125}Te NMR spectroscopy. $Me_2Te[SCO_2(i\text{-}Pr)]_2$ (**2**): $P2_1/n$ (No. 14) with cell parameters a = 6.942(6) Å, b = 25.599(3) Å, c = 9.404(6) Å, β = 94.48(6)°, V = 1666(1) Å^3, Z = 4, R = 0.0648, R_w = 0.0624; $Ph_2Te[SCO_2(i\text{-}Pr)]_2$ (**4**): $P2_1/n$ (No. 14) with a = 12.360(4) Å, b = 12.277(3) Å, c = 15.066(3) Å, β = 102.82(2)°, V = 2229.1(9) Å^3, Z = 4, R = 0.0368, R_w = 0.0312; $Me_2TeCl[SCO_2Me]$ (**5**); $P2_1/c$ (No. 14) with a = 5.193(2) Å, b = 18.118(4) Å, c = 9.613(5) Å, β = 91.31(6)°, V = 904.2(6) Å^3, Z = 4, R = 0.0396, R_w = 0.0361; and $Me_2TeBr[SCO_2(i\text{-}Pr)]$ (**8**): $P2_1/n$ (No. 14) with a = 11.701(2) Å, b = 6.250(2) Å, c = 16.152(2) Å, β = 98.43(1)°, V = 1168.4(4) Å^3, Z = 4, R = 0.0369, R_w = 0.0325. In all molecules, the immediate environment about tellurium is that of the saw-horse structure in which the lone pair is assumed to be stereochemically active and occupying an equatorial position in a distorted trigonal bipyramid. In **2** and **5**, the terminal oxygen atoms are oriented toward tellurium, whereas in **4**, one O(i-Pr) group is oriented toward tellurium, as it is in **8**. In the latter cases, the terminal oxygen atoms act as weak bridges to form a pseudo dimeric species in **4** and a pseudo polymer in **8**. Supramolecular interactions in **2** and **5** lead to a sulfur-bridged dimer in the former and a chlorine-bridged polymer in the latter.

Key words: structure, tellurium, dimethyl, diphenyl, monothiocarbonates.

Résumé : On a préparé les dérivés monothiocarbonates des diorganotellure(IV), $R_2Te[SCO_2R']_2$ et $R_2TeX[SCO_2R']$ dans lesquels R = Me, Ph; R′ = Me, i-Pr; X = Cl, Br et I, et on les a caractérisés par les spectroscopies de vibration et de RMN du ^1H, du ^{13}C et du ^{125}Te. $Me_2Te[SCO_2(i\text{-}Pr)]_2$ (**2**) : $P2_1/n$ (No. 14) avec a = 6,942(6), b = 25,599(3) et c = 9,404(6) Å, β = 94,48(6)°, V = 1666(1) Å^3, Z = 4, R = 0,0648 et R_w = 0,0624; $Ph_2Te[SCO_2(i\text{-}Pr)]_2$ (**4**) : $P2_1/n$ (No. 14) avec a = 12,360(4), b = 12,277(3) et c = 15,066(3) Å, β = 102,82(2)°, V = 2229,1(9) Å^3, Z = 4, R = 0,0368 et R_w = 0,0312; $Me_2TeCl[SCO_2Me]$ (**5**) : $P2_1/c$ (No. 14) avec a = 5,193(2), b = 18,118(4) et c = 9,613(5) Å, β = 91,31(6)°, V = 904,2(6) Å^3, Z = 4, R = 0,0396 et R_w = 0,0361; $Me_2TeBr[SCO_2(i\text{-}Pr)]$ (**8**) : $P2_1/n$ (No. 14) avec a = 11,701(2), b = 6,250(2) et c = 16,152(2) Å, β = 98,43(1)°, V = 1168,4(4) Å^3, Z = 4, R = 0,0369 et R_w = 0,0325. Dans toutes les molécules, l'environnement immédiat du tellure correspond à une structure cavalière dans laquelle on suppose que la paire libre est stéréochimiquement active et qu'elle occupe une position équatoriale dans une bipyramide trigonale déformée. Dans les composés **2** et **5**, les atomes d'oxygène terminaux sont orientés vers le tellure, alors que dans le composé **4**, un groupe O(i-Pr) est orienté vers le tellure, comme c'est le cas dans le composé **8**. Dans ces derniers cas, les atomes d'oxygène terminaux agissent comme de faibles ponts conduisant à la formation d'espèces pseudo-dimériques dans le composé **4** et d'un pseudo-polymère dans le composé **8**. Des interactions supramoléculaires dans les

Received January 30, 1996.

This paper is dedicated to Professor Howard C. Clark in recognition of his contributions to Canadian chemistry.

J.E. Drake,[1] R.J. Drake, L.N. Khasrou, A.G. Mislankar,[2] R. Ratnani,[3] and J. Yang. Department of Chemistry and Biochemistry, University of Windsor, Windsor, ON N9B 3P4, Canada.

[1] Author to whom correspondence may be addressed. Telephone: (519) 253-4232, Ext. 3551. Fax: (519) 973-7098. E-mail: ak4@uwindsor.ca

[2] Present address: Pulp and Paper Centre, University of Toronto, Toronto, ON M5S 1A4, Canada.

[3] Present address: Department of Chemistry, Dayanand College, Ajmer 305001, India.

composés **2** et **5** conduisent à la forme d'un dimère relié par le soufre dans le premier et d'un polymère lié par le chlore dans le dernier.

Mots clés : structure, tellure, diméthyle, diphényle, monothiocarbonates.

[Traduit par la rédaction]

Introduction

There have been a number of reports on the reactions of organotellurium(IV) compounds with a variety of 1,1-dithio ligands, such as *O*-alkyl dithiocarbonates (1–6), *N,N*-dialkyl dithiocarbamates (5–14), and *O,O*-dialkyl(alkylene) dithiophosphates (4–6, 14–21), as well as a recent extensive review of supramolecular associations in tellurium complexes with sulfur ligands (22). In general, the chemistry of monothio ligands has received much less attention but a few reports have appeared relating to main group element derivatives including those on monothiocarbamate compounds of thallium (23), tin (24, 25), and, most recently, tellurium (26) as well as on monothiophosphate compounds of tin (27, 28). No reports are evident on derivatives of monothiocarbonates (monoxanthates).

We report on the synthesis and characterization of a variety of diorganotellurium(IV) monothiocarbonates, $R_2Te[SCO_2R']_2$ and $R_2TeX[SCO_2R']$, where R = Me, Ph; R′ = Me, i-Pr; and X = Cl, Br, and I, and present the molecular structures of $Me_2Te[SCO_2(i\text{-}Pr)]_2$, **2**, $Ph_2Te[SCO_2(i\text{-}Pr)]_2$, **4**, $Me_2TeCl[SCO_2Me]$, **5**, and $Me_2TeBr[SCO_2(i\text{-}Pr)]$, **8**.

Experimental

Materials

$TeCl_4$, Me_4Sn, and COS gas were obtained from Aldrich. $TeBr_4$ and Me_2TeI_2 were obtained from Alfa and Organometallics, Inc., respectively. Ph_2TeCl_2 was prepared by the literature method (29) and Me_2TeCl_2 and Me_2TeBr_2 were prepared by an adaption of this method utilizing the reaction of $TeCl_4$ or $TeBr_4$ with Me_4Sn in toluene at 60°C under reflux for 4 h. The reactions were carried out under anhydrous conditions. All solvents were dried and distilled prior to use.

Preparation of the sodium salts of the *O*-alkyl monothiocarbonic acids

$NaSCO_2Me$ and $NaSCO_2(i\text{-}Pr)$

Sodium metal (approximately 1.0 g) was dissolved in dry methanol (20 mL) or isopropanol (25 mL) under nitrogen followed by the addition of dried benzene or toluene (5 mL). Sodium methoxide or isopropoxide was formed as a white slurry in the mixture accompanied by the evolution of hydrogen gas. Dry COS gas was then bubbled through the mixture for 15–20 min to give a white solid. The solvent and any unreacted alcohol were pumped off and the product washed with dichloromethane and left in the refrigerator for 1 day. The white solid formed was then washed with diethyl ether and dried under vacuum to give $NaSCO_2Me$: yield 81%. IR (cm^{-1}) distinctive features: 1592 vs, vbr, 1428 m, 1188 m, 1120 vs,br, 1040 m, 965 mw, 695 mw; Raman (cm^{-1}): 825 (100); or $NaSCO_2(i\text{-}Pr)$: yield 83%. IR (cm^{-1}): 1550 s, br, 1384 mw, 1371 m, 1186 s, 1086 s, br 973 m , 688 m; Raman (cm^{-1}): 830 (100). Both salts hydrolyse on exposure to the atmosphere.

Preparation of dimethylbis(*O*-methyl and *O*-isopropyl monothiocarbonato)tellurium(IV)

*$Me_2Te[SCO_2Me]_2$, **1**, and $Me_2Te[SCO_2(i\text{-}Pr)]_2$, **2***

Typically, a slight excess of the dried sodium salt of *O*-isopropyl monothiocarbonic acid (0.278 g, 1.96 mmol) was added to a solution of dimethyltellurium dichloride (0.216 g, 0.94 mmol) in dried toluene (20 mL) and the mixture stirred for 2 h. The reaction mixture was filtered to remove NaCl and unreacted materials. The solvent was reduced to 5 mL under vacuum, *n*-hexane (approximately 5 mL) was added, and the solution was left overnight in the refrigerator at −6°C. The resulting precipitate was washed with *n*-hexane and dried under vacuum to give $Me_2Te[SCO_2(i\text{-}Pr)]_2$, **2**: white crystals, mp 72–73°C, yield 87%. IR (cm^{-1}) main features: 1638 vs, 1150 vvs, 1091 vs, 843 s, 683 m; Raman (cm^{-1}): 547 [55], 537 [100], 315 [85]. Anal. calcd. for $C_{10}H_{20}O_4S_2Te$: C 30.33, H 3.56; found: C 30.69, H 3.42. Similarly, using $NaSCO_2Me$, $Me_2Te[SCO_2Me]_2$, **1** was formed: colorless crystals, yield 88.5%. IR (cm^{-1}) main features: 1648 s, 1262 s, 1126 vs, 1022 sh, 842 m, 638 s; Raman (cm^{-1}): 547 [45], 538 [75], 313 [100].

Preparation of diphenylbis(*O*-methyl and *O*-isopropyl monothiocarbonato)tellurium(IV)

*$Ph_2Te[SCO_2Me]_2$, **3**, and $Ph_2Te[SCO_2(i\text{-}Pr)]_2$, **4***

Typically, a slight excess of the sodium salt of *O*-isopropyl monothiocarbonic acid (0.220 g, 1.55 mmol) was added to a solution of diphenyltellurium dichloride (0.262 g, 0.74 mmol) in dried toluene (20 mL). The color of the reaction mixture changed from colorless to yellow in a few minutes, but stirring was continued for 2 h to ensure complete reaction. The mixture was then filtered to remove NaCl and unreacted materials, before the volume of the solvent was reduced to approximately 5 mL under vacuum. Then *n*-hexane (approximately 5 mL) was added and the solution was left overnight in the refrigerator at −6°C. The crystals that formed were washed with *n*-hexane and dried under vacuum to give $Ph_2Te[SCO_2(i\text{-}Pr)]_2$, **4**: pale-yellow crystals, mp 99°C, yield 89%. IR (cm^{-1}) main features: 1653 s, 1149 vs, 1088 vs, 843 ms, 734 ms, 683 ms, 660 sh; Raman (cm^{-1}): 998 [55], 314 [100]. Anal. calcd. for $C_{20}H_{24}O_4S_2Te$: C 46.18, H 4.65; found: C 45.45, H 4.47. Attempts to isolate $Ph_2Te[SCO_2Me]_2$ in pure form using $NaSCO_2Me$, under similar conditions as described above, failed. Thus, an excess of $NaSCO_2Me$ (0.85 mmol) and Ph_2TeCl_2 (0.34 mmol) were added under nitrogen to dichloromethane or toluene (15 mL) and held for 10 min at −78°C. The unreacted materials and NaCl were filtered off and the ^1H NMR spectrum of the solution recorded immediately. Peaks assignable to $Ph_2Te[SCO_2Me]_2$, **3**, were predominant but peaks assignable to the diligand (Table 8) and Ph_2Te were also present even though the solution had been held at −78°C. The first-order rate constants at 295 K, $k_{295} = 3.45 \times 10^{-5}$ s^{-1}, apparent activation energy, $E_a = 41$ kJ mol^{-1}, and Arrhenius

Fig. 1. ^{1}H NMR spectrum of the decomposition of $Ph_2Te[SCO_2Me]_2$ taken after 1, 2, 3, and 6 h. Peaks due to $Ph_2Te[SCO_2Me]_2$, $[SCO_2Me]_2$, Ph_2Te, and $MeOSCO_2Me$ are labelled a, b, c, and d, respectively.

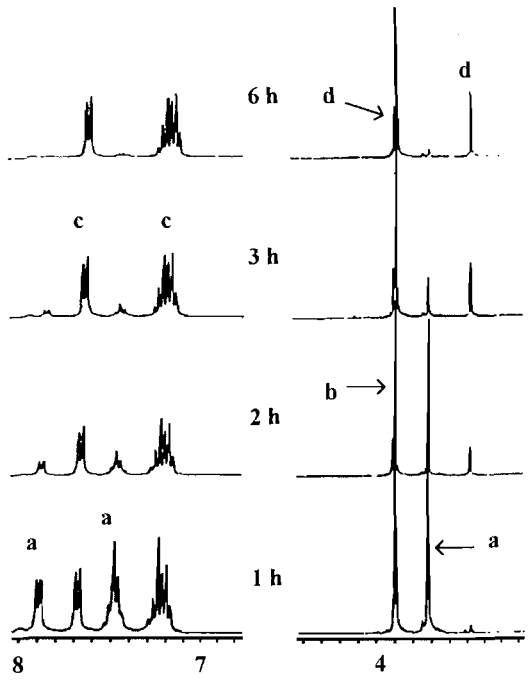

preexponential factor, $A = 6.0 \times 10^2$ s^{-1}. An example of a typical run is given in Fig. 1, which illustrates that additional decomposition occurs with two peaks of equal intensity appearing at 3.92 and 3.48 ppm, possibly attributable to $MeOSCO_2Me$. This requires the elimination of COS, and the infrared spectrum of the gas above the solution showed the strong parallel band centered at 2079 cm^{-1}, as well as weaker features at 859 and 527 cm^{-1}, attributable to COS.

Preparation of halodimethyl(*O*-methyl and *O*-isopropyl monothiocarbonato)tellurium(IV)

*$Me_2TeCl[SCO_2Me]$, **5**, $Me_2TeI[SCO_2Me]$, **6**, $Me_2TeCl[SCO_2(i\text{-}Pr)]$, **7**, $Me_2TeBr[SCO_2(i\text{-}Pr)]$, **8**, and $Me_2TeI[SCO_2(i\text{-}Pr)]$, **9***

Typically, an equimolar amount of dried $NaSCO_2Me$ (0.078 g, 0.68 mmol) was added to a solution of Me_2TeCl_2 (0.158 g, 0.68 mmol) in dichloromethane (20 mL). The mixture was stirred for 2 h before being filtered to remove NaCl and unreacted materials. The solvent was removed under reduced pressure to yield the crude product, which was then recrystallized from a dichloromethane–*n*-hexane mixture to give $Me_2TeCl[SCO_2Me]$, **5**: white crystals, mp 78°C, 84% yield. IR (cm^{-1}) main features: 1655 ms, 1261 s, 1098 vs,br, 1024 sh, 864 mw, 634 vs; Raman (cm^{-1}): 543 [100 br], 319 [25]. Similarly, using $NaSCO_2(i\text{-}Pr)$ (0.160 g, 1.12 mmol) added to a solution of Me_2TeCl_2 (0.257 g, 1.12 mmol) in dichloromethane (20 mL), $Me_2TeCl[SCO_2(i\text{-}Pr)]$, **7** was formed: white crystals, mp 56–57°C, 84% yield. IR (cm^{-1}) main features: 1673 vs,br, 1150 vs, 1090 vs,br, 844 m, 673 m; Raman (cm^{-1}): 544 [60], 535 [100], 325 [90]. Anal. calcd. for $C_6H_{13}O_2SClTe$: C 23.08, H 4.20; found: C 22.72, H 4.32; In a similar fashion as just described for **5** and **7**, the reaction of equimolar amounts of $NaSCO_2Me$ or $NaSCO_2(i\text{-}Pr)$ with Me_2TeBr_2 or Me_2TeI_2 in dichloromethane gave $Me_2TeI[SCO_2Me]$, **6**: yellow viscous oil, 78% yield. IR (cm^{-1}) main features: 1655 s, 1264 vs, 1127 vs, 864 m, 647 ms; Raman (cm^{-1}): 521 [100 br], 315 [55]. $Me_2TeBr[SCO_2(i\text{-}Pr)]$, **8**: pale-yellow crystals, mp 68–69°C, 86% yield. IR (cm^{-1}) main features: 1673 vs, 1153 vs, 1091 vs,br, 845 ms, 677 m; Raman (cm^{-1}): 539 [45], 527 [60], 325 [100]. Anal. calcd. for $C_6H_{13}O_2SBrTe$: C 20.20, H 3.67; found: C 20.52, H 3.77; and $Me_2TeI[SCO_2(i\text{-}Pr)]$, **9**: yellow crystals, 81% yield. IR (cm^{-1}) main features: 1674 s, 1155 s, 1091 s, 1020 sh, 843 ms, 677 w; Raman (cm^{-1}): 539 [45], 527 [60], 325 [100]. Attempts to obtain crystals of $Me_2TeI[SCO_2Me]$, **6**, failed. After 24 h at room temperature, the ^{1}H NMR spectrum of a solution of **6** showed peaks attributable to Me_2TeI_2, and the diligand, $[SCO_2Me]_2$, in approximately equimolar amounts and, after 36 h, these peaks dominated the spectra while two of equal intensity at 3.92 and 3.48 ppm had started to grow in. COS was also identified in the infrared spectrum of the vapour above the solution, as described above.

Preparation of chlorodiphenyl(*O*-methyl and *O*-isopropylmonothiocarbonato)tellurium(IV)

*$Ph_2TeCl[SCO_2Me]$, **10**, and $Ph_2TeCl[SCO_2(i\text{-}Pr)]$, **11***

Typically, an equimolar amount of dried $NaSCO_2Me$ (0.063 g, 0.55 mmol) was added to a solution of Ph_2TeCl_2 (0.195 g, 0.55 mmol) in dichloromethane (20 mL) held at 0°C and the mixture stirred for 1.5 h before being filtered to remove NaCl and unreacted materials. The solvent was removed under reduced pressure to yield $Ph_2TeCl[SCO_2Me]$, **10**: white solid, 82% yield. IR (cm^{-1}) main features: 1656 s,br 1266 m, 1189 sh, 1131 vs,vbr 1059 sh, 843 mw, 736 s, 683 s, 650 sh; Raman (cm^{-1}): 997 [100], 658 [35], 317 [15]. Similarly, using $NaSCO_2(i\text{-}Pr)$ (0.0620 g, 0.44 mmol) added to a solution of Ph_2TeCl_2 (0.154 g, 0.44 mmol) in dichloromethane (20 mL), $Ph_2TeCl[SCO_2(i\text{-}Pr)]$, **11** was formed: white solid, 87% yield. IR (cm^{-1}) main features: 1653 s, 1146 s, 1092 s, 843 ms, 737 ms, 686 ms, 678 ms; Raman (cm^{-1}): 998 [100], 657 [55], 320 [15]. Attempts at work-up to obtain X-ray quality crystals failed. The ^{1}H NMR spectrum of the solutions being used for recrystallization showed peaks attributable to Ph_2TeCl_2, Ph_2Te, and diligand in addition to those attributable to **10** and **11**.

Physical measurements

The elemental analyses were performed at Guelph Chemical Laboratories. Density measurements were performed by the flotation method. The infrared spectra were recorded on a Nicolet 5DX FT spectrometer as CsI pellets and the Raman spectra were recorded on a Ramanor U-1000 spectrometer using the 5145 Å exciting line of an argon ion laser with samples sealed in capillary tubes. The ^{1}H and ^{13}C NMR spectra were recorded on a Bruker 300 FT/NMR spectrometer in $CDCl_3$ using Me_4Si as internal standard. The ^{125}Te NMR spectra were recorded on a Bruker 200 FT/NMR spectrometer in $CDCl_3$ using Me_2Te as external standards as appropriate. The melting points were determined on a Fisher–Johns apparatus.

Table 1. Summary of crystallographic data, intensity collection, and structural refinement for $Me_2Te[SCO_2(i\text{-}Pr)]_2$, **2**, $Ph_2Te[SCO_2(i\text{-}Pr)]_2$, **4**, $Me_2TeCl[SCO_2Me]$, **5**, and $Me_2TeBr[SCO_2(i\text{-}Pr)]_2$, **8**.

Parameter	2	4	5	8
Cell constants				
a (Å)	6.942 (6)	12.360 (4)	5.193 (2)	11.701 (2)
b (Å)	25.599 (3)	12.277 (3)	18.118 (4)	6.250 (2)
c (Å)	9.404 (6)	15.066 (3)	9.613 (5)	16.152 (2)
β (deg)	94.48 (6)	102.82 (2)	91.31 (6)	98.43 (1)
Cell volume (Å^3)	1666(1)	2229.1(9)	904.2(6)	1168.4(4)
Space group	$P2_1/n$	$P2_1/n$	$P2_1/c$	$P2_1/n$
Mol. wt. (g mol^{-1})	395.99	520.13	284.23	356.73
Z	4	4	4	4
ρ_{calcd} (g cm^{-1})	1.58	1.55	2.09	2.03
Absorption coefficient μ (cm^{-1})	20.36	15.43	37.57	60.73
Transmission factors	0.38–1.00	0.90–1.00	0.54–1.00	0.35–1.00
Temperature (°C)	23	23	23	23
Radiation	MoKα 0.71069			
Monochromator	Highly oriented graphite			
Total reflections measured	3401	4340	1844	2395
Unique data used	921	2301	1001	1170
No. of parameters (NP)	104	160	82	100
$R = \Sigma\|\|F_o\| - \|F_c\|\|/\Sigma\|F_o\|$	0.0648	0.0367	0.0396	0.0369
$R_w = [(\Sigma w(\|F_o\| - \|F_c\|)^2/\Sigma wF_o^2)]^{1/2}$	0.0624	0.0310	0.0361	0.0325
Largest shift/esd, final cycle	0.0003	0.0005	0.0004	0.0009
Largest residual electron density (e Å^{-3})	0.87	0.67	0.61	0.61
Atom associated with residual density	Te(1)	C(10)	C(2)	Te(1)

X-ray crystallographic analysis

White needle-like crystals of $Me_2Te[SCO_2(i\text{-}Pr)]_2$, **2**, white block crystals of $Me_2TeCl[SCO_2Me]$, **5**, and yellow block crystals of $Ph_2Te[SCO_2(i\text{-}Pr)]_2$, **4**, and $Me_2TeBr[SCO_2(i\text{-}Pr)]$, **8**, were sealed in thin-walled glass capillaries and mounted on a Rigaku AFC6S diffractometer, with graphite-monochromated Mo Kα radiation.

Cell constants and an orientation matrix for data collection, obtained from a least-squares refinement using the setting angles of 20 carefully centered reflections in the range $12.61 < 2\theta < 19.68°$ (for **2**), $12.70 < 2\theta < 15.67°$ (for **4**), $7.85 < 2\theta < 15.73°$ (for **5**), and $13.00 < 2\theta < 18.21°$ (for **8**) corresponded to monoclinic cells whose dimensions are given in Table 1. For **2**, **4**, and **8**, the systematic absences ($h0l$, $h+l \neq 2n$; $0k0$, $k \neq 2n$) are observed and for **5** they are ($h0l$, $l \neq 2n$; $0k0$, $k \neq 2n$). Based on statistical analyses of intensity distributions and the successful solution and refinement of the structures, the space groups were determined to be $P2_1/n$ (No. 14) for **2**, **4**, and **8**, and $P2_1/c$ (No. 14) for **5**.

The data were collected at a temperature of 23 ± 1°C using the ω–2θ scan technique to a maximum 2θ value of 50.0°. The ω scans of several intense reflections, made prior to data collection, had an average width at half-height of 0.23° for **2** and **5**, 0.30° for **4**, and 0.29° for **8** with a takeoff angle of 6.0°. Scans of $(0.58 + 0.30 \tan\theta)°$ for **2**, $(1.05 + \tan\theta)°$ for **4**, and $(1.63 + 0.30 \tan\theta)°$ for **5** and **8** were made at a speed of 8.0 (**2** and **4**) and 32.0°/min (in ω) for **5** and **8**. The weak reflections ($I < 10.0\sigma(I)$) were rescanned (maximum of two rescans) and the counts were accumulated to assure good counting statistics. Stationary background counts were recorded on each side of the reflection. The ratio of peak counting time to background counting time was 2:1. The diameter of the incident beam collimator was 0.5 mm, and the crystal to detector distance was 400.0 mm.

Of the 3401 (**2**), 4340 (**4**), 1844 (**5**), or 2395 (**8**) reflections that were collected, 3029 (**2**), 4141 (**4**), 1654 (**5**), or 2277 (**8**) were unique (R_{int} = 0.169 (**2**), 0.031 (**4**), 0.183 (**5**), or 0.031 (**8**)). The intensities of three representative reflections, which were measured after every 150 reflections, remained constant throughout data collection, indicating crystal and electronic stability (no decay correction was applied).

The linear absorption coefficient for Mo Kα is 20.36 cm^{-1} (**2**), 15.43 cm^{-1} (**4**), 37.57 cm^{-1} (**5**), and 60.73 cm^{-1} (**8**). An empirical absorption correction, based on azimuthal scans of several reflections, was applied, which resulted in transmission factors ranging from 0.38 to 1.00 (**2**), 0.90 to 1.00 (**4**), 0.554 to 1.00 (**5**) and 0.35 to 1.00 (**8**). The data were corrected for Lorentz and polarization effects.

The structures were solved by direct methods.[4] With the exception of the phenyl rings in compound **2**, which were constrained to a regular hexagon with C—C distances set at 1.40 Å and C-C-C angles at 120°, the non-hydrogen atoms were refined anisotropically and the hydrogen atoms were included in their idealized positions with C—H set at 0.95 Å and with isotropic thermal parameters set at 1.2 times that of the carbon

[4] G.M. Sheldrick. Crystallographic computing 3. *Edited by* G.M. Sheldrick, C. Kruger, and R. Goddard. Oxford University Press, Oxford, England. 1985. p. 175.

atom to which they were attached. The final cycle of full-matrix least-squares refinement[5] (30) was based on 921 (**2**), 2301 (**4**), 1001 (**5**), and 1170 (**8**) observed reflections ($I > 3.00\sigma(I)$) and 104 (**2**), 160 (**4**), 82 (**5**), and 100 (**8**) variable parameters, and converged (largest parameter shift was 0.003 times its esd) with unweighted and weighted agreement factors of $R = \Sigma||F_o| - |F_c||/\Sigma|F_o| = 0.0648$ (**2**), 0.0368 (**4**), 0.0396 (**5**), and 0.0369 (**8**) and $R_w = [(\Sigma w(|F_o| - |F_c|)^2/\Sigma w F_o^2)]^{1/2} = 0.0624$ (**2**), 0.0312 (**4**), 0.0461 (**5**), and 0.0325 (**8**).

The standard deviation of an observation of unit weight[6] was 2.00 (**2**), 1.39 (**4**), 1.69 (**5**), and 1.50 (**8**). The weighting scheme was based on counting statistics and included a factor ($p = 0.007$ (**2** and **5**), 0.008 (**4**), and 0.006 (**8**)) to downweight the intense reflections. Plots of $\Sigma w(|F_o| - |F_c|)^2$ versus $|F_o|$, reflection order in data collection, $\sin\theta/\lambda$, and various classes of indices showed no unusual trends. The maximum and minimum peaks on the final difference Fourier map corresponded to 0.87 and −0.88 e/Å^3, respectively, for **2**, 0.67 and −0.50 e/Å^3, respectively, for **4**, 0.61 and −0.86 e/Å^3, respectively, for **5**, and 0.61 and −0.65 e/Å^3, respectively, for **8**. Neutral-atom scattering factors were taken from Cromer and Waber (30). Anomalous dispersion effects were included in F_c (31); the values for $\Delta f'$ and $\Delta f''$ were those of Cromer (32). All calculations were performed using the TEXSAN (33) crystallographic software package of Molecular Structure Corp. Although the best data sets collected for **2** and **8** were less than ideal, satisfactory solutions of the structures were achieved.

The final atomic coordinates and equivalent isotropic thermal parameters (Tables 2, 3, 4 and 5) are given, respectively, for **2**, **4**, **5**, and **8** for the non-hydrogen atoms, and important distances and bond angles in Tables 6 and 7. The molecular structures of the four compounds are displayed as ORTEP diagrams. Tables of final fractional coordinates and thermal parameters of hydrogen atoms and anisotropic thermal parameters have been deposited.[7]

Calculation of Pauling bond order

The formula proposed by Pauling (34) for calculating the bond orders of partial bonds is given by $d_n - d = -0.60 \log n$, where d_n is the bond length for bond number n, and d is the length of the single bond of the same type. Based on the C—C single bond of 1.54 Å, Pauling's formula gives a bond length of 1.36 Å for $n = 2$; 1.72 Å for $n = 0.5$; and 1.90 Å for $n = 0.25$. These give percentage increases in bond length for the partial bonds of approximately 12 and 23%, respectively, for $n = 0.5$ and 0.25. It is reasonable to assume that similar relationships relating bond order to interatomic distances for the much longer secondary interactions or partial bonds involving Te and S should utilize percentage differences "normalized" to 1.54 as follows rather than absolute differences. Pauling's relationship, which can written as $n = 10^X$, where $X = (d - d_n)/0.6$, can be modified to allow for percentage differences "normalized" to 1.54 to give $X = [1.54(d - d_n)/d]/0.6$ or $X = 2.57(d - d_n)/d$. Based on a Te—S single bond length of 2.63 Å, typical calculated values of the lengths of Te--S partial bonds for various values of n are as follows: 2.63 Å ($n = 1.0$), 2.75 (0.75), 2.94 (0.50) 3.25 (0.25), and 3.66 Å ($n = 0.10$). Based on the assumption that the appropriate Te—Cl and Te—Br single bond lengths are those found in the corresponding Me_2TeX_2 compounds of 2.51 and 2.68 Å, respectively, for X = Cl, Br, then typical values of the lengths of Te--X partial bonds for various values of n are as follows: for Te--Cl, 2.51 Å ($n = 1.0$), 2.63 (0.75), 2.81 (0.50) 3.11 (0.25), and 3.51 Å ($n = 0.10$) and for Te--Br, 2.68 Å ($n = 1.0$), 2.80 (0.75), 3.00 (0.50) 3.32 (0.25), and 3.75 Å ($n = 0.10$). On the basis that a Te—O single bond length is 2.11 Å, then typical calculated values of Te--O partial bonds for various values of n are 2.11 Å ($n = 1.0$), 2.21 (0.75), 2.35 (0.50) 2.60 (0.25), and 2.92 Å ($n = 0.10$). These calculated values appear to be compatible with the sum of the van der Waals radii of Te and S (35).

Results and discussion

A cross section of dimethyl- and diphenyltellurium(IV) monothiocarbonate (monoxanthate) derivatives, $Me_2Te[SCO_2Me]_2$, **1**, $Me_2Te[SCO_2(i\text{-}Pr)]_2$, **2**, $Ph_2Te[SCO_2Me]_2$, **3**, $Ph_2Te[SCO_2(i\text{-}Pr)]_2$, **4**, $Me_2TeCl[SCO_2Me]$, **5**, $Me_2TeI[SCO_2Me]$, **6**, $Me_2TeCl[SCO_2(i\text{-}Pr)]$, **7**, $Me_2TeBr[SCO_2(i\text{-}Pr)]$, **8**, $Me_2TeI[SCO_2(i\text{-}Pr)]$, **9**, $Ph_2TeCl[SCO_2Me]$, **10**, and $Ph_2TeCl[SCO_2(i\text{-}Pr)]$, **11**, are prepared in 80–90% yields by the reaction of the appropriate dimethyl- or diphenyltellurium dihalide with the sodium salt of *O*-methyl or *O*-isopropyl monothiocarbonic acid in appropriate molar ratios in accord with the reactions

[1] $R'_2TeCl_2 + 2NaSCO_2R \rightarrow R'_2Te[SCO_2R]_2 + 2NaCl$
(R′ = Me, Ph; R = Me, i-Pr)

[2] $R'_2TeX_2 + NaSCO_2R \rightarrow R'_2TeX[SCO_2R] + NaX$
(X = Cl, Br, I)

All of the compounds are more susceptible to exposure to the atmosphere than is the case for their dithiocarbonate analogues (1, 36). The halogen derivatives are less soluble than the bis compounds in common organic solvents such as C_6H_6, CS_2, CCl_4, and $CHCl_3$. Only compounds **2**, **4**, **5**, and **8** could be recrystallized as X-ray quality crystals, **2** and **5** being white, and **4** and **8** pale yellow. In general, the Me_2Te derivatives are more stable in solution than the Ph_2Te analogues. Thus, the NMR spectra of the Me_2Te species **1**, **2**, **5**, **7–9**, and even **6**, which is the only derivative that is obtained as a viscous oil, show no signs of decomposition when run immediately after the solutions are formed. By contrast, for the Ph_2Te species **3**, **4**, **10**, and **11**, even the initial spectra of the solutions being used for recrystallization show additional peaks that can be

---

[5] Least-squares: Function minimized: $\Sigma w(|F_o| - |F_c|)^2$, where $w = 4F_o^2(F_o^2)$, $\sigma^2(F_o^2) = [S^2(C + R^2B) + (pF_o^2)^2]/(Lp)^2$, S = scan rate, C = total integrated peak count, R = ratio of scan time to background counting time, Lp = Lorentz-polarization factor, and $p = p$ factor.

[6] Standard deviation of an observation of unit weight: $[\Sigma w(|F_o| - |F_c|)^2/(N_o - N_v)^{1/2}$, where N_o = number of observations and N_v = number of variables.

[7] Copies of material on deposit may be purchased from: The Depository of Unpublished Data, Document Delivery, CISTI, National Research Council Canada, Ottawa, Canada K1A 0S2. The tables of atomic coordinates have also been deposited with the Cambridge Crystallographic Data Centre, University Chemical Laboratory, 12 Union Road, Cambridge, CB2 1EZ, U.K. Structure factor tables are no longer being deposited and may be obtained directly from the author.

Table 2. Final fractional coordinates and B(eq) for non-hydrogen atoms of $Me_2Te[SCO_2(i\text{-}Pr)]_2$, **2**, with standard deviations in parentheses.

Atom	x	y	z	B(eq)
Te(1)	0.0110(3)	0.06442(7)	0.8259(2)	3.89(7)
S(1)	−0.015(1)	−0.0387(3)	0.7940(7)	4.5(4)
S(2)	−0.028(1)	0.1640(3)	0.843(1)	5.9(5)
O(1)	0.340(3)	−0.0086(7)	0.743(2)	7(1)
O(2)	0.290(2)	−0.0935(7)	0.758(2)	5(1)
O(3)	0.327(3)	0.1417(7)	0.790(2)	6(1)
O(4)	0.264(3)	0.2240(8)	0.844(2)	6(1)
C(1)	−0.021(4)	0.071(1)	0.605(3)	7.5(8)
C(2)	−0.290(4)	0.061(1)	0.849(2)	5.4(6)
C(3)	0.221(4)	−0.044(1)	0.764(2)	3.0(5)
C(4)	0.496(5)	−0.101(1)	0.740(4)	7.5(9)
C(5)	0.545(6)	−0.151(1)	0.822(4)	11(1)
C(6)	0.518(5)	−0.105(1)	0.590(4)	9(1)
C(7)	0.218(5)	0.174(1)	0.824(3)	5.8(8)
C(8)	0.467(4)	0.238(1)	0.828(3)	5.9(7)
C(9)	0.509(5)	0.287(1)	0.915(4)	10(1)
C(10)	0.497(6)	0.248(1)	0.677(4)	8.6(9)

Table 3. Final fractional coordinates and B(eq) for non-hydrogen atoms of $Ph_2Te[SCO_2(i\text{-}Pr)]_2$, **4**, with standard deviations in parentheses.

Atom	x	y	z	B(eq)
Te(1)	0.86914(4)	0.13989(4)	0.60241(3)	2.54(2)
S(1)	0.8756(2)	0.3180(1)	0.7005(1)	3.61(9)
S(2)	0.8679(2)	−0.0579(2)	0.5374(1)	3.48(9)
O(1)	0.8071(4)	0.3673(4)	0.5262(3)	4.3(2)
O(2)	0.8463(4)	0.5051(4)	0.6257(3)	4.5(3)
O(3)	0.8641(5)	−0.1025(4)	0.3681(3)	4.9(3)
O(4)	0.8181(4)	0.0694(4)	0.3963(3)	3.8(2)
C(13)	0.8371(5)	0.4002(5)	0.6029(6)	3.4(3)
C(14)	0.8126(7)	0.5864(6)	0.5526(6)	5.0(4)
C(15)	0.9134(9)	0.6291(8)	0.5252(7)	8.8(7)
C(16)	0.7501(8)	0.6719(7)	0.5899(7)	7.0(5)
C(17)	0.8507(6)	−0.0324(6)	0.4202(5)	3.4(3)
C(18)	0.8055(7)	0.1008(7)	0.3003(6)	4.6(4)
C(19)	0.825(1)	0.2198(9)	0.3002(7)	8.6(7)
C(20)	0.6945(9)	0.065(1)	0.2481(7)	9.4(7)
C(1)	0.9232(4)	0.0597(3)	0.7291(2)	2.9
C(2)	1.0126(4)	0.1049(3)	0.7912(3)	3.1
C(3)	1.0569(3)	0.0510(4)	0.8728(3)	3.6
C(4)	1.0116(4)	−0.0479(4)	0.8921(2)	3.7
C(5)	0.9222(4)	−0.0931(3)	0.8300(3)	4.1
C(6)	0.8780(3)	−0.0392(4)	0.7485(3)	3.4
C(7)	0.6956(3)	0.1334(4)	0.5886(3)	3.0
C(8)	0.6474(4)	0.1008(4)	0.6597(2)	3.7
C(9)	0.5322(4)	0.0971(4)	0.6469(3)	5.1
C(10)	0.4652(3)	0.1261(4)	0.5630(4)	4.7
C(11)	0.5134(4)	0.1588(4)	0.4919(3)	4.5
C(12)	0.6286(4)	0.1624(4)	0.5047(3)	3.5

Table 4. Final fractional coordinates and B(eq) for non-hydrogen atoms of $Me_2TeCl[SCO_2Me]$, **5**, with standard deviations in parentheses.

Atom	x	y	z	B(eq)
Te(1)	0.3151(1)	0.33945(4)	0.90493(7)	2.93(3)
Cl(1)	0.5238(5)	0.2629(2)	1.1209(3)	3.7(1)
S(1)	0.0739(6)	0.4022(2)	0.7130(3)	4.5(2)
O(1)	0.427(2)	0.4932(4)	0.8127(8)	4.9(4)
O(2)	0.232(2)	0.5234(4)	0.6117(8)	5.4(5)
C(1)	0.102(2)	0.3963(6)	1.054(1)	4.1(6)
C(2)	0.067(2)	0.2469(6)	0.883(1)	3.7(5)
C(3)	0.275(2)	0.4801(7)	0.723(1)	4.1(6)
C(4)	0.398(3)	0.5893(7)	0.602(1)	6.5(8)

Table 5. Final fractional coordinates and B(eq) for non-hydrogen atoms of $Me_2TeBr[SCO_2(i\text{-}Pr)]$, **8**, with standard deviations in parentheses.

Atom	x	y	z	B(eq)
Te(1)	0.73195(6)	0.1119(1)	0.91551(4)	2.52(3)
Br(1)	0.7565(1)	−0.1891(2)	1.04499(7)	5.18(7)
S(1)	0.7205(3)	0.4187(5)	0.8123(2)	3.6(1)
O(1)	0.5800(6)	0.384(1)	0.6686(4)	4.2(4)
O(2)	0.5468(6)	0.167(1)	0.7741(4)	2.9(3)
C(1)	0.613(1)	0.266(2)	0.9836(7)	4.3(6)
C(2)	0.886(1)	0.259(2)	0.9767(6)	3.6(5)
C(3)	0.6042(9)	0.319(2)	0.7393(6)	2.9(5)
C(4)	0.455(1)	0.048(2)	0.7207(6)	2.9(5)
C(5)	0.343(1)	0.168(2)	0.7144(6)	3.9(6)
C(6)	0.453(1)	−0.166(2)	0.7600(7)	5.0(7)

attributed to the presence of diphenyltellurium and the diligand.

Thus by way of illustration, for $Ph_2Te[SCO_2Me]_2$, **3**, the reductive elimination to Ph_2Te and $[SCO_2Me]_2$ is already underway (*approximately* 40% decomposed) when the first spectrum is run after dissolution (see Fig. 1). The dissociation obeys first-order kinetics reasonably well with a half-life of only 5.5 h at room temperature and an apparent activation energy of 41 kJ mol^{-1}. By comparison, $Ph_2Te[S_2COEt]_2$ had a half-life of 22.9 h and an apparent activation energy of 57 kJ mol^{-1}. The reductive elimination is a general phenomenon for related compounds of this type but in additon, with these monothiocarbonates, COS is eliminated apparently from the diligand to give a species in solution whose NMR is consistent with the formulation $MeOSCO_2Me$.

The NMR spectra of the mixed halide derivatives indicate that their decomposition initially involves disproportionation to the dihalide and bis derivative, with the latter then immediately undergoing reductive elimination.

The crystal structures of $Me_2Te[SCO_2(i\text{-}Pr)]_2$, 2, $Ph_2Te[SCO_2(i\text{-}Pr)]_2$, 4, $Me_2TeCl[SCO_2Me]$, 5, and $Me_2TeBr[SCO_2(i\text{-}Pr)]$, 8

Dimethylbis(*O*-isopropyl monothiocarbonato)tellurium(IV), **2**, and diphenylbis(*O*-isopropyl monothiocarbonato)tellurium(IV), **4**, both crystallize in the space group $P2_1/n$. The ORTEP diagrams (Figs. 2 and 3) illustrate that for both molecules the immediate environment about tellurium can be described as the saw-horse structure typical of tellurium(IV) compounds in which the lone pair is apparently stereochemically active and occupying an equatorial position in a distorted trigonal bipyramid, approximately in the position of the Te1 label. The two carbon atoms of the methyl or phenyl groups occupy the other two equatorial positions with the axial positions being occupied by the sulfur atoms of the monothiocarbonate (monoxanthate) groups. As can be seen from Table 6, the Te—C bond lengths are essentially the same in **2** and **4** (avg. 2.10(3) and 2.115(7) Å, respectively), which is a common feature in diorgano-tellurium(IV) compounds with sulfur ligands (1–21) but is in contrast to Te—C bonds in general where the mean Te—C(aromatic) bond length, 2.116 Å, is shorter than that of Te—C(alkyl), 2.158 Å (37). In the corresponding xanthate derivatives, $Me_2Te[S_2COEt]_2$ and $Ph_2Te[S_2COEt]_2$, the Te—C bond lengths are also similar, 2.12(5) and 2.1339(9) Å, respectively (1).

The S-Te-S angles of 169.9(6)° and 168.10(6)° in **2** and **4**, respectively, are very similar to those reported for $Me_2Te[S_2COEt]_2$, $Ph_2Te[S_2COEt]_2$, $Me_2Te[S_2CNMe_2]_2$, and $Me_2Te[SCONMe_2]_2$ (1, 12, 26) so the slight distortion from linear appears to be independent of whether the organic sub-

Table 6. Interatomic distances (Å) and angles (deg) in compounds **2** and **4**.[a]

$Me_2Te[SCO_2(i\text{-}Pr)]_2$, **2**		$Ph_2Te[SCO_2(i\text{-}Pr)]_2$, **4**	
Te(1)—S(2)	2.569 (8)	Te(1)—S(2)	2.618 (2)
Te(1)—S(1)	2.662 (8)	Te(1)—S(1)	2.630 (2)
Te(1)—C(1)	2.08 (3)	Te(1)—C(1)	2.120 (4)
Te(1)—C(2)	2.12 (3)	Te(1)—C(2)	2.110 (3)
S(1)—C(3)	1.69 (2)	S(1)—C(13)	1.759 (8)
O(1)—C(3)	1.27 (3)	O(1)—C(13)	1.203 (9)
O(2)—C(3)	1.35 (3)	O(2)—C(13)	1.331 (8)
O(2)—C(4)	1.47 (4)	O(2)—C(14)	1.477 (9)
C(4)—C(5)	1.52 (4)	C(14)—C(15)	1.49 (2)
C(4)—C(6)	1.43 (4)	C(14)—C(16)	1.49 (1)
S(2)—C(7)	1.75 (3)	S(2)—C(17)	1.760 (8)
O(3)—C(7)	1.17 (3)	O(3)—C(17)	1.200 (9)
O(4)—C(7)	1.34 (3)	O(4)—C(17)	1.338 (9)
O(4)—C(8)	1.47 (3)	O(4)—C(18)	1.47 (1)
C(8)—C(9)	1.52 (4)	C(18)—C(19)	1.48 (1)
C(8)—C(10)	1.46 (4)	C(18)—C(20)	1.49 (1)
S(1)--O(1)	2.66 (2)	S(1)--O(1)	2.644 (5)
S(2)--O(3)	2.62 (2)	S(2)--O(4)	2.600 (5)
Te(1)--O(1)	3.10 (2)	Te(1)--O(1)	3.051 (5)
Te(1)--O(2)	4.55 (2)	Te(1)--O(2)	4.511 (5)
Te(1)--O(3)	2.99 (2)	Te(1)--O(3)	4.607 (5)
Te(1)--O(4)	4.45 (2)	Te(1)--O(4)	3.150 (5)
Te(1)--S(1)′	3.633 (7)	Te(1)--O(3)″	3.260 (6)
Te(1)--Te(1)′	4.659 (4)	Te(1)--Te(1)″	6.021 (1)
S(2)-Te(1)-S(1)	169.9 (2)	S(2)-Te(1)-S(1)	168.10 (6)
S(2)-Te(1)-C(1)	89 (1)	S(2)-Te(1)-C(1)	83.2 (1)
S(2)-Te(1)-C(2)	85.8 (8)	S(2)-Te(1)-C(7)	90.4 (1)
S(1)-Te(1)-C(1)	88 (1)	S(1)-Te(1)-C(1)	85.2 (1)
S(1)-Te(1)-C(2)	84.8 (8)	S(1)-Te(1)-C(7)	89.4 (1)
C(1)-Te(1)-C(2)	94 (1)	C(1)-Te(1)-C(7)	100.5 (2)
S(1)-Te(1)--O(1)	54.3 (2)	S(1)-Te(1)--O(1)	54.9 (1)
S(2)-Te(1)--O(1)	136.7 (1)	S(2)-Te(1)--O(1)	136.7 (1)
S(1)-Te(1)--O(2)	133.4 (4)	S(1)-Te(1)--O(4)	139.2 (1)
S(2)-Te(1)--O(2)	55.5 (4)	S(2)-Te(1)--O(4)	52.6 (1)
C(1)-Te(1)--S(1)′	172.0 (9)	C(7)-Te(1)--O(3)″	169.5 (2)
S(1)-Te(1)--S(1)′	85.8 (2)		
Te(1)-S(1)--Te(1)′	94.2 (2)		
Te(1)-S(1)-C(3)	93 (1)	Te(1)-S(1)-C(13)	92.2 (3)
S(1)-C(3)-O(1)	128 (2)	S(1)-C(13)-O(1)	125.4 (5)
S(1)-C(3)-O(2)	116 (2)	S(1)-C(13)-O(2)	110.4 (5)
O(1)-C(3)-O(2)	115 (2)	O(1)-C(13)-O(2)	124.2 (7)
C(3)-O(2)-C(4)	119 (2)	C(13)-O(2)-C(14)	117.9 (6)
O(2)-C(4)-C(5)	104 (3)	O(2)-C(14)-C(15)	109.2 (7)
O(2)-C(4)-C(6)	108 (3)	O(2)-C(14)-C(16)	106.2 (7)
C(5)-C(4)-C(6)	114 (3)	C(15)-C(14)	113.1 (7)
Te(1)-S(2)-C(7)	91 (1)	Te(1)-S(2)-C(13)	101.5 (3)
S(2)-C(7)-O(3)	126 (3)	S(2)-C(17)-O(3)	121.6 (6)
S(2)-C(7)-O(3)	110 (3)	S(2)-C(17)-O(4)	113.5 (5)
O(3)-C(7)-O(4)	124 (3)	O(3)-C(17)-O(4)	124.9 (7)
O(4)-C(8)-C(9)	107 (3)	O(4)-C(18)-C(19)	106.1 (7)
O(4)-C(8)-C(10)	111 (3)	O(4)-C(18)-C(20)	109.0 (7)
C(9)-C(8)-C(10)	110 (3)	C(19)-C(18)	115.0 (8)

[a]Symmetry equivalent position $(-x, -y, 2 - z)$ is denoted by a prime and $(2 - x, -y, 1 - z)$ by a double prime.

Table 7. Interatomic distances (Å) and angles (deg) in compounds **5** and **8**.[a]

$Me_2TeCl[SCO_2Me]$, **5**		$Me_2TeBr[SCO_2(i\text{-}Pr)]$, **8**	
Te(1)—Cl(1)	2.703 (3)	Te(1)—Br(1)	2.796 (2)
Te(1)—S(1)	2.481 (3)	Te(1)—S(1)	2.532 (3)
Te(1)—C(1)	2.10 (1)	Te(1)—C(1)	2.13 (1)
Te(1)—C(2)	2.12 (1)	Te(1)—C(2)	2.13 (1)
S(1)—C(3)	1.76 (1)	S(1)—C(3)	1.78 (1)
O(1)—C(3)	1.18 (1)	O(1)—C(3)	1.21 (1)
O(2)—C(3)	1.34 (1)	O(2)—C(3)	1.33 (1)
O(2)—C(4)	1.48 (1)	O(2)—C(4)	1.48 (1)
		C(4)—C(5)	1.50 (1)
		C(4)—C(6)	1.48 (1)
S(1)—O(1)	2.629 (8)	S(1)—O(2)	2.572 (7)
Te(1)—O(1)	2.984 (8)	Te(1)—O(1)	4.459 (6)
Te(1)—O(2)	4.380 (8)	Te(1)—O(2)	2.930 (6)
Te(1)—Cl(1)′	3.494 (3)	Te(1)—O(1)″	3.097 (8)
Te(1)—Te(1)′	5.7974 (8)	Te(1)—Te(1)″	6.260 (1)
Cl(1)-Te(1)-S(1)	173.1 (1)	Br(1)-Te(1)-S(1)	172.68 (8)
Cl(1)-Te(1)-C(1)	86.3 (3)	Br(1)-Te(1)-C(1)	85.5 (3)
Cl(1)-Te(1)-C(2)	84.5 (3)	Br(1)-Te(1)-C(2)	87.5 (3)
S(1)-Te(1)-C(1)	91.1 (3)	S(1)-Te(1)-C(1)	91.2 (3)
S(1)-Te(1)-C(2)	89.6 (3)	S(1)-Te(1)-C(2)	86.5 (3)
C(1)-Te(1)-C(2)	97.3 (4)	C(1)-Te(1)-C(2)	97.8 (5)
S(1)-Te(1)--O(1)	56.6 (2)	S(1)-Te(1)--O(2)	55.6 (2)
Cl(1)-Te(1)--O(1)	129.0 (2)	Br(1)-Te(1)--O(2)	130.2 (1)
Cl(1)-Te(1)--Cl(1)′	101.64 (5)	Br(1)-Te(1)--O(1)″	90.9 (1)
S(1)-Te(1)--Cl(1)′	79.76 (9)	S(1)-Te(1)--O(1)″	91.8 (2)
O(1)-Te(1)--Cl(1)′	101.4 (2)	O(2)-Te(1)--O(1)″	101.8 (2)
C(1)-Te(1)--Cl(1)′	166.3 (3)	C(1)-Te(1)--O(1)″	174.8 (3)
C(2)-Te(1)--Cl(1)′	72.6 (3)	C(2)-Te(1)--O(1)″	78.2 (3)
Te(1)--Cl(1)′-Te(1)′	138.3 (1)	Te--O(1)″-C(3)″	119.1 (7)
Te(1)-S(1)-C(3)	92.1 (4)	Te(1)-S(1)-C(3)	97.7 (4)
S(1)-C(3)-O(1)	126(1)	S(1)-C(3)-O(1)	124.2 (9)
S(1)-C(3)-O(2)	109.6(8)	S(1)-C(3)-O(2)	110.7 (7)
O(1)-C(3)-O(2)	124(1)	O(1)-C(3)-O(2)	125 (1)
C(3)-O(2)-C(4)	115.7(9)	C(3)-O(2)-C(4)	118.9 (7)
		O(2)-C(4)-C(5)	110.0 (9)
		O(2)-C(4)-C(6)	105.1 (8)
		C(5)-C(4)-C(6)	115 (1)

[a]Symmetry equivalent position (x, 1/2 − y, z − 1/2) is denoted by a prime and (3/2 − x, y − 1/2, 3/2 − z) by double prime.

stituent on tellurium is methyl or phenyl, or whether a monothio or dithio group is axial. In $Me_2Te[SCO_2(i\text{-}Pr)]_2$, **2**, the Te(1)—S(1) bond is distinctly longer, 2.662(8) Å, than the Te(1)—S(2) bond, 2.569(8) Å. The sulfur atom associated with the longer bond is 3.663(7) Å from the tellurium atom of an adjacent molecule and this is the only intermolecular contact that is less than the sum of the van der Waals radii of 3.86 Å. The same phenomenon was found in the related dithiocarbonate, $Me_2Te[S_2COEt]_2$, where the Te—S bonds were 2.667(2) and 2.590(2) Å, and a Te--S intermolecular contact of 3.814(2) Å was associated with the longer Te—S bond. Although a distance of 3.633(7) Å corresponds to a Pauling partial bond order of only 0.10, it may be of significance because in $Ph_2Te(SCO_2(i\text{-}Pr)]_2$, **4**, where there are no secondary interactions, the two Te—S bond lengths are similar, with an average value of 2.624(8) Å, which is close to the value of 2.62(2) Å found in $Ph_2Te[S_2COEt]_2$, which also has no secondary Te--S intermolecular interactions (1). In both of the dithiocarbonates, $Me_2Te[S_2COEt]_2$ and $Ph_2Te[S_2COEt]_2$, the second S atom was oriented toward the Te atom at distances ranging from 3.265(2) to 3.336(2) Å, which correspond to Pauling partial bond orders of approximately 0.23. When these sulfur atoms are included in the coordination sphere, the orientation of the atoms about tellurium in $Me_2Te[S_2COEt]_2$ can be described as a pseudo pentagonal bipyramid. In similar fashion, the terminal oxygen atoms of the monoxanthate groups in $Me_2Te[SCO_2(i\text{-}Pr)]_2$, **2**, are oriented toward tellurium at an average Te--O distance of 3.05(8) Å, and the alkoxy groups are oriented away from tellurium at an average Te--O(i-Pr) distance of 4.50(7) Å. Te--O distances of 3.05 Å, which were also observed for the terminal oxygen atoms in the related monothiocarbamate derivative, $Me_2Te[SCONEt_2]_2$

Fig. 2. ORTEP plot of the molecule $Me_2Te[SCO_2(i\text{-}Pr)]_2$, **2**. The atoms are drawn with 30% probability ellipsoids. Hydrogen atoms are omitted for clarity.

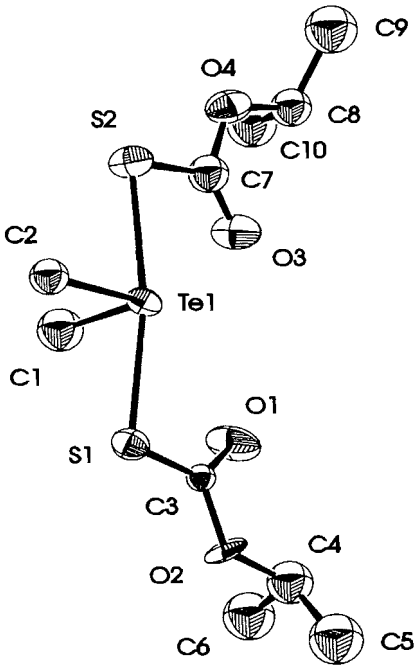

Fig. 3. ORTEP plot of the molecule $Ph_2Te[SCO_2(i\text{-}Pr)]_2$, **4**. The atoms are drawn with 30% probability ellipsoids. Hydrogen atoms are omitted for clarity.

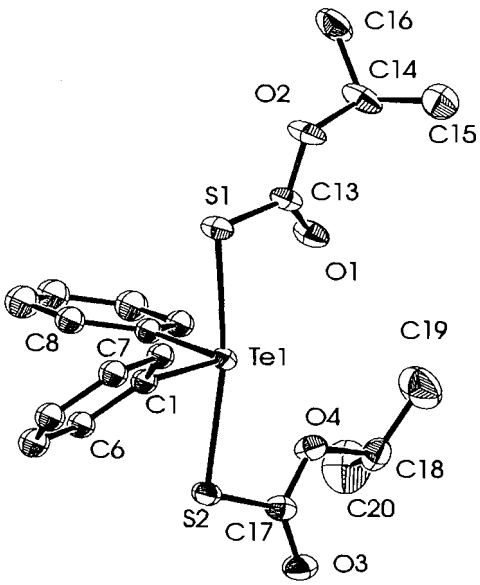

(26), correspond to a Pauling partial bond order of only 0.07, which is closer to the bond order of weak Te--S *inter*molecular interactions rather than Te--S *intra*molecular interactions. Nevertheless, if the weak interactions are included in the coordination sphere, then S(1), S(2), C(2), O(1), and O(3) form a pentagonal plane (mean deviation from plane is 0.032) with Te(1) just below the plane (0.109 Å). The second methyl group

Fig. 4. ORTEP plot of molecules of $Me_2Te[SCO_2(i\text{-}Pr)]_2$, **2**, with both intra- and intermolecular associations shown leading to a dimeric species. The atoms are drawn with 30% probability ellipsoids. Hydrogen atoms are omitted for clarity.

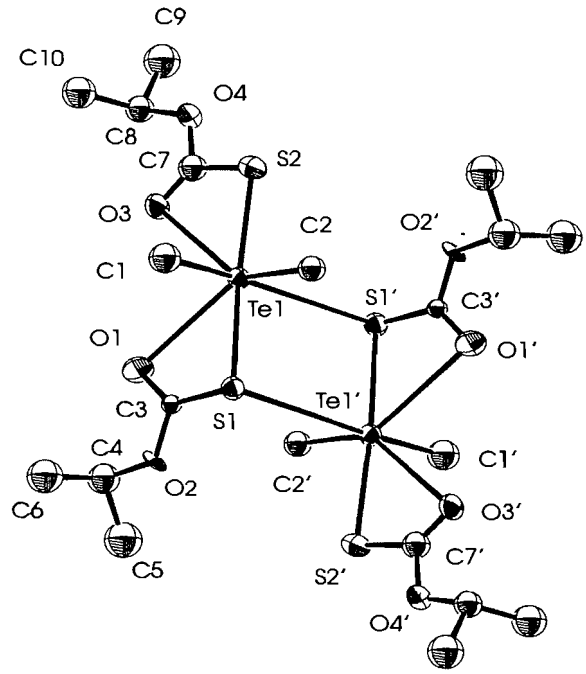

takes up one axial position with C(1) at 1.943 Å above the plane. The intermolecular Te--S bond occupies the other axial position to give a C(1)-Te(1)--S(1)′ angle of 172.0(9)°, which is less distorted from linear than the S(1)-Te(1)-S(2) angle. The resulting approximately rectangular bridge system, with Te(1)-S(1)--Te(1)′ and S(1)-Te(1)--S(1)′ angles of 94.2(2)° and 85.8(2)°, respectively, is seen in Fig. 4 and results in a Te--Te′ distance within the pseudo dimer of 4.659(4) Å. This is essentially the same as was observed in $Me_2Te[SCONEt_2]_2$, where the Te--Te′ distance was 4.575(1) Å. Thus the environment about tellurium in the dimer can be described as that of a distorted pentagonal bipyramid.

By contrast, in $Ph_2Te[SCO_2(i\text{-}Pr)]_2$, **4**, there is no Te--S secondary interaction and both monothiocarbonate groups are not oriented in the same fashion. One group is oriented as in **2**, with a similar Te--O(terminal) distance of 3.051(5) Å, but the second group is turned around so that the oxygen atom of the O(i-Pr) group is now pointed toward tellurium at a similar distance of 3.150(5) Å, and in such a manner that S(1), S(2), C(1)phenyl, O(1), and O(4)alkoxy form a pentagonal plane (mean deviation from plane is 0.057) with Te(1) just below the plane (0.045 Å) and C(7) of the second phenyl group directly above it (2.043 Å). The two planar SCO_2 cores of the monoxanthate groups have a dihedral angle of 21.2(2)°, which is virtually the same as the 20.4(2)° angle found for the SCON planar cores in $Me_2Te[SCONEt_2]_2$ and similar to the 13.5(2)° found in **2**. However, the terminal oxygen atom, which is oriented away from tellurium, is involved in a Te--O intermolecular interaction of a similar distance, 3.260(6) Å, to give a virtual dimer (Fig. 5) in which the Te--Te″ distance of 6.021(1) Å is considerably larger than in **2** or $Me_2Te[SCONEt_2]_2$. When the Te--O intermolecular interac-

Fig. 5. ORTEP plot of molecules of $Ph_2Te[SCO_2(i\text{-}Pr)]_2$, **4**, with both intra- and intermolecular associations shown leading to a dimeric species. The atoms are drawn with 30% probability ellipsoids. Hydrogen atoms are omitted for clarity.

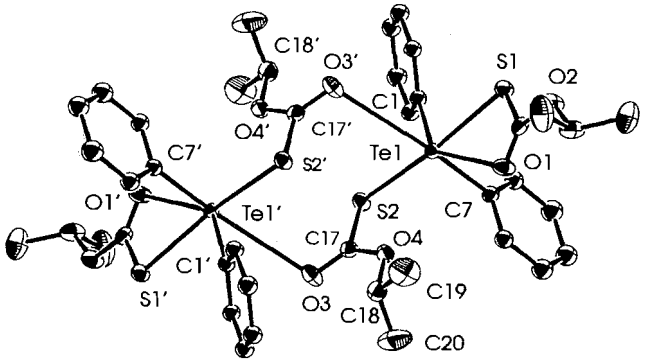

Fig. 6. ORTEP plot of the molecule $Me_2TeCl[SCO_2Me]$, **5**. The atoms are drawn with 30% probability ellipsoids. Hydrogen atoms are omitted for clarity.

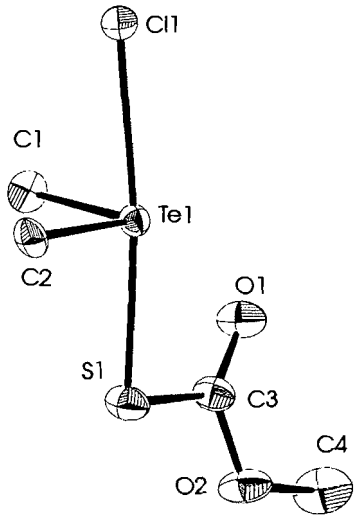

tion is included in the coordination sphere, the environment around Te in **4** becomes that of a distorted pentagonal bipyramid with the axial positions occupied by a phenyl group and the intermolecular terminal oxygen atom to give a C(7)-Te(1)--O(3)″ angle of 169.5(2)° that is no more distorted from linear than the S(1)-Te(1)-S(2) angle.

Chlorodimethyl(*O*-methyl monothiocarbonato)tellurium-(IV), **5**, and bromodimethyl(*O*-isopropyl monothiocarbonato)tellurium(IV), **8**, crystallize in the space groups $P2_1/c$ and $P2_1/n$, respectively. The ORTEP diagrams (Figs. 6 and 7) illustrate that the immediate environment about tellurium can yet again be described as the saw-horse structure typical of tellurium(IV) compounds in which the lone pair is apparently stereochemically active and occupying an equatorial position in a distorted trigonal bipyramid, approximately in the position of the Te1 label. The two methyl groups occupy the other two equatorial positions with the axial positions being occupied by the halogen atom and the sulfur atom of the monothiocarbonate group. It is also clear from the two ORTEP diagrams that the terminal oxygen atom is oriented toward tellurium in $Me_2TeCl[SCO_2Me]$, **5**, with a Te(1)—O(1) distance of 2.984(8) Å (Fig. 7), whereas in $Me_2TeBr[SCO_2(i\text{-}Pr)]$, **8**, the oxygen atom of the alkoxy group is the one oriented toward tellurium (Fig. 8) with the Te(1)—O(2) distance of 2.930(6) Å being similar. As can be seen from Table 7, the Te—C bond lengths in **5** are slightly shorter than in **8**, and are closer to the value in **2** where both terminal oxygen atoms are oriented toward tellurium. However, the differences are close to the error limits and the C-Te-C bond angles show no particular trends for all four molecules.

Fig. 7. ORTEP plot of the molecule $Me_2TeBr[SCO_2(i\text{-}Pr)]$, **8**. The atoms are drawn with 30% probability ellipsoids. Hydrogen atoms are omitted for clarity.

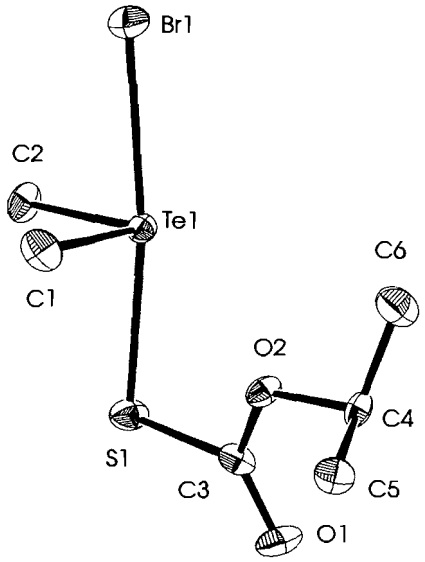

The X-Te-S angles of 173.1(1)° and 172.68(8)° in **5** and **8**, respectively, are similar to those reported for the analogous monothiocarbamates, $Me_2TeCl[SCONEt_2]$ and $Me_2TeBr[SCONEt_2]$ (26). The Te—S bond lengths in **5** and **8** are shorter than even the shorter of the two Te—S bonds in the bis analogues, **2** and **4**, and correspond to bond orders of 1.37 and 1.22, if the average Te—S bond length in the bis species is taken as corresponding to a bond order of 1.0. Correspondingly, the Te—Cl and Te—Br bonds, 2.703(3) and 2.796(2) Å, respectively, are distinctly longer than in α-Me_2TeCl_2, 2.51(3) Å (38), Me_2TeBr_2, 2.67(4) Å, or Ph_2TeBr_2, 2.682(3) Å (39), to give bond orders of 0.63 and 0.78, respectively, which are slightly higher than found for the corresponding monothiocarbamates, $Me_2TeX[SCONEt_2]$. In the latter compounds, the halogen atoms have an intermolecular association with an adjacent tellurium atom to form unsymmetrical Te-X--Te′ bridges in which the X-Te--X′ and Te-X--Te′ angles are close to 90°. The resulting dimeric species with four-center rectangular bridges have Te--Te′ distances of 4.381(1) and 4.556(2) Å, respectively, for $Me_2TeX[SCONEt_2]$, where X = Cl and Br, respectively. Surprisingly, the closest Te--Te distances in **5** and **8** are 5.7974(8) and 6.2496(2) Å, respectively, indicating that similar four-center bridges are not formed with these monothiocarbonates.

Fig. 8. ORTEP plot of a sequence involving the molecule $Me_2TeCl[SCO_2Me]$, **5**, with both intra- and intermolecular associations shown leading to a polymeric chain. The atoms are drawn with 50% probability ellipsoids. Hydrogen atoms are omitted for clarity.

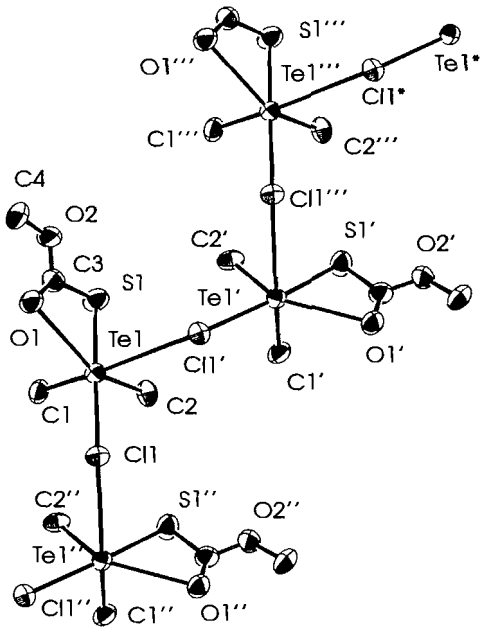

Fig. 9. ORTEP plot of a sequence involving the molecule $Ph_2TeBr[SCO_2(i\text{-}Pr)]$, **8**, with both intra- and intermolecular associations shown leading to a polymeric species. The atoms are drawn with 50% probability ellipsoids. Hydrogen atoms are omitted for clarity.

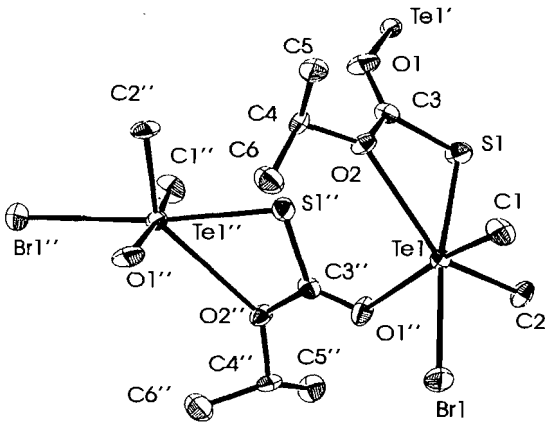

In $Me_2TeCl[SCO_2Me]$, **5**, there is a Te--Cl intermolecular interaction of 3.494(3) Å, which corresponds to a bond order of 0.10 and which is similar to the corresponding interaction in $Me_2TeCl[SCONEt_2]$. However, rather than a Te-Cl--Te′ angle of 89.22(5)° as found in the latter, the angle is 138.3(3)° in **5**, which results in the formation of a zigzag chain rather than a dimer, as can be seen in Fig. 8. The Te--Cl′ interaction is *trans* to a Te–methyl bond at a C(1)-Te(1)--Cl(1)′ angle of 166.3(3)° in a distorted octahedral environment about tellurium. There are no comparable intermolecular interactions involving the bromine atom in $Me_2TeBr[SCO_2(i\text{-}Pr)]$, **8**. However, as in **4**, the terminal oxygen atom, which is oriented away from the tellurium center, is only 3.097(3) Å away from an adjacent tellurium atom and this Te--O intermolecular interaction appears to fulfil the function of the chlorine atom in **5** because it is now *trans* to a Te–methyl bond at a C(1)-Te(1)--O(1)″ angle of 174.8(3)° in a distorted octahedral environment about tellurium, as can be seen in Fig. 9. The lack of Te--Br interactions is surprising because in Me_2TeBr_2 there are two intermolecular interactions with Te--Br distances of 3.560 (4) and 3.661 (4) Å, which are associated with the longer of the two Te—Br bonds, and in Ph_2TeBr_2 the closest such interaction reported is 3.93 Å (39), yet the shortest secondary Te--Br contact in **8** of 4.833(2) Å is considerably longer than the sum of the van der Waals radii. Te--X associations are extensive and in, for example, a series of R_2TeCl_2 compounds with different R groups (36, 38, 40–42), Te--Cl interactions are consistently found (43), with the exception of $(p\text{-}BrC_6H_4)_2TeCl_2$ where Te--Br interactions of 3.71 and 3.80 Å replace those expected for Te--Cl (43). Thus the absence of Te--Br associations in **8** supports the conclusion that even the weak Te--O interactions found in these monoxanthate derivatives are important in establishing the molecular arrangements in the solid state.

Within the four structures described, there are changes involving the orientations of the monoxanthate groups, the intermolecular interactions, the nature of the R groups on tellurium or in the monoxanthate, and different halogen atoms substituting for one of the monoxanthate groups. Despite these variations, the bite angle S—Te--O remains essentially constant regardless of whether the oxygen is terminal or alkoxy, at an average of 54.9(14)° with a S--O bite distance averaging 2.62(3) Å. Further, the bond lengths and angles within the planar SCO_2 core remain relatively unchanged. The SCO(R) angles are consistently distinctly smaller, 112(3)° on average, than the OCO and SCO(terminal) angles, 123(4)° and 125(2)° on average, respectively. The angles are consistent with π-bond character being less significant in the C—OR bonds than in the corresponding C—NR_2 bonds in the monothiocarbamates where the average $SCN(R_2)$ angle was closer to 120°, at 116.8(8)° (26). The C=O(terminal) bonds are, as expected, considerably shorter, 1.21(4) Å on average for all four molecules, than the C—O(alkoxy) bonds at an average of 1.338(8) Å. They are also slightly shorter than those in the monothiocarbamates, yet within values for other C=O bonds involved in secondary interactions (44).

Infrared and Raman spectra

In many respects, given that we have crystal structures of bis and halo derivatives, the vibrational spectra are disappointingly uninformative. In general, these monothiocarbonates appear to be relatively poor scatterers and the quality of the Raman spectra is very variable so that no attempt has been made at extensive assignments. However, certain characteristic features are clearly evident and these are provided in linear form for each compound in the experimental section.

As was to be expected from the vibrational spectra of the related dithiocarbonate (1), dithiocarbamate (7, 8, 12), and monothiocarbamate derivatives (26), three peaks arising primarily from the stretching vibrations of the monothiocarbonate core dominate the infrared spectra of compounds **1–11** in the 1700–1000 cm^{-1} region. These are similar, though not

Table 8. ^{1}H NMR chemical shifts in the spectra of the dimethyl-, diphenyl-, halodimethyl-, and halodiphenyltellurium monothiocarbonates **1–11**.[a,b,c,d]

Compounds	Te-CH_3/C_6H_5	O-CH_n	OCH(CH_3)
$Me_2Te[SCO_2Me]_2$, **1**	2.58 (6 H, s)	3.76 (6 H, s)	
$Me_2Te[SCO_2(i\text{-}Pr)]_2$, **2**	2.56 (6 H, s)	5.04 (2 H, sept)	1.26 (12 H, d)
		[6.3]	[6.3]
$Ph_2Te[SCO_2Me]_2$, **3**	7.91–7.87 (4 H, m)	3.71 (6 H, s)	
	7.50–7.40 (6 H, m)		
$Ph_2Te[SCO_2(i\text{-}Pr)]_2$, **4**	7.91–7.88 (4 H, m)	5.00 (2 H, sept)	1.21 (12 H, d)
	7.47–7.44 (6 H, m)	[6.3]	[6.3]
$Me_2TeCl[SCO_2Me]$, **5**	2.85 (6 H, s)	3.78 (3 H, s)	
$Me_2TeI[SCO_2Me]$, **6**	2.93 (6 H, s)	3.79 (3H, s)	
$Me_2TeCl[SCO_2(i\text{-}Pr)]$, **7**	2.82 (6 H, s)	5.02 (1 H, sept)	1.25 (6 H, d)
		[6.2]	[6.2]
$Me_2TeBr[SCO_2(i\text{-}Pr)]$, **8**	2.86 (6 H, s)	5.02 (1 H, sept)	1.25 (6 H, d)
		[6.3]	[6.3]
$Me_2TeI[SCO_2(i\text{-}Pr)]$, **9**	2.92 (6 H, s)	5.04 (1 H, sept)	1.28 (6 H, d)
		[6.3]	[6.3]
$Ph_2TeCl[SCO_2Me]$, **10**	8.00–7.97 (4 H, m)	3.75 (3 H, s)	
	7.54–7.46 (6 H, m)		
$Ph_2TeCl[SCO_2(i\text{-}Pr)]$, **11**	8.01–7.98 (4 H, m)	5.01 (1 H, sept)	1.23 (6 H, d)
	7.54–7.45 (6 H, m)	[6.3]	[6.3]

[a]The spectra were recorded in $CDCl_3$ and reported in ppm from Me_4Si.
[b]Number of protons and multiplicities are in parentheses (s = singlet; d = doublet; sept = septet, m = multiplet).
[c]Coupling constants in Hz shown in square brackets [ ].
[d]Peaks attributable to the corresponding diligands are seen at 3.91 (s) for $[SCO_2Me]_2$ and at 5.14 (1 H, sept) and 1.31 (6 H, d) for $[SCO_2(i\text{-}Pr)]_2$.

identical, in appearance to corresponding peaks in the starting salts and are generally much stronger and broader than any peaks in the region associated with vibrations attributable to methyl, isopropyl, or phenyl groups. The positions of the peaks indicate that the major contributions involve stretching of the three C—O bonds. Thus, for example, in all of the species containing the SCO_2(i-Pr) moiety, **2**, **4**, **7–9**, **11**, the three peaks are seen at 1638–1674 (mainly C=O stretching), 1146–1155 (mainly C–O stretching), and 1088–1092 cm^{-1} (mainly O–$CH(CH_3)_2$ stretching). In the species containing the SCO_2Me moiety, **1**, **3**, **5**, **6**, **10**, the corresponding peaks are seen at 1638–1656, 1261–1266, and 1098–1131 cm^{-1} (mainly O–CH_3 stretching). The differences probably arise in that mixing with the OCH_3 rocking modes is significant in the latter case as was noted for the $Me_2TeX[S_2COMe]$ derivatives (45). The positions of these three modes may also be compared with those in methylacetate where the assignments are 1768 (C=O stretching), 1268 (C–O stretching), and 1049 cm^{-1} (O–CH_3 stretching). Thus, the proposed assignments are consistent with the assumption that these modes primarily involve the stretching of the C—O bonds but the modes are probably mixed and no doubt involve contributions from S–C stretching as well as from OCH and, in particular, OCH_3 rocking. The fourth stretch of the SCO_2C core is seen between 634 and 683 cm^{-1}, which is the region typical of a single-bonded C–S stretching vibration, and is at lower frequency than in the salts where the C—S bond would have more partial π-bond character. In the Ph_2Te compounds, **3**, **4**, **10**, **11**, the characteristic *f*-phenyl and *v*-phenyl modes, which are both of similar intensity, are observed at ca. 735 and 685 cm^{-1}. As a result, the fourth stretching vibration is normally only observed as a shoulder on the *v*-phenyl mode at 650–660 cm^{-1}. The Raman spectra of the Me_2Te compounds, **1**, **2**, **5**, **6**, **7**, **8**, and **9**, all show peaks of high relative intensity that correspond to the asymmetric and symmetric Te–CH_3 stretching vibrations in similar, though not identical, relative intensities and positions as have been reported for the dihalides, Me_2TeX_2, where X = Cl, Br, and I (46). This is consistent with the C-Te-C bond angles and distances being similar in all species. Unfortunately, as indicated above, the Raman spectra are of such variable quality that, in contrast to the situation with the corresponding halomonothiocarbamates (26) and halodithiocarbonates (45), specific assignments below 400 cm^{-1} to Te–S stretching vibrations and, in particular, to the Te–X stretching vibrations, which are expected in the region below 250 cm^{-1}, cannot be made with confidence.

Nuclear magnetic resonance spectra

The ^{1}H NMR spectral data for compounds **1–11** are presented in Table 8. The methyl group directly attached to tellurium is seen as a sharp singlet at 2.58 and 2.56 ppm, respectively, for $Me_2Te[SCO_2Me]_2$, **1**, and $Me_2Te[SCO_2(i\text{-}Pr)]_2$, **2**. These values for the TeCH_3 chemical shifts are essentially the same as the corresponding bis dithiocarbonate derivatives (1) and slightly larger than those of the bis monothiocarbamates (26). A small, but essentially stepwise, increase is seen in TeCH_3 for $Me_2TeCl[SCO_2Me]$, **5**, compared to $Me_2TeI[SCO_2Me]$, **6**, 2.85 and 2.93 ppm, respectively, and along the series

Table 9. ^{13}C and ^{125}Te NMR chemical shifts for the dimethyl-, diphenyl-, halodimethyl-, and halodiphenyltellurium monothiocarbonates **1–11**.[a]

Compounds	Te-*C*	O-*C*	OC-*C*	SO*C*O	^{125}Te
$Me_2Te[SCO_2Me]_2$, **1**	15.11	54.44		174.68	466.4
$Me_2Te[SCO_2(i\text{-}Pr)]_2$, **2**	15.04	71.57	21.88	173.34	459.3
$Ph_2Te[SCO_2Me]_2$, **3**	134.47, 131.27 130.70, 130.40	54.08		174.80	734.2
$Ph_2Te[SCO_2(i\text{-}Pr)]_2$, **4**	134.32, 130.96 130.77, 130.13	71.40	21.81	173.34	730.0
$Me_2TeCl[SCO_2Me]$, **5**	20.02	55.15		172.10	564.4
$Me_2TeI[SCO_2Me]$, **6**	17.95	55.04		171.09	510.4
$Me_2TeCl[SCO_2(i\text{-}Pr)]$, **7**	19.63	73.09	21.73	170.45	566.1
$Me_2TeBr[SCO_2(i\text{-}Pr)]$, **8**	19.03	73.34	21.61	170.50	544.4
$Me_2TeI[SCO_2(i\text{-}Pr)]$, **9**	17.83	73.38	21.94	171.29	510.0
$Ph_2TeCl[SCO_2Me]$, **10**	134.31, 132.14 131.62, 130.37	55.05		172.22	806.5
$Ph_2TeCl[SCO_2(i\text{-}Pr)]$, **11**	134.34, 132.74 131.58, 130.30	73.14	21.87	170.67	803.5

[a]The spectra were recorded in $CDCl_3$ and reported in ppm from Me_4Si for ^{13}C and from Me_2Te for ^{125}Te.

$Me_2TeCl[SCO_2(i\text{-}Pr)]$, **7**, $Me_2TeBr[SCO_2(i\text{-}Pr)]$, **8**, and $Me_2TeI[SCO_2(i\text{-}Pr)]$, **9**, 2.82, 2.86, and 2.92 ppm, respectively, as one of the monothiocarbonate groups is replaced by Cl, Br, or I. This was also observed in the Me_2TeXL series, where X = $SCONEt_2$ and $SCON(CH_2)_3CH_2$ (26). Changes in the chemical shifts of methyl groups have been related to changes in the electronegativity of the groups attached to the central atom, and the slightly larger shift towards the values observed for Me_2TeCl_2, Me_2TeBr_2, and Me_2TeI_2, of 3.13, 3.26, and 3.27 ppm, respectively, is consistent with the effective electronegativity of the monothiocarbonate being slightly greater than the monothiocarbamate. In the spectra of the bis-substituted diphenyltellurium derivatives $Ph_2Te[SCO_2Me]_2$, **3**, and $Ph_2Te[SCO_2(i\text{-}Pr)]_2$, **4**, the phenyl protons are seen as a pair of multiplets in the regions 7.91–7.87 and 7.50–7.40 ppm with intensities corresponding to 4H and 6H, respectively, as is to be expected for the *meta* and *ortho/para* protons. There is a typical small upfield shift in the corresponding chloro-substituted derivatives, $Ph_2TeCl[SCO_2Me]$, **10**, and $Ph_2TeCl[SCO_2(i\text{-}Pr)]$, **11**.

The relative intensities of the peaks associated with the monothiocarbonate groups are as expected for the formulation of the compounds. The values of the chemical shifts within the monothiocarbonate groups of all of the compounds are found to be similar, though not identical, to each other and to those of the appropriate salts, $NaSCO_2Me$ and $NaSCO_2(i\text{-}Pr)$, from which they were prepared. Thus, there are no significant trends as a result of being linked to tellurium, let alone as a result of changing the organo group or halogen attached to tellurium as illustrated by the fact that in all of the compounds, **2**, **4**, **7**, **8**, **9**, and **11**, the C*H* signal is seen as a septet in the range 5.04–5.00 ppm and the CH_3 signal as a doublet of six times the intensity in the range 1.25–1.21 ppm.

The ^{13}C NMR spectral data for compounds **1–11** are displayed in Table 9. The peaks attributable to the organo groups in the monothiocarbonates again are seen at positions close to those found in the starting salts. However, although the SCO_2R chemical shifts are similar for all 11 compounds, covering the range 170.67–174.68 ppm, they are considerably shifted relative to the values in the starting salts of 186.89 and 185.8 ppm for $NaSCO_2Me$ and $NaSCO_2(i\text{-}Pr)$, respectively. This is consistent with the planar carbon atom of the monothiocarbonate group having essentially the same environment, as is suggested by the X-ray structures of **2**, **4**, **5**, and **8**, in solution in all 11 compounds, which differs from that of the starting salts. Similarly, in the corresponding $R_2Te[S_2COR]_2$ compounds, the S_2COR chemical shifts were all close to 220 ppm compared with values of ca. 232 ppm for the dithiocarbonate salts, and in the monothiocarbamates, $R_2Te[SCONEt_2]_2$ and $R_2TeX[SCONEt_2]$, the S*C*ON chemical shifts were in the range 167–172 ppm with the chemical shift of the salt again close to 12 ppm higher with a value of 183.31 ppm for $NaSCONEt_2$. The chemical shifts of the methyl groups attached to tellurium are essentially the same regardless of the organic group in the monothiocarbonate. The value close to 15.1 ppm for Te*C*H_3 in **1** and **2** is only slightly higher than that found for the monothiocarbamate derivatives, $Me_2Te[SCONR_2]_2$, ca. 14.8 ppm (25) but lower than those reported for related derivatives containing ligands with two sulfur atoms such as $Me_2Te[S_2COR]_2$ (1), $Me_2Te[S_2CNR_2]2$ (8, 12), and $Me_2Te[S_2POGO]_2$ (21) of ca. 15.5, 16.6, and 19.2 ppm, respectively. The halo derivatives, **5–9**, show a slight trend with values of ca. 20, 19, and 18 ppm for $Me_2TeX[SCO_2R]$ where X = Cl, Br, and I, respectively, which places the Te*C*H_3 chemical shifts approximately between those of the bis compounds and those of the dihalides, Me_2TeCl_2, 26.9, Me_2TeBr_2, 25.1, and Me_2TeI_2, 22.0 ppm. The chemical shifts of the phenyl carbon atoms are similar in the bis compounds **3** and **4** as are those in the two chloro derivatives **10** and **11**.

The ^{125}Te NMR chemical shifts for compounds **1–11** are also displayed in Table 9. The peaks attributable to **1** and **2**, of 466.4 and 459.3, respectively, lie between the values of 445–448 ppm found for the bis monothiocarbamate derivatives,

$Me_2Te[SCONR_2]_2$ and those of 475–482 ppm for the bis dithiocarbonates, $Me_2Te[S_2COR]_2$. As with the monothiocarbamates, the substitution of a monothiocarbonate group by a halogen results in an upfield shift toward the chemical shifts of the dihalides to give values of ca. 565 for **5** and **7**, 544.4 for **8**, and 510 ppm for **6** and **9**. The corresponding values for the Me_2TeX_2 species are 733.8, 649.2, and 519.6 ppm for X = Cl, Br, and I, respectively. The values of the chemical shifts for the $Ph_2TeCl[SCO_2R]$ derivatives, **10** and **11**, of 806.5 and 803.5 ppm, respectively, are similarly between those of the corresponding $Ph_2Te[SCO_2R]_2$ derivatives, **3** and **4**, of 734.2 and 730.0 ppm, respectively, and that of Ph_2TeCl_2, 910 ppm. Even the initial ^{125}Te NMR spectra of **3** and **4** show a peak at 690 ppm attributable to the formation of Ph_2Te, which arises from the reductive-elimination of $Ph_2Te[SCO_2R]_2$. This peak increases in intensity as those due to **3** or **4** disappear. Similarly, the spectra of **10** and **11** eventually show a peak at 910 ppm attributable to Ph_2TeCl_2, which arises from the disproportionation of $Ph_2TeCl[SCO_2R]$.

Acknowledgement

We thank the Natural Sciences and Engineering Research Council of Canada and the University of Windsor for financial support. One of us (L.N.K.) thanks the former for an NSERC Research Reorientation Associateship and one of us (R.R.) thanks Dayanand College, Ajmer, India, for granting a leave of absence.

References

1. J.H.E. Bailey, J.E. Drake, L.N. Khasrou, and J. Yang. Inorg. Chem. **34**, 124 (1995).
2. M. Wieber, E. Schmidt, and C. Burschka. Z. Anorg. Allg. Chem. **525**, 127 (1985).
3. A.K. Singh, J.K. Basumatary, T.P. Singh, and B. Padmanabhan. J. Organomet. Chem. **424**, 33 (1992).
4. S. Husebye, K. Maartmann-Moe, and O. Mikalsen. Acta Chem. Scand. **44**, 464 (1990).
5. D. Dakternieks, R. Di Giacomo, R.W. Gable, and B.F. Hoskins. J. Am. Chem. Soc. **110**, 6753 (1988).
6. A.K. Singh and J.K. Basumatary. J. Organomet. Chem. **364**, 73 (1989).
7. J.H.E. Bailey, J.E. Drake, and M.L.Y. Wong. Can. J. Chem. **67**, 1735 (1989).
8. J.H.E. Bailey, J.E. Drake, and M.L.Y. Wong. Can. J. Chem. **69**, 1948 (1991).
9. J.E. Drake and M.L.Y. Wong. J. Organomet. Chem. **377**, 43 (1989).
10. S. Husebye, K. Maartmann-Moe, and W. Steffenson. Acta Chem. Scand. **44**, 139 (1990).
11. S. Husebye, K. Maartmann-Moe, and W. Steffenson. Acta Chem. Scand. **44**, 579 (1990).
12. J.H.E. Bailey and J.E. Drake. Can. J. Chem. **71**, 42 (1993).
13. D. Dakternieks, R. Di Giacomo, R.W. Gable, and B.F. Hoskins. J. Organomet. Chem. **349**, 305 (1988).
14. D. Dakternieks, R. Di Giacomo, R.W. Gable, and B.F. Hoskins. J. Am. Chem. Soc. **110**, 6762 (1988).
15. R.K. Chadha, J.E. Drake, N.T. McManus, B.A. Quinlan, and A.B. Sarkar. Organometallics, **6**, 813 (1987).
16. D. Dakternieks, R. Di Giacomo, R.W. Gable, and B.F. Hoskins. J. Am. Chem. Soc. **110**, 6541 (1988).
17. S. Husebye, K. Maartmann-Moe, and O. Mikalsen. Acta Chem. Scand. **43**, 868 (1989).
18. T.N. Srivastava, J.D. Singh, and S.K. Srivastava. Synth. React. Inorg. Metal. Org. Chem. **20**, 503 (1990).
19. T.N. Srivastava, J.D. Singh, and S.K. Srivastava. Phosphorus Sulfur Silicon Relat. Elem. **55**, 117 (1991).
20. T.N. Srivastava, J.D. Singh, and S.K. Srivastava. Polyhedron, **9**, 943 (1990).
21. J.E. Drake, L.N. Khasrou, A.G. Mislankar, and R. Ratnani. Can. J. Chem. **72**, 1328 (1994).
22. I. Haiduc, R.B. King, and M.G. Newton. Chem. Rev. **94**, 301 (1994)
23. R.J. Magee and M.J. O'Connor. Inorg. Chim. Acta, **5**, 554 (1971).
24. R.F. Dalton and K. Jones. J. Chem. Soc. A, 590 (1970).
25. A.B. Crosby, R.J. Magee, and M.J. O'Connor. Inorg. Chim. Acta, **34**, 107 (1979).
26. J.E. Drake, L.N. Khasrou, A.G. Mislankar, and R. Ratnani. Inorg. Chem. **33**, 6154 (1994).
27. F.A.K. Nasser and J.J. Zuckerman. J. Organomet. Chem. **244**, 17 (1983).
28. I.A. Duncan and C. Glidewell. J. Organomet. Chem. **97**, 51 (1975).
29. R.C. Paul, K.K. Bhasin, and R.K. Chadha. J. Inorg. Nucl. Chem. **37**, 2337 (1975).
30. D.T. Cromer and J.T. Waber. International tables for X-ray crystallography. Vol. IV. The Kynoch Press, Birmingham, England. 1974. Table 2.2 A.
31. J.A. Ibers and W.C. Hamilton. Acta Crystallogr. **17**, 781 (1964).
32. D.T. Cromer. International tables for X-ray crystallography. Vol. IV. The Kynoch Press, Birmingham, England. 1974. Table 2.3.1.
33. TEXSAN-TEXRAY structure analysis package. Molecular Structure Corp., Woodlands, Tex. 1985.
34. L. Pauling. J. Am. Chem. Soc. **69**, 542 (1947); The nature of the chemical bond. 3rd ed. Cornell University Press, Ithaca, N.Y. 1960. p. 255.
35. A. Bondi. J. Phys. Chem. **68**, 441 (1964); Pauling. The nature of the chemical bond. 3rd ed. Cornell University Press, Ithaca, N.Y. 1960. p. 260.
36. N.W. Alcock and W.D. Harrison. J. Chem. Soc Dalton Trans. 251 (1982).
37. F.H. Allen, O. Kennard, D.G. Watson, L. Brammer, A. Orpen, and R. Taylor. J. Chem. Soc. Perkin Trans. 2, S1 (1987).
38. G.D. Christofferson, R.A. Sparks, and J.D. McCullough. Acta Crystallogr. **11**, 782 (1958).
39. G.D. Christofferson and J.D. McCullough. Acta Crystallogr. **11**, 249 (1958).
40. R.K Chada and J.E. Drake. Acta Crystallogr. Sect. C: Cryst. Struct. Commun. **C40**, 1349 (1984).
41. T.S. Cameron, R.B. Amero, and R.E. Cordes. Cryst. Struct. Commun. **9**, 533 (1980); **9**, 539 (1980).
42 J.D. Korp, I. Bernal, J.C. Turley, and G.E. Martin. Inorg. Chem. **19**, 2556 (1980).
43. R.K. Chadha, J.E. Drake, and J.L. Hencher. Can. J. Chem. **61**, 1222 (1983).
44. A.F. Wells. Structural inorganic chemistry. 4th ed. Clarendon Press, Oxford, U.K. 1975. p. 731.
45. J.E. Drake, R.J. Drake, L.N. Khasrow, and R. Ratnani. Inorg. Chem. **35**, 2831 (1996).
46. G.C. Hayward and P.J. Hendra. J. Chem. Soc. A, 1760 (1969).

Organoplatinum(IV) derivatized vinyl monomers and polymers prepared by oxidative addition

Sudhir Achar, Richard J. Puddephatt, and John D. Scott

Abstract: Organoplatinum(IV) complexes of general formula [$PtXMe_2R(NN)$], containing vinyl substituents, have been prepared by oxidative addition of RX, (RX = methyl 2-(bromomethyl)acrylate, 2-(bromomethyl)acrylic acid, 2-bromoethyl methacrylate, acryloyl chloride, and chloromethylstyrene), to [$PtMe_2(NN)$], NN = 2,2′-bipyridine or 4,4′-di-*tert*-butyl-2,2′-bipyridine. Polymers with organoplatinum(IV) substituents have been prepared either by free radical polymerization of the organoplatinum(IV) derivatized monomers or by free radical polymerization of the organic monomers, followed by the oxidative addition of the C-X substituents of these polymers to [$PtMe_2(NN)$]. In the latter method, it is generally not possible to metallate all the C—X bonds, but a high degree of platinum incorporation can be achieved.

Key words: organoplatinum, polymer, oxidative addition, vinyl.

Résumé : On a préparé des complexes organoplatine(IV) de la formule générale [$PtXMe_2R(NN)$], contenant des substituants vinyliques, en faisant appel à une addition oxydante de RX (RX = 2-(bromométhyl)acrylate de méthyle, acide 2-(bromométhyl)acrylique, méthacrylate de 2-bromo-éthyle, chlorure d'acryloyle et chlorométhylstyrène) sur le [$PtMe_2(NN)$], NN = 2,2′-bipyridine ou 4,4′-di-*tert*-butyl-2,2′-bipyridine. On a préparé les polymères contenant des substituants organoplatine(IV) par polymérisation radicalaire des monomères organoplatine(IV) dérivatisés ou par polymérisation radicalaire des monomères organiques, suivie d'une addition oxydante des substituants C-X de ces polymères sur le [$PtMe_2(NN)$]. Dans cette dernière méthode, il n'est généralement pas possible de faire la métallation de toutes les liaisons C—X, mais le degré d'incorporation du platine est élevé.

Mots clés : organoplatine, polymère, addition oxydante, vinyle.

[Traduit par la rédaction]

Introduction

Polymers containing transition metals are of interest as potential catalysts or materials (1); they are often classified based on structure, according to whether the metals are incorporated in the backbone polymer chains (2–4) or are pendant to them (6–8). The metal may be present as an organometallic (contains M—C bonds) or coordination complex (no M—C bonds). Organometallic polymers are often synthesized by polymerizing organometallic monomers or by derivatizing a preformed organic polymer (1–11). We have been interested in using the oxidative addition reaction to introduce organoplatinum functionality into polymerizable monomers or into polymers, with the platinum groups either appended to or incorporated into the polymer backbone (12–15). Routes to both chain and dendrimeric oligomers and polymers have been developed using variants of this methodology. This paper reports details of the application of oxidative addition reactions to the synthesis of monomers and polymers in which organoplatinum groups are appended to a derivatized vinyl functionality. A preliminary account of parts of this work has been published (16). In most other polymers with pendant organotransition metal centres, the metal is bound to the polymer by coordination to η-cyclopentadienyl or η-arene groups or the organometallic group may be bound to the polymer by a group V or VI donor such as a phosphine or a nitrogen or oxygen donor ligand (1–11, 17–23). The methodology described below yields relatively rare examples of vinyl monomers and polymers in which the metals are directly bonded to the monomer or polymer via metal–carbon σ-bonds (22, 23).

The approach used is based on the easy oxidative addition of organic halides to platinum(II), a reaction that occurs in very high yield for alkyl halides containing a wide range of functional groups (24, 25). In particular, addition of alkyl or acyl halides, R-X, to [$PtMe_2$(bipy)], **1a**, bipy = 2,2′-bipyridine, is essentially quantitative and yields [$PtXMe_2R$(bipy)] (26–29). In the present work the group R contains a polymerizable vinyl group and the oxidative addition may be carried out before or after polymerization of the vinyl monomer.

Received January 23, 1996.

This article is dedicated to Professor Howard C. Clark in admiration of his distinguished contributions to chemistry.

S. Achar and R.J. Puddephatt.[1] Department of Chemistry, University of Western Ontario, London, ON N6A 5B7, Canada.
J.D. Scott. Research and Development Laboratories, 3M Canada Inc., CP Box 5757, London, ON N6A 4T1, Canada.

[1] Author to whom correspondence may be addressed. Telephone: (519) 679-2111, ext 6336. Fax: (519) 661-3022. E-mail: pudd@julian.uwo.ca

Scheme 1.

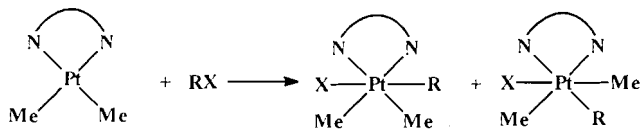

1, NN = bipy
2, NN = bu2bipy

3 4

3a, 4a: NN = bipy, X = Br, R = $CH_2C(CO_2Me)=CH_2$
3b, 4b: NN = bipy, X = Br, R = $CH_2C(CO_2H)=CH_2$
3c, 4c: NN = bipy, X = Br, R = $CH_2CH_2O_2CC(Me)=CH_2$
3d, 4d: NN = bu2bipy, X = Br, R = $CH_2CH_2O_2CC(Me)=CH_2$
3e, 4e: NN = bipy, X = Cl, R = $C(=O)CH=CH_2$
3f, 4f: NN = bu2bipy, X = Cl, R = $C(=O)CH=CH_2$
3g: NN = bipy, X = Cl, R = 4-$CH_2C_6H_4CH=CH_2$
3h: NN = bipy, X = Cl, R = 3-$CH_2C_6H_4CH=CH_2$
3i: NN = bu2bipy, X = Cl, R = 4-$CH_2C_6H_4CH=CH_2$
3j: NN = bu2bipy, X = Cl, R = 3-$CH_2C_6H_4CH=CH_2$

Results and discussion

Synthesis of mononuclear complexes

The complex $[PtMe_2(bipy)]$, **1**, is very reactive in oxidative addition but the products often have limited solubility. To overcome the solubility problem, the new complex $[PtMe_2(bu_2bipy)]$, **2**, bu_2bipy = 4,4′-di-*tert*-butyl-2,2′-bipyridine, was used (15, 30). Both **1** and **2** are red solids, the color arising from the presence of a metal-to-ligand charge transfer (MLCT) band in the visible region of the spectrum (31, 32), and the oxidative addition of alkyl or acyl halides, RX, occurs with bleaching of the colour on formation of the platinum(IV) products $[PtXRMe_2(bipy)]$ and $[PtXRMe_2(bu_2bipy)]$. The reactions can also be monitored by ^1H NMR since the methylplatinum coupling constant, $^2J(PtCH_3)$ decreases from 84–86 Hz in **1** or **2** to 69–72 Hz in the platinum(IV) products (26–29).

The reactions used to prepare potential vinyl monomers with organoplatinum(IV) substituents are shown in Scheme 1. In most cases, the oxidative additions occurred essentially quantitatively but gave the products as a mixture of *trans* and *cis* isomers **3** and **4**. Selected ^1H NMR data and the *trans*/*cis* product ratios are given in Table 1 and complete data are listed in the experimental section. The *trans* isomers **3** have a plane of symmetry perpendicular to the $PtMe_2N_2$ plane and so give a single methylplatinum resonance and, in complexes that contain a CH_2Pt group, a single CH_2Pt resonance. The *cis* isomers **4** have lower symmetry and give two methylplatinum resonances and an "AB" multiplet for the CH^aH^bPt protons (when present). The isomers were readily identified by these characteristic features and the isomer ratios were determined by integration of the ^1H NMR spectra. Attempts to separate the isomers by fractional crystallization or column chromatography were unsuccessful, and they were used in subsequent studies as the mixture of isomers.

Successful reactions were carried out with methyl 2-(bromomethyl)acrylate, 2-(bromomethyl)acrylic acid, 2-bromoethyl methacrylate, acryloyl chloride, and chloromethylstyrene (Scheme 1), thus giving a variety of vinyl monomers containing platinum(IV). All products were isolated as air-stable, pale yellow solids that gave satisfactory analytical data.

The formation of **3b** and **4b** by oxidative addition of 2-(bromomethyl)acrylic acid to **1** is noteworthy because it indicates that the oxidative addition occurs at a much faster rate than methyl–platinum bond cleavage by the carboxylic acid group (33). The reaction of **2** with acryloyl chloride is noteworthy since it was the only case in which the product of *cis* oxidative addition was the major product (Table 1). The sample of chloromethylstyrene used for reaction with **1** and **2** was a mixture of the *meta* and *para* isomers in a 70:30 ratio (the mixture is not readily separable). Fortunately, the oxidative additions occurred selectively to give the *trans* isomers **3** only. Hence the product from **1** was formed a mixture of **3g** and **3h**, and from **2** a mixture of **3i** and **3j**, respectively. In each case, the product ratio corresponded closely to the 30:70 ratio present in the reagent.

Polymeric complexes

Polymeric complexes containing platinum(IV) could be prepared in two ways, as illustrated in Scheme 2 for the case of 2-bromoethyl methacrylate. The free radical polymerization of the mixture of monomers **3c** and **4c** in chlorobenzene, employing azobisisobutyronitrile, AIBN, as initiator, gave the polymer **5** (Scheme 2; note that, for simplicity, the scheme shows only the *trans* isomer **3c** and its product but it is, of course, expected that the polymer will contain platinum(IV) centres with both *cis* and *trans* stereochemistry). The polymer **5** precipitated from solution as it formed and it was not sufficiently soluble to give an NMR spectrum or to allow molecular weight determination.

A similar polymer **6** was prepared by polymerization of the organic monomer 2-bromoethyl methacrylate to its polymer **7** (M_n = 9800, M_w = 16 000, polydispersity 1.6) followed by oxidative addition of the polymer to **1**. However, even using excess **1**, only about 75% of the bromoethyl groups were found to be metallated in the final polymer **6**, which precipitated as it formed (Scheme 2, again only the *trans* oxidative addition product is shown; a more random arrangement of the metallated units than shown is also likely). Hence, the fully metallated polymer can only be obtained from the metallated monomer **3c**,**4c**. The platinum-containing polymers have low solubility in all common organic solvents and it is possible that the precipitation of the partially metallated polymer prevents complete platination. To overcome the solubility problem, additional reactions were carried out with $[PtMe_2(bu_2bipy)]$, **2**. The reactants **2** and the organic polymer **7** were reacted in the molar ratios (based on monomer) of 1:10, 1:4, 1:2, 1:1.33, and 1:1 in acetone to yield the platinated polymers **8a–e**, respectively. Elemental analyses gave a direct measure of the proportion of bromoethyl groups platinated and the results are given in the experimental section. The analytical data indicate a correlation between the amount of platinum used and the amount incorporated, but again it was not possible to metallate all the bromoethyl groups present in the polymer. The solubility of the organoplatinum polymers **8a–e** in THF decreased with increasing platinum content, and samples **8d** and **8e** were not soluble enough for molecular weight determination by gel permeation chromatography. The GPC molecular weight data (experimental section) are similar to that for the organic polymer. It might be expected that the hydrodynamic radius of the platinated polymers would be less than for the organic polymer due to reduced solvation, thus

Table 1. Selected NMR data and isomer ratios for the complexes **3** and **4**.

	trans-isomer, **3**		*cis*-isomer, **4**		
Complex	δ(MePt), ^2J(PtH)	δ(CH_2Pt), ^2J(PtH)	δ(MePtBr), ^2J(PtH)	δ(MePtN), ^2J(PtH)	Isomer ratio
3a,4a	1.39, 70	2.50, 97	0.48, 71	1.30, 70	95:5
3b,4b	1.36, 70	2.47, 98	0.24, 71	1.14, 70	85:15
3c,4c	1.40, 70	2.42, 95	0.55, 72	1.43, 70	60:40
3d,4d	1.36, 70	Obscured	0.53, 74	1.38, 70	55:45
3e,4e	1.46, 72	Absent	0.71, 74	1.39, 72	75:25
3f,4f	1.41, 72	Absent	0.69, 75	1.35, 72	10:90
3g	1.45, 69	2.79, 95			
3h	1.46, 69	2.77, 93			
3i	1.40, 69	2.78, 96			
3j	1.42, 69	2.76, 94			

Scheme 2.

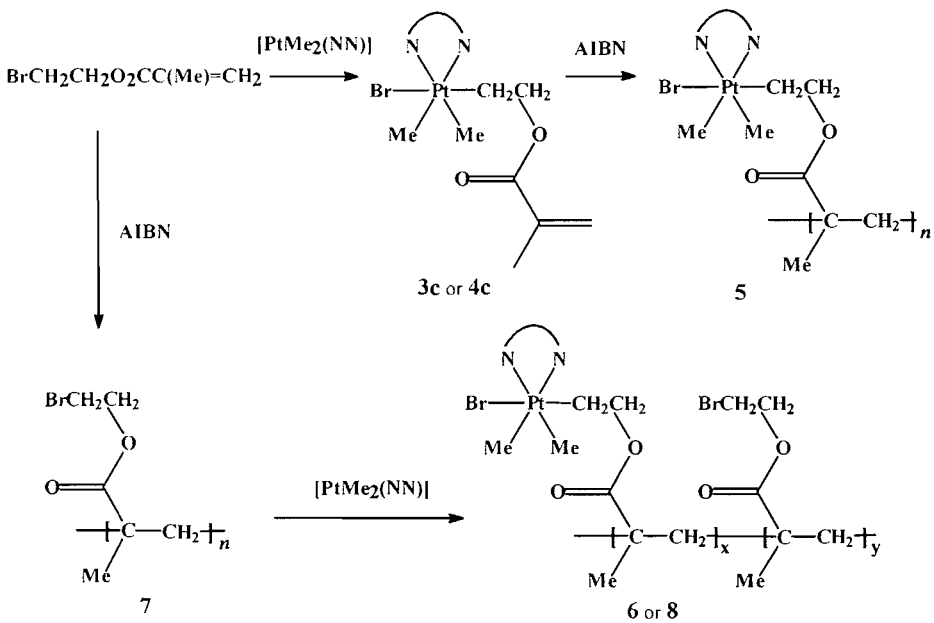

leading to lower GPC molecular weights. Either this is not so or perhaps there is some association between the platinated polymer chains that compensates for this effect. It is reasonable to assume that the chain length is not affected by the metallation step. In the ^{1}H NMR spectra of the polymers **8a–e** in acetone, the peaks due to PtMe, *tert*-butyl, and other aliphatic groups were broad and not completely resolved. To prove the presence of PtMe groups, the polymer **8**–d^6 was synthesized by the oxidative addition of poly(2-bromoethyl methacrylate) to [Pt(CD_3)$_2$(bu_2bipy)] in a ratio of 4:1 and the presence of CD_3Pt groups was then proved by ^{2}H NMR. Two broad resonances were observed in the ^{2}H NMR. The more intense peak at δ = 1.3 was assigned to the CD_3 groups *trans* to nitrogen (present for both *trans* and *cis* oxidative addition), while the less intense resonance at δ = 0.5 was assigned to the CD_3 group *trans* to bromide (present for *cis* oxidative addition only) and integration therefore gave the ratio *trans*:*cis* = 55±5:45±5, essentially the same as for oxidative addition of the monomer to **2** (Table 1). The observation of the CD_3 peaks in the ^{2}H NMR clearly proves the presence of the MePt groups in the polymer **8**.

The platinum(IV) monomers **3g,3h** derived from chloromethylstyrene were sparingly soluble in common organic solvents and hence their solution polymerization could not be carried out. The analogous monomers with bu_2bipy ligands, **3i,3j**, were more soluble but still did not undergo free radical polymerization in the presence of azobis(isobutyronitrile) initiator. The platinated polymer of chloromethylstyrene could only be prepared by polymerization of the organic monomer to give the polymer **9** (M_n = 6800, M_w = 15 000, M_w/M_n = 2.2) followed by reaction with **1** or **2** to give **10** or **11** (Scheme 3; note that only the *meta*-chloromethylstyrene isomer is illus-

Scheme 3.

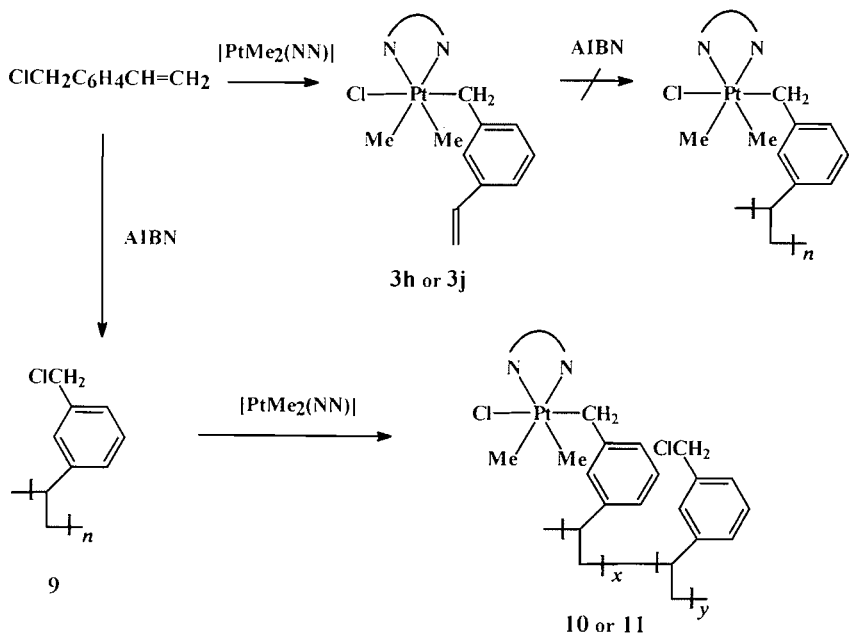

trated for simplicity and that the structure shown is an idealized one and a more random arrangement is likely). The polymers precipitated as pale yellow powders and were sparingly soluble in common organic solvents. Again, complete platination of all chloromethyl groups did not occur on reaction with excess **1** or **2**. It is noteworthy that **11** is more soluble in acetone than **10** and that **11** contains a higher incorporation of platinum (77% of chloromethyl groups platinated) than **10** (62%). This suggests that the precipitation of the partially metallated polymer, with some of the chloromethyl groups coiled back away from the reaction surface, prevents further platination. To check if insolubility alone would prevent further reaction of chloromethyl groups with platinum(II) reagent, Merrifield's resin (which is an insoluble, cross-linked chloromethylated styrene – divinyl benzene copolymer with all chloromethyl groups at the polymer surface) was reacted, as a suspension in acetone, with excess **1** to give the platinated resin, **12**, in which essentially all of the chloromethyl groups were platinated. This clearly shows that the oxidative addition of chloromethyl groups to **1** can occur under heterogeneous conditions provided the chloromethyl groups are located on the polymer surface. Other groups have also successfully derivatized Merrifield's resin to introduce metal substituents, although not by oxidative addition (34–36).

The chemistry of compounds derived from chloromethylstyrene and acryloyl chloride was similar. Thus, the monomers **3e**,**4e** and **3f**,**4f** derived from acryloyl chloride did not undergo free radical polymerization but the organic monomer could be polymerized to give **13** and then platinated to give **14** or **15** (Scheme 4, again simplified for clarity).

As expected, the metallated polymers differ significantly in their physical properties from either the organic polymers or the organometallic monomers. For example, the organoplatinum monomer **3c**,**4c** melts with decomposition at 166°C and the organic polymer **7** exhibits a glass transition in the range 65–79°C, as determined by differential scanning calorimetry (DSC) but is not crystalline and gives no distinct melting endotherm. However, the polymers **5** and **6** each exhibit a very broad endothermic transition over the range 60–160°C, with the peak at 115°C, and there is a melting endotherm that begins at 210°C and peaks at 243°C. When samples of the polymers **5** and **6** were heated to 150°C for 30 min and then cooled and reheated, the broad endotherm in the region 60–160°C was not observed while the melting endotherm was unchanged. Thus, it appears that the polymers **5** and **6** precipitate in a strained conformation that relaxes on heating above 60°C.

TGA studies indicated that the organic polymer, **7**, undergoes complete weight loss over the temperature range 335–395°C, while the organoplatinum polymers decompose over a much wider range. The organoplatinum polymers **5**, **6** and **8a–e** exhibit similar patterns for the TGA thermograms, all decomposing over a wide range of temperature from 240 to 600°C. The decomposition onset temperatures gradually increased with the increase in the platinum content for the series **8a–e**, which clearly reveals the effect of metallation on decomposition characteristics; details for these and other polymers are given in the experimental section.

Experimental

^{1}H NMR spectra were recorded using Varian XL 200 or Gemini 300 MHz spectrometers. FTIR spectra were recorded as KBr disks by using a Bruker IR/32 spectrometer. Thermal analyses were carried out using a Perkin Elmer DSC7 and TAC7/DX differential scanning calorimeter and thermogravimetric analyzer, respectively. The heating rate was 20°C/min and a sample mass of 5–10 mg was used. Nitrogen was used as the purge gas. The molecular weight measurements were carried out using a Waters 600 GPC with Waters 410 differential

Scheme 4.

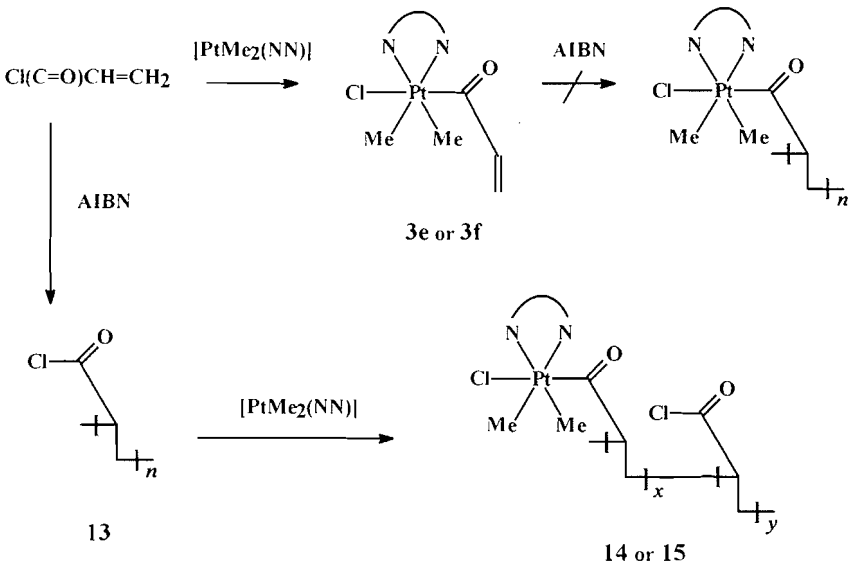

refractometer as the detector. Two ultrastyragel columns were used in series (10^3 Å and 10^2 Å) and THF was used as the solvent. The system was calibrated with linear polystyrene standards. In the NMR listings, a vinyl group is defined as $-CH^a{=}CH^bH^c$, with H^a *trans* to H^b.

[$PtBrMe_2\{CH_2C(COOMe){=}CH_2\}$(bipy)], 3a,4a

To a solution of [$PtMe_2$(bipy)] (0.05 g) in acetone (10 mL) was added methyl 2-(bromomethyl)acrylate (0.02 mL) and the mixture was stirred for 2 h. The solution color changed from red-orange to pale yellow and the product precipitated as a white powder. The product was separated, washed with ether, and dried under vacuum. Yield 86%. IR: ν(CO) = 1714 cm^{-1}, ν(C=C) = 1601 cm^{-1}. ^1H NMR in CD_2Cl_2: **3a**: δ: 1.39 (s, 6H, ^2J(PtH) = 70 Hz, Me_2Pt), 2.50 (s, 2H, ^2J(PtH) = 97 Hz, CH_2Pt), 3.08 (s, 3H, CH_3-O), 4.98 (m, 1H, ^4J(PtH) = 26 Hz, $CH_2{=}$), 5.52 (m, 1H, ^4J(PtH) = 29 Hz, $CH_2{=}$), 7.63 (t, 2H, H^5 of (bipy)), 8.07 (t, 2H, H^4 of (bipy)), 8.21 (d, 2H, H^3 of (bipy)), 8.78 (d, 2H, H^6 of (bipy)); **4a**: δ: 0.48 (s, 3H, ^2J(PtH) = 71 Hz, MePtBr), 1.30 (s, 3H, ^2J(PtH) = 70 Hz, MePtN), 2.46 (s, 2H, ^2J(PtH) = 97 Hz, CH_2Pt), 3.63 (s, 3H, CH_3-O). Anal. calcd. for $C_{17}H_{21}BrN_2O_2Pt$: C 36.4, H 3.8, N 5.0; found: C 36.5, H 3.5, N 4.8.

The following complexes were prepared similarly.

[$PtBrMe_2\{CH_2C(COOH){=}CH_2\}$(bipy)], 3b,4b

Yield 90%. IR: ν(CO) = 1719 cm^{-1}, ν(COOH) = 2899 cm^{-1}. ^1H NMR in CD_3COCD_3: **3b**: δ: 1.36 (s, 6H, ^2J(PtH) = 70 Hz, Me_2Pt), 2.47 (s, 2H, ^2J(PtH) = 98 Hz, CH_2Pt), 4.88 (d, 1H, ^4J(PtH) = 26 Hz, $CH_2{=}$), 5.50 (d, 1H, ^4J(PtH) = 29 Hz, $CH_2{=}$), 7.78 (t, 2H, H^5 of (bipy)), 8.23 (t, 2H, H^4 of (bipy)), 8.55 (d, 2H, H^3 of (bipy)), 8.81 (d, 2H, H^6 of (bipy)); **4b**: δ: 0.24 (s, 3H, ^2J(PtH) = 71 Hz, MePtBr), 1.14 (s, 3H, ^2J(PtH) = 70 Hz, MePtN), 5.25 and 5.62 (m, 1H each, $CH_2{=}$). Anal. calcd. for $C_{16}H_{19}BrN_2O_2Pt$: C 35.2, H 3.5, N 5.1; found: C 35.0, H 3.1, N 5.1.

[$PtBrMe_2\{CH_2CH_2OCOC(CH_3){=}CH_2\}$(bipy)], 3c,4c

Yield 83%. IR: ν(CO) = 1711 cm^{-1}, ν(C=C) = 1634 cm^{-1}. ^1H NMR in CD_2Cl_2: **3c**: δ: 1.40 (s, 6H, ^2J(PtH) = 70 Hz, Me_2Pt), 1.71 (m, 3H, Me-C=), 2.08 and 2.4 (m, 1H each, CH_2Pt), 3.42 (t, 2H, ^3J(PtH) = 42 Hz, CH_2-O), 5.38 (m, 1H, $CH_2{=}$), 5.68 (m, 1H, $CH_2{=}$), 7.76 (m, 2H, H^5 of (bipy)), 8.14 (m, 2H, H^4 of (bipy)), 8.26 (m, 2H, H^3 of (bipy)), 9.2 (m, 2H, H^6 of (bipy)); **4c**: δ: 0.55 (s, 3H, ^2J(PtH) = 72 Hz, MePtBr), 1.43 (s, 3H, ^2J(PtH) = 70 Hz, MePtN), 1.98 (m, 3H, Me-C=), 1.94 and 2.24 (m, 1H each, CH_2Pt), 4.31 and 4.68 (m, 1H each, CH_2-O), 5.55 and 6.11 (m, 1H each, $CH_2{=}$), 7.69 (m, 2H, H^5 of (bipy)), 8.1 (m, 2H, H^4 of (bipy)), 8.29 (m, 2H, H^3 of (bipy)), 8.9 (m, 2H, H^6 of (bipy)). Mass spectrum, (*m/z*): 494 $(M - Br)^+$. Anal. calcd. for $C_{18}H_{23}BrN_2O_2Pt$: C 37.6, H 4.0, N 4.9; found: C 37.7, H 3.8, N 4.9.

[$PtBrMe_2\{CH_2CH_2OCOC(CH_3){=}CH_2\}$($bu_2$bipy)], 3d,4d

Yield 85%. ^1H NMR in CD_2Cl_2: **3d**: δ: 1.36 (s, 6H, ^2J(PtH) = 70 Hz, Me_2Pt), 1.46 (b, 18H, *tert*-butyl protons), 1.71 (m, 3H, Me-C=), 3.41 (t, 2H, ^3J(PtH) = 45 Hz, CH_2-O), 5.37 and 5.7 (m, 1H each, $CH_2{=}$), 7.65, 8.18, 8.78 (2H each, H^5, H^3, and H^6 of (bu_2bipy), respectively); **4d**: δ: 0.53 (s, 3H, ^2J(PtH) = 74 Hz, MePtBr), 1.38 (s, 3H, ^2J(PtH) = 70 Hz, MePtN), 1.98 (m, 3H, Me-C=), 2.2 (m, 1H, CH_2Pt, other H signal is obscured), 4.28 and 4.66 (m, 1H each, CH_2-O), 5.53 and 6.1 (m, 1H each, $CH_2{=}$), 7.75 and 9.06 (2H each, H^5 and H^6 of (bu_2bipy), respectively, H^3 peak obscured).

[$PtClMe_2$(CO-CH=CH_2)(bipy)], 3e,4e

Yield 90%. IR: ν(C=O) = 1653 cm^{-1}. ^1H NMR in CD_3COCD_3: **3e**: δ: 1.46 (s, 6H, ^2J(PtH) = 72 Hz, Me_2Pt), 4.77 (d, 1H, $J(H^cH^a)$ = 11 Hz, H^c), 5.38 (d, 1H, $J(H^bH^a)$ = 17 Hz, H^b) and 6.57 (dd, 1H, $J(H^aH^b)$ = 17 Hz, $J(H^aH^c)$ = 11 Hz, H^a), 7.85 (dt, 2H, H^5 of (bipy)), 8.32 (dt, 2H, H^4 of (bipy)), 8.7 (dd, 2H, H^3 of (bipy)), 9.1 (dd, 2H, H^6 of (bipy)). **4e**: δ: 0.71 (s, 3H, ^2J(PtH) = 74 Hz, MePtCl), 1.39 (s, 3H, ^2J(PtH) = 72 Hz,

MePtN), 4.80 (d, 1H, $J(H^cH^a)$ = 11 Hz, H^c), 5.73 (d, 1H, $J(H^bH^a)$ = 17 Hz, H^b), 7.35 (dd, 1H, $J(H^aH^b)$ = 17 Hz, $J(H^aH^c)$ = 11 Hz, H^a). Anal. calcd. for $C_{15}H_{17}ClN_2OPt$: C 38.2, H 3.6, N 5.9; found: C 37.8, H 3.4, N 6.1.

[$PtClMe_2(CO\text{-}CH{=}CH_2)(bu_2bipy)$], 3f,4f

Yield 80%. ^1H NMR in CD_3COCD_3: **3f**: δ: 1.41 (s, 6H, $^2J(PtH)$ = 72 Hz, Me_2Pt), 4.78 (d, 1H, $J(H^cH^a)$ = 10 Hz, $J(H^cH^b)$ = 2 Hz, H^c), 5.4 (d, 1H, $J(H^bH^a)$ = 17 Hz, $J(H^bH^c)$ = 2 Hz, H^b) and 6.55 (dd, 1H, $J(H^aH^b)$ = 17 Hz, $J(H^aH^c)$ = 10 Hz, H^a). **4f**: δ: 0.69 (s, 3H, $^2J(PtH)$ = 75 Hz, MePtCl), 1.35 (s, 3H, $^2J(PtH)$ = 72 Hz, MePtN), 1.46 (b, 18H, *tert*-butyl), 4.85 (d, 1H, $J(H^cH^a)$ = 10 Hz, $J(H^cH^b)$ = 2 Hz, H^c), 5.72 (d, 1H, $J(H^bH^a)$ = 17 Hz, $J(H^bH^c)$ = 2 Hz, H^b), 7.38 (dd, 1H, $J(H^aH^b)$ = 17 Hz, $J(H^aH^c)$ = 10 Hz, H^a), 7.85, 8.7, and 8.93 (m, 2H each, H^5, H^3, and H^6 of (bu_2bipy)). Anal. calcd. for $C_{23}H_{33}ClN_2OPt$: C 47.3, H 5.7, N 4.8; found: C 47.4, H 5.8, N 4.9.

[$PtClMe_2(CH_2\text{-}C_6H_4\text{-}CH{=}CH_2)$(bipy)], 3g,3h

Yield 88%. ^1H NMR, 300 MHz, $CDCl_3$: **3h**: δ: 1.46 (s, 6H, $^2J(PtH)$ = 69 Hz, Me_2Pt), 2.77 (s, 2H, $^2J(PtH)$ = 93 Hz, CH_2Pt), 4.98 (d, 1H, $J(H^cH^a)$ = 11 Hz, H^c), 5.22 (d, 1H, $J(H^bH^a)$ = 17 Hz, H^b) and 6.2 (dd, 1H, $J(H^aH^b)$ = 17 Hz, $J(H^aH^c)$ = 11 Hz, H^a), 6.1–6.6 (m, 8H, C_6H_4 ring protons of the two isomers), 7.45 (m, 2H, H^5 of (bipy)), 7.9 (m, 4H, H^4 and H^3 of (bipy)), 8.68 (m, 2H, H^6 of (bipy)). Resolved peaks of **3g**: δ: 1.45 (s, 6H, $^2J(PtH)$ = 69 Hz, Me_2Pt), 2.79 (s, 2H, $^2J(PtH)$ = 95 Hz, CH_2Pt), 5.0 (d, 1H, $J(H^cH^a)$ = 11 Hz, H^c), 5.41 (d, 1H, $J(H^bH^a)$ = 17 Hz, H^b) and 6.34 (dd, 1H, $J(H^aH^b)$ = 17 Hz, $J(H^aH^c)$ = 11 Hz, H^a). Anal. calcd. for $C_{21}H_{23}ClN_2Pt$: C 47.2, H 4.3, N 5.2; found: C 46.8, H 4.2, N 5.3.

[$PtClMe_2(CH_2\text{-}C_6H_4\text{-}CH{=}CH_2)(bu_2bipy)$], 3i,3j

Yield 93%. ^1H NMR, 300 MHz, $CDCl_3$: **3j**: δ: 1.36 (b, 36H, *tert*-butyl protons), 1.42 (s, 6H, $^2J(PtH)$ = 69 Hz, Me_2Pt), 2.76 (s, 2H, $^2J(PtH)$ = 94 Hz, CH_2Pt), 4.96 (d, 1H, $J(H^cH^a)$ = 11 Hz, H^c), 5.18 (d, 1H, $J(H^bH^a)$ = 17 Hz, H^b) and 6.17 (dd, 1H, $J(H^aH^b)$ = 17 Hz, $J(H^aH^c)$ = 11 Hz, H^a), 6.0–6.7 (m, 8H, C_6H_4 ring protons of the two isomers), 7.4 (m, 2H, H^5 of (bu_2bipy)), 7.81 (s, 2H, H^3 of (bu_2bipy)), 8.57 (d, 2H, $^3J(PtH)$ = 12 Hz, H^6 of (bu_2bipy)). Resolved peaks of **3i**: δ: 1.40 (s, 6H, $^2J(PtH)$ = 69 Hz, Me_2Pt), 2.78 (s, 2H, $^2J(PtH)$ = 96 Hz, CH_2Pt), 5.01 (d, 1H, $J(H^cH^a)$ = 11 Hz, H^c), 5.42 (d, 1H, $J(H^bH^a)$ = 17 Hz, H^b), 6.32 (dd, 1H, $J(H^aH^b)$ = 17 Hz, $J(H^aH^c)$ = 11 Hz, H^a), 7.42 (m, 2H, H^5 of (bu_2bipy)), 7.86 (s, 2H, H^3 of (bu_2bipy)), 8.52 (d, 2H, $^3J(PtH)$ = 12 Hz, H^6 of (bu_2bipy)). Anal. calcd. for $C_{29}H_{39}ClN_2Pt$: C 53.9, H 6.1, N 4.3; found: C 53.6, H 6.4, N 4.2.

Polymerization of [$PtBrMe_2\{CH_2CH_2OCOC(CH_3){=}CH_2\}$(bipy)] to give 5

A solution of [$PtBrMe_2\{CH_2CH_2OCOC(CH_3){=}CH_2\}$(bipy)] (0.12 g) and azobisisobutyronitrile (0.015 g) in freshly distilled chlorobenzene (5 mL) was degassed by three freeze–pump–thaw cycles at 10^{-5} Torr (1 Torr = 1.33 Pa), then sealed under vacuum and heated to 60°C. After 8 h the product had precipitated, heating was stopped, the solvent was rotoevaporated, and the product was washed with ether and dried. Yield 50%. IR: ν(CO) = 1722 cm^{-1}. Anal. calcd. for $C_{18}H_{23}BrN_2O_2Pt$: C 37.6, H 4.0, N 4.9; found: C 37.1, H 3.9, N 4.6.

Poly(2-bromoethyl methacrylate), 7

A solution of freshly distilled 2-bromoethyl methacrylate (3.5 g) and azobisisobutyronitrile (0.02 g) in dry chlorobenzene (3 mL) was degassed by freeze–pump–thaw cycles at 10^{-5} Torr, then sealed under vacuum and heated to 60°C for 1 day. The solution became more viscous. The polymer was precipitated with methanol and dried. Yield 80%. IR: ν(CO) = 1728 cm^{-1}. ^1H NMR in acetone: δ: 0.9–1.8 (b, Me and C-CH_2), 3.73 (b, CH_2CH_2Br), 4.35 (b, CH_2CH_2Br). GPC (THF): M_n = 9800; M_w = 16 000; polydispersity = 1.63.

[$PtMe_2$(bipy)] with poly(2-bromoethyl methacrylate) to give 6

Solutions of poly 2-bromoethyl methacrylate (0.05 g) in acetone (10 mL) and [$PtMe_2$(bipy)] (0.15 g) in acetone (10 mL) were mixed and stirred at room temperature for 1 day. The precipitated product was separated and washed with ether and dried. Yield 60%. Anal. calcd. for $C_{18}H_{23}BrN_2O_2Pt$-$(C_6H_9BrO_2)_{0.35}$: C 37.6, H 4.1, N 4.4; found: C 37.1, H 4.1, N 4.3. TGA: decomp. onset, 290°C; weight loss: 39% at 630°C. Similarly the organoplatinum polymers **8a–8e** were prepared by the reaction of [$PtMe_2(bu_2bipy)$] and poly 2-bromoethyl methacrylate. The platinum complex **2**, and the preformed polymer **7**, were reacted in ratios corresponding to 1:10, 1:4, 1:2, 1:1.33, and 1:1 to yield the organoplatinum polymers **8a–8e**, respectively. **8a**: Anal. calcd. for $C_{18}H_{23}BrN_2O_2Pt$-$(C_6H_9BrO_2)_{13}$: C 39.1, H 4.9, N 0.8; found: C 39.1, H 4.8, N 0.9. GPC: M_n = 10 000, M_w = 15 500, polydispersity 1.55. TGA: decomp. onset, 240°C; residue: 20% at 580°C. **8b**: Anal. calcd. for $C_{18}H_{23}BrN_2O_2Pt(C_6H_9BrO_2)_{3.57}$: C 41.4, H 5.2, N 2.0; found: C 41.3, H 5.3, N 2.0. GPC: M_n = 9700, M_w = 14 700, polydispersity 1.51. TGA: decomp. onset, 256°C; residue: 26% at 580°C. **8c**: Anal. calcd. for $C_{18}H_{23}BrN_2O_2Pt$-$(C_6H_9BrO_2)_{1.96}$: C 42.6, H 5.4, N 2.6; found: C 43.1, H 5.5, N 2.7. GPC: M_n = 10 300, M_w = 15 000, polydispersity 1.45. TGA: decomp. onset, 260°C; residue: 29% at 580°C. **8d**: Anal. calcd. for $C_{18}H_{23}BrN_2O_2Pt(C_6H_9BrO_2)_{0.92}$: C 43.8, H 5.5, N 3.2; found: C 43.3, H 5.4, N 3.2. GPC: insufficiently soluble. TGA: decomp. onset, 274°C; residue: 34% at 580°C. **8e**: Anal. calcd. for $C_{18}H_{23}BrN_2O_2Pt(C_6H_9BrO_2)_{0.5}$: C 44.5, H 5.6, N 3.6; found: C 43.9, H 5.3, N 3.5. TGA: decomp. onset, 278°C; residue: 35% at 580°C.

Poly(acryloyl chloride), 13

Azobisisobutyronitrile (0.02 g) was added to freshly distilled acryloyl chloride (5 mL) and the mixture was degassed. The sealed ampoule was heated to 70°C for 1 day. Only partial polymerization was observed. The monomer was separated from the polymer by evaporation under vacuum. GPC: M_n = 4300; M_w = 5000; M_w/M_n = 1.16. ^1H NMR in CD_3COCD_3, 200 MHz; δ: 2.3, 2.56 and 3.24 (broad peaks).

The organoplatinum polymers **14** and **15** were prepared as above.

Polymer 14: ^1H NMR, 200 MHz, dmso-d^6; δ: 0.3–2.2 (b, 9H, PtMe, -CH-CH_2-), 7.4–9.8 (b, 6H, (bipy)). Anal. calcd. for $C_{15}H_{17}ClN_2OPt$: C 38.2, H 3.6, N 5.9; found: C 38.0, H 4.2, N 6.0. TGA: decomp. range 200–790°C, weight loss 58%.

Polymer 15: ^1H NMR, 200 MHz, $CDCl_3$; δ: 1.1–2.3 (b, *tert*-butyl, PtMe and -CH-CH_2-), 7.3–9.7 (b, (bipy)). Anal. calcd.

for $C_{23}H_{33}ClN_2OPt(C_3H_3OCl)_{0.9}$: C 46.3, H 5.4, N 4.2; found: C 45.6, H 5.6, N 4.1.

Poly(chloromethylstyrene), 9

To the mixture of the *meta* and *para* isomers of chloromethylstyrene (6 mL) (distilled under reduced pressure) was added azobisisobutyronitrile (0.025 g) and the mixture was then degassed by several freeze–pump–thaw cycles at 10^{-4} Torr and sealed under vacuum. The sealed ampoule was heated to 60°C for 8 h. The polymer was purified by repeated precipitation into methanol from acetone. The polymer was isolated as a white, amorphous material. ^{1}H NMR, 200 MHz, CD_3COCD_3, δ: 1.6 and 1.82 (b, 3H, -CH-CH_2-), 4.56 (b, 2H, CH_2Cl), 6.64, 7.15 (b, 4H, benzene ring protons). GPC: M_n = 6800; M_w = 15 000; M_w/M_n = 2.2. TGA: decomp. 323–600°C, weight loss 63%.

[$PtMe_2$(bipy)] with poly(chloromethylstyrene) to give 10

Solutions of the polymer **9** (0.05 g) in acetone (10 mL) and [$PtMe_2$(bipy)] (0.20 g) in acetone (15 mL) were mixed and stirred at room temperature. The product polymer precipitated from the solution. It was separated, washed with ether, and dried. Yield 70%. ^{1}H NMR, 200 MHz, dmso-d^6, δ: 1.22 (b, 9H, PtMe and -CH-CH_2-), 5.9 (b, 4H, benzene ring protons), 7.36, 7.9 and 8.4 (b, 8H, bipyridine protons). Anal. calcd. for $C_{21}H_{23}ClN_2Pt(C_9H_9Cl)_{0.62}$: C 50.8, H 4.6, N 4.4; found: C 48.9, H 4.7, N 4.3. TGA: decomp. 270–580°C, weight loss 69%. Similarly the polymer **11** was prepared from the polymer **9** and **2**: Yield 78%. ^{1}H NMR, 200 MHz, $CDCl_3$, δ: 1.45 (b, 27H, PtMe, *tert*-butyl and -CH-CH_2-), 4.35 (trace, broad, unreacted chloromethyl groups), broad peaks in the region from δ = 5–9, with peaks at 6.2, 7.15, and 8.05 (10H, benzene ring and bipyridine protons). Anal. calcd. for $C_{29}H_{39}ClN_2Pt(C_9H_9Cl)_{0.32}$: C 55.0, H 6.1, N 4.0; found: C 55.6, H 6.5, N 3.8. TGA: decomp. 300–480°C, weight loss 47%.

[$PtMe_2$(bipy)] with Merrifield's resin

To a suspension of Merrifield's resin (0.05 g) in acetone (10 mL) was added an excess amount of [$PtMe_2$(bipy)] (0.05 g) in acetone (5 mL). The mixture was stirred for 1 day. The resin was separated, washed thoroughly with ether, and dried. Anal. calcd. for $C_9H_8(C_{21}H_{23}ClN_2Pt)_{0.15}$: C 74.4, H 5.9, N 2.1; found: C 72.9, H 6.6, N 2.1.

Acknowledgement

We thank the Natural Sciences and Engineering Research Council (NSERC) of Canada for financial support.

References

1. C.U. Pittman, Jr., C.E. Carraher, Jr., and J.R. Reynolds. *In* Encyclopedia of polymer science and engineering. Vol. 10. 11th ed. Wiley, New York. 1988. p. 451.
2. D.A. Foucher, C.H. Honeyman, J.M. Nelson, B.Z. Tang, and I. Manners. Angew. Chem. Int. Ed. Engl. **32**, 1709 (1993).
3. H.B. Fyfe, M. Mlekuz, D. Zargarian, N.J. Taylor, and T.B. Marder. J. Chem. Soc. Chem. Commun. 188 (1991).
4. K.C. Sturge, A.D. Hunter, R. McDonald, and B.D. Santarsiero. Organometallics, **11**, 3056 (1992).
5. G. Jia, N.C. Payne, J.J. Vittal, and R.J. Puddephatt. Organometallics, **12**, 4771 (1993).
6. P.G. Lacroix, W. Lin, and G.K. Wong. Chem. Mater. **7**, 1293 (1995).
7. E. Lindner, M. Kemmler, H.A. Mayer, and P. Wegner. J. Am. Chem. Soc. **116**, 348 (1994).
8. M.A. Massa and T.B. Rauchfuss. Chem. Mater. **3**, 788 (1991).
9. L.B. Chen, J.X. Jin, J. Lin, H.S. Chen, and X.X. Lin. Makromol. Chem. Rapid Commun. **8**, 187 (1987).
10. S.S. Kher and T.A. Nile. Transition Met. Chem. **16**, 28 (1991).
11. J.M. Nelson, A.J. Lough, and I. Manners. Angew. Chem. Int. Ed. Engl. **33**, 989 (1994).
12. S. Achar and R.J. Puddephatt. Angew. Chem. Int. Ed. Engl. **33**, 847 (1994).
13. S. Achar and R.J. Puddephatt. Organometallics, **14**, 1681 (1995).
14. S. Achar and R.J. Puddephatt. J. Chem. Soc. Chem. Commun. 1895 (1994).
15. S. Achar, J.D. Scott, J.J. Vittal, and R.J. Puddephatt. Organometallics, **12**, 4592 (1993).
16. S. Achar, J.D. Scott, and R.J. Puddephatt. Organometallics, **11**, 2325 (1992).
17. J.C. Lai, T.D. Rounsefell, and C.U. Pittman, Jr. Macromolecules, **4**, 155 (1971).
18. C.U. Pittman, Jr., R.L. Voges, and J. Elder. Macromolecules, **4**, 302 (1971).
19. R.J. Card and D.C. Neckers. J. Am. Chem. Soc. **99**, 7733 (1977).
20. S.N. Gupta and D.C. Neckers. J. Polym. Sci. Polym. Chem. Ed. **20**, 1609 (1982).
21. T. Yamamoto, Y. Yoneda, and T. Maruyama. J. Chem. Soc. Chem. Commun. 1652 (1992).
22. C.U. Pittman, Jr. and R.F. Felis. J. Organomet. Chem. **72**, 389 (1974).
23. N. Funita and K. Sonogashira. J. Polym. Sci. Part A: Polym. Chem. Ed. **12**, 2845 (1974).
24. H.C. Clark and J.D. Ruddick. Inorg. Chem. **9**, 2556 (1970).
25. T.G. Appleton, H.C. Clark, and L.E. Manzer. J. Organomet. Chem. **65**, 275 (1974).
26. P.K. Monaghan and R.J. Puddephatt. Organometallics, **4**, 1405 (1985).
27. J.D. Scott and R.J. Puddephatt. Organometallics, **5**, 1538 (1986).
28. M. Crespo and R.J. Puddephatt. Organometallics, **6**, 2548 (1987).
29. L.M. Rendina, J.J. Vittal, and R.J. Puddephatt. Organometallics, **14**, 2188 (1995).
30. G.M. Bager and W.H.F. Sasse. J. Chem. Soc. 616 (1956).
31. V.F. Sutcliffe and G.B. Young. Polyhedron, **3**, 87 (1984).
32. N. Chaudhury and R.J. Puddephatt. J. Organomet. Chem. **84**, 105 (1975).
33. G.S. Hill, L.M. Rendina, and R.J. Puddephatt. Organometallics, **14**, 4966 (1995).
34. B. Brix and T. Clark. J. Org. Chem. **53**, 3365 (1988).
35. S.M. Baxter, W.E. Jones, Jr., E. Danielson, L. Worl, G. Strouse, J. Younathan, and T.J. Meyer. Coord. Chem. Rev. **111**, 47 (1991).
36. B. Boury, R.J.P. Corriu, D. Leclercq, H. Mutin, J.M. Planeix, and A. Vioux. *In* Inorganic and organic polymers with special properties. *Edited by* R.M. Laine. Kluwer Academic Publishers, Dordrecht. 1992. p. 255.

Synthesis of the complexes [PdClR(cod)] (R = benzyl, ethyl; cod = 1,5-cyclooctadiene). β-Elimination from [PdClEt(cod)] to give the η^1,η^2, and η^3 isomers of $[Pd_2(\mu\text{-}Cl)_2(C_8H_{13})_2]$

Robert A. Stockland, Jr., Gordon K. Anderson, Nigam P. Rath, Janet Braddock-Wilking, and J. Christopher Ellegood

Abstract: Treatment of $[PdCl_2(cod)]$ with tetrabenzyltin gives the benzylpalladium complex $[PdCl(CH_2Ph)(cod)]$ (cod = 1,5-cyclooctadiene), **1a**, whose structure has been determined by X-ray crystallography. It adopts approximate square-planar geometry, with the double bonds perpendicular to the square plane. The corresponding ethylpalladium derivative **1b** has been prepared by a similar method, but it is considerably less stable. It decomposes by β-elimination to produce ethene and a transient hydride complex, which either undergoes migratory insertion to give $[Pd_2(\mu\text{-}Cl)_2(\eta^1,\eta^2\text{-}C_8H_{13})_2]$, **2a**, or dinuclear reductive elimination with a second molecule of **1b** to produce ethane, $[PdCl_2(cod)]$, free cyclooctadiene, and palladium metal. Complex **2a** has also been prepared by reaction of $[PdCl_2(cod)]$ with $NaBH_4$. At higher temperatures **2a** converts to an equilibrium mixture with its η^3-allyl isomer, **2b**. Reactions of $[PdCl_2(cod)]$ or K_2PdCl_4 in the presence of cyclooctadiene in aqueous solution to produce **2a** or **2b** have also been investigated.

Key words: palladium, diene complexes, allyl complexes, isomerization, β-elimination.

Résumé : Le traitement du $[PdCl_2(cod)]$ avec le tétrabenzylétain conduit au complexe benzylpalladium $[PdCl(CH_2Ph)(cod)]$ (cod = cycloocta-1,5-diène), **1a**, dont on a déterminé la structure par diffraction des rayons X. Il adopte une géométrie plan carré dans laquelle les doubles liaisons sont perpendiculaires au plan carré. On a préparé le dérivé éthylpalladium correspondant, **1b**, par une méthode semblable; il est toutefois beaucoup moins stable. Il se décompose par une élimination β pour former de l'éthène et un hydrure complexe transitoire qui peut donner lieu soit à une insertion migratoire conduisant au $[Pd_2(\mu\text{-}Cl)_2(\eta^1,\eta^2\text{-}C_8H_{13})_2]$, **2a**, soit à une élimination réductrice dinucléaire avec une deuxième molécule de **1b** qui fournit de l'éthane, du $[PdCl_2(cod)]$, du cyclooctadiène libre et du palladium métallique. On a aussi préparé le complexe **2a** par réaction du $[PdCl_2(cod)]$ avec le $NaBH_4$. À des températures plus élevées, le composé **2a** se transforme en un mélange à l'équilibre avec l'isomère η^3-allyle **2b**. On a aussi étudié les réactions du $[PdCl_2(cod)]$ ou du K_2PdCl_4 en solution aqueuse, en présence de cyclooctadiène, qui conduisent aux produits **2a** ou **2b**.

Mots clés : palladium, complexes diéniques, complexes allyliques, isomérisation, élimination β.

[Traduit par la rédaction]

Introduction

Since the first platinum complexes of the type [PtClR(cod)] (cod = 1,5-cyclooctadiene) were reported by Clark and Manzer (1), they have served as excellent precursors to a range of organoplatinum species, including bis(phosphine) (2) or diphosphine (3) compounds, or dppm-bridged A-frames (4).

Received March 1, 1996.

This paper is dedicated to Professor Howard C. Clark in recognition of his contributions to Canadian chemistry.

R.A. Stockland, Jr., G.K. Anderson,[1] N.P. Rath, J. Braddock-Wilking, and J.C. Ellegood. Department of Chemistry, University of Missouri – St. Louis, 8001 Natural Bridge Road, St. Louis, MO 63121, U.S.A.

[1] Author to whom correspondence may be addressed. Telephone: (314) 516-5311. Fax: (314) 516-5342. E-mail: ganderson@umsl.edu

The corresponding palladium complexes have proved more elusive. The preparation of [PdClMe(cod)] was first reported in 1977, from the reaction of the dimethyl species with chlorinated solvents or with $[PdCl_2(cod)]$, but it was found to be unstable (5). More recently, a superior synthesis from $[PdCl_2(cod)]$ and tetramethyltin has been reported (6), and we have shown that [PdClMe(cod)] is a suitable precursor to a number of chloride-bridged methylpalladium complexes (7). The pentafluorophenyl complex $[PdCl(C_6F_5)(cod)]$ has been prepared and structurally characterized, and it has been shown to undergo rearrangements that involve migration of the aryl group on to the cyclooctadiene ring (8). In this paper, we report the preparation and structure of $[PdCl(CH_2Ph)(cod)]$, **1a**, and the difficult isolation and facile rearrangement of its ethyl analogue.

Results and discussion

The synthesis of $[PdCl(CH_2Ph)(cod)]$, **1a**, is similar to that of its methyl analogue (6, 7), except that a longer reaction time is required. Thus, refluxing a dichloromethane solution of

Fig. 1. Projection view of the molecular structure of [PdCl(CH_2Ph)(cod)], **1a**, showing the atom-labeling scheme.

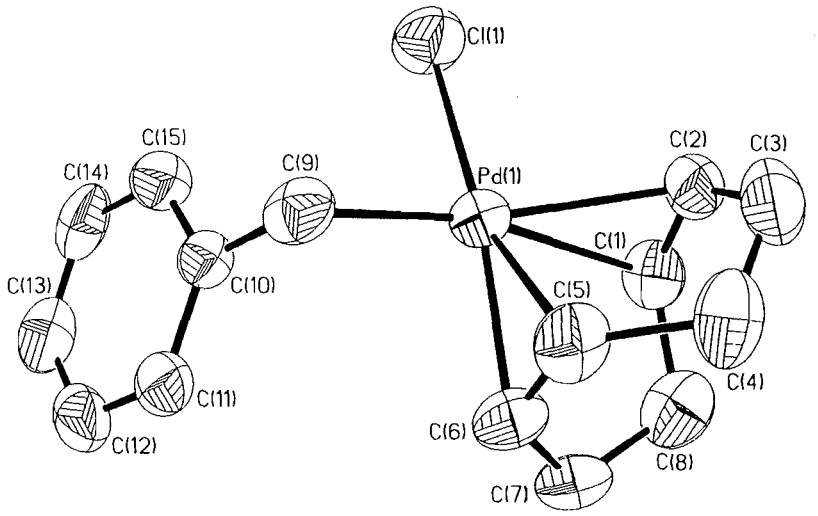

[$PdCl_2$(cod)] with a slight excess of tetrabenzyltin for 7.5 h, followed by purification, gave the product as a yellow solid in good yield. Its ^{1}H and ^{13}C{^{1}H} NMR spectra exhibit the expected resonances. The ^{1}H NMR spectrum displays a singlet at 3.59 ppm due to the benzyl CH_2 hydrogens, and two multiplets at 4.87 and 5.89 ppm due to the coordinated alkene hydrogens *trans* to Cl and CH_2Ph, respectively, in addition to multiplets due to the cyclooctadiene CH_2 groups and the aromatic hydrogens. The significant difference between the two =CH chemical shifts is due to the difference in *trans* influence between the Cl and CH_2Ph groups, the benzyl group weakening the Pd–alkene interaction *trans* to itself and making it more like a free alkene. Consistently, the ^{13}C{^{1}H} NMR spectrum contains two signals due to the nonequivalent alkene moieties, two signals assigned to the aliphatic carbons of cyclooctadiene, a benzylic carbon resonance at 35.8 ppm, and four aromatic signals.

The crystal structure of **1a** belongs to the space group $P2_12_12_1$, and its molecular structure is shown in Fig. 1. Bond distances and angles are given in Table 1. The structure exhibits approximate square planar geometry about palladium, the metal center being coordinated by the two alkene groups of the diene, the benzyl CH_2 group and Cl. The double bonds lie approximately perpendicular to the square plane. The C—C distance for the alkene lying *trans* to the benzyl group is 1.334(10) Å, close to that expected for the free diene, whereas the other C—C bond is lengthened slightly (1.379(10) Å), indicating a stronger alkene–metal interaction *trans* to Cl. The Pd—C and Pd—Cl distances are 2.051(7) and 2.336(2) Å, respectively.

When compared with the few related organopalladium complexes that have been reported previously, namely, [PdClR(cod)] (R = C_6F_5 (8), CH_2SO_2Ph (9)) and the [PdCl{CH($SiMe_3$)PMe_2Ph}(cod)]$^+$ cation (10), the present complex displays the longest Pd—C(alkene) bonds *trans* to the organic fragment and the longest Pd—Cl distance. These features suggest that the benzyl group exhibits the greatest

Table 1. Bond lengths (Å) and angles (deg) for **1a**.

Pd(1)—C(9)	2.051(7)	Pd(1)—C(6)	2.155(7)
Pd(1)—C(5)	2.166(6)	Pd(1)—Cl(1)	2.336(2)
Pd(1)—C(2)	2.363(7)	Pd(1)—C(1)	2.420(7)
C(1)—C(2)	1.334(10)	C(1)—C(8)	1.499(10)
C(2)—C(3)	1.501(11)	C(3)—C(4)	1.507(11)
C(4)—C(5)	1.521(10)	C(5)—C(6)	1.379(10)
C(6)—C(7)	1.509(10)	C(7)—C(8)	1.528(10)
C(9)—C(10)	1.485(9)	C(10)—C(11)	1.382(9)
C(10)—C(15)	1.390(10)	C(11)—C(12)	1.387(9)
C(12)—C(13)	1.339(10)	C(13)—C(14)	1.360(11)
C(14)—C(15)	1.379(10)		
C(9)-Pd(1)-C(6)	91.0(3)	C(9)-Pd(1)-C(5)	93.4(3)
C(6)-Pd(1)-C(5)	37.2(3)	C(9)-Pd(1)-Cl(1)	89.1(2)
C(6)-Pd(1)-Cl(1)	165.9(2)	C(5)-Pd(1)-Cl(1)	156.8(2)
C(9)-Pd(1)-C(2)	162.6(3)	C(6)-Pd(1)-C(2)	93.9(3)
C(5)-Pd(1)-C(2)	80.6(3)	Cl(1)-Pd(1)-C(2)	90.2(2)
C(9)-Pd(1)-C(1)	164.4(3)	C(6)-Pd(1)-C(1)	79.2(3)
C(5)-Pd(1)-C(1)	86.2(3)	Cl(1)-Pd(1)-C(1)	97.4(2)
C(2)-Pd(1)-C(1)	32.4(2)	C(2)-C(1)-C(8)	124.8(8)
C(2)-C(1)-Pd(1)	71.5(4)	C(8)-C(1)-Pd(1)	107.4(5)
C(1)-C(2)-C(3)	126.8(8)	C(1)-C(2)-Pd(1)	76.2(4)
C(3)-C(2)-Pd(1)	102.1(5)	C(2)-C(3)-C(4)	115.6(7)
C(3)-C(4)-C(5)	115.5(7)	C(6)-C(5)-C(4)	124.8(8)
C(6)-C(5)-Pd(1)	71.0(4)	C(4)-C(5)-Pd(1)	111.8(5)
C(5)-C(6)-C(7)	127.0(8)	C(5)-C(6)-Pd(1)	71.8(4)
C(7)-C(6)-Pd(1)	109.1(5)	C(6)-C(7)-C(8)	115.3(7)
C(1)-C(8)-C(7)	113.4(7)	C(10)-C(9)-Pd(1)	112.1(4)
C(11)-C(10)-C(15)	116.8(7)	C(11)-C(10)-C(9)	122.4(7)
C(15)-C(10)-C(9)	120.8(7)	C(10)-C(11)-C(12)	121.5(7)
C(13)-C(12)-C(11)	119.8(8)	C(12)-C(13)-C(14)	120.9(8)
C(13)-C(14)-C(15)	119.9(8)	C(14)-C(15)-C(10)	121.1(7)

trans influence among these organic groups. Within the diene ligand a weaker Pd—C(alkene) interaction *trans* to the benzyl group may induce a stronger Pd—C(alkene) interaction *trans* to Cl which, in turn, results in weakening of the Pd—Cl bond.

Whereas [PdClMe(cod)] reacted with carbon monoxide to produce the corresponding acetyl complex (7), we found that treatment of the benzyl complex with CO (1 atm (101.3 kPa)) at ambient temperature resulted in rapid decomposition.

The reaction of [$PdCl_2$(cod)] with tetraethyltin proved to be more complicated. When the reaction was performed at temperatures above 20°C extensive decomposition took place in addition to formation of dimeric species (vide infra), and long reaction times at ambient temperature also led to decomposition and the formation of palladium mirrors. On the other hand, at 0°C or below the reaction was extremely slow. Excess Et_4Sn also promoted decomposition. We have found that by use of a deficiency of Et_4Sn (ca. 0.6 mol-equiv. per Pd) and relatively short reaction times (ca. 4 h) at 20°C we can isolate [PdClEt(cod)], **1b**, in pure form, albeit in low yield. Since much of the [$PdCl_2$(cod)] is recovered unchanged (and able to be used again), however, the yield of the ethylpalladium complex is 78% based on the amount of [$PdCl_2$(cod)] actually consumed. Longer reaction times result in further reaction of [PdClEt(cod)] and lower isolated yields. The ^1H and $^{13}C\{^1H\}$ NMR spectra of [PdClEt(cod)] are unsurprising, resonances due to the ethyl group being observed in addition to the signals for coordinated cyclooctadiene.

When a C_6D_6 solution of [PdClEt(cod)], **1b**, was allowed to stand at ambient temperature a precipitate formed, along with some palladium metal. Analysis of the remaining solution by ^1H NMR spectroscopy revealed the presence of the dimeric complex [$Pd_2(\mu\ Cl)_2(\eta^1,\eta^2\text{-}C_8H_{13})_2$], **2a**. Signals due to ethene (5.19 ppm) and ethane (0.80 ppm), as well as free 1,5-cyclooctadiene, were also observed. The precipitate was identified as [$PdCl_2$(cod)], which is sparingly soluble in benzene, by its ^1H NMR spectrum in $CDCl_3$ solution. The structure of **2a** was determined from its ^1H and $^{13}C\{^1H\}$ NMR spectra (see Experimental), peak assignments being made from ^1H–^1H and ^{13}C–^1H correlation spectra. The ^1H NMR spectrum shows the expected two olefinic resonances, and the signal due to H1 appears as a multiplet at 3.90 ppm. The resonances for one hydrogen on each of the carbons adjacent to the site of metalation, i.e., C2 and C8, appear at an unusually low frequency (0.40 and 0.60 ppm, respectively), whereas the remaining hydrogens resonate between 1.1 and 2.1 ppm.

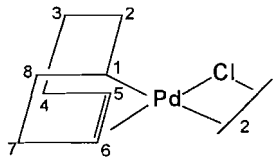

2a

The disappearance of [PdClEt(cod)], **1b**, in benzene solution may be accounted for by the sequence of reactions shown in Scheme 1. β-Hydride elimination from **1b** produces ethene and [PdClH(cod)] (although the latter has not been detected). The hydride complex may follow either of two competing pathways, namely, rearrangement and dimerization to give **2a**, or dinuclear reductive elimination with a molecule of **1b** to produce ethane, [$PdCl_2$(cod)], cyclooctadiene, and palladium metal. It might be anticipated that in the early stages of the reaction, when **1b** is present in relatively high concentration, reaction of [PdClH(cod)] with **1b** would be favored, but this is difficult to ascertain because [$PdCl_2$(cod)] precipitates from solution.

Fig. 2. Plot of the disappearance of **1b** with time (*a*) in dichloromethane, (*b*) in benzene, (*c*) in benzene in the presence of 0.1 mol-equiv. of Et_4Sn, (*d*) in benzene in the presence of 1.0 mol-equiv. of Et_4Sn.

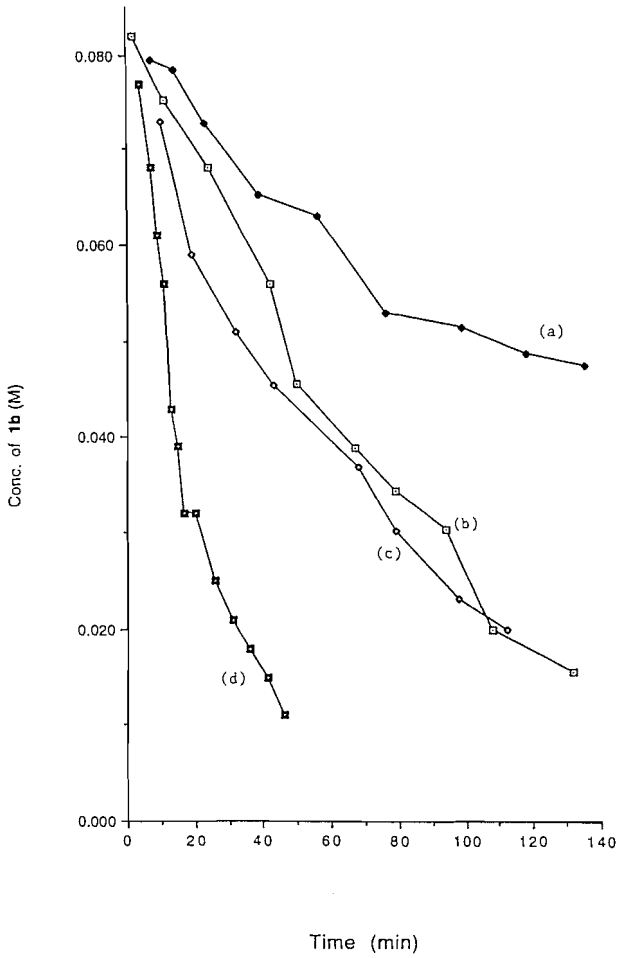

When monitored in C_6D_6 solution, the disappearance of **1b** (which initially contained 10% **2a**) displayed a half-life of 70 min. The reaction occurred more slowly in CD_2Cl_2 solution (Fig. 2), with a half-life of 150 min. Reaction in dichloromethane also resulted in greater conversion to **2a** (ca. 60%). In contrast, when dissolved in CD_3CN **1b** reacted completely within 25 min to produce [$PdCl_2$(cod)] and palladium metal, as well as free cyclooctadiene, ethene, and ethane, with no dimer being detected at all. Integration of the olefinic signals due to [$PdCl_2$(cod)] and cyclooctadiene in the ^1H NMR spectrum indicated that they were formed in equal amounts. When 1 mol-equiv. of Et_4Sn was added to **1b** in C_6D_6 solution decomposition took place much more rapidly (Fig. 2) to give [$PdCl_2$(cod)] and palladium metal, as well as C_2H_4 and C_2H_6, but **2a** was not formed. With 0.1 mol. equiv. of Et_4Sn the disappearance of **1b** was rapid initially (presumably until the

Scheme 1.

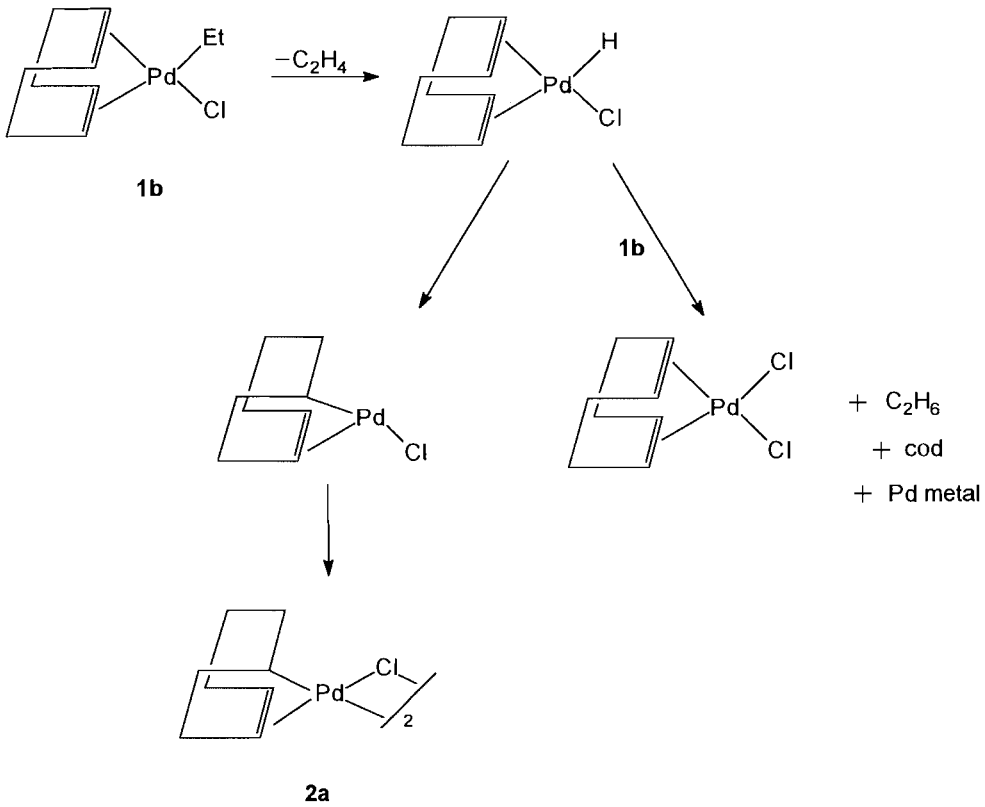

Et_4Sn was exhausted), then the rate of decomposition decreased to that of **1b** alone in benzene solution.

The origin of the observed rate difference in benzene and dichloromethane is uncertain. Acetonitrile may be a sufficiently good nucleophile for palladium to displace cyclooctadiene, and the resulting $[PdClEt(CD_3CN)_2]$ may decompose rapidly to give C_2H_4 and $[PdClH(CD_3CN)_2]$. Further reaction with **1b** would produce C_2H_6 and $[PdCl_2(cod)]$ and Pd metal, thereby accounting for the observed products. Rapid decomposition in the presence of Et_4Sn is consistent with our observations regarding the synthesis of **1b**. Excess Et_4Sn is likely to result in formation of $[PdEt_2(cod)]$, which would decompose by β-hydride elimination followed by reductive elimination of ethane. The dimethyl analogue was also reported to be unstable (5), although it would be susceptible only to Pd—C bond cleavage or reductive elimination. When the reaction of $[PdCl_2(cod)]$ with Et_4Sn was monitored by ^{119}Sn NMR, spectroscopy signals due to Et_4Sn and Et_3SnCl only were observed, indicating that only one ethyl group is transferred to palladium. Even with only 1 mol-equiv. of Et_4Sn, however, it is likely that some $[PdEt_2(cod)]$ is formed (leaving some $[PdCl_2(cod)]$ unreacted), which would decompose readily.

Complex **2a** underwent no further reaction in benzene or dichloromethane solution at ambient temperature, but when a C_6D_6 solution of **2a** was heated to 70°C rearrangement to its allyl isomer $[Pd_2(\mu\text{-}Cl)_2(\eta^3\text{-}C_8H_{13})_2]$, **2b**, occurred. The conversion was 60% complete after 5 h, but then the reaction appeared to reach equilibrium, and further heating caused decomposition. Complex **2b** was identified by its ^1H and $^{13}C\{^1H\}$ NMR spectra. It exhibits triplet and quartet resonances for the allyl functionality in its ^1H NMR spectrum, and the expected five resonances in its $^{13}C\{^1H\}$ NMR spectrum (see Experimental). That an equilibrium between **2a** and **2b** was indeed established was demonstrated by heating a toluene-d_8 solution of **2b** to 100°C for 30 min. Analysis of the solution revealed the presence of **2a** and **2b** in a 1:2 ratio, consistent with that found starting from **2a**.

Espinet and co-workers have shown (8) that $[PdCl(C_6F_5)(cod)]$ undergoes a slow rearrangement in solution at ambient temperature to give a mixture of $[Pd_2(\mu\text{-}Cl)_2(\eta^1,\eta^2\text{-}C_8H_{12}\cdot C_6F_5)_2]$ and $[Pd_2(\mu\text{-}Cl)_2(\eta^3\text{-}C_8H_{12}\cdot C_6F_5)_2]$, the ratio of which was found to depend on the solvent employed. Interconversion of the two isomers was not detected at ambient temperature, and only 20% of $[Pd_2(\mu\text{-}Cl)_2(\eta^1,\eta^2\text{-}C_8H_{12}\cdot C_6F_5)_2]$ was converted to its η^3-allyl isomer after refluxing in chloroform for 80 h. They interpreted this to indicate that $[Pd_2(\mu\text{-}Cl)_2(\eta^1,\eta^2\text{-}C_8H_{12}\cdot C_6F_5)_2]$ is not an intermediate in the formation of the allyl complex, but that both are formed from a common intermediate $[Pd_2(\mu\text{-}Cl)_2(\eta^1\text{-}C_8H_{12}\cdot C_6F_5)_2]$, in which the remaining double bond is uncoordinated (8). In our work **2b** is not formed at 25°C so **2a** could be an intermediate in its formation, but a common intermediate of the type $[Pd_2(\mu\text{-}Cl)_2(\eta^1\text{-}C_8H_{13})_2]$ is also possible with coordination of the free double bond being much faster than rearrangement to the allyl form at ambient temperature. Equilibration of **2a** and **2b** occurs relatively easily at higher temper-

atures, suggesting that there is a lower activation barrier than in the pentafluorophenyl-substituted system. Espinet and coworkers pointed out the significance of slow isomerization of η^1,η^2- to η^3-allyl species and its relevance to organic synthesis via allylmetal complexes (11, 12). Related slow η^1,η^2- to η^3-allyl rearrangements have been observed previously (13, 14).

Although **2a** alone does not convert to **2b** at ambient temperature, we found that addition of free chloride ion (in the form of bis(triphenylphosphine)iminium chloride) to a CD_2Cl_2 solution of **2a** resulted in complete conversion to **2b** within 12 h. In contrast, addition of sodium acetate had no such effect. Addition of chloride to **2a** may result in bridge opening to form a species of the type $[PdCl_2(\eta^1,\eta^2\text{-}C_8H_{13})]^-$, in which rearrangement to the η^3 form occurs more readily. The rearrangement is likely to occur by a series of reversible β-eliminations, and this should be enhanced by the increased electron density on the palladium center in an anionic species. Since acetate is a weaker nucleophile for palladium, the addition of NaOAc resulted in no rate enhancement.

The formation of **2a** from [PtClEt(cod)], and its rearrangement to **2b**, prompted us to investigate alternative methods for the preparation of these dimeric complexes. It had been reported (15) that treatment of $PdCl_2$ with 2.3 equivalents of 1,5-cyclooctadiene in aqueous acetone for 20 h at ambient temperature produced **2a** in high yield. This was shown to occur by Wacker oxidation of one equivalent of cyclooctadiene to cycloocten-5-one, and addition of the HPdCl moiety thus formed to a second cyclooctadiene was proposed to account for the formation of **2a** (15). We have also obtained **2a** by this method. In addition, we found that **2a** can be prepared by treatment of $[PdCl_2(cod)]$ with 1.2 mol-equiv. of $NaBH_4$ in CH_2Cl_2–MeOH solution. When the reaction is carried out at ambient temperature extensive decomposition occurs, but if the reaction is performed at −60°C **2a** is formed cleanly and, although some decomposition to palladium metal occurs during the isolation procedure, the complex can be obtained in good yield. Complex **2b** has been prepared previously, by reaction of $[Pd(\eta^3\text{-}C_8H_{13})(cod)]ClO_4$ with excess LiCl (16). The corresponding bromide-bridged complex was also produced by passing CO through an ethanol solution of $PdCl_2$ and NaCl in the presence of excess 3-bromocyclooctene (17).

Since $[PdCl_2(cod)]$ is formed rapidly from cyclooctadiene and palladium(II) chloride or a tetrachloropalladate(II) salt, it seemed likely that it would be an intermediate in the formation of **2a** from $PdCl_2$ and 1,5-cyclooctadiene (15). Thus, we studied the reactions of $[PdCl_2(cod)]$ with free cyclooctadiene under a variety of conditions. When $[PdCl_2(cod)]$ alone was heated to 70°C for 5 min in water or in aqueous acetone a complex mixture of products was obtained, but when heated with 1 equivalent of cyclooctadiene in water conversion to **2a** occurred within 5 min, although considerable decomposition also took place. Decomposition was inhibited by addition of acetic acid. Thus, heating an aqueous acetic acid solution of $[PdCl_2(cod)]$ with free cyclooctadiene to 70°C for 5 min resulted in very little decomposition to palladium metal, and a mixture of **2a** and **2b** was obtained (eq. [1]). Heating to 100°C gave **2b** only. Whereas the presence of acetic acid appeared to stabilize the system (and promote allyl formation), reaction of $[PdCl_2(cod)]$ was inhibited by addition of hydrochloric acid. Heating a solution of the complex with 1 or 10 equivalents of cyclooctadiene in 6 M HCl resulted in quantitative recovery of $[PdCl_2(cod)]$. Similarly, heating an aqueous solution of $[PdCl_2(cod)]$ with free cyclooctadiene in the presence of 100 equivalents of sodium chloride produced no reaction.

[1] $[PdCl_2(cod)] + cod \xrightarrow[70°C,\ 5\ min]{H_2O/HOAc}$ 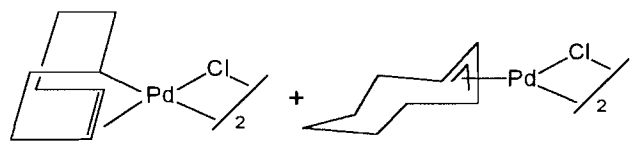 +

2a **2b**

Reactions involving K_2PdCl_4 gave similar results. When an aqueous solution of the salt containing 2 equivalents of cyclooctadiene was heated to 70°C for 5 min a mixture of $[PdCl_2(cod)]$ and **2a** was obtained, but considerable decomposition occurred. Addition of acetic acid again stabilized the system against decomposition. Prolonged heating to 70°C of an aqueous acetic acid solution of K_2PdCl_4 with cyclooctadiene produced a mixture of **2a** and **2b**, whereas heating of the mixture to 100°C gave the allyl complex **2b** as the sole product. Reaction of K_2PdCl_4 with cyclooctadiene was inhibited by excess HCl, only a small amount of $[PdCl_2(cod)]$ being formed after 35 min at 70°C, and neither of the dimeric complexes **2a** or **2b** was observed.

A number of points emerge from these studies. When $[PdCl_2(cod)]$ or K_2PdCl_4 was heated to 70°C in aqueous solution in the presence of excess cyclooctadiene a mixture of **2a** and **2b** was obtained within a few minutes. Thus, **2b** was formed much more rapidly than when **2a** was heated to the same temperature in benzene. At 100°C **2b** was formed as the exclusive product, suggesting that the equilibrium position between the two isomers considerably favors the η^3-allyl form at this temperature in aqueous solution. The role of acetic acid in preventing decomposition is unclear. On the other hand, the presence of excess HCl inhibited reaction of $[PdCl_2(cod)]$ to form **2a** and **2b**. If, as suggested by Stille and James (15), oxidation of cyclooctadiene proceeds by initial attack of water on the coordinated diene of $[PdCl_2(cod)]$ followed by loss of HCl, it would be expected that this process should be suppressed by the presence of HCl.

The observation that excess HCl also inhibits the formation of $[PdCl_2(cod)]$ from K_2PdCl_4 and cyclooctadiene is interesting. The reason for this may simply be that in the presence of a

Table 2. Crystal data and structure refinement for **1a**.

Emperical fomula	$C_{15}H_{19}ClPd$
Formula weight	341.15
Temperature	293(2) K
Wavelength	0.71073 Å
Crystal system	Orthorhombic
Space group	$P2_12_12_1$
Unit cell dimensions	a = 8.0378(12) Å, α = 90°
	b = 10.7825(10) Å, β = 90°
	c = 15.756(3) Å, γ = 90°
Volume, Z	1365.6(4) Å^3, 4
Density (calclulated)	1.659 Mg/m^3
Absorption coefficient	1.530 mm^{-1}
F(000)	688
Crystal size	0.4 × 0.1 × 0.06 mm
θ range for data collection	2.29°–27.50°
Limiting indices	$-10 \le h \le 10$, $-14 \le k \le 14$, $-20 \le l \le 20$
Reflections collected	6024
Independent reflections	3135 (R_{int} = 0.0915)
Absorption correction	Semi-empirical from ψ-scans
Max. and min. transmission	0.7957 and 0.7393
Refinement method	Full-matrix least squares on F^2
Data/restraints/parameters	3134/0/154
Goodness-of-fit on F^2	0.999
Final R indices [$I > 2\sigma(I)$]	$R1$ = 0.0518, $wR2$ = 0.0798
R indices (all data)	$R1$ = 0.0997, $wR2$ = 0.0918
Absolute structure parameter	−0.09(8)
Largest diff. peak and hole	0.583 and −0.498 e Å^{-3}

high concentration of free chloride, dissociation of Cl^- from $PdCl_4^{2-}$ is suppressed, thereby preventing coordination of the diene. This is significant in that reported procedures for the preparation of [$PdCl_2$(cod)] often involve the use of HCl. Whereas the initial report of the synthesis of the complex involved reaction of Na_2PdCl_4 with cyclooctadiene in methanol or acetone solution (18), more recent methods involve the use of a dilute solution of HCl in ethanol (19, 20). The concentration of HCl employed in these cases is considerably lower than that used here, but it should be pointed out that the presence of a high concentration of HCl could have a detrimental effect on the yield of [$PdCl_2$(cod)] prepared by this method.

Experimental

All reactions were carried out under an atmosphere of argon. Solvents were dried and distilled immediately prior to use. Tetraethyltin was obtained from Aldrich. Tetraphenyltin and tetrabenzyltin were prepared from $SnCl_4$ and the appropriate Grignard reagent. [$PdCl_2$(cod)] was prepared according to the method of Chatt et al. (18). NMR spectra were recorded on a Varian XL-300, Varian Unity plus 300, or Bruker ARX-500 spectrometer. ^{1}H and ^{13}C chemical shifts are relative to the residual solvent resonance. Microanalyses were performed by Atlantic Microlab, Inc, Norcross, Ga.

Preparation of [PdCl(CH_2Ph)(cod)], 1a

To a dichloromethane solution of [$PdCl_2$(cod)] (0.50 g, 1.8 mmol) was added $Sn(CH_2Ph)_4$ (1.2 g, 2.4 mmol). The yellow solution was refluxed for 7 h. The resulting black mixture was passed through a Hyflo Supercel column to remove palladium metal, then the solvent was evaporated. The residue was dissolved in a 80:20 mixture of CH_2Cl_2/hexane, and the solution was passed through a 14 × 1 cm silica column. The column was eluted with a total of 1 L of solvent, and the yellow fraction was collected. The solvents were evaporated, leaving the product as a yellow powder that was dried in vacuo (0.39 g, 66%). ^{1}H NMR ($CDCl_3$), δ(H): 2.39 m (CH_2), 3.59 s (CH_2Ph), 4.87 m, 5.89 m (=C*H*), 7.14 m, 7.43 m (C_6H_5). ^{13}C{^{1}H} NMR ($CDCl_3$); δ(C): 27.5, 30.9 (CH_2), 35.8 (CH_2Ph), 104.5, 123.7 (=*C*H), 125.7, 128.6, 129.5, 143.9 (C_6H_5). Anal. calcd for $C_{15}H_{19}ClPd$: C 52.81, H 5.61; found: C 52.81, H 5.66.

Preparation of [PdClEt(cod)], 1b

Tetraethyltin (0.307 mL, 1.55 mmol) was added by syringe to a CH_2Cl_2 (40 mL) solution of [$PdCl_2$(cod)] (0.772 g, 2.71 mmol). The system was protected from light, and stirred for 4 h at 20°C, then cooled in an ice bath. The solvent was evaporated at 0°C. The residue was washed with hexane to remove the tin compounds, then extracted with three 15 mL portions of benzene. The benzene extract was frozen in an ice bath, and the benzene was removed in vacuo, leaving the product as a yellow solid (0.156 g, 36% yield based on Et_4Sn used). ^{1}H NMR (CD_2Cl_2), δ(H): 1.26 t (CH_3), 1.57 m, 1.75 m (CH_2), 2.24 q (CH_2CH_3), 4.98 m, 5.72 m (=C*H*). ^{13}C{^{1}H} NMR (CD_2Cl_2), δ(C): 17.7 (CH_3), 27.3 (CH_2), 30.2 (CH_2CH_3), 30.7 (CH_2), 101.0, 123.6 (=*C*H). The benzene-insoluble material was identified as unreacted [$PdCl_2$(cod)] (0.567 g).

Table 3. Atomic coordinates ($\times 10^4$) and equivalent isotropic displacement parameters ($Å^2 \times 10^3$) for **1a**. U(eq) is defined as one third of the trace of the orthogonalizede U_{ij} tensor.

Atom	x	y	z	U(eq)
Pd(1)	7713(1)	7935(1)	7052(1)	40(1)
Cl(1)	5972(3)	6341(2)	6582(1)	67(1)
C(1)	10114(9)	7409(7)	6198(5)	52(2)
C(2)	9016(9)	8000(8)	5708(4)	52(2)
C(3)	8985(11)	9361(9)	5510(5)	69(3)
C(4)	9378(11)	10212(7)	6241(5)	64(2)
C(5)	8740(10)	9790(6)	7103(6)	55(2)
C(6)	9605(9)	9040(7)	7658(5)	52(2)
C(7)	11280(9)	8445(8)	7511(5)	63(3)
C(8)	11602(9)	8001(8)	6604(5)	65(2)
C(9)	6106(8)	8248(6)	8040(5)	51(2)
C(10)	6327(8)	7336(6)	8737(4)	40(2)
C(11)	7306(10)	7577(6)	9439(4)	50(2)
C(12)	7454(10)	6728(8)	10096(5)	63(2)
C(13)	6669(10)	5635(8)	10047(6)	60(2)
C(14)	5702(11)	5351(7)	9366(5)	60(2)
C(15)	5529(10)	6193(8)	8713(5)	53(2)

Preparation of $[Pd_2(\mu\text{-}Cl)_2(\eta^1,\eta^2\text{-}C_8H_{13})_2]$, 2a

(a) From $[PdCl_2(cod)]$ and Et_4Sn

To a CH_2Cl_2 solution of $[PdCl_2(cod)]$ (0.30 g, 1.05 mmol) was added tetraethyltin (0.30 mL, 1.5 mmol) by syringe. The solution was stirred at ambient temperature for 15 h, during which time a mirror was deposited on the inside of the flask. The resulting solution was passed through a Hyflo Supercel column, and the solvent was evaporated. The yellow residue was washed with hexane, then extracted with benzene. The benzene solution was filtered to remove unreacted $[PdCl_2(cod)]$, then evaporated to dryness to leave the product as a yellow powder (0.12 g, 46%). ^1H NMR (C_6D_6), δ(H): 0.40 (m) H2; 0.60 (dd, 6.2 and 14.4 Hz) H8; 1.45 (dt, 10.8 and 4.4 Hz) H3, H3′; 1.55 (m) H7, H7′; 1.70 (m) H2′, H4; 1.92 (m) H4′; 2.13 (m) H8′; 3.90 (m) H1; 5.60 (m) H5; 5.88 (dt, 6.7 and 8.3 Hz) H6. $^{13}C\{^1H\}$ NMR (C_6D_6), δ(C): 26.3 (C7), 27.0 (C3), 28.7 (C4), 35.7 (C2), 40.2 (C8), 56.0 (C1), 100.7 (C5), 105.2 (C6). Anal. calcd. for $C_{16}H_{26}Cl_2Pd_2$: C 38.27, H 5.22; found: C 38.31, H 5.16.

(b) From $[PdCl_2(cod)]$ and $NaBH_4$

$[PdCl_2(cod)]$ (0.20 g, 0.70 mmol) was dissolved in CH_2Cl_2 (60 mL), and $NaBH_4$ (0.032 g, 0.85 mmol) was added. The mixture was cooled to −60°C and methanol (1 mL), previously cooled to −78°C, was added. After 24 h the solvents were removed in vacuo and the residue was extracted with CH_2Cl_2. After passing through a Hyflo Supercel column, the CH_2Cl_2 was evaporated to leave the product as a light yellow powder, which was washed with hexane and dried (0.134 g, 76%).

Preparation of $[Pd_2(\mu\text{-}Cl)_2(\eta^3\text{-}C_8H_{13})_2]$, 2b

K_2PdCl_4 (0.10 g, 0.31 mmol) was dissolved in a mixture of water (25 mL) and acetic acid (25 mL). The solution was heated to 100°C, then 1,5-cyclooctadiene (0.37 mL, 3.0 mmol) was introduced. The solution changed immediately from red to yellow, then to black. The mixture was maintained at this temperature for 20 min, then cooled in an ice bath, and extracted with CH_2Cl_2 (50 mL). The CH_2Cl_2 solution was washed with water (200 mL), then the solvent was evaporated to leave the product as a light yellow powder (0.043 g, 49%). ^1H NMR ($CDCl_3$), δ(H): 1.45 m, 6H (CH_2), 1.85 m, 2H (CH_2), 2.35 m, 2H (CH_2), 4.75 q, 2H (CH), 5.30 t, 1H (CH). δ(C): 23.2 (1C), 25.1 (2C), 31.1 (2C), 78.6 (2C), 105.0 (1C). Anal. calcd for $C_{16}H_{26}Cl_2Pd_2$: C 38.27, H 5.22; found: C 38.57, H 5.13.

Decomposition of 1b

The conversion of [PdClEt(cod)], **1b**, to $[Pd_2(\mu\text{-}Cl)_2(\eta^1,\eta^2\text{-}C_8H_{13})_2]$, **2a**, under various conditions was monitored by ^1H NMR spectroscopy using a Varian Unity plus 300 spectrometer. A 0.08 M solution of **1b**, containing about 10% **2a**, to which 0.01 M anisole was added as a standard, was prepared. A spectrum was recorded (using either a 1 s or 15 s delay between pulses) at ambient temperature approximately every 15 min. The olefinic signals due to the reactant and product were integrated relative to the anisole signal (3H) at 6.8 ppm.

X-ray structure determination

Light yellow colored rectangular plates were obtained by slow evaporation of a benzene/toluene (1:1) solution of $[PdCl(CH_2Ph)(cod)]$ at 0°C. A crystal of dimensions 0.4 × 0.1 × 0.06 mm was mounted on a glass fiber in random orientation and was coated with Superglue. Preliminary examination and data collection were performed using a Siemens P4RA automated single crystal X-ray diffractometer using monochromated Mo Kα radiation (λ = 0.71073 Å) at 22°C. Autoindexing of 10 centered reflections from the rotation photograph indicated an orthorhombic lattice. Equivalent reflections were checked to confirm the Laue symmetry and a fractional index search was conducted to confirm the cell lengths. Final cell constants and orientation matrix for data collection were calculated by least-squares refinement of the setting angles for 35 reflections ($12° < 2\theta < 25°$). Intensity data were collected using $\overline{\omega}$ scans with fixed scan speed. Friedel pairs were collected to confirm the absolute structure. Three representative reflections measured every 97 reflections showed 13.2% variation during data collection. Crystal data and intensity data collection parameters are listed in Table 2.

Data reduction was carried out using XSCANS and structure solution and refinement were carried out using the SHELXTL-PLUS (5.03) software (21). An absorption correction was applied to the data using equivalent reflections and $\overline{\psi}$ scan reflections. The structure was solved by the Patterson method and refined successfully in the space group $P2_12_12_1$. Full-matrix least-squares refinement was carried out by minimizing $\Sigma\omega(F_o^2 - F_c^2)^2$. The non-hydrogen atoms were refined using the appropriate riding model AFIX = m3. The final residual values were $R(F) = 5.18\%$ for 2042 observed reflections ($I > 2\sigma(I)$) and $wR(F^2) = 9.18\%$; $s = 1.0$ for all data. The absolute structure was confirmed by the Flack method ($x = -0.09(8)$). Structure refinement parameters are listed in Table 2. The atomic coordinates for the non-hydrogen atom are listed in Table 3. A projection view of the molecule, showing the atom labeling, is presented in Fig. 1 (non-hydrogen atoms are represented by 50% probability ellipsoids).

Complete listings of anisotropic displacements for the non-hydrogen atoms, and of positional and isotropic displacement

coefficients for the hydrogen atoms, have been submitted as supplementary material.[2]

Acknowledgments

Thanks are expressed to the donors of the Petroleum Research Fund, administered by the American Chemical Society, and the National Science Foundation (grant numbers CHE-9101834 and CHE-9508228) for support of this work, and to Johnson Matthey Aesar/Alfa for a generous loan of palladium salts. R.A.S. and J.C.E. were supported during summer 1993 and 1994, respectively, as NSF-REU fellows under grant number CHE-9200156. The support of the NSF (grant number CHE-9318696), the U.S. Department of Energy (DE-FG02-92CH10499), and the University of Missouri Research Board for the purchase of the Unity plus and ARX spectrometers is gratefully acknowledged.

References

1. H.C. Clark and L.E. Manzer. J. Organomet. Chem. **59**, 411 (1973).
2. J.W. Ellis, K.N. Harrison, P.A.T. Hoye, A.G. Orpen, P.G. Pringle, and M.B. Smith. Inorg. Chem. **31**, 3026 (1992); K.A. Fallis, G.K. Anderson, and N.P. Rath. Organometallics, **11**, 885 (1992).
3. G.K. Anderson, H.C. Clark, and J.A. Davies. Inorg. Chem. **20**, 3607 (1981); G.K. Anderson and G.J. Lumetta. Organometallics, **4**, 1542 (1985).
4. G.K. Anderson, H.C. Clark, and J.A. Davies. J. Organomet. Chem. **210**, 135 (1981).
5. M. Rudler-Chauvin and H. Rudler. J. Organomet. Chem. **134**, 115 (1977).
6. R.E. Rulke, J.M. Ernsting, A.L. Spek, C.J. Elsevier, P.W.N.M. van Leeuwen, and K. Vrieze. Inorg. Chem. **32**, 5769 (1993).
7. F.T. Ladipo and G.K. Anderson. Organometallics, **13**, 303 (1994).
8. A.C. Albéniz, P. Espinet, Y. Jeannin, M. Philoche-Levisalles, and B.E. Mann. J. Am. Chem. Soc. **112**, 6594 (1990).
9. L. Benchekroun, P. Herpin, M. Julia, and L. Saussine. J. Organomet. Chem. **128**, 275 (1977).
10. R.M. Buchanan and C.G. Pierpont. Inorg. Chem. **18**, 3608 (1979).
11. A.C. Albéniz and P. Espinet. Organometallics **10**, 2987 (1991).
12. A.C. Albéniz, P. Espinet, and Y-S. Lin. Organometallics, **14**, 2977 (1995).
13. G. Albelo, G. Wiger, and M.F. Rettig. J. Am. Chem. Soc. **97**, 4510 (1975).
14. M. Parra-Hake, M.F. Rettig, and R.M. Wing. Organometallics, **2**, 1013 (1983).
15. J.K. Stille and D.E. James. J. Organomet. Chem. **108**, 401 (1976).
16. K.R. Nagasundara, N.M. Nanje Gowda, and G.K.N. Reddy. Indian J. Chem. **19A**, 1194 (1980).
17. H.A. Quinn, W.R. Jackson, and J.J. Rooney. J. Chem. Soc. Dalton Trans. 180 (1972).
18. J. Chatt, L.M. Vallarino, and L.M. Venanzi. J. Chem. Soc. 3413 (1957).
19. D. Drew and J.R. Doyle. Inorg. Synth. **13**, 52 (1972).
20. C.T. Bailey and G.C. Lisensky. J. Chem. Educ. **62**, 896 (1985).
21. G.M. Sheldrick. Siemens Analytical X-Ray Division, Madison, Wis. 1995.

[2] Copies of material on deposit may be purchased from: The Depository of Unpublished Data, Document Delivery, CISTI, National Research Council Canada, Ottawa, Canada K1A 0S2. The table of hydrogen atom parameters has also been deposited with the Cambridge Crystallographic Data Centre, and can be obtained on request from The Director, Cambridge Crystallographic Data Centre, University Chemical Laboratory, 12 Union Road, Cambridge, CB2 1EZ, U.K.

High-pressure methods as a tool in organometallic syntheses: facilitation of oxidative addition to platinum(II)

Andrew R.L. Skauge, Richard D. Shalders, and Thomas W. Swaddle

Abstract: High-pressure (2 GPa) batch reactors now commercially available may offer substantial accelerations of organometallic syntheses, without resort to heating, when the activation process is multicentered or involves the generation and solvation of ions. As an example of the latter class of reactions, the kinetics of the oxidative additions of methyl and ethyl iodides (RI) to dimethyl(2,2′-bipyridine)platinum(II) in acetone have been studied over the pressure range 0–200 MPa. The volumes of activation $\Delta V_I^{\ddagger}$, if assumed to be constant over this range, are -11.7 ± 0.3 and -9.7 ± 0.7 cm^3 mol^{-1}, respectively, implying an acceleration of ca. 3000-fold for a batch synthesis of this sort at 2 GPa. However, a possible slight pressure dependence of $\Delta V_I^{\ddagger}$ may reduce this acceleration to ca. 1 000-fold. The $\Delta V_I^{\ddagger}$ data and the 500-fold retardation on going from R = Me to R = Et are consistent with an S_N2 attack of Pt^{II} on the α-carbon in the alkyl iodides, forming I^- and $[RMe_2Pt(bpy)]^+$.

Key words: volumes of activation, high pressure, oxidative addition, platinum(II), organometallic syntheses.

Résumé : Lorsque le processus d'activation est multicentrique ou qu'il implique la génération ou la solvatation d'ions, les réacteurs discontinus à haute pression (2 GPa) qui sont maintenant disponibles commercialement peuvent s'avérer utiles pour accélérer de façon convaincante les synthèses d'organométalliques, sans chauffage. À titre d'exemple de réaction impliquant une solvatation d'ions, on a étudié la cinétique des additions oxydantes des iodures de méthyle et d'éthyle (RI) sur le diméthyl(2,2′-bipyridine)platine(II), dans l'acétone, à des pressions allant de 0 à 200 MPa. Si l'on fait l'hypothèse qu'ils sont constants sur l'ensemble de ces pressions, les volumes d'activation, $\Delta V_I^{\ddagger}$, de ces deux réactions sont respectivement de $-11,7 \pm 0,3$ et $-9,7 \pm 0,7$ cm^3 mol^{-1} et, pour une synthèse discontinue de cette sorte à 2 GPa, ceci implique une accélération par un facteur de 3000. Toutefois, il est possible qu'une faible dépendance du $\Delta V_I^{\ddagger}$ sur la pression puisse réduire cette accélération à un facteur d'environ 1000. Les données de $\Delta V_I^{\ddagger}$ et un ralentissement par un facteur de 500 en passant de R = Me à R = Et sont en accord avec un mécanisme d'attaque S_N2 du Pt(II) sur le carbone en α des iodures d'alkyles conduisant à la formation de I^- et de $[RMe_2Pt(bpy)]^+$.

Mots clés : volumes d'activation, pression élevée, addition oxydante, platine(II), synthèses d'organométalliques.

[Traduit par la rédaction]

The routine use of pressures on the order of 1 GPa (10 kbar) as a synthetic tool has gained acceptance among organic chemists (1–9), but to date has not found significant application in organometallic chemistry. Apart from the obvious advantage of producing enhanced activities of gaseous reactants, pressure P can influence the maximum attainable *yield* of a reaction through the equilibrium constant K if the reaction volume ΔV (the molar volume of the products minus that of the reactants) is nonzero:

$$[1] \quad \Delta V = -RT(\partial \ln K/\partial P)_T$$

Received January 24, 1996.

This paper is dedicated to Professor Howard C. Clark in recognition of his contributions to Canadian chemistry.

A.R.L. Skauge, R.D. Shalders, and T.W. Swaddle.[1]
Department of Chemistry, The University of Calgary, Calgary, AB T2N 1N4, Canada.

[1] Author to whom correspondence may be addressed. Telephone: (403) 220-5358. Fax: (403) 289-9488. E-mail: swaddle@acs.ucalgary.ca

Similarly, pressure influences the *rate* constant k of the reaction through the volume of activation $\Delta V^{\ddagger}$ (the molar volume of the transition state minus that of the reactants):

$$[2] \quad \Delta V^{\ddagger} = -RT(\partial \ln k/\partial P)_T$$

It is commonly assumed that ΔV and $\Delta V^{\ddagger}$ are independent of pressure, in which case $\ln K$ and $\ln k$ would be linearly dependent upon P. In principle, one can use the quite precise measurements of ΔV or $\Delta V^{\ddagger}$ that can be made at 0.1–200 MPa to predict the outcome of batch syntheses run in autoclaves at 1–2 GPa (pressures now routinely accessible with commercial pressure equipment). In practice, however, $|\Delta V|$ and $|\Delta V^{\ddagger}|$ often become smaller as the pressure is increased beyond 100 MPa. Linear extrapolations of $\ln K$ or $\ln k$ values from low-pressure measurements will therefore tend to overestimate the pressure effect, but at least they place upper limits on what can be achieved for a given reaction with high-pressure techniques.

In this article, we consider only the kinetic aspect — specifically, the potential of high pressures to accelerate syntheses that would otherwise be too slow, without resort to heating that might bring about thermal decomposition. Theoretical expectations for such accelerations, based on typical negative $\Delta V^{\ddagger}$ values (assumed to be independent of P), are given in

Table 1. Rate constants k_P at high pressures relative to atmospheric pressure for some typical volumes of activation.[a]

	k_P/k_0 [b] at 25°C for $\Delta V^{\ddagger}$ =		
P/MPa	−10	−20	−30 cm³/mol⁻¹
0	1	1	1
100	1.50	2.24	3.35
200	2.24	5.02	11.25
400	5.02	25.2	126.6
1000	56.5	3.19×10^3	1.80×10^5
2000	3.19×10^3	1.02×10^7	3.24×10^{10}

[a]Assumed independent of pressure.
[b]Acceleration factors, or retardation factors for the corresponding positive values of $\Delta V^{\ddagger}$.

Table 1. For positive $\Delta V^{\ddagger}$ values, these would be retardation factors; pressure-induced retardation could be useful synthetically in suppressing unwanted side reactions if these have a positive $\Delta V^{\ddagger}$ while that of the reaction of interest is negative or near zero.

An armchair experimentalist might identify at least three types of organometallic reaction as being likely candidates for high-pressure synthetic procedures.

1. **Slow reactions that involve the formation of several bonds between initially separate molecules** (cf. Diels–Alder reactions in conventional organic chemistry). These can be expected to have strongly negative $\Delta V^{\ddagger}$ values, and so to be accelerated by hydrostatic pressure. Ryabov (10) points out that organometallic reactions requiring such multicentered activation tend to have high $\Delta H^{\ddagger}$ and strongly negative $\Delta S^{\ddagger}$, and hence are often too slow for conventional synthetic operations. In general, however, trends in $\Delta V^{\ddagger}$ values tend to parallel those in $\Delta S^{\ddagger}$, so we may anticipate very favorable pressure-induced accelerations for this class of reactions.
2. **Syntheses with unwanted homolytic side reactions.** Homolytic bond fission is generally associated with positive $\Delta V^{\ddagger}$. Indeed, this has been demonstrated for some organometallic cases, viz., Cr—C homolysis pathways in the decompositions of aqueous $(H_2O)_5CrCH(CH_3)_2^{2+}$, $(H_2O)_5CrC(CH_3)_2OH^{2+}$, and $(H_2O)_5CrCH_2C_5H_4NH^{3+}$, for which $\Delta V^{\ddagger} = +26$ (low-pressure limit), +15, and +19 cm³ mol⁻¹, respectively. In these reactions, the homolytic pathway is progressively "squeezed out" and the heterolytic alternative, where significant, emerges as the pressure is increased (11, 12).
3. **Slow reactions involving a substantial increase in solvation.** Any development of electric charge en route to the transition state demands an increase in solvation and hence a negative contribution to the volume of the system. This may overwhelm any positive contributions from bond breaking, so that the overall $\Delta V^{\ddagger}$ can be strongly negative even for a dissociatively activated process (13). Organometallic *oxidative addition* reactions can be of this type; for example, the slow addition of methyl iodide to β-diketonatobis(triphenylphosphite)rhodium(I) complexes evidently involves a rate-determining step that produces iodide and methylrhodium(III) ions, and $\Delta V^{\ddagger}$ values of −9, −18, −19, and −23 cm³ mol⁻¹ were found for the trifluorobenzoylacetone complex in 1,2-dichloroethane, dichloromethane, acetone, and chloroform, respectively (14).

It therefore would seem that pressure acceleration could be used to advantage to force to useful degrees of completion those oxidative addition reactions that are thermodynamically feasible but normally too slow for practical purposes. To evaluate the likely usefulness of this approach in platinum chemistry and to gain mechanistic insights, we have used high-pressure stopped-flow spectrophotometry to study the addition of methyl and ethyl iodides (RI) to dimethyl(2,2′-bipyridine)platinum(II):

$$[3]\quad RI + Me_2Pt(bpy) \xrightarrow{k_1} [RMe_2Pt(bpy)]^+ + I^- \xrightarrow{k_2} RMe_2Pt(bpy)I$$

Reactions of this type are of special interest in that they afford routes to organometallic polymers (15, 16), and in any event they provide informative models of the process of oxidative addition at d^8 square-planar centers, which is of industrial importance (e.g., in the Monsanto process for acetic acid). Thus, for reaction [3] with R = Me in acetonitrile solvent, Crespo and Puddephatt (17) were able, using ^{1}H NMR at −40°C, to detect the actual Pt^{IV} intermediate $[Me_3Pt(bpy)]^+$ and demonstrate that it contained a molecule of coordinated solvent; as the solution warmed to 0°C, iodide ion replaced the coordinated CH_3CN, *trans* to the added methyl group. Detection of major concentrations of the intermediate implied that the rate constant k_1 was greater than k_2 at these temperatures in CH_3CN, but for O-donor solvents such as acetone and methanol (which have less affinity for Pt than does CH_3CN), this was possible only at −80°C. Over the range −7.5 to 20°C in acetone, addition of MeI to $Me_2Pt(bpy)$ proceeded to form $Me_3Pt(bpy)I$ with monophasic second-order kinetics, corresponding to a rate-controlling initial step characterized by k_1 with $\Delta H_1^{\ddagger} = 24.9$ kJ mol⁻¹ and $\Delta S_1^{\ddagger} = -129$ J K⁻¹ mol⁻¹ (18).[2] These kinetic data are consistent with the addition of the solvent molecule to Pt synchronously with the attack of Pt^{II} on the methyl iodide (an S_N2 mechanism, as opposed to radical or radical-chain alternatives (17, 18)) together with the augmented solvation associated with the development of ions in this initial step.

This strongly negative $\Delta S_1^{\ddagger}$ for RI = MeI for reaction [3] in acetone led us to anticipate a correspondingly strongly negative $\Delta V_1^{\ddagger}$, and hence good prospects for synthetically useful pressure-induced accelerations of other, slower, oxidative additions at Pt^{II} centers (e.g., reaction [3] with methyl acetate in place of MeI). The S_N2 mechanism implies slower substitution with more sterically hindered nucleophiles, and we therefore studied reaction [3] with both EtI and MeI to ascertain whether $\Delta V_1^{\ddagger}$ is significantly affected by steric factors.

After this work was completed, we learned of the high-pressure kinetic study by Dücker-Benfer, van Eldik and Canty (19) of the *palladium* analogue of reaction [3] (R = MeI, solvent = acetone), which differs in that both the oxidative addition ($\Delta V^{\ddagger} = -11.9 \pm 0.6$ cm³ mol⁻¹) and subsequent reductive

[2] The activation energy cited in ref. 18 is in fact the enthalpy of activation.

Fig. 1. Pressure dependence of k_1 for addition of MeI to Pt(bpy)Me_2 in acetone at 25°C. Circles: [MeI] = 4.02 mmol L^{-1}. Down triangles: [MeI] = 3.01 mmol L^{-1}. Up triangles: [MeI] = 2.01 mmol L^{-1}. Each data point is the mean of three k_1 values. Broken line: linear regression (eq. [4]). Solid curve: quadratic regression (eq. [5]).

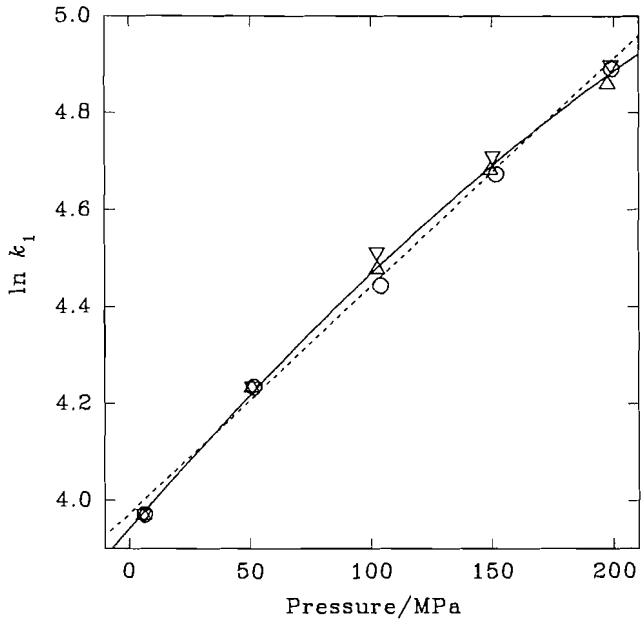

elimination of ethane ($\Delta V^{\ddagger} = -17 \pm 1$ cm^3 mol^{-1}) could be observed — reductive elimination in the Pt^{IV} complex is negligible because of its high activation energy, even though addition of MeI to the Pt^{II} complex is faster than to the Pd^{II} (18). Comparison of our results with $\Delta V^{\ddagger}$ for the latter pathway is instructive.

Experimental

Preparation of dimethyl(2,2′-bipyridine)platinum(II)

In our hands, Pt(bpy)Me_2 was best prepared via Pt(COD)Cl_2 (COD = 1,5-cyclooctadiene), by variations of the methods of Clark and Manzer (20) and Puddephatt et al. (16, 21). Pt(COD)Cl2 was made in 88% yield by heating K_2PtCl_4 (1.7 mmol) in aqueous 1-propanol with COD (1.46 mL) at 60°C for 1.5 h. Addition of NaI to a suspension of Pt(COD)Cl_2 in acetone gave Pt(COD)I_2 quantitatively. Treatment of this solid with methyllithium in diethyl ether under N_2 at 0°C for 2 h, followed by hydrolysis with ice-cold saturated aqueous NH_4Cl, ether extraction, and evaporation of the ether layer gave Pt(COD)Me_2. Reaction of this solid with bpy in acetonitrile gave a 75% yield of moisture-sensitive Pt(bpy)Me_2, which was recrystallized from acetone to give red needles, the authenticity of which was confirmed by CHN analyses and NMR spectroscopy (22).

High-pressure kinetics

Freshly prepared solutions of Pt(bpy)Me_2 and a 20-fold excess of MeI (or 5000-fold excess of EtI) in redistilled anhydrous acetone were loaded into an HPSF-56 high-pressure stopped-flow spectrophotometer (Hi-Tech Scientific Ltd., Salisbury, U.K.) thermostated at 25.0 ± 0.1°C. Pressures were measured with an Autoclave Engineers digital gauge, calibrated (±0.2 MPa) against a Pressurements T3800/4 deadweight gauge. After each pressurization, the system was allowed to re-equilibrate thermally for 30–45 min before firing reagent mixing shots. At least three shots were fired for each pressure and set of concentrations, and the progress of the reaction after mixing was monitored spectrophotometrically through the decay of the absorbance maximum of Pt(bpy)Me_2 at 475 nm (molar absorbance $\varepsilon = 1828 \pm 6$ L mol^{-1} cm^{-1}). The absorbance data were collected and analyzed in terms of a pseudo-first-order rate equation on a dedicated Apple IIe computer. The reaction with EtI at atmospheric pressure was actually slow enough to follow by conventional spectrophotometry with lower [EtI], but the high-pressure experiments required the stopped-flow approach because of the long thermal equilibration times.

Results

It was confirmed by NMR spectroscopy that the products of the reactions of Pt(bpy)Me_2 with MeI and EtI in acetone were indeed Me_3Pt(bpy)I and Me_2EtPt(bpy)I, respectively. The stopped-flow data gave excellent fits to the pseudo-first-order rate equation — better than ±0.1% in the calculated rate constant k_{obsd} — and values of k_{obsd} were accurately proportional to [MeI] or [EtI] (supplementary material, Table S1[3]). There was no evidence for the formation of a long-lived intermediate $[Me_3Pt(bpy)(Me_2CO)]^+$ in the reaction with MeI; furthermore, the reaction of 0.19 mmol L^{-1} Pt(bpy)Me_2 with 4.0 mmol L^{-1} EtI, which was slow enough to follow in a conventional spectrophotometer, showed a strictly maintained isosbestic region at 378–385 nm. Therefore, since the spectra obtained immediately after mixing corresponded to Pt(bpy)Me_2 and the final spectra to RMe_2Pt(bpy)I, k_{obsd}/[RI] values represent k_1 for reaction [3].

Figures 1 and 2 show the pressure dependences of ln k_1 for reaction [3] in acetone with R = Me and Et, respectively. Linear least-squares regression (eq. [4]) represents the data adequately for both MeI and EtI addition, giving $k_1^0 = 53 \pm 1$ L mol^{-1} s^{-1} with $\Delta V_1^{\ddagger} = -11.7 \pm 0.3$ cm^3 mol^{-1} for the combined data for MeI, and $k_1^0 = 0.104 \pm 0.004$ L mol^{-1} s^{-1} with $\Delta V_1^{\ddagger} = -9.7 \pm 0.7$ cm^3 mol^{-1} for EtI, at 25.0°C. The zero (≈ atmospheric) pressure rate constant k_1^0 for MeI agrees satisfactorily with 49 L mol^{-1} s^{-1} extrapolated from the data of Puddephatt et al. (18).

$$[4] \quad \ln k_1 = \ln k_1^0 - (\Delta V_1^{\ddagger}/RT)P$$

For MeI addition, however, a possible slight nonlinearity of the ln k_1 vs. P plot is discernible for the combined data. For simplicity, the data may be fitted to the quadratic expression

$$[5] \quad \ln k_1 = \ln k_1^0 - (\Delta V_1^{0\ddagger}/RT)P + (\Delta\beta^{\ddagger}/2RT)P^2$$

giving $k_1^0 = 51 \pm 1$ L mol^{-1} s^{-1} (in still better agreement with Puddephatt et al. (18)), the limiting zero-pressure volume of activation $\Delta V_1^{0\ddagger} = -14.4 \pm 0.7$ cm^3 mol^{-1}, and the compress-

[3] Table S1, showing pressure dependences of rate constants for the reactions of MeI and EtI with Pt(bpy)Me_2 in acetone at 25°C (1 page) has been deposited as supplementary material and can be purchased from: The Depository of Unpublished Data, Document Delivery, CISTI, National Research Council Canada, Ottawa, Canada K1A 0S2.

Fig. 2. Pressure dependence of k_1 for addition of EtI to Pt(bpy)Me_2 in acetone at 25°C. Each data point is the mean of three k_1 values. Solid line: linear regression (eq. [4]).

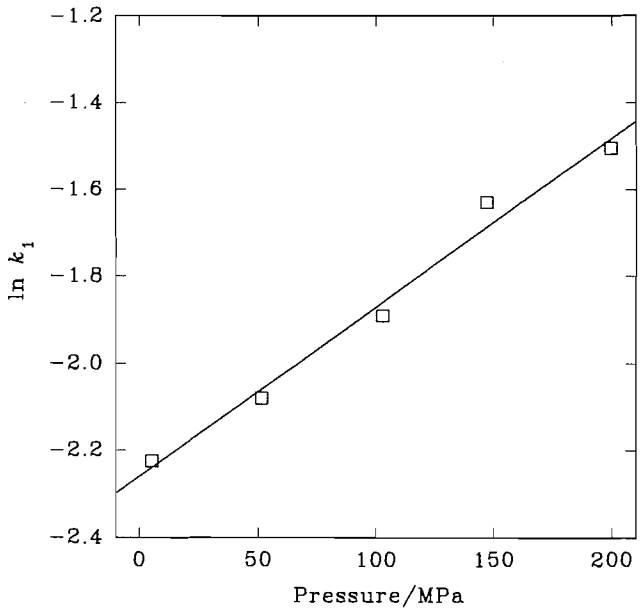

ibility coefficient of activation $\Delta\beta^{\ddagger} = -(\partial\Delta V_1^{\ddagger}/\partial P)_T = -0.027 \pm 0.007$ cm^3 mol^{-1} MPa^{-1} (all uncertainty limits are standard deviations σ). Thus, for reaction [3] with RI = MeI, the curvature of the ln k_1 vs. P plot is significant, though barely so, at the 95% confidence level ($\approx 2\sigma$). If eq. [5] is adopted, then the $\Delta V_1^{\ddagger}$ values from the linear regressions represent the mean or mid-range (100 MPa) value of this parameter. For RI = EtI, use of eq. [5] rather than eq. [4] is clearly unwarranted (Fig. 2).

Discussion

The $\Delta V_1^{\ddagger}$ values from the linear fits are not very different for R = Me and Et, and imply that, if a 2 GPa press for batch samples is available, the greatest pressure accelerations of reactions of the type [3] that might be anticipated would be about 3000-fold at ambient temperature (cf. Table 1). This is probably an overestimate, since the data for MeI suggest that $\Delta\beta^{\ddagger}$ is non-zero, but $|\Delta\beta^{\ddagger}|$ itself can be expected to decrease with pressure — there is no general agreement on equations for extrapolation of the pressure dependences of rate or equilibrium constants far beyond the data base (23), and certainly eq. [5], the simplest nonlinear regression equation, is acceptable only for *interpolation* of data at best. Taking these results together with those for the Pd analogue of reaction [3] (19) and oxidative addition at Rh^I centres (14), we conclude that a synthetic organometallic chemist may expect pressure accelerations of oxidative addition reactions of some three orders of magnitude if a 2 GPa press is used.

The large (500-fold) retardation in reaction [3] in acetone on going from MeI to EtI, together with the similar moderately strongly negative values of $\Delta V_1^{\ddagger}$ for the two reactants, supports Puddephatt's view of the mechanism as an S_N2 process (17, 18). Nucleophilic attack of Pt^{II} on the α-carbon of RI along the axis perpendicular to the plane of the square-planar complex would clearly be very susceptible to steric hindrance from substituent groups on that carbon atom. Volume decreases due to R—Pt bond formation, plus solvation of the incipient ions together with any coordination of solvent in the sixth site of the Pt^{IV} intermediate, will overwhelm the positive contribution to $\Delta V_1^{\ddagger}$ from C—I bond breaking. The striking similarity of our $\Delta V_1^{\ddagger}$ value for reaction [3] with RI = MeI to that reported by van Eldik's group (19) for the ca. 10-fold slower but otherwise analogous Pd^{II} reaction ($\Delta V_1^{\ddagger} = -11.9 \pm 0.6$ cm^3 mol^{-1}) supports this interpretation.

Acknowledgements

We thank Prof. R.J. Puddephatt for discussions, and the Natural Sciences and Engineering Research Council of Canada for equipment and research grants. This article is dedicated to Professor Howard C. Clark, who pioneered the study of the class of platinum complex reactions examined herein.

References

1. N.S. Isaacs. Liquid phase high pressure chemistry. John Wiley & Sons Ltd., Chichester. 1981.
2. J. Jurczak and B. Baranowski (*Editors*). High pressure chemical synthesis. Elsevier, Amsterdam. 1989.
3. K. Matsumoto and R.M. Acheson. Organic synthesis at high pressures. John Wiley & Sons, New York. 1991.
4. K.E. Weale. Chemical reactions at high pressures. E. & F.N. Spon Ltd., London. 1967.
5. W.J. le Noble. *In* High pressure chemistry. *Edited by* H. Kelm. D. Reidel Publishing Co., Dordrecht. 1978. pp. 325, 345.
6. W.J. le Noble. *In* High pressure chemistry and biochemistry. *Edited by* H. Kelm. D. Reidel Publishing Co., Dordrecht. 1987. pp. 279, 295.
7. W.J. le Noble (*Editor*). Pericyclic reactions in organic high pressure chemistry. Elsevier, Amsterdam. 1988.
8. N.S. Isaacs and A. V. George. Chem. Br. **23**, 47 (1987).
9. F.-G. Klärner. Chem. Unserer Zeit **23**, 53 (1989).
10. A.D. Ryabov. Chem. Rev. **90**, 403 (1990).
11. M.J. Sisley, W. Rindermann, R. van Eldik, and T. W. Swaddle. J. Am. Chem. Soc. **106**, 7432 (1984).
12. K. Ishihara and T.W. Swaddle. Can. J. Chem. **64**, 2168 (1986).
13. W.E. Jones, L.R. Carey, and T.W. Swaddle. Can. J. Chem. **50**, 2739 (1972).
14. G.J. van Zyl, G.J. Lamprecht, J.G. Leipoldt, and T.W. Swaddle. Inorg. Chim. Acta, **143**, 223 (1988); J.G. Leipoldt, E.C. Steynberg, and R. van Eldik. Inorg. Chem. **26**, 3068 (1987); J.A. Venter, J.G. Leipoldt, and R. van Eldik. Inorg. Chem. **30**, 2207 (1991).
15. S. Achar, J.D. Scott, and R.J. Puddephatt. Organometallics, **11**, 2325 (1992).
16. S. Achar, J.D. Scott, J.J. Vittal, and R.J. Puddephatt. Organometallics, **12**, 4592 (1993).
17. M. Crespo and R.J. Puddephatt. Organometallics, **6**, 2548 (1987).
18. P.K. Byers, A.J. Canty, M. Crespo, R.J. Puddephatt, and J.D. Scott. Organometallics, **7**, 1363 (1988).
19. C. Dücker-Benfer, R. van Eldik, and A.J. Canty. Organometallics, **13**, 2412 (1994).
20. H.C. Clark and L.E. Manzer. J. Organomet. Chem. **38**, C4I (1972); **59**, 411 (1973).
21. K. Chaudhury and R.J. Puddephatt. J. Organomet. Chem. **84**, 105 (1975).
22. P.K. Monaghan and R.J. Puddephatt. Organometallics, **3**, 444 (1984).
23. M.J. Blandamer. Chemical equilibria in solution: dependence of rate and equilibrium constants on temperature and pressure. Ellis Horwood – PTR Prentice Hall, New York. 1992.

Oxidative fluorination in the Ph_2SO–XeF_2–Cl^- system and fluorine exchange in the $Ph_2S(O)F_2$–$Ph_2S(O)F^+$ system

Xiaobo Ou and Alexander F. Janzen

Abstract: Oxidative fluorination of diphenyl sulfoxide with xenon difluoride occurs under mild conditions in the presence of chloride ion to give $Ph_2S(O)F_2$ in quantitative yield. Chloride ion appears to react with xenon difluoride to generate fluoride ion, and a mechanism of oxidative fluorination is proposed that involves anionic $Ph_2S(O)F^-$ and radical $Ph_2S(O)F^\cdot$ intermediates. Addition of cationic $Ph_2S(O)F^+$ to $Ph_2S(O)F_2$ initiates rapid fluorine exchange, presumably via a symmetrical fluorine-bridged intermediate, and this exchange process was monitored by ^{13}C and ^{19}F NMR spectroscopy. In the presence of chloride ion, $Ph_2S(O)Cl_2$ is formed and can be identified by ^{13}C NMR and by its hydrolysis to Ph_2SO_2. Mechanisms are proposed for these reactions, and ab initio molecular orbital calculations (GAUSSIAN92) were carried out of the postulated intermediates.

Key words: preparation of $Ph_2S(O)F_2$, $Ph_2S(O)F^+$, and $Ph_2S(O)Cl_2$; oxidative fluorination in the Ph_2SO–XeF_2–Cl^- system; fluorine exchange in the $Ph_2S(O)F_2$–$Ph_2S(O)F^+$ system.

Résumé : La fluoration oxydante du diphénylsulfoxyde par le difluorure de xénon s'effectue dans des conditions douces, en présence d'ion chlorure, pour donner le $Ph_2S(O)F_2$, avec un rendement quantitatif. Il semble que l'ion chlorure réagit avec le difluorure de xénon pour générer l'ion fluorure; on propose un mécanisme pour la fluoration oxydante qui implique le $Ph_2S(O)F^-$ anionique et le $Ph_2S(O)F^\cdot$ radicalaire comme intermédiaires. L'addition du $Ph_2S(O)F^+$ cationique sur le $Ph_2S(O)F_2$ initie un échange rapide des ions fluorures, probablement par le biais d'un intermédiaire symétrique à pont fluor; on a suivi ce processus par spectroscopie RMN du ^{13}C et du ^{19}F. En présence d'ion chlorure, il se forme du $Ph_2S(O)Cl_2$ qui a été identifié par RMN du ^{13}C et par son produit d'hydrolyse, le Ph_2SO_2. On propose des mécanismes pour ces réactions et on a effectué des calculs d'orbitales moléculaires ab initio (GAUSSIAN92) sur les intermédiaires postulés.

Mots clés : préparation de $Ph_2S(O)F_2$, $Ph_2S(O)F^+$ et $Ph_2S(O)Cl_2$, fluoration oxydante dans le système Ph_2SO–XeF_2–Cl^-; échange d'ions fluorures dans le système $Ph_2S(O)F_2$–$Ph_2S(O)F^+$.

[Traduit par la rédaction]

Results and discussion

Oxidative fluorination in the Ph_2SO–XeF_2–Cl^- system

The oxidative fluorination of S(IV) to S(VI) derivatives, as well as of Se(IV) and Te(IV), has been carried out with a variety of oxidizing agents such as F_2 (1), ClF (2), BrF_3 (3), XeF_2 (4), CF_3OF (5), CF_3OCl (6), OF_2, SF_5OF (7), AgF_2 (8), and electrochemically (9). Occasionally, CsF or KF is added as a catalyst (10). Zupan and Zajc carried out the oxidation of Ph_2SO by XeF_2, and postulated that $Ph_2S(O)F_2$ was formed as an intermediate that hydrolysed rapidly to the sulfone Ph_2SO_2 (11). Using elemental fluorine, Ruppert prepared $Ar_2S(O)F_2$ and $ArS(O)F_3$, and also characterized the cations $Ar_2S(O)F^+$ and $ArS(O)F_2^+$ (12). Wilson carried out the oxidation of SO_2 with XeF_2 in the presence of fluoride and chloride ions (13). We have studied the oxidation of organo-phosphorus, -sulfur, -tellurium, and -iodine compounds using XeF_2 as the oxidizing agent (14), and noted the catalytic effect of halide ion on the oxidative fluorination of phenyltellurium(IV) compounds (15).

The synthesis of $Ph_2S(O)F_2$ was carried out by adding XeF_2 and ~1% Et_4NCl to Ph_2SO in dichloromethane in a polytetrafluoroethylene (ptfe) bottle at room temperature, eq. [1]. The reaction was complete within 5 min and $Ph_2S(O)F_2$ was formed in essentially quantitative yield. Its ^{13}C NMR spectrum (Table 1 and Fig. 1) is in agreement with that reported by Ruppert (12).

$$[1] \quad Ph_2SO + XeF_2 \xrightarrow[CH_2Cl_2]{Et_4NCl\ (\sim 1\%)} Ph_2S(O)F_2 + Xe$$

During the reaction, the pale green colour of Cl_2 was visible, and traces of the hydrolysis product, Ph_2SO_2, were sometimes detected by ^{13}C NMR, but hydrolysis could be completely eliminated by further drying of solvents and reagents.

In the absence of chloride ion, reaction [1] proceeds sluggishly over a period of 2–6 days. Evidently, chloride ion is an

Received February 21, 1996.

This paper is dedicated to Professor Howard C. Clark in recognition of his contributions to Canadian chemistry.

X. Ou and A.F. Janzen.[1] Department of Chemistry, University of Manitoba, Winnipeg, MB R3T 2N2, Canada.

[1] Author to whom correspondence may be addressed. Telephone: (204) 474-9731. Fax: (204) 275-0905. E-mail: ajanzen@cc.umanitoba.ca

Scheme 1. Proposed mechanism of oxidative fluorination of Ph_2SO by XeF_2 in the presence of fluoride ion.

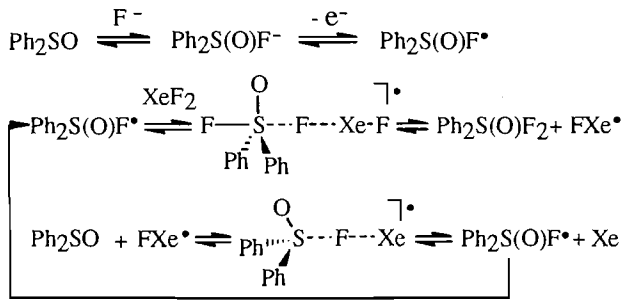

effective catalyst, and we propose that chloride ion is a convenient source of anhydrous and HF-free fluoride ion, as a result of its oxidation by XeF_2, according to eq. [2].

$$[2] \quad 2\,Cl^- + XeF_2 \xrightarrow{CH_2Cl_2} 2\,F^- + Cl_2 + Xe$$

The appearance of the pale green colour of Cl_2 during the synthesis of $Ph_2S(O)F_2$ is in agreement with eq. [2], and previous studies have shown that XeF_2 oxidizes HCl to Cl_2 (16). Anhydrous and HF-free fluoride ion is a powerful base (17) and, as discussed below, molecular orbital calculations point to a reason why F^-, but not Cl^-, catalyzes the oxidation of S(IV).

We propose that oxidative fluorination of Ph_2SO in the presence of fluoride ion proceeds according to the mechanism of Scheme 1, in which the fluoroanion $Ph_2S(O)F^-$ is oxidized to the radical $Ph_2S(O)F^{\cdot}$, followed by cleavage of weak [S--F--Xe]$^{\cdot}$ bridging bonds.

There is support in the literature for the mechanism of Scheme 1. For instance, the addition of fluoride ion to sulfur(IV) compounds produces stable anions, e.g., SO_2F^-, SF_5^-, $CF_3SF_4^-$, etc. (18), and related sulfur(V) radicals are known, e.g., $SOF_3^{\cdot}$, $SF_5^{\cdot}$, $ROSF_4^{\cdot}$, etc. (19). Anion-to-radical oxidation, as proposed in Scheme 1, is known for other fluorinated species, e.g., oxidation of $PhSiF_5^{2-}$ to $PhSiF_5^{\cdot -}$ (20). Our experiments do not allow us to identify the oxidizing agent that converts $Ph_2S(O)F^-$ to $Ph_2S(O)F^{\cdot}$, although Cl_2 or XeF_2 are possibilities. In the case of oxidation of $PhSiF_5^{2-}$ to $PhSiF_5^{\cdot -}$, numerous one-electron acceptors can be used, including metal ions, halogen compounds, tetracyanoethylene, etc. (20). The intermediacy of $FXe^{\cdot}$ has been proposed before (21), and its spectrum is known (22).

The mechanism of Scheme 1 explains why some oxidations, but not others, are carried out in the presence of fluoride ion. A fluoride ion allows the formation of anions, which are then oxidized to radicals. But radicals can be formed without the intermediacy of anions because many oxidizing agents are themselves sources of free radicals, e.g., $SO_3F^{\cdot}$ from $S_2O_6F_2$ (23), or $CF_3O^{\cdot}$ from CF_3OF (24). More vigorous reaction conditions of heating or irradiation may, however, be required if radicals are generated directly from oxidizing agents because bonds of moderate strength must be broken, e.g., RO—OR, Cl—Cl, F—XeF, whereas only very weak bridging bonds, i.e., [S--F--Xe]$^{\cdot}$, are cleaved if oxidation occurs in the presence of fluoride ion.

Such a mechanistic analysis can be extended to other well-known oxidations. For example, the Reed reaction, i.e., the chlorosulfonation of organic compounds with chlorine and SO_2, generally includes the following steps (25):

$$[3] \quad R^{\cdot} \xrightarrow{SO_2} R\text{-}SO_2^{\cdot} \xrightarrow{Cl_2} R\text{-}SO_2Cl + Cl^{\cdot}$$

By analogy with the cleavage of [S--F--Xe]$^{\cdot}$ bonds in Scheme 1, oxidation of sulfur(IV) compounds in the Reed reaction may involve cleavage of the [S--Cl--Cl]$^{\cdot}$ bridged bond, as proposed in eq. [4].

$$[4] \quad R\text{-}SO_2^{\cdot} \xrightleftharpoons{Cl_2} [R(O)_2S\text{--}Cl\text{--}Cl]^{\cdot} \searrow\!\!\nearrow R\text{-}SO_2Cl + Cl^{\cdot}$$

The mechanism of Scheme 1 postulates that F^-, rather than Cl^-, forms an anionic $Ph_2S(O)X^-$ intermediate. In an attempt to uncover any differences between the reactivity of F^- and Cl^- ions, or $F^{\cdot}$ and $Cl^{\cdot}$ radicals, we carried out ab initio calculations of several anionic and radical species **1**–**4** using the GAUSSIAN92 program (26). Phenyl substituents in **1** and **2** have been replaced with fluoro substituents in **3** and **4** in order to simplify the calculation. Experimental structural data are available for compounds such as **5**–**7**, and our analysis is based on a simple comparison between calculated and experimental structures. S—X bond lengths are also known for related compounds such as SOF_2 (158.5 pm), SO_2F_2 (157.0 pm), $SOCl_2$ (207.0 pm), and SO_2Cl_2 (199.0 pm) (27).

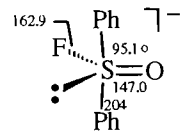

1 (3-21G*)

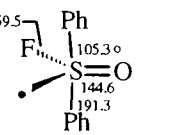

2 (3-21G*)

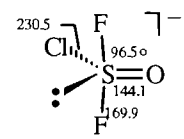

3 (3-21G*)

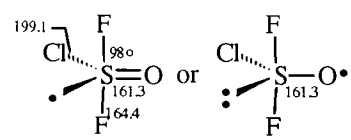

4 (3-21G*)

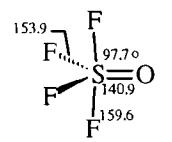

5 (exp)(28)

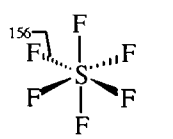

6 (exp)(29)

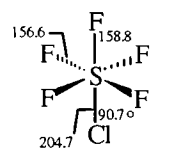

7 (exp)(30)

The calculated structures of fluoroanion **1** and chloroanion **3** reveal a significant difference in S—X bond length. The S—F bond length in **1** is 162.9 pm, which may be compared with experimental S—F bond lengths of 153.9–159.6 pm in **5**–**7**, for an average lengthening of 3.9%. On the other hand, the chloroanion **3** has a calculated S--Cl bond length of 230.5 pm, which is 12.6% longer than the experimental S—Cl bond length of 204.7 pm in **7**. The lengthened/weakened S--Cl bond

Table 1. ^{19}F and ^{13}C NMR chemical shifts (ppm) and C–F coupling constants (Hz) of some sulfur halides.

Compound	δF	δC1	δC2	δC3	δC4
$Ph_2S(O)F^+BF_4^-$	29.5	126.3 (10.8 Hz)	129.8 (1.3 Hz)	132.2	141.5
$Ph_2S(O)F_2$	99.0	147.8 (17.1 Hz)	124.9 (6.1 Hz)	129.2	132.9
$Ph_2S(O)Cl_2$	—	145.9	124.4	129.4	131.1

Scheme 2. Proposed mechanism of fluorine exchange in the $Ph_2S(O)F_2$–$Ph_2S(O)F^+$ system.

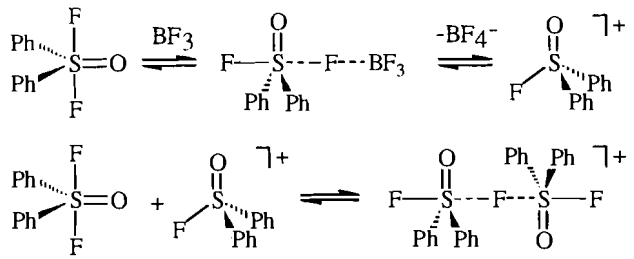

Fig. 1. Distribution of ^{13}C NMR chemical shifts. The 45:55 mixture of $Ph_2S(O)F^+$ and $Ph_2S(O)F_2$ was prepared by adding BF_3 to a solution of $Ph_2S(O)F_2$ in CD_2Cl_2.

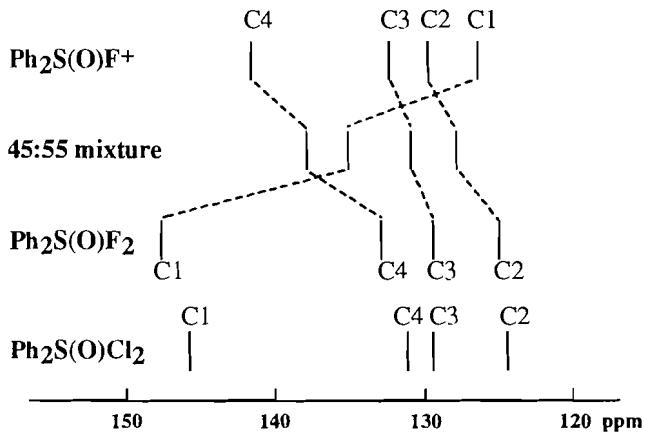

in **3** implies a short-lived intermediate of low concentration, which makes further oxidation to a chloro radical less likely. The relatively short/strong S—F bond in fluoroanion **1**, $Ph_2S(O)F^-$, however, implies a more stable intermediate of greater concentration, which favours subsequent oxidation to the fluoro radical **2**, $Ph_2S(O)F^{\cdot}$. Such an interpretation can explain the unique role of fluoride ion in Scheme 1, and is consistent with catalysis of oxidation reactions by CsF and KF (10).

Quite a different conclusion is reached on the basis of the calculated structures of radical species **2** and **4**. Both S—F and S—Cl bond lengths are shorter/stronger in the radicals than in the anions and, most significantly, both S—F and S—Cl bonds in the radicals are comparable in length to those in the stable compounds **5**–**7**. These results suggest that both fluoro and chloro radicals are reasonable intermediates. According to this interpretation, fluorosulfur(V) radical $Ph_2S(O)F^{\cdot}$ may be formed from sources of $F^{\cdot}$, or by oxidation of fluoroanion $Ph_2S(O)F^-$, whereas chlorosulfur(V) radical $Ph_2S(O)Cl^{\cdot}$ can only be formed from sources of $Cl^{\cdot}$. It is interesting to speculate whether the behaviour of the F^-–$F^{\cdot}$ system in oxidation reactions, as discussed above, is shared by the closely related OH^-–$HO^{\cdot}$ system.

Fluorine exchange in the $Ph_2S(O)F_2$–$Ph_2S(O)F^+$ system

Reaction pathways change abruptly in the presence of a Lewis acid. Addition of BF_3 to $Ph_2S(O)F_2$ gives the cation $Ph_2S(O)F^+$ in essentially quantitative yield. This cation is stable indefinitely in ptfe equipment and can be characterized by ^{19}F and ^{13}C NMR (Table 1 and Fig. 1). Since C1–F and C2–F coupling is clearly visible, there cannot be any fluorine exchange in the cation that is rapid on the NMR time scale. Rapid fluorine exchange does occur on mixing $Ph_2S(O)F_2$ and $Ph_2S(O)F^+$, and such exchange presumably involves the cleavage of a symmetrical intermediate with a weak $[S\text{--}F\text{--}S]^+$ bridging bond, as proposed in Scheme 2.

In support of the mechanism of Scheme 2, it may be noted that related cations of S(VI) are known, e.g., OSF_3^+, OSF_2Cl^+, RSF_4^+ (31), and rapid fluorine exchange between cationic and neutral species via fluorine-bridged intermediates has been studied in related tellurium(VI) fluorides, e.g., the Ph_3TeF_2X–Ph_3TeFX^+ system (X = F, Cl, OH) (32, 33).

Mixtures of $Ph_2S(O)F_2$ and $Ph_2S(O)F^+$ were prepared in two ways, either by mixing samples of $Ph_2S(O)F_2$ and $Ph_2S(O)F^+BF_4^-$, or by adding less than an equivalent of BF_3 to $Ph_2S(O)F_2$. The latter method is generally more convenient because it reduces the handling of moisture-sensitive compounds. Rapid fluorine exchange in the $Ph_2S(O)F_2$–$Ph_2S(O)F^+$ system can be monitored by either ^{13}C or ^{19}F NMR. The ^{13}C NMR chemical shift of C1 moves upfield by 21.6 ppm, as $Ph_2S(O)F_2$ is converted to $Ph_2S(O)F^+$, in agreement with the trend established for a variety of main group fluorides in which C1 shifts upfield by 16 to 26 ppm as F^- is removed (34). In mixtures of $Ph_2S(O)F_2$ and $Ph_2S(O)F^+$, only the weighted average ^{13}C chemical shifts can be observed at ambient temperature because of rapid fluorine exchange, as illustrated in Fig. 1 for a 45:55 mixture.

Typical variable-temperature ^{19}F NMR spectra of the $Ph_2S(O)F_2$–$Ph_2S(O)F^+$ system are shown in Fig. 2. Rapid fluorine exchange is slowed down at −73°C, and integration of

Fig. 2. Variable-temperature ^{19}F NMR spectrum of a 3:1 molar mixture of $Ph_2S(O)F_2$ and $Ph_2S(O)F^+BF_4^-$ in CD_2Cl_2.

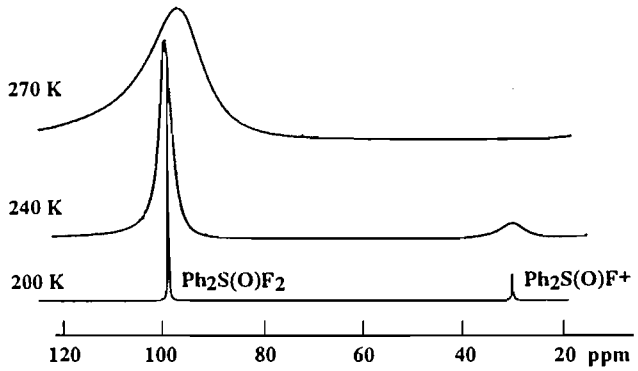

Scheme 3. Proposed mechanism of formation of $Ph_2S(O)Cl_2$.

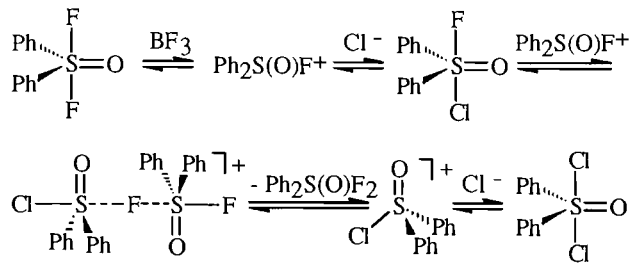

the low-temperature spectrum gives a direct measure of the ratio of $Ph_2S(O)F_2$ and $Ph_2S(O)F^+$. This ratio can also be obtained from the room temperature ^{13}C NMR spectrum and the weighted average of the C1–C4 chemical shifts.

That bridged S--F--S bonds are indeed longer/weaker than terminal S—F bonds in typical sulfur fluorides, as required by the mechanism of Scheme 2, is apparent from the calculated S--F bridge bond of 193.7 pm in **8**. An experimental value of 211.7 pm has been found for the S--F bridge bond in **9** (35). Calculated and experimental terminal S—F bond lengths in **8** and **9** are considerably shorter, in the range 150–173 pm.

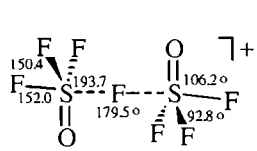

8 (3-21G*)

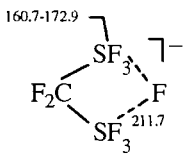

9 (exp)(35)

The mechanism of fluorine exchange in the $Ph_2S(O)F_2$–$Ph_2S(O)F^+$ system can be generalized and applied to the synthesis of $Ph_2S(O)Cl_2$, as proposed in Scheme 3. Both mechanisms of Scheme 2 and Scheme 3 involve cleavage of [S--F--B]$^+$ and [S--F--S]$^+$ bridging bonds.

$Ph_2S(O)Cl_2$ was prepared by adding an excess of Et_4NCl to a solution containing the cation $Ph_2S(O)F^+$, and was identified by ^{13}C NMR and by its hydrolysis to Ph_2SO_2. The C1–C4 chemical shifts of $Ph_2S(O)Cl_2$ are very similar to those of $Ph_2S(O)F_2$, as seen in Table 1 and Fig. 1, and the absence of C1–F and C2–F coupling confirms that no S—F bonds are present. The possibility that an exchange process is responsible for lack of C1–F or C2–F coupling was eliminated by preparing a sample containing a mixture of $Ph_2S(O)Cl_2$ and $Ph_2S(O)F_2$. This mixture showed eight ^{13}C NMR peaks, as expected for a mixture of "rigid" $Ph_2S(O)Cl_2$ and $Ph_2S(O)F_2$. Hydrolysis of this mixture gave only Ph_2SO_2, eq. [5], as confirmed by ^{13}C NMR.

$$[5] \quad Ph_2S(O)Cl_2 + Ph_2S(O)F_2 \xrightarrow{H_2O} Ph_2SO_2 + HX$$

Some evidence for the stoichiometry and mechanism of Scheme 3 was obtained by adding varying amounts of Cl^- to a solution containing $Ph_2S(O)F_2$ and $Ph_2S(O)F^+$. If the amount of Cl^- is less than that of $Ph_2S(O)F^+$, the ^{13}C NMR spectrum shows only four broadened and averaged C1–C4 peaks, as all species in solution undergo rapid halogen exchange in the presence of excess cation $Ph_2S(O)F^+$. If the amount of Cl^- exceeds that of cation $Ph_2S(O)F^+$, then halogen exchange is stopped and the ^{13}C NMR spectrum shows eight carbon peaks expected for a mixture of "rigid" $Ph_2S(O)Cl_2$ and $Ph_2S(O)F_2$. Integration of the ^{13}C NMR spectrum shows that each mole of cation $Ph_2S(O)F^+$ produced half a mole of $Ph_2S(O)Cl_2$ and half a mole of $Ph_2S(O)F_2$, consistent with the stoichiometry of Scheme 3.

Brief investigation by ^{13}C NMR showed that no fluorine exchange occurs in a mixture of $Ph_2S(O)F_2$ and Ph_2SO_2, nor in a mixture of Ph_2SO_2 and $Ph_2S(O)F^+$.

In conclusion, the coordination model of reaction mechanisms (33) denotes the four elementary steps of chemical reactions as +C, −C, $+C^c$, $-C^c$. If cyclic steps, $+C^c$ or $-C^c$, are absent, and if bond formation, +C, is a diffusion-controlled process, then it follows that any mechanistic analysis must focus on the elementary steps of bond cleavage, −C. The mechanism of Scheme 1 identifies the [S--F--Xe]$^\cdot$ bridged bond as the bond that is cleaved during oxidative fluorination in the Ph_2SO-XeF_2-Cl^- system under mild thermal conditions. The mechanisms of Schemes 2 and 3 identify the [S--F--B]$^+$ and [S--F--S]$^+$ bridged bonds as the bonds that are cleaved during fluorine exchange in the $Ph_2S(O)F_2$–$Ph_2S(O)F^+$ system, and during the synthesis of $Ph_2S(O)Cl_2$.

Experimental

NMR spectra were recorded on a Bruker AM300 spectrometer at 282.4 (^{19}F) and 75.47 (^{13}C) MHz, and chemical shifts were measured relative to internal C_6F_6 (−162.9 ppm with respect to $CFCl_3$) and $SiMe_4$, respectively.

XeF_2 (Air Products), Ph_2SO (Matheson, Coleman & Bell), and CD_2Cl_2 (Aldrich) were used without further purification. Et_4NCl and Et_4NBr (Eastman) were recrystallized from dry CH_3CN and stored in a desiccator over P_2O_5. All solvents were dried by distillation and stored over 5 Å molecular sieve, and ptfe equipment was dried at 100°C for several days.

Preparation of $Ph_2S(O)F_2$ with catalyst

Solid Ph_2SO (61 mg, 0.30 mmol) was added to a solution of XeF_2 (54 mg, 0.32 mmol) in CD_2Cl_2 (0.3 mL) at 25°C in an NMR tube with a ptfe insert. Ph_2SO dissolves completely in CD_2Cl_2, but a negligible reaction occurred within 30 min, as judged by exceedingly slow xenon gas evolution. Et_4NCl (2.0 mg, 0.012 mmol) was then added to this mixture, and a rapid

reaction occurred with vigorous evolution of xenon gas. The reaction was complete within 5 min. The ^{13}C NMR spectrum of the solution confirmed that $Ph_2S(O)F_2$ was formed in essentially quantitative yield. ^{13}C NMR of $Ph_2S(O)F_2$: δC1 147.8, J(C1, F) = 17.1 Hz, δC2 124.9, J(C2, F) = 6.1 Hz, δC3 129.2, δC4 132.9. ^{19}F NMR: δF 99.0.

For similar amounts of Ph_2SO and XeF_2, the amount of Et_4NCl catalyst could be reduced to 0.5 mg, without reducing the yield of $Ph_2S(O)F_2$.

In one experiment, 4 mg of Et_4NBr was added to similar amounts of Ph_2SO and XeF_2, and the product $Ph_2S(O)F_2$ was formed in greater than 95% yield.

The use of Ph_3CCl as a catalyst was investigated. Ph_3CCl (20 mg, 0.072 mmol) was added to a mixture of Ph_2SO (60 mg, 0.30 mmol) and XeF_2 (54 mg, 0.32 mmol) in CD_2Cl_2 (0.3 mL) at 25°C in a NMR tube with a ptfe insert. No product, $Ph_2S(O)F_2$, was found after 12 h.

Preparation of $Ph_2S(O)F_2$ without catalyst

Solid XeF_2 (44 mg, 0.26 mmol) and Ph_2SO (50 mg, 0.25 mmol) were dissolved in CD_2Cl_2 (0.3 mL) in a ptfe-lined NMR tube. There was no immediate reaction, as judged by the absence of xenon gas evolution. After 2 days, a 1:2 molar mixture of Ph_2SO and $Ph_2S(O)F_2$ was found. After 6 days, all Ph_2SO was converted to $Ph_2S(O)F_2$, but the C1 peak was exchange broadened and C1–F coupling was not observed in this sample.

Preparation of $Ph_2S(O)F^+$ BF_4^-

Excess BF_3 was bubbled into a solution of $Ph_2S(O)F_2$ (72 mg, 0.30 mmol) in CD_2Cl_2 (0.5 mL) at 25°C to give $Ph_2S(O)F^+$ BF_4^- in essentially quantitative yield. Excess BF_3 was pumped off. ^{13}C NMR of $Ph_2S(O)F^+$ BF_4^-: δC1 126.3, J(C1, F) = 10.9 Hz, δC2 129.8, J(C2, F) = 1.3 Hz, δC3 132.2, δC4 141.5. ^{19}F NMR: δF 29.5.

Preparation of mixtures of $Ph_2S(O)F_2$ and $Ph_2S(O)F^+$

Various amounts of BF_3 were bubbled into a solution of $Ph_2S(O)F_2$ in CD_2Cl_2 at 25°C to generate a mixture of $Ph_2S(O)F_2$ and $Ph_2S(O)F^+$. The ratio of $Ph_2S(O)F_2$ and $Ph_2S(O)F^+$ was determined by ^{13}C or ^{19}F NMR, as described in the text.

Preparation of $Ph_2S(O)Cl_2$

To a 45.55 molar mixture of $Ph_2S(O)F_2$ and $Ph_2S(O)F^+$, prepared from $Ph_2S(O)F_2$ (60 mg, 0.25 mmol) and BF_3 as described above, was added Et_4NCl (18 mg, 0.12 mmol), and the ^{13}C NMR spectrum recorded. An excess of Et_4NCl (50 mg, 0.32 mmol) was then added, and the ^{13}C NMR spectrum recorded and integrated. ^{13}C NMR of $Ph_2S(O)Cl_2$: δC1 145.9, δC2 124.4, δC3 129.4, δC4 131.1.

This mixture of $Ph_2S(O)F_2$ and $Ph_2S(O)Cl_2$ was hydrolyzed by addition of H_2O (25 μL, 1.4 mmol) to give only sulfone Ph_2SO_2.

The $Ph_2S(O)F_2$ and Ph_2SO system

Ph_2SO (30 mg, 0.15 mmol) was added to freshly prepared $Ph_2S(O)F_2$ (75 mg, 0.31 mmol) in CD_2Cl_2 at 25°C. Eight separate ^{13}C NMR signals were observed for $Ph_2S(O)F_2$ and Ph_2SO, however, C1–F and C2–F coupling was not observed in $Ph_2S(O)F_2$ in this sample.

The $Ph_2S(O)F^+$ and Ph_2SO system

Ph_2SO (15 mg, 0.074 mmol) was added to a solution of $Ph_2S(O)F^+$ BF_4^- (72 mg, 0.23 mmol) in CD_2Cl_2 at 25°C. Separate ^{13}C NMR signals were observed for $Ph_2S(O)F^+$ and Ph_2SO, and C1–F coupling was retained in $Ph_2S(O)F^+$.

Molecular orbital calculations

Ab initio molecular orbital calculations were performed with the GAUSSIAN92 system of programs (26) at the 3-21G* level with full optimization, except for the phenyl substituent where a fixed standard geometry was chosen. Calculated structures were compared with related experimental structures.

Acknowledgements

We thank the University of Manitoba for a graduate fellowship award (to X.O.). Dr. R.G. Syvret (Air Products, Allentown, Pa.) is thanked for a sample of XeF_2.

References

1. (*a*) S.P. von Halasz and O. Glemser. Sulfur in organic and inorganic chemistry. Vol. 1. *Edited by* A. Senning. Marcel Dekker, New York. 1971. Chap. 7, p. 209; (*b*) G. Klein and D. Naumann. J. Fluorine Chem. **30**, 259 (1985).
2. (*a*) F. Nyman and H.L. Roberts. J. Chem. Soc. 3180 (1962); (*b*) C.D. Desjardins, C. Lau, and J. Passmore. Inorg. Nucl. Chem. Lett. **9**, 1037 (1973); (*c*) J.M. Shreeve. Sulfur in organic and inorganic chemistry. Vol. 4. *Edited by* A. Senning. Marcel Dekker, New York. 1982. Chap. 4, p. 131.
3. (*a*) R.S. Michalak and J.C. Martin. J. Am. Chem. Soc. **104**, 1683 (1982); (*b*) R.S. Michalak, S.R. Wilson, and J.C. Martin. J. Am. Chem. Soc. **106**, 7529 (1984).
4. N. Bartlett and F.O. Sladky. Chem. Commun. 1046 (1968).
5. (*a*) D.B. Denney, D.Z. Denney, and Y.F. Hsu. J. Am. Chem. Soc. **95**, 8191 (1973); (*b*) G. Pass and H.L. Roberts. Inorg. Chem. **2**, 1016 (1963).
6. T. Kitazume and J.M. Shreeve. J. Am. Chem. Soc. **99**, 4194 (1977).
7. K. Seppelt. Angew. Chem. Int. Ed. Engl. **21**, 877 (1982).
8. (*a*) L.D. Martin, E.F. Perozzi, and J.C. Martin. J. Am. Chem. Soc. **101**, 3595 (1979); (*b*) E.W. Lawless and L.D. Harman. Inorg. Chem. **7**, 391 (1968).
9. (*a*) F.W. Hoffmann, T.C. Simmons, R.B. Beck, H.V. Holler, T. Katz, R.J. Koshar, E.R. Larsen, J.E. Mulvaney, F.E. Rogers, B. Singleton, and R.S. Sparks. J. Am. Chem. Soc. **79**, 3424 (1957); (*b*) H. Baba, K. Kodaira, S. Nagase, and T. Abe. Bull Chem. Soc. Jpn. **51**, 1891 (1978).
10. (*a*) C.W. Tullock, D.D. Coffman, and E.L. Muetterties. J. Am. Chem. Soc. **86**, 357 (1964); (*b*) J.F. Ruff and M. Lustig. Inorg. Chem. **3**, 1422 (1964); (*c*) J.I. Darragh and D.W.A. Sharp. J. Chem. Soc. Chem. Commun. 864 (1969); (*d*) C.J. Schack, R.D. Wilson, J.S. Muirhead, and S.N. Cohz. J. Am. Chem. Soc. **91**, 2907 (1969); (*e*) J.E. Smith and G.H. Cady. Inorg. Chem. **9**, 1442 (1970); (*f*) K. Seppelt. Z. Anorg. Allg. Chem. **428**, 35 (1977).
11. M. Zupan and B. Zajc. J. Chem. Soc. Perkin Trans. 1, 965 (1978).
12. (*a*) I. Ruppert. Angew. Chem. Int. Ed. Engl. **18**, 880 (1979); (*b*) Chem. Ber. **113**, 1047 (1980).
13. I.L. Wilson. J. Fluorine Chem. **5**, 13 (1975).
14. (*a*) J.A. Gibson, R.K. Marat, and A.F. Janzen. Can. J. Chem. **53**, 3044 (1975); (*b*) R.K. Marat and A.F. Janzen. Can. J. Chem. **55**, 3031 (1977).
15. M. Jang and A.F. Janzen. J. Fluorine Chem. **52**, 45 (1991).

16. M.J. Shaw, H.H. Hyman, and R. Filler. J. Org. Chem. **36**, 2917 (1971).
17. (*a*) K.O. Christe and W.W. Wilson. J. Fluorine Chem. **47**, 117 (1990); (*b*) K.O. Christe, E.C. Curtis, D.A. Dixon, H.P. Mercier, J.C.P. Sanders, and G.J. Schrobilgen. J. Am. Chem. Soc. **113**, 3351 (1991).
18. (*a*) F. Seel and L. Riehl. Z. Anorg. Allg. Chem. **282**, 293 (1955); (*b*) K.O. Christe, E.C. Curtis, C.J. Schack, and D. Pilipovich. Inorg. Chem. **11**, 1679 (1972); (*c*) R. Minkwitz and A. Werner. J. Fluorine Chem. **37**, 397 (1987); (*d*) W. Heilemann, R. Mews, S. Pohl, and W. Saak. Chem. Ber. **122**, 427 (1989).
19. (*a*) R.A. De Marco and J.M. Shreeve. Adv. Inorg. Chem. Radiochem. **16**, 109 (1974); (*b*) J.R. Morton and K.F. Preston. J. Chem. Phys. **58**, 2657 (1973).
20. (*a*) K. Tamao, J. Yoshida, H. Yamamoto, T. Kakui, H. Matsumoto, M. Takahashi, A. Kurita, M. Murata, and M. Kumada. Organometallics, **1**, 355 (1982); (*b*) R. Müller and C. Dathe. Chem. Ber. **99**, 1609 (1966).
21. (*a*) R. Filler. Isr. J. Chem. **17**, 71 (1978); (*b*) T.B. Patrick, S. Khazaeli, S. Nadji, K. Hering-Smith, and D. Rief. J. Org. Chem. **58**, 705 (1993).
22. (*a*) J.G. Malm, H. Selig, J. Jortner, and S.A. Rice. Chem. Rev. **65**, 199 (1965); (*b*) G. Zerza, G. Sliwinski, N. Schwentner, G.J. Hoffman, D.G. Imre, and V.A. Apkarian. J. Chem. Phys. **99**, 8414 (1993).
23. F.B. Dudley and G.H. Cady. J. Am. Chem. Soc. **85**, 3375 (1963).
24. J.R. Morton and K.F. Preston. Chem. Phys. Lett. **18**, 98 (1973).
25. J. March. Advanced organic chemistry. 4th ed. John Wiley & Sons, New York. 1992. p. 711.
26. M.J. Frisch, G.W. Trucks, M. Head-Gordon, P.M.W. Gill, M.W. Wong, J.B. Foresman, B.G. Johnson, H.B. Schlegel, M.A. Robb, E.S. Replogle, R. Gomperts, J.L. Andres, K. Raghavachari, J.S. Binkley, C. Gonzalez, R.L. Martin, D.J. Fox, D.J. Defrees, J. Baker, J.J.P. Stewart, and J.A. Pople. Gaussian 92, Revision C. Gaussian, Inc., Pittsburgh Pa. 1992.
27. G. Derflinger and O.E. Polansky. Theor. Chim. Acta (Berl.), **1**, 316 (1963).
28. L. Hedberg and K. Hedberg. J. Phys. Chem. **86**, 598 (1982).
29. F.A. Cotton and G. Wilkinson. Advanced inorganic chemistry. 5th ed. John Wiley & Sons, New York. 1988. p. 509.
30. C.J. Marsden and L.S. Bartell. Inorg. Chem. **15**, 3004 (1976).
31. (*a*) C. Lau, H. Lynton, J. Passmore, and P. Siew. J. Chem. Soc. Dalton Trans. 2535 (1973); (*b*) R.F. Dunphy, C. Lau, H. Lynton, and J. Passmore. J. Chem. Soc. Dalton Trans. 2533 (1973); (*c*) J. Wessel, G. Kleemann, and K. Seppelt. Chem. Ber. **116**, 2399 (1983); (*d*) T. Meier and R. Mews. Angew. Chem. Int. Ed. Engl. **24**, 344 (1985).
32. (*a*) A.S. Secco, K. Alam, B.J. Blackburn, and A.F. Janzen. Inorg. Chem. **25**, 2125 (1986); (*b*) A.F. Janzen, K. Alam, M. Jang, B.J. Blackburn, and A.S. Secco. Can. J. Chem. **66**, 1308 (1988).
33. (*a*) A.F. Janzen. Coord. Chem. Rev. **130**, 355 (1994); (*b*) A.F. Janzen and M. Jang. Can. J. Chem. **67**, 71 (1989).
34. C. Wang, Y. Mo, M. Jang, and A.F. Janzen. Can. J. Chem. **71**, 525 (1993).
35. D. Viets, W. Heilemann, A. Waterfeld, R. Mews, S. Besser, R. Herbst-Irmer, G.M. Sheldrick, and W. Stohrer. J. Chem. Soc. Chem. Commun. 1017 (1992).

Synthesis of dimethylplatinum(IV) compounds, $[\{PtMe_2X_2\}_n]$, $[\{PtMe_2XY\}_n]$, and, in solution, *fac*-$[PtMe_2X(H_2O)_3]^+$, where X and Y are anionic ligands

Trevor G. Appleton, Campbell J. D'Alton, John R. Hall, Michael T. Mathieson, and Mark A. Williams

Abstract: Oxidative addition of X_2 (X = Cl, Br, I) to *cis*-$[PtMe_2L_2]$ (L = pyridine, py, or L_2 = *N,N,N′,N′*-tetramethylethylenediamine (tmen) gave $[PtMe_2X_2L_2]$. For X = Br, I, treatment with aqueous $HClO_4$ gave insoluble $[\{PtMe_2X_2\}_n]$, but for X = Cl, $[PtMe_2Cl_2(H_2O)_2]$ remained in solution, with $[\{PtMe_2Cl_2\}_n]$ depositing only from concentrated solution. $[PtMe_2L_2]$ (L = py, 1/2(tmen)) with water gave $[PtMe_2(OH)_2L_2]$, which, on treatment with $HClO_4$ gave *cis*-$[PtMe_2(H_2O)_4](ClO_4)_2$ in solution. Water also reacted with $[PtMe_2(nbd)]$ (nbd = norbornadiene) to give $[\{PtMe_2\}(OH)_2\}_n]\cdot mH_2O$. Alcohols ROH (R = Me, Et) with *cis*-$[PtMe_2py_2]$ gave $[PtMe_2(OR)(OH)py_2]$, which reacted with aqueous $HClO_4$ solution to give *fac*-$[PtMe_2(OR)(H_2O)_3]ClO_4$ in solution. Addition of chloride to this solution caused precipitation of $[\{PtMe_2(OR)Cl\}_n]$. Reaction of $[\{PtMe_2XY\}_n]$ with $AgNO_3$ in water gave *fac*-$[PtMe_2X(H_2O)_3](NO_3)$ in solution (X = Y = Cl, Br, I or Y = Cl, X = OR); for X = I added acid was necessary to prevent precipitation of $[\{PtMe_2I(OH)\}_n]$. Reaction of a solution of *fac*-$[PtMe_2Br(H_2O)_3](NO_3)$ with $AgNO_2$ gave *fac*-$[PtMe_2(NO_2)(H_2O)_3](NO_3)$ in solution, but an analogous reaction with AgSCN gave a complex in solution formulated as *fac*-$[PtMe_2(SCN)(H_2O)_3](NO_3)$ only in low yield.

Key words: platinum, methyl, pyridine, aqua, alkoxide, oxidative addition, NMR.

Résumé : L'addition oxydante de X_2 (X = Cl, Br, I) sur le *cis*-$[PtMe_2L_2]$ (L = pyridine, py, ou L_2 = *N,N,N′,N′*-tétraméthyléthylènediamine (tmen)) conduit à $[PtMe_2X_2L_2]$. Pour X = Br, I, le traitement de ces derniers produits avec des solutions aqueuse de $HClO_4$ conduit aux complexes insolubles $[\{PtMe_2X_2\}_n]$, mais, avec le produit dans lequel X = Cl, le $[PtMe_2Cl_2(H_2O)_2]$ demeure en solution alors que le $[\{PtMe_2X_2\}_n]$ ne se dépose qu'en solutions concentrées. Le $[PtMe_2L_2]$ (L = py, 1/2(tmen)) réagit avec l'eau pour fournir du $[PtMe_2(OH)_2]$ qui, par traitement avec du $HClO_4$, fournit du *cis*-$[PtMe_2(H_2O)_4](ClO_4)_2$ qui reste en solution. L'eau réagit aussi avec le $[PtMe_2(ndb)]$ (nbd = norbornadiène) pour donner du $[\{PtMe_2\}(OH)_2\}_n]\cdot mH_2O$. Les alcools ROH (R = Me, Et) réagissent avec le *cis*-$[PtMe_2py_2]$ pour conduire au $[PtMe_2(OR)(OH)py_2]$ qui réagissent avec des solutions aqueuses de $HClO_4$ pour fournir du *fac*-$[PtMe_2(OR)(H_2O)_3]ClO_4$ qui reste en solution. L'addition de chlore à cette solution provoque une précipitation de $[\{PtMe_2(OR)Cl\}_n]$. La réaction des produits $[\{PtMe_2XY\}_n]$ avec du $AgNO_3$ dans l'eau fournit les *fac*-$[PtMe_2X(H_2O)_3](NO_3)$ qui restent en solution (X = Y = Cl, Br, I ou Y = Cl, X = OR); pour X = I, il est nécessaire d'ajouter de l'acide pour empêcher la précipitation de $[\{PtMe_2I(OH)\}_n]$. La réaction d'une solution de *fac*-$[PtMe_2Br(H_2O)_3](NO_3)$ avec du $AgNO_2$ fournit du *fac*-$[PtMe_2(NO_2)(H_2O)_3](NO_3)$ qui reste en solution; toutefois, une réaction analogue avec du AgSCN conduit, avec un faible rendement, à un complexe en solution auquel on a attribué la formule *fac*-$[PtMe_2(SCN)(H_2O)_3](NO_3)$.

Mots clés : méthylplatine, pyridine, aqua, alcoolate, addition oxydante, RMN.

[Traduit par la rédaction]

Received February 6, 1996.

This paper is dedicated to Professor Howard C. Clark in recognition of his contributions to Canadian chemistry.

T.G. Appleton,[1,2] C.J. D'Alton, J.R. Hall, M.T. Mathieson, and M.A. Williams. Department of Chemistry, The University of Queensland, Brisbane, Qld. 4072, Australia.

[1] Author to whom correspondence may be addressed. Telephone: +61 (7) 33654005. Fax: +61 (7) 33654299. E-mail: appleton@chem.chemistry.uq.edu.au

[2] The authors express their appreciation of the contributions of Professor Howard C. Clark to the fields of inorganic and organometallic chemistry.

Introduction

An important aspect of the chemistry of methylplatinum(IV) compounds is the remarkable robustness of the mixed alkyl–aqua cations *fac*-$[PtMe_3(H_2O)_3]^+$ (**1**) (1), *fac*-$[PtMe_2Br(H_2O)_3]^+$ (**2**) (2), and *cis*-$[PtMe_2(H_2O)_4]^{2+}$ (**3**) (3). In **1**, all three coordinated water ligands are labilized by the high *trans* effect of the methyl groups (4, 5). In **2** and **3** only the water ligands *trans* to the methyl groups are labile (2, 3, 6). Displacement of water molecules coordinated *cis* to the methyl ligands requires heating or long standing. Exploitation of the differential lability of the aqua ligands in dimethylplatinum(IV) complexes, combined with the photolabilization of coordination sites *trans* to bromide in dimethylbromo compounds (7), has allowed the synthesis of a wide range of derivatives — for example, with amino acids and related ligands (6, 8–14). These compounds were all prepared using **2** or **3** as starting material. The chemistry of dimethylplatinum(IV) compounds containing anionic ligands other than bromide or hydroxide has been much less developed. The possibility exists, with appropriate choice of X^- in *fac*-$[PtMe_2X(H_2O)_3]^+$, of fine-tuning the lability of water bound *trans* to X^- through the *trans* effect of X^-.

In this paper, synthetic routes are described to substances that may be used as starting materials for synthesis of a wide range of dimethylplatinum(IV) compounds, including $[\{PtMe_2X_2\}_n]$, $[\{PtMe_2XY\}_n]$, and *fac*-$[PtMe_2X(H_2O)_3]^+$ for a range of anionic ligands X^- and Y^-. Compounds where X^- is an alkyl or aryl group will be described in a subsequent paper. A preliminary account of some of these results has been published (15).

Results and discussion

General methods for synthesis of $[\{PtMe_2X_2\}_n]$ and $[\{PtMe_2XY\}_n]$

Many dimethylplatinum(IV) complexes $[PtMe_2X_2L_2]$ and $[PtMe_2XYL_2]$ have been prepared by oxidative addition of X_2 or XY to dimethylplatinum(II) compounds *cis*-$[PtMe_2L_2]$ or of MeX to *trans*-$[PtMeYL_2]$, where, for example, L is a tertiary phosphine or arsine (16–19) or L_2 is 2,2′-dipyridyl (bpy) (20, 21). However, ligands of these types bind strongly to the metal, and cannot easily be removed from $[PtMe_2XYL_2]$ to yield $[\{PtMe_2XY\}_n]$.

Clark and Manzer (22) showed that $PtMe_2$(cod) (cod = 1,5-cyclooctadiene) will react with many oxidative addition reagents X_2 or XY to give dimethylplatinum(IV) products. For example, reaction with Br_2 yields $[\{PtMe_2Br_2\}_n]$ (**4**), and reaction with MeI gives $[\{PtMe_3(\mu_3\text{-}I)\}_4]$. These reactions were postulated to proceed through an unstable platinum(IV) intermediate, $[PtMe_2XY(cod)]$, from which the diolefin dissociated. Such a synthesis represents the most direct route to $[\{PtMe_2XY\}_n]$, but is subject to two limitations. The first is that the platinum(II) diolefin compound may not be sufficiently reactive to react with the reagent XY at all. The second is that there is an alternative decomposition route for the intermediate platinum(IV) diolefin compound, reductive elimination of MeY to yield a platinum(II) product. Thus, reaction of $[PtMe_2$(diolefin)] (diolefin = cod or norbornadiene, nbd) with CF_3I produces first $[PtMe(CF_3)$(diolefin)] (23), then $[Pt(CF_3)_2$(diolefin)] (22, 23). We have used $[PtMe_2$(nbd)] (**5**) in reactions with potential oxidants XY, as nbd is more easily displaced from the metal than cod (24).

A second general route is by removal of the pyridine ligands from $[PtMe_2X_2py_2]$ or $[PtMe_2XYpy_2]$ (py = pyridine). Pyridine ligands *trans* to methyl are relatively labile, and may often be removed by treatment with acid under relatively mild conditions. Thus, when $[\{PtMe_2Br_2\}_2]$ (**4**) was first prepared by refluxing $[\{PtMe_3(\mu_3\text{-}I)\}_4]$ with bromine, the crude product was purified by reaction with pyridine to give $[PtMe_2Br_2py_2]$ (**6**), followed by treatment with aqueous $HClO_4$ to regenerate **4** (25). In some cases the desired dimethylbis(pyridine)platinum(IV) complex may be prepared from platinum(IV) precursors, (e.g., $[PtMe_2Cl_2py_2]$ (**7**) (25)), but they are usually prepared by oxidative addition of X_2 or XY to *cis*-$[PtMe_2py_2]$ (**8**). A comparison of the reactions of *cis*-$PtMe_2L_2$ with MeI showed that the compounds where L = py (**8**), L_2 = bpy (**9**), and L_2 = *N*,*N*,*N*′,*N*′-tetramethylethylenediamine, tmen (**10**), were all very reactive, and that acid removed the N-donor ligands from $[PtMe_3Ipy_2]$ and $[PtMe_3I$(tmen)] under conditions where $[PtMe_3I$(bpy)] was unreactive (24). We have included some reactions of **10** in this paper for comparison with those of **8**. We also describe in the experimental section a revised procedure for synthesis of **8**.

The most direct route to the preparation of an ion *fac*-$[PtMe_2X(H_2O)_3]^+$ is by reflux of sparingly soluble

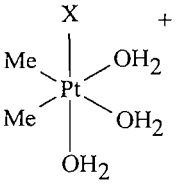

$[\{PtMe_2XY.mH_2O\}n]$

X		X	Y	*m*	
X		Br	Br		**4**
Me	**1**	Cl	Cl		**14**
Br	**2**	I	I		**20**
Cl	**19**	CN	I		**26**
I	**23**	CN	CN		**27**
OMe	**35**	OH	OH	1	**28**
OEt	**39**	OMe	OH	3	**36**
SCN	**46**	OMe	Cl	I	**37**
NO_2	**49**	OEt	OH	0.5	**40**
		OEt	Cl	2	**41**
		SCN	SCN		**44**

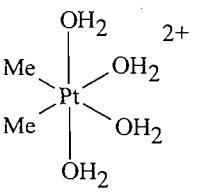

3

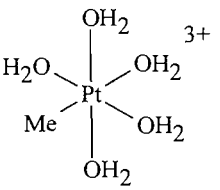

24

$[\{PtMe_2XY\}_n]$ (Y^- = halide) with an aqueous solution of silver ion. In a few cases, the most convenient route to $[\{PtMe_2XY\}_n]$ or *fac*-$[PtMe_2X(H_2O)_3]^+$ was by substitution reactions commencing with one of the available dimethylplatinum(IV) cations, **2** or **3**.

Characterization of products

The most useful information was obtained from ^1H NMR spectra. The protons of each methyl group bound to platinum show a sharp singlet with "satellites" due to coupling with ^{195}Pt (I = $^1/_2$, 34% abundance). It is unlikely that both δ(H) and $^2J_{Pt-CH_3}$ will be coincident for non-equivalent methyl groups. The value of $^2J_{Pt-CH_3}$ is dependent primarily on the ligand *trans* to methyl (26–28), with, for example, typical ranges of 67–74 Hz *trans* to pyridine, and 77–82 Hz *trans* to water. ^{13}C NMR spectra can also provide useful information, although $^1J_{Pt-C}$ tends to be influenced more, relatively, by ligands *cis* to methyl than $^2J_{Pt-CH_3}$ (7, 29). The shielding of the methyl ^{13}C nucleus also depends on the *trans* ligand, with higher nuclear shielding *trans* to water than *trans* to halide (cf., ^1H (28) or ^{15}N (30) bound to platinum). Other resonances in ^{13}C and ^1H NMR can also provide useful confirmation of structure. For example, for complexes $[PtMe_2XYpy_2]$, the number of distinct resonances from pyridine ligands and the values of coupling constants to ^{195}Pt (expected to be small *trans* to methyl) help to confirm the structures assigned.

The dependence of δ(Pt) on the ligand set (especially the donor atoms), including the well-known shielding of the metal nucleus when bound to heavy donor atoms (e.g., I^-, S-donors) (30–32), provided confirmation of the ligands bound to platinum.

NMR data are given in Table 1, and microanalyses in Table 2.

X = Br

As mentioned above, $[\{PtMe_2Br_2\}_n]$ (**4**) was previously prepared by reaction of $[\{PtMe_3(\mu_3\text{-}I)\}_4]$ with bromine (25), or by reaction of $[PtMe_2(cod)]$ with bromine (22). We found that $[PtMe_2(nbd)]$ reacts with bromine in a similar way to give **4** in good yield. IR spectroscopy has shown that there are both terminal and bridging bromide ligands in **4**, and, from comparison of the spectrum with that of $[\{PtMe_3(\mu_3\text{-}Br)\}_4]$, a "cubane" structure with triply bridging bromide, has been proposed (33), analogous to that in $[\{PtBr(\text{-}CH_2CH_2CH_2)(\mu_3\text{-}Br)\}_4]$ (34). **4** is insoluble in non-coordinating solvents and in water, but dissolves in methanol to yield $[PtMe_2Br_2(MeOH)_2]$ (**11**) (29).

$[PtMe_2Br_2py_2]$ (**6**) was previously prepared by reaction of **4** with pyridine (25). This isomer, with pyridine *trans* to the methyl groups, is expected because the high *trans* effect of the methyl groups will direct the incoming pyridine ligands to the *trans* coordination sites. This *trans* effect also facilitates removal of pyridine by acid, to re-form **4**. We have also prepared **6** by reaction of *cis*-$[PtMe_2py_2]$ (**8**) with bromine in choroform. $[PtMe_2(tmen)]$ with bromine in chloroform yielded $[PtMe_2Br_2(tmen)]$ (**12**), which gave **4** when a suspension in dilute aqueous perchloric acid was refluxed for 3 h.

An aqueous solution of *fac*-$[PtMe_2Br(H_2O)_3](NO_3)$ (**3**) was prepared by reaction of a suspension of **4** in water with one mol equivalent of silver nitrate (2).

X = Cl

As noted above, $[PtMe_2Cl_2py_2]$ (**7**) was prepared by reaction of $[PtMe_2Br_2py_2]$ (**6**) with chlorine in refluxing chloroform (25). This preparation worked well provided that sufficient chlorine was passed through the solution. When the supply of chlorine was limited, an additional product was present, which, from NMR data (Table 1), was identified as $[PtMe_2ClBrpy_2]$ (**13**). The ^{195}Pt chemical shift was close to midway between δ_{Pt} for **6** and **7**. There was only one singlet with satellites for the methyl groups, and only one set of pyridine peaks in ^1H and ^{13}C NMR spectra. The Pt–CH_3 coupling constant was consistent with pyridine as the ligand *trans* to methyl (26–28). The ^1H-coupled ^{195}Pt NMR spectrum for each of the compounds **6**, **7**, and **13** showed a septet, as expected from coupling with the protons of two equivalent methyl groups. We have also prepared **7** by reaction of chlorine with *cis*-$[PtMe_2py_2]$ (**8**) in chloroform.

Hall and Swile (33) reported the preparation of

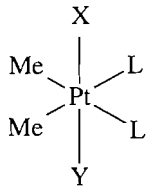

X	Y	L	
Br	Br	py	**6**
Cl	Cl	py	**7**
Br	Br	MeOH	**11**
Br	Br	(tmen)/2	**12**
Br	Cl	py	**13**
Cl	Cl	MeOH	**15**
Cl	Cl	H_2O	**16**
Br	Cl	MeOH	**17**
Br	Cl	H_2O	**18**
I	I	py	**21**
I	I	(en)/2	**22**
CN	I	py	**25**
OH	OH	(bpy)/2	**29**
OH	OH	py	**30**
OH	OH	(tmen)/2	**31**
OMe	OH	(bpy)/2	**32**
OMe	OH	py	**33**
OMe	Cl	py	**34**
OEt	OH	py	**38**

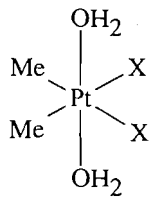

X	
SCN	**42**
NO_2	**47**

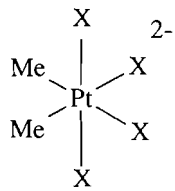

X	
SCN	**43**
NO_2	**48**

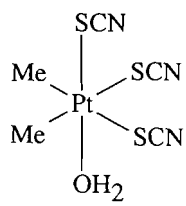

44

Table 1. NMR data.[a]

Compound	Solvent	δ, Pt ppm	δ, H (Me), ppm	$^2J_{Pt-H}$, (Hz)	δ, C (Me), ppm	$^1J_{Pt-C}$, Hz	Other parameters δ (J_{Pt})
$[PtMe_2Cl_2py_2]$ (**7**)	$CDCl_3$	−1821	1.88	69.5	−5.5	525	
$[PtMe_2Br_2py_2]$ (**6**)	$CDCl_3$	−2316	2.08	70.6	−9.6	508	
$[PtMe_2ClBrpy_2]$ (**13**)	$CDCl_3$	−2057	1.98	69.9	−7.5	[b]	
$[PtMe_2I_2py_2]$ (**21**)	$CDCl_3$	[b]	2.54	72.7	−19.4	505	
$[PtMe_2(OH)_2py_2]$ (**30**)	$CDCl_3$	[b]	1.87	71.2	−6.5	648	
$[PtMe_2(OMe)(OH)py_2]$ (**32**)	$CDCl_3$	[b]	1.29	73.2	−6.0	692	OMe: H 3.10 (42.4); C 54.8 (7.8)
$[PtMe_2(OMe)Clpy_2]$ (**34**)	$CDCl_3$	[b]	1.26	73.6	−6.6	710	OMe: H 3.24 (42.3); C 56.0 (5.9)
$[PtMe_2(OEt)(OH)py_2]$	$CDCl_3$	[b]	1.38	72.8	−5.4	695	CH_2: H 3.10(q) (41); C 63.9 (6.8); $^2J_{HH}$ 7.0. CH_3 H 0.83 (t); C 20.2 (14.0)
$[PtMe_2Br_2(tmen)]$ (**12**)	$CDCl_3$	[b]	1.83	70.1	−6.9	669	
$[PtMe_2(OD)_2(tmen)]$ (**31**)	$CDCl_3$	[b]	0.85	73.5	−8.9	685	
$[PtMe_2Cl_2(MeOD)_2]$ (**15**)	CD_3OD	−1516	1.85	79.5	−9.3	597	
$[PtMe_2Br_2(MeOD)_2]$ (**11**)	CD_3OD	−1997	2.02	81.1	−13.0	605	
$[PtMe_2BrCl(MeOD)_2]$ (**17**)	CD_3OD	−1748	1.93	80.1	−11.1	[b]	
$[PtMe_2Cl_2(D_2O)_2]$ (**16**)	D_2O	−1581	1.89	78.3	−7.4	596	
$[PtMe_2BrCl(D_2O)_2]$ (**18**)	D_2O	[b]	1.96	78.4	−9.3	[b]	
$[PtMe_2(SCN)_2(D_2O)_2]$ (**42**)	D_2O	[b]	2.04	65.6	[b]	[b]	
$[PtMe_2(NO_2)_2(D_2O)_2]$ (**47**)	D_2O	[b]	1.96	67.1	[b]	[b]	
$Na[PtMe_2(SCN)_3(D_2O)]$ (**44**)	D_2O	[b]	1.73	68.0	[b]	[b]	
cis-$Na_2[PtMe_2(SCN)_4]$ (**43**)	D_2O	[b]	1.51	69.8	[b]	[b]	
cis-$Na_2[PtMe_2(NO_2)_4]$ (**48**)	D_2O	[b]	1.81	69.7	[b]	[b]	
$[PtMe_2Cl(D_2O)_3](NO_3)$ (**19**)	D_2O	−1159	1.86	77.5	−7.1	596	
$[PtMe_2Br(D_2O)_3](NO_3)$ (**2**)	D_2O	−1387	1.96	76.9	−7.5	592	
$[PtMe_2I(D_2O)_3](NO_3)$ (**23**)	DNO_3/D_2O	−1606	2.13	75.2	−13.1	588	
$[PtMe_2(OMe)(D_2O)_3](NO_3)$ (**35**)	D_2O	−595	1.05	75.6	−3.2	613	OMe: H 2.43 (30.1); C 57.8 (9.8)
$[PtMe_2(OEt)(D_2O)_3](NO_3)$ (**39**)	D_2O	−570	1.14	75.4	−5.3	611	CH_2: H 3.67 (q) (56.4); C 58.8 (8.7). CH_3: H 1.34 (t); C 16.6 (18.6); $^3J_{HH}$ 7.7
$[PtMe_2(SCN)(D_2O)_3](NO_3)$ (**46**)	D_2O	[b]	2.01	75.9	−6.8	709	
$[PtMe_2(^{15}NO_2)(D_2O)_3](NO_3)$ (**49**)	D_2O	−1065 (d)	1.99	79.7	−0.7	658	$^1J_{Pt-N}$ 664 Hz
cis-$[PtMe_2(D_2O)_4](NO_3)_2$	DNO_3/D_2O	−630	2.04	75.7	−4.1	616	

[a]d = doublet, t = triplet, q = quartet; for complexes containing py or tmen the anticipated ligand resonances were observed in ^1H and ^{13}C NMR spectra.
[b]Not measured or not observed.

Table 2. Analytical results.

Compound	Analyses, found (calcd.)		
	C	H	N
$[\{PtMe_2Cl_2\}_n]$ (**14**)	8.4(8.1)	2.1(2.0)	0.2(0.0)
$[\{PtMe_2Br_2\}_n]$ (**4**)	6.3(6.2)	1.7(1.6)	
$[\{PtMe_2I_2\}_n]$ (**20**)	5.5(5.0)	1.4(1.3)	
$[\{PtMe_2(CN)_2\}_n]$ (**27**)	17.2(17.3)	2.2(2.2)	10.2(10.1)
$[\{PtMe_2(SCN)_2\}_n]$ (**45**)	13.8(14.1)	1.9(1.8)	8.2(8.2)
$[\{PtMe_2(OH)_2\cdot H_2O\}_n]$ (**28**)	8.8(8.7)	3.1(3.6)	
$[\{PtMe_2(OMe)Cl\cdot H_2O\}_n]$ (**37**)	11.6(11.6)	3.6(3.6)	
$[\{PtMe_2(OMe)(OH)\cdot 3H_2O\}_n]$ (**36**)	10.7(11.0)	4.7(4.9)	
$[\{PtMe_2(OEt)Cl\cdot 2H_2O\}_n]$ (**41**)	14.1(14.1)	4.1(4.4)	
$[\{PtMe_2(OEt)(OH)\cdot 0.5H_2O\}_n]$ (**40**)	16.3(16.2)	4.4(4.4)	
$[PtMe_2Cl_2py_2]$ (**7**)	31.5(31.7)	3.5(3.5)	5.6(6.2)
$[PtMe_2Br_2py_2]$ (**6**)	26.2(26.5)	2.9(2.9)	4.6(5.2)
$[PtMe_2I_2py_2]$ (**21**)	23.1(22.6)	2.7(2.5)	4.1(4.4)
$[PtMe_2(OH)_2py_2]\cdot 6H_2O$ (**30**)	27.0(27.4)	5.4(5.8)	4.9(5.3)
$[PtMe_2(OMe)Clpy_2]$ (**34**)	34.1(34.7)	3.8(4.3)	6.0(6.2)
$[PtMe_2(OMe)(OH)py_2]\cdot 4H_2O$ (**33**)	31.4(31.0)	5.8(5.6)	5.5(5.6)
$[PtMe_2(OEt)(OH)py_2]\cdot 3H_2O$ (**38**)	34.5(34.9)	5.4(5.4)	5.4(5.8)
$[PtMe_2Br_2(tmen)]$ (**12**)	19.3(19.2)	4.4(4.4)	5.8(5.6)
$[PtMe_2(OH)_2(tmen)]\cdot 7H_2O$ (**31**)	19.4(19.2)	7.3(7.6)	5.4(5.6)

$[\{PtMe_2Cl_2\}_n]$ (**14**) by refluxing a suspension of $[PtMe_2Cl_2py_2]$ (**7**) in aqueous perchloric acid, followed by concentration of the resultant solution. This preparation differs from that of the dibromo analogue, **4**, in that **4** is always present as a solid suspended in the reaction mixture once the pyridine has been removed from **6**, while reaction of **7** under similar conditions yields a clear solution. The desired product, **14**, does indeed precipitate when the solution is concentrated, but care needs to be taken as contamination with $[Hpy]^+(ClO_4)^-$ can occur if too much solvent is removed. The product obtained by following the procedure given in the Experimental Section gave an IR spectrum similar to that described by Hall and Swile (33), who interpreted the spectrum in terms of a tetrameric structure, $[\{PtMe_2Cl(\mu_3\text{-}Cl)\}_4]$. There were no peaks attributable to $[Hpy](ClO_4)$, and no peaks assignable to coordinated water, in the IR spectrum.

The solid **14** was insoluble in chloroform and dichloromethane. Like the dibromo analogue, **4**, it dissolved readily in methanol. NMR data (Table 1) were all consistent with the presence of $[PtMe_2Cl_2(MeOH)_2]$ (**15**) in solution. The ^1H and ^{13}C spectra in CD_3OD each showed a singlet with satellites from the methyl groups. The Pt–CH_3 coupling constant was consistent with methanol as the ligand *trans* to methyl (26–29). The ^1H-decoupled ^{195}Pt NMR spectrum in methanol showed a single peak, at significantly higher frequency than that for $[PtMe_2Br_2(MeOH)_2]$ (**11**), as expected with replacement of bromo by chloro ligands (30–32). The ^1H-coupled ^{195}Pt spectrum showed a septet.

Unlike **4**, the solid **14** dissolved slowly in water. Prolonged standing was required, although the process was accelerated by ultrasonication, but the material was ultimately quite soluble. NMR data were quite similar to those for the methanol complex **15**, including the observation of a septet in the ^1H-coupled ^{195}Pt NMR spectrum. The complex in solution was therefore formulated as $[PtMe_2Cl_2(H_2O)_2]$ (**16**). The ^1H and ^{13}C NMR spectra in D_2O showed no detectable pyridine peaks. The aqua complex **16** is formed when $[PtMe_2Cl_2py_2]$ (**7**) reacts with aqueous perchloric acid, and does not precipitate from dilute solution.

If a small amount of $[PtMe_2BrClpy_2]$ (**13**) was present as an impurity with $[PtMe_2Cl_2py_2]$ (**7**) in the solid that was treated with perchloric acid, and the solid isolated after concentration of the solution was dissolved in methanol, peaks assignable to $[PtMe_2BrCl(MeOH)_2]$ (**17**) were observed in the ^1H, ^{13}C, and ^{195}Pt NMR spectra. A solution of the same solid in D_2O showed peaks from $[PtMe_2BrCl(D_2O)_2]$ (**18**) in the ^1H and ^{13}C NMR spectra.

It was also possible to obtain $[\{PtMe_2Cl_2\}_n]$ (**14**) by reaction of $[PtMe_2(nbd)]$ (**5**) with chlorine, but it was not always easy to separate the product from compounds formed by chlorination of nbd.

Refluxing an aqueous solution of $[PtMe_2Cl_2(H_2O)_2]$ (**16**) with one mol equivalent of silver perchlorate gave a solution of *fac*-$[PtMe_2Cl(H_2O)_3](ClO_4)$ (**19**).

X = I

$[\{PtMe_2I_2\}_n]$ (**20**) was prepared by Clark and Manzer (22) by reaction of $[PtMe_2(cod)]$ with iodine. We prepared **20** by a similar reaction, starting with $[PtMe_2(nbd)]$ (**5**). Hall and Swile (25) reported that $[\{PtMe_2I\cdot PtMe_2I_2\}_n]$ is sometimes formed as a by-product in the preparation of $[\{PtMe_3(\mu_3\text{-}I)\}_4]$ from $K_2[PtCl_6]$ and methyl Grignard reagent. They prepared $[PtMe_2I_2py_2]$ (**21**) and $[PtMe_2I_2(en)]$ (**22**) (en = 1,2-diaminoethane) from reaction of this solid with pyridine and en, respectively, and isolated **20** by reaction of **22** with aqueous $HClO_4$.

We prepared $[PtMe_2I_2py_2]$ (**21**) by reaction of *cis*-$[PtMe_2py_2]$ (**8**) with iodine in chloroform. Reaction of an aqueous suspension of **21** with perchloric acid gave **20**, which, like the dibromo analogue, **4**, was insoluble in nondonor solvents and in water. Reaction of a suspension of **20** in dilute aqueous perchloric acid with one mol equivalent of silver perchlorate gave a solution of *fac*-$[PtMe_2I(H_2O)_3](ClO_4)$ (**23**). Solid $[\{PtMe_2I(OH)\}_n]$ began to precipitate from a solution of **23** if the pH of the solution was increased above 2, so the dilute perchloric acid was necessary to keep **23** in solution. A minor set of methyl peaks (up to 10% of total intensity) was also present in NMR spectra of a D_2O solution (δ(H) 1.22, $^2J_{Pt-CH_3}$ 81.6 Hz; δ(C) −13.2, $^1J_{Pt-C}$ 679.7 Hz) that did not correspond to any previously reported compound. The NMR parameters correspond to a platinum(IV) complex with methyl *trans* to aqua, and the species present has been tentatively formulated as $[PtMe(D_2O)_5]^{3+}$ (**24**).

X = CN

We previously reported (7) the preparation of some dimethylcyano complexes, including $[PtMe_2(CN)Ipy_2]$ (**25**) (by reaction of *cis*-$[PtMe_2py_2]$ (**8**) with ICN), $[\{PtMe_2(CN)I\}_n]$ (**26**) (by reaction of **25** with $HClO_4$), $[\{PtMe_2(CN)Br\}_n]$ (by acidification of a solution of $[PtMe_2Br(CN)_2(H_2O)]^-$), and $[\{PtMe_2(CN)_2\}_n]$ (**27**) (by acidification of a solution of $[PtMe_2(CN)_3(H_2O)]^-$). A solution of *fac*-$[PtMe_2(CN)(MeOH)_3](ClO_4)$ in methanol was prepared by reaction of **25** successively with $AgClO_4$ and $HClO_4$ in methanol, but attempts to obtain a solution of *fac*-$[PtMe_2(CN)(H_2O)_3]^+$ (e.g., by addition of dilute aqueous $HClO_4$ to the methanol solution of *fac*-$[PtMe_2(CN)(MeOH)_3](ClO_4)$) caused precipitation of $[\{PtMe_2(CN)(OH)\cdot 3H_2O\}_n]$ (7).

An attempt was made to prepare **26** directly by reaction of $[PtMe_2(nbd)]$ (**5**) with ICN in chloroform. A white solid precipitated that appeared to be a mixture of **26** and [PtMe(CN)(nbd)].

An alternative method was also used to prepare $[\{PtMe_2(CN)_2\}_n]$ (**27**). A methanol solution of $[PtMe_2(CN)Ipy_2]$ (**25**) was refluxed with one mol equivalent of $AgClO_4$. After removal of precipitated AgI, the solution would then contain $[PtMe_2(CN)py_2(MeOH)](ClO_4)$. One mol equivalent of KCN was added, and the solution was heated. The solution would now contain $[PtMe_2(CN)_2py_2]$. Perchloric acid was added and the solution again refluxed. Solid $[\{PtMe_2(CN)_2\}_n]$ (**27**) precipitated (ν(C≡N) 2201 cm^{-1}). It has been suggested (7) that **27** is a network polymer, with Pt-C≡N-Pt bridging.

X = OH

The amphoteric solid $[\{PtMe_2(OH)_2\}_n]\cdot mH_2O$ (**28**) was previously prepared by reaction of $[\{PtMe_2Br_2\}_n]$ (**4**) with NaOH solution, followed by neutralization with $HClO_4$ solution (3). Monaghan and Puddephatt (21) reported that a complex formulated as $[PtMe_2(OH)(H_2O)(bpy)](OH)$ or as $[PtMe_2(OH)_2(bpy)]\cdot H_2O$ (**29**) was obtained by prolonged stirring of a suspension of $[PtMe_2(bpy)]$ (**9**) in water. We have repeated this preparation with similar results. Addition of $HClO_4$ solution to this compound did not cause displacement of the bpy ligand.

cis-$[PtMe_2py_2]$ (**8**) was sparingly soluble in water, slowly dissolving with prolonged stirring or gentle heating. ^1H and ^{13}C NMR spectra of a D_2O solution showed peaks corresponding to methyl groups bound to platinum(IV) *trans* to pyridine, as well as peaks from coordinated pyridine. The species in solution was formulated as $[PtMe_2(OD)_2py_2]$ (**30**). Removal of solvent water yielded $[PtMe_2(OH)_2py_2]\cdot 6H_2O$ as a white hygroscopic solid. The reaction of water with **8** presumably gives an initial hydrido product, $[PtMe_2(OH)(H)py_2]$, which then reacts with water to give **30** and H_2 (21, 35). When $HClO_4$ solution was added to a solution of **30**, pyridine was displaced to give *cis*-$[PtMe_2(H_2O)_4]^{2+}$ (**3**) in solution, with Hpy^+.

$[PtMe_2(tmen)]$ (**10**) was insoluble in water, and no change occurred when an aqueous suspension was allowed to stand. When the suspension was heated under reflux, the solid dissolved, with some deposition of platinum metal. ^1H and ^{13}C NMR spectra of a D_2O solution were consistent with the presence of $[PtMe_2(OD)_2(tmen)]$ (**31**). Removal of solvent water gave $[PtMe_2(OH)_2(tmen)]\cdot 7H_2O$ as a white hygroscopic solid. Heating a solution of **31** with aqueous $HClO_4$ gave **3** in solution, with $(H_2tmen)^{2+}$.

$[PtMe_2(nbd)]$ (**5**) was insoluble in water, and no change occurred when an aqueous suspension was allowed to stand. When the suspension was heated under reflux for 30 min, the color of the suspended solid changed from cream to white. This solid dissolved in both acid and alkali, and the solution in D_2SO_4–D_2O gave a ^1H NMR spectrum corresponding to *cis*-$[PtMe_2(H_2O)_4]^{2+}$ (**3**). The solid was therefore formulated as $[\{PtMe_2(OH)_2\}_n]\cdot mH_2O$ (**28**), presumably formed by loss of nbd from a platinum(IV) intermediate $[PtMe_2(OH)_2(nbd)]$.

X = OMe

Monaghan and Puddephatt (21) reported that $[PtMe_2(bpy)]$ (**9**) reacts with methanol to give $[PtMe_2(OMe)(H_2O)(bpy)]\cdot OH$. An alternative formulation of this product is $[PtMe_2(OMe)(OH)(bpy)]\cdot H_2O$ (**32**), although the ionic formulation was preferred by Monaghan and Puddephatt because conductivity of an aqueous solution corresponded to a 1:1 electrolyte (21). We have reproduced this synthesis. The bpy ligand was not displaced when a solution in dilute aqueous $HClO_4$ was heated under reflux.

cis-$[PtMe_2py_2]$ (**8**) dissolved in methanol to produce a yellow solution that faded to colorless over 2 h. After 6 h, solvent was removed to give a solid whose ^1H and ^{13}C NMR spectra in D_2O each showed one singlet with satellites from methyl-platinum groups *trans* to pyridine, one set of peaks from coordinated pyridine, and a singlet with satellites assigned to methoxide bound to platinum(IV). No peaks from Pt-H were observed in the ^1H NMR spectrum. The solid analysed for $[PtMe_2(OMe)(OH)py_2]\cdot 4H_2O$, and was nonconducting in aqueous solution. The compound present in solution was therefore formulated as $[PtMe_2(OMe)(OH)py_2]$ (**33**). Heating a solution of **33** in methanol with sodium chloride gave $[PtMe_2(OMe)Clpy_2]$ (**34**).

Heating **33** with aqueous perchloric acid caused removal of the pyridine ligands to give *fac*-$[PtMe_2(OMe)(H_2O)_3](ClO_4)$ (**35**) in solution (with $[Hpy](ClO_4)$). The methoxide ligand remained bound to platinum, as evidenced by the observation of coupling to ^{195}Pt in ^1H and ^{13}C NMR spectra in D_2O. Even several days' standing in 0.5 M $HClO_4$ solution did not cause detectable reaction. Addition of NaOH solution to increase the pH to 4 caused precipitation of a white solid, which, after drying, analysed for $[\{PtMe_2(OMe)(OH)\cdot 3H_2O\}_n]$ (**36**). This

solid slowly redissolved in dilute aqueous $HClO_4$ solution to give a solution of **35**.

Addition of one mol equivalent of NaCl to an aqueous solution of **35** caused slow precipitation of a white solid, which analysed for $[\{PtMe_2(OMe)Cl.H_2O\}_n]$ (**37**). The same product was obtained by reaction of a methanol solution of $[PtMe_2(OMe)Clpy_2]$ (**34**) with $HClO_4$. Refluxing an aqueous suspension of **37** with one mol equivalent of $AgClO_4$ gave AgCl and **35** in solution.

$[PtMe_2(tmen)]$ (**10**) was not soluble in methanol. With standing it did dissolve, but appeared to give a mixture of products. $[PtMe_2(nbd)]$ (**5**) was not soluble in methanol, and did not react, even under reflux.

The chemical stability of these methoxide complexes is remarkable compared with the reactivity of most transition metal alkoxides toward hydrolysis and β-hydride elimination. Monaghan and Puddephatt (21) noted the robustness of **32** and its phenanthroline analogue, and Abbott and co-workers (36) found that non-organometallic platinum(IV) alkoxides such as *trans*-[Pt(malonato)$_2$(OR)(OH)] hydrolysed very slowly in acidic solution. It is noteworthy that in these compounds the robust platinum–alkoxide bonds are all *trans* to ligands with weak to moderate *trans* effects. The trimethylplatinum(IV) alkoxide, $[\{PtMe_2(OMe)\}_n]$, is presumably tetrameric with triply bridging methoxide *trans* to methyl groups, which have high *trans* effect. It is very sensitive to hydrolysis, and has not been completely characterized (37).

X = OEt

Monaghan and Puddephatt (21) found that ethanol reacted with $[PtMe_2(bpy)]$ (**9**) in a manner similar to methanol. We prepared ethoxide complexes by procedures similar to those used for analogous methoxide compounds: $[PtMe_2(OEt)(OH)py_2]\cdot 3H_2O$ (**38**), *fac*-$[PtMe_2(OEt)(H_2O)_3]^+$ (**39**) (in solution), $[\{PtMe_2(OEt)(OH)\cdot 0.5H_2O\}_n]$ (**40**), and $[\{PtMe_2(OEt)Cl\cdot 2H_2O\}_n]$ (**41**). Both $[PtMe_2(tmen)]$ (**10**) and $[PtMe_2(nbd)]$ (**5**) were insoluble in ethanol, and no reaction was observed when these substances were heated with ethanol.

X = SCN

Reaction of an aqueous solution of *cis*-$[PtMe_2(D_2O)_4]^{2+}$ (**3**) with two mol equivalents of NaNCS in D_2O gave a species in solution whose ^1H NMR spectrum showed one singlet with satellites from the methyl groups. The Pt–CH_3 coupling constant, 65.6 Hz, was relatively low, as would be expected if the methyl groups were *trans* to S-bound thiocyanate. The complex present was therefore formulated as $[PtMe_2(SCN)_2(D_2O)_2]$ (**42**) in which thiocyanate ligands have replaced the water molecules initially coordinated *trans* to methyl. Heating a solution of **42** with more NaNCS ultimately gave *cis*-$[PtMe_2(SCN)_4]^{2-}$ (**43**) in solution, with low concentrations of *fac*-$[PtMe_2(SCN)_3(D_2O)]^-$ (**44**) detected as an intermediate when the reaction was monitored by ^1H NMR. **43** was previously obtained by reaction of *fac*-$[PtMe_2Br(H_2O)_3]^+$ (**2**) with excess KNCS (2). When a solution of **42** was allowed to stand, $[\{PtMe_2(NCS)_2\}_n]$ (**45**) slowly precipitated. This solid, which is probably polymeric with Pt-N≡C-S-Pt bridging, was previously obtained when a solution of *fac*-$[PtMe_2Br(SCN)_3]^{2-}$ was allowed to stand (2).

Heating a D_2O suspension of **45** with one mol equivalent of $AgClO_4$ gave *cis*-$[PtMe_2(D_2O)_4]^{2+}$ (**3**) as the only methyl-platinum compound detectable by ^1H NMR (30% yield after 3 h). When a solution of *fac*-$[PtMe_2Br(D_2O)_3](NO_3)$ (**2**) in D_2O was refluxed with excess AgSCN for 3 h, then filtered, three methyl-platinum(IV) species were detected by ^1H and ^{13}C NMR in the filtrate: starting complex **2**, **3**, and a third species that was probably *fac*-$[PtMe_2(SCN)(D_2O)_3]^+$ (**46**). It was present in only 20% yield at this stage of the reaction, and, with further heating, these peaks decreased in intensity. No ^{195}Pt peak was observed in the region corresponding to the anticipated chemical shift of **46** (between −1000 and −2000 ppm). A peak was observed at −318 ppm, which could correspond to a platinum(II) species such as $[Pt(SCN)(D_2O)_3]^+$ (30, 38, 39), which could be formed by reductive elimination of ethane from **46**.

X = NO_2

Reaction of $NaNO_2$ with a D_2O solution of *cis*-$[PtMe_2(D_2O)_4]^{2+}$ (**3**) gave $[PtMe_2(NO_2)_2(D_2O)_2]$ (**47**) in solution, but no solid precipitated from this solution. Heating with excess $NaNO_2$ gave *cis*-$[PtMe_2(NO_2)_4]^{2-}$ (**48**) in solution, previously obtained by heating *fac*-$[PtMe_2Br(H_2O)_3](NO_3)$ (**2**) with excess $NaNO_2$ (2). The Pt–CH_3 coupling constants in these compounds corresponded to methyl groups *trans* to N-bound nitrite.

A solution of *fac*-$[PtMe_2Br(D_2O)_3](NO_3)$ (**2**) in D_2O was refluxed with $Ag(^{15}NO_2)$. A new set of peaks was observed in each of the ^1H and ^{13}C NMR spectra, corresponding to methyl groups *trans* to water. The ^{195}Pt NMR spectrum showed a doublet from coupling with ^{195}Pt, indicating that one nitrite ligand was bound to platinum through nitrogen. The ^{195}Pt–^{15}N coupling constant, 664.1 Hz, was as expected for nitrite bound to platinum(IV) *trans* to a ligand of low *trans* influence (40, 41). The species in solution was therefore formulated as *fac*-$[PtMe_2(^{15}NO_2)(D_2O)_3]^+$ (**49**).

Experimental section

Literature methods were used to prepare the starting materials $[PtMe_2(nbd)]$ (**5**) (24), $[PtMe_2(tmen)]$ (**8**) (24), $[\{PtMe_2Br_2\}_n]$ (**4**) (42), $[\{PtMe_2(OH)_2\}_n]\cdot mH_2O$ (**28**) (42), and *fac*-$[PtMe_2Br(H_2O)_3]^+$ (**2**) in solution (2). Microanalyses were provided by the microanalytical service in this department.

100 MHz ^1H, 25.1 MHz ^{13}C, and 21.4 MHz ^{195}Pt NMR spectra were run on a JEOL FX-100 spectrometer, 200 MHz ^1H and 50.2 MHz ^{13}C NMR spectra on a Bruker ACF 200 spectrometer, and 400 MHz ^1H spectra on a JEOL GX-400 spectrometer. Details of acquisition were as previously described (12, 24). All shifts are positive to higher frequency. Unless otherwise stated, ^{13}C and ^{195}Pt spectra were ^1H-decoupled. For ^1H and ^{13}C spectra in organic solvents, the reference was tetramethylsilane (TMS). For ^{13}C NMR spectra in D_2O, dioxane was used as an internal reference with δ(C) taken as 67.73. For ^1H NMR spectra in D_2O, the reference was the methyl signal of $Na(Me_3Si(CH_2)_3SO_3)$ (TSS). For ^{195}Pt spectra the reference was a separate sample containing 0.5 g $Na_2[PtCl_6]$ per cm^3 (δ(Pt) = 0).

Preparation of *cis*-$[PtMe_2py_2]$ (8)

This procedure described below is a modification of that previously described (24). *cis*-$[PtMe_2(nbd)]$ (**5**) (3.2 g, 10.1 mmol) was dissolved in 25 cm^3 freshly distilled dry diethyl

ether. Dry distilled pyridine (2.45 cm^3, 30.3 mmol) was slowly added while the solution was stirred under nitrogen, and with the flask shielded from light with aluminum foil. Stirring was continued for 30 min, during which time the product deposited from solution. It was filtered off, and washed with small volumes of ether, then with hexane, then dried in the dark under reduced pressure. Yield was 3.1 g (80%). A second crop was obtained if the filtrate was stirred for several hours more in the dark.

Oxidative additions to [$PtMe_2$(nbd)] (5)

The general method is similar to that described by Clark and Manzer for reactions of [$PtMe_2$(cod)] (22), and is illustrated by the reaction of **5** with bromine.

Reaction of 5 with bromine

[$PtMe_2$(nbd)] (**5**) (0.30 g, 0.95 mmol) was dissolved in dichloromethane (10 cm^3), and bromine (0.15 g, 0.94 mmol) was added dropwise. The solution was stirred for 30 min. The yellow product, [{$PtMe_2Br_2$}$_n$] (**4**), precipitated during this time. It was filtered off, washed with dichloromethane, then with ether, and air-dried. Yield was 0.36 g (97%).

Analogous reactions were carried out with other reagents, with variations as noted below.

Reaction of 5 with iodine

Yield of [{$PtMe_2I_2$}$_n$] (**20**) (dark brown solid) was 0.40 g (89%).

Reaction of 5 with water

[$PtMe_2$(nbd)] (**5**) (0.30 g) was suspended in water (20 cm^3) and the suspension was heated under reflux for 1 h. The mixture was cooled, the white solid was filtered off, washed with water, then with acetone, and dried in a vacuum desiccator over phosphorus(V) oxide. Yield of [{$PtMe_2(OH)_2 \cdot 1.5H_2O$}$_n$] (**28**) was 0.12 g (46%).

Oxidative additions to *cis*-[$PtMe_2py_2$] (8)

The general procedure is similar to that previously described (24) for reaction of **8** with MeI, and is illustrated by the reaction with bromine.

Reaction of 8 with bromine

cis-[$PtMe_2py_2$] (**8**) (0.50 g, 1.30 mmol) was dissolved in chloroform (10 cm^3) and bromine (0.20 g, 1.30 mmol) was slowly added, with stirring. The solution was evaporated to dryness under reduced pressure, and the resultant yellow solid, [$PtMe_2Br_2py_2$] (**6**), was washed with ether and dried in air. Yield was 0.70 g (99%).

Variations for analogous reactions with other reagents are noted below.

Reaction of 8 with chlorine

Chlorine gas was bubbled through a chloroform solution (10 cm^3) containing **8** (1.30 mmol) for 10 min, then the solution was taken to dryness. The pale yellow product, [$PtMe_2Cl_2py_2$] (**7**), was obtained in 97% yield.

Reaction of 8 with iodine

The brown solid, [$PtMe_2I_2py_2$] (**21**) was obtained in 56% yield.

Reaction of 8 with cyanogen iodide

The reaction with ICN was carried out in benzene. The white product, [$PtMe_2$(CN)Ipy_2] (**25**), was obtained in 96% yield.

Reaction of 8 with water

cis-[$PtMe_2py_2$] (**8**) (0.20 g, 0.52 mmol) was suspended in water (20 cm^3) and the suspension was stirred for 12 h, during which time the solid dissolved. Solvent water was removed under reduced pressure, and the resultant white solid was dried in a vacuum desiccator over phosphorus(V) oxide. Yield of [$PtMe_2(OH)_2py_2] \cdot 6H_2O$ (**30**) was 0.26 g (95%).

Reaction of 8 with methanol

cis-[$PtMe_2py_2$] (**8**) (0.30 g, 0.78 mmol) was dissolved in dry methanol (20 cm^3). The solution was allowed to stand for 6 h, then taken to dryness under reduced pressure. The oily material was washed with a small volume of water, then with acetone, and dried in air. Yield of the white solid, [$PtMe_2$(OMe)(OH)$py_2] \cdot 4H_2O$ (**33**), was 0.38 g (95%).

Reaction of 8 with ethanol

The reaction was carried out in a similar way to that with methanol, except that the ethanol solution was allowed to stand for 9 h. Yield of the white solid [$PtMe_2$(OEt)-(OH)$py_2] \cdot 3H_2O$ (**38**) was 85%.

Oxidative additions to [$PtMe_2$(tmen)] (10)

Reaction of 10 with bromine

The reaction was carried out in a similar way to that of *cis*-[$PtMe_2py_2$] (**8**) with bromine. Yield of the yellow solid [$PtMe_2Br_2$(tmen)] (**12**) was 94%.

Reaction of 10 with water

[$PtMe_2$(tmen)] (**10**) (0.30 g) was suspended in water (20 cm^3) and the suspension was heated under reflux 20 min. During this time the solid dissolved. The solution was filtered, and water was then removed under reduced pressure. The resultant white solid was washed with a small volume of water, then dried in a vacuum desiccator over phosphorus(V) oxide. Yield of [$PtMe_2(OH)_2$(tmen)] $\cdot 7H_2O$ (**31**) was 0.13 g (72%).

Preparation of [$PtMe_2$(OMe)Clpy_2] (34)

[$PtMe_2$(OMe)(OH)$py_2] \cdot 4H_2O$ (0.30 g, 0.60 mmol) was dissolved in methanol (20 cm^3) and solid sodium chloride (0.035 g, 60 mmol) was added. The mixture was heated at 50°C for 2 h. The solution was then filtered, and taken to dryness. The resultant white solid was washed with ether and air-dried. Yield of **34** was 0.23 g (86%).

Reaction of [$PtMe_2Br_2py_2$] (6) with chlorine

A sample of **6** was prepared, either from *cis*-[$PtMe_2py_2$] (**8**) and bromine as detailed above, or by reaction of [{$PtMe_2Br_2$}$_n$] (**4**) with pyridine (25). To convert **8** completely to [$PtMe_2Cl_2py_2$] (**7**), the following procedure, based on that of Hall and Swile (25) was used. A solution of **6** (3.0 g) in chloroform (50 cm^3) was brought to reflux. Chlorine gas, generated by reaction of MnO_2 with concentrated HCl, was bubbled through the refluxing solution, which turned orange due to the release of Br_2. A pale yellow solid precipitated. Heating and passage of Cl_2 was continued for 30 min. The solid was

filtered off and washed with cold chloroform. To ensure that none of the pyridine ligands were lost in the chlorination treatment, the solid was dissolved in pyridine at ambient temperature, and recovered by removal of pyridine under reduced pressure. It was then redissolved in the minimum volume of hot chloroform, and crystallized by addition of ethanol. Yield of $[PtMe_2Cl_2py_2]$ (**7**) was 2.1 g (85%).

To obtain a product that contained approximately equimolar quantities of **7** and $[PtMe_2BrClpy_2]$ (**13**), a similar procedure was used, except that passage of chlorine was stopped as soon as a solid precipitated.

Removal of coordinated pyridine from $[PtMe_2X_2py_2]$ and $[PtMe_2XYpy_2]$

The general procedure is illustrated by the removal of pyridine from $[PtMe_2Br_2py_2]$ (**6**), based on the procedure of Hall and Swile (25). Variations in particular cases are noted.

Preparation of $[\{PtMe_2Br_2\}_n]$ (4) from $[PtMe_2Br_2py_2]$ (6)

To a suspension of **6** (0.30 g) in water (10 cm^3) was added 0.5 cm^3 70% perchloric acid. The mixture was heated under reflux 3 h. The yellow solid was filtered off, washed with water, then with acetone, and air-dried. Yield of $[\{PtMe_2Br_2\}_n]$ (**4**) was 0.21 g (98%).

Preparation of $[\{PtMe_2I_2\}_n]$ (20) from $[PtMe_2I_2py_2]$ (21)

Yield of the dark brown solid, **20**, was 76%.

Preparation of $[\{PtMe_2Cl_2\}_n]$ (14) from $[PtMe_2Cl_2py_2]$ (7)

To a suspension of **7** (0.40 g) in water (30 cm^3) was added 1 cm^3 70% $HClO_4$. The mixture was heated under reflux 1 h, to give a clear pale yellow solution, which was filtered. Water was removed under high vacuum while the flask was immersed in a water bath at 50°C (higher temperatures could lead to decomposition) until a solid began to precipitate. The flask was stored overnight in a refrigerator. The pale yellow solid was filtered off, washed quickly several times with small volumes of ice-cold water, dried in air, then in a vacuum desiccator over $CaCl_2$. Yield of **14** was 0.17 g (65%).

Preparation of $[\{PtMe_2(CN)_2\}_n]$ (27)

A sample of $[PtMe_2(CN)Ipy_2]$ (**25**) was prepared (7), and 0.4 g (0.75 mmol) was dissolved in methanol (30 cm^3). $AgClO_4$ (0.155 g, 0.75 mmol) was added, and the mixture was heated under reflux for 15 min. Precipitated AgI was filtered off, and KCN (0.49 g, 0.75 mmol) was added to the filtrate, which was then heated under reflux for 15 min. Perchloric acid (0.5 cm^3 70% solution) was added (**CAUTION — HOOD**) and the solution was heated under reflux 1 h. The solution was filtered, then reduced in volume under reduced pressure to 1 cm^3. Water (5 cm^3) was added. A colorless solid formed, which was filtered off, washed with water, then with acetone, and air-dried. Yield of **27** was 0.18 g (77%).

Reaction of $[PtMe_2(OH)_2py_2]\cdot 6H_2O$ (30) with $HClO_4$

30 (0.30 g) was suspended in water (10 cm^3) and 0.5 cm^3 70% $HClO_4$ solution was added. The solid dissolved. The solution was heated at 80°C 30 min, then filtered and concentrated under reduced pressure to 3 cm^3. ^{13}C and ^{195}Pt NMR spectra showed that the solution contained *cis*-$[PtMe_2(H_2O)_4]^{2+}$ (**3**). The solution also contained $[Hpy](ClO_4)$.

Addition of 1 M NaOH solution to increase the pH to 7 caused precipitation of a white solid, which was filtered off, washed with water, then with acetone, and dried in a vacuum desiccator over phosphorus(V) oxide. Yield of $[\{PtMe_2(OH)_2\cdot H_2O\}_n]$ (**28**) was 0.15 g, 91% based on **30**. Dissolution of the solid in the minimum volume of 1M $HClO_4$ solution gave a solution of *cis*-$[PtMe_2(H_2O)_4](ClO_4)_2$ free from pyridinium salts.

Reaction of $[PtMe_2(OMe)(OH)py_2]\cdot 4H_2O$ (33) with $HClO_4$

A sample of **33** was treated in a similar way to that described above for **30**, except that the solution was heated for only 15 min. NMR spectra of the resultant solution were consistent with the presence in solution of *fac*-$[PtMe_2(OMe)(H_2O)_3]^+$ (**35**) as well as Hpy^+.

Addition of 1 M NaOH solution to increase the pH to 4.0 caused precipitation of a white solid that was filtered off, washed with water, and dried in a vacuum desiccator over phosphorus(V) oxide. Yield of $[\{PtMe_2(OMe)(OH)\cdot 3H_2O\}_n]$ (**36**) was 65% based on **33**.

NaCl (0.032 g, 0.54 mmol) was added to 3 cm^3 0.180 M $[PtMe_2(OMe)(H_2O)_3]^+$ solution (containing 0.54 mmol **35**). The mixture was stirred to dissolve the solid, then allowed to stand for 12 h. The white solid that precipitated was filtered off, washed with water, and dried in a vacuum desiccator over phosphorus(V) oxide. Yield of $[\{PtMe_2(OMe)Cl.H_2O\}_n]$ (**37**) was 0.15 g (91%), based on the quantity of **35** initially in solution.

Reaction of $[PtMe_2(OEt)(OH)py_2]\cdot 3H_2O$ (38) with $HClO_4$

Similar procedures to those used for the methoxide complexes gave *fac*-$[PtMe_2(OEt)(H_2O)_3]^+$ (**39**) in solution, and the white solids $[\{PtMe_2(OEt)(OH)\cdot 0.5H_2O\}_n]$ (**40**) (59% yield based on **38**) and $[\{PtMe_2(OEt)Cl\cdot 2H_2O\}_n]$ (**41**) (89% based on the quantity of **39** initially in solution).

Removal of coordinated tmen from $[PtMe_2X_2(tmen)]$

$[\{PtMe_2Br_2\}_n]$ (**4**) was prepared from $[PtMe_2Br_2(tmen)]$ (**12**) in 95% yield by a similar procedure to that described above, starting with the bis(pyridine) analogue, **6**.

A solution of *cis*-$[PtMe_2(H_2O)_4]^{2+}$ (**3**), with H_2tmen^{2+}, was prepared from $[PtMe_2(OH)_2(tmen)]\cdot 7H_2O$ (**31**) by a procedure similar to that described above for the pyridine analogue, **30**.

Preparation of $[\{PtMe_2(SCN)_2\}_n]$ (45)

Solid $[\{PtMe_2(OH)_2\cdot 1.5H_2O\}_n]$ (**28**) (0.20 g, 0.70 mmol) was dissolved, with warming and stirring, in the minimum volume of 1 M $HClO_4$ solution. NaNCS (0.12 g, 1.48 mmol) was added, and the solution stirred to dissolve the solid. The solution was allowed to stand 24 h, during which time a pale yellow solid formed. The solid was filtered off, washed with water, then with acetone, and dried in a vacuum desiccator over silica gel. Yield of **45** was 0.13 g (54%).

Preparation of *fac*-$[PtMe_2X(H_2O)_3]^+$ by halide abstraction from $[\{PtMe_2XY\}_n]$

The general procedure is illustrated by the preparation of *fac*-$[PtMe_2Br(H_2O)_3]NO_3$ (**2**) in solution, based on the procedure of Hall and Swile (2).

*Preparation of **3** in solution*

$[\{PtMe_2Br_2\}_n]$ (**4**) (0.30 g, 0.78 mmol) was suspended in

water (10 cm^3) containing $AgNO_3$ (0.13 g, 0.78 mmol), and the mixture was stirred while heated under reflux 2 h, with protection from light. The mixture was cooled, and precipitated AgBr was filtered off, leaving $[PtMe_2Br(H_2O)_3]^+$ as the only methyl-platinum complex detectable by NMR in the yellow solution. The solution could be concentrated under reduced pressure, and the reaction could be carried out in D_2O, if desired.

Complexes *fac*-$[PtMe_2X(H_2O)_3](NO_3)$ (X = Cl (**19**), OMe (**35**)) were similarly prepared. For X = I (**23**), 0.20 cm^3 70% $HClO_4$ solution was added before the mixture was refluxed, to prevent precipitation of $[\{PtMe_2I(OH)\}_n]$.

Preparation of *fac*-$[PtMe_2(^{15}NO_2)(D_2O)_3](NO_3)$ (49) in solution

$Na(^{15}NO_2)$ (0.182 g, 2.6 mmol) was added to a solution of $AgNO_3$ (0.439 g, 2.6 mmol) in 5 cm^3 water. Solid $Ag(^{15}NO_2)$ precipitated, and was filtered off, washed with ice-cold water, and dried in a vacuum desiccator over silica gel. Yield was 0.272 g (68%).

To 5 cm^3 0.26 M $[PtMe_2Br(D_2O)_3](NO_3)$ (**2**) solution in D_2O (1.3 mmol) was added $Ag(^{15}NO_2)$ (0.20 g, 1.3 mmol), and the mixture was heated under reflux for 1 h while protected from light. The mixture was cooled, and solid was filtered off. From NMR measurements, the yield of **49** in solution was 70%.

An analogous reaction of a solution of **2** with Ag(SCN) gave only 20% yield in solution of a complex formulated as *fac*-$[PtMe_2(SCN)(D_2O)_3]^+$ (**46**).

Acknowledgements

We thank the Australian Research Council for financial support.

References

1. D.E. Clegg and J.R. Hall. Spectrochim. Acta, **21**, 357 (1965).
2. J.R. Hall and G.A. Swile. J. Organomet. Chem. **139**, 403 (1977).
3. J.R. Hall and G.A. Swile. J. Organomet. Chem. **122**, C19 (1976).
4. G.E. Glass and R.S. Tobias. J. Am. Chem. Soc. **89**, 6371 (1967).
5. G.E. Glass, W.B. Schwabacher, and R.S. Tobias. Inorg. Chem. **7**, 2471 (1968).
6. N.H. Agnew, T.G. Appleton, and J.R. Hall. Inorg. Chim. Acta, **41**, 71 (1980).
7. T.G. Appleton, J.R. Hall, and M.A. Williams. Aust. J. Chem. **40**, 1565 (1987).
8. N.H. Agnew, T.G. Appleton, and J.R. Hall. Inorg. Chim. Acta, **41**, 85 (1980).
9. N.H. Agnew, T.G. Appleton, and J.R. Hall. Inorg. Chim. Acta, **50**, 137 (1981).
10. T.G. Appleton, J.R. Hall, and M.A. Williams. Inorg. Chim. Acta, **61**, 51 (1982).
11. T.G. Appleton, J.R. Hall, N.S. Ham, F.W. Hess, and M.A. Williams. Aust. J. Chem. **36**, 673 (1983).
12. T.G. Appleton, R.D. Berry, J.R. Hall, and J.A. Sinkinson. Inorg. Chem. **30**, 3860 (1991).
13. T.G. Appleton, K.A. Byriel, J.R. Hall, C.H.L. Kennard, D.E. Lynch, J.A. Sinkinson, and G. Smith. Inorg. Chem. **33**, 444 (1994).
14. T.G. Appleton, J.R. Hall, T.G. Jones, and J.A. Sinkinson. Polyhedron, **14**, 2613 (1995).
15. T.G. Appleton, J.R. Hall, D.W. Neale, and M.A. Williams. J. Organomet. Chem. **276**, C73 (1984).
16. J. Chatt and B.L. Shaw. J. Chem. Soc. 705 (1959).
17. J.D. Ruddick and B.L. Shaw. J. Chem. Soc. A, 2801 (1969).
18. J.D. Ruddick and B.L. Shaw. J. Chem. Soc. A, 2964 (1969).
19. T.G. Appleton, H.C. Clark, and L.E. Manzer. J. Organomet. Chem. **65**, 275 (1974).
20. J. Kuyper. Inorg. Chem. **17**, 71 (1978).
21. P.K. Monaghan and R.J. Puddephatt. Organometallics, **3**, 444 (1984).
22. H.C. Clark and L.E. Manzer. J. Organomet. Chem. **59**, 441 (1973).
23. T.G. Appleton, J.R. Hall, C.H.L. Kennard, M.T. Mathieson, D.W. Neale, G. Smith, and T.C.W. Mak. J. Organomet. Chem. **453**, 307 (1993).
24. T.G. Appleton, J.R. Hall, and M.A. Williams. J. Organomet. Chem. **303**, 139 (1986).
25. J.R. Hall and G.A. Swile. Aust. J. Chem. **24**, 423 (1971).
26. D.E. Clegg, J.R. Hall, and G.A. Swile. J. Organomet. Chem. **38**, 404 (1972).
27. H.C. Clark and L.E. Manzer. Inorg. Chem. **12**, 362 (1973).
28. T.G. Appleton, H.C. Clark, and L.E. Manzer. Coord. Chem. Rev. **10**, 335 (1973).
29. N.H. Agnew, T.G. Appleton, and J.R. Hall. Aust. J. Chem. **35**, 881 (1982).
30. T.G. Appleton, J.R. Hall, and S.F. Ralph. Inorg. Chem. **24**, 4685 (1985).
31. P.S. Pregosin. Coord. Chem. Rev. **44**, 247 (1982).
32. J.D. Kennedy, W. MacFarlane, R.J. Puddephatt, and P.J. Thompson. J. Chem. Soc. Dalton Trans. 874 (1976).
33. J.R. Hall and G.A. Swile. J. Organomet. Chem. **56**, 419 (1973).
34. S.E. Binns, R.E. Cragg, R.D. Gillard, D.T. Heaton, and M.F. Pilbrow. J. Chem. Soc. A, 1227 (1969).
35. A.J. Canty, R.T. Honeyman, A.S. Roberts, P.R. Traill, R. Colton, B.W. Skelton, and A.H. White. J. Organomet. Chem. **471**, C8 (1994).
36. S.O. Dunham, R.D. Larsen, and E.H. Abbott. Inorg. Chem. **32**, 2049 (1993).
37. O.M. Ivanova and A.D. Gel'man. Zh. Neorg. Khim. **3**, 1334 (1958).
38. T.G. Appleton, J.R. Hall, S.F. Ralph, and C.S.M. Thompson. Inorg. Chem. **23**, 3521 (1984).
39. L.I. Elding and A.B. Groning. Inorg. Chim. Acta, **31**, 243 (1978).
40. S.J.S. Kerrison and P.J. Sadler. J. Chem. Soc. Dalton Trans. 2363 (1982).
41. T.G. Appleton, K.J. Barnham, J.R. Hall, and M.T. Mathieson. Inorg. Chem. **30**, 2751 (1991).
42. J.R. Hall, D.A. Hirons, and G.A. Swile. Inorg. Synth. **20**, 185 (1980).

Synthesis and characterization of mono- and bi-nuclear palladium(II) and platinum(II) complexes containing acetamidine ligands

Anshu Singhal and Vimal K. Jain

Abstract: The reactions of $[M_2Cl_2(\mu\text{-}Cl)_2(PR_3)_2]$ with acetamidines in 1:2 stoichiometry afforded mononuclear complexes, $[MCl_2\{ArNHC(Me)NAr\}(PR_3)]$ (**I**) (M = Pd or Pt; $R_3 = Et_3$, Bu_3, Me_2Ph, $MePh_2$; Ar = Ph or 4-MeC_6H_4 (tol)). Treatment of $[M_2Cl_4(PR_3)_2]$ with Li[ArNC(Me)NAr] under anerobic conditions gave acetamidino-bridged binuclear complexes, $[M_2Cl_2(\mu\text{-}ArNC(Me)NAr)_2(PR_3)_2]$ (**II**). The reaction of $[Pd_2(\mu\text{-}Cl)_2(\eta^3\text{-}allyl)_2]$ with Ag[ArNC(Me)NAr] gave acetamidino-bridged allyl complexes $[Pd_2(\mu\text{-}ArNC(Me)NAr)_2(\eta^3\text{-}allyl)_2]$ (**III**). All the complexes were characterized by elemental analyses and NMR (^1H, ^{31}P, ^{195}Pt) spectroscopy. The mononuclear complexes (**I**) exist in two isomeric forms differing in the coordination of monodentate acetamidine ligand. The ^{31}P and ^{195}Pt NMR data on binuclear complexes (**II**) indicate that there is no significant Pt–Pt interaction. The allyl complexes (**III**) (allyl = C_3H_5) exhibit formation of all three possible isomers, whereas methallyl (allyl = C_4H_7) derivatives exist only in one configuration.

Key words: palladium, platinum, acetamidine, NMR (^1H, ^{31}P, ^{195}Pt), mononuclear complexes, binuclear complexes.

Résumé : Les réactions du composé $[M_2Cl_2(\mu\text{-}Cl)_2(PR_3)_2]$ avec les acétamidines dans un rapport de 1 : 2 conduisent aux complexes mononucléaires $[MCl_2\{ArNHC(Me)NAr\}(PR_3)]$ (**I**) (M = Pd ou Pt; $R_3 = Et_3$, Bu_3, Me_2Ph, $MePh_2$; Ar = Ph ou 4-MeC_6H_4(tol). En traitant le composé $[M_2Cl_4(PR_3)_2]$ avec le Li[ArNC(Me)NAr], dans des conditions anaérobiques, on obtient les complexes binucléaires avec le groupe acétamidino ponté, $[M_2Cl_2(\mu\text{-}ArNC(Me)NAr)_2(PR_3)_2]$ (**II**). La réaction du $[Pd_2(\mu\text{-}Cl)_2(\eta^3\text{-}allyl)_2]$ avec Ag[ArNC(Me)NAr] donne les complexes allyliques avec le groupe acétamidino ponté : $[Pd_2(\mu\text{-}ArNC(Me)NAr)_2(\eta^3\text{-}allyl)_2]$ (**III**). On a caractérisé tous les complexes par analyse élémentaire et par la spectroscopie de RMN du ^1H, ^{31}P, et ^{195}Pt. Le complexe mononucléaire (**I**) existe sous deux formes isomères qui diffèrent par la coordination du ligand acétamide monodentate. Les données de la RMN du ^{31}P et du ^{195}Pt indiquent qu'il n'y a pas d'interaction Pt–Pt significative dans les complexes binucléaires (**II**). Les complexes allyliques (**III**) (allyle = C_3H_5) montrent la formation de tous les trois isomères possibles, tandis que les dérivés méthallyliques (allyl = C_4H_7) existent seulement dans une seule configuration.

Mots clés : palladium, platine, acétamidine, RMN du ^1H, ^{31}P, ^{195}Pt, complexes mononucléaires, complexes binucléaires.

[Traduit par la rédaction]

Introduction

Recently we isolated a series of binuclear palladium(II) and platinum(II) complexes containing one-, two-, and three-atom donor bridging ligands (1–3). The complexes with three-atom donor bridging ligands, e.g., carboxylate (2) and triazenido (3), show unusually strong metal–metal interactions in the d^8 configuration of the metal ion. To assess whether a metal–metal interaction in a d^8 configuration is a general feature of a three-atom bridging ligand, we have chosen amidines that are isoelectronic to carboxylate and triazenes as ligands.

A wide variety of platinum group metal complexes of amidines as well as their anions are now known. The anion acts in a monodentate (4, 5), bidentate chelating (6, 7), or bridging (8–10) fashion and also assists in stabilizing metal–metal bonds (11) in a manner similar to isoelectronic 1,3-disubstituted triazenido, carboxylato groups, etc. The amidino complexes are usually obtained either by the reaction of $[RNCR'NR]^-$ with metal salts or by deprotonation of coordinated neutral amidine in a precursor "M(NRCR'NHR)." Neutral amidines have two possible bonding sites, namely, via the amine-N or the imine-N atom; coordination through the latter is usually observed (4, 5, 12) rather than through more the basic amine-N atom.

In view of the above and in pursuance of our interest in platinum group metal complexes we have synthesized a series of mono- and bi-nuclear palladium(II) and platinum(II) complexes with acetamidines.

Results and discussion

The reaction of the chloro-bridged dimers $[M_2Cl_2(\mu\text{-}Cl)_2(PR_3)_2]$ with acetamidines in 1:2 stoichiometry readily afforded mononuclear complexes of the type

Received December 15, 1995.

This paper is dedicated to Professor Howard C. Clark in recognition of his contributions to Canadian chemistry.

A. Singhal and V.K. Jain.[1] Chemistry Division, Bhabha Atomic Research Centre, Trombay, Bombay-400 085, India.

[1] Author to whom correspondence may be addressed. Telephone: 5511576 and 5563060/2668. Fax: 91-22-556-0750.

Fig. 1. $^{195}Pt\{^1H\}$ (*A*) and $^{31}P\{^1H\}$ NMR spectra (*B*) of the complex $[PtCl_2(PBu_3)\{PhNC(Me)NHPh\}]$ in $CDCl_3$.

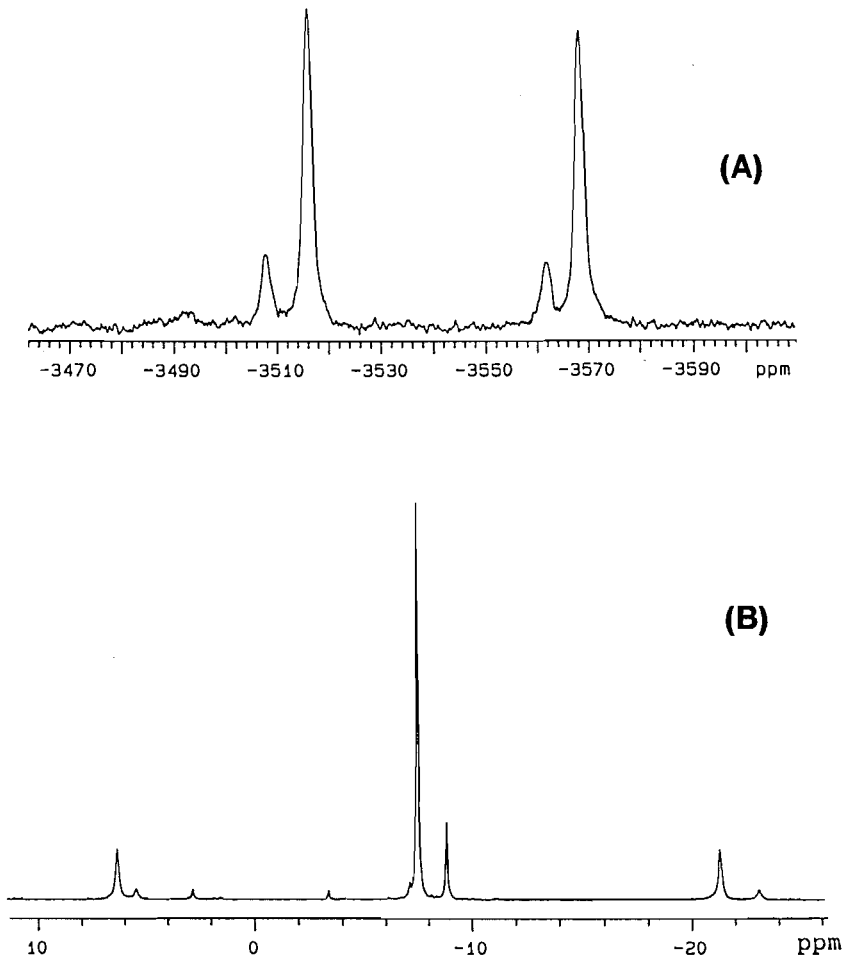

$[MCl_2(PR_3)\{ArNC(Me)NHAr\}]$ (**I**) (M = Pd or Pt; $R_3 = Et_3$, Bu_3, Me_2Ph, $MePh_2$; Ar = Ph or 4-$CH_3C_6H_4$ (tol)). The palladium complexes are yellow while the analogous platinum complexes are pale yellow.

The ^{31}P spectra of most of these complexes showed two resonances, except for a few platinum complexes where one resonance with platinum satellites was observed. Similarly, the ^{195}Pt NMR spectrum of $[PtCl_2(PBu_3)\{PhNC(Me)NHPh\}]$ displayed two doublets (δ −3542.2 ppm (d), ^1J(Pt–P) 3361 Hz (major isomer); δ −3534.8 ppm (d), ^1J(Pt–P) 3474 Hz (minor isomer)) (Fig. 1). The ^1J(Pt–P) coupling constants (Table 1) indicate that in every case nitrogen is *trans* to the phosphine ligand (13). One would expect a magnitude of ^1J(Pt–P) ~3600 Hz for *cis* configuration (phosphine *trans* to chloride). The palladium complexes appear to have a *trans* configuration since the IR spectra in the region 500–200 cm^{-1} for both series of complexes are comparable.

There are two different N donor atoms in amidines. Accordingly, two signals in the ^{31}P NMR spectra can be attributed to the molecules containing amino-N and imino-N coordinated ligand (Fig. 2). No isomerization was noticed on keeping the solution for few hours. We recently reported ligation via different nitrogen atoms in a triazene complex

Fig. 2. Amine–N and imine–N coordination for amidine ligand.

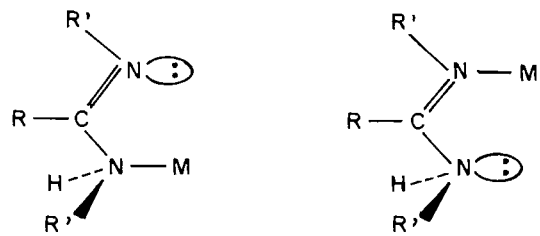

$[PtCl_2(PBu_3)(PhNNNHPh)]$ (3). Interestingly, the X-ray analysis of $[Pt\{C_6H_3)(CH_2NMe_2)_2$-2,6$\}\{tolNC(H)NHtol\}]$-$[CF_3SO_3]$ revealed coordination through imino nitrogen, and this configuration is retained in solution (5). Coordination through imino nitrogen has been suggested for the allyl complexes (5), $[PdCl(\eta^3\text{-}C_3H_5)\{ArNC(H)NHAr\}]$; however, for these complexes Toniolo and co-workers (14) reported ligation via the more basic amine N atom.

In the ^1H NMR spectra the CMe and NH signals for the imine-coordinated isomer appeared at δ ~1.8 and 8.50–9.06 ppm, respectively. The assignment was made by comparison

Table 1. ^{1}H and $^{31}P\{^{1}H\}$ NMR data for palladium and platinum complexes containing acetamidine ligands.

Complex	^{31}P NMR data δ (^{1}J (Pt–P))	^{1}H NMR data[b]
$[PdCl_2(PBu_3)\{PhN{=}C(Me)NHPh\}]$	25.1 25.2	0.86 (apparent q, due to overlapping triplets, P–CH_3), 1.39–1.58 (m, $PCCH_2CH_2$-); 1.85 (br, PCH_2), 2.69 (s, CMe-); 6.45 (s, NH); 7.01–7.43 (m, Ph), 8.64 (s, NH).
$[PdCl_2(PMe_2Ph)\{PhN{=}C(Me)NHPh\}]$	4.68[a] 4.81	1.76 (d, 12.6 Hz, PMe_2); 1.78 (d, 12.3 Hz, PMe_2),[a]1.82 (s, CMe),[a] 2.68 (s, =CMe); 6,42 (s, NH); 7.01 (d, 7.5 Hz), 7.16–7.43 (m), 7.75–7.86 (m) [Ph]; 8.57 (s, NH).[a]
$[PdCl_2(PMePh_2)\{PhN{=}C(Me)NHPh\}]$	14.9 15.0[a]	2.00 (d, 12.3 Hz, PMe), 2.01 (d, 12.0 Hz, PMe),[a] (d, 12.0 Hz, PMe); 1.85 (s, CMe),[a] 2.74 (s, CMe); 6.46 (s, NH); 7.02 (d, 7.3 Hz), 7.22–7.46 (m); 7.67–7.77 (m) [Ph]; 8.64 (s, NH).[a]
$[PdCl_2(PEt_3)\{tolN{=}C(Me)NHtol\}]$	31.8[c]	1.17 (m, $PCCH_3$); 1.80 (s, =CMe-); 1.86 (m, PCH_2-); 2.32, 2.33, 2.35 (each s, tol Me for both isomers), 2.65 (s, =CMe-); 6.40 (s, NH), 6.89 (d, 8 Hz), 7.09–7.30 (m) [C_6H_4]; 8.50 (s, NH).
$[PtCl_2(PEt_3)\{PhN{=}C(Me)NHPh\}]$	0.62[d] (3320 Hz)	1.14 (dt, 17 Hz (d), 7.7 Hz (t), PC-CH_3); 1.84 (m, PCH_2-); 1.87 (s, =CMe); 7.16–7.44 (m, Ph), 9.06 (s, NH).
$[PtCl_2(PBu_3)\{PhN{=}C(Me)NHPh\}]$	–7.5[a] (3357 Hz) –8.8 (3470 Hz)	0.79 (t, 7.3 Hz, P–CH_3),[a] 0.84 (t, 7.3 Hz, P–CH_3), 1.32 (m, P-C-C-CH_2-); 1.45 (s, CMe);[a] 1.49–1.88 (m, PCH_2CH_2); 2.75 (s, CMe), 6.18 (s, NH), 6.74–7.83 (m, Ph); 9.56 (s, NH).
$[PtCl_2(PMe_2Ph)\{PhN{=}C(Me)NHPh\}]$	–23.7[a] (3373 Hz) –25.0 (3482 Hz)	1.74 (d, 11.5 Hz, PMe_2), 1.76 (d, 11.5 Hz, PMe_2);[a] 1.87 (s, =CMe-),[a] 2.73 (s, =CMe-); 6.49 (s, NH), 7.02–7.48 (m), 7.78–7.88 (m) [Ph]; 8.87 (s, NH).[a]
$[PtCl_2(PBu_3)\{tolN{=}C(Me)NHtol\}]$	–7.9[d] (3290 Hz)	0.88 (t, 7.1 Hz, P–CH_3); 1.37–1.60 (m, PC-CH_2-CH_2-), 1.80 (m, PCH_2); 1.86 (s, =CMe-), 2.33 (s), 2.37 (s) (tol Me); 7.11–7.19 (m, C_6H_4); 8.95 (s, NH).
$[PtCl_2(PMe_2Ph)\{tolN{=}C(Me)\text{-}NHtol\}]$	–23.8[a] (3357 Hz) –25.1 (3465 Hz)	1.72 (d, 11.2 Hz, PMe_2), 1.75 (d, 11 Hz, PMe_2),[a] 1.84 (s, =CMe-),[a] 2.88 (s, =CMe-), 2.32, 2.34 (each s, tol-Me); 2.33, 2.35 (each s, tol-Me),[a] 6.43 (s, NH), 6.81 (d), 7.10--7.41, 7.78–7.88 (m) [Ph + C_6H_4]; 8.85 (s, NH).[a]
$[Pd_2Cl_2(\mu\text{-}PhNC(Me)NPh)_2(PEt_3)_2]$	17.3	1.06 (d, t, 15.6 Hz (d), 7.8 Hz (t, P-C-CH_3); 1.62 (m), 1.87 (m) (PCH_2-); 1.72 (s, CMe); 6.78–7.41 (m) [Ph].
$[Pd_2Cl_2(\mu\text{-}PhNC(Me)NPh)_2(PMe_2Ph)_2]$	2.9	1.78 (s, CMe); 1.84 (d), 2.08 (d) (each 12.4 Hz PMe_2); 6.71–7.18 (m), 8.06(m) [Ph].
$[Pd_2Cl_2\{\mu\text{-}PhNC(Me)NPh\}_2(PMePh_2)_2]$	13.7	1.16 (s, CMe); 2.42 (d, 12.0 Hz, PMe); 6.95–7.95 (m) [Ph].
$[Pd_2Cl_2\{\mu\text{-}tolNC(Me)Ntol\}_2(PBu_3)_2]$	10.4	0.94 (t, 7.2 Hz, $PCCCCH_3$); 1.39 (m, $PCCCH_2$-); 1.66 (m, PC-CH_2); 1.94 (s, CMe); 2.06–2.38 (m, PCH_2-); 2.15 (s), 2.16 (s) (tol-Me); 6.76–7.09 (m, C_6H_4).
$[Pd_2Cl_2\{\mu\text{-}tolNC(Me)Ntol\}_2(PMe_2Ph)_2]$	3.7	1.71 (s, CMe); 1.96 (d), 2.00 (d) (each 12.4 Hz PMe_2); 2.24 (s), 2.27 (s) (tol-Me); 6.30 (br, tol, C_6H_4); 6.57 (d), 6.82 (d), 6.83 (d) (each 8.2 Hz, tol, C_6H_4); 7.49 (m), 8.11 (m) [Ph].

Table 1 (*concluded*).

Complex	^{31}P NMR data δ (^{1}J (Pt–P))	^{1}H NMR data[b]
$[Pt_2Cl_2\{\mu\text{-PhNC(Me)NPh}\}_2(PBu_3)_2]$[e]	–8.4 (3630 Hz)	0.80 (t, 7.2 Hz, $PCCCCH_3$); 1.17 (m), 1.46 (m) ($PCH_2CH_2CH_2$]; 1.42 (s, CMe); 6.88–7.40 (m, Ph).
$[Pt_2Cl_2\{\mu\text{-PhNC(Me)NPh}\}_2(PMe_2Ph)_2]$[f]	–23.8 (3690 Hz)	1.48 (d, 11.3 Hz, PMe_2); 1.81 (s, CMe); 6.74–7.72 (m, Ph).
$[Pd_2\{\mu\text{-PhNC(Me)NPh}\}_2(\eta^3\text{-}C_3H_5)_2]$	—	1.70 (s), 1.71 (s) [=CMe]; 2.71 (d, 12.2 Hz, *anti* proton), 3.09 (d, 6.9 Hz, *syn* proton); 5.24 (m, central CH) (for major isomer containing equivalent allyl groups); 2.37 (d), 2.62(d) (each 12 Hz, *anti* proton); 2.99(d), 3.42 (d) (each 7 Hz, *syn* proton); 4.98 (m) (central CH) (second isomer with nonequivalent allyl groups), 2.28 (d, 12.4 Hz, *anti* proton), 3.35 (d, 7 Hz, *syn* proton) (this isomer is present in small concentration); 6.22–7.22 (m, Ph).
$[Pd_2\{\mu\text{-PhNC(Me)NPh}\}_2(\eta^3\text{-}C_4H_7)_2]$	—	1.74 (s, =CMe); 1.81 (s, Me of allyl); 2.54 (s, CH_2 *anti*), 2.82 (s, CH_2 *syn*), 6.75–7.18 (m, Ph).
$[Pd_2\{\mu\text{-tolNC(Me)Ntol}\}_2(\eta^3\text{-}C_3H_5)_2]$	—	1.68, 1.69 (each s, =CMe-), 2.25 (s), 2.27 (s), 2.29 (s), 2.31 (s) (tol-Me + *anti* protons of allyl); 2.68 (d, 12.2 Hz, *anti* proton); 3.06 (d, 6.8 Hz, *syn* proton); 5.22 (m, central CH) (for major isomer containing equivalent allyl groups). 2.59 (d, 12 Hz, *anti* proton),[g] 2.95 (d, 6.8 Hz), 3.38 (d, 6.8 Hz) (*syn* proton); 4.97 (m) (for the isomer with nonequivalent allyl groups); 3.3 (d, 6.8 Hz) (for the isomer with smaller concentration); 6.49–7.02 (m, C_6H_4).
$[Pd_2\{\mu\text{-tolNC(Me)Ntol}\}_2(\eta^3\text{-}C_4H_7)_2]$		1.70 (s, =CMe-); 1.80 (s, Me allyl); 2.27 (s, tol-Me); 2.50 (s, CH_2 *anti*); 2.87 (s, CH_2 *syn*), 6.64 (d, 8 Hz), 6.92 (d, 8 Hz) (C_6H_4).

[a]Due to major isomer.

[b]s = singlet, d = doublet, t = triplet, m = multiplet, dt = doublet of triplet; br = broad.

[c]Chemical shift degeneracy; two isomers are present in a 1:1 ratio as evident from the ^{1}H NMR spectrum.

[d]Only one isomer is formed.

[e]NMR data for the complex prepared from the acetato-bridged platinum complex $^{31}P\{^{1}H\}$ in $CDCl_3$: –8.4 (^{1}J = 3629 Hz, major); –10.3 (minor) ppm. ^{1}H NMR spectrum is similar to the spectrum for the complex prepared from the chloro-bridged platinum derivative.

[f]NMR data for the complex prepared from the acetato-bridged platinum complex $^{31}P\{^{1}H\}$ in C_6D_6: δ –24.3 (^{1}J = 3747 Hz, minor isomer); –25.4 (^{1}J = 3690 Hz, major isomer); ^{1}H in C_6D_6: 1.14 (d, 11.3 Hz, PMe_2, major); 1.19 (d, 11.1 Hz, minor); 1.37 (s, CMe, minor); 1.40 (s, CMe, major); 6.55–7.63 (m, Ph).

[g]Another doublet due to the *anti* protons is merged to tol-Me signal.

with the spectra (5) of $[PdCl(\eta^3\text{-}C_3H_5)(ArNC(H)NHAr)]$ and $[Pt\{C_6H_3(CH_2NMe_2)_2\text{-}2,6\}\{tolNC(H)NHtol\}][CF_3SO_3]$. The resonances for the amine-coordinated isomer were assigned at δ 6.2–6.5 ppm (NH) and ~2.7 ppm (CMe). In general, the imine-coordinated isomer predominated and for a few platinum complexes was formed exclusively. The magnitude of ^1J(Pt–P) for the imine-coordinated isomer is smaller (~110 Hz) than that of the corresponding amine-coordinated complex. This is in agreement with the fact that ^1J(Pt–P) for the complexes containing sp^3 hybridized nitrogen is greater than for those complexes with sp^2 hybridized N donor atom (3).

Acetamidinato-bridged binuclear complexes

The binuclear acetamidinato-bridged palladium(II) and platinum(II) complexes can readily be obtained by the following reaction routes (eqs. [1] and [2])

[1] $[M_2Cl_2(\mu\text{-}X)_2(PR_3)_2] + 2LiAm \longrightarrow [M_2Cl_2(\mu\text{-}Am)_2(PR_3)_2] + 2LiX$

[2] $[Pd_2(\mu\text{-}Cl)_2(\eta^3\text{-allyl})_2] + AgAm \longrightarrow [Pd_2(\mu\text{-}Am)_2(\eta^3\text{-allyl})_2] + 2AgCl$

(M = Pd or Pt; X = Cl or OAc; Am^- = PhNC(Me)NPh or tolNC(Me)Ntol; $R_3 = Et_3$, Bu_3, Me_2Ph, $MePh_2$; allyl = C_3H_5 or C_4H_7).

The palladium complexes are orange while the analogous platinum complexes are lemon-yellow crystalline solids, soluble in common organic solvents. The mass spectrum of $[Pd_2Cl_2(\mu\text{-tolNC(Me)Ntol})_2(PBu_3)_2]$ showed a molecular ion peak at 1163, suggesting binuclear composition of these complexes. Besides a number of other peaks, peaks at *m/e* 581 and 546 can be assigned to mononuclear ions $[PdCl(PBu_3)(tolNC(Me)Ntol)]^+$ and $[Pd(PBu_3)(tolNC(Me)Ntol)]^+$, respectively.

NMR Spectra of II

The ^1H NMR spectra showed the expected integration and peak multiplicities (Table 1). The ^{31}P NMR spectra displayed a single resonance for tertiary phosphines. The ^1J(Pt–P) couplings for these complexes are comparable to those of the corresponding triazenido-bridged complexes (3). The platinum NMR spectra of $[Pt_2Cl_2(\mu\text{-PhNC(Me)NPh})_2(PR_3)_2]$ showed a single doublet ($R_3 = Bu_3$: $\delta^{195}Pt\{^1H\}$ −3244 (d) ppm, ^1J(Pt–P) = 3635 Hz; $R_3 = Me_2Ph$: δ −3220 (d) ppm, ^1J(Pt–P) = 3692 Hz) (Fig. 3). Interestingly, when the complexes were prepared from the acetato-bridged platinum complexes (X = OAc, eq. [1]), two isomeric forms, sym *cis* and sym *trans*, were revealed by the ^{31}P NMR data. One of the peaks had chemical shifts and coupling constant consistent with the spectra of the complexes prepared by the chloro-bridged route (X = Cl, eq. [1]). The second peak showed a slightly higher coupling constant (~57 Hz) than the other, and has been assigned to the sym *cis* isomer based on our earlier data on binuclear complexes. The palladium complexes existed exclusively in one isomeric form irrespective of the method of preparation (X = Cl or OAc; eq. [1]).

The complexes with isoelectronic bridging carboxylate (2) and triazene (3) ligands, $[Pt_2Cl_2(\mu\text{-}Y)_2(PR_3)_2]$ (Y = $RCOO^-$ or

Fig. 3. $^{195}Pt\{^1H\}$ (*A*) and $^{31}P\{^1H\}$ NMR (*B*) spectra of the complex $[Pt_2Cl_2(\mu\text{-PhNC(Me)NPh})_2(PMe_2Ph)_2]$ in $CDCl_3$.

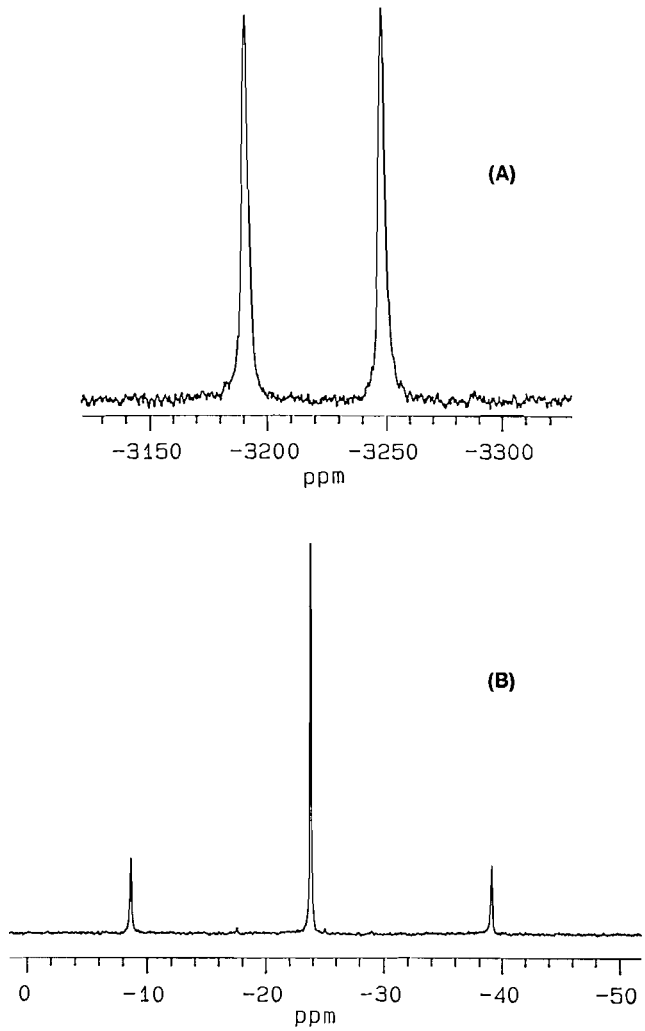

ArNNNAr⁻), show platinum–platinum interaction with formal bond order zero as revealed by presence of ^nJ(Pt–P) and ^nJ(Pt–Pt) couplings in the ^{31}P and ^{195}Pt NMR spectra (2, 3). Accordingly, one would expect similar behaviour for acetamidino-bridged complexes. However, such couplings were not present in the ^{31}P and ^{195}Pt NMR spectra (Fig. 3). This suggests that metal–metal interactions in these complexes are vanishingly small. The observed trend of M—M separation is evident from the X-ray structures of $[Pd_2(\mu\text{-tolNNNtol})_2(\eta^3\text{-allyl})_2]$ (Pd—Pd = 2.856(1) Å) (15), $[Pd_2(\mu\text{-OAc})_2(\eta^3\text{-allyl})_2]$ (Pd—Pd = 2.94 Å) (16), and $[Pd_2(\mu\text{-NHC(Ph)NH})_2(\eta^3\text{-allyl})_2]$ (Pd—Pd = 3.128(1) Å (17). The Pd—Pd separation in the latter can be compared with the pyrazolato-bridged complexes, $[M_2Cl_2(\mu\text{-}Me_2pz)_2(PR_3)_2]$ (M = Pd, 3.115(1) Å; M = Pt, 3.170(1) Å) (18, 19). For bis-pyrazolato-bridged binuclear platinum complexes ^nJ(Pt–P) and ^nJ(Pt–Pt) are not observed. The bite distances of bridging triazenido, carboxylato, and amidino groups in Ni(II), Pd(II), and Pt(II) lantern-type complexes are of the order of ~2.23, ~2.25, and ~2.34 Å, respectively (20). This trend of ligand bite is reflected in the

Fig. 4. Different isomers for the $[Pd_2(\mu\text{-amidino})_2(\eta^3\text{-allyl})_2$ complex.

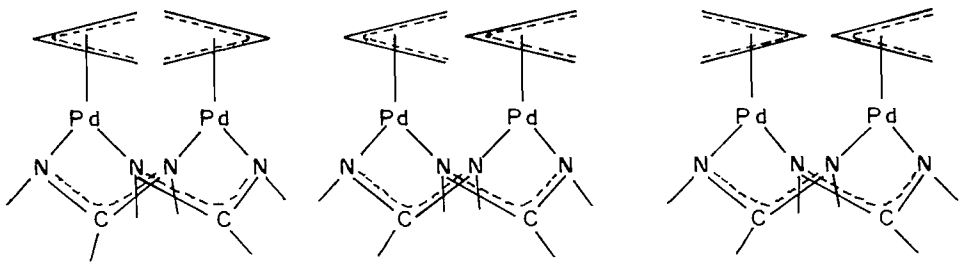

^nJ(Pt–Pt) and ^nJ(Pt–P) couplings for $[Pt_2Cl_2(\mu\text{-}Y)_2(PR_3)_2]$ complexes where Y = $ArNNNAr^-$, $RCOO^-$, $ArNC(Me)NAr^-$. Seemingly, the ligand-induced metal–metal interactions in binuclear d^8 metal complexes stabilized with isoelectronic bridging ligand (e.g., three-atom bridging ligands) are influenced by the ligand bite angle.

NMR spectra of allyl complexes, III

The methallyl palladium complexes showed only one set of resonances in the ^1H NMR spectra, indicating the existence of only one isomer. However, the allyl complexes exhibited three sets of resonances. This indicates that there are all three possible isomers (Fig. 4) in solution. It may be noted that earlier workers have reported one (17), two (21), and three (22) isomers for $[Pd_2(\mu\text{-amidino})_2(\eta^3\text{-allyl})_2]$ complexes.

Experimental

The complexes $[M_2Cl_2(\mu\text{-}Cl)_2(PR_3)_2]$ (M = Pd or Pt; $R_3 = Et_3$, Bu_3, Me_2Ph, $MePh_2$) (23), $[M_2Cl_2(\mu\text{-}OAc)_2(PR_3)_2]$ (2), $[Pd_2(\mu\text{-}Cl)_2(\eta^3\text{-allyl})_2]$ (24, 25), acetamidines (22, 26), ArN=C(Me)-NHAr (Ar = Ph, 4-MeC_6H_4 (tol), and silver amidinate (22) were prepared by literature methods. All reactions were carried out in dried and distilled analytical grade solvents under a nitrogen atmosphere. ^1H and $^{31}P\{^1H\}$ NMR spectra were recorded on a Varian XLR-300 or Bruker AMX-500 spectrometer in freshly prepared $CDCl_3$ or C_6D_6 solutions. Chemical shifts are referred to internal solvent peak ($CHCl_3$ δ 7.26 ppm) for ^1H and 85% H_3PO_4 for ^{31}P. $^{195}Pt\{^1H\}$ NMR spectra were recorded on a Varian XLR-300 instrument operating at 64.49 MHz and the spectra were referenced with external Na_2PtCl_6 in D_2O. Elemental analyses were carried out by the Analytical Chemistry Division of this research centre. Melting points were determined in capillary tubes in the open and were uncorrected. Representative examples of the synthetic routes to the various compounds are reported below. Analytical data for the complexes are given in Table 2.

Preparation of $[PtCl_2\{PhN{=}C(Me)\text{-}NHPh\}(PMe_2Ph)]$

To a dichloromethane solution (15 cm^3) of $[Pt_2Cl_2(\mu\text{-}Cl)_2(PMe_2Ph)_2]$ (111 mg, 0.137 mmol), a solution of *N,N*-diphenylacetamidine (58.6 mg, 0.279 mmol) in dichloromethane (5 cm^3) was added with stirring at room temperature. After an hour of stirring, the solvent was stripped off and the residue was recrystallized from dichloromethane–hexane mixture (1:2, v/v) in 78% (131 mg) yield as a pale yellow crystalline solid.

Preparation of $[Pd_2Cl_2(\mu\text{-}PhNC(Me)NPh\}_2(PMe_2Ph)_2]$

To a THF solution (20 cm^3) of Li[PhNC(Me)NPh], prepared in situ by neutralizing *N,N'*-diphenylacetamidine (70.5 mg, 0.336 mmol) with a hexane solution (0.69 M, 0.5 cm^3) of *n*-BuLi, was added solid $[Pd_2Cl_2(\mu\text{-}Cl)_2(PMe_2Ph)_2]$ (105 mg, 0.166 mmol) with vigorous stirring. The reactants were stirred at room temperature for 2 days. The solvents were stripped off in vacuo. The residue was extracted with benzene and filtered. The filtrate was concentrated in vacuo and the residue was recrystallized from benzene–hexane solution in 59% (95.9 mg) yield.

Preparation of $[Pd_2Cl_2(\mu\text{-}tolNC(Me)Ntol\}_2(PBu_3)_2]$

To a THF solution (20 cm^3) of Li[tolNC(Me)Ntol], prepared as in earlier preparation from *N,N'*-di-*p*-tolylacetamidine (94 mg, 0.395 mmol) and *n*-BuLi solution in hexane (0.8 cm^3, 0.53 M), solid $[Pd_2Cl_2(\mu\text{-}OAc)_2(PBu_3)_2]$ (146 mg, 0.181 mmol) was added. The reaction mixture was stirred at room temperature for 30 h. The solvents were removed in vacuo and the residue was extracted with benzene and filtered. The filtrate was evaporated in vacuo and the residue was recrystallized from hexane (yield, 128 mg, 61%).

Preparation of $[Pt_2Cl_2(\mu\text{-}PhNC(Me)NPh\}_2(PMe_2Ph)_2]$

To a THF solution (10 cm^3) of Li[PhNC(Me)NPh], prepared from *N,N'*-diphenylacetamidine (83 mg, 0.393 mmol) and *n*-BuLi solution (0.8 cm^3, 0.5 M), a benzene solution (10 cm^3) of $[Pt_2Cl_2(\mu\text{-}Cl)_2(PMe_2Ph)_2]$ (154 mg, 0.191 mmol) was added with vigorous stirring. The reaction mixture was stirred at room temperature for 60 h. The solvents were stripped off in vacuo and the residue was extracted with benzene and filtered. The filtrate as concentrated to 2 cm^3 and layered with hexane (5 cm^3), whereupon crystals of the title complex were obtained (yield 133 mg, 60%).

Preparation of $[Pd_2(\mu\text{-}PhNC(Me)NPh\}_2(\eta^3\text{-}C_4H_7)_2]$

To a dichloromethane solution (15 cm^3) of $[Pd_2(\mu\text{-}Cl)_2(\eta^3\text{-}C_4H_7)_2]$ (80 mg, 0.203 mmol) was added silver diphenylacetamidinate (147 mg, 0.42 mmol). The reaction mixture was stirred for 3 h at room temperature. The solvent was removed under reduced pressure and the residue was extracted with dichloromethane and filtered. The filtrate was concentrated in vacuo to 2 cm^3 and layered with hexane (5 cm^3), which on cooling in a freezer gave the crystals of the title complex (yield 49 mg, 33%).

Table 2. Physical and analytical data for the palladium and platinum complexes containing acetamidine ligands.

Complex	Recrystallization solvent (% yield)	Melting point (°C)	% Analysis found (calcd.) C	H	N
$[PdCl_2(PBu_3)\{PhN{=}C(Me)NHPh\}]$	Hexane (52)	Liquid	52.3 (52.9)	6.7 (7.0)	4.8 (4.7)
$[PdCl_2(PMe_2Ph)\{PhN{=}C(Me)NHPh\}]$	Benzene–hexane (74)	160–162	50.4 (50.3)	4.7 (4.8)	5.1 (5.3)
$[PdCl_2(PMePh_2)\{PhN{=}C(Me)NHPh\}]$	Benzene–hexane (65)	155–157	55.8 (55.2)	4.9 (4.6)	5.3 (4.8)
$[PdCl_2(PEt_3)\{tolN{=}C(Me)Ntol\}]$	Ether–hexane (68)	128–130	49.3 (49.5)	6.3 (6.2)	5.8 (5.3)
$[PtCl_2(PEt_3)\{PhN{=}C(Me)NHPh\}]$	Benzene–hexane (63)	135–137	39.8 (40.4)	5.0 (4.9)	4.6 (4.7)
$[PtCl_2(PBu_3)\{PhN{=}C(Me)NHPh\}]$	Hexane (54)	Liquid	45.9 (46.0)	6.2 (6.1)	4.0 (4.1)
$[PtCl_2(PMe_2Ph)\{PhN{=}C(Me)NHPh\}]$	CH_2Cl_2–hexane (78)	165–167	43.0 (43.0)	3.7 (4.1)	5.5 (4.6)
$[PtCl_2(PBu_3)\{tolN{=}C(Me)NHtol\}]$	Hexane (60)	78–80	47.5 (47.6)	7.1 (6.4)	4.2 (4.0)
$[PtCl_2(PMe_2Ph)\{tolN{=}C(Me)NHtol\}]$	CH_2Cl_2–hexane (92)	190–192	44.4 (44.8)	4.2 (4.5)	4.8 (4.4)
$[Pd_2Cl_2\{\mu PhNC(Me)NPh\}_2(PEt_3)_2]$	Ether–hexane (55)	128–130[a]	50.8 (51.1)	5.9 (6.0)	5.9 (6.0)
$[Pd_2Cl_2\{\mu\text{-}PhNC(Me)NPh\}_2(PMe_2Ph)_2]$	Benzene–hexane (59)	186–190[a]	53.3 (54.0)	5.1 (4.9)	5.8 (5.7)
$[Pd_2Cl_2\{\mu\text{-}PhNC(Me)NPh\}_2(PMePh_2)_2]$	Ether–hexane (58)	169–172[a]	58.9 (58.8)	4.8 (4.9)	5.1 (5.2)
$[Pd_2Cl_2\{\mu\text{-}tolNC(Me)Ntol\}_2(PBu_3)_2]$	Hexane (61)	134–136	57.5 (57.8)	8.2 (7.6)	5.1 (4.8)
$[Pd_2Cl_2\{\mu\text{-}tolNC(Me)Ntol\}_2(PMe_2Ph)_2]$	Ether–hexane (65)	188–190[a]	56.1 (55.7)	5.4 (5.4)	4.9 (5.4)
$[Pt_2Cl_2\{\mu\text{-}PhNC(Me)NPh\}_2(PBu_3)_2]$	Paste (49)	—	48.8 (48.6)	6.4 (6.2)	4.1 (4.4)
$[Pt_2Cl_2\{\mu\text{-}PhNC(Me)NPh\}_2(PMe_2Ph)_2]$	Benzene–hexane (56)	126–129	45.6 (45.7)	4.1 (4.2)	5.4 (4.8)
$[Pd_2\{\mu\text{-}PhNC(Me)NPh\}_2(\eta^3\text{-}C_3H_5)_2]$	CH_2Cl_2–hexane (35)	135–137[a]	57.5 (57.2)	5.1 (5.1)	8.4 (7.9)
$[Pd_2\{\mu\text{-}PhNC(Me)NPh\}_2(\eta^3\text{-}C_4H_7)_2]$	CH_2Cl_2–hexane (33)	138–140[a]	58.7 (58.3)	5.2 (5.4)	8.0 (7.6)
$[Pd_2\{\mu\text{-}tolNC(Me)Ntol\}_2(\eta^3\text{-}C_3H_5)_2]$	CH_2Cl_2–hexane (43)	127–130[a]	60.1 (59.3)	5.8 (5.8)	7.6 (7.3)
$[Pd_2\{\mu\text{-}tolNC(Me)Ntol\}_2(\eta^3\text{-}C_4H_7)_2]$	CH_2Cl_2–hexane (71)	100–105[a]	60.8 (60.2)	5.8 (6.1)	8.3 (7.0)

[a]Melts with decomposition or decomposes.

Acknowledgements

We thank Drs. J.P. Mittal and C. Gopinathan for encouragement of this work. We are grateful to authorities of the Regional Sophisticated Instrumentation Centre, Indian Institute of Technology (RSIC, IIT), Powai for providing ^1H, ^{31}P, and ^{195}Pt NMR spectra on a Varian XLR-300 spectrometer, and Head and Mr. V.R. Joshi of the Analytical Chemistry Division, Bhabha Atomic Research Centre, for providing microanalyses for some of the complexes.

References

1. V.K. Jain, R.P. Patel, K.V. Muralidharan, and R. Bohra. Polyhedron, **8**, 2151 (1989); V.K. Jain, R.P. Patel, and K. Venkatasubramanian. Polyhedron, **10**, 851 (1991); V.K. Jain and S. Kannan. J. Organomet. Chem. **405**, 265 (1991); J. Organomet. Chem. **418**, 349 (1991); Polyhedron, **11**, 27 (1992); V.K. Jain, S. Kannan, and R. Bohra. Polyhedron, **11**, 1551 (1992); V.K. Jain and S. Kannan. J. Organomet. Chem. **439**, 231 (1992); V.K. Jain, S. Kannan, R.J. Butcher, and J.P. Jasinski. J. Chem. Soc. Dalton Trans. 1509 (1993); A. Singhal and V.K. Jain. J. Chem.

Soc. Dalton Trans. 1515 (1993); J. Organomet. Chem. **494**, 74 (1995).
2. S. Kannan and V.K. Jain. Magn. Reson. Chem. **28**, 1007 (1990).
3. A. Singhal and V.K. Jain. Polyhedron, **14**, 285 (1995).
4. F.A. Cotton, L.M. Daniels, D.J. Maloney, J.H. Matonic, and C.A. Murillo. Polyhedron, **13**, 815 (1994).
5. D.M. Grove, G. van Koten, H.J.C. Ubbels, K. Vrieze, L.C. Niemann, and C.H. Stam. J. Chem. Soc. Dalton Trans. 717 (1986).
6. J. Barker, N. Cameron, M. Kilner, M.M. Mahoud, and S.C. Wallwork. J. Chem. Soc. Dalton Trans. 1359 (1986).
7. J. Barker, M. Kilner, and R.O. Gould. J. Chem. Soc. Dalton. Trans. 2687 (1987).
8. F.T. Edelmann, W. Ziegler, and U. Behrens. J. Organomet. Chem. **426**, 261 (1992).
9. M. Gomez, G. Muller, and J. Sales. Polyhedron, **12**, 1171 (1993).
10. D.C. Boyd, N.G. Connelly, G.G. Herbosa, M.G. Hill, K.R. Mann, C. Mealli, A.G. Orpen, K.E. Richardson, and P.H. Rieger. Inorg. Chem. **33**, 960 (1994).
11. F.A. Cotton, M. Matusz, R. Poli, and X. Feng. J. Am. Chem. Soc. **110**, 1144 (1988).
12. F. Nicolo, G. Bruno, S.L. Schiavo, M.S. Sinicropi, and P. Piraino. Inorg. Chim. Acta, **223**, 145 (1994).
13. A. Pidcock, R.E. Richards, and L.M. Venanzi. J. Chem. Soc. 1707 (1966).
14. T. Boschi, U. Belluco, L. Toniolo, R. Favez, and R. Roulet. Inorg. Chim. Acta, **23**, 37 (1979).
15. S.C. DeSanctis, N.V. Pavel, and L. Toniolo. J. Organomet. Chem. **108**, 409 (1976).
16. M.R. Churchill and R. Mason. Nature, **204**, 777 (1964).
17. F.T. Edelmann, W. Ziegler, and U. Behrens. J. Organomet Chem. **426**, 261 (1992).
18. V.K. Jain, S. Kannan, and E.R. Tiekink. J. Chem. Soc. Dalton. Trans. 2231 (1992).
19. V.K. Jain, S. Kannan, and E.R. Tiekink. J. Chem. Soc. Dalton Trans. 3625 (1993).
20. K. Umakoshi and Y. Sasaki. Adv. Inorg. Chem. **40**, 187 (1993).
21. L. Toniolo, T. Boschi, and G. Deganello. J. Organomet. Chem. **93**, 405 (1975).
22. P. Hendriks, J. Kuyper, and K. Vrieze. J. Organomet. Chem. **120**, 285 (1976).
23. F.R. Hartley. The chemistry of platinum and palladium. Applied Science Publishers Ltd., London. 1973.
24. Y. Tatsino, T. Yoshida, and S. Otsuka. Inorg. Synth. **19**, 220 (1979).
25. F.R. Hartley and S.R. Jones. J. Organomet. Chem. **66**, 465 (1974).
26. E.C. Taylor and W.A. Ehrhart. J. Org. Chem. **28**, 1108 (1963).

Oxidative addition of a B—B bond by an iridium(I) complex: molecular structure of *mer-cis*-[Ir(PMe$_3$)$_3$Cl(Bcat)$_2$]

Chaoyang Dai, Graham Stringer, Todd B. Marder, R. Thomas Baker, Andrew J. Scott, William Clegg, and Nicholas C. Norman

Abstract: The B—B bond in B_2cat_2 (cat = 1,2-$O_2C_6H_4$) is readily activated by [Ir(PMe$_3$)$_3$Cl(COE)] (COE = η^2-cyclooctene) (**1**) to yield a novel iridium(III) bis(boryl) complex *mer-cis*-[Ir(PMe$_3$)$_3$Cl(Bcat)$_2$] (**2**). This complex is the first structurally characterized iridium bis(boryl) compound, and is the first metal bis(boryl) complex for which two distinct boryl group environments are observed in solution. Colourless crystals of **2** are monoclinic, $P2_1/n$, with unit cell dimensions a = 8.9638(7) Å, b = 32.197(2) Å, c = 9.3980(7) Å, and β = 90.385(2)°.

Key words: iridium, boron, diboron, boryl, oxidative addition, X-ray structure, trimethylphosphine.

Résumé : La liaison B—B du B_2cat_2 (cat = 1,2-$O_2C_6H_4$) est facilement activée par [Ir(PMe$_3$)$_3$Cl(COE)] (COE = η^2-cyclooctène) (**1**) pour conduire à un nouveau complexe bis(boryl)iridium(III), *mer-cis*-[Ir(PMe$_3$)$_3$Cl(Bcat)$_2$] (**2**). Ce complexe est le premier bis(boryl)iridium dont la structure a été caractérisée, et c'est le premier complexe bis(boryl)métal pour lequel on a observé, en solution, deux environnements distincts pour les groupes boryles. Les cristaux de **2** sont incolores, monocliniques, groupe d'espace $P2_1/n$ avec a = 8,9638(7), b = 32,197(2), c = 9,3980(7) Å et β = 90,385(2)°.

Mots clés : iridium, bore, dibore, boryle, addition oxydante, diffraction des rayons X, structure, triméthylphosphine.

[Traduit par la rédaction]

Introduction

Attention has recently been paid to the transition metal catalyzed addition of B—B bonds in $(RO)_2B$—$B(OR)_2$ compounds to alkenes (1) and alkynes (2) and a key step of this process is believed to be the oxidative addition of the B—B bond to the transition metal centre. We have recently reported B—B oxidative addition by the Co(0) complex [Co(PMe$_3$)$_4$] (3*a*), and the Rh(I) complex [Rh(PPh$_3$)$_3$Cl] (3*b*), we (2*c,f,g*) and others (2*a,b,e,h*) have reported this reaction with Pt(0) phosphine complexes such as [Pt(PPh$_3$)$_2$(η^2-C_2H_4)], and He and Hartwig recently observed oxidative addition of B_2cat_2 (cat = 1,2-$O_2C_6H_4$) or its 4-^{t}Bu derivative by [Fe(CO)$_4$] (4*a*) and [Cp$_2$W] (4*b*) fragments. The current work examines the reactivity of B_2cat_2 toward the Ir(I) complex [Ir(PMe$_3$)$_3$Cl(COE)] (COE = η^2-cyclooctene) (**1**) and we report herein the synthesis and molecular structure of a new iridium bis(boryl) complex *mer-cis*-[Ir(PMe$_3$)$_3$Cl(Bcat)$_2$] (**2**)

There were several early reports on the synthesis of metal bis(boryl) complexes by Schmid and Nöth, although none were prepared via B—B oxidative addition, and none were well characterized. Thus, these authors reported (5*a,b,c*) that the reaction of Y_2BX with [Co(dppe)$_2$(H)] (dppe = $Ph_2PCH_2CH_2PPh_2$) gave the 19-electron Co(II) bis(boryl) complexes *trans*-[Co(dppe)$_2$(BY_2)$_2$] (eq. [1]).

[1] $$2Y_2BX + 2\,[Co(dppe)_2(H)] \rightarrow \textit{trans}\text{-}[Co(dppe)_2(BY_2)_2] + [Co(dppe)_2X_2] + H_2$$

(X = Cl, Br, I; Y = Br, I, Ph; Y_2B = Ph_2B, PhClB; Y_2B = $C_{12}H_8B$)

Utilizing these cobalt "boryl transfer reagents" they claimed to have prepared two Ni(II) bis(boryl) compounds [Ni(dppe)$_n$(BPh_2)$_2$] (n = 1, 2) (eq. [2])

Received February 1, 1996.

This paper is dedicated to Professor Howard C. Clark in recognition of his contributions to Canadian chemistry.

C. Dai, G. Stringer, and T.B. Marder.[1] Department of Chemistry, University of Waterloo, Waterloo, ON N2L 3G1, Canada.
R.T. Baker.[1,2] Du Pont Central Research and Development, Corporate Catalysis Center, Science and Engineering Laboratories, E.I. du Pont de Nemours and Co., Experimental Station, Wilmington, DE 19880-0328, U.S.A.
A.J. Scott, W. Clegg,[1] **and N.C. Norman.**[1,3] Department of Chemistry, University of Newcastle upon Tyne, Newcastle upon Tyne NE1 7RU, U.K.

[1] Authors to whom correspondence may be addressed: TBM: Telephone: (519) 888-4582. Fax: (519) 746-0435. E-mail: Marder@UWaterloo.ca; RTB: Telephone: (505) 667-9274. Fax: (505) 667-9905. E-mail: Weg@ LANL.GOV; WC: Telephone: 011-44-191-222-6649. Fax: 011-44-191-222-6929. E-Mail: W.Clegg@Newcastle.ac.uk; NCN: Telephone: 011-44-117-928-7577. Fax: 011-44-117-929-0509. E-Mail: N.C.Norman@Bristol.ac.uk
[2] Present address: CST-18, J514, Los Alamos National Laboratory, Los Alamos, NM 87545, U.S.A.
[3] Present address: School of Chemistry, University of Bristol, Bristol BS8 1TS, England.

[2] $[Co(dppe)_2(BPh_2)_2] + [Ni(dppe)_nBr_2] \rightarrow [Co(dppe)_2Br_2] + [Ni(dppe)_n(BPh_2)_2]$ ($n = 1, 2$)

In addition, the reaction of $[Pt(PPh_3)_4]$ with Me_2BBr in 1:2 ratio gave a compound that was proposed to be a six-coordinate Pt(IV) bis(boryl) complex $[Pt(PPh_3)_2Br_2(BMe_2)_2]$ (*5d*). However, none of the compounds in these early reports were structurally characterized, and their true nature remains unknown.

Among the few recently structurally characterized metal bis(boryl) complexes, $[Co(PMe_3)_3(Bcat)_2]$ is a paramagnetic compound with a distorted square pyramidal structure with an unusually small B-M-B angle of 67.9(4)°. The geometry of this novel cobalt complex can be viewed alternatively as a distorted tetrahedron with the two boryl ligands occupying a single coordination site (*3a*). All reported (*2b,c,e*) Pt(II) bis(boryl) compounds are of the form *cis*-$[Pt(PR_3)_2(Bcat)_2]$ and exhibit the expected four-coordinate square planar geometry and relatively small B-M-B angles of ca. 76°–81°. The

[3] 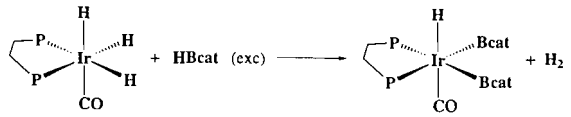

Rh(III) bis(boryl) complex $[Rh(PPh_3)_2Cl(Bcat)_2]$ has a five-coordinate distorted square pyramidal configuration with one boryl group *trans* to Cl, the other *trans* to the vacant site (6). In the solid state, the B-Rh-B angle is 79.0(3)°, and in solution the complex is fluxional, giving only one broad signal in the $^{11}B\{^1H\}$ NMR spectrum. When the 4-^{t}Bu-catB analogue was examined, only one ^{13}C resonance for the ^{t}Bu groups was observed even at −80°C, indicating fast exchange of boryl group environments as might be expected for a five-coordinate complex. The octahedral complex *cis*-$[Fe(CO)_4\{B(1,2\text{-}O_2\text{-}4\text{-}^tBuC_6H_3)\}_2]$ (*4a*) has a B-Fe-B angle of 82.8(4)°. There has been only one Ir bis(boryl) complex reported to date, namely $[IrH(Bcat)_2(CO)(dppe)]$ (7), which was only observed by NMR spectroscopy in the reaction of *fac*-$[IrH_3(CO)(dppe)]$ with excess HBcat (eq. [3]).

It was proposed to have a C_s structure with both boryl groups *trans* to the bidentate chelating phosphines. Compound **2**, *mer-cis*-$[Ir(PMe_3)_3Cl(Bcat)_2]$, reported here is thus the first structurally characterized Ir bis(boryl) compound, and the first metal bis(boryl) complex in which two distinct boryl group environments are observed in solution.

Results and discussion

Addition of B_2cat_2 to a THF solution of **1** at room temperature results in complete conversion (90% isolated yield, see experimental section) to the iridium bis(boryl) complex **2** (eq. [4]). The solution structure of **2** was established by ^1H, $^{13}C\{^1H\}$, $^{31}P\{^1H\}$, and $^{11}B\{^1H\}$ NMR spectroscopy, and its solid state structure was confirmed by a single-crystal X-ray diffraction study on crystals grown by layering hexane over a CH_2Cl_2 solution.

[4] 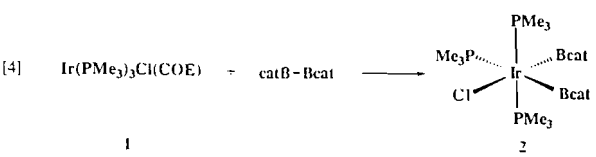

1 2

The $^{31}P\{^1H\}$ NMR spectrum of **2** displays a doublet at −40.9 ppm ($^2J_{P-P}$ = 27.5 Hz) and a broad peak at −50.8 ppm in 2:1 ratio. The latter broad signal clearly indicates that one phosphine ligand is *trans* to a boryl group and the resonance is influenced by the boron nucleus (^{11}B, spin 3/2, 80.4% natural abundance; ^{10}B, spin 3, 19.6% natural abundance) as the resonance of the spin 1/2 nucleus in the *trans* position will display significant broadening due to quadrupolar coupling (8). The $^{11}B\{^1H\}$ NMR spectrum clearly displays two well-separated resonances at 32.6 and 41.7 ppm, respectively, in which the first signal is consistent with a Bcat group *trans* to chloride as shown in the Ir boryl complexes $[Ir(PMe_3)_3(Cl)(H)(Bcat)]$ (9) (δ 32.8 ppm) and $[Ir(PEt_3)_3(Cl)(H)(Bcat)]$ (10) (δ 33.5 ppm), while the other resonance at 41.7 ppm is quite close to the value of δ 44.7 ppm in an iridium tris(boryl) complex *fac*-$[Ir(PEt_3)_3(Bcat)_3]$ (11) in which the boryl groups are all *trans* to the phosphine ligands. Also in the ^1H NMR spectrum, four sets of catecholate proton resonances are observed at (7.07 and 6.76) and (7.12 and 6.83) ppm, and six carbon resonances are observed at (110.53, 120.71, and 149.84) and (115.58, 120.76, and 150.03) ppm in the $^{13}C\{^1H\}$ NMR spectrum in $CDCl_3$. From these results, the structure of **2** can be assigned unambiguously as *mer-cis*-$[Ir(PMe_3)_3Cl(Bcat)_2]$, with one boryl group *trans* to chloride and the other *trans* to the unique trimethylphosphine ligand.

The structure of **2** is further confirmed by single crystal X-ray diffraction. A summary of the crystallographic data and parameters for data collection and refinement is presented in Table 1, selected bond distances and bond angles are given in Table 2, and final atomic coordinates are given in Table 3. The molecular structure of **2** consists of an octahedral arrangement with *mer* phosphine ligands. The two catecholatoboryl groups are mutually *cis* with an unusually large B-Ir-B angle of 91.6 (2)°, vide supra. The two BO_2 planes of these boryl moieties are essentially perpendicular to one another, the angle between the two boryl planes being 107.2°. The boron *trans* to chloride has an iridium–boron distance of 2.024(6) Å, which is the same within statistical error as that in the compound *mer*-$[Ir(PMe_3)_3Cl(H)(Bcat)]$ (**3**) (2.023(10) Å), which was produced through the oxidative addition of the H—B bond in HBcat to **1** (9). The other iridium–boron bond distance is 2.080(6) Å, which is very close to the value of 2.093(7) Å in *fac*-$[Ir(PMe_3)_3H_2(BC_8H_{14})]$, prepared from the reaction of $[Ir(PMe_3)_4H]$ with 9-BBN dimer and in which the BC_8H_{14} boryl group is *trans* to PMe_3 (12). These two Ir—B bond distance values are in accordance with the fact that PMe_3 has a larger *trans* influence than Cl. For further comparison, the Ir—B bond in *trans*-$[Ir(PPh_3)_2Cl(CO)(H)(Bcat)]$ is 2.045(5) Å where boron is *trans* to chloride (10). Crabtree and co-workers reported (13) a novel Ir(IV) boryl complex $[Ir(PMe_3)_3(biphBF)Cl]BPh_4$ prepared by the reaction of $[Ir(PMe_3)_3Cl(biph)]$ (biph = biphenyl-2,2-diyl) with $NOBF_4$. The molecular structure of $[Ir(PMe_3)_3(biphBF)Cl]^+$ was determined and the Ir—B bond distance was found to be 2.00(1) Å with the boryl group *trans* to a phosphine ligand, but, unfortunately, the structure is not very accurate.

Among the Ir—P bond distances in complex **2**, the two mutually *trans* phosphine groups have Ir—P distances of 2.3286(14) and 2.3224(13) Å, respectively, which are very similar to the two *trans* Ir—P distances in compound **3** (2.307(2) and 2.304(2) Å). However, the PMe_3 group *trans* to

Table 1. Summary of X-ray diffraction data for *mer-cis*-[Ir(PMe_3)$_3$Cl(Bcat)$_2$] (**2**).

Parameter	Value
Formula	$C_{21}H_{35}B_2ClIrO_4P_3$
fw	693.67
Crystal system	Monoclinic
a, Å	8.9638(7)
b, Å	32.197(2)
c, Å	9.3980(7)
β, deg	92.385(2)
V, Å^3	2710.0(4)
Z	4
ρ_{calcd}, g cm^{-3}	1.700
Space group	$P2_1/n$
Crystal dimensions, mm	0.42 × 0.24 × 0.08
Crystal colour	Colourless
Temperature, K	160(2)
Radiation	MoK_α
μ, cm^{-1}	52.27
F(000)	1368
Reflections for cell refinement	9778 (θ range 2.26°–25.88°)
Data collection method	Siemens SMART CCD diffractometer, ω rotation with narrow frames
θ range for data collection, deg	2.26–25.90
Index ranges	$-10 \le h \le 4$, $-38 \le k \le 37$, $-10 \le l \le 10$
Reflections collected	12083
Independent reflections	4669 (R_{int} = 0.0539)
Reflections with $I > 2\sigma(I)$	4398
Absorption correction	Semi-empirical
Max. and min. transmission	0.879 and 0.333
Structure solution	Direct methods
Refinement method	Full-matrix least squares on F^2
Refined parameters	299
GOF[a] on F^2	1.148
Final *R* indices [$I > 2\sigma(I)$]	R = 0.0319, wR = 0.0865
R indices (all data)[b]	R = 0.0346, wR = 0.0886
Extinction coefficient χ	0.0008(2)
Largest shift / esd	0.001
Largest diff. peak and hole, e Å^{-3}	1.486 and −1.588

[a] GOF = $[\Sigma w(F_o^2\text{-}F_c^2)^2 / (NO - NV)]^{1/2}$
[b] $R = \Sigma||F_o| - |F_c|| / \Sigma|F_o|$; $wR = [\Sigma w(F_o^2 - F_c^2)^2 / \Sigma w(F_o^2)^2]^{1/2}$.

Bcat in **2** has a significantly longer Ir—P distance of 2.3989(13) Å while the PMe_3 group *trans* to hydride in complex **3** displays an Ir—P bond distance of only 2.351(2) Å. This suggests that the Bcat boryl group has a larger *trans* influence than PMe_3 and even hydride ligands, at least in this octahedral system.

Conclusion

Oxidative addition of the B—B bond in B_2cat_2 to [Ir(PMe_3)$_3$Cl(COE)] readily generates a new iridium bis(boryl) complex *mer-cis*-[Ir(PMe_3)$_3$Cl(Bcat)$_2$], the molecular structure of which demonstrates that there are two distinct boryl groups. NMR studies show that these remain distinct in solution. The boryl group shows a larger *trans* influence than hydride. The reactivity of this novel metal bis(boryl) complex with alkenes and alkynes is currently being investigated, as are the reactions of diborane (4) compounds with other Ir(I) complexes.[4]

Experimental section

General procedures

Reactions and NMR sample preparations were performed under a dry nitrogen atmosphere using glove box techniques. THF was freshly distilled from sodium benzophenone ketyl, hexane from sodium metal, and CH_2Cl_2 from CaH_2 under an N_2 atmosphere. NMR solvents were distilled from CaH_2 ($CDCl_3$) or Na metal (C_6D_6) following three freeze–pump–thaw cycles. [Ir(PMe_3)$_3$Cl(COE)] (**14**) and B_2cat_2 (**15**) were

[4] C. Dai, A. Feiler, F.J. Lawlor, T.B. Marder, N.C. Norman, N.L. Pickett, and E.G. Robins. Unpublished results.

Table 2. Selected bond distances (Å) and angles (°) for *mer-cis*-[Ir(PMe_3)$_3$Cl(Bcat)$_2$] (**2**).

Bond	Distance	Bond	Distance	Bond	Distance
Ir(1)—B(1)	2.080(6)	Ir(1)—B(2)	2.024(6)	Ir(1)—P(1)	2.3989(13)
Ir(1)—P(2)	2.3286(14)	Ir(1)—P(3)	2.3224(13)	Ir(1)—Cl(1)	2.5348(13)
B(1)—O(1)	1.412(7)	B(1)—O(2)	1.422(7)	O(1)—C(1)	1.382(7)
O(2)—C(2)	1.384(6)	C(1)—C(2)	1.366(8)	C(1)—C(6)	1.380(8)
C(2)—C(3)	1.376(8)	C(3)—C(4)	1.391(9)	C(4)—C(5)	1.389(10)
C(5)—C(6)	1.396(10)	B(2)—O(3)	1.420(7)	B(2)—O(4)	1.430(7)
O(3)—C(7)	1.373(7)	O(4)—C(8)	1.375(7)	C(7)—C(8)	1.379(8)
C(7)—C(12)	1.384(8)	C(8)—C(9)	1.380(8)	C(9)—C(10)	1.395(9)
C(10)—C(11)	1.375(10)	C(11)—C(12)	1.395(9)		

Bonds	Angle	Bonds	Angle
B(1)-Ir(1)-B(2)	91.6(2)	B(1)-Ir(1)-P(1)	172.2(2)
B(1)-Ir(1)-P(2)	83.6(2)	B(1)-Ir(1)-P(3)	85.7(2)
B(1)-Ir(1)-Cl(1)	90.6(2)	B(2)-Ir(1)-Cl(1)	177.7(2)
B(2)-Ir(1)-P(1)	96.1(2)	B(2)-Ir(1)-P(2)	87.9(2)
B(2)-Ir(1)-P(3)	87.9(2)	P(1)-Ir(1)-P(2)	96.83(5)
P(1)-Ir(1)-P(3)	94.39(5)	P(1)-Ir(1)-Cl(1)	81.64(4)
P(2)-Ir(1)-P(3)	168.37(5)	P(2)-Ir(1)-Cl(1)	91.93(5)
P(3)-Ir(1)-Cl(1)	92.73(5)	Ir(1)-B(1)-O(1)	124.1(4)
Ir(1)-B(1)-O(2)	128.4(4)	O(1)-B(1)-O(2)	107.5(4)
Ir(1)-B(2)-O(3)	127.0(4)	Ir(1)-B(2)-O(4)	125.9(4)
O(3)-B(2)-O(4)	107.1(4)		

prepared by established methods. NMR spectra were recorded on Bruker AC 200 (^{1}H at 200 MHz, ^{13}C at 50 MHz, ^{31}P at 81 MHz) or AMX 500 (^{1}H at 500 MHz, ^{11}B at 160 MHz) spectrometers. The ^{1}H chemical shifts were referenced to the internal standard tetramethylsilane (TMS) and ^{13}C chemical shifts were referenced to the solvent resonances as an internal standard. The ^{31}P and ^{11}B chemical shifts were referenced to the external standards 85% H_3PO_4 and $F_3B{\cdot}OEt_2$, respectively. The ^{11}B NMR spectrum was obtained using a background subtraction routine to remove resonances due to borosilicate glass in the NMR probe and NMR tube. This was accomplished by recording the spectrum of an NMR tube containing the same volume of pure solvent and with identical acquisition parameters to those of the sample and by subtracting this background FID from that of the sample. Coupling constants are reported in Hz. Multiplicities are reported as (br) broad, (s) singlet, (d) doublet, (vt) virtual triplet, and (m) multiplet. Elemental analysis was obtained from M-H-W Laboratories, Phoenix, Arizona, U. S. A.

Preparation of *mer-cis*-[Ir(PMe_3)$_3$Cl(Bcat)$_2$] (2)

A solution of B_2cat_2 (84 mg, 0.35 mmol) in 2 mL THF was added to a solution of [Ir(PMe_3)$_3$Cl(COE)] (200 mg, 0.35 mmol) in 10 mL THF. The solution turned almost colourless immediately. After stirring for 1 h, the solvent was removed under reduced pressure and the colourless residue was washed with hexane and dried in vacuo to yield 220 mg (90%) of complex **2**. ^{31}P{^{1}H} NMR (81 MHz, 25°C in C_6D_6), δ: −40.9 (d, $^2J_{P-P}$ = 27.5 Hz, 2P, *trans* PMe_3), −50.8 (br, PMe_3). ^{11}B{^{1}H} NMR (160 MHz, 25°C in C_6D_6), δ: 41.7 (br, Bcat), 32.6 (br, Bcat). ^{1}H NMR (500 MHz, 25°C in $CDCl_3$), δ: 1.15 (d, $^2J_{P-H}$ = 7.5 Hz, 9H, PMe_3), 1.48 (vt, $^2J_{P-H}$ = 3.7 Hz, 18H, PMe_3), 7.12, 6.83 (AA′BB′, 4H, Bcat), 7.07, 6.76 (AA′BB′, 4H, Bcat). ^{13}C{^{1}H} NMR (50 MHz, 25°C in C_6D_6), δ: 17.73 (d, J_{P-C} = 26 Hz, PMe_3), 19.52 (dvt, J_{P-C} = 19 Hz, $^3J_{P-C}$ = 4.5 Hz, PMe_3), 110.86 (s), 121.24 (s), 150.65 (s, Bcat), 111.86(s), 121.45 (s, Bcat). In C_6D_6, two resonances due to the inequivalent *C*-O groups of the two Bcat ligands are coincident. ^{13}C{^{1}H} NMR (50 MHz, 25°C in $CDCl_3$), δ: 18.06 (dm, J_{P-C} = 26 Hz, PMe_3), 19.57 (dvt, J_{P-C} = 19.5 Hz, $^3J_{P-C}$ = 4.2 Hz, PMe_3), 110.53(s),

Fig. 1. Thermal ellipsoid plot (50% probability) of the molecular structure of **2**. Hydrogen atoms have been omitted for clarity.

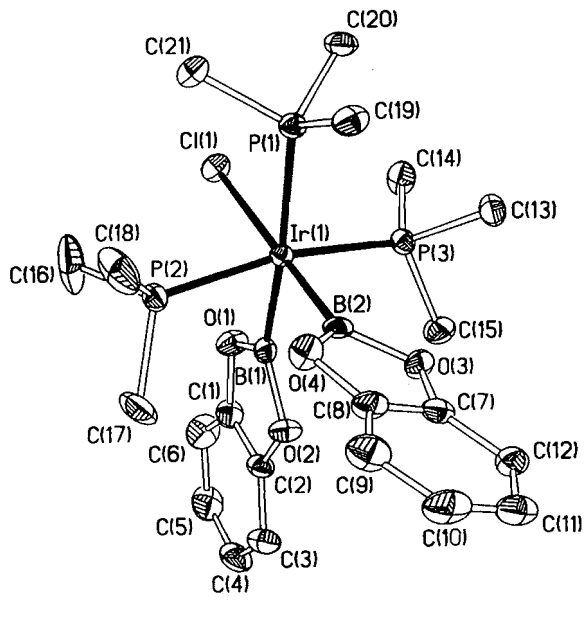

Table 3. Atomic coordinates ($\times 10^4$) and equivalent isotropic displacement parameters (Å $\times 10^3$). U(eq) is defined as one third of the trace of the orthoganalized U_{ij} tensor.

	x	y	z	U(eq)
Ir(1)	7846.3(2)	1564.02(6)	9209.4(2)	14.65(11)
B(1)	9114(7)	1256(2)	10784(6)	18.6(12)
O(1)	10374(4)	1428.1(13)	11516(4)	25.7(9)
O(2)	8922(4)	846.1(12)	11314(4)	23.5(8)
C(1)	10949(6)	1124(2)	12422(6)	25.9(12)
C(2)	10085(6)	776(2)	12300(6)	21.3(11)
C(3)	10408(7)	421(2)	13070(6)	30.7(13)
C(4)	11662(7)	433(2)	13992(7)	36(2)
C(5)	12526(7)	790(2)	14128(7)	40(2)
C(6)	12192(7)	1148(2)	13336(7)	38(2)
B(2)	6434(6)	1076(2)	8971(6)	19.1(12)
O(3)	5362(4)	942.0(12)	9943(4)	23.1(8)
O(4)	6286(4)	812.5(13)	7749(4)	26.4(9)
C(7)	4620(6)	610(2)	9330(6)	23.1(12)
C(8)	5180(6)	530(2)	8013(6)	25.1(12)
C(9)	4677(7)	203(2)	7175(7)	34.3(14)
C(10)	3554(7)	−40(2)	7734(8)	37(2)
C(11)	2998(6)	39(2)	9047(8)	37(2)
C(12)	3514(6)	369(2)	9897(7)	28.7(13)
Cl(1)	9567.9(14)	2187.6(4)	9417.3(13)	22.5(3)
P(1)	6614(2)	1996.8(4)	7446.1(14)	18.5(3)
C(13)	4386(6)	1835(2)	10738(6)	26.3(12)
C(14)	6927(7)	2293(2)	11802(6)	30.2(13)
C(15)	6463(7)	1463(2)	12662(6)	30.3(13)
P(2)	9425(2)	1226.3(4)	7679(2)	20.6(3)
C(16)	11219(8)	1473(3)	7504(11)	62(3)
C(17)	9969(9)	706(2)	8182(8)	47(2)
C(18)	8829(9)	1129(3)	5835(7)	49(2)
P(3)	6404(2)	1792.4(4)	11051.2(14)	19.2(3)
C(19)	4904(6)	1804(2)	6559(6)	27.3(13)
C(20)	6089(7)	2511(2)	8045(6)	26.0(12)
C(21)	7721(7)	2148(2)	5941(6)	25.3(12)

120.71 (s) 149.84 (d, J_{P-C} = 2.6 Hz, Bcat), 111.58 (s), 120.76 (s), 150.03 (s, Bcat). Anal. calcd. for $C_{21}H_{35}B_2ClIrO_4P_3$: C 36.36, H 5.09; found C 37.07, H 5.11.

Molecular structure determination

Crystals of **2** suitable for X-ray diffraction studies were obtained by diffusion of a layer of hexane into a CH_2Cl_2 solution of **2**. Data were collected at low temperature on a Siemens SMART CCD area-detector diffractometer using graphite-monochromated MoK_α radiation (λ = 0.71073 Å) and narrow-frame ω scan methods. The single crystal was mounted on a glass fiber with a coating of perfluoropolyether oil, cell parameters were refined from the observed setting angles for selected reflections, and intensities were measured from a series of frames each covering a 0.3° oscillation in ω. An absorption correction was carried out using a semi-empirical method, based on sets of equivalent reflections measured at different positions.

The structure was solved by direct methods, and refined by full-matrix least-squares techniques (16). The refinement was on F^2 of all independent reflections, to minimize $\Sigma w(F_o^2 - F_c^2)^2$, with weighting $w^{-1} = \sigma^2(F_o^2) + (0.0407P)^2 + 10.1457P$, where $P = (F_o^2 + 2F_c^2)/3$; the refined isotropic extinction parameter χ is defined such that F_c is multiplied by $(1 + 0.001\chi F_c^2\lambda^3/\sin 2\theta)^{-1/4}$. Anisotropic displacement parameters were refined for all non-hydrogen atoms, and isotropic hydrogen atoms were constrained to ride on their parent carbon atoms with fixed bond lengths and idealized bond angles. Programs were standard Siemens control and integration software, version 5 of SHELXTL (16), and local programs.

Details of the crystal determination including complete tables of coordinates, bond distances and angles, and anisotropic displacement parameters have been deposited.[5]

[5] A complete set of data may be purchased from: The Depository of Unpublished Data, Document Delivery, CISTI, National Research Council Canada, Ottawa, Canada K1A 0S2. Tables of bond lengths and angles and atomic coordinates have also been deposited with the Cambridge Crystallographic Data Centre, 12 Union Road, Cambridge, CB2 1EZ, U.K. Structure factor amplitudes are no longer being deposited and may be obtained directly from the authors (either T.B.M. or W.C.).

Acknowledgment

T.B.M. thanks the Natural Sciences and Engineering Research Council of Canada (NSERC) for research funding and Johnson Matthey Ltd. for a loan of Ir salts, N.C.N. thanks the Engineering and Physical Sciences Research Council (EPSRC) for support, W.C. thanks the EPSRC for an equipment grant, A.J.S. thanks the EPSRC for a studentship, and T.B.M. and N.C.N. thank NSERC, The Royal Society (London), and the University of Newcastle upon Tyne for supporting this collaboration through a series of travel grants.

References

1. R.T. Baker, P. Nguyen, T.B. Marder, and S.A. Westcott. Angew. Chem. Int. Ed. Engl. **34**, 1336 (1995).
2. (*a*) T. Ishiyama, N. Matsuda, N. Miyaura, and A. Suzuki. J. Am. Chem. Soc. **115**, 11018 (1993); (*b*) C.N. Iverson and M.R. Smith III. J. Am. Chem. Soc. **117**, 4403 (1995); (*c*) G. Lesley, P. Nguyen, N.J. Taylor, T.B. Marder, A.J. Scott, W. Clegg, and N.C. Norman. Organometallics. In press; (*d*) T. Ishiyama, M. Murata, and N. Miyaura. J. Org. Chem. **60**, 7508 (1995); (*e*) T. Ishiyama, N. Matsuda, M. Murata, F. Ozawa, A. Suzuki, and N. Miyaura. Organometallics, **15**, 713 (1996); (*f*) W. Clegg, A.J. Scott, G. Lesley, T.B. Marder, and N.C. Norman. Acta Crystallogr. Sect. C: Cryst. Struct. Commun. **C52**, 1991 (1996); (*g*) Acta Crystallogr. Sect. C: Cryst. Struct. Commun. **C52**, 1989 (1996); (*h*) C.N. Iverson and M.R. Smith III. Organometallics. Submitted.
3. (*a*) C. Dai, G. Stringer, J.F. Corrigan, N.J. Taylor, T.B. Marder, and N.C. Norman. J. Organomet. Chem. In press; (*b*) P. Nguyen, G. Lesley, N.J. Taylor, T.B. Marder, N.L. Pickett, W. Clegg, M.R.J. Elsegood, and N.C. Norman. Inorg. Chem. **33**, 4623 (1994).
4. (*a*) X. He and J.F. Hartwig. Organometallics, **15**, 400 (1996); (*b*) J.F. Hartwig and H. Xe. Angew. Chem. Int. Ed. Engl. **35**, 315 (1996).
5. (*a*) G. Schmid and H. Nöth. Z. Naturforsch. **20b**, 1008 (1965); (*b*) Chem. Ber. **100**, 2899 (1967); (*c*) G. Schmid. Chem. Ber. **102**, 191 (1969); (*d*) M. Fishwick, H. Nöth, W. Petz, and M.G.H. Wallbridge. Inorg. Chem. **15**, 490 (1976).
6. (*a*) K. Burgess, W.A. van der Donk, S.A. Westcott, T.B. Marder, R.T. Baker, and J.C. Calabrese. J. Am. Chem. Soc. **114**, 9350 (1992); (*b*) R.T. Baker, J.C. Calabrese, S.A. Westcott, P. Nguyen, and T.B. Marder. J. Am. Chem. Soc. **115**, 4367 (1993).
7. B.P. Cleary and R. Eisenberg. Organometallics, **14**, 4525 (1995).
8. R.K. Harris. *In* Nuclear magnetic resonance spectroscopy. Longman Scientific and Technical, Essex, U.K. 1986.
9. J.R. Knorr and J.S. Merola. Organometallics, **9**, 3008 (1990).
10. S.A. Westcott, T.B. Marder, R.T. Baker, and J.C. Calabrese. Can. J. Chem. **71**, 930 (1993).
11. P. Nguyen, H.P. Blom, S.A. Westcott, N.J. Taylor, and T.B. Marder. J. Am. Chem. Soc. **115,** 9329 (1993).
12. R.T. Baker, D.W. Ovenall, J.C. Calabrese, S.A. Westcott, N.J. Taylor, I.D. Williams, and T.B. Marder. J. Am. Chem. Soc. **112,** 9399 (1990).
13. Z. Lu, C. Jun, S.R. de Gala, M. Sigalas, O. Eisenstein, and R.H. Crabtree. J. Chem. Soc. Chem. Commun. 1877 (1993).
14. T. Herskovitz. Inorg. Synth. **21**, 102 (1981).
15. C.N. Welch and S.G. Shore. Inorg. Chem. **7**, 225 (1968).
16. G.M. Sheldrick. SHELXTL. Siemens Analytical X-ray Instruments Inc., Madison, Wis. 1994.

Alkylaluminum complexes containing pyridyl amido ligands. Syntheses and characterization of $AlMe_2[N(CH_2\text{-}2\text{-}Py)_2]$, $Al_2Me_5[N(CH_2\text{-}2\text{-}Py)_2]$, and Al_2Me_4[2,3,5,6-tetra(2-pyridyl)piperazyl], an unusual carbon–carbon bond coupling product

Steven J. Trepanier and Suning Wang

Abstract: The reactions of $AlMe_3$ with di(2-pyridylmethyl)amine have been investigated. Two new complexes, $AlMe_2[N(CH_2\text{-}2\text{-}Py)_2]$ (**1**) and Al_2Me_4[2,3,5,6-tetra(2-pyridyl)piperazyl] (**3**), were obtained as the major and the minor product, respectively, from the reaction of $AlMe_3$ with di(2-pyridylmethyl)amine in a 1:1 ratio in toluene at 23°C. The reaction of $AlMe_3$ with di(2-pyridylmethyl)amine in a 2:1 ratio yielded a dinuclear complex $Al_2Me_5[N(CH_2\text{-}2\text{-}Py)_2]$ (**2**). These complexes were fully characterized by NMR, and elemental and single-crystal X-ray diffraction analyses. Crystal data: **1**, $C_{14}H_{18}N_3Al$, monoclinic, $P2_1/m$, $a = 7.568(2)$, $b = 7.340(1)$, $c = 13.120(8)$ Å, $\beta = 104.17(3)°$, $V = 706.6(4)$ Å^3, $Z = 2$; **2**, $C_{17}H_{27}N_3Al_2$, triclinic, $P\bar{1}$, $a = 8.422(1)$, $b = 16.711(6)$, $c = 7.659(1)$ Å, $\alpha = 91.94(2)°$, $\beta = 113.08(1)°$, $\gamma = 85.17(2)°$, $V = 988.2(4)$ Å^3, $Z = 2$; **3**, $C_{28}H_{32}N_6Al_2$, monoclinic, $P2_1/c$, $a = 7.522(8)$, $b = 15.841(8)$, $c = 11.584(4)$ Å, $\beta = 98.53(5)°$, $V = 1365(1)$ Å^3, $Z = 2$. Compound **1** is a mononuclear complex with the aluminum atom in an approximately trigonal bipyramidal geometry and the amido nitrogen atom in a trigonal planar geometry. Compound **2** contains two aluminum centers bridged by an amido nitrogen atom where one of the aluminum atoms has a tetrahedral geometry while the other has a trigonal bipyramidal geometry. The dinuclear compound **3** can be described as the result of two unusual C—C bonds coupling between the methylene carbon atoms of two molecules of **1**. The aluminum coordination environment in **3** is similar to that of **1**.

Key words: aluminum, amide, pyridyl, 2,3,5,6-tetra(2-pyridyl)piperazine, structure.

Résumé : On a étudié les réactions du $AlMe_3$ avec la di(2-pyridylméthyl)amine. On a obtenu deux nouveaux complexes, le $AlMe_2[N(CH_2\text{-}2\text{-}Py)_2]$ (**1**) (produit majoritaire) et le Al_2Me_4[2,3,5,6-tétra(2-pyridyl)pipérazyl] (**3**) (produit minoritaire), à partir de la réaction de $AlMe_3$ avec la di(2-pyridylméthyl)amine dans un rapport de 1 : 1 dans le toluène à 23°C. La réaction de $AlMe_3$ avec la di(2-pyridylméthyl)amine dans un rapport de 2 : 1 conduit à un complexe dinucléaire $Al_2Me_5[N(CH_2\text{-}2\text{-}Py)_2]$ (**2**). On a caractérisé complètement ces complexes par : la RMN, l'analyse élémentaire et la diffraction de rayons X sur un monocristal. Le composé **1**, $C_{14}H_{18}N_3Al$, appartient au groupe d'espace monoclinique $P2_1/m$, avec $a = 7{,}568(2)$, $b = 7{,}340(1)$, $c = 13{,}120(8)$ Å, $\beta = 104{,}17(3)°$, $V = 706{,}6(4)$ Å^3, $Z = 2$; le composé **2**, $C_{17}H_{27}N_3Al_2$, appartient au groupe d'espace triclinique $P\bar{1}$, avec $a = 8{,}422(1)$, $b = 16{,}711(6)$, $c = 7{,}659(1)$ Å, $\alpha = 91{,}94(2)°$, $\beta = 113{,}08(1)°$, $\gamma = 85{,}17(2)°$, $V = 988{,}2(4)$ Å^3, $Z = 2$; le composé **3**, $C_{28}H_{32}N_6Al_2$, appartient au groupe d'espace monoclinique $P2_1/c$, avec $a = 7{,}522(8)$, $b = 15{,}841(8)$, $c = 11{,}584(4)$ Å, $\beta = 98{,}53(5)°$, $V = 1365(1)$ Å^3, $Z = 2$. Le composé **1** est un complexe mononucléaire avec l'atome d'aluminium dans une géométrie bipyramidale trigonale approximativement et l'atome d'azote du groupe amido dans une géométrie plane trigonale. Le composé **2** contient deux centres aluminium pontés par un atome d'azote du groupe amido; un des atomes d'aluminium a une géométrie tétraédrique tandis que l'autre à une géométrie bipyramidale trigonale. Le composé dinucléaire **3** peut être décrit comme étant le résultat de deux couplages inhabituels des liaisons C—C entre les atomes de carbone méthyléniques de deux molécules du composé **1**. L'environnement de la coordination de l'aluminium du composé **3** est similaire à celui du composé **1**.

Mots clés : aluminium, amide, pyridyl, 2,3,5,6-tétra(2-pyridyl)pipérazine, structure.

[Traduit par la rédaction]

Received January 26, 1996.

This paper is dedicated to Professor Howard C. Clark in recognition of his contributions to Canadian chemistry.

S.J. Trepanier and S. Wang.[1] Department of Chemistry & Biochemistry, University of Windsor, Windsor, ON N9B 3P4, Canada.

[1] Author to whom correspondence may be addressed. Present address: Department of Chemistry, Queen's University, Kingston, ON K6L 3N6, Canada. Telephone: (613) 545-6941. Fax: (613) 545-6669. E-mail: WANGS@CHEM.QUEENSU.CA

Introduction

The chemistry of organoaluminum complexes containing amido or imido ligands has been an area of considerable interest due to the versatile structural and bonding features of the complexes and their potential applications in materials and catalysis (1). Most of the earlier work in this area focuses on the monodentate and bidentate aliphatic amido and imido ligands (1, 2). Our group has been interested in building polynuclear alkylaluminum complexes containing polydentate aromatic amido or imido ligands because the electronic properties and structural features displayed by these complexes are drastically different from those of aliphatic amido or imido complexes (3), but have hardly been explored previously. For example, we observed recently that by coordination, the alkylaluminum moiety can induce or enhance the luminescence of amido ligands containing an aromatic functional group such as pyridyl, which provides a possible new avenue for the development of new chemiluminescent materials. The synthesis and structural elucidation of these organoaluminum complexes are the indispensable steps towards the understanding of their electronic structures, and hence the design of useful luminescent materials. In this report, the syntheses and structures of two novel alkylaluminum complexes with the tridentate ligand, di(2-pyridylmethyl)amido, and a dinuclear complex with a hexadentate diamido ligand, 2,3,5,6-tetra(2-pyridyl)piperazyl, formed through an unusual carbon–carbon bond coupling are described. The luminescence and electronic properties of these compounds are currently under investigation and will be presented in a subsequent report.

Experimental section

The reactions were conducted under an atmosphere of dry and oxygen-free nitrogen or argon, employing either a Vacuum Atmosphere inert atmosphere glove box or standard Schlenk-line techniques. Solvents were distilled from the appropriate drying agents under nitrogen. ^{1}H NMR and ^{13}C NMR spectra were recorded at 300 and 75.4 MHz, respectively, on a Brüker AC-300 spectrometer. Elemental analyses were performed by Desert Analytics, Arizona, or Canadian Microanalytical Service, Delta, British Columbia. Trimethylaluminum was purchased from Aldrich Chemical Co. Di(2-pyridylmethyl)amine was prepared by a modified procedure reported in the literature (4).

Synthesis of $AlMe_2[N(CH_2\text{-}2\text{-}Py)_2]$ (1)

A 2.0 M solution of $Al(CH_3)_3$ (2.0 mL, 4.0 mmol) in toluene was added to di(2-pyridylmethyl)amine (0.80 g, 4.0 mmol) dissolved in 5.0 mL of toluene at 23°C. The solution immediately became pink and was stirred for 0.5 h. Concentration of the solution afforded pink crystals of compound **1**. Yield 80%. ^{1}H NMR (C_6D_6, 298 K, δ, ppm): −0.11 (s, 6H, CH_3), 4.38 (s, 4H, CH_2), 6.62 (m, 2H, Py), 6.86 (m, 2H, Py), 7.13 (m, 2H, Py), 8.48 (m, 2H, Py). ^{13}C NMR (C_6D_6, 298 K, δ, ppm): 55.63 (CH_2), 121.23, 121.57, 136.45, 145.09, 161.23 (py). Anal. calcd. for $C_{14}H_{18}AlN_3$: C 65.89, H 7.06, N 16.47; found: C 64.12 (63.53), H 6.91 (6.76), N 16.15 (15.99). The pure crystals of compound **1** are colorless. However, the surfaces of these crystals are always coated with pink luminescent substances upon crystallization. ^{1}H NMR of the solution obtained by dissolving the single crystals of **1** also indicated the presence of an unknown impurity that could be accountable for the low carbon content of the CHN analysis.

Synthesis of $Al_2Me_5[N(CH_2\text{-}2\text{-}Py)_2]$ (2)

A 2.0 M solution of $Al(CH_3)_3$ (0.5 mL, 1.0 mmol) in toluene was added to di(2-pyridylmethyl)amine (0.10 g, 0.5 mmol) dissolved in 6.0 mL of toluene at 23°C. A colorless solution was obtained. After being stirred for 1.5 h, the solution was evaporated to dryness in vacuo, affording colorless crystalline solids. The ^{1}H NMR spectrum of this solid indicated that it is the pure compound **2**. Yield >90%. Compound **2** can be recrystallized readily from toluene and hexane. ^{1}H NMR (C_6D_6, 298 K, δ, ppm): −0.90 (s, 9H, CH_3), −0.78 (s, 3H, CH_3), 0.12 (s, 3H, CH_3), 3.45 (d, 2H, CH_2, $^2J_{H-H}$ = 16 Hz), 4.44 (d, 2H, CH_2, $^2J_{H-H}$ = 16 Hz), 6.42 (m, 4H, Py), 6.83 (m, 2H, Py), 8.18 (d, 2H, Py). ^{13}C NMR (C_6D_6, 298 K, δ, ppm): 56.04 (CH_2), 121.25, 122.89, 138.49, 144.46, 162.27 (Py). Anal. calcd. for $C_{17}H_{27}Al_2N_3$: C 62.39, H 8.26, N 12.85; found: C 61.46, H 8.02, N 12.86.

Synthesis of Al_2Me_4[2,3,5,6-tetrakis(2-pyridyl)piperazyl] (3)

Compound **3** was isolated as a minor dark-brown product from the reaction of $Al(CH_3)_3$ with di(2-pyridylmethyl)amine as described for the synthesis of compound **1**. Independent syntheses for this compound have not been successful. ^{1}H NMR (C_6D_6, 298 K, δ, ppm): 0.28 (s, 12H, CH_3), 4.78 (d, 2H, CH, $^3J_{H-H}$ = 2.7 Hz), 4.81 (d, 2H, CH, $^3J_{H-H}$ = 2.7 Hz), 6.47 (m, 4H, Py), 6.57 (d, 4H, Py), 6.73 (m, 4H, Py), 8.43 (d, 4H, Py). ^{13}C NMR (C_6D_6, 298 K, δ, ppm): 66.39 (CH), 121.56, 123.49, 135.16, 149.30, 160.91 (Py). Anal. calcd. for $C_{28}H_{32}Al_2N_6$: C 66.40, H 6.32, N 16.60; found: C 66.32, H 6.38, N 16.76.

2,3,5,6-Tetra(2-pyridyl)piperazine

The addition of H_2O to the toluene solution of **3** yielded the free ligand 2,3,5,6-tetra(2-pyridyl)piperazine quantitatively. The free ligand is a light yellow solid. ^{1}H NMR ($CDCl_3$, 298 K, δ, ppm): 4.42 (s, 4H, CH), 6.68 (d, 4H, Py), 7.04 (m, 4H, Py), 7.31 (m, 4H, Py), 8.59 (d, 4H, Py). MS (EI), *m/e*: 395 (M^+, calcd. 394.5).

X-ray crystallographic analysis

All crystals for single-crystal X-ray diffraction were obtained from concentrated toluene/hexane solutions, mounted, and flame sealed in glass capillaries under nitrogen. Data were collected on a Rigaku AFC6S diffractometer with graphite-monochromated Mo-Kα radiation, operated at 50 kV and 35 mA. Three standard reflections were measured every 147 reflections. At the end of data collection, the intensity of the standards of compound **1** and compound **2** decreased by 3% and 5%, respectively, while no decay was observed for **3**. Data were processed on a Silicon Graphics computer using the TEXSAN crystallographic package (5) and corrected for decay and Lorentz-polarization effects. Neutral scattering factors (6) were taken from Cromer and Waber. The systematic absences ($0k0$, $k = 2n + 1$) of **1** agree with the monoclinic space groups $P2_1$ and $P2_1/m$. The space group of **1** was determined to be $P2_1/m$, based on the statistical analysis and the successful solution and refinement of the structure. The crystal of **2** belongs to the triclinic space group $P\bar{1}$. The crystals of **3**

Table 1. Crystallographic data.

Formula	$C_{14}H_{18}N_3Al$ (**1**)	$C_{17}H_{27}N_3Al_2$ (**2**)	$C_{28}H_{32}N_6Al_2$ (**3**)
fw	255.30	326.96	506.6
Space group	$P2_1/m$	$P\bar{1}$	$P2_1/c$
a/Å	7.568(2)	8.422(1)	7.522(8)
b/Å	7.340(1)	16.711(6)	15.841(8)
c/Å	13.120(8)	7.659(1)	11.584(4)
α/deg	90	91.94(2)	90
β/deg	104.17(3)	113.08(1)	98.53(5)
γ/deg	90	85.17(2)	90
U/Å^3	706.6(4)	988.2(4)	1365(1)
Z	2	2	2
D_c/g cm^{-3}	1.20	1.10	1.23
μ(Mo-K$_\alpha$)/cm^{-1}	1.30	1.48	1.30
2θ range/deg	3–50	3–50	3–47
Reflections			
measured	$+h, +k, \pm l$, 1350	$+h, \pm k, \pm l$, 3170	$+h, +k, \pm l$, 2110
observed	793 ($I > 3.0\sigma(I)$)	1410 ($I > 1.9\sigma(I)$)	932 ($I > 1.5\sigma(I)$)
No. of variables	106	199	163
Largest shift/esd in final cycle	0.00	0.00	0.00
Largest electron density peak, e$^-$ Å^{-3}	0.36	0.25	0.37
R^a	0.069	0.053	0.080
R_w^b	0.041	0.035	0.050
Goodness-of-fit,^{c} S	3.07	2.05	1.72

$^aR = \Sigma \| F_o | - | F_c \| / \Sigma | F_o |$.
$^bR_w = (\Sigma w (|F_o| - |F_c|)^2 / \Sigma w F_o^2)^{1/2}$, $w = 1/\sigma^2(F_o)$.
$^cS = (\Sigma w (|F_o| - |F_c|)^2 / (N_o - N_v))^{1/2}$; N_o = number of observations; N_v = number of variables.

belong to the monoclinic space group $P2_1/c$, uniquely determined by the systematic absences ($0k0$, $k = 2n + 1$, $h0l$, $l = 2n + 1$). All structures were solved by direct methods. Full-matrix least-squares refinements minimizing the functions $\Sigma w (|F_o| - |F_c|)^2$ were applied. All non-hydrogen atoms were refined anisotropically. The positions of hydrogen atoms were either calculated or located directly from the difference Fourier maps and not refined. Their contributions in structural factor calculations were included. Crystallographic data are given in Table 1. Tables of hydrogen atom coordinates, anisotropic thermal parameters, and complete lists of bond lengths and angles have been deposited.[2]

Results and discussion

Synthesis and structure of $AlMe_2[N(CH_2\text{-}2\text{-}Py)_2]$ (1)

Compound 1 was isolated as the major product from the reaction of $Al(CH_3)_3$ with di(2-pyridylmethyl)amine in a 1:1 ratio in toluene at 23°C. The structure of **1** was determined by X-ray diffraction analysis. The positional and isotropic thermal parameters of non-hydrogen atoms are listed in Table 2 (*a*). Important bond lengths and angles are given in Table 3 (*a*). An ORTEP diagram showing the molecular structure of **1** is given in Fig. 1.

Fig. 1. An ORTEP diagram showing the molecular structure of **1** with labelling scheme and 50% thermal ellipsoids.

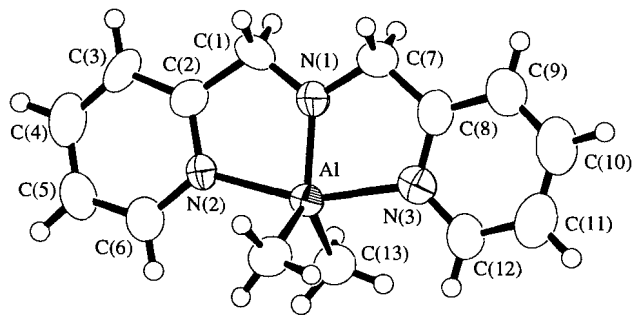

Compound **1** is a mononuclear complex with a C_{2v} symmetry. The molecular plane coincides with the crystallographically imposed reflection plane. The aluminum center in **1** is coordinated by one amido nitrogen atom, two methyl groups, and two pyridyl groups in a distorted trigonal bipyramidal environment as evidenced by the N(2)-Al-N(3) bond angle of 158.5(2)° and the sum of bond angles around the Al atom on the basal plane, 360.0°. The deviation of the N(2)-Al-N(3) angle from linearity is believed to be caused by the geometric

[2] Copies of material on deposit may be purchased from the Depository of Unpublished Data, Document Delivery, CISTI, National Research Council Canada, Ottawa, Canada K1A 0S2. Tables of hydrogen atom parameters and complete lists of bond lengths and angles have also been deposited with the Cambridge Crystallographic Data Centre, and can be obtained on request from The Director, Cambridge Crystallographic Data Centre, University Chemical Laboratory, 12 Union Road, Cambridge, CB2 1EZ, U.K.

constraint of the ligand. Five-coordinate aluminum amido complexes are not very common, but an increasing number of examples are being reported, including $AlMe_2$-$(Et_2NCH_2CH_2NCH_2CH_2NEt_2)$, $Al_2Me_4(2\text{-}NCH_2Py)_2$, and $Al_4(8\text{-quinolylimido})_2(CH_3)_7(OCH_3)$ reported recently by our group (3, 7) and $Al_5H_7(NPr^i)_2(HNPr^i)_2(NCH(CH_3)CH_2N$-$(CH_3)_2)$ reported by Perego and Dozzi (2*d*). The amido N(1)—Al bond length (1.826(4) Å) is significantly shorter than the pyridyl N(2)—Al (2.103(4) Å) and N(3)—Al bond lengths (2.137(5) Å), reflecting the relatively high affinity of the amido atom to the aluminum center. The amido N(1) atom has a trigonal planar geometry. Some contribution of the lone pair to the Al—N(1) bond order is therefore conceivable. The N(1)—Al bond length is indeed significantly shorter than the known amido–aluminum bond lengths (>1.95 Å) where the amido nitrogen atom has a tetrahedral geometry (2, 3, 8), indicative of the participation of the nitrogen lone pair in the Al—N(1) bond. The structure of compound **1** resembles that of $AlMe_2(Et_2NCH_2CH_2NCH_2CH_2NEt_2)$, reported earlier by our group, where the amido ligand has a trigonal planar geometry (7). However, in contrast to the highly fluxional behavior of $AlMe_2(Et_2NCH_2CH_2NCH_2CH_2NEt_2)$ in solution (7), compound **1** retains its solid state structure in solution, as established by NMR spectroscopic studies. The relatively structural rigidity of compound **1** in solution can be attributed to the relatively rigid structure of the di(2-pyridylmethyl)amido ligand (dpa), in comparison with the *N*,*N*,*N*′,*N*′-tetraethyldiethylenediamine amido (tda) ligand (Fig. 2). The corresponding bidentate ligand, 2-(pyridylmethyl)amido, is known to function as a bridging ligand via the amido atom producing the dinuclear compound (3*c*), $Al_2Me_4[N(CH_2\text{-}2\text{-}Py)]_2$. The mononuclear structure of **1** is apparently stabilized by the chelating effect of the tridentate dpa ligand and the coordination saturation of the aluminum center.

Table 2. Atomic coordinates and isotropic thermal parameters B_{eq}

(*a*) Compound **1**

Atom	*x*	*y*	*z*	B_{eq}[a]
Al	0.7648(2)	1/4	0.2486(1)	3.02(4)
N(1)	1.0111(6)	1/4	0.3034(4)	3.9(1)
N(2)	0.8590(6)	1/4	0.1106(3)	3.0(1)
N(3)	0.7764(7)	1/4	0.4130(4)	3.7(1)
C(1)	1.1397(7)	1/4	0.2413(5)	4.5(2)
C(2)	1.0416(8)	1/4	0.1264(5)	3.8(2)
C(3)	1.1266(8)	1/4	0.0441(5)	4.6(2)
C(4)	1.019(1)	1/4	−0.0552(5)	6.5(2)
C(5)	0.831(1)	1/4	−0.0749(5)	5.7(2)
C(6)	0.7596(9)	1/4	0.0094(5)	4.6(2)
C(7)	1.0918(8)	1/4	0.4140(5)	4.2(2)
C(8)	0.9476(9)	1/4	0.4722(5)	4.0(2)
C(9)	0.981(1)	1/4	0.5804(6)	5.9(2)
C(10)	0.839(1)	1/4	0.6285(6)	7.4(3)
C(11)	0.661(1)	1/4	0.5653(7)	6.2(2)
C(12)	0.6387(9)	1/4	0.4591(5)	4.7(2)
C(13)	0.6186(5)	0.0230(6)	0.2150(3)	4.5(1)

(*b*) Compound **2**

Atom	*x*	*y*	*z*	B_{eq}
Al(1)	0.0172(2)	0.3060(1)	0.2182(2)	4.74(5)
Al(2)	0.3531(2)	0.1877(1)	0.5271(2)	3.93(5)
N(1)	0.1261(5)	0.2508(2)	0.4731(5)	3.3(1)
N(2)	0.4323(6)	0.3030(3)	0.6178(6)	4.5(1)
N(3)	0.1837(5)	0.0974(2)	0.4008(6)	3.6(1)
C(1)	0.1528(7)	0.3095(3)	0.6267(8)	4.4(2)
C(2)	0.3148(8)	0.3507(3)	0.6589(8)	4.3(2)
C(3)	0.3438(8)	0.4276(4)	0.7237(8)	5.8(2)
C(4)	0.497(1)	0.4570(4)	0.744(1)	6.8(2)
C(5)	0.6181(9)	0.4098(5)	0.701(1)	6.7(2)
C(6)	0.5817(8)	0.3335(4)	0.6390(9)	6.0(2)
C(7)	−0.0007(6)	0.1945(3)	0.4795(7)	4.1(2)
C(8)	0.0216(7)	0.1167(3)	0.3861(7)	3.6(2)
C(9)	−0.1093(7)	0.0672(3)	0.2947(8)	4.4(2)
C(10)	−0.0712(9)	−0.0036(4)	0.2242(8)	5.3(2)
C(11)	0.095(1)	−0.0260(3)	0.2439(8)	5.2(2)
C(12)	0.2190(7)	0.0270(3)	0.3316(8)	4.7(2)
C(13)	0.4554(7)	0.1396(3)	0.7820(8)	5.5(2)
C(14)	0.4758(7)	0.1729(3)	0.3538(8)	5.9(2)
C(15)	0.163(1)	0.3881(4)	0.2022(9)	10.5(3)
C(16)	−0.0150(7)	0.2247(3)	0.0209(7)	5.6(2)
C(17)	−0.2072(9)	0.3543(4)	0.215(1)	9.9(3)

Table 2 (*concluded*).

(*c*) Compound **3**

Atom	*x*	*y*	*z*	B_{eq}
Al(1)	0.6318(3)	0.1324(1)	0.8455(2)	3.54(6)
N(1)	0.6105(8)	0.0290(3)	0.9169(4)	3.0(1)
N(2)	0.8350(7)	0.1415(4)	0.9935(5)	3.5(2)
N(3)	0.4364(7)	0.0695(4)	0.7196(5)	3.9(2)
C(1)	0.478(1)	0.2291(5)	0.8788(6)	5.3(2)
C(2)	0.798(1)	0.1544(5)	0.7332(6)	6.1(3)
C(3)	0.963(1)	0.2018(5)	1.0127(7)	5.0(2)
C(4)	1.109(1)	0.1920(6)	1.1007(8)	5.9(3)
C(5)	1.124(1)	0.1217(6)	1.1687(7)	5.0(3)
C(6)	0.994(1)	0.0601(5)	1.1492(6)	4.4(2)
C(7)	0.846(1)	0.0744(5)	1.0615(6)	3.2(2)
C(8)	0.690(1)	0.0132(4)	1.0375(5)	3.0(2)
C(9)	0.456(1)	−0.0280(4)	0.8808(5)	3.3(2)
C(10)	0.390(1)	−0.0056(5)	0.7535(6)	3.3(2)
C(11)	0.288(1)	−0.0629(5)	0.6783(6)	3.5(2)
C(12)	0.235(1)	−0.0366(7)	0.5668(7)	5.8(3)
C(13)	0.276(1)	0.0416(7)	0.5308(6)	6.3(3)
C(14)	0.383(1)	0.0953(5)	0.6081(7)	5.1(2)

[a] $B_{eq} = 8/3\ \pi^2(U_{11}(aa^*)^2 + U_{22}(bb^*)^2 + U_{33}(cc^*)^2 + 2U_{12}aa^*bb^*\cos\gamma + 2U_{13}aa^*cc^*\cos\beta + 2U_{23}bb^*cc^*\cos\alpha)$.

Fig. 2.

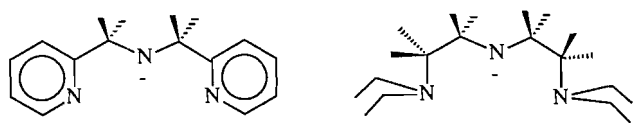

dpa tda

Table 3. Selected bond lengths (Å) and angles (°).

(*a*) Compound **1**

Atom	Atom	Distance	Atom	Atom	Distance
Al	N(1)	1.826(4)	C(1)	C(2)	1.506(7)
Al	N(2)	2.103(4)	C(2)	C(3)	1.394(7)
Al	N(3)	2.137(5)	C(3)	C(4)	1.351(8)
Al	C(13)	1.990(4)	C(4)	C(5)	1.381(8)
N(1)	C(1)	1.420(6)	C(5)	C(6)	1.342(7)
N(1)	C(7)	1.422(6)	C(7)	C(8)	1.478(7)
N(2)	C(2)	1.340(5)	C(8)	C(9)	1.375(7)
N(2)	C(6)	1.355(6)	C(9)	C(10)	1.383(8)
N(3)	C(8)	1.339(6)	C(10)	C(11)	1.386(9)
N(3)	C(12)	1.333(6)	C(11)	C(12)	1.361(8)

Atom	Atom	Atom	Angle	Atom	Atom	Atom	Angle
N(1)	Al	N(2)	79.1(2)	C(8)	N(3)	C(12)	119.7(5)
N(1)	Al	N(3)	79.4(2)	N(1)	C(1)	C(2)	109.3(4)
N(1)	Al	C(13)	123.1(1)	N(2)	C(2)	C(1)	113.4(6)
N(2)	Al	N(3)	158.5(2)	N(2)	C(2)	C(3)	122.1(5)
N(2)	Al	C(13)	95.5(1)	C(1)	C(2)	C(3)	124.4(5)
N(3)	Al	C(13)	96.2(1)	C(7)	C(8)	C(9)	124.5(6)
C(13)	Al	C(13′)	113.8(2)	C(2)	N(2)	C(6)	117.0(5)
Al	N(1)	C(1)	123.4(3)	N(3)	C(12)	C(11)	123.1(6)
Al	N(1)	C(7)	122.9(3)	N(2)	C(6)	C(5)	124.8(6)
Al	N(2)	C(2)	114.6(3)	N(1)	C(7)	C(8)	110.0(4)
Al	N(2)	C(6)	128.4(4)	N(3)	C(8)	C(7)	115.5(5)
Al	N(3)	C(8)	112.3(4)	N(3)	C(8)	C(9)	120.0(6)
Al	N(3)	C(12)	128.0(4)	C(1)	N(1)	C(7)	113.7(4)

(*b*) Compound **2**

Atom	Atom	Distance	Atom	Atom	Distance
Al(1)	N(1)	2.020(4)	N(3)	C(8)	1.338(6)
Al(1)	C(15)	1.952(6)	N(3)	C(12)	1.332(6)
Al(1)	C(16)	1.950(5)	C(1)	C(2)	1.509(7)
Al(1)	C(17)	1.984(6)	C(2)	C(3)	1.368(7)
Al(2)	N(1)	2.002(4)	C(3)	C(4)	1.370(8)
Al(2)	N(2)	2.098(5)	C(4)	C(5)	1.372(8)
Al(2)	N(3)	2.105(4)	C(5)	C(6)	1.363(8)
Al(2)	C(13)	1.967(6)	C(7)	C(8)	1.495(6)
Al(2)	C(14)	1.975(5)	C(8)	C(9)	1.378(6)
N(1)	C(1)	1.467(6)	C(9)	C(10)	1.349(7)
N(1)	C(7)	1.497(5)	C(10)	C(11)	1.372(7)
N(2)	C(2)	1.346(6)	C(11)	C(12)	1.372(7)
N(2)	C(6)	1.346(6)			

Atom	Atom	Atom	Angle	Atom	Atom	Atom	Angle
N(1)	Al(1)	C(15)	110.2(2)	Al(2)	N(2)	C(2)	113.6(4)
N(1)	Al(1)	C(16)	108.3(2)	Al(2)	N(2)	C(6)	128.5(5)
N(1)	Al(1)	C(17)	103.1(2)	C(2)	N(2)	C(6)	117.9(5)
C(15)	Al(1)	C(16)	111.6(3)	Al(2)	N(3)	C(8)	113.6(4)
C(15)	Al(1)	C(17)	111.4(3)	Al(2)	N(3)	C(12)	127.8(4)
C(16)	Al(1)	C(17)	111.7(3)	C(8)	N(3)	C(12)	118.6(5)
N(1)	Al(2)	N(2)	78.3(2)	N(1)	C(1)	C(2)	108.8(4)
N(1)	Al(2)	N(3)	80.3(2)	N(2)	C(2)	C(1)	112.4(5)
N(1)	Al(2)	C(13)	113.5(2)	N(2)	C(2)	C(3)	122.4(6)
N(1)	Al(2)	C(14)	126.3(2)	C(1)	C(2)	C(3)	125.2(6)

Table 3 (*concluded*).

(*b*) Compound **2**

Atom	Atom	Atom	Angle	Atom	Atom	Atom	Angle
N(2)	Al(2)	N(3)	158.4(2)	C(1)	N(1)	C(7)	108.3(4)
N(2)	Al(2)	C(13)	95.2(2)	N(3)	C(12)	C(11)	122.7(5)
N(2)	Al(2)	C(14)	95.5(2)	Al(2)	N(1)	C(7)	108.2(3)
N(3)	Al(2)	C(13)	95.9(2)	N(2)	C(6)	C(5)	122.8(6)
N(3)	Al(2)	C(14)	94.8(2)	N(1)	C(7)	C(8)	110.0(4)
C(13)	Al(2)	C(14)	120.2(2)	N(3)	C(8)	C(7)	114.0(5)
Al(1)	N(1)	Al(2)	116.0(2)	N(3)	C(8)	C(9)	121.4(5)
Al(1)	N(1)	C(1)	110.4(3)	C(7)	C(8)	C(9)	124.5(5)
Al(1)	N(1)	C(7)	106.5(3)	Al(2)	N(1)	C(1)	107.3(3)

(*c*) Compound **3**

Atom	Atom	Distance	Atom	Atom	Distance
Al(1)	N(1)	1.852(5)	C(3)	C(4)	1.39(1)
Al(1)	N(2)	2.125(6)	C(4)	C(5)	1.36(1)
Al(1)	N(3)	2.155(6)	C(5)	C(6)	1.38(1)
Al(1)	C(1)	1.990(8)	C(6)	C(7)	1.408(8)
Al(1)	C(2)	1.962(8)	C(7)	C(8)	1.517(9)
N(1)	C(8)	1.457(7)	C(8)	C(9′)	1.569(9)
N(1)	C(9)	1.483(8)	C(9)	C(10)	1.527(8)
N(2)	C(3)	1.352(8)	C(10)	C(11)	1.403(9)
N(2)	C(7)	1.319(8)	C(11)	C(12)	1.360(9)
N(3)	C(10)	1.316(8)	C(12)	C(13)	1.36(1)
N(3)	C(14)	1.357(8)	C(13)	C(14)	1.40(1)

Atom	Atom	Atom	Angle	Atom	Atom	Atom	Angle
N(1)	Al(1)	N(2)	78.5(2)	C(1)	Al(1)	C(2)	115.9(4)
N(1)	Al(1)	N(3)	78.3(2)	Al(1)	N(1)	C(8)	122.0(4)
N(1)	Al(1)	C(1)	120.2(3)	Al(1)	N(1)	C(9)	121.9(4)
N(1)	Al(1)	C(2)	123.2(5)	N(2)	C(7)	C(6)	122.3(7)
N(2)	Al(1)	N(3)	156.1(3)	N(2)	C(7)	C(8)	115.3(6)
N(2)	Al(1)	C(1)	99.2(3)	C(6)	C(7)	C(8)	122.4(7)
N(2)	Al(1)	C(2)	94.1(3)	N(1)	C(8)	C(7)	105.2(6)
N(3)	Al(1)	C(1)	97.4(3)	N(1)	C(8)	C(9′)	109.2(6)
N(3)	Al(1)	C(2)	94.0(3)	C(7)	C(8)	C(9′)	112.6(6)
Al(1)	N(2)	C(3)	126.2(6)	N(1)	C(9)	C(8′)	109.1(5)
Al(1)	N(2)	C(7)	113.7(5)	N(1)	C(9)	C(10)	105.0(5)
Al(1)	N(3)	C(10)	113.6(5)	C(8′)	C(9)	C(10)	113.0(6)
Al(1)	N(3)	C(14)	125.5(6)	C(8)	N(1)	C(9)	111.0(5)
N(3)	C(10)	C(9)	115.8(6)	N(3)	C(10)	C(11)	123.0(6)
C(9)	C(10)	C(11)	121.2(7)	C(3)	N(2)	C(7)	119.4(6)
C(10)	N(3)	C(14)	120.1(6)	N(3)	C(14)	C(13)	119.1(7)
N(2)	C(3)	C(4)	120.5(7)				

As shown in Fig. 3, the molecules of **1** are packed parallel to each other in the crystal lattice, resulting in extensive π interactions between the aromatic rings. The shortest atomic contact distance between the rings is 3.698(1) Å between the C(3) and C(5′) atoms.

Synthesis and structure of $Al_2Me_5[N(CH_2\text{-}2\text{-}Py)_2]$ (2)

The amido atom in the dpa ligand has two lone pairs of electrons. One can therefore predict that it is possible for the amido atom in **1** to bind to the second aluminum center, forming a dinuclear complex. In fact, it is more common for secondary amido ligands to coordinate to two metal centers as a bridging ligand than to coordinate to one metal center only (1, 3, 7, 8). We therefore performed the reaction of di(2-pyridylmethyl)amine with 2 equivalents of $AlMe_3$, which indeed yielded a new colorless dinuclear complex $Al_2Me_5[N(CH_2\text{-}2\text{-}Py)_2]$ (**2**) in quantitative yield. Compound **2** was fully characterized by NMR and elemental and X-ray diffraction analyses. The posi-

Fig. 3. An unit cell packing diagram showing the intermolecular stacking of compound **1** in the crystal lattice.

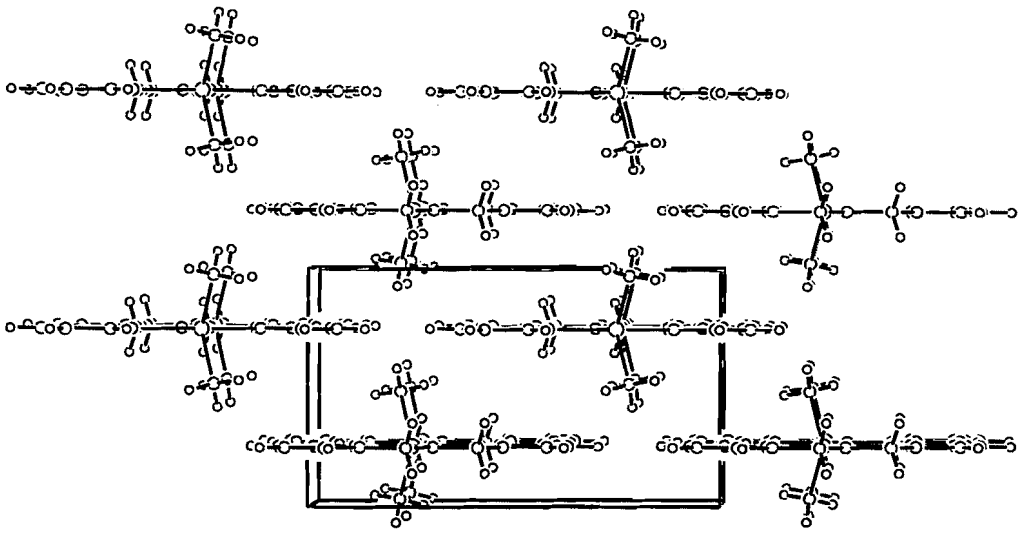

Fig. 4. An ORTEP diagram showing the molecular structure of **2** with labelling scheme and 50% thermal ellipsoids.

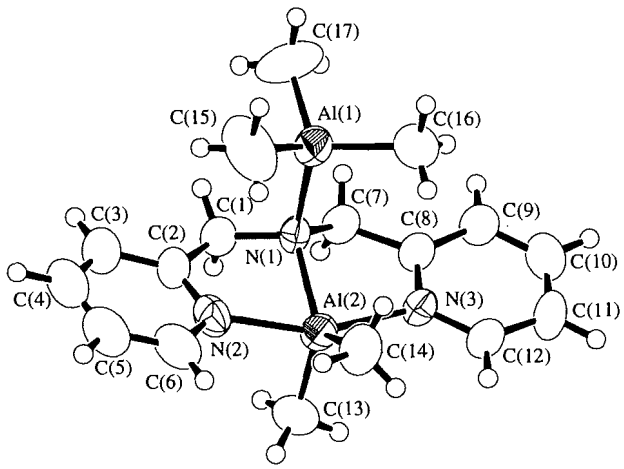

Fig. 5. A diagram showing the intermolecular interactions of compound **2** in the crystal lattice.

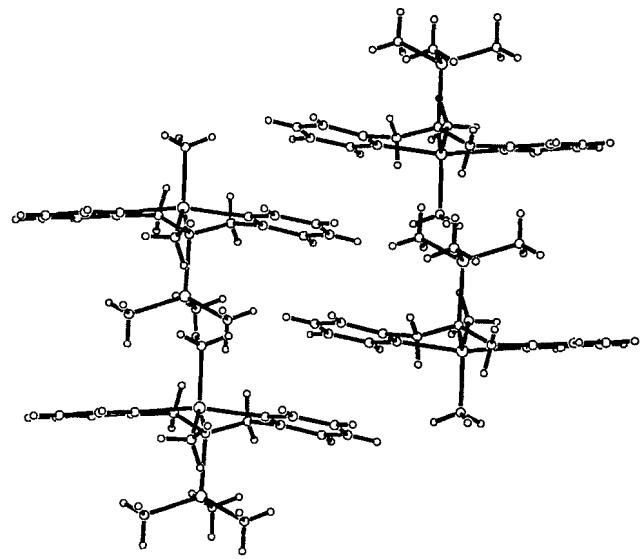

tional and isotropic thermal parameters of nonhydrogen atoms are given in Table 2 (*b*). Selected bond lengths and angles are listed in Table 3 (*b*). An ORTEP diagram showing the molecular structure of compound **2** is given in Fig. 4.

As observed in **1**, the $AlMe_2$ unit is chelated by three nitrogen atoms. The geometry around the Al(2) atom is similar to that in **1**, a distorted trigonal bipyramid. The amido Al(2)—N(1) distance (2.002(4) Å) is, however, significantly longer than that in **1**, consistent with the tetrahedral geometry of the amido N(1) atom. The $AlMe_3$ unit is attached to the N(1) atom with a typical amido nitrogen (tetrahedral) – aluminum bond length (2.020(4) Å). Compound **2** can be considered as the result of the addition of one $AlMe_3$ unit to compound **1**, which removes the C_2 rotational symmetry axis in **1**, resulting in an approximate C_s symmetry. As the consequence of the C_s symmetry, the two methyl groups of the Al(2) atom and the two protons of the methylene groups are inequivalent. In solution, compound **2** retains its solid state structure, as confirmed by the presence of three distinct methyl resonances in a 1:1:3 ratio (two from the Al(2) unit and one from the Al(1) unit) and a well-resolved AB coupling pattern of the CH_2 groups with a typical $^2J_{H-H}$ coupling constant (9) (16 Hz) in the ^1H NMR spectrum of **2**.

In the crystal lattice, the most significant $\pi - \pi$ interactions are between the N(3) and the N(3′) pyridyl rings with the shortest atomic distance being 3.454(7) Å between C(8) and C(10′) (Fig. 5).

Fig. 6. An ORTEP diagram showing the molecular structure of **3** with labelling scheme and 50% thermal ellipsoids.

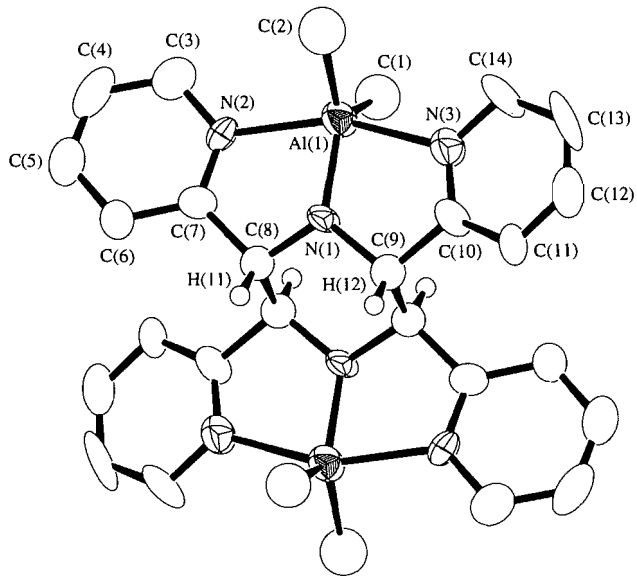

Fig. 7.

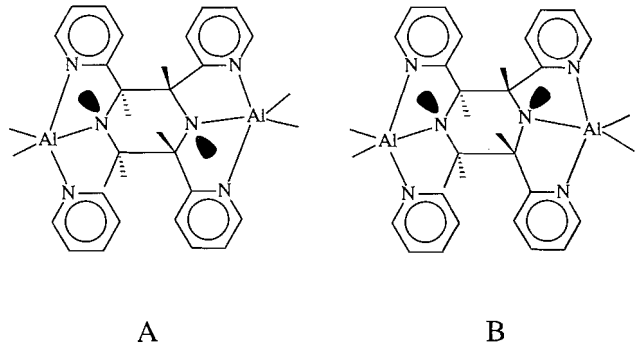

Fig. 8. A unit cell packing diagram showing the intermolecular interactions of compound **3** in the crystal lattice.

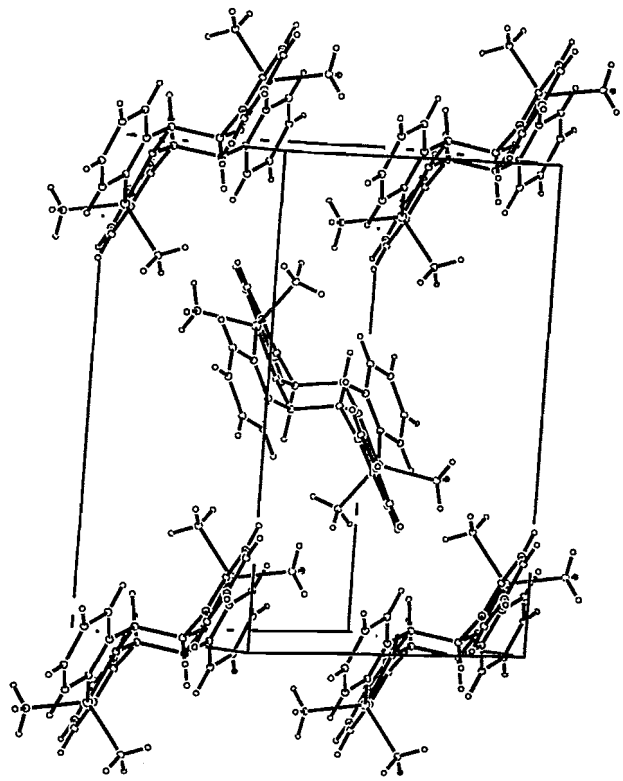

Synthesis and structure of $Al_2(CH_3)_4$[2,3,5,6-tetra(2-pyridyl)piperazyl] (3)

Compound **3** was isolated as a minor dark-brown crystalline product from the reaction of $Al(CH_3)_3$ with di(2-pyridylmethyl)amine in a 1:1 ratio as described for compound **1**. Compound **3** was characterized by elemental, NMR, and X-ray diffraction analyses. Positional and isotropic thermal parameters of non-hydrogen atoms are given in Table 2 (*c*). Selected bond lengths and angles are listed in Table 3 (*c*).

As shown in Fig. 6, compound **3** has two aluminum ions and a crystallographically imposed inversion center symmetry. The coordination environment and bond lengths and angles around each aluminum center resemble that in **1**. There are, however, substantial changes of bond lengths and angles around the amido N(1) atom. The geometry of the N(1) atom is about 5° from planarity (the sum of angles around N(1) is 354.9°). The N(1)—C(8) and N(1)—C(9) distances (1.457(7) Å, 1.483(8) Å) are considerably longer than the corresponding ones in **1**. Each mononuclear unit also deviates significantly from planarity. In comparison with compound **1**, the most interesting feature of **3** is the formation of two carbon–carbon bonds between the two methylene carbon atoms C(8) and C(9′), C(9) and C(8′), leading to the formation of an unprecedented ligand, the deprotonated 2,3,5,6-tetra(2-pyridyl)piperazine (tppz). The C(8)—C(9′) and C(9)—C(8′) distances (1.569(9) Å) are a typical C—C single bond distance. The bond angles around C(8) and C(9) are typical for a tetrahedral geometry (105.0(5)–113.0(6)°). The hydrogen atoms bonded to C(8) and C(9), located directly from the difference Fourier map, are *trans* to the hydrogen atoms on C(8′) and C(9′). The unusual 2,3,5,6-tetra(2-pyridyl)piperazyl ligand could be considered as the consequence of two C—C bond couplings and the elimination of two H_2 molecules between two di(2-pyridylmethyl)amido ligands. Such a C—C coupling reaction is rare. It is conceivable that compound **1** is the direct precursor of compound **3** and converted to **3** through the elimination of two hydrogen molecules. Unfortunately, we have not been able to establish the link between compound **3** and compound **1**. The details of the formation mechanism of **3** have not yet been understood. The free tppz ligand was obtained by hydrolyzing compound **3**.

The presence of the inversion center in the crystal structure of **3** gives the molecule of **3** an approximate C_{2h} symmetry. All the methine protons and the methine carbon atoms are therefore equivalent. Hence, only one proton or carbon resonance due to the methine groups should be observed in the ^1H NMR spectrum or the ^{13}C NMR spectrum of **3**. The ^{13}C NMR spectrum of **3** indeed showed that there is only one type of methine carbon atom. Interestingly, however, two doublet proton resonances of the methine groups with a 2.7 Hz coupling constant

were observed in the ^{1}H NMR spectrum of **3**, indicative of the presence of two different methine protons. Variable temperature ^{1}H NMR spectra recorded at 298–215 K did not reveal any dynamic behavior. One possible explanation for the NMR spectra of **3** is that instead of the trigonal planar geometry, the amido nitrogen atom has a pyramidal geometry in solution. The two lone pairs from the two amido atoms can be either *trans* or *cis* to each other (Fig. 7). In the case of a *trans* geometry, all methine protons are equivalent (**A**). In the case of a *cis* geometry, however, there are two different types of methine protons, one being *cis* to the lone pairs and the other being *trans* to the lone pairs (**B**). The ^{1}H NMR spectrum of **3** is consistent with the structure **B**. We therefore propose that compound **3** has the structure **B** in solution.

Some $\pi - \pi$ interactions appear to be evident as shown by the lattice packing diagram of **3**. The shortest atomic distance between the pyridyl rings is 3.58(1) Å between C(6) and C(7′) (Fig. 8).

The free ligand, di(2-pyridylmethyl)amine, is not luminescent. Compounds **1** and **2**, however, are luminescent at 23°C when irradiated by UV light. The complexation of the alkylaluminum to the ligand clearly plays an important role in promoting the luminescence of the ligand. Efforts are being taken by our group to investigate the luminescent properties of **1** and **2** and the formation mechanism of compound **3**.

Acknowledgement

We thank the Natural Sciences and Engineering Research Council of Canada (NSERC) for financial support.

References

1. (*a*) T. Mole and E.A. Jeffrey. Organoaluminum compounds. Elsevier, New York. 1972; (*b*) M.F. Lappert, P. Power, A.R. Sanger, and R.C. Srivatava. Metal and metalloid amides. Ellis Horwood/Wiley, New York. 1980; (*c*) M. Cesari and S. Cucinella. *In* Aluminum–nitrogen rings and cages in the chemistry of inorganic homo and heterocycles. *Edited by* I. Haiduc and B. Sowerby. Academic Press, London. 1987; (*d*) J.F. Janik, E.N. Duesler, and R.T. Paine. Inorg. Chem. **27**, 4335 (1988); (*e*) Inorg. Chem. **26**, 4341 (1987).
2. (*a*) O.T. Beachley, Jr. and K.C. Racette. Inorg. Chem. **15**, 2110 (1976); (*b*) Inorg. Chem. **14**, 2434 (1975); (*c*) G. Dozzi, C. Busetto, T. Salvatori, and S. Cucinella. J. Organomet. Chem. **192**, 17 (1980); (*d*) G. Perego and G. Dozzi. J. Organomet. Chem. **205**, 21 (1981).
3. (*a*) S.J. Trepanier and S. Wang. Angew. Chem. Int. Ed. Engl. **33**, 1265 (1994); (*b*) J. Chem. Soc. Dalton Trans. 2425 (1995); (*c*) Organomet. **15**, 760 (1996).
4. J.K. Romary, R.D. Zachariasen, J.D. Barger, and H. Schiesser. J. Chem. Soc. (*c*), 2884 (1968).
5. TEXSAN, Crystal Structure Analysis Package, Molecular Structure Corporation, Houston, Tex. 1985 and 1992.
6. D.T. Cromer and J.T. Waber. International tables for X-ray crystallography. Vol. 4. Kynoch Press, Birmingham. 1974. Table 2-2A.
7. S. Trepanier and S. Wang. Organometallics, **13**, 2213 (1994).
8. (*a*) D.M. Choquette, M.J. Timm, J.L. Hobbs, M.M. Rahim, K.J. Ahmed, and R.P. Planalp. Organometallics, **11**, 529 (1992); (*b*) S. Amirkhalili, P.B. Hitchcock, A.D. Jenkins, J.Z. Nyathi, and J.D. Smith. J. Chem. Soc. Dalton Trans. 377 (1981); (*c*) G.H. Robinson, A.D. Rae, C.F. Campana, and S.K. Byram. Organometallics, **6**, 1227 (1987); (*d*) G.H. Robinson, M.F. Self, S.A. Sangokoya, and W.T. Pennington. J. Am. Chem. Soc. **111**, 1520 (1989).
9. D.H. Williams and I. Fleming. Spectroscopic methods in organic chemistry. 4th ed. McGraw-Hill Book Company (UK) Ltd. London. 1987.

The synthesis, and molecular and crystal structure of diphenyl(2-oxidonaphthylmethyliminoacetato)tin(IV)

Frank E. Smith, Lian Ee Khoo, Ngoh Khang Goh, Rosemary C. Hynes, and George Eng

Abstract: The new diorganotin complex ($(C_6H_5)_2Sn(OC_{10}H_6CH{=}NCH_2COO)$) was prepared and characterized by ^1H NMR, IR, elemental analysis, and a single crystal X-ray diffraction study. The crystals are monoclinic, space group $P2_1/a$ with a = 16.9167(9) Å, b = 19.1276(16) Å, c = 26.538(2) Å, β = 100.534(6)°, V = 8442.5(11) Å^3, Z = 16, and D_{calc} = 1.574 Mg m^{-3}. The final discrepancy factors are R_F = 0.030, and R_W = 0.021 for 6524 significant reflections. The tin atom has a distorted trigonal bipyramidal coordination, with no short intermolecular contacts. The two axial Sn—O bonds of 2.12 Å and 2.09 Å and the equatorial Sn—N bond of 2.14 Å are among the shortest found in related complexes.

Key words: diorganotin(IV), bicycloazastannoxide, trigonal bipyramidal, antitumour.

Résumé : On a préparé le nouveau complexe diorganoétain ($(C_6H_5)_2Sn(OC_{10}H_6CH{=}NCH_2COO)$) et l'on l'a caractérisé par IR, RMN du ^1H, analyse élémentaire et diffraction des rayons X sur un cristal unique. Les cristaux sont monocliniques, groupe d'espace $P2_1/a$ avec a = 16,9167(9), b = 19,1276(16) et c = 26,538(2) Å, β = 100,534(6)°, V = 8442,5(11) Å^3, Z = 16. D_{calc} = 1,574 Mg m^{-3}, R_F = 0,030 et R_W = 0,021 pour 6524 réflexions significatives. L'atome d'étain adopte une coordination bipyramidale trigonale déformée et ne comporte pas de contacts intermoléculaires courts. Les longueurs des deux liaisons Sn—O (2,12 et 2,09 Å) et de la liaison équatoriale (2,14 Å) sont parmi les plus courtes observées dans des complexes apparantés.

Mots clés : diorganoétain(IV), bicycloazastannoxyde, bipyramidal trigonal, antitumoral.

[Traduit par la rédaction]

Introduction

The chemotherapeutic properties, especially antitumour activities, of organotins continue to be the focus of many reports (1–5). A variety of organotin complexes structurally related to cis-platin and its derivatives (6, 7) have been investigated for anti-tumour properties (3–5, 8–10). In an encouraging number of instances, the results show the organotins to be more effective than cis-platin or carboplatin (3). Studies of structure–activity relationships have shown that the factors influencing activity may be very subtle differences in bond lengths or bond angles, reinforcing the value of structural investigations in this field (10–13). Recent reports of the activity of certain diorganotin derivatives of pyridine 2,6-dicarboxylic acid and some related compounds (14, 15) against the P388 lymphocytic leukemia tumour, both in vitro and in vivo, led us to report the synthesis and characterization of a series of diorganotin iminodiacetates (16) and diorganotin(IV)-N-arylidene-α-amino acid complexes (17). In line with these developments, we now report the synthesis and characterization of diphenyl(2-oxidonaphthylmethyliminoacetato)tin(IV), including the results of a full X-ray structural analysis. The structure of the ligand (*N*-2-hydroxynaphthalideneglycine) before deprotonation is shown in Fig. 1.

A full X-ray structural analysis of the diphenyltin complex of the deprotonated ligand has been carried out and the results are reported along with a variety of spectroscopic data.

Fig. 1. Structure of *N*-2–hydroxynaphthalideneglycine.

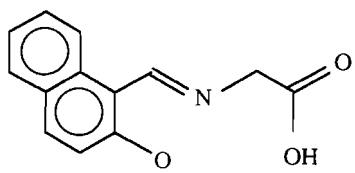

Experimental

Chemicals and reagents

Diphenyltin chloride was purchased from Alfa Inorganics and

Received February 12, 1996.

This paper is dedicated to Professor Howard C. Clark in recognition of his contributions to Canadian chemistry.

F.E. Smith.[1] Department of Chemistry and Biochemistry, Laurentian University, Sudbury, ON P3E 2C6, Canada.
L.E. Khoo and N.K. Goh. School of Science, Nanyang Technological University, 469 Bukit Timah Road, Singapore 259756.
R.C. Hynes. Biochemistry Deptartment, University of Toronto, 1 King's College Circle, Toronto, ON M5S 1J8, Canada.
G. Eng. Chemistry Department and D.C. Agricultural Experiment Station, University of the District of Columbia, Washington D.C. 20005, U.S.A.

[1] Author to whom correspondence may be addressed. Telephone: (705) 675-1151. Fax: (705) 675-4844. E-mail: FSMITH@NICKEL.LAURENTIAN.CA

Table 1. Crystallographic and refinement data for $Ph_2Sn(OC_{10}H_6CH{=}NCH_2COO)$.

Empirical formula:	$SnC_{25}H_{19}NO_3$
Formula weight	500.12
Crystal dimensions	0.25 × 0.20 × 0.15 mm
Crystal system	Monoclinic
2θ range	70.00°–85.00°
Space group	$P2_1/a$
a	16.9167(9) Å
b	19.1276(16) Å
c	26.5385(20) Å
β	100.534(6)°
V	8442.5(11) Å^3
Z value	16
D_{calc}	1.574 Mg m^{-3}
$F(000)$	4011.19
2θ range	70.00°–85.00°
$2\theta_{max}$	99.7°
μ (Cu/Kα)	2.52 mm^{-1}
Radiation	Cu/Kα (λ = 1.54056 Å)
Temperature	295 K
Total reflections	9115
Unique reflections	8640
Reflections with $I_{net} > 2.5\sigma(I_{net})$.	6524
R_F	0.030
R_W	0.021
Goodness-of-fit	1.88

other chemicals were purchased from the Aldrich Chemical Company. All were used without further purification.

Microanalyses

The carbon, hydrogen, and nitrogen microanalyses were carried out on a Control Equipment Corporation 240XA elemental analyser at the School of Chemical Sciences, Universiti Sains Malaysia, Penang, Malaysia.

NMR spectra

The ^1H and ^{13}C NMR spectra were recorded in $CDCl_3$ on a Bruker AC-P 300MHz spectrometer. ^1H NMR data, δ (ppm): 9.18 (^3J(Sn-N=CH) = 64.93 c/s, -CH=N-); 4.49 (^3J(Sn-N-CH_2) = 24.23 c/s, -N-CH_2-), 7.0–8.1 (Ar protons). ^{13}C NMR data, δ (ppm): 166.62 (-CH=N-), 57.80, 172.74 (-N-CH_2-); 171.03, 140.32, 137.36, 136.77, 136.39, 136.02, 133.70, 130.70, 129.64, 129.08, 129.05, 127.28, 124.58, 124.11, 110.40, 108.47 (aromatic C).

IR spectra

The IR spectra were obtained on a Perkin Elmer FTIR 1725 instrument with the samples as KBr discs. ν(O=C-O)$_{asym}$, 1680 cm^{-1}; ν(C=N), 1600 cm^{-1}; ν(O=C-O)$_{sym}$, 1325 cm^{-1}.

Preparation of ligand

A mixture of free (*dl*) glycine (0.1 mol) and 2-hydroxy-1-naphthaldehyde (0.15 mol) in 300 mL of absolute ethanol and 30 mL of methanol was stirred overnight before refluxing for 3–4 h. After cooling in the refrigerator, a crystalline precipitate formed, which was filtered, washed with petroleum ether (60–80°C), dried, and recrystallized from methanol to give the pure product in 50–60% yield.

Analytical data for *N*-2-hydroxynaphthalideneglycine mp 206–208°C (dec.). Anal. calcd. for $C_{13}H_{11}NO_3$: C 68.10, H 4.85, N 6.11; found: C 68.34, H 4.87, N 6.24.

Preparation of diphenyl(2-oxidonaphthylmethyliminoacetato)tin(IV)

Triethylamine (2 cm^3) was added to a stirred solution of *N*-2-hydroxynaphthalideneglycine (10 mmol) in absolute ethanol (25 cm^3). After the dropwise addition of a solution of diphenyltin dichloride (10 mmol) in absolute ethanol (10 cm^3), the mixture was stirred and heated for 2 h on a water bath. Once the resulting mixture was left to stand, the product crystallized, was filtered, dried, and then recrystallized from ethanol. Yield 75%, mp 198–200°C. Anal. calcd. for $C_{25}H_{19}NO_3Sn$: C 60.03, H 3.85, N 2.80; found: C 59.83, H 3.85, N 2.08.

X-ray data collection, structure solution and refinement

The crystallographic data are summarized in Table 1. The intensity data were collected at 295 K on a Nonius diffractometer run by the NRCCAD diffractometer control program (18), using the θ/2θ scan mode and profile analysis (19); 9115 reflections were measured, of which 8640 were unique. Of these, 6524 had $I_{net} > 2.5\sigma(I_{net})$. The h, k, and l ranges were −16 to 16, 0 to 18, and 0 to 26, respectively. The minimum and maximum transmission factors were 0.487 and 0.692. Absorption corrections were made from 4 ψ scans. The structure was solved by direct methods, followed by difference Fouriers. All non-hydrogen atoms were refined anisotropically. Hydrogen atoms were included in calculated positions. Secondary extinction was refined as in Larson (20) as 0.8564(31). The refined parameter is the average length of a mosaic block in μm. The final least-squares cycle was calculated with 196 atoms, 1082 parameters, and 6524 out of 8640 reflections. Weights based on counting statistics were used. Final residuals are $R_F = 0.030$, $R_W = 0.021$ for data with $I_{net} > 2.5\sigma(I_{net})$, $R_F = 0.055$, $R_W = 0.025$ for all data. The goodness of fit was 1.88. Maximum shift/error was 0.023. In the last difference Fourier map, the top peak was 0.36 e/Å^3, and the deepest hole was −0.32 e/Å^3. Scattering factors were taken from the literature (21). All computation was performed using the NRCVAX system of crystal structure solving programs (22).

Results and discussion

In the presence of triethylamine, diphenyltin dichloride reacts with the tridentate ligand *N*-2-hydroxynaphthalideneglycine to give a bicycloazastannoxide. Although organotin carboxylates frequently have di- or polymeric structures resulting from intermolecular bridging by carbonyl oxygen atoms (16, 23), the results of a previous study on similar bicycloazastannoxides, including the crystal and molecular structure of $Bu_2Sn(OC_6H_4CH{=}NCH(i\text{-}Pr)COO)$, shows that these compounds have five-coordinate monomeric structures (17). The title compound shows strong carboxylate absorption bands at 1680 and 1325 cm^{-1}. The separation of 325 cm^{-1} between ν(O=C-O)$_{asym}$ and ν(O=C-O)$_{sym}$ is indicative of a unidentate bonding mode for the carboxylate moiety (24). Further evidence for the fact that the free carbonyl group on the ligand is not involved in coordination with another tin atom can

Fig. 2. Molecular structure and atom numbering scheme.

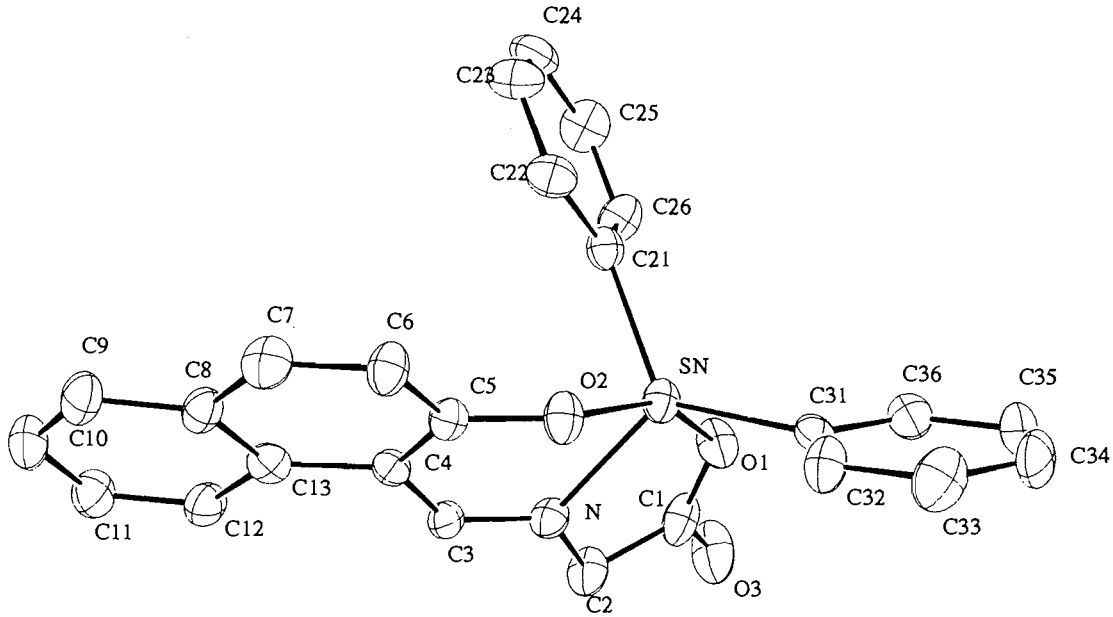

Fig. 3. Packing in the unit cell.

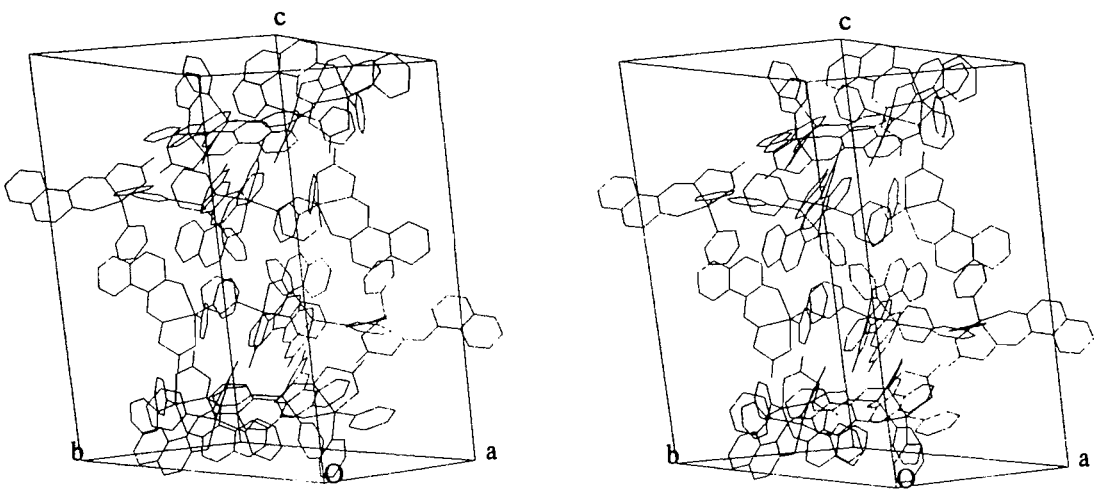

be deduced from the short C—O distance of 1.216(8) Å (mean value). Similar C—O bond lengths of 1.179(13) and 1.213(16) Å have been reported for the corresponding nonbridging carbonyl groups in the compounds $Ph_3SnCl{:}2HOC_6H_4CH{=}NCH_2CO_2Et$ (25) and $Bu_2Sn(OC_6H_4CH{=}NCH(i\text{-}Pr)COO)$, respectively (17). The determination of ^3J(Sn-N=CH) and ^3J(Sn-N-CH_2) coupling constants in the proton NMR spectrum of the complex at 64.93 and 24.23 c/s, respectively, is strongly suggestive of the presence of an intramolecular Sn—N bond (17, 26, 27). An ORTEP (28) plot of the organotin complex, including the atom-numbering scheme, is given in Fig. 2. The unit cell was found to be very large, containing 16 molecules, with 4 molecules in the asymmetric unit. In view of the unusually large size of the unit cell, the structure was checked for missing symmetry using the program MISSYM (29). No additional symmetry was identified. By doubling the tolerances to 0.5 Å displacement for axes and planes and 0.9 Å for inversion centres and translational symmetry, a "pseudo" glide plane (1/2, 0.528, 0), for the tin atoms only, could be located, but even this failed once oxygen and nitrogen atoms were included. The presence of four crystallographically unique molecules per asymmetric unit was therefore verified. A stereo pair showing the packing arrangement of the molecules in the unit cell is shown in Fig. 3. The final fractional coordinates of non-hydrogen atoms with equivalent isotropic thermal parameters are listed in Table 2, while selected bond lengths and bond angles are in Table 3. The bond lengths and angles for the title complex are reported as mean values taken over the four molecules in the asymmetric unit. A complete listing of the bond lengths and angles for each of the molecules in the asymmetric unit, calculated hydrogen atom parameters, and

Table 2. Atomic parameters x, y, z and B_{iso}. ESDs refer to the last digit printed.

	x	y	z	B_{iso}
SnA	0.128731(24)	0.486225(22)	0.117813(14)	3.385(20)
O1A	0.18340 (25)	0.46573 (20)	0.19476 (14)	4.55 (20)
O2A	0.11992 (22)	0.52831 (20)	0.04436 (12)	3.76 (21)
O3A	0.2901 (3)	0.48119 (23)	0.25505 (15)	6.6 (3)
NA	0.2223 (3)	0.56309 (25)	0.13409 (16)	3.4 (3)
C1A	0.2497 (4)	0.4950 (3)	0.21312 (23)	4.5 (4)
C2A	0.2798 (4)	0.5506 (3)	0.18132 (22)	4.4 (3)
C3A	0.2173 (3)	0.6252 (3)	0.11357 (21)	3.2 (3)
C4A	0.1641 (3)	0.6450 (3)	0.06754 (20)	2.8 (3)
C5A	0.1191 (4)	0.5967 (3)	0.03525 (21)	3.1 (3)
C6A	0.0715 (4)	0.6176 (3)	−0.01142 (22)	3.9 (4)
C7A	0.0649 (4)	0.6856 (4)	−0.02391 (21)	4.2 (4)
C8A	0.1068 (4)	0.7387 (3)	0.00715 (22)	3.5 (3)
C9A	0.0960 (4)	0.8095 (4)	−0.00502 (23)	4.7 (4)
C10A	0.1368 (4)	0.8605 (3)	0.0248 (3)	5.3 (4)
C11A	0.1881 (4)	0.8414 (3)	0.06996 (24)	4.5 (4)
C12A	0.1991 (4)	0.7728 (3)	0.08388 (22)	4.0 (4)
C13A	0.1581 (4)	0.7184 (3)	0.05409 (22)	3.3 (3)
C21A	0.0203 (3)	0.5276 (3)	0.13461 (23)	3.3 (3)
C22A	−0.0393 (4)	0.5517 (3)	0.09614 (22)	4.2 (4)
C23A	−0.1091 (4)	0.5784 (4)	0.1074 (3)	5.0 (4)
C24A	−0.1218 (4)	0.5817 (3)	0.1565 (3)	4.9 (4)
C25A	−0.0625 (5)	0.5581 (4)	0.19548 (24)	5.4 (4)
C26A	0.0077 (4)	0.5310 (3)	0.18456 (24)	4.6 (4)
C31A	0.1434 (3)	0.3836 (3)	0.09295 (24)	3.4 (3)
C32A	0.1500 (4)	0.3686 (3)	0.04259 (25)	4.5 (4)
C33A	0.1540 (4)	0.2998 (4)	0.0274 (3)	5.8 (4)
C34A	0.1500 (5)	0.2463 (4)	0.0605 (4)	6.1 (5)
C35A	0.1446 (4)	0.2599 (4)	0.1109 (3)	5.9 (5)
C36A	0.1409 (4)	0.3288 (4)	0.12632 (24)	4.7 (4)
SnB	0.588992(23)	0.510759(22)	0.158540(14)	3.279(20)
O1B	0.70548 (22)	0.53568 (20)	0.20051 (14)	4.30 (22)
O2B	0.47188 (21)	0.47112 (20)	0.14829 (13)	3.78 (21)
O3B	0.79223 (24)	0.52083 (22)	0.27265 (13)	4.82 (22)
NB	0.6086 (3)	0.43289 (24)	0.21793 (16)	3.2 (3)
C1B	0.7314 (4)	0.5042 (3)	0.24316 (22)	3.6 (3)
C2B	0.6810 (3)	0.4447 (3)	0.25707 (20)	3.7 (3)
C3B	0.5699 (4)	0.3751 (3)	0.21732 (19)	3.0 (3)
C4B	0.4971 (3)	0.3556 (3)	0.18331 (21)	3.0 (3)
C5B	0.4519 (4)	0.4053 (3)	0.15134 (22)	3.2 (3)
C6B	0.3765 (4)	0.3860 (3)	0.12171 (22)	4.0 (4)
C7B	0.3508 (4)	0.3188 (4)	0.12176 (23)	4.6 (4)
C8B	0.3961 (4)	0.2656 (3)	0.15144 (23)	3.8 (4)
C9B	0.3681 (4)	0.1965 (4)	0.1508 (3)	5.4 (4)
C10B	0.4109 (5)	0.1459 (4)	0.1797 (3)	5.9 (5)
C11B	0.4831 (4)	0.1624 (4)	0.21097 (25)	5.2 (4)
C12B	0.5124 (4)	0.2300 (3)	0.21221 (22)	4.2 (3)
C13B	0.4700 (4)	0.2841 (3)	0.18323 (21)	3.3 (3)
C21B	0.6265 (4)	0.4683 (3)	0.09235 (21)	3.3 (3)
C22B	0.7065 (4)	0.4660 (3)	0.08877 (24)	4.6 (4)
C23B	0.7295 (4)	0.4455 (4)	0.0436 (3)	5.6 (4)
C24B	0.6716 (4)	0.4280 (4)	0.0016 (3)	5.6 (4)
C25B	0.5921 (5)	0.4293 (3)	0.00465 (24)	4.6 (4)
C26B	0.5682 (4)	0.4496 (3)	0.04971 (25)	4.0 (3)
C31B	0.5472 (4)	0.6147 (3)	0.15797 (21)	3.6 (4)
C32B	0.4690 (5)	0.6310 (4)	0.1350 (3)	5.2 (4)

Table 2 (*continued*).

	x	*y*	*z*	B_{iso}
C33B	0.4451 (5)	0.7007 (5)	0.1314 (3)	7.6 (6)
C34B	0.4976 (6)	0.7518 (4)	0.1494 (4)	8.0 (6)
C35B	0.5747 (6)	0.7366 (4)	0.1714 (3)	6.4 (5)
C36B	0.5997 (4)	0.6683 (4)	0.17623 (22)	4.4 (4)
SnC	0.41745 (3)	0.727709(22)	0.361935(16)	3.676(23)
O1C	0.3684 (3)	0.70533 (21)	0.28358 (14)	4.27 (23)
O2C	0.4193 (3)	0.76782 (22)	0.43574 (14)	4.6 (3)
O3C	0.2763 (3)	0.73084 (23)	0.21556 (16)	6.1 (3)
NC	0.3287 (3)	0.8072 (3)	0.34108 (18)	3.5 (3)
C1C	0.3093 (4)	0.7411 (3)	0.2598 (3)	4.0 (4)
C2C	0.2799 (4)	0.8010 (3)	0.28940 (23)	4.4 (4)
C3C	0.3261 (4)	0.8665 (3)	0.36524 (22)	3.4 (3)
C4C	0.3673 (4)	0.8831 (3)	0.41610 (22)	3.2 (3)
C5C	0.4085 (4)	0.8326 (4)	0.44858 (23)	3.7 (4)
C6C	0.4390 (4)	0.8501 (4)	0.50130 (24)	4.7 (4)
C7C	0.4283 (4)	0.9148 (4)	0.51901 (23)	5.0 (4)
C8C	0.3895 (4)	0.9685 (4)	0.48788 (24)	4.3 (4)
C9C	0.3804 (4)	1.0364 (4)	0.50712 (24)	5.3 (4)
C10C	0.3461 (4)	1.0883 (4)	0.4760 (3)	5.5 (5)
C11C	0.3195 (4)	1.0751 (4)	0.4238 (3)	5.1 (5)
C12C	0.3253 (4)	1.0097 (4)	0.40450 (22)	4.6 (4)
C13C	0.3605 (4)	0.9538 (3)	0.43493 (23)	3.5 (3)
C21C	0.5234 (4)	0.7781 (3)	0.3499 (3)	3.9 (4)
C22C	0.5839 (5)	0.7957 (4)	0.3892 (3)	5.8 (4)
C23C	0.6521 (5)	0.8311 (5)	0.3807 (3)	7.6 (5)
C24C	0.6579 (5)	0.8503 (4)	0.3322 (4)	7.2 (6)
C25C	0.5980 (6)	0.8346 (4)	0.2921 (3)	6.7 (5)
C26C	0.5309 (4)	0.7979 (4)	0.3017 (3)	5.3 (4)
C31C	0.3940 (4)	0.6271 (3)	0.38770 (24)	4.1 (4)
C32C	0.3582 (4)	0.5757 (4)	0.35455 (23)	4.0 (4)
C33C	0.3399 (4)	0.5103 (4)	0.3720 (3)	5.3 (4)
C34C	0.3610 (6)	0.4952 (4)	0.4227 (3)	8.6 (6)
C35C	0.3981 (7)	0.5443 (5)	0.4553 (3)	11.2 (8)
C36C	0.4139 (6)	0.6105 (4)	0.4388 (3)	8.3 (6)
SnD	0.91717 (3)	0.259107(22)	0.358855(16)	3.668(24)
O1D	0.81000 (25)	0.29512 (22)	0.31158 (16)	4.73 (24)
O2D	1.02001 (24)	0.19979 (21)	0.38479 (15)	4.52 (23)
O3D	0.7125 (3)	0.27050 (24)	0.24639 (18)	6.8 (3)
ND	0.8933 (3)	0.17840 (25)	0.30253 (17)	3.3 (3)
C1D	0.7757 (5)	0.2567 (4)	0.2737 (3)	4.5 (4)
C2D	0.8190 (4)	0.1907 (3)	0.26420 (22)	4.2 (3)
C3D	0.9293 (4)	0.1199 (3)	0.30114 (21)	3.2 (3)
C4D	0.9983 (4)	0.0941 (3)	0.33546 (22)	3.2 (3)
C5D	1.0374 (4)	0.1347 (4)	0.37702 (24)	3.8 (4)
C6D	1.1006 (4)	0.1048 (4)	0.41344 (23)	4.7 (4)
C7D	1.1228 (4)	0.0379 (4)	0.4090 (3)	5.1 (4)
C8D	1.0890 (4)	−0.0043 (4)	0.3671 (3)	4.6 (4)
C9D	1.1158 (4)	−0.0736 (4)	0.3616 (3)	5.2 (5)
C10D	1.0839 (5)	−0.1134 (4)	0.3205 (4)	6.4 (6)
C11D	1.0229 (5)	−0.0870 (4)	0.2841 (3)	5.4 (5)
C12D	0.9940 (4)	−0.0209 (4)	0.28775 (24)	4.4 (4)
C13D	1.0257 (4)	0.0228 (3)	0.3294 (3)	3.8 (4)
C21D	0.8584 (4)	0.2300 (3)	0.42076 (23)	3.8 (4)
C22D	0.9024 (4)	0.1976 (4)	0.4637 (3)	5.2 (4)
C23D	0.8640 (4)	0.1751 (4)	0.5022 (3)	6.6 (5)

Table 2 (*concluded*).

	x	*y*	*z*	B_{iso}
C24D	0.7833 (6)	0.1853 (5)	0.4991 (3)	7.6 (6)
C25D	0.7411 (5)	0.2182 (5)	0.4570 (4)	7.2 (5)
C26D	0.7778 (5)	0.2410 (4)	0.4178 (3)	5.2 (4)
C31D	0.9881 (4)	0.3465 (3)	0.34601 (21)	3.6 (4)
C32D	1.0696 (5)	0.3396 (4)	0.3514 (3)	5.3 (4)
C33D	1.1160 (5)	0.3964 (5)	0.3437 (3)	7.2 (5)
C34D	1.0809 (6)	0.4600 (5)	0.3320 (3)	7.5 (6)
C35D	0.9994 (6)	0.4681 (4)	0.3262 (3)	6.2 (5)
C36D	0.9524 (4)	0.4107 (4)	0.33283 (23)	4.6 (4)

Table 3. Comparison of selected bond lengths and angles between the title complex and $Bu_2Sn(OC_6H_4CH{=}NCH(i\text{-}Pr)COO)$ (17)

$Ph_2Sn(OC_{10}H_6CH{=}NCH_2COO$ (Title complex)		$Bu_2Sn(OC_6H_4CH{=}NCH(i\text{-}Pr)COO)$ (see ref. 17)
Bond	Mean[a] bond distance (Å)	Corresponding bond distance (Å)
Sn—O2	2.092(4)	2.078(10)
Sn—O1	2.124(4)	2.151(8)
Sn—C21	2.126(6)	2.138(14)
Sn—C31	2.109(6)	2.100(12)
Sn—N	2.142(5)	2.158(8)
C1—O3	1.216(8)	1.213(16)
Bond angle	Mean[a] bond angle (°)	Corresponding bond angle (°)
O2-Sn-O1	157.24(15)	155.9(3)
O1-Sn-N	76.61(17)	75.3(4)
O2-Sn-N	82.19(16)	81.6(3)
O1-Sn-C31	94.43(21)	93.5(5)
O1-Sn-C21	96.43(21)	93.6(4)
O2-Sn-C21	97.11(21)	100.3(5)
O2-Sn-C31	91.63(21)	94.1(4)
C21-Sn-C31	127.80(21)	125.9(6)
C31-Sn-N	125.40(21)	125.4(4)
C21-Sn-N	106.77(20)	108.3(5)

[a]The means are taken from the values found in the four molecules in the asymmetric unit.

anisotropic thermal parameters have been deposited as Tables T-1, T-2, S-2, and S-3, respectively.[2]

The ligand behaves as a tridentate chelating agent via the phenolic oxygen, the imino nitrogen, and a carboxylate oxygen. The two phenyl groups and the imino nitrogen take up the equatorial positions and the two oxygens the axial sites in a distorted trigonal bipyramidal arrangement around the tin. The tin atom lies in the ligand plane and forms a five-membered and a six-membered chelate ring with the ligand. The closest Sn—O distance between the complexes is 5.3982(8) Å between Sn(b) and O3(d), thus there are no close contacts between the complex entities, and no intermolecular tin–oxygen bridging.

The structure of the title complex is very similar to that reported for $Bu_2Sn(OC_6H_4CH{=}NCH(i\text{-}Pr)COO)$ (17). Lists of the corresponding bond lengths and angles for the two complexes are given in Table 3. The two axial Sn—O bonds of 2.124(4) and 2.092(4) Å and the equatorial Sn—N bond of 2.142(5) Å appear to be the shortest ever reported in complexes of this type. This compound, and a range of similar ones, will be tested for their activities against human tumour cell lines — MCF-7 (a mammary tumour) and WiDr (a colon carcinoma). The results of these tests, along with the structural data reported above, will enable comparison with the active compounds reported previously (3, 4, 5, 13).

[2] Copies of material on deposit may be purchased from: The Depository of Unpublished Data, Document Delivery, CISTI, National Research Council Canada, Ottawa, Canada K1A 0S2. The tables of bond lengths and angles, and of hydrogen atom parameters have also been deposited with the Cambridge Crystallographic Data Centre, and can be obtained on request from The Director, Cambridge Crystallographic Data Centre, University Chemical Laboratory, 12 Union Road, Cambridge, CB2 1EZ, U.K.

Acknowledgements

Financial support from Nanyang Technological University (RO/92/KLE) and the Laurentian University Research Fund (LURF) are gratefully acknowledged.

References

1. A.J. Crowe. Drugs Future, **12**, 40 (1987).
2. B.N. Biddkle and S.J. Gray. Appl. Organomet. Chem. **5**, 43 (1991).
3. M. Gielen. Proceedings of the VIIIth International Conference on the Organometallic Chemistry of Ge, Sn, and Pb, Sendai, Japan, September, 1995.
4. M. Gielen. Metal-Based Drugs, **1**, 213 (1994).
5. M. Gielen, P. Lelieveld, D. de Vos, and R. Willem. *In* Metal-based antitumour drugs. Vol. 2. *Edited by* M. Gielen. Freund Publishing House, Tel Aviv. 1992. pp. 29–54.
6. B. Rosenberg, L. Van Camp, and T. Krigas. Nature, **205**, 698 (1965).
7. J.L. van der Veer and J. Reedijk. Chem. Br. **20**, 775 (1988).
8. A.J. Crowe and P.J. Smith. Chem. Ind. 200 (1980).
9. A.J. Crowe, P. J. Smith, and G. Atassi. Chem.-Biol. Interact. **32**, 171 (1980).
10. A.J. Crowe, P.J. Smith, C.J. Cardin, H.E. Parge, and F.E. Smith. Cancer Lett. **24**, 45 (1984).
11. A. Meriem, R. Willem, J. Meunier-Piret, and M. Gielen. Main Group Met. Chem. **12**, 187 (1989).
12. A. Meriem, M. Gielen, and R. Willem. J. Organomet. Chem. **365**, 91 (1989).
13. M. Gielen, M. Boalam, A. Meriem, B. Mahieu, M. Biesemans, and R.Willem. Heteroat. Chem. **3**, 449 (1992).
14. G. Ruisi, A. Silvestri, M.T. LoGludice, R. Barbieri, G. Atassi, F. Huber, K. Gratz, and L. Lamartina. J. Inorg. Biochem. **25**, 229 (1985).
15. M. Gielen, E. Joosen, T. Mancilla, K. Jurkschat, C. Roobol, J. Bernheim, G. Atassi, F. Huber, E. Hoffmann, H. Perut, and B. Mahieu. Main Group Met. Chem. **10**, 148 (1987).
16. F.L. Lee, E.J. Gabe, L.E. Khoo, W.H. Leong, G. Eng, and F.E. Smith. Inorg. Chim. Acta, **166**, 257 (1989).
17. F.E. Smith, R.C. Hynes, T.T. Ang, L.E. Khoo, and G.Eng. Can. J. Chem. **70**, 1114 (1992).
18. Y. Le Page, P.S. White, and E.J. Gabe. *In* Abstr. Am. Crystallogr. Assoc. Annu. Meeting, 1986. p. 24.
19. D.F. Grant and E.J. Gabe. J. App. Crystallogr. **11**, 114 (1978).
20. A.C. Larson. *In* Crystallographic computing. *Edited by* F.R. Ahmed. Munksgaard, Copenhagen. 1970. p. 291.
21. *In* International tables for X-ray crystallography. Vol. IV. 2nd ed. Kynoch Press, Birmingham, England. 1974. p. 99.
22. E.J. Gabe, Y. Le Page, J-P. Charland, F.L. Lee, and P.S. White. J. Appl. Crystallogr. **22**, 384 (1989).
23. S.W. Ng, C.Wei, and V.G. Kumar Das. J. Organomet. Chem. **345**, 59 (1988).
24. G.B. Deacon, F. Huber, and R.J. Phillips. Coord. Chem. Rev. **33**, 227 (1980).
25. F.L. Lee, E.G. Gabe, L.E. Khoo, G. Eng, and F.E. Smith. Polyhedron, **9**, 653 (1990).
26. K. Kawkami and T. Tanaka. J. Organomet. Chem. **49**, 409 (1973).
27. G. Matsubayashi, T. Tanaka, S. Nisbigaki, and K. Nakatsu. J. Chem Soc. Dalton Trans. 501 (1979).
28. C.K. Johnson. ORTEP-II. Report ORNL-5138, Oak Ridge National Laboratory, Oak Ridge, Tenn. 1976.
29. Y. Le Page. J. Appl. Crystallogr. **21**, 983 (1988).

Pd(0)-catalyzed addition of $Me_3SnSnMe_3$ to α,β-alkynic aldehydes and ketones. Synthesis of (*Z*)-β-trimethylstannyl α,β-alkenic aldehydes and ketones. Preparation and synthetic uses of substituted (*Z*)-4-trimethylstannyl-1,3-butadienes

Edward Piers and Richard D. Tillyer

Abstract: Treatment (dry tetrahydrofuran, reflux) of the α,β-alkynic aldehydes **26**–**28** and ketones **29**–**36** with $Me_3SnSnMe_3$ in the presence of a catalytic amount of $(Ph_3P)_4Pd$ provides fair to excellent yields of the corresponding (*Z*)-β-trimethylstannyl α,β-alkenic aldehydes **41**–**43** and ketones **44**–**51**. The carbonyl compounds **41**–**51**, upon reaction with methylenetriphenylphosphorane under suitable conditions, are smoothly converted into the (*Z*)-4-trimethylstannyl-1,3-butadienes **61**–**71**, respectively. Treatment of the aldehyde **41** with the anion of trimethyl phosphonoacetate and the aldehyde **42** with the anion of the phosphonoacetate **73** produces excellent yields of the 5-trimethylstannyl-2,4-heptadienoates **72** and **74**, respectively. The synthetic potential of (*Z*)-4-trimethylstannyl-1,3-butadienes is illustrated by the conversion of **62** into the functionalized, stereodefined conjugated dienes **76** and **78** and by transformation of **87** into the structurally novel diene **84**. Diels–Alder reactions of **84** with tetracyanoethylene and dimethyl acetylenedicarboxylate provide the spiro[3.5]nonane derivatives **88** and **89**, respectively.

Key words: Diels–Alder cycloaddition, organocopper(I), transmetallation, alkylidenecyclobutane, (*E*)-4-lithio-1,3-butadienes, spiro[3.5]nonane.

Résumé : Le traitement des aldéhydes **26**–**28** et des cétones **29**–**36** α,β-alcyniques avec du $Me_3SnSnMe_3$ (tétrahydrofurane sec, reflux), en présence d'une quantité catalytique de $Pd(PPh_3)_4$, conduit aux aldéhydes **41**–**43** et aux cétones **44**–**51** (*Z*)-β-triméthylstannyl-α,β-alcéniques correspondantes avec des rendements allant de corrects à excellents. Par réaction avec le méthylènetriphénylphosphorane, les composés carbonylés **41**–**51** se transforment facilement en (*Z*)-4-triméthylstannylbuta-1,3-diènes, **61**–**71**, respectivement. Le traitement de l'aldéhyde **41** avec l'anion phosphonoacétate de triméthyle et de l'aldéhyde **42** avec l'anion du phosphonoacétate **73** conduit respectivement à d'excellents rendements aux 5-triméthylstannylhepta-2,4-diénoates **72** et **74**. Le potentiel de synthèse des (*Z*)-4-triméthylstannylbuta-1,3-diènes a été illustré par la conversion du composé **62** en diènes conjugués fonctionnalisé stéréodéfinis **76** et **78** et par la transformation du composé **87** en diène **84** de structure nouvelle. Les réactions de Diels–Alder du composé **84** avec le tétracyanoéthène et l'acétylènedicarboxylate de diméthyle conduisent respectivement aux dérivés spiro[3.5]nonanes **88** et **89**.

Mots clés : cycloaddition de Diels–Alder, organocuivre(I), transmétallation, alkylidènecyclobutane, (*E*)-4-lithiobuta-1,3-diènes, spiro[3.5]nonane.

[Traduit par la rédaction]

Introduction

A recent report (1) from this laboratory disclosed, inter alia, that alkyl 2-alkynoates (general structure **1**), upon treatment with hexamethylditin in the presence of a catalytic amount of tetrakis(triphenylphosphine)palladium(0), are converted into the corresponding alkyl (*Z*)-2,3-bis(trimethylstannyl)-2-alkenoates **2** (eq. [1]). This process, which is generally clean and efficient, is compatible with the presence of a variety of functional groups in R[1]. It was also shown (1) that the *Z* isomers **2** are thermally unstable and, when heated to 75–95°C, rearrange smoothly to the *E* isomers **3** (eq. [2]). We report in this paper that the $(Ph_3P)_4Pd$-catalyzed addition of $Me_3SnSnMe_3$ to α,β-alkynic aldehydes and ketones of general structure **4** does not lead to the formation of the corresponding α,β-bis(trimethylstannyl) α,β-alkenic carbonyl compounds, but instead provides, directly and highly stereoselectively, (*Z*)-β-

Received February 6, 1996.

This paper is dedicated to Professor Howard C. Clark in recognition of his contributions to Canadian chemistry.

E. Piers[1] and R.D. Tillyer. Department of Chemistry, University of British Columbia, 2036 Main Mall, University Campus, Vancouver, BC V6T 1Z1, Canada.

[1] Author to whom correspondence may be addressed. Telephone: (604) 822-3219. Fax: (604) 822-2847. E-mail: epier@unixg.ubc.ca

Table 1. Preparation of α,β-alkynic aldehydes and ketones.

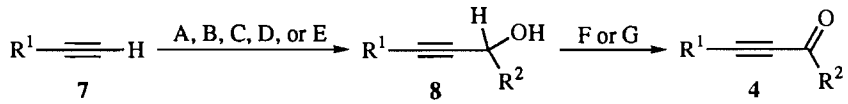

Entry	Starting material 7	R^1	R^2	Conditions[a]	Alcohol 8	Yield (%)[b]	Conditions[a]	Product 4	Yield (%)[b]
1	**9**	TBDMSO$(CH_2)_2$[c]	H	A	**16**	74	F	**26**	72
2	**10**	MOMO$(CH_2)_2$[d]	H	A	**17**	80	F	**27**	57
3	**11**	TBDMSO$(CH_2)_4$[c]	H	A	**18**	81	F	**28**	74
4	**9**	TBDMSO$(CH_2)_2$[c]	Me	B	**19**	92	G	**29**	74
5	**12**	Cl$(CH_2)_3$	Me	B	**20**	85	G	**30**	74
6	**11**	TBDMSO$(CH_2)_4$[c]	Me	B	**21**	60	G	**31**	76
7	**13**	H—≡—$(CH_2)_3$	Me	C	**22**	60	G	**32**	55
8	**14**	i-Pr	Me	B	**23**	—[e]	F	**33**	56[f]
9	**9**	TBDMSO$(CH_2)_2$[c]	i-Pr	D	**24**	85	G	**34**	81
10	**15**	*t*-Bu	*n*-C_6H_{13}	E	**25**	96	G	**35**	72

[a]A: (*i*) MeLi (1 equiv.), THF, −78°C, 10 min; −20°C, 1 h; (*ii*) H_2CO (4 equiv.), warm to room temperature, then stir for 30 min. B: (*i*) as in A; (*ii*) cool to −78°C, add MeCHO (2 equiv.), −78°C, 10 min, then warm to room temperature. C: as in B except that 5 equiv. of MeCHO were used. D: as in B, except that i-PrCHO (1.5 equiv.) was used in place of MeCHO. E: as in B, except that *n*-$C_6H_{13}CHO$ (1.5 equiv.) was used in place of MeCHO. F: pyridinium chlorochromate (PCC) (1.5 equiv.), NaOAc (0.3 equiv.), CH_2Cl_2, room temperature, 2 h. G: PCC (2.5 equiv.), NaOAc (0.3 equiv.), CH_2Cl_2, room temperature, 2.5 h.
[b]Yield of purified, distilled product.
[c]TBDMS = *tert*-butyldimethylsilyl.
[d]MOM = methoxymethyl.
[e]The crude product was not purified.
[f]Overall yield from compound **14**.

trimethylstannyl α,β-alkenic aldehydes and ketones **5** in fair to excellent yields (eq. [3]) (2). Furthermore, we show that substances **5** are excellent precursors for the preparation of synthetically valuable, stereochemically homogeneous (*Z*)-4-trimethylstannyl-1,3-butadienes of general structure **6** (eq. [4]).

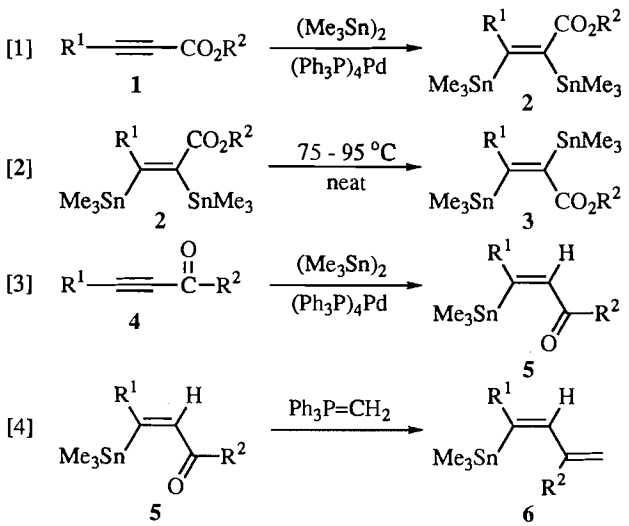

Results and discussion

Preparation of α,β-alkynic aldehydes and ketones

Of the 11 α,β-alkynic aldehydes and ketones employed in this study, substrates **26**–**35** were prepared as summarized in Table 1. Two straightforward synthetic steps were employed in each case. For example, sequential treatment of a solution of 4-*tert*-butyldimethylsilyloxy-1-butyne (**9**) in dry tetrahydrofuran (THF) with methyllithium (1 equiv.) and paraformaldehyde (4 equiv.) gave the primary alcohol **16**, which, upon oxidation with pyridinium chlorochromate in the presence of sodium acetate (3), provided 5-*tert*-butyldimethylsilyloxy-2-pentynal (**26**) (Table 1, entry 1). In a similar fashion, the 1-alkynes **10** and **11** were transformed, via the alcohols **17** and **18**, into the α,β-alkynic aldehydes **27** and **28**, respectively (entries 2 and 3). Analogous chemical processes, using appropriate 1-alkynes as starting materials and ethanal (entries 4–8), 2-methylpropanal (entry 9), and heptanal (entry 10) as electrophilic reagents, afforded the α,β-alkynic ketones **29**–**35**.

All the products listed in Table 1 were distilled, except for the alcohol **23** (entry 8). This substance is quite volatile and, therefore, in order to avoid excessive loss of material, crude **23** was not purified but was oxidized directly to the required ketone **33**. It should also be noted that conversion of 1,6-heptadiyne (**13**) into the secondary alcohol **22** (entry 7) was accompanied by a small amount of a polar, uncharacterized side product that was assumed to be the diol resulting from reaction at both terminal alkyne functions of the starting material.

The final ketonic substrate **36** employed in this study was prepared as shown in Scheme 1. Thus, oxidation of 4-pentyn-1-ol (**37**), followed by reaction of the resultant aldehyde **38** with vinyl magnesium bromide, provided the enynol **39**. Treatment of **39** with *tert*-butyldimethylsilyl chloride under

Scheme 1.

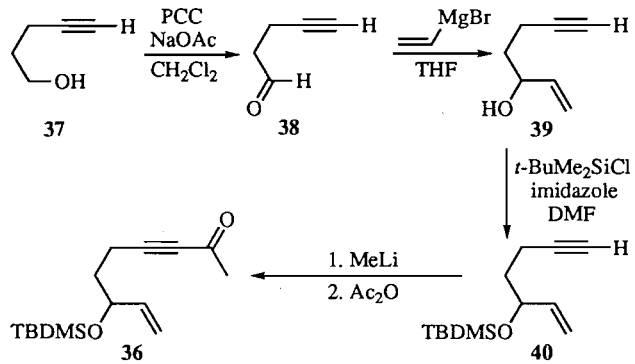

"standard" conditions (4) produced **40**, which, upon sequential treatment with methyllithium and acetic anhydride, afforded the functionalized α,β-alkynic ketone **36**.

Collectively, the substrates **26–36** contain a range of functional groups in addition to the α,β-alkynic aldehyde and ketone moieties. These include primary silyl ether, secondary allylic silyl ether, primary chloride, terminal alkyne, and terminal alkene functions. Based on the results of our earlier studies (1), it seemed highly likely that each of these functional groups would be compatible with the reaction of the substrates with hexamethylditin in the presence of a palladium(0) catalyst.

Pd(0)-catalyzed reaction of the α,β-alkynic aldehydes and ketones 26–36 with hexamethylditin

Initial experiments were carried out using the structurally simple substrate **33**. Thus, employing a procedure similar to that reported previously in connection with the Pd(0)-catalyzed reaction of hexamethylditin with α,β-alkynic esters (1), tetrakis(triphenylphosphine)palladium(0) (5 mol%) was added to a stirred solution of **33** (1 equiv.) and $Me_3SnSnMe_3$ (1 equiv.) in dry THF (argon atmosphere) and the resulting mixture was refluxed (eq. [5]). The progress of the reaction was monitored

[5]

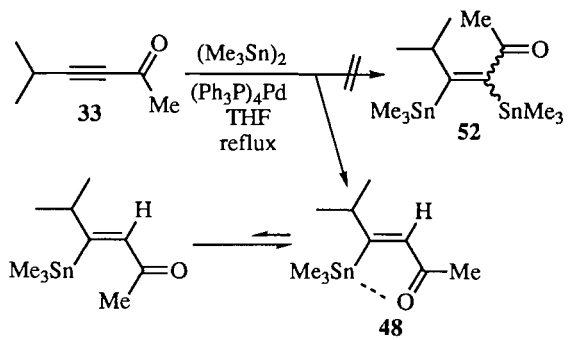

by thin-layer chromatography (tlc), which showed that all of the starting material had been consumed after a reaction period of ~5 h. Removal of most of the solvent and purification of the crude material by flash chromatography on silica gel (5) provided a single product. Inspection of the ^1H nuclear magnetic resonance (nmr) spectrum of this material showed clearly that the product was not the initially expected (*Z*)- (or (*E*))-α,β-bis(trimethylstannyl) α,β-alkenic ketone **52** (1), but was, in fact, (*Z*)-5-methyl-4-trimethylstannyl-3-hexen-2-one (**48**) (eq. [5]). Of particular note in the ^1H nmr spectrum of **48** is the presence of only one 9-proton signal (δ 0.09, $^2J_{Sn-H}$ = 54 Hz) due to the Me_3Sn group and the appearance of a 1-proton doublet (δ 6.77, J = 1.5 Hz, $^3J_{Sn-H}$ = 127 Hz[2]) derived from the alkenic proton at C-3. The magnitude of $^3J_{Sn-H}$ associated with the C-3 proton is characteristic of coupling between tin and a proton that are *trans* to one another on a carbon–carbon double bond (6). This *trans* relationship in product **48** was confirmed by a nuclear Overhauser enhancement (nOe) difference experiment in which irradiation at δ 6.77 caused an increase in the intensity of each of the signals at δ 2.75 (-C*H*Me_2), 1.03 (-CH*Me_2*), and 2.20 (C(O)Me). The enhancement of the methyl resonance of the acetyl group indicates that this substance exists largely in the conformation shown in formula **48**. Presumably, this arrangement is stabilized by coordination of the carbonyl oxygen with the tin atom (see ref. 7 and citations therein). On the other hand, the alternative (planar) conformation (see eq. [5]) would be notably destabilized by steric repulsion between the acetyl methyl group and the Me_3Sn function.

The conversion of **33** into **48** (eq. [5]) was clean and efficient (80% yield of purified product). Examination (tlc, ^1H nmr spectroscopy) of the crude material prior to purification showed that this dark oil did not contain the bis(trimethylstannane) **52**. Furthermore, the geometric isomer of the isolated product **48** could not be detected either. To demonstrate the generality of this process, each member of the structurally diverse set of α,β-alkynic aldehydes and ketones (**26–32**; **34–36**) (vide supra) was subjected to the Pd(0)-catalyzed reaction with hexamethylditin. The results of this study, including the transformation of **33** into **48**, are summarized in Table 2.

The conversion of α,β-alkynic aldehydes and ketones into the corresponding (*Z*)-β-trimethylstannyl α,β-alkenic carbonyl compounds does indeed turn out to be a general reaction. As shown by the data given in Table 2, the starting materials **26-36** are transformed into the products in fair to excellent yields. In each of the summarized conversions, the product was obtained as a single geometric isomer. In the ^1H nmr spectrum of each of the products, the resonance due to the olefinic proton exhibited a $^3J_{Sn-H}$ value consistent with that expected for the *Z* isomer (trans relationship between the trimethylstannyl group and the olefinic hydrogen) (6).

The reactions summarized in Table 2 were carried out in refluxing dry THF, with an initial substrate concentration between 0.3 and 0.6 molar. In each case, 0.05 equiv. of the palladium(0) catalyst ($(Ph_3P)_4Pd$) was employed. Under these conditions, the reactions were generally complete within reasonable reaction times. The products were conveniently purified by flash chromatography (silica gel) (5) of the crude oils derived by removal of most of the solvent (reduced pressure) from the reaction mixtures.

The reactions summarized in entries 7 and 10 of Table 2 require special mention. Reaction of the keto diyne **32** with $Me_3SnSnMe_3$ in the presence of $(Ph_3P)_4Pd$ provided in good yield (69%) (*Z*)-4-trimethylstannyl-3-nonen-8-yn-2-one (**47**) (eq. [6]). The fact that the terminal alkyne function of **32** does not interfere with the "normal" reaction of the alkynic ketone moiety is particularly noteworthy, since it is known (8) that the elements of $Me_3SnSnMe_3$ can be added to 1-alkynes

[2] This value represents the average of the (very similar) $^{117}Sn-H$ and $^{119}Sn-H$ coupling constants.

Table 2. Conversion of α,β-alkynic aldehydes and ketones **26–36** into (*Z*)-β-trimethylstannyl α,β-alkenic aldehydes and ketones **41–51**.

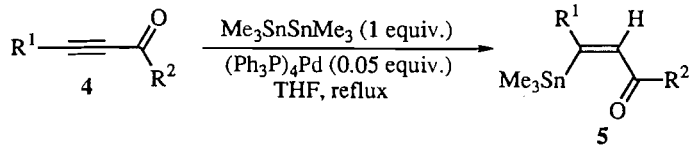

Entry	Starting material 4	R^1	R^2	Reaction time (h)	Product 5	Yield (%)[a]
1	**26**	TBDMSO$(CH_2)_2$[b]	H	2	**41**	87
2	**27**	MOMO$(CH_2)_2$[c]	H	2	**42**	76
3	**28**	TBDMSO$(CH_2)_4$[b]	H	2	**43**	88
4	**29**	TBDMSO$(CH_2)_2$[b]	Me	2	**44**	90
5	**30**	$Cl(CH_2)_3$	Me	3	**45**	81
6	**31**	TBDMSO$(CH_2)_4$[b]	Me	2	**46**	83
7	**32**	H—≡—$(CH_2)_3$	Me	4	**47**	69
8	**33**	i-Pr	Me	5	**48**	80
9	**34**	TBDMSO$(CH_2)_2$[b]	i-Pr	5	**49**	94
10	**35**	*t*-Bu	n-C_6H_{13}	24	**50**	48
11	**36**	H_2C=CH—CH$(CH_2)_2$[b] (OTBDMS)	Me	8	**51**	95

[a]Yield of purified, distilled product.
[b]TBDMS = *tert*-butyldimethylsilyl.
[c]MOM = methoxymethyl.

under conditions similar to those employed for the conversion of **32** into **47** (eq. [6]). The chemoselectivity displayed in the **32** → **47** transformation shows clearly that Pd(0)-catalyzed reactions of terminal alkynes with $Me_3SnSnMe_3$ are appreciably slower than those involving α,β-alkynic aldehydes and ketones.

The reaction involving substrate **35** was found to be sluggish (Table 2, entry 10, eq. [7]). Thus, even after a reaction

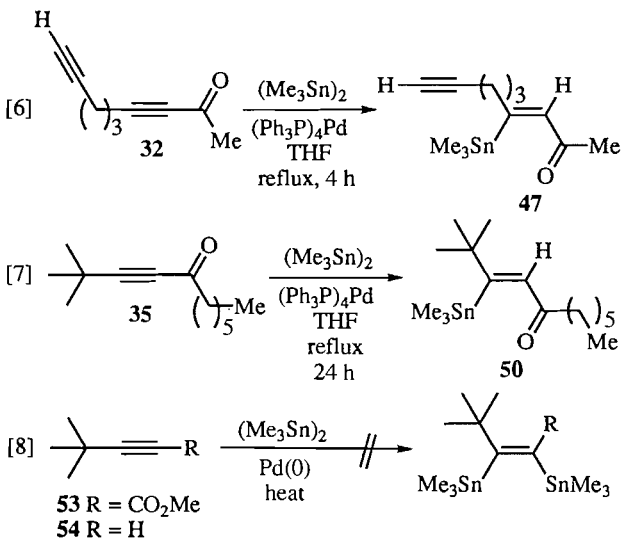

time of 24 h, analyses (tlc, gas–liquid chromatography (glc)) of aliquots of the reaction mixture showed the presence of the starting material **35**, along with $Me_3SnSnMe_3$. Furthermore, monitoring of the reaction mixture by tlc indicated that, as reaction times were increased, a number of minor side products were produced. Work-up and product isolation after a reaction time of 24 h produced product **50** in 48% yield (eq. [7]). The fact that the transformation of **35** into **50** occurred at all is noteworthy, since it has been shown that neither the alkynic ester **53**[3] nor the 1-alkyne **54** (8) react with $Me_3SnSnMe_3$ in the presence of a Pd(0) catalyst, even after prolonged heating of the reaction mixtures (eq. [8]).

Mechanistic considerations

The Pd(0)-catalyzed addition of $Me_3SnSnMe_3$ to α,β-alkynic esters, as summarized in eq. [1], has been proposed to proceed via the catalytic cycle shown in Scheme 2 (1). Furthermore, the thermal rearrangement of the resultant products **2** into the corresponding geometric isomers **3** (eq. [2]) has been rationalized as shown in eq. [9] (1). Thus, according to this proposal, thermolysis of **2** results in (reversible) migration of the α-Me_3Sn group from carbon to the ester carbonyl oxygen to produce the trimethylstannyl allenoate intermediate **55**. A second migration of the Me_3Sn group back to the α carbon, but to the side of the intermediate opposite the β-Me_3Sn function, would provide the *E* isomer **3**. Of the three compounds shown in eq. [9], it is apparent that both **2** and **3** are more stable than the allenoate **55**. However, presumably due primarily to steric repulsion between the two Me_3Sn groups in the *Z* isomer **2**, the equilibrium between **2** and **3** overwhelmingly favors the latter isomer.

Presumably, the Pd(0)-catalyzed reaction of α,β-alkynic

[3] Unpublished work carried out in these laboratories by R.T. Skerlj.

Scheme 2.

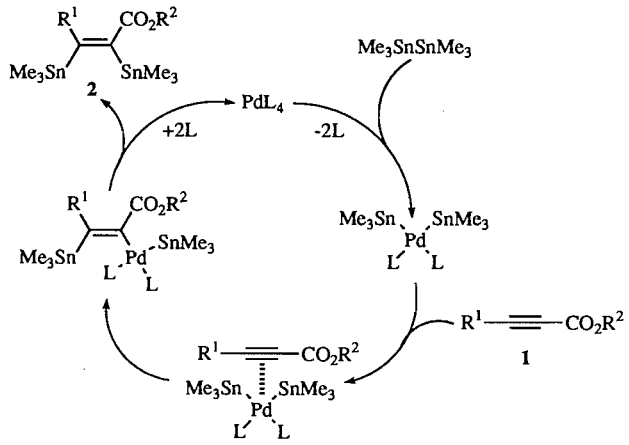

aldehydes and ketones (general formula **4**) with $Me_3SnSnMe_3$ proceeds via a catalytic cycle analogous to that shown in Scheme 2 (see eq. [10]). It seems reasonable to conclude that

[9] 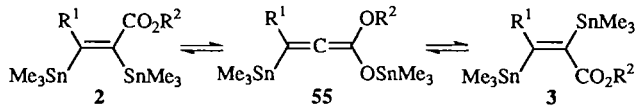

[10] 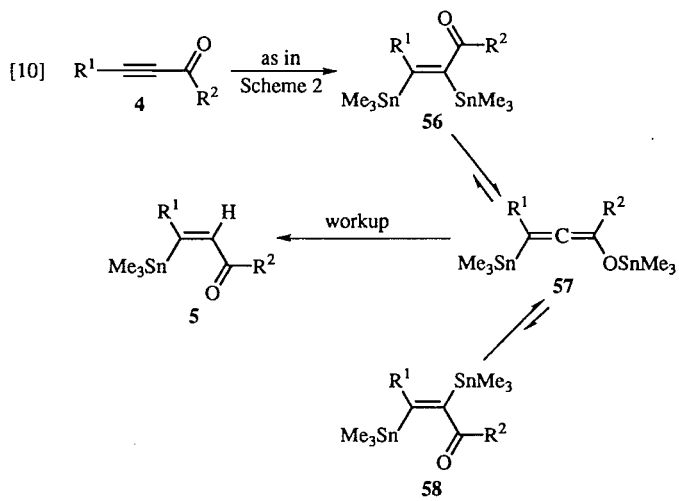

the initial products produced from these processes are the (*Z*)-2,3-bis(trimethylstannyl) α,β-alkenic carbonyl compounds of general structure **56**. To account for the fact that the isolated products are the mono(trimethylstannyl) substances **5**, we propose that **56** and the geometric isomers **58** are unstable with respect to the allenoates **57** (eq. [10]). Thus, in contrast to the ester series, it appears that the first-formed products **56** readily isomerize to the allenoates **57** and that, upon work-up, the latter species are protonated from the side opposite the β-Me_3Sn group to provide the observed products of general structure **5**.

The rationale presented above is supported to some degree by work published by Tsuda et al. (9). These workers reported that the structures of intermediates derived from the reaction of diisobutylaluminum hydride with α,β-alkynic carbonyl compounds are dependent on the nature of the carbonyl group in the substrate. Thus, for example, treatment of methyl propynoate with i-Bu_2AlH in hexamethylphosphoramide (HMPA) produces the alkenylalane **59** (eq. [11]), while an identical reaction involving 1-hexyn-3-one as the substrate affords the diisobutylalanyl allenoate **60** (eq. [12]). The similarities between these results and those derived from our studies (vide supra) are striking.

[11] 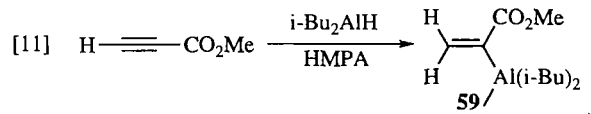

[12] 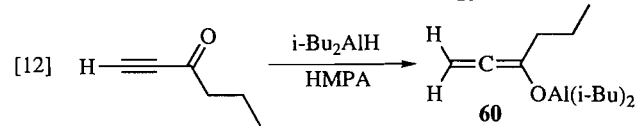

Conversion of the (*Z*)-β-trimethylstannyl α,β-alkenic aldehydes 41–43 and ketones 44–51 into the substituted (*Z*)-4-trimethylstannyl-1,3-butadienes and related compounds

Substituted (*Z*)-4-trimethylstannyl-1,3-butadienes of general structure **6**, along with reagents and synthetic intermediates derived therefrom, are, potentially, valuable substances for organic synthesis. However, prior to the work described herein, a convenient method for preparing **6** had not been reported in the chemical literature and, consequently, the synthetic utility of these materials has not been investigated systematically. The work described above had resulted in the development of a concise, efficient, and experimentally straightforward method for preparing substituted (*Z*)-β-trimethylstannyl α,β-alkenic aldehydes and ketones of general structure **5** (Tables 1 and 2). Obviously, these substances should serve as suitable substrates for the synthesis of the corresponding dienes **6**.

Reaction of the aldehyde **41** with methylenetriphenylphosphorane (prepared from BuLi and $[Ph_3PMe]Br$) in dry THF at room temperature provided, cleanly and efficiently, the trimethylstannyl diene **61** (Table 3, entry 1). In a similar fashion, the aldehydes **42** and **43** were transformed into the dienes **62** and **63**, respectively, in excellent yields (entries 2 and 3).

The (*Z*)-β-trimethylstannyl α,β-alkenic ketones of general structure **5** (R^2 = alkyl) could also be converted into the corresponding dienes **6** using the procedure described above, but, in these cases, complete conversion of the starting materials into products was not complete even after reaction times of several hours at room temperature. Furthermore, long reaction times created "dirty" reaction mixtures and the isolated yields of the desired trimethylstannyl dienes were generally unsatisfactory. In fact, of the ketones subjected to these conditions, only **48** was converted efficiently into the corresponding diene **68** (entry 8), although the reaction time was 10 times that required for the aldehydes **41–43**.

It seems likely that the sluggish nature of the conversion of the ketones **5** into the dienes **6** using $Ph_3P{=}CH_2$ in THF is due to a competition between the required Wittig process and an enolate-forming reaction resulting from the reagent acting as a base rather than a nucleophile. It has been reported (10) that reaction of enolizable ketones with $Ph_3P{=}CH_2$ (prepared from $[Ph_3PMe]Br$ and $NaOC(Et)Me_2$) in benzene provides the corresponding alkenes in good yields. Use of this protocol in

Table 3. Preparation of substituted (*Z*)-4-trimethylstannyl-1,3-butadienes **61–71**.

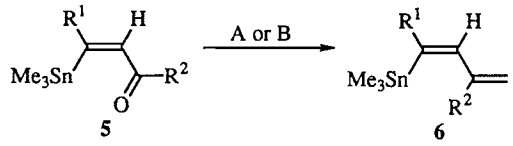

Entry	Starting material **5**	R^1	R^2	Conditions[a]	Reaction time (min)	Product **6**	Yield (%)[b]
1	**41**	TBDMSO$(CH_2)_2$[c]	H	A	30	**61**	87
2	**42**	MOMO$(CH_2)_2$[d]	H	A	30	**62**	82
3	**43**	TBDMSO$(CH_2)_4$[c]	H	A	30	**63**	81
4	**44**	TBDMSO$(CH_2)_2$[c]	Me	B	30	**64**	86
5	**45**	$Cl(CH_2)_3$	Me	B	30	**65**	57
6	**46**	TBDMSO$(CH_2)_4$[c]	Me	B	30	**66**	75
7	**47**	H—≡—$(CH_2)_3$	Me	B	30	**67**	83
8	**48**	i-Pr	Me	A	300	**68**	87
9	**49**	TBDMSO$(CH_2)_2$[c]	i-Pr	B	15	**69**	64
10	**50**	*t*-Bu	*n*-C_6H_{13}	B	30	**70**	81
11	**51**	H_2C=CH—$CH(CH_2)_2$[c] (OTBDMS)	Me	B	30	**71**	85

[a]A: Ph_3P=CH_2 (prepared from $Ph_3P(Me)Br$ and *n*-BuLi in dry THF), THF, room temperature. B: Ph_3P=CH_2 (prepared from $Ph_3P(Me)Br$ and $NaOC(Et)Me_2$ in dry benzene), benzene, room temperature.
[b]Yield of purified, distilled product.
[c]TBDMS = *tert*-butyldimethylsilyl.
[d]MOM = methoxymethyl.

the present work proved to be satisfactory. As can be seen from a perusal of Table 3, subjection of the ketones **44–47** and **49–51** to these reaction conditions provided good to excellent yields of the corresponding dienes (entries 4–7, 9–11).

The aldehydes **41** and **42** also react smoothly with Wittig–Horner reagents. For example, treatment of **41** with the anion of trimethyl phosphonoacetate in dry THF at 0°C afforded the 5-trimethylstannyl-2,4-heptadienoate **72** in 92% yield (eq. [13]). Similarly, reaction of **42** with the reagent derived from treatment of the phosphonate **73** with NaH in dry THF gave the *tert*-butyl ester **74** (91%, eq. [14]).

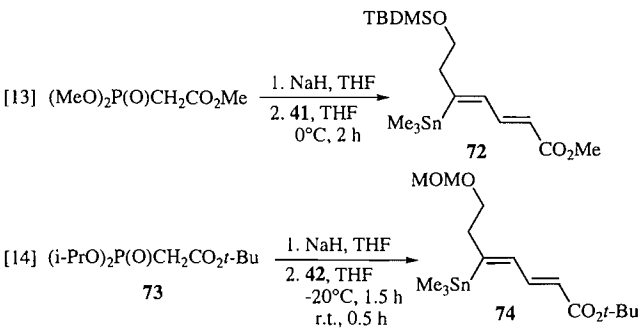

All of the Wittig (**61–71**) and Wittig–Horner (**72**, **74**) products prepared as described above exhibited spectral properties in full accord with the assigned structures. Details are given in the experimental section.

Synthetic uses of (*Z*)-4-trimethylstannyl-1,3-butadienes

We end this discussion with a description of a brief preliminary study on the synthetic utility of the substituted (*Z*)-4-trimethylstannyl-1,3-butadienes. It is evident that these substances should be excellent precursors of organometallic reagents derived by initial transmetallation of the alkenyl Me_3Sn function. Indeed, treatment of (*Z*)-6-methoxymethoxy-4-trimethylstannyl-1,3-hexadiene (**62**) with MeLi (1.1 equiv.) in dry THF at −78°C, followed by addition of ethylene oxide to the resultant solution of the lithio diene reagent **75**, afforded the functionalized diene **76** in 71% yield (Scheme 3). On the other hand, treatment of the lithio diene **75** with 1 equiv. of copper(I) bromide – dimethyl sulfide complex (11) provided the organocopper(I) reagent **77**, which, upon reaction with 2,3-dibromopropene, gave the substituted (*Z*)-1,3,6-hep-

Scheme 3.

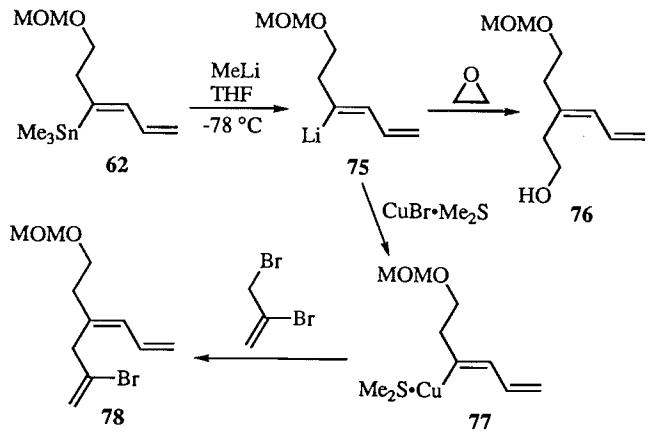

tatriene **78** (83%). Clearly, **62** and related substances of general structure **79** (Table 3 and eqs. [13] and [14]) should serve as suitable precursors for the synthesis of a wide variety of stereochemically defined dienes of general structure **80**.

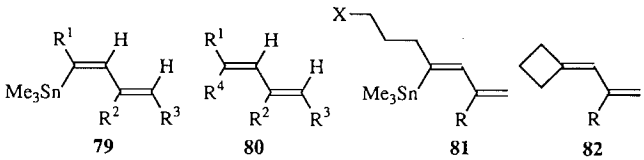

79 **80** **81** **82**

The possibility of employing functionalized (*Z*)-4-trimethylstannyl-1,3-butadienes of general structure **81** (X = leaving group) as synthetic precursors of substituted dienes possessing the novel general structure **82** was also investigated briefly (see Scheme 4). Treatment of (*Z*)-7-chloro-2-methyl-4-trimethylstannyl-1,3-heptadiene (**65**) with MeLi in dry THF at −78°C, followed by warming of the reaction mixture to −48°C, did not lead to a clean reaction. Analyses (glc) of aliquots of the reaction mixture showed the presence of two major products that, on the basis of ^{1}H nmr spectroscopy, appeared to be the desired diene **84** and the noncyclized material **86** (Scheme 4). The ratio of these two products varied somewhat, depending on the reaction conditions, but the most favorable result produced **84** and **86** in a ratio of about 6:1.

It seems reasonable to propose that the mixture of **84** and **86** is produced via a competition between two processes, one involving ring closure of the intermediate **83** (displacement of chloride ion to provide **84**) and the other involving internal proton transfer from the vinyl methyl group to the lithium-bearing carbon (five-membered cyclic transition state) to give the substituted allyllithium **85**. Protonation of the latter species during work-up would produce **86**. If this proposal is correct, increasing the rate of the ring closure reaction without appreciably affecting the rate of the proton transfer process would resolve the difficulty. To that end, treatment of the chloride **65** with NaI in acetone gave the corresponding iodide **87** (Scheme 4). Reaction of the latter compound with MeLi in dry THF (−78 to −48°C), followed by a suitable work-up procedure, gave cleanly a solution of the diene **84** in Et_2O–THF. No other product could be detected by gas–liquid chromatographic analyses.

Due to the volatile nature of the diene **84**, attempts to isolate it free from solvent were not carried out. Instead, the solution of **84** derived from the work-up procedure was placed under an atmosphere of argon and was treated with tetracyanoethylene, which was added in small batches. Upon complete disappearance of the starting material (analyses by glc), the mixture was concentrated and the crude product was purified by flash chromatography. Recrystallization (petroleum ether) of the acquired solid provided, in 69% yield, the functionalized spiro[3.5]nonene **88**. In a similar fashion, when a solution of the diene **84** in benzene was treated with dimethyl acetylenedicarboxylate and the resultant mixture was heated at 70°C for 36 h (argon atmosphere, sealed tube), the substituted spiro[3.5]nonadiene **89** was obtained in 70% yield (Scheme 4).

The Diels–Alder reactivity of the diene **84** is noteworthy and can probably be attributed primarily to two factors. In the conformation required for the cycloaddition reaction (see **84A**), the steric repulsion between H_A and the cyclobutyl methylene group would be less severe than that present

Scheme 4.

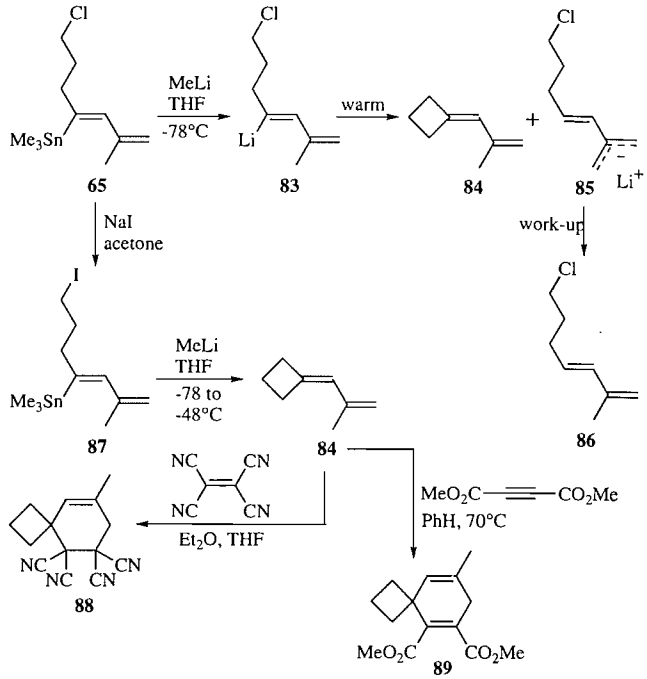

between H_A and a methyl group in, for example, an acyclic diene such as **90**. Therefore, Diels–Alder reactions of **84** would be expected to be more facile than those of acyclic analogs (e.g., **90**). Furthermore, conversion of **84** into a Diels–Alder product is accompanied by a decrease in the angle strain associated with the four-membered ring, since the conversion involves translation of one of the cyclobutyl carbons from an sp^2 to an sp^3 center. This release of strain would be "felt" by the transition state for the cycloaddition process.

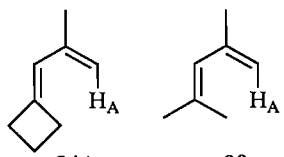

84A **90**

Conclusion

The research results summarized above show that readily prepared α,β-alkynic aldehydes and ketones (general structure **4**) serve as excellent synthetic precursors of the corresponding (*Z*)-β-trimethylstannyl α,β-alkenic aldehydes and ketones (structure **5**) and that the latter substances are readily trans-

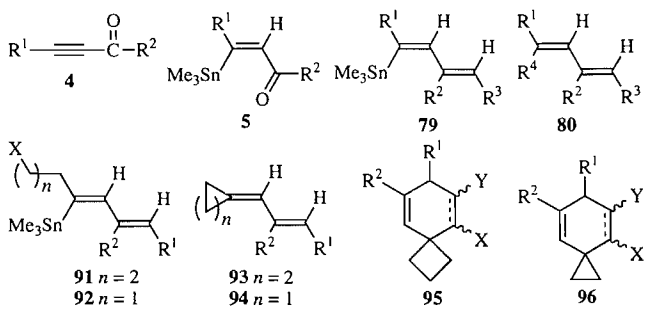

4 **5** **79** **80**

91 $n = 2$
92 $n = 1$

93 $n = 2$
94 $n = 1$

95 **96**

formed into substituted, stereochemically defined dienes of general structure **79**. The possibility of using the alkenyltrimethylstannyl function in **79** as a "handle" for introducing functionalized alkyl substituents was successfully demonstrated and, thus, dienes of general structure **80** are also available via the developed methodology.

It was also shown, by the conversion of **87** into **84** (Scheme 4), that substances of general structure **91** (X = I) should serve as effective precursors for the preparation of alkyldienecyclobutanes (see **93**). Successful Diels–Alder reactions of **93** with suitable dienophiles (see the conversions of **84** into **88** and **89**, Scheme 4) would provide spiro compounds of general structure **95**. It seems likely that similar processes involving conversions of **92** (X = Cl, Br, or I) into functionalized spiro[2.5]octanes **96**, via dienes of general structure **94**, should also be possible. Studies related to these possibilities, along with investigations into further synthetic uses of (*Z*)-β-trimethylstannyl α,β-alkenic carbonyl compounds and dienes derived therefrom, are currently underway in our laboratories.

Experimental

General information

Melting points and distillation temperatures (short-path Kugelrohr distillations) are uncorrected. Infrared (ir) spectra were recorded using potassium bromide pellets or liquid films on sodium chloride discs. Proton (^{1}H) and carbon (^{13}C) nuclear magnetic resonance (nmr) spectra were recorded using $CDCl_3$ solutions. Signal positions in ^{1}H nmr spectra were measured relative to the signals for Me_4Si (δ 0) (internal standard) or $CHCl_3$ (δ 7.25), while resonances in ^{13}C nmr spectra were measured relative to the signal for $CDCl_3$ (δ 77.0). Tin-hydrogen coupling constants (J_{Sn-H}) are given as the average of the ^{117}Sn and ^{119}Sn values. Molecular mass determination (high-resolution mass spectrometry) for substances containing Me_3Sn are based on ^{120}Sn. Flash chromatography (5) and conventional column chromatography were carried out with 230–400 and 70–230 mesh silica gel (E. Merck), respectively. Thin-layer chromatography (tlc) was accomplished with commercial aluminum-backed plates (E. Merck, Type 5554). Gas–liquid chromatography (glc) was performed on instruments equipped with flame ionization detectors and 25 m × 0.21 mm fused silica columns coated with cross-linked SE-54. Commercial $(Me_3Sn)_2$ (Organometallics Inc.) was stored under an inert atmosphere (glove box) and was generally distilled (water aspirator pressure) just prior to use, while commercial $(Ph_3P)_4Pd$ was used without further purification. Aqueous NH_4Cl–NH_4OH (pH 8) was prepared by the addition of ~50 mL of aqueous ammonia (58%) to ~950 mL of saturated aqueous NH_4Cl.

Note: Unless otherwise stated, all reactions were carried out under an atmosphere of dry argon in flamed-dried glassware.

Note: All compounds for which high-resolution mass measurements are given exhibited clean ^{1}H nmr spectra and showed essentially one spot on tlc analyses.

General procedure 1. Preparation of the propargylic alcohols 16–25

To a cold (−78°C), stirred solution of the terminal alkyne (1 equiv.) in dry THF (~3–6 mL per mmol of substrate) was added a solution of MeLi (1 equiv.) in Et_2O. The mixture was stirred at −78°C for 10 min and at −20°C for 1 h. For the preparation of the primary alcohols **16–18**, solid paraformaldehyde (4 equiv.) was added and the mixture was allowed to warm to room temperature. On the other hand, for the synthesis of each of the secondary alcohols **19–25**, the solution of the lithium acetylide was recooled to −78°C prior to addition of the appropriate aldehyde and, after the mixture had been stirred at −78°C for 10 min, it was allowed to warm to room temperature. After each reaction mixture had been stirred for 30 min at room temperature, saturated aqueous $NaHCO_3$ and Et_2O were added. The phases were separated and the aqueous phase was extracted with Et_2O. The combined organic extracts were dried ($MgSO_4$) and concentrated. Each of the crude products, except substance **23** (see Table 1), was purified by flash chromatography, followed by distillation.

The following compounds were prepared via this general procedure.

5-tert-*Butyldimethylsilyloxy-2-pentyn-1-ol (**16**)*

Flash chromatography (130 g of silica gel, 7:3 petroleum ether – Et_2O) of the crude product derived from the terminal alkyne **9** (12) (2.8 g, 15 mmol) and paraformaldehyde (1.8 g, 4 equiv.), followed by distillation (75–80°C/0.5 Torr; 1 Torr = 133.3 Pa) of the acquired material, gave 2.4 g (74%) of the alcohol **16**, a colorless oil that displayed ir (neat): 3394, 2227, 1473, 1109 cm^{-1}; ^{1}H nmr (300 MHz) δ: 0.06 (s, 6H), 0.89 (s, 9H), 1.80–1.95 (br m, 1H), 2.43 (tt, 2H, *J* = 7, 2 Hz), 3.72 (t, 2H, *J* = 7 Hz), 4.24 (br signal, 2H); on addition of D_2O, the signal at δ 1.80–1.95 disappeared and the signal at δ 4.24 sharpened to a t (*J* = 2 Hz). Exact Mass calcd. for $C_7H_{13}O_2Si$ (M^+ − *t*-Bu): 157.0685; found: 157.0679.

*5-Methoxymethoxy-2-pentyn-1-ol (**17**)*

Purification (flash chromatography, 280 g of silica gel, 35:65 petroleum ether – Et_2O; distillation, 110–120°C/0.5 Torr) of the crude product obtained from the 1-alkyne **10** (8.5 g, 74 mmol) and paraformaldehyde (8.9 g, 4 equiv.) provided 8.6 g (80%) of the alcohol **17**, a colorless oil that exhibited ir (neat): 3424, 2227, 1151, 1111, 1029 cm^{-1}; ^{1}H nmr (400 MHz) δ: 0.75–0.90 (br m, 1H), 1.52 (tt, 2H, *J* = 6.5, 2 Hz), 3.38 (s, 3H), 3.65 (t, 2H, *J* = 6.5 Hz), 4.24 (dt, 2H, *J* = 6, 2 Hz), 4.64 (s, 2H); on addition of D_2O, the signal at δ 0.75–0.90 disappeared, and the signal at δ 4.24 collapsed to a br s. Exact Mass calcd. for $C_5H_7O_2$ (M^+ − C_2H_5O): 99.0446; found: 99.0446.

7-tert-*Butyldimethylsilyloxy-2-heptyn-1-ol (**18**)*

This compound was prepared from the terminal alkyne **11** (13) (2.0 g, 9.4 mmol) and paraformaldehyde (1.2 g, 4 equiv.). Flash chromatography of the crude product on silica gel (85 g, 7:3 petroleum ether – Et_2O) and distillation (100–110°C/0.5 Torr) of the derived oil gave 1.9 g (81%) of the alcohol **18**, a colorless oil that showed ir (neat): 3362, 2230, 1256, 1107, 838 cm^{-1}; ^{1}H nmr (300 MHz) δ: 0.04 (s, 6H), 0.86 (s, 9H), 1.57 (m, 4H), 1.78 (br s, 1H), 2.23 (m, 2H), 3.61 (t, 2H, *J* = 7 Hz), 4.24 (br t, 2H, *J* = 2 Hz); on addition of D_2O, the signal at δ 1.78 disappeared. Exact Mass calcd. for $C_9H_{27}O_2Si$ (M^+ − *t*-Bu): 185.0998; found: 185.0997.

6-tert-*Butyldimethylsilyloxy-3-hexyn-2-ol (**19**)*

Purification (flash chromatography, 80 g of silica gel, 7:3

petroleum ether – Et_2O; distillation, 80–90°C/0.5 Torr) of the crude product obtained from the 1-alkyne **9** (1.5 g, 8.2 mmol) and acetaldehyde (0.7 g, 2 equiv.) provided 1.7 g (92%) of the alcohol **19**, a colorless oil that displayed ir (neat): 3368, 2250, 1256, 818 cm^{-1}; ^1H nmr (300 MHz) δ: 0.04 (s, 6H), 0.86 (s, 9H), 1.39 (d, 3H, J = 8 Hz), 2.25 (br s, 1H), 2.38 (dt, 2H, J = 7, 2 Hz), 3.68 (t, 2H, J = 7 Hz), 4.49 (m, 1H); on addition of D_2O, the signal at δ 2.25 disappeared, and the signal at δ 4.49 simplified to a br q (J = 8 Hz). Exact Mass calcd. for $C_8H_{15}O_2Si$ (M^+ − t-Bu): 171.0842; found: 171.0834.

*7-Chloro-3-heptyn-2-ol (**20**)*
This substance was prepared from 5-chloro-1-pentyne (**12**) (4.0 g, 39 mmol) and acetaldehyde (3.4 g, 2 equiv.). Flash chromatography of the crude product on silca gel (150 g, 7:3 petroleum ether – Et_2O) and distillation (65–70°C/0.5 Torr) of the derived oil gave 4.9 g (85%) of the alcohol **20**, a colorless oil that showed ir (neat): 3372, 1089, 1050, 881 cm^{-1}; ^1H nmr (300 MHz) δ: 1.36 (d, 3H, J = 8 Hz), 1.80 (quintet, 2H, J = 8 Hz), 2.33 (td, 2H, J = 8, 2 Hz), 2.75 (br s, 1H), 3.59 (t, 2H, J = 8 Hz), 4.46 (m, 1H); on addition of D_2O, the signal at δ 2.75 disappeared, and the signal at δ 4.46 simplified to a br q (J = 8 Hz). Exact Mass calcd. for $C_7H_{11}{}^{35}ClO$: 146.0499; found: 146.0504.

*8-tert-Butyldimethylsilyloxy-3-octyn-2-ol (**21**)*
Flash chromatography (80 g of silica gel, 7:3 petroleum ether – Et_2O) of the crude product derived from the terminal alkyne **11** (13) (2.0 g, 9.4 mmol) and acetaldehyde (0.8 g, 2 equiv.), followed by distillation (110–120°C/0.5 Torr) of the acquired material, gave 2.2 g (90%) of the alcohol **21**, a colorless oil that displayed ir (neat): 3353, 2248, 1256 cm^{-1}; ^1H nmr (300 MHz) δ: 0.33 (s, 6H), 0.87 (s, 9H), 1.40 (d, 3H, J = 8 Hz), 1.56 (m, 4H), 1.74–1.80 (br m, 1H), 2.22 (m, 2H), 3.60 (t, 2H, J = 6 Hz), 4.50 (m, 1H); on addition of D_2O the signal at δ 1.74–1.80 disappeared and the signal at δ 4.50 simplified to a br q (J = 8 Hz). Exact Mass calcd. for $C_{10}H_{19}O_2Si$ (M^+ − t-Bu): 199.1155; found: 199.1156.

*3,8-Nonadiyn-2-ol (**22**)*
This compound was derived from 1,6-heptadiyne (**13**) (1.0 g, 11 mmol) and acetaldehyde (2.4 g, 5 equiv.). Flash chromatography of the crude product on silica gel (65 g, 65:35 petroleum ether – Et_2O) and distillation (80–85°C/0.5 Torr) of the derived material afforded 0.88 g (60%) of the alcohol **22**, a colorless oil that exhibited ir (neat): 3301, 2247, 2118, 1154, 1013, 882 cm^{-1}; ^1H nmr (400 MHz) δ: 1.41 (d, 3H, J = 6.5 Hz), 1.65–1.75 (m, 3H), 1.95 (t, 1H, J = 2.5 Hz), 2.25–2.40 (m, 4H), 4.49 (m, 1H); on addition of D_2O, the signal at δ 1.65–1.75 collapsed to a quintet (2H, J = 7 Hz), and the signal at δ 4.49 simplified to a br q (J = 6.5 Hz). Exact Mass calcd. for $C_9H_{11}O$ (M^+ − H): 135.0810; found: 135.0815.

*5-Methyl-3-hexyn-2-ol (**23**)*
This substance was derived from 3-methyl-1-butyne (**14**) (3.0 g, 44 mmol) and acetaldehyde (3.9 g, 2 equiv.). After work-up of the reaction mixture, the solution containing the product was concentrated by distillation (atmospheric pressure) through a Vigreaux column (50 × 2 cm). Distillation (80–90°C/10 Torr) of the residual material gave a crude oil (4.6 g) that consisted mainly of the alcohol **23**. This material was used immediately for the next (oxidation) reaction (vide infra).

*7-tert-Butyldimethylsilyloxy-2-methyl-4-heptyn-3-ol (**24**)*
Flash chromatography (300 g of silica gel, 7:3 petroleum ether – Et_2O) of the crude product derived from the terminal alkyne **9** (12) (8.2 g, 45 mmol) and 2-methylpropanal (4.8 g, 1.5 equiv.), followed by distillation (110–120°C/0.5 Torr) of the acquired material, gave 9.7 g (85%) of the alcohol **24**, a colorless oil that displayed ir (neat): 3368, 2218, 1256, 1113, 836, 777 cm^{-1}; ^1H nmr (400 MHz) δ: 0.06 (s, 6H), 0.89 (s, 9H), 0.96, 0.98 (d, d, 3H each, J = 6 Hz in each case), 1.70 (br d, 1H, J = 4 Hz), 1.82 (m, 1H), 2.42 (td, 2H, J = 8, 2 Hz), 3.70 (t, 2H, J = 8 Hz), 4.13 (br m, 1H); on addition of D_2O, the signal at δ 1.70 disappeared, and the signal at δ 4.13 simplified to a br d (J = 6 Hz). Exact Mass calcd. for $C_{11}H_{21}O_2Si$ (M^+ − i-Pr): 213.1311; found: 213.1318.

*2,2-Dimethyl-3-undecyn-5-ol (**25**)*
This material was synthesized from 3,3-dimethyl-1-butyne (**15**) (3.5 g, 43 mmol) and heptanal (7.3 g, 1.5 equiv.). Flash chromatography of the crude product on silica gel (250 g, 7:3 petroleum ether – Et_2O), followed by distillation (80–85°C/0.5 Torr) of the acquired liquid, gave 8.1 g (96%) of the alcohol **25**, a colorless oil that exhibited ir (neat): 3342, 2238, 1460, 1265 cm^{-1}; ^1H nmr (300 MHz) δ: 0.87 (m, 3H), 1.20 (s, 9H), 1.25–1.70 (m, 10H), 2.85 (br s, 1H), 4.33 (br t, 1H, J = 8 Hz); on addition of D_2O, the signal at δ 2.85 disappeared. Exact Mass calcd. for $C_{13}H_{24}O$: 196.1828; found: 196.1819.

General procedure 2. Oxidation of the alcohols 16–25 to the α,β-alkynic aldehydes 26–28 and ketones 29–35
A mixture of the alcohol (1 equiv.), NaOAc (0.3 equiv.), and pyridinium chlorochromate (1.5 equiv. for the alcohols **16–18**, 2.5 equiv. for the alcohols **19–25**) in dry CH_2Cl_2 (~5-10 mL per mmol of alcohol substrate) was stirred (2 h for the alcohols **16–18**, 2.5 h for the alcohols **19–25**) at room temperature. Dry Et_2O (the same volume as that used for the reaction mixture) was added and the mixture was filtered through a column of Florisil® (~30 g per g of propargylic alcohol), using Et_2O as eluant. The material remaining in the reaction vessel was rinsed (and sonicated) thoroughly with Et_2O, and the washings were also passed through the Florisil® column. The combined eluate was dried ($MgSO_4$) and concentrated. The crude product was purified by flash chromatography and (or) distillation.

The following carbonyl compounds were prepared via this general procedure.

*5-tert-Butyldimethylsilyloxy-2-pentynal (**26**)*
Flash chromatography (80 g of silica gel, 5:1 petroleum ether – Et_2O) of the crude product derived from oxidation of the alcohol **16** (2.4 g, 11 mmol), followed by distillation (75–85°C/0.5 Torr) of the acquired liquid, gave 1.7 g (72%) of the aldehyde **26**, a colorless oil that exhibited ir (neat): 2740, 2207, 1673, 1275 cm^{-1}; ^1H nmr (300 MHz) δ: 0.05 (s, 6H), 0.87 (s, 9H), 2.60 (t, 2H, J = 8 Hz), 3.77 (t, 2H, J = 8 Hz), 9.15 (s, 1H). Exact Mass calcd. for $C_7H_{11}O_2Si$ (M^+ − t-Bu): 155.0528; found: 155.0532.

*5-Methoxymethoxy-2-pentynal (**27**)*
This compound was obtained by oxidation of the alcohol **17** (3.6 g, 25 mmol). Flash chromatography of the crude product on silica gel (120 g, 4:6 petroleum ether – Et_2O), followed by distillation (90–95°C/0.5 Torr) of the derived oil, gave 1.9 g

(57%) of the aldehyde **27**, a colorless oil that displayed ir (neat): 2827, 2207, 1669, 1115, 1111, 963 cm^{-1}; ^1H nmr (400 MHz) δ: 2.72 (t, 2H, J = 7 Hz), 3.38 (s, 3H), 3.72 (t, 2H, J = 7 Hz), 4.64 (s, 2H), 9.18 (s, 1H). Exact Mass calcd. for $C_7H_9O_3$ ($M^+ - H$): 141.0551; found: 141.0546.

*7-*tert*-Butyldimethylsilyloxy-2-heptynal (**28**)*
Oxidation of the alcohol **18** (0.9 g, 3.7 mmol), followed by purification (flash chromatography, 40 g of silica gel, 5:1 petroleum ether – Et_2O; distillation, 95–100°C/0.5 Torr) of the crude product gave 0.7 g (74%) of the aldehyde **28**, a colorless oil that showed ir (neat): 2742, 2202, 1673, 838 cm^{-1}; ^1H nmr (300 MHz) δ: 0.05 (s, 6H), 0.90 (s, 9H), 1.65 (m, 4H), 2.46 (t, 2H, J = 8 Hz), 3.63 (t, 2H, J = 6 Hz), 9.18 (s, 1H). Exact Mass calcd. for $C_9H_{15}O_2Si$ ($M^+ - t$-Bu): 183.0842; found: 183.0834.

*6-*tert*-Butyldimethylsilyloxy-3-hexyn-2-one (**29**)*
This substance was derived from oxidation of the alcohol **19** (0.2 g, 0.9 mmol). Flash chromatography of the crude product on silica gel (45 g, 9:1 petroleum ether – Et_2O), followed by distillation (70–80°C/0.5 Torr) of the acquired oil furnished 0.15 g (74%) of the ketone **29**, a colorless oil that displayed ir (neat): 2214, 1680, 1113, 839 cm^{-1}; ^1H nmr (300 MHz) δ: 0.08 (s, 6H), 0.89 (s, 9H), 2.30 (s, 3H), 2.56 (t, 2H, J = 8 Hz), 3.76 (t, 2H, J = 8 Hz). Exact Mass calcd. for $C_8H_{13}O_2Si$ ($M^+ - t$-Bu): 169.0685; found: 169.0684.

*7-Chloro-3-heptyn-2-one (**30**)*
Flash chromatography (80 g of silica gel, 9:1 petroleum ether – Et_2O) of the crude product derived from the alcohol **20** (1.5 g, 10 mmol), followed by distillation (60–65°C/0.5 Torr) of the acquired liquid, gave 1.1 g (74%) of the ketone **30**, a colorless oil that showed ir (neat): 2215, 1677, 1232, 734 cm^{-1}; ^1H nmr (300 MHz) δ: 2.0 (quintet, 2H, J = 7 Hz), 2.30 (s, 3H), 2.54 (t, 2H, J = 7 Hz), 3.51 (t, 2H, J = 7 Hz). Exact Mass calcd. for $C_7H_9{}^{35}ClO$: 144.0343; found: 144.0343.

*8-*tert*-Butyldimethylsilyloxy-3-octyn-2-one (**31**)*
The crude product obtained from oxidation of the alcohol **21** (1.0 g, 3.9 mmol) was purified by flash chromatography (75 g of silica gel, 9:1 petroleum ether – Et_2O) and distillation (95–100°C/0.5 Torr). The resultant product **31** (0.76 g, 76%), a colorless oil, displayed ir (neat): 2212, 1680, 1360, 1104 cm^{-1}; ^1H nmr (300 MHz) δ: 0.04 (s, 6H), 0.88 (s, 9H), 1.62 (m, 4H), 2.30 (s, 3H), 2.38 (t, 2H, J = 7 Hz), 3.62 (t, 2H, J = 6 Hz). Exact Mass calcd. for $C_{10}H_{17}O_2Si$ ($M^+ - t$-Bu): 197.0998; found: 197.1006.

*3,8-Nonadiyn-2-one (**32**)*
This material was obtained by oxidation of the alcohol **22** (0.13 g, 1.0 mmol). Flash chromatography of the crude product on silica gel (35 g, 9:1 petroleum ether – Et_2O), followed by distillation (120–130°C/6.0 Torr) of the derived liquid, gave 0.07 g (55%) of the ketone **32**, a colorless oil that showed ir (neat): 2215, 1680, 1231 cm^{-1}; ^1H nmr (400 MHz) δ: 1.79 (quintet, 2H, J = 7 Hz), 1.98 (t, 1H, J = 2.5 Hz), 2.31 (s, 3H), 2.32 (td, 2H, J = 7, 2.5 Hz), 2.50 (t, 2H, J = 7 Hz). Exact Mass calcd. for C_9H_9O ($M^+ - H$): 133.0653; found: 133.0651.

*5-Methyl-3-hexyn-2-one (**33**)*
Oxidation of the previously prepared, crude 5-methyl-3-hexyn-2-ol (**23**) (vide supra), followed by work-up of the reaction mixture, gave a solution of the ketone **33**. Concentration of this solution by distillation (atmospheric pressure) of the solvent through a Vigreaux column (50 × 2 cm) gave an oil that, upon distillation (80–90°C/10 Torr), provided 2.7 g (57% from 3-methyl-1-butyne (**14**)) of the ketone **33**, a colorless oil that displayed ir (neat): 2208, 1679, 1228 cm^{-1}; ^1H nmr (300 MHz) δ: 1.20 (d, 6H, J = 8 Hz), 2.29 (s, 3H), 2.68 (septet, 1H, J = 8 Hz). Exact Mass calcd. for $C_7H_{10}O$: 110.0732; found: 110.0726.

*7-*tert*-Butyldimethylsilyloxy-2-methyl-4-heptyn-3-one (**34**)*
Flash chromatography (150 g of silica gel, 9:1 petroleum ether – Et_2O) of the crude product derived from the alcohol **24** (2.9 g, 11 mmol), followed by distillation (95–105°C/0.5 Torr) of the acquired liquid, gave 2.4 g (81%) of the ketone **34**, a colorless oil that showed ir (neat): 2214, 1676, 1118, 779 cm^{-1}; ^1H nmr (400 MHz) δ: 0.08 (s, 6H), 0.90 (s, 9H), 1.18 (d, 6H, J = 8 Hz), 2.58–2.68 (m, 3H), 3.80 (t, 2H, J = 6 Hz). Exact Mass calcd. for $C_{10}H_{17}O_2Si$ ($M^+ - t$-Bu): 197.0998; found: 197.1003.

*2,2-Dimethyl-3-undecyn-5-one (**35**)*
This compound was derived from oxidation of the alcohol **25** (4.0 g, 20 mmol). Flash chromatography of the crude product on silica gel (150 g, 9:1 petroleum ether – Et_2O) and distillation (75–80°C/0.5 Torr) of the acquired liquid provided 2.9 g (72%) of the ketone **35**, a colorless oil that exhibited ir (neat): 2213, 1675, 1263, 1142 cm^{-1}; ^1H nmr (300 MHz) δ: 0.87 (m, 3H), 1.28 (br s, 15H), 1.63 (m, 2H), 2.50 (t, 2H, J = 7 Hz). Exact Mass calcd. for $C_{13}H_{22}O$: 194.1672; found: 194.1680.

3-*tert*-Butyldimethylsilyloxy-1-hepten-6-yne (40)
To a stirred solution of 4-pentyn-1-ol (**37**) (3.0 g, 36 mmol) in dry CH_2Cl_2 (100 mL) was added NaOAc (0.9 g, 0.3 equiv.) and PCC (12 g, 1.5 equiv.). After the mixture had been stirred for 2 h at room temperature, dry Et_2O (~100 mL) was added and the mixture was filtered through a column of Florisil® (~100 g, elution with Et_2O). The material remaining in the reaction vessel was rinsed (and sonicated) thoroughly with Et_2O, and the washings were also passed through the Florisil® column. The combined eluate was dried ($MgSO_4$) and most of the solvent was removed by distillation (atmospheric pressure) using a Vigreaux column (50 × 2 cm). The remaining crude product **38** was dissolved in dry THF (100 mL) and the solution was cooled to −78°C. A solution of vinyl magnesium bromide (2 equiv.) in THF was added and the mixture was allowed to warm to room temperature. Saturated aqueous NH_4Cl (~50 mL) and Et_2O (50 mL) were added and the phases were separated. The aqueous phase was extracted with Et_2O and the combined organic extracts were dried ($MgSO_4$) and concentrated by distillation (atmospheric pressure) using a Vigreaux column (50 × 2 cm).

To a stirred solution of the crude oil **39** thus obtained in dry DMF (80 mL) was added imidazole (6.1 g, 2.5 equiv.) and *tert*-butyldimethylsilyl chloride (8.1 g, 1.5 equiv.). The mixture was stirred at room temperature overnight. Saturated aqueous $NaHCO_3$ (~50 mL) and Et_2O (~50 mL) were added and the aqueous phase was extracted with Et_2O. The combined organic extracts were washed with brine, dried ($MgSO_4$), and concentrated. Flash chromatography of the crude product on

silica gel (180 g, 98:2 petroleum ether – Et_2O), followed by distillation (80–90°C/0.5 Torr) of the derived oil gave 2.5 g (31%) of the alkyne **40**, a colorless oil that showed ir (neat): 3314, 3081, 2121, 1254, 838 cm^{-1}; ^1H nmr (400 MHz) δ: 0.02 (s, 3H), 0.06 (s, 3H), 0.89 (s, 9H), 1.68 (m, 2H), 1.92 (t, 1H, J = 4 Hz), 2.22 (m, 2H), 4.22 (m, 1H), 5.05 (ddd, 1H, J = 10, 2, 2 Hz), 5.17 (ddd, 1H, J = 16, 2, 2 Hz), 5.88 (ddd, 1H, J = 16, 10, 6 Hz). Exact Mass calcd. for $C_{13}H_{24}OSi$: 224.1597; found: 224.1593.

7-*tert*-Butyldimethylsilyloxy-8-nonen-3-yn-2-one (36)

To a cold (−78°C), stirred solution of the 1-alkyne **40** (0.44 g, 2.0 mmol) in dry Et_2O (10 mL) was added MeLi (1 equiv.) in Et_2O. After the reaction mixture had been stirred at −78°C for 10 min and at −20°C for 1 h, it was recooled to −78°C and then was transferred slowly (over ~10 min, via cannula) into a cold (−78°C), stirred solution of Ac_2O (2 equiv.) in dry Et_2O (8 mL). After the resultant mixture had been stirred for 10 min at −78°C and 30 min at −48°C, saturated NH_4Cl–NH_4OH (pH 8, 15 mL) was added and the vigorously stirred mixture was allowed to warm to room temperature. The phases were separated and the aqueous phase was extracted with Et_2O. The combined organic extracts were washed with saturated aqueous NH_4Cl, dried ($MgSO_4$), and concentrated. Flash chromatography of the crude product on silica gel (50 g, 9:1 petroleum ether – Et_2O), followed by distillation (90–100°C/0.5 Torr) of the acquired liquid, gave 0.33 g (63%) of the ketone **36**, a colorless oil that displayed ir (neat): 3082, 2211, 1681, 1228, 838 cm^{-1}; ^1H nmr (400 MHz) δ: 0.03 (s, 3H), 0.06 (s, 3H), 0.89 (s, 9H), 1.74 (m, 2H), 2.31 (s, 3H), 2.41 (m, 2H), 4.22 (m, 1H), 5.08 (ddd, 1H, J = 10, 2, 2 Hz), 5.19 (ddd, 1H, J = 17, 2, 2 Hz), 5.77 (ddd, 1H, J = 17, 10, 6 Hz). Exact Mass calcd. for $C_{11}H_{17}O_2Si$ (M^+ − *t*-Bu): 209.0998; found: 209.0995.

General procedure 3. Pd(0)-catalyzed reaction of α,β-alkynic aldehydes 26–28 and ketones 29–36 with hexamethylditin. Preparation of compounds 41–51

To a stirred solution of the α,β-alkynic aldehyde or ketone (1 equiv.) in dry THF (for **26**, **28**, **30**, and **33–35**, ~2 mL per mmol of substrate; for **27**, **29**, **31**, **32**, and **36**, ~3 mL per mmol of substrate) (argon atmosphere) was added $(Me_3Sn)_2$ (1 equiv.) and $Pd(Ph_3)_4$ (5 mol%). The mixture was allowed to reflux for the time indicated in Table 2. In each case, the progress of the reaction was monitored by tlc. When the reaction was complete, the solvent was removed and the viscous residual oil was purified by chromatography and distillation.

The following (*Z*)-β-trimethylstannyl α,β-alkenic aldehydes and ketones were prepared via this general procedure.

*(Z)-5-*tert*-Butyldimethylsilyloxy-3-trimethylstannyl-2-pentenal (41)*

Flash chromatography (100 g of silica gel, 95:5 petroleum ether – Et_2O) of the crude product derived from the aldehyde **26** (1.5 g, 7.1 mmol), followed by distillation (110–120°C/0.5 Torr) of the acquired oil, provided 2.4 g (87%) of the aldehyde **41**, a colorless oil that displayed ir (neat): 2743, 1685, 1563, 1099, 776 cm^{-1}; ^1H nmr (300 MHz) δ: 0.04 (s, 6H), 0.26 (s, 9H, $^2J_{Sn-H}$ = 54 Hz), 0.86 (s, 9H), 2.69 (td, 2H, J = 6.5, 1.3 Hz, $^3J_{Sn-H}$ = 46 Hz), 3.69 (t, 2H, J = 6.5 Hz), 6.68 (dt, 1H, J = 5.5, 1.3 Hz, $^3J_{Sn-H}$ = 114 Hz), 9.56 (d, 1H, J = 5.5 Hz, $^4J_{Sn-H}$ = 5.5 Hz); in nOe difference experiments, irradiation at δ 6.68 caused enhancement of the signals at δ 2.69 and 9.59, irradiation at δ 9.59 caused enhancement of the resonance at δ 6.68, and irradiation at δ 2.69 increased the intensities of the signals at δ 6.68 and 3.69; ^{13}C nmr (75.4 MHz) δ: −7.2, −5.2, 18.4, 26.0, 43.7, 62.2, 140.3, 178.2, 192.4. Exact Mass calcd. for $C_{13}H_{27}O_2SnSi$ (M^+ − Me): 363.0802; found: 363.0806.

(Z)-5-Methoxymethoxy-3-trimethylstannyl-2-pentenal (42)

Flash chromatography (120 g of silica gel, 65:35 petroleum ether – Et_2O) and distillation (100–105°C/0.5 Torr) of the crude product obtained from the aldehyde **27** (1.9 g, 13 mmol) provided 3.1 g (76%) of the product **42**, a colorless oil that showed ir (neat): 1683, 1562, 1151, 1043, 776 cm^{-1}; ^1H nmr (400 MHz) δ: 0.25 (s, 9H, $^2J_{Sn-H}$ = 54 Hz), 2.77 (td, 2H, J = 6.5, 1.3 Hz, $^3J_{Sn-H}$ = 44 Hz), 3.61 (t, 2H, J = 6.5 Hz), 4.58 (s, 2H), 6.72 (dt, 1H, J = 5.5, 1.3 Hz, $^3J_{Sn-H}$ = 113 Hz), 9.59 (d, 1H, J = 5.5 Hz, $^4J_{Sn-H}$ = 5.5 Hz). Exact Mass calcd. for $C_9H_{17}O_3Sn$ (M^+ − Me): 293.0199; found: 293.0201.

*(Z)-7-*tert*-Butyldimethylsilyloxy-3-trimethylstannyl-2-heptenal (43)*

Purification (flash chromatography, 30 g of silica gel, 95:5 petroleum ether – Et_2O; distillation, 120–130°C/0.5 Torr) of the crude product acquired from 0.3 g (1.2 mmol) of the aldehyde **28** furnished 0.45 g (88%) of the product **43**, a colorless oil that exhibited ir (neat): 2742, 1685, 1562, 1256, 1106, 775 cm^{-1}; ^1H nmr (300 MHz) δ: 0.02 (s, 6H), 0.25 (s, 9H, $^2J_{Sn-H}$ = 55 Hz), 0.87 (s, 9H), 1.48 (m, 4H), 2.49 (br t, 2H, J = 6.5 Hz, $^3J_{Sn-H}$ = 47 Hz), 3.59 (t, 2H, J = 6 Hz), 6.62 (dt, 1H, J = 6, 1.3 Hz, $^3J_{Sn-H}$ = 115 Hz), 9.55 (d, 1H, J = 6 Hz, $^4J_{Sn-H}$ = 5.5 Hz); in nOe difference experiments, irradiation at δ 6.62 caused enhancement of the signals at δ 9.55 and 2.49, while irradiations at δ 9.55 and 2.49 caused, in each case, enhancement of the resonance at δ 6.62; ^{13}C nmr (300 MHz) δ: −7.3, −5.2, 18.4, 25.3, 26.0, 32.4, 41.0, 62.7, 138.6, 181.9, 192.6. Exact Mass calcd. for $C_{15}H_{31}O_2SiSn$ (M^+ − Me): 391.1115; found: 391.1112.

*(Z)-6-*tert*-Butyldimethylsilyloxy-4-trimethylstannyl-3-hexen-2-one (44)*

The crude product obtained from the starting material **29** (0.13 g, 0.58 mmol) was purified by flash chromatography (30 g of silica gel, 96:4 petroleum ether – Et_2O) and distillation (110–120°C/0.5 Torr) to produce 0.21 g (90%) of the ketone **44**, a colorless oil,that exhibited ir (neat): 1682, 1573, 1192, 1095, 776 cm^{-1}; ^1H nmr (300 MHz) δ: 0.00 (s, 6H), 0.10 (s, 9H, $^2J_{Sn-H}$ = 54 Hz), 0.84 (s, 9H), 2.19 (s, 3H), 2.63 (td, 2H, J = 6.5, 1.3 Hz, $^3J_{Sn-H}$ = 49 Hz), 3.62 (t, 2H, J = 6.5 Hz), 6.82 (br s, 1H, $^3J_{Sn-H}$ = 121 Hz); in nOe difference experiments, irradiation at δ 6.82 caused enhancement of the signals at δ 2.63 and 2.19, irradiation at δ 2.63 increased the intensity of the resonances at δ 3.62 and 6.82, and irradiation at δ 2.19 caused enhancement of the signal at δ 6.82; ^{13}C nmr (75.4 MHz) δ: −7.4, −5.3, 18.2, 25.9, 30.0, 42.5, 62.0, 136.7, 172.4, 197.3. Exact Mass calcd. for $C_{14}H_{29}O_2SiSn$ (M^+ − Me): 377.0959; found: 377.0966.

(Z)-7-Chloro-4-trimethylstannyl-3-hepten-2-one (45)

Flash chromatography (75 g of silica gel, 95:5 petroleum ether – Et_2O) of the crude product derived from 0.80 g (5.5 mmol) of

the substrate **30**, followed by distillation (100–105°C/0.5 Torr) of the acquired oil produced 1.4 g (81%) of the ketone **45**, a colorless oil that showed ir (neat): 1682, 1572, 1202, 774 cm^{-1}; ^1H nmr (300 MHz) δ: 0.12 (s, 9H, $^2J_{Sn-H}$ = 54 Hz), 1.85 (br quintet, 2H, J = 7 Hz), 2.23 (s, 3H), 2.59 (br t, 2H, J = 7 Hz, $^3J_{Sn-H}$ = 48 Hz), 3.50 (t, 2H, J = 7 Hz), 6.82 (br s, 1H, $^3J_{Sn-H}$ = 120 Hz); in nOe difference experiments, irradiation at δ 6.82 caused enhancement of the resonances at δ 2.59 and 2.23, while irradiation at δ 2.59 increased the intensity of the signals at δ 1.85, 3.50, and 6.82; ^{13}C nmr (75.4 MHz) δ: −7.4, 30.2, 31.6, 36.6, 44.1, 135.6, 174.6, 197.5. Exact Mass calcd. for $C_9H_{16}{}^{35}ClOSn$ (M^+ − Me): 294.9912; found: 294.9912.

*(Z)-8-*tert*-Butyldimethylsilyloxy-4-trimethylstannyl-3-octen-2-one (**46**)*

Purification (flash chromatography, 35 g of silica gel, 96:4 petroleum ether – Et_2O; distillation, 120–130°C/0.5 Torr) of the crude product obtained from 0.16 g (0.63 mmol) of the starting material **31** yielded 0.27 g (83%) of the ketone **46**, a colorless oil that displayed ir (neat): 1682, 1572, 1103, 776 cm^{-1}; ^1H nmr (300 MHz) δ: 0.04 (s, 6H), 0.12 (s, 9H, $^2J_{Sn-H}$ = 53 Hz), 0.88 (s, 9H), 1.35–1.55 (m, 4H), 2.22 (s, 3H), 2.44 (br t, 2H, J = 6.5 Hz, $^3J_{Sn-H}$ = 49 Hz), 3.60 (t, 2H, J = 6.5 Hz), 6.79 (br s, 1H, $^3J_{Sn-H}$ = 122 Hz); in nOe difference experiments, irradiation at δ 6.79 caused enhancement of the signals at δ 2.44 and 2.22, while irradiations at δ 2.22 and 2.44 caused, in each case, enhancement of the resonance at δ 6.79; ^{13}C nmr (75.4 MHz) δ: −7.5, −5.3, 18.3, 25.6, 25.9, 30.1, 32.5, 39.7, 62.9, 134.7, 176.8, 197.6. Exact Mass calcd. for $C_{16}H_{33}O_2SiSn$ (M^+ − Me): 405.1272; found: 405.1266.

*(Z)-4-Trimethylstannyl-3-nonen-8-yn-2-one (**47**)*

Flash chromatography (35 g of silica gel, 95:5 petroleum ether – Et_2O) of the crude product derived from the substrate **32** (0.18 g, 1.3 mmol), followed by distillation (70–80°C/0.5 Torr) of the resultant liquid, gave 0.27 g (69%) of the ketone **47**, a colorless oil that showed ir (neat): 3308, 2119, 1681, 1571, 772 cm^{-1}; ^1H nmr (400 MHz) δ: 0.12 (s, 9H, $^2J_{Sn-H}$ = 54 Hz), 1.63 (quintet, 2H, J = 7.5 Hz), 1.97 (t, 1H, J = 2.5 Hz), 2.19 (td, 2H, J = 7.5, 2.5 Hz), 2.22 (s, 3H), 2.54 (td, 2H, J = 7.5, 1.3 Hz, $^3J_{Sn-H}$ = 48 Hz), 6.62 (br s, 1H, $^3J_{Sn-H}$ = 120 Hz); in nOe experiments, irradiation at δ 6.62 caused signal enhancement at δ 2.54 and 2.22, irradiation at δ 2.54 caused signal enhancement at δ 6.62 and 1.63, and irradiation at δ 2.22 enhanced the signal at δ 6.62. Exact Mass calcd. for $C_{11}H_{17}OSn$ (M^+ − Me): 285.0302; found: 285.0302.

(Z)-5-Methyl-4-trimethylstannyl-3-hexen-2-one (**48**)

The crude product obtained from the substrate **33** (0.20 g, 1.8 mmol), upon subjection to flash chromatography (45 g of silica gel, 98:2 petroleum ether – Et_2O) and distillation (70–75°C/0.5 Torr), furnished 0.40 g (80%) of the ketone **48**, a colorless oil that exhibited ir (neat): 1682, 1568, 1203, 770 cm^{-1}; ^1H nmr (300 MHz) δ: 0.09 (s, 9H, $^2J_{Sn-H}$ = 54 Hz), 1.03 (d, 6H, J = 6.5 Hz), 2.20 (s, 3H), 2.75 (septet of d, J = 6.5, 1.5 Hz, $^3J_{Sn-H}$ = 54 Hz), 6.77 (d, 1H, J = 1.5 Hz, $^3J_{Sn-H}$ = 127 Hz); in nOe difference experiments, irradiation at δ 6.77 produced signal enhancements at δ 1.03, 2.20, and 2.75, while irradiation at δ 2.75 caused enhancement of the resonances at δ 1.03 and 6.77; ^{13}C nmr (75.4 MHz) δ: −6.9, 21.7, 30.1, 36.2, 130.7, 183.0, 197.9. Exact Mass calcd. for $C_9H_{17}OSn$ (M^+ − Me): 261.0301; found: 261.0297.

*(Z)-7-*tert*-Butyldimethylsilyloxy-2-methyl-5-trimethylstannyl-4-hepten-3-one (**49**)*

Flash chromatography (140 g of silica gel, 95:5 petroleum ether – Et_2O) of the crude product obtained from the substrate **34** (2.3 g, 9.2 mmol), followed by distillation (130–135°C/0.5 Torr) of the acquired liquid, afforded 3.6 g (94%) of the ketone **49**, a colorless oil that showed ir (neat): 1678, 1572, 1256, 1098, 777 cm^{-1}; ^1H nmr (400 MHz) δ: 0.04 (s, 6H), 0.12 (s, 9H, $^2J_{Sn-H}$ = 55 Hz), 0.87 (s, 9H), 1.12 (d, 6H, J = 7 Hz), 2.66 (m, 3H), 3.66 (t, 2H, J = 6.5 Hz), 6.88 (br s, 1H, $^3J_{Sn-H}$ = 127 Hz); in nOe difference experiments, irradiations at δ 6.88 and 2.66 caused signal enhancements at δ 2.66 and 6.88, respectively. Exact Mass calcd. for $C_{16}H_{33}O_2SnSi$ (M^+ − Me): 405.1272; found: 405.1269.

*(Z)-2,2-Dimethyl-3-trimethylstannyl-3-undecen-4-one (**50**)*

Purification (flash chromatography, 75 g of silica gel, 97:3 petroleum ether – Et_2O; distillation, 120–130°C/0.5 Torr) of the crude product acquired from 1.0 g (5.2 mmol) of the starting material **35** furnished 0.90 g (48%) of the ketone **50**, a colorless oil that exhibited ir (neat): 1685, 1562, 779, 532 cm^{-1}; ^1H nmr (300 MHz) δ: 0.16 (s, 9H, $^2J_{Sn-H}$ = 53 Hz), 0.86 (m, 3H), 1.13 (s, 9H), 1.27 (br signal, 6H), 1.50–1.67 (m, 2H), 2.49 (t, 2H, J = 7.5 Hz), 6.75 (s, 1H, $^3J_{Sn-H}$ = 130 Hz); in nOe difference experiments, irradiation at δ 6.75 caused signal enhancements at δ 1.13 and 2.49, irradiation at δ 2.49 caused signal enhancements at δ 6.75 and 1.50–1.67, and irradiation at δ 1.13 increased the intensity of the resonance at δ 6.75; ^{13}C nmr (75.4 MHz) δ: −3.6, 14.1, 22.6, 24.3, 29.0, 29.7, 31.6, 40.0, 43.4, 130.3, 184.9, 201.0. Exact Mass calcd. for $C_{15}H_{29}OSn$ (M^+ − Me): 345.1241; found: 345.1237.

*(Z)-7-*tert*-Butyldimethylsilyloxy-4-trimethylstannyl-3,8-nonadien-2-one (**51**)*

Flash chromatography (75 g of silica gel, 95:5 petroleum ether – Et_2O) and distillation (130–135°C/0.5 Torr) of the crude product derived from the substrate **36** (0.84 g, 3.2 mmol) gave 1.3 g (95%) of the ketone **51**, a colorless oil that displayed ir (neat): 1682, 1571, 837, 776 cm^{-1}; ^1H nmr (400 MHz) δ: 0.02 (s, 3H), 0.05 (s, 3H), 0.12 (s, 9H, $^2J_{Sn-H}$ = 54 Hz), 0.89 (s, 9H), 1.45–1.65 (m, 2H), 2.21 (s, 3H), 2.35–2.60 (m, 2H), 4.10 (m, 1H), 5.05 (ddd, 1H, J = 10, 2, 2 Hz), 5.14 (ddd, 1H, J = 18, 2, 2 Hz), 5.80 (ddd, 1H, J = 18, 10, 6 Hz), 6.80 (br s, 1H, $^3J_{Sn-H}$ = 124 Hz). Exact Mass clacd. for $C_{17}H_{33}O_2SiSn$ (M^+ − Me): 417.1272; found: 417.1270.

General procedure 4. Preparation of the (Z)-4-(trimethylstannyl)-1,3-butadienes 61–63 and 68

To a cold (0°C), stirred suspension of methyltriphenylphosphonium bromide (for **61–63**, ~1.8 mmol per mmol of substrate; for **68**, ~2.0 mmol per mmol of substrate) in dry THF (~7 mL per mmol of substrate) was added a solution of *n*-BuLi in hexane (for **61–63**, ~1.3 mmol per mmol of substrate; for **68**, ~1.5 mmol per mmol of substrate). After the resulting yellow solution/suspension had been stirred for 10 min at 0°C and for 30 min at room temperature, a solution of the aldehyde (or ketone) in dry THF (~2 mL per mmol of substrate) was added. The reaction mixture was stirred at room temperature for the time indicated in Table 3. Water (~0.5 mL per mL of reaction solu-

tion) and Et_2O (~0.5 mL per mL of reaction solution) were added and the phases were separated. The aqueous phase was extracted with Et_2O and the combined organic extracts were washed with brine, dried ($MgSO_4$), and concentrated. The crude product was purified by chromatography and distillation.

The following (*Z*)-4-trimethylstannyl-1,3-butadienes were prepared via this general procedure.

*(Z)-6-*tert*-Butyldimethylsilyloxy-4-trimethylstannyl-1,3-hexadiene (**61**)*

Flash chromatography (120 g of silica gel, 98:2 petroleum ether – Et_2O) of the crude product obtained from the aldehyde **41** (2.7 g, 7.2 mmol), followed by distillation (105–110°C/0.5 Torr) of the acquired liquid, gave 2.4 g (87%) of the diene **61**, a colorless oil that showed ir (neat): 3087, 3049, 1621, 1574, 1100, 774 cm^{-1}; ^1H nmr (300 MHz) δ: 0.04 (s, 6H), 0.21 (s, 9H, $^2J_{Sn-H}$ = 53 Hz), 0.88 (s, 9H), 2.49 (br t, 2H J = 7 Hz, $^3J_{Sn-H}$ = 55 Hz), 3.57 (t, 2H, J = 7 Hz), 5.10 (dd, 1H, J = 11, 1.5 Hz), 5.15 (dd, 1H, J = 16, 1.5 Hz), 6.30 (m, 1H), 6.64 (br d, 1H, J = 11 Hz, $^3J_{Sn-H}$ = 131 Hz); ^{13}C nmr (75.4 MHz) δ: −8.0, −5.1, 18.4, 26.0, 43.6, 63.6, 117.1, 137.7, 142.6, 147.3. Exact Mass calcd. for $C_{14}H_{29}OSiSn$ (M^+ − Me): 361.1010; found: 361.1018. Anal. calcd. for $C_{15}H_{32}OSiSn$: C 48.02, H 8.60; found: C 48.00, H 8.70.

*(Z)-6-Methoxymethoxy-4-trimethylstannyl-1,3-hexadiene (**62**)*

Purification (flash chromatography, 230 g of silica gel, 9:1 petroleum ether – Et_2O; distillation, 95–105°C/0.5 Torr) of the crude product derived from the aldehyde **42** (5.84 g, 19.0 mmol) provided 4.76 g (82%) of the diene **62**, a colorless oil that displayed ir (neat): 3086, 1623, 1149, 1045, 771 cm^{-1}; ^1H nmr (300 MHz) δ: 0.02 (s, 9H, $^2J_{Sn-H}$ = 53 Hz), 2.55 (br t, 2H, J = 6 Hz, $^3J_{Sn-H}$ = 53 Hz), 3.24 (s, 3H), 3.50 (t, 2H, J = 6 Hz), 4.60 (s, 2H), 5.10 (br d, 1H, J = 10 Hz), 5.15 (br d, 1H, J = 17 Hz), 6.30 (m, 1H), 6.66 (br d, 1H, J = 11 Hz, $^3J_{Sn-H}$ = 125 Hz); ^{13}C nmr (75.4 MHz) δ: −8.2, 40.3, 55.0, 67.8, 96.2, 117.3, 137.6, 142.4, 147.7. Exact Mass calcd. for $C_{10}H_{19}O_2Sn$ (M^+ − Me): 291.0407; found: 291.0406.

*(Z)-8-*tert*-Butyldimethylsilyloxy-4-trimethylstannyl-1,3-octadiene (**63**)*

The crude product obtained from the aldehyde **43** (0.10 g, 0.25 mmol) was purified by flash chromatography (30 g of silica gel, 98:2 petroleum ether – Et_2O) and distillation (110–115° C/0.5 Torr) to produce 0.08 g (81%) of the diene **63**, a colorless oil that exhibited ir (neat): 3086, 1622, 1574, 1255, 1105, 775 cm^{-1}; ^1H nmr (300 MHz) δ: 0.04 (s, 6H), 0.20 (s, 9H, $^2J_{Sn-H}$ = 53 Hz), 0.88 (s, 9H), 1.30–1.55 (m, 4H), 2.28 (br t, 2H, J = 7 Hz, $^3J_{Sn-H}$ = 56 Hz), 3.59 (t, 2H, J = 6 Hz), 5.06 (dd, 1H, J = 10, 1.5 Hz), 5.13 (dd, 1H, J = 16, 1.5 Hz), 6.13 (m, 1H), 6.59 (br d, 1H, J = 11 Hz, $^3J_{Sn-H}$ = 136 Hz); ^{13}C nmr (75.4 MHz) δ: −8.1, −5.2, 18.4, 26.1, 26.5, 32.5, 40.6, 62.1, 116.5, 137.8, 140.3, 152.1. Exact Mass calcd. for $C_{16}H_{33}OSnSi$ (M^+ − Me): 389.1323; found: 389.1329.

*(Z)-2,5-Dimethyl-4-trimethylstannyl-1,3-hexadiene (**68**)*

Flash chromatography (150 g of silica gel, petroleum ether) of the crude product derived from 3.6 g (13 mmol) of the ketone **48**, followed by distillation (90–105°C/0.5 Torr) of the acquired material, gave 3.1 g (87%) of the diene **68**, a colorless oil that displayed ir (neat): 3083, 1632, 1602, 1188, 769 cm^{-1}; ^1H nmr (300 MHz) δ: 0.14 (s, 9H, $^2J_{Sn-H}$ = 52 Hz), 1.03 (d, 6H, J = 7 Hz), 1.77 (s, 3H), 2.51 (septet of d, J = 7, 1.5 Hz, $^3J_{Sn-H}$ = 60 Hz), 4.74 (br s, 1H), 4.78 (br s, 1H), 6.45 (br s, 1H, $^3J_{Sn-H}$ = 144 Hz); ^{13}C nmr (75.4 MHz) δ: −6.3, 22.7, 23.1, 36.9, 112.6, 138.5, 147.2, 152.9. Exact Mass calcd. for $C_{10}H_{19}Sn$ (M^+ − Me): 259.0509; found: 259.0512.

General procedure 5. Preparation of the (*Z*)-4-(trimethylstannyl)-1,3-butadienes 64–67 and 69–71

To a stirred suspension of methyltriphenylphosphonium bromide (2.5 equiv.) in dry benzene (room temperature, ~9 mL per mmol of ketone substrate used) was added a solution of sodium 2-methyl-2-butoxide (2.5 equiv.) in dry benzene (1.75 M). After the mixture had been stirred for 20 min at room temperature, a solution of the ketone (1 equiv.) in dry benzene (~4 mL per mmol of the ketone) was added and stirring was continued for the time indicated in Table 3. Water (~0.5 mL per mL of reaction solution) and Et_2O (~1 mL per mL of reaction solution) were added and the phases were separated. The aqueous phase was extracted with Et_2O and the combined organic extracts were washed with brine, dried ($MgSO_4$), and concentrated. The crude product was purified by chromatography and distillation.

The following (*Z*)-4-trimethylstannyl-1,3-butadienes were prepared via this general procedure.

*(Z)-6-*tert*-Butyldimethylsilyloxy-2-methyl-4-trimethylstannyl-1,3-hexadiene (**64**)*

Flash chromatography (35 g of silica gel, 98:2 petroleum ether – Et_2O) of the crude product derived from 0.20 g (0.51 mmol) of the ketone **44**, followed by distillation (105–110°C/0.5 Torr) of the acquired liquid, gave 0.17 mg (86%) of the diene **64**, a colorless oil that exhibited ir (neat): 3083, 1633, 1604, 1572, 1255, 774 cm^{-1}; ^1H nmr (300 MHz) δ: 0.04 (s, 6H), 0.13 (s, 9H, $^2J_{Sn-H}$ = 53 Hz), 0.88 (s, 9H), 1.76 (s, 3H), 2.45 (td, 2H, J = 7, 1.3 Hz, $^3J_{Sn-H}$ = 55 Hz), 3.56 (t, 2H, J = 7 Hz), 4.57 (br s, 1H), 4.79 (br s, 1H), 6.53 (br s, 1H, $^3J_{Sn-H}$ = 137 Hz); ^{13}C nmr (75.4 MHz) δ: −7.2, −5.2, 18.4, 22.7, 26.0, 43.6, 63.7, 112.9, 141.8, 144.9, 146.6. Exact Mass calcd. for $C_{15}H_{31}OSiSn$ (M^+ − Me): 375.1166; found: 375.1161.

*(Z)-7-Chloro-2-methyl-4-trimethylstannyl-1,3-heptadiene (**65**)*

Purification (flash chromatography, 35 g of silica gel, 98:2 petroleum ether – Et_2O; distillation, 85–90°C/0.5 Torr) of the crude product obtained from the ketone **45** (0.29 g, 0.73 mmol) gave 0.13 g (57%) of the diene **65**, a colorless oil that displayed ir (neat): 3082, 1632, 1605, 897 cm^{-1}; ^1H nmr (300 MHz) δ: 0.14 (s, 9H, $^2J_{Sn-H}$ = 53 Hz), 1.77 (s, 3H), 1.81 (quintet, 2H, J = 7 Hz), 2.38 (td, 2H, J = 7, 1.3 Hz, $^3J_{Sn-H}$ = 54 Hz), 3.50 (t, 2H, J = 7 Hz), 4.76 (br s, 1H), 4.80 (br s, 1H), 6.52 (br s, 1H, $^3J_{Sn-H}$ = 136 Hz). Exact Mass calcd. for $C_{10}H_{18}{}^{35}ClSn$ (M^+ − Me): 293.0119; found: 293.0114.

*(Z)-8-*tert*-Butyldimethylsilyloxy-2-methyl-4-trimethylstannyl-1,3-octadiene (**66**)*

The crude product obtained from the ketone **46** (0.16 g, 0.37 mmol) was purified by flash chromatography (30 g of silica gel, 97:3 petroleum ether – Et_2O) and distillation (110–115°C/0.5 Torr) to afford 0.12 g (75%) of the diene **66**, a colorless oil that showed ir (neat): 3081, 1572, 1562, 1255, 1103, 775 cm^{-1};

^{1}H nmr (300 MHz) δ: 0.03 (s, 6H), 0.12 (s, 9H, $^2J_{Sn-H}$ = 52 Hz), 0.88 (s, 9H), 1.29–1.55 (m, 4H), 1.76 (s, 3H), 2.24 (br t, 2H, J = 7 Hz, $^3J_{Sn-H}$ = 55 Hz), 3.59 (t, 2H, J = 6 Hz), 4.74 (br s, 1H), 4.79 (br s, 1H), 6.47 (br s, 1H, $^3J_{Sn-H}$ = 139 Hz); ^{13}C nmr (75.4 MHz) δ: −7.4, −5.3, 18.3, 22.7, 26.0, 26.5, 32.4, 40.4, 60.1, 112.6, 142.5, 146.2, 146.6. Exact Mass calcd. for $C_{17}H_{35}OSn$ (M^+ − Me): 403.1479; found: 403.1472.

*(Z)-2-Methyl-4-trimethylstannyl-1,3-nonadien-8-yne (**67**)*

The ketone **47** (1.22 g, 4.07 mmol; in 8 mL of dry benzene) was converted into the diene **67** by treatment with the Wittig reagent (2.5 equiv.; in 15 mL of dry benzene) at room temperature for 30 min. Flash chromatography (65 g of silica gel, petroleum ether) of the crude product, followed by distillation (70–80°C/0.5 Torr) of the liquid obtained, provided 1.01 g (83%) of the diene **67**, a colorless oil that exhibited ir (neat): 3212, 1632, 3082, 2120, 897, 770 cm^{-1}; ^{1}H nmr (400 MHz) δ: 0.13 (s, 9H, $^2J_{Sn-H}$ = 53 Hz), 1.57 (quintet, 2H, J = 7 Hz), 1.76 (s, 3H), 1.94 (t, 1H, J = 2.6 Hz), 2.16 (td, 2H, J = 7, 2.6 Hz), 2.34 (td, 2H, J = 7, 1.3 Hz, $^3J_{Sn-H}$ = 55 Hz), 4.75 (br s, 1H), 4.79 (br s, 1H), 6.51 (br s, 1H, $^3J_{Sn-H}$ = 139 Hz); ^{13}C nmr (75.4 MHz) δ: −7.3, 17.8, 22.7, 28.8, 39.4, 68.4, 84.4, 112.9, 143.5, 144.9, 146.6. Exact Mass calcd. for $C_{12}H_{19}Sn$ (M^+ − Me): 283.0509; found: 283.0510.

*(Z)-6-*tert*-Butyldimethylsilyloxy-2-isopropyl-4-trimethylstannyl-1,3-hexadiene (**69**)*

Purification (flash chromatography, 35 g of silica gel, 97:3 petroleum ether – Et_2O; distillation, 110–115°C/0.5 Torr) of the crude product obtained from the ketone **49** (0.17 g, 0.41 mmol), furnished 0.11 g (64%) of the diene **69**, a colorless oil that showed ir (neat): 3090, 1625, 1461, 1255, 1007, 775 cm^{-1}; ^{1}H nmr (400 MHz) δ: 0.04 (s, 6H), 0.12 (s, 9H, $^2J_{Sn-H}$ = 53 Hz), 0.87 (s, 9H), 1.02 (d, 6H, J = 7 Hz), 2.27 (br septet, 1H, J = 7 Hz), 2.48 (br t, 2H, J = 7 Hz, $^3J_{Sn-H}$ = 53 Hz), 3.56 (t, 2H, J = 7 Hz), 4.71 (br s, 1H), 4.80 (br s, 1H), 6.60 (br s, 1H, $^3J_{Sn-H}$ = 140 Hz); ^{13}C nmr (75.4 MHz) δ: −7.1, −5.2, 18.4, 21.6, 26.0, 34.0, 43.7, 63.8, 108.9, 143.4, 156.4. Exact Mass calcd. for $C_{17}H_{35}OSiSn$ (M^+ − Me): 403.1479; found: 403.1474.

*(Z)-5,5-Dimethyl-2-*n*-hexyl-4-trimethylstannyl-1,3-hexadiene (**70**)*

Flash chromatography (35 g of silica gel, 98:2 petroleum ether – Et_2O) of the crude product obtained from the ketone **50** (0.11 g, 0.31 mmol), followed by distillation (105–110°C/0.5 Torr) of the acquired material, afforded 0.09 g (81%) of the diene **70**, a colorless oil that exhibited ir (neat): 3038, 1630, 899, 770 cm^{-1}; ^{1}H nmr (300 MHz) δ: 0.15 (s, 9H, $^2J_{Sn-H}$ = 52 Hz), 0.88 (m, 3H), 1.07 (s, 9H), 1.30 (br s, 6H), 1.42 (m, 2H), 2.01 (br t, 2H, J = 8 Hz), 4.72 (br s, 1H), 4.77 (br s, 1H), 6.49 (br s, 1H, $^3J_{Sn-H}$ = 151 Hz); ^{13}C nmr (75.4 MHz) δ: −3.6, 14.2, 22.8, 22.7, 29.4, 30.7, 31.8, 37.1, 38.9, 111.2, 137.3, 151.3, 156.6. Exact Mass calcd. for $C_{16}H_{31}Sn$ (M^+ − Me): 343.1448; found: 343.1453.

*(Z)-7-*tert*-Butyldimethylsilyloxy-2-methyl-4-trimethylstannyl-1,3,8-nonatriene (**71**)*

The crude product acquired from the ketone **51** (0.09 g, 0.21 mmol) was purified by flash chromatography (30 g of silica gel, 97:3 petroleum ether – Et_2O) and distillation (125–130°C/0.5 Torr) to afford 0.08 g (85%) of the diene **71**, a colorless oil that displayed ir (neat): 3081, 1632, 1253, 1084, 775 cm^{-1}; ^{1}H nmr (400 MHz) δ: 0.04 (s, 3H), 0.06 (s, 3H), 0.14 (s, 9H, $^2J_{Sn-H}$ = 52 Hz), 0.90 (s, 9H), 1.40–1.60 (m, 2H), 1.78 (s, 3H), 2.19–2.40 (m, 2H), 4.10 (br m, 1H), 4.76 (br s, 1H), 4.80 (br s, 1H), 5.03 (ddd, 1H, J = 10, 2, 2 Hz), 5.14 (ddd, 1H, J = 17, 2, 2 Hz), 5.81 (ddd, 1H, J = 17, 10, 6 Hz), 6.50 (br s, 1H, $^3J_{Sn-H}$ = 139 Hz); ^{13}C nmr (50 MHz) δ: −7.3, −4.8, −4.3, 18.2, 22.7, 25.9, 36.4, 38.9, 73.6, 112.7, 113.7, 141.8, 142.6, 145.9, 146.7. Exact Mass calcd. for $C_{18}H_{35}OSiSn$ (M^+ − Me): 415.1480; found: 415.1478.

Methyl *(2E,4Z)*-7-*tert*-butyldimethylsilyloxy-5-trimethylstannyl-1,4-heptadienoate (72)

To a cold (0°C), stirred suspension of NaH (1.02 g, 21.2 mmol) in 100 mL of dry THF was added dropwise, over a period of ~5 min, trimethyl phosphonoacetate (3.87 g, 21.2 mmol) and the resultant slurry was stirred at 0°C for 5 min and at room temperature for 20 min. The mixture was then recooled to 0°C and a solution of the aldehyde **41** (5.35 g, 14.2 mmol) in 25 mL of dry THF was added. The resulting suspension was stirred at 0°C for 2 h. Water (~50 mL) and Et_2O (~50 mL) were added and the phases were separated. The aqueous phase was extracted with Et_2O (2 × 40 mL) and the combined organic extracts were washed (brine, 40 mL), dried ($MgSO_4$), and concentrated. Flash chromatography (250 g of silica gel, 94:6 petroleum ether – Et_2O) of the crude product and distillation (140–150°C/0.5 Torr) of the acquired liquid provided 5.65 g (92%) of the diene **72**, a colorless oil that displayed ir (neat): 1723, 1626, 1268, 1100, 776 cm^{-1}; ^{1}H nmr (400 MHz) δ: 0.03 (s, 6H), 0.27 (s, 9H, $^2J_{Sn-H}$ = 54 Hz), 0.87 (s, 9H), 2.57 (br t, 2H, J = 7 Hz, $^3J_{Sn-H}$ = 50 Hz), 3.62 (t, 2H, J = 7 Hz), 3.73 (s, 3H), 5.80 (br d, 1H, J = 15 Hz), 6.73 (br d, 1H, J = 11 Hz, $^3J_{Sn-H}$ = 122 Hz), 7.30 (dd, 1H, J = 15, 11 Hz, $^4J_{Sn-H}$ = 7 Hz); in nOe difference experiments irradiation at δ 2.57 caused signal enhancement at δ 6.73 and 3.62, irradiation at δ 5.80 caused resonance enhancement at δ 6.73, and irradiation at δ 6.73 caused enhancement of the signals at δ 5.80 and 2.57. Exact Mass calcd. for $C_{16}H_{31}O_3SnSi$ (M^+ − Me): 419.1065; found: 419.1070.

Preparation of the phosphonate reagent 73

A stirred mixture of triisopropyl phosphite (3.2 g, 15 mmol) and *tert*-butyl bromoacetate (3.0 g, 15 mmol) was heated at 125°C for 1.5 h. Direct distillation (fraction collected between 110 and 115°C/0.5 Torr) of the oil thus obtained gave 3.5 g (81%) of the phosphonate **73**, a colorless oil that exhibited ir (neat): 1730, 1289, 1107, 991 cm^{-1}; ^{1}H nmr (400 MHz) δ: 1.27 (d, 6H, J = 7 Hz), 1.29 (d, 6H, J = 7 Hz), 1.42 (s, 9H), 2.77 (d, 2H, $^2J_{P-H}$ = 22 Hz), 4.68 (m, 2H); ^{13}C nmr (75.4 MHz) δ: 23.8 (d, $^3J_{P-C}$ = 5 Hz), 23.95 (d, $^3J_{P-C}$ = 4 Hz), 27.8, 36.6 (d, $^1J_{P-C}$ = 134 Hz), 70.9 (d, $^2J_{P-C}$ = 6 Hz), 81.6, 164.9 (d, $^2J_{P-C}$ = 6 Hz); ^{31}P nmr (122 MHz) δ: 16.2 (tt, J = 22, 8 Hz).

***tert*-Butyl *(2E,4Z)*-7-methoxymethoxy-5-trimethylstannyl-1,4-heptadienoate (74)**

To a cold (0°C), stirred suspension of NaH (0.26 g, 6.4 mmol) in 25 mL of dry THF was added slowly, over a period of ~5 min, a solution of the phosphonate reagent **73** (1.8 g, 6.4 mmol) in 10 mL of dry THF. After the mixture had been stirred at 0°C for 5 min and at room temperature for 20 min, it

was cooled to −20°C and a solution of the aldehyde **42** (1.17 g, 3.8 mmol) in 10 mL of dry THF was added. The mixture was stirred at −20°C for 1.5 h and was then allowed to warm to room temperature (30 min). Water (~20 mL) and Et_2O (~40 mL) were added and the phases were separated. The aqueous phase was extracted with Et_2O (2 × 20 mL) and the combined organic extracts were washed (brine, 20 mL), dried ($MgSO_4$), and concentrated. Flash chromatography of the crude product on silica gel (65 g, 4:1 petroleum ether – Et_2O), followed by distillation (190–210°C/0.5 Torr) of the acquired material, gave 1.4 g (91%) of the diene **74**, a colorless oil that showed ir (neat): 1703, 1626, 1368, 1045, 770 cm^{-1}; ^1H nmr (400 MHz) δ: 0.25 (s, 9H, $^2J_{Sn-H}$ = 52 Hz), 1.48 (s, 9H), 2.64 (br t, 2H, J = 7 Hz, $^3J_{Sn-H}$ = 49 Hz), 3.33 (s, 3H), 3.54 (t, 2H, J = 7 Hz), 4.58 (s, 2H), 5.72 (br d, 1H, J = 15 Hz), 6.74 (br d, 1H, J = 11 Hz, $^3J_{Sn-H}$ = 120 Hz), 7.21 (dd, 1H, J = 15, 11 Hz, $^4J_{Sn-H}$ = 7 Hz); in nOe difference experiments, irradiation at δ 6.74 caused enhancement of the resonances at δ 5.72 and 2.64, irradiation at δ 2.64 caused signal enhancement at δ 3.54 and 6.74, and irradiation at δ 5.72 increased the intensity of the signal at δ 6.74; ^{13}C nmr (75.4 MHz) δ: −7.8, 28.2, 41.0, 55.3, 67.5, 80.1, 96.4, 123.2, 139.5, 144.2, 160.5, 166.5. Exact Mass calcd. for $C_{15}H_{27}O_4Sn$ (M^+ − Me): 391.0931; found: 391.0938. Anal. calcd. for $C_{16}H_{30}O_4Sn$: C 47.42, H 7.47; found: C 47.59, H 7.39.

(*E*)-3-((2-Methoxymethoxy)ethyl)-3,5-hexadien-1-ol (76)

To a cold (−78°C), stirred solution of the trimethylstannyl diene **62** (0.87 g, 2.84 mmol) in dry THF (50 mL) was added a solution of MeLi (3.1 mmol) in Et_2O. After the mixture had been stirred for 45 min at −78°C, ethylene oxide (~2.5 g, ~57 mmol) was added via a syringe (the barrel of the syringe was cooled using a piece of Dry Ice, in order to facilitate the transfer of the volatile liquid). The resulting mixture was stirred at −78°C for 5 min and at −20°C for 20 min and was then allowed to warm to room temperature (30 min). Saturated aqueous $NaHCO_3$ (10 mL) and Et_2O (30 mL) were added, the phases were separated, and the aqueous phase was extracted with Et_2O (3 × 20 mL). The combined organic extracts were washed (brine, 20 mL), dried ($MgSO_4$), and concentrated. Flash chromatography of the crude product on silica gel (40 g, 2:3 petroleum ether – Et_2O) and distillation (110–120°C/0.5 Torr) of the derived liquid gave 0.38 g (71%) of the alcohol **76**, a colorless oil that exhibited ir (neat): 3401, 3085, 1647, 1150, 1109, 1039 cm^{-1}; ^1H nmr (400 MHz) δ: 1.74 (br s, 1H), 2.39 (br t, 2H, J = 6.5 Hz), 2.49 (t, 2H, J = 6.5 Hz), 3.34 (s, 3H), 3.67 (t, 2H, J = 6.5 Hz), 3.70 (br m, 2H), 4.61 (s, 2H), 5.05 (dd, 1H, J = 10, 1.5 Hz), 5.15 (dd, 1H, J = 17, 1.5 Hz), 6.06 (br d, 1H, J = 11 Hz), 6.60 (ddd, 1H, J = 17, 11, 10 Hz); on addition of D_2O the signal at δ 3.70 sharpened to a t (J = 6.5 Hz), and the signal at δ 1.74 disappeared; ^{13}C nmr (75.4 MHz) δ: 34.4, 37.1, 55.3, 61.2, 66.5, 96.4, 116.8, 129.9, 132.5, 136.3. Exact Mass calcd. for $C_{10}H_{16}O_2$ (M^+ − H_2O): 168.1151; found: 168.1152. Anal. calcd. for $C_{10}H_{18}O_3$: C 64.49, H 9.74; found: C 64.49, H 9.88.

(*Z*)-6-Bromo-4-((2-methoxymethoxy)ethyl)-1,3,6-heptatriene (78)

To a cold (−78°C), stirred solution of the trimethylstannyl diene **62** (0.35 mg, 1.13 mmol) in dry THF (5 mL) was added a solution of MeLi (1.24 mmol) in Et_2O. After the mixture had been stirred for 45 min at −78°C, CuBr·Me_2S (256 mg, 1.24 mmol) was added. The resulting bright pink solution/suspension was stirred at −78°C for 5 min and at −48°C for 15 min. To the resulting bright orange-red solution was added 2,3-dibromopropene (1.5 g, 7.6 mmol) and the resulting colorless solution was stirred at −48°C for 45 min. Aqueous NH_4Cl–NH_4OH (pH 8) (5 mL) and Et_2O (10 mL) were added and the vigorously stirred mixture was allowed to warm to room temperature. The phases were separated and the aqueous phase was extracted with Et_2O (3 × 10 mL). The combined organic extracts were washed (brine, 10 mL), dried ($MgSO_4$), and concentrated. Flash chromatography (40 g of silica gel, 9:1 petroleum ether – Et_2O), followed by distillation (100–110°C/0.5 Torr) of the acquired liquid, furnished 244 mg (83%) of the triene **78**, a colorless oil that showed ir (neat): 3086, 1626, 1150, 1072, 917 cm^{-1}; ^1H nmr (400 MHz) δ: 2.38 (br t, 2H, J = 6 Hz), 3.35 (br s, 5H), 3.62 (t, 2H, J = 6 Hz), 4.60 (s, 2H), 5.12 (dd, 1H, J = 11, 1.5 Hz), 5.20 (dd, 1H, J = 17, 1.5 Hz), 5.48 (br s, 1H), 5.62 (br s, 1H), 6.13 (br d, 1H, J = 11 Hz), 6.54 (ddd, 1H, J = 17, 11, 11 Hz); ^{13}C nmr (75.4 MHz) δ: 36.6, 42.8, 55.2, 66.1, 96.3, 117.5, 117.8, 130.4, 130.9, 132.4, 134.6. Exact Mass calcd. for $C_9H_{12}{}^{79}BrO_2$ (M^+ − C_2H_5O): 215.0072; found: 215.0064. Anal. calcd. for $C_{11}H_{17}BrO_2$: C 50.59, H 6.56; found: C 50.85, H 6.58.

(*Z*)-7-Iodo-2-methyl-4-trimethylstannyl-1,3-heptadiene (87)

A stirred solution of NaI (1.80 g, 11.8 mmol) and the trimethylstannyl diene **65** (0.36 g, 1.18 mmol) in dry acetone (10 mL) was allowed to reflux overnight. Most of the acetone was removed, Et_2O (20 mL) and water (10 mL) were added to the residue, the phases were separated, and the aqueous phase was extracted with Et_2O (3 × 10 mL). The combined organic extracts were washed (water, 10 mL), dried ($MgSO_4$), and concentrated. Flash chromatography of the crude product on silica gel (35 g, 95:5 petroleum ether – Et_2O) and distillation (100–110°C/0.5 Torr) of the derived liquid afforded 0.41 mg (86%) of the diene **87**, a colorless oil that exhibited ir (neat): 3080, 1632, 1215, 896, 769 cm^{-1}; ^1H nmr (400 MHz) δ: 0.16 (s, 9H, $^2J_{Sn-H}$ = 56 Hz), 1.78 (s, 3H), 1.87 (quintet, 2H, J = 7 Hz), 2.34 (br t, 2H, J = 7 Hz, $^3J_{Sn-H}$ = 54 Hz), 3.15 (t, 2H, J = 7 Hz), 4.76 (br s, 1H), 4.80 (br s, 1H), 6.54 (s, 1H, $^3J_{Sn-H}$ = 132 Hz); ^{13}C nmr (50 MHz) δ: −7.3, 6.2, 22.7, 33.6, 40.8, 113.0, 143.8, 144.0, 146.5. Exact Mass calcd. for $C_{10}H_{18}ISn$ (M^+ − Me): 384.9477; found: 384.9476.

5,5,6,6-Tetracyano-8-methylspiro[3.5]non-8-ene (88)

To a cold (−78°C), stirred solution of the trimethylstannyl diene **87** (0.19 g, 0.47 mmol) in dry THF (2 mL) was added a solution of MeLi (0.52 mmol) in Et_2O. After the solution had been stirred for 10 min at −78°C and 20 min at −48°C, water (0.5 mL) and Et_2O (2 mL) were added and the mixture was allowed to warm to room temperature. The phases were separated and the aqueous phase was extracted with Et_2O (2 × 2 mL). The combined organic extracts were dried ($MgSO_4$). The ethereal solution of the reaction product **84** exhibited essentially one non-solvent peak by glc analyses and was used immediately in the next step. To this solution (argon atmosphere) was added (in portions of 5 mg) tetracyanoethylene (~50 mg), until the reaction was shown to be complete (glc analyses). The solvent was removed and the white solid

obtained was dissolved in a minimum amount of Et_2O. Flash chromatography of this solution on silica gel (25 g, 1:1 petroleum ether – Et_2O) and recrystallization of the acquired solid from petroleum ether gave 0.08 mg (69%) of the spiro compound **88** as colorless crystals that displayed mp 166–167°C; ir (KBr disk): 2253, 1440, 883, 696 cm^{-1}; ^1H nmr (400 MHz) δ: 1.88 (br s, 3H), 2.08–2.10 (m, 1H), 2.17–2.24 (m, 3H), 2.73–2.75 (m, 2H), 2.95 (br s, 2H), 5.99 (br s, 1H). Exact Mass calcd. for $C_{14}H_{12}N_4$: 236.1062; found: 236.1056.

5,6-Bis(methoxycarbonyl)-8-methylspiro[3.5]nona-5,8-diene (89)

To a cold (−78°C), stirred solution of the trimethylstannyl diene **87** (0.17 g, 0.43 mmol) in dry THF (2 mL) was added a solution of MeLi (0.47 mmol) in Et_2O. After the solution had been stirred for 10 min at −78°C and 20 min at −48°C, water (0.5 mL) and benzene (2 mL) were added and the mixture was allowed to warm to room temperature. The phases were separated and the aqueous phase was extracted with benzene (3 × 1 mL). The combined organic extracts were dried ($MgSO_4$). To this solution of the crude product **84** was added dimethyl acetylenedicarboxylate (360 mg, 2.6 mmol) and the resultant solution (argon atmosphere) was heated (70°C) in a sealed tube for 36 h. The solvent was removed and the residual oil was purified by flash chromatography (30 g of silica gel, 1:1 petroleum ether – Et_2O) and distillation (100–110°C/0.5 Torr) to give 0.07 g (70%) of the spiro compound **89**, a colorless oil that crystallized on standing. Recrystallization of this material from pentane produced colorless crystals that exhibited mp 55−56°C; ir (KBr disk): 1724, 1635, 1440, 1267, 1051, 754 cm^{-1}; ^1H nmr (400 MHz) δ: 1.72 (br s, 3H), 1.72–1.80 (m, 1H), 1.92–1.96 (m, 3H), 2.58–2.59 (m, 2H), 2.82 (br s, 2H), 3.73 (s, 3H), 3.88 (s, 3H), 5.73 (br s, 1H). Exact Mass calcd. for $C_{14}H_{18}O_4$: 250.1205; found: 250.1203.

Acknowledgements

We are very grateful to the Natural Sciences and Engineering Research Council of Canada for financial support and to the University of British Columbia for a Killam Predoctoral Fellowship (to R. D. T.).

References

1. E. Piers and R.T. Skerlj. Can. J. Chem. **72**, 2468 (1994).
2. E. Piers and R.D. Tillyer. J. Chem. Soc. Perkin Trans. 1, 2124 (1989).
3. E.J. Corey and J.W. Suggs. Tetrahedron Lett. 2647 (1975).
4. E.J. Corey and A. Venkateswarlu. J. Am. Chem. Soc. **94**, 6190 (1972).
5. W.C. Still, M. Kahn, and A. Mitra. J. Org. Chem. **43**, 2923 (1978).
6. A.J. Leusink, H.A. Budding, and J.W. Marsman. J. Organomet. Chem. **9**, 285 (1967).
7. E. Piers and P.D. Coish. Synthesis, 47 (1995).
8. T.N. Mitchell, A. Amamria, H. Killing, and D. Rutschow. J. Organomet. Chem. **304**, 257 (1986).
9. T. Tsuda, T. Yoshida, and T. Saegusa. J. Org. Chem. **53**, 1037 (1988).
10. F. Huet, M. Pellet, and J.M. Conia. Tetrahedron Lett. 3505 (1977).
11. P.G.M. Wuts. Synth. Commun. **11**, 139 (1981).
12. E. Piers and J.S.M. Wai. Can. J. Chem. **72**, 146 (1994).
13. K.C. Nicolaou, T. Ladduwahetty, and E.M. Elisseou. J. Chem. Soc. Chem. Commun. 1580 (1985).

Synthesis, characterization, and reactivity of a ruthenium(II) *N,N′,N″*-tris(2-pyridyl)phosphine complex. X-ray analysis of $RuCl_2(PPh_3)(Ppy_3)$ (py = 2-pyridyl)

Richard P. Schutte, Steven J. Rettig, and Brian R. James

Abstract: Reaction of $RuCl_2(PPh_3)_3$ with Ppy_3 (py = 2-pyridyl) in benzene produced the *N,N′,N″*-Ppy_3 complex $RuCl_2(PPh_3)(Ppy_3)$ **1**. Crystals of $RuCl_2(PPh_3)(Ppy_3)\cdot 2CH_2Cl_2$ ($C_{35}H_{31}Cl_6N_3P_2Ru$) are monoclinic, $a = 17.269(2)$, $b = 10.797(1)$, $c = 20.604(1)$ Å, $\beta = 107.461(6)°$, $Z = 4$, space group $P2_1/c$. The structure was solved by the Patterson method and was refined by full-matrix least-squares procedures to $R = 0.039$ and $R_w = 0.035$ for 4184 reflections with $I \geq 3\sigma(I)$. Complex **1** reacts in MeOH or benzene with two-electron donors (L) to give the chloride-substituted, $[RuCl(L)(PPh_3)(Ppy_3)]PF_6$, or the triphenylphosphine-substituted products, $RuCl_2(L)(Ppy_3)$, (L = CO, MeCN, PhCN), respectively. $[RuCl(MeOH)(PPh_3)(Ppy_3)]BPh_4$ was also isolated. The non-coordinated phosphorus atom in **1** was oxidized to form $RuCl_2(PPh_3)(OPpy_3)$.

Key words: ruthenium, pyridylphosphines, crystal structure

Résumé : La réaction du $RuCl_2(PPh_3)_3$ avec de la Ppy_3 (py = 2-pyridyle) dans le benzène conduit à la formation du complexe *N,N′,N″*-Ppy_3 du $RuCl_2(PPh_3)(Ppy_3)$ **1**. Les cristaux du $RuCl_2(PPh_3)(Ppy_3)\cdot 2CH_2Cl_2$ ($C_{35}H_{31}Cl_6N_3P_2Ru$) sont monocliniques, groupe d'espace $P2_1/c$, avec $a = 17,269(2)$, $b = 10,797(1)$, et $c = 20,604(1)$ Å, $\beta = 107,461(6)°$ $Z = 4$. On a résolu la structure par la méthode de Patterson et on l'a affinée par les méthodes des moindres carrés (matrice complète) jusqu'à des valeurs de $R = 0,039$ et $R_w = 0,035$ pour 4184 réflexions avec $I \geq 3\sigma(I)$. Dans du MeOH ou du benzène, le complexe **1** réagit avec des donneurs à deux électrons (L) pour fournir respectivement des produits substitués par le chlore, $[RuCl(L)(PPh_3)(Ppy_3)]PF_6$, ou des produits substitués par la triphénylphosphine, $RuCl_2(L)(Ppy_3)$, (L = CO, MeCN, PhCN). On a aussi isolé le $[RuCl(MeOH)(PPh_3)(Ppy_3)]BPh_4$. On a oxydé l'atome de phosphore non coordiné du produit **1** pour former du $RuCl_2(PPh_3)(OPpy_3)$.

Mots clés : ruthénium, pyridylphosphines, structure cristalline.

[Traduit par la rédaction]

Introduction

The *N,N′,N″*-coordination mode of tris(2-pyridyl)phosphine (Ppy_3, py = 2-pyridyl), where the ligand binds to the metal centre via the three pyridyl nitrogens, has been observed with a variety of transition metals. All, except one, are cationic sandwich complexes containing two *N,N′,N″*-Ppy_3 ligands and are of the general formula $[M(Ppy_3)_2]^{2+}$ (M = Mn, Co, Ni, Cu, Zn, Ru) (1–3). The X-ray crystal structures of the zinc (2) and the ruthenium (3) complexes have been determined and confirm the *N,N′,N″*-coordination mode. Rarer are the half-sandwich complexes containing only one *N,N′,N″*-Ppy_3 ligand, the only example (prior to this work) being $Zn(Ppy_3)(NO_3)_2$ (2). In this case, the complex is neutral and contains both a monodentate and a bidentate nitrate ligand. Thus, the *N,N′,N″*-coordination mode has generally been observed in sandwich complexes of the first-row transition metals.

This paper reports on the synthesis, characterization, and reactivity of the *N,N′,N″*-Ppy_3, half-sandwich complex $RuCl_2(PPh_3)(Ppy_3)$ **1**. In MeOH, one of the chloro ligands in **1** is labile, and this led to the investigation of some chloride-substitution reactions with neutral two-electron donors. Alternatively, the triphenylphosphine ligand in **1** can be replaced by carrying out the substitution reactions in benzene. This reactivity is similar to that of the well-known $RuCl(PPh_3)_2(Cp)$ complex (Cp = η^5-cyclopentadienyl), which also contains a facial six-electron donor ligand (4). Our interest in 2-pyridylphosphine complexes stems from their potential as homogeneous catalysts in aqueous media (5). This present paper focuses on complex **1**, which turned out to be water insoluble. Related complexes such as $[RuCl(PPh_3)(Ppy_3)_2]Cl$, which contains chelated *P,N*-coordinated Ppy_3 ligands, are water soluble and will be discussed elsewhere (6).

Experimental

All manipulations were carried out under Ar using standard Schlenk techniques. Solvents (Fisher or BDH) were dried and distilled under N_2 prior to use. MeCN and PhCN were dried

Received February 2, 1996.

This paper is dedicated to Professor Howard C. Clark in recognition of his contributions to Canadian chemistry.

R.P. Schutte, S.J. Rettig, and B.R. James.[1] Department of Chemistry, University of British Columbia, 2036 Main Mall, Vancouver, BC, V6T 1Z1, Canada.

[1] Author to whom correspondence may be addressed. Telephone: (604) 822-6645. Fax: (604) 822-2847.

over CaH_2 for 24 h prior to fractional distillation, and stored under argon in the dark. NH_4PF_6 (Aldrich), $NaBPh_4$ (Aldrich), and *m*-$ClC_6H_4C(O)OOH$ (*m*-CPBA) (Aldrich, 80–85% Tech. grade) were used as supplied. $RuCl_2(PPh_3)_3$ (7) and Ppy_3 (8) were prepared according to published procedures.

NMR spectra were recorded at room temperature (r.t.) on a Varian XL-300 MHz (300 MHz for ^1H; 121.4 MHz for ^{31}P) spectrometer. ^1H chemical shifts were recorded using the residual proton of the solvent as internal standard. All ^{31}P chemical shifts were referenced to external 85% H_3PO_4, by setting the chemical shift for $P(OMe)_3$ (Aldrich) at 141.00 ppm (relative to 85% H_3PO_4) in the appropriate solvent (9). Infrared spectra were recorded on a Mattson Genesis Series FTIR spectrometer as Nujol mulls between KBr plates or as KBr pellets. UV–visible spectra were recorded on a Hewlett–Packard-8452A diode array spectrometer. Solid state visible spectra were recorded by dissolving a small amount of complex in either MeOH or CH_2Cl_2 and placing the solution on a glass plate (UV cutoff 300 nm) and allowing the solvent to evaporate so that a thin amorphous film was left behind. The thin film was then placed in the beam of the spectrometer and the spectrum recorded. Conductivity measurements were made at 25°C using a model RCM151B Serfass conductance bridge (A. H. Thomas Co. Ltd.) connected to a 3403 cell from the Yellow Springs Instrument Company. The cell constant was determined by measuring the resistance of an aqueous solution of KCl (0.0100 M, $\sigma = 0.001\,413$ ohm^{-1} cm^{-1} at 25°C) (10). Solutions of $\sim 1 \times 10^{-3}$ M in CH_3NO_2 or MeOH were made just prior to use. Elemental analyses were performed by Mr. P. Borda of this department.

Preparation of $RuCl_2(PPh_3)(Ppy_3)$, 1

Benzene (30 mL) was added to a mixture of $RuCl_2(PPh_3)_3$ (0.48 g, 0.50 mmol) and Ppy_3 (0.13 g, 0.50 mmol). The resulting red solution was refluxed for 7 h in which time a dark red precipitate formed. After the volume was reduced in half, hexanes (40 mL) were added to complete precipitation. The red precipitate was filtered, washed with hexanes (3 × 10 mL) to remove any residual PPh_3, and dried under vacuum (0.32 g, 92%). Anal. calcd. for $C_{33}H_{27}Cl_2N_3P_2Ru$: C 56.66, H 3.89, N 6.01; found: C 56.65, H 3.89, N 5.96%.

Single crystals for an X-ray diffraction study were grown by Et_2O diffusion into a CH_2Cl_2 solution of the complex. The crystals isolated contained two CH_2Cl_2 solvates.

Preparation of $[RuCl(MeOH)(PPh_3)(Ppy_3)]BPh_4$, 2

$NaBPh_4$ (0.022 g, 0.064 mmol) was added to a clear orange solution of **1** (0.042 g, 0.060 mmol) in MeOH (30 mL). After being stirred for 0.5 h, the solution volume was reduced (to ~10 mL) under vacuum during which time an orange precipitate formed. The mixture was stirred for a further 0.5 h and then the precipitate was filtered off and washed with MeOH (2 × 1 mL) and dried under vacuum (24 h), (0.033 g, 54%). Anal. calcd. for $C_{58}H_{51}BClN_3OP_2Ru$: C 68.61, H 5.06, N 4.14; found: C 67.85, H 4.94, N 4.21%.

Preparation of $[RuCl(CO)(PPh_3)(Ppy_3)]PF_6$, 3

To a degassed solution of **1** (0.13 g, 0.19 mmol) and NH_4PF_6 (0.032 g, 0.20 mmol) in MeOH (6 mL), CO gas (1 atm (101.3 kPa)) was added, and the mixture was heated at 65°C for 2 h. The initial red suspension formed a clear yellow solution, which was pumped to dryness and the residue dissolved in acetone (5 mL). The resulting turbid, orange solution was filtered through Celite 545® along with acetone washings (15 mL). The clear filtrate was pumped to dryness and MeOH added (1 mL) to form a yellow precipitate, which was filtered off and dried under vacuum (0.12 g, 75%). Anal. calcd. for $C_{34}H_{27}ClF_6N_3OP_3Ru$: C 48.79, H 3.48, N 5.02; found: C 48.65; H, 3.38; N, 4.96%.

Preparation of $[RuCl(MeCN)(PPh_3)(Ppy_3)]PF_6$, 4

To a suspension of **1** (0.085 g, 0.121 mmol) and NH_4PF_6 (0.020 g, 0.122 mmol) in MeOH (4 mL) was added a solution of MeCN in MeOH (1 mL, made by mixing 0.05 mL of MeCN in 5 mL of MeOH) and the resulting mixture refluxed for 10 min. The orange solution was pumped to dryness and the residue dissolved in acetone (5 mL) and filtered through Celite 545®. The volume was reduced (to ~3 mL) and ether (40 mL) added to form a yellow precipitate. The product was collected by filtration, washed with ether (3 × 5 mL), and dried under vacuum (0.084 g, 82%). Anal. calcd. for $C_{35}H_{30}ClF_6N_4P_3Ru$: C 49.45, H 3.56, N 6.59; found: C 49.58, H 3.64, N 6.73%.

Preparation of $[RuCl(PhCN)(PPh_3)(Ppy_3)]PF_6$, 5

To a red suspension of **1** (0.098 g, 0.14 mmol) and NH_4PF_6 (0.023 g, 0.14 mmol) in MeOH (10 mL) was added PhCN (0.05 mL) with a syringe. The resulting mixture was refluxed for 15 min during which time an orange solution formed. The MeOH was removed under vacuum and the residue dissolved in acetone (50 mL) and filtered through Celite 545®. The filtrate was concentrated (~5 mL) and Et_2O (30 mL) added. The yellow precipitate was filtered off and dried under vacuum (0.091 g, 71%). Anal. calcd. for $C_{40}H_{32}ClF_6N_4P_3Ru$: C 52.67, H 3.53, N 6.14; found: C 52.80, H 3.55, N 5.96%.

Preparation of $RuCl_2(CO)(Ppy_3)$, 6

To a red suspension of **1** (0.13 g, 0.19 mmol) in C_6H_6 (10 mL) was added CO gas (1 atm). The suspension was refluxed for 42 h in which time an orange-brown suspension developed. Hexanes (30 mL) were added to further precipitation and the precipitate collected by filtration. The product was reprecipitated from CH_2Cl_2 (15 mL) by Et_2O (20 mL), filtered, and dried in vacuo (0.05 g, 56%). Anal. calcd. for $C_{16}H_{12}Cl_2N_3OPRu$: C 41.31, H 2.60, N 9.03; found: C 41.05, H 2.64, N 8.91%.

Preparation of $RuCl_2(MeCN)(Ppy_3)$, 7

To a red suspension of **1** (0.13 g, 0.18 mmol) in C_6H_6 (10 mL) was added MeCN (1 mL, 19 mmol). The suspension was refluxed for 17 h. After the mixture was cooled to room temperature, the red precipitate was filtered off, washed with C_6H_6 (4 × 5 mL), and dried in vacuo (24 h), (0.06 g, 68%). Anal. calcd. for $C_{17}H_{15}Cl_2N_4PRu \cdot 1/6C_6H_6$: C 44.00, H 3.28, N 11.40; found: C 44.15, H 3.46, N 11.04%. The $1/6C_6H_6$ solvate was confirmed in the ^1H NMR ($CDCl_3$) spectrum at 7.36 ppm (s). Attempts to remove the solvate by heating (78°C, 24 h) under vacuum caused decomposition of the complex.

Preparation of $RuCl_2(PhCN)(Ppy_3)$, 8

To a red suspension of **1** (0.18 g, 0.25 mmol) in C_6H_6 (10 mL) was added PhCN (1 mL, 11 mmol). The suspension was refluxed for 4 h, then stirred for a further 16 h at room temperature. Hexanes (30 mL) were added and the red precipitate

Table 1. Crystallographic data.[a]

Compound	$RuCl_2(PPh_3)(Ppy_3)\cdot 2CH_2Cl_2$
Formula	$C_{35}H_{31}Cl_6N_3P_2Ru$
fw	869.39
Crystal system	Monoclinic
Space group	$P2_1/c$
a, Å	17.269(2)
b, Å	10.797(1)
c, Å	20.604(1)
β, °	107.461(6)
V, Å^3	3664.6(6)
Z	4
ρ_{calc}, g/cm^3	1.576
$F(000)$	1752
μ(Mo K_α), cm^{-1}	9.83
Crystal size, mm	0.15 × 0.18 × 0.25
Transmission factors (relative)	0.96–1.00
Scan type	ω–2θ
Scan range, deg in ω	1.00 + 0.35 tan θ
Scan speed, deg/min	16 (up to 8 rescans)
Data collected	$+h$, $+k$, $\pm l$
$2\theta_{max}$, deg	55
Crystal decay, %	19.0
Total reflections	9154
Total unique reflections	8870
R_{merge}	0.049
Reflections with $I \geq 3\sigma(F^2)$	4184
No. of variables	424
R	0.039
R_w	0.035
gof	1.78
Max Δ/σ (final cycle)	0.0003
Residual density e/Å^3	−0.64 to 0.72

[a]Temperature 294 K, Rigaku AFC6S diffractometer, Mo K_α (λ = 0.71069 Å) radiation, graphite monochromator, takeoff angle 6.0°, aperture 6.0 × 6.0 mm at a distance of 285 mm from the crystal, stationary background counts at each end of the scan (scan/background time ratio 2:1), $\sigma^2(F^2) = [S^2(C + 4B)]/Lp^2$ (S = scan rate, C = scan count, B = normalized background count), function minimized $\Sigma w(|F_o| - |F_c|)^2$ where $w = 4F_o^2/\sigma^2(F_o^2)$, $R = \Sigma||F_o| - |F_c||/\Sigma|F_o|$, $R_w = (\Sigma w(|F_o| - |F_c|)^2/\Sigma w|F_o|^2)^{1/2}$, and gof = $[\Sigma w(|F_o| - |F_c|)^2/(m-n)]^{1/2}$. Values given for R, R_w, and gof are based on those reflections with $I \geq 3\sigma(I)$.

collected by filtration. This product was reprecipitated from CH_2Cl_2 (5 mL) with Et_2O (50 mL) and dried under vacuum (78°C, 16 h), (0.12 g, 88%). Anal. calcd. for $C_{22}H_{17}Cl_2N_4PRu$: C 48.90, H 3.17, N 10.37; found: C 48.87, H 3.50, N 10.09%.

Preparation of $RuCl_2(PPh_3)(OPpy_3)$, 9

A solution of **1** (0.21 g, 0.29 mmol) with excess *m*-CPBA (0.11 g, 0.51 mmol based on 80% purity) in $CHCl_3$ (25 mL) was stirred for 24 h. Hexanes (160 mL) were added and the resulting brown precipitate filtered. The brown precipitate was redissolved in $CHCl_3$ (5 mL), and hexanes (10 mL) added to form a light brown precipitate that was removed by filtration and discarded. Hexanes (150 mL) were added to the red filtrate causing formation of an orange-red precipitate that was collected and dried under vacuum (78°C, 48 h), (0.15 g, 52%). Anal. calcd. for $C_{33}H_{27}Cl_2N_3OP_2Ru$: C 55.39, H 3.80, N 5.87; found: C 55.14, H 3.80, N 6.06%.

X-ray crystallographic analysis of $RuCl_2(PPh_3)(Ppy_3)\cdot 2CH_2Cl_2$

Crystallographic data appear in Table 1. The final unit-cell parameters were obtained by least squares on 2 sin θ/λ values for 25 reflections with 2θ = 20.1°–29.4°. The intensities of three standard reflections, measured every 200 reflections throughout the data collection, decayed linearly by 19%. The data were processed,[2] for Lorentz and polarization effects, decay, and absorption (semi-empirical, abased on azimuthal scans).

The structure was solved by the Patterson method. The asymmetric unit contains one molecule of the metal complex and two crystallographically independent dichloromethane molecules. Non-hydrogen atoms were refined with anisotropic thermal parameters and hydrogen atoms were fixed in calculated positions (C—H = 0.98 Å, B_H = 1.2 $B_{bonded\ atom}$). No correction for secondary extinction was necessary. Neutral atom scattering factors for all atoms and anomalous dispersion corrections for the non-hydrogen atoms were taken from the *International tables for X-ray crystallography* (11). The largest peak on the final difference map (0.72 e Å^{-3}) was located near the Ru atom. Final atomic coordinates and equivalent isotropic thermal parameters, selected bond lengths, and selected bond angles appear in Tables 2–4, respectively. Hydrogen atom parameters, anisotropic thermal parameters, complete tables of bond lengths and angles, torsion angles, non-bonded contacts, and least-squares planes have been deposited as supplementary material.[3]

Results and discussion

Synthesis and characterization of $RuCl_2(PPh_3)(Ppy_3)$ 1

The synthesis and reactivity of **1** are summarized in Fig. 1 and characterization data for **1–9** are reported in Tables 5–8.

Complex **1** is readily made by reaction of equimolar amounts of $RuCl_2(PPh_3)_3$ and Ppy_3, and its crystal structure is shown in Fig. 2. The Ppy_3 ligand binds facially via the three pyridyl nitrogens, forming three six-membered rings, and the coordination sphere is completed by *cis* chlorides and a PPh_3. The geometry at Ru is close to octahedral with the angles ranging from 84.9(1)° to 94.9(1)°. The Ru(1)—N(3) bond, *trans* to the PPh_3, is slightly longer than the Ru(1)—N(1 and 2) bonds *trans* to Cl, (2.117(4) Å versus 2.075(4) Å and 2.090(4) Å, respectively). These values are similar to those reported for $[Ru(Ppy_3)_2][C_7H_7SO_3]_2$ (2.06(1)–2.09(1) Å) (3), which has two Ppy_3 ligands coordinated facially through the pyridyl nitrogens and is the only other ruthenium structure reported for a Ppy_3 ligand bound in this manner. The Ru(1)—Cl(1 and 2) bond lengths are identical and the Ru(1)—P(2) bond length is typical for that of a Ru(II) phosphine complex (12).

Bond lengths in the Ppy_3 ligand do not change upon coordi-

[2] *teXsan*: Crystal structure analysis package. Molecular Structure Corp. The Woodlands, Tex., 1985 and 1992.

[3] Copies of material on deposit may be purchased from: The Depository of Unpublished Data, Document Delivery, CISTI, National Research Council Canada, Ottawa, Canada K1A 0S2. Tables of hydrogen atom coordinates and bond lengths and angles involving hydrogen atoms have also been deposited with the Cambridge Crystallographic Data Centre and can be obtained on request from The Director, Cambridge Crystallographic Data Centre, University Chemical Laboratory, 12 Union Road, Cambridge CB2 1EZ, UK.

Table 2. Final atomic coordinates (fractional) and B_{eq}.[a]

Atom	*x*	*y*	*z*	B_{eq}
Ru(1)	0.20978(2)	0.25418(4)	0.23526(2)	2.33(1)
Cl(1)	0.14697(8)	0.23833(13)	0.32628(6)	3.44(5)
Cl(2)	0.25879(8)	0.46078(11)	0.27480(7)	3.41(5)
Cl(3)	0.83342(11)	0.1004(2)	0.42094(11)	8.1(1)
Cl(4)	0.67577(13)	0.2093(2)	0.38988(12)	10.2(1)
Cl(5)	0.9186(2)	0.1383(2)	0.1353(2)	14.4(2)
Cl(6)	0.7970(2)	0.0478(3)	0.01523(13)	14.9(2)
P(1)	0.11631(9)	0.20428(14)	0.06668(7)	3.63(6)
P(2)	0.32550(8)	0.14675(12)	0.30009(6)	2.41(5)
N(1)	0.2605(2)	0.2858(3)	0.1574(2)	2.5(2)
N(2)	0.1508(2)	0.0908(4)	0.1933(2)	2.5(2)
N(3)	0.1047(2)	0.3472(4)	0.1754(2)	2.9(2)
C(1)	0.2208(3)	0.2614(5)	0.0911(2)	3.1(2)
C(2)	0.2540(4)	0.2865(5)	0.0397(3)	4.1(3)
C(3)	0.3305(4)	0.3378(6)	0.0546(3)	4.9(3)
C(4)	0.3706(3)	0.3649(5)	0.1213(3)	3.9(3)
C(5)	0.3340(3)	0.3382(5)	0.1707(2)	3.2(2)
C(6)	0.1191(3)	0.0759(5)	0.1251(2)	3.0(2)
C(7)	0.0787(3)	−0.0309(5)	0.0967(3)	4.0(3)
C(8)	0.0673(3)	−0.1260(5)	0.1376(3)	4.4(3)
C(9)	0.0960(3)	−0.1094(5)	0.2070(3)	3.9(3)
C(10)	0.1372(3)	−0.0015(5)	0.2329(2)	2.9(2)
C(11)	0.0719(3)	0.3224(5)	0.1083(3)	3.1(2)
C(12)	0.0038(3)	0.3860(6)	0.0694(3)	4.3(3)
C(13)	−0.0307(3)	0.4765(6)	0.0982(3)	4.8(3)
C(14)	0.0024(4)	0.5024(5)	0.1654(3)	4.5(3)
C(15)	0.0694(3)	0.4360(5)	0.2026(3)	3.6(2)
C(16)	0.3952(3)	0.1074(4)	0.2506(2)	2.8(2)
C(17)	0.3636(3)	0.0443(5)	0.1896(3)	3.4(2)
C(18)	0.4130(4)	0.0110(5)	0.1504(3)	4.6(3)
C(19)	0.4943(4)	0.0416(6)	0.1717(3)	5.6(3)
C(20)	0.5255(4)	0.1068(7)	0.2303(3)	5.8(3)
C(21)	0.4763(3)	0.1412(5)	0.2694(3)	4.3(3)
C(22)	0.3107(3)	−0.0067(4)	0.3343(2)	2.6(2)
C(23)	0.3320(3)	−0.1180(5)	0.3111(3)	3.6(2)
C(24)	0.3189(4)	−0.2279(5)	0.3396(3)	4.5(3)
C(25)	0.2870(4)	−0.2290(6)	0.3929(3)	5.0(3)
C(26)	0.2649(3)	−0.1210(6)	0.4165(3)	4.5(3)
C(27)	0.2772(3)	−0.0089(5)	0.3874(2)	3.4(2)
C(28)	0.3938(3)	0.2088(5)	0.3810(2)	2.8(2)
C(29)	0.3773(3)	0.3182(5)	0.4079(3)	3.7(2)
C(30)	0.4287(4)	0.3606(5)	0.4700(3)	4.9(3)
C(31)	0.4958(4)	0.2927(6)	0.5039(3)	5.0(3)
C(32)	0.5123(4)	0.1807(6)	0.4793(3)	4.5(3)
C(33)	0.4608(3)	0.1397(5)	0.4180(3)	3.9(2)
C(34)	0.7551(4)	0.1747(7)	0.3602(3)	7.0(4)
C(35)	0.8545(5)	0.0185(7)	0.0999(4)	8.8(5)

[a] $B_{eq} = (8/3)\pi^2\Sigma\Sigma U_{ij}a^*_i a^*_j(\mathbf{a}_i \cdot \mathbf{a}_j)$.

nation when compared to data for the free ligand (13), but bond angles do change somewhat. The C(1)-P(1)-C(6) angle (between the two py groups *trans* to Cl) increases slightly to 104.2(2)°, while the C(1)-P(1)-C(11) and C(11)-P(1)-C(6) angles decrease to 98.8(2)°, as compared to an average of 101.9° in the free ligand (13). These angles in **1** are similar to those found in $[Ru(Ppy_3)_2][C_7H_7SO_3]_2$ (100.9(8)°, 99.6(8)°, and 99.6(7)°) (3).

The solution structure of **1** in $CDCl_3$ is consistent with the X-ray structure. The $^{31}P\{^1H\}$ NMR spectrum contains two singlets (Table 5), the result of two uncoupled phosphorus nuclei. The low-field signal is assigned to the PPh_3, while the high-field signal is assigned to the Ppy_3 ligand, the assignments being based on the coordination chemical shift Δ values of 47.7 and 5.56 ppm for the PPh_3 and the Ppy_3 ligands, respectively (14–16). The small Δ value for the Ppy_3 ligand is

Table 3. Selected bond lengths (Å) with estimated standard deviations in parentheses.

Bond	Length	Bond	Length
Ru(1)—Cl(1)	2.438(1)	P(2)—C(16)	1.845(5)
Ru(1)—Cl(2)	2.438(1)	P(2)—C(22)	1.848(5)
Ru(1)—P(2)	2.350(1)	P(2)—C(28)	1.854(5)
Ru(1)—N(1)	2.075(4)	N(1)—C(1)	1.357(5)
Ru(1)—N(2)	2.090(4)	N(1)—C(5)	1.341(6)
Ru(1)—N(3)	2.117(4)	N(2)—C(6)	1.356(6)
P(1)—C(1)	1.829(5)	N(2)—C(10)	1.352(6)
P(1)—C(6)	1.827(5)	N(3)—C(11)	1.354(6)
P(1)—C(11)	1.829(5)	N(3)—C(15)	1.346(6)

Table 4. Selected bond angles (deg) with estimated standard deviations in parentheses.

Bonds	Angle(deg)	Bonds	Angle(deg)
Cl(1)-Ru(1)-Cl(2)	89.84(5)	C(16)-P(2)-C(22)	101.1(2)
Cl(1)-Ru(1)-P(2)	91.54(5)	C(16)-P(2)-C(28)	103.6(2)
Cl(1)-Ru(1)-N(1)	174.4(1)	C(22)-P(2)-C(28)	96.0(2)
Cl(1)-Ru(1)-N(2)	89.1(1)	Ru(1)-N(1)-C(1)	122.9(3)
Cl(1)-Ru(1)-N(3)	88.9(1)	Ru(1)-N(1)-C(5)	120.3(3)
Cl(2)-Ru(1)-P(2)	96.37(5)	C(1)-N(1)-C(5)	116.7(4)
Cl(2)-Ru(1)-N(1)	85.6(1)	Ru(1)-N(2)-C(6)	121.6(3)
Cl(2)-Ru(1)-N(2)	171.0(1)	Ru(1)-N(2)-C(10)	121.6(3)
Cl(2)-Ru(1)-N(3)	84.9(1)	C(6)-N(2)-C(10)	116.7(4)
P(2)-Ru(1)-N(1)	92.1(1)	Ru(1)-N(3)-C(11)	121.6(3)
P(2)-Ru(1)-N(2)	92.6(1)	Ru(1)-N(3)-C(15)	120.7(4)
P(2)-Ru(1)-N(3)	178.6(1)	C(11)-N(3)-C(15)	117.6(4)
N(1)-Ru(1)-N(2)	94.9(1)	P(1)-C(1)-N(1)	120.1(3)
N(1)-Ru(1)-N(3)	87.6(1)	P(1)-C(1)-C(2)	117.3(4)
N(2)-Ru(1)-N(3)	86.2(2)	N(1)-C(1)-C(2)	122.4(5)
C(1)-P(1)-C(6)	104.2(2)	P(1)-C(6)-N(2)	121.0(4)
C(1)-P(1)-C(11)	98.8(2)	P(1)-C(6)-C(7)	116.4(4)
C(6)-P(1)-C(11)	98.8(2)	N(2)-C(6)-C(7)	122.2(5)
Ru(1)-P(2)-C(16)	112.6(2)	P(1)-C(11)-N(3)	120.7(4)
Ru(1)-P(2)-C(22)	117.9(2)	P(1)-C(11)-C(12)	118.4(4)
Ru(1)-P(2)-C(28)	122.4(2)	N(3)-C(11)-C(12)	120.9(5)

consistent with its noncoordination. $^{31}P\{^1H\}$ NMR data for other *N,N',N''*-coordinated Ppy_3 complexes have not been reported. As well, the ^1H NMR ($CDCl_3$) spectrum (Table 6) shows multiple peaks in the phenyl region and is consistent with the complex containing two equivalent (*trans* to Cl) and one inequivalent (*trans* to PPh_3) pyridyl rings. For example, the H6 protons (H adjacent to N in the 2-pyridyl group) give rise to two signals with an integration ratio of 2:1. (That the H6 proton occurs at the most downfield position has been established by others (17, 18).) Thus, the solid state structure of **1** is maintained in $CDCl_3$. However, when **1** is dissolved in MeOH the complex dissociates a chloride (described below).

The synthesis and structure of **1** are similar to those of other Ru(II) complexes containing a facially coordinated six-electron donor ligand. Three examples are $RuCl_2(PPh_3)([9]aneS_3)$ (19), $RuCl(PPh_3)_2(Cp)$ (4), and $RuCl(PPh_3)_2(Tp)$ (20) (where $[9]aneS_3$ = 1,4,7-trithiacyclononane, and Tp = hydrotris(pyrazol-1-yl)borate). The remainder of the coordination spheres is completed by PPh_3 and Cl ligands, relative numbers of each

Fig. 1. Synthesis of compounds. Conditions: (i) Δ, C_6H_6, 7 h; (ii) MeOH, 1 h; (iii) MeOH, 65°C; L = CO, 2 h; L = MeCN, 10 min; L = PhCN, 15 min; (iv) Δ, C_6H_6; L = CO, 42 h; L = MeCN, 17 h; L = PhCN, 4 h, and 16 h at r.t.; (v) $CDCl_3$, r.t.; 1 atm O_2 12 d, or *m*-CPBA, 24 h.

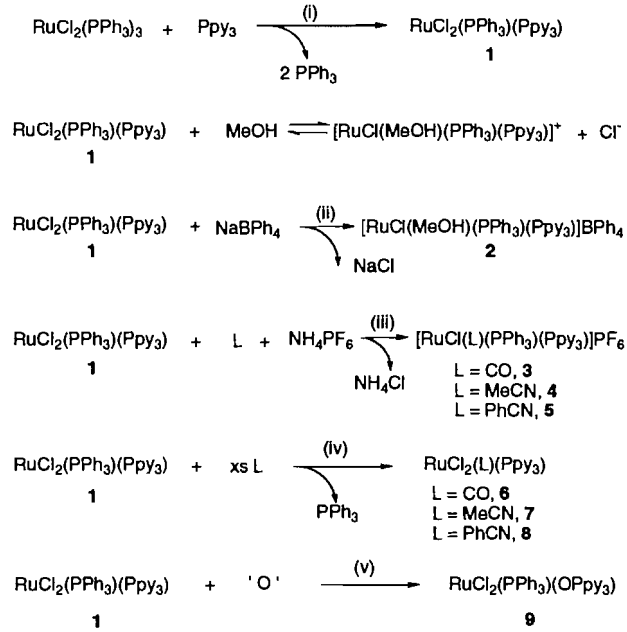

Fig. 2. Perspective view of the $RuCl_2(PPh_3)(Ppy_3)$ molecule; 33% probability thermal ellipsoids are shown for the non-hydrogen atoms. Hydrogen atoms are omitted for clarity.

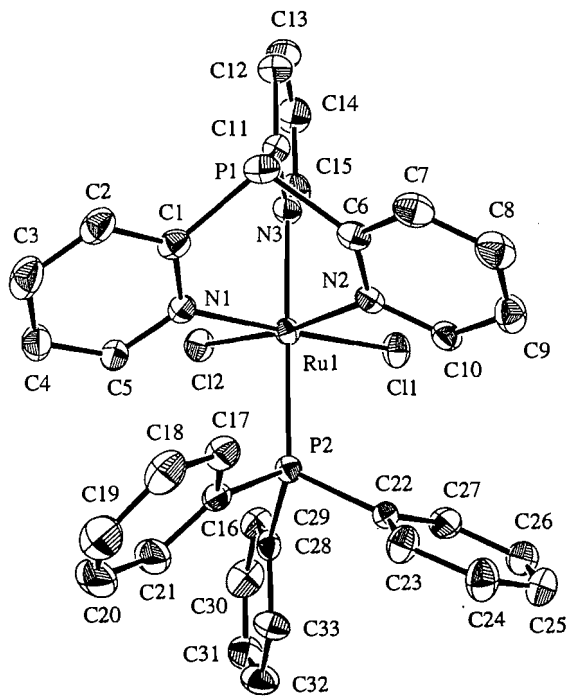

depending on the charge of the facial ligand. Finally, all of the complexes have been synthesized by PPh_3 ligand displacement from $RuCl_2(PPh_3)_3$, although this is not the most convenient method for $RuCl(PPh_3)_2(Cp)$ (4).

Table 5. $^{31}P\{^1H\}$ NMR chemical shifts for *N,N′,N″*-coordinated tris(2-pyridyl)phosphine complexes.

Complex	Solvent	Ppy_3[a] (ppm)	PPh_3[a] (ppm)
$RuCl_2(L)(Ppy_3)$			
L = PPh_3, **1**	$CDCl_3$	4.81	42.3
L = CO, **6**	$CDCl_3$	2.36	—
L = MeCN, **7**	$CDCl_3$	7.71	—
L = PhCN, **8**	$CDCl_3$	7.38	—
$[RuCl(L)(PPh_3)(Ppy_3)]X$			
L = CO; X = Cl[b]	CD_3OD	0.69	36.6
L = CO; X = PF_6, **3**[c]	$CDCl_3$	−0.81	36.7
	CD_3OD	0.69	36.6
L = MeCN; X = PF_6, **4**	$CDCl_3$	2.32	41.4
L = PhCN; X = PF_6, **5**	Acetone-d_6	3.57	42.8
	CD_2Cl_2	2.18	41.2
$RuCl_2(PPh_3)(OPpy_3)$, **9**	$CDCl_3$	3.56[d]	40.4

[a]Singlet; shifts for free Ppy_3 and PPh_3 in $CDCl_3$ are −0.74 and −5.42 ppm, respectively.

[b]In situ.

[c]For the PF_6 salts (**3–5**), the $^{31}P\{^1H\}$ septet for the anion was seen at δ −143 to −145 with $^1J_{PF}$ = 708–713 Hz.

[d]$OPpy_3$.

Fig. 3. Structures of *N,N′,N″*-tris(2-pyridyl)phosphine complexes. (L = PPh_3, **1**; L = CO, **3**, **6**; L = MeCN, **4**, **7**; L = PhCN, **5**, **8**).

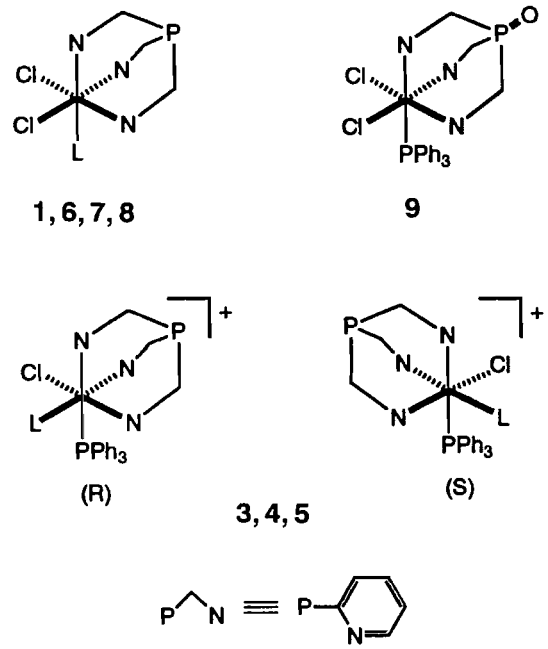

Dissociation of chloride from 1

The molar conductivity of **1** is reported in Table 7. In CH_3NO_2, complex **1** is essentially a nonconductor, while in MeOH the conductivity approaches that expected for a 1:1 conductor. The solvents have comparable dielectric constants (ε = 38.6 for CH_3NO_2, and 32.6 for MeOH (25)), but the higher donor number of MeOH (20.0 vs. 2.7 (25)) leads to the formation of an ionic complex containing a coordinated MeOH (Fig. 1). The complex was isolated as $[RuCl(MeOH)(PPh_3)(Ppy_3)]$-$BPh_4$, **2**, but no NMR data could be recorded because of low solubility. Unfortunately the C analysis for **2** is 0.76% low, but two bands in the IR spectrum can be assigned to a coordinated MeOH: ν_{OH} at 3207 cm^{-1} and ν_{OC} at 1001 cm^{-1}. For neat MeOH the corresponding bands appear at 3342 and 1033 cm^{-1}, respectively (26); the shifts are consistent with MeOH coordination.

The very similar UV–visible spectra of **1** in CH_2Cl_2 and in the solid state (Table 8) imply that the solution structure of **1** in CH_2Cl_2 is the same as that in the solid state (i.e., of the neutral $RuCl_2(PPh_3)(Ppy_3)$). The lower wavelength maxima observed in MeOH are partially attributed to the formation of the coordinated MeOH complex **2**. The spectrum of **2** in CH_2Cl_2, shows a λ_{max} at 414 nm, essentially the same as the 416 nm λ_{max} observed for **1** in MeOH, but the other λ_{max} for **2** (at 368 nm) corresponds to that seen for **1** in CH_2Cl_2. "Solvent effects" on the spectra are clearly important, and this is also evident when addition of a large excess of LiCl (even upto ~10 M) to an MeOH sample of **1** resulted in a change in the 416 nm maximum, to 422 nm, and not the 434 nm position seen for **1** in CH_2Cl_2.

Other ruthenium(II) phosphine complexes containing coordinated MeOH have been reported: the five-coordinate $RuCl_2(PMA)(PPh_3)$ (PMA = *o*-diphenylphosphino-*N,N*-dimethylaniline) reversibly binds MeOH in benzene, as determined by 1H NMR spectroscopy (27); the isolated $Ru(H)_2(CO)(PPh_3)_2(MeOH)$ has been characterized by IR and NMR spectroscopies (28); and $Ru(O_2CCF_3)_2(MeOH)(CO)(PPh_3)_2$ has been characterized by X-ray analysis (29). More closely related, the ionic behaviour observed for **1** parallels that of $RuCl(PPh_3)_2(Cp)$, which is a non-electrolyte in acetone but dissociates appreciably in MeOH (22). Haines and Du Preez isolated the complex $[Ru(MeOH)(PPh_3)_2(Cp)]BPh_4$, which they identified by NMR and IR spectroscopy, although no actual data were presented. As here, the product was not obtained analytically pure. Nevertheless, the ability of $RuCl(PPh_3)_2(Cp)$ to dissociate chloride in MeOH has led to a variety of chloride exchange reactions for the Cp complex (4), and similar reactivity is seen with **1**.

Chloride-substitution reactions

The chloride-substitution reactions are summarized in Fig. 1.

When **1** was heated in CD_3OD under 1 atm CO gas, the initially red suspension changed into a clear yellow solution; the in situ $^{31}P\{^1H\}$ NMR spectrum contained two singlets attributed to the species $[RuCl(CO)(PPh_3)(Ppy_3)]Cl$. However, on a synthetic scale, attempts to isolate this salt always resulted in the formation of an oil. A similar reaction carried out in the presence of NH_4PF_6, however, did allow for isolation of $[RuCl(CO)(PPh_3)(Ppy_3)]PF_6$ **3** as an analytically pure yellow salt.

The $^{31}P\{^1H\}$ NMR (CD_3OD) spectrum of **3** matched that of the in situ species and consisted of two singlets for two uncoupled phosphorus nuclei. The IR spectrum contained a single CO stretch and the compound was a 1:1 conductor in nitromethane. The H6 protons of the Ppy_3 ligand gave rise to three signals in the ^1H NMR spectrum indicating the inequivalence of the three pyridyl groups. These data are consistent with the structure given in Fig. 3, which shows the compound as a racemate.

There is a solvent dependence for the formation of **3**. In ace-

Table 6. ^{1}H NMR chemical shifts for *N,N',N''*-coordinated tris(2-pyridyl)phosphine complexes at room temperature.

Complex	Solvent	δ, ppm (peak[a], no. of H, assignment[b])
$RuCl_2(L)(Ppy_3)$		
L = PPh_3, **1**	$CDCl_3$	6.15(m,2H,Ppy_3);7.17(m,9H,*m-p*-PPh_3);7.29(m,2H,Ppy_3);7.43(m,1H,Ppy_3);7.59(m,6H,*o*-PPh_3);7.68(m,1H,Ppy_3);7.93(m,3H,Ppy_3);8.52(p-d,2H,H6-Ppy_3);10.22(p-d,1H,H6-Ppy_3)
L = CO, **6**	$CDCl_3$	7.30(m,2H,Ppy_3);7.61(m,1H,Ppy_3);7.77(m,2H,Ppy_3);7.90(m,1H,Ppy_3);8.14(m,3H,Ppy_3); 9.47(p-d,2H,H6-Ppy_3);9.98(p-d,1H,H6-Ppy_3)
L = MeCN, **7**	$CDCl_3$	2.67(s,3H,MeCN);7.20(m,3H,Ppy_3);7.62(m,3H,Ppy_3);8.03(m,3H,Ppy_3); 9.69(p-d,2H,H6-Ppy_3); 9.90(p-d,1H,H6-Ppy_3)
L = PhCN, **8**	$CDCl_3$	7.17–7.75(m's,11H,Ppy_3,PhCN);8.08(m,3H,Ppy_3);9.65(p-d,2H,H6-Ppy_3); 9.96(p-d,1H,H6-Ppy_3)
$[RuCl(L)(PPh_3)(Ppy_3)]PF_6$		
L = CO, **3**	$CDCl_3$	6.56(m,1H,Ppy_3);6.74(m,1H,Ppy_3);7.33(m,12H,*o-m*-PPh_3);7.45(m,3H,*p*-PPh_3); 7.54(m,1H,Ppy_3);7.84(m,2H,Ppy_3);7.95(m,2H,Ppy_3);8.26(m,1H,Ppy_3);8.49(m,3H,Ppy_3); 9.56(p-d,1H,H6-Ppy_3)
	CD_3OD	6.66(m,1H,Ppy_3);6.85(m,1H,Ppy_3);7.27(m,12H,*o-m*-PPh_3);7.42(m,3H,*p*-PPh_3); 7.58(m,1H,Ppy_3);7.62(m,1H,Ppy_3);7.75(m,1H,Ppy_3);7.92(m,1H,Ppy_3);7.98(m,1H,Ppy_3); 8.15(p-d,1H,H6-Ppy_3);8.27(m,1H,Ppy_3);8.36(m,1H,Ppy_3);8.48(p-d,1H,H6-Ppy_3); 9.47(p-d,1H,H6-Ppy_3)
L = MeCN, **4**	$CDCl_3$	2.21(s,3H,MeCN);6.53(m,1H,Ppy_3);6.93(m,1H,Ppy_3);7.36(m,15H,PPh_3);7.51(m,1H,Ppy_3); 7.60(m,2H,Ppy_3);7.87(m,1H,Ppy_3);8.20(m,3H,Ppy_3);8.31(p-d,1H,H6-Ppy_3); 8.50(p-d,1H,H6-Ppy_3); 9.61(p-d,1H,H6-Ppy_3)
L = PhCN, **5**	Acetone-d_6	6.80(m,1H,Ppy_3);6.94(m,1H,Ppy_3);7.30–7.65(m's,20H);7.70–7.89(m's,3H);7.93 (m,1H,Ppy_3); 8.13(m,1H,Ppy_3);8.39-8.55(m's,3H);8.60(p-d,1H,H6-Ppy_3); 9.88(p-d,1H,H6-Ppy_3)
$RuCl_2(PPh_3)(OPpy_3)$ 9		
	$CDCl_3$	6.35(m,2H,Ppy_3);7.14–7.33(m's,9H);7.49–7.62 (m's,9H);7.89(m,1H,Ppy_3);8.15(m,3H); 8.45 (p-d,2H,H6-Ppy_3);10.13(p-d,1H,H6-Ppy_3)

[a]s = singlet; m = multiplet; m's = more than one multiplet; p-d = pseudo-doublet(multiplet).

[b]Assignments to specific ligands are made where possible; *o* = *ortho*-H; *m* = *meta*-H; *p* = *para*-H, of Ph groups; H6 = pyridyl-H, adjacent to N of Ppy_3 ligand.

Table 7. Some infrared and conductivity data for *N,N',N''*-coordinated tris(2-pyridyl)phosphine complexes and analogous Cp complexes.

Complex L	IR stretches[a] (cm^{-1}) $RuCl_2(L)(Ppy_3)$	IR stretches[a] (cm^{-1}) $RuCl(L)(PPh_3)(Cp)$	Λ_M (CH_3NO_2, 25°C)[b] (ohm^{-1} mol^{-1} cm^2) $RuCl_2(L)(Ppy_3)$
PPh_3, **1**	—	—	9.9; 67.4[c]
CO, **6**	ν_{CO} = 1942 (s)	ν_{CO} = 1958 (21)[d]	—
MeCN, **7**	ν_{CN} = 2270 (w)	—	—
PhCN, **8**	ν_{CN} = 2224 (m)	—	—
L	$[RuCl(L)(PPh_3)(Ppy_3)]^+$	$[Ru(L)(PPh_3)_2(Cp)]^+$	$[RuCl(L)(PPh_3)(Ppy_3)]^+$
MeOH, **2**	ν_{OH} = 3207 (s), ν_{OC} = 1001(s)	—	—
CO, **3**	ν_{CO} = 1979 (s)	ν_{CO} = 1981 (22)	80.4
MeCN, **4**	ν_{CN} = 2274 (w)	ν_{CN} = 2265 (23)	79.3
PhCN, **5**	ν_{CN} = 2232 (m)	ν_{CN} = 2228 (23)	79.3

[a]s = strong; m = medium; w = weak.

[b]Accepted ranges (ohm^{-1} mol^{-1} cm^2) for 1:1 conductors: in CH_3NO_2 (75-90); in MeOH (80–115) (24).

[c]In MeOH. Calculated using the molecular weight for $RuCl_2(PPh_3)(Ppy_3)$ (699.52 g mol^{-1}). If calculated with the molecular weight of $[RuCl(MeOH)(PPh_3)(Ppy_3)]Cl$ (731.56 g mol^{-1}) the molar conductivity is 64.4.

[d]Appropriate reference appears in parentheses for the Cp complexes.

tone, the reaction at room temperature was slow (11 d) and a mixture of mainly **3** and some $RuCl_2(CO)(Ppy_3)$ **6** (see below) was obtained. The minor product is formed via displacement of the PPh_3 of **1**. In MeOH, the formation of the cationic MeOH intermediate allows for a more efficient mechanism for the formation of **3**.

Use of a procedure similar to that described above for **3** allowed for isolation of the nitrile complexes

Table 8. UV–visible data for *N,N′,N″*-coordinated tris(2-pyridyl)phosphine complexes.

Complex	Solvent	λ_{max} ($\varepsilon_{max} \times 10^{-3}$) nm ($M^{-1}$ cm^{-1})		
$RuCl_2(L)(Ppy_3)$				
L = PPh_3, **1**	CH_2Cl_2	270(20.5)	368(6.40)	434(7.60)
	MeOH	264(20.0)	350(6.00)	416(7.90)
	Solid State[a]	—	368	438
	Solid State[b]	—	368	438
L = CO, **6**	CH_2Cl_2	270(15.6)	350(5.96)	434(3.05)
	MeOH	264(8.92)	338(3.10)	400(1.92)
L = MeCN, **7**	CH_2Cl_2	—	386(7.92)	428(9.31)[c]
	MeOH	—	372(7.67)	418(8.63)[d]
L = PhCN, **8**	CH_2Cl_2	268(24.8)	374(12.0)	434(13.9)
	MeOH	260(22.2)	356(9.10)	414(11.3)
$[RuCl(MeOH)(PPh_3)(Ppy_3)]BPh_4$, **2**	CH_2Cl_2	—	368(~4.84)[e]	414(~5.59)[e]
$[RuCl(L)(PPh_3)(Ppy_3)]PF_6$				
L = CO, **3**	CH_2Cl_2	270(18.0)	366(3.07)	
	MeOH	266(19.0)	352(3.20)	
L = MeCN, **4**	CH_2Cl_2	262(18.9)	336(5.88)	386(7.54)[f]
L = PhCN, **5**	CH_2Cl_2	260(19.1)	324 (10.6)	386(9.61)[g]
$RuCl_2(PPh_3)(OPpy_3)$, **9**	CH_2Cl_2	262(18.5)	362(6.90)	430(7.35)
	MeOH	262(17.8)	346(6.59)	412(7.50)

[a]Amorphous film made from a CH_2Cl_2 solution.
[b]Film made from a MeOH solution.
[c]Shoulder at 466 nm (ε = 6540).
[d]Shoulder at 450 nm (ε = 6630).
[e]Complex not analytically pure.
[f]Shoulder at 424 nm (ε = 5570).
[g]Shoulder at 424 nm (ε = 6330).

$[RuCl(L)(PPh_3)(Ppy_3)]PF_6$, where L = MeCN (**4**) or L = PhCN (**5**). The isolated complexes (Fig. 3) were characterized in the same manner as **3**. Only one equivalent of MeCN was used to make **4**. When excess or neat MeCN was used, the isolated product contained small amounts of impurities, as determined by $^{31}P\{^1H\}$ NMR. Similarly, when $RuCl_2(PPh_3)(Ppy_3)$ and one equivalent of NH_4PF_6 were refluxed in a mixture of PhCN and some acetone (needed to dissolve NH_4PF_6), the isolated product mixture contained **5** and a second product which showed a $^{31}P\{^1H\}$ singlet at δ 6.30 (in acetone-d_6) or 5.05 (in CD_2Cl_2). This second product, also formed from refluxing $RuCl_2(PhCN)(Ppy_3)$ **8** in MeOH with one equivalent of NH_4PF_6 and excess PhCN, is tentatively formulated as $[RuCl(PhCN)_2(Ppy_3)]PF_6$. The complex was not further characterized because of the presence of other minor impurities. Finally, when **1** is refluxed in neat PhCN without NH_4PF_6, $RuCl_2(PhCN)(Ppy_3)$ **8** is formed (see below).

In summary, the best route to chloride-substitution products of **1** is via reactions in MeOH, which allow for dissociation of chloride and disfavour substitution of PPh_3, which occurs in other solvents.

Triphenylphosphine-substitution reactions

By use of a nonpolar solvent such as benzene, the PPh_3 in **1** is readily displaced, the chemistry being similar to that of $RuCl(PPh_3)_2(Cp)$, where the PPh_3 has been replaced by other phosphines, CO, and isocyanides, to name a few (4).

The refluxing of **1** in C_6H_6 under 1 atm CO gas gives two precipitated products, based on the $^{31}P\{^1H\}$ NMR ($CDCl_3$) spectrum which contained two singlets at δ 2.36 (major) and 4.77 (minor). The complex $RuCl_2(CO)(Ppy_3)$ **6** giving rise to the singlet at 2.36 ppm was separated as an orange solid by precipitation from CH_2Cl_2 with Et_2O, while the minor product was not characterized. The ^1H NMR ($CDCl_3$) spectrum of **6** contained two H6 signals integrating in a 2:1 ratio, and the NMR data and the single νCO IR band are consistent with a structure analogous to that of $RuCl_2(PPh_3)(Ppy_3)$ (Fig.3).

Similar reactions of **1** with MeCN and PhCN (Fig. 1) allowed for isolation of $RuCl_2(MeCN)(Ppy_3)$ **7** and $RuCl_2(PhCN)(Ppy_3)$ **8**, respectively, with structures similar to that of the CO complex. These two complexes were isolated in slightly different manners. Complex **8** formed as a red precipitate during the reaction in benzene, the remainder of the product being precipitated by addition of hexanes. The product was then reprecipitated from CH_2Cl_2 with Et_2O to remove a C_6H_6 solvate that otherwise was not removed under vacuum. Finally, **8** was heated under vacuum to remove any remaining solvates, and an analytically pure product was produced. Complex **7** was isolated directly as a red precipitate from the C_6H_6 solution without the addition of hexanes and dried under vacuum for 24 h. The analysis of this complex was calculated including 1/6 mol of C_6H_6 solvate. The C_6H_6 solvate was confirmed by integration of the ^1H NMR ($CDCl_3$) spectrum. When **7** was heated in vacuum (78°C, 24 h) the complex partially decomposed, becoming red-brown in colour; the elemental analysis had a much lower nitrogen percentage, suggesting that MeCN was being lost.

A further factor perhaps assisting the substitution of the PPh_3 in **1** is that the complex is only slightly soluble in C_6H_6, and thus the concentration of the substituting ligand is high,

relative to that of **1**. The longer reaction time required for the CO complex in comparison to the nitrile complexes (42 versus 17–20 h) is probably the result of the relatively low concentration of CO versus that of the nitriles.

There is a striking similarity between the carbonyl and nitrile stretches of the *N,N',N''*-Ppy_3 complexes and those of the analogous Cp complexes (see Table 7; no data could be found for the Cp analogues of **7** and **8**). For example, the cationic carbonyl complexes produced by substitution of the chloride in **1**, or in $RuCl(PPh_3)_2(Cp)$, have essentially the same CO stretches, indicating that the electronic properties of the Ru centre, in terms of back-donation into the π orbital of the CO ligand, are the same. The implication is that the 14-electron fragments $RuCl(Ppy_3)$ and $Ru(PPh_3)(Cp)$ have similar electronic properties. Within either the Ppy_3 or Cp systems, the cationic complexes have the higher ν_{CO} or ν_{CN} values, consistent with the usual property of less π-back-donation from the Ru in the cationic systems.

Reaction of 1 with oxygen and *m*-CPBA

The in situ reaction of **1** with 1 atm O_2 gas in $CDCl_3$ was followed by $^{31}P\{^1H\}$ NMR spectroscopy and, after 3 d at room temperature, signals for **1** and a new species were present in the spectrum. The new signals are for the complex $RuCl_2(PPh_3)(OPpy_3)$ **9** (see Fig. 3), which was synthesized independently using *m*-CPBA as the O-atom donor. In the O_2-system, after 12 d, **9** is the only species present along with a small peak for $OPPh_3$ (δ_P 29.6). Thus, the free phosphorus of the Ppy_3 group in $RuCl_2(PPh_3)(Ppy_3)$ is oxidized to the phosphine oxide, indeed at a rate comparable to that of free Ppy_3. The presence of $OPPh_3$ in the spectrum of the in situ reaction suggests that a second ruthenium product is being formed; this could be a paramagnetic ruthenium-oxo or -peroxo-type species (30) but, because of the relatively small amount of $OPPh_3$ formed, no attempts were made to isolate this other product. In the system of **9** from **1** using *m*-CPBA, the benzoic acid by-product was removed by selective precipitation with hexanes. Reaction of $RuCl_2(PPh_3)_3$ with $OPpy_3$ gave a complex mixture of products including **9**.

Other complexes containing a coordinated $OPpy_3$ ligand have the general formula $[M(OPpy_3)_2][X]_2$ (M = Mn, Co, Ni, Cu, Zn, with $X = ClO_4$ (1); or M = Ru, with $X = PF_6$ (31)), and have been synthesized directly using $OPpy_3$. The $OPpy_3$ ligands coordinate via the three pyridyl nitrogens and form octahedral complexes. Infrared data are not reported for the Ru complex, but the ν_{PO} stretches for the first-row transition metal complexes range from 1231 to 1236 cm^{-1}; **9** gives a similar ν_{PO} stretch at 1235 cm^{-1}. These νPO values are higher than that of the free $OPpy_3$ ligand, 1215 cm^{-1} (1), the increase possibly resulting from the configuration imposed on the ligand upon coordination, or from an increase in $p\pi$–$d\pi$ bonding between the oxygen and phosphorus, caused by an increase in the electronegativity of the phosphorus, induced by the coordinating pyridyl groups (1). This is consistent with the general trend for phosphine oxides (OPR_3) which show an increase in the ν_{PO} wave numbers as R becomes more electronegative (ref. 25, p. 827).

A comparison of the UV–visible spectra of **9** with those of **1** (Table 8) shows that oxidation of the Ppy_3 ligand has only a small influence on the electronic environment at the metal centre, and imply that **9** also dissociates chloride in MeOH.

Acknowledgements

We thank the Natural Sciences and Engineering Research Council of Canada for financial support (research grant for B.R.J. and postgraduate fellowship for R.P.S), and Johnson Matthey Ltd. and Colonial Metals Inc. for loans of $RuCl_3 3H_2O$.

References

1. R.K. Boggess and D.A. Zatko. J. Coord. Chem. **4**, 217 (1975).
2. R. Gregorzik, J. Wirbser, and H. Vahrenkamp. Chem. Ber. **125**, 1575 (1992).
3. F.R. Keene, M.R. Snow, P.J. Stephenson, and E.R.T. Tiekink. Inorg. Chem. **27**, 2040 (1988).
4. S.G. Davies, J.P. McNally, and A.J. Smallridge. Adv. Organomet. Chem. **30**, 1 (1990).
5. I.R. Baird, M.B. Smith, and B.R. James. Inorg. Chim. Acta, **235**, 291 (1995), and references therein.
6. R.P. Schutte. Ph.D. Dissertation, University of British Columbia, 1995.
7. P.S. Hallman, T.A. Stephenson, and G. Wilkinson. Inorg. Synth. **12**, 237 (1970).
8. K. Kurtev, D. Ribola, R.A. Jones, D.J. Cole-Hamilton, and G. Wilkinson. J. Chem. Soc. Datlton Trans. 55 (1980).
9. K.R. Dixon. *In* Multinuclear NMR. *Edited by* J. Mason. Plenum, New York. 1987. Chap. 13.
10. J.E.J. Lind, J.J. Zwolenik, and R.M. Fuoss. J. Am. Chem. Soc. **81**, 1557 (1959).
11. (*a*) International tables for X-ray crystallography. Vol. IV. Kynoch Press. Birmingham, U.K. (present distributor Kluwer Academic Publishers, Boston, Mass.). 1974. pp. 99–102; (*b*) International tables for crystallography. Vol. C. Kluwer Academic Publishers, Boston, Mass. 1992. p. 200–206.
12. P.G. Jessop, S.J. Rettig, C. Lee, and B.R. James. Inorg. Chem. **30**, 4617 (1991).
13. F.R. Keene, M.R. Snow, and E.R.T. Tiekink. Acta Crystallogr. Sect. C: Cryst. Struct. Commun. **C44**, 757 (1988).
14. B.E. Mann, C. Masters, and B.L. Shaw. J. Chem. Soc. (A), 1104 (1971).
15. B.E. Mann, C. Masters, and B.L. Shaw. J. Chem. Soc. Dalton Trans. 704 (1972).
16. P.W. Pregosin and R.W. Kunz. NMR: Basic Principles Prog. **16**, 49 (1979).
17. H.J. Jackobsen. J. Mol. Spectrosc. **34**, 245 (1970).
18. G.E. Griffin and W.A. Thomas. J. Chem. Soc. (B), 477 (1970).
19. N.W. Alcock, J.C. Cannadine, G.R. Clark, and A.F. Hill. J. Chem. Soc. Dalton Trans. 1131 (1993).
20. N.W. Alcock, I.D. Burns, K.S. Claire, and A.F. Hill. Inorg. Chem. **31**, 2906 (1992).
21. S.G. Davies and S.J. Simpson. J. Chem. Soc. Dalton Trans. 993 (1984).
22. R.J. Haines and A.L. Du Preez. J. Organomet. Chem. **84**, 357 (1975).
23. M.I. Bruce, R.C. Wallis, M.L. Williams, B.W. Skelton, and A.H. White. J. Chem. Soc., Dalton Trans. 2183 (1983).
24. W.J. Geary. Coord. Chem. Rev. **7**, 81 (1971).
25. J.E. Huheey. Inorganic chemistry. Harper & Row, New York. 1983. p. 340
26. A.J. Gordon and R.A. Ford. The chemist's companion. Wiley, New York. 1972. p. 191.
27. D.C. Mudalige. Ph.D. Dissertation, University of British Columbia, 1994.
28. B.N. Chaudret, D.J. Cole-Hamilton, R.S. Nohr, and G. Wilkinson. J. Chem. Soc. Dalton. Trans. 1546 (1977).
29. A. Dobson, D.S. Moore, S.D. Robinson, M.B. Hursthouse, and L. New. Polyhedron, **4**, 1119 (1985).
30. B.R. James. Stud. Surf. Sci. Catal. **66**, 195 (1991).
31. F.R. Keene and P.J. Stephenson. Inorg. Chim. Acta, **187**, 217 (1991).

Nucleophilic addition to di- and poly-iron arene complex cations

Alaa S. Abd-El-Aziz, Debbie A. Armstrong, Shelly Bernardin, and Harold M. Hutton

Abstract: Hydride and cyanide addition to a series of di- and polycyclopentadienyliron arene complex cations with etheric bridges is described. Reaction of the di-iron complexes with sodium borohydride resulted in the formation of a number of adducts. *p*-Methyl- and *o,o*-dimethylphenoxybenzene cyclopentadienyliron complexes were used as models in this study to allow for the characterization of the analagous di-iron complexes. The use of HH COSY and CH COSY NMR techniques enabled us to identify the isomeric nature of these adducts. The hydride addition results indicated that the etheric substituent had the predominant effect over the methyl group, leading to a higher addition ratio to the *meta*-, followed by the *ortho*-, then the *para*-positions. It was also clear that in the di-iron system, the hydride addition to each complexed arene ring took place independently. The addition of the cyanide anion to di- and poly-iron arene systems was more selective than that of the hydride anion. Reaction of sodium cyanide with *p*-methyl- or *o*-methyl-substituted arene complexes led to the formation of one adduct, with the cyanide being added to the *meta* position to the etheric bridges. However, cyanide addition to the di-iron complex, with a methyl substituent attached at the *meta* position of each complexed arene, led to the formation of a mixture of adducts. Cyanide addition to the poly-iron system with *p*-substituted arenes proved to be very selective, allowing for the formation of one adduct. Oxidative demetallation with 2,3-dichloro-5,6-dicyano-1,4-benzoquinone (DDQ) produced the uncomplexed polyaromatic ethers with cyano groups in a very good yield.

Key words: cyclopentadienyliron, arene, nucleophilic addition, hydride, cyanide.

Résumé : On décrit l'addition des ions hydrure et cyanure à une série de complexes cationiques di- et polycyclopentadiénylfer–arène avec ponts éthers. La réaction des complexes bi-fer avec le borohydrure de sodium conduit à la formation d'un certain nombre d'adduits. Dans cette étude, on a utilisé les *p*-méthyl- et *o,o*-diméthylphénoxybenzène cyclopentadiénylfer comme modèles permettant de caractériser les complexes di-fer analogues. L'utilisation des techniques de RMN HH COSY et CH COSY ont permis d'identifier la nature des produits isomères de ces adduits. Les résultats obtenus pour l'addition d'hydrure ont indiqué que le substituant éther a un effet plus important que celle du méthyle; ceci conduit à un rapport d'addition plus élevé pour la position *méta*, suivie alors par les positions *ortho* et *para*. Il est également clair que, dans le système bi-fer, l'addition d'hydrure à chacun des noyaux arènes se fait d'une façon indépendante. L'addition de l'anion cyanure aux systèmes di- et poly-fer–arène est plus sélective que celle de l'anion hydrure. La réaction du cyanure de sodium avec les complexes arènes *p*-méthyl- ou *o*-méthyl-substitués conduit à la formation d'un adduit dans lequel le cyanure s'ajoute en position *méta* par rapport au pont éther. Toutefois, l'addition du cyanure au complexe di-fer portant un substituant méthyle en position *méta* de chaque arène complexé conduit à la formation d'un mélange d'adduits. L'addition de cyanure au système poly-fer avec des arènes *p*-substitués s'avère sélective et conduit à la formation d'un seul adduit. La démétallation oxydante de la 2,3-dichloro-5,6-dicyano-1,4-benzoquinone (DDQ) conduit, avec de très bons rendements, à des éthers polyaromatiques non complexés portant des groupes cyano.

Mots clés : cyclopentadiénylfer, arène, addition nucléophile, hydrure, cyanure.

[Traduit par la rédaction]

Introduction

Addition of carbanions, hydrides, phosphorus and nitrogen anions to organometallic complexes has led to novel routes to the functionalization of aromatic compounds (1–15). It is well known that the complexation of a metal moiety, such as $(CO)_3Cr$, $(CO)_3Mn^+$, $(C_6H_6)Fe^{2+}$, or $CpFe^+$ to an aromatic system activates the arene ring towards nucleophilic addition reactions (4-26). In a review by Davies et al., a set of rules was presented to predict the site of nucleophilic addition to organo-transition metal cations containing unsaturated hydrocarbon ligands (1). Other reports have indicated that addition occurs on the *exo* face of the arene ligand, as confirmed by NMR and X-ray crystallographic studies (27, 28).

Due to the ease of complexation of the $(CO)_3Cr$ moiety with aromatic systems, the vast majority of research in this field has involved the use of these types of complexes (8). Addition of

Received February 6, 1996.

This paper is dedicated to Dr. Howard C. Clark for his distinguished contribution to inorganic and organometallic chemistry.

A.S. Abd-El-Aziz,[1] D.A. Armstrong, S. Bernardin, and H.M. Hutton. Department of Chemistry, University of Winnipeg, Winnipeg, MB, R3B 2E9, Canada.

[1] Author to whom correspondence may be addressed. Telephone: (204) 786-9335. Fax: (204) 786-1824. E-mail: abdelaziz@uwinnipeg.ca

nucleophiles to (arene)$Cr(CO)_3$ has led to the formation of anionic [$(CO)_3$Cr(cyclohexadienyl)] intermediates. These adducts are air sensitive and usually undergo oxidative demetallation without isolation, allowing for the functionalization of the arene compounds (2). A novel characteristic of the cyclohexadienyl intermediates is that they may react with electrophilic reagents, enhancing the flexibility of this methodology.

Tremendous effort has been directed toward the use of cationic metal moieties such as $(CO)_3Mn^+$, $CpFe^+$, or $(C_6H_6)Fe^{2+}$ for the activation of arenes, allowing for the formation of neutral functionalized cyclohexadienyl complexes. The use of $(CO)_3Mn^+$ species as an activating group has led to the synthesis of a number of potentially biologically active chiral compounds (16, 17), as well as the functionalization of heterocyclic and cyclohexadiene compounds (15, 18, 19). Addition reactions of a variety of nucleophiles (H^-, CN^-, $CH_3COCH_2^-$, CH_3^-, Cl_3C^-) to cyclopentadienyliron arene cations have also been investigated (27–43). Sutherland et al. examined the hydride addition reactions of various substituted $[(C_6H_5X)FeCp]^+$ systems (37). This study demonstrated that strongly electron-donating substitutents direct hydride addition to the *meta* and *para* positions of the substituent, while the strongly electron-withdrawing substituent directs to the *ortho* position. These results are consistent with those predicted from molecular orbital calculations (32–36). Steric effects from the methyl groups *ortho* to the electron-withdrawing substituent of arene complexes have been reported with hydride addition (41). When *ortho* positions were hindered, addition in the *meta* and *para* positions increased. However, cyanide addition did not display the same sensitivity to steric factors; addition in this case occurred in the *ortho* position only. It was proposed that steric, electronic, and free valency effects all play a role in nucleophilic addition reactions (32, 37).

We have developed an efficient synthetic route to di- and polycyclopentadienyliron arene cations (44–48). The need to devise simple methods for functionalization of these types of complexes led us to the study of nucleophilic substitution and addition reactions. Our recent investigation of the functionalization of polyaromatic arene complexes via nucleophilic substitution has been successful (44–46). In this article we report hydride and cyanide addition to a number of methyl-substituted mono-, di-, and polycyclopentadienyliron complexes.

Results and discussion

Hydride addition

Hydride addition to bis(cyclopentadienyliron) arene di-cations resulted in the formation of a number of isomers. Due to the complexity of the NMR spectra of these adducts, the mono-iron systems were used as models for this investigation. While hydride addition to $CpFe^+$ complexes of monosubstituted arenes has been carefully examined (37), hydride addition to disubstituted arene complexes has not been reported. Reactions of (η^6-isomeric phenoxytoluene-η^5-cyclopentadienyliron) cations with an excess of sodium borohydride gave rise to a mixture of adducts, as illustrated in Scheme 1. The ^1H and ^{13}C NMR spectra were complicated by the number of isomers present; thus it was necessary to characterize the products using HH COSY and CH COSY techniques. For proton assignment, the chemical shifts of the individual isomers were determined from the connectivities in the HH COSY spectrum. Once this information was obtained, ^{13}C chemical shifts were then assigned using CH COSY.

It has been established that a phenoxy substituent attached to the arene $CpFe^+$ complex directs the addition of the nucleophile to *meta* > *ortho* > *para*, whereas a methyl substituent directs *ortho* > *meta* > *para* (29–32, 37). In this study, it was very clear that the phenoxy substituent has a stronger influence on the site of addition than has the methyl substituent due to its greater strength as an electron-donating group. For clarity, we will refer to the site of addition with respect to the etheric bridge. As shown in Scheme 1, the major adduct for complex [**1**] was [**3b**] (66%), formed at the position *meta* to the phenoxy substituent. The second most abundant isomer [**3a**] (30%) displayed addition *ortho* to the phenoxy group. Trace amounts of the product *ipso* to the methyl substituent (*para* to the phenoxy substituent), [**3c**] (4%), were present; however, it was difficult to fully characterize this isomer. For complex [**2**], in which the positions *ortho* to the phenoxy substituent are hindered by methyl groups, the major addition was at the *meta* position with respect to the phenoxy group [**4b**] (60%), as illustrated in Scheme 1. Addition *para* to the phenoxy gave rise to the second most abundant isomer [**4c**] (28%). The minor isomer, [**4a**] (12%), resulted when addition *ipso* to the methyl group took place. Attempts to separate the various isomers by means of column chromatography were

Scheme 1.

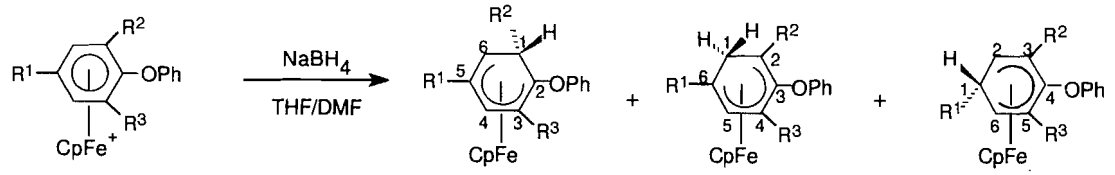

1 $R^1 = CH_3$, $R^2, R^3 = H$ — **3a** (30%) — **3b** (66%) — **3c** (4%)

2 $R^1 = H$, $R^2, R^3 = CH_3$ — **4a** (12%) — **4b** (60%) — **4c** (28%)

Fig. 1. 2D HH COSY for adducts **3a–c** in $CDCl_3$.

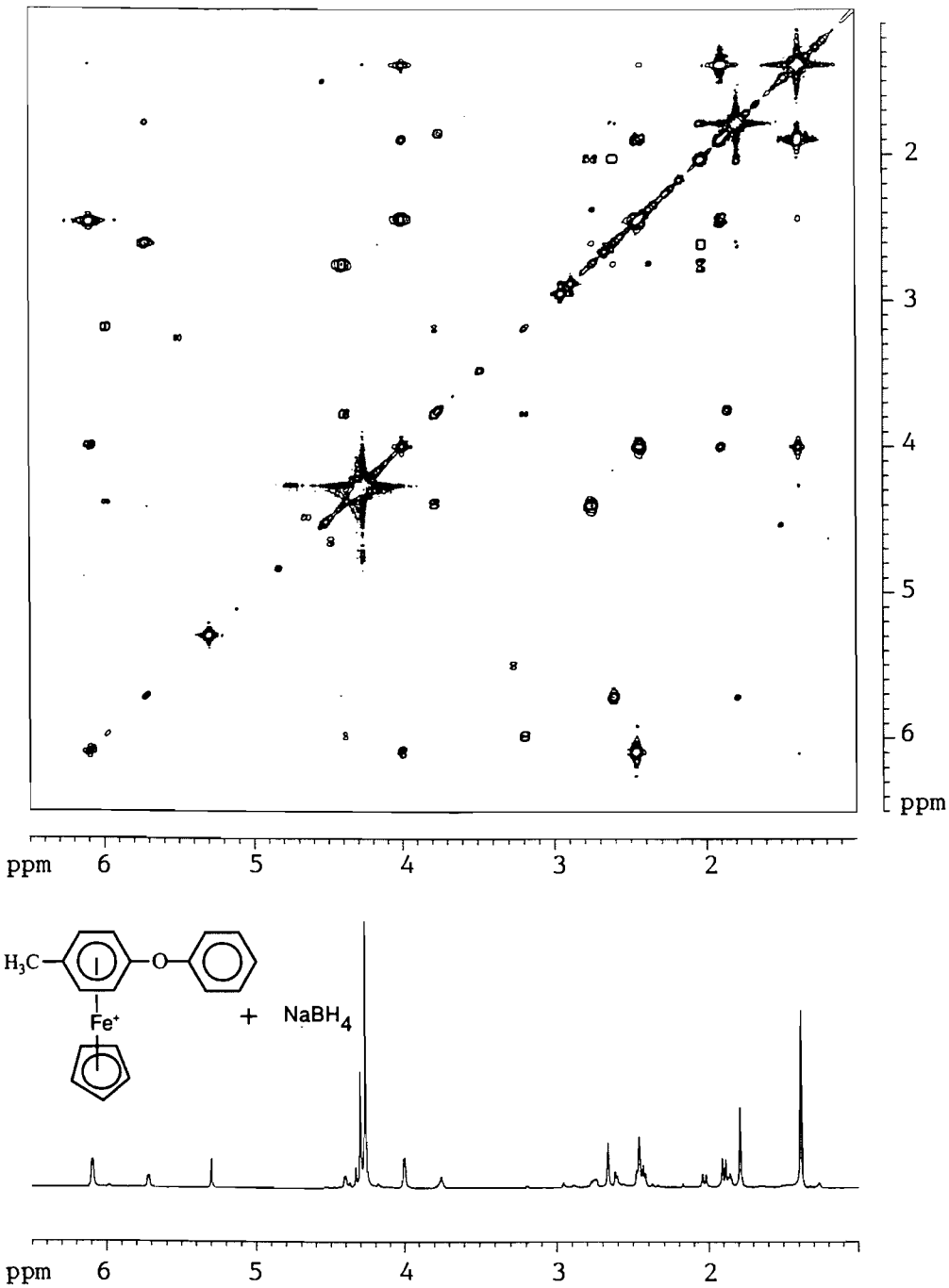

unsuccessful due to the instability of these products. The ^1H and ^{13}C NMR data of the addition products [**3**] and [**4**] are listed in Tables 1 and 2. For the purpose of identification, the site of hydride addition has been designated position one, and numbering proceeds around the ring, so that the phenoxy group is the lowest possible number. As an example, Fig. 1 illustrates the 2D HH COSY for the hydride addition to complex [**1**] (adducts [**3a–c**]).

Reaction of 1.0 mmol of 1,4-bis[(η^6-4-methylphenoxy-η^5-cyclopentadienyl)iron]benzene cation [**5**] with 5.0 mmol of sodium borohydride produced a mixture of isomers, as shown in Scheme 2. Since the complexed arene rings are separated from one another by a (OC_6H_4O) group, as shown in Scheme 2, the addition to each of these rings should be independent. Thus a variety of symmetrical and asymmetrical adducts should be obtained. If the addition takes place at the same site on both rings, there will be no significant change in the chemical shifts between the protons or carbons of one cyclohexadienyl ring and the other. As an example, it was not possible to distinguish between the chemical shift for the *ortho-ortho* isomer [**6a**] and the asymmetric *ortho* addition of isomer [**6c**]. The relative percentage of the addition product calculated

Table 1. ^{1}H NMR data for the adducts **3** and **4**.[a]

Adduct	CH_3	H(1-*exo*)	H(1-*endo*)	H(2)	H(3)	H(4)	H(5)	H(6)	Cp
3a	1.79 s	2.06 (d, 9.8, ex-en)	2.78 (dd, 9.8, en-ex; 5.9, en-6)	—	4.41 (d, 5.1)	5.73 (d, 5.1)	—	2.62 (d, 5.9, 6-en)	4.30 s
3b	1.39 s	1.93 (d, 10.7, ex-en)	2.44 m	2.46 m	—	6.11 (d, 5.1)	4.02 (d, 5.1)	—	4.27 s
4a	1.25, 1.94 s	1.86 s	—	—	—	5.80 (d, 5.9)	4.09 (t, 5.9)	2.09 (d, 5.9)	4.24 s
4b	1.30, 2.51 s	1.82 (d, 12.2, ex-en)	2.37 (dd, 12.2, en-ex; 6.1, en-6)	—	—	—	4.24 (d, 6.2)	2.03 (d, 6.2)	4.18 s
4c	1.96 s	1.57 (d, 12.8, ex-en)	2.35 (dt, 13.1, en-ex; 7.0, en-2,6)	1.79 m	—	—	—	1.79 m	4.26 s

[a]Uncomplexed aromatic peaks appear as multiplet between 6.8 and 7.5 ppm. Coupling constants (Hz) are of adjacent protons unless otherwise indicated.

Table 2. ^{13}C NMR of the adducts **3** and **4**.[a]

Adduct	CH_3	C (1)	C (2)	C (3)	C (4)	C (5)	C (6)	Cp
3a	21.75	31.71	35.99	70.71	74.15	75.11	29.07	74.78
3b	24.89	33.11	24.84	91.87	69.67	75.24	18.79	74.64
4a	29.66, 20.91	28.41	35.42	89.20	98.31	86.20	18.45	75.12
4b	19.97, 16.67	34.28	29.66	98.20	88.00	78.82	17.93	75.37
4c	20.90	28.35	20.11	86.18	94.81	86.18	20.11	76.17

[a]Uncomplexed aromatic peaks appear at 114–128 ppm.

from the NMR spectra for each isomer was based on the total amount of specific addition in each adduct. The *meta* isomer was calculated to be 59%, which was the total of the hydride addition in *meta-meta* [**6b**], *meta-ortho* [**6c**], and the trace *meta-para*. The total *ortho* addition was 35%, which represents the addition *ortho-ortho* [**6a**], *ortho-meta* [**6c**], and a trace of *ortho-para* adduct. Trace amounts of the *para* addition products were also observed (6%). It is also important to note that we did not observe diastereomers for these adducts. The ^{1}H and ^{13}C NMR chemical shifts are shown in Tables 3 and 4, where [**6a**] and [**6b**] represent the symmetrical *ortho* and *meta* isomers, respectively, as well as the *ortho* and *meta* addition of the asymmetrical structure [**6c**].

As part of this study, we blocked the two positions *ortho* to the etheric bridges by two methyl groups in order to enhance addition to the *meta* position. Hydride addition to 1,4-bis[(η^6-(2,6-dimethyl)phenoxy-η^5-cyclopentadienyl)iron]benzene hexafluorophosphate, [**7**], resulted in the formation of three major isomers, as well as traces of a few minor isomers, as shown in Scheme 3. Using the same strategy as described above, the predominant isomer was determined to be the *meta* adduct [**8a**] (51%); *para* [**8b**] (41%) and traces of *ortho* adducts (8%) were also present. The spectral analyses for these adducts are given in Tables 3 and 4. The position of hydride addition was found to be dependent on the substituents on the ring.

Cyanide addition

Nitrile groups are unique in their ease of transformation to other functional groups such as acids, esters, amines, and amides (49, 50). This versatility is valuable in the investigation of synthetic routes for the functionalization of organic and polymeric compounds. In the past few years, we have been involved in the synthesis and characterization of polyaromatic ethers with or without pendant metallic moieties (44–47). In this article, we report the addition of cyanide to a number of $CpFe^+$ polyaromatic ether complexes. Schemes 4 and 5 show the relative distribution of adducts obtained from cyanide addition to isomeric bis(η^6-methylphenoxy-η^5-cyclopentadienyl)ironbenzene hexafluorophosphate [**5**, **9**, and **12**] . In the case of complexes [**5**] and [**9**], single pure products [**10**] and [**11**] were obtained. Cyanide attack on [**5**] and [**9**] took place *meta* to the etheric bridge and *ortho* to the methyl group. In contrast, the *meta* isomer [**12**] gave rise to three possible adducts [**13a–c**]. These isomers displayed *ortho* addition with respect to both etheric and methyl substituents [**13a**] and addition *ortho* to the etheric bridge and *para* to the methyl group [**13b**]. As well, the asymmetrical isomer displayed addition *ortho* to one complexed arene ring with respect to both substituents and *ortho* to the etheric bridge, as well as *para* to the methyl substituent for the second complexed arene [**13c**]. The ^{1}H and ^{13}C NMR of the bimetallic adducts are listed in Tables 5 and 6.

Scheme 2.

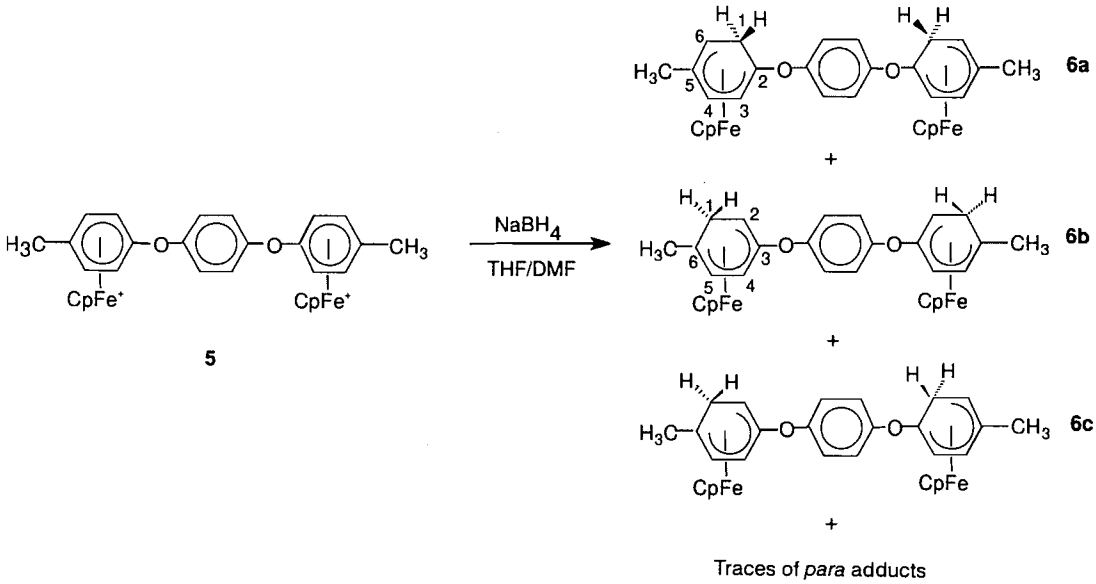

Table 3. ^{1}H NMR data for the adducts **6** and **8**.[a]

Adduct	CH_3	H(1-*exo*)	H(1-*endo*)	H(2)	H(3)	H(4)	H(5)	H(6)	Cp
6a	1.77 s	2.00 (d, 11.0, ex-en)	2.75 (dd, 10.8, en-ex; 5.9, en-6)	—	4.31 (d, 5.6)	5.56 (d, 5.6)	—	2.60 (d, 5.9, 6-en)	4.27 s
6b	1.36 s	1.85 (d, 10.7, ex-en)	2.41 m	2.43 (d, 6.0, 2-en)	—	6.05 (d, 5.7)	3.97 (d, 5.7)	—	4.24 s
8a	1.63, 2.70 s	1.66 (d, 12.7, ex-en)	2.39 (dd, 12.8, en-ex; 7.3, en-6)	—	—	—	4.16 m	2.03 m	4.14 s
8b	2.18 s	1.59 m	2.34 (dd, 12.1, en-ex, 7.3, en-2,6)	1.83 m	—	—	—	1.83 m	4.17 s

[a]Uncomplexed aromatic peaks appear as multiplet between 6.8 and 7.4 ppm. Coupling constants (Hz) are of adjacent aromatic protons unless otherwise indicated.

Table 4. ^{13}C NMR of the adducts **6** and **8**.[a]

Adduct	CH_3	C (1)	C (2)	C (3)	C (4)	C (5)	C (6)	Cp
6a	21.74	31.67	35.92	70.12	73.89	74.96	29.06	74.65
6b	24.87	33.10	18.30	93.85	68.98	75.10	18.79	74.53
8a	19.96, 16.41	34.94	29.74	97.37	89.45	78.17	16.95	75.35
8b	19.45	27.63	19.45	88.42	94.45	88.42	19.45	75.88

[a]Uncomplexed aromatic peaks appear at 117–128 ppm.

The higher selectivity of the cyanide addition was intriguing and prompted us to examine the polyiron systems. Polyaromatic ether complexes with pendant cyclopentadienyliron moieties [**14**]–[**19**] were treated with an excess of NaCN, as described in Scheme 6. Selective addition *meta* to the etheric bridges was obtained in all of these complexes, leading to the formation of the neutral (cyclohexadienyl)FeCp systems [**20**]–[**25**] in yields of 72–81% (based on the recovered starting cationic complexes). Separation of these adducts from their starting cationic complexes was carried out simply by

Scheme 3.

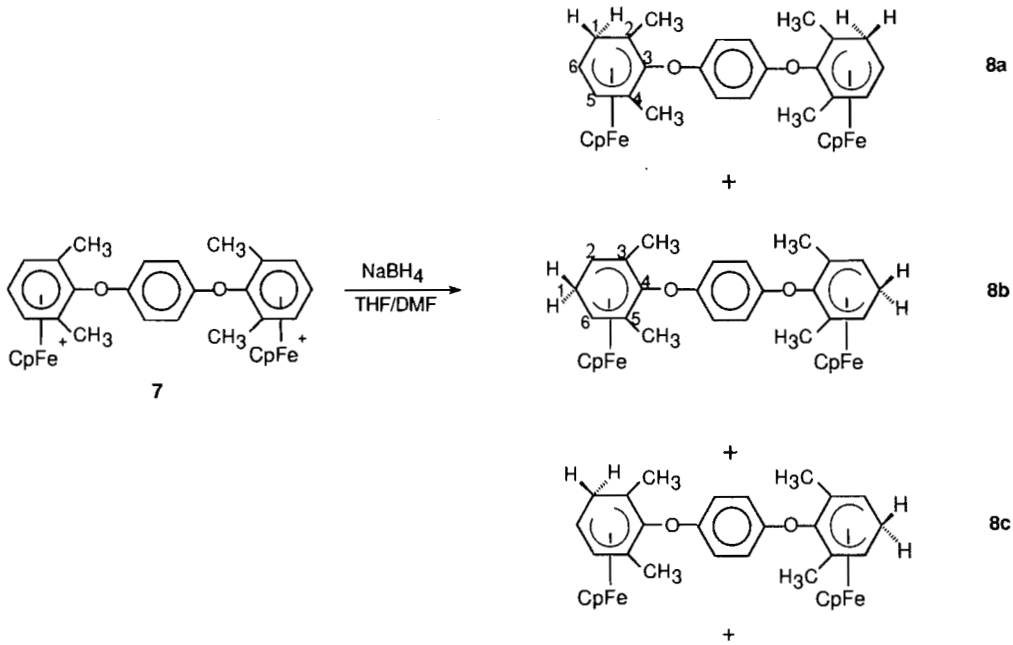

Scheme 4.

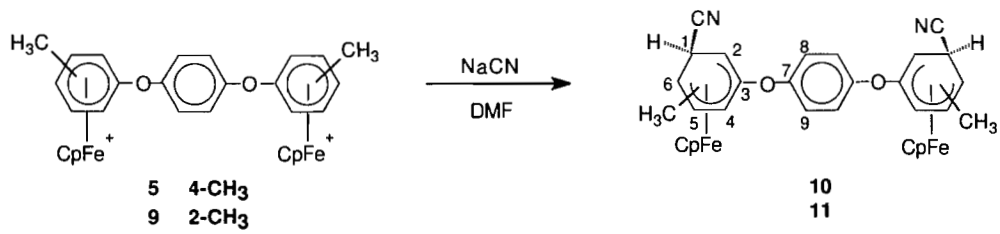

Scheme 5.

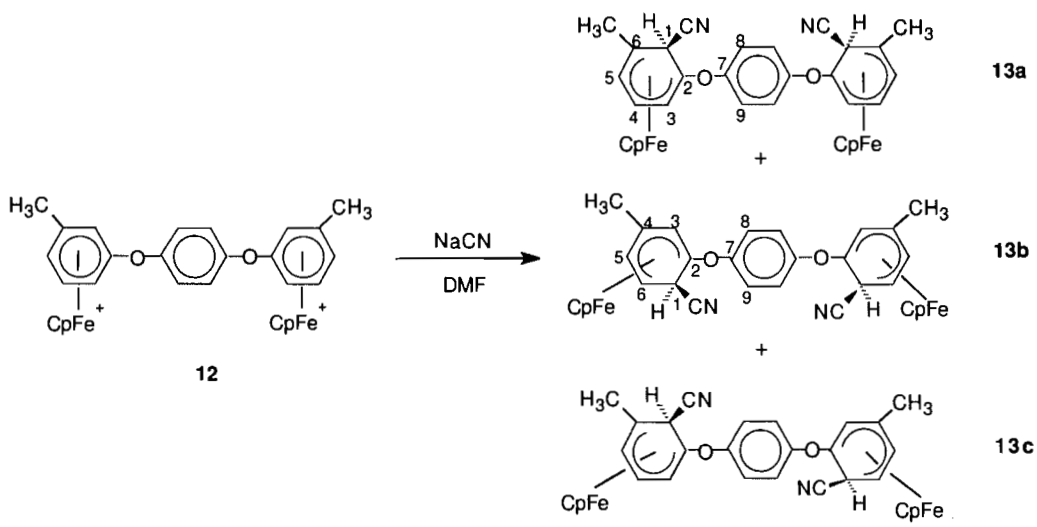

Table 5. ^{1}H NMR data for the adducts **10**, **11**, and **13**.[a]

Adduct	CH_3	H(1 endo)	H(2)	H(3)	H(4)	H(5)	H(6)	Cp	Ph
10	1.93 s	3.52 (d, 5.5, en-2)	3.03 (d, 5.5, 2-en)	—	6.33 (d, 5.4)	5.11 (d, 5.4)	—	4.45 s	6.8–7.3
11	2.19 s	3.54 (d, 5.8, en-6)	—	—	6.33 (d, 5.6)	4.79 (t,5.6)	2.96 (t,5.6, 6-en; t, 6.0)	4.44 s	6.8–7.3
13a	1.71 s	3.51 s	—	5.08 (d, 5.4)	6.25 (t, 5.4)	4.57 (d, 5.4)	—	4.47 s	6.8–7.3
13b	2.58 s	3.46 (d, 6.4, en-6)	—	5.03 s	—	4.77 (d, 6.4)	2.98 (t, 6.4)	4.49 s	6.8–7.3

[a]Coupling constants (Hz) are of adjacent protons unless otherwise indicated.

Table 6. ^{13}C NMR of the adducts **10**, **11**, and **13**.

Adduct	**10**	**11**	**13***a*	**13***b*
CH_3	22.08	20.47	20.93	28.19
C (1)	28.66	28.59	33.62	23.39
C (2)	23.83	28.25	38.54	36.37
C (3)	96.66	94.49	81.14	81.76
C (4)	83.77	83.82	81.55	98.66
C (5)	79.00	80.02	78.36	80.16
C (6)	28.68	23.30	24.90	23.45
C (7)	123.38	122.77	123.61	123.42
C (8)	130.92	130.21	132.49	133.60
C (9)	128.80	126.18	129.17	128.00
CN	116.89	117.00	116.11	117.02
Cp	77.41	77.17	77.50	77.46

extracting the adducts from the mixture with chloroform. These results are consistent with those obtained for the analogous diiron complexes. Figure 2 illustrates ^{1}H NMR of the hepta-iron adduct [**24**] as an example of cyanide addition to the poly-iron series. The detailed NMR data for adducts [**20–25**] are given in Tables 7 and 8. Overall, the *meta* position is influenced by both the etheric and methyl substituents. Infrared spectroscopy was used to confirm the presence of the cyano groups. The ν_{CN} for all cyano adducts were in the range of 2228–2229 cm^{-1}. Our findings are consistant with those of Watts and co-workers, who proposed that addition is influenced by both the inductive and resonance effects of the substituents (29–32).

The free functionalized organic product can be obtained through a simple oxidative demetallation step using 2,3-dichloro-5,6-dicyano-1,4-benzoquinone (DDQ). As an example, a solution of di- or poly-iron cyclohexadienyl adducts [**10**] and [**24**] in acetonitrile was reacted with DDQ for 30 min, leading to the free organic compounds [**26**] and [**27**] in 75 and 78% yield, respectively (Scheme 6). Spectral and analytical data for these compounds are listed in the experimental section of the paper.

In conclusion, spectral data for the hydride reactions of mono- and di-iron arene complexes showed that the etheric substituent has a larger overall effect on the charge distribution on the ring in comparison to the methyl substituent(s). The proportions of the isomers for the bimetallic complexes were in agreement with their analogous monoiron species. In contrast, the reactions of the cyanide anion with di- and poly-iron arenes were selective, with addition at the *meta* position to the etheric bridges. The only isomer that gave a mixture of adducts was the bis[(η^6-3-methylphenoxy-η^5-cyclopentadienyl)iron]benzene hexafluorophosphate [**12**]. In this case, the addition was *ortho* and *para* to the methyl group and *ortho* to the etheric bridges. The oxidative demetallation proved to be successful, allowing for the liberation of the functionalized nitrile compounds from their corresponding iron moieties. The selectivity of the cyanide addition to the poly-iron system provides a unique route to the functionalization of polyaromatic ethers.

Experimental

Measurements

^{1}H and ^{13}C NMR spectra were recorded at 200 and 50 MHz (Gemini 200), respectively, while HH COSY and CH COSY were recorded on a Bruker 500 NMR spectrometer, with chemical shifts calculated from $CDCl_3$ (7.26 for proton and 77.00 for carbon). Coupling constants were measured in Hz. IR spectra were recorded with an FT-IR Bomem MB102 spectrometer.

Reagents

Starting complexes [**1**, **2**, **5**, **7**, **9**, **12**, **13–28**] were prepared by established procedures (45-47). Sodium borohydride (Alfa), DDQ (Aldrich), and sodium cyanide (Aldrich) are commercially available and were used without further purification. All solvents (reagent grade) were used without further purification, with the exception of THF, which was freshly distilled. Silica gel, 60–100 mesh, was used in the column chromatographic purification of the liberated arenes.

Hydride addition reactions

In a 25 mL flask, 0.5 mmol of arene complex and 1.25 mmol of $NaBH_4$ (monoiron complexes) or 2.5 mmol of $NaBH_4$ (diiron complexes) in 10 mL of THF and 1.0 mL of DMF were stirred for 3 h under nitrogen. The bright orange product was then filtered through sintered glass, washed with 10 mL of water, and extracted with $CHCl_3$ (3 × 20 mL). The bright orange extract was washed with water, dried over $MgSO_4$, and the solvent was removed by rotary evaporation, yielding a red or orange oil.

Scheme 6.

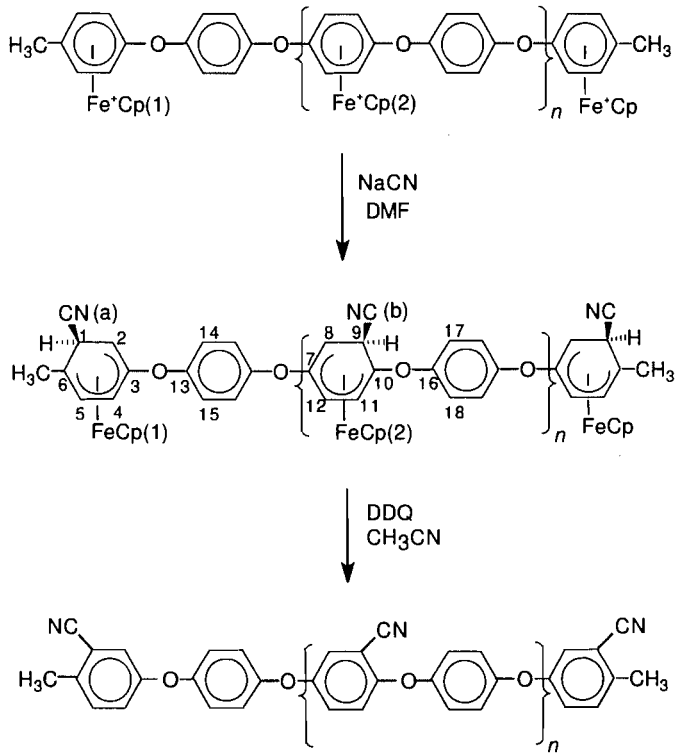

Complex	n
14	1
15	2
16	3
17	4
18	5
19	6

Complex	n
20	1
21	2
22	3
23	4
24	5
25	6

Complex	n
26	0
27	5

Fig. 2. ^{1}H NMR spectrum of adduct **24** in $CDCl_3$.

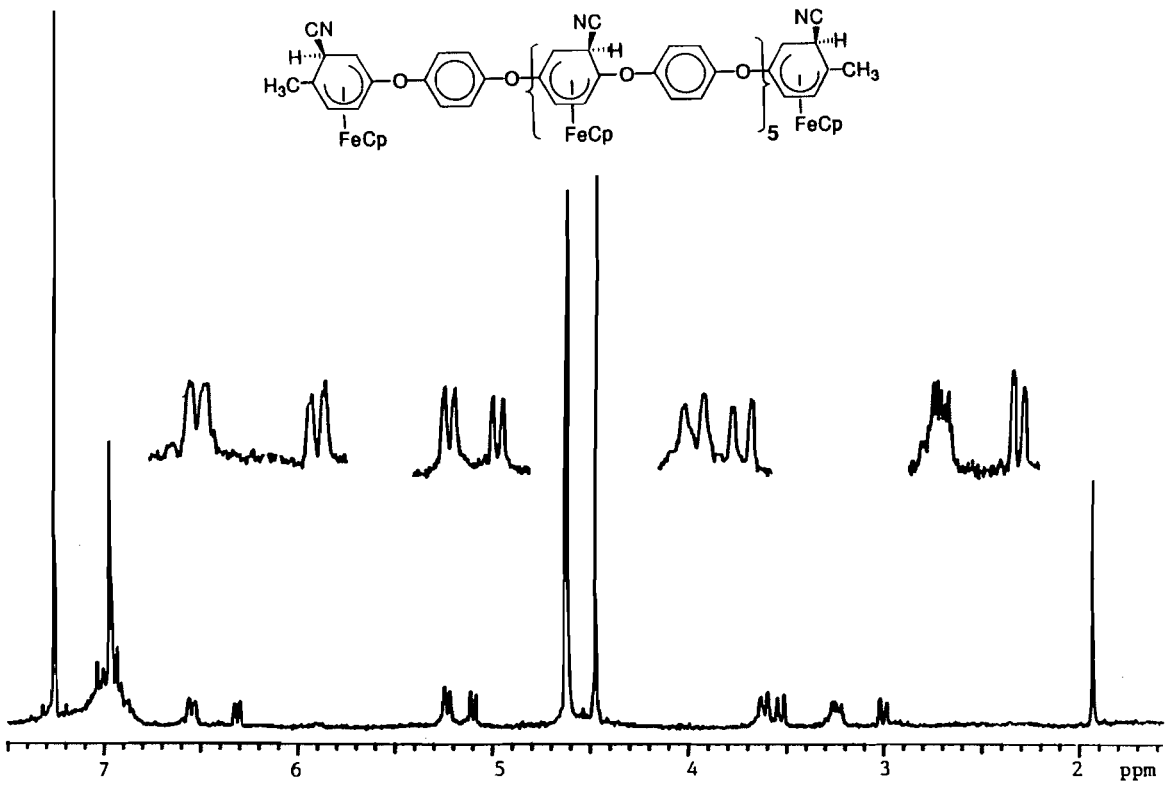

Table 7. ^{1}H NMR of the cyanide addition to the poly-iron series.[a]

Adduct	CH_3	H(1)	H(2)	H(4)	H(5)	H(8)	H(9)	H(11)	H(12)	Cp(1)	Cp(2)	Uncomp. ArH
20	1.93	3.53	3.01	6.31	5.10	3.24	3.61	5.21	6.54	4.48	4.60	6.8–7.4
	s	(d, 6.6)	(d, 6.6)	(d, 5.4)	(d, 5.4)	m	(d, 6.4)	(d, 6.1)	(d, 6.1)	s	s	m
21	1.93	3.55	3.02	6.31	5.12	3.25	3.63	5.25	6.55	4.48	4.62	6.8–7.4
	s	(d, 6.4)	(d, 6.4)	(d, 5.5)	(d, 5.5)	(d, 6.3)	(d, 6.3)	(d, 5.8)	(d, 5.8)	s	s	m
22	1.94	3.56	3.04	6.33	5.13	3.27	3.64	5.26	6.57	4.49	4.59	7.0–7.3
	s	(d, 6.8)	(d, 6.8)	(d, 5.5)	(d, 5.5)	m	(d, 5.9)	(d, 5.8)	(d, 5.8)	s	s	m
23	1.94	3.54	2.99	6.33	5.12	3.26	3.63	5.26	6.56	4.49	4.64	6.7–7.4
	s	(d, 6.7)	(d, 6.7)	(d, 6.5)	(d, 6.5)	m	(d, 6.8)	(d, 6.8)	(d, 6.8)	s	s	m
24	1.94	3.52	3.01	6.31	5.11	3.24	3.62	5.24	6.56	4.48	4.64	6.8–7.2
	s	(d, 5.8)	(d, 5.8)	(d, 5.7)	(d, 5.7)	m	(d, 6.8)	(d, 5.6)	(d, 5.6)	s	s	m
25	1.93	3.54	3.01	6.31	5.09	3.25	3.62	5.24	6.55	4.47	4.63	6.9–7.3
	s	(d, 6.7)	m	(d, 6.5)	(d, 6.5)	(d, 6.9)	(d, 6.9)	(d, 6.7)	(d, 6.7)	s	s	m

[a]Coupling constants (Hz) are of adjacent aromatic protons unless otherwise indicated.

Table 8. ^{13}C NMR of the cyanide addition to the poly-iron series.

Adduct	**20**	**21**	**22**	**23**	**24**	**25**
CN(a)	116.93	116.96	116.34	115.95	116.30	115.91
CN(b)	116.33	116.39	116.38	116.35	116.34	116.27
CH_3	22.09	22.04	22.07	22.02	20.51	20.52
Cp(1)	77.37	77.35	77.38	77.36	77.38	77.41
Cp(2)	78.18	78.17	78.19	78.18	78.19	78.16
C(1)	28.69	28.61	28.88	28.34	28.64	29.71
C(2)	26.06	26.00	25.21	26.06	25.98	25.95
C(3)	96.63	96.63	96.60	96.62	97.21	96.86
C(4)	83.74	83.72	83.68	83.59	83.57	83.58
C(5)	78.94	78.39	78.27	78.40	78.51	78.38
C(6)	29.55	28.88	28.55	28.76	28.57	28.74
C(7)	96.63	96.63	96.60	96.62	97.21	96.86
C(8)	26.00	25.99	26.08	26.04	26.12	26.39
C(9)	29.88	29.87	28.87	36.43	29.90	29.95
C(10)	33.03	29.65	29.78	29.86	29.78	29.83
C(11)	80.12	78.93	78.96	78.96	78.98	78.99
C(12)	83.67	83.64	83.74	83.72	83.72	83.74
C(13)	123.35	122.67	123.35	122.86	123.78	122.52
C(14)	129.95	129.01	129.80	129.67	128.75	128.80
C(15)	130.27	130.27	130.18	130.13	130.21	130.76
C(16)	123.35	122.67	123.35	122.86	123.78	122.52
C(17)	119.58	119.59	119.73	119.28	119.23	119.24
C(18)	119.26	120.12	119.79	119.87	119.81	119.73

Cyanide addition reactions

An example of the cyanide addition reactions: In a 25 mL flask, 0.5 mmol of 1,4-bis[(η^6-4-methylphenoxy-η^5-cyclopentadienyl)iron]benzene hexafluorophosphate and 3.0 mmol of NaCN in 5 mL of DMF and 1 drop of water were stirred for 3 h under a nitrogen atmosphere. The red solution was extracted with $CHCl_3$ (2 × 20 mL), washed with water, and dried over $MgSO_4$. The solvent was evaporated off, yielding a red oily product.

Demetallation reactions

To a solution of the adduct (0.5 mmol) in 10 mL of acetonitrile, 0.5 mmol of DDQ (2,3-dichloro-5,6-dicyano-1,4-benzoquinone) was added, and the resulting mixture was left to stir for 30 min at room temperature. The black solution was then filtered through sintered glass and evaporated to dryness. The product was dissolved in CH_2Cl_2, placed on a short silica gel column and eluted with $CHCl_3$ and CH_2Cl_2; the resulting solutions were dried over $MgSO_4$ and evaporated to dryness to give the free functionalized polyaromatic ethers (**26** and **27**), which have been characterized:

26: ν_{CN}: 2236 cm^{-1}. ^{1}H NMR δ: 2.50 (s, 2CH_3), 6.90 (d, 8.6 Hz, 2H, Ar), 7.11 (d, 8.6 Hz, 2H, Ar), 7.54 (d, 7.8 Hz, 2H, Ar),

7.63 (s, 2H, Ar), 7.71 (d, 8.0 Hz, 2H, Ar); ^{13}C NMR δ: 21.66 (CH_3), 115.81 (CN), 117.74, 120.46, 130.04, 133.38, 133.88 (ArH), 112.90, 115.52, 144.70 (q). Anal. calcd. for $C_{22}H_{16}O_2N_2$: C 77.63, H 4.74, N 8.23; found: C 77.41, H 4.93, N 8.41.

27: ν_{CN}: 2234 cm^{-1}. ^{1}H NMR δ: 2.49 (s, 6H, CH_3), 7.64 (s, 2H, Ar), 7.76 (d, 8.1 Hz, 2H, Ar), 7.54 (d, 8.1 Hz, 2H, Ar), 7.63 (s, 5H, Ar), 7.57 (d, 8.1 Hz, 5H, Ar), 7.73 (d, 8.1 Hz, 5H, Ar), 6.77–7.34 (m, 24H, Ar). ^{13}C NMR δ: 21.70 (CH_3), 115.40, 115.23 (CN), 119.41, 119.82, 121.90 , 122.71, 130.53, 130.92, 134.36, 133.40 (ArH), 112.57, 115.22, 115.30, 144.31 (q). Anal. calcd. for $C_{87}H_{51}O_{12}N_7$: C 75.37, H 3.71, N 7.07; found: C 75.22, H 3.89, N 6.92.

Acknowledgements

Financial support for this work provided by the Natural Sciences and Engineering Reseach Council of Canada (NSERC) and Petroleum Research Funds (ACS-PRF) is gratefully acknowledged. D.A.A. (graduate student, University of Manitoba) also thanks the Department of Chemistry, University of Manitoba.

References

1. S.G. Davies, M.L. Green, and M.P. Mingos. Tetrahedron, **34**, 3047 (1978).
2. M.F. Semmelhack. Comprehensive organic chemistry. Vol. 4. *Edited by* B.M. Frost and I. Fleming. Pergamon, Oxford. 1991 p. 531.
3. P. L. Pauson. J. Organomet. Chem. **200**, 207 (1980).
4. E.P. Kundig, V. Desobry, D.P. Simmons, and E. Wenger. J. Am. Chem. Soc. **111**, 1804 (1989).
5. E.P. Kundig. Pure Appl. Chem. **12**, 1855 (1985).
6. M.F. Semmelhack, H.T. Hall, R. Farina, Jr.,M. Yoshifuji, G. Clark, T. Bargar, K. Hirotsu, and J. Clardy. J. Am. Chem. Soc. **13**, 3535 (1979).
7. E.P. Kundig, A.F. Cunningham, P. Paglia, Jr., and D.P. Simmons. Helv. Chim. Acta, **73**, 386 (1990).
8. M.F. Semmelhack, G.R. Clark, J.L. Garcia, J.J. Harrison, Y. Thebtaranonth, W. Wulff, and A. Yamashita. Tetrahedron, **23**, 3957 (1981).
9. G. Winkhaus, L. Pratt, and G. Wilkinson. J. Chem. Soc. 3807 (1961).
10. D.M. David, L.A.P. Kane-Maguire, and S.G. Pyne. J. Chem. Soc. Dalton Trans. 289 (1994).
11. G.R. Krow, W.H. Miles, P.M. Smiley, W.S. Lester, and Y.J. Kim. J. Org. Chem. **14**, 4040 (1992).
12. W.J. Ryan, P.E. Peterson, Y. Cao, P.G. Williard, D.A. Sweigart, C.D. Baer, C.F. Thompson, Y.K. Chung, and T.M. Chung. Inorg. Chim. Acta, **211**, 1 (1993).
13. R.D. Pike, W.J. Ryan, G.B. Carpenter, and D.A. Sweigart. J. Am. Chem. Soc. **111**, 8535 (1989).
14. R.D. Pike, W.J. Ryan, N.S. Lennhoff, J. Van Epp, and D.A. Sweigart. J. Am. Chem. Soc. **112**, 4798 (1990).
15. Y.K. Chung and D.A. Sweigart. J. Organomet. Chem. **308**, 223 (1986).
16. W.H. Miles and H.R. Brinkman. Tetrahedron Lett. **5**, 589 (1992).
17. W.H. Miles, P.M. Smiley, and H.R. Brinkman. J. Chem. Soc. Chem. Commun. 1897 (1989).
18. R.D. Pike and D.A. Sweigart. Synlett, 565 (1990).
19. P.J. Domaille, S.D. Ittel, J.P. Jesson, and D.A. Sweigart. J. Organomet. Chem. **202**, 191 (1980).
20. A.J. Pearson. Acc. Chem. Res. **13**, 463 (1980).
21. S.L. Grundy and P.M. Maitlis. J. Organomet. Chem. **272**, 265 (1984).
22. S.L. Grundy, A.R.H. Sam, and S.R. Stobart. J. Chem. Soc. Perkin Trans. 1, 1663 (1989).
23. A. Piorko, A.S. Abd-El-Aziz, C.C. Lee, and R.G. Sutherland. J. Chem. Soc. Perkin Trans. **1**, 469 (1989).
24. E.P. Kundig, P. Jeger, and G. Bernardineli. Angew. Chem. Int. Ed. Engl. **19**, 34, (1995).
25. R.P. Alexander and G.R. Stephenson. J. Organomet. Chem. **299**, C1 (1986).
26. T.S. Cameron, M.D. Clerk, A. Linden, K.C. Sturge, and M.J. Zaworotko. Organometallics, **7**, 2571 (1988).
27. C.C. Lee, R.G. Sutherland, and B.J. Thomson. Tetrahedron Lett. **26**, 2625 (1972).
28. A.N. Nesmeyanov, N.A. Vol'kenau, L.S. Shilovtseva, and V. A. Petrakova. J. Organomet. Chem. **85**, 365 (1975).
29. I.U. Khand, P.L. Pauson, and W.E. Watts. J. Chem. Soc. (C), 2261 (1968).
30. I.U. Khand, P.L. Pauson, and W.E. Watts. J. Chem. Soc. (C), 2257 (1968).
31. I.U. Khand, P.L. Pauson, and W.E. Watts. J. Chem. Soc. (C), 116 (1969).
32. J.F. McGreer and W.E. Watts. J. Organomet. Chem. **110**, 103 (1976).
33. D.W. Clack and L.A.P. Kane-Maguire. J. Organomet. Chem. **174**, 199 (1979).
34. D.W. Clack and L.A.P. Kane-Macguire. J. Organomet. Chem. **107**, C40 (1976).
35. D.W. Clack, M. Monshi, and L.A.P. Kane-Macguire. J. Organomet. Chem. **120**, C25 (1976).
36. X. Luo, G.A. Arteca, C. Zhang, and P.G. Mezey. J. Organomet. Chem. **444**, 131 (1993).
37. R.G. Sutherland, C.H. Zhang, R.L. Chowdhury, A. Piorko, and C.C. Lee. J. Organomet. Chem. **333**, 367 (1987).
38. R.G. Sutherland, R.L. Chowdhury, A. Piorko, and C.C. Lee. Can. J. Chem. **64**, 2031(1986).
39. R.G. Sutherland, R.L. Chowdhury, A. Piorko, and C.C. Lee. J. Organomet. Chem. **319**, 379 (1987).
40. R.G. Sutherland, R.L. Chowdhury, A. Piorko, and C.C. Lee. J. Chem. Soc. Chem. Commun. 1296 (1985).
41. C.H. Zhang, R.L. Chowdhury, A. Piorko, C.C. Lee, and R.G. Sutherland. J. Organomet. Chem. **346**, 67 (1988).
42. R.G. Sutherland, C.H. Zhang, A. Piorko, and C.C. Lee. Can. J. Chem. **67**, 137 (1989).
43. R.G. Sutherland, R.L. Chowdhury, A. Piorko, and C.C. Lee. J. Org. Chem. **52**, 4618 (1987).
44. A.S. Abd-El-Aziz, C.R. de Denus, C.R. Zawortko, and L.R. MacGillivray. J. Chem. Soc. Dalton Trans. 3375 (1995).
45. A.S. Abd-El-Aziz, D.C. Schriemer, and C.R. de Denus. Organometallics, **13**, 374 (1994).
46. A.S. Abd-El-Aziz, K.M. Epp, C.R. de Denus, and G. Fisher-Smith. Organometallics, **13**, 2299 (1994).
47. A.S. Abd-El-Aziz, Y. Lei, and C.R. de Denus. Polyhedron, **14**, 1585 (1995).
48. A.S. Abd-El-Aziz and K.M. Epp. Polyhedron, **14**, 957 (1994).
49. W.C. Christopfel and L.L. Miller. J. Org. Chem. **51**, 4160 (1986).
50. L. Anzalone and J.A. Hirsch. J. Org. Chem. **50**, 2128 (1985).

Evidence for an intramolecular transition metal Arbuzov reaction

Zhao Chen, Chet Jablonski, and John Bridson

Abstract: Reaction of [CpCo(C_3F_7)(I)(L)], (L = PPh_2Me (**1***a*), $PPhMe_2$ (**1***b*), PMe_3 (**1***c*), and $PPh(OMe)_2$ (**2**)), with $PPh(OMe)_2$ affords diastereomeric Co- and P-chiral metallophosphinates CpCo(C_3F_7)(L)(P(O)Ph(OMe)), **4***a*,*b*,*c* and **6**, respectively. The solid state structure and relative configuration of the lower R_f diastereomeric phosphinate CpCo(C_3F_7)($PPh(OMe)_2$)(P(O)Ph(OMe)), **6**-2, was determined by X-ray diffraction. *RR*;*SS*-**6**-2 crystallizes in the triclinic system with space group $P\bar{1}$(no. 2), with a = 12.928(4) Å, b = 14.683(4) Å, c = 7.666(2) Å, α = 103.50(2)°, β = 101.31(3)°, γ = 109.50(2)°, V = 1272.8(7) Å^3, Z = 2, and R = 0.036 (R_w = 0.030) for 2867 reflections with $I > 3.00\sigma(I)$. CpCo(C_3F_7)(I)($PPh(OMe)_2$), **2**, reacts with PPh_2Me to yield the same Co- and P-chiral phosphinate products as obtained for the reaction of **1***a* with $PPh(OMe)_2$, albeit with different optical yields. The product stereochemistry is not accounted for by the established mechanism for transition metal Arbuzov-like dealkylations, which requires formation of a common, ionic intermediate [CpCo(C_3F_7)(PPh_2Me)($PPh(OMe)_2$)]$^+$, **3**, via iodide substitution and subsequent nucleophilic attack at carbon. A parallel intramolecular dealkylation pathway is proposed to account for the results.

Key words: stereochemistry, mechanism, Arbuzov, Co(III) complex, chiral metal, X-ray

Résumé : La réaction du [CpCo(C_3F_7)(I)(L)], (L = PPh_2Me (**1***a*), $PPhMe_2$ (**1***b*), PMe_3 (**1***c*) et $PPh(OMe)_2$ (**2**)) avec du $PPh(OMe)_2$ conduit aux métallophosphinates diastéréomériques Co- et P-chiraux CpCo(C_3F_7)(L)(P(O)Ph(OMe)) **4***a*,*b*,*c* et **6** respectivement. Faisant appel à la diffraction des rayons X, on a déterminé les structures solides et les configurations relatives du phosphinate diastéréomère de R_f le plus faible, CpCo(C_3F_7)($PPh(OMe)_2$)(P(O)Ph(OMe)), **6**-2. Le composé *RR*;*SS*-**6**-2 cristallise dans le système triclinique, groupe d'espace $P\bar{1}$ (n° 2) avec a = 12,928(4), b = 14,683(4) et c = 7,666(2) Å, α = 103,50(2)°, β = 101,31(3)° et γ = 109,50(2)°, V = 1272,8(7) Å^3, Z = 2 et R = 0,036 (R_w = 0,030) pour 2867 réflexions avec $I > 3{,}00\sigma(I)$. Le CpCo(C_3F_7)(I)($PPh(OMe)_2$), **2**, réagit avec du PPh_2Me pour conduire aux mêmes produits Co- et P-chiraux que ceux obtenus par réaction du composé **1***a* avec du $PPh(OMe)_2$; les rendements optiques sont toutefois différents. On ne peut pas expliquer la stéréochimie du produit en se basant sur le mécanisme établi pour les réactions de désalkylations de type Arbuzov des métaux de transition pour lesquels il est nécessaire de former un intermédiaire ionique commun, [CpCo(C_3F_7)(PPh_2Me)($PPh(OMe)_2$)]$^+$, **3**, par le biais d'une substitution de l'iodure et d'une attaque nucléophile subséquente au niveau du carbone. Pour expliquer les résultats, on propose une voie réactionnelle parallèle de désalkylation intramoléculaire.

Mots clés : stéréochimie, mécanisme, Arbuzov, complexe de Co(III), métal chiral, rayon X.

[Traduit par la rédaction]

Introduction

Phosphites and phosphonites react readily with transition metal iodides to give metallophosphonates and -phosphinates, respectively (1, 2). Mechanistic studies have identified the predominant mechanism as a two-step sequence (cf. eq. [1]) that parallels the classic organophosphorus Arbuzov rearrangement (3–9). Initial halide substitution at the metal centre gives a cationic phosphite or phosphonite intermediate that can, in favourable circumstance, be directly observed (1, 3–7, 9–12). Subsequent attack of halide ion at carbon occurs with C—O bond cleavage to displace the thermodynamically stable phosphoryl species. In the course of our studies of transition-metal-mediated Arbuzov chemistry as a platform for diastereoselective synthesis of P-chiral phosphinates from prochiral phosphonites, asymmetric Co(III) auxiliaries have been developed that afford P-chiral products with fair to good optical yields (2, 6, 13, 14). In this report we present evidence, derived from product distribution studies, which suggests that a novel, intramolecular dealkylation pathway competes with the accepted mechanism of eq. [1].

Received February 1, 1996.

This paper is dedicated to Professor Howard C. Clark in recognition of his contributions to Canadian chemistry.

Z. Chen, C. Jablonski,[1] and J. Bridson. Department of Chemistry, Memorial University of Newfoundland, St. John's, NF A1B 3X7, Canada.

[1] Author to whom correspondence may be addressed. Telephone: (709) 737-8089. Fax: (709) 737-3702. E-mail: cjablons@morgan.ucs.mun.ca

Results and discussion

Substitution and Arbuzov chemistry of 1 and 2

Treatment of the iodo phosphine complexes η^5-CpCo(C_3F_7)(L)(I) (**1***a*, L = PPh_2Me; **1***b*, L = $PPhMe_2$; **1***c*, L = PMe_3 (5); **2**, L = $PPh(OMe)_2$ (14)) with one equivalent of dimethyl phenylphosphonite in acetone at ambient temperature for 20 h affords a complex reaction mixture containing prod-

[1] $L_n\text{-[M]-X} + P(OR)_nR'_{3-n} \longrightarrow [\,L_n\text{-[M]-P(OR)}_nR'_{3-n}]^+X^- \xrightarrow{-RX} L_n\text{-[M]-P(O)(OR)}_{n-1}R'_{3-n}$

Scheme 1.

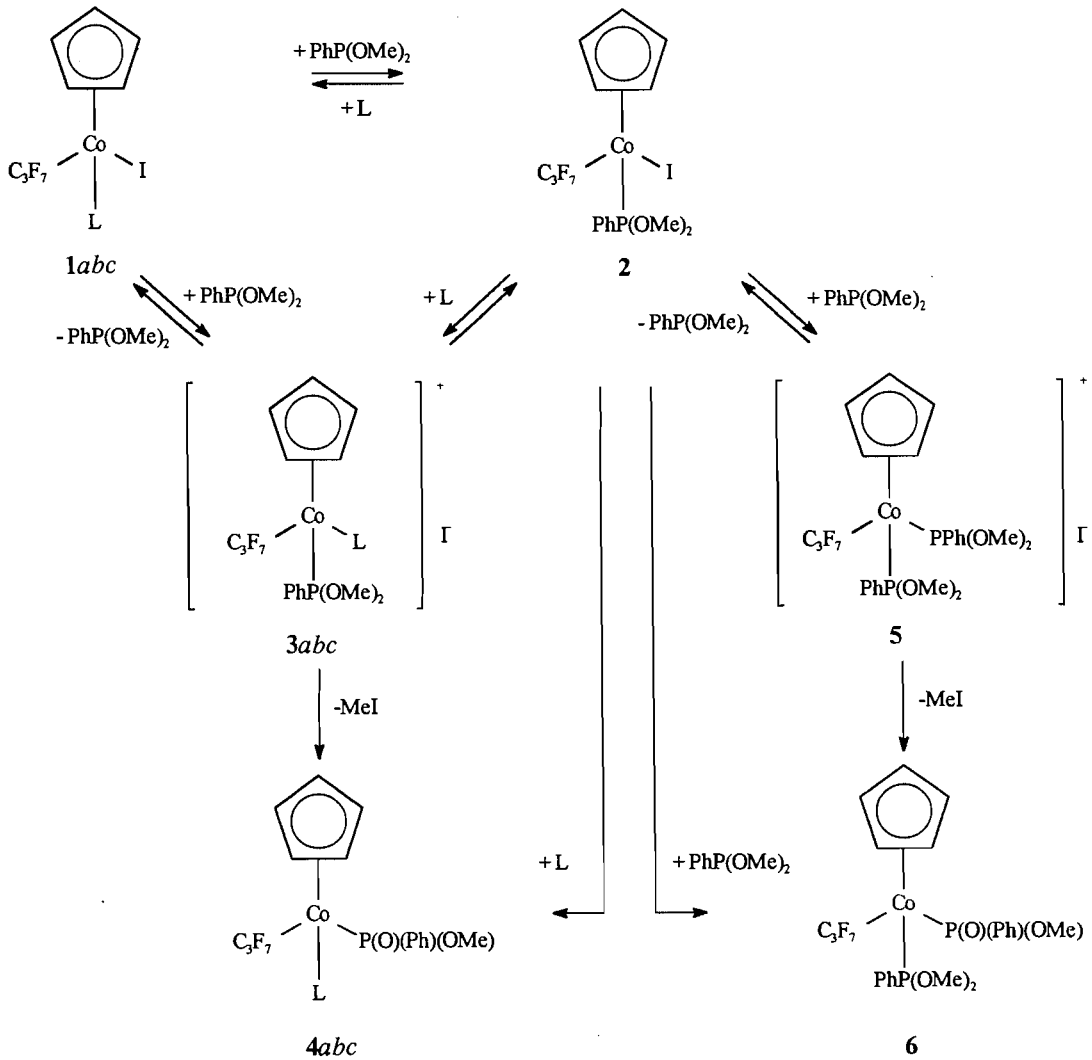

a, PPh_2Me; *b*, $PPhMe_2$; *c*, PMe_3

ucts derived from simple phosphine substitution, halide substitution – Arbuzov dealkylation, as well as combinations of both processes (cf. Scheme 1). Product structure was confirmed by comparison of NMR parameters with known compounds (**1***c* (5) and **2** (14)) and by full analytical and spectroscopic characterization in the case of **1***a* and **1***b* (cf. Tables 1–3). Two diastereomeric pairs of enantiomers with characteristically different ^1H NMR spectra were detected for all Co- and P-chiral metallophosphinates, η^5-$CpCo^*(C_3F_7)(L)(P^*(O)Ph(OMe))$ **4***a*,*b*,*c* and **6**.

Relative stereochemistry at chiral Co and P for the diastereomeric pairs of phosphine-substituted phosphinates **4***a* and **4***b* was empirically assigned by comparison of relative chromatographic R_f values with those of crystallographically determined *RR*;*SS* and *RS*;*SR*-**4***c* (5). We have found that *RR*;*SS* diastereomers of this type consistently elute before the *RS*;*SR* form on silica gel thin-layer chromatographic (TLC) plates. Thus the relative stereochemistry of the higher R_f diastereomers is assigned *RR*;*SS*-**4***a*-1 and *RR*;*SS*-**4***b*-1 and of the lower R_f diastereomers is *RS*;*SR*-**4***a*-2 and *RS*;*SR*-**4***b*-2.

The relative stereochemistry of the lower R_f phosphonite-substituted product **6**-2 was unambiguously established by single crystal X-ray diffraction study. The ORTEP representation of the molecular structure obtained (cf. Fig. 1) shows a

Table 1. Physical data for η^5-CpCo*(C_3F_7)(L)(X).

Compound[a]	L, X	Formula	% yield	Analysis: % C found (calcd.)	Analysis: % H found (calcd.)	Relative config.	Melting point (°C)
1*a*	PPh_2Me, I	$C_{21}H_{18}F_7IPCo$	90.0	40.88 (40.67)	3.03 (2.93)		155–160
1*b*	$PPhMe_2$, I	$C_{16}H_{16}F_7IPCo$	86.6	34.53 (34.43)	2.84 (2.89)		104–108
4*a*-1	PPh_2Me, P(O)(OMe)(Ph)	$C_{28}H_{26}F_7O_2P_2Co$	16.0	48.20 (51.87)	4.04 (4.04)	*RR,SS*	155–158
4*a*-2	$PPhMe_2$, P(O)(OMe)(Ph)	$C_{28}H_{26}F_7O_2P_2Co$	6.0	—	—	*RS,SR*	150–152
4*b*-1	$PPhMe_2$, P(O)(OMe)(Ph)	$C_{23}H_{24}F_7O_2P_2Co$	24.8	47.24 (47.12)	4.10 (4.13)	*RR,SS*	114–116
4*b*-2	$PPhMe_2$, P(O)(OMe)(Ph)	$C_{23}H_{24}F_7O_2P_2Co$	12.0	—	—	*RS,SR*	118–120
6-1	P(O)(OMe)(Ph), P(O)(OMe)(Ph)	$C_{23}H_{24}F_7O_4P_2Co$	34.9	—	—	*RS,SR*	149–151
6-2	P(O)(OMe)(Ph), P(O)(OMe)(Ph)	$C_{23}H_{24}F_7O_4P_2Co$	26.8	44.96 (44.68)	4.05 (3.91)	*RR,SS*	131–138

[a]The designation -1, -2 refers to high and low R_f, respectively.

Table 2. ^1H NMR data for η^5-CpCo*(C_3F_7)(L)(X).[a]

Compound	L, X	C_6H_5	Cp	OMe	PMe
1*a*	PPh_2Me, I	7.83 (m), 7.64 (m), 7.47 (m)	5.09 (s)		2.18 (d, 11)
1*b*	$PPhMe_2$, I	7.90 (m), 7.52 (m)	4.91 (s)		2.12 (d, 11.1) 1.96 (d, 11.1)
4*a*-1	PPh_2Me, P(O)(OMe)(Ph)	7.78 (m), 7.60 (m), 7.45 (m), 7.34 (m)	5.06 (s)	3.09 (d, 11.1)	2.17 (d, 12.3)
4*a*-2	PPh_2Me, P(O)(OMe)(Ph)	7.91 (m), 7.58 (m), 7.47 (m), 7.36 (m)	4.87 (s)	3.34 (d, 11.1)	2.13 (d, 11.7)
4*b*-1	$PPhMe_2$, P(O)(OMe)(Ph)	7.77 (m), 7.64 (m), 7.46 (m), 7.36 (m)	4.86 (s)	3.41 (d, 10.8)	2.06 (d, 11.4) 1.90 (d, 11.4)
4*b*-2	$PPhMe_2$, P(O)(OMe)(Ph)	7.92 (m), 7.79 (m), 7.48 (m), 7.40 (m)	4.64 (s)	3.42 (d, 11.1)	2.01 (d, 11.4) 1.87 (d, 11.4)
6-1	P(O)(OMe)(Ph), P(O)(OMe)(Ph)	7.73 (m), 7.50 (m), 7.33 (m)	5.09 (s)	3.83 (d, 10.8), 3.73 (d, 11,10), 3.41 (d, 10.8)	—
6-2	P(O)(OMe)(Ph), P(O)(OMe)(Ph)	7.75 (m), 7.46 (m), 7.37 (m)	4.98 (s)	3.87 (d, 11.1), 3.81 (d, 10.5), 3.33 (d, 11.1)	—

[a]^1H NMR (300.1 MHZ) chemical shifts in $CDCl_3$ relative to internal TMS; *J* values in Hz; m = multiplet, d = doublet.

typical pseudo-octahedral, three-legged piano-stool structure with average interligand bond angles (93.7°) approaching 90°. The phosphoryl P-atom is distorted from ideal tetrahedral geometry showing a moderate opening of the Co-P=O angle to 117.8° that is accommodated by a closing of the MeO-P-C(10) angle to 100.5°. A substantial multiple bond character (15) for the phosphoryl group is inferred from the P=O distance (1.487(3) Å), which is considerably shorter than the P(1)—O(1) single bond length measured for **6**-2 (1.625(3) Å) but comfortably in the normal range for free (15), P-coordinated (16, 17), or even P=O bridging (18) phosphoryl groups in a wide range of chemical environments (16, 17). The CIP ligand priority sequence Cp > $PPh(OMe)_2$ > P(O)(OMe)Ph > C_3F_7 for Co (19–21) and Co > OMe > O > Ph for P unambiguously fix the relative stereochemistry of **6**-2 as $R_{Co}R_P$. CIP priority differences for phosphonite and phosphine show that

Table 3. ^{13}C and ^{31}P NMR data for η^5-$CpCo^*(C_3F_7)(L)(X)$.[a]

Compound	L, X	C_6H_5	Cp	OMe	PMe	^{31}P (PR_3, P—O)
1*a*	PPh_2Me, I	i: 137.56 (d, 43.3), 134.74 (d, 44.5) *o,m*: 132.65 (d, 7.8), 130.67 (d, 5.7), 128.49 (d,, 8.7), 128.26 (d, 8.7) *p*: 132.80	87.75		19.85 (d, 34.0)	31.44, —
1*b*	$PPhMe_2$, I	i: 139.02 (d, 43.2) *o,m*: 129.56 (d, 7.8), 128.85 (d, 8.3) *p*: 130.45	87.63		16.74 (d, 39.6)	19.02, —
4*a*-1	PPh_2Me, P(O)(OMe)(Ph)	*i*: 143.62 9(d, 49.5), 138.46 (d, 40.7), 136.93 (d, 50.1) *o,m*: 132.96 (d, 8.2), 130.59 (d, 10.3), 128.14 (d, 11.6), 127.40 (d, 12.4) *p*: 130.01, 129.64, 129.16	89.06	50.31 (d, 11.1)	15.84 (d, 29.7)	
4*a*-2	PPh_2Me, P(O)(OMe)(Ph)	*i*: 141.29 (d, 52.5), 137.49 (d, 43.2), 136.71 (d, 49.6) *o,m*: 133.16 (d, 9.9), 132.27 (d, 8.8), 128.33 (d, 9.1), 127.75 (d, 10.9) *p*: 132.62, 130.31, 129.24	89.87	49.77 (d, 11.6)	16.35 (d, 29.5)	
4*b*-1	$PPhMe_2$, P(O)(OMe)(Ph)	*i*: 143.33 (d, 49.6), 140.20 (d, 45.1), 132.24 (d, 51.32) *o,m*: 130.59 (d, 10.0), 130.06 (d, 7.9), 128.47 (d, 9.5), 127.56 (d, 11.2) *p*: 131.75, 129.62, 129.32	88.98	50.46 (d, 9.4)	16.69 (d, 34.7)	
4*b*-2	$PPhMe_2$, P(O)(OMe)(Ph)	*i*: 143.99 (d, 53.1), 139.69, 132.72 (d, 39.6) *o,m*: 130.47 (d, 10.6), 130.20 (d, 7.7), 128.63 (d, 9.0), 127.91 (d, 11.4) *p*: 129.81, 129.45	90.03	49.72 (d, 14.4)	17.77 (d, 30.6)	
6-1	P(O)(OMe)(Ph), P(O)(OMe)(Ph)	*i*: 143.73 (d, 58.2), 137.13 (d, 58.1) *o,m*: 131.25 (d, 10.6), 130.93 (d, 11.2), 128.05 (d, 10.4), 127.15 (d, 10.9) *p*: 131.00, 129.21	89.96	55.44 (d, 11.5), 54.26 (d, 10.4)	—	
6-2	P(O)(OMe)(Ph), P(O)(OMe)(Ph)	*i*: 144.48 (d, 58.3), 136.57, d, 58.7) *o,m*: 131.25 (d, 10.6), 130.58 (d, 10.0), 127.83 (d, 12.9), 127.67 (d, 11.5) *p*: 130.93, 129.29	90.28	55.00 (d, 10.9), 54.74 (d, 10.0), 49.96 (d, 11.8)	—	

[a] ^{13}C (75.47 MHz) chemical shifts in ppm relative to solvent $CDCl_3$; ^{31}P (121.5 MHz) chemical shifts in ppm relative to external 85% H_3PO_4; *J* values in Hz; d = doublet.

RR;*SS*-**6**-2 has the same relative stereochemistry as the lower R_f *RS*;*SR* diastereomers in the phosphine substituted series.

Product distribution was examined in detail for the case of reaction of **1***a* with $PPh(OMe)_2$. Careful preparative thick-layer chromatographic (PLC) isolation gives, in order of decreasing R_f values, unreacted **1***a*, dark-green phosphonite complex η^5-$CpCo^*(C_3F_7)(PPh(OMe)_2)$(I), **2**, two orange, phosphine-metallophosphonate diastereomers η^5-$CpCo^*(C_3F_7)(PPh_2Me)$-(P^*(O)Ph(OMe)), **4***a*-1,2, followed by two light-orange phosphonite-metallophosphinate diastereomers (14) η^5-$CpCo^*(C_3F_7)(PPh(OMe)_2)(P^*(O)Ph(OMe))$, **6**-1,2. The iodo-phosphonite complex **2** is stable for months in the solid state or in acetone solution; however, it reacts readily in the presence of methyldiphenylphosphine to afford the same sequence of products.

Product distribution was also monitored by ^1H NMR spectroscopy. We (14) as well as others (22) have observed that piano-stool Co(III) metallophosphonates such as **4** tend to be substitution inert, hence the phosphonite complexes **6**-1 and **6**-2 must derive from stepwise halide substitution and Arbuzov dealkylation of **2**. The observation that no phosphonite-containing products, **6**, were observed for the reaction of **1***a* with dimethyl phenylphosphonite in the presence of excess PPh_2Me (mole ratio **1***a*:$PPh(OMe)_2$:PPh_2Me = 1:1:10) suggests a facile phosphine substitution that establishes the equilibrium **1***a* + $PPh(OMe)_2$ ⇄ **2** + PPh_2Me. Pre-equilibrium phosphine exchange was confirmed from observation of concentration/time curves vs. starting material ratios in acetone-d_6 solution. A labile species with δ_{Cp} = 5.60 ppm was observed and tentatively assigned as the cationic intermediate **3***a*; how-

Fig. 1. ORTEP plot of η^5-CpCo*(C_3F_7)(PPh(OMe)$_2$)(P*(O)Ph(OMe)), **6**-2.

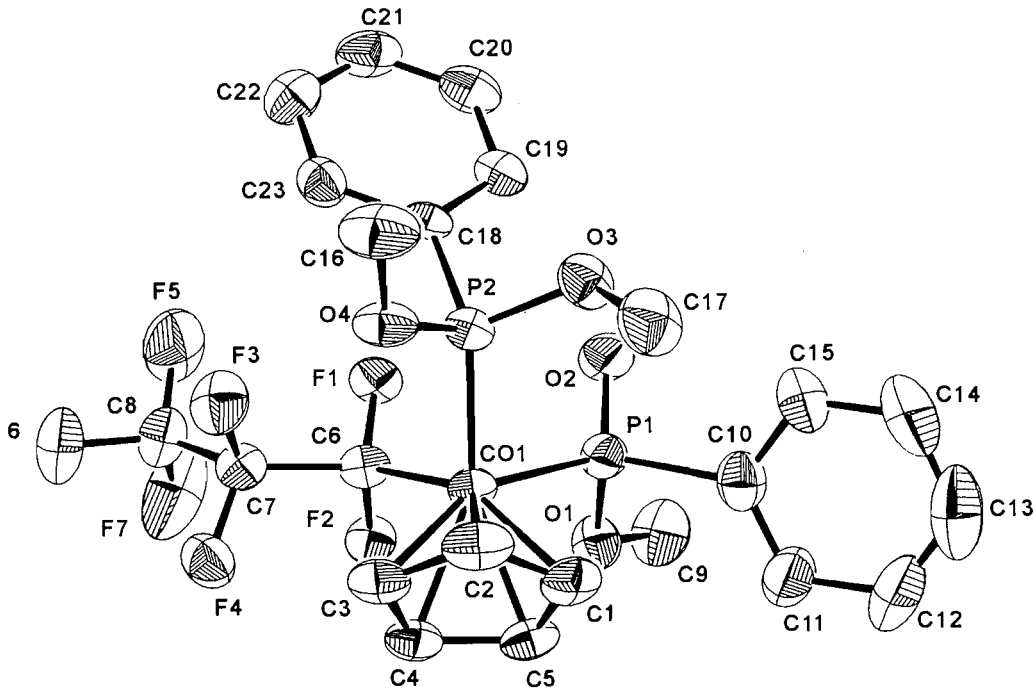

ever, we are unable to unequivocally distinguish whether formation of **4** proceeds by direct phosphine exchange (**2** → **4**) and (or) via the proposed cationic intermediate **3***a* (**1**,**2** → **3** → **4**). Nevertheless, all directly observed products follow directly from consideration of Scheme 1.

Stereochemistry and optical yields

If cationic $[\eta^5$-CpCo(C_3F_7)(PPh$_2$Me)(PPh(OMe)$_2$)$]^+I^-$, **3***a*, is the unique intermediate for transition metal Arbuzov dealkylation (Scheme 1), treatment of the iodo-phosphine complex η^5-CpCo(C_3F_7)(PPh$_2$Me)(I), **1***a*, with dimethyl phenylphosphonite or of the iodo-phosphonite complex η^5-CpCo*(C_3F_7)(PPh(OMe)$_2$)(I), **2**, with methyldiphenylphosphine is expected to produce identical optical yields of P-chiral metallophosphinate product, **4**. In that event %de is fully determined by $\Delta\Delta G^{\ddagger}$ for iodide attack at the diastereotopic methoxy groups of intermediate **3***a* as shown in Scheme 1. In contrast with this hypothesis, we find that the optical yield of phosphinate η^5-CpCo(C_3F_7)-(PPh$_2$Me)(P(O)-Ph(OMe)) (%de = 100 × ([**4***a*-1]−[**4***a*-2])/([**4***a*-1]+[**4***a*-2])) is sensitive to reactant composition in acetone (cf. Table 4). Table 4 shows the dependence of optical yield on reactant composition as determined by integration of ^{1}H NMR spectra in the Cp region. Relative stereochemistry for the Co- and P-chiral metallophosphinates **4***a* and **4***b* was assigned by comparison of TLC R_f values with that of crystallographically determined **4***c*. (5). Reaction of **1***a* with PPh(OMe)$_2$ resulted in increased optical yield for **4***a*-1, **4***a*-2 compared with reaction of **2** with PPh$_2$Me (cf. Table 4 entries 1 and 3). The product distribution studies are inconsistent with the formation of a common intermediate and therefore imply the presence of a parallel reaction channel with a different optical yield. We propose a competing, intramolecular pathway, which is possible only for the iodophosphonite **2**.

There is ample literature precedent that establishes that intramolecular alkyl migrations can lead to metallophosphonates (23–25). We therefore propose an intramolecular attack of iodide at carbon, concerted with associative nucleophilic attack at the metal by PPh$_2$Me. Expulsion of MeI from **2** gives the metallophosphinate **4***a*-1, **4***a*-2 in a single step as illustrated in Scheme 2. Optical yield for **4***a* formation via the intramolecular pathway is then a function of $\Delta\Delta G^{\ddagger}$(intramolecular) rather than $\Delta\Delta G^{\ddagger}$(intermolecular) for iodide attack at diastereotopic OMe (cf. Scheme 2). Optical yields will then reflect the position of the equilibrium connecting the starting materials **1** and **2**. In the presence of excess PPh$_2$Me the equilibrium **1***a* + PPh(OMe)$_2$ ⇄ **2** + PPh$_2$Me shifts to the left and effectively shuts off the intramolecular route. Under these conditions (cf. Table 4, entry 6) the intermolecular sequence **1***a*→**3***a*→**4***a* provides the dominant route to phosphinate product. If our interpretation is correct, higher %de in the presence of excess PPh$_2$Me can be interpreted as less efficient optical induction for the intramolecular vs. intermolecular pathway. Accordingly, the lowest optical yields were measured in methanol solvent (cf. Table 4, entry 8) since hydrogen bonding limits iodide nucleophilicity and the intramolecular pathway operates exclusively (cf. discussion below).

Attempts to further test for the proposed intramolecular Arbuzov reaction mechanism by reacting $[\eta^5$-CpCo(C_3F_7)-(PPh$_2$Me)(PPh(OMe)$_2$)$]^+SbF_6^-$, prepared by iodide abstraction of 2 followed by in situ treatment with PPh$_2$Me, with NaI in acetone failed. Reaction under these conditions resulted in nucleophilic attack of iodide on cobalt rather than carbon. The

Table 4. Product distribution vs. reactant composition for Scheme 1.

Entry no.	Reactant composition (mol ratio)	Solvent	Yield (mol %)[a] 1*a*	2	*RR,SS*-**4***a*-1/ *RS,SR*-**4***a*-2 (%de)[b]	*RS,SR*-**6**-1/ *RR,SS*-**6**-2 (%de)
1	**1***a*:$PPh(OMe)_2$ = 1:1	Acetone	53.4	16.4	16.0/6.0 (46)	4.9/3.3 (19.5)
2	**1***a*:$PPh(OMe)_2$ = 1:3	Acetone	Trace	Trace	3.3/1.1 (50)	46.7/41.6 (5.8)
3	**2**:PPh_2Me = 1:1	Acetone	40.6	4.5	32.1/14.3 (38.2)	5.3/3.2 (25)
4	**2**:PPh_2Me = 1:1	Benzene	69.9	21.8	2.5/1.1 (38.9)	2.8/2.0 (16.7)
5	**2**:**1***a*:PPh_2Me = 1:2:1	Acetone	74.9	11.6	9.6/3.9 (42.2)	Trace
6	**1***a*:$PPh(OMe)_2$:PPh_2Me = 1:1:10	Acetone	51.8	Trace	37.9/10.3 (57.3)	Trace
7	**1***a*:$PPh(OMe)_2$:PPh_2Me = 1:1:10	Acetone:methanol = 3:2	>90	Trace	Trace	Trace
8	**2**:PPh_2Me = 1:1	Acetone:methanol = 3:2	56.9	12.4	12.6/7.4 (26.2)	6.5/4.3 (20.4)

[a]Determined by ^1H NMR integration of the η^5-Cp region.
[b]%de = $|([RR,SS]-[RS,SR])/([RR,SS]+[RS,SR])| \times 100$.

Scheme 2.

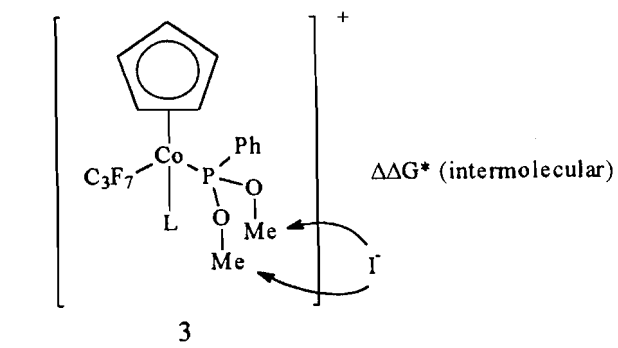

3

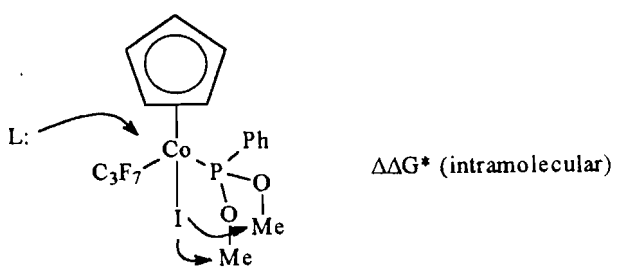

2

iodo complexes, resulting from phosphonite/phosphine substitution, were isolated in a 14.5:1 ratio in > 90% chemical yield.

Brunner's early studies (26) of coordinatively saturated, pseudo-tetrahedral, piano-stool complexes elegantly established dissociative substitution with dominant retention of configuration at chiral metal. Fewer examples of associative activation have been identified (27–30). The latter require an ancillary ligand capable of removing an electron pair in order to avoid formation of high-energy 20 e^- species. Established cases involve hapticity decreases ($\eta^5 \rightarrow \eta^3$ "ring slippage" (27)) of indenyl or cyclopentadienyl or linear→bent NO isomerization (31). In a relevant study Landon and Brill (3) reported second-order kinetics for the Arbuzov rearrangement of η^5-CpCo(dppe)I with $P(OMe)_3$ and steric inhibition for the increased bite-angle ligand dppp (1,3-bis(diphenylphosphino)propane), implying an associative reaction. The stereochemical consequences pursuant to the presence of a prochiral phosphonite in the present study allow detection of an otherwise masked reaction mechanism.

Solvent effects

Solvent effects also support the proposed intramolecular Arbuzov dealkylation. Free iodide ion is strongly solvated in protonic solvents and is considerably less nucleophilic (6), hence attack at carbon required for Arbuzov dealkylation is inhibited. Complex **1***a* reacts with $PPh(OMe)_2$ in the presence of excess PPh_2Me via initial displacement of iodide; however, the second step is effectively blocked in methanol and Arbuzov dealkylation does not proceed readily (cf. Table 4, entry

Fig. 2. GMMX determined conformational energies for **3**.

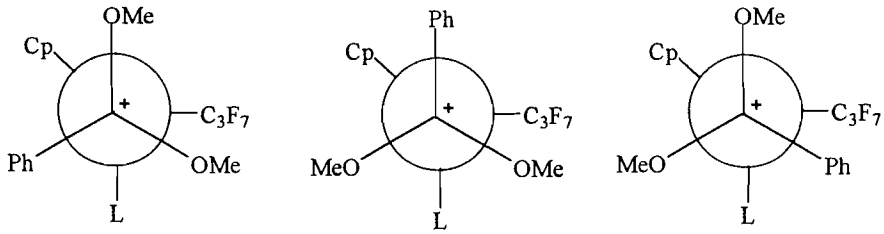

L	E_I (rel) kJ/mol	E_{II} (rel) kJ/mol	E_{III} (rel) kJ/mol
PMe_3	0	9.6	13.4
$PPhMe_2$	0	3.3	>12.5
PPh_2Me	3.8	0	6.3

7). If other reaction pathways were available under these conditions, **4***a*-1, and **4***a*-2 would still be formed.

Strikingly different results were obtained when the reaction was carried out starting with **2** in the methanol-d_4 (cf. Table 4, entry 8). Addition of one equivalent of PPh_2Me resulted in the formation of four Cp peaks in the ^1H NMR spectrum assigned to **1***a*, **2**, **4***a*-1, and **4***a*-2. Arbuzov dealkylation occurs readily from **2** even when the two-step pathway **2**→**3***a*→**4***a* is blocked in protonic media. Since iodide is non-nucleophilic under these conditions, iodide attack at OCH_3 cannot occur from outside the coordination sphere. In contrast, protonic solvent is expected to have little effect on a concerted mechanism involving **3** that avoids formation of free iodide. Optical yields in this experiment are determined exclusively by the intramolecular mechanism and decreased to %de = 28, consistent with a decreased optical induction in the intramolecular route.

It is reasonable to expect that low dielectric media will inhibit iodide substitution since the process involves substantial charge separation. Indeed (cf. Table 4, entry 4) we find that the optical yield for the reaction of **2** with PPh_2Me drops as the solvent changes from acetone (ϵ = 20, %de = 32) to benzene (ϵ = 4, %de = 15).

Ligand sphere effects on optical yield

$\Delta\Delta G^{\ddagger}$ for attack of iodide at the diastereotopic phosphonite methoxy groups will of course determine optical yield. Previous studies of Co→P chiral induction for **1**→**4** (L = $PPh_2NH(C^*H(Me)Ph)$) identified (2, 13, 14) intramolecular N—H···O═P hydrogen bonding as a pivotal parameter for Co→P chiral induction. We were therefore surprised to find that optical yields measured for **1**→**4** (L = phosphine, phosphonite), which cannot reduce the number of low-energy conformers by intramolecular hydrogen bonding, were in some cases superior. Measured optical yields for **1**→**4** decreased along the series L = PPh_2Me (40%) < $PPhMe_2$ (33%) < PMe_3 (18%). It was of interest to determine the effect of ligand steric requirements on the efficacy of Co→P optical induction.

Molecular mechanics global minimum conformational searches for the intermediates **3***a–c* were carried out using the GMMX algorithm (32) with the assumption that insight relevant to diastereoselection in the transition state for intermolecular dealkylation might be provided. Starting structures for the cations **3**, obtained from model compounds derived from crystallographic data, were minimized using the MMX (33) force field, which has been shown to be appropriate for related piano-stool molecules (34, 35). GMMX searches of conformational space used a combined Monte Carlo internal – Cartesian randomization protocol that examined rotations about all specified bonds with less than 3-fold symmetry. Conformations meeting energy criteria were then MMX minimized, checked for redundancy, and retained subsequent to a final energy assessment. Surviving conformations within a 12.5 kJ/mol band containing the lowest energy structure were retained. Further cycles removed/re-added hydrogen atoms in calculated positions and minimized in order to dislodge structures from saddle points. Finally, the surviving conformations were checked for redundancy and energy criteria. The process was continued until no further conformations were lost.

The GMMX conformational searches identified three staggered Co-$P(OMe)_2Ph$ rotamers for the intermediate **3***a,b,c*. Figure 2 shows Newman projections along with the calculated relative MMX energies. Literature evidence (36, 37) strongly suggests that the region between the almost 90° L-Co-C_3F_7 is the least sterically accessible for pseudo-octahedral piano stools. The GMMX calculations concur, and rotamers I and II, which place the least sterically demanding group (OMe) in that region, are always most stable. Face/edge Cp–Ph interactions (38–40) may also contribute to the relative stability of rotamers I and II. Differences are small; however, the relative increase in the energy of rotamer I with respect to II as phenyl groups accumulate on the phosphine donor L can be traced to increasing Ph–L steric interactions.

Curtin–Hammett restrictions (41) preclude a direct relation between conformer population and optical yield, however, based on the GMMX calculations described above, a case can be made for the direction of chiral induction and ligand sphere effects on the measured %de for **1**→**3**→**4**. It is clear that the critical step for chiral induction occurs on attack of iodide at the diastereotopic OMe groups of **3**, which displaces the phosphoryl product. We have previously established a preference for a dominant *anticlinal* Cp-Co-P═O conformation (2, 13, 14, 42, 43) in piano-stool metallophosphonate and metallophosphinate complexes. Assumption of significant product-like character in the transition state predicts a preference for

attack at the *anticlinal* Cp-Co-P-OMe, and conformer II (R_{Co} configuration shown in Fig. 2) is then correctly linked to the major product ($R_{Co}R_P$). Optical yields will then parallel the II/I ratio, which increases along the series PMe_3 (18%de) < $PPhMe_2$ (33%de) < PPh_2Me (40%de).

Experimental

General

All manipulations were performed under a dry nitrogen atmosphere using standard Schlenk techniques. Nitrogen was purified by passing though a series of columns containing granular phosphorus pentoxide, 3A molecular sieves, and BASF DEOX catalyst (100°C). Acetone, methanol, and methylene chloride were distilled from activated 4A molecular sieves. Reactions were monitored by analytical thin-layer chromatography (precoated TLC plates, silica gel F-254, Merck). NMR spectra were recorded on a General Electric GN300-NB spectrometer operating at a proton frequency of 300.1 MHz. Preparative thick-layer chromatographic (PLC) purification was carried out using a Chromatotron (Harrison Associates) with 1–2 mm thick silica $gel_{60}PF_{254}$(Merck) adsorbent. The compounds $CpCo(C_3F_7)(CO)$(I) (44), **1***c* (5), and **2** (14) were prepared using the established procedures. Commercial samples of dimethyl phenylphosphonite, diphenylmethylphosphine, dimethylphenylphosphine, trimethylphosphine, $AgSbF_6$, and perfluoropropyl iodide (Aldrich) were used as received. Melting points were measured in sealed, nitrogen-filled capillaries and are uncorrected. C, H analyses were provided by Canadian Microanalytical Service Inc., Delta, B.C.

Preparation of η^5-$CpCo^*(C_3F_7)(PPh_2Me)$(I) (**1***a*) and η^5-$CpCo^*(C_3F_7)(PPhMe_2)$(I) (**1***b*).

PPh_2Me (90.1 mg, 0.450 mmol) was added dropwise to a stirred 25 mL, black, CH_2Cl_2 solution of η^5-$CpCo^*(C_3F_7)$-(CO)(I) (197.4 mg, 0.4407 mmol) contained in a 100 mL Schlenk flask and stirred at ambient temperature (20°C) for 12 h. Removal of volatiles under water aspirator followed by oil pump vacuum overnight left a dark green solid, which was purified by thick-layer radial PLC on silica gel (CH_2Cl_2) to give **1***a* (245.9 mg, 0.3966 mmol, 90.0%). **1***b* was prepared in 86.6% yield from η^5-$CpCo^*(C_3F_7)$(CO)(I) and $PPhMe_2$ in an analogous manner. Physical, analytical, and spectroscopic data for **1***a,b* are presented in Tables 1–3.

Reaction of η^5-$CpCo^*(C_3F_7)(PPh_2Me)$(I) (**1***a*) with $PPh(OMe)_2$ in acetone

η^5-$CpCo^*(C_3F_7)(PPh_2Me)$(I) (134.0 mg, 0.2161 mmol), $PPh(OMe)_2$ (38.0 mg, 0.2188 mmol), and acetone (25 mL) were mixed in a 50 mL Schlenk flask and stirred at ambient temperature (20°C) for 24 h. Removal of volatiles under water aspirator followed by oil pump vacuum overnight left a dark-green solid, which was purified by PLC on silica gel. Elution with CH_2Cl_2 separated (in order of decreasing R_f values) a dark-green zone containing **1***a* (71.6 mg, 0.115 mmol) and **2** (20.9 mg, 0.0354 mmol). Continued elution with acetone separated two orange zones containing **4***a*-1, **4***a*-2 (**4***a*-1: 22.4 mg, 0.0346 mmol; **4***a*-2: 8.4 mg, 0.013 mmol), followed by two light-orange zones containing **6**-1, **6**-2 (**6**-1: 7.6 mg 0.012 mmo l; **6**-2: 3.1 mg 0.0050 mmol). Physical, analytical, and spectroscopic data for **4***a*-1,2 are presented in Tables 1–3.

Table 5. Positional parameters[a] and *B*(eq) for **6**-2.

Atom	*x*	*y*	*z*	*B*(eq)
Co(1)	0.86631(5)	0.29330(4)	0.09365(7)	2.40(2)
P(1)	0.7104(1)	0.28599(8)	−0.1076(1)	2.95(4)
P(2)	0.7909(1)	0.13075(8)	0.0634(1)	2.65(3)
F(1)	0.8736(2)	0.1979(2)	−0.2712(3)	3.19(7)
F(2)	0.9669(2)	0.3631(2)	−0.1680(3)	3.27(8)
F(3)	1.0482(2)	0.1915(2)	0.0153(3)	4.6(1)
F(4)	1.1412(2)	0.3528(2)	0.0618(3)	4.6(1)
F(5)	1.0409(3)	0.1502(3)	−0.3496(4)	7.9(1)
F(6)	1.2075(2)	0.2376(2)	−0.1636(4)	5.8(1)
F(7)	1.1201(3)	0.3080(3)	−0.3146(4)	7.9(2)
O(1)	0.7527(2)	0.3853(2)	−0.1762(4)	3.6(1)
O(2)	0.6437(2)	0.1908(2)	−0.2704(4)	4.1(1)
O(3)	0.6686(2)	0.0891(2)	0.0997(4)	3.8(1)
O(4)	0.8767(2)	0.1111(2)	0.2178(4)	3.4(1)
C(1)	0.8418(4)	0.3768(3)	0.3323(5)	3.6(1)
C(2)	0.9123(4)	0.3273(3)	0.3888(5)	3.7(2)
C(3)	1.0123(4)	0.3621(3)	0.3351(5)	3.4(1)
C(4)	1.0044(4)	0.4355(3)	0.2452(5)	3.2(1)
C(5)	0.8988(4)	0.4438(3)	0.2430(5)	3.3(1)
C(6)	0.9399(3)	0.2786(3)	−0.1069(5)	2.6(1)
C(7)	1.0567(3)	0.2660(3)	−0.0633(6)	3.0(1)
C(8)	1.1058(4)	0.2405(4)	−0.2265(7)	4.1(2)
C(9)	0.6711(4)	0.3929(4)	−0.3224(7)	5.1(2)
C(10)	0.6082(4)	0.3133(4)	0.0116(6)	3.8(2)
C(11)	0.6180(4)	0.4117(4)	0.0951(7)	4.9(2)
C(12)	0.5393(5)	0.4279(5)	0.1864(8)	6.6(3)
C(13)	0.4520(6)	0.3463(7)	0.1949(9)	7.3(3)
C(14)	0.4400(4)	0.2492(5)	0.1098(8)	6.3(2)
C(15)	0.5168(4)	0.2320(4)	0.0177(7)	4.7(2)
C(16)	0.8434(4)	0.0169(3)	0.2639(6)	5.0(2)
C(17)	0.6508(4)	0.1241(4)	0.2800(7)	5.2(2)
C(18)	0.7575(3)	0.0270(3)	−0.1505(5)	2.7(1)
C(19)	0.6529(3)	−0.0114(3)	−0.2911(6)	3.4(1)
C(20)	0.6257(4)	−0.0947(3)	−0.4479(6)	4.2(2)
C(21)	0.7018(5)	−0.1397(3)	−0.4646(6)	4.4(2)
C(22)	0.8062(4)	−0.1032(4)	−0.3287(7)	4.6(2)
C(23)	0.8335(3)	−0.0195(3)	−0.1728(6)	3.6(1)

[a]Estimated standard deviations in the least significant figure are given in parentheses.

Reaction of η^5-$CpCo^*(C_3F_7)(PPhMe_2)$(I) (**1***b*) with $PPh(OMe)_2$ in acetone

η^5-$CpCo^*(C_3F_7)(PPh_2Me)$(I) (41.3 mg, 0.0749 mmol), $PPh(OMe)_2$ (20.8 mg, 0.122 mmol), and acetone (25 mL) were mixed in a 50 mL Schlenk flask and stirred at 50°C for 12 h. Removal of volatiles under water aspirator followed by oil pump vacuum overnight left a dark-green solid, which was purified by PLC on silica gel. Elution with CH_2Cl_2 separated (in order of decreasing R_f values) a dark-green zone containing **1***b* and **2** (17.6 mg). Continued elution with acetone separated two orange zones containing **4***b*-1, **4***b*-2 (**4***b*-1: 10.9 mg, 0.0186 mmol; **4***b*-2: 5.3 mg, 0.0090 mmol). Physical, analytical, and spectroscopic data for **4***b*-1,2 are presented in Tables 1–3.

Table 6. Selected intramolecular distances[a] and angles for **6**-2.

Atom	Atom	Distance (Å)	Atom	Atom	Distance (Å)
Co(1)	P(1)	2.239(2)	O(3)	C(17)	1.450(5)
Co(1)	P(2)	2.191(1)	O(4)	C(16)	1.453(5)
Co(1)	C(1)	2.095(4)	C(1)	C(2)	1.407(6)
Co(1)	C(2)	2.114(4)	C(1)	C(5)	1.416(5)
Co(1)	C(3)	2.120(4)	C(2)	C(3)	1.403(6)
Co(1)	C(4)	2.112(4)	C(3)	C(4)	1.429(5)
Co(1)	C(5)	2.093(4)	C(4)	C(5)	1.408(6)
Co(1)	C(6)	1.967(4)	C(6)	C(7)	1.563(5)
P(1)	O(1)	1.625(3)	C(7)	C(8)	1.537(6)
P(1)	O(2)	1.487(3)			
P(1)	C(10)	1.843(4)			
P(2)	O(3)	1.599(3)			
P(2)	O(4)	1.603(3)			
P(2)	C(18)	1.820(4)			

Atom	Atom	Atom	Angle (°)	Atom	Atom	Atom	Angle (°)
P(1)	Co(1)	P(2)	93.68(5)	O(2)	P(1)	C(10)	107.3(2
P(1)	Co(1)	C(6)	90.9(1)	Co(1)	P(2)	O(4)	107.3(1)
P(2)	Co(1)	C(6)	96.5(1)	Co(1)	P(2)	C(18)	124.7(1)
Co(1)	P(1)	O(1)	106.3(1)	O(3)	P(2)	O(4)	105.4(2)
Co(1)	P(2)	O(3)	116.8(1)	O(3)	P(2)	C(18)	97.0(2)
Co(1)	P(1)	O(2)	117.8(1)	O(4)	P(2)	C(18)	103.7(2)
Co(1)	P(1)	C(10)	112.2(1)	P(1)	O(1)	C(9)	117.5(3)
O(1)	P(1)	O(2)	111.4(2)	P(2)	O(3)	C(17)	123.0(3)
O(1)	P(1)	C(10)	100.5(2)	P(2)	O(4)	C(16)	122.1(3)

[a]Estimated standard deviations in the least significant figure are given in Parenthesis.

Reaction of η^5-CpCo*(C_3F_7)(PPh(OMe)2)(I) 2 with PPh_2Me in acetone

η^5-CpCo*(C_3F_7)(PPh(OMe)$_2$)(I) (147.0 mg, 0.2491 mmol), PPh_2Me (51.0 mg, 0.255 mmol), and acetone (25 mL) were mixed in a 50 mL Schlenk flask and stirred at ambient temperature (20°C) for 24 h. Removal of volatiles under water aspirator followed by oil pump vacuum overnight left a dark-green solid, which was purified by PLC on silica gel. Elution with CH_2Cl_2 separated (in order of decreasing R_f values) a dark-green zone containing **1***a* (62.1 mg, 0.100 mmol) and **2** (6.6 mg, 0.011 mmol). Continued elution with acetone separated two orange zones containing **4***a*-1, **4***a*-2 (**4***a*-1: 45.1 mg, 0.0696 mmol; **4***a*-2: 21.0 mg, 0.0324 mmol), followed by two light-orange zones containing **6**-1, **6**-2 (**6**-1: 7.9 mg 0.013 mmol; **6**-2: 4.4 mg 0.0071 mmol).

Reaction of η^5-CpCo*(C_3F_7)(PPh(OMe)2)(I) 2 with $AgSbF_6$ following with PPh_2Me and then NaI in acetone

A 10 mL colourless, acetone solution of $AgSbF_6$ (29.1 mg, 0.0847 mmol) was added dropwise with stirring into a 20 mL dark-green acetone solution of η^5-CpCo*(C_3F_7)(PPh(OMe)$_2$)(I) (44.0 mg, 0.0755 mmol) contained in a 50 mL Schlenk flask at ambient temperature (20°C). A white precipitate of AgI formed. Dropwise addition of PPh_2Me (16.6 mg, 0.0829 mmol) resulted in the formation of a brown solution. Treatment of the solution with NaI (22.8 mg, 0.1521 mmol) gave an immediate colour change to deep green. Removal of volatiles under water aspirator pressure followed by oil pump vacuum overnight left a dark-green solid. ^{1}H NMR analysis ($CDCl_3$) of the residue in cyclopentadienyl region showed two resonances corresponding to **1***a* (δ = 5.09 ppm, 75.0%) and **2** (δ = 5.19 ppm, 17.2%). The phosphinate complexes **4***a*-1, **4***a*-2 were not detected.

NMR tube reaction of η^5-CpCo*(PPh(OMe)2)(I), 2, with PPh_2Me in acetone-d_6

A 5 mm NMR tube was charged with η^5-CpCo*(C_3F_7)(PPh(OMe)$_2$)(I) (13.44 mg, 0.02276 mmol), PPh_2Me (4.78 mg, 0.0239 mmol), and acetone-d_6 (0.86 mL) and capped with a septum. The sample was equilibrated at ambient temperature (20°C) for 24 h. The ^{1}H NMR spectrum showed **1***a* (δ = 5.25 ppm, 45.4%), **2** (δ = 5.37 ppm, 5.5%), **4***a*-1 (δ = 5.20 ppm, 23.5%), **4***a*-2 (δ = 4.95 ppm, 8.4%), **6**-1 (δ = 5.18 ppm, 7.1%), **6**-2 (δ = 4.98 ppm, 6.3%), respectively. A parallel reaction was carried out for CpCo*(C_3F_7)-(PPh(OMe)2)(I) with PPh_2Me, resulting in **1***a* (δ = 5.25 ppm, 30.1%), **2** (δ = 5.37 ppm, 4.2%), **4***a*-1 (δ = 5.20 ppm, 26.9%), **4***a*-2 (δ = 4.95 ppm, 13.3%), **6**-1 (δ = 5.18 ppm, 7.6%), **6**-2 (δ = 4.98 ppm, 8.0%), respectively.

Reaction of η^5-CpCo*(C_3F_7)(PPh_2Me)(I), 1*a*, with $PPh(OMe)_2$ in acetone in the presence of excess PPh_2Me

η^5-CpCo*(C_3F_7)(PPh_2Me)(I) (27.0 mg, 0.0435 mmol), $PPh(OMe)_2$ (7.6 mg, 0.045 mmol), and PPh_2Me (95.8 mg, 0.478 mmol) were mixed in 10 mL of acetone in a 50 mL Schlenk flask and stirred at ambient temperature (20°C) for 24

Table 7. Summary of crystallographic data for **6**-2.

Formula	$C_{23}H_{24}O_4F_7P_2Co$
FW (g/mol)	618.31
Crystal habit	Orange column
Crystal size (mm)	0.45 × 0.12 × 0.10
Crystal system	Triclinic
Lattice parameters	
a (Å)	12.928(4)
b (Å)	14.683(4)
c (Å)	7.666(2)
α (°)	103.5(2)
β (°)	101.31(3)
γ (°)	109.50(2)
V (Å^3)	1272.8(4)
Space group	$P\bar{1}$ (no. 2)
Z	2
D_{calcd}(g/cm^3)	1.613
F_{000}	628
$\mu_{(MoK\alpha)}$(cm^{-1})	8.73
Scan width(°)	1.47 + 0.30 tan θ
$2\theta_{max}$ (°)	50.0
No. of reflections measured	
Total	4682
Unique	4469
R_{int}	0.027
Corrections[a]	Lorentz–polarization absorption
Trans.factors:	0.95–1.00
Secondary extinction coeff.	0.25290×10^{-6}
Function minimized	$\Sigma w(\|F_o\| - \|F_c\|)^2$
Least-squares weights	$4F_o^2/\sigma^2(F_o^2)$
p-Factor	0.01
Anomalous dispersion	All non-hydrogen atoms
No. of observations ($I > 2.00\sigma(I)$)	2867
No. of variables	335
Reflection/parameter ratio	8.56
R[b]	0.036
R_w[c]	0.030
Goodness of fit indicator[d]	1.45
Max shift/error in final cycle	0.71
Δρ Final (max/min) (e$^-$/Å^3)	0.33/ − 0.25

[a]cf. ref. 46.
[b]$R = \Sigma||F_o| - |F_c||/\Sigma|F_o|$.
[c]$R_w = [(\Sigma w(|F_o| - |F_c|)^2/\Sigma wF_o^2)]^{1/2}$.
[d]GOF = $(\Sigma(|F_o| - |F_c|)/\sigma)/(n - m)$) where n = no. of reflections, m = no. of variables, and σ^2 = variance of ($|F_o| - |F_c|$).

h. Removal of volatiles under water aspirator followed by oil pump vacuum overnight left a dark-green solid. ^{1}H NMR analysis in $CDCl_3$ showed three cyclopentadienyl resonances corresponding to **1***a* (δ = 5.09 ppm, 51.4%), **4***a*-1 (δ = 5.06 ppm, 40.1%), and **4***a*-2 (δ = 4.87 ppm, 10.8%).

Reaction of η^5-CpCo*(C$_3$F$_7$)(PPh$_2$Me)(I), 1*a*, with PPh(OMe)$_2$ in acetone/methanol

η^5-CpCo*(C$_3$F$_7$)(PPh$_2$Me)(I) **1***a* (21.8 mg, 0.0352 mmol), PPh(OMe)$_2$ (6.0 mg, 0.035 mmol), and PPh$_2$Me (69.1 mg, 0.345 mmol) were combined in 3/2 (v/v) acetone/methanol (10 mL) in a 50 mL Schlenk flask at ambient temperature (20°C) and stirred for 24 h. The ^{1}H NMR spectrum of the crude product showed only one cyclopentadienyl resonance (δ = 5.09 ppm) assigned to the starting material **1***a* in $CDCl_3$. A similar reaction starting with η^5-CpCo(C$_3$F$_7$)(PPh(OMe)$_2$)(I) **2** (43.3 mg, 0.0734 mmol) and PPh$_2$Me (14.7 mg, 0.0735 mmol) in 3/2 (v/v) acetone/methanol gave **1***a* (δ = 5.09 ppm, 50.7%), **2** (δ = 5.19 ppm, 11.0%), **4***a*-1 (δ = 5.06 ppm, 11.25%), **4***a*-2 (δ = 4.87 ppm, 6.6%), respectively.

Reaction of η^5-CpCo*(C$_3$F$_7$)(PMe$_3$)(I) (1*c*) with PPh(OMe)$_2$ in acetone

PPh(OMe)$_2$ (258.6 mg, 1.520 mmol) was added dropwise to a stirred 40 mL dark green acetone solution of η^5-CpCo*(C$_3$F$_7$)(CO)(I) (334.7 mg, 0.7554 mmol) in a 100 mL Schlenk flask at 50°C until the solution became clear yellow in colour (around 5 h). Removal of volatiles under water aspira-

tor pressure followed by oil pump vacuum overnight left an orange solid, which was purified by PLC on silica gel. Elution with 9/1 acetone/methanol separated (in order of decreasing R_f value) a deep orange zone containing **4***c*-1 (236.7 mg, 0.4515 mmol), two yellow-green zones containing **6**-1 (15.6 mg, 0.0298 mmol) and **6**-2 (6.7 mg, 0.0128 mmol), respectively, and an orange zone containing **4***c*-2 (114.2 mg, 0.2178 mmol).

Crystal structure determination of η^5-$CpCo^*(C_3F_7)(PPh(OMe)_2)(P(O)(OMe)Ph)$, 6-2

A diastereomeric mixture of **6**-1 and **6**-2 was prepared as described previously (14). The lower R_f diastereomer was separated using preparative thick-layer radial chromatography and recrystallized by slow evaporation of a methylene chloride – hexane solvent mixture. An orange single crystal was selected and mounted on a glass fibre for X-ray analysis. Crystal data were collected at ambient temperature on a Rigaku AFC6S diffractometer with graphite monochromated Mo Kα radiation, λ = 0.71069 Å, and a 2 kW sealed tube generator using the ω scan technique to a maximum 2θ value of 50.0°. Positional parameters and selected bond distances and angles are given in Tables 5 and 6, respectively. Cell constants and an orientation matrix for data collection were determined from least-squares refinement using the setting angles of the 20 carefully centered reflections in the range $9.22 < 2\theta < 17.73°$ and are given in Table 7. The space group $P\bar{1}$ (no. 2) was assigned on the basis of systematic absences and on the successful solution and refinement of the structure. Omega (ω) scans of several intense reflections, made prior to data collection, had an average width at half-height of 0.31° with a take-off angle of 6.0°. Scans of $(1.47 + 0.30 \tan \theta)°$ were made at a speed of 4.0°/min (in ω). Weak reflections ($I < 10.0\sigma(I)$) were rescanned (max 2) and the counts accumulated to assure good counting statistics. Stationary counts were recorded on each side of the reflection. The ratio of peak counting time to background counting time was 2:1.

The linear absorption coefficient for Mo Kα is 8.7 cm^{-1}. An empirical absorption correction, based on azimuthal scans of several reflections, was applied, resulting in transmission factors ranging from 0.95 to 1.00. The data were corrected for Lorentz and polarization effects. a correction for secondary extinction was applied with coefficient = 0.25290 $\mp 10^{-6}$. The structure was solved by direct methods (45) using the Molecular Structure Corporation TEXSAN software. Non-hydrogen atoms were refined anisotropically. Idealized hydrogen atoms were included at the calculated positions and were not refined.

Tables of atomic coordinates, bond distances and angles, and torsion angles for η^5-$CpCo^*(C_3F_7)(PPh(OMe)_2)(P^*(O)Ph(OMe))$, **6**-2, have been deposited as supplementary material.[2]

[2] Copies of material on deposit may be purchased from: The Depository of Unpublished Data, Document Delivery, CISTI, National Research Council Canada, Ottawa, Canada K1A 0S2. The tables of atomic coordinates and bond lengths and angles have also been deposited with the Cambridge Crystallographic Data Centre, and can be obtained on request from The Director, Cambridge Crystallographic Data Centre, University Chemical Laboratory, 12 Union Road, Cambridge, CB2 1EZ, U.K. Structure factor tables are no longer being deposited, but may be obtained from the author.

Acknowledgement

We thank the Natural Sciences and Engineering Research Council of Canada (NSERC) for a Grant to C.J. and Memorial University for financial support.

References

1. T.B. Brill and S.J. Landon. Chem. Rev. **84**, 577 (1984).
2. H. Brunner, C.R. Jablonski, and P.G. Jones. Organometallics, **7**, 1283 (1988).
3. S.J. Landon and T.B. Brill. J. Am. Chem. Soc. **104**, 6571 (1982).
4. S.J. Landon and T.B. Brill. Inorg. Chem. **23**, 1266 (1984).
5. Z. Zhou, C. Jablonski, and J. Bridson. Organometallics, **13**, 781 (1994).
6. Z. Zhou, C. Jablonski, and J. Bridson. Organometallics, **12**, 3677 (1993).
7. H. Nakazawa, M. Yamaguchi, K. Kubo, and K. Miyoshi. J. Organomet. Chem. **428**, 145 (1992).
8. H. Nakazawa, Y. Kadoi, and K. Miyoshi. Organometallics, **8**, 2851 (1989).
9. H. Nakazawa, Y. Kadoi, T. Mizuta, K. Miyoshi, and H. Yoneda. J. Organomet. Chem. **366**, 333 (1989).
10. E.V. Schleman and T.B. Brill. J. Organomet. Chem. **323**, 103 (1987).
11. H. Nakazawa, T. Fujita, K. Kubo, and K. Miyoshi. J. Organomet. Chem. **473**, 243 (1994).
12. C. Leiva, K. Mossert, A.H. Klahn, and D. Sutton. J. Organomet. Chem. **469**, 69 (1994).
13. B.J. Boone, C.R. Jablonski, P.G. Jones, M.J. Newlands, and Y.F. Yu. Organometallics, **12**, 3042 (1993).
14. C.R. Jablonski, H.Z. Ma, Z. Chen, R.C. Hynes, J.N. Bridson, and M.P. Bubenik. Organometallics, **12**, 917 (1993).
15. D.G. Gilheaney. *In* The chemistry of organophosphorus compounds. Vol. 2. John Wiley, New York. 1992. pp. 1–52.
16. D.M. Roundhill, R.P. Sperline, and W.B. Beaulieu. Coord. Chem. Rev. **26**, 263 (1978).
17. B. Walther. Coord. Chem. Rev. **60**, 67 (1984).
18. S. Neumann, D. Schomburg, and R. Schmutzler. J. Chem. Soc. Chem. Commun. 848 (1979).
19. T.E. Sloan. Top. Stereochem. **12**, 1 (1981).
20. C. Lecomte, Y. Dusavsoy, J. Protas, J. Tirouflet, and A. Dormand. J. Organomet. Chem. **73**, 67 (1974).
21. P. Mata, A.M. Lobo, C. Marshall, and A.P. Johnson. Tetrahedron: Asymmetry, **4**, 657 (1993).
22. H. Nakazawa, K. Morimasa, Y. Kushi, and H. Yoneda. Organometallics, **7**, 458 (1988).
23. J. Reinhard, M. Luksza, W. Malisch, D. Kempf, and G. Kuenzel. J. Organomet. Chem. **266**, C22 (1984).
24. H.A. Kaul, D. Greissinger, M. Luksza, and W. Malisch. J. Organomet. Chem. **228**, C29 (1982).
25. W. Malisch and A. Meyer. J. Organomet. Chem. **198**, C29 (1980).
26. H. Brunner. Adv. Organomet. Chem. **18**, 151
27. J.M. O'Connor and C.P. Casey. Chem. Rev. **87**, 307 (1987).
28. H. Brunner and M. Lappus. Angew. Chem. Int. Ed. Engl. **11**, 923 (1972).
29. H. Brunner and H. Vogt. Chem. Ber. **114**, 2186 (1981).
30. G.W. Parshall and S.D. Ittel. *In* Homogeneous catalysis — The application and chemistry of catalysis by soluble transition metal complexes. 2nd ed. John Wiley & Sons, New York. 1992.
31. M.A. Dewey, Y.L. Zhou, Y.M. Liu, and J.A. Gladysz. Organometallics, **12**, 3924 (1993).
32. M. Saunders, K.N. Houk, Y.-D. Wu, W.C. Still, M. Lipton, G. Chang, and W.C. Guida. J. Am. Chem. Soc. **112**, 1419 (1990).

33. J.J. Gajewski, K.E. Gilbert, and J. McKelvey. *In* Advances in Molecular Modeling. Vol. 2. JAI Press Inc., Creenwich, Conn. 1990. pp. 65–92.
34. S.C. Mackie and M.C. Baird, Conn. Organometallics, **11**, 3712 (1992).
35. J. Polowin, S.C. Mackie, and M.C. Baird. Conn. Organometallics, **11**, 3724 (1992).
36. B.K. Blackburn, S.G. Davies, K.H. Sutton, and M. Whittaker. Chem. Soc. Rev. **17**, 147 (1988).
37. B.K. Blackburn, S.G. Davies, and M. Whittaker. *In* Stereochemistry of organometallic and inorganic compounds. Vol. 3. Elsevier, Amsterdam. 1989. pp. 141–223.
38. H. Brunner, B. Hammer, C. Krueger, K. Angermund, and I. Bernal. Organometallics, **4**, 1063 (1985).
39. S.E. Garner and A.G. Orpen. J. Chem. Soc. Dalton Trans. 533 (1993).
40. H. Brunner, R. Oeschey, and B. Nuber. Angew. Chem. Int. Ed. Engl. **33**, 866 (1994).
41. J.I. Seeman. Chem. Rev. **83**, 83 (1983).
42. C.R. Jablonski, T. Burrow, and P.G. Jones. J. Organomet. Chem. **370**, 173 (1989).
43. C.R. Jablonski, H.Z. Ma, and R.C. Hynes. Organometallics, **11**, 2796 (1992).
44. R.B. King, P.M. Treichel, and F.G.A. Stone. J. Am. Chem. Soc. **83**, 3593 (1961).
45. C.J. Gilmore J. Appl. Crystallogr. **17**, 42 (1984).

Pyridine-2-selenolate and -2-tellurolate as ligands: a multinuclear (^{77}Se, ^{119}Sn, ^{125}Te) magnetic resonance study of some tin(IV) complexes, and X-ray structural analyses of $Sn(SPh)_2(2\text{-}Se\text{-}C_5H_4N\text{-}N,Se)_2$ and $Sn(SPh)_{1.85}(2\text{-}Se\text{-}C_5H_4N)_{2.15}$[1]

Naveen Chopra, Leslie C. Damude, Philip A.W. Dean, and Jagadese J. Vittal

Abstract: Reactions between $Sn(E'Ph)_n$ (E' = S or Se; n = 2 or 4) and the bis(pyridine) dichalcogenides 2,2'-$(C_5H_4NE)_2$ (E = Se or Te), abbreviated py_2E_2, have been studied using multinuclear (^{77}Se, ^{119}Sn, ^{125}Te) magnetic resonance. In this way the occurrence of the pyridine-2-chalcogenate complexes $Sn(E'Ph)_{4-x}(Epy)_x$ (E' = S or Se; E = Se, x = 1–4; E = Te, x = 1 or 2) has been demonstrated. The pattern of ^{119}Sn NMR chemical shifts for $Sn(E'Ph)_{4-x}(Sepy)_x$ (E' = S or Se, x = 0–4) is consistent with bidentate bonding for the $pySe^-$ ligand when x = 1 and 2. The $pyTe^-$ ligand is probably bidentate also in all four complexes containing this ligand. As part of the NMR analysis, ^{77}Se and (or) ^{125}Te NMR data were obtained for py_2Te_2 and for the new mixed dichalcogenides PhE'ER (E' = S, Se, or Te; E ≠ E' = Se or Te; R = 2-py or Ph), which were produced in the systems $Ph_2E'_2$:R_2E_2. The complex $Sn(SPh)_2(Sepy)_2$ (**1**) was isolated pure and its structure determined by the single crystal X-diffraction technique. The compound crystallizes in the monoclinic space group $P2_1/n$, with unit cell dimensions a = 9.7929(9) Å, b = 22.340(2) Å, c = 11.368(1) Å, β = 108.803(7) °, V = 2354.3(4) Å^3, d_{calc} = 1.837 g cm^{-3}, and Z = 4. Refinement by full-matrix least squares on F^2 gave agreement factors $R1$ = 0.0425 and $wR2$ = 0.0882 for 2823 independent reflections with $F_o \geq 4\sigma(F_o)$ and 258 variables. The structure confirms that the $PySe^-$ ligand behaves in a chelating manner. The molecule $Sn(SPh)_2(2\text{-}Se\text{-}C_5H_4N\text{-}N,Se)_2$ has a distorted octahedral structure with the PhS^- ligands in *cis* positions and the two Se donor atoms in *trans* positions. The Sn—Se, Sn—S, and Sn—N distances are 2.6291(8) and 2.6358(8) Å, 2.475(2) and 2.464(2) Å, and 2.325(5) and 2.333(5) Å. The bite angles N-Sn-Se of the chelating ligands are 65.9(1)° and 65.8(1)°. En route to **1**, the yellow crystalline compound $Sn(SPh)_{1.85}(2\text{-}Se\text{-}C_5H_4N)_{2.15}$ (**2**) was isolated. This was shown by ^{119}Sn NMR spectroscopy to contain both $Sn(2\text{-}Se\text{-}C_5H_4N)_2(SPh)_2$ and $Sn(2\text{-}Se\text{-}C_5H_4N)_3(SPh)$. The crystal and molecular structure of **2** was determined by single crystal X-ray diffraction techniques. Crystal data: monoclinic, space group $P2_1/n$, a = 9.795(2) Å, b = 22.355(4) Å, c = 11.362(2) Å, β = 108.87(3)°, V = 2354.2(8) Å^3, d_{calc} = 1.837 g cm^{-3}, d_{obs} = 1.87(5) g cm^{-3}, Z = 4, $R1$ = 0.0306, $wR2$ = 0.0651 for 2756 data ($F_o \geq 4\sigma(F_o)$) and 258 parameters. Crystallographic evidence for the presence of co-crystallized $Sn(2\text{-}Se\text{-}C_5H_4N)_3(SPh)$ occurs only in a minor lengthening of one of the two Sn—S bonds, Sn—S(1) (compared with expectation for **1**), and an excess of electron density at S(1) when the data are modelled as $Sn(2\text{-}Se\text{-}C_5H_4N)_2(SPh)_2$. These effects are attributed to a crystallographic disorder of SPh and η^1-{2-Se-C_5H_4N} at the S(1)Ph site, involving isostructural $Sn(\eta^2\text{-}\{2\text{-}Se\text{-}C_5H_4N\})_2(\{\eta^1\text{-}\{2\text{-}Se\text{-}C_5H_4N\})(SPh)$ and $Sn(\eta^2\text{-}\{2\text{-}Se\text{-}C_5H_4N\})_2(SPh)_2$.

Key words: pyridine-2-selenolate, pyridine-2-tellurolate, tin complexes.

Résumé : Utilisant la résonnance magnétique de noyaux multiples (^{77}Se, ^{119}Sn, ^{125}Te), on a étudié les réactions entre le $Sn(E'Ph)_n$ (E' = S ou Se; n = 2 ou 4) et les dichalcogénures de bis(pyridine) 2,2'-$(C_5H_4NE)_2$ (E = Se ou Te), représentés en abrégé par py_2E_2. On a pu ainsi démontrer la formation des complexes 2-chalcogénates de pyridine $Sn(E'Ph)_{4-x}(Epy)_x$ (E' = S ou Se; E = Se, x = 1–4; E = Te, x = 1 ou 2). L'allure des déplacements chimiques de la RMN du ^{119}Sn du composé $Sn(E'Ph)_{4-x}(Sepy)_x$ (E' = S ou Se, x = 0–4) est en accord avec une liaison bidentate pour le ligand $pySe^-$ lorsque x = 1 et 2. Le ligand $pyTe^-$ est probablement bidentate dans tous les quatre complexes où on le retrouve également. Dans le cadre de cette analyse par RMN, on obtenu les données relatives au complexe py_2Te_2 et aux nouveaux dichalcogénures mixtes PhE'ER (E' = S, Se, ou Te; E ≠ E' = Se ou Te; R = 2-py ou Ph), qui se forment dans les systèmes $Ph_2E'_2$: R_2E_2. On a isolé, à l'état pur, le complexe $Sn(SPh)_2(Sepy)_2$ (**1**) et

Received January 12, 1996.

This paper is dedicated to Professor Howard C. Clark in recognition of his contributions to Canadian chemistry.

N. Chopra, L.C. Damude, P.A.W. Dean,[2] and J.J. Vittal.[2] Department of Chemistry, University of Western Ontario, London, ON N6A 5B7, Canada.

[1] Taken in part from the Honours Research Thesis of Naveen Chopra: University of Western Ontario, 1991.

[2] Authors to whom correspondence may be addressed. Telephone: (519) 679-2111, ext. 6331. Fax: (519) 661-3022. E-mail: pawdean@julian.uwo.ca

on a déterminé sa structure par la technique de diffraction des rayons X sur un monocristal. Le composé cristallise dans le groupe d'espace monoclinique $P2_1/n$, avec a = 9,7929(9) Å, b = 22,340(2) Å, c = 11,368(1) Å, β = 108,803(7)°, V = 2354,3(4) Å^3, d_{calc} = 1,837 g cm^{-3}, et Z = 4. L'affinage par la méthode des moindres carrés, matrice complète, sur F^2 conduit à des facteurs d'agrément $R1$ = 0,0425 et $wR2$ = 0,0882 pour 2823 réflexions indépendantes avec $F_o \geq 4\sigma(F_o)$ et 258 variables. La structure confirme que le ligand PySe$^-$ se comporte de manière chélatante. La molécule $Sn(SPh)_2(2\text{-}Se\text{-}C_5H_4NB\mathit{N,Se})_2$ a une structure octaédrique déformée avec les ligands PhS$^-$ en positions *cis* et les deux atomes donneurs Se en positions *trans*. Les distances Sn—Se, Sn—S et Sn—N sont respectivement de : 2,6291(8) et 2,6358(8) Å, 2,475(2) et 2,464(2) Å, et de 2,325(5) and 2,333(5) Å. Les angles d'attache N-Sn-Se des ligands chélatants sont de 65,9(1)° et de 65,8(1)°. Au cours de la synthèse du composé **1**, on a isolé le composé jaune cristallin $Sn(SPh)_{1,85}(2\text{-}Se\text{-}C_5H_4N)_{2,15}$ (**2**). La spectroscopie de RMN du ^{119}Sn a montré qu'il contient les deux complexes $Sn(2\text{-}Se\text{-}C_5H_4N)_2(SPh)_2$ et $Sn(2\text{-}Se\text{-}C_5H_4N)_3(SPh)$. On a déterminé la structure cristalline et moléculaire du composé **2** par la technique de diffraction des rayons X sur un monocristal. Le composé cristallise dans le groupe d'espace monoclinique $P2_1/n$, avec a = 9,795(2) Å, b = 22,355(4) Å, c = 11,362(2) Å, β = 108,87(3)°, V = 2354,2(8) Å^3, d_{calc} = 1,837 g cm^{-3}, d_{obs} = 1,87(5) g cm^{-3}, Z = 4, $R1$ = 0,0306, $wR2$ = 0,0651 pour 2756 données ($F_o \geq 4\sigma(F_o)$) et 258 paramètres. Les preuves cristallographiques de la présence du composé co-cristallisé $Sn(2\text{-}Se\text{-}C_5H_4N)_3(SPh)$ reposent uniquement sur une élongation mineure de l'une des deux liaisons Sn—S, Sn—S (1) (comparée à ce qui était attendu pour le composé **1**), et sur un excès de la densité électronique en S(1) lorsque les données sont modélisées sur le composé $Sn(2\text{-}Se\text{-}C_5H_4N)_2(SPh)_2$. On attribue ces effets à un désordre cristallographique de SPh et de η^1-{2-Se-C_5H_4N} au niveau du site S(1)Ph, impliquant les composés isostructuraux $Sn(\eta^2\text{-}\{2\text{-}Se\text{-}C_5H_4N\})_2(\{\eta^1\text{-}\{2\text{-}Se\text{-}C_5H_4N\})(SPh)$ et $Sn(\eta^2\text{-}\{2\text{-}Se\text{-}C_5H_4N\})_2(SPh)_2$.

Most clés : 2-sélénolate de pyridine, 2-tellurolate de pyridine, complexes d'étain.

[Traduit par la rédaction]

Introduction

The ligand chemistry of 2-O-$C_5H_4N^-$ and is well developed (1), as is that of 2-S-$C_5H_4N^-$, pyt$^-$ (2–4). In contrast, there appear to be only two published studies of the ligand behaviour of pyridine-2-selenolate, Sepy$^-$, both appearing during the course of the present work (5, 6*a*),[3] and none concerning pyridine-2-tellurolate, pyTe$^-$. As ligands, pySe$^-$ and pyTe$^-$ have several interesting features that make them worthy of study. They contain donor atoms of disparate "hardness"/"softness", the "soft" chalcogen and the "borderline" pyridinic nitrogen (7*a*). Thus an otherwise unstable bond between an acid and base of mismatched "hard"/"soft" character, or an unusual coordination number or geometry (6*a*), may be stabilized by *N,chalcogen*-chelation. As well, coordination of the N along with the chalcogen may help saturate the coordination sites of a metal and so reduce or prevent chalcogen bridging, leading to higher volatility than in the metal chalcogenates themselves (6*a*). Further, the presence of ^{77}Se or ^{125}Te nuclei at the chalcogen may allow use of chalcogen NMR to follow their reactions.

As a contribution to the study of the ligand behaviour of pySe$^-$ and pyTe$^-$, we present here our results for several of their tin(IV) complexes. These complexes were prepared in solution using methods described earlier for tin(IV) complexes of pyt$^-$ and its N-oxide (4). The tin complexes comprise a model system in which information from the ^{77}Se/^{125}Te NMR chemical shifts is bolstered by both ^{119}Sn NMR chemical shifts and one-bond coupling between $^{119/117}$Sn and ^{77}Se/^{125}Te. During the course of the study we were able to isolate $Sn(SPh)_2(Sepy)_2$ and $Sn(SPh)_{1.85}(Sepy)_{2.15}$, and their structures have been determined by X-ray analytical methods.

Experimental

Materials

Diphenyldiselenide (Aldrich) showed no impurities by ^{13}C or ^{77}Se NMR, and was used as received. Literature methods were used for diphenyldisulfide (8), 2,2′-dipyridyldiselenide, py_2Se_2 (9), $Sn(SPh)_4$ and $Sn(SePh)_4$ (10), and $Sn(SPh)_2$ and $Sn(SePh)_2$ (11).

A low yield of 2,2′-dipyridylditelluride, py_2Te_2, was obtained by the method of ref. 12. Exact Mass in mass spectrum, calcd. for $C_{10}H_8N_2{}^{126}Te^{130}Te$: 411.8786; found: 411.8777, 411.8773 (duplicate measurements). Proton and ^{13}C NMR data obtained for this compound are consistent with those reported (13) while our work was in progress.[4]

All solvents for use in NMR sample preparation or synthesis were dried over 3A molecular sieves and sparged with Ar(g) before use.

Syntheses of $Sn(SPh)_2(2\text{-}Se\text{-}C_5H_4N)_2$ (1) and $Sn(SPh)_{1.85}(Sepy)_{2.15}$ (2)

Under Ar, a solution of py_2Se_2 (0.290 g, 0.923 mmol) in CH_2Cl_2 was added to solid $Sn(SPh)_2$ (0.312 g, 0.926 mmol). The mixture was stirred for 2 h, then filtered through a medium sinter under Ar pressure, giving a yellow filtrate and a khaki residue. The volume of the filtrate was reduced to 2 mL in a flow of Ar, and then hexane (1 mL) was added. On standing, bright yellow crystals formed at room temperature, and crystallization was completed by overnight refrigeration at 5°C. The crystals were separated by fitration and washed with CH_2Cl_2:hexane = 1:10 (2 × 1.5 mL). The yield was 0.337 g, but ^{119}Sn NMR showed the presence of ca. 13 mol% $Sn(SPh)(Sepy)_3$, which was not removed by two further recrystallizations from 1:1 CH_2Cl_2:hexane. Anal. of recrystallized product. calcd. for $C_{21.85}H_{17.85}N_{2.15}S_{1.85}Se_{2.15}Sn_1$: C 39.86, H 2.73, N 4.57; found: C: 39.87, 39.74; H: 2.64, 2.59; N: 4.56, 4.51. Single crystal X-ray analysis of the product, **2**, confirmed that $Sn(SPh)_2(Sepy)_2$ and $Sn(SPh)(Sepy)_3$ co-crystallize (see Results and discussion).

An NMR sample of **2** (82 mg in 3 mL of CH_2Cl_2) was prepared in a 10 mm o.d. NMR tube. To this was added $Sn(SPh)_4$ (ca. 5 mg) until the ^{119}Sn NMR spectrum showed the presence

[3] An additional paper describing the synthesis of $Sn(Sepy)_x$ (x = 2,4), $Pb(Sepy)_2$, and $Pb(3\text{-}Me_3Si\text{-}2\text{-}SeC_5H_3N)_2$, and the strucutural analysis of $Sn(Sepy)_2$, appeared after the completion of our manuscript (6*b*).

[4] An incorrect value of δ_{Te} for 2,2′-py_2Te_2 is given in ref. 13 (S.J. Dunne and E.I. von Nagy-Felsobuki, private communication).

Table 1. Crystal data for $Sn(SPh)_2(Sepy)_2$, **1**, and $Sn(SPh)_{1.85}(Sepy)_{2.15}$, **2**.

	1		**2**
Empirical formula	$C_{22}H_{18}N_2S_2Se_2Sn_1$		$C_{21.85}H_{17.85}N_{2.15}S_{1.85}Se_{2.15}Sn_1$
Formula weight	651.11		658.30
Temperature/°C		25	
Wavelength/Å		0.71073	
Crystal system		Monoclinic	
Space group		$P2_1/n$	
Unit cell dimensions			
a/Å	9.7929(9)		9.795(2)
b/Å	22.340(2)		22.355(4)
c/Å	11.368(1)		11.362(2)
β/deg	108.803(7)		108.87(3)
Volume/Å^3	2354.3(3)		2354.2(8)
Z		4	
Density, obsd./g cm^{-3}	—		1.87(5)
Density, calcd./g cm^{-3}	1.837		1.837
Absorption coefficient/mm^{-1}	4.366		4.585
Independent reflections	4126 (R(int) = 0.0331)		4142 (R(int) = 0.0281)
Refinement method		Full-matrix least squares on F^2	
Data/restraints/parameters	2823/0/258		2756/0/258
Goodness-of-fit (GoF) on F^2	1.013		1.021
Final R indices [$F_o > 4\sigma(F_o)$]	$R1$ = 0.0425, $wR2$ = 0.0882		$R1$ = 0.0306, $wR2$ = 0.0651
R indices (all data)	$R1$ = 0.0767, $wR2$ = 0.1012		$R1$ = 0.0706, $wR2$ = 0.0845

$R1 = \Sigma(||F_o| - |F_c||)/\Sigma|F_o|$; $wR2 = [\Sigma w(F_o^2 - F_c^2)^2/\Sigma wF_o^4]^{1/2}$; GoF = $[\Sigma w(F_o^2 - F_c^2)^2/(n - p)]^{1/2}$ where n is the number of reflections and p is the number of parameters refined.

of a small amount of $Sn(SPh)_3(Sepy)$. At this stage, the solvent volume was reduced to ca. 1.5 mL and 1.5 mL of hexane was layered on. Refrigeration overnight yielded 33 mg of bright yellow single crystals, which were isolated by decantation. Tin-119 NMR spectroscopy of a sample of this product, **1**, in CH_2Cl_2 showed the presence of only $Sn(SPh)_2(Sepy)_2$ ($Sn(SPh)(Sepy)_3$:$Sn(SPh)_2(Sepy)_2 < 0.02$). Elemental analysis confirmed the purity of **1**. Anal. calcd. for $C_{22}H_{18}N_2S_2Se_2Sn$: C 40.58, H 2.78, N 4.30; found: C 40.64, H 2.62, N 4.30. A smaller second crop of product was obtained from the decantate on more extended refrigeration.

X-ray structure determination

$Sn(SPh)_2(Sepy)_2$

Yellow crystals of **1** were obtained from a mixture of CH_2Cl_2 and C_6H_{14} as described above. A suitable crystal was selected (size 0.44 × 0.21 × 0.19 mm) and mounted, for diffraction experiments, at the end of a glass fibre using epoxy glue. The diffraction experiments were carried out on a Siemens P4 4-circle diffractometer with XSCANS software package (14*a*) using graphite monochromated Mo Kα radiation at 25°C. The cell constants and orientation matrices were determined (14*a*) by centering 26 high-angle reflections ($24.2° \leq 2\theta \leq 25.0°$). A total of 5170 reflections were collected in the θ range 1.8°–25.0° ($-1 \leq h \leq 11$, $-1 \leq k \leq 26$, $-13 \leq l \leq 13$) in ω–2θ scan mode at variable scan speeds (1–10 deg. min^{-1}). Background measurements were made at the ends of the scan range. Three standard reflections were monitored for every 297 data measured. A Gaussian absorption correction was applied to the data after indexing the faces of the data crystal (six faces and the face indices are {011}, ($\bar{1}$01) and (100)) and measuring the distances between them. SHELXTL (15) programs were used for data processing, solution, and refinements. The space group $P2_1/n$ was unambiguously determined from the systematic absences. All the non-hydrogen atoms in the neutral molecule were refined anisotropically. All the hydrogen atoms were placed in calculated ideal positions and included for the purpose of structure factors calculations only. In the final least-squares refinement cycles on F^2, the model converged at $R1$ = 0.0425, $wR2$ = 0.0882, and Gof = 1.013 for 2823 reflections with $F_o \geq 4\sigma(F_o)$ and 258 parameters, and $R1$ = 0.0767, $wR2$ = 0.1012 for all 4126 data. In the final difference Fourier synthesis the electron density fluctuates in the range 0.533 to −0.453 e Å^{-3}. There is no shift in the final cycles. An extinction correction was refined to 0.00160 (14a). The experimental details and crystal data are shown in Table 1, and the positional and thermal parameters in Table 2.

$Sn(SPh)_{1.85}(Sepy)_{2.15}$

Yellow crystals of **2** were obtained by recrystallization of the crude product from a mixture of CH_2Cl_2 and C_6H_{14} (1:1, v:v) at 5°C, as described above. A suitable crystal was selected (size 0.44 × 0.26 × 0.23 mm) and mounted, for diffraction experiments, at the end of a glass fibre using expoxy glue. Density measurements were made by the neutral buoyancy method using a mixture of CCl_4 and 1,2-$C_2H_4Br_2$. The diffraction experiments were carried out on an Enraf–Nonius CAD4F diffractometer using graphite monochromated Mo Kα radiation at 25°C. The cell constants and orientation matrices were determined (14*b*) by centering 22 high-angle reflections ($25.5° \leq 2\theta \leq 28.0°$). A total of 5194 reflections were

Table 2. Atomic coordinates ($\times 10^4$) and equivalent isotropic displacement parameters ($Å^2 \times 10^3$) for **1**. U(eq) is defined as one third of the trace of the orthogonalized U_{ij} tensor.

Atom	x	y	z	U(eq)
Sn	2576.8(5)	6240.2(2)	1236.4(4)	35.8(2)
Se(1)	3936.3(8)	5836.7(4)	−254.6(6)	52.2(2)
Se(2)	2229.5(8)	6255.6(3)	3441.0(6)	50.5(2)
S(1)	2608.6(22)	7333.7(8)	897.1(20)	60.4(6)
S(2)	92.6(19)	5974.6(9)	−19.6(16)	50.9(5)
N(1)	5076(5)	6297(2)	2059(4)	38(1)
C(1)	5495(7)	6076(3)	1144(6)	42(2)
C(2)	6953(8)	6060(4)	1258(7)	64(2)
C(3)	7922(8)	6284(4)	2300(8)	73(2)
C(4)	7486(8)	6523(4)	3233(8)	64(2)
C(5)	6038(8)	6525(3)	3094(6)	52(2)
N(2)	3075(6)	5330(2)	2296(5)	45(1)
C(6)	2815(7)	5452(3)	3377(6)	48(2)
C(7)	2995(9)	5011(4)	4252(8)	78(3)
C(8)	3436(11)	4461(4)	4036(10)	95(3)
C(9)	3713(11)	4337(4)	2949(11)	93(3)
C(10)	3507(9)	4789(4)	2114(8)	70(2)
C(11)	1321(8)	7545(3)	1610(6)	50(2)
C(12)	−109(9)	7586(4)	935(8)	68(2)
C(13)	−1115(10)	7759(4)	1449(10)	92(3)
C(14)	−738(11)	7886(4)	2686(10)	82(3)
C(15)	690(13)	7856(4)	3395(8)	94(3)
C(16)	1761(9)	7689(3)	2856(7)	70(2)
C(17)	325(7)	5925(3)	−1509(6)	42(2)
C(18)	555(8)	5380(3)	−1965(7)	56(2)
C(19)	735(9)	5338(4)	−3135(7)	66(2)
C(20)	657(9)	5844(4)	−3821(7)	68(2)
C(21)	426(9)	6386(4)	−3375(7)	67(2)
C(22)	258(8)	6434(3)	−2208(7)	53(2)

collected in the θ range 1.8°–25.0° ($-1 \leq h \leq 11$, $-1 \leq k \leq 26$, $-13 \leq l \leq 13$) in ω–2θ scan mode at variable scan speeds (0.97–4.1 deg min^{-1}) and with a scan width of 0.7 + 0.35 tan θ, with a maximum time per datum of 40 s. Background estimates were made by extending the scan by 25%. Three standard reflections were monitored every 120 min of data collection. A Gaussian absorption correction was applied to the data after indexing the faces of the data crystal (six faces and the face indices are {011}, (10$\bar{1}$) and ($\bar{5}4\bar{1}$)) and measuring the distances between them. SHELXTL (15) programs were used for data processing, solution, and the least-square refinements on F^2. The space group $P2_1/n$ was unambiguously determined from the systematic absences. The structure is isomorphous and isostructural with the pure form of the compound, [Sn(Sepy)$_2$(SPh)$_2$]. During the least-squares refinement cycles, it was found that one of the Sn—S bond lengths was longer than the other (Sn—S(1), 2.486(2) Å vs. Sn—S(2), 2.467(2) Å, $\Delta/\sigma = 7.1$). Chemical analysis and solution ^{119}Sn NMR data (see above, and following) show that the data crystal must contain both Sn(Sepy)$_2$(SPh)$_2$ and Sn(Sepy)$_3$(SPh). However, comparison with the structure of **1** (*pure* Sn(Sepy)$_2$(SPh)$_2$) suggests that only the S(1)Ph is contaminated (see below). Assuming that only the S(1)Ph is contaminated, comparison of the electron densities in the S(1) and S(2) positions gave the composition SPh/Sepy = 0.89/0.11, in fair agreement with an average composition (Sn(Sepy)$_{2.15}$(SPh)$_{1.85}$) calculated for **2** from the C, H, and N microanalyses and the average composition [Sn(SPh)$_{\sim 1.87}$(Sepy)$_{\sim 2.13}$] obtained by ^{119}Sn NMR, both for the same batch of crystals from which the data crystal was chosen. The site occupancies of S(1), C(12), C(16), H(12), and H(16) were fixed on the basis of the elemental analysis for the subsequent least-squares cycles (see footnote 5, re: deposited material). All the non-hydrogen atoms in the neutral molecule were refined anisotropically. All the hydrogen atoms were placed in calculated ideal positions and included for the purpose of structure factors calculations only. In the final least-squares refinement cycles on F^2, the model converged at $R1 = 0.0306$, $wR2 = 0.0651$, and Gof = 1.021 for 2756 reflections with $F_o \geq 4\sigma(F_o)$ and 258 parameters, and $R1 = 0.0706$, $wR2 = 0.0845$ for all 4136 data. In the final difference Fourier synthesis the electron density fluctuates in the range 0.41(9) to −0.58(9) e Å^{-3}. The four top peaks resided near the S(2), Se(1), and Sn at distances of 0.67–0.96 Å. There is no shift in the final cycles. An extinction correction was refined to 0.00185 (11). The experimental details and crystal data are shown in Table 1 and Table 3 contains the positional and thermal parameters.

The agreement factors obtained when the crystal was

Table 3. Atomic coordinates ($\times 10^4$) and equivalent isotropic displacement parameters ($Å^2 \times 10^3$) for **2**. U(eq) is defined as one third of the trace of the orthogonalized U_{ij} tensor.

Atom	x	y	z	U(eq)
Sn	2578.5(4)	6239.0(2)	1236.9(3)	35.5(1)
Se(1)	3935.7(6)	5834.1(3)	−255.1(5)	51.8(2)
Se(2)	2239.8(6)	6256.2(3)	3445.7(5)	50.2(2)
S(1)[a]	2613(2)	7336(1)	886(2)	70(1)
S(2)	90(2)	5972(1)	−17(1)	47(1)
N(1)	5077(4)	6298(2)	2063(4)	41(1)
C(1)	5491(6)	6074(2)	1138(5)	43(1)
C(2)	6953(6)	6062(3)	1253(6)	62(2)
C(3)	7937(6)	6287(3)	2318(6)	71(2)
C(4)	7490(6)	6524(3)	3241(6)	63(2)
C(5)	6037(6)	6525(3)	3086(5)	50(2)
N(2)	3064(5)	5329(2)	2303(4)	47(1)
C(6)	2824(5)	5456(3)	3372(5)	46(1)
C(7)	2983(7)	5021(4)	4261(6)	71(2)
C(8)	3416(9)	4468(4)	4046(9)	99(3)
C(9)	3704(9)	4343(3)	2973(9)	93(3)
C(10)	3512(7)	4788(3)	2120(7)	67(2)
C(11)	1324(6)	7554(2)	1619(5)	49(1)
C(12)[b]	−112(7)	7594(3)	931(6)	66(2)
C(13)	−1100(8)	7758(4)	1475(8)	87(2)
C(14)	−708(10)	7881(3)	2700(9)	88(2)
C(15)	712(11)	7846(3)	3409(7)	95(3)
C(16)[b]	1743(8)	7689(3)	2858(6)	79(2)
C(17)	333(5)	5922(3)	−1502(5)	41(1)
C(18)	552(6)	5375(3)	−1973(5)	53(2)
C(19)	726(8)	5344(3)	−3133(6)	70(2)
C(20)	658(7)	5841(4)	−3821(6)	68(2)
C(21)	429(7)	6388(3)	−3374(6)	65(2)
C(22)	257(6)	6429(3)	−2209(5)	55(2)

[a]Occupancy factor 1.16875.
[b]Occupancy factor 1.01250.

assumed to be pure $Sn(Sepy)_2(SPh)_2$ were as follows: $R1$ = 0.0304 and $wR2$ = 0.0686, Gof = 0.993 for 2756 reflections and 258 parameters; $R1$ = 0.0705 and $wR2$ = 0.0906 for all data. In the final Fourier synthesis, the four top peaks, with electron density range 0.58–0.51, resided around S(1) at distances 0.55–0.80 Å. The changes in the interatomic distances, bond angles, thermal parameters, etc., produced by this assumption are otherwise insignificant.

Tables of anisotropic thermal parameters, hydrogen atom coordinates, selected weighted least-squares planes and selected dihedral angles for **1** and **2** have been deposited as the supplementary material.[5]

[5] Copies of tables of anisotropic thermal parameters, hydrogen atom coordinates, selected weighted least-square planes, selected dihedral angles, and selected closest non-bonded distances for **1** and **2** may be purchased from: the Depository of Unpublished Data, Document Delivery, CISTI, National Research Council Canada, Ottawa, Canada K1A 0S2. The tables of hydrogen atom coordinates have also been deposited with the Cambridge Crystallographic Data Centre, and can be obtained on request from The Director, Cambridge Crystallographic Data Centre, University Chemical Laboratory, 12 Union Road, Cambridge, CB2 1EZ, U.K.

NMR spectra

Proton and ^{13}C-{^1H} NMR spectra of samples in 5 mm o.d. NMR tubes were obtained using Varian Gemini-200 or Varian XL-300 NMR spectrometers. For ^{119}Sn-{^1H}, ^{77}Se-{^1H}, and ^{125}Te-{^1H} NMR, samples were prepared in 10 mm o.d. NMR tubes. These spectra were measured using either the XL-300 spectrometer or a Varian XL-200, depending on availability. Internal references for ^1H and ^{13}C NMR spectra were the solvent residuals. External references for ^{119}Sn, ^{77}Se, and ^{125}Te NMR spectra were neat $SnMe_4$, neat Me_2Se, and neat $SnMe_4$ (ν[^{125}Te for Ph_2Te_2 {0.5 M CH_2Cl_2}]/ν[^{119}Sn for neat $SnMe_4$]) = 0.846 409 ± 0.000 002 at 295 ± 2 K (16) and δ_{Te}(neat Me_2Te, external) = δ_{Te} (Ph_2Te_2 {0.5 M in CH_2Cl_2}) + 422 (17*a*), respectively.

Mass spectrum

The mass spectrum of 2,2′-py_2Te_2 was measured with a Finnigan MAT 8230 spectrometer at 70 eV using isobutane for chemical ionization.

Elemental microanalysis

Carbon, hydrogen, and nitrogen microanalyses were carried out by Guelph Chemical Laboratories Ltd.

Results and discussion

(*i*) PhE'Epy (E' = S or Se; E = Se or Te)

When $Sn(E'Ph)_4$ (E' = S or Se) reacts with py_2E_2 (E = Se or Te), PhE'Epy are possible products. So far as we are aware, no NMR data have been reported for these particular mixed dichalcogenides. Therefore, to facilitate analysis of the reaction mixtures described in the following sections, PhE'Epy were prepared separately from $Ph_2E'_2$ and py_2E_2 and their ^{77}Se and (or) ^{125}Te NMR spectra measured. The results are summarized in Table 4. For the sake of completeness, data for PhTeEpy (E = Se or Te) are included in Table 4 as well, and the table also contains data for the series PhE'EPh, for comparison. Again, all these species were prepared by mixing the symmetrical dichalcogenides. The system Ph_2Te_2:py_2Te_2 was used to confirm[4] δ_{Te} for py_2Te_2.

The rate at which redistribution occurs in $Ph_2E'_2$:py_2E_2 or $Ph_2E'_2$:Ph_2E_2 mixtures depends on the lightest chalcogen in the mixture. At the concentrations used in this study (ca. 0.05 mol/L of solvent) the redistributions are complete in minutes at room temperature (in the time of mixing and initial NMR spectroscopic measurement) when the lightest chalcogen is Te, hours when it is Se, and appear not to have reached equilibrium in weeks when it is S. These rates correlate with the energies of homolytic bond cleavage Te—Te < Se—Se < S—S (*7b*).

The assignments for PhE'ER (R = Ph or py) are straightforward except for the diselenide and ditelluride of formula PhE'Epy. We find that the line widths of R_2Se_2 and R_2Te_2 are reproducibly larger for R = py than for R = Ph, $\Delta\Delta\nu_{1/2(Se)} \approx 2$ Hz and $\Delta\Delta\nu_{1/2(Te)} \approx 16$ Hz, probably because of residual coupling to ^{14}N when R = py. In PhE'Epy (E = E' = Se or Te) the two ^{77}Se or ^{125}Te resonances are of similarly disparate line width and we assign the broader line to the -Epy group.

The ^{77}Se and ^{125}Te resonances of PhE'ER (R = py or Ph; E = Se or Te) show behaviour analogous to Normal Halogen Dependence (19): the shielding of ^{77}Se or ^{125}Te in the ER group depends on the chalcogen E' in the order S < Se < Te. In the ^{77}Se and ^{125}Te NMR spectra (E = ^{77}Se or ^{125}Te), the ratio $[\delta_E(PhSeER) - \delta_E(PhTeER)]/[\delta_E(PhSER) - \delta_E(PhTeER)] = 0.23$ for E = ^{77}Se, R = py or Ph, and 0.30 for ^{125}Te, R = py or Ph, providing the assignment for PhEE'py (E = E' = Se or Te) is made as described above. The invariance of the ratios with R lends support to the proposed assignments. The value of 0.30 for E = ^{125}Te is close to the average found for the analogous ratio in halogen-containing species of a variety of elements (20), while the value of 0.23 for E = ^{77}Se is at the lower end of such values.

(*ii*) $Sn(SPh)_{4-x}(Sepy)_x$

Tin-119 NMR spectra show that four new species, each giving one ^{119}Sn signal with ^{77}Se satellites, are formed sequentially when py_2Se_2 is added to $Sn(SPh)_4$ in gradually increasing amount. The ^{77}Se NMR spectra of the mixtures show a corresponding four signals for selenium attached to tin, which can be assigned from their order of appearance and their $^{117/119}Sn$ satellite splittings. The ^{77}Se NMR spectra also show a signal from pySeSPh (see above) and, in py_2Se_2-rich mixtures, a signal from unreacted diselenide. The formation of pySeSPh shows that PhS^- and $pySe^-$ ligands are interchanging in the $Sn(SPh)_4$:py_2Se_2 mixtures, although the existence of unreacted py_2Se_2 in the equilibrium mixtures, even at the lowest $Sn(SPh)_4$:py_2Se_2 ratio investigated (1:0.5), shows that the interchange is incomplete. Evidently $Sn(SPh)_{4-x}(Sepy)_x$ are being formed according to equilibrium [1], E' = S, E = Se. Table 5 contains ^{119}Sn and ^{77}Se NMR data for $Sn(SPh)_{4-x}(Sepy)_x$.

Table 4. Selenium-77 and ^{125}Te NMR data for PhE'ER (R = py or Ph) and the corresponding symmetrical species in CH_2Cl_2 at ambient probe temperature.

Compound	E',E	δ_{Se}[a]	δ_{Te}[b]
PhE'Epy	S,Se	538.7	
	S,Te		1000
	Se,Se	412.4,[c] 486.9[d]	
	Te,Se	308.5	746
	Se,Te	232.7	839
	Te,Te		361,[c] 456[d]
PhE'EPh	S,Se	522.0	
	S,Te		1016
	Se,Te	257.9	836
	Se,Se	461.0[e]	
	Te,Te		417[f,g]
py_2E_2	—,Se	443.0[h]	
	—,Te		410[g]

[a]Reproducibility ±0.5 ppm.
[b]Reproducibility ±1 ppm or better, except as noted; uncertainty from referencing ±3 ppm.
[c]PhE'- (tentative assignment).
[d]-Epy (tentative assignment).
[e]Earlier ^{77}Se NMR data are available for this compound, e.g., ref 17*b*.
[f]Reproducibility approximately ±5 ppm.
[g]Earlier ^{125}Te NMR data are available for this compound, e.g., ref 17*a*.
[h]δ_{Se} = 439 ($CDCl_3$) (18).

[1] $Sn(E'Ph)_4 + n\ py_2E_2 \rightleftarrows Sn(E'Ph)_{4-x}(Epy)_x + m\ pyE_{2-y}E'Ph_y$ (equilibrium mixture)

The complexes $Sn(SPh)_{4-x}(Sepy)_x$ form more readily for x = 1 or 2 than for x = 3 or 4. The latter two species become major components of the mixtures only in the presence of a significant excess of py_2Se_2, e.g., when py_2Se_2:$Sn(SPh)_4$ = 5.5, the relative amounts of the three species present are $Sn(SPh)_2(Sepy)_2 > Sn(SPh)(Sepy)_3 > Sn(SePy)_4$. Redistribution (equilibrium [2])

[2] $2\ Sn(E'Ph)_{4-x}(Epy)_x \rightleftarrows Sn(E'Ph)_{4-x+1}(Epy)_{x-1} + Sn(E'Ph)_{4-x-1}(Epy)_{x+1}$

is significant for x = 1 and 3, but not for x = 2.

Structural information can be deduced from the *pattern* of ^{119}Sn NMR chemical shifts that is observed for $Sn(SPh)_{4-x}(Sepy)_x$. Defining $\Delta\delta_{Sn}$ (*4-x,4-x-1*) as $\delta_{Sn}[Sn(E'Ph)_{4-x}(ER)_x] - \delta_{Sn}[Sn(E'Ph)_{4-x-1}(ER)_{x+1}]$, the data (Table 5) for the series where E' = S, E' Se, R = py give $\Delta\delta_{Sn}(4,3) = 243$, $\Delta\delta_{Sn}(3,2) = 349$, $\Delta\delta_{Sn}(2,1) = 121$, $\Delta\delta_{Sn}(1,0) = 145$ ppm. Significantly, the values of $\Delta\delta_{Sn}$ (*4,3*) and $\Delta\delta_{Sn}$(*3,2*) are relatively large. A different pattern is observed for $Sn(SPh)_{4-x}(SePh)_4$, $\Delta\delta_{Sn}(4,3) = 41.7$, $\Delta\delta_{Sn}$ (*3,2*) = 44.2, $\Delta\delta_{Sn}$ (*2,1*) = 46.8, $\Delta\delta_{Sn}$ (*1,0*) = 49.5

Table 5. Representative metal and chalcogen NMR data for $Sn(E'Ph)_{4-x}(Epy)_x$ in CH_2Cl_2 at ambient probe temperature.

E′,E	x	δ_{Sn}[a]	δ_{Se}[b]	δ_{Te}[c]	$^1J(^{119}Sn-^{77}Se)$/Hz[d]	$^1J(^{119}Sn-^{125}Te)$/Hz[d]
S,Se	0[e]	49.8				
	1	−192.9	468.6		805	
	2	−542.0	471.0		465	
	3	−663.0	462.4		753	
	4	−808.4	477.8		~870	
Se,Se	0[f]	−132.9	183.3		1584	
	1	−382.1	463.0,[g]249.8[h]		843,[g]1479[h]	
	2	−776.9	490.1,[g]370.1[h]		498,[g]1345[h]	
	3	−794.8	476.8,[g]391.3[h]		741,[h]1378[i]	
S,Te	1	−267.7		772		2128
	2	−694[i]		732		1193
Se,Te	1	−433.2	267.2	745	1394	2245
	2	−839.8	396.2	726	[j]	~1510[k]

[a]Relative to external neat $SnMe_4$ at ambient probe temperature. Reproducibility ±0.5 ppm.
[b]Relative to external neat Me_2Se at ambient probe temperature. Reproducibility ±0.5 ppm.
[c]Converted to external neat Me_2Te as external reference as described in the experimental section. Reproducibility ±1 ppm. Uncertainty due to referencing ±3 ppm.
[d]Reproducibility ±5 Hz or better, except as noted.
[e]Earlier data are available, e.g., refs. 21, 22.
[f]Earlier data are available, e.g., refs. 22, 23.
[g]–Sepy.
[h]–SePh.
[i]±3 ppm.
[j]Could not be observed with certainty at ambient probe temperature; at 213 K, $^1J(^{117/119}Sn-^{77}Se)_{Avg}$ ≈1200 Hz.
[k]$^1J(^{117/119}Sn-^{125}Te)_{Avg}$; at 213 K, $^1J(^{117/119}Sn-^{125}Te)_{Avg}$ ≈1040 Hz.

ppm for E = S, E′ = Se, R = Ph (22). Using previous arguments (4), the difference between the two patterns is associated with initial replacement of SPh^- by *chelating* $Sepy^-$ in the series $Sn(SPh)_{4-x}(Sepy)_x$. A similar process cannot occur in $Sn(SPh)_{4-x}(SePh)_x$. For $Sn(SPh)_{4-x}(Sepy)_x$, bi- for mono-dentate replacement occurs until a coordination number of six is reached, after which SPh^- is replaced by *monodentate* $Sepy^-$. In the series $Sn(SPh)_{4-x}(pyt)_x$ (4), this argument was bolstered by a structure determination for $Sn(\eta^2\text{-pyt})_2(\eta^1\text{-pyt})_2\cdot$pytH. Since only one ^{77}Se NMR signal is observed for $Sn(SPh)_{4-x}(Sepy)_x$ (x = 3 or 4), but ^1J(Sn–Se) is maintained, there must be rapid intramolecular exchange of chelating and monodentate $Sepy^-$ in these complexes at ambient probe temperature. There is no dramatic decrease in the magnitude of the time-averaged ^1J when the monodentate $Sepy^-$ is incorporated, and therefore the monodentate $pySe^-$ must be *Se*-bonded. Thus $Sn(SPh)_{4-x}(Sepy)_x$ should be formulated $Sn(SPh)_3$(Sepy-*N,Se*), $Sn(SPh)_2$(Sepy-*N,Se*)$_2$, Sn(SPh)(Sepy-*N,Se*)$_2$(Sepy-*Se*), and Sn(Sepy-*N,Se*)$_2$(Sepy-*Se*)$_2$ for x = 1 through 4. The formulation of $Sn(SPh)_2$(Sepy-*N,Se*)$_2$ is confirmed by the X-ray structural analysis given below, and that of Sn(SPh)(Sepy-*N,Se*)$_2$(Sepy-*Se*) is given strong support by its co-crystallization with $Sn(SPh)_2$(Sepy-*N,Se*)$_2$ in **2** (see below). Pure $Sn(SPh)_2(Sepy)_2$ cannot be isolated in the presence of $Sn(SPh)(Sepy)_3$ (see Experimental), but it can be isolated in the presence of $Sn(SPh)_3$(Sepy-*N,Se*), presumably because co-crystallization is now prevented by the different shapes of the two complexes. The structure of pure $Sn(SPh)_2$(Sepy-*N,Se*)$_2$, **1**, is described below.

(*iii*) $Sn(SePh)_{4-x}(Sepy)_x$

These complexes are formed in the system $Sn(SePh)_4$:py_2Se_2, according to eq. [1], E′ = E = Se. For $Sn(SePh)_{4-x}(Sepy)_x$, 0 < x < 4, two different sets of ^{77}Se satellites are found around each ^{119}Sn NMR signal, and two ^{77}Se NMR signals are observed for each complex. Assignment can be made on the basis of the relative intensities of the two sets of satellites, together with a knowledge of the expected magnitude of $^1J(^{119}Sn-^{77}Sepy)$ from the series $Sn(SPh)_{4-x}(Sepy)_x$ (Table 5). Tin-119 and ^{77}Se NMR data for $Sn(SePh)_{4-x}(Sepy)_x$ are included in Table 5. It can be seen from the data that ^1J is significantly larger for *Sn–Se*Ph coupling than for *Sn–Se*py. Also, the values of $^1J(^{119}Sn-^{77}Sepy)$ vary irregularly with x. The pattern of $\Delta\delta_{Sn}$ is again $\Delta\delta_{Sn}(4,3)$,$\Delta\delta_{Sn}(3,2) > \Delta\delta_{Sn}(2,1)$, $\Delta\delta_{Sn}(1,0)$ and we conclude that the structures of $Sn(SePh)_{4-x}(Sepy)_x$ parallel those of $Sn(SPh)_{4-x}(Sepy)_x$ discussed above. Then the irregularity observed for $^1J(^{119}Sn-^{77}Sepy)$ must reflect changes in coordination number and ratio of bi- and monodenate $Sepy^-$ ligands.

Equilibrium [1] lies further to the right for E′ = E = Se than for E′ = S, E = Se, e.g., when $Sn(SePh)_4$:py_2Se_2 = 1:0.5, no detectable pySeSePh or py_2Se_2 is found at equilibrium, only Ph_2Se_2. Also, unlike $Sn(SPh)_2(Sepy)_2$, discussed above, $Sn(SePh)_2(Sepy)_2$ *does* undergo significant redistribution, eq. [2], x = 2, and we have been unable to isolate pure

[6] In contrast, distorted dodecahedral coordination has been reported for Sn(2-S-C_5H_3N-3-$SiMe_3$-*N,S*)$_4$ (24).

$Sn(SePh)_2(Sepy)_2$. These observations are consistent with the expectation that replacement of $SePh^-$ by another Se-donor ligand should be easier than replacement of PhS^- by the Se-donor ligand, reflecting the greater ease of oxidation of $SePh^-$.

(*iv*) $Sn(SPh)_{4-x}(Tepy)_x$ (x = 1 or 2)

Mixtures of $Sn(SPh)_4$ and py_2Te_2 or of $Sn(SPh)_2$ and py_2Te_2 are not particularly stable, and some decomposition was evident during the extended periods necessary to obtain both ^{119}Sn and ^{125}Te NMR spectra at either ambient probe temperature or at 213 K. However, we were able to fully characterize $Sn(SPh)_3(Tepy)$ and $Sn(SPh)_2(Tepy)_2$. This appears to be the first evidence for ligand behaviour by $Tepy^-$. The complex $Sn(SPh)_3(Tepy)$ was the major species at $Sn(SPh)_4$:py_2Te_2 = 1:1 or 1:5. Both these mixtures contain both unreacted py_2Te_2 and pyTeSPh, as evidenced by ^{125}Te NMR. Solutions in which $Sn(SPh)_2(Tepy)_2$ is the major species can be made by oxidative addition, eq. [3], E′ = S, but some decomposition is indicated by change of the mixture from pale orange to dark brown with the formation of a black insoluble species.

[3] $Sn(E'Ph)_2 + py_2Te_2 \rightarrow Sn(E'Ph)_{4-x}(Tepy)_x$

(with decomposition)

No evidence was found for $Sn(SPh)(Tepy)_3$ or $Sn(Tepy)_4$ when mixing, and NMR spectral measurements were carried out either at ambient probe temperature or at 213 K.

Sn-119 and ^{125}Te NMR data for $Sn(SPh)_{4-x}(Tepy)_x$ (x = 1 or 2) are included in Table 5. It is important to note that for these complexes the values of $\Delta\delta_{Sn}(4\text{-}x,4\text{-}x\text{-}1)$ ($\Delta\delta_{Sn}(4,3)$ = 318, $\Delta\delta_{Sn}(3,2)$ = 427 ppm) are much larger than the corresponding values found (22) for $Sn(SPh)_{4-x}(TePh)_x$ ($\Delta\delta_{Sn}(4,3)$ = 113, $\Delta\delta_{Sn}(3,2)$ = 139 ppm). This suggests that the first two $pyTe^-$ ligands introduced into $Sn(SPh)_{4-x}(Tepy)_x$ behave as *N,Te*-chelates, but data for the full series $Sn(SPh)_{4-x}(Tepy)_x$ are necessary to strengthen this conclusion. It is *possible* that chelation of $Tepy^-$ in $Sn(SPh)_{4-x}(Tepy)_x$ (x = 1 or 2) may be prevented by steric congestion, but then it is not obvious why $Sn(SPh)_{4-x}(pyTe\text{–}Te)_x$ (x = 3,4) should not be formed, since the analogous $TePh^-$-containing species have been prepared in solution by an oxidative addition (22).

(*v*) $Sn(SePh)_{4-x}(Tepy)_x$

The behaviour of mixtures of $Sn(SePh)_4$ and py_2Te_2 (eq. [2]) or of $Sn(SePh)_2$ and py_2Te_2 (eq. [3]) is generally similar to that of the thiolate analogues, except that here both ^{125}Te and ^{77}Se couple to ^{119}Sn. The mixtures provide ^{119}Sn, ^{125}Te, and ^{77}Se NMR evidence for $Sn(SePh)_{4-x}(Tepy)_x$ (x = 1 or 2), along with unreacted py_2Te_2 and pyTeSePh. In no mixture examined was $Sn(SePh)_2(Tepy)_2$ the major tin-containing species.

Details of the NMR spectra are given in Table 5. The magnitudes of $^1J(^{119}Sn\text{–}^{77}Se)$ and $^1J(^{119}Sn\text{–}^{125}Te)$ are quite different for $Sn(SePh)_3(Tepy)$ and, together with the relative satellite intensities in the ^{119}Sn NMR spectrum, this makes assignment of the ^1J couplings straightforward for this species. Even at 213 K, the ^1J couplings of $Sn(SePh)_2(Tepy)_2$ are not completely resolved, but they are evidently of similar magnitude, and it is possible that the assignments should be reversed.

Again, a comparison of $\Delta\delta_{Sn}(4,3)$ and $\Delta\delta_{Sn}(3,2)$ for phenyl (22) and 2-pyridyl analogues shows that $pyTe^-$ is most probably behaving in a chelating manner: the values are 302 and 410 ppm for $Sn(SePh)_{4-x}(Tepy)_x$ and 89 and 102 ppm for $Sn(SePh)_{4-x}(TePh)_x$.

Fig. 1. Perspective view of the molecule $Sn(SPh)_2(2\text{-}Se\text{-}C_5H_4N\text{-}N,Se)_2$.

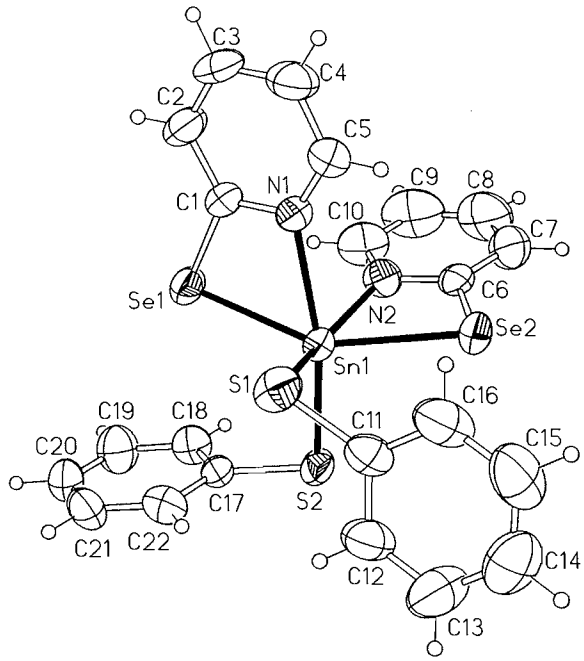

(vi) Structure of $Sn(SPh)_2(Sepy)_2$, 1

The crystal structure of **1** consists of discrete $Sn(SPh)_2(Sepy)_2$ molecules. The closest approach is 2.267 Å between H(16) and H(12) (x − 0.5, 1.5 − y, z − 0.5). Figure 1 shows a perspective view of the molecule and gives the numbering scheme. The bond distances and bond angles are given in Table 6.

Monomeric $Sn(SPh)_2(Sepy)_2$ has the structure $Sn(SPh)_2(C_5H_4NSe\text{-}N,Se)_2$, with bidentate chelating $pySe^-$ ligands. This confirms the conclusion reached from the ^{119}Sn NMR data. There is distorted octahedral coordination about the Sn, with the two S atoms mutually *cis*, the two Se atoms mutually *trans*, and the two N atoms mutually *cis*. The configuration is very similar to that found for $Sn(C_5H_4NS\text{-}N,S)_2Cl_2$, **3** (24), and for $Sn(C_5H_4NS\text{-}N,S)_2(C_5H_4NS\text{-}S)_2$, **4**, in $Sn(pyt)_4pytH$ (4), but quite different from the distorted dodecahedral structure of $Sn(2\text{-}S\text{-}C_5H_3N\text{-}3\text{-}SiMe_3\text{-}N,S)_4$ (25) or the *trans*-diorganyl grossly distorted octahedral (or distorted tetrahedral (26)) structures of various complexes $R_2Sn(pyt)_2$ (R = Me (27), *c*-C_6H_{11} (28), or Ph (29)) and $Bu^n{}_2Sn(2\text{-}S\text{-}5\text{-}NO_2\text{-}C_5H_3)_2$ (26).

The Sn—S distances of 2.464(2) and 2.475(2) Å are very similar to those of the monodentate pyt^- ligands in **4** (4), but slightly lower than those of $Sn(SPh)_4(bipy)$, which range from 2.497(1) to 2.502(1) Å (30) Similarly, the Sn—N distances of 2.325(5) and 2.333(5) Å are identical within experimental uncertainty to those of the chelating ligands in **4**. They are, however, slightly larger than those of **3** (2.271(9) and 2.256(9) Å), and much smaller than the values found (26–29)

Table 6. Bond distances and angles for $Sn(SPh)_2(C_5H_4NSe\text{-}N,Se)_2$, **1**.

(*a*) Bond distances

Atom		Distance	Atom		Distance	Atom		Distance
1	2	(Å)	1	2	(Å)	1	2	(Å)
Sn	Se(1)	2.6291(8)	Sn	S(1)	2.475(2)	Sn	N(1)	2.325(5)
Sn	Se(2)	2.6358(8)	Sn	S(2)	2.464(2)	Sn	N(2)	2.333(5)
Se(1)	C(1)	1.891(6)	S(1)	C(11)	1.769(8)	N(1)	C(1)	1.332(8)
Se(2)	C(6)	1.892(7)	S(2)	C(17)	1.783(6)	N(1)	C(5)	1.347(8)
N(2)	C(6)	1.360(8)	N(2)	C(10)	1.320(9)	C(1)	C(2)	1.392(9)
C(2)	C(3)	1.353(10)	C(3)	C(4)	1.372(11)	C(4)	C(5)	1.376(10)
C(6)	C(7)	1.371(10)	C(7)	C(8)	1.352(12)	C(8)	C(9)	1.376(13)
C(9)	C(10)	1.355(11)	C(11)	C(12)	1.366(10)	C(11)	C(16)	1.379(10)
C(12)	C(13)	1.352(11)	C(13)	C(14)	1.365(12)	C(14)	C(15)	1.372(13)
C(15)	C(16)	1.424(13)	C(17)	C(18)	1.371(9)	C(17)	C(22)	1.376(9)
C(18)	C(19)	1.401(9)	C(19)	C(20)	1.361(10)	C(20)	C(21)	1.359(10)
C(21)	C(22)	1.392(10)						

(*b*) Bond angles

Atom			Angle	Atom			Angle	Atom			Angle
1	2	3	(deg)	1	2	3	(deg)	1	2	3	(deg)
N(1)	Sn	N(2)	79.8(2)	N(1)	Sn	S(2)	163.98(13)	N(2)	Sn	S(2)	95.30(14)
N(1)	Sn	S(1)	86.79(13)	N(2)	Sn	S(1)	158.35(14)	N(2)	Sn	S(1)	101.95(7)
N(1)	Sn	Se(1)	65.93(12)	N(2)	Sn	Se(1)	88.24(13)	S(2)	Sn	Se(1)	98.89(5)
S(1)	Sn	Se(1)	101.74(5)	N(1)	Sn	Se(2)	93.35(12)	N(2)	Sn	Se(2)	65.78(13)
S(2)	Sn	Se(2)	98.53(5)	S(1)	Sn	Se(2)	98.47(5)	Se(1)	Sn	Se(2)	149.86(3)
C(1)	Se(1)	Sn	78.5(2)	C(6)	Se(2)	Sn	79.5(2)	C(11)	S(1)	Sn	98.4(2)
C(17)	S(2)	Sn	99.2(2)	C(1)	N(1)	C(5)	121.2(6)	C(1)	N(1)	Sn	102.4(4)
C(5)	N(1)	Sn	136.2(5)	N(1)	C(1)	C(2)	120.2(6)	N(1)	C(1)	Se(1)	113.1(5)
C(2)	C(1)	Se(1)	126.6(5)	C(3)	C(2)	C(1)	118.7(7)	C(2)	C(3)	C(4)	121.1(7)
C(3)	C(4)	C(5)	118.5(7)	N(1)	C(5)	C(4)	120.3(7)	C(10)	N(2)	C(6)	119.3(6)
C(10)	N(2)	Sn	137.8(5)	C(6)	N(2)	Sn	102.9(4)	N(2)	C(6)	C(7)	119.6(7)
N(2)	C(6)	Se(2)	111.8(5)	C(7)	C(6)	Se(2)	128.6(6)	C(8)	C(7)	C(6)	119.7(8)
C(7)	C(8)	C(9)	120.8(8)	C(10)	C(9)	C(8)	116.9(9)	N(2)	C(10)	C(9)	123.7(8)
C(12)	C(11)	C(16)	119.1(8)	C(12)	C(11)	S(1)	120.9(6)	C(16)	C(11)	S(1)	120.0(6)
C(13)	C(12)	C(11)	122.3(8)	C(12)	C(13)	C(14)	120.8(9)	C(13)	C(14)	C(15)	118.7(9)
C(14)	C(15)	C(16)	120.9(8)	C(11)	C(16)	C(15)	118.2(8)	C(18)	C(17)	C(22)	119.9(6)
C(18)	C(17)	S(2)	120.0(5)	C(22)	C(17)	S(2)	120.1(5)	C(17)	C(18)	C(19)	120.3(7)
C(20)	C(19)	C(18)	119.2(7)	C(21)	C(20)	C(19)	120.8(7)	C(20)	C(21)	C(22)	120.6(7)
C(17)	C(22)	C(21)	119.2(7)								

for the diorganyltinbis(pyridine-2-thiolates) (2.636(4) −2.77(1) Å), consistent with the *semi*-chelating nature of the *N,S* ligand in the latter. The Sn—Se distances, 2.6291(8) and 2.6358(8) Å, are comparable to the values of 2.648(3)–2.669(3) Å observed in the octahedral anion of $(Ph_4As)_2[Sn\{Se_2C{=}C(CN)_2\}_3]$ (31), but longer than analogous distances observed in various tetrahedral species of the general type $Sn(SeR)_4$ (32, 33), as expected.

The geometry of the $Sepy^-$ ligands is unexceptional (5, 6). The bite of the ligands observed in **1**, 65.78(13)° and 65.93(12)° falls outside the range of 58.9(4)°–62.9(4)° found for polymeric $Cd(Sepy)_2$ (6*a*). The Sn-Se-C angles of **1**, 78.5(2)° and 79.5(2)°, are similar to the corresponding intrachelate angles in $Cd(Sepy)_2$, 77.5(5)° and 76.5(6)° (6*a*), but smaller than the corresponding angles found (33) in either form of $Sn(SePh)_4$ (96.0(3)° and 96.5(3)° in the orthorhombic form, 95.1(3)° and 95.7(3)° in the monoclinic form), consistent with the formation of a small chelate ring in **1**. The intrachelate Sn-N-C angles of **1**, 102.4(4)° and 102.9(4)°, are slightly larger than the corresponding angles found for the chelate rings of either **3** (98.1(7)° and 100.0(7)°) or **4** (99.6(4)° and 98.5(4)°). This is consistent with the presence of a longer Sn–chalcogen bond in the chelate rings of **1** than in those of **3** or **4**.

(*vii*) Structure of $Sn(SPh)_{1.85}(Sepy)_{2.15}$, 2

Overall, the structure of the neutral molecule that provides a solution in the X-ray analysis of **2** is remarkably similar to that

Table 7. Bond distances and angles for $Sn(SPh)_{1.85}$ $(2\text{-}Se\text{-}C_5H_4N)_{2.15}$, **2**.

(*a*) Bond distances

Atom		Distance	Atom		Distance	Atom		Distance
1	2	(Å)	1	2	(Å)	1	2	(Å)
Sn	Se(1)	2.6301(8)	Sn	S(1)	2.486(2)	Sn	N(1)	2.324(4)
Sn	Se(2)	2.6360(8)	Sn	S(2)	2.466(2)	Sn	N(2)	2.336(4)
Se(1)	C(1)	1.886(5)	S(1)	C(11)	1.790(6)	N(1)	C(1)	1.340(6)
Se(2)	C(6)	1.889(6)	S(2)	C(17)	1.782(5)	N(1)	C(5)	1.337(7)
N(2)	C(6)	1.340(7)	N(2)	C(10)	1.326(7)	C(1)	C(2)	1.396(7)
C(2)	C(3)	1.375(8)	C(3)	C(4)	1.367(9)	C(4)	C(5)	1.376(8)
C(6)	C(7)	1.374(8)	C(7)	C(8)	1.354(11)	C(8)	C(9)	1.366(11)
C(9)	C(10)	1.359(9)	C(11)	C(12)	1.373(8)	C(11)	C(16)	1.366(8)
C(12)	C(13)	1.357(9)	C(13)	C(14)	1.346(10)	C(14)	C(15)	1.366(11)
C(15)	C(16)	1.394(10)	C(17)	C(18)	1.379(8)	C(17)	C(22)	1.378(8)
C(18)	C(19)	1.384(8)	C(19)	C(20)	1.348(9)	C(20)	C(21)	1.370(9)
C(21)	C(22)	1.390(8)						

(*b*) Bond angles

Atom			Angle	Atom			Angle	Atom			Angle
1	2	3	(deg)	1	2	3	(deg)	1	2	3	(deg)
N(1)	Sn	N(2)	80.1(2)	N(1)	Sn	S(2)	164.15(11)	N(2)	Sn	S(2)	94.94(12)
N(1)	Sn	S(1)	86.68(11)	N(2)	Sn	S(1)	158.57(12)	S(2)	Sn	S(1)	102.02(6)
N(1)	Sn	Se(1)	66.06(11)	N(2)	Sn	Se(1)	88.52(12)	S(2)	Sn	Se(1)	98.95(4)
S(1)	Sn	Se(1)	101.54(4)	N(1)	Sn	Se(2)	93.14(11)	N(2)	Sn	Se(2)	65.56(12)
S(2)	Sn	Se(2)	98.53(4)	S(1)	Sn	Se(2)	98.67(4)	Se(1)	Sn	Se(2)	149.79(3)
C(1)	Se(1)	Sn	78.5(2)	C(6)	Se(2)	Sn	79.1(2)	C(11)	S(1)	Sn	98.4(2)
C(17)	S(2)	Sn	98.8(2)	C(1)	N(1)	C(5)	121.2(5)	C(1)	N(1)	Sn	102.0(3)
C(5)	N(1)	Sn	136.5(4)	N(1)	C(1)	C(2)	119.7(5)	N(1)	C(1)	Se(1)	113.4(4)
C(2)	C(1)	Se(1)	126.8(4)	C(3)	C(2)	C(1)	118.8(6)	C(2)	C(3)	C(4)	120.6(6)
C(3)	C(4)	C(5)	118.5(6)	N(1)	C(5)	C(4)	121.2(6)	C(10)	N(2)	C(6)	119.9(5)
C(10)	N(2)	Sn	137.3(4)	C(6)	N(2)	Sn	102.7(4)	N(2)	C(6)	C(7)	120.3(6)
N(2)	C(6)	Se(2)	112.6(4)	C(7)	C(6)	Se(2)	127.0(5)	C(8)	C(7)	C(6)	118.8(7)
C(7)	C(8)	C(9)	121.0(8)	C(10)	C(9)	C(8)	117.8(8)	N(2)	C(10)	C(9)	122.2(7)
C(12)	C(11)	C(16)	118.8(6)	C(12)	C(11)	S(1)	120.0(5)	C(16)	C(11)	S(1)	121.2(5)
C(13)	C(12)	C(11)	120.6(6)	C(12)	C(13)	C(14)	121.2(8)	C(13)	C(14)	C(15)	119.6(8)
C(14)	C(15)	C(16)	119.8(7)	C(11)	C(16)	C(15)	119.9(7)	C(18)	C(17)	C(22)	119.3(5)
C(18)	C(17)	S(2)	120.6(4)	C(22)	C(17)	S(2)	120.1(5)	C(17)	C(18)	C(19)	119.7(6)
C(20)	C(19)	C(18)	120.9(7)	C(21)	C(20)	C(19)	120.2(6)	C(20)	C(21)	C(22)	119.8(6)
C(17)	C(22)	C(21)	120.0(6)								

observed for **1**. Selected bond distances and angles are given in Table 7, using the same numbering scheme as in Fig. 1. The agreement factors, estimated standard deviations, residual electron density, thermal parameters, etc. indicate that this is a very good X-ray analysis (34, 35). Indeed, if considered in isolation, the X-ray analysis could easily be mistaken for that of **1**; only the NMR and elemental analytical data (see experimental section) tell us that the compound is not **1**. There is, however, a discrepancy involving the Sn—S distances. In **2**, the Sn—S(1) distance exceeds the Sn—S(2) distance by more than in **1** ($\Delta/\sigma = 7.1$ vs. 3.9). As well, if the data measured here are interpreted as due to **1**, there is excess electron density in the vicinity of S(1) (see Experimental). The data are of sufficiently high quality that these admittedly minor discrepancies warrant further discussion.

We can account for the anomalies occurring in **2** as follows: since the Sn—S(2) distances of **1** and **2** are identical (2.466(2) vs. 2.464(2) Å), there is no disorder involving S(2)Ph; partial occupation of the SPh site by Sepy occurs only at S(1)SPh. In our refinement we allowed the pyridyl group of the contaminant to occupy its two possible orientations with equal probability. Since the Sn—Se bond length will exceed the Sn—S bond length, incorporation of 15% of Sepy extends Sn—S(1) in the (average) molecule, which provides a solution for the data. Incorporating the disorder also has the effect of removing the excess electron density in the vicinity of S(1) (see Experimental). It is noteworthy that substitution of Sepy for SPh occurs at only one of the two chemically identical, though crystallographically distinct (see above), SPh sites of $Sn(Sepy)_2(SPh)_2$. Selective substitution of this type has been

observed in other instances (for recent reviews, see ref. 36).

The proof of co-crystallization and resulting disorder in **2** provides another example in support of the crystallographers' maxim, formalized by Parkin (36), that extra caution must be exercised if there are any unusual measured bond lengths. When in doubt, evidence from spectroscopic and chemical analysis should be sought to correctly formulate compounds and to understand the crystallographic anomaly.

It is evident that in order for $Sn(Sepy)_2(SPh)_2$ and $Sn(Sepy)_3(SPh)$ to co-crystallize as **2** in the manner detected, the structure of $Sn(Sepy)_3(SPh)$ must be the same as that of $Sn(Sepy)_2(SPh)_2$ in **1**, i.e., it must be *cis*-$Sn(\eta^2\text{-Sepy})_2(\eta^1\text{-Sepy})(SPh)$. Thus the formulation $Sn(\eta^2\text{-Sepy})_2(\eta^1\text{-Sepy})(SPh)$ proposed from the pattern of ^{119}Sn NMR chemical shifts (see above) is confirmed.

Acknowledgments

This work was made possible by funding from the Natural Sciences and Engineering Research Council of Canada in the form of an Individual Research Grant to P.A.W.D. and an Equipment Grant to the Department of Chemistry for the purchase of the Siemens service X-ray diffractometer. We thank Professor N.C. Payne for access to the Enraf–Nonius X-ray diffractometer, and we are grateful to S. England and V.M. Richardson of this department for expert technical assistance in obtaining some of the NMR spectra.

References

1. J.M. Rawson and R.E.P. Winpenny. Coord. Chem. Rev. **139**, 313 (1995).
2. E.S. Raper. Coord. Chem. Rev. **61**, 143 (1985).
3. R.S. Vagg. *In* Comprehensive coordination chemistry. Vol. 2. *Edited by* G. Wilkinson, R.D. Gillard, and J.A. McCleverty. Pergamon, Oxford. 1987. Chap. 20.4, p. 800.
4. L.C. Damude, P.A.W. Dean, V. Manivannan, R.S. Srivastava, and J.J. Vittal. Can. J. Chem. **68**, 1323 (1990).
5. D.V. Khasnis, M. Buretea, T.J. Emge, and J.G. Brennan. J. Chem. Soc. Dalton Trans. 45 (1995).
6. Y. Cheng, T.J. Emge, and J.G. Brennan. (*a*) Inorg. Chem. **33**, 3711 (1994); (*b*) Inorg. Chem. **35**, 342 (1996)
7. J.E. Huheey, E.E. Keiter, and R.L. Keiter. Inorganic chemistry. 4th ed. HarperCollins, New York. 1993. (*a*) p.346ff, and refs. therein; (*b*) Appendix E, and refs. therein.
8. L. Field. *In* Organic chemistry of sulfur. *Edited by* S. Oae. Plenum, New York. 1977. Chap. 7.
9. A. Toshimitsu, H. Owada, K. Terao, S. Uemura, and M. Okano. J. Org. Chem. **49**, 3796 (1984).
10. R. Kumar, H.E. Mabrouk, and D.G. Tuck. J. Chem. Soc. Dalton Trans. 1045 (1988).
11. J.J.I. Arsenault and P.A.W. Dean. Can. J. Chem. **61**, 1516 (1983).
12. F.P. Colonna, G. Distefano, V. Galasso, K. Irgolic, G.C. Pappalardo, and L. Pope. J. Chem. Soc. Perkin Trans. 2, 281. (1981).
13. S.J. Dunne, L.A. Summers, and E.I. von Nagy-Felsobuki. J. Heterocycl. Chem. **30**, 409 (1993).
14. (*a*) XSCANS. Version 2.1, Siemens Analytical X-Ray Instruments Inc., Madison, Wisconsin, U.S.A. 1994; (*b*) CAD4 Diffractometer Manual. Version 5, Enraf–Nonius Delft, Delft, The Netherlands. April 1988.
15. SHELXTL Version 5.0 Reference Manual. Siemens Analytical X-Ray Instruments Inc., Madison, Wisconsin, U.S.A. 1994.
16. P.A.W. Dean, V. Manivannan, and J.J. Vittal. Inorg. Chem. **28**, 2360 (1989).
17. C. Rodger, N. Sheppard, H.C.E. McFarlane, and W. McFarlane. *In* NMR and the periodic table. *Edited by* R.K. Harris and B.E. Mann. Academic, London. 1978. Chap. 12. (*a*) Table 12.11 and refs. therein; (*b*) Table 12.7 and refs. therein.
18. S.J. Dunne. Ph.D. Thesis, University of Newcastle, New South Wales, Australia. 1992. Chap. 6, p. 212.
19. C.J. Jameson and J. Mason. *In* Multinuclear NMR. *Edited by* J. Mason. Plenum, New York. 1987. Chap. 12, p. 71, and refs. therein.
20. R.G. Kidd. Annu. Rep. NMR Spectrosc, **10**, 5 (1980).
21. J.D. Kennedy and W. McFarlane. J. Chem. Soc. Perkin Trans. 2, 146 (1974).
22. P.A.W. Dean and R.S. Srivastava. Inorg. Chim. Acta, **105**, 1 (1985).
23. J.D. Kennedy, W. McFarlane, G.S. Pyne, P.L. Clarke, and J.L. Wardell. J. Chem. Soc. Perkin Trans. 2, 1234 (1975).
24. M. Masaki, S. Matsunami, and H. Ueda. Bull. Chem. Soc. Jpn. **51**, 3298 (1978).
25. E. Block, G. Ofori-Okai, H. Kang, J. Wu, and J. Zubieta. Inorg. Chim. Acta, **190**, 5 (1991).
26. G. Domazetis, B.D. James, M.F. Mackay, and R.J. Magee. J. Inorg. Nucl. Chem. **41**, 1555 (1979).
27. M.V. Castano, A. Macias, A. Castineiras, A.S. Gonzalez, E.G. Martinez, J.S. Casas, J. Sordo, W. Hiller, and E.E. Castellano. J. Chem. Soc. Dalton Trans. 1001 (1990)
28. M. Boualam, J. Meunier-Piret, M. Biesemans, R.Willem, and M. Gielen. Inorg. Chim. Acta, **198**, 249 (1992).
29. R. Schmiedgen, F. Huber, and H. Preut. Acta Crystallogr. Sect. C: Cryst. Struct. Commun. **C49**, 1735 (1993).
30. J.L. Hencher, M. Khan. F.F. Said, R. Sieler, and D.G. Tuck. Inorg. Chem. **21**, 2787 (1982).
31. D. Gruss and H.-U. Hummel. Acta Crystallogr. Sect. C: Cryst. Struct. Commun. **C49**, 1307 (1993).
32. A.G. Osborne, R.E. Hollands, R.F. Bryan, and S. Lockhart. J. Organometal. Chem. **226**, 129 (1982).
33. D.H.R. Barton, H. Dadoun, and A. Gourdon. Nouv. J. Chim. **6**, 53 (1982).
34. P.G. Jones. Chem. Soc. Rev. **13**, 157 (1984).
35. D. Watkin. Acta Crystallogr. Sect. A: Found. Crystallogr. **A50**, 411 (1994).
36. G. Parkin. Chem. Rev. **93**, 887 (1993); Acc. Chem. Res. **25**, 455 (1992); Adv. Inorg. Chem. **42**, 291 (1993).

Ionically conducting polyether composites

J.R. Stevens and W. Wieczorek

Abstract: Ionic conductivity in polymer–salt electrolytes occurs in the amorphous regions of the complex. Poly(ethylene oxide) (PEO) is the best polyether for complexing salts. Unfortunately, it is partially crystalline at ambient temperatures. With inorganic (i.e., alumina) or organic (i.e., poly(acrylamide) (PAAM)) fillers the crystallization of PEO is inhibited and the room temperature conductivity is enhanced in these mixed phase systems by over two orders of magnitude (to $\sim 10^{-4}$ S/cm) above the base PEO–salt system ($<10^{-6}$ S/cm). Even adding PAAM to an initially amorphous system (oxymethylene-linked PEO–$LiClO_4$) increases the room temperature conductivity by 2 to 3 times. Various alkali metal salts (Li, Na) and NH_4SCN are used with α-Al_2O_3, θ-Al_2O_3, PAAM′ and poly(*N,N*′-dimethyl acrylamide) as fillers. The aluminas stiffen the complex and increase T_g. The addition of the organic fillers lowers T_g, as is to be preferred. It is suggested that changes in the conductivity with changes in salt and filler concentration are due to changes in the ultrastructure and morphology and are the result of an equilibrium between various Lewis acid – Lewis base reactions. Qualified success has been achieved in modelling ionic conductivity in these composite electrolyte systems using an effective medium approach. In this approach it has been assumed that the main conductivity enhancement takes place in thin amorphous layers of the polyether that coat the dispersed polyacrylamide particles separated in a microphase. In the best complexes this layer is identified by a second T_g.

Key words: polyethers, composites, ionic conductivity, phase structure, Lewis acids and bases.

Résumé : La conductivité ionique des électrolytes de la forme sel de polymères se produit dans les régions amorphes du complexe. Le poly(oxyde d'éthylène) («PEO») est le meilleur éther pour la complexation des sels. En présence de garnitures inorganiques (par exemple, de l'alumine) ou organique (par exemple, le poly(acrylamide) (PAAM)), la cristallisation du «PEO» est inhibé; dans ces systèmes de phases mixtes, la conductivité à la température ambiante est de deux ordres de grandeur plus élevée (rehaussée à environ 10^{-4} S/cm) que celle du système de base «PEO»–sel ($<10^{-6}$ S/cm). Même l'addition de PAAM à un système initialement amorphe («PEO»–$LICIO_4$ lié par de l'oxyméthylène) provoque une augmentation (par des facteurs de deux à trois) de la conductivité à la température ambiante. Divers sels de métaux alcalins (Li, Na), de même que la NH_4SCN, peuvent être utilisés comme garnitures de concert avec de l'α-Al_2O_3, du θ-Al_2O_3, du PAAM et du poly (*N,N*′-diméthyl acrylamide). Les alumines solidifent le complexe et augmentent la valeur de T_g. Comme on peut l'espérer, l'addition de garnitures organiques diminue la valeur de T_g. Il a été suggéré que les changements dans la conductivité associés à des changements dans la concentration en sel et en garniture sont dus à des changements dans l'ultrastructure et la morphologie et qu'ils sont le résultat d'un équilibre entre diverses réactions d'acides et de bases de Lewis. Utilisant une approche faisant intervenir le milieu effectif, on a obtenu des résultats mitigés dans le modelage de la conductivité ionique dans ces systèmes électrolytes composites. Dans cette approche, on fait l'hypothèse que l'augmentation principale de la conductivité se produit dans des couches minces amorphes de polyéther qui recouvrent les particules dispersées de polyacrylamide séparées dans une microphase. Dans les meilleurs complexes, cette couche est identifiée par une deuxième valeur de T_g.

Mots clés : polyéthers, composite, conductivité ionique, structure de la phase, acides et bases de Lewis.

[Traduit par la rédaction]

Introduction

Polymer electrolytes are complexes of electronodonor polymers with various inorganic or organic salts or acids (1). The entropic and enthalpic characteristics of the polymer–salt system should promote the dissociation of the dopant salt or acid. For cation solvation it is necessary for the polymer to contain series of heteroatoms each with lone electron pairs (usually O, N, S) that have inter or intramolecular spacings in the polymer matrix conducive to the coordination of the heteroatoms with the acceptor cations. The anions are only weakly coordinated, if at all; they usually simply "dig" into the polymer matrix.

In these systems ionic transport mainly occurs through a coupling of the ions with relaxing polymer segments in the amorphous regions of a highly viscoelastic material; high cationic transport numbers and fast structural and ion relaxation times are important. Another requirement is, then, that the amorphous regions of the material be as far above the liquid–glass transition as possible in the operating temperature and pressure range. The final requirement is structural and chemical stability; such characteristics as degradation, moisture absorption, phase separation, and crystallization over time would be detrimental to a useful polymer electrolyte.

The most intensely studied polymer electrolytes (2–5) are based on poly(oxa alkanes), poly(aza alkanes), or poly(thia alkanes). These studies are motivated by the possibility of a variety of applications among which are (*i*) solid state primary

Received February 6, 1996.

This paper is dedicated to Professor Howard C. Clark in recognition of his contributions to Canadian chemistry.

J.R. Stevens[1] and W. Wieczorek. Department of Physics, University of Guelph, Guelph, ON N1G 2W1, Canada.

[1] Author to whom correspondence may be addressed. (Telephone: (519) 824-4120, Ext. 3852. Fax: (519) 836-9967. E-mail: jrsteven@uoguelph.ca

and secondary microbatteries with a lithium or lithium alloy anode and a composite cathode containing intercalated materials, (*ii*) electrochemical sensors, and (*iii*) electrochromic devices (displays and "smart" windows). The range of conductivities depends on the kind of application and is $10^{-3} - 10^{-4}$ S/cm for batteries; conductivities can be lower for sensors and electrochromic applications.

This report deals with polymer electrolytes based on poly(oxa alkanes) or polyethers and particularly on poly(ethylene oxide) (PEO) based composites complexed with alkali metal salts (Li, Na) and NH_4SCN. These materials have a complicated phase structure consisting of an amorphous phase, a crystalline phase, and at least one in a range of crystalline complex phases formed between the incorporated polymers and the salt. The contribution of each particular phase to the conduction process changes with temperature, causing difficulties in the interpretation of experimental results; the mechanism for ionic conductivity in polymeric electrolytes has yet to be established. PEO is unfortunately about 70% crystalline at ambient temperatures with conductivities in the low range of $10^{-7} - 10^{-8}$ S/cm. The volume of flexible amorphous phase and the ionic conductivity increase dramatically as the polyether melts. For polymer–salt complexes the melting temperatures range between 65°C and 140°C depending on the salt concentration. However, at temperatures exceeding the melting point the mechanical and electrochemical stability of these electrolytes deteriorates.

Since chains containing ethylene oxide (EO) provide just the right spacing and solvation properties to coordinate and encapsulate suitable cations, considerable work has been done to synthesize EO configurations that limit or eliminate crystallization. This research has taken three main directions. The first is to limit the length of the chain segments containing EO monomeric units to between 4 and 15. Such lengths are long enough to effectively complex alkali metal cations but too short to effectively crystallize. Examples are polymer networks, random and block EO – propylene oxide (PO) copolymers, randomly variable length segments of PEO joined by methyleneoxide units, and comblike systems with short chain EO or EO–PO sequences as the comb "teeth" and backbones like poly(dimethyl siloxane) and poly(phosphazene) (5). The second is to use plasticizing salts that form complexes with low-temperature eutectics with the pristine PEO phase, and the third is to add fillers that reduce the crystallizing tendencies of the PEO polymer host.

From the point of view of ease of preparation as well as commercial application the third idea is the simplest. Generally two types of composite polymeric electrolytes are considered. The first is based on inhomogeneous mixtures of polymer and inorganic or organic additives that are not dissolved in a common low molecular weight volatile solvent. These are mixed phase systems and are the subject of this study. Examples of organic additives, and the ones used here, are poly(*N,N'*-dimethylacrylamide) (NNPAAM) and polyacrylamide (PAAM). Hydrogen bonding is possible in PAAM composites but not in NNPAAM composites since NNPAAM lacks an amidic hydrogen. Blend-based composite polymeric electrolytes are the second type (6, 7). Examples are systems obtained by the dissolution of two (usually high molecular weight) components in an appropriate solvent followed by the evaporation of the solvent; miscible or partially miscible blends of both components are formed. In the present work the application of solid inorganic and organic additives is explored in an attempt to prevent crystallization and to enhance the ionic conductivity over that for the basic PEO–salt system. The overall objective has been to understand the role of the filler additives (organic and inorganic powders and high molecular weight polymers with special properties) in ionic conduction in these composite PEO-based electrolytes. Various aspects of this work have been reported previously in different publications (8–12). This paper assembles all of the relevant results from these publications for the purpose of discussing and comparing physical and chemical properties. Gray has reported studies using low molecular weight additives with the objective of improving the mechanical properties of PEO-based electrolytes (3, 6).

Experimental

Sample preparation

NNPAAM ($M_w = 1.3 \times 10^5$, Polysciences, reagent grade) and PEO (Aldrich, reagent grade, $M_w = 5 \times 10^6$) were used without further purification and after drying under vacuum ($<10^{-4}$ Torr; 1 Torr = 133.3 Pa) at 50–70°C for 48 h. The synthesis of oxymethylene-linked PEO (OMPEO) followed that of Nicholas et al. (13). The resulting transparent elastomers were dried under vacuum for 48 h before synthesizing the polymer electrolyte. Polyacrylamide PAAM ($M_w = 1.6 \times 10^5$) was prepared by the free radical polymerization of acrylamide (Aldrich, reagent grade) using benzoyl peroxide (Aldrich reagent grade) as initiator. The product was dried under vacuum at 100°C for 48 h. Commercially available α-Al_2O_3(Aldrich reagent grade, fraction with grain sizes less than 5 μm) and θ-Al_2O_3 (with grain sizes less than 2 μm) were used as inorganic fillers. Amorphous aluminum oxide θ-Al_2O_3 was obtained by thermal dehydration of aluminum hydroxide performed at 1100°C. The details concerning the preparation of these inorganic fillers as well as the separation of these fillers into fraction of different grain sizes have been described elsewhere (14, 15). Acetonitrile (Aldrich, reagent grade) was doubly distilled and stored over type 4A molecular sieves. All of the steps in the preparation procedure were performed in an argon-filled drybox (moisture content lower than 20 ppm). $LiClO_4$ (Aldrich, reagent grade), $NaClO_4$ (Aldrich, reagent grade), NH_4SCN (Aldrich, reagent grade), and NaI (Aldrich, reagent grade) were dried under vacuum ($<10^{-4}$ Torr) at 120°C prior to incorporation. The concentration of salts was equal to 10 mol% with respect to the ether oxygen concentration. The solid components were mixed in appropriate amounts in a small glass reactor and then acetonitrile was added to form an approximately 5 mass% suspension with respect to all solid components. The mixture was magnetically stirred until a homogenous suspension was obtained. Excess acetonitrile was removed by vacuum distillation. The composite electrolytes obtained were dried under vacuum ($<10^{-4}$ Torr) for 48–72 h at 60°C. The concentration of fillers in the composite electrolytes varied between 5 and 50 vol%. All samples were equilibrated at ambient temperature for at least a month before undertaking any experiments.

DSC studies

DSC data were obtained between –110 and 150°C using a

Fig. 1. Comparison of the temperature dependence of ionic conductivity measured for [○] $(PEO)_{10}NaI$ electrolyte and [●] $(PEO)_{10}NaI$–θ-Al_2O_3 (10 mass%) composite electrolyte.

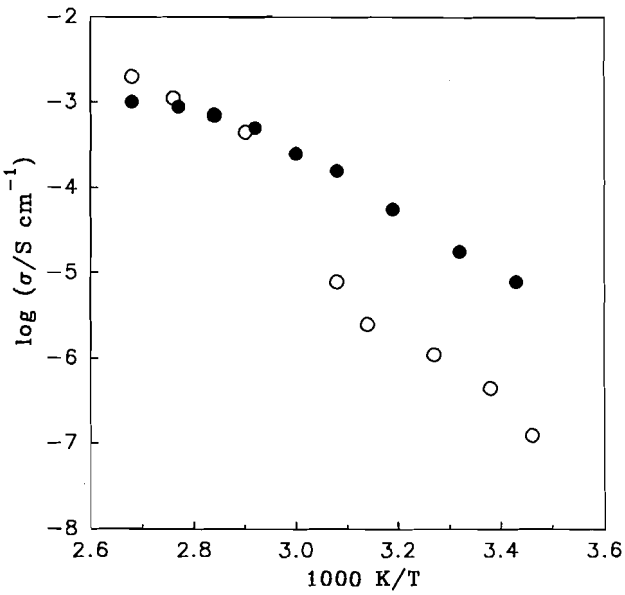

DuPont TA 2910 scanning calorimeter with a low-temperature measuring head and liquid nitrogen cooled heating element. Approximately 15 mg samples in aluminum pans were stabilized by slow cooling to –110°C and then heated at 10°C/min to 150°C. An empty aluminum pan was used as a reference.

Conductivity measurements

Ionic conductivity was determined using the complex impedance method in the temperature range –20 to 100°C. The samples were sandwiched between stainless steel blocking electrodes and placed in a temperature-controlled furnace. The impedance measurements were carried out on a computer-interfaced HP 4192 impedance analyzer over the frequency range 5–13 MHz. The peak-to-peak voltage in impedance experiments was equal to 1 V.

Conductivity results

Figure 1 compares the temperature dependence of the conductivities for the $(PEO)_{10}NaI$ and $(PEO)_{10}NaI$–θ-Al_2O_3 (10 mass%) systems. The θ-Al_2O_3 grain sizes were less than 2 μm. At temperatures up to about 60°C, which roughly corresponds to the melting temperature of the crystalline PEO phase (T_m), conductivities measured for the composite system are higher; above this temperature the ionic conductivities of both systems are comparable. An abrupt change in the conductivity of the $(PEO)_{10}NaI$ electrolyte near T_m for the crystalline PEO phase is evident and is not observed for the composite electrolyte. As can be seen in Table 1, the addition of 10 mass% of θ-Al_2O_3 to the $(PEO)_{10}NaI$ electrolyte reduces the fraction of the crystalline PEO phase (X_c) by 34%, increasing the conductivity as shown for ambient temperatures in Fig. 1. Although lowering X_c improves the conductivity, the addition of stiff filler grains results in lowering the flexibility of the composite electrolyte; the higher glass transition temperature (T_g) measured for the $(PEO)_{10}NaI$–θ-Al_2O_3 system is evidence of this.

Fig. 2. Comparison of isotherms of ionic conductivity of PEO–PAAM–$LiClO_4$ composite electrolytes at [○] 25°C and [▽] 100°C with isotherms of ionic conductivity of PEO–NNPAAM–$LiClO_4$ composite electrolytes at [●] 25°C and [▼] 100°C. [■], [□]: Conductivities measured for the $(PEO)_{10}LiClO_4$ electrolyte at 25°C and 100°C, respectively.

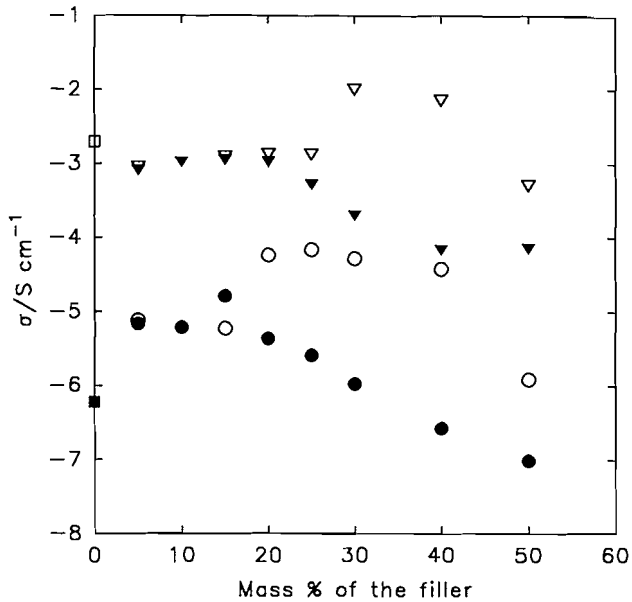

As PAAM is added to the $(PEO)_{10}LiClO_4$ electrolytes, the ambient temperature conductivity increases to a plateau as is observed in Fig. 2. At 25°C the ionic conductivities of the majority of the PEO–PAAM–$LiClO_4$ composite electrolytes are higher than for the $(PEO)_{10}LiClO_4$ electrolyte. For the PEO–NNPAAM–$LiClO_4$ electrolytes, conductivity initially increases with the addition of the filler and then decreases for NNPAAM concentrations higher than 15 mass%. For NNPAAM concentrations higher than ~30 mass%, conductivities are lower than for the $(PEO)_{10}LiClO_4$ system.

At 100°C, conductivities of composite systems containing 20–40 mass% of PAAM are still higher than for the $(PEO)_{10}LiClO_4$ electrolyte. For NNPAAM electrolytes, conductivities are almost the same as for the $(PEO)_{10}LiClO_4$ electrolyte up to 20 mass% of NNPAAM and gradually decrease for higher NNPAAM concentrations. As can be seen from Table 1, PAAM is effective at reducing crystallization in the $(PEO)_{10}LiClO_4$ electrolyte series. The amount of the crystalline PEO phase in these composite electrolytes is lower than for the $(PEO)_{10}LiClO_4$ system. Two T_g's are observed for samples containing 15 and 25 mass% of PAAM. One is comparable to the T_g of the $(PEO)_{10}LiClO_4$ electrolyte, the other is roughly comparable to the T_g of the undoped PEO system. It can be concluded that the addition of PAAM plasticized the PEO–$LiClO_4$ electrolyte and separated out a flexible amorphous phase of low T_g. Similar trends are also observed for the PEO–$LiClO_4$ based composite electrolytes containing NNPAAM. Although the presence of two different T_g's is not observed, the T_g's of PEO–NNPAAM–$LiClO_4$ composite electrolytes are lower than for the $(PEO)_{10}LiClO_4$ system and decrease with an increase in the NNPAAM concentration. For concentrations of NNPAAM below ~25 mass% the addition of NNPAAM reduces the frac-

Table 1. DSC data for composite polyether electrolytes.

Polymer host	Type of salt[a]	Type and conc.[b] of filter	T_{g1}/K	T_{g2}/K	X_c/%[c]
PEO				221	74
OMPEO				215	18
PEO	NaI		249		70
PEO	$LiClO_4$		242		23
PEO	NH_4SCN		256		66
OMPEO	$LiClO_4$		237		
OMPEO	$NaClO_4$		257		
PEO	NH_4SCN	PAAM 40	262		64
PEO	NaI	θ-Al_2O_3 10	260		40
PEO	$LiClO_4$	PAAM 15	254	208	14
PEO	$LiClO_4$	PAAM 25	244	198	4
PEO	$LiClO_4$	PAAM50	239		3
PEO	$LiClO_4$	NNPAAM 15	239		<1
PEO	$LiClO_4$	NNPAAM 25	236		9
PEO	$LiClO_4$	NNPAAM 50	229		43
OMPEO	$LiClO_4$	PAAM 15	234	205	
OMPEO	$LiClO_4$	PAAM 25	228	192	
OMPEO	$LiClO_4$	PAAM 50	234		
OMPEO	$LiClO_4$	NNPAAM 15	238	212	
OMPEO	$LiClO_4$	NNPAAM 25	234	208	
OMPEO	$LiClO_4$	NNPAAM 50	218		12
OMPEO	$NaClO_4$	PAAM 15	254		
OMPEO	$NaClO_4$	PAAM 25	249		
OMPEO	$NaClO_4$	PAAM 50	257		
OMPEO	$NaClO_4$	α-Al_2O_3 15	249		
OMPEO	$NaClO_4$	α-Al_2O_3 25	245		
OMPEO	$NaClO_4$	α-Al_2O_3 50	247		

[a]Concentration of salts in all electrolytes studied is equal to 10 mol% with respect to polyether oxygens.

[b]Concentration of fillers in mass%.

[c]X_c calculated on the basis of DSC data according to the procedure described in ref. 9.

tion of the crystalline PEO phase. For higher concentrations the X_c increases and approaches that for the $(PEO)_{10}LiClO_4$ electrolyte. These changes in X_c account for the decrease in conductivity observed at ambient temperatures for composite PEO–NNPAAM–$LiClO_4$ electrolytes with high concentrations of NNPAAM.

Figure 3 compares the temperature dependence of conductivity measured for the PEO–PAAM (40 mass%) blends (10 mol% of $LiClO_4$) with that for the same blends interchanging the $LiClO_4$ salt with NH_4SCN. As can be seen, conductivities measured for electrolytes containing NH_4SCN are slightly higher over the entire temperature range. This cannot be easily explained on the basis of the differential scanning calorimetry (DSC) results presented in Table 1 since there is no evidence of the presence of the low T_g flexible amorphous phase for the electrolytes doped with NH_4SCN. Also X_c for the electrolyte containing NH_4SCN is higher than for the composite electrolyte with $LiClO_4$. The NH_4^+ cations are less tightly bound to the polyether chains as was shown from FT-IR and Raman measurements (12, 16).

Assuming the facilitating effect of these polyacrylamides on the conductivity of the $(PEO)_{10}LiClO_4$ electrolyte, it is interesting to analyze the effect of the addition of polyacrylamides on the ambient temperature conductivities of the amorphous

Fig. 3. Comparison of the temperature dependence of ionic conductivity of PEO–PAAM (40 mass%) based composite electrolytes with [○] 10 mol% of $LiClO_4$ and [●] 10 mol% of NH_4SCN.

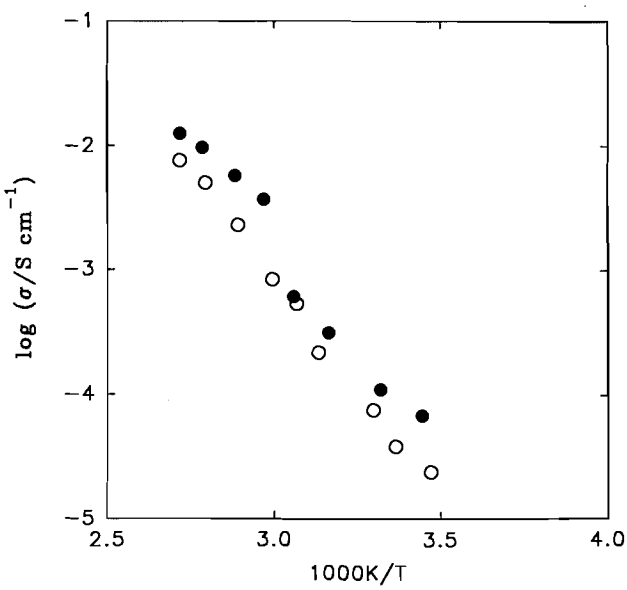

Fig. 4. Comparison of the isotherm of ionic conductivity of OMPEO–PAAM–$LiClO_4$ composite electrolytes at [○] 25°C with the isotherm of ionic conductivity of PEO–NNPAAM–$LiClO_4$ composite electrolytes at [●] 25°C. [□]: Conductivity measured for OMPEO–$LiClO_4$ electrolytes. All samples with 10 mol% of $LiClO_4$ with respect to ether oxygen concentration.

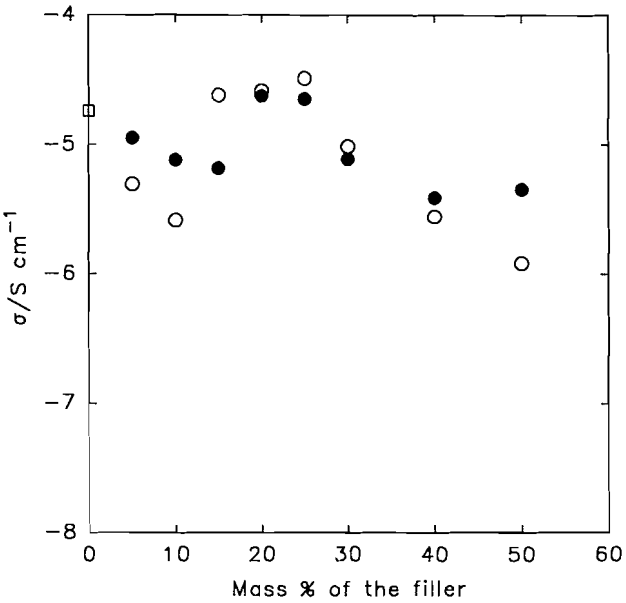

Fig. 5. Comparison of the isotherm of ionic conductivity of OMPEO–PAAM blend-based composite electrolytes doped with [○] $LiClO_4$ and [●] $NaClO_4$. T = 25°C.

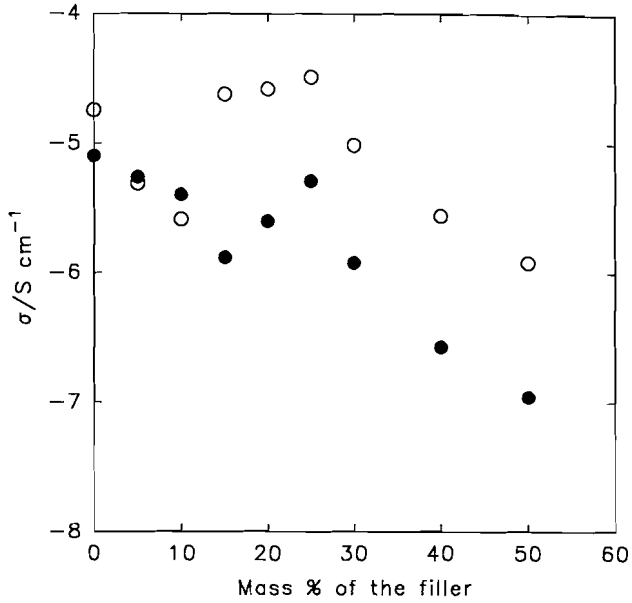

OMPEO–$LiClO_4$ electrolyte. This effect is shown in Fig. 4 in which conductivity isotherms at 25°C for the OMPEO–PAAM–$LiClO_4$ and OMPEO–NNPAAM–$LiClO_4$ systems are presented. As can be seen, the addition of polyacrylamides initially decreases the ionic conductivity for PAAM concentrations up to ~10 mass% and for NNPAAM concentrations ~15 mass%. This trend is reversed for samples containing 20–25 mass% of these polyacrylamides. In this filler concentration range conductivities of composite electrolytes are roughly 2–3 times higher than for the base OMPEO–$LiClO_4$ electrolyte. For concentrations of polyacrylamides exceeding 25 mass%, conductivity again decreases. As can be seen from Table 1, for polyacrylamide concentrations equal to 15 and 25 mass% two T_g's are observed, similar to the $(PEO)_{10}LiClO_4$–PAAM systems. The lower T_g is comparable to the T_g of the undoped OMPEO, the higher to the T_g of the $(OMPEO)_{10}LiClO_4$ electrolyte. Note that for systems containing NNPAAM, the higher T_g decreases with an increase in NNPAAM concentration and, for the sample with 50 mass% of NNPAAM, T_g is roughly the same as for the undoped OMPEO. This effect is similar to that previously described for the PEO–$LiClO_4$–NNPAAM composite electrolytes. The presence of a larger fraction of a flexible amorphous phase accounts for the higher conductivities measured for composite electrolytes in comparison with the base OMPEO–$LiClO_4$ system. As can be seen conductivities measured for most of the electrolytes containing NNPAAM are higher than for systems with PAAM (except in the 15–30 mass% range). The higher conductivities measured for electrolytes containing NNPAAM for concentrations higher than 30 mass% can be explained by the higher flexibility (lower T_g) of the amorphous phase of these electrolytes compared to the OMPEO–PAAM–$LiClO_4$ composite electrolytes.

In Fig. 5 the effect of the addition of various alkali metal salts ($NaClO_4$, $LiClO_4$) on the ambient temperature conductivity of OMPEO–PAAM blends is shown. The shape of the conductivity isotherms measured for both systems is qualitatively the same. However, except for the concentrations of PAAM up to 10 mass%, conductivities measured for the electrolytes containing $LiClO_4$ are higher. This is consistent with the lower T_g values measured for these composite electrolytes as shown in Table 1.

In Fig. 6 the effects of the addition of inorganic (i.e., α-Al_2O_3) and organic (i.e., PAAM) fillers on the ambient temperature conductivity of OMPEO–$NaClO_4$ electrolyte are compared. Conductivity isotherms measured for both systems show the same trend: an initial drop in conductivity followed by an increase in conductivity with the conductivity maximum for samples containing ~25 mass% of the filler, followed by a decrease in conductivity for higher filler concentrations. Up to filler concentrations of ~25 mass%, conductivities measured for both composite systems are roughly the same. For higher filler concentrations conductivities measured for the electrolytes containing α-Al_2O_3 are higher. This is in agreement with the DSC data showing higher flexibility (lower T_g) for the OMPEO–$NaClO_4$–α-Al_2O_3 system in this filler concentration range.

Conductivity mechanism — discussion

The ion conduction behaviour of composite polyether-based electrolytes can be explained in terms of a classification of components as either Lewis acid or Lewis base or as, in the case of the aluminas, amphoteric. Examples of Lewis bases are the ether oxygens of PEO and OMPEO, anions such as ClO_4^-, I^-, SCN^-, the carbonyl oxygens of PAAM or NNPAAM, and the nitrogens of the NH_2 and $N(CH_3)_2$ groups of, respectively, PAAM and NNPAAM. Li^+, Na^+, and NH_4^+, cations can be classified as Lewis acids. Both θ- and α-Al_2O_3

Fig. 6. Comparison of the isotherm of ionic conductivity of OMPEO–PAAM–$NaClO_4$ composite electrolytes at [●] 25°C with the isotherm of ionic conductivity of OMPEO–α-Al_2O_3–$NaClO_4$ composite electrolytes at [○] 25°C. [■]: Conductivity measured for OMPEO–$NaClO_4$ electrolytes. All samples with 10 mol% of $NaClO_4$ with respect to ether oxygen concentration.

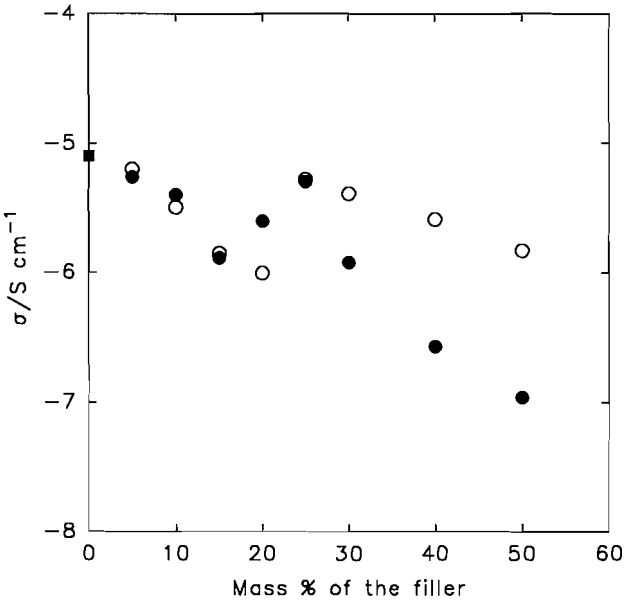

are of an amphoteric Lewis acid–base character, which is manifested through the coexistence of the surface Al (acid) and O (base) groups. In the case of aluminas there is also the possibility of the adsorption of water molecules on the surfaces resulting in the formation of surface OH groups. As discussed below, we believe that the changes in the ultrastructure and morphology of composite electrolytes and therefore the conductivity are the result of an equilibrium between various Lewis acid – Lewis base reactions.

After the addition of alkali metal salts and alumina to the crystalline PEO-based electrolytes there is a competition between alumina acidic surface groups and alkali metal cations for the ether oxygens. Surface Al groups can act as nucleation centres, in the crystallization of PEO from acetonitrile solutions. Since there are a large number of these centres the crystallization proceeds more rapidly and, as a result, more disorder is frozen into the new solid. This is manifested by a decrease in the fraction of the crystalline PEO phase and hence an increase in ambient temperature conductivity as shown in Fig. 1 for the $(PEO)_{10}NaI$–θ-Al_2O_3 composite electrolyte. However, an attachment of acidic θ-Al_2O_3 centres to PEO also results in an increase in T_g. θ-Al_2O_3 has smaller average grain sizes than the α-Al_2O_3 used as an additive to OMPEO-based electrolytes. Also the surface area of θ-Al_2O_3 is larger (approximately 900 m^2/g) in comparison to the surface area of α-Al_2O_3 (approximately 100–150 m^2/g). Therefore there are more active centres in the case of θ-Al_2O_3, which is a stronger acid than α-Al_2O_3. This results in stronger attachment of θ-Al_2O_3 to the PEO polymer host; a stiffening of the system results. For the OMPEO–$NaClO_4$–α-Al_2O_3 electrolytes some of Na^+ cations can be replaced by the acidic α-Al_2O_3 centres in the coordination spheres of ether oxygens. This results in a slight decrease in T_g that is, however, not high enough to enhance the conductivity of these OMPEO–$NaClO_4$ based composite electrolytes.

In the case of systems containing polyacrylamides there is a competition between the base centres of the polyethers and the polyacrylamides in the complexation of alkali metal cations. As has been already discussed in our previous papers (9, 10), there is a possibility of the formation of three different types of complexes.

Type I complexes: polyether–M^+–polyether complexes (M=Li, Na) involving Lewis base ether oxygens from the polyether chain. These complexes incorporate transient cross-links (intra or intermolecular) between the polyether chains via alkali metal cations, which stiffen the polyether host and reduce the electrolyte conductivity.

Type II complexes: mixed polyether–M^+–NNPAAM (PAAM) complexes involving Lewis base ether oxygens from the polyether chain and Lewis base carbonyl oxygens or (and) amide nitrogens from the NNPAAM (PAAM) chains.

Type III complexes: NNPAAM–M^+–NNPAAM complexes involving the Lewis base carbonyl oxygens or (and) amide nitrogens of NNPAAM (PAAM).

The formation of these complexes has been recently observed in FT-IR and FT-Raman studies (9–11). For concentrations of polyacrylamides up to 25 vol% the formation of type II complexes is more probable, thus leading to a reduction in X_c. For the higher polyacrylamide concentrations the probability of the formation of type III complexes increases.

The presence of type II and type III complexes reduces the number of transient cross-links in the polyether phase. This is manifested by a decrease in T_g and in some composite systems by the presence of flexible polyether phase with a T_g comparable to the T_g of undoped polyether (see Table 1). From the results in Table 1 it seems that the Li^+ cation, being a stronger Lewis acid than the Na^+ cation, forms complexes within the polyacrylamide phase more easily than Na^+ and at the expense of Type I complexes. Therefore more Li^+ than Na^+ transient crosslinks are present in the polyacrylamide-rich microphases of these composite electrolytes. As a result there is a lower T_g and therefore a higher conductivity for the lithium electrolytes than for the sodium electrolytes (see Fig. 5 and Table 1). In the case of PAAM the formation of hydrogen bonds between NH_2 groups and oxyanions such as ClO_4^- can occur. This will lower the mobility of ClO_4^- anions and therefore the conductivity is lower, as observed in Figs. 2, 4, and 5 for PAAM-based systems with PAAM concentrations higher than ~25–30 mass%. This might also be an explanation of the lower conductivities observed for OMPEO–PAAM–$NaClO_4$ systems in comparison with OMPEO–$NaClO_4$–α-Al_2O_3 electrolytes for filler concentrations higher than 25 mass%. Another explanation of this behaviour might involve the lower basicity of the surface α-Al_2O_3 groups compared to that of the PAAM Lewis acid groups.

For composite systems with NNPAAM, it was shown from FT-IR studies (11) that Li^+ cations are preferentially coupled to the carbonyl oxygens of NNPAAM. The depletion of Li^+ cations from the polyether phase results in a decrease in conductivity for composite electrolytes containing over ~25–30 mass% of NNPAAM.

Different types of interactions should probably be assumed in the case of the PEO–PAAM–NH_4SCN electrolytes. NH_4^+,

cations are the weakest Lewis acids amongst Li^+, Na^+, and NH_4^+. Drastic changes in the flexibility (T_g) and X_c of PEO–NH_4SCN electrolytes are not observed following the addition of PAAM. However, the conductivity of these systems was the highest among the composite polyether–PAAM electrolytes described. FT-IR experiments (12) showed the formation of $(SCN^-)_2$ dimers as well as the co-coordination of NH_4^+ by both PEO and PAAM. It is also evident from FT-IR experiments (12, 16) that NH_4^+ cations are more loosely bound to polyether oxygens than are Li^+ and Na^+, which is an explanation for the higher conductivities measured for NH_4SCN-doped composite systems. Despite intensive studies the exact mechanisms for ionic conduction in electrolytes containing NH_4SCN is still unknown.

FT-IR experiments performed on various composite systems containing polyacrylamides (9–12) confirm the possibility of the formation of various complexes involving polyether, alkali metal salt (or NH_4SCN), and polyacrylamide. Changes in the positions of the maximum of the C-O-C, C=O, and N-H stretching modes were observed. An analysis of the peak characteristic for the ClO_4^- anions shows that in composite electrolytes there is a reduction in the concentration of contact ion pairs compared to the pure polyether-based electrolytes (11). This also confirms an increase in conductivity in polyether-based composite electrolytes.

Conductivity models

Ion-conducting polymer systems, formed by the dissolution of salts in suitable ion-coordinating polymers, have a great potential for applications in numerous electrochemical devices. Although an understanding of the macroscopic properties associated with an efficient ionic transport in polymer electrolytes has advanced and the specific demands on salt and host structures that give high conductivity are rather well established (5, 17), a detailed microscopic picture of ionic conduction in these materials has not been achieved. Despite the ease of preparation of composite systems such as those discussed in this report, the problem of the mechanism of ionic conduction in such systems is even more acute. The best that we have been able to do is to use an "effective medium" theory (EMT) approach (7, 9–11, 18). This approach has had some success and has been applied assuming that the PEO–polyacrylamide (PAAM or NNPAAM) composites contain three components with different electrical properties. These are (*i*) a highly conductive uncomplexed polyether interface layer surrounding the polyacrylamide core, (*ii*) dispersed insulating polyacrylamide–salt complexes, and (*iii*) a matrix polyether–salt ionic conductor. It was further assumed that components (*i*) and (*ii*) could be combined in a composite unit that was spherically symmetric. Under these assumptions the components were considered to be embedded in a self-consistent effective medium with the same effective conductivity as the composite. The model connects an enhancement of ionic conductivity (see Figs. 2, 4, and 5) with the existence of a highly conductive amorphous layer on the surface of the polyacrylamide, i.e., component (*i*) in the composite unit: a layer within which there has been a depletion of transient cross-links due to the preference of cations for polyacrylamide. This layer has a lower T_g and therefore increased flexibility.

For some of the composite electrolytes the ionic conductivity has an Arrhenius temperature dependence over a certain temperature range (see Fig. 3). For these composites the order–disorder temperature (T_D) is the temperature at which a change in the conduction mechanism is expected. T_D can be calculated using a semiempirical approach (11, 19), which yields a linear relationship between the natural logarithm of the conductivity preexponential factor ($\ln \sigma_0$) and the Arrhenius activation energy for conduction (E_a), and which includes such parameters as T_D, the theoretical cation and anion concentrations, and the frequency of oscillation of the ions as they await the next activated step. For example, for the PEO–PAAM–NH_4SCN composite a linear relation between $\ln \sigma_0$ and E_a has been found for both the experimentally determined dc conductivity and the value of conductivity obtained from the EMT model. The characteristic temperatures T_D calculated from both data sets agree and are equal to 71°C. This temperature roughly corresponds to the melting temperature of the undoped PEO phase. Such behaviour was previously found for other composite polymeric electrolytes (18).

Conclusions

Ionic conductivity in mixed phase composite electrolytes based upon PEO and using inorganic (Al_2O_3) and organic (PAAM, NNPAAM) fillers to inhibit or prevent the crystallization of PEO has been discussed. Various alkali metal salts (Li, Na) and NH_4SCN were used. In general, the room temperature conductivity is enhanced by over two orders of magnitude above the base PEO–salt system. Even adding PAAM and NNPAAM to an initially amorphous system (OMPEO) increases the room temperature conductivity by 2 to 3 times. It is suggested that changes in the conductivity with changes in salt and filler concentration are due to changes in the ultrastructure and morphology and are the result of an equilibrium between various Lewis acid – Lewis base reactions. Qualified success has been achieved in modelling ionic conductivity in these composite electrolyte systems using an effective medium approach. In this approach it has been assumed that the main conductivity enhancement takes place in thin amorphous layers of the polyether that coat the dispersed polyacrylamide particles separated in a microphase. In the best complexes this layer is identified by a second T_g.

References

1. M.B. Armand, J.M. Chabagno, and M. Duclot. *In* Fast ion transport in solids. *Edited by* P. Vashita, J.N. Mundy, and G.K. Shenoy. Elsevier, North Holland, New York. 1979. p. 131.
2. J.R. MacCallum and C.A. Vincent (*Editors*) Polymer electrolyte reviews – 1 and Polymer electrolyte reviews – 2. Elsevier, London. 1987 and 1989.
3. F.M. Gray. Solid polymer electrolytes — fundamentals and technological applications. VCH, Weinheim. 1991.
4. B. Scrosati. Applications of electroactive polymers. Chapman and Hall, London. 1993.
5. P.G. Bruce. Solid state electrochemistry. Cambridge University Press, Cambridge. 1995 pp. 95–162.
6. F.M. Gray. *In* Polymer electrolyte reviews – 1. *Edited by* J.R. MacCallum and C.A. Vincent. Elsevier, London. 1987. pp. 139–172.
7. K. Such, J.R. Stevens, W. Wieczorek, M. Siekierski, and Z. Florjańczyk. J. Polym. Sci. Polym. Phys. Ed. **32**, 2221 (1994).
8. W. Wieczorek, Z. Florjańczyk, and J.R. Stevens. Electrochim. Acta, **40**, 2251 (1995).

9. W. Wieczorek, K. Such, Z. Florjańczyk, and J.R. Stevens. J. Phys. Chem. **98**, 6840 (1994).
10. W. Wieczorek, K. Such, S.H. Chung and J.R. Stevens. J. Phys. Chem. **98**, 9047 (1994).
11. W. Wieczorek, A. Zalewska, D. Raducha, Z. Florjańczyk, J.R. Stevens, A. Ferry, and P. Jacobsson. Macromolecules, **29**, 143 (1996).
12. A. Zalewska, W.Wieczorek, and J.R. Stevens. J. Phys. Chem. **100**, 11382 (1996).
13. C.V. Nicholas, D.J. Wilson, C. Booth, and J.R.M. Giles. Br. Polym. J. **20**, 289 (1988).
14. W. Wieczorek, K. Such, H. Wyciślik, and J. Płocharski. Solid State Ionics, **36**, 255 (1989).
15. J. Płocharski, W. Wieczorek, J. Przyłuski, and K. Such. Appl. Phys. A: Solids Surf. **A49**, 55 (1988).
16. A. Ferry, P. Jacobsson, and J.R. Stevens. J. Phys. Chem. **100**, 12574 (1996).
17. M. Ratner. *In* Polymer electrolyte reviews – 1. *Edited by* J.R. MacCallum and C.A. Vincent. Elsevier, London. 1987. pp. 173–236.
18. W. Wieczorek and M. Siekierski. J. Appl. Phys. **76**, 2220 (1994).
19. D.P. Almond and A.R. West. Solid state ionics, **23**, 27 (1987); Solid State Ionics, **18&19**, 1105 1986).

Novel (fulvalene)dichromium alkyl and acyl complexes of the types $FvCr_2(CO)_{6-n}L_nRR'$ and $Et_4N[FvCr_2(CO)_{6-n}L_nR]$ (R, R′ = Me, CH_2CN, COMe; L = CO, PMe_2Ph; *n* = 0, 1, 2)

István Kovács and Michael C. Baird

Abstract: The compound $FvCr_2(CO)_6Me_2$ (**1**) is obtained, via the intermediate formation of $Et_4N[FvCr_2(CO)_6Me]$ (**2**), by stepwise addition of 2 equivalents of methyl iodide to $(Et_4N)_2[FvCr_2(CO)_6]$; the analogous cyanomethyl compounds $FvCr_2(CO)_6(CH_2CN)_2$ (**3**) and $Et_4N[FvCr_2(CO)_6(CH_2CN)]$ (**4**) are formed similarly. Compound **1** readily undergoes CO insertion upon treatment with 2 equivalents of PMe_2Ph, giving rise to *trans,trans*-$FvCr_2(CO)_4(PMe_2Ph)_2(COMe)_2$ (**6**), also in two steps via *trans*-$FvCr_2(CO)_5(PMe_2Ph)(Me)(COMe)$ (**8**). The neutral methyl "half" of **2** reacts similarly with PMe_2Ph to form $Et_4N[$*trans*-$FvCr_2(CO)_5(PMe_2Ph)(COMe)]$ (**7**), while the anionic "half" of **2** is alkylated with $ClCH_2CN$ to give $FvCr_2(CO)_6(CH_2CN)Me$ (**5**). Treatment of **5** with PMe_2Ph also results in CO insertion into the Cr—Me bond to give *trans*-$FvCr_2(CO)_5(PMe_2Ph)(CH_2CN)(COMe)$ (**10**). Although **3** is inert to both substitution and insertion reactions with PMe_2Ph, the phosphine-substituted dialkyl (fulvalene)dichromium complex *trans,trans*-$FvCr_2(CO)_4(PMe_2Ph)_2(CH_2CN)_2$ (**9**) is prepared by reaction of $ClCH_2CN$ with $(Et_4N)_2[FvCr_2(CO)_4(PMe_2Ph)_2]$.

Key words: chromium, metal–metal bonds, fulvalene.

Résumé : On a obtenu le composé $FvCr_2(CO)_6Me_2$ (**1**), par le biais de la formation de $Et_4N[FvCr_2(CO)_6Me]$ (**2**), par une addition par étapes de deux équivalents d'iodure de méthyle à du $(Et_4N)_2[FvCr_2(CO)_6]$; les composés cyanométhylés analogues, $FvCr_2(CO)_6(CH_2CN)_2$ (**3**) et $Et_4N[FvCr_2(CO)_6(CH_2)]$ (**4**), se forment de la même manière. Par traitement avec deux équivalents de PMe_2Ph, le composé **1** subit facilement une insertion de CO qui conduit en deux étapes au *trans,trans*-$FvCr_2(CO)_4(PMe_2Ph)_2(COMe)_2$ (**6**) par le biais de l'intermédiaire *trans*-$FvCr_2(CO)_5(PMe_2Ph)(Me)(COMe)$ (**8**). De la même manière, la «moitié» méthylée neutre du composé **2** réagit avec le PMe_2Ph pour conduire à la formation de $Et_4N[$*trans*-$FvCr_2(CO)_5(PMePh)(COMe)]$ (**7**) alors que la «moitié» anionique du composé **2** est alkylée par le $ClCH_2CN$ et conduit au $FvCr_2(CO)_2(CH_2CN)Me$ (**5**). Le traitement du composé **5** à l'aide de PMe_2Ph provoque aussi une insertion de CO dans la liaison Cr—Me et fournit le *trans*-$FvCr_2(CO)_5(PMe_2Ph)(CH_2CN)(COMe)$ (**10**). Même si le composé **3** est inerte aux réactions tant de substitution que d'insertion avec le PMe_2Ph, il est possible de préparer le complexe dialkyl(fulvalène)chrome substitué par une phosphine, *trans,trans*-$FvCr_2(CO)_4(PMe_2Ph)_2(CH_2CN)_2$ (**9**), par réaction du $ClCH_2CN$ avec du $(Et_4N)_2[FvCr_2(CO)_4(PMe_2Ph)_2]$.

Mots clés : chrome, liaisons métal–métal, fulvalène.

[Traduit par la rédaction]

Introduction

In previous papers (1), we have explored the chemistry of fulvalenedichromium and -dimolybdenum complexes of the types $FvM_2(CO)_4L_2$, $FvM_2(CO)_4L_2HX$, $FvM_2(CO)_4L_2H_2$, and $FvM_2(CO)_4L_2X_2$ (M = Cr, Mo; X = Cl, Br, I; L = CO, tertiary phosphines). Following our earlier work on 17-electron, metal-centered radicals (2), the main impetus to this work was a desire, ultimately successful (1c,d), to find and study compounds of the type $FvM_2(CO)_4L_2$ that would undergo spontaneous, thermal metal-metal bond homolysis to give the novel biradical isomers $L(CO)_2M(\mu\text{-}Fv)M(CO)_2L$. In the course of our research, the above-mentioned examples of halo and hydrido classes of compounds were also perforce prepared as starting meterials and (or) products of reactions of the compounds $FvM_2(CO)_4L_2$. We (1a) and others (3) have also demonstrated that protonation of anionic complexes of the type $[FvM_2(CO)_4L_2]^{2-}$ results in the formation of the hydrides $FvM_2(CO)_4L_2H_2$, and we now extend our research on fulvalene complexes to examples of alkyl and acyl (fulvalene)dichromium carbonyl complexes, obtained by treating the anionic species $[FvCr_2(CO)_4L_2]^{2-}$ with various alkyl halides.

Received January 25, 1996.

This paper is dedicated to Professor Howard C. Clark in recognition of his distinguished contributions to chemistry in Canada.

I. Kovács[1] **and M.C. Baird.**[2] Department of Chemistry, Queen's University, Kingston, ON K7L 3N6, Canada.

[1] NATO Science Fellow; Rsearch Group for Petrochemistry of the Hungarian Academy of Sciences, Veszprém, Hungary.

[2] Author to whom correspondence may be addressed. Telephone: (613) 545–2616. Fax: 613-545-6669. E-mail: bairdmc@qucdn.queensu.ca

Table 1. Carbonyl stretching frequencies.

Compound	$\nu_{CO}(cm^{-1})^a$
$FvCr_2(CO)_6(CH_3)_2$ (**1**)	2002 (s), 1929 (vs)
$Et_4N[FvCr_2(CO)_6CH_3]$ (**2**)	2000 (s), 1924 (vs), 1902 (s), 1810 (m), 1788 (m), 1727 (m, br)
$FvCr_2(CO)_6(CH_2CN)_2$ (**3**)	2021 (m), 1952 (vs, br)
$Et_4N[FvCr_2(CO)_6CH_2CN]$ (**4**)	2011 (s), 1938 (vs), 1897 (vs), 1795 (vs), 1727 (m, br)
$FvCr_2(CO)_6(CH_2CN)Me$ (**5**)	2021 (m), 2006 (m-s), 1959 (vs), 1931 (s)
trans,trans-$FvCr_2(CO)_4(PMe_2Ph)_2(COMe)_2$ (**6**)	1920 (s), 1840 (vs), 1636 (m)
Et_4N[*trans*-$FvCr_2(CO)_5(PMe_2Ph)COMe$] (**7**)	1920 (s), 1897 (s), 1837.5 (vs), 1808 (m), 1789 (m), 1725 (w, br), 1633 (m)
trans-$FvCr_2(CO)_4(PMe_2Ph)_2(CH_2CN)_2$ (**9**)	1941 (m), 1865 (vs)
trans-$FvCr_2(CO)_5(PMe_2Ph)(CH_2CN)COMe$ (**10**)	2019 (m-s), 1949 (vs), 1922 (m-s, sh), 1844 (s), 1639 (m)
$(Et_4N)_2[FvCr_2(CO)_6]$ ref. (*1d*)	1890 (vs), 1800 (vs), 1717 (s)

[a]In THF.

Experimental section

General comments

All manipulations were carried out under purified nitrogen using standard Schlenk techniques and a Vacuum Atmospheres glovebox. All solvents were freshly distilled under nitrogen from sodium benzophenone ketyl. Deuterated solvents were purchased from CDN Isotopes and CIL, degassed, and stored in the glovebox. PMe_2Ph, methyl iodide, and chloroacetonitrile were products of Aldrich and were used as received. The compound $(Et_4N)_2[FvCr_2(CO)_6]$ was prepared as previously (*1d*). IR spectra were recorded on a Bruker IFS 25 FT-IR spectrometer using a 0.2-mm NaCl cell. NMR spectra were acquired on a Bruker AM-400 (400.1 MHz ^1H, 100.6 MHz $^{13}C\{^1H\}$, 162.0 MHz $^{31}P\{^1H\}$) NMR spectrometer; IR data are compiled in Table 1. FAB(+)-MS analyses were performed on a Fisons VG Quattro triple quadrupole mass spectrometer using 3-nitrobenzyl alcohol as the matrix. Elemental analyses were carried out by Canadian Microanalytical Services Ltd. (Delta, B.C.).

$FvCr_2(CO)_6Me_2$ (1)

A solution of 0.10 g (0.15 mmol) $(Et_4N)_2[FvCr_2(CO)_6]$ in 5 mL THF was treated with 20 μL (0.32 mmol) of chloroacetonitrile at room temperature. The color changed instantly from yellow to brown, and an IR spectrum indicated that formation of $FvCr_2(CO)_6Me_2$ was complete in ~3 h. Although no other products appeared according to both IR and ^1H NMR studies, evaporation of the solvent resulted in the formation of a yellow-brown oil, which could not be obtained free of THF; some decomposition also occurred, and thus microanalytical characterization of **1** was not successful although all spectroscopic data were consistent with the formulation. ^1H NMR (acetone-d_6), δ: 0.62 (s, 6H, Me), 5.10 ("t," 4H, Fv), 5.37 ("t", 4H, Fv). $^{13}C\{^1H\}$ NMR (acetone-d_6), δ: −5.0 (s, Me), 88.3 (s, Fv), 89.8 (s, Fv), 102.5 (s, C-1 Fv), 238.9 (s, CO *cis* to Me), 249.0 (s, CO *trans* to Me). IR spectroscopic data are shown in Table 1.

$Et_4N[FvCr_2(CO)_6Me]$ (2)

This compound was detected by IR spectroscopy in a reaction carried out as above but with only 0.10 mL of methyl iodide added (Table 1). In an NMR experiment, a solution of 15 mg $(Et_4N)_2[FvCr_2(CO)_6]$ in 0.6 mL acetone-d_6, was treated with methyl iodide dropwise until complete consumption of the starting material had occurred. Since some **1** was always present, no attempt was made to isolate the monomethyl compound, which was unambiguously characterized by IR and NMR spectroscopy. ^1H NMR (acetone-d_6), δ: 0.53 (s, 3H, CrMe), 1.36 (tt, $J_1 = 7$ Hz, $J_2 = 2$ Hz, 12H, CH_2*Me*), 3.42 (q, $J = 7$ Hz, 8H, CH_2N), 4.35, 4.71, 4.80, 4.93 ("t," each 2H, Fv). $^{13}C\{^1H\}$ NMR (acetone-d_6), δ: −2.4 (s, CrMe), 7.7 (s, CH_2*Me*), 52.9 (s, CH_2N), 82.0, 82.3, 86.3, 86.7 (s, all Fv), 90.4 (s, C-1 Fv), 112.9 (s, C-1 Fv), 240.3 (s, CO *cis* to Me), 245.8 (s, CO of anionic moiety), 252.7 (s, CO *trans* to Me).

$FvCr_2(CO)_6(CH_2CN)_2$ (3)

Compound **2** (0.10 g, 0.16 mmol) was dissolved in 5 mL of THF and 20 μL (0.32 mmol) of chloroacetonitrile were injected into the stirred solution at room temperature. The yellow reaction mixture instantly turned deep red and an IR analysis carried out ~1 h later indicated complete consumption of the dianion and formation of a single product, $FvCr_2(CO)_6(CH_2CN)_2$ (Table 1). Evaporation of the solvent resulted in the formation of a red-brown oil. Our attempts to purify this material did not meet with success, but spectroscopic characterization unambiguously established its identity. ^1H NMR (acetone-d_6), δ: 1.62 (s, 4H, CH_2), 5.34 ("t", 4H, Fv), 5.74 ("t", 4H, Fv). $^{13}C\{^1H\}$ NMR (acetone-d_6), δ: −15.4 (s, $CrCH_2$), 89.9 (s, Fv), 93.4 (s, Fv), 102.2 (s, C-1 Fv), 127.4 (s, CN), 238.8 (s, CO *cis* to CH_2CN, 248.2 (s, CO *trans* to CH_2CN).

$Et_4N[FvCr_2(CO)_6(CH_2CN)]$ (4)

A solution of 0.10 g (0.16 mmol) **1** in 5 mL of THF was treated with 10 μL (0.16 mmol) $ClCH_2CN$, added dropwise at room temperature (~10 min). The yellow reaction mixture instantly turned deep red and an IR analysis showed complete consumption of the dianion and formation of $Et_4N[FvCr_2(CO)_6(CH_2CN)]$ (Table 1). Addition of an extra 10 mL of $ClCH_2CN$ transformed this intermediate into **3** within ~2 h without color change. Evaporation of the solvent when only $Et_4N[FvCr_2(CO)_6(CH_2CN)]$ was present resulted in the formation of a red-brown oily residue containing THF, which could not be removed. Attempts to purify this compound led to extensive decomposition to unidentified materials, but it was characterized spectroscopically. ^1H NMR (acetone-d_6), δ: 1.30 (s, 2H, CH_2), 1.36 (tt, $J_1 = 7$ Hz, $J_2 = 2$ Hz, 12H, CH_2*Me*), 3.42 (q, $J = 7$ Hz, 8H, CH_2N), 4.42, 4.82, 5.02, 5.19 ("t," each

2H, Fv). $^{13}C\{^1H\}$ NMR (acetone-d_6), δ: −12.8 (s, $CrCH_2$), 7.7 (s, CH_2Me), 52.9 (s, CH_2N), 82.6, 83.0, 86.4 (s, all Fv), 87.9 (s, C-1 Fv), 88.7 (s, Fv), 116.3 (s, C-1 Fv), 128.1 (s, CN), 240.9 (s, CO *cis* to CH_2CN), 245.3 (s, CO of anion), 250.3 (s, CO *trans* to CH_2CN). See Table 1 for IR data.

$FvCr_2(CO)_6(CH_2CN)Me$ (5)

A solution of 0.10 g (0.16 mmol) $(Et_4N)_2[FvCr_2(CO)_6]$ was dissolved in 5 mL of THF and reacted with 10 μL (0.16 mmol) of $ClCH_2CN$, added dropwise at room temperature. The yellow reaction mixture instantly turned deep red and an IR analysis showed complete consumption of the dianion and formation of $Et_4N[FvCr_2(CO)_6(CH_2CN)]$. Addition of 10 μL (0.16 mmol) of methyl iodide transformed this intermediate into compound **5** in ~2 h (IR). Evaporation of the solvent resulted in the formation of a red-brown oil, but attempts to further purify the material were unsuccessful. Nevertheless, **5** was satisfactorily characterized spectroscopically in solution and its identity seems firmly established. ^1H NMR (acetone-d_6): δ: 0.64 (s, 3H, Me), 1.59 (s, 2H, CH_2), 5.11, 5.30, 5.48, 5.64 ("t", each 2H, Fv). $^{13}C\{^1H\}$ NMR (acetone-d_6), δ: −15.8 (s, CH_2), −5.2 (Me), 88.7, 89.1, 90.5, 92.6 (s, all Fv), 100.6 (s, C-1 Fv), 103.9 (s, C-1 Fv), 127.5 (s, CN), 238.6 (s, CO *cis* to Me), 239.2 (s, CO *cis* to CH_2CN), 248.5 (s, CO *trans* to CH_2CN), 248.6 (s, CO *trans* to Me). For IR data see Table 1.

***trans,trans*-$FvCr_2(CO)_4(PMe_2Ph)_2(COMe)_2$ (6)**

A solution of **1**, prepared as above, was evaporated to dryness and the resulting brown material was redissolved in a 2:1 toluene–hexane solvent mixture. Addition of 0.6 mL (4.2 mmol) of PMe_2Ph resulted in precipitation of a yellow solid. A second, smaller crop of precipitate was recovered from the decanted solvent by concentrating under reduced pressure. The combined yellow solids were washed with 5 × 20 mL of hexane and dried. Yield: 0.74 g (1.05 mmol, 86%). The product was recrystallized from THF–hexane at −20°C, but did not give analytically pure samples. However, spectroscopic and mass spectrum data were consistent with the proposed structure. ^1H NMR (acetone-d_6), δ: 1.87 (d, J_{PH} = 9 Hz, 12H, PMe), 2.35 (s, 6H, COMe), 4.26 (m, 4H, Fv), 4.53 (m, 4H, Fv), 7.45 (m, 6H, *m,p*-Ph), 7.69 (m, 4H, *o*-Ph). $^{13}C\{^1H\}$ NMR (acetone-d_6): δ: 18.8 (d, J_{PC} = 30 Hz, PMe), 49.4 (s, CO*Me*), 91.9 (s, Fv), 93.4 (s, Fv), 103.9 (s, C-1 Fv), 129.3 (d, J_{PC} = 9 Hz, *o*-Ph), 130.0 (d, J_{PC} = 8 Hz, *m*-Ph), 130.2 (s, *p*-Ph), 140.8 (d, J_{PC} = 38 Hz, *ipso*-Ph), 250.8 (d, J_{PC} = 45 Hz, CO), 272.4 (d, J_{PC} = 18 Hz, *C*OMe). $^{31}P\{^1H\}$ NMR (acetone-d_6), δ: 58.2. FAB(+)-MS, *m/z*(%): $[M + H]^+$ = 707(0.7), $[M - 3CO - Me]^+$ = 607(1), $[M - 4CO - Me]^+$ = 579(1), $[M - 4CO - 2Me]^+$ = 564(2.5), $[M - PMe_2Ph - 2CO]^+$ = 512(10), $[M - PMe_2Ph - 3CO]^+$ = 484(3), $[M - PMe_2Ph - 4CO]^+$ = 456(8), $[M - PMe_2Ph - 4CO - Me]^+$ = 441(4), $[M - 2PMe_2Ph - 4CO]^+$ = 318(41). IR data are listed in Table 1.

Reaction of freshly generated **3** (0.04 mmol) with 20 μL (0.14 mmol) of PMe_2Ph was attempted in 5 mL THF solution, both thermally and photochemically. In an experiment carried out at room temperature and ambient light over 3 days, the reaction mixture decomposed and a precipitate formed in a green solution; only very weak carbonyl bands were detected in the IR spectrum, at 1944 and 1869 cm^{-1}. Irradiation of a solution of **3** and PMe_2Ph with a 200-W Hanovia lamp led to the same result, but much more quickly (~3 h).

$Et_4N[$*trans*-$FvCr_2(CO)_5(PMe_2Ph)(COMe)]$ (7)

This compound was characterized spectroscopically in situ when an acetone-d_6 solution of $(Et_4N)_2[FvCr_2(CO)_6]$ (15 mg) was "titrated" consecutively with equimolar amounts of methyl iodide and PMe_2Ph at room temperature. ^1H NMR (acetone-d_6), δ: 1.36 (tt, J_1 = 7 Hz, J_2 = 2 Hz, 12H, CH_2Me), 1.89 (d, J_{PH} = 9 Hz, 6H, PMe), 2.37 (s, 3H, COMe), 3.42 (q, J = 7 Hz, 8H, CH_2N), 4.23 ("t", 2H, Fv), 4.40 (m, 2H, Fv), 4.46 (m, 2H, Fv), 4.54 ("t," 2H, Fv), 7.43 (m, 3H, *m,p*-Ph), 7.74 (m, 2H, *o*-Ph). $^{13}C\{^1H\}$ NMR (acetone-d_6), δ: 18.7 (d, J_{PC} = 30 Hz, PMe), 49.5 (s, CO*Me*), 81.6, 82.1, 90.9, 91.7 (s, all Fv), 92.0 (s, C-1 Fv), 111.7 (s, C-1 Fv), 129.1 (d, J_{PC} = 8 Hz, *o*-Ph), 130.0 (s, *p*-Ph), 130.1 (d, J_{PC} = 8 Hz, *m*-Ph), 141.2 (d, J_{PC} = 37 Hz, *ipso*-Ph), 246.2 (s, CO of anion), 251.3 (d, J_{PC} = 44 Hz, CO of CrCOMe). $^{31}P\{^1H\}$ NMR (acetone-d_6), δ: 59.0. For IR see Table 1.

***trans*-$FvCr_2(CO)_5(PMe_2Ph)Me(COMe)$ (8)**

This compound was observed in NMR scale reactions when PMe_2Ph was added slowly to **1** dissolved in 0.6 mL of acetone-d_6, or when methyl iodide was added to the in situ generated $Et_4N[$*trans*-$FvCr_2(CO)_5(PMe_2Ph)(COMe)]$. Both reactions resulted in various mixtures of this compound and **2**. ^1H NMR (acetone-d_6), δ: 0.50 (s, 3H, CrMe), 1.96 (d, J_{PH} = 9 Hz, 6H, PMe), 2.38 (s, 3H, COMe), 4.58 (m, 2H, Fv), 4.72 (m, 2H, Fv), 4.86 ("t," 2H, Fv), 4.93 ("t", 2H, Fv), 7.46 (m, 3H, *m, p*-Ph), 7.74 (m, 2H, *o*-Ph). $^{13}C\{^1H\}$ NMR (acetone-d_6), δ: −4.8 (s, CrMe), 18.8 (d, J_{PC} = 30 Hz, PMe), 49.4 (s, CO*Me*), 88.3, 88.9, 92.4, 93.6 (s, all Fv), 102.7 (s, C-1 Fv), 104.0 (s, C-1 Fv), 129.35 (d, J_{PC} = 9 Hz, *o*-Ph), 130.1 (d, J_{PC} = 8 Hz, *m*-Ph), 130.3 (s, *p*-Ph), 140.7 (d, J_{PC} = 39 Hz, *ipso*-Ph), 239.3 (s, CO cis to Me), 249.5 (CO *trans* to Me), 250.7 (d, J_{PC} = 44 Hz, CO cis to COMe). $^{31}P\{^1H\}$ NMR (acetone-d_6), δ: 57.9.

***trans,trans*-$FvCr_2(CO)_4(PMe_2Ph)_2(CH_2CN)_2$ (9)**

A solution of 0.30 g (0.34 mmol) $FvCr_2(CO)_4(PMe_2Ph)_2I_2$ (4d) was dissolved in 10 mL of THF and mixed with a large excess of sodium suspension (prepared from sodium dispersion in mineral oil (Aldrich) by washing with 3 × 10 mL of hexane) in 10 mL of THF. The reaction mixture immediately changed color from purple to yellow, but stirring was continued for 1 h. The reaction mixture, containing $Na_2[FvCr_2(CO)_4(PMe_2Ph)_2]$ (IR, ν_{CO}: 1778 and 1680 cm^{-1}) (4d), was filtered through Celite to give a clear, golden-yellow filtrate, which was reacted with 30 μL (0.47 mmol) of chloroacetonitrile. After 3 h, the NaCl precipitate was filtered off, the reaction mixture was concentrated to ~3 mL, and the alkyl complex was precipitated with 10 mL of hexane and collected and dried under reduced pressure. *trans,trans*-**9** was obtained as a poorly soluble, yellow powder in 0.22 g (0.31 mmol), 91 % yield. ^1H NMR (acetone-d_6), δ: 1.23 (d, J_{PH} = 2 Hz, 4H, CH_2), 1.91 (d, J_{PH} = 9 Hz, 12H, PMe), 4.55 (m, 4H, Fv), 4.58 (m, 4H, Fv), 7.50 (m, 6H, *m,p*-Ph), 7.74 (m, 4H, *o*-Ph). $^{13}C\{^1H\}$ NMR (DMSO-d_6): δ: −14.9 (d, J_{PC} = 15 Hz, CH_2), 19.2 (d, J_{PC} = 31 Hz, PMe), 88.1, 89.8 (s, both Fv), 100.5 (s, C-1 Fv), 128.5 (d, J_{PC} = 9 Hz, *o*-Ph), 129.3 (s, CN), 129.6 (d, J_{PC} = 7 Hz, *m*-Ph), 129.7 (s, *p*-Ph), 139.1 (d, J_{PC} = 39 Hz, *ipso*-Ph), 251.6 (d, J_{PC} = 46 Hz, CO). $^{31}P\{^1H\}$ NMR (acetone-d_6), δ: 61.2. FAB(+)-MS, m/z(%) $[M + Na]^+$ = 723(1), $[M - 2CO]^+$ = 644(1.5), $[M - 2CO - CH_2CN]^+$ = 604(2), $[M - 4CO - CH_2CN]^+$ = 548(4), $[M - PMe_2Ph - 4CO]^+$ = 450(13.5), [M

$- PMe_2Ph - 4CO - CH_2CN]^+ = 410(25)$, $[M - PMe_2Ph - 4CO - 2CH_2CN]^+ = 370(8)$, $[M - 2PMe_2Ph - 4CO]^+ = 312(31)$, $[M - 2PMe_2Ph - 4CO - CH_2CN]^+ = 272(22.5)$. IR data are listed in Table 1.

***trans*-$FvCr_2(CO)_5(PMe_2Ph)(CH_2CN)(COMe)$ (10)**

A solution of 0.27 g (0.41 mmol) $(Et_4N)_2[FvCr_2(CO)_6]$ in 45 mL of THF was reacted with 25 μL (0.41 mmol) of $ClCH_2CN$, added at room temperature. The mixture turned red instantly, and IR spectroscopic monitoring indicated completion of the formation of $Et_4N[FvCr_2(CO)_6CH_2CN]$ in ~1 h. At this point, 50 μL (0.80 mmol) of methyl iodide were added and complete formation of **3** was observed after ~1 h. The resulting brown solution was then stirred with 0.15 mL (1.05 mmol) of PMe_2Ph for 0.5 h, and an IR spectrum showed that compound **4** was the only carbonyl containing product. The solvent was removed under reduced pressure and 40 mL of a 1:1 THF-hexane mixture was used to extract **4** from the resulting solid. This solution was filtered and evaporated to dryness to give 0.15 g (0.25 mmol, 62%) of a yellow-brown solid. Although attempted recrystallizations did not result in analytically pure product, **4** was thoroughly characterized by spectroscopic means. ^1H NMR (acetone-d_6), δ: 1.43 (s, 2H, CH_2), 1.98 (d, J_{PH} = 9 Hz, PMe), 2.40 (s, 3H, COMe), 4.70 (m, 2H, Fv), 4.76 (m, 2H, Fv), 5.08 ("t," 2H, Fv), 5.22 ("t", 2H, Fv), 7.47 (m, 3H, *m,p*-Ph), 7.76 (m, 2H, *o*-Ph). $^{13}C\{^1H\}$ NMR (acetone-d_6), δ: −15.3 (s, $CrCH_2$), 18.9 (d, J_{PC} = 31 Hz, PMe), 49.4 (s, CO*Me*), 89.2, 91.7, 93.0, 94.0 (s, all Fv), 101.2 (s, C-1 Fv), 105.9 (s, C-1 Fv), 127.6 (s, CN), 129.5 (d, J_{PC} = 9 Hz, *o*-Ph), 130.2 (d, J_{PC} = 7 Hz, *m*-Ph), 130.5 (s, *p*-Ph), 140.7 (d, J_{PC} = 38 Hz, *ipso*-Ph), 239.8 (s, CO cis to CH_2CN), 249.2 (s, CO *trans* to CH_2CN), 250.6 (d, J_{PC} = 44 Hz, CO of CrCOMe), 271.9 (d, J_{PC} = 18 Hz, *C*OMe). $^{31}P\{^1H\}$ NMR (acetone-d_6), δ: 57.5. FAB(+)-MS, *m/z*(%): (No $[M]^+$ appeared) $[M - CO]^+ = 565(2)$, $[M - 2CO]^+ = 537(3)$, $[M - 6CO]^+ = 425(7.5)$, $[M - 6CO - Me]^+ = 410(17)$, $[M - PMe_2Ph - 2CO]^+ = 399(13)$, $[M - 6CO - Me - CH_2CN]^+ = 370(27)$, $[M - PMe_2Ph - 6CO]^+ = 287(15)$, $[M - PMe_2Ph - 6CO - Me]^+ = 272(27)$. IR data are listed in Table 1.

Results and discussion

Dianionic fulvalene complexes, $[FvM_2(CO)_6]^{2-}$ (M = Mo, W), have been shown to undergo nucleophilic reactions with various alkyl halides to give dialkyl derivatives of the types $FvM_2(CO)_6R_2$ (R = Me, CH_2Ph, CH_2OMe, etc.) (3*a*,*b*), Not reported to date, however, are analogous reactions of the anionic complex $[FvCr_2(CO)_6]^{2-}$, which is expected to react with alkyl halides as in eq. [1] to give alkylchromium species. We now report the results of an investigation of such reactions.

[1] $[FvCr_2(CO)_6]^{2-} + 2RX \rightarrow FvCr_2(CO)_6R_2 + 2X^-$

To our surprise, addition of $BrCH_2CN$ to a THF solution of $(Et_4N)_2[FvCr_2(CO)_6]$ did not result in the formation of the anticipated dialkyl product, but resulted instead in oxidation to $FvCr_2(CO)_6$ (1*c*, *d*). Similar reactions with XCH_2CO_2Et (X = Cl, Br, I) were also briefly investigated by IR and ^1H NMR spectroscopy, and all resulted in the formation of $FvCr_2(CO)_6$. ^1H NMR spectra of the reaction mixtures temporarily exhibited very broad fulvalene resonances before those of $FvCr_2(CO)_6$ began to emerge, and it would seem that electron-transfer-initiated radical reactions rather than nucleophilic substitutions take place, resulting in metal-metal bond formation. We obtained similar results for the reaction of $(Et_4N)_2[FvMo_2(CO)_6]$ with $BrCH_2CN$, and similar reactions have been reported for mononuclear metal carbonyl anions (4).

Hexacarbonyl Alkyl Compounds

Not all alkyl halides oxidize the $[FvCr_2(CO)_6]^{2-}$ anion, however. Treatment of $(Et_4N)_2[FvCr_2(CO)_6]$ with 2 equivalents or more of methyl iodide resulted in the formation of the rather unstable dimethyl compound $FvCr_2(CO)_6Me_2$ (**1**) (eq. [2], Scheme 1).

[2] $(Et_4N)_2[FvCr_2(CO)_6] + 2MeI \rightarrow FvCr_2(CO)_6Me_2$ **1**

Compound **1** was thoroughly characterized by spectroscopic methods and the data are fully consistent with the structure shown in Scheme 1. Thus the ^1H NMR spectrum exhibited a Cr-Me resonance at δ 0.62 and fulvalene multiplets at δ 5.10 and 5.37, while the $^{13}C\{^1H\}$ NMR spectrum exhibited a relatively shielded Cr-Me resonance at δ -5.0, fulvalene resonances at δ 88.3, 89.8, and 102.5, and two CO resonances at δ 238.9 (cis to Me) and 249.0 (trans to Me). Assignments of the ^{13}C resonances were made on the basis of data for $CpMo(CO)_3Me$ (5), and the results imply that the CO ligands do not interchange on the NMR time scale. While this work was in progress we learned that compound **1** has also been prepared by McGovern and Vollhardt.[3]

When only 1 equivalent of MeI was slowly added to a solution of dianion, the very sensitive, monoanionic intermediate $Et_4N[FvCr_2(CO)_6Me]$ (**2**) could be identified (Scheme 1). All spectroscopic data for this unstable species are consistent with the suggested structure, the ^1H NMR spectrum exhibiting a methyl resonance (δ: 0.53) and two sets of fulvalene hydrogens. Similarly the $^{13}C\{^1H\}$ NMR spectrum exhibited a Cr-Me resonance at δ −2.4, two sets of fulvalene resonances, and three CO resonances, two for the neutral and one for the anionic "half."

It is interesting to note that the IR spectrum exhibited one set of carbonyl bands of frequencies comparable with those of **1** (2000 and 1924 cm^{-1}) and a second set of considerably lower frequencies (1902, 1810, 1788 and 1727 cm^{-1}), comparable with those of $(Et_4N)_2[FvCr_2(CO)_6]$ (Table 1). Thus the chromium atoms of the two "halves" of **2** appear to be in very different electronic environments. Possibly a result of this dissimilarity is the large difference (22.5 ppm) between the two Fv C-1 carbon resonances, at δ 90.4 and 112.9.

Surprisingly, when $(Et_4N)_2[FvCr_2(CO)_6]$ was treated with an excess not of $BrCH_2CN$ but of $ClCH_2CN$, complete formation of $FvCr_2(CO)_6(CH_2CN)_2$ (**3**) took place at room temperature (eq. [3]), no $FvCr_2(CO)_6$ being formed at all.

[3] $[FvCr_2(CO)_6]^{2-} + 2\ ClCH_2CN \rightarrow FvCr_2(CO)_6(CH_2CN)_2$ **3**

The product was characterized by IR and NMR spectroscopy, although it could not be isolated analytically pure. However,

[3] P.A. McGovern and K.P.C. Vollhardt, private communication.

Scheme 1.

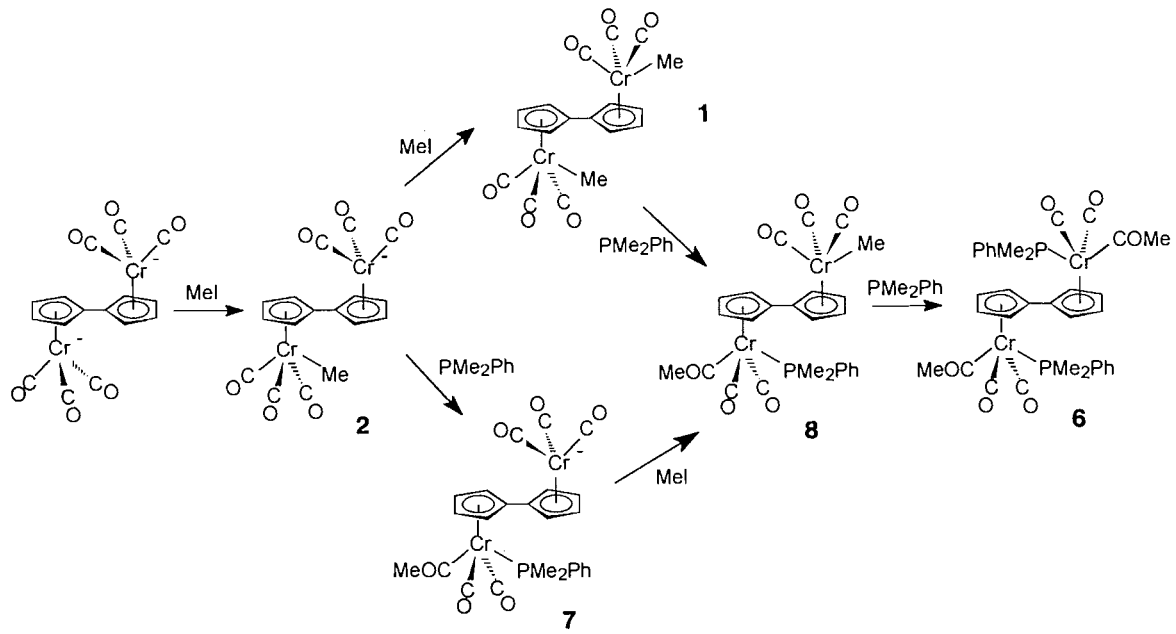

the ^1H and $^{13}C\{^1H\}$ NMR spectra exhibit patterns of resonances similar to those of **1**, the $CrCH_2$ proton and carbon resonances appearing at δ 1.62 and −15.4, respectively. Two resonances were observed in the CO region at δ 238.8 (*cis* to CH_2) and 248.2 (*trans* to CH_2) in about 2:1 ratio, suggesting a lack of interchange of these ligands. The carbonyl stretching bands of **3** are observed at higher frequencies than those of **1**, consistent with the greater electron-withdrawing power of the cyanomethyl group. The reasons for the differences in products from reactions of $(Et_4N)_2[FvCr_2(CO)_6]$ with $BrCH_2CN$ and $ClCH_2CN$ are not at all clear; understanding must await a mechanistic study.

Interestingly, when only 1 equivalent of $ClCH_2CN$ was slowly added to a solution of $(Et_4N)_2[FvCr_2(CO)_6]$, sole formation of the anionic alkyl intermediate $Et_4N[FvCr_2(CO)_6(CH_2CN)]$ (**4**) was observed, confirming the intermediacy of this complex in eq.[3]. This anionic alkyl compound was also too labile to be obtained pure, but was characterized spectroscopically. As is the case with **2**, the IR spectrum of **4** suggests the presence of "neutral" (2011 and 1938 cm^{-1}) and "anionic" (1897, 1795, and 1727 cm^{-1}) "halves," and the ^1H and $^{13}C\{^1H\}$ NMR spectra exhibit two sets of resonances. Also, as with **2**, the $^{13}C\{^1H\}$ NMR spectrum of **4** exhibited an unusually large difference (~28 ppm) between the two fulvalene bridgehead carbon resonances, at δ 87.9 and 116.3. Reaction of **4** with a second equivalent of $ClCH_2CN$ to give **3** was, because of decreased nucleophilicity of the monoanion, rather slow (~1 h) relative to the very rapid reaction with the first equivalent.

Successful formation of the anionic alkyl compounds $(Et_4N)[FvCr_2(CO)_6Me]$ (**2**) and $(Et_4N)[FvCr_2(CO)_6(CH_2CN)]$ (**4**) offered opportunities to synthesize mixed dialkyl complexes, and the compound $FvCr_2(CO)_6(CH_2CN)Me$ (**5**) was prepared as outlined in eq. [4], via addition of MeI to $(Et_4N)[FvCr_2(CO)_6(CH_2CN)]$. The product was thoroughly characterized spectroscopically. As can be seen in Table 1, the IR spectrum clearly exhibited two pairs of carbonyl stretching bands, one pair at 2006 and 1931 cm^{-1} attributable to the methyl "half," and another at 2021 and 1959 cm^{-1} that is attributable to the cyanomethyl "half." (Compare with data for **1** and **3**.) Furthermore, the ^1H NMR spectrum exhibited Me and CH_2 resonances at δ 0.64 and 1.59, respectively, and two sets of fulvalene resonances, while the $^{13}C\{^1H\}$ NMR spectrum exhibited Me and CH_2 resonances at δ −5.2 and −15.8, respectively, a CN resonance, and two sets each of fulvalene and CO resonances.

[4] $(Et_4N)[FvCr_2(CO)_6(CH_2CN)] + MeI \rightarrow$
4

$FvCr_2(CO)_6(CH_2CN)Me$
5

Tertiary phosphine-substituted compounds

In an unsuccessful attempt to synthesize phosphine-substituted analogues of **1**, it was found that **1** readily *added* 2 equivalents of PMe_2Ph at room temperature. The consequence was a sequence of migratory CO insertion reactions into the Cr—Me bonds (eq. [5]), resulting in formation of the diacetyl compound $FvCr_2(CO)_4(PMe_2Ph)_2(COMe)_2$ (**6**) in good yield. Although **6** is also too unstable to be isolated analytically pure, the mass spectrum and ^1H, $^{13}C\{^1H\}$, and $^{31}P\{^1H\}$ NMR spectra are all completely consistent with the *trans,trans* structure shown in Scheme 1. Thus the FAB mass spectrum exhibited a protonated molecular ion and several reasonable fragmentation peaks. In addition, the ^1H and $^{13}C\{^1H\}$ NMR spectra each exhibited only single acetyl Me and PMe resonances and single sets of fulvalene resonances, consistent with a symmetrical *trans,trans* structure (see experimental section), while the $^{31}P\{^1H\}$ NMR spectrum exhibited only one singlet. The $^{13}C\{^1H\}$ NMR spectrum exhibited only one doublet for two CO ligands, at δ 250.8 and with a relatively large (J_{PC} 45 Hz) coupling constant suggestive of a *cis*-P-Cr-CO and consequently a *trans*-P-Cr-COMe arrangement (5). The MeCO res-

onance appeared at δ 272.4 (J_{PC} 18 Hz), quite similar to that of $CpMo(CO)_2(PMe_2Ph)COMe$ (266.8 (12.5)) (5).

[5] $FvCr_2(CO)_6Me_2 + 2PMe_2Ph \rightarrow$
1

trans,trans-$FvCr_2(CO)_4(PMe_2Ph)_2(COMe)_2$
6

To our knowledge, **6** is the first well-characterized acylchromium complex of the type $CpCr(CO)_2L(COMe)$ (L = phosphorus donor) that has been prepared via a spontaneous, ligand-assisted CO insertion into a Cr–alkyl bond. Two other examples of compounds of the type $CpCr(CO)_2L(COMe)$ were prepared as minor products, either in photochemical substitution reactions of $CpCr(CO)_3Me$ with L (L = PPh_3, $P(OMe)_3$) (6*a*) or in an apparent Arbuzov reaction of [$CpCr(CO)_2${P(OMe) 63}] with $P(OMe)_3$ (6*b*); both exist as mixtures of *cis* and *trans* isomers. Indeed, although photochemical substitution reactions of complexes of the type $CpCr(CO)_3R$ (R = alkyl) with phosphorus donors have attracted a great deal of attention, reactions invariably resulted in the formation of mono- and bis-substituted alkyl complexes (7). An attempt to substitute **1** with PPh_3 under thermal conditions failed, and an experiment carried out under UV irradiation resulted in the formation of $FvCr_2(CO)_6$ instead of substitution.

When the reaction of **1** was performed with small aliquots of PMe_2Ph added slowly to the reaction mixture, intermediate formation of the methyl-acetyl complex $FvCr(CO)_5(PMe_2Ph)(Me)(COMe)$ (**8**, Scheme 1) could be detected by NMR spectroscopy. Although this compound could not be obtained selectively, it was characterized in situ by NMR spectroscopy. The ^1H, $^{13}C\{^1H\}$, and $^{31}P\{^1H\}$ NMR spectra are completely compatible with the suggested formulation, with the acetyl group and PMe_2Ph ligands occupying mutually *trans* positions. Thus the ^1H NMR spectrum exhibited CrMe, CrCOMe, and PMe resonances at δ 0.50, 2.38, and 1.96, respectively, in addition to four two-hydrogen fulvalene resonances at δ 4.58, 4.72, 4.86, and 4.93. The $^{13}C\{^1H\}$ NMR spectrum exhibited CrMe, CrCOMe, and PMe resonances at δ −4.8, 49.4 and 18.8, respectively, six fulvalene resonances, three CO resonances, and one MeCO resonance. There is also only a single resonance in the $^{31}P\{^1H\}$ NMR spectrum, confirming the presence of a single geometric isomer.

As indicated in Scheme 1, **8** was also formed by reaction of $Et_4N[FvCr_2(CO)_6Me]$ with first PMe_2Ph, then MeI. As shown, direct addition of PMe_2Ph to the methyl "half" of $Et_4N[FvCr_2(CO)_6Me]$ resulted in the formation of the anionic acetyl compound $Et_4N[FvCr_2(CO)_5(PMe_2Ph)(COMe)]$ (**7**), the IR spectrum of which exhibited carbonyl bands at 1897, 1808, 1789, and 1725 cm^{-1}, similar to those of $(Et_4N)_2[FvCr_2(CO)_6]$, and at 1920, 1837.5, and 1636 (C═O) cm^{-1}, similar to those of **6;** thus **7** presumably assumes the structure shown in Scheme 1, with a *trans* acetyl "half." The ^1H NMR spectrum exhibited a PMe doublet resonance (δ 1.89), an acetyl resonance (δ 2.37), and four fulvalene multiplets (δ 4.23, 4.40, 4.46, and 4.54). The $^{13}C\{^1H\}$ NMR spectrum exhibited single PMe and CO*Me* resonances, as well as six fulvalene, two CO, and one *C*OMe resonance, while the presence of only one resonance in the $^{31}P\{^1H\}$ NMR spectrum confirmed the presence of only a single isomer. As with the other monoanionic complexes **2** and **4**, the $^{13}C\{^1H\}$ NMR spectrum exhibited a large difference (19.7 ppm) between the two bridgehead carbon resonances (δ 92.0 and 111.7).

Contrary to our expectations, addition of an excess of PMe_2Ph to **3** under thermal and photochemical conditions did not result in the formation of a substituted derivative **3**, but rather in decomposition to unidentified precipitates in both cases. The IR spectra indicated the possible formation of trace amounts of a substituted product (1944 and 1869 cm^{-1}), but this reaction was not investigated further.

Consequently, in accord with different substitution behaviours of the homodialkyl compounds **1** and **3**, the mixed alkyl compound **5** reacted with PMe_2Ph only the methyl "half", resulting in the formation in good yield of the mixed alkyl acyl compound $FvCr_2(CO)_5(PMe_2Ph)(CH_2CN)(COMe)$ (**10**) (eq. [6]).

[6] $FvCr_2(CO)_6(CH_2CN)Me + PMe_2Ph \rightarrow$
3

trans-$FvCr_2(CO)_4(PMe_2Ph)(CH_2CN)(COMe)$
10

Although the molecular ion of **10** could not be observed in the mass spectrum, the fragmentation pattern is quite consistent with the formulation suggested. The IR spectrum exhibited sets of carbonyl bands at 2019 and 1949 cm^{-1} and at 1922, 1844, and 1639 (C═O) cm^{-1}, similar to those of **4** and **6**, respectively, and suggesting that the acetyl "half" assumes the *trans* isomeric form. The ^1H NMR spectrum exhibited the expected $CrCH_2$ (δ 1.43), PMe (δ 1.98), and COMe (δ 2.40) resonances, as well as four fulvalene resonances (δ 4.70, 4.76, 5.08, 5.22). The $^{13}C\{^1H\}$ NMR spectrum exhibited single $CrCH_2$ (δ −15.3), PMe (δ 18.9), CO*Me* (δ 49.4), and CN (δ 127.6) resonances, as well as six fulvalene resonances (δ 89.2, 91.7, 93.0, 94.0, 101.2, 105.9). three CO resonances (δ 239.8, 249.2, 250.6), and a *C*OMe resonance (δ 271.9).

Earlier it was shown that reduction of *cis,cis*-$FvMo_2(CO)_4L_2Br_2$ (L = PPh_3, PCy_3, PXy_3) with sodium dispersion readily afforded the corresponding dianions (1*b*). Similar treatment of *cis,cis*-$FvCr_2(CO)_4(PMe_2Ph)_2I_2$ (1*d*) was carried out with an excess of sodium dispersion in THF, resulting in the formation of the very air-sensitive salt $Na_2[FvCr_2(CO)_4(PMe_2Ph)_2]$ (eq. [7]).

[7] *cis*,cis-$FvCr_2(CO)_4(PMe_2Ph)_2I_2$ + excess Na →

$Na_2[FvCr_2(CO)_4(PMe_2Ph)_2]$

This salt was then treated with $ClCH_2CN$ to give **9** in excellent yield (eq. [8]).

[8] $Na_2[FvCr_2(CO)_4(PMe_2Ph)_2] + 2\ ClCH_2CN \rightarrow$

$FvCr_2(CO)_4(PMe_2Ph)_2(CH_2CN)_2$
9

The FAB mass spectrum of **9** exhibited a peak at 723 amu, attributed to the molecular ion plus Na^+, as well as several reasonable fragmentation ions. Consistent with a *trans,trans* structure, the ^1H and $^{13}C\{^1H\}$ spectra are very simple. The

former exhibited single $CrCH_2$ (δ 1.23) and PMe (δ 1.91) resonances and only two fulvalene resonances (δ 4.55, 4.58), while the $^{13}C\{^1H\}$ NMR spectrum exhibited a $CrCH_2$ doublet at δ −14.9 (J_{PC} 15 Hz), confirming the presence of a Cr—C bond. In addition, only three fulvalene resonances (δ 88.1, 89.8, 100.5) and one CO carbon doublet (δ 251.6) were observed in the CO region, consistent with the symmetric structure anticipated for the *trans,trans* isomer. No sign of isomerization to *cis,trans* or *cis,cis* forms could be detected in solutions of **9**.

Acknowledgements

We thank NATO for a Science Fellowship to I.K. (administered by the Natural Sciences and Engineering Research Council of Canada (NSERC)), NSERC for a Research Grant to M.C.B., and the Hungarian Science Fund for additional support to I.K. provided by Grant No. OTKA F7419. We are also indebted to J.A. Stone for assistance in obtaining mass spectra.

References

1. (*a*) I. Kovács and M.C. Baird. Organometallics, **14,** 4074 (1995); (*b*) Organometallics, **14**, 4084 (1995); (*c*) Organometallics, **14**, 5469 (1995); (*d*) Organometallics, **15**, 3588 (1996).
2. (*a*) S. Fortier, M.C. Baird, K.F. Preston, J.R. Morton, T. Ziegler, T.J. Jaeger, W.C. Watkins, J.H. MacNeil, K.A. Watson, K. Hensel, Y. LePage, J.-P. Charland, and A.J. Williams. J. Am. Chem. Soc. **113**, 542 1991; (*b*) K.A.E. O'Callaghan, S.J. Brown, J.A. Page, M.C. Baird, T.C. Richards, and W.E. Geiger. Organometallics, **10**, 3119 (1992); (*c*) W.C. Watkins, T. Jaeger, C.E. Kidd, S. Fortier, M.C. Baird, G. Kiss, G.C. Roper, and C.D. Hoff. J. Am. Chem. Soc. **114**, 907 (1992); (*d*) C.A. MacConnachie, J.M. Nelson, and M.C. Baird. Organometallics, **11**, 2521 (1992); (*e*) T.C. Richards, W.E. Geiger, and M.C. Baird. Organometallics, **13**, 4494 (1994); (*f*) N.A. Cooley, P.T.F. MacConnachie, and M.C. Baird. Polyhedron, **7**, 1965 (1988); (*g*) W.C. Watkins, K. Hensel, S. Fortier, D.H. Macartney, M.C. Baird, and S.J. McLain. Organometallics, **11**, 2418 (1992); (*h*) P.R. Drake and M.C. Baird. J. Organomet. Chem. **363**, 131 (1989); (*i*) M.D. Koeslag and M.C. Baird. Organometallics, **13**, 11 (1994); (*j*) I. Kuksis and M.C. Baird. Organometallics, **13**, 1551 (1994); (*k*) C.A. Goulin, T.A. Huber, J.M. Nelson, D.H. Macartney, and M.C. Baird. J. Chem. Soc. Chem. Commun. 798 (1991); (*l*) T.A. Huber, D.H. Macartney, and M.C. Baird. Organometallics, **12**, 4715 (1993); (*m*) Organometallics, **14**, 592 (1995).
3. (*a*) M. Tilset, K.P.C. Vollhardt, and R. Boese. Organometallics, **13**, 3146 (1994); (*b*) J.S. Drage and K.P.C. Vollhardt. Organometallics, **5**, 280 (1986); (*c*) P.A. McGovern and K.P.C. Vollhardt. Synlett, 493 (1990).
4. I. Kovács, F. Ungváry, and J.F. Garst. Organometallics, **12**, 389 (1993), and refs. therein.
5. L.J. Todd, J.R. Wilkinson, J.P. Hickey, D.L. Beach, and K.W. Barnett. J. Organomet. Chem. **154**, 151 (1978).
6. (*a*) H.G. Alt. J. Organomet. Chem. **124**, 167 (1977); (*b*) L.-Y. Goh, M.J. D'Aniello, S. Slater, E.L. Muetterties, I. Tavanaiepour, M.I. Chang, M.F. Fredrich, and V.W. Day. Inorg. Chem. **18**, 192 (1979).
7. (*a*) H.G. Alt and J.A. Schwarzle. J. Organomet. Chem. **162**, 45 (1978); (*b*) R.M. Medina and J.R. Masaguer. J. Organomet. Chem. **299**, 341 (1986).

Multinuclear NMR spectra of $[Pt(L)Cl_3]^-$ (L = pyridine derivatives) complexes and crystal structure of *trans*-Pt(2,6-di(hydroxymethyl)pyridine)$_2Cl_2.2H_2O$

Fernande D. Rochon, André L. Beauchamp, and Corinne Bensimon

Abstract: Complexes of the type $[Pt(L)Cl_3]^-$ (L = pyridine derivative) were synthesized and studied by ^{13}C and ^{195}Pt NMR spectroscopies. The ^{195}Pt signals were observed between −1720 and −1897 ppm. No correlation between the δ(Pt) and the pK_a of the protonated pyridine derivatives was found. The chemical shifts vary with the substituents on the pyridine ligand. Compounds with substituents in *ortho* positions were observed at lower fields, except for complexes containing hydroxy or amine groups. The latter compounds were observed at higher fields, close to the signals of the Pt-unsubstituted pyridine compound. These results were explained in terms of the solvent effect. The chemical shifts δ(C) and the coupling constants $J(^{13}C–^{195}Pt)$ were measured and the results interpreted with a view of obtaining information on the nature of the Pt—N bond. The possibility of π-bonding between platinum and the pyridine ligand is examined. The conformation of the pyridine ring in relation to the platinum plane and the energies of the rotation barriers around the Pt—N bond in these types of platinum(II) complexes are briefly discussed. The crystal structure of *trans*-$Pt(2,6\text{-}(HOCH_2)_2py)_2Cl_2\cdot 2H_2O$ was determined by X-ray diffraction. The compound is monoclinic, *C2/m*, $a = 7.022(6)$, $b = 15.646(13)$, $c = 8.344(10)$ Å, ß = 93.35(8)°, $Z = 2$, $R = 0.037$. The platinum atom is located at the junction of the twofold axis and the mirror plane, the N atoms and the *para*-C atom of the pyridine ring are situated on the twofold axis, and the chloride ligands are on the mirror plane. The compound crystallizes with molecules of water, which are H-bonded to the hydroxy groups. The Pt—Cl bond distance is 2.306(2) Å, and that of the Pt—N bond is 2.041(6) Å. The dihedral angle between the platinum and the pyridine planes is 79.8°.

Key words: platinum, pyridine derivatives, NMR, crystal structure.

Résumé : Des complexes de type $[Pt(L)Cl_3]^-$ (L = dérivé de la pridine) ont été etudiés par spectroscopie RMN du ^{13}C et du ^{195}Pt. Les signaux ^{195}Pt ont été observés entre −1720 et −1897 ppm. Aucune correlation entre les δ(Pt) et les pK_a des dérivés protonés de la pyridine n'a été déduite. Les déplacements chimiques dépendent des substituants sur la pyridine. Les composés avec des substituants en positions *ortho* été observé à des champs plus faibles, à l'exception des complexes contenant des groupements hydroxy ou amine. Ces derniers ont été observés à champ plus élevé, proche de celui observé pour $[Pt(pyridine)Cl_3]^-$. Ces résultats ont été interprétés en fonction de l'effet de solvant. Les déplacements chimiques δ(C) et les constantes de couplage $J(^{13}C–^{195}Pt)$ ont été mesurés et les résultats interprétés en vue d'obtenir des informations sur la nature de la liaison Pt—N. La possibilité de liaison π dans ce type de complexes a été examinée. La conformation du noyau de la pyridine par rapport au plan du platine ainsi que les énergies des barrières de rotation autour du lien Pt—N dans ce type de complexes de platine(II), sont brièvement discutées. La structure cristalline du composé *trans*-$Pt(2,6\text{-}(HOCH_2)_2py)_2Cl_2]\cdot 2H_2O$ a été déterminée par diffraction des rayons -X. Le composé cristallise dans le groupe d'espace monoclinique *C2/m*, $a = 7,022(6)$, $b = 15,646(13)$, $c = 8,344(10)$ Å, β = 93,35(8)°, Z = 2 et R = 0,037. L'atome de platine est situé à la jonction de l'axe de rotation 2 et du miroir, les ligands Cl^- sont localisés sur le miroir et les atomes N et C (para) sont sur l'axe 2. Les liens Pt—Cl et Pt—N sont 2,306(2) et 2,041(6) Å. L'angle dièdre entre le plan de la pyridine et celui du platine est 79,8°. Le composé cristallise avec des molécules d'eau qui forment des ponts hydrogènes avec les groupements hydroxy des ligands.

Mots clés : platine, dérivés de la pyridine, résonance magnétique nucléaire, structure cristalline.

Received February 27, 1996.

This paper is dedicated to Professor Howard C. Clark in recognition of his contributions to Canadian chemistry.

F.D. Rochon[1] **and C. Bensimon.** Department of Chemistry, Université du Québec à Montréal, C.P. 8888, Montréal, QC H3C 3P8, Canada.
A.L. Beauchamp. Department of Chemistry, Université de Montréal, C.P. 6128, Montréal, QC H3C 3J7, Canada.

[1] Author to whom correspondence may be addressed. Telephone: (514) 987-3000, ext. 4896. Fax: (514) 987-4054. E-mail: rochon.fernande@uqam.ca

Introduction

Pyridine complexes of platinum(II) have been known for a long time, but studies of the nature of the metal–ligand bond are relatively scarce in the literature. Pyridine has six π molecular orbitals (1). The three bonding orbitals are filled, while the three higher energy antibonding orbitals are empty and could accept electron density from the metal. The orientation of the pyridine ring in the platinum complexes can give useful information on the type of orbitals involved in the Pt—L (L = pyridine derivatives) bonding. Bond lengths are usually sensitive to the presence of multiple bonding but, in this case, bond length values are generally not accurate enough to provide unambiguous conclusions. Multinuclear NMR spectroscopy can also give some indication of the strength of the Pt—L bond. The σ bond will cause a deshielding effect on the ligand and a shielding effect on the metal, while back-donation from the metal to the ligand should produce the opposite effect.

The ^{195}Pt NMR signals are particularly sensitive to the presence of substituents on the ligands, especially those in *ortho* positions of the pyridine ligands. These effects are not always predictable in NMR spectroscopy and the origins of the different observed chemical shifts are not well understood. A few authors have made systematic ^{195}Pt NMR studies of platinum(II)–pyridine complexes. Motschi, Sze, and Pregosin have characterized a series of compounds of the type trans-Pt(py-X)$(C_2H_4)Cl_2$ (2), while Marzilli et al. (3) have studied three types of complexes: *cis*- and *trans*-Pt(py-X)$(DMSO)Cl_2$ and *cis*-$[Pt(py\text{-}X)(DMSO)_2Cl]^+$. These authors tried to correlate the pK_a of the protonated py-X ligands to the ^{195}Pt chemical shifts of the complexes. They observed correlations for pyridine ligands containing substituents in *para* position only. For Pt(py-X)$(DMSO)Cl_2$, the authors found, for the *cis* isomer, a very small shielding on the platinum atom as the pK_a values increase, and the reverse for the *trans* isomer. But the differences in chemical shifts are very small and we believe that the observed correlations might not be highly significant. ^{13}C NMR spectroscopy can also give useful information on the nature of the metal–ligand bond. Unfortunately, it is not easy to interpret the overall effects.

Compounds of the type $[Pt(py)Cl_3]^-$ are simple (no isomers), easy to prepare with a good purity, and very soluble in water. We have now synthesized a long series of these complexes with pyridine ligands containing different substituents and we have measured their ^{13}C and ^{195}Pt NMR spectra. The results were interpreted with a view to obtaining information on the factors governing their chemical shifts and also on the nature of the Pt–pyridine bond and molecular conformation. A few disubstituted compounds of the type *trans*-Pt$(L)_2Cl_2$ were studied in order to evaluate approximately the rotation barriers in these complexes. In an attempt to crystallize the monosubstituted complex with 2,6-di(hydroxymethyl)pyridine, we obtained single crystals of the disubstituted compound. Disubstituted complexes are always obtained in these reactions as a by-product, and they are usually filtered out of the solution. The crystal was studied by X-ray diffraction and the results are described below.

Experimental

The ^{195}Pt NMR spectra were measured on a Bruker WH-400 (85.832 MHz) spectrometer, while the ^{13}C NMR spectra were obtained on a Bruker WP-80 operating at 20.15 MHz. The spectra of the platinum complexes were measured at concentrations near saturation in 10 mm tubes, while the ^{13}CNMR spectra of the ligands were measured in the normal 5 mm tubes. Most of the spectra were measured in D_2O (or chloroform). The external standard for the ^{195}Pt spectra was $[Pt(H_2O)_6]^{4+}$ (δ = 0 ppm). The decomposition points were measured on a Fisher–Johns instrument. The ligands were bought from Aldrich and K_2PtCl_4 from Johnson Matthey and Co. The latter was recrystallized from water before use.

Synthesis of K[Pt(L)Cl_3]

The complexes were synthesized according to the published method (4) with slight modifications. The reaction time varied between 3 and 48 h depending on the ligand. The compounds with pyridine (3 h at 75°C), 4-methylpyridine (3 h at 75°C), and 2,6-dimethylpyridine (12 h at 65°C) have already been reported (4). The complex with 3-methylpyridine was prepared by the same method (3 h. at 75°C). Yield: 30%. mp 180–195°C (dec.).

L = 2-methylpyridine, 2-(methylamino)pyridine, 2,3-dimethylpyridine, 2,4-dimethylpyridine, 2,5-dimethylpyridine, 3,4-dimethylpyridine, 3,5-dimethylpyridine, 4-cyanopyridine, 4-acetylpyridine, 4-tert-butylpyridine, and 4-(hydroxymethyl)pyridine

Two mmoles each of K_2PtCl_4 and of the ligand were dissolved in 50 mL of DMF and the solution was stirred during 3 h at 80°C. The mixture was filtered and the filtrate evaporated to dryness under reduced pressure. The residue was washed with ether and dried. It was then dissolved in acetone and the mixture was filtered to eliminate KCl and K_2PtCl_4. The filtrate was evaporated to dryness and the residue was washed with chloroform and finally dried. The ^{195}Pt and ^{13}C NMR spectra confirmed the purity of the compounds. 2-Methylpyridine, yield 81%, mp 160–170°C (dec.); 2-(methylamino)pyridine, yield 45%, mp 155–165°C (dec.); 2,3-dimethylpyridine, yield 79%, mp 205–220°C (dec.); 2,4-dimethylpyridine, yield 70%, mp 220–230°C (dec.); 2,5-dimethylpyridine, yield 46%, mp 210–220°C (dec.); 3,4-dimethylpyridine, yield 51%, mp 155–160°C (dec.); 3,5-dimethylpyridine, yield 40%, mp 160–165°C (dec.); 4-cyanopyridine, yield 45%, mp 185–200°C (dec.); 4-acetylpyridine, yield 48%, mp 195–205°C (dec.); 4-*tert*-butylpyridine, yield 45%, mp 200–205°C (dec.); 4-(hydroxymethyl)pyridine, yield 35%, mp 210–220°C (dec.).

L = 2,3,6-trimethylpyridine and 2,4,6-trimethylpyridine

Two mmoles each of K_2PtCl_4 and of the ligand were dissolved in 75 mL of DMF. The mixture was stirred for 48 h at 60°C and then filtered. The filtrate was then treated as described for 2-methylpyridine. Yields: 45% and 34%, mp 195–200°C (dec.) and 155–165°C (dec.), respectively.

L = 2-(aminomethyl)pyridine, 2-(hydroxymethyl)pyridine, 2-methoxypyridine, 2,6-dimethoxypyridine, and 2,6-di(hydroxymethyl)pyridine

Two mmoles each of K_2PtCl_4 and of the ligand were dissolved in 50 mL of water. The mixture was stirred overnight at room temperature and then filtered. The filtrate was then evaporated to dryness under reduced pressure and the residue was washed with ether and dried. The product was then dissolved in ace-

Table 1. Crystal data of *trans*-Pt(2,6-$(HOCH_2)_2$py)$_2Cl_2 \cdot 2H_2O$.

Formula	$C_{14}H_{22}N_2O_6Cl_2Pt$
fw	580.34
space group	*C2/m*
a (Å)	7.022(6)
b (Å)	15.646(13)
c (Å)	8.344(10)
ß (°)	93.35(8)
Volume (Å^3)	915(1)
Z	2
F(000)	560
ρ_{calcd} (Mg m^{-3})	2.106
μ(MoKα) (mm^{-1})	8.073
$R = (\Sigma\|\|F_o\| - \|F_c\|\|)/\Sigma\|F_o\|$	0.037
$R_w = [\Sigma w(\|F_o\| - \|F_c\|)^2/\Sigma w\|F_o\|^2]^{1/2}$	0.042

tone to eliminate KCl and K_2PtCl_4, which were filtered out. The filtrate was finally evaporated to dryness and the residue washed with chloroform and dried. 2-(Aminomethyl) pyridine, yield 55%, mp 155–160°C (dec.); 2-(hydroxymethyl)pyridine, yield 35%, mp 170–180°C (dec.); 2-methoxypyridine, yield 75%, mp 160–165°C (dec.); 2,6-dimethoxypyridine, yield 64%, mp 175–180°C (dec.); 2,6-di(hydroxymethyl)pyridine), yield 64%, mp 155–160°C (dec.).

Synthesis of *trans*-Pt(py)$_2Cl_2$ complexes (L = 2-methylpyridine and 3-methylpyridine)

These complexes were synthesized according to the method described by Kauffman for the synthesis of the pyridine complex (5). Yields: 68%, 75%; mp 210–220°C (dec.) and 195–205°C (dec.), respectively.

Data collection and resolution of the crystal structure

The data collection (2θ/θ) was made at room temperature, on a Syntex $P\bar{1}$ diffractometer, with graphite-monochromatized MoKα radiation (0.71069 Å). The unit cell parameters were calculated from the least-squares refinement of the angles of 15 centered reflections. A rapid data collection suggested a *C* Bravais lattice. Therefore a slower collection was made assuming a *C* lattice. The crystal data are summarized in Table 1. The scan rate varied between 1 and 24° min^{-1}. The intensity data were corrected for absorption (Gaussian integration) and for the effects of Lorentz and polarization. The coordinates of the Pt atom were determined from a three-dimensional Patterson synthesis and the positions of all the other non-hydrogen atoms were obtained by structure factor and Fourier-map calculations. The positions of the H atoms (except those on O atoms, which could not be located) were fixed at their calculated positions with isotropic $U = 0.076$ Å^2. The refinement of the structure was done using full-matrix least-squares calculations minimizing $\Sigma w(F_o - F_c)^2$. Isotropic secondary-extinction corrections (6) were included in the calculations. Individual weights $w = 1/\sigma^2(F)$ were applied. The scattering curves of Cromer and Waber (7) were used for Pt, Cl, N, and C and that of Stewart, Davidson and Simpson (8) was used for H. The anomalous dispersion terms of Pt and Cl were included (9). The calculations were performed using the programs already described (10).[2]

Results and discussion

The complexes K[Pt(L)Cl_3] (L = pyridine derivative) were synthesized by modifying the reported method (4). For most of the complexes, the reaction of K_2PtCl_4 with the ligand was done in dimethyl formamide, in a Pt–ligand mole ratio close to 1:1. The time of reaction varied with the ligand, between 3 and 48 h. A longer time was required for ligands that have substituents in positions 2 and 6. The reactions were performed between 60 and 80°C, except for 2-(aminomethyl)pyridine, 2-(hydroxymethyl)pyridine, 2-methoxypyridine, 2,6-dimethoxypyridine, and 2,6-di(hydroxymethyl)pyridine, whose reactions were done at room temperature and in aqueous medium. These compounds were studied by multinuclear NMR spectroscopy.

^{195}Pt NMR

The variation of the electronic effects on the platinum atom, by the presence of different substituents on the pyridine ligands, can be studied by ^{195}Pt NMR spectroscopy. While the σ bond causes a shielding effect on the δ(Pt), back-donation from the metal to the ligand will produce the opposite effect. An increase of the intrinsic basicity of the ligand should lead to a stronger σ bond and a larger electron density on the platinum atom. As a result, the δ(Pt) should shift towards higher fields. The intrinsic basicity of the ligands can be evaluated from the gas phase protonic affinities or by the Hammett constants but these values are not easily accessible. The pK_a values of the protonated ligands are available for most pyridine derivatives and they should give useful information on the strength of the σ bond.

The ^{195}Pt NMR spectra of the platinum(II) complexes were measured in D_2O and the results are shown in Table 2. The signals were observed between −1720 and −1897 ppm. An attempt was made to find a correlation between the δ(Pt) of all the complexes and the pK_a of the protonated pyridine derivatives. No general relation was found. The chemical shifts of the complexes were found to vary with the substituents on the ligand, and the compounds can be classified into four groups. The signals of the first group of complexes, which contain ligands with no substituents in *ortho* positions, were observed between −1805 and −1818 ppm. The pK_a values for these protonated ligands vary between 1.77 and 6.46 (11). The second group of complexes contains pyridine derivatives with a methyl or methoxy substituent in position 2 (pK_a between 3.20 and 6.63) and the δ(Pt) were found at slightly lower field,

[2] **Supplementary material available:** The following tables and figures have been deposited: Experimental details of the crystallographic study (S1), anisotropic thermal factors (S2), H coordinates (S3), and weighted best planes (S4). This material may be purchased from: The Depository of Unpublished Data, Document Delivery, CISTI, National Research Council Canada, Ottawa, Canada K1A 0S2. Tables S1 and S3 have also been deposited with the Cambridge Crystallographic Data Centre, and can be obtained on request from The Director, Cambridge Crystallographic Data Centre, University Chemical Laboratory, 12 Union Road, Cambridge, CB2 1EZ, U.K.

Table 2. ^{195}Pt chemical shifts of the complexes and pK_a of the protonated ligands (from ref. 11).

py	δ(Pt)	pK_a
Pyridine	−1816	5.22
3-CH_3py	−1816	5.63
4-CH_3py	−1817	5.98
4-NCpy	−1812	1.90
4-CH_3COpy	−1811	1.77
4-$HOCH_2$py	−1814	5.62
4-$(CH_3)_3$Cpy	−1818	5.99
3,4-$(CH_3)_2$py	−1805	6.46
3,5-$(CH_3)_2$py	−1806	6.15
2-CH_3py	−1796	5.96
2-CH_3Opy	−1789	3.20
2,3-$(CH_3)_2$py	−1763	6.57
2,4-$(CH_3)_2$py	−1784	6.63
2,5-$(CH_3)_2$py	−1785	6.40
2,6-$(CH_3)_2$py	−1754	6.72
2,6-$(CH_3O)_2$py	−1735	
2,3,6-$(CH_3)_3$py	−1720	7.40
2,4,6-$(CH_3)_3$py	−1747	7.48
2-$HOCH_2$py	−1820	5.60
2-CH_3NHpy	−1897	8.10
2-$H_3N^+CH_2$py	−1857	3.31
2,6-$(HOCH_2)_2$py	−1839	

between −1763 and −1796 ppm. The compounds containing methyl or methoxy substituents in positions 2 and 6 (pK_a between 6.72 and 7.48), which form the third group, showed resonances at the lowest field, between −1720 and −1754 ppm. The fourth group, which is composed of platinum compounds containing pyridine derivatives with hydroxy or amine groups in positions 2 or (and) 6, were observed at the highest fields, between −1820 and −1897 ppm. The pK_a of these protonated ligands vary between 3.31 and 8.10. These observations do not show any relation between the δ(Pt) and the pK_a values. It seems that factors other than the basicity of the ligands influence the ^{195}Pt NMR signals of the complexes.

The data obtained from the three first groups of platinum(II) complexes are in agreement with the results observed by Pregosin (12), who reported a ^{195}Pt downfield shift when the ligand became more sterically demanding, close to the binding site. Therefore, the bulkiness around the binding N atom seems to be the first factor governing the ^{195}Pt chemical shifts. The compounds with two substituents in *ortho* positions (third group) are observed at the lowest field (≈−1740 ppm) while those with no substituent in *ortho* positions (first group) are observed at higher field (≈−1810 ppm).

The complexes of the fourth group, which contain ligands with hydroxy or amine groups in positions 2 and (or) 6, do not follow this rule. Compounds with -CH_2OH groups in positions 2 and (or) 6 were observed at higher fields (−1820 and −1839 ppm), close to those of complexes with no substituents in *ortho* positions. Two hypotheses were investigated in order to explain these data. The observed different chemical shifts might be attributed to different Pt–ligand π-bonding or (and) to the solvent effect around the platinum atom. In both explanations, the effects depend on the conformation of the complexes, namely, on the orientation of the pyridine ring with respect to the platinum coordination plane.

Orientation of the pyridine ligands in the Pt(II) complexes

A crystallographic review of pyridine–platinum(II) complexes was made in order to determine the conformation of the pyridine ring in these complexes. We have chosen only the compounds that have chloride ligands in *cis* positions to the pyridine ligand. The results have shown that for pyridine ligands without *ortho* substituents, the dihedral angles between the coordination plane of the platinum atom and the plane of the pyridine ring vary from 44° to 59° (13–19). For the 2-methylpyridine complex, the angle is 72° (20). For complexes containing ligands with substituents in positions 2 and 6, they vary from 82° to 89° (16, 21–25). Obviously, the pyridine ring is frozen in a nearly perpendicular orientation by the *ortho* substituents. For a dihedral angle of 72°, the Cl --- C_{methyl} distance (~3.2 Å) is substantially less than the sum of the van der Waals radii (~3.9 Å), and further reducing this angle would be energy costly. Thus, oscillation of the pyridine ligand is restricted to a narrow ±15° range about 90°, and 180° rotation to reach the other vertical orientation is probably obstructed by very high repulsion when the pyridine ligand tries to become coplanar with the coordination plane. For ligands without *ortho* substituents, at the lower limit of 45°, the H --- Cl distance (~2.77 Å) is also less than the sum of the van der Waals radii (~3.1 Å), but it increases rapidly as the pyridine is rotated towards the vertical orientation. Therefore, these ligands can freely oscillate over a large ±45° range about 90°.

Simple molecular mechanics calculations were run with the PC-MODEL package[3] to estimate the contribution of nonbonded contacts to the rotation barrier in these systems. Energy was calculated as the pyridine was rotated about the Pt—N bond with respect to the coordination plane, over the representative 0°–90° range of dihedral angles. Rigid idealized bond lengths and bond angles were used, but for each dihedral angle the methyl groups were allowed to adopt the orientation of lowest energy. The energy vs. dihedral angle curve showed a maximum for 0° (coplanar), as expected, with values (kJ/mol) of 150 for pyridine, 1280 for 2-methylpyridine, and 2700 for 2,6-dimethylpyridine. These values are certainly overestimated, since steric strain can be relieved by relatively energy-inexpensive variations of other geometrical parameters (e.g., small changes of bond angles or out-of-plane deformations). For instance, increasing the N—Pt—Cl angle to 93° reduces the above values to 90, 850, and 1580 kJ/mol, and for 97°, they become 40, 440, and 860 kJ/mol, respectively. It is noteworthy that even for the latter fairly large distortion, the rotation barrier remains very high for 2- and 2,6-substituted ligands. When the dihedral angle between the platinum and the pyridine planes is about 45°, the maximum energies (assuming *cis* bonds of 90°) are drastically reduced to approximately <10, 120, and 185 kJ/mol for the pyridine, 2-methylpyridine, and

[3] PCMODEL Program, Version 88.0, Serena Software.

2,6-dimethylpyridine complexes, respectively. Therefore, for pyridine complexes the angle can vary between 45 and 90° with almost no loss of energy due the repulsion of the *cis* ligands. For 2,6-dimethylpyridine, the most stable conformation is greater than 70° where the *cis* repulsions become negligible.

Variable-temperature NMR experiments were run to check this different behavior with respect to rotation. For this purpose, $[PtLCl_3]^-$ compounds are useless, since rotation about the Pt—N bond would not generate distinguishable rotamers. Instead, *trans*-PtL_2Cl_2 complexes were used, with the ligands 2-methyl- and 3-methylpyridine, which can form two unequivalent rotamers (methyl groups on the same or opposite sides of the PtN_2 plane, respectively). The ^1H spectrum of *trans*-Pt(2-methylpyridine)$_2Cl_2$ was measured in chloroform. The aromatic multiplets were too complicated to be analyzed, but the methyl signal at ~2.25 ppm appeared as two sharp peaks 11 Hz apart. The relative intensities (65:35) indicate that the two forms have comparable stabilities, as expected. These peaks remained unaffected as temperature was increased to the maximum possible temperature of 50°C. Therefore, the energy barrier can be calculated to be >71 kJ/mol. For *trans*-Pt(3-methylpyridine)$_2Cl_2$, the ^{13}C and ^1H NMR spectra were measured in a mixture of chloroform and Freon-21 between 25° and −100°C. A single sharp methyl resonance was observed over the whole temperature range covered. The other signals all showed single peaks also. This can be due to the presence of a single rotamer (unlikely), the resonances are too close to be resolved (possible), or fast exchange between the two rotamers because of a low rotation barrier (likely). Considering that no broadening was detected at the lowest temperature used (−100°C) and assuming that the separation of the methyl signals for the two rotamers would be the same as above, an upper limit of 29 kJ/mol can be calculated for the rotation barrier.

Although these results provide only rough estimates, they support the overall picture of a highly restricted perpendicular orientation for *ortho*-substituted pyridines and much greater orientation flexibility for ligands without *ortho* substituents.

^{195}Pt data and solvation effects

These observations on the conformation of the complexes suggest that the main factor influencing the δ(Pt) of the platinum complexes is the solvent effect. For the pyridine complex, the two H atoms in positions 2 and 6 are not large enough to prevent the approach of water molecules, especially when the angle is close to 45°. The molecules of solvent are attracted towards the platinum centre below and above the platinum plane, thus increasing the electron density in the close environment of the Pt atom. Therefore the δ(Pt) should be observed at higher field. With compounds containing two $-CH_3$ substituents in positions 2 and 6, the pyridine and platinum planes must be perpendicular to each other. The two hydrophobic methyl groups are then located directly above and below the platinum plane, preventing the approach of water molecules. Therefore the electron density on the platinum atom is reduced compared to the pyridine compound. The platinum chemical shift of the 2,6-dimethylpyridine complex is observed at lower field than those of the compounds without hydrophobic substituents in *ortho* positions.

To demonstrate this solvent effect, platinum compounds containing ligands with substituents in positions 2 and 6, which can recreate an environment similar to the solvent effect, were studied. One such example is $[Pt(2,6\text{-}(HOCH_2)_2py)Cl_3]^-$, whose platinum resonance was observed at much higher field (−1839 ppm) than the other 2,6-disubstituted complexes with hydrophobic groups (−1720 to −1754 ppm) . In fact, it was observed very close to the value measured for $[Pt(py)Cl_3]^-$ (−1816 ppm). Other platinum complexes containing hydroxy or amine groups in *ortho* positions (which form the fourth group) were also observed at similar higher fields. The hydrophilic groups in *ortho* positions are located above and below the platinum plane and create an environment similar to that observed in the pyridine complex. These observations confirm the hypothesis on the importance of the solvent effect on the chemical shifts in ^{195}Pt NMR spectroscopy.

Nevertheless, even if the solvent effect can explain the δ(Pt), the presence of Pt–pyridine π-bonding is not excluded. In Zeise's salt (26), the π bond is formed from the overlap of the filled d_{yz} orbital of platinum (the platinum plane is in the *xy* plane and ethylene is along the y axis) with the vacant π* of ethylene, since C_2H_4 is perpendicular to the platinum plane. Considering that all the π* orbitals of pyridine have a nodal plane through the six-membered ring, back-donation could take place via $d_{xy} \rightarrow \pi^*$, if the pyridine ring is perpendicular to the coordination plane, or via $d_{yz} \rightarrow \pi^*$, if it is coplanar. For pyridine, π_4^* (LUMO) has the right symmetry (1) for accepting back-donation from the metal, since it has no nodal plane on the N atom (contrary to π_5^*). In the conformation with a dihedral angle of ≈90°, which is accessible for all ligands, $d_{xy} \rightarrow \pi^*$ interaction could occur, but this type of back-donation is not believed to be appreciable. The fact that complexes with ligands, without *ortho* substituents, have dihedral angles around 50° has led a few authors to suggest that $d_{yz} \rightarrow \pi^*$ bonding would exist (16, 26). Therefore, the observed dihedral angle would result from two factors: the π bond ($d_{yz} \rightarrow \pi^*$), which would tend to bring the pyridine ring in the coordination plane, while the Cl ··· H(ortho) steric repulsions would tend to bring the two planes perpendicular to each other. Furthermore, the d_{xy} orbital was suggested to contribute in the bonding of the two *cis* Pt—Cl bonds, which would reduce its involvement in the Pt—L π bond (26).

Since ^{13}C NMR spectroscopy had provided information on similar π-bonding problems in Ru(II) and Rh(III) compounds (27), the spectra were recorded for our $[Pt(L)Cl_3]^-$ complexes.

^{13}C NMR

The ^{13}C NMR spectra of pyridine and its methyl derivatives and their Pt(II) complexes were measured in D_2O. The experimental data for the ligands are shown in Table 3, while those of the complexes, along with $\Delta\delta(\delta_{complex} - \delta_{ligand})$ are shown in Table 4.

For the free pyridine molecules, three factors will influence the electron density on the carbon atoms, and thus the chemical shifts of the ligands. There are three different mesomeric forms of pyridine produced by the delocalization of the π electrons, two of which have a δ^- charge on the N atom and a δ^+ charge on the *ortho* or *para* C atoms. These mesomeric forms decrease the electron density on the carbon atoms in positions 2, 4, and 6 (28). The second factor is the inductive effect of the nitrogen atom, which is more important for closer carbon

Table 3. ^{13}C chemical shifts (δ, ppm) of the pyridine derivatives measured in D_2O.

	2-CH_3	3-CH_3	4-CH_3	5-CH_3	6-CH_3	C(2)	C(3)	C(4)	C(5)	C(6)
Pyridine (py)						149.43	125.00	137.84	125.00	149.43
3-CH_3(py)		18.40				149.58	134.70	138.20	124.49	146.44
3,5-CH_3(py)		18.06		18.06		146.15	134.76	139.65	134.76	146.15
3,4-CH_3(py)		19.23	16.31			148.34	134.47	149.65	126.01	145.93
2-CH_3(py)	23.29					158.40	124.49	138.13	121.94	148.70
2,3-CH_3(py)	21.70	18.86				157.10	133.01	138.70	122.43	145.93
2,4-CH_3(py)	23.50		20.95			158.04	125.22	149.72	122.89	148.19
2,5-CH_3(py)	23.14			17.96		155.34	124.13	138.86	131.57	148.63
2,6-CH_3(py)	23.72				23.72	157.75	121.21	138.06	121.21	157.75
2,4,6-CH_3(py)	22.63		21.02		22.63	156.73	123.04	150.31	123.04	156.73
2,3,6-CH_3(py)	21.39	18.40			22.99	156.07	129.60	139.15	121.87	154.68

Table 4. ^{13}C chemical shifts (δ, ppm) of the $K[Pt(py)Cl_3]$ complexes and (Δδ, ppm) (δ of the complex – δ of the ligand) measured in D_2O.

Ligand	2-CH_3	3-CH_3	4-CH_3	5-CH_3	6-CH_3	C(2)	C(3)	C(4)	C(5)	C(6)
Pyridine (py)						154.25	126.97	139.88	126.97	154.25
						(4.82)	(1.92)	(2.04)	(1.97)	(4.82)
3-CH_3(py)		18.18				154.25	137.11	140.10	126.03	151.47
		(–0.22)				(4.67)	(2.41)	(1.90)	(1.54)	(5.03)
3,5-CH_3(py)		18.06		18.06		151.33	136.88	141.26	136.88	151.33
		(0.00)		(0.00)		(5.18)	(2.12)	(1.61)	(2.12)	(5.18)
3,4-CH_3(py)		19.15	16.38			153.01	136.73	151.62	127.54	151.04
		(–0.08)	(0.07)			(4.67)	(2.26)	(1.97)	(1.53)	(5.11)
Mean Δδ (ligands with no *ortho* substituents)						4.84	2.19	1.88	1.79	5.03
2-CH_3(py)	26.78					162.12	127.27	139.30	123.91	154.39
	(2.99)					(3.72)	(2.78)	(1.17)	(1.97)	(5.69)
2,3-CH_3(py)	24.56	19.88				160.82	136.37	140.09	123.96	151.77
	(2.85)	(1.02)				(3.72)	(2.36)	(1.39)	(1.53)	(5.84)
2,4-CH_3(py)	26.45		20.69			161.18	128.12	152.06	125.13	153.32
	(2.95)		(–0.26)			(3.14)	(2.90)	(2.34)	(2.24)	(5.33)
2,5-CH_3(py)	26.23			17.70		158.99	126.95	140.46	134.47	154.10
	(3.09)			(–0.26)		(3.65)	(2.82)	(1.60)	(2.90)	(5.47)
Mean Δδ (ligands with substituent in position 2)						3.56	2.71	1.63	2.16	5.51
2,6-CH_3(py)	27.66				27.66	162.05	124.20	139.88	124.20	162.05
	(3.94)				(3.94)	(4.30)	(2.99)	(1.82)	(2.99)	(4.30)
2,4,6-CH_3(py)	27.44		20.44		27.44	161.17	125.00	152.06	125.00	161.17
	(4.81)		(–0.58)		(4.81)	(4.44)	(1.96)	(1.75)	(1.96)	(4.44)
2,3,6-CH_3(py)	25.32	19.71			27.36	160.52	132.59	140.90	124.13	159.20
	(3.93)	(1.31)			(4.37)	(4.45)	(2.99)	(1.75)	(2.26)	(4.52)
Mean Δδ (ligands with substituent in positions 2 and 6)						4.39	2.64	1.77	2.40	4.42

atoms. Therefore the carbon atoms in positions 3 and 5 are influenced only by the inductive effect and are observed at higher fields. Those located in position 4 are only slightly influenced by the inductive effect of the N atom, and appear at intermediate chemical shifts. The chemical shifts of the pyridine C atoms in D_2O were found at 149.43, 137. 84, and 125.00 ppm for atoms in positions 2, 4, and 3, respectively. The last factor that influences the C chemical shifts is a local effect due to the presence of substituents at different positions. The addition of a methyl group increases the ionic mesomeric forms of the pyridine derivative, and the electron density on the C atoms to which it is bonded decreases. When a -CH_3 substituent is in position 2, the δ(C) of C2 varies between 155.34 and 158.40 ppm, an increase of about 7.5 ppm when compared to pyridine. A substituent in position 3 or 5 increases the δ(C) of C3 or C5 by about 9.5 ppm, and a -CH_3 substituent in position 4 increases the δ(C) of C4 by about 12 ppm (Table 3). The presence of a -CH_3 group creates a greater deshielding on its ring C atom when it is far from the N atom. The chemical shifts of the methyl groups vary between 16.31 to 23.72 ppm and those located in positions 2 and 6 are the most deshielded.

Upon coordination of the pyridine ligand to the platinum atom, the formation of the σ bond will decrease the electron density on the ligand and especially on the atoms close to the binding site, namely, those in positions 2 and 6. Furthermore, the ionic mesomeric forms will be more favored, reducing the electron density in positions 2, 4, and 6. As a result, all the chemical shifts of the carbon atoms are shifted towards lower field upon coordination.

Since it was postulated that pyridine would form multible bonding with platinum, while the 2,6-disubstituted compounds would only form *a* σ bond, attempts were made to study this hypothesis by ^{13}C NMR spectroscopy. The chemical shifts of the complexes containing ligands with methyl groups in positions 2 and (or) 6, were compared with those of the complexes with pyridine ligands with no substituents in ortho positions. A comparison of $\Delta\delta$ ($\delta_{complex} - \delta_{ligand}$) for the different complexes should give useful information. The average $\Delta\delta$ for the pyridine complexes with no *ortho* substituents are 4.84 for C(2), 2.19 for C(3), 1.88 for C(4), 1.79 for C(5), and 5.03 ppm for C(6) (Table 4). For Pt compounds containing ligands with a methyl substituent in position 2, the corresponding $\Delta\delta$ values are 3.56, 2.71, 1.63, 2.16, and 5.58 ppm, while they are 4.40, 2.65, 1.77, 2.40, and 4.42 ppm for the 2,6-disubstitued compounds. If π-bonding is more important in complexes containing ligands with no *ortho* substituents, the electronic density on the ligand should be larger for these complexes, and the $\Delta\delta$ should be smaller. In our case, we have not observed smaller shifts for the compounds containing ligands with no substituents in *ortho* positions, compared to the *ortho*-disubstituted complexes. Therefore, our results do not support the hypothesis that π-bonding would be less important in the 2,6-disubstituted pyridine complex.

It could be argued that the aquation reactions of the different ligands are different. The extent of hydration for unsubstituted pyridine might be more important than the hydration reaction with 2,6-dimethylpyridine. To study this influence, a second comparison was done using the chemical shifts of three ligands measured in chloroform. The $\Delta\delta$ ($\delta_{complex\ in\ D_2O} - \delta_{ligand\ in\ CDCl_3}$) values are 4.57, 3.45, and 4.17 ppm for pyridine, 4.20, 4.47, 3.52, 3.67, and 5.70 ppm for 2-methylpyridine, and 4.46, 4.16, and 3.48 ppm for 2,6-dimethylpyridine. Again, the $\Delta\delta$ values are similar for the pyridine and the 2,6-dimethylpyridine complexes. Therefore, these results confirm that π-bonding, if present, is probably similar for all the platinum complexes.

Attempts were made to confirm the presence of Pt→L π-bonding from the ^{13}C NMR spectra of the complexes. We can compare our results with a Ru(II) compound known to form metallic multiple bonding with pyridine (27). According to the authors, C(4) is the most reliable probe to study this effect. The chemical shift of C(4) of the pyridine ligand in $[Ru(NH_3)_5(pyridine)]^{2+}$ is 134.6 ppm, for a $\Delta\delta$ value of −3.2 ppm (δ of pyridine measured in D_2O). Therefore, upon coordination of pyridine to ruthenium(II), the electron density on the ligand is increased. For the corresponding Rh(III) and Co(III) compounds $[M(NH_3)_5(pyridine)]^{3+}$ (Rh(III) and Co(III) are harder metals than Ru(II)), the π-bonding should be reduced and the chemical shifts of C(4) were observed at 141.9 ($\Delta\delta$ = 4.1 ppm) and 142.7 ppm ($\Delta\delta$ = 4.9 ppm), respectively. Our values vary from 1.17 to 2.04 ppm. This comparison seems to confirm the multiple nature of the Pt—N bond in pyridine–platinum(II) complexes. Nevertheless, its extent seems much less important than in Ru(II) pyridine complexes, but probably more than in Rh(III) and Co(III) compounds. Yet, the strength of the σ bond might vary with different metals and different oxidation states.

Table 5. $J(^{13}C-^{195}Pt)$ coupling constants (Hz) of the complexes $K[Pt(py)Cl_3]$.

Ligand	^3J 2-CH_3	^3J 6-CH_3	^3J C(3)	^4J C(4)	^3J C(5)
py			41.2	11.8	41.2
2-CH_3(py)	30.9		33.8		39.7
3-CH_3(py)			n.o.		44.1
2,3-CH_3(py)	22.1		30.9		42.7
2,4-CH_3(py)	30.9		33.8		39.7
2,5-CH_3(py)	30.9		33.8		39.7
2,6-CH_3(py)	27.9	27.9	30.9		30.9
3,4-CH_3(py)			n.o.		42.7
3,5-CH_3(py)			42.7	14.7	42.7
2,3,6-CH_3(py)	22.1	25.0	27.7		32.4
2,4,6-CH_3(py)	22.1	22.1	30.9		30.9

n.o., not observed.

The $J(^{13}C-^{195}Pt)$ coupling constants were also measured and are shown in Table 5. The ^3J couplings were observed on C3 and C5 and vary from 27.7 to 44.1 Hz. The ^4J (with C4) are much smaller (11.8–14.7 Hz) and they could be measured only on two complexes. For the ligands with methyl substituents in positions 2 and 6, the ^3J vary between 22.1 and 30.9 Hz. The smaller values for the methyl C atoms are caused by the different hydridizations (sp^3 vs. sp^2). No ^2J values could be measured. These values are usually too small to be observed, due to the inadequate orientation of the different orbitals. Grim, Keiter, and McFarlane (29) have made a ^{31}P NMR study of compounds of the type *cis*- and *trans*-$Pt(PR_3)_2Cl_2$. The authors have observed larger $J(^{31}P-^{195}Pt)$ coupling constants when the extent of π-bonding increased. In our work, we have not observed any differences between the coupling constants of the different platinum complexes.

Structure of *trans*-$Pt(2,6\text{-}(HOCH_2)_2py)_2Cl_2$

The crystal structure of a platinum complex containing ligands with substituents in positions 2 and 6 capable of recreating the solvent effect around the platinum atom was determined. The ligand chosen for this study was 2,6-di(hydroxymethyl)pyridine. The two hydroxy groups could be located close to the Pt atom above and below the plane, as suggested from ^{195}Pt NMR spectroscopy. The monosubstituted complex did not produce crystals suitable for X-ray diffraction. Therefore, the disubstituted compound was analyzed. The refined atomic parameters of the complex are listed in Table 6. A labelled diagram of the molecule is shown in Fig. 1. The platinum atom is located at the junction of a 2-fold axis and a mirror plane, the chloro ligands are on the mirror plane, while the N and C(4) atoms are on the 2-fold axis. The compound crystallized with molecules of water that are also situated on a 2-fold axis. As expected, the coordination around Pt(II) is square planar (perfect plane by symmetry). The six atoms of the pyridine ring are in a plane with deviations N, 0.000; C(2), −0.003(5); C(3),

Fig. 1. Labelled diagram of *trans*-Pt(2,6-$(HOCH_2)_2$py)$_2Cl_2 \cdot 2H_2O$.

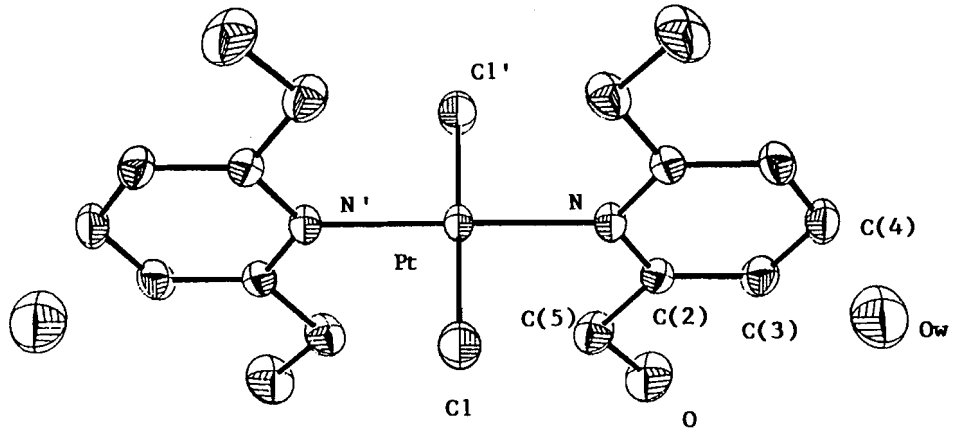

Table 6. Positional parameters with their e.s.d.'s and temperature factors (10^4) $U_{eq} = 1/3\ \Sigma_i\Sigma_j U_{ij} a_i^* a_j^* a_i . a_j$.

Atom	x	y	z	U_{eq} (Å^2)
Pt	0	0	0	205
Cl	2886(3)	0	1467(3)	356
N	0	1304(4)	0	225
C(2)	532(7)	1742(3)	−1306(7)	246
C(3)	533(8)	2626(4)	−1332(7)	297
C(4)	0	3068(5)	0	323
C(5)	1152(9)	1222(4)	−2711(7)	330
O	1639(7)	1753(3)	−4010(5)	459
O(w)	0	3976(7)	5000(7)	873

Table 7. Bond distances (Å) and angles (°).

Pt—Cl	2.306(2)	Cl-Pt-Cl′	180.0
Pt—N	2.041(6)	Cl-Pt-N	90.0
N—C(2)	1.358(6)	N-Pt-N′	180.0
C(2)—C(3)	1.382(7)	Pt-N-C(2)	120.3(3)
C(3)—C(4)	1.380(7)	N-C(2)-C(3)	121.1(5)
C(2)—C(5)	1.512(8)	N-C(2)-C(5)	117.1(4)
C(5)—O	1.422(8)	C(2)-N-C(2)′	119.4(4)
		C(2)-C(3)-C(4)	119.3(5)
		C(3)-C(4)-C(3)′	119.7(4)
		C(3)-C(2)-C(5)	121.7(5)
		C(2)-C(5)-O	111.5(5)

N′: 0, −y, 0; Cl′: −x, 0, −z.

−0.003(6); C(4), 0.001; C(2′), 0.003(6); and C(3′), −0.003(6) Å. The C(5) and the hydroxyl−O atoms are also in the pyridine plane, with deviations of −0.037(6) and −0.012(5) Å, respectively. The dihedral angle between the platinum and the pyridine planes is 79.8°, close to the value of 81.6° observed in K[Pt(2,6-dimethylpyridine)Cl_3] (21).

The crystal Pt(2,6-$(HOCH_2)_2$py)$_2Cl_2$ is the *trans* isomer as expected for 2,6-disubstituted compounds. It has been shown that it is not possible to synthesize *cis* isomers containing two pyridine ligands with substituents in positions 2 and 6 (4, 25). The bond distances and angles are listed in Table 7. The Pt—Cl bond length is normal (2.306(2) Å), and the Pt—N bond distance is 2.041(6) Å. Pt—N bond distances for pyridine ligands usually seem slightly shorter than those observed for similar Pt – primary amine compounds, but it is difficult to compare since the *trans* ligand must be taken into consideration and few compounds of these types have been reported. The Pt—N bonds in *trans*-Pt(*tert*-butylamine)$_2Cl_2$ are 2.041(6) and 2.053(6) Å (30), while in a *trans* pyridine derivative compound, the Pt—N (pyridine) bonds are slightly shorter, 2.013(4) Å (31). In *trans*-Pt(pyridine)$_2Cl_2$, the bond distance is 1.98(1) Å (13) and it is 1.991(11) Å in *trans*-Pt(4-EtCOOpy)$_2Cl_2$ (15). The slightly shorter bond observed in Pt–pyridine compounds might indicate the presence of π bonds, but there are not enough data available at the moment in the literature to reach such a conclusion. The present structure does not show any evidence of bonds shorter than those observed in Pt – primary amine complexes. The presence of two bulky substituents in *ortho* positions might be an important factor in slightly increasing the Pt—N distances.

The O atoms in the hydroxy groups are located in the plane of the pyridine ring, but away from the platinum atom. The crystal *trans*-Pt(2,6-$(HOCH_2)_2$py)$_2Cl_2$ is stabilized by intermolecular hydrogen bonding between the hydroxy groups and the water molecules. The distance O ··· O is 2.754(6) Å with an angle C(5)—O ··· O of 103.1(3)° and the distance O ··· O(w) is 2.789(6) Å, with an angle C(5)—O ··· O(w) = 103.4(3)°. These results indicate that the conformations of the hydroxy groups in the crystal are different from those suggested by the ^{195}Pt NMR spectra. The presence of lattice molecules of water is probably a major factor responsible for the different conformation in the solid state, since hydrogen bonds provide an important contribution to crystal packing energy. This observation does not weaken the conclusion reached from ^{195}Pt NMR spectroscopy. Since the dihedral angle between the Pt plane and the pyridine plane is close to 90°, rotations around the -CH_2OH groups within the free species could easily bring the hydroxy groups in the close environment of the platinum atom on both sides of the Pt plane.

A packing diagram of the molecules is shown in Fig. 2. The Pt atoms are located at $z = 0$ and the lattice water molecules are all located at $z = {}^1/_2$. The pyridine rings are stacked in the crystal along the x direction, at approximately $y \approx {}^1/_4$ and ${}^3/_4$ and $z = 0$.

Fig. 2. Packing diagram in the crystal *trans*-Pt(2,6-$(HOCH_2)_2py)_2Cl_2 \cdot 2H_2O$.

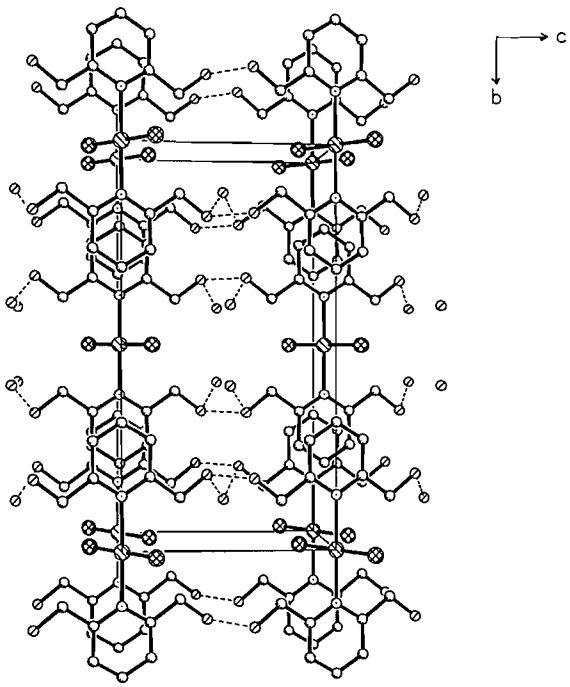

Conclusion

The ^{13}C NMR spectra of the platinum(II) complexes do not rule out the multiple nature of the Pt—N bond, but the extent of π-bonding is small compared to ruthenium(II)–pyridine complexes. In this work, we have assumed that the extent of the σ bond remains the same when substituents are added on the pyridine ring. This hypothesis might not be acceptable, but it is not easy to separate the two types of bonding since only the overall effect can be observed. ^{15}N NMR spectroscopy might bring more information on the nature of the Pt—N bond than a ^{13}C NMR study. Nevertheless, except for pyridine, most of the ^{15}N enriched ligands are not easily available.

The ^{195}Pt NMR spectroscopic results have provided useful information in the study of this series of platinum(II) complexes. The solvent effect plays a major role in the determination of the platinum chemical shifts. Complexes containing ligands with no substituents in the *ortho* position would allow the molecules of solvent (water) to approach the platinum atom on both sides of the platinum plane, thus increasing the electron density in the close environment of the metallic center. On the other hand, compounds containing 2,6-dimethylpyridine with two hydrophobic methyl groups on each side of the platinum plane (since the Pt and pyridine planes are perpendicular to each other), do not allow the approach of the molecules of solvent in the close environment of the Pt atom, thus reducing the electronic density around the Pt atom. The latter compounds are observed at lower fields. The Pt compounds with ligands that can recreate the solvent effect, such as 2,6-di(hydroxymethyl)pyridine, are observed again at higher fields, like the pyridine complex.

The crystal structure determination of *trans*-Pt(2,6-$(HOCH_2)_2py)_2Cl_2$ has shown that all the hydroxy groups are in the same plane as the pyridine ring and point away from the platinum atom. In aqueous solution, the ^{195}Pt NMR spectra of $K[Pt(2,6\text{-}(HOCH_2)_2py)Cl_3]$ and related compounds have shown that the hydroxy groups seem to be close to the platinum atom. If we assume that the angle between the platinum plane and the pyridine plane is close to 90°, the hydroxy groups could be thought of as recreating, around the Pt atom, a hydrophilic environment similar to the solvent effect. The different orientation of the hydroxy groups observed in the solid state results from the formation of hydrogen bonds with the molecules of lattice water, which would stabilize this conformation. A rotation around the $-CH_2OH$ groups could bring the hydroxy groups into the close environment of the platinum atom on both sides of the Pt plane as suggested by the solution spectra.

This work confirms that π-bonding, if present, is not different for *ortho*-unsubstituted or *ortho*-substituted ligands in the Pt(II) complexes. But the presence of multiple bonding is not essential to explain the conformation of the ligands in the Pt(II) complexes. The energy difference for dihedral angles of 45° and 90° in $[Pt(pyridine)Cl_3]^-$ is very small (<10 kJ mol^{-1}) and could easily be overcome, for example, by very weak dipole–dipole attractions between the *ortho* H atoms and the *cis* chloro ligands. Some interesting results from the literature might strengthen this suggestion. The crystal structures of the compounds *trans*-Pt(DMSO)(3,5-dimethylpyridine)I_2 (32) and *trans*-Pt(pyridine)$_2I_2$ (33) have shown that the dihedral angles between the Pt and the pyridine ring are 79° and 75°, respectively. These angles are much larger than those observed for Pt-dichloro compounds containing ligands with no substituents in positions 2 and 6 (44°–59°). The larger angle might be caused by the absence of dipole–dipole attractions between the *ortho* H atoms of the pyridine derivative and the cis iodo ligands.

Acknowledgment

The authors are grateful to the Natural Sciences and Engineering Research Council of Canada for financial support.

References

1. K.B. Wiberg. Physical organic chemistry. John Wiley, New York. 1972. p 76.
2. H. Motschi, S.N. Sze, and P.S. Pregosin. Helv. Chim. Acta, **62**, 2086 (1979).
3. L.G. Marzilli, Y. Hayden, and M.D. Reily. Inorg. Chem. **25**, 974 (1986).
4. P.C. Kong and F.D. Rochon. Can. J. Chem. **56**, 441 (1978).
5. G.B. Kauffman. Inorg. Synth. **2**, 249 (1946).
6. P. Coppens and W.C. Hamilton. Acta Crystallogr. Sect. A: Cryst. Phys. Diffr. Theor. Gen. Crystallogr. **A26**, 71 (1970).
7. D.T. Cromer and J.T. Waber. Acta Crystallogr. **18**, 104 (1965).
8. R.F. Stewart, E.R. Davidson, and W.T. Simpson. J. Chem. Phys. **42**, 3175 (1965).
9. D.T. Cromer. Acta Crystallogr. **18**, 17 (1965).
10. R. Melanson and F.D. Rochon. Can. J. Chem. **53**, 2371 (1975).
11. D.D. Derrin. Dissociation constants of organic bases in aqueous solution. Butterworths, London. 1965. pp. 140–183.
12. P.S. Pregosin. Coord. Chem. Rev. **44**, 247 (1982).
13. P. Colamarino and P.L. Orioli. J. Chem. Soc. Dalton Trans. 1656 (1975).
14. F. Caruso, R. Spagna, and L. Zambonelli. Acta Crystallogr. Sect. B: Struct. Crystallogr. Cryst. Chem. **B36**, 713 (1980).

15. M. Camalli, F. Caruso, and L. Zambonelli. Cryst. Struct. Commun. **9**, 721 (1980).
16. F. Caruso, R. Spagna, and L. Zambonelli. J. Cryst. Mol. Struct. **8**, 46 (1978).
17. M.A.M. Meester and K. Olie. Cryst. Struct. Commun. **4**, 725 (1975).
18. V.K. Bel'skii, V.Y. Kukushkin, V.E. Konovalov, A.I. Moiseev, and V.N. Yakovlev. Zh. Obshch. Khim. **60**, 2180 (1990).
19. V.Y. Kukushkin, V.K. Bel'skii, E.A.A. Aleksandrova, E.Y. Pan'kova, V.E. Konovalov, V.N. Yakovlev, and A.I. Moiseev. Zh. Obshch. Khim. **61**, 318 (1991).
20. R. Melanson and F.D. Rochon. Acta Crystallogr. Sect. B: Struct. Crystallogr. Cryst. Chem. **B34**, 1125 (1978).
21. R. Melanson and F.D. Rochon. Can. J. Chem. **54**, 1002 (1976).
22. F.D. Rochon and R. Melanson. Acta Crystallogr. Sect. B: Struct. Crystallogr. Cryst. Chem. **B36**, 691 (1980).
23. F.D. Rochon and R. Melanson. Acta Crystallogr. Sect. B: Struct. Crystallogr. Cryst. Chem. **B37**, 690 (1981).
24. F. Caruso, R. Spagna, and L. Zambonelli. Inorg. Chim. Acta, **32**, L23 (1979).
25. F.D. Rochon, P.C. Kong, and R. Melanson. Can. J. Chem. **58**, 97 (1980).
26. T.A. Albright, R. Hoffmann, J.C. Thibeault, and D.L. Thorn. J. Am. Chem. Soc. **101**, 3801, (1979).
27. D.K. Lavallee, M. D. Baughman, and M.P. Phillips. J. Am. Chem. Soc. **99**, 718 (1977).
28. R.T. Morisson and R.N. Boyd. Organic chemistry. Allyn and Bacon, Boston, Mass. 1979.
29. S.O. Grim, R.L. Keither, and W. McFarlane. Inorg. Chem. **6**, 1133 (1967).
30. R. Melanson and F.D. Rochon. Acta Crystallogr. Sect. C: Cryst. Struct. Commun. **C41**, 350 (1985).
31. F.D. Rochon and R. Melanson. Acta Crystallogr. Sect. B: Struct. Crystallogr. Cryst. Chem. **B35**, 2313 (1979).
32. T.T.B. Ha, F.L. Wimmer, J.P. Souchard, N.P. Johnson, and J. Jaud. J. Chem. Soc. Dalton Trans. 1251 (1990).
33. G. Thiele and D. Wagner. Chem. Ber. **111**, 3162 (1978).

Bis- and tris(amidine)fluoroboron cations and mixed tetrahaloborate anions: NMR studies of mixed boron trihalide adduct redistribution reactions involving amidines as strong nitrogen bases[1]

J. Stephen Hartman, Zheng Yuan, Arnold Fox, and Anh Nguyen

Abstract: Amidines as strong Lewis bases react with amidine–mixed boron trihalide adduct systems $D{\cdot}BF_nCl_{3-n}$ ($n = 0$–3) in the presence of excess boron trihalide to give complex mixtures of products including the mixed tetrahaloborate anions $BF_nCl_{4-n}^-$ and the fluoroboron cations $D_2BF_2^+$ and D_3BF^{2+}, which coexist with the neutral adducts $D{\cdot}BF_nCl_{3-n}$. Excess amidine rapidly displaces chloride ion from the chlorofluoroborate anions and neutral mixed boron trihalide adducts to give high yields of the fluoroboron cations. The D_3BF^{2+} cations of the amidines 1,8-diazabicyclo[5,4,0]undec-7-ene (DBU) and 1,5-diazabicyclo[4,3,0]non-5-ene (DBN) are inert and have been isolated as their hexafluorophosphate salts. $(DBN)_2BF_2^+$ is inert and has been isolated as its hexafluorophosphate salt, but $(DBU)_2BF_2^+$ is highly reactive.

Key words: amidines, fluoroboron cations, mixed boron trihalide adducts, redistribution reactions, fluorine-19 NMR, boron-11 NMR, 1,8-diazabicyclo[5,4,0]undec-7-ene (DBU), 1,5-diazabicyclo[4,3,0]non-5-ene (DBN)

Résumé : Les amidines, comme de fortes bases de Lewis, réagissent avec les systèmes d'adduits amidine–trihalogénures de bore mixtes, $D{\cdot}BF_nCl_{3-n}$ ($n = 0$–3), en présence d'un excès de trihalogénure de bore, pour donner des mélanges complexes de produits contenant les anions mixtes tétrahalogénoborates, $BF_nCl_{4-n}^-$, ainsi que les cations fluorure de bore $D_2BF_2^+$ et D_3BF^{2+} qui coexistent avec les adduits neutres $D{\cdot}BF_nCl_{3-n}$. L'excès d'amidine déplace rapidement l'ion chlorure des anions chlorofluoroborate et des adduits trihalogénures de bore mixtes neutres pour conduire, avec des rendements élevés, aux cations fluorure de bore. Les cations D_3BF^{2+} des amidines 1,8-diazabicyclo[5.4.0]undéc-7-ène (DBU) et 1,5-diazabicyclo[4.3.0]non-5-ène (DBN) sont inertes et ont été isolés sous la forme de sels hexafluorophosphate. Le $(DBN)_2BF_2^+$ est inerte et a été isolé comme son sel hexafluorophosphate: toutefois, le $(DBU)_2BF_2^+$ est extrêmement réactif.

Mots clés : amidines, cations fluorure de bore, adduits mixtes de trihalogénures de bore, réactions de redistribution, RMN du fluor-19, RMN du bore-11, 1,8-diazabicyclo[5.4.0]undéc-7-ène (DBU), 1,5-diazabicyclo[4.3.0]non-5-ène (DBN).

[Traduit par la rédaction]

Introduction

Earlier work in this laboratory (1,2) has shown that low-steric-hindrance tertiary amines selectively displace heavy halide ion X^- (X = Cl, Br) from nitrogen-donor mixed boron trihalide adducts $D{\cdot}BF_2X$ to form bis(amine)difluoroboron cations (eq. [1]). With pyridines the adducts $D{\cdot}BFX_2$ also react, and form bis(pyridine)fluorohaloboron and tris(pyridine)fluoroboron cations as in eq. [2] (3). We now report the extension of our

[1] $$D{\cdot}BF_2X + D' \rightarrow DD'BF_2^+ + X^-$$

[2] $$D{\cdot}BFX_2 + D' \rightarrow DD'BFX^+ + X^- \xrightarrow{D'} DD'_2BF^{2+} + X^-$$

work to mixed boron trihalide adducts of amidines (4), which as strong nitrogen bases of low steric hindrance should be capable of driving the formation of fluoroboron cations even more effectively than is possible with pyridines as donors.

The basicity of the amidine functional group >N—CR=N— is enhanced by electron delocalization toward the imino nitrogen as in structure **1b**. The substituent on the imino nitrogen atom, the site of protonation and of complex formation, has the strongest influence on amidine basicity (5), although basicity is also affected by substitution at the central

Received January 5, 1996.

This paper is dedicated to Professor Howard C. Clark in recognition of his contributions to Canadian chemistry.

J.S. Hartman,[2] Z. Yuan,[3] A. Fox,[4] and A. Nguyen. Department of Chemistry, Brock University, St. Catharines, ON L2S 3A1, Canada.

[1] Presented in part at the Third Chemical Conference of the North American Continent, Toronto, Ontario, June 1988.

[2] Author to whom correspondence should be addressed. Telephone: (905) 688-5550, ext. 3849. Fax: (905) 682-9020. E-mail: shartman@chemiris.labs.brocku.ca

[3] Present address: Watkins-Johnson Company, Scotts Valley, CA 95066, U.S.A.

[4] Present address: General Ballistics, Alliston, ON L9R 1V5, Canada.

1a 1b

carbon atom and the amino nitrogen (6). Amidines with their strong basicity have interesting coordination chemistry (7). Monomeric, dimeric, and cluster metal amidine complexes have been studied. N-H containing acyclic amidines can lose a proton to form [R′—N═CR—N—R″]$^-$ species, which can act as bridging ligands (7, 8). To avoid problems of N-H proton transfer, we have limited our work to *N,N,N′*-trialkyl-substituted amidines. Following preliminary studies with *N,N,N′*-trimethylacetamidine (Me_2N-CMe═NMe) and *N,N,N′*-trimethylbenzamidine, which are not commercially available, our work on amidine interactions with mixed boron trihalide adducts has involved 1,8-diazabicyclo[5,4,0]undec-7-ene (DBU, **2**) and 1,5-diazabicyclo[4,3,0]non-5-ene (DBN, **3**). Both of these amidines are readily available and have become

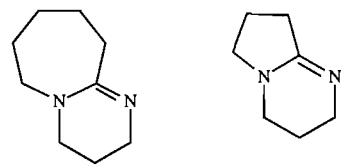

2, DBU 3, DBN

well established as strongly basic yet non-nucleophilic reagents in organic synthesis (9, 10). DBN is one of the strongest amidine bases, with a pK_b of about 0.5 in 50% aqueous ethanol (11). DBU is almost as basic, with a pK_b of 1.1 in 1 M aqueous solution and 0.6 in 10% aqueous solution (Table I of ref. 10). This compares to pK_b values of 2.9–3.4 for simple aliphatic trialkylamines and 7.2–8.8 for simple pyridines (12).

Despite the reputation of DBU and DBN as strongly basic yet non-nucleophilic reagents (9, 10), a number of recent reports have shown that these bases can indeed act as nucleophiles (13), notably towards halogenated derivatives of main group elements (14), and a few DBU–metal complexes have recently been reported (15).

Experimental

Materials

Most compounds utilized in this work are moisture sensitive. They were handled with standard inert-atmosphere Schlenk line and glove bag techniques (16). Carefully dried solvents were used.

Boron trifluoride gas (Matheson) was passed through a glass tube packed with sodium fluoride in order to remove traces of HF. Boron trichloride gas (Matheson, bp 12.7°C) was condensed with a slush bath at −63°C on the Schlenk line, and a trap-to-trap distillation was carried out. The pure liquid BCl_3, which is clear and colorless, was diluted to 0.5 M in $CDCl_3$ and stored at −10°C in a closed Schlenk vessel.

Boron tribromide (Alfa Inorganics) was treated with mercury to remove bromine and was transferred into small ampoules by trap-to-trap distillation on a high-vacuum line. The sealed ampoules were stored in the dark to prevent photochemical formation of bromine and were opened as needed in the glove bag.

Commercial DBU (Abbott Laboratories; Air Products and Chemicals, Inc.) was distilled under reduced pressure and dry nitrogen (130–134°C at 20 Torr (1 Torr = 133.3 Pa)) using microdistillation apparatus sealed with Apiezon M grease and linked to a Schlenk line. The purified DBU (clear and almost colourless) and DBN (Aldrich, 95%) were stored over Lindé 5 Å molecular sieves prior to use.

N,N,N′-Trimethylacetamidine and *N,N,N′*-trimethylbenzamidine were synthesized according to the procedure of Wilson et al. (17), using $Ti(NMe_2)_4$ that had been synthesized by the procedure of Bradley and Thomas (18) and vacuum distilled. The amidine products were vacuum distilled and stored in tightly sealed 5 mL flasks over activated Lindé 3 Å molecular sieves before use.

Hexane was dried with sodium wire. Deuterated chloroform (Merck, minimum isotopic purity 99.8% D) was dried with Lindé 5 Å molecular sieves that were baked in advance in a muffle furnace at 400°C for more than 3 h and cooled over a period of 0.5 h in a vacuum desiccator. Sodium tetraphenylborate (Fisher, 99.6%), sodium hexafluorophosphate (Alfa, 98%), and ammonium hexafluorophosphate (Aldrich, 99.5%) were used as supplied.

C_6F_6 (Whittaker) was used as a secondary internal reference for ^{19}F chemical shifts (−162.7 ppm from $CFCl_3$). $Et_2O{\cdot}BF_3$, prepared by reaction of BF_3 with diethyl ether and fractionation of the liquid product, was used as the ^{11}B external reference. Nitromethane (Fisher), distilled at 101–102°C, was used as the external reference for ^{15}N.

Boron trihalide adducts

Boron trihalide adducts were synthesized as described previously (2, 19), with a bubbler added to control the flow rate of the gas. BF_3 or BCl_3 was slowly bubbled into an anhydrous hexane solution of the amidine (hexane:amidine = 5:1– 10:1 v/v) under a positive nitrogen atmosphere until no additional precipitation occurred. The reaction took place at 0°C in an ice bath, with stirring. DBU·BF_3 and DBN·BF_3 are very stable in water, and DBU·BF_3 did not change over a month on standing in air. The separation of boron trifluoride adducts from the solution was initially carried out by syringe/septum methods (2, 3), but in view of the stability of DBU·BF_3 and DBN·BF_3 to hydrolysis, in later work the adducts were filtered in air and washed with hexane and water to remove organic and inorganic impurities, followed by drying in air and under vacuum and storage in a Schlenk vessel.

Synthesis and isolation of fluoroboron cations

Difluoroboron cations $D_2BF_2^+$ and monofluoroboron cations D_3BF^{2+} were formed by similar methods. In most situations, a solution of 0.05–0.10 mL 1.0 M BCl_3 in $CDCl_3$ was added to a solution of 0.3–0.4 mL 0.3–0.5 M D·BF_3 in $CDCl_3$ in a 5 mm NMR tube. Both of these solutions were kept at −63°C in a slush bath. After 10–20 min, during which time D·BF_nCl_{3-n} formed (2, 3, 19), a solution of 0.2–0.4 mL of 1 M amidine in $CDCl_3$ was added. Syringes (1 mL and 50 μL) were used to

inject the various reagents. A very narrow glass rod with an enlargement at the bottom was especially useful for mixing reagents in the NMR tube. The whole process was carried out in a glove bag under a nitrogen atmosphere. Since redistribution reactions occur rapidly in these systems, only a few minutes were required for the fluoroboron cations to form.

Monitoring by ^{19}F NMR showed that the best ratio of Cl to F for the formation of the $D_2BF_2^+$ cations of DBU and DBN is 0.8:1. For the D_2BFCl^+ and D_3BF^{2+} cations the best ratio of Cl to F is (1.2–1.5):1. Both have the same precursor, $D{\cdot}BFCl_2$, and only half as much free amidine is needed for D_2BFCl^+ formation as for D_3BF^{2+}. Some D_2BFCl^+ was always formed along with D_3BF^{2+}.

Neither $D_2BF_2^+$ nor D_3BF^{2+} was isolated directly from the $CHCl_3$ mother solution by precipitating as $D_2BF_2^+Cl^-$ or $D_3BF^{2+}Cl_2^-$. A precipitate that did form in such a solution containing $(DBU)_2BF_2^+$ gave a fast atom bombardment mass spectrum (FAB spectrum (20)) with only one strong peak corresponding to $DBU{\cdot}H^+$, indicating that the precipitate is $[DBU{\cdot}H]^+Cl^-$.

Sodium tetraphenylborate was added in an attempt to precipitate fluoroboron cations as their tetraphenylborate salts, as in related systems (2, 3). However, FAB analysis indicated that only $[D{\cdot}H]^+BPh_4^-$ (D = DBU, DBN) were isolated in 1:1 $CHCl_3$–EtOH solution.

$(DBU)_3BF^{2+}$, $(DBN)_3BF^{2+}$, and $(DBN)_2BF_2^+$ were isolated by selective precipitation as their hexafluorophosphate salts. A white precipitate appeared immediately when a saturated $NaPF_6$ or NH_4PF_6 solution in ethanol was added to a cation-containing 1:1 $CHCl_3$–EtOH solution. Recrystallization was carried out from a 1:1 acetone–EtOH solution. The fluoroboron hexafluorophospates are soluble in acetone and insoluble in EtOH.

High-quality single crystals suitable for X-ray crystallography were grown by a solvent diffusion process. The key to growing these crystals is that absolute EtOH must be very gently added to fluoroboron cation-containing hexafluorophosphate-containing acetone solution along the glass wall of a 10 mm diameter tube to keep the surface in an undisturbed state. The acetone solution must be a little less than saturated. The slower the diffusion process, the higher the quality of the crystal. After 20 h of solvent diffusion, excellent crystals began to appear.

Since $(DBU)_2BF_2^+$ decomposes in water and alcohol, it could not be isolated by the general method. Other unsuccessful attempts included use of a large amount of hexane to precipitate it from the mother solution, and the direct addition of a saturated solution of $NaPF_6$ or NH_4PF_6 in $CHCl_3$ to the mother solution.

Tris(DBU)monofluoroboron hexafluorophosphate

In a −63°C slush bath, a solution of BCl_3 in $CHCl_3$ was added to a solution of $DBU{\cdot}BF_3$ in $CHCl_3$ in a 1:0.8 molar ratio. After stirring for 10 min, a fourfold excess (over BCl_3) of 1 M DBU in $CHCl_3$ was added and the solution was stirred for another 10 min. This solution was mixed with absolute ethanol in a 1:1 volume ratio. NH_4PF_6, as a saturated solution in ethanol, was slowly added with vigorous stirring until no additional precipitate formed. The white solid, very stable to hydrolysis, was washed with several portions of water and ethanol. ^{19}F NMR spectrum in acetone: δ −129.9 ppm, 1:1:1:1 quartet; δ −70.8 ppm, 1:1 doublet (quartet:doublet ~ 1:12); ^{11}B NMR spectrum: δ 4.7 ppm, 1:1 doublet; $J(^{11}B–^{19}F)$ = 50.7 Hz; $J(^{19}F–^{31}P)$ = 710.6 Hz; no ^{19}F or ^{11}B extraneous peaks. FAB spectrum (NBA matrix): peak at *m/z* 631 having an isotope pattern consistent with $\{[(DBU)_3BF^{2+}](PF_6^-)\}^+$. The elemental analysis is given in Table 1.

Table 1. Elemental analyses of (amidine)fluoroboron hexafluorophosphates.

	Element	Calcd. (%)	Found (%)	
$[(DBU)_3BF^{2+}](PF_6^-)_2$	C	41.75	43.05	42.92
	H	6.23	6.44	6.59
	N	10.83	10.47	10.51
	F	31.82	31.67	32.07
	B	1.39	1.59	1.83
$[(DBN)_3BF^{2+}](PF_6^-)_2$	C	36.42	37.17	37.33
	H	5.24	5.32	5.43
	N	12.14	11.66	11.93
	F	35.68	36.42	36.13
	B	1.56	0.96	1.05
$[(DBN)_2BF_2^+](PF_6^-)$	C	38.01	37.47	37.16
	H	5.47	5.05	4.97
	N	12.68	12.56	12.47

Tris(DBN)monofluoroboron hexafluorophospate

Needle-like transparent crystals of tris(DBN)monofluoroboron hexafluorophosphate were obtained by using a procedure similar to that for the DBU analogue. Since $(DBN)_3BF^{2+}$ was always present with $(DBN)_2BF_2^+$ and both of them could be precipitated by PF_6^-, the amount of PF_6^- was controlled so that only the doubly charged cation was precipitated and the singly charged cation remained in solution. ^{19}F NMR spectrum in acetone: δ −141.1 ppm, 1:1:1:1 quartet; δ −70.8 ppm, 1:1 doublet; ^{11}B NMR spectrum in acetone: δ 3.6 ppm, 1:1 doublet; $J(^{11}B–^{19}F)$ = 47.8 Hz; no additional ^{19}F or ^{11}B NMR peaks. The elemental analysis is given in Table 1.

Bis(DBN)difluoroboron hexafluorophosphate

1M BCl_3 in $CHCl_3$ was added to a solution of $DBN{\cdot}BF_3$ in $CHCl_3$, in a 1:3 molar ratio in a −63°C slush bath. After stirring for 5 min, a twofold excess of 1 M DBN in $CHCl_3$ solution was added, and the solution was stirred for 5 min. A twofold excess (v/v) of water was added to the $CHCl_3$ solution and the mixture was shaken for 5 min in a separatory funnel. Addition of saturated $NaPF_6$ to the water phase with stirring gave a white precipitate that was filtered, washed with several portions of water and $CHCl_3$, and recrystallized from 1:1 acetone–EtOH. ^{19}F NMR spectrum in acetone: δ −146.5 ppm, 1:1:1:1 quartet; δ −70.8 ppm, 1:1 doublet (quartet:doublet ~ 1:6). ^{11}B NMR spectrum in acetone: $J(^{11}B–^{19}F)$ = 31.6 Hz; no ^{19}F or ^{11}B extraneous peaks. FAB spectrum: *m/z* at 297 $[(DBN)_2BF_2]^+$(100%) and 173 $[(DBN)BF_2]^+$. The elemental analysis is given in Table 1.

Instrumentation

Most spectra of the DBU and DBN systems were obtained on a Bruker AC-200 multinuclear Fourier Transform NMR spectrometer operating at 188.31 MHz (^{19}F), 64.20 MHz (^{11}B), and

Fig. 1. 188.2 MHz ^{19}F NMR spectrum of a DBU·BF_nCl_{3-n} solution in $CDCl_3$ with mole ratio DBU:BF_3:BCl_3 = 2:1:1.

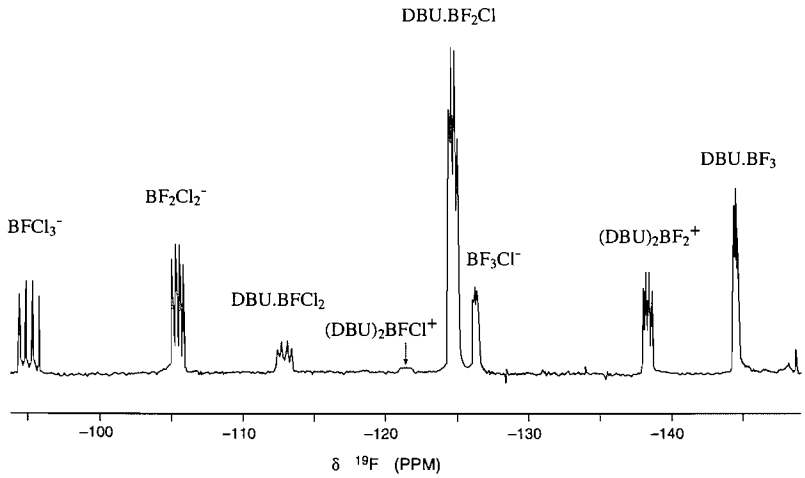

20.29 MHz (^{15}N), with 8K FIDs and spectral windows varying from 6000 Hz (^{11}B) to 35 000 Hz (^{19}F). For ^{19}F, between 200 and 2000 30° pulses were usually accumulated, with a relaxation delay of 1.1 s. ^{19}F spin-lattice relaxation times were determined on the AC-200 instrument using the inversion–recovery (180°–τ–90°) pulse sequence. ^{15}N spectra of DBN and DBU were obtained by the INEPT technique (21), but low signal strength prevented ^{15}N NMR studies of the adducts.

Variable-temperature ^{19}F NMR studies of the trimethylacetamidine and trimethylbenzamidine systems were carried out on a Bruker WP-60 multinuclear Fourier Transform NMR spectrometer operating at 56.4 MHz. High-field ^{11}B spectra of the DBU and DBN systems were obtained on a Bruker AM-500 spectrometer at 160.64 MHz, with a spectral width of 20 000 Hz and 8K and 16K FIDs, and 1000–2000 30° pulses. High-field ^{11}B spectra of the trimethylacetamidine and trimethylbenzamidine systems were obtained on a Bruker WH-400 instrument operating at 128.51 MHz.

FAB spectra were obtained on an AEI MS-30 (Kratos Ltd, Manchester) double-beam mass spectrometer coupled to a saddle field atom gun (Ion Tech Ltd, Teddington, U.K.), retrofitted with a Kratos FAB source in beam 1. The accelerating voltage was 4 kV. 3-Nitrobenzyl alcohol (NBA) was used as a liquid matrix in most cases. Data were collected on a DS-55 Kratos data system. A Hewlett–Packard 2631G printer was used to plot the spectra and mass intensity data. Signals from the matrix were subtracted automatically in the computer system in most situations. The BMASROS program was utilized for interpretation of isotope patterns.

Results

The DBU·BF_nCl_{3-n} system

Figures 1 and 2 show ^{19}F and ^{11}B NMR spectra of solutions of DBU·BF_3 following (*i*) BCl_3 addition to induce F,Cl exchange and form the mixed boron trihalide adducts DBU·BF_nCl_{3-n}, and (*ii*) addition of sufficient DBU to complex the excess Lewis acid. Large amounts of the mixed chlorofluoroborate anions $BFCl_3^-$, $BF_2Cl_2^-$, and BF_3Cl^-, identified by their chemical shifts and coupling constants (22), are present in addition

Fig. 2. 160.4 MHz ^{11}B NMR spectra of DBU·BF_nCl_{3-n} solutions in $CDCl_3$. (*a*) Cl < F; (*b*) Cl > F.

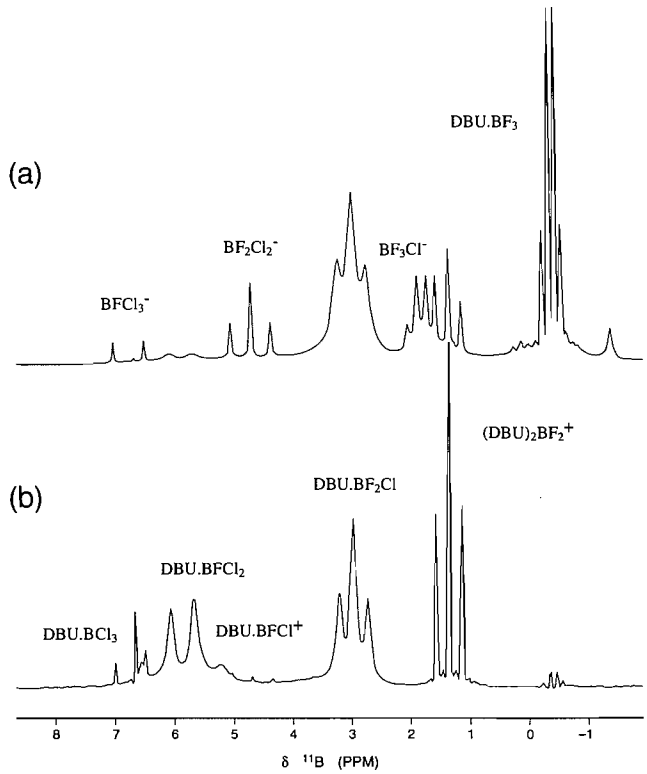

to the neutral boron trihalide adducts DBU·BF_nCl_{3-n} (n = 0–3) and the $(DBU)_2BF_2^+$ cation. There are also small amounts of DBU·BCl_3 and $(DBU)_2BFCl^+$. In samples with higher Cl:F ratios a signal arising from $(DBU)_3BF^{2+}$ can also be detected, and the DBU·BCl_3 peak is large. Most ^{19}F signals are 1:1:1:1 quartets due to coupling to ^{11}B (I = 3/2), and most ^{11}B signals give first-order multiplets that confirm the number of fluorines attached. The ^{11}B–^{19}F coupling constants are consistent in both ^{11}B and ^{19}F spectra and confirm our peak assignments, except $(DBU)_3BF^{2+}$ and $(DBU)_2BFCl^+$, which give broad ^{19}F

Table 2. ^{19}F and ^{11}B NMR parameters of amidine–haloboron cations, amidine – boron trihalide adducts, and fluorochloroborate anions.

Amidine	Adduct	Chemical shift[a] (ppm) ^{19}F	Chemical shift[a] (ppm) ^{11}B	$J(^{11}B–^{19}F)$ (Hz)
DBU[b]	D·BF_3	−144.3	−0.4	17.3
	D·BF_2Cl	−124.6	2.9	36.3
	D·$BFCl_2$	−112.8	5.8	62.7
	D·BCl_3		6.7	
	$D_2BF_2^+$	−138.4	1.4	34.0
	D_2BFCl^+	−121.6	5.4	
	D_3BF^{2+}	−132.8	3.6	
	D_3BF^{2+}[c]	−129.9	4.7	50.7
DBN[b]	D·BF_3	−149.9	−0.6	17.4
	D·BF_2Cl	−129.2	3.0	34.1
	D·$BFCl_2$	−118.1	6.0	62.6
	D·BCl_3		6.5	
	$D_2BF_2^+$	−149.4	0.7	31.6
	$D_2BF_2^+$[c]	−146.5		31.6
	D_2BFCl^+	−131.6	4.5	
	D_3BF^{2+}	−143.4	2.2	
	D_3BF^{2+}[c]	−141.1	3.6	47.8
Me_3acetamidine[d]	D·BF_3	−144.4	−0.7	17.6
	D·BF_2Cl	−125.6	2.9	35.7
	D·$BFCl_2$	−115.2	5.7	60.7
	D·BCl_3		6.3	
	D·BF_2Br[e]	−119.1	−2.7	
	D·$BFBr_2$[e]	−106.5		80.4
	$D_2BF_2^+$	−141.6	0.6	33.8
Me_3benzamidine[d]	D·BF_3	−145.6	−0.5	17.0
	D·BF_2Cl	−120.4	3.0	38.1
	D·$BFCl_2$	−110.1	5.8	62.7
	D·BCl_3		6.4	
	$D_2BF_2^+$	−145.4	0.7	33.8
	D_3BF^{2+}[f]		4.2	46.2
Chloro-fluoroborate anions[b,g]	BF_4^-	−154.1	−2.3	~0
	BF_3Cl^-	−126.2	1.8	24.3
	$BF_2Cl_2^-$	−105.4	4.6	54.7
	$BFCl_3^-$	−95.4	6.8	81.6
	BCl_4^-	6.7		

[a] ^{19}F, ppm to high frequency of $CFCl_3$; ^{11}B, ppm to high frequency of $Et_2O·BF_3$.
[b] ambient temperature; $CDCl_3$ solvent unless otherwise noted.
[c] Determined from the PF_6^- salt in acetone solvent.
[d] CD_2Cl_2 solvent. ^{19}F: −53°C; values can vary with temperature by up to 2.5 ppm between −53°C and ambient temperature. ^{11}B, ambient temperature.
[e] Collapsed by rapid chemical exchange in most samples.
[f] Assigned by analogy with the ^{11}B NMR spectra of the DBU and DBN systems.
[g] For literature values (CH_2Cl_2 solvent) see ref. 22.

signals because of more efficient quadrupole relaxation of boron (23). Better resolution is obtained from a solution of the hexafluorophosphate salt of $(DBU)_3BF^{2+}$ in acetone than from the $CDCl_3$ solutions described above. Table 2 gives the NMR parameters of the amidine–haloboron cations and amidine – boron trihalide adducts, and chlorofluoroborate anions. At −40°C most ^{11}B NMR signals become very broad due to increased efficiency of ^{11}B quadrupole relaxation, with only the DBU·BCl_3 peak remaining sharp, and several small peaks appear in the 6.3–6.9 ppm region of the spectrum that might arise from species such as $(DBU)_2BCl_2^+$ or $(DBU)_3BCl^{2+}$ (3).

Positive ion fast atom bombardment mass spectra (FAB spectra) (20) obtained directly from these solutions confirm the presence of the fluoroboron cations. Parent ion peaks were observed for $(DBU)_2BF_2^+$, *m/z* 353, and $(DBU)_2BFCl^+$, *m/z* 369 (isotope cluster). Our FAB results will be reported in more detail elsewhere.

Monitoring the DBU·BF_3 + BCl_3 system by ^{19}F NMR as DBU is added to the system is instructive. Before adding any DBU, all redistribution reactions are so rapid that separate ^{19}F signals could not be observed for any individual species. Chemical exchange was slowed sufficiently at the DBU:BF_3:BCl_3 ratio of 1.6:1:1 that some resonances were resolved, despite the excess of Lewis acid (Fig. 3*a*). The broad peaks at −144 ppm (DBU·BF_3) and −126 ppm indicate that rapid chemical exchange occurs among some species. However, the peaks assigned to $BFCl_3^-$, $BF_2Cl_2^-$, and DBU·BF_2Cl are sufficiently well resolved to show splittings due to $^{11}B–^{19}F$ coupling. Fluorine exchange occurs at very different rates in different species, as we observed previously in the mixed tetrahaloborate anions (22) where the BFX_3^- species underwent the slowest exchange, followed by successively faster exchange in $BF_2X_2^-$ and BF_3X^-. The same pattern occurs here, with exchange slow in $BFCl_3^-$ and $BF_2Cl_2^-$ but faster in BF_3Cl^-.

When no excess Lewis acid remains (DBU:BF_3:BCl_3 = 2:1:1), chemical exchange is slow on the NMR time scale and all of the peaks are well resolved (Fig. 3*b*). Further additions of DBU (Figs. 3*c* and 3*d*) led to diminution and eventual disappearance of all of the signals arising from chlorofluoroboron species, adducts and anions alike, so that only the $(DBU)_2BF_2^+$ and DBU·BF_3 ^{19}F signals remained as major signals, along with a very small $(DBU)_3BF^{2+}$ signal. As the titration proceeded, the DBU·BF_2Cl and DBU·$BFCl_2$ signals first increased and then decreased and disappeared. This is consistent with the following reactions:

[3] $$BF_nCl_{4-n}^- + DBU \rightarrow DBU·BF_nCl_{3-n} + Cl^-$$

[4] $$DBU·BF_2Cl + DBU \rightarrow (DBU)_2BF_2^+ + Cl^-$$

Figure 4 shows the changes in relative concentrations of the BF_2-containing species, and is consistent with stepwise formation of $(DBU)_2BF_2^+$ from $BF_2Cl_2^-$ by chloride ion displacement as the amount of DBU increases. Redistribution reactions among BF, BF_2, and BF_3-containing species must also be taking place since the mole percentage of BF_2-containing species as a whole, compared to total fluorine in the system, is increasing throughout the reaction.

Formation of $(DBU)_3BF^{2+}$ and $(DBU)_2BFCl^+$ (very minor species in the samples described above, with a 1:1 ratio of Cl to F) is favoured by higher ratios of Cl to F. This gives larger proportions of DBU·$BFCl_2$ and $BFCl_3^-$ in the initial solution, and these then undergo stepwise displacement of Cl^- by DBU as in eq. [5]. Figure 5 shows the ^{19}F and ^{11}B spectra of a sample

Fig. 3. ^{19}F NMR monitoring of the titration of a DBU·BF_3 + BCl_3 solution with DBU. The DBU:BF_3: BCl_3 ratios are: (*a*) 1.6:1:1; (*b*) 2:1:1; (*c*) 2.6:1:1; (*d*) 3.4:1:1.

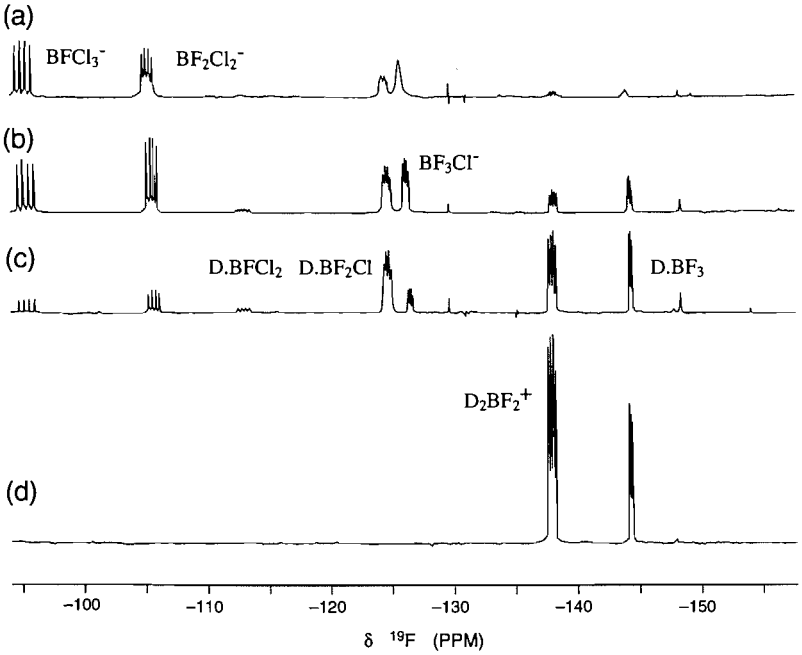

Fig. 4. Formation of $(DBU)_2BF_2^+$ from $BF_2Cl_2^-$ and DBU·BF_2Cl in a DBU·BF_nCl_{3-n} solution by successive additions of DBU, as monitored by ^{19}F NMR. ○, $BF_2Cl_2^-$; □, DBU·BF_2Cl; △, $(DBU)_2BF_2^+$; X, percent of total ^{19}F intensity arising from all three of the BF_2 species.

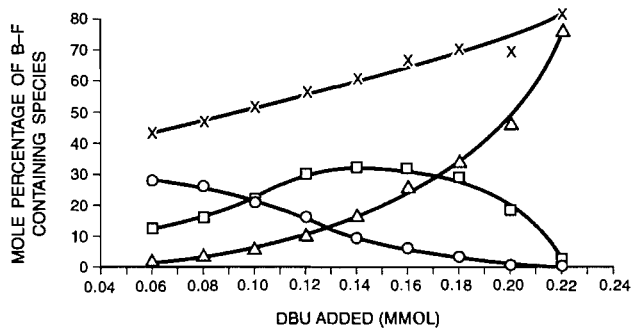

[5] $$BFCl_3^- \xrightarrow[-Cl^-]{DBU} DBU{\cdot}BFCl_2 \xrightarrow[-Cl^-]{DBU} (DBU)_2BFCl^+ \xrightarrow[-Cl^-]{DBU} (DBU)_3BF^{2+}$$

with a higher Cl:F ratio following the addition of two equivalents of DBU. There are strong $(DBU)_3BF^{2+}$ and $(DBU)_2BF_2^+$ ^{19}F signals and no other major peaks. The $(DBU)_3BF^{2+}$ ^{19}F signal has a partially collapsed ^{11}B–^{19}F coupling pattern (23). The ^{11}B spectrum has strong peaks from both of these cations and also a strong DBU·BCl_3 peak, but no other peaks. Note that DBU·BCl_3 is inert to Cl^- displacement by DBU under our conditions. $(DBU)_3BF^{2+}$ was isolated from such solutions as its PF_6^- salt, and is very stable to hydrolysis, as are the analogous ions D_3BH^{2+} (24) and D_3BBr^{2+} (25). $(DBU)_2BF_2^+$ is immediately decomposed by water, methanol, and ethanol, as determined by addition of these compounds to $CDCl_3$ solutions containing $(DBU)_2BF_2^+$. Its high reactivity contrasts with the inertness of most $D_2BF_2^+$ (2, 3) and $D_2BH_2^+$ (26) cations, including $(DBN)_2BF_2^+$, which is described below, and also with DBU·BF_3 and $(DBU)_3BF^{2+}$, which are very stable to hydrolysis. It is surprising that $(DBU)_2BF_2^+$, which is intermediate between the latter two compounds and has intermediate values of ^{19}F and ^{11}B NMR parameters, should be so different in its properties.

The reaction of DBU·BF_3, BCl_3, and a slight excess of DBU in $CDCl_3$ in a sealed thick-walled 5 mm NMR tube at 50°C was monitored by ^{19}F NMR. Initially the spectrum resembled Fig. 1, with peaks of the chlorofluoroborate anions, DBU – mixed boron trihalide adducts, and DBU–fluoroboron cations, but all of the ion peaks, cations and anions alike, diminished in intensity while the DBU·BF_2Cl and DBU·$BFCl_2$ peaks increased to become the major species. Table 3 gives the changes in relative ^{19}F peak intensities wth time of reaction. DBU·BF_3 diminished slightly and then stayed constant. $(DBU)_2BFCl^+$ first increased and then diminished. These results show conclusively that the initial mixture containing the chlorofluoroborate anions is far from equilibrium, at least in the presence of a small excess of DBU.

The resolution of the $BF_nCl_{4-n}^-$ ^{19}F NMR signals is always in the order $BFCl_3^- > BF_2Cl_2^- > BF_3Cl^-$. Some samples give an especially sharp $BFCl_3^-$ resonance, with the septet of equal-intensity peaks arising from ^{10}B–^{19}F coupling (^{10}B, 20% abundant, $I = 3$) being well resolved in addition to the 1:1:1:1 quartet arising from ^{11}B–^{19}F coupling (^{11}B, 80% abundant, $I = 3/2$)

Fig. 5. The ^{11}B and ^{19}F NMR spectra of $(DBU)_3BF^{2+}$ and $DBU)_2BF_2^+$, obtained from $CDCl_3$ solutions of $DBU{\cdot}BF_nCl_{3-n}$ to which an excess of DBU was added.

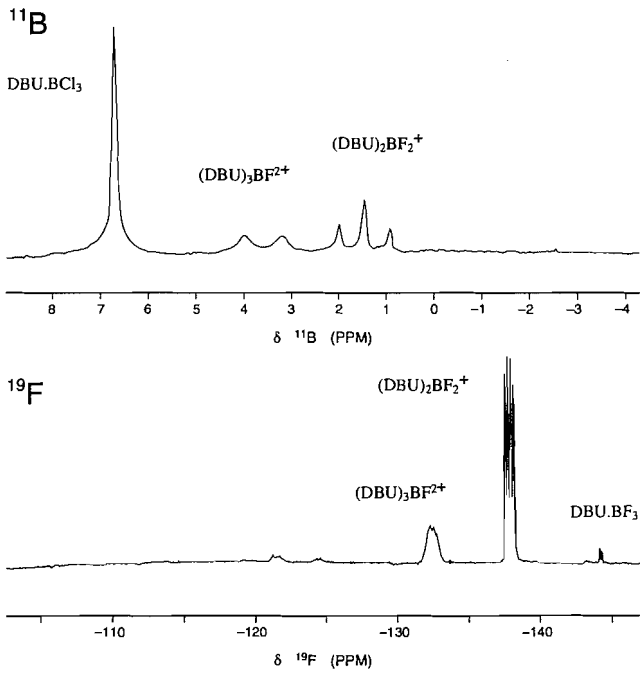

Table 3. Changes in relative ^{19}F peak intensities of a $DBU/BF_3/BCl_3$ sample[a] on reaction in a sealed tube at 50°C.

Time (h)	0	1	3	6	22	40
$BFCl_3^-$	5	8	5	4	2	2
$BF_2Cl_2^-$	4	4	4	2	2	2
BF_3Cl^-	2	1	1	1	0	0
$(DBU)\cdot BFCl_2$	7	10	15	18	27	29
$(DBU)\cdot BF_2Cl$	24	27	31	37	43	47
$(DBU)\cdot BF_3$	9	5	4	5	5	5
$(DBU)_2BFCl^+$	7	9	12	9	9	6
$(DBU)_2BF_2^+$	43	36	29	25	13	8

[a]0.15 mmol $DBU\cdot BF_3$, 0.15 mmol BCl_3, and 0.18 mmol DBU in $CDCl_3$.

(Fig. 6). Since the magnetogyric ratio of ^{10}B is only 1/3 that of ^{11}B, the magnitude of $J(^{10}B–^{19}F)$ is only 1/3 that of $J(^{11}B–^{19}F)$ (27). The ^{19}F isotope shift between $^{10}BFCl_3$ and $^{11}BFCl_3$ is 0.092 ppm, appreciably greater than the corresponding value for BF_4^-, 0.050 ppm (28), ketone$\cdot BF_3$ adducts, 0.066 ppm (29), or $(quinuclidine)_2BF_2^+$, 0.064 ppm, in accord with heavier nearby atoms increasing the effect (30).

^{19}F spin-lattice relaxation times in a typical $DBU{\cdot}BF_nCl_{3-n}$ solution in $CDCl_3$ were as follows: $DBU\cdot BF_3$, 0.93 s; $DBU\cdot BF_2Cl$, 0.60 s; $DBU\cdot BFCl_2$, 0.61 s; $(DBU)_2BF_2^+$, 0.23 s; $(DBU)_2BFCl^+$, 0.14 s. Because of the strong dependence of spin-lattice relaxation on solvent viscosity the relative times are more significant than the individual values. The more hindered the molecular tumbling about boron, the shorter is the spin-lattice relaxation time, as we observed in an analogous series of pyridine adducts and cations (3). The cations, with two large substituents on boron, are unable to tumble effectively about either donor–boron bond since the second donor interferes, and the cations have by far the shortest spin-lattice relaxation times.

Fig. 6. 188.2 MHz ^{19}F spectrum of $BFCl_3^-$ in $CDCl_3$, showing multiplets arising from spin–spin coupling to ^{10}B and ^{11}B.

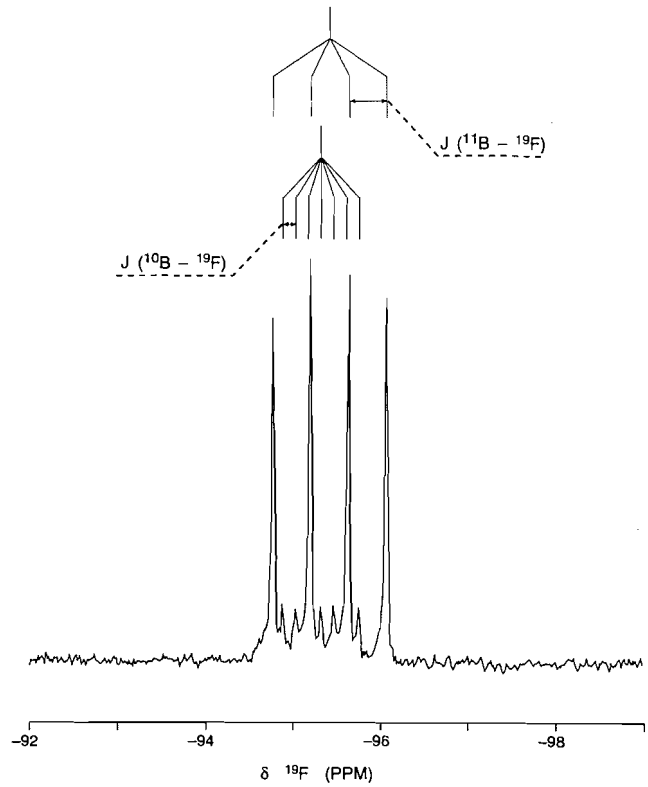

The $DBU{\cdot}BF_nBr_{3-n}$ system

Chemical exchange that is rapid on the NMR time scale restricts ^{19}F NMR monitoring of species containing B—Br bonds in the $DBU{\cdot}BF_nBr_{3-n}$ system. A moderate excess of DBU slows chemical exchange sufficiently to give a well-resolved ^{19}F 1:1:1:1 quartet for $(DBU)_2BF_2^+$, in addition to broad peaks at δ −117 ppm, −133 ppm ($(DBU)_3BF^{2+}$), and −144 ppm ($DBU\cdot BF_3$) (Fig. 7*a*), and in some solutions −114 ppm. The $(DBU)_3BF^{2+}$ peak remains broad due to ^{11}B quadrupole relaxation effects, but broadening of the other peaks must be caused by chemical exchange. On further addition of DBU, the $DBU\cdot BF_3$ peak becomes a well-resolved 1:1:1:1 quartet and the low-field absorption, apparently arising from rapidly exchanging bromofluoroboron species, disappears (Fig. 7*b*), consistent with complete displacement of Br^- from the bromofluoroboron species. Changing the proportions of Br to F changes the proportions of the $(DBU)_3BF^{2+}$ and $(DBU)_2BF_2^+$ cations as in the $DBU{\cdot}BF_nCl_{3-n}$ system.

The $DBU/BF_3/BCl_3/BBr_3$ system gives ^{19}F spectra similar to those of the $DBU{\cdot}BF_nCl_{3-n}$ system if $BCl_3 > BBr_3$, and similar to spectra of the $DBU{\cdot}BF_nBr_{3-n}$ system if $BBr_3 > BCl_3$. The DBU·BFClBr adduct resonance could not be detected.

Fig. 7. 188.2 MHz ^{19}F NMR spectra of the DBU·BF_nBr_{3-n} system. (*a*) DBU:BF_3:BBr_3 = 8:3:2; (*b*) excess DBU added.

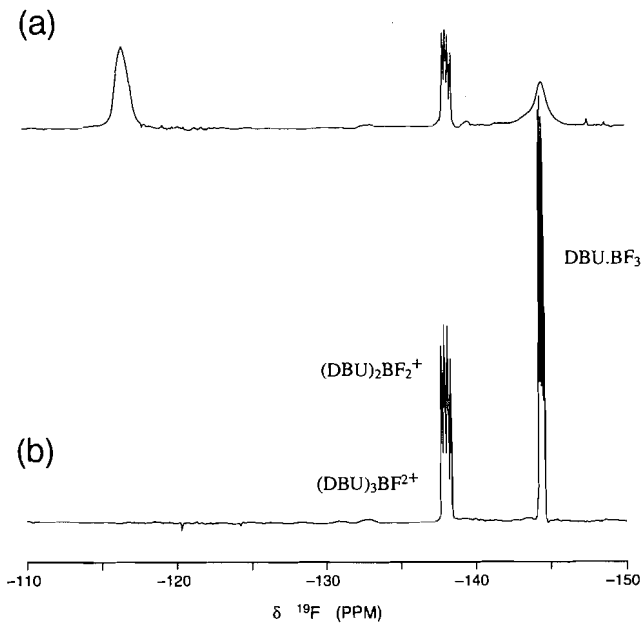

The DBN·BF_nCl_{3-n} system

The DBN·BF_nCl_{3-n} system behaves similarly to the corresponding DBU adduct system. All of the DBN·BF_nCl_{3-n} adducts, the mixed chlorofluoroborate anions, and the DBN fluoroboron cations are readily formed and detected by NMR. The reactivity of DBN·BF_2Cl is similar to that DBU·BF_2Cl, with excess amidine displacing chloride very rapidly, but DBN·$BFCl_2$ reacts with DBN much faster than DBU·$BFCl_2$ reacts with DBU, consistent with the decreased steric hindrance of DBN compared to DBU. The chemical shifts of some adducts and cations differ by several ppm from those of the corresponding DBU species (Table 2). $(DBN)_3BF^{2+}$ formation is favoured by a high ratio of Cl to F, and its ^{19}F signal, like that of its DBU analogue, is poorly resolved in $CDCl_3$ due to ^{11}B quadrupole relaxation effects. $(DBN)_2BFCl^+$, which gives a broad ^{19}F NMR signal in $CDCl_3$, is an intermediate in the formation of $(DBN)_3BF^{2+}$ from DBN·$BFCl_2$, and its ^{19}F signal first increases and then decreases in intensity when excess DBN is added. $(DBN)_2BF_2^+$ and $(DBN)_3BF^{2+}$ are inert and both have been isolated as their hexafluorophosphate salts. $(DBN)_2BF_2^+$ is stable in water up to 85°C but decomposes at 100°C generating fluoride ion (^{19}F δ −119.9 ppm; confirmed by dissolving NaF) and boric acid (^{11}B δ ~19 ppm; broad band (31); also generated by decomposition of the chloroboron species by water extraction).

All cations were confirmed by FAB. For $(DBN)_2BF_2^+$, peaks at *m/z* 297, ($(DBN)_2BF_2^+$) and at *m/z* 173, ($(DBN)BF_2^+$) were observed both from solution and from the PF_6^- salt; for $(DBN)_2BFCl^+$, peaks at *m/z* 313, ($(DBN)_2BFCl^+$) and at *m/z* 189, ($(DBN)BFCl^+$) were observed from solution. The PF_6^- salt of $(DBN)_3BF^{2+}$ gave a peak at *m/z* 547 that was confirmed as $\{[(DBN)_3BF](PF_6)\}^+$ by its isotope pattern.

The DBN·BF_nBr_{3-n} system

Addition of excess DBN to a DBN·BF_3 + BBr_3 solution at −63°C in $CDCl_3$ gave a ^{19}F 1:1:1:1 quartet at δ −79.6 ppm, $J(^{11}B-^{19}F)$ = 113.3 Hz, assigned to $BFBr_3^-$ (lit. (22) δ: −78.6 ppm, $J(^{11}B-^{19}F)$ = 111.3 Hz in CH_2Cl_2), and a very broad band that moved to lower frequency (higher field) as the amount of DBN increased, consistent with (*i*) rapid chemical exchange among species containing both fluorine and bromine, and (*ii*) rapid displacement of bromide ion by DBN. Surprisingly, addition of excess DBN gave only a large DBN·BF_3 and a small BF_4^- ^{19}F resonance, without the expected large DBN–fluoroboron cation peaks. This system merits further study.

MeC(=NMe)NMe_2 and PhC(=NMe)NMe_2 mixed boron trihalide adduct systems

The *N,N,N'*-trimethylacetamidine and *N,N,N'*-trimethylbenzamidine BF_nCl_{3-n} and BF_nBr_{3-n} adduct systems in $CDCl_3$ and CD_2Cl_2 behave similarly to the corresponding DBU and DBN systems. Their low-temperature ^{19}F and ambient-temperature ^{11}B NMR parameters are included in Table 2. As with DBU and DBN, mixed tetrahaloborate anions were present. ^{19}F chemical shifts change appreciably (up to 2.5 ppm) between ambient temperature and −53°C. Low temperatures slow the exchange processes and allow ^{19}F NMR detection of signals that apparently arise from amidine·BF_nBr_{3-n} adducts and additional bromofluoroborate anions, whereas $BFBr_3^-$ is the only bromofluoroboron species that can be observed at ambient temperature. However, the low-temperature ^{19}F spectra were poorly resolved, with most $^{11}B-^{19}F$ spin–spin multiplets collapsed due to increased efficiency of ^{11}B quadrupole relaxation. (More efficient ^{11}B quadrupole relaxation also broadens the ^{11}B spectra of all of the amidine adduct systems at low temperatures.)

Discussion

General

Of the various classes of organic Lewis bases that form mixed boron trihalide adducts (32), amidines are at one extreme in their high ability to form fluoroboron cations by heavy halide ion displacement (eqs. [1] and [2]). Weak donors such as dimethyl ether (33) amd methyl acetate (34) do not undergo these reactions at all, whereas benzoate esters (35) and tetramethylurea (36), like the lowest-steric-hindrance tertiary-amine mixed boron trihalide adducts (1, 2), form $D_2BF_2^+$ only. Pyridine adducts form $D_2BF_2^+$ very rapidly from D·BF_2X and, unlike the above bases, also form D_2BFCl^+, $D_2BFBr_2^+$, and D_3BF^{2+} from pyridine·BFX_2, but the reaction is slow (3). In the amidine – mixed boron trihalide adduct systems all of the above cation types form rapidly. The amidine·BF_2Cl and amidine·$BFCl_2$ adducts give fluoroboron cations within minutes, while redistribution reactions in the amidine·BF_nBr_{3-n} are rapid even on the NMR time scale so NMR signals of individual amidine–bromofluoroboron species cannot be detected at ambient temperature. The strong basicity of amidines (stronger than trialkylamines and far stronger than pyridines) and their low steric hindrance (only two substituents on the donor nitrogen) clearly favour fluoroboron cation formation. Except for those prepared from mixed boron trihalide adducts, the relatively few four-coordinate fluoroboron cations known are primarily formed with chelating donors (37).

While heavy halide ion displacement from mixed boron trihalide adducts by amidine occurs rapidly, other reactions are

much slower. For example, days at 50°C are required to attain equilibrium in the sealed-tube reaction of Table 3. A wide range of reaction rates is not surprising in complex exchanging systems, and has been noted in other $D{\cdot}BF_nX_{3-n}$ adduct systems (3, 32).

The ^{19}F and ^{11}B NMR parameters of the amidine – mixed boron trihalide adducts and fluoroboron cations follow the patterns seen in other adduct systems (2, 3, 19, 38), with the number and type of heavy halogen atoms having greater effects than the donor or the fluorines. ^{19}F chemical shifts are also affected by donor steric hindrance (3, 19). DBU has greater steric hindrance than DBN since the five-membered ring of DBN holds back the amidine substituents from the imino nitrogen donor site more effectively than the seven-membered ring of DBU. The approximately 5 ppm shift to high frequency (low field) of the ^{19}F chemical shifts of the $DBU{\cdot}BF_nCl_{3-n}$ adducts, compared to the corresponding DBN adducts (Table 2), reflects the greater steric hindrance. This effect doubles to 10–11 ppm in the $D_2BF_2^+$ and D_2BFCl^+ ions where the presence of two donor molecules should lead to greater steric interaction about boron. Interestingly, the chemical shift difference between the D_3BF^{2+} ions of DBU and DBN does not increase further but remains at 11 ppm.

We attempted ^{15}N NMR of these systems but low signal intensities, even with the INEPT sequence (21), prevented this. Our ^{15}N chemical shift values for the pure liquid amidines (DBU: −179 ppm (imino N); −289 ppm (amino N); DBN: −195 ppm (imino N); −288 ppm (amino N)) are consistent

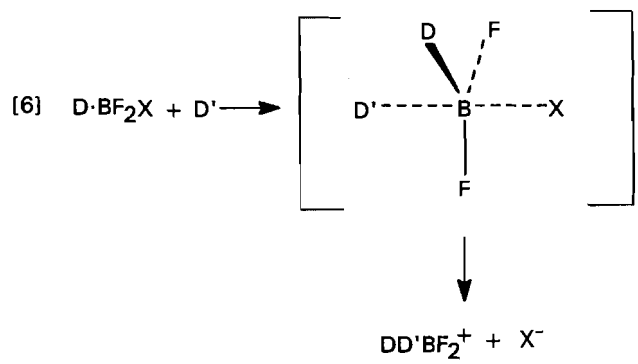

with other amidine ^{15}N chemical shifts (39), although our DBU values differ appreciably from a published value (−172 ppm (imino N); −295 ppm (amino N) (15)). The 16 ppm difference between the imino nitrogen chemical shifts of DBU and DBN is consistent with somewhat greater steric inhibition of resonance, i.e., of planarity of the >N—C=N— system, in DBU: the imino nitrogen moves slightly closer to the chemical shift range for simple imines, −30 to −75 ppm (39*b*). Steric inhibition of resonance is also consistent with the decreased Bronsted basicity of DBU compared to DBN. The greater reactivity of $(DBU)_2BF_2^+$ compared to $(DBN)_2BF_2^+$ can be rationalized in terms of the greater steric hindrance introduced by DBU, but the extreme difference in stability between these cations, as well as between $(DBU)_2BF_2^+$ and $(DBU)_3BF^{2+}$, is surprising.

Chloride ion is readily displaced from $DBU{\cdot}BF_2Cl$ and $DBU{\cdot}BFCl_2$ by excess DBU but $DBU{\cdot}BCl_3$ is unaffected (Fig. 5). This is typical of the differences in reactivity of mixed vs. unmixed boron trihalide adducts: the mixed-halogen adducts are always far more susceptible to displacement of halide ion than the unmixed-halogen adducts of the same donor (1–3). However, we cannot completely exclude the possibility that the large low-field ^{11}B NMR peak of Fig. 5 arises from BCl_4^- rather than from $DBU{\cdot}BCl_3$, since BCl_4^- and $D{\cdot}BCl_3$ adducts give ^{11}B singlets of very similar chemical shift (3). Even if BCl_4^- were present in place of $DBU{\cdot}BCl_3$, the same argument would apply: it would be equally noteworthy that no Cl^- is displaced from BCl_4^- while all of the available Cl^- is displaced from the mixed chlorofluoroboron species, and our conclusion, that chloride displacement occurs much more easily from mixed- than from unmixed-halogen species, would remain valid.

A unique feature of the amidine adduct systems is the formation of large amounts of the mixed chlorofluoroborate anions along with the mixed boron trihalide adducts and fluoroboron cations. These anions cannot be detected in the pyridine or tertiary-amine mixed boron trihalide adduct systems that do give fluoroboron cations (1–3). Mixed chlorofluoroborate anions have, however, been formed in the tetramethylurea (TMU) BF_nCl_{3-n} adduct system, along with $(TMU)_2BF_2^+$, although preparation conditions were different (36), but there was no evidence for $(TMU)_2BFCl^+$ or $(TMU)_3BF^{2+}$ formation.

High-field ^{11}B NMR would be a useful supplement to ^{19}F NMR as a routine monitoring technique for detecting the non-fluorine-containing boron species. Because it was not routinely available, and because of the very small chemical shift dispersion of the various D_nBCl_{4-n} species including BCl_4^- (3), we know less about the behaviour of the non-fluorine-containing boron species in these systems than the fluorine-containing ones.

Mechanistic implications

Heavy halide ion displacement from mixed boron trihalide adducts is highly selective, in the order of $BF_2X \gg BFX_2 \gg BX_3$, and we have previously explained this in terms of fluorine-to-boron π-bonding stabilization of the transition state, the stabilization increasing with the number of fluorines. Evidence from our earlier studies (2, 3) supports an associative (S_N2) reaction mechanism (eq. [6]), although the same π-bonding considerations would lead to similar selectivity if there were a dissociative mechanism with a three-coordinate intermediate or transition state. π-Bonding in the transition state, from the donor molecule as well as from halogen, can also account for the far more rapid reaction in adduct systems in which the donor can π-bond to boron in the transition state, e.g., pyridines (3), than in cases where it cannot, e.g., aliphatic tertiary amines (2). Amidines resemble pyridines in that they can stabilize the transition state by π-bonding to boron (structure **4c**). Together with the high basicity and low steric hindrance of amidines, this can account for the very rapid formation of amidine–fluoroboron cations.

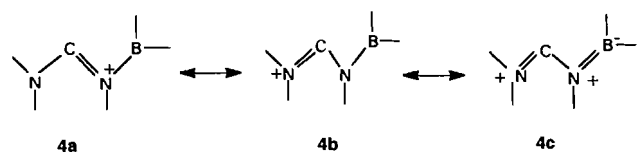

The large and varying amounts of mixed tetrahaloborate

anions that are present in freshly prepared amidine – mixed boron trihalide adduct solutions are a complicating factor. We (32, 36) and others (40) have discussed possible exchange reactions about boron, including donor-for-halogen exchange that would lead to both mixed tetrahaloborate anions and haloboron cations. The formation, and disappearance on standing, of mixed chlorofluoroborate anions in the tetramethylurea adduct system, from solutions containing both $TMU{\cdot}BF_3$ and $TMU{\cdot}BCl_3$ (36) seems consistent with this pattern. We proposed that redistribution of substituents about boron is caused by an initial dissociation of the weak $TMU{\cdot}BF_3$ donor–acceptor bond, followed by rapid fluorine exchange between the freed BF_3 with the four-coordinate boron species, giving a generalized redistribution reaction including donor-for-halogen as well as halogen-for-halogen exchange, generating the mixed chlorofluoroborate anions as well as $(TMU)_2BF_2^+$, a typical reaction being eq. [7], in which the chlorine bridge in the transition state or reactive intermediate is similar to the fluorine bridge of the $B_2F_7^-$ ion (41). Mechanisms of this type have been dealt with in detail by Janzen and co-workers (42).

[7] $D{\cdot}BCl_3 + BF_3 \longrightarrow$ 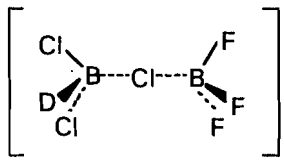

$D{\cdot}BCl_2^+ + BF_3Cl^-$

A number of features are different in the amidine – mixed boron trihalide adduct systems. One is that the amidine–boron donor–acceptor bond should be much stronger than the oxygen–donor donor–acceptor bond of the TMU adducts, and at least as strong as the nitrogen–boron donor–acceptor bonds in tertiary amine – boron trihalide adducts (43) because of the greater base strength and lower steric hindrance of amidines compared to tertiary amines. The strength of the amidine–boron donor–acceptor bond would prevent an initial BF_3 dissociation step. However, our solutions are prepared using an excess of BCl_3, and the following reaction is plausible:

[8] $DBU{\cdot}BF_3 + BCl_3 \longrightarrow$ 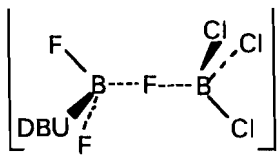

$DBU{\cdot}BF_2^+ + BFCl_3^-$

There is, however, experimental evidence suggesting that the formation of large amounts of the chlorofluoroborate ions is extraneous to the amidine$\cdot BF_nX_{3-n}$ adduct systems, and is an artifact of the preparation method. ^{19}F spectra of freshly prepared samples (e.g., Fig. 1) show a mismatch between high chlorofluoroborate anion concentrations and lower concentrations of the boron cations than would be required to balance the charge. The total negative charge of the boron-containing anions would have to equal the total positive charge of the boron-containing cations if the only source of ionic species were donor-for-halogen redistribution reactions about boron. A non-boron-containing cation must be present in these cases, and this has been confirmed by the precipitation from some solutions of solids that by FAB analysis are the amidine hydrochlorides, $[amidine{\cdot}H]^+{\cdot}Cl^-$. (An excess of haloboron cations over haloborate anions would not be a problem since since Cl^- and Br^- are well known to be counterions in related fluoroboron cation-forming mixed boron trihalide adduct systems (1–3).)

Furthermore, sealed-tube equilibration studies (Table 3) show that the initial mixtures, with chlorofluoroborate anions present in large and varying amounts, are not at equilibrium. The closest approach to equilibrium observed by us (Table 3, 40 h at 50°C) gives relative proportions that resemble other mixed boron trihalide adduct systems (2, 3, 32) far more closely than do the initial mixtures, with the neutral mixed boron trihalide adducts as the major species. Only two of the three mixed tetrahaloborate anions can still be detected, and the BF_3 adduct, $D_2BF_2^+$, and D_2BFCl^+ are present in similar low concentrations. Since the chlorofluoroborate ion concentrations diminish markedly, they cannot be major species at equilibrium.

Equation [8] cannot be the whole story because (*i*) the chlorofluoroborate ions are present initially, without sufficient fluoroboron cation counterion present to balance the charge; and (*ii*) amidinium hydrochloride salts instead of fluoroboron cation salts precipitate from solution, showing the presence of large amounts of protonated amidine in solution, despite preparation and handling of the amidines and solvent under rigorously dry conditions so that water is unlikely to be a source of $amidine{\cdot}H^+$. However, these observations are accounted for if the $amidine{\cdot}H^+$ cations and the chlorofluoroborate anions are both formed through reaction of amidine with the chloroform solvent. Strong bases can attack chloroform with the generation of carbenes (44):

[9] $D + CHCl_3 \rightarrow D{\cdot}H^+ + CCl_3^-$

$\downarrow$

$CCl_2 + Cl^-$

Since the chlorofluoroborate anions are formed initially when excess boron trihalide is present but not under excess-base conditions, a concerted mechanism is likely in which the boron trihalide assists by facilitating the removal of chloride ion from chloroform:

[10] $D + CHCl_3 + BF_nCl_{3-n} \longrightarrow$ 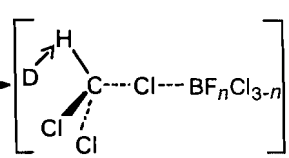

$D{\cdot}H^+ + CCl_2 + BF_nCl_{4-n}^-$

Alternatively, reaction [9] might continue under excess amidine conditions, but the chlorofluoroborate anions would undergo chloride displacement by amidine (eq. [3]) so that their concentrations would not build up.

Thus the greater base strength of amidines, compared to trialkylamines or pyridines, leads to the formation of chlorofluoroborate ions in solution, but indirectly through attack on the chloroform solvent rather than directly through donor-for-halogen redistribution reactions about boron. A similar reaction in methylene chloride, the solvent in much of our work with *N,N,N'*-trimethylacetamidine and *N,N,N'*-trimethylbenzamidine, is possible as well, although CHCl is a less stable carbene than CCl_2 (44), and can account for the formation of mixed tetrahaloborate anions in this solvent as well.

Conclusions

The combination of high basicity, π-bonding stabilization of the transition state, and low steric hindrance makes the amidines the most effective Lewis bases studied to date for generating fluoroboron cations from mixed boron trihalide adducts. Only the amidine·BF_nCl_{3-n} adduct systems have been studied in detail because the amidine·BF_nBr_{3-n} systems undergo extremely rapid chemical exhange and displacement of all B—Br bonds by excess amidine. The presence of large and variable amounts of the mixed chlorofluoroborate anions $BF_nCl_{4-n}^-$ in our freshly prepared samples appears to be related to attack of amidine on the chloroform solvent, via a carbene mechanism, rather than an integral part of the redistribution equilibria in the amidine·BF_nCl_{3-n} systems. We cannot exclude the possibility that the chlorofluoroborate anions may also form by donor-for-halogen redistribution reactions in the amidine·BF_nCl_{3-n} adduct systems, as they apparently do in the TMU·BF_nCl_{3-n} adduct system.

Acknowledgements

We are indebted to the late Mel Farquharson for his assistance in the early stages of the DBU work. We also thank Abbott Laboratories, North Chicago, Illinois, U.S.A., for providing a sample of DBU, Tim Jones for technical assistance, Prof. Alex F. Janzen for helpful discussions, the Department of Chemistry, University of Manitoba, for its hospitality to J.S.H. while this paper was being written, the Departments of Chemistry at McMaster University and the University of Guelph for access to high-field ^{11}B nmr, and the Natural Sciences and Engineering Research Council of Canada for financial support.

References

1. M.J. Farquharson and J.S. Hartman. J. Chem. Soc. Chem. Commun. 256 (1984).
2. M.J. Farquharson and J.S. Hartman. Can. J. Chem. **67**, 1711 (1989).
3. M.J. Farquharson and J.S. Hartman. Can. J. Chem. **74**, 1309 (1996).
4. S. Patai and Z. Rappaport (*Editors*). The chemistry of functional groups. The chemistry of amidines and imidates. Vol. 2. John Wiley and Sons, New York. 1991.
5. J. Oszczpowicz and E. Raczynska. J. Chem. Soc. Perkin Trans. 2, 1643 (1984).
6. J. Oszczpowicz and K. Ciszkowski. J. Chem. Soc. Perkin Trans. 2, 663 (1987); E. Raczynska, J. Oszczpowicz, and M. Walczak. J. Chem. Soc. Perkin Trans. 2, 1087 (1985).
7. J. Barker and M. Kilner. Coord. Chem. Rev. **133**, 219 (1994); K. Vrieze and G. Van Koten. *In* Comprehensive coordination chemistry. The synthesis, reactions, properties, and applications of coordination compounds. Vol. 2. *Edited by* G. Wilkinson, R.D. Gillard, and J.A. McCleverty. Pergamon Press, Oxford. 1987. Chap. 13, Sect. 13.5.
8. F.A. Cotton, T. Inglis, K. Milner, and T.R. Webb. Inorg. Chem. **14**, 2023 (1975); F.A. Cotton, W.H. Ilsley, and W. Kaim. Inorg. Chem. **18**, 3569 (1979).
9. H. Oediger, F. Möller, and K. Eiter. Synthesis, 591 (1972).
10. I. Hermecz. Adv. Heterocycl. Chem. **42**, 84 (1987).
11. D.H.R. Barton, J.D. Elliott, and S.D. Géro. J. Chem. Soc. Perkin Trans. 1, 2085 (1982).
12. D.R. Perrin. Dissociation constants of organic bases in aqueous solutions. Butterworths, London. 1965; and Supplement, 1972.
13. H. Lammers, P. Cohen-Fernandes, and C.L. Habraken. Tetrahedron, **50**, 865 (1994).
14. R. Reed, R. Reau, F. Dahan, and G. Bertrand. Angew. Chem. Int. Ed. Engl. **32**, 399 (1993); G. Bouhadir, R.W. Reed, R. Reau, and G. Bertrand. Heteroat. Chem. **6**, 371 (1995); H.H. Karsch, T. Rupprich, and M. Heckel. Chem. Ber. **128**, 959 (1995).
15. J.V. Barkley, C.J. Davies, B.T. Heaton, and C. Jacob. J. Chem. Soc. Dalton Trans. 2861 (1995), and references therein.
16. D.F. Shriver. The manipulation of air-sensitive compounds. McGraw–Hill, New York. 1969.
17. J.D. Wilson, J.S. Wager, and H. Weingarten. J. Org. Chem. **36**, 1613 (1971).
18. D.C. Bradley and I.M. Thomas. J. Chem. Soc. 3857 (1960).
19. A. Fox, J.S. Hartman, and R.E. Humphries. J. Chem. Soc. Dalton Trans. 1275 (1982).
20. J.M. Miller. Mass Spectrom. Rev. **9**, 319 (1990); K. Balasanmugam, J.S. Hartman, J.M. Miller, and Z. Yuan. Can. J. Chem. **67**, 685 (1989).
21. R.K. Harris. Nuclear magnetic resonance spectroscopy. Pitman, London. 1983. Chap. 7.
22. J.S. Hartman and G.J. Schrobilgen. Inorg. Chem. **11**, 940 (1972).
23. J. Bacon, R.J. Gillespie, and J.W. Quail. Can. J. Chem. **41**, 3063 (1963); M.J. Bula and J.S. Hartman. J. Chem. Soc. Dalton Trans. 1047 (1973).
24. M.A. Mathur and G.E. Ryschkewitsch. Inorg. Chem. **19**, 887 (1980).
25. C. Makosky, G.L. Galloway, and G.E. Ryschkewitsch. Inorg. Chem. **6**, 1972 (1967).
26. J. Emri and B. Györi. In Comprehensive coordination chemistry. The synthesis, reactions, properties, and applications of coordination compounds. Vol. 3. *Edited by* G. Wilkinson, R.D. Gillard, and J.A. McCleverty. Pergamon Press, Oxford. 1987. Chap. 24, pp. 81–104; G.E. Ryschkewitsch. *In* Boron hydride chemistry. *Edited by* E.L. Muetterties. Academic Press, New York. 1975. Chap. 6.
27. E. D. Becker. High resolution NMR. Theory and chemical applications. 2nd ed. Academic Press, New York. 1980. Chap. 5, pp. 93–94.
28. K. Kuhlmann and D.M. Grant. J. Phys. Chem. **68**, 3208 (1964); R.J. Gillespie and J.S. Hartman. J. Chem. Phys. **45**, 2712 (1966).
29. R.J. Gillespie and J.S. Hartman. Can. J. Chem. **46**, 2147 (1968).
30. P.E. Hansen. Annu. Rep. NMR Spectrosc. **15**, 105 (1983); G.A. Webb. *In* NMR of newly accessible nuclei. Vol. 1. *Edited by* P. Laszlo. Academic Press, New York. 1983. Chap. 4, pp. 94–95.
31. H. Nöth and B. Wrackmeyer. *In* Nuclear magnetic resonance spectroscopy of boron compounds. NMR. Basic principles and progress. Vol. 14. *Edited by* P. Diehl, E. Fluck, and R. Kosfeld. Springer-Verlag, Berlin. 1978. Table XI.
32. J.S. Hartman and J.M. Miller. Adv. Inorg. Chem. Radiochem. **21**, 147 (1978).

33. M.J. Bula, D.E. Hamilton, and J.S. Hartman. J. Chem. Soc. Dalton Trans. 1405 (1972).
34. M.J. Bula, J.S. Hartman, and C.V. Raman. J. Chem. Soc. Dalton Trans. 725 (1974).
35. J.S. Hartman and B.D. McGarvey. Inorg. Chim. Acta **44**, L39 (1980); J.S. Hartman, B.D. McGarvey, and C.V. Raman. Inorg. Chim. Acta **49**, 63 (1981).
36. J.S. Hartman and G.J. Schrobilgen. Inorg. Chem. **13**, 874 (1974).
37. Gmelin handbook of inorganic chemistry. Boron compounds. 2nd Supplement, Vol. 37. 1976. pp. 114–125.
38. J.S. Hartman and J.M. Miller. Inorg. Chem. **13**, 1467 (1974).
39. (*a*) J. Oszczapowicz, I. Wawer, M. Dargatz, and E. Kleinpeter. J. Chem. Soc. Perkin Trans. 2, 1127 (1995), and references therein; (*b*) G.J. Martin, M.L. Martin, and J.-P. Gouesnard. *In* ^{15}N NMR spectroscopy. NMR. Basic principles and progress. Vol. 18. *Edited by* P. Diehl, E. Fluck, and R. Kosfeld. Springer-Verlag, Berlin. 1981. Fig. 1–1.
40. A.G. Massey. Adv. Inorg. Chem. Radiochem. **10**, 1 (1967).
41. J.S. Hartman and P. Stilbs. J. Chem. Soc. Chem. Commun. 566 (1975).
42. A.F. Janzen. Coord. Chem. Rev. **130**, 355 (1994); X. Ou, R. Wallace, and A.F. Janzen. Can. J. Chem. **71**, 51 (1993).
43. H.C. Brown. J. Chem. Soc. 1248 (1956).
44. J. March. Advanced organic chemistry. Reactions, mechanisms, and structure. 4th ed. John Wiley and Sons, New York. 1992. pp. 195–202; T.L. Gilchrist and C.W. Rees. Carbenes, nitrenes and arynes. Thomas Nelson and Sons, London. 1969. Chap. 2.

Photochemical nucleophile–olefin combination, aromatic substitution (photo-NOCAS) reaction, Part 12. Factors controlling the regiochemistry of the reaction with alcohol as the nucleophile[1]

Donald R. Arnold, Mary S.W. Chan, and Kimberly A. McManus

Abstract: The photo-NOCAS reaction that combines methanol, serving as the nucleophile, and the radical cation of 4-methyl-1,3-pentadiene (**14**$^{+\bullet}$), substituting on the 1,4-dicyanobenzene radical anion (**1**$^{-\bullet}$), yields (*E*)-1-(4-cyanophenyl)-4-methoxy-4-methyl-2-pentene (**15**) as the major product. This regioisomer arises from bonding of methanol to C-4, the more heavily alkyl-substituted carbon of the diene, giving the less alkyl-substituted allylic radical. All previous examples of the photo-NOCAS reaction have yielded major adduct(s) having regiochemistry consistent with the *anti*-Markovnikov rule; the more heavily substituted (more stable?) β-alkoxyalkyl radical was the predominant intermediate. Empirically derived heats of formation and high-level ab initio molecular orbital calculations (MP2/6-31G*//HF/6-31G*) provide convincing evidence that of the two alternative allylic radicals, generated upon addition of methanol to **14**$^{+\bullet}$, that which has the more alkyl substituted allylic radical moiety is, in fact, **not** the more stable. Of course, the total structure of the intermediate must be considered; the stabilizing effect of alkyl substitution on the carbon next to the oxygen of the ether moiety cannot be ignored. Ab initio molecular orbital calculations (MP2/6-31G*//HF/6-31G*) are reported for the radical cations of 2-methylpropene (**2**$^{+\bullet}$), 2-methyl-2-butene (**6**$^{+\bullet}$), 2-methyl-1,3-butadiene (**9**$^{+\bullet}$), 4-methyl-1,3-pentadiene (**14**$^{+\bullet}$), and 2,4-dimethyl-1,3-pentadiene (**18**$^{+\bullet}$). Calculations were also carried out on possible intermediates (bridged radical cations, distonic radical cations, and β-alkoxyalkyl radicals) involved upon reaction of these radical cations with methanol. Results of these calculations provide a basis for explaining/predicting the regiochemistry of the photo-NOCAS reaction involving methanol as the nucleophile: the major adduct(s) result(s) from attachment of methanol to that end of the alkene or diene which gives rise to the more stable intermediate radical. The more stable radical is **not** necessarily the more heavily alkyl substituted.

Key words: photoinduced electron transfer, radicals, radical cations, ab initio molecular orbital calculations.

Résumé : La réaction de photo-NOCAS permet de combiner le méthanol, qui agit comme nucléophile, et le cation radical du 4-méthylpenta-1,3-diène (**14**$^{+\bullet}$), qui se substitue sur l'anion radical du 1,4-dicyanobenzène (**1**$^{-\bullet}$), et fournit du (*E*)-1-(4-cyanophényl)-4-méthoxy-4-méthylpent-2-ène (**15**) comme produit principal. Le régioisomère résulte d'une liaison du méthanol au C-4, le carbone du diène le plus substitué par des groupes alkyles, qui conduit au radical allylique le moins substitué par des groupes alkyles. Tous les exemples de réactions photo-NOCAS rapportés antérieurement ont toujours fourni des produits majoritaires dont la régiochimie était en accord avec la règle *anti*-Markovnikov correspondant à un intermédiaire prédominant comportant le radical β-alkoxyalkyle le plus substitué (le plus stable?). Les chaleurs de formation que l'on peut obtenir empiriquement de même que des calculs d'orbitales moléculaires ab initio à des niveaux élevés (MP2/6-31G*//HF/6-31G*) fournissent des données qui permettent de conclure d'une façon convaincante que, des deux radicaux allyliques alternatifs générés par l'addition de méthanol sur **14**$^{+\bullet}$, le radical qui porte la moitié radicalaire allylique la plus substituée par des groupes alkyles n'est, en fait, pas le plus stable. Il est évident que l'on doit considérer la structure totale de l'intermédiaire; on ne peut pas faire abstraction de l'effet stabilisant de la substitution alkyle sur le carbone voisin de l'oxygène de la portion éther. Des calculs d'orbitales moléculaires ab initio (MP2/6-31G*//HF/6-31G*) ont été effectués sur les cations radicaux 2-méthylpropène (**2**$^{+\bullet}$), 2-méthylbut-2-ène (**6**$^{+\bullet}$), 2-méthylbuta-1,3-diène (**9**$^{+\bullet}$), 2-méthylpenta-1,3-diène (**14**$^{+\bullet}$) et 2,4-diméthylpenta-1,3-diène (**18**$^{+\bullet}$). On a aussi effectué des calculs sur des intermédiaires possibles, des cations radicaux pontés, des cations radicaux distoniques et des radicaux β-alkoxyalkyles impliqués lors des réactions de ces cations radicaux avec le méthanol. Les résultats de ces calculs fournissent une base pour expliquer/prédire la régiochimie de la réaction de photo-NOCAS impliquant le méthanol comme

Received March 22, 1996.

This paper is dedicated to Professor Howard C. Clark in recognition of his contributions to Canadian chemistry.

D.R. Arnold,[2] M.S.W. Chan, and K.A. McManus. Department of Chemistry, Dalhousie University, Halifax, NS B3H 4J3, Canada.

[1] This is also Part 39 of the series Radical Ions in Photochemistry. See refs. 1 and 2 for preceding parts of these series.

[2] Author to whom correspondence may be addressed. Telephone: (902) 494-3714. Fax: (902) 494-1310. E-mail: arnold@ac.dal.ca

nucléophile : les produits majoritaires proviennent de la fixation du méthanol à l'extrémité de l'alcène ou du diène qui conduit au radical intermédiaire le plus stable. Le radical le plus stable n'est pas nécessairement celui qui est le plus substitué par des groupes alkyles.

Mots clés : transfert d'électron photoinduit, radicaux, cations radicaux, calculs d'orbitales moléculaires ab initio.

[Traduit par la rédaction]

Introduction

From the first examples of the photochemically induced nucleophile–olefin combination, aromatic substitution (photo-NOCAS) reaction, involving methanol, 2-methylpropene (**2**), and 1,4-dicyanobenzene (**1**) (reaction [1] (1*a*,*b*)) and of methanol, 2-methyl-2-butene (**6**), and 1,4-dicyanobenzene (**1**) (reaction [2] (1*f*)), the regiochemistry of the combination has been described as *anti*-Markovnikov (1*a*,*b*). That is, the nucleophile (methanol) bonds with the most hydrogenated of the ethenoid carbon atoms (3). Upon first consideration, since the combination of a nucleophile with an olefin radical cation leads ultimately to a radical intermediate (Scheme 1), the regiochemistry might be expected to be analogous to that of radicals adding to alkenes, which generally does follow the *anti*-Markovnikov rule (4). Originally, of course, Markovnikov's rule was developed for predicting the regiochemistry of electrophilic addition (hydrogen halide) to alkenes (3). While both of these rules are useful, they are hardly explanations for the observed reactivity.

The original electronic interpretation of Markovnikov's rule, *the electrophile adds to the alkene to produce the more stable carbocation intermediate*, is still accepted (3*b*, 5). Generally, the more heavily alkyl-substituted carbocation is also the more stable. This rule is followed even when the carbocation is bridged with the electrophile (6). On the other hand, the original mechanistic explanation for the *anti*-Markovnikov rule for radical addition to alkenes, *the radical adds to the alkene to produce the more stable radical intermediate,* has been shown to be incorrect (7). The regiochemistry of the radical addition to alkenes is generally controlled by polar and steric factors; the transition state is early along the reaction coordinate, and the regiochemistry is determined before differences in the stability of the alternative free-radical intermediates becomes important. The addition of radicals to alkenes may also be influenced by bridging within the radical intermediate (8). Clearly, to be able to predict the regiochemistry of product formation from the photo-NOCAS reaction, *all* of the factors that influence the regiochemistry must be understood.

The results that forced this study at this time involve a photo-NOCAS reaction that combines methanol and an unsymmetrically substituted diene, followed by substitution on 1,4-dicyanobenzene (**1**). One previous example of this type has been reported: the photo-NOCAS reaction that combines methanol, 2-methyl-1,3-butadiene (**9**), and 1,4-dicyanobenzene (**1**), behaves "normally." Four 1:1:1 adducts are obtained (reaction [3] (1*c*)). Accepting the fact that the regiochemistry is determined upon addition of methanol to the diene radical cation, step 3 of the proposed mechanism (Scheme 1), the major products (**10**, **11**, and **12**, 0.89) arise from attack of methanol at C-1 of the diene. Attack at C-1 gives the more heavily substituted, (presumably) more stable allylic radical, that is, *anti*-Markovnikov addition (1c). The need for additional thought on the matter arose with new results from the photo-NOCAS reaction combining methanol, 4-methyl-1,3-pentadiene (**14**), and 1,4-dicyanobenzene (**1**) (reaction [4]). This reaction is *not* regioselective; in fact, more than half of the products (**15**, 0.57) result from attack of methanol at C-4. Attack at C-4 leads to formation of a less alkyl-substituted, *less stable (?)*, allylic radical than does attack at C-1. Attack at C-4 is also significantly *more sterically hindered* than attack at C-1.

The regiochemistry returns to "normal" with the combination of methanol and the radical cation of 2,4-dimethyl-1,3-pentadiene (**18**$^{+\bullet}$) (reaction [5]). The isomeric photo-NOCAS adducts **19**, **20**, and **21** result from addition of methanol to the

Reaction [1] (1a,b)

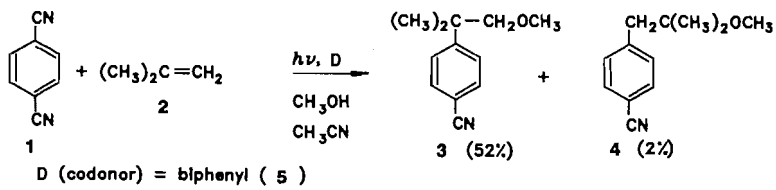

D (codonor) = biphenyl (5)

Reaction [2] (1f)

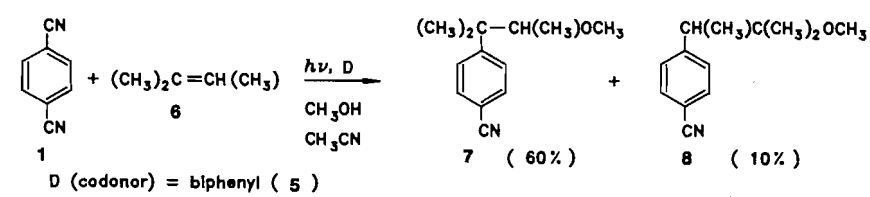

D (codonor) = biphenyl (5)

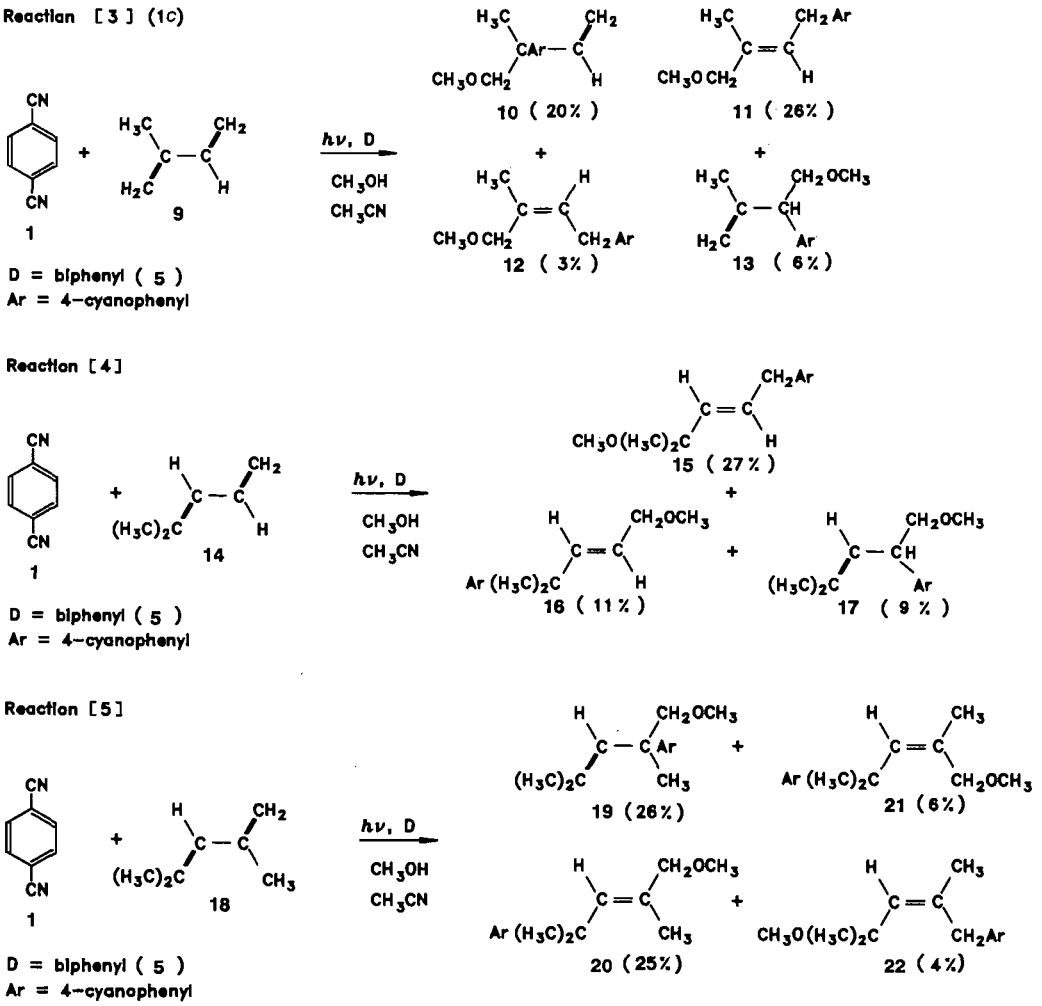

less alkyl-substituted position, giving the more heavily alkyl-substituted allylic radical. The combined yields of these adducts make this, *anti*-Markovnikov, the major (0.93) mode of addition.

The main objective of this project was to establish criteria useful for explaining/predicting the regiochemistry of the photo-NOCAS reaction, involving the combination of an alcohol (methanol) and the radical cation of an alkene or diene, substituting on 1,4-dicyanobenzene (**1**).

Results

An acetonitrile–methanol (3:1) solution of 4-methyl-1,3-pentadiene (**14**), 1,4-dicyanobenzene (**1**), and biphenyl (**5**) was irradiated with a medium-pressure mercury vapour lamp through Pyrex (reaction [4]). Progress of the reaction was followed by capillary column gas chromatography with a flame ionization detector (gc/fid). The ratio of products was determined by integration of the peak areas in the gc/fid. The yields of isolated products, based upon the amount of **1** consumed, were consistent with this ratio. While the efficiency of the reaction was increased upon the addition of biphenyl (**5**), serving as a codonor (Scheme 1, steps *6a* and 7), the ratio of products was similar with and without biphenyl (**5**). The product ratio was also independent of the extent of conversion, irradiating in the presence of 5. The first indication of the structure of the major product, (*E*)-1-(4-cyanophenyl)-4-methoxy-4-methyl-2-pentene (**15**, 27%), was evident from the mass spectrum (gc/ms) where major peaks were 73 *m/z* for the methoxypropyl fragment (C_4H_9O) and 142 *m/z* ($C_{10}H_8N$) for the ion resulting upon loss of the methoxypropyl fragment. Another fragment is dominant in the other two adducts: both (*E*)-4-(4-cyanophenyl)-1-methoxy-4-methyl-2-pentene (**16**, 11%) and 4-(4-cyanophenyl)-5-methoxy-2-methyl-2-pentene (**17**, 9%) have a major peak at 170 *m/z* ($C_{12}H_{12}N$) due to loss of the methoxymethylene fragment.

Similar irradiation of an acetonitrile–methanol solution of 2,4-dimethyl-1,3-pentadiene (**18**), **1**, and **5** gave four photo-NOCAS adducts: 4-(4-cyanophenyl)-5-methoxy-2,4-dimethyl-2-pentene (**19**, 26%), (*E*)-4-(4-cyanophenyl)-1-methoxy-2,4-dimethyl-2-pentene (**20**, 25%), (*Z*)-4-(4-cyanophenyl)-1-methoxy-2,4-dimethyl-2-pentene (**21**, 6%), and (*Z*)-1-(4-cyanophenyl)-4-methoxy-2,4-dimethyl-2-pentene (**22**, 4%) (reaction [5]). Again, the regiochemistry of the adducts was readily established from the mass spectral fragmentation pattern. Adducts **19**, **20**, and **21** have a major fragment at 184 *m/z* ($C_{13}H_{14}N$) indicative of the loss of the methoxymethylene fragment. The base peak in the mass spectrum of **20** and **21** is 85 *m/z* (C_5H_9O) for the ion resulting from loss of the arylpropyl fragment. Major fragments from **22** had 116 *m/z* (C_8H_6N),

Scheme 1.

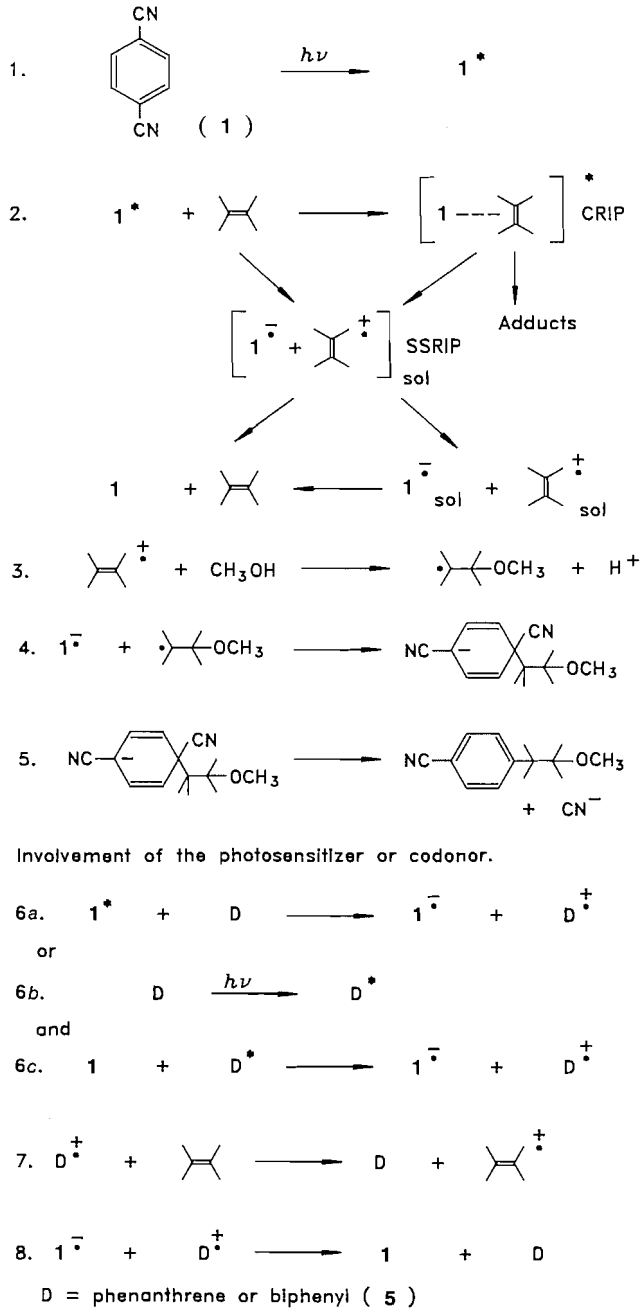

for the ion resulting from loss of the arylmethyl fragment, and 73 *m/z*, for the methoxypropyl fragment (C_4H_9O).

Structural assignments

Structural assignments of the products were based primarily upon detailed analysis of ^1H and ^{13}C nmr spectra. Mass and infrared spectra and elemental analyses were also useful. Adduct **15**, from reaction [4], was identified as (*E*)-1-(4-cyanophenyl)-4-methoxy-4-methyl-2-pentene. The ^1H nmr spectrum exhibits a singlet (3.11 ppm) indicative of a methoxy methyl group. A doublet at 3.40 ppm represents an aryl-substituted methylene group. A doublet and a doublet of triplets appear in the vinyl region of the ^1H nmr spectrum, representing a vinyl proton adjacent to a quaternary carbon and a vinyl proton adjacent to a methylene group, respectively. The coupling constant (16.2 Hz) between these vinyl protons is indicative of the *E* configuration. An AA′XX′ pattern in the aromatic region of the ^1H nmr spectrum is indicative of the 4-cyanophenyl group. In the ^{13}C nmr spectrum of **15**, there is a low-field quartet (50.31 ppm) that is consistent with the methyl of the methoxy group, and a singlet (74.65 ppm), which indicates a quaternary carbon bonded to the methoxy group. The aryl-substituted methylene gives a triplet at higher field (38.83 ppm). Two vinyl methine groups are also present (127.04 and 138.28 ppm).

Compound **16** was identified as (*E*)-4-(4-cyanophenyl)-1-methoxy-4-methyl-2-pentene. The ^1H nmr spectrum exhibits a singlet (3.33 ppm) indicative of a methoxy methyl group. A low-field doublet (3.93 ppm) represents a methylene group, methoxy substituted. A doublet and a doublet of triplets appear in the vinyl region of the ^1H nmr spectrum, representing a vinyl proton adjacent to a quaternary carbon and a vinyl proton adjacent to a methylene group, respectively. The coupling constant (15.9 Hz) between these vinyl protons is indicative of the *E* configuration. An AA′XX′ pattern in the aromatic region of the ^1H nmr spectrum is indicative of the 4-cyanophenyl group. There is a low-field quartet (58.09 ppm) in the ^{13}C nmr spectrum of **16** that is consistent with the methyl of the methoxy group. The methoxy-substituted methylene group shows up as a triplet at 73.09 ppm. A higher field singlet (40.88 ppm) indicates a quaternary carbon bonded to the aryl group. Two vinyl methine groups are also present (123.98 and 141.79 ppm).

Compound **17** was identified as the 1,2-addition product resulting from attack of methanol at the less substituted end of the diene: 4-(4-cyanophenyl)-5-methoxy-2-methyl-2-pentene. The low-field singlet in the ^1H nmr spectrum (3.32 ppm) is indicative of the methoxy methyl group. An ABX pattern (3.51, 3.55, and 3.84 ppm) was observed for the protons on the methylene group next to an oxygen and the benzylic/allylic methine group. The presence of a trisubstituted alkene is indicated by the protons of two methyl groups exhibiting two doublets at 1.64 and 1.74 ppm, resulting from long-range coupling to the vinyl proton. The signal for this vinyl proton appears at 5.27 ppm as a broad doublet due to long-range coupling to the methyl protons and typical vicinal coupling (8.8 Hz) to the benzylic/allylic methine proton. The AA′XX′ pattern in the aromatic region of the ^1H nmr spectrum is indicative of the 4-cyanophenyl group. In the ^{13}C nmr spectrum of **17**, there is a low-field quartet (58.98 ppm) that is consistent with the methyl of the methoxy group and a triplet at 76.54 ppm supports a methylene group substituted with a methoxy group. A higher field doublet (44.82 ppm) indicates a methine group, aryl substituted. A vinyl methine carbon and a vinyl quaternary carbon are also present (123.48 and 135.27 ppm, respectively).

Compound **19**, from reaction [5], was identified as the 1,2-addition product resulting from attack of methanol at the less substituted end of the diene: 4-(4-cyanophenyl)-5-methoxy-2,4-dimethyl-2-pentene. The ^1H and ^{13}C nmr spectra of **19** were similar to those of compound **17**. Unlike **17**, **19** has a benzylic/allylic methyl group, which eliminates the coupling of the vinyl proton with the benzylic/allylic proton observed in **17**. As a result, the vinyl proton in **19** appears as a multiplet

due to long-range couplings to the vinyl methyl protons. Also, the ABX pattern that was observed with compound **17** has now been simplified to an AB pattern (3.29 and 3.37 ppm, 8.8 Hz), indicating a methylene group adjacent to a quaternary stereogenic centre. In the ^{13}C nmr spectrum, an aryl-substituted quaternary carbon (44.68 ppm) and a lower field methoxy-substituted methylene (82.58 ppm) are observed. There is also a vinyl methine carbon and a vinyl quaternary carbon (129.71 and 134.99 ppm, respectively).

Compound **20** was identified as the 1,4-addition product resulting from attack of methanol at the less substituted end of the diene: (*E*)-4-(4-cyanophenyl)-1-methoxy-2,4-dimethyl-2-pentene. The ^1H and ^{13}C nmr spectra of **20** are similar to those of compound **16**. The differences can be attributed to the additional methyl group, which shows up as a doublet in the ^1H nmr spectrum, due to long-range coupling to the vinyl proton. A singlet at 3.76 ppm represents a methoxy-substituted methylene group. A multiplet appears in the vinyl region of the ^1H nmr spectrum, representing the vinyl proton adjacent to a quaternary carbon with long-range coupling (1.2 Hz) to the vinyl methyl protons. In the ^{13}C nmr spectrum of **20**, there is a low-field quartet (57.68 ppm) that is consistent with the methyl of the methoxy group The methoxy-substituted methylene shows up as a triplet at 78.94 ppm. A higher field singlet (39.95 ppm) indicates a quaternary carbon bonded to the aryl group. A vinyl methine group and a vinyl quaternary carbon are also evident (134.15 and 136.33 ppm). The decision in favour of the *E* configuration for **20** was based upon the results of a double-irradiation experiment leading to a nuclear Overhauser effect (nOe). When the vinyl proton was irradiated, an enhanced signal was observed for the protons on the methyl groups attached to the benzylic carbon, the protons on the methylene group (methoxy substituted), and for the *ortho*-aryl protons.

Compound **21**, (*Z*)-4-(4-cyanophenyl)-1-methoxy-2,4-dimethyl-2-pentene, was identified as the configurational isomer of **20**. The ^1H and ^{13}C nmr spectra show characteristic patterns similar to those of compound **20**. The *Z* configuration was assigned on the basis of the observed nOe. In this case, when the vinyl proton was irradiated, an enhancement was observed in the signals due to the protons on all three of the methyl groups and for the *ortho*-aryl protons. The configurations of **20** and **21** were further substantiated by use of the ACD/CNMR ^{13}C simulation program (Version 1.1, 1995); calculated and observed ^{13}C chemical shifts were in good agreement.[3]

Compound **22** was identified as the 1,4-addition product resulting from attack of methanol at the more substituted end of the diene: (*Z*)-1-(4-cyanophenyl)-4-methoxy-2,4-dimethyl-2-pentene. The ^1H and ^{13}C nmr spectra of **22** are similar to those of compound **15**. The differences can be attributed to the additional methyl group, which shows up as a doublet in the ^1H nmr spectrum, long-range coupled to the vinyl proton. A singlet at 3.78 ppm represents a methylene group, aryl substituted, which is further supported by a triplet at 37.75 ppm in the ^{13}C nmr spectrum. A multiplet appears in the vinyl region of the ^1H nmr spectrum, representing the vinyl proton adjacent to a quaternary carbon and having long-range coupling (1.2 Hz) to the vinyl methyl protons. In the ^{13}C nmr spectrum of **22**, there is a low-field quartet (50.16 ppm) that is consistent with the methyl of the methoxy group, and a singlet (75.09 ppm), which indicates a quaternary carbon bonded to the methoxy group. A vinyl methine group and a vinyl quaternary carbon are also present (132.24 and 135.25 ppm). The decision in favour of the *Z* configuration for **22** was based upon the results of a double-irradiation experiment leading to a nuclear Overhauser effect (nOe). When the vinyl proton was irradiated, enhancement was observed in the signals due to the protons on all three of the vicinal methyl groups.

Calculations

Ab initio molecular orbital calculations were carried out, using the GAUSSIAN 92 package of programs (9, 10), to obtain fully optimized structures (UHF/6-31G*) of the radical cations of 2-methylpropene (**2**), 2-methyl-2-butene (**6**), 2-methyl-1,3-butadiene (**9**), 4-methyl-1,3-pentadiene (**14**), and 2,4-dimethyl-1,3-pentadiene (**18**). The results of these calculations: optimized structures, and spin and charge density distribution obtained from Mulliken population analysis, are shown in Tables 1–5 and Figs. 1–5. The total energies, corrected for spin contamination, were obtained from single point calculations with Møller–Plesset perturbation theory (MP2) at the HF/6-31G* geometries. A thorough search was made for possible intermediates involved upon reaction of methanol with these alkene and diene radical cations.

Discussion

The proposed mechanism for the photo-NOCAS reaction is shown in Scheme 1, specifically for the combination of methanol adding to the radical cation of an alkene (1). The dominant issue here is the determination of those factors which influence the regiochemistry of the reaction, presumably established during step 3 of this scheme. The products obtained upon combination of methanol with the dienes provide strong support for this, step 3, as the initial bonding event. All of the photo-NOCAS adducts bear the methoxy group at a terminal carbon of the initial diene. Multiple products result from subsequent addition of the resulting intermediate allylic radical, at either of the ambident ends, to an *ipso* position of the 1,4-dicyanobenzene radical anion ($\mathbf{1}^{-\bullet}$) during step 4.

This deceptively simple representation of the initial bonding (Scheme 1, step 3) has been expanded (Scheme 2): step 3*a* represents the initial formation of a dipole-induced radical-ion complex; step 3*b* represents formation of a bridged radical cation; step 3*c* involves the formation of the new carbon–oxygen bond resulting in a distonic radical cation, and, finally, step 3*d* is the deprotonation from the oxygen of the distonic radical cation that yields the β-alkoxyalkyl radical. Similar species have been proposed to explain reactions of radical cations in the gas phase, observed by mass spectrometry (11). In principle, of course, not all of these steps may be necessary and some of them may be reversible. Our approach is now clear: we will consider the structure, energy, and the spin and charge distribution for all of these hypothetical intermediates and search for agreement between theory and the experimentally observed product ratios.

The results of the calculations relevant to the reaction of 2-methylpropene (**2**) (reaction [1]) are summarized in Tables 1, 6, 7, 8, and 9, and in Figs. 1, 6, 7, 8, and 9. The alkene radical

[3] Software available from: Advanced Chemical Development Inc., 141 Adelaide Street, West, Suite 1501, Toronto, ON M5H 3L5, Canada.

Table 1. (*a*) Optimized (UHF/6-31G*) structure for the 2-methylpropene radical cation (**2**$^{+\bullet}$).

Bond length (Å)		Bond angle (deg)		Dihedral angle (deg)	
C1—C2	1.417	C1C2C3	120.3	C4C3C2C1	180.0
C2—C3	1.483	C3C2C4	119.4		

Table 1. (*b*) Spin and charge densities (**2**$^{+\bullet}$).

Atom number	Charge density summed into heavy atoms	Spin density
1	0.34	0.82
2	0.23	0.31
3	0.22	−0.04
4	0.22	−0.04

Table 2. (*a*) Optimized (UHF/6-31G*) structure for the 2-methyl-2-butene radical cation (**6**$^{+\bullet}$).

Bond length (Å)		Bond angle (deg)		Dihedral angle (deg)	
C1—C2	1.492	C1C2C3	121.3	C1C2C3C4	0.0
C2—C3	1.415	C1C2C5	118.6	C1C2C3C5	−180.0
C3—C4	1.484	C2C3C4	126.8		
C2—C5	1.487	C3C2C5	120.0		

Table 2. (*b*) Spin and charge densities (**6**$^{+\bullet}$).

Atom number	Charge density summed into heavy atoms	Spin density
1	0.19	−0.07
2	0.19	0.44
3	0.25	0.66
4	0.18	−0.09
5	0.19	−0.05

Table 3. (*a*) Optimized (UHF/6-31G*) structure for the 2-methyl-1,3-butadiene radical cation (**9**$^{+\bullet}$).

Bond length (Å)		Bond angle (deg)		Dihedral angle (deg)	
C1—C2	1.400	C1C2C3	116.5	C4C3C2C1	−180.0
C2—C3	1.408	C1C2C5	120.4	C5C2C3C1	0.0
C3—C4	1.379	C2C3C4	124.0		
C2—C5	1.505	C3C2C5	123.1		

Table 3. (*b*) Spin and charge densities (**9**$^{+\bullet}$).

Atom number	Charge density summed into heavy atoms	Spin density
1	0.28	0.78
2	0.13	−0.06
3	0.13	−0.27
4	0.28	0.74
5	0.17	0.00

Table 4. (*a*) Optimized (UHF/6-31G*) structure for the 2-methyl-1,3-pentadiene radical cation (**14**$^{+\bullet}$).

Bond length (Å)		Bond angle (deg)		Dihedral angle (deg)	
C1—C2	1.384	C1C2C3	121.2	C4C3C2C1	180.0
C2—C3	1.395	C2C3C4	125.7	C5C4C3C2	−180.0
C3—C4	1.402	C3C4C5	119.2	C6C4C3C2	0.0
C4—C5	1.494	C3C4C6	124.5		
C4—C6	1.494	C5C4C6	116.2		

Table 4. (*b*) Spin and charge densities (**14**$^{+\bullet}$).

Atom number	Charge density summed into heavy atoms	Spin density
1	0.23	0.82
2	0.15	−0.37
3	0.11	0.24
4	0.17	0.46
5	0.17	−0.06
6	0.17	−0.06

Table 5. (*a*) Optimized (UHF/6-31G*) structure for the 2,4-dimethyl-1,3-pentadiene radical cation (**18**$^{+\bullet}$).

Bond length (Å)		Bond angle (deg)		Dihedral angle (deg)	
C1—C2	1.399	C1C2C3	115.4	C4C3C2C1	179.2
C2—C3	1.404	C2C3C4	130.3	C7C4C3C2	−1.5
C3—C4	1.398	C3C4C7	125.8	C5C4C3C2	178.3
C4—C5	1.499	C3C4C5	118.4	C6C2C1C3	−179.8
C4—C7	1.495	C5C4C7	115.9		
C2—C6	1.508	C1C2C6	118.6		

Table 5. (*b*) Spin and charge densities (**18**$^{+\bullet}$).

Atom number	Charge density summed into heavy atoms	Spin density
1	0.20	0.86
2	0.12	−0.31
3	0.06	0.12
4	0.18	0.48
7	0.15	−0.05
5	0.15	−0.07
6	0.14	0.03

cation, **2**$^{+\bullet}$, remains planar, the dihedral angle C-1,C-2,C-3,C-4 is −180°. A significant proportion, almost half, of the positive charge density is borne by the methyl groups, leaving one-third on the terminal methylene carbon (C-1). The vertical ionization potential (9.39 eV), taken from the eigenvalue for the HOMO of the neutral molecule (**2**), and the adiabatic ionization potential (8.81 eV), taken as the difference in the calculated (MP2/6-31G*//HF/6-31G*) total energies of the fully optimized structures of the neutral molecule and the radical cation, are in good agreement with the experimental value (9.24 eV, vertical ionization potential) obtained from the photoelectron spectra (12).

A thorough search was made for the distonic radical cation,

Fig. 1. 2-Methylpropene radical cation ($2^{+\bullet}$).

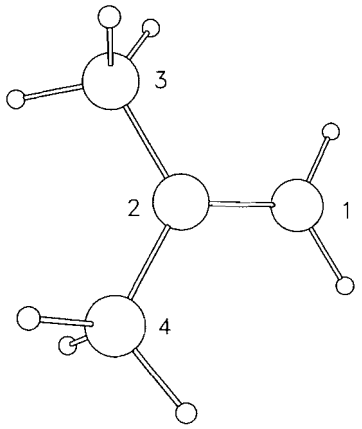

Fig. 2. 2-Methyl-2-butene radical cation ($6^{+\bullet}$).

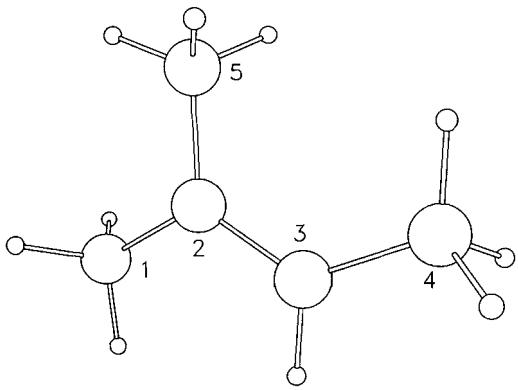

Fig. 3. 2-Methyl-1,3-butadiene radical cation ($9^{+\bullet}$).

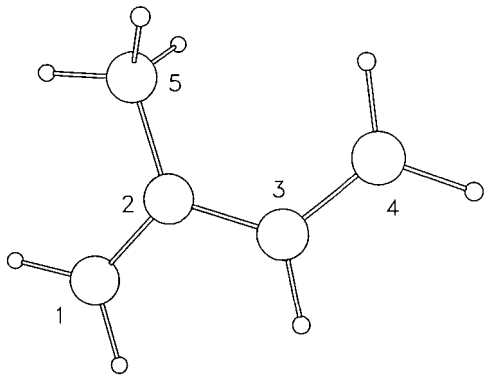

with methanol bonded to C-1; several conformers were found, the structure of the fully optimized global minimum (*anti*), $\mathbf{2a}^{+\bullet}$, is depicted in Table 6*a*,*b* and Fig. 6*a*. This structure is accurately described as **distonic** (11). The C-1,O-5 bond length is relatively long (1.57 Å), there is no evidence for bridging; the C-2,O-5 distance is 2.47 Å. The excess α-spin density resides largely (1.12) on C-2 while the positive charge density (0.79) is distributed over C-1, O-5, and C-6. This structure is significantly (92 kJ mol^{-1}) more stable than the components, i.e., the alkene radical cation, $\mathbf{2}^{+\bullet}$, and methanol.

An analogous fully optimized structure was found with

Fig. 4. 4-Methyl-1,3-pentadiene radical cation ($14^{+\bullet}$).

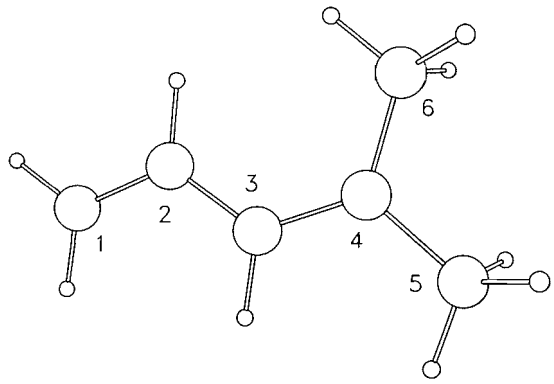

Fig. 5. 2,4-Dimethyl-1,3-pentadiene radical cation ($18^{+\bullet}$).

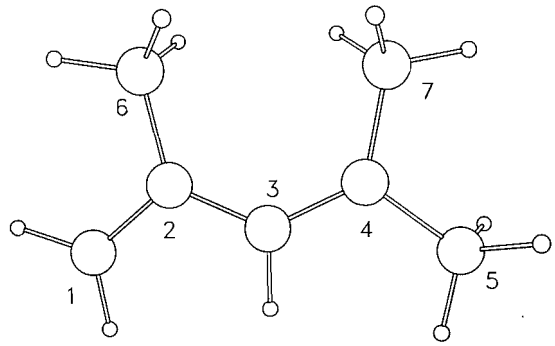

Scheme 2.

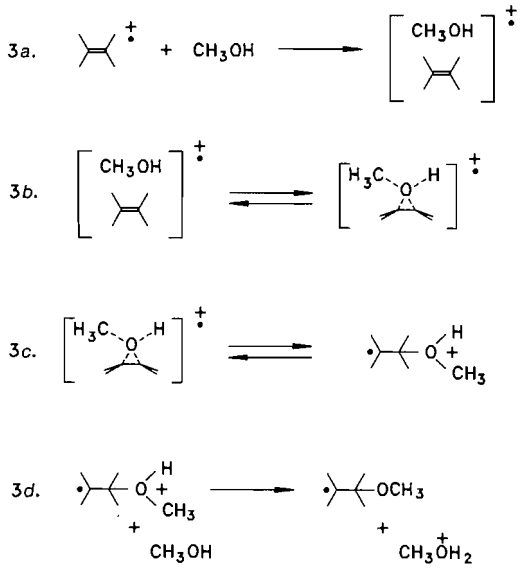

methanol bonded to C-2 ($\mathbf{2b}^{+\bullet}$, Table 6*c*,*d* and Fig. 6*b*). In fact, this distonic radical cation (*gauche*), $\mathbf{2b}^{+\bullet}$, is more stable (6.1 kJ mol^{-1}) than $\mathbf{2a}^{+\bullet}$. A factor contributing to the stability of $\mathbf{2b}^{+\bullet}$ is the additional charge delocalization; the methyl groups, C-3 and C-4, each bear significant (0.16) positive charge density.

Starting the calculation with a bridged structure, symmetrically constrained to have equal C-1,O-5 and C-2,O-5 bond

Table 6. (*a*) Optimized (UHF/6-31G*) structure for the 2-methylpropene–methanol distonic radical cation (C-1 bonded) (**2a**$^{+\bullet}$).

Bond length (Å)		Bond angle (deg)		Dihedral angle (deg)	
C1—C2	1.469	C1C2C3	120.0	C1C2C3C4	174.1
C2—C3	1.503	C1C2C4	120.5	C3C2C1O5	81.1
C2—C4	1.504	C3C2C4	119.2	C6O5C1C2	179.9
C1—O5	1.566	C2C1O5	109.2		
C2—O5	2.474	C1O5C6	119.4		
O5—C6	1.466				

Table 6. (*b*) Spin and charge densities (**2a**$^{+\bullet}$).

Atom number	Charge density summed into heavy atoms	Spin density
1	0.43	−0.06
2	0.01	1.12
3	0.10	−0.15
4	0.09	−0.15
5(O)	−0.16	0.04
6	0.52	0.01

Table 6. (*c*) Optimized (UHF/6-31G*) structure for the 2-methylpropene–methanol distonic radical cation (C-2 bonded) (**2b**$^{+\bullet}$).

Bond length (Å)		Bond angle (deg)		Dihedral angle (deg)	
C1—C2	1.476	C1C2C3	114.8	C1C2C3C4	−136.3
C2—C3	1.512	C1C2C4	115.3	C3C2C1O5	110.5
C2—C4	1.512	C3C2C4	114.3	C6O5C2C1	−56.4
C1—O5	2.506	C1C2O5	106.3		
C2—O5	1.653	C2O5C6	123.8		
O5—C6	1.459				

Table 6. (*d*) Spin and charge densities (**2b**$^{+\bullet}$).

Atom number	Charge density summed into heavy atoms	Spin density
1	0.14	1.18
2	0.22	−0.06
3	0.16	0.00
4	0.16	0.00
5(O)	−0.20	0.05
6	0.50	0.00

lengths, also converges to a minimum (no negative vibrational frequencies) **2c**$^{+\bullet}$ (Table 7 and Fig. 7). However, when this structure is fully optimized upon removing the symmetry constraint, the structure reverts to the distonic radical cation **2b**$^{+\bullet}$. This bridged structure may be an intermediate, preceding formation of the distonic radical cations, or may form during the equilibration of the distonic radical cations. The energy of this structure would then set a lower limit (24–30 kJ mol^{-1}), presumably only slightly below the activation energy for this equilibration.

Table 7. (*a*) Optimized (UHF/6-31G*) structure for the 2-methylpropene–methanol symmetrically bridged (constrained) radical cation (**2c**$^{+\bullet}$).

Bond length (Å)		Bond angle (deg)		Dihedral angle (deg)	
C1—C2	1.410	C1C2C3	120.7	C1C2C3C4	179.4
C2—C3	1.485	C1C2C4	120.5	C3C2C1O5	−81.4
C2—C4	1.485	C3C2C4	118.8	C6O5C1C2	−119.3
C1—O5	2.776	C2C1O5	75.3		
C2—O5	2.776	C1O5C6	122.6		
O5—C6	1.419				

Table 7. (*b*) Spin and charge densities (**2c**$^{+\bullet}$).

Atom number	Charge density summed into heavy atoms	Spin density
1	0.33	0.80
2	0.26	0.32
3	0.19	−0.04
4	0.19	−0.04
5(O)	−0.32	0.01
6	0.36	0.00

Fig. 6. (*a*) 2-Methylpropene–methanol distonic radical cation (C-1 bonded) (**2a**$^{+\bullet}$); (*b*) 2-methylpropene–methanol distonic radical cation (C-2 bonded) (**2b**$^{+\bullet}$).

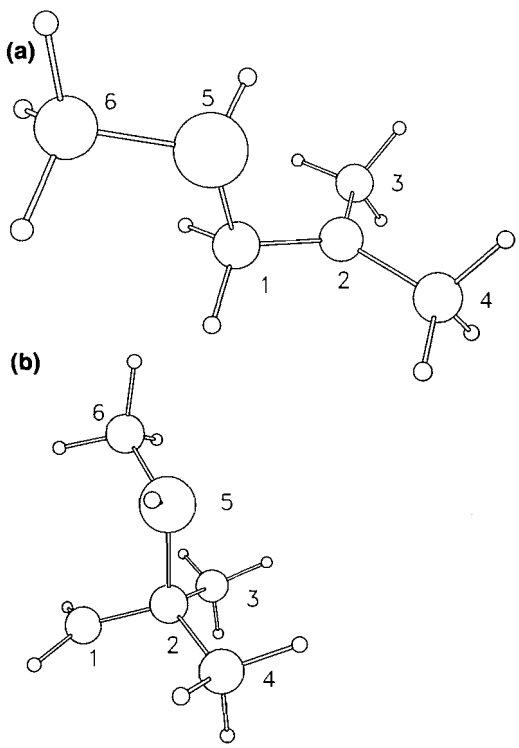

The next step in the sequence (Scheme 2, step 3*d*) involves deprotonation from the oxygen of the distonic radical cations to give the alternative β-alkoxyalkyl radicals. Two conformers of each radical were found; these correspond to the *gauche*

Table 8. (*a*) Optimized (UHF/6-31G*) structure for the 2-methylpropene–methanol radical (C-1 bonded) (**2a•**).

Bond length (Å)		Bond angle (deg)		Dihedral angle (deg)	
C1—C2	1.501	C1C2C3	116.6	C2C1O5C6	178.0
C2—C3	1.504	C1C2C4	118.5	C1C2C3C4	151.2
C2—C4	1.502	C3C2C4	118.3	C3C2C1O5	166.3
C1—O5	1.396	C2C1O5	110.6		
C2—O5	2.382	C1O5C6	114.1		
O5—C6	1.391				

Table 8. (*b*) Spin and charge densities (**2a•**).

Atom number	Charge density summed into heavy atoms	Spin density
1	0.30	−0.14
2	0.03	1.18
3	−0.02	−0.16
4	0.01	−0.15
5(O)	−0.61	0.01
6	0.30	0.00

Table 8. (*c*) Optimized (UHF/6-31G*) structure for the 2-methylpropene–methanol radical (C-2 bonded) (**2b•**).

Bond length (Å)		Bond angle (deg)		Dihedral angle (deg)	
C1—C2	1.508	C1C2C3	110.9	C1C2O5C6	−64.6
C2—C3	1.533	C1C2C4	110.1		
C2—C4	1.532	C3C2C4	109.9		
C2—O5	1.414	C1C2O5	110.3		
C1—O5	2.400	C2O5C6	118.4		
O5—C6	1.395				

Table 8. (*d*) Spin and charge densities (**2b•**).

Atom number	Charge density summed into heavy atoms	Spin density
1	−0.01	1.26
2	0.32	−0.13
3	0.00	0.01
4	0.03	0.03
5(O)	−0.64	0.01
6	0.30	0.01

and *anti* rotamers around the C-1,O-5 and C-2,O-5 bonds (Table 8 and Fig. 8). From $\mathbf{2a}^{+\bullet}$, the *anti* conformer, **2a•**, was the more stable, while from $\mathbf{2b}^{+\bullet}$, the *gauche* conformer, **2b•**, was preferred. Consistent with experimental results, there is no evidence for bridging in the β-alkoxyalkyl radical (8c). The calculations show the expected trend, the tertiary radical (**2a•**) is more stable (by only 1.3 kJ mol^{-1} !) than the primary radical (**2b•**).

The relative energies (MP2/6-31G*//HF/6-31G*) of these species are shown in Table 9 and Fig. 9. The values for the β-alkoxyalkyl radicals have been incorporated in this plot by

Fig. 7. 2-Methylpropene–methanol symmetrically bridged (constrained) radical cation ($\mathbf{2c}^{+\bullet}$).

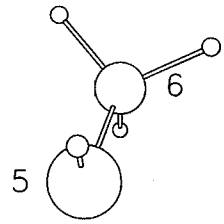

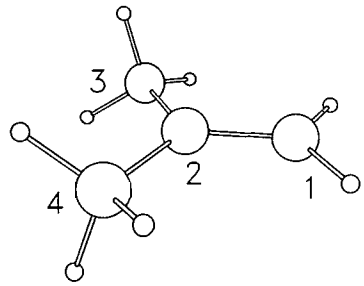

Fig. 8. (*a*) 2-Methylpropene–methanol radical (C-1 bonded) (**2a•**); (*b*) 2-methylpropene–methanol radical (C-2 bonded) (**2b•**).

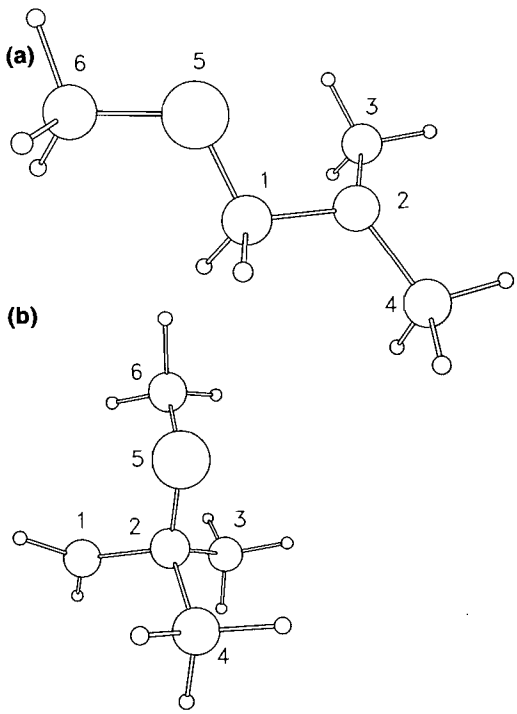

including a molecule of methanol to serve as a base in the deprotonation step (Scheme 2, step 3*d*). It must be emphasized that these calculations are relevant to the individual species in the gas phase. This, of course, is a gross oversimplification considering the charge separation and resulting large dipole of some of these species. In an attempt to assess the importance of solvent interaction, the Onsager reaction field model has been applied (SCRF/MP2/6-31G*//SCRF/HF/6-31G*) (13). The radius of the solute cavity was calculated using the volume key word in the GAUSSIAN program, and the dielectric constant was set at 35.0 (ca. acetonitrile). The most significant effect of including solvent interaction is a reversal of the rela-

Table 9. Relative total energies (MP2/6-31G*//HF/6-31G*) for 2-methylpropene intermediates (total energies obtained by including the solvent dielectric are reported in parentheses).

($2^{+\bullet}$)	−156.302 59 (−156.303 58)
Methanol	−115.344 94 (−115.346 13)
Methanol	−115.344 94 (−115.346 13)
Sum	−386.992 47 (−386.995 84)
($2a^{+\bullet}$)	−271.682 25 (−271.690 98)
Methanol	−115.344 94 (−115.346 13)
Sum	−387.027 19 (−387.037 11)
($2b^{+\bullet}$)	−271.684 59 (−271.687 38)
Methanol	−115.344 94 (−115.346 13)
Sum	−387.029 53 (−387.033 51)
($2c^{+\bullet}$)	−271.673 27 (−271.675 66)
Methanol	−115.344 94 (−115.346 13)
Sum	−387.018 21 (−387.021 79)
($2a^{\bullet}$)	−271.355 28 (−271.355 96)
Protonated methanol	−115.644 29 (−115.646 53)
Sum	−386.999 57 (−387.002 49)
($2b^{\bullet}$)	−271.354 79 (−271.355 34)
Protonated methanol	−115.644 29 (−115.646 53)
Sum	−386.999 08 (−387.001 87)

Fig. 9. Relative energies (MP2/6-31G*//HF/6-31G*) for 2-methylpropene intermediates.

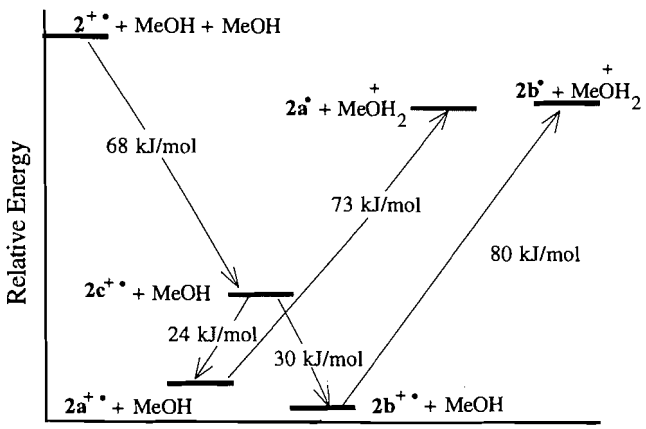

tive order of stability of the two distonic radical cations. In the gas phase, $\mathbf{2b}^{+\bullet}$ is more stable than $\mathbf{2a}^{+\bullet}$ (6.1 kJ mol^{-1}); including the solvent dielectric renders $\mathbf{2a}^{+\bullet}$ more stable than $\mathbf{2b}^{+\bullet}$ (9.5 kJ mol^{-1}). As expected, there is essentially no solvent effect upon the difference in the relative stability of the radicals $\mathbf{2a}^{\bullet}$ and $\mathbf{2b}^{\bullet}$ ($\Delta\Delta$ = 0.34 kJ mol^{-1}).

The difference in the calculated total energy of the alternative β-alkoxyalkyl radicals, $\mathbf{2a}^{\bullet}$ and $\mathbf{2b}^{\bullet}$, is consistent with the observed product ratio (reaction [1]). The major product (**3**, 0.96) results from methanol bonding to C-1. **Hypothesis**: rapid equilibration of the distonic radical cations, through the bridged radical cation, is followed by irreversible deprotonation. The irreversibility of the deprotonation is a logical consequence of the low acidity of the media. The observed product regiochemistry therefore reflects the relative rates of formation of the alternative β-alkoxyalkyl radicals; formation of the more stable β-alkoxyalkyl radical is favoured.

Fig. 10. (*a*) 2-Methyl-2-butene–methanol distonic radical cation (C-3 bonded) ($\mathbf{6a}^{+\bullet}$); (*b*) 2-methyl-2-butene–methanol distonic radical cation (C-2 bonded, C2—O6 bond length constrained) ($\mathbf{6b}^{+\bullet}$).

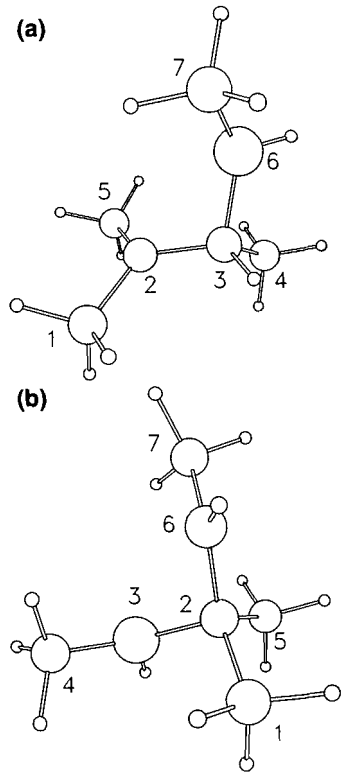

For the photo-NOCAS reaction involving 2-methyl-2-butene (**6**), the products (reaction [2]), and the calculations (Tables 2, 10, 11, 12, 13 and Figs. 2, 10, 11, 12, 13) are consistent with this hypothesis. The vertical ionization potential (8.93 eV) and the adiabatic ionization potential (8.27 eV) are in good agreement with the experimental value (8.68 eV, vertical ionization potential) taken from the photoelectron spectra (12). The radical cation $\mathbf{6}^{+\bullet}$ is planar, the dihedral angle C-1,C-2,C-3,C-5 is −180°. The methyl groups bear a significant share of the positive charge density. The local charge density is, in fact, highest (0.25) on the less substituted alkene carbon (C-3).

The structure of the distonic radical cation with methanol bonded to C-3 ($\mathbf{6a}^{+\bullet}$) was fully optimized. The C-3,O-6 bond length is 1.58 Å, and there is no evidence for bridging; the C-2,O-6 distance is long, 2.46 Å. Calculations on the alternative structure, with methanol bonded to C-2 ($\mathbf{6b}^{+\bullet}$), converged only with a structural constraint; the C-2,O-6 bond length was held to 1.58 Å. Nevertheless, this distonic radical cation ($\mathbf{6b}^{+\bullet}$), with methanol bonded to C-2, is more stable (3.5 kJ mol^{-1}) than the alternative structure ($\mathbf{6a}^{+\bullet}$), with methanol bonded to C-3. Again, in this case, the methyl groups C-1 and C-5 of the distonic radical cation, $\mathbf{6b}^{+\bullet}$, each bear significant (0.14) positive charge density (Table 10*d*).

Table 10. (*a*) Optimized (UHF/6-31G*) structure for the 2-methyl-2-butene–methanol distonic radical cation (C-3 bonded) (**6a**$^{+\bullet}$).

Bond length (Å)		Bond angle (deg)		Dihedral angle (deg)	
C1—C2	1.505	C1C2C3	119.1	C1C2C3C4	119.4
C2—C3	1.483	C1C2C5	119.4	C1C2C3O6	−124.4
C2—C5	1.504	C2C3C4	117.7	C2C3O6C7	65.3
C3—C4	1.514	C3C2C5	120.0		
C2—O6	2.458	C2C3O6	106.6		
C3—O6	1.580	C3O6C7	120.5		
O6—C7	1.462				

Table 10. (*b*) Spin and charge densities (**6a**$^{+\bullet}$).

Atom number	Charge density summed into heavy atoms	Spin density
1	0.09	−0.15
2	0.02	1.15
3	0.33	−0.08
4	0.14	0.02
5	0.09	−0.15
6(O)	−0.17	0.02
7	0.51	0.01

Table 10. (*c*) Optimized (UHF/6-31G*) structure for the 2-methyl-2-butene–methanol distonic radical cation (C-2 bonded, C2—O6 bond length contrained) (**6b**$^{+\bullet}$).

Bond length (Å)		Bond angle (deg)		Dihedral angle (deg)	
C1—C2	1.520	C1C2C3	114.7	C1C2C3C4	42.1
C2—C3	1.488	C1C2C5	113.4	C3C2O6C7	−61.1
C2—C5	1.516	C2C3C4	123.4	C4C3C2O6	−68.7
C3—C4	1.499	C3C2C5	113.8	C1C2O6C7	179.1
C2—O6	1.580	C1C2O6	101.9		
C3—O6	2.434	C2O6C7	123.7		
O6—C7	1.462				

Table 10. (*d*) Spin and charge densities (**6b**$^{+\bullet}$).

Atom number	Charge density summed into heavy atoms	Spin density
1	0.14	0.00
2	0.22	−0.07
3	0.08	1.18
4	0.09	−0.16
5	0.14	0.01
6(O)	−0.18	0.02
7	0.51	0.01

The structure of the bridged radical cation, **6c**$^{+\bullet}$ (Table 11 and Fig. 11), was fully optimized without structural constraints; in fact, removing the constraint from **6b**$^{+\bullet}$ gave **6c**$^{+\bullet}$. Both carbon–oxygen distances, C-2,O-6 and C-3,O-6, are long (2.81 and 2.95 Å). In this case, the differences in energy

Table 11. (*a*) Optimized (UHF/6-31G*) structure for the 2-methyl-2-butene–methanol bridged radical cation (**6c**$^{+\bullet}$).

Bond length (Å)		Bond angle (deg)		Dihedral angle (deg)	
C1—C2	1.488	C1C2C3	120.2	C1C2C3C4	179.0
C2—C3	1.411	C1C2C5	118.0	C3C2O6C7	118.6
C2—C5	1.489	C2C3C4	126.2	C2C3O6C7	−89.0
C3—C4	1.486	C3C2C5	121.8		
C2—O6	2.806	C3C2O6	81.7		
C3—O6	2.954	C2O6C7	150.7		
O6—C7	1.418				

Table 11. (*b*) Spin and charge densities (**6c**$^{+\bullet}$).

Atom number	Charge density summed into heavy atoms	Spin density
1	0.17	−0.05
2	0.24	0.41
3	0.24	0.69
4	0.16	−0.09
5	0.17	−0.06
6 (O)	−0.32	0.01
7	0.35	0.00

Fig. 11. 2-Methyl-2-butene–methanol bridged radical cation (**6c**$^{+\bullet}$).

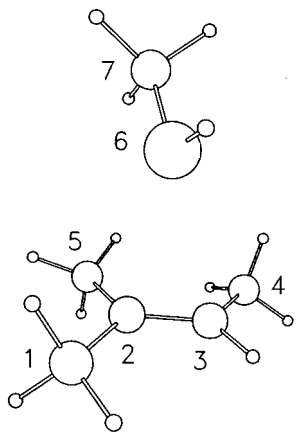

between the alternative distonic radical cations and this bridged radical cation is small (±5 kJ mol^{-1}); it seems likely that equilibration among these intermediates would be rapid. Deprotonation of the distonic radical cation **6a**$^{+\bullet}$ leads to the tertiary β-alkoxyalkyl radical, **6a**$^{\bullet}$, which is more stable (6.4 kJ mol^{-1}) than the secondary β-alkoxyalkyl radical, **6b**$^{\bullet}$, resulting from deprotonation of **6b**$^{+\bullet}$ (Table 12 and Fig. 12).

The relative energies (MP2/6-31G*//HF/6-31G*) of these intermediates are shown in Table 13 and Fig. 13. Again, in this case, the major effect of including the solvent dielectric is to reverse the relative stabilities of the distonic radical cations: **6a**$^{+\bullet}$ becomes more stable than **6b**$^{+\bullet}$ (5.1 kJ mol^{-1}). The relative stability of the β-alkoxyalkyl radicals (**6a**$^{\bullet}$ and **6b**$^{\bullet}$) is unaffected.

The formation of **7** as the major (0.86) photo-NOCAS adduct in reaction [2] is consistent with the hypothesis: rapid equilibration of the initially formed intermediates, followed

Isodesmic Reactions

[1a] $H_3C-O-C(CH_3)_2-\dot{C}H_2$ ⇌ $H_3C-O-CH_2-\dot{C}(CH_3)_2$

2b• 2a•

ΔH (kJ mol^{-1}) −1.3 (calc'd)[a] +1.8 (calc'd)[b] −58.4 (calc'd)[c]

[1b] $H_3C-O-C(CH_3)_3 + CH_3CH_2\bullet$ ⇌ $H_3C-O-CH_2-CH_3 + (CH_3)_3C\bullet$

ΔH (kJ mol^{-1}) −2.9 (calc'd)[a] +2.5 (calc'd)[b] −61.9 (calc'd)[c] −2.1 (exp.)[d]

[1c] $H_3C-O-C(CH_3)_3$ ⇌ $H_3C-O-CH_2-CH(CH_3)_2$

ΔH (kJ mol^{-1}) +15.3 (calc'd)[a] +21.3 (calc'd)[b] −21.3 (calc'd)[c]

[1d] $(CH_3)_2CH-\dot{C}H_2$ ⇌ $(CH_3)_3C\bullet$

ΔH (kJ mol^{-1}) −24.0 (calc'd)[a] −18.8 (calc'd)[b] −40.2 (calc'd)[c] −15.9 (exp.)[d]

[1e] $H_3C-O-C(CH_3)_3 + (CH_3)_2CH-\dot{C}H_2$ ⇌ $H_3C-O-CH_2-CH(CH_3)_2 + (CH_3)_3C\bullet$

ΔH (kJ mol^{-1}) −8.7 (calc'd)[a] +2.5 (calc'd)[b] −61.5 (calc'd)[c]

[2a] $H_3C-O-C(CH_3)_2-\dot{C}H(CH_3)$ ⇌ $H_3C-O-CH(CH_3)-\dot{C}(CH_3)_2$

6a• 6b•

ΔH (kJ mol^{-1}) −6.4 (calc'd)[a] −2.1 (calc'd)[b]

[2b] $H_3C-O-C(CH_3)_3 + (CH_3)\dot{C}H(CH_3)$ ⇌ $H_3C-O-CH(CH_3)_2 + (CH_3)_3C\bullet$

ΔH (kJ mol^{-1}) −4.1 (calc'd)[a] −1.9 (calc'd)[b] −6.7 (exp.)[d]

[2c] $H_3C-O-C(CH_3)_2(C_2H_5)$ ⇌ $H_3C-O-CH(CH_3)-CH(CH_3)_2$

ΔH (kJ mol^{-1}) +5.0 (calc'd)[a] +6.3 (calc'd)[b]

[2d] $(CH_3)_2CH-\dot{C}H(CH_3)$ ⇌ $(C_2H_5)\dot{C}(CH_3)_2$

ΔH (kJ mol^{-1}) −9.8 (calc'd)[a] −8.1 (calc'd)[b]

[2e] $H_3C-O-C(CH_3)_2(C_2H_5) + (CH_3)_2CH-\dot{C}H(CH_3)$ ⇌ $H_3C-O-CH(CH_3)-CH(CH_3)_2 + (C_2H_5)\dot{C}(CH_3)_2$

ΔH (kJ mol^{-1}) −4.8 (calc'd)[a] −1.8 (calc'd)[b]

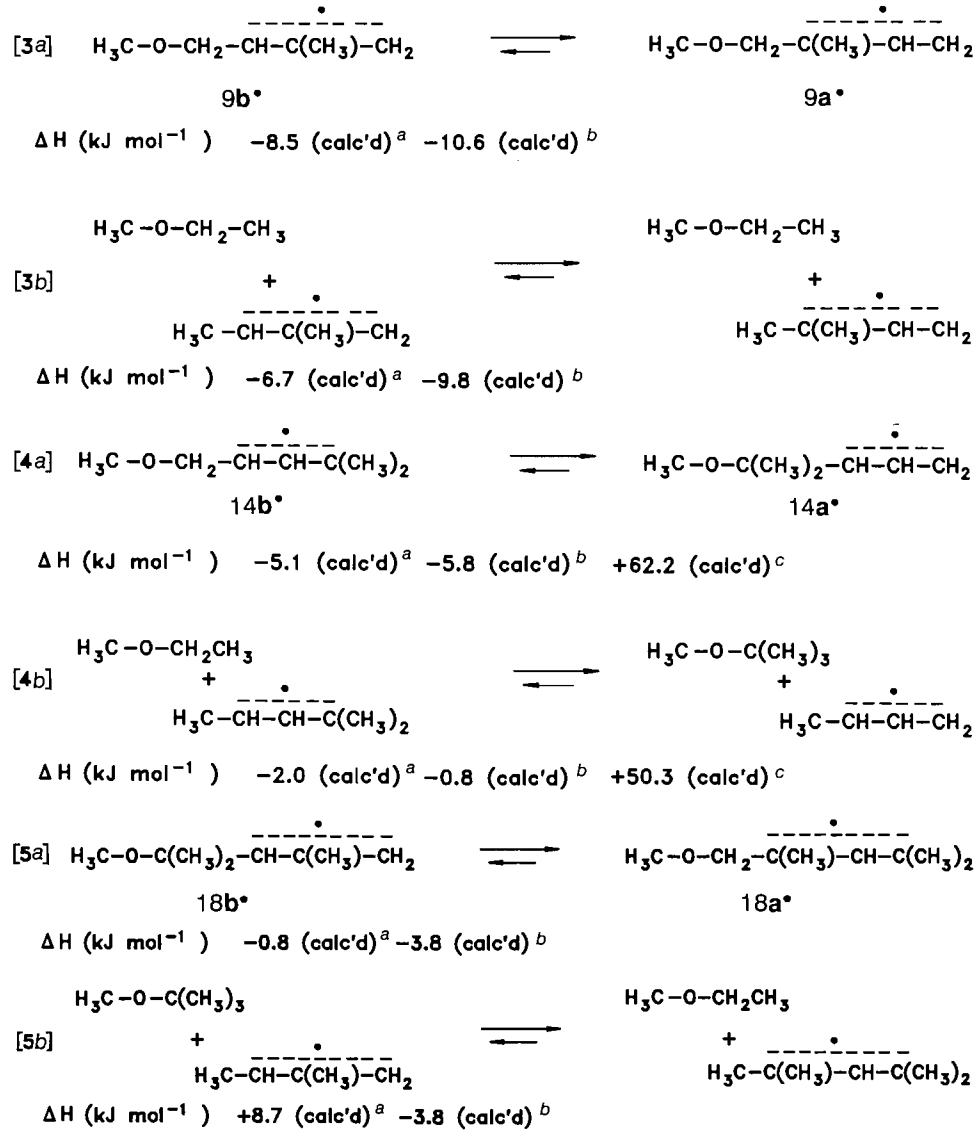

[a] *Ab initio* molecular orbital calculations (MP2/6-31G*//HF/6-31G*) (10).

[b] Empirically derived heats of formation, Benson's empirical rules (16).

[c] Derived by the semi-empirical molecular orbital method (AM1) (17).

[d] Experimentally determined heats of formation (14).

by irreversible deprotonation from the distonic radical cations, with preferential formation of the more stable β-alkoxyalkyl radical, **6a**•.

For both of these reactions (reactions [1] and [2]), it is interesting to note the alternation in the order of relative stability (MP2/6-31G*//HF/6-31G*) between the distonic radical cations, **2b**$^{+\bullet}$ more stable than **2a**$^{+\bullet}$, and **6b**$^{+\bullet}$ more stable than **6a**$^{+\bullet}$, and the relative stability of the β-alkoxyalkyl radicals, **2a**• more stable than **2b**•, and **6a**• more stable than **6b**•. An indication of the cause of this effect is the significant positive charge density borne by the methyl group(s) on the carbon next to the protonated oxygen atom of the distonic radical cations. For the distonic radical cations, the increased stability resulting from additional positive charge delocalization is greater than the difference in stability between secondary (or even primary) versus tertiary alkyl radicals. Since results to be described later will further challenge the general statement, "The more heavily substituted radical is the more stable," additional consideration has been given to this generalization. For reaction [1], relevant isodesmic reactions are shown (reactions [1*a*] – [1*e*]).

The isodesmic reaction [1*b*] involves a dissection of the alternative intermediates **2a**• and **2b**•. The calculated heat of reaction [1*b*] agrees well with that for reaction [1*a*]. In addi-

Table 12. (*a*) Optimized (UHF/6-31G*) structure for the 2-methyl-2-butene–methanol radical (C-3 bonded) (**6a**•).

Bond length (Å)		Bond angle (deg)		Dihedral angle (deg)	
C1—C2	1.503	C1C2C3	118.5	C1C2C3C4	85.6
C2—C3	1.513	C1C2C5	118.0	C1C2C3O6	−156.5
C2—C5	1.504	C2C3C4	112.7	C5C2C3O6	48.0
C3—C4	1.528	C3C2C5	119.0	C2C3O6C7	70.6
C2—O6	2.425	C2C3O6	112.3		
C3—O6	1.405	C3O6C7	115.3		
O6—C7	1.394				

Table 12. (*b*) Spin and charge densities (**6a**$^{+\bullet}$).

Atom number	Charge density summed into heavy atoms	Spin density
1	0.00	−0.16
2	0.01	1.20
3	0.30	−0.13
4	0.02	0.04
5	−0.01	−0.16
6(O)	−0.62	0.01
7	0.30	0.01

Table 12. (*c*) Optimized (UHF/6-31G*) structure for the 2-methyl-2-butene–methanol radical (C-2 bonded) (**6b**•).

Bond length (Å)		Bond angle (deg)		Dihedral angle (deg)	
C1—C2	1.532	C1C2C3	110.7	C1C2C3C4	−66.2
C2—C3	1.514	C1C2C5	109.7	C3C2O6C7	64.9
C2—C5	1.532	C2C3C4	121.8	C4C3C2O6	48.4
C3—C4	1.500	C3C2C5	110.4	C1C2O6C7	−176.3
C2—O6	1.416	C3C2O6	110.8		
C3—O6	2.413	C2O6C7	118.3		
O6—C7	1.395				

Table 12. (*d*) Spin and charge densities (**6b**$^{+\bullet}$).

Atom number	Charge density summed into heavy atoms	Spin density
1	0.00	0.01
2	0.31	−0.13
3	0.00	1.23
4	0.01	−0.16
5	0.03	0.03
6(O)	−0.64	0.01
7	0.30	0.01

tion, in this case, experimentally determined heats of formation of the components are available (14); the agreement is encouraging.

The dissection illustrated in the isodesmic reaction [1*e*] is, in fact, the combination of two isodesmic reactions, [1*c*] and [1*d*]. The isodesmic reaction [1*c*] reveals the fact that alkyl substitution on the carbon bonded to oxygen of the ether leads

Fig. 12. (*a*) 2-Methyl-2-butene–methanol radical (C-3 bonded) (**6a**•); (*b*) 2-methyl-2-butene–methanol radical (C-2 bonded) (**6b**•).

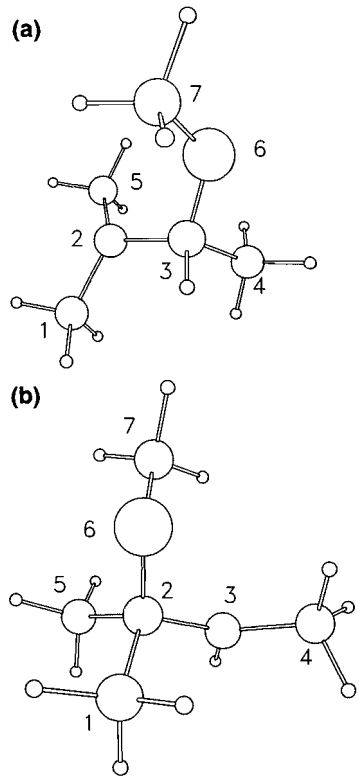

to increased stability. The calculated (MP2/6-31G*//HF/6-31G*) total energies of the isomeric *tert*-butyl and isobutyl radicals show the expected trend; the tertiary radical is 24.0 kJ mol^{-1} more stable than the primary radical (reaction [1*d*]). Combining these two equations gives an indication of the relative importance of these two factors influencing the stability of the radicals **2a**• and **2b**•. This isodesmic reaction, [1*e*], is significantly less exothermic (−8.7 kJ mol^{-1}) than indicated upon consideration of "radical" stability alone (reaction [1*d*]).

Analogous isodesmic reactions, relevant to reaction [2], are shown (reactions [2*a*] – [2*e*]). Again, in this case, experimental data is available for reaction [2*b*]; the calculated value is in good agreement with the experimental results (14). The same trend is observed: the *tert*-radical is more stable than the *sec*-radical (reaction [2*d*]), but the difference is attenuated by the stabilizing influence of alkyl substitution on the carbon adjacent to the oxygen of the ether (reaction [2*c*]). The relevant isodesmic reaction (reaction [2*e*]) lies in favour of the *tert*-radical over the *sec*-radical by only 4.2 kJ mol^{-1}.

The optimized structure for the radical cation of 2-methyl-1,3-butadiene (**9**$^{+\bullet}$) has the expected planar structure with normal bond lengths and angles (Table 3 and Fig. 3). The vertical ionization potential (8.67 eV) and the adiabatic ionization potential (8.45 eV) are in good agreement with the experimental value (8.85 eV, vertical ionization potential) taken from the photoelectron spectra (12). The charge densities at the two termini, C-1 and C-4, are identical. The charge densities at C-2 and C-3 are also identical. These values provide no basis for

Table 13. Relative total energies (MP2/6-31G*//HF/6-31G*) for 2-methyl-2-butene intermediates (total energies obtained by including the solvent dielectric are reported in parentheses).

(**6**$^{+\bullet}$)	−195.488 39 (−195.488 60)
Methanol	−115.344 94 (−115.346 13)
Methanol	−115.344 94 (−115.346 13)
Sum	−426.178 27 (−426.180 86)
(**6a**$^{+\bullet}$)	−310.856 96 (−310.866 53)
Methanol	−115.344 94 (−115.346 13)
Sum	−426.201 90 (−426.212 66)
(**6b**$^{+\bullet}$)	−310.858 28 (−310.864 59)
Methanol	−115.344 94 (−115.346 13)
Sum	−426.203 22 (−426.210 72)
(**6c**$^{+\bullet}$)	−310.856 51 (−310.859 38)
Methanol	−115.344 94 (−115.346 13)
Sum	−426.201 45 (−426.205 51)
(**6a**$^{\bullet}$)	−310.528 57 (−310.531 49)
Protonated methanol	−115.644 29 (−115.646 53)
Sum	−426.172 86 (−426.178 02)
(**6b**$^{\bullet}$)	−310.526 14 (−310.528 98)
Protonated methanol	−115.644 29 (−115.646 53)
Sum	−426.170 43 (−426.175 51)

Fig. 13. Relative energies (MP2/6-31G*//HF/6-31G*) for 2-methyl-2-butene intermediates.

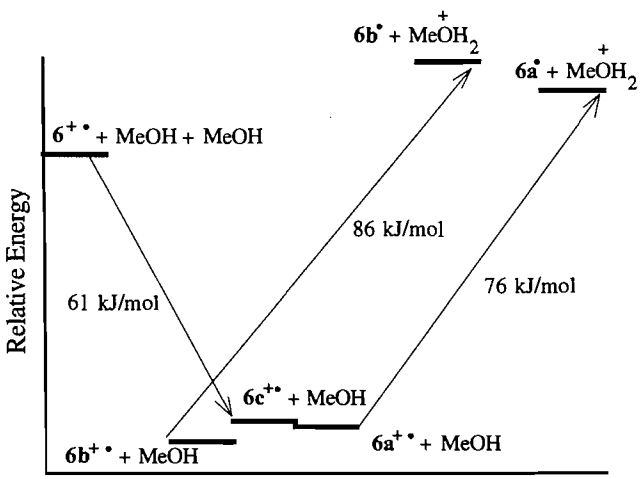

predicting the regiochemistry of the addition. There is, however, significant charge density on the methyl group (C-5). If this charge is summed in with the charge on C-1 and C-2, the argument could be made that more than half (0.58) of the positive charge is in this region; the major products (0.89) do arise from methanol attack at C-1 (reaction [3]).

Two fully optimized structures were obtained for the alternative distonic radical cations (Table 14 and Fig. 14), methanol bonded to C-1 (**9a**$^{+\bullet}$) or to C-4 (**9b**$^{+\bullet}$); **9a**$^{+\bullet}$ is 7.3 kJ mol^{-1} more stable than **9b**$^{+\bullet}$. These structures are accurately described as distonic; the charge and spin are separated. The positive charge is largely associated with the ether moiety, the ether-methyl, and methylene (C-1 or C-4) groups. For **9a**$^{+\bullet}$, the C-1,O-6 bond is 1.54 Å. There is no evidence for bridging; the C-2,O-6 distance is 2.44 Å, and the dihedral angle C-3,C-

Table 14. (*a*) Optimized (UHF/6-31G*) structure for the 2-methyl-1,3-butadiene–methanol distonic radical cation (C-1 bonded) (**9a**$^{+\bullet}$).

Bond length (Å)		Bond angle (deg)		Dihedral angle (deg)	
C1—C2	1.481	C1C2C3	118.1	C1C2C3C4	178.3
C2—C3	1.399	C1C2C5	118.2	C5C2C1C3	178.2
C3—C4	1.389	C2C3C4	125.3	C3C2C1O6	105.7
C2—C5	1.517	C2C1O6	107.9	C2C1O6C7	−178.2
C1—O6	1.540	C1O6C7	119.9		
C2—O6	2.442				
O6—C7	1.466				

Table 14. (*b*) Spin and charge densities (**9a**$^{+\bullet}$).

Atom number	Charge density summed into heavy atoms	Spin density
1	0.42	−0.06
2	−0.01	0.91
3	0.04	−0.75
4	0.08	1.00
5	0.09	−0.11
6 (O)	−0.15	0.02
7	0.53	0.01

Table 14. (*c*) Optimized (UHF/6-31G*) structure for the 2-methyl-1,3-butadiene–methanol distonic radical cation (C-4 bonded) (**9b**$^{+\bullet}$).

Bond length (Å)		Bond angle (deg)		Dihedral angle (deg)	
C1—C2	1.397	C1C2C3	118.7	C1C2C3C4	178.9
C2—C3	1.396	C1C2C5	119.3	C5C2C1C3	178.7
C3—C4	1.476	C2C3C4	124.4	C2C3C4O6	103.5
C2—C5	1.517	C3C4O6	107.9	C3C4O6C7	−174.2
C4—O6	1.539	C4O6C7	120.1		
C3—O6	2.437				
O6—C7	1.465				

Table 14. (*d*) Spin and charge densities (**9b**$^{+\bullet}$).

Atom number	Charge density summed into heavy atoms	Spin density
1	0.06	1.01
2	0.09	−0.72
3	−0.02	0.89
4	0.45	−0.05
5	0.05	0.08
6(O)	−0.15	0.02
7	0.52	0.01

Fig. 14. (*a*) 2-Methyl-1,3-butadiene–methanol distonic radical cation (C-1 bonded) (**9a**$^{+\bullet}$); (*b*) 2-methyl-1,3-butadiene–methanol distonic radical cation (C-4 bonded) (**9b**$^{+\bullet}$).

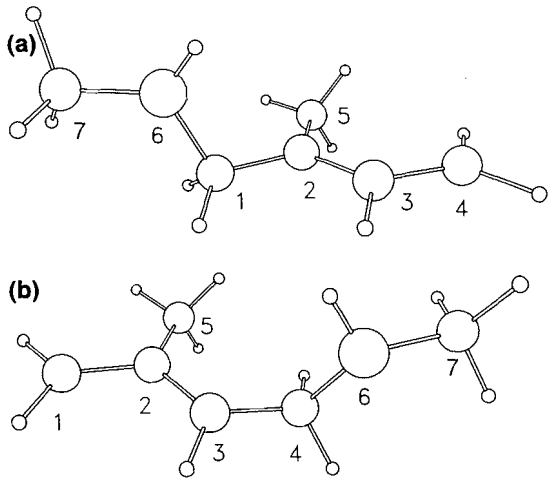

Fig. 15. (*a*) 2-Methyl-1,3-butadiene–methanol radical (C-1 bonded) (**9a**$^{\bullet}$); (*b*) 2-methyl-1,3-butadiene–methanol radical (C-4 bonded) (**9b**$^{\bullet}$).

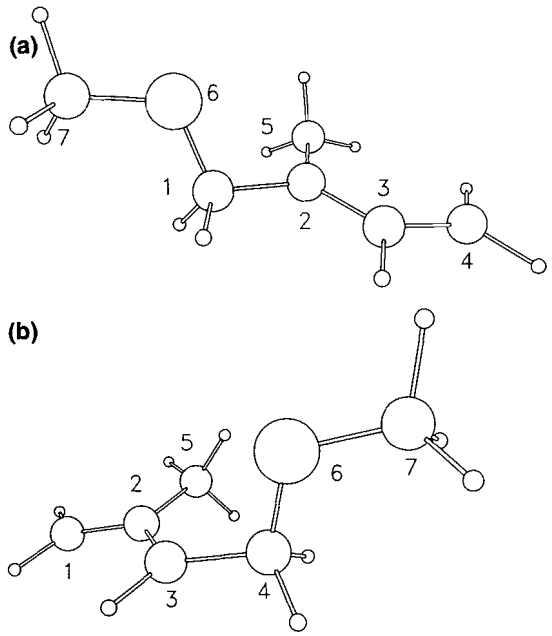

2,C-1,O-6 is 106°. The allylic radical moiety is essentially planar (dihedral angle C-1,C-2,C-3,C-4 is 178°). The structure of **9b**$^{+\bullet}$ is similar, with no evidence for bridging. A thorough search was made for a bridged radical cation(s) and none was found. Deprotonation from the oxygen of the distonic radical cations, **9a**$^{+\bullet}$ and **9b**$^{+\bullet}$, gave the radicals, **9a**$^{\bullet}$ and **9b**$^{\bullet}$ (Table 15 and Fig. 15). The radical with methanol bonded to C-1 (**9a**$^{\bullet}$) is the more stable (8.5 kJ mol^{-1}). In this case, the more stable radical cation (**9a**$^{+\bullet}$) and the more stable radical (**9a**$^{\bullet}$) both have the methanol bonded to C-1; the allylic radical moiety is the more heavily alkyl-substituted.

The relevant isodesmic reaction shows the calculated (MP2/6-31G*//HF/6-31G*) total energies of the isomeric 1,1-dimethyl- and 1,2-dimethyl-substituted allylic radicals follow the expected trend; the 1,1-disubstituted radical is 6.7 kJ mol^{-1} more stable than the 1,2-disubstituted radical (reaction [3*b*]). Calculations of the relative stability of the radicals (**9a**$^{\bullet}$ and **9b**$^{\bullet}$, reaction [3*a*]) and the isodesmic reaction [3*b*] are consistent with the observed product ratio (reaction [3]).

The radical cation of 4-methyl-1,3-pentadiene (**14**$^{+\bullet}$), in the s-*trans* conformation, is planar (dihedral angle C-1,C-2,C-

Table 15. (*a*) Optimized (UHF/6-31G*) structure for the 2-methyl-1,3-butadiene–methanol radical (C-1 bonded) (**9a**$^{\bullet}$).

Bond length (Å)		Bond angle (deg)		Dihedral angle (deg)	
C1—C2	1.504	C1C2C3	119.9	C1C2C3C4	179.1
C2—C3	1.396	C1C2C5	115.8	C5C2C1C3	−179.8
C3—C4	1.391	C2C3C4	127.5	C3C2C1O6	125.2
C2—C5	1.506	C2C1O6	109.5	C2C1O6C7	176.2
C1—O6	1.400	C1O6C7	114.1		
C2—O6	2.371				
O6—C7	1.392				

Table 15. (*b*) Spin and charge densities (**9a**$^{+\bullet}$).

Atom number	Charge density summed into heavy atoms	Spin density
1	0.28	−0.10
2	0.04	1.00
3	0.00	−0.80
4	−0.03	1.03
5	0.02	−0.12
6 (O)	−0.61	0.01
7	0.30	0.00

Table 15. (*c*) Optimized (UHF/6-31G*) structure for the 2-methyl-1,3-butadiene–methanol radical (C-4 bonded) (**9b**$^{\bullet}$).

Bond length (Å)		Bond angle (deg)		Dihedral angle (deg)	
C1—C2	1.390	C1C2C3	120.2	C1C2C3C4	−178.1
C2—C3	1.403	C1C2C5	119.6	C5C2C1C3	179.8
C3—C4	1.500	C2C3C4	124.5	C2C3C4O6	78.3
C2—C5	1.516	C3C4O6	109.9	C3C4O6C7	179.1
C4—O6	1.403	C4O6C7	113.8		
C3—O6	2.377				
O6—C7	1.392				

Table 15. (*d*) Spin and charge densities (**9b**$^{+\bullet}$).

Atom number	Charge density summed into heavy atoms	Spin density
1	−0.06	1.01
2	0.10	−0.80
3	−0.02	1.04
4	0.29	−0.11
5	0.00	0.09
6(O)	−0.60	0.02
7	0.30	0.01

Table 16. Relative total energies (MP2/6-31G*//HF/6-31G*) for 2-methyl-1,3-butadiene intermediates (total energies obtained by including the solvent dielectric are reported in parentheses).

(**9**$^{+\bullet}$)	−194.290 91 (−194.291 65)
Methanol	−115.344 94 (−115.346 13)
Methanol	−115.344 94 (−115.346 13)
Sum	−424.980 79 (−424.983 91)
(**9a**$^{+\bullet}$)	−309.667 73 (−309.685 68)
Methanol	−115.344 94 (−115.346 13)
Sum	−425.012 67 (−425.031 81)
(**9b**$^{+\bullet}$)	−309.664 96 (−309.684 46)
Methanol	−115.344 94 (−115.346 13)
Sum	−425.009 90 (−425.030 59)
(**9a**$^{\bullet}$)	−309.341 21 (−309.347 11)
Protonated methanol	−115.644 29 (−115.646 53)
Sum	−424.985 50 (−424.993 64)
(**9b**$^{\bullet}$)	−309.337 97 (−309.343 79)
Protonated methanol	−115.644 29 (−115.646 53)
Sum	−424.982 26 (−424.990 32)

Fig. 16. Relative energies (MP2/6-31G*//HF/6-31G*) for 2-methyl-1,3-butadiene intermediates.

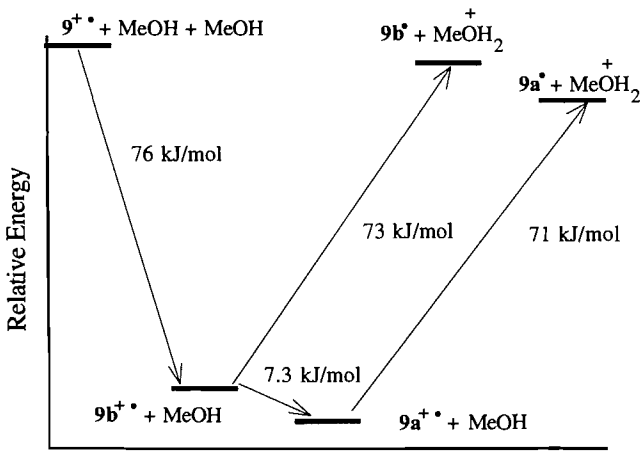

3,C-4 is −180°, C-2,C-3,C-4,C-5 is 180°, Table 4, Fig. 4). The calculated vertical ionization potential (8.23 eV) and the adiabatic ionization potential (7.90 eV) are in good agreement with the experimental value (8.28 eV, vertical ionization potential) taken from the photoelectron spectra (12). The charge density, at a single position, is greatest at C-1 (0.23); however, significant charge is borne by the methyl groups and if the positive charges on C-3,C-4,C-5, and C-6 are summed, this is the region of highest charge density (0.62).

A fully optimized structure for a distonic radical cation, with methanol bonded to C-4, was obtained (**14a**$^{+\bullet}$, Table 17*a*,*b* Fig. 17*a*). The C-4,O-7 bond length was relatively long (1.71 Å) and there was no evidence for bridging. An analogous structure with methanol bonded to C-1, **14b**$^{+\bullet}$, was obtained; with a C-1,O-7 bond length of 1.56 Å, and no evidence for

Table 17. (*a*) Optimized (UHF/6-31G*) structure for the 4-methyl-1,3-pentadiene–methanol distonic radical cation (C-4 bonded) (**14a**$^{+\bullet}$).

Bond length (Å)		Bond angle (deg)		Dihedral angle (deg)	
C1—C2	1.389	C1C2C3	122.9	C1C2C3C4	179.4
C2—C3	1.393	C2C3C4	125.4	C2C3C4C6	−15.1
C3—C4	1.477	C3C4C6	118.5	C2C3C4C5	−153.8
C4—C5	1.512	C3C4C5	114.6	C2C3C4O7	94.9
C4—C6	1.509	C3C4O7	105.3	C3C4O7C8	61.8
C4—O7	1.708	C4O7C8	123.8		
O7—C3	2.537				
O7—C8	1.452				

Table 17. (*b*) Spin and charge densities (**14a**$^{+\bullet}$).

Atom number	Charge density summed into heavy atoms	Spin density
1	0.09	0.99
2	0.06	−0.73
3	0.05	0.89
4	0.20	−0.03
5	0.16	0.00
6	0.16	0.00
7(O)	−0.21	0.04
8	0.48	0.00

Table 17. (*c*) Optimized (UHF/6-31G*) structure for the 4-methyl-1,3-pentadiene–methanol distonic radical cation (C-1 bonded) (**14b**$^{+\bullet}$).

Bond length (Å)		Bond angle (deg)		Dihedral angle (deg)	
C1—C2	1.472	C1C2C3	120.8	C1C2C3C4	179.5
C2—C3	1.391	C2C3C4	127.3	C2C3C4C6	0.6
C3—C4	1.394	C3C4C6	124.2	C2C3C4C5	−178.3
C4—C5	1.505	C3C4C5	120.1	C3C2C1O7	98.2
C4—C6	1.505	C2C1O7	111.0	C2C1O7C8	82.0
C1—O7	1.556	C1O7C8	119.9		
O7—C2	2.496				
O7—C8	1.466				

Table 17. (*d*) Spin and charge densities (**14b**$^{+\bullet}$).

Atom number	Charge density summed into heavy atoms	Spin density
1	0.43	−0.05
2	0.01	0.87
3	0.01	−0.67
4	0.07	0.93
5	0.06	−0.11
6	0.06	−0.11
7(O)	−0.15	0.03
8	0.52	0.00

Fig. 17. (*a*) 4-Methyl-1,3-pentadiene–methanol distonic radical cation (C-4 bonded) (**14a**$^{+\bullet}$); (*b*) 4-methyl-1,3-pentadiene–methanol distonic radical cation (C-1 bonded) (**14b**$^{+\bullet}$).

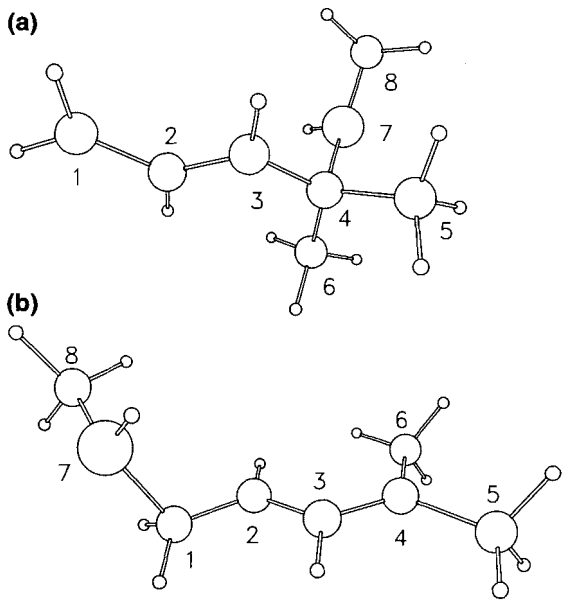

bridging (Table 17*c*,*d*, Fig. 17*b*). The calculations reveal that **14b**$^{+\bullet}$ is of higher energy (9.2 kJ mol^{-1}) than **14a**$^{+\bullet}$. A major factor contributing to the relative stability of **14a**$^{+\bullet}$ must be the significant charge density borne by the methyl groups, C-5 and C-6. Deprotonation from the oxygen of the distonic radical cation **14a**$^{+\bullet}$ gives the radical **14a**$^{\bullet}$, which is more stable (5.1 kJ mol^{-1}) than the analogous radical, **14b**$^{\bullet}$, obtained from **14b**$^{+\bullet}$ (Tables 18, 19, and Figs. 18, 19). Including the solvent dielectric in these calculations has a large effect upon the relative energies of the distonic radical cations; **14b**$^{+\bullet}$ is now more stable (49.8 kJ mol^{-1}) than **14a**$^{+\bullet}$. As expected, there is little solvent effect on the relative energies of the radicals, **14a**$^{\bullet}$ and **14b**$^{\bullet}$.

The 1,4-adducts from **14** have the *E* configuration (**15** and **16**); the *Z* isomers were not detected. This stereochemistry is a reflection of the preferred configuration of the starting diene; the s-*trans* conformer of **14** is favoured. The calculated (MM3) difference in energy between **14** s-*cis* and **14** s-*trans* is 14 kJ mol^{-1}. The s-*trans* conformation is planar while the s-*cis* conformer is twisted with a calculated dihedral angle, C-1,C-2,C-3,C-4, of 43°. The configuration of the intermediate allylic radicals, **14a**$^{\bullet}$ and **14b**$^{\bullet}$, is a reflection of the conformation of the initial diene.

While the observed product ratio, preferential addition of methanol to C-4 (reaction [4]), and the calculated relative energies of the alternative radicals, **14a**$^{\bullet}$ more stable than **14b**$^{\bullet}$ (reaction [4*a*]), are consistent with the proposed hypothesis, this is the only reaction studied, so far, where the order of radical stability was not anticipated. The more stable radical, **14a**$^{\bullet}$, has the *mono*-substituted (C-3) allylic radical, compared to **14b**$^{\bullet}$, with a *tri*-substituted (C-2,C-4,C-4) allylic radical. Calculations based upon the isodesmic reaction (reaction [4*b*]) support the notion that the total structure of the intermediate radical, not just the allylic radical moiety, must be taken into account. Formation of the more heavily substituted ether, less substituted allylic radical, is favoured in this case.

Table 18. (*a*) Optimized (UHF/6-31G*) structure for the 4-methyl-1,3-pentadiene–methanol radical (C-4 bonded) (**14a**$^{\bullet}$).

Bond length (Å)		Bond angle (deg)		Dihedral angle (deg)	
C1—C2	1.392	C1C2C3	124.0	C1C2C3C4	−177.2
C2—C3	1.390	C2C3C4	127.5	C2C3C4C6	109.9
C3—C4	1.516	C3C4C6	109.2	C2C3C4C5	−12.9
C4—C5	1.531	C3C4C5	113.7	C2C3C4O7	−137.3
C4—C6	1.531	C3C4O7	109.2	C3C4O7C8	65.9
C4—O7	1.417	C4O7C8	118.3		
O7—C3	2.391				
O7—C8	1.396				

Table 18. (*b*) Spin and charge densities (**14b**$^{+\bullet}$).

Atom number	Charge density summed into heavy atoms	Spin density
1	−0.03	1.03
2	0.03	−0.80
3	−0.01	1.00
4	0.30	−0.11
5	0.00	0.01
6	0.04	0.02
7 (O)	−0.64	0.01
8	0.30	0.00

Table 18. (*c*) Optimized (UHF/6-31G*) structure for the 4-methyl-1,3-pentadiene–methanol radical (C-1 bonded) (**14b**$^{\bullet}$).

Bond length (Å)		Bond angle (deg)		Dihedral angle (deg)	
C1—C2	1.509	C1C2C3	123.0	C1C2C3C4	177.4
C2—C3	1.392	C2C3C4	127.8	C2C3C4C5	−0.3
C3—C4	1.395	C3C4C5	124.4	C2C3C4C6	179.9
C4—C5	1.506	C3C4C6	120.3	C3C2C1O7	27.6
C4—C6	1.507	C2C1O7	114.3	C2C1O7C8	77.0
C1—O7	1.397	C1O7C8	114.9		
O7—C2	2.442				
O7—C8	1.395				

Table 18. (*d*) Spin and charge densities (**14b**$^{+\bullet}$).

Atom number	Charge density summed into heavy atoms	Spin density
1	0.33	−0.12
2	−0.07	1.02
3	0.01	−0.81
4	0.05	0.97
5	0.00	−0.12
6	−0.01	−0.13
7(O)	−0.61	0.00
8	0.30	0.00

The fully optimized (MP2/6-31G*//HF/6-31G*) global minimum structure for the radical cation of 2,4-dimethyl-1,3-pentadiene (**18**$^{+\bullet}$) is essentially planar with dihedral angles C-1,C-2,C-3,C-4 and C-7,C-2,C-1,C-3 of −179° and −180°

Table 19. Relative total energies (MP2/6-31G*//HF/6-31G*) for 4-methyl-1,3-pentadiene intermediates (total energies obtained by including the solvent dielectric are reported in parentheses).

(**14**$^{+\bullet}$)	−233.479 93 (−233.481 88)
Methanol	−115.344 94 (−115.346 13)
Methanol	−115.344 94 (−115.346 13)
Sum	−464.169 81 (−464.174 14)
(**14a**$^{+\bullet}$)	−348.845 14 (−348.853 56)
Methanol	−115.344 94 (−115.346 13)
Sum	−464.190 08 (−464.199 69)
(**14b**$^{+\bullet}$)	−348.841 62 (−348.872 51)
Methanol	−115.344 94 (−115.346 13)
Sum	−464.186 56 (−464.218 64)
(**14a**$^{\bullet}$)	−348.512 59 (−348.518 41)
Protonated methanol	−115.644 29 (−115.646 53)
Sum	−464.156 88 (−464.164 94)
(**14b**$^{\bullet}$)	−348.510 64 (−348.516 67)
Protonated methanol	−115.644 29 (−115.646 53)
Sum	−464.154 93 (−464.163 20)

Fig. 18. (*a*) 4-Methyl-1,3-pentadiene–methanol radical (C-4 bonded) (**14a**$^{\bullet}$); (*b*) 4-methyl-1,3-pentadiene–methanol radical (C-1 bonded) (**14b**$^{\bullet}$).

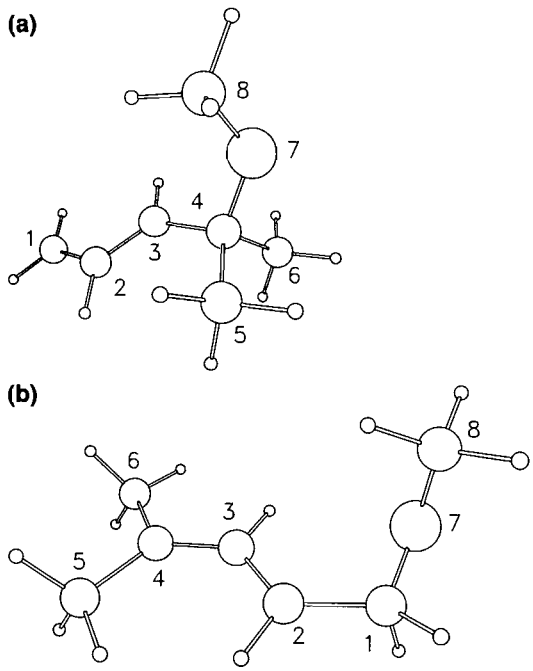

(Table 5, Fig. 5). The calculated vertical ionization potential (8.62 eV) and the adiabatic ionization potential (7.58 eV) are in good agreement with the experimental values (8.49 eV, vertical, and ≤8.08 adiabatic) taken from the photoelectron spectra.[4] Almost half (0.48) of the positive charge density on this

[4] D. Klapstein. St. Francis Xavier Univeristy, Antigonish, N.S., Canada, unpublished results.

Fig. 19. Relative energies (MP2/6-31G*//HF/6-31G*) for 4-methyl-1,3-pentadiene intermediates.

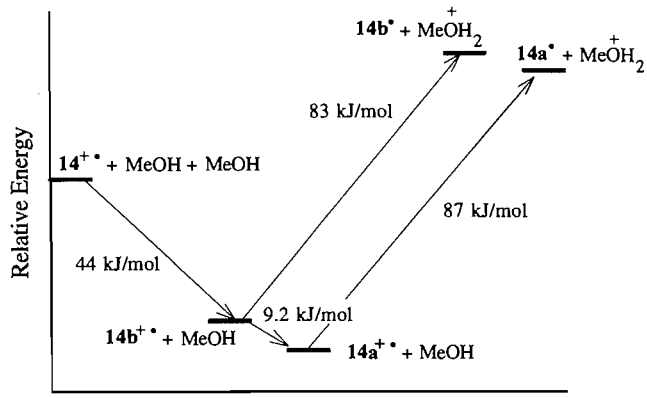

radical cation, **18**$^{+\bullet}$, is on C-4,C-5, and C-6, with only 0.20 on C-1. The major mode of addition, forming **19**, **20**, and **21** (reaction [5]), results from initial bonding of methanol to C-1, giving the more heavily substituted allylic radical, which is, in this case, the more stable (reaction [5*a*]).

There is convincing experimental evidence that the neutral molecule, **18**, is significantly (ca. 50°) twisted from the s-*cis* conformer (15*a*). Published calculations (HF/6-31G) on the neutral molecule indicate a global minimum structure with a dihedral angle C-1,C-2,C-3,C-4 of 52°, i.e., twisted from s-*cis*, and another conformer C-1,C-2,C-3,C-4 of 180°, s-*trans*, 9.3 kJ mol^{-1} higher energy (15*b*). Higher level calculations (MP2/6-31G*//HF/6-31G*) reduce this energy difference to 7.9 kJ mol^{-1}. Earlier molecular mechanics calculations (MMP1) found two twisted conformers, dihedral angles C-1,C-2,C-3,C-4, of 52° and 163°, with a difference in energy of only 1.3 kJ mol^{-1} (15c). MM3 calculations also give two twisted conformers, C-1,C-2,C-3,C-4 of 49° and 149°; in this case, 0.5 kJ mol^{-1} in favour of the twisted s-*trans* conformer. In view of the twist in this neutral molecule, it is not surprising that both *Z* (**21** and **22**) and *E* (**20**) 1,4-adducts have been identified among the products.

The planarity (calculated) of the radical cation, **18**$^{+\bullet}$, is in marked contrast with the significant twist in the neutral molecule. A thorough search was made for conformational minima of **18**$^{+\bullet}$; two were found. The lowest energy conformer is essentially planar s-*trans* (dihedral angle, C-1,C-2,C-3,C-4 of −179°). A twisted s-*cis* (C-1,C-2,C-3,C-4 of −12°) shallow minimum was also found, 12.3 kJ mol^{-1} above the global minimum. These minima are separated by a rotational barrier estimated (MP2/6-31G*//HF/6-31G*) to be 73 kJ mol^{-1} above the global minimum, s-*trans* conformer. The total overlap between C-2 and C-3, obtained by Mulliken population analysis, is 0.48 for both conformers of **18**$^{+\bullet}$. These values can be compared with a barrier of only 11 kJ mol^{-1} for rotation around the C-2—C-3 bond of the neutral molecule, s-*cis* twisted **18**, and the total overlap between C-2 and C-3 of 0.37 (s-*trans*, 0.41). Clearly, the radical cation, **18**$^{+\bullet}$, is inherently more planar than the neutral molecule.

An important question generated by this discussion is: what is the best/easiest method for obtaining the relative heats of formation of these intermediate radicals? The ab initio calculations discussed so far utilized reasonably large basis sets and included electron correlation (MP2/6-31G*//HF/6-31G*, cor-

Table 20. Heats of formation and total energies of (**2a**•) and (**2b**•).

Method	(**2a**•)	(**2b**•)	Δ (kJ mol^{-1})
AM1	−175.1 kJ	−116.7 kJ	−58.4
Benson's rules	−83.3 kJ	−85.1 kJ	−1.8
HF/STO-3G//HF/STO-3G	−267.245 69 au	−267.235 09 au	21.8
HF/3-21G//HF/3-21G	−269.052 54 au	−269.052 84 au	−0.8
HF/6-31G*//HF/6-31G*	−270.549 05 au	−270.544 09 au	13.0
MP2/6-31G*//HF/6-31G*	−271.353 17 au	−271.352 79 au	1.3
SCRF/HF/6-31G*//SCRF/HF/6-31G*	−270.549 41 au	−270.544 38 au	13.2
SCRF/MP2/6-31G*//SCRF/HF/6-31G*	−271.355 96 au	−271.355 34 au	1.6

Table 21. Heats of formation and total energies of *tert*-butyl methyl ether and isobutyl methyl ether.

Method	*tert*-Butyl methyl ether	Isobutyl methyl ether	Δ (kJ mol^{-1})
AM1	−271.271 kJ	−293.175 kJ	−21.9
Benson's rules	−286.604 kJ	−257.734 kJ	28.9
Experimental	−283.672 kJ		
HF/6-31G*//HF/6-31G*	−271.175 63 au	−271.174 95 au	1.8
MP2/6-31G*//HF/6-31G*	−272.013 15 au	−272.007 31 au	15.3
MP2/6-31G*//MP2/6-31G*	−272.014 96 au	−272.009 20 au	15.1
MP2/6-311+G*//MP2/6-31G*	−272.135 46 au	−272.129 44 au	15.8

rected for spin contamination). These numbers are basis-set dependent. The results of the calculations for the isodesmic reactions, using various basis sets, and other methods (16, 17), have been listed (reactions [1*a*]–[5*b*] and Tables 20 and 21). For example, the difference in stability of the alternative intermediate radicals, **2a**• and **2b**•, is very basis-set/method dependent. Calculations on the isodesmic reaction (reaction [1*c*]) reveal that a major contribution can be attributed to variation in the calculated total energy for the ethers (*tert*-butyl methyl ether and isobutyl methyl ether) upon inclusion of electron correlation. The differences in the heats of formation of these two ethers, determined by various methods, are summarized in Table 21. It was, to some extent, reassuring to note that further increasing the basis set (MP2/6-311+G*//MP2/6-31G*) had little effect on the calculated total energies of these species. It was also interesting to note the general agreement between the energies calculated (MP2/6-31G*//HF/6-31G*) and those derived by Benson's empirical rules (16). In only two cases, reactions [1*b*] and [2*b*], were experimental data available (14); there is good agreement between the experimental and calculated values (±3 kJ mol^{-1}). In marked contrast, the agreement between both the values derived from the ab initio calculations and the experimental values with results obtained from a semi-empirical molecular orbital method (AM1 (17)) is generally poor.

An additional observation worthy of note deals with the relative abundance of 1,4- versus 1,2-adducts from the conjugated dienes. This regiochemistry is determined during the coupling of the allylic radical with the 1,4-dicyanobenzene radical anion (**1**$^{-\bullet}$), step 4, Scheme 1. Previous results have led to the hypothesis that preferential coupling occurs at that end of the ambident allylic radical with highest spin density, moderated by steric interactions. Two 1,2-adducts were observed, **17** from reaction [4] and **19** from reaction [5]. In both cases, these adducts are less sterically hindered than the alternative pair of isomers, which were not observed.

Conclusions

1. The regiochemistry of the photo-NOCAS reaction (step 3, Scheme 1) with methanol acting as the nucleophile, combining with the radical cation of an alkene or diene, can be predicted on the basis of the *anti*-Markovnikov rule. Addition occurs at that position which yields the most stable intermediate radical.

2. The regiochemistry is not controlled by steric factors. The nucleophile (methanol) does not always add preferentially to the least hindered site.

3. The nucleophile (methanol) does not always add preferentially to the carbon bearing the greatest positive charge density.

4. The more heavily alkyl-substituted radical is not (necessarily) the more stable.

5. Ab initio molecular orbital calculations (MP2/6-31G*// HF/6-31G*, corrected for spin contamination) lend support to the hypothesis that the addition proceeds by initial formation of bridged radical cation complexes, followed by formation of alternative distonic radical cations. Subsequent deprotonation from the oxygen of the distonic radical cations to give β-alkoxyalkyl radicals determines the regiochemistry.

6. Isodesmic reactions based upon empirically derived heats of formation (Benson's rules) are also useful for predicting relative free-radical stability.

7. Not surprisingly, in view of the small differences in the

stability of these radicals, the agreement between theory and experiment is not absolute.

8. The alternative 1,2- versus 1,4-addition is controlled by spin density and steric factors.

9. The stereochemistry of the photo-NOCAS 1,4-adducts involving dienes is a reflection of the relative stability of the alternative s-*cis* and s-*trans* conformers of the starting neutral diene. This ratio is accurately predicted, based upon relative energies of the conformers calculated by molecular mechanics (MM3).

10. The regiochemistry of the photo-NOCAS reaction is dependent upon the nucleophile. Preliminary results indicate that the regiochemistry of the reaction with cyanide anion is different from that reported here for the addition of methanol.

Experimental

General information

^1H and ^{13}C nmr spectra were obtained from a Bruker 250 or 400 MSL spectrometer. Spectra were recorded in parts per million and frequencies are relative to tetramethylsilane. Infrared spectra (ir) were recorded on a Nicolet 205 spectrometer and are reported in wave numbers (cm^{-1}). Elemental analyses were performed by Canadian Microanalytical Service Ltd., B.C. Exact Mass determinations were obtained using a CEC 21-110 mass spectrometer. Progress of the reaction was followed by gas chromatography using a Hewlett–Packard (HP) 5890 gas chromatograph fitted with a DB-1701 fused silica WCOT column (30 m × 0.25 mm, 0.25-μm film thickness) and a calibrated flame ionization detector (gc/fid). An HP 3392A integrator was interfaced with the gc/fid to obtain peak areas. An HP 5890 gas chromatograph with a 5% phenyl methyl silicone fused silica WCOT column (25 m × 0.20 mm, 0.33-μm film thickness) interfaced with an HP 5970 mass selective detector (gc/ms) was also used for product analyses. Mass spectra are reported as *m/z* (relative intensity). Separation of product mixtures was generally carried out using preparative medium-pressure liquid chromatography (mplc) (1*a*). The mplc consists of a 2.5 cm × 1 m column packed with thin-layer chromatography (tlc) grade silica gel (with binder) (cat. no. 81632, Rose Scientific Ltd.) at a pressure of 20 psi using helium (1psi = 6.9 kPa). Connected to the mplc was a UV spectrophotometer – fraction collector that collects ca. 10-mL fractions. Preparative gas chromatography (prep-gc) was carried out on a Varian Aerograph model 920 instrument using a 1/4 in. × 6 ft aluminum column packed with 20% SE-30 on Chromasorb W 60/80 NAM.

Materials

Acetonitrile (Fisher ACS grade) was distilled twice, first from sodium hydride and then from phosphorus pentoxide. It was then passed through a column of basic alumina, refluxed over calcium hydride for 24 h (under a nitrogen atmosphere), fractionally distilled (under nitrogen), and stored over molecular sieves (3 Å) (18). Methanol was distilled and then stored over molecular sieves (4 Å). 1,4-Dicyanobenzene (**1**) (Aldrich) was purified by treatment with Norite in methylene chloride, followed by recrystallization from 95% ethanol. Tetraethylammonium perchlorate (TEAP) (Aldrich) was recrystallized three times from water and then dried in a vacuum oven for 15 h, 70°C, 0.25 Torr (1 Torr = 133.3 Pa). Biphenyl (**5**) (Eastman Kodak Co.) was recrystallized from methanol. 4-Methyl-1,3-pentadiene (**14**) (≥98%) was obtained from Fluka Chemika-BioChemika. 2,4-Dimethyl-1,3-pentadiene (**18**) (≥98%) was obtained from Aldrich Chemical Co.

Irradiations

Irradiations were generally carried out on solutions of acetonitrile–methanol (3:1) with 1,4-dicyanobenzene (**1**), the diene, and biphenyl (**5**) serving as a codonor. Solutions were irradiated in either 2 cm i.d. Pyrex tubes or 5 mm Pyrex nmr tubes, which were degassed by nitrogen ebullition. These samples were irradiated at 10°C using a CGE 1-kW medium-pressure mercury vapour lamp contained in a water-cooled quartz immersion well.

Combination of methanol, 4-methyl-1,3-pentadiene (14), and 1,4-dicyanobenzene (1) to form photo-NOCAS adducts 15, 16, and 17: reaction [4]

A solution of 4-methyl-1,3-pentadiene (**14**) (0.40 g, 0.55 mL, 0.005 mol), 1,4-dicyanobenzene (**1**) (0.6 g, 0.005 mol), and biphenyl (**5**) (0.4 g, 0.003 mol) in acetonitrile–methanol (3:1, 40 mL) was degassed by nitrogen ebullition for 5 min and irradiated for 44 h. The solvent was removed to yield a crude photolysate. The crude photolysate was separated by mplc using a linear solvent gradient of hexanes – (5% diethyl ether, 95% hexanes). The products eluted in the order **17**, **16**, and **15**.

(E)-1-(4-Cyanophenyl)-4-methoxy-4-methyl-2-pentene (15)

The yield of **15** was 27%: infrared (Nicolet 205) *ν*: 3034(w), 2977(s), 2934(m), 2905(m), 2824(m), 2228(s), 1608(m), 1506(m), 1466(w), 1413(w), 1379(m), 1363(m), 1256(w), 1170(m), 1137(m), 1076(s), 977(m), 844(m), 822(m); ^1H nmr (250.13 MHz, $CDCl_3$) δ_{TMS}: 1.22 (s, 6H, 2 CH_3), 3.11 (s, 3H, OCH_3), 3.40 (d, 2H, $^3J_{1-2}$ = 6.1 Hz, methylene, aryl substituted (1-H)), 5.50 (d, 1H, $^3J_{2-3}$ = 16.2 Hz, vinyl H (3-H)), 5.64 (dt, 1H, $^3J_{2-3}$ = 16.2 Hz, $^3J_{1-2}$ = 6.1 Hz, vinyl H (2-H)), 7.24 (d, 2H, $^3J_{2'-3'}$ = 7.9 Hz, $^3J_{5'-6'}$ = 7.9 Hz, H's adjacent to alkyl-substituted aryl carbon (2′-H, 6′-H)), 7.53 (d, 2H, $^3J_{2'-3'}$ = 7.9 Hz, $^3J_{5'-6'}$ = 7.9 Hz, H's adjacent to cyano-substituted aryl carbon (3′-H, 5′-H)); ^{13}C nmr (62.90 MHz, $CDCl_3$) δ: 25.73 (q, 2 CH_3), 38.83 (t, CH_2, aryl substituted), 50.31 (q, OCH_3), 74.65 (s, quaternary carbon adjacent to oxygen), 109.99 (s, quaternary aryl carbon, cyano substituted), 119.00 (s, CN), 127.04 (d, vinyl CH), 129.32 (d, aromatic CH adjacent to alkyl-substituted aryl carbon), 132.27 (d, aromatic CH adjacent to cyano-substituted aryl carbon), 138.28 (d, vinyl CH), 146.06 (s, quaternary aryl carbon, alkyl-substituted); ms *m/z*: 73(19), 99(39), 116(17), 141(17), 142(33), 153(22), 168(43), 200(100), 201(14). Anal. calcd. for $C_{14}H_{17}NO$: C 78.10, H 7.96, N 6.51; found: C 78.55, H 7.96, N 6.40; repeat: C 77.62, H 7.92, N 6.45.

(E)-4-(4-Cyanophenyl)-1-methoxy-4-methyl-2-pentene (16)

The yield of **16** was 11%: infrared (Nicolet 205) *ν*: 2970(s), 2931(s), 2874(m), 2822(m), 2228(s), 1606(m), 1504(m), 1467(m), 1452(m), 1402(w), 1386(m), 1379(m), 1364(m), 1194(m), 1121(s), 1109(s), 1076(w), 1062(w), 1019(w), 977(s), 839(s); ^1H nmr (250.13 MHz, $CDCl_3$) δ_{TMS}: 1.41 (s, 6H, 2 CH_3), 3.33 (s, 3H, OCH_3), 3.93 (d, 2H, $^3J_{1-2}$ = 6.1 Hz, OCH_2 (1-H)), 5.58 (dt, 1H, $^3J_{2-3}$ = 15.9 Hz, $^3J_{1-2}$ = 6.1 Hz, vinyl H (2-H)), 5.84 (d, 1H, $^3J_{2-3}$ = 15.9 Hz, vinyl H (3-H)), 7.43 (d, 2H, $^3J_{2'-3'}$ = 7.9 Hz, $^3J_{5'-6'}$ = 7.9 Hz, H's adjacent to

alkyl-substituted aryl carbon (2′-H, 6′-H)), 7.57 (d, 2H, $^3J_{2'-3'}$ = 7.9 Hz, $^3J_{5'-6'}$ = 7.9 Hz, H's adjacent to cyano-substituted aryl carbon (3′-H, 5′-H)); ^{13}C nmr (62.90 MHz, $CDCl_3$) δ: 28.36 (q, 2 CH_3), 40.88 (s, quaternary carbon, aryl substituted), 58.09 (q, OCH_3), 73.09 (t, OCH_2), 110.00 (s, quaternary aryl carbon, cyano substituted), 118.95 (s, CN), 123.98 (d, vinyl CH), 127.06 (d, aromatic CH adjacent to alkyl-substituted aryl carbon), 132.04 (d, aromatic CH adjacent to cyano-substituted aryl carbon), 141.79 (d, vinyl CH), 154.08 (s, quaternary aryl carbon, alkyl-substituted); ms *m/z*: 71(100), 115(15), 116(35), 140(16), 142(47), 153(27), 154(15), 157(47), 168(47), 170(47), 215(1). Anal. calcd. for $C_{14}H_{17}NO$: C 78.10, H 7.96, N 6.51; found: C 77.93, H 7.95, N 6.44.

*4-(4-Cyanophenyl)-5-methoxy-2-methyl-2-pentene (**17**)*

The yield of **17** was 9%: infrared (Nicolet 205) *ν*: 2975(m), 2927(s), 2891(m), 2877(m), 2826(m), 2228(s), 1607(m), 1504(m), 1458(m), 1449(m), 1377(m), 1192(m), 1177(m), 1113(s), 834(m); ^{1}H nmr (250.13 MHz, $CDCl_3$) δ_{TMS}: 1.64 (s, 3H, CH_3), 1.74 (s, 3H, CH_3), 3.32 (s, 3H, OCH_3), 3.51 (dd, 1H, $^3J_{5-5'}$ = 10.9 Hz, $^3J_{4-5}$ = 7.0 Hz, H of methylene group, methoxy substituted (5-H)), 3.55 (dd, 1H, $^3J_{5-5'}$ = 10.9 Hz, $^3J_{4-5'}$ = 6.7 Hz, H of methylene group, methoxy substituted (5′-H)), 3.84 (m, 1H, $^3J_{3-4}$ = 8.8 Hz, $^3J_{4-5}$ = 7.0 Hz, $^3J_{4-5'}$ = 6.7 Hz, H of methine group (4-H)), 5.27 (br d, 1H, $^3J_{3-4}$ = 8.8 Hz, vinyl H (3-H)), 7.34 (d, 2H, $^3J_{2'-3'}$ = 8.4 Hz, $^3J_{5'-6'}$ = 8.4 Hz, H's adjacent to alkyl-substituted aryl carbon (2′-H, 6′-H)), 7.58 (d, 2H, $^3J_{2'-3'}$ = 8.4 Hz, $^3J_{5'-6'}$ = 8.4 Hz, H's adjacent to cyano-substituted aryl carbon (3′-H, 5′-H)); ^{13}C nmr (62.90 MHz, $CDCl_3$) δ: 18.32 (q), 25.90 (q), 44.82 (d, CH, aryl substituted), 58.98 (q, OCH_3), 76.54 (t, OCH_2), 109.99 (s, quaternary aryl carbon, cyano substituted), 119.12 (s, CN), 123.48 (d, vinyl CH), 128.61 (d, aromatic CH adjacent to alkyl-substituted aryl carbon), 132.24 (d, aromatic CH adjacent to cyano-substituted aryl carbon), 135.27 (s, vinyl quaternary carbon), 148.92 (s, quaternary aryl carbon, alkyl-substituted); ms *m/z*: 89(12), 115(12), 116(25), 127(14), 128(15), 140(10), 142(30), 143(13), 153(12), 154(14), 170(100), 171(14), 215(13). Anal. calcd. for $C_{14}H_{17}NO$: C 78.10, H 7.96, N 6.51; found: C 77.79, H 8.02, N 6.26.

Combination of methanol, 2,4-dimethyl-1,3-pentadiene (18), and 1,4-dicyanobenzene (1) to form photo-NOCAS adducts 19, 20, 21, and 22: reaction [5]

A solution of 2,4-dimethyl-1,3-pentadiene (**18**) (3.0 g, 4.0 mL, 0.031 mol), 1,4-dicyanobenzene (**1**) (2.5 g, 0.020 mol), and biphenyl (**5**) (1.6 g, 0.010 mol) in acetonitrile–methanol (3:1, 160 mL) was degassed by nitrogen ebullition for 5 min and irradiated for 94 h. The solvent was removed to yield a crude photolysate. The crude photolysate was separated by mplc using a linear solvent gradient of hexanes – (5% diethyl ether, 95% hexanes). Further purification was achieved via additional chromatography using mplc. Four 1:1:1 adducts eluted in the order **19**, (**21** and **22**; together) and **20**. Some additional separation of **21** and **22** was achieved using prep-gc.

*4-(4-Cyanophenyl)-5-methoxy-2,4-dimethyl-2-pentene (**19**)*

The yield of **19** was 26%: infrared (Nicolet 205) *ν*: 2972(s), 2929(s), 2876(s), 2829(m), 2227(s), 1606(s), 1503(m), 1475(m), 1450(s), 1408(m), 1386(m), 1376(m), 1196(m), 1169(m), 1116(s), 1104(s), 1066(m), 1019(m), 985(m), 963(m), 841(s), 822(m); ^{1}H nmr (250.13 MHz, $CDCl_3$) δ_{TMS}: 1.10 (d, 3H, $^4J_{1-3}$ = 1.2 Hz, vinyl CH_3 (1-H)), 1.46 (s, 3H, CH_3), 1.70 (d, 3H, $^4J_{1'-3}$ = 1.2 Hz, vinyl CH_3 (1′-H)), 3.26 (s, 3H, OCH_3), 3.29 (d, 1H, $2J_{5-5'}$ = 8.8 Hz, H of methylene group, methoxy substituted (5-H)), 3.37 (d, 1H, $^2J_{5-5'}$ = 8.8 Hz, H of methylene group, methoxy substituted (5′-H)), 5.48 (m, 1H, $^4J_{1-3}$ = 1.2 Hz, $^4J_{1'-3}$ = 1.2 Hz, vinyl H (3-H)), 7.47 (d, 2H, $^3J_{2'-3'}$ = 8.6 Hz, $^3J_{5'-6'}$ = 8.6 Hz, H's adjacent to alkyl-substituted aryl carbon (2′-H, 6′-H)), 7.55 (d, 2H, $^3J_{2'-3'}$ = 8.6 Hz, $^3J_{5'-6'}$ = 8.6 Hz, H's adjacent to cyano-substituted aryl carbon (3′-H, 5′-H)); ^{13}C nmr (62.90 MHz, $CDCl_3$) δ: 19.73 (q), 23.92 (q), 26.83(q), 44.68 (s, quaternary carbon, aryl substituted), 59.33 (q, OCH_3), 82.58 (t, OCH_2), 109.37 (s, quaternary aryl carbon, cyano substituted), 119.25 (s, CN), 128.14 (d, aromatic CH adjacent to alkyl-substituted aryl carbon), 129.71 (d, vinyl CH), 131.71 (d, aromatic CH adjacent to cyano-substituted aryl carbon), 134.99 (s, vinyl quaternary carbon), 153.21 (s, quaternary aryl carbon, alkyl-substituted); ms *m/z*: 51(5), 53(5), 77(7), 89(5), 103(5), 115(9), 116(12), 127(8), 128(6), 129(5), 130(11), 140(7), 142(100), 143(12), 153(7), 154(11), 156(8), 168(8), 184(59), 185(9), 229(9). Anal. calcd. for $C_{15}H_{19}NO$: C 78.56, H 8.35, N 6.11; found: C 78.73, H 8.29, N 6.04.

*(E)-4-(4-Cyanophenyl)-1-methoxy-2,4-dimethyl-2-pentene (**20**)*

The yield of **20** was 25%: infrared (Nicolet 205) *ν*: 2967(s), 2928(s), 2875(m), 2819(m), 2228(s), 1606(m), 1503(m), 1467(m), 1450(m), 1401(m), 1382(m), 1363(m), 1192(m), 1114(s), 1096(s), 1062(m), 1020(w), 839(s); ^{1}H nmr (250.13 MHz, $CDCl_3$) δ_{TMS}: 1.14 (d, 3H, $^4J_{2-3}$ = 1.2 Hz, vinyl CH_3 (2-H)), 1.44 (s, 6H, 2 CH_3's), 3.31 (s, 3H, OCH_3), 3.76 (s, 2H, methylene group, methoxy substituted), 5.77 (m, 1H, $^4J_{2-3}$ = 1.2 Hz, vinyl H (3-H)), 7.47 (d, 2H, $^3J_{2'-3'}$ = 8.5 Hz, $^3J_{5'-6'}$ = 8.5 Hz, H's adjacent to alkyl-substituted aryl carbon (2′-H, 6′-H)), 7.58 (d, 2H, $^3J_{2'-3'}$ = 8.5 Hz, $^3J_{5'-6'}$ = 8.5 Hz, H's adjacent to cyano-substituted aryl carbon (3′-H, 5′-H)); The nOe experiment: the vinyl proton was irradiated. An nOe was observed for the signals due to protons on the methyl groups (benzylic), protons on the methylene group (methoxy substituted), and the *ortho*-aryl protons; ^{13}C nmr (62.90 MHz, $CDCl_3$) δ: 15.10 (q), 30.96 (q, 2 CH_3's), 39.95 (s, quaternary carbon, aryl substituted), 57.68 (q, OCH_3), 78.94 (t, OCH_2), 109.23 (s, quaternary aryl carbon, cyano substituted), 119.15 (s, CN), 127.02 (d, aromatic CH adjacent to alkyl-substituted aryl carbon), 132.07 (d, aromatic CH adjacent to cyano-substituted aryl carbon), 134.15 (s, vinyl quaternary carbon), 136.33 (d, vinyl CH), 156.16 (s, quaternary aryl carbon, alkyl-substituted); ms *m/z*: 55(19), 72(27), 73(15), 85(100), 115(11), 116(27), 140(13), 142(59), 154(20), 156(11), 167(21), 168(10), 182(32), 184(28). Exact Mass calcd. for $C_{15}H_{19}NO$: 229.1467; found: 229.1462.

*(Z)-4-(4-Cyanophenyl)-1-methoxy-2,4-dimethyl-2-pentene (**21**)*

The yield of **21** was 6%: ^{1}H nmr (250.13 MHz, $CDCl_3$) δ_{TMS}: 1.41 (s, 6H, 2 CH_3's), 1.75 (d, 3H, $^4J_{2-3}$ = 1.5 Hz, vinyl CH_3 (2-H)), 2.90 (s, 3H, OCH_3), 3.29 (s, 2H, methylene group, methoxy substituted), 5.71 (m, 1H, $^4J_{2-3}$ = 1.5 Hz, vinyl H (3-H)), 7.48 (d, 2H, $^3J_{2'-3'}$ = 8.8 Hz, $^3J_{5'-6'}$ = 8.8 Hz, H's adjacent

to alkyl-substituted aryl carbon (2′-H, 6′-H)), 7.58 (d, 2H, $^3J_{2'-3'}$ = 8.8 Hz, $^3J_{5'-6'}$ = 8.8 Hz, H's adjacent to cyano-substituted aryl carbon (3′-H, 5′-H)); The nOe experiment: the vinyl proton was irradiated. An nOe was observed for the signals due to protons on the methyl groups (benzylic), protons on the vinyl methyl group, and the *ortho*-aryl protons; ^{13}C nmr (62.90 MHz, $CDCl_3$) δ: 21.79 (q), 31.84 (q, 2 CH_3's), 40.10 (s, quaternary carbon, aryl substituted), 57.94 (q, OCH_3), 71.06 (t, OCH_2), 109.28 (s, quaternary aryl carbon, cyano substituted), 119.16 (s, CN), 127.03 (d, aromatic CH adjacent to alkyl-substituted aryl carbon), 131.99 (d, aromatic CH adjacent to cyano-substituted aryl carbon), 134.52 (s, vinyl quaternary carbon), 137.78 (d, vinyl CH), 156.56 (s, quaternary aryl carbon, alkyl-substituted); ms *m/z*: 51(7), 53(8), 55(22), 72(20), 73(35), 77(7), 85(100), 115(8), 116(19), 127(7), 140(8), 142(28), 154(11), 167(10), 182(13), 184(8). Exact Mass calcd. for $C_{15}H_{19}NO$ (50/50 mixture of **21** and **22**): 229.1467; found: 229.1455.

(Z)-1-(4-Cyanophenyl)-4-methoxy-2,4-dimethyl-2-pentene (22)

The yield of **22** was 4%: ^{1}H nmr (250.13 MHz, $CDCl_3$) δ_{TMS}: 1.34 (s, 6H, 2 CH_3's), 1.59 (d, 3H, $^4J_{2-3}$ = 1.2 Hz, vinyl CH_3 (2-H)), 3.20 (s, 3H, OCH_3), 3.78 (s, 2H, methylene group, aryl substituted), 5.34 (m, 1H, $^4J_{2-3}$ = 1.2 Hz, vinyl H (3-H)), 7.29 (d, 2H, $^3J_{2'-3'}$ = 7.9 Hz, $^3J_{5'-6'}$ = 7.9 Hz, H's adjacent to alkyl-substituted aryl carbon (2′-H, 6′-H)), 7.57 (d, 2H, $^3J_{2'-3'}$ = 7.9 Hz, $^3J_{5'-6'}$ = 7.9 Hz, H's adjacent to cyano-substituted aryl carbon (3′-H, 5′-H)); The nOe experiment: the vinyl proton was irradiated. An nOe was observed for the signals due to protons on the three methyl groups; ^{13}C nmr (62.90 MHz, $CDCl_3$) δ: 23.96 (q), 28.17 (q, 2 CH_3's), 37.77 (t, CH_2, aryl substituted), 50.16 (q, OCH_3), 75.09 (s, quaternary carbon adjacent to oxygen), 109.63 (s, quaternary aryl carbon, cyano substituted), 119.16 (s, CN), 129.57 (d, aromatic CH adjacent to alkyl-substituted aryl carbon), 132.14 (d, vinyl CH), 132.24 (d, aromatic CH adjacent to cyano-substituted aryl carbon), 135.25 (s, vinyl quaternary carbon), 146.13 (s, quaternary aryl carbon, alkyl substituted); ms *m/z*: 53(13), 55(12), 73(21), 89(18), 113(16), 116(29), 140(12), 142(13), 154(19), 155(11), 156(13), 167(25), 182(100), 183(15), 197(30), 214(22). Exact Mass calcd. for $C_{15}H_{19}NO$ (50/50 mixture of **21** and **22**): 229.1467; found: 229.1455.

Acknowledgements

This work was supported financially by the Natural Sciences and Engineering Research Council of Canada. M.S.W. Chan thanks the Izaak Walton Killiam Memorial Foundation for a scholarship. We thank Drs. D.L. Hooper and M. Lumsden at the Atlantic Regional Magnetic Resonance Centre at Dalhousie University for the high-field nmr spectra. We are also grateful to Drs. P.D. Pacey and Y.-R. Luo for helpful discussions regarding the empirically derived heats of formation.

References

1. (*a*) D.R. Arnold and M.S. Snow. Can. J. Chem. **66**, 3012 (1988); (*b*) R.M. Borg, D.R. Arnold, and T.S. Cameron. Can. J. Chem. **62**, 1785 (1984); (*c*) K.A. McManus and D.R. Arnold. Can. J. Chem. **72**, 2291 (1994); (*d*) D.R. Arnold, X. Du, and H.J.P. de Lijser. Can. J. Chem. **73**, 522 (1995); (*e*) D.A. Connor, D.R. Arnold, P.K. Bakshi, and T.S. Cameron. Can. J. Chem. **73**, 762 (1995); (*f*) K.A. McManus and D.R. Arnold. Can. J. Chem. **73**, 2158 (1995); (*g*) D.R. Arnold, D.A. Connor, K.A. McManus, P.K. Bakshi, and T.S. Cameron. Can. J. Chem. **74**, 602 (1996).
2. (*a*) D.R. Arnold, X. Du, and J. Chen. Can. J. Chem. **73**, 307 (1995); (*b*) A.L. Perrott and D.R. Arnold, Can. J. Chem. **70**, 272 (1992); (*c*) H.J.P. de Lijser and D.R. Arnold. J. Phys. Chem. **100**, 3996 (1996).
3. (*a*) W. Markovnikov. Ann. Chem. Pharm. **153**, 256 (1870); (*b*) C.K. Ingold. Structure and mechanism in organic chemistry. Cornell Univ. Press, Ithaca, N.Y. 1953. p. 646.
4. (*a*) M.S. Kharasch and F.R. Mayo. J. Am. Chem. Soc. **55**, 2468 (1933); (*b*) F.R. Mayo and C. Walling. Chem. Rev. **27**, 351 (1940).
5. (*a*) H.J. Lucas and A.Y. Jameson. J. Am. Chem. Soc. **46**, 2475 (1924); (*b*) J. March. Advanced organic chemistry, 4th ed. Wiley–Interscience, Toronto. 1992. pp. 750–753.
6. J.-E. Dubois and J.R. Chretien. J. Am. Chem. Soc. **100**, 3506 (1978).
7. (*a*) J.M. Tedder and J.C. Walton. Tetrahedron, **36**, 701 (1980); (*b*) J.M. Tedder. Angew. Chem. Int. Ed. Engl. **21**, 401 (1982); (*c*) B. Giese. Angew Chem. Int. Ed. Engl. **22**, 753 (1983); (*d*) K.N. Houk, M.N. Paddon-Row, D.C. Spellmeyer, N.G. Rondan, and S. Nagase. J. Org. Chem. **51**, 2874 (1986).
8. (*a*) P.S. Skell and K.J. Shea. *In* Free radicals. Vol. II. *Edited by* J.K. Kochi. Wiley–Interscience, New York. 1973. Chap. 26; (*b*) H.L. Goering, P.I. Abell, and B.F. Aycock. J. Am. Chem. Soc. **74**, 3588 (1952); (*c*) P.J. Krusic and J.K. Kochi. J. Am. Chem. Soc. **93**, 846 (1971).
9. M.J. Frisch, G.W. Trucks, H.B. Schlegel, P.M.W. Gill, B.G. Johnson, M.W. Wong, J.B. Foresman, M.A. Robb, M. Head-Gordon, E.S. Replogle, R. Gomperts, J.L. Andres, K. Raghavachari, J.S. Binkley, C. Gonzales, R.L. Martin, D.J. Fox, D.J. Defrees, J. Baker, J.J.P. Stewart, and J.A. Pople. GAUSSIAN 92/DFT, Revision F.2. Gaussian, Inc., Pittsburgh, Pa. 1993.
10. (*a*) C. Møller and M.S. Plesset. Phys. Rev. **46**, 618 (1934); (*b*) W.J. Hehre, L. Radom, P.v.R. Schelyer, and J.A. Pople. Ab initio molecular orbital theory. Wiley–Interscience, New York. 1987; (*c*) R.S. Mulliken. J. Chem. Phys. **23**, 1983 (1955).
11. (*a*) B.F. Yates, W.J. Bouma, and L. Radom. J. Am. Chem. Soc. **106**, 5805 (1984); (*b*) J.L. Holmes, F.P. Lossing, J.K. Terlouw, and P.C. Burgers. Can. J. Chem. **61**, 2305 (1983); (*c*) K.L. Busch, W.B. Nixon, and M.M. Bursey. J. Am. Chem. Soc. **100**, 1621 (1978); (*d*) B.T. Golding and L. Radom. J. Am. Chem. Soc. **98**, 6331 (1976); (*e*) J. Fossey and J.-Y Nedelec. Tetrahedron, **37**, 2967 (1981); (*f*) H. Zipse. J. Am. Chem. Soc. **117**, 11798 (1995).
12. (*a*) G. Bieri, F. Burger, E. Heilbronner, and J.P. Maier. Helv. Chim. Acta, **60**, 2213 (1977); (*b*) P. Masclet, D. Grosjean, G. Mouvier, and J. Dubois. J. Electron Spectrosc. Relat. Phenom. **2**, 225 (1973); (*c*) M. Beez, G. Bieri, H. Bock, and E. Heilbronner. Helv. Chim. Acta, **56**, 1028 (1973).
13. (*a*) L. Onsager, J. Am. Chem. Soc. **58**, 1486 (1938); (*b*) M.W. Wong, K.B. Wiberg, and M.J. Frisch. J. Am. Chem. Soc. **114**, 523 (1992); (*c*) J. Am. Chem. Soc. **114**, 1645 (1992); (*d*) M.W. Wong, M.J. Frisch, and K.B. Wiberg. J. Am. Chem. Soc. **113**, 4776 (1991); (*e*) M.W. Wong, K.B. Wiberg, and M.J. Frisch. J. Chem. Phys. **95**, 8991 (1991).
14. D.R. Lide (*Editor*). C.R.C handbook of chemistry and physics. 76th ed. (1995–1996). CRC Press, Inc., New York. 1995.
15. (*a*) A.V. Cunliffe and R.K. Harris. Org. Magn. Reson. **6**, 121 (1974); (*b*) H. Guo and M. Karplus. J. Mol. Struct. (Theochem), **260**, 347 (1992); (*c*) N.L. Allinger and J.C. Tai. J. Am. Chem. Soc. **99**, 4256 (1977).

16. (*a*) S.W. Benson. Thermochemical kinetics. 2nd ed. Wiley–Interscience, New York. 1976; (*b*) H.E. O'Neal and S.W. Benson. *In* Free radicals. Vol. II. *Edited by* J.K. Kochi. Wiley–Interscience, New York. 1973. Chap. 17; (*c*) N. Cohen,and S.W. Benson. Chem. Rev. **93**, 2419 (1993); (*d*) T. Ni, R.A. Caldwell, and L.A. Melton. J. Am. Chem. Soc. **111**, 457 (1989).
17. M.J.S. Dewar, E.G. Zoebisch, E.F. Healy, and J.J.P. Stewart. J. Am. Chem. Soc. **107**, 3902 (1985).
18. A. Okamoto, M.S. Snow, and D.R. Arnold. Tetrahedron, **42**, 6175 (1986).

Synthesis of some phosphino- and arsinobenzenechromium tricarbonyl derivatives and metal carbonyl clusters

William R. Cullen, Steven J. Rettig, and Hongli Zhang

Abstract: The synthesis of a number of new phosphino- and arsinobenzenechromium tricarbonyl ligands $ER_2C_6H_5Cr(CO)_3$ (ER_2 = PEt_2, PPr^i_2, PBu^t_2, PPh_2, $AsPh_2$ $AsMe_2$), $ER[C_6H_5Cr(CO)_3]_2$ (ER = PEt, PBu^t, PPh, AsPh) has been achieved by reacting lithium derivatives of benzenechromium tricarbonyl with appropriate chlorophosphines or iodoarsines. The spectroscopic properties of these ligands are described. The structure of $Pr^i_2PC_6H_5Cr(CO)_3$ was determined by an X-ray crystallographic study. This is the first solid state structure to be reported for a phosphinobenzenechromium tricarbonyl derivative. The structures of four metal carbonyl cluster complexes were also determined. Crystals of $Pr^i_2PC_6H_5Cr(CO)_3$ (**3**, $C_{15}H_{19}CrO_3P$) are monoclinic, space group $P2_1/c$, a = 8.150(2) Å, b = 13.490(2) Å, c = 15.125(1) Å, β = 100.19(1)°, Z = 4; those of $Ru_3(CO)_{11}[PPr^i_2C_6H_5Cr(CO)_3]$ (**15**, $C_{26}H_{19}CrO_{14}PRu_3$) are monoclinic, space group $P2_1/n$, a = 8.565(2) Å, b = 21.808(3) Å, c = 17.167(3) Å, β = 97.41(2)°, Z = 4; those of $Ru_3(CO)_{10}[PPh_2C_6H_5Cr(CO)_3]_2$ (**19**, $C_{32}H_{15}CrO_{14}PRu_3$) are orthorhombic, space group $Pbca$, a = 17.367(4) Å, b = 24.471(5) Å, c = 16.096(3) Å, Z = 8; those of $Ru_3(CO)_{10}[PPr^i_2C_6H_5Cr(CO)_3]_2 \cdot CH_2Cl_2$ (**16**, $C_{40}H_{38}Cr_2O_{16}P_2Ru_3 \cdot CH_2Cl_2$) are orthorhombic, space group $P2_12_12$, a = 13.832(3) Å, b = 17.558(2) Å, c = 10.144(1) Å, Z = 2; and those of $Os_3(CO)_9[PEt_2C_6H_5Cr(CO)_3]_3$ (**26**, $C_{48}H_{45}Cr_3O_{18}Os_3P_3$) are trigonal, space group $P\bar{3}$, a = 15.7558(4) Å, c = 12.662(1) Å, Z = 2. The structures were solved by the Patterson method and were refined by full-matrix least-squares procedures to R = 0.031, 0.027, 0.029, 0.025, and 0.029 (R_w = 0.027, 0.024, 0.024, 0.023, and 0.025) for 2326, 4110, 3878, 3046, and 4093 reflections with $I \geq 3\sigma(I)$, respectively.

Key words: metal carbonyl clusters, phosphinobenzenechromium tricarbonyl derivatives, arsinobenzenechromium tricarbonyl derivatives, crystal structures.

Résumé : On a synthétisé un certain nombre de nouveaux ligands, les phospino et arsinobenzène chrome tricarbonyle $ER_2C_6H_5Cr(CO)_3$ (ER_2 = PEt_2, PPr^i_2, PBu^t_2, PPh_2, $AsPh_2$, $AsMe_2$), $Er[C_6H_5Cr(CO)_3]_2$, (ER = PEt, PBu^t, PPh, AsPh) en faisant réagir des dérivés lithiés du benzène chrome tricarbonyle avec les chlorophosphines ou les iodoarsines appropriés. On décrit les propriétés spectroscopiques de ces ligands. On a déterminé, par cristallographie de rayons X, la structure du composé $Pr^i_2PC_6H_5Cr(CO)_3$. Cette publication représente la première étude d'un dérivé phosphinobenzène chrome tricarbonyle dans l'état solide. On a également déterminé la structure des complexes de quatre agrégats de métal tricarbonyle. Les cristaux de $Pr^i_2C_6H_5Cr(CO)_3$ (**3**, $C_{13}H_{19}CrO_3P$) appartiennent au groupe d'espace monoclinique $P2_1/c$, avec a = 8,150(2) Å, b = 13,490(2) Å, c = 15,125(1) Å, β = 100,19(1)°, Z = 4; les cristaux de $Ru_3(CO)_{11}$ $[PPr^i_2C_6H_5Cr(CO)_3]$ (**15**, $C_{26}H_{19}CrO_{14}PRu_3$) appartiennent au groupe d'espace monoclinique $P2_1/n$, avec a = 8,565(2) Å, b = 21,808(3) Å, c = 17,167(3) Å, β = 97,41(2)°, Z = 4; les cristaux de $Ru_3(CO)_{10}[PPh_2C_6H_5Cr(CO)_3]_2$ (**19**, $C_{32}H_{15}CrO_{14}PRu_3$) appartiennent au groupe d'espace orthorhombique $Pbca$, avec a = 17,367(4) Å, b = 24,471(5) Å, c = 16,096(3) Å, Z = 8; les cristaux de $Ru_3(CO)_{10}[PPr^i_2C_6H_5Cr(CO)_3]_2 \cdot C_2Cl_2$ (**16**, $C_{40}H_{38}Cr_2O_{16}P_2Ru_3 \cdot CH_2Cl_2$) appartiennent au groupe d'espace orthorhombique $P2_12_12$, avec a = 13,832(3) Å, b = 17,558(2) Å, c = 19,144(1) Å, Z = 2; et les cristaux de $Os_3(CO)_9[PEt_2C_6H_5Cr(CO)_3]_3$ (**26**, $C_{48}H_{45}Cr_3O_{18}Os_3P_3$) appartiennent au groupe d'espace trigonal $P\bar{3}$, avec a = 15,7558(4) Å, c = 12,662(1) Å, Z = 2. On a résolu les structures par la méthode de Patterson et on les a affinées par la méthode des moindres carrés, matrice complète, jusqu'à des valeurs de R = 0,031, 0,027, 0,029, 0,025 et 0,029 (R_w = 0,027, 0,024, 0,024, 0,023 et 0,025) pour respectivement 2326, 4110, 3878, 3046 et 4093 réflexions avec $I \geq 3\sigma(I)$.

Mots clés : agrégats de métal carbonyle, dérivés phosphinobenzène chrome tricarbonyle, dérivés arsinobenzène chrome tricarbonyle, structures des cristaux.

[Traduit par la rédaction]

Received January 16, 1996.

This paper is dedicated to Professor Howard C. Clark in recognition of his contributions to Canadian chemistry.

W.R. Cullen,[1] S.J. Rettig, and H. Zhang. Department of Chemistry, University of British Columbia, 2036 Main Mall, Vancouver, BC V6T 1Z1, Canada.

[1] Author to whom correspondence may be addressed. Telephone: (604) 822-4435. Fax: (604) 822-2847. E-mail: wrc@chem.ubc.ca

Introduction

The pyrolysis of metal cluster derivatives of arylphosphines and arsines has proved to be a fruitful procedure for the preparation of cluster-bound arynes such as benzyne, ferrocyne, and naphthyne (1–3). We have also described how similar reactions give rise to derivatives of benzynechromium tricarbonyl (4). The present paper is principally concerned with the preparation and characterization of some metal carbonyl derivatives of the type $M_3(CO)_{12-n}(ER_2Ar')_n$ (M = Ru, Os; E = As, P; R = alkyl, aryl; Ar' = $(\eta^6\text{-}C_6H_5)Cr(CO)_3$; n = 1, 2) that have been used as precursors in the synthesis of aryne derivatives. We also describe the preparation of seven new phosphines and arsines containing the $(\eta^6\text{-}C_6H_5)Cr(CO)_3$ moiety.

Experimental

Unless otherwise stated, all reactions and subsequent manipulations involving organometallic reagents were conducted under an argon atmosphere by using standard Schlenk and vacuum line techniques.

Phosphorus trichloride, chlorodiethylphosphine, dichloroethylphosphine, chlorodiphenylphosphine, and dichlorophenylphosphine were purchased from Strem Chemicals Inc. They were stored under argon after distillation under reduced pressure. The purity of all phosphines was ascertained by using $^{31}P\{^1H\}$ NMR spectroscopy. Ruthenium trichloride (kindly loaned by Johnson Matthey Ltd.), *n*-butyllithium (Aldrich), chromium hexacarbonyl (Strem), and osmium carbonyl (Steck) were used as received.

Column chromatography was carried out by using silica gel (230–400 mesh) or neutral alumina (80–200 mesh, Brockman Activity I) obtained from BDH Co.

^1H NMR spectra were recorded on Varian XL-300 (299.94 MHz), Bruker WH-400 or a WH-200FT (400.00 MHz, or 200.00 MHz) spectrometers, and are referenced to $CDCl_3$ or CD_2Cl_2 set at 7.25 ppm, and 5.32 ppm, respectively, at ambient temperature. $^{31}P\{^1H\}$ NMR spectra were recorded on Varian XL-300 (121.42 MHz) or Bruker WH-200 (80.96 MHz) spectrometers and are referenced to external PPh_3 ($CDCl_3$) set at −5.6 ppm relative to 85% H_3PO_4 (aq) unless otherwise indicated. All chemical shifts are reported in ppm and coupling constants in Hz.

Infrared spectra were recorded by using a Perkin–Elmer 598, 783 or 1710 FTIR spectrophotometer. The spectra were calibrated by using the 1601 cm^{-1} band of polystyrene.

Low-resolution electron impact (EI) mass spectra were obtained by using a Kratos/AEI MS902 mass spectrometer, which was operated in the direct insertion mode (70 eV, 120–150°C source temperature). Fast atom bombardment (FAB) mass spectra were measured using an updated MS-9 mass spectrometer equipped with a FAB source. The matrix was 3-nitrobenzyl alcohol.

The following reagents were prepared by literature methods: $C_6H_5Cr(CO)_3$ (5), $Ru_3(CO)_{12}$ (6), $Os_3(CO)_{11}(CH_3CN)$, $Os_3(CO)_{10}(CH_3CN)_2$ (7), $(CH_3)_2AsI$ (8), Bu^t_2PCl (9), $(CH_3CN)_3Cr(CO)_3$ (10), $Ru_3(CO)_{11}(CH_3CN)$ (11), $Na[(C_6H_5)_2CO]$ (~0.025 M in THF) (12).

Scheme 1. Key to compounds.

$R_2EC_6H_5Cr(CO)_3$

R_2E =		
	Ph_2P,	**1**
	Bu^t_2P,	**2**
	Pr^i_2P,	**3**
	Et_2P,	**4**
	Me_2As,	**5**

$RE[C_6H_5Cr(CO)_3]_2$

RE =		
	PhP,	**7**
	Bu^tP,	**8**
	EtP,	**9**
	PhAs,	**10**

$Ru_3(CO)_{11}L$

L =		
	5,	**11**
	3,	**15**
	1,	**19**
	4,	**22**
	7,	**27**
	6,	**29**

$Ru_3(CO)_{10}L_2$

L =		
	5,	**12**
	3,	**16**
	1,	**20**
	4,	**23**

$Os_3(CO)_{11}L$

L =		
	5,	**13**
	3,	**17**
	1,	**21**
	4,	**24**
	7,	**28**

$Os_3(CO)_{10}L_2$

L =		
	5,	**14**
	3,	**18**
	4,	**25**

$Os_3(CO)_9L_3$

L =		
	4,	**26**

Preparation of Bu^tPCl_2

A freshly prepared Grignard solution of Bu^tMgCl (2 M, 250 mL) was added dropwise with stirring to phosphorus trichloride (68.5 g, 44 mL, 0.5 mol) dissolved in diethyl ether (200 mL) at −20°C: the temperature of the reaction mixture was then allowed to rise to room temperature. The mixture was refluxed for 1 h and then filtered to remove the white solid. Distillation of the filtrate under reduced pressure gave Bu^tPCl_2 as a colorless liquid (35 g, 45%), which solidified on standing, bp 143–148°C (760 Torr; 1 Torr = 133.3 Pa). $^{31}P\{^1H\}$ NMR (121.4 MHz, C_6D_6) δ: 199.9 (s). ^1H NMR (300 MHz, C_6D_6) δ: 1.0 (d).

Preparation of Pr^iPCl_2

A Grignard solution of Pr^iMgCl in ether (1.25 M, 800 mL) was added dropwise to a stirred diethyl ether solution of PCl_3 (55.0 g, 26 mL, 0.4 mol). A white precipitate formed during the addition and the reaction mixture was refluxed for an additional 2 h. The solution was separated from the precipitate by filtration through a medium porosity Schlenk filter. The ether solvent was removed by distillation at atmospheric pressure and the oily residue was distilled under reduced pressure. The product was an air-sensitive, colorless liquid (30 g, 65%), bp 27°C (3 mmHg). $^{31}P\{^1H\}$ NMR (121.4 MHz, $CDCl_3$) δ: 139.2 (s). ^1H NMR (300 MHz, $CDCl_3$) δ: 1.80–1.91 (m, 2H), 1.05 (q, 6H).

Preparation of $[C_6H_5Cr(CO)_3]PBu^t_2$, 2

A solution of $C_6H_6Cr(CO)_3$ (1.0 g, 4.7 mmol) in THF (20 mL) in a Schlenk tube was cooled to −78°C and treated dropwise with *n*-BuLi in hexane (3.0 mL, 1.6 M, 4.8 mmol). The resulting solution was stirred at −78°C for 50 min, when Bu^t_2PCl (1.0 mL, 5.2 mmol) was added. The reaction mixture was stirred at −78°C for 1 h, warmed to room temperature, and stirred continuously for an additional hour. After evaporating the solvent in vacuo, the residual oil was dissolved in CH_2Cl_2 (20 mL) and then filtered under nitrogen through a frit packed with Celite to remove LiCl. The solvent was removed in vacuo to afford a red oil. Hexane (5 mL) was added to the red oil, the resultant suspension was stirred vigorously, and a yellow pre-

cipitate was obtained. The solid was further purified by recrystallization from hexane–CH_2Cl_2 (2/1) to yield **2** as a yellow crystalline solid: yield 80%. IR (KBr) ν(CO): 1960 (vs), 1900 (vs), 1880 (s), 1870 (sh), 1865 (s) cm^{-1}. $^{31}P\{^1H\}$ NMR (121.42 MHz, $CDCl_3$) δ: 42.8 (s). ^1H NMR (300 MHz, $CDCl_3$) δ: 5.7 (t, J(H-H) = 6Hz, 2H), 5.6 (t, *J*(H–H) = 6 Hz, 1H), 5.2 (t, *J*(H–H) = 6 Hz, 2H), 1.2 (d, *J*(P–H) = 10 Hz, 18H). MS (EI) *m/e*: 358 [P^+]. Anal. calcd. for $C_{17}H_{23}CrO_3P$: C 56.97, H, 6.47; found: C 56.80, H 6.52.

Preparation of $[C_6H_5Cr(CO)_3]PPr^i_2$, 3

Compound **3** was synthesized by the procedure described for the preparation of **2** except that Pr^i_2PCl (0.75 mL, 5.0 mmol) was used instead of Bu^t_2PCl. Yellow crystals of **3** were obtained after recrystallization from hexanes–CH_2Cl_2 (2:1) at −30°C (1.1 g, 70%). IR (KBr) ν(CO): 1970 (s), 1880 (s, br) cm^{-1}. $^{31}P\{^1H\}$ NMR (121.42 MHz, $CDCl_3$) δ: 13.9 (s). ^1H NMR (300 MHz, $CDCl_3$) δ: 5.33 (t, *J*(H–H) = 5 Hz, 3H), 5.18 (t, *J*(H–H) = 5 Hz, 2H), 1.95 (q, 2H), 1.05 (dd, *J*(H–H) = 5.5 Hz, 12H). MS (EI) *m/e*: 330 [P^+]. Anal. calcd. for $C_{15}H_{19}CrO_3P$: C 54.55, H 5.76; found: C 54.72, H 5.87.

Preparation of $[C_6H_5Cr(CO)_3]PEt_2$, 4

Chlorodiethylphosphine (0.97 mL, 8.0 mmol) was similarly used to afford **4** as a red oil, which was ~90% pure according to its ^{31}P NMR spectrum. ν(CO): 1978 (s), 1885 (s) cm^{-1}. $^{31}P\{^1H\}$ NMR (121.42 MHz, $CDCl_3$) δ: −13 (s). ^1H NMR (300 MHz, $CDCl_3$) δ: 5.4 (t, *J*(H–H) = 6 Hz, 3H), 5.2 (t, *J*(H–H) = 6 Hz, 2H), 1.8 (q, 4H), 1.2 (m, 6H). IR (CH_2Cl_2) MS (EI) *m/e*: 302 [P^+].

Preparation of $[C_6H_5Cr(CO)_3]AsMe_2$, 5

A similar procedure was used to prepare **5** from Me_2AsI as a yellow solid (70% yield). IR (KBr) ν(CO): 1960 (s), 1880 (s, br) cm^{-1}. ^1H NMR (300 MHz, $CDCl_3$) δ: 1.4 (S, 6H), 5.5 (t, *J*(H–H) = 5.5 Hz, 3H), 5.3 (t, *J*(H–H) = 5.5 Hz, 2H). MS (EI) *m/e*: 318 [P^+]. Anal. calcd. for $C_{11}H_{11}AsCrO_3$: C 41.53, H 3.49; found: C 41.63, H 3.49.

Preparation of $[C_6H_5Cr(CO)_3]PPh_2$, 1

A similar procedure was used to prepare **1** from Ph_2PCl as a yellow crystalline solid (85% yield). IR (KBr) ν(CO): 1980 (s), 1900 (s, br) cm^{-1}. $^{31}P\{^1H\}$ NMR (121.42 MHz, $CDCl_3$) δ: −5.2 (s). ^1H NMR (300 MHz, $CDCl_3$) δ: 7.4 (br s, 10H), 5.4 (t, 1H), 5.2 (m, 4H). MS (EI) *m/e*: 398 [P^+].

Preparation of $[C_6H_5Cr(CO)_3]_2AsPh_2$, 6

A similar procedure was used to synthesize **6** from Ph_2AsI as a yellow crystalline solid (80% yield). ^1H NMR (300 MHz, $CDCl_3$) δ: 7.4 (br s, 10H), 5.3 (br s, 1H), 5.2 (br s, 4H). MS (EI) *m/e*: 358 [P^+]. Anal. calcd. for $C_{21}H_{15}O_3AsCr$: C 57.03, H 3.42. Found: C 56.74, H 3.21.

Preparation of $[C_6H_5Cr(CO)_3]_2PBu^t$, 8

Benzenechromium tricarbonyl (1.62 g, 7.55 mmol) was dissolved in THF (25 mL) at −78°C. A solution of *n*-butyllithium in hexane (4.8 mL, 1.6 M, 7.7 mmol) was added slowly with a syringe to the cold, stirred solution. The solution was then stirred at −78°C for 50 min. Cl_2PBu^t (0.65 g, 4 mmol) in THF (10 mL) was then added dropwise with a syringe to the solution. The reaction mixture was stirred at −78°C for an additional hour and allowed to warm to room temperature. The solvent was evaporated in vacuo. The residual red oil was dissolved in CH_2Cl_2 (20 mL) and then filtered through a short column of silica gel under nitrogen. Dark red impurities and LiCl were left on the top of the column. Evaporation of the eluate followed by crystallization of the solid residue from CH_2Cl_2–hexanes (1:2) afforded **8** (70% yield) as a yellow crystalline solid. IR (KBr) ν(CO): 1970 (s), 1890 (s, br) cm^{-1}. $^{31}P\{^1H\}$ NMR (121.42 MHz, $CDCl_3$) δ: 20.7 (s). ^1H NMR (300 MHz, $CDCl_3$) δ: 5.7 (t, *J*(H–H) = 6 Hz, 2H), 5.4 (t, *J*(H–H) = 6 Hz, 4H), 5.2 (d, *J*(H–H) = 6 Hz, 4H). 1.2 (d, *J*(P–H) = 10 Hz, 9H). MS (EI) *m/e*: 514 [P^+]. Anal. calcd. for $C_{22}H_{21}Cr_2O_3P$: C 51.37, H 3.72; found: C 51.27, H 3.71.

Preparation of $[C_6H_5Cr(CO)_3]_2PEt$, 9

The same procedure used for the synthesis of **8** was followed for the preparation of **9** from $EtPCl_2$, as a yellow crystalline solid (65% yield). IR (KBr) ν(CO): 1962 (s), 1851 (s, br) cm^{-1}. $^{31}P\{^1H\}$ NMR (121.42 MHz, $CDCl_3$) δ: −5.5 (s). ^1H NMR (300 MHz, $CDCl_3$) δ: 5.4 (t, *J*(H–H) = 6 Hz, 6H), 5.2 (t, *J*(H–H) = 6 Hz, 4H), 1.8 (q, *J*(H–H) = 6 Hz, 4H), 1.2 (m, 6H). MS (EI) *m/e*: 486 [P^+]. Anal. calcd. for $C_{20}H_{15}O_6Cr_2P$: C 49.39, H 3.12; found: C 49.75 H 3.34.

Preparation of $[C_6H_5Cr(CO)_3]PPh$, 7

The same procedure was followed for the preparation of **7** from $PhPCl_2$ as a yellow crystalline solid (70% yield). IR (Nujol) νCO): 1970 (s), 1900 (s, br), cm^{-1}. $^{31}P\{^1H\}$ NMR (121.42 MHz, $CDCl_3$) δ: −4.0 (s). ^1H NMR (300 MHz, $CDCl_3$) δ: 7.3–7.6 (m, 5H), 5.6 (t, *J*(H–H) = 6 Hz, 4H), 5.3 (t, *J*(H–H) = 6 Hz, 2H), 5.2 (d, *J*(H–H) = 6 Hz, 4H). MS (EI) *m/e*: 534 [P^+]. Anal. calcd. for $C_{24}H_{15}CrO_6P$: C 53.94, H 2.83; found: C, 53.60, H 2.85.

Preparation of $[C_6H_5(CO)_3]AsPh_2$, 10

The same procedure was followed for the preparation of **10** from $PhAsI_2$ as a yellow solid (70% yield). MS (EI) *m/e*: 578 [P^+]. ^1H NMR (300 MHz, $CDCl_3$) δ: 7.4 (br s, 5H), 5.5 (t, 4H), 5.3 (t, 2H), 5.15 (s, 4H). Anal. calcd. for $C_{24}H_{15}CrO_6As$: C 49.84, H 2.62; found: C 49.50, H 2.43.

Procedure A. Preparation of $Ru_3(CO)_{11}][AsMe_2(C_6H_5Cr(CO)_3)]$, 11

A freshly prepared $Na(Ph_2CO)$ solution was added dropwise to a rapidly stirred solution of $Ru_3(CO)_{12}$ (200 mg, 0.31 mmol) and $(CH_3)_2As[C_6H_5Cr(CO)_3]$ (100 mg, 0.31 mmol) in THF (25 mL) until the solution darkened in color (typically 5–10 drops). When TLC examination of the reaction mixture showed that no starting material remained, the solvent was removed *in vacuo*. The resulting dark red oil was dissolved in CH_2Cl_2 (3 mL) and was chromatographed on a silica gel column with CH_2Cl_2–hexanes (1:1.4) as eluent to give three bands. Band 1 (yellow) was $Ru_3(CO)_{12}$ (trace amount) identified by IR spectroscopy and TLC. Band 3 was the disubstituted ruthenium cluster $Ru_3(CO)_{10}[AsMe_2(C_6H_5Cr(CO)_3)]_2$ **8** (trace amount). Band 2 gave red crystalline **11** (245 mg, 85% yield). IR (KBr) ν(CO): 2100 (m), 2040 (s), 2020 (s), 1890 (sh), 1900 (s) cm^{-1}. ^1H NMR (300 MHz, $CDCl_3$) δ: 1.9 (s, 6H), 5.3 (t, *J*(H–H) = 6.6 Hz, 2H), 5.4 (d, *J*(H–H) = 6 Hz, 2H), 5.6 (t, *J*(H–H) = 6.6 Hz, 1H). Mass spectrum (FAB): *m/e*: 931 [P^+]. Anal. calcd. for $C_{22}H_{11}AsCrO_{14}Ru_3$: C 28.43, H 1.20; found: C 28.14, H 1.23.

Procedure B. Preparation of $Ru_3(CO)_{10}[AsMe_2(C_6H_5Cr\text{-}(CO)_3)]_2$, 12

The title compound was prepared in a way similar to that used for the monosubstituted compound **11** except that a little over 2 equivalents of the arsine (210 mg, 0.62 mmol) was used. The product was purified by using column chromatography with CH_2Cl_2–hexanes (1:1) as eluent and was isolated in 70% yield. ^1H NMR (300 MHz, $CDCl_3$) δ: 5.5 (t, J(H–H) = 6 Hz, 2H), 5.4 (d, J(H–H) = 6.3 Hz, 4H), 5.2 (m, 4H), 1.8 (s, 12H). Mass spectrum (FAB): *m/e*: 1223 [P^+]. Anal. calcd. for $C_{32}H_{22}As_2Cr_2ORu_3$: C 31.51, H 1.82; found: C 31.29, H 1.93.

Procedure C. Preparation of $Os_3(CO)_{11}[AsMe_2(C_6H_5Cr(CO)_3)]$, 13

The compound $[Os_3(CO)_{11}(MeCN)]$ (200 mg, 0.22 mmol) was stirred in CH_2Cl_2 (30 mL) with $Me_2AsC_6H_5Cr(CO)_3$ (70 mg, 0.22 mmol) for 2 h at room temperature to afford a clear yellow solution. Silica gel (200–400 mesh, 5 mL) was then added to the crude solution and the solvent was removed *in vacuo*. The dried residual silica gel was added to the top of a silica gel column. By using CH_2Cl_2–hexanes (1:1:8) as eluent, the pure yellow **13** was obtained in 90% yield (235 mg) from the first band. ^1H NMR (300 MHz, $CDCl_3$) δ: 5.5 (t, 1H), 5.4 (d, 2H), 5.2 (t, 2H), 2.0 (s, 6H). Mass spectrum (FAB) *m/e*: 1198 [P^+]. Anal. calcd. for $C_{22}H_{11}AsCrO_{14}Os_3$: C 22.08, H 0.93; found: C 22.16, H 0.98. The second band that was eluted gave a small amount of the disubstituted cluster derivative identified by using mass spectrometry.

Procedure D. Preparation of $Os_3(CO)_{10}[AsMe_2C_6H_5Cr(CO)_3]_2$, 14

The procedure used for the preparation of **14** was identical to that used for **13** with the exception that $[Os_3(CO)_{10}(MeCN)_2]$ (100 mg, 0.1 mmol) was used. Pure **14** was thus obtained in 70% yield. ^1H NMR (300 MHz, $CDCl_3$) δ: 5.5 (t, 4H), 5.2 (t, 6H), 1.9 (s, 12H).Mass spectrum (FAB) *m/e*: 1487 [P^+]. Anal. calcd. for $C_{32}H_{22}As_2Cr_2O_{16}Os_3$: C 25.85, H 1.49; found: C 25.71, H 1.57.

Procedure E. Preparation of $Ru_3(CO)_{11}[PPr^i2C_6H_5Cr(CO)_3]$, 15

Addition of PPN^+Cl^- (10 mg) to a solution of $Ru_3(CO)_{12}$ (200 mg, 0.31 mmol) and $Pr^i{}_2PC_6H_5(CO)_3$ (103 mg, 0.31 mmol) in THF (40 mL) resulted in gas evolution. After stirring for 30 min, the solvent was removed from the red solution under reduced pressure. The residue was dissolved in CH_2Cl_2 (2 mL) and applied to a silica gel column, with CH_2Cl_2–hexanes (1:1.7) as eluent. The first band proved to contain $Ru_3(CO)_{12}$ and the third band was characterized as $Ru_3(CO)_{10}[PPr^i{}_2C_6H_5(CO)_3]_2$. The major second band afforded **15** as a red powder in 80% yield after solvent evaporation. Crystals of **15** were grown from CH_2Cl_2–hexanes (1:2.5) at −30°C. The crystals thus obtained were washed with hexanes and dried in vacuo for 1 min. IR (CH_2Cl_2) ν(CO): 2100 (s), 2049 (vs), 2017 (vs), 1978 (vs), 1907 (vs) cm^{-1}. 942 [P^+]. $^{31}P\{^1H\}$ NMR (121.4 MHz, $CDCl_3$) δ: 58.9 (s). ^1H NMR (300 MHz, $CDCl_3$) δ: 5.7 (t, J(H–H) = 6.2 Hz, 3H), 5.2 (t, J(H–H) = 6.3 Hz, 2H), 2.5 (m, 2H), 1.2–1.4 (m, 12H). Mass spectrum (FAB) *m/e*: Anal. calcd. for $C_{26}H_{19}CrO_{14}PRu_3$: C 33.16, H 2.03; found: C 32.84, H 1.90.

Procedure F. Preparation of $Ru_3(CO)_{10}[Pr^i{}_2PC_6H_5Cr(CO)_3]_2$, 16

The title complex was prepared in the same manner as described for the preparation of the monosubstituted cluster **15** except that a little over 2 molar equivalents of $Pr^i{}_2PC_6H_5Cr(CO)_3$ (215 mg, 0.65 mmol) was used. Following chromatography with CH_2Cl_2–hexanes (1:1.3) as eluent, pure **16** was obtained in 70% yield as a dark red powder. X-ray-quality crystals were grown from CH_2Cl_2–hexanes (1:2.5) at −4°C. IR (KBr) ν(CO): 2022 (s), 1973 (vs), 1903 (vs) cm^{-1}. $^{31}P\{^1H\}$ NMR (121.4 MHz, $CDCl_3$) δ: 54.6 (s). ^1H NMR (300 MHz, $CDCl_3$) δ: 5.75 (t, 6H), 5.2 (t, J(H–H) = 6.3 Hz, 4H), 2.5 (m, J(H–H) = 6.1 Hz, 4H), 1.2–1.4 (m, 24H). Mass spectrum (FAB) *m/e*: 1244 [P^+]. Anal. calcd. for $C_{41}H_{40}Cl_2Cr_2O_{16}P_2Ru_3$: C 37.06, H 3.04. found: C 37.03, H 2.97.

Preparation of $Os_3(CO)_{11}[Pr^i{}_2PC_6H_5Cr(CO)_3]$, 17

The yellow complex **17** was obtained in 80% yield by using procedure **C**. IR (KBr) ν(CO): 2100 (w), 2050 (s), 2030-2000 (vs, br), 1990-1960 (vs, br), 1940 (w), 1910 (s), 1890 (s) cm^{-1}. $^{31}P\{^1H\}$ NMR (121.4 MHz, $CDCl_3$) δ: 27.8 (s). ^1H NMR (300 MHz, $CDCl_3$) δ: 5.7 (t, 3H), 5.2 (t, 2H), 2.5 (m, 2H), 1.2-1.4 (m, 12H). Mass spectrum (FAB) *m/e*: 1209 [P^+]. Anal. calcd. for $C_{26}H_{19}CrO_{14}Os_3P$: C 25.83, H 1.59; found: C 25.89, H 1.59.

Preparation of $Os_3(CO)_{10}[Pr^i{}_2PC_6H_5Cr(CO_3]_2$, 18

The yellow complex **18** was isolated in 80% yield by using procedure **D**. IR (KBr) ν(CO): 2080 (m), 2010 (sh), 2000 (vs), 1970 (vs), 1900 (s, br) cm^{-1}. $^{31}P\{^1H\}$ NMR (121.4 MHz, $CDCl_3$) δ: 21.7 (s). ^1H NMR (300 MHz, $CDCl_3$) δ: 5.7 (t, 6H), 5.2 (t, 4H), 2.4 (m, 4H), 1.1–1.4 (m, 24H). Mass spectrum (FAB) *m/e*: 1513 [P^+]. Anal. calcd. for $C_{40}H_{38}Cr_2O_{16}Os_3P_2$: C 31.79, H 2.54; found: C 31.63, H 2.50.

Preparation of $Ru_3(CO)_{11}[Ph_2PC_6H_5Cr(CO)_3]$, 19

The complex **19** was isolated, by following procedure **A**, as a red powder (~70% yield). This powder was dissolved in CH_2Cl_2 (10 mL), layered with hexanes (20 mL), and stored in a freezer for a week to give red-orange prism-like crystals. IR (Nujol) ν(CO): 2100 (s), 2060 (sh), 2040 (s), 2020 (vs), 2000 (vs), 1970 (vs), 1960 (sh), 1900 (s) cm^{-1}. $^{31}P\{^1H\}$ NMR (121.4 MHz, $CDCl_3$) δ: 37.3 (s). ^1H NMR (300 MHz, $CDCl_3$) δ: 7.4–7.6 (br s, 10H), 5.6 (t, J(H–H) = 6 Hz, 3H), 5.1 (t, J(H–H) = 6 Hz, 2H). Mass spectrum (FAB) *m/e*: 1011 [P^+]. Anal. calcd. for $C_{32}H_{15}CrO_{14}PRu_3$: C 38.07, H 1.50; found: C 38.21, H 1.55.

$Ru_3(CO)_{10}[Ph_2PC_6H_5Cr(CO)_3]_2$, 20

Compound **20** was isolated in 60% yield by following procedure **B**. $^{31}P\{^1H\}$ NMR (121.4 MHz, $CDCl_3$) δ: 36.5 (s). ^1H NMR (300 MHz, $CDCl_3$) δ: 7.4–7.6 (br s, 5H), 5.5 (t, 6H), 5.1 (t, 4H). Mass spectrum (FAB) *m/e*: 1381 [P^+]. Anal. calcd. for $C_{52}H_{30}Cr_2O_{16}P_2Ru_3$: C 45.26, H 2.20; found: C 45.39, H 2.28.

Preparation of $Os_3(CO)_{11}[Ph_2PC_6H_5Cr(CO)_3]$, 21

Solid **21** was obtained in 80% yield by following procedure **C**. IR (KBr): ν(CO) 2150 (s), 2060 (vs), 2020 (vs), 2000 (vs), 1970 (vs), 1900 (vs) cm^{-1}. $^{31}P\{^1H\}$ NMR (121.4 MHz, CD_2Cl_2) δ: 0.3 (s). ^1H NMR (300 MHz, CD_2Cl_2) δ: 7.5 (m, 10H), 5.8 (td, J(H–H) = 5.8 Hz, 1H), 5.6 (td, J(H–H) = 5.7 Hz,

2H), 5.2 (td, J(H–H) = 5.8 Hz, 2H). Mass spectrum (FAB) *m/e*: 1277 [P^+]. Anal. calcd. for $C_{32}H_{15}CrO_{14}Os_3P$: C 30.07, H 1.19; found: C 30.15, H 1.23.

Preparation of $Ru_3(CO)_{11}[Et_2PC_6H_5Cr(CO)_3]$, 22

Compound **22** was obtained in 85% yield by using procedure **A**. $^{31}P\{^1H\}$ NMR (121.4 MHz, $CDCl_3$) δ: 28.2 (s). IR (KBr): 2100 (s), 2040 (s), 2020 (s), 1980 (vs), 1970 (vs), 1950 (s), 1900 (s), 1870 (s) cm^{-1}. ^1H NMR (300 MHz, $CDCl_3$) δ: 5.5 (td, J(H–H) = 7 Hz, 1H), 5.3 (td, J(H–H) = 7 Hz, 2H), 5.2 (2dd, J(H–H) = 7 Hz, 2H), 2.0–2.4 (m, 4H), 1.2–1.4 (2t, J(H–H) = 7 Hz, 6H). Mass spectrum (FAB) *m/e*: 915 [P^+]. Anal. calcd. for $C_{24}H_{15}CrO_{14}PRu_3$: C 31.55, H 1.66; found: C 31.47, H 1.66.

Preparation of $Ru_3(CO)_{10}[Et_2PC_6H_5Cr(CO)_3]_2$, 23

The dark red product **23** was isolated in 75% yield by using procedure **B**. IR (KBr) ν(CO): 2070 (w), 2020 (s), 2000–1910 (s, br), 1910–1880 (s, br), cm^{-1}. $^{31}P\{^1H\}$ NMR (121.4 MHz, $CDCl_3$) δ: 28.4 (s). ^1H NMR (300 MHz, $CDCl_3$) δ: 5.6 (t, J(H–H) = 7 Hz, 1H), 5.4 (t, J(H–H) = 7 Hz, 2H), 5.2 (d, J(H–H) = 7 Hz, 2H), 2.0–2.4 (m, 8H), 1.2–1.5 (2t, J(H–H) = 7 Hz, 12H). Mass spectrum (FAB) *m/e*: 1189 [P^+]. Anal. calcd. for $C_{38}H_{32}Cl_2Cr_2O_{16}P_2Ru_3$: C 34.91, H 2.54; found: C 34.74, H 2.59.

Preparation of $Os_3(CO)_{11}[Et_2PC_6H_5Cr(CO)_3]$, 24

The yellow product **24** was obtained in 80% yield by following procedure **E**.IR (KBr) ν(CO): 2100 (m), 2060 (s), 2030 (s), 2000 (vs), 1980 (sh), 1970 (vs), 1910 (s), 1900 (sh), 1880 (s), 1870 (sh), cm^{-1}. $^{31}P\{^1H\}$ NMR (121.4 MHz, $CDCl_3$) δ: −9.1 (s). ^1H NMR (300 MHz, $CDCl_3$) δ: 5.5 (t, J(H–H) = 7 Hz, 1H), 5.4 (t, J(H–H) = 7 Hz, 2H), 5.2 (d, J(H–H) = 7 Hz, 2H), 2.2–2.4 (m, 4H), 1.2–1.4 (t, J(H–H) = 7 Hz, 6H). Mass spectrum (FAB) *m/e*: 1182 [P^+]. Anal. calcd. for $C_{24}H_{15}CrO_{14}Os_3P$: C 24.40, H, 1.28; found: C 24.56, H 1.31.

Preparation of $Os_3(CO)_{10}[Et_2PC_6H_5Cr(CO)_3]_2$, 25

The use of procedure **D** afforded **25** in 70% yield. IR (KBr) ν(CO): 2075 (m), 2010 (sh), 1980 (vs, br), 1890 (s, br) cm^{-1}. $^{31}P\{^1H\}$ NMR (121.4 MHz, $CDCl_3$) δ: −9.8 (s). ^1H NMR (300 MHz, $CDCl_3$) δ: 5.5 (t, J(H–H) = 7 Hz, 1H), 5.3 (t, J(H–H) = 7 Hz, 2H), 5.2 (d, J(H–H) = 7 Hz, 2H), 2.2–2.6 (m, 4H), 1.2–1.5 (2t, J(H–H) = 7 Hz, 6H). Mass spectrum (FAB) *m/e*: 1456 [P^+]. Anal. calcd. for $C_{36}H_{30}Cr_2O_{16}Os_3P_2$: C 29.71, H 2.08. found: C 29.96, H 2.14.

Preparation of $Os_3(CO)_9[Et_2PC_6H_5Cr(CO)_3]_3$, 26

A solution of $Os_3(CO)_{11}[Et_2PC_6H_5Cr(CO)_3]$ (300 mg) was heated in refluxing n-octane under a nitrogen atmosphere for 15 h. After this time TLC showed that no starting material was present. The solvent was then removed under reduced pressure and the resulting brown oil was transferred to a silica gel column. Elution with hexane gave one yellow band, which was $Os_3(CO)_{12}$, as identified by IR spectroscopy. Subsequent elution with hexanes–CH_2Cl_2 (1:1.7) afforded three bands. Bands 1 and 3 contained trace amounts of unidentified products. The major band 2 contained the complex **26**. Orange crystals suitable for X-ray structure analysis were grown from hexanes–CH_2Cl_2 (3:1) at −30°C. IR (KBr) ν(CO): 1965 (vs, br), 1930 (s), 1890 (vs, Br) cm^{-1}. $^{31}P\{^1H\}$ NMR (121.4 MHz, $CDCl_3$) δ: −15.9 (s). ^1H NMR (300 MHz, $CDCl_3$) δ: 5.6 (t, J(H–H) = 7 Hz, 3H), 5.4 (t, J(H–H) = 7 Hz, 6H), 5.2 (d, J(H–H) = 7 Hz, 6H), 2.0–2.5 (m, 12H), 1.2–1.4 (m, 18H). Mass spectrum (FAB) *m/e*: 1729 [P^+]. Anal. calcd. for $C_{48}H_{45}Cr_3Os_3P_3$: C 33.33, H 2.63; found: C 32.93, H 2.62.

Preparation of $Ru_3(CO)_{11}[PhP\{C_6H_5Cr(CO)_3\}_2]$, 27

The title compound was prepared by three different methods but always in low yield. Method **A** resulted in 25% yield and method **E** in 15% yield. An excess of $PhP[C_6H_5Cr(CO)_3]_2$ (200 mg) was added to a cool solution of $Ru_3(CO)_{11}(MeCN)$ (100 mg, 0.15 mmol, 20 mL of CH_2Cl_2) generated in situ. The resulting solution was stirred for 1 h and the solvent was removed *in vacuo*. The ^{31}P NMR spectrum of the crude product indicated the presence of **27** in low yield.

27: yellow solid. IR (CH_2Cl_2) ν(CO): 2100 (s), 2050 (s), 2040 (s), 1970 (s), 1900 (s) cm^{-1}. $^{31}P\{^1H\}$ NMR (121.4 MHz, $CDCl_3$) δ: 37.6 (s). ^1H NMR (300 MHz, $CDCl_3$) δ: 7.4–7.6 (m, 5H), 5.8 (m, 6H), 5.3 (m, 4H). Mass spectrum (FAB) *m/e*: 1147 [P^+]. Anal. calcd. for $C_{35}H_{15}Cr_2O_{17}PRu_3$: C 36.69, H 1.32; found: C 36.65, H 1.40.

Preparation of $Os_3(CO)_{11}[PhP\{C_6H_5Cr(CO)_3\}_2]$, 28

The yellow solid **28** was isolated in 50% yield by using procedure **C**. $^{31}P\{^1H\}$ NMR (121.4 MHz, $CDCl_3$) δ: 0.1 (s). ^1H NMR (300 MHz, $CDCl_3$) δ: 7.6 (m, 2H), 7.4 (m, 3H), 5. 7 (t, 6H), 5.4 (q, 4H). Mass spectrum (FAB) *m/e*: 1415 [P^+]. Anal. calcd. for $C_{35}H_{15}Cr_2O_{17}Os_3P$: C 29.75, H, 1.07; found: C 29.50, H 1.31.

Preparation of $Ru_3(CO)_{11}[Ph_2AsC_6H_5Cr(CO)_3]$, 29

The red product **29** was obtained in 10% yield by following procedure **A**. $^{31}P\{^1H\}$ NMR (121.4 MHz, $CDCl_3$) δ: 7.3 (m, 10H), 5.3 (t, 2H), 5.1 (3H). Mass spectrum (FAB) *m/e*: 1054 [P^+]. Anal. calcd. for $C_{32}H_{15}AsCrO_{14}Ru_3$: C 36.48, H 1.44; found: C 36.64, H 1.56.

X-ray crystallographic analyses

Crystallographic data appear in Table 1. The final unit-cell parameters were obtained by least-squares on the setting angles for 25 reflections with 2θ = 27.8–33.1° for **3**, 35.7–40.1° for **15**, 20.1–30.7° for **19**, 30.1°–36.8° for **16**, and 40.1°–45.5° for **26**. The intensities of three standard reflections, measured every 200 reflections throughout the data collections, decayed linearly by 7.8% for **15** and by 2.1% for **19** and showed only small random fluctuations for other complexes. The data were processed and corrected for Lorentz and polarization effects, decay (where appropriate), and absorption (empirical, based on azimuthal scans for three reflections).[2]

The structures were solved by the Patterson method. The structural analysis of **26** was initiated in the centrosymmetric space group $P\bar{3}$ on the basis of the E-statistics and the Patterson function. This choice was confirmed by subsequent calculations. Complex **16** has exact (crystallographic) C_2 symmetry and complex **26** has exact C_3 symmetry.

The dichloromethane solvent in **16** was modeled as 1:1 disordered over two sites, both carbon atoms lying on the twofold

[2] *teXsan*: Crystal structure analysis package. Molecular Sturcture Corp., The Woodlands, Tex. 1985 and 1992.

Table 1. Crystallographic data.[a]

Compound	**3**	**15**	**19**	**16**	**26**
Formula	$C_{15}H_{19}CrO_3P$	$C_{26}H_{19}CrO_{14}PRu_3$	$C_{32}H_{15}CrO_{14}PRu_3$	$C_{40}H_{38}Cr_2O_{16}P_2Ru_3 \cdot CH_2Cl_2$	$C_{48}H_{45}Cr_3O_{13}Os_3P_3$
Fw	330.28	941.61	1009.64	1328.81	1729.38
Color, habit	Yellow, prism	Golden, prism	Red-orange, prism	Black, prism	Red-brown, prism
Crystal system	Monoclinic	Monoclinic	Orthorhombic	Orthorhombic	Trigonal
Space group	$P2_1/c$	$P2_1/n$	$Pbca$	$P2_12_12$	$P\bar{3}$
a, Å	8.150(2)	8.565(2)	17.367(4)	13.832(3)	15.7758(4)
b, Å	13.490(2)	21.808(3)	24.471(5)	17.558(2)	15.7758(4)
c, Å	15.125(1)	17.167(3)	16.096(3)	10.144(1)	12.662(1)
α, deg	90	90	90	90	90
β, deg	100.19(1)	97.41(2)	90	90	90
γ, deg	90	90	90	90	120
V, Å^3	1636.8(4)	3179.5(10)	6840(2)	2463.7(7)	2722.2(3)
Z	4	4	8	2	2
ρ_{calc}, g/cm^3	1.340	1.967	1.960	1.791	2.110
$F(000)$	688	1832	3920	1316	1644
μ(Mo-K_α), cm^{-1}	8.00	18.10	16.89	15.65	77.00
Crystal size, mm	0.40 × 0.40 × 0.50	0.18 × 0.30 × 0.40	0.25 × 0.35 × 0.45	0.16 × 0.25 × 0.39	0.20 × 0.25 × 0.40
Transmission factors	0.84–1.00	0.84–1.00	0.89–1.00	0.88–1.00	0.54–1.00
Scan type	ω–2θ	ω–2θ	ω	ω–2θ	ω–2θ
Scan range, ω°	1.10 + 0.35 tan θ	1.30 + 0.35 tan θ	0.94 + 0.35 tan θ	1.26 + 0.35 tan θ	1.42 + 0.35 tan θ
Scan, ° min^{-1}	32	16	16	16	32
Data collected	$+h, +k, \pm l$	$+h, +k, \pm l$	$+h, +k, +l$	$+h, +k, +l$	$\pm h, +k, +l$
$2\theta_{max}$, deg	55	55	55	60	70
Crystal, decay, %	7.8	2.1	Negligible	Negligible	
Total reflections	4195	7987	8579	4035	8652
Unique reflections	3929	7492	8579	4035	8006
R_{merge}	0.020	0.029	—	—	0.044
Number with $I \geq 3\sigma(I)$	2326	4410	3878	3046	4093
Variables	182	406	460	307	227
R	0.031	0.027	0.029	0.025	0.029
R_w	0.027	0.024	0.024	0.023	0.025
gof	2.25	1.67	1.41	1.68	1.35
Max Δ/σ (final cycle)	0.001	0.001	0.003	0.01	0.001
Residual density e/Å^3	−0.21 to 0.23	−0.38 to 0.38	−0.44 to 0.42	−0.45 to 0.41	−1.36 to 1.28 (near Os)

[a]Temperature 294 K, Rigaku AFC6S diffractometr, MoK_α (λ = 0.71069 Å) radiation, graphite monochromator, takeoff angle 6.0°, aperture 6.0 × 6.0 mm at a distance of 285 mm from the crystal, stationary background counts at each end of the scan (scan/background time ratio 2:1), $\sigma U2.(F^2) = [S^2(C + 4B)]/Lp^2$ (S = scan rate, C = scan rate, C = scan count, B = normalized background count), function minimized $\Sigma w(|F_o| - |F_c|)^2$ where $w = 4F_o^2/\sigma^2(F_o^2)$, $R = \Sigma||F_o| - |F_c||/\Sigma|F_o|$, $R_w = (\Sigma w(|F_o| - |F_c|)^2/\Sigma w|F_o|^2)^{1/2}$, and gof = $[\Sigma w(|F_o| - |F_c|)^2/(m - n)]^{1/2}$. Values given for R, R_w, and gof are based on those reflections with $I \geq 3\sigma(I)$.

axis. All non-hydrogen atoms were refined with anisotropic thermal parameters. Hydrogen atoms were fixed in calculated positions (C—H = 0.98 Å, $B_H = 1.2\ B_{bonded\ atom}$). Secondary extinction corrections were applied for **3** and **26**, the final values of the extinction coefficients being $1.13(3) \times 10^{-6}$ and $3.9(2) \times 10^{-7}$, respectively. Neutral atom scattering factors for all atoms and anomalous dispersion corrections for the non-hydrogen atoms were taken from the *International Tables for X-Ray Crystallography* (13). A parallel refinement of the mirror image of **16** gave significantly higher residuals, the R and R_w ratios being 1.083 and 1.100, respectively. Final atomic coordinates and equivalent isotropic thermal parameters, selected bond lengths, and selected bond angles appear in Tables 2–4, respectively. Hydrogen atom parameters, anisotropic thermal parameters, bond lengths, bond angles, torsion angles, intermolecular contacts, and least-squares planes are included as supplementary material.[3]

Results and Discussion

Two different strategies were utilized previously to prepare

[3] Copies of material on deposit may be purchased from: The Depository of Unpublished Data, Document Delivery, CISTI, National Research Council Canada, Ottawa, Canada K1A 0S2. Tables of hydrogen atom coordinates and bond lengths and angles involving hydrogen atoms have also been deposited with the Cambridge Crystallograhic Data Centre and can be obtained on request from The Director, Cambridge Crystallographic Data Centre, University Chemical Laboratory, 12 Union Road, Cambridge CB2 1EZ, UK.

Table 2. Final atomic coordinates and B_{eq} (Å^2).[a]

Atom	x	y	z	B_{eq}
3				
Cr(1)	0.47528(5)	0.16413(3)	0.12765(3)	3.656(9)
P(1)	0.76735(9)	0.36299(5)	0.22499(5)	4.19(2)
O(1)	0.1355(3)	0.0742(2)	0.1022(2)	8.49(8)
O(2)	0.4576(3)	0.1604(2)	−0.0705(1)	7.20(7)
O(3)	0.3048(3)	0.3606(2)	0.1004(2)	8.29(8)
C(1)	0.2675(4)	0.1075(2)	0.1126(2)	5.40(8)
C(2)	0.4637(3)	0.1607(2)	0.0065(2)	4.56(7)
C(3)	0.3710(4)	0.2850(2)	0.1128(2)	5.25(8)
C(4)	0.7011(3)	0.2328(2)	0.2097(2)	3.68(6)
C(5)	0.7506(3)	0.1647(2)	0.1493(2)	3.98(6)
C(6)	0.6944(3)	0.0654(2)	0.1457(2)	4.63(7)
C(7)	0.5893(4)	0.0330(2)	0.2030(2)	5.03(7)
C(8(	0.5387(4)	0.0998(2)	0.2638(2)	4.90(8)
C(9)	0.5927(3)	0.1977(2)	0.2666(2)	4.46(7)
C(10)	0.8522(3)	0.3950(2)	0.1231(2)	4.73(7)
C(11)	0.7138(4)	0.4044(2)	0.0413(2)	6.20(9)
C(12)	0.9466(4)	0.4939(2)	0.1398(2)	7.1(1)
C(13)	0.9581(4)	0.3441(2)	0.3116(2)	5.54(8)
C(14)	0.9106(5)	0.3100(3)	0.4000(2)	8.4(1)
C(15)	1.0892(4)	0.2768(3)	0.2851(2)	7.4(1)
15				
Ru(1)	0.26285(4)	0.14078(2)	0.25719(2)	2.724(7)
Ru(2)	0.00277(4)	0.05429(2)	0.21906(2)	2.878(7)
Ru(3)	0.27305(4)	0.04980(2)	0.13654(2)	3.212(8)
Cr(1)	0.19885(9)	0.13304(3)	0.55400(4)	3.64(2)
P(1)	0.2265(1)	0.21630(5)	0.35364(6)	2.98(2)
O(1)	0.5887(4)	0.1710(2)	0.2216(2)	5.27(10)
O(2)	0.4018(4)	0.0553(2)	0.3903(2)	4.89(9)
O(3)	0.1380(4)	0.2368(2)	0.1352(2)	5.8(1)
O(4)	0.1494(4)	−0.0580(2)	0.0350(2)	5.9(1)
O(5)	0.5758(5)	0.0710(2)	0.0657(3)	9.4(2)
O(6)	0.4497(5)	−0.0354(2)	0.2599(2)	8.2(1)
O(7)	0.1279(5)	0.1411(2)	0.0116(2)	5.9(1)
O(8)	−0.1799(5)	−0.0426(2)	0.1158(2)	6.0(1)
O(9)	−0.2494(4)	0.0740(2)	0.3250(2)	6.0(1)
O(10)	0.1477(5)	−0.0424(2)	0.3362(2)	7.2(1)
O(11)	−0.1429(4)	0.1556(2)	0.1103(2)	5.34(10)
O(12)	0.5510(5)	0.1270(2)	0.5793(3)	9.0(2)
O(13)	0.2065(6)	−0.0008(2)	0.5185(3)	8.3(1)
O(14)	0.2194(5)	0.0989(2)	0.7237(2)	7.0(1)
C(1)	0.4659(5)	0.1601(2)	0.2374(2)	3.6(1)
C(2)	0.3427(5)	0.0844(2)	0.3402(2)	3.2(1)
C(3)	0.1776(5)	0.1986(2)	0.1788(3)	3.7(1)
C(4)	0.1952(5)	−0.0183(2)	0.0737(3)	4.0(1)
C(5)	0.4663(6)	0.0637(3)	0.0946(3)	5.3(1)
C(6)	0.3803(5)	−0.0025(3)	0.2181(3)	5.3(1)
C(7)	0.1742(5)	0.1088(2)	0.0609(3)	4.1(1)
C(8)	−0.1091(5)	−0.0075(2)	0.1541(3)	3.8(1)
C(9)	−0.1531(5)	0.0681(2)	0.2865(3)	3.9(1)
C(10)	0.1033(5)	−0.0054(2)	0.2935(3)	4.4(1)
C(11)	−0.0790(5)	0.1198(2)	0.1510(3)	3.6(1)
C(12)	0.4160(7)	0.1304(3)	0.5678(3)	5.4(1)
C(13)	0.2032(7)	0.0504(3)	0.5301(3)	5.1(1)
C(14)	0.2129(6)	0.1109(2)	0.6580(3)	4.8(1)
C(15)	0.1565(5)	0.1945(2)	0.4463(2)	3.11(10)
C(16)	0.0389(5)	0.1488(2)	0.4444(2)	3.5(1)
C(17)	−0.0519(5)	0.1413(2)	0.5062(3)	4.3(1)
C(18)	−0.0232(6)	0.1786(2)	0.5720(3)	4.8(1)
C(19)	0.0984(6)	0.2224(2)	0.5774(3)	4.9(1)
C(20)	0.1891(6)	0.2290(2)	0.5164(3)	4.0(1)
C(21)	0.4053(5)	0.2631(2)	0.3845(3)	4.0(1)
C(22)	0.0755(5)	0.2755(2)	0.3206(3)	3.8(1)
C(23)	0.5425(5)	0.2239(2)	0.4187(3)	4.5(1)
C(24)	0.4469(6)	0.3033(2)	0.3169(3)	5.1(1)
C(25)	0.0626(7)	0.3285(2)	0.3785(3)	4.9(1)
19				
Ru(1)	0.19333(2)	0.05218(2)	0.07377(3)	2.543(9)
Ru(2)	0.29899)3)	−0.03793(2)	0.07451(3)	3.048(10)
Ru(3)	0.32885(2)	0.05400(2)	−0.03040(3)	2.637(9)
Cr(1)	0.05471(5)	0.19116(4)	0.23157(5)	3.50(2)
P(1)	0.13848(7)	0.13703(6)	0.03412(9)	2.46(3)
O(1)	0.0924(3)	0.0013(2)	0.2055(3)	6.1(1)
O(2)	0.0886(2)	−0.0016(2)	−0.0563(3)	5.4(1)
O(3)	0.2784(2)	0.1028(2)	0.2212(2)	4.2(1)
O(4)	0.4324(3)	−0.1146(2)	0.0361(3)	7.2(2)
O(5)	0.2184(2)	−0.1068(2)	0.2047(3)	5.9(1)
O(6)	0.2050(3)	−0.0903(2)	−0.0658(3)	5.7(1)
O(7)	0.3977(2)	0.0135(2)	0.2131(2)	4.4(1)
O(8)	0.4722(2)	−0.0026(2)	−0.0969(3)	5.8(1)
O(9)	0.4191(2)	0.1142(2)	0.1060(2)	5.0(1)
O(10)	0.3431(3)	0.1596(2)	−0.1275(3)	5.4(1)
O(11)	0.2320(2)	0.0078(2)	−0.1725(3)	5.1(1)
O(12)	0.1279(3)	0.1023(2)	0.3315(3)	6.8(2)
O(13)	0.1997(3)	0.2559(2)	0.2468(3)	7.4(2)
O(14)	0.0055(3)	0.2341(2)	0.3975(3)	6.5(1)
C(1)	0.1277(3)	0.0212(2)	0.1550(4)	3.6(2)
C(2)	0.1317(3)	0.0179(2)	−0.0118(4)	3.5(1)
C(3)	0.2514(3)	0.0836(2)	0.1638(3)	3.0(1)
C(4)	0.3837(4)	−0.0855(3)	0.0487(4)	4.4(2)
C(5)	0.2482(3)	−0.0808(3)	0.1556(4)	3.9(2)
C(6)	0.2384(4)	−0.0688(2)	−0.0163(4)	4.1(2)
C(7)	0.3605(3)	−0.0020(2)	0.1610(4)	3.3(1)
C(8)	0.4191(3)	0.0181(2)	−0.0724(4)	3.7(1)
C(9)	0.3826(3)	0.0900(2)	0.0601(3)	2.2(1)
C(10)	0.3352(3)	0.1209(2)	−0.0900(3)	3.3(1)
C(11)	0.2644(3)	0.0233(2)	−0.1164(4)	3.4(1)
C(12)	0.1000(4)	0.1358(3)	0.2919(4)	4.5(2)
C(13)	0.1453(4)	0.2307(3)	0.2410(4)	4.8(2)
C(14)	0.0241(3)	0.2180(3)	0.3329(4)	4.3(2)
C(15)	0.0626(3)	0.1649(2)	0.1004(3)	2.8(1)
C(16)	0.0466(3)	0.2215(2)	0.1033(3)	3.7(1)
C(17)	−0.0162(4)	0.2419(3)	0.1472(4)	4.8(2)
C(18)	−0.0643(3)	0.2059(3)	0.1902(4)	5.1(2)
C(19)	−0.0517(3)	0.1497(3)	0.1883(4)	4.5(2)
C(20)	0.0127(3)	0.1297(2)	0.1445(3)	3.4(1)
C(21)	0.0857(3)	0.1330(2)	−0.0648(3)	2.7(1)
C(22)	0.0066(3)	0.1287(3)	−0.0653(4)	4.5(2)
C(23)	−0.0313(4)	0.1230(3)	−0.1402(5)	6.1(2)
C(24)	0.0071(4)	0.1211(3)	−0.2143(4)	5.1(2)
C(25)	0.0854(4)	0.1254(3)	−0.2133(4)	4.6(2)
C(26)	0.1238(3)	0.1311(2)	−0.1389(4)	3.7(1)
C(27)	0.2022(3)	0.1964(2)	0.0211(3)	2.5(1)
C(28)	0.2630(3)	0.2044(2)	0.0749(4)	3.6(1)
C(29)	0.3118(3)	0.2480(2)	0.0658(4)	4.8(2)
C(30)	0.3010(4)	0.2841(2)	0.0043(4)	4.8(2)

Table 2. (*continued*).

Atom	*x*	*y*	*z*	B_{eq}
C(31)	0.2414(4)	0.2782(3)	−0.0493(4)	5.2(2)
C(32)	0.1916(3)	0.2344(2)	−0.0407(4)	4.2(2)
16				
Ru(1)	0.58555(2)	0.54730(2)	0.38033(4)	2.289(6)
Ru(2)	0.50000	0.50000	0.62732(6)	2.777(10)
Cr(1)	0.66145(6)	0.74385(4)	0.06072(7)	3.04(2)
Cl(1)[b]	0.9173(7)	0.4902(5)	0.7263(7)	17.7(3)
Cl(1a)[b]	0.9088(7)	0.4983(4)	0.869(1)	20.4(4)
P(1)	0.71732(7)	0.63485(6)	0.3805(1)	2.21(2)
O(1)	0.6220(3)	0.4810(2)	0.1118(4)	6.0(1)
O(2)	0.7180(2)	0.4255(2)	0.4954(5)	5.4(1)
O(3)	0.4366(3)	0.6702(2)	0.3082(4)	4.91(10)
O(4)	0.6652(3)	0.5154(2)	0.8228(4)	6.0(1)
O(5)	0.4504(3)	0.6694(2)	0.6260(5)	5.19(10)
O(6)	0.5142(3)	0.6345(2)	−0.0431(5)	6.6(1)
O(7)	0.4999(3)	0.8191(2)	0.2073(4)	5.5(1)
O(8)	0.6058(4)	0.8496(3)	−0.1568(5)	9.2(2)
C(1)	0.6080(3)	0.5096(3)	0.2105(4)	3.5(1)
C(2)	0.6631(3)	0.4707(3)	0.4611(5)	3.4(1)
C(3)	0.4921(3)	0.6255(3)	0.3358(4)	3.13(10)
C(4)	0.6033(4)	0.5123(3)	0.7494(5)	3.6(1)
C(5)	0.4721(3)	0.6073(3)	0.6141(6)	3.8(1)
C(6)	0.5708(4)	0.6764(3)	−0.0035(6)	4.4(1)
C(7)	0.5632(3)	0.7894(3)	0.1536(5)	3.5(1)
C(8)	0.6281(5)	0.8085(4)	−0.0744(6)	5.5(2)
C(9)	0.7205(3)	0.7115(3)	0.5048(5)	2.82(10)
C(10)	0.6332(3)	0.7645(3)	0.4963(5)	3.5(1)
C(11)	0.7316(4)	0.6795(3)	0.6431(5)	3.9(1)
C(12)	0.8355(3)	0.5864(2)	0.4058(4)	2.90(9)
C(13)	0.9214(3)	0.6407(3)	0.4217(6)	4.5(1)
C(14)	0.8600(3)	0.5267(3)	0.2997(6)	4.2(1)
C(15)	0.7428(3)	0.6871(3)	0.2259(4)	2.38(9)
C(16)	0.7535(3)	0.6456(3)	0.1078(5)	3.03(9)
C(17)	0.7893(4)	0.6793(3)	−0.0072(5)	3.8(1)
C(18)	0.8122(4)	0.7572(4)	−0.0089(5)	4.5(1)
C(19)	0.7998(3)	0.8004(3)	0.1057(5)	3.8(1)
C(20)	0.7663(3)	0.7662(3)	0.2208(5)	3.08(10)
C(21)[b]	1.0000	0.5000	0.835(3)	8.9(7)
C(21a)[b]	1.0000	0.5000	0.950(2)	5.6(4)
26				
Os(1)	0.54927(1)	0.24356(1)	0.18923(1)	2.046(6)
Cr(1)	0.27052(5)	0.37220(6)	0.28488(6)	2.94(3)
P(1)	0.39383(8)	0.21974(8)	0.2305(1)	2.29(4)
O(1)	0.4554(3)	0.9372(2)	0.1023(3)	4.4(2)
O(2)	0.5768(3)	0.2010(3)	0.4216(3)	4.0(1)
O(3)	0.5356(3)	0.3167(3)	−0.0319(3)	4.3(2)
O(4)	0.1073(3)	0.3081(4)	0.1290(3)	6.0(2)
O(5)	0.1798(3)	0.4673(3)	0.4094(3)	5.3(2)
O(6)	0.1349(3)	0.1917(3)	0.4079(4)	6.4(2)
C(1)	0.3852(3)	0.3308(3)	0.2454(4)	2.6(2)
C(2)	0.3690(3)	0.3751(3)	0.1564(4)	3.1(2)
C(3)	0.3775(4)	0.4685(4)	0.1655(5)	4.0(2)
C(4)	0.4015(4)	0.5179(4)	0.2613(5)	4.3(2)
C(5)	0.4168(4)	0.4746(4)	0.3505(5)	4.0(2)
C(6)	0.4081(3)	0.3822(3)	0.3436(4)	3.1(2)
C(7)	0.3039(3)	0.1465(4)	0.1297(4)	3.4(2)
C(8)	0.1959(4)	0.1130(4)	0.1482(5)	5.1(3)
C(9)	0.3418(3)	0.1531(3)	0.3537(4)	3.2(2)
C(10)	0.3264(4)	0.0499(4)	0.3552(4)	4.1(2)
C(11)	0.4924(3)	0.1135(3)	0.1405(4)	2.8(2)
C(12)	0.5705(3)	0.2190(3)	0.3354(4)	3.0(2)
C(13)	0.5455(3)	0.2940(3)	0.0525(4)	2.9(2)
C(14)	0.1713(4)	0.3340(4)	0.1879(4)	4.0(2)
C(15)	0.2152(4)	0.4315(4)	0.3609(4)	3.4(2)
C(16)	0.1888(4)	0.2599(4)	0.3608(5)	4.1(2)

[a] $B_{eq} = (8/3)\pi^2\Sigma\Sigma U_{ij}a^*_i a^*_j(\mathbf{a}_i \cdot \mathbf{a}_j)$.
[b] Occupancy 0.50.

phosphino- and arsinobenzenechromium tricarbonyl derivatives. The first was the thermal replacement of three carbonyls from $Cr(CO)_6$ by an aryl group attached to the phosphine. Thus, refluxing the arylphosphine and chromium hexacarbonyl in a decalin solution gives rise to two series of complexes: monomeric $R_2PC_6H_5Cr(CO)_3$ and dimeric $[R_2PC_6H_5Cr(CO)_2]_2$. This route gives low yields, requires considerable time, and is limited in scope (14). For some phosphines, such as Ph_3P and $(m\text{-tolyl})_3P$, only the dimers are isolated (14).

The second strategy employed for the formation of $R_2PC_6H_5Cr(CO)_3$ involves the reaction of a chlorophosphine with the lithium derivative of benzenechromium tricarbonyl $(\eta^6\text{-}LiC_6H_5)Cr(CO)_3$, in THF or Et_2O, at low temperature. Two indirect routes to the lithiated intermediate have been developed; one involves a *trans*-metallation reaction between bis(η^6-phenyltricarbonylchromium)mercury and *n*-butyllithium (15). The second, more efficient, route involves *trans*-metallation of $[\eta^6\text{-}(Bu^n{}_3Sn)C_6H_5]Cr(CO)_3$ with *n*-BuLi in THF at −78°C (16). The butyltin derivative can be synthesized by the reaction of $(MeCN)_3Cr(CO)_3$ with (tributylstannyl)benzene.

Semmelhack et al. (17) developed a high-yield direct lithiation method involving addition of *n*-BuLi to $C_6H_6Cr(CO)_3$ in THF at −78°C in the presence of TMEDA. Subsequent addition of halophosphine or arsine affords the desired phosphino- and arsinobenzenechromium tricarbonyl derivatives. This method was adopted for the present investigation; 10 complexes (**1–10**) were prepared in this work including the three known compounds $Ph_2PC_6H_5Cr(CO)_3$ **1**, $PhP[C_6H_5Cr(CO)_3]_2$ **7**, and $Ph_2AsC_6H_5Cr(CO)_3$ **6**, which were isolated in higher yields than previously reported (16*a*, 18). In our hands the yields of the $R_2P[C_6H_5Cr(CO)_3]$ phosphines are higher than those of $RP[C_6H_5Cr(CO)_3]_2$. Recrystallization is best employed as a purification method because of the possibility of decomposition of the compounds on silica gel or alumina. Compounds **1–10** are all yellow solids, except $Et_2PC_6H_5Cr(CO)_3$, **4**, which is a red oily liquid; all are soluble in a range of organic solvents. In the solid state, the compounds are stable for long periods of time under an inert atmosphere. In general, their spectroscopic properties are much as expected. The ^{31}P NMR shifts can be fitted reasonably well to the Grim and McFarlane equation (19): δ (w.r.t. 85% H_3PO_4) = $-62 + \Sigma\sigma^P$ if σ^P for the $C_6H_5Cr(CO)_3$ moiety is taken as +20.

The crystal structure of $Pr^i{}_2P(C_6H_5)Cr(CO)_3$ **3** is shown in Fig. 1 and selected bond lengths and bond angles appear in

Fig. 1. Molecular structure of $Pr^i_2PC_6H_5Cr(CO)_3$, **3**; 33% probability thermal ellipsoids are shown for the non-hydrogen atoms.

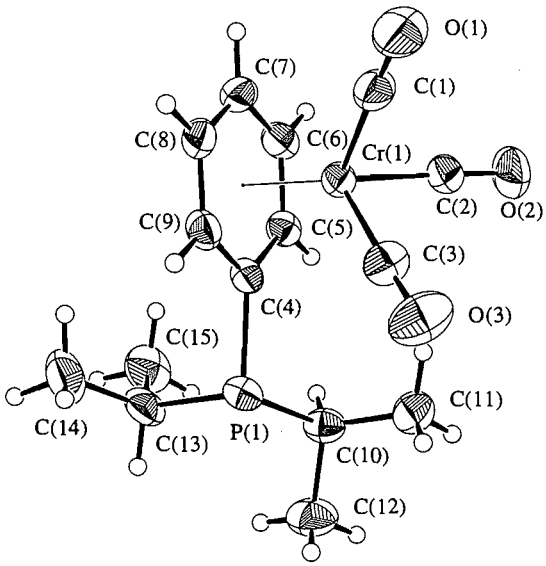

Table 3. The "three-legged piano-stool" geometry is typical of (η^6-arene)$Cr(CO)_3$ complexes. The CO-Cr-CO angles range from 87.6(1)° to 89.0(1)° and the $Cr(CO)_3$ moiety is partially eclipsed (i.e., midway between eclipsed and staggered relative to the η^6-phenyl ring). A staggered structure is rare for monosubstituted arenes (20).

One of the isopropyl groups in the Pr^i_2 moiety is oriented almost perpendicular to the π-arene moiety. This conformation forces the remaining isopropyl group below the plane of the π-arene ring, with the $Cr(CO)_3$ moiety.

The structure of $Ph_2AsC_6H_5Cr(CO)_3$, **6** (21), is very similar to that of **3**. In fact the change from Ph_2As to Pr^i_2P is barely discernible in the $C_6H_5Cr(CO)_3$ moiety. The ring C—C bonds of **3** vary between 1.391(4) and 1.419(3) Å in an apparently random manner; however, in **6** there appears to be some tendency towards an alternation in the bond lengths.

With the advent of mild synthetic routes (22), many tertiary phosphine and arsine derivatives of $Ru_3(CO)_{12}$ and $Os_3(CO)_{12}$ have been prepared; however, only one contains a benzene chromium tricarbonyl moiety. To fill in this gap, 10 new derivatives of $Ru_3(CO)_{12}$, **11**, **12**, **15**, **16**, **19**, **20**, **22**, **23**, **27**, and **29** were synthesized and characterized. Most reactions employed sodium benzophenone ketyl (BPK) as catalyst. PPN salts were also used to assist the substitution reactions although this method is less satisfactory. The catalyzed reactions with the ligands $(R_2EC_6H_5)Cr(CO)_3$ (R_2E = Me_2As, Pr^i2P, Et_2P, Ph_2P) afford the expected mono- or di-substituted products in good yield with the yields of the monosubstituted derivatives being higher. However, under the same conditions $Ph_2AsC_6H_5Cr(CO)_3$ and $PhP[C_6H_5Cr(CO)_3]_2$ yield only the monosubstituted products **27** and **29**. $Bu^t_2PC_6H_5Cr(CO)_3$ appears to react only to a limited extent under these conditions and $PhAs[C_6H_5Cr(CO)_3]_2$ or $Bu^tP[C_6H_5Cr(CO)_3]_2$ not at all. The bulk of the ligands is probably the determining factor; however, it should be noted that the very bulky PFc_2Ph (Fc = ferrocenyl) forms $Ru_3(CO)_{10}(PFc_2Ph)_2$ in high yield (23).

Fig. 2. Molecular structure of $Ru_3(CO)_{11}[Pr^i_2PC_6H_5Cr(CO)_3]$, **15**; 33% probability thermal ellipsoids are shown for the non-hydrogen atoms.

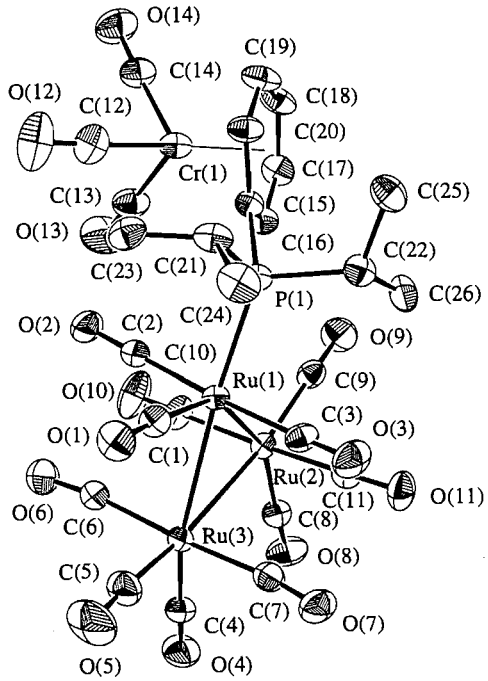

Substitution reactions of $Os_3(CO)_{12}$ are facilitated by the use of the activated clusters, $Os_3(CO)_{11}(MeCN)$ and $Os_3(CO)_{10}(MeCN)_2$ (24), and the new complexes **13**, **14**, **17**, **18**, **21**, **24**, **25**, **28** were prepared by using this methodology. The bulky ligands $Bu^tP[C_6H_5Cr(CO)_3]_2$ and $Bu^t_2PC_6H_5Cr(CO)_3$ failed to react. The trisubstituted derivative $Os_3(CO)_9[(Et_2PC_6H_5)Cr(CO)_3]_3$, **26**, was obtained by refluxing $Os_3(CO)_{11}[Et_2PC_6H_5Cr(CO)_3]$ in *n*-octane: compound **26** was the major product in addition to $Os_3(CO)_{12}$. The spectroscopic properties of the cluster derivatives are much as expected.

The crystal structures of two monosubstituted complexes **15** and **19** have been determined. ORTEP plots are shown in Figs. 2 and 3. Metrical data are summarized in Tables 3 and 4. The phosphine ligands are equatorial and the longest of the Ru—Ru bonds is *cis* to the ligand. The average metal–metal distances in **15** and **19** are 2.8908 and 2.8729 Å, respectively, which is greater than the 2.854 Å found for $Ru_3(CO)_{12}$. This expansion has been attributed to the bulk of the ligands. The cone angles of the isopropyl-and phenyl- phosphines are estimated to be 164° and 154°, respectively, by using data from the structure of $Ru(CO)_3[Pr^i_2PC_6H_5Cr(CO)_3]_2$.[4]

The disubstituted ruthenium cluster $Ru_3(CO)_{10}[Pr^i_2P(C_6H_5Cr(CO)_3)]_2$ **16** also has been crystallographically characterized and the structure is shown in Fig. 4. Selected metrical data for the 1:1 dichloromethane solvate are listed in Tables 3 and 4.

The structure is that commonly found for $M_3(CO)_{10}L_2$ clusters where the two ligands occupy equatorial positions at opposite ends of one of the Ru—Ru bonds. The structure of

[4] W.R. Cullen, S.J. Rettig, and H. Zhang. Unpublished results.

Table 3. Bond lengths (Å) with estimated standard deviations in parentheses.[a]

Bond	Length	Bond	Length
3			
Cr(1)—C(1)	1.835(3)	P(1)—C(10)	1.849(3)
Cr(1)—C(2)	1.819(3)	P(1)—C(13)	1.865(3)
Cr(1)—C(3)	1.834(3)	O(1)—C(1)	1.151(3)
Cr(1)—C(4)	2.231(2)	O(2)—C(2)	1.157(3)
Cr(1)—C(5)	2.209(2)	O(3)—C(3)	1.154(3)
Cr(1)—C(6)	2.206(3)	C(4)—C(5)	1.404(3)
Cr(1)—C(7)	2.218(3)	C(4)—C(9)	1.419(3)
Cr(1)—C(8)	2.211(3)	C(5)—C(6)	1.414(4)
Cr(1)—C(9)	2.197(3)	C(6)—C(7)	1.393(4)
Cr(1)—A	1.71	C(7)—C(8)	1.400(4)
P(1)—C(4)	1.840(3)	C(8)—C(9)	1.391(4)
15			
Ru(1)—Ru(2)	2.9276(6)	Cr(1)—A	1.72
Ru(1)—Ru(3)	2.8776(5)	P(1)—C(15)	1.834(4)
Ru(1)—P(1)	2.384(1)	P(1)—C(21)	1.859(4)
Ru(1)—C(1)	1.863(4)	P(1)—C(22)	1.863(5)
Ru(1)—C(2)	1.938(5)	O(1)—C(1)	1.145(5)
Ru(1)—C(3)	1.919(5)	O(2)—C(2)	1.134(5)
Ru(2)—Ru(3)	2.8672(7)	O(3)—C(3)	1.141(5)
Ru(2)—C(8)	1.923(5)	O(4)—C(4)	1.130(5)
Ru(2)—C(9)	1.901(5)	O(5)—C(5)	1.128(5)
Ru(2)—C(10)	1.945(5)	O(6)—C(6)	1.127(6)
Ru(2)—C(11)	1.921(5)	O(7)—C(7)	1.134(5)
Ru(3)—C(4)	1.904(5)	O(8)—C(8)	1.134(5)
Ru(3)—C(5)	1.912(5)	O(9)—C(9)	1.129(5)
Ru(3)—C(6)	1.943(5)	O(10)—C(10)	1.123(5)
Ru(3)—C(7)	1.943(5)	O(11)—WC(11)	1.139(5)
Cr(1)—C(12)	1.845(6)	O(12)—C(12)	1.150(6)
Cr(1)—C(13)	1.850(6)	O(13)—C(13)	1.136(6)
Cr(1)—C(14)	1.838(5)	O(14)—C(14)	1.153(5)
Cr(1)—C(15)	2.274(4)	C(15)—C(16)	1.413(5)
Cr(1)—C(16)	2.207(4)	C(15)—C(20)	1.417(6)
Cr(1)—C(17)	2.205(5)	C(16)—C(17)	1.405(6)
Cr(1)—C(18)	2.203(5)	C(17)—C(18)	1.388(6)
Cr(1)—C(19)	2.187(5)	C(18)—C(19)	1.407(7)
Cr(1)—C(20)	2.190(5)	C(19)—C(20)	1.390(6)
19			
Ru(1)—Ru(2)	2.8686(6)	Cr(1)—A	1.70
Ru(1)—Ru(3)	2.8900(7)	P(1)—C(15)	1.828(5)
Ru(1)—P(1)	2.372(1)	P(1)—C(21)	1.840(5)
Ru(1)—C(1)	1.893(6)	P(1)—C(27)	1.838(5)
Ru(1)—C(2)	1.935(6)	O(1)—C(1)	1.129(6)
Ru(1)—C(3)	1.925(6)	O(2)—C(2)	1.141(6)
Ru(2)—Ru(3)	2.8602(6)	O(3)—C(3)	1.138(6)
Ru(2)—C(4)	1.921(6)	O(4)—C(4)	1.125(6)
Ru(2)—C(5)	1.892(6)	O(5)—C(5)	1.140(6)
Ru(2)—C(6)	1.953(7)	O(6)—C(6)	1.119(6)
Ru(2)—C(7)	1.963(6)	O(7)—C(7)	1.124(6)
Ru(3)—C(8)	1.920(6)	O(8)—C(8)	1.124(6)
Ru(3)—C(9)	1.941(6)	O(9)—C(9)	1.140(6)
Ru(3)—C(10)	1.902(6)	O(10)—C(10)	1.131(6)
Ru(3)—C(11)	1.932(6)	O(11)—C(11)	1.131(6)
Cr(1)—C(12)	1.843(7)	O(12)—C(12)	1.146(7)
Cr(1)—C(13)	1.854(6)	O(13)—C(13)	1.132(6)

Table 3. (*concluded*).

Bond	Length	Bond	Length
Cr(1)—C(14)	1.837(6)	O(14)—C(14)	1.158(6)
Cr(1)—C(15)	2.211(5)	C(15)—C(16)	1.414(7)
Cr(1)—C(16)	2.199(6)	C(15)—C(20)	1.413(7)
Cr(1)—C(17)	2.213(6)	C(16)—C(17)	1.392(7)
Cr(1)—C(18)	2.202(6)	C(17)—C(18)	1.398(8)
Cr(1)—C(19)	2.221(6)	C(18)—C(19)	1.393(8)
Cr(1)—C(20)	2.181(5)	C(19)—C(20)	1.410(7)
16			
Ru(1)—Ru(1)[b]	2.8914(8)	P(1)—C(9)	1.845(5)
Ru(1)—Ru(2)	2.8927(6)	P(1)—C(12)	1.861(4)
Ru(1)—P(1)	2.384(1)	P(1)—C(15)	1.851(4)
Ru(1)—C(1)	1.872(4)	O(1)—C(1)	1.137(5)
Ru(1)—C(2)	1.905(5)	O(2)—C(2)	1.153(5)
Ru(1)—C(3)	1.939(5)	O(3)—C(3)	1.133(5)
Ru(2)—C(4)	1.903(5)	O(4)—C(4)	1.137(6)
Ru(2)—C(5)	1.928(5)	O(5)—C(5)	1.137(6)
Cr(1)—C(6)	1.843(5)	O(6)—C(6)	1.148(6)
Cr(1)—C(7)	1.837(5)	O(7)—C(7)	1.155(6)
Cr(1)—C(8)	1.839(6)	O(8)—C(8)	1.146(7)
Cr(1)—C(15)	2.251(4)	C(15)—C(16)	1.411(6)
Cr(1)—C(16)	2.197(5)	C(15)—C(20)	1.427(6)
Cr(1)—C(17)	2.211(5)	C(16)—C(17)	1.399(7)
Cr(1)—C(18)	2.214(5)	C(17)—C(18)	1.405(8)
Cr(1)—C(19)	2.204(5)	C(18)—C(19)	1.398(8)
Cr(1)—C(20)	2.212(5)	C(19)—C(20)	1.392(7)
Cr(1)—A	1.71		
26			
Os(1)—Os(1)[c]	2.9013(3)	P(1)—C(1)	1.831(4)
Os(1)—P(1)	2.344(1)	P(1)—C(7)	1.826(5)
Os(1)—C(11)	1.884(5)	P(1)—C(9)	1.829(5)
Os(1)—C(12)	1.954(5)	O(1)—C(11)	1.148(5)
Os(1)—C(13)	1.918(5)	O(2)—C(12)	1.144(5)
Cr(1)—C(1)	2.263(4)	O(3)—C(13)	1.162(5)
Cr(1)—C(2)	2.233(5)	O(4)—C(14)	1.152(6)
Cr(1)—C(3)	2.207(5)	O(5)—C(15)	1.149(6)
Cr(1)—C(4)	2.209(5)	O(6)—C(16)	1.149(6)
Cr(1)—C(5)	2.210(5)	C(1)—C(2)	1.414(6)
Cr(1)—C(6)	2.222(5)	C(1)—C(6)	1.429(6)
Cr(1)—C(14)	1.837(6)	C(2)—C(3)	1.415(7)
Cr(1)—C(15)	1.837(5)	C(3)—C(4)	1.387(8)
Cr(1)—C(16)	1.853(6)	C(4)—C(5)	1.401(8)
Cr(1)—A	1.72	C(5)—C(6)	1.394(7)

[a]Here and elsewhere, A refers to the unweighted centroid of the η^6-coordinated aromatic ring.

[b]Symmetry operation: x, y, z.

[c]Symmetry operation: $1 - y, x - y, z$.

$Os_3(CO)_{10}(PFc_2Ph)_2$ provides a rare example of the alternative 1,2-*trans*,*cis* arrangement of the phosphine ligands (25). In **16** the three Ru—Ru bond distances (mean value 2.8923 Å) are the same within experimental error. This is in contrast to the monosubstituted complexes **15** and **19** in which there are significant differences in the three Ru—Ru separations with the Ru—Ru bond *cis* to the phosphine ligand being significantly elongated. In other disubstituted complexes, $Ru_3(CO)_{10}L_2$, the

Table 4. Bond angles (deg) with estimated standard deviations in parentheses.[a]

Bonds	Angle (deg)	Bonds	Angle (deg)
3			
C(1)-Cr(1)-C(2)	89.0(1)	C(10)-P(1)-C(13)	103.3(1)
C(1)-Cr(1)-C(3)	87.6(1)	Cr(1)-C(1)-O(1)	178.3(3)
C(1)-Cr(1)-A	126.5	Cr(1)-C(2)-O(2)	178.7(3)
C(2)-Cr(1)-C(3)	87.6(1)	Cr(1)-C(3)-O(3)	177.8(3)
C(2)-Cr(1)-A	125.9	P(1)-C(4)-C(5)	125.5(2)
C(3)-Cr(1)-A	127.5	P(1)-C(4)-C(9)	116.3(2)
C(4)-P(1)-C(10)	105.2(1)	C(5)-C(4)-C(9)	117.2(2)
C(4)-P(1)-C(13)	98.5(1)		
15			
Ru(2)-Ru(1)-Ru(3)	59.19(1)	Ru(2)-Ru(3)-C(6)	90.0(2)
Ru(2)-Ru(1)-P(1)	115.89(3)	Ru(2)-Ru(3)-C(7)	89.9(1)
Ru(2)-Ru(1)-C(1)	143.7(1)	C(4)-Ru(3)-C(5)	99.6(2)
Ru(2)-Ru(1)-C(2)	86.7(1)	C(4)-Ru(3)-C(6)	92.8(2)
Ru(2)-Ru(1)-C(3)	93.3(1)	C(4)-Ru(3)-C(7)	92.7(2)
Ru(3)-Ru(1)-P(1)	174.27(3)	C(5)-Ru(3)-C(6)	90.7(2)
Ru(3)-Ru(1)-C(1)	84.8(1)	C(5)-Ru(3)-C(7)	88.1(2)
Ru(3)-Ru(1)-C(2)	93.0(1)	C(6)-Ru(3)-C(7)	174.5(2)
Ru(3)-Ru(1)-C(3)	89.6(1)	C(12)-Cr(1)-C(13)	87.1(2)
P(1)-Ru(1)-C(1)	100.3(1)	C(12)-Cr(1)-C(14)	85.9(2)
P(1)-Ru(1)-C(2)	89.6(1)	C(12)-Cr(1)-A	131.7
P(1)-Ru(1)-C(3)	87.8(1)	C(13)-Cr(1)-C(14)	87.6(2)
C(1)-Ru(1)-C(2)	91.6(2)	C(13)-Cr(1)-A	126.6
C(1)-Ru(1)-C(3)	90.2(2)	C(14)-Cr(1)-A	123.9
C(2)-Ru(1)-C(3)	177.0(2)	Ru(1)-P(1)-C(15)	120.6(1)
Ru(1)-Ru(2)-Ru(3)	59.54(1)	Ru(1)-P(1)-C(21)	113.6(1)
Ru(1)-Ru(2)-C(8)	152.7(1)	Ru(1)-P(1)-C(22)	114.5(1)
Ru(1)-Ru(2)-C(9)	109.6(1)	C(15)-P(1)-C(21)	104.2(2)
Ru(1)-Ru(2)-C(10)	91.4(1)	C(15)-P(1)-C(22)	98.7(2)
Ru(1)-Ru(2)-C(11)	82.2(1)	C(21)-P(1)-C(22)	102.7(2)
Ru(3)-Ru(2)-C(8)	93.6(1)	Ru(1)-C(1)-O(1)	176.7(4)
Ru(3)-Ru(2)-C(9)	169.0(1)	Ru(1)-C(2)-O(2)	173.2(4)
Ru(3)-Ru(2)-C(10)	89.1(1)	Ru(1)-C(3)-O(3)	173.4(4)
Ru(3)-Ru(2)-C(11)	88.8(1)	Ru(3)-C(4)-O(4)	178.5(4)
Ru(8)-Ru(2)-C(9)	97.3(2)	Ru(3)-C(5)-O(5)	176.0(5)
Ru(8)-Ru(2)-C(10)	93.3(2)	Ru(3)-C(6)-O(6)	173.3(5)
Ru(8)-Ru(2)-C(11)	93.0(2)	Ru(3)-C(7)-O(7)	172.5(4)
Ru(9)-Ru(2)-C(10)	89.5(2)	Ru(2)-C(8)-O(8)	177.4(4)
Ru(9)-Ru(2)-C(11)	91.3(2)	Ru(2)-C(9)-O(9)	176.9(4)
C(10)-Ru(2)-C(11)	173.4(2)	Ru(2)-C(10)-O(10)	173.4(4)
Ru(1)-Ru(3)-Ru(2)	61.28(1)	Ru(2)-C(11)-O(11)	172.6(4)
Ru(1)-Ru(3)-C(4)	154.7(1)	Cr(1)-C(12)-O(12)	176.9(5)
Ru(1)-Ru(3)-C(5)	105.7(2)	Cr(1)-C(13)-O(13)	177.3(5)
Ru(1)-Ru(3)-C(6)	86.6(1)	Cr(1)-C(14)-O(14)	177.6(5)
Ru(1)-Ru(3)-C(7)	88.5(1)	P(1)-C(15)-C(16)	118.3(3)
Ru(2)-Ru(3)-C(4)	93.5(1)	P(1)-C(15)-C(20)	123.2(3)
Ru(2)-Ru(3)-C(5)	166.8(2)	C(16-C(15)-C(20)	117.2(4)
19			
Ru(2)-Ru(1)-Ru(3)	59.56(2)	Ru(2)-Ru(3)-C(10)	170.4(2)
Ru(2)-Ru(1)-P(1)	158.58(4)	Ru(2)-Ru(3)-C(11)	90.7(2)
Ru(2)-Ru(1)-C(1)	94.3(2)	C(8)-Ru(3)-C(9)	94.6(2)
Ru(2)-Ru(1)-C(2)	91.4(2)	C(8)-Ru(3)-C(10)	99.7(2)
Ru(2)-Ru(1)-C(3)	88.2(2)	C(8)-Ru(3)-C(11)	92.5(2)
Ru(3)-Ru(1)-P(1)	99.06(4)	C(9)-Ru(3)-C(10)	87.7(2)
Ru(3)-Ru(1)-C(1)	153.8(2)	C(9)-Ru(3)-C(11)	172.9(2)
Ru(3)-Ru(1)-C(2)	92.6(2)	C(10)-Ru(3)-C(11)	90.4(2)

Table 4. (*continued*).

Bonds	Angle (deg)	Bonds	Angle (deg)
Ru(3)-Ru(1)-C(3)	90.2(2)	C(12)-Cr(1)-C(13)	88.7(3)
P(1)-Ru(1)-C(1)	107.1(2)	C(12)-Cr(1)-C(14)	85.4(3)
P(1)-Ru(1)-C(2)	88.0(2)	C(12)-Cr(1)-A	128.0
P(1)-Ru(1)-C(3)	93.6(2)	C(13)-Cr(1)-C(14)	89.2(3)
C(1)-Ru(1)-C(2)	89.1(2)	C(13)-Cr(1)-A	126.7
C(1)-Ru(1)-C(3)	87.5(2)	C(14)-Cr(1)-A	125.7
C(2)-Ru(1)-C(3)	176.5(2)	Ru(1)-P(1)-C(15)	117.3(2)
Ru(1)-Ru(2)-Ru(3)	60.59(2)	Ru(1)-P(1)-C(21)	112.7(2)
Ru(1)-Ru(2)-C(4)	162.6(2)	Ru(1)-P(1)-C(27)	118.7(2)
Ru(1)-Ru(2)-C(5)	97.5(2)	C(15)-P(1)-C(21)	99.6(2)
Ru(1)-Ru(2)-C(6)	87.1(2)	C(15)-P(1)-C(27)	101.9(2)
Ru(1)-Ru(2)-C(7)	90.4(2)	C(21)-P(1)-C(27)	104.0(2)
Ru(3)-Ru(2)-C(4)	102.1(2)	Ru(1)-C(1)-O(1)	175.8(6)
Ru(3)-Ru(2)-C(5)	158.0(2)	Ru(1)-C(2)-O(2)	172.4(5)
Ru(3)-Ru(2)-C(6)	87.7(2)	Ru(1)-C(3)-O(3)	172.7(5)
Ru(3)-Ru(2)-C(7)	88.1(2)	Ru(2)-C(4)-O(4)	177.2(6)
C(4)-Ru(2)-C(5)	99.9(3)	Ru(2)-C(5)-O(5)	179.1(6)
C(4)-Ru(2)-C(6)	90.9(3)	Ru(2)-C(6)-O(6)	174.6(5)
C(4)-Ru(2)-C(7)	90.5(2)	Ru(2)-C(7)-O(7)	173.0(5)
C(5)-Ru(2)-C(6)	92.9(2)	Ru(3)-C(8)-O(8)	179.6(5)
C(5)-Ru(2)-C(7)	90.7(2)	Ru(3)-C(9)-O(9)	171.8(5)
C(6)-Ru(2)-C(7)	175.8(2)	Ru(3)-C(10)-O(10)	175.8(5)
Ru(1)-Ru(3)-Ru(2)	59.85(1)	Ru(3)-C(11)-O(11)	172.7(5)
Ru(1)-Ru(3)-C(8)	149.6(2)	Cr(1)-C(12)-O(12)	178.0(6)
Ru(1)-Ru(3)-C(9)	87.9(2)	Cr(1)-C(13)-O(13)	178.4(6)
Ru(1)-Ru(3)-C(10)	110.7(2)	Cr(1)-C(14)-O(14)	178.6(6)
Ru(1)-Ru(3)-C(11)	86.4(2)	P(1)-C(15)-C(16)	121.7(4)
Ru(2)-Ru(3)-C(8)	89.8(2)	P(1)-C(15)-C(20)	120.5(4)
Ru(2)-Ru(3)-C(9)	90.1(2)	C(16)-C(15)-C(20)	117.5(5)
16			
Ru(1)[b]-Ru(1)-Ru(2)	60.014(9)	C(6)-Cr(1)-C(7)	87.6(2)
Ru(1)[b]-Ru(1)-P(1)	174.92(3)	C(6)-Cr(1)-C(8)	87.8(3)
Ru(1)[b]-Ru(1)-C(1)	86.1(1)	C(6)-Cr(1)-A	126.5
Ru(1)[b]-Ru(1)-C(2)	93.2(1)	C(7)-Cr(1)-C(8)	85.9(2)
Ru(1)[b]-Ru(1)-C(3)	82.0(1)	C(7)-Cr(1)-A	130.2
Ru(2)-Ru(1)-P(1)	119.81(3)	C(8)-Cr(1)-A	125.1
Ru(2)-Ru(1)-C(1)	139.8(2)	Ru(1)-P(1)-C(9)	119.3(1)
Ru(2)-Ru(1)-C(2)	69.8(1)	Ru(1)-P(1)-C(12)	112.1(1)
Ru(2)-Ru(1)-C(3)	97.6(1)	Ru(1)-P(1)-C(15)	117.7(1)
P(1)-Ru(1)-C(1)	95.9(1)	C(9)-P(1)-C(12)	102.6(2)
P(1)-Ru(1)-C(2)	91.4(1)	C(9)-P(1)-C(15)	102.3(2)
P(1)-Ru(1)-C(3)	93.1(1)	C(12)-P(1)-C(15)	100.1(2)
C(1)-Ru(1)-C(2)	93.1(2)	Ru(1)-C(1)-O(1)	174.4(5)
C(1)-Ru(1)-C(3)	98.4(2)	Ru(1)-C(2)-O(2)	170.7(5)
C(2)-Ru(1)-C(3)	167.2(2)	Ru(1)-C(3)-O(3)	178.7(4)
Ru(1)-Ru(2)-Ru(1)[b]	59.97(2)	Ru(2)-C(4)-O(4)	176.2(5)
Ru(1)-Ru(2)-C(4)	102.9(1)	Ru(2)-C(5)-O(5)	169.3(5)
Ru(1)-Ru(2)-C(4)[b]	154.6(1)	Cr(1)-C(6)-O(6)	179.7(6)
Ru(1)-Ru(2)-C(5)	75.0(2)	Cr(1)-C(7)-O(7)	177.3(5)
Ru(1)-Ru(2)-C(5)[b]	98.0(2)	Cr(1)-C(8)-O(8)	178.4(6)
C(4)-Ru(2)-C(4)[b]	98.8(3)	P(1)-C(15)-C(16)	118.9(3)
C(4)-Ru(2)-C(5)	94.8(2)	P(1)-C(15)-C(20)	123.8(3)
C(4)-Ru(2)-C(5)[b]	90.3(2)	C(16)-C(15)-C(20)	116.7(4)
C(5)-Ru(2)-C(5)[b]	172.0(3)		
26			
Os(1)[c]-Os(1)-Os(1)[d]	60.00	C(14)-Cr(1)-A	124.8

Table 4. (*concluded*).

Bonds	Angle (deg)	Bonds	Angle (deg)
Os(1)[c]-Os(1)-P(1)	164.42(3)	C(15)-Cr(1)-A	125.2
Os(1)[c]-Os(1)-C(11)	102.1(1)	C(16)-Cr(1)-A	130.9
Os(1)[c]-Os(1)-C(12)	78.0(1)	Os(1)-P(1)-C(1)	116.1(1)
Os(1)[c]-Os(1)-C(13)	97.0(1)	Os(1)-P(1)-C(7)	111.3(2)
Os(1)[d]-Os(1)-P(1)	110.63(3)	Os(1)-P(1)-C(9)	114.5(2)
Os(1)[d]-Os(1)-C(11)	154.5(1)	C(1)-P(1)-C(7)	105.7(2)
Os(1)[d]-Os(1)-C(12)	96.1(1)	C(1)-P(1)-C(9)	103.6(2)
Os(1)[d]-Os(1)-C(13)	72.8(1)	C(7)-P(1)-C(9)	104.5(2)
P(1)-Os(1)-C(11)	90.5(1)	P(1)-C(1)-C(2)	120.5(3)
P(1)-Os(1)-C(12)	91.4(1)	P(1)-C(1)-C(6)	120.9(3)
P(1)-Os(1)-C(13)	91.2(1)	C(2)-C(1)-C(6)	118.1(4)
C(11)-Os(1)-C(12)	97.5(2)	Os(1)-C(11)-O(1)	173.5(4)
C(11)-Os(1)-C(13)	93.3(2)	Os(1)-C(12)-O(2)	175.8(4)
C(12)-Os(1)-C(13)	168.8(2)	Os(1)-C(13)-O(3)	173.9(4)
C(14)-Cr(1)-C(15)	88.6(2)	Cr(1)-C(14)-O(4)	178.2(5)
C(14)-Cr(1)-C(16)	87.9(2)	Cr(1)-C(15)-O(5)	178.9(5)
C(15)-Cr(1)-C(16)	86.2(2)	Cr(1)-C(16)-O(6)	176.7(5)

[a]Here and elsewhere, A refers to the unweighted centroid of the η^6-coordinated aromatic ring.

[b]Symmetry operation: x, y, z.

[c]Symmetry operation: $1 - y, x - y, z$.

[d]Symmetry operation: $1 - x + y, 1 - x, z$.

Fig. 3. Molecular structure of $Ru_3(CO)_{11}[Ph_2PC_6H_5Cr(CO)_3]$, **19**; 33% probability thermal ellipsoids are shown for the non-hydrogen atoms.

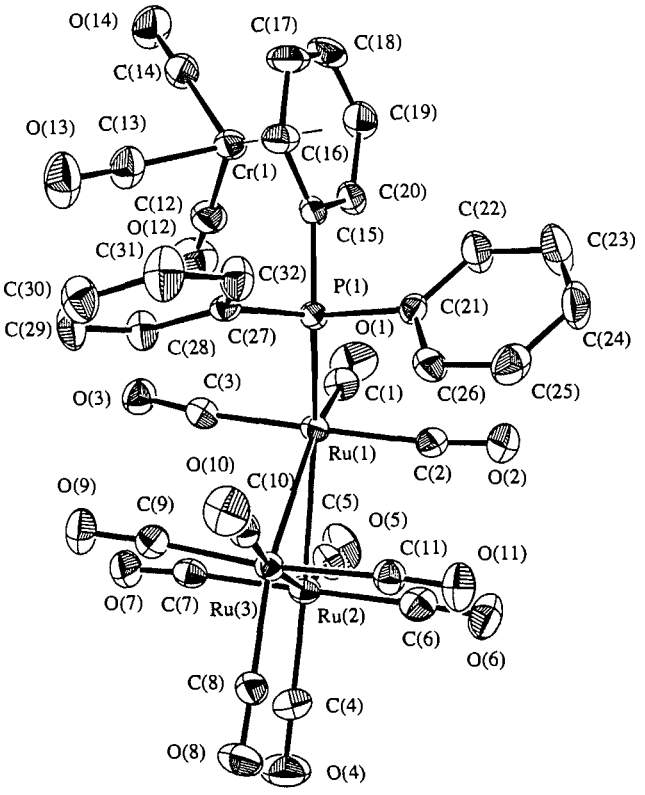

Fig. 4. Molecular structure of $Ru_3(CO)_{10}[Pr^i_2PC_6H_5Cr(CO)_3)]_2$, **16**; 33% probability thermal ellipsoids are shown for the non-hydrogen atoms.

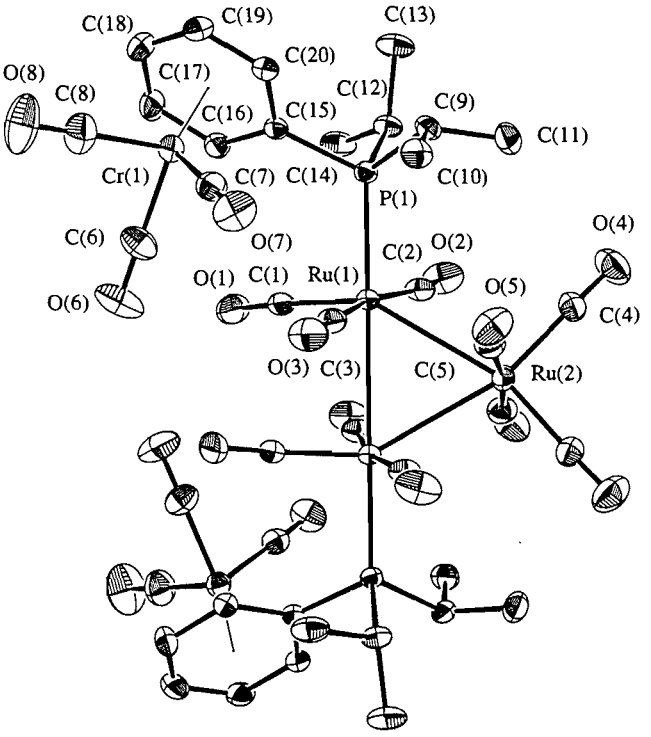

Fig. 5. Molecular structure of $Os_3(CO)_9[Et_2PC_6H_5Cr(CO)_3]_3$, **26**; 33% probability thermal ellipsoids are shown for the non-hydrogen atoms.

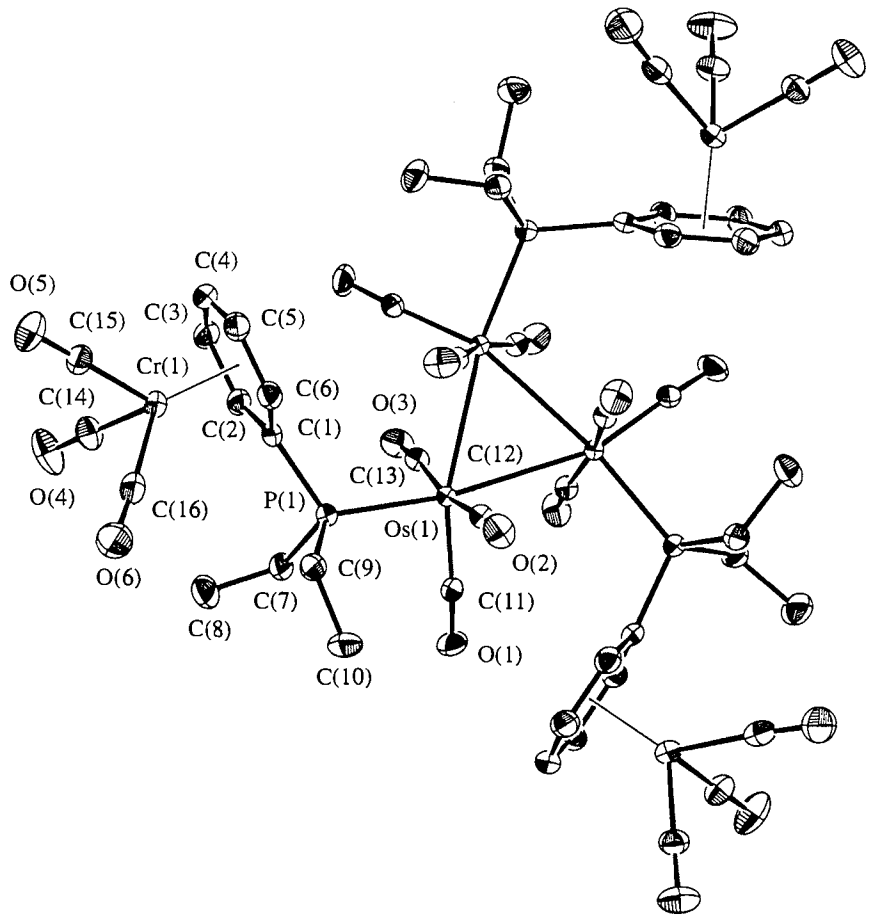

M_3 frame is essentially an isosceles triangle (26). The average Ru—Ru bond distance in **16** is longer than that in the parent carbonyl (mean 2.854 Å) by 0.04 Å and is not significantly different from that in the monosubstituted complex **15** (mean 2.8908 Å).

In **16** the introduction of two phosphine ligands results in considerable twisting of the RuL'_4 units about the Ru—Ru bonds. Unlike the monosubstituted complexes, none of the equatorial carbonyls are found on the Ru_3 plane; for example, CO(1) and CO(4) lie on opposite sides of the Ru_3 plane by 0.73 Å and 0.64 Å, respectively. As a result, all the axial carbonyls are also moved from their idealized positions. Consequently there are no pronounced differences in the bond distances between axial carbonyls and equatorial carbonyls (mean 1.911 Å); the pseudoequatorial Ru—CO(1) bond at the substituted ruthenium atom is the shortest (1.872(4) Å).

The molecular structure of the trisubstituted derivative $Os_3(CO)_9[Et_2PC_6H_5Cr(CO)_3]_3$ **26** has been determined. The relevant bond distances and angles are tabulated in Tables 3 and 4 and an ORTEP plot of the structure is shown in Fig. 5. The molecule **26** has a crystallographic threefold axis, and the structure contains an equilateral triangular Os_3 core with the three phosphine ligands bound one to each osmium atom in pseudo-equatorial sites. The Os-Os bond distances are identical at 2.9013(3) Å and are longer than those in the parent carbonyl (average 2.877 Å (27)), by 0.024 Å. In $Os_3(CO)_9(PPh_3)_3$ the average Os—Os bond distance is also increased to 2.91 Å, but in trisubstituted ruthenium clusters the average Ru—Ru separation is essentially the same as that found in $Ru_3(CO)_{12}$ (28).

In **26** the phosphorus atoms are coordinated at pseudo-equatorial sites and are all situated away from the Os_3 plane by 0.52 Å in the same direction. The Os—P bond at 2.344(1) Å is surprisingly shorter than the Ru—P bond found in **19** (2.372(1) Å) and **15** (2.384(1) Å). In some other trisubstituted complexes the phosphine ligands are arranged in such a way that one lies below the M_3 plane, while the other two lie above it (28).

The products of the thermal decomposition of some of these cluster complexes will be reported in a forthcoming publication (29).

Acknowledgments

We thank the Natural Sciences and Engineering Research Council of Canada for financial support.

References

1. M.A. Bennet and H.P. Schwemln. Angew. Chem. Int. Ed. Engl. **28**, 1296 (1989).

2. W.R. Cullen, S.J. Rettig, and T.-C. Zheng. Organometallics, **11**, 928 (1992).
3. W.R. Cullen, S.J. Rettig, and T.-C. Zheng. Organometallics, **14**, 1466 (1995).
4. (*a*) W.R. Cullen, S.J. Rettig, and H. Zhang. Organometallics, **10**, 2965 (1991); (*b*) Organometallics, **11**, 1000 (1992); (*c*) Organometallics, **12**, 1964 (1993).
5. C.A.L Mahaffy and P.L. Pauson. Inorg. Synth. **19,** 154 (1979).
6. (*a*) M.I. Bruce, J.G. Matisons, R.C. Wallis, J.M. Patrick, and A.H. White. J. Chem. Soc. Dalton Trans. 2365 (1983); (*b*) M.I. Bruce, C.M. Jensen, and N.L. Jones. Inorg. Synth. **28**, 216 (1990).
7. B.F.G. Johnson, J. Lewis, and D.A. Pippard. J. Chem. Soc. Dalton Trans. 407 (1981).
8. E. Roberts, E.E. Turner, and F. W. Bury. J. Chem. Soc. 1443 (1926).
9. M. Fild, O. Stelzer, and R. Schmutzler. Inorg. Synth. **14**, 4 (1973).
10. D.P. Tate, W.R. Knipple, and J.M. Augl. Inorg. Chem. **1**, 433 (1962).
11. G.A. Foulds, B.F.G. Johnson, and J. Lewis. J. Organomet. Chem. **296**, 147, (1985).
12. M.I. Bruce, J.G. Matisons, and B.K. Nicholson. J. Organomet. Chem. **247**, 321 (1983).
13. (*a*) International tables for X-ray crystallography. Vol. IV. Kynoch Press. Birmingham, U.K. (present distributor Kluwer Academic Publishers, Boston, Mass, U.S.A.). 1974. pp. 99–102; (*b*) International tables for crystallography. Vol. C. Kluwer Academic Publishers, Boston, Mass, U.S.A. 1992. pp. 200–206.
14. J.A. Bowden and R. Colton. Aust. J. Chem. **24**, 2471 (1971).
15. M.D. Rausch and R.E. Gloth. J. Organomet. Chem. **153**, 59 (1978).
16. (*a*) M.E. Wright. Organometallics, **8**, 407 (1989); (*b*) M.E. Wright, L. Lawson, R.T. Baker, and D.C. Roe. Polyhedron, **11**, 323 (1992).
17. M.F. Semmelhack, J. Bisaha, and M. Czarny. J. Am. Chem. Soc. **101**, 768 (1979).
18. (*a*) H.J. Wasserman, M.J. Wovkulich, J.D. Atwood, and M.R. Churchill. Inorg. Chem. **19**, 2831 (1980); (*b*) M.D. Rausch and R.E. Gloth. J. Organomet. Chem. **153**, 59 (1978).
19. S.O. Grim and W. McFarlane. Nature, **208**, 995 (1965).
20. J. Li, A.D. Hunter, S.G. Bott, and J.L. Atwood. Organometallics, **11**, 3050 (1992).
21. H.J. Wasserman, M.J. Wovkulich, J.D. Atwood, and M.R. Churchill. Inorg. Chem. **19**, 2831 (1980).
22. (*a*) M. Arewgoda, B.H. Robinson, and J. Simpson. J. Chem. Soc. Chem. Commun. 284 (1982); J. Am. Chem. Soc. **105**, 1893 (1983); (*b*)M.I. Bruce, J.G. Matisons, and B.K. Nicholson. J. Organomet. Chem. **247**, 321 (1983); (*c*) G. Lavigne and H.D. Kaze. J. Am. Chem. Soc. **106**, 4647 (1984); (*d*) M.O. Albers, E. Singleton, and N.J. Coville. J. Organomet. Chem. **326**, 229 (1987).
23. S.T. Chacon, W.R. Cullen, M.I. Bruce, O.B. Shawkataly, F.W.B. Einstein, R.H. Jones, and A.C. Willis. Can. J. Chem. **68**, 2001 (1990).
24. (*a*)B.F.G. Johnson, J. Lewis, and D.A. Pippard. J. Chem. Soc. Dalton Trans. 407 (1987); (*b*) B.F.G. Johnson, J. Lewis, T.I. Odiaka, and P.R. Raithby. J. Organomet. Chem. **216**, C56 (1981).
25. W.R. Cullen, S.J. Rettig, and T.-C. Zheng. Can. J. Chem. **70**, 2329 (1992).
26. M.I. Bruce, M.J. Liddell, C.A. Hughes, J.M. Patrick, B.W. Skelton, and A.H. White. J. Organomet. Chem. **347**, 181 (1988).
27. M.R. Churchill, F.J. Hollander, and P.J. Hutchinson. Inorg. Chem. **16**, 2655 (1977).
28. M.I. Bruce, M.J. Liddell, O.B. Shawkataly, C.A. Hughes, B.W. Skelton, and A.H. White. J. Organomet. Chem. **347**, 207 (1988).
29. W.R. Cullen, S.J. Rettig, and H. Zhang. Inorg. Chim. Acta. In press.

Synthesis of *meso*-phenyl-4,6-dipyrrins, preparation of their Cu(II), Ni(II), and Zn(II) chelates, and structural characterization of bis[*meso*-phenyl-4,6-dipyrrinato]Ni(II)

Christian Brückner, Veranja Karunaratne, Steven J. Rettig, and David Dolphin

Abstract: *meso*-Phenyldipyrromethanes can be oxidized by 2,6-dicyano-3,5-dichloro-*para*-benzoquinone (DDQ) to the corresponding *meso*-phenyldipyrrins. As expected, these novel, stable bipyrrolic pigments readily form metal chelates with copper(II), nickel(II), and zinc(II). Their UV–VIS spectra are compared with a series of known alkyl-substituted dipyrrin chelates and, based on the UV–VIS spectral analysis, the dihedral angle between the two ligands in the bis[*meso*-phenyldipyrrinato]Ni(II) complex was calculated to be 42°. The molecular structure of this complex was determined by X-ray crystallography, essentially confirming the calculation. Crystals of $C_{30}H_{22}N_4Ni$ are orthorhombic, $a = 17.156(3)$, $b = 35.217(1)$, $c = 7.886(1)$ Å, $Z = 8$, space group *Fddd*. The structure was solved by direct methods and refined by full-matrix least-squares procedures to $R = 0.040$ and $R_w = 0.031$ for 1058 reflections with $I \geq 3\sigma(F^2)$. The central nickel is coordinated in a distorted square-planar fashion by four nitrogens. The pair of the planar dipyrrinato ligands enclose a dihedral angle of 38.5°. This is the lowest angle reported for nickel(II) complexes of this kind. As a result of this, and in sharp contrast to previously described nickel(II) dipyrrin chelates, the central metal is diamagnetic.

Key words: *meso*-phenyldipyrromethanes, *meso*-phenyldipyrrins, *meso*-phenyldipyrrinato transition metal chelates, X-ray crystallography.

Résumé : Sous l'influence de la 2,6-dicyano-3,5-dichloro-*para*-benzoquinone (DDQ), on peut oxyder les *méso*-phényldipyrrométhanes en *méso*-phényldipyrrines correspondantes. Comme on pouvait s'y attendre, ces nouveaux pigments bipyrroliques stables forment des chélates métalliques avec le cuivre(II), le nickel(II) et le zinc(II). On a comparé leurs spectres UV–VIS avec ceux d'une série de chélates connus de dipyrrines substitutées par des groupes alkyles et, sur la base d'une analyse des spectres UV–VIS, on a calculé que l'angle dièdre entre les deux coordinats du complexe bis[*méso*-phényldipyrrinato]Ni(II) est de 42°. La structure moléculaire de ce complexe, telle que déterminée par diffraction des rayons X, confirme essentiellement les conclusions obtenues par calculs. Les cristaux du $C_{30}H_{22}N_4Ni$ sont orthorhombiques, groupe d'espace *Fddd*, avec $a = 17,156(3)$, $b = 35,217(1)$ et $c = 7,886(1)$ Å et $Z = 8$. La structure a été résolue par des méthodes directes et affinée par la méthode des moindres carrés jusqu'à des valeurs de $R = 0,040$ et $R_w = 0,031$ pour 1058 réflexions avec $I \geq 3\sigma(F^2)$. Le nickel central est coordiné d'une façon plan carré déformée par les quatre azotes. La paire de coordinats dipyrrinato plans forme un angle dièdrdre de 38,5°. Cette valeur correspond à l'angle le plus faible rapporté pour des complexes de nickel(III) de cette espèce. Il en résulte que, par opposition à ce qui a été décrit antérieurement pour les chélates de nickel(II) dipyrrine, le métal central est diamagnétique.

Mots clés : *méso*-phényldipyrrométhanes, *méso*-phényldipyrrines, *méso*-phényldipyrrinato, chélates des métaux de transition, diffraction des rayons X.

[Traduit par la rédaction]

Introduction

Dipyrrins (**1**), also known as dipyrromethenes, are basic, brightly colored, fully conjugated flat bipyrrolic molecules. Their propensity to strongly chelate transition metals has long been recognized (1, 2). Their structure, atom numbering scheme, and the formal nomenclature for dipyrrins is shown below. Positions 1 and 9 are also referred to as α positions, positions 2, 3, 7, and 8 as β positions, and position 5 as the *meso* position.

Received December 1, 1995.

This paper is dedicated to Professor Howard C. Clark in recognition of his contributions to Canadian chemistry.

C. Brückner, V. Karunaratne, S.J. Rettig, and D. Dolphin.[1]
Department of Chemistry, University British Columbia, 2036 Main Mall, Vancouver, BC V6T 1Z1, Canada.

[1] Author to whom correspondence may be addressed. Telephone: (604) 822-7881. Fax: (604) 822-9678. E-mail: david@dolphin.chem.ubc.ca

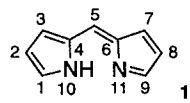

1

4,6-Dipyrrin
2-(2-*H*-Pyrrol-2-ylidenemethyl)pyrrole

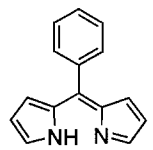

2

5-Phenyl-4,6-dipyrrin
2-(2-*H*-Pyrrol-2-ylidene-methyl-phenyl)pyrrole

Scheme 1.

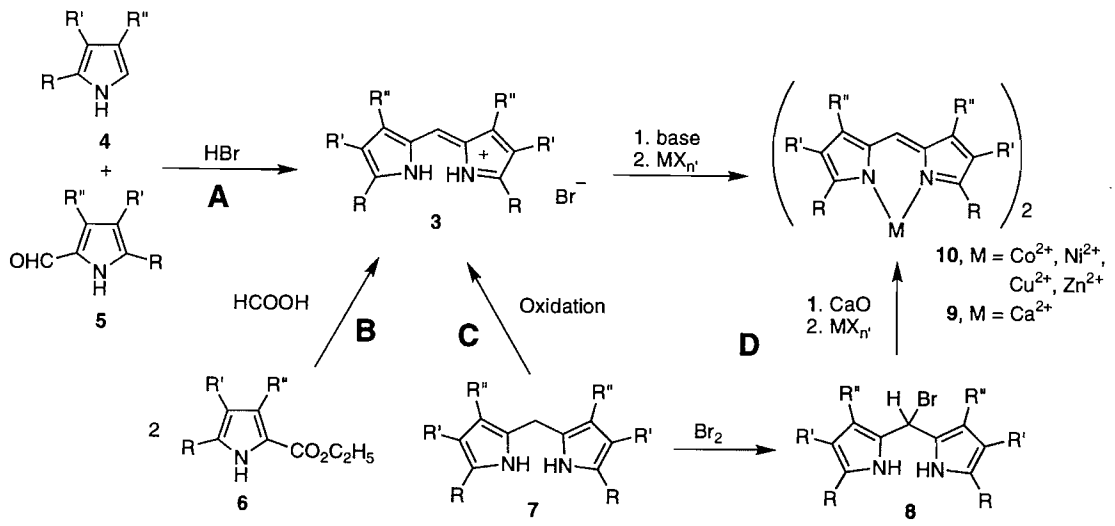

Scheme 2.

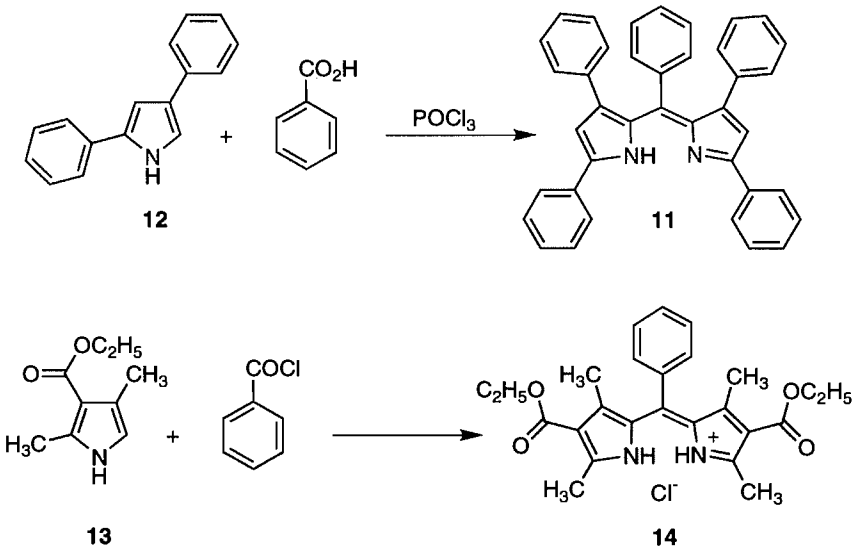

Scheme 1 outlines the principal pathways for the synthesis of α- and β-alkyldipyrrins (3) and their chelate-type mode of metal complex formation. Four main synthetic pathways can be distinguished:

A: The "classic" acid-catalyzed reaction of an α,β-alkyl-α′-free pyrrole (**4**) with a trialkylpyrrole-α-aldehyde (**5**) (1, 4);

B: The reaction of an α,β-alkyl-α′-ethyloxycarbonylpyrrole (**6**) in concentrated formic acid (5).

C: The oxidation of hexaalkyl-dipyrromethanes (**7**) by ferrous chloride (1) or 2,3-dichloro-5,6-dicyano-1,4-benzoquinone (DDQ) (6).

D: The *meso*-bromination of a dipyrromethane to yield the *meso*-bromo-dipyrromethane **8**, and subsequent reaction with calcium oxide to form the calcium chelate (**9**), yields directly a metal chelate. The calcium chelate can easily be transmetallated with a variety of transition metals (7–9).

In all other cases, reaction of dipyrrin (**3**) with a divalent transition metal salt yields the corresponding dipyrrinato complexes **10**. None of the methods A, B, or D has the potential to give access to *meso*-substituted, α,β-free dipyrrins (**2**). Only route C offers access to the title compounds by oxidation of a *meso*-phenyldipyrromethane (10). As will be outlined later in detail, this route was, indeed, successful in providing the title compounds.

meso-Alkyl-substituted dipyrrins are less common (1, 11–13) and the synthesis of *meso*-phenyl-substituted dipyrrins is even rarer, in fact, we are only aware of four previous syntheses, two of them shown in Scheme 2. Rogers (14, 15) confirmed in 1943 a finding of Gabriel from 1908 (16) that described the formation of **11** by reaction of 2,4-diphenylpyrrole (**12**) with in situ generated benzoyl chloride. In a similar approach, Treibs et al. reacted pyrrole **13** with benzoyl chloride to yield the hexasubstituted *meso*-phenyldipyrrin hydrochloride **14** (5). It is noteworthy that in both instances the pyrroles were substituted, particularly at one α and at least one β position. This prevents polymerization of the pyrroles during the harsh reaction conditions, consequently, these methods are not options to synthesize *meso*-phenyl, α-unsubstituted dipyrrins. A disadvantage of the protecting α-phenyl moieties is that they introduce severe steric interligand interactions

Scheme 3.

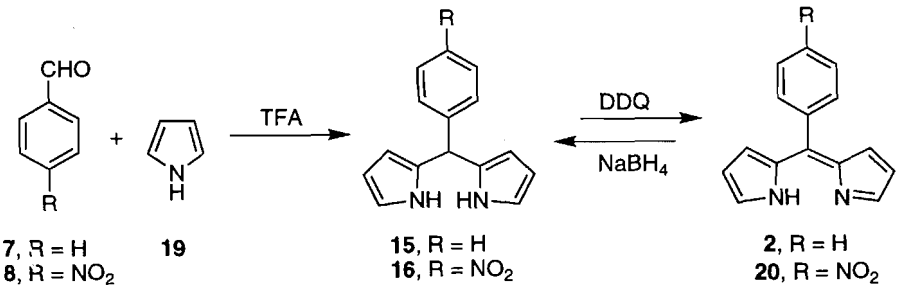

17, R = H
18, R = NO_2

19

15, R = H
16, R = NO_2

2, R = H
20, R = NO_2

upon metal complex formation. Moreover, *meso*-phenyl substitution concomitant with β-substituents also introduces intra-ligand steric interactions that can, for instance in the case of **14**, lead to deviations from planarity and even chemical instability (17). No reports were made on the metal complexation properties of either **11** or **14**. In 1985 the X-ray structure of bis[1-(2,6-dichlorobenzyl)-5-(2,6-dichlorophenyl)-dipyrrinato]zinc(II) was reported (18). This *meso*-phenyl and α-substituted dipyrrin complex was the kinetic product in the Rothemund-type condensation of the sterically hindered 2,6-dichlorobenzaldehyde with pyrrole, and its isolation was unexpected and fortuitous. Similarly unanticipated, Cavaleiro et al. isolated and crystallized *meso*-aryl-substituted dibenzofuranyldipyrrin in an attempted tetraarylporphyrin synthesis from *o*-acetoxybenzaldehyde and pyrrole (19). These synthetic pathways towards *meso*-phenyl dipyrrins and their metal complexes cannot be generalized. Recently two reports appeared in the literature in which *meso*-phenyl-substituted dipyrrin moieties were integral parts of larger molecules. The BF_2 complex of an α-methyl-*meso*-phenyldipyrrin unit was the input unit of a molecular photonic wire (20) and an α-thiophenyl and β-alkyl-substituted *meso*-phenyldipyrrin was synthesized in the course of research towards polyheterocyclic ligands; however, neither the complexing properties nor the conformation of this compound were reported (21).

The stereochemistry of pyrrin ligands around the metal is dependent on the bulkiness of the substituents in the α and α′ positions, and has found interest (22) since Porter (23) called attention to this phenomenon; however, only a limited number of structural data are available (18, 22, 24, 25). Few α-unsubstituted dipyrrinato complexes have been prepared (26, 27) and in no case has a crystal structure been described. Therefore, it was interesting to investigate the complex geometry of the α′-unsubstituted *meso*-phenyldipyrrin ligands of type **2** and to contrast these findings with published data. This and the general interest for novel ligand classes for use in transition metal catalysis (28), photometric metal detection (29), or biomedical purposes (30) prompted us to investigate the synthesis and the metal complexing properties of α,β-unsubstituted *meso*-phenyldipyrrins.

Results and discussion

Synthesis of 5-phenyldipyrromethanes 15 and 16

The *meso*-phenyldipyrromethanes **15** and **16** were synthesized by the acid- catalyzed condensation of benzaldehyde (**17**) or *p*-nitrobenzaldehyde (**18**), with pyrrole (**19**). Pyrrole was also used as solvent according to a procedure of Lee and Lindsey (10) (see Scheme 3). The synthesis of **16** offers the great practical advantage over the synthesis of **15** or other dipyrromethanes described by Lee and Lindsey, in avoiding any chromatography during the work-up or purification of the compound; thus it is amenable to large-scale (≥10.0 g product per experiment) preparations. The higher electrophilicity of *p*-nitrobenzaldehyde compared to benzaldehyde likely results in a faster reaction rate and a stabilization of the resulting dipyrromethane towards acid-catalyzed decompositions. Both these aspects in combination with the simple work-up explain the high overall yield of 82% for **15** vs. the reported 49% (10) for **16**.

Preparation and characterization of *meso*-phenyldipyrrins 2 and 20

Dehydrogenations with DDQ have found wide application in the synthesis of pyrrolic pigments (31). In particular, DDQ is useful in the conversion of any type of reduced porphyrins (e.g., porphyrinogens or chlorins) to the corresponding fully unsaturated porphyrins (32). Porphyrinogens are intermediates (33) in the synthesis of *meso*-tetraarylporphyrins according to the methods of Adler et al. (34) or Lindsey and Wagner (35), i.e., the acid-catalyzed cyclization of pyrrole and benzaldehydes. Hence, it was not unexpected that the reaction of *meso*-phenyldipyrromethanes **15** or **16** with one equivalent of DDQ smoothly formed the desired dipyrrins **20** and **2** (Scheme 3). *p*- and *o*-Chloranil are equally well suited to perform the conversion. Reduction of **2** or **20** with $NaBH_4$ in MeOH regenerates the leuko form **16** or **15**. In dilute solution, the oxidation products are bright yellow in color. The optical spectrum of **2** under acidic and basic conditions is shown in Fig. 1. The two-band pattern of the protonated species is analogous to that of 1, 2, 3, 7, 8, 9-hexamethyldipyrrin hydrobromide (11), but ~14 nm hypsochromically shifted, with slightly lower extinction coefficients. The bands have been assigned to $\pi^* \leftarrow \pi$ transitions and are indicative of the marked planarity of these fully conjugated aromatic systems. Addition of acid protonates the basic imine-type nitrogen of the 2*H*-pyrrole unit and this removal of non-degeneracy of the linear resonator in combination with the presence of a positive charge induces a bathochromic shift of 42 nm and a tripling of the extinction coefficient (36). For steric reasons, it can be inferred that the phenyl moiety is approximately perpendicular to the plane of the dipyrrin. Consequently, the phenyl group is not in full conjugation with the pyrrolic system and substituents on the phenyl group minimally influence the π-cloud of the dipyrrin. This explains the close similarity of the optical spectrum of **2** and its *p*-nitro derivative **20**; a similar

Fig. 1. Optical spectra of **2** in CH_2Cl_2 – 0.5% MeOH – trace NH_4OH (broken line) and in CH_2Cl_2 – 0.5% MeOH – trace HCl (dotted line), and of **20** in CH_2Cl_2 – 0.5% MeOH – trace HCl (solid line).

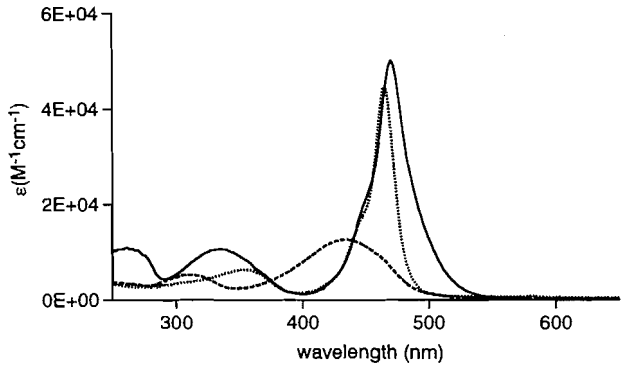

situation is also found in variously phenyl-substituted *meso*-tetraphenylporphyrins (37). The nitro compound **20**, and its metal complexes, exhibit a band at ~260 nm that we attribute to the *p*-nitro moiety. The optical spectrum of **2** is closer to that of the hexamethyldipyrrin than to the spectrum of **11**, which is about 110 nm bathochromically shifted (17), possibly reflecting the extended conjugation (and distortion) of this system by the α-phenyl groups.

The signals in the ^1H and ^{13}C NMR of the *meso*-phenyldipyrrins indicate a plane of symmetry. This is consistent with formulating the dipyrrins as adopting a planar conformation and a rapid tautomeric exchange of the NH proton between the two nitrogens. The ^1H NMR shifts for the β-protons of **2** of 6.39 and 6.47 ppm and for the α-protons of 7.78 ppm attest to the aromatic character of these compounds.

Alkyldipyrrins of type **3** are, owing to their basicity, generally isolated and purified as their hydrobromide or hydrochloride salts (1). Although conditions for thin-layer and column chromatography of dipyrrin hydrobromides have been described (mixture of formic acid, methanol, and chloroform – silica gel (38)), it is not common practice. Their free bases are also reportedly less stable. We were surprised to find that in case of the *meso*-phenyldipyrrins, column chromatography (CH_2Cl_2 – silica gel) of their free bases posed no difficulty.

Formation and characterization of transition metal chelates of the *meso*-phenyldipyrrins

General data and synthesis

A concentrated MeOH solution of the *meso*-phenylpyrrins **2** or **20**, when mixed with a methanolic solution of the divalent metal ions Ni^{2+}, Cu^{2+}, and Zn^{2+}, as their acetates, yields the corresponding highly colored metal complexes (Scheme 4). The complexes are stable and do not require any special handling. Analyses confirmed the stoichiometry of the precipitates as $M(ligand)_2$. The metal complexes formed X-ray quality dichroic (metallic green–red) crystals.

The vibrational spectra of the metal complexes are similar to those of their ligands. This is not unexpected as conjugation is already attained in the planar ligand moiety before coordination to a metal. Thus, intraligand vibrations will undergo only minor shifts upon metal chelation. This has been rationalized before for the metal complexes of hexaalkylpyrrins (39).

Scheme 4.

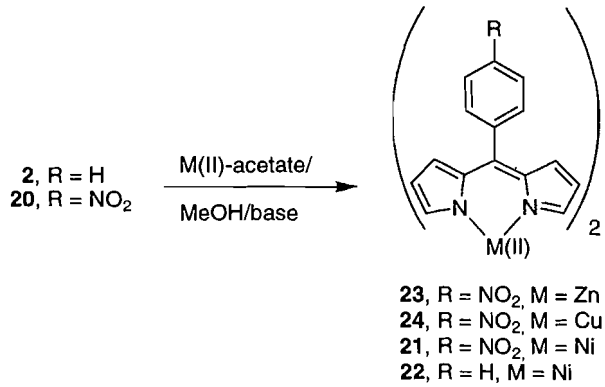

23, R = NO_2, M = Zn
24, R = NO_2, M = Cu
21, R = NO_2, M = Ni
22, R = H, M = Ni

Fig. 2. Optical spectra of **21** in $CHCl_3$ (broken line) and **22** in $CHCl_3$ (solid line).

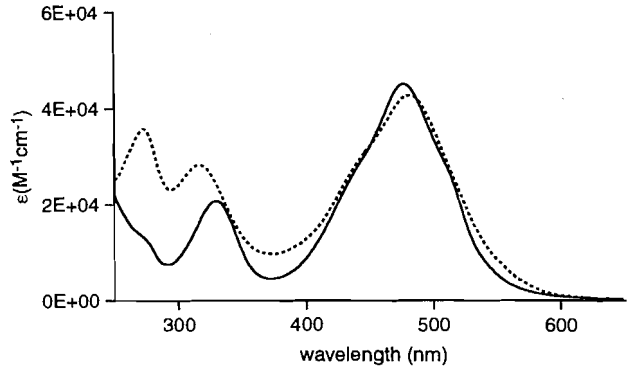

UV–VIS spectra

The optical properties of the metal compounds are strongly dependent on the central metal but the nickel chelates **21** and **22** are very similar (Fig. 2). This similarity, in particular with respect to λ_{max} and log ϵ, is indicative of a very similar stereochemistry of these two compounds. The UV–VIS spectrum of the zinc chelate **23** resembles that of the protonated ligand, suggesting the absence of any metal ← metal transitions (see Fig. 3). However, metal ← ligand charge transfer transitions are generally observed in this energy region and they cannot be excluded (27), though other authors have assigned this band exclusively to intraligand π* ← π transitions and the bands in the 320–350 nm region to charge transfer transitions (40). The electronic spectra of the nickel and the copper chelates **20**, **21**, and **24** follow the same general pattern as that of **23** (see Figs. 2 and 3). The UV–VIS spectra of the metal chelates are nearly indistinguishable in non- or weakly coordinating solvents such as benzene, methanol, methylene chloride, or chloroform but show changes in pyridine, most noticeable for the zinc chelate, as also shown in Fig. 3. Table 1 lists selected UV–VIS data of some known dipyrrinato-metal complexes (**25**–**40**) and of the novel compounds **21**, **23**, and **24**.

When comparing the longest wavelength absorption of the Zn-chelate **23** at 486 nm against the equivalent transitions of

Fig. 3. Optical spectra of **23** in CH_2Cl_2 (dotted line) and pyridine (dashed line), and **24** in $CHCl_3$ (solid line).

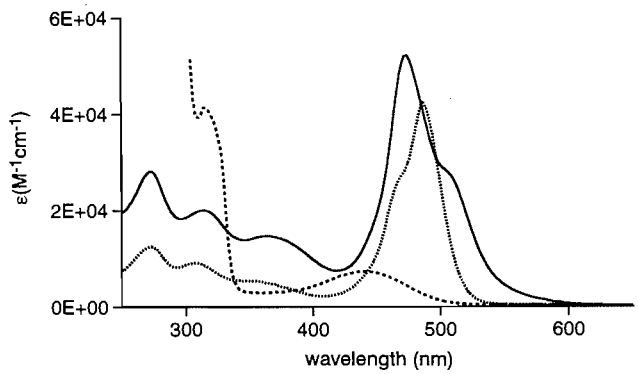

the alkyl-substituted analogues **25–32**, it is remarkable that the *meso*-phenylpyrrin chromophore is distinguished by the highest transition energy. An equivalent trend can be seen in the nickel (**22** vs. **33–36**) and copper (**24** vs. **37–40**) chelate series. Hyperconjugation effects have been suggested for the progressive bathochromic shift with increasing methyl substitution (27). Extended π-conjugation can be evoked for the bathochromically shifted optical spectrum in case of dipyrrins **28** and **32**. The absence of both effects in the zinc, nickel, and copper chelates **21–24** rationalize their relatively high transition energies. The introduction of a *meso*-methyl substituent in chelates **29** and **30** leads, when compared to their *meso*-unsubstituted analogues **27** and **28**, to a relatively small change in the energy of the longest wavelength transition; however, their extinction coefficients significantly decrease. This, based on theoretical considerations, may be taken as a sign of distortion from planarity (17). Based on the foregoing, the high extinction coefficients of the metal chelates of the *meso*-phenyldipyrrins seem to indicate that the ligands are flat. In the absence of any β-substituent and hence any intraligand steric crowding, and in analogy to the conformation of *meso*-tetraphenylporphyrins (42), this appears to be a reasonable assumption. As will be detailed later, the single crystal X-ray structure of **22** shows that the assumption of planarity is, in fact, valid.

The stereochemistry of the ligands around the central metal is strongly dependent on the metal type. The preference of zinc(II) for a tetrahedral, and of nickel(II) and, even more so, of copper(II) for a square-planar coordination sphere is well documented (43). Regardless of the α substituents present in the dipyrrin ligands, the realization of a tetrahedral coordination sphere poses no interligand steric interactions. Consequently, and in analogy to the stereochemistry of the zinc chelates of alkyldipyrrins, compound **23** can be assigned a tetrahedral structure (9, 22, 27, 40). The picture is more complex for the nickel and copper chelates. It has been found in previous studies that α substituents prevent square-planar coordination due to interligand crowding. This forces the complex into a distorted tetrahedral structure in which the two approximately planar α-methyldipyrrinato ligands are inclined (as determined by X-ray crystal structure analysis) at an angle (referred to as dihedral angle) of 76.3° for nickel chelate **33** (24) and 66° for copper chelate **39** (25). With hydrogen as the sole α substituents no a priori statement can be made about the stereochemistry around the metal. It has been suggested that some electronic interaction exists between the π-systems of the two dipyrrin units coordinated to the same metal ion in the "tetrahedral" Co(II) and Cu(II) complexes (44). Motekaitis and Martell presented an MO theory model and derived a relationship (eq. [1]) in which the intensity of the longest wavelength transition is assumed to change with the tetrahedral angle θ between the ligands:

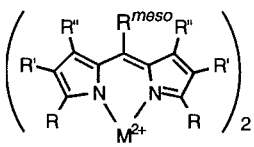

Compound no.	R	R′	R″	R^{meso}	M^{2+}
25	-H	-Me	-Me	-H	Zn
26	-Me	-H	-Me	-H	Zn
27	-Me	-Me	-Me	-H	Zn
28	-Me	$-CO_2Et$	-Me	-H	Zn
29	-Me	$-CO_2Et$	-Me	-Me	Zn
30	-Me	-Me	-Me	-Me	Zn
31	$-CO_2Et$	-Cl	-Cl	-H	Zn
32	-Ph	-H	-H	-H	Zn
33	-Me	-H	-Me	-H	Ni
34	-Me	-Me	-Me	-H	Ni
35	-Me	$-CO_2Et$	-Me	-H	Ni
36	-Ph	-H	-H	-H	Ni
37	-H	-Me	-Me	-H	Cu
38	-Me	-Me	-Me	-H	Cu
39	-Me	$-CO_2Et$	-Me	-H	Cu
40	-Ph	-H	-H	-H	Cu

Table 1. Selected UV–VIS data and dihedral angles of dipyrrinato chelates.

Compound no.	λ_{max} (log ε)[a] (nm)	Dihedral angle (°)[b]	Reference
23	486 (4.97)[d]	90[g]	This work
25	500 (5.08)[e]	90[g]	27
	483 (4.97)		
26	488 (4.22)[e]	90[g]	27
	469, sh		
27	505 (4.93)[e]	90[g]	27
	487 (5.07)		
28	490 (5.33)[e]	90[g]	22
	446, sh		
29	501 (5.05)[f]		11
30	505 (4.06)[f]		11
31	537 (5.13)[e]		9, 41
32	552 (4.93)[e]	90[g]	27
	510 (5.06)		
22	484 (4.63)[d]	42,[h] 38.5[i]	This work
33	512 (4.85)[e]	76.3[i]	24, 39
34	531 (4.70)UIe		
		39	
	462 (4.57)		
35	495 (4.99)[e]		40
36	540 (4.85)[e]	60,[j] 66[h]	26
24	474 (4.72)[e]	48[h]	This work
37	471 (4.85)[e]	50,[h] 63[j]	26
	409 (4.61)		
38	525 (4.65)[e]	68[j]	39
	471 (4.76)		
39	495 (5.05)[e]	66[i]	25, 40
40	564 (4.93)[e]	90,[h] 73[j]	26
	509 (4.70)		

[a]Longest wavelength $\pi^* \leftarrow \pi$ transition.
[b]Between planes formed by the ligands.
[c]*p*-NO_2-phenyl.
[d]In CH_2Cl_2.
[e]In $CHCl_3$.
[f]Solvent not specified.
[g]Assumed angle.
[h]Calculated according to Motekaitis et al. (9).
[i]From X-ray single crystal structure.
[j]Based on ligand field transition analysis (26).

$$[1] \quad \frac{\epsilon^{\theta}}{\epsilon^{90}} = \sin^2 \theta$$

θ is the tetrahedral angle, ϵ^{θ} is the extinction coefficient of a reference compound known to be tetrahedral, i.e., θ = 90°, and ϵ^{θ} is the extinction coefficient of a similar compound whose geometry is to be determined. According to eq. [1], the calculated tetrahedral angle in the *meso*-phenyldipyrrin nickel complex **22** would be 42°, and in the copper complex **24**, 48°. There are, however, precautions to be taken when applying Martell's methodology for determination of the interligand dihedral angle. The prerequisite that the ligands are flat and coordinate in exactly the same MN_4 fashion to the complexes to be compared must be strictly fullfilled. Fergusson and coworkers (22), for instance, published the crystal structure analysis of the palladium chelate of 3,3′,5,5′-tetramethyl-4,4′-diethoxycarbonyldipyrrin in which the dipyrrin unit was *not* planar. The tendency for palladium to achieve square-planar coordination geometry is strong enough to distort the planar ligand and to enforce a stepped arrangement of the ligands around the metal centre. With little change in transition energy, the extinction coefficients were reduced compared to the analogous tetrahedral cadmium, mercury, or zinc complexes. However, the application of eq. [1] gives incorrect results when compared to the actual structures. A second example can be derived from examination of the literature. Based on the extinction coefficient of **31**, Martell determined the dihedral angle of the copper analogue to be 40° (9). However, considering the steric requirement of the ethoxycarbonyl moiety and setting it against the crystallographically determined dihedral angle of 66° for **39** or values determined for the complexes **37**–**40**, this value appears to be considerably too low. Murakami et al. investigated the IR spectrum and the ligand-field bands of this complex and proposed the involvement of the carbonyl oxygen in this copper chelate, giving a CuN_4O_2 coordination (41). In light of this it becomes apparent that the dihedral angle predicted by Martell's method had to be in error. In the present case, however, the prerequisites of similarly flat ligands forming in all cases a MN_4 coordination sphere are most likely fullfilled and, consequently, the theoretically determined values may be significant. Indeed, the X-ray crystal structure analysis for nickel complex **22** proved the value determined by Martell's method to be fairly accurate (3.5° deviation, Table 1). As for the copper chelate, a final experimental proof of the calculated value still awaits, but the value of 48° is in agreement with the calculated value of one other α-unsubstituted copper chelate **37** and, as expected, is significantly smaller than for the α-alkyl-substituted chelates. The calculated values for the copper chelates have to be taken with some reservation as shown by the discrepancies of the values determined by ligand field transition band analysis and by Martell's method.

The change of the optical spectrum of **23** upon the addition of pyridine (Fig. 3) results from an expansion of the Zn-coordination sphere from tetrahedral ZnN_4 to a distorted tetragonal pyramid ZnN_5. This forces the dipyrrinato ligands to take up a smaller dihedral angle, which probably accounts for the observed spectrum. The nickel chelate UV–VIS spectrum shows only a slight change upon addition of pyridine. This is analogous to, for instance, the reluctance of the square- planar nickel(II) porphyrins to expand their coordination sphere and the small changes in their optical spectrum associated with any additional coordination (45). This effect is even more pronounced in the case of the Jahn–Teller ion copper(II).

Magnetic properties

The magnetic properties of nickel(II) complexes with N-donor ligands may permit conclusions regarding their coordination geometry. Square-planar complexes are typically diamagnetic, and tetrahedral complexes paramagnetic (43). All

Fig. 4. ORTEP plot (stereoview) of **22**; 33% probability thermal ellipsoids are shown for the non-hydrogen atoms.

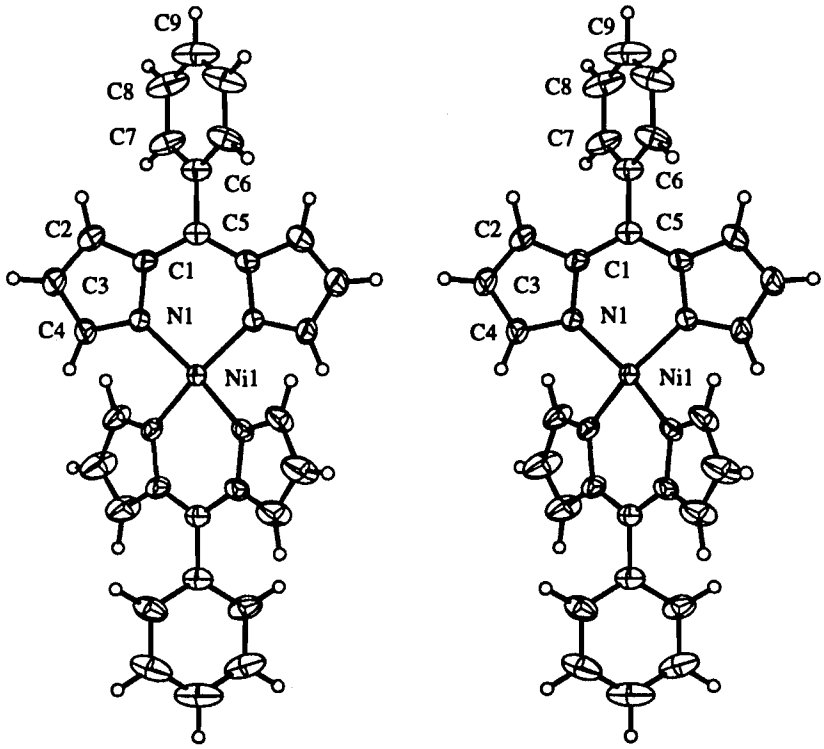

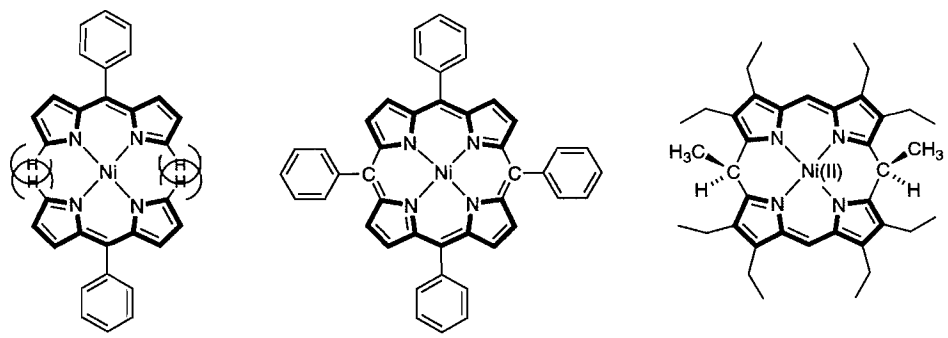

22 41 42

nickel(II) chelates of dipyrrins have been described as paramagnetic and, therefore, their description as distorted tetrahedral rather than distorted square planar is plausible regardless of the actual dihedral angle between the ligands. To our surprise, the nickel chelates **21** and **22**, as judged by the sharp ^1H and ^{13}C NMR, proved to be diamagnetic. This suggests that they are (distorted) square planar. On the basis of a comparison of the steric interactions in the cyclic and planar [meso-tetraphenylporphyrinato]nickel(II) (**41**) or the cyclic and saddle-shaped [5,15-dimethyl-5,15-dihydrooctaethylporphyrinato]-nickel(II) (**42**) (46), it becomes clear that a planar coordination can be excluded since the two α-hydrogens of the opposing ligands would occupy the same space (given standard Ni—N bond lengths) in case of square- planar coordination. To unambiguously answer the question about the dihedral angles in the nickel chelate, an X-ray crystal structure analysis of a single crystal of **22** was undertaken.

Crystal structure analysis

An ORTEP representation of **22** as it exists in the crystal together with the numbering system employed in Tables 2 and 3 is shown in Fig. 4. Atom coordinates and B_{eq} are listed in Table 2. Selected bond parameters are listed in Table 3, and the crystallographic data are listed in Table 4.

The molecule has D_2 symmetry, which makes the two ligands equivalent and endows a C_2-axis passing through the *p*-hydrogens of the *meso* substituent, the methine carbons, and the central metal. The planes of the two essentially planar dipyrrin ligands enclose a dihedral angle of 38.5°, in close agreement with the calculated value of 42°. The equivalent angle in [3,3′,5,5′-tetramethylpyrrinato]nickel(II) (**33**) is, as mentioned above, 76.3° (24). The small angle results directly from the smaller size of the α-H as compared to the α-methyl group. The bite angle N–Ni–N_a of the ligand is 94.3°, which is, within the experimental uncertainty, equal to the bite angle

Table 2. Atom coordinates and B_{eq}[a] for **22**.

Atom	*x*	*y*	*z*	B_{eq}
Ni(1)	0.12500	0.12500	0.62500	3.07(1)
N(1)	0.0990(1)	0.16291(5)	0.4630(2)	3.61(5)
C(1)	0.0985(1)	0.20166(7)	0.4808(3)	3.91(6)
C(2)	0.0592(2)	0.21708(8)	0.3404(4)	6.72(9)
C(3)	0.0340(2)	0.18773(9)	0.2426(4)	8.0(1)
C(4)	0.0592(2)	0.15443(8)	0.3215(3)	5.29(7)
C(5)	0.1250	0.22034(9)	0.6250	3.50(7)
C(6)	0.1250	0.26307(9)	0.6250	4.18(8)
C(7)	0.1658(2)	0.28288(8)	0.5040(4)	5.70(8)
C(8)	0.1666(2)	0.32263(8)	0.5060(6)	7.5(1)
C(9)	0.1250	0.3416(1)	0.6250	8.6(2)

[a] $B_{eq} = 8/3\pi^2(\Sigma\Sigma U_{ij} a_i^* a_j^* (\mathbf{a}_i \cdot \mathbf{a}_j)$.

Table 3. Selected bond distances and bond angles for **22**.[a]

Atoms	Distance (Å)	Atoms	Angle (°)
Ni(1)—N(1)	1.879(2)	N(1)-Ni(1)-N(1)$_a$	94.3(1)
N(1)—C(4)	1.336(3)	N(1)-Ni(1)-N(1)$_c$	92.1(1)
C(1)—C(5)	1.390(3)	Ni(1)-N(1)-C(4)	123.4(2)
C(3)—C(4)	1.396(4)	N(1)-C(1)-C(2)	108.0(2)
C(6)—C(7)	1.374(3)	C(2)-C(1)-C(5)	128.2(2)
C(8)—C(9)	1.355(4)	C(2)-C(3)-C(4)	106.7(3)
N(1)—C(1)	1.404(3)	C(1)-C(5)-C(1)$_c$	123.5(3)
C(1)—C(2)	1.405(4)	C(5)-C(6)-C(7)	120.5(2)
C(2)—C(3)	1.360(4)	C(6)-C(7)-C(8)	120.3(3)
C(5)—C(6)	1.505(4)	C(8)-C(9)-C(8)$_c$	120.9(4)
C(7)—C(8)	1.400(4)	N(1)-Ni(1)-N(1)$_b$	152.5(1)
		Ni(1)-N(1)-C(1)	128.6(2)
		C(1)-N(1)-C(4)	106.2(2)
		N(1)-C(1)-C(5)	123.4(2)
		C(1)-C(2)-C(3)	107.8(2)
		N(1)-C(4)-C(3)	111.3(3)
		C(1)-C(5)-C(6)	118.2(1)
		C(7)-C(6)-C(7)$_c$	118.9(3)
		C(7)-C(8)-C(9)	119.7(3)

[a] Symmetry operations: (*a*) 1/4 – *x*, 1/4 – *y*, *z*; (*b*) *x*, 1/4 – *y*, 5/4 – *z*; (*c*) 1/4 – *x*, *y*, 5/4 – *z*.

observed for **33**. The N–Ni–N$_b$ angle is 152.5°. Unlike in the latter structure, no distortion in the sense of a deviation of colinearity of the two local twofold axes of each Ni-ligand group can be detected. The four Ni—N distances are equal (1.879(2) Å), and unusually short for complexes of this kind. We regard this effect to be partially due to the reduced ionic radius of the d^8 low spin ion vs. the high-spin congener in **33** (47) and partially due to the reduced interligand steric interactions. The extent of the steric effect becomes perceptible if the bond length is compared to those in related nickel complexes **33**, nickel porphyrin (**41**), a ruffled nickel porphyrin (**42**), and a 5,10-dihydroporphyrin system (**43**) as listed in Table 5. The quasi-rigid porphyrin core (in complex **41**) resists undue radial expansions or contractions in the equatorial plane of the core. Therefore, the metal – porphyrin nitrogen bond lengths are

Table 4. Crystallographic data for compound **22**.[a]

Formula	$C_{30}H_{22}N_4Ni$
fw	497.23
Crystal system	Orthorhombic
Space group	*Fddd*
a, Å	17.156(3)
b, Å	35.217(1)
c, Å	7.886(1)
V, Å^3	4764.4(9)
Z	8
D_{cacl}, g/cm^3	1.386
F(000)	2964
μ. cm^{-1}	8.41
Crystal size, mm	0.20 × 0.30 × 0.40
Transmission factors	0.877–1.000
Scan type	ω–2θ
Scan range, deg in ω	0.94 + 0.35 tan θ
Scan speed, deg/min	16 (up to 8 rescans)
Data collected	+*h*, +*k*, +*l*
$2\theta_{max}$, deg	70
Crystal decay, %	2.3
Total reflections	2874
Total unique reflections	2874
Reflections with $I \leq 3\sigma(F^2)$	1058
No. of variables	82
R	0.040
Rw	0.031
gof	2.00
Max Δ/σ (final cycle)	0.0002
Residual density e/Å^3	–0.44 to 0.42

[a] Temperature 294 K, Rigaku AFC6S diffractometer, Mo Kα radiation (λ = 0.71069 Å), graphite monochromator, takeoff angle 6.0°, aperture 6.0 × 6.0 mm at a distance of 285 mm from the crystal, stationary background counts at each end of the scan (scan/background time ratio 2:1); $\sigma^2(F^2) = [S_2(C + 4B)]/Lp_2$ (*S* = scan rate, *C* = scan count, *B* = normalized background count), function minimized $\Sigma w (|F_o| - |F_c|)^2$ where $w = 4F_o^2/\sigma^2(F_o^2)$, $R = \Sigma||F_o| - |F_c||/\Sigma|F_o|$, $R_w = (\Sigma w(|F_o| - |F_c|)^2/\Sigma w|F_o|^2)^{1/2}$, and gof = $[\Sigma w(|F_o| - |F_c|)^2/(m - n)]^{1/2}$. Values given for *R*, R_w, and gof are based on those reflections with $I \leq 3\sigma(F^2)$.

Table 5. Ni—N bond lengths of selected tetrapyrrolic nickel complexes.

Compound no.	Ni—N bond length (Å)	Reference
22	1.879(2)	This work
27	1.952(7) (averaged)	24
42	1.904(5) (3 out of 4)	46
43	1.929	48
41	1.96[a]	49, 51

[a] Typical value for nickel porphyrins.

restricted relative to the normal range of values that are found in metal – monodentate nitrogen ligand bond lengths, which results in a "stretched" bond length of ~1.96 Å. Ruffled nickel porphyrins can reduce the bond length by about 0.03 Å; in the saddle-shaped **42**, which is essentially a strapped bisdipyrri-

Fig. 5. Intraligand bond lengths, and limiting resonance structures of the dipyrrinato ligand.

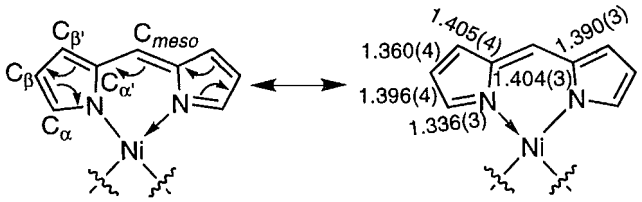

nato nickel(II) compound, the bond length is a further 0.025 Å shorter. The removal of the ligand strap concomitant with the introduction of α-methyl groups introduces severe steric interactions in **33** but allows for a large dihedral angle, nonetheless, a long Ni—N bond length is recorded for this class of complexes. Removal of a large portion of this interaction by the replacement of the methyl groups with hydrogens in **22** allows the two ligands to achieve "pseudo-planarity" and results in the shortest Ni—N bond length of its class.

Inspection of the intraligand bond lengths reveals that two types of C—N bonds exist, a short C_{α}—N bond and a long $C_{\alpha'}$—N bond. The differences can be accounted for in terms of a resonance description of the π-electrons in the ligand molecule. Figure 5 shows the two limiting resonance structures and the associated bond lengths. According to this simplified picture, the C_{α}—N bond would receive partial π-contribution, the $C_{\alpha'}$—N bond would not. The difference in double bond character of these bonds explains the observed bond length differences in a qualitative way. The deviation of the $C_{\alpha'}$–N bond length from the expected 1.42 Å for a C—N single bond reflects the aromatic character of the pyrrole unit itself, albeit the analogous bond length in pyrrole is about 0.04 Å shorter (50). The $C_{\alpha'}$—C_{meso} bond and the C_{α}—C_{β} bond have a formal bond order of 1.5, and hence their bond lengths are as expected. The mean plane of the *meso*-phenyl group is tilted 58.1° with respect to the mean plane of the dipyrrin unit. This deviation from the, perhaps, expected orthogonal finds its parallels in the structure of *meso*-tetraphenylporphyrins (38, 51).

NMR spectroscopy

The ^1H and ^{13}C NMR data of the diamagnetic metal chelates **21–23** are largely as expected, and similar to the spectra of the protonated ligands. One noticeable exception is a large low field shift of the α-protons in the nickel chelates **21** and **22**, i.e., a shift of +2.48 ppm for **22** as compared to the zinc analog **23**. This also is evidence of the small dihedral angle of the ligand mean planes in the nickel complex. The α-protons experience shielding effects of both the aromatic dipyrrinato systems and thus are more shielded than in the tetrahedral zinc complex, where such "double" shielding cannot occur.

Conclusion

The *meso*-phenyl-4,6-pyrrins can be conveniently prepared from the corresponding dipyrromethanes. They exhibit properties similar to previously described alkyl-substituted dipyrrins with the exception that they exhibit a significantly higher $\pi^* \leftarrow \pi$ transition energy as judged by their hypsochromically shifted UV–VIS spectra. The *meso*-phenyldipyrrins form metal complexes with nickel(II), copper(II), and zinc(II). Their spectroscopic data can be rationalized in the context of the previously described dipyrrinato complexes; however, the lack of a bulky α-substituent allows unique properties to this class of ligands. Based on optical and ^1H NMR data, the zinc complex can be assigned a tetrahedral structure. Both the nickel and the copper complex can be described as distorted square-planar complexes. The distortion from planarity of the nickel complex was predicted to be 42°, based on UV–VIS data analysis. An X-ray crystal structure analysis determined the angle to be 38.5° and the Ni—N distance to be 1.879(2) Å. This is the smallest angle and the shortest Ni—N bond length recorded for dipyrrinato complexes. As a consequence of this, and in contrast to previously described [dipyrrinato]nickel(II) complexes, the [*meso*-phenyldipyrrinato]nickel(II) complexes are diamagnetic. The stereochemistry of the copper complex is assumed to be similar to that of the nickel complex. Studies to utilize the unique steric requirement of the *meso*-phenyldipyrrin ligand, e.g., to form coordination polyhedra with no precedent in the dipyrrinato field, such as octahedral M(III)(ligand)$_3$ complexes, are currently under way in our laboratories.

Experimental section

Instrumentation and materials

Melting points were determined on a Thomas model 40 Micro Hot Stage and are uncorrected. The infrared spectra were measured with a Perkin–Elmer model 834 FT-IR instrument. The NMR spectra were measured with a Bruker AC 200 FT spectrometer and are expressed in parts per million (δ) relative to the external standard TMS. The low- and high-resolution mass spectra were obtained by Dr. G. Eigendorf and co-workers of this department using an AEI MS9 and a Kratos MS50 spectrometer, respectively. The electronic spectra were measured on a HP 8452A photodiode array spectrophotometer. Elemental analyses were performed by Mr. P. Borda of this department on a Fisons CHN/O Analyzer, model 1108.

meso-Phenyldipyrromethane **15** was synthesized according to the procedure of Lee and Lindsey (10). All other reagents and solvents were commercially available and of reagent grade or higher, and were, unless otherwise specified, used as recieved. The silica gel used in flash chromatographies was Merck Silica Gel 60, 230–400 mesh.

5-(4-Nitrophenyl)dipyrromethane (16)

Nitrobenzaldehyde (**18**) (3.0 g, 19.87 mmol) was dissolved in freshly distilled pyrrole (**19**) (44.0 g, 0.66 mol). The mixture was degassed by bubbling with N_2 for 10 min. TFA (0.15 mL, 0.1 equiv based on the benzaldehyde) was added and the mixture was stirred under N_2 until no starting aldehyde could be detected by TLC (ca. 15 min). The volume of the slightly yellow mixture was reduced under high vacuum at 50°C to a viscous oil. This oil was dissolved in CH_2Cl_2 (100 mL) and cyclohexane (50 mL) was added. Without heating, the mixture was reduced on the rotary evaporator until precipitation just began. Scratching with a glass rod caused rapid crystallization of an slightly greenish solid which, after drying at 50°C/0.2 Torr (1 Torr = 133.3 Pa) for 24 h gave 3.85 g (71.2%) of analytically pure compound **16**. A second crop of lesser purity was obtained from the mother liquor upon further evaporation

(0.55 g, 10.3%); mp 158°C; UV–VIS (MeOH) λ_{max} nm (rel. intensity): 222 (1.0), 266 (0.77); ^{1}H NMR (200 MHz) δ: 5.58 (s, 1H), 5.87 (m, 2H), 6.18 (dd, J = 11.8, 2.5 Hz, 2H), 6.74 (m, 2H), 7.37 (d, J = 11.8 Hz, 2H), 7.95 (br s, 2H), 8.14 (d, J = 11.8 Hz, 2H); ^{13}C NMR (50 MHz) δ: 43.8, 107.8, 108.8, 118.0, 123.8, 129.2, 130.8, 146.9, 149.7; LR-MS (EI) *m/e*: 267 (100.0, M^+), 220 (9.7, $MH^+ - NO_2$), 201 (16.3, $M^+ - C_4H_4N$), 154 (9.7), 145 (47.3, $MH^+ - Ph - NO_2$). Exact Mass calcd. for $C_{15}H_{13}N_3O_2$: 267.10078; found: 267.10080. Anal. calcd. for $C_{15}H_{13}N_3O_2$: C 67.41, H 4.9, N 15.72; found: C 67.23, H 4.98, N 15.62.

5-Phenyl-4,6-dipyrrin (2)

meso-Phenyldipyrromethane (15) (500 mg, 2.25 mmol) was dissolved with the help of a heat gun in benzene (25 mL). A solution of 2,3-dichloro-5,6-dicyano-1,4-benzoquinone (537 mg, 2.35 mmol) dissolved in benzene (5 mL) was added and the mixture stirred until no starting material could be detected by tlc (1 h). The black precipitate was filtered off and air-dried to provide 440 mg (85 %) of crude 2, which was used for metal complex formation. An analytical sample was purified by column chromatography (silica gel, 25 g, 1% MeOH in $CHCl_3$). The bright yellow main fraction was collected and evaporated to dryness. The yellow film was dissolved in acetone (20 mL) and precipitated by diffusion of cyclohexane into this solution to yield a yellow-brown precipitate (55.0 % based on crude material); mp 184°C; IR (neat): 1555, 1450, 1435, 1340, 1055 cm^{-1}; UV–VIS (CH_2Cl_2 – 0.5% MeOH – trace NH_4OH) λ_{max} (log ε): 310 (3.75), 434 (4.10) nm; (CH_2Cl_2 – 0.5% MeOH – trace HCl) λ_{max} (log ε): 354 (4.02), 466 (4.65) ^{1}H NMR (200 MHz, acetone-d_6) δ: 6.39 (m, 2H), 6.47 (d, J = 3.5 Hz, 2H), 6.39–6.47 (m, 5H), 7.78 (s, 2H), ~12.5 (s, very broad, 1H); ^{13}C NMR (50 MHz, acetone-d_6) δ: 118.3, 128.5, 129.2, 129.7, 131.3, 135.0, 138.0, 144.6; nm; LR-MS (EI, 180°C) *m/e*: 220 (77, M^+), 219 (100, $M^+ - H$). Exact Mass calcd. for $C_{15}H_{12}N_2$: 220.10005; found: 220.10012. A consistent elemental analysis (deviation 3.0% from the calculated values) could not be achieved, possibly due to varying amounts of solvation and (or) salt formation.

5-(4-Nitrophenyl)-4,6-pyrrin (20)

This compound was prepared from **16** by a method analogous to that used for the preparation of compound **2**. Yield after chromatography: 59%; mp 189–191°C; IR (neat): 1555, 1520, 1515, 1510, 1450, 1340, 1050 cm^{-1}; UV–VIS (CH_2Cl_2 – 0.5% MeOH – trace NH_4OH) λ_{max} (log ε): 264 (3.99), 300 (4.08), 434 (4.38) nm; (CH_2Cl_2 – 0.5% MeOH – trace HCl) λ_{max} (log ε): 258 (4.16), 336 (4.17), 470 (4.74) nm; ^{1}H NMR (200 MHz, acetone-d_6) δ: 6.21 (m, 2H), 6.40 (m, 2H), 7.36 (d, J = 8 Hz, 2H), 7.55 (s, 2H), 7.96 (d, J = 8 Hz, 2H), ~12.0 (very broad, 1H); ^{13}C NMR (50 MHz, acetone-d_6) δ: 119.0, 123.7, 128.8, 128.9, 132.4, 139.5, 140.9, 144.6, 145.6; LR-MS (EI, 150°C) *m/e*: 265 (100, M^+), 234 (18.8, $MH^+ - 2O$), 228 (68.2), 218 (96.5, $M^+ - HNO_2$). Exact Mass calcd. for $C_{15}H_{11}O_2N_3$: 265.0851; found: 265.08501.

Bis[5-(4-nitrophenyl)-4,6-pyrrinato]Zn(II) (23)

To a solution of dipyrrin **20** (100 mg, 3.77×10^{-4} mol) in MeOH (10 mL) was added zinc acetate dihydrate (420 mg, 5 equiv.) in MeOH (10 mL) and the mixture was heated on a water bath for 4 h. The mixture was evaporated to dryness on the rotary evaporator and the remaining solids were tritrurated with $CHCl_3$. The resulting bright orange-yellow solution was filtered though a short plug of silica gel and allowed to slowly evaporate. Compound **23** was obtained as dark orange lumps with a bright green metallic lustre, which were, after drying (0.1 Torr/50°C), analytically pure (180 mg, 81%); mp > 300°C; IR (neat): 1590, 1541, 1515, 1405, 1372, 1335, 1243, 1190, 1025, 995 cm^{-1}; UV–VIS (CH_2Cl_2) λ_{max} (log ε): 486 (4.97), 352 (4.08), 308 (4.30), 272 (4.42) nm; (pyridine) λ_{max} (rel. intensity): 440 (0.2), 316 (1.0); ^{1}H NMR (200 MHz, $CDCl_3$) δ: 6.45 (dd, J = 0.8, 4.2, 1H), 6.59 (dd, J = 0.8, 4.2, 1H), 7.59 (s, 1H), 7.75 (d, 9.2 Hz, 1H), 8.35 (d, 9.2 Hz, 1H); LR-MS (EI) *m/e*: 592 (40.3, M^+), 295 (88.8), 280 (48.7), 265 (100, ligand$^+$). Anal. calcd. for $C_{30}H_{20}N_6O_4Zn$: C 60.63, H 3.39, N 14.1; found: C 60.71, H 3.3, N 14.00.

Bis[5-(4-nitrophenyl)-4,6-pyrrinato]Ni(II) (21)

Compound **20** was prepared using the procedure for the preparation of **23**. Slow evaporation of a $CHCl_3$ – 1% MeOH solution of **21** yielded a dark brown-orange microcrystalline material, which was, after drying (0.1 Torr/50°C) analytically pure; mp, 230°C; IR (neat): 1595, 1555, 1520, 1335, 1370, 1240, 1040, 1020, 995 cm^{-1}; UV–VIS (CH_2C_2) λ_{max} (log 274 (4.58), 318 (4.47), 484 (4.63) nm; (MeOH) λ_{max} (rel. intensity): 272 (0.47), 292, sh (0.45), 466, sh (0.96), 482 (1.0) nm; (pyridine) λ_{max} (rel. intensity): 316 (1.0), 456, br (0.43), 486 (0.48); ^{1}H NMR (200 MHz) δ: 6.66 (d, J = 4.1 Hz, 1H), 7.52 (d, J = 8.6 Hz, 1H), 8.26 (2 overlapping d, 2H), 10.83 (s, 1H); LR-MS (EI, 180°C) *m/e*: 586 (48.3, M^+), 539 (15.6, $M^+ - HNO_2$), 464 (15.3, $M^+ - Ph - NO_2$). Exact mass calcd. for $C_{30}H_{20}N_6NiO_4$: 586.08997; found: 586.08992. Anal. calcd. for $C_{30}H_{20}N_6NiO_4$: C 61.36, H 3.43, N 14.31; found: C 6.57, H 3.36, N 14.20.

Bis[5-(4-nitrophenyl)-4,6-pyrrinato]Cu(II) (24)

Dipyrrin (20) (100 mg, 3.77 mmol) was dissolved in minimal warm MeOH (~5 mL) and, with stirring, a solution of copper acetate monohydrate (380 mg, 5 equiv) in MeOH (5 mL) and concentrated ammonia (0.5 mL) was added. The metal complex precipitated from the dark orange solution almost instantaneously. The precipitate was filtered off after stirring for 12 h at room temperature, then dried and chromatographed on a short (10 × 2.5 cm, 1% MeOH – $CHCl_3$) column of silica gel. The first intensely orange band was collected and slow evaporation of the solvent furnished 160 mg (72%) of the metal complex 24 as black needles with a green metallic lustre. Alternatively, repeated recrystallization from $CHCl_3$–MeOH yields dark green, dichroic microcrystals with a metallic lustre. After drying (0.1 Torr/50°C) an analytically pure sample was obtained; mp > 300°C; UV–VIS ($CHCl_3$) λ_{max} (log ε): 274 (4.52), 314 (4.21), 368 (4.26), 474 (4.72) nm; (MeOH) λ_{max} (rel. intensity): 268 (0.72), 308 (0.47), 374 (0.39), 468 (1.0), 502, sh (0.53); LR-MS (EI) *m/e*: 591 (6.6, M^+), 295 (100), 280 (68.6), 264 (44.3), 248 (26.5), 234 (49.0). Exact Mass calcd. for $C_{30}H_{20}O_4N_6{}^{65}Cu$: 593.08240; found: 593.08305. Anal. calcd. for $C_{30}H_{20}CuN_6O_4$: C 60.63, H 3.39, N 14.15; found: C 60.70, H 3.54, N 14.03.

Bis[5-phenyl-4,6-pyrrinato]Ni(II) (22)

Prepared in 76% yield in an analogous fashion as described for **23**. Slow evaporation of an acetone solution gave **22** as dichroic crystals; mp (dec.) 240°C; IR (neat): 1575, 1535, 1505,

1410, 1380, 1345, 1245, 1035, 1030, 1000 cm^{-1}; UV–VIS ($CHCl_3$) λ_{max} (log ϵ): 324 (4.33), 472 (462) nm; (MeOH) λ_{max} (rel. intensity): 264 (0.18), 314 (0.23), 458 (0.83), 478 (1.0); ^1H NMR (300 MHz, $CDCl_3$) δ: 6.73 (d, J = 4.6 Hz, 4H), 7.38–7.46 (m, 10H), 7.60 (d, J = 4.5 Hz, 4H), 9.63 (s, 4H); ^{13}C NMR (50 MHz, $CDCl_3$) δ: 127.4, 129.1, 130.7, 134.5, 136.8, 139.4, 143.7, 147.7, 173.0; LR-MS (EI, 200°C) *m/e*: 496 (100, M^+), 430 (18.8), 419 (18.2), 219 (74.8). Exact Mass calcd. for $C_{30}H_{22}N_4Ni$: 496.11978; found: 496.12071. Anal. calcd. for $C_{30}H_{22}N_4Ni$: C 72.47, H 4.46, N 11.27; found: C 72.33, H 4.70, N 11.3.

X-ray crystallographic analysis of bis[5-phenyl-4,6-pyrrinato]Ni(II) (22)

Crystallographic data appear in Table 4. The final unit-cell parameters were obtained by least squares on the setting angles for 25 reflections with 2θ = 23.3°–33.6°. The intensities of three standard reflections, measured every 200 reflections throughout the data collection, decayed linearly by 2.3%. The data were processed, corrected for Lorentz and polarization effects, decay, and absorption (empirical, based on azimuthal scans for three reflections). The structure was solved by direct methods, the coordinates of the non-hydrogen atoms being determined from an *E*-map or from subsequent difference Fourier syntheses (52). The molecule has exact D_2 (crystallographic 222) symmetry. Non-hydrogen atoms were refined with anisotropic thermal parameters and hydrogen atoms were fixed in calculated positions with C—H = 0.98 Å and $B_H = 1.2\ B_{bonded\ atom}$. No correction for secondary extinction was necessary. Neutral atom scattering factors for all atoms and anomalous dispersion corrections for the non-hydrogen atoms were taken from the *International Tables for X-Ray Crystallography* (53). Hydrogen atom parameters, anisotropic thermal parameters, torsion angles, intermolecular contacts, scheme of the unit cell, symmetry operators, and least-squares planes are included as supplementary material.[2]

Acknowledgements

We thank the Natural Sciences and Engineering Council of Canada for financial support.

Note added in proof:

Since the submission of the manuscript, another report describing *meso*-phenyl-4,6-dipyrrin and its BF_2 complex has appeared in the literature: R.W. Wagner and J.S. Lindsey. Pure Appl. Chem. **68**, 1373 (1996).

[2] Supplementary material metioned in the text may be purchased from: The Depository of Unpublished Data, Document Delivery, CISTI, National Research Council of Canada, Ottawa, Canada, K1A 0S2. Tables of hydrogen atom coordinates and bond lengths and angles involving hydrogen atoms have also been deposited with the Cambridge Crystallographic Data Centre and can be obtained on request from The Director, Cambridge Crystallographic Data Centre, University Chemical Laboratory, 12 Union Road, Cambridge CB2 1EZ, U.K.

References

1. H. Fischer, and H. Orth. Die Chemie des Pyrrols. Vol. 2, erste Hälfte. Akademische Verlagsgesellschaft m.b.H., Leipzig. 1940. pp. 1–151.
2. H. Falk. The chemistry of linear oligopyrroles and bile pigments. Springer Verlag, Vienna, New York. 1989.
3. A. Gossauer and J. Engel. *In* The porphyrins. Vol 2. *Edited by* D. Dolphin. Academic Press, New York, San Francisco, London. 1987. pp. 197–253.
4. A.H. Corwin and J.S. Andrews. J. Am. Chem. Soc. **58**, 1086 (1936).
5. A. Treibs, M. Strell, I. Strell, and D. Grimm. Liebigs Ann. Chem. 289 (1978).
6. P.A. Jacobi and J. Guo. Tetrahedron Lett. **36**, 2717 (1995).
7. K. Brunnings and A. Corwin. J. Am. Chem. Soc. **66**, 331 (1944).
8. H. Fischer and R. Nussler. Liebigs Ann. Chem. **491**, 167 (1931).
9. R.J. Motekaitis and A.E. Martell. Inorg. Chem. **9**, 1832 (1970).
10. C.-H. Lee and J.S. Lidsey. Tetrahedron, **50**, 11427 (1994).
11. A.W. Johnson, I.T. Kay, E. Markham, R. Price, and K.B. Shaw. J. Chem. Soc. 3416 (1959).
12. A. Treibs and K. Hintermeier. Liebigs Ann. Chem. **592**, 11 (1955).
13. H. Xie, D.A. Lee, M.O. Senge, and K.M. Smith. J. Chem. Soc. Chem. Commun. 791 (1994).
14. M.A.T. Rogers. J. Chem. Soc. 596 (1943).
15. M.A.T. Rogers. J. Chem. Soc. 598 (1943).
16. S. Gabriel. Ber. Dtsch. Chem. Ges. **14**, 1138 (1908).
17. R.A. Jeffreys and E.B. Knott. J. Chem. Soc. 1028 (1951).
18. C.L. Hill and M.M. Williamson. J. Chem. Soc. Chem. Commun. 1228 (1985).
19. A.S. Cavaliero, M. de F. P.. Condesso, M.M. Olmstead, D.E. Oram, K.M. Snow, and K.M. Smith. J. Org. Chem. **53**, 5847 (1988).
20. R.W. Wagner and J.S. Lindsey. J. Am. Chem. Soc. **116**, 9759 (1994).
21. F.H. Carré, R.J.P. Corriu, G. Bolin, J.J.E. Moreau, and C. Vernhet. Organometallics, **12**, 2478 (1993).
22. F.C. March, D.A. Couch, K. Emerson, J.E. Fergusson, and W.T. Robinson. J. Chem. Soc. (A) , 440 (1971).
23. R.C. Porter. J. Chem. Soc. 368 (1938).
24. F.A. Cotto, B.G. DeBoer, and J.R. Pipal. Inorg. Chem. **9**, 783 (1970).
25. M. Elder and B.R. Penfold. J. Chem. Soc. (A), 2556 (1969).
26. Y. Murakami, Y. Matsuda, and K. Sakata. Inorg. Chem. **10**, 1728 (1971).
27. Y. Murakami and K. Sakata. Bull. Chem. Soc. Jpn. **47**, 3025 (1974).
28. A. Pfaltz. Acc. Chem. Res. **26**, 339 (1993).
29. H.M..H. Irving. *In* Comprehensive coordination chemistry. Vol. 1. *Edited by* G. Wilkinson. Pergamon Press, Oxford. 1987. pp. 521–563.
30. H.E. Howard-Lock and C.J.L. Lock. *In* Comprehensive coordination chemistry. Vol. 6. *Edited by* G. Wilkinson. Pergamon Press, Oxford. 1987. pp. 755–778.
31. J. S. Lindsey. *In* Metalloporphyrins catalyzed reactions. *Edited by* F. Montanari and L. Casella. Kluwer Academic Publishers, Dordrecht, The Netherlands. 1994. pp. 49–86.
32. (*a*) G. H. Barnett, M.F. Hudson, and K.M. Smith. Tetrahedron Lett. **30**, 2887 (1973); (*b*) J. Chem. Soc. Perkin Trans. 1, 1401 (1975).
33. D. Dolphin. J. Heterocycl. Chem. **7**, 275 (1970).
34. A.D. Adler, F.R. Longo, J.D. Finarelli, J. Goldmacher, J. Assour, and L. Korsakoff. J. Org. Chem. **32**, 476 (1966).
35. J.S. Lindsey and R.W. Wager. J. Org. Chem. **54**, 828 (1989).

36. L.G.S. Brooker and R.H. Sprague. J. Am. Chem. Soc. **63**, 3203 (1941).
37. A. Treibs and N. Häberle. Liebigs Ann. Chem. **718**, 183 (1968).
38. E.F. Meyer, Jr. and D.R. Cullen. *In* The porphyrins. Vol. 3. *Edited by* D. Dolphin. Academic Press, New York, San Francisco, London. 1978. pp. 513–529.
39. Y. Murakami and K. Sakata. Iorg. Chim. Acta, **2**, 273 (1968).
40. J.E. Fergusson and C.A. Ramsay. J. Chem. Soc. (A) , 5222 (1965).
41. Y. Murakami, Y. Matsuda, K. Sakata, and A.E. Martell. J. Chem. Soc. Dalton Trans. 1, 1729 (1973).
42. W.R. Scheidt. *In* The porphyrins. Vol. 3. *Edited by* D. Dolphin. Academic Press, New York, San Francisco, London. 1978. pp. 463–511.
43. F.A. Cotton and G. Wilkinson. *In* Advanced inorganic chemistry. John Wiley & Sons, New York. 1988. pp. 741–754.
44. D. Eley and D. Spivey. Trans. Faraday Soc. **58**, 405 (1962).
45. J.W. Buchler. *In* The porphyrins. Vol.1. *Edited by* D. Dolphin. Academic Press, New York, San Francisco, London. 1978. pp. 389–483.
46. P.N. Dwyer, J.W. Buchler, and W.R. Scheidt. J. Am. Chem. Soc. **96**, 2789 (1974).
47. R.D. Shao. Acta Crystallogr. Sect. A: Cryst. Phys. Diffr. Theor. Gen. Crystallogr. **A32**, 751 (1976).
48. E.F. Meyer, Jr. Acta Crystallogr. Sect. B. Struct. Crystallogr. Cryst. Chem. **B28**, 2162 (1972).
49. D.M. Collins, W.R. Scheidt, and J.L. Hoard. J. Am. Chem. Soc. **94**, 6689 (1972).
50. D.J. Chadwick. *In* Pyrroles: the synthesis and the physical and chemical properties of the pyrrole ring. Vol. 48. Part 1. *Edited by* A. Jones. John Wiley & Sons, New York, Chichester, Brisbane, Toronto, and Singapore. 1990. pp. 8–33.
51. E.B. Fleischer, C.K. Miller, and L.E. Webb. J. Am. Chem. Soc. **86**, 2342 (1964).
52. (*a*) A. Altomare, M.C. Burla, M. Camalli, M. Cascarano, C. Giacovazzo, A. Guagliardi, and G. Polidori. SIR92: J. Appl. Crystallogr. **27**, 435 (1994); (*b*) P.T. Beurskens, G. Admiraal, G. Beurskens, W.P. Bosman, S. Garcia-Granda, R.O. Gould, J.M.M. Smits, and C. Smykala. DIRDIF92: The DIRDIF program system. Technical Report of the Crystallography Laboratory, University of Nijmegen, The Netherlands. 1992; (*c*) *teXsan*: Crystal Structure Analysis Package. Molecular Structure Corporation. The Woodlands, Tex., U.S.A. 1985 and 1992.
53. (*a*) International tables for crystallography. Vol. IV. The Kynoch Press, Birmigham, U.K. (Present distributor: Kluwer Academic Publishers, Boston, Mass.) 1974. pp. 99–102; (*b*) International tables for crystallography. Vol. C. Kluwer Academic Publishers, Boston, Mass. 1992. pp. 219–222.

Absorption spectroscopy of (Ind)Ni(PPh_3)X (Ind = indenyl, 1-Me-indenyl; X = Cl, Br, Me) and M(Ind)$_2$ (M = Ni, Ru; Ind = indenyl)

Malken Bayrakdarian, Martin J. Davis, Christian Reber, and Davit Zargarian

Abstract: The electronic structures of two types of transition metal indenyl complexes have been studied. The first type, a series of (Ind)Ni(PPh_3)X compounds (Ind = indenyl, 1-Me-indenyl; X = Cl, Br, Me) was investigated by absorption spectroscopy and Extended Hückel Molecular Orbital calculations. The energy differences between calculated levels are in good agreement with experimental band positions. For example, the lowest energy singlet–singlet band maximum for (Ind)Ni(PPh_3)Cl is at 19 500 cm^{-1} and the calculated HOMO−LUMO difference is 19 817 cm^{-1}. For X = Me, the calculated energy difference increases to 21 930 cm^{-1} and the corresponding absorption band is at 22 500 cm^{-1}. The influence of the metal–ligand interactions on the molecular orbitals is discussed. The second category of indenyls, the bis(indenyl) compounds of Ni and Ru, show absorption spectra that are markedly different from those of nickelocene and ruthenocene. For example, in comparison to nickelocene, the first absorption band of Ni(Ind)$_2$ is 5700 cm^{-1} higher in energy and is more intense by two orders of magnitude; in contrast, the first absorption maximum of Ru(Ind)$_2$ is 6600 cm^{-1} lower in energy than observed for ruthenocene. The characteristics and relaxation dynamics of the lowest energy excited states are discussed.

Key words: absorption spectroscopy, indenyl, nickel, ruthenium, EHMO analysis.

Résumé : Nous avons étudié la spectroscopie électronique de deux types de composés dont l'élément de transition est lié à un ou deux ligands indényle. Les spectres d'absorption des composés (Ind)Ni(PPh_3)X (Ind = indényle, 1-méthylindényle; X = Cl, Br, méthyle) sont présentés. Les maxima des bandes sont comparés aux différences d'énergie entre orbitales moléculaires calculées avec la méthode «Extended Hückel». Un exemple illustratif en est la première bande singulet–singulet du (Ind)Ni(PPh3)Cl qui est mesurée à 19 100 cm^{-1}, très proche à la différence d'énergie HOMO − LUMO calculée de 19 817 cm^{-1}. Pour le composé (Ind)Ni(PPh3)Me la bande correspondante est décalée vers une énergie plus élevée dont le maximum est à 22 500 cm^{-1}. La différence HOMO−LUMO calculée est de 21 930 cm^{-1}. L'influence des différents ligands sur les caractéristiques des orbitales moléculaires est discutée. Les composés de la 2^e catégorie étudiée sont du type M(Ind)$_2$, avec M = Ni, Ru. Leurs spectres sont comparés à ceux du nickélocène et du ruthénocène. La première bande du Ni(Ind)$_2$ est à une énergie de 5700 cm^{-1} plus élevée que celle du nickelocène et son intensité est plus grande de deux ordres de grandeur. La première bande du Ru(Ind)$_2$ se trouve à une énergie de 6600 cm^{-1} plus basse que celle du ruthénocène. Les caractéristiques du premier état excité et les mécanismes de relaxation sont discutés.

Mots clés : spectroscopie d'absorption, indényle, nickel, ruthénium, analyse EHMO.

Introduction

Metallocene and mono-Cp (Cp = cyclopentadienyl) complexes of transition metals have fascinated chemists over the past four decades for many reasons, including their unusual electronic structures, interesting patterns of reactivity, and the particular symmetry inherent in their molecular structures. The nature of the interaction between the orbitals of the Cp ligand and the metal centre (M) is of key importance to these properties and has been the subject of numerous theoretical and experimental investigations (1, 2). In contrast, the chemistry of complexes containing ligands analogous to Cp, such as the indenyl and the fluorenyl ligands, remains much less developed. The limited studies of this class of complexes have nevertheless demonstrated that the presence of benzo moieties in these ligands often leads to significant changes in the properties of their complexes. For instance, certain indenyl and fluorenyl complexes exhibit ligand substitution reaction rates that are orders of magnitude larger than those seen for their Cp analogues (3). Similarly, a number of stoichiometric and catalytic reactions are better promoted by some indenyl complexes relative to the Cp analogues (4–6). Such enhancement of reactivity is conventionally attributed to the flexible hapticity of the indenyl and fluorenyl ligands, which provides a means for stabilizing the reaction intermediates (3).

Received March 12, 1996.

This paper is dedicated to Professor Howard C. Clark in recognition of his contributions to Canadian chemistry.

M. Bayrakdarian, M.J. Davis, C. Reber,[1] and D. Zargarian.[1]
Département de chimie, Université de Montréal, C.P. 6128, succursale Centre-ville, Montréal, QC H3C 3J7, Canada.

[1] Authors to whom correspondence may be addressed. Telephone: (514) 343-7332 (C.R.) and (514) 343-2247 (D.Z.). Fax: (514) 343-7586. E-mail: reber@ere.umontreal.ca and davitz@ere.umontreal.ca.

As part of an ongoing research program to develop the chemistry of late metal Ind complexes (Ind = indenyl and its substituted derivatives), we have begun a systematic investigation of the electronic spectra of a series of late metal mono- and bis-Ind complexes. This investigation has two main components: on the one hand, comparisons of structural and spectroscopic features of analogous Cp and Ind complexes are used to pinpoint the salient differences in the M–Cp and M–Ind interactions; on the other hand, Extended Hückel Molecular Orbital (EHMO) calculations are carried out where necessary in order to determine the relative energies of metal and ligand orbitals and their varying contributions to the overall bonding picture in these complexes. An attempt is then made to draw correlations between the emerging MO diagrams and the observed structural and spectral differences for the species considered. This approach has the potential to improve our understanding of some of the underlying reasons for the major differences between Cp and Ind complexes. The present paper reports the results of our studies on the indenyl complexes IndNi(PPh_3)X and M($Ind)_2$ (M = Ni and Ru).

Experimental

Materials

The preparative work was carried out using standard Schlenk techniques and an argon-filled dry box; the solvents were dried and distilled before use following established procedures. The complexes $NiCp_2$ and $RuCp_2$ were purchased from Aldrich and purified by vacuum sublimation prior to use. Ni($Ind)_2$ (7, 8) and Ru($Ind)_2$ (9) were prepared according to literature procedures. Reacting $(PPh_3)_2NiX_2$ (X = Cl and Br) with IndLi (Ind = indenyl and 1-Me-indenyl) furnished the complexes (Ind)Ni(PPh_3)X, which were, in turn, reacted with MeMgBr or MeLi to give the methyl derivatives (X = Me). A more detailed description of the preparation and characterization of the compounds (Ind)Ni(PPh_3)X, including their solid state structures, is given elsewhere (10).

Spectroscopy

The sample solutions were prepared in a glove box using dry solvents. Typical concentrations were on the order of 10^{-3} M. Absorption spectra were measured in 1 cm quartz cells capped with recessed Suba•Seal septa (Aldrich) on a Varian Cary 5E spectrometer.

Extended Hückel Molecular Orbital (EHMO) calculations

EHMO calculations were carried out using a program package based on the ICON code (11, 12). Atomic coordinates and unit cell parameters obtained from X-ray diffraction data (10) were transformed to a Cartesian coordinate system by the program package. Standard values were used for all parameters describing atomic orbitals. A maximum of 58 atoms and 156 valence orbitals were used. Atomic coordinates and summaries of the output for the EHMO calculations presented in Fig. 2 and Table 2 are provided as supplementary material.[2]

[2] Copies of material on deposit may be purchased from: The Depository of Unpublished Data, Document Delivery, CISTI, National Research Council Canada, Ottawa, Canada K1A 0S2.

Fig. 1. Schematic views of the two different Ind hapticities observed in (Ind)Ni(PPh_3)X compounds.

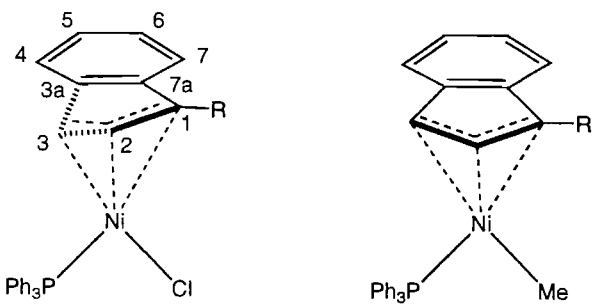

Results and discussion

(a) Indenyl hapticity in (Ind)Ni(PPh_3)X

In theory, an idealized pentahapto indenyl ligand is one in which all carbon atoms of the five-membered ring are symmetrically coordinated to the metal atom. In reality, however, most indenyl complexes display some deviation from this ideal η^5 mode whereby the metal atom is somewhat less strongly coordinated to the ring-junction carbons (C3a and C7a). A number of parameters are used to measure the extent of such deviations, or "slip-fold distortions," including the so-called slip value, which is defined as $\Delta M—C = M—C_{avg.}$ (for C3a and C7a) − $M—C_{avg.}$ (for C3 and C1) (8); thus, the smaller the slip value the less significant the distortion. The extent of "slippage" normally depends on the formal electron count of the complex such that most compounds with 18 or fewer electrons exhibit little distortion (e.g., Fe(η^5-$Ind)_2$ with $\Delta M—C = 0.04$ Å (8)), whereas significant distortions are usually found in compounds in which a pentahapto indenyl would place more than 18 electrons in the metal valence orbitals (e.g., (η^3-Ind)Ir($PMe_2Ph)_3$ with $\Delta M—C = 0.79$ Å (13)). In some cases, however, slip-fold distortions might be larger than expected even in formally 18-electron compounds. For instance, even though the complexes (Ind)Ni(PPh_3)Cl would be 18-electron species with pentahapto indenyls, their solid state structures show significantly slipped indenyls with $\Delta M—C \approx 0.25$ Å (10). The relatively large distortion observed here might be attributed to the tendency of Ni(II) complexes to prefer 16- vs. 18-electron configurations.

An even more unusual feature of the indenyl hapticity in the complexes (Ind)Ni(PPh_3)Cl is that the displacement of Ni away from C3a and C7a is not towards C-2, as expected, but rather towards C-3, as illustrated in Fig. 1. This "sideways slippage" leads to unequal distances between the nickel atom and the carbons of the five-membered ring such that Ni—C7a > Ni—C3a > Ni—C1 > Ni—C2 > Ni—C3 (10). Therefore, the hapticity of the indenyl ligand in these compounds appears to lie somewhere in the continuum defined by the η^5, η^3, and the (η^1,η^2) coordination modes. We have suggested that this sideways slippage is caused by the different *trans* influences of the PPh_3 and Cl ligands (10). Consistent with this reasoning, replacing Cl in the Ind complexes by the higher *trans* influence ligand Me results in a "symmetrically slipped" indenyl ligand, i.e., Ni—C1 = Ni—C3 and Ni—C3a = Ni—C7a (Fig. 1). A similar situation exists in the analogous Cp complexes: in the complex (Me-Cp)Ni(PPh_3)I the Ni—C distance for the carbon atom *trans* to PPh_3 is longer than that *trans* to iodide

Table 1. Wavelengths and wave numbers of absorption bands (molar absorptivities).

Compound	λ_{max} (nm); E_{max} (cm^{-1}) (ε)
(Indenyl)Ni(PPh_3)Cl[a]	512; 19 500 (1400) 413; 24 200 (2920)
(indenyl)Ni(PPh_3)Br[a]	709; 14 100 (20) sh 518; 19 300 (570) 416; 24 000 (>1500)
(1-Me-indenyl)Ni(PPh_3)Cl[a]	512; 19 500 (820) 412; 24 300 (1680)
(1-Me-indenyl)Ni(PPh_3)Br[a]	514; 19 400 (1000) 416; 24 000 (1950) 337; 29 700 (>5000)
(1-Me-indenyl)Ni(PPh_3)Me[a]	543; 18 400 (80) 445; 22 500 (510) sh 384; 26 000 (2640) 339; 29 500 (10 200)
Ni(indenyl)$_2$[b]	496; 20 200 (3180)
Ru(indenyl)$_2$[b]	423; 23 460 (750) 344; 29 100 (1700)

[a]In THF.
[b]In Et_2O.

(14), whereas in the alkyl analogue CpNi(PPh_3)(CF_3) all Ni—C bonds are fairly equal (15).

To study the effect of the indenyl hapticity on the MO diagram and the electronic transitions of the complexes (Ind)Ni(PPh_3)X, we have recorded their absorption spectra and carried out EHMO calculations, as described below.

(b) Absorption spectra, band assignments, and EHMO calculations for (Ind)NiPPh$_3$X

The results of the absorption spectra for the complexes (Ind)NiPPh$_3$X are summarized in Table 1, and the spectra for three selected indenyl compounds are presented in Fig. 2. The halo derivatives show similar absorption spectra consisting of a broad band (B) at approximately 520 nm followed by a more intense band centered at 410 nm (C), as illustrated in Fig. 2*a*. Methyl substitution at the 1 position of the indenyl ligand has only a small effect on transition energies, but appears to change the band intensities, as shown by the comparison in Fig. 2a and Table 1. Based on their intensities, these transitions are spin-allowed bands from the singlet electronic ground state, which have typical molar absorptivities of 10^3–10^4 M^{-1} cm^{-1} (16). Weak, low-energy bands were observed for these complexes at ca. 700 nm (A), which most likely correspond to the spin-forbidden transition to the lowest energy triplet state. The weak intensity of this band is caused by the magnitude of the spin-orbit coupling, which for 3*d* metal ions normally leads to absorption bands ca. 100 times weaker than spin-allowed transitions (17).

Fig. 2. Absorption spectra of (Ind)Ni(PPh_3)X compounds. (*a*) X = Cl; Ind = indenyl (solid line), 1-Me-indenyl (dotted line); (*b*) X = Me; Ind = 1-Me-indenyl.

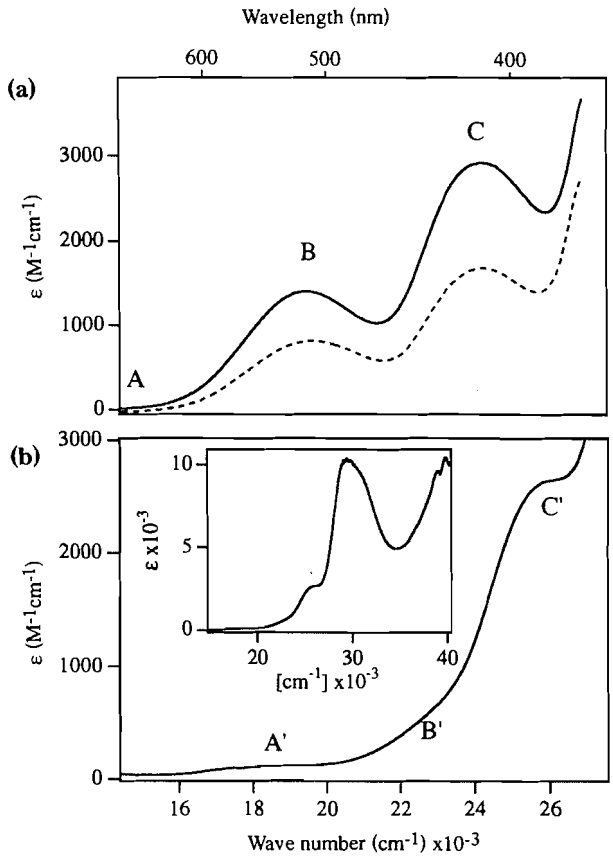

The methyl derivative (1-Me-indenyl)Ni(PPh_3)Me shows a different spectrum than the halo compounds, as illustrated in Fig. 2*b*. A weak, low-energy band is observed at 543 nm (A′), again most likely corresponding to the transition to the lowest energy triplet state. A band of comparable intensity to the first spin-allowed band for the halide compounds is observed as a shoulder at 445 nm (B′), higher in energy by approximately 3000 cm^{-1} than for the compounds in Fig. 2*a*. A second band (C′), comparable in intensity to the band C of the halide complexes, is observed at an energy higher by 2000 cm^{-1}. The inset to Fig. 2*b* shows the absorption spectrum of the methyl compound up to higher energy. An intense band is observed at 339 nm, most likely corresponding to an allowed electronic transition; similar intense bands at this energy were observed for dilute solutions of some of the halide compounds (Table 1).

The spectra for the Ind complexes show qualitative similarities to those reported for the analogous Cp complexes (18). The latter show only one absorption band between 600 nm and 400 nm with a molar absorptivity similar to those of the two bands observed for the Ind complexes in this region (Table 1). For example, the band maximum for CpNi(PPh_3)Cl is at 512 nm, the same wavelength as for the analogous Ind compound, and has a molar absorptivity of 900 M^{-1} cm^{-1} (18). At higher energy, an intense band is observed at 331 nm (ϵ = 8500 M^{-1} cm^{-1}), very similar to the bands of the (Ind)Ni(PPh_3)Cl com-

Table 2. Molecular orbital energies from EHMO calculations and main contributions from atomic orbitals in %.[a]

Compound	HOMO-2	HOMO-1	HOMO	LUMO	LUMO+1	LUMO+2
(indenyl)Ni(PPh_3)Cl						
eV	−12.187	−12.091	−11.382	−8.925	−8.474	−8.322
cm^{-1}	−6493	−5718	0	19 817	23 454	24 680
Ni (3*d*)	28	33	38	27	2	<1
Cl (3*p*)	<1	4	<1	3	<1	<1
C (2*p*, indenyl)	34	19	48	41	75	<1
P (3*p*)	2	3	<1	3	<1	<1
C (2*p*, phenyl)	11	14	<1	7	2	84
(1-Me-indenyl)Ni(PPh_3)Cl						
eV	−12.157	−12.036	−11.376	−8.909	−8.473	−8.328
cm^{-1}	−6299	−5323	0	19 898	23 414	24 584
Ni (3*d*)	37	20	36	26	2	<1
Cl (3*p*)	<1	3	<1	3	<1	<1
C (2*p*, indenyl)	10	35	48	39	82	<1
P (3*p*)	3	4	<1	3	<1	<1
C (2*p*, phenyl)	16	10	<1	9	<1	82
(1-Me-indenyl)Ni(PPh_3)Me						
eV	−12.171	−11.768	−11.291	−8.572	−8.444	−8.254
cm^{-1}	−7098	−3847	0	21 930	22 693	24 495
Ni (3*d*)	28	9	37	19	2	<1
C (2*p*, methyl)	<1	14	<1	10	<1	<1
C (2*p*, indenyl)	2	48	44	23	75	<1
P (3*p*)	4	<1	<1	2	<1	<1
C (2*p*, phenyl)	30	2	<1	17	<1	88

[a]The energy of the HOMO was set to 0 cm^{-1} to simplify comparison to the spectra. Atomic orbitals contributing less than 1% to the MO are not included in the sums for indenyl and phenyl fragments.

pounds in this region. Weak triplet transitions are reported between 600 and 800 nm. The maximum of the first spin-allowed band for CpNi(PPh_3)Me is observed at an energy higher by 5800 cm^{-1} than in the Cl analogue (18). A shift in the same direction, albeit smaller (3000 cm^{-1}), was observed in the Ind compounds.

The results of EHMO calculations carried out on the complexes (Ind)Ni(PPh_3)X (Ind = indenyl and X = Cl; Ind = 1-Me-indenyl and X = Cl and Me) allow a qualitative assignment of the bands observed in the absorption spectra and can be used to discuss some of the important spectroscopic differences between the Cl and the Me compounds. The energy levels and orbital characteristics for the HOMO–LUMO energy range, which is the region of interest for low-energy electronic transitions, are summarized in Fig. 3 and in Table 2. Very similar orbital energies were obtained for (indenyl)Ni(PPh_3)Cl and (1-Me-indenyl)Ni(PPh_3)Cl, in good qualitative agreement with their similar solid state structures and absorption spectra. The calculated HOMO–LUMO gaps of 19 817 cm^{-1} and 19 898 cm^{-1} for the indenyl and 1-Me-indenyl compounds, respectively, are in excellent agreement with the energy of the first spin-allowed transition in the absorption spectra observed at approximately 19 500 cm^{-1}. The energy of the second band in the spectra presented in Fig. 2*a* (ca. 24 000 cm^{-1}) corresponds to a number of energy gaps, so that in principle several transitions (e.g., HOMO-2→LUMO, HOMO-1→LUMO, HOMO→LUMO+1, and HOMO→LUMO+2) could contribute to this band.

In the case of (1-Me-indenyl)Ni(PPh_3)Me, we calculate a HOMO–LUMO gap of 21 930 cm^{-1}, again in good agreement with the experimental transition energy of 22 500 cm^{-1}. A number of orbital energy gaps correspond to the transition energy of the second, more intense band in the spectrum of this complex. Due to the absence of a center of inversion in our compounds, parity selection rules do not apply and even *d–d* bands have considerable intensities. The highest energy level included in Fig. 3 has mainly π^* character on both the Ind ligands and the phenyl groups of PPh_3, leading to an allowed transition from the HOMO. This transition corresponds to the intense band observed at approximately 29 500 cm^{-1} in dilute solutions and calculated at 27 360 cm^{-1}, showing once again good agreement between the calculated energies and the spectroscopic data.

In the chloro compounds, the HOMO and LUMO are primarily a combination of nickel 3*d* and indenyl π orbitals (Table 2). The main contribution to the higher energy orbitals LUMO+1 and LUMO+2 comes from the Ind ligand and the phenyl groups of PPh_3, respectively; this explains their fairly constant energy levels in all three compounds. The main difference between the EHMO energies for the compounds in Fig. 3 concerns the LUMO and HOMO-1 orbitals, both of which are higher in energy for (Ind)Ni(PPh_3)Me than for the

Fig. 3. EHMO energy levels for the three compounds whose spectra are presented in Fig. 2. The wave number scale applies to (1-Me-indenyl)Ni(PPh_3)Me, with the energy of the HOMO set to 0 cm^{-1} for comparison with the spectroscopic data.

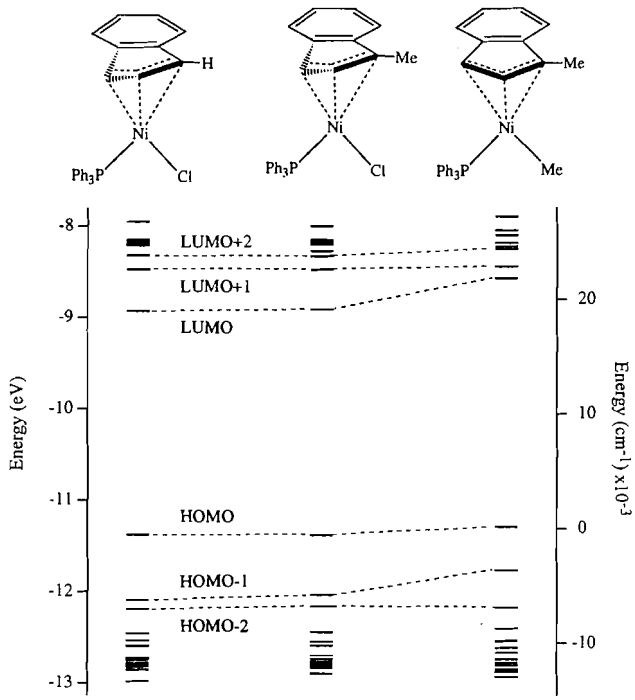

two chloro derivatives. The higher LUMO energy leads to a shorter wavelength for the first spin-allowed transition in the Ni–Me compound, as observed in the spectra. The higher energy of the HOMO-1 level decreases the difference between the first and the following absorption transitions, a likely reason for the overlapping bands in Fig. 2*b*. The contributions from the Me ligand to the LUMO and HOMO-1 orbitals are 3–4 times larger than those of the Cl ligand, as summarized in Table 2.

The use of EHMO calculations to analyze the electronic spectra of our complexes seems justified in light of the general agreement between experimental transition energies and calculated energy gaps. The close correspondence between measured absorption bands and calculated orbital energies is remarkable, especially in view of the simplifications involved in the EHMO scheme and the neglected electron–electron repulsions (19). To be sure, the observed agreement might arise from a fortuitous cancellation of contributions from electron-pairing energies and Madelung-type ionic interactions (20), both of which are neglected in the EHMO methodology. Nevertheless, our comparison indicates that the spectroscopic signatures for the different electronic structures of the compounds (Ind)Ni(PPh_3)X are reflected in the EHMO calculations. The match between spectroscopic and calculated data for the indenyl complexes studied here is in contrast to the difficulties encountered in rationalizing the spectroscopic data for the analogous Cp compounds using semi-empirical MO calculations (18). We plan to undertake a broader study of a number of Ind and Cp complexes and to use more advanced semi-empirical MO techniques in order to investigate the origins of this discrepancy and the limitations of our approach.

(c) Indenyl hapticity in $Ni(Ind)_2$ and $Ru(Ind)_2$

Detailed descriptions of the solid state structures of $Ni(Ind)_2$ (8) and $Ru(Ind)_2$ (21) have been reported in the literature. It is instructive for our analysis to briefly compare these structures to the corresponding Cp analogues. For example, nickelocene adopts a centrosymmetric structure with parallel, staggered, and very nearly planar Cp rings (approximate D_{5d} symmetry), and the Ni atom is displaced by only 0.03 Å from the fivefold axes of the rings (22). In contrast, the two Ind ligands in $Ni(Ind)_2$ are highly distorted toward trihapto coordination, with an average slip value of ca. 0.42 Å. Thus, the flexible hapticity of the Ind ligands stabilizes $Ni(Ind)_2$ by avoiding an unfavorable 20 electron configuration obtained in the presence of two η^5-Ind ligands. A different situation exists in the two Ru compounds where the rings are planar, nearly parallel, and fully eclipsed and show no significant deviation from a pentahapto coordination. The similarity in the structures of $Ru(Ind)_2$ and ruthenocene reflects the formal electron count of these complexes (18 electrons), which does not necessitate any distortions in the Ind compounds.

We set out to study the electronic spectra of these bis(indenyl) complexes and compare them to the corresponding spectra for the metallocenes in order to examine the electronic consequences of replacing Cp ligands by Ind. The results of this study are described in the following section.

(d) Absorption spectra and electronic structures of $Ni(Ind)_2$ and $Ru(Ind)_2$

The absorption spectra of the two bis-indenyl compounds are shown in Fig. 4 and their band energies and intensities are summarized in Table 1. The UV–visible spectrum of $Ni(Ind)_2$ shows an intense, broad absorption band in the green spectral region with its maximum at 20 200 cm^{-1} and a molar absorptivity of 3180 M^{-1} cm^{-1}, very different from nickelocene whose lowest-energy absorption band is in the red spectral region with a first maximum at 14 500 cm^{-1} and a much lower molar absorptivity of 60 M^{-1} cm^{-1} (23–25). The band maximum of $Ni(Ind)_2$ is higher in energy by 5700 cm^{-1} and more intense by almost two orders of magnitude than in nickelocene. This dramatic difference can not be explained by the lower symmetry alone since $Ni(Ind)_2$ retains its center of inversion in the solid state and hence parity selection rules apply. Even if the symmetry of $Ni(Ind)_2$ is somewhat relaxed in solution, we would still expect the molar absorptivities for formally Laporte-forbidden *d–d* bands to be significantly lower than those reported in Fig. 2 and Table 1 for indenyl compounds without a center of inversion. The intensity of this band indicates that the lowest excited state is no longer a ligand-field level but involves important contributions from ungerade parity molecular orbitals, leading to allowed electronic transitions.

The width of the first absorption band for both compounds is 5000 cm^{-1}, but nickelocene shows two maxima at low temperatures, due to at least two different overlapping *d–d* transitions (24, 26). In contrast, the first absorption band in $Ni(Ind)_2$ is symmetric, indicating that one electronic state determines the band shape. These observations imply that the character of the lowest energy excited state of $Ni(Ind)_2$ is not similar to that of nickelocene where all low-energy transitions are parity forbidden *d–d* bands (25). The large width for a single band is caused by large structural changes between the ground- and

Fig. 4. Absorption spectra of $Ni(Ind)_2$ (solid line) and $Ru(Ind)_2$ (dotted line).

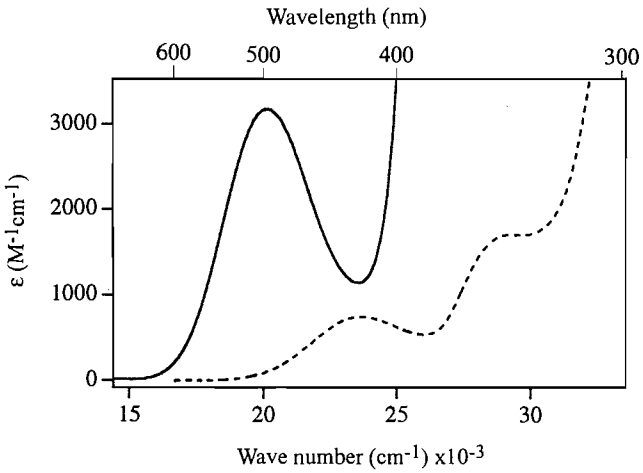

excited states, as expected for bands with significant charge transfer character.

Further supporting this assignment is the absence of luminescence from $Ni(Ind)_2$ at temperatures higher than 5 K. We observed no luminescence from $Ni(Ind)_2$ doped into ruthenocene between 500 and 1800 nm with the same instrumentation used for detecting weak near-infrared and visible luminescence for nickelocene and cobaltocene doped into single crystals of ruthenocene (26, 27). Large structural changes between the ground- and lowest energy excited states are probably responsible for the efficient nonradiative relaxation processes, which quench luminescence from $Ni(Ind)_2$. All observations illustrate that the first excited state of $Ni(Ind)_2$ is dramatically different from nickelocene.

The spectroscopic comparison of ruthenocene and $Ru(Ind)_2$ also reveals significant differences in the nature of the lowest energy excited state. $Ru(Ind)_2$ shows a more intense first band than ruthenocene for which the lowest energy *d–d* transition occurs at 30 000 cm^{-1} with a molar absorptivity of 200 M^{-1} cm^{-1} (28). However, the increase in intensity for the Ru compounds is less dramatic than for the analogous nickel compounds, consistent with the similar solid state structures for $Ru(Ind)_2$ and ruthenocene. Although precise bandwidths are difficult to determine quantitatively for the overlapping bands of ruthenocene, widths larger than 3000 cm^{-1} are observed for both ruthenocene and $Ru(Ind)_2$, with the first band maximum of the latter being 6600 cm^{-1} lower in energy. A detailed EHMO study of $M(Ind)_2$ (M = Fe, Ru) has established that the first excited electronic state of these compounds has significant indenyl π character (9). The metal d orbitals and one of the indenyl π orbitals are at the same energy, leading to a large π contribution to the LUMO; this is in agreement with our observation of a large, intense band for the transition from HOMO, which is mainly metal *d* to LUMO, which is a combination of metal *d* and indenyl π.

As was found for $Ni(Ind)_2$, we did not observe any luminescence for $Ru(Ind)_2$. The absence of luminescence in these bis(Ind) complexes is in agreement with a detailed study on the photophysics and photochemistry of bis(arene)ruthenium compounds that showed that ring-tilting in the excited state favors nonradiative relaxation and quenches luminescence (29). Large excited state distortions of this type are quite probable in both the $Ru(Ind)_2$ and the $Ni(Ind)_2$ compounds, given the well-documented facility with which indenyl ligands undergo hapticity changes accompanied by folding (3), but they are much less likely for the metal-centered *d–d* transitions in metallocenes. Another possible source of luminescence quenching is the number of high-energy C—H oscillators that can act as potential acceptors for the electronic excitation energy. Although this is found to be a less important factor in bis(arene)ruthenium compounds (29), its importance in lowering the luminescence quantum yield for bis(indenyl) compounds cannot be ignored given that the latter compounds possess 14 C—H oscillators compared to 10 in the corresponding metallocenes.

Conclusion

The comparison of absorption spectra for indenyl compounds and their cyclopentadienyl analogues shows that this method offers a very sensitive probe into metal – aromatic ligand bonding and molecular symmetry. Our results indicate strong correlations between structural characteristics, spectroscopic parameters, and metal – aromatic ligand bonding. In addition, this combination of techniques provides some insight into the nature and properties of the low-energy excited electronic states, information not routinely available with other techniques. In this sense, the present approach, which focuses on the HOMO–LUMO energy differences, complements past work on the photoelectron spectroscopy of Ind complexes (9) where the focus is the relative energies of low-lying occupied MOs. Future work will involve preparing related derivatives and investigating them with structural, spectroscopic, and more sophisticated molecular orbital studies.

Acknowledgements

This work was made possible by research grants from the Natural Sciences and Engineering Research Council of Canada and Fonds pour la formation de chercheurs et l'aide à la recherche (Province of Quebec).

References

1. A. Haaland. Acc. Chem. Res. **12**, 415 (1979).
2. J.M. Manriquez, M.D. Ward, W.M. Reiff, J.C. Calabreses, N.L. Jones, P.J. Carroll, E.E. Bunel, and J.S. Miller. J. Am. Chem. Soc. **117**, 6182 (1995).
3. J.P. Collman, L.S. Hegedus, J.R. Norton, and R.G. Finke. Principles and applications of organotransition metal chemistry. University Science Books, Mill Valley, 1987. pp. 255, 256.
4. H. Bonneman and W. Brijoux (Editors). Aspects of homogeneous catalysis. Vol. 5. D. Reidel, Dordrecht, The Netherlands. 1984. p. 75.
5. H. Bonneman. Angew. Chem. Int. Ed. Engl. **24**, 248 (1985).
6. T.B. Marder, D.C. Roe, and D. Milstein. Organometallics, **7**, 1451 (1988).
7. F.H. Köhler. Chem. Ber. **107**, 570 (1974).
8. S.A. Westcott, A.K. Kakkar, G. Stringer, N.J. Taylor, and T.B. Marder. J. Organomet. Chem. **394**, 777 (1990).
9. N.S. Crossley, J.C. Green, A. Nagy, and G. Stringer. J. Chem. Soc. Dalton Trans. 2139 (1989).
10. (*a*) T.A. Huber, F.B.-Gariépy, and D. Zargarian. Organometallics, **14**, 4997 (1995); (*b*) T.A. Huber, M. Bayrakdarian, I.

Dubuc, S. Dion, F.B.-Gariépy, and D. Zargarian. Manuscript in preparation.
11. R. Hoffmann. J. Chem. Phys. **39**, 1397 (1963).
12. C. Mealli and D.M. Proserpio. J. Chem. Educ. **67**, 399 (1990).
13. J.S. Merola, R.T. Kacmarcik, and D. Van Engen. J. Am. Chem. Soc. **108**, 329 (1986).
14. L. Ballester, S. Perez, A. Gutierrez, M. F. Perpinan, E. Gutierrez-Puebla, A. Monge, and C. Ruiz. J. Organomet. Chem. **414**, 411 (1991).
15. M.R. Churchill and T. A. O'Brien. J. Chem. Soc. A, 161 (1970).
16. A.J. Lees. Chem. Rev. **87**, 711 (1987).
17. C.J. Ballhausen. Introduction to ligand field theory. McGraw–Hill, New York. 1962.
18. J. Thomson and M.C. Baird. Can. J. Chem. **51**, 1179 (1973).
19. E. Heilbronner and H. Bock. Das HMO Modell und seine Anwendung. Vol. 1. Verlag Chemie, Weinheim, Germany. 1968. Chap. 11.
20. E.G. Bakalbassis, M.-A.D. Stiakaki, A.C. Tsipis, and C.A. Tsipis. J. Chem. Educ. **73**, 111 (1996).
21. N.C. Webb and R.E. Marsh. Acta Crystallogr. **22**, 382 (1967).
22. P. Seiler and J.D. Dunitz. Acta Crystallogr. Sect. B: Struct. Crystallogr. Cryst. Chem. **B36**, 2255 (1980).
23. K.R. Gordon and K.D. Warren. Inorg. Chem. **17**, 987 (1978).
24. J.H. Ammeter and J.D. Swalen. J. Chem. Phys. **57**, 678 (1972).
25. L. Pavlik, V. Cerny, and E. Maxova. Collect. Czech Chem. Commun. **35**, 3045 (1970).
26. M.J. Davis and C. Reber. Inorg. Chem. **35**, 3320 (1996).
27. M.J. Davis and C. Reber. Inorg. Chem. **34**, 4585 (1995).
28. Y.S. Sohn, D.N. Hendrickson, and H.B. Gray. J. Am. Chem. Soc. **93**, 3603 (1971).
29. T. Karlen, A. Hauser, and A. Ludi. Inorg. Chem. **33**, 2213 (1994).

A pentaammineruthenium(III) dimer with the novel bridging ligand 4,4′-dicyanamidobiphenyl dianion

Manuel A.S. Aquino, Christopher A. White, Corinne Bensimon, J.E. Greedan, and Robert J. Crutchley

Abstract: The novel ligand 4,4′-dicyanamidobiphenyl dianion (bp^{2-}) has been synthesized and characterized by ^{13}C NMR spectroscopy, cyclic voltammetry, and crystallography. The crystal structure of $[Ph_4As]_2[bp]\cdot H_2O$ showed that bp^{2-} is approximately planar with a dihedral angle of 8.2° between phenyl ring planes and the cyanamide groups in an *anti* conformation. The water of crystallization is asymmetrically hydrogen bonded between cyanamide groups of adjacent bp^{2-} ions. The crystal data for $C_{62}H_{48}N_4As_2+H_2O$ are monoclinic crystal system and space group $P2_1/c$ with $a = 12.998(5)$ Å, $b = 13.465(4)$ Å, $c = 28.703(13)$ Å, $\beta = 98.94(3)°$, $V = 4963(3)$ Å^3, and $Z = 4$. The structure was refined by using 4555 reflections with $I > 2.5\sigma(I)$ to an R factor of 0.058. The complex, $[\{(NH_3)_5Ru\}_2(\mu\text{-bp})][X]_4$, where X = tosylate or PF_6^- ions, was also synthesized and characterized by ^1H NMR spectroscopy, cyclic voltammetry, spectroelectrochemistry, and temperature-dependent magnetic susceptibility measurements. From cyclic voltammetry measurements, the comproportionation constants to form the mixed-valence complex $[\{(NH_3)_5Ru\}_2(\mu\text{-bp})]^{3+}$ were estimated to be 4.1, 16, and 22 in water, acetonitrile, and nitromethane, respectively. The trend and magnitude of K_c suggests solvent valence trapping of a weakly coupled Class II ion. The MMCT band of the mixed-valence complex had to be deconvoluted from the low-energy LMCT band and had the following properties in acetonitrile, $\nu_{max} = 8400$ cm^{-1}, $\varepsilon_{max} = 3300$ M^{-1} cm^{-1}, and $\Delta\nu_{1/2} = 3300$ cm^{-1}. The weak superexchange mediating properties of bp^{2-} compared to 1,4-dicyanamidobenzene dianion were suggested to arise from the larger barrier to the formation of the radical anion bp^-.

Key words: cyanamido, mixed valence, superexchange, ruthenium.

Résumé : On a synthétisé le nouveau ligand dianionique, 4,4′-dicyanamidobiphényle (bp^{2-}) et on l'a caractérisé par la spectroscopie de RMN, la voltampérométrie cyclique et par cristallographie. La structure du cristal de $[Ph_4As]_2[bp]\cdot H_2O$ montre que l'anion bp^{2-} est approximativement plan avec un angle dièdre de 8,2° entre les cycles phényles plans, et les groupes cyanamides sont dans une conformation *anti*. L'eau de cristallisation est liée de façon asymétrique par des liaisons hydrogènes entre les groupes cyanamides adjacents aux ions bp^{2-}. Les cristaux de $C_{62}H_{48}N_4As_2 + H_2O$ appartiennent au groupe d'espace monoclinique $P2_1/c$ avec $a = 12,998(5)$ Å, $b = 13,465(4)$ Å, $c = 28,703(13)$ Å, $\beta = 98,94(3)°$, $V = 4963(3)$ Å^3 et $Z = 4$. On a affiné la structure en utilisant 4555 réflexions avec $I > 2,5\sigma(I)$ jusqu'à un facteur de R de 0,058. On a également synthétisé le complexe $[\{(NH_3)_5Ru\}_2(\mu\text{-bp})][X]_4$, X = ion tosylate ou PF_6^-, et on l'a caractérisé par la spectroscopie de RMN, la voltampérométrie cyclique, la spectroélectrochimie et par les mesures de susceptibilité magnétique en fonction de la température. À partir des mesures de voltampérométrie cyclique, on a évalué la constante de compropornation à 4,1, 16 et 22 dans l'eau, dans l'acétonitrile et dans le nitrométhane respectivement. La tendance et l'importance de K_c suggèrent une capture de valence d'un ion de classe II faiblement couplé par le solvant. La bande de valence mixte du complexe MMCT doit être déconvolutée à partir de la bande LMCT de faible énergie et a les propriétés suivantes dans l'acétonitrile, $\nu_{max} = 8400$ cm^{-1}, $\varepsilon_{max} = 3300$ M^{-1} et $\Delta\nu_{1/2} = 3300$ cm^{-1}. On suggère que les propriétés de suréchange faible de l'ion bp^{2-} compares avec celles du dianion 1,4-dicyanobenzène, sont dues à la plus grande barrière à la formation de l'anion radicalaire bp^-.

Mots clés : cyanamido, valence-mixte, suréchange, ruthénium.

[Traduit par la rédaction]

Received February 8, 1996.

This paper is dedicated to Professor Howard C. Clark in recognition of his contributions to Canadian chemistry.

C.A. White, C. Bensimon, and R.J. Crutchley.[1] Ottawa–Carleton Chemistry Institute, Carleton University, Ottawa, ON K1S 5B6, Canada.
M.A.S. Aquino. Department of Chemistry, St. Francis Xavier University, P.O. Box 5000, Antigonish, NS B2G 2W5, Canada.
J.E. Greedan. Institute for Materials Research, McMaster University, Hamilton, ON L8S 4M1, Canada.

[1] Author to whom correspondence may be addressed. Telephone: (613) 520-2600, ext. 3848. Fax: (613) 520-3749. E-mail: rcrutch@ccs.carleton.ca

Introduction

Biphenyl spacers have played an important role in elucidating the effect of medium on electron transfer rates and spin interactions (1–4). For example, McLendon and co-workers (1) have examined the dependence of the rate of electron transfer between porphyrins on the dihedral angle between phenyl rings of a biphenyl spacer. The rate of electron transfer was shown not to follow the expected cos θ relationship but to qualitatively follow a cos 2θ function, with maxima at 0 and 90° and a minimum at 45°. This dependence was anticipated by a theory for bis-porphyrin systems developed by Cave, Marcus, and Siders (5). More recent studies have focussed on incorporating polyphenyl spacers into supramolecular assemblies (6) and, in this regard, the long-range (nm scale) transfer of electrons or energy will depend on the geometric and electronic properties of the bridge. The effect of these properties can be described by the intercomponent

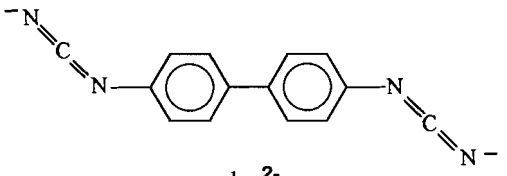

bp^{2-}

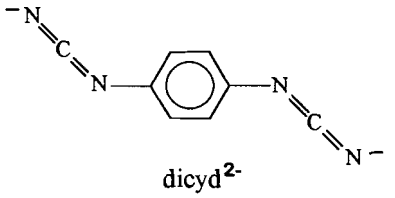

$dicyd^{2-}$

interaction energy, H, whose distance dependence is expected (7) to follow

$$[1] \quad H = H_0 \exp(-\beta r)$$

where β is an attenuation factor and r is the separation between two metal ions. It has been suggested (6) that β for hole transfer superexchange through polyphenylene bridges is approximately equal to zero. These investigations have practical application to poly(*p*-phenylene), a polymer that has been studied extensively (8) for its possible electronic and photonic applications.

Because our research program is uniquely suited to the study of hole transfer superexchange through π-donor aromatic systems, we decided to synthesize dicyanamidobiphenyl dianion (bp^{2-}) in order to compare its abilities as a superexchange mediator with those of 1,4-dicyanamidobenzene dianion ($dicyd^{2-}$). The complexes, $[\{(NH_3)_5Ru\}_2(\mu\text{-dicyd})]^{4+}$ where $dicyd^{2-}$ can be unsubstituted, 2,5-dimethyl, 2,5-dichloro, or 2,3,5,6-tetrachloro-1,4-dicyanamidobenzene dianion, possess Ru(III) ions that are strongly antiferromagnetically coupled (9, 10). The mechanism for metal–metal exchange was suggested to be hole transfer superexhange via the highest occupied orbital (HOMO) of the bridging $dicyd^{2-}$ ligand. In addition, the mixed-valence complexes $[\{(NH)_5Ru\}_2(\mu\text{-dicyd})]^{3+}$ are also strongly coupled systems that show a remarkable solvent dependence of metal–metal coupling (11, 12).

The bp^{2-} ligand should be one in which the conditions for superexchange within a biphenyl moiety are considerably enhanced and a comparison with the $dicyd^{2-}$ ligand will lead to greater insight into those factors controlling hole transfer superexchange.

Experimental

Physical measurements

Ultraviolet–visible near-infrared absorption spectra were taken on a Cary 5 spectrophotometer. The IR spectra of the samples in KBr discs were obtained with a Perkin-Elmer 1600 series FTIR spectrophotometer. ^1H and ^{13}C NMR spectra were run on a Varian XL-200 NMR spectrometer or a Bruker AMX-400 NMR spectrometer at 300 K and referenced to TMS (0.00 ppm). C, H, and N elemental analyses were performed by Canadian Microanalytical Services Ltd. The experimental setup used to perform non-aqueous (13) and aqueous (14) cyclic voltammetry experiments has already been described. The ferricenium/ferrocene couple with E^0 = 665 mV vs. NHE (15) was used in nonaqueous solvents as an internal calibrant. Spectroelectrochemistry was performed with a Pyrex–quartz cell of published design (16). Tetrabutylammonium hexafluorophosphate (TBAH) was recrystallized twice from ethanol and vacuum dried at 110°C overnight. Temperature-dependent magnetic susceptibility measurements were performed on a Quantum Design S.Q.U.I.D. magnetometer from 5 to 300 K in a 1.0 T field.

Materials

All chemicals and solvents were reagent grade or better. Benzidine (Anachemia), tetraphenylarsonium chloride hydrate $[Ph_4As][Cl]\cdot H_2O$ (Aldrich), and anhydrous acetonitrile (99+%, Aldrich) were used as received. Nitromethane (99+%, Aldrich) had to be distilled to remove impurities that decomposed the Ru(III) dimer. $[(NH_3)_5Ru(OH_2)][PF_6]_2$ was prepared according to literature procedures (17).

Preparation of N,N′-dicyano-4,4′-diaminobiphenyl·H_2O, $bpH_2\cdot H_2O$

To a gently refluxing solution of ammonium thiocyanate (7.6 g) in 100 mL of acetone was added dropwise a solution of benzoyl chloride in 100 mL of acetone. Over the 15 min. addition, the stirred solution became yellow and ammonium chloride precipitated. An acetone solution of benzidine (9.2 g in 100 mL) was then added dropwise over a 30 min. period to the refluxing reaction mixture. After addition was complete, the reaction mixture was allowed to reflux for 1 h, and then added to 1.5 L of water to ensure complete precipitation of the yellow benzoyl thiourea intermediate, which was filtered off and washed with water. This intermediate was then transferred to a 1 L Erlenmeyer flask containing 350 mL of 2.5 M NaOH solution. The reaction mixture was brought to a boil and maintained at that temperature for 5 min and then allowed to cool to 65°C. A solution of $Pb(acetate)_2\cdot 3H_2O$ (24 g) in 120 mL water was added, causing the reaction mixture to turn brown and then slowly black with the formation of lead sulfide. The formation of lead sulfide should take no more than 10 min, after which the reaction mixture is filtered into an ice-cooled suction flask. Immediate addition of glacial acetic acid (55 mL) to

the filtrate precipitated the white product, which was filtered and washed copiously with water. Recrystallization from acetone–water yields fine white needles. Yield: 5.9 g (50%); mp: decomposes >200°C. IR: ν(NCN) = 2224 cm^{-1}. Dimer formation is indicated by a strong ν(C=N) band centered at 1680 cm^{-1} that is absent in the monomer (18). ^{13}C NMR: 5 peaks at 137.7, 133.8, 127.5, 115.4, and 112.0 ppm in DMSO-d_6. ^1H NMR: 7.62 (doublet, 4H), 7.05 (doublet, 4H), and 10.23 (broad singlet, 2H) ppm in DMSO-d_6. The presence of a water of recrystallization was confirmed by a water resonance at 3.44 ppm which integrated for two protons. Anal. calcd.for $C_{14}H_{12}N_4O$: C 66.65, H 4.79, N 22.21; found: C 66.69, H 4.63, N 22.34.

Preparation of bis(tetraphenyl arsonium) 4,4′-dicyanamidobiphenyl, $[Ph_4As]_2[bp]\cdot H_2O$

To a solution of bpH_2 (0.23 g) in 2 M NaOH (30 mL) was added a solution of $[Ph_4As][Cl]$ (0.82 g) in water (10 mL). A canary-yellow precipitate immediately formed. This was filtered and washed with water and vacuum dried. The crude product was dissolved in boiling acetonitrile (60 mL) and the solution gravity filtered. Ether was allowed to diffuse into the filtrate, which over 2 days gave golden crystals. Yield: 0.79 g (83%). IR: ν(NCN) = 2088 cm^{-1}. Anal. calcd. for $C_{62}H_{50}As_2N_4O$: C 73.23, H 4.96, N 5.51; found: C 72.77, H 5.13, N 5.69.

Preparation of $[\{(NH_3)_5Ru\}_2(\mu\text{-}bp)][PF_6]_4\cdot$acetone

Under argon, $[(NH_3)_5Ru(OH_2)][PF_6]_2$ (1.0 g) and bpH_2 (0.25 g) were dissolved in 75 mL acetone. The solution was allowed to stir for 16 h at room temperature, then filtered, and exposed to air. Upon stirring for 2 h, the complex oxidized, turning the solution from a light green to a dark blue-green colour. Tetrabutylammonium bromide (1.5 g) was added to the solution to precipitate the green bromide complex. This was filtered, washed with acetone and allowed to dry. The bromide salt was then dissolved in water (35 mL), filtered and the filtrate added to a solution of NH_4PF_6 (3.3 g) in water (10 mL). The resulting blue-green precipitate was filtered, washed with ice-cold water, and vacuum dried. Recrystallization was achieved by diffusing ether into an acetone solution of the complex. Yield: 1.02 g (82%). IR: ν(NCN) = 2110 cm^{-1}. Anal. calcd.for $C_{17}H_{44}F_{24}N_{14}OP_4Ru_2$: C 16.43, H 3.57, N 15.77; found: C 16.70, H 3.57, N 15.26.

Preparation of $[\{(NH_3)_5Ru\}_2(\mu\text{-}bp)][tosylate]_4\cdot 2H_2O$

Metathesis of the bromide complex (as prepared above) in aqueous solution with potassium tosylate yielded the tosylate complex in 80% yield. The complex was recrystallized by acetone diffusion into an acetone–water solution of the complex. IR: ν(NCN) = 2106 cm^{-1}. Anal. calcd.for $C_{42}H_{70}N_{14}O_{14}Ru_2S_4$: C 38.06, H 5.32, N 14.79; found: C 37.64, H 5.05, N 14.72.

Crystal structure determination of $[Ph_4As]_2[bp]\cdot H_2O$

A suitable cubic crystal was grown by allowing a saturated warm DMSO solution to slowly cool to room temperature. The crystal was mounted on a glass capillary and measurements made on a Picker diffractometer with Cu $K\alpha_1$ radiation. Cell constants and an orientation matrix for data collection were obtained from least-squares refinement using the setting angles of 30 reflections in the range $80 < 2\theta < 100$ and corresponded to a monoclinic cell. Based on systematic absences, the space group was determined to be $P2_1/c$. For $Z = 4$ and fw = 1016.95 g, the calculated density is 1.361 g/cm^3.

The data were collected using the ω-2θ scan technique to a maximum 2θ value of 119.9°. A total of 8182 reflections were collected with a unique set of only 6270 reflections. The standards were measured after every 150 reflections and no crystal decay was noticed. The data were corrected for Lorentz and polarization effects (19). No absorption correction was made.

The structure was solved by direct methods. All the atoms were refined anisotropically except the hydrogen atoms, which were calculated. The final cycle of full-matrix least-squares refinement was based on 4555 observed reflections ($I > 2.5\sigma(I)$) and 623 variable parameters. Weights based on counting statistics were used. The maximum and minimum peaks on the final differences Fourier map corresponded to −0.490 and 1.250 e/A^3, respectively. All the calculations were performed using the NRC VAX crystallographic software package (20).

Full listings of positional and thermal parameters, bond angles and lengths, and dihedral angles have been deposited as supplementary material.[2]

Results and discussion

The bridging ligand

Crystals of the free dianion ligand $[Ph_4As]_2[bp]$ are air stable, unlike those of $[Ph_4As]_2[dicyd]$ that must be stored under argon. Crystal data and atomic parameters for $[Ph_4As]_2[bp]$ are compiled in Tables 1 and 2, respectively. The structure of bp^{2-} is shown in Fig. 1 and selected bond lengths and angles are given in Table 3. As shown in Fig. 1, bp^{2-} adopts an approximately planar geometry suggesting significant π interactions between the two phenyl rings and between the cyanamide groups and their respective phenyl rings. The π interaction between the phenyl rings favours a planar geometry but this is opposed by steric repulsion between *ortho* hydrogens, which results in a small but significant dihedral angle of 8.2° between the phenyl ring planes. There are many crystal structures of phenylcyanamide ligands (9, 10, 21–23) that show cyanamide groups coplanar with phenyl rings. Crystal structures of uncoordinated 1,4-dicyanamidobenzene dianion ($dicyd^{2-}$) and its substituted derivatives (10, 23) have all shown the cyanamide groups to adopt an *anti* conformation, as do those of bp^{2-}. The apparent stability of the *anti* conformation arises in part from its minimal repulsion between cyanamide anion groups. An additional feature in the crystal structure of bp^{2-} is the presence of a water of crystallization, hydrogen bonded between adjacent bp^{2-} ligands to form a chain of alternating bp^{2-} and water molecules within the crystal lattice. The nitrogen to oxygen separations (Table 3) are

[2] A complete set of data may be purchased from: The Depository of Unpublished Data, CISTI, National Research Council Canada, Ottawa, Canada K1A 0S2. Tables of atomic parameters and bond lengths and angles have also been deposited with the Cambridge Crystallographic Data Centre, and can be obtained on request from The Director, Cambridge Crystallographic Data Centre, University Chemical Laboratory, 12 Union Road, Cambridge, CB2 1EZ, U.K.

Table 1. Crystal data for $[Ph_4As]_2[bp]\cdot H_2O$.

Empirical formula	$C_{62}H_{48}N_4As_2 + H_2O$
fw	1016.95
Crystal system	Monoclinic
Space group	$P2_1/c$
Crystal dimensions (mm)	$0.30 \times 0.15 \times 0.10$
a, Å	12.998(4)
b, Å	13.465(4)
c, Å	28.703(3)
β, deg	98.94(3)
V, Å^3	4963(3)
Z	4
ρ_{calcd}, g/cm^3	1.361
T, °C	20
Radiation (λ, Å)	CuKα$_1$ (1.540 56)
μ, cm^{-1}	2.02
R_f (sig refl)	0.058
R_w (sig refl)	0.054
R_f (all refl)	0.077
R_w (all refl)	0.062
Goodness of fit	4.03

Table 2. Atomic parameters and B_{iso}[a] for the anion of $[Ph_4As]_2[bp]\cdot H_2O$.

Atom	x	y	z	B_{iso}[b]
N1	0.1931(7)	0.8601(6)	0.1875(3)	9.2(5)
N2	0.1194(5)	0.8983(5)	0.105544(24)	6.3(4)
N3	−0.5425(6)	0.6245(6)	−0.0693(3)	8.5(5)
N4	−0.6069(7)	0.6496(7)	−0.1533(3)	11.4(6)
C1	0.1526(7)	0.8756(6)	0.1489(3)	6.4(4)
C2	0.0312(6)	0.8523(5)	0.0814(3)	5.5(4)
C3	−0.0307(6)	0.7841(5)	0.1008(3)	5.5(4)
C4	−0.1213(6)	0.7460(5)	0.0752(3)	5.3(4)
C5	−0.1557(6)	0.7729(5)	0.0290(3)	5.5(4)
C6	−0.0907(7)	0.8392(6)	0.0082(3)	6.1(4)
C7	−0.0011(7)	0.8753(6)	0.0338(3)	6.1(4)
C8	−0.2553(7)	0.7370(5)	0.0025(3)	5.5(4)
C9	−0.3148(7)	0.6625(6)	0.0208(3)	7.0(5)
C10	−0.4087(7)	0.6299(7)	−0.0033(3)	7.2(5)
C11	−0.4498(7)	0.6648(7)	−0.0469(3)	7.2(5)
C12	−0.3922(7)	0.7379(6)	−0.0674(3)	6.6(5)
C13	−0.2993(7)	0.7713(6)	−0.0420(3)	6.6(5)
C14	−0.5734(7)	0.6393(7)	−0.1122(4)	8.9(6)
O	0.7989(6)	0.3758(7)	0.2099(3)	12.0(6)

[a]Estimated standard deviations are in parentheses.
[b]B_{iso} is the mean of the principal axes of the thermal ellipsoid, Å^2.

well within hydrogen bonding range (24) but are asymmetric and this may account for the non-equivalence of respective cyanamide and phenyl groups in the bp^{2-} ion. The crystal structures of $dicyd^{2-}$ and its substituted derivatives (23) show no solvent of crystallization and in these cases the $dicyd^{2-}$ ion possesses a center of symmetry.

Cyclic voltametry of the bp^{2-} ion, in acetonitrile (Table 4), shows two couples consistent with the reactions in Scheme 1. The anodic to cathodic peak separations of these couples are

Table 3. Selected crystal structure data for $[Ph_4As]_2[bp]\cdot H_2O$.

Bond lengths, Å			
O—N1	2.936(11)	O—N4	2.780(12)
N1—C1	1.170(12)	C5—C6	1.423(11)
N2—C1	1.291(11)	C5—C8	1.477(12)
N2—C2	1.388(11)	C6—C7	1.367(12)
N3—C11	1.386(12)	C8—C9	1.417(12)
N3—C14	1.249(14)	C8—C13	1.394(12)
N4—C14	1.202(15)	C9—C10	1.378(13)
C2—C3	1.393(11)	C10—C11	1.365(13)
C2—C7	1.400(11)	C11—C12	1.419(13)
C3—C4	1.385(12)	C12—C13	1.385(13)
C4—C5	1.381(11)		
Bond angles, deg			
N1-O-N4	117.7(4)[a]	N2-C2-C7	119.1(7)
C1-N2-C2	120.1(7)	N3-C11-C10	118.7(9)
C11-N3-C14	121.3(9)	N3-C11-C12	123.7(9)
N1-C1-N2	172.4(10)	N3-C14-N4	176.5(12)
N2-C2-C3	125.4(70		

[a]Note: N1 and N4 are on different molecules.

Table 4. Solvent-dependent cyclic voltammetry data[a] of $[Ph_4As]_2[bp]$, $[Ph_4As]_2[dicyd]$, and $[\{(NH_3)_5Ru\}_2(\mu\text{-bp})]^{4+}$ salts.

	L_1	L_2	Ru(III/II)	ΔE[b]
$[\{(NH_3)_5Ru\}_2(\mu\text{-bp})]^{4+}$				
H_2O[c]		0.91(190)	−0.02(60)	0.036
CH_3CN[d]	1.04(80)	1.21(85)	0.05(100)	0.072
CH_3NO_2[d]	1.10(75)	1.35(90)	0.16(110)	0.080
bp^{2-}				
CH_3CN[e]	0.31(60)	0.54(60)		
$dicyd^{2-}$				
CH_3CN[f]	−0.46(125)	0.21(65)		

[a]All data in volts versus NHE (anodic to cathodic peak separations in mV in parentheses).
[b]Separation between Ru(III/II) couples, see ref. 25.
[c]Tosylate salt, 100 mV/s, 0.1 M $NaClO_4$.
[d]PF_6^- salt, 100 mV/s, 0.1 M TBAH.
[e]200 mV/s, 0.1 M TBAH.
[f]100 mV/s, 0.1 M TBAH.

Scheme 1.

$$bp^{2-} \underset{L_1}{\overset{-e^-}{\rightleftharpoons}} bp^{\cdot-}$$

$$bp^{\cdot-} \underset{L_2}{\overset{-e^-}{\rightleftharpoons}} bp$$

consistent with one-electron redox processes and good reversibility is shown by equivalent anodic and cathodic currents at scan rates greater than or equal to 200 mV s^{-1}. In addition, the ratio of anodic peak current functions, $i_p/\nu^{1/2}$ found for the electrochemical responses of bp^{2-} with those of equimolar fer-

Fig. 1. ORTEP drawing of bp^{2-}. The tetraphenyl arsonium counterions and water molecule have been excluded for clarity.

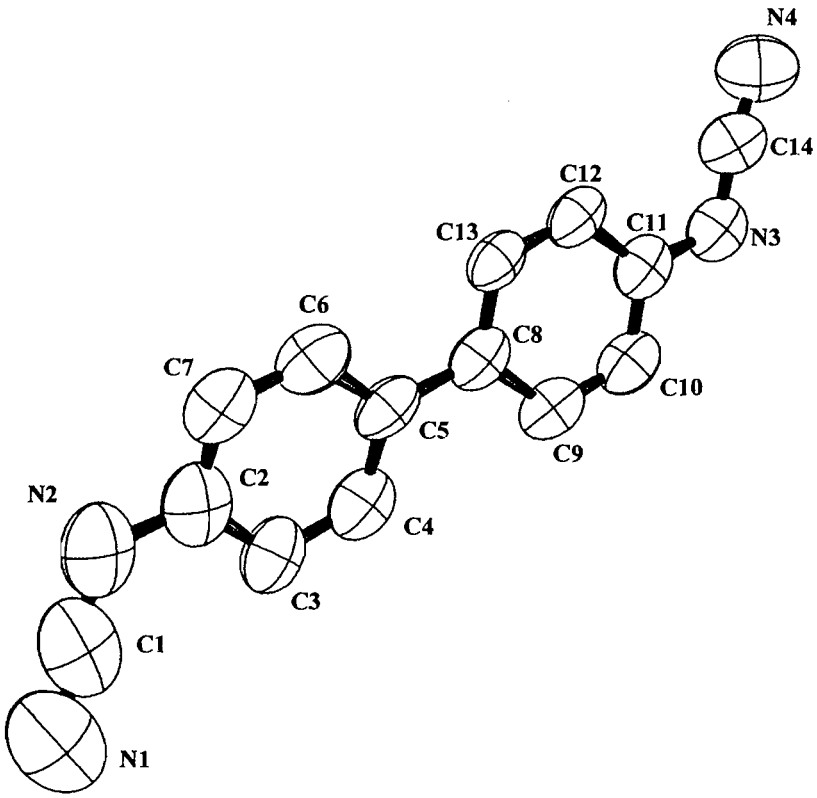

rocene gave for L_1 a value of 0.90 and for L_2 a value of 0.95. At slower scan rates, reversibility of the L_2 couple is significantly decreased as shown by the reduction of both anodic and cathodic currents relative to the L_1 couple and by the fouling of the working electrode. Drying the solvent did not appear to improve reversibility.

The complex

The cyclic voltammogram of $[\{(NH_3)_5Ru\}_2(\mu\text{-bp})]^{4+}$ in acetonitrile (Fig. 2), and the electrochemical data in this solvent as well as water and nitromethane (Table 4), are indicative of a weakly coupled mixed-valence state for this complex. In Fig. 2, the overlap of Ru(III/II) couples results in only a single cathodic and anodic peak of twice the current intensity of the one-electron ligand couples at more positive potentials. Richardson and Taube (25) have given a graphical method of evaluating the separation between overlapping Ru(III/II) couples (ΔE in Table 4) from the separation of anodic and cathodic peaks in the cyclic voltammetry experiment. From the values of ΔE, the estimated comproportionation constants K_c for $[\{(NH_3)_5Ru\}_2(\mu\text{-bp})]^{3+}$ in water, acetonitrile, and nitromethane are 4.1, 16, and 22, respectively. We have interpreted similar but much greater solvent dependence in K_c for $[\{(NH_3)_5Ru\}_2(\mu\text{-dicyd})]^{4+}$ complexes as due to solvent-induced valence trapping (11, 12) and this may play a role here as well. However, in the case of very weakly coupled mixed-valence complexes, a considerable contribution to K_c is derived from the electrostatic repulsion between metal ions. Ferrere and Elliott (26) have proposed the following expression for this electrostatic contribution,

Fig. 2. Cyclic voltammogram of $[\{(NH_3)_5Ru\}_2(\mu\text{-bp})][PF_6]_4$, platinum disk working electrode (1.6 mm diameter), scan rate 200 mV/s, 0.1 M TBAH in acetonitrile.

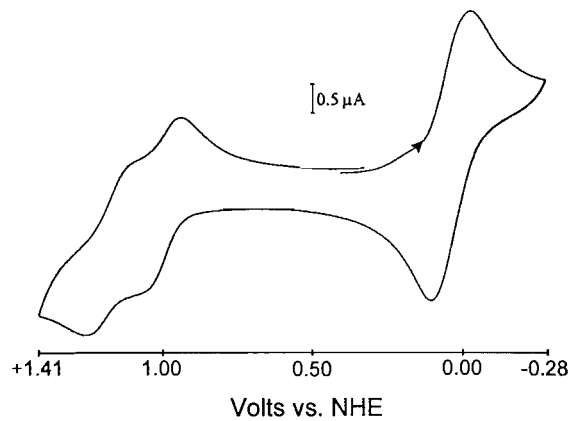

[2] $\Delta E_e = 1/(4\pi\varepsilon\varepsilon_0 R)$

where ε is the dielectric constant of the solvent, ε_0 is the vacuum permittivity constant, and R is the separation between metal ions. For $[\{(NH_3)_5Ru\}_2(\mu\text{-bp})]^{3+}$, the metal–metal separation is estimated at 15.6 Å, assuming the cyanamides retain an *anti* conformation upon coordination, and thus ΔE_e is esti-

Table 5. Solvent-dependent electronic absorption spectroscopy data[a] for $[\{(NH_3)_5Ru\}_2(\mu\text{-bp})]^{4+}$.

		LMCT	
Solvent	$\pi^* \leftarrow \pi$	$b_1^* \leftarrow b_2$	$b_1^* \leftarrow b_1$
H_2O[b]	299(4.51)	393(3.76)[c]	751(4.07)
CH_3CN[d]	207(4.69), 301(4.47)	398(3.93)	869(4.18)
CH_3NO_2[d]		404(3.94)	988(4.27)

[a]Data in nm with log ε in M^{-1} cm^{-1} in parentheses.
[b]Tosylate salt of complex.
[c]Shoulder.
[d]PF_6^- salt of the complex.

Fig. 3. Spectroelectrochemical reduction of $[\{(NH_3)_5Ru\}_2(\mu\text{-bp})][PF_6]_4$ at fixed potential to form the mixed-valence complex; 0.1 M TBAH in acetonitrile. The initial spectrum is that of the Ru(III,III) complex with the other spectra taken at approximately 3 min intervals.

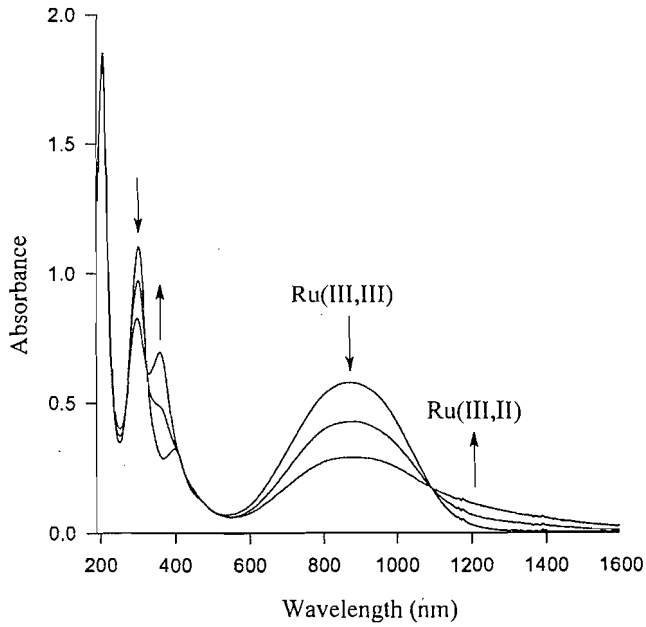

mated to be 12, 23, and 25 mV in water, acetonitrile and nitromethane, respectively. The over 35 mV separation in ΔE (see Table 4) between water and either acetonitrile or nitromethane can therefore not be entirely accounted for by differences in electrostatic repulsion and may indicate some degree of solvent trapping of the mixed-valence state in water. Indeed, the magnitude of K_c in aqueous solution is very close to that predicted on purely statistical grounds and suggests no metal–metal coupling (Class I behavior) (27). Further evidence of metal–metal coupling can be found in the spectroelectrochemical studies.

The solvent-dependent electronic absorption spectral data together with assignments for $[\{(NH_3)_5Ru\}_2(\mu\text{-bp})]^{4+}$ are given in Table 5 and a representative spectrum of the complex in acetonitrile is shown in Fig. 3. A spectroscopic analysis of the Ru(III)–cyanamide chromophore (28) showed that two ligand-to-metal charge transfer (LMCT) transitions can be expected from the interaction of the two nonbonding π symmetry electron pairs of the cyanamide moiety with the Ru(III) ion. In Table 5, the energy and extinction coefficient of lowest energy LMCT band, $b_1^* \leftarrow b_1$, are clearly dependent on the solvent. Similar effects have been seen for both inner (22) and outer sphere (29) perturbations of the Ru(III)-cyanamide moiety and have been rationalized in terms of the Ru(III)–cyanamide π overlap integral.

Spectroelectrochemical reduction of $[\{(NH_3)_5Ru\}_2(\mu\text{-bp})]^{4+}$ to the mostly mixed-valence complex in solution is shown in Fig. 3. The platinum mesh working electrode was held at fixed potential (−85 mV vs. NHE) and the spectra shown in Fig. 3 were taken at approximately 3 min intervals. Because the Ru(III/II) couples overlap, it was assumed that reduction to the mixed-valence complex was complete when the intensity of the $b_1^* \leftarrow b_1$ LMCT band of the Ru(III,III) complex was reduced by approximately one-half. It was possible to cycle between the extremes shown in Fig. 3 with no change in isosbestic points and the absorbance maxima of the Ru(III, III) complex spectrum. However, upon further reduction with loss of LMCT band intensity, the instability of the Ru(II, II) complex became apparent because oxidation of the solution did not regenerate the Ru(III, III) spectrum. The Ru(II, II) complex is not expected to absorb at all above 500 nm and will therefore not interfere with deconvolution of the metal-to-metal charge transfer (MMCT) band from the $b_1^* \leftarrow b_1$ LMCT band.[3] The MMCT band appears in Fig. 3 as the low-energy tail that grows in with the formation of the Ru(III, II) complex. The process to deconvolute the MMCT transition from the low energy band envelope has been described in detail (11) but the main assumptions are that the MMCT transition can be represented by a single Gaussian band and the energy and band shape of the LMCT transition does not change upon reduction of one of the Ru–cyanamide chromophores. The spectral data for the deconvoluted MMCT band are ν_{max} = 8400 cm^{-1}, ε_{max} = 2200 M^{-1} cm^{-1}, and $\Delta\nu_{1/2}$ = 3300 cm^{-1}. The high-energy tail of the the MMCT band does not significantly contribute (<1%) to the intensity of the LMCT band maximum. Nevertheless, the MMCT extinction coefficient needs to be corrected for the comproportionation equilibrium for which the actual proportion of mixed-valence species is defined (30) as

$$[3] \quad P = [\text{Ru(III, II)}]/([\text{Ru(III, II)} + [\text{Ru(III, III)} + [\text{Ru(II, II)}])$$

or in terms of the comproportionation constant

$$[4] \quad P = K_c^{1/2}/(2 + K_c^{1/2})$$

Because K_c = 16 in acetonitrile, P = 0.67, and the corrected intervalence absorption band has ε_{max} = 3300 M^{-1} cm^{-1}. The comproportionation constant and Hush theory resonance exchange integral (31, 32), estimated at H_{ad} = 400 cm^{-1}, are consistent with a weakly coupled Class II mixed-valence com-

[3] The Ru(II,II) dimer possesses no charge transfer chromophores that would absorb in the visible or NIR regions and ligand field transitions would be at wavelengths much lower than 500 nm.

plex (27). However, the value of $\Delta\nu_{1/2}$ derived by nonlinear curve fitting analysis is far narrower than that predicted by Hush theory, $\Delta\nu_{1/2}$(calc) = 4400 cm^{-1}, and may be an artifact in this instance.

Metal–metal coupling and the nature of the bridging ligand

Metal-metal coupling in the mixed-valence complex $[\{(NH_3)_5Ru\}_2(\mu\text{-dicyd})]^{3+}$ is substantially greater than that found for the bp^{2-} analogue. For $[\{(NH_3)_5Ru\}_2(\mu\text{-dicyd})]^{3+}$ in acetonitrile (10), $K_c = 6.8 \times 10^4$ and its MMCT band has ν_{max} = 6910 cm^{-1}, ε_{max} = 4090 M^{-1} cm^{-1}, and $\Delta\nu_{1/2}$ = 2640 cm^{-1}. The magnitude of its comproportionation constant and narrowness of the MMCT band (Hush theory $\Delta\nu_{1/2}$ = 4000 cm^{-1}) support a strongly coupled Class II assignment for the $[\{(NH_3)_5Ru\}_2(\mu\text{-dicyd})]^{3+}$ ion (27, 32, 33). In addition, previous studies have shown that intramolecular antiferromagnetic coupling of the Ru(III,III) complex $[\{(NH_3)_5Ru\}_2(\mu\text{-dicyd})]^{4+}$ is sufficiently strong to render the complex diamagnetic in the solid state (9) and, in poor donor solvents, an essentially diamagnetic ^1H NMR spectrum is observed (34), slightly perturbed by the trace Boltzmann population of the triplet excited state (e.g., in nitromethane-d_3: *trans* ammine, 18.24; *cis* ammine, 4.90; phenyl, 6.12 ppm). In contrast, temperature-dependent magnetic susceptibility studies of $[\{(NH_3)_5Ru\}_2(\mu\text{-bp})][PF_6]_4$ showed no evidence of intramolecular antiferromagnetic coupling and a Curie–Weiss fit of the data between 60 to 300 K gave $\theta = -42$ K, indicating intermolecular antiferromagnetic exchange. The ^1H NMR spectrum of this complex in acetonitrile-d_3 is dramatically affected by its paramagnetism, with the *cis* ammine protons appearing as a broad singlet resonance contact shifted to 57.3 ppm and two singlet phenyl ring proton resonances pseudocontact shifted to −41.2 and 20.7 ppm. The *trans* ammine protons were not observed and are believed to be >250 ppm.

From the above, it is clear that $dicyd^{2-}$ is a superior mediator of superexchange metal–metal coupling compared to bp^{2-}. If it is assumed that the dominant mechanism for superexchange is hole transfer via the HOMO of the bridging ligand,[4] the differences in metal–metal coupling must be due to the nature of the HOMO, its energy, and continuity. A measure of the relative energies of free bp^{2-} and $dicyd^{2-}$ HOMOs is the difference in L_1 redox couples in Table 4. Because the L_1 of bp^{2-} is 780 mV more positive than that of the oxidized ligand, there must exist a larger energy barrier to the creation of the oxidized ligand virtual state from the bp^{2-} ligand, as is required by the hole transfer superexchange mechanism. The energy barrier to oxidation exists because the steric repulsion between *ortho* hydrogens of the phenyl rings forces the biphenyl moiety to be nonplanar and thereby weakens the π interactions between phenyl rings. If the energy of the π superexchange pathway could be raised, this would reduce the energy gap between metal orbitals and the superexchange pathway. The hypothetical biphenyl dianion bridging ligand, for which the protons at the 4 and 4′ ring positions have been removed, meets these requirements and would optimize hole transfer superexchange within the biphenyl moiety.

[4] This seems reasonable because both are π-donor aromatic dianion ligands.

An example of a bridging ligand that contains a biphenyl dianion spacer is 3,3′,5,5′-tetrapyridylbiphenyl dianion ($tpbp^{2-}$) (35). The mixed valence complex, $[\{(ttrpy)Ru\}_2(\mu\text{-tpbp})]^{3+}$ where ttrpy is 4′-*p*-tolyl-2,2′,6′,2″-terpyridine, possesses an extraordinarily intense MMCT band centered at 1820 nm with ε_{max} = 27 000 M^{-1} cm^{-1} in acetonitrile (35*a*). The comproportionation constant of the complex is approximately 600 and its Hush resonance exchange integral is estimated to be 1200 cm^{-1} These values are significantly greater than those found for $[\{(NH_3)_5Ru\}_2(\mu\text{-bp})]^{3+}$; however, the nature of the spectator ligands has changed and because this can have a dramatic effect on ruthenium 4d-orbital energies, the relative superexchange mediating properties of bp^{2-} and $tpbp^{2-}$ cannot be properly evaluated. In addition, superexchange via $tpbp^{2-}$, can occur by both electron transfer, owing to the presence of the pyridine moieties, and hole transfer, through σ and π pathways of the biphenyl moiety, whereas for the bp^{2-} ligand, effective superexchange is probably restricted to hole transfer via its π HOMO.

There are only a few other examples of multi-atom bridging ligands that are likely to mediate hole transfer superexchange coupling in mixed-valence complexes. These are: malonitrile anion derivatives (36), triazole anion derivatives (37), bibenzimidazolate dianion (38), and finally the azodicarbonyl dianion ligands (39). Importantly, the magnitude of coupling in $[\{Ru(bpy)_2)\}_2(\mu\text{-adc})]^{3+}$, where adc^{2-} is an azodicarbonyl dianion derivative and bpy is 2,2′-bipyridine, is so great that the authors have suggested that the Ru(II)-adc^{-}(radical)-Ru(II) resonance form may make an significant contribution to the mixed-valence state (39). While this magnitude of coupling may be possible through the $dicyd^{2-}$ ligand, the nonplanarity of bp^{2-} limits its superexchange mediating properties. Work to synthesize the 2,7-dicyanamidophenanthrene dianion ligand, which should contain a planar biphenyldicyanamido moiety, is in progress.

Acknowledgements

R.J.C, M.A.S.A., and J.E.G. thank the Natural Sciences and Engineering Research Council of Canada for financial support. We also thank Johnson-Matthey PLC for the loan of ruthenium trichloride.

References

1. (*a*) A. Helms, D. Heiler, and G. McLendon. J. Am. Chem. Soc. **114**, 6227 (1992); (*b*) J. Am. Chem. Soc. **113**, 4325 (1991).
2. M. Minato, P.M. Lahti, and H. van Willigen. J. Am. Chem. Soc. **115**, 4532 (1993).
3. A. Osuka, S. Nakajima, K. Maruyama, N. Mataga, T. Asahi, I. Yamazaki, Y. Nishimura, T. Ohno, and K. Nozaki. J. Am. Chem. Soc. **115**, 4577 (1993).
4. Y. Kim and C.M. Lieber. Inorg. Chem. **28**, 3990 (1989).
5. R. Cave, R.A. Marcus, and P. Siders. J. Phys. Chem. **90**, 1436 (1986).
6. (*a*) F. Barigelletti, L. Flamigni, M. Guardigli, A. Juris, M. Beley, S. Chodorowski-Kimmes, J.-P. Collin and J.-P. Sauvage. Inorg. Chem. **35**, 136 (1996); (*b*) F. Barigelletti, L. Flamigni, V. Balzani, J.-P. Collin, J.-P. Sauvage, A. Sour, E.C. Constable, and A.M.W. Cargill Thompson. J. Am. Chem. Soc. **116**, 7692 (1994).
7. R.A. Marcus and N. Sutin. Biochem. Biophys. Acta, **811**, 265 (1985).

8. J.J.S. Lamba and J.M. Tour. J. Am. Chem. Soc. **116**, 11723 (1994), and refs. therein.
9. M.A.S. Aquino, F.L. Lee, E.J. Gabe, C. Bensimon, J.E. Greedan, and R.J. Crutchley. J. Am. Chem. Soc. **114**, 5130 (1992).
10. M.A.S. Aquino, F.L. Lee, E.J. Gabe, J.E. Greedan, and R.J. Crutchley. Inorg. Chem. **30**, 3234 (1991).
11. M.L. Naklicki and R.J. Crutchley. Inorg. Chim. Acta, **225**, 123 (1994).
12. M.L. Naklicki and R.J. Crutchley. J. Am. Chem. Soc. **116**, 6045 (1994).
13. A.R. Rezvani and R.J. Crutchley. Inorg. Chem. **33**, 170 (1994).
14. M.A.S. Aquino, A.E. Bostock, and R.J. Crutchley. Inorg. Chem. **29**, 3641 (1990).
15. T. Gennett, D.F. Milner, and M.J. Weaver. J. Phys. Chem. **89**, 2787 (1985).
16. K.J. Brewer, M. Calvin, R.S. Lummpkin, J.W. Otvos, and L.O. Spreer. Inorg. Chem. **28**, 4446 (1989).
17. R.W. Callahan, G.M. Brown, and T.J. Meyer. Inorg. Chem. **14**, 1443 (1975).
18. M.L. Naklicki and R.J. Crutchley. Inorg. Chem. **28**, 4226 (1989).
19. D.F. Grant and E.J. Gabe. J. Appl. Crystallogr. **11**, 114 (1978).
20. E.J. Gabe, F.L. Lee, and Y. Lepage. J. Appl. Crystallogr. **22**, 384 (1989).
21. (*a*) R.J. Crutchley, R. Hynes, and E.J. Gabe. Inorg. Chem. **29**, 4921 (1990); (*b*) M.L. Brader, E.W. Ainscough, E.N. Baker and A.M. Brodie. Polyhedron, **8**, 2219 (1989); (*c*) R.J. Letcher, W. Zhang, C. Bensimon, and R.J. Crutchley. Inorg. Chim. Acta, **210**, 183 (1993); (*d*) W. Zhang, C. Bensimon, and R.J. Crutchley. Inorg. Chem. **32**, 5808 (1993).
22. R.J. Crutchley, K. McCaw, F.L. Lee, and E. J. Gabe. Inorg. Chem. **29**, 2576 (1990).
23. M.A.S. Aquino, R.J. Crutchley, F.L. Lee, E.J. Gabe, and C. Bensimon. Acta Crystallogr. Sect. C: Cryst. Struct. Commun. **C49**, 1543 (1993).
24. T. Moeller. Inorganic chemistry. John Wiley & Sons, Toronto. 1982. p. 252.
25. D.E. Richardson and H. Taube. Inorg. Chem. **20**, 1278 (1981).
26. S. Ferrere and C.M. Elliott. Inorg. Chem. **34**, 5818 (1995).
27. M.B. Robin and P. Day. Adv. Inorg. Chem. Radiochem. **10**, 247 (1967).
28. (*a*) R.J. Crutchley and M.L. Naklicki. Inorg. Chem. **28**, 1955 (1989); (*b*) C.E.B. Evans, D. Ducharme, M.L. Naklicki, and R.J. Crutchley. Inorg. Chem. **34**, 1350 (1995).
29. (*a*) A.A. Saleh and R.J. Crutchley. Inorg. Chem. **29**, 2132 (1990); (*b*) R.J. Crutchley, A.A. Saleh, K. McCaw, and M.A.S. Aquino. Mol. Cryst. Liq. Cryst. **194**, 93 (1991).
30. J.-P. Launay, M. Tourrel-Pagis, J.-F. Lipskier, V. Marvaud, and C. Joachim. Inorg. Chem. 30, 1033 (1991).
31. N.S. Hush. Prog. Inorg. Chem. **8**, 391 (1967).
32. C. Creutz. Prog. Inorg. Chem. **30**, 1 (1983).
33. R.J. Crutchley. Adv. Inorg. Chem. **41**, 273 (1994).
34. M.L. Naklicki. Ph.D. Thesis, Carleton University. Ottawa, Ont. 1995.
35. (*a*) M. Beley, J.-P. Collin, R. Louis, B. Metz, and J.-P. Sauvage. J. Am. Chem. Soc. **113**, 8521 (1991); (*b*) M. Beley, S. Chodorowski, J.-P. Collin, J.-P. Sauvage, L. Flamigni, and F. Barigelletti. Inorg. Chem. **33**, 2543 (1994).
36. H. Krentzien and H.Taube. J. Am. Chem. Soc. **98**, 6379 (1976).
37. R. Hage, J.G. Haasnoot, J. Reedijk, R. Wang, and J.G. Vos. Inorg. Chem. **30**, 3263 (1991).
38. (*a*) M. Haga, T. Matsumura-Inoue, and S. Yamabe. Inorg. Chem. **26**, 4148 (1987). (*b*) M. Haga and A.M. Bond. Inorg. Chem. **30**, 475 (1991); (*c*) T. Ohno, K. Nozaki, and M. Haga. Inorg. Chem. **31**, 4256 (1992); (*d*) D.P. Rillema, R. Sahai, P. Matthews, A.K. Edwards, and R.J. Shaver. Inorg. Chem. **29**, 167 (1990).
39. (*a*) W. Kaim, V. Kasack, H. Binder, E. Roth, and J. Jordanov. Angew. Chem. Int. Ed. Engl. **27**, 1174 (1988); (*b*) W. Kaim and V. Kasack. Inorg. Chem. **29**, 4696 (1990); (*c*) V. Kasack, W. Kaim, H. Binder, J. Jordanov, and E. Roth. Inorg. Chem. **34**, 1924 (1995).

Preparation and structure of 2-chloro-1,3-dimethyldiaza-2-arsenane, 1,3-dimethyldiaza-2-arsenanium tetrachlorogallate, and butadiene cycloadducts of diazarsenium cations

Neil Burford, Charles L.B. Macdonald, Trenton M. Parks, Gang Wu, Borzena Borecka, Witold Kwiatkowski, and T. Stanley Cameron

Abstract: 1,3-Dimethyldiaza-2-arsenanium tetrachlorogallate (crystal data: $C_5H_{12}AsCl_4GaN_2$, $M = 386.61$, orthorhombic, space group $Pca2_1$, $a = 14.432(3)$ Å, $b = 6.7580(14)$ Å, $c = 13.905(3)$ Å, $V = 1356.2(5)$ Å^3) is synthesized by the routine chloride ion abstraction procedure from 2-chloro-1,3-dimethyldiaza-2-arsenane (crystal data: $C_5H_{12}AsClN_2$, $M = 210.54$, monoclinic, space group $P2_1/n$, $a = 7.206(1)$ Å, $b = 9.650(1)$ Å, $c = 13.021(2)$ Å, $\beta = 99.61(2)°$, $V = 892.8(2)$ Å^3). X-ray crystallographic studies of both compounds are described together with that for 2-chloro-1,3-dimethyldiaza-2-arsolidine (crystal data: $C_4H_{10}AsClN_2$, $M = 196.51$, monoclinic, space group $P2_1/n$, $a = 6.959(7)$ Å, $b = 9.23(2)$ Å, $c = 12.14(2)$ Å, $\beta = 95.4(1)°$, $V = 777(4)$ Å^3) providing useful structural comparisons. In contrast to the closely related arsolidinium salts, the diazarsenanium gallate exhibits a monomeric solid state structure. Rapid and quantitative cycloaddition reactions of the diazarsolidinium and diazarsenanium cations with 2,4-dimethylbutadiene give similar cycloadducts. The Diels–Alder type arsolidinium adduct is structurally characterized (crystal data: $C_{10}H_{20}AsCl_4GaN_2$, $M = 454.73$, orthorhombic, space group $Pca2_1$, $a = 18.471(2)$ Å, $b = 7.000(2)$ Å, $c = 13.738(1)$ Å, $V = 1776.2(8)$ Å^3), and the related structure of the arsenanium cycloadduct is confirmed by 2D NMR.

Key words: arsenium, cycloadditions, arsenanium, Diels–Alder, cyclochloroarsines.

Résumé : On peut synthétiser le tétragallate de 1,3-diméthyldiaza-2-arsénanium (données cristallographiques : $C_5H_{12}AsCl_4GaN_2$, $M = 386,61$, orthorhombique, groupe d'espace $Pca2_1$, $a = 14,432(3)$ Å, $b = 6,7580(14)$ et $c = 13,905(3)$ Å, $V = 1356,2(5)$ Å^3) par la méthode usuelle d'enlèvement de l'ion chlorure du 2-chloro-1,3-diméthyldiaza-2-arsénane (données cristallographiques : $C_5H_{12}AsClN_2$, $M = 210,54$, monoclinique, groupe d'espace $P2_1/n$, $a = 7,206(1)$, $b = 9,650(1)$ et $c = 13,021(2)$ Å, $\beta = 99,61(2)°$, $V = 892,8(2)$ Å^3). Afin de pouvoir faire des comparaisons de structures utiles, on décrit les études de diffraction des rayons X de ces deux composés en même temps que celle du 2-chloro-1,3-diméthyldiaza-2-arsolidine (données cristallographiques : $C_4H_{10}AsClN_2$, $M = 196,51$, monoclinique, groupe d'espace $P2_1/n$, $a = 6,959(7)$, $b = 9,23(2)$ et $c = 12,14(2)$ Å, $\beta = 95,4(1)°$, $V = 777(4)$ Å^3). Par opposition aux structures très apparentées des sels d'arsolidinium, le gallate de diazarsénanium présente une structure monomérique à l'état solide. Des réactions de cycloadditions rapides et quantitatives des cations diazarsolidinium et diazarsénanium avec le 2,4-diméthylbutadiène conduisent à des cycloadduits semblables. On a caractérisé la structure de l'adduit de type Diels–Alder du cation arsolidinium (données cristallographiques : $C_{10}H_{20}AsCl_4GaN_2$, $M = 454,73$, orthorhombique, groupe d'espace $Pca2_1$, $a = 18,471(2)$, $b = 7,000(2)$ et $c = 13,738(1)$ Å, $V = 1776,2(8)$ Å^3) et on a confirmé la structure apparentée du cycloadduit du cation arsénanium par RMN en 2D.

Mots clés : arsénium, cycloadditions, arsénanium, Diels–Alder, cyclochloroarsines.

[Traduit par la rédaction]

Introduction

The structural simplicity of systems containing coordinatively unsaturated (low coordinate) centres makes them attractive for reactivity studies. In this context, pnictogenium cations **1** have garnered attention due to their structure and bonding analogy with carbenes. Numerous phosphenium **1***a* derivatives have been reported (1, 2) since their initial discovery (3) and isola-

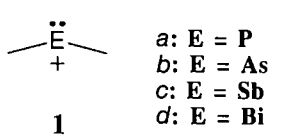

1

***a*: E = P**
***b*: E = As**
***c*: E = Sb**
***d*: E = Bi**

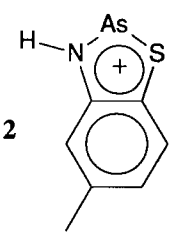

2

Received February 21, 1996.

This paper is dedicated to Professor Howard C. Clark in recognition of his contributions to Canadian chemistry.

N. Burford,[1] C.L.B. Macdonald, T.M. Parks, G. Wu, B. Borecka, W. Kwiatkowski, and T.S. Cameron. Department of Chemistry, Dalhousie University, Halifax, NS B3H 4J3, Canada.

[1] Author to whom correspondence may be addressed. Telephone: (902) 494-3681. Fax: (902) 494-1310. E-mail: Burford@is.Dal.ca

tion (4), establishing them as a principal focus in the development of phosphorus chemistry. Despite the identification of various arsenium cations **1***b* (5, 6), few examples have been comprehensively characterized (7), and the heavier congeneric systems **1***c* (8, 9) and **1***d* (9, 10) are rarely mentioned in the literature. The use of a Hückel framework **2** allowed for the isolation of the first arsenium derivative (11). However, in the absence of such charge delocalization, heterolytic As—Cl bond cleavage from the chloroarsolidines **3Cl** and **4Cl** provided dimeric structures **6** in the solid state (7), in contrast to the phospholidinium **7** analogue (2).

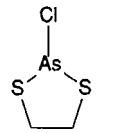

3Cl

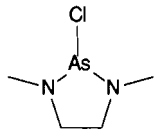

4Cl

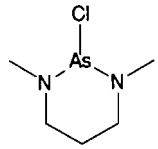

5Cl

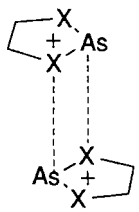

6

a: **X** = **S**
b: **X** = **NMe**

We present here the preparation and structures of the six-membered diazarsenane **5Cl** and the tetrachlorogallate salt of the corresponding diazarsenanium cation **5**, which is clearly

3

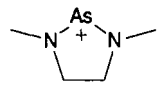

4

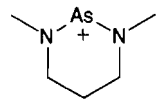

5

monomeric in the solid state. In addition, we describe the rapid and quantitative cycloaddition reactions of **4** (preliminary communication, see ref. 12) and **5** with 2,3-dimethylbutadiene, which contrast the spirocyclic formation **8** observed for **7** (13). The Diels–Alder type adduct **4BD**[$GaCl_4$] has been

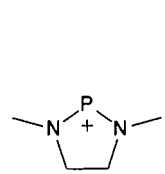

7

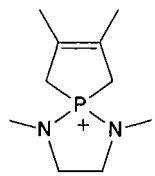

8

structurally characterized, and the related structure of the cycloadduct **5BD** is confirmed by 2D NMR.

Experimental procedures

Arsenic trichloride and triethylamine (BDH) were distilled under nitrogen before use. Gallium trichloride and 2,3-dimethyl-1,3-butadiene (Aldrich) were sublimed in vacuo before use. *N*,*N*′-dimethyl-1,3-propanediamine and *N*,*N*′-dimethylethylenediamine (Aldrich) were used as received.

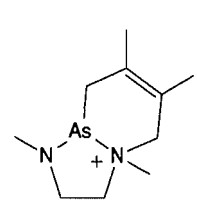

4BD

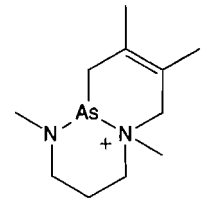

5BD

Compounds **4Cl** and $\mathbf{4}_2[GaCl_4]_2$, were prepared as previously reported (7). Diethyl ether was dried over sodium with benzophenone, CCl_4 was dried over P_2O_5, CD_2Cl_2 and CH_2Cl_2 were dried over P_2O_5 and CaH_2, and all solvents were stored in evacuated bulbs. Solids were handled in VAC Vacuum/Atmospheres or MBraun nitrogen-filled glove box while liquids were manipulated in a nitrogen-filled glove bag. Unless otherwise indicated, all reactions were performed in sealed reactors (14), which were flame-dried before use. Melting points were recorded on a Fisher–Johns apparatus and are uncorrected. Elemental analyses were performed by Beller Laboratories, Göttingen, Germany. Infrared spectra were recorded as Nujol mulls on CsI plates using a Nicolet 510P FT-IR spectrometer. NMR spectra were recorded on either a Bruker AC-250 spectrometer with samples flame sealed in 5 mm Pyrex tubes or a Bruker AMX400 spectrometer with samples sealed in 5 mm commercial thin-walled NMR tubes. All chemical shifts are reported in ppm relative to an external standard (TMS for ^1H and ^{13}C). Variable temperature (VT) NMR studies involved equilibration times of 10 min at each temperature. NMR samples of reaction mixtures were prepared by decanting an aliquot of the reaction mixture into an NMR tube, removing the volatiles in vacuo, and introducing an appropriate amount of CD_2Cl_2 in vacuo. Unless otherwise indicated, crystalline samples were obtained by slow removal of solvent and were washed by cold spot back-distillation (14).

Preparation of 5Cl[2]

A solution of *N*,*N*′-dimethyl-1,3-propanediamine (4.96 g, 48.5 mmol) and triethylamine (25 mL) in diethyl ether (20 mL) was slowly added (45 min) dropwise to a solution of $AsCl_3$ (8.80 g, 48.5 mmol) in diethyl ether (125 mL) in a 3-neck flask, under a continuous stream of dry nitrogen gas. Immediate reaction produced a copious white precipitate; the mixture was stirred overnight then filtered under nitrogen and the solid was washed with two portions (25 mL) of fresh ether. The washings were added to the filtrate and the volume of the solution was reduced by removal of the solvent in vacuo and cooling to −18°C produced colourless crystals that were recrystallized from fresh ether and characterized as 2-chloro-1,3-dimethylcyclo-1,3-diaza-2-arsahexane (2-chloro-1,3-dimethyldiaza-2-arsenane), 5.81 g, 27.6 mmol, 57%; mp 47.0–48.5°C; IR (cm^{-1}): 2744(m), 2718(m), 2702(m), 2687(w), 1276(vs), 1227(vs), 1207(m), 1146(vs), 1133(vs), 1125(vs,sh), 1091(s), 1050(vs), 1037(vs), 941(vs), 925(s), 891(s), 837(vs), 570(vs), 540(m), 414(m), 361(vs), 342(m), 320(w), 285(s,sh), 263(vs), 239(vs), 233(vs); ^1H NMR (CD_2Cl_2): 2.88 (CH_2N, m, 4H), 2.63 (CH_3, s, 6H), 1.94 (CH_2, m, 2H); $^{13}C\{^1H\}$ NMR (CD_2Cl_2): 48.4 (CH_2N), 40.3 (CH_3), 27.8 (CH_2).

[2] First reported briefly in ref. 6.

Preparation of 5[$GaCl_4$]

A solution of **5Cl** (0.45 g, 2.1 mmol) in CH_2Cl_2 (20 mL) was slowly added to a solution of $GaCl_3$ (0.38 g, 2.1 mmol) in CH_2Cl_2 (40 mL) over a period of 15 min. Approximately 90% of the solvent was removed in vacuo and the solution was cooled to 5°C to produce yellow crystals characterized as 1,3-dimethyldiaza-2-arsenanium tetrachlorogallate, 0.39 g, 1.0 mmol, 48%; mp 52.0–54.5°C; IR (cm^{-1}): 1347(w), 1284(vs), 1242(vs), 1205(s), 1184(w), 1152(vs), 1118(vs), 1102(m), 1084(s), 1049(vs), 1040(vs), 955(vs), 913(w), 879(s), 862(m), 806(w), 752(w), 601(s), 588(s), 551(w), 493(w), 387(vs, sh), 378(vs), 362(vs), 339(vs), 301(w), 266(w), 255(w), 232(s); ^1H NMR (CD_2Cl_2): 3.49 (CH_2N, m, 4H), 3.34 (CH_3, s, 6H), 2.29 (CH_2, m, 2H); $^{13}C\{^1H\}$ NMR (CD_2Cl_2): 51.6 (CH_2N), 42.6 (CH_3), 26.2 (CH_2). Anal. (%) calcd.: C 15.53, H 3.13, N 7.25; Found C 15.97, H 3.29, N 7.35.

Preparation of 4BD[$GaCl_4$] (ref. 12)

2,3-Dimethylbutadiene (0.11 g, 1.3 mmol) in CH_2Cl_2 (7 mL) was added dropwise (8 min) to a stirred solution of **4**[$GaCl_4$] (0.32 g, 0.42 mmol) in CH_2Cl_2 (40 mL). Slow removal of the solvent in vacuo afforded air-sensitive colourless crystals, which were characterized as 1-azonia-1,3,4,7-tetramethyl-7-aza-6-arsabicyclo(4.3.0)non-3-ene tetrachlorogallate, **4BD**[$GaCl_4$], 0.21 g, 0.46 mmol, 55%; mp 139–140°C; IR (cm^{-1}): 1657(w), 1413(m), 1325(w), 1300(w), 1270(m), 1241(m), 1171(m), 1116(m), 1073(m), 1058(w), 1009(m), 984(m), 967(s), 940(w), 924(w), 885(w), 867(m), 798(w), 784(m), 737(w), 655(w), 597(w), 581(m), 569(m), 525(w), 453(w), 423(w), 383(vs), 366(s), 349(m), 313(w), 228(w); ^1H NMR (CD_2Cl_2): 3.90 (d of d of d, 1H), 3.85 (d, 1H), 3.69 (d of d, 1H), 3.55 (d, 1H), 3.49 (d of d, 1H), 3.22 (s, 3H), 3.15 (t of d), 1H), 3.10 (d, 1H), 2.97 (s, 3H), 2.67 (d, 1H), 1.95 (m, 6H); $^{13}C\{^1H\}$ NMR (CD_2Cl_2): 130.4, 128.8, 62.8, 62.2, 59.1, 52.2, 41.8, 37.6, 20.7, 20.3; see discussion for COSY analysis. Anal.(%) calcd.: C 26.41, H 4.43; found: C 26.02, H 4.49. ^1H and ^{13}C NMR spectra of the reaction mixture show **4BD**[$GaCl_4$] as the only product.

Preparation of 5BD[$GaCl_4$]

2,3-Dimethyl-1,3-butadiene (0.24 g, 2.9 mmol) in CH_2Cl_2 (6 mL) was added over a period of 4 min to a solution of **5**[$GaCl_4$] (1.11 mmol) in CH_2Cl_2 (90 mL) prepared in situ. The mixture was allowed to stir for 20 min. The solvent was removed in vacuo to give a viscous yellow oil that solidified upon standing overnight and was characterized as 1-azonia-1,3,4,7-tetramethyl-7-aza-6-arsabicyclo(4.4.0)dec-3-ene tetrachlorogallate, **5BD**[$GaCl_4$], 0.849 g, 1.81 mmol, 82%; mp 83.5–87.5°C; IR (cm^{-1}): 1343(w), 1313(m), 1301(m), 1286(w), 1267(m), 1234(m), 1204(s), 1200(s), 1184(m), 1156(vs), 1135(s), 1123(m), 1097(w), 1074(m), 1051(m), 1042(s), 1029(m), 1003(s), 982(vs), 946(s), 913(s), 884(s), 847(vs), 806(w), 788(w), 770(vs), 738(w), 657(m), 611(m), 583(s), 548(w), 503(s), 405(m,sh), 381(vs,br), 365(vs), 343(s), 317(m), 288(w), 257(w); ^1H NMR (ppm, CD_2Cl_2): 3.71 (m, 3H), 3.69 (m, 3H), 3.39 (d, 1H), 3.36 (d, 1H), 3.14 (s, 3H), 3.05, (s, 3H), 3.01 (m, 2H), 2.47 (d, 1H), 2.39 (m, 1H), 1.90 (s, 3H), 1.74 (m, 1H); $^{13}C\{^1H\}$ NMR (ppm, CD_2Cl_2): 124.6, 122.8, 65.0, 57.4, 48.9, 45.6, 43.9, 33.1, 22.2, 19.5, 19.0; see discussion for COSY analysis. ^1H and ^{13}C NMR spectra of the reaction mixture show **5BD**[$GaCl_4$] as the only product.

Recrystallization of 4Cl

Evacuated samples of **4Cl** stored at 4°C for weeks sublimed onto the glass walls of the vessel or tube. The crystals (mp 19°C) were mounted in a nitrogen-filled glove bag under a stream of cold nitrogen (liquid nitrogen boil-off). The X-ray diffraction data were collected at −60°C.

X-ray crystallography

Crystals were selected and mounted in Pyrex capillaries in the drybox. Pertinent crystallographic data are summarized in Table 1. Unit-cell parameters were obtained from the setting angles of 18 accurately centered reflections with $6.13 < 2\theta < 50.04°$ for **5**[$GaCl_4$], 24 accurately centered reflections with $20 < 2\theta < 26°$ for **4Cl**, 20 accurately centered reflections with $35 < 2\theta < 40°$ for **5Cl**, and 22 accurately centered reflections with $30.31 < 2\theta < 45.55°$ for **4BD**[$GaCl_4$]. The choice of space groups was based on systematically absent reflections and was confirmed by the successful solution and refinement of the structures. The stability of the crystals was monitored using three standard reflections; significant decay was not observed. Data were corrected for Lorentz and polarization effects, and the absorption corrections were applied based on the program DIFABS (15). Scattering factors (16) were corrected for anomalous dispersion.

Structures were solved by direct methods to find the heavy atoms with the remaining atoms located from difference Fourier synthesis (18). The hydrogen atoms were placed in geometrically calculated positions with a C—H distance of 0.96 Å (**5**[$GaCl_4$]), 0.95 Å (**4Cl** and **5Cl**), or 1.08 Å (**4BD**[$GaCl_4$]); their positions were not refined, and they were assigned fixed isotropic temperature factors with a value of 1.2 B_{eq} of the atom to which each was bonded. The models were refined using full-matrix least-squares techniques based on F, minimizing the function $\Sigma w(|F_o| - |F_c|)^2$, where the weight is defined as $w = 4F_o^2/\sigma^2(F_o^2)$ $(\sigma^2(F_o) + (p\ F_o/2)^2)^{-1}$ and σ is derived from counting statistics (18). Supplementary material containing crystal data, atomic positional parameters, anisotropic thermal parameters, and bond lengths and angles for **5**[$GaCl_4$], **4Cl**, **5Cl**, and **4BD**[$GaCl_4$] has been deposited.[3]

Results and discussion

Chlorodiazarsenane and diazarsenanium tetrachlorogallate

The halide ion abstraction technique, now commonplace in the preparation of phosphenium salts (1), is also applicable for the formation and isolation of arsenium derivatives. The first examples, **3**[$GaCl_4$] and **4**[$GaCl_4$], were shown to adopt novel dimeric structures **6** in the solid state (7). We have now extrapolated the synthetic procedure to the six-membered (cyclohexane derivative) diazarsenane framework (6). 2-Chloro-1,3-

[3] Copies of the supplementary material may be purchased from: The Depository of Unpublished Data, Document Delivery, CISTI, National Research Council Canada, Ottawa, Canada K1A 0S2. With the exception of the anisotropic thermal parameters, these data have also been deposited with the Cambridge Crystallographic Data Centre, and can be obtained on request from The Director, Cambridge Crystallographic Data Centre, University Chemical Laboratory, 12 Union Road, Cambridge, CB2 1EZ, U.K.

Table 1. Crystal data for **5** $[GaCl_4]$, **4Cl**, **5Cl**, and **4BD**$[GaCl_4]$.

	5$[GaCl_4]$	**4Cl**	**5Cl**	**4BD**$[GaCl_4]$
Formula	$C_5H_{12}AsCl_4GaN_2$	$C_4H_{10}AsClN_2$	$C_5H_{12}AsClN_2$	$C_{10}H_{20}AsCl_4GaN_2$
fw	386.61	196.51	210.54	454.73
Crystal system	Orthorhombic	Monoclinic	Monoclinic	Orthorhombic
Space group	$Pca2_1$ (no. 29)	$P2_1/n$ (no. 14)	$P2_1/n$ (no. 14)	$Pca2_1$ (no. 29)
a, Å	14.432 (3)	6.959 (7)	7.206 (1)	18.471 (2)
b, Å	6.7580 (14)	9.23 (2)	9.650 (1)	7.000 (2)
c, Å	13.905 (3)	12.14 (2)	13.021 (2)	13.738 (1)
β, °		95.4 (1)	99.61 (2)	
V, Å^3	1356.2 (5)	777 (4)	892.8 (2)	1776.2 (8)
Z	4	4	4	4
Radiation	MoK_α λ = 0.71069 Å	MoK_α λ = 0.71069 Å	MoK_α λ = 0.71069 Å	MoK_α λ = 0.71069 Å
μ, cm^{-1}	124.60	46.24	40.27	39.84
Temperature, K	293 ± 2	213 ± 1	296 ± 1	291 ± 1
Diffractometer	Rigaku AFC5R	Rigaku AFC5R	Rigaku AFC5R	Rigaku AFC5R
Scan type	ω–2θ	ω–2θ	ω–2θ	ω–2θ
D_{calcd}, g cm^{-3}	1.893	1.681	1.566	1.700
No. of reflections	739	1160	1459	1470
No. of observations ($I > 3.00\ \sigma(I)$)	378[a]	814	828	951
Reflection/parameter ratio	4.50	11.2	9.98	5.87
No. of variables	84	73	83	162
Residuals: R, Rw	0.0505, 0.1074	0.0431, 0.0587	0.0259, 0.0289	0.0437, 0.0437

[a] $I > 2.00\ \sigma(I)$

dimethyldiaza-2-arsenane **5Cl** reacts with $GaCl_3$, in an essentially identical fashion to the arsolidine **4Cl** (7), to give chloro-1,3-dimethyldiaza-2-arsenanium **5** tetrachlorogallate. Compounds **5Cl** and **5**$[GaCl_4]$ have been comprehensively characterized and crystallographic views of the solid state structures are illustrated in Figs. 1 and 2, respectively. The structure of 2-chloro-1,3-dimethyldiaza-2-arsolidine **4Cl** (−60°C; Fig. 3) is also described for comparison. Selected bond lengths and angles for the three compounds are compared with those for **4**$_2[GaCl_4]_2$ (7) in Table 2.

Crystals of **5**$[GaCl_4]$ were of poor quality and provided only limited data. Nevertheless, the distinctly ionic structure shows no evidence of interaction between cations (shortest intercationic As–N 5.62(2) Å) (Fig. 4) in contrast to the dimeric **6** structure of **4**$[GaCl_4]$ (as well as **3**$[GaCl_4]$) (7). This implies that the association between monomers in **6** is weak, consistent with the relatively long intermonomer bonds observed in **6**, and ^{1}H NMR spectroscopic data for **4**$_2[GaCl_4]_2$, which indicate a monomer–dimer equilibrium in solution (7). Cation–anion contacts in **5**$[GaCl_4]$ (3.363(9) and 3.58(1) Å) (Fig. 4) are within the sum of the van der Waals' radii for As and Cl (As, 2.0 Å; Cl, 1.7 Å (19)), but are significantly longer than the As—Cl bonds in **4Cl** (2.390(5) Å) and **5Cl** (2.357(2) Å), and are comparable to the cation-anion contacts observed in the structure of **4**$_2[GaCl_4]_2$ (3.296(2) and 3.424(2) Å) (7). The resulting polymeric lattice of **5**$[GaCl_4]$ is reminiscent of the solid state structures observed for $(Me_2Si(N^tBu)_2E)[GaCl_4]$ (E = Sb, Bi) (9). The As—N bonds (1.68(3) and 1.67(2) Å) are significantly shorter than the shortest bond of **4**$_2[GaCl_4]_2$ (1.752(5) and 1.949(4) Å(7)), implicating a degree of π-bonding over the N-As-N moiety.

In spite of the monomeric structure observed for **5**$[GaCl_4]$, the neutral arsenane **5Cl** also adopts a dimeric arrangement involving a four-membered As_2N_2 intermonomer contact that is similar to that of the corresponding arsolidines **3Cl** and **4Cl** as well as the dications **6**. Such arrangements contrast that observed for related chloroarsines (11, 20), which involve four-membered As_2Cl_2 contacts. The intermonomer contact is significantly shorter in **4Cl** (As–N′ 2.84(1) Å) than in **5Cl** (As–N′ 3.250(5) Å), and both are substantially longer than observed for **4**$[GaCl_4]$ (2.103(8) Å) (7). These interactions are well within the sum of the van der Waals' radii for As and N (As, 2.0 Å; N, 1.5 Å (19)) and impose a pseudo-tetracoordinate environment on N(2). The shorter interaction in **4Cl** has a measurable impact on the structural features of the arsolidine heterocycle, which exhibits slight differences in the As–N bond lengths as well as the geometries at the nitrogen centres. N(1) is essentially planar (sum of the angles 359.3°), while N(2) is clearly pyramidalized (sum of the angles 339.4°). The geometrically indistinguishable nitrogen centres of **5Cl** have bond angle sums (N(1), 348°; N(2), 347°) that are substantially greater than expected for an sp^3 (328.5°) hybridized site. In this context, the relatively long (see for example refs. 20 and 21) As—Cl bonds (**4Cl**, 2.390(5) Å; **5Cl**, 2.357(2) Å) and relatively short endocyclic As—N bonds (**4Cl**, 1.77(1) Å, 1.870(8) Å; **5Cl**, 1.796(4) Å, 1.803(5) Å; typical range 1.82-1.88 Å (see for example ref. 22)) in both compounds implicate a degree of As—N π-bonding.

Fig. 1. ORTEP view (50% probability ellipsoids) of the dimeric unit of **5Cl** showing the closest intermolecular interactions, As(1)–N(2)′ 3.250(5) Å (hydrogen atoms omitted for clarity).

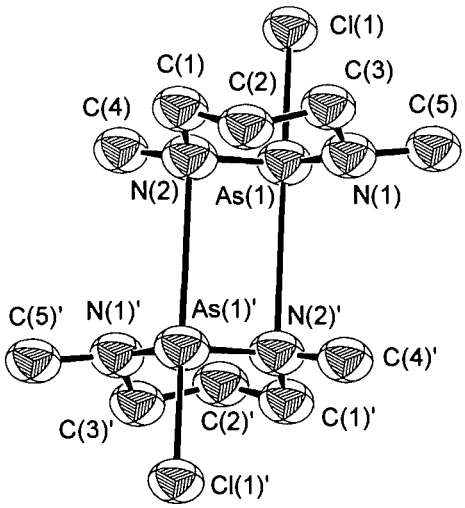

Fig. 2. PLUTO view of $5[GaCl_4]$.

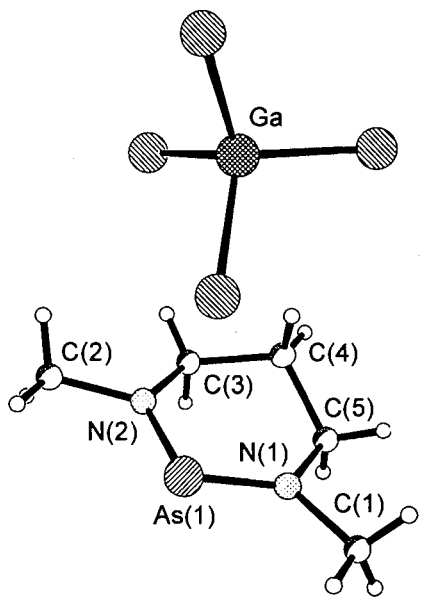

Fig. 3. ORTEP view (50% probability ellipsoids) of the dimeric unit of **4Cl** showing the closest intermolecular interactions, As(1)–N(2)′ 2.84(1) Å (Hydrogen atoms omitted for clarity).

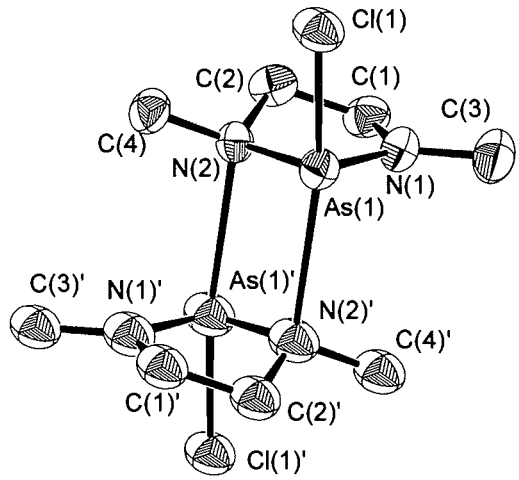

Fig. 4. The unit cell of $5[GaCl_4]$, showing the closest cation–anion contacts.

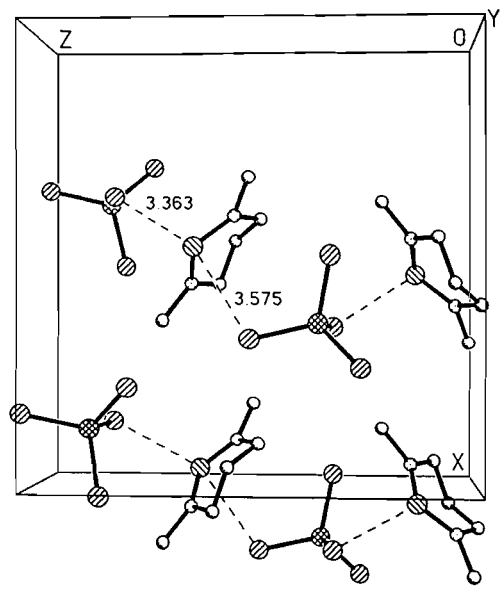

The ^1H NMR spectra for **5Cl** (δ: 2.88m, 2.63s, 1.94m) and $5[GaCl_4]$ (δ: 3.49m, 3.34s, 2.29m) are interpreted as very similar AA′BB′CD spin systems and differ only in chemical shift, with the salt exhibiting the expected deshielding. Consistent with integration values, the lower frequency multiplet is assigned to the azamethylene protons and the singlet to the methyl protons. Neither spectrum shows significant changes at −80°C.

Diazarsenium-butadiene cycloaddition

Compounds $4[GaCl_4]$ and $5[GaCl_4]$ react rapidly with 2,3-dimethylbutadiene in CH_2Cl_2 to give a single product, as shown by ^1H NMR spectra of the reaction mixtures. The isolated products are spectroscopically similar and an X-ray crystallographic study of the product from $4[GaCl_4]$ reveals a tetrachlorogallate salt of cycloadduct **4BD**, in which the diene is assymmetrically bound to the arsolidinium heterocycle (across one of the As—N bonds).

The bicyclic structure of the cation is shown in Fig. 5 and selected bond lengths and angles are given in Table 2. The cross-ring As(1)—N(2) bond is significantly longer (2.056(10) Å) than that of As(1)—N(1) (1.797(11) Å), and is comparable (within experimental error) to the corresponding bond observed in the dication **6b** (As – tetracoordinate N, 1.949(4) Å; As – tricoordinate N, 1.752(5) Å). The cross-ring bond in **4BD** is anomalously long in comparison to the As—N bonds in **4Cl**, **5Cl**, and $4[GaCl_4]$, and may be considered an intramolecular donation to an amino-alkyl-arsenium centre. Consistently, intermolecular donor interactions to the dithiarsolidinium cation are also long (7), as are those to phosphe-

Table 2. Selected bond lengths (Å) and angles (°) for $\mathbf{4}_2$ $[GaCl_4]_2$ (7), **5** $[GaCl_4]$, **4Cl**, **5Cl**, and **4BD**$[GaCl_4]$.

$\mathbf{4}_2[GaCl_4]_2$ (7)		**5**$[GaCl_4]$		**4Cl**		**5Cl**		**4BD**$[GaCl_4]$	
				As(1)—Cl(1)	2.390 (5)	As(1)—Cl(1)	2.357 (2)		
As(1)—N(1)	1.752 (5)	As(1)—N(1)	1.68 (3)	As(1)—N(1)	1.77 (1)	As(1)—N(1)	1.796 (4)	As(1)—N(1)	1.797 (11)
As(1)—N(2)	1.949 (4)	As(1)—N(2)	1.67 (2)	As(1)—N(2)	1.830 (8)	As(1)—N(2)	1.803 (5)	As(1)—N(2)	2.056 (10)
N(2)—C(4)	1.506 (8)	N(2)—C(2)	1.505 (12)	N(2)—C(4)	1.47 (1)	N(1)—C(3)	1.459 (8)	N(1)—C(1)	1.50 (2)
N(2)—C(2)	1.500 (9)	N(2)—C(3)	1.487 (12)	N(2)—C(2)	1.46 (1)	N(1)—C(5)	1.456 (8)	N(1)—C(3)	1.49 (2)
N(1)—C(3)	1.487 (8)	N(1)—C(1)	1.489 (12)	N(1)—C(3)	1.44 (1)	N(2)—C(1)	1.459 (8)	N(2)—C(2)	1.50 (2)
N(1)—C(1)	1.462 (8)	N(1)—C(5)	1.489 (12)	N(1)—C(1)	1.43 (1)	N(2)—C(4)	1.465 (7)	N(2)—C(4)	1.53 (2)
				Cl(1)-As(1)-N(1)	100.8 (3)	Cl(1)-As(1)-N(1)	99.8 (2)		
				Cl(1)-As(1)-N(2)	97.8 (3)	Cl(1)-As(1)-N(2)	99.1 (2)		
N(1)-As(1)-N(2)	87.2 (2)	N(1)-As(1)-N(2)	102.2 (11)	N(1)-As(1)-N(2)	87.8 (4)	N(1)-As(1)-N(2)	98.4 (2)	N(1)-As(1)-N(2)	98.3 (4)
As(1)-N(2)-C(2)	107.6 (3)	As(1)-N(2)-C(3)	126 (2)	As(1)-N(2)-C(2)	108.7 (7)	As(1)-N(1)-C(3)	121.9 (4)	As(1)-N(2)-C(2)	104.2 (8)
As(1)-N(2)-C(4)	114.9 (4)	As(1)-N(2)-C(2)	121 (2)	As(1)-N(2)-C(4)	116.8 (7)	As(1)-N(1)-C(5)	113.7 (4)	As(1)-N(2)-C(4)	107.8 (9)
C(2)-N(2)-C(4)	110.9 (4)	C(3)-N(2)-C(2)	113 (2)	C(2)-N(2)-C(4)	113.9 (9)	C(3)-N(1)-C(5)	112.3 (5)	C(2)-N(2)-C(4)	109.7 (11)
As(1)-N(1)-C(1)	116.2 (4)	As(1)-N(1)-C(5)	130 (2)	As(1)-N(1)-C(1)	115.9 (7)	As(1)-N(2)-C(1)	121.1 (4)	As(1)-N(1)-C(1)	110.0 (9)
As(1)-N(1)-C(3)	124.4 (4)	As(1)-N(1)-C(1)	121 (2)	As(1)-N(1)-C(3)	124.4 (8)	As(1)-N(2)-C(4)	113.2 (4)	As(1)-N(1)-C(3)	117.2 (10)
C(1)-N(1)-C(3)	119.1 (5)	C(1)-N(1)-C(5)	108 (2)	C(1)-N(1)-C(3)	119 (1)	C(1)-N(2)-C(4)	112.6 (5)	C(1)-N(1)-C(3)	112.6 (12)
N(1)-C(1)-C(2)	106.0 (5)	N(1)-C(5)-C(4)	109 (2)	N(1)-C(1)-C(2)	107.4 (9)	N(2)-C(1)-C(2)	112.0 (5)	N(1)-C(1)-C(2)	107.4 (12)
N(2)-C(2)-C(1)	107.2 (5)	N(2)-C(3)-C(4)	113 (2)	N(2)-C(2)-C(1)	107.4 (9)	N(1)-C(3)-C(2)	111.3 (5)	N(2)-C(2)-C(1)	106.4 (11)
		C(3)-C(4)-C(5)	113 (3)			C(1)-C(2)-C(3)	113.1 (5)		

Fig. 5. ORTEP view (50% probability ellipsoids) of the cation in **4BD**[$GaCl_4$] and closest chlorine atom, As(1)–Cl(3) 3.382(6) Å, of the tetrachlorogallate anion (hydrogen atoms omitted for clarity).

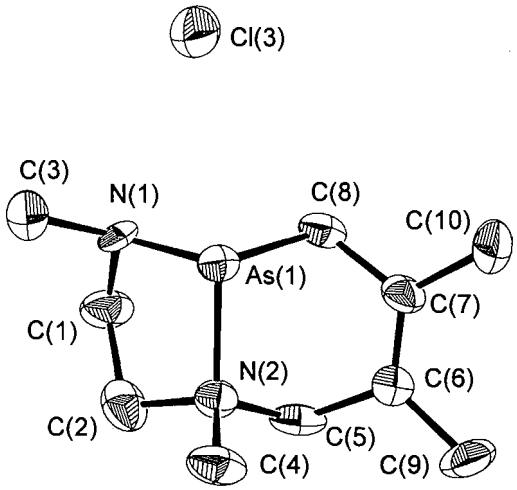

nium centres (23). In the other extreme, the bicyclic structure of **4BD** can be viewed as an ammonium-arsine.

The complex ^1H NMR spectra of **4BD**[$GaCl_4$] (previously reported (24)) and **5BD**[$GaCl_4$] (Fig. 6) in CD_2Cl_2 were resolved by COSY techniques at 400 MHz. Methyl groups 1, 2, 3, and 4 (illustrated in **9**) are observed as singlets at 1.90, 1.74, 3.05, and 3.14 ppm, respectively. The six methylene protons are observed in the usual region, with the signals for those closest to the nitrogen atoms farther downfield. While it has been possible to identify the signals produced by each of the protons in a vicinal pair, it has not been possible to identify which of the two protons is responsible for which of the signals. Protons 1 and 2 are observed as multiplet signals at 3.01 and 3.71 ppm. Likewise, protons 3 and 4 exhibit multiplets at 1.74 and 2.39 ppm. Protons 5 and 6 exhibit a doublet at 3.36 ppm and a multiplet at 3.69 ppm, while protons 7 and 8 each

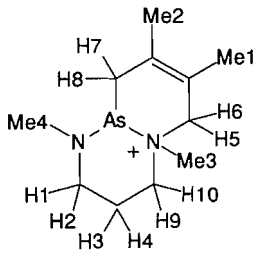

9

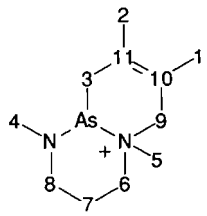

10

produce a doublet at 2.47 ppm and 3.39 ppm. Finally, protons 9 and 10 each produce multiplet signals at 3.01 ppm and 3.71 ppm.

A (^1H, ^{13}C) HETCOR spectrum has allowed for unambiguous assignment of the carbon signals for **5BD**[$GaCl_4$] (illustrated in **10**): 1, 22.2 ppm; 2, 19.0 ppm; 3, 33.1 ppm; 4, 43.9 ppm; 5, 48.9 ppm; 6, 57.4 ppm; 7, 19.5 ppm; 8, 45.6 ppm; and 9, 65.0 ppm. Two quaternary carbon signals were found at 122.8 and 124.6 ppm. The lower field signal is presumably due to carbon 10.

Formation of cations **4BD** and **5BD** are in contrast to the butadiene cycloaddition reaction observed for the diazaphospholidinium cation **7**, which results in the oxidative cycloaddition phosphonium product **8** (13). The arsenium cycloaddition reactions may be classified as Diels–Alder-type reactions with the As-N unit behaving as a "hetero-dienophile," and in the context of reactions observed for phosphaalkynes (25), phosphaalkenes (26) and phosphinines (27). Qualitative MO analysis reveals that the HOMO of the diene and the LUMO of the dienophile can be considered as the dominant interaction determining the structure of the transition state in a "normal electron-demand" process (see for example ref. 28). A comprehensive theoretical study of these reactions is in progress.

Fig. 6. Two-dimensional (^1H, ^1H) COSY NMR of **5BD**[$GaCl_4$].

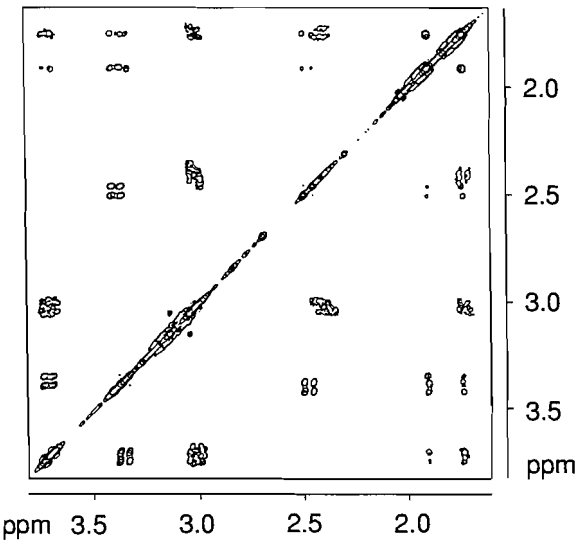

Conclusions

The diazarsenanium tetrachlorogallate salt adopts a monomeric structure in the solid state, in contrast to the corresponding arsolidinium salt. Nevertheless, both salts undergo quantitative Diels–Alder-like cycloaddition reactions with 2,3-dimethylbutadiene, involving one As-N bond as the olefin, and contrasting the observations for the corresponding phospholidinium cation.

Acknowledgements

We thank the Natural Sciences and Engineering Research Council of Canada and the Isaac Walton Killam Foundation (C.L.B.M.) for funding, the Atlantic Region Magnetic Resonance Centre for NMR facilities, and Kathy Robertson for assistance with the X-ray crystallography.

References

1. M. Sanchez, M.R. Mazieres, L. Lamande, and R. Wolf. *In* Multiple bonds and low coordination in phosphorus chemistry. *Edited by* M. Regitz and O.J. Scherer. Georg Thieme Verlag, Stuttgart. 1990. pp. 129–148; A.H. Cowley and R.A. Kemp. Chem. Rev. **85**, 367 (1985); A.H. Cowley, M.C. Cushner, M. Lattman, M.L. McKee, J.S. Szobota, and J.C. Wilburn. Pure Appl. Chem. **52**, 789 (1980).

2. N. Burford, P. Losier, C. Macdonald, V. Kyrimis, P.K. Bakshi, and T.S. Cameron. Inorg. Chem. **33**, 1434 (1994).
3. S. Fleming, M.K. Lupton, and K. Jekot. Inorg. Chem. **11**, 2534 (1972); B.E. Maryanoff and R.O. Hutchins. J. Org. Chem. **37**, 3475 (1972).
4. A.H. Cowley, M.C. Cushner, and J.S. Szobota. J. Am. Chem. Soc. **100**, 7784 (1978); J. Luber and A. Schmidpeter. Angew. Chem. Int. Ed. Engl. **15**, 111 (1976); J. Chem. Soc. Chem. Commun. 887 (1976); P. Friedrich, G. Huttner, J. Luber, and A. Schmidpeter. Chem. Ber. **111**, 1558 (1978).
5. R.H. Anderson and R.H. Cragg, J. Chem. Soc. Chem. Commun. 1414 (1971).
6. C. Payrastre, Y. Madaule, J.G. Wolf, T.C. Kim, M.-R. Mazieres, R. Wolf, and M. Sanchez. Heteroat. Chem. **3**, 157 (1992).
7. N. Burford, T.M. Parks, B.W. Royan, B. Borecka, T.S. Cameron, J.F. Richardson, E.J. Gabe, and R. Hynes. J. Am. Chem. Soc. **114**, 8147 (1992).
8. A.P. Coleman, M. Nieuwenhuyzen, H.N. Rutt, and K.R. Seddon. J. Chem. Soc. Chem. Commun. 2369 (1995); N. Burford and B.W. Royan. J. Chem. Soc. Chem. Commun. 19 (1989).
9. M. Vieth, B. Bertsch, and V. Huch. Z. Anorg. Allg. Chem. **559**, 73 (1988).
10. L.P. Battaglia, A. Bonamartini Corradi, G. Pelizzi, and M.E. Vidoni Tani. J. Chem. Soc. Dalton Trans. 1141 (1977); G.B. Jameson, E. Blaszo, and H.R. Oswald. Acta Crystallogr. Sect. C: Cryst. Struct. Commun. **C40**, 350 (1984); W. Frank, J. Weber, and E. Fuchs. Angew. Chem. Int. Ed. Engl. **26**, 74 (1987); N.W. Alcock, M. Ravindran, and G.R. Willey. J. Chem. Soc. Chem. Commun. 1063 (1989); M. Schäfer, G. Frenzen, B. Neumuller, and K. Dehnicke. Angew. Chem. Int. Ed. Engl. **31**, 334 (1992); R.D. Rogers, A.H. Bond, S. Aguinaga, and A. Reyes. J. Am. Chem. Soc. **114**, 2967 (1992); W. Clegg, L.J. Farrugia, A. McCamley, N.C. Norman, A.G. Orpen, N.L. Pickett, and S.L. Stratford. J. Chem. Soc. Dalton Trans. 2579 (1993); T. Allman, R.G. Goel, and H.S. Prasad. J. Organomet. Chem. **166**, 365 (1979); C.J. Carmalt, N.C. Norman, A.G. Orpen, and S.E. Stratford. J. Organomet. Chem. **460**, C22 (1993); L. Agocs, N. Burford, T.S. Cameron, J.M. Curtis, J.F. Richardson, K.N. Robertson, and G.B. Yhard. J. Am. Chem. Soc. In press.
11. N. Burford, T.M. Parks, B.W. Royan, and P.S. White. Can. J. Chem. **71**, 702 (1992).
12. N. Burford, T.M. Parks, P.K. Bakshi, and T.S. Cameron. Angew. Chem. Int. Ed. Engl. **33**, 1267 (1994).
13. C.K. SooHoo and S.G. Baxter. J. Am. Chem. Soc. **105**, 7443 (1983); A.H. Cowley, R.A. Kemp, J.G. Lasch, N.C. Norman, and C.A. Stewart. J. Am. Chem. Soc. **105**, 7444 (1983). A.H. Cowley, R.A. Kemp, J.G. Lasch, N.C. Norman, and C.A. Stewart, B.R. Whittlesey, and T.C. Wright. Inorg. Chem. **25**, 740 (1986).
14. N. Burford, J. Müller, and T.M. Parks. J. Chem. Educ. **71**, 801 (1994).
15. N. Walker and D. Stuart. Acta. Crystallogr. Sect. A: Found. Crystallogr. **A39**, 158 (1983).
16. International tables for X-ray crystallography. Vol. IV. Kynoch, Birmingham, England. 1974.
17. TEXSAN-TEXRAY single crystal structure analysis package, Version 5.0. Molecular Structure Corporation, The Woodlands, Texas. 1989.
18. W.R. Busing, K.O. Martin, and H.A. Levy. ORFLS. A Fortran crystallographic least-squares program; Report ORNL-TM-305, Oak Ridge National Laboratory, Oak Ridge, Tennessee. 1962.
19. CRC handbook of chemistry and physics. 67th ed. CRC Press, Boca Raton, Florida. 1986. D-188.
20. M. Veith and B. Bertsch. Z. Anorg. Allg. Chem. **557**, 7 (1988).
21. A. Camerman and J. Trotter. J. Chem. Soc. 730 (1965).
22. J. Wiess and W. Eisenhuth. Z. Anorg. Allg. Chem. **350**, 9 (1967); A. Gieren, H. Betz, T Hübner, V. Lamm, M. Herberhold, and K. Guldner. Z. Anorg. Allg. Chem. **513**, 160 (1984); R. Bohra, H.W. Roesky, M. Noltemeyer, and G.M. Sheldrick. Acta. Crystallogr. Sect. C: Cryst. Struct. Commun. **C40**, 1150 (1984); H. Grützmacher and H. Pritzkow. Chem. Ber. **122**, 1417 (1989).
23. N. Burford, P. Losier, P.K. Bakshi, and T.S. Cameron. J. Chem. Soc. Chem. Commun. 307 (1996).
24. N. Burford, T.M. Parks, and G. Wu. Phosphorus, Sulfur Silicon, **93–94**, 397 (1994).
25. M. Regitz. *In* Multiple bonds and low coordination in phosphorus chemistry. *Edited by* M. Regitz and O.J. Scherer. Georg Thieme Verlag, Stuttgart. 1990. p. 84.
26. R. Appel. *In* Multiple bonds and low coordination in Pposphorus chemistry. *Edited by* M. Regitz and O.J. Scherer. Georg Thieme Verlag, Stuttgart. 1990. p. 165.
27. G. Märkl. *In* Multiple bonds and low coordination in phosphorus chemistry. *Edited by* M. Regitz and O.J. Scherer. Georg Thieme Verlag, Stuttgart. 1990. p. 244.
28. I. Fleming. Molecular orbitals in organic Chemistry. J. Wiley and Sons, New York. 1976.

Secondary ion mass spectroscopy (SIMS) and kinetics of the catalysis of bisulphite oxidation by aqueous iron

R.R. Martin and Jinjiang Li

Abstract: The catalytic activity of Fe(II) and Fe(III) in the aqueous oxidation of bisulphite by molecular oxygen at bisulphite concentrations similar to those in cloud water has been studied. Secondary Ion Mass Spectroscopy (SIMS) of insoluble sulphates derived from bisulphite after oxidation by $^{18}O_2$ gives different $^{18}O/^{32}S$ ratios for Fe(II) and Fe(III), indicating that the oxidation mechanism is different in these two species.

Key words: oxidation, bisulphite, iron, secondary ion mass spectroscopy.

Résumé: On a étudié l'activité catalytique du Fe(II) et du Fe(III) sur l'oxydation aqueuse du bisulfite par l'oxygène moléculaire, à des concentrations de bisulfite semblables à celles que l'on rencontre dans l'eau de pluie. La spectroscopie de masse des ions secondaires (SMIS) des sulfates insolubles obtenus par oxydation du bisulfite par du $^{18}O_2$ conduit à des rapports différents de $^{18}O/^{32}S$ pour le Fe(II) et le Fe(III); ce résultat indique que le mécanisme de l'oxydation est différent avec ces deux espèces.

Mots clés : oxydation, bisulfite, fer, spectroscopie de masse des ions secondaires.

[Traduit par la rédaction]

Introduction

The rate of oxidation of S(IV) in solution has been the subject of considerable study (1). Transition metal ions in solution are known to act as catalysts, as is the case with Fe(III)(2). Recent work has shown synergistic interactions between Fe(III) and Cu(II) (3). The mechanism for the reaction has been the subject of debate, which is likely to continue since the reaction, complex in itself, has kinetics strongly dependent on both the pH and ionic strength of the solution (4).

The archetypical mechanism advanced by Backstrom (5) suggests that in the oxidation of bisulphite the metal ion is reduced, leading to formation of a bisulphite radical that reacts rapidly with molecular oxygen. Kraft and van Eldick (6) proposed a mechanism for the oxidation of aqueous HSO_3^- in which Fe(III) is reduced to Fe(II), followed by reaction of the Fe(II)–HSO_3^- complex to produce sulphate, peroxide, $S_2O_6^{2-}$, and Fe(III). More recently van Eldick et al. (7) have proposed that oxidative cycling of Fe(III) and Fe(II) in the presence of molecular oxygen occurs with the pseudo-zero-order oxidation of Fe(II) by SO_5 species. Other mechanisms have been suggested, see for instance Conklin and Hoffman (8). In this paper we examine the kinetics of the oxidation of dilute HSO_3^- by molecular oxygen in solution at pH 4.6 maintained by an acetate – acetic acid buffer with Fe(III) and Fe(II) as catalysts. Reaction has been attempted in the absence of oxygen and in solutions in equilibrium with air and pure oxygen. The effect of adding the complexing agent 1,10-phenanthroline was also studied. Secondary Ion Mass Spectroscopy (SIMS) can be used in conjunction with isotopically enriched reactants to study the oxidation reactions (9). In this work SIMS is used to estimate the $^{18}O/^{32}S$ ratio in $BaSO_4$ precipitated from solution after oxidation of bisulphite with $^{18}O_2$; differences in this ratio obtained with Fe(III) and Fe(II) as catalysts can give an indication of differences in the reaction mechanisms.

Received August 10, 1995.

This paper is dedicated to Professor Howard C. Clark in recognition of his contributions to Canadian chemistry.

R.R. Martin[1] and J. Li. Department of Chemistry, University of Western Ontario, London, ON N6A 5B7, Canada.

[1] Author to whom correspondence may be addressed. Telephone: (519) 679-2111. Fax: (519) 661-3022. E-mail: rrhm@julian.uwo.ca

Experimental

The kinetics of the oxidation of bisulphite was measured using 100 ppb ferrous or ferric iron and 20 ppm bisulfite at 25°C in a solution buffered to a pH of 4.6 by a 0.01 M acetate – acetic acid buffer. The effect of oxygen was examined by excluding oxygen completely or by bubbling either air or pure oxygen through the system. The effects of varying both iron and buffer concentrations were also examined. An additional set of experiments was carried out using 20 ppm bisulphite and 100 ppb ferrous and (or) ferric iron at 25, 30, and 35°C to establish the activation energies for the reactions. In all cases the temperature was controlled to within 0.05°C.

Two further experiments were carried out using 20 ppm bisulphite and 100 ppb solutions of ferrous and ferric iron in 3.3×10^{-3} M 1,10-phenanthroline. The concentration of the Fe(II)–1,10-phenanthroline complex was measured using the absorption band centred at 508 nm with a Shimadzu 160 UV spectrometer. All solutions were prepared using reagent grade materials and distilled deionized water. Bisulphite solutions were prepared fresh daily. Analysis for ionic species was carried out using a Dionex DX-100 ion chromatograph.

Table 1. Specific rate constant for bisulfite oxidation as a function of temperature in the Fe(III) and Fe(II) systems.

Iron species	T/°C	k
Fe(III)	25 ± 0.05	0.019 ± 0.0005
Fe(III)	30 ± 0.05	0.035 ± 0.0009
Fe(III)	35 ± 0.05	0.50 ± 0.00125
Fe(II)	25 ± 0.05	0.015 ± 0.0004
Fe(II)	30 ± 0.05	0.025 ± 0.0006
Fe(II)	35 ± 0.05	0.038 ± 0.001

The SIMS experiment was carried out by preparing a solution 0.1 M in bisulphite and 0.1 M in either Fe(II) or Fe(III) buffered to a pH of 4.6 as before. Argon was bubbled through the solution for 3 h and the resulting solution was exposed to 20 kPa of $^{18}O_2$ for 48 h at 23°C. The resulting sulphate was precipitated from solution with $BaCl_2$, and the precipitate was dried and pressed into indium foil to reduce charging during SIMS analysis. The mass spectrum was obtained using a Cameca IMS 3f instrument with a 5 nA Cs^+ primary ion beam at 7.5 keV net energy rastered over a square 250 μm on edge, while secondary ions were collected from a central spot 150 μm in diameter to avoid edge effects from the ion crater created by the primary ion beam. A 100 V offset was applied to the sample holder to suppress molecular secondary ions.

Results and discussion

The reaction did not proceed in the absence of molecular oxygen, showing that it is the sole oxidizing agent in our system. The reaction was pseudo zero order in oxygen and first order for bisulphite in the presence of either Fe(II) or Fe(III), a result consistent with reports by other authors (10). The oxygen result is not surprising considering the large excess of oxygen used. The result confirmed that it was not necessary to use pure oxygen in our work.

No sulphur-containing ions other than HSO_3^- and SO_4^{2-} were detected during analysis using ion chromatography. Parenthetically, the kinetics were the same in unstirred solutions in contact with air. In addition, we noted that the oxidation rate is negatively correlated with buffer concentration. The latter observation is consistent with the series of iron complexes formed with the acetate buffer system (11).

The variation in specific rate constants with temperature between 25 and 35°C for both iron species is shown in Table 1. The activation energies determined from these data using the Arrhenius equation were 73.8 ± 2 and 70.9 ± 2 kJ mol^{-1} for the ferric and ferrous systems, respectively, in agreement with Hara and Okita (10). These activation energies fall within experimental error for both species, a result consistent with oxidative cycling between Fe(III) and Fe(II) as suggested elsewhere (6, 7).

Figure 1 shows a plot of the concentration of bisulphite vs. time in Fe(II) and Fe(III) solutions in the presence of 1,10-phenanthroline. Little reaction is observed in the complexed Fe(II) system while reaction ceases in the Fe(III) solution after 10–20 min. Such reaction as may be inferred during the initial few minutes in the Fe(II) solution may be attributed either to Fe(III) impurity in the standards used and (or) reaction prior to the relatively slow sequestration of Fe(II) by 1,10-phenanthroline. Cessation of reaction in the Fe(III) system corresponds to quantitative recovery of the Fe(III) as the Fe(II)–1,10-phenanthroline complex. Clearly the Fe(II)–1,10-phenanthroline complex suppresses the catalytic action of Fe(II). This result is consistent with observations by Lee et al. (12) who have shown the formation constant for the Fe(II) complex to be seven orders of magnitude greater than that for Fe(III); as well, Fe(II) will displace Fe(III) from 1,10-phenanthroline.

Fig. 1. Plot of concentration of bisulfite vs. time in the presence of either Fe(III) or Fe(II).

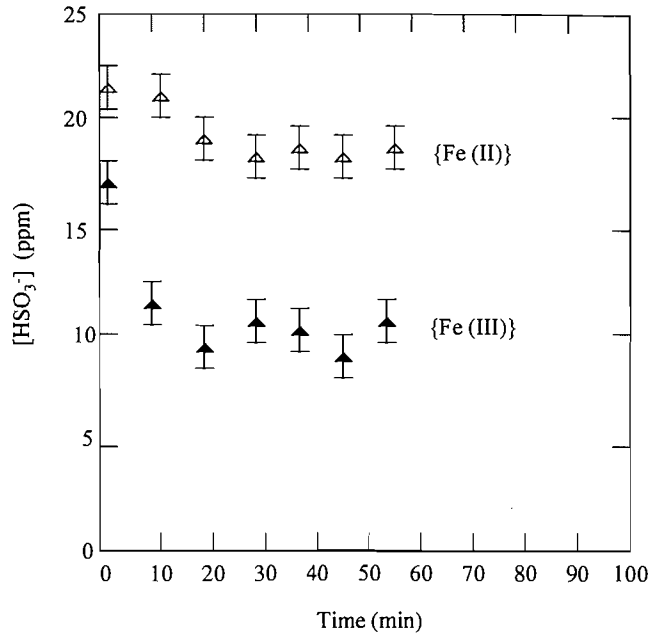

Fig. 2. Development of the 1,10-penanthroline/Fe(II) complex in the Fe(III)-catalyzed system.

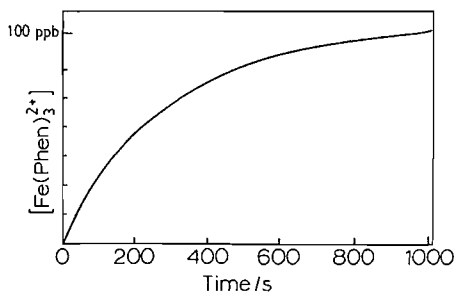

It should be noted that the Fe(II)–1,10-phenanthroline complex develops relatively slowly, taking about 10 min to develop fully under our experimental conditions. The growth in the absorbance attributed to the complex formation with time is shown in Fig. 2, which was obtained directly from the spectrometer.

Behra and Sigg (13) have reported that Fe(II) is the predominant oxidation state in fog water with a half-life for oxidation to Fe(III) at pH 5 and 5°C of 4.6 years. Our results support redox cycling of iron during oxidation since complexation of Fe(II) by 1,10-phenanthroline interrupts the cycle by sequestering Fe(II). It should be noted, however, that Fe(II) is a catalyst for bisulphite oxidation in its own right. Redox cycling is also consistent with our observation that the oxidation kinetics

Table 2. Ratio $^{18}O/^{32}S$ secondary ion yield in sulphate after oxidation with $^{18}O_2$ with Fe(III) and Fe(II) as catalysts.

Iron species	Ratio, secondary ion yield $^{18}O/^{32}S$
Fe(III)	0.34 ± 0.15
Fe(II)	1.20 ± 0.03

are essentially independent of the starting material, Fe(II) or Fe(III).

The SIMS experiment was undertaken to estimate the $^{18}O/^{32}S$ ratio obtained by oxidation of bisulphite by $^{18}O_2$ in systems dominated by either Fe(II) or Fe(III). Significant differences would be indicative of different reaction mechanisms. The results, shown in Table 2, give ratios of 1.2/1 and 0.34/1 for Fe(II) and Fe(III) systems, respectively. The SIMS data used in constructing Table 2 were based on analysis of three distinct sites on the surface of the barium sulfate precipitates mounted on indium foil. These results are subject to large relative errors due to differential charging, which arises because the particle distribution and size is non-uniform and varies from site to site. Changes in surface charging have a significant effect on secondary ion yield.

It is difficult to propose a unique reaction mechanism from our results, both because the system is complicated by the presence of a buffer that forms a series of complexes with the iron species and because more than one mechanism is consistent with the results. It is reasonable to suggest that the Fe(III) reacts in a manner similar to that proposed in the original Backstrom (5) mechanism:

$$Fe(III) + HSO_3^- \rightarrow Fe(II) + HSO_3^{\bullet}$$

$$HSO_3^{\bullet} + \tfrac{1}{2}O_2 + H_2O \rightarrow 2SO_4^{2-} + 4H^+$$

When the bisuphite is oxidized in $^{18}O_2$ this step yields an $^{18}O/^{32}S$ ratio of 0.5.

Benson (14) has suggested that peroxide complexes of Fe(II) and O_2 are formed during oxidative cycling of Fe:

$$Fe(II) + O_2 \rightarrow Fe(II)O_2$$

followed by slow oxidation of Fe(II) to Fe(III) by molecular oxygen. Reaction of the peroxide with bisulphite in $^{18}O_2$:

$$Fe(II)O_2 + 2HSO_3^- \rightarrow Fe(II) + 2SO_4^{2-} + 2H^+$$

yields an $^{18}O/^{32}S$ ratio of 1:1.

At any rate it appears that the ratio of $^{18}O/^{32}S$ will be lower in the Fe(III) system than that obtained with Fe(II). The preponderance of Fe(II) in cloud water suggests that this is the principle iron catalyst responsible for oxidation of bisulphite. The Fe(II) peroxide species may play an important role in the oxidation mechanism.

The behaviour of the system is consistent with that expected for the following simplified mechanism:

$$Fe(III) + HSO_3^- \rightarrow Fe(II) + HSO_3^{\bullet}$$

$$HSO_3^{\bullet} + \tfrac{1}{4}O_2 + \tfrac{1}{2}H_2O \rightarrow SO_4^{2-} + 2H^+$$

$$Fe(II) + O_2 \rightarrow Fe(II)O_2$$

$$Fe(II)O_2 + 2HSO_3^- \rightarrow Fe(II) + 2SO_4^{2-} + 2H^+$$

Net: $Fe(III) + 3HSO_3^- + \tfrac{5}{4}O_2 + \tfrac{1}{2}H_2O \rightarrow Fe(II) + 3SO_4^{2-} + 4H^+$

followed by slow oxidation of Fe(II) to Fe(III):

$$4Fe(II) + O_2 + 4H^+ \rightarrow 4Fe(III) + 2H_2O$$

As long as Fe(II) oxidation is slow, Fe(II) will become the dominant catalytic agent as the concentration of Fe(III) falls. While we do not suggest that this is a definitive mechanism, especially in a system such as the buffer used in our work, it does explain our observations. First, reaction with Fe(II) does not proceed when the system contains 1,10-phenanthroline, while reaction with Fe(III) is quenched after a 10 min induction period when 1,10-phenanthroline is added. Further, this induction period corresponds to quantitative recovery of the 1,10-phenanthroline–Fe(II) complex. Second, the activation energies for the two systems are within experimental error, reflecting the strong coupling between Fe(III) and Fe(II). Third, the ratio of $^{18}O/^{32}S$ for the Fe(II)-catalyzed oxidation is close to unity (1.2/1) while it is 0.34/1 for the Fe(III) system.

Conclusions

The kinetics of iron-catalyzed bisulphite oxidation are consistent with oxidative cycling of ferrous and ferric iron, as reported elsewhere.

SIMS analysis of sulfates precipitated after oxidation of bisulphite in systems dominated by each of the iron species yields significantly different $^{18}O/^{32}S$ ratios when oxidation is carried out in the presence of $^{18}O_2$. Fe(III) yields a ratio of $^{18}O/^{32}S$ less than unity, suggesting that H_2O is an oxygen source. The Fe(II) system yields a ratio close to unity; a species such as Fe(II) peroxide is thus implicated in the reaction mechanism. SIMS provides a powerful tool for probing the reaction mechanism.

These results, combined with those obtained by Behra and Sigg, imply that Fe(II) is the dominant iron catalyst in cloud water.

References

1. L.R. Martin. *In* SO_2, NO and NO_2 oxidation mechanisms: atmospheric considerations. *Edited by* J.G. Calvert. Butterworths, London. 1984. pp. 63–100.
2. T.E. Graedel and M.L. Mandich. J. Geophys. Res. **91**, 5205 (1986).
3. W. Stumm, Xue Hangbin, Maria de Lurdes, S. Goncalvez, M. Reutlinger, and L. Sigg. Environ. Sci. Technol. **25**, 1716, (1991).
4. L.R. Martin and W.H. Michael. Atmos. Environ. **21**, 2267 (1987).
5. H. Backstrom. Z. Phys. Chem. **256**, 122 (1934)
6. J. Kraft and R. van Eldik. Atmos. Environ. **23**, 2709 (1989).
7. R. van Eldick, C. Brandt, and I. Fabian. Inorg. Chem. **33**, 687 (1994).
8. M.H. Conklin and M.R. Hoffman. Environ. Sci. Technol. **22**, 899 (1988).
9. T. Kyotani, S. Hayashi, A. Tomita, J.A. MacPhee, and R.R. Martin. Fuel, **71**, 655 (1992).

10. H. Hara and T. Okita. Atmos. Environ. Part A: **24A**, 1427 (1990).
11. D.P. Douglas. *In* Stability constants of metal-ion complexes. Pergamon Press, London. 1979.
12. T.S. Lee, I.M. Kolthoff, and L.J. Leussing. J. Am. Chem. Soc. **70**, 2348 (1948).
13. P. Behra and L. Sigg. Nature, **344**, 419 (1991).
14. D. Benson. *In* Mechanisms of inorganic reactions in solution. An introduction. McGraw–Hill, London. 1968. p. 140.

Study of formation and fragmentation of ionic complexes of polydentate ligands with Al(III) and glycerol by fast atom bombardment mass spectrometry. Part 1: Polydentate ligands

Mandapati Saraswathi and Jack M. Miller

Abstract: The complexation reactions of aluminum ions with polydentate ligands such as 12-crown-4, 15-crown-5, 18-crown-6, 1,10-dithia-18-crown-6, dicyclohexyl-18-crown-6, dibenzo-18-crown-6, and dibenzo-24-crown-8 and acyclic analogs mono-, di-, tri-, tetra-, penta-, and hexaethylene glycols were studied using FAB mass spectrometry. These cyclic ligands form $(M + 117)^+$, $(M + 157)^+$, $(M + 231)^+$, and $(M + 253)^+$ ions with different aluminum-containing species. Collisionally activated dissociations of these adduct ions gave fragment ions, initially due to the loss of ligands directly attached to aluminum, followed by insertion of aluminum into the remaining ligand skeleton. Further fragmentation of the metal-containing species gave ions corresponding to consecutive losses of C_2H_4O units. Fragmentations of deuterium-labelled ions were used to help in establishing fragmentation pathways. Selectivity towards metal chelation is observed in this order: 12-crown-4 < 15-crown-5 < 18-crown-6. The elemental compositions of adduct ions were confirmed by high-resolution measurements. The formation of $(M + Al - 2H)^+$ ion, obtained by the displacement of two hydroxy protons, is more favored for tetra- and pentaethylene glycols.

Key words: crown ethers, polyethylene glycols, aluminum(III)–glycerol, ionic complexes and ion dissociations.

Résumé : Utilisant la spectrométrie de masse BAR, on a étudié les réactions de complexation des ions aluminium avec des ligands polydentates suivants : 12-couronne-4, 15-couronne-5, 18-couronne-6, 1, 10-dithia-18-couronne-6, dicyclohexyl-18-couronne-6, dibenzo-18-couronne-6 et le dibenzo-24-couronne-8 et avec les analogues mono, di, tri, tétra, penta et hexaéthylène. Ces ligands cycliques forment des ions $(M + 117)^+$, $(M + 157)^+$, $(M + 231)^+$ et $(M + 253)^+$ avec différentes espèces contenant de l'aluminium. Les dissociations, activées par des collisions, de ces ions adduits donnent des ions fragments, initialement à cause de la perte du ligand attaché directement à l'aluminium suivie de l'insertion de l'aluminium dans le squelette du ligand restant. Une fragmentation plus poussée de l'espèce contenant le métal donne des ions correspondants à la perte consécutive d'unités C_2H_4O. On a utilisé les fragmentations d'ions marqués au deutérium dans le but de déterminer le processus de fragmentation. On observe une sélectivité dans la chélation du métal dans l'ordre suivant : 12-couronne-4 < 15-couronne-5 < 18-couronne-6. Des mesures à haute résolution ont permis de confirmer la composition élémentaire de ces ions adduits. La formation de l'ion $(M + Al - 2H)^+$, obtenu par le déplacement de deux protons hydroxyliques, est plus favorisée pour les tétra et pentaéthylène glycol.

Mots clés : éthers couronnes, polyéthylène glycol, aluminium(III)–glycérol, complexes ioniques et dissociation d'ions.

[Traduit par la rédaction]

Introduction

The host–guest chemistry of crown ethers has been studied extensively because of the importance of these complexes in synthesis, in phase transfer catalysis, and as complexing agents for unwanted or dangerous ionic contaminants (1). The strength of metal–ligand complexes formed from crown ethers in solution depends on the size of the ring, on the metal ion, and on the solvent in which the reaction occurs (2). These multidentate systems have also been studied extensively by molecular mechanics methods (3). Mass spectrometry offers conditions useful for evaluating cation–ligand complexation in the absence of solvents. Recent studies on crown ether complexation reactions in the gas phase also show selectivity in binding with alkali metal ions and are useful in assessment of cation–ligand interaction (4). However, in some cases these cation complexation reactions are dependent on the matrix used in fast atom bombardment mass spectrometry (5).

Fast atom bombardment and electrospray ionization methods are useful techniques for the evaluation of both strong and weak interactions. Metal complexes arising from binding of cations with ligands such as cyclodextrins (6), bleomycin (7), bipyridyl amino acid (8), arylmethyl ethers (9), amines (10), nitriles (11), and nucleobase-substituted polyethers (12) were studied by these techniques. A recent study suggests the possibility of chiral recognition by using chiral crown ethers in the gas phase (13). Bowers and co-workers (14) predicted gas

Received March 1, 1996.

This paper is dedicated to Professor Howard C. Clark in recognition of his contributions to Canadian chemistry.

M. Saraswathi and J.M. Miller.[1] Department of Chemistry, Brock University, St. Catharines, ON L2S 3A1, Canada.

[1] Author to whom correspondence may be addressed. Telephone: (905) 688-5550, ext. 3402. Fax: (905) 682-9020. E-mail: jmiller@sandcastle.cosc.brocku.ca

phase conformations by accurate measurements of collision cross sections of alkali metal ion complexes of 18-crown-6 using ion chromatography techniques. Collisionally activated dissociation (CAD) of metal – crown ether complexes resulted in the formation of distonic radical cations by the homolytic cleavage of C—C bonds and elimination of neutral C_2H_4O units from the complex to yield abundant fragment ions (4*c*–*e*,15), which is analogous to the fragmentation of protonated crown ethers (16). During the CAD process, cations residing within the binding cavity of a ligand behave very differently from the cations binding from the outside of the ligand cavity. The dissociation of the larger metal ion – ligand complexes led to the formation of metal ions in greater abundance (4*c*, 12).

Crown ethers, which often serve to transport ionic species to specific sites (17), have not been studied with aluminum ions in the mass spectrometer. Therefore, we undertook the study of the interaction of aluminum ions with crown ethers and their open-chain counterparts. In the present study, the formation and fragmentation processes of cation–ligand complexes and the generation of cyclic ions between aluminum ions and polyethylene glycols are also discussed.

Experimental

All mass spectrometric experiments were conducted using a Kratos (Manchester, U.K.) Concept 1S double focusing (EB configuration) mass spectrometer, fitted with an Ion Tech. (Teddington, U.K.) fast atom gun. The gun was operated at 6–8 kV with the gun current 0.5–1 μA, using xenon as a bombarding gas. Source pressure was maintained at (1–2) × 10^{-5} Torr (1 Torr = 133.3 Pa). All data were recorded at 8 kV accelerating voltage at a scan rate of 8 s/decade, over a mass range of 11–950 u at 1100 resolution with an inter scan delay of 2 s. Samples were prepared by dissolution of the ether in a matrix mixture containing $AlCl_3$ (~0.5 mg) in glycerol (25–30 mg) water, (2 μL), and TFA (2 μL). One microlitre of solution was loaded on to the stainless steel FAB probe tip. The *m/z* measurements were calibrated with 2,4,6-tris(perfluoroheptyl)-1,3,5-triazine. For each run, 8–10 scans were averaged and the background was subtracted using the Kratos DART / MACH3 data system. Equimolar solution data were recorded by using equal volumes of sample solution and constant amounts of glycerol (25–30 mg), water (2 μL), and TFA (2 μL) and equal quantities of $AlCl_3$ (~0.5 mg). High-resolution mass measurements were made at a resolving power of 10 000. Linked scan spectra were recorded keeping the *B/E* or B^2/E constant for daughter and precursor ion analysis, respectively. The main beam intensity was reduced to 45–50% of its original value, using helium in the first field-free region collision cell, to obtain CAD spectra.

All samples were commercially available (Aldrich, Parish) and used without further purification. Glycerol-d_3 was prepared by exchange reactions with deuterium oxide.

Results and discussion

Crown ethers

To study the complexation of aluminum ions with crown ethers, aluminum chloride was first dissolved in glycerol. As for other metal chlorides used to make metal–ligand complexes, a few microlitres of water were added to make the solution homogeneous. This process led to partial hydrolysis of the aluminum chloride. Finally, crown ether was mixed with the metal ion – matrix solution and spectra were recorded. Some ions were observed above the molecular ion region but the spectrum is complicated by chemical noise. By increasing the concentration of the crown ether, a FAB spectrum of the crown ether is ultimately obtained.

Scheme 1. Ions produced from $AlCl_3$/glycerol/TFA/H_2O.

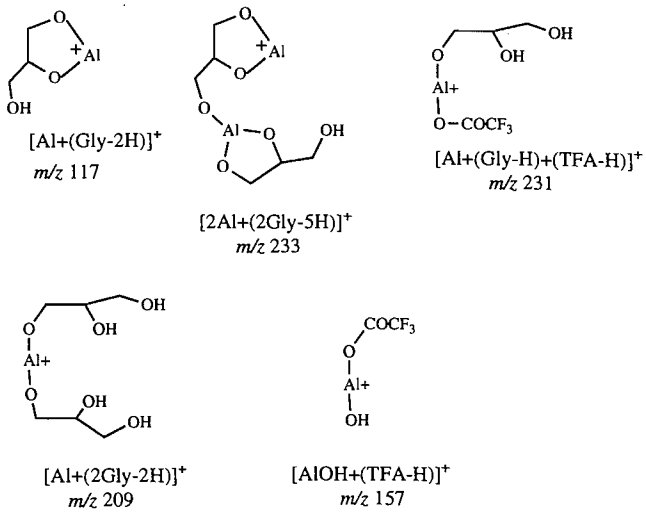

On analyzing the spectrum of the matrix mixture of $AlCl_3$ with glycerol and water, we found that the spectrum is dominated by glycerol ions and some ions containing aluminum and glycerol. The noise level, however, was not reduced. Addition of a few microlitres of trifluoroacetic acid (TFA) to the matrix reduced the noise and produced ions with predictable masses at *m/z* 27, $\{Al^+\}$, 93 $\{(Gly + H)^+\}$, 117 $\{[Al + (Gly - 2H)]^+\}$, 209 $\{[Al + (2Gly - 2H)]^+\}$, 231 $\{[Al + (Gly - H) + (TFA - H)]^+\}$, 233 $\{[Al_2 + (2Gly - 5H)]^+\}$. In addition, clusters of these ions with 116 [Al + (Gly − 3H)] and 114 (TFA) units are also observed. The spectrum recorded with the substitution of glycerol and water by glycerol-d_3 and D_2O showed increase in *m/z* according to the number of hydroxy groups present in an ion: *m/z* 117 shifted to 118, *m/z* 209 to 213, and *m/z* 231 and 233 to *m/z* 233 and 234, respectively. Structures proposed for these ions are given in Scheme 1. Replacement of TFA with acetic acid and the use of a solution of $AlCl_3$ do not produce good spectra.

Aluminum foil and anhydrous aluminum chloride were used by other workers to generate aluminum ions (Al^+) (18). Finally, we tried using the combination of $AlCl_3$ (instant mixing) in glycerol with 2 μL each of TFA and water. The spectrum obtained with crown ether produced ions with an addition of 117, 157, 231, and 253 units to the crown ether. Use of monothioglycerol in place of the glycerol matrix produced the $(M + 18)^+$ ion as the base peak due to trace amounts of ammonium salts present in the thioglycerol. The formation of the $(M + 133)^+$ ion further suggested that the *m/z* 117 ion formed in a glycerol matrix was a complex of aluminum and glycerol. Other ions were not significant enough to check the presence of the thioglycerol unit.

The mass spectra of the crown ethers 12-crown-4 (**1**), 15-

Table 1. Relative abundances of ions obtained from crown ethers in the $AlCl_3$–glycerol–TFA–water matrix.

Compound No.	$(M + H)^+$	$(M + 117)^+$	$(M + 157)^+$	$(M + 231)^+$	$(M + 253)^+$	*m/z* 45	87	89	133	175
1	79	35	11	13	6	100	24	37	10	13
2	22	33	31	16	5	100	21	33	15	—
3	23	47	31	25	19	100	32	47	18	—
4	64	7	—	8	—	100				
5	11	19	4	6	4	100				
6	31	14	4	7	—	60				
7	28	22	9	15	10	100				
Other ions										
2	219 (7) $(MH - H_2)^+$									
3	263 (8) $(MH - H_2)^+$, 535 (6) $(M + 271)^+$, 175 (7), 177 (7)									
4	295 (26) $(MH - H_2)^+$, 149 (42) $(C_6H_{13}O_2S)^+$, 147 (14) $(C_6H_{11}O_2S)^+$									
5	81 (82) $(C_6H_9)^+$, 187 (11) $(C_{10}H_{19}O_3)^+$, 141 (10), 371 (5) $(MH - H_2)^+$									
6	93 (29) $(C_6H_4OH)^+$, 109 (44) $(C_6H_4O_2H)^+$, 121 (100) $(C_6H_4O_2CH)^+$, 136 (38) $(C_6H_4O_2C_2H_4)^+$, 137 (26) $(C_6H_4OHOC_2H_4)^+$, 163 (23) $(C_6H_4O_2C_4H_7)^+$, 181 (11) $(C_{10}H_{13}O_3)^+$, 359 (5) $(MH - H_2)^+$									
7	93 (51) $(C_6H_4OH)^+$, 109 (40) $(C_6H_4O_2H)^+$, 121 (96) $(C_6H_4O_2CH)^+$, 136 (37) $(C_6H_4O_2C_2H_4)^+$, 137 (37) $(C_6H_4OHOC_2H_4)^+$, 163 (23) $(C_6H_4O_2C_4H_7)^+$, 225 (11) $(C_{12}H_{17}O_4)^+$									

Table 2. High-resolution measurements of *m/z* 381, 421, 495, and 517 from 18-crown-6.

m/z	Formula	Observed mass	Theoretical mass	Deviation (Δ ppm)
381	$C_{15}H_{30}O_9Al$	381.1780	381.17051	3.3
421	$C_{14}H_{25}O_9F_3Al$	421.12649	421.12660	0.2
495	$C_{17}H_{31}O_{11}F_3Al$	495.1614	495.16338	3.9
517	$C_{16}H_{24}O_{10}F_6Al$	517.10790	517.1089	1.9

crown-5 (**2**), 18-crown-6 (**3**), 1,10-dithia-18-crown-6 (**4**), dicyclohexyl-18-crown-6 (**5**), dibenzo-18-crown-6 (**6**), and dibenzo-24-crown-8 (**7**) were analyzed in the aluminum–glycerol – TFA–water matrix. Relative abundances of ions obtained from these cyclic ligands are listed in Table 1. All compounds yield the *m/z* 45 $(C_2H_5O)^+$ ion as the most abundant ion, except for dibenzo-18-crown-6, which produced *m/z* 121 $\{(C_6H_4O_2CH)^+\}$as the base peak in the spectrum. Formation of the *m/z* 121 ion is a characteristic fragmentation of dibenzocrowns (19). Other abundant ions are $(M + H)^+$, $(M + 117)^+$, $(M + 157)^+$, $(M + 231)^+$, and $(M + 253)^+$. Less abundant ions due to the consecutive losses of C_2H_4O units from $(M + H)^+$ ions were also seen in the spectrum.

Spectra obtained with glycerol-d_3 and D_2O instead of glycerol and water show that the mass of $(M + H)^+$, $(M + 117)^+$, and $(M + 157)^+$ ions increased by one unit, and the mass of $(M + 231)^+$ ions by two units. There is no change in the mass of the $(M + 253)^+$ ion.

Experiments with 1,2-propanediol as the matrix in place of glycerol gave ions from 18-C-6 corresponding to $(M + H)^+$, $(M + 101)^+$, $(M + 157)^+$, $(M + 215)^+$, and $(M + 253)^+$ in addition to the other ions below the molecular ion region. Similarly, in ethylene glycol the spectrum of 18-C-6 also shows $(M + H)^+$, $(M + 157)^+$ and $(M + 253)^+$ ions in addition to the formation of $(M + 87)^+$ and $(M + 201)^+$ ions above the molecular region. Formation of $(M + 117)^+$, $(M + 101)^+$, and $(M + 87)^+$ from glycerol, 1,2-propanediol, and ethylene glycol, respectively, indicates that these complexes correspond to the adduct ions of the $\{Al + (matrix - 2H)\}^+$ complex. Similar changes with respect to the matrix are also observed in the mass of $(M + 231)^+$, $(M + 215)^+$, and $(M + 201)^+$ ions, which suggests the participation of the matrix in the formation of these ions. However, there is no change in the mass of $(M + 157)^+$ and $(M + 253)^+$ ions. The spectrum of 18-C-6 recorded in $AlCl_3$, glycerol, acetic acid, and water gave $(M + H)^+$, $(M + 117)^+$, $(M + 61)^+$, and $(M + 177)^+$ ions but no $(M + 157)^+$ ion. Therefore, we conclude that TFA participates in the formation of $(M + 157)^+$, $(M + 231)^+$, and $(M + 253)^+$ ions. The $(M + 231)^+$ ion is a complex of $\{Al + (Gly-H) + (TFA - H)\}^+$ with 18-C-6, which shows a mass increase of 2 u in D_2O experiments. The $(M + 253)^+$ ion is a complex of $\{[Al + (2TFA - 2H)] + M\}^+$, and remains unchanged during D_2O exchange. Finally, the composition of the $(M + 157)^+$ ion can be accounted for with one exchangable proton as the $\{M + [AlO,H + (TFA-H)]\}^+$ ion. High-resolution mass measurements of $(M + 117)^+$, $(M + 157)^+$, $(M + 231)^+$, and $(M + 253)^+$ ions fit with the proposed formula (Table 2). Despite the use of $AlCl_3$, no chloride-containing species are observed in the spectra. Thus the aluminum coordinates to the crown and matrix-derived anions to form a unipositive complex cation.

Experiments carried out with equimolar solutions of analytes **1**, **2**, and **3** under identical conditions can give metal-

Scheme 2. Collisionally activated dissociation of $(M + 117)^+$ ion from 18-crown-6.

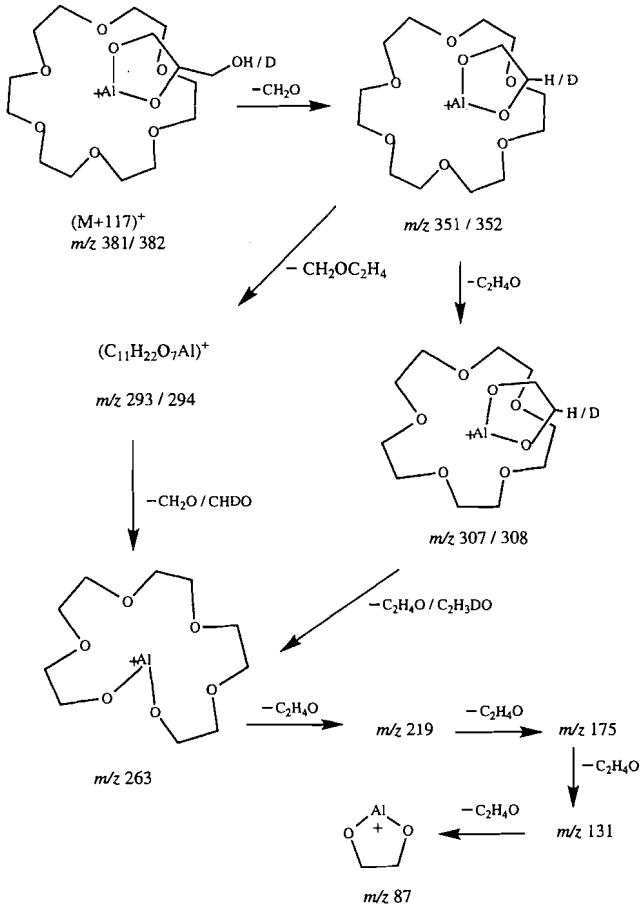

complexed ions in relative complexation by aluminum ions. Relative abundances of $(M + 117)^+$, $(M + 157)^+$, $(M + 231)^+$, and $(M + 253)^+$ ions directly indicate the metal ion binding strengths with crown ethers. These are in the order of 18-C-6 > 15-C-5 > 12-C-4. Experiments with an equimolar solution of mixed ligands 12-C-4 / 15-C-5 and 15-C-5 / 18-C-6 showed the selectivity in the formation of metal-complexed ions. The abundances of the significant cluster ions $(M + 117)^+$, $(M + 157)^+$, $(M + 231)^+$, and $(M + 253)^+$ vary as 18-C-6 > 15-C-5 > 12-C-4. This analysis was not extended to other crown ethers that are less polar and have solubility problems on mixing with a polar matrix. Although, regular spectra of 1,10-dithia-18-crown-6, dicyclohexyl-18-crown-6, dibenzo-18-crown-6, and dibenzo-24-crown-8 have been collected using solutions of these compounds prepared from 1,2-dibromoethane and methanol, this process does not keep the sample in the matrix for sufficiently long to run the competitive analysis.

Ion dissociations

The dissociation of $(M + 117)^+$, $(M + 157)^+$, $(M + 231)^+$, and $(M + 253)^+$ ions from 12-C-4, 15-C-5, and 18-C-6 shows similar types of fragmentation. Hence, the fragmentation processes of ions from 18-C-6 only are discussed (Scheme 2). These metal chelated ions $(M + 117)^+$, $(M + 157)^+$, $(M + 231)^+$, and $(M + 253)^+$ show formation of precursor ions, which are cluster ions of crown with various ionic aluminum species surrounded by glycerol, TFA, and OH groups.

$\{M + (Al + Gly - 2H)\}^+$, m/z *381*

Unimolecular dissociation and collisionally activated dissociation differ in the removal of neutral fragments to produce *m/z* 293 and 307 ions from the most abundant ion at *m/z* 351, which is formed from the parent ion by the loss of CH_2O. Formation of *m/z* 293 is a facile process in unimolecular decomposition whereas formation of *m/z* 307 is favored under the CAD conditions. This suggests that formation of *m/z* 307 is a higher energy process. Further dissociation of ions at *m/z* 293 and 307 gives rise to *m/z* 263 by the loss of CH_2O and C_2H_4O units, respectively.

Fragmentation of *m/z* 263 by consecutive losses of C_2H_4O units led to the formation of ions at *m/z* 219, 175, 131, and 87. The normal FAB mass spectrum of 18-C-6 shows $(M + H)^+$ at *m/z* 265 and $(M + H - H_2)^+$ at *m/z* 263 ions in glycerol matrix. If the ion at *m/z* 263 obtained during CAD of the $(M + 117)^+$ ion corresponds to the $(MH - H_2)^+$ ion of 18-C-6, the further fragmentation of *m/z* 263 should produce ions at *m/z* 177, 133, and 89. They have significant abundances as observed in the CAD spectrum of the $(MH - H_2)^+$ ion from 18-C-6 in a glycerol matrix. The CAD spectrum of the $(M + H)^+$ ion of 18-C-6 also shows the formation of similar ions at *m/z* 177, 133, and 89 (16). However, formation of *m/z* 87 is a less significant process from *m/z* 263 and 265 of 18-C-6. Therefore, there probably is another structure accounting for some of *m/z* 263 that is different from that normally expected from the $(MH - H_2)^+$ ion. It might have been produced by the insertion of an AlO^+ ion into the crown. Crown ethers have been shown to undergo more facile bond insertion reactions than open-chain analogs with Fe^+ and Co^+ (20). Abundant ions at *m/z* 175, 131, and 87 arising from *m/z* 263 should have an aluminum ion in them (Scheme 2). The dissociation of $(M + 118)^+$ at the *m/z* 382 ion shows the retention of deuterium in the $(P - 30)^+$, $(P - 74)^+$, and $(P - 88)^+$ ions. This suggests that the formation of $(P - CH_2O)^+$ comes from a glycerol moiety. Further loss of C_2H_4O and $CH_2OC_2H_4$ is exclusively from the crown, since the loss of C_2H_4O and $CH_2OC_2H_4$ from glycerol would involve loss of D, to give an ion at *m/z* 308 and 294, respectively. The processes of formation of *m/z* 263 may be directly from the $(P - CH_2O)^+$ (*m/z* 352) ion and from the $(P - CH_2O,C_2H_4O)^+$ (*m/z* 308) ion and (or) by the elimination of CHDO from *m/z* 294 (Scheme 2).

$\{M + [AlOH + (TFA - H)]\}^+$, m/z *421*

This ion, on fragmentation, produces major ions at *m/z* 328 and 327 from labelled and unlabelled parent ions, respectively. The ion at *m/z* 327/328 is due to a characteristic loss of CF_2CO_2 from the parent ion by the migration of F to the metal ion. Formation of another abundant ion at *m/z* 329 is explained by losses of ($C_2H_4OCH_2O$ and H_2O/DHO) groups from the parent ion (Scheme 3). This ion, on elimination of HF, forms *m/z* 309. Fragmentation of *m/z* 327/328 by the removal of HF/DF may produce *m/z* 307. Other fragment ions at *m/z* 263, 219, 175, 131, and 87 are also observed.

Fragmentation of the $(M + 231)^+$ ion (m/z *495)*

This ion contains two exchangeable protons with primary and secondary hydroxyl groups from glycerol. The decomposition

Scheme 3. Fragmentation of $(M + 157)^+$ ion under CAD from 18-crown-6.

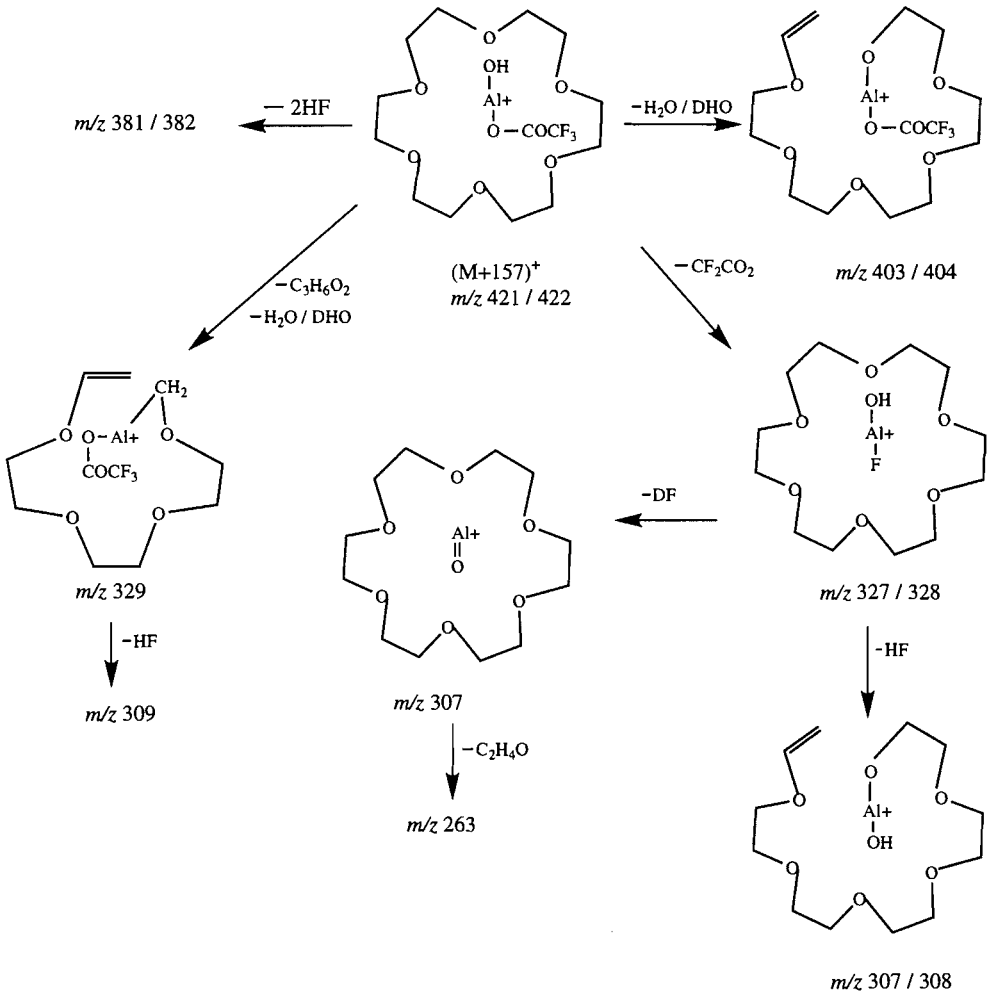

of the ion at *m/z* 495/497 involves the loss of one of the deuteriums during the elimination of CF_3CO_2D to give the ion at *m/z* 381/382. The dissociation of a partially labelled ion $(M + 231)^+$ at *m/z* 496 shows mainly the loss of CF_3CO_2H. Elimination of unlabelled TFA as the major process can be explained in terms of the bond fission energies of O–D and O–H and the ease of exchange of protons on the glycerol moiety of this ion during the analysis. Further dissociation of *m/z* 381/382 is similar to the fragmentation of the $(M + 117)^+$ ion.

Fragmentation of $(M + 253)^+$ (m/z *517)*

Fragmentation of this ion produces an abundant ion at *m/z* 423 due to the loss of CF_2CO_2, by transfer of F to the metal (Scheme 4). Further fragmentation also involves the loss of another CF_2CO_2 moiety, which is a characteristic of the presence of another TFA group in the ion. The migration of an F to the aluminum yields an abundant ion at *m/z* 329. This ion is a complex of 18-C-6 and $(AlF_2)^+$. Interestingly AlF_2^+ ion interactions are detected while $AlCl_2^+$ ions are not seen. The elimination of HF is also observed from the *m/z* 423 and 329 ions. Other significant ions produced from *m/z* 329 are at *m/z* 175, 153, and 109. The fragmentation of *m/z* 329 into *m/z* 175 may involve the transfer of F from Al back to the ligand skeleton and binding of aluminum to oxygens of the ether is shown. Formation of *m/z* 153 involves transfer to the ether fragment instead of the Al-containing species. Formation of low-abundance ions due to consecutive losses of C_2H_4O units from *m/z* 423 and 329 is also observed.

Mass spectra of glycols obtained from $AlCl_3$–glycerol–TFA

The FAB mass spectra of mono- (**8**), di- (**9**), tri- (**10**), tetra- (**11**), penta- (**12**), and hexaethylene glycols (**13**) were run in the $AlCl_3$ – glycerol – water and TFA matrix mixture. Relative abundances of ions obtained from these compounds are listed in Table 3. Commonly observed ions from glycols are $(M + Al - 2H)^+$ and $(M + 117)^+$. In addition, ions due to consecutive losses of C_2H_4O units from these $(M + Al - 2H)^+$ and $(M + 117)^+$ ions are also observed. Ethylene glycol does not form an $(M + 117)^+$ ion and gives ions corresponding to $(C_2H_5O)^+$, $(HOAlOC_2H_4OH)^+$, and $\{(HOC_2H_4O)_2Al\}^+$ with significant abundances. D_2O experiments with tetraethylene glycol show no mass shift in the formation of the $(M + Al - 2H)^+$ ion. Therefore, the two hydroxyl protons of the glycol are substituted by Al^{3+} in producing the $(M + Al - 2H)^+$ ion, which forms a cyclic ether with aluminum ion. The $(M + 117)^+$ ion

Scheme 4. Collisionally activated dissociation of {M + Al (TFA − H)$_2$}$^+$ ion from 18-crown-6.

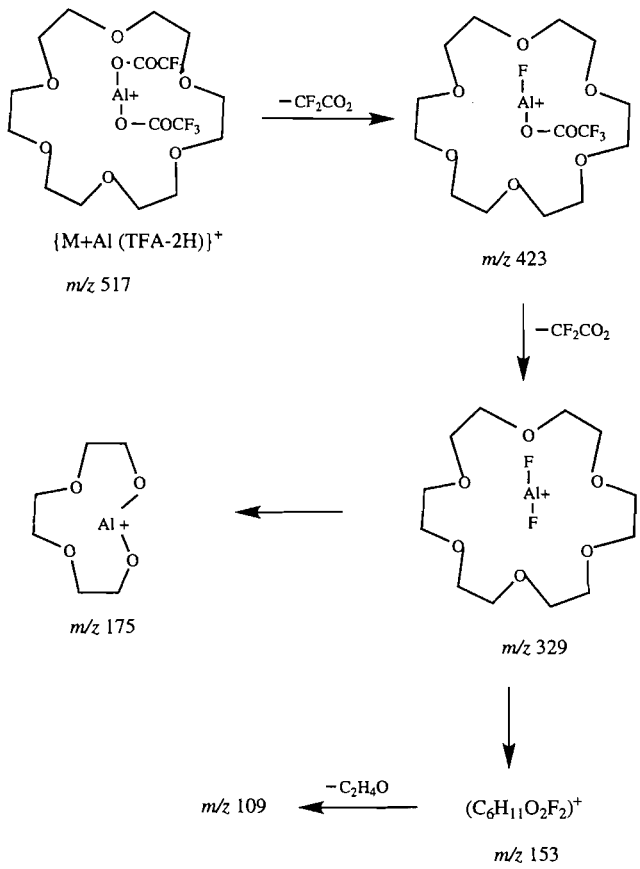

shows an increase in the mass by 1 u during D_2O exchange. Exact Mass measurements of the $(M + Al - 2H)^+$ ion from triethylene glycol at *m/z* 175 show a good fit for $(C_6H_{12}O_4Al)^+$ with an error of 3.4 ppm (observed 175.05449, theoretical 175.05509).

Formation of a cyclic $(M + Al - 2H)^+$ ion depends on the number of ethylene oxide (C_2H_4O) units and is observed from triethylene glycol to pentaethylene glycol as the base peak. Although in hexaethylene glycol the abundance of $(M + Al - 2H)^+$ ion is significant, the $(C_2H_5O)^+$ ion is the base peak. Formation of this ion from hexaethylene glycol is less favoured because of a lower probability of the two ends meeting for the intra-molecular substitution process to occur. Diethylene glycol does not give the $(M + Al - 2H)^+$ ion and formation of the $(M + 117)^+$ ion predominates. In 11-, 14-, 17-, and 20-membered rings derived from tri-, tetra-, penta-, and hexaethylene glycols, respectively, on formation of the $(M + Al - 2H)^+$ ion, the existence of donor–acceptor interactions between ethereal oxygens and aluminum results in highly stable metal–ligand complexes. In diethylene glycol this type of coordination may not be possible in the 8-membered ring to form $(M + Al - 2H)^+$ ion.

Ions $(M + H)^+$, $(M + Al - 2H)^+$, and $(M + 117)^+$ obtained from equimolar solutions of glycols under identical conditions can be compared to obtain the relative metal ion affinity of glycols. A ratio of the intensity of $(M + H)^+$, $(M + Al - 2H)^+$, and $(M + 117)^+$ ions individually and total ion intensity vs.

Fig. 1. A ratio of ion intensity of $(M + Al - 2H)^+$, $(M + H)^+$, and $(M + 117)^+$ ions and total ion intensity vs. glycols. $(M + Al\text{-}2H)^+$ -■-; $(M + H)^+$ -□-; $(M + 117)^+$ -◆-.

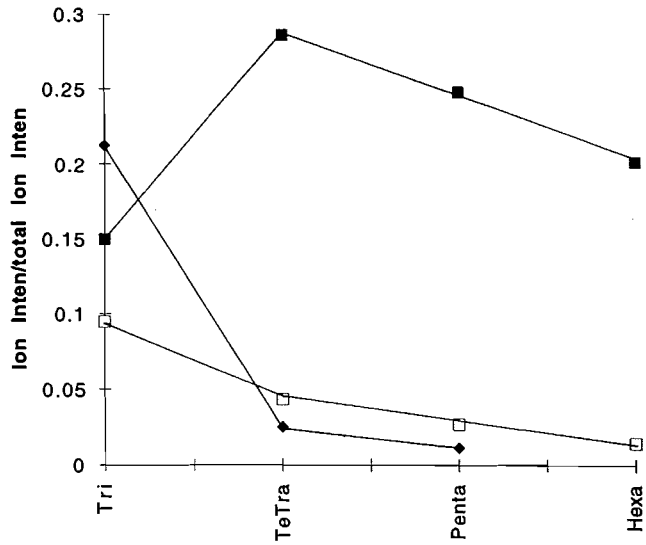

glycol chain length is presented as a graph (Fig. 1). The cyclic $(M + Al - 2H)^+$ ion formation is highly favored in tetraethylene glycol and formation of $(M + H)^+$ and $(M + 117)^+$ ions is gradually decreased as the chain length increases. Ethylene glycol and diethylene glycol are less effective at complexing in the presence of glycerol matrix and only reagent ions dominated the spectrum at constant molar concentrations. 1,3-Propanediol and 2-butene1,4-diol also yield abundant $(M + 117)^+$ ions (Table 3).

Ion dissociations

The CAD spectra of $(M + Al - 2H)^+$ ions from tri- and pentaethylene glycols show ions corresponding to the elimination of C_2H_4O units, which ultimately leads to the formation of *m/z* 87 [$(C_2H_4O_2Al)^+$]. The further decomposition of *m/z* 87 gives rise to *m/z* 43 [$(AlO)^+$]. $(M + 117)^+$ from triethylene glycol yields an ion at *m/z* 175, i.e., $(M + Al - 2H)^+$, by the elimination of glycerol. The further fragmentation of this ion is identical with the fragmentation of the $(M + Al - 2H)^+$ ion. Another adduct from the same glycol corresponding to the {(M − H) + [Al (TFA − H)]}$^+$ ion dissociates to produce ions at *m/z* 175 by the removal of CF_3CO_2H. Another abundant ion is at *m/z* 235. The $(M + 233)^+$ ion of pentaethylene glycol gives ions due to loss of C_2H_4O units from the parent ion in addition to the formation of the most abundant $(M + Al - 2H)^+$ ion at *m/z* 263. Further fragmentation of *m/z* 263 also involves the loss of ethylene oxide units. The fragmentation of the $(M + Al - 2H)^+$ ion (*m/z* 263) from pentaethylene glycol is similar to the fragmentation of *m/z* 263 produced from the decomposition of the $(M + 117)^+$ ion of 18-C-6 (Scheme 2).

The metastable ion analysis at constant B^2/E of the $(M + Al - 2H)^+$ ion at *m/z* 263 gives $(M + 117)^+$ and {M + (Al_2 + 2Gly − 5H)}$^+$ ions as precursors. However, the $(M + Al - 2H)^+$ ion from trigol has another abundant precursor ion at *m/z* 193 corresponding to {(M − H) + AlOH)}$^+$ in addition to the $(M + 117)^+$ ion.

Table 3. Relative abundances of ions obtained from glycols in the $AlCl_3$ / glycerol / TFA / H_2O matrix.

Compound No.	$(M + H)^+$	$(M + Al-2H)^+$	$(M + 117)^+$	$(M + 231)^+$	$(M + 233)^+$	*m/z* 45	87	89	131	133	175
8	10	28	—	—	—	55	—	—	—	—	—
9	49	—	100	16	12	54	—	—	—	—	—
10	18	100	51	6	12	67	25	31	20		
11	13	100	8	9	9	81	9	22	6	5	9
12	9	100	2	2	—	95	9	24	5	6	8
13	2	24	—	—	—	100	16	5	10	—	—
1,3-Propanediol	16	—	100	26	14						
2-Butene-1,4-diol[a]	53	—	64	63	—	9					
Other ions											
8	105 (100) $[(M - H) + AlOH)]^+$, 149 (76) $(2M + Al - 2H)^+$										
10	289 (42) $[(M - H) + Al + (TFA - H)]^+$, 405 (16) $[(M - H) + 2Al + (Gly - 3H) (TFA - H)]^+$										
12	219 (6) $(C_8H_{16}O_4AlO)^+$, 379 (11) $(M + 2Al + Gly - 5H)^+$										
13	59 (10) $(C_2H_4OCH_3)^+$, 73 (37) $(C_2H_5OC_2H_4)^+$, 219 (7) $(C_8H_{16}O_4AlO)^+$, 263 (8) $(C_{10}H_{20}O_5AlO)^+$										

[a]71 (100) $(MH - H_2O)^+$.

Conclusions

These polydentate ligands formed abundant adduct ions with various ionic aluminum species. The complexation reactions of these crown ethers in the gas phase showed selectivity in binding with respect to ligand in the order 18-C-6 > 15-C-5 > 12-C-4. Dissociations of adduct ions initially give fragment ions due to loss of the non-crown species attached directly to aluminum. The insertion of aluminum ion into the crown ether chain was also observed. Formation of analogous $(M + Al - 2H)^+$ ions was observed in the FAB spectra of tri-, tetra-, penta-, and hexaethylene glycols. The stability of these ions depends on the distribution of charge through electrostatic interaction with ethereal oxygens. In mono- and diethylene glycols such types of charge distribution may not be possible. Since aluminum reagents are strong Lewis acids, strong binding of aluminum to donor molecules is observed. The complexation reactions of crown ethers with aluminum ions may fall into a distinct class of aluminum host–guest chemistry.

Acknowledgement

The authors are grateful to the Natural Sciences and Engineering Research Council of Canada for financial support in the form of operating and equipment grants to J.M.M. and to T.R.B. Jones for technical assistance.

References

1. (*a*) C.J. Pedersen. J. Am. Chem. Soc. **89**, 7017 (1967); (*b*) F. Vogtle and E. Wever (Editors). Host–guest complex chemistry — macrocycles. Springer-Verlag, New York. 1985; (*c*) J-M. Lehn. Angew. Chem. Int. Ed. Engl. **29**, 1304 (1990); (*d*) R.M. Izatt, J.S. Bradshaw, S.A. Nielsen, J.D. Lamb, J.J. Christensen, and D. Sen. Chem. Rev. **85**, 271 (1985); (*e*) R.M. Izatt, K. Pawlak, J.S. Bradshaw, and R. Bruening. Chem. Rev. **91**, 1721 (1991); (*f*) R.M. Izatt, J.S. Bradshaw, K. Pawlak, R.S. Bruening, and B.J. Tarbet. Chem Rev. **92**, 1261 (1992).
2. (*a*) D.M. Dishong and G.W. Gokel. J. Org. Chem. **47**, 147 (1982); (*b*) G.W. Gokel, D.M. Goli, C. Minganti, and L. Echegoyen. J. Am. Chem. Soc. **105**, 6786 (1983).
3. (*a*) G. Wipff, P. Wiener, and P. Kollman. J. Am. Chem. Soc. **104**, 3249 (1982); (*b*) L.X. Dang and P. Kollman. J. Am. Chem. Soc. **112**, 5716 (1990).
4. (*a*) H. Zhang, I-H. Chu, S. Leming, and D.V. Dearden. J. Am. Chem. Soc. **113**, 7415 (1991); (*b*) H. Zhang and D.V. Dearden. J. Am. Chem. Soc. **114**, 2754 (1992); (*c*) I-H. Chu, H. Zhang, and D.V. Dearden. J. Am. Chem. Soc. **115**, 5736 (1993); (*d*) S. Maleknia and J.S. Brodbelt. J. Am. Chem. Soc. **114**, 4295 (1992); (*e*) C.C. Liou and J.S. Brodbelt. J. Am. Soc. Mass Spectrom. **3**, 543 (1992); (*f*) M. Vincenti. J. Mass Spectrom. **30**, 925 (1995).
5. G.J. Langley, D.G. Hamilton, and M.C. Grossel. J. Chem. Soc. Perkin Trans. 2, 929 (1995).
6. (*a*) P.S. Bates, R. Kataky, and D. Parker. J. Chem. Soc. Chem. Commun. 691 (1993).
7. J.W. Sam, X-J. Tang, and J. Peisach. J. Am. Chem. Soc. **116**, 5250 (1994)
8. S.R. Wilson, A. Yasmin, and Y. Wu. J. Org. Chem. **57**, 6941 (1992).
9. K. Wang, X. Han, R.W. Gross, and G.W. Gokel. J. Am. Chem. Soc. **117**, 7680 (1995).
10. (*a*) L-Z. Chen and J.M. Miller. Rapid. Commun. Mass Spectrom. **6**, 492 (1992); (*b*) J. Organomet. Chem. **448**, 225 (1993).
11. (*a*) L-Z. Chen and J.M. Miller. J. Am. Soc. Mass Spectrom. **2**, 120 (1991); (*b*) Can. J. Chem. **69**, 2002 (1991); (*c*) Org. Mass Spectrom. **27**, 19 (1992); (*d*) J. Am. Soc. Mass Spectrom. **3**, 451 (1992); (*e*) Org. Mass Spectrom. **27**, 883 (1992); (*f*) L-Z. Chen, J.M. Miller, and V.S. Murthy. Rapid Commun. Mass Spectrom. **6**, 721 (1992).
12. M. Saraswathi and J.M. Miller. J. Am. Soc. Mass Spectrom. **7**, 42 (1996); (*b*) J. Mass Spectrom. **31**, 1011 (1996).
13. M. Sawada, Y. Takai, H. Yamada, T. Kaneda, K. Kamada, T. Mizooku, K. Hirose, Y. Tobe, and K. Naemura. J. Chem. Soc. Chem. Commun. 2497 (1994); (*b*) M. Sawada, Y. Takai, H. Yamada, S. Hirayama, T. Kaneda, T. Tanaka, K. Kamada, T. Mizooku,S. Takeuchi, K. Ueno, K. Hirose, Y. Tobe, and K. Naemura. J. Am. Chem. Soc. **117**, 7726 (1995).

14. S. Lee, T. Wyttenbach, G. von Helden, and M.T. Bowers. J. Am. Chem. Soc. **117**, 10159 (1995).
15. S. Maleknia and J.S. Brodbelt. Rapid Commun. Mass Spectrom. **6**, 376 (1992).
16. (*a*) O. Curcuruto, P. Traldi, G. Moneti, L. Corda, and G. Podda. Org. Mass Spectrom. **26**, 713 (1991); (*b*) S. Maleknia, C-C. Liou, and J. Brodbelt. Org. Mass Spectrom. **26**, 997 (1991).
17. R.W. Kozak, T.A. Waldman, R.W. Atcher, and O.A. Gansow. Trends Biotechnol. **4**, 259 (1995).
18. R.V. Hodges, P.B. Armentrout, and J.L. Beauchamp. Int. J. Mass Spectrom. Ion Phys. **29**, 375 (1979); (*b*) A.K. Chowdhury and C.L. Wilkins. Int. J. Mass Spectrom. Ion Processes, **82**, 163 (1988).
19. A.S. Gomes and C.M.F. Oliveira. Org. Mass Spectrom. **12**, 407 (1977).
20. (*a*) S.K. Huang and J. Allison. Organometallics, **2**, 883 (1983); (*b*) S.K. Huang, Y.C. Lee, J. Allison, and A.I. Popov. Spectrosc. Lett. **16**, 215 (1983).

Structure and bonding of organosilicon compounds containing silicon–silicon and silicon–germanium bonds: an X-ray absorption fine structure study

Jian Z. Xiong, Detong Jiang, Craig E. Dixon, Kim M. Baines, and T.K. Sham

Abstract: Si K-edge X-ray Absorption Fine Structures (XAFS) spectroscopy has been used to study the structure and bonding of a series of highly symmetric organosilicon compounds, $Si(CH_3)_4$, $Ge[Si(CH_3)_3]_4$, $Si[Ge(CH_3)_3]_4$, and $Si[Si(CH_3)_3]_4$, in the gas phase. It was found that there is a significant difference in the absorption coefficient in the near-edge region between local Si–Si interactions in these compounds and long-range Si–Si interactions in crystalline solids and that the Si—Si bond length in the molecule $Si[Si(CH_3)_3]_4$ is 2.364(10) Å and the Si—Ge bond lengths in $Si[Ge(CH_3)_3]_4$ and $Ge[Si(CH_3)_3]_4$ are 2.38(3) Å and 2.396(15) Å, respectively. These results and their comparison to Si—Si and Si—Ge interatomic distances in crystalline solids are discussed.

Key words: XAFS, EXAFS, organosilicon, Si—Ge bond length.

Résumé : On a utilisé la spectroscopie d'absorption des structures fines de rayons X du Si («XAFS») pour étudier la structure et les modes de liaison d'une série de composés organosiliciés hautement symétriques, $Si(CH_3)_4$, $Ge[Si(CH_3)_3]_4$, $Si[Ge(CH_3)_3]_4$ et $Si[Si(CH_3)_3]_4$, en phase gazeuse. On a observé des différences importantes dans les coefficients d'absorption, dans la région près de la surface, entre les interactions locales Si–Si de ces composés et les interactions Si–Si à longue distance dans les solides cristallins; on a aussi trouvé que la longueur de la liaison Si—Si dans la molécule de $Si[Si(CH_3)_3]_4$ est de 2,364(10) Å alors que les longueurs des liaisons Si—Ge dans les composés $Si[Ge(CH_3)_3]_4$ et $Ge[Si(CH_3)_3]_4$ sont respectivement de 2,38(3) et 2,396(15) Å. On discute de ces résultats et de leur comparaison avec les distances interatomiques Si—Si et Si—Ge observées dans des solides cristallins.

Mots clés : «XAFS», «EXAFS», organosilicié, longueur de la liaison Si—Ge.

[Traduit par la rédaction]

1. Introduction

The structure and electronic properties of molecular systems containing group IV elements with Si—C, Si—Si, and Ge—Si bonds are of particular interest in connection with their implications for the structure and electronic properties of group IV based electronic materials. Si–Ge atomic layer superlattice materials (1), for example, play an important role in modern electronic devices.

The objective of this research is to use the X-ray absorption fine structure (XAFS) technique to investigate the structure and bonding properties of prototype molecules of high symmetry: $Si(CH_3)_4$ (TMS), $Ge[Si(CH_3)_3]_4$, $Si[Ge(CH_3)_3]_4$, and $Si[Si(CH_3)_3]_4$. These compounds are selected because the central metal atom (Si or Ge) is in a perfect tetrahedral site. For example, the central atom in $Si[Si(CH_3)_3]_4$ and $Si[Ge(CH_3)_3]_4$ is bonded to four Si or Ge atoms, respectively. The local geometry of Si and Ge in their pure crystalline state has the same local symmetry. It would be interesting to compare the local structure (first shell) of Si and Ge in these model compounds to those of crystalline Si, Ge, Si–Ge alloys, and Si–Ge superlattices and ask questions about the structure and bonding relationship in terms of the local metal–metal interaction in the $SiSi_4$ and $SiGe_4$ moieties versus the extended metal–metal interaction in the corresponding semiconductors.

X-ray Absorption Fine Structure (XAFS) spectroscopy deals with the measurement and interpretation of the photon energy-dependent X-ray absorption coefficient above a specific core level threshold (edge) of an element in a chemical environment (2). XAFS is essentially the modulation (due to the presence of surrounding atoms) of the otherwise smooth monotonic atomic absorption coefficient (in the free atom) and it extends to as much as 1000 eV above the threshold. For molecules in the gas phase, for example, the absorption coefficient increases abruptly as the photon energy approaches the ionization threshold of a core level (Si 1*s* in this study). These features arise from the excitation of a core electron into previ-

Received February 16, 1996.

This paper is dedicated to Professor Howard C. Clark in recognition of his contributions to Canadian chemistry.

J.Z. Xiong, D. Jiang,[1] C.E. Dixon, K.M. Baines, and T.K. Sham.[2] Department of Chemistry, The University of Western Ontario, London, ON N6A 5B7, Canada.

[1] Present address: Department of Physics, Simon Fraser University, Burnaby, BC V5A 1S6, Canada.

[2] Author to whom correspondence may be addressed. Telephone: (519) 679-2111, ext. 6341. Fax: (519) 661-3022. E-mail: sham@uwo.ca

ously unoccupied atomic (Rydberg) and molecular orbitals that are bound, and into resonance states that are quasi-bound (potential barrier states, sometime known as shape resonance) (3). These processes often result in sharp absorption features at the edge followed by resonance characteristic of the local environment extending to ~50 eV above the threshold. This region has been traditionally called NEXAFS (Near Edge X-ray Absorption Fine Structures) or XANES (X-ray Absorption Near Edge Structures) (4). It contains information about the symmetry and bonding of the molecular system surrounding the absorbing atom. Beyond this region and up to as much as 1000 eV above, the absorption coefficient exhibits oscillations and this region is called EXAFS (Extended X-ray Absorption Fine Structures) (2). EXAFS arises from the interference of the outgoing photoelectron wave with the backscattering photoelectron wave. Thus, it contains information about the nature of the absorbing and backscattering atoms (usually the nearest neighbouring atoms), the interatomic distances (bond length), and the dynamic behaviour (vibrational motion of the neighbouring atoms relative to the absorbing atom that stretches and compresses the bond). EXAFS is now a reasonably established technique for the determination of local structures (5). It can be used to extract bond lengths, R; coordination numbers, N; and Debye–Waller factors, $\exp(-2\sigma^2k^2)$, where σ^2 is the mean-square relative displacement of the interatomic distance between the absorbing atom and the backscattering atom for a disordered system such as molecules in the gas phase or in solution. In this paper, we report the Si K-edge X-ray absorption measurements of the above-mentioned compounds with emphasis on the analysis of the EXAFS. The results are compared with other structure analysis methods such as electron diffraction and X-ray crystallography. It should be noted that the advantage of EXAFS over standard X-ray crystallography is that it does not require a single crystal. As it turns out, growing good quality single crystals for these high vapour pressure solids is quite challenging. The phase function and amplitude function of the Si–Ge pair obtained from the EXAFS analysis are also reported; they can be used as model functions for the analysis of Si K-edge EXAFS for semiconductor systems containing Si—Ge bonds.

The paper is organized as follows. In Sect. 2, the experimental procedures are briefly described, followed by a more detailed description of the EXAFS analysis procedures in Sect. 3. A discussion on the X-ray Absorption Near Edge Structure (XANES), followed by the EXAFS results and their comparison with literature values, is given in Sect. 4. A summary and conclusion can be found in Sect. 5.

2. Experimental procedures

TMS was obtained commercially (from Petrarch System Inc.). $Si[Si(CH_3)_3]_4$ (6), $Ge[Si(CH_3)_3]_4$ (7), and $Si[Ge(CH_3)_3]_4$ (8) were synthesized according to literature procedures. Except for TMS, all the samples are white solids with vapour pressure sufficient (milliTorr to tens of milliTorr at room temperature) for gas phase measurements at room temperature.

The XAFS (both XANES and EXAFS) experiments were performed using the Ontario Centre for Materials Research–Canadian Synchrotron Radiation Facility (OCMR–CSRF), high-vacuum double-crystal (DCM) beamline at the Aladdin ring (SRC); which is operated by the University of Wisconsin–Madison. The monochromator was equipped with a pair of InSb (111) crystals for these measurements and has a resolution of 0.8 eV at the Si K-edge (9). All the spectra were recorded with a gas ionization chamber (with a cell length of 6.625 in.) in total ion yield mode. The ion yield signal is normalized to the incoming flux, which was at $\sim 10^9$ photons/s as monitored by an in-line ion chamber filled with N_2 gas to ~1.0 Torr (1 Torr = 133.3 Pa) (9). The photon energy was calibrated by setting the K-edge inflection point of the absorption spectrum of a clean Si (100) wafer at 1839.1 eV as determined by the first peak position in the first derivative of the Si K-edge XANES.

All the measurements were carried out at room temperature except for $Si[Ge(CH_3)_3]_4$. The gas pressure was maintained at about 100, 30, and 10 mTorr for TMS, $Si[Si(CH_3)_3]_4$, and $Ge[Si(CH_3)_3]_4$, respectively. The pressure fluctuation, which was quite small, was also simultaneously monitored during the measurement. For $Si[Ge(CH_3)_3]_4$, the temperature of the ionization chamber was maintained at 65°C in order to increase its vapour pressure to about 20 mTorr. Extreme care was taken to eliminate any cross-contamination of the samples: the ion chamber was rinsed with organic solvent and baked before another sample was introduced. A background spectrum was also recorded before the sample was introduced. All spectra reported here are the sum of as many as 10 scans (35 min/scan) to ensure a quality signal-to-noise ratio.

Fig. 1. A raw Si K-edge XAFS data set of TMS, where the XANES and EXAFS regions are noted.

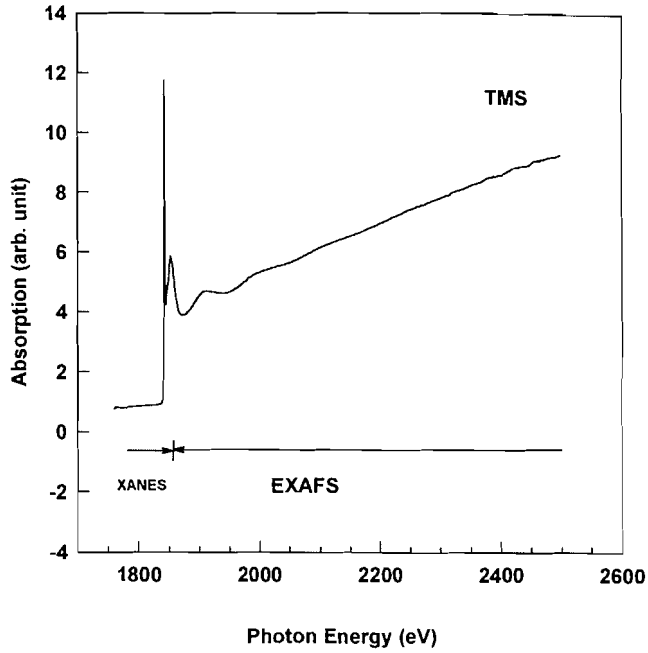

3. EXAFS data analysis

Figure 1 shows a typical set of Si K-edge X-ray absorption data for TMS before data reduction, where the XANES and EXAFS regions are noted. The reproducibility of data from multiple scans for each sample was checked in both E (X-ray photon energy) space and k (photoelectron wave number) space to identify any suspicious features in the spectra due to experimental artifacts.

Fig. 2. $k^3\chi(k)$ of (*a*) $SiMe_4$ (Me = CH_3), (*b*) $Si(SiMe_3)_4$, and (*c*) $Ge(SiMe_3)_4$; $\chi(k)$ of (*d*) $Si(GeMe_3)_4$; and the magnitude of Fourier transform of (*e*) $SiMe_4$, (*f*) $Si(SiMe_3)_4$, (*g*) $Ge(SiMe_3)_4$, and (*h*) $Si(GeMe_3)_4$.

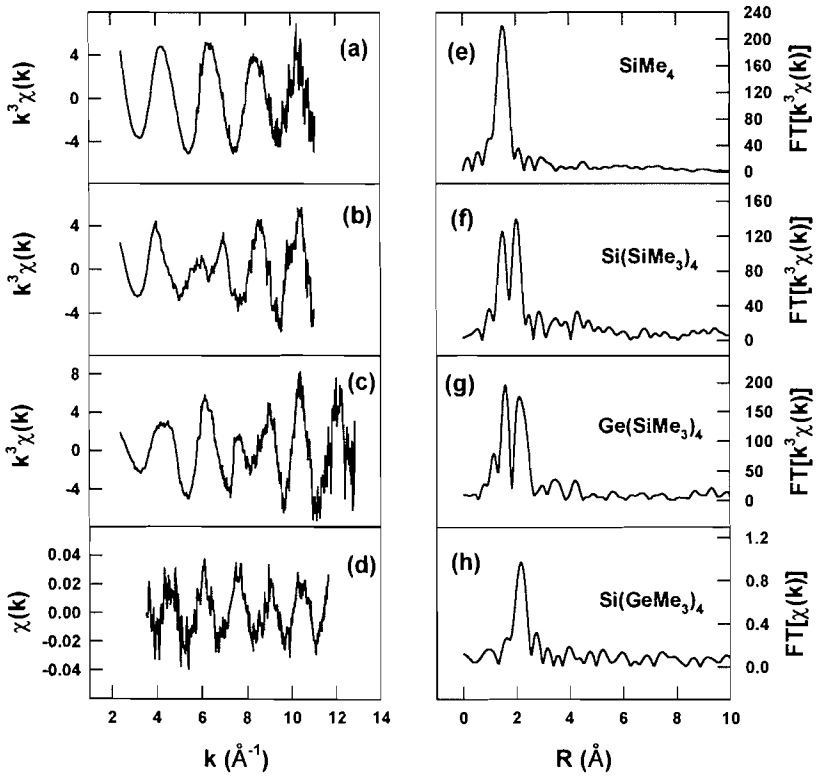

The EXAFS interference function is defined by $\chi(k) = [\mu(E) - \mu_0(E)]/\mu_0(E)$, where $\mu_0(E)$ is the atomic absorption coefficient. The experimental energy origin (E_0) is set at 1843 eV for all the compounds. The difference between the energy origin of the samples and the reference phase functions was used as a floating parameter in the later curve-fitting analysis. Following the usual data reduction procedure (2), in which the post-edge background was removed by a 3-section cubic spline fit and then normalized by the edge jump obtained by extrapolation of a straight line fit above the edge using the software package BAN (10), the k^3-weighted $\chi(k)$ for TMS, $Ge[Si(CH_3)_3]_4$, and $Si[Si(CH_3)_3]_4$ (Figs. 2(*a*)–(*c*)) and $\chi(k)$ for $Si[Ge(CH_3)_3]_4$ (Fig. 2(*d*)) were extracted from the respective raw data. Figures 2(*e*)–(*h*) show the magnitude of the Fourier transforms of the k-weighted $\chi(k)$ data. It can be seen that for a simple molecule such as TMS, there exists a single sinusoidal oscillation in its EXAFS, while in more complicated molecules, such as $Ge[Si(CH_3)_3]_4$ where Si has two different types of neighbouring atoms (Ge and C), the spectrum exhibits a beating of two sinusoidal waves in k space.

The data analysis in this work was conducted using the nonlinear least-squares curve-fitting program EXAFIT of K.R. Bauchspiess (11). The parameterized function used to fit the data is

$$\chi(k) = \sum_{j=1}^{n} \frac{N_j}{k_j R_j^2} S_0^2 S(k_j) f_j(k_j)\, e^{-2k_j^2\sigma_j^2} e^{-2R_j/\lambda} \sin[2k_j R_j + \phi_j(k_j)]$$

where the sum is over all the neighbouring atomic shells. The physical meaning of all the variables in this formula has been discussed extensively in the literature (2, 11, 12); it will not be repeated here. The effective backscattering amplitude

$$S_0^2 S(k_j)\, |f_j(k_j)|\, e^{-2k_j^2\sigma_j^2} e^{-2R_j/\lambda}$$

and the phase $\phi_j(k_j)$ used in the fitting were calculated using ab initio XAFS theory (FEFF, version 5.03) (13). The curve-fitting was performed in both R-space and k-space. In a typical curve-fitting for a single shell, four parameters, namely, ΔE_0, R, σ^2, and N, were varied simultaneously, where ΔE_0 is the difference between the energy origin calculated from FEFF and 1843 eV, σ^2 is the mean-square relative displacement of the interatomic distance R between the absorbing atom and the backscattering atom, and N is the coordination number.

The residual sum of squares used in this work is defined as (12)

$$\chi^2 = \frac{N_{pts}}{N_{pts} - n} \frac{1}{N} \sum_{j=1}^{N} (\text{Data}_j - \text{Model}_j)^2$$

where $N_{pts} = 2 + 2\Delta k \Delta R/\pi$ is the number of relevant independent points (14), n is the number of fitting parameters used, and N is the number of total data points. This is the quantity minimized in the nonlinear least-squares curve-fitting. The uncertainties of the results were estimated by finding the deviation of a parameter from its best-fit value (by fixing this parameter while leaving all others floating), which doubles the residual sum of squares between the fit and data. These uncer-

Fig. 3. Normalized Si K-edge XANES of TMS, $Ge(SiMe_3)_4$, $Si(SiMe_3)_4$, $Si(GeMe_3)_4$, and crystalline Si (100).

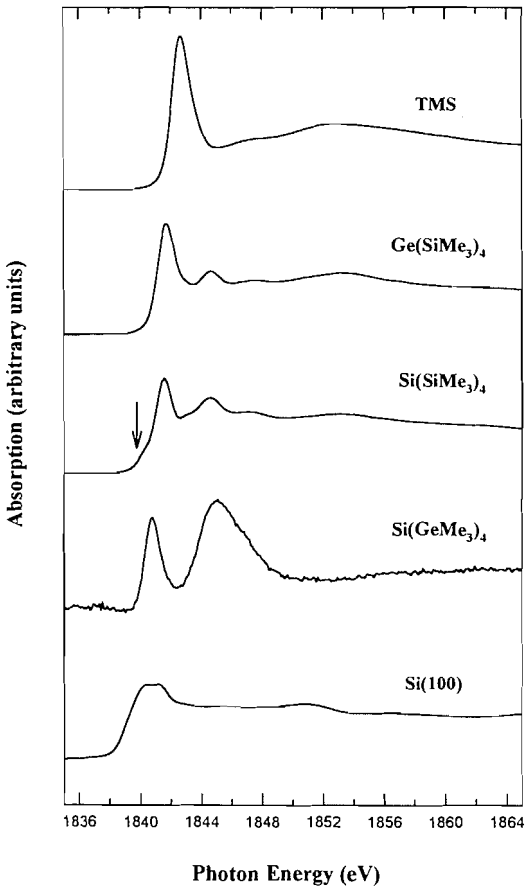

Fig. 4. Comparison of (*a*) experimental $Si(SiMe_3)_4$ XANES with (*b*) simulated $Si(SiMe_3)_4$ XANES (see text).

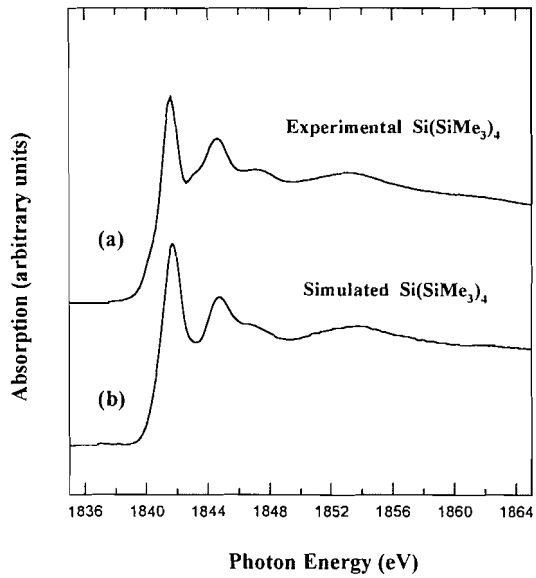

tainties include all the effects of correlations between all the parameters, and the error bars estimated in this way are found to be too conservative (15).

In the nonlinear least-squares minimization analysis, a major source of uncertainties on the EXAFS structural parameters is the parameter correlation (e.g., between R and ΔE_0 and between N and σ^2). It is then sometimes desirable to use the structural parameters obtained from model compounds that are structurally similar to the sample to limit the number and the physically meaningful range of the fitting parameters in the nonlinear least-squares fitting process. The structural results obtained for the well-defined molecules in this study could, to a certain extent, serve the purpose of providing EXAFS empirical references to disentangle more complicated structural problems, e.g., in a Si—Ge atomic layer superlattice.

4. Results and discussion

Figure 3 shows the Si K-edge absorption of TMS, $Si[Si(CH_3)_3]_4$, $Si[Ge(CH_3)_3]_4$, and $Ge[Si(CH_3)_3]_4$ as well as crystalline Si(100). In this section, the XANES features are first discussed briefly, followed by a detailed analysis of the EXAFS and their implications.

4.1. Si K-edge XANES: general observations

Figure 3 shows the Si K-edge XANES of all the four compounds together with that of a single crystal Si(100). Although the spectra for some of these compounds have been published before (16), the spectra in Fig. 3 are of higher quality in the signal-to-noise ratio and are free of contamination. These data agree generally with the previously published results (16) (except that the energy position for TMS is now recalibrated to 2 eV higher binding energy than in the previous report and the low-energy shoulder for $Si[Ge(CH_3)_3]_4$ reported earlier is no longer seen as the result of the precaution described in Sect. 2 to eliminate contamination[3]). In this paper, we will only summarize the qualitative observation of the XANES features and point out some important observations that have not been reported previously.

Several interesting features from Fig. 3 are noted. First, TMS exhibits a single intense resonance at the threshold followed by some weak ones, while the other molecules exhibit more intense multiple resonances. Second, the spectra of $Si[Si(CH_3)_3]_4$ and $Ge[Si(CH_3)_3]_4$ appear to be quite similar with the exception of the small low-energy shoulder in the former. Third, the first peak of the $Si[Ge(CH_3)_3]_4$ spectrum is located at about the same energy as the low-energy shoulder of the $Si[Si(CH_3)_3]_4$ spectrum. Based on comparison of the experimental spectra of $Si[Si(CH_3)_3]_4$, $Ge[Si(CH_3)_3]_4$, and $Si[Ge(CH_3)_3]_4$, the low-energy shoulder in $Si[Si(CH_3)_3]_4$ (see Fig. 3, noted by an arrow) is assigned to transitions from Si 1*s*, originating from the central Si (Si^a), to molecular orbitals of essentially Si–Si character. The remaining features are dominated by transitions originating from the surrounding

[3] $Si[Ge(CH_3)_3]_4$ is a very difficult sample to run in the gas phase because it has very low vapour pressure and low mass percentage of Si. Therefore, it is easily contaminated by $Si[Si(CH_3)_3]_4$ or $Ge[Si(CH_3)_3]_4$, which have higher vapour pressures and a higher edge jump. It is believed that the previously reported spectrum (16) was contaminated with $Si[Si(CH_3)_3]_4$. The spectrum reported in Fig. 3 was taken with extreme care. It was reproducible with heating and even after being sealed in the ion chamber for hours during the long EXAFS scans.

four silicon atoms (Si^b). The above assignment is derived from the following procedure: the spectra of $Si[Si(CH_3)_3]_4$, $Ge[Si(CH_3)_3]_4$, and $Si[Ge(CH_3)_3]_4$ were normalized to an edge jump of unity, and then the $Si[Ge(CH_3)_3]_4$ spectrum, which represents the contribution from the central atom Si^a, was added to the scaled spectrum of $Ge[Si(CH_3)_3]_4$ (by a factor of 4 in the vertical), which represents the contribution from the four surrounding atoms Si^b. The resultant spectrum was normalized to an edge jump of unity. The simulated $Si[Si(CH_3)_3]_4$ spectrum, shown in Fig. 4, is very similar to that of $Si[Si(CH_3)_3]_4$. This procedure assumes that the chemical and structural (symmetry) environment at the Si in $Si[Ge(CH_3)_3]_4$ is the same as that of Si^a in $Si[Si(CH_3)_3]_4$, that the environment of the surrounding silicon atoms in $Ge[Si(CH_3)_3]_4$ is similar to that in $Si[Si(CH_3)_3]_4$, and that the Si K-edge spectrum is the sum of contributions from all the Si atoms. In other words, the Si—Si and Si—Ge bonds are assumed to be chemically very similar (in valence electron distribution) and the nearest neighbouring atoms are primarily responsible for the general shape of the XANES. These assumptions are valid, as supported by Fig. 4, which shows nearly identical features implying that Si—Si and Si—Ge bonds are quite similar chemically. Since the absorption feature in the near edge region is sensitive to multiple scattering processes that involve primarily valence electrons, the absorbing atoms with similar electron distribution and local symmetry would yield similar XANES, as shown in Fig. 4. This point was not adequately addressed previously (16). The same cannot be said for the EXAFS (vide infra) because in the EXAFS region, the kinetic energy of the photoelectron increases considerably and the core electrons become more important in the single scattering process that is the dominant contribution to the EXAFS. This is why the Si K-edge EXAFS between the Si–Si and Si–Ge pairs look very different, although the nature of these two chemical bonds is generally considered similar (in valence electron distribution) in main group chemistry. It should also be noted that the more intense second resonance (1844.6 eV) in $Si[Ge(CH_3)_3]_4$ relative to the progressively weaker second resonance in the Si–Si and Si–C systems may indicate a more effective caging effect (potential barrier) in the $Si[Ge(CH_3)_3]_4$ system. More detailed MS-Xα analysis of these features will be presented elsewhere (17).

Another interesting point is that the first resonance in crystalline Si is split despite the fact that its local structure is identical to the central atom in $Si[Si(CH_3)_3]_4$ and $Si[Ge(CH_3)_3]_4$, which exhibit a single resonance peak in this region (Fig. 3). The splitting of the intense Si K-edge absorption peak in crystalline Si is the result of long-range order effects (band structure). It is interesting to note that this splitting is rounded off even in nano-structure Si such as porous silicon, which contains networks of crystalline Si of nm dimension (18), indicating that the long-range order has to go beyond nanometers to produce this effect.

4.2. EXAFS analysis

Figure 2 shows the k^n-weighted EXAFS data ($n = 0$ or 3) $\chi(k)$ for all the compounds and their corresponding Fourier Transform (FT) of ($k^n \chi(k)$). The FT technique is an established procedure that separates the phase and the amplitude of the EXAFS (2, 19). As expected, only one noticeable shell is observed for TMS (the Si–C shell) and $Si[Ge(CH_3)_3]_4$ (the Si–

Fig. 5. (*a*) Magnitude of the Fourier transform (solid line) and the fit (broken line) in *R*-space (transform range is 2.6–10.9 $Å^{-1}$); (*b*) $k^{2.5}$-weighted data (solid line) and the fit (broken line) in *k*-space; (*c*) Fourier filtered data (solid line) and the fit (broken line) (filtering window range is 0.6–2.4 C) for TMS. The vertical lines define the fitting range. The insertion in (*a*) shows the schematic structure of the molecule (hydrogen atoms were neglected).

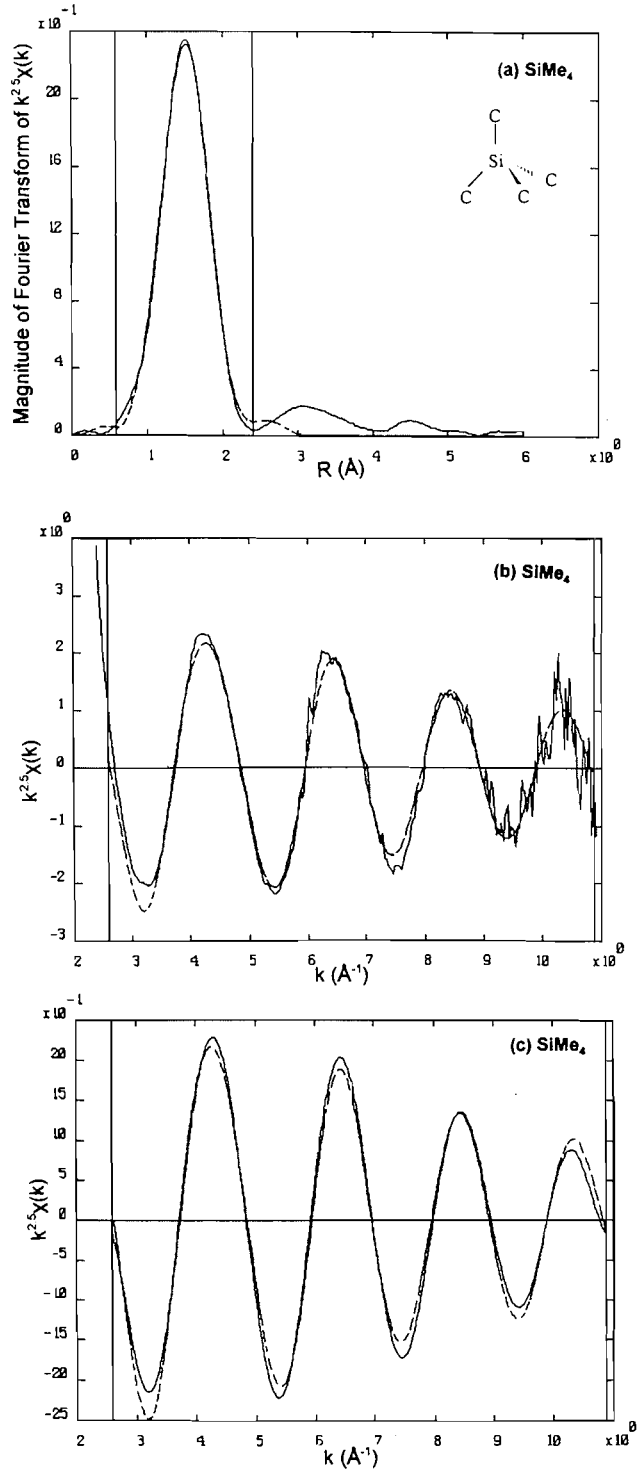

Table 1. EXAFS fitting range and results for $Si(CH_3)_4$ and $Ge(Si(CH_3)_3)_4$ in k-space (with Fourier filtering) and R-space.

Molecule		Parameter	k-space	R-space
$Si(CH_3)_4$	N_{pts} = 11	Data range	2.6–10.9 Å^{-1}	0.6–2.4 Å
	Si–C shell	ΔE_0 (eV)	8.5 ± 2	7 ± 3
		R (Å)	1.887 ± 0.015	1.879 ± 0.015
		σ^2 (Å^2)	0.003 ± 0.002	0.003 ± 0.002
		N	4.2 ± 0.8	4.5 ± 0.6
$Ge(Si(CH_3)_3)_4$	N_{pts} = 12	Data range	2.4–12.4 Å^{-1}	1.2–2.8 Å
	Si–C shell	ΔE_0 (eV)	6.2 ± 3	5.9 ± 3
		R (Å)	1.889 ± 0.020	1.888 ± 0.015
		σ^2 (Å^2)	0.003 (fixed)	0.003 (fixed)
		N	3.9 ± 1	3.9 ± 0.5
	Si–Ge shell	ΔE_0 (eV)	6.2[a]	5.9[a]
		R (Å)	2.394 ± 0.015	2.397 ± 0.015
		σ^2 (Å^2)	0.004 ± 0.003	0.004 ± 0.002
		N	1.2 ± 0.5	1.2 ± 0.4

[a]The difference between this value and that of the Si–C shell was fixed at zero in fitting.

Ge shell),[4] while two shells are seen for $Si[Si(CH_3)_3]_4$ (Si–C and Si–Si shells) and $Ge[Si(CH_3)_3]_4$ (Si–C and Si–Ge shells), in both k- and R-space. The detailed analyses for each of the four compounds are discussed below.

4.2.1. $Si(CH_3)_4$ (TMS)

TMS is a stable compound with a very high vapour pressure (boiling point of 26.5°C). Its structure is well known: T_d symmetry with a Si—C bond length of 1.875(2) Å as determined from electron diffraction analysis (20). TMS was used as a test case for our experimental and data analysis procedures.

As described in Sect. 3, the EXAFS data ($k^{2.5}$ weighted) have been fitted in both R-space and k-space (Fig. 5) using a single Si–C shell model. Figure 5(*a*) shows the R-space data and fit. Figure 5(*b*) shows the k-space normalized data and the fit. Figure 5(*c*) shows the Fourier filtered data and the k-space fit. A Hamming window has been applied as a filter in the analysis. Some of the side lobes of the main peak in Fig. 2(*e*) have disappeared in Fig. 5(*a*) due to the application of the filter window, but the bump at around 3 Å is present in both figures, indicating that it is a true peak. This peak is most probably due to the (Si-C-C-Si) triangle scattering path. No fitting attempt was made for it is too weak to obtain quantitative results.

The k-space (with Fourier filtering) and R-space fitting results, which are given in Table 1 together with those for $Ge[Si(CH_3)_3]_4$, are practically the same. The number of relevant independent points N_{pts}, calculated based on the data range ($2 + 2\Delta k\Delta R/\pi$) (14), is also listed in Table 1. The bond length, 1.883(15) Å (average of k- and R-space results), is in good agreement with the electron diffraction (ED) data 1.875(2) Å (20). The coordination number is slightly higher than 4, but it is within a reasonable range (20% uncertainty) for N in EXAFS analysis. This is because coordination number N, the atomic backscattering amplitude f_j (k_j,π) and the Debye–Waller factor are highly correlated and it is often difficult to separate them unequivocally.

It should be noted that the σ^2 in the Debye–Waller factor, which is approximated as a Gaussian, represents the mean-square relative displacement of the interatomic distance (21). Although it should contain all vibrational mode contributions as well as static disorder in principle, the dominant one in TMS and tetrahedral molecules is the mean-square relative displacement resulting from the totally symmetric vibration mode of the Si—C bonds. The theoretical mean square relative displacement resulting from the totally symmetric vibration at a given temperature can be calculated from its vibrational frequency (1250 cm^{-1} for Si–CH_3) and the result thus obtained is σ^2_{vib} = 0.0009 Å^2 for TMS according to the theory (22). This result sets the lower bound for this value. The fact that it is smaller than the value obtained from the EXAFS analysis indicates that we have not underestimated the σ^2 in the analysis.

The error bars for all the parameters listed in Table 1 were determined using the method described in Sect. 3. They are probably too conservative. For each of the parameters, a well-defined minimum was found, so we conclude that we have found a very good fit for TMS. With the result of the TMS analysis, which is very satisfactory, we are confident that our experimental and data analysis procedures will work for other compounds. A similar procedure has been used for $Ge[Si(CH_3)_3]_4$, $Si[Si(CH_3)_3]_4$, and $Si[Ge(CH_3)_3]_4$. These results are presented below.

4.2.2. $Ge[Si(CH_3)_3]_4$

From the molecular structure of $Ge[Si(CH_3)_3]_4$, it is expected that there should be two major single backscattering shells for each of the four chemically equivalent Si atoms in the molecule, the Si–C and the Si–Ge shell. From Figs. 2(*c*) and (*g*), which show a simple beating of two sinusoidal waves and two

[4] The methyl hydrogen, due to its lack of core electrons, has little scattering power to high-energy electrons, therefore contributes little to the EXAFS. The Si–C single scattering pathway in $Si[Ge(CH_3)_3]_4$ is too long to make a significant contribution to the overall amplitude because of the $1/R_j^2$ dependence and short attenuation length of the electrons.

Fig. 6. (*a*) Magnitude of the Fourier transform (solid line) and the fit (broken line) in *R*-space (transform range is 2.4–12.4 Å^{-1}); (*b*) k^3-weighted data (solid line, the sharp feature at $k = 7.3$ is due to a glitch of the monochromator) and the fit (broken line) in *k*-space; (*c*) Fourier filtered data (solid line) and the fit (broken line) (filtering window range is 1.2–2.8 Å) for $Ge(SiMe_3)_4$. The vertical lines define the fitting range. The insertion in (*a*) shows the schematic structure of the molecule (hydrogen atoms were neglected).

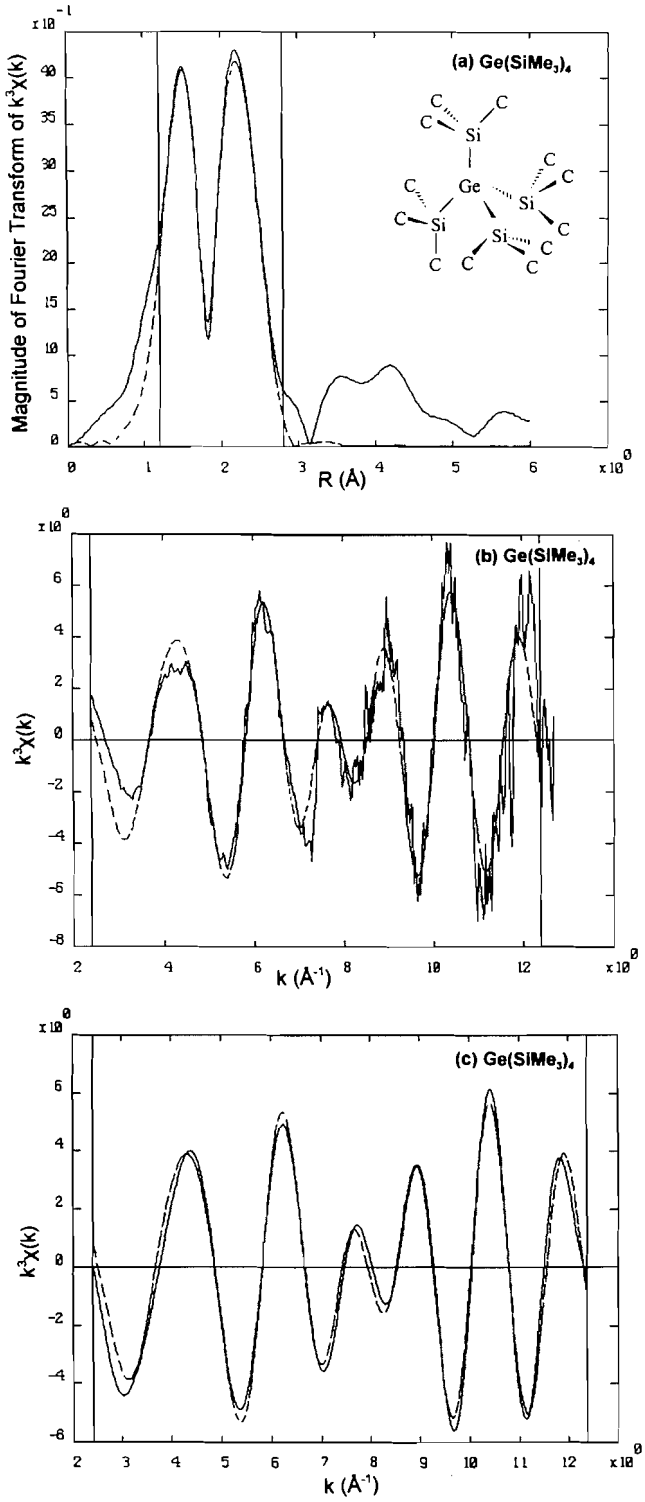

maxima in the Fourier transform (FT), respectively, it is apparent that a two-shell model should be adequate to account for most of the spectral features. The contribution of the Si–C-C-Si triangle path is ignored by properly limiting the *R*-space fitting range and the filtering range for *k*-space fitting. A two-shell fit was carried out for $Ge[Si(CH_3)_3]_4$. Due to the strong correlation of the parameters, only six parameters were allowed to vary independently in the fitting. The σ^2 for the Si–C shell was fixed at 0.003, the same as TMS. This is not an unreasonable assumption, since the Si–C bond in these two compounds should be very similar. We also allowed ΔE_0 of the Si–Ge shell to be the same as that of the Si–C shell; since they have the same central Si atom, ΔE_0 should not vary significantly. Figure 6(*a*) shows the *R*-space data and fit. Figure 6(*b*) shows the *k*-space normalized data (k^3 weighted) and the fit. Figure 6(*c*) shows the Fourier filtered data and the *k*-space fit.

It can be seen from Table 1 that both *k*-space (with Fourier filtering) and *R*-space fits gave similar results. The Si—Ge bond length is determined to be 2.396(15) Å (average of *R*- and *k*-space results), which is comparable to the reported 2.370(1) Å in $Ge(SiH_3)_4$ as determined by electron diffraction (ED) analysis (23), and close to the reported average bond length of 2.405 Å in a series of strained-layer $(Si_m/Ge_n)_p$ superlattices (1). The Si—C bond length for $Ge[Si(CH_3)_3]_4$ is the same as that of TMS within experimental uncertainty. The σ^2 for the Si—Ge bond is larger than for the Si—C bond. Using the same method as that for TMS (22), the calculated F^2_{vib} for $Ge[Si(CH_3)_3]_4$ is about 0.0011 Å^2 based on the stretching frequency of 312 cm^{-1} (24) for the Si–Ge pair. The number of nearest neighbours is larger than theory. It should be noted, however, that both the Debye–Waller factor and the coordination number are within the range of acceptable uncertainty (2). As for TMS, a well-defined minimum was found for each of the parameters. It is reassuring to find that the magnitude of the error bar for $Ge[Si(CH_3)_3]_4$ is comparable to that of TMS, although the former has more fitting variables.

4.2.3. $Si[Si(CH_3)_3]_4$

From Figs. 2(*b*) and (*f*), we observe a similar EXAFS pattern for $Si[Si(CH_3)_3]_4$ as for $Ge[Si(CH_3)_3]_4$, with the beating occurring at different *k* values. In $Si[Si(CH_3)_3]_4$, there are two different kinds of Si atoms: Si^a (bonded to four Si) and Si^b (bonded to one Si and three CH_3 groups). The observed $\chi(k)$ of $Si[Si(CH_3)_3]_4$ is the sum of $\chi(k)$ of Si^a and $\chi'(k)$ of Si^b. The χ' for Si^b should be slightly different from the χ for Si^a despite the fact that the bond length and the mean-square relative displacement along the bond are the same in both cases, this is because they have different threshold energies E_0, and they are chemically different locally. The central atom Si^a exhibits a 1 eV shift to lower binding energy relative to the surrounding four Si^b atoms as deduced from both XANES (this work) and photoelectron measurements (25).

A multi-shell fit (one shell for Si^a and two shells for Si^b) was carried out for $Si[Si(CH_3)_3]_4$: Si^a–Si^b (core hole on Si^a), Si^b–C (core hole on Si^b), and Si^b–Si^a (core hole on Si^b). The calculated backscattering amplitude for these three shells (Si^a–Si^b, Si^b–C, and Si^b–Si^a) using the FEFF scheme has been weighted by 0.2, 0.8, and 0.8, respectively, so that the coordination number, N_j, given in the fitting should be 4 for the Si^a–Si^b shell, 3 and 1 for the Si^b–C shell and the Si^b–Si^a shell,

Table 2. EXAFS fitting range and results for $Si^a(Si^b(CH_3)_3)_4$[a] and $Si(Ge(CH_3)_3)_4$ in *k*-space (with Fourier filtering) and *R*-space.

Molecule		Parameter	*k*–space	*R*–space
$Si^a(Si^b(CH_3)_3)_4$	N_{pts} = 11	Data range	2.4–10.8 $Å^{-1}$	0.9–2.7 Å
	Si^a–Si^b shell	ΔE_0 (eV)	6.4 ± 5	6.8 ± 1.5
		R (Å)	2.364 ± 0.015	2.364 ± 0.005
		σ^2 ($Å^2$)	0.004 ± 0.003	0.004 ± 0.001
		N	4 (fixed)	4 (fixed)
	Si^b–C shell	ΔE_0 (eV)	5.7 ± 2	6.5 ± 0.8
		R (Å)	1.875 ± 0.012	1.875 (fixed)
		σ^2 ($Å^2$)	0.0015 ± 0.002	0.0016 ± 0.0015
		N	3 (fixed)	3 (fixed)
	Si^b–Si^a shell	ΔE_0 (eV)	5.7[b]	6.5[b]
		R (Å)	2.364[c]	2.364[c]
		σ^2 ($Å^2$)	0.004[c]	0.004[c]
		N	0.8 ± 0.6	0.8 ± 0.2
$Si(Ge(CH_3)_3)_4$	N_{pts} = 8	Data range	4.1–10.1 $Å^{-1}$	1.2–3.0 Å
	Si–Ge shell	ΔE_0 (eV)	4.4 ± 6	2.6 ± 5
		R (Å)	2.38 ± 0.03	2.37 ± 0.03
		σ^2 ($Å^2$)	0.004 ± 0.004	0.004 ± 0.003
		N	2.9 ± 1	2.8 ± 0.6

[a]The uncertainties of the parameters for this compound are decided differently (see text).
[b]The difference between this value and that of the Si^b–C shell was fixed at zero in fitting.
[c]The difference between this value and that of the Si^a–Si^b shell was fixed at zero in fitting.

respectively. By fixing and linearly constraining some of the parameters, the number of independent variables in the fitting was reduced from 12 to 7 and 6 in *k*-space and *R*-space, respectively (see Table 2), to obtain a fit (Fig. 7). The results are tabulated in Table 2. The uncertainty estimation scheme described in Sect. 3 broke down for ΔE_0 and *R*, probably because there are too many shells and the correlations between the parameters are too strong. The uncertainties listed in Table 2 for the ΔE_0's for both shells were obtained when the *R*'s were fixed at 2.364 and 1.875 Å for Si—Si and Si—C bonds, while those for the *R*'s were obtained by fixing the ΔE_0's at 6.4 eV (*k*-space) and 6.8 eV (*R*-space) for the Si^a–Si^b shell and 5.7 eV (*k*-space) for the Si^b–C shell.

The Si—Si and Si—C bond lengths of 2.364(10) and 1.875(12) Å (average of *k*- and *R*-space results) agree very well with the ED results (26) of 2.361(3) and 1.889(3) Å and X-ray crystallography results (27) of 2.346(1) and 1.879(4) Å. It should be noted that this particular compound is a very interesting case for testing the additive model of EXAFS in that altogether there are 8 Si—Si single scattering paths with identical interatomic distances and mean-square relative displacement, yet there is a small difference in the E_0 between the two absorbing Si atoms. The result of the analysis indicates that the small difference is clearly noticeable in the near-edge region but does not have a noticeable effect in *k*-space EXAFS, particularly in the high-*k* region where a 1 eV difference in $(E - E_0)^{1/2}$ has little effect on its corresponding *k* value.

4.2.4. $Si[Ge(CH_3)_3]_4$

This compound has a very low vapour pressure and a relative low mass percentage of Si, which makes it difficult to obtain very high-quality data under our experimental conditions. The ionization chamber was maintained at about 65°C to get a reasonable signal-to-noise ratio in the EXAFS region with multiple scans. The fluctuation of temperature (±1°C) may contribute slightly to the noisier data compared to those of the other compounds. Fortunately the data set is dominated by a single sinusoidal wave arising from the Si–Ge pair as expected. The $k^{0.5}$-weighted data were fitted with a single Si–Ge shell. Figure 8 and Table 2 show the fit and the parameters. As expected, the error bar for the parameters is a little larger than that of TMS and $Ge[Si(CH_3)_3]_4$ because of the data quality. Noticeably, the coordination numbers obtained from both *k*- and *R*-space fits are lower than the theoretical value, in contrast to the trend found in TMS and $Ge[Si(CH_3)_3]_4$. This is probably due to the large uncertainty in normalizing the edge jump because, for $Si[Ge(CH_3)_3]_4$, the signal-to-background ratio is considerably smaller than those for the other compounds reported here.

Figure 9 shows the phase shift and amplitude functions of the Si–Ge pair derived experimentally using the BAN program (10), where

$$\text{Amplitude} = \frac{N}{kR^2} S_0^2 S(k) f(k)\, e^{-2k^2\sigma^2} e^{-2R/\Lambda}$$

with $N = 4$ and $R = 2.38$ Å for the Si–Ge pair and phase shift is $\phi(k)$ ($2kR$ term was subtracted).

Since the EXAFS function of $Si[Ge(CH_3)_3]_4$ results from a dominant single Si–Ge shell backscattering, the phase shift

Fig. 7. (*a*) Magnitude of the Fourier transform (solid line) and the fit (broken line) in *R*-space (transform range is 2.4–10.8 Å^{-1}); (*b*) k^3-weighted data (solid line) and the fit (broken line) in *K*-space; (*c*) Fourier filtered data (solid line) and the fit (broken line) (filtering window range is 0.9–2.7 Å) for $Si(SiMe_3)_4$. The vertical lines define the fitting range. The insertion in (*a*) shows the schematic structure of the molecule (hydrogen atoms were neglected).

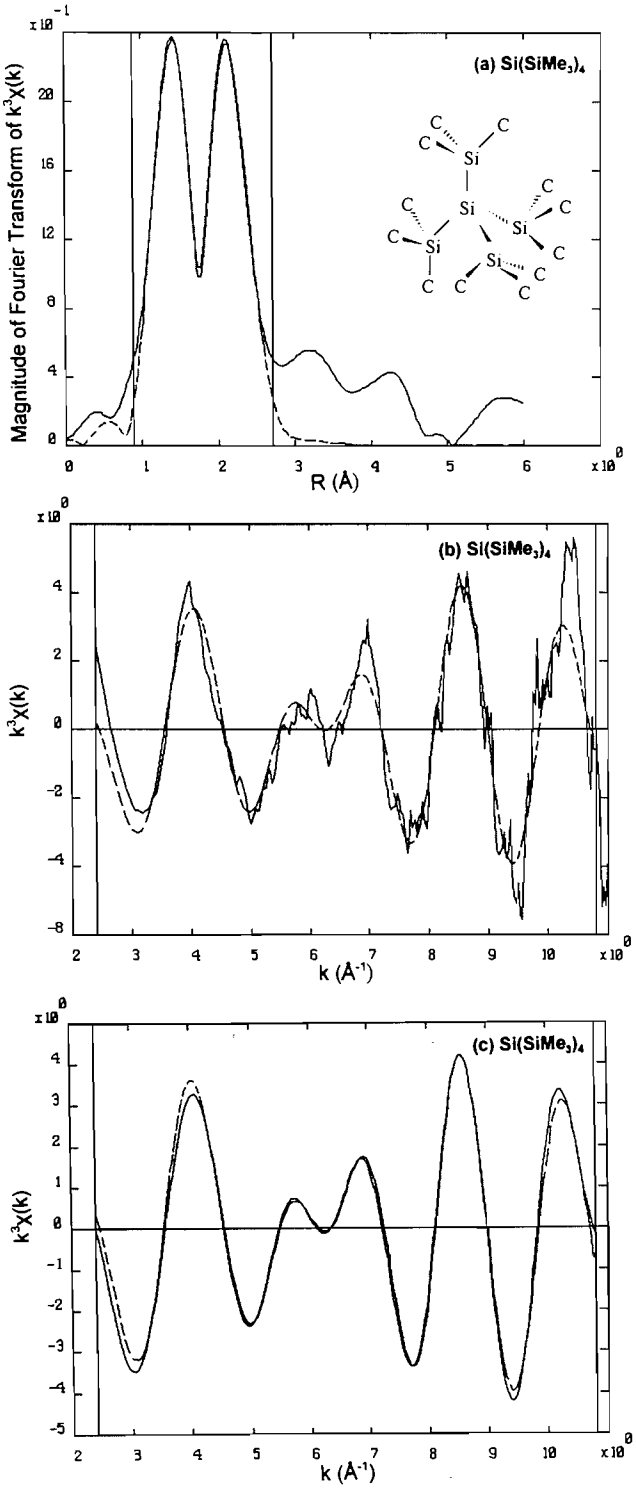

Fig. 8. (*a*) Magnitude of the Fourier transform (solid line) and the fit (broken line) in *R*-space (transform range is 4.1–10.1 Å^{-1}); (*b*) $k^{0.5}$-weighted data (solid line) and the fit (broken line) in *K*-space; (*c*) Fourier filtered data (solid line) and the fit (broken line) (filtering window range is 1.2–3.0 Å) for $Si(GeMe_3)_4$. The vertical lines define the fitting range. The insertion in (*a*) shows the schematic structure of the molecule (hydrogen atoms were neglected).

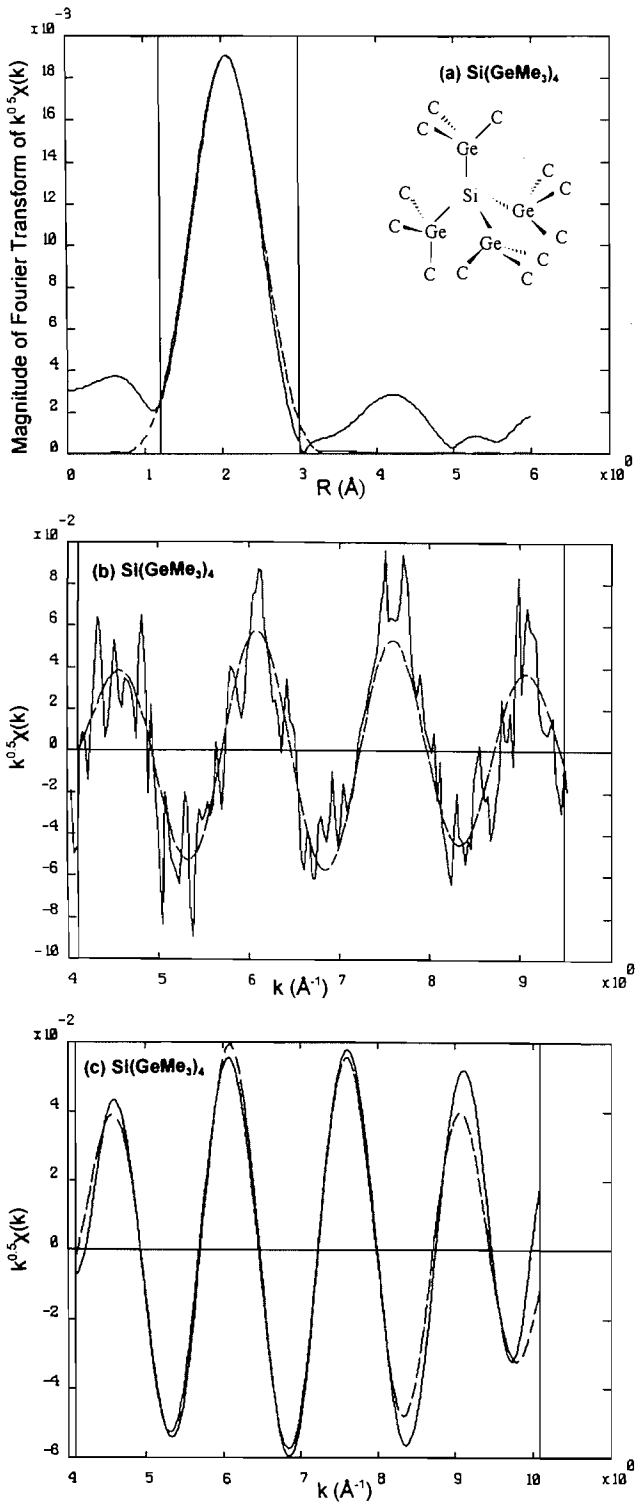

Fig. 9. Experimental (*a*) amplitude and (*b*) phase shift functions (see text for definitions) for the Si–Ge pair extracted from the EXAFS of $Si(GeMe_3)_4$.

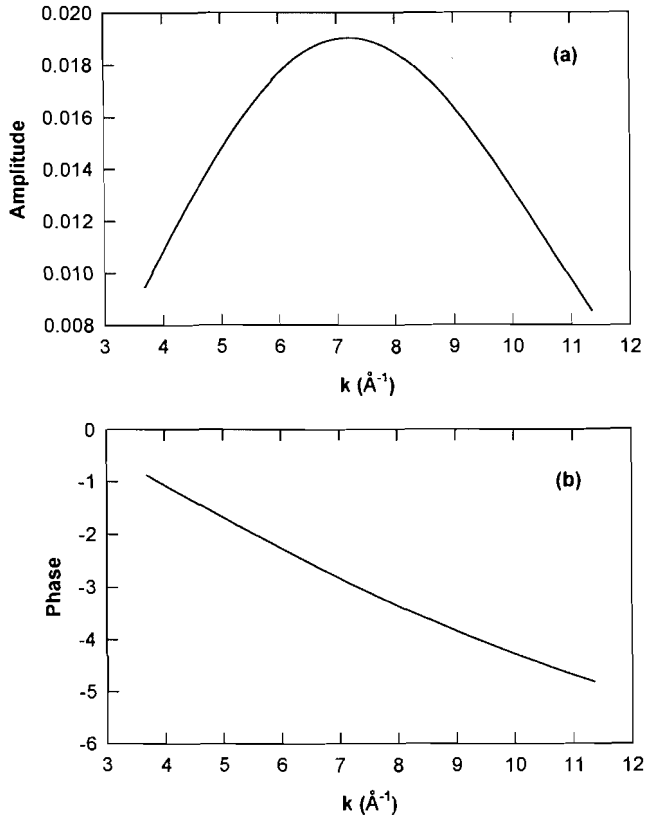

and amplitude functions can be obtained with fewer artifacts relative to $Ge[Si(CH_3)_3]_4$, where the Si–C shell and the Si–Ge shell are difficult to separate. As discussed in Sect. 3, these functions may be a very helpful reference in analyzing the structure of more complicated Si–Ge systems.

4.3. Comparison of Si—Si and Si—Ge bond lengths in molecules and in solid state semiconductors

From the above analysis it is clear that Si K-edge EXAFS indeed provides accurate local structural information about bond length and related parameters for these molecules. The $Si[Si(CH_3)_3]_4$ results (Si—Si bond length = 2.364(10)Å) are in good agreement with the electron diffraction result of 2.361(3) Å (26) and the X-ray crystallography result of 2.346(1) Å (27). The Si—Ge bond lengths are reported for these compounds for the first time.

The Si—Si bond length values reported here are in fact comparable within experimental uncertainty with the Si—Si bond length found in related organosilicon compounds: 2.373(2) and 2.390(2) Å for the peripheral and central Si—Si bonds in $[(CH_3)_3Si]_3Si—Si[Si(CH_3)_3]_3$ (27) and 2.340(9) Å in $(CH_3)_3Si—Si(CH_3)_3$ (28).

Let us compare the Si—Si bond length of Si—Si in $Si[Si(CH_3)_3]_4$ (of which the central Si has the same local structure as that of Si in crystalline Si) with that of crystalline Si (2.350Å) (29). It is immediately apparent that the crystalline value falls within the range of values exhibited by organosilicon compounds. Thus it is quite reasonable to state that in the absence of significant steric effects, the Si—Si bond in an organosilicon compound is comparable to that of crystalline silicon. Returning to Fig. 3, it is interesting to see how dramatic an effect the long-range Si–Si interaction in the semiconductor has on the XANES (the splitting of the threshold resonance that was absent in the organometallic compounds). It is quite clear that the interatomic distance observed in these systems is not very sensitive to long-range electronic interactions.

A similar comparison can be made between the Si—Ge bond lengths reported here, 2.396(15) Å for $Ge[Si(CH_3)_3]_4$ and 2.38(3) Å for $Si[Ge(CH_3)_3]_4$, and the average nearest neighbour distance in the relaxed Si–Ge alloys with the same Si—Ge stoichiometry grown on Si (2.372 Å for 20% Ge and 2.430 Å for 20% Si in $Si_{1-x}Ge_x$) (1). Taking into account the fact that the solid state value includes some relatively short Si—Si and long Ge-Ge bonds, and the experimental uncertainty, the molecular results are comparable to the solid state results. Since the observed Si—Ge bond length for these molecular systems is typical of bond lengths found in organosilicon compounds containing Si—Ge bonds, 2.384(1), 2.394(1), and 2.416(1) Å for $(C_6H_5)_3Ge—Si(CH_3)_3$, $(C_6H_5)_3Si—Ge(CH_3)_3$, and $(C_6H_5)_3Ge—Si[Si(CH_3)_3]_3$, respectively (30), this observation again suggests that the Si—Ge bond length in organometallic compounds is comparable to the Si—Ge interatomic distance in solid state Si–Ge semiconductors. The Si XANES in the solid state compounds (16), however, exhibits the threshold splitting characteristic of long-range electronic interaction as was the case in crystalline silicon. Thus, the bond length (derivable from EXAFS) is not very sensitive to the long-range electronic interaction but the Si K-edge XANES is.

5. Summary and conclusions

We have reported Si K-edge XAFS spectra for a series of organosilicon compounds containing Si—Si and Si—Ge bonds and have shown that reliable structural and bonding properties can be extracted from the EXAFS and the XANES of these compounds, respectively, without the use of high-quality single crystals. Comparison of the gas phase results with solid state results reveals that the Si—Si and Si—Ge interatomic distances in the latter fall within the range of corresponding bond lengths found in the molecular system. Thus the bond length is not very sensitive to the extended electronic interaction in the solid state. The Si K-edge XANES, however, clearly reveals the difference between the more localized electronic structure (molecular orbitals) in the molecular system and the delocalized electronic structure (densities of states) in the solid state semiconductors. The EXAFS amplitude and phase for the Si–Ge absorber–backscatterer pair has been extracted from the experimental data. These functions may be of some use for the extraction of EXAFS parameters in systems containing the Si—Ge bond.

Acknowledgements

Financial support for this work was provided by the Ontario Centre for Materials Research and the Natural Sciences and Engineering Research Council of Canada. We are grateful to Drs. K.H. Tan, X.H. Feng, and B.W. Yates for their technical support. Thanks are also due to the staff of SRC for their

expert operation of Aladdin, which is supported by the National Science Foundation under award DMR-9212658.

References

1. P. Aebi, T. Tyliszczak, A.P. Hitchcock, K.M. Baines, T.K. Sham, T.E. Jackman, J.-M. Baribeau, and D.J. Lockwood. Phys. Rev. B: Condens. Matter, **45**, 13579 (1992).
2. D.C. Koningsberger and R. Prins. (*Editors*). X-ray absorption: principles, applications, techniques of EXAFS, SEXAFS and XANES. J. Wiley, New York. 1988.
3. T.K. Sham, B.X. Yang, J. Kirz, and J.S. Tse. Phys Rev. A: Gen. Phys. **40**, 652 (1989).
4. J. Stöhr. *In* NEXAFS spectroscopy. Springer-Verlag, Berlin. 1992.
5. XAFS VIII, Proc. Int. Conf. X-ray Absorpt. Fine Struct. 8th, Berlin, 1994. Physica, B: **208 & 209**, (1995).
6. H. Gilman and C.L. Smith. J. Organomet. Chem. **8**, 245 (1967).
7. A.G. Brook, F. Abdesaken, and H. Soellradl. J. Organomet. Chem. **299**, 95 (1986).
8. K.M. Baines, K.A. Mueller, and T.K. Sham. Can J. Chem. **70**, 2884 (1992).
9. B.X. Yang, F. Middleton, B. Olssen, G.M. Bancroft, J.M. Chen, T.K. Sham, K.H. Tan, and D. Wallace. Rev. Sci Instrum. **63**, 1355 (1992).
10. T. Tyliszczak. Version 4.54, Tolmar Instruments, Hamilton, ON, Canada. 1993.
11. K.R. Bauchspiess. Jpn. J. Appl. Phys. **32**, 131 (1993), Suppl. 32-2.
12. D.T. Jiang, S.M. Heald, T.K.Sham, and M.J. Stillman. J. Am. Chem. Soc. **116**, 11004 (1994).
13. (*a*) J.J. Rehr, J. Mustre de Leon, S.I. Zabinsky, and R.C. Albers. J. Am. Chem. Soc. **113**, 5135 (1991); (*b*) J. Mustre de Leon, J.J. Rehr, S.I. Zabinsky, and R.C. Albers. Phys. Rev. B: Condens. Matter, **44**, 4146 (1991).
14. E.A. Stern. Phys. Rev. B: Condens. Matter, **48**, 9825 (1993).
15. F.W. Lytle, D.E. Sayer, and E.A. Stern. Physica, B: **158**, 701 (1988).
16. A.P. Hitchcock, T. Tyliszczak, P. Aebi, J.Z. Xiong, T.K. Sham, K.M. Baines, K.A. Mueller, X.H. Feng, J.M. Chen, B.X. Yang, Z.H. Lu, J.M. Baribeau, and T.E. Jackman. Surf. Sci. **291**, 349 (1993).
17. J.Z. Xiong and T.K. Sham. XAFS IX, Proc. Int. Conf. X-ray Absorpt. Fine Struct. 9th, Grenoble, 1996. J. Phys. Colloq. In press.
18. T.K. Sham, X.H. Feng, D.T. Jiang, B.X. Yang, J.Z. Xiong, A. Bzowski, D.C. Houghton, B. Bryskiewicz, and E. Wang. Can. J. Phys. **70**, 813 (1992).
19. B.K. Teo. *In* EXAFS: basic principles and data analysis. Springer-Verlag, Berlin. 1985.
20. K.H. Hellwege and A.M. Hellwege. (*Editors*). Landolt–Börnstein New Series Group II, Vol. 7. Structure data of free polyatomic molecules. Springer-Verlag, Berlin. 1987.
21. T.K. Sham. Acc. Chem. Res. **19**, 99 (1986).
22. S.J. Cyvin. *In* Molecular vibrations and mean square amplitudes. Elsevier, Amsterdam. 1968.
23. T. Lobreyer, H. Oberhammer, and W. Sundermeyer. Angew. Chem. Int. Ed. Engl. **32**, 586 (1993).
24. S. Mohan and M. Baskaran. Spectrochim. Acta, Part A: **46A**, 757 (1990).
25. D.G.J. Sutherland, G.M. Bancroft, and K.H. Tan. J. Chem. Phys. **97**, 7918 (1992).
26. L.S. Bartell, F.B. Clippard, Jr., and T.L. Boates. Inorg. Chem. **9**, 2436 (1970).
27. A. Heine, R. Herbst-Irmer, G.M. Sheldrick, and D. Stalke. Inorg. Chem. **32**, 2694 (1993).
28. B. Beagley, J.J. Monaghan, and T.G. Hewitt. J. Mol. Struct. **8**, 401 (1971).
29. C. Kittel. *In* Introduction to solid state physics. John Wiley & Sons, Inc., New York. 1986.
30. K.M. Baines and W.G. Stibbs. Coord. Chem. Rev. **145**, 157 (1995).

Variable-energy photoelectron spectroscopy of $CpM(CO)_3$ (M = Mn, Re) and $CpFe(CO)_2I$

Yong-Feng Hu, G. Michael Bancroft, Kim H. Tan, John S. Tse, and Dong-Sheng Yang

Abstract: Photoelectron spectra of the valence, inner-valence, and core levels of $CpM(CO)_3$ (M = Mn, Re) and $CpFe(CO)_2I$ were obtained using He I radiation and synchrotron radiation between 21 eV and 150 eV photon energies. The high-resolution Mn 3*p*, Fe 3*p*, and I 4*d* core level spectra are reported. Broadening of the I 4*d* spectrum is due to vibrational and ligand field splittings. Observation of the 3*p* spectra is critical to fully interpreting the *np*→*nd* resonance effect in the valence band spectra. This resonance effect is very useful for assigning the metal *d* orbital bands in the valence spectra. A Xα-SW calculation of $CpMn(CO)_3$ was used to confirm the assignment of the valence and inner-valence orbitals. The experimental and theoretical branching ratios are in good agreement. The general trend of the metal *d* orbital ionization potentials for $CpML_3$ (M = transition metal) complexes is also discussed.

Key words: photoelectron, synchrotron radiation, $CpMn(CO)_3$, $CpRe(CO)_3$, $CpFe(CO)_2I$, *np*→*nd* resonance, Xα-SW calculation.

Résumé : On a obtenu les spectres photoélectoniques de valence, de valence interne et des niveaux d'énergie de l'atome central des complexes $CpM(CO)_3$ (M = Mn, Re) et $CpFe(CO)_2I$ en utilisant une radiation He I et une radiation du synchrotron avec des énergies de photon se situant entre 21 eV et 150 eV. On rapporte les spectres à haute résolution des niveaux d'énergie Mn 3*p*, Fe 3*p* et I 4*d*. L'élargissement du spectre du niveau I 4*d* est dû au dédoublement du champ vibrationnel et du champ du ligand. L'observation des spectres 3*p* est critique pour interpréter entièrement l'effet de résonnance *np*→*nd* dans le spectre de la bande de valence. Cet effet de résonnance est très utile pour l'attribution des bandes de l'orbitale *d* du métal dans les spectres de valence. On a utilisé un calcul Xα-SW du composé $CpM(CO)_3$ pour confirmer l'attribution des orbitales de valence et de valence interne. Les rapports expérimentaux et théoriques de ramification sont en parfait accord. On discute également de la tendance générale des potentiels d'ionisation de l'orbitale *d* du métal dans le complexes $CpML_3$ (M = métal de transition).

Mots clés : photoélectron, radiation du synchrotron, $CpM(CO)_3$, $CpRe(CO)_3$, $CpFe(CO)_3I$, résonnance *np*→*nd*, calcul Xα-SW.

[Traduit par la rédaction]

Introduction

The electronic structures of transition metal cyclopentadienyl carbonyl complexes have been the subject of a wealth of photoelectron spectroscopic (1) and theoretical studies (2). $CpMn(CO)_3$ and $CpFe(CO)_2L$ are central complexes not only for the understanding of the electronic structure of these complexes, but also because they are widely used in transition-metal-aided organic synthesis. Conventional He I/He II photon energies have been used exclusively to obtain the photoelectron spectra of these complexes, and the assignments of the spectra have been aided by comparing the relative He I/He II band intensities. However, the He I/He II spectra, even combined with various theoretical calculations, have failed to yield firm assignments of the valence spectra of some relatively simple molecules, such as $CpPtMe_3$ (3) and $Ni(C_3H_5)_2$ (4). The definitive assignment can only be obtained by combining the variable-energy synchrotron radiation spectra and Xα-SW intensity calculations (3*b*, 4*c*).

The variable-energy synchrotron photoelectron spectra of $CpPtMe_3$ (3*b*) showed that the lowest binding energy peak arises from an MO of largely ligand character, in contrast to the previous experimental and theoretical study that assigned this peak to Pt 5*d* orbitals (3*a*). This result is not consistent with the well-established, qualitative MO descriptions for molecules with general formula $CpML_3$ (M is a transition metal and L is an arbitrary ligand with only σ-donor capability (2*e*)), which shows that the HOMO is a metal orbital. To examine the periodic trend in metal *d* binding energies, we have undertaken detailed variable-energy photoelectron studies of organometallic molecules across and down the transition metal series. We recently published the $M(\eta^3\text{-}C_3H_5)_2$ (M = Ni, Pd, Pt) (4*c*) and $CpM(CO)_2$ (M = Co, Rh, Ir) (5) spectra. In the present study, we investigate the electronic structures of earlier transition metal complexes $CpM(CO)_3$ (M = Mn, Re) and $CpFe(CO)_2I$, using variable-energy photoelectron spectroscopy and Xα-SW calculations. In addition, we wanted to demonstrate the use of synchrotron radiation to study the

Received February 22, 1996.

This paper is dedicated to Professor Howard C. Clark in recognition of his contributions to Canadian chemistry.

Y.-F. Hu, G.M. Bancroft,[1] K.H. Tan, J.S. Tse, and D.S. Yang. Department of Chemistry, University of Western Ontario, London, ON N6A 5B7, Canada.

[1] Author to whom correspondence may be addressed. Telephone: (519) 661-3122. Fax: (519) 661-3022. E-mail: scigmb@uwoadmin.uwo.ca.

inner-valence and core level spectra of organometallic complexes. For example, the high intensity of synchrotron radiation is critical to observing the broad, weak, inner-valence spectra. The high intensity is also essential in observing the Mn 3*p* and Fe 3*p* peaks, which are important in studying the effects of the *np*→*nd* resonance in the valence band spectra (6). The high resolution of synchrotron radiation is also essential in discussing the causes of the broadening in the I 4*d* spectra.

Experimental section

High-purity samples are purchased from Aldrich Chemicals Co., and used directly without further purification.

The photoelectron spectra were measured using two different photoelectron spectrometers. He I spectra were obtained using our McPherson ESCA-36 photoelectron spectrometer. The Ar $2p_{3/2}$ at a binding energy (BE) of 15.759 eV is used for internal calibration with a resolution of ~23 meV. The spectra at higher photon energies (22–150 eV) were obtained with our modified ESCA-36 spectrometer (7) at the Canadian Synchrotron Radiation Facility (CSRF) at the Aladdin storage ring, University of Wisconsin – Madison (8). A 600 g/mm grating gave photon energies between 22 and 72 eV, and a 1800 g/mm grating gave photon energies between 70 and 150 eV. The Xe 5*s* line at a BE of 23.397 eV was used as the calibrant when the 600 g/mm grating was employed, giving a total line width of ~70 meV at 45 eV photon energy. The Kr $3d_{5/2}$ line at a BE of 97.795 eV was used as the calibrant when the 1800 g/mm grating was employed, giving a resolution of ~230 meV at 128 eV photon energy. A Quantar no. 36 position sensitive detector (9) was used to enhance greatly the intensity of the signal, which allowed us to record a broad-scan spectrum spanning 40–50 eV in about 10 min.

All the samples were introduced through the heatable probe into the gas cell of the spectrometer. $CpMn(CO)_3$ was volatile enough to obtain spectra at room temperature. $CpRe(CO)_3$ and $CpFe(CO)_2I$ were less volatile and required heating at temperatures of 50 and 85°C, respectively. The pressure in the sample chamber was controlled at around 3×10^{-5} Torr, while the pressure in the gas cell was around 5×10^{-3} Torr (1 Torr = 133.3 Pa).

Spectra were deconvoluted with a Gaussian–Lorentzian lineshape using a nonlinear least-squares procedure described previously (10). Band areas were taken from the above fitting results and the experimental branching ratios were calculated based on the branching ratio definition ($BR_i = A_i/\Sigma A_i$).

Computational details

A transition state Xα-SW calculation (11) for $CpMn(CO)_3$ was performed to calculate the valence orbital energies, compositions, and theoretical cross sections. The bond distances and bond angles were taken from the crystal structure of $CpMn(CO)_3$ reported by Berndt and Marsh (12). The molecule was idealized to have C_s symmetry. The exchange α parameters were chosen from the literature (13). An l_{max} of 3 was used for outer sphere, and l_{max} values of 2, 1, 1, and 0 were used for Mn, C, O, and H atoms, respectively. The Xα-SW cross sections were calculated using Davenport's program (14) with a Latter tail added to correct the asymptotic behaviour. The resulting partial ionization cross sections (σ_i) were then used to calculate the theoretical branching ratios ($BR_i = \sigma_i/\Sigma\sigma_i$) for each orbital.

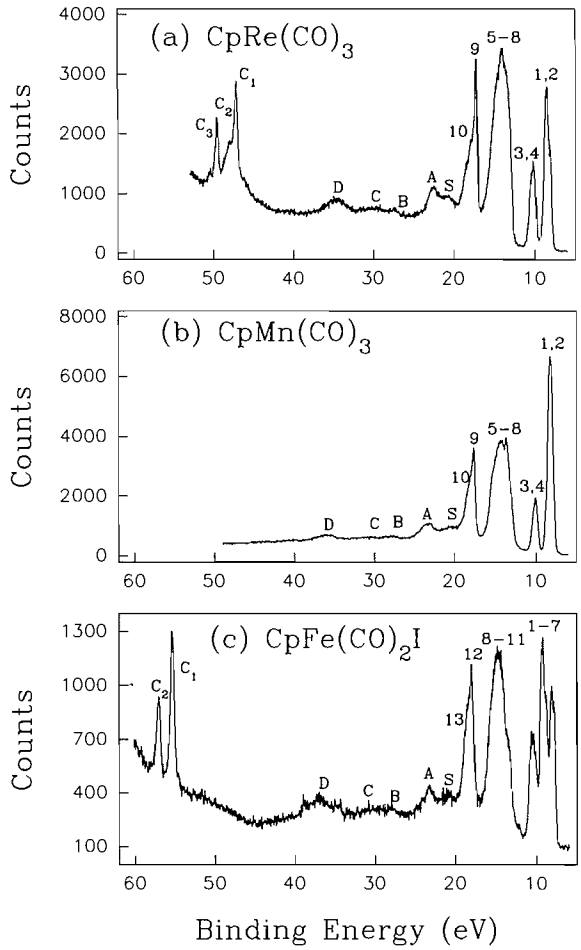

Fig. 1. The high-resolution broad-scan photoelectron spectra of (*a*) $CpRe(CO)_3$ at 72 eV photon energy, (*b*) $CpMn(CO)_3$ at 72 eV photon energy, and (*c*) $CpFe(CO)_2I$ at 70 eV photon energy. See text for explanation of the labelling.

Results and discussion

A. General features of the spectra

Photoelectron spectra of (*a*) $CpRe(CO)_3$, (*b*) $CpMn(CO)_3$, and (*c*) $CpFe(CO)_2I$ spanning 7 eV to 50–60 eV binding energies (BE) are presented in Fig. 1. These spectra were taken at a total resolution of ≤0.2 eV. It is evident that our spectra clearly show three distinctive regions: the intense, relatively narrow valence levels with BE less than 20 eV (labelled 1–13 and S), the weak, broad inner-valence levels with BE between 20 and 40 eV (labelled A–D), and the core levels with BE greater than 40 eV in Figs. 1(*a*) and (*c*) (labelled C_1, C_2, C_3).

The general features of the valence levels in Fig. 1 are in very good agreement with the previous He I/He II studies of these molecules (2*a*, 15). The bands between 7 and 12 eV BE show very different peak shapes and intensities and they are sensitive to metal and ligand substitution. In contrast, the bands from 13 to 20 eV are very similar and therefore insensitive to metal and ligand substitution. Lichtenberger et al.

assigned the valence levels up to 17 eV BE of these molecules based on the He I/He II techniques and a Fenske–Hall calculation (2*a*). The results in the following sections will generally confirm Lichtenberger's previous assignments, but also clarify the assignments of two peaks in the $CpFe(CO)_2I$ spectrum.

The inner-valence spectra of these d^6 cyclopentadienyl metal carbonyl complexes are very similar in peak shapes and positions, like the high-BE valence region. We have shown that the inner-valence spectra of $Re(CO)_5X$ (X = Cl, Br) complexes (16) are dominated by the contribution of carbonyl satellites and CO 3σ orbitals, but not the halogen *s* orbitals. Similarly, a contribution from the I 5*s* orbital around 20 eV BE cannot be seen in the inner-valence region of $CpFe(CO)_2I$. Therefore, the inner-valence spectrum of $CpFe(CO)_2I$ can be assigned in the same way as the spectra of $CpM(CO)_3$ (M = Mn, Re) and $CpM(CO)_2$ (M = Co, Rh and Ir) (5) complexes. That is, the peak (peak S) around 20 eV BE is the shakeup peak from CO 1π and 5σ orbitals; the next peak A around 23 eV is a CO satellite peak but has a higher percentage of Cp ring character; the next two peaks between 24 and 31 eV are the satellite peaks due to CO 4σ orbitals; and the broad and relatively intense peak around 35 eV is due to the CO 3σ orbital (also see Sec. C).

The remaining ionization bands of $CpRe(CO)_3$ and $CpFe(CO)_2I$ in Figs. 1(*a*) and 1(*c*) belong to the core levels, and they can be assigned easily. Two sharp peaks at 47.21 and 49.63 eV BE in Fig. 1(*a*) are the two Re 4*f* spin-orbit components. The shoulder on the higher BE side of $4f_{7/2}$ at 47.5 eV is due to the Re $5p_{3/2}$ ionization. These results are in very good agreement with our high-resolution Re 4*f* results for $Re(CO)_5X$ (X = $(CO)_5$, Cl and Br) complexes (16). The I 4*d* spin-orbit components of $CpFe(CO)_2I$ can be found at 55.20 and 56.92 eV BE in Fig. 1(*c*). The broadening effect of the I 4*d* peaks will be discussed in the next section.

B. Core level study

Recently we demonstrated the importance of high resolution and high intensity in the study of core level photoelectron spectra of organometallic complexes. Vibrational fine structure was resolved on the metal 4*f* core level of heavy metal carbonyl compounds (17). Ligand field broadening was also shown to be present in the Os 4*f* core level of $Os(CO)_5$ (16). In the present paper, we wanted to show: first, the importance of high intensity of synchrotron radiation in the observation of the Mn 3*p* and Fe 3*p* core levels, which are important to the valence level $3p \rightarrow 3d$ resonance studies (6, 16) (see next section); second, the importance of the high resolution of synchrotron radiation in the study of the broadening of the I 4*d* spectrum; and third, the importance of the tunability of synchrotron radiation in a core level cross-section study of the Fe 3*p* and I 4*d* levels in $CpFe(CO)_2I$.

Observation of metal core *p* levels has been shown to be important in the study of $np \rightarrow nd$ resonances (6, 16). However, due to the extremely low cross section of these 3*p* levels at Al Kα energies (~0.02 Mb (18)), these spectra have not been observed in the gas phase. With synchrotron radiation, we can tune the photon energy to the maximum of the 3*p* cross section (~1 Mb at 120–150 eV (18)), and obtain these weak spectra for the first time. Figure 2 presents the high-resolution (total instrumental resolution <0.3 eV) Mn 3*p* spectrum of $CpMn(CO)_3$ at 130 eV photon energy. Our Mn 3*p* BE of 56.3 eV is much larger than the Mn 3*p* BE for Mn metal of 47.2 eV referenced to the vacuum level (19). The broad line width of 2.32 eV is due to the very short lifetime of the 3*p* hole state.

Fig. 2. Photoelectron spectrum of the Mn 3*p* level of $CpMn(CO)_3$, taken at 130 eV photon energy.

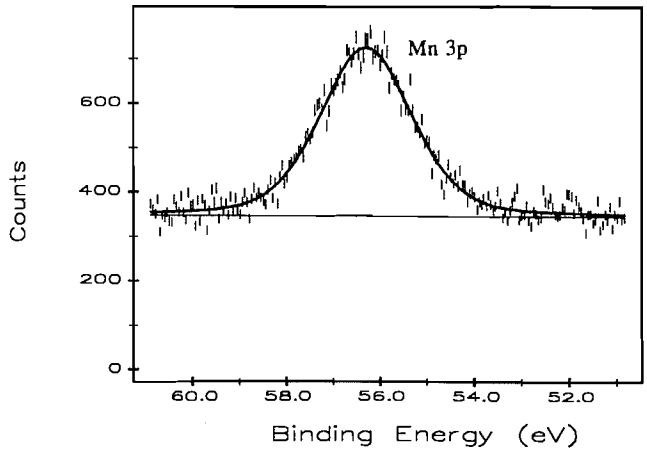

Fig. 3. Core level photoelectron spectra of $CpFe(CO)_2I$ at (*a*) 130, and (*b*) 150 eV photon energies, showing the increase of the relative intensity of Fe 3*p* orbital relative to those of I 4*d* orbitals.

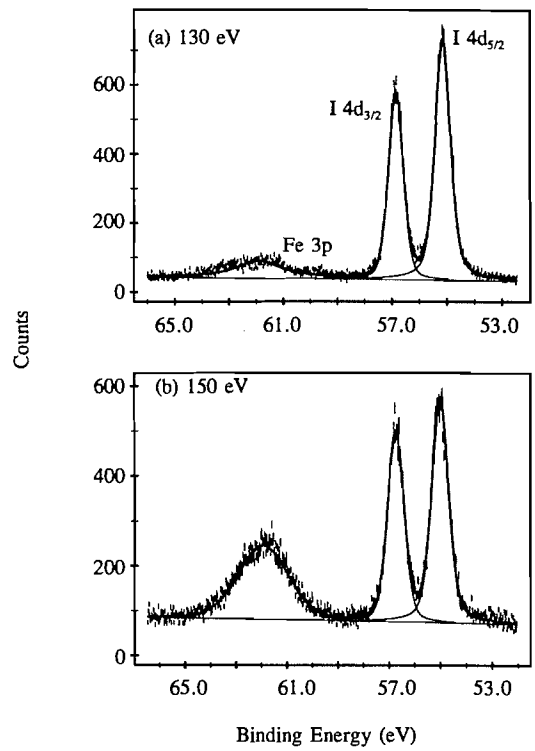

Figure 3 illustrates the Fe 3*p* and I 4*d* core level spectra of $CpFe(CO)_2I$: the broad Fe 3*p* level at 62.0 eV, and the I $4d_{5/2}$ and $4d_{3/2}$ levels at 55.20 and 56.92 eV, respectively. The Fe 3*p* BE will again be useful for studying the $np \rightarrow nd$ resonance effects on the valence band (see next section). These spectra were taken at medium resolution, and gave I 4*d* line widths of 0.75 eV in Fig. 3(*b*). I 4*d* spectra taken at 106 eV photon energy and ≤0.15 eV resolution gave I $4d_{5/2}$ and $4d_{3/2}$ line-

Table 1. Binding energies, C_2^0 values, and nuclear quadrupole splittings for I molecules.

Compounds	Binding energies (eV) I $4d_{5/2}$[a]	I $3d_{5/2}$[b]	C_2^0 (meV) I 4d[a]	e^2qQ (MHz) ^{129}I[c]
HI	57.50	627.6	+31.7	
I_2	57.20	627.3	+27.8	−2238
$CpFe(CO)_2I$	55.20	(625.3)[d]	(+17.5)	(−1400)
$Mn(CO)_5I$		625.2		
CsI		623.6		
$Fe(CO)_4I_2$				−1397

[a]Reference 23.
[b]Reference 20.
[c]Reference 22.
[d]Values in parentheses for $CpFe(CO)_2I$ are calculated using eq. [1].

widths of 0.52 and 0.54 eV, respectively. The I $4d_{5/2}$ binding energy of 55.20 eV is much smaller than that of other small covalent molecules such as HI and I_2 (Table 1). However, assuming that the differences in I $4d_{5/2}$ and $3d_{5/2}$ binding energies are the same, the calculated I $3d_{5/2}$ BE for $CpFe(CO)_2I$ is 625.3 eV, in good agreement with that previously observed for $Mn(CO)_5I$ (20), and midway between the I $3d_{5/2}$ BE for I_2 and CsI (Table 1). The $CpFe(CO)_2I$ BE shows that the I atom is really rather negative for a covalent molecule, in agreement with conclusions from ^{129}I and ^{127}I Mossbauer spectroscopy on transition metal iodine compounds (21, 22).

The I $4d_{5/2}$ and $4d_{3/2}$ total line widths (0.54 and 0.52 eV) are very broad compared to the I 4*d* inherent line widths of <0.2 eV, or the total line widths of ~0.2 eV previously observed at similar resolution for I_2 and ICl (23). As for CF_3I, the large line widths are due to a combination of vibrational broadening and ligand field splitting (23), with the major part of this broadening due to unresolved vibrational broadening (23, 24). Using the core equivalent approximation (24), the core equivalent of I 4*d* core-ionized $CpFe(CO)_2I$ is $CpFe(CO)_2Xe^+$. The Fe—Xe^+ bond length is likely to be much longer than the Fe—I bond length of 2.66 Å (2*a*). This would yield a long Fe–Xe^+ vibrational progression (the Fe–I symmetric stretching frequency is only 202 cm^{-1}) (25). It is also possible that CO vibrational splitting could broaden the I 4*d* line, as was seen in the W 4*f* spectrum in $W(CO)_6$ (17).

Ligand field splitting will also contribute to the broadening of these lines. The larger line width of the I $4d_{5/2}$ line is an indication of the importance of this effect. A semiquantitative estimate of the ligand field splitting (as expressed by C_2^0) (23) can be made because C_2^0 is proportional to the nuclear quadrupole coupling constant, e^2qQ at the I nucleus (23). Thus, we can write

$$[1]\quad \frac{C_2^0[CpFE(CO)_2I]}{C_2^0[I_2]} = \frac{e^2qQ[CpFe(C)^2I]}{e^2qQ[I_2]}$$

C_2^0 and e^2qQ are well known (Table 1), and we assume that e^2qQ for $CpFe(CO)_2I$ is close to that for cis-$Fe(CO)_4I_2$ (Table 1). Substituting into eq. [1], C_2^0 for $CpFe(CO)_2I$ is 17.5 meV. This value gives a $4d_{3/2}$ splitting of only 0.14 eV, and $4d_{5/2}$ splittings of less than this. Fitting five peaks to the doublet with these splittings gives an individual line width of 0.45 eV, showing that vibrational broadening is still the dominant broadening mechanism.

Fig. 4. Comparison of the theoretical and experimental branching ratios of Fe 3*p* and I 4*d* orbitals of $CpFe(CO)_2I$. Errors are ±2%.

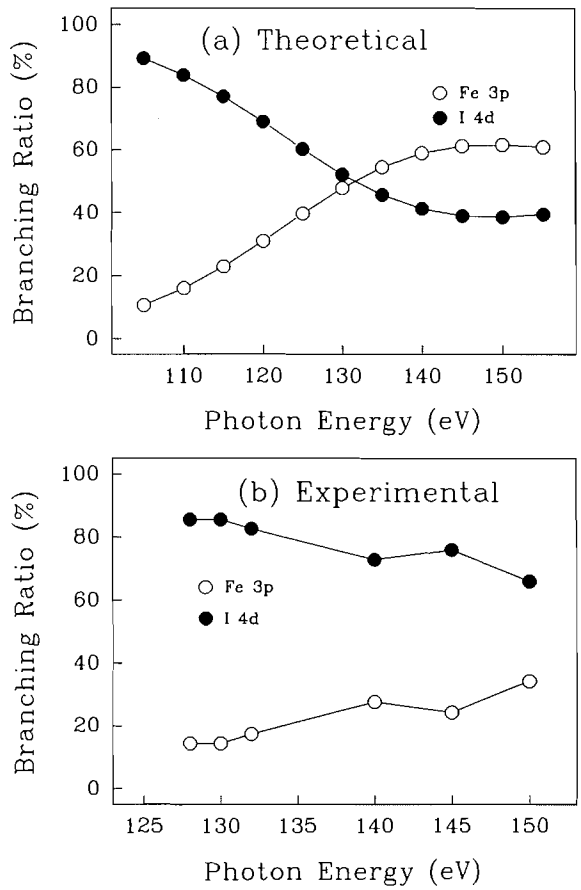

Figure 3 shows the increase in the relative intensity of Fe 3*p* compared with those of I 4*d* from 130 to 150 eV photon energy. This phenomenon is expected when compared with the atomic cross sections of these orbitals. Figure 4 plots the experimental and theoretical (18) branching ratios of Fe 3*p*

Fig. 5. Representative valence-level photoelectron spectra of $CpMn(CO)_3$ at (*a*) 21.22, (*b*) 40, (*c*) 60, and (*d*) 80 eV photon energies.

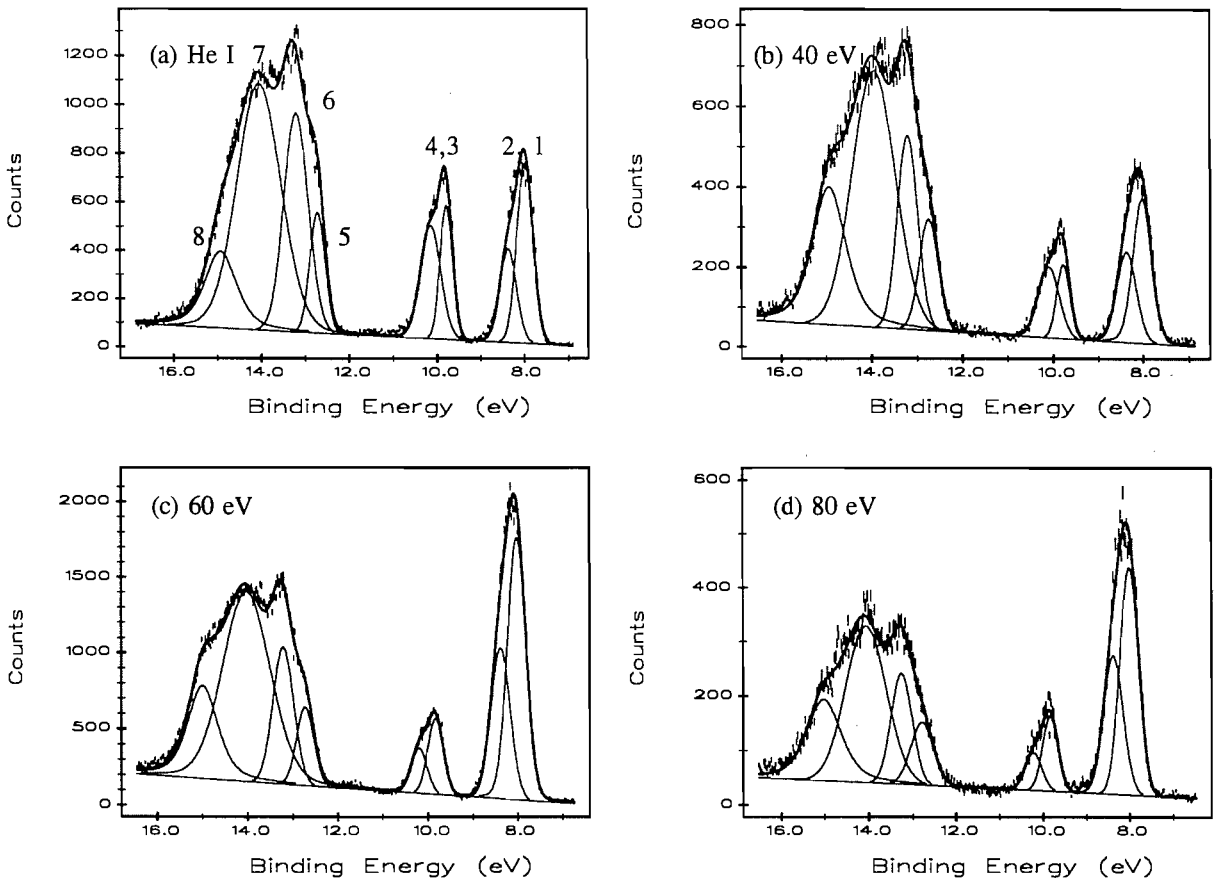

and I 4*d* orbitals. It is obvious that the intensity of the Fe 3*p* orbital peak increases between photon energies of 100 and 145 eV, while the intensity of I 4*d* decreases continuously in the same region. Branching ratios of these orbitals cross each other at about 130 eV photon energy theoretically, but well above 150 eV from our experimental results. Clearly, the position of the I 4*d* Cooper minimum is at higher energy than predicted from the atomic calculation. Shifts in the Cooper minimum from atomic values have recently been seen on the Pd 4*d* orbitals in $Pd(\eta^3\text{-}C_3H_5)_2$ (4*c*, 26).

C. Variable photon energy results

(a) $CpM(CO)_3$ (M = Mn, Re) complexes

Representative variable-energy photoelectron spectra at 21.22, 40, 60, and 80 eV photon energies of $CpMn(CO)_3$ and $CpRe(CO)_3$ are presented in Figs. 5 and 6. These four photon energies were typically chosen to represent the spectra taken (*a*) by He I radiation with the best resolution, (*b*) by He II radiation, (*c*) at a photon energy higher than the threshold of the *np*→*nd* resonance, and (*d*) at a photon energy well above the *np*→*nd* resonance. It is immediately obvious that the relative intensities of the bands vary dramatically with the photon energy. Especially noticeable is that the relative intensities of the first band in Fig. 5 and 6 increase continually with the increase of the photon energy between 21.22 and 60 eV photon energy, and then show a decrease in the relative intensity from 60 to 80 eV photon energy. This provides us with direct experimental evidence for the assignment of the metal *d* orbitals to peaks 1 and 2.

Using synchrotron radiation, we observed the metal *np*→*nd* resonance on the first band (peaks 1 and 2) to be around 58 eV photon energy for $CpMn(CO)_3$ and around 50 eV for $CpRe(CO)_3$, respectively, also indicating that peaks 1 and 2 arise from orbitals of very high *d* character compared with the other peaks (16). This assignment is in agreement with Lichtenberger's previous He I/He II studies combined with a Fenske–Hall calculation (15).

Xα-SW calculations have proven to be a useful tool for assignment of the valence-level photoelectron spectra of organometallic molecules (27), and we have successfully utilized this technique in the calculation of photoionization cross sections in the study of variable-energy synchrotron radiation photoelectron spectra of some organometallics (3*b*, 4*c*, 5, 28). We performed an Xα-SW calculation on $CpMn(CO)_3$ to further confirm the valence band assignment, to assign the inner valence peaks, and to explain the experimental branching ratio results.

In Table 2, we list the Xα-SW orbital energies and the composition of the resulting wave functions for the upper valence orbitals of $CpMn(CO)_3$. The experimental ionization potentials and the assignments of valence-level bands are also pre-

Fig. 6. Representative valence-level photoelectron spectra of $CpRe(CO)_3$ at (*a*) 21.22, (*b*) 40, (*c*) 60, and (*d*) 80 eV photon energies.

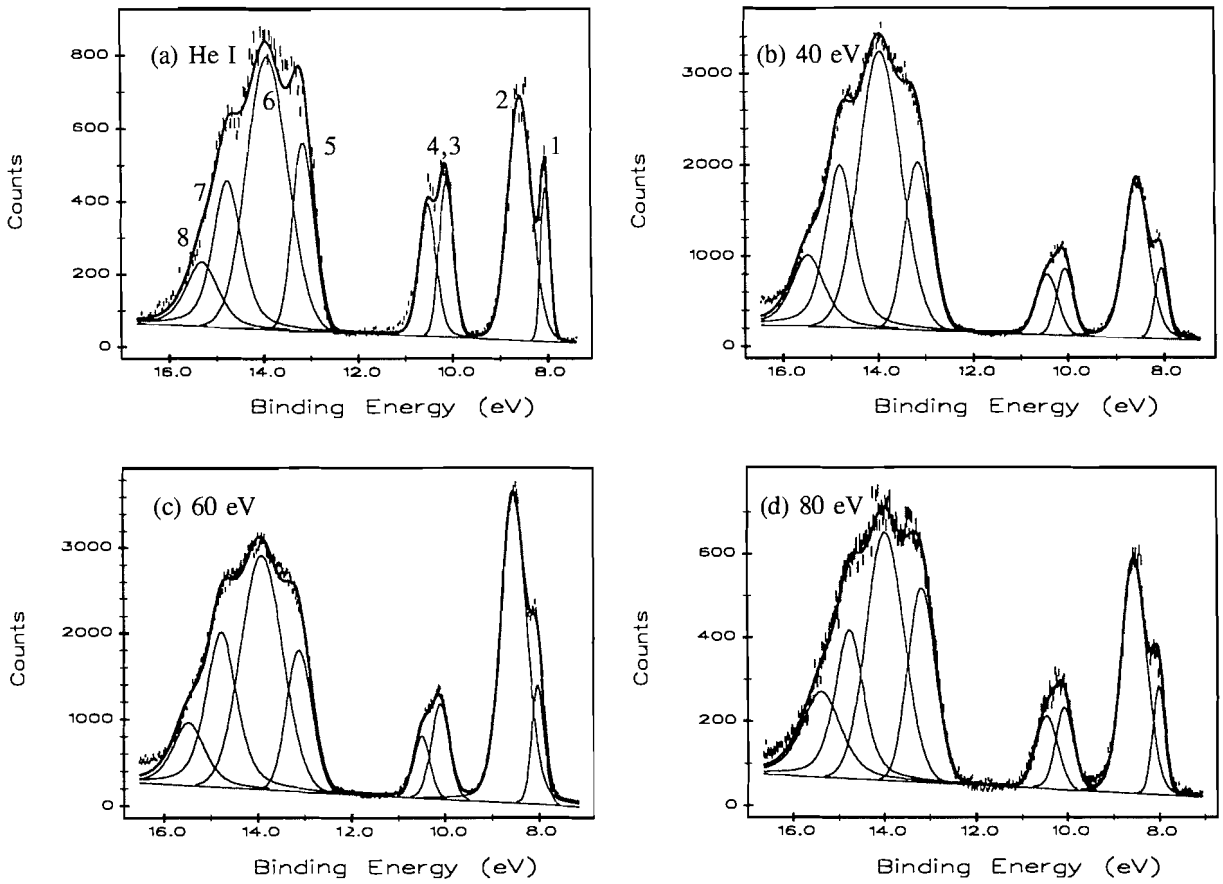

sented in Table 2. The first two MOs in the ground state of $CpMn(CO)_3$ are almost degenerate in energy and both have high (65%) Mn 3*d* contribution. They are derived from Mn $3d_{x^2-y^2}$ and $3d_{xy}$ orbitals and assigned as peak 1 in Fig. 5(*a*). The next MO 18*a*′ is 0.18 eV lower than the HOMO, and this MO also has high Mn 3*d* character (80%). This orbital interacts more with the CO group, but very little with the Cp ring. This orbital can be assigned to peak 2, which is mostly derived from the Mn $3d_{z2}$ orbital. Our Xα results are in good agreement with the previous INDO-type calculation result (2*d*) and strongly support the conclusion that peaks 1 and 2 are the metal *d*-based peak from our variable-energy synchrotron radiation study. The next pair of MO orbitals 11*a*″ and 17*a*′ are almost degenerate in energy and have about 50% Cp ring character. These two orbitals can be easily assigned to peaks 3 and 4, which has also been assigned by Lichtenberger et al. (2*a*) as predominantly ring e_1″ ionization. Peaks 5, 6, 7, and 8 relate to the MO orbitals mainly from CO and Cp groups, and we must point out that the labelling of these peaks and their assignments is somewhat arbitrary because of the many overlapping orbitals involved in this region. However, our Xα results do show that the first three MO orbitals 16*a*′, 10*a*″, and 15*a*′ all have very high Cp ring contribution compared to the rest of the MO orbitals. This allows us to firmly assign these three orbitals to peak 5, since a distinct shoulder between 11 and 13 eV BE has been observed in methyl-substituted ring compounds (2*a*).

The Xα-SW orbital energies and compositions of outer-valence and inner-valence levels of $CpMn(CO)_3$ are listed in Table 3. The inner-valence levels of the three titled compounds are very similar in BE and all are very weak in intensity compared with the valence levels. They were not studied before due to the limitations of the photon source. The first peak (peak 9, see Fig. 1) at 17.63 eV BE is derived from three Cp ring-based orbitals. Peak 10 is at the shoulder of peak 9. It has a BE of 18.23 eV and can be assigned to the contribution of the three CO 4σ orbitals. The next four peaks (peaks S, A, B, C) were assigned previously to the contributions of CO shakeup and satellite peaks that our calculation does not address. However, our Xα results show that there are three Cp orbitals overlapping with the first CO satellite peak at 23.4 eV. The last band in the inner-valence level at 35.6 eV can be assigned readily to the well-known CO 3σ orbitals.

The Xα-SW branching ratio (BR) calculation has been shown to be very valuable for the confirmation of the Xα-SW energy orbital assignment for many molecules. The photoionization cross sections of $CpMn(CO)_3$ were calculated using the Xα-SW method. The BRs of peaks 1, 2 and 3, 4 were then calculated based on the cross sections. Figure 7 presents the comparison of the experimental and theoretical BRs of peaks 1, 2 and 3, 4 for $CpMn(CO)_3$. Both the experimental and Xα calculation BRs show that the BR of peaks 1 and 2 generally increases with photon energies between 20 and 55 eV, while the reverse holds true for peaks 3 and 4. This can be easily

Table 2. Valence-level Xα-SW result for $CpMn(CO)_3$ and band assignment.

	Energy (eV)			Mn			
Orbital	Xα	Expt.	Assignment	3*d* (%)	3*p* (%)	CO (%)	Cp (%)
12*a*″	7.66	7.98	Mn 3*d*	65.0	2.6	16.8	15.5
19*a*′	7.67			65.7	2.5	16.9	14.9
18*a*′	7.84	8.37	Mn 3*d*	79.9	0.6	18.2	1.0
11*a*″	8.75	10.01	Cp *e*″	41.6	2.2	5.7	50.5
17*a*′	8.77	(10.3)		40.5	2.2	5.6	51.7
16*a*′	11.26	12.72	Cp	2.6	5.5	6.9	84.2
10*a*″	13.08			0.7	0.1	24.3	74.9
15*a*′	13.10			0.9	0.1	14.8	84.2
9*a*″	13.17	13.20	CO 1σ, 5π	2.7	0.1	93.0	4.2
14*a*′	13.17			2.5	0	79.8	17.7
8*a*″	13.20	14.05	CO	0.2	0	73.8	26.0
6*a*″	13.53		Cp	5.0	0.6	73.2	21.2
13*a*′	13.54			5.4	0.4	85.6	8.6
7*a*″	13.58			0	0.7	24.5	74.9
12*a*′	13.62			2.0	0.1	92.7	4.3
11*a*′	13.63			0.5	1.1	16.3	82.0
5*a*″	14.47	14.93	CO 1σ, 5π	25.3	4.7	59.8	10.2
10*a*′	14.48			24.7	4.5	58.2	12.6
9*a*′	15.34			18.2(s)	5.2	74.2	2.4

Table 3. Xα-SW result for $CpMn(CO)_3$ and band assignment, outer-valence, and inner-valence levels.

	Energy (eV)			Mn			
Orbital	Xα	Expt.	Assignment	3*d* (%)	3*p* (%)	CO (%)	Cp (%)
8*a*′	16.80	17.63	Cp	0.8	0.2	0.2	98.7 (C 2*p*, H 1*s*)
4*a*″	17.38			0.4	0	0.4	99.2
7*a*′	17.39			0.4	0	0.4	99.2
6*a*′	18.44	18.23	CO 4σ	0.2	0.1	99.6 (O 2*s*, 2*p*)	0.1
3*a*″	18.46			0.1	0.2	99.6	0.1
5*a*′	18.53			0.6(*s*)	0.2	99.2	0
		20.33	CO shakeup				
2*a*″	21.31	23.44	Cp and	0.8	0.3	0	98.9 (C 2*s*)
4*a*′	21.36		CO satellite	0.8	0.3	0	98.9
3*a*′	25.31			0.5(1.1 *s*)	0.8	0.1	97.5
		27.53	CO satellite				
		30.61	CO satellite				
1*a*′	35.38	35.63	CO 3σ	0	0	100 (C,O 2*s*, 2*p*)	0
1*a*″	35.42			0	0	100	0
2*a*′	35.42			0	0	100	0

explained because the atomic cross section of Mn 3*d* increases from its threshold to about 60 eV photon energy, while the atomic cross sections of ligand orbitals decrease in the same region. It is noteworthy that only BRs up to 55 eV photon energy are presented in Fig. 7 in order to avoid the interference of Mn 3*p*→3*d* resonance at band 1 after about 56 eV photon energy. The good agreement between the experimental and Xα-calculated BRs strongly confirms once again that peaks 1 and 2 arise from mainly metal-based orbitals and peaks 3 and 4 arise from orbitals with higher ligand character.

Fig. 7. Comparison of experimental (▼, ●) and Xα (▽, ○) branching ratios of peaks 1, 2 and 3, 4 of $CpMn(CO)_3$.

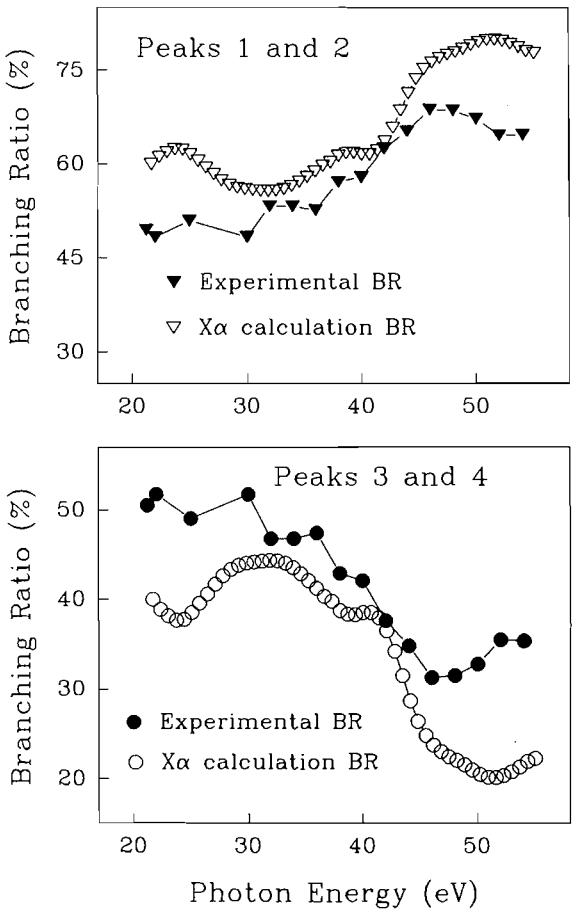

(b) $CpFe(CO)_2I$

We chose to study the electronic structure of $CpFe(CO)_2I$ using variable-energy synchrotron radiation for two reasons. Firstly, the valence level spectrum of $CpFe(CO)_2I$ is much more complex than that of the above two compounds (seven well-resolved peaks between 7.5 and 11.5 eV BE) and the previous assignment was not firm (2*a*). We will demonstrate the value of the observation of the *np*→*nd* resonance for confident assignment of these seven peaks. Secondly, as mentioned earlier, we want to study more and different types of $CpML_3$ complexes, using synchrotron radiation, to see the trend in M 3*d* IPs across the periodic table.

Variable-energy photoelectron valence spectra of $CpFe(CO)_2I$ at 21.22, 52, 60, and 80 eV photon energy are shown in Fig. 8, representing: (*a*) a high-resolution He I spectrum, and synchrotron radiation spectra corresponding to the photon energies of (*b*) before, (*c*) around, and (*d*) after the expected Fe 3*p*→3*d* resonance at ~62 eV from the Fe 3*p* BE. These spectra clearly demonstrate the different trends in the change of the relative intensity of different peaks. Especially noticeable is that the relative intensities of peaks 3 and 4 increase as the photon energy increases, suggesting that both peaks 3 and 4 arise from orbitals of high Fe 3*d* character.

In the previous He I study, Lichtenberger and Fenske (2*a*) assigned the valence spectrum of this compound based on the Fenske calculation and by comparison with the spectra of $Mn(CO)_5X$ complexes. Briefly, peaks 1 and 2 were due to ionizations from the Fe–I antibonding π levels. Peak 4 was assigned to the ionizations from two of the three orbitals of high Fe 3*d* character corresponding to peak 1 in $CpMn(CO)_3$. Peaks 6 and 7, around 10.5 eV BE, were assigned to the ionizations from cyclopentadienyl ring e_1'' orbitals, similar to those of $CpMn(CO)_3$ and $CpRe(CO)_3$. But no conclusive assignments could be made for peaks 3 and 5, since the He I spectrum alone could not distinguish between the predominant Fe 3*d* b_2 orbital and the Fe–I σ orbital, which is mostly of iodine character. Our variable-energy results in Fig. 8 show that the relative intensity of peak 3 increases with the photon energy compared with that of peak 5. This implies that peak 3 should be the predominantly metal b_2-type orbital, which can be confirmed with the observation of *np*→*nd* resonance results for this peak.

Figure 9 presents the valence spectra of $CpFe(CO)_2I$ close to the Fe 3*p* BE of 62.0 eV at 58, 60, 63, and 65 eV photon energy. It is obvious that the relative intensities of peaks 3 and 4 increase, relative to peaks 5, 6, and 7, on going from 60 to 63 eV photon energy, then begin to decrease on going from 63 to 65 eV photon energy. On the other hand, there is no noticeable increase in the intensity of shoulder 5 relative to peak 6. This observation supports the assignment of peak 3 as the Fe 3*d*-based b_2 orbital and peak 5 as the ligand-based a_1 orbital, without any further theoretical calculation.

It is also apparent that the intensities of peaks 1 and 2 increase relative to peaks 5, 6, and 7 above 60 eV photon energy (Fig. 8 and 9). This increase is perhaps unexpected because the I 5*p* cross section decreases sharply at these energies (18, 29). However, another multielectron effect — interchannel coupling — enhances the I 5*p* intensity above the I 4*d* ionizations at 55 eV (29). The I 4d cross section increases rapidly to ~90 eV photon energy, offsetting the expected decrease in I 5*p* cross section.

Conclusion

High-resolution photoelectron spectra of valence, inner-valence, and core levels of $CpM(CO)_3$ (M = Mn, Re) and $CpFe(CO)_2I$ have been studied using monochromatized synchrotron radiation (SR). The high intensity and tunability of SR is important for observing the weak inner valence and M 3*p* (M = Fe, Mn) core level spectra for the first time. The high resolution is critical in defining the broadening mechanisms on the I 4*d* spectrum. The tunability of the radiation is necessary for obtaining the relative intensity of the valence band peaks as a function of photon energy. These intensities, when combined with Xα-SW calculations, yield definitive assignments for the valence and inner-valence molecular orbital ordering. For example, the valence band MOs of $CpMn(CO)_3$ and $CpFe(CO)_2I$ can be readily assigned with the aid of the Xα-SW intensity calculations and the *np*→*nd* resonances. Apart from the I lone pair orbitals in $CpFe(CO)_2I$, the metal *d* orbitals in these complexes are the HOMOs, as predicted earlier (2). In the late second- and third-row transition metal organometallic complexes, such as $CpPtMe_3$ and $Pt(\eta^3\text{-}C_3H_5)_2$, the metal *d* orbitals are at appreciably lower BE (5), resulting in the HOMO being a ligand-based orbital.

Fig. 8. Representative valence-level photoelectron spectra of $CpFe(CO)_2I$ at (*a*) 21.22, (*b*) 52, (*c*) 60, and (*d*) 80 eV photon energies.

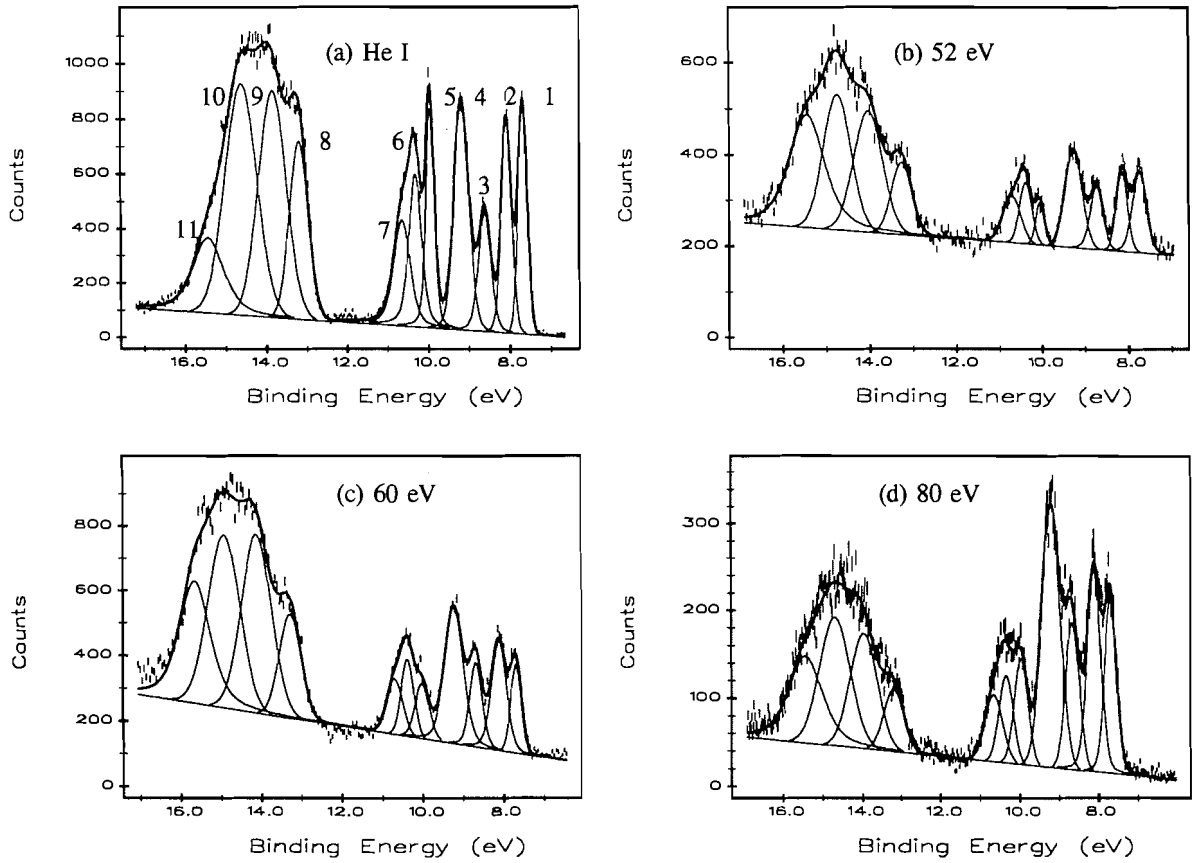

Fig. 9. The valence-level spectra of $CpFe(CO)_2I$ at (*a*) 58, (*b*) 60, (*c*) 63, and (*d*) 65 eV photon energy, showing the increase of the relative intensities of peaks 3 and 4 around 63 eV photon energy.

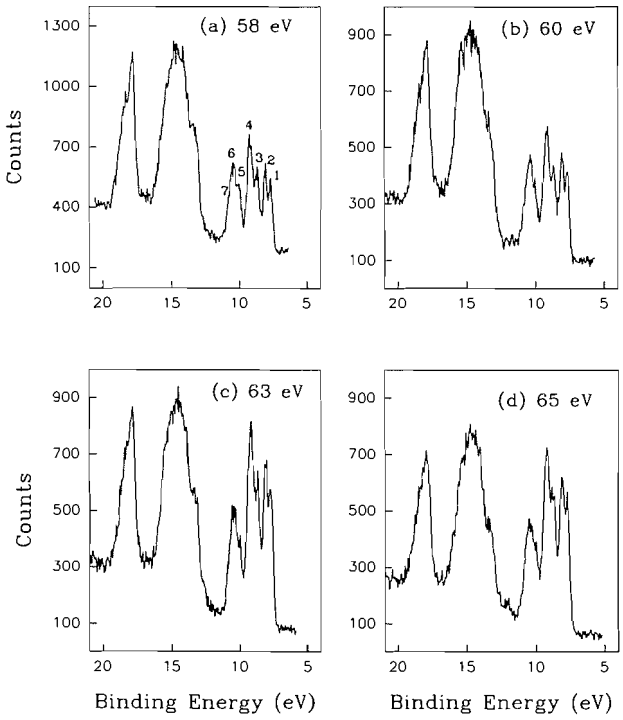

Acknowledgment

We are grateful for the financial support of Natural Sciences and Engineering Research Council (NSERC) of Canada. We also thank the continued assistance from the staff at the Synchrotron Radiation Center, Stoughton, Wis. G.M.B. is very pleased to dedicate this paper to H.C. Clark, as a small token of appreciation for his help and friendship.

References

1. (*a*) D.L. Lichtenberger, A. Rai-Chaudhuri, and R.H. Hogan. *In* Organometallic chemistry. *Edited by* T.P. Fehlner. Plenum, New York. 1992. Chap. 5; (*b*) D.L. Lichtenberger and G.E. Kellogg. Acc. Chem. Res. **20**, 379 (1987); (*c*) J.C. Green. Struct. Bonding (Berlin), **43**, 37 (1981); (*d*) D.L. Lichtenberger, D.C. Calabro, and G.E. Kellogg. Organometallics, **3**, 1623 (1984); (*e*) D.L. Lichtenberger and A. Rai-Chaudhuri. J. Am. Chem. Soc. **113**, 2923 (1991); (*f*) D.L. Lichtenberger, S.K. Renshaw, and R.M. Bullock. J. Am. Chem. Soc. **115**, 3276 (1993).
2. (*a*) D.L. Lichtenberger and R.F. Fenske. J. Am. Chem. Soc. **98**, 50 (1976); (*b*) M. Elian, M.M.L. Chen, M.P. Mingos, and R. Hoffmann. Inorg. Chem. **15**, 1148 (1976); (*c*) B.E. Schilling, R. Hoffmann, and D.L. Lichtenberger. J. Am. Chem. Soc. **101**, 585 (1979); (*d*) M. Bohm and R. Gleiter. J. Comput. Chem. **1**, 407 (1980); (*e*) T.A. Albright, J.K. Burdett, and M.H. Whangbo. *In* Orbital interactions in chemistry. John Wiley & Sons, New York. 1985.
3. (*a*) D.S. Yang, G.M. Bancroft, R.J. Puddephatt, B.E. Bursten, and S.D. McKee. Inorg. Chem. **28**, 873 (1989); (*b*) D.S. Yang,

G.M. Bancroft, R.J. Puddephatt, K.H. Tan, J.N. Cutler, and J.D. Bozek. Inorg. Chem. **29**, 4956 (1990).
4. (*a*) D. Moncrieff, I.H. Hillier, V.R. Saunder, and W. von Niessen. Chem. Phys. Lett. **131**, 545 (1986); (*b*) P. Decleva, G. Fronzoni, and A. Lisini. Chem. Phys. **134**, 307 (1989); (*c*) X. Li, G.M. Bancroft, R.J. Puddephatt, Z.F. Liu, Y.F. Hu, and K.H. Tan. J. Am. Chem. Soc. **116**, 9543 (1994).
5. X. Li, G.M. Bancroft, R.J. Puddephatt, Y.F. Hu, and K.H. Tan. Organometallics, **15**, 2890 (1996).
6. J.C. Green. Acc. Chem. Res. **27**, 131 (1994).
7. J.D. Bozek, J.N. Cutler, G.M. Bancroft, K.H. Tan, D.S. Yang, and R.G. Cavell. Chem. Phys. Lett. **165**, 1 (1990).
8. K.H. Tan, G.M. Bancroft, L.L. Coatsworth, and B.W. Yates. Can. J. Phys. **60**, 131 (1982).
9. Z.F. Liu, G.M. Bancroft, L.L. Coatsworth, and K.H. Tan. Chem. Phys. Lett. **203**, 337 (1993).
10. G.M. Bancroft, L. Adams, L.L. Coatsworth, C.D. Bennewitz, J.D. Brown, and W.D. Westwood. Anal. Chem. **47**, 586 (1975).
11. (*a*) K.H. Johnson. Adv. Quantum Chem. **7**, 147 (1973); (*b*) F. Herman, A.R. William, and K.H. Johnson. J. Chem. Phys. **61**, 3508 (1974); (*c*) D.A. Case and C.Y. Yang. Int. J. Quantum Chem. **18**, 1091 (1980); (*d*) M. Cook and D.A. Case. QCPE, **12**, 465 (1982).
12. A.F. Berndt and R.E. Marsh. Acta Crystallogr. **16**, 118 (1963).
13. (*a*) K. Schwarz. Phys. Rev. B: Solid State, **5**, 2466 (1972); (*b*) Theor. Chim. Acta, **34**, 225 (1974).
14. J.W. Davenport. Phys. Rev. Lett. **36**, 945 (1976).
15. D.C. Calabro, J.L. Hubbard, C.H. Blevins II, A.C. Campbell, and D.L. Lichtenberger. J. Am. Chem. Soc. **103**, 6839 (1981).
16. Y.F. Hu, G.M. Bancroft, Z.F. Liu, and K.H. Tan. Inorg. Chem. **34**, 3716 (1995).
17. Y.F. Hu, G.M. Bancroft, J.D. Bozek, Z.F. Liu, D.G.J. Sutherland, and K.H. Tan. J. Chem. Soc. Chem. Commun. 1276 (1992).
18. J.J. Yeh and I. Lindau. At. Data Nucl. Data Tables, **32**, 1 (1985).
19. J.C. Fuggle and N. Mårtensson. J. Electron Spectrosc. Relat. Phenom. **21**, 275 (1980).
20. W.L Jolly, K.D. Bomben, and C.J. Eyermann. At. Data Nucl. Data Tables, **31**, 433 (1984).
21. G.M. Bancroft and K.D. Butler. J. Am. Chem. Soc. **96**, 7208 (1974).
22. R.V. Parish. *In* Mossbauer spectroscopy applied to inorganic chemistry. Vol.2. *Edited by* G.J. Long. Plenum Press, New York. 1987. Chap. 9. p. 391.
23. J.N. Cutler, G.M. Bancroft, and K.H. Tan. J. Chem. Phys. **97**, 7932 (1992).
24. D.J. Bristow and G.M. Bancroft. J. Am. Chem. Soc. **105**, 5634 (1983).
25. D.J. Parker. J. Chem. Soc. A, 1382 (1970).
26. X. Li, G.M. Bancroft, R.J. Puddephatt, Y.F. Hu, Z. Liu, D.G.J. Sutherland, and K.H. Tan. J. Chem. Soc. Chem. Commun. 67 (1993).
27. (*a*) D.S. Yang, G.M. Bancroft, J.D. Bozek, R.J. Puddephatt, and J.S. Tse. Inorg. Chem. **28**, 1 (1989); (*b*) D.S. Yang, G.M. Bancroft, and R.J. Puddephatt. Inorg. Chem. **29**, 2118 (1990); (*c*) D.S. Yang, G.M. Bancroft, L. Dignard-Bailey, R.J. Puddephatt, and J.S. Tse. Inorg. Chem. **29**, 2487 (1990); (*d*) D.S. Yang, G.M. Bancroft, R.J. Puddephatt, and J.S. Tse. Inorg. Chem. **29**, 2496 (1990); (*e*) B.E. Bursten, M. Casarin, S. DiBella, A. Fang, and I.L. Fragala. Inorg. Chem. **24**, 2169 (1985); (*f*) F.A. Cotton, G.G. Stanley, A.H. Cowley, and M. Lattman. Organometallics, **7**, 835 (1988); (*g*) G. Guimon, G. Pfister-Guillouzo, B. Chaudret, and R. Poilblanc. J. Chem. Soc. Dalton Trans. 43 (1985); (*h*) S. Elbel, M. Grodzicki, L. Pille, and G. Ünger. J. Mol. Struct. **175**, 441 (1988); (*i*) A.J. Bridgeman, L. Davis, S.J. Dixon, J.C. Green, and I.N. Wright. J. Chem. Soc. Dalton Trans. 1023 (1995).
28. (*a*) B.W. Yates, K.H. Tan, G.M. Bancroft, L.L. Coatsworth, J.S. Tse, and G.J. Schrobilgen. J. Chem. Phys. **84**, 3603 (1986); (*b*) D.G.J. Sutherland, J.Z. Xiong, Z. Liu, T.K. Sham, G.M. Bancroft, K.M. Baines, and K.H. Tan. Organometallics, **13**, 3671 (1994).
29. G.M. Bancroft, B.W. Yates, K.H. Tan, and L.L. Coatsworth. J. Chem. Soc. Chem. Commun. 1613 (1984).

Redox activity of tryptophan residues in recombinant cytochrome c peroxidase and its W51F and W191F mutants

George Tsaprailis and Ann M. English

Abstract: Tryptophan oxidation mediated via the heme was initiated by adding 2, 6, and 20 equivalents of H_2O_2 to 5 μM recombinant CCP (CCP(MI)) and its W51F and W191F mutants at pH 7.0. Addition of the proteins to 8 M urea (pH 1.5) relieved heme quenching of Trp fluorescence. CCP(MI)-I, W51F-I, and W191F-I, the two-electron oxidized species (Fe^{IV}=O,$R^{\cdot+}$) formed on addition of 2 equivalents of H_2O_2, exhibited decreased fluorescence relative to the Fe^{III} forms. Loss of 0.7 Trp in CCP(MI)-I and W51F-I, and 0.2 Trp in W191F-I implies that $R^{\cdot+}$ is located on Trp191 in CCP(MI)-I and W51F-I. Spontaneous decay of the Fe^{IV}=O hemes back to Fe^{III}, followed by reaction with 2 more equivalents of H_2O_2 after 24 h, resulted in a *combined* loss of 2.7 (CCP(MI)), 1.5 (W51F), and ~1 (W191F) Trp. Also, addition of 6 equivalents of H_2O_2 to the *resting* Fe^{III} enzymes resulted in loss of ~2 Trps in CCP(MI) but only ~1 in W51F and W191F, suggesting that Trp51 becomes redox active in CCP(MI) when >2 equivalents of H_2O_2 are reduced. Addition of 20 equivalents of H_2O_2 resulted in a *total* loss of ~4, 2.5, and 2 Trp in CCP(MI), W51F, and W191F, respectively. Activity loss largely paralleled Trp loss, and the residual activity of CCP(MI) and W51F exposed to 20 equivalents of H_2O_2 was 5–19%, while W191F exhibited ~50% activity. SDS PAGE analysis revealed that oxidized CCP(MI) and W191F were 60–70% monomeric, and W51F 27% monomeric following its reaction with >2 equivalents H_2O_2. Amino acid analyses confirmed Trp loss and also showed significant Tyr, but *not* Met, loss in the oxidized proteins. Donors to the heme and pathways of electron migration are proposed based on the combined results.

Key words: cytochrome c peroxidase, Trp mutants, H_2O_2 oxidation, redox-active residues.

Résumé : On a induit l'oxydation du tryptophane par l'hème en ajoutant 2, 6 et 20 équivalents de H_2O_2 à 5 μM de recombinant CCP (CCP(M)) et ses mutants W51F et W191F à pH 7,0. L'addition de protéines à 8 M d'urée (pH 1,5) diminue l'extinction de la fluorescence du Trp par l'hème. CCP(MI)-I, W51F-I et W191F-I, les espèces oxydées à deux électrons (Fe^{IV}=O,$R^{\cdot+}$) formées lors de l'addition de deux équivalents de H_2O, exhibent une diminution de la fluorescence par rapport à la forme Fe^{III}. La perte de 0,7 Trp dans le CCP(MI)-I et dans le W51F-I et de 0,2 Trp dans le W191F-I implique que $R^{\cdot+}$ est localisé sur le Trp191 dans le CCP(MI)-I et dans le W51F-I. La dégradation spontanée de l'hème Fe^{IV}=O en Fe^{III}, suivie de la réaction avec deux équivalents supplémentaires de H_2O_2 après 24 h résulte en une perte *combinée* de 2,7 (CCP(MI)), de 1,5 (W51F) et d'environ 1 (W191F) Trp. De même, l'addition de 6 équivalents de H_2O_2 à l'enzyme Fe^{III} à l'état fondamental résulte en une perte d'environ 2 Trps dans le CCP(MI) mais la perte est seulement de l'ordre de 1 dans le W51F et dans le W191F, suggérant que Trp51 devient une agent redox actif dans le CCP(MI) lorsque plus de deux équivalents de H_2O_2 sont réduits. L'addition de 20 équivalents de H_2O_2 conduit à une perte *totale* d'environ 4, 2,5 et 2 Trp dans le CCP(MI), W51F et W191F respectivement. La perte d'activité va de pair avec la perte de Trp, et l'activité résiduelle du CCP(MI) et du W51F, lorsque ces substances sont soumises à 20 équivalents de H_2O_2, est de l'ordre de 5–19% tandis que le W191F exhibe une activité de 50% environ. L'analyse SDS PAGE révèle que le CCP(MI) et le W191F oxydés sont à 60–70% sous forme monomère et le W51F existe à 27% sous la forme monomère par suite de la réaction avec plus de deux équivalents de H_2O_2. L'analyse des acides aminés confirme la perte de Trp et révèle une perte significative de Tyr, mais *pas* de perte de Met, dans la protéine oxydée. Sur la base des résultats combinés on propose des donneurs pour l'hème et un mécanisme de migration d'électron.

Mots clés : cytochrome c peroxydase, mutants du Trp, H_2O_2 oxydation, résidus actifs comme agent redox.

[Traduit par la rédaction]

Received March 4, 1996.

This paper is dedicated to Professor Howard C. Clark in recognition of his contributions to Canadian chemistry.

G. Tsaprailis and A.M. English.[1] Department of Chemistry and Biochemistry, Concordia University, 1455 de Maisonneuve Boulevard West, Montreal, QC H3G 1M8, Canada.

[1] Author to whom correspondence may be addressed. Telephone: (514)848-3338. Fax: (514) 848-2868. E-mail: english@vax2.concordia.ca

Introduction

The identification of a Trp radical in yeast CCP-I[2] (1) was the first instance that a Trp residue was shown to play a redox-active role in an enzyme (2). Recently, however, a redox-active Trp has been identified in ribonucleotide reductase (3) and, in addition to Trp, a number of other amino acid radicals, including tyrosyl, cysteinyl, and glycyl radicals are known to play catalytic roles in enzymatic reactions (4). Reversible redox activity of protein residues involves the formation of one-electron oxidized free radical species, which are stabilized by the surrounding polypeptide. Thus, a full understanding of the use of protein free radicals in redox catalysis (free radical enzymology) requires characterization of their storage sites, and elucidation of their migration and quenching mechanisms in protein matrices.

The catalysis of two-electron redox chemistry by Fe^{III} heme centres necessitates the generation of radical species. Hence, small plant and fungal heme peroxidases can provide important insight into the reactivity of protein radicals in redox catalysis. Binding of H_2O_2 to the Fe^{III} ion in heme peroxidases (Fe^{III}, P) results in heterolytic cleavage of the O—O bond, and formation of a two-electron oxidized intermediate (Fe^{IV}=O,$P^{\cdot+}$), termed compound I (eq. [1]). Reduction of the latter in one-electron steps (eqs. [2] and [3]) back to the resting enzyme occurs via formation of the one-electron oxidized intermediate (Fe^{IV}=O,P), termed compound II.

[1] $Fe^{III}P + H_2O_2 \rightarrow Fe^{IV}{=}O,P^{\cdot+} + H_2O$

[2] $Fe^{IV}{=}O,P^{\cdot+} + 1e^- \rightarrow Fe^{IV}{=}O,P$

[3] $Fe^{IV}{=}O,P + 1e^- \rightarrow Fe^{III}P + H_2O$

In most heme peroxidases $P^{\cdot+}$ is initially a porphyrin π-cation radical, but a protein-based radical is observed for CCP-I (5, 6). Of the 7 Trps, Trp191, which is in van der Waals contact with the heme (Fig. 1), has been identified as the redox-active amino acid residue in CCP-I. The broad EPR signal characteristic of native CCP-I was not observed in the spectrum of W191F-I (7, 8), and this mutant also exhibited a transient porphyrin radical on reaction with peroxide (9). Trp51, which is only 4 Å from the heme (Fig. 1), was eliminated as the radical site since W51F-I exhibited EPR and ENDOR spectra almost identical to those of CCP(MI)-I (7).

We have shown previously that steady-state protein fluorescence can be used to probe the loss of Trp residues in H_2O_2-oxidized yeast CCP (10). Since heme is a highly efficient quencher of CCP fluorescence (11), protein denaturation in 8 M urea at pH 1.5 is required to relieve quenching and allow fluorescence loss to be equated with Trp loss. Furthermore, since denaturation of CCP occurs rapidly in 8 M urea, it is assumed that radical migration does not occur during this process (10), and that protein-based radicals are converted to stable oxidation products on exposure to the solvent.

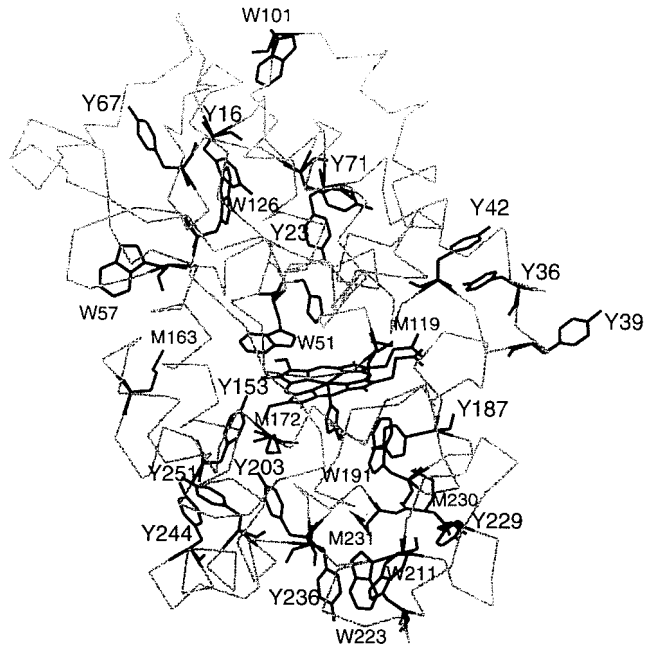

Fig. 1. The C_α backbone of CCP showing the location of the 7 Trp (W), 14 Tyr (Y), and 6 Met (M) residues relative to the heme.

The fluorescence measurements are extended here to the recombinant enzyme (CCP(MI)) and two mutants, W51F and W191F, in which the Trp residues closest to the heme are singly mutated to phenylalanine. In lignin peroxidase (LIP), where Phe46 and Phe193 correspond to Trp51 and Trp 191 (12), $P^{\cdot+}$ is a porphyrin π-cation radical in compound I (13). Since it is more difficult to oxidize the side chain of phenylalanine than the indole side chain of Trp (14), the rapid transfer of oxidizing equivalents from the porphyrin to a protein-based radical is presumably prevented in LIP-I (6). Despite the Trp191 → Phe mutation, a porphyrin π-cation radical is only transiently formed ($t_{1/2}$ ~14 ms) in W191F-I (9). The porphyrin radical is transferred to the protein, resulting in an EPR signal for W191F-I that has been assigned to a tyrosyl radical (7, 8). Hence, an examination of compound I of the two Trp → Phe mutants will provide a test of the EPR data and also demonstrate if fluorescence measurements on the denatured proteins can clearly distinguish between Trp and Tyr radicals.

In the absence of oxidizable substrates, CCP(MI)-I, W51F-I, and W191F-I spontaneously decay to give products with absorption spectra similar to their resting Fe^{III} forms. The half-life of the Fe^{IV}=O heme in CCP(MI)-I and W191F-I is ~3 h (15), but that of W51F-I is only ~3–4 s (16). EPR studies revealed that the protein radical signal in yeast CCP-I decays on a slightly faster time scale than the Fe^{IV}=O centre (17). However, a protein-based radical persists in W191F-I for only ~10 min (18), clearly indicating that the Fe^{IV}=O heme is not reduced by the removal of a second electron from the EPR-

[2] Abbreviations: ABTS, 2,2′-azinobis[3-ethylbenzthiazoline-6-sulfonic acid]; CCP(MI), recombinant cytochrome c peroxidase (EC 1.11.1.5) from *E. coli*; CCP(MI)-I, W51F-I, W191F-I, compounds I of CCP(MI), W51F, and W191F, where compound I is the two-electron oxidized species formed when stoichiometric H_2O_2 reacts with the peroxidases; CCP(MI)-II, compound II, species formed on one-electron reduction of compound I; ENDOR, electron-nuclear double resonance; EPR, electron spin resonance; LC–MS, liquid chromatography with mass spectrometric detection; LIP, lignin peroxidase; NATA, *N*-acetyltryptophanamide; SDS–PAGE, sodium dodecyl sulphate – polyacrylamide gel electrophoresis.

active species. To probe Trp loss due to the combined effects of protein radical decay and endogenous electron transfer to the Fe^{IV}=O heme, the decay products were examined by fluorescence at time intervals between 15 s and 24 h following the addition of H_2O_2. Furthermore, the 24-h decay products were exposed to another two oxidizing equivalents of H_2O_2 and rapidly unfolded to see if Trp residues were also electron donors in the decay products.

Millimolar H_2O_2 readily oxidizes methionine residues in proteins but not aromatic residues (19). However, yeast CCP reduces up to 20 equiv. of H_2O_2 at micromolar concentrations using endogenous donors on the polypeptide (20), including ~3 Trps (10). A mechanism consistent with the reduction of 2 equiv. of $H_2O_2$by compound I would be the following:

[4] $Fe^{IV},P^{\cdot+} \rightarrow Fe^{III},P^{\cdot+},P_x^{\cdot}$

[5] $Fe^{III},P^{\cdot+},P_x^{\cdot} + H_2O_2 \rightarrow Fe^{IV}=O,P^{\cdot+},P_x^{\cdot},P_y^{\cdot} + H_2O$

where $P_x^{\cdot}$ and $P_y^{\cdot}$ are additional protein-based radicals generated by the transfer of the two oxidizing equivalents from peroxide via the heme to the polypeptide. Exposure to 6 and 20 equiv. of H_2O_2 was undertaken to estimate the *maximum* number of Trp donors in each of the mutants examined here. As carried out previously with yeast wild-type CCP (10), amino acid analyses were performed to probe the loss of non-Trp residues, and ferrocytochrome c and ferrocyanide oxidizing activities were measured just prior to denaturation to compare fluorescence loss with activity loss. H_2O_2 titres and the extent of radical-mediated *intermolecular* protein cross-linking were also measured. Finally, interpretation of the combined data, in terms of possible sites of protein-based free radical formation and possible radical and electron migration pathways, is attempted.

Experimental

Materials

Wild-type recombinant cytochrome c peroxidase (CCP(MI)) and its W51F and W191F mutants, prepared as described (16), were generous gifts from Dr Mark Miller (University of California, San Diego). Horse heart cytochrome c (Type III), *N*-acetyltryptophanamide (NATA), and guanidinium chloride were obtained from Sigma; ABTS was purchased from Boehringer Mannheim as the diammonium salt, and analytical grade urea was purchased from Anachemia. All chemicals were used without further purification. Distilled water (specific resistance 18 MΩ cm) was prepared using a Banstead Nanopure system. SDS–PAGE was performed on 7.5% acrylamide gels using a Mini Protean II Electrophoresis Dual Slab Cell and silver staining (Bio-Rad). Densitometer tracings of the gels were obtained on a FisherBiotech transmission densitometer. Fluorescence and absorption measurements were carried out on a Shimadzu model RF 5000 spectrofluorometer and a Hewlett Packard 8451A diode-array spectrophotometer, respectively.

H_2O_2 oxidation

Protein stock solutions of 5 μM were prepared in 0.1 M sodium phosphate buffer (pH 7.0) using ϵ_{408} (mM^{-1} cm^{-1}) values of 102 (CCP(MI)), 141 (W51F) (16), and 109 (W191F) (21). Stock H_2O_2 solutions (0.2–2 mM) were prepared in the same buffer and H_2O_2 concentrations were determined spectrophotometrically by monitoring the CCP-catalyzed oxidation of excess ABTS ($\Delta\varepsilon_{405}$ = 36.8 mM^{-1} cm^{-1}). Protein and H_2O_2 stocks were mixed to give the desired ratios. Formation of Fe^{IV}=O heme was followed spectrophotometrically at 424 nm (17).

Enzyme activities

Assay solutions contained 180 μM H_2O_2, 25 μM ferrocytochrome c, or 20 mM ferrocyanide as reducing substrate and 25 nM native or oxidized peroxidase in 0.1 M phosphate buffer (pH 7.0). Activity measurements were performed by following substrate oxidation spectrophotometrically (ferrocytochrome c, $\Delta\varepsilon_{550}$ = 18 mM^{-1} cm^{-1} (22); ferrocyanide, $\Delta\varepsilon_{420}$ = 1.0 mM^{-1} cm^{-1} (23, 24)). Activities of the H_2O_2-oxidized enzymes are reported relative to the unoxidized enzymes maintained under the same conditions.

H_2O_2 turnover, H_2O_2 titres, SDS–PAGE, and amino acid analysis

ABTS (700 μM) oxidation was monitored at 724 nm to determine the time course and extent of H_2O_2 turnover by 5 μM enzyme. The 24-h decay products were titrated with H_2O_2 and the absorbance change at 424 nm monitored to determine the extent of Fe^{IV}=O heme formation. Cross-linking of the proteins following addition of H_2O_2 was investigated by SDS–PAGE (10), and amino acid analysis was carried out as previously described (10).

Relative fluorescence

At various time intervals (15 s – 24 h) after the addition of H_2O_2 to 5 μM protein in 0.1 M phosphate buffer (pH 7.0), the samples were diluted with urea to give a final concentration of 1 μM protein in 8 M urea at pH 1.5. Following 280-nm excitation, fluorescence intensities were measured at 350 nm, which is the emission maximum of CCP in urea (11). The Raman peak of water was subtracted from all emission spectra, and inner-filter effects were corrected using the formula (25):

[6] $F = F_o \text{ antilog}[A_{ex} + A_{em})/2]$

where F is the corrected fluorescence intensity, F_o the observed intensity, A_{ex} and A_{em} are the absorbances at the excitation and emission wavelengths, respectively. Relative fluorescence intensities (%F) were calculated assuming %F = 100 for unoxidized protein maintained under the same conditions.

Results

Relative fluorescence

The fluorescence increase, observed within the mixing time (2–3 s) upon denaturation of CCP(MI), W51F, and W191F in urea, is accompanied by a red shift in emission maximum to 350 nm, characteristic of Trp exposure to the aqueous environment (11). After correcting for inner-filter effects (eq. [6]), the proteins exhibit fluorescence intensities in 8 M urea at pH 1.5 equal to that of Trp model compound NATA, indicating that each of the 6 or 7 Trp residues in the denatured proteins possesses the same fluorescence quantum yield as NATA (10). Heme quenching is totally eliminated under these conditions

Fig. 2. Relative fluorescence intensities at 350 nm of 1 μM H_2O_2-oxidized protein in 8 M urea (pH 1.5) at 22°C. 5 μM protein was reacted with H_2O_2 in 0.1 M phosphate buffer, pH 7.0, and diluted with urea at various times after addition of H_2O_2. Circles, 2 equiv. of H_2O_2 added (compound I); triangles, 6 equiv. of H_2O_2 added; squares, 20 equiv. of H_2O_2 added. Data points are the corrected (eq. [6]) relative fluorescence intensities (*%F*) and represent the averages of four measurements. (*A*) CCP(MI), (*B*) W51F, and (*C*) W191F. Experimental conditions: 280-nm excitation; slits, 5 nm; scan rate, 114 nm/min.

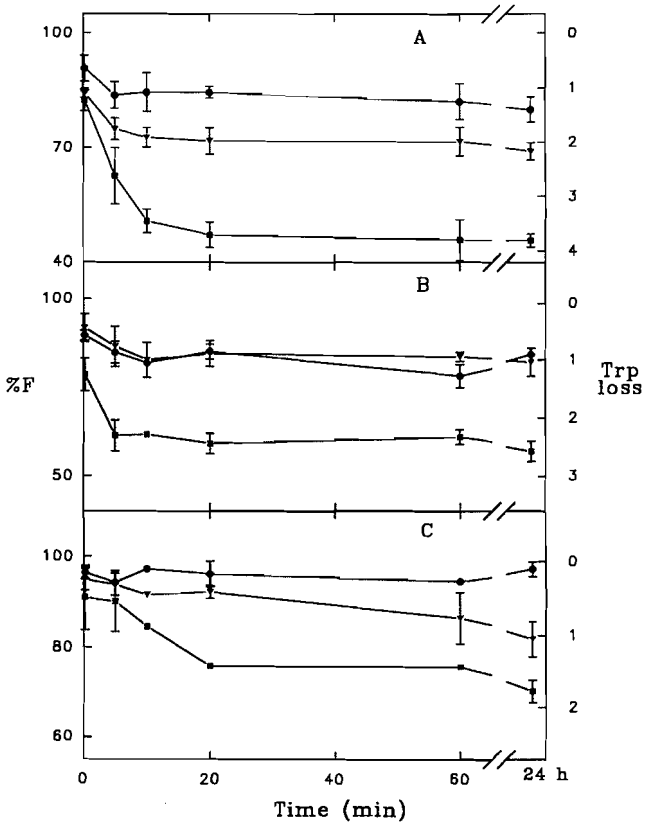

due to dissociation of the heme from the polypeptide as evidenced by the appearance of free-heme spectra (10).

Figure 2*A* summarizes the fluorescence intensities at 350 nm following denaturation of CCP(MI) at various time intervals after the addition of 2, 6, and 20 equiv. of H_2O_2. Addition of CCP(MI)-I to 8 M urea at pH 1.5 reveals loss of fluorescence due to heme-mediated Trp oxidation by H_2O_2 (10). CCP(MI)-I formed 15 s prior to denaturation retains 91 ± 3% fluorescence relative to resting CCP(MI), which corresponds to the oxidation of 0.7 ± 0.2 Trp residues. In the 24-h decay product of CCP(MI)-I the number of Trps lost increases to 1.4 ± 0.2. Addition of 6 equiv. of H_2O_2 to CCP(MI) 15 s and 5 min prior to denaturation resulted in loss of ~1 and 2 Trps, and when 20 equiv. of H_2O_2 were added for the same time intervals, ~1 and 3 Trps were oxidized; this increased to a total of ~4 when the 20:1 sample was denatured after 24 h. Clearly, the number of Trps oxidized increases with time and the amount of H_2O_2 added. Addition of aliquots of the CCP(MI)–H_2O_2 mixtures to an ABTS solution indicated that 3 H_2O_2 were turned over in ~1 min and 10 in ~5 min.

Upon denaturation 15 s following its generation, W51F-I exhibits 89 ± 1% relative fluorescence in 8 M urea (pH 1.5), indicating loss of 0.7 ± 0.1 Trps out of a total of 6. Samples of W51F-I denatured over 24 h exhibit loss of 1.0–1.3 Trps, and addition of 6 equiv. of H_2O_2 to W51F resulted in oxidized species with essentially the same fluorescence vs. time profile as W51F-I (Fig. 2*B*). The fluorescence loss 15 s after the addition of 20 equiv. of H_2O_2 to W51F reveals the immediate loss of ~1 Trp, and at longer times (≥5 min), a total loss of ~2.5 Trps is observed (Fig. 2*B*).

Fig. 3. Horse heart ferrocytochrome c oxidizing activities relative to unoxidized protein in 0.1 M phosphate buffer (pH 7.0) of the (*A*) CCP(MI) and (*B*) W51F samples in Fig. 2 just prior to denaturation.

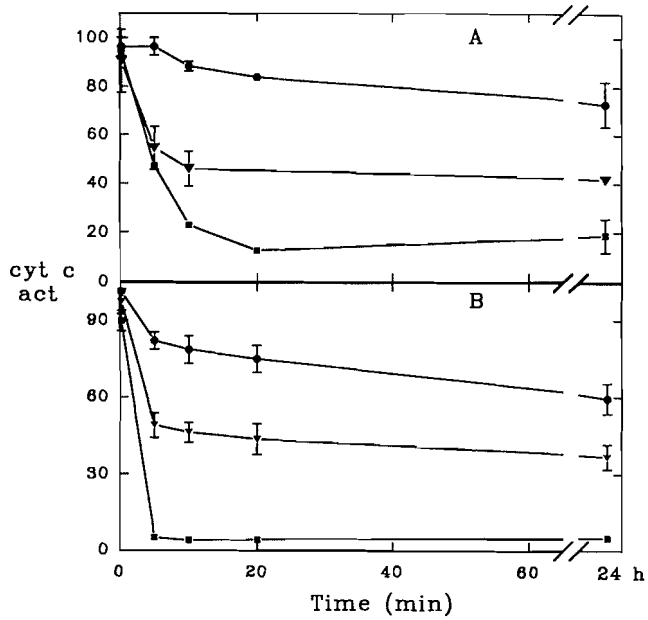

W191F-I and its 24-h decay product retain 96–97% relative fluorescence in 8 M urea (pH 1.5), indicating oxidation of only ~0.2 Trp (Fig. 2*C*). The 6:1 and 20:1 W191F samples lose Trp slowly over time, resulting in the oxidation of ~1 and 2 Trps, respectively, in their 24-h decay products (Fig. 2*C*). Addition of aliquots of the W191F–H_2O_2 mixtures to an ABTS solutions indicated that 3 H_2O_2 were turned over in ~1 min and 10 in ~ 30 min.

Enzyme activities

Using ferrocytochrome c as reducing substrate, the activities of CCP(MI) and W51F are shown in Fig. 3. CCP(MI)-I and W51F-I formed 15 s before commencing the assays exhibit ~96% ferrocytochrome c oxidizing activity, but this is reduced to 60–70% in the 24-h decay products. Preincubation for 5–10 min with 6 equiv. of H_2O_2 further reduces the activity to 50–55%, and exposure to 20 equiv. results in 5% activity in W51F and ~19% activity in CCP(MI) (Fig. 3 and Table 1). W191F has negligible ferrocytochrome oxidizing activity because the presence of Trp191 is necessary for rapid reduction of the heme by ferrocytochrome c (18).

Ferrocyanide oxidizing activities of CCP(MI), W51F, and W191F as a function of preincubation time with 2–20 equiv. of H_2O_2 are summarized in Fig. 4. The overall dependence of activity on the number of oxidizing equivalents added and on

Table 1. Properties of the 24-h decay products of H_2O_2-oxidized CCP(MI), W51F, and W191F[a].

	2 equiv. H_2O_2			6 equiv. H_2O_2			20 equiv. H_2O_2		
Property (%)[b]	CCP(MI)	W51F	W191F	CCP(MI)	W51F	W191F	CCP(MI)	W51F	W191F
H_2O_2 titer[c]	72	—[g]	94	54	—[g]	82	18	—[g]	51
Monomer[d]	100	60	67	68	26	65	60	28	65
Cyt c act.[e]	73	59	—	42	37	—	19	5	—
$Fe(CN)_4^4$act.[e]	55	56	86	25	27	77	9	11	53
Trp loss[f]	~1.3	~0.5	~0.7	~1.2	~0.2	0	~0.4	~0.2	0

[a]Properties measured 24 h after oxidation of 5 μM protein in 0.1 M phosphate buffer (pH 7.0).
[b]Relative to unoxidized samples maintained under the same conditions.
[c]From H_2O_2 titrations (see text).
[d]From Table 2.
[e]Activities from Figs. 3 and 4.
[f]Trp loss 15 s following addition of 2 equiv. of H_2O_2 to the decay products. The loss was estimated from the change in fluorescence of the decay products in 8 M urea (pH 1.5) before and after addition of H_2O_2 (see text).
[g]Fe^{IV}=O forms of W51F are too unstable to measure H_2O_2 titres spectrophotometrically.

Fig. 4. Ferrocyanide oxidizing activities relative to unoxidized protein in 0.1 M phosphate buffer (pH 7.0) of the (*A*) CCP(MI), (*B*) W51F, and (*C*) W191F samples in Fig. 2 just prior to denaturation.

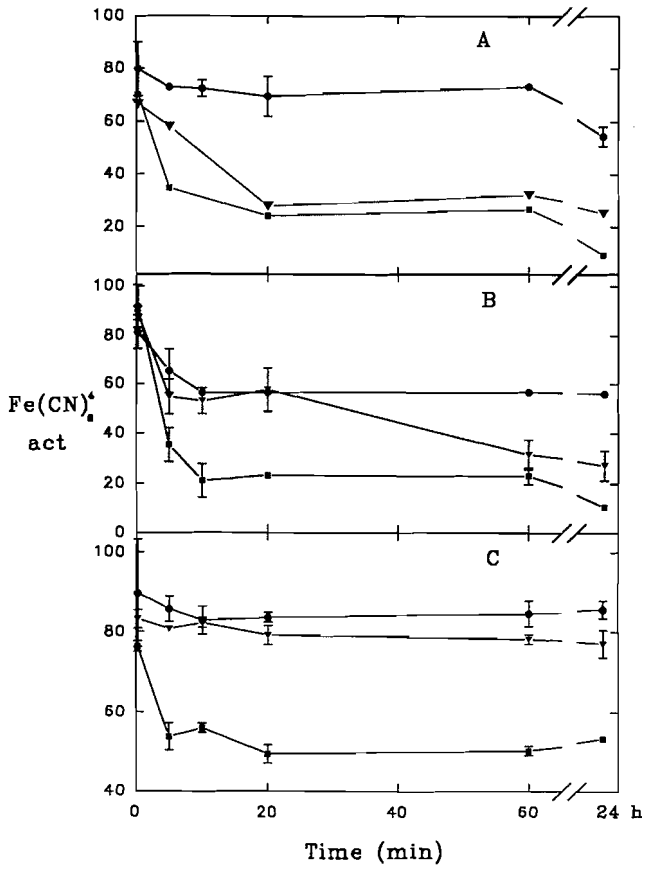

preincubation time is similar to that shown in Fig. 3. CCP(MI) and W51F shows similar activity vs. preincubation time profiles except that the 6:1 W51F samples lose activity more slowly than the corresponding CCP(MI) samples. The loss in ferrocyanide oxidizing activity of the W191F samples preincubated for only 15 s with H_2O_2 is comparable to that of the other mutants; however, W191F retains considerably greater activity after 2 h, with the 2:1, 6:1, and 20:1 samples exhibiting 86, 77, and 53% activity, respectively, compared to 55, 25, and 9% for CCP(MI) (Table 1).

H_2O_2 titres

Using the relative absorbance change at 424 nm (the maximum in the difference spectrum of the Fe^{III} and Fe^{IV}=O forms), the 24-h decay products of oxidized CCP(MI) and W191F were titrated with H_2O_2 to determine the extent of their ability to reform Fe^{IV}=O heme (reaction [1]). The decay products of W191F possess the highest titres, and these match the ferrocyanide oxidizing activities closely (Table 1). There is also a good correspondence between the titres and ferrocytochrome c oxidizing activities for CCP(MI), but its ferrocyanide oxidizing activities are significantly lower (Table 1). The instability of the Fe^{IV}=O heme of W51F ($t_{1/2}$ ~3–4 s) prevented measurement of its titre; nonetheless, the decay products of this mutant exhibit comparable activity to CCP(MI) with both reducing substrates (Table 1).

SDS–PAGE

Table 2 summarizes the percent monomer in the H_2O_2-oxidized enzymes at pH 7.0. Gels of CCP(MI)-I and its 24-h decay product showed no polymerized protein, whereas the monomeric content of the 6:1 and 20:1 24-h decay products is 60–70%. W51F-I gives rise to 85% monomeric protein when denatured within 15 s, but the monomeric content of its decay product is reduced to 60% within ≥1 h. The 6:1 and 20:1 W51F samples show extensive polymerization, with a monomer content of ≤28% after 24 h. The percent monomer in oxidized W191F falls within the narrow range of 60–80% for all samples (Table 2), with the remainder forming dimeric forms exclusively, in agreement with published results (18).

Amino acid analyses

Analyses of the 24-h decay products of CCP(MI) and W191F were carried out (insufficient W51F was available for these

Table 2. Percent monomer in H_2O_2-oxidized CCP(MI), W51F, and W191F.[a]

	%Monomer[b]								
	2 equiv. H_2O_2			6equiv.H_2O_2			20 equiv.H_2O_2		
Time	CCP(MI)	W51F	W191F	CCP(MI)	W51F	W191F	CCP(MI)	W51F	W191F
15 s	100	85	78	100	60	65	100	68	70
5 min	100	73	70	69	35	66	68	25	60
1 h	100	60	65	72	26	70	67	28	65
24 h	100	60	67	68	26	65	60	28	65

[a]2, 6, and 20 equivalents of H_2O_2 were added to 5 μM protein in 0.1 M phosphate buffer (pH 7.0) and the samples were denatured at the times indicated.
[b]Percent monomer relative to unoxidized samples as estimated by integration of the densitometer tracings of the gels.

analyses). For both proteins the Trp loss was in good agreement with that observed by fluorescence. Loss of 0.7, 1.5, and 4.4 Tyr was observed for the 2:1, 6:1, and 20:1 decay products of CCP(MI), and the 20:1 product also lost 0.8 Met but 0 Cys. The corresponding Tyr losses for W191F were 1.5, 2.0, and 3.8, but no peroxide-induced loss of Met or Cys was observed for this mutant. Although the side chains of Met and Cys residues are readily oxidized, the amino acid analyses suggest that the endogenous donors to the heme are largely Trp and Tyr residues, rather than Met residues (Fig. 1) or the single Cys residue in CCP.

Discussion

CCP(MI)-I exhibits 91 ± 3% fluorescence at 350 nm relative to unoxidized CCP(MI) in 8 M urea at pH 1.5, corresponding to the loss of 0.7 ± 0.2 Trp. This result is the same as that observed for yeast wild-type CCP (10), and supports the assignment of Trp191 as the redox-active residue in CCP-I and CCP(MI)-I (1). W51F-I exhibits the same Trp loss (0.7 ± 0.1) as CCP(MI)-I, but the fluorescence loss in denatured W191F-I is negligible (Fig. 2*C*). These results are consistent with the assignment of the EPR signals to a tyrosyl radical in W191F-I and an indolyl radical in W51F-I (7, 8), and confirm that Tyr- and Trp-based radicals can be distinguished by the fluorescence method employed here.

Dissipation of the oxidizing equivalents (Fe^{IV}=O,$P^{\cdot+}$) stored in compound I increases the Trp loss in CCP(MI)-I and W51F-I to ~1.4. The Fe^{III} heme of the decay products reacts rapidly with H_2O_2, and this leads to the immediate loss of 1.3, 0.5, and 0.7 extra Trps in CCP(MI), W51F, and W191F (Table 1), corresponding to a *combined* loss of 2.7, 1.5, and 0.9 Trps, respectively. Oxidation of Trp51 on addition of H_2O_2 to the decay product of CCP(MI)-I is likely since Trp51 → Phe mutation significantly decreases Trp oxidation on the addition of H_2O_2 to the decay product of W51F-I. Trp51 is also a possible electron donor in the 24-h decay product of W191F-I given that reaction with H_2O_2 results in the loss of ~0.7 Trp (Table 1).

Addition of 6 equiv. of H_2O_2 to the *resting* enzymes prior to denaturation results in the loss of ~2 Trps in CCP(MI) and ~1 in each of the mutants (Fig. 2). This provides further evidence that oxidizing equivalents generated at the heme are transferred to Trp191 and Trp51 in CCP(MI) by a mechanism such as that given in eqs. [4] and [5]. The ABTS results reveal that CCP(MI) and W191F turn over 6 equiv. of H_2O_2 in less than 1 min, and the amino acid analyses show loss of 1.5 and 2 Tyr residues in CCP(MI) and W191F, respectively, in addition to the Trps oxidized in these proteins. To reduce 6 equiv. of H_2O_2 would require that three oxidized aromatic residues act as two-electron donors. However, additional donors may have gone undetected, given the experimental errors associated with amino acid analyses and the fluorescence measurements (see error bars in Fig. 2). LC-MS characterization of the oxidized proteins using an electrospray source is under way to determine the nature and location of the modified residues.

After standing for 24 h, the 6:1 decay products were reacted with more H_2O_2. The results revealed that an additional Trp was oxidized in CCP(MI) (Table 1), to give a *combined* loss of >3 Trps. No extra Trps were oxidized in the mutants (Table 1), where only one Trp was initially oxidized (Fig. 2). Thus, both Trp191 → Phe and Trp51 → Phe mutation must shut down pathways of endogenous electron transfer to the heme that access redox-active Trp residues in the wild-type enzyme.

Following exposure to 20 equiv. of H_2O_2 a maximum Trp loss of ~4, 2.5, and 2 is observed for CCP(MI), W51F, and W191F, respectively (Fig. 2). Amino acid analysis shows that ~4 Tyr residues were lost in both CCP(MI) and W191F, and ~1 Met in CCP(MI), and the ABTS results reveal that the 20 equiv. of H_2O_2 are turned over by CCP(MI) and W191F in 5 and 30 min, respectively. Thus, in the absence of catalatic activity ($2H_2O_2 \rightarrow O_2 + 2H_2O$), 20 electrons would have to be transferred to peroxide via the heme. Two-electron oxidation of the 9 residues found to be lost in CCP(MI) would supply 18 electrons, but only 12 electrons would be available from the 6 residues lost in W191F. It has been shown previously that yeast wild-type CCP can turn over 20 equiv. of H_2O_2 with no detectable oxygen evolution, which eliminates turnover via catalatic activity (20). It is possible that CCP(MI) also turns over 20 equiv. of H_2O_2 by utilizing endogenous donors, but this is less likely for W191F, and possible catalatic activity of this mutant is under investigation. It is noteworthy that an extra Trp is oxidized in the 20:1 decay product of CCP(MI) compared to the yeast enzyme (10); furthermore, CCP(MI) turns over 20 equiv. of H_2O_2 almost five times faster than yeast CCP (10). Hence, despite the very similar X-ray structures of the two wild-type proteins (26), they may not utilize a common set of pathways for endogenous electron donation to

the heme.

Oxidation of amino acid residues significantly reduces the ability of CCP(MI), and that of W191F to a lesser extent, to undergo reaction with H_2O_2 (eq. [1]). This is reflected in the H_2O_2 titres of the 24-h decay products listed in Table 1. Since one of the oxidizing equivalents of peroxide is transferred to the protein in reaction [1], depletion of endogenous donors around the heme (Fig. 1) may inhibit further reaction with peroxide. In addition, oxidation of the distal His52 could prevent Fe^{IV}=O formation, since this residue plays a key role in the heterolytic cleavage of peroxide, and His52 → Leu mutation results in a 10^5-fold decrease in the rate of reaction [1] (27, 28). Amino acid analysis shows loss of 0.3–0.6 His in the decay products of CCP(MI) and 0.1–0.4 His in those of W191F. Thus, the slightly greater His loss in the wild-type enzyme, coupled with the greater loss of redox-active aromatic residues, may account for the lower H_2O_2 titres of the CCP(MI) decay products.

The ferrocytochrome c oxidizing activities of the 24-h decay products of CCP(MI), and the ferrocyanide oxidizing activities of the W191F products are similar to their H_2O_2 titres (Table 1). Hence, the decreased activities of these species can be attributed to the same factors that prevent Fe^{IV}=O heme formation. However, the ferrocyanide oxidizing activities of the CCP(MI) decay products are ~10–20% lower than the corresponding ferrocytochrome c oxidizing activities (Table 1), unlike oxidized yeast CCP where both activities were found to be the same (10). Ferrocyanide and ferrocytochrome c are oxidized at different sites on CCP. The small molecule diffuses up the peroxide-access channel and is oxidized at the δ-*meso* heme edge (29). Reconstitution of CCP with δ-*meso*-substituted heme groups blocks ferrocyanide oxidation and selectively inhibits the ferrocyanide oxidizing activity of the enzyme (29). Retardation of ferrocyanide oxidation would thus be possible by diminishing access to the heme in the decay products by a mechanism such as radical-mediated *intra*molecular cross-linking in the neighbourhood of the substrate channel.

Oxidation of ferrocytochrome c involves complex formation between the proteins. A putative electron transfer path via Trp191 has been proposed based on the X-ray structure of the CCP – cyt c complex (18, 30), in which the heme edges are separated by at least 17 Å (18). It has been demonstrated that formation of an indolyl radical at Trp191 is necessary for the efficient ferrocytochrome c oxidizing activity of CCP(MI) (18). Since Trp loss is observed for the three CCP(MI) decay products (Table 1), it is possible that Trp191 is not 100% *irreversibly* oxidized in the fractions with ferrocytochrome c oxidizing activity. However, it is also possible that new ferrocytochrome c oxidation sites open up in the decay products, which do not require that Trp191 remains unaltered.

A comparison of Figs. 2, 3, and 4 indicates that the time course of activity loss is similar to that for fluorescence loss. Both change rapidly over the first 10–20 min, and then slowly over the next 24 h. Hence, fluorescence is a good probe of the time course of other changes, in addition to Trp loss, induced in CCP(MI) and its mutants following reaction with peroxide.

Table 2 summarizes the radical-mediated *inter*molecular cross-linking in CCP(MI) and its mutants. The percent dimer observed in the oxidized W191F samples falls within the range of 20–40% at all time intervals, irrespective of the extent of H_2O_2 turnover. Approximately 30% dimerization of W191F-I has been reported previously (18), which is roughly the average of the values listed for this mutant in Table 2. CCP(MI) exhibits a similar amount of dimerization as W191F, and also a small fraction of polymerization to higher molecular weight species, following the loss of 2 or more Trps (exposure to 6 equiv. of H_2O_2 for ≥5 min). The reaction of metmyoglobin with H_2O_2 also produces protein-based radicals, and a Tyr151–Tyr151 intermolecular cross-link has been established in sperm whale myoglobin (31). Tyrosine radicals readily dimerize, so the dityrosine bond in myoglobin is assumed to arise from radical formation at Tyr151, which is 12 Å from the heme (31). Peptide mapping of the dimer formed in H_2O_2-oxidized yeast CCP indicated that an intermolecular cross-link is localized between residues 32 and 48 (23, 32), a sequence that includes Tyr36, Tyr39, and Tyr42. These three Tyr residues are highly solvent exposed and are within 5–14 Å from the heme (Fig. 1); hence, cross-linking in W191F and CCP(MI) is likely to involve dityrosine formation between these Tyr-rich regions. It is of note that ≤40% of oxidized CCP(MI) and W191F undergo cross-linking (Table 2). This suggests that the radical migration pathway(s) leading to cross-linking are shut down once alternate pathways are chosen, or that the proteins are heterogeneous. Variation in the extent of post-translational processing of the N-terminal Met (33) in CCP(MI) and its mutants has been detected by electrospray MS (G. Tsaprailis, unpublished results), and the effects of such heterogeneity are under investigation. W51F-I exhibits similar cross-linking behaviour to W191F-I (Table 2), but on exposure to 6 equiv. of H_2O_2, extensive conversion to higher molecular weight species is observed.

The fluorescence, activity, and cross-linking data presented here on oxidized CCP(MI) and its Trp mutants underscore the important role played by Trp residues in the redox chemistry of the enzyme. Previously, we had suggested that a ring of aromatic residues on the proximal side of the heme of yeast CCP act as donors to peroxide (10); these residues include the 3 proximal Trps (191, 211, 223) and 3 Tyr residues (187, 229, 236) (Fig. 1). The fluorescence results obtained here support the loss of the 3 proximal Trps in recombinant CCP(MI), and the distal Trp51 appears to be also oxidized on addition of more than 2 equiv. of H_2O_2 to CCP(MI), as discussed previously. At least 4 Tyr residues are oxidized in CCP(MI) and these could include three from the proximal side, and one from sequence 32–48, which is likely to be involved in intramolecular cross-linking.

Mutation of Trp191 → Phe results in immediate cross-linking on W191F-I formation. Thus, electron transfer from a Tyr residue in sequence 32–48 to the porphyrin is likely to occur in W191F-I. Since Trp loss is observed following addition of >2 equiv. of H_2O_2 to W191F, oxidation of Trp51 may follow that of the initial Tyr. It is difficult to speculate on the identity of the remaining Tyr and Trp residues oxidized in W191F; however, their oxidation does not lead to further cross-linking of the protein.

Mutation of Trp51 → Phe gives rise to a protein that undergoes extensive cross-linking following addition of >2 equiv. of H_2O_2. Loss of 1 Trp on denaturation of W51F-I suggests than Trp191 is the first protein-based radical formed, but formation and dissipation of additional protein radicals in this mutant results in over 70% polymerization of

the protein.

The ability of CCP to reduce more than 2 equiv. of H_2O_2 in the absence of its donor substrate may be important under conditions of oxidative stress in yeast (34). Another of CCP's proposed functions is the regulation of mitochondrial respiration rates by controlling the flow of reducing equivalents to cytochrome c oxidase, which CCP does by competing for the same reducing substrate, ferrocytochrome c (34). To carry out both of these functions, the presence of Trp51 and Trp191 is critical. Mutation of the former results in an enzyme that undergoes extensive cross-linking, presumably due to radical migration to its surface. Exposed radicals in vivo would lead to damage of other cellular components. Removal of Trp191 leads to a "well-behaved" mutant, but one with negligible ferrocytochrome c oxidizing activity.

Acknowledgments

We wish to thank Dr Mark Miller (University of California, San Diego) for providing us with the CCP(MI), W51F, and W191F proteins used in this study. This research was supported by a grant from the Natural Sciences and Engineering Research Council of Canada (NSERC) to A.M.E.

References

1. M. Sivaraja, D.B. Goodin, M. Smith, and B.M. Hoffman. Science, **245**, 738 (1989).
2. R.C. Prince and G.N. George. Trends Biochem. Sci. **15**, 170 (1990).
3. J.M. Bollinger, Jr., W.H. Tong, N. Ravi, B.H. Huynh, D.E. Edmondson, and J. Stubbe. J. Am. Chem. Soc. **116**, 8024 (1994).
4. H. Sigel and A. Sigel (*Editors*) Metal ions in biological systems: Vol. 30. Metalloenzymes involving amino acid-residue and related radicals. Marcel Dekker, New York. 1994.
5. J.H. Dawson. Science, **240**, 433 (1989).
6. A.M. English and G. Tsaprailis. Adv. Inorg. Chem. **43**, 79 (1995).
7. C.P. Scholes, Y. Liu, L.A. Fishel, M.F. Farnum, J.M. Mauro, and J. Kraut. Isr. J. Chem. **29**, 85 (1989).
8. L.A. Fishel, M.F. Farnum, J.M. Mauro, M.A. Miller, and J. Kraut. Biochemistry, **30**, 1986 (1991).
9. J.E. Erman, L.B. Vitello, J.M. Mauro, and J. Kraut. Biochemistry, **28**, 7992 (1989).
10. T. Fox, G. Tsaprailis, and A.M. English. Biochemistry, **33**, 186 (1994).
11. T. Fox, L. Ferreira-Rajabi, B.C. Hill, and A.M. English. Biochemistry, **32**, 6938 (1993).
12. T.L. Poulos, S.L. Edwards, H. Wariishi, and M.H. Gold. J. Biol. Chem. **268**, 4429 (1993).
13. L. Marquez, H. Wariishi, H.B. Dunford, and M.H. Gold. J. Biol. Chem. **263**, 10549 (1988).
14. S.S. Isied. *In* Metal ions in biological systems. Vol. 27. Electron transfer reactions in metalloproteins, *Edited by* H. Sigel and A. Sigel. Marcel Dekker, New York. 1991. pp. 1–56.
15. J.E. Erman, L.B. Vitello, M.A. Miller, and J. Kraut. J.Am. Chem. Soc. **114**, 6592 (1992).
16. L.A. Fishel, J.E. Villafranca, J.M. Mauro, and J. Kraut. Biochemistry, **26**, 351 (1987).
17. J.E. Erman and T. Yonetani. Biochim. Biophys. Acta, **393**, 350 (1975).
18. M.A. Miller, L. Vitello, and J.E. Erman. Biochemistry, **34**, 12048 (1995).
19. N.P. Neumann. Methods Enzymol. **11**, 485 (1967).
20. J.E. Erman and T. Yonetani. Biochim. Biophys. Acta, **393**, 343 (1975).
21. J.M. Mauro, L.A. Fishel, J.T. Hazzard, T.E. Meyer, G. Tollin, M.A. Cusanovich, and J. Kraut. Biochemistry, **27**, 6243 (1988).
22. T. Yonetani and G.S. Ray. J. Biol. Chem. **240**, 4503 (1965).
23. B.D. Spangler. Ph.D. Dissertation, Northern Illinois University, Dekalb, Ill. 1984.
24. H.C. Jordi and J.E. Erman. Biochemistry, **13**, 3741 (1974).
25. J.R. Lakowicz. Principles of fluorescence spectroscopy. Plenum, New York. 1983. p. 44.
26. J. Wang, J.M. Mauro, S.L. Edwards, S.J. Oatley, L.A. Fishel, V.A. Ashford, N. Xuong, and J. Kraut. Biochemistry, **29**, 7160 (1990).
27. J.E. Erman and L.B. Vitello, J. Am. Chem. Soc. **114**, 6592 (1992).
28. J.E. Erman, L.B. Vitello, M.A. Miller, A. Shaw, K.A. Brown, and J. Kraut. Biochemistry, **32**, 9798 (1993).
29. G.D. DePhillis, B.P. Sishta, A.G. Mauk, and P.R. Ortiz de Montellano. J. Biol. Chem. **266**, 19334 (1991).
30. H. Pelletier and J. Kraut. Science, **258**, 1748 (1992).
31. A. Wilks and P.R. Ortiz de Montellano. J. Biol. Chem. **267**, 8827 (1992).
32. B.D. Spangler and J.E. Erman. Biochim. Biophys. Acta, **872**, 155 (1986).
33. F. Sherman, J.W. Stewart, and S. Tsunasawa. BioEssays, **3**, 27 (1985).
34. A.M. English. *In* Encyclopedia of inorganic chemistry. Vol. 4. *Edited* by R.B. King. Wiley, Chichester. 1994. pp. 1682–1697.

The metal-mediated conversion of octachlorocycloheptatriene into dodecachloroheptafulvalene: a synthetic, structural, and EHMO study

James A. Dunn, Hari K. Gupta, Alex D. Bain, and Michael J. McGlinchey

Abstract: Octachlorocycloheptatriene, C_7Cl_8, **3**, reacts with a variety of organometallic precursors, e.g., $Fe_2(CO)_9$, $Co_2(CO)_8$, $[(C_5H_5)Fe(CO)_2]^-$, to give dodecachloroheptafulvalene, $C_{14}Cl_{12}$, **12**, in yields ranging from 54 to 68%. There is no evidence to support the intermediacy of carbene complexes of the type $C_7Cl_6{=}ML_n$, and it is suggested that the reaction proceeds by the dechlorination of C_7Cl_8 to give hexachlorotropylidene, which dimerizes to the observed product. Extended Hückel molecular orbital calculations are used to show that the chlorinated carbene, C_7Cl_6, should be more stable than the corresponding parent system, C_7H_6. The EHMO calculations also reveal that planar heptafulvalenes are electronically disfavored and should exist preferentially in the *S-anti* conformation, as is the case for $C_{14}H_{12}$. The molecule $C_{14}Cl_{12}$, **12**, is shown by X-ray crystallography to be formed only as the *syn* conformer, which isomerizes to the *anti* structure only at high temperature. The conformations of the two seven-membered rings in **12** closely resemble that found in octachlorocycloheptatriene itself. C_7Cl_8, **3**, crystallizes in the orthorhombic space group *Pnma* with $a = 7.140(1)$ Å, $b = 13.329(3)$ Å, $c = 12.595(3)$ Å, and $V = 1198.7(4)$ Å^3 for $Z = 4$. **3** adopts a severely bent boat structure in which the planes C(1)-C(7)-C(6) and C(2)-C(3)-C(4)-C(5) make angles of 51.8° and 32.4°, respectively, with the C(1)-C(2)-C(5)-C(6) plane.

Key words: octachlorocycloheptatriene, heptafulvalenes, metal-mediated dimerization.

Résumé : L'octachlorocycloheptatrième C_7Cl_8, **3**, réagit avec divers précurseurs organométalliques, par exemple : $Fe_2(CO)_9$, $Co_2(CO)_8$, $[(C_5H_5)Fe(CO)_2]^-$, pour donner le dodécachloroheptafulvène, $C_{14}Cl_{12}$, **12**, avec des rendements allant de 54 à 68%. Il n'y a pas de preuve qui permet de confirmer la présence d'un complexe carbène intermédiaire du type $C_7Cl_6{=}ML_n$, et on suggère que la réaction s'effectue par la déchloration du C_7Cl_8 pour donner l'hexachlorotropylidène qui, par dimérisation, conduit au produit observé. On a utilisé des calculs étendus d'orbitale moléculaire de Hückel pour montrer que le carbène chloré, C_7Cl_6, doit être plus stable que le système apparenté correspondant, C_7H_6. Les calcluls OMEH révèlent également que les heptafulvènes plans sont défavorisés électroniquement et doivent exister préférentiellement dans une conformation *S-anti*, comme dans le cas du $C_{14}Cl_{12}$. On montre, par cristallographie de rayons X, que la molécule $C_{14}Cl_{12}$, **12**, existe uniquement sous forme de conformère *syn* qui s'isomérise seulement à haute température en une structure *anti*. La conformation des deux cycles à sept chaînons dans le composé **12** ressemble étroitement à celle trouvée dans l'octachlorocycloheptatrième lui-même. Le composé C_7Cl_8, **3**, cristallise dans le groupe d'espace orthorhombique *Pnma* avec $a = 7{,}140(1)$ Å, $b = 13{,}329(3)$ Å, $c = 12{,}595(3)$ Å, et $V = 1198{,}7(4)$ Å^3 pour $Z = 4$. Le composé **3** adopte une structure bateau fortement courbée dans laquelle les plans C(1)-C(7)-C(6) et C(2)-C(3)-C(4)-C(5) font respectivement un angle de 51,8° et de 32.4° avec le plan C(1)-C(2)-C(5)-C(6).

Mots clés : octachlorocycloheptatrième, heptafulvènes, dimérisation assistée par un métal.

[Traduit par la rédaction]

Introduction

In continuation of our studies on organometallic derivatives of seven-membered rings (1), we chose to prepare octachlorocycloheptatriene, C_7Cl_8, as an example of a sterically hindered molecule. Although perfluorinated ligands, such as C_5F_5, C_6F_6, or C_8F_8, have received considerable attention (2–4), perchlorinated systems appear to have been less thoroughly investigated. A number of perchlorocyclopentadienyl complexes, e.g., $(\eta^1\text{-}C_5Cl_5)Mn(CO)_5$, $(\eta^5\text{-}C_5Cl_5)Mn(CO)_3$, and $(\eta^5\text{-}C_5Cl_5)_2Ru$, are known (5, 6), and recently $(\eta^6\text{-}C_6Cl_6)Cr(CO)_3$ was obtained by repeated lithiation and chlorination procedures (7). We are unaware of any organometallic derivatives possessing a C_7Cl_7 ligand. It has been claimed (8) that $Fe_2(CO)_9$ reacts with perchloro(3,4-dimethylenecyclobutene) and with perchlorofulvene to give organo-iron complexes, but their identity has not been confirmed by X-ray crystallography. We here report the X-ray crystal structure of C_7Cl_8, its reaction with a series of metal carbonyls to give *syn*-

Received March 7, 1996.

This paper is dedicated to Professor Howard C. Clark in recognition of his contributions to Canadian chemistry.

J.A. Dunn, H.K. Gupta, A.D. Bain, and M.J. McGlinchey.[1]
Department of Chemistry, McMaster University, Hamilton, ON L8S 4M1, Canada.

[1] Author to whom correspondence may be addressed. Telephone: (905) 525-9140, ext. 23303. Fax: (905) 522-2509. E-mail: mcglinc@mcmaster.ca

Scheme 1. Synthetic route to C_7Cl_8, **3**.

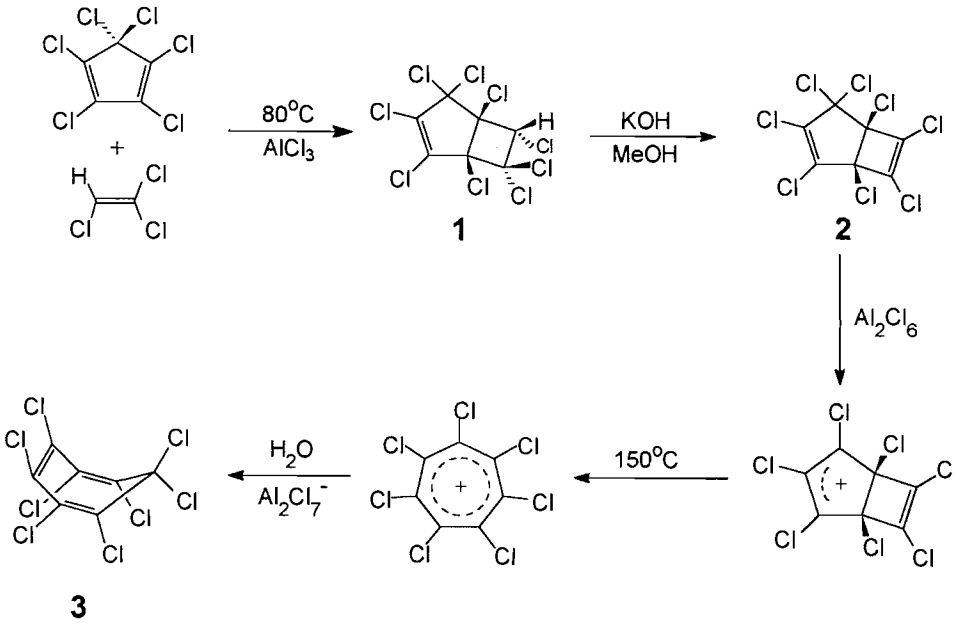

$C_{14}Cl_{12}$, and EHMO calculations to rationalize the observed nonplanar geometry of heptafulvalenes.

Results and discussion

The structure of C_7Cl_8

The synthesis of octachlorocycloheptatriene, first described by West and co-workers in 1968 (9, 10), involves the reaction of hexachlorocyclopentadiene, C_5Cl_6, with trichloroethylene to give the bicyclo[3.2.0]heptene, **1**, which can be dehydrochlorinated to produce the diene **2**, as in Scheme 1. Subsequent thermolysis in the presence of aluminum chloride yields octachlorocycloheptatriene, **3**, presumably by the symmetry-forbidden disrotatory ring opening of the intermediate cation to the heptachlorotropylium ion which can recapture a chloride from the chloroaluminate anion.

Although the position of the unique hydrogen in C_7Cl_9H, **1**, is not known with certainty, the structure of the related molecule $C_7Cl_8H_2$, **4**, has been established by an X-ray diffraction study (11). The two isomers of C_7Cl_8, namely **2** and **3**, give readily interpretable mass spectra since their chlorine isotope patterns are immediately evident. However, to characterize such highly chlorinated molecules, nuclear quadrupole resonance spectroscopy is arguably more useful than are the conventional NMR techniques. The NQR spectrum of **3** was described in the original synthetic report (10), but the signal-to-noise was rather unsatisfactory and we now report more accurate parameters. Figure 1 shows the ^{35}Cl NQR spectrum of octachlorocycloheptatriene, **3**, acquired on a solid state NMR spectrometer by removing the probe from the magnet and tuning to the ^{35}Cl frequency range. The excellent signal-to-noise ratio obtainable by this technique is evident, and five peaks are found in the expected 2:2:2:1:1 ratio; the first three resonances are found in the region for vinylic chlorines, while the latter two are typical of a CCl_2 moiety.

The boat-shaped geometry of cycloheptatriene, **5**, was originally established from electron diffraction measurements.

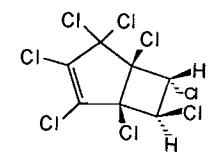

4

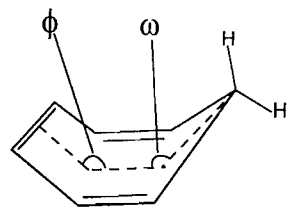

5

The dihedral angles between C(6)-C(7)-C(1) (plane 1), (C(1)-C(2)-C(5)-C(6) (plane 2), and (C(2)-C(3)-C(4)-C(5) (plane 3) are $\omega = 144°$ for (plane 1)/(plane 2), and $\phi = 140°$ for (plane 2)/(plane 3), respectively (12). In the severely hindered heptaphenyl analogue C_7Ph_7H, **6**, the corresponding values of ω and ϕ are 125° and 145°. That molecule is initially generated (see Scheme 2) as conformation **6a** whereby the unique phenyl substituent occupies an equatorial site; however, the ring flips irreversibly to the axial conformer **6b**, which has been structurally characterized (1).

There is a report that in hexachlorotropone, C_7Cl_6O, **7**, the bulky chlorines do not permit the ring to maintain the electronically favored planar geometry, but rather it adopts a boat conformation with ω and ϕ values of 151° and 156°, respectively.[2] Analogously, the seven-membered ring in the do-

[2] R.P. Dodge, R.J. Sime, and D.H. Templeton, personal communication cited in ref. 13.

Fig. 1. ^{35}Cl NQR spectrum of C_7Cl_8, **3**.

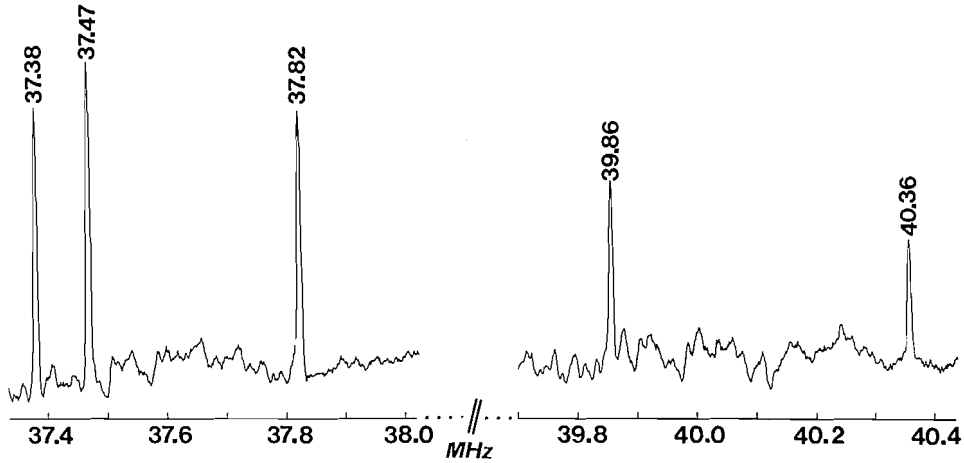

Scheme 2. Synthesis and isomerization of C_7Ph_7H, **6**.

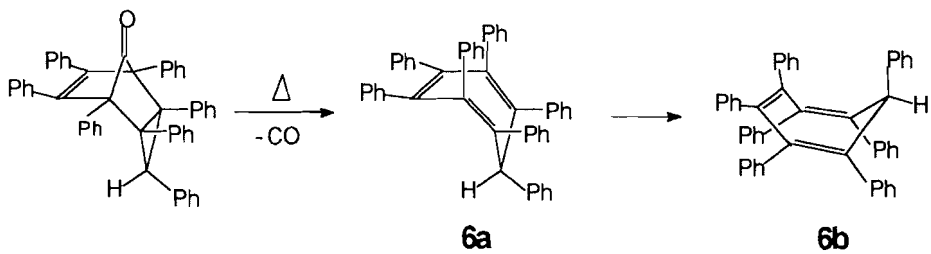

decachloro[1.6.7]quinarene, **8**, is also markedly nonplanar (14).

Since we had in hand X-ray quality crystals of C_7Cl_8, **3**, we obtained diffraction data, and the resulting structure appears as Fig. 2. Crystallographic data, together with bond lengths and angles, are collected in Tables 1–3. Octachlorocycloheptatriene adopts a boat conformation in which the CCl_2 unit is bent up through 51.8° from the C(1)-C(2)-C(6)-C(7) plane, (i.e., $\omega = 128.2°$) while the C(3)—C(4) unit is bent up by 32.4° ($\phi = 147.6°$). There is clear bond alternation whereby the single bonds average 1.479 Å, and the mean double bond length is 1.336 Å. There is no indication of a norcaradiene-type structure, **9**, as is known for 7,7-dicyanocycloheptatriene (15). Overall, these data suggest that the steric hindrance within polychlorinated seven-membered rings is substantial, and that the system should exhibit a high barrier towards boat-to-boat conformational flipping.

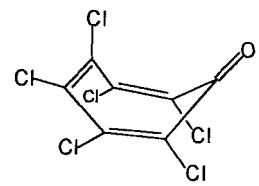

7

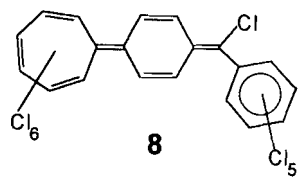

8

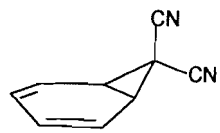

9

Reactions of C_7Cl_8 with organometallics

We are aware of only a single reaction of C_7Cl_8, **3**, with a transition metal complex (16). Treatment of octachlorocycloheptatriene with nickelocene resulted in coupling of a C_5H_5 fragment with a C_7Cl_7 unit (see Scheme 3); subsequent intramolecular Diels–Alder addition yielded the cage compound **10**. The perchloro analogue of **10**, viz. **11**, has been characterized crystallographically as the product resulting from the reaction of **3** with tetrachlorodiazocyclopentadiene (17).

In an attempt to prepare metal carbonyl complexes possessing a C_7Cl_7 fragment, we treated **3** with a number of organometallic precursors, viz. $[(C_5H_5)Fe(CO)_2]^-$, $Fe_2(CO)_9$, $Co_2(CO)_8$, $(acac)Rh(C_2H_4)_2$, and $(Ph_3P)_2Rh(CO)Cl$. In all cases, the sole organic product isolated was *syn*-perchloroheptafulvene, **12**. This molecule, previously found in 80% yield from the reaction of C_7Cl_8 with methyllithium, had been structurally characterized by X-ray diffraction, despite a crystallo-

Table 1. Structure determination summary.

	3
Empirical formula	C_7Cl_8
Formula wt.	367.67
Dimensions, mm	0.36 x 0.31 x 0.20
Crystal system	Orthorhombic
Space group	*Pnma*
a, Å	7.140(1)
b, Å	13.329(3)
c, Å	12.595(3)
V, Å^3	1198.7(4)
F(000)	712
Z	4
ρ_{calc}, g.cm^{-3}	2.037
Radiation(λ, Å)	Ag Kα (0.56086)
Monochromator	graphite
Temp, K	293(2)
μ(Ag Kα), mm^{-1}	0.928
Absorption correction	ψ scan
Transmission max,min	0.794,0.600
Scan method	θ–2θ
2θ range, deg	3.52–40.1
Index ranges	$-1 \le h \le 8$, $-16 \le k \le 1$, $-1 \le l \le 15$
No. of measd rflcns	1928
No. of unique rflcns	1202
No. of obsd rflcns	1202 ($I \ge -3\sigma(I)$)
No. of variables	73
*R*1 ($I > 2\sigma(I)$)	0.0335
R_w (all data)	0.0767
GOF	0.848
Weighting scheme	[a]
Largest diff. peak, e Å^{-3}	0.279
Largest diff. hole, e Å^{-3}	−0.302

[a] $w = [\sigma^2F_o^2 + (0.0410p)^2 + (0.00p)]^{-1}$, where $p = [\max(F_o^2, 0) + 2F_c^2]/3$.

Table 2. Atomic coordinates (×10^4) and equivalent isotropic displacement parameters (Å^2 × 10^3) for **3**.

	x	*y*	*z*	*U*(eq)[a]
Cl(7A)	1709(2)	2500	4120(1)	61(1)
Cl(7B)	23322(2)	2500	6166(1)	86(1)
Cl(1)	652(1)	4115(1)	6850(1)	72(1)
Cl(2)	−2870(2)	4683(1)	5600(1)	65(1)
Cl(3)	−3427(1)	3642(1)	3406(1)	65(1)
C(7)	−1140(6)	2500	5516(3)	51(1)
C(1)	−33(4)	3406(2)	5792(2)	45(1)
C(2)	−1627(4)	3618(2)	5287(2)	43(1)
C(3)	−2424(4)	3003(2)	4452(2)	42(1)

[a] *U*(eq) is defined as one third of the trace of the orthogonalized U_{ij} tensor.

Table 3. Bond lengths (Å) and angles (deg) for **3**.

Cl(7A)—C(7)	1.804(4)
Cl(7B)—C(7)	1.760(5)
Cl(1)—C(1)	1.705(3)
Cl(2)—C(2)	1.720(3)
Cl(3)—C(3)	1.725(3)
C(7)—C(1)	1.511(4)
C(1)—C(2)	1.334(4)
C(2)—C(3)	1.450(4)
C(3)—C(4)	1.340(5)
C(1)-C(7)-C(6)	106.2(3)
C(1)-C(7)-Cl(7B)	112.6(2)
C(1)-C(7)-Cl(7A)	110.4(2)
Cl(7A)-C(7)-C(7B)	104.7(2)
C(2)-C(1)-C(7)	122.2(3)
C(2)-C(1)-Cl(1)	120.0(2)
C(7)-C(1)-Cl(1)	117.6(3)
C(1)-C(2)-C(3)	124.1(3)
C(1)-C(2)-Cl(2)	120.4(2)
C(3)-C(2)-Cl(2)	115.5(2)
C(4)-C(3)-C(2)	124.4(2)
C(4)-C(3)-Cl(3)	119.6(1)
C(2)-C(3)-Cl(3)	116.0(2)
Cl(1)-C(1)-C(2)-Cl(2)	7.1(4)
Cl(2)-C(2)-C(3)-Cl(3)	38.5(3)
Cl(3)-C(3)-C(4)-Cl(4)	0.0

Fig. 2. X-ray crystal structure of C_7Cl_8, **3**, showing the atom numbering scheme.

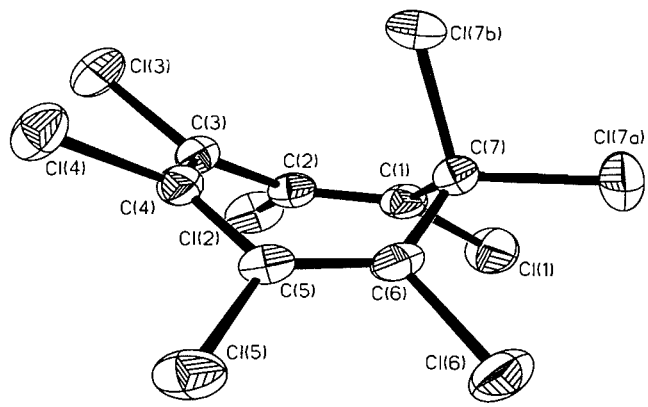

graphic disorder problem (18). Since we had obtained crystals by a different route, we collected a data set in the hope of resolving the disorder but encountered the same difficulty. The bivalvular (clam-shaped) geometry allows the molecules to pack randomly with the central double bond "up" or "down," as indicated in Fig. 3. The structure can be modelled by assigning half occupancies to all atoms except C(3), C(6), C(10), C(13), and their attached chlorines. Figure 3 illustrates this crystallographic disorder (showing only the carbon framework for clarity), while Fig. 4 depicts the geometry of a single

Scheme 3. Syntheses of chlorinated cages derived from C_7Cl_8, **3**.

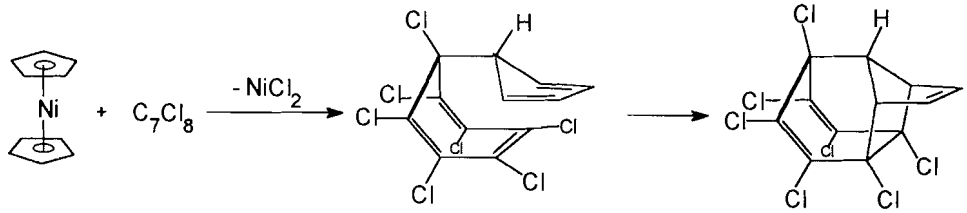

10

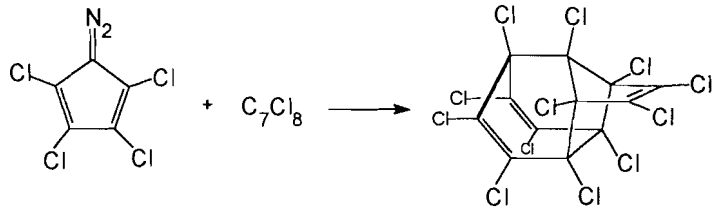

11

molecule of **12**. The seven-membered rings are severely bent with interplanar angles ω and ϕ of 124.7° and 147.5°, respectively. The central carbon–carbon double bond is markedly pyramidal such that the atoms C(1) and C(8) lie 0.09 Å out of the plane containing C(2), C(7), C(9), and C(14). Another way to describe this facet of the structure is to define an angle θ (= 173.5°) between the plane containing C(1), C(2), and C(7), and the C(1)═C(8) vector. Each Cl-C═C-Cl moiety is essentially planar and appears to be isolated from its neighboring double-bonded fragment.

It has been suggested (18) that *syn*-$C_{14}Cl_{12}$, might arise by lithiation at one of the dichloro positions of C_7Cl_8 to give C_7Cl_7Li that, in turn, could attack a second molecule of **3** to produce perchloroditropyl, **14**, as in Scheme 4. A second lithiation, followed by *cis* elimination of LiCl, could yield **12**. Prolonged heating of *syn*-$C_{14}Cl_{12}$, **12**, yields the known *anti*-$C_{14}Cl_{12}$, **13**, originally described by West, Dahl, and their colleagues (19). Continued heating of **13** to 340°C brings about loss of chlorine and rearrangement to decachlorophenanthrene.

Our own speculations have focussed on the possible intermediacy of a hexachlorotropylidene–metal complex. Analogous C_7H_6 carbene complexes of iron, tungsten, and ruthenium have been synthesized (20), as typified in Scheme 5. However, despite repeated efforts, we have been unable to obtain any evidence for such perchlorocarbene complexes; the metal-containing products are merely well-known materials such as $CoCl_2$ or $FeCl_2$. Moreover, if *syn*-$C_{14}Cl_{12}$ arises as the result of a metal–template-induced coupling, one must still account for the observed *syn* stereochemistry. On the other hand, if, as we suspect, the metal merely dechlorinates C_7Cl_8 to give hexachlorotropylidene, C_7Cl_6, then one must consider the possible fate of this carbene intermediate. It is relevant to note that the reaction of decachloro(4-allylidenecyclopentene), **15**, with $Fe_2(CO)_9$ leads to the cyclization product octachlorobicyclo[3.3.0]octa-1,3,7-triene, **16** (21). One could envisage metal-promoted dechlorination, as in Scheme 6, to produce an intermediate carbene **17** that inserts into a C—Cl bond and, after a chlorine [1,5] sigmatropic shift, yields the bicyclo species **16**.

Fig. 3. X-ray crystal structure of *syn*-$C_{14}Cl_{12}$, **12**, showing the molecular disorder of the carbon skeleton; chlorines have been omitted for clarity.

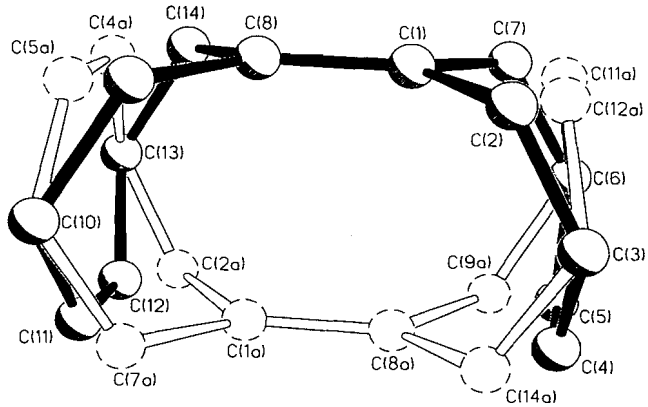

Fig. 4. X-ray crystal structure of *syn*-$C_{14}Cl_{12}$, **12**, showing the atom numbering scheme.

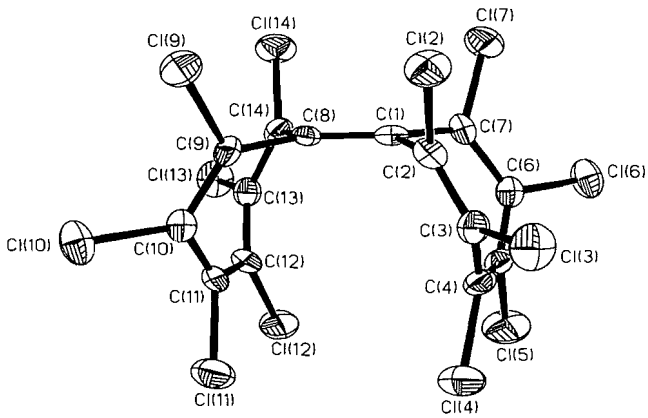

In recent years, the chemistry of the so-called "nucleophilic carbenes" has received much attention (22). These species, typified by $(MeO)_2C$:, have singlet character whereby the electron deficiency at the carbene center is considerably alle-

Scheme 4. Proposed lithiation route to *syn*-$C_{14}Cl_{12}$, **12**, and its isomerization to *anti*-$C_{14}Cl_{12}$, **13**.

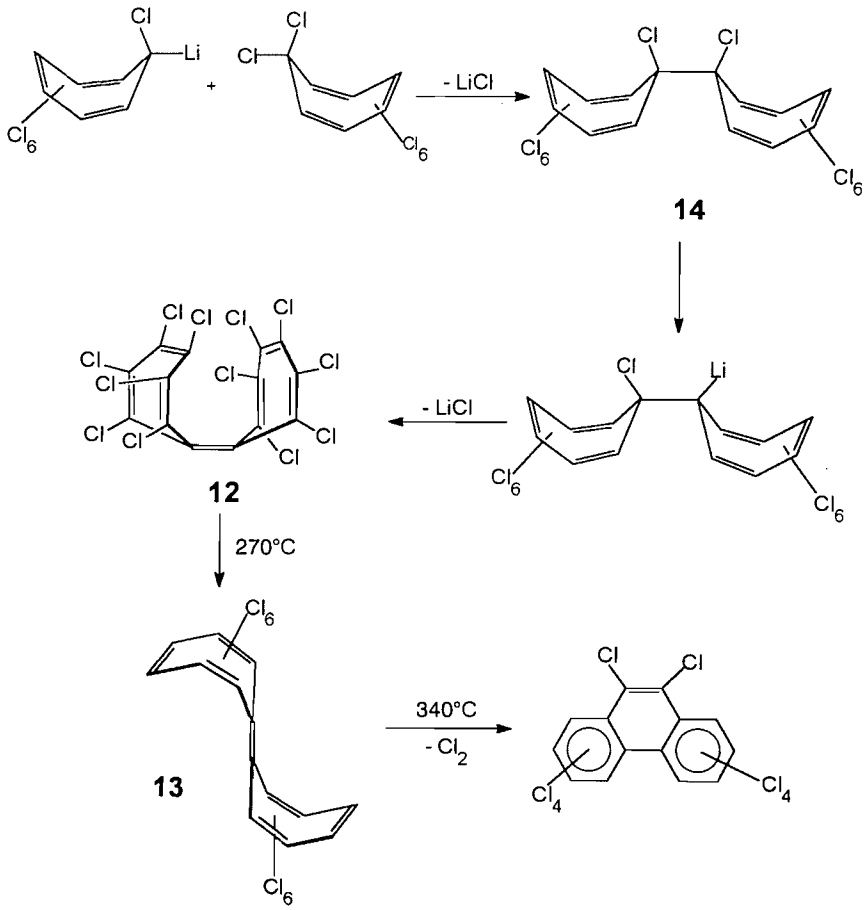

Scheme 5. Route to metal-tropylidene complexes.

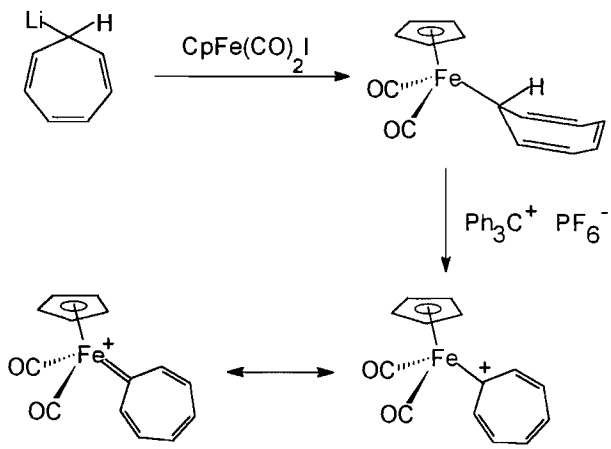

Scheme 6. Proposed carbene mechanism of $Fe_2(CO)_9$-promoted cyclization.

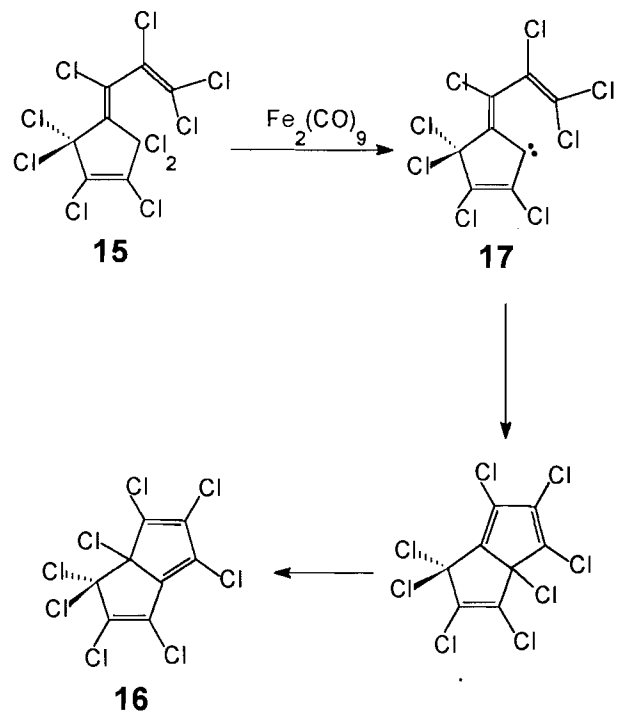

viated by π donation from adjacent oxygen (or nitrogen) atoms to the formally vacant p_z orbital on carbon. These carbenes are sufficiently long lived that, in the absence of a suitable trap, they can give good yields of dimer. We show in Fig. 5 a comparison of the EHMO-derived frontier orbital patterns for planar C_7H_6 and for C_7Cl_6.

The structure of C_7H_6 has been intensively studied with respect to the relative stabilities of the planar tropylidene carbene and the allene-like cyclohepta-1,2,4,6-tetraene (23).

Scheme 7. Proposed route to heptafulvalene via a cyclic allene dimer.

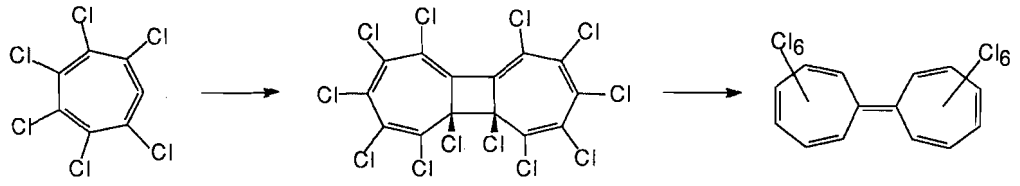

Fig. 5. Frontier orbitals of C_7Cl_6 and of C_7H_6.

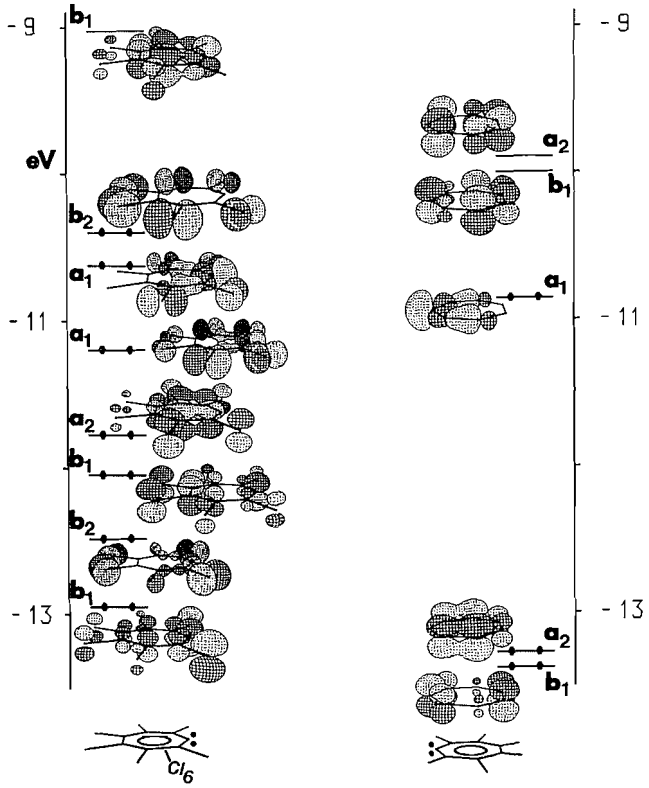

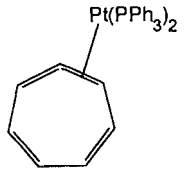

18

Indeed, it has even been claimed that the carbene form does not represent an energy minimum, but rather is merely the transition state for the interconversion of enantiomeric allenes (24*a*).[3] As mentioned previously, numerous metal–tropylidene systems have been described (20), but there is a report that the cyclohepta-1,2,4,6-tetraene form has been trapped as a stable $(Ph_3P)_2Pt(C_7H_6)$ complex, **18** (25).

When we compare the planar tropylidenes, we note that, in C_7H_6, the HOMO has a large in-plane component on the carbene carbon, while the LUMO has predominant π^* character (23). By way of contrast, in C_7Cl_6 the HOMO is localized entirely on the peripheral chlorines, and lies just above the "σ lone pair" on the carbene carbon, as anticipated for a singlet species. We see from Fig. 5 that there is a markedly enhanced HOMO–LUMO gap in the chlorinated system that can be traced to participation of the chlorine p_z orbitals with the π manifold of the ring. One may conclude that C_7Cl_6 should be a relatively long-lived nucleophilic carbene with a high propensity to dimerize. Such an interaction between two carbenes would presumably involve donation of the in-plane lone pair of electrons on the carbene carbon of one C_7Cl_6 fragment into the LUMO of its reaction partner. Moreover, the *syn* stereochemistry may well arise as the result of secondary orbital interactions — a phenomenon commonly invoked to account for the formation of *endo* adducts in the Diels–Alder reaction (26). An alternative scenario would invoke dimerization of the cyclic allenes to give a tricyclic system that could open up to give the observed heptafulvalene, as in Scheme 7 (27). Calculations to clarify these aspects are in progress.

It is noteworthy that the conversion of *syn*-$C_{14}Cl_{12}$, **12**, to *anti*-$C_{14}Cl_{12}$, **13**, requires prolonged heating at 275°C (19); clearly, this process has a very large activation energy! Of course, the steric problems encountered by a planar C_7Cl_6 moiety as it manoeuvers its way past the neighboring chlorines in the other half of the molecule impose a large barrier but, even in the absence of large chlorine substituents, heptafulvalenes are not planar. Early calculations by Dewar and Gleicher suggested that planar $C_{14}H_{12}$ would exhibit bond fixation rather than a delocalized structure in which all bond lengths were rather similar (28). A subsequent X-ray crystal structure confirmed this prediction of alternating single and double bonds, but also showed the molecule to be nonplanar (29). As shown in Fig. 6, $C_{14}H_{12}$ adopts the *anti* conformation with interplanar angles θ, ω, and ϕ of 173°, 155°, and 164°, respectively.

This result may be rationalized with the aid of molecular orbital calculations at the extended Hückel level. Figure 7 presents a Walsh diagram depicting the gradual flattening of $C_{14}H_{12}$. The energy minimum is found for θ, ω, and ϕ values each within one degree of those found in the X-ray crystal structure. We see that bending the molecule symmetrically into an *S* shape (i.e., after breaking the D_{2h} symmetry of the planar molecule we preserve C_{2h} symmetry throughout the process) stabilizes the HOMO and raises the LUMO. In the planar molecule, the HOMO reveals a substantial π^* overlap between the central C=C moiety and the two outer fragments; this destabilizing interaction is decreased as the molecule bends. Concomitantly, the LUMO loses some degree of in-phase π-type overlap, and the net result is to augment the HOMO–LUMO gap. The bent structure is calculated to be approximately 8.5 kcal mol^{-1} more stable than the planar form.

These effects are not just the result of crystal packing

[3] For a very recent summary of the current status of the C_7H_6 problem, see ref. 24*b*.

Fig. 6. X-ray crystal structure of *anti*-$C_{14}H_{12}$; data taken from ref. 29.

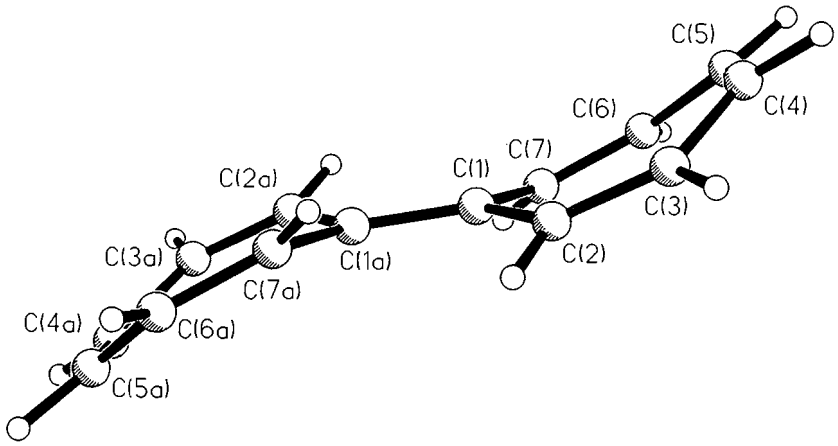

forces; heptafulvalene is known to undergo symmetry-allowed $[_{\pi}14_a+_{\pi}2_s]$ cycloaddition with tetracyanoethylene whereby the twisted shape of the $C_{14}H_{12}$ is ideally suited for *antara* addition to the 14π system to give the adduct **19**.[4]

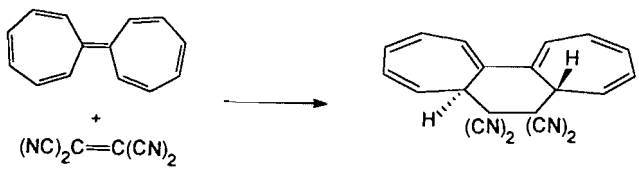

19

In conclusion, we report that octachlorocycloheptatriene, **3**, adopts a severely bent boat conformation, closely analogous to that found for C_7Ph_7H. Treatment of C_7Cl_8 with metal carbonyls does not yield isolable organometallic complexes but rather leads to dechlorination and dimerization to *syn*-perchloroheptafulvalene, **12**. The high barrier to conformational change from **12** to its *anti*-isomer **13** may be attributed principally to unfavorable steric interactions between chlorines. However, it is also shown that electronic factors favor nonplanar conformations for heptafulvalenes.

Experimental section

All reactions were carried out under an atmosphere of dry nitrogen employing conventional benchtop and glovebag techniques. All solvents were dried according to standard procedures before use (31). Silica gel (particle size: 20–45 μm) was employed for flash column chromatography. ^1H and ^{13}C solution NMR spectra were recorded on a Bruker AC-200 spectrometer. Mass spectra were obtained on a VG analytical ZAB-ZE spectrometer.

NQR spectra were run on a Bruker MSL 100 NMR spectrometer equipped with a 10 mm wideline solenoid probe and a fast digitizer. Approximately a gram of sample was used, and good spectra were obtained in under 10 min. The low-power transmitter in the spectrometer gave a null in the signal, which is similar to a 180° pulse in NMR (32), at a pulse width of 17 μs. Spectra were obtained with a 1 μs pulse and digitized over a sweep range of 1 MHz, with a delay between pulses of 50 ms.

[4] W. von E. Doering, personal communication cited in ref. 30.

Fig. 7. EHMO-derived Walsh diagram depicting the symmetrical flattening of *anti*-$C_{14}H_{12}$ from a C_{2h} geometry to D_{2h}. The HOMO is marked with an asterisk. (The broken line represents the total electronic energy and is drawn to a different scale.)

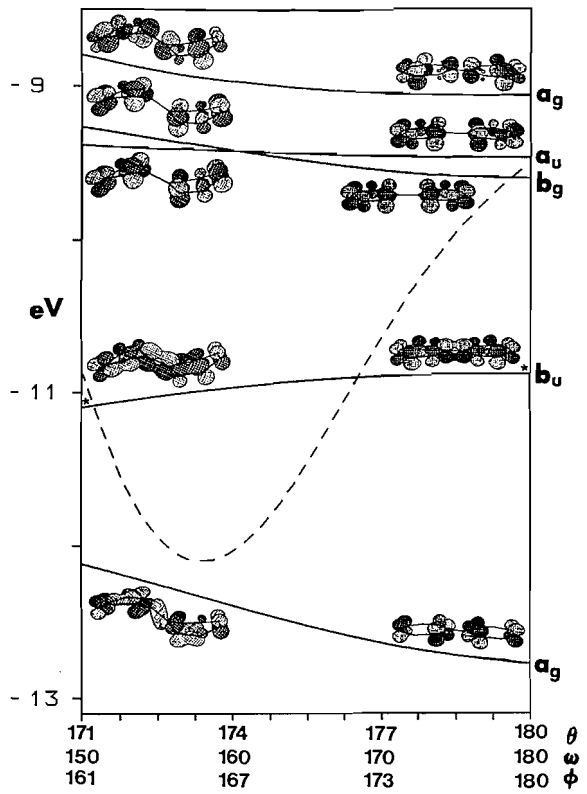

Reaction of C_7Cl_8 with $Fe_2(CO)_9$

Octachlorocycloheptatriene (0.184 g, 0.50 mmol), prepared by West's method (10) and $Fe_2(CO)_9$ (0.182 g, 0.50 mmol) were heated under reflux in tetrahydrofuran (THF) (10 mL) for 24 h. The mixture was cooled, filtered to remove the inorganic salts, and the volume was reduced under vacuum. Addition of hexane eventually led to the precipitation of light yellow crystals of $C_{14}Cl_{12}$, **12**, (0.080 g, 0.134 mmol, 54%). ^{13}C NMR (CD_2Cl_2) δ: 137.0, 132.8, 128.6, 124.0. Mass spectrum *m/z* (%): 588 $[M]^+$, 553 $[M - Cl]^+$, 518 $[M - 2Cl]^+$, 483 $[M - 3Cl]^+$, 448 $[M - 4Cl]^+$, 378 $[M - 6Cl]^+$, 294 $[C_7Cl_6]^+$,

259 $[C_7Cl_5]^+$, 224 $[C_7Cl_4]^+$, 189 $[C_7Cl_3]^+$. Peaks quoted are in each case the lowest mass in the envelope and correspond to ^{35}Cl; the observed isotopic abundances correctly matched the pattern required for the number of chlorines in the fragment ion.

Reaction of C_7Cl_8 with $Co_2(CO)_8$

$Co_2(CO)_8$ (0.372 g, 1.09 mmol) dissolved in THF (30 mL) was added to a solution of C_7Cl_8 (0.400 g, 1.09 mmol) in THF (10 mL) and allowed to stir at room temperature for 24 h. Filtration, concentration to half volume, and treatment with hexane gave a crude solid that was purified by flash chromatography (hexanes) to yield as the sole product $C_{14}Cl_{12}$, **12**, (0.177 g, 0.30 mmol, 55%), identified by its mass spectrum.

Reaction of C_7Cl_8 with $(Ph_3P)_2Rh(CO)Cl$

A mixture of $(Ph_3P)_2Rh(CO)Cl$ (0.345 g, 0.50 mmol) and C_7Cl_8 (0.184 g, 0.50 mmol) in THF (20 mL) was heated under reflux for 24 h. Filtration, concentration to half volume, and treatment with hexane gave a crude solid that was recrystallized from $CHCl_3$ to yield as the sole product $C_{14}Cl_{12}$, **12**, (0.095 g, 0.16 mmol, 64%), identified by its mass spectrum.

Reaction of C_7Cl_8 with $Na[Fe(CO)_2(C_5H_5)]$

To a solution of $[(C_5H_5)Fe(CO)_2]_2$ (0.145 g, 0.40 mmol) in THF (10 mL) was added excess Na–Hg. The resulting red solution was filtered, treated with C_7Cl_8 (0.270 g, 0.80 mmol), and allowed to stir at room temperature for 3.5 h, after which time the solution had become brown. Filtration, concentration to half volume, and treatment with hexane gave a crude solid that was purified by flash chromatography (hexanes) to yield as the sole product $C_{14}Cl_{12}$, **12**, (0.133 g, 0.224 mmol, 56%), identified by its mass spectrum.

Reaction of C_7Cl_8 with $(acac)Rh(C_2H_4)_2$

A mixture of $(acac)Rh(C_2H_4)_2$ (0.129 g, 0.50 mmol) and C_7Cl_8 (0.184 g, 0.50 mmol) in THF (10 mL) was heated under reflux for 24 h. Filtration, concentration to half volume, and treatment with hexane gave a crude solid that was recrystallized from $CHCl_3$ to give X-ray quality crystals of $C_{14}Cl_{12}$, **12**, (0.125 g, 0.34 mmol, 68%), identified by its mass spectrum.

X-ray crystallography

X-ray crystallographic data for **3** and **12** were collected on a Siemens R3m/V diffractometer with Ag Kα radiation (λ = 0.560 86 Å). The structures were solved by using the Direct Methods routine contained in the SHELXTL-PLUS program library (33). Crystal data collection parameters for C_7Cl_8 are listed in Table 1. Atom coordinates and selected bond lengths and angles for **3** are collected in Tables 2 and 3. Anisotropic displacement parameters for **3** have been deposited as supplementary material.[5] The molecular parameters for **12** were in agreement with those previously published (18); however, in that report, the molecular disorder was not clearly illustrated, and we show this phenomenon in Fig. 3.

[5] Copies of this table may be purchased from: The Depository of Unpublished Data, Document Delivery, CISTI, National Research Council Canada, Ottawa, Canada K1A 0S2.

Molecular orbital calculations

These calculations were performed via the extended Hückel method using weighted H_{ij}'s (34); orbital drawings were obtained by use of the program CACAO (35).

Acknowledgements

Financial support from the Natural Sciences and Engineering Research Council of Canada, and also from the donors of the Petroleum Research Fund, administered by the American Chemical Society, is gratefully acknowledged. Mass spectra were obtained courtesy of Dr. Richard Smith of the McMaster Regional Centre for Mass Spectrometry. We thank Dr. J.F. Britten for X-ray crystallographic advice, and Dr. Carlo Mealli, CNR, Florence, Italy, for the program CACAO.

References

1. L.C.F. Chao, H.K. Gupta, D.W. Hughes, J.F. Britten, S.S. Rigby, A.D. Bain, and M.J. McGlinchey. Organometallics, **14**, 1139 (1995).
2. R.P. Hughes, X. Zheng, R.L. Ostrander, and A.L. Rheingold. Organometallics, **13**, 1567 (1994).
3. (*a*) M.J. McGlinchey and T-S. Tan. J. Am. Chem. Soc. **98**, 2271 (1976); (*b*) R. Middleton, J.R. Hull, S.R. Simpson, C.H. Tomlinson, and P.L. Timms. J. Chem. Soc. Dalton Trans. 120 (1973); (*c*) J.J. Barker, A.G. Orpen, A.J. Seeley, and P.L. Timms. J. Chem. Soc. Dalton Trans. 3097 (1993).
4. R.T. Carl, E.W. Corcoran, R.P. Hughes, and D.E. Samkoff. Organometallics, **9**, 838 (1990), and refs. therein.
5. K.J. Reimer and A. Shaver. Inorg. Chem. **14**, 2707 (1975).
6. F.L. Hedberg and H. Rosenberg. J. Am. Chem. Soc. **95**, 870 (1973).
7. P.G. Gassman and P.A. Deck. Organometallics, **13**, 1934 (1994).
8. T. Matsukura, K. Mano, and A. Fujino. Bull. Chem. Soc. Jpn. **48**, 2464 (1975).
9. R. West and K. Kusuda. J. Am. Chem. Soc. **90**, 7354 (1968).
10. K. Kusuda, R. West, and V.N.M. Rao. J. Am. Chem. Soc. **93**, 3627 (1971).
11. J. Buddrus and H. Preut. Chem. Ber. **124**, 2373 (1991).
12. M. Traetteberg. J. Am. Chem. Soc. **86**, 4265 (1964).
13. K.V. Scherer, Jr. J. Am. Chem. Soc. **90**, 7352 (1968).
14. S. Drüecke, P. Imming, T. Kämpchem, and G. Seitz. Chem. Ber. **121**, 1595 (1988).
15. E. Ciganek. J. Am. Chem. Soc. **89**, 1454 (1967).
16. C. Moberg and M. Nilsson. Tetrahedron Lett. 4521 (1974).
17. V.N.M. Rao, C.J. Hurt, K. Kusuda, J.C. Calabrese, and R. West. J. Am. Chem. Soc. **97**, 6785 (1975).
18. H.M. Hügel, E. Horn, and M.R. Snow. Aust. J. Chem. **38**, 383 (1985).
19. M. Ishimori, R. West, B.K. Teo, and L.F. Dahl. J. Am. Chem. Soc. **93**, 7101 (1971).
20. (*a*) N.T. Allison, Y. Kawada, and W.M. Jones. J. Am. Chem. Soc. **100**, 5224 (1978); (*b*) P.E. Riley, R.E. Davis, N.T. Allison, and W.M. Jones. Inorg. Chem. **21**, 1321 (1982); (*c*) J.R. Lisko and W.M. Jones. Organometallics, **5**, 1890 (1986).
21. K. Kusuda. Bull. Chem. Soc. Jpn. **56**, 481 (1983).
22. (*a*) R.A. Moss. Acc. Chem. Res. **13**, 58 (1980); (*b*) K. Kassam and J. Warkentin. J. Org. Chem. **59**, 5071 (1994), and refs. therein.
23. (*a*) R. Gleiter and R. Hoffmann. J. Am. Chem. Soc. **90**, 5457 (1968); (*b*) S.D. McGregor and W.M. Jones. J. Am. Chem. Soc. **90**, 123 (1968); (*c*) L. Radom, H.F. Schaefer III, and M.A. Vincent. Nouv. J. Chim. **4**, 411 (1980); (*d*) M.J.S. Dewar and D. Landman. J. Am. Chem. Soc. **99**, 6179 (1977); (*e*) R.L. Tyner,

W.M. Jones, Y. Ohrn, and J.R. Sabin. J. Am. Chem. Soc. **96**, 3765 (1974); (*f*) W. Kirmse, K. Loosen, and H.D. Sluma. J. Am. Chem. Soc. **103**, 5935 (1981); (*g*) P.R. West, O.L. Chapman, and J.P. LeRoux. J. Am. Chem. Soc. **104**, 1779 (1982); (*h*) J.W. Harris and W.M. Jones. J. Am. Chem. Soc. **104**, 7329 (1982).

24. (*a*) E.E. Waali. J. Am. Chem. Soc. **103**, 3604 (1981); (*b*) S. Matzinger, T. Bally, E.V. Patterson, and R.J. McMahon. J. Am. Chem. Soc. **118**, 1535 (1996).
25. (*a*) W.R. Winchester and W.M. Jones. Organometallics, **4**, 2228 (1985); (*b*) K.A. Abboud, Z. Lu, and W.M. Jones. Acta Crystallogr. Sect. C: Cryst. Struct. Commun. **C48**, 909 (1992).
26. T.L. Gilchrist and R.C. Storr. Organic reactions and orbital symmetry, 2nd ed. Cambridge University Press, Cambridge, U.K. 1979. pp 118–120.
27. (*a*) K. Untch. Int. Symp. on the Chemistry of Non-benzenoid Aromatic Compounds, 1st Sendai, Japan, August, 1970; (*b*) R.J. McMahon, C.J. Abelt, O.L. Chapman, J.W. Johnson, C.L. Kreil, J-P. LeRoux, A.M. Mooring, and P.R. West. J. Am. Chem. Soc. **109**, 2456 (1987).
28. M.J.S. Dewar and G.J. Gleicher. J. Am. Chem. Soc. **87**, 685 (1965).
29. R. Thomas and P. Coppens. Acta Crystallogr. Sect. B: Struct. Crystallogr. Cryst. Chem. **B28**, 1800 (1972).
30. R.B. Woodward and R. Hoffmann. The conservation of orbital symmetry. Verlag Chemie, Weinheim, Germany. 1970. p. 88.
31. D.D. Perrin, W.L.F. Armarego, and D.R. Perrin. Purification of laboratory chemicals. Pergamon Press, New York. 1980.
32. A. Ramamoorthy, N. Chandrakumar, A.K. Dubey, and P.T. Narasimhan. J. Magn. Reson. Ser. A, **102**, 274 (1993).
33. G.M. Sheldrick. SHELXTL PC Release 4.1. Siemens Crystallographic Research Systems, Madison, Wis. 1990.
34. (*a*) R. Hoffmann. J. Chem. Phys. **39**, 1397 (1963); (*b*) R. Hoffmann and W.N. Lipscomb. J. Chem. Phys. **36**, 2179 (1962); **36**, 3489 (1962); (*c*) J.H. Ammeter, H-B. Bürgi, J.C. Thibeault, and R. Hoffmann. J. Am. Chem. Soc. **100**, 3686 (1978).
35. C. Mealli and D.M. Proserpio. J. Chem. Educ. **67**, 3399 (1990).

Photoinduced oxidative degradation of unsaturated $M_3(dppm)_3CO^{2+}$ clusters (M = Pd, Pt) by chlorocarbons and chloride ion

Pierre D. Harvey, Réjean Provencher, Jonathan Gagnon, Tianle Zhang, Daniel Fortin, Karine Hierso, Marc Drouin, and Steve M. Socol

Abstract: Both $M_3(dppm)_3CO^{2+}$ clusters (M = Pd, Pt) photoreact with chlorocarbons (Cl—R; R = CCl_3, $CHCl_2$, CH_2Cl, C_6H_5, $C_{10}H_{15}$ (adamantyl)) and chloride ion (slowly) to produce the oxidized mononuclear species $M(dppm)Cl_2$ as a sole isolated M-coordinated inorganic product. Such reactions do not proceed in the dark, except for R = $CH_2C_6H_5$. Among the organic products, the coupling compound R–R (R = C_6H_5) is observed along with many phosphine compounds such as $P(C_6H_5)_3$. In an attempt to elucidate the photoinduced mechanism at the early stage of the phototransformations, the following have been investigated : the ground state binding constants (K_{11} for M = Pd in methanol), the photochemical quantum yields of cluster disappearance (Φ_{dis} for M = Pd) as a function of substrates, substrate concentrations, excitation wavelengths, solvents (ethanol vs toluene), and presence of CO, and the emission lifetimes (τ_e for M = Pt) at 77 K as a function of substrate concentrations (CH_2Cl_2 and $CHCl_3$) in ethanol and toluene. Some of the experimental conclusions have also been corroborated theoretically using density functional theory. Geometry optimization calculations have been performed for the model compounds $Pd_3(PH_3)_6CO^{2+}\cdots Cl^-$, $Pd_3(PH_3)_6^{2+}$, $Pd_3(PH_3)_6CO^{2+}\cdots Cl^0$, $Pd_3(PH_3)_6CO^{2+}\cdots Cl\text{-}CH_3$, and $Pd_3(PH_3)_6CO^{3+}$ in their ground states.

Key words: atom abstraction, photochemistry, C-Cl bond, clusters, host-guest.

Résumé : Les agrégats $M_3(dppm)_3CO^{2+}$ (M = Pd, Pt) photoréagissent tous les deux avec les chlorocarbones (Cl-R; CCl_3, $CHCl_2$, CH_2Cl, C_6H_5, $C_{10}H_{16}$ (adamantyle)) et avec l'ion chlorure (lentement) pour conduire à des espèces mononucléaires oxydées $M(dppm)Cl_2$ qui correspondent au seul produit inorganique M-coordiné à être isolé. Ces réactions ne se produisent pas à la noirceur, excepté pour le composé R = $CH_2C_6H_5$. Parmi les composés organiques, on observe le composé de couplage R–R (R = C_6H_5) ainsi que plusieurs phosphines telle que la $P(C_6H_5)_3$. Dans le but d'élucider le mécanisme photoinduit dans l'étape initiale des phototransformations, on a examiné les caractéristiques suivantes : les constantes d'association dans l'état fondamental (K_{11}, pour M = Pd dans le méthanol), les rendements quantiques photochimiques pour la disparition des agrégats (Φ_{dis} pour M = Pd) en fonction des substrats, des concentrations de substrat, des longueurs d'onde d'excitation, des solvants (éthanol vs. toluène) et de la présence de CO et les durées de vie d'émissions (τ_e pour M = Pt), à 77 K, en fonction des concentrations de substrat (CH_2Cl_2 et $CHCl_3$) dans l'éthanol et le toluène. Un certain nombre de conclusions expérimentales ont aussi été corroborées d'une façon théorique en faisant appel à la théorie de la densité fonctionnelle. On a effectué des calculs d'optimisation de géométrie pour les composés modèles $Pd_3(PH_3)_6CO^{2+}\cdots Cl^-$, $Pd_3(Ph_3)_6^{2+}$, $Pd_3(PH_3)_6CO^{2+}\cdots Cl^0$, $Pd_3(PH_3)_6CO^{2+}\cdots Cl\text{-}CH_3$ et $Pd_3(PH_3)_6CO^{3+}$ dans leurs états fondamentaux.

Mots clés : enlèvement d'atome, photochimie, liaison C—Cl; agrégats, hôte–invité.

[Traduit par la rédaction]

Introduction

The photoinduced oxidation of bi- and polynuclear organometallic complexes has been a topic of long term interest (1). The two possible mechanisms are the electron transfer from the excited complex to the substrate, and the atom transfer from the substrate to the excited complex (1). These key processes occur in the early stage of the transformations, and the elucidation of which mechanism is proceeding requires carefully designed experiments. In metal–metal bonded complexes, another pathway is possible, and involves photoinduced homolytic metal–metal bond scission in the excited states (1), generating radical species that exhibit redox and atom transfer properties that are different from those of the ground state metal–metal bonded species. Relevant to this study are recent photochemical and spectroscopic studies reported by our group (2, 3) and others (4, 5) on low-valent Pd–Pd bonded isocyanide complexes, and which have demonstrated the rich photochemistry that these species offer and the diversity of primary photoinduced processes that have been observed. More recently, our group has been interested in the photoactivation of small molecules, notably $O_2(g)$ by the low-valent $Pd_3(dppm)_3CO^{2+}$ cluster (dppm = $((C_6H_5)_2P)_2CH_2$) (6).

Received February 6, 1996.

This paper is dedicated to Professor Howard C. Clark in recognition of his contributions to Canadian chemistry.

P.D. Harvey,[1] R. Provencher, J. Gagnon, T. Zhang, D. Fortin, K. Hierso, M. Drouin,[2] and S.M. Socol. Département de chimie, Université de Sherbrooke, Sherbrooke, QC J1K 2R1, Canada.

[1] Author to whom correspondence may be addressed. Telephone: (819) 821-7092. Fax: (819) 821-8017. E-mail: pharvey@structure.chimie.usherb.ca

[2] Laboratoire de chimie structurale.

[3] Present address: Southern Utah University, Department of Physical Sciences, Cedar City, UT 84720, U.S.A.

The observed product was the $Pd_3(dppm)_3(O_2)_2^{2+}$ species, which was formed with a quantum yield efficiency of about 3% (at λ_{exc} ~500 nm). This work extends the photochemistry of the $M_3(dppm)_3CO^{2+}$ clusters (M = Pd, Pt) towards the activation of chlorocarbon molecules, and provides a series of experiments that help elucidate the possible mechanisms responsible for the phototransformations *at the early stage* of the photoinduced processes. Density functional theory is also used in order to corroborate some of the experimental findings by the means of geometry optimization computations of some proposed intermediate species. This work will provide experimental evidence for a double- pathway mechanism, one involving a photoinduced Cl atom abstraction followed by a degradation of the cluster, and another involving a fragmentation followed by subsequent reaction with the chlorocarbon molecules.

Experimental

Materials

$[Pd_3(dppm)_3CO](Y = CF_3CO_2,PF_6)_2$ (7) and $[Pt_3(dppm)_3CO](PF_6)_2$ (8) were prepared according to literature procedures. Methanol (BDH), dichloromethane (BDH), chloroform (BDH), carbon tetrachloride (Anachemia), sodium chloride (Fisher), benzyl chloride (Aldrich Chem. Co.), chlorobenzene (BDH), and 1-chloroadamantane (1-Cl-ada; Aldrich Chem. Co.) were purchased at the highest purity grade possible (eg., spectrograde) and were used as received. Ethanol (Les alcools de commerces, 95%) and toluene (BDH) were dried over Na(s) and distilled by fractionation. The formation of a glass at 77 K, with no sign of cracking, was used as the test of solvent dryness.

The complex $[Pd_3(dppm)_3(CO)(N_2C_6H_4NEt_2)](CF_3CO_2)_2(BF_4)$ was prepared via a direct reaction between $[Pd_3(dppm)_3CO](CF_3CO_2)_2$ and the diazonium salt [*para*-$N_2C_6H_4NEt_2](BF_4)$ (Aldrich Chem. Co) in methanol in a 1:1 stoichiometric ratio for 2–3 h. The complex has been characterized by IR ($\nu(N\equiv\overset{+}{N})$ = 2162 cm^{-1}, ν(CO) = 1830 cm^{-1} (solid state)); ^1H NMR ($\delta(CH^aH^bP_2)$: 4.75 and 4.98 ppm (AB quartet; $^2J(H^aH^b)$ = 15 Hz in $(CD_3)_2CO$)), and UV visible spectroscopy (λ_{max} = 464 (br), 380, and 308 nm). The complex $[Pd_3(dppm)_3(CO)(Cl)]BF_4 \cdot 2CH_2Cl_2$ was prepared from daylight irradiation of $[Pd_3(dppm)_3(CO)N_2C_6H_4NEt_2](CF_3CO_2)_2(BF_4)$ in neat CH_2Cl_2. This reaction does not proceed in the dark. The product was characterized by X-ray crystallography using single crystals formed during the photoreaction as CH_2Cl_2 solvate. Its report is appropriate at this time for the purpose of this work (supplementary material, see footnote 4). The full characterization and investigation of the diazonium adducts will be reported in due course.

Instrumentation

The emission spectra were measured on a PTI LS 100 spectroflurometer. The emission lifetimes (τ_e) were measured on the same instrument fitted with a tungsten EG & G model FX-280 microsecond flash-lamp source (~1 μs fwhm) and a phosphorimeter component. To obtain data that are of sufficient quality for this work, multi-scanning and pulsing techniques were employed.

Photochemical studies

The photochemical reactions were performed with a home-made immersion cell using an Ace Hanovia Hg–Xe 200-W lamp. The photoreactions proceeded with broadband irradiation using a uranium sleeve glass filter (λ_{cutoff} ~340 nm). For the quantum yield measurements, ferrioxalate actionometry was employed (9–11). The actinometer excitation slits were set at 0.5 mm, and excitation was set at 488 nm for all samples and standards unless stated otherwise. The excitation wavelength was selected using a Aminco-Bomem monochromator, also equipped with a Hg–Xe 200-W lamp. The absorbance of the complex and standard solutions was adjusted to a value of ~0.4–0.5 at λ_{max} ~487 nm for M = Pd and at λ_{max} ~380 nm for M = Pt prior the measurements. Typical concentrations range from 1.5×10^{-5} to 2.0×10^{-5} M. The calibrations of the standard ferrioxalate actinometric solutions were performed carefully in the dark. The absorbance change at a given irradiation time was followed by UV–visible spectroscopy (Hewlett–Packard 8452A) at a value of λ_{max} that varied between 466 and 490 nm depending upon the nature of the solvent mixture. All measurements and calibration experiments were performed at least 3 times and before 10% photoconversion.

Binding Constant Measurements

The K_{11} measurements were performed by UV–visible spectroscopy (12) at room temperature, and were extracted by plotting the Benesi–Hildebrand graphs (~$1/\Delta A$ vs. 1/[substrate] with ΔA as the absorbance change upon the increase in substrate concentration). The ratio intercept/slope in this plot gives K_{11}. As a counter check, the K_{11} values were also evaluated using Scatchard and Scott plots ($-\Delta A$/[substrate] vs. $-\Delta A$, K_{11} = −slope (Scatchard); −[substrate]/ΔA vs. [substrate], K_{11} = slope/intercept (Scott)). The measured K_{11} values are all found to be the same within the experimental uncertainties, generally ±10% based upon the maximum and minimum values obtained, except for the Cl^- ion, which turned out to be irreproducible (see text below). Typically between 6 and 10 data points were acquired for each measurement, which was repeated three times. Details on the methodology employed can be found in ref. 13.

Computational details

The reported density functional calculations were all carried out utilizing the program called Amsterdam Density Functional that was developed by Baerends et al. (14, 15) and vectorized by Raveneck (16). The numerical integration procedure applied for the calculations was developed by te Velde and co-workers (17). The geometry optimization procedure was based on the method developed by Versluis and Ziegler (18). The electronic configurations of the molecular systems were described by an uncontracted double-ζ basis set (19) on palladium for 4*s*, 4*p*, and 5*s*, and triple-ζ for 5d. Double- ζ STO basis sets (20) were used for chloride (3*s*, 3*p*), phosphorus (3*s*, 3*p*), oxygen (2*s*, 2*p*), carbon (2*s*, 2*p*), and hydrogen (1*s*), augmented with a single 4*d* polarization function for Cl and P, a single 3*d* one for O, and C, and a 2*p* function for H. No polarization function was used for palladium. The $1s^2\ 2s^2\ 2p^6\ 3s^2\ 3d^{10}$ configuration on palladium, the $1s^2\ 2s^2$ configuration on chloride and on phosphorus, and the $1s^2$ configurations on oxygen, carbon, and nitrogen were treated by the frozen-core approximation (15). A set of auxiliary (21) *s*, *p*, *d*, *f*, and *g* STO functions, centered on all nuclei, was used

in order to fit the molecular density and present Coulomb and exchange potentials accurately in each SCF cycle. Energy differences were calculated by including the local exchange-correlation potential by Vosko et al. (22). No nonlocal exchange and correlation corrections were made for the geometry optimizations.

Crystal structure of $[Pd_3(dppm)_3(\mu\text{-}CO)(\mu\text{-}Cl)](BF_4)\cdot CH_2Cl_2$

Intensity data were collected at 190 K on an Enraf–Nonius CAD-4 automatic diffractometer using graphite monochromated Mo$K\alpha$ radiation. The NRCCAD (23*a*) programs were used for centering, indexing, and data collection. The unit cell dimensions were obtained by least-squares fit of 24 centered reflections in the range of $30° \leq 2\theta \leq 36°$. During data collection, the intensities of two standard reflections were monitored every 60 min. No significant decay was observed. The structure was solved by the application of direct methods using the NRCVAX (23*b*) program and refined by least squares. The atomic scattering factors in stored NRCVAX are from Cromer and Waber (International tables for X-ray crystallography, Vol IV). Hydrogen atoms were geometrically placed at idealized position and not refined. At convergence the final discrepancy indices were $R = 0.063$, $wR = 0.066$, and $SC = 1.55$. The residual positive and negative electron densities in the final maps were 1.27 and -1.67 e/Å^3 and were located in the vicinity of the BF_4^- anion. The C═O bond distance was fixed at 1.15 Å in the refinement. The ORTEP (23*c*) diagram was generated from NRCVAX. The crystal has one solvent molecule (CH_2Cl_2). The BF_4^- molecule is disordered and was treated as a B atom surrounded by two interlocking ideal tetrahedra of F atoms (all U_{ij} restrained to be equal) with B---F distances restrained to 1.36 Å; a 63:37 occupancy ratio is observed. Only the higher occupancy site was retained. Restrain refinement was used on U_{ij} to be all equal for C1 to C6 atoms because of thermal motion leading to large U parameters.

Results and discussion

1. Photoreactions

The $M_3(dppm)_3CO^{2+}$ clusters undergo photooxidative degradation in the presence of chlorocarbons either as a neat solvent or in acetonitrile solutions, and also in the presence of Cl^- ions. These photoinduced chemical processes form the known corresponding $M(dppm)Cl_2$ complexes as sole isolated metal-coordinated inorganic products (for M = Pd, Pt) as identified from comparison of ^1H and ^{31}P NMR spectra with authentic samples (eq. [1]).

$$[1] \quad M_3(dppm)_3CO^{2+} \xrightarrow[h\nu]{\text{R-Cl or } Cl^-} M(dppm)Cl_2$$

The reactions do not proceed in the dark. To establish the mechanistic step of the $Pd_3(dppm)_3CO^{2+}$ photoconversion to $Pd(dppm)Cl_2$, the model system $Pd_3(dppm)_3(CO)(Y)^{3+}$ (Y = $N_2C_6H_4NEt_2$) (13) was investigated. This compound is prepared from the binding of $Pd_3(dppm)_3CO^{2+}$ with $[N_2C_6H_4NEt_2]^+$ (as the BF_4^- salt) (13). This complex is surprisingly unstable to light in the presence of CH_2Cl_2 to slowly form $[Pd_3(dppm)_3(CO)(Cl)]BF_4$ as identified by X-ray crystallography (as a CH_2Cl_2 solvate). This cationic cluster is essentially identical to that reported by Puddephatt and co-workers (24) and the bulk of the data have been deposited as supplementary material.[4] Only minor structural differences have been noticed such as the absence of disorder between the Cl^- ion and CO group, and minor changes in bond lengths and angles. Further light irradiation of the cluster also forms $Pd(dppm)Cl_2$. This later photoreaction is significantly slower. Based upon these observations, it is believed that this Cl^- adduct species may be one of the intermediate products prior to the formation of the final oxidized mononuclear $M(dppm)Cl_2$ complex.

By GC–MS, one of the organic products was identified as biphenyl for the chlorobenzene substrate. Possibly due to volatility problems, the expected ethylene and acetylene products for dichloromethane and chloroform were not observed under the same experimental conditions. The presence of biphenyl indicates the formation of the highly reactive radical phenyl group. Numerous other organics (for M = Pd) are also unselectively photoproduced, but their identity is not known at this time. This was not the purpose of this work. By GC–MS, the molecular weights of the fragments indicate that large organic molecules have been generated, along with various phosphine-containing compounds such as $P(C_6H_5)_3$. For the Cl^- substrates, the photolyses are very slow and only $Pd(dppm)Cl_2$ and dppm decomposition products are observed (as expected). There was no evidence of acetonitrile solvent participation in the products.

2. Thermodynamics

The emission spectra of the $M_3(dppm)_3CO^{2+}$ clusters reveal that the triplet energies (E_T) are determined from emission band maxima, located at 1.76 eV (14 200 cm^{-1}, M = Pd) and 1.91 eV (16 100 cm^{-1}, M = Pt) (25). From cyclic voltammetry, both clusters exhibit an irreversible electrochemical oxidation wave at +1.38 V and +1.05 V vs. SCE for the $Pd_3(dppm)_3CO^{2+}$ and $Pt_3(dppm)CO^{2+}$, respectively, both as PF_6^- salts, in degassed acetonitrile solutions containing 0.1 M tetrabutylammonium hexafluorophosphate. The coulometric experiments establish that the electrochemical process is a multielectron process, which places an upper limit for the one-electron oxidation of the clusters (i.e., $\leq$+1.38 V (M = Pd) and $\leq$+1.05 V (M = Pt) vs. SCE). The excited state driving forces in the lowest energy triplet excited state ($E^{*/+}$) would then be evaluated to be in the order of 0.38 V and 0.86 V vs. SCE for M = Pd and Pt, respectively. These values are not great enough to spontaneously reduce most simple chlorocarbons such as C_6H_5Cl ($E^{0/-} = -2.32$ V vs. NHE), CH_2Cl_2 ($E^{0/-} = -2.23$ V vs. NHE), $CHCl_3$ ($E^{0/-} = -1.67$ V vs. NHE), and CH_3Cl ($E^{0/-} = -2.23$ V vs. NHE) (26). In these cases, the photoinduced electron transfer mechanism from the $M_3(dppm)_3CO^{2+}$ cluster in their lowest energy $^3A_2$ states to the chlorocarbon molecules is clearly thermodynamically unfavorable. This is obviously also true for the cluster oxidation in the presence of the Cl^- anion. Con-

[4] Copies of material on deposit may be purchased from: The Depository of Unpublished Data, Document Delivery, CISTI, National Research Council Canada, Ottawa, Canada K1A 0S2. These data, with the exemption of anisotropic thermal parameters and torsion angles, have also been deposited with the Cambridge Crystallograhic Data Centre, and can be obtained on request from The Director, Cambridge Crystallograhic Data Centre, University Chemical Laboratory, 12 Union Road, Cambridge, CB2 1EZ, U.K.

Fig. 1. Typical UV–visible spectroscopic changes when additions of $CHCl_3$ are made to a solution of $Pd_3(dppm)_3CO^{2+}$ in methanol at 298 K ([cluster] $\sim 1 \times 10^{-5}$ M).

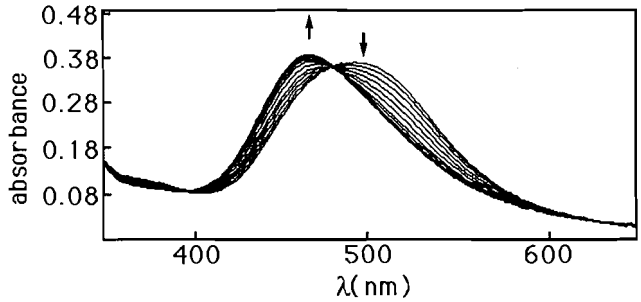

Scheme 1.

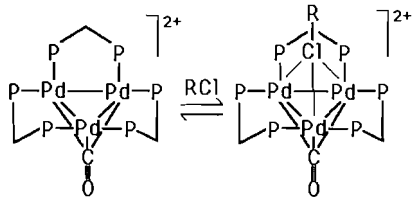

versely, substrates such as $C_6H_5CH_2Cl$ ($E^{o/-} = -1.0$ V vs. SCE (27)) and CCl_4 ($E^{0/-} = -0.78$ and -1.67 V) offer the possibility that such a photoinduced process occurs for $Pt_3(dppm)_3CO^{2+}$. For CCl_4, the presence of a fourth Cl atom renders the molecule an excellent electron scavenger. For $C_6H_5CH_2Cl$, scission of the reduced species generates the Cl^- ion and the benzyl radical ($C_6H_5{\cdot}CH_2$), which is stabilized by resonance. In these cases, electron transfer could also be considered.

3. Binding studies

From a thermodynamic standpoint, a photoinduced atom abstraction mechanism must be considered. In such a mechanism, the substrate R—Cl *must* physically approach the excited M_3^{2+} center. Recently published flash photolysis measurements indicate that the excited state lifetimes range from 25 (M = Pd) to a few hundred picoseconds (M = Pt) (25), which are not long enough to allow a diffusion of the $M_3(dppm)_3CO^{2+*}$ ($^3A_2$) species to the substrates. The photoprocess (atom abstraction) must be *unimolecular*, involving a ground state preassembling of the clusters and the substrates. Since the chromophoric unsaturated M_3^{2+} center is located at the bottom of a cavity formed by six dppm-phenyl groups, the substrate must act as a guest molecule in this pocket.

This section addresses the ground state host–guest behavior of the $M_3(dppm)_3CO^{2+}$–chlorocarbon systems. The cluster of choice is $Pd_3(dppm)_3CO^{2+}$ since its absorption spectrum exhibits a well-defined absorption band at around 480 nm, where isosbestic points can be clearly observed upon association with a substrate (13). Methanol was chosen as solvent since previous studies established that this solvent interacts the least with the cavity (13), and offers good solubility for the cluster and substrates.

Figure 1 shows UV–visible spectra changes upon addition of chloroform. Clear isosbestic points are evident at ~479 and ~398 nm, indicating a 1:1 stoichiometric ratio (Scheme 1).

Fig. 2. Typical Benesi–Hildebrand, Scatchard, and Scott plots associated with the addition of $CHCl_3$ to a solution of $Pd_3(dppm)_3CO^{2+}$ in methanol at 298 K.

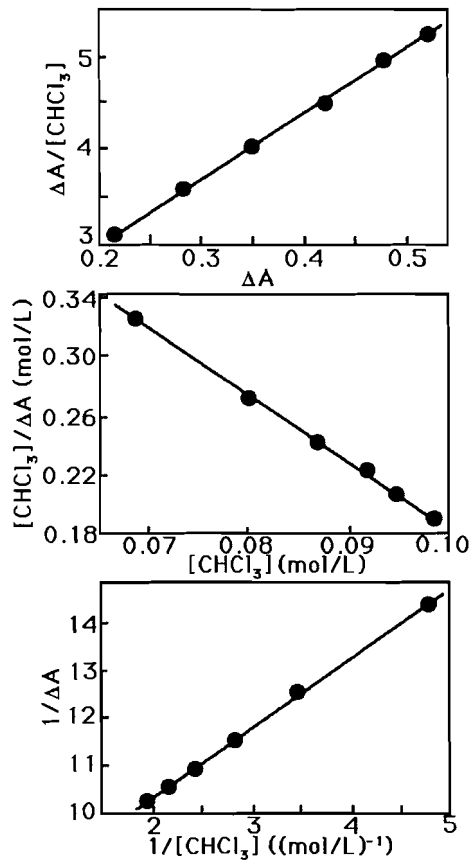

The K_{11} values extracted from the Benesi–Hildebrand plots (Fig. 2) are listed in Table 1. These constants have also been verified by also extracting them from the Scatchard and Scott plots (Fig. 2). Except for Cl^-, reversibility can be observed from the displacement of the substrate by adding a second substrate monitoring the progression by UV–visible spectroscopy (each substrate exhibits its own λ_{max}). In the Cl^- case, the binding constant is very large (>10 000 M^{-1}) and somewhat hard to obtain with precision. There is no obvious trend between the molecular dimension and K_{11} (Table 1). However, some rationalization can be made. Chloride is the smallest substrate of this series and is charged ($Cl^-\cdots Pd_3^{2+}$); it is the most efficient guest of the series. C_6H_5Cl compares structurally to toluene, which was investigated earlier ($K_{11} = 0.08 \pm 0.02$ M^{-1} (13)). The slight increase in K_{11} here ($K_{11} = 0.16 \pm 0.01$ M^{-1}) could be associated with some extra binding between the Cl atom and the Pd_3 center. Furthermore, adding extra Cl atoms on a given substrate should then slightly increase K_{11} if the substrate is not too sterically demanding. This is indeed observed for CH_2Cl_2 (0.25 ± 0.03 M^{-1}) and $CHCl_3$ (4.9 ± 0.5 M^{-1}). However, a slight decrease is observed for CCl_4 (3.4 ± 0.1 M^{-1}), which could be due to the slight increase in molecular dimensions.

Two unexpected results come from 1-Cl-ada (35 ± 5 M^{-1}) and $C_6H_5CH_2Cl$ (7.3 ± 0.1 M^{-1}), which were used for their bulkiness (1-Cl-ada), and low bond dissociation energy and reduction potential ($C_6H_5CH_2Cl$), respectively. The increase

Table 1. Comparison of K_{11} values and substrate sizes.

Substrate	K_{11}/M^{-1}[a]	Dimensions[b]
Cl^-	[c]	van der Waals diam. = 3.6 Å, ionic diam. = 3.4 Å
CH_3Cl	Not measured	Average diameter ~4.7 Å
CH_2Cl_2	0.25 ± 0.03	Average diameter ~5.2 Å
$CHCl_3$	4.9 ± 0.5	Average diameter ~5.7 Å
CCl_4	3.4 ± 0.1	Average diameter ~6.1 Å
1-Cl-ada	35 ± 5	Average diameter ~6.5 Å
C_6H_5Cl[d]	0.16 ± 0.1	Assuming a rectangular shape ~8.7 × 3.6 × 6.9 Å
$C_6H_5CH_2Cl$	7.3 ± 0.1	Assuming a rectangular shape ~9.4 × 3.6 × 6.9 Å

[a]The uncertainties are defined by the difference between the average value and the maximum and minimum values measured.

[b]The average diameters have been calculated by averaging the four dimensions (diameters) of the four tetrahedral axes. These tetrahedral dimensions have been calculated using r_{vdw} (H) = 1.30 Å and r_{rdw} (Cl) = 1.80 Å, and bond length extracted from the PC MODEL computer software.

[c]Not accurate since the system is not reversible. However, the few data extracted from the Benesi–Hildebrand plots indicate that K_{11} is very large (>10 000 M^{-1}).

[d]A slow thermal reaction has been observed at high concentrations. At low concentrations (~10^{-3} M in $C_6H_5CH_2Cl$ for ~10^{-5} M in cluster) no reaction is observed.

Table 2. Comparison of Φ_{dis} with E(C—Cl) and $E^{0/-}$.

	Φ_{dis}	E(C—Cl)/kcal mol^{-1}[a]	$E^{0/-}$/V[b]
Cl^-	~1.5×10^{-5} 0.86 M (in ethanol)	—	—
Neat C_6H_5Cl	0.00044 ± 0.00010	95 (CRC)	−2.32
Neat CH_2Cl_2	0.00051 ± 0.00023	82.8 (JPC)	−2.23
Neat $CHCl_3$	0.0030 ± 0.0005	79.2 (JPC)	−1,67
Neat CCl_4	0.00080 ± 0.00015	70.3 (JPC)	−0.78, −1.71
1-Cl-ada	0.000048 ± 0.000010 3.43 M (in toluene)	[c]	[d]
Neat $C_6H_5CH_2Cl$	Thermal	69 (CRC)	−1.0 (vs. SCE)[e]

[a]1 kcal = 4.18 kJ. From ref. 37.

[b]In 75% dioxane vs. NHE (unless stated otherwise) from ref. 26.

[c]The E(C—Cl) for CH_3CH_2Cl is 81 kcal mol^{-1} (CRC handbook).

[d]$E^{0/-}$ for chlorobicyclo[7,1^{1,5}]heptane is −1.99 V. It is highly suspected that $E^{0/-}$ for 1-Cl-ada is also ~−2 V.

[e]From ref. 27.

by at least one order of magnitude on going from Cl—CH_2Cl (0.25 M^{-1}) to C_6H_5—CH_2Cl (~7.3 M^{-1}) is not unprecedented. The K_{11} increases from acetate to benzoate, nitroethane to nitrobenzene, and acetonitrile to benzonitrile are also all around an order of magnitude (13). Cooperation between the binding of the Cl atom with the Pd_3 center, and the binding of the hydrophobic phenyl group and the cavity dppm-phenyl groups, appears to be responsible for this phenomenon. Finally, the unexpectedly large K_{11} value for 1-Cl-ada can only be explained by a binding involving only the hydrophobic portions of the host–guest pair. In this case the multiple hydrophobic intermolecular contacts could lead to a large K_{11} value. No attempt was made to further investigate this phenomenon.

4. Quantum Yields

The photochemical quantum yields (Φ) were measured by ferrioxalate actinometry following the rate of $Pd_3(dppm)_3CO^{2+}$ consumption by UV–visible spectroscopy (λ_{max} ~ 480 nm). First, $Pd_3(dppm)_3CO^{2+}$ was investigated in neat solvents (Table 2). We noticed that in neat $C_6H_5CH_2Cl$, $Pd_3(dppm)_3CO^{2+}$ reacted slowly (thermally) at room temperature, so no Φ value could be measured. However, at [R—Cl] ~ 10^{-3} M (typical concentration range for K_{11} measurements), no detectable reaction was noticed. This reactivity is tentatively attributed to the relatively high stability of the benzyl radical ($C_6H_5CH_2^{\cdot}$); and it is concluded that the homolytic C—Cl bond cleavage by $Pd_3(dppm)_3CO^{2+}$ is facile in this case. For C_6H_5Cl, CH_2Cl_2, and $CHCl_3$, Φ increases with both the decrease in E(C—Cl) and $E^{0/-}$ values. Surprisingly, Φ decreases for CCl_4 while E(C—Cl) and $E^{0/-}$ continue to decrease in this series. This result further supports the conclusion that the primary process in the mechanism cannot be an

Fig. 3. Graph of $\Phi_{dis}(Pd_3(dppm)_3CO^{2+})$ vs. % $CHCl_3$ (V:V) in toluene (top) and ethanol (bottom).

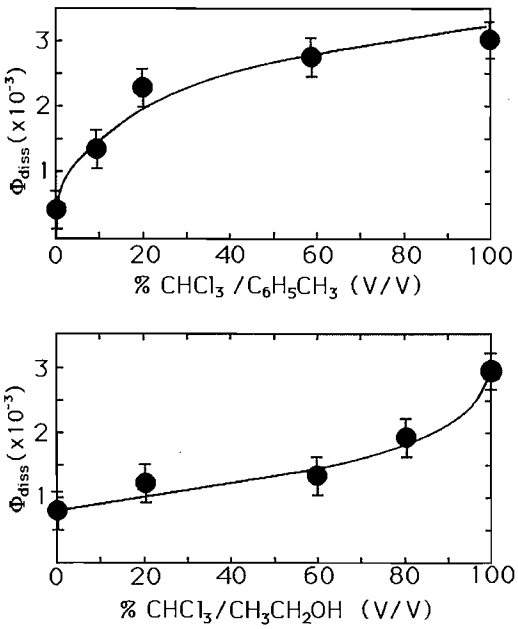

decrease in this series. This result further supports the conclusion that the primary process in the mechanism cannot be an outer-sphere electron transfer. On the other hand, an atom transfer mechanism is not ruled out since "steric considerations" can also affect the rates of reaction. One has to note that the K_{11} data also arise from measurements that also consider the steric effects in the complex stability. By ignoring the experimental uncertainties, Φ varies as $C_6H_5Cl < CH_2Cl_2 < CCl_4 < CHCl_3$ in neat solvents, which parallels the trend in K_{11}. For the chloride substrate, at $[Cl^-] = 0.86$ M (as Bu_4N^+ salt) in ethanol, $\Phi \sim 1.5 \times 10^{-5}$ (extremely weak)! Again no reaction is observed in the dark. One has to note that the Cl^- ion is very strongly bonded to the $Pd_3(dppm)_3CO^{2+}$ cluster, so no direct comparison of the Φ values can be made. The extremely low Φ value indicates that the photodecomposition is slow. This is indeed observed during the bulk photolysis reactions for $Pd_3(dppm)_3(CO)(Cl)^+$ (i.e., the photoproduct of the $Pd_3(dppm)_3(CO)(N_2C_6H_4NEt_2)^{3+}$ photodecomposition in CH_2Cl_2, believed to be one of the intermediates).

For comparison purposes, Φ's for the photochemical reactions between $Pt_3(dppm)_3CO^{2+}$ and $CHCl_3$, and CH_2Cl_2 (neat) were also measured. As expected, the Φ value is greater for M = Pt with $CHCl_3$ ($\Phi = 0.0041 \pm 0.0005$ at $\lambda = 380$nm) than that of $Pd_3(dppm)_3CO^{2+}$ (0.0030 ± 0.0005). For CH_2Cl_2, Φ is about the same for both clusters, considering the uncertainties. Both the triplet energy and the excited state driving forces are greater for $Pt_3(dppm)_3CO^{2+}$. These experiments did not provide any evidence of one mechanism or another.

Based upon the hypothesis that an atom transfer mechanism involves a physical approach of the R-Cl molecule towards the M_3 center, Φ should be sensitive to the presence of a competitive molecule (solvent). Figure 3 shows the relationship of Φ for the $Pd_3(dppm)_3CO^{2+}$–$CHCl_3$ photoreactions as a function of the % (V/V) for two different solvents (toluene and ethanol). The toluene graph shows an upward curvature, while the

Scheme 2.

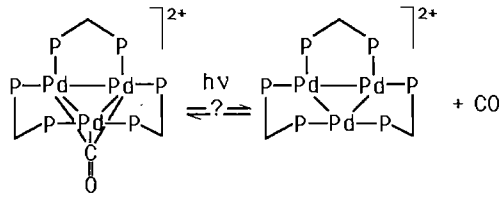

ethanol graph shows a downward curvature, with the increase in %(V/V), in $CHCl_3$, confirming the expected difference. Except for CH_2Cl_2, the other substrates were not investigated as a function of %(V/V) substrate and solvent. For CH_2Cl_2, Φ increases (slightly) with % (V/V) CH_2Cl_2, but the large uncertainties prevent us from determining the curvature trend. Based upon the K_{11} measurements reported elsewhere (13), ethanol appears to be a better binder than toluene with $Pd_3(dppm)_3CO^{2+}$. Figure 3 indicates that ethanol inhibits the increase in Φ values with the increase in $[CHCl_3]$. On the other hand, the sharp increase in Φ's in the toluene graph at low $[CHCl_3]$ indicates that toluene does not efficiently inhibit the photoreactions. These results are also consistent with this substrate–cavity model where toluene does not compete as efficiently as ethanol for the cavity.

The most surprising result is the non-zero value at 0% quantity of $CHCl_3$ (~0.0005), indicating that $Pd_3(dppm)_3CO^{2+}$ is photo-consumed even in the absence of chlorocarbons. We note that these values are even greater than that of the Cl^- substrate stated above. This observation clearly indicates the presence of a second photochemical pathway since with short periods of time in the dark, this instability does not occur. This pathway is clearly inefficient with such low quantum yields, but cannot be neglected for the CH_2Cl_2, CCl_4, 1-Cl-ada, and C_6H_5Cl substrates. The design of experiments in order to elucidate this second pathway is not obvious. Two proposed mechanisms can be anticipated: (*i*) photolabilisation of the CO group (Scheme 2) as observed in many organometallic polynuclear complexes (1) followed by a breakdown of the cluster, and (*ii*) photoinduced fragmentation of the cluster according to eq. [2]:

$$[2] \quad Pd_3(dppm)_3CO^{2+} \underset{\text{dark}}{\overset{h\nu}{\rightleftharpoons}} \text{"Pd(dppm)"} + \text{"}Pd_2(dppm)_2(CO)(S)_2^{2+}\text{"} \longrightarrow \text{products}$$

where S is a two-electron donor (counter anion or solvent molecule). This second reaction is essentially the last step prior to the synthesis of the $Pd_3(dppm)_3CO^{2+}$ cluster as demonstrated by Puddephatt and co-workers (7, 8). The following experiments are performed: (*i*) measurements of Φ in the presence of CO(g), and (*ii*) measurements of Φ for the PF_6^- and $CF_3CO_2^-$ salts. The first set of experiments (Φ vs. CO(g)) demonstrates that Φ is independent (within the experimental uncertainties) in the presence of 1 atm of CO(g) (1 atm = 101.3 kPa). The synthesis of $Pd_3(dppm)_3CO^{2+}$ does not require high pressures of CO (7). This experiment was attempted in order to slow down the CO loss, if any. The most revealing experiments are the measurements of Φ for $Pd_3(dppm)_3CO^{2+}$ as a PF_6^- and as a $CF_3CO_2^-$ salt. Using different solvents (ethanol and acetonitrile) and atmospheres (Ar, CO_2, O_2, CO, and H_2), we find that

Scheme 3.

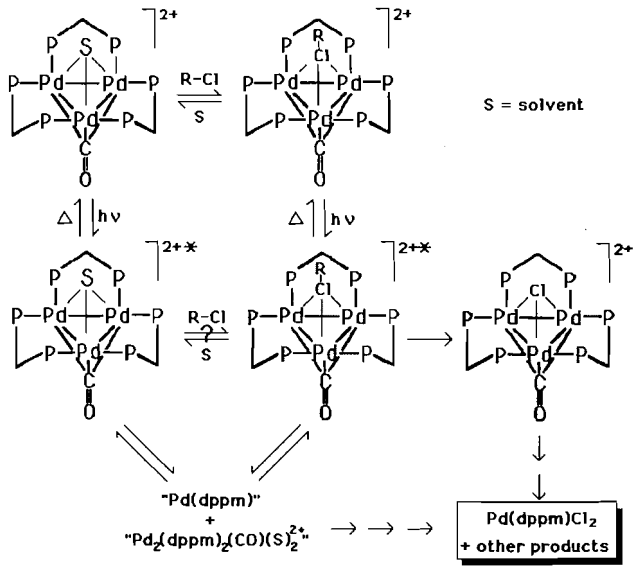

is a better binder than PF_6^- (13) which should indicate that the cavity is competitively blocked by the carboxylate molecule, if one assumes the host–guest mechanism. However, this result is consistent with eq. [2] shifting the reaction to the right when S is a better two-electron donor. Interestingly we find Φ (ethanol) > Φ (toluene) (at [substrate] = 0, see Fig. 3), where ethanol is a two-electron donor. The next question is whether or not the formation of $Pd_3(dppm)_3^{2+}$ (first scenario: Scheme 2) can lead to an *efficient* subsequent fragmentation of the cluster. Theory predicts that it cannot (see section below), corroborating the experimental results (Φ vs. CO(g)). Then, will the intermediates generated in eq. [2] subsequently react with R—Cl to produce the final observed products? Previous studies strongly indicate that it is indeed possible. The highly reactive "Pd(dppm)" species is expected to be thermally active towards R—Cl based upon the known chemistry for "$Pd(R_2PCH_2CH_2PR_2)$" where R = C_6H_{11} (28). For the CO bridged d^9-d^9 proposed intermediates (eq. [2]), a recent work on an isoelectronic CNR bridged "$Pd_2(dppm)_2$" d^9-d^9 compound demonstrated that this complex was efficiently photoconverted to $Pd(dppm)Cl_2$ in the presence of CH_2Cl_2 (29). Thus, experimental and literature results favor scenario (*ii*) for the second pathway of R—Cl activation. The overall proposed pathways are summarized in Scheme 3. The C—Cl homolytic bond cleavage involves the formation of the $Pd_3(dppm)_3(CO)(Cl)^{2+}$ intermediate, which represents one of the mechanistic steps of the photoinduced photodegradation of the cluster.

Considering the K_{11} measured for 1-Cl-ada, one would expect Φ to be large. However, the binding does not necessarily involve the C-Cl bond oriented inside the cavity. Indeed, Φ(1-Cl-ada) = 0.000048 ± 0.000010 for [1-Cl-ada] = 3.43 M in toluene. This value is by far the smallest one (excluding the Cl^- case). Further, the CPK models demonstrate that the bulkiness of 1-Cl-ada precludes strong R—Cl··Pd_3^{2+} interactions, confirming that homolytic bond cleavage by $Pd_3(dppm)_3CO^{2+*}$ ($^3A_2$) is not anticipated to be efficient.

5. Emission lifetimes

This section addresses the first proposed pathway (host–guest chemistry). Perturbation studies of the photophysical properties of the $M_3(dppm)_3CO^{2+}$ complexes indicate that the presence of a substrate in the cavity always induces a decrease in excited state lifetimes (25). This general behavior has also been observed for metal complexes of calix[4]arene derivatives for which a metal atom is located at the lower rim acting either as a luminescent probe (Ir(I); ref. 30) or a strong Lewis acid (W = O (31)), and the recently investigated $Cu_3(dppm)_3OH^{2+}$ cluster (32). This phenomenon is attributable to the "loose bolt effect" (for small perturbations) or to the formation of an "exciplex" (for larger change in lifetimes) (33). For $Pt_3(dppm)_3CO^{2+}$ both 298 K flash photolysis and 77 K emission lifetime measurements established that toluene as a pure solvent provided the shortest lifetimes among the solvent molecules investigated (25). The hypothesis is that toluene binds more strongly to $Pt_3(dppm)_3CO^{2+}$ than do most common solvents. This difference with $Pd_3(dppm)_3CO^{2+}$ is not understood at this time.

To further understand the difference between the photochemical quantum yield behavior in toluene and ethanol, the emission decay traces for $Pt_3(dppm)_3CO^{2+}$ at 77 K in the presence of CH_2Cl_2 and $CHCl_3$ were investigated. $Pt_3(dppm)_3CO^{2+}$ was selected because of its greater emission quantum yield at 77 K (34). At such a temperature, cluster degradation is not anticipated to be an inefficient mechanism for the excited state deactivation; solely the Pt_3^{2+}···Cl—R interactions are governing the changes in τ_e with [Cl—R]. In pure solvent, the emission decays are rigorously monoexponential (τ_e = 10.2 ± 0.5 μs, toluene; τ_e = 18.0 ± 0.1 μs, ethanol). In the presence of $CHCl_3$ or CH_2Cl_2, the carefully measured decays become biexponential (Fig. 4). The biexponential behavior is demonstrated from deconvolution decay analysis. The emission spectra exhibit no band shift but show a gradual decrease in intensity with chlorocarbon concentration. The long component exhibits a τ_e value of 10.2 or 18.0 μs characteristic of the solvent, and does not change (within ±0.5 μs) with an increase in chlorocarbon concentration up to 40% (V/V). Such a result further rules out the possibility of an outer-sphere electron transfer in the excited state in these cases ($CHCl_3$, CH_2Cl_2), since generally the emission decay traces exhibit monoexponential behaviors with lifetimes decreasing with the substrate concentration. The short component exhibits a lifetime of 450 ± 150 ns for both CH_2Cl_2 and $CHCl_3$. The relative intensity ratio for short component/long component after deconvolution increases proportionally with the chlorocarbon/solvent ratio (V/V). This experiment demonstrates that the short and long components are associated with the luminescence of $Pt_3(dppm)_3CO^{2+}$ interacting (or hosting) a chlorocarbon and a solvent molecule, respectively. The very short lifetimes in the $Pt_3(dppm)_3CO^{2+}$··· chlorocarbon cases strongly indicate the formation of exciplexes. The exciplex emissions appear to be weak since the emission intensity of the mixture steadily decreases with the increase in chlorocarbon concentration. Also these emissions are anticipated to be located very close to the $Pt_3(dppm)_3CO^{2+}$··· solvent emissions, since no change in λ_{max} emission was observed in all the experiments. The most important finding is that the short component/long component intensity ratio always differs greatly between the two solvents (ethanol, toluene) at a given chloro-

Fig. 4. Typical emission decay traces for the $Pt_3(dppm)_3CO^{2+}$ clusters at 77 K. Top: in toluene containing 30% CH_2Cl_2 (V:V) Bottom: in ethanol containing 3% CH_2Cl_2 (V:V). The peaks marked with an X are instrumental artifacts. The double arrow markings indicate the short-lived components (~18% of the total intensity).

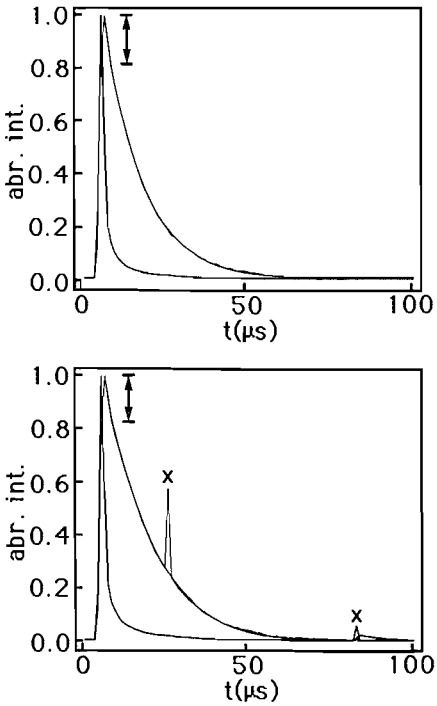

carbon/solvent ratio. As a typical example, Fig. 4 compares two 77 K emission decays of $Pt_3(dppm)_3CO^{2+}$: the first in toluene containing 30% CH_2Cl_2, and the second in ethanol containing 3% CH_2Cl_2. Both decays exhibit the same short component/long component ratio (~18%). This result indicates that the halocarbon molecule competes relatively more efficiently to occupy the $Pt_3(dppm)_3CO^{2+}$ cavity in ethanol. Essentially, this confirms that ethanol is a weaker binder for $Pt_3(dppm)_3CO^{2+}$ than toluene and further supports the above hypothesis.

6. Geometry optimizations

Density functional theory was used to optimize geometries in the ground state of some proposed intermediates in order to explain and corroborate some experimental results. For $Pd_3(dppm)_3CO^{2+}$ in its ground ($^1A_1$) and lowest energy triplet excited states ($^3A_2$, (T_1), $^3E_2$ (T_2)), the geometry compounds have already been computed (35). The computations compared very favorably with the experimental data, particularly for the Pd—Pd bond lengths. For comparison purposes, these data are reported in Table 3. The geometry of the model $Pd_3(PH_3)_6(CO)(Cl)^+$ cluster has also been optimized (Table 3 and Fig. 5) in order to address the weak interactions between the Pd_3^{2+} center and the substrate. The comparison of the Pd—Pd bond lengths is also excellent, but some differences are noted for the covalent Pd—P and Pd—C bonds. These differences can be up to 0.055 Å. For the more ionic Pd···Cl interactions, the computed Pd···Cl distance is significantly shorter

Fig. 5. Optimized ground state geometry of the model compound $Pd_3(PH_3)_6(CO)(Cl)^+$. The geometry for $Pd_3(PH_3)_6(CO)(Cl)^{2+}$ is the same except that some distances and angles have changed (see details in Table 4).

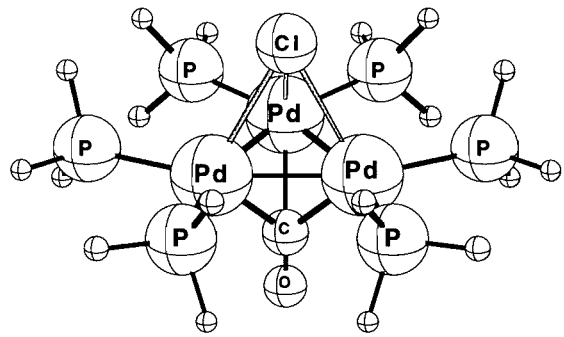

Fig. 6. Optimized geometry of the model association complex $Pd_3(PH_3)_6(CO)^{2+}\cdots ClCH_3$ in the ground state.

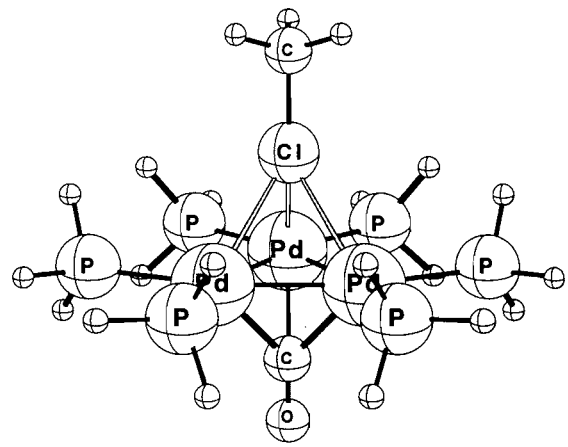

than that of the crystal structures. The differences are up to 0.23–0.26 Å from the average X-ray values. Steric effects with the H-dppm atoms and the nature of the theoretical methods employed are likely to be at the origin of these differences. Investigations should concentrate mainly on the metal–metal bonds.

The first optimization considered is the ground state interactions between $Pd_3(PH_3)_6CO^{2+}$ and chloromethane (Fig. 6). The number of atoms is kept low in order to reduce the computer time, and the optimization was performed under the restricted C_{3v} symmetry. The results of the computations are compared in Table 4. The first and most important prediction is that the Pd···Cl interactions are expected to be very weak as the computed Pd···Cl distances are in the order of 2.83 Å. This distance compares to average distances of the X-ray results reported for $Pd_3(dppm)_3(CO)(Cl)^+$ (Table 3), but is in fact larger than that of the $Pd_3(PH_3)_6(CO)(Cl)^+$ computed distance (2.628 Å). This result may be due to the lack of electrostatic interaction between Pd_3^{2+} and neutral $ClCH_3$. The calculated Pd—Pd bond length (2.63 Å) compares favorably to that of most "$Pd_3(dppm)_3CO^{2+}$" complexes reported so far (see ref. 36 for examples). The r(Pd—P), r(C═O), and r(Pd—C) calculated values also compare with the $Pd_3(PH_3)_6(CO)(Cl)^+$ and

Table 3. Comparison of the calculated and experimental structures for Pd_3 clusters (bond lengths in Å).

	$Pd_3(PH_3)_6CO^{2+}$ ground state calculated	$Pd_3(dppm)CO^{2+}$ X-ray[a]	$Pd_3(PH_3)_6CO^{2+}$, $^3A_2$, calculated[b]	$Pd_3(dppm)_3CO^{2+}$, $^3A_2$ excited state distortion[b]	$Pd_3(PH_3)_6(CO)(Cl)^+$ calculated	$Pd_3(dppm)_3(CO)(Cl)^+$ Puddephatt (X-ray)[c]	$Pd_3(dppm)_3(CO)(Cl)^+$ This work (X-ray)
r(Pd—Pd)	2.592	2.604(30)	2.778	~2.78	2.594	2.591(11)	2.595(17)
r(Pd—C)	2.317	2.318(30)	2.376	—	2.287	2.310(11)	2.311(30)
r(Pd—C)	2.080	2.105(17)	2.057	—	2.189	?	2.244
r(C═O)	1.170	1.165(5)	1.169	—	1.156	?	[d]
r(Pd—Cl)					2.628	2.741	2.668
						2.796	2.903
						3.161	3.011
						2.899(average)	2.861(average)

[a]These data are taken from ref. 13.
[b]These data are taken form ref. 35.
[c]From ref. 24, and CSD (Cambridge Structural Database).
[d]This value is fixed in the refinement.

$Pd_3(PH_3)_6(CO)^{2+}$ data. We conclude that the interactions between the Cl atom of R—Cl and the Pd_3^{2+} center is very weak, causing little perturbation to the host skeleton. The following set of calculations addresses the possibility of the photoinduced labilization of CO (Scheme 2). The optimized geometry of $Pd_3(PH_3)_6^{2+}$ was calculated and the results at convergence (Table 4) indicate that the Pd—Pd and Pd—P distances undergo practically no, or very little, perturbation (within 0.03 Å). If the Pd—Pd bond length had significantly increased, one may have suspected that fragmentation would occur. This is not the case.

To shed light on the steps following the homolytic C—Cl bond cleavage, the geometries of the model compounds $Pd_3(PH_3)_6CO^{3+}$ and $Pd_3(PH_3)_6(CO)(Cl)^{2+}$ were also investigated. The question is, what may happen after the Cl· radical starts interacting with the Pd_3^{2+} center? One hypothesis is an intramolecular electron transfer from the Pd_3^{2+} center to the strongly oxidant Cl· radical. To test this hypothesis, the structure of the $Pd_3(PH_3)_6CO^{3+}$ compound is optimized (Table 4). While the r(Pd—P), r(C·O), and r(Pd—C) data resemble the rest of the data reported in Table 4, the calculated Pd—Pd distance has significantly increased to ~2.73 Å. This distance is very close to the limit of a formal Pd—Pd single bond (see data reported in ref. 3). It is also close to the distance found experimentally in the $Pd_3(dppm)_3CO^{2+}$ cluster in its lowest energy triplet excited state ($^3A_2$; ~2.78 Å) (35). If a formal electron is indeed transferred from the Pd_3^{2+} to the Cl· center to form the Pd_3^{3+} and Cl^- species, then the calculated Pd—Pd bond length in $Pd_3(PH_3)_6(CO)(Cl)^{2+}$ should be close to 2.73 Å also. This is not quite the case as the computed distance converges to 2.68 Å, indicating that the structure is an intermediate between the two forms ($Pd_3^{2+}\cdots Cl^{\cdot}$ and $Pd_3^{3+}\cdots Cl^-$). The r(Pd—P), r(Pd—C), and r(C═O) data are also "normal" (Table 4), but the Pd···Cl distance has significantly decreased, down to ~2.54 Å. This increase in interactions may appear to be due to an increase in electrostatic interactions (i.e., $Pd_3^{3+}\cdots Cl^-$ form). Nonetheless, with a distance of ~2.68 Å typical for a Pd—Pd dppm bridged single bond, the homolytic scission of the Pd—Pd bond after the Cl abstraction does not seem obvious at this point. However, the electrochemical cyclic voltammograms recorded for both $M_3(dppm)_3CO^{2+}$ clusters (M = Pd,Pt) exhibit irreversible oxidation waves, suggesting that further events are obviously taking place after the transfer of the first electron ($Pd_3^{2+} \rightarrow Pd_3^{3+} + 1e^-$). The intramolecular electron transfer between the Pd_3^{2+} and Cl· centers forming Pd_3^{3+} and Cl^-, which subsequently degrade into products, still appears as a possible mechanism of photoinduced fragmentation.

Final remarks

The photoinduced degradation of $M_3(dppm)_3CO^{2+}$ in the presence of chlorocarbons and chloride ion proceeds via very complicated pathways. This work has addressed only a fraction of them, notably for the primary steps. There is no evidence of an electron transfer mechanism involving the excited clusters in their $^3A_2$ states and the R—Cl and Cl^- substrates. On the other hand, the series of measurements performed were all consistent with an atom abstraction mechanism. The well-established host–guest behavior of the cluster was used to confirm this mechanism in the $^3A_2$ states. To our knowledge such a strategy does not seem to have been employed before.

Table 4. Comparison of the calculated structures for Pd_3 clusters (bond lengths in Å).[a]

	$Pd_3(PH_3)_6^{2+}$	$Pd_3(PH_3)_6CO^{3+}$	$Pd_3(PH_3)_6(CO)(Cl)^{2+}$	$Pd_3(PH_3)_6(CO)(Cl)^{+}$	$Pd_3(PH_3)_6(CO)(ClCH_3)^{2+}$	$Pd_3(PH_3)_6(CO)^{2+}$
r(Pd—Pd)	2.606	2.733	2.680	2.594	2.634	2.592
r(Pd—P)	2.191	2.335	2.331	2.287	2.317	2.317
r(C═O)	—	1.157	1.161	1.156	1.158	1.170
r(Pd—d)	—	2.097	2.115	2.189	2.117	2.080
r(Pd—Cl)	—	—	2.541	2.628	2.830	—

[a]Data for $Pd_3(PH_3)_6(CO)(Cl)^+$ are also compared in Table 3, and data for $Pd_3(PH_3)_6(CO)^{2+}$ are from ref. 35. All calculations were performed under a C_{3v} restricted geometry.

One very important observation is clearly the very low photochemical quantum yields, demonstrating the rather inefficient capacity of the clusters to photoactivate the C—Cl bond. For stronger C—X bonds (such as C—H), this observation allows us to predict that the cleavage of this C—X bond will simply not occur, but rather the second pathway (primary photoinduced fragmentation of the cluster) may become dominant in order to promote reactivity in these cases. Thus cluster degradation and decomposition should be observed. This is consistent with the nature of the organic photoproducts observed with the chloride substrate, which are all phosphine derivatives (issued from the coordinated dppm). This decomposition mechanism is complex since high molecular weight fragments are observed (higher than dppm in some cases), indicating that the processes involved formation of free radicals. The very low photochemical quantum yields (Φ) have been commented on in one of our studies on O_2 activation (6). There are many possible explanations for the low Φ values: (*i*) the excited state lifetimes are found to be extremely short ($\tau_1 < 40$ ps, M = Pd; $\tau_1 < 40$ ps, $70 < \tau_2 < 400$ ns, intensity ratio for $\tau_1/\tau_2 = 95/5$, M = Pt; (ref. 25)); (*ii*) access to the lumophore is sterically hindered by another interacting substrate in the ground and excited states; and (*iii*) the biradical-type excited state is delocalized over three metal centers, not localized as in the case of the $M_2(CO)_{10}$ dimers ($2 \times M(CO)_5$; M = Mn, Re; ((ref. 1*a*)). Further studies in this area are in progress.

Acknowledgements

This research was funded by the Natural Sciences and Engineering Research Council of Canada (NSERC) and FCAR (Fonds concertés pour l'avancement de la recherche). J.G. is grateful to FCAR and R.P. to the Université de Sherbrooke for the award of graduate scholarships. P.D.H. also thanks Professor Yves Mugnier (Université de Bourgogne, Dijon) for kindly measuring the cyclic voltammograms of the two clusters (as PF_6 salts).

References

1. (*a*) G.L. Geoffroy and M.S. Wrighton. Organometallic photochemistry. Academic Press, New York. 1979; (*b*) T.J. Meyer and J.V. Caspar. Chem. Rev. **85**, 187 (1985); (*c*) P. D. Harvey. J. Cluster. Sci. **4**, 377 (1993).
2. D. Perreault, M. Drouin, A. Michel, and P.D. Harvey. Inorg. Chem. **31**, 2740 (1992).
3. P.D. Harvey and Z. Murtaza. Inorg. Chem. **32**, 4721 (1993).
4. F.R. Lemke, R.M. Granger, D.A. Morgenstern, and C.P. Kubiak. J. Am. Chem. Soc. **112**, 4052 (1990).
5. (*a*) P.A. Metcalf and C.P. Kubiak. J. Am. Chem. Soc. **108**, 4682 (1986); (*b*) M.K. Reinking, M.L. Kullberg, A.R. Culter, and C.P. Kubiak. J. Am. Chem. Soc. **107**, 3517 (1985).
6. P.D. Harvey, M. Crozet, and K.T. Aye. Can. J. Chem. **73**, 123 (1995).
7. L. Manojlovic-Muir, K.W. Muir, B.R. Lloyd, and R.J. Puddephatt. J. Chem. Soc. Chem. Commun. 1336 (1983).
8. G. Ferguson, B.R. Lloyd and R.J. Puddephatt. Organometallics, **5**, 344 (1986).
9. H.J. Kuhn, S.E. Braslavsky, and R. Schmidt. Pure Appl. Chem. **61**, 187 (1989).
10. S.L. Murov, I. Carmichael, and G.L. Hug. Handbook of photochemistry. 2nd ed. Marcel Dekker, Inc., New York. 1993. pp. 299–301.
11. E.E. Wegner and A.W. Adamson. J. Am. Chem. Soc. **88**, 394 (1966).
12. K.A. Connors. Binding constants: the measurement of molecular complex stability. J. Wiley & Sons, New York. 1987.
13. R. Provencher, K.T. Aye, M. Drouin, J. Gagnon, N. Boudreault, and P.D. Harvey. Inorg. Chem. **33**, 3689 (1994).
14. E.J. Baerends, D.E. Ellis, and P. Ros. Chem. Phys. **2**, 41 (1973).
15. E.J. Baerends. Ph.D. Thesis, Vrije Universiteit, Amsterdam (1975).
16. W. Raveneck. Algorithms and applications on vector and parallel Computers. *Edited by* H.J.J. Rigie, Th. J. Dekkor, and H.A. van de Vorst. Elsevier, Amsterdam. 1987.
17. P.M. Boerrigter, G. te Velde, and E.J. Baerends. Int. J. Quantum Chem. **33**, 87 (1988).
18. L. Verluis and T. Ziegler. J. Chem. Phys. **88**, 322 (1988).
19. (*a*) G.J. Snijders, E.J. Baerends, and P. Vernooÿs. At. Nucl. Data Tables, **26**, 483 (1982); (*b*) P. Vernooÿs, G.J. Snijders, and E.J. Baerends. J. Int. Slater Type Basis Functions for the Whole Periodic System; Internal Report. Free University of Amsterdam, Amsterdam. 1981.
20. (*a*) L. Noodleman and J.G. Nownan. J. Chem. Phys. **70**, 4903 (1979); (*b*) L. Noodleman. J. Chem. Phys. **74**, 5737 (1981); (*c*) L. Noodleman and E.J. Baerends. J. Am. Chem. Soc. **106**, 2316 (1984).
21. J. Krijn and E.J. Baerends. *In* Fit function in the HFS method, Internal Report (in Dutch). Free University of Amsterdam, Amsterdam. 1984.
22. S.D. Vosko, L. Wilk, and M. Nusair. Can. J. Phys. **58**, 1200 (1990).
23. (*a*) Y. LePage, P.D. White, and E.J. Gabe. NRCCAD. An enhanced CAD-4 control program. Proc. Am. Crystallogr., Hamiton Meeting, 1986, Abstract PA 23; (*b*) E.J. Gabe, Y. LePage, J.-P. Charland, F.L. Lee, and P.S. White. J. Appl. Crystallogr. **22**, 384 (1989); (*c*) C.K. Johnson. ORTEP — A Fortran thermal ellipsoid

ploprogram. Technical Report ORNL-5138, Oakridge, Tenn. 1976.
24. L. Manojlovic-Muir, K.W. Muir, B.R. Lloyd, and R.J. Puddephatt. J. Chem. Soc. Chem. Commun. 536 (1985).
25. P.D. Harvey, S.M. Hubig, and T. Ziegler. Inorg. Chem. **33**, 3700 (1994).
26. M.R. Rifi and F.H. Covitz. Introduction to organic chemistry. Marcel Dekker, New York 1974. pp. 200–204.
27. P. Zuman. Handbook series in organic electrochemistry. Vol. 1. CRC Press, Inc., Cleveland, Ohio. 1977. p. AG22.
28. Y. Pan, J.T. Mague, and M.J. Fink. J. Am. Chem. Soc. **115**, 3842 (1993).
29. M.A. Khan and A.J. McAlees. Inorg. Chim. Acta, **104**, 109 (1985).
30. J. Gagnon, C. Loeber, D. Matt, and P.D. Harvey. Inorg. Chim. Acta. **242**, 137 (1996).
31. P.D. Harvey, J. Gagnon, R. Provencher, B. Xu, and T. Swager. Can. J. Chem. **74**, 000 (1996).
32. R. Provencher and P.D. Harvey. Inorg. Chem. **35**, 2235 (1996).
33. N.J. Turro. Modern molecular photochemistry. The Benjamin/Cummings Publishing Co. Inc., Menlo Park, Calif. 1978, pp. 138 and 172.
34. R. Provencher and P.D. Harvey. Inorg. Chem. **32**, 61 (1993).
35. R. Provencher and P.D. Harvey. Inorg. Chem. **35**, 2113 (1996).
36. R.J. Puddephatt, L. Manojlovic-Muir, and K.W. Muir. Polyhedron, **9**, 2767 (1990).
37. (*a*) R.C. Weast, D.R. Lide, M.J. Astle, and W.H. Beyer (*Editor*). CRC handbook of chemistry and physics. 75th ed. CRC Press, Boca Roton, Fla. 1995. p.F. 234; (*b*) M. Weissman and S.W. Benson. J. Phys. Chem. **87**, 243 (1983).

Tungsten and molybdenum oxo complexes of tetrakis(phenyldiazenyl)calix[4]arene substituted derivatives : EHMO calculations, spectroscopic characterization, and perturbations of the photophysical properties by neutral guest molecules

Pierre D. Harvey, Jonathan Gagnon, Réjean Provencher, Bing Xu, and Timothy M. Swager

Abstract: Bowl-shaped chromophores fabricated with tungsten and molybdenum oxo complexes of calix[4]arenes substituted at the *para* positions with phenyldiazenyl ($R_2C_6H_3N_2$) derivatives are investigated. The nature of the lowest energy excited states has been addressed theoretically using Extended Hückel Molecular Orbital (EHMO) calculations and experimentally using UV–visible, luminescence, and polarized emission spectroscopy at 77 K. The lowest energy excited states are intraligand (azobenzene fragment) $\pi\pi^*$ (S_2 and T_2) and $n\pi^*$ states (S_1 and T_1). The compounds are weakly luminescent in the 600–630 nm range exhibiting emissions arising from the $^1(\pi\pi^*)$ states ($S_2 \rightarrow S_0$, $1 < \tau_e < 4$ ns, and $3 \times 10^{-4} < \phi < 3 \times 10^{-3}$). The region located above 900 nm was not investigated. Evidence for guest–host chemistry has been demonstrated by ^{1}H-NMR spectroscopy, and the binding constants for two of the compounds with pyridine in toluene as a solvent were obtained by UV–visible spectroscopy. The presence of a guest molecule inside the luminescent metal oxo complex of a calix[4]arene hosts decreases the emission lifetimes.

Key words: host–guest, photophysics, calix[4]arene, EHMO, fluorescence

Résumé : On a étudié des chromophores en forme de bol préparés à partir de complexes oxo-tungstène et oxo-molybdène de calix[4]arènes substitués en positions *para* par des dérivés phényldiazényles ($R_2C_6H_3N_2$). On a étudié la nature des états excités de plus faible énergie par le biais de calculs d'orbitales molécules étendues de Hückel («EHMO») ainsi que par des expériences faisant appel aux spectroscopies UV–visible, de luminescence et d'émission polarisée à 77 K. Les états excités de plus faible énergie sont les états intraligands (fragment azobenzène) $\pi\pi^*$ (S_2 et T_2) et les états $n\pi^*$ (S_1 et T_1). Les composés sont faiblement luminescents dans le région de 600 à 630 nm et ils présentent des émissions dérivant des états $^1(\pi\pi^*)$ $S_2 \rightarrow S_0$, $1 < \tau_e < 4$ ns et $3 \times 10^{-4} < \phi < 3 \times 10^{-3}$). On n'a pas étudié la région située en dessus de 900 nm. On a mis en évidence de la chimie hôte–invité grace à la spectroscopie RMN du ^{1}H et, faisant appel à la spectroscopie UV–visible, on a déterminé les constantes de liaison de deux des composés avec la pyridine dans le toluène comme solvant. La présence d'une molécule invitée à l'intérieur du complexe luminescent oxo-métal d'un hôte calix[4]arène diminue la durée de vie d'émission.

Mots clés : hôte–invité, photophysique, calix[4]arène, EHMO, fluorescence,

[Traduit par la rédaction]

Introduction

The chemistry of calixarene compounds is well established (1), and has been exploited over the past few years in order to take advantage of the guest–host interactions that these compounds provide (2). Applications include cation extractions and alkali metal sensors. These compounds can be considered as bifunctional recognition devices where the lower rim acts as an ionophoric cavity and the upper rim behaves as a hydrophobic pocket. Molecules such as chloroform and toluene have been found to bind in the cavities of various calixarene compounds (1, 2*i*). More recently much progress has been made in improving the sensorial and binding properties of these compounds by attaching metal or organometallic centers (3). Tungsten oxo complexes of calix[4]arene derivatives have been used to produce bowlic liquid crystals (4).

We now wish to report the spectroscopic and photophysical properties of a series of metal oxo complexes of tetrakis(phe-

Received February 6, 1996.

This paper is dedicated to Professor Howard C. Clark in recognition of his contributions to Canadian chemistry.

P.D. Harvey,[1] J. Gagnon, and R. Provencher. Département de chimie, Université de Sherbrooke, Sherbrooke, QC J1K 2R1, Canada.

B. Xu and M. Swager. Department of Chemistry, University of Pennsylvania, Philadelphia, PA 19104-6323, U.S.A.

[1] Author to whom correspondence may be addressed. (Telephone: (819) 821-7092. Fax: (819) 821-8017. E-mail: pharvey@structure.chimie.usherb.ca

Scheme 1.

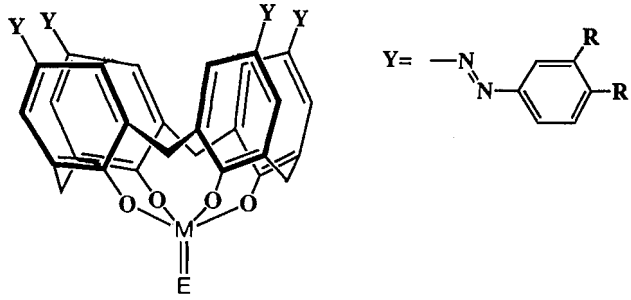

1: M=W, E=O, R=$OC_{10}H_{21}$

2: M=W, E=O, R=CH_3

3: M=Mo, E=O, R=$OC_{10}H_{21}$

4: free ligand, R=$OC_{10}H_{21}$

nyldiazenyl)calix[4]arene derivatives (M = W, Mo) (Scheme 1). These systems exhibit multifunctional properties, two of which are designed for the binding of organic substrates (the M = O groups are strong Lewis acids, and the phenyl groups provide hydrophobic pockets), and one for the luminescent probe at 77 K (azobenzene). The metal centers were observed to influence the absorption and emission band maxima (λ_{max}) and the emission lifetimes (τ_e). The photophysical properties are also found to be somewhat sensitive to the solvent (methylcyclohexane, pyridine, butyronitrile, etc.). Finally, one of the tungstenoxocalix[4]arene derivatives was investigated in its polymeric associated form where the molecules act as both guests and hosts at the same time and organize in a head-to-tail fashion.

Experimental section

Materials

The syntheses of the free ligands and the complexes have been reported (4), or will be reported, elsewhere (5), except for compound **2**, which is described below. Compounds **1–4** are solvated by one dimethylformamide molecule (DMF) inside the cavity as demonstrated by ^{1}H NMR integration.

Compound 2

To a solution of $NaBF_4$ (11.5 g, 104.7 mmol) in 30 mL of water cooled with an ice bath was added 18 mL of concentrated hydrochloric acid followed by 3,4-dimethylaniline (10 g, 82.5 mmol). To this mixture $NaNO_2$ (5.72 g, 82.5 mmol) in 15 mL of water was slowly added while keeping the reaction temperature below 10°C. After 0.5 h, the reaction mixture was filtered, then washed with 50 mL of a cool $NaBF_4$ solution, then with 50 mL of cool methanol, finally with 50 mL of ether, and finally dried and cooled in a desiccator with cooling to obtain 3,4-dimethylbenzene-diazonium tetrafluoroborate as a white solid. This product was dissolved in 100 mL THF, cooled to 0°C, and then pyridine (4 mL) and calix[4]arene (2 g, 4.7 mmol) were added. After 3 h, the solution was filtered and washed with THF and methanol. The solid was dissolved in pyridine and treated with activated carbon, filtered, and evaporated, and was then dispersed in 200 mL of 5% HCl and stirred for 1.5 h at room temperature. Filtering and drying gave 2.1 g of tetrakis-3,4-dimethylphenydiazenylcalix[4]arene as a red-orange solid (47% yield). ^{1}H NMR (DMSO-d_6): 7.70 (s, Ph, 8H), 7.59 (s, Ph, 4H), 7.50 (d, Ph, 4H), 7.22 (d, Ph, 4H), 3.61 (s, $PhCH_2$, 8H), 2.23 (s, CH_3, 12H), 2.21 (s, CH_3, 12H). Tetrakis-3,4-dimethylphenylazocalix[4]arene, 0.5 g (0.52 mmol), and $WOCl_4$, 178 mg (0.52 mmol), in 15 mL of dry toluene were then refluxed for 12 h under argon. Evaporation of the solvent gave a residue that was recrystallized from DMF, to give 0.45 g of tungstenoxotetrakis-3,4-dimethylphenydiazenylzocalix[4]arene as a yellow solid (70% yield). ^{1}H NMR ($CDCl_3$): 7.70 (s, Ph, 8H), 7.61 (s, Ph, 4H), 7.59 (d, Ph, 4H), 7.23 (d, Ph, 4H), 4.84 (d, $PhCH_2$, 4H), 3.56 (s, $PhCH_2$, 4H), 2.30 (s, CH_3, 24H), and 8.0, 4.1 (formyl H of DMF), 2.95, 2.85, 1.30, 0.55 (methyl H of DMF).

Preparation of the pyridine complex

The pyridine complex of tungstenoxodidodecanoxylbenzenediazenylcalix[4]arene was obtained by recrystallizing tungstenoxodidodecanoxylbenzenediazenylcalix[4]arene in pyridine – THF – MeOH. ^{1}H NMR ($CDCl_3$) 8.58, 7.65, 7.25 (free pyridine), 7.9–6.7 (m, phenyl H of azocalix[4]arene and guest pyridine, 25H), 5.00, 4.82, 4.43 (d, d, d, $PhCH_2$, 4H), 4.2–3.8 (m, OCH_2, 16H), 3.63, 3.43 (d, d, $PhCH_2$, 4H), 2.0–0.8 (m, alkyl H). The upfield shift of the pyridine protons is indicative of the binding of the molecule in the cavity. For other examples of this effect see ref. 4.

Instruments

The absorption spectra were acquired on a Hewlett Packard 8452 A diode array spectrophotometer. The emission and excitation spectra were obtained using either a Spex Fluorolog II spectrometer or a PTI LS100 spectrometer. The emission lifetime measurements were performed on a photon counting system coupled with the PTI LS100 instrument, using a homemade N_2(g) flash lamp source under the following conditions: electrode gap, 1.6 mm; gas, 15 Torr (1 Torr = 133.3 Pa); applied voltage, 40 kV; repetition rate, 40 kHz. Under these conditions, the lamp pulse exhibits a full width at half-maximum (fwhm) of 2.5 ns (when the electrodes are freshly cleaned). A PTI software package for the deconvolution technique was used to extract the lifetimes from the data. Each lifetime measurement was performed at least three times from the same freshly prepared samples. The reproducibility was found to be within ±0.05 ns. The FT-Raman spectrum was obtained with an IFS 55 FRA106 Bruker instrument.

Experimental procedures

The emission quantum yields were measured using 9,10-diphenylanthracene as the standard according to published procedures (6). The polarization ratios (N) were measured according to literature procedures (see examples in ref. 7). The binding constants were determined using the methodology outlined in details in ref. 8.

Computational details

All MO calculations were of the extended Hückel type (EHMO) using a modified version of the Wolfsberg–Helmholz formula (9). The atomic parameters used for C, H, O, N,

Fig. 1. EHMO energy levels (left) for the diazobenzene chromophoric molecule. EHMO pictures (right) for the LUMO (32; $4b_g$), HOMO (33; $14a_g$), and HOMO-1 (34; $4a_u$).

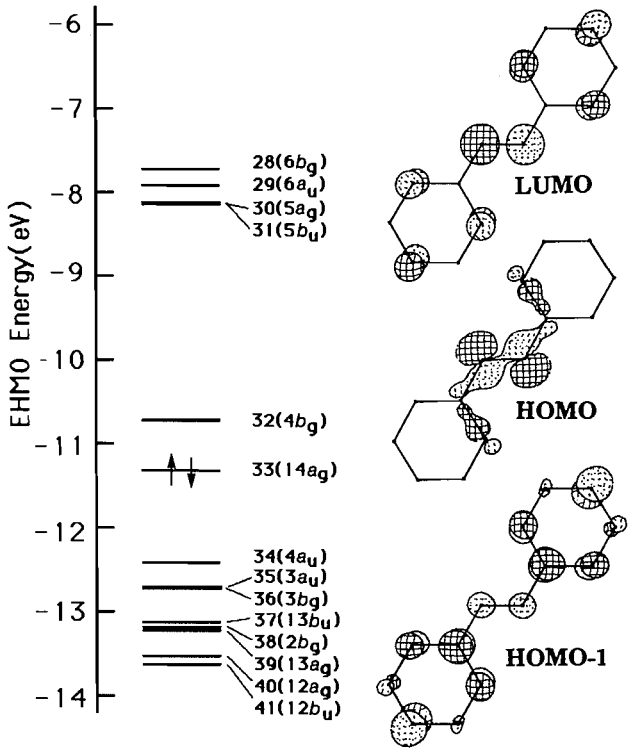

Fig. 2. EHMO energy levels for the tungsten oxo complex of the tetrakis-(phenyldiazenyl)calix[4]arene.

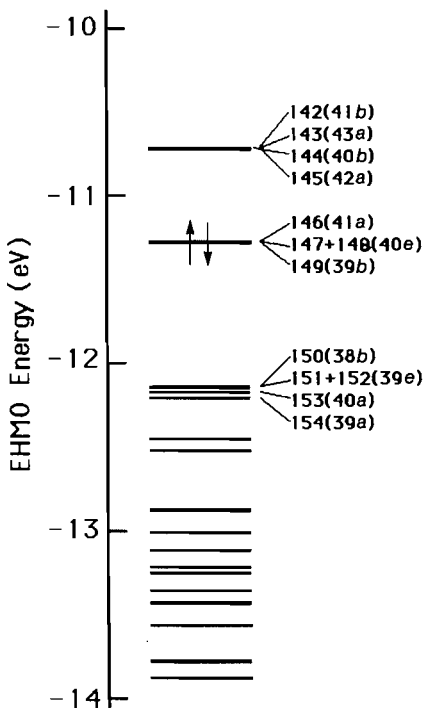

and W are taken from refs. 9 and 10. The bond lengths and angles used for the computations are those found crystallographically in the literature (3*f*) and are *r*(C—C) = 1.4 Å, *r*(C—O) = 1.47 Å, *r*(C—H) = 1.05 Å, *r*(N=N) = 1.25 Å, *r*(W=O) = 1.70 Å, *r*(W—O) = 1.89 Å, ∠O-W-O = 181°, ∠W-O-C = 135°, ∠C-C-C = 120°. The long alkyl chains and methylene groups were not included in the computations, since they are of very little consequence to the lowest energy excited states. Pictorial representations of the orbitals were obtained using the CACAO graphics package included in the software (11). The absorption spectrum of compound **1** was calculated using Heller's time-dependent theory, giving equivalent results to a traditional Franck–Condon analysis (12 and, for a recent applications, ref. 13).

Results and discussion

1. Excited state characterization (EHMO)

The nature of the frontier MO's has been addressed theoretically using the Extended Hückel Molecular Orbital methods (EHMO). The electronic structures of the *trans*-azobenzene compound (C_{2h}), the tungsten oxo complex of the mono(phenyldiazenyl)calix[4]arene (C_1), and the tungsten oxo complex of the tetrakis(phenyldiazenyl)calix[4]arene (C_4) have been investigated. The tungsten oxo complex of the mono(phenyldiazenyl)calix[4]arene was investigated because it exhibits an intermediate level of complication (i.e., low number of MOs) between the *trans*-azobenzene and the tungsten oxo complex of the tetra-substituted ligand.[2] A summary of the key results is presented here.

The EHMO calculations for all three model compounds indicate that the energy ordering of the three MOs of interest in this work is that of the intraligand π(HOMO-1), *n*(HOMO), and π*(LUMO) MOs localized in the azobenzene fragments (Figs. 1–3). The HOMO and LUMO are localized at −11.26 and −10.70 eV, respectively, for all three computed compounds. In the tetrakis(phenyldiazenyl)calix[4]arene case, the HOMO defined as MO no. 33 ($14a_g$) in Fig. 1 becomes MOs no. 146–149 (41*a*, 40*e*, 39*b*). These four MOs, all *n* in nature, have the same EHMO energy (accidently degenerate Fig. 2). The LUMO defined as MO no. 32 ($4b_g$) for azobenzene becomes MOs no. 142–145 (41*b*, 43*a*, 40*b*, 42*a*), also with the same energy, for the tungsten oxo complex of tetrakis(phenyldiazenyl)calix[4]arene. The π(HOMO-1) (MOs no. 34; $4a_u$) for azobenzene is located at –12.18 eV according to the EHMO calculations. This MO becomes MOs no. 150–153 (38*b*, 39*e*, 40*a*) in the tungsten oxo complex of the calix[4]arene derivative. These MOs are all π systems. The MO representations of one of the π* systems (designated as LUMO for analogy with the azobenzene molecule), one of the *n* systems (designated as HOMO), and one of the π systems are presented in Fig. 3. These are not described here since they are very similar to that of the well-known azobenzene molecule. Above the LUMO in the tungsten oxo complex of the tetra- and mono(phenyldiazenyl) compounds are localized a

[2] Supplementary information: as a typical example, the MO energies, atomic contributions, occupancies, and MO drawings for six of the frontier MOs for the tungsten oxo complex of the mono(phenyldiazenyl)calix[4]arene are supplied. Copies of material on deposit may be purchased from: The Depository of Unpublished Data, Document Delivery, CISTI, National Research Council Canada, Ottawa, Canada K1A 0S2.

Fig. 3. EHMO pictures for the LUMO (MO no. 149; 39*b*), the HOMO (MO no. 150; 38*b*), and MOs no. 151 + 152 (39*c*) designated by HOMO-1 for the tungsten oxo complex of the tetrakis (phenyldiazenyl)calix[4]arene.

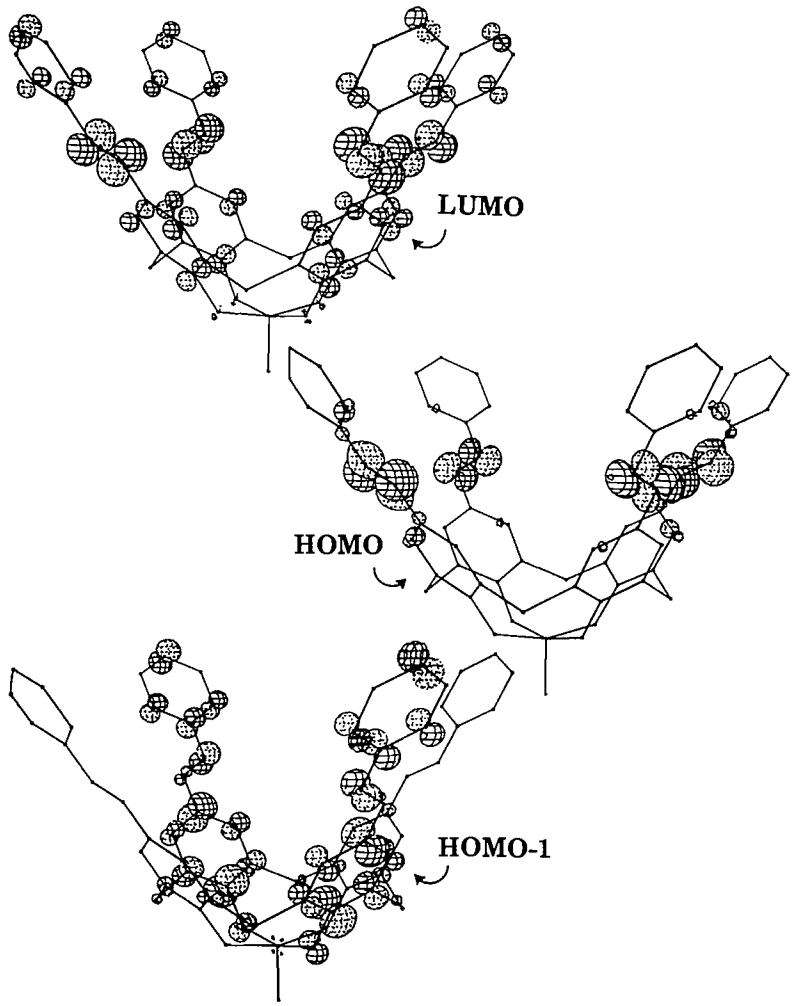

series of MOs that are a W═O π* system using the W d_{xz}, and the O p_y and p_x atomic orbitals. The atomic contributions are in the order of ~84% W and ~7% O. These contributions are the square of the LCAO coefficients used in the EHMO approximations; these are normalized to 100%. These MOs are localized ~2 eV above the LUMO π* system, and are also of little consequence to this work. For the π*, *n*, and π systems designated by the LUMO, HOMO, and HOMO-1 for all three model compounds, the atomic contributions are very similar from one compound to the other (see Figs. 1 and 3; tables for atomic contributions for the tungsten oxo complex of the mono(phenyldiazenyl) compound are supplied in the Supplementary Information as examples).

To summarize, the EHMO computations predict that the metal oxo complexes of the tetrakis(phenyldiazenyl)-calix[4]arene derivatives should exhibit absorption spectra where the lowest energy bands arise from $n \rightarrow \pi^*$ electronic transitions localized in the azobenzene fragments, followed by higher energy absorptions assignable to $\pi \rightarrow \pi^*$ transitions, also localized primarily within the ligand.

2. Excited state characterization (UV–vis spectra)

Typical absorption spectra and data are shown in Fig. 4 and Table 1, respectively. The spectra are characterized by a strong absorption ($78\,000 < \varepsilon$ (M^{-1} cm^{-1}) $< 108\,000$, toluene at 298 K) in the 370–440 nm region, which exhibits some poorly resolved features attributable to the presence of vibrational progressions. Due to the large intensity, the $n \rightarrow \pi^*$ band assignment is readily ruled out (14). Rather a $\pi \rightarrow \pi^*$ assignment is more appropriate (14). The $n \rightarrow \pi^*$ band was not located at 298K. To insure our assignments, as well as to locate the $n \rightarrow \pi^*$ absorption band, the spectra at 77 K were measured (Fig. 5) and calculated using Heller's time-dependent theory (12). At 77 K, the spectra are somewhat better resolved, and a vibrational progression is readily seen with a spacing of 1500 cm^{-1}, which is consistent with an excited state C═C stretching mode and not an Ṅ═Ṅ mode. Figure 6 compares the experimental spectrum for **1** and the calculated band located at 400 nm (i.e., 25 000 cm^{-1}). In this analysis we define a model using the lowest number of parameters to correctly calculate the experimental spectra, consisting of two-dimen-

Table 1. Absorption spectroscopic data in toluene.

Compounds	ν_{max}/±100 cm^{-1}	λ_{max}/±2 nm	ε/M^{-1} cm^{-1} ±10%	Comments
1	26 500	378	88 000	
	25 100	398	74 000	Shoulder
	23 600	424	38 000	Shoulder
2	28 700	348	78 000	
	23 300	430	6 300	Shoulder
3	26 500	378	108 000	Broad band
4	27 200	368	88 000	
	25 900	386	74 100	Shoulder
	22 400	446	8 830	Shoulder

Fig. 4. UV–visible spectra for compounds **1**–**4** in toluene at 298 K (from top to bottom).

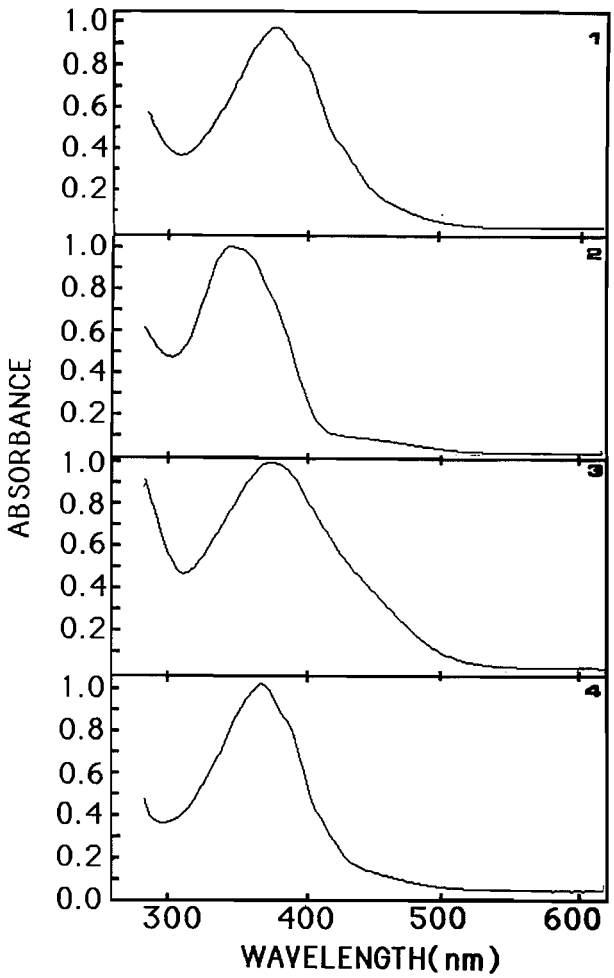

Fig. 5. UV-visible spectra for compound **1** in 2-MeTHF showing the vibrational progression of the $\pi \rightarrow \pi^*$ electronic band.

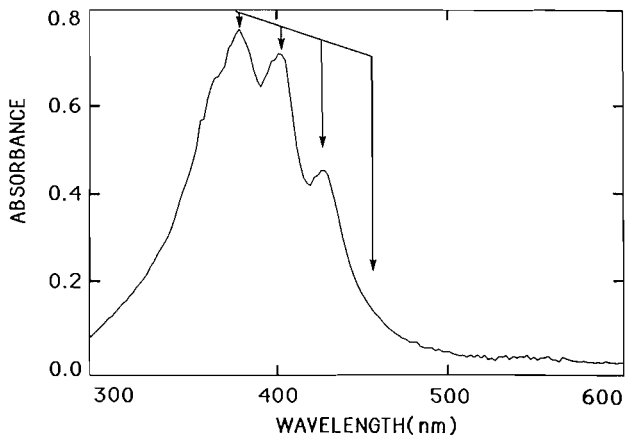

sional harmonic oscillator potential energy surfaces for both the ground and excited electronic states. No satisfactory results were obtained using a single Franck–Condon active mode. In the two-mode model, the vibrational frequencies were fixed at 1510 and 1110 cm^{-1}, for the calculations that are close to the vibrational frequencies observed in the Raman spectrum (peaks observed at 1590 and 1152 or 1107 cm^{-1}).[3] A variation of these frequencies by more than 10% does not affect the agreement between calculated and experimental spectra. The Huang–Rhys parameters, S (15), for both vibrational modes were treated as adjustable parameters in the fitting process, using the 15 000 – 35 000 cm^{-1} region of the absorption spectrum. The agreement between calculated and experimental spectra (Fig. 6) is excellent in view of the simple model with only two adjustable parameters. At the best fit, values of 1.99 and 1.10 were obtained for S along the excited electronic 1510 and 1110 cm^{-1} modes, respectively. If one lowers all S values by 2-3%, the agreement between experiments and calculations is no longer acceptable; an augmentation of 2–3% also leads to unacceptable calculations. These modes are easily assigned to ν(C=C) (1590, and 1152 or 1107 cm^{-1} in the ground state), and the possibility of ν(N=N) as potential assignment is ruled out since this mode is generally found at around 1400 cm^{-1} (16). We conclude that the 400 nm band undoubtedly arises from an intraligand $\pi \rightarrow \pi^*$ type electronic transition. The excited state distortions (ΔQ) are calculated, and are 0.12 and 0.11 Å for the two modes, respectively. These values are of the same order of magnitude as that

[3] The solid state FT-Raman spectrum is provided as supplementary information (see footnote 2).

Fig. 6. Comparison between the experimental (full line) and calculated spectra (full line with dotted line on top using Heller's time-dependent theory) for compound **1**. The $n \rightarrow \pi^*$ band belonging to the N = N groups becomes apparent at ~18 000 cm^{-1} (~550 nm).

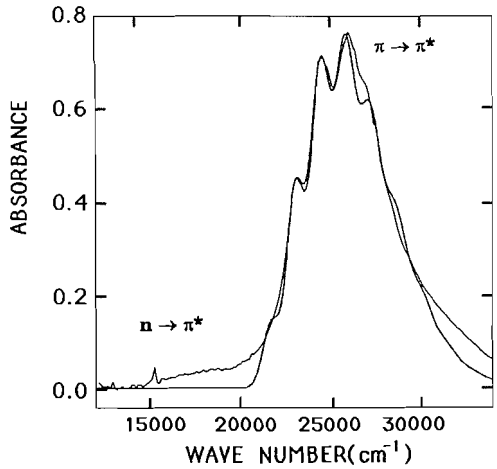

reported for the $Ru(bpy)_3^{2+}$ cation (bpy = bipyridine) for which a lowest energy metal-to-ligand charge transfer (MLCT) excited state is assigned (17). In this case, ΔQ averages ~+0.07 Å along the C—C bonds in the bpy ligands (17). Since the MOs associated with this $\pi \rightarrow \pi^*$ electronic transition (HOMO-2 and LUMO) are C—C bonding and anti-bonding, respectively, the ΔQ values calculated must be positive (i.e., C=C bond lengthenings).

The two regions where agreement between the calculated and measured spectra are poor (~20 000 cm^{-1} (~500 nm) and ~33 000 cm^{-1} (~300 nm)) are due to the presence of overlapping electronic bands. With respect to the ~300 nm feature, other $\pi \rightarrow \pi^*$ electronic bands are likely to appear in this region, based upon the EHMO findings. The second region (~20 000 cm^{-1}; ~500 nm) is of more interest since it indicates the presence of a low-intensity electronic transition (~5% of the 400 nm band) that we confidently assign to $n \rightarrow \pi^*$ (N=N). The energy gap between this band and the 400 nm band (~800 – 900 cm^{-1}) measured at ν_{max} is essentially the same as that reported for azobenzene (18). No other absorption band was observed below 15 000 cm^{-1}. No attempt was made to deconvolute these higher and lower energy bands.

A comparison of **1**, **3**, and **4** (Table 1) shows weak metal dependence on λ_{max} of the absorption (400 nm $\pi \rightarrow \pi^*$) band. On the other hand, the substituent effect observed between compounds **1** and **2** ($OC_{10}H_{21}$ vs. CH_3) on λ_{max} clearly indicates the presence of a greater substituent perturbation on the (azobenzene) chromophore, which reinforces this assignment.

3. Emission properties

The compounds are found to be weakly emissive in the 600–630 nm range at 77 K (Fig. 7. $3 \times 10^{-4} < \phi_e < 3 \times 10^{-3}$), while no luminescence was observed at room temperature either in solution or in the solid state. Although the absence of vibronic structure in the emission spectra would suggest that the luminescence does not arise from a $\pi\pi^*$ state (15), polarized emission photoselection spectroscopy (7) is used for assignment. By knowing that the transition moments for $\pi \rightarrow \pi^*$ and $n \rightarrow \pi^*$ electronic transitions (without a change of spin multiplicity) are polarized parallel and perpendicular to the aromatic plane, respectively, and that these same electronic transitions with a multiplicity change (singlet–triplet) are perpendicular and parallel polarized to the plane, respectively, one can predict the relative polarization of the two electronic bands (14). Since the 400 nm band is securely assigned ($\pi \rightarrow \pi^*$), one can use its in-plane polarization as a reference point. Scheme 2 shows all possible scenarios for the relative polarization of the emission transition moment for both fluorescence and phosphorescence.

The polarization ratio, N, is given by $(I_{BB}/I_{BE})_V \cdot (I_{EE}/I_{EB})_H$, where $(I_{BB}/I_{BE})_V$ is the ratio of the intensities of vertically to horizontally polarized emission when excited with vertically polarized light, and $(I_{EE}/I_{EB})_H$ is the ratio of the intensities of

Fig. 7. Emission spectra for compounds **1–4** in ethanol at 77 K. The intensities have been normalized and baselines have been adjusted vertically for clarity.

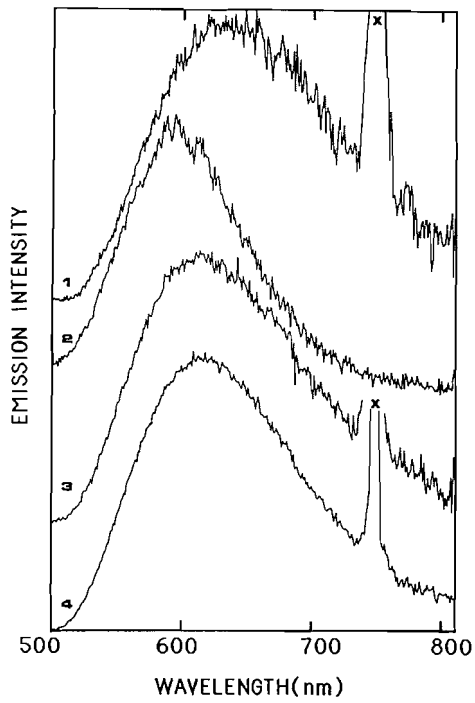

Scheme 2.

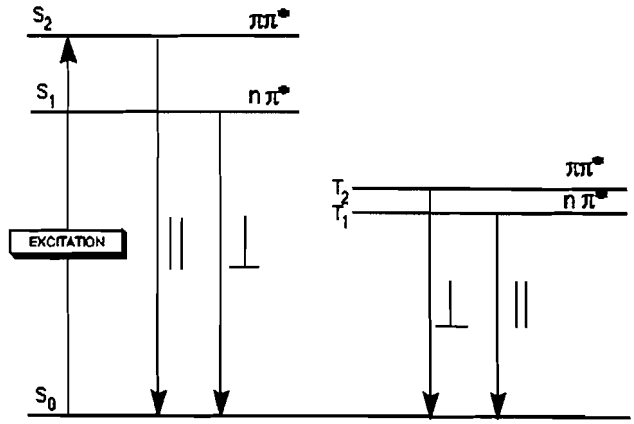

Fig. 8. Polarization ratio for the emission spectra for compound **1** using λ_{exc} = 430 nm (top), for compound **1** using λ_{exc} = 375 nm (middle), and for compound **4** also using λ_{exc} = 375 nm. Solvent was ethanol.

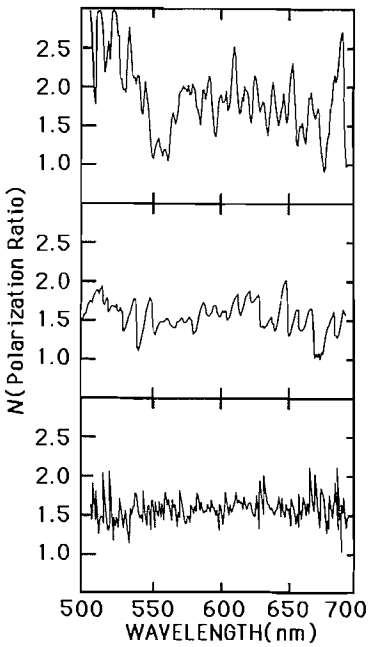

parallel and perpendicular polarized emission with horizontally polarized excitation. N is then related to the relative orientation of the transition moments in absorption and emission. The theoretical value of $N = 3$ indicates that absorption polarized on a single molecular axis is followed by an emission along the same axis. $N = 0.5$ indicates that single axis absorption is followed by emission along a perpendicular axis. In practice, the theoretical values were never obtained due in part to the natural depolarization of the glass. In a situation where N = 1.0, then the emission is depolarized. For this work, it is assumed that absorption is followed by an emission arising from the same azobenzene lumophore group (no energy transfer from one azobenzene center to another in the calix[4]arene), and two different λ_{exc} at 375 and 430 nm were used for comparison purposes. Figure 8 shows N vs. λ for compounds **1** and **4**. Referring to Figs. 5, and 6, the 430 nm absorption region appears to be free from overlap with other absorption bands, and it is reasonable to assume that the polarization of the absorbed light is pure. For compound **1** when λ_{exc} = 430 nm, N varies from ~3 at 500 nm, to ~2 at λ_{max}, to ~1.5 at ~700 nm (Fig. 8), indicating that the emission exhibits a significant component polarized parallel to the absorption ($S_0 \rightarrow S_1$, $\pi \rightarrow \pi^*$). The signal-to-noise ratio is poor because of the lower emission quantum yield. The decrease in N with λ could be indicative of the presence of a non-totally symmetric vibrational mode under the emission band envelope (7). At λ_{exc} = 375 nm, the polarization ratios are now ~1.5, and appear to be constant with λ_{emi}. The 375 nm region (~26 700 cm^{-1}) exhibits a difference between the calculated (full line with dotted line on top) and experimental (full line) absorption spectrum (Fig. 6), which is due to the fact that other absorption bands are not taken into account. Excitation is taking place in two different absorption systems at 375 nm (26 700 cm^{-1}), and mixing of the polarized light will occur (if the transition moments are not parallel).[4] Similar results are also obtained for compound **4** (the free ligand). Hence, the emission is polarized parallel to the absorption, thereby leaving only two possible assignments for the luminescence: $^1\pi\pi^* \rightarrow$ ground state or $^3n\pi^* \rightarrow$ ground state.

The emission spectra of azobenzene ($C_6H_5N{=}N\text{-}C_6H_5$) are known and are described as follows: the first emission is an $S_2 \rightarrow S_0$ fluorescence (high-energy emission) arising from the $^1(\pi\pi^*)$ state with λ_{max} ~425 nm (23 500 cm^{-1}), and τ_F <5 ps; the second emission (low-energy emission) is an $S_1 \rightarrow S_0$ fluorescence arising from the $^1(n\pi^*)$ state with λ_{max} >800 nm (<12 500 cm^{-1}), and $\tau_F \approx$ 25 ps (18). At room temperature the $S_0 \rightarrow S_2$ ($\pi\pi^*$) absorption is localized at ~320 nm (31 300 cm^{-1}) in azobenzene (18). For all compounds investigated, this $\pi\pi^*$ absorption, which fits the one for the azobenzene, is localized at ~380 nm (26 300 cm^{-1}). The difference represents a ~60 nm red shift (i.e., ~5000 cm^{-1}). Such a shift would place the high-energy emission band at ~540 nm (i.e., 23 500 (azobenzene) – 5000 = 18 500cm^{-1}) for the investigated complexes. The emission maxima are observed between 600 (167 00 cm^{-1}) and 630 nm (15 900 cm^{-1}; Table 2)! The emission arising from the $^1(n\pi^*)$ state (if observed) is also expected to red shift with respect to the unsubstituted azobenzene. Similarly a 5000 cm^{-1} red shift of the low energy emission band going from azobenzene to the investigated compounds would place the $^1(n\pi)^* \rightarrow S_0$ fluorescence band in the 7500 cm^{-1} range (or lower), which is well above 900 nm; a range that was not investigated here. The lowest energy triplet state in azobenzene, $^3(n\pi^*)$, is located at 990 nm (i.e., 10 100 cm^{-1}) according to literature (18). Based upon these λ_{max} considerations, the emission bands are assigned to $S_n(^1\pi\pi^*) \rightarrow S_0$ transitions similar to that of the high-energy fluorescence observed in azobenzene. The absence of vibronic structure could be indicative of a change in conformation in the $^1(\pi\pi^*)$ state. Azobenzene is known to undergo photoinduced *cis-trans* isomerization (18*b*).

The photophysical data (Table 2) for **4** indicate very low values for τ_e (emission lifetime) and ϕ_e (emission quantum yield). These low values are also consistent with an $S_n \rightarrow S_0$ fluorescence (14, 18). Here S_n indicates an higher energy $\pi\pi^*$ singlet excited state, bypassing the $n\pi^*$ singlet and triplet states. From then on, this S_n emissive state will be designated as "S_2" by analogy with azobenzene. In comparison with the reported data for azobenzene ($\tau_F < 5$ ps, $\Phi_F < 1 \times 10^{-4}$) (18*b*), the larger values in the study are due to an increase in both medium (77 K glass) and molecular rigidity. It is not possible to comment on the Φ_e, τ_e, k_r (radiative rate constants), and k_{nr} (non-radiative rate constants) data due to the low number of compounds investigated. Heavy-atom effects, "loose bolt effects," molecular rigidity, and host–guest interactions may affect the magnitude of these values. Further investigation is necessary.

4. Guest–host chemistry

Typically one can assign the intraligand bands ($\pi \rightarrow \pi^*$ vs.

[4] Allowed $\pi \rightarrow \pi^*$ electronic transitions can be polarized in-plane with respect to an aromatic molecule, but the relative polarization of these may be different (*x*-polarized vs. *y*-polarized).

Table 2. Photophysical data for the metallocalix[4]arenes.[a]

Compounds	ν_{max}/cm^{-1}[b]	λ_{max}/nm[b]	τ_e/ns[c]	ϕ_e[d]	k_r/s^{-1}[e]	k_{nr}/s^{-1}[f]
1	15 900	630	1.56	3.77×10^{-4}	2.4×10^5	6.4×10^8
2	16 700	600	2.61	Not measured	—	—
3	16 300	614	3.55	7.06×10^{-4}	2.0×10^5	2.8×10^8
4	16 300	615	1.57	3.24×10^{-3}	2.1×10^6	6.3×10^8

[a]77 K in ethanol.
[b]±3 nm, ±100 cm^{-1}.
[c]~±0.05 ns.
[d]±10%.
[e]$k_r = \phi_e/\tau_e$.
[f]$k_{nr} = (1 - \phi_e)/\tau_e$.

Fig. 9. Typical example of the spectroscopic changes that occur in the absorption spectra for compound **1** when pyridine is added to the toluene solutions. Inset: typical Benesi–Hildebrand plot used for the K_{11} measurements.

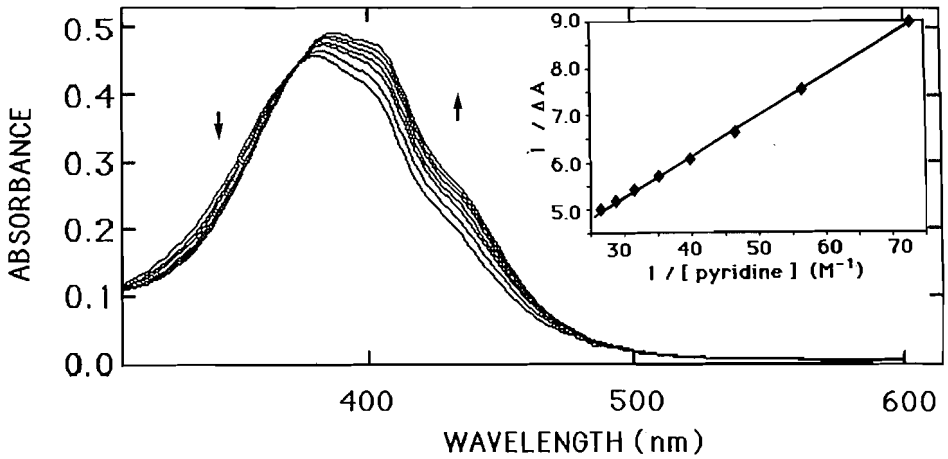

$n \rightarrow \pi^*$) on the basis of band shift with of polarity the medium (14, 19). However, this was not possible in this work due to the presence of guest molecules in the cavities of the calix[4]arene moieties. In fact, the measurements of λ_{max} (of the 400 nm band) as a function dielectric constant of the medium lead to a quasi-random relationship. Such behavior is not new to us since similar behavior was also observed previously with the $M_3(dppm)_3CO^{2+}$ clusters (M = Pd, Pt; dppm = $((C_6H_5)_2P)_2CH_2$) (8*a*), where the guest–host chemistry was well established with X-ray crystal structures and UV–vis spectroscopy (20).

The binding constants, K_{11}, were measured for the following ground state associated complexes: compound **1** – pyridine and compound **4** – pyridine using UV–visible spectroscopy, and toluene as solvent. Typical pyridine concentrations used for compound **1** ranged from 0.010 to 0.050 M and, for compound **4**, from 0 to 0.11 M. The K_{11} data were extracted from the Benesi–Hildebrand plots (8*a*,*b*) and confirm that the associated complexes are 1:1 stoichiometric complexes. The data are as follows: compound **1** – pyridine, $K_{11} = 35 \pm 4\ M^{-1}$; compound **4** – pyridine, $K_{11} \leq 1\ M^{-1}$. The host concentration in toluene solutions was kept constant for all measurements (the absorbance was ~0.45–0.50 at λ_{max}). A typical set of spectroscopic changes and plots is presented in Fig. 9. The increase in K_{11} (≥35-fold) on going from compound **4** to compound **1** clearly demonstrates that the $W^{+6}\cdots N$ interactions are present and contribute to the binding. The rigidity could also contribute to the increase in the K_{11} value.

Table 3 compares the 77 K emission lifetimes for compounds **1–4** in various solvents. For comparison purposes, methylcyclohexane was also investigated because of its size, its lack of Lewis basicity, its ability to form glass at 77 K (when dry), and the solubility of the compounds in this solvent. It is reasonable to assume that methylcyclohexane is a very weak binder within the calix[4]arene cavity. From Table 3 a clear trend is observed: τ_e(methylcyclohexane) > τ_e(ethanol) > τ_e(butyronitrile). All decay traces were monoexponential. By adding pyridine (proven above to be acting as guest molecule) up to 20% in volume, the emission lifetimes decrease further regardless of the solvent or the compound. For instance, compound **1** in ethanol exhibits a decrease from 1.56 to 0.81 ns, and compound **3** in butyronitrile presents a change from 1.85 down to 0.71 ns. This observation is consistent with the previously reported data for $Pd_3(dppm)_3CO^{2+}$, which showed that the addition of an interacting substrate within the cavity always resulted in a decrease in excited state lifetimes (20*b*).

The last system investigated is compound **1** quenched from

Table 3. Solvent dependence of the emission lifetimes for compounds **1**–**4**.[a,b]

Compound	τ_e Ethanol	τ_e Butyronitrile	τ_e Methylcyclohexane
1	1.56 (630)	0.92 (630)	— [c]
2	2.61 (600)	1.44 (592)	— [c]
3	3.55 (614)	1.85 (620)	3.89 (~626)
4	1.57 (615)	1.14 (620)	1.88 (623)

[a]Data in ns (±0.05).
[b]The values in parentheses are the emission wavelength maxima in nm.
[c]Not measured.

Fig. 10. Balls and sticks, and space-filling representations of two tungsten oxo complexes of the tetrakis(phenyldiazenyl)-calix[4]arene stacking together in a host–guest fashion.

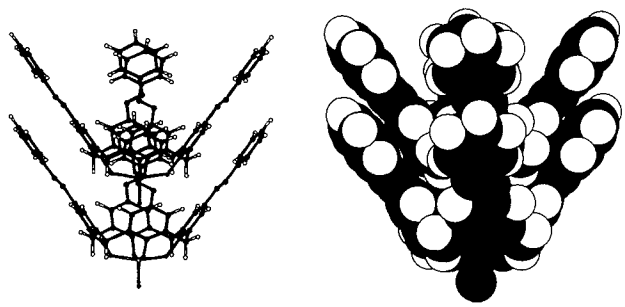

the liquid crystal state. Upon heating, the guest DMF molecule escapes the cavity and the host molecule self-assembles in a head-to-tail fashion to form an associated material exhibiting mesomorphic properties (4). Computer modeling (Fig. 10) clearly indicates that W═O···W═O close contacts are not possible in this self-assembly (the WO···WO distance is in the order of 4.35 Å while the C···C contacts are set to 3.55 Å, similar to graphite). The 77 K emission band for this material is red shifted to 650 nm along with the absorption maxima, which is red shifted by 30 nm (at 298 K). The 77 K emission lifetime is 1.98 ± 0.05 ns (compared to 1.56 ns for compound **1** in its monomeric form). This datum suggests that DMF binds more strongly to the host molecule than the host itself. This result is consistent with the fact that the mesomorphic properties vanish when DMF is added to the material (4), and with the fact that the associated structure is mostly based upon hydrophobic interactions with little or no W anchoring contribution.

Concluding remarks

The chromophoric centers in these host molecules are the diazobenzene fragments with practically no, or very little, perturbation of the metal atoms on the MOs. The nature of the lowest excited states is $\pi\pi^* > n\pi^*$, identical to that of diazobenzene. The observed ~615 ± 15 nm weak emissions arise from an upper singlet $\pi\pi^*$ state, not from the lowest energy triplet $n\pi^*$ state. Only the 400–900 nm range was investigated. The emissions arising from the $n\pi^*$ states are expected to be located above 900 nm. Finally, the photophysical data establish that additions of a neutral substrate inside the cavity of the calix[4]arene moieties result invariably in a decrease in τ_e.

Acknowledgements

This research was supported by the Natural Sciences and Engineering Research Council of Canada (NSERC) and FCAR (Fonds pour la formation de chercheurs et l'aide à la recherche) (P.D.H.), and by the Office of Naval Research (T.M.S.). P.D.H. also thanks le Ministère des Affaires Internationales du Québec, Coopération Québec/États-Unis for a cooperative grant.

References

1. C.D. Gutsche. Calixarenes Royal Society of Chemistry, Cambridge. 1989.
2. (*a*) I. Aoki and S.J. Shinkai. J. Chem. Soc. Chem. Commun. 730 (1992); (*b*) N. Sato and S.J. Shinkai. Chem. Soc. Perkin Trans. **2**, 621 (1993); (*c*) M. McCarrick, B. Wu, S.J. Harris, D. Diamond, G. Barret, and M.A. Mc Kervey., J. Chem. Soc. Chem. Commun. 1286 (1992); (*d*) S. Kanamathareddy and C.D. Gutsche. J. Am. Chem. Soc. **115**, 6572 (1993); (*e*) D. Matt, C. Loeber, J. Vicens, and Z. Asfari. J. Chem. Soc. Chem. Commun. 604 (1993); (*f*) J.K. Moran and D.M. Roundhill. Inorg. Chem. **31**, 4213 (1992); (*g*) R. K. Juneja, K.D. Robinson, C.P. Johnson, and J.L. Atwood. J. Am. Chem. Soc. **115**, 3818 (1993); (*h*) P. Guilbaud, A. Varnek, and G. Wipff. J. Am. Chem. Soc. **115**, 8298 (1993); (*i*) J.L. Atwood, G.W. Orr, S.G. Bott, and K.D. Robinson. Angew. Chem. Int. Ed. Engl. **32**, 1093 (1993).
3. (*a*) W. Xu, J.P. Rourke, J.J. Vittal, and R.J. Puddephatt. J. Chem. Soc. Chem. Commun. 145 (1993); (*b*) W. Xu, J.J. Vittal, and R.J. Puddephatt. J. Am. Chem. Soc. **115**, 6456 (1993); (*c*) P.D. Beer, M.G.B. Drew, C. Hazlewood, D. Hesek, J. Hodacova, and S.E. Stokes. J. Chem. Soc. Chem. Commun. 229 (1993); (*d*) P.D. Beer, C.A.P. Dickson, N. Fletcher, A.J. Goulden, A. Grieve, J. Hodacova, and T. Wear. J. Chem. Soc. Chem. Commun. 828 (1993); (*e*) C. Loeber, D. Matt, A. De Cian, and J. Fisher. Organomet. Chem. **475**, 297 (1994); (*f*) F. Carazza, C. Floriani, A. Chiesi-Villa, and C. Rizzoli. Inorg. Chem. **30**, 4465 (1991).
4. B. Xu and T.M. Swager. J. Am. Chem. Soc. **115**, 1159 (1993).
5. B. Xu and T.M. Swager. To be published.
6. E.C. Lim, J.D. Lapora, and J.M. H. Yu. J. Mol. Spectrosc. **19**, 412 (1966), and refs. therein.
7. (*a*) B. Zelent, P.D. Harvey, and G. Durocher. Can. J. Spectrosc. **29**, 23 (1984); (*b*) Can. J. Spectrosc. **28**, 188 (1983); (*c*) Spectroscopy (Amsterdam), **2**, 128 (1983).
8. (*a*) R. Provencher, K.T. Aye, M. Drouin, J. Gagnon, N. Boudreault, and P.D. Harvey. Inorg. Chem. **33**, 3689 (1994); (*b*) K.A. Connors. Binding constants. The measurement of molecular complex stability. Wiley, New York. 1987. pp. 130–156.
9. (*a*) J.H. Ammeter, H.B. Burgi, J.C. Thibeault, and R. Hoffmann. J. Am. Chem. Soc. **100**, 3686 (1978); (*b*) R. Hoffmann and W.N. Lipscomb. J. Chem. Phys. **36**, 2179 (1962); (*c*) J. Chem. Phys. **37**, 2872 (1963); (*d*) R. Hoffmann. J. Chem. Phys. **39**, 1397 (1963).
10. A. Dedieu, T.A. Albright, and R. Hoffmann. J. Am. Chem. Soc. **101**, 3141 (1979).
11. C. Mealli and D. Proserpio. J. Chem. Educ. **67**, 339 (1990).
12. E. Heller. Acc. Chem. Res. **14**, 368 (1981).
13. P.D. Harvey. Inorg. Chem. **34**, 2019 (1995).
14. N.J. Turro. Modern molecular photochemistry. Benjamin/Cummings Publishing Co., Menlo Park, Calif. 1978.

15. K. Huang and A. Rhys. Proc. R. Soc. London, Ser. A, **204**, 406 (1958).
16. J.B. Lambert, H.F. Shurvell, D. Lightner, and R.G. Cooks. Introduction to organic spectroscopy. Macmillan Publishing Company, New York. 1987. p. 179.
17. R.F. Dallinger and W.H. Woodruff. J. Am. Chem. Soc. **101**, 1355 (1979).
18. (*a*) C.G. Morgante and W.S. Struve. Chem. Phys. Lett. **68**, 267 (1979); (*b*) W.S. Struve. Chem. Phys. Lett. **46**, 15 (1977); (*c*) E.J. Chambers and I.S. Haworth. J. Chem. Soc. Chem. Commun. 1631 (1994); (*d*) S.L. Murov, I. Carmichael, and G.L. Hug. Handbook of photochemistry. 2nd ed. Marcel Dekker, Inc., New York. 1993. p. 56.
19. P.D. Harvey and B. Daoust. Can. J. Chem. **71**, 5375 (1992).
20. (*a*) R. Provencher and P.D. Harvey. Inorg. Chem. **32**, 61 (1993); (*b*) P.D. Harvey, S. Hubig, and T. Ziegler. Inorg. Chem. **33**, 3700 (1994).

Parallel vs. perpendicular alkyne coordination in binuclear complexes. The first examples of reactivity differences in isomers differing in their alkyne coordination modes

Darren S.A. George, Robert McDonald, and Martin Cowie

Abstract: The reaction of $[Ir_2(CO)_3(dppm)_2]$ (dppm = $Ph_2PCH_2PPh_2$) with dimethyl acetylenedicarboxylate (DMAD) first yields $[Ir_2(CO)_2(\mu\text{-}\eta^1\text{:}\eta^1\text{-DMAD})(dppm)_2]$ (**2**) in which the alkyne is bound parallel to the metal–metal axis and the diphosphines are bound in a *trans* arrangement at both metals. This metastable isomer slowly rearranges to the stable form, $[Ir_2(CO)_2(\mu\text{-}\eta^2\text{:}\eta^2\text{-DMAD})(dppm)_2]$ (**3**), in which the alkyne is now bound perpendicular to the metals and the diphosphines are bent back in a *cis* arrangement at both metals. The analogous species can be prepared by substituting hexafluoro-2-butyne (HFB) for DMAD; however, for the HFB adduct the isomer having the parallel geometry is seen only as a transient species; only $[Ir_2(CO)_2(\mu\text{-}\eta^2\text{:}\eta^2\text{-HFB})(dppm)_2]$ (**5**) was isolated. Compound **2** reacts readily with PMe_3 to yield $[Ir_2(CO)(PMe_3)(\mu\text{-CO})(\mu\text{-}\eta^1\text{:}\eta^1\text{-DMAD})(dppm)_2]$, and with $CH_3OSO_2CF_3$ to yield $[Ir_2(CH_3)(CO)_2(\mu\text{-}\eta^1\text{:}\eta^1\text{-DMAD})(dppm)_2][SO_3CF_3]$, whereas **3** reacts with neither reagent. Both **2** and **3** react with $HBF_4{\cdot}OEt_2$ to yield the respective alkyne-bridged hydrides, $[Ir_2H(CO)_2(\mu\text{-}\eta^1\text{:}\eta^1\text{-DMAD})(dppm)_2][BF_4]$ and $[Ir_2H(CO)_2(\mu\text{-}\eta^2\text{:}\eta^2\text{-DMAD})(dppm)_2][BF_4]$, in which the gross structural features and the alkyne coordination mode of the precursor are retained in each case. The latter species rearranges readily at ambient temperature, via migratory insertion, to give the vinyl-bridged product, $[Ir_2(CO)_2(\mu\text{-}\eta^1\text{:}\eta^2\text{-RC = C(H)R})(dppm)_2][BF_4]$ (R = CO_2Me); however, the former is inert under these conditions, yielding the above vinyl species together with other decomposition products only upon reflux in benzene for several hours. Protonation of the perpendicular hexafluoro-2-butyne adduct also yields the corresponding vinyl product, together with decomposition products. The structure of **3**, as the methylene chloride disolvate, was established by X-ray analysis. Crystal data are as follows. $\mathbf{3}{\cdot}2CH_2Cl_2$: $C_{60}H_{54}Cl_4O_6P_4Ir_2$, monoclinic, $P2/c$, a = 26.088(5) Å, b = 9.896(4) Å, c = 23.954(3) Å, β = 109.27(1)°, Z = 4, $R(F)$ = 0.038, $R_w(F^2)$ = 0.0997 (all data).

Key words: diiridium alkyne complexes, parallel and perpendicular alkyne coordination.

Résumé : La réaction du $[Ir_2(CO)_3(dppm)_2]$ (dppm = $Ph_2PCH_2PPh_2$) avec l'acétylènedicarboxylate de diméthyle (ADDM) donne en premier lieu le $[Ir_2(CO)_2(\mu\text{-}\eta^1\text{:}\eta^1\text{-ADDM})(dppm)_2]$ (**2**) dans lequel l'alcyne est lié parallèlement à l'axe métal–métal et les diphosphines sont liés selon un arrangement *trans* par rapport aux deux atomes métalliques. Cet isomère métastable se transpose lentement pour donner l'isomère stable $[Ir_2(CO)_2(\mu\text{-}\eta^2\text{:}\eta^2\text{-ADDM})(dppm)_2]$ (**3**), dans lequel l'alcyne se retrouve lié perpendiculairement aux deux atomes métalliques et les diphosphines sont ramenés à un arrangement *cis* au niveau des deux atomes métalliques. On peut préparer les espèces analogues en remplaçant l'ADDM par l'hexafluoro-2-butyne (HFB), cependant dans l'adduit HFB, l'isomère ayant la géométrie parallèle semble uniquement une espèce transitoire; on a seulement isolé le $[Ir_2(CO)_2(\mu\text{-}\eta^2\text{:}\eta^2\text{-HFB})(dppm)_2]$ (**5**). Le composé **2** réagit facilement avec PMe_3 pour donner $[Ir_2(CO)(PMe_3)(\mu\text{-CO})(\mu\text{-}\eta^1\text{:}\eta^1\text{-ADDM})(dppm)_2]$, et avec $CH_3OSO_2CF_3$ pour donner $[Ir_2(CH_3)(CO)_2(\mu\text{-}\eta^1\text{:}\eta^1\text{-ADDM})(dppm)_2][SO_3CF_3]$, tandis que le composé **3** ne réagit pas avec aucun de ces réactifs. Les composés **2** et **3** reagissent avec le $HBF_4{\cdot}OEt_2$ pour conduire respectivement aux hydrures avec le groupe alcyne en position de pont : $[Ir_2H(CO)_2(\mu\text{-}\mu^1\text{:}\eta^1\text{-ADDM})(dppm)_2][BF_4]$ et $[Ir_2H(CO)_2(\mu\text{-}\eta^2\text{:}\eta^2\text{-ADDM})(dppm)_2][BF_4]$, dans lesquels les caractéristiques structurales principales et le mode de coordination de l'alcyne du précurseur sont retenus dans chacun des case. La dernière espèce se transpose facilement à la température ambiante, via une insertion migratoire, pour donner le produit avec un groupe vinyle en position de pont $[Ir_2(CO)_2(\mu\text{-}\eta^1\text{:}\eta^2\text{-RC=C(H)R})(dppm)_2][BF_4]$ (R = CO_2Me); toutefois le premier composé est inerte dans ces conditions et donne l'espèce vinylique ci-dessus ainsi que d'autres produits de décomposition uniquement au reflux du benzène pendant plusieurs heures. La protonation de l'adduit hexafluoro-2-butyne perpendiculaire donne également le produit vinylique

Received June 3, 1996.

This paper is dedicated to Professor Howard C. Clark in recognition of his contributions to Canadian chemistry.

D.S.A. George, R. McDonald, and M. Cowie.[1] Department of Chemistry, University of Alberta, Edmonton, AB T6G 2G2, Canada.

[1] Author to whom correspondence may be addressed. Telephone: (403) 492-5581. Fax: (403) 492-8231. E-mail: martin.cowie@ualberta.ca

correspondant ainsi que des produits de décomposition. On a établi la structure du composé **3** comme produit de solvatation double du chlorure de méthylène. Les données cristallines sont les suivantes : **3**·2CH_2Cl_2 : $C_{60}H_{54}Cl_4O_6P_4Ir_2$, monoclinique, groupe d'espace *P2/c*, a = 26,088(5) Å, b = 9,896(4) Å, c = 23,954(3) Å, β = 109,27(1)°, Z = 4, $R(F)$ = 0,038, $R_w(F^2)$ = 0,0997 (tous les données).

Mots clés : complexes de diiridium alcyne, coordination parallèle et perpendiculaire de l'alcyne.

[Traduit par la rédaction]

Introduction

The ability of transition-metal complexes to facilitate important transformations of unsaturated substrates has provoked much interest in complexes containing coordinated alkynes (1–4). In such complexes, coordination to a metal centre serves to activate the alkyne group, so it follows that reactivity should depend on the nature of the alkyne binding. In binuclear complexes, which constitute the simplest systems in which more than one metal can be involved, three simple bonding modes can be distinguished. In the first, the alkyne can coordinate terminally to one metal, in which case the bonding is readily described in terms of the Dewar–Chatt–Duncanson model, originally proposed for olefin binding (5). Introduction of the second metal also introduces two alkyne bridging modes, in which the alkyne is oriented either parallel to (μ-η^1:η^1-coordination), or perpendicular to (μ-η^2:η^2-coordination), the metal–metal axis. These are sometimes referred to as dimetallacyclobutene and dimetallatetrahedrane structures, respectively, when there is an accompanying metal–metal bond, or *cis* dimetallated olefins and dimetallabicyclobutanes, respectively, when there is no metal–metal bond. As was pointed out by Hoffmann et al. (6), the preference for one orientation over the other is a function of the electronic requirements of the metals. The parallel-bound alkyne can be

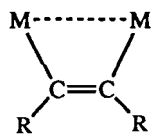

μ-η^1:η^1

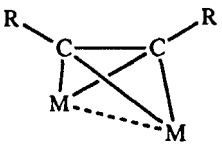

μ-η^2:η^2

considered as a *neutral* two-electron donor (or alternatively as a *dianionic* four-electron donor), while in the perpendicular orientation it is normally viewed as a *neutral* four-electron donor, and the preference for one or the other will often depend on the number of electrons needed by the metals to achieve a favourable electron count. In addition, the bridging alkyne can modulate its donor ability by changing binding modes upon gain or loss of ancillary ligands, in order to satisfy the electron demands of the metals (7).

Reactions of alkynes with diphosphine-bridged, homo- and heterobinuclear complexes of rhodium and iridium have been of long-standing interest to this research group (8), with a view towards developing an understanding of how the alkyne coordination mode influences its subsequent reactivity. In the majority of diphosphine-bridged complexes characterized, the alkyne has been found to coordinate in the parallel orientation, although the dirhodium complexes, $[Rh_2(CO)_2(\mu\text{-}RC{\equiv}CPh)(dppm)_2]$(dppm = $Ph_2PCH_2PPh_2$, R = H, Ph) (9), are notable exceptions, resembling a number of dicobalt analogs (10) in having a perpendicular alkyne binding mode. This bonding for the dirhodium species is even more surprising when comparison is made to the isoelectronic Pd and Pt complexes $[MM'Cl_2(\mu\text{-}CF_3C_2CF_3)(dppm)_2]$ (MM' = Pd_2 (11), PtPd (12), Pt_2 (13)), which have a parallel binding mode for the alkyne. A metastable isomer of $[Rh_2(CO)_2(\mu\text{-}HC{\equiv}CPh)(dppm)_2]$, which was proposed to have a parallel-bound alkyne, was prepared from $[Rh_2(CO)_2(\mu\text{-}H)_2(dppm)_2]$ (9); however, it rearranged readily to the more stable isomer having a perpendicular alkyne.

We undertook a related study, attempting to prepare the diiridium alkyne complexes, $[Ir_2(CO)_2(\mu\text{-}RC_2R)(dppm)_2]$ (R = CO_2Me, CF_3). In these target complexes a perpendicular alkyne binding mode would result in an Ir(0) oxidation state assignment for both metals, whereas the parallel geometry could be viewed as giving rise to an Ir(+1) formulation. It was felt that by using an alkyne such as dimethyl acetylenedicarboxylate (DMAD) or hexafluoro-2-butyne (HFB), having strongly electron-withdrawing substituents, the dianionic formulation of the ligand and the corresponding Ir(+1) oxidation state might be favoured. In this context, it had previously been noted in the Pd_2 complexes, that the parallel alkyne geometry had only been obtained with alkynes having electronegative substituents (11*b*). In addition, it was reasoned that the use of a third-row metal should favour the higher oxidation state, and the lower lability of Ir compared to Rh may assist in deterring any rearrangement from a parallel to a perpendicular alkyne coordination, as occurred in the dirhodium system. It was also of interest to establish whether the different alkyne binding modes would give rise to reactivity differences. Surprisingly, no study has yet addressed this relationship between reactivity and the two different bridging modes.

Experimental section

All solvents, including deuterated solvents used for NMR experiments, were dried, degassed, and distilled before use and were stored under N_2. Reactions were carried out using standard Schlenk procedures. Dinitrogen was passed through columns of Ridox and 4A molecular sieves to remove traces of oxygen and water, respectively. Carbon monoxide (Matheson) was used as received. Hydrated iridium(III) chloride was purchased from Engelhard Scientific, ammonium hexachloroiridate (IV) was obtained from Victoria Precious Metals, and bis(diphenylphosphino)methane (dppm) was purchased from Organometallics Inc. Dimethyl acetylenedicarboxylate (DMAD) was obtained from Aldrich and stored under N_2 over molecular sieves in the dark. The complex $[Ir_2(CO)_3(dppm)_2]$ (**1**) was prepared as previously reported (14). All other chemicals were used as received without further purification.

NMR spectra were recorded on a Bruker AM-400 spec-

trometer operating at 400 MHz for ^1H and $^1H\{^{31}P\}$ spectra and at 161.9 MHz for $^{31}P\{^1H\}$ spectra; $^{13}C\{^1H\}$ spectra were obtained on Bruker WH-200 and AM-400 instruments operating at 50.32 and 100.61 MHz, respectively. In these cases an internal deuterated solvent lock was employed. Phosphorus chemical shifts are reported with respect to external 85% H_3PO_4, while carbon and proton shifts are with respect to TMS with the solvent as internal standard. Infrared spectra were run on a Nicolet 7199 Fourier transform interferometer, as either solids (Nujol mulls on KBr disks) or solutions (KCl cell windows, 0.5 mm path length). A Perkin–Elmer 883 infrared spectrophotometer was also employed to monitor the progress of some reactions. Elemental analyses were performed by the microanalytical service within the department.

(a) Preparation of $[Ir_2(CO)_2(\mu\text{-}\eta^1\text{:}\eta^1\text{-DMAD})(dppm)_2]$ (2)

To a solution of **1** (35 mg, 28.3 μmol) in 4 mL of THF or benzene was added DMAD (3.6 μL, 29.3 μmol), followed by gentle warming of the solution in a water bath at 40–45°C, resulting in a colour change from orange to intense blue (about 3 min). The solution volume was then reduced to 1 mL by evaporation under a stream of nitrogen. Pentane (10 mL) was added, giving a blue microcrystalline precipitate (purple from benzene), which was washed twice with 10 mL aliquots of pentane and dried, first under nitrogen, then under vacuum. Due to the high air-sensitivity of this compound, an elemental analysis was not obtained. IR (THF solution): 1934 (s, Ir-CO), 1701 (s, ester CO) cm^{-1}. NMR (THF, 22°C), δ: $^{31}P\{^1H\}$: 5.28 (singlet); ^1H: 8.2–6.3 (multiplet, 40H, C_6H_5), 4.36 and 3.42 (multiplets, each 2H, CH_2), 2.70 (singlet, 6H, CH_3); $^{13}C\{^1H\}$: 191.0 (singlet, Ir-*C*O).

(b) Preparation of $[Ir_2(CO)_2(\mu\text{-}\eta^2\text{:}\eta^2\text{-DMAD})(dppm)_2]$ (3)

To a solution of **1** (100 mg, 80.8 μmol) in toluene (10 mL) was added one equivalent of DMAD (9.9 μL, 11.5 mg, 80.8 μmol). An immediate darkening of the orange reaction mixture occurred, with a change to dark green within 5 min. The solution was then refluxed for 10 min, during which time the colour changed to dark blue then to lighter green. Upon slow cooling of the mixture to room temperature the green colour faded to light yellow, accompanied by formation of a pale yellow microcrystalline solid. Ether (20 mL) was added to complete precipitation, and the yellow solid obtained was recrystallized from CH_2Cl_2–Et_2O. The pale yellow powder was dried under an N_2 stream, then under vacuum, yielding 69 mg (64% isolated yield) of product. IR (Nujol mull): 1938 (vs, Ir-*CO*), 1682 (s, ester *CO*) cm^{-1}; (CH_2Cl_2 solution): 1943 (vs), 1690 (s) cm^{-1}. NMR (CD_2Cl_2, 22°C), δ: $^{31}P\{^1H\}$: –12.6 (singlet); ^1H: 7.45–6.87 (multiplet, 40H, C_6H_5), 5.70, 3.39 (multiplets, each 2H, CH_2), 3.61 (singlet, 6H, CH_3); $^{13}C\{^1H\}$: 173.8 (singlet, Ir-*CO*). Anal. calcd. for $C_{58}H_{50}Ir_2O_6P_4$: C 51.55, H 3.73, found: C 51.78, H 3.94.

(c) Preparation of $[Ir_2(CO)_2(\mu\text{-}\eta^2\text{:}\eta^2\text{-HFB})(dppm)_2]$ (5)

A 50-mL flask was charged with 100 mg of **1** (80.8 μmol) and 30 mL of CH_2Cl_2. Hexafluoro-2-butyne was passed over the solution for a few minutes, and the solution was stirred for 4 days, over which time the solution slowly changed from orange to green to brown to orange. The solvent was removed under vacuum, and the residue recrystallized from 4 mL of benzene and 12 mL of pentane. The yellow precipitate was then washed twice with 10 mL of ether. Yield: 43 mg (39%). IR (Nujol mull): 1947 (Ir-CO) cm^{-1}; (CH_2Cl_2 solution): 1950 (Ir-CO) cm^{-1}. NMR (CD_2Cl_2, 22°C), δ: $^{31}P\{^1H\}$: –13.1 (m); ^1H: 8.0–6.9 (m, 40H, C_6H_5), 5.35 and 3.70 (m, each 2H, CH_2); ^{19}F: –48.56 (m).

(d) Reaction of 1 with HFB

An NMR tube was charged with **1** (21.2 mg, 17.1 μmol) and 0.5 mL of CD_2Cl_2 and was capped with a rubber septum. Hexafluoro-2-butyne (420 μL, 17.0 μmol) was added via gas-tight syringe, and the tube was sealed with Parafilm and shaken. After 45 min, the orange solution had acquired a slight green cast; however, the $^{31}P\{^1H\}$ NMR spectrum showed only starting material. After 1 day, the solution, which had been stored under nitrogen, had become a much darker green colour, and the NMR showed, in addition to starting material, a small amount of compound **5**, along with larger quantities of the known compound $[Ir_2(CO)_4(dppm)_2]$ (14) and a new compound **4** ($^{31}P\{^1H\}$: δ: 1.31 (s). $^{13}C\{^1H\}$: 190.2 (t, J_{CP} = 5.4 Hz, Ir-CO). ^1H: 3.55 and 3.85 (m, 2H each, CH_2)). After 5 days, this species had disappeared, leaving only **5** and the tetracarbonyl species, in a 1:1 ratio.

(e) Preparation of $[Ir_2(CO)(PMe_3)(\mu\text{-}CO)(\mu\text{-}DMAD)(dppm)_2]$ (6)

To an NMR tube charged with **2** (prepared from 53 mg (42.8 μmol) of **1**) in 0.5 mL of CD_2Cl_2 was added trimethylphosphine (4.5 μL, 43.5 μmol), causing a slow colour change from intense blue to a dark olive green, then to brown. This product was only characterized in solution owing to its high solubility and facile loss of trimethylphosphine. IR (CH_2Cl_2 solution): 1967 (s, Ir-CO), 1701 (s, Ir-CO, ester CO) cm^{-1}; IR (Nujol mull): 1964 (s, Ir-CO), 1702, 1677 (broad, s, μ-CO, ester CO) cm^{-1}. NMR (CD_2Cl_2, 22°C); δ: $^{31}P\{^1H\}$: –3.57 (dddd; J_{AB} = 109.6 Hz, J_{AC} = 64.5 Hz, J_{AD} = 14.6 Hz, J_{AE} = 27.1 Hz), –23.66 (dddd; J_{AB} = 109.6 Hz, J_{BC} = 7.9 Hz, J_{BD} = 52.5 Hz, J_{BE} = 4.54 Hz), –49.44 (dddd; J_{AC} = 64.5 Hz, J_{BC} = 7.9 Hz, J_{CD} = 82.2 Hz, J_{CE} = 24.2 Hz), –51.9 (dddd; J_{AD} = 14.6 Hz, J_{BD} = 52.5 Hz, J_{CD} = 82.2 Hz, J_{DE} = 3.15 Hz), –62.37 (m, PMe_3); ^1H: 8.2–6.3 (m, 40H, C_6H_5), 5.25, 4.55, 3.97, and 3.42 (m, each 1H, CH_2), 2.75 and 2.67 (s, each 3H, CO_2CH_3), 1.70 (d, 9H, $P(CH_3)_3$); $^{13}C\{^1H\}$: 182.8 (m, Ir-*C*O), 230.3 (t of m; J_{CP} = 63 Hz, μ-CO).

(f) Attempted reaction of 3 with PMe_3

An NMR tube was charged with 18 mg (13.3 μmol) of **3** and 0.5 mL of CD_2Cl_2. Trimethylphosphine (9.1 μL, 66.3 μmol) was added, resulting in no apparent reaction as seen by the lack of change in the $^{31}P\{^1H\}$ NMR spectrum over a 24 h period.

(g) Reaction of 2 with $CH_3O_3SCF_3$

To a solution of **2** (prepared from 30 mg (24.2 μmol) of **1**) in 4 mL of CH_2Cl_2 was added methyl triflate (2.8 μL, 24.7 μmol) at –80°C. The solution was stirred for 1 h, during which time the solution slowly turned a reddish orange. This was warmed to room temperature, and the solution volume reduced to 1 mL by evaporation under a rapid stream of nitrogen. The brown precipitate obtained by addition of ether (10 mL) was washed twice with ether and dried under nitrogen and under vacuum. The NMR spectrum of this sample showed it to be chiefly

$[Ir_2(CH_3)(CO)_2(\mu\text{-}\eta^1\text{:}\eta^1\text{-DMAD})(dppm)_2][SO_3CF_3]$ (**7**), which has been previously characterized (15). IR (CH_2Cl_2 solution): 2009 (s), 1980 (s, Ir-CO), 1702, 1683 (broad, ester CO) cm^{-1}. NMR (CD_2Cl_2, 22°C) δ: $^{31}P\{^1H\}$: 7.69 (m), –9.34 (m); ^1H: 7.7–7.0 (m, 40H, C_6H_5), 4.30 and 3.45 (m, each 2H, CH_2), 3.00 and 2.25 (s, each 3H, CH_3), 0.60 (t, 3H, $IrCH_3$); $^{13}C\{^1H\}$: 193.6 (t, J_{CP} = 9.16 Hz, Ir-*C*O), 182.4 (t, J_{CP} = 7.9 Hz, Ir-*C*O).

(h) Attempted reaction of 3 with $CH_3O_3SCF_3$

An NMR tube was charged with **3** (20.4 mg, 15.1 μmol) and 0.5 mL of CD_2Cl_2. Methyl triflate (1.8 μL, 15.9 μmol) was added, and the mixture allowed to stand for several hours. Phosphorus-31 NMR showed only slight (≤10%) reaction to form **11**, probably due to adventitious water.

(i) Preparation of $[Ir_2(H)(CO)_2(\mu\text{-}\eta^1\text{:}\eta^1\text{-DMAD})(dppm)_2][BF_4]$ (8)

A sample of compound **2** (synthesized as above, from 35 mg **1** and 3.6 μL of DMAD) was dissolved in 4 mL of CH_2Cl_2 and cooled to –80°C. Addition of tetrafluoroboric acid – diethyl ether complex (4.1 μL, 29.9 μmol) caused a colour change from intense blue to dark brown. This mixture was allowed to warm to room temperature, and the solvent was removed by evaporation under a stream of nitrogen, giving an orange solid that was recrystallized from dichloromethane and ether (v/v 1:10), and washed twice with ether. Yield: 33 mg (81%). IR (Nujol mull): 2022 (vs), 1991 (s, Ir-CO), 1702 (s, ester CO) cm^{-1}. NMR (CD_2Cl_2, 22°C) δ: $^{31}P\{^1H\}$: 11.84 (m), –5.90 (m); $^{13}C\{^1H\}$: 193.3 (t, $^2J_{CP}$ = 8.95 Hz), 181.5 (broad, Ir-*C*O): ^1H: 8.0–6.9 (m, 40H, C_6H_5), 2.41 and 2.34 (s each 3H, CH_3), –21.54 (t, $^2J_{HP}$ = 12.2 Hz, 1H).

(j) Preparation of $[Ir_2(CO)_3(H)(\mu\text{-}\eta^1\text{:}\eta^1\text{-DMAD})(dppm)_2][BF_4]$ (9)

Carbon monoxide was passed over 5 mL of a CH_2Cl_2 solution of **8** (40 mg, 27.7 μmol), resulting in a colour change from orange to yellow. The solution was evaporated to 1 mL under a steady flow of nitrogen, and the product was precipitated by the addition of 15 mL of ether. IR (CH_2Cl_2 solution): 2051 (m), 2024 (s), 1984 (m, Ir-CO), 1706, 1690 (broad, ester CO) cm^{-1}; (Nujol mull); 2019 (broad, Ir-CO), 1695 (broad, ester CO) cm^{-1}. NMR (CD_2Cl_2, 22°C), δ: $^{31}P\{^1H\}$: –11.58 (m), –26.77 (m); ^1H: 8.0–6.9 (multiplet, 40H, C_6H_5), 4.40 and 4.55 (multiplets, each 2H, CH_2), 2.45 and 2.80 (singlets, each 3H, CH_3), –12.04 (triplet, $^2J_{HP}$ = 26.9 Hz, 1H).

(k) Low-temperature protonation of 2

An NMR tube was charged with a solution of **2** (prepared from 21 mg (17.0 μmol) of **1** and 2.1 μL of DMAD) in 0.5 mL of CD_2Cl_2 and cooled to –80°C. Triflic acid (1.5 μL, 17.0 μmol) was added, causing a colour change from blue to orange. By $^{31}P\{^1H\}$ NMR, this solution was shown to contain almost pure **8** at –80°C, with no intermediates detectable.

(l) Preparation of $[Ir_2(H)(CO)_2(\mu\text{-}\eta^2\text{:}\eta^2\text{-DMAD})(dppm)_2][BF_4]$ (10)

To a solution of **3** (32 mg, 23.7 μmol) in 2 mL of CH_2Cl_2 (cooled to –10°C by a salt–ice bath) was added one equivalent of $HBF_4{\cdot}OEt_2$ (3.2 μL, 23.3 μmol). The solution changed colour from pale yellow to bright yellow immediately, and then turned golden brown over the course of about 5 min. This solution was stirred for 15 min, and the product precipitated by the addition of 20 mL of pentane. The supernatant was removed, and the brown precipitate was washed twice with pentane, then dried first under a flow of nitrogen, and then under vacuum. NMR (CH_2Cl_2, 22°C), δ: $^{31}P\{^1H\}$: 20.24 (m), 2.44 (m); $^{13}C\{^1H\}$: 174.9 (broad, Ir-*C*O), 167.2 (t, $^2J_{CP}$ = 8.8 Hz, Ir-*C*O); ^1H: 8.0–6.9 (m, 40H, C_6H_5), 4.18 and 3.45 (m, each 2H, CH_2), 3.45 and 2.75 (s, each 3*H*, CH_3), –21.20 (t, 1H).

(m) Preparation of $[Ir_2(CO)_2(\mu\text{-}\eta^1\text{:}\eta^2\text{-}CH_3O_2CC{=}C(H)CO_2CH_3)(dppm)_2][BF_4]$ (11)

To a solution of **3** (50 mg, 37.0 μmol) in 15 mL of CH_2Cl_2 was added one equivalent of $HBF_4{\cdot}OEt_2$ (5.6 μL, 40.8 μmol). The solution changed colour from pale yellow to a clear golden brown, then quickly changed to clear bright yellow, and was stirred for half an hour. The solvent was reduced to about 1 mL by evaporation under a steady stream of nitrogen, and the compound precipitated by the addition of 15 mL of ether. The supernatant was removed, and the yellow precipitate was washed twice with ether. Yield 33 mg (62%). IR (Nujol mull): 1984, 1961 (vs, Ir-CO), 1656 (s, ester CO) 1552 (s, C=C stretch) cm^{-1}; (CH_2Cl_2 solution): 2004, 1978 (s, Ir-CO), 1710, 1688 (m, ester CO) 1550 (m, C=C) cm^{-1}. NMR (CD_2Cl_2, 20°C), δ: $^{31}P\{^1H\}$: –8.45 (apparent triplet, $J_{AB} = J_{AC}$ = 44.5 Hz), –9.68 (ddd, J_{AB} = 44.5 Hz, J_{BC} = 3.5 Hz, J_{BD} = 9.2 Hz), –18.96 (ddd, J_{BC} = 3.5 Hz, J_{AC} = 44.5 Hz, J_{CD} = 58 Hz), –24.53 (dd, J_{CD} = 58 Hz, J_{BD} = 9.2 Hz); ^1H: 7.7–6.8 (m, 40H, C_6H_5), 6.47, 5.39, 4.36 and 4.04 (m, each 1H, CH_2), 4.62 (m, vinyl), 3.18 and 2.42 (s, each 3H, CH_3); $^{13}C\{^1H\}$: 176.00, 175.39 (m, Ir-*C*O, J_{CC} = 9.41 Hz), 194.45, 175.21 (m, ester *C*O); Anal. calcd. for $C_{58}H_{55}O_8BF_4Ir_2P_4$: C 48.27, H 3.84, found: C 47.77, H 3.54.

(n) Low-temperature protonation of 3

An NMR tube was charged with **3** (17.1 mg, 12.7 μmol) and 0.5 mL of CD_2Cl_2 and cooled to –80°C. Triflic acid (1.1 μL, 12.4 μmol) was added, causing a colour change from pale yellow to bright yellow. The NMR of this yellow solution showed the presence of one symmetrical species (–70°C), δ: $^{31}P\{^1H\}$: –14.41 (s). $^{13}C\{^1H\}$: 170.33 (s). ^1H: 20.0 (s, 1H), 6.61 and 3.93 (broad, 2H each, CH_2), 3.38 (broad, 6H, CH_3)). Allowing this to warm up to –20°C caused it to convert to compound **10**, which, in turn, converted to compound **11**.

(o) Attempted protonation of 5

To an NMR tube containing 10.0 mg (7.3 μmol) of **5** dissolved in 0.5 mL of CD_2Cl_2 was added 1.0 μL (7.3 μmol) of $HBF_4{\cdot}OEt_2$. The $^{31}P\{^1H\}$ NMR spectrum showed the appearance of four resonances reminiscent of **11** after several hours. However, upon further standing a number of unidentified decomposition products began to appear. Based on the $^{31}P\{^1H\}$ and ^1H NMR spectra of the initial product, this species was shown to be the analogue of **11**, namely, $[Ir_2(CO)_2(\mu\text{-}\eta^1\text{:}\eta^2\text{-}CF_3C{=}C(H)CF_3)(dppm)_2][BF_4]$. Owing to its instability this product was not characterized further. NMR (CD_2Cl_2, 20°C), δ: $^{31}P\{^1H\}$: –8.67 (apparent triplet, $J_{AB} = J_{AC}$ = 44.9 Hz), –9.46 (ddd, J_{AB} = 46.2 Hz, J_{BC} = 3.4 Hz, J_{BD} = 13.5 Hz), –16.25 (doublet of unresolved multiplets,

Table 1. Crystallographic experimental details.

A. Crystal data	
Formula	$C_{60}H_{54}Cl_4Ir_2O_6P_4$
Formula weight	152.11
Crystal dimensions (mm)	0.82 × 0.22 × 0.05
Crystal system	Monoclinic
Space Group	*P2/c* (No. 13)
Unit cell parameters[a]	
a (Å)	26.088 (5)
b (Å)	9.896 (4)
c (Å)	23.954 (3)
β (deg)	109.273 (11)
V (Å^3)	5837.9 (28)
Z	4
ρ_{calcd} (g cm^{-3})	1.731
μ (mm^{-1})	4.897

B. Data collection and refinement conditions	
Diffractometer	Enraf-Nonius CAD4[b]
Radiation (λ[Å])	Mo Kα (0.71073)
Monochromator	Incident-beam, graphite crystal
Temperature (°C)	22
Scan Type	θ-2θ
Data collection 2θ limit (deg)	50.0
Total data collected	10446 ($0 \le h \le 30$, $0 \le k \le 11$, $-28 \le l \le 28$)
Independent reflections	10202
Number of observations (NO)	6943 ($F_o^2 \ge 2\sigma(F_o^2)$)
Structure solution method	Patterson (location of Ir atoms)
Refinement method	Full-matrix least-squares on F^2 (SHELXL-93[c])
Absorption Correction method	DIFABS[d]
Range of absorption correction factors	1.276–0.832
Data/restraint/parameters	10187 [$F_o^2 \ge -3\sigma(F_o^2)$]/0/685
Goodness-of-fit (S)[e]	1.027 [$F_o^2 \ge -3\sigma(F_o^2)$]
Final R indices[f]	
$F_o^2 > 2\sigma(F_o^2)$	R_1 = 0.0380, wR_2 = 0.0814
All data	R_1 = 0.0926, wR_2 = 0.0997
Largest difference peak and hole	0.922 and –0.958 e Å^{-3}

[a]Obtained from least-squares refinement of 24 reflections with 19.9° < 2θ < 22.9°.

[b]Programs for diffractometer operation and data collection were those supplied by Enraf–Nonius.

[c]G.M. Sheldrick. SHELXL-93. Program for crystal structure determination. University of Göttingen, Germany, 1993. Refinement on F_o^2 for all reflections except for 15 having $F_o^2 < -3\sigma(F_o^2)$. Weighted *R*-factors wR_2 and all goodness of fit *S* are based on F_o^2; conventional *R*-factors R_1 are based on F_o, with F_o set to zero for negative F_o^2. The observed criterion of $F_o^2 > 2\sigma(F_o^2)$ is used only for calculating R_1, and is not relevant to the choice of reflections for refinement. *R*-factors based on F_o^2 are statistically about twice as large as those based on F_o, and *R*-factors based on ALL data will be even larger.

[d] Reference 16.

[e]$S = [\Sigma w(F_o^2 - F_c^2)^2/(n-p)]^{1/2}$ (n = number of data; p = number of parameters varied; $w = [\sigma^2(F_o^2) + (0.0376P)^2 + 20.0739P]^{-1}$ where $P = [\mathrm{Max}(F_o^2,0) + 2F_c^2]/3$).

[f]$R_1 = \Sigma||F_o| - |F_c||/\Sigma|F_o|$; $wR_2 = [\Sigma w(F_o^2 - F_c^2)^2/\Sigma w(F_o^4)]^{1/2}$.

J = 52.4 Hz), –22.59 (broad unresolved multiplets); ^{1}H: 7.7–6.8 (m, 40H, C_6H_5), 5.85, 5.33, 4.38, and 3.80 (m, each 1H, CH_2), 4.65 (m, vinyl).

X-ray data collection

Diffusion of ether into a concentrated CH_2Cl_2 solution of complex **3** produced yellow prismatic crystals, several of which were mounted and flame-sealed in glass capillaries under N_2 and solvent vapor to minimize decomposition and (or) solvent loss. Data were collected on an Enraf–Nonius CAD4 diffractometer using Mo Kα radiation. Unit-cell parameters at 22°C were obtained from a least-squares refinement of the setting angles of 24 reflections in the range 19.9° ≤ 2θ ≤ 22.9°. The monoclinic diffraction symmetry and the systematic absences ($h0l$ $l \ne 2n$) were consistent with the space groups *Pc* or *P2/c* (the latter was confirmed as the correct space group by the successful solution and refinement of the structure).

Intensity data were collected as outlined in Table 1. Three

Table 2. Atomic coordinates and equivalent isotropic displacement parameters.

	(*a*) Molecule 1				(*b*) Molecule 2			
Atom	*x*	*y*	*z*	U_{eq},Å^2	*x*	*y*	*z*	U_{eq}, Å^2
Ir(1)	–0.042739(13)	0.10110(3)	–0.231097(13)	0.03042(9)*	0.502424(13)	0.21756(3)	0.306364(12)	0.02696(9)*
P(1)	–0.00021(9)	0.2376(2)	–0.14990(9)	0.0334(5)*	0.58088(9)	0.0860(2)	0.33671(8)	0.0299(5)*
P(2)	0.08985(9)	0.2677(2)	–0.20458(9)	0.0334(5)*	0.56105(9)	0.0477(2)	0.20409(8)	0.0292(5)*
O(1)	–0.1352(3)	–0.0168(8)	–0.1970(4)	0.080(2)*	0.4973(4)	0.3357(7)	0.4204(3)	0.078(2)*
O(2)	–0.0100(3)	–0.2510(8)	–0.3248(4)	0.088(3)*	0.4375(3)	0.5734(6)	0.1960(3)	0.064(2)*
O(3)	–0.0905(3)	–0.1560(7)	–0.3476(3)	0.072(2)*	0.3935(3)	0.4683(6)	0.2486(3)	0.054(2)*
C(1)	–0.1002(4)	0.0290(9)	–0.2104(4)	0.042(2)*	0.4997(4)	0.2889(8)	0.3770(4)	0.041(2)*
C(2)	–0.0187(3)	–0.0431(8)	–0.2797(3)	0.032(2)*	0.4711(3)	0.3641(7)	0.2420(3)	0.029(2)*
C(3)	–0.0376(4)	–0.1619(9)	–0.3183(4)	0.040(2)*	0.4337(3)	0.4767(8)	0.2258(3)	0.035(2)*
C(4)	–0.1130(6)	–0.2621(12)	–0.3898(5)	0.101(5)*	0.3530(4)	0.5720(10)	0.2322(5)	0.065(3)*
C(5)	0.0478(3)	0.3534(8)	–0.1677(3)	0.033(2)*	0.5806(3)	–0.0326(8)	0.2777(3)	0.030(2)*

Anisotropically-refined atoms are marked with an asterisk (*). The form of the anisotropic displacement parameter is: $\exp[-2\pi^2(h^2a^{*2}U_{11} + k^2b^{*2}U_{22} + l^2c^{*2}U_{33} + 2klb^*c^*U_{23} + 2hla^*c^*U_{13} + 2hka^*b^*U_{12})]$.

reflections were chosen as intensity standards, being remeasured after 120 min of X-ray exposure time. Although one of these standards lost 10% of its original intensity, the other two remained constant; recentering the crystal did not lead to a significant change in intensities. Since this intensity loss was not uniform a decomposition correction was not applied to the data. Absorption corrections were applied to the data according to the method of Walker and Stuart (16).

Structure solution and refinement

The structure of **3** was solved in the space group *P*2/*c* using standard Patterson and Fourier techniques. The unit cell was found to contain two independent molecules of **3**, each located on a crystallographic twofold axis (vide infra). The structure was refined on F^2 using full-matrix least-squares methods.[2] Positional parameters for the hydrogens attached to the carbon atoms of the complex and solvent molecules were calculated from the geometries about the attached carbon. These hydrogens were given thermal parameters 20% greater than the equivalent isotropic *B*'s of their attached atoms, and included as fixed contributions.

The final model for complex **3**, with 685 parameters varied, converged to a value of $R = 0.038$. The positional and thermal parameters for the non-hydrogen core atoms are given in Table 2, and selected bond lengths and angles are given in Tables 3 and 4, respectively.[3]

[2] Programs used were those of SHELXL-93 by G.M. Sheldrick, University of Göttingen, Germany, 1993.

[3] Tables of atomic coordinates for all atoms, a complete listing of bond lengths and angles, anisotropic thermal parameters, derived positions for the hydrogen atoms, and ORTEP diagrams of molecule 2 of complex **3** are available as supplementary material and can be purchased from: The Depository of Unpublished Data, Document Delivery, CISTI, National Research Council Canada, Ottawa, Canada K1A 0S2. Bond lengths and angles and hydrogen positions have also been deposited at the Cambridge Crystallographic Data Centre and can be obtained on request from The Director, Cambridge Crystallographic Data Centre, University Chemical Laboratory, 12 Union Road, Cambridge, CB2 1EZ, United Kingdom. Structure factors are no longer being deposited and can be obtained on request from the author.

Table 3. Selected interatomic distances (Å).

		Distance	
Atom 1	Atom 2	Molecule 1	Molecule 2
Ir(1)	Ir(1′)	2.6695(7)	2.6612(7)
Ir(1)	P(1)	2.327(2)	2.330(2)
Ir(1)	P(2′)	2.314(2)	2.315(2)
Ir(1)	C(1)	1.867(9)	1.855(9)
Ir(1)	C(2)	2.065(7)	2.077(8)
Ir(1)	C(2′)	2.098(8)	2.110(7)
P(1)	C(5)	1.849(8)	1.834(7)
P(2)	C(5)	1.828(8)	1.847(7)
O(1)	C(1)	1.158(10)	1.159(9)
O(2)	C(3)	1.182(10)	1.217(9)
O(3)	C(3)	1.327(11)	1.335(9)
O(3)	C(4)	1.441(12)	1.433(10)
C(2)	C(2′)	1.43(2)	1.428(15)
C(2)	C(3)	1.476(11)	1.447(11)

Primed are related to unprimed atoms via the crystallographic twofold axis at (0, *y*, –¼) in molecule 1 and at (½, *y*, ¼) in molecule 2.

Along with two dichloromethane molecules of crystallization, the asymmetric unit in the structure of complex **3** contains half of each of two crystallographically independent molecules; the molecules are essentially mirror images of each other. Molecule **1** is generated by rotation of the unique moiety containing Ir(1) about the twofold axis at 0, *y*, –¼, while rotation of the corresponding unit containing Ir(2) about the twofold axis at ½, *y*, ¼ generates molecule **2**. The tables of bond lengths and angles list parameters for both independent molecules side-by-side; it can be seen that there are no significance differences between the geometries of the two.

Results and compound characterization

The addition of one equivalent of dimethyl acetylenedicarboxylate (DMAD) to a solution of $[Ir_2(CO)_3(dppm)_2]$ (**1**) in toluene produces an initially deep blue-green solution containing

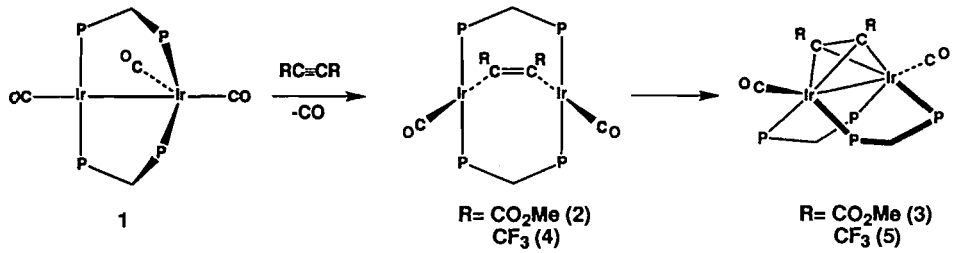

Table 4. Selected interatomic angles (deg).

			Angle	
Atom 1	Atom 2	Atom 3	Molecule 1	Molecule 2
Ir(1′)	Ir(1)	P(1)	93.57(6)	93.39(5)
Ir(1′)	Ir(1)	P(2′)	95.37(5)	95.60(5)
Ir(1′)	Ir(1)	C(1)	157.4(3)	157.2(2)
Ir(1′)	Ir(1)	C(2′)	50.7(2)	51.1(2)
Ir(1′)	Ir(1)	C(2′)	49.6(2)	50.0(2)
P(1)	Ir(1)	P(2′)	98.32(8)	98.70(8)
P(1)	Ir(1)	C(1)	101.7(3)	102.8(3)
P(1)	Ir(1)	C(2)	136.3(2)	135.3(2)
P(1)	Ir(1)	C(2′)	99.1(2)	98.2(2)
P(2′)	Ir(1)	C(1)	98.8(3)	97.7(3)
P(2′)	Ir(1)	C(2)	108.1(2)	109.6(2)
P(2′)	Ir(1)	C(2′)	141.5(2)	142.4(2)
C(1)	Ir(1)	C(2)	107.7(3)	106.7(3)
C(1)	Ir(1)	C(2′)	110.8(3)	110.9(3)
C(2)	Ir(1)	C(2′)	40.3(4)	39.9(4)
Ir(1)	P(1)	C(5)	109.8(3)	109.7(3)
Ir(1′)	P(2)	C(5)	112.4(3)	112.2(2)
C(3)	O(3)	C(4)	116.8(8)	116.9(7)
Ir(1)	C(1)	O(1)	179.0(8)	178.4(8)
Ir(1)	C(2)	Ir(1′)	79.8(3)	78.9(3)
Ir(1)	C(2)	C(2′)	71.1(4)	71.3(4)
Ir(1)	C(2)	C(3)	143.4(6)	143.3(5)
Ir(1′)	C(2)	C(2′)	68.6(4)	68.8(4)
Ir(1′)	C(2)	C(3′)	134.6(6)	134.1(5)
C(2′)	C(2)	C(3)	126.8(5)	129.1(5)
O(2)	C(3)	O(3)	122.5(8)	121.1(8)
O(2)	C(3)	C(2)	125.8(9)	125.8(8)
O(3)	C(3)	C(2)	111.7(8)	113.1(7)
P(1)	C(5)	P(2)	112.6(4)	113.0(4)

Primed are related to unprimed atoms via the crystallographic twofold axis at (0, *y*, –¼) in molecule 1 and at (½, *y*, ¼) in molecule 2.

$[Ir_2(CO)_2(\mu\text{-}\eta^1\text{:}\eta^1\text{-DMAD})(dppm)_2]$ (**2**), which has been assigned the structure shown above. The $^{31}P\{^1H\}$ NMR spectrum of this species shows a singlet at δ 5.28, indicative of only one chemical environment for the phosphorus nuclei, and the ^1H NMR spectrum shows signals for two different types of methylene protons (multiplets at δ 4.36 and 3.42) and a singlet at δ 2.70 for the methyl protons of the alkyne ligand, in a 2:2:6 ratio of intensities, implying front–back asymmetry in the complex and a symmetrical orientation of the alkyne. The $^{13}C\{^1H\}$ NMR spectrum of species **2** (prepared by the addition of DMAD to ^{13}CO-enriched compound **1**) shows a singlet at δ 191.0, with no resolved coupling to the phosphorus atoms bound to iridium ($^2J_{P-C} < 2$ Hz). No additional resonances are observed, confirming that **2** contains only a pair of equivalent CO groups. The carbonyl stretch, at 1934 cm^{-1}, is consistent with the geometry shown; unfortunately, a C≡C stretch due to the coordinated acetylenic moiety (which would usually be observed in the region 1550–1650 cm^{-1}) could not be identified. Although these data alone do not distinguish between a formulation for the complex in which the alkyne is coordinated as a *cis*-dimetallated olefin or one containing a dimetallatetrahedrane unit, crystallographic characterization of complex **3**, which is subsequently formed from **2** (vide infra), confirms the latter geometry for **3**, implying a different geometry for **2**. Species **2** is thus an isoelectronic analogue of the structurally characterized compounds $[MM'Cl_2(\mu\text{-HFB})(dppm)_2]$ (MM′ = Pd, Pt; HFB = hexafluoro-2-butyne) (11–13) and is also analogous to the rhodium species $[Rh_2(CO)_2(\mu\text{-}HC_2Ph)(dppm)_2]$, previously reported (9*b*).

Compound **2** is unusual in that, although diphosphine-bridged rhodium or iridium A-frame complexes containing two terminal carbonyls and a dianionic bridge are well known (e.g., $[MM'(CO)_2(\mu\text{-S})(dppm)_2]$, MM′ = Rh_2 (17), Ir_2 (18), RhIr (19)), this is one of the few cases in which an alkyne is spanning the metals with no metal–metal bond or other bridging atoms present. Most of the previous examples do not involve bridging dppm ligands and have the alkyne in a perpendicular arrangement (20). Only the dppm-bridged complexes of Pd_2 (11), PtPd (12), Pt_2 (13), and Rh_2 (9*b*) have a parallel-alkyne arrangement and fit into this category. The only examples in which an alkyne is parallel in the absence of metal–metal bonding, but in which there are no dppm groups, are $[Ir_2(NO)_2(PPh_3)_2(\mu\text{-HFB})_2]$ (21) and $[Pt_2(COD)_2(\mu\text{-HFB})_2)]$ (22), which in fact have two parallel, bridging alkynes. Although the dirhodium compound has a structure exactly analogous to **2**, it was apparently not obtained from the reaction of the analogous tricarbonyl dirhodium precursor, but was obtained in the reaction of $[Rh_2(CO)_2(\mu\text{-H})_2(dppm)_2]$ with two equivalents of phenylacetylene, yielding styrene as the other product. Presumably, the metastable dirhodium analogue was not observed in reactions of $[Rh_2(CO)_3(dppm)_2]$ because, under the refluxing conditions necessary for reaction to be observed, facile transformation to the perpendicular-alkyne complex is expected. Related bis(dimethylphosphino)methane-bridged dirhodium complexes of formula $[Rh_2(CO)_2(\mu\text{-RCCR})(dmpm)_2]$ (R = CO_2Me, CF_3) have also been reported (8*k*) but the orientation of the alkyne group could not be unequivocally established based on the spectroscopic data. However, the dark purple colour of these dmpm species is reminiscent of both complex **2** and its Rh_2 analogue, suggesting a parallel alkyne arrangement for these products also.

Fig. 1. Perspective view of one of the two crystallographically independent $[Ir_2(CO)_2(\mu\text{-}CH_3O_2C\text{—}C\equiv C\text{—}CO_2CH_3)(dppm)_2]$ molecules (molecule 1) showing the atom labelling scheme. Primed atoms are related to unprimed ones via the crystallographic twofold axis (0, *y*, –¼) bisecting the Ir(1)—Ir(1′) and C(2)—C(2′) bonds. Non-hydrogen atoms are represented by Gaussian ellipsoids at the 20% probability level. Hydrogen atoms are shown with arbitrarily small thermal parameters for the carboxymethyl (C(4), C(4′)) and dppm methylene (C5, C(5′)) groups, and are not shown for the dppm phenyl groups.

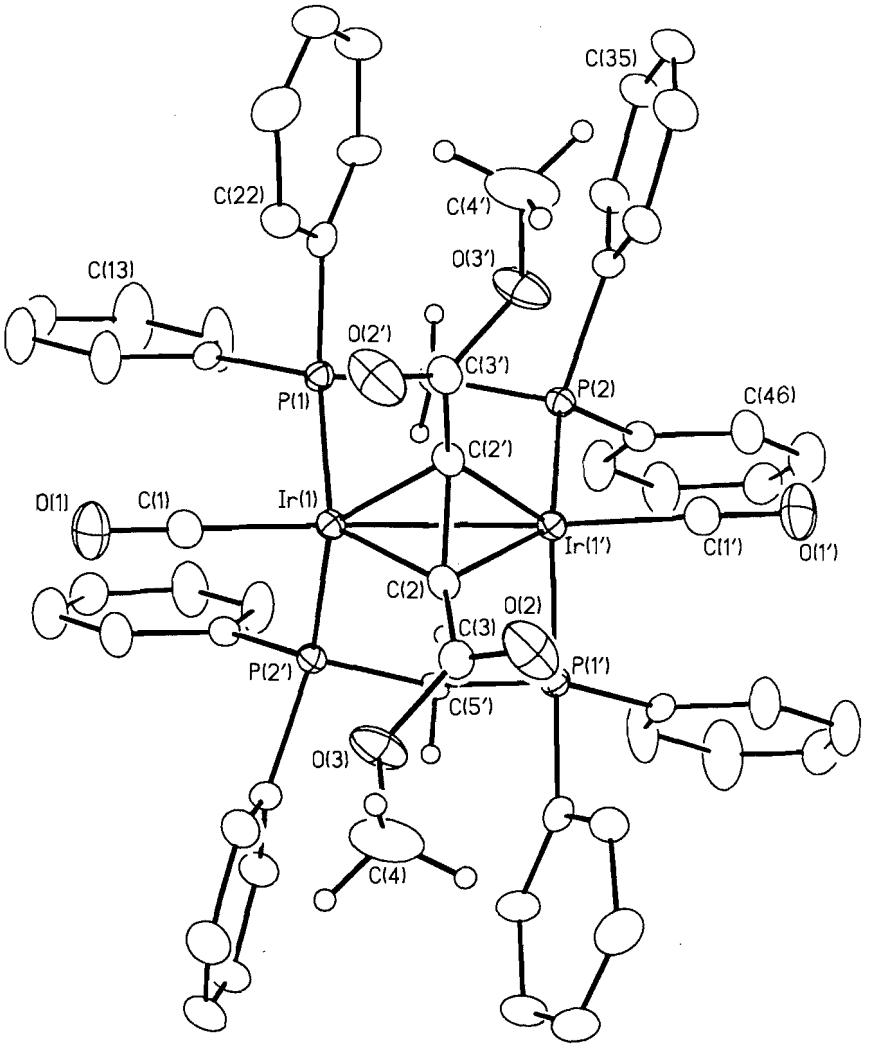

Solid samples of **2** are stable indefinitely in the absence of air, but slowly (1–2 days) turn to light orange-yellow in solution. Unfortunately, we have not yet succeeded in obtaining X-ray quality crystals of **2**. The orange-yellow product obtained from **2** upon standing has been identified as the isomer **3**, in which the alkyne now has a perpendicular orientation with respect to the metals, as has been established by an X-ray study. Compound **3** is obtained routinely in the reaction of **1** with DMAD in refluxing toluene.

As noted in the experimental section, compound **3** crystallizes with two independent molecules (each having a twofold axis bisecting the metal–metal and acetylenic C—C bonds). Figure 1 gives a view of one molecule showing all non-hydrogen atoms, whereas Fig. 2 is an alternate view in which only the ipso carbons of the dppm phenyl groups are shown. Similar views for the second molecule, which is essentially identical to the first, are given in the Supplementary Material.[3] Compound **3** is structurally reminiscent of the previously characterized compounds $[Rh_2(CO)_2(\mu\text{-}\eta^2\text{:}\eta^2\text{-PhCCPh})(dppm)_2]$ (9), $[Co_2(CO)_2(\mu\text{-}\eta^2\text{:}\eta^2\text{-MeCCMe})(dppm)_2]$ (10*a*), $[Co_2(CO)_2(\mu\text{-}\eta^2\text{:}\eta^2\text{-PhCCPh})(dpam)_2]$ (10*b*) (dpam = bis(diphenylarsino)methane), $[Co_2(CO)_4(\mu\text{-}\eta^2\text{:}\eta^2\text{-PhCCPh})(dppm)]$ (10*b*), and $[Co_2(CO)_6(\mu\text{-}\eta^2\text{:}\eta^2\text{-RCCR})]$ (R = Ph (10*c*), Bu^t (10*d*)), having alkyne ligands oriented essentially perpendicular to the metal–metal bond. This binding mode of the DMAD ligand in **3** is accommodated by a bending back of the diphosphine ligands (P(1)-Ir-P(2′) = 98.32(8)°(98.70(8)°)[4] as observed in

[4] In discussions of the structure, the first number given refers to molecule **1** and the number following, in parentheses, refers to molecule **2**.

Fig. 2. Alternate view of molecule 1, with only the *ipso* carbons of the dppm phenyl groups shown.

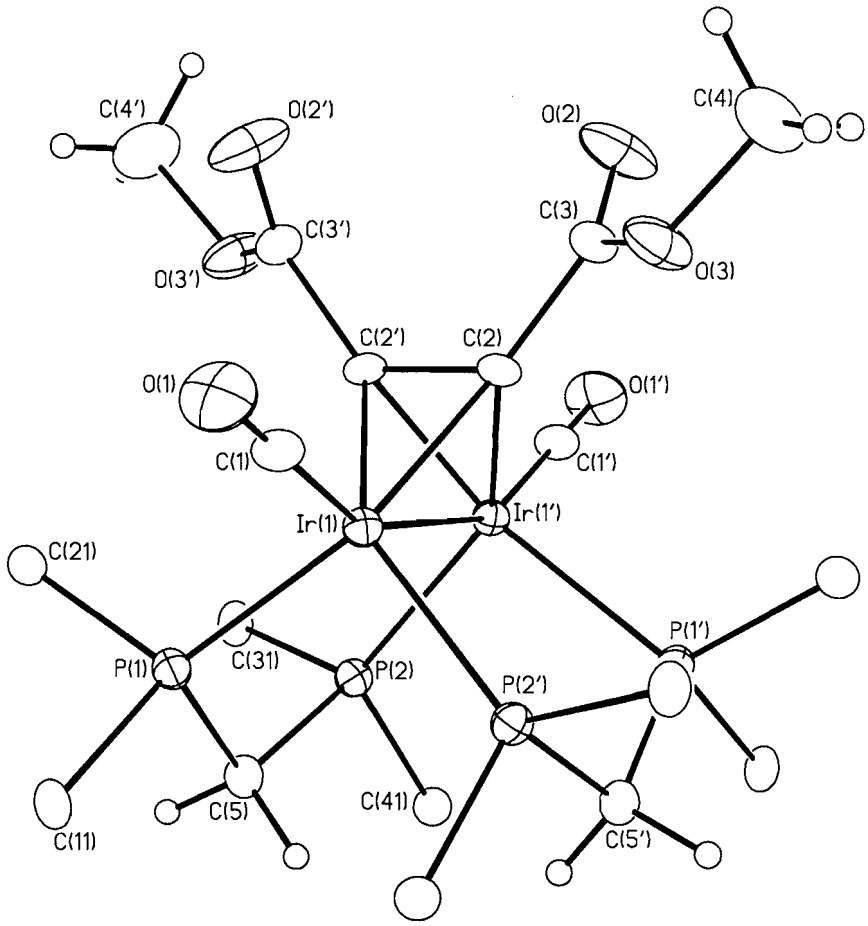

several of the above alkyne-bridged species, as well as in the complexes $[Ir_2(H)_2(CO)_2(\mu\text{-SiRPh})(dppm)_2]$ (R = H, Ph) (23), $[Rh_2(CO)_2(\mu\text{-SiHR})_2(dppm)_2]$ (R = Et, Ph) (24), $[Rh_2Cl_2(\mu\text{-X})_2(dppm)_2]$ (X = Cl, CH_3CO_2, $Ph_2P(C_6H_4)$ (25), $[(Rh(PNP))_2(\mu\text{-}\eta^1\text{:}\eta^1\text{DMAD})(\mu\text{-PNP})_2]$ (PNP = $(MeO)_2PN(Me)P(OMe)_2$) (26), $[Pt_2Me_4(dRpm)_2]$ (dRpm = dppm, dmpm) (27), and $[Ir_2(CNC_6H_3Me_2)_4(dmpm)_2]$ (28). Although a number of species having this diphosphine arrangement have been characterized, this nevertheless constitutes a relatively uncommon class of complexes (see also ref. 29). A number of complexes have also been characterized in which a *cis* arrangement is observed at one metal while the more normal *trans* arrangement is found at the other (30).

The coordination geometry about Ir(1) can be described as distorted trigonal bipyramidal, with C(1) and Ir(1′) acting as axial ligands while P(1), P(2′), and the C(2)—C(2′) unit (the latter being viewed as a neutral two-electron π donor to each of Ir and Ir′) occupy the equatorial sites. Distortions from this model, especially the severely acute Ir(1′)-Ir(1)-C(2) and Ir(1′)-Ir(1)-C(2′) angles 50.7(2)° (51.1(2)°) and 49.6(2)° (50.0(2)°), respectively, and the offset of the terminal carbonyl group C(1)O(1) from the Ir–Ir axis (Ir(1′)-Ir(1)-C(1) = 157.4(3)°, (157.2(2)°)), result from the bridging geometry of the alkyne. The deviation of the carbonyls from the Ir–Ir′ axis can be readily rationalized in terms of a "bent" metal–metal interaction as diagrammed below. In this view the axial site at each metal, opposite the carbonyl group, is the orbital that gives rise to the Ir—Ir bond. The tilting of the (alkyne) IrP_2 planes together with the Ir–CO vectors is suggestive of such a "bent" overlap. This view is not unlike that held for the carbonyl-bridged isomer of $Co_2(CO)_8$ (31), which has a very similar structure to that of the present species, with two bridging carbonyls replacing the alkyne bridge, and is supported by more recent theoretical studies (6, 32).

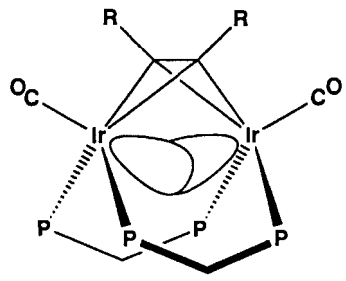

As expected, coordination to the metal centres has resulted in a change in the geometry of the DMAD group as a result of rehybridization of the acetylenic carbons. Furthermore, the acetylenic C(2)—C(2′) distances of 1.43(2) Å (1.43(2)Å) are much longer than observed in structures having the parallel geometry, in which values of near 1.34 Å, consistent with a

dimetallated olefinic formulation for this group, are normally observed (6, 8, 10, 33–39). These distances are even substantially longer than that reported (1.33(1) Å) in the dirhodium analogue (9) and in a number of related species (10, 40–43) having a bridging diphenylacetylene group, where distances near 1.35 Å appear typical. These distances in **3** are comparable to those between the acetylenic and carboxylate carbons (C(2)—C(3) = 1.48(1) Å (1.45(1)Å)), and as such are consistent with a loss of much of the multiple-bond character. The perpendicular binding mode is known to be more effective at lowering the alkyne bond order than the parallel mode, as seen from the significantly lower acetylenic C—C stretches in the IR spectra of the former (from ca. 1530–1642 cm^{-1} to ca. 1425 cm^{-1}). This can be understood on this basis of electron donation from *both* orthogonal π orbitals in the former case and concomitant π back-donation into *both* π^* sets. In the parallel mode one π bond remains intact and essentially unperturbed. The rehybridization at the alkyne carbons is also seen by the C(2′)-C(2)-C(3) angles of 126.8(5)°(129.1(5)°), which are distinctly more acute than is usually observed (133–145°); only $[Co_2(CO)_6(\mu\text{-}\eta^2\text{:}\eta^2\text{-}C_6F_6)]$ (C_6F_6 = 3,4,5,5,6,6-hexafluorocyclohexa-1-yne-3-ene) (44) possesses smaller C_{ac}-C_{ac}-R angles (118(2)°, 122(2)°), probably due to their endocyclic nature. In contrast, the closely related compound $[Rh_2(CO)_2(\mu\text{-}\eta^2\text{:}\eta^2\text{-PhCCPh})(dppm)_2]$ shows a separation of only 1.33(1) Å between the acetylenic carbons, and the C_{ac}-C_{ac}-R angles (133.0(8)° and 134.2(8)°) are normal (9). Overall the Ir_2C_2 core of **3** can be described as a dimetallatetrahedrane unit, with the distortions from this model (especially from the ideal bond angles of 60°) arising mainly due to the inherent inequality of the Ir—Ir, Ir—C, and C—C bond lengths.

The Ir(1)—Ir(1′) distances of 2.6695(7) (2.6612(7)) Å are the shortest so far observed within the class of similar diphosphine-bridged systems involving these metals, for which the metal–metal distances usually fall within the range 2.77–2.89 Å (8*b*, 8*g*, 12, 38, 45); the distances observed herein are more comparable to that found in another perpendicular-alkyne bridged complex, $[Ir_2(CO)_4(PPh_3)_2(\mu\text{-}\eta^2\text{:}\eta^2\text{-PhCCH})]$ (Ir—Ir = 2.691(1) Å) (46) and to the Rh—Rh distance of 2.644(1) Å in $[Rh_2(CO)_2(\mu\text{-}\eta^2\text{:}\eta^2\text{-PhCCPh})(dppm)_2]$ (9). Presumably the short metal–metal separation is a consequence of the bite imposed by the alkyne bridge, which requires a decreased Ir—Ir distance in order to maximize Ir—Ir and Ir—C overlaps, as mentioned above. In spite of the short metal–metal separation and the long distance between acetylenic carbons (vide supra), the Ir – alkyne carbon distances (2.065(7) – 2.110(7) Å) are within the range previously observed (2.05–2.13 Å) for iridium atoms bound to alkyne residues in related systems (8*b*,*d*,*g*,*h*). The Ir—P distances are similar to those observed in other $Ir_2(dppm)_2$ complexes, and despite the short Ir—Ir distance and the tilting of the equatorial planes at the metals, the intraligand P···P separations (3.059(3) Å (3.069(3) Å)) are normal.

The spectral data for the two isomers **2** and **3** serve to clearly distinguish the two. In the $^{31}P\{^1H\}$ NMR spectra the resonances for these species differ by almost 18 ppm. However, both appear as singlets owing to the chemical equivalence of the four phosphorus nuclei in both compounds, so yield no further structural information. The upfield chemical shift seen in the $^{13}C\{^1H\}$ NMR spectrum on proceeding from **2** to **3** (δ 191.10, 173.8) is unexpected in the context of the metal oxidation states. The lower oxidation state of Ir in compound **3** (0 versus +1) should give rise to more π back-donation to the carbonyls and a concomitant downfield ^{13}C shift (47). We propose that the alkyne group in the perpendicular mode functions as a better π acceptor by virtue of using both orthogonal sets of π^* orbitals. The lower electron density remaining for π back-donation to the carbonyls is then manifest in the upfield ^{13}C shift for the carbonyl resonances in **3**. Such an argument is also consistent with the solution IR spectra, which show a somewhat higher frequency carbonyl stretch for **3** (1943 cm^{-1}) than for **2** (1934 cm^{-1}). Of course, metal oxidation state assignments in such species are somewhat artificial, and **3** could equally well be viewed as a metallatetrahedrane complex having localized Ir—C σ bonds to the carbon atoms, in which case the metals could be viewed as Ir(+2).

The analogous hexafluoro-2-butyne complexes, $[Ir_2(CO)_2(\mu\text{-}\eta^1\text{:}\eta^1\text{-HFB})(dppm)_2]$ (**4**) and $Ir_2(CO)_2(\mu\text{-}\eta^2\text{:}\eta^2\text{-HFB})(dppm)_2]$ (**5**) are prepared much as are the DMAD compounds, by reaction **1** with the alkyne. However, unlike the DMAD reaction, the reaction with HFB is very slow at ambient temperature, and only the final product **5** can be isolated. Intermediate **4**, analogous to the blue species **2**, appears at intermediate times (giving solutions a green tinge) but is always obtained together with varying amounts of starting material **1** and product **5**. Attempts to synthesize analogs of these parallel and perpendicular alkyne compounds, using alkynes such as phenylacetylene and diphenylacetylene, gave no indications of reaction at ambient or slightly elevated temperatures, even after 24 h. Refluxing compound **1** in the presence of these alkynes resulted in a large number of unidentified decomposition products.

Although conversion from the parallel to the perpendicular alkyne-bridged coordination is irreversible in these compounds, the reversible transformation has been observed in a number of cases; the first examples were accompanied by ligand loss or gain (7), but recently two reports have appeared in which two isomers differed in their orientations of the alkyne groups (8*n*, 20*a*). In the former examples it is difficult to compare alkyne reactivities, owing to the differing ancillary ligand counts, however, such a comparison should be more meaningful in the isomeric compounds, where at least the ancillary ligands are the same. In a previous study on two RhMn-containing isomers, which differed in their alkyne binding, protonation gave different intermediates, but the same final product (8*n*). Compounds **2** and **3** in this paper offer another opportunity to compare the reactivities of an alkyne group in the two bridging coordination modes, since both species can be isolated free of the other. To our knowledge, no other study comparing such reactivities has been reported.

Possibly the most obvious difference in the two isomers (**2** and **3**) relates to the electron counts at the metals. With the alkyne functioning as a 2-electron donor in **2** the metals each have a 16-electron count, whereas in **3**, in which the alkyne is a 4-electron donor, both metals are saturated. This difference shows up clearly in the attempted reactions with PMe_3. Whereas compound **3** shows no reaction with excess PMe_3 over extended periods of time, compound **2** reacts readily with one equivalent of the phosphine to yield the adduct $[Ir_2(CO)(PMe_3)(\mu\text{-CO})(\mu\text{-DMAD})(dppm)_2]$ (**6**). This product displays five $^{31}P\{^1H\}$ resonances for the chemically distinct phosphorus nuclei. The maximum coupling between these

nuclei is found to be ca. 110 Hz, indicating a *cis* arrangement of the phosphines at each metal; by comparison, *trans* phosphines in such systems typically show coupling of ca. 300 Hz. The $^{13}C\{^1H^1\}$ NMR spectrum shows one terminal carbonyl resonance at δ 182.8 and one due to the bridging group at δ 230.3. This latter resonance displays large coupling (63 Hz) to P_A and P_B, indicating that these phosphorus nuclei are almost *trans* to this carbonyl (by comparison, *cis* $^2J_{P-C}$ values are typically less than 15 Hz). Movement of the one carbonyl from a terminal to a bridging site presumably results from the steric crowding upon coordination of PMe_3. We assume that this is also a major reasons for the transformation from *trans* to *cis* diphosphine groups that occurs. Complex **6** is chiral, but will be present as a racemic mixture, resulting from PMe_3 attack at either metal.

Attempts to generate a tricarbonyl species analogous to **6** by reacting **2** or **3** with CO failed, as no reaction was observed in either case. A species, believed to be a tricarbonyl, alkyne-bridged complex, was observed at intermediate times in the reaction of **1** with DMAD, having all carbonyls terminal ($^{13}C\{^1H\}$ NMR, δ: 199, 183, 178). However, owing to its facile loss of CO to yield **2**, this intermediate was incompletely characterized.

We next turned our attention to the reactions of **2** and **3** with the electrophiles, CH_3^+ and H^+, in attempts to obtain alkyl and hydride products. It was hoped that the alkynes in the two different bridging modes might display different tendencies to undergo migratory insertion with the alkyl or hydride moieties. Compound **2** reacts with methyl triflate to yield the alkyl product $[Ir_2(CH_3)(CO)_2(\mu\text{-DMAD})(dppm)_2][SO_3CF_3]$ (**7**), having the structure diagrammed below. This product is identical to the product previously obtained in the reaction of

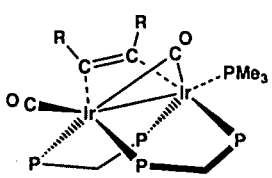

6

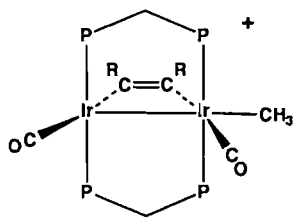

7

$[Ir_2(CH_3)(CO)(\mu\text{-CO})(dppm)_2][SO_3CF_3]$ with DMAD (**15**) and is the product expected from electrophilic attack at a filled d_{z^2} orbital on one of the metal centres in **2**. All spectroscopic parameters are consistent with the structure shown. No migratory insertion of the alkyne and the methyl group has been observed in this or the previous study, in spite of a favourable mutually *cis* arrangement of the two groups.

Surprisingly perhaps, compound **3** does not react with methyl triflate. We had expected that the 18e, formally Ir(0) centres would be susceptible to electrophilic attack, but this appears not to be case with Me^+. Possibly the reaction is inhibited by more severe steric crowding than is present in **2**.

Protonation also proceeds differently for the two isomers. Reaction of **2** with $HBF_4{\cdot}OEt_2$ yields the hydrido species $[Ir_2H(CO)_2(\mu\text{-DMAD})(dppm)_2][BF_4]$ (**8**) as shown in Scheme 1. The hydride is shown to be terminally bound to one metal, displaying coupling to only two adjacent ^{31}P nuclei. An alternate structure, in which the carbonyl and hydride ligands on one metal are interchanged, is ruled out for two reasons. First, the structure shown is analogous to that of the previously characterized methyl complex **7** (15), with both species having very comparable spectral parameters, and second, the reaction of **8** with CO yields the tricarbonyl $[Ir_2H(CO)_3(\mu\text{-DMAD})(dppm)_2][BF_4]$ (**9**), in which the hydride ligand remains adjacent to the DMAD unit. If complex **8** had the alternate geometry, its product upon reaction with CO would be the isomer **9b**, which has the hydrido ligand opposite the alkyne; this latter product has been previously characterized (48) and is clearly distinguishable from **9**. No migratory insertion of the alkyne and hydrido ligands in **8** is observed at ambient temperature in spite of their mutually *cis* arrangement. However, refluxing **8** in benzene for several hours yielded a mixture of products, one of which (in approximately 50% yield) was identified as the migratory insertion product **11** (vide infra).

Compound **3** reacts readily with $HBF_4{\cdot}OEt_2$ at −10°C to yield $[Ir_2H(CO)_2(\mu\text{-DMAD})(dppm)_2][BF_4]$ (**10**) in which the hydride group is found to be terminally bound to one metal. Although the orientation of the alkyne group is equivocal, the facile conversion from **3** suggests that it has remained perpendicular to the metals. As such, compound **10** resembles the isoelectronic species $[RhMn(CO)_3(\mu\text{-}\eta^2\text{:}\eta^2\text{-}RC_2R)(dppm)_2]$ (R = CO_2Me, CF_3) (8*n*), in which the "$Mn(CO)_2$" moiety is replaced by "$IrH(CO)^+$". In addition, the final product (**11**) in the subsequent transformation of **10** is shown to also have a *cis*-diphosphine arrangement, so it seems likely that the diphosphines have remained *cis* in the transformation **3** to **10** to **11**. The appearance of two methyl resonances seems at first to be inconsistent with the structure shown for **10**, however, reference to Fig. 2 shows that one methyl group is tipped towards one metal whereas the second is aimed at the other; protonation at one metal would render these methyl groups inequivalent. Warming to ambient temperature results in the smooth transformation of **10** to $[Ir_2(\mu\text{-}\eta^1\text{:}\eta^2\text{-}(MeO_2C)C{=}C(H)CO_2Me)(CO)_2(dppm)_2][BF_4]$ (**11**) in which migration of the hydride to the alkyne group to give a bridging vinyl group has occurred. This transformation is accompanied by the disappearance of the hydride resonance of **10** and the appearance of the vinyl signal at δ 4.62 in the ^1H NMR spectrum. Also observed, is the C=C stretch of this vinyl group at ca. 1550 cm^{-1}; significantly, none of the alkyne-bridged species displayed the expected C—C stretches for these alkyne moieties. The $^{31}P\{^1H\}$ NMR spectrum shows four separate resonances, consistent with the structure shown, and the maximum coupling (58 Hz) between these nuclei confirms the *cis*–*cis* diphosphine arrangement. In the $^{13}C\{^1H\}$ NMR spectrum the carbonyls display a mutual coupling of 9.4 Hz, suggesting an arrangement in which both are approximately opposite the Ir—Ir bond, facilitating their coupling.

Protonation of **3** at temperatures below −20°C suggests that the initial site of protonation is at the DMAD carboxylate oxygens, as seen by the low-field shift of the proton at δ 20.0, which is consistent with a strongly hydrogen-bonded proton (49). Reference to Fig. 2 shows that protonation at these groups could easily give rise to a species in which the proton bridges both groups. The other spectroscopic parameters (^1H, ^{13}C, and ^{31}P) are all very similar to those of **3**, consistent with protonation occurring on the periphery of the molecule. Transfer of the proton from the carboxylate groups to one of the metals in **10** would require very little movement of any of the groups.

Scheme 1.

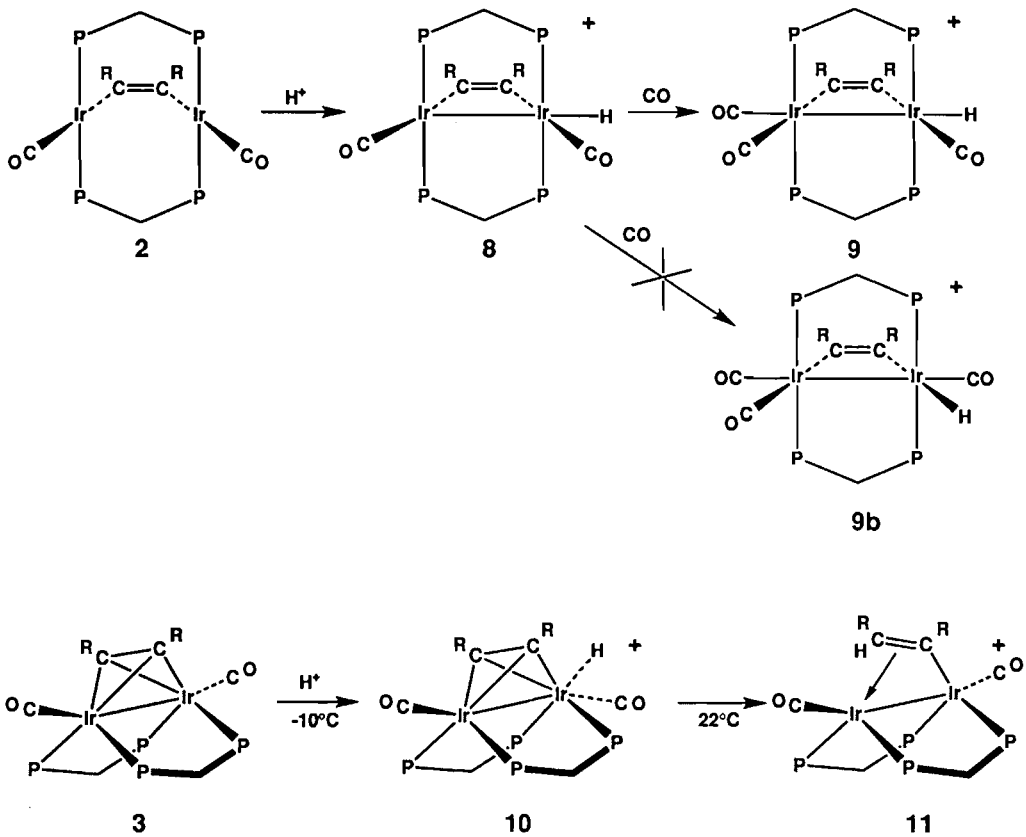

Scheme 2.

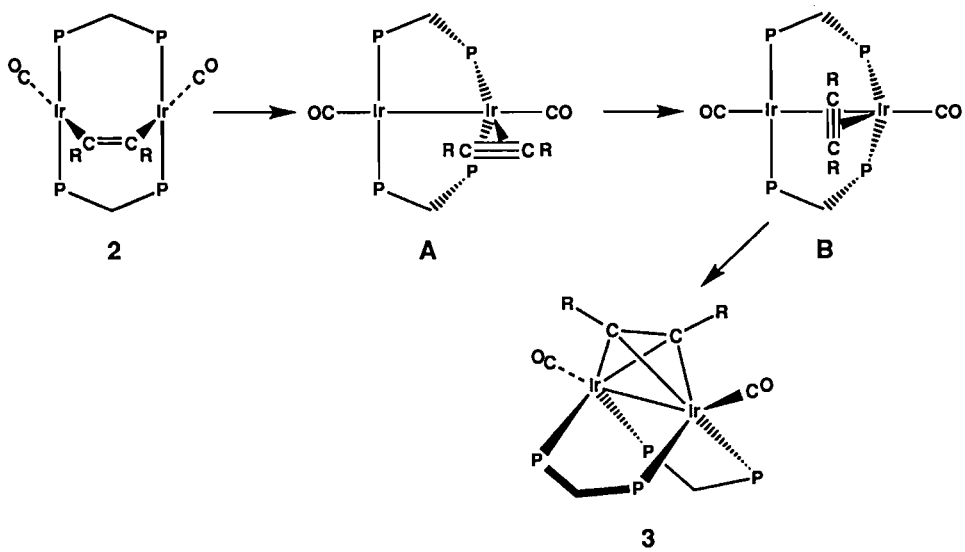

We had hoped that protonation of the HFB analogue $[Ir_2(CO)_2(\mu\text{-}\eta^2\text{:}\eta^2\text{-HFB})(dppm)_2]$ (**5**) would yield the corresponding vinyl product, and that the additional NMR coupling involving the fluorine nuclei would yield additional information about the binding of the vinyl group. However, although the vinyl product $[Ir_2(CO)_2(\mu\text{-}\eta^1\text{:}\eta^2\text{-}(CF_3)C{=}C(H)CF_3)(dppm)_2][BF_4]$ could be identified in the NMR spectra, its facile decomposition to several species did not allow the appropriate heteronuclear decoupling experiments to be carried out.

Discussion

At the outset, it was our intention to isolate an iridium ana-

logue of the blue, metastable $[Rh_2(CO)_2(\mu\text{-}\eta^1\text{:}\eta^1\text{-}RC_2R')(dppm)_2]$ (9), having a parallel alkyne bonding mode. This has been achieved using the activated alkyne, dimethyl acetylenedicarboxylate, generating $[Ir_2(CO)_2(\mu\text{-}\eta^1\text{:}\eta^1\text{-}DMAD)(dppm)_2]$ (**2**). With the closely related hexafluoro-2-butyne, the analogous product was observed as a transient species, but was never isolated. Attempts to prepare the phenyl- and diphenylacetylene adducts, more closely resembling the dirhodium compound, were unsuccessful, with no reaction observed at mild temperatures and decomposition occurring under harsher conditions. As anticipated, the combination of the activated alkyne and the less labile Ir centres allows the isolation of the target species **2**, although the effect of changing just the alkyne or the metal could not be assessed, since activated alkynes were not used in the dirhodium study. In spite of the extended lifetime of **2**, it still slowly rearranges (over a 24–48 h period) in solution to the more stable isomer **3**, having a perpendicular-alkyne bonding mode. The greater stability of the perpendicular product can be rationalized, at least for the activated alkynes, on the basis that this geometry allows the alkyne to function as a better π acceptor from the electron-rich Ir(0) centres, with donation into both orthogonal π^* orbitals. It should also be noted that the transformation from **2** to **3** should also be favoured by increased bond formation. In addition to more π back-donation, which formally corresponds to stronger Ir—C bonds, there is an additional metal–metal bond in **3**. Both effects should outweigh the concomitant slight weakening of the alkyne C—C bond that occurs. This being said, it nevertheless remains a mystery that the palladium and platinum analogues, $[MM'Cl_2(\mu\text{-}\eta^1\text{:}\eta^1\text{-}RC_2R)(dppm)_2]$, retain a *parallel*-alkyne geometry (11–13).

Superficially it would appear that rearrangement from **2** to **3**, via alkyne rotation and bending back of the phosphines, should be facile. This is not the case, taking up to 48 h in solution at ambient temperature. Hoffmann has argued that simple alkyne rotation by 90° in these binuclear systems is symmetry forbidden (6). We therefore propose that alkyne rotation occurs at a single metal centre, as shown in Scheme 2. The structures of proposed intermediates **A** and **B** are analogous to that of **1**, having a *cis* diphosphine arrangement at one metal and one carbonyl replaced by an η^2-alkyne. The bent-back diphosphine arrangement at one metal would facilitate alkyne rotation by moving the dppm phenyl rings away from the alkyne substituents. Alkyne rotation at a single metal has been reported (50), and is presumably analogous to the more studied olefin rotation (51). In the final step, movement of the perpendicular alkyne from one metal to the bridging position would then be accompanied by bending back of the diphosphines at the second metal.

The isolation of the two isomeric forms of $[Ir_2(CO)_2(\mu\text{-}RC{\equiv}CR)(dppm)_2]$ (R = CO_2Me), having either a parallel (**2**) or a perpendicular (**3**) alkyne-bridged arrangement, has allowed an investigation of the reactivity differences of the two species. Even the mere exposure to air shows a dramatic difference in the two, with the parallel isomer decomposing instantly, while the perpendicular isomer is stable indefinitely. It is well recognized that the two binding modes give rise to differing valence electron counts at the metals. In **2**, each metal has a 16e configuration so is coordinatively unsaturated, whereas the metals are saturated in **3**. In keeping with these configurations, **2** reacts readily with PMe_3, ultimately yielding saturated metal centres, whereas **3** fails to react. The product of PMe_3 attack on **2**, $[Ir_2(CO)(PMe_3)(\mu\text{-}CO)(\mu\text{-}DMAD)(dppm)_2]$ (**6**), retains the parallel-alkyne bridge although the diphosphines adopt a *cis* arrangement at both metals. Based on the data available, it is not possible to rationalize the transformation from *trans* to *cis*-diphosphines, in which the bridging carbonyl and DMAD groups end up in adjacent positions. We would have anticipated a *trans*-diphosphine arrangement, having the carbonyl and alkyne on opposite faces of the dimer.

Although we have rationalized the failure of **3** to react with PMe_3 as due to the saturation at both metals, this is only part of the story, since the analogous $[Cp_2Rh_2(\mu\text{-}CO)(\mu\text{-}CF_3C_2CF_3)]$ reacts with nucleophiles, in spite of the saturated metal configurations (4). It was proposed that rotation of the alkyne from perpendicular to parallel generates unsaturation, allowing ligand coordination. In compound **3** it seems that this alkyne rotation is very unfavorable, as noted above, so the metals retain their saturated configurations, and do not allow ligand addition to occur.

Not unexpectedly, the electron-rich species **2** and, to a lesser extent, **3** react with electrophiles such as CH_3^+ and H^+. In **2**, an orbital, corresponding to the filled d_{z^2} orbital on each square-planar Ir centre is the obvious site of electrophilic attack, and both CH_3^+ and H^+ react to yield analogous products $[Ir_2(E)(CO)_2(\mu\text{-}DMAD)(dppm)_2]^+$ (E = CH_3 (**7**), H (**8**)), in which the electrophile is coordinated at one metal, adjacent to the $\mu\text{-}\eta^1\text{:}\eta^1$-alkyne group. In neither case does migratory insertion, to give the appropriate vinyl ligand, occur. Although insertion involving a bridging alkyne and an alkyl group is not common, that involving a hydride is well documented (8*k*, 8*n*, 36, 52), so the failure of **8** to transform to a vinyl-containing product is surprising.

The reactivity of **3** with electrophiles is significantly different from that of **2**. First **3** does not react with methyl triflate, presumably owing to the greater congestion at the metals when the alkyne is perpendicular. Although the smaller proton does find access to one of the metals, yielding, at low temperature, a product analogous to **8** except having a perpendicular alkyne and a *cis*-diphosphine arrangement (see Scheme 1), warming to ambient temperature results in migratory insertion and formation of a vinyl-bridged product (**11**). The latter transformation is not surprising, but the failure of the isomeric **8** to undergo the analogous rearrangement is curious, particularly since a number of parallel alkyne-to-vinyl transformations have been reported (51). The reason for this difference is not understood.

In conclusion, we have for the first time demonstrated that the bridged, parallel and perpendicular, alkyne binding modes in binuclear complexes can give rise to significant reactivity differences. Although the failure of the isomer, containing the perpendicular-bound alkyne, to react with PMe_3 or $MeOSO_2CF_3$, can be rationalized based on the saturated metal configurations or the crowded metal environments, respectively, the different reactivities of the two isomers upon protonation remains a mystery. The facile conversion of the perpendicular alkyne to a vinyl group upon protonation, is in marked contrast to the failure of the other isomer, in which the parallel alkyne is adjacent to the terminal hydride ligand, to undergo migratory insertion to give a vinyl group under similarly mild conditions.

Acknowledgements

We thank the Natural Sciences and Engineering Research Council of Canada and the University of Alberta for financial support, and Professor C.P. Casey for communicating results prior to their publication.

References

1. J.P. Collman, L.S. Hegedus, J.R. Norton, and R.G. Finke. Principles and applications of organotransition metal chemistry. University Science Books, Mill Valley, Calif. 1987. Chaps. 11 and 18, and references therein.
2. J.L. Davidson. *In* Reactions of coordinated ligands. Vol. 1. *Edited by* P.S. Braterman. Plenum Press, New York. 1986. p. 825.
3. (*a*) E.L. Muetterties. Bull. Soc. Chim. Belg. **84**, 953 (1975); (*b*) Bull Soc. Chim. Belg. **85**, 451 (1976); (*c*) Angew. Chem. Int. Ed. Engl. **17**, 545 (1978); (*d*) E.L. Muetterties, R.N. Rhodin, E. Band, C.F. Brucker, and W.R. Pretzer. Chem. Rev. **79**, 91 (1979); (*e*) E. Sappa, A. Tiripicchio, and P. Braunstein. Chem. Rev. **83**, 203 (1983).
4. R.S. Dickson. Polyhedron, **10**, 1995 (1991).
5. (*a*) M.J.S. Dewar. Bull. Soc. Chim. Fr. **18**, C79 (1951); (b) Annu. Rep. Chem. Soc. **48**, 112 (1951); (*c*) J. Chatt and L.A. Duncanson. J. Chem. Soc. 2339 (1953); (*d*) M.J.S. Dewar, R.C. Haddon, A. Komornicki, and H. Rzepa. J. Am. Chem. Soc. **99**, 377 (1977); (*e*) M.J.S. Dewar and G.P. Ford. J. Am. Chem. Soc. **101**, 783 (1979).
6. D.M. Hoffman, R. Hoffmann, and C.R. Fisel. J. Am. Chem. Soc. **104**, 3858 (1982).
7. (*a*) R.S. Dickson and G.N. Pain. J. Chem. Soc. Chem. Commun. 277 (1979); (*b*) M.R. Gagné and J. Takats. Organometallics, **7**, 561 (1988).
8. (*a*) M. Cowie and T.G. Southern. Inorg. Chem. **21**, 246 (1982); (*b*) B.R. Sutherland and M. Cowie. Organometallics, **3**, 1869 (1984); (*c*) M. Cowie, R.S. Dickson, and B.W. Hames. Organometallics, **3**, 1879 (1984); (*d*) B.R. Sutherland and M. Cowie. Organometallics, **4**, 1801 (1985); (*e*) J.A. Jenkins, J.P. Ennett, and M. Cowie. Organometallics, **7**, 1845 (1988); (*f*) I.R. McKeer, S.J. Sherlock, and M. Cowie. J. Organomet. Chem. **352**, 205 (1988); (*g*) B.A. Vaartstra and M. Cowie. Organometallics, **8**, 2388 (1989); (*h*) B.A. Vaartstra and M. Cowie. Organometallics, **9**, 1594 (1990); (*i*) R.W. Hilts, R.A. Franchuk, and M. Cowie. Organometallics, **10**, 304 (1991); (*j*) B.A. Vaartstra, J. Xiao, J.A. Jenkins, R. Verhagen, and M. Cowie. Organometallics, **10**, 2708 (1991); (*k*) J.A. Jenkins and M. Cowie. Organometallics, **11**, 2767 (1992); (*l*) J. Xiao and M. Cowie. Organometallics, **12**, 463 (1993); (*m*) B.T. Sterenberg, R.W. Hilts, G. Moro, R. McDonald, and M. Cowie. J. Am. Chem. Soc. **117**, 245 (1995); (*n*) L.-S. Wang and M. Cowie. Can. J. Chem. **73**, 1058 (1995); (*o*) Organometallics, **14**, 3040 (1995); (*p*) F.H. Antwi-Nsiah, O. Oke, and M. Cowie. Organometallics, **15**, 506 (1996).
9. (*a*) D.H. Berry and R. Eisenberg. Organometallics, **6**, 1796 (1987); (*b*) S.I. Hommeltoft, D.H. Berry, and R. Eisenberg. J. Am. Chem. Soc. **108**, 5345 (1986).
10. (*a*) R.P. Aggarwal, N.G. Connelly, M.C. Crespo. B.J. Dunne, P.J. Hopkins, and A.G. Orpen. J. Chem. Soc. Chem. Commun. 33 (1989); (*b*) P.H. Bird, A.R. Fraser, and D.N. Hall. Inorg. Chem. **16**, 1923 (1977); (*c*) W.G. Sly. J. Am. Chem. Soc. **81**, 18 (1959); (*d*) F.A. Cotton, J.D. Jamerson, and B.R. Stults. J. Am. Chem. Soc. **98**, 1774 (1976).
11. (*a*) A.L. Balch, C.-L. Lee, C.H. Lindsay, and M.M. Olmstead. J. Organomet. Chem. **177**, C22 (1979); (*b*) C.-L. Lee, C.T. Hunt, and A.L. Balch. Inorg. Chem. **20**, 2498 (1981).
12. P.G. Pringle and B.L. Shaw. J. Chem. Soc. Dalton Trans. 889 (1983).
13. R.J. Puddephatt and M.A. Thomson. Inorg. Chem. **21**, 725 (1982).
14. B.R. Sutherland and M. Cowie. Organometallics, **4**, 1637 (1985).
15. J.R. Torkelson and M. Cowie. Manuscript in preparation.
16. N. Walker and D. Stuart. Acta Crystallogr. Sect. A: Found. Crystallogr. **A39**, 158 (1983).
17. C.P. Kubiak and R. Eisenberg. Inorg. Chem. **19**, 2726 (1980).
18. C.P. Kubiak, C. Woodcock, and R. Eisenberg. Inorg. Chem. **19**, 2733 (1980).
19. B.A. Vaartstra and M. Cowie. Inorg. Chem. **28**, 3138 (1989).
20. (*a*) C.P. Casey, R.S. Cariño, R.K. Hayashi, and K.D. Schladetzky. J. Am. Chem. Soc. **118**, 1617 (1996); (*b*) N.M. Boag, M. Green, J.A.K. Howard, F.G.A. Stone, and H. Wadepohl. J. Chem. Soc. Dalton Trans. 862 (1981); (*c*) N.M. Boag, M. Green, J.A.K. Howard, J.L. Spencer, R.F.D. Stansfield, M.D.O. Thomas, F.G.A. Stone, and P. Woodward. J. Chem. Soc. Dalton Trans. 2181 (1980); (*d*) G.M. Villacorta, D. Gibson, I.D. Williams, and S.J. Lippard. J. Am Chem. Soc. **107**, 6732 (1985); (*e*) G.M. Villacorta, D. Gibson, I.D. Williams, E. Whang, and S.J. Lippard, Organometallics, **6**, 2426 (1987); (*f*) H.L. Aalten, G. van Koten, E. Reithorst, and C.H. Stam. Inorg. Chem. **28**, 4140 (1989); (*g*) C. Bianchini, D. Masi, A. Meli, M. Peruzzini, A. Vaaca, F. Laschi, and P. Zanello. Organometallics, **10**, 636 (1991); (*h*) E. Spaltenstein and J. M. Mayer. J. Am. Chem. Soc. **113**, 7744 (1991); (*i*) J. Krause, W. Bonrath, and K.R. Pörchke. Organometallics, **11**, 1158 (1992); (*j*) D.L. Reger and M.F. Huff. Organometallics, **11**, 69 (1992).
21. J. Clemens, M. Green, M.-C. Kuo, C.J. Fritchie, J. Mague, and F.G.A. Stone. J. Chem. Soc. Chem. Commun. 53 (1972).
22. L.E. Smart, J. Browning, M. Green, A. Laguna, J.L. Spencer, and F.G.A. Stone. J. Chem. Soc. Dalton Trans. 1777 (1977).
23. R. McDonald and M. Cowie. Organometallics, **9**, 2468 (1990).
24. (*a*) W.-D. Wang, S.I. Hommeltoft and R. Eisenberg. Organometallics, **7**, 2417 (1988); (*b*) W.-D. Wang and R. Eisenberg. J. Am. Chem. Soc. **112**, 1833 (1990).
25. F.A. Cotton, K.R. Dunbar, and M.G. Verbruggen, J. Am. Chem. Soc. **109**, 5498 (1987).
26. J.T. Mague. Inorg. Chem. **28**, 2215 (1989).
27. L. Manojlović-Muir, K.A. Muir, A.A. Frew, S.S.M. Ling, M.A. Thomson, and R.J. Puddephatt. Organometallics, **3**, 1637 (1984).
28. J. Wu, P.E. Fanwick, and C.P. Kubiak. J. Am. Chem. Soc. **111**, 7812 (1989).
29. (*a*) J. Wu, P.E. Fanwick, and C.P. Kubiak. J. Am. Chem. Soc. **110**, 1319 (1988); (*b*) P. Braunstein, B. Oswald, A. DeCian, and J. Fischer, J. Chem. Soc. Dalton Trans. 2685 (1991).
30. M.P. Brown, S.J. Cooper, A.A. Frew, L. Manojlović-Muir, K.W. Muir, R.J. Puddephatt, K.R. Seddon, and M.A. Thomson. Inorg. Chem. **20**, 1500 (1981); (*b*) R.J. Haines, E. Meintjies, M. Laing, and P. Sommerville. J. Organomet. Chem. **216**, C19 (1981); (*c*) W.S. McDonald, P.G. Pringle, and B.L. Shaw. J. Chem. Soc. Chem. Commun. 861 (1982); (*d*) A.T. Hutton, P.G. Pringle, and B.L. Shaw. Organometallics, **2**, 1889 (1983); (*e*) C. Woodcock and R. Eisenberg. Inorg. Chem. **24**, 1287 (1985); (*f*) A.L. Balch, R.R. Guimerans, J. Linehan, M.M. Olmstead, and D.E. Oram. Organometallics, **4**, 1445 (1985); (*g*) D.L. DeLaet, R. Del Rosario, P.E. Fanwick, and C.P. Kubiak. J. Am. Chem. Soc. **109**, 754 (1987); (*h*) D.J. Elliot, G. Ferguson, D.G. Holah, A.N. Hughes, M.C. Jennings, V.R. Magnuson, D. Potter, and R.J. Puddephatt. Organometallics, **9**, 1336 (1990); (*i*) M.K. Reinking. Ph.D. Thesis, Purdue University, 1989. Chap. 3.
31. G.G. Sumner, H.P. Klug, and L.E. Alexander. Acta Crystallogr. **17**, 732 (1964).
32. H. van Dam, D.J. Stufkens, A. Oskan, M. Doran, and I.H. Hillier. Electron Spectrosc. Relat. Phenom. **21**, 47 (1980).

33. K.A. Johnson and W.L. Gladfelter. Organometallics, **8**, 2866 (1989).
34. J.L. Davidson, W. Harrison, D.W.A. Sharp, and G.A. Sim. J. Organomet. Chem. **46**, C42 (1972).
35. Y. Koie, S. Shinoda, Y. Saito, B.J. Fitzgerald, and C.G. Pierpont. Inorg. Chem. **19**, 770 (1980).
36. R.S. Dickson, S.H. Johnson, H.P. Kirsch, and D.J. Lloyd. Acta Crystallogr. Sect. B: Crystallogr. Cryst. Chem. Struct. **B33**, 2057 (1977).
37. J.T. Mague, Organometallics, **5**, 918 (1986).
38. J.T. Mague, C.L. Klein, R.J. Majeste, and E.D. Stevens. Organometallics, **3**, 1860 (1984).
39. R.J. Puddephatt and M.A. Thomson. Inorg. Chem. **21**, 725 (1982).
40. M.A. Bennett, R.N. Johnson, G.B. Robertson, T.W. Turney, and P.O. Whimp. Inorg. Chem. **15**, 97 (1976).
41. T.R. Jack, C.J. May, and J. Powell. J. Am. Chem. Soc. **99**, 4707 (1977).
42. E.L. Muetterties, W.R. Pretzer, M.G. Thomas, B.F. Beier, D.L. Thorn, V.W. Day, and A.B. Anderson. J. Am. Chem. Soc. **100**, 2090 (1978).
43. B.H. Freeland, J.E. Huz, N.C. Payne, and K.G. Tyers. Inorg. Chem. **19**, 693 (1980).
44. N.A. Bailey and R. Mason. J. Chem. Soc. A, 1293 (1968).
45. (*a*) C.P. Kubiak, C. Woodcock, and R. Eisenberg. Inorg. Chem. **19**, 2733 (1980); (*b*) B.R. Sutherland and M. Cowie. Inorg. Chem. **23**, 2324 (1984); (*c*) Can. J. Chem. **64**, 464 (1986); (*d*) J. Wu, M.K. Reinking, P.E. Fanwick, and C.P. Kubiak. Inorg. Chem. **26**, 247 (1987); (*e*) R. McDonald, B.R. Sutherland, and M. Cowie. Inorg. Chem. **26**, 3333 (1987). (*f*) J. Wu, P.E. Fanwick, and C.P. Kubiak. Organometallics, **6**, 1805 (1987); (*g*) A.L. Balch, K.M. Waggoner, and M.M. Olmstead. Inorg. Chem. **27**, 4511 (1988).
46. M. Angoletta, P.L. Bellon, F. Demartin, and M. Sansoni. J. Organomet. Chem. **208**, C12 (1981).
47. B.E. Mann and B.F. Taylor. ^{13}C NMR data for organometallic compounds. Academic Press; London. 1981. pp. 14–15.
48. J.R. Torkelson, F.H. Antwi-Nsiah, and M. Cowie. Manuscript in preparation.
49. H. Friebolin. Basic one- and two-dimensional NMR spectroscopy. VCH Verlagsgesellschaft mbH, Weinheim. 1991. pp. 54, 284.
50. M.J. Burn, G.-Y. Kiel, F. Seils, J. Takats, and J. Washington. J. Am. Chem. Soc. **111**, 6850 (1989).
51. R. Cramer, J.B. Kline, and J.D. Roberts. J. Am. Chem. Soc. **91**, 2519 (1969).
52. (*a*) R.S. Dickson, C. Mok, and G. Pain. J. Organomet. Chem. **166**, 385 (1979); (*b*) J.J. Bonnet, R. Mathieu, and J.A. Ibers. Inorg. Chem. **19**, 2448 (1980); (*c*) N.M. boag, M. Green, and F.G.A. Stone. J. Chem. Soc. Chem. Commun. 1281 (1980); (*d*) S.A.R. Knox. J. Organomet. Chem. **400**, 255 (1990).

Steric effects of bulky phosphines on ^{95}Mo NMR shieldings

Shuquan Song and Elmer C. Alyea

Abstract: Three sets of substituted molybdenum carbonyl complexes of the type $Mo(CO)_{6-n}(PY_3)_n$ (n = 1–3) with a wide range of phosphorus ligands (Y = Ar, R, OR, NR_2, Cl, H) were synthesized and their respective ^{95}Mo NMR spectral data were collected. The steric effect of PY_3 plays an unexpectedly important role in the paramagnetic shielding term determining $\delta(^{95}Mo)$, and is even observed in the least crowded $M(CO)_5(PY_3)$ complexes. It is deduced that the steric requirement reduces the commonly accepted π-ability of phosphites by weakening the M—P bonds, making $\delta(^{95}Mo)$ positions move toward higher frequency in going from $M(CO)_5(PY_3)$ to *fac*-$M(CO)_3(PY_3)_3$. A detailed correlation analysis in the case of phosphite ligands has shown that the free cone space to accommodate a PY_3 ligand may be as low as 95° in $Mo(CO)_{6-n}(PY_3)_n$ (n = 1–3) derivatives. The fair linearity of these correlations suggests indirectly that the σ-component in phosphite bonding is relatively less important. These linear correlations of $\delta(^{95}Mo)$ against the Tolman cone angle θ provide an empirical estimation of the bulkiness of any phosphite ligand.

Key words: metal–phosphorus bonds, ^{95}Mo NMR, steric effects.

Résumé : On a synthétisé trois ensembles de complexes de molybdène carbonyle substitués du type $Mo(CO)_{6-n}(PY_3)_n$ (n = 1–3) avec une grande variété de ligands phosphores (Y = Ar, R, OR, NR_2, Cl, H) et on a recueilli leurs données spectrales respectives en RMN du ^{95}Mo. L'effet stérique du PY_3 joue un rôle important inattendu dans le terme de blindage paramagnétique déterminant $\delta(^{95}Mo)$, et on l'observe même dans les derniers complexes $M(CO)_5(PY_3)$ encombrés. On en déduit que l'encombrement stérique réduit la tendance-π communément acceptée pour les phosphites en affaiblissant la liaison M—P de telle sorte que la position de $\delta(^{95}Mo)$ se déplace vers les plus hautes fréquences en allant de $M(CO)_5(PY_3)$ vers *fac*-$M(CO)_3(PY_3)$. Une analyse détaillée de corrélation dans le cas du ligand phosphite montre que l'espace conique libre pour accommoder le ligand PY_3 peut être aussi faible que 95° dans les dérivés $Mo(CO)_{6-n}(PY_3)_n$ (n = 1–3). La linéarité assez grande de ces corrélations suggère indirectement que la composante σ dans la liaison du phosphite est relativement moins importante. Ces corrélations linéaires de $\delta(^{95}Mo)$ contre l'angle θ du cône de Tolman fournissent une estimation empirique de l'encombrement de tout ligand phosphite.

Mots clés : lien métal–phosphore, RMN du ^{95}Mo, effet stérique.

[Traduit par la rédaction]

Introduction

The importance of steric effects of trivalent phosphorus ligands on various reactivities of phosphine complexes has been well studied and reviewed several times (1) since the introduction of the cone angle concept by Tolman (1*a*). At least five different steric parameters defining the bulkiness of these important ligands were proposed previously (1*d*) and, quite recently, another steric parameter, E_r, has been developed for trivalent phosphorus and nitrogen donors by T.L. Brown using molecular mechanics methods (2). The benefits and limitations for the various steric parameters have also been considered by various researchers in their interpretations of the thermodynamic and (or) kinetic behaviour of phosphorus ligands in the formation of (1, 3), isomerization (4), *trans* effects (5), and σ/π bonding (6), in transition metal complexes. Applications of these steric parameters have mainly been qualitative due to the inherent uncertainty of each parameter and the overlapping effect of electronic components. Previous studies suggest that the steric effect exerts a significant influence on magnetic shielding of the transition metal nucleus (7), which can be measured to high precision, and therefore steric contributions to M—P bonding might be estimated more precisely from ^{95}Mo and ^{31}P NMR spectrometry if a wide range of bulky P(III) ligands were investigated. This paper focuses on evaluations of the steric component in M—P bonding by analysis of ^{95}Mo NMR shielding parameters for a wide range of $Mo(CO)_{6-n}(PY_3)_n$ (n = 1–3) derivatives.

Received February 12, 1996.

This paper is dedicated to Professor Howard Clark in recognition of his contributions to Canadian chemistry.

S. Song and E.C. Alyea.[1] Guelph–Waterloo Centre for Graduate Work in Chemistry, Guelph Campus, Department of Chemistry and Biochemistry, University of Guelph, Guelph, ON N1G 2W1, Canada.

[1] Author to whom correspondence may be addressed. Telephone: (519) 824-4120, ext. 3031. Fax: (519) 766-1499. E-mail: alyea@chembio.uoguelph.ca

Experimental

The molybdenum carbonyl complexes $Mo(CO)_{6-n}(PY_3)_n$ (n = 1–3) of trivalent phosphine and phosphite ligands were prepared according to published procedures (8*b*, 8*c*). $Mo(CO)_3CHT$ (9*a*), $Mo(CO)_4NBD$ (9*a*), and $Mo(CO)_5NMe_3$

Fig. 1. ^{95}Mo (*a*) and ^{31}P (*b*) NMR spectra for *fac*-$Mo(CO)_3(PPh_2Bz)_3$ in dichloromethane; in the ^{31}P spectrum, the ^1J(Mo–P) coupling constants, which can be clearly resolved on an enlarged scale, are consistent with the values obtained directly from the ^{95}Mo spectrum, and the peak at higher field is due to free ligand.

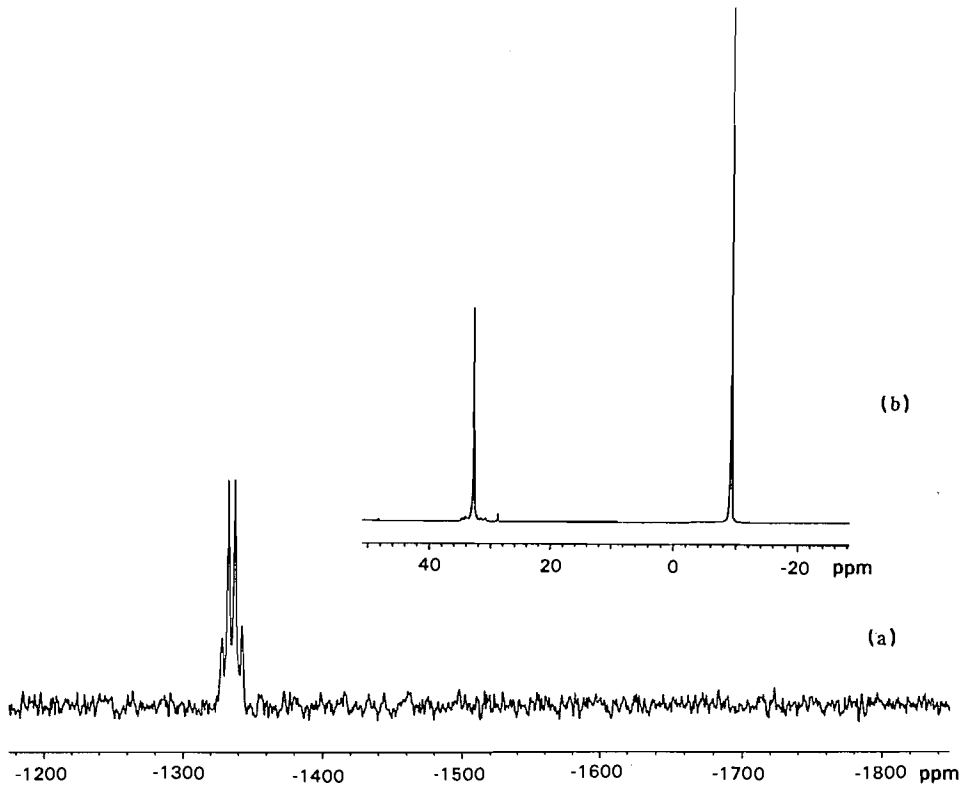

(10) or $Mo(CO)_5$(piperidine) (9*b*) were used as precursors to make *fac*-, *cis*-, and mono displaced Mo derivatives, respectively, which are listed in Table 1. Many of them are known (11), as indicated in the footnotes to the table. The phosphite complexes are usually colourless and the phosphine complexes are yellowish. In most displacement reactions of $Mo(CO)_3$CHT, $Mo(CO)_4$NBD, and $Mo(CO)_5(NMe_3)$ or $Mo(CO)_5$(piperidine) by this class of ligands, a single product was formed, easily identified by IR and ^{31}P and ^{95}Mo NMR spectrometry. Several typical spectra are presented in Figs. 1–3. In some cases of very bulky ligands, such as $P(OSiMe_3)_3$ or $P(NMe_2)_3$, either the f3 and m3 were obtained together, as shown in Fig. 4, or c2 and t2 coexisted, as illustrated in Fig. 5. The isomers were still clearly differentiated by their ^{95}Mo and ^{31}P NMR spectra, although their IR bands in the carbonyl region were overlapped. Several Mo complexes were isolated and purified: *fac*-$Mo(CO)_3[PPh_2(C{\equiv}CPh)]_3$ (yield: 53%); *fac*-$Mo(CO)_3[P(OPh)_3]_3$ (yield: 80%); *fac*-$Mo(CO)_3(ETPB)_3$ (yield: 88%); *cis*-$Mo(CO)_4(ETPB)_2$ (yield: 79%); *cis*-$Mo(CO)_4(PPh_2Bz)_2$ (yield:68%); *cis*-$Mo(CO)_4[P(OSiMe_3)_3]_2$ (yield: 23%); *cis*-$Mo(CO)_4(PPh_2Cy)_2$ (61%); $Mo(CO)_5P$(2-MeO-Ph)$_3$ (43%). However, because of their air sensitivity and prior characterization, the spectral data for most complexes in Table 1 were collected in situ under a nitrogen atmosphere without further purification and isolation. Every species was unambiguously characterized in terms of geometry by ^{95}Mo, ^{31}P, ^{13}C NMR, and IR spectroscopy (13), but only representative data (Tables 4–6) are presented in this paper.

^{31}P and ^{13}C NMR spectra were obtained on a Varian Unity 400 MHz instrument at 161.9 and 100.6 MHz, respectively, using 85% aqueous H_3PO_4 and TMS in $CDCl_3$ as external standards. ^{95}Mo NMR spectra were collected at 26.08 MHz at 10 Hz/pt resolution in 10 mm tubes, using CH_2Cl_2 (normally) as solvent and concentrations as near 0.1 M as possible; the external standard was 2 M Na_2MoO_4 in D_2O (pH 11).

Data precision for the ^{95}Mo NMR spectral results has been described in related papers (7). To briefly summarize the line width data for the present $Mo(CO)_{6-n}(PY_3)_n$ (n = 1–3) complexes, $W_{1/2}$ had the following ranges: 5–120 Hz (n = 1), 10–490 Hz (n = 2), and 5–40 Hz (n = 3). Compared to the line width for m1 complexes, $W_{1/2}$ was, on average, 2.3 times greater for c2 complexes and 0.5 lower magnitude for f3 complexes.

Results and discussion

^{95}Mo NMR spectral parameters

Tables 1 and 2 list the ^{95}Mo NMR data for $Mo(CO)_{6-n}(PY_3)_n$ for a wide range of trivalent phosphorus ligands in the order of their Tolman cone angle. Immediately, a general trend is seen, as shown graphically in Fig. 6. As the degree of displacement (DD) increases from 1 to 3, the ^{95}Mo NMR chemical shifts move dramatically to high frequency with several crossovers for DD = 3. As observed previously by ^{31}P and ^{51}V NMR for carbonyl phosphine vanadium complexes (7*d*), the greatly reduced Mo—P bonding ability as DD increases (especially

Fig. 2. ^{95}Mo NMR spectrum (*a*) and IR bands in carbonyl region (*b*) for *cis*-$Mo(CO)_4(P(OSiMe_3)_3)_2$; both are in dichloromethane.

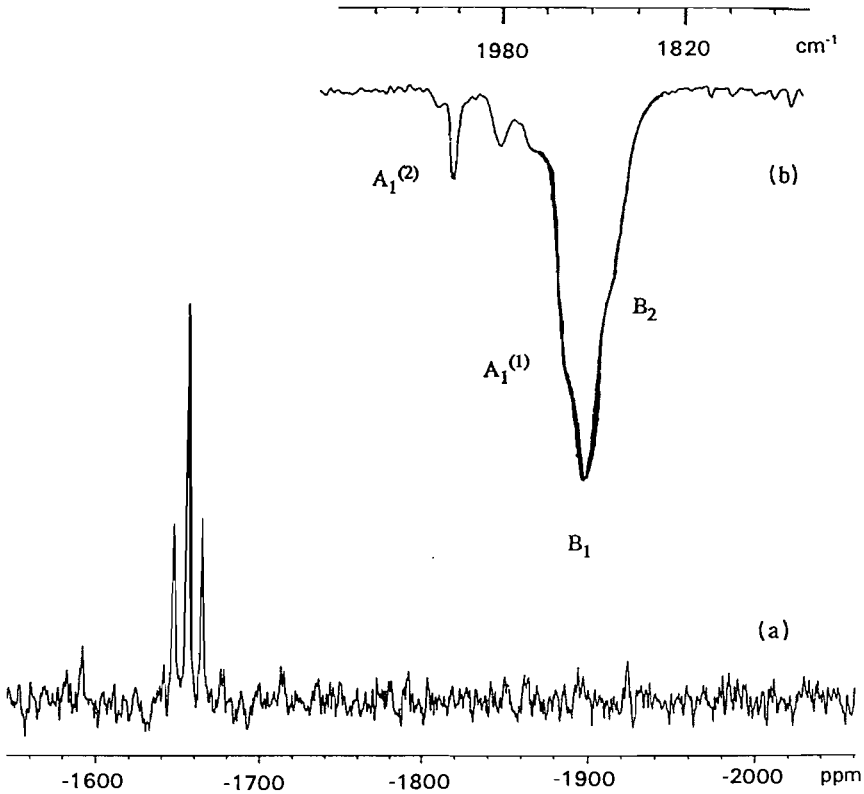

from 2 to 3) indicates that the steric component imposes a serious deshielding shift on $\delta(^{95}Mo)$, which is also the direction of weak π and weak σ effects of ligands such as chlorophenylphosphines (7*b*).

As commonly accepted (7, 8, 12, 13), ^{95}Mo NMR chemical shift trends as interpreted by the Ramsey equation ($\sigma = \sigma_d + \sigma_p$) are dominated by the paramagnetic (σ_p) term, since the diamagnetic term (σ_d) is small and constant for a similar series. Hence, factors affecting the average electronic excitation energy (ΔE) term of the σ_p expression mainly influence ^{95}Mo nuclear shielding.

We now hypothesize that there may be a quantitative expression such as eq. [1]:

$$[1] \quad \delta_M = A\,\theta + B\,\sigma + C\,\pi + D$$

which describes the multi-parameter dependencies of $\delta(^{95}Mo)$ (or screening constant, σ_p), in which θ, σ, and π are measures of steric, σ, and π components, respectively. An attempt to estimate the steric component in eq. [1] is the goal of this paper. This would form a significant basis for the future separation of σ and π contributions for the phosphorus ligands. Our detailed analysis of the magnetic shielding in the molybdenum complexes for a few selected phosphorus ligands is presented in the following order:

(*a*) Strong π-ligands: PF_3, ETPB, $P(OMe)_3$, and $P(OPh)_3$

(*b*) Strong σ- and (or) moderate π-ligands: PEt_3, $P(n\text{-}Bu)_3$, and PMe_3,

(*c*) Extra bulky ligands: $P(OSiMe_3)_3$, PCy_3, $P(2\text{-}Me\text{-}Ph)_3$, and $P(2,6\text{-}Me_2\text{-}OPh)_3$

(*a*) Strong π-ligands: PF_3(104°), ETPB(101°), $P(OMe)_3$(107°), and $P(OPh)_3$(128°)

These four ligands are well known as good π-acceptors, based on the high stretching frequencies of *trans* CO's in transition metal complexes (6, 13), shorter M—P bond distances (14), high stability of the M—P link (15, 16), high reactivity toward displacement of CO in metal carbonyl moieties (1, 3, 4), and other electrochemical (12*f*, 17) and spectroscopic studies (6, 8*a*, 18). In agreement with these observations and the expectation that the ΔE term in the σ_p term is enhanced by good π-acceptor ability, the phosphites indeed make the ^{95}Mo nuclei in their molybdenum carbonyl derivatives quite shielded compared with most other ligands, whether in m1 or f3 derivatives (Fig. 7). The folded lines for the three phosphites in Fig. 7 exhibit, in going from m1 to f3 geometry, the deshielding contributions of the steric component, already discussed in previous papers (7) but further reinforced below. However, it cannot be easily interpreted at this point that in its f3 complex the less bulky ETPB ($\theta = 101°$) brings σ_p to high frequency by 55 ppm with respect to PF_3 ($\theta = 104°$). Notably, the ^{95}Mo resonance for the m1–$P(OPh)_3$ complex occurs 45 ppm at high frequency compared to that for m1–$P(OMe)_3$ in this least bulky geometry and this relationship changes little in going to c2 and f3 geometries. This undoubtedly reflects the weaker bonding ability of $P(OPh)_3$ compared to $P(OMe)_3$ (and perhaps other small alkylphosphites). It will be shown that an important interligand repulsion exists even in $Mo(CO)_5L$ derivatives, usually considered to be steric-interaction-free structures. If the extra deshielding occurring in m1–$P(OPh)_3$ were due to steric factors, then the two δ/n folded lines for

Fig. 3. ^{95}Mo NMR spectrum (bottom) and IR carbonyl stretching bands (top) for $Mo(CO)_5(P(2\text{-}MeO\text{-}Ph)_3)$; both are in dichloromethane.

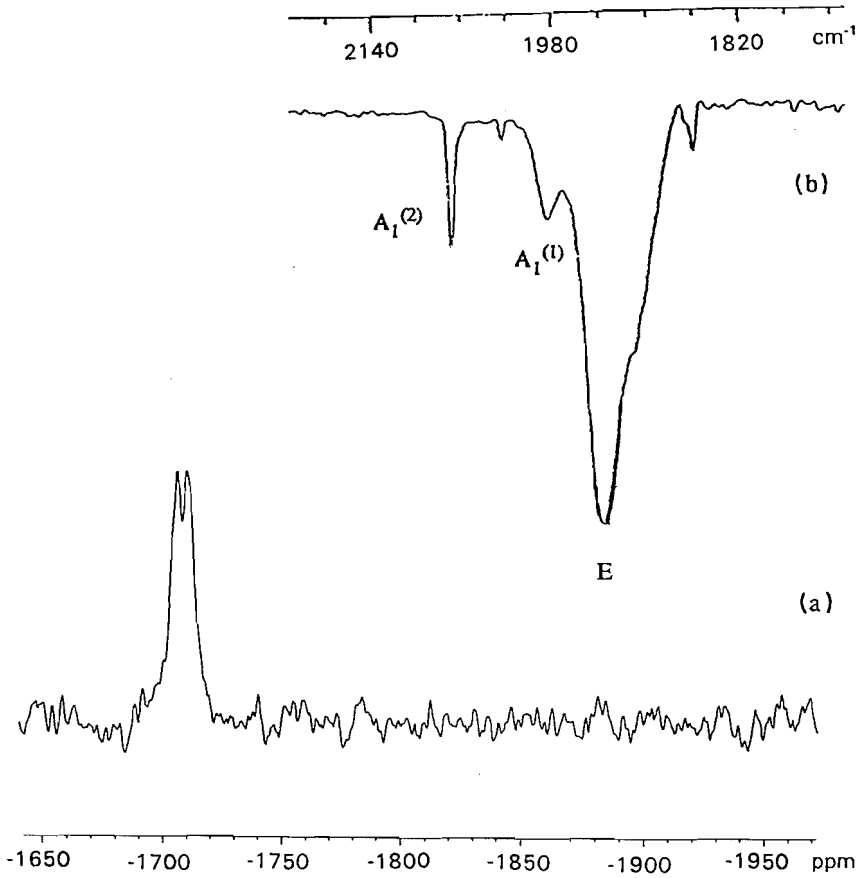

Fig. 4. The ^{95}Mo (bottom) and ^{31}P (top) NMR spectra recorded in dichloromethane in situ from an attempt to produce *fac*-$Mo(CO)_3(P(OSiMe_3)_3)_3$ using $Mo(CO)_3CHT$; the facial isomer could not be isolated, and only a mixture of *mer*-3 and *fac*-3 was obtained. The ^{31}P NMR spectrum unambiguously indicates the formation of the *fac*-3 complex; the stronger signal is due to free ligand and the singlet with six ^{95}Mo satellites is due to the three phosphorus ligands in the *fac*-3 complex. The ^{95}Mo resonances for *fac*-3 are obscured by those for the *mer*-3 isomer.

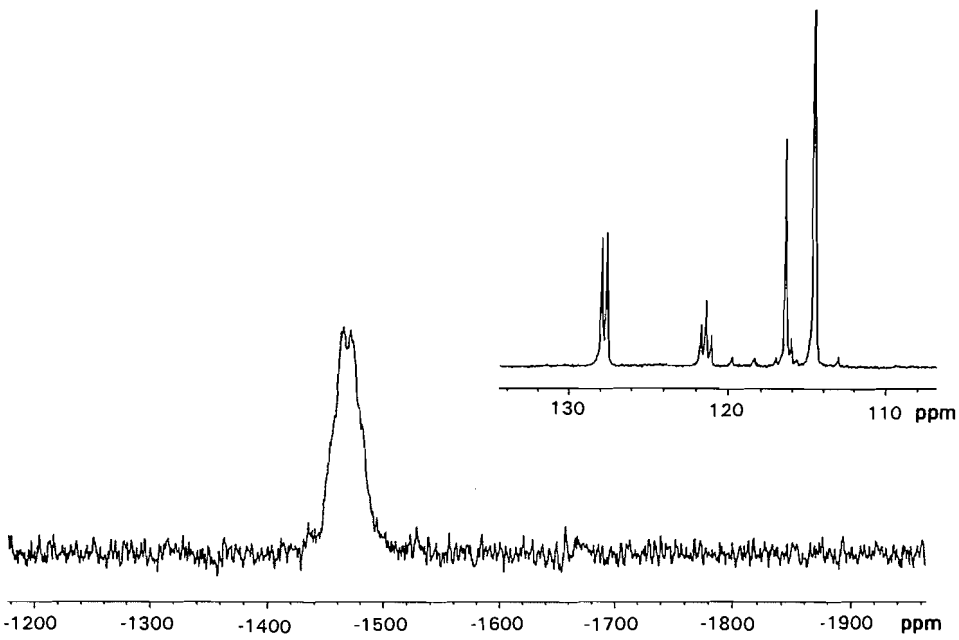

Table 1. ^{95}Mo NMR chemical shifts for molybdenum complexes of various P(III) ligands, $Mo(CO)_{6-n}(PY_3)_n$ (n = 1, 2, and 3) (in ppm).[a]

No.	Ligands	θ[b] (°)	δ(C_{4v})[c] (n = 1)	δ(C_{2v}) (n = 2)	δ(C_{3v}) (n = 3)
1	$P(mes)_3$	212	NR[d]	NR	NR
2	$P(2\text{-tol})_3$	194	NR	NR	NR
3	$P(O\text{-}2,6\text{-}Me_2\text{-}Ph)_3$	190	−1747[f]	NR	NR
4	$P(2\text{-MeO-Ph})_3$	(185)[e]	−1709	NR	NR
5	$P(t\text{-Bu})_3$	182	−1708	NR	NR
6	$P(O\text{-}t\text{-Bu})_3$	172	(−1716)	−1626	NR
7	$P(O\text{-SiMe}_3)_3$	(≤172)	−1790	−1657	−1468
8	$P(Cy)_3$	170	−1825[g]	NR[h]	NR
9	$P(Bz)_3$	165	−1804	−1645[i]	NR
10	$P(i\text{-Pr})_3$	160	Fail	−1684	NR
11	$P(NMe_2)_3$	157	−1804[a]	−1619	−1484[j]
12	$PCyPh_2$	153	—	Insol[k]	NR
13	$PBzPh_2$	152	(−1786)	−1614	−1336
14	$P(4\text{-MeO-Ph})_3$	145	−1744[l]	−1560[l]	−1265[l]
15	PPh_3	145	−1742[l]	−1558[l]	−1265[l]
16	$P(O\text{-}2\text{-tol})_3$	141	−1812	−1722	−1572
17	$PPh_2(CH{=}CH_2)$	(140)	(−1780)	−1632	−1428
18	PPh_2Et	140	−1789[m]	−1657[a,n]	−1414[o]
19	PPh_2Cl	138	−1702[a]	−1522[a,p]	−1319
20	PPh_2Me	136	−1772[m]	−1637[a]	−1427[a,q]
21	5-PhDBP[r]	(132)	−1795[s]	−1714[s]	−1494[s]
22	$PPh_2(C{\equiv}CPh)$	(132)	−1736	−1601	−1468
23	$PPh_2(OMe)$	132	−1791[a,t]	−1670[a,u]	−1454[v]
24	PEt_3	132	−1856[a]	−1764[a,w]	−1558
25	$P(n\text{-Bu})_3$	132	−1842[a]	−1743[a]	−1521[a]
26	$P(CH_2CH_2CN)_3$	132	−1829[m]	−1737[x]	Insol
27	PCl_2Ph	131	−1617	−1371	−1124
28	PBr_3	131	−1396	−977	NR(−500)
29	$P(O\text{-}i\text{-Pr})_3$	130	−1835[a]	−1762[a]	−1728
30	$P(OPh)_3$	128	−1819[a]	−1752[y]	−1673[z]
31	$PHPh_2$	128	—	−1726	−1639
32	PCl_3	124	−1523	−1206	−910
33	$PPhMe_2$	122	−1788[a]	−1672	−1486[z]
34	$PPh(OMe)_2$	120	−1816[a]	−1740	−1611[z,aa]
35	PMe_3	118	−1818	−1722	−1586
36	$P(OCH_2CF_3)_3$	(110)	−1837	−1803	−1743
37	$P(OCH_2CH_2Cl)_3$	110	−1844	−1807	−1734
38	$P(OEt)_3$	109	−1854[a]	−1807[a]	−1721[a,bb]
39	$P(OMe)_3$	107	−1864[a]	−1828[a]	−1756[a]
40	PH_2Ph	106	—	−1771	−1703
41	ETPB	101	−1859[a,cc]	−1847	−1805
42	PF_3	104	−1860[dd]	−1860[dd]	−1860[dd]
43	PH_3	87	—	—	(−1755)[ee]
44	CO	95[ff]	−1857.0	−1857.0	−1857.0

[a]In this table, 70% of δ(^{95}Mo) values were recorded in this work, including several remeasurements; others are taken from ref. 8*a* unless specifically noted. For the remeasurements, the literature values have always been taken instead of the values recorded here unless the former have been proved to be incorrect.

[b]Tolman cone angles from ref. 1*a*.

[c]C_{4v}, C_{2v}, and C_{3v} represent the ideal geometries for penta-, *cis*-L_2-tetra-, and *fac*-L_3-tri-carbonyl complexes.

[d]NR denotes no reaction was observed according to ^{31}P and ^{95}Mo NMR; or fast decomposition occurred even if the reaction took place, such as PCy_3 substitution from $Mo(CO)_4$NBD or $Mo(CO)_3$CHT precursors.

[e]The values in parentheses are estimated because no literature data were available.

[f]1,2-Dichloroethane has to be used for refluxing due to the low reaction rate at 40° in CH_2Cl_2.

[g]Taken from ref. 12*b*; a same value of −1825 ppm with ^1J(M–P) = 129 Hz was recorded here.

Table 1 (*concluded*).

[h]A value of −1765 ppm was reported for *trans*-$Mo(CO)_4[P(Cy)_3]_2$ in ref. 12*c*.

[i]Another broader unresolved resonance at −1706 ppm ($W_{1/2}$ = 7810 Hz) was observed; so the assignment might be either signal.

[j]This value is taken for *mer*-3 (see text) and is not used in the correlation analyses.

[k]*cis*-$Mo(CO)_4[P(Ph)_2Cy]_2$ is insoluble in the organic solvents tried.

[l]See ref. 7*a* for $P(X\text{-}Ph)_3$ derivatives.

[m]Taken from ref. 12*b*.

[n]−1655 ppm with ^1J(M–P) = 139 Hz was observed here.

[o]Taken from ref. 12*d*; −1412 ppm with ^1J(M–P) = 125 Hz and $W_{1/2}$ = 14 Hz was recorded here.

[p]The same value of −1522 ppm with ^1J(M–P) = 161 Hz was recorded here.

[q]The same value of −1427 ppm with ^1J(M–P) = 128 Hz and $W_{1/2}$ = 15 Hz was measured here.

[r]5-PhDBP = 5-phenyldibenzophosphole.

[s]Taken from ref. 12*e*.

[t]The same value of −1791 ppm with ^1J(M–P) = 163 Hz was obtained here.

[u]Two quite different values of −1677 (^1J(M–P) = 161 Hz, $W_{1/2}$ = 30 Hz) and −1707 ppm (^1J(M–P) = 153 Hz, $W_{1/2}$ = 40 Hz) were reported in ref. 8*a*. The listed value of −1670 ppm with ^1J(M–P) = 142 Hz was recorded here.

[v]Taken from ref. 12*f*; the same value of −1456 ppm with ^1J(M–P) = 142 Hz was recorded here.

[w]Another same value of −1765 ppm with ^1J(M–P) = 129 Hz and $W_{1/2}$ = 26 Hz was reported in ref. 12*d*.

[x]Taken from ref. 12*c*.

[y]The same value of −1751 ppm with ^1J(M–P) = 229 Hz and $W_{1/2}$ = 50 Hz was recorded here. Reported ^1J(M–P) of 250 Hz in ref. 12*b* is too high (see text).

[z]Taken from ref. 12*f*.

[aa]The same value of −1610 ppm with ^1J(M–P) = 184 Hz and $W_{1/2}$ = 18 Hz was measured here.

[bb]The same value of −1721 ppm was recorded here.

[cc]The same value of −1860 ppm with ^1J(M–P) = 224 Hz and $W_{1/2}$ = 8 Hz was recorded here.

[dd]Taken from ref. 12*g* (see also ref. 7*c*).

[ee]Estimated value by extrapolation.

[ff]95° was proposed by refs. 1*a* and 12*h*.

$P(OPh)_3$ and $P(OMe)_3$ should be more diverging (splayed) rather than parallel because the greater bulk of $P(OPh)_3$ (128°) relative to $P(OMe)_3$ (107°) should cause a large separation between the values for the most congested f3 derivatives. Thus, the weaker bonding ability of $P(OPh)_3$ may not be determined solely by the steric effect. On the other hand, the $\delta(^{95}Mo)$ (−1728 ppm) for f3–$P(O\text{-}i\text{-}Pr)_3$ (note that $P(O\text{-}i\text{-}Pr)_3$ (130°) has a similar ligand cone angle to $P(OPh)_3$) appears at 55 ppm lower frequency from the value for f3–$P(OPh)_3$ and only 28 ppm higher frequency from the f3-$P(OMe)_3$ value. This suggests that if the steric parameters for $P(OPh)_3$ and $P(O\text{-}i\text{-}Pr)_3$ were not underestimated and overestimated, respectively, the weaker bonding ability or the extra deshielding effect of $P(OPh)_3$ could only be attributed to a weaker σ component ($pK_a = -2.0$). It must be pointed out that there have already been many observations indicating the weak bonding ability (4, 16, 19) of the $P(OPh)_3$ ligand even though the short Cr—P distance in $Cr(CO)_5(P(OPh)_3)$ is usually interpreted in terms of strong π-acceptor character (20) of this common ligand. It was also noted experimentally in this work that the substitution of pyridines from *fac*-$Mo(CO)_3(Py)_3$ by $P(OPh)_3$ is much more difficult than by $P(OMe)_3$ or ETPB.

The IR stretching frequencies for *trans* carbonyls of phosphite complexes are approximately the same, within experimental error, for each of the three geometries (see Table 3) except that the f3–$P(OPh)_3$ complex does have higher ν_{co} (and force constant) values. The observation of this anomalous effect for $P(OPh)_3$ is in agreement with the previous suggestion that the stretching frequency is more likely reflecting the weak σ component (7). Only the A_1(highest) mode is used here because of a higher precision (sharper line), the lack of ambiguity in its assignment, and its relation to (covering) all force constants. Taking into account the recording error of ν_{co}'s and the ambiguous assignments of the IR bands, one can see again that IR parameters are not as reliable as NMR chemical shift data for evaluation of ligand effects. Although most common phosphites are thought to be strong π-ligands, ^{95}Mo NMR spectrometry shows, consistent with the weaker M—$P(OPh)_3$ bonding (4, 16, 19), that $P(OPh)_3$ has some special electronic property different from other phosphites. Unfortunately, there previously was no structural information on a higher displaced phosphite–molybdenum compound available in the literature. The crystal structures of *cis*-$Mo(CO)_4(P(OPh)_3)_2$ and *fac*-$Mo(CO)_3(P(OPh)_3)_3$ were recently determined in our laboratory (22). The Mo—P bond distances (both are 2.44 Å) are much shorter than most known Mo—P bonds (ca. 2.54 Å). As concluded for M—PCl_3 bonding (7*c*), the short distance may be partially caused by the weak σ ability of $P(OPh)_3$, without the need to invoke strong π bonding to rationalize the bond shortening. The P-Mo-P bond angles are 90° in both cases, though the range is 82–94° in the *fac* complex, indicating the more significant steric distortion in the latter complex. Many authors (4*d–f*, 16*d*) also observed that the reactivity of $P(OPh)_3$ (θ = 128°) toward transition metals is even lower than that of PPh_3 (θ = 145°) even though the latter is bulkier and supposedly a weaker π-acceptor. For example, the rate of substitution for diamine (N–N) from *cis*-$W(CO)_4$(N–N) by $P(OPh)_3$ is lower than by PPh_3, and much lower than by ETPB

Table 2. ^1J(Mo–P) coupling constants for molybdenum complexes of various P(III) ligands, $Mo(CO)_{6-n}L_n$ (n = 1, 2 and 3) (in Hz).[a]

No.	Ligands	θ (°)	$^1J(C_{4v})$ (n = 1)	$^1J(C_{2v})$ (n = 2)	$^1J(C_{3v})$ (n = 3)
1	$P(mes)_3$	212	NR	NR	NR
2	$P(2\text{-tol})_3$	194	NR	NR	NR
3	$P(O\text{-}2,6\text{-}Me_2\text{-}Ph)_3$	190	227	NR	
4	$P(2\text{-MeO-Ph})_3$	(185)	107	NR	NR
5	$P(t\text{-Bu})_3$	182	122	NR	NR
6	$P(O\text{-}t\text{-Bu})_3$	172	215	216	NR
7	$P(O\text{-}SiMe_3)_3$	(≤172)		222	228[b]
8	$P(Cy)_3$	170	129	NR	NR
9	$P(Bz)_3$	165	138	125(PR)[c]	NR
10	$P(i\text{-Pr})_3$	160	F	122	NR
11	$P(NMe_2)_3$	157	173	167	U
12	$PCyPh_2$	153		Insol	NR
13	$PBzPh_2$	152		125(PR)	122
14	$P(4\text{-MeO-Ph})_3$	145	135	U[d]	119
15	PPh_3	145	137	U	120
16	$P(O\text{-}2\text{-tol})_3$	141	234	232	242(PR)
17	$PPh_2(CH{=}CH_2)$	(140)	—	140(PR)	125
18	PPh_2Et	140	137	131	124
19	PPh_2Cl	138	165	166	155
20	PPh_2Me	136	135	133	126
21	5-PhDBP	(132)	132	134	126
22	$PPh_2(C{\equiv}CPh)$	(132)	137	128(PR)	135
23	$PPh_2(OMe)$	132	156	142[e]	142[e]
24	PEt_3	132	131	125	125
25	$P(n\text{-Bu})_3$	132	133	124	124
26	$P(CH_2CH_2CN)_3$	132	140	128	insol.
27	PCl_2Ph	131	197	194	198
28	PBr_3	131	242	235	NR
29	$P(O\text{-}i\text{-Pr})_3$	130	215	209	211
30	$P(OPh)_3$	128	237	229[f]	239
31	$PHPh_2$	128	—	127	126
32	PCl_3	124	250	250	251
33	$PPhMe_2$	122	131	130	127
34	$PPh(OMe)_2$	120	183	184	185
35	PMe_3	118	130	129	127
36	$P(OCH_2CF_3)_3$	(110)	235	227	232
37	$P(OCH_2CH_2Cl)_3$	110	213	221	215
38	$P(OEt)_3$	109	214	213	210
39	$P(OMe)_3$	107	218	215	214
40	PH_2Ph	106	—	120	123
41	ETPB	101	227	225	226
42	PF_3	104	284	281	290
43	PH_3	87			
44	CO	95			

[a]The ^1J(M–P) values have the same reference sources as chemical shifts in Table 1, unless otherwise designated.

[b] ^1J(M–P) = 228 Hz was obtained from ^{95}Mo satellite lines in the ^{31}P NMR spectrum because the Mo-95 resonance was overlapped by a dominant and poorly resolved quartet for the *mer* isomer.

[c]PR = "poorly resolved," which means there is probably a larger error in these values.

[d]U = "unresolved."

[e] ^1J(M–P) of 142 Hz for both c2 and f3 derivatives of this ligand was recorded in this work, while two values of 161 Hz (ref. 12*i*) and 153 Hz (ref. 12*j*) have been reported.

[f] ^1J(M–P) of 229 Hz for c2 derivative was recorded in this work.

Fig. 5. ^{95}Mo NMR spectrum for molybdenum complexes of the $P(NMe_2)_3$ ligand recorded in dichloromethane. The sample is from an attempt to make the *fac*-$Mo(CO)_3L_3$ derivative: (*a*) *trans*-$Mo(CO)_4L_2$; (*b*) *cis*-$Mo(CO)_4L_2$; (*c*) *mer*-$Mo(CO)_3L_3$.

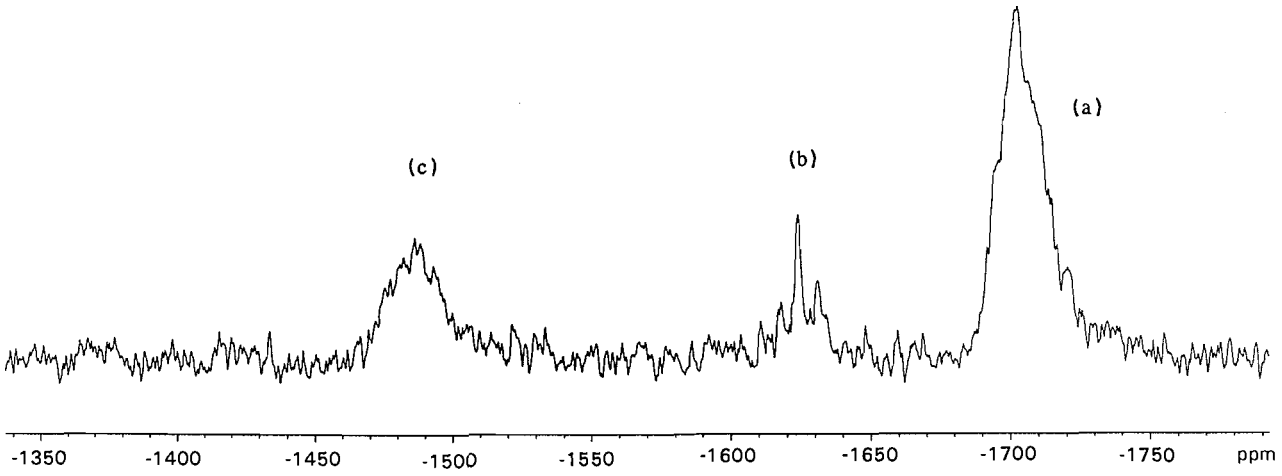

Fig. 6. An overview for the influence of ligand size on ^{95}Mo shielding with increasing degree of displacement (*n*). Py represents pyridine.

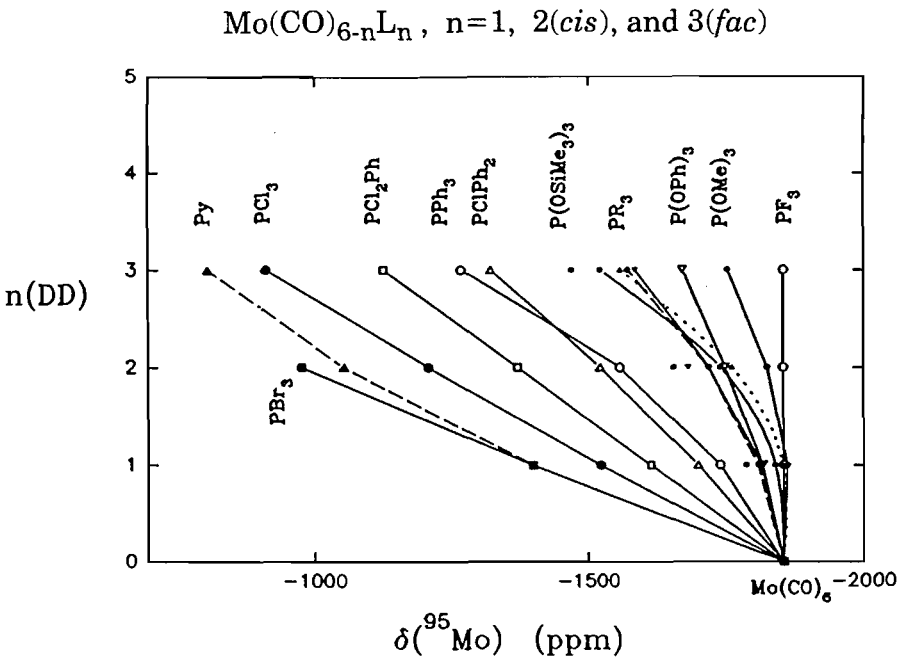

and $P(O\text{-}i\text{-}Pr)_3$. Thus, the weak σ character of $P(OPh)_3$ might play a dominant role in bonding (13). Although the ^{31}P NMR chemical shift is less sensitive than the corresponding ^{95}Mo shift to steric interaction (7*c*, 13) (see the text below), the smaller $\Delta\delta(^{31}P)$ value (16.6 ppm) for f3–$P(OPh)_3$ than that for c2–$P(OPh)_3$ (24.1 ppm), opposite to the trend of consistently increasing $\Delta\delta(^{31}P)$ values from m1 to f3 for the other three smaller ligands, indicates a detectable steric effect, at least in solution, active in the f3–$P(OPh)_3$ complex.

PF_3 gives rise to almost the same $\delta(^{95}Mo)$ value in $Mo(CO)_5L$ as ETPB and $P(OMe)_3$, but the CO stretching frequency for its m1 complex is 20 cm^{-1} higher than those for the other two analogues. Such a big difference is most likely due to a combination of the remarkably weak σ ability and strong π character of PF_3. As analyzed before (6), both strong π and weak σ character of a *trans* ligand enhance the infrared parameter of carbonyls. It is worth noting that the magnitude of ^1J(Mo—P) (where $^1J_{M-P}$ is normally assumed to be only

Table 3. Spectroscopic properties for Mo complexes of putatively strong π-acceptor ligands.[a]

Parameters	Structure[b]	Ligands			
		PF_3	ETPB	$P(OMe)_3$	$P(OPh)_3$
$\nu_{co}(A1)$	m1	2104	2084	2080	2083
(cm^{-1})	c2	2087	2044	2037	2046
	f3	2065	1988	1976	1994
k_1	m1	16.57	15.76	15.88	15.95
(mdyn/Å)	c2	16.23	15.42	15.25	15.45
	f3	16.62	15.05	14.74	15.16
k_2	m1	16.53	16.15	16.02	16.17
(mdyn/Å)	c2	16.82	15.76	15.67	15.90
$\Delta\delta(^{31}P)$	m1	50	44.4	21	26
(ppm)	c2	51.5	46.3	23	24.1
	f3	53.5	47.5	25.2	16.6
^1J(Mo–P)	m1	284	227	218	237
(Hz)	c2	281	225	215	229
	f3	290	226	214	239

[a]See refs. 13 and 21 for the sources of IR and $\Delta\delta(^{31}P)$ NMR information, respectively.
[b]m1 is mono, c2 is *cis*, f3 is *fac* isomer.

related to the *s* character) (6*a*, 7*b*) for different phosphorus ligands (23), is roughly correlated with that of ν_{co}, implying that these two parameters are somewhat similar in their correlations with the σ component.

(*b*) Strong σ- and (or) moderate π-ligands: PEt_3 (132°), $P(n\text{-}Bu)_3$ (132°), and PMe_3 (118°)

A noteworthy feature in Fig. 7 is the parallel $\delta(^{95}Mo)/n$ lines between PEt_3 and $P(n\text{-}Bu)_3$, and the overlapping lines between PMe_3 and $P(O\text{-}o\text{-}Tol)_3$. The dramatic shift of $\delta(^{95}Mo)$ for PEt_3 and $P(n\text{-}Bu)_3$ complexes to high frequency with higher DD starts even with their c2 derivatives, indicating that they might be bulkier than Tolman's estimation. There is no argument about the strong σ-donor ability of these two phosphines; probably they are the strongest ones among trivalent phosphorus ligands in complexes of octahedral geometry. (The stronger σ-donor ability of other extra bulky ligands such as $P(t\text{-}Bu)_3$ (pK_a = 11.4) and P(2,4,6-trimethoxy-Ph)$_3$ (pK_a = 11.2) (12*a*, 24) would only be exerted in much less sterically hindered situations.) It must be kept in mind, however, that strong electronic donation will always lead to magnetic shielding on the central metal nucleus through enhancement of LFSE (ΔE_σ) and expansion of *d* electrons. It is not yet clear at this point why $\delta(^{95}Mo)$ for m1–PEt_3 or m1–$P(n\text{-}Bu)_3$ occur on the shielding side by 38 ppm and 24 ppm, respectively, relative to m1–PMe_3, in spite of their similar pK_a values (8.69 and 8.43; 8.65 for PMe_3) and smaller cone angle for PMe_3. This anomaly might have its origin in the low proton affinity (PA) of PMe_3 in the gas phase (25). In other words, the high pK_a value of PMe_3 in aqueous solution may be overestimated due to solvation effects. If the σ ability of PMe_3 is truly lower than PPh_3, as argued by gas phase PA or gas phase IP, however, a great number of experimental observations such as stable M—PMe_3 bond strengths (16) are not easily explained. An answer to this anomaly is more likely related to the π ability of PMe_3 (6, 13, 26). The markedly high frequency shift of $\delta(^{95}Mo)$ for the f3 and c2 derivatives of PEt_3 and PBu_3 ligands can be attributed only to the steric interaction. Some researchers have estimated the cone angle of these two donors to be 142° (4*c*), 10° larger than the 132° originally calculated by Tolman (1*a*), based on their observation that the *trans*:*cis* ratio in the formation of $W(CO)_4L_2$ is much higher than expected for L = $P(n\text{-}Bu)_3$ or PEt_3. In the crystal structures of *cis*-$Mo(CO)_4L_2$ (L = PMe_3, PEt_3 and $P(n\text{-}Bu)_3$) determined in the early 1980s by F.A. Cotton et al. (27*a*), the M—P bond distances are 2.522(1), 2.544(4), and 2.552(8) Å, respectively; P-Mo-P bond angles are 97.54(4)°, 100.27(3)°, and 99.29(4)°, respectively. The differences have been ascribed to steric interactions. More notable is the conformation of PEt_3, and $P(n\text{-}Bu)_3$ in these complexes: within the same complex, the three β carbons of one phosphine are opened further along the P—C_α bonds while the three β carbons of the other phosphine tend to be closer. The smaller average C_α-P-C_α angle for PMe_3 is accounted for by its smaller bulk relative to those for PEt_3 and PBu_3. Meanwhile, the three β carbons of $P(CH_2CH_2CN)_3$ in $Mo(CO)_5L$ are opened (27*b*). This might mean that the "open" conformation is more energetically stable in the two free PEt_3 and $P(n\text{-}Bu)_3$ ligands and the closeness in highly displaced derivatives is the consequence of steric congestion. In fact, the anomalous steric effects of PEt_3 and PBu_3 have been noted in many other related studies (4*a*, 17*g*, 28). This steric feature of PBu_3 may have led to its initial designation by QALE (Quantitative Analysis of Ligand Effects) as a "π donor" (17*a*). Attempts to obtain crystals suitable for X-ray analysis for *fac*-

Fig. 7. A locally enlarged picture for the influence of ligand size on ^{95}Mo shielding with increasing degree of displacement (n).

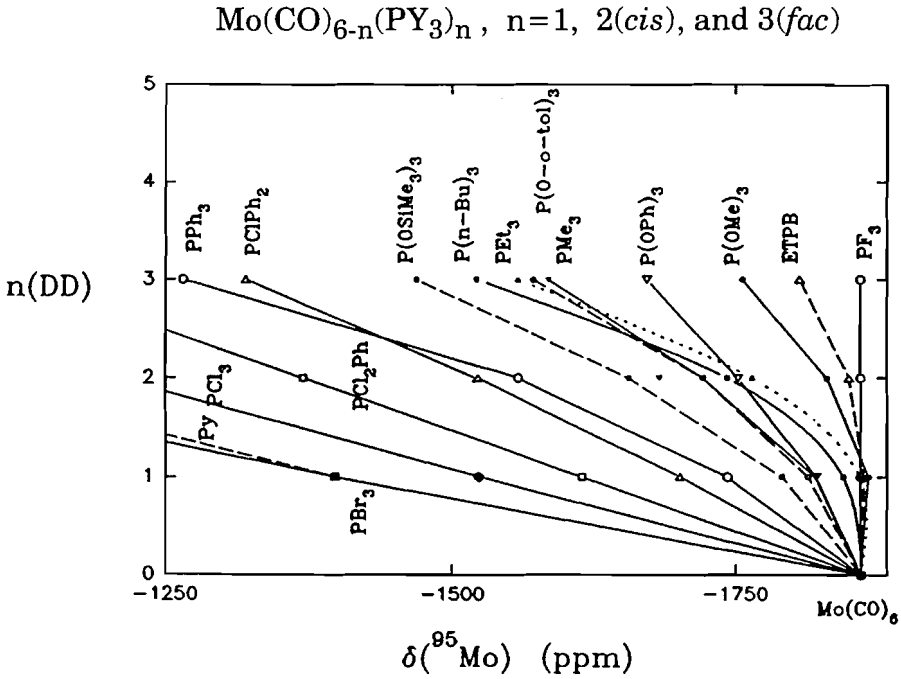

$Mo(CO)_3(PR_3)_3$ of any of the three trialkylphosphines are still underway. It can be anticipated that the much more strained structural features, e.g., longer Mo—P bond distance, smaller C_α-P-C_α angles, and compressed β carbon orientations, or much lower Mo—P bond strengths, will be found more likely in *fac*-PEt_3 and *fac*-P(*n*-Bu)$_3$ complexes than in the *fac*-PMe_3 analogue. Fortunately, the molecular structure for *fac*-$Cr(CO)_3(PEt_3)_3$ has been reported (29). The longer Cr—P bond distance (2.429(8) Å) compared to other known Cr—P lengths suggests a weakening of the Cr—P bond due to steric interactions between the adjacent PEt_3 ligands. The shorter Cr—C_{trans} bond (1.829(8) Å) and longer O—C_{trans} bond can be associated with strong d_π–π^*(CO) back-donation. It is noted that the authors suggested that PEt_3 behaves essentially as a σ-donor ligand, with little or no π-acceptor capacity. The average P-Cr-P angle of 95.77(5)° is smaller than the P-Mo-P angle of 97.54(5)° in *cis*-$Mo(CO)_4(PMe_3)_2$ and much smaller than the P-Mo-P angle of 100.27(5)° in *cis*-$Mo(CO)_4(PEt_3)_2$ (12*h*). In addition to the smaller size of Cr relative to the Mo atom, this may also suggest that in f3 geometry a cone space of 180° (vide infra) can only accommodate three ligands having ca. 95° cone angle without steric interaction. The steric repulsion among nine alkyl groups forces their reorientation toward the three CO's, which, on the other hand, resist deformation because of three strong M—CO bonds.

The ν_{co} values for the three alkylphosphine derivatives in m1, c2, and f3 geometries are the same within experimental error (see Table 4). For both PEt_3 and P(*n*-Bu)$_3$ ligands, however, $\Delta\delta(^{31}P)$ and ^1J(Mo–P) values decrease greatly in the c2 and f3 derivatives. In contrast, only a small change occurs for the f3 geometry in $\Delta\delta(^{31}P)$, with a slight reduction in ^1J(Mo–P), for L = PMe_3. These decreases are most likely related, at least partly, to the greater steric bulk of the former two ligands (also discussed in refs. 7*a*–*c*, 13).

The bulky phosphite P(O-*o*-Tol)$_3$ (141°) and small PMe_3 (118°) ligands exhibit almost identical overall ^{95}Mo shielding patterns (−1818 vs. −1812 for m1, −1722 vs. −1722 for c2, and −1586 vs. −1572 for f3) despite a difference of 23° in their cone angles. Phosphite ligands are usually thought to be strong π-acceptors and the donor:acceptor ratio is much lower than for trimethylphosphine, which is commonly thought to be a strong σ-donor. The π ability of PMe_3 is still being debated (26). Why are these two ligands so similar in ^{95}Mo shielding? First, the increased $\Delta\delta(^{95}Mo)$ values between P(O-*o*-Tol)$_3$ and $P(OPh)_3$ from m1 to f3 (7 ppm, 30 ppm, and 101 ppm) can be attributed unambiguously to steric factors in the high DD derivatives for the former (see Fig. 7). Also, the consistently greater deshielding behaviour of $P(OPh)_3$ in all the three geometries (m1, c2, and f3) compared to $P(OMe)_3$ and P(O-i-Pr)$_3$ has been attributed to the weaker σ ability of $P(OPh)_3$ (see above). Thus, the greater ^{95}Mo shielding observed for $P(OPh)_3$ than for PMe_3 might be ascribed to a better π ability for $P(OPh)_3$. But as a strong-and-small σ donor, as well as a possible modest π-acceptor, PMe_3 ligand might not have an up to 87 ppm greater deshielding effect compared with bulkier $P(OPh)_3$ especially in the most congested f3 derivatives. If the π ability of $P(OPh)_3$ is considered to be the dominant factor, then the differences in m1 geometry should also be large and comparable to those for c2 or f3 geometries. Therefore, the anomalous deshielding behaviour of PMe_3 and the similarity of PMe_3 to P(O-*o*-Tol)$_3$ are more likely caused by two factors, i.e., either a practically larger cone angle (ca.125°–130°) or a weaker π character for PMe_3. Certainly, the practical π ability of P(O-*o*-Tol)$_3$ is smaller than that of $P(OPh)_3$, due to steric hindrance.

It is noted again that no differences are observed in ν_{co} and force constant values for the above three alkylphosphine complexes in each geometry, as pointed out earlier (Table

Table 4. Spectroscopic properties for Mo complexes of $P(alkyl)_3$ ligands.[a]

Parameters	Structures	Ligands			
		PEt_3	PBu_3	PMe_3	$P(O\text{-}o\text{-}Tol)_3$
$\nu_{co}(A_1)$	m1	2069	2070	2071	
(cm^{-1})	c2	2016	2015	2016	
	f3	1926	1922	1931	1984
k_1	m1	15.48	15.47	15.61	
(mdyn/Å)	c2	14.86	14.63	14.56	
	f3	13.91	13.85	14.04	15.06
k_2	m1	15.87	15.81	15.86	
(mdyn/Å)	c2	15.24	15.24	15.27	
$\Delta\delta(^{31}P)$	m1	39	44.5	43.7	20.5
(pm)	c2	32	41.2	46.5	15.4
	f3	28.2	34.2	44.5	10.8
^1J(Mo–P)	m1	131	133	130	234
(Hz)	c2	125	124	129	232
	f3	125	124	127	242

[a]See refs. 13 and 21 for the sources of IR and $\Delta\delta(^{31}P)$ NMR information, respectively.

4). Moreover, ν_{co} and k values for the $P(O\text{-}o\text{-}Tol)_3$ complexes are remarkably greater than those for the alkylphosphine analogues, indicating the sensitive dependence of CO IR parameters on the σ component of the P(III) ligands.

(*c*) Extra bulky ligands ($\theta > 145°$)

As seen in the experimental section and the data in Tables 1–3, the bulkier the ligand, the more difficult is the multiple displacement, and the more the central molybdenum nucleus is deshielded. Fig. 8 presents many $\delta(^{95}Mo)/n$ plots for Mo complexes of extra bulky ligands. A significant deshielding trend, even in m1 derivatives, can be seen relative to the corresponding less bulky analogues (see Figs. 6 and 7). A dramatic shifting of $\delta(^{95}Mo)$ toward higher frequency with increased degree of displacement, n (such as for f3–PPh_2Bz (152°) and f3-$P(OSiMe_3)_3$ (172°)), is observed. Most f3 complexes of extra bulky phosphines with cone angles greater than 160° could not be synthesized except in the case of $P(OSiMe_3)_3$. The cone angle value for this ligand has not been reported, and a value of 172° (overestimated?) from the analogous phosphite, $P(O\text{-}t\text{-}Bu)_3$, is assumed in Fig. 8. Quite surprisingly, the crowded *fac*-$Mo(CO)_3[P(OSiMe_3)_3]_3$ complex, as well as the *mer* isomer, have been successfully generated in situ, according to ^{31}P NMR (see Fig. 4).

Several points can be summarized from Fig. 8:

(*i*) The $\delta(^{95}Mo)$ for m1–PCy_3 occurs at the most shielded position while the $\delta(^{95}Mo)$ for m1–$P(t\text{-}Bu)_3$ at the most deshielded position in defining the extremes for m1 complexes of a dozen extra bulky ligands. The huge difference in ^{95}Mo shielding observed between $Mo(CO)_5(P(t\text{-}Bu)_3)$ and $Mo(CO)_5(PCy_3)$ is important because these two ligands are both bulky and are both strong bases. There seems to be a very small steric influence on $\delta(^{95}Mo)$ in the m1–PCy_3 compound in spite of its large cone angle (170°). Many crystallographic studies have indicated a smaller cone angle (157°–168°) for the PCy_3 ligand in practice due to a suitable orientation to allow the intermeshing of the cyclohexyl groups and compression into each other (30). It has been pointed out many times by others that cyclohexyl ligands adopt stable configurations, which corresponds to a considerable interpenetration of their rings. Despite many attempts, the synthesis of the *cis* isomer of $Mo(CO)_4(PCy_3)_2$ has only recently been reported (10*d*, 31). The X-ray analyses shows extreme steric hindrance, with the Mo—P distance being elongated to 2.654(4) Å (31*d*). The complex $Pt(PCy_3)_3$ has been studied by X-ray crystallography (30*a*). A steric space of 240° by 180° for two P ligands in $Pt(PCy_3)_3$ is much larger than the 180° (estimated by 270-2(45), see below for the thresholds) by 90° measured for two P ligands in *cis*-$M(CO)_4L_2$. In contrast, the other bulky ligand, $P(t\text{-}Bu)_3$ (182°), also a strong base (pK_a 11.40, pK_a 9.70 for PCy_3), brings the $\delta(^{95}Mo)$ for its m1 complex 117 ppm to high frequency. This remarkable deshielding behaviour of $P(t\text{-}Bu)_3$ must be related to the steric rigidity of this ligand. As a matter of fact, PCy_3 is very similar to other alkylphosphines in shielding behaviour in their $M(CO)_5L$ analogues ($\delta(^{95}Mo)$, m1): −1829 ppm for $P(CH_2CH_2CN)_3$, −1842 ppm for $P(n\text{-}Bu)_3$, −1856 ppm for PEt_3, −1818 ppm for PMe_3, and −1825 ppm for PCy_3); the basicities for other alkylphosphines are only one pK_a unit lower than for PCy_3 (17). Thus, if there are considerable steric differences in $Mo(CO)_5(PCy_3)$ and $Mo(CO)_5(P(t\text{-}Bu)_3)$, the former would be expected to be more stable than the latter.

(*ii*) Although tribenzylphosphine PBz_3 ($pK_a = 6.0$, $\theta = 165°$) is larger than $P(NMe_2)_3$ (pK_a not measured, $\theta = 157°$), it promotes a 26 ppm greater shielding in c2 derivatives than does the latter. Possible reasons for the greater deshielding effect of

Table 5. $\delta(^{95}Mo)$ and $\delta(^{31}P)$ data for Mo complexes of some bulky phosphorus ligands.[a]

Ligands	θ(°)	m1(ppm) $\delta_M/\Delta\delta_P$	c2(ppm) $\delta_M/\Delta\delta_P$	f3(ppm) $\delta_M/\Delta\delta_P$
$P(O\text{-}2,6\text{-}Me_2Ph)_3$	190	−1747/8.6		
$P(2\text{-}MeOPh)_3$	(185)	−1709/56.1		
$P(t\text{-}Bu)_3$	182	−1708/43.5		
$P(O\text{-}t\text{-}Bu)_3$	172	(−1716)	−1626	
$P(OSiMe_3)_3$	(≤172)	−1790/14.3	−1657/12.2	−1468/6.8
PCy_3	170	−1825/		
PBz_3	165	−1804/36.8	−1645/27.9	
$P(i\text{-}Pr)_3$	160		−1684/25.9	
$P(NMe_2)_3$	157	−1804/23.3	−1619/21.3	−1484
$PBzPh_2$	152		−1614/43.4	−1336/42.0
PPh_3	145	−1742/42.9	−1558/43.3	−1265/40.0

[a]See ref. 21 for the sources of $\Delta\delta(^{31}P)$ NMR information.

Fig. 8. Extra bulky effects of P(III) ligands on Mo shielding with increasing degrees of displacement (*n*).

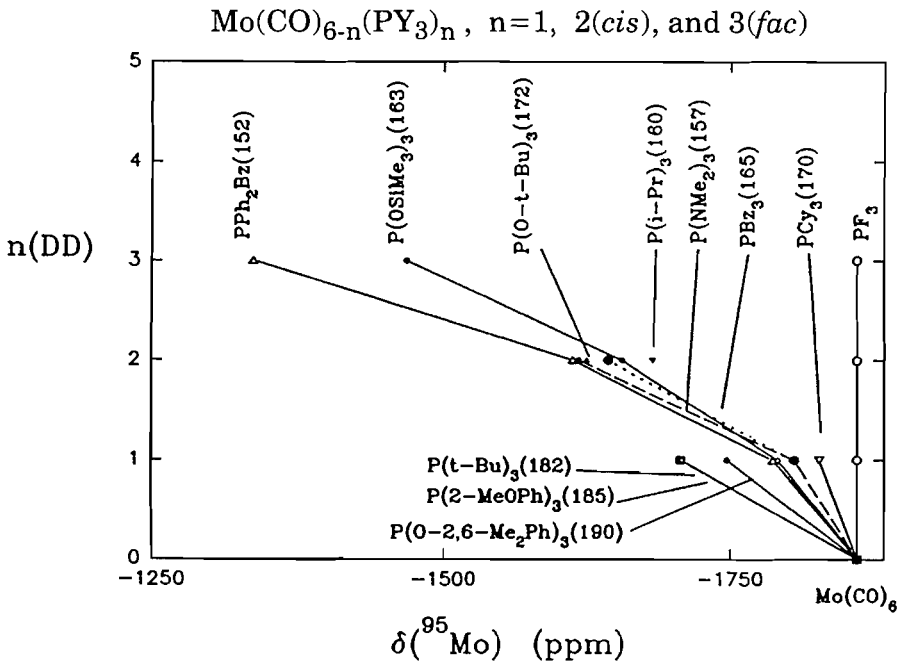

the less bulky $P(NMe_2)_3$ (than PBz_3 and $P(i\text{-}Pr)_3$) are that the aminophosphine might have a weaker π-acceptor ability or that it has a more rigid molecular framework.

(*iii*) $P(2\text{-}MeOPh)_3$ (θ = 185°, estimated) shows a similar overall deshielding effect compared to $P(t\text{-}Bu)_3$ (θ = 182°) in its m1 complex. However, the $\delta(^{95}Mo)$ value for the even more sterically crowded m1–$P(O\text{-}2,6\text{-}Me_2Ph)_3$ (θ = 190° for L) lies at 30 ppm to lower frequency, implying that there is greater Mo—P π interaction in this phosphite complex.

(*iv*) The most deshielded value in Fig. 8 is observed for f3–PPh_2Bz. The steeper rise in $\delta(^{95}Mo)$ from m1 to f3 (double $\Delta\delta(^{95}Mo)$'s) for this ligand illustrates, once more, the significant contribution of steric bulk to the paramagnetic shielding term. It should be stressed here that if their cone angles are accurate, a 70 ppm (δ = −1265 ppm) deshielding for the less bulky PPh_3 (145°) in its f3 derivative compared with f3-PPh_2Bz (152°) is most likely due to the weaker π and (or) weaker σ ability of PPh_3. Similarly, the shielding power of the larger $P(OSiMe_3)_3$ (172°) in its highly displaced derivatives compared to PPh_2Bz (152°) can be attributed to the greater π-character of the former.

Table 5 lists the spectroscopic data for the Mo complexes of some extra bulky ligands (θ > 145°). It can be seen that all those complexes with phosphine ligands have large ^{31}P coordination chemical shifts (30-40 ppm), indicating a strong σ-donating property. In contrast, $\Delta\delta(^{31}P)$ values for phosphite derivatives are very small, reflecting fewer *sp* electrons available on phosphorus for σ-bonding. Such a small coordination

Fig. 9. Correlation of $\delta(^{95}Mo)$ for $Mo(CO)_5(PY_3)$ with ligand cone angle, θ. The phosphites complexes are labelled by square double points.

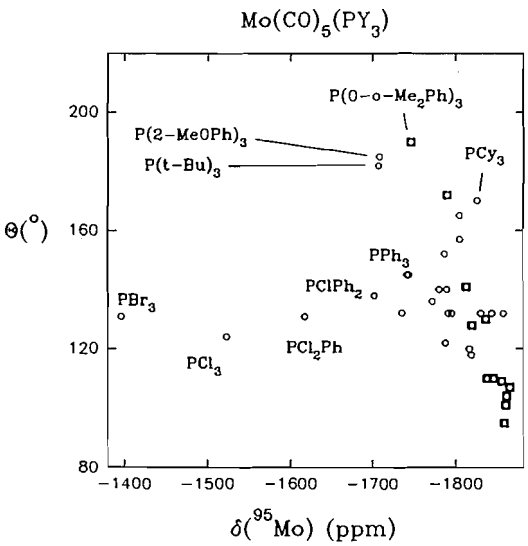

Fig. 10. Correlation of $\delta(^{95}Mo)$ for *cis*-$Mo(CO)_4(PY_3)_2$ with ligand cone angle, θ. The phosphites complexes are labelled by square double points.

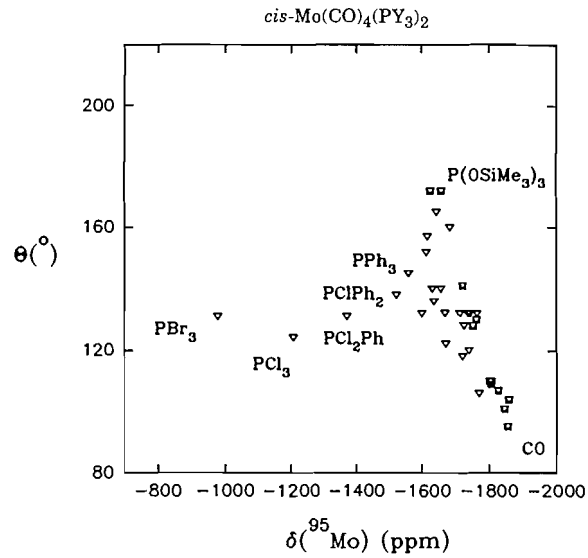

chemical shift for these bulky phosphite complexes is also due partially to the decreased π interaction (which should shift $\delta(^{31}P)$ to high frequency (7*c*)) under the high steric conditions. ^1J(Mo–P) data (Table 2) cannot provide firm information about the steric effects because the coupling constant is dominantly controlled by the electronegativity of substituent groups or *s* character (7*c*) and (or) the (small) variation of M—P bond distance. However, its magnitude does decrease when a significant steric requirement exists, such as in the f3–PPh_3 or f3–PPh_2R cases. Although some ^1J(Mo–P) values appear to get larger "abnormally" in quite bulky phosphite f3 derivatives such as the f3–$P(OSiMe_3)_3$ or f3–P(O-2-Tol)$_3$ complexes, these anomalous values may result from measurement error due to very poor resolution of the relevant resonances.

Why do *mer*-3 isomers have δ_M values quite close to those for corresponding *fac*-3 analogues? Also, the resonance for any *trans*-$M(CO)_4L_2$ is close to that for the *cis* isomer. In a *mer*-3 isomer, the steric strain is usually thought to be alleviated. Due to the steric contribution to deshielding, the *mer*-3 or *trans*-2 isomers should resonate at much lower frequency than their *fac*-3 and *cis*-2 analogues because of the lessened steric repulsion in *mer*-3 and *trans*-2 isomers. What makes the $\Delta\delta_M$ between *fac*/*mer* or *cis*/*trans* so small is possibly attributable to (*a*) the nearly invariable paramagnetic circulation density, which is reflected by the close E° between the t2 and c2 isomers (7*c*, 17*g*–*i*) or between the f3 and m3 isomers (12*f*, 17*h*–*i*); (*b*) the released but still existing steric effects, because only a free cone space of ca. 95° (see below) is available for each L.

Correlations of $\delta(^{95}Mo)$ with ligand steric parameters

To analyze, quantitatively, the dependence of ^{95}Mo magnetic shielding on the size of donating ligands, correlations of $\delta(^{95}Mo)$ for the three sets (m1, c2, and f3) of derivatives with Tolman cone angles were examined (Figs. 9–11). It can be seen very clearly that the magnetic deshielding trend or δ_M is proportional to both the steric size of phosphorus ligands in

Fig. 11. Correlation of $\delta(^{95}Mo)$ for *fac*-$Mo(CO)_3(PY_3)_3$ with ligand cone angle, θ. The phosphite complexes are labelled by square double points.

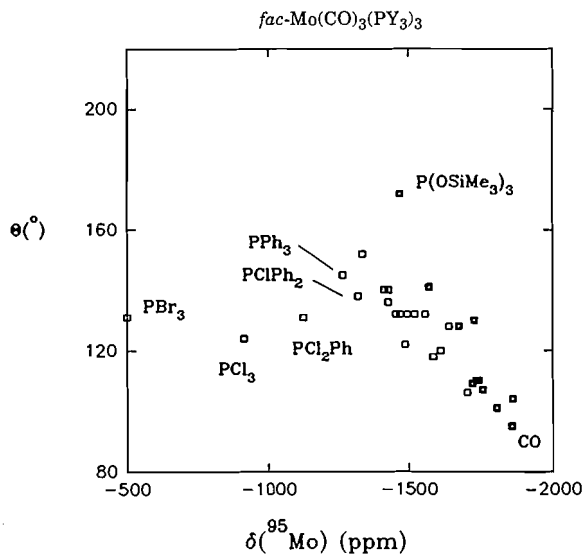

each set of derivatives and the degree of displacement, increasing from m1 (Fig. 9), c2 (Fig. 10) to f3 (Fig. 11).

Except for the chloro- or bromo-phosphorus ligands, the deshielding magnitude increases generally with the cone angles in each of the three series of complexes, and the rate of this increase is faster for *fac*-$Mo(CO)_3L_3$ than for *cis*-$Mo(CO)_4L_2$, and lowest for the $Mo(CO)_5L$ series in which the steric requirement is smallest. This offers firm evidence for an important steric contribution to δ_M (see also ref. 7). Examining Figs. 9–11 closely, one can delineate many significant features, which are summarized below. Again it must be kept in

mind whenever analyzing these correlations that (*i*) the values of $\delta(^{95}Mo)$ are much more accurate (*the experimental error is definitely smaller than the dimension of plot points!*) than other measures including steric bulk parameters cited here; and (*ii*) the σ/π electronic components definitely contribute to the magnetic shielding, being comparable to steric effects for the least congested structures.

(*a*) All the δ/θ points seem to fall in a fan area. The *phosphites* represented by double points (square) form a linear trend, indicating two important features. First, the π character of phosphites tends to stabilize Mo—P bonds, and so the ^{95}Mo nucleus resonates at lower frequency with respect to other complexes of isosteric ligands. Second, the roughly linear increase in deshielding on the Mo occurring for phosphite complexes with increased ligand cone angles is evidently a direct result of steric interaction. The strong interligand repulsion makes the Mo—P bonds longer and weaker for these good π-acceptor complexes, hence leading to a decrease in ΔE and a shrinking of the metal 4*d* orbitals. It should be emphasized that the primary reason for the above deshielding trend in phosphite complexes is a steric requirement, resulting in an indirect weakening of π ability in all of the three displacement sets. Although the basicities of various phosphites are quite different (pK_a varies from -2 to 4.5), they apparently make only a small contribution to the roughly linear trend. The steric interaction contributes to the $\delta(^{95}Mo)$ almost linearly even in $Mo(CO)_5L$ complexes of phosphites, although there is usually supposed to be no serious steric congestion in a $M(CO)_5L$ complex (more detailed discussion below).

(*b*) The $\delta(^{95}Mo)$ chemical shifts for phosphine complexes are scattered over the entire fan area in all three sets of derivatives, as shown by the single open points in Figs. 9–11, instead of giving a linear pattern. The phosphines display an irregular and complicated shielding trend. However, a seemingly linear correlation between δ_M and θ for the f3 series in Fig. 11 reflects, strongly, the increasingly important role that steric factors play in paramagnetic shielding of ^{95}Mo in these most crowded derivatives. The increased irregularity of δ_M/θ plots for *cis*-$Mo(CO)_4L_2$, and particularly for the $Mo(CO)_5L$ derivatives, is undoubtedly an indication of a complicated combination of three factors: steric effects, and σ and π electronic effects.

(*c*) The weak σ and weak π effects in PX_3 (X = Cl, Br) complexes: the electronic and steric effects of the PX_3 ligands have been discussed in detail in a previous paper (*7b*). The three δ_M/θ correlations here indicate further that phosphorus trihalide ligands are quite different from other P(III) ligands. Actually a linear trend of δ_M/θ for PF_3, PCl_3, and PBr_3 exists for each of the three derivatives, as can be seen from Figs. 9–11. PF_3 happens to join the class of regular P(III) ligands that are good π-acceptors.

(*d*) As noted in Fig. 9, (*i*) the δ_M/θ correlation shows a more irregular relationship for m1-phosphines and slightly poor linearity for phosphite complexes (mainly due to several points for very small ligands at the bottom); and (*ii*) many phosphines such as PCy_3, PBz_3, $P(NMe_2)_3$, PEt_3, and $P(n\text{-}Bu)_3$ exhibit an unusually stronger shielding ability than their isosteric phosphites.

As to the above point (*i*), the more irregular $\delta(^{95}Mo)/\theta$ correlation for m1–phosphine complexes compared with those for c2's and f3's might be attributed to the minimum steric effects

Fig. 12. Correlation of $\delta(^{95}Mo)$ for $Mo(CO)_5(P(OR)_3)$ with respective ligand cone angles, θ.

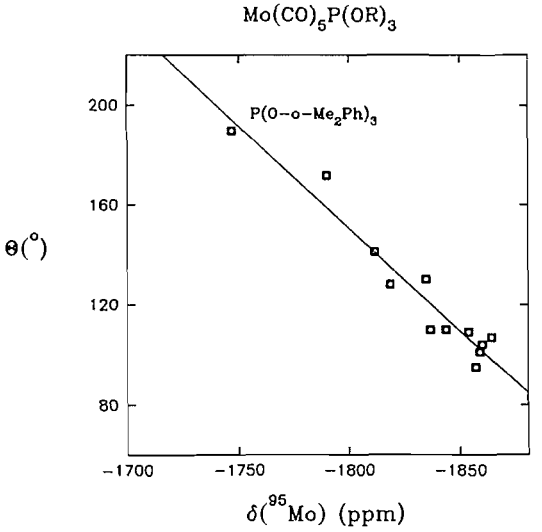

and the variations in (not necessarily dominant) electronic effects, as pointed out previously. It is well known that the phosphine ligands PRR_1R_2 with various R groups have quite different σ and π electronic properties, which have been described by pK_a, Tolman's electronic parameter, χ_i, and electrochemical parameters. The electronic effects of phosphines are much more complex than those for phosphites and vary greatly from one to another. Usually the σ/π ratio for this class of ligands is larger than for phosphites, as concluded by a number of authors. However, whether the σ character is dominant and *whether the π character is actually weak for these phosphines* are not yet clear. Nevertheless, the more irregular correlation in Fig. 12 is simply an indication of increasingly important electronic effects with respect to the steric effects in m1 derivatives.

As to the above point (*ii*), it can be noted that so-called "strong" alkylphosphines are just strong σ-donors. Quite importantly, three phosphines, PEt_3, $P(n\text{-}Bu)_3$, and $P(CH_2CH_2CN)_3$, of the same size (132°) shield the Mo centre better than two isosteric phosphites, $P(OPh)_3$ (128°) and P(O-i-Pr)$_3$ (132°), which are putatively good π-acceptors. There should be no significant differences in steric interaction in the $M(CO)_5L$ geometry for these five ligands, which have virtually the same fairly small cone angles. There are two possible reasons for such a shielding difference. The former three phosphines may *also be good π-acceptors* and the synergic effect operates. Alternatively, the π ability of phosphites may be reduced seriously if their bulkiness exceeds a certain threshold, e.g., $\theta = 128°$ (?). A quantitative separation of these contributing σ and π electronic effects first needs to filter out the steric component.

Semiquantitative estimation of steric bulkiness

According to the above qualitative discussion and cited X-ray results, it is believed that intramolecular steric interactions in c2 and f3 geometries are important. In m1 derivatives, the steric effect can also be observed and estimated, as illustrated by the double points in Fig. 9, but with greater error. Three roughly linear relationships between $\delta(^{95}Mo)$ for phosphite complexes and θ are presented in Figs. 12–14 and eq. [2],

Table 6. Re-estimated phosphite cone angles from $\delta(^{95}Mo)$ data of molybdenum complexes, $Mo(CO)_{6-n}L_n$ (n = 1, 2, and 3).

No.	Ligands	θ^a (°)	θ_s (n = 1)	θ_s (n = 2)	θ_s (n = 3)
3	$P(O\text{-}2,6\text{-}Me_2Ph)_3$	190	199		
6	$P(O\text{-}t\text{-}Bu)_3$	172		176	
7	$P(O\text{-}SiMe_3)_3$	(≤172)	162	165	170
16	$P(O\text{-}2\text{-}tol)_3$	141	142	142	149
29	$P(O\text{-}i\text{-}Pr)_3$	130	122	129	117
30	$P(OPh)_3$	128	136	132	128
36	$P(OCH_2CF_3)_3$	(110)	120	114	114
37	$P(OCH_2CH_2Cl)_3$	110	114	113	116
38	$P(OEt)_3$	109	105	113	119
39	$P(OMe)_3$	107	97	105	111
41	ETPB	101	100	99	101
42	PF_3	104	101	94	90
44	CO	95	102	95	91

[a]Tolman cone angle taken from ref. 1*a*.

Fig. 13. Correlation of $\delta(^{95}Mo)$ for *cis*-$Mo(CO)_4(P(OR)_3)_2$ with respective ligand cone angles, θ.

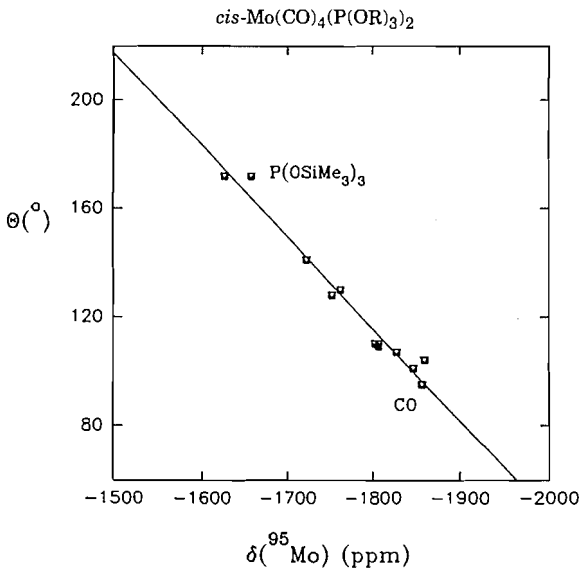

Fig. 14. Correlation of $\delta(^{95}Mo)$ for *fac*-$Mo(CO)_3(P(OR)_3)_3$ with respective ligand cone angles, θ.

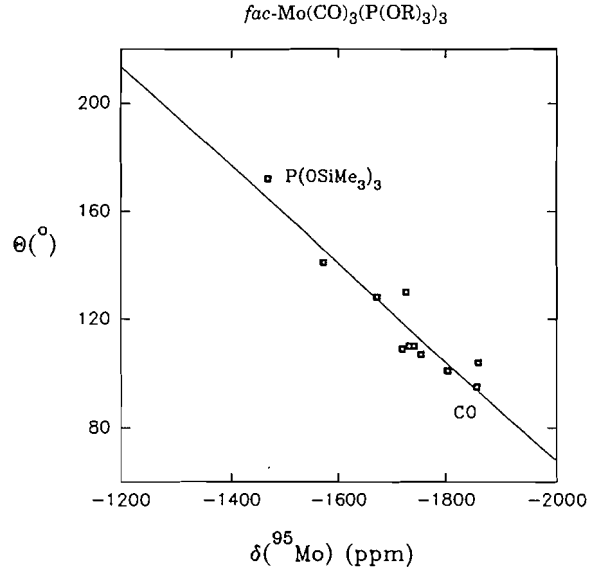

allowing for an approximate re-estimation of the steric parameters for phosphites.

[2] $\delta(^{95}Mo) = A\theta + B$

[2*a*] m1: $A = 1.14$, $B = -1974$; ($r = 0.968$, $N = 12$)

[2*b*] c2: $A = 2.86$, $B = -2130$; ($r = 0.986$, $N = 12$)

[2*c*] f3: $A = 4.90$, $B = -2302$; ($r = 0.945$, $N = 11$)

Table 6 lists many θ_s (steric size estimated by metal shielding) values for phosphites obtained by a linear analysis, as well as the original Tolman cone angles for the sake of comparison. As an experimentally derived value, θ_s will be a genuine (but approximate since it is combined with unisolated electronic effects) measure of interligand repulsion in pseudo-O_h geometry. If the electronic effects could be separated, then it should be a characteristic measure of both stable conformation and the interpenetration of ligands in solution.

An unexpected but important observation is that even for $Mo(CO)_5PY_3$ complexes, ^{95}Mo shielding has a roughly linear dependence on the size of phosphite ligands (Fig. 12). In agreement with the estimation by Cotton et al. (12*h*) and Tolman (1*a*), the cone angle for the small linear molecule CO is derived by extrapolation to be ca. 95° in *cis*-$Mo(CO)_4L_2$ (see the bottom line of Table 6 for relevant values). This value is consonant with the above observation of steric interaction existing in m1 derivatives; that is, *the maximum cone angle for an incoming ligand without interligand repulsion occurring is only ca. 95°*.

Conclusions

1. An analysis of $\delta(^{95}Mo)$ NMR values for a wide range of $Mo(CO)_{6-n}(PY_3)_n$ complexes indicates that steric effects play

an unexpectedly important role in the paramagnetic shielding terms. This cooperating contribution that causes deshielding has even been observed in the least crowded $M(CO)_5(PY_3)$ complexes. A detailed correlation analysis shows that the free cone space to accommodate an incoming ligand is equal to that estimated for CO itself in $Mo(CO)_{6-n}(PY_3)_n$ (n = 1–3) derivatives.

2. Three linear dependencies of $\delta(^{95}Mo)$ on phosphite cone angles, θ, have been observed, including even one for the m1 series. It can be inferred that the steric requirement reduces the commonly accepted π ability of phosphites by extending or weakening the M—P bonds, making $\delta(^{95}Mo)$ positions move toward lower field. The linearity of these correlations suggests that the σ component in phosphite bonding is relatively less important. Based on these linear correlations, a new set of more practical steric measures of phosphites were estimated.

Acknowledgments

This research was supported by a research grant from the Natural Sciences and Engineering Research Council of Canada.

References

1. (*a*) C.A. Tolman. Chem. Rev. **77**, 313 (1977); (*b*) G. Wilkinson, F.G.A. Stone, and E.W. Abel (*Editors*). Comprehensive organometallic chemistry. Pergamon Press, Oxford. 1982; (*c*) W. Levason. *In* The chemistry of organophosphorus compounds. Vol. 1. *Edited by* F.R. Hartley. Wiley, Chichester. 1990. Chapt. 15; (*d*) B.P. Dias, M.E.M. Piedade, and J.A.M. Simoes. Coord. Chem. Rev. **135/136**, 737 (1994).
2. (*a*) M.L. Caffery and T.L. Brown. Inorg. Chem. **30**, 3907 (1991); (*b*) K.J. Lee and T.L. Brown. Inorg. Chem. **31**, 289 (1992); (*c*) T.L. Brown. Inorg. Chem. **31**, 1286 (1992); (*d*) M.G. Choi and T.L. Brown. Inorg. Chem. **32**, 1548 (1993); (*e*) T.L. Brown and K.J. Lee. Coord. Chem. Rev. **128**, 89 (1993); (*f*) K.J. Lee and T.L. Brown. Inorg. Chem. **26**, 1852 (1987).
3. (*a*) J.P. Collman, L.S. Hegedus, J.R. Norton, and R.G. Finke. Principles and applications of organotransition metal chemistry. University Science Books, Mill Valley, Calif. 1987; (*b*) O. Stelzer. *In* Topics in phosphorus chemistry. Vol 9. *Edited by* E.J. Griffith and M. Grayson. 1977. p. 1; (*c*) R. Mason and D.W. Meek. Angew. Chem. **17**, 183 (1978); (*d*) N.E. Burke, A. Singhal, M.J. Hintz, J.A. Ley, H. Hui, L.R. Smith, and D.M. Blake. J. Am. Chem. Soc. **101**, 74 (1979); (*e*) E.C. Alyea and D.W. Meek (*Editors*). Catalytic aspects of metal phosphine complexes. Advances in Chemistry 196, American Chemical Society: Washington, D.C. 1982; (*f*) F.P. Pruchnik. Organometallic chemistry of the transition elements. Plenum Press, New York. 1990; (*g*) J.D. Atwood. Inorganic and organometallic reaction mechanisms. Brooks/Cole, Monterey, Calif. 1985.
4. (*a*) D.T. Dixon, J.C. Kola, and J.A.S. Howell. J. Chem. Soc. Dalton Trans. **1307** (1984); (*b*) D.J. Darensbourg and A.H. Graves. Inorg. Chem. **18**, 1257 (1979); (*c*) M.L. Boyles, D.V. Brown, D.A. Drake, and C.K. Hostetler. Inorg. Chem. **24**, 3126 (1985); (*d*) G.R. Dobson and A. Moradi-Araghi. Inorg. Chim. Acta. **31**, 263 (1978); (*e*) S. Ching and D.F. Shriver. J. Am. Chem. Soc. **111**, 3238 (1989); (*f*) R.J. Angelici and C.M. Ingemanson. Inorg. Chem. **8**, 83 (1969).
5. (*a*) P.B. Hitchcock, B. Jacobson, and A. Pidcock. J. Chem. Soc. Dalton Trans. 2043 (1977); (*b*) I. Macleod, L. Manojlovic-Muir, D. Millington, K.W. Muir, D.W.A. Sharp, and R. Walter. J. Organomet. Chem. **97**, C7 (1975); (*c*) R. Brady, W.H. De Camp, B.R. Flynn, and M.L. Schneider. Inorg. Chem. **14**, 2669 (1975); (*d*) W.A. Schenk. J. Organomet. Chem. **179**, 253 (1979); (*e*) L.M. Ounapu, J.A. Mosbo, J.M. Risley, and B.N. Storhoff. J. Organomet. Chem. **194**, 337 (1980); (*f*) A. Pidcock, R.E. Richards, and L.M. Venanzi. J. Chem. Soc. (A), 1707 (1966); (*g*) M.J. Wovkulich and J.D. Atwood. Organometallics, **1**, 1316 (1982).
6. (*a*) S.-Q. Song and E.C. Alyea. Comments Inorg. Chem. **18**, 145 (1996); (*b*) E.C. Alyea and S.-Q. Song. Comments Inorg. Chem. **18**, 189 (1996).
7. (*a*) E.C. Alyea and S.-Q. Song. J. Chem. Soc. Dalton Trans. Submitted; (*b*) S.-Q. Song and E.C. Alyea. Inorg. Chem. **34**, 3864 (1995); (*c*) E.C. Alyea and S.-Q. Song. J. Chem. Soc. Dalton Trans. Submitted; (*d*) D. Rehder. J. Magn. Reson. **38**, 419 (1980); (*e*) G.M. Gray and R.J. Gray. Organometallics, **2**, 1026 (1983).
8. (*a*) M. Minelli, J.H. Enemark, R.T.C. Brownlee, M.J. O'Connor, and A.G. Wedd. Coord. Chem. Rev. **68**, 169 (1985); (*b*) E.W. Abel, M.A. Bennett, and G. Wilkinson. J. Chem. Soc. 2323 (1959); (*c*) M.S. Davies, R.K. Pierens, and M.J. Aroney. J. Organomet. Chem. **458**, 141 (1993).
9. (*a*) J.J. Eisch and R.B. King (*Editors*). Organometallic syntheses. Vol. 1. Academic Press, New York. 1965; (*b*) D.J. Darensbourg and T.L. Brown. Inorg. Chem. **7**, 959 (1968).
10. (*a*) T.Y. Luh. Coord. Chem. Rev. **60**, 255 (1984); (*b*) T.S.A. Hor. J. Organomet. Chem. **319**, 213 (1987); (*c*) T.S.A. Hor. Inorg. Chim. Acta, **149**, 169 (1988); (*d*) J.K. Shen, Y.C. Gao, Q.Z. Shi, and F. Basolo. Coord. Chem. Rev. **128**, 68 (1993).
11. S.W. Kirtley. *In* Comprehensive organometallic chemistry. Vol. 3. *Edited by* G. Wilkinson, F.G.A. Stone, and E.W. Abel. Pergamon Press, Oxford. 1982. Chap. 26.1.
12. (*a*) G. Wilkinson, R.D. Gillard, J.A. McCleverty (*Editors*). Comprehensive coordination chemistry. Vol. 2. Pergamon Press, Oxford. 1987. p. 1030; (*b*) E.C. Alyea and A. Somogyvari. Transition Met. Chem. **12**, 310 (1987); (*c*) Can. J. Chem., **66**, 397 (1988); (*d*) Magn. Reson. Chem. **24**, 357 (1986); (*e*) S. Affandi, J.H. Nelson, N.W. Alcock, O.W. Howarth, E.C. Alyea, and G.M. Sheldrick. Organometallics, **7**, 1724 (1988); (*f*) A.M. Bond, S.W. Carr, and R. Colton. Organometallics, **3**, 541 (1984); (*g*) J.T. Bailey, R.J. Clark, and G.C. Levy. Inorg Chem. **21**, 2085 (1982); (*h*) F.A. Cotton, D.J. Darensbourg, S. Klein, and B.W.S. Kolthammer. Inorg. Chem. **21**, 2661 (1982); (*i*) G.T. Andrews, I.J. Colquhoun, and W. McFarlane. J. Chem. Soc. Dalton Trans. 2353 (1982); (*j*) G.M. Gray and C.S. Kraihanzel. Inorg. Chem. **22**, 2959 (1983).
13. S.-Q. Song. Ph.D. Thesis, University of Guelph, Guelph, Ont. 1994. Chapts. 2 and 7.
14. (*a*) M.T. Tribble and J.G. Traynham. *In* Advances in linear free energy relationships. *Edited by* N.B. Chapman and J. Shorter. Plenum, London. 1972. Chap. 4; (*b*) D.M. Bridges, G.C. Holywell, D.W.H. Rankin, and J.M. Freeman. J. Organomet Chem. **32**, 87 (1971); (*c*) H.J. Plastas, J.M. Steward, and S.O. Grim. Inorg. Chem. **12**, 265 (1973); (*d*) H.S. Preston, J.M. Stewart, H.J. Plastas, and S.O. Grim. Inorg. Chem. **11**, 161 (1972).
15. (*a*) T. Kruck. Angew Chem. **6**, 53 (1967); (*b*) J.R. Nixon. *In* Adv. Inorg. Chem. Radiochem. Vol. 29. *Edited by* H.J. Emeleus and A.G. Sharpe. Academic Press, New York. 1985; (*c*) L. Stahl and R.D. Ernst. J. Am. Chem. Soc. **109**, 7585 (1987).
16. (*a*) S.P. Nolan and C.D. Hoff. J. Organomet. Chem. **290**, 365 (1985); (*b*) S.L. Mukerjee, R.F. Lang, T. Ju, G. Kiss, and C.D. Hoff. Inorg. Chem. **31**, 4885 (1992); (*c*) S.P. Nolan, R.L. Vega, and C.D. Hoff. Organometallics, **5**, 2529 (1986); (*d*) H. Daamen, D.J. Van Der Poel Stufkens, and A. Oskama. Thermochim. Acta, **34**, 69 (1979).
17. (*a*) M.N. Golovin, M.M. Rahman, J.E. Belmonte, and W.P. Giering. Organometallics, **4**, 1981 (1985); (*b*) M.M. Rahman, H.Y. Liu, A. Prock, and W.P. Giering. Organometallics, **6**, 650 (1987); (*c*) M.M. Rahman, H.Y. Liu, K. Eriks, A. Prock, and W.P. Giering. Organometallics, **8**, 1 (1989); (*d*) H.Y. Liu, K.

Eriks, W.P. Giering, and A. Prock. Inorg. Chem. **28**, 1759 (1989); (*e*) H.Y. Liu, K. Eriks, A. Prock, and W.P. Giering. Organometallics, **9**, 1758 (1990); (*f*) M.R. Wilson, D.C. Woska, A. Prock, and W.P. Giering. Organometallics, **12**, 1742 (1993); (*g*) A.M. Bond, D.J. Darensbourg, E. Mocellin, and B.J. Stewart. J. Am. Chem. Soc. **103**, 6827 (1981); (*h*) R.N. Bahchi, A.M. Bond, G. Brain, R. Cotton, T.L.E. Henderson, and J.E. Kevekordes. Organometallics, **3**, 4 (1984); (*i*) A.M. Bond, S.W. Carr, and R. Cotton. Inorg. Chem. **23**, 2343 (1984).

18. (*a*) J. Mason (*Editor*). Multinuclear NMR. Plenum Press, New York. 1987; (*b*) R.K. Harris and B.E. Mann (*Editors*). NMR and the periodic table. Academic Press, London. 1978; (*c*) J.G. Verkade and L.D. Quin (*Editors*). Phosphorus-31 NMR spectroscopy in stereochemical analysis. VCH Publishers, Inc., Florida. 1987; (*d*) J.R. Van Wazer and J.H. Letcher. *In* Topics in phosphorus chemistry. Vol. 5. *Edited by* M. Grayson and E.J. Griffith. Wiley & Sons, New York. 1967. p. 169; (*e*) P.S. Pregosin and R.W. Kunz. ^{31}P and ^{13}C NMR of transition metal phosphine complexes. Springer-Verlag, Berlin. 1979; (*f*) P.S. Pregosin (*Editor*). Transition metal nuclear magnetic resonance. Elsevier, Amsterdam. 1991.
19. J. Emsley and D. Hall. *In* The chemistry of phosphorus. Harper & Row, London. 1976. Chap. 5.
20. J.E. Huheey. Inorganic chemistry. 3rd ed. Harper & Row, New York. 1983.
21. (*a*) J. Mason (*Editor*). Multinuclear NMR. Plenum Press, New York. 1987. Chap. 12; (*b*) S.-Q. Song. Ph.D. Thesis, University of Guelph, Guelph, Ont. 1994. Chap. 6.
22. (*a*) E.C. Alyea, G. Ferguson, and M. Zwikker. Acta Crystallogr. Sect. C: Cryst. Struct. Commun. **C50**, 676 (1994); (*b*) E.C. Alyea, G. Ferguson, and S.-Q. Song. Acta Crystallogr. Sect. C: Cryst. Struct. Commun. **C51**, 2238 (1995).
23. (*a*) J.G. Verkade. Coord. Chem. Rev. **9**, 1 (1972/73); (*b*) S.O. Grim, D.A. Wheatland, and W. McFarlane. J. Am. Chem. Soc. **89**, 5573 (1967); (*c*) S.O. Grim, P.R. McAllister, and R.W. Singer. Chem. Commun. 38 (1969).
24. (*a*) M. Wada and S. Higashizaki. J. Chem. Soc. Chem. Commun. 482 (1984); (*b*) M. Wada, S. Higashizaki, and A. Tsuboi. J. Chem. Res. (S), **38** (M), 467 (1985).
25. (*a*) A. Immirzi and A. Musco. Inorg. Chim. Acta, **25**, L41 (1977); (*b*) D.G. Gilheany. *In* The chemistry of organophosphorus compounds. Vol. 1. *Edited by* F.R. Hartley. Wiley & Sons, Chichester. 1990. Chap. 2.
26. (*a*) S.X. Xiao, W.C. Trogler, D.E. Ellis, and Z.B. Yellin. J. Am. Chem. Soc. **105**, 7033 (1983); (*b*) S.P. Wang, M.G. Richmond, and M. Schwartz. J. Am. Chem. Soc. **114**, 7595 (1992); (*c*) S.T. Krueger, R. Poli, A.L. Rheingold, and D.L. Staley. Inorg. Chem. **28**, 4599 (1989).
27. (*a*) F.A. Cotton, D.J. Darensbourg, A. Fang, B.W.S. Kolthammer, D. Reed, and S.L. Thompson. Inorg. Chem. **20**, 4090 (1981); (*b*) F.A. Cotton, D.J. Darensbourg, and W.H. Ilsley. Inorg. Chem. **20**, 578 (1981).
28. R.C. Bush and J. Angelici. Inorg. Chem. **27**, 681 (1988).
29. A. Holladay, M.R. Churchill, and A. Wong. Inorg. Chem. **19**, 2195 (1980).
30. (*a*) A. Immirzi and A. Musco. Inorg. Chim. Acta, **21**, L37 (1977); (*b*) D.F. Mullica, J.D. Oliver, and D.A. Grossie. Acta Crystallogr. Sect. C: Cryst. Struct. Commun. **C43**, 591 (1987); (*c*) G. Ferguson, P.J. Roberts, E.C. Alyea, and M. Khan. Inorg. Chem., **17**, 2965 (1978).
31. (*a*) G.J. Kubas and C. Hoff. Inorg. Synth. **27**, 1; (1990); (*b*) H.J. Wasserman, G.J. Kubas, and R.R. Ryan. J. Am. Chem. Soc. **108**, 2294 (1986); (*c*) G.J. Kubas. Acc. Chem. Res. **21**, 120 (1988); (*d*) M. Watson, S. Woodward, G. Conole, M. Kessler, and G. Sykara. Polyhedron, **13**, 2455 (1994).

In situ FTIR studies of 4-cyanopyridine adsorption at the Au(111) electrode

A.C. Chen, S.G. Sun, D.F. Yang, B. Pettinger, and J. Lipkowski

Abstract: In situ electromodulated reflectance Fourier transform infrared (FTIR) spectroscopy has been employed to study the adsorption of 4-cyanopyridine (4-CNPy) at an Au(111) electrode surface. The vibrational spectra have been used to study (*i*) the dependence of the band intensity on the surface coverage, (*ii*) the character of surface coordination, and (*iii*) the stability of adsorbed 4-CNPy molecules. It has been observed that the vibrational bands in the spectra acquired in the electroreflection experiment are significantly broader than the corresponding spectra acquired in a transmission cell. Some weaker bands seen in the spectra recorded in transmission were not observed in the electroreflectance experiment. The electroreflectance spectra were dominated by the two ring deformation bands observed at 1416 cm^{-1} and 1554 cm^{-1}. The intensities of these bands correlated well with the surface concentrations of 4-CNPy molecules determined from independent electrochemical studies. The integrated absorption intensities of the bands recorded in the electroreflection experiments were larger by a factor of five than the absorption intensities measured in the transmission cell. This indicates that the electric field of the photon acting on a molecule, present in front of the gold electrode, is significantly enhanced by reflection from the electrode. The infrared experiments suggest that at positive potentials the 4-CNPy molecules are coordinated to the metal surface through the nitrogen atom of the aromatic ring. The 4-CNPy molecules are oxidized at the Au electrode at potentials higher than 0.6 V (SCE) and are reduced to form $(4\text{-CNPy})^{-\bullet}$ ion at potentials lower than −1.1 V (SCE).

Key words: adsorption, infrared spectroscopy, 4-cyanopyridine, gold electrode.

Résumé : On a utilisé la spectroscopie infrarouge avec transformation de Fourier et réflectance électromodulée in situ pour étudier l'adsorption de la 4-cyanopyridine (4-CNPy) à la surface d'une électrode d'or(111). On fait appel aux spectres de vibration pour étudier : (*i*) l'influence du recouvrement de la surface sur l'intensité de la bande, (*ii*) le caractère de la coordination de la surface et (*iii*) la stabilité des molécules de 4-CNPy adsorbées. On a observé que les bandes de vibration dans les spectres enregistrés dans l'expérience d'électroréflexion sont de façon significative plus larges que celles des spectres enregistrés dans les cellules de transmission. Quelques bandes plus faibles apparaissant dans les spectres entregistrés par transmission n'apparaissent pas dans l'expérience d'électroréflectance. Dans les spectres d'électroréflectance on observe deux bandes importantes de déformations de cycle à 1416 cm^{-1} et à 1554 cm^{-1}. Les intensités de ces bandes correspondent bien avec les concentrations de surface des molécules de 4-CNPy déterminées à partir des études électrochimiques indépendantes. Les intensités d'absorption intégrées enregistrées dans l'expérience d'électroréflectance sont cinq fois plus élevées que les intensités d'absorption mesurées dans la cellule de transmission. Ceci indique que le champ électrique du photon agissant sur une molécule, présente en face de l'électrode d'or, est renforcé de façon significative par la réflexion à partir de l'électrode. Les expériences réalisées dans l'infrarouge suggèrent qu'à des potentiels positifs, les molécules de 4-CNPy sont coordonnées à la surface du métal via l'atome d'azote du cycle aromatique. Les molécules de 4-CNPy sont oxydées à l'électrode d'or à des potentiels plus élevés que 0,6 V (SCE) et sont réduites pour former l'ion $4\text{-CNPy}^{-\bullet}$ à des potentiels inférieurs à −1,1 V (SCE).

Mots clés : adsorption, spectroscopie infrarouge, 4-cyanopyridine, électrode d'or.

[Traduit par la rédaction]

Received March 19, 1996.

This paper is dedicated to Professor Howard C. Clark in recognition of his contributions to Canadian chemistry.

A.C. Chen, D.F. Yang, and J. Lipowski.[1] Guelph–Waterloo Center for Graduate Study in Chemistry, Guelph Campus, University of Guelph, Guelph, ON N1G 2W1, Canada.
S.G. Sun. Department of Chemistry, Xiamen University, Xiamen, Fujian, 361005, China.
B. Pettinger. Fritz Haber Institut der Max Planck Gesellschaft, Faradayweg 4-6, D 14195, Berlin, Germany.

[1] Author to whom correspondence may be addressed. Telephone: (519) 824-4120, ext. 8543. Fax: (519) 766-1499. E-mail: Lipkowski@chembio.uoguelph.ca

1. Introduction

FTIR spectroscopy is a powerful in situ technique to study electrified interfaces (1, 2). It has been used to identify intermediates and products of electrocatalytic oxidation of small organic molecules (3, 4). The electric field of the *s*-polarized IR photon has a zero strength at metal surfaces and hence the adsorbed molecules are optically inactive in this polarization. In contrast, the field has a nonzero strength in the solution and the molecules present in the solution are IR active for *s*-polarized radiation. Polarization-resolved IR spectroscopy has therefore been used to determine whether the intermediate (or product) of these reactions is an adsorbed or solution species (5–7). Finally, the surface selection rules of FTIR spectroscopy have been used to study the orientation of molecules adsorbed on the metal surface; for example, difluorobenzene at a polycrystalline platinum (8), isoquinoline (9) and flavine adenosine (10) at a mercury, and acetonitrile (11) at a gold electrode. Most of the past in situ FTIR studies were concerned with either the identification of species generated at the electrode surface or the determination of the character of their surface coordination. Less work has been done to develop FTIR spectroscopy as a tool for quantitative analysis of adsorbed species that could provide information about the composition of the interfacial region.

In this work, we will employ in situ FTIR spectroscopy to investigate adsorption of 4-caynopyridine (4-CNPy) at the Au(111) electrode surface. This study constitutes one part of a broader project the objective of which is to describe coordination of organic molecules to metal electrodes. The 4-CNPy was selected for the present study because we wanted to evaluate the relative strength of the surface coordination of this organic molecule through the CN group and through the nitrogen atom of the aromatic ring. We recently determined the surface concentrations of these molecules and observed that 4-CNPy assumes a flat π-bonded surface coordination at the negatively charged interface while at low bulk concentrations, and a vertical (N-bonded) orientation at the positively charged surface while at higher bulk concentrations (12). When potential is moved from a negative limit in the positive direction, the 4-CNPy molecules progressively reorient from the flat to the vertical position. The adsorption of 4-CNPy at Ag, Cu, and Pt electrodes has been investigated extensively by Raman spectroscopy (surface-enhanced Raman scattering (SERS)) (13–16). These studies revealed that 4-CNPy molecules may be reduced at these electrodes at negative potentials and various schemes were proposed to explain the mechanism of this reaction (13, 14). The specific objectives of our work were therefore threefold: (*i*) to correlate surface concentrations of 4-CNPy molecules determined from electrochemical studies in ref. 12 with the intensities of selected IR bands for adsorbed molecules to cross-check the surface concentration data, (*ii*) to employ surface selection rules of IR spectroscopy to study the potential-induced reorientation of the adsorbed molecules, and (*iii*) to use IR spectroscopy to determine the potential range within which the molecules are stable at the electrode surface and the potential of the onset of 4-CNPy reduction.

2. Experimental

Water and chemicals

All solutions were prepared from Milli-Q water. The supporting electrolyte was 0.1 M $KClO_4$ purified according to the procedure described in our previous papers (17, 18). The concentrations of 4-CNPy used in this study were 0.1 M and 0.01 M. The 4-CNPy was purified by sublimation twice under vacuum. The electrolyte solution was deaerated by purging argon for about 30 min prior to each experiment.

Cell and electrodes

A syringe-type IR cell with a flat CaF_2 window was used in the in situ FTIR studies. An Au(111) single-crystal electrode grown, cut, and polished in our laboratory was used as the working electrode. The working electrode was flame annealed and before each experiment it was additionally cleaned by applying slow (20 mV/s) repetitive oxidation–reduction cycles in the pure supporting electrolyte solution. During the IR experiment, the working electrode was pushed against the CaF_2 window to form a thin layer. A platinum foil was used as the counter electrode, and the reference electrode was a Ag/AgCl (3 M KCl saturated with AgCl) electrode. For the sake of comparison with previous electrochemical results, all potentials measured with respect to the Ag/AgCl were converted to the saturated calomel electrode (SCE) scale. All experiments were performed at 20±2°C.

Experimental procedures

In situ FTIR experiments were carried out on a Nicolet 20SX/C FTIR apparatus equipped with a MCT-B detector cooled by liquid nitrogen. The sample compartment of the FTIR apparatus was purged throughout the experiment using CO_2 and H_2O-free air provided by the Puregas Heatless Dryer. The electrode potential was controlled with the help of a PAR 173 potentiostat. Equipment and data processing procedures used to determine the cyclic voltammogram have been described in our previous publications (12, 17, 18).

Subtractively Normalized Interfacial Fourier Transform Infrared Spectroscopy (SNIFTIRS) was employed to record the IR spectra (1). The spectra were determined using a multiple potential step (MPS) procedure in which the electrode potential was stepped m times between a reference potential E_1 and a sample potential E_2. During a portion of the cycle the electrode potential was held either at potential E_1 or at E_2 while n interferograms were acquired. The acquisition was delayed for 30 s with respect to the time of the potential change to allow the interface to reach thermodynamic equilibrium at the imposed polarization. The change of the electrode potential was synchronized with the acquisition of the interferograms by connecting the external trigger port of the PAR 173 potentiostat to the communication port of a DX 486 computer that controlled the FTIR instrument. This procedure was repeated m times until a total number of $N = n \times m$ interferograms was acquired for each of the two potentials. Typical values of n and m employed in this study were $n = 100$ and $m = 20$. The interferograms were added, Fourier transformed, and used to calculate a relative change of the electrode reflectivity defined as:

$$[1] \quad \Delta R/R = (R(E_2) - R(E_1))/R(E_1)$$

where $R(E_1)$ and $R(E_2)$ are the electrode reflectivities at potentials E_1 and E_2, respectively. Since $\Delta R/R$ represents a difference between reflectivities at potentials E_1 and E_2, the sign of

$\Delta R/R$ may be positive or negative or may change with the wavelength. In the $\Delta R/R$ spectrum, the band that does not change its sign is referred to as a monopolar band. In contrast, a band that displays a change of sign is called a bipolar. The spectra were recorded with a resolution of 8 cm^{-1}, at an angle of incidence approximately equal to 60°. The transmission spectra were determined by squeezing an investigated solution between two flat CaF_2 windows. The thickness of the gap between the two tightly pressed CaF_2 windows was determined using the interference fringe method, where the frequency of the oscillations on the interference pattern were measured for the empty thin-layer cell. The gap thickness was determined to be 6 μm and its reproducibility was 10%. The gap thickness was additionally calibrated by filling the gap with neat benzene and recording the intensity of the band at 1960 cm^{-1}, which has an absorbance of 0.10 for every 0.01 mm thickness (19).

3. Results and discussion

3.1. Adsorption of 4-CNPy at the Au(111) electrode surface

To determine experimental conditions for FTIR studies, the adsorption of 4-CNPy was initially characterized using cyclic voltammetry. Figure 1*a* shows the cyclic voltammogram (CV) recorded for the Au(111) electrode in 0.1 M $KClO_4$ + 0.01 M 4-CNPy solution. The CV was acquired employing the hanging electrolyte configuration in which only the Au(111) plane of the electrode was in contact with the electrolyte solution (12, 17). Multiple peaks can be seen on the CV curve. The nature of these peaks can be explained with the help of the adsorption isotherm taken from our previous work (12) and shown in Fig. 1*b*. The peaks located near −0.65 V(SCE) may be identified as corresponding to the adsorption/desorption of 4-CNPy. The peaks at about +0.2 V can be assigned to the reorientation of adsorbed molecules. In the half cycle moving in the positive direction, a large peak is seen at potentials close to +0.7 V(SCE); we will show later that this corresponds to the oxidation of 4-CNPy molecules. Figure 1 shows also that at a potential of −0.8 V (SCE) the organic molecules are desorbed from the electrode surface. The potential E_1 = −0.8 V (SCE) was therefore chosen as the reference potential for the FTIR experiments.

Figure 2 shows a series of subtractively normalized IR spectra determined for a 0.1 M $KClO_4$ + 0.01 M 4-CNPy solution, by stepping the potential between the reference potential (E_1 = −0.8 V (SCE)) and a sample potential (E_2) that varied from −0.60 to +0.75 V (SCE). To facilitate interpretation of these spectra, we additionally measured a spectrum of 4-CNPy solution in $CHCl_3$ and in the aqueous solution of the investigated electrolyte, using the thin-layer transmission cell. Figure 3 shows the transmission spectrum of 4-CNPy in $CHCl_3$ and two bands at 2245 cm^{-1} and at 1416 cm^{-1} for the aqueous solution of 4-CNPy. In the aqueous solution, all other bands of 4-CNPy overlapped with a much more intense water band and hence they are not shown in the figure. For comparison, a selected SNIFTIRS spectrum is also included in Fig. 3. The major features of the IR spectra may be summarized as follows:

(*a*) The SNIFTIRS spectra display four bands for 4-CNPy in the region between 1400 and 1610 cm^{-1} at frequencies 1416, 1505, 1554, and 1601 cm^{-1}, respectively. With the exception of the band at 1554 cm^{-1} the bands are blue shifted

Fig. 1. For the Au(111) electrode in 0.1 M $KClO_4$ + 0.01 M 4-CNPy solution: (*a*) cyclic voltammogram recorded at the sweep rate of 20 mV s^{-1}; (*b*) the Gibbs excess versus electrode potential plot.

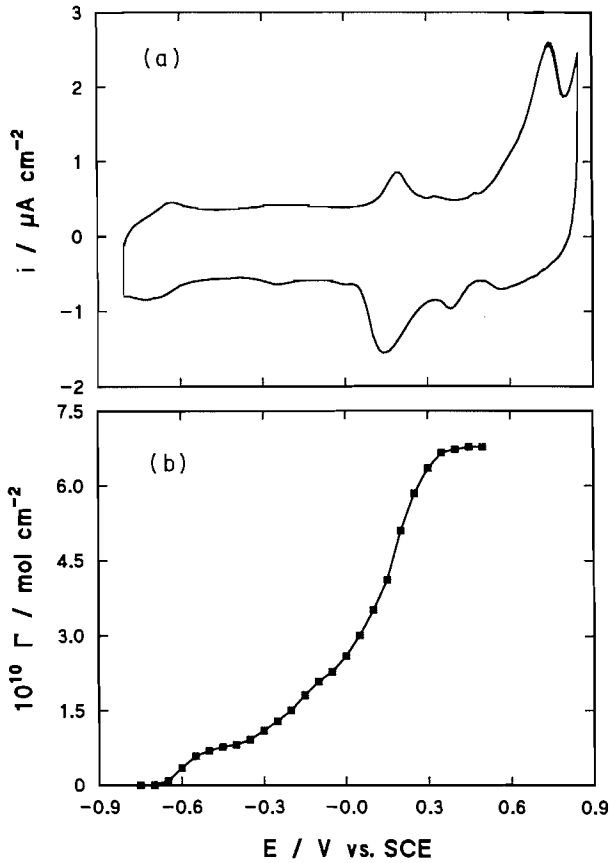

with respect to the bands determined in transmission in $CHCl_3$. However, the band at 1416 cm^{-1} determined in reflection has the same position as the band measured in transmission for the aqueous solution of 4-CNPy. This feature suggests that the blue shift is due chiefly to the solvent effect. All bands determined in the electroreflectance experiments are significantly broader than the bands measured in the transmission experiments. The band broadening for molecules either adsorbed at or in front of a metal surface is a general behavior. It may be explained in terms of a reduced lifetime of the excited state due to the energy transfer to the metal (20). The bands at 1601 and 1505 cm^{-1} may be identified as bands of a_1 symmetry corresponding to the C–C stretching vibrations. The bands at 1416 and 1554 cm^{-1} may be assigned as bands of b_2 symmetry corresponding to anti-symmetric in-plane ring deformations (21). At potentials more positive than 0.15 V (SCE) another small band can also be seen at 1220 cm^{-1}; it could be assigned to the ring bending vibration α(CC), which has b_2 symmetry.

(*b*) When sample potential becomes greater than 0.60 V (SCE), a negative band appears in the spectrum near 2342 cm^{-1}. The intensity of this band significantly increases when the sample potential becomes more positive. This band can be assigned to the asymmetrical stretching of CO_2 (22). Its appearance indicates that 4-CNPy molecules are oxidized at E >0.6 V (SCE). This result suggests that the large

Fig. 2. SNIFTIRS spectra for 4-CNPy adsorbed at the Au(111) electrode from a 0.1 M $KClO_4$ + 0.01 M 4-CNPy solution. For each spectrum, the reference potential E_1 was equal to −0.8 V (SCE) and the value of E_2 is indicated in the figure.

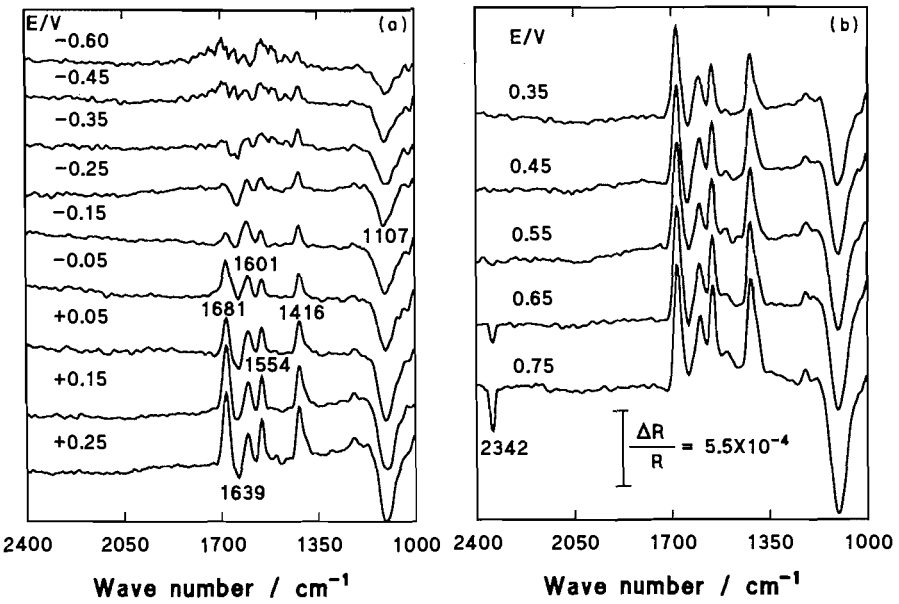

Fig. 3. Comparison of the transmission and SNIFTIRS spectra for 4-CNPy; (*a*) transmission spectrum (100 scans) for a 1.5 M 4-CNPy solution in $CHCl_3$, (*b*) selected bands of the transmission spectrum (100 scans) of a 0.1 M 4-CNPy + 0.1 M $KClO_4$ aqueous solution, (*c*) SNIFTIRS spectrum for a 0.01 M 4-CNPy + 0.1 M $KClO_4$ solution acquired using $E_1 = -0.8$ V (SCE) and $E_2 = 0.45$ V (SCE).

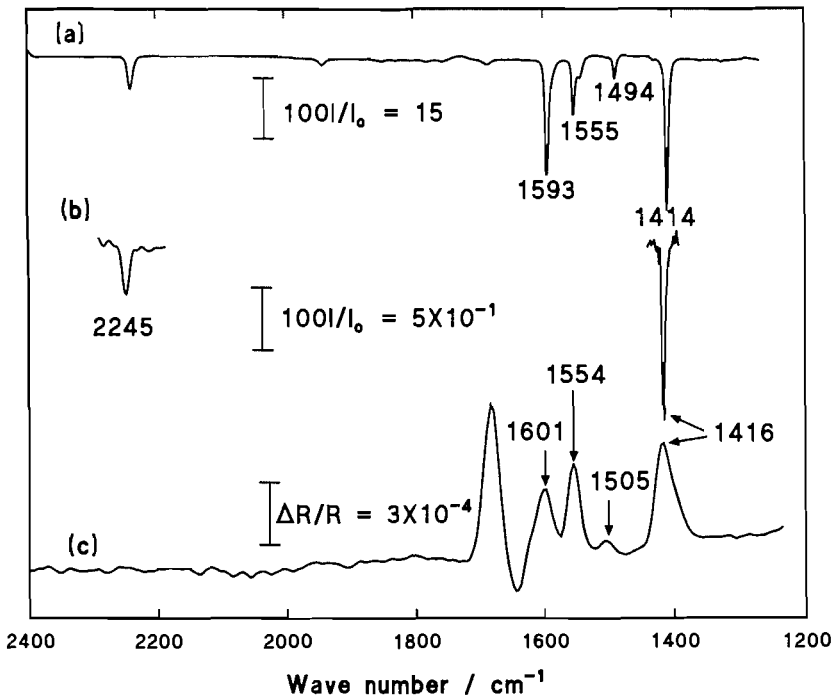

peak observed on the "positive-going" half cycle of the cyclic voltammogram at $E \approx 0.7$ V (SCE) is due to the oxidation of 4-CNPy.

(*c*) A negative band centered at 1107 cm^{-1} can be assigned to the vibrations of perchlorate ions (11). The band intensity increases with the electrode potential since the concentration of perchlorate ions in the double layer increases when E (and hence the electrode charge density) becomes more positive.

Fig. 4. Comparison of the SNIFTIRS spectra acquired in a 0.1 M $KClO_4$ + 0.01 M 4-CNPy solution using nonpolarized light for spectra (*a*) and (*c*) (2000 scans), and *s*-polarized light for spectra (*b*) and (*d*) (3000 scans). The spectra were determined using $E_1 = -0.8$ V (SCE) and $E_2 = 0.05$ V (SCE) for spectra (*a*) and (*b*) and $E_2 = 0.45$ V (SCE) for spectra (*c*) and (*d*).

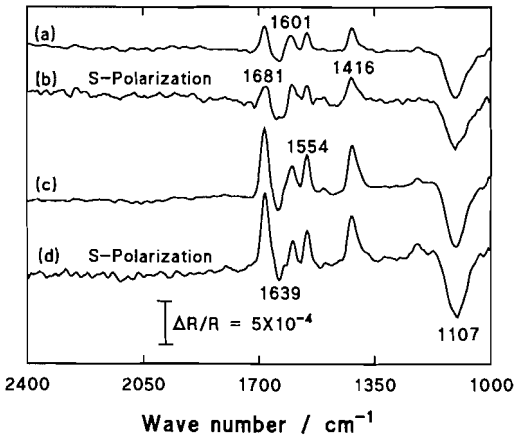

Fig. 5. Schematic diagram representing in-plane ring deformations for the 4-CNPy molecule corresponding to the bands at 1416 and 1554 cm^{-1}; squares represent the CN group, open circles the carbon atoms, and closed circles the nitrogen heteroatom. For the sake of clarity the hydrogen atoms are not shown in this diagram.

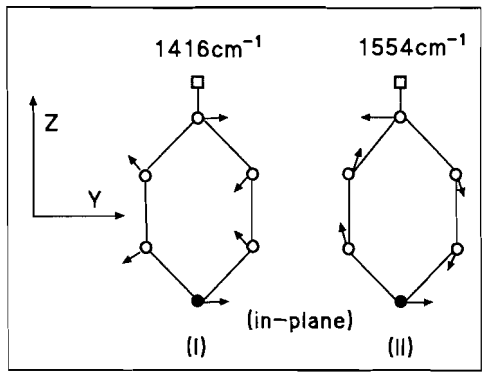

(*d*) A positive band at 1681 cm^{-1} can be assigned to the vibrations of chemisorbed H_2O (11). The potential-induced change of the water bands may be caused either by a substitution of water molecules at the surface by the adsorbed molecules of 4-CNPy or may be due to the change in the concentration of ions within the diffuse part of the double layer.

There are two other features of the IR spectra that are important to note. (*i*) The band due to the CN group stretching mode should be seen at approximately 2245 cm^{-1}; however, this band is absent in all SNIFTIRS spectra shown in Figs. 2 and 3. (*ii*) The intensity of all bands changes with the sample potential; in contrast, the frequencies of these bands are independent of E_2.

For 4-CNPy, the potential difference spectra shown in Fig. 2 may, as a good approximation, be equated to the difference between the absorbance of Γ molecules adsorbed at the sample potential E_2 and desorbed at the reference potential E_1:

$$[2] \quad \Delta R/R \approx 2.3\,\Gamma\,(\varepsilon_{des}(E_1) - \varepsilon_{ads}(E_2))$$

where ε_{des} and ε_{ads} are the molar absorption coefficients of the solution and the adsorbed species respectively. We use the term "desorbed" to describe molecules that at potential E_2 were adsorbed at the electrode surface and at potential E_1 are present in the bulk of the thin layer. The b_2 bands at 1220, 1416, 1554 cm^{-1} are apparently monopolar; they have a positive sign and the band frequency does not depend on the sample potential. These features suggest that the spectra are dominated by IR absorption from the solution species. To confirm this conclusion we performed a few additional experiments and acquired SNIFTIRS spectra using *s*-polarized photons. At the surface of a gold electrode, the electric field of an *s*-polarized photon is equal to zero and hence the adsorbed 4-CNPy is optically inactive for this polarization. Figure 4 shows the potential difference spectra acquired using nonpolarized and *s*-polarized IR radiation for two selected values of the sample potential E_2. In each case, the spectra acquired using either the nonpolarized or *s*-polarized radiation display the same features. This behavior indicates that all the b_2 bands correspond to IR absorption by the solution species. These data also indicate that the IR absorption bands for adsorbed 4-CNPy molecules are either much weaker than the bands of the solution species or that the adsorbed molecules are optically inactive.

We can employ surface selection rules to prove that vibrations corresponding to b_2 bands at 1416 and 1554 cm^{-1} are likely to be IR inactive in molecules adsorbed at the gold electrode surface. Figure 5 shows that the 1416 cm^{-1} band (Model I) is due to the deformation in which one semicircle of the ring is stretching while the other is contracting, and the 1554 cm^{-1} band (Model II) is due to the deformation in which opposite quadrants of the ring are stretching while the intervening quadrants are contracting (23). The two bands correspond to in-plane ring vibrations (18). Since the 4-CNPy molecule exhibits a planar structure and has C_{2v} symmetry the dipole moment for the vibration with b_2 symmetry changes along the *y* axis of the molecule (24). For a molecule adsorbed at a gold electrode, surface selection rules state that the vibration will be allowed if a change in the dipole derivative has a nonzero component in the direction normal to the surface (25). The 4-CNPy molecules are likely to assume either a flat (π-bonded) or a vertical (N-bonded) surface coordination. In the first case, the dipole moment will change in the direction parallel to the metal surface and its component in the direction normal to the surface will be zero. In the second case, depending on the magnitude of the tilt angle, the dipole moments of the two vibrations will change predominantly in the direction that is parallel to the surface. For adsorbed molecules, these two vibrations are expected to be IR inactive and $\varepsilon_{ads}(E_2)$ in eq. [2] will be equal to zero. In contrast, the molecules that are desorbed from the electrode surface and remain in the thin layer are randomly oriented. There is always a significant fraction of the molecules that are either far away from the electrode surface or whose dipole change has a nonzero component in the direction normal to the surface. Therefore the desorbed molecules are IR active and ε_{des} has a nonzero value. In conclusion, the subtractively normalized spectrum of a molecule that is IR inactive in the adsorbed state but is IR active in the

Fig. 6. The black points and solid lines show the dependence of the integrated intensities of the IR bands at 1416 cm^{-1} (Fig. 6*a*) and at 1554 cm^{-1} (Fig. 6*b*) on the electrode potential. The open points and broken lines show the potential dependence of the Gibbs excess of 4-CNPy molecules adsorbed at the Au(111) electrode from a 0.01 M 4-CNPy + 0.1 M $KClO_4$ solution. The inset represents the molar absorption coefficients calculated from the integrated intensities of the IR bands and the Gibbs excess values.

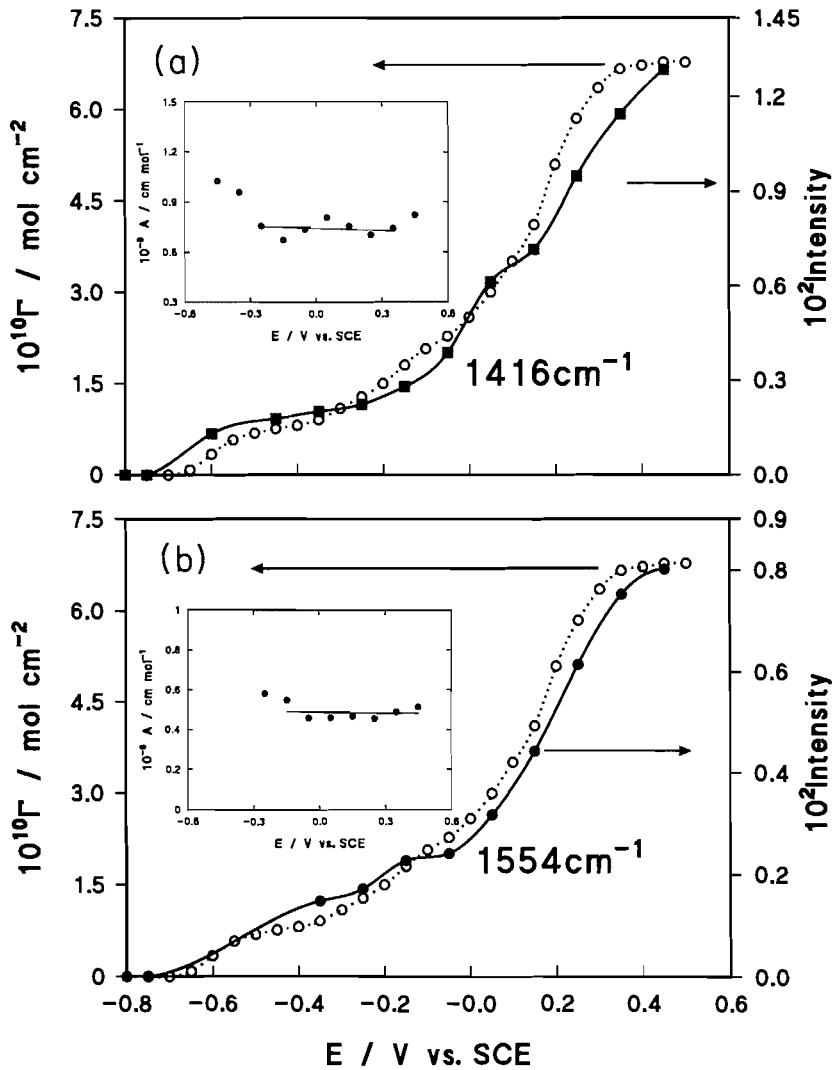

solution phase should be monopolar and its sign should be positive, consistent with the shape and sign of the spectra shown in Fig. 2.

Equation [2] shows that the intensity of a subtractively normalized spectrum that is dominated by the features of the desorbed species should be proportional to the surface concentration of molecules initially adsorbed at the sample potential E_2. The integrated intensity of the absorption bands at 1416 and 1554 cm^{-1} are plotted (black points and solid lines) against the sample potential in Figs. 6*a* and *b*, respectively. For comparison, open points and dotted lines in these figures represent the Gibbs surface excess of 4-CNPy determined from chronocoulometric experiments in ref. 12. The changes in the integrated band intensity follow the changes of the 4-CNPy surface concentration determined from chronocoulometic studies, which is consistent with the predictions from eq. [2]. The integrated band intensities and the Gibbs excess data may be used to calculate the integrated absorptivity A defined as:

$$[3] \quad A = \frac{1}{2.3\Gamma} \int_{\text{band}} \frac{\Delta R}{R} \, d\bar{\nu}$$

The integrated absorptivities are plotted against the electrode potential in the insets for Figs. 6*a* and *b*. Their values are apparently independent of the electrode potential and are equal to 7.2×10^6 mol^{-1} cm and 4.6×10^6 mol^{-1} cm for the bands at 1416 and 1554 cm^{-1}, respectively. In these calculations, we assumed that the desorbed molecules in the thin-layer cell experience a standing wave of IR photons and that the light makes only a single passage, rather than a double passage through the reflecting cavity. It is interesting to compare the

integrated absorptivities determined from the potential modulation experiments to the values obtained by means of transmission infrared measurements as defined by :

$$[4] \quad A = \frac{1}{bc} \int_{\text{band}} \log \frac{I_0}{I} \, d\bar{\nu}$$

where b is the thickness of the cell, c is the concentration of 4-CNPy, and I_0 and I are the incident and transmitted beam intensities. The integrated absorptivities, determined with the help of eq. [4], are equal to 1.5×10^6 mol^{-1} cm and 8.7×10^5 mol^{-1} cm for the two bands, respectively. The values determined from transmittance are about 5 times smaller than the values obtained from the relative change of the electrode reflectivity. Such differences between absorptivities determined in the transmission and reflection experiments are expected when the thickness of the thin-layer cavity of the spectro-electrochemical cell is comparable to the wavelength of the infrared radiation. These differences result from the strong spatial variation in the electric field vector of the light close to the reflecting metal surface. In the spectro-electrochemical experiment, the desorbed molecules are residing in a thin layer of solution (ca. 10 μm thick) in front of the electrode that acts as a reflecting mirror. The distance between the desorbed molecule and the mirror is comparable to the wavelength of the infrared radiation. The mirror changes the field of the infrared photons, resulting in the effective value of A being much larger than the value measured in a transmission experiment (25, 26). For the angle of incidence and the estimated thickness of the thin layer in the spectro-electrochemical cell an enhancement factor of five is consistent with the estimates reported in (refs. 25 and 26). This has serious implications for the use of IR spectroscopy as an analytical tool for measuring the amount of adsorbed species. Since the absorption coefficients measured in the transmission experiment and in the thin-layer electrochemical cell may differ significantly, IR spectroscopy may not be used to measure the absolute surface concentrations of adsorbed ions or molecules. On the other hand, insets to Figs. 4*a* and *b* show that the effective absorption coefficient is independent of the electrode potentials and, therefore, IR spectroscopy could be used as a good measure of a relative change in the electrode coverage by adsorbed ions or molecules. This point is well illustrated by studies of ionic adsorption at gold electrodes by Corrigan and Weaver (27, 28).

We have emphasized in the preceding paragraph that b_2 bands are expected to be IR inactive in adsorbed molecules and hence they cannot be used to study potential-induced reorientation of the 4-CNPy molecules. To extract information about the orientation of adsorbed molecules, we have to rely on the two bands of a_1 symmetry. For this symmetry, the dipole moment changes are in the plane of the molecule along the C_{2v} axis (z direction in Fig. 4). The a_1 bands for adsorbed molecules are therefore expected to be IR inactive for the flat (π-bonded) and to be IR active for the vertical (N-bonded) surface coordination. The first of the two a_1 bands (at 1601 cm^{-1}) overlaps with the band of water and hence it cannot be used to extract this structural information. The second band (at 1505 cm^{-1}) is weak; however, the signal-to-noise ratio in our experiments was large enough to allow the use of this band in the estimation of the surface orientation for the adsorbed molecules. Figure 7 shows enlarged sections of the SNIFTIRS spectra in the region corresponding to the position of the 1505 cm^{-1} band. The band is poorly discernible from the background for potentials that are more negative than 0.15 V (SCE), that is, in the region where the 4-CNPy molecules are expected to assume the π-bonded orientation. At more positive potentials, where 4-CNPy reorients to assume the vertical orientation, the band becomes much stronger than the background and displays well-defined bipolar features. The positive portion of this band corresponds to IR absorption by the desorbed species while the negative segment may be identified as corresponding to the vibrations of adsorbed molecules. The band for adsorbed species is apparently red shifted with respect to the position of the band for desorbed molecules. This shift may reflect the differences between the chemical environment of 4-CNPy molecules in the adsorbed and the desorbed states rather than a Stark effect. The negative portions of the bands correspond to the molecules adsorbed at positive potentials where they form a compact organic film at the electrode surface. The molecules in this film experience chiefly a nonaqueous environment. In contrast, the positive segment of the bipolar spectrum corresponds to the molecules desorbed from the electrode surface at $E_1 = -0.8$ V (SCE). The spectral properties of these molecules are in principle similar to their spectral behavior in an aqueous solution. The differences between the band positions for the adsorbed and desorbed species are likely to be of the same origin as the differences between the band frequencies for the aqueous and $CHCl_3$ solutions of 4-CNPy, seen in the transmission spectra shown in Fig. 3. Overall, the absence of the band at $E < 0.15$ V (SCE) and the appearance of the bipolar band at the more positive potential is consistent with the potential-induced

Fig. 7. SNIFTIRS spectra in the 1540–1440 cm^{-1} region, for 4-CNPy adsorbed at the Au(111) electrode from a 0.1 M $KClO_4$ + 0.01 M 4-CNPy solution. For each spectrum, the reference potential E_1 was equal to −0.8 V (SCE) and the value of E_2 is indicated in the figure.

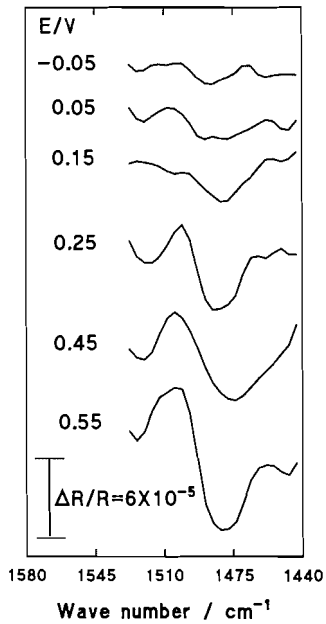

Fig. 8. SNIFTIRS spectra for a 0.01 M 4-CNPy + 0.1 M KClO4 solution acquired using E_1 = 0.4 V (SCE) and negative values of E_2 indicated in the figure for each spectrum.

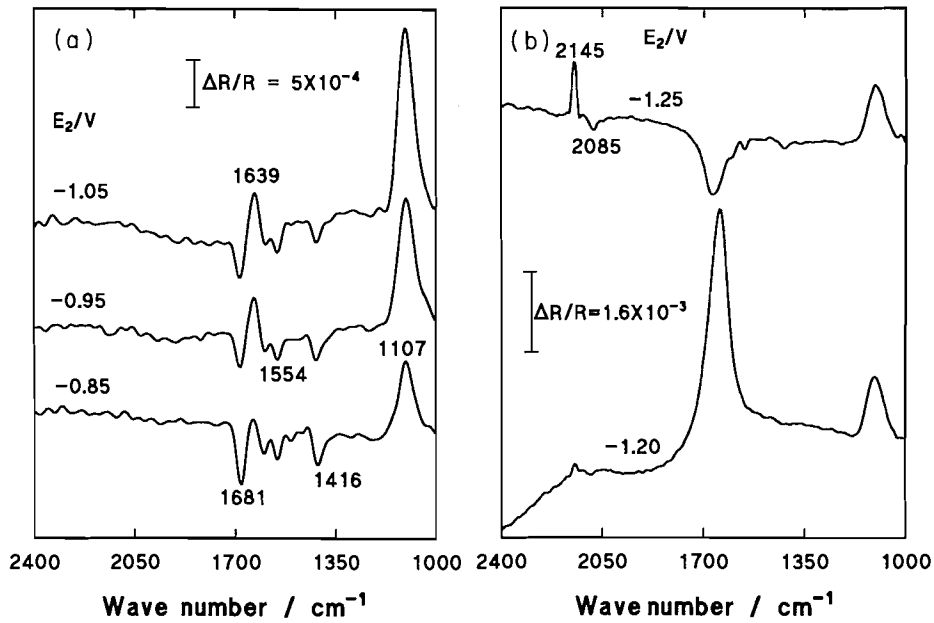

reorientation of the adsorbed molecules, from flat at negative potentials to a vertical position at the positive potentials. Some additional information about the orientation of adsorbed species may be obtained from the total absence of the CN stretching band on the SNIFTIRS spectrum, which should be observed at about 2245 cm^{-1} wave number. The CN stretching band has the same a_1 symmetry as the C–C stretching band at 1505 cm^{-1}. We note that on the transmission spectrum shown in Fig. 3, the two bands have approximately similar intensities. Therefore, the total absence of the CN band in the SNIFTIRS spectra, even for $E_2 > 0.15$ V, may be tentatively interpreted either in terms of a much more significant broadening of this band or as a result of a cancellation in the absorptivities of the adsorbed and solution species. For the vertical orientation of the molecules, a cancellation would be expected if the 4-CNPy molecules are coordinated to the metal surface through the N atom of the aromatic ring, with the CN group facing the solution side of the interface. In this orientation, the CN group would experience a predominantly aqueous environment. The band positions for the adsorbed and the desorbed species should be identical and, hence, if subtracted, they should cancel each other.

3.2. Reduction of 4-CNPy at the Au(111) electrode

Previous studies of 4-CNPy adsorption at Ag, Cu, and Pt electrodes revealed that 4-CNPy molecules may be reduced at these metals at negative potentials (13–16) and various reaction schemes were proposed to explain the mechanism of this reaction (28). For example it was suggested in ref. 13 that 4-CNPy molecules were reduced to give CN^- ion and pyridine molecule as the reaction products. In contrast, it was suggested in ref. 14 that the reduction leads to the formation of a $(4\text{-CNPy})^{-\cdot}$ radical ion. To determine the potential range in which the 4-CNPy molecules are stable at the Au(111) electrode surface, we employed SNIFTIRS to study the behavior of 4-CNPy molecules at very negative potentials. Figures 8*a* and *b* show SNIFTIR spectra obtained by choosing the reference potential E_1 = +0.40 V (SCE) and stepping to the sample potential E_2, which varied from −0.85 to −1.25 V (SCE). At the reference potential, the electrode surface is covered by a monolayer of adsorbed 4-CNPy molecules, and at the sample potentials, the molecules are mostly desorbed from the electrode surface.

For sample potentials that are higher than −1.1 V, the spectra shown in Fig. 8*a* are essentially mirror images of the spectra presented earlier in Figs. 2 and 3. They display the same absorption bands; however, since the direction of the potential step is changed, the bands in Fig. 8 are predominantly negative rather than positive. The shape of the spectrum changes when E_2 decreases below −1.05 V (SCE). The band at 1681 cm^{-1}, due to IR absorption by H_2O, becomes very strong at E_2 = −1.2 V (SCE). Hydrogen evolution takes place at this potential and the formation of H_2 bubbles in the thin layer can be observed. As a result, the concentration of water molecules in the thin layer changes significantly when the potential is stepped between E_1 and E_2. In addition, a new bipolar band appears in the spectrum. Its positive branch has a maximum at 2145 cm^{-1} and the negative portion has a minimum at 2085 cm^{-1}. These bands grow further by decreasing the potential to E_2 = −1.25 V. The bands are not observed on the spectra acquired using *s*-polarized radiation and hence they may be identified as corresponding to the adsorbed species. The positive branch of the band at 2145 cm^{-1} corresponds to the species adsorbed at the reference potential (E_1 = 0.4 V (SCE)), and the negative section at 2085 cm^{-1} is related to the species adsorbed at the sample potential E_2. According to ref. 13, the band at 2085 cm^{-1} may be assigned to CN^-, formed by the reduction of 4-CNPy molecules, which involves a cleavage of the CN–ring bond and the formation of a cyanide ion and a pyridine molecule (see also reduction scheme in ref. 29). However, accord-

Fig. 9. Comparison of three SNIFTIRS spectra recorded at the Au(111) electrode by stepping the potential between $E_1 = 0.4$ V (SCE) and $E_2 = -0.55$ V (SCE). Spectrum (*a*) corresponds to 3×10^{-3} M pyridine in 0.1 M $KClO_4$ solution. Spectra (*b*) and (*c*) correspond to 0.01 M 4-CNPy + 0.1 M $KClO_4$ solution; spectrum (*b*) was acquired without exposing the electrode to the very negative polarization; spectrum (*c*) was recorded after pre-electrolysis at $E = -1.2$ V (SCE).

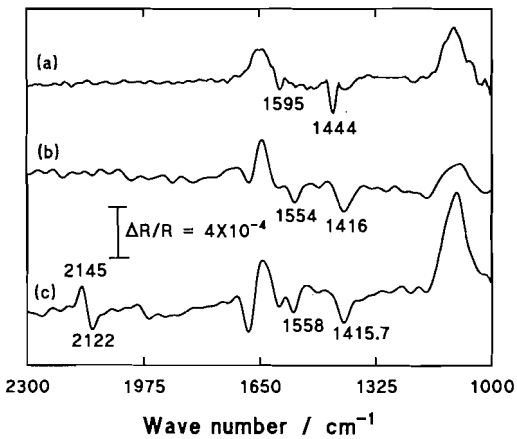

ing to ref. 14 this band may also be assigned to the ν_{CN} mode of the $(4\text{-CNPy})^{\cdot -}$ radical anion. To test these two hypotheses, we have recorded SNIFTIRS spectrum for a 3×10^{-3} M solution of pyridine molecules. The potential was modulated between a value E_1 at which pyridine molecules form a compact monolayer at the Au(111) surface and a potential E_2 where they are desorbed from the surface (12). In Fig. 9, the spectrum for pyridine (curve (*a*)) is compared to the spectrum for 4-CNPy (curve (*b*)), corresponding to the potential modulation between $E_1 = 0.4$ V (SCE) and E_2 equal to –0.8 V. Curve (*c*) in Fig. 9 shows the spectrum recorded after a prolonged electrolysis at $E = -1.2$ V (SCE) used to generate the product of 4-CNPy reduction. The spectrum was acquired after this pre-electrolysis by stepping the potential between $E_1 = 0.4$ V (SCE) and $E_2 = -0.55$ V (SCE). The spectrum for pyridine displays a strong ring stretching band at 1444 cm^{-1}. In contrast, the ring stretching bands for the 4-CNPy molecule in spectra (*b*) and (*c*) are observed at 1416 and 1558 cm^{-1}. Apparently, the appearance of the bipolar band in the 2145–2122 cm^{-1} range, due to reduction of 4-CNPy at the negative potentials, is not accompanied by a change in the ring stretch frequencies. The ring stretching band characteristic for the pyridine molecule is not observed in spectrum (*c*), and this behavior indicates that the reduction of 4-CNPy molecules does not involve a cleavage of the CN–ring bond. The band at 2085 cm^{-1} may therefore be assigned to the formation of the $(4\text{-CNPy})^{\cdot -}$ radical anion. Overall, the spectral behavior of 4-CNPy molecules at negative potentials, described above for the Au(111) surface, are very similar to that observed for a Cu electrode by Rubim and Sala (14). In conclusion, our SNFTIRS experiments indicate that 4-CNPy molecules are stable at the Au(111) electrode surface in the potential range of -1.1 V (SCE) $< E <$ 0.6 V (SCE). The molecules are reduced at more negative potentials and are oxidized at more positive potentials.

4. Summary

Subtractively normalized Fourier transform infrared spectroscopy was employed to study adsorption of 4-cyanopyridine at the Au(111) electrode surface. In these experiments, the potential was modulated between the value $E_1 = -0.8$ V (SCE), at which 4-CNPy molecules are desorbed from the electrode, and the value E_2, at which 4-CNPy molecules are adsorbed at the Au(111) surface. The measured spectra were considered to be equal to the difference between the absorbance of the desorbed molecules at E_1 and the adsorbed molecules at E_2. The IR spectra were used to study (*i*) the dependence of the band intensity on the surface coverage, (*ii*) the character of surface coordination, and (*iii*) the stability of adsorbed 4-CNPy molecules. We observed that the IR bands acquired during the the electroreflectance experiments are significantly broader than the bands from a transmission cell. Some weaker bands recorded in transmission were not observed in the electroreflectance experiment. The electroreflectance spectra were dominated by four bands corresponding to the in-plane ring deformations. Two of them had b_2 symmetry while the other two had a_1 symmetry. All b_2 bands were monopolar in character and their sign was positive; they were dominated by the absorbance of the desorbed 4-CNPy molecules. The intensity of these bands correlated well with the surface concentrations of 4-CNPy molecules, determined from independent electrochemical studies. The integrated absorption intensities for these bands were larger by a factor of five than the absorption intensities of the bands recorded in the transmission cell. This indicates that the photon field, acting on the molecules in front of the gold electrode, is significantly enhanced by reflection from the electrode. One of the two a_1 bands overlapped with the band for water. The second a_1 at 1505 cm^{-1} was quite weak; however, the signal-to-noise ratio in our experiments was sufficiently large to study its potential-induced changes. The band was bipolar and its character varied with the electrode potential. The changes were consistent with a progressive reorientation of 4-CNPy molecules from a flat (π-bonded) coordination at negative potentials, to a vertical N-bonded geometry at positive potentials. The total absence of the band due to the CN stretch in the SNIFTIRS spectra suggested that, in the vertical orientation, 4-CNPy molecules are oriented with the nitrogen atom from the ring pointing towards the metal while the CN group faces the solution. The IR spectra acquired at either very negative or very positive potentials indicate that 4-CNPy is reduced at $E < -1.1$ V (SCE) and it is oxidized at $E > 0.6$ V (SCE).

Acknowledgment

This work was supported by a grant from the Natural Sciences and Engineering Research Council of Canada.

References

1. S. Pons. J. Electroanal. Chem. **150**, 495 (1983).
2. A. Bewick and S. Pons. *In* Advances in infrared and Raman spectroscopy. Vol. 2. *Edited by* R.J.H. Clark and R.E. Hester. John Wiley & Sons, Chichester. 1985. pp. 1–63.
3. A.C. Chen and S.G. Sun. Gaodeng Xuexiao Huaxue Xuebao, **15**, 401 (1994); **15**, 548 (1994).
4. S.G. Sun, D.F. Yang, and Z.W. Tian. J. Electroanal. Chem. **289**, 177 (1990).

5. M.G. Samant, K. Kunimatsu, H. Seki, and M.R. Philpott. J. Electroanal. Chem. **280**, 391 (1990).
6. S.C. Chang and M.J. Weaver. J. Phys. Chem. **94**, 5095 (1990).
7. S. Watanabe, J. Inukai, and M. Ito. Surf. Sci. **293**, 1 (1993).
8. S. Pons and A. Bewick. Langmuir, **1**, 141 (1985).
9. D. Blackwood, C.Korzeniewski, W. Mckenna, J. Li, and S. Pons. ACS Symp. Ser. **378**, 338 (1988).
10. V.I Birss, A.S. Hinman, C.E. McGarvey, and J. Segal. Electrochim. Acta, **39**, 2449 (1994).
11. P.W. Faguy, W.R. Fawcett, G. Liu, and A.J. Motheo. J. Electroanal. Chem. **339**, 339 (1992).
12. D.F. Yang and J. Lipkowski. Elektrokhimiya, **31**, 836 (1995).
13. H. Furukawa, M. Takahashi, and M. Ito. Chem. Phys. Lett. **132**, 498 (1986).
14. J.C. Rubim and O. Sala. J. Mol. Struct. **145**, 157 (1986).
15. J.C. Rubim. J. Electroanal. Chem. **220**, 339 (1987).
16. C.S. Allen and R.R. Van Duyne. Chem. Phys. Lett. **63**, 455 (1979).
17. D.F. Yang. Ph.D. Thesis, University of Guelph, Guelph, Ont. 1995.
18. J. Richer and J. Lipkowski. J. Electrochem. Soc. **133**, 121 (1986).
19. H.H. Willard, L.L. Merritt, J.A. Dean, and F.A. Settle. *In* Instrumental methods of analysis. 6th ed. Wadswarth Publishing Company, Belmont, Calif. 1981. pp. 202–207.
20. A.M. Bradshaw and E. Schweitzer. *In* Spectroscopy of surfaces. *Edited by* R.J.H. Clark and R.E. Hester. John Wiley & Sons Ltd., Chichester. 1988. pp. 413–478.
21. J.H.S. Green and D.J. Harrison. Spectrochim. Acta, Part A, **33**, 75 (1977).
22. S.G. Sun and A.C. Chen. J. Electroanal.Chem. **323**, 319 (1992).
23. N.B. Colthup, L.H. Daly, and S.E. Wiberley. *In* Introduction to infrared and Raman spectroscopy. Academic Press, New York. 1990. pp. 261–280.
24. H.H. Jaffe and M. Orchin. Theory and applications of ultraviolet spectroscopy. John Wiley and Sons, Inc., New York. 1964.
25. M. Moskovits. Rev. Mod. Phys. **99**, 783 (1985).
26. R.G. Greenler. J. Chem. Phys. **44**, 310 (1966).
27. D.S. Corrigan and M.J. Weaver. J. Phys. Chem. **90**, 5300 (1986).
28. D.S. Corrigan and M.J. Weaver. J. Electroanal. Chem. **239**, 55 (1988).
29. J. Volke and V. Skala. J. Electroanal. Chem. **36**, 383 (1972).

The reactions of $[Pd_2Cl_2(\mu\text{-}PP)_2]$ (PP = dppm, dmpm) with $Et_2NC{\equiv}CNEt_2$ in methylene chloride solution: X-ray crystal structures of $[Pd_2Cl_2(\mu\text{-}CH_2)(\mu\text{-}dppm)_2]$ and hexakis(diethylamino)benzene, $C_6(NEt_2)_6$

Sean R. Klopfenstein, Constanze Kluwe, Kristin Kirschbaum, and Julian A. Davies

Abstract: The binuclear palladium(I) complex, $[Pd_2Cl_2(\mu\text{-}dppm)_2]$ (dppm = bis(diphenylphosphino)methane), has been shown to react with bis(diethylamino)acetylene, $Et_2NC{\equiv}CNEt_2$, in methylene chloride solution to yield two isolable products, the known methylene-bridged complex, $[Pd_2Cl_2(\mu\text{-}CH_2)(\mu\text{-}dppm)_2]$, and hexakis(diethylamino)benzene, $C_6(NEt_2)_6$, both of which have been characterized crystallographically. The source of the bridging methylene group in $[Pd_2Cl_2(\mu\text{-}CH_2)(\mu\text{-}dppm)_2]$ has been shown to be the methylene chloride solvent. A mechanism that accounts for the formation of the two isolable products is proposed. The complex, $[Pd_2Cl_2(\mu\text{-}dmpm)_2]$ (dmpm = bis(dimethylphosphino)methane), was similarly found to react with $Et_2NC{\equiv}CNEt_2$ in methylene chloride solution to yield $[Pd_2Cl_2(\mu\text{-}CH_2)(\mu\text{-}dmpm)_2]$, which was identified spectroscopically.

Key words: acetylene, palladium, cyclooligomerization, aminoacetylene, hexakis(diethylamino)benzene.

Résumé : On montre que le complexe binucléaire de palladium(I), $[Pd_2Cl_2(\mu\text{-}dppm)_2]$ (dppm = bis(diphénylphosphino)-méthane, réagit avec le bis(diéthylamino)acétylène, $Et_2NC{\equiv}CNEt_2$, dans une solution de chlorure de méthylène pour donner deux produits que l'on peut isoler : un complexe avec un méthylène ponté $[Pd_2Cl_2(\mu\text{-}dppm)_2]$ qui est connu, et l'hexakis(diéthylamino)benzène, $C_6(NEt_2)_6$; ces deux complexes sont caractérisés par cristallographie. On montre que le groupe méthylène en position de pont dans le complexe $[Pd_2Cl_2(\mu\text{-}CH_2)(\mu\text{-}dppm)_2]$ vient du solvant. On propose un mécanisme qui tient compte des deux produits que l'on peut isoler. De façon similaire, on a trouvé que le complexe $[Pd_2Cl_2(\mu\text{-}dmpm)_2]$ (dmpm = bis(diméthylphosphino)méthane) réagit avec $Et_2NC{\equiv}CNEt_2$ en solution dans le chlorure de méthylène pour conduire au complexe $[Pd_2Cl_2(\mu\text{-}CH_2)(\mu\text{-}dmpm)_2]$ que l'on a identifié par spectroscopie.

Mots clés : acétylène, palladium, cyclooligomérisation, aminoacétylène, hexakis(diéthylamino)benzène.

[Traduit par la rédaction]

Introduction

Binuclear palladium(I) complexes of the type $[Pd_2X_2(\mu\text{-}PP)_2]$ (X = anionic ligand, PP = dppm, dmpm, etc.) are known (1) to react with simple acetylenes bearing electron-withdrawing substituents (e.g., $-CF_3$, $-CO_2Me$) to yield the acetylene complexes, $[Pd_2X_2(\mu\text{-}RC{\equiv}CR)(\mu\text{-}PP)_2]$. Acid catalysis (2, 3) facilitates acetylene addition to the metal-metal bond of $[Pd_2X_2(\mu\text{-}PP)_2]$ and allows generation of $[Pd_2X_2(\mu\text{-}RC{\equiv}CR)(\mu\text{-}PP)_2]$ complexes from acetylenes *without* electron-withdrawing substituents (e.g., -H, -Ph), Fig. 1. We have shown (4, 5) that the heteroatom-substituted acetylene, $MeSC{\equiv}CSMe$, reacts with $[Pd_2Cl_2(\mu\text{-}dppm)_2]$ to yield the acetylene complex, $[Pd_2Cl_2(\mu\text{-}MeSC{\equiv}CSMe)(\mu\text{-}dppm)_2]$, which undergoes a Lewis-acid-promoted rearrangement to the vinylidene isomer, $[Pd_2Cl_2(\mu\text{-}C{=}C\{SMe\}_2)(\mu\text{-}dppm)_2]$, Fig. 2. Vinylidene complexes, formed via 1,2-heteroatom shift reactions, have similarly been isolated from the reactions of haloacetylenes (6) with $[Pd_2Cl_2(\mu\text{-}dppm)_2]$.

Amino-substituted acetylenes and alkoxyacetylenes, $MeC{\equiv}CY$ (Y = NMe_2, OEt) have been shown (7) to undergo 1,2-heteroatom shifts in reactions with $[Mn_2(CO)_9(NCMe)]$. In these cases the 1,2-heteroatom shift reactions are accompanied by CO insertion into the C—Y bond of the newly formed vinylidene, Fig. 3. Such processes are not typical of the reactions of manganese carbonyls with heteroatom-substituted acetylenes. For example, $[Mn_2(CO)_{10}]$ reacts with $PhC{\equiv}CNEt_2$ to yield the expected acetylene complex, $[Mn_2(CO)_8(PhC{\equiv}CNEt_2)]$ (8). Other nitrogen-containing acetylenes have been shown (8) to react with metal carbonyl

Received February 15, 1996.

This paper is dedicated to Professor Howard C. Clark in recognition of his contributions to Canadian chemistry.

S.R. Klopfenstein, C. Kluwe, K. Kirschbaum, and J.A. Davies.[1] Department of Chemistry, The University of Toledo, Toledo, OH 43606, U.S.A.

[1] Author to whom correspondence may be addressed. Telephone: (419) 530-2254. FAX: 419-530-4033. E-mail: JDAVIES@UOFT02.UTOLEDO.EDU

Fig. 1. Acetylene addition to the metal–metal bond of $[Pd_2X_2(\mu\text{-}PP)_2]$.

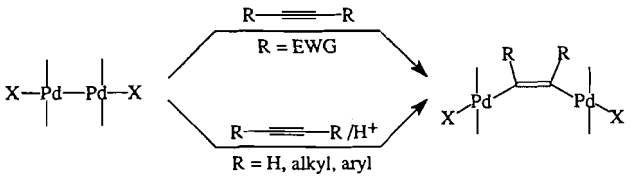

Fig. 2. Reactions of MeSC≡CSMe with $[Pd_2Cl_2(\mu\text{-dppm})_2]$.

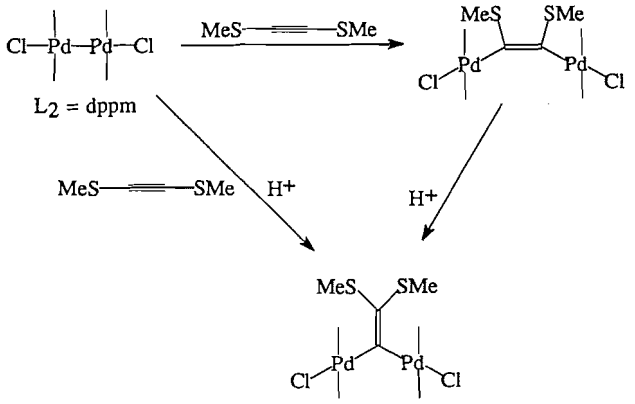

complexes to yield products that arise either from acetylene oligomerization or from C-N bond cleavage, Fig. 4.

In this paper, the reactions between the palladium(I) complexes, $[Pd_2Cl_2(\mu\text{-}PP)_2]$ (PP = dppm, dmpm), and bis(diethylamino)acetylene, $Et_2NC{\equiv}CNEt_2$, in methylene chloride solution are described. Neither acetylene complexes nor the vinylidene isomers could be identified among the reaction products. Two compounds were isolated from the reaction of $Et_2NC{\equiv}CNEt_2$ with $[Pd_2Cl_2(\mu\text{-dppm})_2]$ in CH_2Cl_2, the known methylene-bridged complex, $[Pd_2Cl_2(\mu\text{-}CH_2)(\mu\text{-dppm})_2]$, **1**, and hexakis(diethylamino)benzene, $C_6(NEt_2)_6$, **2**, both of which were characterized crystallographically (**1**·$2CH_2Cl_2$ and **2**). From the reaction of $[Pd_2Cl_2(\mu\text{-dmpm})_2]$ with $Et_2NC{\equiv}CNEt_2$ in methylene chloride solution the analogous methylene-bridged complex, $[Pd_2Cl_2(\mu\text{-}CH_2)(\mu\text{-dmpm})_2]$, was isolated and characterized spectroscopically.

Experimental

Materials

All solvents were deoxygenated prior to use. Reactions were performed under argon or nitrogen using standard Schlenck techniques. Methylene chloride was distilled from calcium carbide under nitrogen. Diethyl ether was distilled from sodium ribbon under nitrogen. Diethylamine was dried over finely ground potassium hydroxide and used without further purification. The compounds $[Pd_2Cl_2(\mu\text{-dppm})_2]$ (9) and $[Pd_2Cl_2(\mu\text{-dmpm})_2]$ (10) were prepared by literature methods. Bis(diethylamino)acetylene was prepared by a procedure modified from three published reports (11–13), as detailed below.

Physical measurements

NMR spectra were measured on Varian VXR-400, Varian Gemini-200, and JEOL FX-90Q NMR spectrometers. Internal tetramethylsilane was employed as a shift standard in ^1H and $^{13}C\{^1H\}$ NMR measurements and $^{31}P\{^1H\}$ NMR spectra were referenced to external 85% phosphoric acid. Data for GC–MS experiments were collected on a HP-5890 instrument with mass-sensitive detector.

Fig. 3. Reactions of MeC≡CY (Y = NMe_2, OEt) with $[Mn_2(CO)_9(NCMe)]$.

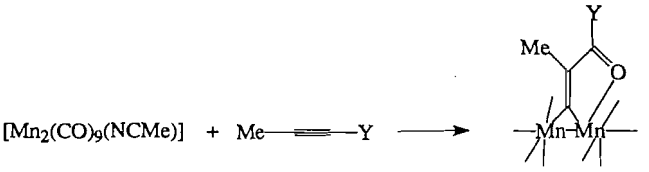

Fig. 4. Reactions of nitrogen-containing acetylenes with metal carbonyl complexes.

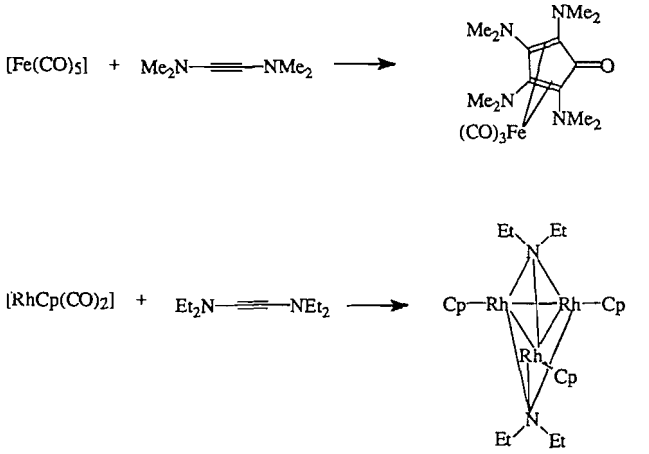

X-ray crystallography[2]

General methods

Single crystals of 1·$2CH_2Cl_2$ and 2 were selected for data collection and mounted on glass fibers in random orientations. X-ray diffraction data were collected with an Enraf–Nonius CAD4 diffractometer in the ω–2θ mode. Data were collected for 1·$2CH_2Cl_2$ to a maximum of 2θ of 44° and for 2 to a maximum of 2θ of 52°. Lorentz and polarization corrections were applied to the data. Absorption effects were corrected by a semiempirical method on the basis of a series of ψ-scans. The structures were refined in full-matrix least squares where the function minimized was

$$\Sigma\omega(|F_o| - |F_c|)^2$$

[2] Copies of tables of all bond distances and angles and thermal parameters may be purchased from: The Depository of Unpublished Data, Document Delivery, CISTI, National Research Council Canada, Ottawa, Canada K1A 0S2. Tables of bond distances and angles have also been deposited with the Cambridge Crystallographic Data Centre, and can be obtained on request from The Director, Cambridge Crystallographic Data Centre, University Chemical Laboratory, 12 Union Road, Cambridge, CB2 1EZ, U.K.

and the weight ω was defined as $4F_o^2/\sigma^2(F_o^2)$. Scattering factors were taken from the standard literature (14). Anomalous dispersion effects were included in F_c. The unweighted and weighted agreement factors are defined as

$$R = \Sigma||F_o| - |F_c||/\Sigma|F_o|,\ R_w = (\Sigma\omega(|F_o| - |F_c|)^2/\Sigma\omega(|F_o|^2)^{1/2}$$

All calculations were performed on a VAX 3100 computer using MolEN (15).

Synthesis of bis(diethylamino)acetylene

(i) Preparation of lithium diethylamide

A three-necked, 300-mL, round-bottomed flask was equipped with a magnetic stirrer bar, dropping funnel, gas inlet, and mineral oil bubbler. The flask was charged with diethylamine (10.5 mL, 0.20 mol) and freshly distilled diethyl ether (50 mL). The contents of the flask were cooled to 0°C and a solution of *n*-butyllithium in hexanes (50 mL, 0.20 mol) was added dropwise under an atmosphere of argon. The resulting lithium diethylamide was used directly in the next step.

*(ii) Preparation of 1,2-dichloro-1-(*N,N*-diethylamino)ethene*

A three-necked, 1000-mL, round-bottomed flask was equipped with a mechanical stirrer, reflux condenser, gas inlet, and mineral oil bubbler. An atmosphere of argon was maintained throughout the procedure. To the flask was added freshly distilled diethyl ether (120 mL), and trichloroethylene (18 mL, 0.20 mol). The solution was cooled to −90°C with a Dry Ice – diethyl ether cooling bath. To the stirring solution, the lithium diethylamide solution (see above) was added via cannula over a period over 10 min while maintaining a temperature below −70°C. Additional diethylamine (21 mL, 0.4 mol) was then added and the flask allowed to warm slowly to 30°C using a water bath. The mixture was allowed to stir for 45 min at 30°C and then the water bath was removed and the reaction flask allowed to come to room temperature over a period of 1 h. The resulting brown, heterogeneous mixture was filtered through a coarse frit covered with dry, finely ground, potassium carbonate. The flask and frit were washed with three 20-mL portions of dry diethyl ether and the washings combined with the filtrate. The filtrate was concentrated to a volume of 100 mL with a rotary evaporator while maintaining a bath temperature below 40°C. The resulting brownish-red solution was analyzed by GC–MS and used without further purification for conversion to the chloroketeneaminal.

(iii) Preparation of 2-chloro-1,1-bis(diethylamino)ethene

The product from (*ii*) was placed in a three-necked, 250-mL, round-bottomed flask with diethylamine (15 mL, 0.30 mol). The flask was equipped with a magnetic stirrer bar and a reflux condenser while an atmosphere of argon was maintained. The contents of the flask were brought to reflux by use of a water bath maintained at 70°C. After 1 h of reflux, some separation of solid material was noted. Additional diethylamine (15 mL, 0.30 mol) was then added in three equal portions over a period of 1 h. The mixture was allowed to reflux for 12 h at which time additional diethylamine (5 mL, 0.10 mol) was added and reflux continued for 8 h longer. The water bath was removed and the flask allowed to cool to room temperature over a period of 1 h. The mixture was then filtered through a coarse frit and the reaction flask and frit were washed with three 20-mL portions of dry diethyl ether and the washings combined with the filtrate. The filtrate was then reduced to a volume of 50 mL with a rotary evaporator while maintaining a bath temperature below 40°C. The resulting brown-red solution was analyzed by GC–MS and used without further purification for the final step.

(iv) Preparation of bis(diethylamino)acetylene

To a three-necked, 250-mL, round-bottomed flask equipped with a magnetic stirrer bar, dropping funnel, gas inlet, and mineral oil bubbler, the chloroketeneaminal (50 mL, 80% by GC–MS) was added with freshly distilled diethyl ether (75 mL). The flask was cooled to 0°C with an ice bath and freshly prepared lithium diethylamide (10.5 mL, 0.20 mol, see (*i*), above) was added via cannula. The solution was allowed to warm to room temperature and stirred overnight under flowing argon. Analysis by GC–MS showed complete conversion. The brown suspension was filtered through a coarse frit covered with Celite using a water aspirator equipped with a potassium hydroxide tube for protection. The Celite was washed with three 10-mL portions of diethyl ether and the washings combined with the filtrate. The solvent was removed by distillation through a 40-cm Vigreux column while maintaining the bath temperature below 70°C. The resulting red-brown liquid (40 mL, 84% by GC–MS) was transferred via cannula to a 100-mL, three-necked, round-bottomed flask equipped for vacuum distillation. The acetylene distilled as a clear oil at 30°C and 0.25 Torr (1 Torr = 133.3 Pa). Yield: 28 mL, 25 g, 74%. ^{1}H NMR ($CDCl_3$): δ 1.1 (CH_3, t), 2.8 (CH_2, q); J(H, H) 7.15 Hz; $^{13}C\{^1H\}$ NMR ($CDCl_3$), δ: 12.9 (CH_3), 49.6 (CH_2), 74.3 (-C≡C-); MS: M* = 168 (100%).

Reaction of $[Pd_2Cl_2(\mu\text{-dppm})_2]$ with $Et_2NC{\equiv}CNEt_2$ in methylene chloride solution

$[Pd_2Cl_2(\mu\text{-dppm})_2]$ (0.135 g, 1.3×10^{-4} mol) was placed in a 25-mL, argon-filled Schlenck tube containing a magnetic stirrer bar and freshly distilled methylene chloride (25 mL) was added. The solution was cooled to −78°C in a Dry Ice – acetone bath. In a separate flask, freshly distilled methylene chloride (10 mL) was added to bis(diethylamino)acetylene (0.24 mL, 0.22 g, 1.3×10^{-3} mol, 10× excess). The acetylene solution was added via cannula to the cooled solution of $[Pd_2Cl_2(\mu\text{-dppm})_2]$. The reaction mixture was allowed to warm to room temperature by slow evaporation of carbon dioxide from the cooling bath over a period of 6 h. The color of the reaction mixture changed from orange to red. The reaction mixture was then filtered via cannula into a Schlenk flask and concentrated to a volume of 7 mL on a vacuum line. Freshly dried diethyl ether (25 mL) was layered onto the methylene chloride solution and the flask cooled in a freezer for 24 h. A solid precipitate formed that was filtered from the orange supernatant liquid (see below). The yellow-gold solid was washed with two 10-mL portions of diethyl ether and dried under vacuum for 3 h. The product was identified as $[Pd_2Cl_2(\mu\text{-}CH_2)(\mu\text{-dppm})_2]$ as follows: $^{31}P\{^1H\}$ NMR (CD_2Cl_2): δ 14.9; ^{1}H NMR (CD_2Cl_2): δ 1.65 (quintet) (μ-CH_2), $J_{(P,H)}$ = 7.7 Hz, δ 7.90 (m), 7.64 (m), 7.42 (m), 7.28 (m) 7.13 (t) (Ph_2P-), δ 3.5 (m) (P-CH_2-P), $J_{(P,H)}$ = 4.7 Hz, $J_{(H,H)}$ = 14 Hz, δ 2.8 (m) (P-CH_2-P) $J_{(P,H)}$ = 3.4 Hz, $J_{(H,H)}$ = 14 Hz. Anal. calcd. (found) for $C_{51}H_{46}Cl_2P_4Pd_2$: C 57.4 (56.9), H 4.3

Table 1. X-ray data for $1{\cdot}2CH_2Cl_2$ and **2**.

	$1{\cdot}2CH_2Cl_2$	**2**
Formula	$C_{53}H_{50}Cl_6Pd_2P_4$	$C_{18}H_{60}N_6$
fw	1236.40	360.72
$F(000)$	2488	630
Crystal dimensions, mm	0.24 × 0.18 × 0.12	0.30 × 0.20 × 0.15
Radiation (λ, Å)	Mo K_α (0.71073)	Mo K_α (0.71073)
Temperature, K	190 ± 1	294 ± 1
Space group	$P4_3$	$R\bar{3}$
Cell dimensions		
a, Å	21.129(5)	18.147(3)
c, Å	14.267(4)	8.151(1)
V, Å^3	6369(5)	2325(1)
Z	4	3
D_{calc}, g/cm^3	1.29	0.78
μ, cm^{-1}	9.4	0.45
No. of parameters	509	95
R	0.062	0.038
R_w	0.096	0.044
S	2.83	1.41
Maximum residual density, e/Å^3	1.83	0.15

(4.3). Yield = 39.2 mg (36% based on Pd). Crystals of $[Pd_2Cl_2(\mu\text{-}CH_2)(\mu\text{-dppm})_2]{\cdot}2CH_2Cl_2$ suitable for X-ray diffraction experiments were obtained by slow evaporation of methylene chloride.

The orange supernatant liquid (see above) was reduced in volume to 2 mL under vacuum. The resulting oily liquid was cooled in a freezer at 0°C for 7 days during which time clear, colorless crystals formed that were found to be suitable for X-ray diffraction and were identified as hexakis(diethylamino)benzene (<5% yield).

X-ray crystallography

(i) $[Pd_2Cl_2(\mu\text{-}CH_2)(\mu\text{-}dppm)_2]{\cdot}2CH_2Cl_2$ ($1{\cdot}2CH_2Cl_2$)

Slow evaporation of the solvent, CH_2Cl_2, yielded yellow single crystals. The crystals diffracted X-rays poorly. They lost solvent and turned into a yellow powder within about 10 min at room temperature. Rapid handling and cooling (190 K) circumvented this problem. The tetragonal unit cell constants and the orientation matrix for data collection were obtained from least-squares refinement, using the setting angles of 25 reflections in the range $10 < \Theta < 13°$. As a check on crystal stability the intensities of three representative reflections were measured every 60 min, indicating a total loss in intensity of 1.9%. An anisotropic decay correction was applied with correction factors on I in the range from 0.963 to 1.103. A total of 4340 reflections were collected, of which 4077 were unique. Intensities of equivalent reflections were averaged, the agreement factors were 3.0% based on I and 2.1% based on F_o. A total of 3321 reflections with $F_o^2 > 3.0\sigma(F_o^2)$ were used in the calculations.

Structure solution and refinement: The positions of the two palladium atoms were found by direct methods. The remaining atoms were located by repeated least-squares refinements followed by difference Fourier syntheses. A total of two equivalents of highly disordered CH_2Cl_2 were found per metal complex. The disorder was modeled and refined in the following ways. C(60), Cl(5), Cl(5a), Cl(6), and Cl(6a) comprised 3/4 equivalent of CH_2Cl_2 disordered over two positions with occupancies for C(60) of 3/4, for Cl(5) and Cl(6) of 1/2, and for Cl(5a) and Cl(6a) of 1/4. Similarly, another 3/4 equivalent of CH_2Cl_2 included C(61) (multiplicity = 3/4), Cl(7) and Cl(8) (occupancy = 1/2), as well as Cl(7a) and Cl(8a) (occupancy = 1/4). C(62), C(19) and Cl(10) represented another 1/2 equivalent of CH_2Cl_2. The atomic positions of the solvent were fixed and only isotropic thermal parameters were refined. The relatively high maximum residual electron density (1.83 e/Å^3) might be due to further small quantities of disordered solvent that we were unable to include in our model. The carbon atoms, C(2), C(7), C(11), C(41), C(47), C(50), and C(51), of the metal complex were refined with isotropic thermal parameters. All other non-hydrogen atoms were refined with anisotropic thermal parameters. The positions of the hydrogen atoms of the metal complex were calculated and included in the least-squares refinement as riding atoms, $U_{iso} = 1.3U_{eq}$ (bonding atom). The hydrogen positions for the disordered CH_2Cl_2 were not calculated. The final cycle of refinement included 509 variable parameters and converged with unweighted and weighted agreement factors of $R = 0.062$ and $R_w = 0.096$. Further details are given in Table 1.

*(ii) $C_6(NEt_2)_6$ (**2**)*

Cooling a solution of **2** in CH_2Cl_2 yielded colorless single crystals. The rhombohedral unit cell constants and the orientation matrix for data collection were obtained from least-squares refinement, using the setting angles of 25 reflections in the range $4 < \Theta < 15°$. As a check on crystal stability the intensities of three representative reflections were measured every 60 min, indicating a total gain in intensity of 0.2%. An

Fig. 5. Synthesis of $Et_2NC{\equiv}CNEt_2$.

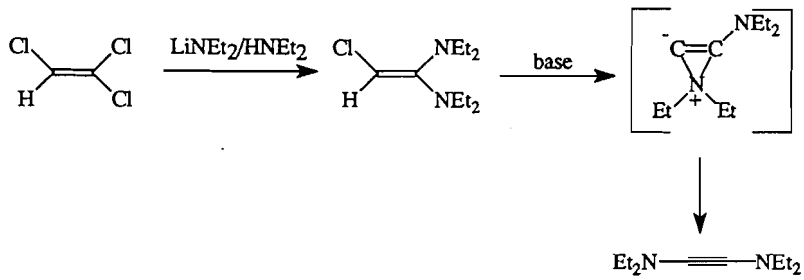

anisotropic decay correction was applied with correction factors on I in the range from 0.983 to 1.035. A total of 1111 reflections were collected, of which 1011 were unique. Intensities of equivalent reflections were averaged, the agreement factors were 1.6% based on I and 1.6% based on F_o. A total of 624 reflections with $F_o^2 > 3.0\sigma(F_o^2)$ were used in the calculations.

Structure solution and refinement: The positions of six atoms were found by direct methods. The remaining atoms were located in succeeding difference Fourier syntheses. The molecule lies on a $\bar{3}$. All non-hydrogen atoms were refined with anisotropic thermal parameters. Hydrogen atoms were refined with isotropic thermal parameters. The final cycle of refinement included 95 parameters and converged with unweighted and weighted agreement factors of $R = 0.038$ and $R_w = 0.044$. Further details are given in Table 1.

Reaction of $[Pd_2Cl_2(\mu\text{-dmpm})_2]$ with $Et_2NC{\equiv}CNEt_2$ in methylene chloride solution

$[Pd_2Cl_2(\mu\text{-dmpm})_2]$ (0.110 g, 2.0×10^{-4} mol) was placed in a 100-mL, nitrogen-filled Schlenck tube containing a magnetic stirrer bar, and freshly distilled methylene chloride (25 mL) was added. Bis(diethylamino)acetylene (50 μL, 2.65×10^{-4} mol) was added slowly via syringe over a period of 5 min. The reaction mixture was allowed to stir for 6 h at room temperature. The color of the reaction mixture changed from yellow to dark red. The reaction mixture was then filtered via cannula into a Schlenck flask and concentrated to a volume of less than 10 mL on a vacuum line. Freshly dried diethyl ether (15 mL) was layered onto the methylene chloride solution and the flask allowed to stand at room temperature overnight followed by cooling in a freezer for 24 h. A solid precipitate formed that was filtered from the orange supernatant liquid. The yellow-black solid was washed with two 10-mL portions of diethyl ether and dried under vacuum for 2 h. The solid was then dissolved in the minimum amount of methylene chloride and allowed to stand overnight during which time a black precipitate formed. The yellow supernatant was filtered from the black solid via cannula, and diethyl ether (15 mL) was layered onto the methylene chloride solution. After 24 h at room temperature a yellow solid had formed that was isolated by cannula filtration, washed with two 25-mL portions of diethyl ether, and dried under vacuum for 8 h. The product was identified as $[Pd_2Cl_2(\mu\text{-}CH_2)(\mu\text{-dmpm})_2]$ as follows: $^{31}P\{^1H\}$ NMR (CD_2Cl_2): δ −4.1; ^1H NMR (CD_2Cl_2): δ 1.3 (quintet) (μ-CH_2), $J_{(P,H)}$ = 7.7 Hz, δ 1.7 (s) 1.6 (s) (Me_2P-), δ 2.26 (m), 1.52 (m) (P-CH_2-P), $J_{(P,H)}$ = 4.7 Hz, $J_{(H,H)}$ = 14 H. $^{13}C\{^1H\}$ NMR (CD_2Cl_2): δ 20.9 (s) (μ-CH_2), δ 23.0 (t) (P-CH_2-P), δ 15.6 (qn), 14.6 (qn) (Me_2P-). Anal. calcd. (found) for $C_{11}H_{30}Cl_2P_4Pd_2$: C 23.2.(23.3), H 5.3 (5.2). Yield = 28.6 mg (25.3% based on Pd).

Results and discussion

Simple acetylenes, such as $CF_3C{\equiv}CCF_3$, react with dinuclear palladium(I) complexes of the type $[Pd_2X_2(\mu\text{-PP})_2]$ to yield acetylene-bridged products (1–3), as illustrated in Fig. 1, while the sulfur-substituted acetylene MeSC≡CSMe reacts according to the pathways illustrated in Figure 2, with formation of a vinylidene-bridged complex under Lewis-acid-promoted conditions (4, 5). Other heteroatom-substituted acetylenes, such as IC≡CI (6), ClC≡CCl (16), PhC≡CCl (17), MeSC≡CMe (4, 5), and MeOC≡CMe[3] have also been shown to yield vinylidene-bridged products in reactions with $[Pd_2X_2(\mu\text{-PP})_2]$ complexes via 1,2-heteroatom shifts under certain conditions. Since the nitrogen-substituted acetylene, $MeC{\equiv}CNMe_2$, is known (7) to undergo a 1,2-heteroatom shift in the reaction with $[Mn_2(CO)_9(NCMe)]$, we sought to investigate the reactions of nitrogen-substituted acetylenes with dinuclear palladium(I) complexes. Our work with sulfur-substituted acetylenes has revealed significant differences in reactivity between symmetrically substituted acetylenes and unsymmetrically substituted acetylenes (e.g., MeSC≡CSMe vs. MeSC≡CMe (4,5)) and so we first began to investigate the reactivity of the symmetrically substituted, nitrogen-containing acetylene, $Et_2NC{\equiv}CNEt_2$, with $[Pd_2X_2(\mu\text{-PP})_2]$ (X = anionic ligand, PP = dppm, dmpm) complexes.

The synthesis of $Et_2NC{\equiv}CNEt_2$, detailed in the experimental section, was derived from literature reports (11–13) and followed the pathway outlined in Fig. 5. Our modifications to the reported methods led to isolation of $Et_2NC{\equiv}CNEt_2$ in a 74% overall yield.

The reaction of $[Pd_2Cl_2(\mu\text{-dppm})_2]$ with a tenfold excess of $Et_2NC{\equiv}CNEt_2$ in methylene chloride solution was investigated. The reaction was monitored by removal of aliquots and measurement of the $^{31}P\{^1H\}$ NMR spectra, which revealed a complex mixture of species in solution. Precipitation with diethyl ether allowed isolation of a single complex (δP = 14.9 ppm) whose ^1H NMR spectrum revealed, in addition to resonances attributed to the bridging dppm ligands, a quintet at

[3] J.A. Davies, C. Kluwe, and J. Müller. Unreported results.

Fig. 6. ORTEP diagram of $[Pd_2Cl_2(\mu\text{-}CH_2)(\mu\text{-}dppm)_2]$ (**1**).

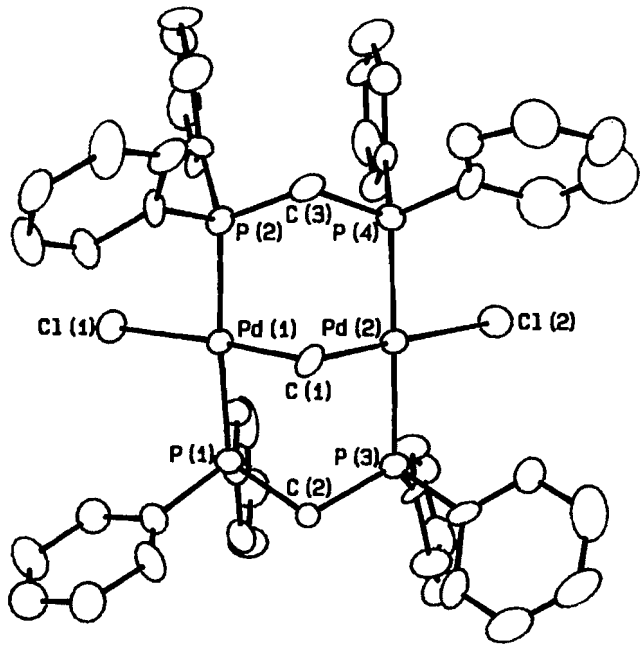

Table 2. Selected bond angles and distances for $\mathbf{1}\cdot 2CH_2Cl_2$.

(*a*) Bond angles (°).

Atom 1	Atom 2	Atom 3	Angle
Cl(1)	Pd(1)	P(1)	90.4(2)
Cl(1)	Pd(1)	P(2)	95.3(2)
Cl(1)	Pd(1)	C(1)	174.8(7)
P(1)	Pd(1)	P(2)	174.3(2)
P(1)	Pd(1)	C(1)	88.1(6)
P(2)	Pd(1)	C(1)	86.2(6)
Cl(2)	Pd(2)	P(3)	92.6(2)
Cl(2)	Pd(2)	P(4)	92.0(2)
Cl(2)	Pd(2)	C(1)	176.6(6)
P(3)	Pd(2)	P(4)	174.2(2)
P(3)	Pd(2)	C(1)	87.3(6)
P(4)	Pd(2)	C(1)	87.9(6)
Pd(1)	C(1)	Pd(2)	103(1)

(*b*) Bond lengths (Å).

Atom 1	Atom 2	Distance
Pd(1)	Cl(1)	2.429(5)
Pd(1)	P(1)	2.311(6)
Pd(1)	P(2)	2.321(6)
Pd(1)	C(1)	2.04(2)
Pd(2)	Cl(2)	2.419(6)
Pd(2)	P(3)	2.300(6)
Pd(2)	P(4)	2.319(6)
Pd(2)	C(1)	2.03(2)
Pd(1)	Pd(2)	3.171(2)[a]

[a]Refers to the Pd(1)·····Pd(2) separation.

1.65 ppm. A comparison to literature data (18–20) suggested that this signal could be attributed to a methylene group bridging the palladium centers and that the complex, isolated in 36% yield, was $[Pd_2Cl_2(\mu\text{-}CH_2)(\mu\text{-}dppm)_2]$. Single crystals of $[Pd_2Cl_2(\mu\text{-}CH_2)(\mu\text{-}dppm)_2]\cdot 2CH_2Cl_2$ ($\mathbf{1}\cdot 2CH_2Cl_2$) suitable for X-ray diffraction were obtained from a methylene chloride solution by slow solvent evaporation. The structure of $[Pd_2Cl_2(\mu\text{-}CH_2)(\mu\text{-}dppm)_2]$ is shown in Fig. 6, selected bond angles and distances are presented in Table 2, and positional parameters and B_{eq} are shown in Table 3.

The two palladium centers are spanned by two bridging dppm ligands and the bridging methylene group. The structure adopts the typical "A-frame" coordination mode common to related systems. Each palladium center is approximately square-planar with terminal chloride ligands *trans* to the bridging methylene group. The most significant deviations from square-planar geometry occurred in the angles P1-Pd1-P2 (174.3(2)°), P3-Pd2-P4 (174.2(2)°), Cl1-Pd1-P2 (95.3(2)°), P1-Pd1-C1 (88.1(6)°), and P2-Pd1-C1 (86.2(6)°). These deviations most likely arise from the incompatibility of the optimum Pd·····Pd separation and the ideal tetrahedral geometry of the bridging methylene group. The structure corresponds closely to that reported previously for the platinum analog (21).

The origin of the methylene bridge in $[Pd_2Cl_2(\mu\text{-}CH_2)(\mu\text{-}dppm)_2]$ was shown to be the methylene chloride solvent by repeating the reaction of $[Pd_2Cl_2(\mu\text{-}dppm)_2]$ with $Et_2NC{\equiv}CNEt_2$ in d_2-methylene chloride solution. The resulting product exhibited an identical $^{31}P\{^1H\}$ NMR spectrum to that described above ($\delta P = 14.9$ ppm), but the ^1H NMR spectrum lacked the quintet at 1.65 ppm, confirming incorporation of a $\mu\text{-}CD_2$ group in place of $\mu\text{-}CH_2$. In the absence of $Et_2NC{\equiv}CNEt_2$, $[Pd_2Cl_2(\mu\text{-}dppm)_2]$ was shown to be unreactive towards methylene chloride under conditions comparable to those employed in the reaction. Thus, stirring a methylene chloride solution of $[Pd_2Cl_2(\mu\text{-}dppm)_2]$ at room temperature for 3 weeks or refluxing a methylene chloride solution of $[Pd_2Cl_2(\mu\text{-}dppm)_2]$ overnight gave no evidence for formation of $[Pd_2Cl_2(\mu\text{-}CH_2)(\mu\text{-}dppm)_2]$ by $^{31}P\{^1H\}$ NMR spectroscopy. These data suggest that $[Pd_2Cl_2(\mu\text{-}dppm)_2]$ reacts with $Et_2NC{\equiv}CNEt_2$ to generate one or more species capable of further reaction with methylene chloride to form $[Pd_2Cl_2(\mu\text{-}CH_2)(\mu\text{-}dppm)_2]$.

The second product isolated in low yield from the reaction of $[Pd_2Cl_2(\mu\text{-}dppm)_2]$ with a tenfold excess of $Et_2NC{\equiv}CNEt_2$ in methylene chloride solution was identified crystallographically as hexakis(diethylamino)benzene, the cyclotrimerization product derived from $Et_2NC{\equiv}CNEt_2$. The structure of $C_6(NEt_2)_6$ is shown in Fig. 7, selected bond angles and distances are presented in Table 4, and positional parameters and B_{eq} are shown in Table 5.

The molecule possesses approximate C_{6h} symmetry. The bond lengths and angles have normal values and correspond well to those reported for $C_6(NMe_2)_6$ (22). The diethylamino substituents adopt a conformation such that the nitrogen lone pair does not participate in the aromatic π-system and the C_{Ar}—N bond distances reflect the single bond character.

Palladium-promoted cyclotrimerization reactions of acetylene are well known (23) but much of the reported work concerns reactions of simple acetylenes promoted by complexes of palladium(0) or palladium(II). Reactions of functionalized

Table 3. Positional parameters and B_{eq} for **1**·2CH_2Cl_2.

Atom	*x*	*y*	*z*	B^a (Å^2)
Pd(1)	0.51034(7)	0.21788(7)	0.477	1.58(3)
Pd(2)	0.43228(8)	0.11260(7)	0.5856(2)	1.72(3)
Cl(1)	0.6076(2)	0.2790(3)	0.4710(5)	2.6(1)
Cl(2)	0.4314(3)	0.0440(3)	0.7213(4)	2.9(1)
Cl(5)	0.293	0.238	0.256	6.9(4)*
Cl(5a)	0.310	0.225	0.288	4.5(6)*
Cl(6)	0.404	0.276	0.158	3.0(2)*
Cl(6a)	0.419	0.249	0.207	8(1)*
Cl(7)	0.204	0.174	0.023	5.5(3)*
Cl(7a)	0.185	0.164	−0.003	9(1)*
Cl(8a)	0.239	0.313	0.001	6.6(8)*
Cl(8)	0.243	0.296	−0.017	4.9(3)*
Cl(9)	0.251	0.124	0.471	8.8(5)*
Cl(10)	0.224	0.083	0.280	10.6(7)*
P(1)	0.5596(3)	0.1346(3)	0.4017(4)	1.9(1)
P(2)	0.4516(3)	0.2958(3)	0.5520(4)	1.8(1)
P(3)	0.4747(3)	0.0352(2)	0.4913(4)	1.9(1)
P(4)	0.3834(3)	0.1938(3)	0.6677(4)	1.9(1)
C(1)	0.4279(9)	0.1680(9)	0.470(2)	2.0(4)
C(2)	0.5116(9)	0.0636(9)	0.380(1)	1.4(4)*
C(3)	0.3773(9)	0.2709(9)	0.603(2)	2.0(5)
C(4)	0.583(1)	0.154(1)	0.283(2)	2.7(5)
C(5)	0.548(1)	0.146(1)	0.205(1)	2.4(5)
C(6)	0.568(1)	0.166(1)	0.119(2)	3.5(6)
C(7)	0.626(1)	0.192(1)	0.109(2)	3.5(5)*
C(8)	0.667(1)	0.201(1)	0.185(2)	4.2(6)
C(9)	0.644(1)	0.182(1)	0.275(2)	3.1(6)
C(10)	0.629(1)	0.103(1)	0.461(2)	2.5(5)
C(11)	0.6479(9)	0.126(1)	0.546(2)	2.0(4)*
C(12)	0.700(1)	0.098(1)	0.590(2)	4.4(6)
C(13)	0.732(1)	0.046(1)	0.549(2)	3.2(6)
C(14)	0.712(1)	0.026(1)	0.465(2)	3.8(6)
C(15)	0.664(1)	0.052(1)	0.422(2)	3.1(5)
C(16)	0.4252(9)	0.3541(9)	0.470(2)	2.0(4)
C(17)	0.367(1)	0.3844(9)	0.480(2)	2.7(5)
C(18)	0.350(1)	0.430(1)	0.408(2)	3.9(6)
C(19)	0.393(1)	0.447(1)	0.339(2)	3.0(5)
C(20)	0.451(1)	0.416(1)	0.334(2)	3.4(5)
C(21)	0.464(1)	0.371(1)	0.395(2)	2.5(5)
C(22)	0.487(1)	0.340(1)	0.650(2)	2.0(5)
C(23)	0.456(1)	0.392(1)	0.688(2)	3.3(6)
C(24)	0.481(1)	0.423(1)	0.766(2)	4.0(6)
C(25)	0.535(1)	0.403(1)	0.802(2)	3.2(6)
C(26)	0.569(1)	0.354(1)	0.765(2)	3.7(6)
C(27)	0.5441(9)	0.3211(9)	0.686(1)	1.7(4)
C(28)	0.533(1)	−0.0174(9)	0.540(2)	2.0(5)
C(29)	0.564(1)	−0.005(1)	0.620(2)	2.2(5)
C(30)	0.611(1)	−0.043(1)	0.653(2)	3.4(6)
C(31)	0.628(1)	−0.100(1)	0.607(2)	3.7(6)
C(32)	0.597(1)	−0.114(1)	0.520(2)	4.5(7)
C(33)	0.548(1)	−0.0728(9)	0.491(2)	2.7(5)
C(34)	0.413(1)	−0.017(1)	0.451(2)	2.5(5)
C(35)	0.416(1)	−0.046(1)	0.362(2)	3.4(6)
C(36)	0.366(1)	−0.084(1)	0.331(2)	4.2(6)
C(37)	0.317(1)	−0.097(1)	0.391(2)	3.8(6)
C(38)	0.312(1)	−0.070(1)	0.479(2)	5.0(7)
C(39)	0.362(1)	−0.029(1)	0.509(2)	3.7(6)
C(40)	0.423(1)	0.216(1)	0.776(1)	1.9(5)
C(41)	0.396(1)	0.265(1)	0.833(2)	2.7(4)*
C(42)	0.434(1)	0.286(1)	0.913(2)	4.3(7)
C(43)	0.489(1)	0.258(1)	0.931(2)	3.1(6)
C(44)	0.515(1)	0.210(1)	0.878(2)	3.5(6)
C(45)	0.4813(9)	0.191(1)	0.798(2)	2.1(5)
C(46)	0.301(1)	0.180(1)	0.701(2)	3.6(6)
C(47)	0.251(1)	0.220(1)	0.680(2)	2.9(5)*
C(48)	0.192(1)	0.199(1)	0.702(2)	5.0(7)
C(49)	0.176(1)	0.146(1)	0.740(2)	4.2(7)
C(50)	0.221(2)	0.112(2)	0.766(3)	8(1)*
C(51)	0.289(2)	0.120(2)	0.746(3)	6.4(8)*
C(60)	0.363	0.277	0.258	8(1)*
C(61)	0.268	0.077	0.380	6(2)*
C(62)	0.252	0.224	−0.044	5(1)*

[a]Starred atoms were refined isotropically. Anisotropically refined atoms are given in the form of the isotropic equivalent displacement parameter defined as: $(4/3)[a^2B(1,1) + b^2B(2,2) + c^2B(3,3) + ab(\cos\gamma)B(1,2) + ac(\cos\beta)B(1,3) + bc(\cos\alpha)B(2,3)]$.

Table 4. Selected bond angles and distances for **2**.

(*a*) Bond angles (°).

Atom 1	Atom 2	Atom 3	Angle
C(1)	N(1)	C(2)	115.3(1)
C(1)	N(1)	C(4)	115.6(1)
C(2)	N(1)	C(4)	110.9(1)
N(1)	C(2)	C(3)	115.2(1)
N(1)	C(1)	C(1′)	117.0(1)
N(1)	C(1)	C(1″)	123.0(1)
C(1″)	C(1)	C(1)′	120.0(1)

(*b*) Bond lengths (Å).

Atom 1	Atom 2	Distance
N(1)	C(1)	1.447(2)
N(1)	C(2)	1.469(2)
N(1)	C(4)	1.468(2)
C(2)	C(3)	1.507(3)
C(1)	C(1′)	1.409(1)

[a]Symmetry transformation (′): $1 + y, 1 - x + y, 2 - z$; (″): $x - y, -1 + z, 2 - z$.

acetylenes and reactions promoted by palladium(I) are much less common. The cyclotrimerization of the dimethyl ester of acetylene dicarboxylic acid to yield hexamethyl mellitate, promoted by [Pd_2Cl_2(μ-dppm)$_2$], has been described and a mechanism proposed (24). In the case of the cyclotrimerization of $Et_2NC{\equiv}CNEt_2$, a comparable mechanism suggests pathways by which [Pd_2Cl_2(μ-CH_2)(μ-dppm)$_2$] might be formed. Fig-

Table 5. positional parameters and B_{eq} for **2**.

Atom	*x*	*y*	*z*	B^a (Å^2)
N(1)	0.87327(7)	0.04885(7)	1.0173(2)	2.52(3)
C(1)	0.93566(8)	0.02184(9)	1.0018(2)	2.15(3)
C(2)	0.8230(1)	0.0225(1)	1.1692(2)	3.39(4)
C(3)	0.8726(1)	0.0311(1)	1.3232(2)	3.95(5)
C(4)	0.81828(9)	0.0327(1)	0.8739(2)	3.32(4)
C(5)	0.7790(1)	0.0894(1)	0.8690(3)	4.94(5)
H(21)	0.799(1)	0.062(1)	1.179(2)	4.4(4)*
H(22)	0.7741(9)	−0.0373(9)	1.160(2)	3.7(4)*
H(31)	0.917(1)	0.091(1)	1.342(2)	5.8(5)*
H(32)	0.835(1)	0.014(1)	1.421(2)	5.3(4)*
H(33)	0.898(1)	−0.005(1)	1.321(2)	5.4(4)*
H(41)	0.770(1)	−0.031(1)	0.871(2)	4.2(4)*
H(42)	0.8546(9)	0.0444(9)	0.772(2)	3.4(4)*
H(51)	0.738(1)	0.076(1)	0.960(3)	7.0(6)*
H(52)	0.820(1)	0.149(1)	0.884(2)	6.9(5)*
H(53)	0.752(1)	0.086(1)	0.761(3)	7.7(6)*

[a]Starred atoms were refined isotropically. Anisotropically refined atoms are given in the form of the isotropic equivalent displacement parameter defined as: $(4/3)[a^2B(1,1) + b^2B(2,2) + c^2B(3,3) + ab(\cos\gamma)B(1,2) + ac(\cos\beta)B(1,3) + bc(\cos\alpha)B(2,3)]$.

Fig. 7. ORTEP diagram of $C_6(NEt_2)_6$ (**2**).

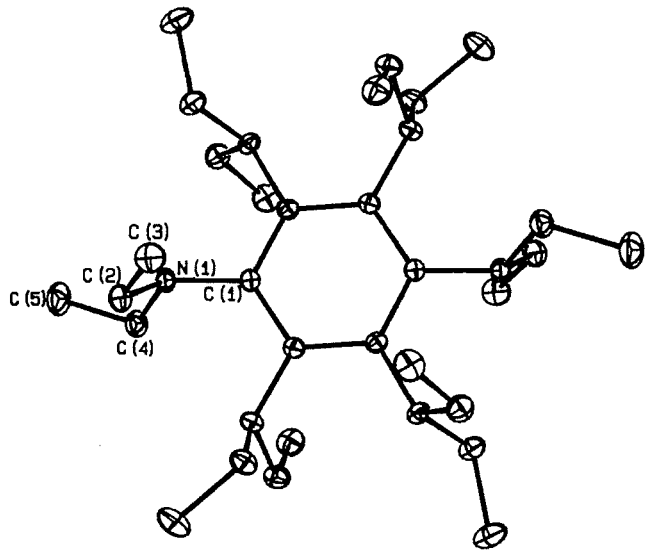

Fig. 8. Possible mechanism for cyclotrimerization of $Et_2NC{\equiv}CNEt_2$.

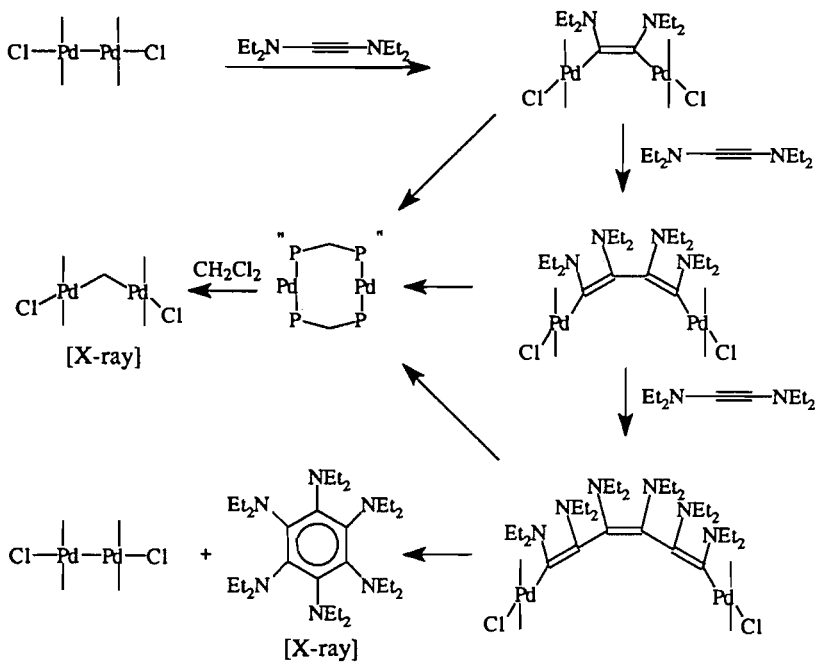

ure 8 outlines a possible mechanism for cyclotrimerization of $Et_2NC{\equiv}CNEt_2$ that is based upon that proposed for hexamethyl mellitate formation (24).

Included in the pathway are intermediates capable of reductive elimination of chlorinated organic fragments. Such processes would lead to the generation of palladium(0) species that might subsequently react with methylene chloride to form $[Pd_2Cl_2(\mu\text{-}CH_2)(\mu\text{-}dppm)_2]$. It is noteworthy that $[Pd_2Cl_2(\mu\text{-}CH_2)(\mu\text{-}dppm)_2]$ was synthesized earlier by the reaction between the binuclear palladium(0) complex, $[Pd_2(\mu\text{-}dppm)_3]$, and methylene chloride (21). Binuclear palladium(0) complexes of the type $[Pd_2(\mu\text{-}PP)_2]$, although not known with dppm as the bridging ligand, have been isolated and characterized crystallographically with the sterically demanding

$Cy_2P(CH_2)_2PCy_2$ ligand to provide kinetic stabilization (25). Thus, the mechanism illustrated in Fig. 8 appears to be a reasonable pathway, which accounts for the formation of both $[Pd_2Cl_2(\mu\text{-}CH_2)(\mu\text{-dppm})_2]$ and $C_6(NEt_2)_6$ from the reaction between $[Pd_2Cl_2(\mu\text{-dppm})_2]$ and $Et_2NC{\equiv}CNEt_2$ in methylene chloride solution. However, all attempts, by GC–MS, to detect chlorinated organic products resulting from the various reductive elimination pathways in Fig. 8 failed (26) and so the possibility exists that reactive palladium(0) species, capable of oxidative addition of methylene chloride, arise from other pathways distinct from those illustrated in Fig. 8. Similarly, we cannot exclude the possibility that cyclotrimerization is promoted by a palladium-containing decomposition product.

The complex $[Pd_2Cl_2(\mu\text{-dppm})_2]$ was found to be unreactive towards $Et_2NC{\equiv}CNEt_2$ in chloroform and monitoring a $CHCl_3$ solution of these compounds by $^{31}P\{^1H\}$ NMR spectroscopy over a period of several hours gave no evidence for any reaction. $[Pd_2Cl_2(\mu\text{-dmpm})_2]$ was found to react with $Et_2NC{\equiv}CNEt_2$ in methylene chloride solution and $[Pd_2Cl_2(\mu\text{-}CH_2)(\mu\text{-dmpm})_2]$ could be isolated in pure form from the reaction mixture in 25.3% yield.

Conclusions

The palladium(I) complex, $[Pd_2Cl_2(\mu\text{-dppm})_2]$, has been shown to react with $Et_2NC{\equiv}CNEt_2$ in methylene chloride solution to yield the product of acetylene cyclotrimerization, $C_6(NEt_2)_6$, and the methylene-bridged complex, $[Pd_2Cl_2(\mu\text{-}CH_2)(\mu\text{-dppm})_2]$, as isolable products. Formation of $C_6(NEt_2)_6$ suggests initial generation of an acetylene complex capable of further reaction, via two insertion steps and a reductive elimination step, to generate the hexasubstituted benzene. Isolation of $[Pd_2Cl_2(\mu\text{-}CH_2)(\mu\text{-dppm})_2]$ is suggestive of a deactivation pathway that involves generation of a palladium(0) intermediate capable of oxidative addition of the methylene chloride solvent. The results, together with those extant in the literature (24) show that binuclear palladium(I) complexes serve as promoters for the synthesis of hexasubstituted benzenes by acetylene cyclotrimerization and that this reaction is possible even with heteroatom-substituted acetylenes that lead to highly functionalized aromatics. In the case described here, however, the possibility of catalysis by unidentified palladium-containing decomposition products cannot be excluded.

Acknowledgments

Thanks are expressed to the Petroleum Research Fund, administered by the American Chemical Society, for support of this work and to the College of Arts and Sciences Instrumentation Center at The University of Toledo for X-ray crystallographic facilities.

References

1. A.L. Balch, C.-L. Lee, C.H. Lindsay, and M.M. Olmstead. J. Organomet. Chem. **177**, C22 (1979).
2. B.L. Shaw and S.J. Higgins. J. Chem. Soc. Chem. Commun. 1629 (1986).
3. B.L. Shaw and S.J. Higgins. J. Chem. Soc. Dalton Trans. 457 (1988).
4. J.A. Davies, K. Kirschbaum, and C. Kluwe. Organometallics, **13**, 3664 (1994).
5. C. Kluwe and J.A. Davies. Organometallics, **14**, 4257 (1995).
6. J.A. Davies, A.A. Pinkerton, R. Syed, and M.J. Vilmer, J. Chem. Soc., Chem. Commun. 47 (1988).
7. R.D. Adams, G. Chen, L. Chen, M.P. Pompeo, and J. Yin. Organometallics, **10**, 2541 (1991).
8. R.B. King and C.A. Harmon. Inorg. Chem. **15**, 879 (1976).
9. A.L. Balch and L.S. Benner. Inorg. Synth. **21**, 47 (1982).
10. J.A. Davies, S. Dutremez, and M. Vilmer, J. Prakt. Chem. **334**, 34 (1992).
11. L. Brandsma and R. van der Heiden. Synthesis, 76 (1987).
12. L. Brandsma and H.D. Verkruijsse. Synth. Commun. **21**, 811 (1991).
13. H.G. Viehe and S.Y. Delavarenne. Chem. Ber. **103**, 1209 (1970).
14. D.T. Cromer and J.T. Waber. International tables for X-ray crystallography. Vol. IV. Kynoch Press, Birmingham, England. 1974.
15. C.K. Fair. MolEN: An interactive intelligent system for crystal structure analysis; User Manual. Enraf–Nonius, Delft, The Netherlands. 1990.
16. M. Vilmer. Ph.D. Thesis, University of Toledo, 1991.
17. S. Zheng. M.S. Thesis, University of Toledo, 1993.
18. H.G. Viehe and M. Reinstein. Angew. Chem. Intl. Ed. Engl. **3**, 506 (1964).
19. M.P. Brown, J.R. Fisher, R.J. Puddephatt, and K.R. Seddon. Inorg. Chem. **18**, 2808 (1979).
20. A.L. Balch, C.T. Hunt, C.L. Lee, M.M. Olmstead, and J.P. Farr. J. Am. Chem. Soc. **103**, 3764 (1981).
21. R.J. Puddephatt, K.A. Azam, A.A. Frew, B.R. Lloyd, L. Monojlovic-Muir, and K.W. Muir. Organometallics, **4**, 1400 (1985).
22. K. Mislow, J.P. Toscano, A.B. Buda, B. Kahr, and J.M. Chance. J. Org. Chem. **53**, 3226 (1988).
23. J.A. Davies. *In* Comprehensive organometallic chemistry II. Vol. 9. *Edited by* E.W. Abel, F.G.A. Stone, and G. Wilkinson (Volume edited by R.J. Elsevier, Oxford. 1995. Puddephatt) p. 291.
24. A.L. Balch, C.T. Hunt, and C.-L. Lee. Inorg. Chem. 20, 2498 (1981).
25. Y. Pan, J.T. Mague, and M.J. Fink. J. Am. Chem. Soc. **115**, 3842 (1993).
26. S. Klopfenstein. M.S. Thesis, University of Toledo, 1995.

Thiophenophane metal complexes. IV. Effects from ligand changes outside the coordination sphere

C. Robert Lucas and Shuang Liu

Abstract: Preparation of two thiophenophane polythioether macrocycles and 11 of their complexes of Cu(I), Cu(II), Ag(I), and Pd(II) is described. The single crystal X-ray structure of $[(CuBr)_2(L1)]_x$ is reported: space group *Pcma*, $a = 8.7120(6)$, $b = 10.7791(5)$, $c = 12.0929(5)$ Å, $Z = 2$, $R_f = 0.052$, $R_w = 0.036$ for 521 reflections. Variable-temperature magnetic susceptibility measurements for $[(CuCl_2)_2(L1)]$ and $[(CuCl_2)_2(L2)]$ reveal weak antiferromagnetic and weak ferromagnetic coupling, respectively. Cyclic voltammograms of these compounds display two unequal waves in acetonitrile solvent but only one in nitromethane or dimethyl sulfoxide. ^{1}H NMR spectra of $\{[(\eta\text{-}C_3H_5)Pd]_2(L1)\}\{PF_6\}_2$ and $\{[(\eta\text{-}C_3H_5)Pd]_2(L2)\}\{PF_6\}_2$ in various solvents show different temperature responses. These magnetic, electrochemical, and NMR effects are discussed in the light of structural differences at sites in the two ligands that are outside the coordination spheres.

Key words: magnetic susceptibility, copper, thioether, electrochemistry.

Résumé : On décrit la préparation de deux thiophénophanes, des polyéthers macrocycliques, et de onze le leurs complexes de Cu(I), Cu(II), Ag(I) et Pd(II). On rapporte la structure par rayons X sur un cristal unique du complexe $[(CuBr)_2(L1)]_x$. Le cristal appartient au groupe d'espace *Pnma* avec $a = 8{,}7120(6)$, $b = 10{,}7791(5)$, $c = 12{,}0929(5)$ Å, $Z = 2$. $R_f = 0{,}052$, $R_w = 0{,}036$ pour 521 réflexions. Les mesures de susceptibilité magnétique à température variable révèlent que les composés $[(CuCl_2)_2(L1)]$ et $[CuCl_2)_2(L2)]$ ont respectivement de faibles couplages antiferromagnétiques et ferromagnetiques. Les voltampérogrammes cycliques de ces composés montrent deux ondes inégales dans l'acétonitrile comme solvant, mais seulement une onde dans le nitrométhane ou dans le diméthylsulfoxyde. Les spectres de RMN du ^{1}H des complexe $\{[(\eta\text{-}C_3H_5)Pd]_2(L1)\}\{PF_6\}_2$ et $\{[(\eta\text{-}C_3H_5)Pd_2(L2)\}\{PF_6\}_2$ dans différents solvants donnent des résultats différents selon la température. On discute des effets magnétique, électrochimique et RMN à la lumière des différences structurales au niveau des sites qui, dans les deux ligands, sont en dehors des sphères de coordination.

Mots clés : susceptibilité magnétique, cuivre, thioéther, électrochimie.

[Traduit par la rédaction]

Introduction

Changes in bond lengths and angles in the coordination sphere have been widely studied as a means of tuning the properties of metal complexes once the gross features of these properties have been determined by the choice of a metal, its oxidation state, and its donor atoms (1). We have been interested for some time in the often more subtle effects that can be achieved by changes in a ligand's skeleton or its conformation at sites that are remote from the coordination sphere (2, 3). These changes can have quite dramatic effects and are believed to be involved, in ways that are not yet well understood, in long-range (>10 Å) transmission of magnetic or electronic influences through enzymes and other large structures (4, 5). In this report, we describe studies of the consequences of structural change at sites in the ligands L1 and L2 that are outside a coordination sphere.

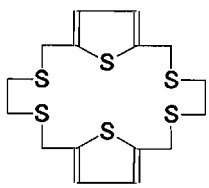

L1

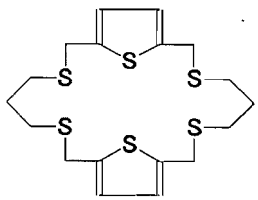

L2

Experimental

Commercially available reagents were obtained from the Aldrich Chemical Co. Inc., or from Morton Thiokol Alfa Products Inc. and were used without further purification.

Received November 6, 1995.

This paper is dedicated to Professor Howard C. Clark in recognition of his contributions to Canadian chemistry.

C.R. Lucas[1] and S. Liu.[2] Department of Chemistry, Memorial University of Newfoundland, St. John's, NF A1B 3X7, Canada.

[1] Author to whom correspondence may be addressed. Telephone: (709) 737-8118. FAX: (709) 737-3702. E-mail: rlucas@plato.ucs.mun.ca

[2] Present address: Dupont Merck Pharmaceutical Co., Radiopharmaceutical Division, 331 Treble Cove Rd., N. Billerica, MA 01862, U.S.A.

Those used for cyclic voltammetry measurements were spectroscopic grade. Spectroscopic data were obtained by using the following instruments: IR, Mattson Polaris FT; UV–VIS, Cary model 17; ESR, Bruker ESP-300 X-band spectrometer operating at ~9.5 GHz; NMR, General Electric 300-NB; mass spectra, VG micromass 7070 HS. FAB mass spectra were obtained by using a matrix composed of glycerol and *p*-toluenesulfonic acid (PTSA). Solution "glasses" for ESR measurements were prepared by plunging sealed capillaries containing ~10^{-4} mol/L solutions into liquid nitrogen. Magnetic susceptibility data were obtained at room temperature by the Faraday method. Variable-temperature magnetic susceptibility data on powder samples were obtained in the range 5–300 K by using an Oxford Instruments superconducting Faraday magnetic susceptibility system with a Sartorius 4432 microbalance. Main solenoid fields of 1.5 and 2.0 T and a gradient field of 10 T m^{-1} were employed and the susceptibility data were corrected for diamagnetism by using Pascal constants. A value of 60 × 10^{-6} cgsu/mol of copper atoms was used as a correction for temperature-independent paramagnetism (TIP) (6). The calibrant was $HgCo(NCS)_4$. Curve fittings were carried out by using a locally modified program for nonlinear weighted least squares as proposed by Wentworth (7) on the basis of work by Deming (8). Electrochemical measurements were carried out under a nitrogen atmosphere at room temperature by using a Cypress Systems, Inc., CS-1087 computer-controlled potentiostat. Solution concentrations were 10^{-3} mol/L in complex and 0.1 mol/L in supporting electrolyte (tetraethylammonium perchlorate). Voltammograms were recorded in acetonitrile by using a glassy carbon working electrode that was pre-polished with 0.3 μm Al_2O_3, a platinum counter electrode, and an aqueous saturated calomel reference electrode checked periodically relative to a 1.0 × 10^{-3} mol/L solution of ferrocene in acetonitrile containing 0.1 mol/L tetraethylammonium perchlorate for which the ferrocene/ferrocenium reduction potential was 400 mV. The reference electrode was separated from the bulk of the solution by a porous Vycor tube. Junction potential corrections were not used. Voltages reported versus the normal hydrogen electrode were obtained by adding 244 mV to the potential measured versus SCE. Analyses were performed by Canadian Microanalytical Service Ltd.

Ligands

(a) (Ligand L1)

Sodium (2.35 g, 0.102 mol) was dissolved in commercial absolute ethanol (300 mL) under an atmosphere of dry nitrogen. To this solution 1,2-ethanedithiol was added slowly and, after the addition was complete, the solution was refluxed gently for 10 min. To the refluxing solution 2,5-bis(chloromethyl)thiophene (9) in commercial absolute ethanol (200 mL) was added with vigorous stirring over 10 h. The mixture was refluxed for an additional 12 h. and then volatiles were removed under reduced pressure. The solid residue was dissolved in $CHCl_3$ and the solution washed several times with water before being dried over $CaCl_2$. The solvent was removed under reduced pressure, leaving a white solid that was recrystallized from benzene to give needle-like crystals; mp 126–127°C. Yield 2.11 g (20.8%). NMR: ($CDCl_3$, ppm from TMS internal standard, assignments based on ^{13}C–^1H heteronuclear correlation and attached proton test, position identification from Fig. 1), ^{13}C: 142.9 C2, 125.2 C1, 32.3 C4, 31.6 C3; ^1H: 6.70 (s) C1 (4H), 3.87 (s) C3 (8H), 2.67 (s) C4 (8H). Mass spectrum: parent ion $[C_{16}H_{20}S_6]^+$, calcd., *m/z*: 404; found, *m/z*: 404. Anal. calcd. for $C_{16}H_{20}S_6$: C 47.48, H 4.98; found: C 47.89, H 5.07.

(b) (Ligand L2)

The procedure was similar to that for L1 (above) except that 1,3-propanedithiol (5.50 g, 0.0501 mol) was used and, after removing ethanol, the residue was dissolved in CH_2Cl_2 instead of $CHCl_3$. Recrystallization from benzene gave white needle-like crystals; mp 122–123°C. Yield 2.69 g (24.8%). NMR: ($CDCl_3$, ppm from TMS int. std., assignments based on ^{13}C-^1H heteronuclear correlation and attached proton test, position identification from Fig. 1), ^{13}C: 141.9 C2, 125.7 C1, 30.9 C3, 30.1 C4, 28.3 C5; ^1H: 6.75 (s) C1 (4H), 3.86 (s) C3 (8H), 2.49 (t, J = 7.2 Hz) C4 (8H), 1.72 (q, J = 7.2 Hz) C5 (8H). Mass spectrum: parent ion $[C_{18}H_{24}S_6]^+$, calcd., *m/z*: 432; found, *m/z*: 432. Anal. calcd. for $C_{18}H_{24}S_6$: C 49.96, H 5.59; found: C 50.01, H 5.66.

Complexes

NOTE: *Perchlorate salts are often treacherously explosive (10) and although we have been unable to cause the compounds described below to detonate from shock or heat we recommend suitable precautions be taken whenever perchlorates are handled.*

(a) [$(CuCl_2)_2$(L1)]

To a solution of $CuCl_2 \cdot 2H_2O$ (70 mg, 0.41 mmol) in the mixed solvent tetrahydrofuran–methanol (15 mL:2 mL) was added a solution of L1 (81 mg, 0.20 mmol) in CH_2Cl_2 (5 mL). The dark-green solution was filtered immediately and the filtrate was allowed to evaporate slowly in air until dark-green crystals formed that were collected by filtration, washed with small amounts of chloroform and then diethyl ether, and dried in air; mp 140–143°C (dec.). Yield 105 mg (78%). Anal. calcd. for $C_{16}H_{20}Cl_4Cu_2S_6$: C 28.53, H 2.99, Cl 21.06 Cu 18.87; found: C 29.34, H 3.16, Cl 21.29, Cu 18.40.

(b) [$(CuCl)_2$(L1)]

To a solution of CuCl (25 mg, 0.25 mmol) in acetonitrile (20 mL) was added a solution of L1 (51 mg, 0.13 mmol) in CH_2Cl_2 (5 mL). The yellow-coloured solution of cuprous chloride darkened to a deeper yellow upon addition of the ligand and after filtration this solution was left standing in air to evaporate solvent. Dark yellowish-brown crystals were deposited and were separated by filtration. The crystals were washed with small amounts of dichloromethane and then diethyl ether and dried in air; mp 200–205°C (dec.) Yield 67 mg (89%). Anal. calcd. for $C_{16}H_{20}Cl_2Cu_2S_6$: C 31.89, H 3.34, Cl 11.77, Cu 21.09; found: C 32.18, H 3.44, Cl 12.30, Cu 20.08.

(c) [$(CuBr)_2$(L1)]$_x$

To a solution of $CuBr \cdot S(CH_3)_2$ (60 mg, 0.29 mmol) in acetonitrile (15 mL) was added a solution of L1 (50 mg, 0.12 mmol) in dichloromethane (5 mL). The solution was filtered and left standing in air to evaporate solvent. Light-yellow crystals formed that were separated and washed with small amounts of dichloromethane and then diethyl ether and dried in air; mp 191–194°C (dec.) Yield 70 mg (84%). Anal. calcd. for

$C_{16}H_{20}Br_2Cu_2S_6$: C 27.79, H 2.91, Br 23.11, Cu 18.38; found: C 28.16, H 2.92, Br 23.89, Cu 17.8.

(d) [Ag(L1)][ClO$_4$]

To a solution of $AgClO_4 \cdot H_2O$ (41 mg, 0.18 mmol) in acetonitrile (10 mL) was added a solution of L1 (81 mg, 0.20 mmol) in CH_2Cl_2 (5 mL). The colourless solution was filtered and left standing in air to evaporate solvent. Colourless crystals formed that were separated and washed with small amounts of dichloromethane and then diethyl ether and dried in air; mp 176–180°C (dec.). Yield 105 mg (95%). Anal. calcd. for $C_{16}H_{20}AgClO_4S_6$: C 31.40, H 3.29, Ag 17.63; found: C 31.54, H 3.39, Ag 18.7.

(e) {[(η-C$_3$H$_5$)Pd]$_2$(L1)}{PF$_6$}$_2$

To a solution of $[(\eta\text{-}C_3H_5)PdCl]_2$ (74 mg, 0.20 mmol) in acetonitrile (10 mL) was added a solution of $AgPF_6$ (105 mg, 0.42 mmol) in acetonitrile (10 mL). A white precipitate formed immediately and after stirring for 5 min the precipitate was removed by filtration. To the filtrate was added a solution of L1 (81 mg, 0.20 mmol) in CH_2Cl_2 (5 mL). The solution was filtered and left standing in air to evaporate solvent. Bright-yellow crystals formed that were separated and washed with small amounts of CH_2Cl_2 and then diethyl ether and dried in air; mp 170–175°C (dec.) Yield 152 mg (77%). Anal. calcd. for $C_{22}H_{30}F_{12}P_2Pd_2S_6$: C 26.70, H 3.06; found: C 27.10, H 3.05.

(f) [(CuCl$_2$)$_2$(L2)]

To a solution of $CuCl_2 \cdot 2H_2O$ (43 mg, 0.25 mmol) in tetrahydrofuran (10 mL) was added a solution of L2 (108 mg, 0.25 mmol) in CH_2Cl_2 (5 mL). The deep-green solution was filtered and left standing in air to evaporate solvent. The deep green crystals that formed were separated and washed with small amounts of CH_2Cl_2 and then diethyl ether and dried in air; mp 140–145°C (dec.) Yield 67 mg (76%). Anal. calcd. for $C_{18}H_{24}Cl_4Cu_2S_6$: C 30.81, H 3.45, Cl 20.21, Cu 18.10; found: C 31.62, H 3.51, Cl 19.46, Cu 17.6.

(g) [(CuCl)$_2$(L2)]

To a solution of CuCl (25 mg, 0.25 mmol) in acetonitrile (10 mL) was added a solution of L2 (56 mg, 0.13 mmol) in CH_2Cl_2 (5 mL). The resulting solution was filtered and left standing in air to evaporate solvent. The light brown crystals that formed were separated, washed with small amounts of CH_2Cl_2 and then diethyl ether, and dried in air; mp 200–205°C (dec.) Yield 65 mg (82%). Anal. calcd. for $C_{18}H_{24}Cl_2Cu_2S_6$: C 34.28, H 3.84, Cl 11.24, Cu 20.15; found: C 33.97, H 3.81, Cl 10.93, Cu 19.6.

(h) [Ag(L2)][ClO$_4$]

To a solution of $AgClO_4 \cdot H_2O$ (45 mg, 0.20 mmol) in acetonitrile (10 mL) was added a solution of L2 (87 mg, 0.20 mmol) in CH_2Cl_2 (5 mL). The colourless solution was filtered and left standing in air to evaporate solvent. The colourless crystals that formed were separated, washed with small amounts of CH_2Cl_2 and then diethyl ether, and dried in air; mp 150–153°C (dec.) Yield 81 mg (94%). FAB mass spectrum: calcd. for $[C_{18}H_{24}{}^{109}AgS_6]^+$ and $[C_{18}H_{24}{}^{107}AgS_6]^+$, *m/z*: 541 and 539; found; *m/z*: 541 and 539. Anal. calcd. for $C_{18}H_{24}AgClO_4S_6$: C 33.78, H 3.78; found: C 34.13, H 3.87.

(i) [(PdCl$_2$)$_2$(L2)]

To a refluxing solution of $PdCl_2$ (89 mg, 0.50 mmol) in CH_3CN (60 mL) was added dropwise a solution of L2 (108 mg, 0.25 mmol) in CH_2Cl_2 (20 mL). The solution was refluxed for a further 4 h during which time the colour changed to orange. The hot solution was filtered, concentrated to 30 mL, and cooled in an ice bath to give orange crystals that were separated, washed with a little diethyl ether, and dried in air; mp 147–155°C (dec.) Yield 124 mg (63%). Anal. calcd. for $C_{18}H_{24}Cl_4Pd_2S_6$: C 27.46, H 3.07; found: C 27.81, H 3.10.

(j) {[(η-C$_3$H$_5$)Pd]$_2$(L2)}{PF$_6$}$_2$

To a solution of $[(\eta\text{-}C_3H_5)PdCl]_2$ (74 mg, 0.20 mmol) in acetone (15 mL) was added $AgPF_6$ (105 mg, 0.42 mmol) in acetone (5 mL). The white precipitate that formed was removed by filtration and to the filtrate was added L2 (45 mg, 0.10 mmol) in CH_2Cl_2 (10 mL). The solution was filtered and left standing in air to evaporate solvent. The yellow crystals that formed were separated, washed with small amounts of CH_2Cl_2 and then diethyl ether, and dried in air; mp 163–167°C (dec.) Yield 62 mg (71%). Anal. calcd. for $C_{24}H_{34}F_{12}P_2Pd_2S_6$: C 28.33, H 3.37; found: C 28.60, H 3.38.

(k) [Cu$_2$(L2)][ClO$_4$]$_2$·6CH$_3$CN

To a solution of CuCl (50 mg, 0.50 mmol) in acetonitrile (15 mL) was added $AgClO_4 \cdot H_2O$ (113 mg, 0.50 mmol) in acetonitrile (15 mL). The white precipitate that formed was removed by filtration and to the filtrate was added L2 (108 mg, 0.25 mmol) in CH_2Cl_2 (15 mL). The solution was filtered and left standing in air to evaporate solvent. The brown crystals that formed were separated, washed with small amounts of CH_2Cl_2 and then diethyl ether, and dried in air; mp 185–190°C (dec.) Yield 191 mg (76%). Anal. calcd. for $C_{30}H_{42}N_6Cl_2Cu_2O_8S_6$: C 35.85, H 4.21, N 8.36, Cu 12.65; found: C 35.49, H 4.20, N 7.82, Cu 12.4.

X-ray

A summary of crystallographic data for $[(CuBr)_2(L1)]_x$ is found in Table 1. X-ray diffraction data were collected by using a Nonius CAD-4 diffractometer. All measurements were made with graphite monochromated Mo Kα radiation and the θ–2θ scan technique with profile analysis (11) at a scan speed of 4°/min. Three standards were measured after every 100 reflections and no significant crystal decay was detected. Cell constants and an orientation matrix for data collection, obtained from a least-squares refinement of the setting angles of 20 carefully centred reflections in the range $30.00° < 2\theta < 40.00°$, corresponded to an orthorhombic cell with dimensions as shown in Table 1. The space group was determined by systematic absences, a statistical analysis of intensity distribution, packing considerations, and the successful solution and refinement of the structure. Of the 1011 reflections collected 779 were unique. The data were corrected for Lorentz and polarization effects but no corrections were made for absorption.

The structures were solved with MULTAN (12) plus a difference Fourier map and refined by full-matrix least squares with counting statistics weights. All calculations were performed with the NRC VAX Crystal Structure programs (13). Non-hydrogen atoms were refined anisotropically. The final cycle of full-matrix least-squares refinement was based on 521 observed

Table 1. Crystal data for $[(CuBr)_2(L1)]_x$.

Parameter	Value
Empirical formula	$C_{16}H_{20}Br_2Cu_2S_6$
Formula weight	691.62
Crystal dimensions, mm	0.07 × 0.07 × 0.15
Space group	Orthorhombic *Pcma*
a, Å	8.7120(6)[a]
b, Å	10.7791(5)
c, Å	12.0929(5)
Z (molecules/cell)	2
F(000) electrons	659.89
Volume, Å^3	1135.61
d_{calc}, g/cm^3	1.964
Linear absorption coefficient (μ), mm^{-1}	5.90
Radiation (MoKα), Å	λ = 0.70930
2θ (max), deg	44.9
No. reflections measured	1011
No. of unique reflections	779
No. unique reflections, $I_{net} > 2.5\sigma I_{net}$	521
Last least-squares cycle calculated with	8 atoms 64 parameters 521 reflections
R_f (sig. refl.)	0.052
R_w (sig. refl.)	0.036
Goodness of fit (last cycle)[b]	2.31
R_f (all refl.)	0.090
R_w (all refl.)	0.038
Maximum shift/σ	0.000
Last *D*-map:	
Deepest hole, e/Å^3	−0.740
Highest peak, e/Å^3	0.820

[a]Throughout this article, esd's are in parentheses and refer to the last digit printed.

[b]Goodness of fit = $[\Sigma w(|F_o| - |F_c|)^2/(\text{no. of reflections} - \text{no. of parameters})]^{1/2}$.

reflections ($I > 2.50\sigma(I)$) and 64 variables and converged with unweighted and weighted agreement factors ($R = \Sigma||F_o| - |F_c||/\Sigma|F_o|$ and $R_w = [(\Sigma w(|F_o| - |F_c|)^2/\Sigma wF_o^2)]^{1/2}$) equal to 0.052 and 0.036, respectively. Neutral atom scattering factors were from the usual source (14). A description of the experimental procedure, anisotropic thermal parameters, and a full listing of bond lengths and bond angles are available as supplementary data.[3]

Discussion

The X-ray study of $[(CuBr)_2(L1)]_x$ reveals (Fig. 1) a two-dimensional polymeric structure consisting of an extended series of fused rings, some of which contain Cu_2Br_2 subunits and some of which contain thiophene subunits. For the macrocyclic ligand, all thioether sulfur lone pairs are exocyclic in a manner reminiscent of other thiophenophanes as free ligands or in some of their complexes (15–19). Rigidity imposed by the thiophene units on the macrocyclic ring limits the ring's ability to place its thioether electron pairs endocyclic during complex formation, as has been noted previously in thiophenophane complexes (15).

Overall, the structure of $[(CuBr)_2(L1)]_x$ can be described as a series of sheets stacked in such a way that one is slipped with respect to the next along one axis only (the vertical axis in Fig. 1) so that the macrocyclic ligand ring cavities in every second sheet are superimposed. The coordination geometry about copper is distorted tetrahedral. Each copper atom is coordinated to two thioether sulfur atoms in two different macrocyclic rings with a bond angle at copper that is substantially larger (134.93(21)°) than the tetrahedral angle. One pair of equivalent S-Cu-Br angles is closed slightly (99.94(11)°) while the remaining equivalent pair is less disturbed at 105.36(12)°. The Cu_2Br_2 rings are roughly at right angles to the plane of the polymer sheet and have internal angles of 109.52(13)° at copper and 70.48(10)° at bromine. This structure may be compared to that of $[Cu(L)Br]_x$ (L = 1,4,8,11-tetrathia[11](3,6)pyridizinophane) (20), which is also a two-dimensional extended polymer with Cu_2Br_2 and macrocyclic ligand rings and distorted tetrahedral coordination about each copper consisting of two bromines and two thioether sulfurs from separate macrocycles. The Cu–S distance of 2.298(4) Å in our $[(CuBr)_2(L1)]_x$ is somewhat shorter than the Cu–S distances in $[CuBr(L)]_x$ (2.321(2) and 2.315(2) Å) and is in fact shorter than the Cu–S distances in [Cu(L′)Cl] (L′ = 2,5,8-trithia[9](1,2)benzenophane (2.303(2), 2.311(2), 2.398(2) Å) (21) or the shortest Cu-S distance in $[Cu(L'')_2]^+$ (L″ = 2,5,8-trithia[9](2,5)thiophenophane) (2.301(3) Å) (16). It is longer, however, than the shortest Cu–S distances in $[Cu([15]aneS_5)]^+$ (2.243(5) Å) (22) or in $[Cu(DTO)_2]^+$ (DTO = 3,6-dithiaoctane) (2.280(4) Å) (23). The Cu—Br distances in the Cu_2Br_2 rings of $[(CuBr)_2(L1)]_x$ are unequal (2.490(4) and 2.577(3) Å) and slightly longer than the comparable pair of unequal Cu—Br distances in $[Cu(L)Br]_x$ (2.458(1) and 2.507(1) Å) (20).

The structures of $[(CuCl)_2(L1)]$ and $[(CuCl)_2(L2)]$ were not determined but their poor solubility in all solvents is similar to that of $[(CuBr)_2(L1)]_x$ and it is assumed that they too are polymeric with solid state structures analogous to that of $[(CuBr)_2(L1)]_x$. Likewise, structures of $[Cu(L2)][ClO_4]$, $[Ag(L1)][ClO_4]$ and $[Ag(L2)][ClO_4]$ have not been determined but probably also involve exocyclic ligand electron lone pairs and oligomeric or polymeric natures. The fact that the FAB mass spectrum of $[Ag(L2)][ClO_4]$ detected a mononuclear parent ion is not proof of a mononuclear structure since the thiophenophane complex $[Ag_2(L)_2][ClO_4]_2$ (L = 2,5,8,11-tetrathia[12](2,5)thiophenophane), which is known to be dinuclear from X-ray studies, also gives a mononuclear parent ion under similar conditions (15).

The IR spectrum of $[(CuCl_2)_2(L1)]$ has strong bands at 312 and 288 cm^{-1} that are similar to those in other dinuclear copper(II) species having asymmetric double Cl-bridges, which we have described previously (19). Those substances and, by inference, $[(CuCl_2)_2(L1)]$ as well involve-square pyramidal coordination about each copper by two bridging chlorines, a terminal chlorine, and two thioether donors. The bridging is asymmetric and goes from apex to base through both bridges.

[3] A complete set of data may be purchased from: The Depository of Unpublished Data, CISTI, National Research Council Canada, Ottawa, Canada K1A 0S2. Except for the anisotropic thermal parameters, the data mentioned above have also been deposited with the Cambridge Crystallographic Data Centre, University Chemical Laboratory, 12 Union Road, Cambridge, CB2 1EZ, U.K.

Fig. 1. X-ray structure for $[(CuBr)_2(L1)]_x$. (*a*) Details near the Cu coordination sphere. (Thermal ellipsoids at 50% probability level.) (*b*) A single polymer sheet.

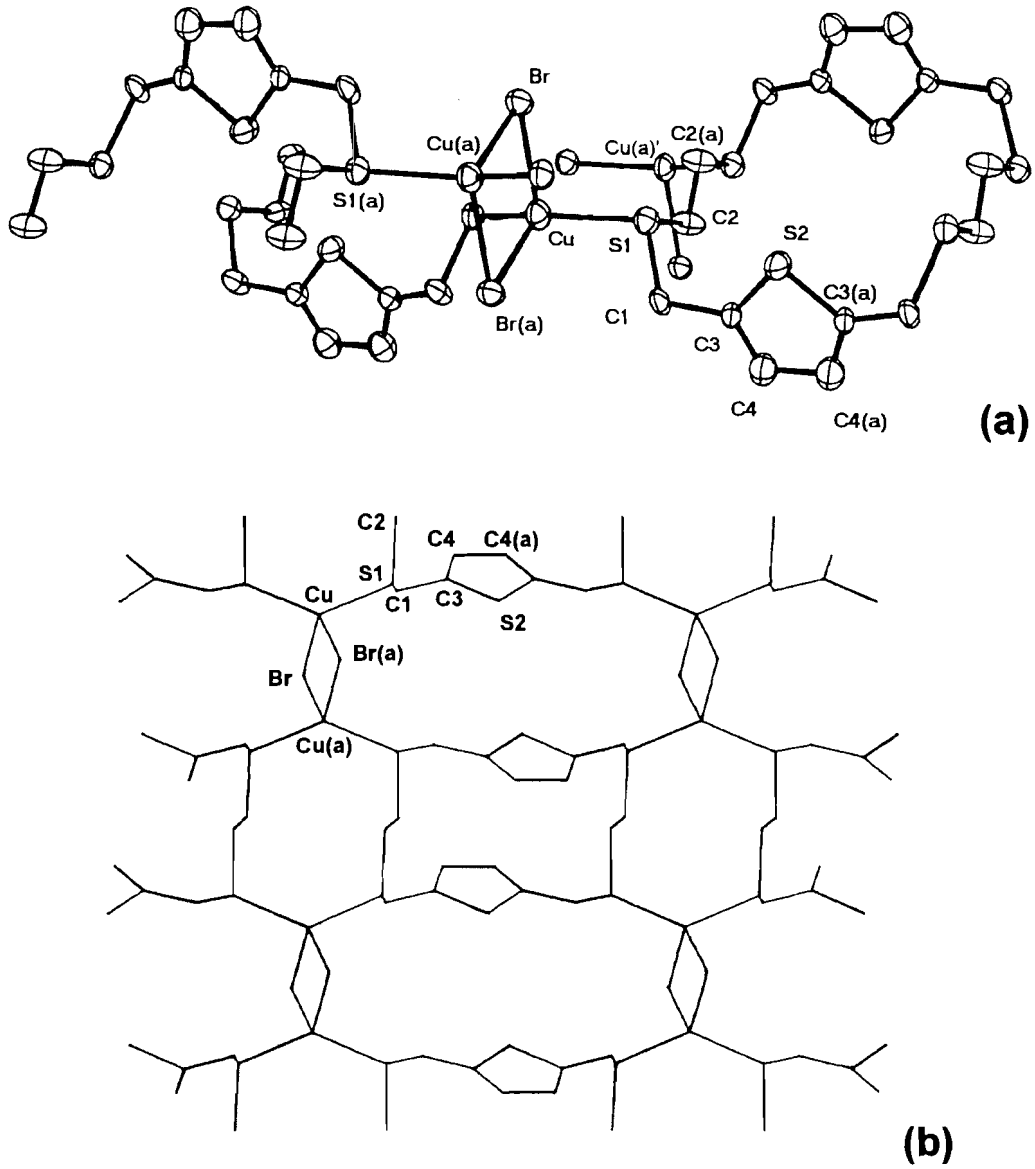

This geometry is similar to that described above for $[(CuBr)_2(L1)]_x$ except that a terminal Cu–halogen bond is missing from each copper's coordination sphere as would be expected since $[(CuBr)_2(L1)]_x$ involves Cu(I), not Cu(II). The spectrum of $[(CuCl_2)_2(L2)]$ has a single strong, broad band at 340 cm^{-1} that may or may not represent two unresolved bands plus a weak band at 312 cm^{-1}. In either case, it suggests that the bridge bond lengths and angles of the Cu_2Cl_2 system in $[(CuCl_2)_2(L2)]$ are probably just slightly different from those in $[(CuCl_2)_2(L1)]$. This conclusion is of importance with respect to subsequent interpretation of the temperature-dependent magnetic properties of this substance.

Electronic spectral details for the two copper(II) compounds are given in Table 4. The energies of both charge transfer and *d–d* envelope bands and the shapes of the *d–d* envelopes are very similar to those observed previously (19) for species discussed above in connection with the infrared spectra. The electronic spectral data therefore also indicate that the coordination spheres in $[(CuCl_2)_2(L1)]$ and $[(CuCl_2)_2(L2)]$ are similar to each other and to those in the substances described previously. A slight difference in the position of the *d–d* envelopes also indicates distortional differences in otherwise similar coordination spheres as did the infrared spectra.

ESR spectra are consistent with the results from infrared and electronic spectroscopy and indicate axial systems in both solids and *N,N*-dimethylformamide (DMF) solutions. The spectra of solid $[(CuCl_2)_2(L1)]$ and $[(CuCl_2)_2(L2)]$ are indistinguishable at 77 K and at 278 K as are those of DMF solutions at room temperature or as "glasses" at 77 K. At both 77 K and 278 K, all spectra of solid samples have $g_{\|} = 2.174$ and $g_{\perp} = 2.025$, which gives $g_{av} = 2.076$. In DMF solution at room temperature, the spectra are isotropic with $g_{iso} = 2.172$. In

Table 2. Positional parameters and equivalent isotropic temperature factors for $[(CuBr)_2(L1)]_x$.

Atom	x	y	z	B_{iso}[a]
Br	0.4359(3)	0	0.16475(16)	2.77(11)
Cu	0.3402(3)	0	−0.03687(20)	3.04(15)
S(1)	0.2400(5)	0.1969(3)	−0.0469(3)	2.66(20)
S(2)	0.3150(8)	1/2	−0.1141(4)	3.3(3)
C(1)	0.2994(17)	0.2472(9)	−0.1866(9)	2.5(7)
C(2)	0.0280(16)	0.2025(11)	−0.0593(9)	2.4(7)
C(3)	0.2642(18)	0.3827(10)	−0.2054(10)	1.8(7)
C(4)	0.2065(17)	0.4298(10)	−0.2982(10)	2.9(7)

[a] B_{iso} is the means of the principal axes of the thermal ellipsoid.

Table 3. Selected bond lengths and angles in $[(CuBr)_2(L1)]_x$.

Bond	Distance (Å)	Bonds	Angle (deg)
Cu—Br	2.577(3)	Cu-Br-Cu(a)	70.48(10)
Cu-Br(a)	2.490(4)	Br-Cu-Br(a)	109.52(13)
Cu-S(1)	2.298(4)	Br-Cu-S(1)	99.94(11)
		Br(a)-Cu-S(1)	105.36(12)
		S(1)-Cu-S(1a)	134.93(21)

Table 4. Electronic spectra.

	λ_{max} in nanometers (ε)			
Complex	Solids[a]	Solutions		Assignment
$[(CuCl_2)_2(L1)]$	690	900[b] (120)	925[c] (175)	*d–d* envelope
	470	430 (1030)	430 (620)	$\sigma(S) \rightarrow dx^2 - y^2$
	340	350 (sh)	350 (sh)	$Cl \rightarrow dx^2 - y^2$
$[(CuCl_2)_2(L2)]$	645	925[c] (170)		*d–d* envelope
	460	425 (550)		$\sigma(S) \rightarrow dx^2 - y^2$
	340	350 (sh)		$Cl \rightarrow dx^2 - y^2$

[a] Nujol mull.
[b] CH_3CN.
[c] $HCON(CH_3)_2$.

DMF solution "glass" at 77 K, overlapping signals due to two components can be seen. The major component has $g_{\|} = 2.343$, $g_{\perp} = 2.051$ and $A_{\|} = 120 \times 10^{-4}$ cm^{-1}, giving $g_{av} = 2.148$. The minor component has $g_{\|} = 2.396$, $g_{\perp} = 2.052$, and $A_{\|} = 126 \times 10^{-4}$ cm^{-1} giving $g_{av} = 2.167$. The major component is $[CuCl{\cdot}n(DMF)]^+$ and the minor component is $[CuCl(L)]^+$. These components are commonly seen in solutions of related substances and arise from a solvent-driven dissociative equilibrium (3, 24).

Cyclic voltammograms of $[(CuCl_2)_2(L1)]$ and $[(CuCl_2)_2(L2)]$ show interesting similar solvent dependencies (Table 5). In acetonitrile, each compound gives two unequal waves but in nitromethane or dimethyl sulfoxide (DMSO) only one is detected. The possibility that there is a stepwise reduction of the dinuclear species in acetonitrile is unlikely because of the inequality of the two waves and the large separation of the two $E_{1/2}$ values (~500 mV). No evidence for a (Cu(II)/Cu(I)) dinuclear species (25, 26) has been found by either electrochemical or chemical reduction methods and the two waves are therefore due to two different electroactive species in solution. The species giving the larger current response in each case (Components 1, Table 5), have wave characteristics ($E_{1/2}$, ΔE_p) similar to each other and to those of several CuS_2Cl^+ solvates that we have studied previously (24). The Component 2 species are slightly different in each case but are more like each other than they are like Components 1. The Component 2 wave is not produced as a result of ligand conformation changes in solution because the wave shape does not change with scan rate (27). It is most likely therefore, that the Component 2 waves arise from further solvolysis of the dominant Component 1 species (28–31). Whether this involves loss of the second chloride or loss of a thioether donor is unclear and electronic spectra (Table 4) shed no light on this question except to indicate that the chromophore in solution is different from that in the solid state. We have, however, observed only single waves for three square-pyramidal $[CuS_2Cl_2]_2$ species with thiophenophane ligands, similar except for their hydrocarbon parts to those in the present study, which give two waves. Thus, there is a factor involving the ligand skeleton rather than the coordination sphere that controls the rate of solvolysis and hence the presence or absence of the second wave.

That solvent also plays a vital role in the electrochemical response of these substances is readily apparent from the solvent dependence of their electrochemical parameters (Table 5). Comparison of the results of our studies (3, 24) of solution structures with those of others (29–31) suggests that coordination spheres of the solvated species are quite dependent on the nature of the solvent, which influences, among other things, the degree to which original ligands are lost, the extent of solvation, and the stereochemistry.

Results from variable-temperature magnetic susceptibility experiments for $[(CuCl_2)_2(L1)]$ and $[(CuCl_2)_2(L2)]$ are displayed in Fig. 2. For $[(CuCl_2)_2(L1)]$, the shape of the χT versus T curve and the values of χT and μ_{eff} (1.77 B.M.) at room temperature indicate only very weak antiferromagnetic coupling (32) between the Cu(II) atoms. The best fit of the data to the Friedberg magnetization expression (32, 33) obtained by using g, $-2J$ (the intradimer coupling), and J' (the interdimer coupling) as parameters gives $g = 2.041(4)$, $-2J = 2.5(3)$ cm^{-1}, and $J' = -1.99(5)$ cm^{-1} (assuming four nearest-neighbour dimers in the solid). This value of g (2.041) obtained by the fitting process compares reasonably with that obtained by ESR (2.075) and gives some confidence in the values of $-2J$ and J' also obtained by curve fitting.

For $[(CuCl_2)_2(L2)]$, the shape of the χT versus T curve is consistent with very weak ferromagnetic interactions between Cu(II) atoms. In fact, the shape of this curve is quite unusual throughout the higher temperature region where most χT values are larger than normal for a Curie Law or a Curie–Weiss Law Cu(II) system with weak coupling and decrease with temperature instead of remaining constant. In its low-temperature region, there is clear indication of very weak ferromagnetic interactions in the sample. Due to the weakness of these interactions, a plot of χ versus T appears normal for a magnetically dilute system. A plot of $1/\chi$ versus T (Fig. 3), however, reveals both the weakness of the ferromagnetic interactions (a

Table 5. Cyclic voltammetry.[a]

	Solvent			
	CH_3CN[b]			
Complex	Component 1	Component 2	CH_3NO_2[c]	DMSO[c]
$[(CuCl_2)_2(L1)]$	532 (105)	58 (79)	570 (160)	293 (222)
$[(CuCl_2)_2(L2)]$	536 (105)	64 (81)	550 (120)	260 (286)

[a]$E_{1/2}$ in mV vs. SCE (ΔE_p in mV).
[b]At 50, 100, 200 or 400 mV/s.
[c]At 200 mV/s.

Fig. 2. (*a*) χT vs. T for $[(CuCl_2)_2(L1)]$ and (*b*) χT vs. T for $[(CuCl_2)_2(L2)]$. Experimental (△); calculated (—).

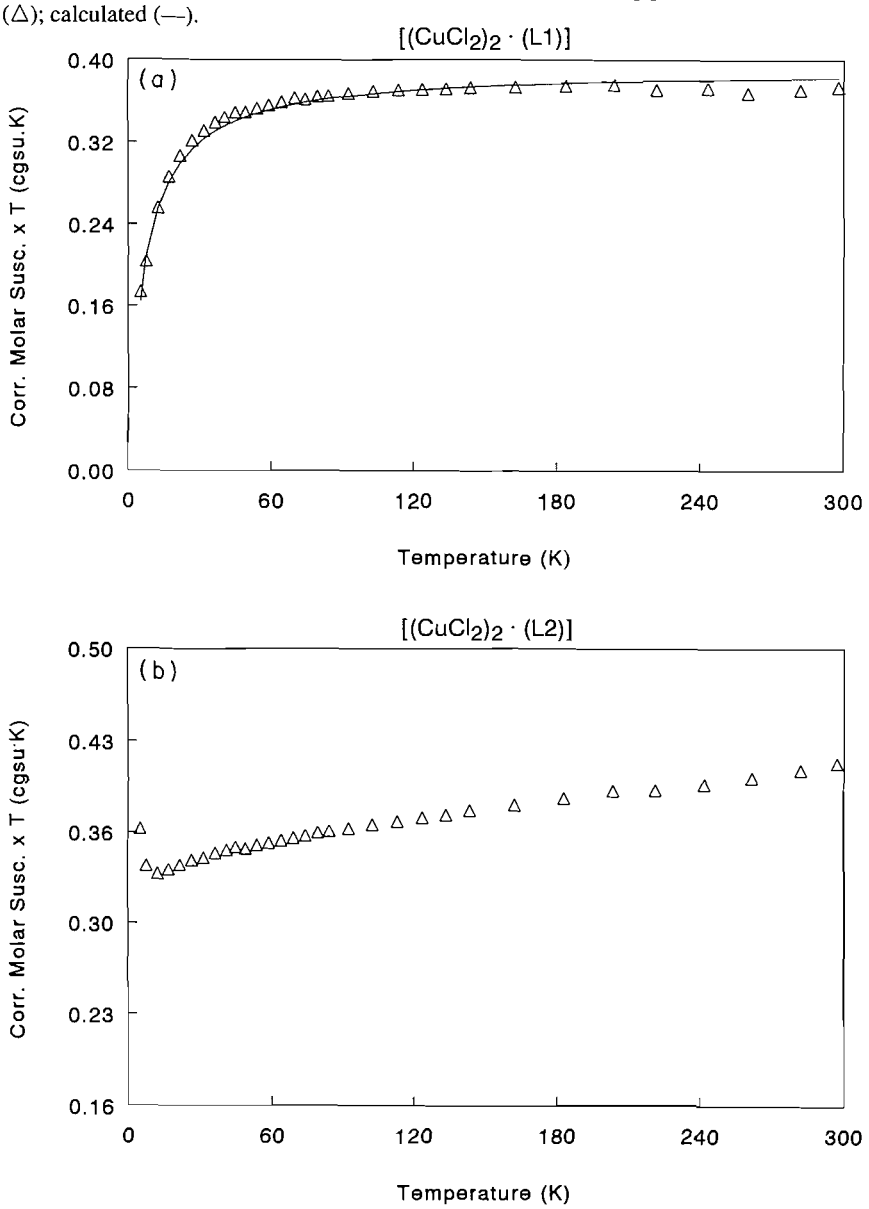

nearly zero intercept) and a curious increasing deviation from linearity as the temperature is raised. Both effects are reflected in the slightly higher than usual value at room temperature for μ_{eff} (1.86 B.M.). We believe that the high temperature effects are due to spin-orbit coupling since other explanations based on alternating chains of dimers or one dimensional chains with inter-chain interactions fail to give acceptable fits of the data to known models (34). This hypothesis is the subject of an

Fig. 3. $1/\chi$ vs. T for $[(CuCl_2)_2(L2)]$. Curie Law (----); experimental (△).

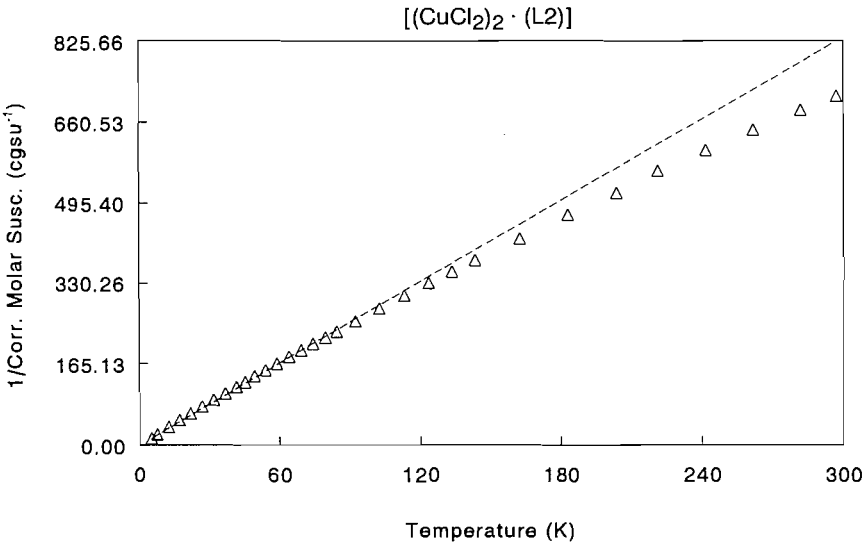

Table 6. ^{1}H NMR data in ppm from TMS.

Thiophene	Allyl centre H	Allyl *syn*-H's	Thiophene α-CH_2	Allyl *anti*-H's	-$(CH_2)_2$- or -$CH_2CH_2CH_2$-	-$CH_2CH_2CH_2$-	Temp. (°C)
{[Pd(allyl)]$_2$(L1)} in CD_3NO_2							
7.020(s)	5.85(br)	4.91(br)	4.30(br)	3.61(br)	3.20(br)		25
{[Pd(allyl)]$_2$(L2)} in CD_3NO_2							
7.014(s)	5.84(br)	4.608(d) J = 6.6 Hz	4.440(s)	3.473(d) J = 11.5 Hz	2.99(br)	1.90(br)	90
7.021(s)	5.85(br)	4.60(br)	4.45(br)	3.50(br)	3.03(br)	1.90(br)	60
7.07(br)	5.97(br)	4.74(br)	4.487(m)	3.63(br)	2.95(br)	2.07(br)	25
6.98(br)		4.28(br)		3.11(br)	2.50(br)		
{[Pd(allyl)]$_2$(L2)} in d_6-dimethyl sulfoxide							
6.997(s)	5.788(m)		4.42(br)	3.36(br)	2.834(t) J = 5.6 Hz	2.04(m)	60
7.003(s)	5.790(m)		4.44(br)	3.36(br)	2.82(br)	2.00(br)	50
7.008(s)	5.793(m)		4.45(br)	3.36(br)	2.82(br)	2.00(br)	40
7.013(s)	5.798(m)		4.47(br)	3.36(br)	2.81(br)	1.99(br)	30
{[Pd(allyl)]$_2$(L2)} in CD_3CN							
6.923(s)	5.720(m)	4.430(d) J = 7.1 Hz	4.282(s)	3.304(d) J = 12.8 Hz	2.754(t) J = 4.7 Hz	1.97(m)	25

ongoing theoretical study. The ferromagnetic interactions detected at low temperature in $[(CuCl_2)_2(L2)]$ that appear instead as antiferromagnetic in $[(CuCl_2)_2(L1)]$ are believed to arise from a small change in the Cu-Cl-Cu bridge angle between the two complexes. This change could be caused by differences in environmental strain on the Cu_2Cl_2 rings in the two complexes originating from the extra CH_2 groups in L2 compared to L1. As a result, the bridge angle just barely provides weak antiferromagnetic coupling via super-exchange in $[(CuCl_2)_2(L1)]$ but provides accidental orthogonality of the magnetic orbitals in the bridge of $[(CuCl_2)_2(L2)]$. This would eliminate antiferromagnetic coupling from $[(CuCl_2)_2(L2)]$ and leave only weak ferromagnetic coupling as observed.

The ^{1}H NMR spectra of $\{[(\eta\text{-}C_3H_5)Pd]_2(L1)\}\{PF_6\}_2$ and $\{[(\eta\text{-}C_3H_5)Pd]_2(L2)\}\{PF_6\}_2$ were examined in a variety of solvents as a function of temperature. The purpose of this examination was to search for differences between the L1 and L2 complexes that could be explained on the basis of structural variation. Any such differences found would provide support for the hypothesis presented above to explain the differing magnetic behaviour of the copper(II) complexes of these two ligands. The results are in Table 6 and the important conclusions are that the complexes exhibit stereochemical nonrigidity and that the L2 complex does so at lower temperature than that of L1. Stereochemical nonrigidity of palladium–thioether complexes is now well documented (17, 18,

35–37) and may involve dissociative equilibria, inversions at coordinated sulfur, or sigmatropic rearrangements of the metal atom over several heteroatom binding sites in a ligand. Precisely which are involved in the present cases is not immediately obvious but it is clear that the L1 complex, $\{[(\eta\text{-}C_3H_5)Pd]_2(L1)\}\{PF_6\}_2$, undergoes the processes with greater difficulty than its L2 counterpart. This is evident from the fact that, in CD_3NO_2 at room temperature, the spectrum of $\{[(\eta\text{-}C_3H_5)Pd]_2(L1)\}\{PF_6\}_2$ is only beginning to show broadening of its peaks due to the onset of the processes whereas the spectrum of $\{[(\eta\text{-}C_3H_5)Pd]_2(L2)\}\{PF_6\}_2$ is already indicating discrimination between two types of thiophene hydrogens, two kinds of allyl groups, and two different three-carbon bridges in the macrocyclic ring. In other words, the greater flexibility of L2 proposed above to account for the Cu(II) magnetic phenomena is apparent in the Pd(II) NMR spectra also.

Conclusions

IR, ESR, and electronic spectroscopic evidence and an X-ray diffraction study of the analogous Cu(I) species all indicate that the Cu(II) coordination spheres of the dinuclear complexes described herein are probably distorted square pyramids linked apex-to-base and apex-to-base by two Cl bridges. Together with their macrocyclic ligands, these dinuclear units would give a two-dimensional polymeric sheet, and the sheets when stacked in a staggered array would give the isolated three-dimensional solids. Although the coordination spheres in the Cu(II) L1 and L2 complexes are similar, the evidence indicates their dimensions are probably slightly different due to influences arising from skeletal changes in remote portions of the ligands. Electronic spectroscopic, electrochemical, and ESR evidence indicate dissolving is accompanied by solvolysis, the extent of which is controlled by structural details outside the coordination sphere. Thus, the nature of the ligand framework outside the coordination sphere influences magnetic properties in the solid state, and in solution it influences the extent of solvolysis, which in turn affects the degree of dissociation, stereochemistry of the coordination sphere, and electrochemistry. The same ligand framework differences affect the stereochemical nonrigidity of palladium complexes of these ligands as well.

Acknowledgements

The assistance of Dr. E.J. Gabe (National Research Council) and Dr. L.K. Thompson (Memorial University of Newfoundland) (X-ray and variable temperature magnetic susceptibility data collection, respectively) is gratefully acknowledged as is that of Ms. M. Baggs and Dr. B. Gregory with collection of the FAB and EI mass spectral data. Financial support was provided by the Natural Sciences and Engineering Research Council of Canada and Memorial University of Newfoundland.

References

1. P. Comba. Coord. Chem. Rev. **123**, 1 (1993).
2. B. Adhikary, S. Liu, and C.R. Lucas. Inorg. Chem. **32**, 5957 (1993).
3. S. Liu, C.R. Lucas, R.C. Hynes, and J.P. Charland. Can. J. Chem. **70**, 1773 (1992).
4. P. Chaudhuri, K. Oder, K. Wieghardt, S. Gehring, W. Haase, B. Nuber, and J. Weiss. J. Am. Chem. Soc. **110**, 3657 (1988).
5. O. Farver and I. Pecht. J. Am. Chem. Soc. **114**, 5764 (1992).
6. N.J. Hill. J. Chem. Soc. Faraday Trans. 631 (1976).
7. W.E. Wentworth. J. Chem. Educ. **42**, 96 (1965).
8. W.E. Deming. Statistical adjustment of data. John Wiley and Sons, New York. 1943.
9. J.M. Griffing. J. Am. Chem. Soc. **70**, 3416 (1948).
10. H.-J. Küppers, K. Wieghardt, B. Nuber, J. Weiss, B. Eckhard, and A.X. Trautwein. Inorg. Chem. **26**, 3762 (1987).
11. D.F. Grant and E.J. Gabe. J. Appl. Crystallogr. **11**, 114 (1978).
12. G. Germain, P. Main, and M.M. Woolfson. Acta Crystallogr. Sect. A: Cryst. Phys. Diffr. Theor. Gen. Crystallogr. **A27**, 368 (1971).
13. E.J. Gabe, F.L. Lee, and Y. LePage. *In* Crystallographic computing 3. *Edited by* G. Sheldrick, C. Kruger, and R. Goddard. Clarendon Press, Oxford. 1985. p. 167.
14. *In* International Tables for X-ray crystallography. Vol. IV. Kynoch Press, Birmingham, England. 1974. Table 2.2A.
15. C.R. Lucas, S. Liu, M.J. Newlands, J.P. Charland, and E.J. Gabe. Can. J. Chem. **68**, 644 (1990).
16. C.R. Lucas, S. Liu, M.J. Newlands, J.P. Charland, and E.J. Gabe. Can. J. Chem. **66**, 1506 (1988).
17. S. Liu, C.R. Lucas, M.J. Newlands, and J.P. Charland. Inorg. Chem. **29**, 4380 (1990).
18. C.R. Lucas, S. Liu, M.J. Newlands, and E.J. Gabe. Can. J. Chem. **68**, 1357 (1990).
19. C.R. Lucas, S. Liu, M.J. Newlands, J.P. Charland, and E.J. Gabe. Can. J. Chem. **67**, 639 (1989).
20. L. Chen, L.K. Thompson, S.S. Tandon, and J.N. Bridson. Inorg. Chem. **32**, 4063 (1993).
21. L. Escriche, M.P. Almajano, J. Casabo, F. Teixidor, J. Rius, C. Miravitlles, R. Kivekas, and R. Sillampaa. J. Chem. Soc. Dalton Trans. 2969 (1993).
22. P.W.R. Corfield, C. Ceccarelli, M.D. Glick, I.W.Y. Moy, L.A. Ochrymowycz, and D.B. Rorabacher. J. Am. Chem. Soc. **107**, 2399 (1985).
23. E.N. Baker and G.E. Norris. J. Chem. Soc. Dalton Trans. 877 (1977).
24. H. Wu and C.R. Lucas. Inorg. Chem. **32**, 526 (1993).
25. S. Karunakaran and M. Kandaswamy. J. Chem. Soc. Dalton Trans. 1595 (1994).
26. S.S. Tandon, L.K. Thompson, J.N. Bridson, V. McKee, and A.J. Downard. Inorg. Chem. **31**, 4635 (1992).
27. T. Sakurai and S. Suzuki. J. Inorg. Biochem. **40**, 197 (1990).
28. M.M. Bernardo, M.J. Heeg, R.R. Schroeder, L.A. Ochrymowycz, and D.B. Rorabacher. Inorg. Chem. **31**, 191 (1992).
29. M.F. Cabral, J. de O. Cabral, E. Bouwman, W.L. Driessen, and J. Reedijk. Inorg. Chim. Acta, **167**, 205 (1990).
30. M.F. Cabral, J de O. Cabral, E. Bouwman, W.L. Driessen, J. Reedijk, U. Turpeinen, and R. Hämälainen. Inorg. Chim. Acta, **196**, 137 (1992).
31. M.F. Cabral, J. de O. Cabral, J. Van Rijn, and J. Reedijk. Inorg. Chim. Acta, **87**, 87 (1984).
32. C.R. Lucas, S. Liu, and L.K. Thompson. Inorg. Chem. **29**, 85 (1990).
33. B.E. Myers, L. Berger, and S.A. Friedberg. J. Appl. Phys. **40**, 1149 (1969).
34. O. Kahn. Molecular magnetism. VCH, New York. 1993.
35. C.R. Lucas and S. Liu. J. Chem. Soc. Dalton Trans. 185 (1994).
36. H. Wu and C.R. Lucas. Inorg. Chem. **31**, 2354 (1992).
37. C.R. Lucas and S. Liu. Inorg. Chim. Acta, **230**, 133 (1995).

Polycarbon ligands: synthesis and characterization of the phosphinodiynes $Ph_2PC{\equiv}C\text{-}C{\equiv}CR$ (R = Bu^t, Ph, $SiMe_3$), the $\mu\text{-}\eta^1,\eta^2_{\alpha,\beta}$-butadiynyl complexes $Ru_2(CO)_6(\mu\text{-}PPh_2)(\mu\text{-}\eta^1,\eta^2_{\alpha,\beta}\text{-}C{\equiv}C\text{-}C{\equiv}CR)$, and the molecular structure of a cobalt carbonyl derivative $Ru_2(CO)_6(\mu\text{-}PPh_2)(\mu\text{-}\eta^1,\eta^2_{\alpha,\beta}\text{:-}\mu\text{-}\eta^2,\eta^2_{\gamma,\delta}\text{-}C{\equiv}C\text{-}C{\equiv}CBu^t)Co_2(CO)_6$

Peter Blenkiron, John F. Corrigan, Didier Pilette, Nicholas J. Taylor, and Arthur J. Carty

Abstract: The phosphino-diynes ($PPh_2C{\equiv}C\text{-}C{\equiv}CR$) (R = Bu^t, Ph, $SiMe_3$) are obtained in excellent yield from the corresponding diyne anions $RC{\equiv}C\text{-}C{\equiv}C^-$ by quenching with PPh_2Cl. Monosubstitution on $Ru_3(CO)_{12}$ yields the trinuclear clusters $Ru_3(CO)_{11}(PPh_2C{\equiv}C\text{-}C{\equiv}CR)$, which upon thermolysis afford the butadiynyl complexes $Ru_2(CO)_6(\mu\text{-}\eta^1,\eta^2_{\alpha,\beta}\text{-}C{\equiv}C\text{-}C{\equiv}CR)(\mu\text{-}PPh_2)$ (R = Bu^t, **7***a*; R = Ph, **7***b*; R = $SiMe_3$, **7***c*) as the major products. The full characterization of the series of compounds (**7***a–c*) $Ru_2(CO)_6(\mu\text{-}\eta^1,\eta^2_{\alpha,\beta}\text{-}C{\equiv}C\text{-}C{\equiv}CR)(\mu\text{-}PPh_2)$ is reported including an X-ray diffraction study of **7***a*. Crystals of **7***a* are monoclinic, a = 9.849(2), b = 9.886(2), c = 28.368(9) Å, β = 95.18(2)°, space group $P2_1/n$, and Z = 4; refinement converged to R = 0.0243 (R_w = 0.0253). The structure shows that the tetracarbon chain is bonded to the first metal atom by a simple M—C σ bond and to the second via a dative π interaction leaving an outer alkyne unit uncoordinated. In the reaction between **7***a* and cobalt carbonyl, a $Co_2(CO)_6$ moiety becomes attached to the $\text{-}C_\gamma{\equiv}C_\delta\text{-}$ bond in a tetrahedral arrangement to give the tetranuclear mixed-metal species $Ru_2(CO)_6(\mu\text{-}PPh_2)(\mu\text{-}\eta^1,\eta^2_{\alpha,\beta}\text{:}\mu\text{-}\eta^2,\eta^2_{\gamma,\delta}\text{-}C{\equiv}C\text{-}C{\equiv}CBu^t)Co_2(CO)_6$ **8**, as confirmed by X-ray crystallography: triclinic, a = 9.9969(9), b = 11.3018(9), c = 17.268(1) Å, α = 90.653(6)°, β = 100.911(6)°, γ = 110.465(5)°, space group $P\bar{1}$ and Z = 2; refinement converged to R = 0.0222 (R_w = 0.0264).

Key words: diruthenium complexes, butadiynyl, synthesis, structure.

Résumé : On a obtenu les phosphino-diynes ($PPh_2C{\equiv}C\text{-}C{\equiv}CR$) (R = Bu^t, Ph, $SiMe_3$), avec un excellent rendement, par désactivation des anions diynes correspondants $RC{\equiv}C\text{-}C{\equiv}C^-$ avec le PPh_2Cl. La monosubstitution sur le composé $Ru_3(CO)_{12}$ donne les clusters trinucléaires $Ru_3(CO)_{11}(PPh_2C{\equiv}C\text{-}C{\equiv}CR)$ qui, sur thermolyse, donnent les complexes butadiynls $Ru_2(CO)_6(\mu\text{-}\eta^1,\eta^2_{\alpha,\beta}\text{-}C{\equiv}C\text{-}C{\equiv}CR)(\mu\text{-}PPh_2)$ (R = Bu^t, **7***a*; R = Ph, **7***b*; R = $SiMe_3$, **7***c*) comme produits majoritaires. On rapporte la caractérisation complète de la série de composés (**7***a–c*) $Ru_2(CO)_6(\mu\text{-}\eta^1,\eta^2_{\alpha,\beta}\text{-}C{\equiv}C\text{-}C{\equiv}CR)(\mu\text{-}PPh_2)$ en incluant les études de diffraction de rayons X du composé **7***a*. Les cristaux du composé **7***a* appartiennent au groupe d'espace monoclinique $P2_1/n$ avec a = 9,849(2), b = 9,886(2), c = 28,368(9) Å, β = 95,18(2)°, et Z = 4; l'affinement converge vers des valeurs de R = 0,0243 (R_w = 0,0253). La structure montre que la chaîne tétracarbonée est liée au premier atome métallique par une liaison σ simple M—C et au second via une interaction dative π laissant l'unité alcyne externe non coordonnée. Dans l'interaction entre le composé **7***a* et le cobalt carbonyle, l'unité $Co_2(CO)_6$ devient attachée à la liaison $\text{-}C_\gamma{\equiv}C_\delta\text{-}$ selon un arrangement tétraédrique pour donner l'espèce métallique mixte tétranucléaire $Ru_2(CO)_6(\mu\text{-}PPh_2)(\mu\text{-}\eta^1,\eta^2_{\alpha,\beta}\text{:}\mu\text{-}\eta^2,\eta^2_{\gamma,\delta}\text{-}C{\equiv}C\text{-}$

Received February 12, 1996.

This paper is dedicated to Professor Howard C. Clark in recognition of his contributions to Canadian chemistry.

P. Blenkiron and A.J. Carty.[1] Guelph–Waterloo Centre for Graduate Work in Chemistry, Waterloo Campus, Department of Chemistry, University of Waterloo, Waterloo, ON N2L 3G1, Canada, and Steacie Institute for Molecular Sciences, National Research Council of Canada, 100 Sussex Drive, Ottawa, ON K1A 0R6, Canada.

J.F. Corrigan, D. Pilette, and N.J. Taylor. Guelph–Waterloo Centre for Graduate Work in Chemistry, Waterloo Campus, Department of Chemistry, University of Waterloo, Waterloo, ON N2L 3G1, Canada.

[1] Author to whom correspondence may be addressed. Telephone: (613) 993-2024. Fax: (613) 957-8850. E-mail: arthur.carty@nrc.ca

C≡CBu^t)$Co_2(CO)_6$ **8**, tel que confirmé par cristallographie de rayons X : les cristaux sont tricliniques, a = 9,9969(9), b = 11,3018(9), c = 17,268(1) Å, α = 90,653(6)°, β = 100,911(6)°, γ = 110,465(5)°, groupe d'espace $P\bar{1}$ et Z = 2; l'affinement converge vers des valeurs de R = 0,0222 (R_w = 0,0264).

Mots clés : complexes de diruthénium, butadiynyl, synthèse, structure.

[Traduit par la rédaction]

Introduction

Polyyne-yl **1**, polyyne-diyl **2**, alkapolyene-ylidene **3**, and alkapolyene-bis(ylidene) **4** ligands offer exciting possibilities for linking metal centres in extended linear chains via metal–

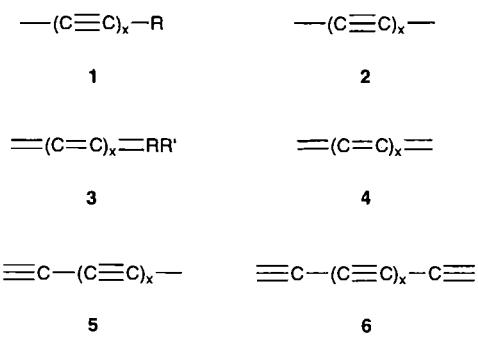

1 **2**

3 **4**

5 **6**

carbon single (M—C_{sp}) (e.g., **2**) and double (M=C_{sp}) (e.g., **4**) bonds or three-dimensional arrays by using both the σ and π electrons of the polycarbon fragment. Much attention has focussed on linear bis(acetylide)-based metal complexes due to the interesting nonlinear optical and liquid crystalline properties of rodlike oligomers and polymers derived from these building blocks (see, for example, ref. 1). Metal fragment terminated polyyne-diyls L_nM-$(C{\equiv}C)_x$-ML_n (2) are also being examined in detail in an effort to prepare materials known as molecular wires where the potential for electronic communication along an extended unsaturated C_n chain can be explored (3). Monometallic and bimetallic cumulenes such as the pentatetraenylidene ruthenium complex [Ru=C=C=C=C=CPh_2(Cl)$(DPPE)_2$][PF_6] (4) and the butatrienebis(ylidene) rhenium compounds [Re]=C=C=C=C=[Re] ([Re] = Cp*(NO)$(PPh_3)^+$) (3*c*) have also been synthesized to probe the materials, and the electronic and chemical properties of these linear polyunsaturated metal complexes. Yet another unsaturated unit for assembling rodlike materials is the polyynylalkylidyne **5** where metal fragments terminate a chain via M≡C_{sp} or M—C_{sp} bonds.[2] There are now many examples of organometallic complexes built from the structural entities represented by **1**–**5**. The polyyne bis(alkylidyne) **6** represents another potential building block. In each of these ligands, the polyunsaturated carbon chains, as well as the metal–carbon multiple bonds in **3**–**6**, are potential sites for further metal complexation and these additional π-bonding capabilities offer enormous scope for the development of new classes of metal-adorned polycarbon materials. Yet to date, few attempts have been made to exploit this carbon–carbon unsaturation to build new polymetallic compounds (5*c*,*d*, 6).

[2] Examples of polyynylalkylidynes are known. See for example, ref. 5.

As an extension of our detailed investigations on the chemistry of bi- and polynuclear compounds bearing μ-η-bound acetylides (7) we have initiated a program to synthesize polymetallic complexes with diynyl -$(C{\equiv}C)_2$-R and diyne-diyl -$(C{\equiv}C)_2$- ligands where one or both C—C multiple bonds are bound in η-fashion to metal fragments. We have found that the phosphino-diynes ($PPh_2C{\equiv}C$-C≡CR) (R = Bu^t, Ph, $SiMe_3$) provide convenient entry to this area of chemistry, undergoing facile P—C bond cleavage in the metal coordination sphere to access complexes containing the butadiynyl ligand. In this paper, we describe the synthesis of these phosphinodiynes and the generation of the first series of binuclear compounds with μ-η^1,η^2 diynyl ligands, namely $Ru_2(CO)_6$(μ-η^1,$\eta^2_{\alpha,\beta}$-C≡C-C≡CR)(μ-PPh_2) (R = Bu^t, **7***a*; R = Ph, **7***b*; R = $SiMe_3$, **7***c*). In this series of compounds, in addition to a metal–C_{sp} bond to one metal, one of the two carbon–carbon triple bonds of the diynyl ligand is attached in η^2 fashion to a second metal atom via a π interaction. The remaining triple bond is free. A further incentive for the study of molecules of type **7** is the opportunity to compare reactivity patterns for coordinated vs. free triple bonds in the same molecule and we report here the reactivity of **7***a* towards $Co_2(CO)_8$. To our knowledge, such a comparison has not been made for alkyne triple bonds.

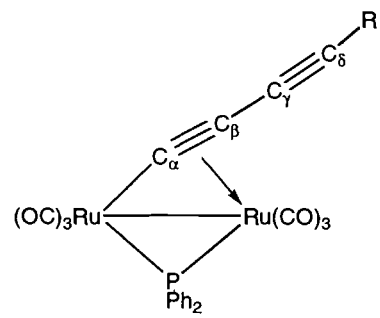

7

a, R = Bu^t

b, R = Ph

c, R = $SiMe_3$

Results and discussion

Synthesis and characterization of $PPh_2C{\equiv}C$-C≡CR (R = Bu^t, Ph, $SiMe_3$)

The phosphinodiynes $PPh_2C{\equiv}C$-C≡CR (R = Bu^t, Ph) were obtained in good yields from the corresponding terminal butadiyne by low-temperature deprotonation followed by addition of PPh_2Cl. The diynes Bu^{t}C≡C-C≡CH and PhC≡C-C≡CH were prepared according to a literature procedure involving the Cadiot–Chodkiewicz coupling of an

Scheme 1.

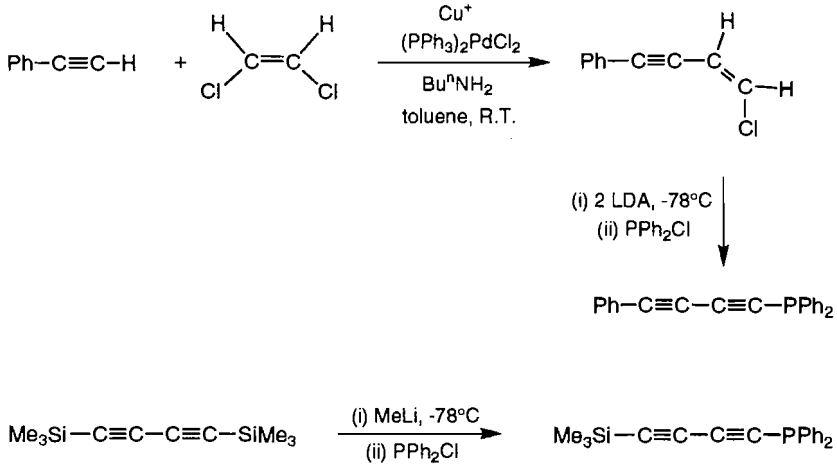

appropriately substituted 1-bromoalkyne and the alkynol $HC{\equiv}CCMe_2OH$ (8). This method, however, is a multistep process that provides the diynes in low to moderate overall yield and is particularly unreliable in the case of R = Ph because of a facile polymerization pathway. We have found that a relatively simple two-step route can give direct access to $PPh_2C{\equiv}C\text{-}C{\equiv}CPh$, thus avoiding the necessity of isolating the parent diyne. As shown in Scheme 1, the Pd-catalyzed coupling of *cis*-1,2-dichloroethylene and $PhC{\equiv}CH$ gives the chloro-enyne (9), which is then treated with two equivalents of base to give the diyne anion. Quenching of this solution with PPh_2Cl affords the desired acetylenic phosphine in much improved yield (56%) compared with the Cadiot–Chodkiewicz route (17%). The attempted coupling of $Bu^tC{\equiv}CH$ and $HClC{=}CHCl$ under identical conditions proved unsuccessful, however. A GC–MS analysis of the reaction mixture gave a strong signal corresponding to $Bu^tC{\equiv}CC{\equiv}CBu^t$ and, while reductive elimination of the alkynyl ligands in first-formed $(PPh_3)_2Pd(C{\equiv}CR)_2$ followed by C–C coupling is thought to be the first stage in the catalytic process (10), it seems that subsequent oxidative addition of more alkyne is favoured over addition of $HClC{=}CHCl$.

The $SiMe_3$-substituted phosphinodiyne was prepared in almost quantitative yield (92%) by monodesilylation of $Me_3SiC{\equiv}C\text{-}C{\equiv}CSiMe_3$ using MeLi to give the diyne anion $Me_3SiC{\equiv}C\text{-}C{\equiv}C^-$ (11). Subsequent in situ treatment with PPh_2Cl afforded the desired $PPh_2C{\equiv}C\text{-}C{\equiv}CSiMe_3$ quantitatively and this was isolated as a pale yellow powdery solid.

The series of phosphinodiynes has been characterized by elemental analysis and by IR, NMR, and mass spectroscopies. The latter show the molecular ion at the expected mass and in addition each gives a strong signal corresponding to a PPh_2C_4 fragment. ^{31}P spectra exhibit the expected high-field resonance at $\sim \delta -30$ while ^1H data are in accord with expectation. All four butadiynyl carbons ($PPh_2C_\alpha{\equiv}C_\beta\text{-}C_\gamma{\equiv}C_\delta\text{-}R$) are observed in the ^{13}C spectra and, in common with previously reported alkynylphosphines $PR_2C{\equiv}CR'$ (12), C_β resonates downfield of C_α. Assignment of the ^{13}C signals was achieved on the basis of the magnitude of the J_{PC} coupling constant and by comparing $C\{^1H\}$ and proton-coupled spectra. Thus distinct doublets are observed for C_α (J_{PC} = 9–15 Hz) and C_β (J_{PC} = ~ 6 Hz) (cf. J_{PC} = 15.8 and 5.2 Hz for C_α and C_β, respectively, in the bisphosphine $PPh_2\text{-}C_\alpha{\equiv}C_\beta\text{-}C{\equiv}C\text{-}PPh_2$ (13)) while C_γ and C_δ appear as singlets in the $C\{^1H\}$ spectra. For $PPh_2C{\equiv}C\text{-}C{\equiv}CPh$, C_γ is considerably broadened and this effect may be due to communication along the unsaturated carbon chain. Identification of C_δ is readily apparent in the proton-coupled ^{13}C spectra, occurring either as a multiplet (R = Bu^t, Ph) or as a broadened singlet (R = $SiMe_3$). The remaining quaternary carbon resonance is thus ascribed to C_γ.

Synthesis and chemistry of $Ru_2(CO)_6(\mu\text{-}\eta^1,\eta^2_{\alpha,\beta}\text{-}C{\equiv}C\text{-}C{\equiv}CR)(\mu\text{-}PPh_2)$ (R = Bu^t, Ph, $SiMe_3$)

Addition of a few drops of sodium benzophenone ketyl catalyst to a room temperature THF solution of $Ru_3(CO)_{12}$ and a slight excess of $PPh_2C{\equiv}C\text{-}C{\equiv}CR$ allows rapid and quantitative conversion to the monosubstituted product $Ru_3(CO)_{11}(PPh_2C{\equiv}C\text{-}C{\equiv}CR)$. Thermolysis of this solution effects P—C bond cleavage and cluster fragmentation (Scheme 2) to afford the yellow dinuclear σ–π complexes $Ru_2(CO)_6(\mu\text{-}\eta^1,\eta^2_{\alpha,\beta}\text{-}C{\equiv}C\text{-}C{\equiv}CR)(\mu\text{-}PPh_2)$ in reasonable yield (R = Bu^t, 31%, **7***a*; R = Ph, 24%, **7***b*; R = $SiMe_3$, 20%, **7***c*) after work-up.

The spectroscopic properties of the series **7** are entirely in accord with expectation and correlate closely with those observed in the acetylide analogue $Ru_2(CO)_6(\mu\text{-}\eta^1,\eta^2\text{-}C{\equiv}CR)(\mu\text{-}PPh_2)$ (**A**). Thus six ν(CO) bands are found in the IR spectrum. These appear at slightly higher wave numbers than in their acetylide counterparts and presumably reflect the electron-withdrawing effect of the outer alkyne group.

The ^{31}P NMR spectra show the expected single peak in the chemical shift range 122.0 – 124.6 with frequencies typical of phosphido-bridged Ru—Ru bonds (14). In the corresponding acetylides $Ru_2(CO)_6(\mu\text{-}\eta^1,\eta^2\text{-}C{\equiv}CR)(\mu\text{-}PPh_2)$ (R = Bu^t, Ph) $\delta^{31}P$ values are 125.2 and 130.5 ppm, respectively (15). As was observed in the case of the acetylides (**A**), **7***a–c* show dynamic behaviour in solution and thus exhibit only three CO resonances in the ^{13}C NMR spectrum. This occurs as a result of σ–π interconversion in which the coordinated C_4R ligand undergoes rapid exchange between the two metal sites, via the well-known windshield wiper fluxional process. All three CO resonances are phosphorus-coupled and consist of a characteristically large J_{PC} coupling for the CO *trans* to the phosphido bridge (J_{PC} ~ 72 Hz) and two smaller *cis* couplings (J_{PC} ~ 12

Scheme 2.

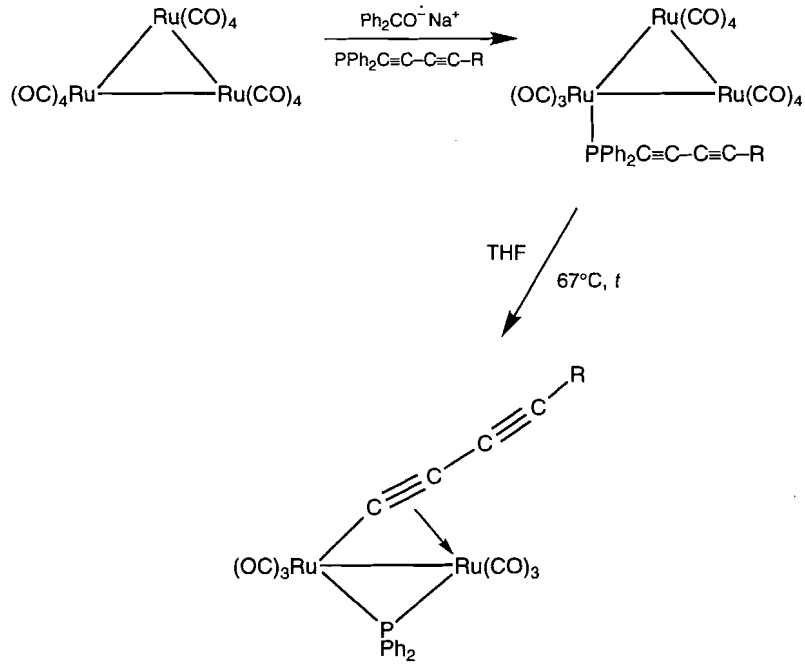

7

a, R = Bu^t, t = 4 h
b, R = Ph, t = 2.5 h
c, R = SiMe$_3$, t = 2 h

Hz, *trans* to M—C_β bond; J_{PC} ~ 5 Hz, *trans* to M—M bond) (16). The four *sp* diyne carbon resonances of **7***a–c* were all located and lie in the range δ 74–109. Chemical shifts for C_α–C_δ were assigned on the basis of their J_{PC} coupling constants.[3] Thus in each case C_α appears as a doublet with a coupling to phosphorus of ~28 Hz and is found downfield of the other quaternary carbons, consistent with its unique coordination to both metal centres. The signal ascribed to C_β shows a J_{PC} of ~8 Hz and these couplings match almost exactly those observed in $Ru_2(CO)_6(\mu\text{-}\eta^1,\eta^2\text{-}C{\equiv}CR)(\mu\text{-}PPh_2)$. In the latter compounds the chemical shift of C_α and C_β is dependent on the nature of the R group; for the archetypal electron-withdrawing group R = Ph, C_α is downfield of C_β while for the electron-donating Bu^t and Pr^i substituents the positions of the signals are reversed. This picture is consistent with our observation that in **7***a–c*, C_α occurs at lower field than C_β due to the presence of an electronegative outer alkynyl functionality.

Whereas in **7***a* and **7***c* P–C coupling extends only to C_γ, the resonance of C_δ in the ^{13}C spectrum of **7***b* appears as a doublet with $^5J_{PC}$ = 3 Hz. It is tempting to attribute this to increased communication along the C_4 chain when the terminal group is a phenyl substituent attached to C_δ via an sp^2 Ph_{ipso} carbon atom. A paucity of ^{13}C NMR data for butadiynyl complexes prevents any assessment of the generality of this phenomenon; however, it is worth noting that in the η^1-butadiynyl species $Rh(C{\equiv}CC{\equiv}CPh)(CO)(PPr^i_3)_2$, P–C coupling also extends to the C_δ carbon (6*a*). In contrast, for the diynyl complexes $Cp^*Re(NO)(PPh_3)C_4R$ (R = H, Me, $SiMe_3$), P–C coupling to C_δ is absent (5*a*). Long-range, six-bond P–H coupling in the terminal butadiynyl compounds *trans*-$Ru(CO)_2(PEt_3)_2(C{\equiv}CC{\equiv}CH)_2$ has also been cited as evidence of electronic communication along a C_4 chain (1*f*). In the free ligands $PPh_2C{\equiv}CC{\equiv}CR$, J_{PC} coupling extends only to C_β, with C_γ and C_δ resonating as singlets, although in the case of R = Ph, the signal corresponding with C_γ is considerably broadened. Thus it appears that the binding of the C_4 ligand to the metal enhances electronic communication between the phosphorus atom and the butadiynyl carbons.

Since **7***a–c* represent the first known $\mu\text{-}\eta^1,\eta^2$-butadiynyl complexes, it was of interest to determine precise details of the structure for comparison with the acetylide analogues. Thus an X-ray diffraction study of $Ru_2(CO)_6(\mu\text{-}\eta^1,\eta^2{}_{\alpha,\beta}\text{-}C{\equiv}C\text{-}C{\equiv}CBu^t)(\mu\text{-}PPh_2)$ **7***a* was undertaken and the molecular structure is shown in Fig. 1. In the dinuclear molecule two $Ru(CO)_3$ units are bonded via a short (Ru(1)-Ru(2) 2.769(1) Å) bond and are bridged by a symmetrical phosphido group (Ru(1)-P-Ru(2) 71.9(1)°) and a butadiynyl ligand. The tetracarbon fragment is attached to the diruthenium unit via the inner C_α—C_β triple bond, leaving the outer alkyne group unattached. The bonding mode is thus constituted from a σ interaction between Ru(1) and C(7) (2.031(3) Å) and a π-type coordination of the C(7)—C(8) triple bond to Ru(2) (Ru(2)—C(7) 2.284(3) Å, Ru(2)—C(8) 2.408(3) Å). The C(7)—C(8)

[3] See illustration for designation of C_α, C_β, C_δ, C_γ.

Fig. 1. The molecular structure of $Ru_2(CO)_6(\mu\text{-}\eta^1,\eta^2_{\alpha,\beta}\text{-}C{\equiv}C\text{-}C{\equiv}CBu^t)(\mu\text{-}PPh_2)$ **7***a* showing the atomic numbering scheme. Hydrogen atoms are omitted for clarity.

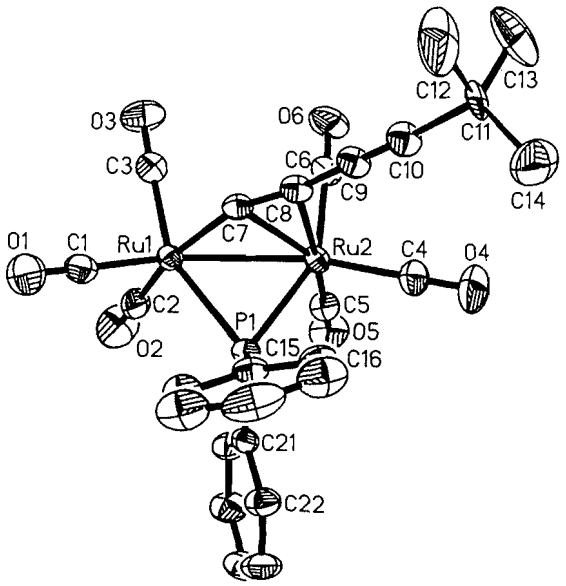

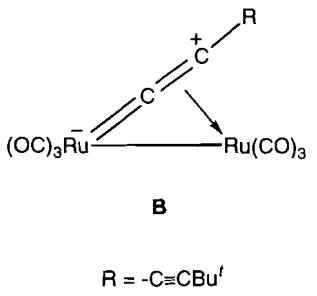

Fig. 2. Key bond lengths and angles in the Ru-C≡C-C≡C fragment of **7***a*.

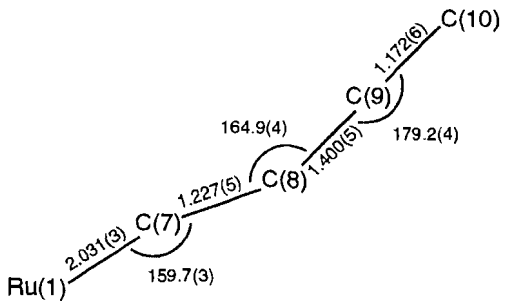

distance of 1.227(5) Å in **7***a* compares favourably with that found in the corresponding acetylide $Ru_2(CO)_6(\mu\text{-}\eta^1,\eta^2\text{-}C{\equiv}CBu^t)(\mu\text{-}PPh_2)$ (1.218(4) Å) but is significantly longer than values normally found for C≡C bond lengths in metal-alkynyl complexes where the triple bond is uncoordinated. Indeed, transition metal-alkynyl C≡C bond lengths fall into a relatively narrow range of values and show only small structural perturbations across a wide array of chemical and electronic environments. A recent compilation by Manna et al. revealed that two-thirds of the C≡C distances recorded fall in the range 1.190–1.214 Å (mean value 1.201(16) Å (17). Thus the influence of $\mu\text{-}\eta^1,\eta^2$ coordination is to effect a small but noticeable elongation of the C≡C triple bond with respect to free acetylene (1.2033(2) Å) and in metal η^1-alkynyl complexes. It is interesting that in the molecules *trans*-$Ru(CO)_2(PEt_3)_2(C{\equiv}CC{\equiv}CSiMe_3)_2$ where the butadiynyl ligands are terminal, the C_α—C_β bond length of 1.226(2) Å is essentially identical to that in **7***a*. In this case -C≡C- bond lengthening was attributed to greater delocalization along the $RuC{\equiv}CC{\equiv}CSiMe_3$ chain in the Me_3Si-substituted diynyl complex. This can be represented by a contribution of the type $^-Ru{=}C{=}C{=}C{=}SiMe_3^+$ to the ground state and implies both Ru*d*π–C*p*π* and Si*d*π–polyyne π interactions.

A comparison of the Ru(1)—C(7) distance (2.031(3) Å) in **7***a* with Ru—C_{sp} bond lengths in ruthenium η^1-ynyls and diynyls (*trans*-$Ru(CO)_2(PEt_3)_2(C{\equiv}CPh)_2$, Ru(1)—$C_{sp}$ 2.074(3) Å; *trans*-$Ru(CO)_2(PEt_3)_2(C{\equiv}CSiMe_3)_2$, Ru(1)—$C_{sp}$ 2.062(2) Å; *trans*-$Ru(CO)_2(PEt_3)_2(C{\equiv}CC{\equiv}CSiMe_3)_2$, Ru(1)—$C_{sp}$ 2.057(2) Å) (1*f*) indicates significant Ru—C_α bond shortening in **7***a* consistent with some degree of Ru—C_α multiple bonding as represented by the vinylidene-like structure **B**.

This shortening of the formal single bond between the σ-bound metal atom and C_α of an acetylide coordinated in $\mu\text{-}\eta^1,\eta^2$- fashion at a dinuclear centre becomes even more apparent in trinuclear acetylides. Thus, for example, in $Ru_3(CO)_9$ $(\mu_3\text{-}\eta^1,\eta^2,\eta^2\text{-}C{\equiv}CPr^i)(\mu\text{-}PPh_2)$ the Ru(2)—C(10) *sp* bond length is 1.960(6) Å (18) and in $\{Ru_3(CO)_9(\mu\text{-}PPh_2)\}_2(\mu_6\text{-}C_4)$ where a diyne-diyl unit is bonded in $\mu_3\text{-}\eta^1,\eta^2,\eta^2$- fashion to two separate Ru_3 centres the formal Ru—C_{sp} σ bonds are of length 1.936(6) Å (19). These latter values approach the Ru—CO distances. The presence of partial metal–carbon multiple bonding in the vinylidene-like resonance form **B** has implications for the chemistry of these ruthenium diynyl complexes towards unsaturated metal fragments, as will be described in a forthcoming communication.

The uncoordinated alkyne -C≡C- bond of **7***a* is very short (C(9)—C(10) 1.172(6) Å and in the normal range for free alkynes (cf. HC≡CH 1.2033(2) Å). Thus it appears that the outer, uncoordinated alkyne in **7***a* serves as an electronegative substituent on the $\mu\text{-}\eta^1,\eta^2$-ynyl fragment, enhancing Ru*d*π—C*p*π* backbonding, shortening Ru—C_α, and elongating the -C≡C- triple bond of the π-coordinated ynyl group.

As expected, there is a marked deviation from linearity in the butadiynyl group on coordination, as shown schematically in Fig. 2, with a C(7)-C(8)-C(9) angle of 164.9(4)°, indicative of some carbon atom rehybridization. This compares closely with corresponding angles in the related tetrairon butadiynediyl complex $\{Fe_2(CO)_6(\mu\text{-}PPh_2)\}_2(\mu_4\text{-}C_4)$ reported by Bruce and co-workers (164.2(4), 165.8(5)°) (19) and approaches those recorded for π-coordinated substituted butadiyne complexes (2*c*, 6*a*, 20). The Ru(1)-C(7)-C(8)-C(9) fragment is *trans* bent as opposed to the normal *cis* bending of an alkyne on η^2 coordination.

The C(8)—C(9) (1.400(5) Å) bond linking the two alkyne units is shorter than its formal single designation would suggest and is evidence for a certain amount of electronic delocalization along the C_4 fragment. This effect has been noted in structural studies of organic diynes (21) as well as in other transition metal butadiynyl complexes (1*f*, 2*c*,*d*, 3*a*, 22).

A rational mechanism for the formation of **7***a–c* involves

Scheme 3.

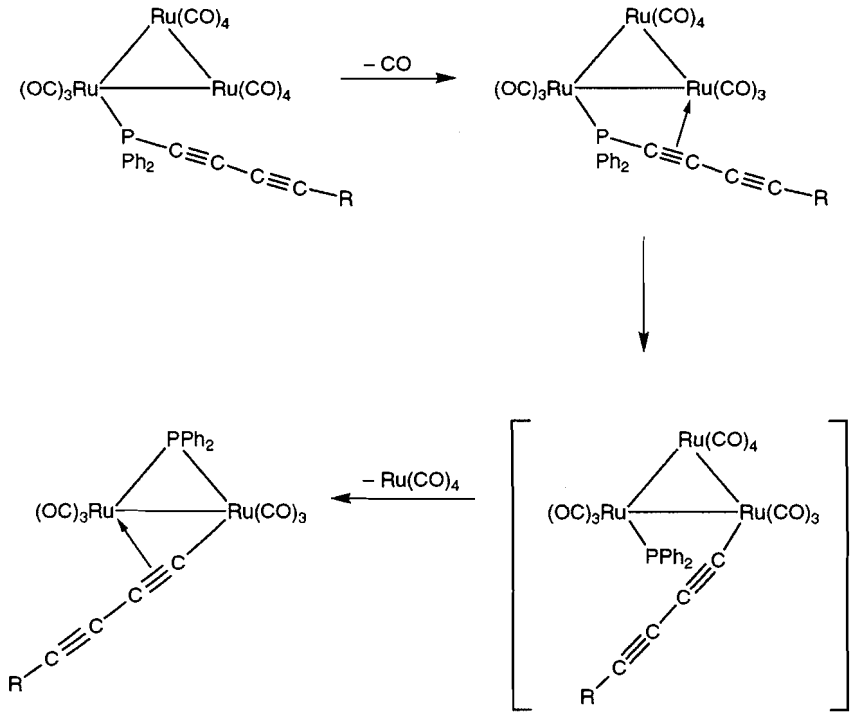

Scheme 4.

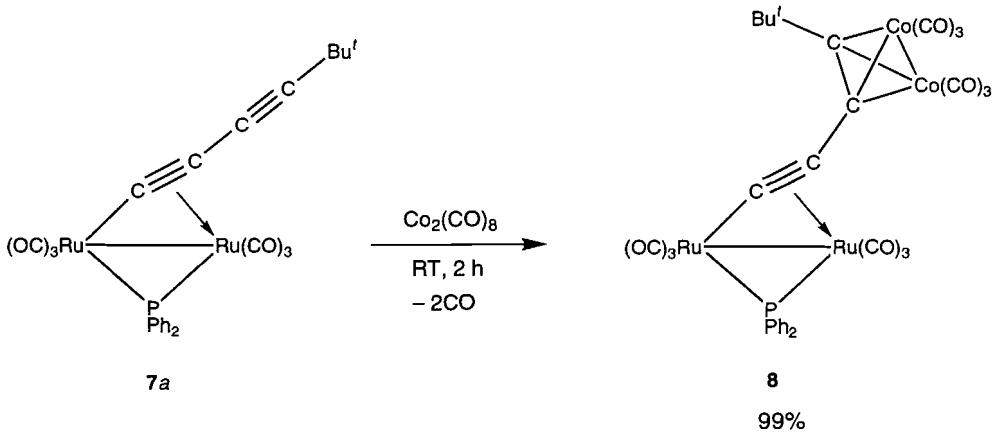

initial attachment of the phosphinobutadiyne via phosphorus to an $Ru_3(CO)_{11}$ moiety followed by intra- (Scheme 3) or intermolecular π coordination of one triple bond, subsequent P—C bond scission, and formation of μ-phosphido and μ-η-alkynyl groups. This mechanism allows the generation of both dinuclear μ-η^1,η^2- and trinuclear alkynyl complexes.

We were interested in exploring the chemical behaviour of the butadiynyl ligand in **7** and as an initial test of its reactivity we investigated the reaction with dicobalt octacarbonyl, $Co_2(CO)_8$ (Scheme 4). From the crystal structure of ***7a*** it appears that the outer alkyne unit is fairly accessible and so it seemed possible that a $Co_2(CO)_6$ group might coordinate perpendicular to the triple bond to furnish the well-known tetrahedral Co_2C_2 arrangement. Thus addition of $Co_2(CO)_8$ to ***7a*** at room temperature gave smooth and quantitative conversion to a single red-brown product after 2 h. A single crystal X-ray diffraction study confirmed the coordination of a $[Co_2(CO)_6]$ unit to the alkyne function to give the mixed-metal tetranuclear compound $Ru_2(CO)_6(\mu\text{-}PPh_2)(\mu\text{-}\eta^1,\eta^2_{\alpha,\beta}\text{:}\mu\text{-}\eta^2,\eta^2_{\gamma,\delta}\text{-}C{\equiv}C\text{-}C{\equiv}CBu^t)Co_2(CO)_6$ **8**. The molecular structure of **8** is shown in Fig. 3.

The structural parameters of the Co_2C_2 tetrahedrane unit in which the alkyne acts as a bridging μ_2 ligand to the dicobalt system are consistent with those reported for other compounds containing this fragment. Thus the Co(1)—Co(2) and C(15)—C(16) separations of 2.462(1) and 1.365(4) Å, respectively, compare with the ranges 2.453(4)–2.477(2) and 1.32(4)–1.36(3) Å found for five other $Co_2(CO)_6(\mu$-diyne) complexes (13, 23). Similarly, the Co—C distances in the Co_2C_2 core fall in the ranges found for these same compounds. The structure provides an interesting comparison of the effect of a three-electron donor σ–π alkynyl group versus a four-electron

Fig. 3. The molecular structure of $Ru_2(CO)_6(\mu\text{-}PPh_2)$-$(\mu\text{-}\eta^1,\eta^2_{\alpha,\beta}\text{:}\mu\text{-}\eta^2,\eta^2_{\gamma,\delta}\text{-}C{\equiv}C\text{-}C{\equiv}CBu^t)Co_2(CO)_6$ **8** showing the atomic numbering scheme. For clarity, only the *ipso* carbons of the phenyl rings are drawn and the hydrogen atoms are omitted.

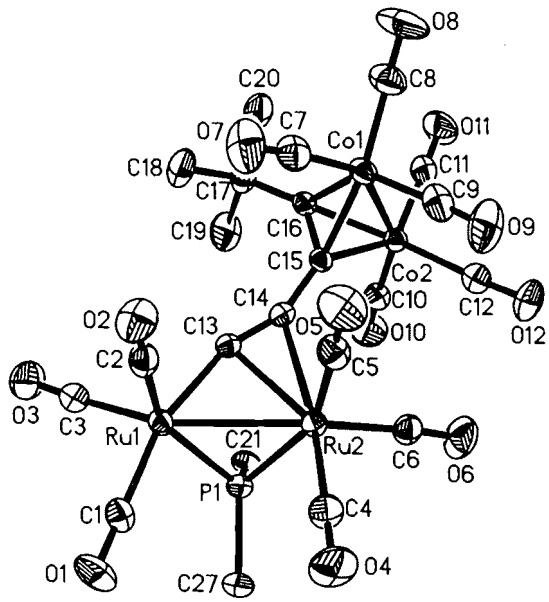

donor 2π acetylene functionality. The effect is most apparent in the C≡C bond lengths of the two alkyne units with the 2π-bonded moiety giving a greater separation (C(15)—C(16) 1.365(4) Å) than that seen in the σ–π-bound unit (C(13)—C(14) 1.241(3) Å). The Co_2 axis in **8** is bound essentially symmetrically to the C≡C bond (Co(1)—C(15) 1.971(2), Co(1)—C(16) 1.968(3), Co(2)—C(15) 1.963(2), Co(2)—C(16) 1.960(3) Å) with the C–C and Co–Co vectors lying perpendicular to one another. Addition of the dicobalt moiety produces a bending back of the outer alkyne substituents (C(14)-C(15)-C(16) 135.0(2)°, C(15)-C(16)-C(17) 136.8(2)°) and an increase in the *trans*-bending of the inner Ru_2-coordinated alkyne, C(13)-C(14)-C(15) 158.2(3)° (vs. 164.9(4)° in **7***a*). The *cis*-bending in the C(14)-C(15)-C(16)-C(17) fragment is slightly greater than normal (e.g., 138.9(6)° and 144.6(6)° in $\{Co_2(CO)_6\}PhC{\equiv}C\text{-}C{\equiv}CPh$ (**23***b*)) and may be caused by the steric constraints of the Bu^t and $Ru_2(CO)_6(PPh_2)(C_2)$ substituents.

The complexes **7***a–c* provide a unique opportunity to compare directly the reactivity of free and coordinated alkyne units and to assess the impact of a second alkynyl group. It is clear from initial studies that **7** exhibits distinctly different reactivity patterns in comparison with its monoynyl counterpart (24). Further investigations in this area are currently underway.

Experimental section

General procedures

All manipulations and reactions were carried out under an atmosphere of dinitrogen using standard Schlenk-line techniques or in a dry-box. Solvents for reactions, chromatography, and crystallizations were distilled under nitrogen from appropriate drying agents prior to use. Reactions were monitored by thin-layer chromatography (Baker-flex IB2-F) and infrared spectroscopy (carbonyl region). Purification of products was performed by column chromatography using oven-dried (150°C, 24 h) silica gel (70–230 mesh) on a dry-packed column or by thin-layer chromatography (TLC). Triruthenium dodecacarbonyl, dicobalt octacarbonyl, and chlorodiphenylphosphine were purchased from Strem, *cis*-1,2-dichloroethylene, 3-3-dimethyl-1-butyne, and 1,4-bis(trimethylsilyl)-1,3-butadiyne from Aldrich and were used without further purification. 5,5-Dimethyl-hexa-1,3-diyne was prepared according to the literature procedure (8).

IR spectra were recorded on Nicolet 520 FTIR and Bio-Rad FTS-40A instruments, using sodium chloride cells of 0.5 mm path length for solution spectra (*n*-hexane) or as KBr pellets. NMR spectra were recorded on Bruker AC 200, AM 200 (^{1}H, 200 MHz; $^{31}P\{^1H\}$ 81.0 MHz; $^{13}C\{^1H\}$ 50.3 MHz) and MSL 300 (^{1}H, 300 MHz; $^{31}P\{^1H\}$ 121.5 MHz) instruments. The $^{31}P\{^1H\}$ spectra are referenced externally to 85% H_3PO_4 and ^{1}H, ^{13}C to solvent sources. Mass spectrometric data were obtained by GC–MS on a Hewlett–Packard 5790A GC with a Hewlett–Packard 5970A mass selective detector (EI, 70 eV). Elemental analyses were performed by M-H-W Laboratories, Phoenix, Arizona, and by the Microanalysis Service of the Institute for Biological Sciences, NRC, Ottawa.

Syntheses

$PPh_2C{\equiv}C\text{-}C{\equiv}C\text{-}Bu^t$

A two-necked round-bottomed flask (250 mL) was charged with Bu^{t}C≡C-C≡C-H (3.60 g, 33.9 mmol) and diethyl ether (25 mL) and cooled to −78°C. To this was added a slight excess of 1.6 M Bu^{n}Li (22.0 mL, 35.2 mmol) over 20 min using a dropping funnel and the solution allowed to stir for 1 h before the addition of PPh_2Cl (6.2 mL, 34.5 mmol) in ether (10 mL). After warming to room temperature and further stirring for 1 h the solvent was partially removed and benzene added. The resulting white precipitate (LiCl) was filtered off to yield a pale yellow oil on drying. Addition of *n*-hexane precipitated an off-white microcrystalline solid. Yield = 6.90 g, 70%; mp 72°C.

$PPh_2C{\equiv}C\text{-}C{\equiv}C\text{-}Bu^t$: IR ν(C≡C)/cm^{-1}, (C_6H_{14}): 2249 vs, 2208 s, 2102 s; (KBr): 2250 m, 2207 s, 2100 w. ^{1}H NMR ($CDCl_3$) δ: 7.53–7.22 (m, 10H, Ph), 1.17 (s, 9H, Bu^t). $^{13}C\{^1H\}$ NMR ($CDCl_3$) δ: 135.3 (d, J_{PC} 5.9 Hz, PC_{ipso}), 132.7–128.6 (m, Ph), 92.0 (d, J_{PC} 6.0 Hz, C_β), 91.74 (s, C_δ), 74.3 (d, J_{PC} 8.8 Hz, C_α), 64.2 (s, C_γ), 30.4 (s, CMe_3), 28.2 (s, CMe_3). Proton-coupled ^{13}C NMR ($CDCl_3$) δ: 135.4–127.0 (m, Ph), 92.0 (d, J_{PC} 5.8 Hz, C_β), 91.7 (m, C_δ), 74.3 (d, J_{PC} 12.5 Hz, C_α), 64.2 (s, C_γ), 30.4 (virtual qt, CMe_3), 28.2 (m, CMe_3). $^{31}P\{^1H\}$ NMR ($CDCl_3$) δ: −31.4 (s). MS: 290 (M)$^+$, 233 (M − Bu^t)$^+$, 57 (Bu^t)$^+$. Anal. calcd. for $C_{20}H_{19}P$: C 82.74, H 6.60; found: C 82.64, H 6.70.

$PPh_2C{\equiv}C\text{-}C{\equiv}C\text{-}Ph$

Synthesis of $PhC{\equiv}C\text{-}CH{=}CHCl$:[4] Phenylacetylene (5.90 mL, 53.7 mmol), and 2.5 molar equivalents of *cis*-1,2-dichloroethylene (13.0 g, 134 mmol) were placed in a 250 mL round-

[4] This synthesis is based on the method reported by Kende and Smith (9*a*). We found that use of *trans*-$Pd(PPh_3)_2Cl_2$ gave slightly better yields than $Pd(PPh_3)_4$ (90% vs. 75%).

Table 1. X-ray crystallographic and data processing parameters for **7***a* and **8**.

Formula	$C_{26}H_{19}O_6PRu_2$	$C_{32}H_{19}Co_2O_{12}PRu_2$
Molecular weight	660.5	946.4
Crystal size (mm)	0.60 × 0.36 × 0.25 × 0.36	0.56 × 0.54 × 0.24 × 0.31 × 0.54 × 0.48
Crystal system	Monoclinic	Triclinic
Space group	$P2_1/n$	$P\bar{1}$
a (Å)	9.849(2)	9.9969(9)
b (Å)	9.886(2)	11.3018(9)
c (Å)	28.368(9)	17.268(1)
α (°)	—	90.653(6)
β (°)	95.18(2)	100.911(6)
γ (°)	—	110.465(5)
V (Å^3)	2751.1(12)	1788.4(3)
Z	4	2
D_c (g cm^{-3})	1.595	1.758
Radiation (MoKα, Å)	0.71073	0.71073
F(000)	1304	928
μ (cm^{-1})	11.92	18.43
Scan type	ω	ω
2θ range (°)	4.0–50.0	4.0–52.0
Scan width (°)	1.20	1.20
Scan speed (° min^{-1})	2.02–29.30	3.00–30.00
Reflections measured	5169	7441
Reflections observed	3886 ($F \geq 6.0\sigma(F)$)	6329 ($F \geq 6.0\sigma(F)$)
R	0.0243	0.0222
R_w	0.0253	0.0264
GoF	1.89	2.29

bottomed flask along with n-butylamine (25 mL, 253 mmol), copper iodide (0.30 g, 1.58 mmol) and *trans*-$Pd(PPh_3)_2Cl_2$ (0.30 g, 0.43 mmol). The solution was stirred for 16 h after which the solvent was removed under reduced pressure to afford a red-brown oil. Column chromatography on SiO_2 yielded a pale yellow oil identified by GC–MS as the chloro-enyne PhC≡C-CH=CHCl (7.90 g, 90%).

Synthesis of $PPh_2C{\equiv}C\text{-}C{\equiv}C\text{-}Ph$: The enyne PhC≡C-CH=CHCl (5.80 g, 35.7 mmol) was dissolved in THF (150 mL) and cooled to −78°C. Addition of two molar equivalents of LDA gave an orange-brown solution, which was stirred at low temperature for 3 h before treating with PPh_2Cl (7.0 mL, 39.0 mmol). After 20 min the low-temperature bath was removed and the solution stirred for a further 2 h after temperature equilibration. Partial evaporation of the solvent, filtration, and then drying yielded a brown oil, which was chromatographed on silica. Elution with dichloromethane–n-hexane (3:10) and evaporation of the solvent gave $PPh_2C{\equiv}C\text{-}C{\equiv}C$-Ph as a pale yellow powdery solid. Yield 6.90 g, 62%, mp 54°C.

$PPh_2C{\equiv}C\text{-}C{\equiv}C$-Ph: IR ν(C≡C)/cm^{-1}, (C_6H_{14}): 2205 vs, 2208 s, 2111 m; (KBr): 2201 s, 2104 w. ^{1}H NMR ($CDCl_3$) δ: 7.64–7.27 (m, Ph). $^{13}C\{^1H\}$ NNMR ($CDCl_3$) δ: 134.9 (d, J_{PC} 6.1 Hz, PC_{ipso}), 132.7–128.5 (m, Ph), 121.1 (s, Ph_{ipso}), 91.4 (d, J_{PC} 6.2 Hz, C_β), 81.0 (s, C_δ), 80.9 (d, J_{PC} 12.8 Hz, C_α), 74.1 (s, br, C_γ). Proton-coupled ^{13}C NMR ($CDCl_3$) δ: 134.9–126.7 (m, Ph), 121.1 (m, Ph_{ipso}), 91.4 (d, J_{PC} 5.9 Hz, C_β), 81.0 (m, C_δ), 80.9 (d, J_{PC} 14.4 Hz, C_α), 74.1 (s, br, C_γ). $^{31}P\{^1H\}$ NMR ($CDCl_3$) δ: −30.0 (s). MS: 310 $(M)^+$, 233 $(M - Ph)^+$. Anal. calcd. for $C_{22}H_{15}P$: C 85.15, H 4.87; found: C 85.24; H 4.57.

$PPh_2C{\equiv}C\text{-}C{\equiv}C\text{-}SiMe_3$

A solution of $Me_3SiC{\equiv}C\text{-}C{\equiv}CSiMe_3$ (4.0 g, 20.6 mmol) in THF (90 mL) was cooled to −78°C and treated with a slight excess of MeLi (16.0 mL, 22.4 mmol). After a few minutes a fine off-white precipitate had formed. Stirring at −78°C was continued for 2 h before allowing the solution to warm to −40°C for 30 min. On cooling to −78°C, PPh_2Cl (4.0 mL, 22.3 mmol) was added. After 30 min, the cooling bath was removed and the solution was allowed to warm to room temperature. Removal of the solvent under reduced pressure produced a brown oil, which was chromatographed on silica. Elution with dichloromethane–*n*-hexane (1:1) yielded a single colourless band that afforded $PPh_2C{\equiv}C\text{-}C{\equiv}C\text{-}SiMe_3$ as a pale yellow solid on evaporation of the solvent. Yield 5.78 g (92%); mp 32°C.

$PPh_2C{\equiv}C\text{-}C{\equiv}C\text{-}SiMe_3$: IR ν(C≡C)/cm^{-1}, (C_6H_{14}): 2228 vw, 2165 w, 2073 s. ^{1}H NMR ($CDCl_3$) δ: 7.61–7.33 (m, 10H, Ph), 0.21 (s, 9H, $SiMe_3$). $^{13}C\{^1H\}$ NNMR ($CDCl_3$) δ: 135.6 (d, J_{PC} 6.1 Hz, PC_{ipso}), 133.4–129.5 (m, Ph), 92.5 (d, J_{PC} 6.4 Hz, C_β), 91.5 (s, C_δ), 88.3 (s, C_γ), 77.0 (d, J_{PC} 14.9 Hz, C_α), 0.03 (s, $SiMe_3$). Proton-coupled ^{13}C NMR ($CDCl_3$) δ: 135.5–127.9 (m, Ph), 92.5 (d, J_{PC} 5.9 Hz, C_β), 91.5 (s, br, C_δ), 88.3 (s, C_γ), 77.0 (d, J_{PC} 15.2 Hz, C_α), 0.0 (q, J_{CH} 120 Hz, $SiMe_3$). $^{31}P\{^1H\}$ NMR ($CDCl_3$) δ: −31.7 (s). MS: 306 $(M)^+$, 233 $(M - SiMe_3)^+$, 73 $(SiMe_3)^+$. Anal. calcd. for $C_{19}H_{19}PSi$: C 74.48, H 6.25; found: C 74.25. H 6.39.

Table 2. Atomic coordinates ($\times 10^4$) and equivalent isotropic displacement coefficients ($Å^2 \times 10^4$) for $Ru_2(CO)_6(\mu\text{-}\eta^1,\eta^2\text{-}C{\equiv}C\text{-}C{\equiv}CBu^t)(\mu\text{-}PPh_2)$ **7***a*.

Atom	*x*	*y*	*z*	*U*(eq)
Ru(1)	2693.7(3)	−1060.9(3)	1024.8(1)	39.54(9)
Ru(2)	2282.2(3)	1542.3(3)	681.0(1)	40.31(9)
P(1)	1852.7(9)	784.3(9)	1440.6(3)	40.4(3)
O(1)	3940(4)	−2908(4)	1804(1)	124(2)
O(2)	41(3)	−2632(4)	825(2)	118(2)
O(3)	3832(3)	−2372(4)	156(1)	92(1)
O(4)	2335(4)	4632(3)	749(1)	105(2)
O(5)	−667(3)	1348(3)	301(1)	82(1)
O(6)	3153(3)	999(3)	−321(1)	88(1)
C(1)	3459(4)	−2228(5)	1513(1)	67(2)
C(2)	1028(4)	−2049(4)	917(2)	64(2)
C(3)	3390(4)	−1912(4)	472(1)	56(1)
C(4)	2315(4)	3485(4)	723(1)	63(2)
C(5)	435(4)	1421(4)	452(1)	51(1)
C(6)	2847(4)	1234(4)	43(1)	55(1)
C(7)	4149(3)	389(4)	1005(1)	42(1)
C(8)	4665(3)	1506(4)	960(1)	48(1)
C(9)	5540(4)	2624(4)	981(1)	53(1)
C(10)	6263(4)	3568(4)	1003(1)	59(1)
C(11)	7223(19)	4815(18)	978(6)	48(4)
C(11A)[a]	7129(34)	4566(31)	1082(13)	77(9)
C(12)	8605(5)	4263(6)	1115(3)	167(4)
C(13)	7453(12)	5129(11)	470(3)	127(6)
C(13A)[a]	6633(16)	5791(14)	725(6)	100(7)
C(14)	6664(12)	5952(10)	1214(6)	140(7)
C(14A)[a]	7289(13)	5211(14)	1588(5)	95(6)
C(15)	2963(3)	1412(4)	1945(1)	49(1)
C(16)	3498(4)	2689(5)	1958(2)	66(2)
C(17)	4350(5)	3128(6)	2342(2)	87(2)
C(18)	4664(5)	2277(7)	2716(2)	100(3)
C(19)	4152(5)	997(7)	2707(2)	91(2)
C(20)	3312(4)	543(5)	2323(1)	67(2)
C(21)	153(3)	836(4)	1653(1)	45(1)
C(22)	−86(4)	1531(4)	2060(1)	62(2)
C(23)	−1403(5)	1556(5)	2210(2)	84(2)
C(24)	−2455(5)	913(6)	1954(2)	87(2)
C(25)	−2228(4)	227(5)	1556(2)	77(2)
C(26)	−939(4)	188(4)	1401(1)	61(1)

[a]Atoms C(11A), C(13A), and C(14A) arise from a disorder about the *tert*-butyl group.

Table 3. Bond lengths (Å) for $Ru_2(CO)_6(\mu\text{-}\eta^1,\eta^2\text{-}C{\equiv}C\text{-}C{\equiv}Bu^t)(\mu\text{-}PPh_2)$ **7***a*.

Ru(1)—Ru(2)	2.769 (1)	Ru(1)—P(1)	2.362 (1)
Ru(1)—C(1)	1.905 (4)	Ru(1)—C(2)	1.910 (4)
Ru(1)—C(3)	1.958 (4)	Ru(1)—C(7)	2.031 (3)
Ru(2)—P(1)	2.355 (1)	Ru(2)—C(4)	1.924 (4)
Ru(2)—C(5)	1.880 (4)	Ru(2)—C(6)	1.965 (4)
Ru(2)—C(7)	2.284 (3)	Ru(2)—C(8)	2.408 (3)
P(1)—C(15)	1.830 (3)	P(1)—C(21)	1.831 (4)
O(1)—C(1)	1.135 (6)	O(2)—C(2)	1.140 (5)
O(3)—C(3)	1.127 (5)	O(4)—C(4)	1.136 (5)
O(5)—C(5)	1.132 (5)	O(6)—C(6)	1.124 (5)
C(7)—C(8)	1.227 (5)	C(8)—C(9)	1.400 (5)
C(9)—C(10)	1.172 (6)	C(10)—C(11)	1.560 (19)
C(10)—C(11A)	1.310 (31)	C(11)—C(12)	1.485 (19)
C(11)—C(13)	1.511 (20)	C(11)—C(14)	1.443 (22)
C(11A)—C(12)	1.478 (33)	C(11A)—C(13A)	1.624 (36)
C(11A)—C(14A)	1.568 (38)	C(15)—C(16)	1.367 (6)
C(15)—C(20)	1.392 (5)	C(16)—C(17)	1.384 (6)
C(17)—C(18)	1.366 (8)	C(18)—C(19)	1.362 (9)
C(19)—C(20)	1.382 (6)	C(21)—C(22)	1.381 (5)
C(21)—C(26)	1.393 (5)	C(22)—C(23)	1.402 (6)
C(23)—C(24)	1.367 (7))	C(24)—C(25)	1.355 (7)
C(25)—C(26)	1.380 (6)		

$Ru_2(CO)_6(\mu\text{-}\eta^1,\eta^2_{\alpha,\beta}\text{-}C{\equiv}C\text{-}C{\equiv}CBu^t)(\mu\text{-}PPh_2)$ **7**a

Triruthenium dodecacarbonyl (2.50 g, 3.91 mmol) was dissolved in tetrahydrofuran (300 mL, three freeze–pump–thaw cycles) and treated with a slight excess of $PPh_2C{\equiv}C\text{-}C{\equiv}CBu^t$ (1.20 g, 4.13 mmol). A few drops of sodium benzophenone ketyl catalyst in THF were added, causing an immediate colour change to deep red. After stirring for 10 min an IR (2098 w, 2047 s, 2031 ms, 2016 s cm^{-1}) indicated the complete consumption of $Ru_3(CO)_{12}$ while a spot TLC showed a single red-orange band that we assign as the monosubstituted species $Ru_3(CO)_{11}(PPh_2C{\equiv}C\text{-}C{\equiv}CBu^t)$. The solution was then heated to reflux for 4 h, causing considerable darkening. On cooling, the solvent was partially evaporated in vacuo and the residue absorbed onto a small amount of silica gel. Column chromatography on silica yielded a minor band of $Ru_3(CO)_{12}$ (identified by IR) using *n*-hexane as eluant. With dichloromethane–*n*-hexane (1:49), a broad band of pale yellow **7***a* was then removed. Reducing the volume to ~5 mL and overnight cooling to −10°C yielded 0.805 g (31%) of a yellow crystalline solid; mp 119°C.

7*a*: IR(C_6H_{14}) ν(CO)/cm^{-1}: 2085 s, 2057 s, 2021 s, 2010 m, 2002 s, 1990 mw. ^1H NMR ($CDCl_3$) δ: 7.48–7.20 (m, 10H, Ph), 1.10 (s, 9H, Bu^t). $^{13}C\{^1H\}$ NMR ($CDCl_3$) δ: 197.4 (d, J_{PC} 12.6 Hz, CO), 195.0 (d, J_{PC} 72.5 Hz, CO), 193.6 (d, J_{PC} 4.5 Hz, CO), 138.9 (d, J_{PC} 28.7 Hz, PC_{ipso}), 134.2 (d, J_{PC} 32.7 Hz, PC_{ipso}), 134.2–128.0 (m, Ph), 100.2 (d, J_{PC} 27.7 Hz, C_α), 88.1 (s, C_δ), 74.5 (d, J_{PC} 7.5 Hz, C_β), 66.8 (d, J_{PC} 3.5 Hz, C_γ), 30.6 (s, CMe_3), 28.0 (s, CMe_3). $^{31}P\{^1H\}$ NMR ($CDCl_3$) δ: 124.6 (s). Anal. calcd. for $C_{26}H_{19}O_6PRu_2$: C 47.26, H 2.87; found: C 47.20, H 2.78.

$Ru_2(CO)_6(\mu\text{-}\eta^1,\eta^2_{\alpha,\beta}\text{-}C{\equiv}C\text{-}C{\equiv}CPh)(\mu\text{-}PPh_2)$ **7**b

Compound **7***b* was prepared in a manner similar to that described above, using $PPh_2C{\equiv}C\text{-}C{\equiv}CPh$ (reflux time 2.5 h). Yield: 24%; mp 38°C. ($Ru_3(CO)_{11}(PPh_2C{\equiv}C\text{-}C{\equiv}CPh$: IR, 2098 w, 2047 s, 2028 ms, 2014 s cm^{-1}.)

7*b*: IR(C_6H_{14}) ν(CO)/cm^{-1}: 2085 s, 2058 s, 2022 s, 2012 m, 2003 s, 1992 mw. ^1H NMR ($CDCl_3$) δ: 7.61–7.21 (m, Ph). $^{13}C\{^1H\}$ NMR (CD_2Cl_2) δ: 197.7 (d, J_{PC} 11.6 Hz, CO), 195.2 (d, J_{PC} 72.0 Hz, CO), 193.8 (d, J_{PC} 5.0 Hz, CO), 139.0 (d, J_{PC} 29.0 Hz, PC_{ipso}), 133.6 (d, J_{PC} 33.2 Hz, PC_{ipso}), 134.5–128.5 (m, Ph), 122.3 (s, Ph_{ipso}), 109.0 (d, J_{PC} 27.7 Hz, C_α), 78.2 (d, J_{PC} 2.5 Hz, C_δ), 77.4 (d, J_{PC} 4.5 Hz, C_γ), 74.0 (d, J_{PC} 8.2 Hz, C_β). $^{31}P\{^1H\}$ NMR ($CDCl_3$) δ: 123.8 (s). Anal. calcd. for $C_{28}H_{15}O_6PRu_2$: C 49.42, H 2.22; found: C 49.26, H 1.98.

Table 4. Bond angles (°) for $Ru_2(CO)_6(\mu\text{-}\eta^1,\eta^2\text{-}C{\equiv}C\text{-}C{\equiv}Bu^t)(\mu\text{-}PPh_2)$ **7***a*.

Ru(2)-Ru(1)-P(1)	53.9(1)	Ru(2)-Ru(1)-C(1)	148.7(1)
P(1)-Ru(1)-C(1)	103.8(1)	Ru(2)-Ru(1)-C(2)	108.8(1)
P(1)-Ru(1)-C(2)	98.1(1)	C(1)-Ru(1)-C(2)	94.8(2)
Ru(2)-Ru(1)-C(3)	99.7(1)	P(1)-Ru(1)-C(3)	153.6(1)
C(1)-Ru(1)-C(3)	100.3(2)	C(2)-Ru(1)-C(3)	90.6(2)
Ru(2)-Ru(1)-C(7)	54.2(1)	P(1)-Ru(1)-C(7)	75.5(1)
C(1)-Ru(1)-C(7)	102.4(2)	C(2)-Ru(1)-C(7)	162.6(2)
C(3)-Ru(1)-C(7)	89.0(1)	Ru(1)-Ru(2)-P(1)	54.2(1)
Ru(1)-Ru(2)-C(4)	154.7(1)	P(1)-Ru(2)-C(4)	105.3(1)
Ru(1)-Ru(2)-C(5)	99.7(1)	P(1)-Ru(2)-C(5)	92.8(1)
C(4)-Ru(2)-C(5)	95.5(2)	Ru(1)-Ru(2)-C(6)	97.8(1)
P(1)-Ru(2)-C(6)	152.0(1)	C(4)-Ru(2)-C(6)	102.0(2)
C(5)-Ru(2)-C(6)	91.0(2)	Ru(1)-Ru(2)-C(7)	46.2(1)
P(1)-Ru(2)-C(7)	71.2(1)	C(4)-Ru(2)-C(7)	117.7(1)
C(5)-Ru(2)-C(7)	145.7(1)	C(6)-Ru(2)-C(7)	90.5(1)
Ru(1)-Ru(2)-C(8)	76.3(1)	P(1)-Ru(2)-C(8)	86.8(1)
C(4)-Ru(2)-C(8)	89.1(1)	C(5)-Ru(2)-C(8)	175.4(1)
C(6)-Ru(2)-C(8)	87.2(1)	C(7)-Ru(2)-C(8)	30.2(1)
Ru(1)-P(1)-Ru(2)	71.9(1)	Ru(1)-P(1)-C(15)	116.1(1)
Ru(2)-P(1)-C(15)	117.6(1)	Ru(1)-P(1)-C(21)	123.9(1)
Ru(2)-P(1)-C(21)	122.5(1)	C(15)-P(1)-C(21)	103.5(2)
Ru(1)-C(1)-O(1)	178.5(4)	Ru(1)-C(2)-O(2)	176.0(4)
Ru(1)-C(3)-O(3)	177.5(4)	Ru(2)-C(4)-O(4)	180.0(5)
Ru(2)-C(5)-O(5)	178.1(3)	Ru(2)-C(6)-O(6)	176.8(3)
Ru(1)-C(7)-Ru(2)	79.6(1)	Ru(1)-C(7)-C(8)	159.7(3)
Ru(2)-C(7)-C(8)	80.5(2)	Ru(2)-C(8)-C(7)	69.3(2)
Ru(2)-C(8)-C(9)	125.5(3)	C(7)-C(8)-C(9)	164.9(4)
C(8)-C(9)-C(10)	179.2(4)	C(9)-C(10)-C(11)	174.3(8)
C(9)-C(10)-C(11A)	172.7(15)	C(10)-C(11)-C(12)	104.0(11)
C(10)-C(11)-C(13)	110.5(11)	C(12)-C(11)-C(13)	96.5(12)
C(10)-C(11)-C(14)	109.6(13)	C(12)-C(11)-C(14)	122.9(13)
C(13)-C(11)-C(14)	112.3(13)	C(10)-C(11A)-C(12)	118.7(22)
C(10)-C(11A)-C(13A)	107.5(22)	C(12)-C(11A)-C(13A)	115.4(22)
C(10)-C(11A)-C(14A)	118.1(25)	C(12)-C(11A)-C(14A)	90.4(19)
C(13A)-C(11A)-C(14A)	105.5(19)	P(1)-C(15)-C(16)	122.3(3)
P(1)-C(15)-C(20)	118.8(3)	C(16)-C(15)-C(20)	118.8(3)
C(15)-C(16)-C(17)	120.9(4)	C(16)-C(17)-C(18)	119.8(5)
C(17)-C(18)-C(19)	120.1(5)	C(18)-C(19)-C(20)	120.6(5)
C(15)-C(20)-C(19)	119.7(5)	P(1)-C(21)-C(22)	121.2(3)
P(1)-C(21)-C(26)	120.3(3)	C(22)-C(21)-C(26)	118.4(3)
C(21)-C(22)-C(23)	119.7(4)	C(22)-C(23)-C(24)	120.5(4)
C(23)-C(24)-C(25)	120.1(4)	C(24)-C(25)-C(26)	120.4(4)
C(21)-C(26)-C(25)	120.9(4)		

$Ru_2(CO)_6(\mu\text{-}\eta^1,\eta^2{}_{\alpha,\beta}\text{-}C{\equiv}C\text{-}C{\equiv}CSiMe_3)(\mu\text{-}PPh_2)$ **7c**

Compound **7***c* was prepared in a manner similar to that described above, using $PPh_2C{\equiv}C\text{-}C{\equiv}CSiMe_3$ (reflux time 2 h). Yield: 20%; mp 84°C. ($Ru_3(CO)_{11}(PPh_2C{\equiv}C\text{-}C{\equiv}CSiMe_3$): IR, 2098 w, 2048 s, 2031 ms, 2018 s cm^{-1}.)

7*c*: IR(C_6H_{14}) ν(CO)/cm^{-1}: 2086 s, 2059 s, 2024 s, 2013 m, 2004 s, 1993 mw. ^1H NMR ($CDCl_3$) δ: 7.59–7.24 (m, 10H, Ph), 0.10 (s, 9H, $SiMe_3$). $^{13}C\{^1H\}$ NMR ($CDCl_3$) δ: 197.1 (d, J_{PC} 11.7 Hz, CO): 194.5 (d, J_{PC} 72.4 Hz, CO), 193.3 (d, J_{PC} 5.5 Hz, CO), 138.5 (d, J_{PC} 30.7 Hz, PC_{ipso}), 132.7 (d, J_{PC} 33.5 Hz, PC_{ipso}), 134.0–128.0 (m, Ph), 106.4 (d, J_{PC} 27.3 Hz, C_α), 91.0 (d, J_{PC} 6.9 Hz, C_β), 85.7 (s, C_δ), 74.0 (d, J_{PC} 5.5 Hz, C_γ), −0.33 (s, $SiMe_3$). $^{31}P\{^1H\}$ NMR ($CDCl_3$) δ: 122.0 (s). Anal. calcd. for $C_{25}H_{19}O_6PRu_2Si$: C 44.38, H 2.83; found: C 44.05, H 2.76.

$Ru_2(CO)_6(\mu\text{-}PPh_2)(\mu\text{-}\eta\text{-}C{\equiv}C\text{-}C{\equiv}CBu^t)Co_2(CO)_6$ **8**

Compound **7***a* (0.20 g, 0.30 mmol) was dissolved in toluene (20 mL) and treated with an excess of $Co_2(CO)_8$ (0.15 g, 0.44 mmol). A darkening of the solution was evident after a few minutes and an IR spectrum recorded after 2 h stirring showed complete consumption of **7***a*. The solvent was removed under reduced pressure and the resulting brown residue loaded onto TLC plates. Elution with dichloromethane–*n*-hexane (1:4) gave a red-brown band as the major product (crude yield 0.284 g, 99%). Crystallization from *n*-hexane at −10°C produced

Table 5. Atomic coordiantes ($\times 10^4$) and equivalent isotropic displacement coefficients ($Å^2 \times 10^4$) for $Ru_2(CO)_6(\mu\text{-}PPH_2)$-$(\mu\text{-}\eta^1,\eta^2_{\alpha,\beta}\text{:}\mu\text{-}\eta^2,\eta^2_{\gamma,\delta}\text{-}C{\equiv}C\text{-}C{\equiv}CBu^t)Co_2(CO)_6$ **8**.

Atom	*x*	*y*	*z*	*U*(eq)
Ru(1)	−1056.5(2)	1520.4(2)	3189.3(1)	22.23(7)
Ru(2)	1208.0(2)	2335.5(2)	2393.1(1)	21.49(7)
Co(1)	3965.3(4)	6523.1(3)	3726.4(2)	26.7(1)
Co(2)	2927.2(3)	7022.8(3)	2416.8(2)	22.4(1)
P(1)	−1278.4(7)	1822.7(6)	1838.5(4)	22.8(2)
O(1)	−2625(2)	−1352(2)	2847(1)	48.6(9)
O(2)	921(2)	1390(2)	4767(1)	49(1)
O(3)	−3485(2)	2052(2)	3789(1)	54(1)
O(4)	1085(3)	−279(2)	1902(2)	58(1)
O(5)	3774(2)	2692(2)	3805(1)	60(1)
O(6)	2664(3)	3656(2)	1076(1)	57(1)
O(7)	3312(3)	4986(3)	5053(1)	63(1)
O(8)	5856(3)	9063(2)	4497(2)	75(1)
O(9)	5926(3)	5391(3)	3193(1)	60(1)
O(10)	514(2)	6892(2)	1109(1)	52.0(9)
O(11)	4310(2)	9802(2)	2656(1)	51.2(9)
O(12)	4813(2)	6330(2)	1514(1)	46.6(9)
C(1)	−2034(3)	−291(2)	2984(2)	31(1)
C(2)	163(3)	1420(3)	4199(2)	32(1)
C(3)	−2622(3)	1817(3)	3560(2)	32(1)
C(4)	1125(3)	711(3)	2079(2)	35(1)
C(5)	2862(3)	2565(3)	3279(2)	34(1)
C(6)	2149(3)	3207(2)	1585(2)	33(1)
C(7)	3606(3)	5625(3)	4560(2)	39(1)
C(8)	5136(3)	8085(3)	4206(2)	45(1)
C(9)	5211(3)	5838(3)	3412(2)	38(1)
C(10)	1419(3)	6921(3)	1623(2)	32(1)
C(11)	3785(3)	8734(3)	2559(2)	32(1)
C(12)	4071(3)	6573(2)	1851(2)	31(1)
C(13)	255(3)	3341(2)	3158(1)	21.2(8)
C(14)	1155(3)	4315(2)	2976(1)	21.7(8)
C(15)	2060(3)	5600(2)	3026(1)	20.9(8)
C(16)	2065(3)	6704(2)	3358(1)	22.5(8)
C(17)	1027(3)	7131(2)	3713(2)	31(1)
C(18)	604(4)	6320(3)	4395(2)	44(1)
C(19)	−353(3)	6917(3)	3076(2)	50(1)
C(20)	1723(4)	8530(3)	4021(2)	50(1)
C(21)	−1893(3)	3060(2)	1414(1)	25.3(9)
C(22)	−2680(3)	3598(3)	1782(2)	38(1)
C(23)	−3185(3)	4490(3)	1421(2)	48(1)
C(24)	−2899(3)	4858(3)	689(2)	45(1)
C(25)	−2115(3)	4342(3)	320(2)	44(1)
C(26)	−1619(3)	3441(3)	676(2)	36(1)
C(27)	−2279(3)	490(2)	1095(2)	28.4(9)
C(28)	−3751(3)	−149(3)	1063(2)	38(1)
C(29)	−4553(4)	−1156(3)	502(2)	49(1)
C(30)	−3910(4)	−1519(3)	−24(2)	65(2)
C(31)	−2479(5)	−883(4)	−19(3)	87(2)
C(32)	−1640(4)	135(3)	549(2)	61(2)

red-brown crystals overnight (crystalline yield 0.252 g, 88%); mp 111°C.

8: IR(C_6H_{14}) ν(CO)/cm^{-1}: 2095 m, 2080 s, 2058 vs, 2035 m, 2030 m sh, 2022 s, 2002 m, 1988 w. ^1H NMR ($CDCl_3$) δ: 7.60–7.14 (m, 10H, Ph), 1.11 (s, 9H, Bu^t). $^{13}C\{^1H\}$ NMR ($CDCl_3$) δ: 199.07 (br, CO), 197.3 (d, J_{PC} 11.2 Hz, CO), 195.2 (d, J_{PC} 71.2 Hz, CO), 194.1 (d, J_{PC} 6.5 Hz, CO), 139.4 (d, J_{PC} 30.6 Hz, PC_{ipso}), 134.1 (d, J_{PC} 32.1 Hz, PC_{ipso}), 133.9–128.3 (m, Ph), 115.7 (s, C_δ), 113.1 (d, J_{PC} 31.8 Hz, C_α), 93.6 (d, J_{PC} 7.6 Hz, C_β), 74.6 (d, J_{PC} 3.0 Hz, C_γ), 37.0 (s, CMe_3), 32.2 (s, CMe_3). $^{31}P\{^1H\}$ NMR ($CDCl_3$) δ: 120.0 (s). Anal. calcd. for $C_{32}H_{19}Co_2O_{12}PRu_2$: C 40.61, H 2.02; found: C 40.07, H 1.96.

Table 6. Bond lengths (Å) for $Ru_2(CO)_6(\mu\text{-}PPh_2)$-$(\mu\text{-}\eta^1,\eta^2_{\alpha,\beta}\text{:}\mu\text{-}\eta^2,\eta^2_{\gamma,\delta}\text{-}C{\equiv}C\text{-}C{\equiv}Bu^t)Co_2(CO)_6$ **8**.

Ru(1)—Ru(2)	2.759(1)	Ru(1)—P(1)	2.341(1)
Ru(1)—C(1)	1.929(2)	Ru(1)—C(2)	1.958(3)
Ru(1)—C(3)	1.928(3)	Ru(1)—C(13)	2.024(2)
Ru(2)—P(1)	2.347(1)	Ru(2)—C(4)	1.878(3)
Ru(2)—C(5)	1.968(3)	Ru(2)—C(6)	1.919(3)
Ru(2)—C(13)	2.267(3)	Ru(2)—C(14)	2.465(3)
Co(1)—Co(2)	2.462(1)	Co(1)—C(7)	1.791(3)
Co(1)—C(8)	1.823(3)	Co(1)—C(9)	1.834(4)
Co(1)—C(15)	1.971(2)	Co(1)—C(16)	1.968(3)
Co(2)—C(10)	1.805(3)	Co(2)—C(11)	1.813(3)
Co(2)—C(12)	1.827(3)	Co(2)—C(15)	1.963(2)
Co(2)—C(16)	1.960(3)	P(1)—C(21)	1.823(3)
P(1)—C(27)	1.825(2)	O(1)—C(1)	1.135(3)
O(2)—C(2)	1.129(3)	O(3)—C(3)	1.121(4)
O(4)—C(4)	1.141(4)	O(5)—C(5)	1.128(3)
O(6)—C(6)	1.137(4)	O(7)—C(7)	1.137(4)
O(8)—C(8)	1.134(4)	O(9)—C(9)	1.123(5)
O(10)—C(10)	1.133(3)	O(11)—C(11)	1.130(3)
O(12)—C(12)	1.125(4)	C(13)—C(14)	1.241(3)
C(14)—C(15)	1.408(3)	C(15)—C(16)	1.365(4)
C(16)—C(17)	1.506(4)	C(17)—C(18)	1.532(4)
C(17)—C(19)	1.536(4)	C(17)—C(20)	1.529(4)
C(21)—C(22)	1.381(5)	C(21)—C(26)	1.396(4)
C(22)—C(23)	1.383(5)	C(23)—C(24)	1.385(5)
C(24)—C(25)	1.365(5)	C(25)—C(26)	1.383(5)
C(27)—C(28)	1.383(4)	C(27)—C(32)	1.363(5)
C(28)—C(29)	1.386(4)	C(29)—C(30)	1.343(6)
C(30)—C(31)	1.356(6)	C(31)—C(32)	1.407(5)

Crystal structure determination of complex 7*a*

Yellow crystals of **7***a* were grown from a saturated *n*-hexane solution at −10°C. Data were collected at 295 K on a Siemens R3m/V diffractometer. Background measurements using the stationary crystal, stationary counter method were made at the beginning and end of each scan, each for 25.0% of the total scan time. Two standard reflections were monitored every 100 measurements; no significant decay was detected over the time of data collection. Data were corrected for Lorentz and polarization effects and absorption corrections were applied using the face-indexed numerical method. Relevant crystal and data collection parameters for the present study are given in Table 1.

The structure was solved by Patterson and Fourier methods and refined by full-matrix least squares, first with isotropic thermal parameters and then with anisotropic thermal parameters for all non-hydrogen atoms. A difference Fourier map revealed the positions of the hydrogen atoms, which were

Table 7. Bond angles (°) for $Ru_2(CO)_6(\mu\text{-}PPh_2)(\mu\text{-}\eta^1,\eta^2_{\alpha,\beta}\text{:}\mu\text{-}\eta^2,\eta^2_{\gamma,\delta}\text{-}C{\equiv}C\text{-}C{\equiv}Bu^t)Co_2(CO)_6$ **8**.

Ru(2)-Ru(1)-P(1)	54.1(1)	Ru(2)-Ru(1)-C(1)	109.8(1)
P(1)-Ru(1)-C(1)	92.5(1)	Ru(2)-Ru(1)-C(2)	95.3(1)
P(1)-Ru(1)-C(2)	149.0(1)	C(1)-Ru(1)-C(2)	94.5(1)
Ru(2)-Ru(1)-C(3)	149.0(1)	P(1)-Ru(1)-C(3)	109.1(1)
C(1)-Ru(1)-C(3)	95.6(1)	C(2)-Ru(1)-C(3)	100.2(1)
Ru(2)-Ru(1)-C(13)	54.0(1)	P(1)-Ru(1)-C(13)	75.7(1)
C(1)-RU(1)-C(13)	163.6(1)	C(2)-Ru(1)-C(13)	90.3(1)
C(3)-Ru(1)-C(13)	99.0(1)	Ru(1)-Ru(2)-P(1)	53.9(1)
Ru(1)-Ru(2)-C(4)	95.9(1)	P(1)-Ru(2)-C(4)	91.5(1)
Ru(1)-Ru(2)-C(5)	99.6(1)	P(1)-Ru(2)-C(5)	153.4(1)
C(4)-Ru(2)-C(5)	92.3(1)	Ru(1)-Ru(2)-C(6)	153.7(1)
P(1)-Ru(2)-C(6)	103.0(1)	C(4)-Ru(2)-C(6)	97.1(1)
C(5)-Ru(2)-C(6)	102.7(6)	Ru(1)-Ru(2)-C(13)	46.2(1)
P(1)-Ru(2)-C(13)	71.3(1)	C(4)-Ru(2)-C(13)	141.8(1)
C(5)-Ru(2)-C(13)	89.9(1)	C(6)-Ru(2)-C(13)	119.6(1)
Ru(1)-Ru(2)-C(14)	76.2(1)	P(1)-Ru(2)-C(14)	87.0(1)
C(4)-Ru(2)-C(14)	171.2(1)	C(5)-Ru(2)-C(14)	85.2(1)
C(6)-Ru(2)-C(14)	91.7(1)	C(13)-Ru(2)-C(14)	30.0(1)
Co(2)-Co(1)-C(7)	146.1(1)	Co(2)-Co(1)-C(8)	102.6(1)
C(7)-Co(1)-C(8)	101.7(1)	Co(2)-Co(1)-C(9)	97.9(1)
C(7)-Co(1)-C(9)	98.2(2)	C(8)-Co(1)-C(9)	105.0(1)
Co(2)-Co(1)-C(15)	51.1(1)	C(7)-Co(1)-C(15)	95.9(1)
C(8)-Co(1)-C(15)	142.9(1)	C(9)-Co(1)-C(15)	104.4(1)
Co(2)-Co(1)-C(16)	51.0(1)	C(7)-Co(1)-C(16)	100.2(1)
C(8)-Co(1)-C(16)	103.7(1)	C(9)-Co(1)-C(16)	141.7(1)
C(15)-Co(1)-C(16)	40.5(1)	Co(1)-Co(2)-C(10)	152.6(1)
Co(1)-Co(2)-C(11)	98.3(1)	C(10)-Co(2)-C(11)	98.3(1)
Co(1)-Co(2)-C(12)	97.9(1)	C(10)-Co(2)-C(12)	99.4(1)
C(11)-Co(2)-C(12)	102.9(1)	Co(1)-Co(2)-C(15)	51.4(1)
C(10)-Co(2)-C(15)	102.7(1)	C(11)-Co(2)-C(15)	138.7(1)
C(12)-Co(2)-C(15)	108.1(1)	Co(1)-Co(2)-C(16)	51.3(1)
C(10)-Co(2)-C(16)	104.3(1)	C(11)-Co(2)-C(16)	99.7(1)
C(12)-Co(2)-C(16)	144.2(1)	C(15)-Co(2)-C(16)	40.7(1)
Ru(1)-P(1)-Ru(2)	72.1(1)	Ru(1)-P(1)-C(21)	121.7(1)
Ru(2)-P(1)-C(21)	118.9(1)	Ru(1)-P(1)-C(27)	120.6(1)
Ru(2)-P(1)-C(27)	121.9(1)	C(21)-P(1)-C(27)	101.5(1)
Ru(1)-C(1)-O(1)	178.5(2)	Ru(1)-C(2)-O(2)	176.8(3)
Ru(1)-C(3)-O(3)	176.4(2)	Ru(2)-C(4)-O(4)	178.7(3)
Ru(2)-C(5)-O(5)	177.4(3)	Ru(2)-C(6)-O(6)	175.8(2)
Co(1)-C(7)-O(7)	175.2(2)	Co(1)-C(8)-O(8)	179.2(3)
Co(1)-C(9)-O(9)	177.0(2)	Co(2)-C(10)-O(10)	177.0(3)
Co(2)-C(11)-O(11)	179.2(3)	Co(2)-C(12)-O(12)	177.8(2)
Ru(1)-C(13)-Ru(2)	79.8(1)	Ru(1)-C(13)-C(14)	163.1(2)
Ru(2)-C(13)-C(14)	83.8(2)	Ru(2)-C(14)-C(13)	66.2(2)
Ru(2)-C(14)-C(15)	134.1(2)	C(13)-C(14)-C(15)	158.2(3)
Co(1)-C(15)-Co(2)	77.5(1)	Co(1)-C(15)-C(14)	130.0(2)
Co(2)-C(15)-C(14)	144.8(2)	Co(1)-C(15)-C(16)	69.6(1)
Co(2)-C(15)-C(16)	69.5(1)	C(14)-C(15)-C(16)	135.0(2)
Co(1)-C(16)-Co(2)	77.6(1)	Co(1)-C(16)-C(15)	69.9(2)
Co(2)-C(16)-C(15)	69.8(1)	Co(1)-C(16)-C(17)	137.1(2)
Co(2)-C(16)-C(17)	136.6(2)	C(15)-C(16)-C(17)	136.8(2)
C(16)-C(17)-C(18)	108.6(3)	C(16)-C(17)-C(19)	108.5(2)
C(18)-C(17)-C(19)	108.8(2)	C(16)-C(17)-C(20)	111.2(2)
C(18)-C(17)-C(20)	109.7(2)	C(19)-C(17)-C(20)	109.9(3)

Table 7 (*concluded*).

P(1)-C(21)-C(22)	122.2(2)	P(1)-C(21)-C(26)	119.2(2)
C(22)-C(21)-C(26)	118.5(3)	C(21)-C(22)-C(23)	120.4(3)
C(22)-C(23)-C(24)	120.4(4)	C(23)-C(24)-C(25)	120.2(3)
C(24)-C(25)-C(26)	119.7(3)	C(21)-C(26)-C(25)	121.0(3)
P(1)-C(27)-C(28)	118.9(2)	P(1)-C(27)-C(32)	122.2(2)
C(28)-C(27)-C(32)	118.8(2)	C(27)-C(28)-C(29)	120.7(3)
C(28)-C(29)-C(30)	120.3(3)	C(29)-C(30)-C(31)	120.1(3)
C(30)-C(31)-C(32)	120.7(4)	C(27)-C(32)-C(31)	119.5(3)

included in calculated positions. The hydrogen atoms were treated using the riding model method with refined isotropic thermal parameters for phenyl hydrogens and fixed isotropic thermal parameters for the methyl hydrogen atoms. Atoms C(11A), C(13A), and C(14A) arise from a disorder about the *tert*-butyl group. A satisfactory model was refined with an occupancy of 60:40 (C:C(A)) for these three atoms. Atom C(12) was refined with full occupancy. In the final cycles of refinement a weighting scheme, $w = [s^2(F_o)]^{-1}$ was used. The function minimized in the least-squares refinement was $\Sigma w(|F_o| - |F_c|)^2$. The weighted R value, R_w, is defined as $[\Sigma w(|F_o|—|F_c|)^2/\Sigma w|F_o|^2]^{1/2}$, where the weights, w, are optimized on moderate intensities. The atomic scattering factors, corrected for the real and imaginary parts of anomalous dispersions, were taken from ref. 25; for hydrogen, those of Stewart et al. were used (26). Programs used are described elsewhere (27). Final atomic coordinates for the non-hydrogen atoms and equivalent isotropic displacement coefficients are presented in Table 2 (equivalent isotropic U (U_{eq} = 1/3 × orthogonalized U_{ij} tensor). Bond lengths and angles are presented in Tables 3 and 4, respectively. Anisotropic displacement coefficients and hydrogen atom parameters have been deposited as supplementary material.[5]

Crystal structure determination of complex 8

Red-brown crystals of **8** were grown from a saturated *n*-hexane solution at −10°C. Data were collected at 200 K on a Siemens P4 diffractometer. Background measurements using the stationary crystal, stationary counter method were made at the beginning and end of each scan, each for 25.0% of the total scan time. Three standard reflections were monitored every 100 measurements; no significant decay was detected over the time of data collection. Data were corrected for Lorentz and polarization effects and absorption corrections were applied using the face-indexed numerical method. Relevant crystal and data collection parameters are given in Table 1.

The structure was solved and refined as for **7***a*. Final atomic coordinates for the non-hydrogen atoms and equivalent isotropic displacement coefficients are presented in Table 5. Bond lengths and angles are presented in Tables 6 and 7, respectively. Anisotropic displacement coefficients and hydrogen atom parameters have been deposited as supplementary material.[5]

[5] This supplementary data may be purchased from: The Depository of Unpublished Data, Document Delivery, CISTI, National Research Council Canada, Ottawa, Canada K1A 0S2. Complete crystallographic data for **7***a* have been deposited at the Cambridge Crystallographic Data Centre and can be obtained on request from The Director, Cambridge Crystallographic Data Centre, University Chemical Laboratory, 12 Union Road, Cambridge, CB2 1EZ, UK. Lists of structure factors are available from the authors.

Acknowledgements

This work was supported by the National Research Council of Canada and by the Natural Sciences and Engineering Research Council of Canada in the form of an operating grant (to A.J.C.) and a Canada International Fellowship Award (to P.B.). We thank Dr Todd B. Marder (University of Waterloo) for many helpful suggestions on ligand synthesis.

References

1. (*a*) C.W. Faulkner, S.L. Ingham, M.S. Khan, J. Lewis, N.J. Long, and P.R. Raithby. J. Organomet. Chem. **482**, 139 (1994); (*b*) J. Lewis, M.S. Khan, A.K. Kakkar, B.F.G. Johnson, T.B. Marder, H.B. Fyfe, F. Wittmann, R.H. Friend, and A.E. Dray. J. Organomet. Chem. **425**, 165 (1992); (*c*) M.J. Irwin, G. Jia, N.C. Payne, and R.J. Puddephatt. Organometallics, **15**, 51 (1996); (*d*) J.P. Rourke, D.W. Bruce, and T.B. Marder. J. Chem. Soc. Dalton Trans. 317 (1995); (*e*) L.K. Myers, C. Langhoff, and M.E. Thompson. J. Am. Chem. Soc. **114**, 7560 (1992); (*f*) Y. Sun, N.J. Taylor, and A.J. Carty. Organometallics, **11**, 4293 (1992); (*g*) R.R. Tykwinski and P.J. Stang. Organometallics, **13**, 3203 (1994); (*h*) L.D. Field, A.V. George, T.W. Hambley, E.Y. Malouf, and D.L. Young. J. Chem. Soc. Chem. Commun. 931 (1990); (*i*) S. Takahashi, H. Morimoto, E. Murato, S. Kataoka, K. Sonogashira, and N. Hagihara. J. Polym. Sci. Polym. Chem. Ed. **20**, 565 (1982); (*j*) I. Manners. Chem. Br. **32**, 46 (1996); (*k*) N. Pirio, D. Touchard, P.H. Dixneuf, M. Fettouhi, and L. Ouahab. Angew. Chem. Int. Ed. Engl. **32**, 651 (1992).
2. (*a*) H. Lang. Angew. Chem. Int. Ed. Engl. **33**, 673 (1994); (*b*) H. Werner, T. Rappert, and J. Wolf. Isr. J. Chem. **30**, 377 (1990); (*c*) T. Rappert, O. Nürnberg, and H. Werner. Organometallics, **12**, 1359 (1993); (*d*) M.I. Bruce, P. Hinterding, E.R.T. Tiekink, B.W. Skelton, and A.H. White. J. Organomet. Chem. **450**, 209 (1993); (*e*) A. Wong, P.C.W. Kang, C.D. Tagge, and D.R. Leon. Organometallics, **9**, 1992 (1990); (*f*) H.B. Fyfe, M. Mlekuz, D. Zargarian, N.J. Taylor, and T.B. Marder. J. Chem. Soc. Chem. Commun. 188 (1991); (*g*) M. Brady, W. Weng, and J.A. Gladysz. J. Chem. Soc. Chem. Commun. 2655 (1994).
3. (*a*) N. Le Narvor, L. Toupet, and C. Lapinte. J. Am. Chem. Soc. **117**, 7129 (1995); (*b*) N. Le Narvor and C. Lapinte. Organometallics, **14**, 634 (1995); (*c*) Y. Zhou, J.W. Seyler, W. Weng, A.M. Arif, and J.A. Gladysz. J. Am. Chem. Soc. **115**, 8509 (1993); (*d*) J.W. Seyler, W. Weng, Y. Zhou, and J.A. Gladysz. Organometallics, **12**, 3802 (1993); (*e*) N. Le Narvor and C. Lapinte. J. Chem. Soc. Chem. Commun. 357 (1993); (*f*) W. Weng, T. Bartik, M. Brady, B. Bartik, J.A. Ramsden, A.M. Arif, and J.A.

Gladysz. J. Am. Chem. Soc. **117**, 11922 (1995); (*g*) F. Coat and C. Lapinte. Organometallics, **15**, 477 (1996).
4. (*a*) D. Touchard, P. Haquette, A. Daridor, L. Toupet, and P.H. Dixneuf. J. Am. Chem. Soc. **116**, 11157 (1994); (*b*) D. Peron, A. Romero, and P.H. Dixneuf. Gazz. Chim. Ital. **124**, 497 (1994).
5. (*a*) W. Weng, T. Bartik, and J.A. Gladysz. Angew. Chem. Int. Ed. Engl. **33**, 2199 (1994); (*b*) W. Weng, J.A. Ramsden, A.M. Arif, and J.A. Gladysz. J. Am. Chem. Soc. **115**, 3824 (1993); (*c*) W. Weng, A.M. Arif, and J.A. Gladysz. Angew. Chem. Int. Ed. Engl. **32**, 891 (1993); (*d*) G.H. Worth, B.H. Robinson, and J. Simpson. Organometallics, **11**, 501 (1992).
6. (*a*) H. Werner, O. Gevert, P. Steinert, and J. Wolf. Organometallics **14**, 1786 (1995); (*b*) C.J. Adams, M.I. Bruce, E. Horn, B.W. Skelton, E.R.T. Tiekink, and A.H. White. J. Chem. Soc. Dalton Trans. 3299 (1993); (*c*) J. Chem. Soc. Dalton Trans. 3313 (1993).
7. A.A. Cherkas, S. Doherty, M. Cleroux, G. Hogarth, L.H. Randall, S.M. Breckenridge, N.J. Taylor, and A.J. Carty. Organometallics, **11**, 1701 (1992), and refs. therein.
8. L. Brandsma. Preparative acetylenic chemistry. Elsevier, Amsterdam. 1988.
9. (*a*) A.S. Kende and C.A. Smith. J. Org. Chem. **53**, 2655 (1988). (*b*) D. Chemin and G. Linstrumelle. Tetrahedron, **50**, 5335 (1994).
10. (*a*) K. Sonogashira, Y. Tohda, and N. Hagihara. Tetrahedron Lett. **50**, 4467 (1975); (*b*) J.K. Stille. Angew. Chem. Int. Ed. Engl. **25**, 508 (1986); (*c*) C. Amatore, M. Azzabi, and A. Jutand. J. Am. Chem. Soc. **113**, 1670 (1991).
11. (*a*) A.B. Holmes, C.L.D. Jennings-White, A.H. Schultess, B. Akinde, and D.R.M. Walton. J. Chem. Soc. Chem. Commun. 840 (1979); (*b*) J.L. Bréfort, R.J.P. Corriu, Ph. Gerbier, C. Guérin, B.J.L. Henner, A. Jean, Th. Kuhlmann, F. Garnier, and A. Yassar. Organometallics, **11**, 2500 (1992).
12. B. Wrackmeyer and K. Horchler. Prog. NMR Spectrosc. **22**, 209 (1990).
13. C.J. Adams, M.I. Bruce, E. Horn, and E.R.T. Tiekink. J. Chem. Soc. Dalton Trans. 1157 (1993).
14. S.A. MacLaughlin, D. Nucciarone, and A.J. Carty. *In* Phosphorus-31 NMR spectroscopy in stereochemical analysis; organic compounds and metal complexes. *Edited by* J.G. Verkade and L.D. Quinn. VCH Publishers, New York. 1987. Chap. 16.
15. A.A. Cherkas, L.H. Randall, S.A. MacLaughlin, G.N. Mott, N.J. Taylor, and A.J. Carty. Organometallics, **7**, 969 (1988).
16. L.H. Randall, A.A. Cherkas, and A.J. Carty. Organometallics, **8**, 568 (1989).
17. J. Manna, K.D. John, and M.D. Hopkins. Adv. Organomet. Chem. **38**, 79 (1995).
18. D. Nucciarone, S.A. MacLaughlin, N.J. Taylor, and A.J. Carty. Organometallics, **7**, 106 (1988).
19. C.J. Adams, M.I. Bruce, B.W. Skelton, and A.H. White. J. Organomet. Chem. **450**, C9 (1993).
20. G.G. Cash and R.C. Pettersen. J. Chem. Soc. Dalton Trans. 1630 (1979).
21. (*a*) Y. Rubin, S.S. Lin, C.B. Knobler, J. Anthony, A.M. Boldi, and F. Diederich. J. Am. Chem. Soc. **113**, 6943 (1991); (*b*) B.F. Coles, P.B. Hitchcock, and D.R.M. Walton. J. Chem. Soc. Dalton Trans. 442 (1975); (*c*) J.J. Mayerle and T.C. Clarke. Acta Crystallogr. Sect. B: Struct. Crystallogr. Cryst. Chem. **B34**, 143 (1978); (*d*) F.H. Allen, O. Kennard, D.G. Watson, L. Brammer, A.G. Orpen, and R. Taylor. J. Chem. Soc. Perkin Trans. 2, S1 (1987).
22. (*a*) A. Romero, D. Peron, and P.H. Dixneuf. J. Chem. Soc. Chem. Commun. 1410 (1990); (*b*) T.B. Marder, G. Lesley, Z. Yuan, H.B. Fyfe, P. Chow, G. Stringer, I.R. Jobe, N.J. Taylor, I.D. Williams, and S.K. Kurtz. ACS Symp. Ser. **455**, 605 (1991).
23. (*a*) C.E. Housecroft, B.F.G. Johnson, M.S. Khan, J. Lewis, P.R. Raithby, M.E. Robson, and D.A. Wilkinson. J. Chem. Soc. Dalton Trans. 3171 (1992); (*b*) B.F.G. Johnson, J. Lewis, P.R. Raithby, and D.A. Wilkinson. J. Organomet. Chem. **408**, C9 (1991).
24. P. Blenkiron, D. Pilette, J.F. Corrigan, N.J. Taylor, and A.J. Carty. J. Chem. Soc. Chem. Commun. 2165 (1995).
25. International tables for X-ray crystallography. Vol IV. Kynoch Press, Birmingham. 1974.
26. R.F. Stewart, E.R. Davidson, and W.T. Simpson. J. Chem. Phys. **42**, 3175 (1965).
27. A.J. Carty, G.N. Mott, N.J. Taylor, and J.E. Yule. J. Am. Chem. Soc. **100**, 3051 (1978).

A density functional study of the bonding in tertiary phosphine chalcogenides and related molecules

Nicole Sandblom, Tom Ziegler, and Tristram Chivers

Abstract: The nature of the phosphorus–tellurium bond in tertiary phosphine tellurides is not well understood. There is also controversy over the nature of multiple bonding in the lighter chalcogenides and the related ylides and imides. Density functional theory (DFT) was used to investigate the interactions in the molecule, Me_3PE (E = O, S, Se, Te, BH_3, CH_2, NH). The calculated PE bond energies and orbital populations reveal contributions from both σ donation from the phosphine and π back-donation to the phosphine in all of the above cases. Down the group from oxygen to tellurium, the PE bond weakens from 544 kJ mol^{-1} to 184 kJ mol^{-1}, but multiple bonding becomes more significant with respect to the single bond. For E = BH_3, the PB bond energy is 166 kJ mol^{-1}. Trimethylphosphine ylide was found to have a π-bond order of 0.5, while that of trimethylphosphine imine is 0.6. For comparison, the oxides of trimethylamine and trimethylarsine were also calculated to examine the pnictogen–oxygen bond; Me_3N does not participate in multiple bonding with oxygen, while the π-bond orders for Me_3PO and Me_3AsO were calculated as 0.7 and 0.6, respectively.

Key words: phosphine chalcogenides, phosphine ylides, phosphine imides, DFT calculations

Résumé : La nature de la liaison phosphore–tellure dans les tellurures de phosphine tertiaires n'est pas très bien comprise. Il ya a également une controverse relativement à la nature de la liaison multiple dans les chalcogénures plus légères et dans les ylures et imides apparentés. On a fait appel à la théorie de la densité fonctionnelle (TDF) pour étudier les interactions dans la molécule de Me_3PE (E = O, S, Se, BH_3, CH_2, NH). Les énergies de liaison PE calculées et les populations des orbitales révèlent des contributions à la fois du transfert σ à partir de la phosphine et du transfert en retour π vers la phosphine dans tous les cas ci-dessus. La liaison PE s'affaiblit lorsqu'on descend dans la famille de l'oxygène vers le tellure, elle passe de 544 kJ mol^{-1} à 184 kJ mol^{-1}, mais la liaison multiple devient plus significative par rapport à la liaison simple. Pour E = BH_3, l'énergie de la liaison PB est de 166 kJ mol^{-1}. On a trouvé que l'ylure de la triméthylphosphine a une liaison π de l'ordre de 0,5, tandis que pour l'imine de la triméthylphosphine l'ordre est de 0,6. Pour fins de comparaison, on a également calculé les oxydes de la triméthylamine et de la triméthylarsine, pour examiner la liaison oxygène–azote; Le Me_3N ne participe pas à la liaison multiple avec l'oxygène, alors que calcul des ordres de la liaison π pour le Me_3PO et le Me_3AsO donnent 0,7 e 0,6 respectivement.

Mots clés : chalcogénures de phosphine, ylure de phosphore, imides de phosphine, calculs de TDF.

[Traduit par la rédaction]

1. Introduction

The useful electrical properties of certain metal tellurides have sparked research into developing single-source precursors for these semiconductors (1, 2). Many research groups now routinely use trialkylphosphine tellurides, R_3PTe, as tellurium transfer agents; for example, the reaction of Et_3PTe with low-valent transition-metal compounds generates metal-tellurium clusters that can be subsequently pyrolyzed to binary metal tellurides (3). Other important applications of R_3PTe reagents as a source of reactive tellurium include the preparation of terminal metal tellurides (4), chalcogen exchange reactions (5), insertions into metal–carbon (6) and metal–metal (7) bonds, and in the titanium-mediated heterohydrocoupling of Te and Bu_3SnH (8).

Relatively little is known about the bonding in phosphine tellurides. The three crystallographically characterized structures suggest that the phosphorus–tellurium bond has an order of about 1.5, where PTe is 2.368 Å for $^tBu_3PTe$ (9), 2.365 Å in the case of $^iPr_3PTe$ (10), and 2.371 Å in $^tBu_2[NH(C_6H_{11})]PTe$ (11). ^{125}Te solution NMR spectroscopy at room temperature and ^{125}Te Mössbauer spectroscopy at 4.2 K provide results that have been interpreted as inconsistent with the presence of π bonding (12). The controversy is not confined to tellurium. Although phosphine oxides are commonly described as $R_3P{=}O$, there is still debate over the nature of the PO bond in these molecules (13). The possible resonance contributors range from a single to triple bond (Fig. 1). Several experimental observations, e.g. bond energies of oxides and sulfides,

Received March 12, 1996.

This paper is dedicated to Professor Howard C. Clark in recognition of his contributions to Canadian chemistry.

N. Sandblom, T. Ziegler,[1] and T. Chivers. Department of Chemistry, The University of Calgary, Calgary, AB T2N 1N4, Canada.

[1] Author to whom correspondence may be addressed. Telephone: (403)-220-5368. Fax: (416)-289-9488. E-mail: ziegler@acs.ucalgary.ca

Fig. 1. Resonance contributions to the PO bond in tertiary phosphine oxide.

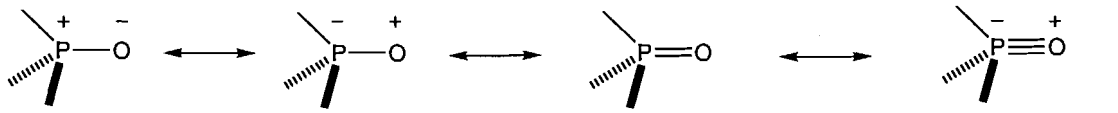

single σ–bond I | single π–bond II | 1 σ–bond + 1 π–bond III | 1 σ–bond + 2 π–bond IV

bond lengths, dipole moments, NMR shifts and coupling constants when E = Se, and infrared stretching frequencies of the P—E bond in the oxides, sulfides, and selenides, suggest multiple bonding (14). However, in a recent paper, Power (15) studied the chemical shift tensors of Me_3PO and related molecules, and concluded that the phosphorus–oxygen bond is dative.

Ab initio studies of phosphine chalcogenides have been limited to oxygen and sulfur, and the most extensive work focuses on H_3PO (14). Given the proven ability of density functional theory (DFT) to predict geometries and energies accurately (16), we decided to study the orbital interactions involved in the trimethylphosphine chalcogenide bond. For comparison purposes, trimethylphosphine-borane, trimethylphosphine ylide, and trimethylphosphine imide, and the oxides of trimethylamine and trimethylarsine were also considered.

2. Computational details

All calculations were based on approximate density functional theory within the local density approximation (17), LDA, in the parameterization by Vosko et al. (18). In addition, we used Becke's (19) nonlocal exchange correction as well as inhomogenous gradient corrections for correlation due to Perdew (20), NL-SCF. The reported calculations were performed utilizing the vectorized version of the ADF program system developed by Baerends et al. (21, 22) and vectorized by Ravenek (23). The numerical integration procedure applied for the calculations was developed by te Velde and co-workers (24). All molecules were optimized with C_{3v} symmetry with the following exceptions: borane (D_{3h}), methylene (C_{2v}), trimethylphosphine ylide (C_s), imine (C_{2v}), trimethylphosphine imide (C_s). The geometry optimization procedure was based on the method developed by Versluis and Ziegler (25). A double ζ-STO basis set (25) was employed for the *ns* and *np* shells of the main group elements. The basis set was augmented by a single *3d* STO function except for hydrogen, where a *2p* STO was used as polarization. Electrons in lower shells were considered as core and treated according to the procedure due to Baerends and co-workers. (26). An auxiliary (27) set of *s*, *p*, *d*, *f*, and *g* STO functions, centered on all nuclei, was used in order to fit the molecular density and present Coulomb and exchange potentials accurately in each SCF cycle. All structures were optimized at the LDA level of theory. The calculated bond energies include nonlocal corrections evaluated from LDA densities.

3. Results and discussion

General bonding scheme in Me_3PE and related systems

The PE bond in trimethylphosphine chalcogenides (Me_3PE) can be analysed by considering the frontier orbitals on the two fragments Me_3P and E. The orbitals of interest on Me_3P are the occupied σ-type HOMO, **1a**, of a_1 symmetry, and the empty e_1 pair, **1b** and **1c**. The three *p* orbitals on the chalcogens (E) are shown as **2a**, **2b**, and **2c**. The σ component of the P—E bond involves donation of charge from the occupied orbital **1a** on Me_3P to the empty orbital **2a** on the chalcogen. This process is illustrated in **3a**. The π interactions are represented by donation from the filled π-type *p* orbitals, **2b** and **2c**, on E to the empty σ* orbitals on Me_3P. This type of donation, as shown in **3b** and **3c**, has been termed negative hyperconjugation (28). We note further that each of the orbitals **3b** and **3c** has π symmetry with respect to the PE bond. Interaction **3a** represents the singly bonded σ-resonance structure I of Fig. 1, whereas **3b** and **3c** each represent the π-resonance structure II of Fig. 1.

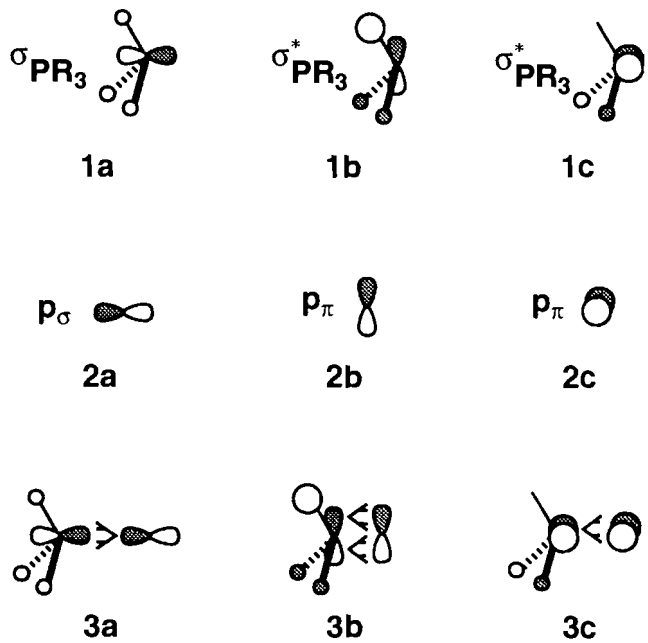

A number of fragments have frontier orbitals analogous to the chalcogens. They are, in the terminology of Hoffmann (29), isolobal with the chalcogens and form similar bonds with tertiary phosphines. Thus the transition metal fragment, $Cr(CO)_5$, with the frontier orbitals, **4a–c**, is isolobal with the chalcogens; its bonding to R_3P has been studied previously (30). Other isolobal fragments are borane, **5a–c**, methylene, **6a–c**, and imine, **7a–c**. The frontier orbital energies of the chalcogens as well as those of BH_3, CH_2, and NH are compared to those of Me_3N, Me_3P, and Me_3As in Fig. 2.

General bond energy decomposition scheme

In general, the molecules under consideration are of the form

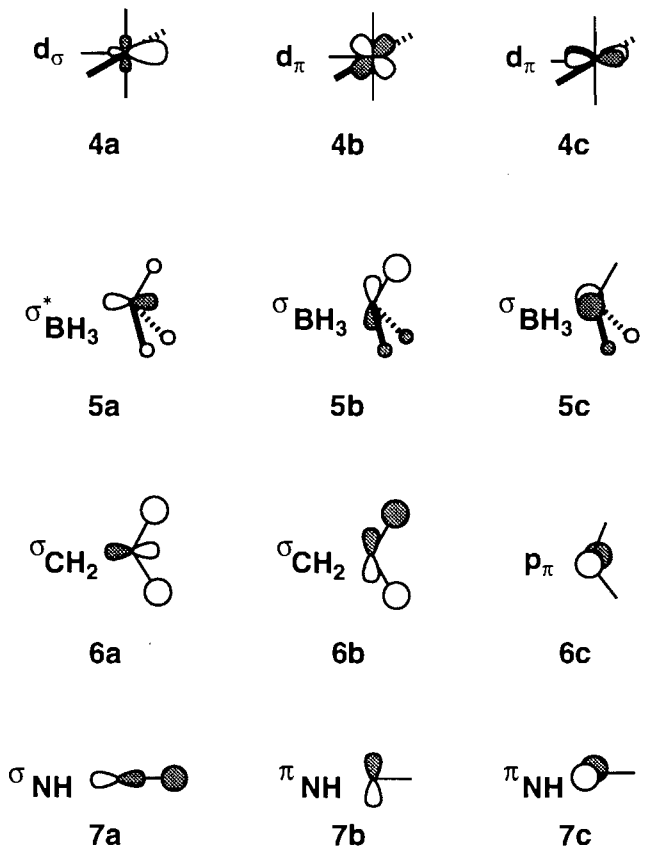

Fig. 2. Orbital energies for the frontier orbitals of the Me_3X and E fragments.

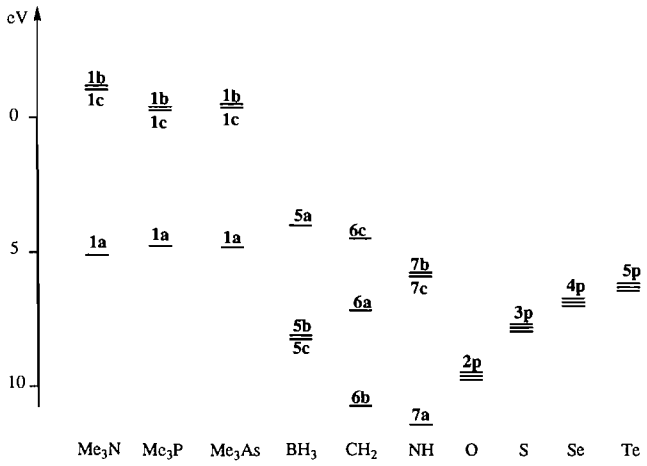

Me_3XE where X = N, P, As and E = O, S, Se, Te, BH_3, CH_2, NH. Using the generalized transition state method (31), we are able to separate steric and electronic contributions to the XE bond energy:

[1] $\Delta H_{XE} = E(E) + E(Me_3X) - E(Me_3XE)$

according to

[2] $\Delta H_{XE} = -[\Delta E_{prep} + \Delta E^0 + \Delta E_{el}]$

Table 1. Bond energy analysis (kJ mol^{-1}) and selected orbital populations for Me_3PE (E = O, S, Se, Te).

	$\Delta E^{Me_3P}_{prep}$ [a]	ΔE^{E}_{prep} [b]	$\Delta E^0 + \Delta E_{res}$ [c]	ΔE_{don} [d]	e_{don} [e]	ΔE_{bdon} [f]	e_{bdon} [g]	ΔE_{syn} [h]	e^{syn}_{don} [i]	e^{syn}_{bdon} [j]	ΔH_{PE} [k]
Me_3PO	21	276	771	−1210	1.0	−37	0.1	−365	1.4	0.4	−544(−582)[l]
Me_3PS	15	167	178	−497	0.7	−51	0.2	−149	1.0	0.6	−337(−383)[m]
Me_3PSe	14	152	117	−379	0.7	−50	0.2	−120	0.9	0.5	−266
Me_3PTe	13	132	53	−243	0.5	−49	0.2	−90	0.7	0.5	−184

[a] Preparation energy of Me_3P.
[b] Preparation energy of E.
[c] Steric interaction energy and residual energy.
[d] Energy from donation interaction.
[e] Electrons accepted in donation interaction.
[f] Energy from back-donation interaction.
[g] Electrons accepted in back-donation interaction.
[h] Energy from synergic effect.
[i] Electrons accepted in synergic donation interaction.
[j] Electrons accepted in synergic back-donation interaction.
[k] PE bond energy.
[l] Experimental energy for Me_3PO from ref. 32.
[m] Experimental energy for Pr_3PS from ref. 32.

Table 2. Optimized bond lengths (Å) and angles (°) for Me_3P and Me_3PE[a] (E = O, S, Se, Te).

	r_{PE}	r_{CP}	∠CPE	∠CPC	Reference
Me_3P		1.857(1.847)		100.2(98.6)	33
Me_3PO	1.497(1.476)	1.816(1.809)	112.8(114.4)	106.0(104.1)	34
Me_3PS	1.945(1.940)	1.828(1.818)	113.7(114.1)	104.9(104.5)	34
Me_3PSe	2.083(2.091)	1.827(1.816)	113.6(113.8)	105.0(104.8)	35
Me_3PTe	2.303(2.368)	1.830(1.896)	113.7(108.7)	105.0(110.2)	9[b]

[a]Experimental values are given in parentheses.
[b]For $^tBu_3PTe$.

Here ΔE_{prep} is the energy required to alter the Me_3X and E fragments from their ground state conformation to the geometry they adopt in the combined complex. The term ΔE_{prep} in the fragments E = O, S, Se, Te, CH_2, and NH also contains a promotion energy from the electronic ground state to a valence state suitable for σ donation and π back-donation with Me_3X, as explained in detail later.

The term ΔE^0 represents the steric interaction energy between Me_3X and E. It includes the stabilizing electrostatic interaction between the two fragments and the exchange repulsion component resulting from the destabilizing interactions between occupied orbitals on E and Me_3X. The steric interaction energy, ΔE^0, is obtained as ΔH_{XE} of eq. [1] from a calculation of Me_3XE and E(Me_3XE) in which only the occupied orbitals of E and Me_3X are used as basis functions.

Finally, ΔE_{el} of eq. [2] accounts for the stabilizing interactions between occupied and empty fragment orbitals. The stabilizing electronic interaction energy ΔE_{el} is further decomposed into

$$[3] \quad \Delta E_{el} = \Delta E_{don} + \Delta E_{bdon} + \Delta E_{syn} + \Delta E_{res}$$

Here ΔE_{don} represents the stabilizing contribution to ΔH_{XE} due to σ donation, **3a**, of charge from the σ-donor orbital, **1a**, on Me_3X to an empty σ-acceptor orbital (**2a**, **5a**, **6a**, or **7a**) on E. It is obtained as the additional energy gained by adding one of the σ-acceptor orbitals (**2a**, **5a**, **6a**, or **7a**) on E to the basis of occupied E and Me_3X fragment orbitals in a calculation of Me_3XE. The orbital population, e_{don}, shows how many electrons the orbital on E (**2a**, **5a**, **6a**, or **7a**) accepts in this calculation. The term ΔE_{bdon} is due to the π donations, **3b** and **3c**, in which charge is transferred to **1b** and **1c** on Me_3X from two occupied π-donor orbitals on E such as **2b** and **2c**. The term is obtained in a way similar to ΔE_{don}, except that the added virtual orbitals now are **1b** and **1c**. Similarly, the orbital population, e_{bdon}, now refers to the electrons accepted by **1b** and **1c**. The third contribution, ΔE_{syn}, is a measure of the synergic effect, the degree to which donation, **3a**, and back-donation, **3b** + **3c**, reinforce each other. It is the extra stabilization of the XE bond gained by including the virtual fragment orbitals, **1b** and **1c**, as well as **2a**, or its equivalent, at the same time. This calculation gives the synergic orbital populations, e_{don} and e_{bdon}, which represent the number of electrons in the σ-acceptor orbital on E (**2a**, **5a**, **6a**, or **7a**) and in the σ*-acceptor orbitals on Me_3X (**1b** and **1c**), respectively. Finally, ΔE_{res} measures the additional stabilization gained by including the remaining virtual fragment orbitals in the calculation. It is often combined with the steric interaction energy since it stems from interactions that serve to reduce the exchange repulsion.

Trimethylphosphine chalcogenides

Table 1 describes the bond energy decomposition and orbital populations of the trimethylphosphine chalcogenides. The preparation energy of trimethylphosphine is due to a slight geometric distortion from the free phosphine; it is relatively small for all of the chalcogens. The preparation energy for the chalcogens is electronic. It represents a promotion of the chalcogen from its ^3P ground state to the $(2p_\sigma)^0(2p_\pi)^4$ valence configuration. The promotion energy is due to the loss of exchange stabilization as two electrons of parallel spin in the ^3P ground state are given opposite spin orientations in the $(2p_\sigma)^0\ (2p_\pi)^4$ valence configuration. This requires much more energy for oxygen, 276 kJ mol^{-1}, with contracted p orbitals and high exchange stabilization, than for tellurium, 132 kJ mol^{-1}, with the most diffuse p orbitals and the smallest exchange stabilization.

The combined steric interaction energy, $\Delta E^0 + \Delta E_{res}$, is dominated by destabilizing overlaps between occupied orbitals on the Me_3P and E fragments (Table 1). It is most repulsive, 771 kJ mol^{-1}, for Me_3PO with the shortest distance between the two fragments and decreases gradually from Me_3PS, 178 kJ mol^{-1}, to Me_3PTe, 53 kJ mol^{-1}, as the PE distance increases.

The stabilization, $-\Delta E_{don}$, due to the σ donation is largest for E = O with $-\Delta E_{don}$ = 1210 kJ mol^{-1}, and decreases gradually from Me_3PS, 497 kJ mol^{-1}, to Me_3PTe, 243 kJ mol^{-1}. The trend is understandable, when we observe that the donation from the occupied σ orbital on Me_3P, **1a**, to the empty p_σ orbital on E is most favorable for oxygen with the p_σ orbital of lowest energy (Fig. 2). The gain in stabilization decreases gradually from E = S to E = Te as the energy of the p_σ orbital approaches that of **1a**. The actual charge transfered is 1.0 e for Me_3PO with a drop from 0.7 e in Me_3PS to 0.5 e in Me_3PTe (Table 1).

The contribution, $-\Delta E_{bdon}$, from the back-donations, **3b** and **3c**, is not very large. This is not surprising since the p_π donor orbitals on E are of much lower energy than the π-acceptor orbitals **1b** and **1c** on Me_3P, Fig. 2. This is especially true in the case of oxygen where the back-donation amounts to 0.1 e and $-\Delta E_{bdon}$ = 37 kJ mol^{-1}. For the remaining chalcogens, the energy gap is reduced and the back-donation somewhat larger at 0.2 e with $-\Delta E_{bdon}$ = 50 kJ mol^{-1}.

Table 3. Bond energy analysis (kJ mol^{-1}) and selected orbital populations for Me_3PE (E = BH_3, CH_2, NH, O).

E	$\Delta E_{prep}^{Me_3P}$ [a]	ΔE_{prep}^{E} [b]	$\Delta E^0 + \Delta E_{res}$ [c]	ΔE_{don} [d]	e_{don} [e]	ΔE_{bdon} [f]	e_{bdon} [g]	ΔE_{syn} [h]	e_{don}^{syn} [i]	e_{bdon}^{syn} [j]	ΔH_{PE} [k]
BH_3	16	54	80	−256	0.6	−24	0.1	−36	0.7	0.3	−166
CH_2	14	343	193	−600	0.9	−69	0.2	−172	1.1	0.5	−357
NH	14	970	730	−1724	1.8	−272	0.6	−51	1.6	0.6	−333
O	21	276	771	−1210	1.0	−37	0.1	−365	1.4	0.7	−544(−582)[l]

[a]Preparation energy of Me_3P.
[b]Preparation energy of E.
[c]Steric interaction energy and residual energy.
[d]Energy from donation interaction.
[e]Electrons accepted in donation interaction.
[f]Energy from back-donation interaction.
[g]Electrons accepted in back-donation interaction.
[h]Energy from synergic effect.
[i]Electrons accepted in synergic donation interaction.
[j]Electrons accepted in synergic back-donation interaction.
[k]PE bond energy.
[l]Experimental energy for Me_3PO from ref. 32.

Fig. 3. Bond lengths and angles in Me_3XE.

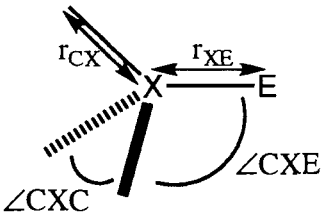

The synergic effect substantially increases the multiple bonding character of the PE linkage. Thus the back-donation for oxygen is increased by 0.6 *e* to a total of 0.7 *e* (Table 1). Now the PO bond has the most pronounced π components, **3b** and **3c**. By equating the total π-bond order with the electron charge back-donated we get an order of 0.7 for the PO linkage. The corresponding π-bond orders for E = S, Se, and Te are 0.6, 0.5, and 0.5, respectively.

The σ component of the PE bond, **3a**, is also enhanced by the synergic effect. For the PO bond, 1.4 *e* is donated to oxygen. (Table 1) For the other chalcogens, the σ donations are 1.0 *e* (S), 0.9 *e* (Se), and 0.7 *e* (Te), respectively.

It is clear that both the σ and π components are important for the PE linkage after the synergic effect has been taken into account. Both σ and π bonding have the largest contributions for oxygen. Their contributions decrease from sulfur to tellurium, and σ bonding is always more pronounced than π bonding. However, in relative terms, the two bonding modes become more comparable in importance upon descending Group 16 from oxygen towards tellurium.

The synergic contribution to the PE bond, $-\Delta E_{syn,}$ is substantial, starting at 365 kJ mol^{-1} for E = O and decreasing to 90 kJ mol^{-1} for E = Te (Table 1). The calculated PE bond energies for oxygen and sulfur compare well with the experimental estimates obtained for Me_3PO (32), and Pr_3PS (32), respectively. The overall phosphorus–chalcogen bond energy is predicted to decrease down the group (Table 1).

Table 2 contains calculated bond lengths and angles (as defined in Fig. 3) for the Me_3PE systems. The optimized structures are in good agreement with the experimentally observed data. The deviation is largest in the case of tellurium, because the experimental data are those of the tri-*tert*-butylphosphine telluride. This molecule has bulkier substituents than trimethylphosphine telluride, so it is not surprising that the ∠CPC angle is larger and the PC distance longer in tri-*tert*-butylphosphine telluride as the result of the steric interaction between the *tert*-butyl groups. Indeed, the PTe bond length in tri-*tert*-butylphosphine telluride has been described as anomalous and suspiciously long (14). Therefore, the calculated bond length of 2.303 Å is probably a more realistic value.

The PH_3 molecule has a ∠HPH angle of 93°. Thus, electronically, the optimal ∠CPC angle for phosphines should be close to 90°. However, the bulk of the R groups attached to phosphorus tends to increase the ∠CPC angle, and PC distance, in order to relieve the steric repulsion. The ∠HPH bond angle in PH_4^+ is 109°. Thus the ∠CPC angle in R_3PE should open up towards 109° if, to a first approximation, we consider the chalcogenides as pure electrophiles with a σ-acceptor orbital, **3a**, but without any π-donation ability, **3b** and **3c**. We see, in fact, that the ∠CPC angles in R_3PE are larger than in

Table 4. Optimized bond lengths (Å) and angles (°) for Me_3P, E, and Me_3PE[a] (E = BH_3, CH_2, NH).

	r_{PE}	r_{CP}	∠CPE	∠CPC	Additional lengths and angles	Ref.
Me_3P		1.857(1.847)		100.2(98.6)		33
BH_3					r_{BH} = 1.202, ∠HBH = 120.0	
Me_3PBH_3	1.863(1.894)	1.823(1.811)	113.0(113.8)	105.8(104.8)	r_{BH}: 1.222(1.201); ∠HBH: 113.6(109.2); ∠HBP: 104.9(109.8)	6
CH_2					r_{CH}: 1.090(1.078); ∠HCH: 138.0(136)	7
Me_3PCH_2	1.659(1.640)	1.833(1.815)	114.2(116.5)	104.4(101.6)	r_{CH}: 1.091(1.060); ∠HCH: 119.5; ∠HCP:120.2(128)	8
NH					r_{NH}: 1.058(1.035)	7
Me_3PNH	1.564(1.652)	1.827(1.913)	113.9(109.6)	104.6(109.4)	r_{NH}: 1.021(1.020); ∠PNH: 118.9 (114)	9[b]

[a]Experimental values are given in parentheses.
[b]For $^tBu_3PNH$.

R_3P, both experimentally and theoretically. Further, the PC distance is somewhat shorter in R_3PE as the larger ∠CPC angle allows the R groups to move closer to the phosphorus atom for the same amount of steric repulsion as in R_3P. The effect of π donation, **3b** and **3c**, would be to increase the PC distance and close the ∠CPC angle as the σ* orbitals, **1b** and **1c**, accept electron density. Obviously, the PE σ bonding in R_3PE is dictating the changes of the R_3P framework. However, the degree of increase in the ∠CPC angle and decrease in the PC distance is likely modified by the opposing trends from the π back-donation, **3b** and **3c**. This balance between the σ and π effects on geometry is evident in the trend down the group. The telluride has the longest PC bonds, and has the most π character relative to the σ contribution.

Me_3PBH_3, Me_3PCH_2, and Me_3PNH

Table 3 contains the bond energies and orbital populations of the isoelectronic series, Me_3PE (E = BH_3, CH_2, and NH), and compares them to those of the oxide. The preparation energies of the phosphine are due to a slight distortion of geometry and are fairly small in these cases. The preparation of borane distorts it from a planar to a pyramidal conformation, and ΔE_{prep} is only 54 kJ mol^{-1}. We shall explain the reason for the distortion of BH_3 as well as the NH and CH_2 fragments later (Table 4). For imine, the preparation involves shortening the NH bond and promoting electrons from the $^3\Sigma^-$ ($\mathbf{7a}^2\mathbf{7b}^1\mathbf{7c}^1$) ground state to a paired $\mathbf{7a}^0\mathbf{7b}^2\mathbf{7c}^2$ valence state. The preparation of NH requires the most energy, 970 kJ mol^{-1}. The preparation of methylene is both electronic and geometric; the ∠HCH angle opens up and the $^3B1$ ($\mathbf{6a}^1\mathbf{6b}^2\mathbf{6c}^1$) ground state is promoted to a $\mathbf{6a}^0\mathbf{6b}^2\mathbf{6c}^2$ valence state . The preparation of CH_2 takes substantially less energy, 343 kJ mol^{-1}, than NH because it only involves the promotion of one electron out of a bonding orbital to pair up with another electron in the nonbonding $2p_C$ π orbital, **6c**.

Across the row from boron to oxygen, the combined steric interaction energy, $\Delta E^0 + \Delta E_{res}$, increases from 80 to 771 kJ mol^{-1}. This trend can be explained in terms of the distance between the two fragments. The PE distance decreases from left to right across the row, giving rise to a more and more repulsive interaction between occupied orbitals on the two fragments.

The relative energies of **5a**, **6a**, and **7a** (Fig. 2), explain the differences in stabilization due to σ donation, $-\Delta E_{don}$. It is greatest for E = NH, $-\Delta E_{don}$ = 1724 kJ mol^{-1}, which has the lowest energy acceptor orbital, **7a**. For E = CH_2 and BH_3, $-\Delta E_{don}$ equals 600 and 256 kJ mol^{-1}, respectively; this trend is expected since the orbital energies decrease by **7a** < **6a** < **5a**. The charge transferred by σ bonding decreases from 1.8 *e* for the imine to 0.6 *e* for the borane.

Back-donation in the borane is not very favourable because of the large gap between the donor orbitals, **5b** and **5c**, and the back-donation acceptor orbitals, **1b** and **1c** (Fig. 2). The stabilization is quite small in this case, $-\Delta E_{bdon}$ = 24 kJ mol^{-1}. The imine donor orbitals, **7b** and **7c**, are higher in energy; the stabilization is greater here, $-\Delta E_{bdon}$ = 272 kJ mol^{-1}. There is some back-donation in the case of the methylene fragment, and almost all of the stabilization, $-\Delta E_{bdon}$ = 69 kJ mol^{-1}, comes from the higher energy orbital, **6c**. While **6b** has the proper symmetry to be involved as a donor, its overlap with **1b** is very small, and there is a wide energy gap between these two orbitals. The trimethylphosphine ylide does not have equal contributions in the two back-donation interactions, and can be represented by the resonance structure III in Fig. 1 with only one σ and one π bond.

There is a synergic effect for all of the isoelectronic analogues, but none is as substantial as that for E = O. For the borane and imine adducts, the stabilization is quite small, $-\Delta E_{syn}$ = 36 and 51 kJ mol^{-1}, respectively. For methylene, the stabilization, 172 kJ mol^{-1}, is still not as large as the synergic effect for oxygen, 365 kJ mol^{-1}. However, all of these compounds have some multiple bonding. The π-bond order for borane is 0.3 *e*, for methylene, 0.5 *e*, and for imine, 0.6 *e*. The overall bond energy for PE decreases from −333 kJ mol^{-1} for E = NH, to −166 kJ mol^{-1} for E = BH_3.

The optimized geometries for this series are described in Table 4 along with some experimental comparisons; in the case of Me_3PNH, no experimental data are available; instead, the data for $^tBu_3PNH$ are given. For the C_s optimized molecules, Me_3PCH_2 and Me_3PNH, average PC bond lengths and ∠CPC are shown. The experimental electron diffraction study of Me_3PCH_2 assumed C_3 symmetry for the Me_3P fragment, so in this case the calculated numbers may be more realistic (13*a*). As observed for the trimethylphosphine chalcogenides, the PC bonds in Me_3PBH_3, Me_3PCH_2, and Me_3PNH are slightly shorter than those in trimethylphosphine and the CPC

Table 5. Bond energy analysis (kJ mol^{-1}) and selected orbital populations for Me_3XO (X = N, P, As).

	$\Delta E^{Me_3X}_{prep}$ [a]	ΔE^0_{prep} [b]	$\Delta E^0 + \Delta E_{res}$ [c]	ΔE_{don} [d]	e_{don} [e]	ΔE_{bdon} [f]	e_{bdon} [g]	ΔE_{syn} [h]	e^{syn}_{don} [i]	e^{syn}_{bdon} [j]	ΔH_{XO} [k]
Me_3NO	70	276	318	−859	0.7	−1	0.0	−1	0.7	0.0	−197
Me_3PO	21	276	771	−1210	1.0	−37	0.1	−365	1.4	0.7	-544(−582)[l]
Me_3AsO	26	276	555	−918	0.9	−18	0.1	−264	1.2	0.6	−343

[a]Preparation energy of Me_3X
[b]Preparation energy of O
[c]Steric interaction energy and residual energy.
[d]Energy from donation interaction.
[e]Electrons accepted in donation interaction.
[f]Energy from back-donation interaction.
[g]Electrons accepted in back-donation interaction.
[h]Energy from synergic effect.
[i]Electrons accepted in synergic donation interaction.
[j]Electrons accepted in synergic back-donation interaction.
[k]XO bond energy.
[l]Experimental energy for Me_3PO from ref. 32.

angle also opens up. The changes here are not as significant as the change to Me_3PO, but are on the order of the changes observed for the heavier chalcogens. As mentioned above, this is indicative of the σ-bonding interaction dominating the geometry. The π-bonding effects of PC bond lengthening and ∠CPC decreasing must also play a part, but are overshadowed. For E = BH_3, the PC bond is the shortest for this isoelectronic series; while the σ-donation energy is not the largest, it has the smallest back-donation energy, so the shortening effect (σ) is not significantly cancelled by the lengthening effect (π). Trimethylphosphine imine has both the largest $-\Delta E_{don}$ and largest $-\Delta E_{bdon}$ for this series; a balance between these two factors leads to an overall shortening of the PC bond.

In these molecules, the fragments bonded to Me_3P also change geometry. The boron–hydrogen bonds in the phosphine adduct are longer than those in borane. The σ interaction populates **5a**, which is nonbonding in the planar ground state of BH_3 and becomes B—H bonding in the pyramidal BH_3 fragment, while the π interactions depopulate the BH bonding orbitals **5b** and **5c**. The geometry at boron becomes pyramidal in order to stabilize the now populated **5a** by allowing bonding overlaps between $2p_B$ and $1s$ on each hydrogen, **5a**.

The carbon–hydrogen bonds in methylene stay approximately the same. This is understandable because the ground state methylene has one electron in the bonding orbital **6a**, which is also the population of **6a** in coordinated CH_2. The π interaction involves back-donation from a nonbonding orbital, **6c**, which holds 1.5 *e* in the ylide compound. The main change in the methylene fragment is the decrease in ∠HCH from 138.0° in free CH_2 to 119.5° in the ylide. The decrease in the ∠HCH angle stabilizes the **6a** acceptor orbital by enhancing the bonding overlap. Steric factors might also decrease the ∠HCH angle in the ylide compound.

The **7a** orbital of NH is a slightly anti-bonding combination between an *sp* lobe on nitrogen and $1s$ on hydrogen. It is thus understandable that the NH bond in coordinated imine shortens, since **7a** holds 1.6 *e* in complexed NH, compared to 2.0 *e* in free NH (Table 3). The optimized structure of Me_3PNH has ∠PNH of 118.9°; this structure is 39 kJ mol^{-1} lower in energy than a structure with a linear PNH.

Me_3NO, Me_3PO, and Me_3AsO

Table 5 gives the bond energy decomposition for the oxides of the second-, third-, and fourth-row pnictogens. We shall show that in the case of the trimethylpnictogen oxides there is a balance between a favourable steric arrangement with a long Me_3X—O distance and optimal orbital interactions between Me_3X and O. The optimized bond lengths and angles of the trimethylpnictogens and the oxides are shown in Table 6.

The preparation energy for Me_3N is the most substantial (70 kJ mol^{-1}), compared to the relatively small preparations for Me_3P and Me_3As (21 and 22 kJ mol^{-1}, respectively). The amine must distort significantly by expanding the length of the CN bonds in order to reduce crowding, as it is smaller than the heavier pnictogens. Trimethylarsine oxide slightly distorts in a manner similar to trimethylphosphine oxide. While both σ donation and π back-donation affect the geometry, the dominant σ contribution leads to slightly longer CAs bonds and an opening of ∠CAsC.

Because of the small size of nitrogen and the closer contacts

Table 6. Optimized bond lengths (Å) and angles (°) for Me_3X and Me_3XO[a] (X = N, P, As).

	r_{XO}	r_{CX}	∠CXO	∠CXC	Ref.
Me_3N		1.433(1.451)		110.8(110.9)	37
Me_3NO	1.337(1.388)	1.521(1.479)	109.1(109.9)	109.8(109.1)	40
Me_3P		1.857(1.847)		100.2(98.6)	33
Me_3PO	1.497(1.476)	1.816(1.809)	112.8(114.4)	106.0(104.1)	34
Me_3As		1.996(1.964)		97.1(96.0)	35
Me_3AsO	1.666(1.631)	1.960(1.967)	112.6(112.6)	106.2	34

[a]Experimental values are given in parentheses.

in Me_3NO, one might expect Me_3NO to have a larger steric contribution, $\Delta E^0 + \Delta E_{res}$, than either Me_3PO or Me_3AsO, but this is not the case. In fact, trimethylamine oxide has the lowest contribution, 318 kJ mol^{-1}, compared to 771 kJ mol^{-1} for trimethylphosphine oxide and 555 kJ mol^{-1} for trimethylarsine oxide. We shall comment on this shortly.

The donation stabilization for Me_3N is smaller, $-\Delta E_{don}$ = 859 kJ mol^{-1}, than those of Me_3P and Me_3As, where $-\Delta E_{don}$ = 1210 and 918 kJ mol^{-1}, respectively. The energies of the donation orbitals are all about the same, **1a**, and the overlap between this orbital and **2a** is similar in all three pnictogens. When Me_3XO forms, the energy of **1a** will drop as it donates electrons and forms a bond. This drop in energy is more drastic in the case of amine, which makes further donation more difficult, and only 0.7 *e* is donated, as compared to the phosphine (1.0 *e*) and the arsine (0.9 *e*).

Figure 2 shows that the back-donation acceptor orbitals, **1b** and **1c**, of the amine are much higher in energy than the phosphine and arsine orbitals, and thus are less likely to interact with the full orbitals on oxygen, **2b** and **2c**. There is virtually no stabilization from back-donation for Me_3N, $-\Delta E_{bdon}$ = 1 kJ mol^{-1}, whereas both Me_3P and Me_3As have contributions due to back-donation. The energy of **1b** and **1c** is slightly lower and the overlap with **2b** and **2c** is slightly better for Me_3P than for Me_3As, and $-\Delta E_{bdon}$ reflects this with 37 kJ mol^{-1} (Me_3P) compared to 18 kJ mol^{-1} (Me_3As).

The synergic effect is considerable for the heavier pnictogens and nonexistent for nitrogen. As mentioned earlier, the π-bond order of X = P increases to 0.7 due to the synergic effect; for X = As, there are similar effects and the π-bond order is 0.6. The different pnictogen–oxygen bonds vary in strength in the order phosphorus (−544 kJ mol^{-1}) > arsenic (−343 kJ mol^{-1}) > nitrogen (−197 kJ mol^{-1}).

Me_3NO could have acquired stronger σ and π interactions by decreasing the NO distance at the expense of enhancing the steric repulsion as well. Apparently, the potential gain in σ and π bonding from shortening the NO bond is offset by higher steric crowding.

4. Conclusions

DFT calculations were used to study the nature of the trimethylphosphine chalcogenide bond. All of the chalcogens participate in π back-donation to a pair of low-lying PC σ* orbitals with *e* symmetry in the C_{3v} point group. The π-bond order was found to decrease down Group 16 from 0.7 for oxygen to 0.5 for tellurium. The phosphorus–oxygen bond is strongest, ΔH_{PO} = −544 kJ mol^{-1}. Other elements bonded to trimethylphosphine were also considered in terms of the isoelectronic series, BH_3, CH_2, and NH. The trimethylphosphine imine had the strongest bonding with ΔH_{PN} = −333 kJ mol^{-1}. Trimethylphosphine ylide was found to bond by σ donation from the phosphine and one π back-donation interaction from the nonbonding *p* orbital of methylene. The borane adduct participated in σ bonding and also had a π-bond order of 0.3. Further comparison of bonding in trimethylpnictogen oxides revealed no multiple bonding in Me_3NO, but a π-bond order of 0.6 for Me_3AsO. The inability of Me_3N to π-bond to O affects the geometry of Me_3NO. Compared to Me_3N, the CN bonds are longer in trimethylamine oxide, due to the steric crowding around nitrogen.

5. Acknowledgements

We thank the Natural Sciences and Engineering Research Council of Canada (NSERC) for financial support.

6. References

1. T. Chivers. J. Chem. Soc. Dalton Trans. 1185 (1996).
2. H.B. Singh and N. Sudha. Polyhedron, **15**, 745 (1996).
3. (*a*) M.L. Steigerwald, T. Siegrist, S.M. Stuczynski, and Y.-U. Kwon. J. Am. Chem. Soc. **114**, 3155 (1992); (*b*) M.L. Steigerwald, T. Siegrist, and S.M. Stuczynski. Inorg. Chem. **30**, 2256 (1991); (*c*) J.G. Brennan, T. Siegrist, S.M. Stuczynski, and M.L. Steigerwald. J. Am. Chem. Soc. **112**, 9233 (1990); (*d*) J. Am. Chem. Soc. **111**, 9240 (1989); (*e*) M.L. Steigerwald and C.E. Rice. J. Am. Chem. Soc. **110**, 4228 (1988).
4. D. Rabinovich and G. Parkin. J. Am. Chem. Soc. **110**, 4228 (1988).
5. J.M. McConnachie, J.C. Bollinger, and J.A. Ibers. Inorg. Chem. **32**, 3923 (1993).
6. (*a*) M.L. Steigerwald and C.R. Sprinkle. Organometallics, **7**, 245 (1988); (*b*) K. McGregor, G.B. Deacon, R.S. Dickson, G.D. Fallon, R.S. Rowe, and B.O. West. J. Chem. Soc. Chem. Commun. 1293 (1990); (*c*) W. Piers, D.J. Parks, L.R. MacGillivray, and M.J. Zawarotko. Organometallics, **13**, 4547 (1994).
7. W. Uhl, U. Schütz, W. Hiller, and M. Heckel. Organometallics, **14**, 1073 (1995).
8. J.M. Fischer, W.E. Piers, S.D.P. Batchilder, and M.J. Zaworotko. J. Am. Chem. Soc. **118**, 283 (1996).
9. N. Kuhn, H. Schumann, and G. Wolmershäuser. Z. Naturforsch. B: Anorg. Chem. Org. Chem. **42B**, 674 (1987).
10. N. Kuhn, G. Henkel, H. Schumann, and R. Fröhlich. Z. Naturforsch. B: Anorg. Chem. Org. Chem. **45B**, 1010 (1990).
11. (*a*) M. Bochmann, G.C. Bwembya, N. Whilton, X. Song, M.B. Hursthouse, S.J. Coles, and A. Karanlov. J. Chem. Soc. Dalton Trans. 1887 (1995); (*b*) M. Bochmann, G.C. Bwembya, M.B.

Hursthouse, and S.J. Coles. J. Chem. Soc. Dalton Trans. 2813 (1995).
12. C.H.W. Jones and R.D. Sharma. Organometallics, **6**, 1419 (1987).
13. (*a*) D.G. Gilheany. Chem. Rev. **94**, 1339 (1994); (*b*) N. Burford. Coord. Chem. Rev. **112**, 1 (1992).
14. D.G. Gilheany. *In* The chemistry of organophosphorus compounds. Vol. 2. *Edited by* F.R. Hartley. Wiley–Interscience, Chichester, U.K. 1992. pp. 1–52.
15. W.P. Power. J. Am. Chem. Soc. **117**, 1800 (1995).
16. T. Ziegler. Chem. Rev. **91**, 651 (1991).
17. (*a*). O. Gunnarsson and I. Lindquist. Phys. Rev. B: Condens. Matter, **B10**, 1319 (1974); (*b*) Phys. Rev. B: Condens. Matter, **B13**, 4274 (1976); (*c*) O. Gunnarsson, M. Johnson, and I. Lindquist. Phys. Rev. B: Condens. Matter, **B20**, 3136 (1979).
18. S.H. Vosko, L. Wilk, and M. Nusair. Can. J. Phys. **58**, 1200 (1990).
19. A.D. Becke. Phys. Rev. A: Gen. Phys. **A38**, 3098 (1988).
20. (*a*) J.P. Perdew. Phys. Rev. B: Condens. Matter, **B33**, 8822 (1986); (*b*) Phys. Rev. B: Condens. Matter, **B34**, 7406 (1986).
21. E.J. Baerends, D.E. Ellis, and P. Ros. Chem. Phys. **2**, 41 (1973).
22. E.J. Baerends. Ph.D. Thesis, Frije Universiteit, Amsterdam. 1975.
23. W. Ravenek. *In* Algorithms and applications on vector and parallel computers. *Edited by* H.J.J. Riele, Th.J. Dekker, and H.A. van de Horst. Elsevier, Amsterdam. 1987.
24. (*a*) P.M. Boerrigter, G. te Velde, and E.J. Baerends. Int. J. Quantum Chem. **33**, 87 (1988); (*b*) G. te Velde, and E.J. Baerends. J. Comput. Chem. **99**, 84 (1992).
25. L. Versluis and T. Ziegler. J. Chem. Phys. **88**, 322 (1988).
26. (*a*) J.G. Snijders, E.J. Baerends, and P. Vernoijs. At. Data Nucl. Data Tables, **26**, 483 (1982); (*b*) P. Vernoijs, J.G. Snijders, and E.J. Baerends. Slater type basis functions for the whole periodic system, Internal Report. Frije Universiteit, Amsterdam. 1981.
27. J. Krijn and E.J. Baerends. Fitfunctions in the HFS method, Internal Report. Frije Universiteit, Amsterdam. 1984.
28. P.v.R. Schleyer and A.J. Kos. Tetrahedron, **39**, 1141 (1983).
29. R. Hoffmann. Angew. Chem. Int. Ed. Engl. **21**, 711 (1982).
30. H.-B. Kraatz, H. Jacobsen, T. Ziegler, and P.M. Boorman. Organometallics, **12**, 76 (1993).
31. T. Ziegler and A. Rauk. Theor. Chim. Acta, **46**, 1 (1977).
32. S.B. Hartley, W.S. Holmes, J.K. Jacques, M.F. Mole, and J.C. McCoubrey. Q. Rev. Chem. Soc. **17**, 204 (1963).
33. L.S. Bartell and L.O. Brockway. J. Chem. Phys. **32**, 512 (1960).
34. C.J. Wilkins, K. Hagen, L. Hedberg, Q. Shan, and K. Hedberg. J. Am. Chem. Soc. **97**, 6352 (1975).
35. E.J. Jacob and S. Samdal. J. Am. Chem. Soc. **99**, 5656 (1977).
36. K. Iijima, Y. Hakamata, T. Nishikawa, and S. Shibata. Bull. Chem. Soc. Jpn. **61**, 3033 (1988).
37. M.D. Harmony, V.W. Laurie, R.L. Kuczkowski, R.H. Schwendeman, D.A. Ramsay, F.J. Lovas, W.J. Lafferty, and A.G. Maki. J. Phys. Chem. Ref. Data, **8**, 619 (1979).
38. E.A.V. Ebsworth, T.E. Fraser, and D.W.H. Rankin. Chem. Ber. **110**, 3494 (1977).
39. D.W.H. Rankin, H.E. Robertson, R. Seip, H. Schmidbaur, and G. Blaschke. J. Chem. Soc. Dalton Trans. 827 (1985).
40. A. Caron, G.J. Palenik, E. Goldish, and J. Donohue. Acta Crystallogr. **17**, 102 (1964).

An unusually large value of $^1J(^{31}P,^{31}P)$ for a solid triphenylphosphine phosphadiazonium cationic complex: determination of the sign of *J* from 2D spin-echo experiments

Klaus Eichele, Roderick E. Wasylishen, Robert W. Schurko, Neil Burford, and W. Alex Whitla

Abstract: Phosphorus-31 NMR spectra of a solid triphenylphosphine phosphadiazonium salt, [Mes*NP-PPh_3][SO_3CF_3], have been acquired at 4.7 and 9.4 T. Analysis of the spectra obtained with magic-angle spinning indicates that the two phosphorus nuclei are strongly spin–spin coupled, $|^1J(^{31}P,^{31}P)| = 405(5)$ Hz, despite the unusually long P—P separation, $r_{P,P} = 2.625$ Å. Two-dimensional spin-echo spectra provide convincing evidence that $^1J(^{31}P,^{31}P)$ is negative. Semi-empirical molecular orbital calculations at the INDO level support the negative sign for $^1J(^{31}P,^{31}P)$. A large span, 576 ppm, is observed for the chemical shift tensor of the two-coordinate phosphorus centre ($\delta_{11} = 307$ ppm, $\delta_{22} = 174$ ppm, $\delta_{33} = -269$ ppm), which is very similar to the value previously reported for the non-coordinated phosphorus centre in the free Lewis acid, [Mes*NP][$AlCl_4$]. The principal components and orientations of the phosphorus shielding tensors of these compounds are compared with those calculated for $[HNP]^+$ and its phosphine adduct using the ab initio Gauge-Including Atomic Orbitals method. The phosphorus chemical shift tensor of the triphenylphosphine moiety has a relatively small span of 33 ppm.

Key words: spin–spin coupling constants, solid-state NMR, ^{31}P NMR, MO calculations, phosphadiazonium cation, P—P bonds.

Résumé : Les spectres de la RMN du phosphore-31 du sel de phosphadiazonium de la triphénylphosphine, [Mes*NP-PPh_3][SO_3CF_3] ont été enregistré à 4,7 et 9,4 T. L'analyse des spectres obtenus avec la rotation de l'angle-magique indiquent que les deux noyaux de phosphore ont un couplage spin–spin très fort, $|^1J(^{31}P,^{31}P)| = 405(5)$ Hz, en dépit de la longue distance de séparation inhabituelle P—P, $r_{P,P} = 2{,}65$ Å. Les spectres en deux dimensions spin-écho fournissent une preuve convaincante de la valeur négative de $^1J(^{31}P,^{31}P)$. Les calculs d'orbitale moléculaire semi empirique au niveau INDO confirment le signe négatif de $^1J(^{31}P,^{31}P)$. On a observé un graqnd étalement, 576 ppm, pour le déplacement chimique du tenseur des deux centre phosphore coordonnés $\delta_{11} = 307$ ppm, $\delta_{22} = 174$ ppm, $\delta_{33} = -269$ ppm, ce quei est très voisin des valeurs rapportées antérieurement pour les centres phosphore non coordonnées dans les acides de Lewis libres [Mes*NP][$AlCl_4$]. On a comparé les composantes principales et les orientations du tenseur de blindage du phosphore avec celles calculées pour le $[HNP]^+$ et ses adduits phosphine en utilisant les calculs ab initio de Gauge incluant la méthode de l'orbitale atomique. Le déplacement chimique du tenseur phosphore de l'unité triphénylphosphine s'étale relativement peu 33 ppm.

Mots clés : constantes de couplage spin–spin, RMN à l'état solide, RMN du ^{31}P, calculs de OM, cation phosphadiazonium, liaison P—P.

[Traduit par la rédaction]

Introduction

The magnitudes of $^{31}P,^{31}P$ spin–spin coupling constants between directly bonded phosphorus nuclei, $^1J(^{31}P,^{31}P)$, have been reported for numerous compounds (1–5). Although the sign of $^1J(^{31}P,^{31}P)$ has been determined for very few compounds, some general patterns have emerged. Values of $^1J(^{31}P,^{31}P)$ can be of either sign and vary from at least +766 Hz (6) to −451 Hz (7). The largest positive values have been observed for tetracoordinate–hexacoordinate adducts such as R_3P–PF_5, $J \approx +723$ Hz (8), pentacoordinate–pentacoordinate compounds, $J \approx +750$ Hz (9), and hypodiphosphate anions such as $[FO_2P$–$PO_2F]^{2-}$, $J \approx +766$ Hz (6). In each case, one or both of the phosphorus nuclei are bonded to several electronegative substituents. On the other hand, negative values of $^1J(^{31}P,^{31}P)$ seem to be associated with systems containing low-coordinate phosphorus nuclei, e.g., systems such as H_2P–PH_2 and $(t\text{-Bu})_2P$–$P(t\text{-Bu})_2$, where $^1J(^{31}P,^{31}P)$ is −108 Hz (10) and −451 Hz (7), respectively. Similarly, values of $^1J(^{31}P,^{31}P)$ involving a dicoordinate centre bound to a di-, tri-, or tetracoordinate centre are thought to be negative (4, 5), but these have not been confirmed experimentally. Interestingly, the lat-

Received February 29, 1996.

This paper is dedicated to Professor Howard C. Clark for his distinguished contributions to inorganic and organometallic chemistry.

K. Eichele, R.E. Wasylishen,[1] R.W. Schurko, N. Burford, and W.A. Whitla. Department of Chemistry, Dalhousie University, Halifax, NS B3H 4J3, Canada.

[1] Author to whom correspondence may be addressed. Telephone: (902) 494-2564. Fax: (902) 494-1310. E-mail: rodw@is.dal.ca or Roderick.Wasylishen@dal.ca

ter couplings cover a wide range, (−)232 Hz to (−)684 Hz, and it has been suggested that $^1J(^{31}P,^{31}P)$ in these systems increases (i.e., becomes more negative) with increasing phosphorus–phosphorus bond order (4, 5, 11).

The purpose of this communication is to demonstrate the power of solid-state ^{31}P NMR experiments in determining the absolute sign and magnitude of $^1J(^{31}P,^{31}P)$ for an adduct composed of a phosphadiazonium cation, [Mes*NP]$^+$ (Mes* = 2,4,6-tri-*tert*-butylphenyl), and triphenylphosphine, bound by an unusually long P—P bond of 2.625 Å (12). The results of this study clearly demonstrate that there is no simple, general relationship between $^1J(^{31}P,^{31}P)$ and P—P bond order. Finally, information concerning the phosphorus shielding tensors is also derived.

Experimental

Materials

The preparation of [Mes*NP-PPh_3][SO_3CF_3] from its precursor [Mes*NP][SO_3CF_3] has been previously reported (12).

Solid-state ^{31}P NMR experiments

Solid-state ^{31}P NMR experiments were carried out using Bruker MSL-200 (B_0 = 4.7 T) and AMX-400 (B_0 = 9.4 T) spectrometers. Phosphorus-31 NMR spectra obtained with cross-polarization and magic-angle spinning (CP/MAS) were acquired using Bruker double-bearing MAS probes, with 3.5 μs proton pulse widths and recycle delays of 4–10 s. Chemical shifts were referenced with respect to external 85% aqueous H_3PO_4 by setting the peak of external solid [NH_4][H_2PO_4] to 0.8 ppm.

The 2D spin-echo spectrum of [Mes*-NP-PPh_3][SO_3CF_3] was obtained at 4.7 T. A standard spin-echo pulse sequence was used under CP and high-power ^1H decoupling conditions (14). For each t_1 increment, 32 transients were collected. A total of 64 t_1 increments were acquired. After zero-filling once in each dimension, the data size for 2D FT was 512 × 128. Gaussian window-functions were applied to FIDs in both dimensions prior to 2D FT, and the final 2D spectrum was displayed in magnitude mode.

Calculations of the spectra due to static powder samples or samples spinning at the magic angle were performed using a 80586 microprocessor. The program WSolids, written in the C++ language and developed in our laboratory, was used for all calculations.

Quantum mechanical calculations

The ab initio Gauge-Including Atomic Orbitals (GIAO) calculations of phosphorus chemical shieldings were performed using a 6-311G basis set, augmented with two sets of polarization functions on all atoms. Absolute chemical shieldings were converted to chemical shifts using the absolute chemical shielding of 85% aqueous H_3PO_4, σ = 328.35 ppm. All calculations were performed using an IBM RS6000/580 workstation.

Semiempirical molecular orbital calculations of $^1J(^{31}P,^{31}P)$ were carried out using the self-consistent field finite-perturbation approach of Pople and Beveridge (17). The Fermi contact contribution was calculated using the Intermediate Neglect of Differential Overlap (INDO) approximation (17). Values of the one-centre exchange integrals *G*1 and *F*2 were taken as 0.276 and 0.190, respectively.[2] The phosphorus *s*-orbital density, $1s|0|^2$, was taken as 5.6251 (19).

Results and discussion

Phosphorus-31 NMR spectra of a polycrystalline powder sample of [Mes*NP-PPh_3][SO_3CF_3] are shown in Fig. 1. The lower spectrum, obtained with magic-angle spinning (MAS), shows two doublets and associated spinning side bands. One of the phosphorus centres has a relatively large chemical shift anisotropy, indicated by the numerous spinning side bands, and is assigned to the dicoordinate phosphorus centre. The magnitude of the indirect homonuclear spin–spin coupling constant $^1J(^{31}P,^{31}P)$ determined from the doublets is 405(5) Hz. Identical splittings, 405(5) Hz, were observed in ^{31}P NMR spectra obtained at 9.4 T, thereby ruling out crystallographic nonequivalence as the origin of the splittings. The doublets arising from the phosphorus centre, which is directly bonded to nitrogen, show additional asymmetric splittings of 100 Hz due to residual dipolar coupling with the quadrupolar ^{14}N nucleus (see insert, Fig. 1). This phenomenon is well documented (20). Since the C-N-P bond angle is approximately linear, 169.5°, it is reasonable to assume that the electric field gradient at the nitrogen centre will be nearly axially symmetric, with the largest component along the formal PN triple bond. From the known internuclear separation, $r_{P,N}$ = 1.486(4) Å (12), the dipolar coupling constant, $R(I,S) = (\mu_0/4\pi)(\gamma_I\gamma_S/r_{I,S}^3)(\hbar/2\pi)$, can be calculated, 1070 Hz. With these values, analysis of the asymmetric doublets yields an upper limit for $|^1J(^{31}P,^{14}N)|$ of 25 Hz and a nitrogen nuclear quadrupolar coupling constant, $\chi(^{14}N)$, of −1.7(2) MHz. This relatively small value of $\chi(^{14}N)$ is reasonable, given that in typical isonitriles (21), N-bonded thiocyanates (22), and the central nitrogen nucleus of hydrazoic acid (23), HN_3, values of $\chi(^{14}N)$ between −0.3 and −2.0 MHz have been reported.

The ^{31}P NMR spectrum of the stationary powder sample is also depicted in Fig. 1. In contrast to the MAS spectrum, in which all homo- and heteronuclear spin–spin interactions anticipated for the three-spin system (^{31}P–^{31}P–^{14}N) are resolved, no clear evidence for couplings is apparent from the spectrum of the static sample. The only exception is a distinct splitting of 2.6 kHz observed in the high-frequency region of the spectrum, corresponding to δ_{11} of the chemical shift tensor for the dicoordinate phosphorus centre. To obtain more detailed information about the homonuclear spin–spin interactions, a two-dimensional spin-echo experiment was performed. This experiment is analogous to the *J*-resolved experiment in high-resolution NMR spectroscopy, with the exception that homonuclear direct dipolar coupling and anisotropy in the indirect spin–spin coupling also contribute to the line shape. The experimental 2D spin-echo experiment, together with the F_1 projection, is shown in Fig. 2. Small separate "islands" in the contour plot confirm that the large splitting at 307 ppm is indeed due to homonuclear $^{31}P,^{31}P$ spin–spin interactions.

From the internuclear separation, $r_{P,P}$ = 2.625 Å, the direct dipolar coupling constant $R(^{31}P,^{31}P)$ is calculated as 1090 Hz.

[2] R. Sebastian and T. Schaefer, private communication; obtained by extrapolation of the values given by Galasso (18).

Fig. 1. Solid-state ^{31}P NMR spectra of [Mes*NP-PPh_3][SO_3CF_3] obtained at 4.7 T. The bottom trace shows the MAS spectrum for a sample spinning at 3.6 kHz (360 scans), the upper trace was obtained for the stationary sample (14 086 scans). Asterisks denote the isotropic peaks. The expansion shows the isotropic multiplet of the dicoordinate phosphorus centre, with the large splitting due to $^1J(^{31}P,^{31}P)$. The smaller asymmetric splitting is due to $^{31}P,^{14}N$ spin–spin interactions.

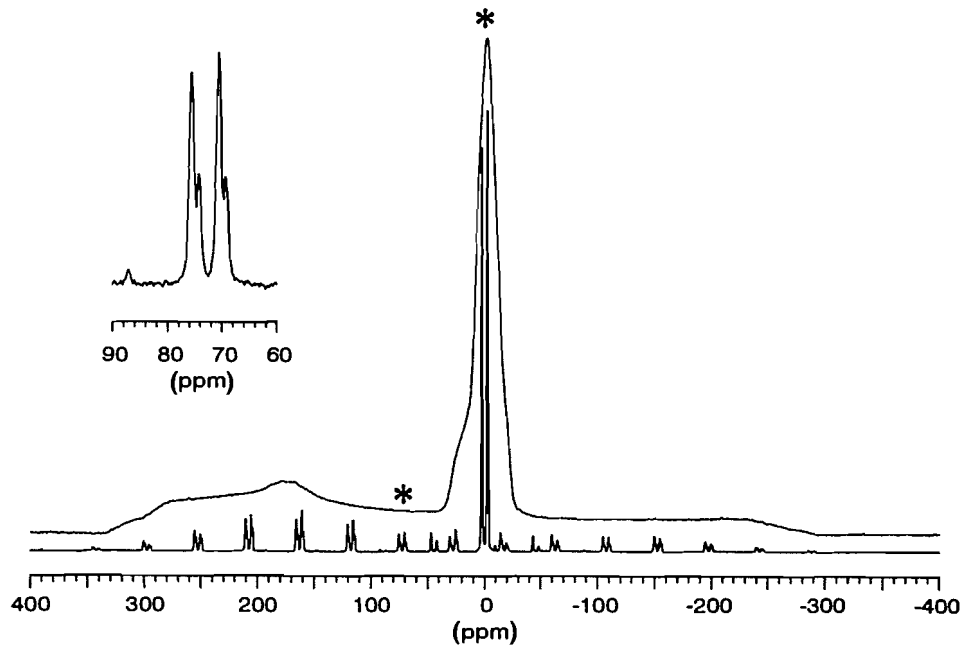

Thus, considering only the direct dipolar interaction for an AX spin system, one would anticipate a Pake doublet for the F_1 projection with a maximum splitting of $2R$, or 2.2 kHz. The experimental observation of 2.6 kHz for the maximum splitting indicates that the indirect spin–spin coupling cannot be neglected in this case. Idealized Pake-like powder patterns for $^1J(^{31}P,^{31}P) = -405$, 0 and +405 Hz are shown in Fig. 2*b*. Also included is the Pake doublet arising from an A_2 spin system (in which case J is not an observable). The F_1 projection will be a mixture arising from the sum of A_2, AB, and AX type coupling patterns (24); however, given the significant differences in chemical shift anisotropies for the two phosphorus nuclei, the AX-type coupling is expected to dominate. Indeed, a comparison between calculated and observed projections reveals that the AX-type couplings prevail in this spin system (the small features at ± 800 Hz might be attributed to contributions from A_2-type spectra). The comparison further shows that the sign of $^1J(^{31}P,^{31}P)$ is opposite to that of the dipolar coupling constant, $R(^{31}P,^{31}P)$. In principle, the direct dipolar coupling may contain contributions from the anisotropy in the indirect spin–spin coupling, ΔJ (25). Therefore, ambiguity arises as to the absolute sign of the effective dipolar coupling constant, $R_{eff} = R - \Delta J/3$, which cannot be resolved at room temperature. However, in the case of a negative effective dipolar coupling constant, ΔJ would be required to be 6.54 kHz, while the alternative results in $\Delta J = 0$ Hz. Given that the isotropic value of $|^1J(^{31}P,^{31}P)|$ is 405 Hz, anisotropies on the order of 6.54 kHz seem unreasonably large. Therefore, our results indicate that the absolute sign of $^1J(^{31}P,^{31}P)$ is negative.

Having obtained this information about the homonuclear spin–spin interactions, the lineshape of the static powder pattern can be simulated to extract information about the phosphorus shift tensors. This line shape depends on the relative orientations of the chemical shift and dipolar coupling tensors (26). For the dicoordinate phosphorus centre, the occurrence of the maximum dipolar splitting at 307 ppm indicates that the P—P vector is close to the direction of δ_{11}. That is, δ_{11} is approximately perpendicular to the NP bond axis, since the NPP bond angle is 109.8(2)°. Similar orientations of the phosphorus chemical shift tensor have also been established for related systems containing the $[Mes*NP]^+$ (27) and Mes*CP (28) fragments. Interestingly, for the triphenylphosphine ligand the direction of least shielding also appears to be along the direction of the P—P bond. The field dependence of the NMR spectrum arising from the triphenylphosphine ligand is illustrated in Fig. 3. The results for the principal components of the phosphorus chemical shift tensors and their orientations are summarized in Table 1 and compared to experimental values reported for [Mes*NP][$AlCl_4$] (27). Surprisingly, the chemical shift tensors of $[Mes*NP]^+$ and its triphenylphosphine adduct are very similar; it appears that the short N—P bond in the adduct still dominates the shielding characteristics of the dicoordinate phosphorus in this compound and is hardly affected by the coordination of PPh_3. To confirm this notion, we have carried out ab initio molecular orbital (MO) calculations of phosphorus chemical shieldings on the simple model compound $[HNP]^+$ and its phosphine adduct, $[HNP–PH_3]^+$, using the GIAO method (15). The results of these calculations are included in Table 1. The calculations are successful in that they qualitatively predict the span of the phosphorus chemical

Fig. 2. The left side shows the experimental solid-state ^{31}P 2D spin-echo experiment on a stationary sample of $[Mes^*NP\text{-}PPh_3][SO_3CF_3]$ obtained at 4.7 T. The right-hand side displays several Pake-like doublets calculated for AX and A_2 spin systems using the values of J indicated. In each case, R was kept at 1090 Hz.

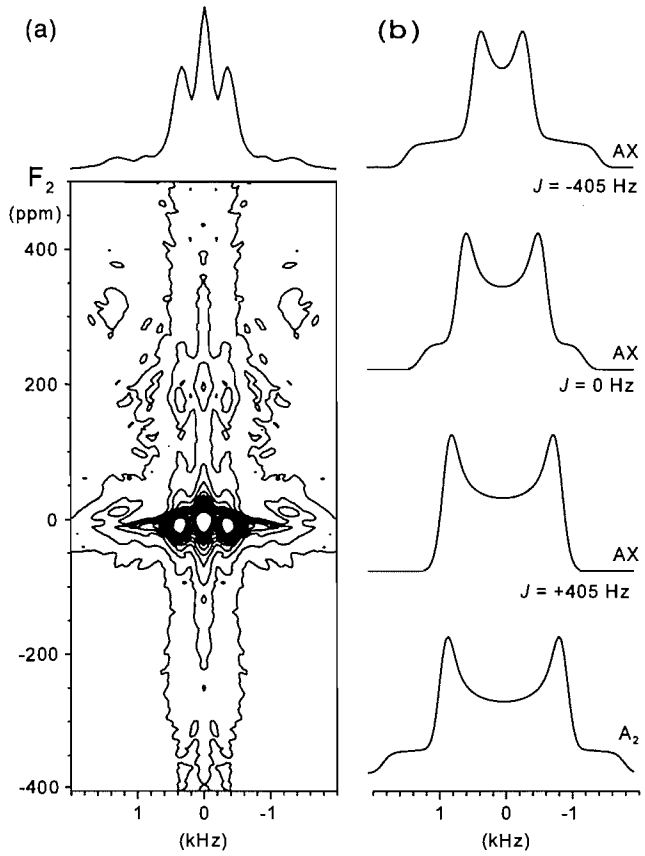

shift tensor for the two-coordinate phosphorus to be much greater than that of the four-coordinate phosphorus. Furthermore, the calculated phosphorus chemical shift tensor of the two-coordinate phosphorus is only marginally perturbed by the PH_3 ligand. However, for the geometries indicated, the calculations predict an increase in shielding of the dicoordinate phosphorus upon coordination that is greater than observed experimentally for $[Mes^*NP]^+$ and $[Mes^*NP\text{-}PPh_3]^+$. Given the simplicity of our model compounds, this is not unexpected. Finally, the calculated orientation of the phosphorus chemical shift tensor of the dicoordinate centre corroborates our experimental finding that the direction of least shielding is close to the internuclear vector.

The minor change of the phosphorus chemical shift tensor of the dicoordinate centre upon formation of the adduct can be rationalized in terms of a weak P-P interaction consistent with the long P–P distance. However, the observation of a relatively large indirect $^{31}P,^{31}P$ spin–spin coupling for this compound is counterintuitive, indicating that there is, nevertheless, a strong communication of nuclear spins via the electronic framework. For comparison, in the donor-stabilized methylenediylphosphenium cation $[R_2C{=}P\text{-}PPh_3]^+$, the $|^1J(^{31}P,^{31}P)|$ has been reported as 450.5 Hz; however, the P—P separation is about

Table 1. Experimental and calculated[a] phosphorus chemical shift tensors (in ppm) of iminophosphine centres.

	δ_{iso}	δ_{11}	δ_{22}	δ_{33}
$[Mes^*\text{-}NP\text{-}PPh_3][SO_3CF_3]$	71[b,c]	307	174	−269
$[Mes^*\text{-}NP\text{-}PPh_3][SO_3CF_3]$	−1[b,c]	15	0	−18
$[Mes^*\text{-}NP][AlCl_4]$[d]	77	308	196	−273
$[H\text{-}NP]^+$ ∠HNP = 180°	−12	299	299	−633
∠HNP = 176.4°	−13	298	297	−633
$[H\text{-}NP\text{-}PH_3]^+$ r = 2.625 Å	−58[e,f]	342	200	−716
r = 2.400 Å	−46[e,g]	400	130	−667
r = 2.200 Å	12[e,h]	544	55	−563
$[H\text{-}NP\text{-}PH_3]^+$ r = 2.625 Å	−240[i,j]	−229	−241	−252
r = 2.400 Å	−243[i,k]	−226	−246	−256
r = 2.200 Å	−256[i,l]	−230	−247	−291

[a]Calculated phosphorus chemical shieldings have been converted to chemical shifts using δ = 328 ppm − σ (ref. 16). Errors in the values of the principal components are estimated to be less than 5 ppm.
[b]$^1J(^{31}P, ^{31}P)$ = −405(5) Hz.
[c]Euler angles relating the chemical shift tensor to the ^{31}P, ^{31}P dipolar tensor are 0°, 90°, 0°.
[d]Reference 27.
[e]δ_{22} is perpendicular to the mirror plane. PNH = 169.5°.
[f]Angle between PN and δ_{33} is 9°, between PP and δ_{11} is −11°.
[g]Angle between PN and δ_{33} is 17°, between PP and δ_{11} is −3°.
[h]Angle between PN and δ_{33} is 28°, between PP and δ_{11} is 8°.
[i]δ_{11} is perpendicular to the mirror plane.
[j]Angle between PP and δ_{33} is 29°.
[k]Angle between PP and δ_{33} is 66°.
[l]Angle between PP and δ_{33} is 88°.

2.267(2) Å (19). The negative value of $^1J(^{31}P,^{31}P)$ for $[Mes^*NP\text{-}PPh_3][SO_3CF_3]$ provides further evidence that $^1J(^{31}P,^{31}P)$ is negative in compounds with phosphorus in low coordination environments (2, 4, 5).

In spite of the large amount of experimental data available for $^1J(^{31}P,^{31}P)$, such couplings are not well understood. Several researchers have suggested that in systems containing formal phosphorus lone-pairs, the orientations of these electron lone pairs are of paramount importance (30, 31). However, other than qualitatively recognizing that the lone pairs reduce $^1J(^{31}P,^{31}P)$, the reasons behind this are not obvious. For many years it was assumed that mechanisms other than the Fermi contact must be important even in systems containing single P—P bonds because large anisotropies in $^1J(^{31}P,^{31}P)$ were reported for $R_2(S)P\text{–}P(S)R_2$ (32). Reinvestigation of one of these compounds indicates that ΔJ is in fact small (25), thus there may be no need to suppose that mechanisms other than the Fermi contact are important for these systems. In systems containing formal phosphorus–phosphorus double bonds, theoretical calculations predict mechanisms other than the Fermi contact to be important (33); however, the reliability of these theoretical calculations has not been established. While some workers have indicated that a clear relationship exists between the magnitude of $^1J(^{31}P,^{31}P)$ and the P—P bond order for some systems (4, 5, 11), the generality of such claims must be limited. For the system under examination in the present study, the phosphorus–phosphorus separation is well beyond values typical of P—P "single-bond" lengths (≈2.2 Å), yet the value of $^1J(^{31}P,^{31}P)$ is −405 Hz. The lability of the P—P interaction

Fig. 3. Expansion of the ^{31}P NMR spectra of static samples obtained at 4.7 (14 086 scans) and 9.4 T (10 000 scans), showing the field dependence of the lineshape due to contributions by the triphenylphosphine ligand. The top depicts the experimental spectra, the bottom shows spectra calculated using the values listed in Table 1. The detailed lineshape depends upon both the phosphorus chemical shift tensor and the $^{31}P,^{31}P$ spin-spin interactions.

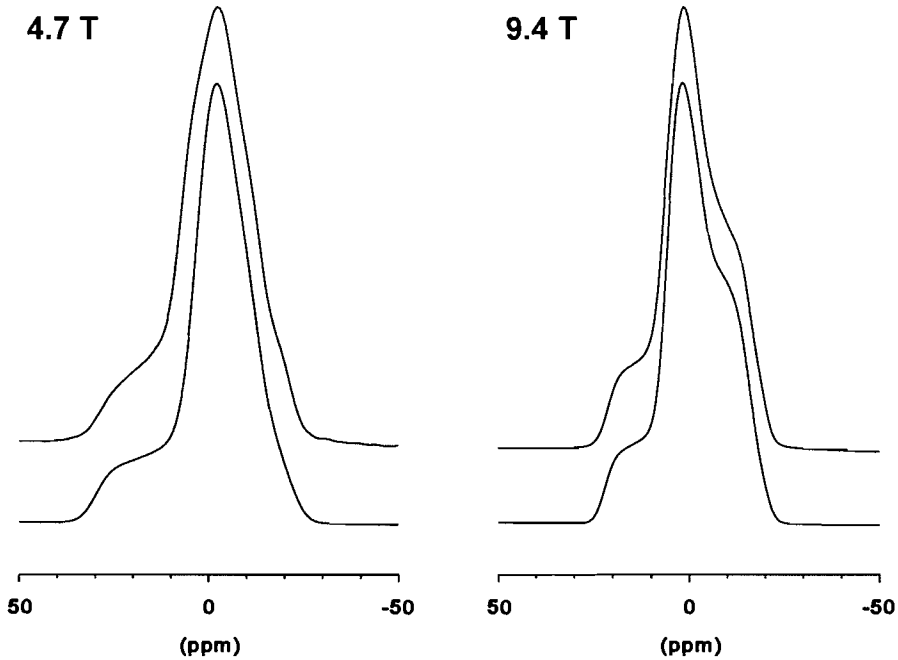

Table 2. Calculated values of $^1J(^{31}P, ^{31}P)$ for several simple model compounds.

Molecule	$r_{P,P}$ (Å)	$^1J(^{31}P,^{31}P)$ (Hz)
$[HNP\text{-}PH_3]^+$	2.2	−360
	2.4	−620
	2.6	−650
	2.8	−590
	3.0	−450
	3.2	−260
	3.4	−100
	3.6	−20
$[H_2C{=}P\text{-}PH_3]^+$	2.267	−390
$[HP{=}\mathit{P}\text{-}\mathit{P}H_3]^+$	2.206	−450
$[H\mathit{P}{=}\mathit{P}\text{-}PH_3]^+$	2.0	+560
trans-H-P=P-H	2.0	+830
$H_2P\text{–}PH_2$[a]	2.218	−80
$H_3P\text{–}PF_5$	2.2	+960
$[FO_2P\text{-}PO_2F]^{2-}$	2.18	+1800

[a]*gauche* conformation, 74° between formal lone pairs.

in [Mes*NP-PPh$_3$][SO_3CF_3] is further highlighted by its dissociation in solution: no evidence of $^1J(^{31}P,^{31}P)$ is observed by solution ^{31}P NMR spectroscopy at 190 K.

Semiempirical molecular orbital calculations have been successful in reproducing many experimental trends in spin–spin coupling constants involving first-row elements (17, 34); therefore, it is of interest to calculate $^1J(^{31}P,^{31}P)$ as a function of $r_{P,P}$ in a simple model compound, $[HNP\text{-}PH_3]^+$. The orientation of the PH_3 group relative to the linear $[HNP]^+$ moiety was fixed to mimic that found experimentally for [Mes*NP-PPh$_3$][SO_3CF_3]. The results of the INDO calculations are summarized in Table 2. A negative sign is calculated for $^1J(^{31}P,^{31}P)$, and the value is of the correct magnitude. Negative values of $^1J(^{31}P,^{31}P)$ are also calculated for the related cations, $[H_2C{=}P\text{-}PH_3]^+$ and $[HP{=}P\text{-}PH_3]^+$. Only the Fermi contact interaction is considered in these calculations. To check the reliability of the INDO method for calculating $^1J(^{31}P,^{31}P)$, additional calculations have been carried out for model compounds related to systems where the sign of $^1J(^{31}P,^{31}P)$ is experimentally known. While the calculations correctly predict large and positive values for $^1J(^{31}P,^{31}P)$ in $H_3P\text{–}PF_5$ (8) and the difluorohypodiphosphate anion (6), the magnitude of $^1J(^{31}P,^{31}P)$ is overestimated. Calculations on $H_2P\text{–}PH_2$ indicate that $^1J(^{31}P,^{31}P)$ is very sensitive to molecular conformation, in agreement with previous semiempirical (35–37) and ab initio calculations (38). A negative value of $^1J(^{31}P,^{31}P)$ is also calculated for the *gauche* conformation in agreement with previous INDO calculations (36, 37) and experiment (10). For *trans*-diphosphene, $^1J(^{31}P,^{31}P)$ is predicted to be positive. As already mentioned, it has been suggested that this value is negative (2–5). Ab initio calculations of $^1J(^{31}P,^{31}P)$ in *trans*-diphosphene indicate that the orbital mechanism dominates and that its contribution is large and negative (33). Similar arguments have been used to rationalize the negative value of $^1J(^{15}N,^{15}N)$ in a *trans*-diazene, where the Fermi contact con-

tribution is positive on the basis of INDO calculations (39), while ab initio calculations predict a small but negative Fermi contact contribution (33). Clearly, much more research will be required before an understanding of $^1J(^{31}P,^{31}P)$ values is realized. Further measurements of the sign of $^1J(^{31}P,^{31}P)$ in systems containing low-coordinate phosphorus nuclei would be helpful. Also, solid-state NMR measurements that might shed light on the anisotropy of $^1J(^{31}P,^{31}P)$ tensors would be desirable. Finally, we hope that this work will stimulate further theoretical interest in $^1J(^{31}P,^{31}P)$ tensors. Clearly, the semi-empirical approaches such as the INDO method used in this study are qualitative at best and consequently of limited value.

In summary, we have observed a large $^{31}P-^{31}P$ spin–spin coupling constant between two phosphorus nuclei that are separated by more than 2.6 Å! Clearly, there is no simple relationship between $^1J(^{31}P,^{31}P)$ and bond order or bond length. To our knowledge, this is the first example where the absolute sign of J has been determined using the 2D spin-echo experiment. It also appears to be the first sign determination of $^1J(^{31}P,^{31}P)$ where one of the phosphorus nuclei is associated with a low-coordinate phosphorus centre.

Acknowledgements

The authors are indebted to the Natural Sciences and Engineering Research Council of Canada for financial support and to Dr. Jason A.C. Clyburne for helpful discussions. We are grateful to Dr. Michael D. Lumsden for his assistance in obtaining the AMX-400 spectra. All spectra were obtained at the Atlantic Region Magnetic Resonance Centre, which is also supported by NSERC.

References

1. E.G. Finer and R.K. Harris. Prog. Nucl. Magn. Reson. Spectrosc. **6**, 61 (1971).
2. (*a*) C.J. Jameson. *In* Phosphorus-31 NMR spectroscopy in stereochemical analysis, organic compounds and metal complexes. *Edited by* J.G. Verkade and L.D. Quin. VCH Publishers, Deerfield Beach, Fla. 1987. pp. 205–230; (*b*) J.G. Verkade and J.A. Mosbo. *In* Phosphorus-31 NMR spectroscopy in stereochemical analysis, organic compounds and metal complexes. *Edited by* J.G. Verkade and L.D. Quin. VCH Publishers, Deerfield Beach, Fla. 1987. pp. 450–452.
3. (*a*) C.J. Jameson. *In* Multinuclear NMR. *Edited by* J. Mason. Plenum Press, New York. 1987. pp. 89–131; (*b*) K.R. Dixon. *In* Multinuclear NMR. *Edited by* J. Mason. Plenum Press, New York. 1987. pp. 369–402.
4. S. Lochschmidt and A. Schmidpeter. Phosphorus Sulfur **29**, 73 (1986).
5. K. Karaghiosoff. *In* Multiple bonds and low coordination in phosphorus chemistry. *Edited by* M. Regitz and O.J. Scherer. Georg Thieme Verlag, Stuttgart. 1990. pp. 463–471.
6. H. Falius and M. Murray. J. Magn. Reson. **10**, 127 (1973).
7. H.C.E. McFarlane, W. McFarlane, and J.A. Nash. J. Chem. Soc. Dalton Trans. 240 (1980).
8. C.W. Schultz and R.W. Rudolph. J. Am. Chem. Soc. **93**, 1898 (1971).
9. L. Lamandé and A. Munoz. Tetrahedron, **46**, 3527 (1990).
10. R.M. Lynden-Bell. Trans. Faraday Soc. **57**, 888 (1961).
11. A.H. Cowley and N.C. Norman. Prog. Inorg. Chem. **34**, 1 (1986).
12. N. Burford, T.S. Cameron, J.A.C. Clyburne, K. Eichele, K.N. Robertson, S. Sereda, R.E. Wasylishen, and W.A. Whitla. Inorg. Chem. **35**, 5460 (1996).
13. E. Niecke, R. Detsch, M. Nieger, F. Reichert, and W.W. Schoeller. Bull. Soc. Chim. Fr. **130**, 25 (1993).
14. (*a*) K.W. Zilm, G.G. Webb, A.H. Cowley, M. Pakulski, and A. Orendt. J. Am. Chem. Soc. **110**, 2032 (1988); (*b*) M. Rance and R.A. Byrd. J. Magn. Reson. **52**, 221 (1983).
15. (*a*) K. Wolinski, J.F. Hinton, and P. Pulay. J. Am. Chem. Soc. **112**, 8251 (1990); (*b*) P. Pulay. Theor. Chim. Acta, **50**, 299 (1979).
16. C.J. Jameson, A. De Dios, and A.K. Jameson. Chem. Phys. Lett. **167**, 575 (1990).
17. J.A. Pople and D.L. Beveridge. Approximate molecular orbital theory. McGraw–Hill, New York. 1970.
18. V. Galasso. Theor. Chim. Acta, **34**, 137 (1974).
19. (*a*) D.H. Whiffen. J. Chim. Phys. **61**, 1589 (1964); (*b*) T.A. Albright. Org. Magn. Reson. **8**, 489 (1976).
20. R.K. Harris and A.C. Olivieri. Prog. NMR Spectrosc. **24**, 435 (1992).
21. (*a*) E.A.C. Lucken. *In* Nuclear quadrupolar coupling constants. Academic Press, London. 1969; (*b*) W. Gordy and R.L. Cook. *In* Microwave molecular spectra. John Wiley & Sons, New York. 1984; (*c*) A. Loewenstein. Adv. Nucl. Quadrupole Reson. **5**, 53 (1983).
22. (*a*) K. Eichele and R.E. Wasylishen. Angew. Chem. Int. Ed. Engl. **31**, 1222 (1992); (*b*) Inorg. Chem. **33**, 2766 (1994).
23. J. Murgich and Y. Aray. J. Chem. Phys. **87**, 3580 (1987).
24. T. Nakai and C.A. McDowell. J. Am. Chem. Soc. **116**, 6373 (1994).
25. K. Eichele, G. Wu, R.E. Wasylishen, and J.F. Britten. J. Phys. Chem. **99**, 1030 (1995).
26. K. Eichele and R.E. Wasylishen. J. Magn. Reson. Ser. A, **106**, 46 (1994).
27. R.D. Curtis, M.J. Shriver, and R.E. Wasylishen. J. Am. Chem. Soc. **113**, 1493 (1991).
28. J.C. Duchamp, M. Pakulski, A.H. Cowley, and K.W. Zilm. J. Am. Chem. Soc. **112**, 6803 (1990).
29. G. David, E. Niecke, M. Nieger, and J. Radseck. J. Am. Chem. Soc. **116**, 2191 (1994).
30. R.E. Wasylishen. *In* Nuclear magnetic resonance spectroscopy of nuclei other than protons. *Edited by* T. Axenrod and G.A. Webb. John Wiley & Sons, New York. 1974. pp. 105–125.
31. V.M.S. Gil and W. von Philipsborn. Magn. Reson. Chem. **27**, 409 (1989).
32. (*a*) P.N. Tutunjian and J.S. Waugh. J. Chem. Phys. **76**, 1223 (1982); (*b*) J. Magn. Reson. **49**, 155 (1982).
33. V. Galasso. Chem. Phys. **83**, 407 (1984).
34. (*a*) I. Ando and G.A. Webb. Theory of NMR parameters. Academic Press, London. 1983; (*b*) J. Kowalewski. Annu. Rep. NMR Spectrosc. **12**, 81 (1982); (*c*) R.H. Contreras and J.C. Facelli. Annu. Rep. NMR. Spectrosc. **27**, 255 (1993).
35. A.H. Cowley and W.D. White. J. Am. Chem. Soc. **91**, 1917 (1969).
36. V. Galasso. J. Magn. Reson. **36**, 181 (1979).
37. S. Duangthai and G.A. Webb. Org. Magn. Reson. **21**, 199 (1983).
38. J.P. Albrand, H. Faucher, D. Gagnaire, and J.B. Robert. Chem. Phys. Lett. **38**, 521 (1976).
39. Y. Kuroda, Y. Fujiwara, A. Kuwae, and K. Matsushita. J. Chem. Soc. Perkin Trans. 2, 675 (1986).

Synthesis and characterization of phosphinimine-substituted trifluoro- or trichloro-*p*-benzoquinones and their cationic Rh(I) complexes. The crystal and molecular structure of 3,5,6-trichloro-2-(triphenylphosphinimino)-*p*-benzoquinone

Jin Li, Kattesh V. Katti, A. Alan Pinkerton, Herbert Nar, and Ronald G. Cavell

Abstract: Reaction of tetrafluoro- or tetrachloro-*p*-benzoquinone with silylated phosphoranimines $R_2R'P{=}NSiMe_3$ (R = Ph, Me) yields very highly colored monosubstituted derivatives of the *p*-quinone that act as two-electron acceptors showing clean, reversible CV traces. The molar absorptivity values are typical of dyes. These ligands also form chelate complexes with Rh(I) precursors using the quinone oxygen and the imine nitrogen donor sites. One of the quinone derivatives, 3,5,6-trichloro-2-(triphenylphosphinimino)-*p*-benzoquinone, has been structurally characterized. The iminated quinone shows a normal P═N bond length (1.597(2) Å) and P-N-C angle (P-N-C(3) 132.7(2)°). The N—C(3) bond, 1.327(3) Å, is a little shorter as is expected for the establishment of a conjugated structure between the phosphinimine substituent and the quinone ring. Some steric crowding pushes the Cl and N substituents on the quinone ring out of the plane of the ring.

Key words: quinones, phosphinimines, fluorine, chlorine, rhodium.

Résumé : La réaction de la tétrafluoro- ou de la tétrachloro-*p*-benzoquinone avec des phosphoranimines silylées $R_2R'P{=}NSiMe_3$ (R = Ph, Me) fournit des dérivés monosubstitués fortement colorés de la *p*-quinone qui agissent comme des accepteurs de deux électrons et qui présentent de courbes de CV réversibles propres. Les valeurs d'absorption molaire sont typiques des colorants. Ces coordinats forment aussi des chélates complexes avec des précurseurs Rh(I); ils utilisent l'oxygène de la quinone et l'azote de l'imine comme sites donneurs. On a caractérisé la structure de l'un des dérivés de la quinone, la 3,5,6-trichloro-2-(triphénylphosphinimino)-*p*-benzoquinone. Pour la quinone iminée la longueur de la liaison P═N (1,597(2) Å) et l'angles P-N-C (P-N-C(3), 132,7(2)°) sont normaux. La liaison N—C(3), 1,327(3) Å, est un peu plus courte que celle à laquelle on pourrait s'attendre pour une structure conjuguée entre le substituant phosphinimine et le noyau quinone. Un encombrement stérique force les substituants Cl et N attachés au noyau quinone à adopter des positions hors-plan.

Mots clés : quinones, phosphinimines, fluorure, chlorure, rhodium.

[Traduit par la rédaction]

Introduction

The quinone–hydroquinone system is a well-known redox couple widely used synthetically as an oxidant or as a dehydrogenating agent. In the context of the present study it is also notable that there is a fairly extensive phosphorus chemistry (1, 2) although not by any means as large as that of the general organic derivatives. Several important biochemicals (for example, Vitamins E and K) belong to the quinone system and such species have been implicated in photosynthesis and respiration processes (3–6). Benzoquinone is also an efficient oxidant for metallocenes (7, 8). Many quinone derivatives are very highly coloured and so find applications as dyes and pigments (9–11). Some benzoquinone, anthraquinone, and naphthoquinone derivatives absorb light above 700 nm and thus find use as laser filters (12–14).

The first examples of phosphinimine derivatized *p*-quinones (15) were obtained from the reaction of azido-*p*-benzoquinone with phosphines (eq. [1]). It was claimed that these compounds would be useful as dyestuffs, insecticides, and synthetic intermediates.

An alternate route (16) to such compounds was provided by the reaction of phosphorus pentachloride with 1-aminoanthraquinone to first form *N*-tetrachlorophosphoranyl-1-aminoanthraquinone, which was then converted into the trichlorophosphazoanthraquinone by treatment with tertiary bases (B) (eq. [2]).

Received February 14, 1996.

This paper is dedicated to Professor Howard C. Clark in recognition of his contributions to Canadian chemistry.

J. Li, K.V. Katti, and R.G. Cavell.[1] Department of Chemistry, University of Alberta, Edmonton, AB T6G 2G2, Canada.
A.A. Pinkerton and H. Nar. Department of Chemistry, University of Toledo, Toledo, OH 43606-3390, U.S.A.

[1] Author to whom correspondence may be addressed. Telephone: (403) 492-5310. Fax: (403) 492-8231. E-mail: Ron.Cavell@Ualberta.ca

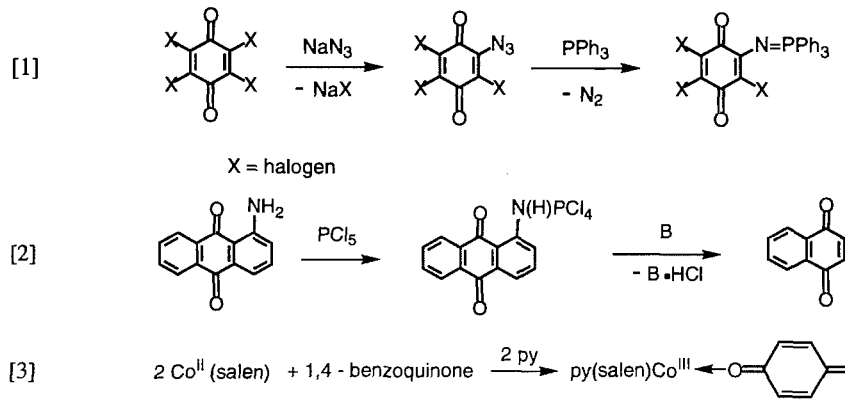

Although the *o*-benzoquinones are known to be good chelating agents, forming numerous stable transition-metal compounds (17–20), there are only a few examples of σ-coordinated *p*-benzoquinones. These systems typically form bridged complexes and most of the systems studied have yielded polymeric products. Less condensed examples are the dimeric products obtained from the reaction of *p*-benzoquinone with the pentacyanocobaltate anion (21) or Schiff's base metal complexes; for example, $Co^{(II)}$(salen) (eq. [3]) yields the pyridine-stabilized Co^{III}[*N*,*N*′-ethylenebis(salicylideneiminato) product. In these latter examples, however, only the parent quinone reacted in this way. Tetrachloro-*p*-benzoquinone did not react with the $Co^{(II)}$ precursor (22).

If these *o*-quinone ligands are combined with metal salts in a 1:1 ratio, polymeric products are obtained (23, 24). Formation of polymeric products can be prevented by blocking the coordination positions with other polydentate ligands. In such cases dimetallic complexes are obtained. The Fe(III) quinone complex (23) contains both bridging and terminal dihydroxybenzoquinone ligands. Dimetallic complexes of Ni and Cu are known, with several structurally characterized examples being reported (25–27). Recently, Calvo et al. reported the crystal structure of a dimetallic complex of Rh(I) (28). Related is 2,5-bis(arylamino)-*p*-benzoquinone, obtained from the reaction of phenylamine with *p*-benzoquinone, which combines with the first-row transition metals to form polymeric metal complexes (29). Unfortunately, the ligands themselves generally have very poor solubility and the resultant polymeric materials are also generally insoluble.

Recent interest in the design of new charge transfer complexes of quinones using a selection of donor groups (30)[2] has been sparked by the metal-like electrical conductivity of single crystals of the tetrathiafulvalene–tetracyanoquinodimethane (TTF–TCNQ) charge transfer complex (32). Although many different substituents have been attached to the quinone framework to supply electron density, there has been little use of electron-rich inorganic functionalities such as phosphazenes or thiazenes for such purposes. Monophosphazenes of the type $RPh_2P{=}NR'$ are themselves versatile one-, two-, or four-electron donors to transition and actinide metals (33–36) and this property suggested that such functionalities might provide suitable electron donor sources for the quinone framework while simultaneously conferring unique reactivity, high thermal stability, and structural diversity beyond that available with strictly organic substituents. In addition, the proximity of the N and O ligating centers that can be developed with phosphazene-substituted *p*-quinones suggested that chelate complexes could be readily formed with transition metals. These metals might have interesting electrical and optical properties. Therefore, as part of a study of iminophosphorane substitutional chemistry, we have explored the attachment of iminophosphoranes to halogenated quinones and herein report the formation and characterization of chloro- and fluoro-*p*-quinones derivatized with one iminophosphorane substituent. These species are notably highly colored and also act as complexing agents toward metals.

Results and discussion

Synthesis and properties of the ligands

Derivatization of the halogenated quinones is readily achieved by extension of the process in which an activated halogenoaromatic reacts with a silyliminophosphorane to eliminate trimethylsilylhalide, binding the imine center to the aromatic (34–36). In the present case, reaction of tetrafluoro- or tetrachloro-*p*-benzoquinone with one equivalent of trimethylsilylphosphinimines in CH_2Cl_2 proceeded smoothly in the same fashion as the activated aromatics (34–36), giving the corresponding monosubstituted *p*-benzoquinone derivatives **1–5** in good yield (eq. [4]). The elimination of trimethylsilylchloride, which was not previously demonstrated in the developments of our system of substituted ligands (34–36), is as effective as the elimination of trimethylsilyl fluoride.

The monosubstituted phosphoraniminequinones are very highly colored, air-stable, solids that are soluble in most common organic solvents. The solid compounds appear black. Upon dissolution, intense purple or blue solutions are obtained. The large values of their UV–visible molar extinction coefficients place them in the category of dye molecules (Table 1). The composition and structure of each of the compounds has been determined from the analytical data, mass spectra, and ^1H, ^{31}P, and ^{19}F NMR spectroscopy. Molecular ions for each of the compounds have been observed in the mass spectra. Phosphorus-31 NMR data are also given in Table 1.

We have structurally characterized 3,5,6-trichloro-2-(triphenylphosphinimino)-*p*-benzoquinone (**3**) and the structure is illustrated in Fig. 1. Crystallographic experimental details are given in Table 2, the positional parameters in Table 3, and selected important bond angles and lengths are given in Table

[2] For leading references of quinones with extended π-systems see ref. 31.

[4]

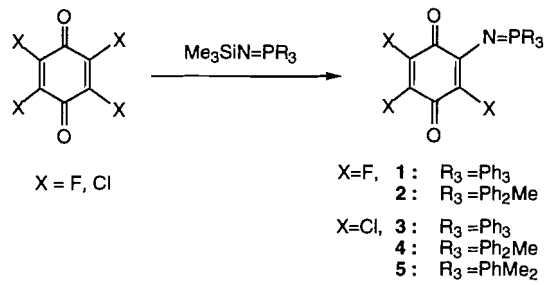

Fig. 1. ORTEP drawing of **3** with 30% probability ellipsoids for all non-hydrogen atoms.

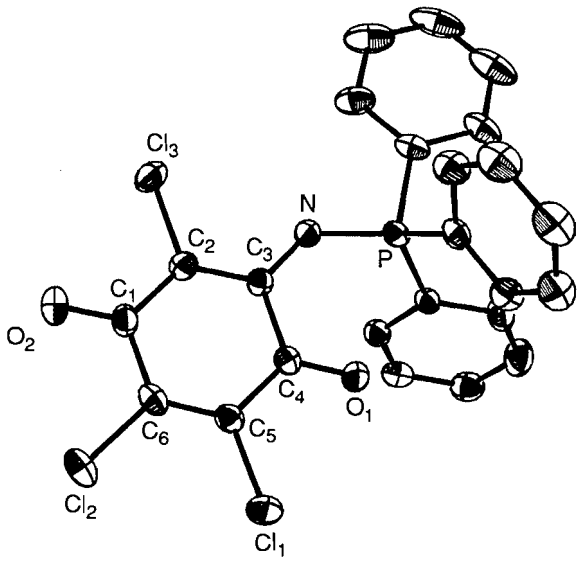

4. The P=N bond length of 1.597(2) Å is comparable to those we observed earlier (36) for iminophosphoranophosphines and is not exceptionally short, but the N—C(3) distance, 1.327(3) Å, is short compared to those in previously evaluated systems (36). This shortening suggests stronger binding between the quinone framework and the phosphinimine. The angle subtended at the imine nitrogen, P-N-C(3), 132.7(2)°, is comparable to those observed for fluoroaromatic iminophosphinimines (36). The environment around the quinone ring is quite crowded. This leads to a distortion in which Cl(1) and Cl(2) are pushed to opposite sides of the aromatic plane (+0.067 and −0.087 Å, respectively, with respect to the aromatic plane defined by the framework carbons C(1) thru C(6)) and, similarly, Cl(3) and N are also pushed out of the plane (+0.099 and −0.119 Å, respectively).[3]

Complexation reaction of the ligands with [Rh(cod)Cl]$_2$

Reactions of **1** or **4** with 1/2[Rh(cod)Cl]$_2$ and $AgClO_4$ in acetone at 25°C proceed smoothly to give complexes **6** and **7** in high yield (see eq. [5]).

The monocation for each of the cationic complexes is observed in the mass spectra (FAB). The ^{31}P NMR chemical shift of complex **6** shows a single peak at 39.2 ppm, which is 23.9 ppm downfield from the signal for the corresponding uncoordinated ligand **1**. The ^{19}F NMR of complex **6** showed three signals: at −140.4 ppm (a doublet of doublets with splittings of 1.5 and 4.9 Hz), which is due to the fluorine *meta* to the phosphinimine, at −148.3 ppm (a doublet with a splitting of 4.9 Hz), which is due to the fluorine *para* to the phosphinimine, and at −158.8 ppm (a singlet) due to the fluorine that is *ortho* to the phosphinimine. In comparison, the uncoordinated ligand **1** shows corresponding ^{19}F NMR chemical shift signals at −141.92 ppm (d, 7.5 Hz) for the *meta* fluorine, −148.4 ppm (dd, 3.8 and 7.5 Hz) for the *para* fluorine, and −152.6 ppm (d, 3.8 Hz) for the *ortho* fluorine. Comparing the complex and the ligand ^{19}F NMR spectra reveals that the signal at −140.4 ppm showed only a small (1.5 ppm) downfield shift and there is no significant shift for the signal at −148.3 ppm. However, the third signal (at −158.8 ppm), which belongs to the fluorine closest to the phosphinimine, shows a 6 ppm upfield shift compared to the uncoordinated ligand. These data are consistent with a structure in which the imine nitrogen is coordinated to the Rh(I) center. There is no evidence for Rh—F coupling, which has been observed in some similar compounds (37). The infrared spectrum of complex **6** showed two quinone carbonyl stretching bands at 1692 and 1664 cm^{-1} compared with bands at 1709 and 1685 cm^{-1} for the corresponding free ligand (**1**). These changes in frequency can be attributed to π backdonation from the Rh center to the C=O π^* orbital. All of the spectral evidence suggests that complex **6** contains rhodium(I) coordinated by the ligand via both an oxygen and an imine nitrogen, as illustrated in eq. [5].[4]

The ^{31}P NMR spectrum for complex **7** showed a single peak at 31.2 ppm, 16 ppm downfield from the value for the corresponding uncoordinated ligand **4**. The quinone carbonyl infrared stretching frequencies for complex **7** are 1681 and 1629 cm^{-1}, which are to be compared with the corresponding bands at 1725 and 1679 cm^{-1} for the free ligand **4**. The IR and NMR evidence suggests that **7** has the same structure as **6** with the small numerical differences in the spectral parameters arising from and in accord with the differences between the nature of the halogenated quinones. The chloroquinone more readily allows electron density to flow toward the metal center upon coordination, resulting in larger coordination shifts than for the fluoroquinone.

[3] Details of the crystal structure determination of **3** including crystal and data collection parameters, temperature factor expressions (U's), and positional parameters and their estimated standard deviations (14 pages) are available as supplementary material and may be purchased from: The Depository of Unpublished Data, Document Delivery, CISTI, National Research Council Canada, Ottawa, Canada K1A 0S2. With the exception of the temperature factor expressions, these data have also been deposited with the Cambridge Crystallographic Data Centre, and can be obtained on request from The Director, Cambridge Crystallographic Data Centre, University Chemical Laboratory, 12 Union Road, Cambridge, CB2 1EZ, U.K.

[4] One referee suggested that the Rh(I) center was oxidized either by Ag^+ or by the quinone to yield Rh(III) complexes. The evidence that no oxidation occurs in these preparations is provided by independent reactions of ligand **3** with [Rh(cod)Cl]$_2$ and KPF_6 to give a Rh(I) complex of **3** with ^{31}P NMR parameters very similar to those of **6** and **7**. Reaction of this product with dppe displaces the quinone ligands and generates the well-known $Rh(dppe)_2^+$ cation (38), thus the Rh(I) center is not oxidized by the quinone ligands or reagents used in the formation of the Rh(I) precursor from the original source dimer.

[5] 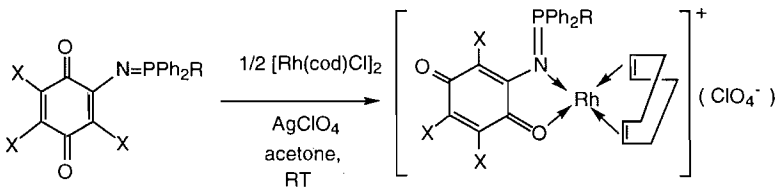

6: X = F, R = Ph
7: X = Cl, R = Me

Table 1. Phosphorus-31 NMR[a] data and UV spectral data for compounds **1–7**.

Compounds	No.	δ_P (ppm)	λ_{max} (nm)	log ε
3,5,6-Trifluoro-2-(triphenylphosphinimino)-*p*-benzoquinone	**1**	15.27(s)	544	3.61
3,5,6-Trifluoro-2-(methyldiphenylphosphinimino)-*p*-benzoquinone	**2**	16.56(s)	536	3.47
3,5,6-Trichloro-2-(triphenylphosphinimino)-*p*-benzoquinone	**3**	14.44(s)	570	3.46
3,5,6-Trichloro-2-(methyldiphenylphosphinimino)-*p*-benzoquinone	**4**	15.42(s)	572	3.46
3,5,6-Trichloro-2-(dimethylphenylphosphinimino)-*p*-benzoquinone	**5**	19.52(s)	554	3.12
[(3,5,6-Trifluoro-2-(triphenylphosphinimino)-*p*-benzoquinone){σ-O, N} Rh(cod)](ClO_4)	**6**	39.2(s)	546	3.20
[(3,5,6-Trichloro-2-(methyldiphenylphosphinimino)-*p*-benzoquinone){σ-O,N}Rh(cod)](ClO_4)	**7**	31.19(s)	550	3.21

[a]Spectra obtained in $CDCl_3$ solution; ppm vs. 85% H_3PO_4. Positive values indicate resonance to low field of standard.
[b]$^2J_{PP}$ = 52.90 Hz.
[c]$^2J_{PP}$ = 52.70 Hz.

Electrochemistry of phosphinimine-*p*-benzoquinone derivatives

The electrochemical data for the mono-phosphinimine derivatives of the chloro- and fluoroquinones show that they reversibly accept two electrons as do the parent quinones. The CV traces are clean and well shaped, showing the classic "duck-bill" shape and a pair of reverse sweep peaks that match the forward, reduction sweep. Numerical data for the potentials and the differences between peak positions in the forward and the reverse sweeps (ΔE) are given in Table 5. The CV trace of 3,5,6-trichloro-2-(triphenylphosphinimino)-*p*-benzoquinone (**3**) showed, on occasion, extra features that appear to be due to hydrolysis of the compound. The fluoroquinones **1** and **2** and the related chloroquinones **4** and **5** did not appear to be so susceptible nor do a number of related chloro-cyano-phosphinimine quinones that we have investigated (37).

Conclusions

Halogenated quinones can be readily substituted with phosphinimine moieties and the resultant compounds are highly colored species with potential for dye applications. These quinones demonstrate reversible two-electron redox behaviour and they also readily form complexes with transition metals. There would appear to be considerable potential for the utilization of the properties shown by these new ligands.

Experimental

All experimental manipulations were performed under an atmosphere of dry argon using Schlenk techniques. Solvents were dried and distilled under argon prior to use: CH_2Cl_2, CH_3CN, THF, and toluene were distilled from P_2O_5, P_2O_5–CaH_2, Na–benzophenone, and Na, respectively. The deuterated solvent, $CDCl_3$, was distilled and stored under argon before use. Commercial (Aldrich) supplies of dppm, Me_3SiN_3, 1,4-tetrachloro- and 1,4-tetrafluoro-quinones were used as obtained. $Ph_3P{=}NSiMe_3$, $(CH_3)Ph_2P{=}NSiMe_3$, and $Ph(CH_3)_2P{=}NSiMe_3$ were prepared from the reaction of the appropriate phosphine with Me_3SiN_3 as previously described (39). Nuclear magnetic resonance spectra were recorded on Bruker WH-200 and 400 spectrometers using as the reference the deuterium signal of the solvent employed (respective operating frequencies: ^1H = 200.133 and 400.135 MHz, ^{13}C = 50.323 and 100.614 MHz, ^{31}P = 81.015 and 161.977 MHz, ^{19}F = 188.313 and 376.503 MHz). The ^1H chemical shifts are reported in ppm from external Me_4Si, the ^{31}P NMR spectra are reported in ppm from external 85% H_3PO_4, and the ^{19}F NMR spectra are reported in ppm from external $CFCl_3$. Positive values are shifts downfield. Low-resolution mass spectra (Electron Impact, EI) were recorded at 16 or 70 eV on an AEI MS50 spectrometer. Positive ion fast atom bombardment mass spectra (FAB-MS) were obtained by using Xe fast atoms on a customized AEI MS9 spectrometer. Infrared spectra were recorded using a Nicolet 7199 infrared spectrometer. UV–visible spectra were recorded using a Hewlett Packard 8450A diode array spectrophotometer. Elemental analyses were performed by the Microanalytical Services Laboratory at the University of Alberta. Melting points were ascertained by visual methods in unsealed capillaries. Osmometry measurements were made in CH_2Br_2 or *o*-dichlorobenzene solutions using a Corona Wescan vapor pressure osmometer operated by the University of Alberta Microanalytical Services Laboratory. The crystal structure was determined at the University of Toledo. Details are given in Tables 2–4.

Synthesis of the substituted quinone ligands

Synthesis of 3,5,6-trifluoro-2-(triphenylphosphinimino)-*p*-

Table 2. Crystallographic experimental details.

A. Crystal data	
Formula	$C_{24}H_{15}C_{13}NO_2P$
F.W.	486.73
$F(000)$	496
Crystal dimensions (mm)	0.28 × 0.16 × 0.10
Peak width at half-height (deg)	0.28
Radiation MoK$_\alpha$ (Å)	λ = 0.71073
Instrument:	Enraf–Nonius CAD4 diffractometer
Monochromator	Graphite crystal, incident beam
Attenuator	Zr foil, factor 19.5
Takeoff angle (deg)	2.8
Detector aperture (mm) horizontal	2.2–2.3
vertical	4.0
Crystal to detector dist. (cm)	21
Scan type	ω–2θ
Scan rate (min^{-1})	1–7° (in ω)
ω scan width, (deg)	0.8 + 0.34 tan θ
θ scan width, (deg)	0.833 ω width
Maximum 2θ (deg)	50.0
T°C	21 ± 1
Space group	Triclinic $P\bar{1}$
Cell dimensions a (Å)	10.249(2)
b (Å)	13.429(2)
c (Å)	8.917(2)
α (deg)	103.26(1)
β (deg)	112.38(2)
γ (deg)	89.21(1)
V (Å^3)	1100.9
Z	2
ρ (g/cm^3)	1.47
μ (cm^{-1})	5.1
No. of reflections measured	4095 total, 3859 unique
Data corrections	Lorentz–polarization, Linear decay (from 0.959 to 1.056 on I), Reflection averaging (agreement on I = 1.8%), Empirical absorption (from 0.95 to 1.00 on I).
B. Structure solution and refinement[a]	
Solution	Direct methods
Hydrogen atoms	Refined as riding atoms
Refinement	Full-matrix least-squares
Minimization function	$\Sigma w(\|F_o\| - \|F_c\|)^2$
Least-squares weights	$4F_o^2/\sigma^2(F_o^2)$
Anomalous dispersion	All non-hydrogen atoms
Reflections included ($F_o^2 > 3.0\sigma(F_o^2)$)	2732
Parameters refined	280
R	0.037
R_w	0.049
Esd of obs. of unit weight	1.44
Convergence, largest shift	0.03σ
High peak in final diff. map	0.23 (5) e/Å^3
Low peak in final diff. map	–0.21(3) e/Å^3

[a]Computer hardware, VAX11/750; computer software, SDP/VAX (Enraf–Nonius and B.A. Frenz & Associates, Inc.).

benzoquinone (**1**): To a solution of 1,4-tetrafluorobenzoquinone (1.00 g, 5.55 mmol) in CH_2Cl_2 (40 mL), maintained at 0°C using an ice–water bath, was added dropwise a solution of $Me_3SiN{=}PPh_3$ (1.941 g, 5.55 mmol), also in CH_2Cl_2 (20 mL). A purple color formed immediately. The reaction mixture was stirred at 0°C for about 1 h, then at room temperature for 12 h. The solution was taken to dryness in vacuum and the resultant purple solids were washed with hexane (20 ml × 3)

Table 3. Positional parameters and their estimated standard deviations for **3**.

Atom	*x*	*y*	*z*	*B* (Å^2)
Cl(1)	0.64996(7)	0.42734(6)	0.41313(8)	4.55(2)
Cl(2)	0.32482(9)	0.37445(7)	0.19136(9)	5.96(2)
Cl(3)	0.27354(7)	0.16116(6)	0.61191(9)	4.69(2)
P	0.72315(7)	0.25552(5)	0.96579(7)	3.04(1)
N	0.5679(2)	0.2414(2)	0.8224(2)	3.41(5)
O(1)	0.7307(2)	0.3508(1)	0.7152(2)	3.82(4)
O(2)	0.1888(2)	0.2495(2)	0.3218(2)	5.62(5)
C(1)	0.3130(3)	0.2709(2)	0.4138(3)	3.62(6)
C(2)	0.3793(3)	0.2378(2)	0.5659(3)	3.20(6)
C(3)	0.5160(2)	0.2661(2)	0.6761(3)	2.84(5)
C(4)	0.6072(2)	0.3275(2)	0.6255(3)	2.93(6)
C(5)	0.5425(3)	0.3586(2)	0.4654(3)	3.21(6)
C(6)	0.4051(3)	0.3343(2)	0.3712(3)	3.69(6)
C(7)	0.7886(3)	0.3857(2)	1.0799(3)	3.02(6)
C(8)	0.9280(3)	0.4122(2)	1.1929(3)	4.41(8)
C(9)	0.9686(3)	0.5116(3)	1.2886(4)	5.49(9)
C(10)	0.8730(3)	0.5854(2)	1.2739(4)	4.88(8)
C(11)	0.7352(3)	0.5597(2)	1.1620(3)	4.08(7)
C(12)	0.6944(3)	0.4614(2)	1.0652(3)	3.40(6)
C(13)	0.7014(3)	0.1953(2)	1.1176(3)	3.73(6)
C(14)	0.8172(4)	0.1930(2)	1.2628(3)	5.16(8)
C(15)	0.7997(4)	0.1516(3)	1.3836(4)	7.0(1)
C(16)	0.6699(4)	0.1112(3)	1.3586(4)	7.2(1)
C(17)	0.5558(4)	0.1118(3)	1.2142(4)	6.99(9)
C(18)	0.5698(3)	0.1548(2)	1.0924(3)	5.22(8)
C(19)	0.8543(3)	0.1871(2)	0.9043(3)	3.40(6)
C(20)	0.8328(3)	0.0806(2)	0.8562(3)	4.73(8)
C(21)	0.9279(4)	0.0231(2)	0.8050(4)	5.68(9)
C(22)	1.0458(3)	0.0716(3)	0.8058(4)	5.60(9)
C(23)	1.0674(3)	0.1763(3)	0.8524(4)	5.19(8)
C(24)	0.9709(3)	0.2348(2)	0.8995(3)	4.17(7)

[a]Anisotropically refined atoms are given in the form of the isotropic equivalent displacement parameter defined as: $(4/3)*[a^2*B(1,1) + b^2*B(2,2) + c^2*B(3,3) + ab(\cos\gamma)*B(1,2) + ac(\cos\beta)*B(1,3) + bc(\cos\alpha)*B(2,3)]$.

Table 4. Selected bond distances (Å) and angles for **3**.

Distances	
P—N	1.597(2)
N—C(3)	1.327(3)
C(1)—C(2)	1.436(4)
C(1)—C(6)	1.484(5)
C(2)—C(3)	1.366(3)
C(3)—C(4)	1.507(4)
C(4)—C(5)	1.482(3)
C(5)—C(6)	1.335(3)
O(1)—C(4)	1.211(3)
O(2)—C(1)	1.218(3)
Cl(1)—C(5)	1.703(3)
Cl(2)—C(6)	1.709(3)
Cl(3)—C(2)	1.723(3)
Angles	
P-N-C(3)	132.7(2)

and dried in vacuum (yield 2.18 g; 90%; purple powder). ^{19}F NMR ($CDCl_3$): δ(F_1 (*ortho* to N=PPh_3)) −152.55 (d, 1F, $^5J_{F_1-F_3}$ = 3.8 Hz), δ(F_2 (*para* to N=PPh_3)) −141.92 (d, 1F, $^3J_{F_2-F_3}$ = 7.5 Hz), δ(F_3 (*meta* to N=PPh_3)) −148.35 (dd, 1F, $^3J_{F_2-F_3}$ = 7.5 Hz, $^5J_{F_1-F_3}$ = 3.8 Hz). ^{1}H NMR ($CDCl_3$): phenyl rings δ 7.45, 7.80 (m, 15H). MS (EI, *m/z*): 437 (M^+, 100%). Anal. calcd. for $C_{24}H_{15}NF_3O_2P$: C 65.91, H 3.46, N 3.20; found: C 65.22, H 3.37, N 3.34.

Synthesis of 3,5,6-trifluoro-2-(methyldiphenylphosphinimino)-*p*-benzoquinone (**2**): To a solution of 1,4-tetrafluorobenzoquinone (1.00 g, 5.55 mmol) in CH_2Cl_2 (40 mL), maintained at 0°C using an ice–water bath, was added dropwise a solution of Me_3SiN=PPh_2Me (1.560 g, 5.55 mmol), also in CH_2Cl_2 (20 mL). A purple color formed immediately. The reaction mixture was stirred at 0°C for about 1 h, then at room temperature for 12 h. The solution was taken to dryness in vacuum and the resultant purple solids were washed with hexane (20 mL × 3) and dried in vacuum (yield 1.10 g; 56%; purple powder). ^{19}F NMR ($CDCl_3$): δ(F_1 (*ortho* to N=PPh_3)) −154.30 (s, 1F), δ(F_2 (*para* to N=PPh_3)) −141.00 (d, 1F, $^3J_{F_2-F_3}$ = 3.8 Hz), δ(F_3 (*meta* to N=PPh_3)) −148.90 (d, 1F, $^3J_{F_2-F_3}$ = 3.8 Hz). ^{1}H NMR ($CDCl_3$): phenyl rings δ 7.45, 7.80 (m, 10H), methyl group δ 2.30 (d, 3H, $^2J_{P-H}$ = 16.0 Hz). MS (EI, *m/z*): 475 (M^+, 100%). Anal. calcd. for $C_{19}H_{13}NF_3O_2P$: C 60.81, H 3.49, N 3.73; found: C 59.67, H 3.31, N 4.33.

Synthesis of 3,5,6-trichloro-2-(triphenylphosphinimino)-*p*-benzoquinone (**3**): To a solution of 1,4-tetrachlorobenzoquinone (2.500 g, 10.17 mmol) in THF (80 mL) at room temperature (RT) was added dropwise a solution of Me_3SiN=PPh_3 (3.554 g, 10.17 mmol), also in THF (20 mL). The reaction mixture was refluxed for 12 h. The deep blue solution was taken to dryness in vacuum and the resultant solids were washed with hexane (20 mL × 3) and dried in vacuum (yield 4.25 g; 88%; blue powder; mp 227–229°C). ^{1}H NMR ($CDCl_3$): phenyl rings δ 7.55, 7.70 (m, 15H). MS (EI, *m/z*): 487 (M^+, 100%). Anal. calcd. for $C_{24}H_{15}NCl_3O_2P$: C 59.23, H 3.11, N 2.88, Cl 21.85; found: C 59.19, H 3.09, N 2.86, Cl 21.80.

Synthesis of 3,5,6-trichloro-2-(methyldiphenylphosphinimino)-*p*-benzoquinone (**4**): To a solution of 1,4-tetrachlorobenzoquinone (2.567 g, 10.44 mmol) in THF (40 mL) at RT was added dropwise a solution of Me_3SiN=PPh_2Me (3.00 g, 10.44 mmol), also in THF (10 mL). The reaction mixture was refluxed for 12 h. The deep blue solution was taken to dryness in vacuum and the resultant solids were washed with hexane (20 mL × 3) and dried in vacuum (yield 2.30 g; 52%; blue powder; mp 208–210°C). ^{1}H NMR ($CDCl_3$): phenyl rings δ 7.55, 7.85 (m, 10H), methyl group δ 2.35 (d, 3H, $^2J_{P-H}$ = 16.0 Hz). MS (EI, *m/z*): 425 (M^+, 100%). Anal. calcd. for $C_{19}H_{13}NCl_3O_2P$: C 53.74, H 3.09, N 3.30, Cl 25.05; found: C 53.73, H 3.17, N 3.54, Cl 23.82.

Synthesis of 3,5,6-trichloro-2-(dimethylphenylphosphinimino)-*p*-benzoquinone (**5**): To a solution of 1,4-tetrachlorobenzoquinone (0.436 g, 1.78 mmol) in THF (25 mL) at room temperature was added dropwise a solution of Me_3SiN=$PPhMe_2$ (0.400 g, 1.78 mmol), also in THF (10 mL). The reaction mixture was refluxed for 12 h. The deep blue solution was taken to dryness in vacuum and the resultant solids were washed with hexane (20 mL × 3) and dried in vac-

Table 5. Reduction potential ($E^{0'}$) data for monosubstituted quinone derivatives and selected reference systems.

Compound	$E^{0'}$ (V)	ΔE (meV)
p-Benzoquinone[a]	−0.10	70
	−0.85	150
Tetrachloro-*p*-benzoquinone[b]	+0.34	80
	−0.43	100
Tetrafluoro-*p*-benzoquinone	+0.28	
	−0.66	
3,5,6-Trifluoro-2-(triphenylphosphinimino)-*p*-benzoquinone (**1**)	0.00	90
	−0.76	120
3,5,6-Trifluoro-2-(methyldiphenylphosphinimino)-*p*-benzoquinone (**2**)	−0.05	70
	−0.79	90
3,5,6-Trichloro-2-(triphenylphosphinimino)-*p*-benzoquinone (**3**)	+0.03	105
	−0.73	95
3,5,6-Trichloro-2-(methyldiphenylphosphinimino)-*p*-benzoquinone (**4**)	−0.11	110
	−0.84	120
3,5,6-Trichloro-2-(dimethylphenylphosphinimino)-*p*-benzoquinone (**5**)	−0.14	100
	−0.88	130

[a]Literature: $E^{0'}$ = −0.15 and −0.81 V (vs. Ag/AgCl in DMF at 19°C with [*n*-Bu_4N]ClO_4 (0.1 M) as electrolyte) (3).
[b]Literature: $E^{0'}$ = +0.35 and −0.43 V (vs. Ag/AgI in CH_2Cl_2 at 25°C with [*n*-Bu_4N]ClO_4 (0.5 M) as electrolyte) (3).

uum to obtain (**5**) (yield 0.52 g; 81%; blue powder). ^{1}H NMR ($CDCl_3$): phenyl rings δ 7.55, 7.80 (m, 5H), methyl groups δ 2.02 (d, 3H, $^2J_{P-H}$ =16.0 Hz). MS (EI, *m/z*): 361 (M^+, 100%). Anal. calcd. for $C_{14}H_{11}NCl_3O_2P$: C 46.38, H 3.06, N 3.86, Cl 29.33; found: C 44.07, H 2.76, N 3.85, Cl 30.83.

Synthesis of rhodium (I) complexes

Synthesis of [(3,5,6-trifluoro-2-(triphenylphosphinimino)-*p*-benzoquinone){σ-O,N}Rh(cod)](ClO_4) (**6**): To a 100 mL Schlenk flask were added [(cod)RhCl]$_2$ (0.049 g, 0.100 mmol), $AgClO_4$ (0.042 g, 0.20 mmol), and acetone (15 mL). The mixture was stirred for 15 min whereupon a light yellow solution and a white precipitate formed. This solution was filtered into a purple solution of **1** (0.088 g, 0.200 mmol), also in acetone (15 mL), and the mixed solutions were stirred for 1 h. The solution was taken to near dryness; then hexane (10 mL) was added, whereupon a precipitate formed. The product was filtered and washed with hexane (10 mL × 2) and dried in vacuum. Recrystallization from CH_2Cl_2 gave the one-eighth dichloromethane solvate of **6** (yield: 0.11 g; 73%; brown powder). ^{19}F NMR ($CDCl_3$): δ −140.43 ppm (dd, 1F, coupling constant: 1.5 Hz and 4.9 Hz), δ −148.33 ppm (d, 1F, coupling constant: 4.9 Hz), δ −158.76 ppm (s, 1F). ^{1}H NMR ($CDCl_3$): phenyl rings: δ 7.55, 7.65 ppm (m, 15H), cod groups: δ 4.20 ppm (s, 4H, HC═), δ 2.45 ppm (m, 4H, H_2C), δ 1.65 ppm (broad, 4H, H_2C). MS (FAB): 648 (monocation). Anal. calcd. for $C_{32}H_{27}NClF_3O_6PRh \cdot 1/8CH_2Cl_2$: C 50.87, H 3.62, N 1.85, Cl 5.84; found: C 49.06, H 3.63, N 1.87, Cl 5.65.

A similar procedure to that described above was used to prepare [3,5,6-trichloro-2-(methyldiphenylphosphinimino)-*p*-benzoquinone){σ-O,N}Rh(cod)](ClO_4) (**7**) from [(cod)RhCl]$_2$, $AgClO_4$, and **4**, again in acetone (yield: 0.102 g; 69%; brown powder). ^{1}H NMR ($CDCl_3$): phenyl rings: δ 7.60, 7.80 ppm (m, 10H), cod groups: δ 4.23 ppm (s, 4H, HC═), δ 2.50 ppm (m, 4H, H_2C), δ 1.70 ppm (broad, 4H, H_2C). Methyl group: δ 2.80 ppm (d, $^2J_{P-H}$ = 12 Hz). MS (FAB): 636 (monocation). Mol. Wt.: 511.4 (solvent: CH_2Br_2). Anal. calcd. for $C_{27}H_{25}NCl_4O_6PRh$: C 44.11, H 3.43, N 1.91, Cl 19.29; found: C 44.08, H 3.49, N 1.93, Cl 17.96.

Electrochemistry

An electrochemical cell was constructed to provide a small-volume (ca. 10 mL) inert-gas-blanketted environment for the measurements. Three electrodes were introduced through a sealed glass cap extending to the base of the tube where they projected into the solution volume. A gas inlet was provided as well as a rotatable bent side arm on the cell to hold the solid sample ready for addition. The procedure was as follows: first, the sample was put in the sidearm tube and solvent was added to the cell. A blank cyclovoltammetric scan was done. Then the sample tube was turned to drop the sample into the solvent. The sample was allowed to dissolve completely, and then the CV scan of the solution was taken. The working electrode was a small (1 mm diameter) Pt bead sealed in soft glass. A coiled Pt wire (15 cm in length) was used as the auxiliary electrode. The compartment for the Ag/AgCl quasi-reference electrode was separated from the working electrode compartment by a fine frit. The support electrode was [*n*-Bu_4N]BF_4. The solvent (dichloromethane, Spectrograde, BDH) was degassed and dried over alumina (ICN Biomedical, neutral, W200 Super 1). The working electrode was cleaned by placing the electrode tip over boiling HNO_3 (reagent grade) for 0.5 h, rinsing with distilled water (2 L), and soaking in a saturated ferrous ammonium sulphate solution (made up in 1 M H_2SO_4) for 0.5 h. Finally, it was rinsed with distilled water (2 L) and reagent acetone (1 L), and dried with a hot air gun immediately before

use. The potential was supplied by a EG&G model 273 potentiostat, and the resulting cyclic voltammograms were recorded using a Hewlett Packard 7015B X-Y recorder. The solutions employed during cyclic voltammetry were typically (5–7) × 10^{-4} M in organometallic complex and 0.1 M in [n-Bu_4N]BF_4. These experiments were carried out at ambient temperatures (about 23°C). The formal oxidation or reduction potential, $E^{0'}$, for reversible couples is defined as the average of the anodic ($E_{p,a}$) and cathodic ($E_{p,c}$) peak potentials. The separation of the cathodic and anodic potentials is ΔE, $|E_{p,c} - E_{p,a}|$. The cathodic to anodic peak current ratio is defined as $i_{p,c}/i_{p,a}$ (40). The oxidation of ferrocene is reported to be highly reversible in many solvents (41) and was used as an internal reference (under our experimental conditions, $E^{0'}$ = +0.47 V vs. Ag/AgCl, $i_{p,c}/i_{p,a}$ = 1.0, ΔE = 100 mV) (42). A scan rate of 0.1 V s^{-1} was used for all the compounds measured. The ratio $i_{p,c}/i_{p,a}$ was used to establish chemical reversibility for the compounds studied.

Acknowledgment

R.G.C., J.L., and K.V.K. thank the Natural Sciences and Engineering Research Council of Canada for support. A.A.P. and H.N. thank the College of Arts and Sciences of the University of Toledo for support of the X-ray facilities. We thank Dr D. Law for some assistance with experimental work.

References

1. A.A. Kutyrev and V.V. Moskva. Russ. Chem. Rev. **56**, 1028 (1987).
2. R. Burgada and R. Setton. *In* The chemistry of organophosphorus compounds. Vol. 3. *Edited by* F.R. Hartley. Wiley, London. 1994.
3. S. Patai (*Editor*). The chemistry of the quinonoid compounds. John Wiley & Sons, New York. 1974.
4. C.A. Wraight. Biochim. Biophys. Acta, **459**, 525 (1977).
5. C.A. Wraight. FEBS Lett. **93**, 283 (1978).
6. G.R. Cliff and G. Jones. J. Chem. Soc. (C), 3418 (1971).
7. G. Wilkinson, M. Rosenblum, M.C. Whiting, and R.B. Woodward. J. Am. Chem. Soc. **74**, 2125 (1952).
8. R.L. Brandon, J.H. Osiecki, and A. Ottenberg. J. Org. Chem. **31**, 1214 (1966).
9. K. Venkataraman. The chemistry of synthetic dyes. Academic Press, New York. 1952.
10. H.A. Lubs. The chemistry of synthetic dyes and pigments. Reinhold, New York. 1955.
11. T.S. Gore, B.S. Joshi, S.V. Sunthankar, and B.D. Tilak. (*Editors*). Recent progress in the chemistry of natural and synthetic colouring materials. Academic Press, New York. 1962.
12. K. Takagi, M. Kawabe, M. Matsuoka, and T. Kitao. Dyes Pigm. **6**, 177 (1985).
13. H. Nishi, Y. Hatada, and K. Kitahara. Bull. Chem. Soc. Jpn. **56**, 1482 (1983).
14. J. Fabian. Chem. Rev. **92**, 1197 (1992).
15. W.L. Mosby and M.L. Silva. US Patent 3,387,004 (1968).
16. Y.G. Shermolovich, R.I. Vlyazlo, and L.N. Markovskii. Zh. Obshch. Khim. **48**, 539 (1978).
17. C.G. Pierpont and R.M. Buchanan. Coord. Chem. Rev. **38**, 45 (1981).
18. C.G. Pierpont and C.W. Lange. Prog. Inorg. Chem. **41**, 381 (1993).
19. C.G. Pierpont and H.H. Downs. Inorg. Chem. **15**, 343 (1975).
20. A.B.P. Lever, H. Masui, R.A. Metcalfe, D.J. Stufkens, E.S. Dodsworth, and P.R. Auburn. Coord. Chem. Rev. **125**, 317 (1993).
21. A.A. Vlcek and J. Hanzlik. Inorg. Chem. **6**, 2053 (1967).
22. C. Floriani, G. Fachinetti, and F. Calderazzo. J. Chem. Soc. Dalton Trans. 765 (1973).
23. J.T. Wrobleski and D.B. Brown. Inorg. Chem. **18**, 498 (1979).
24. (*a*) R.S. Bottei and J.T. Fangman. J. Inorg. Nucl. Chem. **28**, 1259 (1966); (*b*) R.S. Bottei and D.L. Green. J. Inorg. Nucl. Chem. **30**, 1469 (1968); (*c*) A.M. Talati and V.N. Mistry. Indian J. Chem. **11**, 296 (1973); (*d*) S. Kanda and Y. Saito. Bull. Chem. Soc. Jpn. **30**, 192 (1957); (*e*) D.K. Cabbiness and E.S. Amis. Bull. Chem. Soc. Jpn. **40**, 435 (1967); (*f*) A.M. Talati and V.N. Mistry. J. Indian Chem. Soc. **50**, 225 (1973); (*g*) H. Kobayashi, T. Haseda, and S. Kanda. J. Phys. Soc. Jpn. **18**, 349 (1963); (*h*) C. Yoshimura, H. Noguchi, T. Inoue, and H. Hara. Bunseki Kagaku, **15**, 918 (1966); (*i*) M.A.A. Beg. Pak. J. Sci. Ind. Res. **14**, 452 (1971); (*j*) T.R. Rao, P.R. Rao, P. Lingaiah, and L. Sirdeshmukh. J. Indian Chem. Soc. **67**, 832 (1990).
25. C.G. Pierpont, L.C. Francesconi, and D.N. Hendrickson. Inorg. Chem. **16**, 2367 (1977).
26. F. Tinti, M. Verdaguer, O. Kahn, and J. Savariault. Inorg. Chem. **26**, 2380 (1987).
27. J. Folgado, R. Ibanez, E. Coronado, D. Beltran, J.M. Savariault, and J. Galy. Inorg. Chem. **27**, 19 (1988).
28. M.A. Calvo, A.M.M. Lanfredi, L.A. Oro, M.T. Pinillos, C. Tejel, A. Tiripicchio, and F. Ugozzoli. Inorg. Chem. **32**, 1147 (1993).
29. A.A. Berlin, B.I. Liogon'kii, and E.A. AbdullaZade. Vysokomol. Soedin. Ser. A, **9**, 1725 (1967).
30. (*a*) A.M. Kine, D.O. Cowan, F. Gerson, and R.J. Mockel. J. Am. Chem. Soc. **107**, 556 (1985); (*b*) A. Aumuller and S. Hunig. Liebig. Ann. Chem. 618 (1984); (*c*) T. Mitsuhashi, M. Goto, K. Honda, K. Maroyama, T. Sugawara, T. Inabe, and T. Watanabe. J. Chem. Soc. Chem. Commun. 810 (1987).
31. (*a*) P.W. Kenney, T.H. Jozefiak, and L.L. Miller. Org. Chem. **53**, 5007 (1988); (*b*) W.C. Christopfel and L.L. Miller. J. Org. Chem. **51**, 4149 (1986); (*c*) T. Chiba, P.W. Kenny, and L.L. Miller. J. Org. Chem. **52**, 4328 (1987); (*d*) P.W. Kenny and L.L. Miller. J. Chem. Soc. Chem. Commun. 84 (1987).
32. J. Ferraris, D.O. Cowan, V.V. Waltka, and H.H. Perlstein. J. Am. Chem. Soc. **94**, 948 (1977).
33. (*a*) E. Bohm, K. Dehnicke, A. Maurer, and D. Fenske. Z. Naturforsch. B: Chem. Sci. **43**, 138 (1988); (*b*) D. Fenske, E. Bohm, K. Dehnicke, and J. Strahle. Z. Naturforsch. B: Chem. Sci. **43**, 1 (1988); (*c*) A. Maurer, D. Fenske, J. Beck, W. Hiller, J. Strahle, E. Bohm, and K. Dehnicke. Z. Naturforsch. B: Chem. Sci. **43**, 5 (1988); (*d*) H.W. Roesky, U. Sesake, M. Noltemeyer, P.G. Jones, and G.M. Sheldrick. J. Chem. Soc. Dalton Trans. 1309 (1986); (*e*) H.W. Roesky, K.V. Katti, U. Seseke, U. Scholtz, E. Herbst, E. Egert, and G.M. Sheldrick. Z. Naturforsch. B: Chem. Sci. **41**, 1509 (1986); (*f*) R.E. Cramer, F. Edelmann, A.L. Mori, S. Roth, J.W. Gilge, K. Tatsumi, and A. Nakamura. Organometallics, **7**, 841 (1988), and refs. therein.
34. K.V. Katti and R.G. Cavell. Organometallics, **8**, 2147 (1989).
35. K.V. Katti and R.G. Cavell. Inorg. Chem. **28**, 413 (1989).
36. K.V. Katti, B.D. Santarsiero, A.A. Pinkerton, and R.G. Cavell. Inorg. Chem. **32**, 5919 (1993).
37. J. Li. Ph. D. Thesis, University of Alberta, 1996.
38. A.R. Sanger. J. Chem. Soc. Dalton Trans. 120 (1977).
39. L. Birkhofer and A. Ritter. Angew, Chem. Int. Ed. Engl. **4**, 417 (1965); L. Birkhofer, A. Ritter, and P. Richter. Chem. Ber. **96**, 2750 (1963).
40. R.S. Nicholson. Anal. Chem. **38**, 1406 (1966).
41. J.D.L. Holloway and W.E. Geiger. J. Am. Chem. Soc. **101**, 2038 (1979).
42. R.R. Gagne, C.A. Koval, and G.C. Lisensky. Inorg. Chem. **19**, 2854 (1980).

$Mo_2(OCH_2{}^tBu)_6(Cp)Na(DME)$. Preparation, structure, and solution behavior

Theodore A. Budzichowski, Malcolm H. Chisholm, and William E. Streib

Abstract: From the reaction between $Mo_2(OCH_2{}^tBu)_6$ and NaCp (Cp = C_5H_5) in THF the title complex was obtained as a crystalline product in the presence of DME (DME = dimethoxyethane). Crystal data for $Mo_2(OCH_2{}^tBu)_6(Cp)Na(DME)$ at −167°C: a = 11.885(2) Å, b = 19.240(1) Å, c = 11.562(2) Å, α = 102.73(1)°, β = 106.95(1)°, γ = 98.55(1)°, Z = 2 and space group of $P\bar{1}$. In the solid state there is an unbridged Mo≡Mo bond of distance 2.276(1) Å. One Mo atom is bonded to four alkoxides, two of which are also bonded to Na^+ while the other is η^5-bonded to the Cp ligand, with Mo—C distances ranging from 2.34 to 2.66 Å, and to two OR groups, one of which is bound to the Na^+ ion. In addition to the coordination to three OR groups the Na^+ ion binds one DME molecule via both of its ether oxygen atoms. The Mo—O distances fall in the range 1.91–2.01 Å with the longer distances being associated with those groups that are also bonded to the Na^+ ion. In polar solvents the title complex dissociates to give $Mo_2(OCH_2{}^tBu)_6$ and Na^+ Cp^-.

Key words: molybdenum, alkoxide, cyclopentadienyl, metal–metal triple bonds.

Résumé : On a obtenu le composé mentionné dans le titre sous forme cristalline à partir de la réaction entre le $Mo_2(OCH_2{}^tBu)_6$ et le NaCp (Cp = C_2H_5) dans le THF. Les données cristallines pour le composé $Mo_2(OCH_2{}^tBu)_6(CP)Na(DME)$ à −167°C sont les suivantes : a = 11,885(2) Å, b = 19,240(1) Å, c = 11,562(2) Å, α = 102,73(1)°, β = 106,95(1)°, γ = 98,55(1)°, Z = 2 et groupe d'espace $P\bar{1}$. À l'état solide il y a une distance de liaison Mo≡Mo non ponté de 2,276(1) Å. Un atome de Mo est lié à quatre groupes alcoolates, dont deux sont également liés à l'ion Na^+ tandis que l'autre est lié par une liaison η^5 au ligand Cp avec des distances de liaison allant de 2,34 à 2,066 Å et à deux groupes OR dont l'un est lié à l'ion Na^+. En plus de la coordiantion aux trois groupes OR, l'ion Na^+ est lié à une molécule de DME par l'intermédiaire de ses deux atomes d'oxygène. Les distances Mo—O se situent dans un intervalle de 1,91 à 2,01 Å, la plus grande distance étant associée aux groupes qui sont également liés à l'ion Na^+. Dans les solvants polaires, le composé mentionné dans le titre se dissocie pour donner le complexe $Mo_2(OCH_2{}^tBu)_6$ et Na^+Cp^-.

Mots clés : molybdène, alcoolate, cyclopentadiényle, triple liaison métal–métal.

[Traduit par la rédaction]

Introduction

We have for some time been exploring the chemistry associated with dinuclear complexes of the formula $M_2(OR)_6$ where M = Mo and W (1). These are members of a class of so-called ethane-like dimers having a cylindrical M—M triple bond of electronic configuration $\sigma^2\pi^4$. The metal atoms are weakly Lewis acidic since the metal d_{xy}, $d_{x^2-y^2}$ orbitals are vacant and are only weakly involved in π-bonding to the alkoxide oxygen p_π orbitals. This allows for substrate uptake and often subsequent activation at the dinuclear center (2). Recently we have been examining the uptake of anionic ligands such as CN^- (3*a*) and OR^- (3*b*), which may bind reversibly according to eqs. [1] and [2].

[1] $M_2(OR)_6 + X^- \rightleftharpoons [M_2(OR)_6X]^-$

[2] $[M_2(OR)_6X]^- + X^- \rightleftharpoons [M_2(OR)_6(X)_2]^{2-}$

The position of the equilibria in eqs. [1] and [2] is sensitive to the steric properties of R and the metal. For given systems the $\Delta H°$ value is more negative by ca. 3 kcal/mol for M = W relative to M = Mo and weak nucleophiles such as halides and NCS^- do not bind to the $M_2(OR)_6$ complexes.

We describe here our studies of the binding of the cyclopentadienyl ligand, which was of interest to us in part because earlier studies of $M_2(NMe_2)_4Cp_2$ complexes were inconclusive concerning the mode of coordination of the C_5H_5 moiety to the $Mo_2{}^{6+}$ center (4).

Results and discussion

Syntheses and solution behavior

The reaction between NaCp and $Mo_2(OCH_2{}^tBu)_6$ proceeds quickly in THF, based on the rapid color change from yellow to deep purple that occurs when the two are mixed at room temperature. The product may be obtained by simply evaporating the solvent in vacuo (0.01 Torr, 25°C; 1 Torr = 133.3 Pa) and retains at least two equivalents of THF (depending on the drying time) based on ^1H NMR spectroscopic analysis. Surprisingly, the spectrum is quite simple and belies the color

Received February 20, 1996.

This paper is dedicated to Professor Howard C. Clark in recognition of his contributions to Canadian chemistry.

T.A. Budzichowski, M.H. Chisholm,[1] and W.E. Streib.
Department of Chemistry and Molecular Structure Center, Indiana University, Bloomington, IN 47405 U.S.A.

[1] Author to whom correspondence may be addressed. Telephone: (812) 855-6606. Fax: (812) 855-7148. E-mail: chisholm@indiana.edu

Fig. 1. Stacked plot of ^{1}H NMR spectra (-CH_2- region, toluene-d_8, 300 MHz, 23°C to –80°C) showing the changes that occur upon cooling. Resonances marked with an asterisk are due to DME.

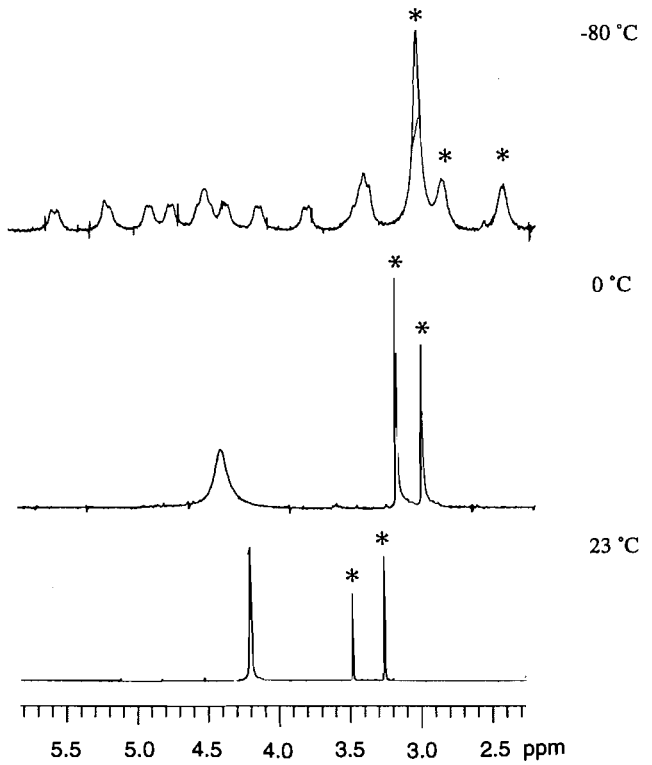

of the material since the chemical shifts of the alkoxide resonances are only slightly altered from those of pure $Mo_2(OCH_2{}^tBu)_6$, but are significantly broadened. When DME is added, however, the product crystallizes nicely from cold THF solution (−34°C) as large purple parallelopipeds. The ^{1}H NMR spectrum is similarly straightforward and consists of single resonances for the –$OCH_2{}^tBu$ (both methylene and methyl) groups, DME (both methyl and methylene groups), and cyclopentadienyl moieties. The normalized ratio of these resonances (alkoxide:DME:Cp) is 6:1:1, consistent with the analytical data and the solid state structure observed by single-crystal X-ray diffraction (vide infra).

Once again, the neopentoxide resonances are only slightly shifted and broadened from those of $Mo_2(OCH_2{}^tBu)_6$ at room temperature (23°C, toluene-d_8), which is consistent with fluxional behavior and *dissociation* of the cyclopentadienyl moiety from the dimolybdenum center. Upon cooling, the spectrum becomes quite complex and at very low temperature (–80°C, toluene-d_8) it is clear that the solid state structure is maintained in solution: the molecule is asymmetric, possessing six different alkoxide groups. These give rise to 6 ^{t}Bu resonances and 12 doublets (6 doublets of doublets) for the methylene groups, which are all diastereotopic. Furthermore, the methylene groups of the DME are split into two broad resonances, but the signal for the methyl groups of this moiety is only broadened. Apparently, the process that equilibrates these groups of the DME is not completely frozen out at –80°C since one would anticipate two resonances, and two doublets of doublets for the methylene groups, based on the observed molecular structure in the solid state.

Fig. 2. ORTEP plot of the core atoms for Na(DME)Mo_2-$(OCH_2tBu)_2(\eta^5$-$C_5H_5)$ with ellipsoids at the 50% probability level. This view is roughly perpendicular to the Mo≡Mo axis.

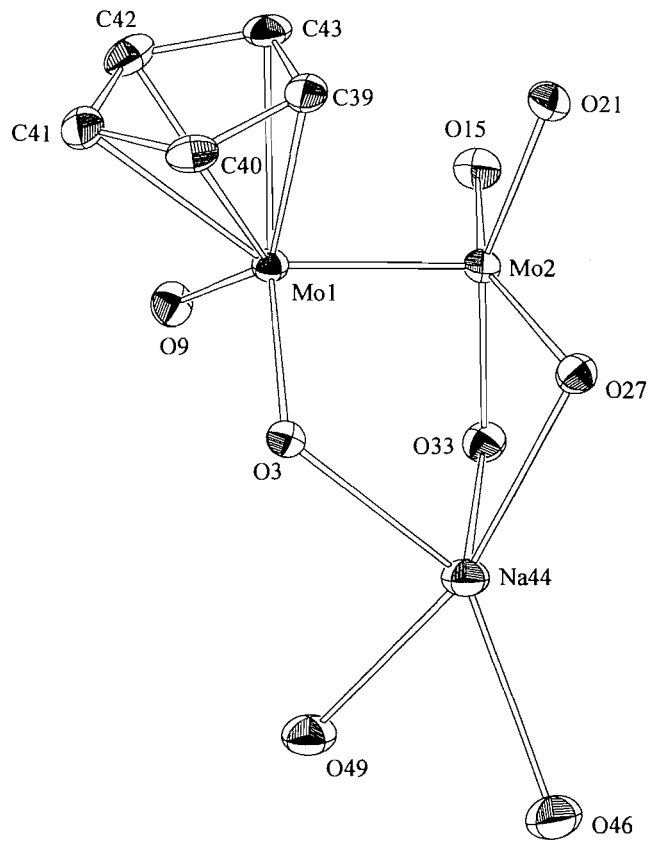

In contrast, warming a solution of the complex briefly (60°C, 2–3 min) in toluene-d_8 produces sharper resonances (for free $Mo_2(OCH_2{}^tBu)_6$) and a distinctive color change to yellow that may be readily observed prior to decomposition. The process is reversible and cooling causes reassociation. Unfortunately, because of the fluxionality of the adduct, (DME)$NaMo_2(OCH_2{}^tBu)_6(\eta^5$-$C_5H_5)$, data could not be obtained with the precision necessary for computation of $\Delta H°$ and $\Delta S°$ for the equilibrium. These changes are shown in Fig. 1.

It was clear at this point that the enthalpy of η^5-C_5H_5 association is only modestly favorable and is balanced with the unfavorable loss in entropy that occurs when NaCp, $Mo_2(OCH_2{}^tBu)_6$, and the molecule of DME are brought together in the adduct. With this in mind, 18-crown-6 was introduced as a potential complexing agent for the sodium cation. Unfortunately, no appreciable changes could be observed spectroscopically, and recrystallization from DME:THF produced (DME)$NaMo_2(OCH_2{}^tBu)_6(\eta^5$-$C_5H_5)$, not a charge-separated complex such as $[Na(18\text{-crown-}6)]^+[Mo_2(OCH_2{}^tBu)_6$-$(\eta^5$-$C_5H_5)]^-$. Addition of pyridine to solutions of (DME)$NaMo_2(OCH_2{}^tBu)_6(\eta^5$-$C_5H_5)$ resulted in the formation of $Mo_2(OCH_2{}^tBu)_6(py)_2$, NaCp, and DME. This is an unusual result in the sense that the sodium cations, which are bound to alkoxide ligands in the adduct, dissociate along with the cyclopentadienyl moiety.

Metathesis of alkoxide for Cp might otherwise have been

Fig. 3. ORTEP plot of $Na(DME)Mo_2(OCH_2{}^tBu)_6(\eta^5\text{-}C_5H_5)$ showing all non-hydrogen atoms at the 40% probability level (for clarity). The view is roughly parallel to the Mo≡Mo axis and highlights the staggered and asymmetric arrangement of the ligands.

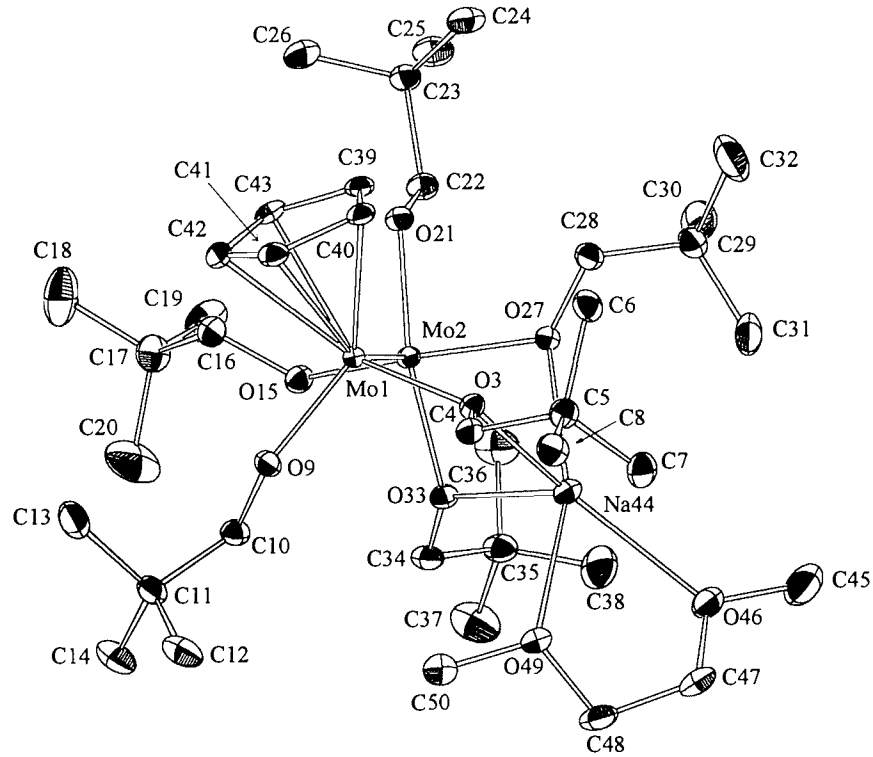

anticipated based on hard–soft acid–base principles. Numerous complexes are known that contain η^5-cyclopentadienyl ligands and metal–ligand multiple bonds (e.g., $[(\eta^5\text{-}C_5Me_5)Ta(\equiv N)(Me)]_3$ (5). Given the isolobal analogy between triply-bonded ligands (such as nitride) and the $\eta^5\text{-}C_5H_5$ ligand it is somewhat perplexing that a formation of $CpMo(OR)_2(\equiv Mo(OR)_3)$ would be energetically unfavorable relative to $Mo_2(OR)_6(py)_2$.

Solid-state structure

A view of the central $CpO_6Mo_2NaO_2$ skeleton giving the atom number scheme is given in Fig. 2 and an ORTEP view of the complex is given in Fig. 3. A listing of atomic coordinates is given in Table 1, selected bond distances and bond angles are given in Tables 2 and 3, and a summary of structural data is given in Table 4.

The Mo—Mo distance of 2.276 Å is typical of that for a triple bond. One molybdenum atom Mo(1) is coordinated to two $OCH_2{}^tBu$ groups and the Cp ligand, which may be considered as $\eta^5\text{-}C_5H_5$, with Mo(1)—C distances spanning a relatively narrow range 2.34–2.66 Å. There are two short, 2.34 and 2.36 Å, and three longer, 2.51, 2.54, and 2.66 Å, Mo(1) to C distances. These distances do not lend themselves to either the η^1 or $\eta^3\text{-}C_5H_5$ bonding pattern. The other Mo atom is bonded to four $OCH_2{}^tBu$ groups. Of the six $OCH_2{}^tBu$ ligands, three are bonded to both Mo and the Na ion, one from Mo(1) and two from Mo(2), and coordination to the Na ion results in a slight lengthening of the Mo—O distance from 1.98 to 2.01 Å. The coordination of the Na ion is completed by the η^2-DME ligand such that Na is five coordinate. The Na—O distances span a narrow range 2.31–2.51Å.

Experimental section

All synthetic procedures were performed under an inert atmosphere utilizing standard procedures in conjunction with a Vacuum Atmospheres Corporation Dri-Lab. The solvents used were dried by standard procedures and stored over 4 Å molecular sieves prior to use. $Mo_2(OCH_2{}^tBu)_6$ was prepared as described in the literature (7) and was recrystallized from cold hexanes and dried in vacuo prior to use. Sodium cyclopentadienide was prepared from freshly cracked cyclopentadiene (Aldrich) and sodium hydride (Aldrich) in THF. The soluble portion was collected by filtration, and the volatile components were removed in vacuo (25°C, 0.01 Torr) to afford NaCp as a pure white powder. The crown ether (18-crown-6) was purchased from Aldrich and was purified by repeated sublimation (100°C, 0.001 Torr) prior to use. NMR spectra were recorded on Varian XL-300 (300.1 MHz) and Bruker AM-500 (500.0 MHz) spectrometers and were referenced to residual protio impurities of the deuterated solvents.

Synthesis of $Na(DME)Mo_2(OCH_2{}^tBu)_6(\eta^5\text{-}C_5H_5)$

Yellow crystalline $Mo_2(OCH_2{}^tBu)_6$ (800 mg, 1.12 mmol) and NaCp (110 mg, 1.24 mmol) were weighed into a 30 mL

Table 1. Fractional coordinates and isotropic thermal parameters for $Mo_2(OCH_2{}^tBu)_6CpNa(DME)$.

Atom	10^4x	10^4y	10^4z	$10B_{iso}$
Mo(1)	6751.9(2)	6626.3(1)	1222.3(2)	10
Mo(2)	7806.0(2)	7805.1(1)	1760.4(2)	11
O(3)	8122(1)	6260(1)	2138(1)	13
C(4)	7951(2)	5489(1)	1958(2)	16
C(5)	8654(2)	5279(1)	3125(2)	18
C(6)	8195(2)	5536(1)	4216(2)	20
C(7)	9992(2)	5619(1)	3511(2)	23
C(8)	8450(2)	4444(1)	2760(2)	21
O(9)	6562(1)	6305(1)	−527(1)	15
C(10)	6892(2)	6613(1)	−1434(2)	17
C(11)	6273(2)	6095(1)	−2767(2)	20
C(12)	6723(3)	5389(1)	−2878(2)	27
C(13)	4911(3)	5925(2)	−3055(2)	32
C(14)	6592(3)	6484(2)	−3695(2)	9
O(15)	7064(1)	8201(1)	378(1)	16
C(16)	5842(2)	8192(1)	−194(2)	19
C(17)	5656(3)	8711(2)	−1029(2)	27
C(18)	4299(3)	8642(2)	−1581(3)	44
C(19)	6273(3)	9493(2)	−238(3)	31
C(20)	6175(4)	8497(2)	−2088(3)	52
O(21)	6899(1)	8297(1)	2720(1)	15
C(22)	7223(2)	9071(1)	3184(2)	16
C(23)	6367(2)	9369(1)	3835(2)	18
C(24)	5084(2)	9166(2)	2903(3)	27
C(25)	6810(2)	10204(1)	4302(3)	26
C(26)	6404(2)	9066(1)	4953(2)	25
O(27)	9067(1)	7878(1)	3411(1)	14
C(28)	8824(2)	7790(1)	4509(2)	17
C(29)	9899(2)	8163(1)	5718(2)	23
C(30)	10155(3)	8987(2)	5919(3)	34
C(31)	11015(3)	7888(2)	5622(3)	33
C(32)	9565(3)	7975(2)	6806(3)	48
O(33)	9132(1)	7657(1)	1063(1)	14
C(34)	9612(2)	8085(1)	390(2)	18
C(35)	10561(2)	8785(1)	1218(2)	22
C(36)	10003(3)	9309(1)	1951(3)	31
C(37)	11028(3)	9150(2)	350(3)	38
C(38)	11600(3)	8602(2)	2143(3)	35
C(39)	5640(2)	6867(1)	2604(2)	15
C(40)	5528(2)	6110(1)	2440(2)	16
C(41)	4800(2)	5731(1)	1194(2)	16
C(42)	4492(2)	6255(1)	563(2)	18
C(43)	4988(2)	6963(1)	1426(2)	16
Na(44)	10044(1)	7051.3(5)	2467(1)	17
C(45)	13205(3)	7393(2)	4282(3)	54
O(46)	12257(1)	7062(1)	3121(2)	27
C(47)	12461(2)	6409(1)	2426(3)	24
O(48)	11683(2)	6233(1)	1083(3)	25
O(49)	10447(1)	6122(1)	1013(2)	20
C(50)	9635(2)	5935(1)	−247(2)	25

Schlenk flask equipped with a Teflon-coated magnetic stirring bar in the dry box. THF (~15 mL) was added via cannula under N_2 outside the box resulting in the formation of a deep purple solution, which was stirred for 2 h. After this time the volatile components were evaporated in vacuo (0.01 Torr, 25°C) and the purple foamy residue dried for 2 h. Despite numerous attempts, crystalline material could not be obtained from Et_2O or THF (even in the presence of 18-crown-6) by the addition of hexanes or pentane in which the product is insoluble. However, the addition of DME dramatically improves the crystallinity of the product, which vigorously retains one equivalent of this chelating ether and is easily isolated as large crystals from 2:1 THF:DME (5 mL total volume, 0°C). One of these was eventually used for the single-crystal X-ray diffraction experiment. The product was reasonably soluble in benzene-d_6 and toluene-d_8 and analyzed satisfactorily for $Na(DME)Mo_2(OCH_2{}^tBu)_6(\eta^5\text{-}C_5H_5)$. For $Na(DME)Mo_2(OCH_2{}^tBu)_6(\eta^5\text{-}C_5H_5)$: ^1H NMR (toluene-d_8, 0°C); δ: 6.62 (s, 5H), 4.20 (s, 12H), 3.14 (s, 6H), 3.01 (s, 4H), 1.11 (br s, 54H). ^1H NMR (toluene-d_8, −80°C), δ: 6.71 (s, 5H), 5.49, 5.12, 4.87, 4.72, 4.51, 4.47, 4.36, 4.13, 3.72 (d, 1H each for $-CH_2$), 3.43 (m, 3 overlapping d, 3H total for $-CH_2$), 3.08 (br s, 6H, $CH_3OCH_2CH_2OCH_3$), 2.91 (br s, 2H, $CH_3OCH_2CH_2OCH_3$), 2.52 (br s, 2H, $CH_3OCH_2CH_2OCH_3$), 1.57, 1.48, 1.29, 1.25, 1.00, 0.85 (s, 9H each for $-CH_2C(CH_3)_3$. Anal. calcd. for $C_{39}H_{81}O_8Mo_2Na$: C 52.46, H 9.14; found: C 52.95, H 9.29.

Table 2. Selected bond distances (Å) for $Mo_2(OCH_2{}^tBu)_6CpNa(DME)$.

A	B	Distance
Mo(1)	Mo(2)	2.2759(5)
Mo(1)	O(3)	1.9833(15)
Mo(1)	O(9)	1.9124(15)
Mo(1)	C(39)	2.3646(22)
Mo(1)	C(40)	2.5419(22)
Mo(1)	C(41)	2.6629(23)
Mo(1)	C(42)	2.5102(23)
Mo(1)	C(43)	2.3432(22)
Mo(2)	O(15)	1.9547(15)
Mo(2)	O(21)	1.9553(15)
Mo(2)	O(27)	2.0129(15)
Mo(2)	O(33)	1.9961(15)
Na(44)	O(3)	2.4266(18)
Na(44)	O(27)	2.3643(17)
Na(44)	O(33)	2.3120(18)
Na(44)	O(46)	2.5110(19)
Na(44)	O(49)	2.3760(19)
C(39)	C(40)	1.408(3)
C(39)	C(43)	1.422(3)
C(40)	C(41)	1.405(3)
C(41)	C(42)	1.399(3)
C(42)	C(43)	1.420(3)

Single crystal X-ray study

General operating procedures and listings of programs have been given previously (8).

An irregular crystal of suitable size was obtained by cleaving a large piece of the sample in a nitrogen atmosphere filled glove bag. The crystal was mounted using silicone grease and it was then transferred to a goniostat where it was cooled to −167°C for characterization and data collection. A systematic

Table 3. Selected angles (deg) for $Mo_2(OCH_2{}^tBu)_6CpNa(DME)$.

A	B	C	Angle
Mo(1)	Mo(1)	O(3)	95.51(5)
Mo(2)	Mo(1)	O(9)	101.62(5)
Mo(2)	Mo(1)	C(39)	94.89(6)
Mo(2)	Mo(1)	C(40)	125.32(5)
Mo(2)	Mo(1)	C(41)	146.35(5)
Mo(2)	Mo(1)	C(42)	123.79(6)
Mo(2)	Mo(1)	C(43)	93.63(6)
O(3)	Mo(1)	O(9)	106.58(6)
O(3)	Mo(1)	C(39)	105.47(7)
O(3)	Mo(1)	C(40)	88.41(7)
O(3)	Mo(1)	C(41)	104.21(7)
O(3)	Mo(1)	C(42)	135.40(7)
O(3)	Mo(1)	C(43)	140.31(7)
O(9)	Mo(1)	C(39)	142.09(7)
O(9)	Mo(1)	C(40)	129.32(7)
O(9)	Mo(1)	C(41)	98.54(7)
O(9)	Mo(1)	C(42)	86.90(7)
O(9)	Mo(1)	C(43)	109.20(8)
C(39)	Mo(1)	C(40)	33.11(8)
C(39)	Mo(1)	C(41)	53.88(8)
C(39)	Mo(1)	C(42)	55.83(8)
C(39)	Mo(1)	0(43)	35.16(8)
C(40)	Mo(1)	C(41)	31.22(7)
C(40)	Mo(1)	C(42)	53.12(8)
C(40)	Mo(1)	C(43)	55.47(8)
C(41)	Mo(1)	C(42)	31.19(8)
C(41)	Mo(1)	C(43)	54.10(8)
C(42)	Mo(1)	C(43)	33.80(8)
Mo(1)	Mo(2)	O(15)	105.96(5)
Mo(1)	Mo(2)	O(21)	100.08(5)
Mo(1)	Mo(2)	O(27)	101.43(5)
Mo(1)	Mo(2)	O(33)	100.16(5)
O(15)	Mo(2)	O(21)	88.81(6)
O(15)	Mo(2)	O(27)	152.55(6)
O(15)	Mo(2)	O(33)	89.65(6)
O(21)	Mo(2)	O(27)	88.20(6)
O(21)	Mo(2)	O(33)	159.33(6)
O(27)	Mo(2)	O(33)	83.74(6)
O(3)	Na(44)	O(27)	91.84(6)
O(3)	Na(44)	O(46)	140.08(7)
O(3)	Na(44)	O(49)	90.11(6)
O(27)	Na(44)	O(33)	69.80(6)
O(27)	Na(44)	O(46)	128.16(7)
O(27)	Na(44)	O(49)	162.39(7)
O(33)	Na(44)	O(46)	123.56(7)
O(33)	Na(44)	O(49)	98.00(6)
O(46)	Na(44)	O(49)	68.98(6)

search of a limited hemisphere of reciprocal space revealed no symmetry among the observed intensities. An initial choice of space group $P\bar{1}$ was later proven correct by the successful solution of the structure. Following complete data collection, data processing gave a residual of 0.023 for the averaging of 6291 unique intensities that had been observed more than once. Four standards measured every 400 data showed no significant trends. No correction was made for absorption.

Table 4. Summary of crystal data for $Mo_2(OCH_2{}^tBu)_6$-CpNa(DME).

Empirical formula	$C_{39}H_{81}Mo_2NaO_8$
Color of crystal	Violet
Crystal dimensions (nm)	0.15 × 0.25 × 0.50
Space group	$P\bar{1}$
Temp (°C)	−167
Cell dimensions	
a (Å)	11.885(2)
b (Å)	19.240(3)
c (Å)	11.546(2)
α (deg)	102.73(1)
β (deg)	106.95(1)
γ (deg)	98.55(1)
Z (molecule/cell)	2
Volume (Å)	2398.35
Calculated density (g/cm^3)	1.236
Wavelength (Å)	0.71069
Molecular weight	892.93
Linear absorption coefficient (cm^{-1})	5.586
Detector to sample distance (cm)	22.5
Sample to source distance (cm)	23.5
Average ω scan width at half height	0.25
Scan speed (deg/min)	8.0
Scan width (deg + dispersion)	2.0
Individual background (s)	4
2θ Range (deg)	6–45
Total number of reflections collected	12 722
Number of Unique Intensities	6291
Number with $F > 3*\sigma(F)$	5724
$R(F)$	0.0211
$Rw(F)$	0.0234
Goodness of fit for last cycle	0.913
Maximum δ/σ for last cycle	0.30

The structure was solved by using a combination of direct methods (MULTAN78) and Fourier techniques. The positions of the molybdenum atoms were determined from an initial E-map. The positions of the remaining non-hydrogen atoms were obtained from subsequent iterations of least-squares refinement and difference Fourier calculation. Only a few of the hydrogens were observed. Hydrogens were included in fixed calculated positions with thermal parameters fixed at one plus the isotropic thermal parameter of the atom to which they were bonded.

In the final cycles of refinement, the non-hydrogen atoms were varied with anisotropic thermal parameters to a final $R(F) = 0.021$. The final difference map was featureless, the largest peak being 0.328 e/Å^3 and the deepest hole being −0.331 e/Å^3.

The nonbonded Mo—Na distances, not shown in the tables, are: Mo(1)—Na(44), 3.646(1) Å, and Mo(2)—Na(44), 3.201(1) Å.

Acknowledgments

We thank the National Science Foundation for support.

References

1. (*a*) M.H. Chisholm. Acc. Chem. Res. **23**, 419 (1990); (*b*) J. Organomet. Chem. **400**, 235 (1990).
2. (*a*) T.A. Budzichowski, M.H. Chisholm, and K. Folting. Chem. –Eur. J. **2**, 110 (1996); (*b*) M.H. Chisholm. J. Chem. Soc. Dalton Trans. 1781 (1996).
3. (*a*) T.A. Budzichowski and M.H. Chisholm. Polyhedron, **13**, 2035 (1994); (*b*) T.A. Budzichowski, M.H. Chisholm, K. Folting, J.C. Huffman, and W.E. Streib. J. Am. Chem. Soc. **117**, 7428 (1995).
4. M.H. Chisholm, M.J. Hampden-Smith, K.A. Stahl, J.C. Huffman, J.D. Martin, and K.G. Moodley. Polyhedon, **7**, 1991 (1988).
5. M.B. Holl, M.Kersting, B.Pendley, and P.T. Wolczanski. Inorg. Chem. **29**, 1518 (1990).
6. (*a*) R.Hoffmann. Angew. Chem. Int. Ed. Engl. **21**, 711 (1982); (*b*) T.A. Albright, J.K. Burdett, and M.-H. Whangbo. *In* Orbital interactions in chemistry. Wiley, New York. 1995.
7. M.H. Chisholm, F.A. Cotton, C.A. Murillo and, W.W. Reichert. Inorg. Chem. **16**, 1801 (1977).
8. M.H. Chisholm, K. Folting, J.C. Huffman and C.C. Kirkpatrick. Inorg. Chem. **23**, 1021 (1984).

COMMUNICATION

Synthesis and spectroscopic characterization of bis(trifluorophosphinyl)-gold(I) undecafluorodiantimonate(V) $[Au(PF_3)_2][Sb_2F_{11}]$

B. Bley, M. Bodenbinder, G. Balzer, H. Willner, G. Hägele, F. Mistry, and F. Aubke

Abstract: The synthesis of $[Au(PF_3)_2][Sb_2F_{11}]$, the first example of a linear, thermally stable metal bis(trifluorophosphine) complex is achieved by CO substitution of $[Au(CO)_2][Sb_2F_{11}]$ by PF_3. The $[Au(PF_3)_2]^+$ cation can also be generated by reductive phosphorylation by an excess of PF_3 in fluorosulfuric acid. Spectroscopic characterization involves ^{19}F and ^{31}P NMR in HSO_3F and SO_2 solution including spectral simulation by the WIN-DAISY method and FT-IR and Raman spectra. Spectroscopic evidence suggests that the metal–ligand bond involves predominantly σ-bonding with drastically reduced π-back-donation.

Key words: gold(I) complex, linear; gold(I) PF_3 complex; ^{31}P NMR; ^{19}F NMR; vibrational spectra.

Résumé : On a réalisé la synthèse du $[Au(PF_3)_2][Sb_2F_{11}]$, le premier exemple d'un complexe de bis(trifluorophosphine) d'un métal, linéaire et thermiquement stable, en substituant le groupe CO du composé $[Au(CO)_2][Sb_2F_{11}]$ par le groupe PF_3. Le cation $[Au(PF_3)_2]^+$ peut également être généré par phosphorylation réductrice avec un excès de PF_3 dans l'acide fluorosulfurique. Les caractérisations par spectroscopie impliquent la RMN du ^{19}F et du ^{31}P en solution dans du HSO_3F et du SO_2 incluant la simulation spectrale par la méthode du WIN-DAISY et des spectres FT-IR et Raman. Les preuves spectroscopiques suggèrent que la liaison ligand–métal implique de façon prédominante une liaison σ qui réduit drastiquement le transfert en retour π.

Mots clés : complexe d'or(I), linéaire; complexe de PF_3 or(I); RMN du ^{31}P; RMN du ^{19}F; spectres vibrationnels.

[Traduit par la rédaction]

While a substantial number of transition metal complexes with trifluorophosphine, PF_3, have become known (1–3), compounds containing homoleptic metal–PF_3 cations are rare. The known examples involve $[M(PF_3)]^+$ complexes of d^{10} metal ions like Ag^+ (4), Cu^+ (5), and Hg_2^{2+} (4) with $[AsF_6]^-$ as anion (4, 5). The salts are frequently thermally unstable (4) and incompletely characterized. We want to report here the synthesis of $[Au(PF_3)_2][Sb_2F_{11}]$ and the spectroscopic characterization of the linear $[Au(PF_3)_2]^+$ cation by IR, Raman, and ^{19}F and ^{31}P NMR spectroscopy. Two earlier publications by us form the basis for the synthesis of $[Au(PF_3)_2][Sb_2F_{11}]$. The recently reported compound $[Au(CO)_2][Sb_2F_{11}]$ (6) provides a convenient starting material and the molecular structure determination of $[Hg(CO)_2][Sb_2F_{11}]$ (7) demonstrates why the very weakly basic $[Sb_2F_{11}]^-$ anion is so eminently suited to stabilize unusual, highly electrophilic cations by weak, secondary interionic SbF--CO contacts. Moreover, additional homoleptic metal carbonyl cations like $[M(CO)_4]^{2+}$ (8), M = Pd and Pt, and $[M(CO)_6]^{2+}$ (9), M = Ru or Os, have $[Sb_2F_{11}]^-$ as counter anion.

The synthesis of $[Au(PF_3)_2][Sb_2F_{11}]$ is readily accomplished by the displacement of CO by PF_3 using a slight excess of gaseous PF_3 according to:

$$[1]\quad [Au(CO)_2][Sb_2F_{11}]_{(s)} + 2\,PF_{3\,(g)} \xrightarrow{25°C} [Au(PF_3)_2][Sb_2F_{11}] + 2\,CO_{(g)}$$

Received March 13, 1996.

This paper is dedicated to Professor Howard C. Clark in recognition of his contributions to Canadian chemistry.

B. Bley, M. Bodenbinder, G. Balzer, and H. Willner.[1] Institut für Anorganische Chemie der Universität Hannover, Callinstr. 9, D-30167 Hannover, Germany.
G. Hägele. Institut für Anorganische Chemie und Strukturchemie, Heinrich-Heine-Universität, Universitätsstr. 1, D-40225 Düsseldorf, Germany.
F. Mistry and F. Aubke.[1] Department of Chemistry, The University of British Columbia, Vancouver, BC V6T 1Z1, Canada.

[1] Authors to whom correspondence may be addressed. Telephone: 011-49-511-762 2401 (H.W.), (604) 822 3817 (F.A.); Fax: 011-49-511-762 3006 (H.W.), (604) 822 2847 (F.A.); E-mail: willner@mbox.acc.uni-hannover.de and aubke@chem.ubc

The white, moisture-sensitive product decomposes at 105°C in a N_2 atmosphere. The composition is established by the mass balance of the reaction, by PF_3 uptake measurements, and by the identification of CO by IR in the gas phase after displacement. The substitution of CO by CH_3CN to give $[Au(CH_3CN)_2][SbF_6]$ (6) provides a precedent. In $[Au(CO)_2]^+$, where CO is predominantly a σ-donor ligand, displacement by a better σ-donor is possible. Hence substitution of CO by PF_3 suggests that PF_3 is a better σ-donor towards univalent gold then is CO. An alternative approach starts from $Au(SO_3F)_3$ dissolved in HSO_3F and allows the in situ generation of the $[Au(PF_3)_2]^+$ cation according to:

$$[2]\quad Au(SO_3F)_3 + 3\ PF_3 \xrightarrow{HSO_3F,25°C} [Au(PF_3)_2]^+_{(solv)} + OPF_3 + S_2O_5F_2 + SO_3F^-_{(solv)}$$

The cation and the products of the reduction, OPF_3 and $S_2O_5F_2$, are detected in the ^{19}F and ^{31}P NMR spectra. The volatile compounds OPF_3 and $S_2O_5F_2$ are also detected by gas phase IR. Hence the formation of solvated $[Au(PF_3)_2]^+$ in HSO_3F proceeds in complete analogy to the reported reductive carbonylation of $Au(SO_3F)_3$ to produce $[Au(CO)_2]^+_{(solv)}$ (10).

The observed vibrational bands of $[Au(PF_3)_2][Sb_2F_{11}]$ are listed in Table 1, together with estimated intensities, an approximate description of the vibrational modes, and the previously reported fundamentals for free PF_3 (11). Bands attributed to the $[Sb_2F_{11}]^-$ anion are observed in similar positions in both IR and Raman spectra, as was reported for $[Au(CO)_2][Sb_2F_{11}]$ (6).

For $[Au(PF_3)_2]^+$ the partial coincidence of bands in the IR and Raman spectrum, most noticeable in the P–F stretching range at 963–974 cm^{-1}, would suggest a linear cation with eclipsed PF_3 groups (point group D_{3h}) rather than D_{3d} where the PF_3 groups are staggered. A clear distinction between both possibilities cannot be made using vibrational data. A complete assignment of bands will have to await a molecular structure determination and successful depolarization measurements on $[Au(PF_3)_2]^+_{(solv)}$.

The $\bar{\nu}$ (PF_3) modes are clearly separated from bands due to the anion and are easily identified. In $[Au(PF_3)_2]^+$, $\bar{\nu}$ (PF_3) vibrations are shifted to higher wave numbers relative to free PF_3 (11). This shift, previously attributed to reduced M to PF_3 π-back-bonding (4, 5), is even more pronounced than in $[Ag(PF_3)]^+$ (4), $[Hg_2(PF_3)_n]^{2+}$, $n = 1$ or 2 (4), or in $[Cu(PF_3)]^+$ (5), all with $[AsF_6]^-$ as anion. Since in metal–PF_3 complexes the π-acceptor orbital on the ligand has some antibonding character (3), a reduction in π-back-bonding results in increased P—F bond strength. The implication for $[Au(PF_3)_2]^+$ is that metal–ligand bonding as in $[Au(CO)_2]^+$ (6) involves predominantly σ-bonds. The ability of univalent gold to form strong covalent σ-bonds, resulting largely in linear complexes, is well documented (12), and seemingly aided by relativistic effects (13).

For NMR measurements in solution, two different samples are employed. In sample 1, solid $[Au(PF_3)_2][Sb_2F_{11}]$ is dissolved in SO_2. In sample 2 the $[Au(PF_3)_2]^+$ cation is generated in HSO_3F by reduction of $Au(SO_3F)_3$ with PF_3. In the second sample, HSO_3F together with SO_3F^- (14), uncoordinated PF_3 (4), and the reduction products $S_2O_5F_2$ (14) and OPF_3 (15) are identified by comparison to published precedents. Broad resonances in the ^{19}F spectrum of sample 1 at −90.6 (F br.), −110.1 (F eq.), and −132.0 ppm (F ax.) are attributed to the $[Sb_2F_{11}]^-$ anion (15).

Table 1. Vibrational wave numbers (cm^{-1}) of $[Au(PF_3)_2][Sb_2F_{11}]$ and an approximate band description.

IR	Raman	PF_3	Description of mode
	991 (w)		
		892	
974 (vs)	974 (w)		
966 (s,sh)	963 (m)		ν(PF_3)
		860	
927 (sh)			
915 (vs)			
697 (sh)	692 (m)		
685 (vs)			
659 (s)			ν($Sb_2F_{11}^-$)
	651 (s)		
597 (w)	598 (m)		
	540 (w)		
		487	δ(PF_3)
532 (w)			
512 (sh)			
503 (m)			ν($Sb_2F_{11}^-$)
490 (w)			
381 (s)	376 (vw)		
		344	δ(PF_3)
	296 (m)		
283 (vs)			δ($Sb_2F_{11}^-$)
227 (w)	231 (m)		ν(Au–P)
	202 (m)		δ($Sb_2F_{11}^-$)
173 (w)	168 (m)		ρ(PF_3)
	132 (w)		

m = medium, s = strong, sh = shoulder, v = very, w = weak.

Since ^{19}F and ^{31}P NMR spectra at room temperature exhibit rather broad, poorly resolved peaks, ^{19}F spectra are recorded at 215 K and ^{31}P NMR spectra at 225 K. The results are compiled in Table 2, together with the parameters obtained by automated analysis and spectral simulations, using the WIN-DAISY (16) method. Experimental and simulated ^{19}F and ^{31}P NMR spectra are shown in Figs. 1 and 2. The spectra of the species present in SO_2 and HSO_3F solution are identical and the species is clearly identified as $[Au(PF_3)_2]^+_{(solv)}$. The observed splitting pattern is consistent with a $[AX_3]_2$ spin system. The coupling constant $^1J_{PF}$ is with −1414.6 Hz (at 215 K) slightly larger than in free PF_3 in SO_2 solution (−1403 Hz). This suggests, according to observations reported for $[Ag(PF_3)]^+$ and $[Hg_2(PF_3)]^{2+}$ (4), reduced metal to PF_3 π-back-donation. In neutral metal PF_3 compounds $^1J_{PF}$ values are smaller and fall between −1230 and −1350 Hz (3). Finally, the rather large $^2J_{PP}$ value of 922.7 Hz (at 215 K) is consistent with a *trans* geometry in $[Au(PF_3)_2]^+$, because *cis* complexes such as, for example, $Mo(CO)_4(PF_3)_2$ have much smaller values of 55 Hz (17). It is interesting to note that the long-range coupling constant $^4J_{FF}$, which has significant influence on the spectral theory of $[AX_3]_2$ systems, is not zero but between −1.8 Hz (from ^{19}F NMR) and −0.7 Hz (from ^{31}P NMR), respectively.

In summary, $[Au(PF_3)_2]^+$, the first example of a linear, ther-

Table 2. ^{19}F and ^{31}P NMR parameters of the linear cation $[Au(PF_3)_2]^+$. Results from automated analysis of the $[AX_3]_2$ spectra using WIN-DAISY.

Sample	$[Au(PF_3)_2][Sb_2F_{11}]^a$		$[Au(PF_3)_2][SO_3F]^b$	
Solvent	SO_2		HSO_3F	
Temperature	215 K	225 K	215 K	225 K
Observed	^{19}F	^{31}P	^{19}F	^{31}P
δ_F (ppm)	−39.7	—	−42.5	—
δ_P (ppm)	—	126.7	—	125.5
$^1J_{PF}$ (Hz)	c	c	−1414.6	−1412.8
$^3J_{PF}$ (Hz)	c	c	55.0	53.3
$^4J_{FF}$ (Hz)	c	c	−1.8	−0.7
$^2J_{PP}$ (Hz)	c	c	922.7	921.6

References: ^{19}F: ext. $CFCl_3$ in $CDCl_3$ at 215 K, ^{31}P: ext. 85% H_3PO_4 at 298 K.

[a] $[Sb_2F_{11}]^-$, δ_F (ppm): −90.6 (bridging F); −110.1 (eq. F); −123.0 (ax. F).

[b] $[SO_3F^-]/HSO_3F$, δ_F (ppm): 40.3.

[c] No iteration performed. Spectral patterns and coupling constants are identical with data obtained from $[Au(PF_3)_2][SO_3F]$ in HSO_3F.

Fig. 1. 188.3 MHz ^{19}F NMR spectrum of $[Au(PF_3)_2]^+$, dissolved in HSO_3F, at 215 K. Upper: experimental, lower: simulated spectrum. Resonance frequencies (Hz) referenced vs. ext. $CFCl_3$ in $CDCl_3$.

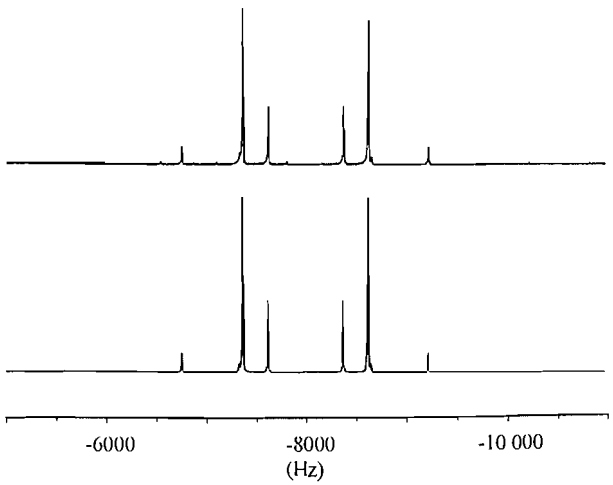

mally stable metal–bis(PF_3) complex, is obtained either in HSO_3F or SO_2 solution, or as solid material in $[Au(PF_3)_2][Sb_2F_{11}]$. As in $[Au(CO)_2]^+$ (6, 10), the metal–ligand bonds in $[Au(PF_3)_2]^+$ are predominantly σ-bonds. Both cations are 14-e$^-$ species and violate the noble gas formalism. The formation of $[Au(PF_3)_2]^+_{(solv)}$ in HSO_3F by reduction of $Au(SO_3F)_3$ with PF_3 is unusual and proceeds in analogy to the formation of $[Au(CO)_2]_{(solv)}$, with PF_3 replacing CO both as reducing agent and as ligand. It is hoped that $[Au(PF_3)_2]^+$ will be the first member of a new class of thermally stable, homoleptic $[M(PF_3)_n]^{m+}$ cations.

Acknowledgement

Financial support by the Deutsche Forschungsgemeinschaft (DFG) (to H.W. and G.H.), the Natural Sciences and Engineering Research Council of Canada (NSERC) (to F.A.), NATO (to H.W. and F.A.), Fonds der Chemischen Industrie (to B.B.), and the A. v. Humboldt Foundation (to F.A.) is gratefully acknowledged.

Fig. 2. 81 MHz ^{31}P NMR spectrum of $[Au(PF_3)_2]^+$, dissolved in HSO_3F, at 225 K. Upper: experimental, lower: simulated spectrum. Resonance frequencies (Hz) referenced vs. ext. 85% H_3PO_4.

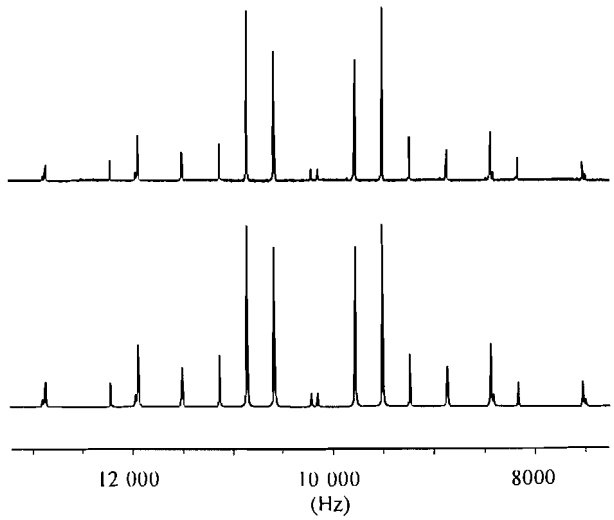

References

1. Th. Kruck. Angew. Chem. **79**, 27 (1967).
2. J.F. Nixon. Adv. Inorg. Chem. Radiochem. **13**, 363 (1970).
3. J.F. Nixon. Adv. Inorg. Chem. Radiochem. **29**, 41 (1985).
4. P.A.W. Dean and D.G. Ibbott. Can. J. Chem. **54**, 177 (1976).
5. C.D. Desjardins, D.B. Edwards, and J. Passmore. Can. J. Chem. **57**, 2714 (1979).
6. H. Willner, J. Schaebs, G. Hwang, F. Mistry, R. Jones, J. Trotter, and F. Aubke. J. Am. Chem. Soc. **114**, 8972 (1992).
7. M. Bodenbinder, G. Balzer-Jöllenbeck, H. Willner, R.J. Batchelor, F.W.B. Einstein, and F. Aubke. Inorg. Chem. **36**, 82 (1996).
8. G. Hwang, C. Wang, F. Aubke, M. Bodenbinder, and H. Willner. Can. J. Chem. **71**, 1532 (1993).
9. C. Wang, B. Bley, G. Balzer-Jöllenbeck, A.R. Lewis, S.C. Siu, H. Willner, and F. Aubke. J. Chem. Soc. Chem. Commun. 2071 (1995).
10. H. Willner and F. Aubke. Inorg. Chem. **29**, 2195 (1990).
11. K. Nakamoto. Infrared spectra of inorganic and coordination compounds. 3rd ed. John Wiley and Sons, New York. 1970. p. 124.
12. (*a*) R.J. Puddephatt. The chemistry of gold. Elsevier, Amsterdam. 1978; (*b*) *In* Comprehensive coordination chemistry. Vol. 7. *Edited by* G. Wilkinson. Pergamon Press, Oxford. 1987. p. 861.
13. (*a*) P. Pyykkö. Chem. Rev. **88**, 563 (1988), and references therein; (*b*) P. Schwerdtfeger. J. Am. Chem. Soc. **111**, 7261 (1989).
14. W.V. Cicha, F.G. Herring, and F. Aubke. Can. J. Chem. **68**, 102 (1990).
15. S. Berger, S. Braun, and H.-O. Kalinowski. NMR-Spektroskopie von Nichtmetallen. Vol. 3, p. 69, and Vol. 4, p. 86. Thieme, Stuttgart. 1994.
16. U. Weber, R. Spiske, H.W. Höffken, G. Hägele, and H. Thiele. WIN-DAISY: WIN-DAISY manual, Bruker. 1993.
17. J.F. Nixon. J. Fluorine Chem. **3**, 179 (1973).

1996 Bader Award Lecture
Aminoacyl ethyl phosphates. Biomimetically activated amino acids[1]

Ronald Kluger, Xianfeng Li, and Richard W. Loo

Abstract: Aminoacyl ethyl phosphates are functional analogues of aminoacyl adenylates, the activated intermediates formed by ribosomal enzymes from the reaction of amino acids with ATP. The aminoacyl ethyl phosphates are prepared by DCC-mediated coupling of a tetraalkylammonium salt of ethyl phosphate and an *N*-*t*-Boc-amino acid, followed by deprotection. The efficiency of the synthesis and the solubility properties of the product depend on the alkyl group in the ammonium counterion of the phosphate. *N*-Protected and free aminoacyl ethyl phosphates hydrolyze slowly ($t_{1/2}$ in neutral solution, 25°C, ~100 h). These materials are potentially useful in biomimetic peptide synthesis, protein modification, and aminoacylation of RNA.

Key words: amino acids, acyl phosphates, aminoacyl phosphates, biomimetic aminoacylation.

Résumé : Les éthylphosphates d'aminoacyles sont des analogues fonctionnels des adénylates d'aminoacyles, les intermédiaires activés formés par les enzymes ribosomaux par réaction des acides aminés avec l'ATP. Les éthylphosphates d'aminoacyle se préparent par le couplage, sous l'action du DCC, d'un sel tétraalkylammonium de l'éthylphosphate et d'un acide *N*-*t*-Boc-aminé, suivi d'une déprotection. L'efficacité de la synthèse et la solubilité du produit dépendent de la nature du groupe alkyle du contreion ammonium du phosphate. Les éthylphosphates portant des groupes aminoacyles libres ou *N*-protégés s'hydrolysent lentement ($t_{1/2}$, en solution neutre, 25°C, est d'environ 100 h). Ces produits présentent un intérêt potentiel dans les synthèses biomimétiques des peptides, dans la modification des protéines ainsi que dans l'aminoacétylation de l'ARN.

Mots clés : acides aminés, phosphates d'acyles, phosphates d'aminoacyles, aminoacétylation biomimétique.

The formation of peptides and proteins from amino acids is a central biosynthetic process in all living systems. Each amino acid that is added to the growing peptide does so against inherently large thermodynamic and kinetic barriers, following the sequence specified by the bases of DNA. In this process, the carboxyl portion of the amino acid is chemically activated, overcoming the thermodynamic barrier and kinetic pathway by formation of a suitable intermediate (1). In most organisms, including all eukaryotes, this is accomplished in reactions promoted by aminoacyl *t*-RNA synthetases (one for each of the types of amino acid) (1, 2). The specific amino acid is added to the appropriate *t*-RNA to form a 3′-terminal ester, providing the amino acid with a nucleic acid-coded "tag."

The initial step in the process catalyzed by the synthetase is activation of the specified amino acid by reaction with ATP to form the aminoacyl adenylate. ATP undergoes a substitution reaction at its α-phosphorus to produce the 5′-adenosyl ester of the acyl phosphate of amino acid, an aminoacyl adenylate, along with inorganic pyrophosphate. The aminoacyl adenylates are enzymic reaction intermediates, reacting on the same enzyme with the appropriate tRNA to form an aminoacyl *t*RNA (1).

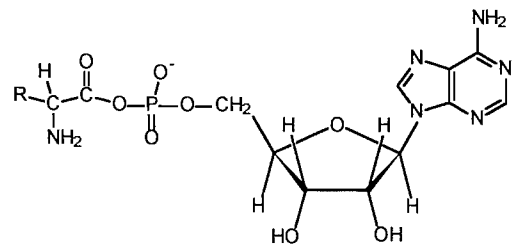

Aminoacyl adenylate

Aminoacyl adenylates are acyl phosphate monoesters and their reactions occur at the acyl phosphate functional site. The adenosine portion of the molecule adds chemical complexity and is a direct result of the enzymic reaction of ATP with the amino acid. Since the aminoacyl adenylates are intermediates in the enzymic reaction and do not accumulate, chemical characterization required their synthesis. The presence of the adenosyl group caused considerable difficulty and resulted in impure materials (3–6). However, the general properties and their validity as intermediates were established by these studies.

As mixed anhydrides of amino acids and phosphate esters, the materials are of interest for chemical study. They are acti-

Received August 8, 1996.

R. Kluger,[2] X. Li, and R.W. Loo. Department of Chemistry, University of Toronto, 80 St. George Street, Toronto, ON M5S 3H6, Canada.

[1] This paper expands upon a portion of the Alfred Bader Award Lecture presented by Ronald Kluger at the Annual Conference of the Canadian Society for Chemistry in St. John's, Newfoundland, June 1996.

[2] Author to whom correspondence may be addressed. Telephone and Fax: (416) 978-3582. E-mail: rkluger@alchemy.chem.utoronto.ca

vated amino acids, presenting the possibility of aminoacylating various acceptors under conditions that are compatible with biochemical materials. However, the complexity arising from the adenosine portion has made their synthesis inefficient. While this group has many sites for binding to a protein, the inherent reactions it undergoes should be found in materials with less complex alkyl groups. Based on these considerations, we reasoned that simpler monoesters of aminoacyl phosphates might retain the potentially chemically useful properties of aminoacyl adenylates while avoiding the complexity that arises from the adenosyl group.

The reported syntheses of aminoacyl adenylates utilize the reaction of 5′-adenylic acid with acyl chlorides, mixed carboxylic anhydrides, or DCC-activated amino acids (4, 6, 7). Berg's pioneering synthesis used free amino acids (3), giving the product in very low yield. The use of *N*-protected amino acids gives improved yields (4, 6).

We found no reports of the isolation of simple aminoacyl alkyl phosphates. In an early study, Chantrenne proposed that *Z*-glycyl phenyl phosphate was present in the reaction of *Z*-glycyl chloride and disilver phenyl phosphate (8).

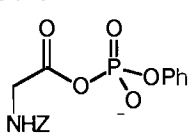

Katchalsky and Paecht (9) used an extension of Lynen's acyl phosphate synthesis (10) to make an aminoacyl aryl phosphate. They reacted the silver salt of *Z*-leucine with dibenzyl phosphorochloridate and removed the protecting groups with HBr. The resulting leucyl phosphate contained benzyl bromide that could not be removed without destroying the acyl phosphate.

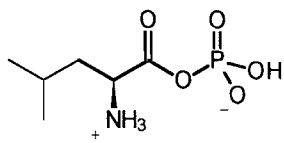

Leucyl phosphate

Based on the reaction patterns of acyl phosphate esters (11, 12) and properties of amino protecting groups (13) we have now achieved a convenient synthesis of aminoacyl ethyl phosphates. We made a diverse group of examples and assessed their properties. The general structure is shown below. Variation occurs in the "R" group that defines the amino acid and the "R"' group of the tetralkylammonium ion.

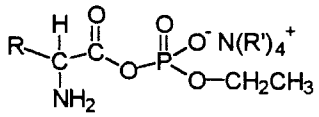

Aminoacyl ethyl phosphate

Experimental section

Synthesis of aminoacyl ethyl phosphates

These were prepared as a variety of tetralkylammonium salts whose properties were assessed. The materials are in general hygroscopic and give inconsistent results in elemental analysis. However, they are readily analyzed by a combination of NMR (^{1}H, ^{31}P), mass spectrometry, and HPLC. NMR chemical shifts are reported relative to tetramethyl silane (^{1}H) and 85% phosphoric acid (^{31}P).

Bis(tetraalkylammonium) ethyl phosphates

Ethyl dichlorophosphate (5.9 mL, 50 mmol) was added (over 10 min) to 20 mL of water in an ice-cooled round-bottom flask and stirred for 1 h. The water was removed on a rotary evaporator. To the residue was added two equivalents of a tetraalkylammonium hydroxide solution. After titration to pH 7.0 with hydrochloric acid, the resulting solution was lyophilized to yield a white paste that was used for coupling reactions without further purification. ^{31}P NMR spectra indicated that only a single compound was present.

Bis(tetramethylammonium) ethyl phosphate: ^{1}H NMR (D_2O) δ: 3.70 (2H, m), 3.00 (24H, s), 1.04 (2H, t); ^{31}P NMR (D_2O) δ: 1.68. *Bis(tetraethylammonium) ethyl phosphate:* ^{1}H NMR (D_2O) δ: 3.74 (2H, m), 2.98 (16H, t), 1.07 (3H, t), 0.74 (24H, t); ^{31}P NMR (D_2O) δ: 1.68. *Bis(tetrapropylammonium) ethyl phosphate:* ^{1}H NMR (D_2O) δ: 3.74 (2H, m), 2.98 (16H, t), 1.55 (16H, m), 1.07 (3H, t), 0.74 (24H, t); ^{31}P NMR (D_2O) δ: 1.68. *Bis(tetrabutylammonium) ethyl phosphate:* ^{1}H NMR (D_2O) δ: 3.63 (2H, m), 2.97 (16H, t), 1.42 (16H, m), 1.13 (16H, m), 1.00 (3H, t), 0.72 (24H, t); ^{31}P NMR (D_2O) δ:1.68.

Synthesis of tetraethylammonium salts of *N*-protected aminoacyl ethyl phosphates

Dicyclohexylcarbodiimide (1.0 mmol) was added to a stirred solution of an *N*-protected amino acid (1.2 mmol) in dry dichloromethane (20 mL). The resulting solution (cloudy) was stirred for 5 min, then bis(tetraethylammonium) ethyl phosphate (1 mmol), dissolved in 5 mL of dichloromethane, was added. ^{31}P NMR was used to follow the reaction. Upon completion, the resulting white suspension was collected by filtration and washed with 10 mL dichloromethane. The clear dichloromethane solution was then washed twice with water and the aqueous phase was collected, frozen, and lyophilized overnight to give a white paste. The paste was dissolved in acetone (5 mL) and the mixture was passed through a silica Sep-pak cartridge to remove inorganic salts. The eluent was evaporated to give the *N*-protected aminoacyl ethyl phosphate as a glassy material. The following compounds were prepared from the reaction of an *N*-protected amino acid and bis(tetraethylammonium) ethyl phosphate. Each product gave a single peak in reverse phase HPLC analysis as well as appropriate NMR and mass spectral results. The first example contains full details.

Tetraethylammonium N-t-*Boc phenylalanyl ethyl phosphate*

To a stirred solution of *N*-(*tert*-butoxycarbonyl)-L-phenylalanine (318 mg, 1.2 mmol) in dry dichloromethane (20 mL) was added DCC (247 mg, 1.2 mmol). The resulting white cloudy solution was stirred for 5 min and tetraethylammonium ethyl phosphate (385 mg, 1.0 mmol) dissolved in 5 mL of dichloromethane was added. The reaction was stirred at room temperature for 1 h. After the reaction was complete, the resulting white suspension was filtered and washed with 10 mL of dichloromethane. The clear dichloromethane solution was then washed twice with water and the aqueous phase was collected. The aqueous solution was frozen and lyophilized over-

night to give a white solid. The solid was dissolved in 5 mL of acetone and the mixture was passed through a silica Sep-pak cartridge to remove inorganic salts. The eluent was evaporated to give *N-t*-Boc phenylalanyl ethyl phosphate as a glassy material (453 mg, 87%). ^{1}H NMR ($CDCl_3$) δ: 7.23 (5H, m), 5.03 (1H, d), 4.56 (1H, m), 4.03 (2H, m), 3.37 (8H, q), 3.20 (2H, m), 1.38 (9H, s), 1.30 (12H, t), 1.24 (3H, t); ^{31}P NMR ($CDCl_3$) δ: −6.8; FAB mass spectrum (–, glycerol): 125 (100, $EtHPO_4^-$), 372 (51.4, M). Other derivatives were made by the same general procedure.

Tetraethylammonium N-t-*Boc alanyl ethyl phosphate:* (73% yield) ^{1}H NMR ($CDCl_3$) δ: 5.17 (1H, d), 4.24 (1H, m), 4.00 (2H, m), 3.38 (8H, q), 1.40 (9H, s), 1.36 (3H, d), 1.32 (12H, t), 1.22 (3H, t); ^{31}P NMR ($CDCl_3$) δ: −6.8; FAB mass spectrum (–, glycerol): 296 (100, M).

Tetraethylammonium N-t-*Boc*-O-*Bn serinyl ethyl phosphate:* (58% yield) ^{1}H NMR ($CDCl_3$) δ: 7.30 (5H, m), 5.42 (1H, d), 4.52 (2H, s), 4.42 (1H, m), 3.98 (2H, m), 3.80 (2H, m), 3.35 (8H, q), 1.41 (9H, s), 1.28 (12H, t), 1.18 (3H, t); ^{31}P NMR ($CDCl_3$) δ: −7.1; FAB MS (–, glycerol): 402 (95.5, M).

Tetraethylammonium N-t-*Boc*-S-B*n cysteinyl ethyl phosphate:* (76% yield) ^{1}H NMR ($CDCl_3$) δ: 7.28 (5H, m), 5.40 (1H, d), 4.52 (1H, m), 4.02 (2H, m), 3.78 (2H, s), 3.38 (8H, q), 2.93 (2H, m), 1.42 (9H, s), 1.30 (12H, t), 1.25 (3H, t); ^{31}P NMR ($CDCl_3$) δ: −6.9; FAB mass spectrum (–, glycerol): 418 (100, M).

Tetraethylammonium N-t-*Boc valyl ethyl phosphate:* (72% yield) ^{1}H NMR ($CDCl_3$) δ: 5.14 (1H, d), 4.17 (1H, m), 4.00 (2H, m), 3.38 (8H, q), 2.18 (1H, m), 1.40 (9H, s), 1.32 (12H, t), 1.22 (3H, t), 0.91 (6H, dd); ^{31}P NMR ($CDCl_3$) δ: −7.7; FAB mass spectrum (–, glycerol): 324 (100, M).

Tetraethylammonium N-t-*Boc tryptophanyl ethyl phosphate:* (85% yield) ^{1}H NMR ($CDCl_3$) δ: 6.90–7.60 (6H, m), 5.01 (1H, d), 4.62 (1H, m), 4.08 (2H, m), 3.36 (2H, m), 3.05 (8H, q), 1.39 (9H, s), 1.29 (3H, t), 1.10 (12H, t); ^{31}P NMR ($CDCl_3$) δ: −7.7; FAB mass spectrum (–, glycerol): 411 (100, M).

Hydrolysis

The rate of hydrolysis of *N-t*-Boc phenylalanyl ethyl phosphate was measured using ^{31}P NMR. *N-t*-Boc phenylalanyl ethyl phosphate (0.04 M) was incubated in 1 mL of 0.5 M 3-(*N*-morpholino])propanesulfonate (MOPS) pH 7.0, at 25.0°C. The hydrolysis was followed by integrating signals for the aminoacyl phosphate ester (δ −6.6 ppm) and the product, ethyl phosphate (δ 2.8 ppm). The hydrolysis was monitored to 90% completion.

General procedure for the deprotection of *N-t*-Boc protected aminoacyl phosphates

The *N-t*-Boc protected aminoacyl alkyl phosphate was dissolved in a minimum amount of trifluoroacetic acid (TFA). After the dissipation of gases, the TFA was removed by rotary evaporation (30°C) and vacuum pumping. The resulting oil was dissolved in acetone or diethyl ether. The resulting precipitate was then collected by vacuum filtration and washed several times with acetone or diethyl ether. After air drying for 10 min aminoacyl alkyl phosphate was isolated.

(l)-*Alanyl ethyl phosphate*
White solid; mp 120°C (dec.); $[\theta] = +2.9 \times 10^3$ deg cm^2 decimol^{-1} (λ_{max} = 216.5 nm); IR (KBr): 1764, 1623, 1574, 1251, 1230, 1075, 1047 cm^{-1}; ^{1}H NMR (400 MHz, D_2O) δ: 1.20 (t, 3H, J = 7.1 Hz), 1.53 (d, 3H, J = 7.3 Hz), 3.98 (m, 2H), 4.19 (q, 1H, J = 7.3 Hz); ^{13}C NMR (100 MHz, D_2O) δ: 15.71, 16.30 (d, J_{C-P} = 6.6 Hz), 50.01 (d, J_{C-P} = 7.3 Hz), 64.83 (d, J_{C-P} = 5.8 Hz), 167.92 (d, J_{C-P} = 8.8 Hz); ^{31}P NMR (121 MHz, D_2O) δ: −6.58. FAB MS calcd.: 197; found (*m/z*): 196 $(M - H)^-$, 170 $(M - Et)^+$. TLC: R_f = 0.44, red-brown spot.

(l)-*Phenylalanyl ethyl phosphate*
White solid; mp 133°C (dec.); $[\theta] = +1.1 \times 10^4$ deg cm^2 decimol^{-1} (λ_{max} = 220.0 nm); IR (KBr): 1764, 1567, 1237, 1082, 1040 cm^{-1}; ^{1}H NMR (400 MHz, D_2O) δ: 1.07 (t, 3H, J = 7.1 Hz), 3.12 (dd, 2H, J = 7.4, 14.7 Hz), 3.21 (dd, 2H, J = 6.3, 14.7 Hz), 3.79 (m, 2H), 4.33 (dd, 1H, J = 6.3, 7.4 Hz), 7.26–7.41 (m, 5H); ^{13}C NMR (100 MHz, D_2O) δ: 16.33 (d, J_{C-P} = 6.6 Hz), 36.16, 55.25 (d, J_{C-P} = 8.1 Hz), 64.83 (d, J_{C-P} = 6.4 Hz), 128.87, 130.03, 130.19, 134.26, 166.80 (d, J_{C-P} = 8.1 Hz); ^{31}P NMR (121 MHz, D_2O) δ: −6.80. FAB MS calcd.: 273, found (*m/z*): 272 $(M - H)^-$, 274 $(M + H)^+$, 246 (M − Et). TLC: R_f = 0.66, purple spot. HPLC: retention time = 4.5 min.

(d)-*Phenylalanyl ethyl phosphate*
Identical ^{1}H and ^{31}P NMR to (l)-phenylalanyl ethyl phosphate. $[\theta] = -1.1 \times 10^4$ deg cm^2 decimol^{-1} (λ_{max} = 220.0 nm).

(l)-*Valyl ethyl phosphate*
White solid; mp 160°C (dec.); $[\theta] = 4.6 \times 10^3$ deg cm^2 decimol^{-1} (λ_{max} = 218.5 nm); IR (KBr): 1766, 1612, 1572, 1280, 1239, 1081, 1041 cm^{-1}; ^{1}H NMR (400 MHz, D_2O) δ: 0.90 (d, 3H, J = 4.4 Hz), 0.91 (d, 3H, J = 4.4 Hz), 1.10 (t, 3H, J = 7.3 Hz), 2.24 (m, 1H), 3.88 (m, 2H), 3.93 (d, 1H, J = 4.4 Hz); ^{13}C NMR (100 MHz, D_2O) δ: 16.33 (d, J_{C-P} = 6.6 Hz), 17.81, 18.07, 29.97, 59.50 (d, J_{C-P} = 7.3 Hz), 64.80 (d, J_{C-P} = 6.6 Hz), 167.05 (d, J_{C-P} = 8.8 Hz); ^{31}P NMR (121 MHz, D_2O) δ: −6.76. FAB MS calcd.: 225; found (*m/z*): 224 $(M - H)^-$, 226 $(M + H)^+$, 198 $(M - Et)^+$.

O-*Benzyl*-(l)-*seryl ethyl phosphate*
White solid; ^{1}H NMR (200 MHz, D_2O) δ: 1.11 (t, 3H, J = 6.9 Hz), 3.79–3.97 (m, 4H), 4.35 (m, 1H), 4.53–4.55 (m, 2H), 7.33 (m, 5H); ^{31}P NMR (121 MHz, D_2O) δ: −6.83.

(l)-*Tryptophanyl ethyl phosphate*
Light yellow solid; ^{1}H NMR (200 MHz, D_2O) δ: 1.14 (t, 3H, J = 7.1 Hz), 3.41 (m, 2H), 3.84 (m, 2H), 4.49 (m, 1H), 7.18 (m, 2H), 7.29 (s, 1H), 7.47 (d, 1H, J = 7.5 Hz), 7.64 (d, 1H, J = 7.0 Hz); ^{31}P NMR (121 MHz, D_2O) δ: −6.74.

β-*Alanyl ethyl phosphate*
White solid; ^{1}H NMR (200 MHz, D_2O) δ: 1.20 (t, 3H, J = 7.0 Hz), 1.8 (m, 2H), 2.80 (m, 2H), 3.95 (m, 2H); ^{31}P NMR (121 MHz, D_2O) δ: −6.51.

α-*Methylalanyl ethyl phosphate*
White solid; ^{1}H NMR (200 MHz, D_2O) δ: 1.13 (t, 3H, J = 7.0 Hz), 1.51 (s, 6H), 3.92 (m, 2H); ^{31}P NMR (121 MHz, D_2O) δ: −6.35.

Scheme 1.

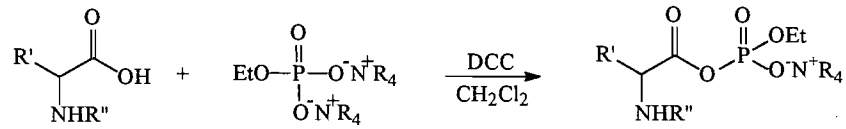

Table 1. Aminoacyl phosphates synthesized from *N-t*-Boc-phenylalanine and bis(tetraalkylammonium) ethyl phosphates and their solvent affinities.

Alkyl group R	Reaction time, h	% Yield (±5%)[a]	Solvent
Methyl	3.0	55[b]	H_2O
Ethyl	1.0	95	H_2O
n-Propyl	1.0	95	Dichloromethane–H_2O
n-Butyl	1.0	95	Dichloromethane

[a]Determined from ^{31}P NMR spectra of reaction mixtures except for reactions with bis(tetramethylammonium) ethyl phosphate.
[b]Determined from ^{31}P NMR spectra of an aqueous extract of the reaction mixture.

Detection of racemization

The retention of chiral integrity in the aminoacyl phosphate during the coupling reaction was determined by first removing the protecting group and then hydrolyzing the resulting aminoacyl phosphate. The resulting amino acid was treated with Mosher's acid chloride (14). The ^{19}F and ^{1}H NMR spectra of the amides were compared with pure standards.

Results

The preparation of aminoacyl ethyl phosphates is readily accomplished by coupling an amino-protected amino acid with a salt of ethyl phosphate, followed by removal of the protecting group. The removal is done under conditions that do not affect the acyl phosphate. Both natural L α-amino acids and "unnatural" amino acids were converted. Since acyl phosphates are unstable in base, the protecting group should be selected to permit removal in acidic solutions, principally carbobenzyloxy (Cbz) and the more readily removed *tert*-butyloxycarbonyl (*t*-Boc). Thus, we chose *t*-Boc as the protecting group for our studies.

The activation of the amino acid for formation of the acyl phosphate is best accomplished under conditions that do not lead to racemization. Reaction with *N,N'*-dicyclohexylcarbodiimide (DCC) fulfills these requirements (13). This dehydrating–coupling reagent functions most efficiently in organic solvents such as dichloromethane (15). Since phosphate salts are not normally soluble in dichloromethane, we utilized tetraalkylammonium salts of phosphates (16, 17). These dissolve in organic solvents and the phosphate oxygens are highly nucleophilic. (Scheme 1).

Results from the reaction of *N-t*-Boc-phenylalanine and various bis(tetraalkylammonium) ethyl phosphates are shown in Table 1. Except for the case of bis(tetramethylammonium) ethyl phosphate, all coupling reactions went to completion in 1 h. The reaction with bis(tetramethylammonium) phosphate gave the product in 55% yield in 3 h due to its poor solubility in dichloromethane.

The solubility of these aminoacyl phosphates depends critically upon the nature of their counterions. A longer alkyl chain increases solubility in nonpolar solvents while a shorter chain improves aqueous solubility. The effect of the nature of alkyammonium is useful for the separation and purification of the product. For bis(tetrabutylammonium) ethyl phosphate salts, the product is isolated from the organic phase while unreacted starting material is removed by an aqueous wash. *N,N'*-Dicyclohexylurea (DCU) is the by-product from DCC. For products isolated in an organic phase, most of the DCU is removed by precipitation in acetonitrile, but the product inevitably contains some DCU. Further purification of the *N*-protected aminoacyl phosphate was attempted by silica and ion exchange chromatography. However, both treatments led to some hydrolysis.

The product from the reaction of an amino acid and bis (tetrapropylammonium) ethyl phosphate partitions into both water and dichloromethane. This also gives mixtures that are difficult to purify. With tetramethylammonium or tetraethylammonium ethyl phosphates, the resulting aminoacyl phosphate is preferentially soluble in water. Therefore, a slight excess of amino acid can be used to ensure the complete conversion of the phosphate. The product is collected in the aqueous layer and isolated by freeze-drying. In this case, after removal of inorganic salts, the protected aminoacyl phosphate is obtained without contamination by DCU.

The tetraethylammonium salts of a diverse group of amino acids were efficiently converted to the corresponding tetraethylammonium salt of aminoacyl phosphates by this method (Table 2). As a test of the generality of the method, different *N*-protection groups were used, including *tert*-butyloxycarbonyl (*t*-Boc), carbobenzyloxy (Cbz), 9-fluorenylmethoxycarbonyl (Fmoc), and *N-o*-nitrophenyl sulfenyl (Nps). Completion of the reaction was checked by ^{31}P NMR of the reaction mixture. The coupling reaction was complete in 1–12 h, giving aminoacyl phosphates in 58–88% isolated yields. The *N*-Fmoc aminoacyl phosphates could not be isolated in the same way, presumably due to the hydrophobic nature of Fmoc group. We have developed alternative methods for the preparation of *N*-Fmoc aminoacyl phosphate esters (unpublished work of Z. Huang and N. Branda). However, since the protecting group is designed for removal in base, conditions

Table 2. Aminoacyl phosphates synthesized from *N*-protected amino acids and bis(tetraethylammonium) ethyl phosphate.

Amino acid	% Yield[a]	Optical rotation $[\alpha]_D^{25}$	FAB mass (calcd./found)
N-*t*-Boc-Phe	87.4	+ 21.9 (*c* 0.90, $CHCl_3$)	372.1/372.2
N-*t*-Boc-Ala	73.0	+ 1.0 (*c* 0.60, $CHCl_3$)	296.1/296.2
N-*t*-Boc-Ser(Bn)	57.9	+ 14.7 (*c* 0.76, $CHCl_3$)	402.1/402.1
N-*t*-Boc-Cys(Bn)	75.7	+ 5.8 (*c* 6.02, $CHCl_3$)	418.1/418.0
N-*t*-Boc-Val	71.9	+ 1.3 (*c* 18.5, $CHCl_3$)	324.1/324.0
N-*t*-Boc-Trp	85.0	+ 5.1 (*c* 7.65, $CHCl_3$)	411.1/411.0
N-Cbz-Ala	86.7	+ 4.4 (*c* 0.83, $CHCl_3$)	330.1/330.3
N-Cbz-Val	72.1	+ 4.3 (*c* 0.52, $CHCl_3$)	358.1/358.3
N-Fmoc-Val	95.0[b]		
N-Nps-Val	62.0	−1.1 (*c* 0.54, $CHCl_3$)	377.0/377.0

[a]Yields are from bis(tetraethylammonium) ethyl phosphate.
[b]Product not isolated, estimate from ^{31}P NMR.

that also cleave acyl phosphate, we did not generalize the development of this class.

The aminoacyl ethyl phosphates have appropriate ^1H, ^{13}C, and ^{31}P NMR spectra as well as mass spectra for the parent peak (FAB (−) with glycerol). Although carboxyl-activated amino acids are prone to racemization, we observed that the aminoacyl ethyl phosphates retain their stereochemical integrity using NMR analysis of diastereomeric amides derived from Mosher's acid (14). This is consistent with the optical activity we observe.

Stability toward hydrolysis

The utility of *N*-protected aminoacyl ethyl phosphates depends on reactions with nucleophiles proceeding more rapidly than reactions with water. *N*-*t*-Boc-phenylalanyl ethyl phosphate (0.04 M) was incubated in 1 mL of 0.5 M MOPS, pH 7.0, at 25 0°C. The reaction was followed by integrating signals for the disappearance of the starting material and the formation of ethyl phosphate in the ^{31}P NMR. The hydrolysis is slow with an observed first-order rate constant of 2×10^{-6} s^{-1}, corresponding to a half-life of about 100 h.

Removal of the *N*-*t*-Boc group from *N*-*t*-Boc-aminoacyl ethyl phosphates is readily achieved with trifluoroacetic acid under conditions that do not cleave the acyl phosphate. The resulting aminoacyl ethyl phosphate is sufficiently resistant to hydrolysis to be useful for reaction with the amino group of a free amino acid or the *N*-terminus of a growing peptide chain. The hydrolysis of phenylalanyl ethyl phosphate follows first-order kinetics, $k_{obsd} = 1.9 \times 10^{-6}$ s^{-1}. The half-life is over 100 h, indicating that these reagents do not hydrolyze rapidly in neutral solution, even if the protecting group is removed.

Acylation reactions

The biosynthesis of proteins involves the formation of the 3′-terminus ester of *t*RNA and the approproiate amino acid. Direct reaction of aminoacyl ethyl phosphate and *t*RNA in the absence of an enzyme requires that alcohols react readily with aminoacyl ethyl phosphates. Combination of isopropanol, a model for the secondary alcohol in *t*RNA, and aminoacyl ethyl phosphates gave no reaction. In fact, isopropanol is a good solvent for other reactions. Extended reaction in methanol produces the amino acid methyl ester.

We are in the process of developing catalytic systems that will enhance the reaction of alcohols with aminoacyl ethyl phosphates. We have found that divalent metal ions promote the reaction (18). In another study we found that amino-alcohols, such as triethanolamine, react at their hydroxyl centre with monoesters of acyl phosphates (19). This information may provide the basis for the development of a route to aminoacylation of RNA. We have assessed the utility of aminoacyl ethyl phosphates as activated aminoacids for the chemical synthesis of peptides in water (19). The reaction occurs efficiently and will be reported in detail in a separate paper. Preliminary studies also indicate that the reagents can serve as site-directed inactivators of enzymes that promote reactions of amino acids (Y. Song, unpublished). Such inactivation is consistent with the report that aminoacyl adenylates react with lysines in enzymes (20).

Conclusions

N-*t*-Boc-protected aminoacyl ethyl phosphates are readily prepared as their tetralkylammonium salts by DCC-mediated coupling. The reaction efficiency depends on the choice of solvent in relation to the alkyl group of the tetralkylammonium ion. Deprotection is readily achieved with trifluoroacetic acid, conditions that leave the acyl phosphate intact. The convenient preparation, hydrolytic stability, and retention of chiral integrity make these aminoacyl ethyl phosphates a new class of activated amino acids that function in aqueous solution.

Acknowledgements

Financial support of this research was provided by the Natural Sciences and Engineering Research Council of Canada through an operating grant (to Ronald Kluger) as well as by a postgraduate fellowship to Richard W. Loo. Helpful preliminary experiments were performed by Neil Branda and Zheng Huang.

References

1. T. McKee. *In* Biochemistry. William C. Brown, Co., Dubuque, Iowa. 1995. p. 536.
2. P. Schimmel. Annu. Rev. Biochem. **56**, 125 (1987).
3. P. Berg. J. Biol. Chem. **233**, 608 (1958).
4. K. Moldave, P. Castelfranco, and A. Meister. J. Biol. Chem. **234**, 841 (1959).
5. R. Lewinsohn, M. Paecht-Horowitz, and A. Katchalsky. Biochim. Biophys. Acta, **140**, 24 (1967).
6. D. W. Armstrong, R. Seguin, M. Saburi, and J.H. Fendler. J. Mol. Evol. **13**, 103 (1979).
7. J.A. DeMoss, S.M. Genuth, and G.D. Novelli. Proc. Nat. Acad. Sci. U.S.A. **42**, 325 (1956).
8. H. Chantrenne. Nature, **164**, 576 (1949).
9. A. Katchalsky and M. Paecht. J. Am. Chem. Soc. **76**, 6042 (1954).
10. F. Lynen. Chem. Ber. **73**, 367 (1940).
11. R. Kluger, A.S. Grant, S.L. Bearne, and M.R. Trachsel. J. Org. Chem. **55**, 2864 (1990).
12. G. Disabato and W.P. Jencks. J. Am. Chem. Soc. **83**, 4393 (1961).
13. M. Bodanszky, Y. Z. Klausner, and M.A. Ondetti. Peptide synthesis. 2nd ed. Wiley, New York. 1988.
14. W. Breuer and I. Ugi. J. Chem. Res. (M) , 2901 (1982).
15. H.G. Khorana and A.R. Todd. J. Chem. Soc. 2257 (1953).
16. A.B. Woodside, Z. Huang, and C.D. Poulter. Org. Synth. **66**, 211 (1988).
17. R. Kluger and Z. Huang. J. Am. Chem. Soc. **113**, 5124 (1991).
18. V. Mazza. M.Sc., University of Toronto (1996).
19. X. Li. Ph.D., University of Toronto (1996).
20. D. Kern, B. Lorber, Y. Boulanger, and R. Giege. Biochemistry, **24**, 1321 (1985).

Dihydrofurans from α-diazoketones due to facile ring opening – cyclization of donor–acceptor cyclopropane intermediates

Elizabeth A. Lund, Isaac A. Kennedy, and Alex G. Fallis

Abstract: A series of α-diazoketones, **8**, **25**, **28**, **31**, and **34**, have been synthesized and their reaction with ethyl vinyl ether examined under various reaction conditions. In the presence of metal salts ($Rh_2(OAc)_4$, $Pd(OAc)_2$, CuCl) the ethoxydihydrofurans **12**, **37**, **39**, **41**, and **43** are produced. Sensitized irradiation of the α-diazoketone **8** afforded the dihydrofuran **12** plus cyclobutanone **7**, while direct photolysis of α-diazoketones **8**, **25**, **28**, **31**, and **34** gave the cyclobutanones **7**, **38**, **40**, **42**, and **44**, respectively. A sample of the cyclopropylketone **45** was isolated from the rhodium(II) acetate mediated reaction of **34** and its facile rearrangement to dihydrofuran **43** demonstrated. Collectively, these results indicate that the initial product from the reaction of an α-diazoketone with an electron-rich alkene such as ethyl vinyl ether is a cyclopropylketone. The donnor–acceptor substitution pattern of this intermediate results in spontaneous rearrangement to a dihydrofuran. Thus a direct dipolar cycloaddition mechanism is not involved when α-diazoketones react with enol ethers under metal-mediated conditions. Instead, these reactions follow a cyclopropanation rearrangement or, more accurately, cyclopropanation – ring opening – cyclization pathway.

Key words: diazoketone, rhodium acetate, dihydrofuran, cyclopropylketone, vinyl ether.

Résumé : On a synthétisé une série d'α-diazocétones **8**, **25**, **28**, **31** et **34** et on a étudié, dans différentes conditions, leur réaction avec l'éther éthylvinylique. En présence de sels métalliques ($RH_2(OAc)_4$, $Pd(OAC)_2$, CuCl) on obtient les éthoxydihydrofurannes **12**, **37**, **39**, **41** et **43**. L'irradiation sensibilisée de l'α-diazocétones **8** produit le dihydrofuranne **12** et la cyclobutanone **7**, tandis que la photolyse directe des α-diazocétones **8**, **25**, **28**, **31** et **34** donne les cyclobutanones **7**, **38**, **40**, **42** et **44** respectivement. On a isolé un échantillon de cyclopropylcétone **45** de la réaction du composé **34** en présence de l'acétate de rhodium et on démontre sa transposition facile en dihydrofuranne **43**. Collectivement, ces résultats indiquent que le produit initial de la réaction d'une α-diazocétone avec un alcène riche en électrons tel l'éther éthylvinylique est une cyclopropylcétone. Le modèle de substitution donneur–accepteur de cet intermédiaire provient d'une transposition spontanée en dihydrofuranne. Ainsi un mécanisme de cycloaddition dipolaire directe n'est pas impliqué lorsque une α-diazocétone réagit avec des éthers énoliques en présence d'un métal. Au lieu de cela ces réactions suivent une transposition cyclopropanique ou plus précisément un processus de cyclopropanation, d'ouverture du cycle du cyclopropane et de cyclisation.

Mots clés : diazocétone, acétate de rhodium, dihydrofuranne, cyclopropylcétone, éther vinylique.

[Traduit par la rédaction]

Introduction

Motivated by our interest in the total synthesis of the potent anti-tumor agent paclitaxel (Taxol®) (1) we initially envisaged a strategy that depended upon the successful application of an α-cyclopropyl radical ring opening – conjugate addition sequence (**1**–**3**, Scheme 1) for the construction of the congested tricyclo[9.3.1.$0^{3,8}$]pentadecene nucleus. This ring opening should install both the bridgehead double bond at C_{11}—C_{12} and generate a radical center in a relatively flat precursor suitably disposed to add in an 8-*endo* fashion to a ring C enone (2). We therefore required precursors that would give rise to a radical intermediate of type **A** (Scheme 2) in order to examine this strategy.

Initial results

A variety of standard Simmons–Smith based methods for cyclopropanation of appropriately substituted olefins to generate systems related to **A** were unsuccessful. Thus a different approach was investigated. The α-diazoketone **8** was synthesized from the cyclohexenone **4** (1*d*) as follows. Conjugate addition of lithium dimethylcuprate generated the enolate, which reacted in situ with ethyl formate to provide the ketone **5**. Diazo transfer was effected with tosylazide and triethylamine followed by treatment with potassium hydroxide to generate the α-diazoketone **8**. It was anticipated that treatment of this material with rhodium(II) acetate in the presence of ethyl vinyl ether would afford the requisite spiro cyclopropyl system **9**. However, treatment of **8** with $Rh_2(OAc)_4$ (2 mol %, 21°C) in the presence of excess ethyl vinyl ether afforded neither the expected cyclopropylcyclohexanone **9** nor the cyclobutanone **7** that would have arisen from Wolff rearrangement of **8** to the ketene **10** followed by conventional [2+2] cycloaddition. Instead, a new compound was isolated, whose spectra

Received May 14, 1996.

E.A. Lund, I.A. Kennedy, and A.G. Fallis.[1] Ottawa–Carleton Chemistry Institute, Department of Chemistry, University of Ottawa, 10 Marie Curie, Ottawa, ON K1N 6N5, Canada.

[1] Author to whom correspondence may be addressed. Telephone: (613) 562-5732. FAX: (613) 562-5170. E-mail: AFALLIS@OREO.CHEM.UOTTAWA.CA

Scheme 1. Potential radical rearrangement – conjugate addition route to taxanes.

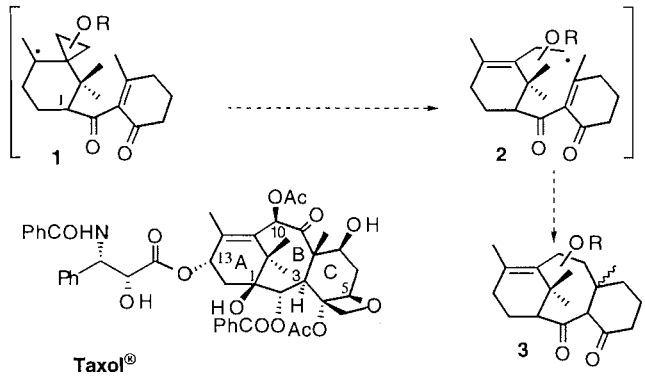

Scheme 2. Synthesis and reaction pathways for α-diazoketone **8**.

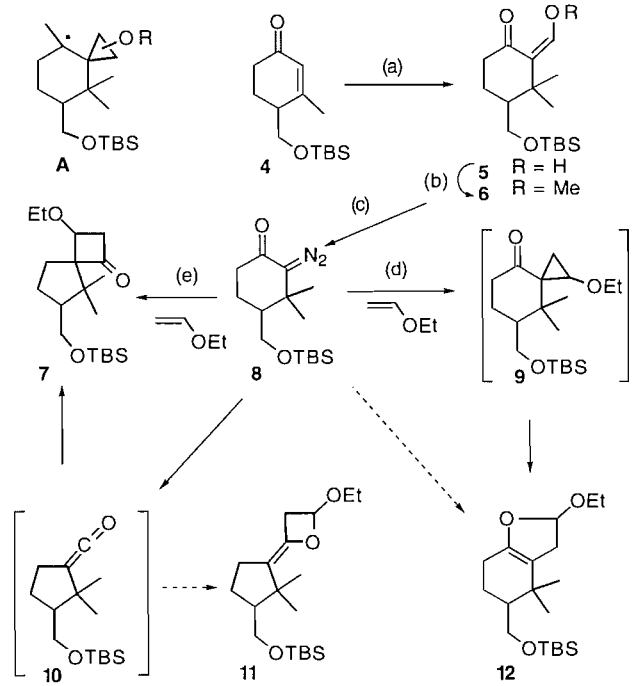

(a) Me_2CuLi, ether, 0 °C, 1.5 h, HCO_2Et, 0.5 h, 20%; (b) CH_2N_2, ether, 21 °C, 3 h, 83%; (c) Et_3N, TsN_3, CH_2Cl_2, -15 to 21 °C, 2 h; KOH (aq), 15 min; 20%; (d) $Rh_2(OAc)_4$ (cat), ether, $CH_2C{=}HOEt$, syringe pump, 21 °C, 4 h, 70%; (e) hv, $CH_2{=}CHOEt$, 2.5 h, 88%.

suggested the presence of two tertiary vinyl carbons (^{13}C NMR δ 102.4, 148.3 ppm) and an acetal carbon (δ 104.6 ppm) with an attached proton (^1H NMR δ 5.45 ppm). These features were consistent with both the oxetane structure **11** and the dihydrofuran system **12**. The oxetane could arise from the formal [2+2] addition of ethyl vinyl ether to the carbonyl group of the ketene **10**, while the dihydrofuran **12** could have been formed directly from a dipolar cycloaddition to ethyl vinyl ether or alternatively could have arisen from a ring opening – rearrangement – ring closure of the intermediate cyclopropyl ketone **9**. In spite of the visual difference between these two ring systems, various NMR experiments were inconclusive.

In addition, standard acid hydrolysis and oxidative cleavage

Scheme 3. Carbonyl-ether substituted cyclopropanes.

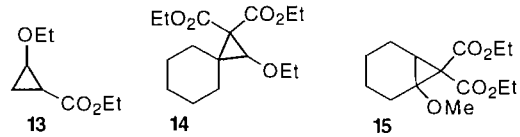

reactions (ozone, RuO_4) gave mixtures that did not permit a definitive structural assignment with only one compound available. As described below, the structures of **12** and related dihydrofurans were ultimately established by acid-catalyzed hydrolysis and in situ trapping to form a new keto-acetal. However, based on additional studies with related α-diazoketone systems, it is now clear that with electron-rich olefins such as ethyl vinyl ether, cyclopropylketones are formed initially but do not survive the standard reaction work-up at room temperature (21°C), and rapidly rearrange to dihydrofurans related to **12**. Thus, in contrast to literature examples that invoke dipolar cycloaddition mechanisms to rationalize dihydrofuran formation, with cyclopropanes containing both electron-donating and -withdrawing substituents the normal mechanism involves cyclopropanation followed by rearrangement (ring opening – cyclization) to afford the cyclic ethers (3).

Background

Donor–acceptor (push–pull) cyclopropanes have received considerable attention (4). Generally cyclopropanes with a single electron-donating and an electron-withdrawing group (e.g., 1-ethoxy-2-carboethoxycyclopropane, **13**) are stable at room temperature and require more forcing conditions for rearrangement to a dihydrofuran acetal, although cyclopropyl β-amino acids ring open readily, indicating the donating ability of the donor is a key feature (Scheme 3). Thus, for oxygen-substituted systems direct rearrangement usually requires either two donor or two acceptor groups. The ease with which the initial cyclopropane undergoes a 1,3-sigmatropic shift is therefore both substituent and substrate dependent (4). For example, the spirosystem **14** may be isolated, but the related cyclopropane **15** was not detected when dimethyl diazomalonate reacted in the presence of copper with 1-methoxycyclohexene (5). Other methoxy cyclopropanes also rearranged more readily than the corresponding ethoxy-substituted derivatives (6). However, the reaction conditions markedly influence the course of diazocarbonyl rearrangements, particularly solvent polarity (pentane versus CH_2Cl_2) (7) and the catalyst ($Rh_2(OAc)_4$ versus $Rh_2(OPiv)_4$) (8). Cyclopropanes were the presumed intermediates generated from cyclic β-diazodiketones in the presence of furans and rhodium carboxylate salts (9).

Discrete ketene carbonyl cycloadditions are rare and have received limited attention. The two previously reported cases involved strong electron-withdrawing groups in the ketene. One case involved the reaction of bis(trifluoromethyl)ketene (**16**) with vinyl ether **17** to give a mixture of the oxetane **18** and the expected [2+2] cycloaddition product **19** (Scheme 4) (10). A related example employed the sterically hindered silyl enol ether of *tert*-butyl methyl ketone (**21**) with diphenylketene (**20**) to provide the oxetane **22** and the ketone **23** from ring opening of the initial cyclobutanone adduct followed by silyl

Scheme 4. Ketene carbonyl cycloadditions.

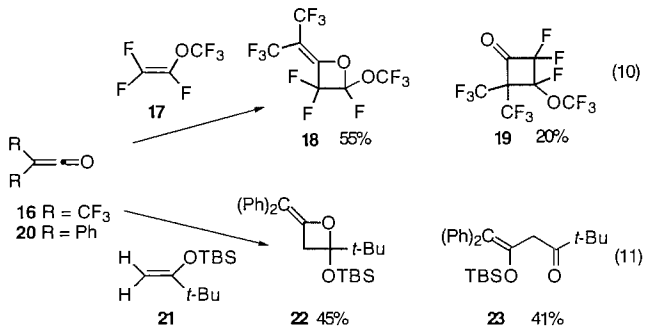

migration (11). In addition, ab initio molecular orbital calculations have demonstrated that alkene addition to the ketene carbonyl is usually energetically disfavoured relative to cyclobutanone formation (12).

Results

Is the dihydrofuran structure **12** correct, or do the methyl groups in the ketene **10**, derived from Wolff rearrangement of **8**, provide sufficient steric hindrance to alter the normal [2+2] cycloaddition reaction to give the oxetane **11** rather than the cyclobutanone **7**?

To learn more about the reactivity of the α-diazoketone **8**, other metal salts ($Pd(OAc)_2$, CuCl) were examined as well as its photolytic behaviour. In addition, other diazo ketones **25**, **28**, **31**, and **34** with various substitution patterns were synthesized (Scheme 5) and subjected to a parallel set of conditions. The initial enolate, derived from the conjugate addition of lithium dimethylcuprate to **4**, underwent rapid proton transfer to the sterically less hindered enolate when allowed to warm to 21°C, so that condensation with ethyl formate afforded the keto-aldehyde **24** directly. Diazo transfer as above generated the α-diazoketone **25**. Parallel reactions afforded **28** from **26**, while **31** was synthesized by treatment of acyl chloride **30** with diazomethane. The diphenyl system **34** (azibenzil, 2-diazo-1,2-diphenyl-1-ethanone) was prepared by silver oxide oxidation of **33** (13).

The results of the catalytic reactions and the irradiation experiments are summarized in Table 1. In the case of **8**, the major product from the metal-catalyzed reaction with ethyl vinyl ether was the dihydrofuran **12**, although the yield varied with the catalyst selected. Thus the reactions with $Pd(OAc)_2$ or CuCl afforded **12** in isolated yields of 72% and 30%, respectively. However, when standard alkenes, rather than electron-rich olefins, were used, the dihydrofuran products were not observed. Instead, cyclopropylketone **35** was isolated in 25% yield in the rhodium(II) acetate catalyzed reaction with 2,5-dihydrofuran in place of ethyl vinyl ether (Scheme 6). In a similar manner, addition to cyclohexene afforded **36** (25%). Clearly the methyl groups are not a major factor as the other α-diazoketones listed in Table 1 also afforded acetal products. In all cases direct irradiation generated the [2+2] cycloaddition products illustrated, which arise from Wolff rearrangement to the ketene followed by conventional cycloaddition.

The dihydrofuran-acetal structures observed above in the metal-catalyzed reactions of the various α-diazoketones

Scheme 5. Synthesis of α-diazoketone substrates.

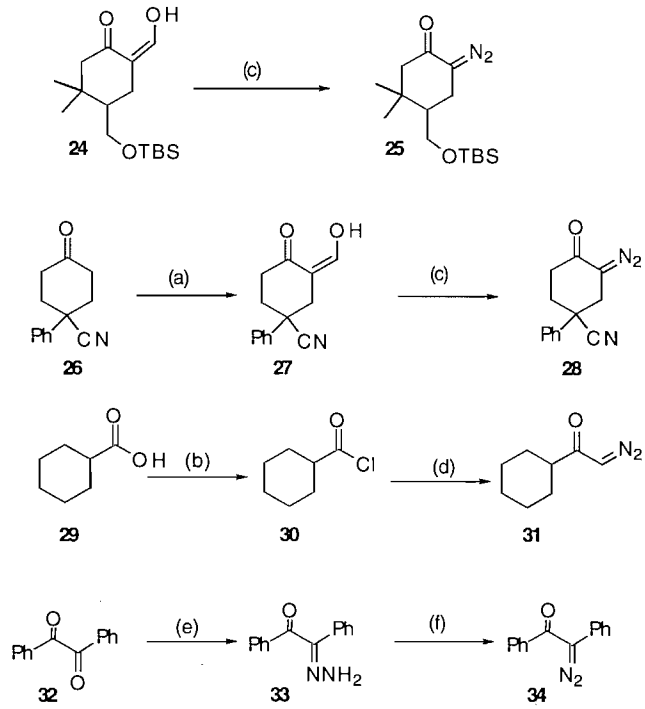

(a) NaH, ether, HCO_2Et; (b) $(COCl)_2$, C_6H_6, 21 °C, 97%; (c) Et_3N, TsN_3, CH_2Cl_2, -15 to 21 °C, 2 h; KOH (aq), 15 min; 40-70% (d) CH_2N_2, ether, 0 °C, 95%; (e) ref 13; (f) Ag_2O, THF, 67 °C, 5 h, 84%.

Scheme 6. Cyclopropane products with standard alkenes.

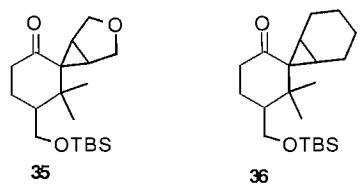

require additional experimental data to establish their structures unambiguously. To ascertain the decomposition pathways of these systems, the model system azibenzil (**34**) was examined in detail, particularly its behaviour with ethyl vinyl ether and rhodium(II) acetate. Direct pathways to the dihydrofuran **43** or the oxetane **48** from the α-diazoketone **34** (Scheme 7) are feasible after initial reaction of the carbenoid intermediate. Both of these products may arise from zwitterionic intermediates such as **46** or **47** that possess both enolate and oxacarbenium ion character. Surprisingly, the acetal product from the reaction could not be established from its spectral data. High-resolution mass spectroscopy confirmed the molecular formula ($C_{18}H_{18}O_2$). Both structures contain an equal number of CH, CH_2, CH_3, and quaternary carbons plus one methine attached directly to two ether oxygens, two methylene groups, and the methyl group of an ethoxy substituent. Unfortunately two-dimensional ^1H–^1H COSY, ^1H–^1H ROESY, and ^1H–^{13}C HETCOR experiments were inconclusive. A ^{13}C–^{13}C coupling INADEQUATE experiment should have allowed differentiation of the two different olefin substitution patterns, but the olefin carbon atoms had long relaxation

Table 1. Metal-catalyzed and photochemical reactions of α-diazoketones in ethyl vinyl ether.

Diazo ketone	Catalyst	Yield (%)	Dihydrofuran	Photolysis yield (%)	Cyclobutanone
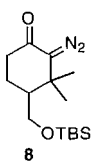 **8**	$Rh_2(OAc)_4$	70	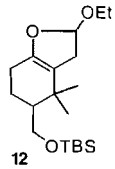 **12**	88	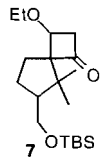 **7**
	$Pd(OAc)_2$	72			
	CuCl	30			
	$h\nu$,Ph_2CO	25		30, Ph_2CO	
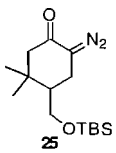 **25**	$Rh_2(OAc)_4$	75	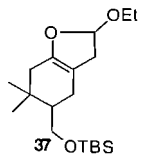 **37**	88	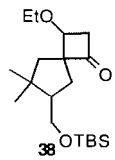 **38**
	$Pd(OAc)_2$	72			
	CuCl	35			
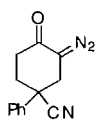 **28**	$Rh_2(OAc)_4$	40	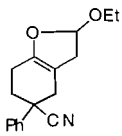 **39**	60	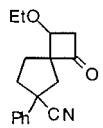 **40**
	$Pd(OAc)_2$	36			
	CuCl	10			
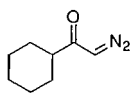 **31**	$Rh_2(OAc)_4$	71	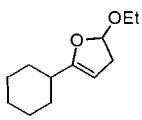 **41**	88	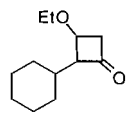 **42**
	$Pd(OAc)_2$	37			
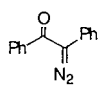 **34**	$Rh_2(OAc)_4$	68	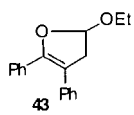 **43**	77	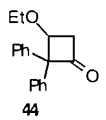 **44**
				44, Ph_2CO	

times (approximately 10 s), making it impossible to resolve the structural differences.

To establish the structure unambiguously the acetal product was subjected to acid-catalyzed hydrolysis with in situ trapping of the resulting keto-aldehyde with 2,2-dimethyl-1,3-propanediol. These experiments confirmed the upper pathway was followed (Scheme 7), since treatment of the presumed acetal **43** with *p*-toluenesulfonic acid in the presence of 3,3-dimethyl-1,3-propanediol afforded ketone **49** (68% yield), which could be distinguished from **50** by its ^1H NMR spectrum. The spectrum exhibited a characteristic one-proton doublet of doublets at δ 4.91 ppm (J = 7.8, 7.0 Hz) that was assigned to the acetal proton H_a coupled with each of the diastereotopic methylene protons. A second one-proton doublet of doublets at δ 4.31 ppm (J = 4.9, 5.6 Hz) was assigned to the methine proton H_b adjacent to the carbonyl group. The splitting pattern seen with this signal also arises from independent couplings with each of the diastereotopic methylene protons H_e and H_f. This type of coupling is only possible in structure **49**. Proton H_b in structure **50** has no adjacent carbons bearing protons and would therefore be expected to appear as a singlet in the ^1H NMR spectrum. In a similar manner the dihydrofuran **39** derived from diazoketone **28** afforded the keto-acetal **51** and thus established that the dihydrofurans are the final products of these α-diazoketones upon treatment with various metal catalysts in the presence of ethyl vinyl ether.

Diphenyl ketene, the putative Wolff rearrangement product from azibenzil (**34**) is relatively stable. It was synthesized independently to determine its reactivity with ethyl vinyl ether and its behaviour in the presence of rhodium(II) acetate and to establish with certainty that neither dihydrofuran **43** nor oxetane **48** were formed from the ketene. Diphenylketene (**20**) was prepared from acid chloride **52** upon treatment with triethylamine (Scheme 8) (14). For the thermal reaction a solution of diphenyl ketene (**20**) and ethyl vinyl ether in freshly distilled ether was stirred overnight under argon. Cyclobutanone **44** was obtained in 88% yield (IR, 1779 cm^{-1}). A metal-ketene intermediate, if formed, does not appear to alter the course of the reaction, as only the cyclobutanone **44** was isolated (89%) in the presence of $Rh_2(OAc)_4$.

The use of benzophenone as a triplet sensitizer during the photolysis of α-diazoketones is known to promote cyclopropane formation (15), although a large excess of sensitizer is required (16). It was anticipated that these conditions would allow detection of the cyclopropane. However, benzophenone (10 equiv.) sensitized photolysis of **8** failed to provide the cyclopropane **9**. A mixture of cyclobutanone **7** (30%) and dihydrofuran **12** (25%) was formed instead (Table 1). This

Scheme 7. Rearrangement pathways for α-diazoketone **34**.

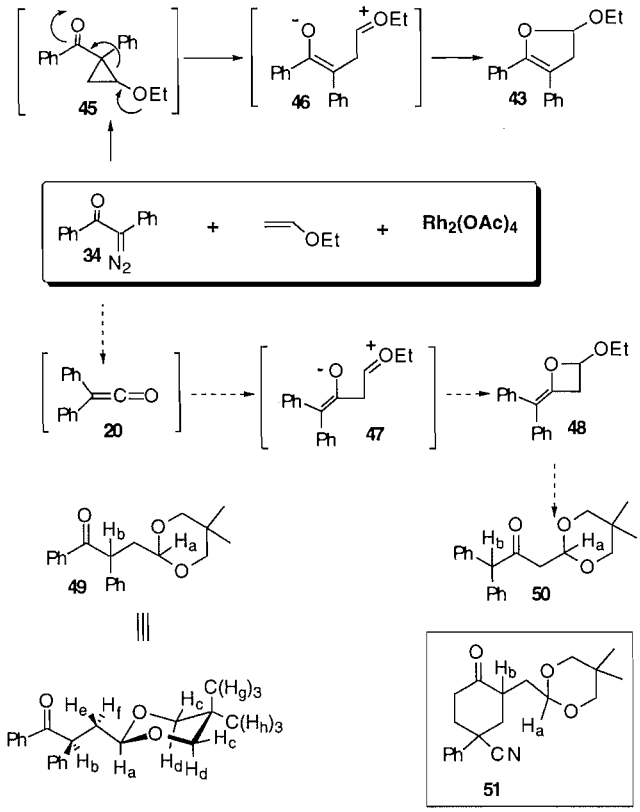

Scheme 8. Diphenylketene cycloadditions.

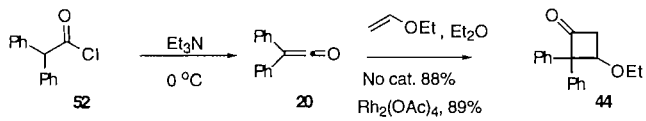

result was unexpected since Wolff rearrangement is considered to arise only from the singlet carbene (16, 17). Upon direct irradiation, no acetal products could be detected and clean conversion to the cyclobutanone **7** from [2+2] cycloaddition to the ketene double bond was observed. As mentioned above, this same pattern was observed with the other α-diazoketones **25**, **28**, **31**, and **34** to give **38**, **40**, **42**, and **44**, respectively. Decomposition of **8** under various conditions that are known to promote cyclopropanation ($Rh_2(OAc)_4$, pentane/ethyl vinyl ether, 30:1, 0°C; $Rh_2(OPiv)_4$, pentane/ethyl vinyl ether, 30:1, 0°C) (7, 8) also afforded **12** as the major product. A similar result was obtained with $Rh_2(OAc)_4$ in ethyl vinyl ether at −78°C, although immediate GC–MS analysis indicated the presence of a minor component (~10%) consistent with cyclopropylketone **9.**

A final attempt was made to prepare a sample related to **9**, the methoxy cyclopropane **B**, by addition of dimethyloxosulfonium methylide (18) to the enol ether ketone **6**. It was anticipated that conjugate addition would occur in accord with literature precedent (18, 19) to generate the methoxy cyclopropanone **B**. However, the product was a new methoxydihydrofuran system that differed from the dihydrofuran **12** by more than the substitution pattern. The ^1H NMR signal at δ 5.55 and

Table 2. NMR data for dihydrofurans.

Compound	δ H5 (ppm)	δ C2 (ppm)	δ C3 (ppm)
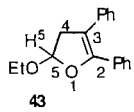 43	5.62 (dd, J = 7.2, 2.6 Hz)	148.2	102.6
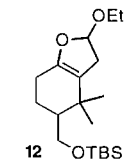 12	5.45 (m)	148.3	102.4
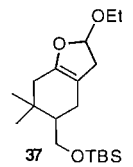 37	5.45 (m)	147.3	102.4
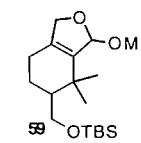 59	5.55	148.2	113.2

the olefinic carbon signals at δ 113.2 and 148.0 did not fit the chemical shift pattern observed for the other isomers, as tabulated in Table 2. In addition, it was not the product **57** from closure of the oxygen anion on the sulfinyl bearing carbon. In contrast to literature examples, the ylide adds preferentially to the carbonyl group, possibly as a consequence of the steric interference of the geminal dimethyl groups. Closure of **55** should afford the epoxide **56**, but this material was not detected. Instead it opens in a similar manner to the cyclopropanes to generate a dipolar zwitterionic species **58**, which collapses to give the observed product **59** (Scheme 9).

Discussion

The experiments above have established that the major product isolated from the reaction of structurally diverse α-diazoketones in the presence of rhodium(II) acetate and related catalysts with an electron-rich olefin such as ethyl vinyl ether is a dihydrofuran. There are two possible mechanisms for this process. The dihydrofuran may arise from a concerted or stepwise dipolar cycloaddition to the enol ether or, alternatively, the ethoxy-substituted cyclopropylketone is a true intermediate that undergoes rapid fragmentation and subsequent ring closure to the dihydrofuran.

Doyle et al. (20) have examined cyclopropanations with ethyl diazoacetate. The regio- and stereochemical control in catalytic cyclopropanation reactions is derived from the transition metal, its associated ligands, the diazo compound, and the olefin. The influence of the olefin is the weakest, while the electronic influence of the transition metal provides the dominant regio- and stereochemical control. Studies with chiral catalysts confirmed (21–24) that the transition metal is directly involved in the product-forming step. The more stable *trans* cyclopropanes usually predominate and the stereoselec-

Scheme 9. Attempted synthesis of cyclopropylketone **B**.

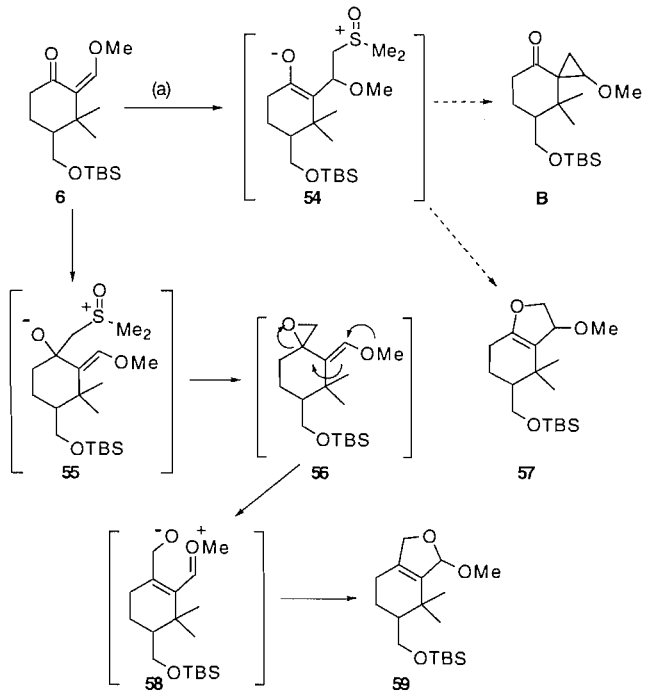

(a) Me_2SOCH_3I, NaH, DMF, 21 °C, 2h, 40%

tivities are not altered by the catalyst concentration, the rate of addition of the diazo compound, or the molar ratio of olefin to diazo compound. The cyclopropanation process was proposed by Doyle et al. (6, 20, 25) to occur through an initial interaction between the olefinic π bond and the electrophilic centre of the metal carbenoid, followed by σ-bond formation with backside displacement of the catalyst (Scheme 10). As the reaction proceeds the π-complexed olefin may rotate around the electrophilic centre to place the C—C bond of the olefin parallel to the metal–carbon bond. Thus the substituted carbon of the olefin is oriented *anti* to the metal. Two transition states, *trans* and *cis*, are possible in which the energy difference due to the interactions between R/R_1 and COPh determines the predominant isomer **61** or **62**. A study by Noels, Hubert, and co-workers supports the existence of a free carbene–carbenoid equilibrium (26).

The product distribution is influenced by an increase in the nucleophilicity of the carbonyl oxygen and (or) the electrophilicity of the β-carbon in the metaloid complex. This favours the dihydrofuran products as a consequence of the increased stabilization provided by both the carbonyl group and the developing electrophilic centre on the vinyl ether (Scheme 10). Due to the absence of an ether oxygen this stabilization is less with a standard olefin. This influence is usually only observed with α-diazoketones, as α-diazoesters are less nucleophilic. Dihydrofurans have also been obtained from copper-catalyzed reactions of diazomalonates and related diazoketones with various vinyl ethers (27, 28). These subtle effects are illustrated by the finding that dihydrofuran **63** (9%) was the minor product (cyclopropane 83%) in the $Rh_2(OAc)_4$ catalyzed reaction of α-diazopropiophenone (**60**) with ethyl vinyl ether, but **64** was the major product (40%) with 2-methoxypropene (6).

Scheme 10. Possible combined cyclopropanation–dihydrofuran mechanism.

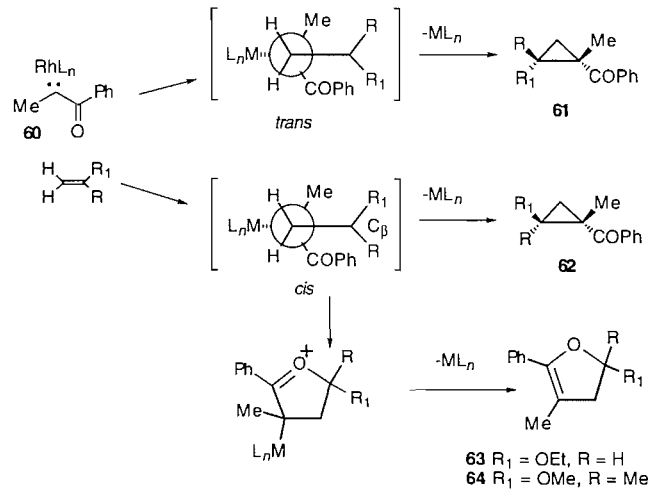

Scheme 11. Possible dipolar mechanism for dihydrofuran formation.

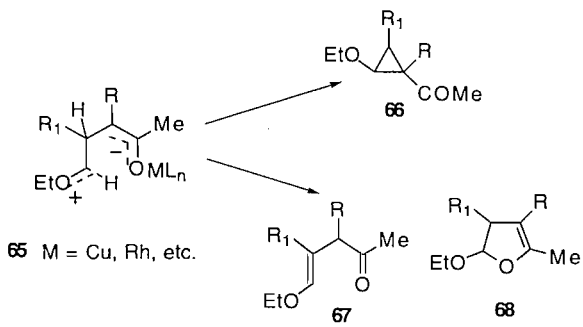

Alonso et al. (27) suggested a direct dipolar mechanism to explain the formation of dihydrofuran and acyclic products from various cyclopropanation reactions (Scheme 11) (27, 29). The dipolar intermediate **65** was proposed as the precursor to both the acyclic **67** and dihydrofuran **68** products. In this case, 1,3 ring closure to **66** is disfavoured with respect to the 1,5 ring closure. The stabilization of the dipolar intermediate is consistent with Doyle's mechanism where an increase in the nucleophilicity of the enolate oxygen increases the ease of 1,5-cyclization compared to 1,3-cyclization (6).

Variation of the catalyst ligands and solvent polarity has a significant effect on the outcome of rhodium(II) carboxylate catalyzed cyclopropanation reactions (7, 8, 30). Padwa, Doyle, and co-workers have established that the products that may arise from a dipolar mechanism are inhibited in pentane relative to dichloromethane (30). Competition experiments between cyclopropanation and bond insertion (tertiary C—H) provided a 44:56 product ratio with $Rh_2(OAc)_4$. More electrophilic metal carbenoids (perfluoroborate ligands) resulted in hydrogen insertion exclusively. In contrast, only cyclopropanation products were obtained with the less electrophilic rhodium(II) caprolactamate catalyst, which suppresses the carbene insertion into the C—H bond. Cyclopropanation is enhanced relative to dihydrofuran formation with rhodium(II) pivalate as catalyst (31, 32). Thus azibenzil (**34**) and ethyl vinyl ether

Scheme 12. Reduction of cyclopropylketone **45**.

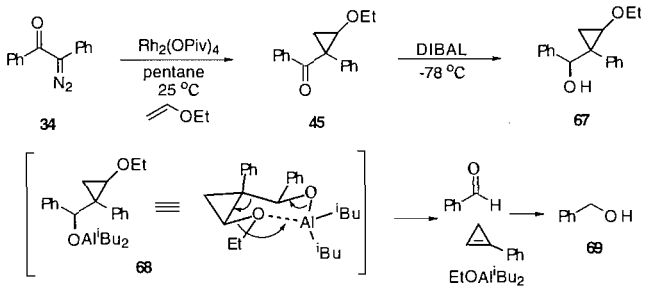

were treated with $Rh_2(OAc)_4$ in ether and pentane in separate experiments to provide the dihydrofuran **43** in yields of 97% and 91%. However, unexpectedly, the use of rhodium pivalate also gave the same product **43** (93%) in each case.

Dowd et al. (33) found that $Rh_2(OAc)_4$ catalyzed reactions of ketene acetals with methyl diazoacetate yielded unstable cyclopropyl esters that were reacted in situ with lithium aluminum hydride, albeit in low yield. They concluded that with diazoacetone the cyclopropylketone was too reactive to be isolated and probably rearranged through a dipolar intermediate to yield a small amount of a dihydrofuran product.

It is standard practice to purify reaction products prior to spectroscopy by filtration and chromatography. To discern the influence of the work-up conditions on the presumed cyclopropylketone intermediates the following experiments were conducted. Reactions with **34** were conducted separately with $Rh_2(OAc)_4$–ether and $Rh_2(OPiv)_4$–pentane, excess solvent was evaporated under a stream of argon, and the crude material was dissolved in $CDCl_3$ (which had been passed through basic alumina immediately prior to use). The ^1H NMR spectrum of this material displayed the characteristic cyclopropane signals expected at δ 0.6–0.9 ppm and a ^{13}C NMR signal at δ 194.5 ppm. In addition, an IR absorption at 1675 cm^{-1} was consistent with the cyclopropyl ketone **45**. Storage at −15°C (24 h) or further purification resulted in complete conversion to dihydrofuran **43**. A further attempt was made to detect the cyclopropylketone by in situ reduction with DIBAL at −78°C (Scheme 12). GC–MS analysis of the red reaction solution indicated a new compound (23%) had been formed with a mass corresponding to that of cyclopropanol **67** (*m/z* 268). Aqueous work-up and chromatography afforded dihydrofuran **43** plus benzyl alcohol (**69**), which appears to result from a Grob-type fragmentation (34) to generate benzaldehyde from the intermediate aluminate **68** followed by further reduction (Scheme 12).

Conclusions

The results of the acetal hydrolysis trapping experiments, together with the spectroscopic evidence for the formation of cyclopropane **45**, indicate that dihydrofuran **43** is not formed by either a direct concerted or a stepwise mechanistic pathway involving a dipolar cycloaddition. Rather the dihydrofuran arises from a facile rearrangement of the initially formed cyclopropane due to its donor–acceptor substitution pattern. This conclusion finds support in related metal-catalyzed systems (27) in which cyclopropanation of enol ethers or ketene acetals is followed by rearrangement as the preferred pathway (6, 35, 36). In addition, mild oxidation of 1-hydroxymethyl-2-ethoxycyclopropane to the corresponding ethoxy-aldehyde resulted in spontaneous rearrangement to a dihydrofuran (37). In the case of vinyl diazoester addition to vinyl ethers ($Rh_2(OAc_4)$, the initial vinyl cyclopropanes undergo a Et_2AlCl catalyzed rearrangement to cyclopentenes (36). Over 35 years ago D'Yakonov and Komendantov concluded that furans arose from copper-catalyzed cyclopropanations with ethyl diazoacetate and acetylenes by rearrangement of the initial cyclopropene (38). By analogy, the same conclusion can be extended to the other α-diazoketones in this study with ethyl vinyl ether. Indeed the majority of alkene–diazocarbonyl combinations produce cyclopropanes in good yields with standard alkenes. Only when the "electronics" of both the reacting partners are "tuned" to stabilize a dipolar intermediate due to their donor–acceptor or push–pull properties, are appreciable amounts of dihydrofuran formed (6, 8, 31, 33, 37).

Thus, in keeping with current knowledge, it is reasonable to suggest that the α-diazoketone initially forms a metal carbenoid intermediate, which adds to the olefin to form an α-cyclopropylketone. In the majority of cases with a standard olefin, the stable cyclopropane product is isolated. However, with electron-rich enol ethers the electronic substitution pattern precipitates further rearrangement, resulting in ring opening and subsequent cyclization to afford the observed dihydrofurans. In these cases, exposure to most purification conditions (filtration through a plug of Celite®, TLC, or standing at −10 to −15°C, ~24 h) assists the rearrangement. Variation in the polarity of the reaction medium has no significant effect on the outcome of the reaction, and it is therefore unlikely that a dipolar-type mechanism, as illustrated in Schemes 10 and 11, is involved. Thus, we favour the intermediacy of the cyclopropane in the majority of literature examples that involve electron-rich alkenes. Therefore, a common mechanism should be applied to most metal-catalyzed α-diazoketone cyclopropanations with all olefins. The product distribution reflects, in large measure, the relative stability of the three-membered ring system and its substitution pattern. Consistent with this conclusion, the literature experimental data are (naturally) not reported on crude reaction products before the dihydrofurans are formed but after purification, by which time, in most cases, the primary donor–acceptor substituted cyclopropanes have rearranged by ring opening and subsequent cyclization (Scheme 7). This implies that much of the mechanistic work and corresponding conclusions compiled to date concerned with cyclopropanation – dihydrofuran formation would benefit from further study under controlled, neutral conditions.

In summary, spontaneous dihydrofuran formation from α-diazoketones usually requires diactivated cyclopropyl carbonyl systems. This mild route from cyclic α-diazoketones via monoactivated cyclopropyl ketones provides an attractive sequence to generate compounds for further synthetic manipulation in view of the widespread occurrence of five-membered oxygen-containing heterocyclic ring systems in nature (39).[2]

Finally, it would be beneficial to have a standard, recognized nomenclature to describe this rhodium(II) mediated cyclopropanation–rearrangement process to afford dihydro-

[2] For a spiro-dihydrobenzofuran system see ref. 39*c*.

furans. This conversion has a formal resemblance to a dipolar cycloaddition. For example, in a nice synthesis of aflatoxin B_2, the intermolecular addition of an α-diazodiketone to 2,3-dihydrofuran via a cyclopropanation–rearrangement sequence is described as a "rhodium carbenoid dipolar cycloaddition", a "rhodium-mediated dipolar cycloaddition", or "the formal dipolar cycloaddition of cyclic diazodicarbonyl compounds with vinyl ethers mediated by dirhodium catalysts" (40). Clearly a cycloaddition is an addition reaction that forms a ring; however, this term also has mechanistic implications implying the reaction is either of a pericyclic or dipolar nature. In the present context these dihydrofuran-forming reactions may be characterized as a sequence involving a metal carbenoid or metal-mediated cyclopropanation – ring opening – cyclization pathway in which the cyclopropane cleavage step is similar to a Grob-type fragmentation,[3] which affords a dipolar intermediate that closes to the dihydrofuran.

Experimental (see ref. 1*d* for general procedures)

2-Formyl-3,3-dimethyl-4-*tert*-butyldimethylsilyloxymethylcyclohexanone (5)

Copper(I) iodide (3.80 g, 20 mmol) suspended in ether (200 mL) was cooled to 0°C and methyllithium (28.6 mL, 40 mmol) was added to the stirred suspension. After stirring for 15 min, an ether solution of the enone **4** (1*d*) (2.56 g, 20 mmol) was added dropwise over 10 min. After 90 min, ethyl formate (9 mL) was added and, after a further 20 min at 0°C, the reaction was poured into aqueous 10% NH_4Cl solution (150 mL). The organic layer was washed (3×) with dilute aqueous 1% HCl solution, dried, and concentrated. Chromatography (ethyl acetate/petroleum ether; 1:20) gave **5** (0.64 g, 20%). ^{1}H NMR (200 MHz) δ: 0.03 (s, 6H), 0.90 (s, 9H), 1.11 (s, 3H), 1.30 (s, 3H), 1.55 (m, 2H), 1.95 (m, 1H), 2.40 (m, 2H), 3.42 (dd, 1H, J = 8.4, 5.3 Hz), 3.83 (dd, 1H, J = 4.3, 8.7 Hz), 8.90 (d, 1H, J = 3.2 Hz), 15.22 (d, 1H, J = 3.2 Hz); ^{13}C (50.3 MHz) δ: 188.3, 185.6, 117.9, 62.5, 46.0, 33.3, 30.2, 29.0, 25.6, 19.9, 18.0, −5.7; HRMS calcd. for $C_{12}H_{21}O_3Si$ ($M^+ - C_4H_9$): 241.1259; found: 241.1252.

2-Formyl-5,5-dimethyl-4-*tert*-butyldimethylsilyloxymethylcyclohexanone (24)

This compound was a component of the reaction above and was prepared selectively when the reaction was allowed to warm to 21°C prior to adding the ethyl formate. After a further 4 h, work-up as above afforded **24** (2.5 g, 78%). ^{1}H NMR (200 MHz) δ: 0.02 (s, 6H), 0.85 (s, 12H), 0.98 (s, 3H), 1.55 (m, 1H), 2.09 (d, 2H, J = 11.4 Hz), 2.51 (dd, 1H, J = 5.8, 15.7 Hz), 3.41 (dd, 1H, J = 8.4, 5.3 Hz), 3.75 (dd, 1H, J = 4.3, 8.7 Hz), 8.73 (d, 1H, J = 1.6 Hz), 15.0 (d, 1H, J = 1.6 Hz); ^{13}C (50.3 MHz) δ: 188.3, 185.6, 117.9, 62.5, 46.0, 33.3, 30.2, 29.0, 25.6, 19.9, 18.0, −5.7. HRMS calcd. for $C_{12}H_{21}O_3Si$ ($M^+ - C_4H_9$): 241.1259; found: 241.1254.

2-(Methoxymethylidene)-3,3-dimethyl-4-*tert*-butyldimethylsilyloxymethylcyclohexanone (6)

Treatment of **5** (200 mg, 0.067 mmol) in ether (1 mL) at 22°C with excess diazomethane (prepared from *N*-nitrosomethylurea) in ether afforded **6** directly. Concentration followed by chromatography (20% acetone – petroleum ether) gave the product **6** (174 mg, 83%). ^{1}H NMR (acetone-d_6) (200 MHz) δ: 0.08 (s, 6H), 0.90 (s, 9H), 1.11 (s, 3H), 1.34 (s, 3H), 1.56–2.32 (m, 5H), 3.50 (dd, 1H, J = 8.15, 10 Hz), 3.85–3.92 (m, 4H), 7.22 (s, 1H); ^{13}C (50.3 MHz) δ: 201.8, 160.6, 123.5, 62.7, 61.9, 47.8, 37.1, 36, 26.9, 25.8, 21.1, 20.7, 18.2, −5.4; HRMS calcd. for $C_{13}H_{23}O_3$ ($M^+ - C_4H_9$): 255.1416; found: 255.1409.

2-Diazo-3,3-dimethyl-4-*tert*-butyldimethylsilyloxymethylcyclohexanone (8)

Standard diazo transfer procedure

2-Formyl-3,3-dimethyl-4-*tert*-butyldimethylsilyloxymethylcyclohexanone (**5**) (3.6 g, 12 mmol) was dissolved in dichloromethane (25 mL) and freshly distilled triethylamine (3.37 mL, 0.024 mmol) was added. The solution was cooled in an external ice–salt bath (−10°C) and *p*-toluenesulfonyl azide (1.8 g, 10 mmol, prepared from *p*-toluenesulfonyl chloride and sodium azide) was added with vigorous stirring over a period of approximately 1 h. Stirring was continued for an additional 2 h as temperature rose to 0°C. A solution of KOH (0.672 g, 12 mmol) in water (25 mL) was added and the mixture was stirred at 21°C for 15 min. The resulting emulsion was placed in a separatory funnel (100 mL), the dichloromethane layer separated, and the aqueous layer extracted twice with dichloromethane (5 mL). The combined dichloromethane extracts were washed with aqueous KOH solution (0.05 g in 15 mL water), water, and dried. Concentration and chromatography (5% ethyl acetate – petroleum ether) gave the product in 20% yield from **4**. IR (neat): 2100, 1740 cm^{-1}; ^{1}H NMR (200 MHz) δ: 3.85 (dd, 1H, J = 10.0, 4.4 Hz) 3.54 (dd, 1H, J = 10.0, 7.5 Hz), 2.41 (m, 2H), 2.1 (m, 1H), 1.71 (m, 2H), 1.39 (s, 3H), 11.17 (s, 3H), 0.93 (s, 9H), 0.1 (s, 6H); ^{13}C (50.3 MHz) δ: 193.9, 62.5, 62.2, 51.4, 44.2, 32.6, 28.4, 25.6, 22.3, 17.9, −5.8; HRMS calcd. for $C_{15}H_{28}O_2Si$: 268.1858; found: 268.1865.

2-Diazo-4-(*tert*-butyldimethylsilyloxy)methyl-5,5-dimethylcyclohexanone (25)

70% yield from **24**. IR (neat): 2100, 1740 cm^{-1}; ^{1}H NMR (200 MHz) δ: 3.82 (dd, 1H, J = 10.0, 4.4 Hz), 3.5 (dd, 1H, J = 10.0, 7.5 Hz), 2.85 (m, 1H), 2.60 (m, 1H) 2.08 (s, 2H), 1.68 (m, 1H,), 0.97 (s, 3H), 0.89 (s, 3H), 0.85 (s, 9H), 0.15 (s, 6H); ^{13}C (50.3 MHz) δ: 193.9, 62.5, 62.2, 51.4, 44.2, 32.6, 28.4, 25.6, 22.5, 17.9, −5.8; HRMS calcd. for $C_{15}H_{28}O_2Si$: 268.1858; found: 268.1865.

2-Diazo-4-cyano-4-phenylcyclohexanone (28)

40% yield from the parent ketone **26**. IR (CCl_4) 2238, 2110, 1727 cm^{-1}; ^{1}H NMR (200 MHz) δ: 2.34 (dd, 2 H, J = 8.1, 4.2 Hz), 2.57 (dt, 1 H, J = 18.4, 4.1 Hz), 2.80 (dt, 1 H, J = 18.4, 9.5 Hz), 3.22 (s, 2 H), 7.42 (m, 5 H); ^{13}C (50.3 MHz) δ: 190.4, 137.7, 129.5, 129.0, 125.5, 120.8, 62.5 (C-2), 41.2, 34.3, 33.7, 32.2; MS *m/z*: 225, 197, 168, 154, 141, 129.

2-Diazo-1-cyclohexyl-1-oxoethane (31)

Oxalyl chloride (4.8 mL, 54.6 mmol) was added dropwise to a stirred solution of cyclohexanecarboxylic acid (1 g, 7.8 mmol)

[3] For a Grob-type fragmentation in cyclopropanone acetals see ref. 41.

in benzene (40 mL). Concentration gave the acid chloride (97%), which was reacted directly with an ethereal solution of diazomethane to generate the diazoketone **31** (95%). IR (neat): 2104, 1636 cm^{-1}; ^1H NMR (200 MHz) δ: 1.25 (m, 6H), 1.71 (m, 4H), 5.22 (s, 1H), 2.10 (br, 1H); ^{13}C (50 MHz) δ: 198.5, 29.1, 25.6; HRMS calcd. for $C_8H_{12}N_2O$: 152.0950; found: 152.0942.

2-Diazo-1,2-diphenyl-1-ethanone (34)

A suspension of benzil monohydrazone **33** (2.0 g, 8.92 mmol) in THF (200 mL) was heated at reflux until the mixture became homogeneous. Powdered Ag_2O (2.26 g, 9.75 mmol) was added in small portions over 15 min and the resulting mixture was heated at reflux for 5 h with vigorous stirring. The silver residue was removed by hot filtration (gravity, over Celite®) and washed with two 5 mL portions of THF. The filtrate was concentrated to give ~2 g of oily orange crystals. Recrystallization from pentane yielded 1.66 g (84%) of azibenzil **34** as bright orange crystals, mp 66–67°C (lit. (13*b*) mp 67–67.5°C); IR (KBr pellet): 3051, 2075,1605 cm^{-1}; ^{13}C NMR (50.3 MHz): δ: 182.5, 132.0, 125.9, 125.7, 123.4, 123.1, 122.6, 122.1, 121.5, 120.1 ppm.

2-Formyl-4-cyano-4-phenylcyclohexanone (27)

A stirred mixture of sodium hydride (0.376 g, 12.5 mmol, 80% in mineral oil, Aldrich), anhydrous ether (100 mL), and ethyl alcohol (0.25 mL) was cooled (0°C) and a solution of ketone **26** (2.5 g, 12.5 mmol) and redistilled ethyl formate (1.52 mL, 18.8 mmol) was added dropwise over 1 h. After 66 h, ethanol (1 mL) and water (10 mL) were added and the mixture was poured into a separatory funnel (500 mL). The organic layer was separated, washed with water (5 mL), and the combined aqueous extract was washed with ether (100 mL). The aqueous layer was acidified with 6 N HCl (4 mL) and the mixture extracted twice with ether (30 mL). The combined ether solutions were washed with brine (25 mL), dried, filtered, and concentrated to give the product **27** (2.5 g), which was used directly in the diazo transfer step.

2,2-Dimethyl-3-*tert*-butyldimethylsilyloxymethyl-7-oxa-8-ethoxybicyclo[4.3.0]non-1,6-ene (12)

Standard catalytic procedure

An anhydrous diethyl ether (1.5 mL) solution of α-diazoketone **8** (100 mg, 0.34 mmol) was added over 4 h by syringe pump (Sage model 341A) to a stirred solution (dichloromethane, anhydrous ether, pentane, or benzene) of the catalyst ((1 mg, 4.5 mmol, palladium(II) acetate) or (0.7 mg, 1.7 mmol, rhodium(II) acetate or rhodium(II) pivalate) or (1.7 mg, 16.8 mmol, cuprous chloride)) and excess alkene (1 mL) at room temperature (21°C). The needle of the syringe was placed just below the surface of the reaction solution. Once the addition was complete, the mixture was concentrated, flushed through a small amount of silica gel (70–230 mesh) or Celite®, and reconcentrated. The product was purified by chromatography (5% ethyl acetate – petroleum ether) to give **12** in 70% yield (rhodium(II) acetate). IR (neat): 1100 cm^{-1}; ^1H NMR (200 MHz) δ: 0.15 (s, 6H), 0.85 (s, 9H), 1.05 (s, 3H), 1.24 (t, 3H, J = 7.1 Hz), 1.27 (s, 3H), 1.71–2.80 (m, 7H), 3.35 (m, 1H), 3.50 (m, 1H), 3.75 (m, 2H), 5.45 (m, 1H); ^{13}C (50.3 MHz) δ: 148.3, 104.6, 102.4, 63.4, 63.2, 45.7, 39.5, 39.4, 32.6, 28.8, 25.7, 23.8, 23.0, 18.0, 15.0, −5.7; DEPT (50.3 MHz) δ: 104.6 (CH), 63.4 (CH_2), 63.2 (CH_2), 45.7 (CH), 39.5 (CH_2), 38.4 (CH_2), 28.8 (CH_3), 25.7 (CH_3), 23.8 (CH_2), 23.0 (CH_3), 15.0 (CH_3), −5.7 (CH_3); HRMS calcd. for $C_{19}H_{36}O_3Si$: 340.2433; found: 340.2433.

4,4-Dimethyl-3-*tert*-butyldimethylsiloxymethyl-7-oxa-8-ethoxybicyclo[4.3.0]non-1,6-ene (37)

75% yield from diazoketone **25** with rhodium(II) acetate catalyst. IR (neat): 1100 (vs, C-O) cm^{-1}; ^1H NMR (200 MHz) δ: 0.14 (s, 6H), 0.85 (s, 9H), 0.86 (s, 3H), 0.96 (s, 3H), 1.19 (t, 3H, J = 7.1 Hz), 1.70–2.60 (m, 7H), 3.35 (m, 1H), 3.53 (m, 1H), 3.75 (m, 2H), 5.50 (m, 1H); ^{13}C (50.3 MHz) δ: 147.3, 105.0, 102.4, 63.6, 63.2, 45.5, 39.4, 39.2, 31.6, 28.6, 25.5, 23.8, 22.9, 18.0, 15.1, −5.6; HRMS calcd. for $C_{19}H_{36}O_3Si$: 340.2433; found: 340.2425.

3-Cyano-3-phenyl-7-oxa-8-ethoxybicyclo[4.3.0]non-1,6-ene (39)

40% yield from cyclohexanone **27** with rhodium(II) acetate catalyst. IR (CCl_4): 1098, 2241 cm^{-1}; ^1H NMR (200 MHz) δ: 1.23 (t, 3H, J = 7.1 Hz), 2.40 (m, 8H), 3.71 (m, 2H), 5.55 (m, 1H), 7.33 (m, 5H); ^{13}C (50.3 MHz) δ: 149.3, 139.9, 129.0, 102.0, 64.0, 39.3, 35.9, 32.8, 21.2, 14.9; HRMS calcd. for $C_{17}H_{19}NO$: 269.1411; found: 269.1382.

2,3-Diphenyl-5-ethoxy-4,5-dihydrofuran (43)

The $Rh_2(OAc)_4$ catalyzed addition of ethyl vinyl ether to **34** (21°C) (500 mg, 2.25 mmol) followed the general method described above. The ^1H NMR spectrum of the crude product showed no remaining starting material and GC–MS analysis indicated a 97% conversion to the dihydrofuran **43**. Analysis (TLC, silica gel, 20:1 petroleum ether/ethyl acetate) indicated rapid decomposition of the acetal. Dihydrofuran **43** was decomposed on exposure to $CDCl_3$ that had not been passed through basic alumina immediately prior to use. A purified sample was obtained by flash chromatography (20:1, hexanes/ether) to give **43** (68%) as a pale yellow oil.

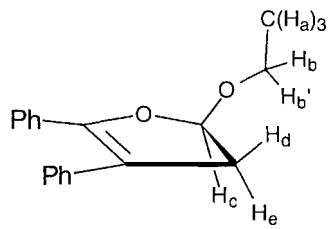

43

43: IR (film, NaCl): 1011, 760, 694 cm^{-1}; ^1H NMR (200 MHz) δ: 7.53–7.10 (m, 10H, aromatic protons), 5.62 (dd, H_c, $J_{c,e}$ = 7.2 Hz, $J_{c,d}$ = 2.6 Hz), 3.97 (dq, H_b, $J_{b,a}$ = 9.6 Hz, $J_{b,b'}$ = 7.1 Hz), 3.66 (dq, $H_{b'}$, $J_{b',a}$ = 9.6 Hz, $J_{b',b}$ = 7.1 Hz), 3.41 (dd, H_e, $J_{e,d}$ = 16.4 Hz, $J_{e,c}$ = 7.2 Hz), 2.93 (dd, H_d, $J_{d,e}$ = 16.4 Hz, $J_{d,c}$ = 2.6 Hz), 1.06 (dd, 3H_a, $J_{a,b}$ = $J_{a,b'}$ = 9.6 Hz); ^{13}C NMR (50.3 MHz, DEPT) δ: 148.2 (s, Ph(O)*C*=C), 135.1 and 131.7 (s, phenyl *ipso* C), 128.5, 128.2, 128.1, 127.9, 127.5, 126.1 (d, phenyl *C*H), 109.3 (s, C=*C*Ph(CH_2)), 102.6 (d, O*C*HO), 63.7 (t, CCH_2CH(O)(O)), 42.3 (t, OCH_2CH_3), 15.3 (q, CH_2CH_3) ppm; HRMS calcd. for $C_{18}H_{18}O_2$: 266.1307; found: 266.1331.

3,3-Dimethyl-4-*tert*-butyldimethylsilyloxymethyl-2-(spiro-3-oxabicyclo[3.1.0]hexyl)cyclohexanone (35)

The standard reaction with **8** and rhodium(II) acetate with 2,5-dihydrofuran afforded the cyclopropyl product **35** (25%). IR (neat): 1710 cm^{-1}; ^1H NMR (200 MHz) δ: 0.0 (s, 6H), 0.81 (s, 3H), 0.87 (s, 9H), 1.21 (s, 3H), 1.23–1.50 (m, 2H), 1.9 (m, 1H), 2.1–2.7 (m, 4H), 3.31–3.60 (m, 2H), 3.70–3.85 (m, 2H), 4.21 (m, 1H), 4.70 (m, 1H); ^{13}C (50.3 MHz) δ: 210.2, 75.0, 62.7, 54.0, 46.0, 38.5, 36.1, 33.0, 29.5, 26.0, 21.2, 18.0, −6.4; HRMS calcd. for $C_{19}H_{34}O_3Si$ ($M^+ - H_2O$): 320.2099; found: 320.2097.

3,3-Dimethyl-4-*tert*-butyldimethylsilyloxymethyl-2-(spiro[4.1.0]heptanyl)cyclohexanone (36)

The standard reaction with rhodium(II) acetate and **8** plus cyclohexene gave the product **36** in 25% yield. IR (neat): 1710 1093 cm^{-1}; ^1H NMR (200 MHz) δ: 0.04 (s, 6H), 0.88 (s, 12H), 1.03 (s, 3H), 1.06–2.31 (m, 15H), 3.84 (m, 1H); HRMS calcd. for $C_{21}H_{38}O_2Si$: 350.2641; found: 350.2661.

Diphenylketene (20) (ref. 14)

A Schlenk flask (100 mL) containing a solution of diphenyl acyl chloride **52** (4.2 g, 5.64 mmol) in Et_2O (50 mL) was cooled to 0°C. Triethylamine (2.36 mL, 16.9 mmol, 3 equiv.) was added dropwise over 5 min to give a canary-yellow solution. The flask was sealed under argon and placed in the fridge overnight to precipitate $Et_3N{\cdot}HCl$. The salt was removed by filtration through a medium glass frit under an atmosphere of argon. Concentration under vacuum followed by flash vacuum distillation gave **20** as a thick yellow oil (0.91 g, 83%), bp 120–122°C at 0.15 Torr (1 Torr = 133.3 Pa). The distillation must be done rapidly to avoid formation of the ketene dimer. IR (KBr): 1762 cm^{-1}; IR (film, NaCl): 2097 (s) cm^{-1}; ^1H NMR (200 MHz) δ: 7.1–7.8 (m, 10H).

2,2-Diphenyl-3-ethoxycyclobutanone (44)

Standard photolysis procedure

A solution of α-diazoketone **34** (100 mg, 0.45 mmol) in ethyl vinyl ether (5 mL, 52.3 mmol) was placed in an oven-dried quartz tube (15 mm × 120 mm) that had been cooled under a stream of argon. The solution was degassed with dry deoxygenated argon (20 min) and irradiated with a medium-pressure Hanovia mercury lamp for 2.5 h until TLC analysis indicated that the starting material was consumed. Concentration and chromatography (11:1 petroleum ether/ethyl acetate) gave the cyclobutanone **44** (103 mg, 87%). IR (film): 1779 cm^{-1}; ^1H NMR (200 MHz) δ: 7.5–7.1 (m, 10H, aromatic protons), 4.82 (m, 1H), 3.6–3.11 (m, 4H), 1.06 (t, 3H); HRMS calcd. for $C_{18}H_{18}O_2$: 266.1307; found: 266.1316.

*Sensitized photolysis of α-diazoketone **34** with ethyl vinyl ether*

The procedure above was modified by the addition of benzophenone (0.813 g, 4.46 mmol, 10 equiv.) to the solution of α-diazoketone **34** (100 mg, 0.446 mmol) and ethyl vinyl ether (5 mL, 52.3 mmol). The mixture was degassed and irradiated (4.5 h). Concentration and chromatography (11:1 petroleum ether/ethyl acetate) gave 63 mg of cyclobutanone **44** and 8 mg of crude dihydrofuran **43** (7%)). Further radial chromatography (silica gel, 4 mm plates, 20:1 petroleum ether/ethyl acetate) afforded cyclobutanone **44** (52 mg, 44%).

Thermal reaction, no catalyst: Ethyl vinyl ether (246 μL, 2.57 mmol), diphenylketene **20** (200 mg, 1.03 mmol), and freshly distilled ether (25 mL) were placed in a 5 mL round-bottom flask and stirred under argon overnight. The IR of the reaction mixture contained no diphenylketene absorption (2096 cm^{-1}). Excess ethyl vinyl ether was removed under vacuum and the last traces of the ether were removed under a stream of argon. Chromatography (silica gel, 5:1 petroleum ether/ethyl acetate) gave **44** (241 mg (88%) as a bright yellow oil. The less polar product was the dimer of diphenylketene (IR (neat): 1814 (s) cm^{-1}; ^1H NMR (200 MHz) δ: 7.84–7.72 (m, 1.5H), 7.62–7.38 (m, 2H), 7.3–7.1 (m, 1.5H) 7.84–7.10 (m, aromatic protons)).

With catalyst: A solution of diphenylketene **20** (200 mg, 1.03 mmol) and freshly distilled ether (9 mL) was added by syringe pump to a mixture of ethyl vinyl ether (~1 mL, excess) and $Rh_2(OAc)_4$ (9 mg, 2 mol %) over a period of 7 h. The reaction mixture, after column chromatography (silica gel, 5:1 petroleum ether/ethyl acetate), yielded cyclobutanone **44** (206 mg, 89%).

5,5-Dimethyl-3-ethoxy-6-*tert*-butyldimethylsilyloxymethylspiro[3.4]heptan-1-one (7)

Direct photolysis of **8** in ethyl vinyl ether gave **7** in 88% yield. IR (neat): 1780, 1100 cm^{-1}; ^1H NMR (200 MHz) δ: 0.15 (s, 6H), 0.85 (s, 12H), 1.05 (s, 3H), 1.20 (m, 3H), 1.71 (m, 4H), 2.11 (m, 1H), 3.02 (m, 2H), 3.45 (m, 4H), 3.87 (m, 1H); HRMS calcd. for $C_{19}H_{36}O_3Si$: 283.1734; found: 283.1715.

6-Phenyl-6-cyano-3-ethoxyspiro[3.4]heptan-1-one (40)

Direct photolysis of **28** in ethyl vinyl ether gave **40** in 60% yield. IR (CCl_4): 2234, 1779 cm^{-1}; ^1H NMR (200 MHz) δ: 1.23 (m, 3H), 2.52 (m, 6H), 3.19 (m, 2H), 3.63 (m, 2H), 4.11 (m, 1H), 7.34 (m, 5H); HRMS calcd. for $C_{17}H_{19}O_2N$: 269.1411; found: 269.1411.

2-Cyclohexyl-3-ethoxycyclobutanone (42)

Direct photolysis of **31** in ethyl vinyl ether gave **42** in 80% yield. IR (neat): 1780 cm^{-1}; ^1H NMR (200 MHz) δ: 1.00 (m, 9H), 1.83 (m, 5H), 2.91 (m, 3H), 3.45 (m, 2H), 4.15 (m, 1H); MS *m/z*: 197, 196, 168, 154, 150, 132, 122, 108, 80, 67.

3,4-Diphenylbutan-4-oxo-(2,2-dimethylpropylenedioxy) acetal (49)

Dihydrofuran **43** (17 mg, 0.064 mmol) and 2,2-dimethyl-1,3-propanediol (20 mg, 0.192 mmol, 3 equiv.) were dissolved in dry benzene (10 mL) and a single crystal of PPTS was added. The mixture was stirred at room temperature until there was no remaining dihydrofuran by TLC analysis. The crude reaction mixture was concentrated and chromatographed (5:1 petroleum ether/ethyl acetate) to give acetal **49** (14 mg, 68%). ^1H NMR (500 MHz, COSY) δ: 8.00–7.98 (m), 7.97–7.20 (m) (10H, phenyl protons), 4.91 (dd, H_a, J = 7.8, 7.0 Hz), 4.31 (dd, H_b, J = 5.6, 4.9 Hz), 3.38 (ddd, $2H_c$, J = 18.8, 10.9, 2.7 Hz), 3.29 (dd, $2H_d$, J = 17.2, 11.0 Hz), 2.60 (ddd, H_e, J = 13.8, 7.9, 5.8 Hz), 2.15 (ddd, H_f, J = 13.8, 6.8, 4.8 Hz), 1.14 (s, $3H_g$), 0.67 (s, $3H_h$); ^{13}C NMR (125 MHz, DEPT) δ: 199.2 (s, C=O),

139.0 (s), 136.6 (s), 134.8 (d), 132.7 (d), 129.8 (d), 128.9 (d), 128.9 (d), 128.6 (d), 128.3 (d), 128.2 (d), 127.0 (d), 100.0 (d, C_a), 77.71 (t, $C_{c,d}$), 48.1 (d, C_b), 38.5 (t, $C_{e,f}$), 30.0 (s, $C(CH_3)_2$), 22.9 (q, C_g), 21.7 (q, C_h) ppm; HRMS calcd. for $C_{21}H_{24}O_3$: 324.1726; found: 324.1741.

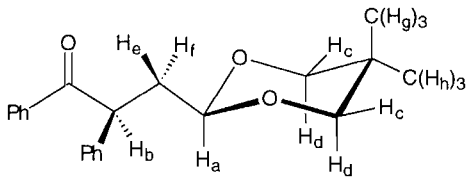

49

Ethan-2-(4-cyano-4-phenyl-2-ethyl-1-oxocyclohexyl)-2,2-dimethylpropylenedioxy acetal (51)

Compound **39** (18 mg, 0.067 mmol) and 2,2-dimethyl-1,3-propanediol (35 mg, 0.33 mmol, 5 equiv.) were dissolved in anhydrous benzene (4 mL). A single crystal of PPTS was added and the solution was stirred at 21°C for 13 h. Chromatography (5:1 petroleum ether/ethyl acetate) provided **51** (12.3 mg, 56%).

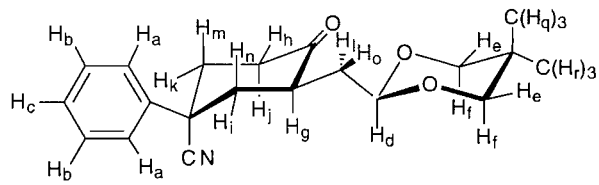

51

51: ^{1}H NMR (500 MHz, COSY) δ: 7.50–7.48 (m, 2H_a), 7.42–7.39 (m, 2H_b), 7.36–7.34 (m, H_c), 4.58 (dd, H_d, J = 5.9, 3.9 Hz), 3.56 (dm, 2H, J = 11.3 Hz, H_e), 3.40 (d, 1H, J = 11.3 Hz, H_f), 3.37 (d, 1H, J = 11.3 Hz, H_f'), 3.24 (m, H_g), 2.97 (m, H_h), 2.67 (ddd, H_i, J = 13.6, 5.4, 3.7 Hz), 2.57 (ddd, H_j, J = 14.3, 4.2, 2.5 Hz), 2.450 (m, H_k), 2.32 (ddd, H_l, J = 3.91, 6.14, 14.31 Hz), 2.25 (ddd, H_m, J = 14.0, 14.0, 4.2 Hz), 1.98 (ddd, H_n, J = 13.6, 13.6, 13.6 Hz), 1.45 (ddd, H_o, J = 5.9, 5.9, 14.3 Hz), 1.16 (s, 3H_q), 0.69 (s, 3H_r). In ^{1}H–^{1}H decoupling experiments, irradiation of the methine proton at δ 3.24 (H_g) caused the collapse of the following signals: δ 2.67 (H_i) to a dd, J = 13.6, 3.7 Hz; δ 2.32 (H_l) to a dd, J = 14.3, 3.9 Hz; δ 1.98 (H_n) to a dd, J = 13.6, 13.6 Hz; and δ 1.45 (H_o) to a dd, J = 14.3, 5.9 Hz. Irradiation of the acetal methine proton at δ 4.58 (H_d) caused the collapse of the signal at δ 2.32 (H_l) to a dd, J = 14.3, 6.1 Hz and the signal at δ 1.45 (H_o) to a dd, J = 14.3, 5.9 Hz; ^{13}C NMR (125 MHz, DEPT) δ: 208.4 (s, *C*=O), 138.7 (s, phenyl=*C*(C)(C)), 129.2 (d, C_b), 128.5 (d, C_c), 125.5 (d, C_a), 121.6 (s, *C*N), 100.1 (d, C_d), 77.2 (t, $C_{e,f}$), 76.7 (t, $C_{l,o}$), 44.6 (s, *C*-CN), 42.9 (d, C_g), 39.0 (t, $C_{k,m}$), 38.0 (t, $C_{n,l}$), 33.5 (t, $C_{h,j}$), 30.1 (s, $C(CH_3)(CH_3)$), 23.0 (q, C_q), 21.8 (q, C_r); MS (EI) *m/z*: 326 (M−1, 1.0%), 283 (M−44, 8.1%), 197 (20.3%), 149 (74%), 129 (43%), 115 (37%), 105 ($C_6H_5C{=}O^+$, 16%), 77 (22%, $C_6H_5^+$), 57 (base peak), 41(81%); HRMS calcd. for $C_{20}H_{24}NO_3$ (M^+ −H): 326.1834; found: 326.1801.

9-Methoxy-2,2-dimethyl-3-*tert*-butyldimethylsilyloxymethyl-8-oxabicyclo[4.3.0]non-1,6-ene (59)

Trimethyloxosulfonium iodide (38.2 mg, 0.17 mmol) in DMF (0.5 mL) was added to a suspension of NaH (4 mg) in DMF (1 mL) at 21°C. After stirring for 20 min, a solution of **6** (53 mg, 0.17 mmol) in DMF (0.5 mL) was added in one portion and stirring was continued for 2 h. Cold water was added and the reaction mixture was extracted several times with ether. The combined ether extracts were washed with water and brine, dried, and chromatographed (5% Et_2O – petroleum ether) to give **59** (22 mg, 40%). ^{1}H NMR (300 MHz) δ: 0.02 (s, 6H), 0.86 (s, 3H), 0.87 (s, 9H), 1.1 (s, 3H), 1.43–1.50 (m, 2H), 1.90–1.96 (m, 1H), 2.04–2.09 (m, 2H), 2.38–2.35 (m, 1H), 2.64–2.68 (m, 1H), 3.40 (dd, 1H, J = 8.8, 10 Hz), 3.42 (s, 3H), 3.75 (dd, 1H, J = 3.6, 10 Hz), 5.34 (dd, 1H, J = 2.6, 7.2 Hz); ^{13}C (75 MHz) δ: 148.2, 113.2, 105.6, 63.5, 55.4, 47, 35.4, 26.9, 25.9, 22.4, 22.18, 22, 21.8, −5.3; DEPT (75 MHz) δ: 105.6 (CH), 63.5 (CH_2), 55.4 (CH_3), 47 (CH), 35.4 (CH_2), 26.9 (CH_3), 25.9 (CH_3), 22.4 (CH_2), 22.2 (CH_2), 22 (CH_3), −5.3 (CH_3); HRMS calcd. for $C_{18}H_{34}O_3$: 326.2276; found: 326.2285.

1-Phenacyl-1-phenyl-2-ethoxycyclopropane (45)

Trapping experiment with DIBAL

Diazo compound **34** (0.050 g, 0.223 mmol) in pentane (30 mL) with $Rh_2(OPiv)_4$ (2 mol%) as the catalyst was reacted as above. After the addition of **34** was complete the lime-green reaction mixture was cooled to −78°C and DIBAL (1.5 M in toluene, 300 μL, 0.446 mmol) added in one portion. The solution immediately turned bright red. This mixture was allowed to stir at −78°C for 15 min. GC–MS analysis indicated the presence of a new peak (23% of the mixture) with a mass corresponding to the α-cyclopropyl alcohol **67**. The reaction was quenched with a saturated aqueous solution of sodium potassium tartrate (5 mL). This mixture was extracted with ether (3 × 10 mL). The combined extracts were washed with brine, filtered, dried, and concentrated to give 54 mg of crude product as a thick red-brown oil. Chromatography (5:1 petroleum ether/ethyl acetate) afforded benzyl alcohol (6 mg) and the cyclopropyl alcohol **67** (10 mg).

The standard reaction rhodium(II) acetate reaction was conducted with ethyl vinyl ether and **34** but filtration was bypassed and the lime-green crude solution was concentrated directly under a stream of argon. It was dissolved in $CDCl_3$ that had been passed through basic alumina immediately prior to use. The ^{1}H and ^{13}C NMR and IR spectra of this opaque suspension were recorded immediately. The sample was stored in the freezer, without solvent, under an atmosphere of argon. Attempts to purify cyclopropane **45**, other than by filtration under an inert atmosphere, resulted in either partial or complete conversion to dihydrofuran **43**. Slow conversion of **45** to **43** occurred on storage (−10–15°C) in a sealed flask under an inert atmosphere. Compound **45**: IR (film, NaCl): 3062, 1722 cm^{-1}; ^{1}H NMR (200 MHz) δ: 7.92–7.78 (m, 5H), 7.62–6.90 (m, 5H), 3.38 (q, 2H), 1.41–0.90 (m, 5H, overlapping t at 1.12), 0.90–0.62 (m, 1H) ppm; ^{13}C NMR (50.3 MHz) δ: 194.5, 134.8, 132.9, 129.9, 129.1, 129.0, 128.7, 128.6, 128.2, 128.1, 128.0, 65.8, 32.4, 29.7, 23.2, 15.3 ppm.

Acknowledgment

We are grateful to the Natural Sciences and Engineering Research Council of Canada and to Merck Frosst Canada for

financial support of this research and to J. Axon, P. Wilson, T. Wong, and S. Woo for fruitful discussion.

References

1. (*a*) Y.-F. Lu and A.G. Fallis. Tetrahedron Lett. **34**, 3367 (1993); (*b*) Y.-F. Lu, C.W. Harwig, and A.G. Fallis. J. Org. Chem. **58**, 4202 (1993); (*c*) T. Wong, M.A. Romero, and A.G. Fallis. J. Org. Chem. **59**, 5527 (1994); (*d*) Y.-F. Lu and A.G. Fallis. Can. J. Chem. **73**, 2239 (1995); (*e*) Y.-F. Lu, C.W. Harwig, and A.G. Fallis. Can. J. Chem. **73**, 2253 (1995); (*f*) M.W. Tjepkema, P.D. Wilson, T. Wong, M.A. Romero, H. Audrain, and A.G. Fallis. Tetrahedron Lett. **36**, 6039 (1995); (*g*) T. Wong, M.W. Tjepkema, H. Audrain, P.D. Wilson, and A.G. Fallis. Tetrahedron Lett. **37**, 755 (1996).
2. (*a*) A.L.J. Beckwith and C.H. Schiesser. Tetrahedron, **41**, 3925 (1985); (*b*) G.A. Molander and J.A. McKie. J. Org. Chem. **59**, 3186 (1994).
3. E.A. Lund, I.A. Kennedy, and A.G. Fallis. Tetrahedron Lett. **34**, 6841 (1993).
4. H.-U. Ressig. Top. Curr. Chem. **144**, 73 (1988).
5. E. Wenkert, M.E. Alonso, B.L. Buchwalter, and J.C. Kechia. J. Am. Chem. Soc. **99**, 4778 (1977).
6. M.P. Doyle, J.H. Griffin, V. Bagheri, and R.L. Dorow. Organometallics, **3**, 53 (1984).
7. A. Padwa, D.J. Austin, and S.L. Xu. J. Org. Chem. **57**, 1330 (1992).
8. H.M.L. Davies, J. Clark, and G.F. Kimmer. J. Org. Chem. **56**, 6440 (1991).
9. M.C. Pirrung, J. Zhang, and A.T. McPhail. J. Org. Chem. **56**, 6269 (1991).
10. D.C. England and C.G. Krespan. J. Org. Chem. **35**, 3312 (1970).
11. P.W. Raynolds and J.A. DeLoach. J. Am. Chem. Soc. **106**, 4566 (1984).
12. F. Bernardi, A. Bottoni, M.A. Robb, and A.J. Venturini. J. Am. Chem. Soc. **112**, 2106 (1990).
13. (*a*) A.K. Cotter and S.S. Wang. J. Org. Chem. **27**, 1517 (1962); (*b*) J. Tsuji, H. Takahashi, and T. Kajimoto. Tetrahedron Lett. 4573 (1973).
14. E.C. Taylor, A. McKillop, and A.H. Hawks. Org. Synth. **52**, 36 (1972); **52**, 37 (1972).
15. M. Jones and W. Ando. J. Am. Chem. Soc. **90**, 2200 (1968).
16. Y. Yamamoto, S.I. Murahashi, and I. Moritana. Tetrahedron, **31**, 2663 (1975).
17. A. Padwa and R. Layton. Tetrahedron Lett. 2167 (1967).
18. E.J. Corey and M.Chaykovsky. J. Am. Chem. Soc. **87**, 1353 (1965).
19. C.R. Johnson, C.W. Schroeck, and J.R. Shanklin. J. Am. Chem. Soc. **95**, 7424 (1973).
20. M.P. Doyle, R.L. Dorow, W.E. Buhro, J.H. Griffin, W.H. Tamblyn, and M.L. Trudell. Organometallics, **3**, 44 (1984).
21. A.J. Anciaux, A.J. Hubert, A.F. Noels, N. Pertinot, and P. Teyssie. J. Org. Chem. **45**, 695 (1980).
22. W.R. Moser. J. Am. Chem. Soc. **91**, 1135 (1969).
23. A. Nakamura, A. Konishi, R. Tsujitani, M. Kudo, and S. Otsuka. J. Am. Chem. Soc. **100**, 3449 (1978).
24. T. Aratani. Tetrahedron Lett. 2599 (1977).
25. M.P. Doyle. Acc. Chem. Res. **19**, 348 (1986).
26. A. Demonceau, A.F. Noels, J.-L. Costa, and A.J. Hubert. J. Mol. Catal. **58**, 21 (1990).
27. M. Alonso, A. Morales, and A.W. Chitty. J. Org. Chem. **47**, 3747 (1982).
28. (*a*) E. Wenkert. Acc. Chem. Res. **13**, 27 (1980); (*b*) E. Wenkert, M.E. Alonso, B.L. Buckwalter, and E.L. Sanchez. J. Am. Chem. Soc. **105**, 2021 (1983); (*c*) E. Wenkert and T.S. Arrhenius. J. Am. Chem. Soc. **105**, 2030 (1983); (*d*) E. Wenkert, M.E. Alonso, B.L. Buckwalter, and K.J. Chou. J. Am. Chem. Soc. **99**, 4778 (1977).
29. M.E. Alonso, P. Jano, M.I. Hernandez, R.S. Greenberg, and E. Wenkert. J. Org. Chem. **48**, 3047 (1983).
30. (*a*) A. Padwa, D.J. Austin, A.T. Price, M.A. Semones, M.P. Doyle, M.N. Protopopova, W.R. Winchester, and A. Tran. J. Am. Chem. Soc. **115**, 8669 (1993); (*b*) A. Padwa, D.J. Austin, and S.F. Hornbuckle. J. Org. Chem. **61**, 63 (1996).
31. J. Adams and D.M. Spero. Tetrahedron, **47**, 1765 (1991).
32. H.M.L. Davies, E. Saikali, T.J. Clark, and E.H. Chee. Tetrahedron Lett. **31**, 6299 (1990).
33. P. Dowd, C. Kaufman, and Y.H. Paik. Tetrahedron Lett. **26**, 2283 (1985).
34. (*a*) W.C. Still and M.-Y. Tsai. J. Am. Chem. Soc. **102**, 3654 (1980); (*b*) H.E. Zimmerman. J. Am. Chem. Soc. **76**, 2285 (1954).
35. M.L. Graziano and R. Scarpati. J. Chem. Soc. Perkin Trans. 1, 289 (1985).
36. H.M.L. Davies and B. Hu. J. Org. Chem. **57**, 3186 (1992).
37. R. Menicagli, C. Malanga, and L. Lardicci. J. Chem. Res. (S), 20 (1985).
38. I.A. D'Yakonov and M.I. Komendantov. Zh. Obsch. Khim. (USSR), **29**, 1749 (1959)
39. (*a*) B.H. Lipshutz. Chem. Rev. **86**, 795 (1986); (*b*) M.V. Sargent. *In* Comprehensive heterocyclic chemistry. Vol. 4. Part 3. *Edited by* C.W. Bird and G.W.H. Cheeseman. Pergamon Press, New York. 1984; (*c*) W.A. Ayer and S. Miao. Can. J. Chem. **71**, 487 (1993).
40. M.C. Pirrung and Y.R. Lee. Tetrahedron Lett. **37**, 2391 (1996).
41. P.D. Wilson, D. Friedrich, and L.A. Paquette. J. Chem. Soc. Chem. Commun. 1351 (1995).

Extended chain 2,3-pyrazinedicarboxylate complexes of manganese(II) and cadmium(II); synthesis and structure and magnetic properties

Long Mao, Steven J. Rettig, Robert C. Thompson, James Trotter, and Shihua Xia

Abstract: Manganese and cadmium complexes of singly and doubly deprotonated 2,3-pyrazinedicarboxylic acid ($pyzdcH_2$) have been prepared and studied. Crystal data: $[H_3O]_{2x}[Mn(pyzdc)_2]_x$, **1**, monoclinic, $C2/c$ (no. 15), a = 14.472(1) Å, b = 8.475(2) Å, c = 13.0771(9) Å, β = 114.753(4)°, Z = 4; $[H_3O]_{2x}[Cd(pyzdc)_2]_x$, **2**, monoclinic, $C2/c$ (no. 15), a = 14.4857(9) Å, b = 8.502(1) Å, c = 14.9803(7) Å, β = 126.951(2)°, Z = 4; $[Mn(pyzdc)(H_2O)_2]_x \cdot 2xH_2O$, **3**, monoclinic, $P2_1/c$ (no. 14), a = 6.5523(7) Å, b = 7.6702(7) Å, c = 20.5815(6) Å, β = 93.605(5)°, Z = 4; $[Cd(pyzdc)(H_2O)_3]_x \cdot xH_2O$, **4**, monoclinic, Cc (no. 9), a = 6.088(1) Å, b = 11.5410(9) Å, c = 15.0624(7) Å, β = 96.532(8)°, Z = 4. The structures were solved by Patterson (**1**, **4**) or direct (**2**, **3**) methods and were refined by full-matrix least-squares procedures to R = 0.036, 0.025, 0.034, and 0.022 (R_w = 0.032, 0.025, 0.036, and 0.023) for 2825, 4961, 1672, and 2641 reflections with $I \geq 3\sigma(F^2)$, respectively. The structures of **1** and **2** consist of extended anionic chains of metal ions that are linked by double-bridging $pyzdc^{2-}$ groups, with electrical neutrality maintained by the presence of H_3O^+ cations in the lattice. In **3** double chains of manganese ions are cross-linked by $pyzdc^{2-}$ ligands forming a "ladder-like" motif. The structure of **4** consists of extended chains of cadmium ions in which single $pyzdc^{2-}$ groups bridge metal centres. Magnetic susceptibility studies indicate, at most, only weak antiferromagnetic exchange in **1** but moderately strong antiferromagnetic interactions in **3**, mediated by bridging carboxylate groups ($J = -0.27$ cm^{-1}).

Key words: extended chains, manganese, cadmium, 2,3-pyrazinedicarboxylates, X-ray structures, antiferromagnetism.

Résumé : On a préparé et on a étudié des complexes de manganèse et de cadmium de l'acide pyrazinedicarboxylique ($pyzdcH_2$) déprotoné et doublement déprotoné. Les données cristallines sont les suivantes : $[H_3O]_{2x}[Mn(pyzdc)_2]_x$, **1**, monoclinique, $C2/c$ (no. 15), a = 14,472(1) Å, b = 8,475(2) Å, c = 13,0771(9) Å, β = 114,753(4)°, Z = 4; $[H_3O]_{2x}[Cd(pyzdc)_2]_x$, **2**, monoclinique, $C2/c$ (no. 15), a = 14,4857(9) Å, b = 8,502(1) Å, c = 14,9803(7) Å, β = 126,951(2)°, Z = 4; $[Mn(pyzdc)(H_2O)_2]_x \cdot 2xH_2O$, **3**, monoclinique, $P2_1/c$ (no. 14), a = 6,5523(7) Å, b = 7,6702(7) Å, c = 20,5815(6) Å, β = 93,605(5)°, Z = 4; $[Cd(pyzdc)(H_2O)_3]_x \cdot xH_2O$, **4**, monoclinique, Cc (no. 9), a = 6,088(1) Å, b = 11,5410(9) Å, c = 15,0624(7) Å, β = 96,532(8)°, Z = 4. On a résolu les structures par la méthode de Patterson (**1**, **4**) ou la méthode directe (**2**, **3**) et on les a affinées par la méthode des moindres carrés matrice complète jusqu'à des valeurs de R = 0,036, 0,025, 0,034, et 0,022 (R_w = 0,032, 0,025, 0,036 et 0,023) pour 2825, 4961, 1672 et 2641 réflexions avec $I \geq 3\sigma(F^2)$, respectivement. Les structures des composés **1** et **2** consistent en des chaînes anioniques allongées d'ions métalliques qui sont liées par des groupes $pyzdc^{2-}$ doublement pontés, avec la neutralité électrique maintenue par la présence de cations H_3O^+ dans le réseau. Dans le composé **3** des chaînes doubles d'ions manganèse sont réticulées par les ligands $pyzdc^{2-}$ formant un motif en forme d'échelle. La structure du composé **4** consiste en des chaînes allongées d'ions cadmium dans lesquelles un seul groupe $pyzdc^{2-}$ forme un pont entre les centres métalliques. Les études de susceptibilité magnétique indiquent, tout au plus, uniquement un faible échange ferromagnétique dans le composé **1** mais des interactions antiferromagnétiques modérément fortes dans le composé **3** au moyen du groupe carboxylate en position de pont ($J = -0,27$ cm^{-1}).

Mots clés : chaînes allongées, manganèse, cadmium, 2,3-pyrazinedicarboxylates, structures aux rayons X, antiferromagnétisme.

[Traduit par la rédaction]

Received June 7, 1996.

This paper is dedicated to Professor Howard C. Clark in recognition of his contributions to Canadian chemistry.

L. Mao, S.J. Rettig, R.C. Thompson,[1] J. Trotter, and S. Xia. Department of Chemistry, University of British Columbia, 2036 Main Mall, Vancouver, BC V6T 1Z1, Canada.

[1] Author to whom correspondence may be addressed. Telephone: (604) 822-4979. Fax: (604) 822-2847. E-mail: robert.c.thompson@mtsg.ubc.ca

Fig. 1. 2,3-Pyrazinedicarboxylate bridging modes

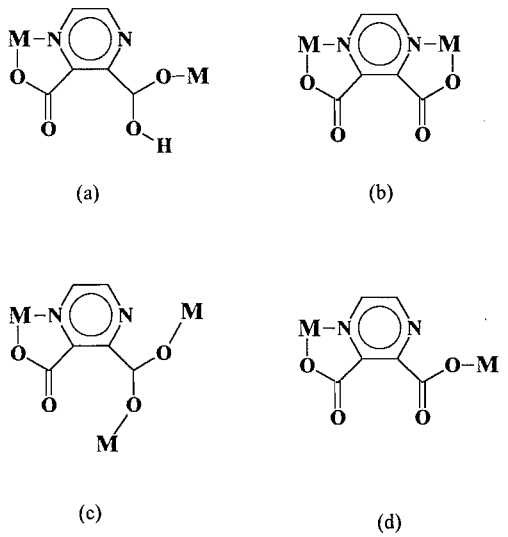

Introduction

The ligands formed by the single and double deprotonation of 2,3-pyrazinedicarboxylic acid ($pyzdcH_2$) can, by virtue of their six donor atoms, bind to metal ions in a variety of ways, including bridging, the latter generating extended polymeric materials. Pyrazine itself (1,4-diazine) has attracted considerable attention as a linear bridge between metals in extended covalent network solids (1–3) and the pyrazinedicarboxylate ligands under consideration here have the added characteristic of potentially forming chelate-supported bridges. Such structural features have been observed in the compound $[Cu(pyzdcH)_2]_x \cdot 2xH_2O$ (4), for example, which has extended chains of copper ions linked by double-bridging $pyzdcH^-$ groups. The bridging mode, depicted in Fig. 1(a), involves chelate interactions to one metal and bonding through single carboxylate oxygens to the second metal. $[M(pyzdc)(H_2O)_2]_x \cdot 2xH_2O$ (where M = Co, Ni, or Cu) (4) and $[Co(pyzdc)(H_2O)_2]_x$ (5), on the other hand, have extended chain structures in which single $pyzdc^{2-}$ ligands bridge the metals by 1,4-diazine links that are supported by chelate formation to both metals (Fig. 1(b)). The compound $Zn(pyzdc) \cdot 3H_2O$ exhibits a different type of structure (6), one in which double chains of metal ions are cross-linked by $pyzdc^{2-}$ groups. The ligands in this structure chelate to a metal in one chain and bridge two metals in the second chain by O-C-O links involving the second carboxylate group (Fig.1(c)).

The dependence of structural type on the nature of the metal in 2,3-pyrazinedicarboxylate complexes has prompted us to extend our detailed structural investigations of this class of compound to complexes of other metals, specifically those of manganese(II) and cadmium(II). By employing dilute aqueous solutions to obtain products, as described previously (4), polymer formation is slow and as a result all four compounds reported here were obtained in crystalline form suitable for single crystal X-ray diffraction studies.

A second interest in studying these complexes concerns the potential of pyrazinedicarboxylate ligands to mediate magnetic exchange interactions in poly- or oligo-metallic complexes. Previous studies revealed only weak antiferromagnetic interactions in polymetallic Co(II), Ni(II), and Cu(II) complexes of these ligands (4) and it was suggested that stronger interactions might be found in systems such as those of manganese(II) in which the metals incorporate unpaired electron density in t_{2g} orbitals. The magnetic properties of two manganese complexes are examined here.

There have been earlier reports on 2,3-pyrazinedicarboxylates of manganese(II) that focused mainly on syntheses and characterization by thermochemical and spectroscopic means (7, 8). No crystal structure determinations or detailed cryomagnetic studies on these systems have been published prior to the present work.

Experimental

Syntheses

Chemicals of at least reagent grade quality were used without further purification. All products are air stable.

*Oxonium poly-bis-μ-(2,3-pyrazinedicarboxylato)manganate(II), $[H_3O]_{2x}[Mn(pyzdc)_2]_x$, **1***

2,3-Pyrazinedicarboxylic acid (0.42 g, 2.5 mmol) was dissolved in 100 mL water and slowly added to a 60 mL aqueous solution of $MnCl_2 \cdot 4H_2O$ (0.25 g, 1.25 mmol). After standing for ~48 h, the solution yielded yellow crystals. After selecting suitable crystals for X-ray analysis, the rest of the product was collected by filtration, washed with water, and dried in vacuo at room temperature for 24 h. Anal. calcd. for $C_{12}H_{10}MnN_4O_{10}$: C 33.90, H 2.37, N 13.18; found: C 33.96, H 2.42, N 13.15.

*Oxonium poly-bis-μ-(2,3-pyrazinedicarboxylato)-cadmiumate(II), $[H_3O]_{2x}[Cd(pyzdc)_2]_x$, **2***

Procedure was as described above for **1**, employing 1.25 mmol $CdCl_2 \cdot 2.5H_2O$ in 60 mL water and 2.5 mmol $pyzdcH_2$ in 70 mL water. Crystals of $[H_3O]_{2x}[Cd(pyzdc)_2]_x$ are colourless. Anal. calcd. for $C_{12}H_{10}CdN_4O_{10}$: C 29.86, H 2.09, N 11.61; found: C 29.89, H 2.08, N 11.81.

*Poly-diaqua-μ-2,3-pyrazinedicarboxylatomanganese(II) dihydrate, $[Mn(pyzdc)(H_2O)_2]_x \cdot 2xH_2O$, **3***

2,3-Pyrazinedicarboxylic acid (0.42 g, 2.5 mmol) was dissolved in 120 mL water and the solution was adjusted to pH = 5 with 1.0 M aqueous NaOH. This solution was added slowly to a 60 mL aqueous solution of $MnCl_2 \cdot 4H_2O$ (0.50 g, 2.5 mmol). Pale yellow, very thin, crystals deposited after the solution was left standing for ~12 h. Crystal growth was allowed to continue for ~2 weeks, then crystals suitable for X-ray diffraction studies were selected. The remainder of the crystals were separated by filtration, washed with water, and dried in vacuo at room temperature for 24 h. Anal. calcd. for $C_6H_{10}MnN_2O_8$: C 24.58, H 3.44, N 9.56; found: C 24.65, H 3.47, N 9.42.

*Poly-triaqua-μ-2,3-pyrazinedicarboxylatocadmium(II) monohydrate, $[Cd(pyzdc)(H_2O)_3]_x \cdot xH_2O$, **4***

Procedure was as described above for **3**, employing 2.5 mmol $CdCl_2 \cdot 2.5H_2O$ in 60 mL water and 2.5 mmol $pyzdcH_2$ in 85 mL water. Colourless crystals deposited after the solution was left standing for ~48 h. Crystals suitable for X-ray diffraction studies were selected and the remainder were separated by filtration, washed with water, and dried in vacuo at room temper-

Table 1. Crystallographic data.[a]

Compound	**1**	**2**	**3**	**4**
Formula	$C_{12}H_{10}MnN_4O_{10}$	$C_{12}H_{10}CdN_4O_{10}$	$C_6H_{10}MnN_2O_8$	$C_6H_{10}CdN_2O_8$
fw	425.17	482.64	293.09	350.56
Color, habit	Yellow, octahedron	Colorless, prism	Pale yellow, needle	Colorless, prism
Crystal system	Monoclinic	Monoclinic	Monoclinic	Monoclinic
Space group	*C*2/*c*	*C*2/*c*	$P2_1/c$	*Cc*
a, Å	14.472(1)	14.4857(9)	6.5523(7)	6.088(1)
b, Å	8.475(2)	8.502(1)	7.6702(7)	11.5410(9)
c, Å	13.0771(9)	14.9803(7)	20.5815(6)	15.0624(7)
β, deg	114.753(4)	126.951(2)	93.605(5)	96.532(8)
V, Å^3	1456.7(4)	1474.3(2)	1032.3(1)	1051.5(2)
Z	4	4	4	4
ρ_{calc}, g/cm^3	1.939	2.174	1.886	2.214
F(000)	860	952	596	688
Radiation	Mo	Mo	Cu	Mo
μ, cm^{-1}	9.39	15.56	108.66	21.16
Crystal size, mm	0.23 × 0.23 × 0.23	0.20 × 0.25 × 0.35	0.06 × 0.09 × 0.35	0.10 × 0.20 × 0.20
Transmission factors	0.94–1.00	0.92–1.00	0.76–1.00	0.85–1.00
Scan type	ω–2θ	ω–2θ	ω–2θ	ω–2θ
Scan range, ω°	1.31+0.35 tan θ	1.37+0.35 tan θ	1.10+0.20 tan θ	1.10+0.35 tan θ
Scan rate, °min^{-1}	32 (up to 8 rescans)	32 (up to 8 rescans)	32 (up to 8 rescans)	32 (up to 8 rescans)
Data collected	+*h*, +*k*, ±*l*	+*h*, +*k*, ±*l*	+*h*, +*k*, ±*l*	+*h*, +*k*, ±*l*
$2\theta_{max}$, deg	90	100	155	80
Crystal. decay, %	Negligible	Negligible	Negligible	Negligible
Total reflections	6428	8119	2473	3606
Unique reflections	6263	7929	2267	3376
R_{merge}	0.038	0.018	0.020	0.023
Number with $I \geq 3\sigma(I)$	2825	4961	1672	2641
Variables	144	144	195	152
R	0.036	0.025	0.034	0.022
R_w	0.032	0.025	0.036	0.023
gof	1.59	1.60	2.40	1.20
Max Δ/σ (final cycle)	0.0003	0.006	0.004	0.002
Residual density e/Å^3	−0.74 to 0.64	−0.30 to 0.19	−0.29 to 0.40	−0.27 to 0.18

[a]Temperature 294 K, Rigaku AFC6S diffractometer, Mo K_α (λ = 0.71069 Å) or Cu K_α (λ = 1.54178 Å) radiation, graphite monochromator, takeoff angle 6.0°, aperture 6.0 × 6.0 mm at a distance of 285 mm from the crystal, stationary background counts at each end of the scan (scan/background time ratio 2:1), $\sigma^2(F^2) = [S^2(C + 4B)]/Lp^2$ (S = scan rate, C = scan count, B = normalized background count), function minimized $\Sigma w(|F_o|-|F_c|)^2$ where $w = 4F_o^2/\sigma^2(F_o^2)$, $R = \Sigma||F_o|-|F_c||/\Sigma|F_o|$, $R_w = (\Sigma w(|F_o|-|F_c|)^2/\Sigma w|F_o|^2)^{1/2}$, and gof = $[\Sigma w(|F_o|-|F_c|)^2/(m-n)]^{1/2}$. Values given for *R*, R_w, and gof are based on those reflections with $I \geq 3\sigma(I)$.

ature for 24 h. Anal. calcd. for $C_6H_{10}CdN_2O_8$: C 20.56, H 2.87, N 7.99; found: C 20.60, H 2.85, N 7.91.

X-ray crystallographic analyses of 1–4

Crystallographic data appear in Table 1. The final unit-cell parameters were obtained by least squares on the setting angles for 25 reflections with 2θ = 37.7°–44.7° for **1**, 61.9°–73.7° for **2**, 102.9°–110.3° for **3**, and 45.0°-51.2° for **4**. The intensities of three standard reflections, measured every 200 reflections throughout the data collections, showed only small random fluctuations for all four compounds. The data were processed and corrected for Lorentz and polarization effects, and absorption (empirical, based on azimuthal scans).[2]

The structures were solved by Patterson (**1**, **4**) or direct (**2**, **3**) methods. The structural analyses of **1** and **2** were initiated in the centrosymmetric space group *C*2/*c* and that of **4** in the non-centrosymmetric space group *Cc* on the basis of the E-statistics. These choices were confirmed by subsequent calculations. The metal atoms in **1** and **2** are situated on crystallographic C_2 axes. It should be noted that **1** and **2** are *not* isostructural even though they are nearly isomorphous and the polymeric chains in the two structures are very similar.

All non-hydrogen atoms were refined with anisotropic thermal parameters. Hydrogen atoms of **1**, **2**, and **3** were refined with isotropic thermal parameters and those of **4** were fixed in calculated positions (O—H = 0.88 Å, C—H = 0.98 Å, $B_H = 1.2\ B_{bonded\ atom}$, O—H hydrogen orientations based on difference map peak positions). Secondary extinction corrections were applied for **1**, **2**, and **3**, the final values of the extinction coefficients being $1.7(2) \times 10^{-7}$, $4.07(9) \times 10^{-7}$, and $2.02(5) \times 10^{-5}$, respectively. Neutral atom scattering factors for all atoms (9) and anomalous dispersion corrections for the non-hydrogen

[2] *teXsan*: Crystal structure analysis package. Molecular Structure Corp. the Woodlands, Tex. 1985 & 1992.

Table 2. Final atomic coordinates (fractional) and B_{eq} (10^3 Å^2).[a]

Atom	*x*	*y*	*z*	B_{eq}
		1		
Mn(1)	0	−0.01093(4)	1/4	1.450(5)
O(1)	0.12682(8)	0.0398(1)	0.40711(8)	1.97(2)
O(2)	0.18588(7)	0.1753(1)	0.56784(8)	2.14(2)
O(3)	0.08342(10)	0.4505(1)	0.66891(9)	2.53(2)
O(4)	0.08245(8)	0.2004(1)	0.71933(8)	1.93(2)
O(5)	0.35500(9)	0.0469(1)	0.63133(10)	2.32(2)
N(1)	−0.06109(8)	0.1511(1)	0.34954(9)	1.47(2)
N(2)	−0.11058(9)	0.3225(2)	0.49969(9)	1.70(2)
C(1)	0.01003(10)	0.1881(2)	0.4521(1)	1.27(2)
C(2)	−0.01486(10)	0.2718(2)	0.5284(1)	1.31(2)
C(3)	−0.1807(1)	0.2846(2)	0.3978(1)	1.91(3)
C(4)	−0.1564(1)	0.1972(2)	0.3228(1)	1.79(2)
C(5)	0.11626(10)	0.1297(2)	0.4772(1)	1.38(2)
C(6)	0.05798(10)	0.3093(2)	0.6489(1)	1.39(2)
		2		
Cd(1)	0	0.25533(1)	1/4	1.523(1)
O(1)	0.03518(8)	0.2078(1)	0.41645(7)	2.04(1)
O(2)	0.13543(8)	0.0652(1)	0.57223(7)	2.19(2)
O(3)	0.33613(10)	−0.2094(1)	0.66853(8)	2.57(2)
O(4)	0.38720(8)	0.0382(1)	0.72517(7)	1.94(1)
O(5)	0.02801(9)	0.1925(1)	0.63518(8)	2.25(2)
N(1)	0.16801(8)	0.0988(1)	0.35722(7)	1.49(1)
N(2)	0.36534(8)	−0.0747(1)	0.50639(8)	1.69(1)
C(1)	0.19672(8)	0.0604(1)	0.45812(8)	1.28(1)
C(2)	0.29726(8)	−0.0249(1)	0.53389(8)	1.30(1)
C(3)	0.3360(1)	−0.0346(2)	0.40629(9)	1.92(2)
C(4)	0.2375(1)	0.0538(1)	0.33147(9)	1.80(2)
C(5)	0.11510(9)	0.1159(1)	0.48332(8)	1.42(1)
C(6)	0.34212(8)	−0.0666(1)	0.65215(8)	1.39(1)
		3		
Mn(1)	0.19247(7)	0.26787(5)	0.38768(2)	1.632(9)
O(1)	0.1934(3)	0.5436(3)	0.40903(9)	2.05(4)
O(2)	0.2635(4)	0.7513(3)	0.4833(1)	2.75(5)
O(3)	0.1372(3)	0.7557(3)	0.6248(1)	2.53(5)
O(4)	0.4741(3)	0.7451(3)	0.6269(1)	2.40(4)
O(5)	0.2072(5)	−0.0075(3)	0.3898(1)	3.03(5)
O(6)	0.1889(4)	0.3007(4)	0.2838(1)	2.82(5)
O(7)	0.4585(5)	0.5508(4)	0.2428(1)	3.75(7)
O(8)	−0.1419(5)	0.2439(4)	0.2033(1)	3.10(6)
N(1)	0.2398(4)	0.2926(3)	0.4987(1)	1.75(5)
N(2)	0.3095(4)	0.3724(3)	0.6302(1)	2.29(5)
C(1)	0.2561(4)	0.4596(4)	0.5190(1)	1.51(5)
C(2)	0.2896(4)	0.4988(4)	0.5850(1)	1.64(5)
C(3)	0.2920(6)	0.2091(4)	0.6090(2)	2.53(6)
C(4)	0.2567(5)	0.1685(4)	0.5435(2)	2.40(7)
C(5)	0.2361(4)	0.5976(4)	0.4663(1)	1.64(5)
C(6)	0.3005(5)	0.6827(3)	0.6128(1)	1.82(5)

atoms (10) were taken from the *International tables for X-ray crystallography*. A parallel refinement of the structure of **4** having the opposite polarity gave significantly higher residuals, the R and R_w ratios being 1.059 and 1.058, respectively.

Final non-hydrogen atomic coordinates and equivalent isotropic thermal parameters, bond lengths, bond angles, and hydrogen bond geometry appear in Tables 2–5, respectively. Hydrogen atom parameters, anisotropic thermal parameters,

Table 2 (*concluded*).

Atom	*x*	*y*	*z*	B_{eq}
		4		
Cd	0.9993	0.13990(1)	0.5003	1.742(2)
O(1)	0.7818(6)	0.1233(3)	0.3689(2)	2.43(5)
O(2)	0.5935(4)	0.2729(2)	0.4152(1)	2.65(4)
O(3)	0.7676(6)	0.3725(3)	0.1152(2)	2.80(6)
O(4)	0.8644(4)	0.3388(2)	0.2608(2)	2.74(4)
O(5)	0.7725(6)	−0.0018(3)	0.5518(2)	3.53(7)
O(6)	1.2242(5)	0.0133(3)	0.4313(2)	2.61(5)
O(7)	1.1377(4)	0.3027(2)	0.4290(2)	2.59(4)
O(8)	0.7380(4)	0.0412(2)	0.7286(2)	3.21(5)
N(1)	0.3070(4)	0.1332(2)	0.2725(1)	1.94(4)
N(2)	0.3987(4)	0.2443(2)	0.1178(1)	1.70(3)
C(1)	0.4903(4)	0.1962(2)	0.2707(1)	1.45(3)
C(2)	0.5373(4)	0.2530(2)	0.1931(1)	1.43(3)
C(3)	0.2146(5)	0.1805(3)	0.1192(2)	2.14(5)
C(4)	0.1703(5)	0.1254(3)	0.1972(2)	2.22(5)
C(5)	0.6368(4)	0.2004(2)	0.3586(2)	1.79(4)
C(6)	0.7392(4)	0.3278(2)	0.1896(2)	1.80(4)

[a] $B_{eq} = (8/3)\pi^2 U_{ij} a_i^* a_j^* (\boldsymbol{a}_i \cdot \boldsymbol{a}_j)$.

complete tables of bond lengths and bond angles, torsion angles, intermolecular contacts, and least-squares planes are included as supplementary material.[3]

Physical measurements

Thermal Gravimetric Analysis (TGA) was performed on powdered samples using a TA Instruments TGA 51 thermogravimetric analyzer. Samples of 5–20 mg were heated at 10°C min^{-1} in an atmosphere of dry nitrogen at a flow rate of 100 mL min^{-1}. Magnetic susceptibilities over the temperature range ~4–82 K were measured at applied fields of 7 501 Oe using a P.A.R. model 155 vibrating sample magnetometer as previously described (11). Samples were held in Kel-F capsules and corrections were made for background signal over the entire temperature range studied. Magnetic susceptibilities were corrected for diamagnetism of all atoms (manganese, −14; $pyzdc^{2-}$ −68; H_2O, −12 (all corrections in units of 10^{-6} cm^3 mol^{-1})). Complete magnetic data have been deposited as supplementary material. Carbon, hydrogen, and nitrogen analyses were performed by P. Borda of this department.

Results and discussion

$[H_3O]_{2x}[M(pyzdc)_2]_x$, 1 (M = Mn), 2 (M = Cd)

Single crystal X-ray diffraction studies reveal that although **1** and **2** have similar unit-cell dimensions and crystallize in the same space group, the two materials are neither isomorphous nor isostructural. The extended chain structures of **1** and **2** (see below), however, are essentially superimposable. Part of the structure of **1**, with the atom numbering scheme, is shown in Fig. 2. In this structure each metal ion is *cis*-coordinated by chelation interactions (involving a ring nitrogen, N(1), and an adjacent carboxylate oxygen, O(1)) to two ligands forming $M(pyzdc)_2^{2-}$ units. The other two *cis* positions are occupied by oxygen atoms, O(4), from carboxylate groups not involved in chelation on two neighbouring units. This results in extended chains of metal ions double-bridged by $pyzdc^{2-}$ ligands, each ligand coordinating in the manner depicted in Fig. 1(d). Electrical neutrality is maintained by the presence of H_3O^+ ions in the lattice. In all four structures described in this work hydrogen-bonding interactions involving the lattice entities H_3O^+ (**1** and **2**) or H_2O (**3** and **4**) link chains in a 3-dimensional network. As an example, part of the network is shown for **1** in Fig. 3.

The stoichiometry of **1** and **2** is the same as that of the previously characterized $[Co(pyzdcH)_2(H_2O)_2]$ (12), $[Ni(pyzdcH)_2(H_2O)_2]$ (4), and $[Cu(pyzdcH)_2]_x \cdot 2xH_2O$ (4), yet the five compounds encompass three very distinct structures. Structurally, **1** and **2** are more closely related to the copper compound, which has a chain structure with double-bridging $pyzdcH^-$ ligands (Fig 1(a)). This contrasts structurally with the cobalt and nickel complexes which are monometallic. Whereas $[Cu(pyzdcH)_2]_x \cdot 2xH_2O$ has H_2O molecules in the lattice, in **1** and **2** the lattice entity is H_3O^+. In effect, the hydroxyl protons of the $pyzdcH^-$ ligands, which are H-bonded to the lattice waters in the copper compound, are transferred to the lattice waters in **1** and **2**, thus forming the H_3O^+ ions. Evidence for this "transfer" comes from the X-ray analyses in which the hydrogen atoms in both structures were located and refined, clearly indicating the presence of H_3O^+ entities. In considering

[3] Supplementary material mentioned in the text may be purchased from: The Depository of Unpubliahed Data, Document Delivery, CISTI, National Research Council of Canada, Ottawa, Canada K1A 0S2. Tables of hydrogen atom coordinates and bond lengths and angles involving hydrogen atoms have also been deposited with the Cambridge Crystallographic Data Centre and can be obtained on request from The Director, Cambridge Crystallographic Data Centre, University Chemical Laboratory, 12 Union Road, Cambridge CB2 1EZ, U.K.

Fig. 2. The structure of $[H_3O]_{2x}[Mn(pyzdc)_2]_x$ (**1**), with atom numbering scheme; 33% probability thermal elipsoids are shown.

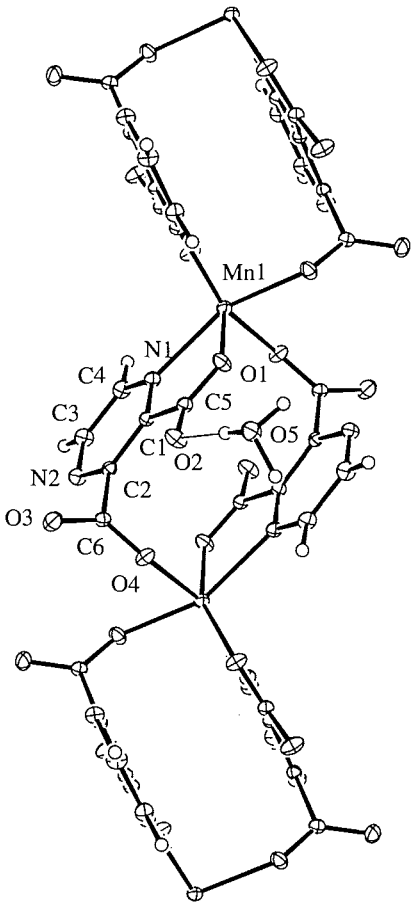

why the ligand proton should be "transferred" from the hydroxyl group in the Mn and Cd compounds but not in the Cu compound, we note that in the latter the oxygen, O(4), of the carboxylic acid group is only weakly coordinated to a metal ion (Cu—O(4) distance 2.405(2) Å versus 1.948(1) Å for the distance involving the chelating oxygens, O(1)). Hence the acidity of the hydroxyl proton is not greatly enhanced by electron polarization effects of the metal ion and the proton remains bonded to O(3). In both **1** and **2**, however, each ligand has one oxygen from each of its carboxylate groups involved in comparable and relatively strong coordination to a metal (Mn—O(1) = 2.1486(9) Å, Mn—O(4) = 2.136(1) Å, Cd—O(1) = 2.2611(8) Å, and Cd—O(4) = 2.2716(8) Å); thus, the other carboxylate oxygens on each ligand, O(2) and O(3), are rendered weakly basic and the hydroxyl protons are transferred to water molecules, forming H_3O^+ entities. The weak Cu—O(4) interaction is a consequence of the preference of Cu(II) for distorted geometries, a factor not relevant for Mn(II) or Cd(II).

Interestingly the thermal properties of these compounds clearly reflect the difference in the lattice units. Whereas $[Cu(pyzdcH)_2]_x \cdot 2xH_2O$ undergoes dehydration with relative ease, losing the lattice water over the temperature range 50–160°C (4), **1** and **2** are thermally stable to significantly higher temperatures. Thermogravimetric analysis, TGA, of **1** shows it to be stable to about 150°C, decomposing with loss of two moles of H_2O and two moles of CO_2 over the range 150–265°C. This is in good agreement with an earlier thermal study on a structurally uncharacterized compound of the same stoichiometry as **1** (8). TGA studies on **2** show the compound to be stable to 165°C, decomposing with loss of two moles of H_2O and one mole of CO over the range 165–268°C.

Octahedral complexes of manganese(II), by virtue of their high unpaired spin density and orbitally non-degenerate ground state ($^6A_{1g}$ in O_h), are ideally suited for studies on magnetic exchange interactions. The possibility of magnetic exchange interactions mediated by the bridging $pydzdc^{2-}$ ligands in **1** was investigated by examining the magnetic prop-

Table 3. Bond lengths (Å) with estimated standard deviations in parentheses.[a]

Bond	Length	Bond	Length
1			
Mn(1)—O(1)	2.1486(9)	Mn(1)—O(4)′	2.136(1)
Mn(1)—N(1)	2.308(1)	O(1)—C(5)	1.250(2)
O(2)—C(5)	1.253(2)	O(3)—C(6)	1.247(2)
O(4)—C(6)	1.246(2)	N(1)—C(4)	1.332(2)
N(1)—C(1)	1.342(2)	N(2)—C(3)	1.333(2)
N(2)—C(2)	1.345(2)	C(1)—C(5)	1.515(2)
C(1)—C(2)	1.389(2)	C(3)—C(4)	1.388(2)
C(2)—C(6)	1.518(2)		
2			
Cd(1)—O(1)	2.2611(8)	Cd(1)—O(4)′	2.2716(8)
Cd(1)—N(1)	2.3609(9)	O(1)—C(5)	1.249(1)
O(2)—C(5)	1.255(1)	O(3)—C(6)	1.252(1)
O(4)—C(6)	1.248(1)	N(1)—C(4)	1.332(1)
N(1)—C(1)	1.345(1)	N(2)—C(3)	1.334(1)
N(2)—C(2)	1.345(1)	C(1)—C(5)	1.516(1)
C(1)—C(2)	1.396(1)	C(3)—C(4)	1.390(2)
C(2)—C(6)	1.517(1)		
3			
Mn(1)—O(1)	2.160(2)	Mn(1)—O(3)′	2.167(2)
Mn(1)—O(4)″	2.226(2)	Mn(1)—O(5)	2.115(2)
Mn(1)—O(6)	2.151(2)	Mn(1)—N(1)	2.294(2)
O(1)—C(5)	1.264(3)	O(2)—C(5)	1.240(3)
O(3)—C(6)	1.246(4)	O(4)—C(6)	1.251(3)
N(1)—C(1)	1.349(3)	N(1)—C(4)	1.326(4)
N(2)—C(2)	1.344(4)	N(2)—C(3)	1.328(4)
C(1)—C(2)	1.393(4)	C(1)—C(5)	1.516(4)
C(2)—C(6)	1.523(4)	C(3)—C(4)	1.389(4)
4			
Cd—O(1)	2.261(3)	Cd—O(3)′	2.246(4)
Cd—O(5)	2.329(4)	Cd—O(6)	2.327(3)
Cd—O(7)	2.366(2)	Cd—N(2)′	2.354(2)
O(1)—C(5)	1.250(4)	O(2)—C(5)	1.245(3)
O(3)—C(6)	1.263(4)	O(4)—C(6)	1.249(3)
N(1)—C(1)	1.335(3)	N(1)—C(4)	1.331(4)
N(2)—C(2)	1.338(3)	N(2)—C(3)	1.343(4)
C(1)—C(2)	1.398(3)	C(1)—C(5)	1.511(3)
C(2)—C(6)	1.508(4)	C(3)—C(4)	1.388(4)

[a]Symbols refer to the symmetry operations: (for **1**): (*) $-x, y, 1/2-z$; (′) $x, -y, -1/2+z$; (″) $1/2-x, 1/2+y, 3/2-z$; (for **2**): (′) $-1/2+x, 1/2-y, -1/2+z$; (″) $1/2-x, 1/2-y, 1-z$; (*) $-x, y, 1/2-z$; (for **3**): (′) $-x, 1-y, 1-z$; (″) $1-x, 1-y, 1-z$; (for **4**): (′) $1/2+x, 1/2-y, 1/2+z$; (″) $-1/2+x, 1/2-y, -1/2+z$.

Fig. 3. Stereoscopic view showing part of the H-bonding network in $[H_3O]_{2x}[Mn(pyzdc)_2]_x$ (**1**).

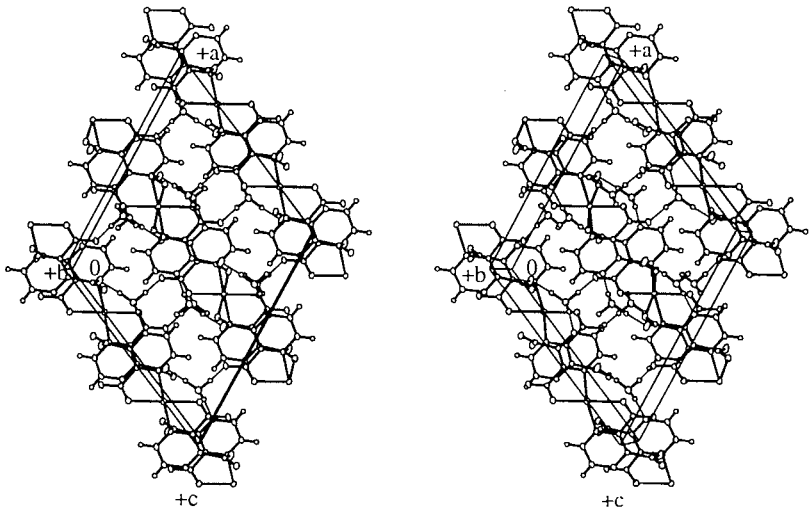

erties of a powdered sample of the compound at low temperatures. The magnetic moment of **1** is 5.90 μ_B at 82 K and decreases only slightly to 5.70 μ_B at 4.4 K. In view of the known structure of the compound, the magnetic susceptibilities were analysed according to the Weng Heisenberg model for antiferromagnetically coupled linear chains of metal ions with the coefficients generated by Hiller et al. (13) for $S = 5/2$. Accordingly

$$[1] \quad \chi_M = [Ng^2\beta^2/kT]\,[A + BX^2]\,[1 + CX + DX^3]^{-1}$$

where for $S = 5/2$, $A = 2.9167$, $B = 208.04$, $C = 15.543$, $D = 2707.2$, and $X = |J|/kT$. Fits of the experimental data to the model were made using a nonlinear least-squares procedure with the following function minimized:

$$[2] \quad F = \left[\frac{1}{n}\sum_{i=1}^{n}\left(\frac{\chi^i_{calc} - \chi^i_{obs}}{\chi^i_{obs}}\right)^2\right]^{1/2}$$

where n is the number of data points. F provides a measure of the goodness of fit between theory and experiment. In the fitting procedure g was fixed at 2.00 and J, the exchange coupling constant, was allowed to vary. The best agreement between experiment and theory was obtained with $J = -0.017$ cm^{-1} ($F = 0.0094$).[4] The experimental magnetic moments as well as the line calculated using the best fit value of J are shown in Fig. 4. The magnitude of J is small and, particularly since zero field splitting effects can account for minor decreases in moment at low temperatures (14), not too much quantitative significance should be attached to it. Clearly though, the results place an upper limit of 0.017 cm^{-1} on the magnitude of the exchange coupling constant in **1** and show that antiferromagnetic exchange in the compound, if it exists at all, is very weak. It is of interest to compare the results for **1** with those reported earlier for the structurally related $[Cu(pyzdcH)_2]_x \cdot 2xH_2O$. To compare complexes with different d^n configurations it is appropriate to compare values of $4S^2J$ (where S is the total spin) rather than J (15). The upper limit of this parameter for **1** is 0.43 cm^{-1}, comparable to, though greater than, the value 0.11 cm^{-1} for $[Cu(pyzdcH)_2]_x \cdot 2xH_2O$ (4). A structural feature of the $pyzdc^{2-}$ bridge in **1** that is not seen in the depiction in Fig. 1(d) but is seen in the detailed representation in Fig. 2 concerns the CO_2 group engaged in the non-chelate metal binding; the plane of this group is almost orthogonal to the plane of the heterocyclic ring. This feature was noted previously in the case of the $pyzdcH^-$ bridging ligands in $[Cu(pyzdcH)_2]_x \cdot 2xH_2O$ (4) and, as discussed there, such a situation would not favor magnetic exchange interactions as it eliminates a delocalized π-electron pathway for exchange.

[4] Here and elsewhere in this work the uncertainty in J is estimated to be approximately 10%.

$[Mn(pyzdc)(H_2O)_2]_x \cdot 2xH_2O$, 3, and $[Cd(pyzdc)(H_2O)_3]_x \cdot xH_2O$, 4

Compounds **3** and **4** have the same stoichiometry as that of the previously studied complexes of composition $[M(pyzdc)(H_2O)_2]_x \cdot 2xH_2O$ (M = Co, Ni, or Cu) (4). Structurally though, **3** and **4** are different from one another and each has different structures from the other three. The Co, Ni, and Cu compounds are isomorphous (4) and have structures involving extended chains of metal ions linked by $pyzdc^{2-}$ ligands coordinated to two metal centres via chelate interactions as depicted in Fig. 1(b). Part of the structure of **3** with the atom numbering scheme is shown in Fig. 5. This structure consists of double chains of manganese ions in which $pyzdc^{2-}$ ligands provide O(3)-C(6)-O(4) bridges between metals in each chain and, through chelate interactions with metals in the other chain (involving a ring nitrogen, N(1), and a carboxylate oxygen, O(1) of the second carboxylate group), cross-link the chains forming a "ladder-like" motif. A similar double chain structure was reported earlier for $Zn(pyzdc) \cdot 3H_2O$ (6) and a simplified representation of the $pyzdc^{2-}$ bridging mode in **3** and in the zinc compound is shown in Fig. 1(c). There are, in addition, two *cis*-coordinated and two lattice water molecules per metal in **3**. We note that the metal – ligand chromophore in **3** is MNO_5 while in the analogous Co, Ni, and Cu complexes the chromophore is MN_2O_4. Manganese(II) often shows a prefer-

Table 4. Bond angles (deg) with estimated standard deviations in parentheses.[a]

Bonds	Angle(deg)	Bonds	Angle(deg)
1			
O(1)—Mn(1)—O(1)*	156.93(6)	O(1)—Mn(1)—O(4)′	90.52(4)
O(1)—Mn(1)—O(4)″	106.94(4)	O(1)—Mn(1)—N(1)	73.58(4)
O(1)—Mn(1)—N(1)*	92.56(4)	O(4)′—Mn(1)—O(4)″	82.54(6)
O(4)′—Mn(1)—N(1)	158.32(4)	O(4)′—Mn(1)—N(1)*	88.02(4)
N(1)—Mn(1)—N(1)*	106.95(6)	Mn(1)—O(1)—C(5)	120.36(9)
Mn(1)″—O(4)—C(6)	133.42(9)	Mn(1)—N(1)—C(4)	128.71(9)
Mn(1)—N(1)—C(1)	112.83(9)	C(2)—N(2)—C(3)	117.8(1)
C(1)—N(1)—C(4)	118.1(1)	N(1)—C(1)—C(5)	115.1(1)
N(1)—C(1)—C(2)	121.1(1)	N(2)—C(2)—C(1)	120.6(1)
C(2)—C(1)—C(5)	123.8(1)	C(1)—C(2)—C(6)	125.2(1)
N(2)—C(2)—C(6)	114.2(1)	N(1)—C(4)—C(3)	120.8(1)
N(2)—C(3)—C(4)	121.5(1)	O(1)—C(5)—C(1)	117.7(1)
O(1)—C(5)—O(2)	125.8(1)	O(3)—C(6)—O(4)	126.0(1)
O(2)—C(5)—C(1)	116.5(1)	O(4)—C(6)—C(2)	118.1(1)
O(3)—C(6)—C(2)	115.8(1)		
2			
O(1)—Cd(1)—O(1)*	159.43(5)	O(1)—Cd(1)—O(4)′	88.95(3)
O(1)—Cd(1)—O(4)″	107.12(3)	O(1)—Cd(1)—N(1)	72.08(3)
O(1)—Cd(1)—N(1)*	96.11(3)	O(4)′—Cd(1)—O(4)″	78.77(5)
O(4)′—Cd(1)—N(1)	153.24(3)	O(4)′—Cd(1)—N(1)*	88.76(3)
N(1)—Cd(1)—N(1)*	111.39(4)	Cd(1)—O(1)—C(5)	118.81(7)
Cd(1)″—O(4)—C(6)	129.86(7)	Cd(1)—N(1)—C(4)	127.90(7)
Cd(1)—N(1)—C(1)	113.41(7)	C(2)—N(2)—C(3)	117.82(9)
C(1)—N(1)—C(4)	118.59(9)	N(1)—C(1)—C(5)	116.35(8)
N(1)—C(1)—C(2)	120.44(9)	N(2)—C(2)—C(1)	120.88(9)
C(2)—C(1)—C(5)	123.21(8)	C(1)—C(2)—C(6)	125.16(8)
N(2)—C(2)—C(6)	113.94(8)	N(1)—C(4)—C(3)	120.64(10)
N(2)—C(3)—C(4)	121.57(10)	O(1)—C(5)—C(1)	118.71(9)
O(1)—C(5)—O(2)	125.37(10)	O(3)—C(6)—O(4)	125.57(10)
O(2)—C(5)—C(1)	115.92(9)	O(4)—C(6)—C(2)	119.21(9)
O(3)—C(6)—C(2)	115.07(9)		
3			
O(1)—Mn(1)—O(3)′	95.52(8)	O(1)—Mn(1)—O(4)″	94.63(8)
O(1)—Mn(1)—O(5)	167.0(1)	O(1)—Mn(1)—O(6)	95.00(9)
O(1)—Mn(1)—N(1)	73.62(8)	O(3)′—Mn(1)—O(4)″	163.69(8)
O(3)′—Mn(1)—O(5)	87.9(1)	O(3)′—Mn(1)—O(6)	86.75(10)
O(3)′—Mn(1)—N(1)	101.34(8)	O(4)″—Mn(1)—O(5)	85.08(10)
O(4)″—Mn(1)—O(6)	79.67(9)	O(4)″—Mn(1)—N(1)	93.76(8)
O(5)—Mn(1)—O(6)	97.7(1)	O(5)—Mn(1)—N(1)	93.4(1)
O(6)—Mn(1)—N(1)	166.49(9)	Mn(1)—O(1)—C(5)	120.5(2)
Mn(1)′—O(3)—C(6)	143.2(2)	Mn(1)″—O(4)—C(6)	146.9(2)
Mn(1)—N(1)—C(1)	113.0(2)	Mn(1)—N(1)—C(4)	129.4(2)
C(1)—N(1)—C(4)	117.6(2)	C(2)—N(2)—C(3)	116.8(2)
N(1)—C(1)—C(2)	120.8(3)	N(1)—C(1)—C(5)	116.0(2)
C(2)—C(1)—C(5)	123.2(2)	N(2)—C(2)—C(1)	121.4(3)
N(2)—C(2)—C(6)	114.1(2)	C(1)—C(2)—C(6)	124.5(3)
N(2)—C(3)—C(4)	122.3(3)	N(1)—C(4)—C(3)	121.1(3)
O(1)—C(5)—O(2)	126.5(3)	O(1)—C(5)—C(1)	116.3(2)
O(2)—C(5)—C(1)	117.2(2)	O(3)—C(6)—O(4)	124.2(3)
O(3)—C(6)—C(2)	118.1(3)	O(4)—C(6)—C(2)	117.5(3)

ence for O over N donors and this may, in part at least, account for the different structure adopted by **3**.

Consistent with the presence of lattice water in **3**, the compound undergoes decomposition at fairly low temperatures. TGA analysis revealed loss of water in two distinct steps involving loss of three moles over the range 50–175°C and a fourth water from 175 to 320°C. This is in good agreement with thermal studies reported previously (7) on a structurally uncharacterized compound of the same stoichiometry as **3**. The inconsistency of the pattern of

Table 4 (*concluded*).

Bonds	Angle(deg)	Bonds	Angle(deg)
4			
O(1)—Cd—O(3)′	166.35(9)	O(1)—Cd—O(5)	85.5(1)
O(1)—Cd—O(6)	82.6(1)	O(1)—Cd—O(7)	82.73(9)
O(1)—Cd—N(2)′	122.00(10)	O(3)′—Cd—O(5)	96.0(1)
O(3)′—Cd—O(6)	83.7(1)	O(3)′—Cd—O(7)	97.8(1)
O(3)′—Cd—N(2)′	71.66(9)	O(5)—Cd—O(6)	96.26(10)
O(5)—Cd—O(7)	164.5(1)	O(5)—Cd—N(2)′	86.2(1)
O(6)—Cd—O(7)	92.17(10)	O(6)—Cd—N(2)′	155.38(9)
O(7)—Cd—N(2)′	91.53(8)	Cd—O(1)—C(5)	112.5(2)
Cd″—O(3)—C(6)	119.8(2)	C(1)—N(1)—C(4)	117.6(2)
Cd″—N(2)—C(2)	113.7(2)	Cd″—N(2)—C(3)	127.8(2)
C(2)—N(2)—C(3)	118.3(2)	N(1)—C(1)—C(2)	121.6(2)
N(1)—C(1)—C(5)	114.3(2)	C(2)—C(1)—C(5)	124.2(2)
N(2)—C(2)—C(1)	120.3(2)	N(2)—C(2)—C(6)	116.8(2)
C(1)—C(2)—C(6)	122.9(2)	N(2)—C(3)—C(4)	120.5(2)
N(1)—C(4)—C(3)	121.8(3)	O(1)—C(5)—O(2)	126.6(3)
O(1)—C(5)—C(1)	115.1(2)	O(2)—C(5)—C(1)	118.1(3)
O(3)—C(6)—O(4)	126.0(3)	O(3)—C(6)—C(2)	117.3(3)
O(4)—C(6)—C(2)	116.7(2)		

[a]Symbols refer to the symmetry operations: (for **1**): (*) $-x$, y, $1/2-z$; (′) x, $-y$, $-1/2+z$; (″) $1/2-x$, $1/2+y$, $3/2-z$; (for **2**): (′) $-1/2+x$, $1/2-y$, $-1/2+z$; (″) $1/2-x$, $1/2-y$, $1-z$; (*) $-x$, y, $1/2-z$; (for **3**): (′) $-x$, $1-y$, $1-z$; (″) $1-x$, $1-y$, $1-z$; (for **4**): (′) $1/2+x$, $1/2-y$, $1/2+z$; (″) $-1/2+x$, $1/2-y$, $-1/2+z$.

Fig. 4. Magnetic moment and magnetic susceptibility versus temperature plots: triangles and squares are moment data for **1** and **3**, respectively; circles are susceptibility data for **3**; lines are calculated from theory as described in the text.

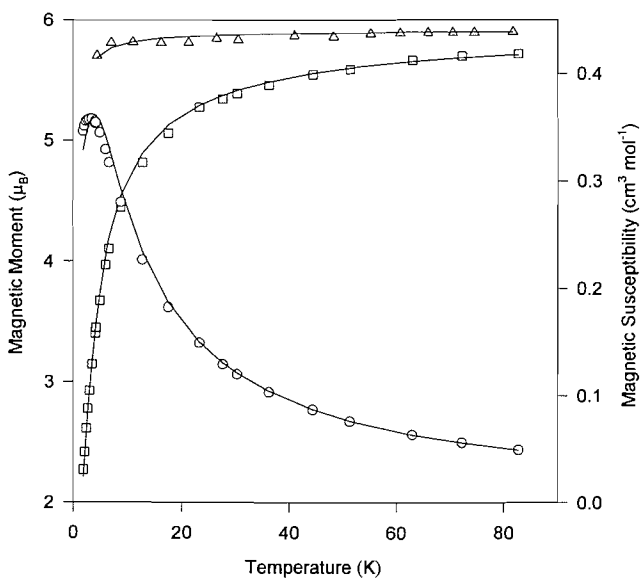

water loss in relation to the structure of the original compound (two lattice and two coordinated water molecules) suggests that considerable structural rearrangement occurs during dehydration.

Cryomagnetic studies on **3** show the magnetic moment to decrease from 5.71 μ_B at 82 K to 2.27 μ_B at 1.9 K. Such behaviour indicates the presence of significant antiferromag-

Fig. 5. The structure of $[Mn(pyzdc)(H_2O)_2]_x \cdot 2xH_2O$ (**3**), with atom numbering scheme; 33% probability thermal elipsoids are shown.

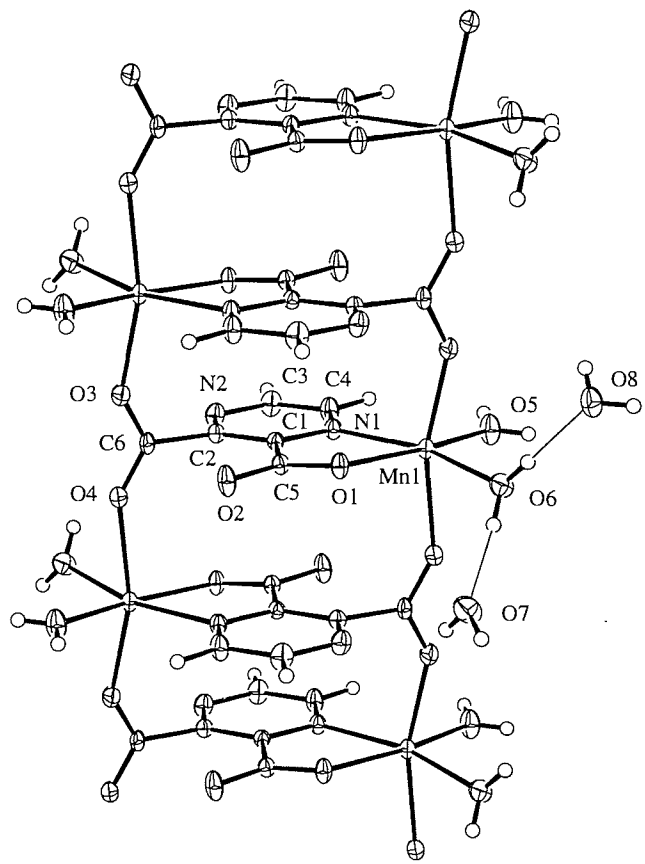

Table 5. Hydrogen bond geometry (Å, deg).[a]

D—H...A	D—H	H...A	D...A	D—H...A
		1		
O(5)—H(3)...O(2)	0.99(3)	1.51(3)	2.482(2)	169(3)
O(5)—H(4)...O(3)[a]	1.09(2)	1.45(2)	2.517(2)	165(2)
O(5)—H(5)...N(2)[b]	0.92(2)	1.83(2)	2.747(2)	174(2)
C(3)—H(1)...O(4)[c]	0.91(2)	2.52(2)	3.242(2)	137(1)
		2		
O(5)—H(3)...O(2)	0.91(2)	1.59(2)	2.499(1)	177(2)
O(5)—H(4)...O(3)[d]	1.13(3)	1.39(3)	2.501(1)	168(2)
O(5)—H(5)...N(2)[e]	1.05(3)	1.74(3)	2.779(1)	170(2)
C(3)—H(1)...O(4)[f]	0.92(2)	2.51(2)	3.214(1)	134(1)
		3		
O(5)—H(1)...O(2)[g]	0.84(4)	1.85(5)	2.679(3)	166(4)
O(5)—H(2)...O(8)[h]	0.77(5)	1.98(5)	2.718(4)	161(5)
O(6)—H(3)...O(8)	0.78(4)	1.90(4)	2.680(4)	178(4)
O(6)—H(4)...O(7)	0.83(4)	1.95(4)	3.077(4)	169(4)
O(7)—H(5)...N(2)[i]	0.79(6)	2.31(6)	3.000(4)	147(5)
O(7)—H(6)...O(4)[j]	0.86(5)	2.04(5)	2.860(3)	161(4)
O(8)—H(7)...O(7)[h]	0.69(4)	2.17(4)	2.832(5)	160(5)
O(8)—H(8)...O(1)[h]	0.80(6)	1.99(6)	2.779(3)	173(6)
C(4)—H(10)...O(2)[g]	0.94(3)	2.52(3)	3.433(4)	165(3)
		4		
O(5)—H(2)...O(8)	0.88	1.98	2.741(4)	144
O(6)—H(3)...N(1)[k]	0.88	1.98	2.858(4)	172
O(7)—H(5)...O(2)[k]	0.88	1.95	2.827(4)	178
O(7)—H(6)...O(4)	0.88	2.03	2.899(3)	170
O(8)—H(7)...O(4)[l]	0.88	1.88	2.752(3)	173
O(8)—H(8)...O(1)[m]	0.88	1.95	2.830(4)	174
C(3)—H(9)...O(2)[c]	0.98	2.33	3.124(3)	138
C(4)—H(10)...O(8)[n]	0.98	2.37	3.337(4)	167

[a]Superscripts refer to symmetry operations: (a) 1/2–x, –1/2+y, 3/2–z; (b) 1/2+x, –1/2+y, z; (c) –1/2+x, 1/2–y, –1/2+ z; (d) 1/2–x, 1/2+y, 3/2– z; (e) –1/2+x, 1/2+y, z; (f) x, –y, –1/2+ z; (g) x, –1+y, z; (h) –x, –1/2+y, 1/2– z; (i) 1–x, 1–y, 1– z; (j) x, 3/2–y, –1/2+ z (k) 1+x, y, z; (l) –1/2+x, 1/2–y, 1/2+z; (m) x, –y, 1/2+z; (n) –1+x, –y, –1/2+z.

netic exchange, a fact confirmed by the observation of a maximum in the susceptibility versus temperature plot at about 3 K (Fig. 4). The structure of **3** shows each metal bonded to two nearest neighbours via O-C-O bridges and to a third nearest neighbour metal in the attached chain by the heterocyclic ring. This suggests the possibility of a fairly complex coupling scheme with at least two J's needed to characterize the system. However, in view of our results for **1** it seems likely that exchange mediated by the ligands between the chains will be very weak and, to a good approximation, may be ignored. The behaviour under such circumstances should follow that expected for isolated chains. Under this assumption, we examined fits of the magnetic susceptibility to the Weng linear chain model as described above and obtained a satisfactory best fit for $J = -0.27$ cm^{-1} with g fixed at 2.00 (F = 0.027). The experimental magnetic moments and susceptibilities as well as the lines calculated using the best fit value of J are shown in Fig. 4. In a classic paper on linear chain antiferromagnetism (16) Wagner and Friedberg determined that in $Mn(HCO_2)_2 \cdot 2H_2O$ chains of manganese(II) ions, linked by double-bridging carboxylate groups, are antiferromagnetically coupled with $J = -0.56$ cm^{-1}, while manganese ions linked by single-bridging carboxylates in the same structure are more weakly antiferromagnetically coupled. Consistent with these early results, our analysis shows that in **3** the single carboxylate-bridged manganese(II) ions are coupled antiferromagnetically with the magnitude of the exchange coupling constant approximately half that observed for the double carboxylate-bridged manganese chains in the formate compound.

Figure 6 shows part of the structure of **4** along with the atom numbering scheme. This structure consists of extended chains of cadmium ions in which single bridging $pyzdc^{2-}$ groups bind to metal centres as in **1** and **2** (Fig. 1(d)) and six-coordination about each metal is achieved with three water molecules coordinating in a *mer* fashion. There is one lattice water per metal in this structure and, consistent with this, the compound is thermally unstable above 60°C. TGA studies reveal loss of four H_2O over the temperature range 60–270°C. There are no other known examples of pyrazinedicarboxylates with the structure exhibited by **4**.

Summary and conclusions

All four of the compounds studied in this work have extended

Fig. 6. The structure of $[Cd(pyzdc)(H_2O)_3]_x \cdot xH_2O$ (**4**), with atom numbering scheme; 33% probability thermal elipsoids are shown.

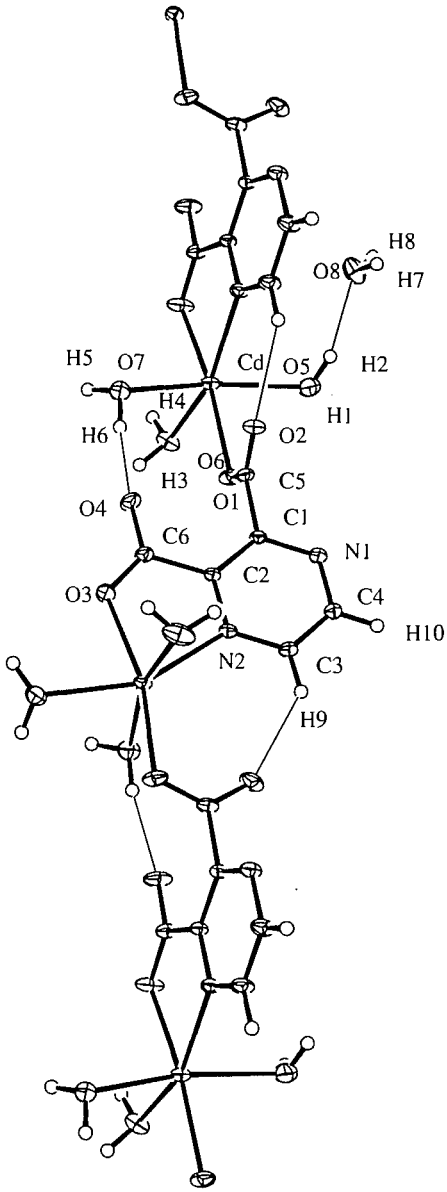

chain structures. The novel "ladder-like" double chain structure of **3** is known to occur in one other pyrazinedicarboxylate structure, $Zn(pydc) \cdot 3H_2O$ (6), while the structural types exhibited by **1**, **2**, and **4** have not been reported previously. Cryomagnetic studies on **1** reveal, at best, only weak antiferromagnetic interactions and confirm an earlier observation that 2,3-pyrazinedicarboxylate ligands are not strong mediators of magnetic exchange when the π-pathway for exchange is disrupted. In **3**, moderate antiferromagnetic coupling occurs between magnetic centres where the pathway for exchange does not involve the heterocyclic part of the ligand but involves single O-C-O bridges. The magnitude of the exchange is consistent with that observed previously for carboxylate-bridged chains of manganese(II) ions.

Acknowledgments

Financial support from the Natural Sciences and Engineering Research Council of Canada is gratefully acknowledged.

References

1. B.F. Hoskins and R. Robson. J. Am. Chem. Soc. **112**, 1546 (1990).
2. T. Otieno, S.J. Rettig, R.C. Thompson, and J. Trotter. Inorg. Chem. **32**, 1607 (1993).
3. L.R. MacGillivary, S. Subramanian, and M.J. Zaworotko. J. Chem. Soc. Chem. Commun. 1325 (1994).
4. L. Mao, S.J. Rettig, R.C. Thompson, J. Trotter, and S. Xia. Can. J. Chem. **74**, 433 (1996).
5. P. Richard, D. Tran Qui, and E.F. Bertaut. Acta Crystallogr. Sect. B: Struct. Crystallogr. Cryst. Chem. **B29**, 111 (1973).
6. P. Richard, D. Tran Qui, and E.F. Bertaut. Acta Crystallogr. Sect. B: Struct. Crystallogr. Cryst. Chem. **B30**, 628 (1974).
7. R.L. Chapman, F.S. Stephens, and R.S. Vagg. Inorg. Chim. Acta, **26**, 247 (1977).
8. A.L. Magri, A.D. Magri, F. Balestrieri, E. Cardarelli, G. D'Ascenzo, and A. Pazanelli. Thermochim. Acta, **48**, 253 (1981).
9. International tables for X-ray crystallography. Vol. IV. Kynoch Press, Birmingham, U.K. (present distributor Kluwer Academic Publishers. Boston, Mass., U.S.A.). 1974. pp. 99–102.
10. International tables for crystallography. Vol. C. Kluwer Academic Publishers, Boston, Mass., U.S.A. 1992. pp. 200–206.
11. J.S. Haynes, K.W. Oliver, S.J. Rettig, R.C. Thompson, and J. Trotter. Can. J. Chem. **62**, 891 (1984).
12. C.L. Klein, C.J. O'Connor, R.J. Majeste, and L.M. Trefonas. J. Chem. Soc. Dalton Trans. 2419 (1982).
13. W. Hiller, J. Strahle, A. Datz, M. Hanack, W.E. Hatfield, L.W. terHaar, and P. Gutlich. J. Am. Chem. Soc. **106**, 329 (1984).
14. W.E. Hatfield, W.E. Estes, W.E. Marsh, M.W. Pickens, L.W. ter Haar, and R.W. Weller. *In* Extended linear chain compounds. Vol. 3. *Edited by* J.S. Miller. Plenum Press, New York. 1983. Chap. 2.
15. S.L. Lambert and D.N. Hendrickson. Inorg. Chem. **18**, 2683 (1979).
16. G.R. Wagner and S.A. Friedberg. Phys. Lett. **9**, 11 (1964).

Ryanoids and related compounds. Identification of five new ryanoids from the plant *Ryania speciosa* Vahl. Formal total syntheses of 3-deoxyryanodol (cinnzeylanol), 10-*O*-acetyl-3-deoxyryanodol (cinnzeylanine), 2-deoxyryanodol, 2-deoxy-2-epiryanodol, 2,3-dideoxy-2,3-dihydroryanodol, 2-deoxy-3-epiryanodol, and 2-deoxy-3-epiryanodine[1]

Luc Ruest and Marco Dodier

Abstract: In the course of a preliminary investigation on the relationships between the chemical structure of ryanoids and their affinity to the ryanodine binding site, we have isolated, from the plant *Ryania speciosa* Vahl, four new members of this family of natural insecticidal compounds (ryanoids **3**, **4**, **5**, and **6**) and corrected the reported structure of a fifth one (ryanoid **7**). In addition, we have synthesized, from anhydroryanodol (**10**), new members of this family having fewer hydroxyl groups in ring A: cinnzeylanol (**14**) and cinnzeylanine (**15**), 2,3-dideoxy-2,3-dihydroryanodol (**16**), 2-deoxy-3-epiryanodol (**18**), and 2-deoxy-3-epiryanodine (**19**), 2-deoxyryanodol (**20**), and 2-deoxy-2-epiryanodol (**21**).

Key words: ryanoids synthesis, cinnzeylanine, 2-deoxyryanodols, 2-deoxy-3-epiryanodine.

Résumé : Dans le cadre d'une étude préliminaire des relations structures chimiques – activité biologique des ryanoïdes et de leur affinité au site récepteur de la ryanodine, nous avons isolé de la plante *Ryania speciosa* Vahl, quatre nouveaux membres de cette famille d'insecticides naturels (les ryanoïdes **3**, **4**, **5** et **6**) et corrigé la structure déjà rapportée d'un cinquième (le ryanoïde **7**). Par ailleurs, à partir de l'anhydroryanodol (**10**), nous avons synthétisé quelques membres de cette famille, moins oxygénés au cycle A : le cinnzeylanol (**14**) et la cinnzeylanine (**15**), le 2,3-didéoxy-2,3-dihydroryanodol (**16**), le 2-déoxy-3-épiryanodol (**18**) et la 2-déoxy-3-épiryanodine (**19**), le 2-déoxyryanodol (**20**) et le 2-déoxy-2-épiryanodol (**21**).

Mots clés : synthèse de ryanoïdes, cinnzeylanine, 2-déoxyryanodols, 2-déoxy-3-épiryanodine.

Introduction

Ryanodine (**1**) (Fig. 1) (1–3) is an interesting and important calcium release channel modulator in mammalian muscles (4).[3] In a search to identify the structural features that are necessary to maintain biological activity, we (5–7) and others (8–14) have recently focused on the characterization of new ryanoids from the plant *Ryania speciosa* Vahl, and also on skeleton and functional group modifications (5, 6, 8, 10, 15–24) in order to obtain more information on their eventual role in the affinity of these molecules to the ryanodine binding site.

Received June 3, 1996.

L. Ruest[2] and M. Dodier. Département de Chimie, Université de Sherbrooke, Sherbrooke, QC J1K 2R1, Canada.

[1] Taken in part from M. Dodier: M. Sc. Thesis, 1996.

[2] Author to whom correspondence may be addressed. Telephone: (819) 821-7922. Fax: (819) 821-8017. E-mail: lruest@structure.chimie.usherb.ca

[3] A recent review on ryanodine will appear shortly in Pharmacological Reviews.

Recently, we have identified four new ryanoids (**3**–**6**) (Fig. 1) and corrected the structure of a fifth one (**7**) reported earlier (10). We have also modified the oxidation level of ring A of the ryanodine skeleton, which resulted in the syntheses of two natural diterpenes, cinnzeylanol (**14**) and cinnzeylanine (**15**) (25, 26), and of several other compounds (**16**, **18**–**20**, **21**).

Results and discussion

New natural ryanoids

The new natural ryanoids were obtained by chromatographic separation of the crude extracts of powdered *Ryania speciosa* wood after removal of the most abundant ryanoids (5, 8, 12, 13). We noted that simple crystallization of column-purified ryanodine left, in the mother liquors, an enriched mixture of ryanodine (**1**), 9,21-didehydroryanodine (**2**), and two new compounds: 9α,21-epoxyryanodine (**3**) and 3-*O*-benzoyl-18-hydroxyryanodol (**5**). The epoxide **3** was obtained in pure form via HPLC. Epoxide **3** has been synthesized previously by epoxidation of 9,21-didehydroryanodine (**2**) (10, 19, 23).

Benzoate **5** and ryanodine (**1**) have the same HPLC reten-

Fig. 1.

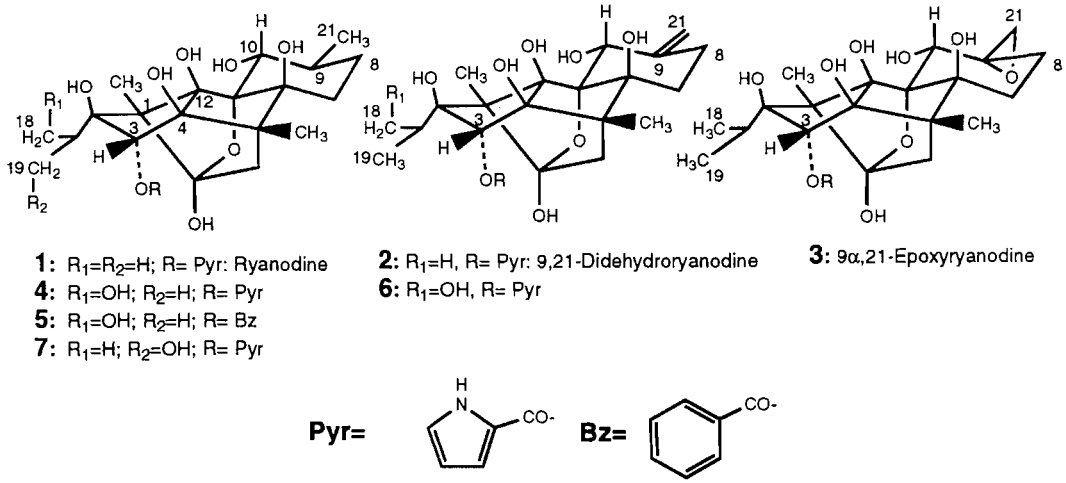

1: $R_1=R_2=H$; R= Pyr: Ryanodine
4: $R_1=OH$; $R_2=H$; R= Pyr
5: $R_1=OH$; $R_2=H$; R= Bz
7: $R_1=H$; $R_2=OH$; R= Pyr

2: $R_1=H$, R= Pyr: 9,21-Didehydroryanodine
6: $R_1=OH$, R= Pyr

3: 9α,21-Epoxyryanodine

tion time and were first obtained as a 1:5 mixture. Fractional crystallization of ryanodine from this mixture gave mother liquors enriched in benzoate (ca. 40%). The resulting mixture was reacted with ozone (10), which cleaved the pyrrole moiety of ryanodine but left benzoate unaltered. A final TLC purification of the ozonolysis mixture gave pure compound **5**. The location of the hydroxyl group in **5** at position 18 follows the discussion below, which combines both NMR and X-ray diffraction analyses and offers the possibility of discriminating between 18- and 19-hydroxylated ryanoids when an aromatic ring is present at position 3.

From the group of ryanoids more polar than 9,21-dehydroryanodine (**2**), we isolated three other compounds, **4**, **7**, and **6** (in order of increasing polarity), hydroxylated at the isopropyl group, and fortunately crystallized the one that showed the same NMR data as a ryanoid reported previously (10). X-ray analysis of that ryanoid (see **7**, Fig. 2) (27), showed that the isopropylic hydroxyl group is located at position 19, close to the shielding area of the pyrrole ring attached as a pyrrole-2-carboxylate at C3. The remaining protons at C19 appear as an ABX pattern centered at about 3.6 ppm while the C18 methyl group occurs as a doublet at about 1.27 ppm. For the other isomer **4**,[4] which carries the OH at C18, the unshielded ABX pattern and shielded methyl doublet are found at 3.9 and 0.9 ppm, respectively. The same concordant arguments have been applied to the new 9,21-didehydroryanodine **6**, hydroxylated at position 18, and also to benzoate **5**, which both show an ABX pattern close to 3.9 ppm and a shielded methyl doublet at 0.89 ppm.

Synthetic achievements

The ryanodine molecule has been derivatized extensively, first by Wiesner and co-workers (2, 28) to elucidate its structure and subsequently by several groups to establish the structural features important for biological activity and to make experimentally useful analogs. Since 1984, most of the modifications done by us and others have involved ryanodine (**1**), 9,21-didehydroryanodine (**2**), and ryanodol (**8**). Several modifications were made at positions 8, 9, 10, and 21 in ring C (10, 15, 16, 18, 29–24). Various nucleophiles have recently been introduced at C4 and C12 (17). Some years ago, we described (18) the epimerization of ryanodine at position 3 and we wish now to report other modifications in ring A that led us to the syntheses of the title compounds.

Syntheses of cinnzeylanol (14) and cinnzeylanine (15) from anhydroryanodol (10)

Cinnzeylanol (**14**) and cinnzelanine (**15**) (Scheme 1) were isolated from *Cinnamomi Cortex* by Nohara et al. (25). Very recently, compounds of this family were also isolated from *Persea indica* by Fraga and co-workers (26). These natural diterpenes are closely related to ryanodol (**8**), being its 3-deoxy analogs. Synthetically, the specific removal of the 3-*endo* hydroxyl group from the ryanodol molecule appears not a trivial operation. Previously (18), we showed (Scheme 2) how either ryanodine (**1**) or ryanodol (**8**) can lead to olefin **11** through anhydroryanodine (**9**) or anhydroryanodol (**10**). Based on the conversion of ryanodine (**1**) to anhydroryanodine (**9**) (2, 28), we proceeded to the treatment of the olefin **11** (Scheme 1) with strong acid, which resulted in the formation (89%) of anhydrocinnzelanol (**12**) by C1—C15 bond cleavage, promoted by protonation of the C2—C3 double bond. Compound **12** was oxidized (18) to epoxide **13**, which underwent a transannular cyclization to give cinnzeylanol (**14**), in 75% yield, under the reductive action of lithium in ammonia. This intramolecular cyclization had been used in the total syntheses of ryanodol (29, 30) and of 3-epiryanodol (18). The structure of compound **14** was confirmed by X-ray diffraction analysis (see Fig. 2) (27). Acetylation of **14** gave cinnzeylanine (**15**).

Synthesis of 2,3-dideoxy-2,3-dihydroryanodol (16)

Removal of a second oxygen atom (the one at C2) from the

[4] This ryanoid, 18-hydroxyryanodine (**4**), was also observed recently by Prof. H.R. Besch, Jr. and Dr K.R. Bidasee, Department of Pharmacology and Toxicology, Indiana University School of Medicine, Indianapolis, Indiana 46202, U.S.A. (personal communication, 1995).

Fig. 2. ORTEP perspective view of crystalline **7**, **14**, **16**, and **18**: 30% probability thermal ellipsoids are shown for the non-hydrogen atoms.

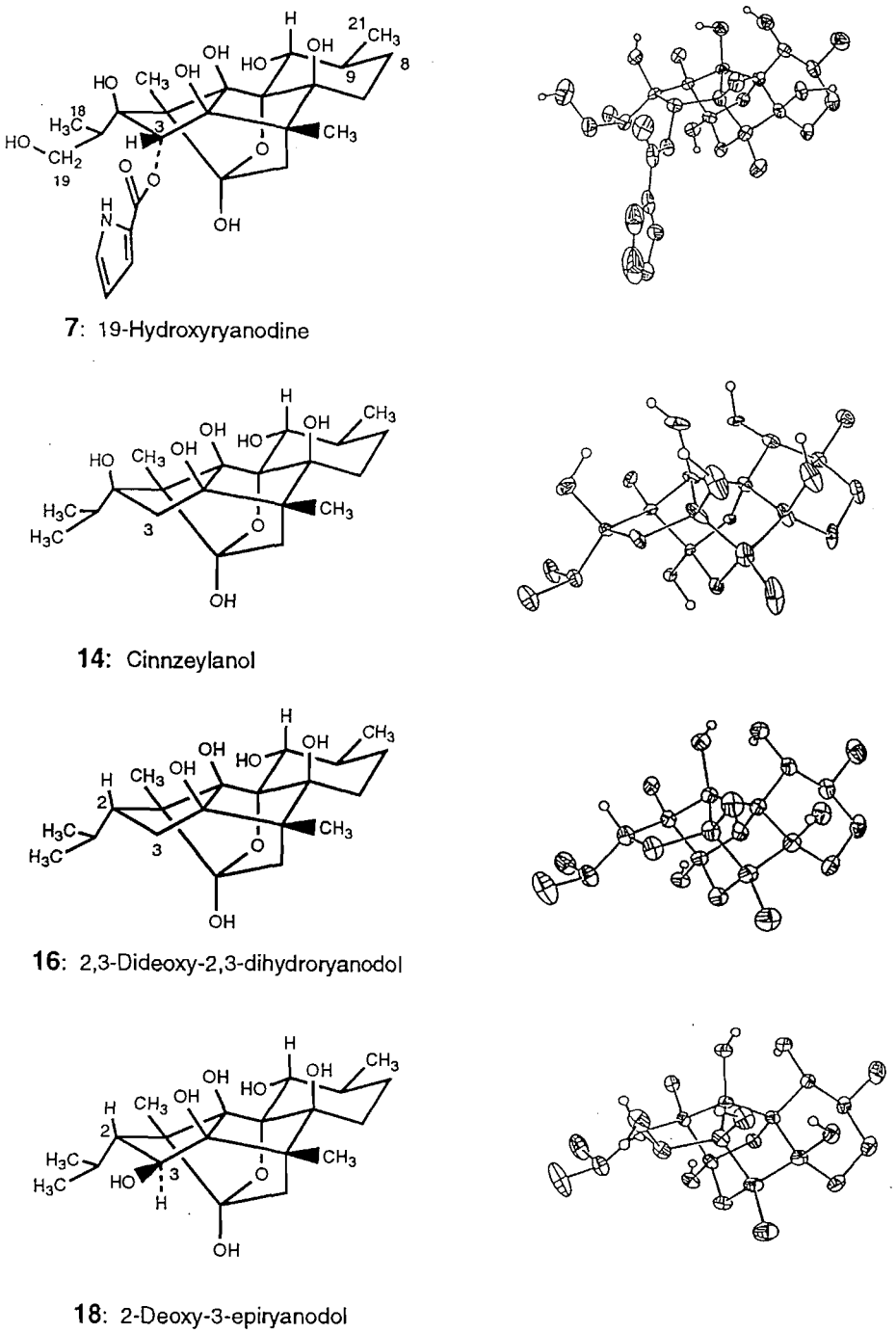

ryanodol molecule also became possible by submitting anhydrocinnzeylanol (**12**) (Scheme 3) directly to the reducing action of lithium in ammonia. Thus was obtained, in 92% yield, compound **16**, which has no hydroxyl group in ring A aside from those common with ring B at positions 4 and 12. The stereochemistry at position 2 of that compound was clearly established by X-ray diffraction (see Fig. 2) (27). We did not observe the presence of the possible epimer at that position. An attack (see Fig. 3, path a) of the unactivated C1—C2 double bond by the proximate radical anion, first developed at the lactone carbonyl group (see **12A**), has to be invoked as a possible mechanistic explanation (18, 31–33). Subsequent fast reduction of this radical species would give a highly basic alkyl anion at C2 (see **12B**) that would be protonated immediately in this medium from the "*exo*" face of the molecule, to give **16**.

Scheme 1.

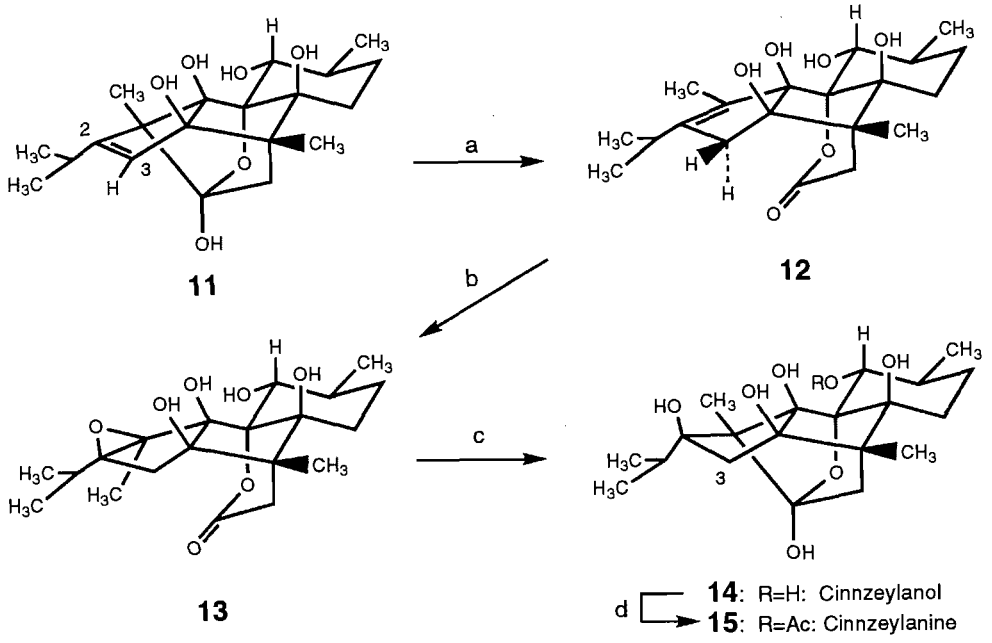

Reaction conditions: a: H_2SO_4, CH_3OH, 89%; b: CF_3CO_3H, $NaHCO_3$, $(CH_2Cl)_2$, 71%; c: Li, NH_3, THF, 75%; d: Ac_2O, Et_3N, DMAP, THF, 18%.

Scheme 2.

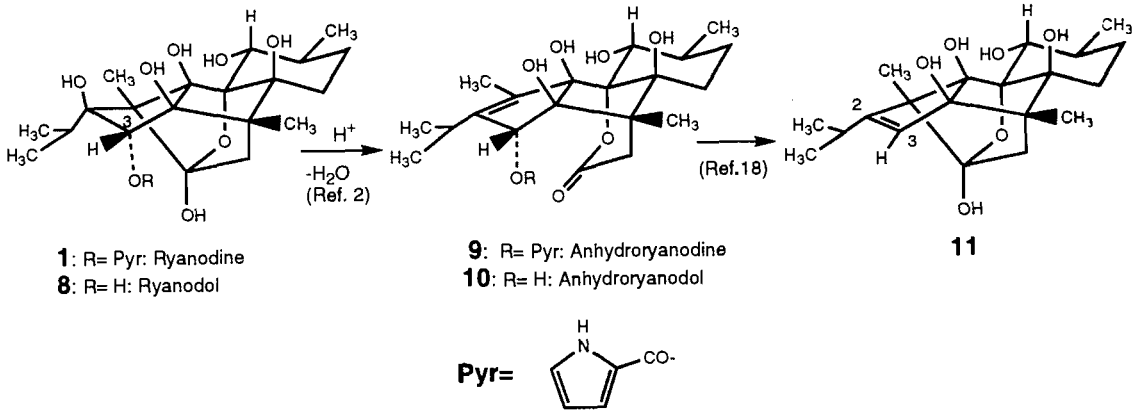

Synthesis of 2-deoxy-3-epiryanodol (18) and 2-deoxy-3-epiryanodine (19)

Oxidation of anhydroryanodol (**10**) with manganese dioxide (30) gave enone **17**, which was submitted to lithium in ammonia and furnished 2-deoxy-3-epiryanodol (**18**) in 69% yield. The stereochemistry at position 2 was clearly established by X-ray diffraction analysis (see Fig. 2) (27). A possible mechanistic explanation (see Fig. 3, path b) involves a dianion (or a radical anion) formed in the enone moiety that could attack, from C1, the lactone carbonyl (or, respectively, a lactone radical anion), thus forming the C1—C15 bond. Rapid *exo*-protonation at C2 of the resulting enolate **17A** would then give cyclopentanone **17B**, which would be reduced by lithium and protonated to give the most stable 3-*exo* hydroxyl group, with "*anti*" substituents at positions 2 and 3. Selective acylation of the 3-*epi*-hydroxyl group of **18** with 2-pyrrolecarboxylic acid (34) furnished 2-deoxy-3-epiryanodine (**19**).

Synthesis of 2-deoxyryanodol (20) and 2-deoxy-2-epiryanodol (21)

Anhydroryanodol (**10**), when first submitted (Scheme 3) to the action of a strong base, then transferred into the usual lithium–ammonia reducing medium, furnished a mixture of 2-deoxy epimers (24%) of ryanodol **20** and **21** together with the already known alkene **11** (54%). The basic treatment was used to deprotonate (see Fig. 3, path c) the 3-*endo* hydroxyl group, thus removing its reactivity as a leaving group (which, otherwise, gives alkene **11**). This alkoxide **10A** would be reduced to

Scheme 3.

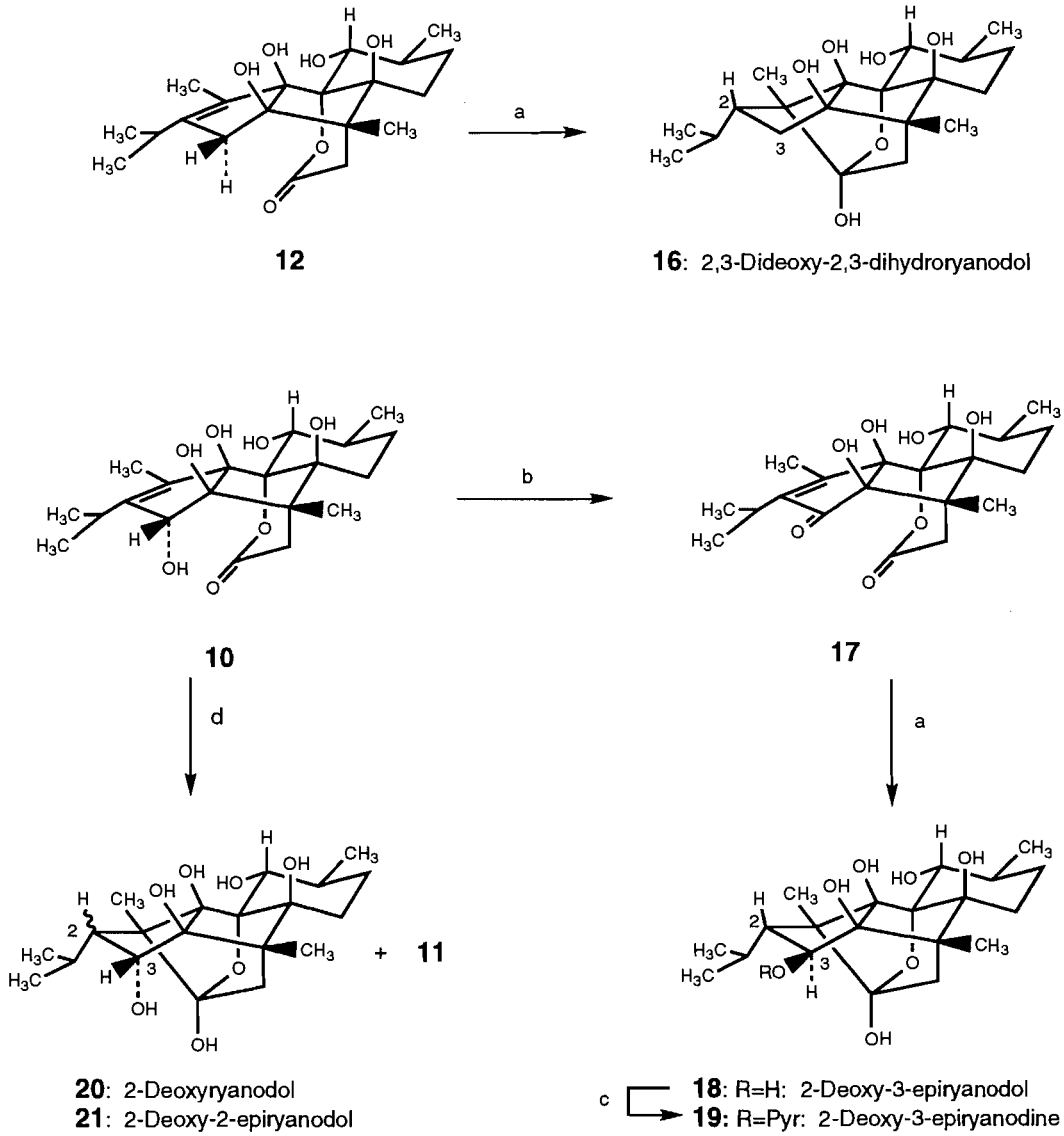

Reaction conditions: a: Li, NH_3, THF, 92% in **16**; 69% in **18**; b: MnO_2, $CHCl_3$, 69%; c: Pyrrole-2-carboxylic acid, Diphenylphosphorylazide (DPPA), Et_3N, DMF, 13%; d: LDA, THF then condition a, 24% in **20** and **21**; 54% in **11**.

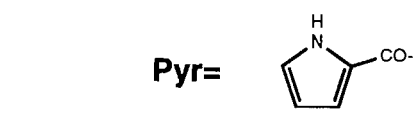

10B and the usual C1—C15 reductive cyclization previously described would occur and lead to an anion (see **10C**) located at C2. Based on steric arguments this species should normally invert at C2 towards "*anti*" mutual orientation of the isopropyl and hydroxyl groups (see **10D**), leading to compound **21** after protonation. By calculation (see **20**, **21A**, and **21B**, Fig. 4), isomer **21** should be sterically favored by more than ~2.0 kcal/mol over the "*syn*" isomer. On the other hand, stereoelectronic arguments (delocalization of the anion at C2 in the antibonding orbital of the C3—O bond; n–σ^* interaction) (35), suggest an enhanced stability of the "*syn*" stereochemistry that would allow a protonation of **10C** from the *exo* face to yield compound **20**. The presence of a 1:1 mixture (see experimental) of these 2-epimers (besides favoring **21** by >95:5) suggests that stereoelectronic effects indeed play a significant role in the stabilization of anion **10C**.

In conclusion, we identified five new minor ryanoids in the extracts of *Ryania speciosa*. In a preliminary attempt to relate the structure of ryanoids to their affinity to the ryanodine receptor, we have focused on ring A and showed that positions

Fig. 3.

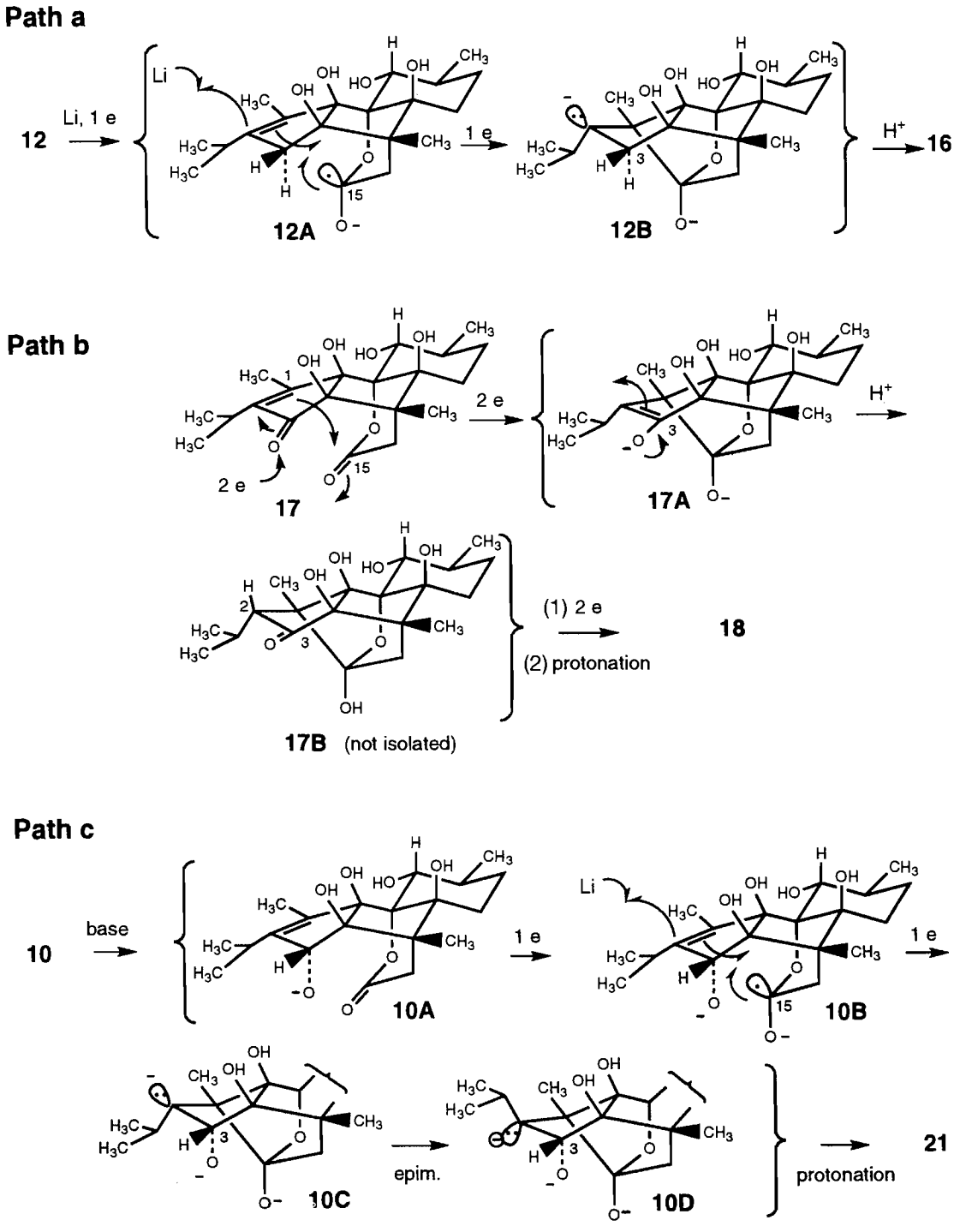

2 and 3 of these molecules can be specifically deoxygenated, leading to hydrophobic ring A. The impact of the reported modifications on affinity is currently under analysis[5] through measurements of the affinities of a number of specific derivatives of each of these compounds and the results of this analysis will be reported elsewhere. Access to other positions of the ryanodine molecule are currently under investigation.

Experimental section

Melting points were recorded on a Reichert hot stage apparatus and are uncorrected Mass spectra (ms) and peak matching (HRMS) data were determined at 70 eV on a VG Micromass

[5] Prof. William Welch, Department of Biochemistry, and Prof. John. L. Sutko, Department of Pharmacology, University of Nevada, School of Medicine, Reno, Nevada 89557, U.S.A.

Fig. 4. ORTEP view of **20** and representations of minimized **20** and **21**. The geometry optimizations and energy calculations were carried out using the MOPAC program by means of the semiempirical methods AM1.

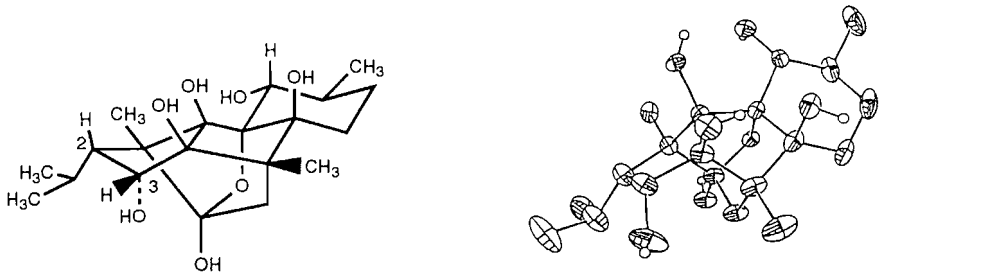

20: 2-Deoxyryanodol

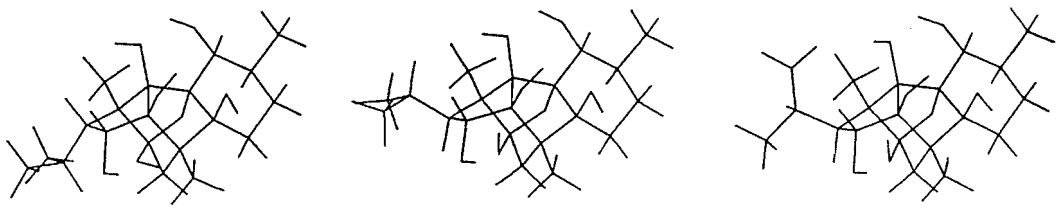

ΔE (relative): 4.6 kcal/mol — **20**

ΔE (relative): 2.0 kcal/mol — **21A**

ΔE (relative): 0.0 kcal/mol — **21B**

ZAB-1F spectrometer. Infrared absorption spectra were measured on a FT-IR Perkin–Elmer 1600 spectrophotometer. The ^1H (300 MHz) and ^{13}C (75 MHz) NMR spectra were recorded on a Bruker AC-300 instrument (with CHD_2OD as internal standard centered at 3.30 or 49.15δ). Some ^{13}C peaks are obscured by the strong solvent signal at ~49δ. The usual standard abbreviations have been used to indicate the multiplicity of the proton signals. Analytical and preparative thin-layer chromatography were carried out on glass plates 0.25 or 0.5 mm precoated with silica gel 60F-250 (Merck). Column chromatography was performed with Merck silica gel (200–400 mesh). HPLC utilized a Waters model 510 instrument equipped with a Vydac C18 reverse-phase preparative column (15 μm, 2.5 × 25 cm) and a Waters 484 tunable UV detector set at 254 nm. A typical solvent for HPLC preparative separation was a mixture of 40% methanol in water. All reactions were performed under argon atmosphere and in solvents purified by standard methods. Reaction mixtures were extracted with at least five portions of distilled ethyl acetate. Solutions in organic solvents were washed with brine, dried over anhydrous magnesium sulfate or anhydrous sodium sulfate, filtered, and then stripped of solvents with a rotatory evaporator connected to a water aspirator. Molecular modelling was performed using the MOPAC program by means of semiempirical AM1 methods.

Isolation of the new ryanoids

Extraction of powdered Ryania wood was done as previously described in the literature (1, 5, 13) but over a longer period of time (average 11 compared to 3–4 days). The crude extract was partitioned into three main fractions by column chromatography: in the fraction less polar than ryanodine we did not observe the presence of any new ryanoid other than the ones already described. The intermediate main fraction containing ryanodine–dehydroryanodine mixture was thoroughly crystallized from acetone–hexane to give the usual crystalline mixture of ryanodine (**1**) and dehydroryanodine (**2**) and leave the mother liquors, enriched in two new compounds: epoxide **3** and benzoate **5**. A sample of this mixture was purified by HPLC under the general conditions described above and gave (in order of decreasing polarity) pure epoxide **3**, pure dehydroryanodine (**2**), and a ~5:1 mixture of ryanodine (**1**) and benzoate **5**, along with small quantities of other known ryanoids. By further crystallization (acetone–hexane) of ryanodine from this new mixture, the proportion became ~3:2. Treatment with ozone of a sample of this mixture following a known procedure (10) gave a mixture of several compounds from which unaltered benzoate **5** was easily purified by plate chromatography (0.5 mm, 10% methanol in chloroform). The third fraction, more polar than the main one, furnished compounds **4**, **7**, and **6** (in order of increasing polarity) by HPLC separation, along with other known polar ryanoids already reported (7, 11, 13, 14).

9α,21-Epoxyryanodine (3): mp 212–214°C; ^1H NMR (CD_3OD, δ ppm): 7.03, 6.88, and 6.24 (3 dd for pyrrole ring hydrogens), 5.64 (s, 1H, HC3), 4.38 (s, 1H, HC10), 2.84 (d, 5.1 Hz, 1H, H_AC21), 2.58 (d, 13.8 Hz, 1H, H_AC14), 2.37 (d, 5.1 Hz, 1H, H_BC21), 2.5–2.3 (m, 2H), 2.26 (m, 1H, HC13), 1.96 (d, 13.8 Hz, H_BC14), 1.45–1.20 (m, 2H), 1.34 (s, 3H, CH_3C1), 1.10 (d, 6.7 Hz, 3H, CH_3C13), 0.92 (s, 3H, CH_3C5),

0.75 (d, 6.4 Hz, 3H, CH_3C13); ms *m/e*: 507 (M^+, weak); HRMS calcd. for $C_{25}H_{33}O_{10}N$: 507.2104 (M^+); found: 507.2097.

18-Hydroxy-3-O-benzoylryanodol (5): ^1H NMR (CD_3OD, δ ppm): 8.06 (2H), 7.66 (1H) and 7.53 (2H) (3 m for Ar-H), 5.72 (s, 1H, HC3), 3.91 (app. d, 4.8 Hz, 2H, 2H, H_2C18), 3.79 (d, 10.1 Hz, HC10), 2.51 (d, 13.7 Hz, 1H, H_AC14), 2.25 (m, 1H, HC13), 2.10 (m, 1H, $H_{ax}C7$), 1.98 (d, 13.7 Hz, 1H, H_BC14), 1.85 (m, 1H, HC9), 1.50 (m, 2H, $H_{ax}C8$, $H_{eq}C7$), 1.42 (s, 3H, CH_3C1), 1.22 (m, 1H, $H_{eq}C8$), 1.01 (d, 6.5 Hz, 3H, CH_3C9), 0.88 (d, 6.5 Hz, 3H, CH_3C13), 0.82 (s, 3H, CH_3C5); ms *m/e*: 502 ($M^+ - H_2O$); HRMS calcd. for $C_{27}H_{34}O_9$ ($M^+ - H_2O$): 502.2203; found: 502.2198.

18-Hydroxyryanodine (4): ^1H NMR (CD_3OD, δ ppm): 7.03, 6.87, and 6.23 (3 m for pyrrole hydrogens), 5.59 (s, 1H, HC3), 3.94 (dd, 10.3 and 5.4 Hz, 1H, H_AC18), 3.85 (dd, 10.3 and 3.9 Hz, H_BC18), 3.79 (d, 10.2 Hz, 1H, HC10), 2.50 (d, 13.8 Hz, 1H, H_AC14), 2.21 (m, 1H, H_XC13), 2.09 (m, 1H, $H_{ax}C7$), 1.94 (d, 13.8 Hz, 1H, H_BC14), 1.89 (m, 1H, HC9), 1.50 (m, 2H, $H_{eq}C7$, $H_{ax}C8$), 1.41 (s, 3H, CH_3C1), 1.23 (m, 1H, $H_{eq}C8$), 1.00 (d, 6.4 Hz, CH_3C9), 0.90 (d, 7.3 Hz, CH_3C13), 0.88 (s, 3H, CH_3C5); ms *m/e*: 491 ($M^+ - H_2O$); HRMS calcd. for $C_{25}H_{33}O_9N$ ($M^+ - H_2O$): 491.2155; found: 491.2148.

19-Hydroxyryanodine (7): NMR data of this ryanoid in CD_3OD are slightly different from those reported in a mixture of $CDCl_3$ and CD_3OD (10). We confirmed that addition of $CDCl_3$ to a solution of **7** in CD_3OD almost removes these differences; mp 153–155°C (CH_3OH); ^1H NMR (CD_3OD, δ ppm): 6.98, 6.91, and 6.21 (3 m for pyrrole hydrogens), 5.55 (s, 1H, HC3), 3.78 (d, 10.2 Hz, 1H, HC10), 3.54 (dd, 10.8 and 4.6 Hz, 1H, H_AC19), 3.46 (dd, 10.8 and 2.4 Hz, 1H, H_BC19), 2.33 (d, 13.8 Hz, 1H, H_AC14), 2.18 (m, 1H, H_XC13), 1.98 (m, 1H, $H_{ax}C7$), 1.87 (d, 13.8 Hz, 1H, H_BC14), 1.77 (m, 1H, HC9), 1.50–1.35 (m, 2H, $H_{eq}C7$, $H_{ax}C8$), 1.34 (s, 3H, CH_3C1), 1.27 (d, 6.8 Hz, 3H, CH_3C13), 1.23 (m, 1H, $H_{eq}C8$), 0.97 (d, 6.5 Hz, CH_3C9), 0.81 (s, 3H, CH_3C5); ms *m/e*: 491 ($M^+ - H_2O$); HRMS calcd. for $C_{25}H_{33}O_8N$ ($M^+ - H_2O$): 491.2155; found: 491.2148.

18-Hydroxy-9,21-dehydroryanodine (6): ^1H NMR (CD_3OD, δ ppm): 7.03, 6.88, and 6.23 (3 m for pyrrole hydrogens), 5.61 (s, 1H, HC3), 5.05 and 4.86 (2 br s, 1H each, H_2C21), 4.74 (br s, 1H, HC10), 3.94 (dd, 10.4 and 5.3 Hz, 1H, H_AC18), 3.89 (dd, 10.4 and 3.8 Hz, 1H, H_BC18), 2.49 (d, 13.8 Hz, 1H, H_AC14), 2.29–2.07 (m, 3H, HC13, HC7, HC8), 1.92 (d, 13.8 Hz, 1H, H_BC14), 1.42 (s, 3H, CH_3C1), 1.38–1.26 (m, 2H, HC7, HC8), 0.91 (s, 3H, CH_3C5), 0.90 (d, 6.4 Hz, 1H, CH_3C13); ms *m/e*: 489 ($M^+ - H_2O$); HRMS calcd. for $C_{25}H_{31}O_9N$ ($M^+ - H_2O$): 489.1999; found: 489.2010.

Synthesis of 3-deoxyryanodol (cinnzeylanol) (14) and cinnzeylanine (15)

Anhydrocinnzeylanol (3-deoxyanhydroryanodol) (12)
Concentrated sulfuric acid (0.1 mL) was added, at 25°C, to a solution of olefin **11** (26 mg, 0.074 mmol) in methanol (10 mL) and the mixture refluxed for 40 h. The cooled mixture was transferred into aqueous sodium bicarbonate (5%) and extracted with ethyl acetate. The crude product was chromatographed on silica plate (0.5 mm, 10% methanol in chloroform) to give pure **12** (23 mg, 89%); mp 110–112°C (MeOH); IR (film, ν cm^{-1}): 3389, 2922, 1732, 1461; ^1H NMR (CD_3OD, δ ppm): 4.02 (d, 10.0 Hz, 1H, HC10), 2.70 (m, 1H, HC13), 2.61 (dq, 17.5 and 1.7 Hz, 1H, H_AC3), 2.45 (d, 19.5 Hz, 1H, H_AC14), 2.36 (d, 19.5 Hz, 1H, H_BC14), 2.10 (dq, 17.5 and 2.6 Hz, H_BC3), 1.80 (m, 1H, HC9), 1.72 (br s, 3H, CH_3C1), 1.63–1.48 (m, 4H, H_2C7), 1.07 (d, 6.4 Hz, 3H, CH_3C9), 1.02 (s, 3H, CH_3C5), 1.00 (d, 7.0 Hz, 3H, CH_3C13), 0.94 (d, 7.0 Hz, 3H, CH_3C13); ^{13}C NMR (CD_3OD, δ ppm): 174.2, 148.6, 137.6, 87.1, 75.6, 75.4, 43.3, 39.9, 37.6, 31.4, 30.9, 29.3, 23.3, 23.0, 21.4, 16.1, 14.5; ms *m/e*: 349 ($M^+ - H_2O$); HRMS calcd. for $C_{20}H_{29}O_5$ ($M^+ - H_2O$): 349.2015; found: 349.2008.

1,2-Epoxyanhydrocinnzeylanol (13)
At ambient temperature, solid sodium bicarbonate (2 mg) was added to a solution of anhydrocinnzeylanol (**12**) (27 mg, 0.074 mmol) in a mixture of 1,2-dichloroethane (2 mL) and acetonitrile (1 mL). To this mixture was added a solution of trifluoroperacetic acid (1 N, 120 μL) in 1,2-dichloroethane. After 20 h at room temperature and addition of aqueous sodium thiosulfate (0.1 N, 2 mL), the mixture was extracted with ethyl acetate and the crude product was chromatographed (flash, 5–10% methanol in chloroform) to give epoxide **13** (19 mg, 71%); mp 182–184°C (MeOH); IR (film, ν cm^{-1}): 3426, 2968, 1731; ^1H NMR (CD_3OD δ ppm): 4.04 (d, 10.5 Hz, 1H, HC10), 2.78 (d, 20.0 Hz, 1H, H_AC3), 2.63 (d, 20.0 Hz, 1H, H_BC3), 2.25 (d, 15.6 Hz, 1H, H_AC14), 1.75 (m, 1H, HC9), 1.60 (d, 15.6 Hz, 1H, H_BC14), 1.65–1.50 (m, 4H, H_2C7, H_2C8), 1.54 (s, 3H, CH_3C1), 1.06 (d, 6.3 Hz, 3H, CH_3C9), 1.00 (d, 6.9 Hz, 3H, CH_3C13), 0.96 (d, 5.9 Hz, CH_3C13), 0.94 (s, 3H, CH_3C5); ^{13}C NMR (CD_3OD, δ ppm): 173.2, 95.4, 87.5, 80.6, 78.9, 75.4, 43.8, 38.1, 37.4, 33.1, 29.4, 21.2, 20.7, 17.3, 16.4; ms *m/e*: 382 (M^+); HRMS calcd. for $C_{20}H_{30}O_7$: 382.1991; found: 382.1989.

Cinnzeylanol (3-deoxyryanodol) (14)
A solution of epoxide **13** (29 mg, 0.076 mmol) in tetrahydrofuran (THF) (3 mL) was transferred (cannula) into a blue solution of lithium (50 mg) in ammonia (10 mL, −78°C). The mixture was stirred for 30 min, then treated with solid ammonium chloride (100 mg) and stirred until discoloration (~5 min). Ammonia was allowed to escape while raising the temperature to 25°C and the residue was dissolved in water and extracted with ethyl acetate. Pure cinnzeylanol (**14**) (22 mg, 75%) was obtained from the crude product by flash chromatography (10% methanol in chloroform); mp 140–141°C (MeOH) (lit (26) mp 140–141°C (25) 139–142°C); IR (film, ν cm^{-1}): 3366, 2937, 1469, 1017; ^1H NMR (CD_3OD, δ ppm): 3.79 (d, 10.2 Hz, 1H, HC10), 2.41 (d, 15.5 Hz, 1H, H_AC3), 2.10 (app td, 12.5 and 5.8 Hz, $H_{ax}C7$), 1.92 (m, 1H, HC13), 1.84 (d, 13.6 Hz, H_AC14), 1.80 (m, 1H, HC9) 1.76 (d, 15.5 Hz, 1H, H_BC3), 1.73 (d, 13.6 Hz, 1H, H_BC14), 1.60–1.40 (m, 2H, $H_{ax}C8$, $H_{eq}C7$), 1.31 (s, 3H, CH_3C1), 1.28 (m, 1H, $H_{eq}C8$), 1.00 (d, 6.4 Hz, 3H, CH_3C9), 0.99 (d, 6.7 Hz, 3H, CH_3C13), 0.95 (d, 6.7 Hz, 3H, CH_3C13), 0.86 (s, 3H, CH_3C5); ^{13}C NMR (CD_3OD, δ ppm): 102.4, 98.3, 90.2, 87.3, 86.3, 72.8 (2), 43.4, 35.3, 34.2, 29.5, 27.3, 19.1, 18.9, 18.8, 11.1, 9.7; ms *m/e*: 366 ($M^+ - H_2O$); HRMS calcd. for $C_{20}H_{30}O_6$ ($M^+ - H_2O$): 366.2042; found: 366.2050.

Cinnzeylanine (10-O-acetyl-3-deoxyryanodol) (15)

To a solution of alcohol **14** (25 mg, 0.065 mmol) in THF (10 mL) was successively added triethylamine (19 μL, 0.14 mmol), acetic anhydride (1.0 mL of a 0.1 M solution in THF, 0.10 mmol), and 4-dimethylaminopyridine (DMAP) (3 mg). After 48 h at room temperature, the mixture was poured onto aqueous sodium bicarbonate (5%) and extracted with ethyl acetate. The crude product was chromatographed on two silica plates (0.5 mm, 10% methanol in chloroform) to furnish cinnzeylanine (**15**) (4.9 mg, 18%), anhydrocinnzeylanol (**12**) (2.9 mg), and anhydrocinnzeylanine (2.4 mg), along with unchanged starting material **14** (11 mg); this yield was not optimized; ^{1}H NMR (CD_3OD, δ ppm): 5.26 (d, 10.7 Hz, 1H, HC10), 2.39 (d, 15.5 Hz, 1H, H_AC3), 2.12 (m, 1H, HC9), 2.05 (s, 3H, CH_3CO), 1.92 (app td, 13.5 and 6.6 Hz, 1H, $H_{ax}C7$), 1.89 (m, 1H, HC13), 1.85 (d, 13.7 Hz, 1H, H_AC14), 1.74 (d, 13.7 Hz, 1H, H_BC14), 1.72 (d, 15.5 Hz, 1H, H_BC3), 1.56 (m, 2H, $H_{ax}C8$, $H_{eq}C7$), 1.34 (m, 1H, $H_{eq}C8$), 1.33 (s, 3H, CH_3C1), 1.00 (d, 6.6 Hz, 3H, CH_3C9), 0.94 (d, 6.9 Hz, 3H, CH_3C13), 0.87 (s, 3H, CH_3C5), 0.84 (d, 6.6 Hz, 3H, CH_3C13); ms *m/e*: 426 (M^+, weak), 408 ($M^+ - H_2O$); HRMS calcd. for $C_{22}H_{32}O_7$ ($M^+ - H_2O$): 408.2148; found: 408.2142.

Synthesis of 2,3-dideoxy-2,3-dihydroryanodol (16)

A solution of anhydrocinnzeylanol (**12**) (18 mg, 0.049 mmol) in THF (2 mL) was transferred (cannula) into a cold (−78°C) blue solution of lithium (20 mg) in ammonia (10 mL). After 30 min of stirring and addition of solid ammonium chloride (100 mg), the discolored mixture was allowed to warm to room temperature (evaporation of ammonia). The solid residue was dissolved in water and extracted with ethyl acetate to give pure compound **16** (17 mg, 92%); this compound was recrystallized (MeOH) for monocrystal X-ray diffraction analysis: mp 217–220°C; IR (film, ν cm^{-1}): 3282, 2944, 1459, 1005; ^{1}H NMR (CD_3OD, δ ppm): 3.80 (d, 10.2 Hz, 1H, HC10), 2.13 (app td, 12.3 and 5.9 Hz, 1H, $H_{ax}C7$), 1.90–1.70 (m, 7H, HC13, HC9, H_2C14, H_2C3, HC2), 1.55–1.43 (m, 2H, $H_{ax}C8$, $H_{eq}C7$), 1.28 (m, 1H, $H_{eq}C8$), 1.21 (s, 3H, CH_3C1), 1.03 (d, 5.7 Hz, 3H, CH_3C13), 1.00 (d, 6.5 Hz, 3H, CH_3C9), 0.90 (d, 5.7 Hz, 3H, CH_3C13), 0.86 (s, 3H, CH_3C5); ^{13}C NMR (CD_3OD, δ ppm): 103.5, 97.5, 90.8, 87.2, 73.1, 61.9, 50.9, 43.4, 39.0, 35.4, 30.4, 29.5, 27.4, 24.1, 23.7, 18.9, 11.2; ms *m/e*: 368 (M^+); HRMS calcd. for $C_{20}H_{32}O_6$: 368.2199; found: 368.2192.

Syntheses of 2-deoxy-3-epiryanodol (18) and 2-deoxy-3-epiryanodine (19)

3-Oxoanhydroryanodol (17)

Following a slightly modified procedure (30), a solution of anhydroryanodol (**10**) (17 mg, 0.044 mmol) in chloroform (10 mL) was reacted with activated manganese dioxide (25 mg) at 25°C for 3 h. Filtration (cotton, Celite) of the mixture and evaporation of the solvent left a residue that was purified by flash chromatography (5% methanol in chloroform) to give pure enone **17** (11 mg, 66%); IR (film, ν cm^{-1}): 3439, 2966, 1745, 1691, 1622, 1021; ^{1}H NMR (CD_3OD, δ ppm): 4.04 (d, 10.4 Hz, 1H, HC10), 2.75 (heptuplet, 7.0 Hz, 1H, HC13), 2.58 (d, 19.8 Hz, 1H, H_AC14), 2.23 (d, 19.8 Hz, 1H, H_BC14), 2.21 (s, 3H, CH_3C1), 1.76 (m, 1H, HC9), 1.61–1.46 (m, 4H, H_2C8), 1.15, 1.13, and 1.08 (3 d, 7.0 Hz, 3H each, 3 CH_3CH), 1.09 (s, 3H, CH_3C5); ms *m/e*: 380 (M^+); HRMS calcd. for $C_{20}H_{28}O_7$: 380.1835; found: 380.1826.

2-Deoxy-3-epiryanodol (18)

A solution of enone **17** (50 mg, 0.131 mmol) in THF (5 mL) was transferred into a blue solution (−78°C) of lithium (25 mg) in ammonia (10 mL). After 30 min, extraction was performed as described above. Flash chromatography of the crude product gave compound **18** (34.8 mg, 69%); mp 304–308°C (MeOH); IR (film, ν cm^{-1}): 3396, 2929, 1634, 1453; ^{1}H NMR (CD_3OD, δ ppm): 3.81 (d, 10.0 Hz, 1H, HC10), 3.59 (d, 5.2 Hz, 1H, HC3), 2.15–2.00 (m, 1H, $H_{ax}C7$), 1.95 (m, 1H, HC13), 1.83 (m, 1H, HC9), 1.81 (d, 13.7 Hz, 1H, H_AC14), 1.58 (d, 13.7 Hz, 1H, H_BC14), 1.55–1.43 (m, 3H, HC2, $H_{ax}C8$, $H_{eq}C7$), 1.24 (s, 3H, CH_3C1), 1.08 (d, 6.4 Hz, 3H, CH_3C13), 1.07 (d, 6.6 Hz, 3H, 3H, CH_3C13), 1.00 (d, 3H, 6.4 Hz, 3H, CH_3C9), 0.87 (s, 3H, CH_3C5); ^{13}C NMR (CD_3OD, δ ppm): 103.0, 87.6, 86.2, 75.3, 61.8, 42.1, 35.4, 29.6, 27.1, 24.3, 23.7, 18.9, 14.9, 11.3; ms *m/e*: 384 (M^+); HRMS calcd. for $C_{20}H_{32}O_7$: 384.2148; found: 384.2139.

2-Deoxy-3-epiryanodine (19)

Following a modified method form the literature (34), a solution of alcohol **18** (18 mg, 0.046 mmol) and 2-pyrrolecarboxylic acid (7.6 mg, 0.069 mmol) in dimethylformamide (DMF) (1.5 mL) was treated with diphenylphosphorylazide (DPPA) (20 μL, 0.092 mmol) and triethylamine (39 mL, 0.276 mmol) and stirred for 64 h at room temperature. The mixture was transferred into aqueous sodium bicarbonate and extracted with ethyl acetate. The crude product was chromatographed on silica plate (0.5 mm, 10% methanol in chloroform) to give unreacted starting material (15 mg) along with compound **19** (3 mg, 13%). No attempt was made to increase this yield; IR (film, ν cm^{-1}): 3391, 2935, 1693, 1412, 1324, 1148; ^{1}H NMR (CD_3OD, δ ppm): 6.95, 6.90, and 6.18 (3 m for pyrrole hydrogens), 5.16 (d, 5.7 Hz, 1H, HC3), 3.79 (d, 10.2 Hz, 1H, HC10), 2.13 (app td, 12.5 and 6.1 Hz, $H_{ax}C7$), 2.04 (m, 1H, HC13), 1.94 (dd, 10.6 and 5.7 Hz, 1H, HC2), 1.92 (d, 14.2 Hz, 1H, H_AC14), 1.84 (m, 1H, HC9), 1.74 (d, 14.2 Hz, 1H, H_BC14), 1.52 (m, 2H, $H_{ax}C8$, $H_{eq}C7$), 1.32 (s, 3H, CH_3C1), 1.23 (m, 1H, $H_{eq}C8$), 1.07 (d, 6.2 Hz, 3H, CH_3C13), 1.01 (s, 3H, CH_3C5), 1.00 (d, 6.1 Hz, 3H, CH_3C9), 0.91 (d, 6.4 Hz, 3H, CH_3C13); ms *m/e*: 477 (M^+); HRMS calcd. for $C_{25}H_{35}O_8N$: 477.2362; found: 477.2365.

Synthesis of 2-deoxyryanodol (20) and 2-deoxy-2-epiryanodol (21)

To a cold (−78°C) solution of anhydroryanodol (13 mg, 0.034 mmol) in THF (3 mL) was added a solution of lithium diisopropylamide (100 μL, ~2 M in THF). After 30 min of stirring at −78°C, this preparation was transferred (cannula) to a cold (−78°C) blue solution of lithium (~50 mg) in ammonia (10 mL) and the mixture was stirred for 1 h. After the addition of solid ammonium chloride (100 mg) and warming to 25°C (evaporation of ammonia), the residue was dissolved in water and extracted with ethyl acetate. The crude extract was chromatographed on silica plate (0.5 mm, 10% methanol in chloroform) to give the known olefin **11** (6.7 mg, 54%) (18) and a 1:1 mixture (by NMR evidence) of 2-deoxyryanodol (**20**) and 2-deoxy-2-epiryanodol (**21**) (3.1 mg, 24%). In our hands, these epimers were inseparable by the usual silica plate chromatography. Fortunately, fractional crystallization (methanol) of their mixture furnished pure compound **20**. Stereochemistry at C2 was revealed by X-ray diffraction analysis (see Fig. 4) (27).

2-Deoxyryanodol (20): mp 243°C (dec.) (MeOH); ^{1}H NMR (CD_3OD, δ ppm): 4.34 (d, 11.4 Hz, 1H, HC3), 3.78 (d, 10.2 Hz, 1H, HC10), 2.52 (d, 13.2 Hz, 1H, H_AC14), 2.14–2.00 (m, 2H, $H_{ax}C7$, HC9), 1.83 (m, 1H, HC13), 1.81 (app t, 11.4 Hz, 1H, HC2), 1.72 (d, 13.2 Hz, 1H, H_BC14), 1.58–1.40 (m, 2H, $H_{eq}C7$, $H_{ax}C8$), 1.24 (m, 1H, $H_{eq}C8$), 1.20 (s, 3H, CH_3C1), 1.12 (s, 3H, CH_3C5), 1.09 (d, 6.6 Hz, 1H, CH_3C9), 1.01 (d, 5.2 Hz, 3H, CH_3C13), 0.99 (d, 5.8 Hz, 3H, CH_3C13); ms *m/e*: 384 (M^+); HRMS calcd. for $C_{20}H_{32}O_7$: 384.2148; found: 384.2143.

2-Deoxy-2-epiryanodol (21): NMR data of this compound were obtained from the spectrum of a mixture with epimer **20**: ^{1}H NMR (CD_3OD, δ ppm): 4.22 (d, 6.7 Hz, 1H, HC3), 3.75 (d, 10.2 Hz, 1H, HC10), 2.32 (d, 13.4 Hz, 1H, H_AC14), 2.08 (m, 2H, $H_{ax}C7$, HC9), 1.83 (m, 1H, HC13), 1.72 (d, 13.4 Hz, 1H, H_BC14), 1.62 (dd, 6.7 and 3.5 Hz, 1H, HC2), 1.59–1.40 (m, 2H, $H_{eq}C7$, $H_{ax}C8$), 1.27 (m, 1H, $H_{eq}C8$), 1.20 (s, 3H, CH_3C1), 1.11 (s, 3H, CH_3C5), 1.05–0.99 (m, 9H, CH_3C9, and 2 CH_3C13).

Acknowledgments

We thank Mr. M. Drouin and Mr. G. Boulé, Département de Chimie, Université de Sherbrooke, for their technical assistance (X-ray diffraction, molecular mechanics calculations of compounds **20** and **21**, and mass spectrometry). We also thank Mr. C. Berthelette as a summer student for his help in isolating and purifying natural ryanoids from *Ryania speciosa*. We are grateful to Professor W. Welch, Department of Biochemistry, University of Nevada, Reno, who made this work possible by funding us with research subcontracts from the National Science Foundation (NSF) and the American Heart Association (AHA). We wish also to thank the Université de Sherbrooke for financial support from the Fonds de Recherche à Allocation Interne (FRAI).

References

1. E.F. Rogers, F.R. Koniuszy, J. Shavel, Jr., and K. Folkers. J. Am. Chem. Soc. **70**, 3086 (1984).
2. K. Wiesner. Adv. Org. Chem. **8**, 295 (1972).
3. S.N. Srivastava and M. Przybylska. Can. J. Chem. **46**, 795 (1968).
4. (*a*) D.J. Jenden and A.S. Fairhurst. Pharmacol. Rev. **21**, 1 (1969); (*b*) J.L. Sutko, E. Robinson, F.A. Lattanzio, Jr., R.G. Schlatterer, P. Deslongchamps, and L. Ruest. *In* Transduction in biological systems. *Edited by* C. Hidalgo, J. Bacigalupo, E. Jaimovich, and J. Vergara. Plenum Publishing Corporation, New York. 1990. Chap. 31. pp. 465–473.
5. L. Ruest, D.R. Taylor, and P. Deslongchamps. Can. J. Chem. **63**, 2840 (1985).
6. J.L. Sutko, L.J. Thompson, R.G. Schlatterer, F.A. Lattanzio, A.S. Fairhurst, C. Campbell, S.F. Martin, P. Deslongchamps, L. Ruest, and D.R. Taylor. J. Labelled Compd. Radiopharm. **23**, 215 (1986).
7. R.D. Humerickhouse, H.R. Besch, Jr., K. Gerzon, L. Ruest, J.L. Sutko, and J.T. Emmick. Mol. Pharmacol. **44**, 412 (1993).
8. A.L. Waterhouse, I. Holden, and J.E. Casida. J. Chem. Soc. Chem. Commun. 1265 (1984).
9. A.L. Waterhouse, I. Holden, and J.E. Casida. J. Chem. Soc. Perkin Trans. 2, 1011 (1985).
10. A.L. Waterhouse, I.N. Pessah, A.O. Francini, and J.E. Casida. J. Med. Chem. **30**, 710 (1987).
11. R.A. Humerickhouse, J. Paschal, T. Elvey, D. Berry, and H.R. Besch, Jr. Pharmacologist, **31**, 185 (1989) (Program and Abstracts ASPET, Abstracts 363).
12. P.R. Jefferies, R.F. Toia, and J.E. Casida. J. Nat. Products, **54**, 1147 (1991).
13. P.R. Jefferies, R.F. Toia, B. Brannigan, I.N. Pessah, and J.E. Casida. J. Agric. Food Chem. **40**, 142 (1992).
14. P.R. Jefferies, W.-W. Lam, R.F. Toia, and J.E. Casida. J. Agric. Food Chem. **40**, 509 (1992).
15. D.E. Mais, N. Bowling, and A.M. Watanabe. Biochem. Biophys. Res. Commun. **182**, 462 (1992).
16. K. Gerzon, R.A. Humerickhouse, H.R. Besch, J.R. Bidasee, J.T. Emmick, R.W. Roeske, Z. Tian, L. Ruest, and J.L. Sutko. J. Med. Chem. **36**, 1319 (1993).
17. P.R. Jefferies, E. Lermberg, W.-W. Lam, and J.E. Casida. J. Med. Chem. **36**, 1128 (1993).
18. L. Ruest and P. Deslongchamps. Can. J. Chem. **71**, 634 (1993).
19. W. Welch, S. Ahmad, J.A. Airey, K. Gerzon, R.A. Humerickhouse, H.R. Besch, Jr., L. Ruest, P. Deslongchamps, and J.L. Sutko. Biochemistry, **33**, 6074 (1994).
20. R.A. Humerickhouse, K.R. Bidasee, K. Gerzon, J.T. Emmick, S. Kwon, J.L. Sutko, L. Ruest, and H.R. Besch, Jr. J. Biol. Chem. **269**, 30242 (1994).
21. D.R. Witcher, P.S. Mcpherson, S.D. Kahl, T. Lewis, P. Bentley, M.J. Mullinix, J.D. Windass, and K.P. Campbell. J. Biol. Chem. **269**, 13076 (1994).
22. S.D. Kahl, P.S. Mcpherson, T. Lewis, P. Bentley, M.J. Mullinnix, J.D. Windass, and K.P. Campbell. Anal. Biochem. **218**, 55 (1994).
23. W. Welch, A.J. Williams, A. Tinker, L. Ruest, K. Mitchell, P. Deslongchamps, J. Lamothe, K. Gerzon, H.R. Besch, Jr., and J.L. Sutko. Biochemistry. In press.
24. W. Welch, J.L. Sutko, K.E. Mitchell, J. Airey, and L. Ruest. Biochemistry, **35**, 7165 (1996).
25. T. Nohara, Y. Kashiwada, K. Murakami, T. Tomimatsu, M. Kido, A. Yagi, and I. Nishioka. Chem. Pharm. Bull. **29**, 2451 (1981).
26. A. Gonzalez-Coloma, D. Terrero, A. Perales, P. Escoubas, and B.M. Fraga. J. Agric. Food Chem. **44**, 296 (1996).
27. M. Drouin, M. Dodier, and L. Ruest. Acta Crystallogr. Sect. C: Submitted.
28. R.B. Kelly, D.J. Whittingham, and K. Wiesner. Can. J. Chem. **29**, 905 (1951).
29. A. Bélanger, D.J.F. Berney, H.J. Borschberg, R. Brousseau, A. Doutheau, R. Durand, H. Katayama, R. Lapalme, D.M. Leturc, C.C. Liao, F.N. MacLachlan, J.P. Maffrand, F. Marazza, R. Martino, C. Moreau, L. St-Laurent, R. Saintonge, P. Soucy, L. Ruest, and P. Deslongchamps. Can. J. Chem. **57**, 3348 (1979).
30. P. Deslongchamps, A. Bélanger, D.J.F. Berney, H.J. Borschberg, R. Brousseau, A. Doutheau, R. Durand, H. Katayama, R. Lapalme, D.M. Leturc, C.C. Liao, F.N. MacLachlan, J.P. Maffrand, F. Marazza, R. Martino, C. Moreau, L. Ruest, L. St-Laurent, R. Saintonge, and P. Soucy. Can. J. Chem. **68**, 115 (1990) (a series of four papers).
31. L.A. Paquette, J. Reagan, S.L. Schreiber, and C.A. Teleha. J. Am. Chem. Soc. **111**, 2331 (1989).
32. L.A. Paquette and Y.J. Shi. J. Am. Chem. Soc. **112**, 8478 (1990).
33. Z. Cekovic. Tetrahedron Lett. 749 (1972).
34. S. Yamada, Y. Yokoyama, and T. Shiori. J. Org. Chem. **39**, 3302 (1974).
35. P. Deslongchamps. *In* Stereoelectronic effects in organic chemistry. Organic Chemistry Series. Vol. 1. *Edited by* J.E. Baldwin. Pergamon Press, Oxford, England. 1983. p. 283.

A revised structure for the piperidine alkaloid andrachamine

Sibel Mill and Claude Hootelé

Abstract: A new method for the synthesis of *trans*-2,6-disubstituted piperidine derivatives is described. The transformation of cyclic α-methoxycarbamates **5** and **6** affords *trans* ketones **17** and **18**. The synthesis of diols **1–4** from **17** and **18** has shown that the structure proposed in the literature for the piperidine alkaloid andrachamine is incorrect. A reexamination of the original spectral data of this alkaloid suggested that it is a *meso* 2,6-disubstituted piperidine derivative. Unambiguous syntheses of **23** and **24** and comparison with a sample of andrachamine have established that this alkaloid possesses structure **23**.

Key words: *N*-acyliminium, piperidine, alkaloid, andrachamine.

Résumé : Une nouvelle méthode de synthèse de dérivés pipéridiniques *trans*-2,6-disubstitués est décrite. La transformation des carbamates cycliques α-méthoxylés **5** et **6** conduit aux cétones *trans* **17** et **18**. La synthèse des diols **1–4** au départ de **17** et **18** a montré que la structure proposée dans la littérature pour l'alcaloïde pipéridinique andrachamine est erronée. Un réexamen des propriétés spectrales de cet alcaloïde a permis de conclure qu'il s'agit d'un dérivé pipéridinique 2,6-disubstitué *méso*. Des synthèses non ambiguës des dérivés **23** et **24** et la comparaison avec un échantillon d'andrachamine ont établi que cet alcaloïde possède la structure **23**.

Mots clés : *N*-acyliminium, piperidine, alcaloïde, andrachamine.

In 1986, the isolation of a new piperidine alkaloid from extracts of the shrub *Andrachne aspera* (Euphorbiaceae), collected near Karachi, was reported (1). The new base was called andrachamine. A second piperidine derivative, andrachcine, was described shortly afterwards from the same species (2). Structure **1** was proposed for andrachamine, based mainly upon spectroscopic studies. Of particular importance for the structural attribution was the assignment to C4 of a signal appearing at 18.7 ppm in the ^{13}C NMR spectrum of andrachamine; comparison of this value with ^{13}C values reported in the literature for C4 in *cis*- and *trans*-2,6-disubstituted piperidine derivatives led to the assignment of the *trans* configuration to the alkaloid (1).

More recently, an unambiguous nitrone-based synthesis of the aminodiol (±)**1** was published (3). No direct comparison was possible but the authors claimed the correspondence, based on the alleged agreement of the spectroscopic properties, between their synthetic compound and andrachamine. Indeed, although the ^{13}C chemical shift for C4 (19.12 ppm) in (±)**1** is close to the value reported for andrachamine, some of the other ^{13}C values reported for (±)**1** do *not* agree with those reported for the alkaloid: the chemical shifts of C2 and C6 for instance differ by more than 10 ppm between the two spectra. An examination of the evidence accumulated convinced us that the structure of andrachamine could not be **1**. As the presence of the C4 signal at 18.7 ppm in the ^{13}C NMR spectrum of andrachamine appeared as a definite argument in favour of a *trans*-disubstituted piperidine structure, we decided to synthesize the four racemic *trans* diastereomers **1–4** and to compare their spectral properties with those of the alkaloid.

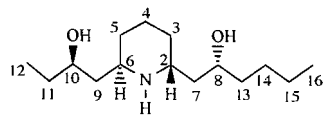

1

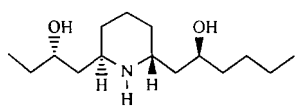

3

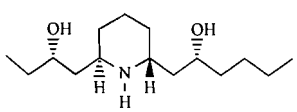

2

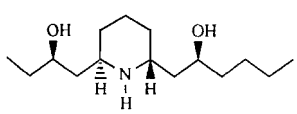

4

The stereoselective synthesis of *trans*-2,6-disubstituted piperidines is generally more difficult than the synthesis of the corresponding *cis* derivatives. Recent work from our laboratory has shown that the sequence: anodic methoxylation – elimination – nucleophilic addition provides an efficient route for the synthesis of *cis*-2,6-disubstituted piperidine derivatives from 2-substituted compounds (4). The high stereoselectivity observed in favour of the *cis* compounds results from the stereoelectronically preferred axial attack of the nucleophile (5, 6) on the *N*-acyliminium intermediate whose favoured conformation has a pseudoaxial alkyl group at C2 (Fig. 1*a*) (7, 8). On the basis of the above model we reasoned that the presence of a cyclic 6-membered carbamate would force the C2 side chain in a pseudoequatorial orientation in the *N*-acyliminium ion and that the preferred axial attack of an incoming nucleophile should therefore lead to a *trans*-2,6-disubstituted derivative (Fig. 1*b*). One related example was reported in the literature (9) and a few more appeared after the present work was complete (10).

Received February 15, 1996.

S. Mill and C. Hootelé.[1] Organic Chemistry Department, Faculty of Sciences, Free University of Brussels, B-1050 Brussels, Belgium.

[1] Author to whom correspondence may be addressed. Telephone: 32-2-650-30-39. Fax: 32-2-650-27-98.

Fig. 1.

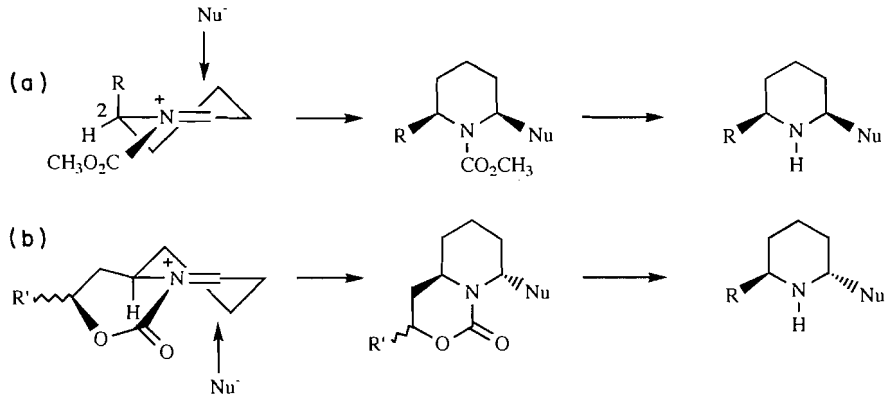

Scheme 1.

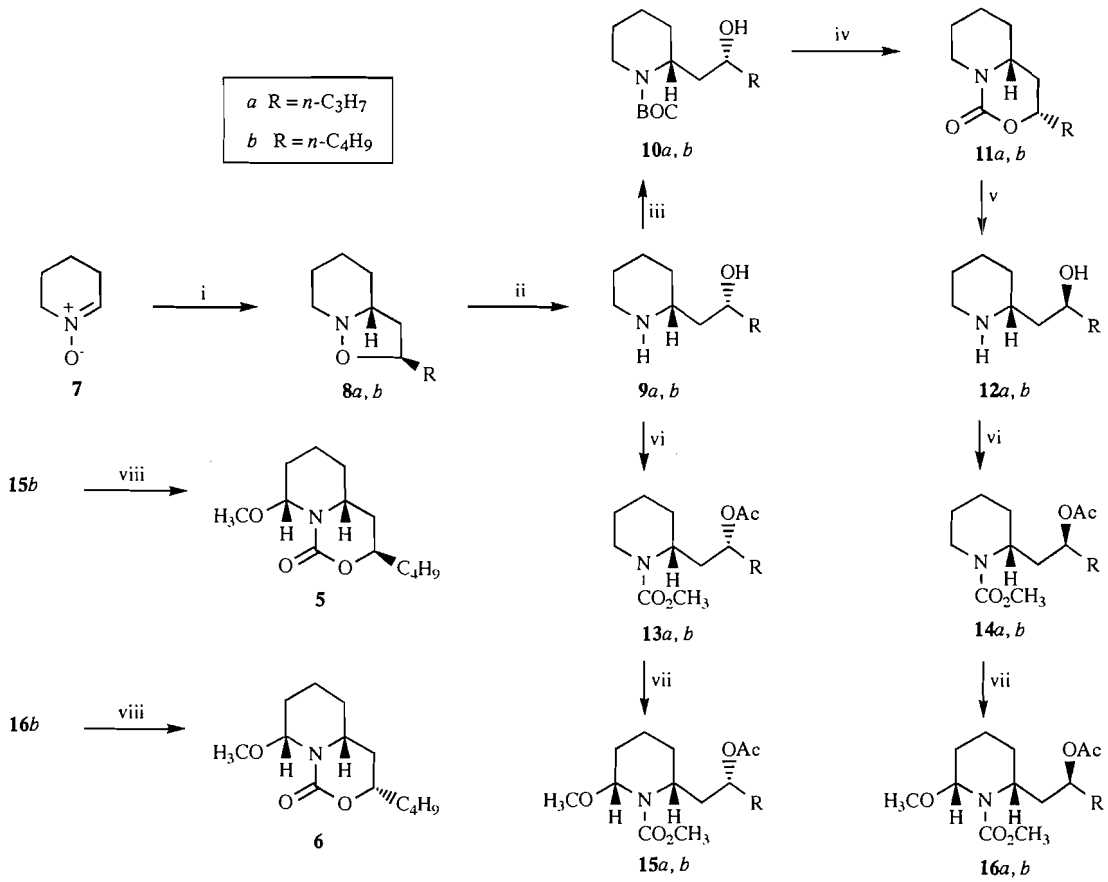

i: $CHCl_3$:EtOH (1:1), sealed tube (*a*: 1-pentene, 50°C, 90 h, 87%; *b*: 1-hexene, 60°C, 70 h; 93%); ii: Ni/Al, 1 M aqueous KOH solution, MeOH, r.t., 17 h (*a*: 98%; *b*: 95%); iii: BOC_2O, THF, r.t., 3 h (*a*: 80%; *b*: 95%); iv: MesCl, pyridine, r.t., 24 h, (*a*: 96%; *b*: 91%); v: 2 M ethanolic KOH, r.t., 17 h + 1 h reflux (*a*: quant.; *b*: 94%); vi: (*a*) $ClCO_2CH_3$, K_2CO_3, H_2O, r.t., 3 h; (*b*) Ac_2O, pyridine, r.t., 17 h (**13***a*: 79%; **13***b*: 91%; **14***a*: 69%; **14***b*: 86%); vii: −2e, Et_4NOTs, MeOH, 8 V; 8 F/mol (**15***a*: 99%; **15***b*: 99%; **16***a*: 92%; **16***b*: 83%); viii: *t*BuOK, THF, r.t., 1 h (**5**: 97%; **6**: 97%).

Indeed, we established that access to *trans*-2,6-piperidine derivatives through cyclic 6-membered carbamates was possible and a pathway was developed in which cyclic α-methoxycarbamates **5** and **6** serve as precursors of diastereomers **1**–**4** (see Scheme 2).

The synthesis of carbamates **5** and **6** is outlined in Scheme 1. Cycloadditions between nitrones and terminal alkenes are known to be highly regio- and diastereoselective (11–13). *exo* Addition of nitrone **7** to 1-hexene gave 93% of isoxazolidine **8***b*; the isolated *exo*/*endo* ratio was found to be 99/1. Reduc-

Scheme 2.

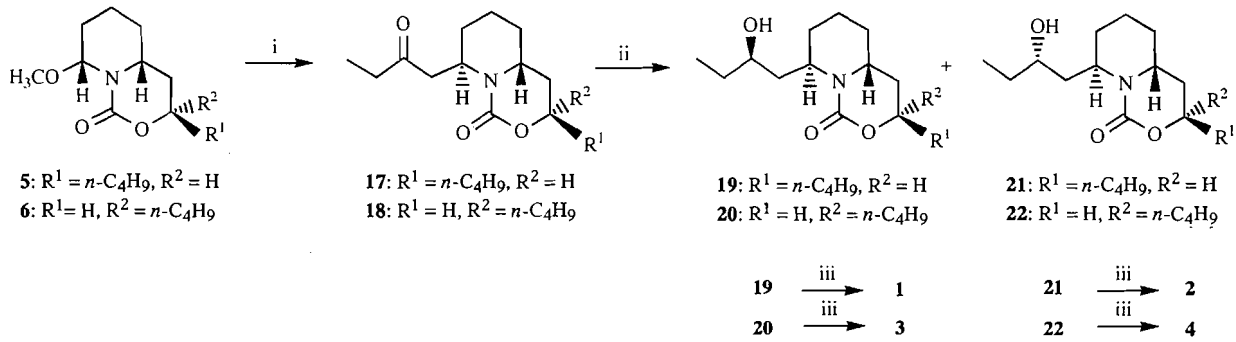

5: $R^1 = n\text{-}C_4H_9$, $R^2 = H$
6: $R^1 = H$, $R^2 = n\text{-}C_4H_9$

17: $R^1 = n\text{-}C_4H_9$, $R^2 = H$
18: $R^1 = H$, $R^2 = n\text{-}C_4H_9$

19: $R^1 = n\text{-}C_4H_9$, $R^2 = H$
20: $R^1 = H$, $R^2 = n\text{-}C_4H_9$

21: $R^1 = n\text{-}C_4H_9$, $R^2 = H$
22: $R^1 = H$, $R^2 = n\text{-}C_4H_9$

i: $TiCl_4$, CH_2Cl_2, 0°C, 5 min, then −45°C, $CH_2{=}CH\text{-}(OSiMe_3)CH_2CH_3$, 2 h (**17**: 58%; **18**: 55%); ii: $NaBH_4$, MeOH, r.t., 25–50 min, (**19**: 38%; **20**: 51%; **21**: 54%; **22**: 34%); iii: 2 M ethanolic KOH, reflux 1–18 h (**1**: quant.; **3**: 95%; **4**: 91%).

tive cleavage of the N—O bond of **8***b* with Ni/Al alloy and KOH in aqueous methanol afforded γ-aminoalcohol **9***b* in 95% yield. The epimeric alcohol **12***b* was obtained from **9***b* after a three-step sequence: protection of **9***b* as the N-BOC derivative **10***b* followed by treatment with mesyl chloride afforded the corresponding cyclic carbamate **11***b* with inversion at carbon 8; hydrolysis and decarboxylation of this carbamate led to γ-aminoalcohol **12***b* in 81% overall yield. The two epimeric γ-aminoalcohols **9***b* and **12***b* were then submitted to the same reaction sequence; after protection of the amine and alcohol functions, anodic oxidation of the resulting carbamates **13***b* and **14***b* was performed in the conditions described previously (4). The cyclic carbamates **5** and **6** were obtained by treatment of α-methoxycarbamates **15***b* and **16***b* with *t*BuOK in THF.

The synthesis of aminodiols **1**–**4** from **5** and **6** is outlined in Scheme 2.

The nucleophilic displacement of the methoxy group of **5** and **6** was performed by treatment with an excess of 2-(trimethylsilyloxy)but-1-ene (14) in the presence of $TiCl_4$ at low temperature to give the expected *trans*-2,6-piperidine derivatives **17** and **18** with yields of 58 and 55%, respectively. No *cis* product was detected. The desired *trans* aminodiols **1**–**4** were obtained by subsequent $NaBH_4$ reduction of the ketone function of **17** and **18**, separation of the resulting diastereomeric alcohols, and finally cleavage of the carbamate function under basic conditions.

The ^{13}C chemical shifts of the aminodiols **1**–**4** are given in Table 1.

These values deserve some comments. The *trans*-2,6 configuration of the four diastereomers is confirmed by the chemical shifts of C4: they range from 19.8 to 20.6 ppm, in agreement with typical values reported for *trans*-2,6-disubstituted piperidine models (15). Comparison of the ^1H and ^{13}C NMR properties of **1** and its *N*-benzyl derivative with those published (3) clearly shows the identity of Carruthers' compound with ours. The complete relative configurations of **1** and **2** (**2** only differs from **1** at C10) are therefore established. On this basis, examination of the C2, C6, C8, and C10 chemical shifts through the series and comparison with mono- and disubstituted piperidine derivatives of established configuration (16)[2] allow the unambiguous determination of the relative configurations of **3** and **4**.

Comparison of the ^{13}C chemical shifts of the four aminodiols **1**–**4** with the values published for andrachamine clearly establishes that none of them is identical with andrachamine. *The structure of andrachamine has therefore been misassigned.* When this work was complete, it came to our knowledge that the same conclusion had been reached independently in another laboratory (17). As an authentic specimen of the alkaloid was no longer available, a reexamination of the spectral properties of andrachamine appeared necessary. The original ^1H and ^{13}C NMR spectra were kindly supplied by Professor Ahmad; their study revealed that the alkaloid was not isolated as a pure compound as indicated inter alia by the relative intensities of the signals in the ^{13}C NMR spectrum. Indeed, on a given spectrum, signals corresponding to equally substituted carbon atoms are expected to display nearly equal intensities. However, on the original ^{13}C spectrum of andrachamine the intensities associated with the 73.6/71.0 (assigned to C10 and C8) and 9.9/13.9 (assigned to C12 and C16) signal pairs for instance appear in a 1/3 ratio. In a similar way, the low intensities of the signals at 31.0 and 39.6 ppm did not match those of the other major signals of the spectrum. It therefore appears that the signals at 73.6, 39.6, 31.0, and 9.9 ppm are due to the presence of impurities and that only the eight following ^{13}C signals are attributable to the major constituent: δ 71.0, 59.1, 40.3, 40.1, 29.4, 23.0, 18.7, and 13.9 ppm (Table 2). The signal at 23.0 ppm being only attributable to C4, a C_2 symmetric *trans*-2,6-disubstituted derivative can be ruled out. It is likely therefore that the alkaloid is a *meso* 2,6-disubstituted piperidine derivative corresponding either to structure **23** or to structure **24**.

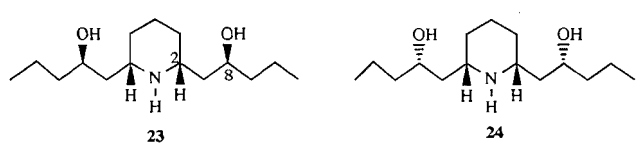

23 **24**

[2] Also, S. Mill and C. Hootelé, unpublished results.

Scheme 3.

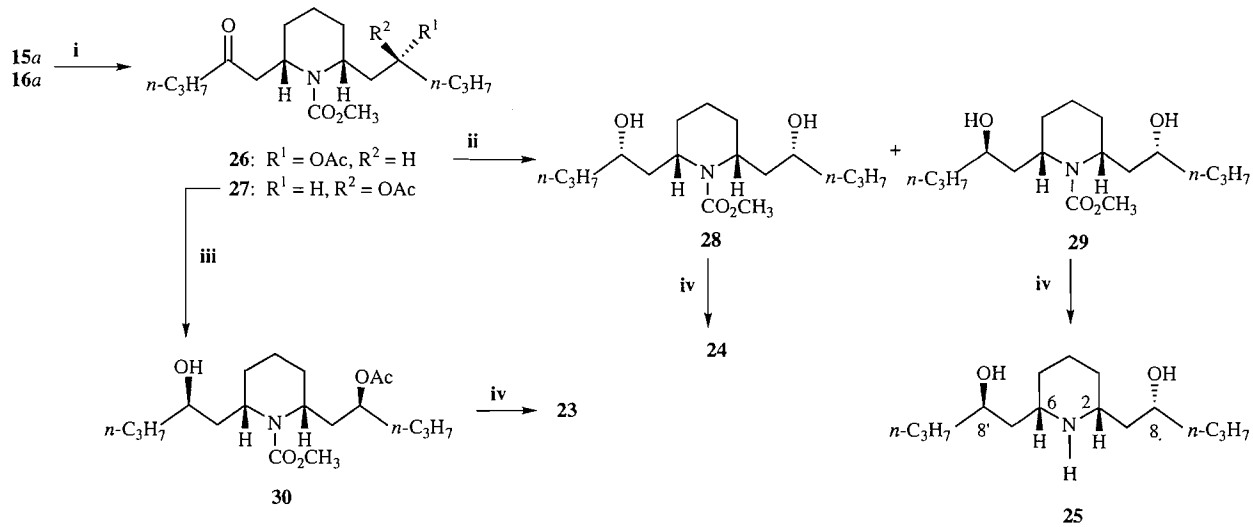

i: $CF_3SO_3SiMe_3$ or $TiCl_4$, $CH_2{=}C(OSiMe_3)CH_2CH_2CH_3$, CH_2Cl_2, −78°C, 1 h (**26**: 56%; **27**: 81%); ii: (*a*) K_2CO_3, MeOH, r.t., 23 h (84%); (*b*) $NaBH_4$, MeOH, r.t., 30 min (**28**: 10%; **29**: 62%); iii: $LiAl(OtBu)_3H$, THF, 0°C, 1 h (84%); iv: 1–2 M ethanolic KOH, 1–5 h, reflux (**23**: 95%, **24**: quant.; **25**: 99%).

Table 1. ^{13}C chemical shifts (ppm) of aminodiols **1**–**4** (62.8 MHz) and of andrachamine according to ref. 1 (75.5 MHz).

Attribution	1	2	3	4	Andrachamine according to ref. 1
C10	70.9	75.1	73.0	69.1	73.6
C8	69.6	67.9	71.7	73.7	71.0
C6	47.7*	53.0	50.5*	46.3	59.1
C2	47.6*	46.5	50.3*	53.1	59.1
C7	39.4**	43.1*	40.4**	42.4*	31.0
C9	39.2**	38.1*	40.0**	38.2*	40.3
C13	37.8**	37.1*	37.9**	37.0*	39.6
C3	32.6***	33.5**	32.6	33.2**	40.1
C5	32.5***	32.8**	32.6	32.4**	40.1
C11	30.8	31.2	30.8	30.8	29.4
C14	28.7	28.5	27.7	27.8	29.4
C15	23.2	23.2	22.8	23.1	23.0
C4	20.4	20.6	19.8	20.3	18.7
C16	14.5	14.5	14.1	14.3	13.9
C12	10.7	10.1	9.8	10.4	9.9

*, **, ***These values may be interchanged.

The synthesis of the two *meso* isomers **23** and **24** was achieved as outlined in Scheme 3.

Carbamates **15***a* and **16***a* were obtained by the same cycloaddition, C8 inversion, and anodic methoxylation pathway as described above for the synthesis of **15***b* and **16***b* (Scheme 1). The elimination – nucleophilic addition, respectively, yielded the two *cis* ketones **26** and **27**. Methanolysis of the ester function of **26** followed by $NaBH_4$ reduction yielded a mixture of diols **28** and **29**; they were separated on alumina and transformed under basic conditions into the aminodiols **24** and **25**. The relative configurations of **24** and **25** rest on the analysis of their ^{13}C NMR spectra. On the other hand, **23** was obtained after stereoselective reduction of the ketone **27** followed by basic hydrolysis of **30**. The complete analysis of the ^1H and ^{13}C NMR spectra of **23**, **24**, and **25** could be achieved using COSY and HMQC experiments.

Unexpectedly, we observed that the ^{13}C chemical shifts of neither **23** nor **24** were identical with the eight values retained for andrachamine (Table 2). However, significant differences only affect the α and β positions relative to the nitrogen atom and suggest that the values reported for andrachamine do not refer to the free base but to a salt of the alkaloid (18). Indeed,

Table 2. ^{13}C (90.6 MHz) chemical shifts (ppm) of **23**, **24**, the corresponding trifluoroacetates, and the major signals of the original spectrum of andrachamine.

Attribution	**23**	**24**	**23**·CF_3COOH	**24**·CF_3COOH	Major signals of the original spectrum (1)
C8	71.5	69.3	72.6	69.1	71.0
C2	56.8	54.9	58.8	56.9	59.1
C7	44.5	43.9	40.8*	39.4*	40.3*
C9	40.8	41.0	40.4*	38.2*	40.1*
C3	34.3	32.6	30.2	27.5	29.4
C4	25.2	25.4	23.3	23.1	23.0
C10	19.1	19.6	19.0	18.7	18.7
C11	14.6	14.8	14.3	13.8	13.9

*These values may be interchanged.

Table 3. ^{13}C (90.6 MHz) chemical shifts (ppm) of andrachamine from *Andrachne aspera* and its trifluoroacetate.

Attribution	Andrachamine from *A. aspera*	Andrachamine·CF_3COOH
C8	71.7	72.9
C2	57.0	58.8
C7	43.7	40.3*
C9	40.7	40.1*
C3	33.5	29.9
C4	24.7	23.0
C10	18.9	18.6
C11	14.4	14.0

*These values may be interchanged.

the chemical shift values observed after protonation of **23** (by addition of one equivalent of trifluoroacetic acid) are in complete accordance with the retained values while the ^{13}C spectrum of **24** after protonation is quite different (Table 2). The values of the ^1H NMR spectrum of **23**·CF_3COOH (i.a. δ(H2): 3.13 ppm, δ(H8): 3.77 ppm) are in perfect agreement with the published ones (1); in the free base, however, H2 occurs at 2.72 ppm.

From the evidence accumulated above, it appears that the alkaloid andrachamine is correctly depicted by structure **23**. To obtain a definite confirmation of this attribution a sample of andrachamine was reisolated from *Andrachne aspera* and compared with synthetic **23**; the two samples appeared identical. Moreover, after protonation, our sample of andrachamine exhibited eight ^{13}C signals corresponding to the eight major signals appearing on the original spectrum of Professor Ahmad (Table 3).

Experimental

Mass spectral data were obtained on a Micromass 7070 or a Fisons Autospec spectrometer (high-resolution measurements). NMR spectra were recorded on a Bruker WM 250 (^1H: 250 MHz, ^{13}C: 62.8 MHz), an AMX 400 (^1H: 360 MHz, ^{13}C: 90.6 MHz), or a Varian Unity 600 (^1H: 600 MHz, ^{13}C: 150.7 MHz) spectrometer in $CDCl_3$ with TMS as internal standard. IR spectral data were recorded on a Brucker IFS 25 spectrometer, as liquid films unless otherwise stated.

Analytical thin-layer chromatography was performed on Polygram Sil G/UV254 plates and on Merck aluminium sheets, aluminium oxide 60 F 254 neutral, type E. Visualization was accomplished either by ethanolic phosphomolybdic acid solution followed by heating or by iodine followed by Dragendorff's reagent.

General procedure for the cycloaddition reactions

To a stirred solution of 1-hydroxypiperidine (0.023 mol) in dichloromethane (20 mL) at 0°C, yellow mercuric oxide (0.047 mol) is slowly added. The solution is then allowed to warm up to room temperature, stirred until the hydroxylamine has disappeared (TLC), and then filtered through Celite. After evaporation of the solvent under reduced pressure, the residue is mixed with the terminal alkene (0.159 mol), ethanol (20 mL), and chloroform (20 mL) in a sealed tube. After 70–90 h at 50–60°C, the solvent is evaporated under reduced pressure; after one or two successive flash chromatographies (Kieselgel 60 Merck; ether:hexane 2:3), the pure *exo* isoxazolidine is isolated.

The ^1H NMR spectra of **8***a* and **8***b* indicate a "slow" nitrogen inversion process at room temperature: all signals are enlarged, due to interconversion between the *trans* conformer (*t*, ca. 89%) and the *cis* pair (*c*).

Isoxazolidine **8**a, *87%*: ^1H NMR, δ ppm: 4.35 (m, H8(*c*)), 4.04 (m, H8(*t*)), 3.5–3.4 (m, H6e(*t*) + H2(*c*)), 3.02 (m, H6e(*c*)), 2.73 (m, H6a(*c*)), 2.46 (m, H6a(*t*)), 1.18–2.40 (13H, m), 0.93 (3H, m); ^{13}C NMR, δ ppm: 76.3 (C8), 66.9 (C2), 55.6 (C6), 40.6, 38.0, 30.0, 25.3, 24.4, 19.6, 14.5 (CH_3); MS *m/z*: 169 ($M^{+\cdot}$ 15%), 168 (10) (calcd. for $C_{10}H_{18}NO$ ($M^{+\cdot}$ −H): 168.1388; found: 168.1386), 126 (4), 100 (100), 84 (21).

Isoxazolidine **8**b, *93%*: ^1H NMR, δ ppm: 4.33 (m, H8(*c*)), 4.02 (m, H8(*t*)), 3.5–3.4 (m, H6e(*t*) + H2(*c*)), 3.02 (m, H6e(*c*)), 2.66 (m, H6a(*c*)), 2.44 (m, H6a(*t*)), 1.14–2.32 (15H, m), 0.90 (3H, m); ^{13}C NMR, δ ppm: 76.6 (C8), 66.9 (C2), 55.7 (C6), 40.6, 35.6, 30.0, 28.6, 25.3, 24.5, 23.2, 14.5 (CH_3); MS *m/z*: 183 ($M^{+\cdot}$, 24%), 182 (8) (calcd. for $C_{11}H_{20}NO$ ($M^{+\cdot}$ −H): 182.1545; found: 182.1547), 126 (5), 100 (100), 84 (37).

General procedure for the hydrogenolysis of isoxazolidines 8 *a*, *b*

A 1 M aqueous KOH solution (10 mL) is added to a stirred solution of the isoxazolidine (1.48 mmol) in methanol, (10 mL). The Ni/Al alloy (twice the weight of isoxazolidine) is slowly added. The reaction mixture is left overnight and then filtered through Celite and rinsed with methanol (200 mL). After evaporation of the methanol under reduced pressure, aqueous NaOH (30 mL) is added to the residue and the aqueous phase is extracted with chloroform (3 × 40 mL). Removal of the solvent under reduced pressure gives the pure γ-aminoalcohol.

9a, (±/−)-halosaline, 97%: IR (CCl_4 solution), cm^{-1}: 3350, 2956, 2932, 2872; ^1H NMR, δ ppm: 3.88 (1H, m, H8), 3.17 (2H, m, OH, NH), 3.05 (1H, dd, J = 11 and 2 Hz, H2), 2.86 (1H, m, H6e), 2.56 (1H, dt, J = 12 and 3 Hz, H6a), 1.26–1.80 (12H, m), 0.92 (3H, t, J = 7 Hz); ^{13}H NMR, δ ppm: 69.1 (C8), 55.1 (C2), 47.3, 42.6 (C6, C7), 40.4 (C9), 32.0, 26.5 (C3, C5), 25.1, 19.3 (C10, C4), 14.4 (CH_3); MS *m/z*: 171 ($M^{+\cdot}$, 36%) (calcd. for $C_{10}H_{21}NO$: 171.1623; found: 171.1620), 154 (17), 128 (100), 98 (68).

9b, *95%*: IR (CCl_4 solution), cm^{-1}: 3326, 2933, 2859; ^1H NMR, δ ppm: 3.86 (1H, m, H8), 3.29 (2H, m, OH, NH), 3.04 (1H, m), 2.86 (1H, m), 2.56 (1H, dt, J = 12 and 3 Hz, H6a), 1.23–1.81 (14H, m), 0.90 (3H, t, J = 7 Hz); ^{13}C NMR, δ ppm: 69.3 (C8), 55.0 (C2), 47.2, 42.5 (C6, C7), 37.8 (C9), 31.9, 28.3, 26.5 (C3, C5, C10); 25.1, 23.0 (C4, C11), 14.3 (CH_3); MS *m/z*: 185 ($M^{+\cdot}$, 5%) (calcd. for $C_{11}H_{23}NO$: 185.1780; found: 185.1783), 128 (13), 112 (6), 98 (11), 84 (100).

General procedure for the synthesis of *N*-carbomethoxy derivatives of 9 *a*, *b* and 12*a*, *b*

K_2CO_3 (7.87 mmol) and methyl chloroformate (5.30 mmol) are successively added to a stirred solution of γ-aminoalcohol (1.06 mmol) in water. After 3 h at room temperature, NH_4OH is added and the basic solution is extracted with $CHCl_3$ (3 × 20 mL). The combined $CHCl_3$ phases are evaporated under reduced pressure and the residue is filtered through a short column of alumina to afford the corresponding *N*-carbomethoxy derivative.

N-*Carbomethoxy derivative of* ***9***a, *95.5%*: IR (CCl_4 solution), cm^{-1}: 3346, 2942, 2872, 1682; ^1H NMR, δ ppm: 4.50 (1H, m, H2), 3.98 (2H, m, H6e and OH), 3.72 (3H, s, NCO_2CH_3), 3.36 (1H, m, H8), 2.74 (1H, dt, J = 13 and 2Hz, H6a), 2.00 (1H, dt, J = 14 and 2Hz), 1.16–1.76 (11H, m), 0.91 (3H, t, J = 7 Hz); ^{13}C NMR, δ ppm: 157.9, 67.7 (C2), 53.4 (NCO_2CH_3), 47.9 (C8), 39.7, 39.6, 38.1, 30.0, 26.0, 19.7, 14.6 (CH_3); MS *m/z*: 229 ($M^{+\cdot}$, 2%) (calcd. for $C_{12}H_{23}NO_3$: 229.1678; found: 229.1686), 186 (2), 170 (1), 168 (1), 142 (100).

N-*Carbomethoxy derivative of* ***9***b, *95%*: ^1H NMR, δ ppm: 4.50 (1H, m, H2), 3.98 (2H, m, OH and H8), 3.72 (3H, s, NCO_2CH_3), 3.34 (1H, m, H6e), 2.73 (1H, m, H6a), 2.03 (1H, m), 1.16–1.96 (13H, m), 0.90 (3H, t, J = 7 Hz); ^{13}C NMR, δ ppm: 157.6, 67.6 (C2), 53.0 (NCO_2CH_3), 47.5 (C8), 39.3, 37.7, 36.7, 29.6, 28.3, 25.6, 22.9, 19.3, 19.3, 14.1 (CH_3); MS *m/z*: 243 ($M^{+\cdot}$, 3%) (calcd. for $C_{13}H_{25}NO_3$: 243.1834; found: 243.1836), 186 (2), 184 (2), 168 (3), 142 (100).

N-*Carbomethoxy derivative of* ***12***a, *74%*: IR (CCl_4 solution), cm^{-1}: 3446, 2955, 2937, 2865, 1697, 1679; ^1H NMR, δ ppm: 4.40 (1H, m, H2), 3.98 (1H, m, H6e), 3.69 (3H, s, NCO_2CH_3), 3.62 (1H, m, H8), 2.88 (1H, m, H6a), 2–3 (1H, OH), 1.31–1.80 (12H, m), 0.92 (3H, m); ^{13}C NMR, δ ppm: 156.5, 69.9 (C2), 52.5 (NCO_2CH_3), 48.9 (C8), 39.8, 39.6, 38.2, 29.1, 25.5, 19.0, 18.9, 14.0 (CH_3); MS *m/z*: 229 ($M^{+\cdot}$, 2%) (calcd. for $C_{12}H_{23}NO_3$: 229.1678; found: 229.1684), 186 (1), 170 (1), 168 (1), 142 (100).

N-*Carbomethoxy derivative of* ***12***b, *86%*: ^1H NMR, δ ppm: 4.39 (1H, m, H2), 3.99 (1H, m), 3.69 (3H, s, NCO_2CH_3), 3.64 (1H, m), 2.88 (1H, dt, J = 13 and 2.5 Hz, H6a), 1.26–2.5 (15H, m), 0.90 (3H, t, J = 7 Hz); ^{13}C NMR, δ ppm: 156.7, 70.4 (C2), 52.8 (NCO_2CH_3), 49.1 (C6), 39.7, 38.4, 37.5, 29.4, 28.1, 25.7, 22.9, 19.2, 14.2 (CH_3); MS *m/z*: 243 ($M^{+\cdot}$, 1%) (calcd. for $C_{13}H_{25}NO_3$: 243.1834; found: 243.1835), 186 (2), 168 (2), 142 (100).

General procedure for the acetylation reactions

The *N*-carbomethoxy derivative (4.58 mmol) is treated at room temperature for 17 h with a mixture of pyridine (15 mL) and acetic anhydride (0.046 mol). After evaporation of the solvent, filtration of the residue through a short column of alumina yields the corresponding *O*-acetyl derivative.

13a, *83%*: IR (CCl_4 solution), cm^{-1}: 2956, 2937, 2867, 1740, 1699; ^1H NMR, δ ppm: 4.74 (1H, m, H8), 4.38 (1H, m, H2), 4.02 (1H, m, H6e), 3.64 (3H, s, NCO_2CH_3), 2.75 (1H, dt, J = 2.5 and 13 Hz, H6a), 2.03 (3H, s, $OCOCH_3$), 1.97 (1H, m), 1.27–1.68 (11H, m), 0.91 (3H, t, J = 7 Hz); ^{13}C NMR, δ ppm: 171.0, 156.4, 71.8 (C8), 52.9 (NCO_2CH_3), 47.9 (C2), 39.5, 37.0, 34.2, 29.4, 26.0, 21.6 ($OCOCH_3$), 19.5, 18.9, 14.4 (CH_3); MS *m/z*: 271 ($M^{+\cdot}$, <1%), 212 (4), 211 (7) (calcd. for $C_{12}H_{21}NO_2$ ($M^{+\cdot}$ −AcOH): 211.1572; found: 211.1578), 168 (7), 155 (6), 142 (100).

13b, *96%*: IR, cm^{-1}: 2954, 2937, 2862, 1740, 1683; ^1H NMR, δ ppm: 4.73 (1H, m, H8), 4.38 (1H, m, H2), 4.02 (1H, m, H6e), 3.64 (3H, s, NCO_2CH_3), 2.75 (1H, dt, J = 2.5 and 13 Hz, H6a), 2.03 (3H, s, $OCOCH_3$), 2.00 (1H, m), 1.21–1.68 (13H, m), 0.89 (3H, t, J = 7 Hz); ^{13}C NMR δ ppm: 171.0, 156.3, 71.9 (C8), 52.8 (NCO_2CH_3), 47.8 (C2), 39.4, 34.5, 34.2, 29.4, 27.7, 26.0, 23.0, 21.6 ($OCOCH_3$), 19.5, 14.3 (CH_3); MS *m/z*: 285 ($M^{+\cdot}$, 1%) (calcd. for $C_{15}H_{27}NO_4$: 285.1940; found: 285.1939), 242 (1), 225 (7), 169 (7), 155 (10), 142 (100).

14a, *93%*: ^1H NMR, δ ppm: 4.83 (1H, m, H6), 4.33 (1H, m, H2), 4.01 (1H, m, H6e), 3.67 (3H, s, NCO_2CH_3), 2.90 (1H, m, H6a), 2.03 (3H, s, $OCOCH_3$), 1.96 (1H, m), 1.27–1.71 (11H, m), 0.90 (3H, t, J = 7 Hz); ^{13}C NMR, δ ppm: 171.2, 156.4, 72.6 (C8), 52.9 (NCO_2CH_3), 48.4 (C2), 39.7, 36.7, 34.5, 28.9, 26.0, 21.6 ($OCOCH_3$), 19.4, 19.0, 14.3 (CH_3); MS *m/z*: 271 ($M^{+\cdot}$, <1%), 212 (3), 211 (7) (calcd. for $C_{12}H_{21}NO_2$ ($M^{+\cdot}$ −AcOH): 211.1572; found: 211.1561), 168 (7), 155 (5), 142 (100).

14b, *quant.*: ^1H NMR, δ ppm: 4.82 (1H, m, H8), 4.33 (1H, m), 3.99 (1H, m), 3.67 (3H, s, NCO_2CH_3), 2.90 (1H, m, H6a), 2.03 (3H, s, $OCOCH_3$), 1.97 (1H, m), 1.21–1.69 (13H, m), 0.89 (3H, t, J = 7 Hz); ^{13}C NMR, δ ppm: 170.7, 155.9, 72.3 (C8), 52.3 (NCO_2CH_3), 47.9 (C2), 39.1, 33.9, 33.7, 28.3, 27.3, 25.4, 22.4, 21.1 ($OCOCH_3$), 18.9, 13.9 (CH_3); MS *m/z*: 285 ($M^{+\cdot}$, <1%) (calcd. for $C_{15}H_{27}NO_4$: 285.1940; found: 285.1946), 242 (<1), 225 (5), 168 (6), 155 (8), 142 (100).

Preparation of the *N*-carbotertiobutoxy derivatives 10*a*, *b*

To a stirred solution of γ-aminoalcohol (0.32 mmol) in THF (6 mL) at room temperature, ditertiobutyl dicarbonate (0.41 mmol) is added. After 3 h, the solvent is evaporated under reduced pressure and after a flash chromatography (Kieselgel

60 Merck; ethyl acetate:hexane 1:9), the pure N-Boc derivative is isolated.

10a, *80%*: IR, cm^{-1}: 3452, 2936, 2870, 1660; ^1H NMR, δ ppm: 4.46 (1H, m), 4.21 (1H, m), 3.95 (1H, m), 3.32 (1H, m), 2.67 (1H, dt, J = 11 and 2.5 Hz, H6a), 1.12–2.04 (21H, m), 0.91 (3H, t, J = 7 Hz); ^{13}C NMR, δ ppm: 80.2, 67.2 (C2), 46.8 (C8), 39.5 (C6), 39.1, 37.8, 29.7, 28.6 (*t*Bu), 25.7, 19.5, 19.4, 14.2 (CH_3); MS *m/z*: 271 ($M^{+\cdot}$, 8%), 215 (7), 198 (11), 184 (21) (calcd. for $C_{10}H_{18}NO_2$ ($M^{+\cdot} - C_5H_{11}O$): 184.1337; found: 184.1346), 172 (20), 170 (16), 154 (8), 142 (12), 128 (100), 84 (84).

10b, *95%*: ^1H NMR, δ ppm: 4.46 (1H, m), 4.23 (1H, m), 3.95 (1H, m), 3.15 (1H, m), 2.65 (1H, dt, J = 14 and 2.5 Hz, H6a), 1.99 (1H, dt, J = 12 and 2 Hz), 1.12–1.78 (22H, m), 0.90 (3H, t, J = 7 Hz); ^{13}C NMR, δ ppm: 156.2, 80.4, 67.7 (C2), 47.0 (C8), 39.7 (C6), 38.0, 36.9, 29.9, 28.8 (*t*Bu), 28.6, 26.0, 23.1, 19.6, 14.4 (CH_3); MS *m/z*: 285 ($M^{+\cdot}$, 1%) (calcd. for $C_{16}H_{31}NO_3$: 285.2304; found: 285.2311), 229 (1), 212 (3), 184 (13), 172 (5), 143 (3), 128 (100).

Preparation of 11*a*, *b*

To a solution of **10** (0.30 mmol) in pyridine (3 mL) at room temperature, freshly distilled mesyl chloride (6.6 mmol) is added. After 24 h, water (10 mL) is added and the solution is extracted with dichloromethane (3 × 15 mL). The organic phase is evaporated under reduced pressure and after a flash chromatography (Kieselgel 60 Merck; ethyl acetate:hexane 1:2), the pure cyclic carbamate is isolated.

11a, *96%*: ^1H NMR, δ ppm: 4.46 (1H, m, H8), 4.14 (1H, m, H6e), 3.28 (1H, ddt, J = 11, 5.5, and 2.5 Hz, H2), 2.65 (1H, dt, J = 13 and 3 Hz, H6a), 2.04 (1H, ddd, J = 14, 5.5, and 2 Hz), 1.10–1.90 (11H, m), 0.93 (3H, t, J = 7 Hz); ^{13}C NMR, δ ppm: 154.0, 74.9 (C8), 54.2 (C2), 44.8 (C6), 37.1, 36.0, 33.8, 25.1, 23.8, 18.0, 13.9 (CH_3); MS *m/z*: 197 ($M^{+\cdot}$, 30%) (calcd. for $C_{11}H_{19}NO_2$: 197.1416; found: 197.1419), 168 (12), 154 (31), 127 (60), 110 (18), 84 (100).

11b, *91%*: ^1H NMR, δ ppm: 4.45 (1H, m, H8), 4.09 (1H, m, H6e), 3.25 (1H, ddt, J = 11, 5.5, and 2.5 Hz, H2), 2.63 (1H, dt, J = 13 and 3 Hz, H6a), 2.02 (1H, ddd, J = 14, 5.5, and 2 Hz), 1.08–1.83 (13H, m), 0.89 (3H, t, J = 7 Hz); ^{13}C NMR, δ ppm: 154.3, 75.4 (C8), 54.5 (C2), 45.1 (C6), 36.3, 35.0, 34.1, 27.2, 25.4, 24.1, 22.9, 14.2 (CH_3); MS *m/z*: 211 ($M^{+\cdot}$, 19%) (calcd. for $C_{12}H_{21}NO_2$: 211.1572; found: 211.1581), 168 (27), 166 (7), 154 (13), 127 (54), 110 (17), 84 (100).

Preparation of 12*a*, *b* from 11 *a*, *b*

The cyclic carbamate (1.34 mmol) is mixed with 20 mL of a 2 M ethanolic KOH solution. After 17 h at room temperature and 1 h at reflux, the solvent is evaporated under reduced pressure. The residue is diluted with water (30 mL) and the aqueous phase is extracted with CH_2Cl_2 (3 × 30 mL). Evaporation of the solvent gives the pure γ-aminoalcohol.

12a, *quant.*: IR (CCl_4 solution), cm^{-1}: 3307, 2957, 2931, 2871, 2859, 1552; ^1H NMR, δ ppm: 2.5–4 (1H, m, OH), 3.80 (1H, m, H8), 3.02 (1H, m), 2.64 (2H, m), 1.82 (1H, m), 1.05–1.67 (12H, m), 0.91 (3H, t, J = 7 Hz); ^{13}C NMR, δ ppm: 72.8 (C8), 58.3 (C2), 46.1 (C6), 42.7, 40.5, 34.5, 27.4, 24.6, 18.7, 14.2 (CH_3); MS *m/z*: 171 ($M^{+\cdot}$, 2%) (calcd. for $C_{10}H_{21}NO$: 171.1623; found: 171.1620), 128 (5), 112 (2), 98 (3), 84 (100).

12b, *94%*: IR (CCl_4 solution), cm^{-1}: 3322, 2932, 2860; ^1H NMR, δ ppm: 3.80 (1H, m, H8), 2–3.5 (1H, m, OH), 3.03 (1H, m), 2.64 (2H, m), 1.81 (1H, m), 1.02–1.67 (14H, m), 0.90 (3H, t, J = 7 Hz); ^{13}C NMR, δ ppm: 73.0 (C8), 58.2 (C2), 46.1 (C6), 42.7, 37.9, 34.5, 27.7, 27.5, 24.6, 22.8, 14.0 (CH_3); MS *m/z*: 185 ($M^{+\cdot}$, 1%) (calcd. for $C_{11}H_{23}NO$: 185.1780; found: 185.1784), 128 (5), 84 (100).

General procedure for anodic methoxylations and preparation of 15*a*, *b* and 16*a*, *b*

The anodic methoxylations are carried out at room temperature in methanol (analytical grade) containing Et_4NOTs as a supporting electrolyte, in an undivided cell equipped with two vitreous carbon electrodes, an exit tube (containing $CaCl_2$) for venting purposes, and a magnetic stirring bar. The carbon electrodes (3 mm in diameter, immersed 3.5 cm in the solution) are 1.0 cm apart. The potentiostat is a homemade apparatus.

The carbamate (0.52 mmol), Et_4NOTs (0.13 mmol), and methanol (15 mL) are placed in the electrolysis cell. The solution is stirred for 10 min and then a constant potential of 8.00 V is applied. After 8 F/mol of electricity is passed, a few drops of NH_4OH are added to the solution and the solvent is evaporated. The residue is then dissolved in water (200 mL), basified with NH_4OH, and extracted with $CHCl_3$ (3 × 50 mL). The combined $CHCl_3$ phases are evaporated and the residue is filtered ($CHCl_3$) through a short column of alumina to afford the 6-methoxy derivative.

15a, *99%*: ^1H NMR, δ ppm: presence of a mixture of conformers: 5.47 and 5.28 (1H, 2 br m, H6), 4.82 (1H, m, H8), 4.24–4.36 (1H, 2 br m, H2), 3.67 (3H, br s, NCO_2CH_3), 3.30 (3H, s, OCH_3), 1.25–2.21 (15H, m), 0.91 (3H, t, J = 7 Hz); ^{13}C RMN, δ ppm: 171.0, 157.5, 83.1 (C6), 72.5 (C8), 56.2 (OCH_3), 53.1 (NCO_2CH_3), 48.0 (C2), 38.7, 37.3, 30.9, 29.9, 28.8, 21.7 ($OCOCH_3$), 18.7, 14.5 (CH_3), 14.3; MS *m/z*: 301 ($M^{+\cdot}$, <1%), 286 (1), 270 (8) (calcd. for $C_{14}H_{24}NO_4$ ($M^{+\cdot} - OCH_3$): 270.1705; found: 270.1696), 269 (8), 242 (4), 241 (9), 226 (4), 210 (14), 209 (15), 172 (100).

15b, *99%*: ^1H NMR (360 MHz), δ ppm: presence of a mixture of conformers: 5.47 and 5.28 (1H, 2 br m, H6), 4.80 (1H, m, H8), 4.23–4.36 (1H, 2 br m, H2), 3.69 (3H, br s, NCO_2CH_3), 3.31 (3H, br s, OCH_3), 1.23–2.27 (17H, m), 0.91 (3H, t, J = 7 Hz); ^{13}C NMR (90.6 MHz), δ ppm: 171.1, 170.7, 157.3, 156.5, 82.9 (C6), 72.5 (C8), 56.0 (OCH_3), 52.9 (NCO_2CH_3), 47.8 (C2), 38.5 and 38.1, 34.6, 30.7, 29.7, 28.6, 27.3, 22.9 ($OCOCH_3$), 21.5, 14.2 (CH_3), 14.0; MS *m/z*: 315 ($M^{+\cdot}$, <1%), 284 (6) (calcd. for $C_{15}H_{26}NO_4$ ($M^{+\cdot} - OCH_3$): 284.1862; found: 284.1855), 283 (8), 255 (8), 224 (12), 172 (100), 140 (51).

16a, *92%*: ^1H NMR, δ ppm: presence of a mixture of conformers: 5.44 and 5.30 (0.5 H, 2 br m), 4.85 (1H, m, H8), 3.98–4.32 (1.5 H, 3 br m), 3.72 and 3.67 (3H, 2 br s, NCO_2CH_3), 3.27 (3H, br s, OCH_3), 1.13–2.90 (15H, m), 0.91 (3H, 2t, J = 7 Hz); ^{13}C NMR, δ ppm: 82.9 (C6), 72.2 (C8), 55.6 (OCH_3), 53.1 and 52.9 (NCO_2CH_3), 48.0 (C2), 39.7, 37.5, 36.8, 34.5, 31.0, 28.9, 27.3, 26.0, 21.6 ($OCOCH_3$), 19.4, 19.1, 14.4 (CH_3), 14.0; MS *m/z*: 301 ($M^{+\cdot}$, <1%), 270 (8), 269 (13) (calcd. for $C_{14}H_{23}NO_4$ ($M^{+\cdot} - CH_3OH$): 269.1627; found: 269.1609), 242 (2), 241 (5), 210 (21), 209 (18), 172 (100).

16b, *83%*: ^1H NMR (360 MHz), δ ppm: presence of a mixture of conformers: 5.30–5.46 (1H, 2 br m, H6), 4.90 (1H, m, H8), 4.11–4.24 (1H, 2 br m, H2), 3.72 (3H, br s, NCO_2CH_3), 3.28 (3H, br s, OCH_3), 1.23–2.14 (12H, m), 0.89 (3H, t, J = 7 Hz);

^{13}C NMR (90.6 MHz), δ ppm: presence of a mixture of conformers: 171.0, 157.1 and 156.4, 82.4 (C6), 72.1 and 71.8 (C8), 55.6 and 55.2 (OCH_3), 52.7 (NCO_2CH_3), 47.7 and 47.4 (C2), 38.2 and 37.5, 34.6, 30.6, 27.5, 27.0 and 26.8, 22.7, 21.3 ($OCOCH_3$), 14.1 (CH_3), 13.6; MS *m/z*: 315 ($M^{+\cdot}$, <1%), 284 (9) (calcd. for $C_{15}H_{26}NO_4$ ($M^{+\cdot}$ $-OCH_3$): 284.1862; found: 284.1843), 283 (14), 255 (6), 224 (14), 223 (13), 172 (100), 140 (48).

Preparation of 5 and 6 from 15*b* and 16*b*

To a solution of **15***b* or **16***b* (6.1×10^{-5} mol) in THF (2 mL), *t*BuOK (1.3×10^{-4} mol) is added under stirring. The reaction mixture is left at room temperature for 1 h, a few drops of water are added, and the THF is evaporated under reduced pressure. The residue is dissolved in water (20 mL) and extracted with CH_2Cl_2 (3×20 mL). The organic phase is evaporated to give the pure 6-methoxy derivative.

***5**, 97%*: IR (CCl_4 solution), cm^{-1}: 3367, 2958, 2934, 2873, 2863, 1704; ^1H NMR, δ ppm: 5.40 (1H, m, H6), 4.36 (1H, m, H8), 3.41 (1H, m, H2), 3.40 (3H, s, OCH_3), 1.18–2.08 (14H, m), 0.91 (3H, t, $J = 7$ Hz); ^{13}C NMR, δ ppm: 154.5, 82.9 (C6), 75.8 (C8), 56.1 (OCH_3), 46.8 (C2), 35.1, 33.9, 27.9, 27.7, 25.4, 22.8, 14.7, 14.2 (CH_3); MS *m/z*: 241 ($M^{+\cdot}$, 1%) (calcd. for $C_{13}H_{23}NO_3$: 241.1678; found: 241.1671), 226 (5), 211 (35), 210 (25), 184 (5), 182 (8), 166 (100), 127 (19), 98 (19), 82 (37).

***6**, 97%*: ^1H NMR, δ ppm: 5.38 (1H, m, H6), 4.26 (1H, m, H8), 3.45 (1H, m, H2), 3.41 (3H, s, OCH_3), 1.20–2.10 (14H, m), 0.91 (3H, t, $J = 7$ Hz); ^{13}C NMR, δ ppm: 153.7, 82.4 (C6), 77.0 (C8), 55.8 (OCH_3), 50.4 (C2), 35.2, 35.2, 27.0, 26.7, 25.0, 22.4, 14.3, 13.8 (CH_3); MS *m/z*: 241 ($M^{+\cdot}$, <1%) (calcd. for $C_{13}H_{23}NO_3$: 241.1678; found: 241.1676), 226 (5), 211 (37), 210 (33), 184 (1), 182 (6), 166 (100), 127 (17), 98 (11), 82 (40).

Nucleophilic displacement of the methoxy group of 5 and 6

To a stirred solution of $TiCl_4$ (1.18 mmol) in dichloromethane (1 mL) at 0°C under a nitrogen atmosphere is added a solution of the methoxy derivative (0.67 mmol); after 5 min under stirring at 0°C, the temperature is lowered to −45°C and trimethylsilyloxybut-1-ene (contaminated with ca. 20% of trimethylsilyloxybut-2-ene) (4.44 mmol) is added. The resulting mixture is left at −45°C for 2 h. Water (20 mL) is then added, the mixture extracted with $CHCl_3$ (3×20 mL), the organic phase evaporated, and the residue submitted to a flash chromatography (Kieselgel 60 Merck; acetone:hexane 1:5), to afford the pure ketone.

***17**, 58%*: IR (CCl_4 solution), cm^{-1}: 2957, 2939, 2873, 1702; ^1H NMR, δ ppm: 4.95 (1H, m, H6), 4.16 (1H, m, H8), 3.50 (1H, m, H2), 2.42–2.74 (4H, m), 1.29–1.98 (14H, m), 1.03 (3H, t, $J = 7$ Hz), 0.91 (3H, t, $J = 7$ Hz); ^{13}C NMR, δ ppm: 209.8 (CO), 154.2, 73.8 (C8), 49.0, 47.8 (C6, C2), 43.3, 36.2, 34.4, 33.7, 33.3, 28.6, 27.5, 22.8, 19.5, 14.3 (CH_3), 8.0 (CH_3); MS *m/z*: 281 ($M^{+\cdot}$, 14%) (calcd. for $C_{16}H_{27}NO_3$: 281.1991; found: 281.1998), 224 (10), 210 (14), 194 (25), 180 (37), 166 (100).

***18**, 55%*: ^1H NMR, δ ppm: 5.05 (1H, m, H6), 4.09 (1H, m, H8), 3.48 (1H, ddt, $J = 11$, 5, and 3 Hz, H2), 2.36–2.73 (4H, m), 2.02 (1H, ddd, $J = 13.5$, 5, and 2 Hz), 1.12–1.88 (13H, m), 1.03 (3H, t, $J = 7$ Hz), 0.90 (3H, t, $J = 7$ Hz); ^{13}C NMR, δ ppm: 210.0 (CO), 154.0, 75.2 (C8), 49.8, 47.9 (C6, C2), 43.4, 36.2, 35.9, 34.8, 33.4, 28.3, 26.9, 22.8, 18.4, 14.1 (CH_3), 7.9 (CH_3); MS *m/z*: 281 ($M^{+\cdot}$, 8%) (calcd. for $C_{16}H_{27}NO_3$: 281.1991; found: 281.1985), 224 (4), 210 (17), 194 (16), 180 (32), 166 (100).

Nucleophilic displacement of the methoxy group of 15*a* and 16*a*

To a stirred solution of the 6-methoxy derivative (0.28 mmol) in dichloromethane (3 mL) at −78°C under a nitrogen atmosphere is added a solution of trimethylsilyloxy-pent-1-ene contaminated with ca. 50% of ethylbenzene (2.8 mmol) and TMSOTf (0.62 mmol; preparation of **26**) or $TiCl_4$ (0.34 mmol; prep. of **27**). The resulting mixture is left at −78°C for 1 h. This mixture is then poured into a saturated $NaHCO_3$ solution (50 mL) and extracted with $CHCl_3$ (3×50 mL); the organic phase is evaporated and the residue submitted to a flash chromatography (Kieselgel 60 Merck; ethyl acetate:hexane 1:3), to afford the pure ketone.

***26**, 56%*: IR cm^{-1}: 2957, 2937, 2874, 1700 (broad); ^1H NMR, δ ppm: 4.69 (2H, m), 4.23 (1H, m), 3.66 (3H, s, NCO_2CH_3), 2.42–2.66 (4H, m), 2.05 (3H, s, $OCOCH_3$), 1.29–2.04 (14H, m), 0.92 (6H, 2t, $J = 7$ Hz); ^{13}C NMR, δ ppm: 209.1, 171.1, 156.6, 72.8 (C8), 53.0 (NCO_2CH_3), 48.0, 47.9, 46.9, 45.2, 39.2, 36.6, 28.5, 28.4, 21.7 ($OCOCH_3$), 18.8, 17.6, 14.4, 14.4 (CH_3), 14.1 (CH_3); MS *m/z*: 355 ($M^{+\cdot}$, <1%), 296 (40) (calcd. for $C_{17}H_{30}NO_3$ ($M^{+\cdot}$ $-OAc$): 296.2226; found: 296.2228), 210 (14), 226 (22), 140 (100).

***27**, 81%*: ^1H NMR, δ ppm: 4.89 (1H, m, H8), 4.64 (1H, br m), 4.21 (1H, br m), 3.68 (3H, s, NCO_2CH_3), 2.64 (2H, m), 2.43 (2H, m), 2.07 (3H, s, $OCOCH_3$), 1.23–1.80 (14H, m), 0.92 (6H, 2t, $J = 7.5$ Hz); ^{13}C NMR, δ ppm: 209.4, 171.3, 156.6, 72.2 (C8), 53.0 (NCO_2CH_3), 48.0, 47.6, 46.9 (C2, C6), 45.3, 39.6, 37.1, 28.5, 27.9, 21.6 ($OCOCH_3$), 19.1, 17.7, 15.4 (CH_3), 14.4, 14.2 (CH_3); MS *m/z*: 355 ($M^{+\cdot}$, <1%) (calcd. for $C_{19}H_{33}NO_5$: 355.2359; found: 355.2340), 296 (24), 226 (13), 210 (17), 140 (100).

General procedure for the reductions with $NaBH_4$

To a methanolic solution (2 mL) of ketone **17** or **18** (7.05×10^{-5} mol) is added $NaBH_4$ (0.46 mmol) at room temperature. After complete disappearance of the ketone (TLC), water is added and the mixture is extracted with chloroform. After evaporation of the organic phase, the residue is flash chromatographed on silica gel (acetone:hexane 1:1–4:1) to yield the two epimeric alcohols.

***19**, 38%*: IR (CCl_4 solution), cm^{-1}: 3445, 2959, 2938, 2873, 1674; ^1H NMR, δ ppm: 4.63 (1H, m, H6e), 4.17 (1H, m, H8), 3.33 (2H, m), 1.15–2.08 (19H, m), 0.93 (6H, 2t, $J = 7.5$ and 7 Hz); ^{13}C NMR, δ ppm: 156.3, 73.7 (C8), 68.7, 49.2, 47.7 (C2, C6), 37.5, 34.6, 33.9, 33.7, 30.0, 29.9, 27.4, 22.9, 20.1, 14.3 (CH_3), 10.8 (CH_3); MS *m/z*: 283 ($M^{+\cdot}$, 5%) (calcd. for $C_{16}H_{29}NO_3$: 283.2147; found: 283.2150), 254 (14), 211 (18), 210 (29), 166 (100), 96 (10), 82 (17).

***20**, 51%*: IR (CCl_4 solution), cm^{-1}: 3475, 2958, 2938, 2873, 1671; ^1H NMR, δ ppm: 4.82 (1H, m, H6e), 4.08 (1H, m, H8), 3.28 (2H, m), 1.15 −2.08 (19H, m), 0.96 (3H, t, $J = 7.5$ Hz), 0.91 (3H, t, $J = 7$ Hz); ^{13}C NMR (90.6 MHz), δ ppm: 155.4, 75.7 (C8), 68.6, 49.7, 47.5 (C2, C6), 38.2, 35.7, 34.9, 33.8, 29.8, 29.6, 26.9, 22.8, 18.8, 14.1 (CH_3), 10.7 (CH_3); MS *m/z*: 283 ($M^{+\cdot}$, 4%) (calcd. for $C_{16}H_{29}NO_3$: 283.2147; found: 283.2150), 254 (7), 211 (12), 210 (29), 166 (100), 96 (12), 82 (26).

21, 54%: IR (CCl_4 solution), cm^{-1}: 3420, 2959, 2937, 2874, 2865, 1674; ^1H NMR, δ ppm: 4.56 (1H, m, H6e), 4.16 (1H, m, H8), 3.56 (2H, m), 2–3 (1H, OH), 1.16–1.98 (18H, m), 0.95 (3H, t, J = 7 Hz), 0.90 (3H, t, J = 7 Hz); ^{13}C NMR, δ ppm: 155.7, 73.7, 73.3, 51.1, 48.0 (C2, C6), 38.2, 34.6, 33.8, 33.7, 30.8, 30.5, 27.5, 22.9, 20.0, 14.3 (CH_3), 10.5 (CH_3); MS *m/z*: 283 ($M^{+\cdot}$, 6%) (calcd. for $C_{16}H_{29}NO_3$: 283.2147; found: 283.2151), 254 (8), 211 (28), 210 (22), 166 (100), 96 (14), 82 (22).

22, 34%: IR (CCl_4 solution), cm^{-1}: 3431, 2958, 2936, 2873, 1680; ^1H NMR, δ ppm: 4.75 (1H, m, H6e), 4.10 (1H, m, H8), 3.66 (1H, m), 3.49 (1H, ddt, J = 11, 5, and 3 Hz, H2), 2.26 (1H, br m, OH), 2.04 (1H, ddd, J = 14, 5, and 2 Hz), 1.13–1.97 (17H, m), 0.94 (3H, t, J = 7.5 Hz), 0.90 (3H, t, J = 7 Hz); ^{13}C NMR, δ ppm: 154.8, 75.1, 72.0, 49.7, 49.6 (C2, C6), 38.2, 36.0, 34.9, 33.7, 31.1, 29.4, 27.0, 22.7, 18.6, 14.1 (CH_3), 10.1 (CH_3); MS *m/z*: 283 ($M^{+\cdot}$, 5%) (calcd. for $C_{16}H_{29}NO_3$: 283.2147; found: 283.2148), 254 (4), 211 (21), 210 (32), 166 (100), 96 (10), 82 (17).

Preparation of 1, 2, 3, and 4 from 19, 20, 21, and 22

Cyclic carbamate (0.024 mmol) is mixed with a 2 M ethanolic solution of potassium hydroxide. After 1–18 h at reflux, the solvent is evaporated under reduced pressure. The residue is diluted with water (10 mL) and the aqueous phase is extracted with $CHCl_3$ (3 × 10 mL). Evaporation of the chloroform yields the pure aminodiol.

1, quant.: IR (CCl_4 solution), cm^{-1}: 3382, 2958, 2933, 2873; ^1H NMR, δ ppm: 3.67–3.82 (2H, m, H8 and H10), 3.44 (3H, br, NH and 2 OH), 3.27 (2H, m, H2 and H6), 1.26–1.88 (18H, m), 0.91 (6H, 2t, J = 7 Hz); MS *m/z*: 257 ($M^{+\cdot}$, 2%) (calcd. for $C_{15}H_{31}NO_2$: 257.2355; found: 257.2353), 228 (8), 200 (14), 184 (93), 156 (100), 138 (16), 84 (14), 82 (21).

2: IR (CCl_4 solution), cm^{-1}: 3452–3311, 2958, 2934, 2873; ^1H NMR, δ ppm: 3.70–3.80 (4H, m, H8, H10 and 2 OH), 3.18 (2H, m, H2 and H6), 1.17–1.81 (19H, m), 0.90 (6H, t, J = 7 Hz); MS *m/z*: 257 ($M^{+\cdot}$, 2%) (calcd. for $C_{15}H_{31}NO_2$: 257.2355; found: 257.2346), 228 (8), 200 (8), 184 (74), 156 (100), 138 (22), 84 (11), 82 (27).

3, 95%: IR (CCl_4 solution), cm^{-1}: 3347, 2965, 2932, 2880, 2861; ^1H NMR, δ ppm: 3.64–3.78 (2H, m, H8 and H10), 3.13 (2H, m, H2 and H6), 1.7–3 (3H, NH and 2 OH), 1.15–1.69 (18H, m), 0.92 (6H, t, J = 7 Hz); MS *m/z*: 257 ($M^{+\cdot}$, 2%) (calcd. for $C_{15}H_{31}NO_2$: 257.2355; found: 257.2373), 240 (2), 228 (7), 200 (10), 184 (82), 166 (23), 156 (100), 138 (20), 84 (13), 82 (20).

4, 91%: IR (CCl_4 solution), cm^{-1}: 3322, 2958, 2934, 2874, 2788; ^1H NMR, δ ppm: 3.66–3.84 (2H, m, H8 and H10), 2–3.6 (3H, NH and 2 OH), 3.20 (2H, m, H2 and H6), 1.14–1.91 (18H, m), 0.92 (6H, t, J = 7 Hz); MS *m/z*: 257 ($M^{+\cdot}$, 2%) (calcd. for $C_{15}H_{31}NO_2$: 257.2355; found: 257.2345), 228 (6), 200 (12), 184 (100), 166 (29), 156 (26), 138 (21), 84 (18), 82 (24).

Transformation of 26 into 28 and 29

K_2CO_3 (1.29 mmol) is added to a stirred methanolic (6 mL) solution of **26** (2.15×10^{-4} mol). After 23 h at room temperature, the methanol is evaporated under reduced pressure and the residue is taken up in water (15 mL). The aqueous phase is extracted with $CHCl_3$ (3 × 15 mL), the chloroform evaporated, and the corresponding alcohol is obtained in 84% yield. This derivative is immediately submitted to reduction with $NaBH_4$ (same procedure as above, r.t. for 30 min). The diastereomeric alcohols **28** and **29** are separated by chromatography on alumina (ethyl acetate:hexane 1:2).

28, 10%: ^1H NMR, δ ppm: 3.77 (3H, s, NCO_2CH_3), 2–4.5 (6H, m), 1.28–1.82 (18H, m), 0.92 (6H, t, J = 7 Hz); ^{13}C NMR, δ ppm: 158.5, 68.7 (C2), 53.7 (NCO_2CH_3), 48.2 (C8), 43.9, 39.8, 30.7, 19.5, 15.3, 14.6 (CH_3); MS *m/z*: 315 ($M^{+\cdot}$, 1%) (calcd. for $C_{17}H_{33}NO_4$: 315.2410; found: 315.2415), 272 (2), 256 (14), 228 (45), 10 (23), 156 (8), 142 (100), 140 (60).

29, 62%: ^1H NMR, δ ppm: 4.40 (3H, br m, H2, H6, and OH), 3.74 (3H, s, NCO_2CH_3), 3.49 (2H, br m), 3–4 (1H, OH), 1.25–1.92 (18H, m), 0.92 (6H, 2t, J = 7 Hz); ^{13}C NMR, δ ppm: 158.3, 69.9, 68.2 (C2, C6), 53.6 (NCO_2CH_3), 48.2, 47.8, 43.5, 43.5, 40.7, 39.7, 30.5, 28.2, 19.5, 19.3, 14.8, 14.6 (CH_3), 14.5 (CH_3); MS *m/z*: 315 ($M^{+\cdot}$, <1%) (calcd. for $C_{17}H_{33}NO_4$: 315.2410; found: 315.2408), 256 (17), 228 (47), 210 (24), 156 (8), 142 (100), 140 (71).

Reduction of 27 into 30

To a stirred solution of ketone **27** (3.77×10^{-4} mol) in THF (13 mL) is added $LiHAl(OtBu)_3$ (1.53 mmol) at 0°C. After 1 h, a few drops of water are added and the mixture is filtered through Celite. The solvent is then evaporated under reduced pressure and the residue is chromatographed on alumina (ethyl acetate:hexane 2:1) to afford the alcohol **30** in 84% yield.

30: ^1H NMR, δ ppm: 4.88 (1H, m, H8), 4.27 (1H, m), 4.17 (1H, m, H10), 3.69 (3H, s, NCO_2CH_3), 3.54 (1H, m), 2.06 (3H, s, $OCOCH_3$), 1.24–1.83 (19H, m), 0.92 (6H, 2t, J = 7 Hz); ^{13}C NMR, δ ppm: 171.2, 157.0, 72.1, 70.0, 52.9 (NCO_2CH_3), 48.3, 47.6, 44.3, 40.3, 40.2, 39.4, 37.0, 29.0, 27.8, 22.5, 21.4 ($OCOCH_3$), 19.1, 18.9, 14.3 (CH_3), 14.2 (CH_3); MS *m/z*: 357 ($M^{+\cdot}$, <1%) (calcd. for $C_{19}H_{35}NO_5$: 357.2515; found: 357.2499), 298 (30), 270 (11), 238 (9), 228 (20), 210 (50), 142 (48), 140 (100).

General procedure for the basic hydrolysis of carbamates 28, 29, and 30

The carbamate (0.182 mmol) is mixed with a 1–2 M ethanolic solution of potassium hydroxide. After 1–5 h at reflux, the solvent is evaporated under reduced pressure. After 1–5 h at reflux, the solvent is evaporated under reduced pressure. The residue is diluted with water (20 mL) and the aqueous phase is extracted with $CHCl_3$ (3 × 20 mL). Evaporation of the chloroform yields the pure aminodiol.

23 (synthetic andrachamine), 95%: ^1H NMR (600 MHz), δ ppm: 3.79 (2H, m, H8), 2.72 (2H, m, H2), 1.84 (1H, dqn, J = 13 and 3.5 Hz, H4e), 1.71 (2H, dq, J = 13 and 3 Hz, H3e), 1.54 (1H, qt, J = 13 and 4 Hz, H4a), 1.48 (2H, dt, J = 14 and 4 Hz, H7e), 1.46–1.32 (13H, m), 0.97 (2H, qd, J = 13 and 4 Hz, H3a), 0.92 (6H, t, J = 7 Hz, H11; MS *m/z*: 257 ($M^{+\cdot}$, 3%) (calcd. for $C_{15}H_{31}NO_2$: 257.2355; found: 257.2369), 240 (2), 228 (2), 214 (11), 184 (2), 170 (100).

24, quant.: ^1H NMR (600 MHz), δ ppm: 3.85 (2H, m, H8), 2.88 (2H, m, H2), 1.83 (2H, m, H4), 1.21–1.59 (19H, m), 0.92 (6H, t, J = 7 Hz, H11); MS *m/z*: 257 ($M^{+\cdot}$, 4%) (calcd. for $C_{15}H_{31}NO_2$: 257.2355; found: 257.2342), 240 (3), 228 (2), 214 (16), 184 (2), 170 (100).

25, 99%: ^1H NMR (600 MHz), δ ppm: 3.87 (1H, m, H8), 3.82 (1H, m, H8′), 2.85 (1H, m, H2), 2.73 (1H, m, H6), 1.84 (1H, m, H4e), 1.64 (3H, H3e, H5e, OH), 1.22–1.56 (15H, m), 1.10

(1H, m, H5a), 1.01 (1H, m, H3a), 0.92 (3H, t, J = 7 Hz), 0.91 (3H, t, J = 7 Hz); ^{13}C NMR, δ ppm: 72.4, 68.0, 57.8 (C6), 53.6 (C2), 43.9, 43.3, 40.6, 40.5, 33.7, 33.0 (C3, C5), 24.8 (C4), 18.9, 18.7, 14.2 (CH_3), 14.1 (CH_3); MS *m/z*: 257 ($M^{+\cdot}$, 4%) (calcd. for $C_{15}H_{31}NO_2$: 257.2355; found: 257.2342), 240 (2), 228 (2), 214 (16), 184 (3), 170 (100).

Isolation of andrachamine from *Andrachne aspera*

Dried plants of *Andrachne aspera* (870 g) collected near Karachi (Pakistan) were immersed in methanol (3 L) for 4 days. Methanol was filtered and the process repeated three times. The combined MeOH phases were evaporated under reduced pressure and the residue was digested overnight with 2% aqueous HCl (100 mL). The solution was filtered through Celite, basified with NaOH, and extracted with $CHCl_3$ (3 × 1 L). The organic phase was then washed with water (50 mL), concentrated to ca. 20 mL, and extracted with 2% aqueous HCl (3 × 25 mL). The aqueous phase was basified (NaOH) and extracted with $CHCl_3$ (3 × 100 mL). The combined organic phases were washed with water (25 mL) and evaporated under reduced pressure to give 1.22 g of crude alkaloids (0.14% dry weight).

The crude extract (254 mg) was submitted to two successive chromatographies (Kieselgel 60 Merck; $CHCl_3$:isopropylamine 50:1) to give crystalline andrachamine **23** (3.5 mg). The alkaloid was found identical with synthetic **23** (TLC, MS, ^{1}H and ^{13}C NMR).

Natural andrachamine: ^{1}H NMR, δ ppm: 3.80 (2H, m, H8), 2.76 (2H, m, H2), 1.26–1.88 (20H, m), 1.01 (1H, m, H3a), 0.92 (6H, t, J = 7 Hz, H11); MS *m/z*: 257 ($M^{+\cdot}$, 2%) (calcd. for $C_{15}H_{31}NO_2$: 257.2355; found: 257.2357), 240 (2), 228 (2), 214 (13), 184 (5), 170 (100).

Acknowledgments

The authors wish to thank Professor V.U. Ahmad (University of Karachi) for his kind collaboration and Professor S.I. Ali (University of Karachi) for collecting and identifying the vegetal material. They are also grateful to Dr. R. Ottinger for the NMR spectra. S.M. wishes to thank the Fonds pour la formation à la Recherche dans l'Industrie et dans l'Agriculture (FRIA, Belgium), C.H. is a Research Associate of the Fonds National de la Recherche Scentifique (FNRS, Belgium).

References

1. V.U. Ahmad and M.A. Nasir. Heterocycles, **24**, 2841 (1986).
2. V.U. Ahmad and M.A. Nasir. Phytochemistry, **26**, 585 (1987).
3. W. Carruthers, P. Coggins, and J.B. Weston. J. Chem. Soc. Perkin Trans. 1, 2323 (1990).
4. F. Driessens and C. Hootelé. Can. J. Chem. **69**, 211 (1991).
5. P.D. Palasz, J.H.P. Hutley, and J.D. Hardstone. J. Chem. Soc. Perkin Trans. 2, 807 (1984).
6. P. Deslongchamps. *In* Stereoelectronic effects in organic chemistry. Pergamon, New York. 1983. Chap. 6.
7. P. Beak and W.J. Zajdel. J. Am. Chem. Soc. **106**, 1010 (1984).
8. D.L. Comins and M.A. Foley. Tetrahedron Lett. **29**, 6711 (1988).
9. M.A. Ciufolini, C.W. Hermann, K.H. Whitmire, and N.E. Byrne. J. Am. Chem. Soc. **111**, 3473 (1989).
10. (*a*) D.S. Brown, P. Charreau, T. Hansson, and S.V. Ley. Tetrahedron, **47**, 1311 (1991); (*b*) D.L. Comins and H. Hong. J. Am. Chem. Soc. **115**, 8851 (1993); (*c*) Y. Matsumura, and T. Tomita. Tetrahedron Lett. **35**, 3737 (1994).
11. J.J. Tufariello. Acc. Chem. Res. **12**, 396 (1979).
12. E. Gössinger. Monatsh. Chem. **112**, 1017 (1981).
13. C. Hootelé, W. Ibebeke-Bomangwa, F. Driessens, and S. Sabil. Bull. Soc. Chim. Belg. **96**, 57 (1987).
14. E.J. Corey and A.W. Gross. Tetrahedron Lett. **25**, 495 (1984).
15. E.L. Eliel, D. Kandasamy, C. Yen, and K.D. Hargrave. J. Am. Chem. Soc. **102**, 3698 (1989).
16. C. Hootelé, F. Halin, S. Thomas, and D. Tourwé. Tetrahedron, **41**, 5563 (1985).
17. M. Osterhout. Diss. Abstr. Int. B: **53**, 2876-B (1992).
18. C.G. Beguin, M.N. Deschamps, V. Boubel, and J.J. Delpuech. Org. Magn. Reson. **11**, 418 (1978).

Synthesis of β-hydroxypiperidine alkaloids by anodic oxidation of carbamates and hydroboration

Mark Plehiers and Claude Hootelé

Abstract: The β-hydroxypiperidine alkaloids (±)-pseudoconhydrine, (±)-*N*-methylpseudoconhydrine, (−)-5-hydroxysedamine, and (+)-sedacryptine were synthesized. Successive functionalization of the piperidine ring via anodic methoxylation allowed the regio- and stereoselective introduction of the substituents. The α and α′ substituents were introduced by application of the sequence elimination – nucleophilic addition from 2- or 2,5-substituted 6-methoxycarbamates. Hydroboration – oxidation of enecarbamates, obtained by elimination of methanol from α-methoxycarbamates, allowed the introduction of the β-hydroxy function.

Key words: alkaloid, Sedum, *N*-acyliminium, enecarbamate.

Résumé : La synthèse des alcaloïdes pipéridiniques β-hydroxylés tels que la (±)-pseudoconhydrine, la (±)-*N*-méthylpseudoconhydrine, la (−)-5-hydroxysédamine et la (+)-sédacryptine est décrite. L'oxydation anodique de carbamates permet l'introduction successive, de manière régio- et stéréosélective, des substituants sur le cycle pipéridinique. Les substituants α et α′ sont introduits par application de la séquence élimination–addition nucléophile aux carbamates 6-méthoxylés, 2- ou 2,5-substitués. La fonction β-hydroxy est aménagée par hydroboration–oxydation d'ènecarbamates obtenus, au départ d'α-méthoxycarbamates, par élimination de méthanol.

Mots clés : alcaloïde, Sedum, *N*-acyliminium, ènecarbamate.

Development of efficient methods for the elaboration of polysubstituted piperidine compounds is an important goal in the area of natural product synthesis. Indeed, the increasing interest observed in this field is related to the search for new strategies for the synthesis of potentially bioactive compounds and was stimulated recently, among others, by the glycosidase inhibitory properties of polyhydroxylated piperidine derivatives (1). While numerous methods are known for the introduction of a substituent α to the nitrogen atom of the piperidine nucleus, functionalization of β and (or) γ positions has seldom been described in the literature.

The anodic methoxylation of carbamates followed by elimination and nucleophilic substitution now emerges as a powerful method for the synthesis of 2- and 2,6-substituted piperidine derivatives (2–4); the success of this method rests on the highly regioselective preparation of intermediate α-methoxycarbamates from the parent heterocycles. These intermediates are protected forms of reactive *N*-acyliminium cations that can be generated by treatment with Lewis acids and can add a number of nucleophiles. On the other hand, treatment of α-methoxycarbamates in acidic or thermolytic conditions leads to the formation of enecarbamates; these enamine-type compounds allow the introduction of electrophiles at the β position on the piperidine ring (5, 6).

Received June 5, 1996.

M. Plehiers and C. Hootelé.[1] Organic Chemistry Department, Faculty of Sciences, Free University of Brussels, B-1050 Brussels, Belgium.

[1] Author to whom correspondence may be addressed. Telephone: 32-2-650 30 39. Fax: 32-2-650 27 98.

In this paper, we wish to report a new route for the synthesis of β-hydroxy α- and α,α′-substituted piperidine derivatives based on successive functionalizations via anodic oxidation. As an illustration, norsedamine **10** was efficiently functionalized at position 5 (via hydroboration of the enecarbamate **12**) to yield 5-hydroxysedamine **20**; the immediate precursor of ent-**20** was substituted at position 6 to furnish (+)-sedacryptine **28** after functional group transformations.

Results and discussion

Synthesis of β-hydroxypiperidine derivatives

In a preceding communication (6), we briefly reported that hydroboration–oxidation of piperidine enecarbamates constitutes an efficient procedure for the preparation of β-hydroxypiperidine derivatives; the reaction proceeds with good yields to furnish *trans*/*cis* isomers in ratios ranging from 2/1 (20°C) to 6/1 (−78°C to −10°C). Although the last ratio was recently questioned (7), it appears reproducible in our hands. The stereoselectivity observed in favour of the *trans* compound results from a preferential attack of borane from the less hindered side of the enecarbamate **A** (Scheme 1).

Enecarbamate hydroboration was first applied to the model derivative ***3a*** and then exploited to realize short syntheses of pseudoconhydrine **8** (8) and *N*-methylpseudoconhydrine **9** (9), which have a 2,5-*trans* relative stereochemistry (Scheme 1).

On the other hand, we established that alcohols possessing a 2,5-*cis* relative stereochemistry can be efficiently obtained by stereoselective reduction of the corresponding ketone. The method is illustrated by the synthesis of (−)-5-hydroxysedamine **20**.

(2*S*,8*S*)-Norsedamine **10** was prepared in optically pure form, protected, and anodically oxidized in methanol to give

Scheme 1.

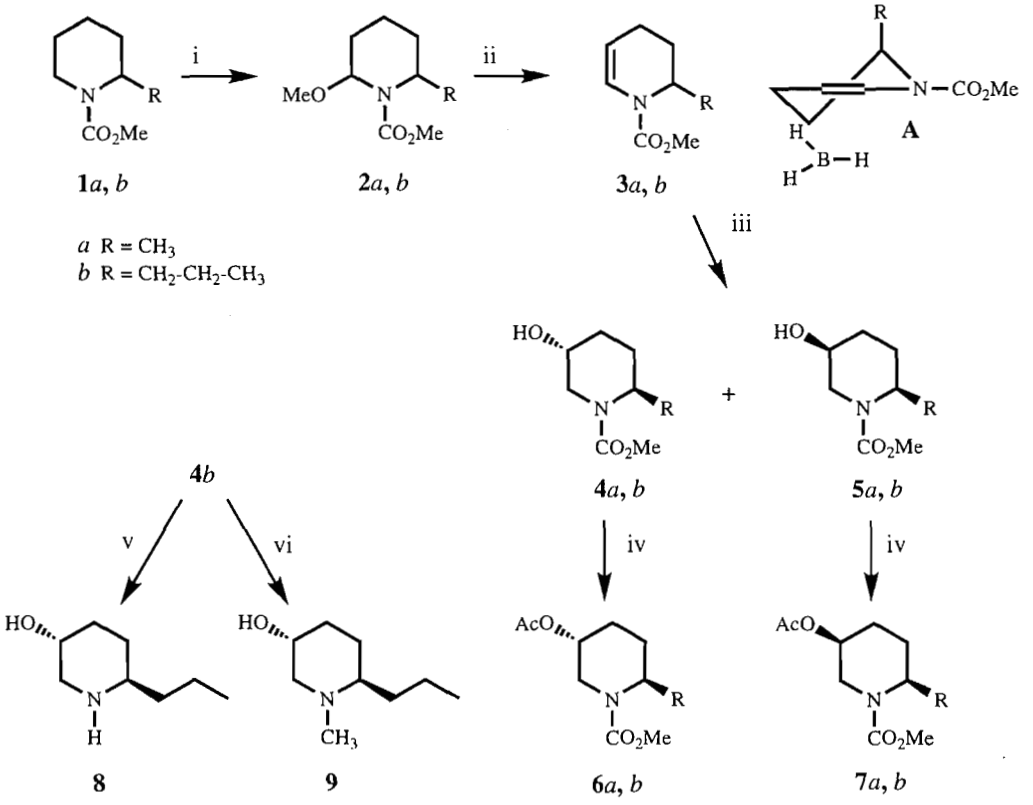

i: MeOH, $Et_4N^+OTs^-$, 8 V, **2***a*: 2.6 F/mol, 77%, **2***b*: 3 F/mol; ii: *p*-TSA (10% w/w); ΦH, **3***a*: 80%, **3***b*: 91% from **1***b*; iii: from **3***a*: (1) $BH_3{\cdot}SMe_2$, THF, rt; (2) H_2O_2, NaOH, 71% (*c*/*t*: 1/2); from **3***b*: (1) $BH_3{\cdot}SMe_2$, THF, −78°C to −10°C; (2) H_2O_2, NaOH, 71% (*c*/*t*: 1/6); iv: Ac_2O, pyridine; v: (1) TMSI, CH_2Cl_2; (2) MeOH, 89%; vi: $LiAlH_4$, THF, 80%.

Scheme 2.

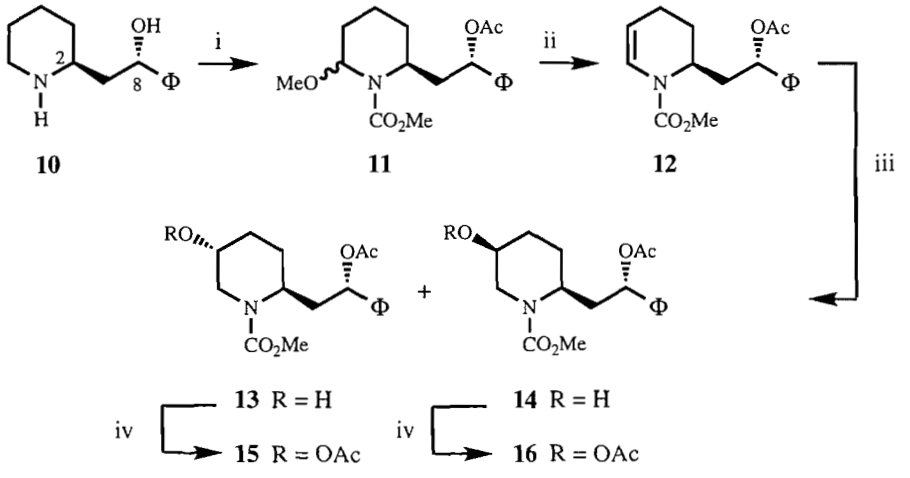

i: (1) $ClCO_2CH_3$, K_2CO_3, H_2O; (2) Ac_2O, pyridine; (3) MeOH, $Et_4N^+OTs^-$, 8 V, 8 F/mol, 95%; ii: *p*-TSA 10%, ΦH, 93%; iii: (1) $BH_3{\cdot}SMe_2$, THF, 20°C; (2) H_2O_2, NaOH, 75%, *t*/*c* 3/1; iv: Ac_2O, pyridine.

11 (3); the enecarbamate **12** was readily obtained by smooth elimination of MeOH from **11** using *p*-toluenesulfonic acid (10% w/w) in benzene as described previously (6) (Scheme 2).

Hydroboration of the enecarbamate **12** (Scheme 2) at room temperature, using the commercially available borane dimethyl sulfide complex, and subsequent hydrogen peroxide oxidation of the intermediate boranes furnished a 3:1 mixture of the alcohols **13** and **14**, which were easily separated by flash

Table 1. Selected ^{1}H NMR chemical shifts of **6***a*, **15**, **7***a*, and **16** (250 MHz, $CDCl_3$, *J* in Hz).

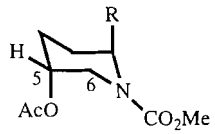

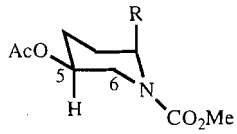

6*a* R = CH_3 **7***a* R = CH_3
15 R = $CH_2CH(OAc)\Phi$ **16** R = $CH_2CH(OAc)\Phi$

Derivative	H5	H6e	H6a
6*a*	4.87, m	4.13, bd (15)	3.03, dd (15, 2)
15	4.87, m	4.23, bd (15)	3.11, dd (15, 2)
7*a*	4.64, tt (11, 5)	4.14, ddd (13, 5, 2)	2.76, dd (13, 11)
16	4.65, tt (11, 5)	4.2, m	2.84, dd (13, 11)

Scheme 3.

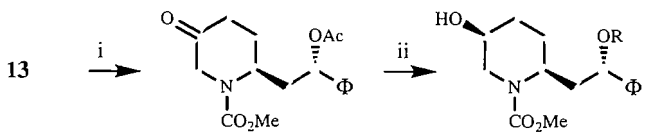

17

18 R = H
14 R = Ac

i: PCC 4 equiv., CH_2Cl_2, reflux, 1 h, 71% or Swern oxidation, 3 equiv., 92%; ii: $LiAl(O\text{-}t\text{Bu})_3H$, THF, 0°C, 2 h, 88%.

chromatography. Attribution of the 2,5 relative stereochemistry of alcohols **13** and **14** rests on the analysis of the ^{1}H (coupling connectivity by 2D-COSY) and ^{13}C NMR spectra of the corresponding diacetyl derivatives **15** and **16** and comparison with those of the model compounds **6***a* and **7***a*. In all these compounds, $A^{(1,3)}$ interactions between the N-acyl moiety and the C2 substituent force this last one in an axial orientation (10). Selected diagnostical values from the ^{1}H NMR spectra are reported in Table 1.

Attempts to prepare ketone **17** by oxidation of the intermediate boranes only proceeded with low yield but we observed that this unstable ketone was readily obtained by oxidation of the alcohol **13** or the mixture of **13** and **14** (Scheme 3). Swern oxidation (11) was found to give higher and more reproducible yields of **17** than PCC (12).

Reduction of the keto function of **17** with $NaBH_4$ yielded a 1/8 ratio of the alcohols **13** and **14**. Use of lithium tri-*tert*-butoxyaluminium hydride resulted in the formation of the *cis* alcohol **14** only, with concomitant deacetylation (88% global yield of *cis* derivatives **14** and **18**).

The procedure described above provides the 2,5-*cis* alcohol **14** in a global yield of 60% from the enecarbamate **12**.

Lithium aluminium hydride reduction of the carbamates **14** and **13** furnished (−)-5-hydroxysedamine **20** and its C5 epimer **19**. Spectral and specific rotation values of synthetic and natural **20** (13) are in perfect agreement.

The preferred solution conformation of sedamine was established previously (14): the hydroxyl function at C8 is involved in an intramolecular hydrogen bonding with the nitrogen lone pair and the base exists predominantly in a *cis*-fused conformation. The ^{1}H NMR spectra of **19** and **20** indicate that the hydroxyl function at C5 and the phenyl group are both equatorial in the two diols; the C2 side chain is therefore equatorial in **19** and axial in 5-hydroxysedamine **20**. On the other hand, the diacetyl derivatives (13) obtained from **19** and **20** present a chair conformation in which the C2 substituent has an equatorial orientation and the acetoxy at C5 occupies, respectively, an equatorial and an axial orientation.

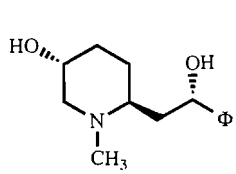

19

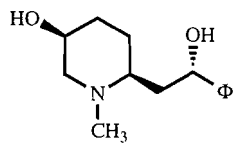

20

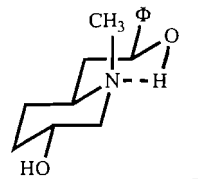

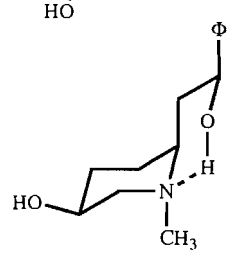

Synthesis of 2,5,6-trisubstituted piperidine compounds

To our knowledge, no example of transformation of a 2,5-disubstituted piperidine into a 2,5,6-trisubstituted derivative by anodic methoxylation has been described in the literature. The anodic oxidations of piperidine carbamates we described previously were generally carried out in MeOH containing $Et_4N^+OTs^-$ as supporting electrolyte in an undivided cell equipped with two vitreous carbon electrodes (3, 4) and the electrolysis was performed by application of a constant potential of 8 V between the electrodes. Before undertaking the oxidation of compound ent-**16**, precursor of (+)-sedacryptine **28**, we studied the influence of the supporting electrolyte ($Et_4N^+OTs^-$ and $Bu_4N^+BF_4^-$) and of the electrode (carbon and platinum) on the oxidation of the model compound **7***a*. Some significant results are given in Table 2.

It appeared that the anodic oxidation performed under our usual conditions (3, 4) (entry 1) furnished the methoxy compound **21** with a moderate yield. The replacement of the carbon rod anode by a platinum foil allowed a substantial

Table 2. Anodic oxidation of acetate 7*a*.

Entry	Electrolyte	Mol. ratio electrolyte/ acetate 7*a*	Anode	*n*, F/mol	Yield[a] of **21** (%)
1	$Et_4N^+OTs^-$	1/16	C	8	50
2	$Et_4N^+OTs^-$	1/7	Pt	8	50
3	$Et_4N^+OTs^-$	1/14	Pt	8	75
4	$Bu_4N^+BF_4^-$	1/4	Pt	5	71

[a]Isolated yields.

Table 3. Anodic oxidation of acetate ent-**16**.

Entry	Electrolyte	Mol. ratio electrolyte/ acetate ent-**16**	Anode	*n*, F/mol	Yield[a] of **23** (%)
1	$Bu_4N^+BF_4^-$	1/4	Pt	6	43
2	$Et_4N^+OTs^-$	1/10	Pt	8	40
3	$Et_4N^+OTs^-$	1/10	C	8	58[b]
4	$Et_4N^+OTs^-$	1/10	C	10	32

[a]Isolated yields.
[b]28% of recovered starting material.

increase of the yield (entry 3). During our systematic study we observed that in the case of $Et_4N^+OTs^-$ as electrolyte the best yields were obtained when the electrolyte/carbamate molar ratio was kept below a 0.1 value; on the other hand, in the case of $Bu_4N^+BF_4^-$, electrolyte/carbamate ratios ranging from 0.1 to 1 gave comparable yields. Of course, a high relative concentration of the electrolyte is suitable in that it allows shorter reaction times.

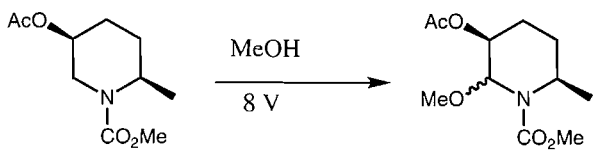

7*a* **21**

Application to the diacetoxy derivative ent-**16** (2*R*,5*R*,8*R*) of the best conditions found for the oxidation of 7*a* appeared disappointing as a yield of less than 50% of **23** was obtained. A new series of experiments was therefore undertaken and the results are reported in Table 3.

For the anodic oxidation of ent-**16**, the highest yield of the methoxy derivative **23** was achieved using $Et_4N^+OTs^-$ as supporting electrolyte and a vitreous carbon rod as anode. In all cases the reaction appeared incomplete and a substantial amount of starting material could be recovered. It was observed that an increase in the number of Faraday did not improve the yield (entry 4) but led to the formation of degradation products. The α-methoxycarbamates **21** and **23** were found to be stable compounds and they can be stored for months without noticeable degradation.

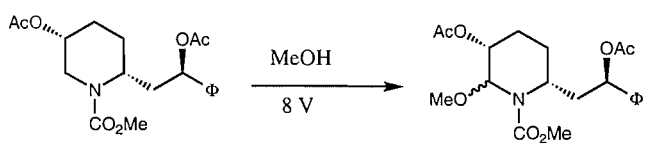

ent-**16** **23**

The elimination – nucleophilic addition sequence was first performed on the model compound **21**. The iminium cation was formed at −45°C with $TiCl_4$ as a Lewis acid and reacted with 2-trimethylsilyloxypropene at −78°C to yield a 76/24 mixture of the expected ketones **22** in 73% yield.

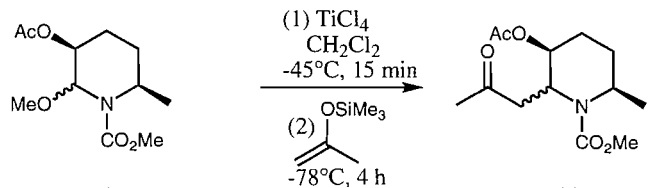

21 **22** (*c*+*t*)

The same sequence was applied to the methoxy derivative **23**. The reaction was first conducted at low temperature (−78°C to −45°C, 4 h), furnishing a mixture in which the expected *cis* and *trans* compounds **24** were present in low yield (ca. 25%); the other major constituents were identified as the starting material (ca. 50%) and a 6-hydroxy derivative **25** (ca. 25%) originating from the addition of water to the iminium cation during the work-up. These observations indicate that the formation of the iminium cation was not complete under these conditions. When the two steps were conducted at 0°C a 77/23 mixture of the two expected diastereoisomers was isolated in 60% yield. The *cis* relative stereochemistry is attributed to the major compound on the basis of our previous results on related compounds.

Simple functional group transformations of **24** allowed the synthesis of (+)-sedacryptine **28** (Scheme 4).

After protection of the keto group of the *cis* and *trans*

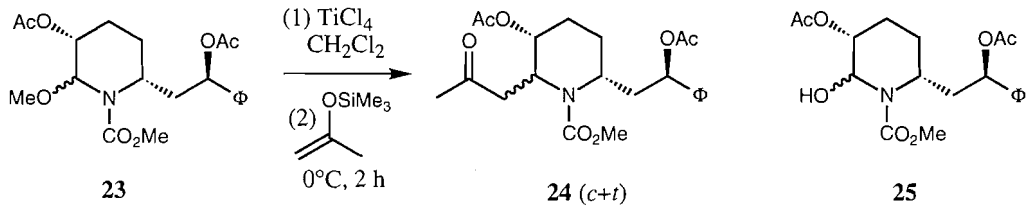

23 **24** (*c+t*) **25**

Scheme 4.

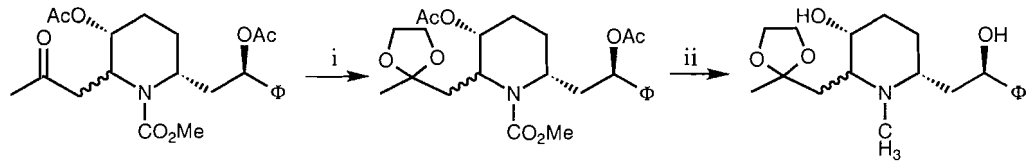

24 (*c+t*) **26** (*c+t*) **27** (*c+t*)

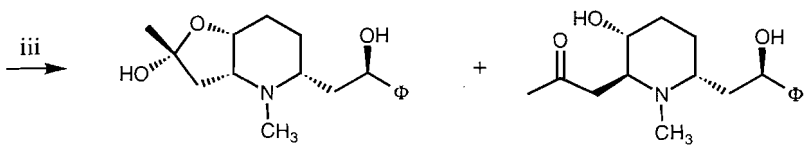

28 **29**

i: ethylene glycol, $TsOH \cdot H_2O$, benzene, reflux; ii: $LiAlH_4$, THF, reflux, 67% from **24**; iii: 0.1 N HCl, reflux.

trisubstituted compounds **24**, reduction of the carbamate and acetate functions furnished the corresponding amino alcohols **27** in 67% yield without modification of the diastereoisomeric ratio. Deprotection of the acetal function was performed in boiling 0.1 N aqueous hydrogen chloride, providing, after neutralization, a mixture of (+)-sedacryptine **28** and its C6-epimer **29** in a 60/40 ratio.

Compounds possessing a β-amino ketone moiety are able to epimerize under a variety of conditions (4, 15). We observed that pure sedacryptine as well as the above 60/40 mixture epimerizes in methanol at room temperature affording a 80/20 mixture of **28** and **29**. On the other hand, this last ratio shifted to >95/5 in cyclohexane. Spectral properties of our synthetic (+)-sedacryptine **28** were identical with those of the natural compound; the optical rotations of both samples were identical in magnitude but of opposite sign. The above synthesis confirms the absolute configuration (2*S*,5*S*,6*S*,8*S*,10*S*) previously attributed to the alkaloid (16).

Experimental

Mass spectral data were obtained on a Micromass 7070 spectrometer or a Fisons Autospec spectrometer. Unless otherwise stated, NMR spectra were recorded on a Bruker WM 250 spectrometer in $CDCl_3$ with TMS as internal standard. IR spectral data were recorded on a Brucker IFS 25 spectrometer. Analytical thin-layer chromatography was performed on Polygram Sil G/UV254 plates and on Merck aluminium sheets, aluminium oxide 60 F_{254} neutral, type E. Visualization was accomplished either by ethanolic phosphomolybdic acid solution followed by heating or by iodine followed by spraying Dragendorff reagent.

Anodic methoxylations were carried out at room temperature in methanol (analytical grade) containing the supporting electrolyte, in an undivided cell equipped with two vitreous carbon electrodes (unless otherwise stated) and a magnetic stirring bar. The carbon electrodes (0.3 cm diameter, immersed 3.5 cm into the solution) were placed 1.0 cm apart. The platinum foil anode (0.3 × 4 cm) was immersed 2 cm into the solution at 1 cm of the carbon cathode. The potentiostat was a homemade apparatus; the potential between the electrodes was fixed at 8 V.

Anodic oxidation of 1*a*

The carbamate **1***a* (521 mg, 3.3 mmol), $Et_4N^+OTs^-$ (50 mg, 0.16 mmol), and 15 mL of methanol were introduced into the electrolysis cell. The solution was stirred for 10 min and then a constant potential of 8 V was applied. After 2.6 F/mol of electricity was passed, some drops of NH_4OH were added to the solution and the solvent was evaporated; the residue was dissolved in water (30 mL), basified with NH_4OH, and extracted with $CHCl_3$ (2 × 30 mL). The combined $CHCl_3$ layers were evaporated and the residue was filtered through a short column of silica gel (ethyl acetate/hexane 1:2) to afford the 6-methoxy derivative **2***a* (oil, 476 mg, 2.54 mmol, 77%): ^1H NMR δ: 5.39 (1H, m, H6), 4.33 (1H, m, H2), 3.72 (3H, s, NCO_2CH_3), 3.26 (3H, broad s, CH_3O), 1.2–2.1 (6H, m), 1.28 (3H, d, J = 7 Hz, CH_3); ^{13}C NMR δ: 82.6, 55.3, 52.9, 47.0, 30.8, 30.5, 19.9, 14.0; MS, *m/z*: 187 ($M^{+\bullet}$, 3%), 186 (5), 172 (33), 156 (100), 142 (76), 71 (86).

Preparation of the enecarbamate 3*a* from 2*a*

The 6-methoxy derivative **2***a* (100 mg, 0.53 mmol) was dissolved in dry benzene (10 mL); $TsOH \cdot H_2O$ (10 mg, 0.052

mmol) was added and the reaction mixture was stirred at room temperature. After 1.5 h, some drops of NH_4OH were added to the reaction mixture and the solvent was evaporated; the residue was dissolved in water (30 mL) and the solution extracted with $CHCl_3$ (2 × 30 mL). The combined organic layers were evaporated and the residue was filtered through a short column of alumina to afford the enecarbamate **3***a* (65 mg, 0.42 mmol, 80%) as a colourless oil: ^{1}H NMR δ: 6.69 (1H, m, H6), 4.86 (1H, m, H2), 4.40 (1H, m, H5), 3.75 (3H, s, NCO_2CH_3), 1.7–2.2 (4H, m), 1.12 (3H, d, J = 7 Hz, CH_3); ^{13}C NMR δ: 124.1, 105.8, 53.1, 46.7, 26.9, 17.6, 17.1; MS, *m/z*: 155 ($M^{+\bullet}$, 36%), 140 (100).

Synthesis of *N*-carbomethoxyconiine 1*b*

N-Carbomethoxypiperidine (5.04 g, 35 mmol), $Et_4N^+OTs^-$ (550 mg, 1.8 mmol), and 50 mL of methanol were introduced into the electrolysis cell. The solution was stirred for 10 min and a constant potential of 8 V was applied. After 2.7 F/mol of electricity was passed, some drops of NH_4OH were added to the solution and the solvent was evaporated; the residue was dissolved in water (400 mL), basified with NH_4OH, and extracted with $CHCl_3$ (3 × 400 mL). The combined $CHCl_3$ layers were evaporated and the residue was filtered through a short column of silica gel (ethyl acetate/hexane 1:2) to afford 2-methoxy-*N*-carbomethoxypiperidine (6 g, 34 mmol).

To a solution of $TiCl_4$ (7.2 g, 38 mmol) in CH_2Cl_2 at −78°C, under an atmosphere of nitrogen, was added dropwise a solution of allyltrimethylsilane (9.5 g, 59 mmol) and 2-methoxy-*N*-carbomethoxypiperidine (6 g) in 40 mL of CH_2Cl_2. After 1 h at −78°C, the reaction mixture was poured into 400 mL of water and extracted with 2 × 400 mL of CH_2Cl_2. The combined CH_2Cl_2 layers were evaporated to dryness. Distillation of the residue under reduced pressure afforded the substitution derivative (4.98 g, 27.2 mmol, 77% global yield) as a colourless oil, bp 94–98°C (3 Torr;): ^{1}H NMR δ: 5.7 (1H, ddt, J = 17, 10 and 7 Hz), 5.01 (1H, dd, J = 17 and 2 Hz), 4.98 (1H, dt, J = 2 and 10 Hz), 4.28 (1H, m, H2), 3.96 (1H, broad d, J = 14 Hz, H6e), 3.64 (3H, s, NCO_2CH_3), 2.79 (1H, td, J = 2 and 14 Hz, H6a), 2.35 (1H, dt, J = 14 and 7 Hz), 2.26 (1H, dt, J = 14 and 7 Hz), 1.3–1.6 (6H, m); ^{13}C NMR δ: 156.6, 135.7, 117.1, 52.8, 50.8, 39.7, 34.8, 28.0, 25.9, 19.2; MS, *m/z*: 182 ($M^{+\bullet}$ − 1, 4%), 142 (100).

The above derivative (4.5 g, 24.5 mmol) in 300 mL of ethanol containing 10% Pd/C (0.5 g) was hydrogenated (1 atm (101.3 kPa)). After filtration through Celite and evaporation of the solvent, a distillation under reduced pressure of the residue furnished *N*-carbomethoxyconiine **1***b* (3.7 g, 20 mmol, 81%), bp 92–96°C (2 Torr; 1 Torr = 133.3 Pa): ^{1}H NMR δ: 4.24 (1H, m, H2), 3.98 (1H, broad d, J = 13 Hz, H6e), 3.67 (3H, s, NCO_2CH_3), 2.80 (1H, td, J = 13 and 3 Hz, H6a), 1.2–1.7 (10H, m), 0.91 (3H, t, J = 7 Hz); ^{13}C NMR δ: 156.7, 52.8, 51.0, 39.5, 32.3, 28.8, 26.1, 19.9, 19.4, 14.4; MS, *m/z*: 185 ($M^{+\bullet}$, 2%), 142 (100).

Preparation of the enecarbamate 3*b* from 1*b*

The carbamate **1***b* (2.52 g, 13 mmol), $Et_4N^+OTs^-$ (250 mg, 0.83 mmol), and 50 mL of methanol were introduced into the electrolysis cell. The solution was stirred for 10 min and a constant potential of 8 V was applied. After 3F/mol of electricity was passed, some drops of NH_4OH were added to the solution and the solvent was evaporated; the residue was dissolved in water (400 mL), basified with NH_4OH, and extracted with $CHCl_3$ (3 × 400 mL). The combined $CHCl_3$ layers were evaporated to dryness to afford the 6-methoxy derivative **2***b* (2.8 g, 13 mmol): ^{1}H NMR δ: 5.45 (1H, m, H6), 4.14 (1H, m, H2), 3.71 (3H, s, NCO_2CH_3), 3.28 (3H, s, OCH_3), 1.2–1.9 (10H, m), 0.92 (3H, t, J = 7 Hz); ^{13}C NMR δ: 82.9, 55.8, 53.0, 51.3, 36.3, 31.1, 27.9, 20.9, 14.4, 14.2; MS, *m/z*: 215 ($M^{+\bullet}$, <1%), 200 (4), 184 (32), 172 (64), 142 (22), 140 (20), 71 (100).

The crude 6-methoxy derivative **2***b* was dissolved in dry benzene (200 mL); $TsOH{\cdot}H_2O$ (300 mg, 1.57 mmol) was added and the reaction mixture was stirred at room temperature. After 1 h, some drops of NH_4OH were added to the reaction mixture and the solvent was evaporated. The residue was dissolved in 30 mL of dilute NH_4OH and extracted with 2 × 30 mL of $CHCl_3$. The combined $CHCl_3$ layers were evaporated to dryness and the residue was filtered through a short column of alumina ($CHCl_3$) to afford the enecarbamate **3***b* (2.18 g, 11.9 mmol, 91% from **1***b*): ^{1}H NMR δ: 6.75 (1H, m, H6), 4.8 (1H, m, H2), 4.3 (1H, m, H5), 3.74 (3H, s, NCO_2CH_3), 1.2–2.1 (8H, m), 0.92 (3H, t, J = 7 Hz); ^{13}C NMR δ: 124.2, 106.4, 53.2, 50.7, 33.2, 24.5, 19.6, 18.0, 14.4; MS, *m/z*: 183 ($M^{+\bullet}$, 12%), 140 (100).

General procedure for the acetylation reactions

The alcohol was treated with a mixture of pyridine and acetic anhydride for 1 night at room temperature. After addition of ethanol and chloroform, the solvents were evaporated and the residue was filtered through a short column of alumina to yield the corresponding O-acetyl derivative.

General procedure for the hydroboration of enecarbamates

All the glassware was dried in an oven, assembled hot, and cooled under a stream of dry nitrogen. THF was distillated from lithium aluminium hydride, into the reaction flask containing the enecarbamate; the flask was then equipped with a rubber septum and a positive pressure of nitrogen was maintained. The hydroboration was carried out by adding a 2 M solution of borane in THF (Aldrich) through the septum via a hypodermic syringe previously flushed with dry nitrogen. After the reaction was complete, the reaction flask was immersed in a cooling bath at 0°C, and the excess of borane was destroyed by adding some drops of water. The oxidation step was carried out under magnetic stirring at room temperature by adding the proper amounts of aqueous NaOH and hydrogen peroxide.

Hydroboration of the enecarbamate 3*a*

The enecarbamate **3***a* (267 mg, 1.72 mmol) was subjected to hydroboration, according to the general procedure described above, in 25 mL of THF with addition of a 2 M $BH_3{\cdot}SMe_2$ solution (0.86 mL, 1.72 mmol). After 3 h, the reaction was stopped and the oxidation was performed by adding 1 mL of 3 M NaOH and 1 mL of H_2O_2 (35% w/w). After 2 h at room temperature, the reaction mixture was basified by addition of 100 mL of dilute NH_4OH and extracted with $CHCl_3$ (3 × 100 mL). The combined $CHCl_3$ layers were evaporated to dryness and the residue was submitted to flash chromatography (silica gel, ethyl acetate/hexane 1:1) to furnish successively the *cis* alcohol **5***a* (69 mg, 0.39 mmol, 22%), and the *trans* alcohol **4***a* (148 mg, 0.85 mmol, 49%); **4***a*: ^{1}H NMR δ: 4.44 (1H, m, H2),

4.02 (1H, broad d, J = 14 Hz, H6e), 3.93 (1H, m, H5), 3.69 (3H, s, NCO_2CH_3), 3.06 (1H, dd, J = 14 and 2 Hz, H6a), 1.3–2.1 (4H, m), 1.15 (3H, d, J = 7 Hz, CH_3); ^{13}C NMR δ: 157.4, 64.8, 53.0, 46.7, 45.1, 25.6, 24.1, 15.8; MS, *m/z*: 173 ($M^{+\bullet}$, 10%), 158 (100), 140 (48), 125.9 (m*), 124.0 (m*), 114 (16), 102 (11), 88 (11); **5***a*: ^{1}H NMR δ: 4.36 (1H, m, H2), 4.12 (1H, ddd, J = 13, 5 and 1 Hz, H6e), 3.68 (3H, s, NCO_2CH_3), 3.57 (1H, tt, J = 5 and 11 Hz, H5), 2.66 (1H, dd, J = 11 and 13 Hz, H6a), 1.5–1.8 (4H, m), 1.15 (3H, d, J = 7 Hz, CH_3); ^{13}C NMR δ: 156.4, 67.7, 53.1, 45.9, 45.7, 28.9, 28.5, 16.0; MS, *m/z*: 173 ($M^{+\bullet}$, 28%), 158 (100), 140 (69), 126 (17), 116 (32), 114 (16), 102 (24), 88 (22).

The O-acetyl derivatives **6***a* and **7***a* were prepared according to the procedure described above; **6***a*: ^{1}H NMR δ: 4.87 (1H, m, H5), 4.47 (1H, m, H2), 4.13 (1H, broad d, J = 15 Hz, H6e), 3.67 (3H, s, NCO_2CH_3), 3.03 (1H, dd, J = 15 and 2 Hz, H6a), 1.2–2 (4H, m), 2.01 (3H, s, OAc), 1.15 (3H, d, J = 7 Hz, CH_3); ^{13}C NMR δ: 170.8, 156.8, 67.5, 52.9, 46.3, 42.2, 24.7, 23.2, 21.5, 15.9; MS, *m/z*: 215 ($M^{+\bullet}$, <1%), 200 (3; calcd. for $C_9H_{14}NO_4$: 200.0922; found: 200.0927), 155 (66), 140 (100), 126.4 (m*). **7***a*: ^{1}H NMR δ: 4.64 (1H, tt, J = 5 and 11 Hz, H5), 4.39 (1H, m, H2), 4.14 (1H, ddd, J = 13, 5, and 2 Hz, H6e), 3.68 (3H, s, NCO_2CH_3), 2.76 (1H, dd, J = 13 and 11 Hz, H6a), 2.03 (3H, s, OAc), 1.5–1.9 (4H, m), 1.15 (3H, d, J = 7 Hz, CH_3); ^{13}C NMR δ: 170.4, 156.2, 69.6, 53.0, 45.9, 42.3, 28.5, 25.2, 21.5, 15.9; MS, *m/z*: 215 ($M^{+\bullet}$, <1%), 200 (2; calcd. for $C_9H_{14}NO_4$: 200.0922; found: 200.0920), 155 (66), 140 (100), 126.4 (m*).

Hydroboration of the enecarbamate 3*b*

The enecarbamate **3***b* (108 mg, 0.59 mmol) was submitted to hydroboration, according to the general procedure described above, in 5 mL of THF with the addition, at −78°C, of a 2 M $BH_3{\cdot}SMe_2$ solution (0.3 mL, 0.59 mmol). Once the addition was complete, the reaction mixture was maintained at −10°C for 20 h; the reaction was then stopped and the oxidation was performed by adding 0.5 mL of 3 M NaOH and 0.5 mL of H_2O_2 (35% w/w). After 2 h at room temperature, the reaction mixture was poured into 20 mL of dilute NH_4OH and extracted with $CHCl_3$ (3 × 20 mL). The combined $CHCl_3$ layers were evaporated to dryness and the residue was submitted to flash chromatography (silica gel, ethyl acetate/hexane 1:1) to furnish successively the *cis* alcohol **5***b* (11 mg, 0.054 mmol, 9%) and the *trans* alcohol **4***b* (74 mg, 0.36 mmol, 62%). **4***b*: ^{1}H NMR δ: 4.27 (1H, m, H2), 4.05 (1H, broad d, J = 14 Hz, H6e), 3.91 (1H, m, H5), 3.69 (3H, s, NCO_2CH_3), 3.0 (1H, dd, J = 14 and 2 Hz, H6a), 1.1–2.1 (8H, m), 0.92 (3H, t, J = 7 Hz, CH_3); ^{13}C NMR δ: 64.6, 52.6, 50.4, 44.8, 31.3, 25.5, 22.1, 19.5, 13.9; MS, *m/z*: 201 ($M^{+\bullet}$, 3%), 170 (3), 158 (100), 140 (50); **5***b*: ^{1}H NMR δ: 4.1 (2H, m, H2 and H6e), 3.66 (3H, s, NCO_2CH_3), 3.55 (1H, tt, J = 10.5 and 5 Hz, H5), 2.58 (1H, dd, J = 13 and 10.5 Hz, H6a), 1.2–1.9 (8H, m), 0.89 (3H, t, J = 7 Hz, CH_3); ^{13}C NMR δ: 67.2, 52.6, 49.5, 45.4, 31.5, 28.5, 26.8, 19.4, 13.9; MS, *m/z*: 201 ($M^{+\bullet}$, 3%), 170 (3), 158 (100), 140 (51).

The O-acetyl derivatives **6***b* and **7***b* were prepared according to the procedure described above; **6***b*: ^{1}H NMR δ: 4.86 (1H, m, H5), 4.33 (1H, m, H2), 4.18 (1H, broad d, J = 15 Hz, H6e), 3.68 (3H, s, NCO_2CH_3), 2.97 (1H, dd, J = 15 and 2 Hz, H6a), 2.02 (3H, s, OAc), 1.2–2.0 (8H, m), 0.92 (3H, t, J= 7 Hz, CH_3); ^{13}C NMR δ: 170.9, 157.2, 67.5, 52.9, 50.4, 42.2, 31.8, 23.6, 23.2, 21.5, 19.9, 14.3; MS, *m/z*: 243 ($M^{+\bullet}$, 2%), 212 (2), 200 (42; calcd. for $C_9H_{14}NO_4$: 200.0922; found: 200.0922), 183 (15), 158 (6), 140 (100); **7***b*: ^{1}H NMR δ: 4.67 (1H, tt, J = 5 and 11 Hz, H5), 4.2 (2H, m, H2 and H6e), 3.71 (3H, s, NCO_2CH_3), 2.74 (1H, dd, J = 11 and 13 Hz, H6a), 2.06 (3H, s, OAc), 1.2–1.9 (8H, m), 0.95 (3H, t, J = 7Hz, CH_3); ^{13}C NMR δ: 170.4, 156.8, 69.5, 53.1, 50.1, 42.4, 31.9, 26.9, 25.6, 21.5, 19.9, 14.4; MS, *m/z*: 242 ($M^{+\bullet}$, <1%), 212 (1), 200 (30; calcd. for $C_9H_{14}NO_4$: 200.0922; found: 200.0926), 183 (28), 158 (13), 140 (100).

Hydroboration of the enecarbamate 12

The enecarbamate **12** (252 mg, 0.83 mmol) was subjected to hydroboration, according to the general procedure described above, in 20 mL of THF with addition of a 2 M $BH_3{\cdot}SMe_2$ solution (0.45 mL, 0.91 mmol). After 1.5 h, the reaction was stopped and the oxidation was performed by adding 1 mL of 3 M NaOH and 1 mL of H_2O_2 (35% w/w). After 2 h at room temperature, the reaction mixture was basified with 50 mL of dilute NH_4OH and extracted with $CHCl_3$ (3 × 50 mL). The combined $CHCl_3$ layers were evaporated to dryness and the residue was submitted to flash chromatography (silica gel, ethyl acetate/hexane 9:1) to furnish successively the *cis* alcohol **14** (49 mg, 0.15 mmol, 18%) and the *trans* alcohol **13** (154 mg, 0.47 mmol, 57%). **13**: ^{1}H NMR δ: 7.3 (5H, m), 5.71 (1H, dd, J = 6 and 7 Hz, H8), 4.32 (1H, m, H2), 4.12 (1H, m H6e), 3.95 (1H, m, H5), 3.66 (3H, s, NCO_2CH_3), 3.15 (1H, dd, J = 2 and 14 Hz, H6a), 2.05 (3H, s, OAc), 1.2–2.4 (7H, m); ^{13}C NMR δ: 157.1, 140.2, 128.5, 128.2, 126.7, 74.4, 64.4, 52.7, 48.3, 45.1, 36.1, 25.6, 22.5, 21.3; MS, *m/z*: 321 ($M^{+\bullet}$, 1%), 261 (25), 202 (15), 158 (100), 156.3 (m*), 140 (41), 124.0 (m*). **14**: ^{1}H NMR δ: 7.3 (5H, m), 5.7 (1H, dd, J = 5 and 8 Hz, H8), 4.17 (2H, m, H2 and H6e), 3.66 (3H, s, NCO_2CH_3), 3.58 (1H, m, H5), 2.73 (1H, dd, J = 11 and 13 Hz, H6a), 2.04 (3H, s, OAc), 1.4–2.4 (7H, m); ^{13}C NMR δ: 170.6, 156.3, 140.7, 128.9, 128.5, 127.0, 74.7, 67.4, 53.2, 47.9, 46.1, 36.7, 28.9, 27.6, 21.6; MS, *m/z*: 321 ($M^{+\bullet}$, <1%), 278 (6), 261 (55), 202 (35), 158 (100), 140 (50).

The O-acetyl derivatives **15** and **16** were prepared according to the procedure described above. **15**: ^{1}H NMR δ: 7.3 (5H, m), 5.72 (1H, dd, J = 6 and 8 Hz, H8), 4.87 (1H, m, H5), 4.37 (1H, m, H2), 4.23 (1H, broad d, J = 15 Hz, H6e), 3.66 (3H, s, NCO_2CH_3), 3.11 (1H, dd, J = 15 and 2 Hz, H6a), 2.04 (3H, s, OAc), 2.01 (3H, s, OAc), 1.3–2.4 (6H, m); ^{13}C NMR δ: 170.8, 170.5, 156.9, 140.6, 128.9, 128.5, 127.0, 74.6, 67.2, 53.0, 48.2, 42.5, 36.5, 23.6, 23.4, 21.5; MS, *m/z*: 363 ($M^{+\bullet}$, <1%; calcd. for $C_{19}H_{25}NO_6$: 363.1681; found: 363.1688), 320 (2), 303 (17), 252.9 (m*), 244 (12), 243 (9), 200 (40), 194.8 (m*), 158 (10), 156 (10), 140 (100), 110.2 (m*), 98 (m*); **16**: ^{1}H NMR δ: 7.3 (5H, m), 5.72 (1H, dd, J = 6 and 8 Hz, H8), 4.65 (1H, tt, J = 5 and 11 Hz, H5), 4.2 (2H, m, H2 and H6e), 3.67 (3H, s, NCO_2CH_3), 2.84 (1H, dd, J = 11 and 13 Hz, H6a), 2.04 (3H, s, OAc), 2.05 (3H, s, OAc), 1.2–2.4 (6H, m); ^{13}C NMR δ: 170.1, 169.9, 155.8, 140.2, 128.5, 128.2, 126.6, 74.2, 68.9, 52.8, 47.4, 42.3, 36.3, 26.7 25.2, 21.2, 21.1; MS, *m/z*: 363 ($M^{+\bullet}$, <1%; calcd. for $C_{19}H_{25}NO_6$: 363.1681; found: 363.1687), 304 (4), 303 (7), 260 (4), 244 (10), 243 (8), 200 (37), 140 (100), 110.2 (m*), 98 (m*).

Preparation of pseudoconhydrine 8

To a solution of **4***b* (46 mg, 0.22 mmol) in 5 mL of CH_2Cl_2 was added TMSI (0.32 mL, 2.28 mmol) distilled over copper pow-

der just before use. The reaction mixture was refluxed for 1 h and after addition of some drops of MeOH was allowed to stand at room temperature during 10 min. The solvent was evaporated to dryness and the residue was dissolved in dilute NH_4OH and extracted with $CHCl_3$ (3 × 15 mL). Evaporation of the $CHCl_3$ layers furnished **8** as a colourless oil (28 mg, 0.19 mmol, 89 %). Mass and ^1H NMR spectra were identical with those reported in the literature (17).

Preparation of *N*-methylpseudoconhydrine 9

To a solution of **4***b* (30 mg, 0.15 mmol) in THF (10 mL) was added $LiAlH_4$ (50 mg). The mixture was refluxed for 2.5 h. Some drops of water were added at room temperature, the mixture was filtered through Celite, and the solvent was evaporated to dryness. The residue was dissolved into 10 mL of $CHCl_3$ and extracted with 0.1 N HCl (2 × 10 mL). The organic phase was discarded and the aqueous phase basified with NH_4OH and extracted with $CHCl_3$ (2 × 100 mL). The combined $CHCl_3$ layers were evaporated to dryness and the residue was filtered through a short column of alumina ($CHCl_3$/MeOH 9:1) to afford **9** (20 mg, 0.12 mmol, 80%). Mass and ^1H NMR spectra were identical with those reported in the literature (18).

Swern oxidation of alcohol 13

DMSO (102 μL, 1.45 mmol) was added to a stirred solution of oxalyl chloride (126 μL, 1.45 mmol) in 2 mL of CH_2Cl_2 at −78°C under a nitrogen atmosphere. After 10 min, alcohol **13** (156 mg, 0.48 mmol) dissolved in 1 mL of CH_2Cl_2 was added; the reaction flask was then cooled at −40°C and after 10 min at −78°C triethylamine (1 mL) was added dropwise. The reaction mixture was allowed to reach room temperature and after 15 min poured into 30 mL of water. After neutralization with concentrated HCl and extraction with CH_2Cl_2 (30 mL), the organic phase was washed with dilute NH_4OH, dried, evaporated, and filtered through a short column of silica gel (ethyl acetate/hexane 4:1) to give the ketone **17** (142 mg, 0.44 mmol, 92%). IR: (CCl_4 solution) cm^{-1}: 2955, 1739, 1708, 1450, 1234; ^1H NMR δ: 7.3 (5H, m), 5.83 (1H, dd, J = 5 and 9 Hz, H8), 4.3 (2H, m, H2 and H6e), 3.71 (3H, s, NCO_2CH_3), 3.62 (1H, d, J = 19Hz, H6a), 2.07 (3H, s, OAc), 1.6–2.4 (6H, m); ^{13}C NMR δ: 206.8, 170.6, 156.2, 140.5, 129.0, 128.7, 126.9, 73.8, 53.5, 50.9, 48.8, 39.7, 36.0, 26.7, 21.6; MS, *m/z*: 319 ($M^{+\bullet}$, 1%), 291 (2), 275 (15), 260 (11), 156 (100),128 (32).

PCC oxidation of the alcohol 13

PCC adsorbed on alumina (1 g, 0.9 mmol) was added under stirring to a solution of **13** (73 mg, 0.22 mol) in 10 mL of CH_2Cl_2. The mixture was refluxed and stirred for 1 h, cooled, and then filtered through a column of Florisil (CH_2Cl_2, then AcOEt). The combined organic layers were evaporated to dryness and the residue was filtered through a short column of silica gel (AcOEt). Evaporation of the solvent furnished the ketone **17** as a colourless oil (50 mg, 0.15 mmol, 71%).

Reduction of ketone 17 with $NaBH_4$

$NaBH_4$ (60 mg, 1.6 mmol) was added to a solution of ketone **17** (103 mg, 0.32 mmol) in 5 mL of absolute ethanol at 0°C. After 15 min some drops of water were added and the solvent was evaporated to dryness. The residue was dissolved in 10 mL of dilute NH_4OH and extracted with CH_2Cl_2 (3 × 10 mL). The combined CH_2Cl_2 layers were evaporated and the residue was submitted to flash chromatography (silica gel, ethyl acetate/hexane 4:1) to furnish successively the alcohols **14** (84 mg, 0.26 mmol, 81%) and **13** (10 mg, 0.031 mmol, 10%).

Reduction of ketone 17 with $LiAl(O\text{-}t\text{Bu})_3H$

$(t\text{BuO})_3AlLiH$ (24 mg, 0.094 mmol) was added to a solution of ketone **17** (20 mg, 0.062 mmol) in THF (2 mL) at 0°C. After 2 h some drops of water were added and the mixture was filtered through Celite. After evaporation of the solvent, dilute NH_4OH was added to the residue and the solution was extracted with $CHCl_3$. Evaporation of the solvent followed by a flash chromatography (silica gel, AcOEt/hexane 1:9) furnished the *cis* acetate **14** (12 mg, 0.037 mmol, 60%) and the *cis* diol **18** (5 mg, 0.017 mmol, 28%). **18**: ^1H NMR δ: 7.3 (5H, m), 4.73 (1H, m, H8), 4.36 (1H, m, H2), 4.07 (H, m, H6e), 3.66 (3H, s, NCO_2CH_3), 3.58 (1H, m, H5), 2.61 (1H, dd, J = 11 and 12 Hz, H6a), 1.4–2.2 (8H, m); MS, *m/z*: 279 ($M^{+\bullet}$, 3%), 261 (4), 244 (m*), 202 (4), 186 (4), 173 (3), 158 (100), 140 (78), 124.0 (m*).

Preparation of alcohol 19

To a solution of the carbamate **13** (33 mg, 0.1 mmol) in THF (5 mL) was added $LiAlH_4$ (35 mg). The mixture was then refluxed for 3.5 h. After addition of some drops of water the mixture was filtered through Celite and the solvent was evaporated to dryness. The residue was filtered through a short column of alumina ($CHCl_3$, MeOH 5%, NH_4OH) to give **19** as a colourless oil (15 mg, 0.063 mmol, 63%): $[\alpha]_D^{20}$ −80.5 (c = 0.9, MeOH); ^1H NMR δ: 7.34 (5H, m), 4.82 (1H, dd, J = 3 and 10 Hz, H8), 3.79 (1H, tt, J = 4 and 8 Hz, H5), 2.99 (1H, ddd, J = 12, 4, and 1 Hz, H6e), 2.56 (1H, m, H2), 2.40 (3H, s, NCH_3), 2.26 (1H, dd, J = 8 and 12 Hz, H6a), 1.36–2.08 (6H, m); ^{13}C NMR δ: 128.8, 127.7, 125.9, 73.5, 65.7, 61.2, 60.3, 41.4, 39.9, 32.5, 25.9; MS, *m/z*: 235 ($M^{+\bullet}$, 3%), 128 (3), 114 (100), 96 (10).

Preparation of (−)-5-hydroxysedamine 20

The alcohol **14** (18 mg, 0.056 mmol) was reduced with $LiAlH_4$ (20 mg) in THF (5 mL) as described for **13** to afford alcohol **20** as a colourless oil (10 mg, 0.045 mmol, 80%). The mass, ^1H, and ^{13}C spectra were identical with those reported in the literature (13); $[\alpha]_D^{20}$ −53 (c = 0.3, MeOH).

Anodic oxidation of carbamate 7*a*

The carbamate **7***a* (59 mg, 0.27 mmol), $Bu_4N^+BF_4^-$ (22 mg, 0.068 mmol), and 5 mL of methanol were introduced into the electrolysis cell equipped with a platinum anode and a vitreous carbon cathode. A constant potential of 8 V was applied. After 5F/mol of electricity was passed, the usual work-up was applied; the crude fraction (68 mg) was flash chromatographed (silica gel, AcOEt/hexane 1:2) to give **21** (47 mg, 0.19 mmol, 71%): ^1H NMR δ: 5.5 (1H, m, H6), 4.70 (1H, dt, J ≈ 4 and 12 Hz, H5), 4.3 (1H, m, H2), 3.73 (3H, s, NCO_2CH_3), 3.33 (3H, broad s, OCH_3), 2.10 (3H, s, OAc), 1.64–2.14 (4H, m), 1.29 (3H, d, J = 7 Hz, CH_3); ^{13}C NMR δ: 170.7, 156.3, 82.9, 72.2, 55.8, 53.2, 46.2, 29.1, 21.5, 19.8; MS, *m/z*: 245 ($M^{+\bullet}$, <1%), 214 (8), 202 (4), 198 (5), 185 (23), 172 (11), 170.4 (m*), 170 (7), 142 (25), 140 (11), 118 (100).

Preparation of 22 from 21

To a solution of $TiCl_4$ (21 μL, 0.19 mmol) in 0.2 mL of

CH_2Cl_2 at −45°C, under an atmosphere of nitrogen, was added a solution of **21** (32 mg, 0.13 mmol) in 0.6 mL of CH_2Cl_2. After 15 min the solution was cooled to −78°C and 2-trimethylsilyloxypropene (112 mg, 0.65 mmol) contaminated by ca. 25% of $(CH_3)_3SiOSi(CH_3)_3$ was added. After 4 h at −78°C, the solution was poured into 10 mL of water and NaCl was added; extraction with CH_2Cl_2 (2 × 10 mL), evaporation to dryness, and two successive flash chromatographies (silica gel, ethyl acetate/hexane 1:1) furnished **22** as a 76:24 mixture of diastereoisomers (26 mg, 0.096 mmol, 73%): MS, *m/z* (*c* + *t*): 271 ($M^{+\bullet}$, <1%), 256 (2), 240 (2), 214 (14), 211 (100), 198 (16), 196 (17), 172 (50), 171 (46), 169 (65), 168 (54), 156 (28), 154 (47), 152 (30), 140 (64), 102 (75), 85 (86). The following NMR values were extracted from the spectra of the mixture: major constituent: ^{1}H NMR δ: 4.8–5.07 (2H, m, H5 and H6), 4.35 (1H, m, H2), 3.69 (3H, s, NCO_2CH_3), 2.99 (1H, dd, *J* = 16 and 9 Hz, H7), 2.35 (1H, dd, *J* = 16 and 3 Hz, H7′), 2.19 (3H, s, CH_3), 1.95 (3H, s, OAc), 1.6–1.8 (4H, m), 1.18 (3H, d, *J* = 7 Hz, CH_3); ^{13}C NMR δ: 205.4, 169.7, 156.1, 70.4, 53.0, 48.6, 45.6, 45.4, 30.0, 28.3, 21.0, 20.2, 20.1; minor constituent: ^{1}H NMR δ: 4.78 (1H, m), 4.27 (1H, m), 4.01 (1H, m), 3.64 (3H, s, NCO_2CH_3), 3.12 (1H, dd, *J* = 16 and 8 Hz, H7), 2.60 (1H, dd, *J* = 16 and 7 Hz, H7′), 2.19 (3H, s, CH_3), 2.03 (3H, s, OAc), 1.3–1.9 (4H, m), 1.33 (3H, d, *J* = 7 Hz, CH_3); ^{13}C NMR δ: 205.8, 169.7, 156.2, 70.9, 52.4, 51.4, 49.0, 44.9, 30.0, 26.9, 24.8, 21.3, 18.4.

Anodic oxidation of ent-16

(+)-ent-**16** (93 mg, 0.25 mmol), $Et_4N^+OTs^-$ (8 mg, 0.026 mmol), and 5 mL of methanol were introduced into the electrolysis cell. The solution was stirred for 10 min and a constant potential of 8 V was applied. After 8F/mol of electricity was passed, some drops of NH_4OH, were added to the solution and the solvent was evaporated; the residue was dissolved in water (50 mL), basified with NH_4OH, and extracted with $CHCl_3$ (2 × 50 mL). The combined $CHCl_3$ layers were evaporated and the residue was filtered through a short column of silica gel (ethyl acetate/hexane 1:1) to afford a mixture of **23** and unreacted ent-**16**. This mixture was submitted to column chromatography on alumina (ethanol-free $CHCl_3$) to furnish the mixture of the diastereomeric methoxy compounds **23** (57 mg, 0.145 mmol, 58%): MS, *m/z* (*cis* and *trans*): 362 ($M^{+\bullet}-CH_3O^\bullet$, 3%), 333 (17), 319 (20), 259 (27), 231 (41), 230 (20), 202 (23), 198 (100), 170.4 (m*), 170 (18), 156 (61). The following NMR values were extracted from the spectra of the mixture: major constituent: ^{1}H NMR δ: (330 K): 7.31 (5H, m), 5.79 (1H, dd, *J* = 7 Hz, H8), 5.5 (1H, m, H6), 4.67 (1H, dt, *J* = 12 and 4 Hz, H5), 4.24 (1H, m, H2), 3.72 (3H, s, NCO_2CH_3), 3.35 (3H, s, OCH_3), 2.28 (m, 2H), 2.06 (6H, s, OAc), 1.6–1.94 (4H); ^{13}C NMR δ: (330 K): 170.7, 156.9, 141.2, 129.0, 128.5, 127.0, 83.5, 74.2, 72.2, 57.0, 53.3, 47.8, 40.5, 26.6, 21.4, 20.0; minor constituent: ^{1}H NMR δ (330K): 7.3 (5H, m), 5.8 (1H, m, H8), 5.19 (1H, d, *J* = 2 Hz, H6), 4.91 (1H, dt, *J* = 6 and 3 Hz, H5), 3.70 (3H, s, NCO_2CH_3), 3.60 (1H, m, H2), 3.28 (3H, s, OCH_3), 2.58 (1H, ddd, *J* = 5, 9, and 14 Hz, H7), 2.25 (1H, m, H7′), 2.04 (3H, s, OAc), 1.96 (3H, s, OAc), 1.6–1.9 (4H, m); ^{13}C NMR δ (330 K): 170.7, 170.3, 157.7, 141.2, 129.0, 128.5, 127.1, 85.8, 74.5, 69.2, 56.0, 52.6, 49.2, 39.8, 23.7, 23.4, 21.3, 21.2.

Nucleophilic displacement of the methoxy group of 23

To a stirred solution of $TiCl_4$ (43 μL, 0.39 mmol) in 1 mL of CH_2Cl_2 at 0°C, under an atmosphere of nitrogen, was added a solution of **23** (139 mg, 0.35 mmol) in 3 mL of CH_2Cl_2 and 2-trimethylsilyloxypropene (303 mg, 1.75 mmol) contaminated by ca. 25% of $(CH_3)_3SiOSi(CH_3)_3$. The solution was stirred for 2 h at 0°C, then poured into 50 mL of water and, after addition of NaCl, extracted with CH_2Cl_2 (4 × 50 mL). The combined CH_2Cl_2 layers were evaporated to dryness and the residue was submitted to two successive flash chromatographies (silica gel ethyl acetate/hexane 1:1) to furnish **24** as a 77/23 mixture of *c/t* diastereoisomers (88 mg, 0.21 mmol, 60%): MS, *m/z* (*cis* + *trans*): 419 ($M^{+\bullet}$, <1%; calcd. for $C_{22}H_{29}NO_7$: 419.1944; found: 419.1938), 362 (2), 359 (38), 316 (6), 299 (61), 298 (21), 270 (6), 256 (64), 249.0 (m*), 198 (70), 197 (27), 196 (37), 195 (50), 194 (35), 156 (61), 154 (60), 153.1 (m*), 150.0 (m*), 138 (40), 114 (100). The following NMR values were extracted from the spectra of the mixture: major constituent: ^{1}H NMR δ: 7.35 (5H, m), 5.76 (1H, dd, *J* = 10 and 4 Hz, H8), 5.07 and 4.93 (2H, m, H5 and H6), 4.29 (1H, m, H2), 3.69 (3H, s, NCO_2CH_3), 2.92 (1H, dd, *J* = 16 and 9 Hz, H9), 2.39 (1H, dd, *J* = 16 and 3 Hz, H9′), 2.17 (3H, s, CH_3), 2.09 (3H, s, OAc), 1.93 (3H, s, OAc), 1.9–2.2 (2H, m, H7), 1.2–1.7 (4H, m); ^{13}C NMR δ: 205.4, 170.5, 169.7, 156.1, 140.4, 128.8, 128.4, 126.6, 73.7, 70.1, 53.2, 48.5, 46.9, 45.2, 40.9, 30.1, 25.8, 21.8, 21.4, 20.3; minor constituent: ^{1}H NMR δ (characteristic values): 5.87 (1H, dd, *J* = 8 and 6 Hz, H8), 4.73 (1H, m), 4.2 (1H, m), 3.8 (1H, m), 3.58 (3H, s, NCO_2CH_3), 3.10 (1H, dd, *J* = 17 and 8 Hz, H9), 2.58 (2H, m), 2.17 (3H, s, CH_3), 2.06 (3H, s, OAc), 2.00 (3H, s, OAc), 1.6–2.1 (5H, m).

25: ^{1}H NMR δ: 7.3 (5H, m), 5.90 (1H, broad s, H6), 5.78 (1H, dd, *J* = 5 and 9 Hz, H8), 4.72 (1H, dt, *J* = 12 and 4 Hz, H5), 4.23(1H, m, H2), 3.72 (3H, s, NCO_2CH_3), 2.98 (1H, m, OH), 1.79 (1H, m, H7), 2.09 and 2.07 (6H, 2s, 2 × OAc), 1.7–2.1 (5H, m); MS, *m/z*: 379 ($M^{+\bullet}$, <1%), 319 (9), 318 (5), 301 (5), 259 (16), 241 (6), 231 (11), 216 (8), 198 (33), 156 (100), 121 (73).

Preparation of 27

A solution of **24** (68 mg, 0.16 mmol), ethylene glycol (17 mg, 3.2 mmol), and $TsOH{\cdot}H_2O$ (7 mg) in 20 mL of benzene was refluxed for 3 h in a Dean–Stark apparatus. After evaporation of the solvent, the residue was dissolved in dilute NH_4OH and extracted with CH_2Cl_2 (3 × 15 mL). The combined organic layers were evaporated to dryness to furnish **26** as a colourless oil (70 mg).

To a solution of the crude acetal **26** in THF (15 mL) was added $LiAlH_4$ (116 mg). The mixture was heated under reflux for 3 h. Some drops of water were added and the mixture was filtered through Celite and evaporated to dryness. The combined CH_2Cl_2 layers were evaporated and a chromatography on alumina of the residue furnished the diol **27** as a *c/t* mixture (36 mg, 1.1 mmol, 67% from **24**). The following NMR values (major constituent) were extracted from the spectra of the mixture: ^{1}H NMR δ: 7.3 (5H, m), 4.90 (1H, dd, *J* = 3 and 11 Hz, H8), 3.96 (4H, m, -OCH_2CH_2O-), 3.92 (1H, m, H5), 3.04 (1H, m), 2.91 (1H, td, *J* = 5 and 2 Hz, H6), 2.49 (3H, s, NCH_3), 1.2–2.1 (10H, m), 1.35 (3H, s, CH_3); ^{13}C NMR δ: 145.6, 128.6, 127.4, 125.9, 109.6, 75.9, 68.2, 65.0, 64.7, 64.2, 61.1, 40.8, 39.1, 32.4, 32.3, 24.4, 20.7; MS, *m/z*: 335 ($M^{+\bullet}$, 8%), 320 (2), 292 (6), 234 (14), 214 (97), 112 (29), 87 (100), 58.6 (m*).

Preparation of sedacryptine 28 from 27

A solution of the acetal **27** (36 mg, 1.1 mmol) in 0.1 N aqueous HCl (5 mL) was heated under reflux for 30 min. The mixture was then cooled, basified with NH_4OH, and extracted with CH_2Cl_2 (3 × 15 mL). The combined CH_2Cl_2 layers were evaporated to dryness to furnish a mixture of sedacryptine **28** and **29** in a 60/40 ratio (25 mg, 0.086 mmol, 80 %). After epimerization in MeOH the diastereoisomeric ratio moved to 80/20. Crystallization from cyclohexane furnished pure (+)-sedacryptine **28** as colourless crystals, mp 122–123°C; $[\alpha]_D^{20}$ +14 (c = 0.54, $CHCl_3$); ^1H NMR δ (360 MHz): 7.34 (5H, m), 4.85 (1H, dd, J = 10 and 3 Hz, H8), 4.07 (1H, q, J = 3 Hz, H5), 2.69 (1H, t, J = 3 Hz, H6), 2.31 (1H, m, H2), 2.28 (3H, s, NCH_3), 2.24 (1H, d, J = 13 Hz, H9), 2.20 (1H, m, H7), 2.09 (1H, ddt, J = 14, 3 and 3 Hz, H4e), 1.91 (1H, dd, J =13 and 4 Hz, H9′), 1.83 (1H, m, H3e), 1.54–1.65 (3H, m, H3a, H4a, H7′), 1.5–1.9 (2H, OH), 1.48 (3H, s, CH_3); MS, m/z: 291 ($M^{+\bullet}$, 4%), 273 (12), 234 (2), 230 (4), 170 (100), 152 (83), 135.9 (m*), 112 (44), 95 (75).

Acknowledgements

M.P. wishes to thank the "Institut pour l'Encouragement de la Recherche Scientifique dans l'Industrie et l'Agriculture" (IRSIA) for the award of a fellowship. C.H. is a Research Associate of the National Fund for Scientific Research (FNRS).

References

1. K. Burgess and I. Henderson. Tetrahedron, **48**, 4045 (1992).
2. T. Shono, Y. Matsumura, and K. Tsubata. J. Am. Chem. Soc. **103**, 1172 (1981).
3. F. Driessens and C. Hootelé. Can. J. Chem. **69**, 211 (1991).
4. A. Durant and C. Hootelé. Can. J. Chem. **70**, 2722 (1992).
5. T. Shono, Y. Matsumura, K. Tsubata, Y. Sugihara, S. Yamane, T. Kanazawa, and T. Aoki. J. Am. Chem. Soc. **104**, 6697 (1982).
6. M. Plehiers and C. Hootelé. Tetrahedron Lett. **34**, 7569 (1993).
7. W. Oppolzer and C.G. Bochet. Tetrahedron Lett. **36**, 2959 (1995).
8. H.S. Yanai and W.N. Lipscomb. Tetrahedron, **6**, 103 (1959).
9. M.F. Roberts and R.T. Brown. Phytochemistry, **20**, 447 (1981).
10. R.W. Hoffman. Chem. Rev. **89**, 1841 (1989).
11. A.J. Mancuso, S-L. Huang, and D. Swern. J. Org. Chem. **43**, 2480 (1978).
12. E.J. Corey and J.W. Suggs. Tetrahedron Lett. **31**, 2647 (1975).
13. W. Ibebeke-Bomangwa and C. Hootelé. Tetrahedron, **43**, 935 (1987).
14. C. Hootelé, F. Halin, S. Thomas, and D. Tourwé. Tetrahedron, **41**, 5563 (1985).
15. F. Galinovsky, G. Bianchetti, and O. Vogl. Monatsh. Chem. **84**, 1221 (1953).
16. C. Hootelé, B. Colau, F. Halin, J.P. Declercq, G. Germain, and M. Van Meerssche. Tetrahedron Lett. **21**, 5061 (1980).
17. K.E. Harding and S.R. Burks. J. Org. Chem. **49**, 40 (1984).
18. T. Shono, Y. Matsumura, O. Onomura, and M. Sato. J. Org. Chem. **53**, 4118 (1988).

Study of the coordinated system Pb(II) – neutral valine – valinate ion

Teresa María Borges Miquel, Mercedes Lemus Sánchez, Josefa Castro Macías, and Jesús César Rodríguez Placeres

Abstract: The polarographic method has been applied to the study of the mixed-coordinated system (Pb(II) – neutral valine – valinate ion, in aqueous medium, I = 1.0 mol L^{-1} ($NaClO_4$) and 25 ± 0.1°C. The stabilization of the following complexes: $[Pb(HV)]^{2+}$ (β_{10} = 9.7), $[Pb(HV)_2]^{2+}$ (β_{20} = 28), $[Pb(HV)(V)]^{+}$ ($\beta_{11} = 3.3 \times 10^4$), $[Pb(V)]^{+}$ ($\beta_{01} = 3.7 \times 10^4$), and $[Pb(V)_2]$ ($\beta_{02} = 2.8 \times 10^7$) was observed.

Key words: polarography, Pb(II), valine, speciation.

Résumé : On a appliqué la méthode polarographique à l'étude du système coordiné mixte Pb(II) – valine neutre – ion valinate, en solution aqueuse, I = 1,0 mol L^{-1} ($NaClO_4$), à 25 ± 0,1°C. On a observé la stabilisation des complexes suivants : $[Pb(HV)]^{2+}$ (β_{10} = 9,7), $[Pb(HV)_2]^{2+}$ (β_{20} = 28), $[Pb(HV)(V)]^{+}$ ($\beta_{11} = 3{,}3 \times 10^4$), $[Pb(V)]^{+}$ ($\beta_{01} = 3{,}7 \times 10^4$), et $[Pb(V)_2]$ ($\beta_{02} = 2{,}8 \times 10^7$).

Mots clés : polarographie, Pb(II), valine, espéciation.

[Traduit par la rédaction]

Introduction

The study of the coordinated systems metal ion – amino acids has become increasingly important in recent times, and from different points of view. Increasing worldwide interest was confirmed in 1991, when EC countries selected "Biocoordination Chemistry" as one of seven priority research fields.

One of the most interesting procedures currently followed to investigate the structures and functions of complex macromolecules consists in the analysis of simple molecules that present properties similar to those characteristic of macromolecules. The model compounds are, generally, easier to study and the information obtained has frequently been successfully extrapolated to macromolecules. Thus, for example, Freeman (1) has shown the utility of the information obtained in the study of some simple complexes for understanding the structure of the active sites of carboxypeptidase.

Likewise, diverse observations have led to the study of the formation of metal ion complexes of small molecular weight since this is the way in which metal ions are mobilized during prolonged periods of nutrition. The reliability of the stability constant values of both simple and mixed complexes with simple amino acids is also of importance since they represent the main form of administration in the nutritive mixture or the form of excretion. Thus, the reinvestigation of the coordinated system Zn(II)–cysteinate–hystidinate (2) led to a reduction of the initial estimate of the daily dosage of zinc from 38 mg to 32 mg in some nutritive mixtures studied.

On the other hand, studies of the coordinated systems metallic ion – amino acid have generally taken into account only the anion is ligand, disregarding the complexing nature of the neutral species. It was therefore thought worthwhile to undertake a systematic analysis of these systems from the wider standpoint of considering the complexation of the metallic ion by both species.

Lastly, the fact must be pointed out that the majority of studies of coordinated metallic ion – amino acid systems have been carried out by adjusting the ionic strength with weakly complexing electrolytes. We have shown and verified experimentally (3) that the constants determined under these conditions do not in fact respond to true stability constants but rather to defined arrangements of formation constants of simple and mixed species existing in the medium. The importance of this particular results became evident on finding that the use of this type of electrolyte was generalized, and it provided a solid basis for questioning the greater part of the data previously reported in the literature on coordination chemistry.

In this work we report on the analysis of the mixed coordinated system Pb(II) – neutral valine – valinate ion, which has been studied (4,5), Table 1, but never at the standard temperature of 25°C. Only the formation of two complexes with the valinate ion; $[Pb(V)]^{+}$ and $[Pb(V)_2]$, has been described. The scatter of the results is quite remarkable and requires experimental revision. No stabilization of any complex with neutral valine has been detected.

Theoretical

If the molecule of neutral valine (HV), the zwitterion form of

Received September 15, 1995.[1]

T.M. Borges Miquel. Department of Analytical Chemistry, University of La Laguna, Tenerife, Canary Islands, Spain.
M. Lemus Sánchez, J. Castro Macías, and J.C. Rodríguez Placeres.[2] Department of Physical Chemistry, University of La Laguna, Tenerife, Canary Islands, Spain.

[1] Revision received August 7, 1996.
[2] Author to whom correspondence may be addressed. Telephone: 34-22-635 636. Fax: 34-22-635 601.

Table 1. Values reported in the literature for the system Pb(II)–valine – valinate ion.

Method	T (°C)	Medium	$\beta_{01} \times 10^{-4}$	$\beta_{02} \times 10^{-7}$	Ref.
Polarography	30	1.0 M KNO_3	1.58	7.8	4
Glass	35	0.1 M $NaClO_4$	12.6	2512	5

Table 2. Conditions for sets of experiments.

Set	pH	$C_v \times 10^2$ mol l^{-1}	[V] mol l^{-1}	[HV] $\times 10^2$ mol l^{-1}
1	4.16	2–16	$(6.366–53.87) \times 10^{-8}$	1.967–15.54
2	4.17	2–18	$(4.677–62.14) \times 10^{-8}$	1.954–17.51
3	4.22	2–18	$(8.231–55.45) \times 10^{-8}$	1.975–17.53
4	6.12	2–18	$(6.438–56.56) \times 10^{-6}$	1.990–17.89
5	6.52	2–18	$(1.008–14.20) \times 10^{-5}$	1.966–17.88
6	6.53	3–18	$(2.422–14.25) \times 10^{-5}$	2.980–17.94
7	6.58	2–18	$(1.865–16.68) \times 10^{-5}$	1.998–17.88
8	6.77	2–18	$(2.782–25.30) \times 10^{-5}$	1.969–17.91
9	6.95	2–18	$(4.252–38.04) \times 10^{-5}$	1.989–17.79
10	7.33	2–18	$(1.035–8.903) \times 10^{-4}$	1.990–17.76

which widely predominates, and the valinate ion (V) are considered to be possible ligands of Pb(II) and we admit that, as occurs in the studies of alanine (6), leucine (7), and isoleucine (7), only two ligands can be coordinated, the F_{00} function of Schaap and McMasters (8) will be developed as follows:

$$[1] \quad F_{00} = \{1 + \beta_{10}[HV] + \beta_{20}[HV]^2\} + \{\beta_{01} + \beta_{11}[HV]\}[V] + \{\beta_{02}\}[V]^2$$

It is evident that at sufficiently high values of pH the complexes with the anion will predominate since their concentration will be significative and their stability constants must be much greater than those of the neutral form.

At sufficiently low values of pH it is to be expected that the high concentration of the neutral species with respect to that of the anionic species compensates greatly for its much lower stability constant and its complexes with the metallic cation under study can be determined.

Between the limits mentioned, determination of the constants of the mixed coordinated species will be possible.

In any case, it is understood that if the pH required is very low, the concentration of the protonated form may be high, appreciably modifying the ionic strength. This effect can be minimized by decreasing the total concentration of amino acid.

Likewise, in every case it will be necessary to work with the concentration of complexing forms of amino acid such that their complexation will prevail appreciably over the formation of hydroxo-complexes.

The studies were carried out at constant pH but modifying the total concentration of amino acid, such that [HV] and [V] vary with V_T.

With regard to the expression $K_{a2} = [V][H^+]/[HV]$, eq. [1] transforms to:

$$[2] \quad F_{00} = 1 + \{\beta_{10} + \beta_{01}(K_{a2}/[H^+])\}[HV] + \{\beta_{20} + \beta_{11}(K_{a2}/[H^+]) + \beta_{02}(K_{a2}/[H^+])^2\}[HV]^2$$

a relationship that at constant pH will reduce to

$$[3] \quad F_{00} = 1 + B[HV] + C[HV]^2$$

where, if $m = [H^+]/K_{a2}$, the B and C coefficients will be defined by:

$$[4] \quad B = \beta_{10} + \beta_{01} m^{-1}$$

$$[5] \quad C = \beta_{20} + \beta_{11} m^{-1} + \beta_{02} m^{-2}$$

and can be calculated in the usual manner.

The knowledge of an appropriate number of values of the B and C coefficients would allow us to determine the stability constants of the coordinated species present in the medium.

If substitution is made in terms of [V] the expressions would be analogous

$$[6] \quad F_{00} = 1 + \{\beta_{01} + \beta_{10}([H^+]/K_{a2})\}[V] + \{\beta_{02} + \beta_{11}([H^+]/K_{a2}) + \beta_{20}([H^+]/K_{a2})^2\}[V]^2$$

$$[7] \quad F_{00} = 1 + B'[V] + C'[V]^2$$

where:

$$[8] \quad B' = \beta_{01} + \beta_{10} m$$

$$[9] \quad C' = \beta_{02} + \beta_{11} m + \beta_{20} m^2$$

Experimental

Each of the i vs. E curves was plotted with an Inelecsa PDC1212 electrochemistry system. An Ag/ClAg/NaCl sat. Metrohm EA427 electrode and a Pt (EA285) electrode were employed as reference and auxiliary electrode, respectively. The temperature was always 25 ± 0.1°C and the drop time was set at 3 s. The ionic strength was maintained constant at I = 1.0 mol L^{-1} by addition of $NaClO_4$. The pH measurements were carried out with a pHM84 digital pH-meter (± 0.002) and a Radiometer GK2401C combination electrode. The lead perchlorate, Merck p.a., was prepared by weight and it was standardized complexometrically. Sodium perchlorate was also Merck p.a. and the L-valine was from Sigma p.a. The values of the acidity constants (9) were pK_{a1} = 2.35 ± 0.01 and pK_{a2} = 9.62 ± 0.01.

Procedures

The studies were carried out at constant pH, varying the concentration of total valine between the limits indicated in Table 2. In every case, the plots in absence of ligand were made at low pH (2.00 – 3.00) and $[Pb^{2+}] \simeq 1.0 \times 10^{-4}$ M.

All adjustments were carried out utilizing Sigma Plot 5.01.

Results

In all the solutions studied the polarograms show good symmetry and a regular outline. The plot of log $[i_d–i/i]$ vs. E shows that the discharges occurred by a reversible bielectronic pro-

Fig. 1. Plot of the functions F_{00} and F_{10} vs. [HV] at pH 4.16.

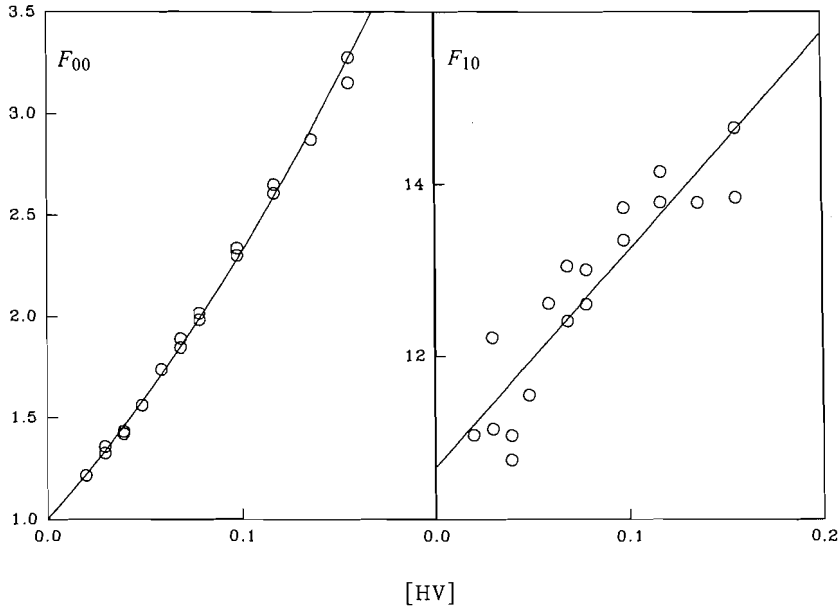

Fig. 2. Plot of the functions F_{00} and F_{10} vs. [HV] at pH 6.95.

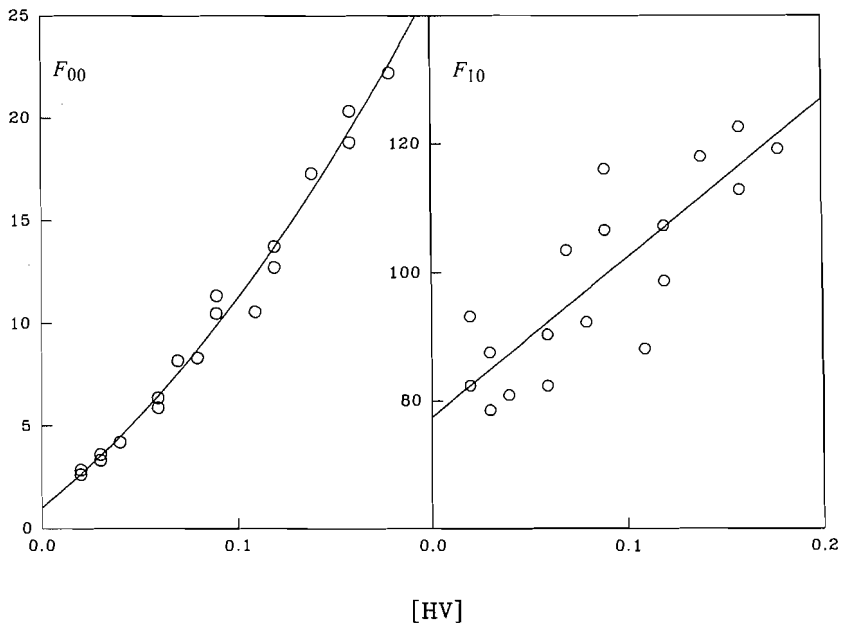

cess. The values for the reversible half-wave potentials were obtained directly from those plots. With few exceptions, the accuracy was better than ± 0.5 mV.

Figures 1–3 present the plots of the F_{i0} functions vs. the concentration of the ligand indicated. In each case, eq.[3] is confirmed. Adjusting by least squares provides the values of B and C given in Table 3.

The studies performed were planned such that studies 1–3 correspond to low values of pH, in which the complexes with neutral valine should prevail. The sets carried out at higher values of pH (4–10) allow the determination of the simple and mixed complexes with the anionic form.

Determination of the β_{10} and β_{20} constants

It will be shown that in eqs. [4] and [5] the summands other than β_{10} and β_{20} are negligible with respect to the corresponding coefficients, B and C, which leads us to propose the following values of the formation constants of the complexes $[Pb(HV)]^{2+}$ and $[Pb(HV)_2]^{2+}$: $\beta_{10} = 9.7 \pm 1.3$ and $\beta_{20} = 28 \pm 7$.

Determination of the β_{01} constant

Equation [4] indicates that a plot of the coefficient B vs. m^{-1} must be a straight line. By fitting to the previously determined ordinate, $\beta_{10} = 9.7$, from the slope of the said plot, Fig. 4, the

Fig. 3. Plot of the functions F_{00} vs. [HV] at pH 7.33.

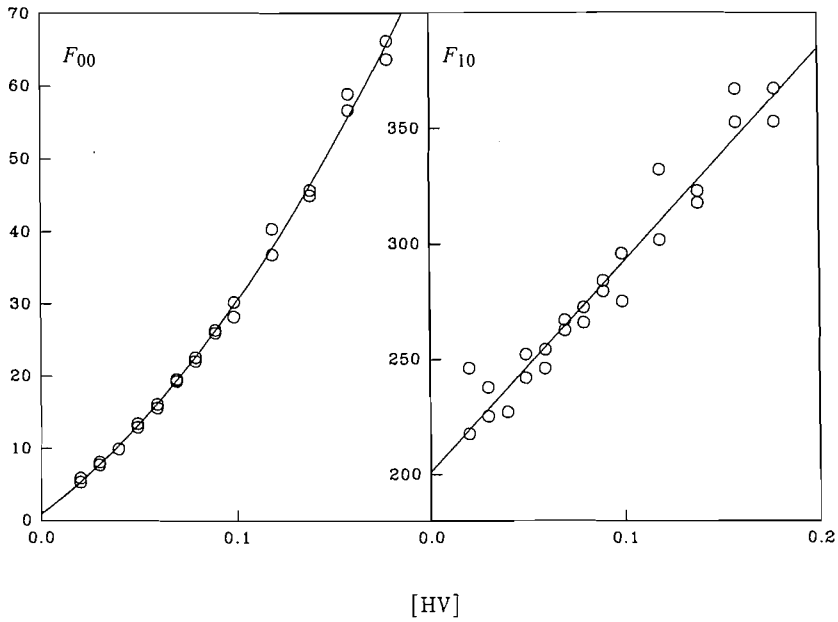

Fig. 4. Plot of B vs. m^{-1}.

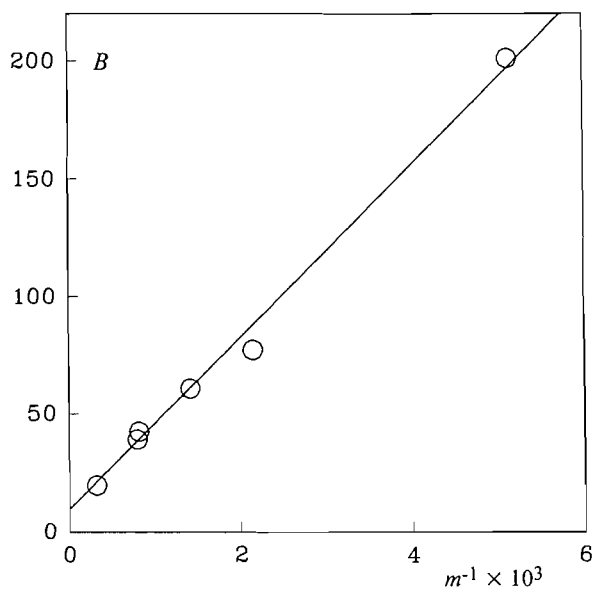

Fig. 5. Plot of $(C - \beta_{20})/m^{-1}$ vs. m^{-1}.

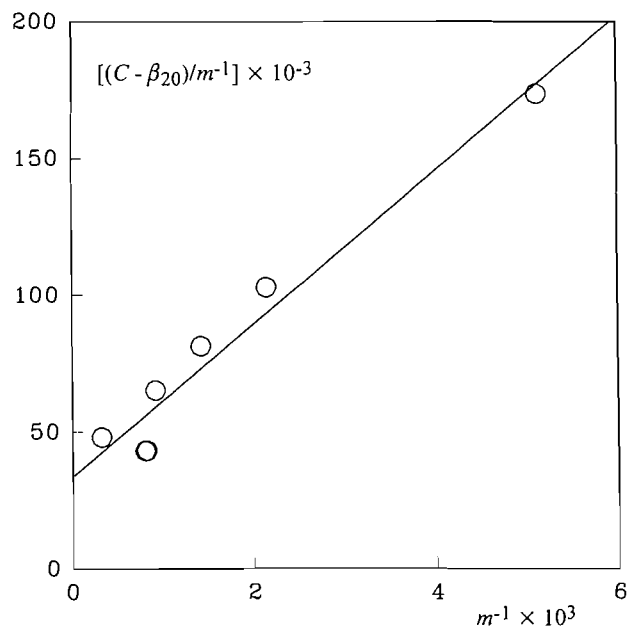

value of the stability constant of the complex $[Pb(V)]^+$ will be obtained:

$$\beta_{01} = (3.7 \pm 0.2) \times 10^4$$

Determination of the β_{02} and β_{11} constants

Taking into account that β_{20} is known, and that the coefficient C is defined by

$$C = \beta_{20} + \beta_{11}\, m^{-1} + \beta_{02}\, m^{-2}$$

the plot of the function $(C - \beta_{20})/m^{-1}$ vs. m^{-1} will determine a straight line with the ordinate in the origin β_{11} and the slope β_{02}.

Figure 5 shows the above-mentioned dependence, which by least squares allows the formation constant of the complexes $[Pb(V)_2]$ and $[Pb(HV)(V)]^+$ to be determined as: $\beta_{02} = (2.8 \pm 0.3) \times 10^7$ and $\beta_{11} = (3.3 \pm 0.6) \times 10^4$.

Discussion

This is the first experimental confirmation of the stabilization of the complexes $[Pb(HV)]^{2+}$, $[Pb(HV)_2]^{2+}$, and $[Pb(HV)(V)]^+$.

Fig. 6. Distribution curves of the lead–valine complexes as a function of pH.

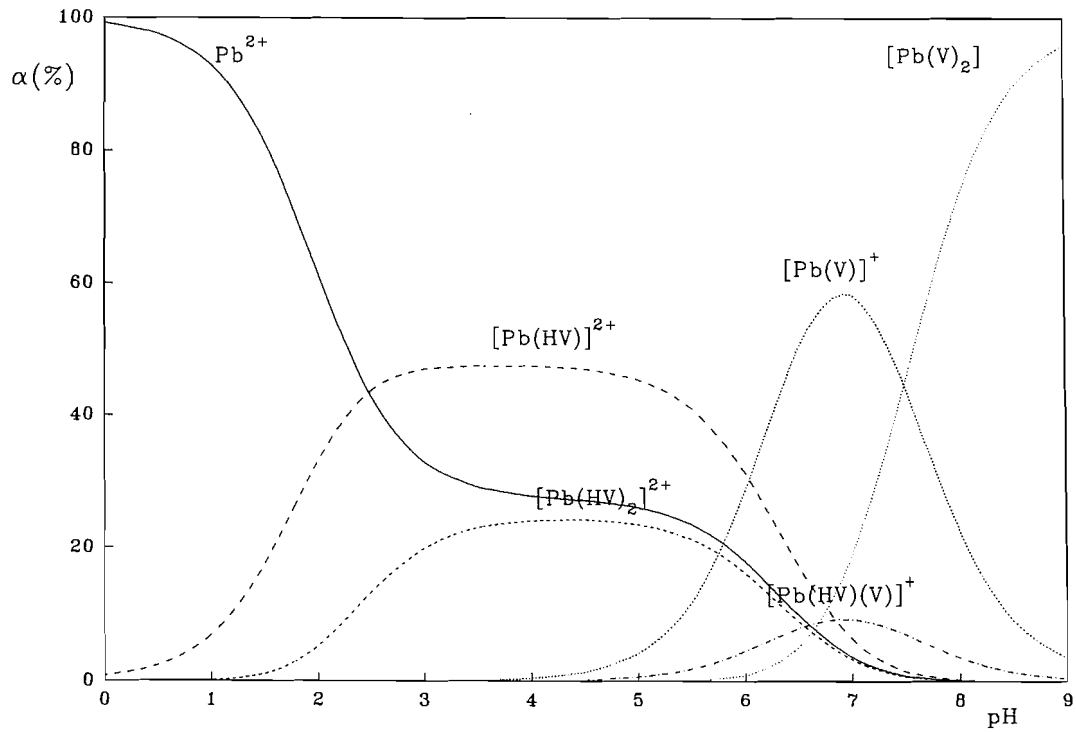

Table 3. Coefficients of the polynomial $F_{00} = 1 + B[HV] + C[HV]^2$.

Set	pH	$m^{-1} \times 10^6$	B	C
1	4.16	3.467	10.70 ± 0.3	25.26 ± 3
2	4.17	3.548	8.446 ± 0.2	35.13 ± 3
3	4.22	3.981	9.807 ± 0.4	22.68 ± 4
4	6.12	316.2	19.72 ± 1	42.92 ± 14
5	6.52	794.8	39.18 ± 2	62.01 ± 16
6	6.53	812.8	42.64 ± 2	62.86 ± 16
7	6.58	912.0	78.35 ± 5	87.27 ± 44
8	6.77	1413	61.04 ± 3	142.9 ± 24
9	6.95	2138	77.43 ± 3	248.1 ± 34
10	7.33	5122	201.2 ± 5	916.4 ± 45

A comparison is only possible with the theoretical value from the equations of Watters and Dewitt (10) using the constants of the simple complexes and from purely statistical considerations: $\beta_{11} = 2\ \beta_{20}^{1/2} \cdot \beta_{02}^{1/2} = 2.8 \times 10^4$. This is in remarkable agreement with the experimental value, $\beta_{11} = 3.3 \times 10^4$.

In relation to the stability constants of the species with one and two valinate ligands, $\beta_{01} = 3.7 \times 10^4$ and $\beta_{02} = 2.8 \times 10^7$, they are of the order of those obtained by Rao and Subrahmanya (4): $\beta_{01} = 1.58 \times 10^4$ and $\beta_{02} = 7.8 \times 10^7$.

In Table 4, the constants obtained in this work are compared with those previously determined for the coordinated system Pb(II)–alanine – alaninate ion (6). A marked parallelism can be observed in the stability of the complexes $[Pb(HX)]^{2+}$, $[Pb(HX)_2]^{2+}$, and $[Pb(X)]^+$, a little higher for those of alanine than the others.

Table 4. Stability constants of Pb(II)–alanine and Pb(II)–valine systems.

System	β_{10}	β_{20}	$\beta_{01} \times 10^{-4}$	$\beta_{02} \times 10^{-7}$	$\beta_{11} \times 10^{-4}$
Pb(II)–alanine	13	25	3.8	6.7	10
Pb(II)–valine	9.7	28	3.7	2.8	3.3

Figure 6 shows the distribution in percentages as a function of the pH for the solution: ($C_{Pb} = 1.0 \times 10^{-4}$ M; $A_T = 0.18$ M).

Acknowledgement

The authors wish to acknowledge financial support for this work from the Consejería de Educación de la Comunidad Autónoma Canaria.

We are grateful to the Spanish Ministry of Education for financial support for J. Castro Macías.

References

1. H.C. Freeman. *In* Inorganic biochemistry. *Edited by* G.E. Eichhorn. Elsevier, Amsterdam. 1973. p. 121.
2. T. Alemdaroglu and G. Berthon. Bioelectrochem. Bioenerg. **8**, 49 (1971).
3. J.C. Rodríguez Placeres, M. Barrera, R.M. Fernández, and A. Arévalo. J. Electroanal. Chem. **169**, 69 (1984).

4. G.N. Rao and R.S. Subrahmanya. Proc. Indian Acad. Sci. **60**, 185 (1964).
5. S. Singh, B.R. Rani, M. Vyas, and K.L. Yadava. Chim. Scr. **26**, 363 (1986).
6. J.C. Rodríguez Placeres, J. Castro Macías, M. Lemus Sánchez, and T.M. Borges Miquel. Collect. Czech. Chem. Commun. **56**, 1200 (1991).
7. J. Castro Macías. Thesis. University of La Laguna, Tenerife (1996).
8. W.B. Schaap and D.L. McMasters. J. Am. Chem. Soc. **83**, 4699 (1961).
9. M.M. Ramel and M.R. Paris. Bull. Soc. Chim. Fr. **4**, 1359 (1967).
10. J.I. Watters and R. Dewitt. J. Am. Chem. Soc. **82**, 1333 (1960).

Quantitative elemental and structural analysis of dissolved organic carbon fractions from lakes near Sudbury, Ontario

Roy Carl Boerschke, Elizabeth Ann Gallie, Nelson Belzile, Richard Neville Gedye, and James Robert Morris

Abstract: Dissolved organic carbon (DOC) was quantitatively isolated as five separate fractions from two Sudbury area lakes (Ontario, Canada) using the tandem XAD-8/XAD-4 resin technique. Fulvic acids made up ≈48% of the total, humic acids ≈8%, hydrophobic neutrals ≈8%, XAD-4 acids ≈11%, and XAD-4 acetonitrile extracts ≈13%. Hydrophobic:hydrophilic ratios were about 65:35. Solid-state CPMAS ^{13}C NMR indicated a primarily aliphatic nature in all fractions. Percent aromaticity was in the order humic acids > fulvic acids > XAD-4 acetonitrile extracts ≈ XAD-4 acids ≈ hydrophobic neutrals. Titration analysis showed that the ^{13}C NMR peaks of fulvic acids, humic acids, and XAD-4 acids from 160–190 ppm were primarily carboxyl in nature. The XAD-4 acids were the most acidic, suggesting that they may be important geochemical agents. ^{13}C NMR indicated that polysaccharides formed <20% of any fraction. The two neutral fractions (hydrophobic neutrals and XAD-4 acetonitrile extracts) had relatively high N contents, possibly due to the acetonitrile used to extract them. However, the ^{13}C NMR spectra did not show significant quantities of acetonitrile. The elemental and structural composition covaries in the three acid fractions, such that if one acid is enriched or depleted, so are the others. This suggests that the humic and non-humic acids form a continuum in which all fractions are affected by the same formative processes. Compared to published data for other freshwater samples, the three acid fractions from the Sudbury area lakes have low or very low aromaticity. This may indicate that the acid and metal loadings in the Sudbury area have affected the structure of the organic acids, despite the circumneutral character of the study lakes. These are the first quantitative ^{13}C NMR results published for the hydrophobic neutrals and XAD-4 acetonitrile extracts, so comparisons are not possible.

Key words: aquatic DOC, organic acids, ^{13}C NMR, humic substances, non-humic substances.

Résumé : Le carbone organique dissous a été isolé de façon quantitative en cinq fractions distinctes à partir de deux lacs de la région de Sudbury (Ontario, Canada), en utilisant le tandem de résines XAD-8/XAD-4. Les acides fulviques forment ≈48% du total, les acides humiques ≈8%, les hydrophobiques neutres ≈8%, les acides XAD-4 ≈11% et l'extrait acétonitrile de résine XAD-4 ≈13%. Les rapports hydrophobiques:hydrophiliques sont respectivement de 65:35 et 62:38 pour les lacs Ramsey et Nepewassi. Les analyses RMN ^{13}C CPMAS montrent que toutes les fractions ont une nature principalement aliphatique. Les pourcentages d'aromaticité se situent dans l'ordre suivant : acides humiques > acides fulviques > extrait acétonitrile XAD-4 ≈ acides XAD-8 ≈ hydrophobiques neutres. L'analyse par titrage a démontré que les pics RMN ^{13}C des acides fulviques, humiques et XAD-4 de la région 160–190 ppm sont principalement carboxyliques. Les acides XAD-4 étaient les plus acides ce qui suggère qu'ils puissent être des agents géochimiques importants. L'étude RMN ^{13}C indique aussi que les polysaccharides forment <20% de toutes les fractions isolées. Les deux fractions neutres (les hydrophobiques neutres et l'extrait acétonitrile de résine XAD-4) ont montré des contenus en azote relativement élevés possiblement reliés à l'acétonitrile utilisé pour les extraire. Cependant, les spectres RMN ^{13}C n'ont montré aucune quantité significative de ce produit. Les compositions élémentaire et structurelle covarient dans les trois fractions acides de telle sorte que si un des acides est enrichi ou déficient, les autres le sont aussi. Cela suggère que les acides humiques et non-humiques forment un continuum dans lequel toutes les fractions se trouvent affectées par les mêmes processus de formation. En comparant avec les données publiées sur d'autres échantillons d'eau douce, on constate que les trois fractions acides des lacs de la région de Sudbury affichent de basses ou très basses aromaticités. Cela pourrait indiquer que les déversements d'acide et de métaux dans cette région ont pu affecter la structure des acides organiques et ce, malgré le caractère neutre des lacs étudiés. Puisque les résultats sur l'analyse quantitative RMN ^{13}C sur les hydrophobiques neutres et l'extrait acétonitrile XAD-4 sont les premiers à être publiés, la comparaison avec d'autres milieux n'est pas possible.

Mots clés : carbone organique dissous, acides organiques, RMN ^{13}C, matières humiques, matières non-humiques.

Received April 15, 1996.

R.C. Boerschke,[1] E.A. Gallie,[2] N. Belzile, R.N. Gedye, and J.R. Morris. Laurentian University, Sudbury, ON P3E 2C6, Canada.

[1] Present address: Department of Chemistry and Geochemistry, Colorado School of Mines, Golden, CO 80401, U.S.A.

[2] Author to whom correspondence may be addressed. Telephone: (705) 675-1151, ext 2349. Fax: (705) 673-6508. E-mail: agallie@nickel.laurentian.ca

Introduction

Dissolved organic carbon (DOC) is an ubiquitous and pivotal component of aquatic ecosystems. Recognized as a major reservoir of carbon, DOC plays an important role in many physical, chemical, and metabolic processes occurring in water. Whether acting as a food source for bacteria and microorganisms (1), providing mechanisms for the mobilization of metals and organic pollutants and mediating their effects (2–5), or performing a number of other biological or geochemical functions (6), DOC has been identified as a major player in natural processes.

To understand the role DOC plays in aquatic environments, it is necessary to be concerned with the character of its component molecules. DOC in aquatic environments can range from simple compounds such as CH_4 to high molecular weight polymers, and may contain functional groups ranging from hydrocarbons to complex multifunctional compounds (7). However, DOC consists primarily of a complex mixture of organic acids, along with small amounts of bases and neutral compounds (8).

In general, DOC can be divided into six fractions: hydrophilic acids, bases, and neutrals; and hydrophobic acids, bases, and neutrals (9). The hydrophobic acids, which are composed of fulvic and humic acids, make up the humic substances. All other fractions are considered non-humic. Humic substances have been intensively studied. Forming the largest fraction of the DOC, humic substances have been reported to constitute from 40 to 60% (10) to as high as 60–80% (2) of total carbon present.

Many studies on the characterization of aquatic humic substances involve degradative and non-degradative techniques. Degradative methods, including oxidative and reductive degradations (11, 12), hydrolysis (13), and pyrolysis (14, 15) have all been used with some success to elucidate the molecular structure of humic substances. Non-degradative methods such as fluorescence and ultraviolet spectroscopy (16) and infrared spectroscopy (17) have shown limited utility in the determination of humic substance structure. Elemental analysis provides the elemental composition of humic substances, from which the sources of DOC can be inferred from C/H, C/N, and O/C ratios (18). Unfortunately, use of these traditional techniques provides primarily qualitative results concerning the character of humic substances.

Recently, carbon-13 nuclear magnetic resonance (^{13}C NMR) has become a valuable non-degradative approach in the characterization of humic substances. Analysis using ^{13}C NMR has shown that distinct differences in structure exist between humic substances isolated from different environments (19, 20). Furthermore, if determinations employ favourable T_{CP} (cross-polarization time), T_{1P} (proton relaxation time) constants, and repeat times, and if any organic free radicals and (or) inorganic paramagnetic species in the sample are identified, then quantitative evaluation of the spectra is possible (21). The importance of quantitative spectra is that they allow for valuable structural relationships to be determined, from which the origin of the humic fractions can be inferred.

The study of non-humic DOC has not been as extensive. Although some work has been done on the fractional distribution of DOC (22–24), little information concerning the structural characterization of the non-humic DOC is available.

Table 1. Physical and chemical characteristics for Ramsey Lake[a] and Nepawassi Lake (26).

Characteristic	Ramsey Lake	Nepawassi Lake
Area (ha)	795.0	1125.0
Maximum depth (m)	20.5	39.0
pH	7.5	6.9
Conductivity (μS/cm)	305.0	53.3
TIP alkalinity (mg/L)	26.5	8.4
Calcium (mg/L)	15.5	4.6
Magnesium (mg/L)	4.5	1.8
Sodium (mg/L)	n/a	1.4
Potassium (mg/L)	1.5	0.8
Sulphate (mg/L)	21.3	11.4
Silica (mg/L)	0.5	1.2
Chloride (mg/L)	59.8	1.1
Total Kjeldahl *N* (μg/L)	420.0	340.0
Ammonium (μg/L)	18.0	12.0
Nitrite (μg/L)	5.0	2.0
Nitrate (μg/L)	15.0	10.0
Total phosphorus (μg/L)	15.0	11.0
Soluble phosphorus (μg/L)	8.0	1.0
Zinc (μg/L)	7.4	5.0
Copper (μg/L)	17.0	4.7
Nickel (μg/L)	92.0	8.3
Iron (μg/L)	14.0	123.0
Aluminum (μg/L)	12.0	35.7
Manganese (μg/L)	8.2	29.7

[a]Ontario Ministry of the Environment and Energy, unpublished data, 1993.

Thus the purposes of this study were: (*i*) to isolate DOC quantitatively from two lakes near Sudbury, Ontario, (*ii*) to fractionate the DOC into its major humic and non-humic components, and (*iii*) to characterize all fractions quantitatively using elemental analysis and solid-state cross-polarization magic angle spinning (CPMAS) ^{13}C NMR. This information will broaden the base of data on DOC from different environments, in particular Canadian environments, and will add fundamental structural information for three non-humic fractions on which little has been published.

Materials and methods

Samples for the study were collected from two lakes near Sudbury, Ontario. Both lakes fall within the Sudbury deposition zone, an area of high anthropogenic sulphate loading (25), but they have not been strongly acidified due to local natural buffering. Ramsey Lake (46°29′N, 80°57′W), a mesotrophic lake located in the centre of Sudbury, covers an area of approximately 795 ha. It has a maximum depth of 20.5 m and a pH of 7.5 (Table 1). Ramsey Lake is primarily spring fed. Primary allochthonous sources of DOC are wetland outflow on the southern and eastern ends of the lake. The balance of Ramsey Lake's watershed is urbanized.

Nepewassi Lake (46°22N, 80°38W), a mesotrophic lake located approximately 40 km southeast of Sudbury, covers an area of 1125 ha. It has a maximum depth of 39 m and a pH of 6.9 (Table 1). Nepewassi Lake has one major and several

minor inflowing tributaries. Roughly 20% of the lake is surrounded by wetlands, with the balance of the lake being encompassed by recreational properties and forest.

Bulk water samples were collected over a 2 week period from November 8 to 25, 1993. This period was about 1 month after fall overturn had begun. Water samples were collected from a depth of approximately 1 m using a manual bilge pump. Immediately upon arrival at the lab, samples were filtered using 0.45 μm Gelman Supor 450 membrane filters, and acidified to pH 1.9 using 1.0 M HCl.

Tandem XAD-8/XAD-4 resin setup

Two 5.3 L columns, containing Rohm and Haas XAD-8 and XAD-4 resins, respectively, were set up. The predicted capacity factor for these columns for $k' = 50$ was determined to be 150 L. Columns were eluted and regenerated after passage of each 150 L batch.

The previously filtered, acidified water was pumped first onto XAD-8 resin at a rate of 400 mL/min. The XAD-8 resin adsorbed the fulvic acids, humic acids, and hydrophobic neutrals. Effluent from the XAD-8 resin was collected in a reservoir before being pumped onto the XAD-4 resin at 400 mL/min. The XAD-4 resin adsorbed most of the remaining DOC (XAD-4 acids and XAD-4 acetonitrile extracts). Hydrophobic and hydrophilic bases, and some hydrophilic neutrals passed through both the XAD-8 and XAD-4 resins and were discarded.

The humic and fulvic acids were eluted from the XAD-8 resin, and the XAD-4 acids from the XAD-4 resin, with dilute 0.1 M NaOH. Humic and fulvic acids were separated by acidification to pH 1 followed by centrifugation. All three fractions were then protonated by cation exchange, vacuum-concentrated, and freeze-dried. Following this, the hydrophobic neutrals were extracted from the XAD-8 resin, and the XAD-4 acetronitrile extracts from the XAD-4 resin, by processing each resin separately with acetonitrile and water in a Soxhlet apparatus for 2 days. These two fractions were also vacuum-concentrated and freeze-dried. All the detailed steps and recommendations of previous researchers were followed (10, 24).

DOC analysis

For each 150 L batch, samples of the filtered unacidified and filtered acidified water were taken to determine initial DOC values. Samples of the effluent from both the XAD-8 and the XAD-4 resins were taken at 25 L intervals from 0 L to 150 L to determine quantitatively the DOC adsorbed by each resin. The ratio of hydrophobic:hydrophilic DOC was also determined through adsorption on the XAD-8 resin, with hydrophobic DOC considered to be the fraction that was adsorbed to the XAD-8 resin.

Following the cation exchange phase for the humic acids, fulvic acids, and XAD-4 acids, samples of each fraction (for all batches combined) were taken to quantitatively determine the relative percentage of each DOC fraction. The relative percentage of each DOC fraction was also calculated after freeze-drying to determine losses incurred during isolation.

DOC analysis was done using an automated Oceanographic International Carbon Analyzer. The carbon analyzer was standardized for a range of 0.1 to 10.0 mgC/L, with sample accuracy ±0.03 mgC/L using potassium acid phthalate and fulvic acid standards. Sample precision was ±0.02 mgC/L determined with standards run every tenth sample.

Elemental analysis

Analyses of C, H, O, N, S, P, and ash were conducted by Huffman Laboratories, Inc., Golden, Colorado. All analyses were carried out using direct methods of determination. Carbon and hydrogen were determined through sample combustion at 1000°C in oxygen, producing carbon dioxide (CO_2) and water (H_2O), respectively. CO_2 was measured using a Coulometrics model 5010 detector. H_2O was quantitatively exchanged with CO_2, by passage through 1,1-carbonyldiimidozole, which was then measured using a second coulometer. Nitrogen was ascertained using a Carlo Erba N 1500 analyzer, which employed a Dumas method with thermal conductivity detection (TCD). Oxygen was resolved using a Coulometrics model 5060 oxygen analyzer, utilizing the Unterzaucher method and a Coulometrics model 5010 for detection. Sulphur was measured using a Leco model SC 132 sulphur analyzer. Ash was determined through oxidation of the sample in a furnace until a constant weight was obtained. Phosphorus was measured by Inductively Coupled Plasma–Atomic Emission Spectrometry.

NMR spectra

The solid state CPMAS ^{13}C NMR analyses were performed by the U.S. Geological Survey, Denver, Colorado. Spectrometer frequency for the ^{13}C NMR was 50.30 MHz, 90 degree pulse width of 4.50 s, contact time of 1.00 ms, pulse delay of 1.00 s, sweep width of 30.030 kHz, and 1000 scans were collected for each spectrum. Optimum contact and relaxation times were determined prior to ^{13}C NMR analysis being performed.

The percent carbon in each shift range was determined by planimetering the areas under the curve three times and averaging. Percent aromaticity was determined using (19):

$$[1] \quad fa_1 = \frac{\text{Area of 110–160 ppm}}{\text{Total Area}} \times 100$$

Titrations

Titrations to estimate the concentration of carboxyl groups were performed with an automated Radiometer titrator. Samples were titrated twice and results averaged. The titer to pH 8 was assigned solely to carboxyl groups (27).

Results and discussion

Dissolved organic carbon

Initial DOC values determined immediately after filtration indicated an average of 5.53 mgC/L for Ramsey Lake and 7.84 mgC/L for Nepewassi Lake. Analysis of effluent from the XAD-8 resin indicated that an average of 3.59 mgC/L and 4.86 mgC/L was adsorbed to the resin from Ramsey and Nepewassi lakes, respectively. Because XAD-8 removes all the hydrophobic DOC, the ratio of hydrophobic:hydrophilic was 65:35 in Ramsey Lake and 62:38 in Nepewassi Lake, values that are probably not significantly different. (Hydrophobic bases, which do not sorb to either XAD-8 or XAD-4 resin, usually make up only 1–2% of the total DOC (24).) From the DOC remaining in the XAD-8 effluent, XAD-4 resin adsorbed a further 1.27 mgC/L and 2.27 mgC/L of hydrophilic material from

Table 2. DOC fraction by weight, elemental composition, atomic ratios, and ash content of DOC fractions isolated from Ramsey Lake and Nepewassi Lake. Elemental composition is corrected for ash content.

Isolate	% of DOC	%C	%H	%O	%N	%S	%P	C/N	C/H	O/C	%Ash
Ramsey Lake											
Fulvic acids	48	53.01	4.63	40.45	1.32	0.81	0.01	46.9	0.95	0.57	0.89
Humic aids	8	53.76	4.60	38.94	2.36	1.02	0.05	26.6	0.97	0.54	2.78
HPO neutrals	9	50.57	7.23	34.90	5.17	5.39	0.02	11.4	0.59	0.52	8.42
XAD-4 acids	10	48.47	4.56	42.76	2.45	0.95	0.01	23.1	0.89	0.66	4.87
XAD-4 ace ex.	13	54.46	6.60	33.68	5.44	0.47	0.03	11.7	0.67	0.46	3.31
Nepewassi Lake											
Fulvic acids	48	53.61	4.57	40.14	1.08	0.64	0.01	57.9	0.98	0.56	1.54
Humic acids	7	54.85	4.66	39.33	1.77	0.86	0.02	36.2	0.98	0.54	3.79
HPO neutrals	7	n/a	n/a	n/a	n/a	n./a	n/a	n/a	n/a	n/a	14.66
XAD-4 acids	11	49.18	4.52	43.22	2.02	0.67	0.01	28.4	0.91	0.66	5.14
XAD-4 ace ex.	18	52.56	6.48	32.12	5.95	1.25	0.01	10.3	0.68	0.46	4.92

Ramsey Lake and Nepewassi Lake, respectively. The remaining 12% of the DOC or about 0.67 mgC/L from Ramsey Lake, and 9% or 0.71 mgC/L from Nepewassi Lake, were discarded. The material discarded was assumed to be mostly bases and hydrophilic neutrals, though some acids may have been present (28).

DOC was isolated as five major fractions: fulvic acids, humic acids, hydrophobic neutrals, XAD-4 acids (sometimes called hydrophilic acids or low-molecular-weight acids), and XAD-4 acetonitrile-removed substances (hereafter referred to as XAD-4 ace extracts). Fulvic acids constitute the largest fraction of the DOC in both lakes (48%) (Table 2). The ratio of fulvic acid to humic acid is 6:1 and 7:1 in Ramsey and Nepawassi lakes, respectively. The ratio for an average of about 100 rivers in the United States is 9:1 (10). However, there is a trend to lower ratios as one moves north into more DOC-rich, organically coloured waters (10), and values as low as 2.5:1 are reported for some Scandanavian lakes (24).

Hydrophobic neutrals are one of the smallest fractions of DOC in the study lakes (Table 2). Published data on hydrophobic neutrals are scanty, but may indicate a trend toward a higher proportion in more northerly lakes. The average percentage in 100 U.S. rivers is 6% (10), in the study lakes it is 7–9%, and in Lake Skjervatjern in Norway it is 9–11% (24).

XAD-4 acids commonly make up 20–25% of freshwater DOC (10, 24, 28). However, in the study lakes, XAD-4 acids make up only 10–11%. There are other freshwaters with documented percentages as low or lower (Yakima River, Wash., U.S.A. at 8–12%; two Antarctic lakes at 7–9%), but these waters also all had much lower fulvic acid percentages (23–26%) (28). Until more data are available for comparison, it is difficult to know how to interpret the difference.

The XAD-4 ace extracts made up 13–18% of the DOC in the study lakes, and 9–12% of the DOC was not captured on either resin. Presumably these final two components are largely made up of non-elutable low-molecular-weight acids, hydrophilic neutrals, and bases. Malcolm (10) indicates that hydrophilic neutrals make up 15% and bases 4% of freshwater DOC, on average, in U.S. rivers. In Lake Skjervatjern, the XAD-4 ace extracts and the lost DOC together made up 13–15% of the total. However, there is no information available for the XAD-4 ace extracts alone.

Elemental and ^{13}C NMR analyses

Fulvic Acid

The elemental composition of fulvic acids is similar in both study lakes (Table 2) and is consistent with fulvic acids from other freshwater sources (Table 3). Of the five fractions isolated, fulvic acids have the lowest N content, giving them the highest C/N ratio. They also have the lowest ash content (Table 2).

The ^{13}C NMR spectra for fulvic acids show the four major peaks and three minor peaks common to lake and stream fulvic acids (29) (Fig. 1; Table 4). The largest peak for fulvic acids is aliphatic carbon (0–62 ppm), accounting for approximately 43% of the total carbon. (The main chemical shift assignments used to interpret the ^{13}C NMR spectra are given in Table 5.)

Aliphatic carbons singly bonded to oxygen or nitrogen (62–90 ppm) are considered to be mainly C-O because of the low N content. Polysaccharides, which have major peaks in this region, may account for the majority of the carbon present in this shift. This suggestion is based on the size of the anomeric peak (90–110 ppm), which can be used to estimate roughly the polysaccharide or carbohydrate-like fraction (19, 30). Up to half the anomeric peak is assumed to result from the C_1 anomeric carbon of polysaccharides (R. Malcolm, personal communication). The total carbon due to polysaccharides is then six times this amount, while the C-O carbon due to polysaccharides is five times this amount (29). These calculations suggest that polysaccharides make up <15% of the total carbon in fulvic acids in Ramsey and Nepawassi lakes, and about two-thirds of the C-O carbon. Any remaining carbon in the C-O region is probably a variety of alcohol and ether carbons. A significant contribution from free saccharides is unlikely given the XAD-8 isolation procedure (29).

Titration analysis to pH 8 used 5.8 and 5.5 mequiv./g for

Table 3. Comparison of elemental composition (ash free), atomic ratios, and ash content from Ramsey Lake and Nepewassi Lake with those from other studies.

Sample	%C	%H	%O	%N	%S	C/N	C/H	O/C	%Ash
				Fulvic acids					
Ramsey Lake	53.0	4.6	40.5	1.3	0.8	46.9	0.95	0.57	0.9
Nepewassi Lake	53.6	4.6	40.1	1.1	0.6	57.9	0.98	0.56	1.5
Skjervatjern Lake (21)	54.7	4.0	38.5	0.7	0.3	92.5	1.14	0.53	0.1
Suwannee River (16)	53.8	4.3	40.5	0.7	0.5	92.2	1.04	0.56	0.8
IHSS Nordic Ref. (16)	48.7	3.4	45.9	0.9	1.1	63.3	1.19	0.71	0.4
Yakima R, Kiona (28)	56.1	4.95	35.5	2.2	1.0	29.8	0.94	0.47	1.1
Yakima R, CleElum (28)	57.2	4.9	35.9	1.0	0.6	66.7	0.97	0.47	8.5
Lake Fryxell (28)	55.0	5.5	34.9	3.1	1.3	20.7	0.83	0.48	1.0
				Humic acids					
Ramsey Lake	53.8	4.6	38.9	2.4	1.0	26.6	0.97	0.54	2.8
Nepewassi Lake	54.9	4.7	39.3	1.8	0.9	36.2	0.98	0.54	3.8
Skjervatjern Lake (21)	56.6	3.5	35.5	1.2	0.5	53.2	1.01	0.48	1.3
Suwannee River (16)	54.2	4.1	39.0	1.2	0.8	52.3	1.09	0.54	3.2
IHSS Nordic Ref. (16)	50.7	3.5	43.3	1.6	0.9	37.3	1.21	0.64	0.9
				XAD-4 acids					
Ramsey Lake	48.5	4.6	42.8	2.5	1.0	23.1	0.89	0.66	4.9
Nepewassi Lake	49.2	4.5	43.2	2.0	0.7	28.4	0.91	0.66	5.1
Yakima R, Kiona (28)	50.5	4.4	40.6	3.0	1.2	19.6	0.96	0.60	3.9
Yakima R, CleElum (28)	52.2	4.6	40.8	1.5	0.6	40.6	0.95	0.59	3.1
Lake Fryxell (28)	49.3	4.8	39.2	4.8	1.8	12.0	0.86	0.60	8.9

Ramsey Lake and Nepewassi Lake, respectively. This indicates that carboxyl groups account for about 13% of total carbon and the majority of the carboxyl and ester carbon (160–190 ppm).

The diverse spectra in the ketonic regions (190–230 ppm) is indicative of a variety of aromatic and aliphatic ketones. The ketonic peak is weak but distinct, similar to other lake (29) and stream fulvic acids (19).

Percent aromaticity for the lakes was approximately 15% for fa_1. This falls at the low end of the range of 16–25% for streams (average 21%) (28, 29), and is comparable to data from an alpine oligotrophic lake with fa_1 of 17% (29).

Humic acids

Humic acids from Ramsey and Nepawassi lakes have a similar elemental composition (Table 2), although the Ramsey Lake humic acids have a slightly higher N and P content, possibly related to this urban lake's slightly more productive nature (Table 1). The humic acids are consistent with humic acids from other lakes (Table 3). The humic acids resemble the fulvic acids in many ways. However, the N and ash contents are higher, and the C/N ratio is lower. This is illustrated in Fig. 2 where the points plot above the 1:1 line for %N and ash, and below for the C/N ratio, for both the study lakes and the comparison lakes (16, 21). Figure 2 also illustrates that the elemental composition of fulvic acid covaries with the composition of humic acid. This is not surprising if one accepts that humic and fulvic acids form a continuum, operationally divided into two arbitrary fractions. Thus the processes affecting the composition of one may well affect the composition of the other.

Three significant differences can be seen in the ^{13}C NMR spectra between the humic and fulvic acids (Fig. 1; Table 4). The first difference is the increased resolution in the 0–50 ppm region in humic acids. The sharp peaks at 28 and 40 ppm suggest that terminal methyl and methylene groups in alkyl chains are important compositional features of humic acids.

The second difference is the presence of a methoxyl peak (50–62 ppm). Methoxyl groups appear to be present in all freshwater humic acids (29). They account for about 8% of the carbon present in Ramsey and Nepewassi lake humic acid samples.

The final difference is an increase in the percent aromaticity of humic acids to about 21% (Table 4). This increase is due in part to a pronounced peak for phenolic aromatic carbon (140–160) that is present only as a weak shoulder in the fulvic acids. A phenolic aromatic peak is a signature of stream and lake humic acids (29). In the study lakes, the peak is well resolved, though the total carbon represented (≈5%) is lower than reported for other lakes (29). The overall aromaticity of the Ramsey and Nepawassi humic acids ($fa_1 \approx$ 21%) is much lower than occurs in one alpine oligotrophic lake ($fa_1 \approx$ 37%: (29)) and lower than in rivers where fa_1 averages 34% (range 30–35%) (29). However, there is very little literature published on lakes so it is difficult to know how to interpret the difference.

The ^{13}C NMR spectra for C-O groups (62–90 ppm) and anomeric carbon (90–110 ppm) demonstrate that polysaccharides do not make up a large fraction of humic acids (<15%), though they may account for virtually all of the C-O carbon. The small polysaccharide component is a point of difference from humic acid characterizations based on soil humates (29, 31).

Humic acid titrations to pH 8 used 4.2 and 4.3 mequiv./g for Ramsey and Nepawassi lakes, respectively. This indicates that humic acids are less acidic than fulvic acids, with carboxyl groups accounting for only about 10% of total carbon.

Hydrophobic neutrals

The hydrophobic neutrals differ in elemental composition and atomic ratios from the other fractions, especially with regard to nitrogen and sulphur contents (Table 2). However, they also have high ash contents[3] and, for Nepawassi samples especially, that introduced some uncertainty in the results and interfered with ^{13}C NMR analyses. For this reason, only the hydrophobic neutrals from Ramsey Lake will be discussed.

The hydrophobic neutrals and XAD-4 ace extracts both have relatively high N contents (Table 2). Since both are isolated from their respective resins using acetonitrile, the question arises whether some of the N could be an artifact of the extraction method. This could happen in two ways. First, it is possible that hydrolysis of the acetonitrile during the refluxing step could break some of the C≡N bonds in the acetonitrile and form ammonium ions (NH_4^+). The ammonium ions might then react with functional groups present in the hydrophobic neutrals, increasing nitrogen levels. A second possibility is that some residual acetonitrile remained in the fraction due to inadequate washing of the isolated hydrophobic neutrals with distilled water (32). Both acetonitrile and its breakdown products (acetic acid and acetamide) should reveal themselves in the ^{13}C NMR spectra. The peak where acetonitrile should fall (117 ppm) is very small. It accounts for <1% of total carbon, which if it were due to acetonitrile would correspond to <10% of the N in the hydrophobic neutrals. Peaks for the breakdown products, however, would be masked by other signals (e.g., amides at 173 ppm would be masked by carboxyl and ester carbons). Nevetheless, this suggests that the N in the hydrophobic neutrals may be a natural part of the material.

The sulphur content is more than five times higher in hydrophobic neutrals than in any other fraction (Table 2). The study lakes have elevated sulphate levels (Table 1) due to years of sulphate loading from local smelting operations. Although XAD-8 resins have no affinity for inorganic anions (28), it is possible that sulphates do not have time to diffuse out of the resins during the rapid elution process in which humic substances are removed. Later, during the longer extraction process in which hydrophobic neutrals are removed, sulphates may have time to escape (J.A. Leenheer, personal communication). Further research is needed on the extent to which elevated S is a contaminant or a real characteristic of hydrophobic neutrals in acidified lakes.

The ^{13}C NMR spectra reveal that the non-humic hydrophobic neutrals are quite different from the humic substances (Fig. 1, Table 4). Aliphatic chains play a more important role in hydrophobic neutrals. Related to the higher aliphatic content, the percent aromaticity is the lowest of all five materials examined, about one-half to one-third the aromaticity of the humic substances. The small quantity of anomeric carbon (90–110 ppm) indicates that polysaccharides form the smallest proportion (<10%) of the total carbon of any of the five materials. Equally, polysaccharides appear to account for less than a third of the carbon in the C-O shift (62–90 ppm). The remaining carbon in this shift could be ethers and alcohols, but may also be carbon singly bonded to N, whether such N is a natural com-

[3] The resins were desalted until conductivity fell below 30 μS/cm. Thus it seems unlikely that NaCl was a large component of the ash.

Fig. 1. Solid state CPMAS ^{13}C NMR spectra for humic fractions (fulvic acids, humic acids) and non-humic fractions (hydrophobic neutrals, XAD-4 acids, XAD-4 ace extracts) isolated from (*a*) Ramsey Lake and (*b*) Nepawassi Lake.

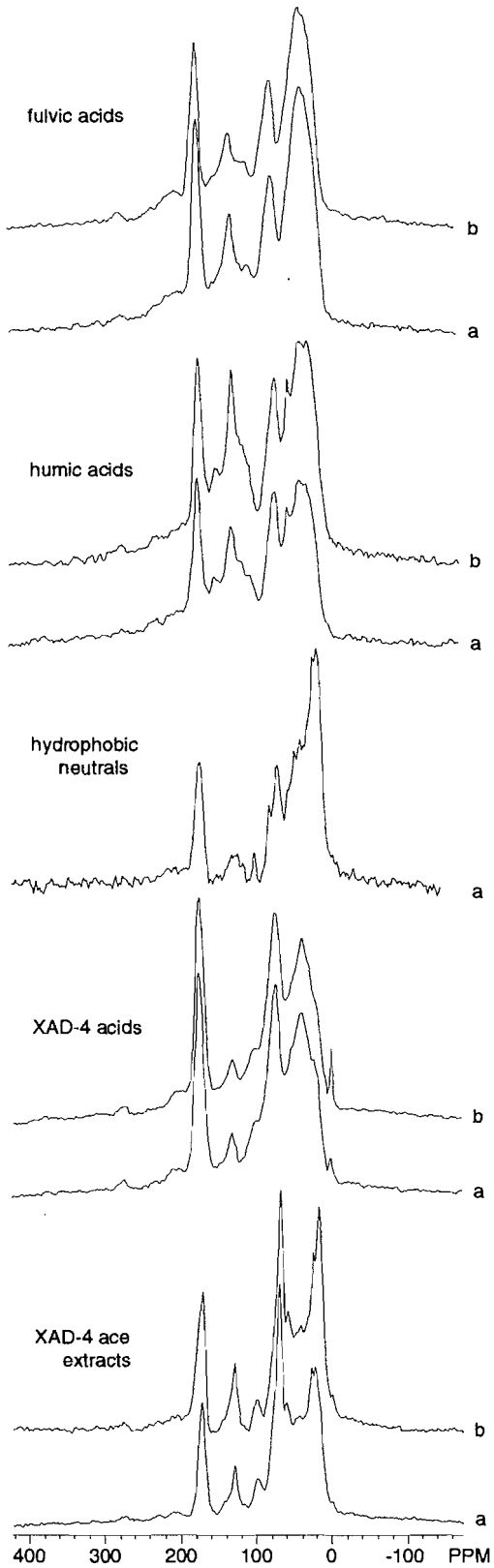

Table 4. Percentage of carbon associated with chemical shifts of ^{13}C NMR for DOC fractions isolated from Ramsey Lake and Nepewassi Lake. Data from Yakima River (28), the only other published data for XAD-4 acids, is included for comparison.

Shift (ppm)	Peak (ppm)	Assignment	Ramsey Lake	Nepewassi Lake	Yakima R Kiona	Yakima R CleElum
Fulvic acids						
00–62	38	Aliphatic	43.7	43.1	34.2	33.7
62–90	73	C-O	16.3	16.6	12.8	13.8
90–110	106	Anomeric	4.4	5.1	)	)
110–140	131	Aromatic	12.5	12.1	30.1	33.1
140–160		Phenolic	1.8	3.2	)	)
160–190	176	Carboxyl and ester	16.7	15.6	19.3	17.2
190–230		Ketonic	4.7	5.1	3.6	4.1
		fa_1 aromaticity	14.2	15.2		
Humic acids						
00–50	28, 40	Aliphatic	29.6	31.0		
50–62	57	Methoxyl	7.6	7.9		
62–90	75	C-O	15.8	15.1		
90–110	104	Anomeric	5.7	5.7		
110–140	130	Aromatic	15.0	16.9		
140–160	150	Phenolic	5.5	5.0		
160–190	175	Carboxyl and ester	16.2	14.2		
190–230		Ketonic	4.6	4.1		
		fa_1 aromaticity	20.6	21.9		
Hydrophobic Neutrals						
00–50	22, 27	Aliphatic	54.4			
50–62		Methoxyl	4.5			
62–90	72	C-O	15.9			
90–110	104	Anomeric	2.3			
110–140	130	Aromatic	5.4			
140–160		Phenolic	1.7			
160–190	175	Carboxyl and ester	11.9			
190–230		Ketonic	4.0			
		fa_1 aromaticity	7.1			
XAD-4 acids						
00–62	32	Aliphatic	39.8	38.4	32.0	30.5
62–90	70	C-O	24.7	24.8	18.0	20.5
90–110	98	Anomeric	6.1	6.5	}	}
110–160	130	Aromatic	7.7	7.9	} 23.4	} 22.1
160–190	175	Carboxyl and ester	19.1	19.9	22.8	21.0
190–230		Ketonic	2.5	2.6	3.8	5.8
		fa_1 aromaticity	7.7	7.9		
XAD-4 acetonitrile extracts						
00–50	18, 27	Aliphatic	38.6	43.2		
50–62	58	Methoxyl	8.7	6.6		
62–90	70	C-O	26.8	23.2		
90–110	100	Anomeric	4.6	3.0		
110–160	130	Aromatic	8.1	7.2		
160–190	170	Carboxyl and ester	11.7	13.7		
190–230		Ketonic	1.5	3.1		
		fa_1 aromaticity	8.1	7.2		

ponent or not. Finally, the carboxyl and ester peak (160–190 ppm) is smaller than for humics, and must be primarily esters since the material has a neutral character.

There are some similarities to humic acids. A weak shoulder from 50–62 ppm is attributed to methoxyl groups, and a very weak phenolic peak is discernable (140–160 ppm). Such features are charactersitic of freshwater humic acids and may characterize freshwater hydrophobic neutrals as well.

The authors are not aware of any published quantitative information on hydrophobic neutrals for comparison.

XAD-4 acids

The elemental composition of XAD-4 acids is similar in

Table 5. General chemical shift assignments for the CPMAS ^{13}C NMR spectra (19, 29).

Shift range (ppm)	Assignment
00 – 62	Short-chained and (or) highly branched aliphatic carbon.
00 – 50	Unsubstituted and saturated aliphatic carbon. Individual peaks are taken to indicate terminal methyl groups, and methylene and methine groups in alkyl chains.
50 – 62	Methoxyl (-OCH_3); aliphatic esters and ethers.
62 – 90	Aliphatic carbons singly bonded to oxygen or nitrogen; ring carbons of polysaccharides; alcohols and ether-bonded aliphatic carbon (C-O).
90 – 110	Anomeric carbon (carbon singly bonded to two oxygen atoms); C_1 anomeric carbon in polysaccharides.
110 – 140	Aromatic carbon with protonated functional groups (110–120 ppm) and unsubstituted and alkyl-substituted aromatic carbon (120–140 ppm).
140 – 160	Aromatic carbon substituted by oxygen or nitrogen; phenol.
160 – 190	Carboxyl carbon; ester carbon.
190 – 230	Aromatic and aliphatic ketones (C=O); aldehydes.

Fig. 2. Comparison of elemental content, ash content, and atomic ratios of fulvic acids vs. humic acids. The line on each graph is the 1:1 line. Triangles represent Ramsey and Nepawassi lakes. Squares represent data for Skjervatjern Lake (21), Suwannee River (16), and IHSS Nordic Reference (16). See Table 3 for more detail.

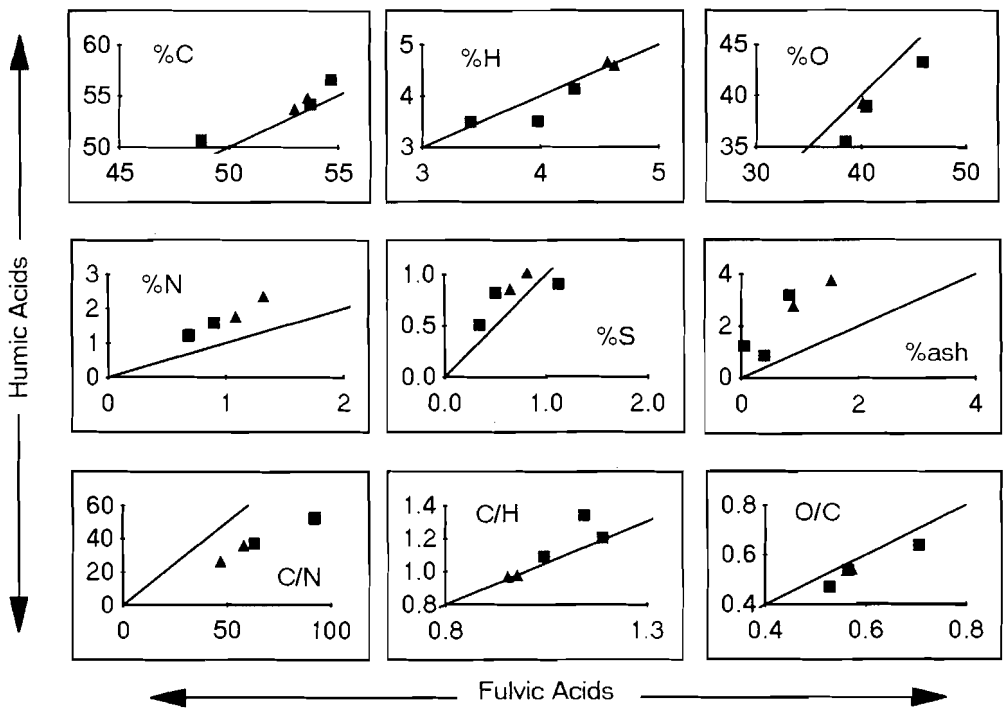

Nepewassi and Ramsey lakes (Table 2), though the Ramsey Lake acids have a slightly higher N content (again attributed to the slightly more productive conditions in Ramsey). Compared to other freshwater XAD-4 acids, those in the study lakes may have a slightly higher O content, but are similar with regard to other elements (Table 3).

The non-humic XAD-4 acids differ from fulvic acids in several ways. They have less C, and more O, N, and ash, and hence plot below and above the 1:1 line, respectively, in Fig. 3. This gives the XAD-4 acids consistently lower C/N ratios, and higher O/C ratios. The latter may imply either a higher carboxylic or polysaccharide content than in fulvic acids. Aiken et al. (28) is the only source of published data for comparison. Aiken et al. (28) found similar elemental differences between XAD-4 acids and fulvic acids in the Yakima River and Lake Fryxell, with one exception. They concluded that XAD-4 acids were enriched in S in comparison to fulvic acids, but our data do not confirm this (Fig. 3). The data in Fig. 3 also show that there is a strong covariance for most of the

Fig. 3. Comparison of elemental content, ash content, and atomic ratios of fulvic acids vs. XAD-4 acids. The line on each graph is the 1:1 line. Triangles represent Ramsey and Nepawassi lakes. Squares represent data for Yakima River at Kiona and Cle Elum (28) and Lake Fryxell (28). See Table 3 for more detail.

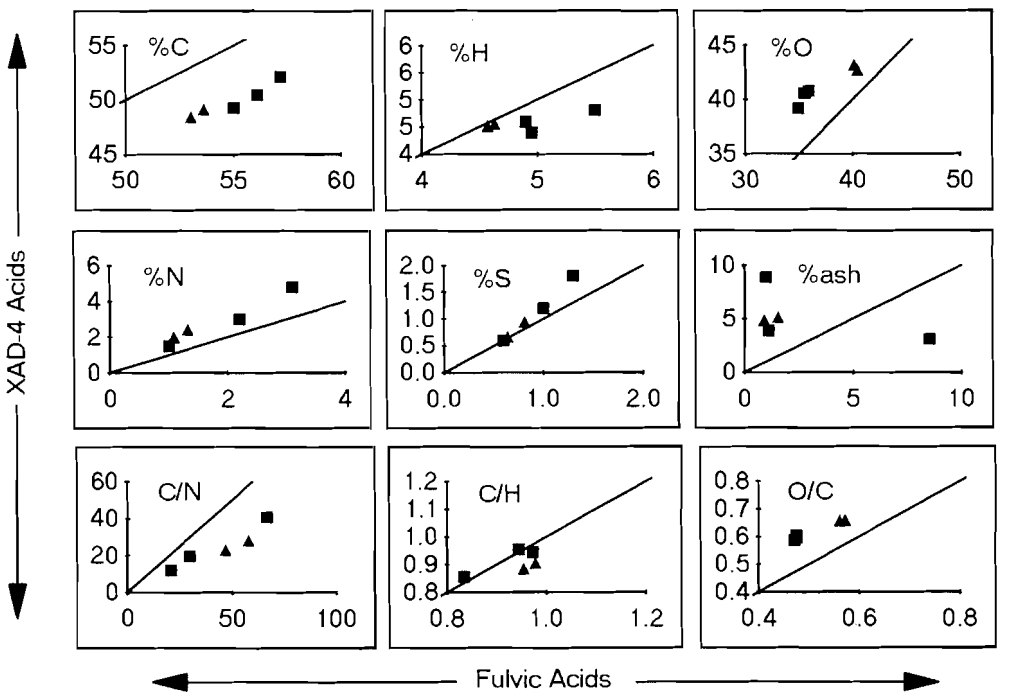

elements in fulvic acids and XAD-4 acids. This suggests that the non-humic components isolated on XAD-4 resin form a continuum with the humic substances, with similar formational processes affecting the composition of all.

The XAD-4 acids distinguish themselves in several ways in the ^{13}C NMR spectra (Fig. 1, Table 4). The anomeric region (90–110 ppm) is larger than in any of the other four fractions. Thus, polysaccharides probably form more of the total carbon (<20%) than in other fractions. In comparison to humic and fulvic acids, the fa_1 aromaticity is low, as with the other non-humic fractions. The carboxyl and ester region (110–160 ppm) is larger than in any other fraction. Titration analysis to pH 8 required 5.9 and 6.0 mequiv./g for Ramsey and Nepawassi lakes, respectively, indicating that approximately 15% of the total carbon and the major part of the carboxyl and ester carbon (110–160 ppm) were carboxyl in nature. Thus, the elevated O/C ratio mentioned above probably indicates both a higher saccharide and higher acidic content. Finally, the XAD-4 acids produce a distinct ketonic (190–230 ppm) peak, similar to fulvic acids.

The only published quantitative ^{13}C NMR spectra for XAD-4 acids are solution-state spectra for two samples from the Yakima River (28) (Table 4). The aromaticity of these samples is reported for the 90–160 ppm shift rather than as fa_1. The Ramsey and Nepawassi samples have much less carbon (about 14% vs. 23%) in the aromatic shift so defined. Thus it appears that all three acids from the study lakes are less aromatic than other freshwater samples. The decrease in aromaticity is offset by an increase in aliphatic carbon, and to a lesser extent heteroaliphatic (C-O) carbon, with little change in the proportion of carboxylic carbon.

Despite the difference described above, the Yakima River samples show the same structural differences between XAD-4 acids and fulvic acids as our data. That is, XAD-4 acids are less aromatic and aliphatic, but more heteroaliphatic (C-O) and carboxylic than fulvic acids from the same body of water (Fig. 4). Given that XAD-4 acids can compose up to 25% of the DOC (28), the acidic component is especially significant, and may contribute to an important geochemical role in weathering, metal interactions, and other environmental processes (28). The same covariance as is noted in elemental composition is present for some structural groups (Fig. 4); that is, where fulvic acids are enriched or depleted in aliphatic, heteroaliphatic, or aromatic components, and possibly carboxylic components, so are the XAD-4 acids. There are few data points on the graphs and one should interpret them with caution, but the covariance again reinforces the sense that the non-humic and humic components form a continuum, in which all fractions are affected by similar formative processes.

XAD-4 acetonitrile extract

XAD-4 ace extracts from both study lakes are alike elementally (Table 2). As with the hydrophobic neutrals that are also extracted with acetonitrile, N content is high, and it is uncertain whether this is an artifact of the isolation procedure or represents a natural component of the extracts. There is virtually no peak at 117 ppm in the ^{13}C NMR spectra, however, which suggests that the N is not due to acetonitrile contamination. The O/C ratio is the lowest of the five fractions. This suggests a less acidic nature, particularly when examined in context with the low to moderate C/H ratio.

Fig. 4. Comparison of ^{13}C NMR functional group content in fulvic acids vs. XAD-4 acids. The line on each graph is the 1:1 line. Triangles represent Ramsey and Nepawassi lakes. Squares represent data for Yakima River at Kiona and Cle Elum (28). 0–62 ppm is aliphatic carbon; 62–90 ppm is C-O; 90–160 ppm is primarily aromatic; 160–190 ppm is carboxyl or ester carbon; and 190–230 ppm is ketonic carbon. The ketonic peak for the Yakima samples was integrated from 190–220 ppm. See Table 4 for more detail.

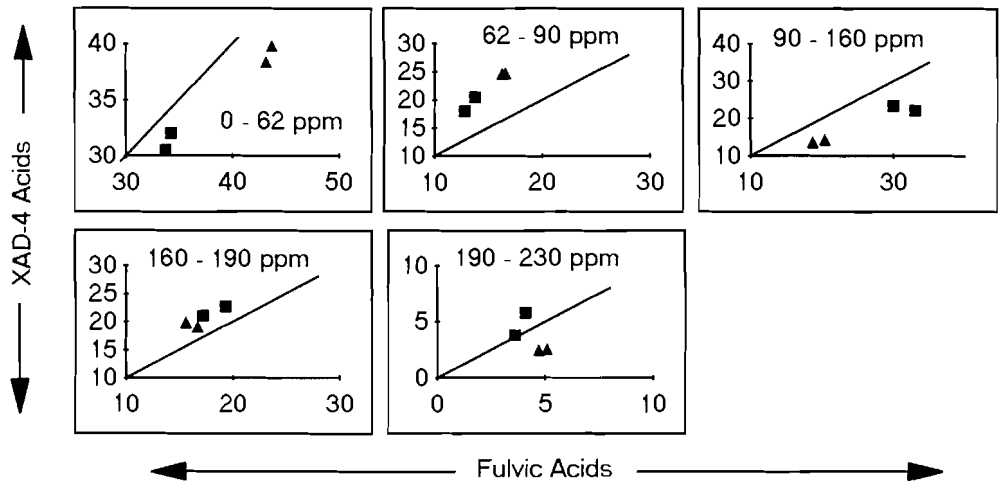

The ^{13}C NMR spectra (Fig. 1; Table 4) show that the XAD-4 ace extracts have low aromaticity, in common with the other non-humic fractions. The C-O region is large, as with the XAD-4 acids, but the anomeric peak indicates that polysaccharides account for <10–15% of the total carbon, and less than half of the C-O carbons. It is possible that some of the remaining C-O carbons are in fact carbon singly bonded to N. The carboxyl and ester region is small, as with the hydrophobic neutrals, and presumably represents primarily esters since the material did not elute with NaOH. The low O/C and C/H ratios also suggest the predominance of esters. Finally, the XAD-4 ace extracts have a higher methoxyl peak (50–62 ppm) than either the humic acids or hydrophobic neutrals. There are no other published ^{13}C NMR results for XAD-4 ace extracts for comparison.

Conclusions

Quantitative elemental and structural analyses were carried out on five DOC fractions isolated from two circumneutral freshwater lakes within the zone of influence of the large mining and smelting industry at Sudbury, Ontario. The isolated fractions were as follows: humic acids and fulvic acids, which have been extensively studied by others, and hydrophobic neutrals, XAD-4 acids (hydrophilic acids), and XAD-4 acetonitrile extracts, which to date have not been well described in the literature.

The ratio of hydrophobic (XAD-8) to hydrophilic (XAD-4) DOC is approximately 65:35. The fulvic acids constitute the largest fraction of the total DOC in both lakes at 48%, with a fulvic acid:humic acid ratio of 6:1 and 7:1 in Ramsey and Nepawassi lakes, respectively. The remaining fractions each make up from ≈7 to 18% of the total DOC.

The key factor distinguishing the humic substances from the non-humic is aromaticity. The former have fa_1 = 14–22% whereas the three non-humic components have fa_1 = 7–9%. Making up for the low aromaticity, the non-humic components are more aliphatic or heteroaliphatic, though, for all five fractions, aliphatic carbon is the single largest carbon group.

Although the humic components are often thought of as the prime source of organic acidity, the XAD-4 acids were found to have a slightly higher carboxylic content. This was seen in the size of the carboxyl shift, and confirmed by titration analysis. The XAD-4 acids in the study lakes make up just less than 20% of the organic acids (10% of DOC). Given their more intense acidity, and the fact that they compose a higher percentage of the DOC in other lakes (28), it is clear that they may be a significant geochemical agent. To date, they have been largely ignored, but with the relative ease of the XAD-8/XAD-4 tandem extraction, their role in weathering, metal transport, and other environmental processes (28) should be investigated.

Both primarily neutral fractions, the hydrophobic neutrals and the XAD-4 ace extracts, have a resolvable methoxyl component. In this they resemble the humic acids. Both neutral fractions appear to have a high N content. Since both are extracted with acetonitrile, the N could be a contaminant. However, the ^{13}C NMR spectra suggest that acetonitrile cannot account for more than about 10% of the N. Both neutral fractions share a small carboxylic-ester peak, assumed to be mostly esters, in keeping with their neutral character. Although the interpretation of ^{13}C NMR spectra for polysaccharide content is difficult, it appears that the neutral fractions have the lowest polysaccharide content. The two neutral fractions are, however, not identical. The hydrophobic neutrals are substantially more aliphatic (54% vs. 39%). They also have the highest sulphur of any of the five fractions, though the sulphur is probably a contaminant from the lakewater.

The two hydrophilic fractions isolated on the XAD-4 resin

have C-O shifts that are substantially higher than those found in the hydrophobic fractions. Other than this, however, there is little that distinguishes the fractions isolated on the two different resins.

Compared to samples from other freshwaters, the three acid fractions in Ramsey and Nepawassi lakes do not appear to be unusual with regard to elemental composition. However, there do appear to be some structural differences. All three acids are either at the low end of the normal range for aromaticity, or are much less aromatic than samples from other freshwaters. There are few lakes with which to compare so it is difficult to interpret the results, but they may indicate that DOC and its formative mechanisms have been affected by the acid rain and metal loadings of the Sudbury area (25), despite the circumneutral character of the study lakes. The results also show that several characteristics of the suite of acid fractions covary, such that when one fraction is richer in an element or functional group, so are the others. Some of the covariance could be due to methodological artifacts, such as the operationally defined fractions not being fully separated (28). However, since the full suite of humic and non-humic fractions form in the same environment and are exposed to the same geochemical milieu, it seems reasonable that they share some elemental and structural characteristics.

Acknowledgements

The authors wish to thank Dr. R.L. Malcolm and the U.S. Geological Survey for providing access to their laboratory facilities and for performing the solid-state CPMAS ^{13}C NMR used in this study. The authors also wish to thank the Natural Sciences and Engineering Research Council of Canada (NSERC) for providing financial support.

References

1. R.G. Wetzel, P.H. Rich, M.C. Miller, and H.L. Allen. Mem. Inst. Ital. Idrobiol. **29** (Supp.), 185 (1972).
2. J.H Reuter and E.M. Perdue. Geochim. Cosmochim. Acta, **41**, 325 (1977).
3. C.W. Carter and I.H. Suffet. Environ. Sci. Technol. **16**, 735 (1982).
4. E.T. Gjessing, G. Riise, R.C. Petersen, and E. Andruchow. Sci. Total Environ. **81/82**, 683 (1989).
5. F.R. Livens. Environ. Pollut. **70**, 183 (1991).
6. D.M. McKnight. *In* Organic acids in aquatic ecosystems. *Edited by* E.M. Perdue and E.T Gjessing. John Wiley and Sons Ltd., New York. 1990. pp. 223–243.
7. S. Boggs, Jr., D.G. Livermore, and M.G. Seitz. J. Macromol. Sci. Rev. Macromol. Chem. Phys. **C25**, 599 (1985).
8. W.H. Glaze. *In* Organic acids in aquatic ecosystems. *Edited by* E.M. Perdue and E.T Gjessing. John Wiley and Sons Ltd., New York. 1990. pp. 75–95.
9. J.A. Leenheer. Environ. Sci. Technol. **15**, 578 (1981).
10. R.L Malcolm. *In* Humic substances in the aquatic and terrestrial environment. *Edited by* B. Allard, H. Boren, and A. Grimvall. Springer-Verlag, New York. 1991. pp. 9–46.
11. R.F. Christman, D.L. Norwood, Y. Seo, and F.H. Frimmel. *In* Humic substances II: In search of structure. *Edited by* M.H.B. Hayes, P. MacCarthy, R.L. Malcolm, and R.S. Swift. John Wiley and Sons Ltd., Chichester. 1989. pp. 33–67.
12. F.J. Stevenson. *In* Humic substances II: In search of structure. *Edited by* M.H.B. Hayes, P. MacCarthy, R.L. Malcolm, and R.S. Swift. John Wiley and Sons Ltd., Chichester. 1989. pp. 121–142.
13. J.W. Parsons. *In* Humic substances II: In search of structure. *Edited by* M.H.B. Hayes, P. MacCarthy, R.L. Malcolm, and R.S. Swift. John Wiley and Sons Ltd., Chichester. 1989. pp. 99–120.
14. H.L.C. Meuzelaar, K. Haider, B.R. Nagar, and J.P. Martin. Pyrolysis – mass spectrometry of recent and fossil biomaterials – compendium and atlas. Elsevier, Amsterdam. 1977.
15. J.M. Bracewell, K. Haider, S.R. Larter, and H.R. Schulten. *In* Humic substances II: In search of structure. *Edited by* M.H.B. Hayes, P. MacCarthy, R.L. Malcolm, and R.S. Swift. John Wiley and Sons Ltd., Chichester. 1989. pp. 181–222.
16. N Senesi, T.M. Miano, M.R. Provenzano, and G. Brunetti. Sci. Total Environ. **81/82**, 143 (1989).
17. A.U. Baes and P.R. Bloom. Soil Sci. Soc. Am. J. **53**, 695 (1989).
18. C. Steelink. *In* Humic substances in soil, sediment and water. *Edited by* G.R. Aiken, D.M. McKnight, R.L. Wershaw, and P. MacCarthy. John Wiley and Sons Ltd., New York. 1985. pp. 457–476.
19. R.L. Malcolm. Anal. Chem. Acta, **232**, 19 (1990).
20. M. Schnitzer. Soil Sci. **151**, 41 (1991)
21. R.L. Malcolm. Environ. Int. **18**, 609 (1992).
22. R.A. Bourbonniere. Org. Geochem. **14**, 97 (1989).
23. P. Kortelainen, M.B. David, T. Roila, and I. Mäkinen. Environ. Int. **18**, 621 (1992).
24. R.L. Malcolm and P. MacCarthy. Environ. Int. **18**, 597 (1992).
25. W. Keller. Can. J. Fish. Aquat. Sci. **49**, 3 (1992).
26. R. Pitblado and W. Keller. Data report: Monitoring of Northeastern Ontario Lakes, 1981–1985. Government of Ontario Press, Toronto. 1983.
27. D.M. McKnight, K.A. Thorn, R.L. Wershaw, J.M. Bracewell, and G.W. Robertson. Limnol. Oceanogr. **33**, 1527 (1988).
28. G.R. Aiken, D.M. McKnight, K.A.Thorn, and E.M. Thurman. Org. Geochem. **18**, 567 (1992).
29. R.L. Malcolm. *In* Humic substances II: In search of structure. *Edited by* M.H.B. Hayes, P. MacCarthy, R.L. Malcolm, and R.S. Swift. John Wiley and Sons Ltd., Chichester. 1989. pp. 339–372.
30. A.L. Bates and P.G. Hatcher. Org. Geochem. **18**. 407 (1992).
31. F.J. Stevenson. *In* Humic substances in soil, sediments, and water. *Edited by* G.R. Aiken, D.M. McKnight, R.L. Wershaw, and P. MacCarthy. John Wiley and Sons Ltd., New York. 1985. pp. 13–52.
32. G.R. Aiken. *In* Humic substances and their role in the environment. *Edited by* F.H. Frimmel and R.F. Christman. John Wiley & Sons, Toronto. 1988. pp. 15–28.

Labdane diterpenes from the marine pulmonate gastropod *Trimusculus peruvianus*

Aurelio San-Martín, Elías Quezada, Pilar Soto, Yolanda Palacios, and Juana Rovirosa

Abstract: The marine gastropod mollusk *Trimusculus peruvianus* collected on the coast of Central Chile yielded four new labdane metabolites. The structural elucidation of all compounds was accomplished by spectral analysis. One diterpenoid showed modest antimicrobial activity.

Key words: *Trimusculus peruvianus*, labdanes, marine mollusk.

Résumé : Le mollusque gastéropode marine *Trimusculus peruvianus* recueilli sur les côtes du centre du Chili a fourni quatre nouveaux métabolites de la famille du labdane. On a élucidé les caractéristiques structurales de chacun de ces composés par le biais d'analyses spectrales. L'un des diterpénoïdes présente une modeste activité antibactérienne.

Mots clés : *Trimusculus peruvianus*, labdanes, mollusques marins.

[Traduit par la rédaction]

Among marine organisms, the most chemically studied are sponges and mollusks. The chemistry of shell-less marine mollusks (e.g., *Aplysia* and nudibranchs) has attracted much interest, mostly because these organisms obtain metabolites present in defensive secretions directly from dietary sources (algae and sponges, respectively) (1). Other mollusks, such as cone shells, produce peptide toxins to catch prey organisms (2). Intertidal gastropods employs a wide variety of tactics in dealing with predators. In addition to morphological adaptations, both behavioral and chemical defenses are employed. Several compounds have been isolated from pulmonate mollusks that presumably play important ecological roles. Polyproprionate metabolites have been identified in the genera *Onchidium* (3) and *Siphonaria* (4), and labdane diterpenes are present in the genus *Trimusculus* (5). Continuing our interest in the structure of secondary metabolites present in marine organisms from Chilean coasts, we report the chemical study of *Trimusculus peruvianus* (6).

Materials and methods

General experimental procedures

The ir spectra were recorded on a Perkin Elmer System 2000 ft-ir spectrophotometer. Low-resolution mass spectra were recorded on a Hewlett–Packard 5995 mass spectrometer. The ^{1}H and ^{13}C nmr spectra as well as ^{1}H–H COSY, ^{13}C (DEPT), HMQC (optimized for $^1J_{H-C}$ = 140 Hz), HMBC (mixing time of 75 ms), and ROESY (mixing time of 250 ms) data were obtained on a Bruker AM-300 spectrometer. All chemical shifts are reported with respect to TMS (δ = 0). Solvents and chemicals were of analytical grade.

Isolation

Specimens of *T. peruvianus* (dry wt. after extraction ca. 850 g) were collected on intertidal rocks near El Tabo, V Region, Chile, during November 1992. The organisms was identified by Prof. C. Osorio, Universidad de Chile. The voucher specimens are on deposit at the Facultad de Ciencias, Universidad de Chile collection. The extraction was carried out at room temperature using acetone by percolation every 48 h (5 × 6 L). The aqueous acetone was concentrated under reduced pressure and extracted with EtOAc and then the organic solvent was dried over anhydrous $MgSO_4$.

Evaporation of the solvent gave a green gum (35 g), which was chromatographed over Sephadex LH-20 using MeOH as eluant. The fractions obtained were then chromatographed on Silica gel and eluted with petroleum ether – EtOAc (0–100% EtOAc). Further normal phase hplc with 2% isopropanol in hexane yielded diterpenes **1** (0.086 g), **2** (0.162 g), **3** (0.012 g), **4** (0,014 g), and **5** (0.005 g).

7α,15-Diacetoxylabda-8,13-dien-6β-ol (2): Oil; ^{1}H nmr, see Table 1: ^{13}C nmr, see Table 2; ir (film) ν_{max}: 3450 (w), 2960 (s), 2940 (s), 1750 (s), 1645 (w), 1360 (s), 1230 (s), 1050 (m); eims (70 eV) *m/z* (rel. int): 347 (2), 346 (2), 288 (2), 287 (5), 286 (6), 271 (6), 260 (15), 219 (44), 218 (30), 205 (39), 203 (26), 201 (17), 135 (74), 43 (100).

6β,7α,15-Triacetoxylabda-8,13-diene (3): Yellow oil; ^{1}H nmr, see Table 1; ^{13}C nmr, see Table 2; ir (film) ν_{max}: 3450 (w), 2940 (s), 1750 (s), 1650 (w), 1370 (s), 1220 (s), 1050 (m); lrms *m/z* (%): 328 (1), 219 (26), 218 (26), 205 (24), 191 (12), 135 (71), 119 (44), 107 (34), 105 (53), 55 (100).

Received April 17, 1996.

A. San-Martin,[1] **E. Quezada, P. Soto, and J. Rovirosa.** Departamento de Química, Facultad de Ciencias, Universidad de Chile, Casilla 653, Santiago 1, Chile.
Y. Palacios. Instituto de Salud Pública, Marathon 1000, Santiago, Chile.

[1] Author to whom correspondence may be addressed. Telephone: 56-2-2713881. Fax: 56-2-2713888. E-mail: aurelio@abello.dic.uchile.cl

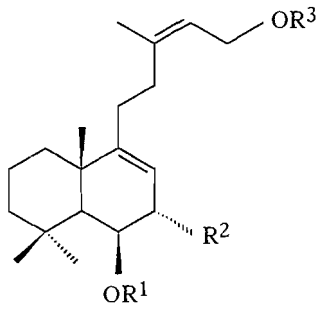

	R^1	R^2	R^3
1	Ac	OH	H
2	H	OAc	Ac
3	Ac	OAc	Ac
4	Ac	OAc	H
5	Ac	H	H

6β,7α-Diacetoxylabda-8,13-dien-15-ol (4): Viscous yellow oil; H nmr, see Table 1; ^{13}C nmr, see Table 2; ir (film) ν_{max}: 3450 (m), 2950 (s), 1740 (s), 1660 (w), 1380 (s), 1220 (s), 1100 (s), 760 (s) cm^{-1}; lrms *m/z* (%): 347 (1), 288 (1), 287 (3), 286 (5), 271 (5), 260 (31), 219 (52), 218 (71), 205 (46), 203 (24), 201 (15), 135 (100).

6β-Acetoxylabda-8,13-dien-15-ol (5): Oil, ^{1}H nmr, see Table 1; ^{13}C nmr, see Table 2; ir (film) ν_{max}: 3450 (m), 2950 (s), 1750 (s), 1660 (w), 1280 (s), 1210 (s), 1050 (m); eims (70 eV) *m/z* (rel. int): 348 (2), 306 (1), 270 (3), 202 (5), 187 (36), 133 (44), 119 (100).

Antimicrobial assays

The qualitative assays were performed using an agar well-diffusion assay. Antimicrobial activity was recorded as the diameter (in mm) of the zone of inhibition, measured from the edge of the agar well to the zone edge. The compounds **1**, **2**, **3**, **4**, and **5** were tested at a concentration of 100 μg/mL against *Klebsiella bronchiseptica, Bacillus anthracis, Bacillus pumilus, Bacillus subtilis, Staphylococcus aureus, Staphylococcus epidermidis, Pseudomonas aeruginosa, Bordetella bronchiseptica, Sarcina lutea, Micrococcus flavus, Proteus vulgaris,* and *Escherichia coli.*

Minimum inhibitory concentration (MIC)

The lowest concentration of the test compounds in which no growth occurred was defined as the MIC.

The quantitative assay for determination of MIC was performed using a twofold serial dilution technique (7). Only compound **3** was tested against all eight organisms, which were highly sensitive to it. See Table 3.

Results and discussion

The concentrated acetone extract of *T. peruvianus* was partitioned between EtOAc and H_2O to give a crude organic extract (see Experimental). This extract was repeatedly subjected to Sephadex LH-20 cc, Si gel open and medium-pressure column chromatography, and hplc, to yield the known diterpene **1**, 6β-acetoxylabda-8,13-dien-7-α,15-diol (6) and four new analogs.

The ^{1}H nmr spectrum of the major compound **2** showed one vinyl proton signal at δ 5.36 (1H, t, J = 7.3 Hz). Two vinylic methyl signals at δ 1.82 (3H, bs) and 1.69 (3H, s) together with four signals in the ^{13}C nmr spectra belonging to sp^2 carbons at δ 148.1 (s), 143.1 (s), 121.0 (s), and 118.8 (d) established the presence of two double bonds. The chemical shifts in ^{1}H nmr and ^{13}C nmr spectra of the vinylic methyl (Me-16), olefinic protons (H-14), and C-12, together with the magnitude of the coupling constant (7.3 Hz) are only compatible with a *Z* configuration for the trisubstituted double bond (5, 8–10). The presence of two 3H singlets at δ 2.06 and 2.08 in its ^{1}H nmr spectrum indicated the presence of two acetate ester groups. The carbonyl groups were confirmed by the strong band at 1740 cm^{-1} in the ir spectrum and the signals at δ 171.1 (s) and 170.0 (s) in the ^{13}C nmr spectrum. The nature of the ester groups as primary and secondary was confirmed by the presence of ^{13}C nmr signals at δ 60.8 (t) and 78.0 (d). In addition, the ^{1}H nmr spectrum showed signals at δ 4.56 (2H, d, J = 7.3 Hz), 4.85 (1H, bs), and 4.16 (1H, bs). The ^{1}H–^{1}H COSY spectrum revealed that the two last signals are strongly coupled and the first one has correlations to an olefinic proton and a vinylic methyl group (Me-16). That the secondary hydroxyl was attached to C-6 was shown by ir, ^{13}C nmr, and ^{1}H nmr data: 3500 cm^{-1}, δ 68.7 (d), and δ 4.16 (1H, bs), respectively. Detailed analysis of ^{1}H and ^{13}C nmr spectra plus ^{1}H–^{1}H COSY, HMQC, and HMBC experiments allowed unambiguous assignment of the ^{1}H and ^{13}C signals shown in Tables 1 and 2, respectively, and indicated a labdane skeleton with two vicinal oxygenated groups in a *trans* diaxial disposition that could be placed at C-6 (hydroxyl group) and C-7 (ester group). The other ester group was assigned to C-15. The relative configurations were assigned by comparison with related compounds (5, 6) and ROESY data. The molecular ion peak was not observed in lrms. The highest mass detected was *m/z* 347 [$M^+ - CH_3OO^-$]. The molecular formula was deduced as $C_{24}H_{38}O_5$ from the ^{13}C and ^{1}H nmr spectra. These data showed compound **2** to be 7α,15-diacetoxylabda-8,13-dien-6β-ol. As far as we know, this is a new natural compound.

Compound **3** yielded spectroscopic data similar to **2**. The absence of an alcoholic function was the main difference. Instead, three acetate groups were present. That this compound is the acetylated derivative of the previous one was evident by the signals in the ^{1}H nmr spectrum at δ 5.32 (1H, bs) instead of 4.16 (1H, bs) in **2**. Also, this spectrum showed three acetyl groups at δ 2.09, 2.05, and 2.04. The ^{13}C nmr spectra also showed the presence of these functions (see Table 2). Acetylation of **2** (Ac_2O/Py, room temperature) gave **3**. The ms did not exhibit a molecular ion peak and gave the highest mass peak at *m/z* 328 [$M^+ - 2 \times CH_3COOH$]. The molecular formula was suggested as $C_{26}H_{40}O_6$ from the analysis of it DEPT ^{13}C nmr spectrum, which showed the presence of 26 carbon atoms (see Table 2). Compound **3** is therefore described as 6β,7α,15-triacetoxylabda-18,13-diene. To our knowledge **3** is a novel natural product.

Compound **4** had analogous spectral features to the previous diterpenes **2** and **3**. The ir spectrum displayed absorption bands at 3450 and 1750 cm^{-1}, indicating the presence of hydroxyl and ester functionalities in its molecule. The hydroxyl group was located at C-15, based on the signals at δ 4.05 (2H, d, J = 7.0 Hz) in the ^{1}H nmr. The ^{1}H–^{1}H COSY spectrum revealed that this signal is strongly coupled with one ole-

Table 1. The ^{1}H nmr data of compounds **2–5**.

	δ (multiplicity) *J*, Hz			
Proton	**2**	**3**	**4**	**5**
1	Hα 1.19 (bd) *J* = 14.8 Hβ 1.76 (dd) *J* = 14.8, 3.7		Hα 1.18 (bd) *J* = 14.0 Hβ 1.75 (bd) *J* = 14.0	
2	Hα 1.55 (dt) *J* = 15.3 Hβ 1.71 (dt) *J* = 15.3		H2 1.61 m	
3	Hα 1.20 (bd) *J* = 14.5 Hβ 1.40 (bd) *J* = 14.5		Hα 1.15 (dd) *J* = 14.0, 5.3 Hβ 1.38 (bd) *J* = 14.5	
5	1.27 (bs)	1.50 (bs)	1.42 (bs)	1.25 (bs)
6	4.16 (bs)	5.32 (bs)	5.25 (bs)	5.45 (d) *J* = 5.5
7	4.85 (bs)	4.98 (bs)	4.90 (bs)	Hα 1.94 (d) *J* = 18.9 Hβ 2.38 (dd) *J* = 5.5, 18.9
11	H2 2.15 (m)	H2 2.05 (m)	H2 2.18 (m)	
12	H2 2.21 (m)	H2 2.1 (m)	H2 2.19 (m)	
14	5.36 (bt) *J* = 7.3	5.36 (t) *J* = 7.3	5.34 (t) *J* = 7.0	5.34 (bt) *J* = 6.7
15	4.56 (d) *J* = 7.3	4.59 (d) *J* = 7.3	4.05 (d) *J* = 7.0	4.00 (d) *J* = 6.7
16	1.82 (bs)	1.82 (bs)	1.73 (bs)	1.78 (bs)
17	1.69 (s)	1.66 (s)	1.58 (s)	1.63 (s)
18	1.31 (s)	1.30 (bs)	1.21 (s)	1.26 (s)
19	1.19 (s)	0.98 (s)	0.90 (s)	1.05 (s)
20	0.93 (s)	0.97 (s)	0.89 (s)	1.05 (s)
CH_3CO	2.06 (s) 2.08 (s)	2.09 (s) 2.05 (s) 2.04 (s)	2.02 (s) 1.97 (s)	1.97 (s)

finic proton (δ 5.34 (1H, t, *J* = 7.0)) and one vinylic methyl (Me-16, δ 1.73 (3H, bs)). The ^{13}C nmr spectrum exhibited signals due to this system (δ 124.7 d, 139.6 s, 23.6 q, and 59.1 t) The ms did not exhibit the molecular ion peak and gave the highest mass peak at *m/z* 347 [M − CH_3COO^-]. Its molecular formula was suggested as $C_{24}H_{38}O_5$ from the analysis of its DEPT ^{13}C nmr spectrum, which showed the presence of 24 carbon atoms (see Table 2). Acetylation of **4** (Ac_2O–Py, rt) gave **3**. The structure of compound **3** is assigned as 6β,7α-diacetoxylabda-8,13-dien-15-ol. To our knowledge this is the first natural occurrence of this compound.

The principal spectroscopic characteristics of compound **5** are similar to the other diterpenes of this animal. It contained a free hydroxyl group, as was evident by the signals at 3450 cm^{-1}, δ 58.4 (t), and 4.00 (2H, d, *J* = 6.7 Hz) in ir, ^{13}C nmr, and ^{1}H nmr spectra, respectively. Only one acetate ester group was present and it was assigned to C-6 by the signals at 1750 cm^{-1} (ir spectrum), δ5.45 (1H, d, *J* = 5.5 Hz) (^{1}H nmr spectra). The ^{13}C nmr spectra exhibited signals for six quaternary carbons (four of them olefinic and one belonging to the carbonyl group), three methine carbons (one of them olefinic), six methyl carbons, (one of them olefinic), six methyl carbons,

Table 2. The ^{13}C nmr data for compounds **2–5**[a].

Carbon	**2**[b]	C coupled with H	**3**	**4**	**5**
1	38.9 t	C-2, C-20	39.1 t	39.1 t	39.4 t
2	18.9 t		19.2 t	19.2 t	19.1 t
3	43.0 t		43.3 t	43.2 t	43.2 t
4	33.5 s		33.4 s	33.6 s	33.4 s
5	50.0 d	C-4, C-9, C-10, C-19, C-20	49.3 d	49.3 d	52.6 d
6	68.7 d	C-4, C-10, C-5, C-7, C-8	73.6 d	73.7 d	66.9 d
7	78.0 d	C-5, C-6, C-8, C-9, C-18, C=O	69.4 d	69.7 d	38.7 t
8	121.0 s		122.1 s	121.9 s	122.2 s
9	148.1 s		147.8 s	148.0 s	139.6 s
10	39.1 s		39.7 s	39.6 s	39.9 s
11	27.0 t	C-10, C-12, C-13, C-14	27.2 t	27.1 t	26.6 t
12	32.0 t	C-11, C-13, C-14, C-16	32.3 t	32.3 t	32.6 t
13	143.1 s		143.1 s	139.6 s	139.1 s
14	118.8 d	C-12, C-15, C-16	119.3 d	124.7 d	124.7 d
15	60.8 t	C-13, C-14, C=O	61.1 t	59.1 t	58.4 t
16	23.8 q	C-12, C-13, C-14	23.6 q	23.6 q	23.2 q
17	17.4 q	C-7, C-8, C-9	17.3 q	17.3 q	19.4 q
18	21.0 q	C-3, C-5, C-19	21.7 q	21.7 q	21.2 q
19	23.2 q	C-3, C-5, C-18	23.3 q	23.3 q	23.0 q
20	33.2 q	C-1, C-3, C-4,	33.2 q	33.2 q	33.8 q
CH_3CO	171.1 s		171.2 s	170.1 s	168.6 s
	171.0 s		170.1 s	169.9 s	
			169.9 s		
CH_3CO	2 × 21.1 q	C=O	2 × 21.4 q	21.3 q	21.0 q
			21.3 q	21.2 q	

[a]The ^{13}C nmr shift multiplicities were determined by DEPT.
[b]By HMBC experiment.

Table 3. Antibacterial spectra (MIC) of compound **3**.

Test organism	μg/mL
Klebsiella bronchiseptica	50
Bacillus anthracis	50
Bacillus pumilus	50
Bacillus subtilis	50
Staphylococcus aureus	65
Staphylococcus epidermidis	75
Pseudomonas aeruginosa	80
Bordetella bronchiseptica	85

and seven methylene carbons, consistent with the molecular ion *m/z* 348 in the mass spectrum and with a molecular formula $C_{22}H_{36}O_3$. Compound **5** was thus established to be 6β-acetoxylabda-8,13-dien-15-ol. To the best of our knowledge this compound is new.

All the compounds were evaluated in the agar well diffusion assay for antimicrobial activity against microorganisms, as indicated in the experimental section. Only compound **3** exhibited a modest activity, and its MIC values were determined by the twofold serial macrobroth dilution assay. The results of these assays are summarized in Table 3.

Compound **3** showed a marginal activity against the Gram-positive bacteria *Bacillus anthracis, B. pumilus, B. subtilis*, and Gram-negative *Klebsiella bronchiseptica*. None of the other compounds showed any remarkable activity.

Acknowledgments

This work was supported by grants from Universidad de Chile (D.T.I.) and Fondecyt (No. 1038-92). The mass spectral were provided by the Instituto de Productos Naturales y Agrobiologia de Canarias. The authors thank María Inés Polanco for assistance with the antimicrobial assays.

References

1. D.J. Faulkner. Nat. Prod. Rep. **9**, 324 (1992), and earlier reviews in this series.
2. P.J. Scheuer. Bioorganic marine chemistry 3. Springer-Verlag, Berlin, Heidelberg. 1989. pp. 81–94.
3. J. Rodriguez, R. Riguera, and C. Debitus. J. Org. Chem. **57**, 4624 (1992).
4. J. Rovirosa, E. Quezada, and A. San-Martín. Bol. Soc. Chil. Quim. **36**, 233 (1991).
5. D. Manker and D.J. Faulkner. Tetrahedron, **43**, 3677 (1987).

6. J. Rovirosa, E. Quezada, and A. San Martín. Bol. Soc. Chil. Quim. **37**, 143 (1992).
7. R.N. Jones, A.L. Barry, T.L. Gavan, and J.A. Washington III. *In* Manual of clinical microbiology. *Edited by* E.H. Lennette, A. Balows, W.J. Hausler, and H.J. Shadomy. American Society for Microbiology, Washington, D.C. 1985. pp. 51–96.
8. D.P. O'Mathúna and R.W. Doskotch. J. Nat. Prod. **57**, 1382 (1994).
9. C. Zdero, F. Bohlmann, R.M. King, and H. Robinson. Phytochemistry, **25**, 2841 (1986).
10. A. San Feliciano, M. Medarne, J.L. Lopez, J.M. Miguel del Corral, P. Puebla, and A.F. Barrero. Phytochemistry, **27**, 2241 (1988).

Theoretical study of the PSi_2 radical

Jose M. Elorza and Jesus M. Ugalde

Abstract: G2 methodology has been used to characterize minima on both doublet and quartet potential energy surfaces of the PSi_2 radical system. We found that for states with doublet spin multiplicity the most stable isomer is the cyclic $^2A_1$. Linear isomers lie more than 24 kcal/mol above in energy. For the quartets the most stable state isomer is the cyclic $^4A_2$, and the most stable linear isomer, i.e., Si-Si-P($^4\Sigma^-$), lies 10.68 kcal/mol higher in energy. The structural features of the various isomers characterized have been rationalized in terms of the bonding features of the molecular orbitals involved.

Key words: ab initio, excited states, radical.

Résumé : On a utilisé la méthodologie G2 pour caractériser les minimums des surfaces d'énergie potentielle tant du doublet que du quadruplet du système radicalaire PSi_2. On a trouvé que, pour les états avec une multiplicité de spin doublet, l'isomère le plus stable est la forme cyclique $^2A_1$. L'énergie des isomères linéaires est plus élevée de 24 kcal/mol. L'état cyclique $^4A_2$ des quadruplets correspond á celle de l'isomére le plus stable; l'énergie de l'isomère linéaire le plus stable, c'est-à-dire Si-Si-P($^4\Sigma^-$) est 10,68 kcal/mol plus élevée. On a rationalisé les caractéristiques structurales des divers isomères étudiés en faisant appel à des caractéristiques de liaison des orbitales moléculaires impliquées.

Mots clés : ab initio, états excités, radicaux.

[Traduit par la rédaction]

1 Introduction

Hypersilicon molecules $Si_nX(n = 3, 2)$ with electronegative X atoms such as oxygen or nitrogen, have been the subject of recent theoretical (1) and experimental (2) studies. In particular, the gas phase experiments of Iraqui et al. (2) have shown that both OSi_2 and NSi_2 radicals have triangular ground state geometries. Both of the linear isomers Si-Si-X and Si-X-Si are higher in energy than these triangular isomers. These species are important in surface science, since they may be viewed as prototypes for the interaction between the X atom and silicon sites in clusters and surfaces (3).

Recently, theory has predicted (4) a linear geometry for the ground state of the C_2P radical, a species isovalent with the NSi_2 radical. However, contrary to the NSi_2, there exists a cyclic isomer of the C_2P ($^2B_2$ state), which is found to be 6.1 kcal/mol above the C-C-P linear $^2\Pi$ ground state, at the G1 level of theory (4). Notice also that both species are predicted to have large dipole moments, 3.293 D and 2.535 D, respectively, which encourages their experimental detection. On the quartet potential energy surface, the linear C-C-P ($^4\Sigma$) structure is found to be the lowest energy structure, with the cyclic $^4A_2$ state lying 17.2 kcal/mol higher in energy, at the MP4/6-311G(d)//MP2/6-31G(d) level of theory. The C_2P radical, on the other hand, is a species relevant for the chemistry of dense clouds, as pointed out by Millar and Astron (5). Indeed, it should be detectable, provided that it is unreactive with oxygen.

In this paper, we use ab initio molecular orbital theory to investigate the nature of the chemical bonds and determine the energy ordering of the various isomers of the PSi_2 radical system, a species isovalent with the previously studied C_2P and NSi_2 radicals.

2 Methods

All structures were optimized at the MP2/6-31G(d) level of theory (6). Geometries of these species can be found in Figs. 1 and 2. Analytical frequencies at the stationary points were calculated at the MP2/6-31G(d) level of theory and all of them were found to be positive. G2 methodology (7) was used to evaluate the energies. All G2 calculations were performed using the GAUSSIAN 92 code of programs (8). G2 energies with their corresponding corrections to the MP4/6-311G(d,p) base energy can be found in Tables 1 and 2.

Note that we found some spin contamination for some of the structures studied in this paper, as indicated by the expectation values of S^2 given in Tables 1 and 2. However, it is worth mentioning that the G2 procedure, through its quadratic configuration interaction correction term, ΔE^{QCI}, has been shown to be reliable for accurate calculations of energies of small molecules with spin-contaminated single configuration wave functions such as the CN and HCO radicals (8). Therefore, even though we recognize that other approaches, such as multireference configuration interaction (MRCI) with spin-adapted wave functions, would lead to more accurate relative energies, they are considerably more demanding from the computational viewpoint than the G2 method, and would likely not alter substantially the energy ordering of the present calculations, at least for the less spin-contaminated species.

We have explored the bonding characteristics of these

Received July 19, 1996.

J.M. Elorza and J.M. Ugalde.[1] Kimika Fakultatea, Euskal Herriko Unibertsitatea, P.K. 1072, 20080 Donostia, Euskadi, Spain.

[1] Author to whom correspondence may be addressed. Telephone: +34-43-216600. Fax: +34-43-212 236. E-mail: ugalde@sq.ehu.es

Fig. 1. MP2/6-31G(d) optimized geometries and electronic structure terms and the expectation value of S^2, in parentheses, for the doublet PSi_2 system. Bond lengths are in Å and angles are in degrees.

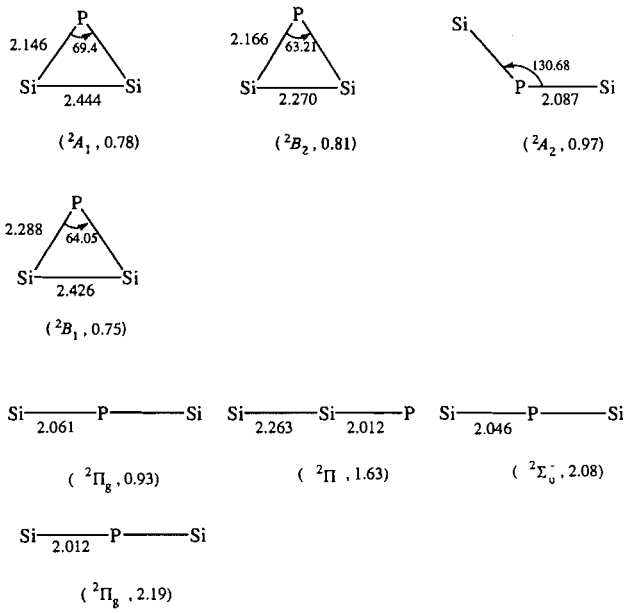

Fig. 2. MP2/6-31G(d) optimized geometries and electronic structure terms and the expectation value of S^2, in parentheses, for the quartet PSi_2 system. Bond lengths are in Å and angles are in degrees.

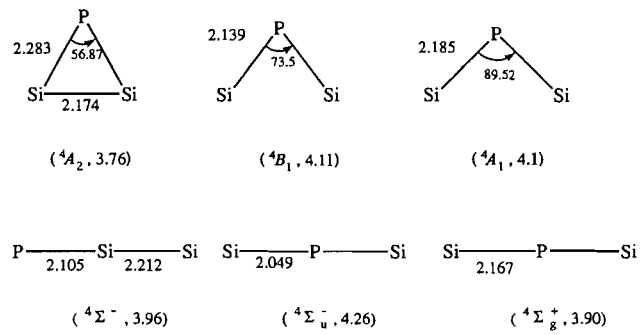

complexes by means of Bader's topological analysis of the electron charge density $\rho(\boldsymbol{r})$ and its associated Laplacian $\nabla^2(\rho\boldsymbol{r})$ (10–13), using the AIMPAC series of programs (14). The MP2/6-31G(d)//MP2/6-31G(d) wave functions were used to build up the electron density. Properties of the bond critical point (r_c), such as $\rho(r_c)$, $\nabla^2\rho(r_c)$, and the value of the energy density $H(r_c)$ have also been calculated. The energy density at the bond critical point indicates a bond to be covalent if $H(r_c) < 0$, and ionic if $H(r_c) > 0$ (11, 12).

3 Results and discussion

The doublet and quartet stable structures, optimized at the MP2/6-31G(d) level of theory, may be found in Figs. 1 and 2, respectively. The energies of the less spin-contaminated structures are shown in Tables 1 (doublets) and 2 (quartets).

3.1 Cyclic doublets

We found four stable triangular PSi_2 structures with the following electronic configurations:

$PSi_2(^2B_2)$ core $8a_1^2\,9a_1^2\,6b_2^2\,10a_1^2\,3b_1^2\,11a_1^2\,7b_2^1$

$PSi_2(^2A_1)$ core $8a_1^2\,9a_1^2\,6b_2^2\,10a_1^2\,3b_1^2\,7b_2^2\,11a_1^1$

$PSi_2(^2A_2)$ core $8a_1^2\,9a_1^2\,6b_2^2\,10a_1^2\,3b_1^2\,7b_2^2\,2a_2^1$

$PSi_2(^2B_1)$ core $8a_1^2\,9a_1^2\,6b_2^2\,10a_1^2\,11a_1^2\,7b_2^2\,3b_1^1$

The structure with the shortest Si—Si bond length belongs to the $^2B_2$ electronic state, which, unlike its isovalent C_2P radical (4), is not the most stable cyclic isomer. Its $8a_1^2$ molecular orbital is mainly composed of the $3s$(P) lone pair with minor contributions from the $3s$ atomic orbitals on the two silicon atoms, the $9a_1$ corresponds to the bonding σ(Si—Si) molecular orbital, the $6b_2$ and the $10a_1$ orbitals correspond to the σ(P—Si) skeletal bonds, and the $3b_1$ and the $11a_1$ are the Si—Si π bonds. The unpaired electron resides on the $7b_2$ orbital, which is Si—Si antibonding and P—Si bonding. Thus, promoting one electron from the doubly occupied $11a_1$ molecular orbital of the $^2B_2$ electronic state to the $7b_2$ orbital yields the most stable cyclic structure, which belongs to the $^2A_1$ electronic state. Note that for the resulting $^2A_1$ structure, the Si—Si bond length has increased and the P—Si bond length has decreased with respect to the $^2B_2$ structure.

The $^2A_2$ electronic state comes from promoting the unpaired $11a_1$ electron, of the $^2A_1$ electronic state, to its virtual $2a_2$ molecular orbital, which is a Si—Si π* antibonding orbital. Accordingly, its Si—Si distance, namely 3.79 Å, is too long to think of an Si—Si bond. The $^2A_2$ electronic state is, therefore, an open triangular structure.

Finally, the $^2B_1$ electronic state, which arises from the $^2A_1$ electronic state by promotion of one electron from the doubly occupied $3b_1$ molecular orbital to the $11a_1$ SOMO, is the least stable of the cyclic PSi_2 doublet structures. Note that this $^2B_1$ structure has the longest P—Si bond length of all the isomers characterized in the study, namely, 2.288 Å.

3.2 Linear doublets

Four stable linear doublet structures have been characterized for the PSi_2 radical system, with the following electronic configurations

Si-P-Si($^2\Pi_g$) core $6\sigma_g^2\,5\sigma_u^2\,7\sigma_g^2\,3\pi_u^4\,6\sigma_u^2\,2\pi_g^1$

Si-P-Si($^2\Sigma^+$) core $6\sigma_g^2\,5\sigma_u^2\,7\sigma_g^2\,3\pi_u^4\,2\pi_g^2\,6\sigma_u^1$

Si-P-Si($^2\Pi_g$) core $6\sigma_g^2\,5\sigma_u^2\,7\sigma_g^2\,3\pi_u^4\,2\pi_g^2\,2\pi_g^1$

Si-Si-P($^2\Pi$) core $10\sigma^2\,11\sigma^2\,12\sigma^2\,4\pi^4\,13\sigma^2\,5\pi^1$

We have also characterized one more linear structure, namely,

Si-P-Si($^2\Pi_u$) core $6\sigma_g^2\,5\sigma_u^2\,7\sigma_g^2\,3\pi_u^4\,6\sigma_u^2\,4\pi_u^1$

which corresponds to the transition state for the inversion of the open PSi_2 ($^2A_2$) isomer, and is 45.12 kcal/mol less stable than the latter, at the G2 level of theory. Hence, such inversion is not accessible at moderate temperatures. Inspection of the optimized Si-P-Si structures shown in Fig. 1 reveals that the Si—P bond length decreases as the instability increases. This behavior can be rationalized in terms of the valence molecular orbitals. Thus, we observed that the population of the $2\pi_g$ MOs increases and the population of the $6\sigma_u$

Table 1. Total energies (in hartree) at the MP4/6-311G(d) G2 level of theory. Additive energy corrections (in mhartree) and G2 relative energies ΔE_{G2} (in kcal/mol) for the doublet PSi_2 radical system.

		$\langle S_2 \rangle$	MP4/6-311G(d)	ΔE^+	ΔE^{2df}	ΔE^{QCI}	ΔE^{ZPE}	E_{G2}	ΔE_{G2}
PSi_2	$^2A_1$	0.78	−918.841 1641	−6.342	−98.211	−2.006	3.086	−919.049 651	0.0
PSi_2	$^2B_2$	0.81	−918.809 7884	−5.857	−97.931	−3.094	3.757	−919.018 581	19.50
PSi_2	$^2A_2$	0.97	−918.801 6659	−4.602	−90.618	−11.068	2.221	−919.013 960	22.40
Si-P-Si	$^2\Pi_g$	0.93	−918.800 3893	−3.428	−90.542	−8.787	3.013	−919.011 097	24.19
Si-Si-P	$^2\Pi$	0.63	−918.767 5579	−2.866	−87.178	−27.119	2.205	−918.992 448	35.89
PSi_2	$^2B_1$	0.75	−918.768 9217	−6.864	−102.081	−4.479	2.892	−918.984 248	41.04

Table 2. Total energies (in hartree) at the MP4/6-311G(d) G2 level of theory. Additive energy corrections (in mhartree) and G2 relative energies ΔE_{G2} (in kcal/mol) for the quartet PSi_2 radical system.

		$\langle S_2 \rangle$	MP4/6-311G(d)	ΔE^+	ΔE^{2df}	ΔE^{QCI}	ΔE^{ZPE}	E_{G2}	ΔE_{G2}
PSi_2	$^4A_2$	3.76	−918.772 6249	−5.428	−96.371	−1.735	3.311	−918.973 215	0.0
PSi_2	$^4B_1$	4.11	−918.748 1451	−5.881	−97.770	−13.330	2.291	−918.962 278	6.86
P-Si-Si	$^4\Pi^-$	3.96	−918.748 0979	−3.409	−91.735	−9.938	2.301	−918.956 195	10.68
Si-P-Si	$^4\Pi_u^-$	4.26	−918.732 6033	−2.671	−88.483	−14.371	2.547	−918.940 570	20.48
Si-P-Si	$^4\Pi_g^+$	3.90	−918.729 7733	−3.850	−82.805	−14.828	2.066	−918.931 999	25.86
PSi_2	$^4A_1$	4.1	−918.671 0286	−6.353	−96.322	−10.923	3.022	−918.881 797	57.36

MO decreases as the bond length decreases. Indeed, the $2\pi_g$ MOs have a node on the central phosphorus atom, while the $6\sigma_u$ has a substantial participation of the $3p_z$ atomic orbital of the phosphorus atom. Hence, populating the $2\pi_g$ MOs at the expense of depopulating the $6\sigma_u$ MO enables the Si—P distance to shrink, so it allows for a better overlap of the atomic orbitals of the bonding $3\pi_u$ MOs. Conversely, as the two degenerate $2\pi_g$ MOs depopulate gradually to populate the $6\sigma_u$ MO, a compromise should be reached for the overall optimum overlap of the atomic orbitals of both the $3\pi_u$ and $6\sigma_u$ MOs, resulting in a steady increase of the Si—P bond length.

The Si-Si-P ($^2\Pi$) structure has one imaginary frequency of $i74.3$ cm^{-1}, on the HF/6-31G(d) potential energy surface, which corresponds to the bending mode. However, reoptimization and subsequent frequency calculation at the MP2/6-31(d) level of theory leads to the stable $^2\Pi$ structure shown in Fig. 1, with all frequencies positive.

3.3 Cyclic quartets

The electronic configurations of the three cyclic quartet structures found on the MP2/6-31G(d,p) potential energy surface are

$PSi_2(^4A_1)$ core $8a_1^2\ 9a_1^2\ 6b_2^2\ 10a_1^2\ 3b_1^2\ 7b_2^1\ 4b_1^1\ 2a_2^1$

$PSi_2(^4A_2)$ core $8a_1^2\ 9a_1^2\ 6b_2^2\ 10a_1^2\ 3b_1^2\ 7b_2^1\ 11a_1^1\ 4b_1^1$

$PSi_2(^4B_1)$ core $8a_1^2\ 9a_1^2\ 6b_2^2\ 10a_1^2\ 3b_1^2\ 7b_2^1\ 11a_1^1\ 2a_2^1$

On the HF/6-31G(d,p) potential energy surface the $^4B_2$ state has an open triangular structure, which collapses to the linear $^4\Sigma_u^-$ state at the MP2/6-31G(d,p) level of theory. The $^4A_1$ state has an Si—Si distance of 3.076 Å at the MP2/6-31G(d,p) level of theory, too long to think of a chemical bond. Indeed further analysis of the electron charge density revealed that no Si—Si bond exists, for no bond critical point was found along the Si—Si path. Therefore, the $^4A_1$ state has an optimum noncyclic triangular structure. The calculated activation energy for the inversion around the phosphorus atom is 9.37 kcal/mol at the G2 level of theory. So, our calculations predict a floppy structure for the $^4A_1$ state, since the calculated activation energy of the inversion process is accessible at moderate temperatures.

The $^4A_2$ state might be thought of as arising from the $^2A_1$ state by promoting one electron from the doubly occupied $7b_2$ orbital to the empty $4b_1$ orbital, the latter being P—Si antibonding and Si—Si bonding. Hence, the P—Si bond length increases and the Si—Si bond length decreases, yielding a SiPSi bond angle even more acute than for the doublets. Concomitantly, replacing the $4b_1$ MO of the $^4A_2$ electronic state by the $2a_2$ MO results in the $^4B_1$ electronic state, whose optimized geometry shows a short P—Si bond length, i.e., 2.139 Å, and a longer Si—Si distance of 2.562 Å, at the MP2/6-31G(d,p) level of theory. Inspection of the gradient paths of the electron charge density, $\rho(r)$, shown in Fig. 3, reveals that there is no bond between the two silicon atoms, though the strain engendered by the bridging phosphorus forces the silicons to lie within the average single bond distance range.

3.4 Linear quartets

The electronic structure of the three stable linear quartets of Fig. 2 are

Si-P-Si($^4\Sigma_u^-$) core $6\sigma_g^2\ 5\sigma_u^2\ 3\pi_u^4\ 7\sigma_g^2\ 6\sigma_u^1\ 2\pi_g^1\ 2\pi_g^1$

Si-P-Si($^4\Sigma_g^+$) core $6\sigma_g^2\ 5\sigma_u^2\ 2\pi_g^4\ 6\sigma_u^2\ 7\sigma_g^1\ 3\pi_u^1\ 3\pi_u^1$

Si-Si-P($^4\Sigma^-$) core $10\sigma^2\ 11\sigma^2\ 12\sigma^2\ 4\pi^4\ 13\sigma^1\ 5\pi^1\ 5\pi^1$

A stable excited state with $^4\Sigma_g^+$ symmetry and the following electronic configuration,

Si-P-Si($^4\Sigma_g^+$) core $6\sigma_g^2\ 5\sigma_u^2\ 3\pi_u^4\ 6\sigma_u^2\ 7\sigma_g^1\ 2\pi_g^1\ 2\pi_g^1$

has also been characterized on the HF/6-31G(d,p) potential

Fig. 3. Gradient map of the electron charge density for the triangular $^4B_1$ state of PSi_2.

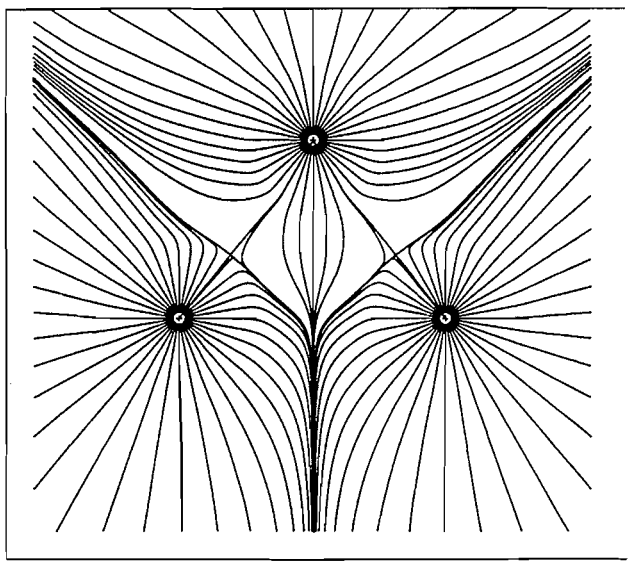

energy surface. However, when reoptimized at the MP2/6-31G(d,p) level, the two degenerate bending vibrational modes become imaginary. In fact, on the latter potential energy surface, this linear structure corresponds to the saddle point for the umbrella motion of the $^4B_1$ triangular state. The estimated activation energy at the MP2/6-31G(d,p)//MP2/6-31G(d,p) + ΔZPVE is 56.79 kcal/mol, a barrier too high to overcome at moderate temperatures.

The SiPSi($^4\Sigma_u^-$) arises from the $^2\Pi_g$ state by $2\pi_g \leftarrow 6\sigma_u$ electron promotion. Note that the quartet state results in a shorter Si—P bond length than the doublet, confirming further our earlier remark about the shrinking of the SiP bond length, as a consequence of depopulating the $6\sigma_u$ orbital in favour of the $2\pi_g$ degenerate orbitals. Accordingly, the $^4\Sigma_g^+$ state, which has the $6\sigma_u$ orbital doubly occupied and the $2\pi_g$ orbitals empty, shows the largest Si—P bond length of both the linear doublet and quartet states, namely, 2.167 Å at the MP2/6-31G(d,p) level of theory.

Finally, the $^4\Sigma^-$ state of the Si-Si-P isomer, which originates from the $^2\Pi$ state, by the $5\pi \leftarrow 13\sigma$ electron promotion, has a larger Si—P bond length and a shorter Si—Si bond length than its precursor, as dictated by the bonding features of the 5π and 13σ orbitals; namely, the 13σ is both Si—Si and Si—P σ-bonding, while the 5π is Si—Si π-bonding and Si—P π-antibonding.

3.5 Energies

Energies of the systems with a too large spin contamination will not be discussed, because it is unlikely that ΔE^{QCI} will be able to compensate for the likely poorer behavior of the G2 procedure, with respect to the less spin-contaminated systems. Therefore, we will not comment on the energies of the $^2\Sigma_u^-$ and the first excited $^2\Pi_g$ electronic states of SiPSi, and would also like to add a word of caution about the energies of the linear SiSiP $^2\Pi$ state, for it bears considerably large spin contamination, namely, $\langle S^2 \rangle = 1.63$.

As evidenced by the energies shown in Tables 1 and 2, in general, the cyclic structures of both doublet and quartet spin states are more stable than their corresponding linear isomers. The exceptions are the $^2B_1$ and the $^4A_1$ electronic states, for which the linear $^2\Pi_g$ and $^2\Pi$, and the $^4\Sigma_g^+$ electronic states, respectively, are found to be more stable. Relative energies, however, are not too large. Thus, at the G2 level of theory five quartet states, two cyclic and three linear, are found within a 25 kcal/mol energy range, while on the doublet PES, four states, three with cyclic optimum structure and one with linear optimum structure, are found within this energy range. Therefore, it is only at high temperatures that several isomers with different electronic configurations are predicted to coexist. Note also that the G2 energy ordering is not modified at the less demanding MP4/6-311G(d) level of theory except in one case, namely, for the $^2B_1$ and $^2\Pi$ states. Indeed, at the MP4/6-311G(d) level of theory the cyclic $^2B_1$ state is 0.9 kcal/mol more stable than the $^2\Pi$ state, but the latter is 5.15 kcal/mol more stable at the G2 level. Inspection of Table 1 reveals that the energy correction terms arising from the deficiencies of the basis set of the base level energy (i.e., ΔE^+, which is due to the lack of diffuse function, and ΔE^{2df}, due to the lack of high polarization functions on non-hydrogen atoms) are larger for the cyclic $^2B_1$ state than for the $^2\Pi$. However, they do not compensate for the much larger energy correction term, ΔE^{QCI}, which accounts for the correlation effects beyond the fourth-order perturbation theory. Thus, ΔE^{QCI} is 22.64 mhartree larger for the $^2\Pi$ state than for the $^2B_1$ state, and determines the higher stability of the former electronic state, at the G2 level of theory, as shown in Table 1. Nevertheless, it is worth noting that the relative base level energy differences between various isomers are modified noticeably with respect to the final G2 values. In particular the $^4B_1$ and $^4\Sigma^-$ optimum structures differ by only 0.1 kcal/mol at the MP4/6-311G(d) base level of theory, but by 3.8 kcal/mol at the G2 level. Once again the ΔE^{QCI} correction is found to be crucial for a reliable estimation of the relative energies.

4 Conclusions

An ab initio molecular orbital study has been carried out for the doublet and quartet potential energy surfaces of the PSi_2 radical system. We have found that the ground state of the doublet spin multiplicity species is a cyclic $^2A_1$ state. The most stable Si-P-Si linear structure, with the $^2\Pi_g$ electronic state, lies 24.19 kcal/mol higher in energy. The Si-Si-P $^2\Pi$ isomer lies even higher in energy than the $^2\Pi_g$ one, opposite to the behavior found for its isovalent C_2P system. On the quartet potential energy surface, the $^4A_2$ cyclic state is the most stable of all the isomers. The Si-Si-P ($^4\Sigma^-$) isomer is the most stable linear isomer, 10.68 kcal/mol less stable than the $^4A_2$ state. The symmetrical Si-P-Si linear isomer ($^4\Sigma_u^-$ electronic state) is found to be 9.8 kcal/mol above the Si-Si-P $^4\Sigma^-$ isomer. Structural features have been discussed in terms of the bonding characteristics of the molecular orbitals involved, and for one case, namely, the $^4B_1$, we carried out Bader's topological analysis of the electron charge density, to determine that it is an open triangular structure, with no Si—Si bond.

5 Acknowledgment

This research has been supported by the Basque Provincial Government of Guipuzcoa (Gipuzkoako Foru Aldundia), the Basque Government (Eusko Jaurlaritza), and the University of the Basque Country (Euskal Herriko Unibertsitatea), Grant No. 203.215-49/94. The authors thank Dr. X. Lopez for many useful suggestions.

References

1. A.I. Boldyrev and J. Simons. J. Phys. Chem. **97**, 5875 (1993).
2. M. Iraqui, N. Goldberg, and H. Schwarz. J. Phys. Chem. **97**, 11371 (1993).
3. C.-M. Chang, B.R. Zegarski, and L.H. Dubois. J. Phys. Chem. **97**, 6948 (1993).
4. A. Largo, C. Barrientos, X. Lopez, and J.M. Ugalde. J. Phys. Chem. **98**, 3985 (1994).
5. J.J. Millar. Astron. Astrophys. **242**, 241 (1991).
6. J.A. Pople, M. Head-Gordon, D.J. Fox, K. Raghavachari, and L.A. Curtiss. J. Chem. Phys. **90**, 5622 (1989).
7. L.A. Curtiss, K. Raghavachari, G.W. Trucks, and J.A. Pople. J. Chem. Phys. **94**, 7221 (1991).
8. M.J. Frisch, G.W. Trucks, M. Head-Gordon, P.M.W. Gill, M.W. Wong, J.B. Foresman, B.G. Johnson, H.B. Schlegel, M.A. Robb, E.S. Replogle, R. Gomperts, J.L. Andres, K. Raghavachari, J.S. Binkley, C. Gonzalez, R.L. Martin, D.J. Fox, D.J. Defrees, J. Baker, J.J.P. Stewart, and J.A. Pople. Gaussian 92, Revision C. Gaussian, Inc., Pittsburgh, Pa. 1992.
9. L.A. Curtiss, C. Jones, G.W. Trucks, K. Raghavachari, and J.A. Pople. J. Chem. Phys. **93**, 2537 (1990).
10. R.F.W. Bader. Atoms in molecules. A quantum theory. Clarendon Press, Oxford. 1990.
11. D. Cremer and E. Kraka. Croat. Chem. Acta. **57** (1984), 1259.
12. E. Kraka and D. Cremer *In* Theoretical models of chemical bonding. Vol 2. The concept of the chemical bond. *Edited by* Z.B. Maksic. Springer Verlag, Berlin. 1990. p. 453.
13. R.J. Boyd and J.M. Ugalde. *In* Computational chemistry. Part A. *Edited by* S. Fraga. Elsevier, Amsterdam. 1992.
14. F.W. Biegler-Konig, R.F.W. Bader, and T.H. Tang. J. Comput. Chem. **27**, 1924 (1980).

Solvent and substrate isotope effects on the enolization and carbon-acid ionization of isobutyrophenone

J.R. Keeffe and A.J. Kresge

Abstract: Bromine scavenging was used to measure rates of acid-catalyzed enolization of isobutyrophenone in H_2O and in D_2O solution and of isobutyrophenone-α-*d* in D_2O solution. The results provide the solvent isotope effect $k_{H^+}/k_{D^+} = 0.56$ and the substrate isotope effect $k_H/k_D = 6.2$ on the enolization reaction, both of which are consistent with the generally accepted mechanism for this process. The present results in combination with literature information also provide the solvent isotope effect on the enolization equilibrium, $K_E(H_2O)/K_E(D_2O) = 0.92$, and the solvent isotope effect on the ionization of isobutyrophenone as a carbon acid, $k_a^K(H_2O)/k_a^K(D_2O) = 5.4$, as well as the product of isotopic fractionation factor and medium effect, $\phi\Phi = 0.90$, for isobutyrophenone enol and the medium effect, $\Phi = 0.47$, for its enolate ion. The isotope effect on K_E is the first ever determined for the keto–enol equilibrium of a simple aldehyde or ketone; its near-unit value is consistent with expectation on the basis of fractionation factors for the species involved.

Key words: isobutyrophenone, keto–enol equilibrium, carbon-acid ionization, solvent isotope effects, isotopic fractionation factors.

Résumé : On a utilisé le piégeage par le brome pour mesurer les vitesses d'énolisation acidocatalysées de l'isobutyrophénone en solution dans le H_2O ou le D_2O et de l'α-*d*-isobutyrophénone en solution dans le D_2O. Les résultats permettent de déduire l'effet isotopique du solvant, $k_{H^+}/k_{D^+} = 0{,}56$, ainsi que l'effet isotopique du substrat, $k_H/k_D = 6{,}2$, sur la réaction d'énolisation; ces deux valeurs sont en accord avec le mécanisme généralement accepté pour ce processus. Les résultats obtenus, combinés aux informations disponibles dans la littérature, permettent aussi de déduire l'effet isotopique du solvant sur l'équilibre d'énolisation, $K_E(H_2O)/K_E(D_2O) = 0{,}92$, et l'effet isotopique du solvant sur l'ionisation de l'isobutyrophénone au niveau du carbone acide $k_a^K(H_2O)/k_a^K(D_2O) = 5{,}4$, ainsi que le produit du facteur de fractionnement isotopique et l'effet du solvant, $\phi\Phi = 0{,}90$, pour l'énol de l'isobutyrophénone, et l'effet du milieu, $\Phi = 0{,}47$, pour l'ion énolate. Dans le cas de l'effet isotopique sur K_E, il s'agit de la première mesure de ce genre réalisée sur l'équilibre céto–énolique d'un aldéhyde ou d'une cétone simple; sa valeur, qui est proche de l'unité, est en accord avec celle à laquelle on pourrait sur la base des facteurs de fractionnement des espèces impliquées.

Mots clés : isobutyrophénone, équilibre céto-énolique, ionisation de carbones acides, effets isotopiques du solvant, facteurs de fractionnement isotopiques.

[Traduit par la rédaction]

Introduction

The recent developement of methods for generating simple enols in greater than equilibrium amount under conditions where they can be observed directly has produced a renaissance of interest in the chemistry of these unstable substances (see, e.g., ref. 1). Among the wealth of new information that has become available are directly measured rate constants for ketonization of simple enols to their carbonyl tautomers, k_K, and these, in combination with rate constants for enolization, k_E, have led to accurate keto-enol equilibrium constants, K_E, by application of the relationship shown in eq. [1]. Solvent isotope effects have been measured on both k_E and k_K for a

$$[1] \qquad K_E = k_E/k_K$$

number of substrates, but up until the present study, enough information had not been supplied for the same system to determine the solvent isotope effect on K_E. We have now filled this gap using the keto–enol isomerization of isobutyrophenone, eq. [2].[3]

[2] 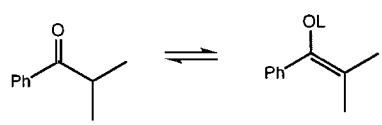

Received August 21, 1996.

J.R. Keeffe[1] **and A.J. Kresge.**[2] Department of Chemistry, University of Toronto, Toronto, ON M5S 3H6, Canada.

[1] Permanent address: Department of Chemistry, San Francisco State University, 1600 Holloway Avenue, San Francisco, CA 94132, U.S.A.

[2] Author to whom correspondence may be addressed. Telephone: (416) 978-7259. Fax: (416) 978-8775. E-mail: akresge@alchemy.chem.utoronto.ca

[3] The symbol "L" is used to denote either protium or deuterium, i.e., L = H or D.

We chose isobutyrophenone for this purpose because the keto–enol equilibrium constant for this substance in H_2O, $K_E(H_2O)$, had already been determined (2), and the hydronium-ion catalytic coefficient for ketonization of the enol in D_2O, $(k_K)_{D^+}$, had been measured as well (3); this ketone also has only one enolizable hydrogen, which simplifies matters considerably. The missing piece of information that we have now supplied is the hydronium-ion catalytic coefficient for enolization of the deuterated substrate in D_2O, $(k_E)^D_{D^+}$, eq. [3].

[3] 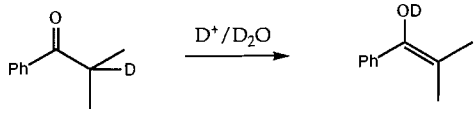

We have also in the present study determined hydronium-ion catalytic coefficients for the enolization of the protiated substrate in H_2O, $(k_E)^H_{H^+}$, eq. [4], and in D_2O, $(k_E)^H_{D^+}$, eq. [5]. This additional information has provided solvent and substrate kinetic isotope effects on the enolization of isobutyrophenone. The present results, in combination with other information already in the literature, have also led to the solvent equilibrium isotope effect on the ionization of isobutyrophenone as a carbon acid, and to isotopic fractionation factors for isobutyrophenone enol and enolate ion.

[4] 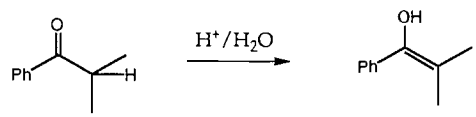

[5] 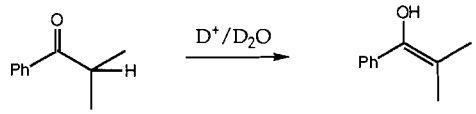

Experimental section

Kinetics

Rates of enolization of isobutyrophenone were determined by using bromine to scavenge the enol as it formed. Reactions were conducted in hydrobromic acid solutions under conditions where the bromine is complexed as Br_3^- ion, and changes in absorbance of this species at $\lambda = 310$ nm were used to monitor the reaction; measurements were made with a Cary 118 spectrometer whose cell compartment was thermostatted at 25.0 ± 0.05°C. Initial bromine concentrations were ca. 3×10^{-4} M and initial isobutyrophenone concentrations were $(2–3) \times 10^{-3}$ M. Zero-order initial rates were measured over times corresponding to 0.5–0.8% of the enolization reaction, and observed first-order rate constants were calculated using eq. [6] (4), in which $-dA/dt$ is

$$[6] \qquad k_{obs} = \frac{(-dA/dt\{1 + 1/(K[Br^-])\}}{\varepsilon[S]}$$

the zero-order rate of change of absorbance at $\lambda = 310$ nm, ε is the extinction coefficient of Br_3^- at this wavelength (determined here as 7535 M^{-1} cm^{-1}), [S] is the isobutyrophenone concentration, and K is the equilibrium constant for the $Br_2 + Br^-$ association reaction. Values of K for the conditions employed were interpolated using literature data (5), and [S] was measured spectrophotometrically before each reaction using $\varepsilon = 265$ M^{-1} cm^{-1} for isobutyrophenone at $\lambda = 300$ determined here.

Deuterated isobutyrophenone for the runs with deuterated substrate in D_2O was generated directly in the reaction solutions by first allowing unlabelled substrate to undergo isotope exchange with the solvent via enolization. Since base-catalyzed enolization is much faster than the very slow acid-catalyzed reaction (2), 0.1 M NaOD solutions were used for this purpose. Exchange was allowed to proceed for times judged to be sufficient to effect at least 99.5% deuteration; enough concentrated hydrobromic acid was then added to neutralize the base and produce a final acid concentration of the desired value, and bromination was begun by adding bromine to these acidic solutions. Isobutyrophenone concentration measurements made before and after the exchange process showed no change. Acid concentrations of these and other reaction mixtures were determined by titrating aliquots after the rate measurements had been completed.

Results

The bromine scavenging method of measuring rates of enolization requires enolization to be the rate-determining stage of the bromination process; thus, in the acidic solutions used here, the rate of bromination of the enol, $k_{Br}[Br_2]$, eq. [7], must be

[7] 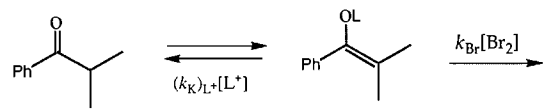

much greater than the rate of acid-catalyzed reketonization, $k_{K^+}[L^+]$. This requirement was amply fulfilled under the present experimental conditions. The reaction of enols with bromine is known to be nearly encounter-controlled, with rate constants of the order of 10^9 M^{-1} s^{-1} (6). At the bromine concentrations used here, the rate of the bromination reaction was therefore $k \cong 10^5$ s^{-1}, which is much greater than the $k \cong 1$ s^{-1} that can be estimated for reketonization using the known rate constants for this reaction in H_2O (2) and D_2O (3) solution. It is thus safe to conclude that enolization was indeed the rate-determining stage under the present reaction conditions.

These measurements were made in hydrobromic acid solutions over the concentration range [LBr] = 0.1 – 0.5 M. Three sets of runs were carried out using (*a*) unlabelled isobutyrophenone in H_2O, (*b*) unlabelled isobutyrophenone in D_2O, and (*c*) isobutyrophenone-α-*d* in D_2O. These data are summarized in Table 1.

For the measurements in D_2O, hydrobromic acid was supplied as 48% HBr in H_2O, and these solutions therefore contained small, variable amounts of protium. The rate constants obtained in these solutions were therefore extrapolated to 100% D_2O. A formalism generally applied to rate data in H_2O–D_2O mixtures (7) was used for this purpose, and, because the extrapolations were short, the linear form of this formalism shown as eq. [8] was employed. In this expression k_x is the observed rate constant

$$[8] \qquad k_x/k_H = 1 - x + x\phi$$

determined in the D_2O solution containing some protium, x is

the atom fraction of deuterium of that solution, k_H is the rate constant in H_2O, and ϕ is a fractionation factor. The fractionation factor in this case is equal to the rate constant in 100% D_2O divided by that in H_2O, as shown in eq. [9], which may be obtained from eq. [8] by setting x equal to 1.

$$[9] \qquad k_D/k_H = \phi$$

Elimination of k_H between eqs. [8] and [9] then leads to eq. [10], which may be

$$[10] \qquad k_D = \phi k_x/(1 - x + x\phi)$$

used to convert k_x into k_D.

The value of k_D needed to obtain ϕ for the application of eq. [10] is of course not known before the extrapolation is made, but a first approximation can be obtained by using k_x instead. The extrapolated value of k_D obtained in this way is then used to get a second approximation of ϕ, and the process is repeated until a self-consistent set of results is obtained.

This method was employed in the present case for the runs with unlabelled substrate; good convergence (ϕ changing by less than 0.1%) was reached after only three iterations. The procedure could not be used for the labelled substrate, because the method of introducing the label into this substance (isotopic exchange with the solvent) precluded rate measurements in H_2O, and the value of k_H needed to estimate ϕ was consequently not available. However, solvent isotope effects can be expected to be the same for isotopologs to a very good degree of approximation,[4] and the converged values of ϕ for the unlabelled substrate were consequently used for the labelled material as well.

Least-squares analysis of the relationship between enolization rate constants and acid concentration showed the presence of an "uncatalyzed" as well as an acid-catalyzed pathway. The mechanisms of these two pathways will of course be different and different values of ϕ will apply. Our rate constants were therefore separated into contributions from the two pathways and eq. [10] was applied separately to each. As Fig. 1 illustrates, corrected rate constants proved in all cases to be hardly different from uncorrected values, and both sets were accurately proportional to acid concentration. The results obtained by linear least-squares analysis are listed in Table 1.

One of the hydronium-ion catalytic coefficients determined here, that for enolization of isobutyrophenone-α-*h* in H_2O, had been determined before (2), and the value obtained, $(k_E)^H_{H^+} = (7.02 \pm 0.69) \times 10^{-7}$ M^{-1} s^{-1}, agrees well with the present result, $(k_E)^H_{H^+} = (8.13 \pm 0.45) \times 10^{-7}$ M^{-1} s^{-1}.

The isotope effects provided by the present results plus some related values from the literature are summarized in Table 2.

[4] Any difference would be an isotope effect upon an isotope effect, also known as a departure from the rule of the geometric mean (8). Such departures are produced by coupling of vibrational motions of bonds involving the isotopically substituted atoms; the effects are small even when these bonds are in the same molecule (9), and they will be even smaller, and consequently negligible, in a situation such as the present where one bond is in the substrate and the other is in the solvent.

Fig. 1. Relationship between acid concentration and rate constants for the enolization of isobutyrophenone-α-*h* in D_2O solution; uncorrected rate constants: O, corrected rate constants: Δ.

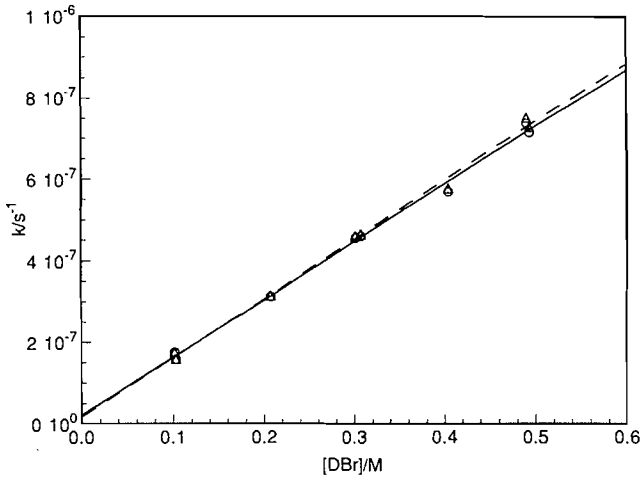

Table 1. Summary of rate data for the enolization of isobutyrophenone in aqueous solution at 25°C.[a]

[LBr]/M	%H[b]	$k_{obs}/10^{-7}$ s^{-1}
Isobutyrophenone-*h*/H_2O		
0.104	100	1.30
0.105	100	1.71
0.205	100	2.27
0.302	100	3.17
0.307	100	3.30
0.340	100	3.58
0.402	100	3.62
0.455	100	4.63
0.488	100	4.51
0.498	100	4.71
$k_{obs}/s^{-1} = (6.72 \pm 1.57) \times 10^{-8} + (8.13 \pm 0.45) \times 10^{-7}$ [HBr]		
Isobutyrophenone-*h*/D_2O		
0.103	1.1	1.58
0.208	2.3	3.14
0.302	3.0	4.55
0.308	3.0	4.59
0.405	4.0	5.69
0.491	4.9	7.36
0.494	4.9	7.14
$k_{corr}/s^{-1} = (1.64 \pm 1.24) \times 10^{-8} + (1.45 \pm 0.04) \times 10^{-6}$ [DBR]		
Isobutyrophenone-*d*/D_2O		
0.211	3.2	1.05
0.278	4.2	1.18
0.407	5.1	1.50
0.478	6.1	1.68
$k_{corr}/s^{-1} = (5.01 \pm 0.32) \times 10^{-8} + (2.35 \pm 0.09) \times 10^{-7}$ [DBr]		

[a]Ionic strength = [LBr].
[b]Atom% protium in the solvent.

Table 2. Summary of isotope effects for the isobutyrophenone keto–enol system.[a]

Process	Isotope effect[b]
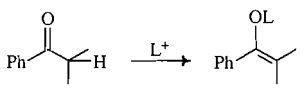	$(k_E)^H_{H^+}/(k_E)^H_{D^+} = 0.562 \pm 0.034$
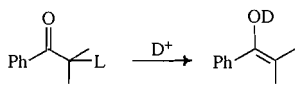	$(k_E)^H_{D^+}/(k_E)^D_{D^+} = 6.16 \pm 0.28$
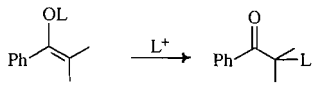	$(k_K)_{H^+}/(k_K)_{D^+} = 3.30 \pm 0.07$[b]
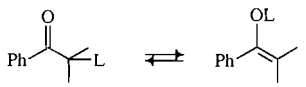	$K_E(H_2O)/K_E(D_2O) = 0.917 \pm 0.058$
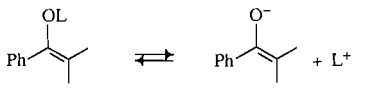	$K^E_a(H_2O)/K^E_a(D_2O) = 5.88 \pm 0.32$[c]
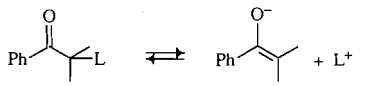	$K^K_a(H_2O)/K^K_a(D_2O) = 5.40 \pm 0.40$
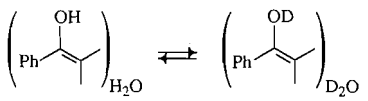	$\phi_E\Phi_E = 0.902 \pm 0.059$
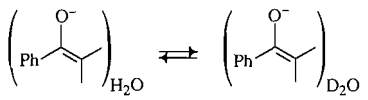	$\Phi_{E^-} = 0.466 \pm 0.035$
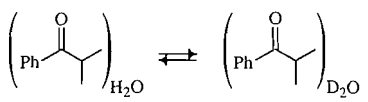	$\Phi_K = 0.827 \pm 0.013$[d]

[a]Ionic strength = 0.10 M.

[b]The error limits cited are statistical uncertainties and do not include possible systematic errors.

[c]From ref. 3.

[d]From ref. 18.

Discussion

Kinetic isotope effects

The rate measurements made here of the acid-catalyzed enolization of isobutyrophenone-α-*h* in H_2O and D_2O provide the solvent isotope effect $(k_E)^H_{H^+}/(k_E)^H_{D^+} = 0.56$. The inverse direction of this isotope effect ($k_H/k_D < 1$) is consistent with the generally accepted reaction mechanism for the hydronium-ion-catalyzed enolization of simple carbonyl compounds, which consists of rapid and reversible hydronation of the substrate on oxgyen followed by rate-determining removal of a carbon-bound hydron by a molecule of water, eq. [11] (10). The isotope effect is inverse because the hydrogen–oxygen bonds in water are stronger than those in the hydronium ion (11), and the bond tightening that this produces in the pre-equilibrium step is not fully compensated by the bond loosening that occurs as the hydronium ion is regenerated in the transition state of the rate-determining step. The present result is consistent with solvent isotope effects on the enolization of other carbonyl compounds, such as $k_{H^+}/k_{D^+} = 0.46$–0.54 for acetone (12) and $k_{H^+}/k_{D^+} = 0.57$ for acetaldehyde (13).

[11] 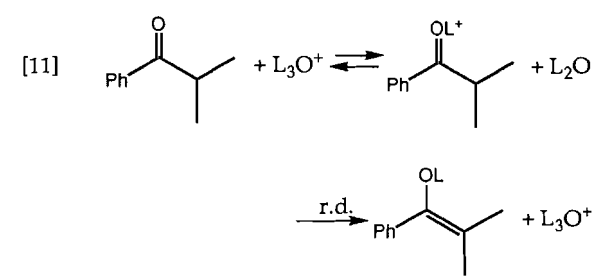

The present rate measurements of the acid-catalzyed enolization of isobutyrophenone-α-*h* and isobutyrophenone-α-*d* in D_2O also provide the substrate isotope effect $(k_E)^H_{D^+}/(k_E)^D_{D^+}$ = 6.2. This is a large, near-maximum, primary effect, which implies a central, symmetrical, rate-determining transition state, with the hydron about half-transferred and the free energy change for the hydron transfer step close to zero (14). This again is consistent with the mechanism of eq. [11], for the acidity of the oxygen-protonated conjugate acid intermediate may be estimated as $pK_a \cong -3.5$ (15), which translates into $\Delta G° = 4.8$ kcal mol^{-1} for the oxygen-hydronation step, and that together with $pK_E = 6.5$ (2), $\Delta G° = 8.8$ kcal mol^{-1}, for the overall reaction, leaves $\Delta G° = 4.0$ kcal mol^{-1} for the hydron transfer step.

Equilibrium isotope effects

A keto–enol equilibrium constant for isobutyrophenone in D_2O solution may be obtained by combining the presently determined acid-catalyzed enolization rate constant for the labelled substrate in D_2O with a literature value of the rate constant for acid-catalyzed ketonization of the enol in D_2O (3): $K_E(D_2O) = (k_E)^D_{D^+}/(k_K)_{D^+} = \{(2.35 \pm 0.09) \times 10^{-7}\}/\{(6.48 \pm 0.07) \times 10^{-1}\} = (3.63 \pm 0.14)\ 10^{-7}$, $pK_E(D_2O) = 6.44 \pm 0.02$.[5] Combination of this result with the value of K_E in H_2O (2) then gives the solvent isotope effect on the keto–enol equilibrium: $K_E(H_2O)/K_E(D_2O) = 0.917 \pm 0.058$.[5] This, as far as we are aware, is the first determination of a solvent isotope effect on the keto–enol isomerization of a simple monofunctional carbonyl compound.

The ionization of a carbonyl compound as a carbon acid may be split formally into two steps, enolization followed by acid ionization of the enol, as shown in eq. [12].

[12] 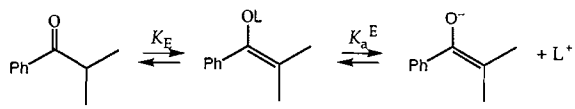

The carbon-acid ionization constant, K^K_a, then becomes the product of the keto–enol equilibrium constant and the acidity constant of the enol, $K^K_a = K_E K^E_a$. Since the present work has provided a value of K_E for isobutyrophenone in D_2O and K^E_a for isobutyrophenone enol in D_2O is available from the literature (3), the acidity constant of isobutyrophenone-α-*d* ionizing as a carbon acid in D_2O solution may be determined as $K^K_a(D_2O) = K_E(D_2O)\ K^E_a(D_2O)$: $\{(3.63 \pm 0.14) \times 10^{-7}\}\{(2.83 \pm 0.14) \times 10^{-13}\} = (1.03 \pm 0.05) \times 10^{-19}$ M, $pK^Ka(D_2O) = 18.99 \pm 0.02$.[5,6] Combination of this result with the value for isobutyrophenone-α-*h* in H_2O solution then gives the solvent isotope effect $K^K_a(H_2O)/K^K_a(D_2O) = 5.40 \pm 0.40$.[5] This is a reasonable value for an acid of this strength (16).

Isotopic fractionation factors

It is useful to separate isotope effects into contributions from individual hydrogens by expressing the overall effect in terms of fractionation factors for all of the isotopically substituted sites involved (9). The solvent isotope effect on the keto–enol equilibrium of isobutyrophenone, for example, may be formulated as shown in eq. [13],

$$[13] \quad \frac{K_E(H_2O)}{K_E(D_2O)} = \frac{\phi_K \Phi_K}{\phi_E \Phi_E}$$

where ϕ_K is the fractionation factor for the enolizable hydrogen of the keto form, ϕ_E is the fractionation factor for the hydroxyl group hydrogen of the enol, and Φ_K and Φ_E are medium effects produced by the solvation shells of the keto and enol isomers, respectively. It is likely that ϕ_K will have a value close to unity and consequently make no significant contribution to the overall isotope effect: fractionation factors for hydrogens in sp^3 bonds to carbon are not very different from unity (9), and $\phi = 1.0$ has in fact been determined for the enolizable hydrogen of 3-methylacetylacetone (17). With this assumption and the directly determined medium effect on the keto form, $\Phi_K = 0.827 \pm 0.013$[5] (18), plus the overall isotope effect determined here, the product of fractionation factor and medium effect for the enol may be evaluated as $\phi_E\Phi_E = 0.902 \pm 0.059$.[5] The near-unit value for this product is consistent with the fact that fractionation factors for hydrogens bound to uncharged oxygen, as well as medium effects for neutral solutes, are themselves generally close to unity (9).

A similar analysis of the overall isotope effect on the carbon acid ionization of isobutyrophenone according to eq. [14], in which ℓ {= 0.69 (6809, 19)} is the fractionation factor for the

$$[14] \quad \frac{K^K_a(H_2O)}{K^K_a(D_2O)} = \frac{\phi_K \Phi_K}{\ell^3 \Phi_{E^-}}$$

hydronium ion, gives $\Phi_{E^-} = 0.466 \pm 0.035$[5] for the medium effect on the isobutyrophenone enolate ion. This, again, is a reasonable result inasmuch as enolate ions, like alkoxide ions, can be expected to be strongly solvated by water molecules, to which they are associated by hydrogen bonding, and hydrogen bonding is known to produce low fractionation factors (20). In fact, on the assumption that the solvation shell of the enolate ion consists of three such water molecules, as is the case for the aqueous hydroxide ion, $\phi = 0.78 \pm 0.02$[5] can be calculated for each of the hydrogen-bonded hydrogens; this is not unlike $\phi = 0.7$, which has been deduced for the corresponding hydrogens solvating the hydroxide ion (9, 21).

[5] The error limits cited are statistical uncertainties and do not include possible systematic errors.

[6] This is a *concentration* dissociation constant applicable at ionic strength = 0.10 M.

Acknowledgement

We are grateful to the Natural Sciences and Engineering Research Council of Canada and the United States National Institutes of Health for financial support of this work.

References

1. Z. Rappoport (*Editor*). The chemistry of enols. Wiley, New York. 1990; Y. Chiang and A.J. Kresge. Science, **253**, 395 (1991).
2. P. Pruszynski, Y. Chiang, A.J. Kresge, N.P. Schepp, and P.A. Walsh. J. Phys. Chem. **90**, 3760 (1986).
3. Y. Chiang, A.J. Kresge, and P.A. Walsh. Z. Naturforsch. A: Phys. Sci. **44A**, 406 (1989).

4. N.P. Schepp. Ph.D. Thesis, Univ. of Toronto. 1989. pp. 30–33.
5. R.O. Griffith, A. McKeown, and A.G. Winn. Trans. Farady Soc. **28**, 101 (1932).
6. R. Hochstrasser, A.J. Kresge, N.P. Schepp, and J. Wirz. J. Am. Chem. Soc. **110**, 7875 (1988).
7. A.J. Kresge. Pure Appl. Chem. **8**, 243 (1964).
8. J. Bigeleisen. J. Chem. Phys. **23**, 2264 (1955).
9. A.J. Kresge, R.A. More O'Ferrall, and M.F. Powell. *In* Isotopes in organic chemistry. Vol. 7. *Edited by* E. Buncel and C.C. Lee. Elsevier, New York. 1987. Chap. 4.
10. J.R. Keeffe and A.J. Kresge. *In* The chemistry of enols. *Edited by* Z. Rappoport. Wiley, New York. 1990. Chap. 7.
11. R.A. More O'Ferrall, G.W. Koeppl, and A.J. Kresge. J. Am. Chem. Soc. **93**, 1 (1971); **93**, 9 (1971).
12. O. Reitz. Naturwissenschaften, **24**, 814 (1936); W.J. Albery and J.S. Gelles. J. Chem. Soc. Faraday Trans. 1, **78**, 1569 (1982); K.P. Shelly, S. Venimadhavan, K. Nagarajan, and R. Stewart. Can. J. Chem. **67**, 1274 (1989).
13. Y. Chiang, M. Hojatti, J.R. Keeffe, A.J. Kresge, N.P. Schepp, and J. Wirz. J. Am. Chem. Soc. **109**, 4000 (1987).
14. A.J. Kresge. *In* Isotope effects on enzyme-catalyzed reactions. *Edited by* W.W. Cleland, M.H. O'Leary, and D.B. Northrop. Univ. Park Press, Baltimore, Md. 1977. pp. 37–63.
15. A. Bagno, G. Scorrano, and R.A. More O'Ferrall. Rev. Chem. Int. **7**, 313 (1987).
16. P.M. Laughton and R.E. Robertson. *In* Solute–solvent interactions. *Edited by* J.F. Coetzee and C.D. Ritchie. Marcel Dekker, New York. 1969. Chap. 7.
17. D.B. Dahlberg and F.A. Long. J. Am. Chem. Soc. **95**, 3825 (1973).
18. J.R. Keeffe and A.J. Kresge. Can. J. Chem. **67**, 792 (1989).
19. A.J. Kresge and A.L. Allred. J. Am. Chem. Soc. **85**, 1541 (1963).
20. M.M. Kreevoy and T.M. Liang. J. Am. Chem. Soc. **102**, 3315 (1980).
21. V. Gold and S. Grist. J. Chem. Soc. Perkin Trans. 2, 89 (1972); W.J. Albery. *In* Proton transfer reactions. *Edited by* E.F. Caldin and V. Gold. Chapman and Hall, London. 1975. Chap. 9.

Folding strain stereocontrol in cyclohexane ring formation by means of an intramolecular ester enolate alkylation reaction

Takashi Tokoroyama and Hisashi Kusaka

Abstract: Diastereoselectivity in the cyclization of ethyl 7-bromo-2-methylheptanoates with an additional substituent at various positions in the chain, by LDA treatment, was investigated in connection with the concept of folding strain stereocontrol. Cyclization of 3-, 4-, and 6-methyl-substituted substrates revealed high selectivity, which demonstrates the prevalence of folding strain stereocontrol and the usefulness of this approach for stereoselective ring construction. In particular, reactions of the latter two substrates resulted in the stereodivergent preparation of diastereomeric 1,3-dimethylcyclohexanecarboxylates. In the case of the 5-methyl-substituted substrate, the selectivity of ring closure was only moderate. ^{1}H and ^{13}C NMR spectroscopic data were useful for determining the conformation of 1-methylcyclohexanecarboxylate derivatives. The origin of the diastereoselectivity was examined through the qualitative comparison of the strain in the diastereomeric folding in the transition state. Various factors that might affect stereoselectivity were examined in the cyclization of 5-substituted substrates to better understand this concept. As predicted, the selectivity increased as the substituent became bulkier: Ph < Me ≈ Et < i-Pr < *t*-Bu. The effects of other factors — solvent, base counter cation, and leaving group — on selectivity agree with results predicted from the reactivity–selectivity relationship.

Key words: folding strain stereocontrol; diastereoselectivity in ring-closure reaction; remote asymmetric induction; ethyl 2-methylcyclohexanecarboxylate derivatives, ^{1}H and ^{13}C NMR; stereoselective synthesis of substituted cyclohexane derivatives.

Résumé : Dans le cadre de travaux sur le concept du stéréocontrôle par le plissement des chaînes, on a étudié la diastéréosélectivité de la cyclisation, sous l'influence du LDA, de 7-bromo-2-méthylheptanoates d'éthyle portant un substituant additionnel dans diverses positions. Les cyclisations des substrats substitués par des groupes méthyles en positions 3, 4 ou 6 se produisent avec une grande sélectivité; ceci met en évidence la prévalence du stéréocontrôle par le plissement de la chaîne et démontre l'utilité de cette approche pour la formation stéréosélective de cycles. Ceci est particulièrement vrai avec les deux derniers substrats qui conduisent à la préparation stéréoconvergente des 1,3-diméthylcyclohexanecarboxylates diastéréomères. Dans le cas du substrat portant un groupe méthyle en position 5, la sélectivité de la formation du cycle n'est que modérée. Les données de la spectroscopie RMN du ^{1}H et du ^{13}C se sont avérées utiles pour la détermination de la conformation des dérivés 1-méthylcyclohexanecarboxylates. On a étudié l'origine de la diastéréosélectivité par le biais d'une comparaison qualitative de la tension dans le plissement diastéréomère dans l'état de transition. Dans le but de mieux comprendre ce concept, on a examiné divers facteurs pouvant affecter la stéréosélectivité lors de la cyclisation de substrats substitués en position 5. Tel qu'on pouvait le prévoir, la sélectivité augmente avec une augmentation de l'encombrement du substituant : Ph < Me ≈ Et < i-Pr < *t*-Bu. Les effets des autres facteurs — solvant, contre-ion basique et le groupe partant — sur la sélectivité sont en accord avec les résultats prédits sur la base de la relation réactivité–sélectivité.

Mots clés : stéréocontrôle par le plissement de la chaîne; diastéréosélectivité lors de réactions de cyclisation; induction asymétrique à distance; RMN ^{1}H et ^{13}C de dérivés du 2-méthylcyclohexanecarboxylate d'éthyle; synthèse stéréosélective de dérivés du cyclohexane substitué.

[Traduit par la rédaction]

Introduction

Diastereoselective cyclization is an efficient approach for the synthesis of ring compounds, with stereoselective installation of substituents on the ring (1). For this reason, cycloaddition reactions, such as the Diels–Alder reaction, are considered a powerful synthetic tool (2). In contrast, diastereocontrol in a simple ring-closure reaction has attracted far less attention. In connection with the stereoselective synthesis of natural products (3), we previously found that the cyclization of 2-(3′,4′-dimethyl-6′-trimethylsilylhex-4′-enyl)cyclohex-2-enone (**1**) proceeded with twofold stereocontrol to give the decalone derivative (**2**) as a single diastereomer (Scheme 1) (4). One of the stereocontrol factors involved the diastereofacial selection based on the conformational preference of the 3′-methyl group with respect to the diastereomeric folding of the acyclic chain in the transition state. We have pointed out the general utility

Received March 14, 1995.[1]

T. Tokoroyama[2] and H. Kusaka. Faculty of Science, Osaka City University, Sumiyoshi-ku, Osaka 558, Japan.

[1] Revision received September 12, 1996.

[2] Author to whom correspondence may be addressed. Present address: 3-25-1, Makizuka-dai, Sakai-shi, Osaka 590-01, Japan. Telephone and Fax: 81-722-93-6492.

Scheme 1.

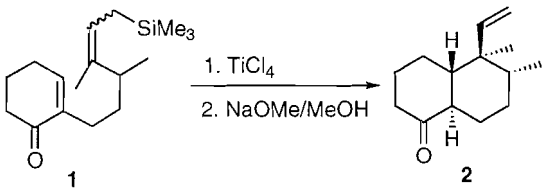

of this type of stereoselection for the diastereoselective construction of ring compounds in terms of folding strain stereocontrol (5–7).

For the intermolecular reaction of acyclic molecules, diastereoselection is generally effective only for 1,2-asymmetric induction without the intervention of chelation or other special conditions. However, for intramolecular reactions, the relative steric strain in the diastereomeric folding of the chain may greatly affect the stereoselectivity, and thus the asymmetric induction, more than a 1,3-relationship to the stereogenic center, could be effective in the folding strain stereocontrol. We believe that the diastereofacial selectivity in a ring-closure reaction is determined by the difference in the total strain energy ($\Delta(SE)_{AB}^{*}$), between the diastereomeric transition states (A,B) and that, even if the stereocenter in the chain is remote from the bond-forming atom, the energy difference could be great enough for the diastereoselection to be effective. Moreover, the design of a stereoselective cyclization may be possible by estimating the strain energy involved. Just as diastereodifferentiation in some acyclic stereocontrols is due to the energy difference between diastereomeric cyclic transition states (e.g., aldol reaction and the Claisen rearrangement) (8), the relative energy of diastereomeric foldings in the transition state determines diastereoselection in the ring-closure reaction. Particularly in carbocyclic six-membered ring formation, the difference in conformational energy between the transition states could be more distinct than that in systems involving many sp^2 carbon atoms and hetero atoms, and a better diastereoselectivity would be reasonably expected. Thus, a high possibility of remote diastereocontrol could be anticipated in carbocyclic ring formation. Although several examples of stereocontrols of this type can be found in the literature, a systematic investigation to demonstrate the underlying concept is lacking (for notable examples, see ref. 9). To further test the feasibility of our concept, we investigated diastereofacial selectivity in the cyclization of ethyl 7-bromo-2-methylheptanoates **3** with a substituent at various positions in the chain to diastereomeric cyclohexanecarboxylates **4** and **5** via an intramolecular ester enolate alkylation reaction (Scheme 2). Kim et al. have used cyclization reactions of this type for the stereoselective synthesis of cyclic natural products (*9f–9n*).

Results and discussion

Synthesis of cyclization substrates

Ethyl 7-bromo-2,3-dimethylheptanoate (**11**) was synthesized by the alkylation of acetoacetate dianion with 3-benzyloxypropyl bromide (**7**) and subsequent successive introduction of methyl groups at the 3 and 2 positions as shown in Scheme 3. To introduce the 3-methyl group, the combination of Nozaki and Weiler methods (10) was used and the resultant trisubstituted olefin was catalytically hydrogenated.

Scheme 2.

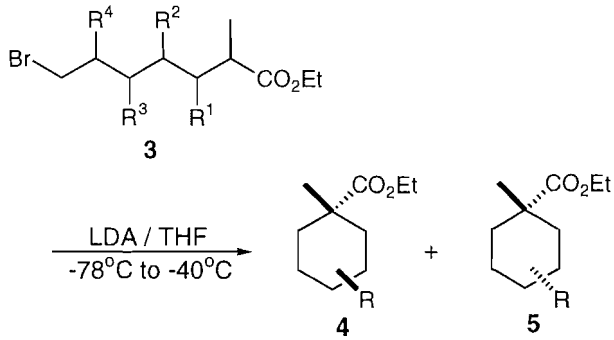

Ethyl 7-bromo-2,4-dimethylheptanoate (**15**) was synthesized by homologation of 2-methyl-δ-valerolactone (**12**) using in situ reduction and the Horner–Emmons reaction (11) (Scheme 4). The synthesis of *ethyl 7-bromo-2,5-dimethylheptanoate* (**19**) was achieved in the same way by starting from 3-methyl-δ-valerolactone (**17**) obtained by the NaBH4 reduction (12) of 3-methylglutaric anhydride (**16**) (Scheme 5). Substrates **25** and **26**, which have a 5-ethyl and a 5-isopropyl group, respectively, were synthesized by the introduction of the alkyl groups through the copper-catalyzed conjugate addition (13) of Grignard reagents to 2-penten-5-olide (**20**) and the subsequent transformations were similar to those described above (Scheme 5). To synthesize the *5-phenyl substrate* **30** the requisite 3-phenyl-δ-valerolactone (**28**) was prepared by the $NaBH_4$ reduction of 3-phenylglutaric anhydride (**27**). To synthesize the 5-*tert*-butyl substrate **35**, since the anhydride corresponding to **27** could not be obtained by the Michael reaction of methyl 4,4-dimethyl-2-pentenoate with dimethyl malonate, the other method shown in Scheme 6 was used. *Ethyl 7-bromo-2,6-dimethylheptanoate* (**39**) was synthesized by the homologation of 4-methyl-δ-valerolactone (**37**) (Scheme 7). The substrates **11**, **15**, **19**, **25**, **26**, **30**, **35**, and **39** were all obtained as a mixture of diastereomers, as seen distinctly from their ^{13}C NMR spectra.

Cyclization and stereochemical assignment of the diastereomeric products

Cyclization was performed in THF using three equivalents of LDA at −78°C for 1 h, and moderate to good yields of the cyclization products were generally obtained under these conditions. The isomer ratios were determined by capillary GPC. Stereochemical assignment of the diastereomeric products was carried out effectively by the analysis of 400 MHz ^1H and ^{13}C NMR spectra with reference to those reported in the literature, when available. The results are shown in Tables 1–5.

Ethyl trans-*1,2-dimethylcyclohexanecarboxylate (40)*[3]

The ^1H NMR spectra of the major product in the cyclization of ethyl 7-bromo-2,3-dimethylheptanoate (**11**) agree well with the data reported for the methyl ester corresponding to the *trans* compound **40**, except with regard to the signal due to the

[3] Throughout this paper, the *cis–trans* notation for the relative configuration of substituted cyclohexanecarboxylate derivatives refers to the ester groups.

Scheme 3.

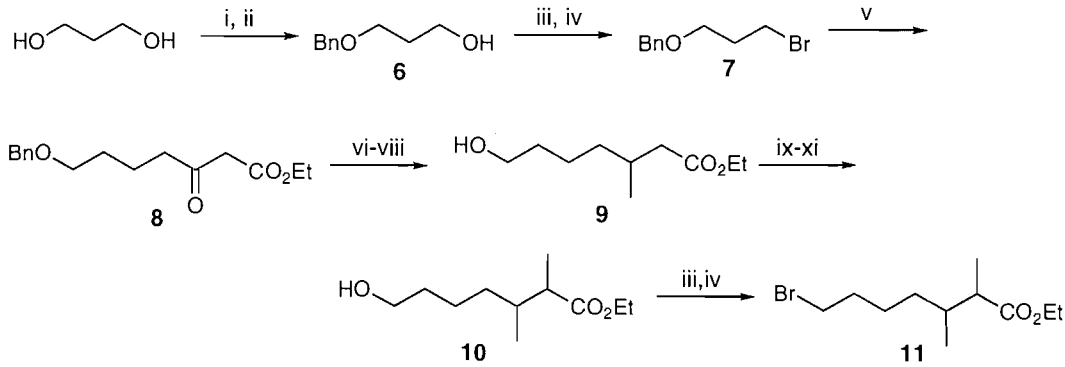

(i) PhCHO, TsOH; (ii) $LiAlH_4$, $AlCl_3$; (iii) MsCl, Et_3N; (iv) LiBr; (v) ethyl acetoacetate dianion; (vi) $(EtO)_2P(O)Cl$, NaH; (vii) $Pd(PPh_3)_2Cl_2$, Me_3Al; (viii) H_2, Pd-C; (ix) MOMCl, $i\text{-}Pr_2NEt$; (x) MeI, NaH; (xi) 6 N HCl

Scheme 4.

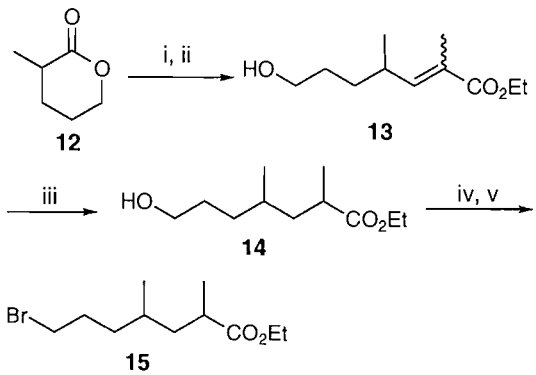

(i) DIBAL; (ii) $(EtO)_2P(O)CHMeCO_2Et$, BuLi; (iii) H_2, Pd-C; (iv) MsCl, Et_3N; (v) LiBr

Scheme 5.

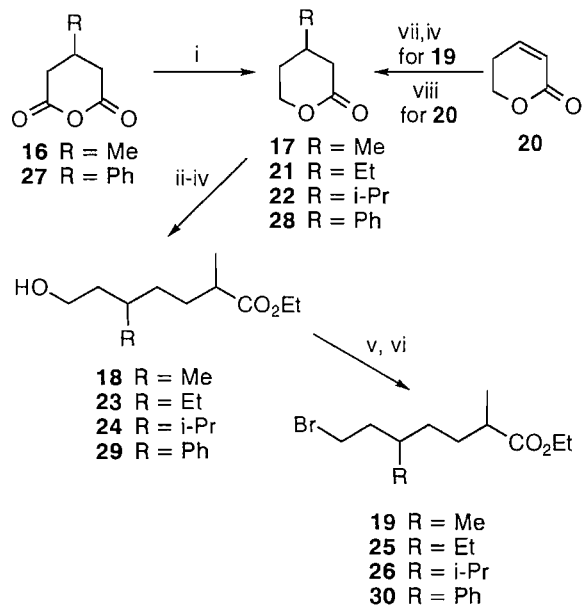

(i) $NaBH_4$, THF; (ii) DIBAH; (iii) $(EtO)_2P(O)CHMeCO_2Et$, BuLi; (iv) H_2, Pd-C; (v) MsCl, Et_3N; (vi) LiBr; (vii) CH_2=CHMgBr, CuI; (viii) $Me_2CHMgBr$, CuI

ester groups (14, 15). When the ^1H NMR spectra of **40** was analyzed using a COSY experiment, the coupling constants between the resonances of the 2-H proton and 3-methylene protons were found to be 3.1 and 10.5 Hz. Therefore, the 2-H proton was concluded to be axial, and the 2-methyl group was considered to assume an equatorial conformation. Moreover, the appearance of the 2-H proton signal at a rather deshielded position (δ 2.01) indicated that the ethoxycarbonyl group is in an equatorial conformation (vide infra).

Ethyl cis- *and* trans-*1,3-dimethylcyclohexanecarboxylates (42 and 43)*

The diastereomers **42** and **43** were obtained as the major products, respectively, in the cyclization of 2,4- and 2,6-dimethyl-7-bromoheptanoic acid esters **15** and **39**. Comparison of the ^1H NMR data with those reported previously (15, 16) suggested that they represented *cis* and *trans* compounds, respectively. The difference between **42** and **43** was more distinct in the ^{13}C NMR spectra in which the signals due to the tertiary methyl groups were observed higher upfield in the former (δ 20.5) than in the latter (δ 28.7). This fact indicates that the former methyl group is axial and the latter is equatorial. Furthermore, in the ^1H NMR spectra, the *trans* ester **43** exhibited signals due to the equatorial C-2 and C-6 protons at deshielded positions (δ 2.13 and 2.16, respectively), while those of the *cis* ester **42** appeared in a normal range, with the ethoxycarbonyl group in **42** and **43** in equatorial and axial orientation, respectively. The ^{13}C resonances of the secondary methyl groups in **42** and **43** were located at a similar field (δ 22.8 and 22.4).

Ethyl trans- *and* cis-*1,4-dimethylcyclohexanecarboxylates (44 and 45)*

The mixture of diastereomers obtained by the cyclization of **19** was separated by flash chromatography, and their conformation was studied by ^1H and ^{13}C NMR spectroscopy. In ^{13}C NMR spectra of the major and minor products, the signals due to tertiary and secondary methyl groups were observed at δ 20.8, 22.7 and δ 28.3, 22.4, respectively. Thus, the former was

Scheme 6.

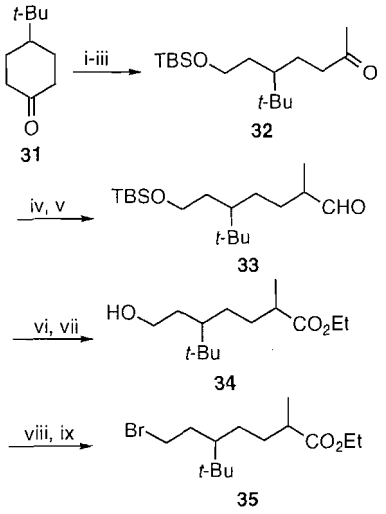

(i) MCPBA; (ii) MeLi; (iii) TBDMSCl, imidazole; (iv) $Ph_3P{=}CHOMe$; (v) $HClO_4$, H_2O; (vi) $KMnO_4$, NaH_2PO_4; (vii) EtOH, TsOH; (viii) MsCl. Et_3N; (ix) LiBr.

considered to have the *trans* structure (**44**) and the latter the *cis* structure (**45**). This assignment was consistent with the difference in the ^1H NMR spectra for both products. The signals of the 2-H_{eq} (= 6-H_{eq}) and 3-H_{ax} (= 5-H_{ax}) protons for **45** appeared at a deshielded (δ 2.17 vs. 1.58 for **44**) and shielded position (δ 0.96 vs. 1.69 for **44**), respectively, which was ascribed to the axial conformation of an ethoxycarbonyl group in **45**.

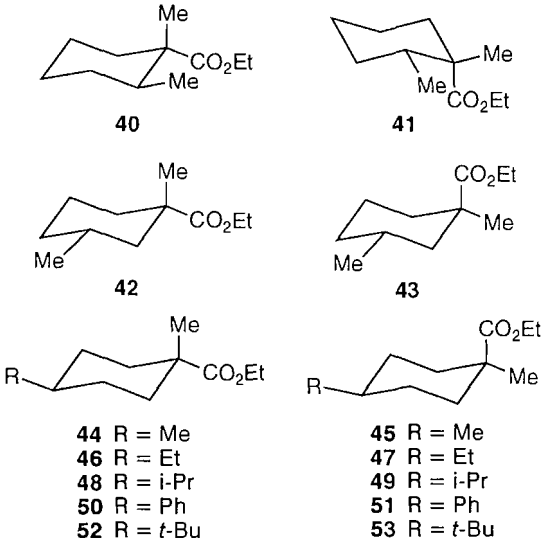

Ethyl trans- *and* cis-*4-ethyl-, 4-isopropyl-, 4-phenyl-, or 4-tert-butyl-1-methylcyclohexanecarboxylates (46–53)*

In these compounds C-4 substituents are believed to lock the conformation, in which they are disposed equatorially, even more strictly than in the 4-methyl analogs above. Thus, the configurations of the diastereomeric products were most readily assigned by comparing the chemical shift values of the signals due to 1-methyl groups in ^{13}C NMR spectra; i.e., the compound with the larger δ value was considered to be *cis* and the one with the smaller δ value *trans*. Additional support for these assignments was obtained by analyzing ^1H NMR spectra, as with the 4-methyl analog described above.[4]

Scheme 7.

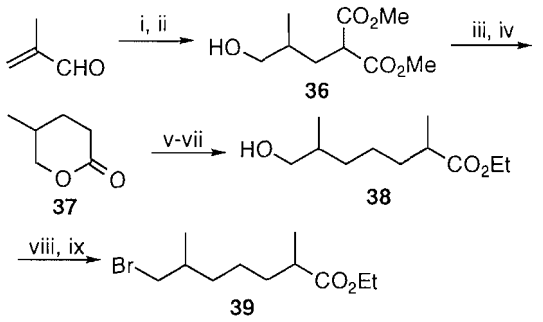

(i) $CH_2(CO_2Me)_2$, Et_3N; (ii) $NaBH_4$; (iii) KOH; (iv) H_2SO_4; (v) DIBAH; (vi) $(EtO)_2P(O)CHMeCO_2Et$, BuLi; (vii) H_2, Pd-C; (viii) MsCl, Et_3N; (ix) LiBr.

Diastereoselectivity in the cyclization of ethyl 7-bromo-2-methylheptanoates with a methyl substituent at various positions in the chain

The ratios of the diastereomeric products observed in the cyclization of substrate **3** with a methyl group at various positions are summarized in Table 1. The reaction shows generally good selectivity, except in the case of 5-methyl-substituted substrate **19**. These results indicate that the remote stereocontrol in a simple ring-closure reaction would have greater potential than is generally thought (1) for the stereoselective synthesis of cyclic compounds, even though the bulkiness of the substituent and the type of the reaction concerned must be taken into account. In the following discussion, the relationship between the degree of diastereoselectivity and the energy difference of the diastereomeric transition states estimated qualitatively from the folding strains is addressed separately for the individual substrates. We have made two assumptions regarding the conformation of the transition state for the sake of simplification.[5] First, we assume that the chair conformation is decidedly preferred over the twist-boat conformation. Second, we assume that the eclipsed (skew) form **54** is favored over the bisected (*gauche*) form **55**, as has been pointed out also by D. Kim et al. (9*g*, 9*k*). The latter assumption is based on the generally accepted view regarding allylic systems, which is supported by the results of computational studies (17, 18). However, these studies have also revealed that the energy difference between the skew and *gauche* forms is much smaller in the model enolate system **56** than in the crotyl analog **57** (1.7 vs. 3.4 kcal/mol) (17). If the presence of the C-2

[4] The ^1H NMR spectral data for the *trans* and *cis* methyl esters corresponding to **52** and **53** were given in ref. 15, but these could not be used to distinguish between the diastereomeric products.

[5] The cyclization is considered to proceed mainly via *E*-enolates (19). The effect of enolate geometry on this issue is unknown, though it is not believed to be very important. A cyclization experiment with the substrates with bulkier ester alkyl groups might be informative in this regard.

Table 1. Remote diastereocontrol in the cyclization of ethyl 7-bromo-2-methylheptanoates with a methyl group at various positions in the chain.[a]

Entry	Subrates	Cyclization products		Diastereomeric ratio (yield)
1	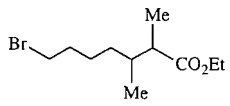 **11**	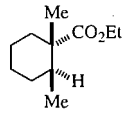 **40**	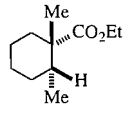 **41**	**40** : **41** = 96 : 4 (78%)
2	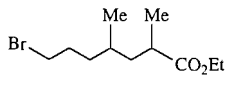 **15**	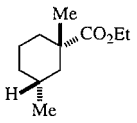 **42**	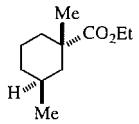 **43**	**42** : **43** = >99 : 4 (83%)
3	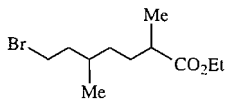 **19**	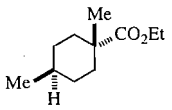 **44**	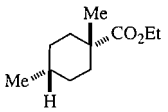 **45**	**44** : **45** = 79 : 21 (66%)
4	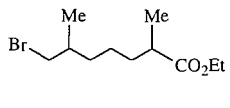 **39**	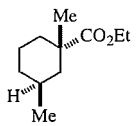 **43**	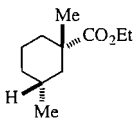 **42**	**43** : **42** = 93 : 7 (53%)

[a]The reactions were conducted with 3 equivalents of LDA in THF at −78°C.

methyl group is taken into account, the energy difference between the transition states (TS) **54** and **55** could be considerably less than the former value, since the *gauche* interaction between the 2-methyl group and the C-3—C-4 bond might destabilize TS **54**.

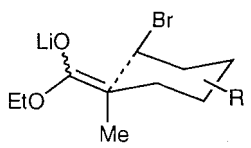

54

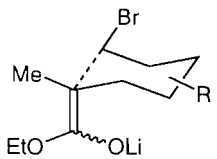

55

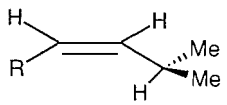

56 R = OMe
57 R = Me

*Cyclization of ethyl 7-bromo-2,3-dimethylheptanoate (**11**)*
In this cyclization, a stereogenic center exists next to the bond-forming carbon atom of an allylic system. Our dually stereocontrolled cyclization reaction mentioned at the outset (Scheme 1) involves this type of stereocontrol. Most of the stereocontrols used by Kim et al. (9) also belong to this category. They have reported an overall selectivity of 98:2 in the cyclization of substrate analogous to **11** (2-butyl and 7-tosyloxy groups instead of 2-methyl and 7-bromo, respectively) (9*f*). The major factors that affect selectivity include the $A^{1,3}$ strain (18, 20) and the additional *gauche* repulsion (quasi-axial vs. quasi-equatorial conformations of the 3-methyl group), both of which make TS **59** unfavorable and lead to the *cis* product through TS **58**.[6] The latter effect is inherent in the

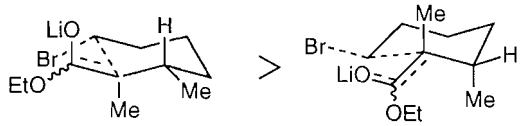

58 > **59**

ring-closure reaction of a carbon chain and should not be neglected (~ 1.8 kcal). In contrast to the models (21, 22) postulated to explain the diastereofacial selectivity in the intermolecular reaction of ester enolates with a β-stereogenic center, where the stereoelectronic effect plays an important role, the steric constraint resulting from the folding of the chain is an additional significant factor in determining the selectivity in the ring-forming reaction. Selectivity in the cyclization of substrates with a substituent remote from the atom on which the bonding occurs largely depends on the extent of the strain energy involved in the chain folding (1,*n*-asymmetric induction, $n \geq 3$).

*Cyclization of 7-bromo-2,4-dimethylheptanoate (**15**)*
The diastereoselectivity for the *cis* product **42** was excellent, and formation of the *trans* product **43** was not detected. TS **61**,

[6] The sign of the inequality between formulas for the transition state conformations denotes the energy (or kinetic) preference.

which leads to the *trans* product **43**, is destabilized relative to *cis*-TS **60** by *gauche* repulsion (~1.8 kcal/mol) and 1,3-diaxial dimethyl interaction (3.7 kcal/mol) (23, 24). This energy difference (<5.5 kcal/mol)[7] is sufficient to explain the selectivity of greater than 99%. Incidentally, the *gauche* transition state **62**, which has no destabilization due to severe 1,3-diaxial dimethyl repulsion, must have a strain energy lower than that of **61**, but higher than that of **60**.

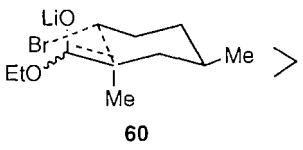

60

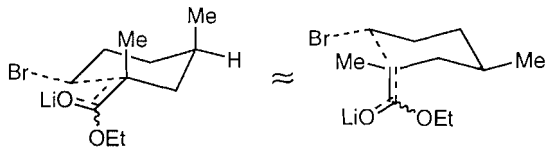

61 **62**

Cyclization of ethyl 7-bromo-2,5-dimethylheptanoate (19)

In this cyclization, formation of the *trans* product **44** was preferred to that of the *cis* product **45** by a ratio of 79:21, which corresponds roughly to the energy difference of 0.8 kcal/mol between the diastereomeric transition states. This selectivity is lower than that expected from the conformational energy difference between **63** and **64** (quasi-equatorial vs. quasi-axial methyl groups, ~1.8 kcal/mol). One of the bonds (C-5—C-6) *gauche* to the axial methyl group in TS **64** located at an end is less sterically constrained, provided that the C-1—C-6 bond remains loose and that the ester enolate alkylation reaction involves an early transition state, as generally postulated (19). This situation would account for the lower selectivity.

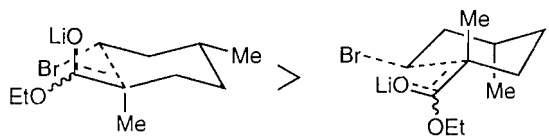

63 **64**

Cyclization of ethyl 7-bromo-2,6-dimethylheptanoate (39)

In this case, the *trans* product **43** was formed predominantly rather than the *cis* isomer **42**, which indicates that TS **66** is preferred to **65**. This fact might be explained by the presence of a severe torsional strain between the 6-methyl and the bromine bonds in TS **65**, which are nearly synperiplanar. While the diastereomeric TS **66** appears to suffer from 1,3-diaxial dimethyl interaction (~3.7 kcal/mol) (23, 24), twist-boat TS **66a** is unlikely since it is doubly disadvantaged (twist-boat form and the *gauche* form). Also, the 1,3-diaxial dimethyl interaction in TS **66** might not be as strong as in a normal cyclohexane ring since the loose C-1—C-6 bond intervenes between the two carbon atoms bearing methyl groups, which differs from the situation in TS **61**. The strong dependence of van der Waals repulsion on the distance between the atoms is well known (25).

[7] The energy difference between the transition states should be less than that estimated for the cyclohexane products, due to the looseness of the emerging bond.

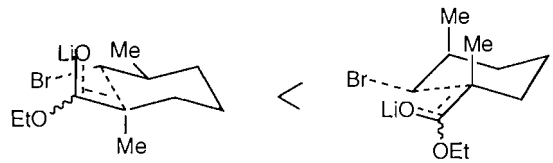

65 **66**

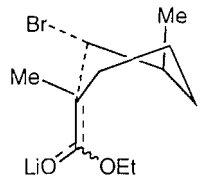

66a

Factors influencing diastereoselectivity

Various parameters that may affect the diastereofacial selectivity, including the size of 5-substituents, were investigated to better understand the parameters governing the cyclization of ethyl 7-bromo-2,5-dimethylheptanoate (**19**), which shows only moderate stereoselectivity.

Relationship between diastereoselectivity and bulkiness of the substituent in the chain

The steric bulkiness of the substituents is believed to greatly affect the energy difference between the diastereomeric transition states, and hence the diastereoselectivity. This subject was investigated in the cyclization of substrate **3**, which carries substituents of various sizes at the 5-position. The results are shown in Table 2 with the relevant conformational free energy (*A*-values) (ref. 24, pp. 433–436, and ref. 26). Generally, selectivity was enhanced as the bulkiness of the 5-substituents increased, as anticipated. However, two points should be mentioned. First, a change in the 5-substituent from methyl to phenyl resulted in a decrease in selectivity, which was contrary to the result predicted from the *A*-values. This result is supported by the fact that in the equilibrium of 1-methyl-1-phenylcyclohexane conformers, the methyl group prefers the equatorial position by 0.3 kcal/mol (27, 28; see also ref. 12). A computational study on a simple allylic system (17) also showed that a phenyl group can be less effective than a methyl group in providing a conformational lock, depending on its disposition. Second, the diastereoselectivity observed for the 5-*tert*-butyl substrate **35** was not as high as expected, considering the ability of the *tert*-butyl group to lock the cyclohexane conformation. This result might indicate the intervention of a *gauche* TS **69** or a twist-boat TS **70** rather than a chair TS **68**, which would definitely be energetically unfavorable.

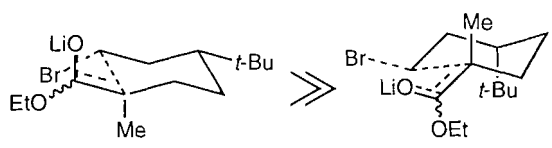

67 **68**

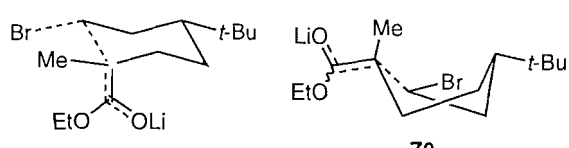

69 **70**

Table 2. Effect of the bulkiness of the substituent on diastereoselectivity in the cyclization of 5-substituted 7-bromo-2-methylheptanoates.

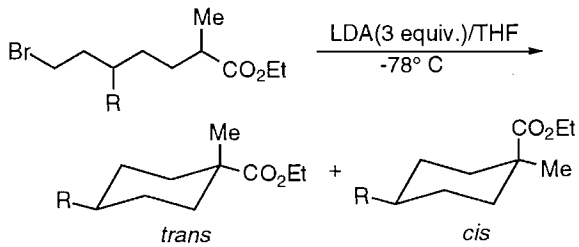

Entry	Substrate R	Substrate No.	Diastereomeric yield (%)	Products ratio (*trans*/*cis*)	A-value (kcal/mol)
1	Me	**19**	66	**44/45** = 79:21	1.8
2	Et	**25**	89	**46/47** = 79:21	1.8
3	i-Pr	**26**	85	**48/49** = 86:14	2.1
4	Ph	**30**	80	**50/51** = 74:26	2.9
5	*t*-Bu	**35**	77	**52/53** = 89:11	>4.5

Table 3. Effect of the solvent on diastereoselectivity in the cyclization of ethyl 7-bromo-2,5-dimethylheptanoate.[a]

Entry	Solvent	Reaction temp. (°C)	Yield (%)	Product ratio *trans*/cis (**44/45**)
1	Et_2O	−20[b]	72.9	73:27
2	THF	−78	66.0	79:21
3	DME	−78	77.5	69:31
4	THF/HMPA[c]	−78	71.9	52:48

[a]The reaction was conducted using 2.5 molar equivalents of LDA.
[b]The reaction did not proceed to completion at −78°C.
[c]HMPA was used in 13.4 molar equivalents.

Effect of the solvent

The effect of the solvent on the diastereoselectivity was examined in the cyclization of the 5-methyl substrate **19** (Table 3). Excluding the reaction in diethyl ether (entry 1), which was conducted at an elevated temperature, selectivity decreased in the order THF > DME > THF/HMPA. This order parallels the well-known increase in enolate reactivity due to the greater dissociation of the enolate cation ion pair and ion aggregate (ref. 26, p. 428). Based on the reactivity–selectivity principle (29), the increase in reactivity should diminish selectivity.

Effect of base counter cation

Kim et al. reported for one of their cyclization reactions that the use of LDA as a base gave better selectivity than potassium hexamethyldisilazide (KHMDS), albeit in poorer yield (9*g*). The results of our investigation in this regard are shown in Table 4. In comparing entries 2 and 4, the selectivity is slightly higher in the reaction with lithium hexamethyldisilazide

Table 4. Effect of the base on diastereoselectivity in the cyclization of ethyl 7-bromo-2,5-dimethylheptanoate.

Entry	Base[a]	Reaction temp. (°C)	Yield (%)	Product ratio *trans*/cis (**44/45**)
1	LDA	−78	66.0	79:21
2	LHMDS	r.t.	72.0	73:27
3	KHMDS	−25	67.6	71:29
4	KHMDS	r.t.	75.0	69:31

[a]Three equivalents were used.

(LHMDS) than with KHMDS. This result is consistent with the trend predicted from the reactivity–selectivity relationship, since the degree of ion-pair dissociation is greater in potassium enolate than in lithium enolate and the former should be more reactive.

Leaving group effect

In the cyclization reactions described thus far, the observed selectivity is generally lower than that predicted from an estimation of the energy difference between the diastereomeric transition states based on the conformation of the product cyclohexane derivatives. This discrepancy may be largely attributed to the fact that the transition state involves a looser conformation than the product. The extent of the discrepancy should increase as the transition state occurs earlier in the reaction. This influence on selectivity is similar to Hammond–BEP behavior (29). Thus, we can predict that diastereoselectivity should decrease as the ease with which the leaving group dissociates increases. Our results are summarized in Table 5.

Conclusion

Diastereoselectivity in cyclohexane ring formation by the intramolecular ester enolate alkylation reaction has been investigated as a case study of the folding strain stereocontrol concept. In the cyclization of ethyl 7-bromo-2-methylheptanoates (**3**) with a methyl substituent at various positions in the chain under LDA treatment, good to excellent selectivities were obtained, with the exception of the case of 5-methyl, where the selectivity was only moderate. It would be valuable from a synthetic point of view that either of the diastereomeric 1,3-dimethylcyclohexanecarboxylates could be obtained stereoselectively merely by choosing the cyclization substrates. Thus, folding strain control could influence a ring-closure reaction to a greater extent than generally thought, and stereoselective ring construction using this approach would be useful. The direction of the selectivity can be explained by a qualitative consideration of the strain factors in the diastereomeric transition states. In this approach, the location of the bond formed relative to the stereogenic center is extremely important. Noteworthy results in this study include the difference in the degree of diastereoselectivity in cyclization between the 2,5-dimethyl and 2,6-dimethyl substrates **15** and **19**, and the unexpected preference for diastereomer **43** over **42** in the cyclization of substrate **39**. Our assumption requires further support from computational studies. Quantitative estima-

Table 5. Effect of leaving group variation on diastereoselectivity in the cyclization of 7-substituted ethyl 2,5-dimethylheptanoate.

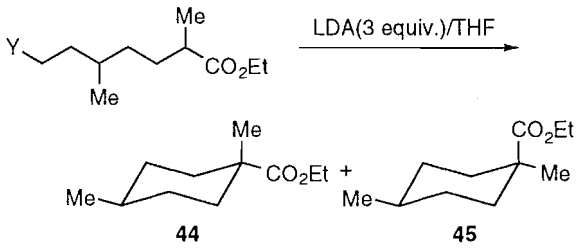

44 45

Entry	Leaving gr. Y	Reaction temp. (°C)	Yield (%)	Product ratio (**44/45**)
1	Cl	–20	60.4	70:30
2	TsO	–78	79.0	81:19
3	Br	–78	66.0	79:21
4	TfO	–78	75.0	73:27
5	I	–78	73.0	69:31

tion of the difference in strain energy between diastereomeric foldings in the transition state is desirable, and future studies should addresss this problem by a combination of MO and force field calculations (30, 31). The effect of bulkiness of the substituent on selectivity was examined in the 5-substituted substrate, and selectivity increased in the order Ph < Me ≈ Et < i-Pr < *t*-Bu, as predicted. The effects of the solvent, the base counter cation, and the leaving group are related to enolate reactivity. A greater reactivity is associated with a lower selectivity, i.e., in accord with the normal reactivity–selectivity relationship. These effects should be taken into account when working with diastereoselective ring contruction.

Experimental

IR spectra were obtained on a JASCO A-100 spectrometer. ^1H and ^{13}C NMR spectra were recorded in $CDCl_3$ on a Hitachi R-90-H, a JEOL FX-100, or a JEOL JMN-GX-400 spectrometer. Proton chemical shifts are reported in ppm on the δ scale relative to TMS as an internal reference (0.00), and carbon chemical shifts are reported in ppm relative to the center line of the $CDCl_3$ triplet (77.03). Carbon signal multiplicities were determined by INEPT experiments. The superscript asterisks on chemical shift values denote the observation of signals for the diastereomer at separate positions. MS spectra (EI) were determined on a JEOL JMS D-300 or a JMX AX-500 high-resolution mass spectrometer. GC analyses were performed on a Shimazu GC-9A apparatus using an OV-1 or Shimazu CBP-20-M-25-20 capillary column. TLC was performed on a precoated thin-layer plate (Merck Art 5744 silica gel $60F_{254}$; 0.25 or 0.5 mm). Silica gel (Fuji–Davison BW-820, BW-300, or BW-200) was used for column chromatography. Et_2O, THF, and DME were distilled from sodium benzophenone ketyl under N_2. HMPA, DMSO, Et_3N, and diglyme were distilled from CaH_2. Benzene, CH_2Cl_2, and CCl_4 were distilled from P_2O_5. MeOH and EtOH were dried by distillation from the corresponding magnesium alkoxide. All reactions were conducted in dry glassware under argon or N_2. The organic extracts were dried over $MgSO_4$ prior to solvent removal on a rotary evaporator.

*3-Benzyloxy-1-propanol (**6**) (32)*

A solution of benzaldehyde (20.4 mL, 200 mmol), 1,3-propanediol (17.4 mL, 240 mmol), and $TsOH{\cdot}H_2O$ (1.9 g) in benzene (300 mL) was refluxed overnight. The reaction mixture was cooled to room temperature, washed successively with 1 N NaOH and water, and dried over anhydrous K_2CO_3. After removal of the solvent the product was distilled to give *3-phenyl-1,3-dioxacyclohexane* (31.4 g, 96%) as a colorless oil; ^1H NMR (90 MHz) δ: 1.20–1.80 (m, 2H, $CH_2CH_2CH_2$), 3.81–4.35 (m, 4H, 2 × OCH_2CH_2), 5.48 (s, 1H, CHPh), 7.20–7.50 (m, 5H, Ph). A solution of this product (15.4 mL, 93.9 mmol) in Et_2O (70 mL) was added to the solution prepared by stirring a mixture of $AlCl_3$ (30.7 g, 230 mmol) in Et_2O (80 mL) and $LiAlH_4$ (2.20 g, 57.5 mmol) in Et_2O (40 mL) at 0°C for 30 min and the resulting mixture was refluxed for 4 h. Water was added carefully to the cooled mixture to destroy the excess hydride and then it was acidified by the addition of dilute H_2SO_4. The mixture was extracted with Et_2O and the combined organic layers were washed with aqueous Na_2CO_3 solution and brine. The product, after removal of the solvent, distilled to afford the title compound **6** (11.2 g, 71%) as a colorless oil; 1H NMR (90 MHz) δ: 1.84 (2H, quintet, J = 5.9 Hz, $CH_2CH_2CH_2$), 1.90 (1H, s, OH), 3.63 (2H, t, J = 5.9 Hz, CH_2CH_2OH), 3.74 (2H, t, J = 5.9 Hz, CH_2CH_2OBn), 4.49 (2H, s, OCH_2Ph), 7.30 (5H, s, Ph).

*1-Benzyloxy-3-bromopropane (**7**)*

To a mixture of 3-benzyloxy-1-propanol (**6**) (11.2 g, 66.7 mmol) and Et_3N (14.0 mL, 100 mmol) cooled to 0°C was added $MeSO_2Cl$ (6.2 mL, 80 mmol). The mixture was stirred for 15 min and the reaction was quenched by the addition of NH_4Cl. The product was extracted with Et_2O and the combined organic phases were washed successively with 1 N HCl, aqueous Na_2CO_3, and brine. The solvent was evaporated to afford the crude mesylate; ^1H NMR (90 MHz) δ: 2.02 (2H, quintet, J = 5.9 Hz, $CH_2CH_2CH_2$), 2.92 (3H, s, O*Ms*), 3.58 (2H, t, J = 5.9 Hz, CH_2OBn), 4.34 (2H, t, J = 5.9 Hz, CH_2OMs), 4.50 (2H, s, OCH_2Ph), 7.31 (5H, s, Ph). A solution of the mesylate thus obtained (16.3 g, 66.7 mmol) in acetone (150 mL) was refluxed overnight with LiBr (14.5 g, 167 mmol) with stirring. Et_2O and water were added and the organic phase was washed with water. The crude product obtained by evaporation of the solvent was purified by silica gel chromatography to furnish the title bromide **7** (12.7 g, 83%) as an oil: ^1H NMR (90 MHz) δ: 2.13 (2H, quintet, J = 6.2 Hz, $CH_2CH_2CH_2$), 3.53 (2H, t, J = 6.2 Hz, CH_2CH_2OBn), 3.66 (2H, t, J = 6.2 Hz, CH_2CH_2Br), 4.51 (2H, s), 7.32 (5H, s, Ph); ^{13}C NMR (25 MHz) δ: 128.5, 127.7, 73.2, 67.7, 32.9, 30.7.

*Ethyl 7-benzyloxy-3-oxoheptanoate (**8**)*

To a stirred suspension of NaH (1.9 g, 39.4 mmol) in THF (50 mL) cooled to 0°C was added a solution of ethyl acetoacetate (4.28 mL, 32.8 mmol) in THF (30 mL). After the mixture had been stirred for 15 min, *n*-butyllithium solution (1.6 M in hexane, 22.0 mL, 35.2 mmol) was added and the mixture was stirred for 15 min at 0°C. To the dianion solution thus prepared was added 3-bromo-1-benzyloxypropane (**7**) (7.51 g, 32.8

mmol) in THF (30 mL) and the reaction mixture was stirred at room temperature for 3 h, then quenched by the addition of 1 N HCl. The product was extracted with Et_2O and the combined organic layers were washed with aqueous $NaHCO_3$ and brine. The residue left after evaporation of the solvent was purified by chromatography on a silica gel column to give the title ester **8** (6.47 g, 71%) as a colorless oil: IR (neat): 1740, 1710 cm^{-1}; ^1H NMR (400 MHz) δ: 1.27 (3H, t, J = 7.3 Hz, $MeCH_2O$), 1.60–1.74 (4H, m, CH_2CH_2), 2.56 (2H, t, J = 6.7 Hz, CH_2CH_2CO), 3.41 (2H, s, $COCH_2CO2$), 3.47 (2H, t, J = 6.7 Hz, CH_2OBn), 4.18 (2H, q, J = 7.3 Hz, OCH_2Me), 4.48 (2H, s, OCH_2Ph), 7.33 (5H, m, Ph); ^{13}C NMR (25 MHz) δ: 202.6 (s), 167.2 (s), 138.5 (s), 128.3 (d), 127.6 (d), 72.9 (t), 69.9 (t), 61.3 (t), 49.3 (t), 42.6 (t), 29.0 (t), 20.3 (t), 14.1 (q).

*Ethyl 7-hydroxy-3-methylheptanoate (**9**)*

To a suspension of NaH (1.46 g, 30.5 mmol) in Et_2O was added a solution of ethyl 7-benzyloxy-3-oxoheptanoate (**8**) (7.7 g, 27.7 mmol) in Et_2O (30 mL) at 0°C. After stirring for 15 min, diethyl chlorophosphate (4.42 mL, 30.5 mmol) in Et_2O (30 mL) was introduced dropwise and stirring was continued at room temperature for 2 h. The reaction mixture was quenched by the addition of aqueous NH_4Cl and washed with aqueous $NaHCO_3$. The solvent was evaporated to leave the enol phosphate. A solution of zero valent palladium reagent was prepared in situ from $PdCl_2(PPh)_3$ (0.38 g, 0.55 mmol) in THF (11 mL) and a solution of DIBAL in toluene (2.25 M, 0.49 mL, 1.1 mmol) at 0°C for 10 min and to this was added successively the enol phosphate (11.4 g, 27.5 mmol), obtained above and dissolved in CH_2Cl_2 (55 mL), and a Me_3Al solution (2 M, 42 mL, 82 mmol) in THF (11 mL). The mixture was stirred at room temperature for 5 days. The reaction mixture was diluted with Et_2O and poured into 1 N HCl. The organic layer was separated and washed with saturated $NaHCO_3$ and brine. The chromatographic purification (silica gel) of the residue left after removal of the solvent afforded *ethyl 7-benzyloxy-3-methyl-2-heptenoate* (6.54 g, 86%) as an oil; ^1H NMR (400 MHz) δ: 1.27 (3H, t, J = 7.3 Hz, $MeCH_2O$), 1.50–1.70 (4H, m), 2.14 (3H, s, =CMe), 2.14 (2H, t, J = 6.1 Hz, CH_2CH_2C=), 3.47 (2H, t, J = 6.1 Hz, CH_2CH_2OBn), 4.14 (2H, q, J = 7.3 Hz, OCH_2Me), 4.49 (2H, s, OCH_2Ph), 5.65 (1H, s, CH=C), 7.33 (5H, m, Ph); ^{13}C NMR (100 MHz) δ: 166.8, 159.6, 138.6, 128.4, 127.6, 127.5, 115.8, 72.9, 70.0, 59.4, 40.6, 29.3, 24.1, 18.6, 14.3. Exact Mass calcd. for $C_{17}H_{24}O_3$: 276.1725; found: 276.1716. A portion of the product (2.4 g, 8.8 mmol) was dissolved in EtOH (50 mL) and hydrogenated in the presence of 10% palladium on charcoal (0.2 g) overnight at room temperature. The catalyst was removed by filtration and the filtrate was evaporated to leave a residue that was purified by chromatography on a silica gel column. The product **9** (1.65 g, 100%) was obtained as a colorless oil; ^1H NMR (400 MHz) δ: 0.93 (3H, d, J = 6.2 Hz, $MeCH$), 1.24 (3H, t, J = 7.0 Hz, $MeCH_2O$), 1.00–2.40 (10H, m), 3.64 (2H, t, J = 5.9 Hz, CH_2CH_2OH), 4.13 (2H, q, J = 7.0 Hz, $MeCH_2O$); ^{13}C NMR (25 MHz) δ: 173.3, 62.9, 60.1, 41.8, 36.4, 32.8, 30.3, 23.1, 19.7, 14.2.

*Ethyl 7-hydroxy-2,3-dimethylheptanoate (**10**)*

A mixture of ethyl 7-hydroxy-3-methylheptanoate (**9**) (1.65 g, 8.8 mmol) and diisopropylethylamine (1.99 mL, 11.4 mmol) in CH_2Cl_2 (35 mL) was stirred for a while at 0°C and then chloromethyl methyl ether (0.87 mL, 11.4 mmol) was added. The resulting mixture was allowed to warm slowly to room temperature, where it was stirred for 5 h, then quenched by the addition of 1 N HCl. The product was extracted with Et_2O, and the extract solution was washed with aqueous $NaHCO_3$ and brine. The residue obtained after evaporation of the solvent was purified by chromatography on a silica gel column to afford *ethyl 7-methoxymethoxy-3-methylheptanoate* (1.92 g, 94%) as an oil: ^1H NMR (400 MHz) δ: 0.94 (3H, d, J = 6.1 Hz, $MeCH$), 1.26 (3H, t, J = 7.3 Hz, $MeCH_2O$), 1.18–2.28 (9H, m), 3.36 (3H, s, $MeOCH_2O$), 3.52 (2H, t, J = 6.1 Hz, CH_2CH_2OMOM), 4.13 (2H, q, J = 7.3 Hz, $MeCH_2O$), 4.62 (2H, s, $MeOCH_2O$). The LDA solution, prepared from diisopropylamine (1.4 mL, 10 mmol) in THF (20 mL) and *n*-butyllithium solution in hexane (1.5 M, 6.8 mL, 10.2 mmol), was cooled to −78°C and to this was added, with stirring, a solution of the MOM ether above dissolved in THF (20 mL) and HMPA (7 mL). After stirring for 30 min, iodomethane (0.62 mL, 10 mmol) was introduced. The cooling bath was removed and the reaction mixture was allowed to warm slowly to room temperature. After 3 h it was quenched by the addition of 1 N HCl and the product was extracted with Et_2O. The organic layers were washed with aqueous $NaHCO_3$ and brine. The residue left after evaporation of the solvent was purified by silica gel chromatography to furnish *ethyl 7-methoxymethoxy-2,3-di-methylheptanoate* (1.69 g, 83%) as an oil: ^1H NMR (400 MHz) δ: 0.86, 0.90* (3H, d, J = 6.6 Hz, $MeCH$), 1.06, 1.10* (3H, d, J = 6.8 Hz, $MeCH_2$), 1.25 (3H, t, J = 7.1 Hz, $MeCH_2O$), 1.10–2.00 (8H, m), 3.36 (3H, s, $MeOCH_2O$), 3.52 (2H, t, J = 6.4 Hz, CH_2CH_2OMOM), 4.13 (2H, q, J = 7.1 Hz, $MeCH_2O$), 4.62 (2H, s, $MeOCH_2O$); ^{13}C NMR (25 Hz) δ: 176.5, 96.5, 67.8, 60.0, 55.1, 44.7,* 44.3, 35.4, 34.6, 33.2,* 29.9, 23.9, 23.7,* 17.2,* 15.7, 14.3, 14.0,* 12.4. Demethoxymethylation of the crude product above (2.35 g) was performed by its treatment with 6 N HCl (4 mL) in THF (47 mL) at room temperature overnight. After dilution with water the reaction mixture was extracted with Et_2O and the combined organic layers were washed with aqueous $NaHCO_3$ and brine. Purification of the product by silica gel chromatography afforded a diastereomeric mixture of the title compound (**10**) (1.76 g, 66% from 9) as an oil: IR (neat): 3375, 1720 cm^{-1}; ^1H NMR (400 MHz) δ: 0.86, 0.91* (3H, d, J = 6.7 Hz, $MeCH$), 1.06, 1.10* (3H, d, J = 6.7 Hz, $MeCH_2$), 1.25 (3H, t, J = 7.3 Hz, $MeCH_2O$), 1.14–1.85 (8H, m), 2.35 (1H, quintet, $CHCHMe$), 3.64 (2H, t, J = 6.1 Hz, CH_2CH_2OH), 4.13 (2H, q, J = 6.7 Hz, $MeCH_2O$); ^{13}C NMR (100 MHz) δ: 176.5(s), 62.9(t), 60.1(t), 60.0(t),* 44.7(d),* 44.3(d), 36.0(d),* 35.4(d), 34.5(t), 33.1(t),* 32.9(t), 23.3(t), 23.2(t),* 17.1(t),* 15.7(q), 14.3(q), 13.9(q), 12.4(q). Exact Mass calcd. for $C_{11}H_{22}O_3$: 202.1569; found: 202.1662.

*Ethyl 7-bromo-2,3-dimethylheptanoate (**11**)*

A mixture of the alcohol **10** (0.57 g, 2.8 mmol) and Et_3N (0.59 mL, 4.2 mmol) in CH_2Cl_2 (10 mL) was stirred at 0°C for 5 min and then $MeSO_2Cl$ (0.26 mL, 3.4 mmol) was added. After the reaction mixture had been stirred for 15 min, it was quenched by the addition of aqueous NH_4Cl. The product was extracted with Et_2O and the extract solution was washed successively with 1 N HCl, aqueous Na_2CO_3, and brine. Evaporation of the solvent gave crude *ethyl 7-mesyloxy-2,3-dimethylheptanoate* as an oil: ^1H NMR (90 MHz) δ: 0.87, 0.91* (3H, d, J = 6.8 Hz, $MeCH$), 1.07, 1.10* (3H, d, J = 7.1 Hz, $MeCH_2$), 1.26 (3H, t, J

= 7.1 Hz, *Me*CH_2O), 1.00–2.00 (7H, m), 2.35 (1H, quintet, J = 6.8 Hz, CHC*H*Me), 3.01 (3H, s, O*Ms*), 4.13 (2H, q, J = 7.3 Hz, MeC*H_2*O), 4.22 (2H, t, J = 6.1 Hz, CH_2CH_2OMs). A solution of the mesylate above in acetone (20 mL) was refluxed with LiBr (0.78 g, 8.9 mmol) overnight. After addition of water the product was extracted with Et_2O and the organic layer was washed with water. The evaporation of the solvent and subsequent purification of the residue by silica gel chromatography afforded the title compound (**11**) (0.50 g, 67%); IR (neat) 1730 cm^{-1}; ^{1}H NMR (400 MHz) δ: 0.87, 0.89* (3H, d, J = 7.3 Hz, *Me*CH), 1.07, 1.11* (3H, d, J = 7.3 Hz, *Me*CH), 1.26 (3H, t, J = 6.7 Hz, *Me*CH_2O), 1.15–1.58 (4H, m), 1.76–1.87 (3H, m), 2.35 (1H, quintet, J = 6.7 Hz, CHC*H*Me), 3.41 (2H, t, J = 6.7 Hz, CH_2CH_2Br), 4.14 (2H, q, J = 6.7 Hz, CH_2CH_2O); ^{13}C NMR (100 MHz) δ: 176.4(s), 60.1(t), 44.6(d),* 44.3(d), 35.8(d),* 35.2(d), 33.8(t), 33.7(t), 32.9(t), 25.8(t), 25.6(t),* 17.1(q),* 15.7(q), 14.3(q), 13.8(q),*12.5(q). Exact Mass calcd. for $C_{11}H_{21}O_2Br$: 265.0725; found: 265.0820.

*2-Methyl-5-pentanolide (**12**)*

To a solution of LDA prepared from diisopropylamine (11.9 mL, 85 mmol), THF (100 mL), and *n*-butyllithium solution in hexane (1.3 M, 65 mL, 85 mmol) was added δ-valerolactone (4.63 g, 50 mmol) at −78°C under stirring. After the mixture had been stirred for 30 min, iodomethane (9.34 mL, 150 mmol) dissolved in a mixture of HMPA (10.4 mL) and THF (15 mL) was added dropwise (33). The reaction mixture was allowed to warm slowly, by removal of the cooling bath, up to −40°C, where it was quenched by the addition of water. After acidification with 3 N HCl, the product was extracted with Et_2O and the organic layers were washed with aqueous $NaHCO_3$ and brine. Distillation gave the methylated product **12** (3.57 g, 63%) as a colorless oil; IR (neat): 1730 cm^{-1}; ^{1}H NMR (400 MHz) δ: 1.26 (3H, d, J = 6.7 Hz, *Me*CH), 1.56 (1H, m, 3-H_{ax}), 1.92 (2H, m, 3-H_{eq}, 4-H_{eq}), 2.10 (1H, sextet, J = 6.7 Hz, 4-H_{ax}), 2.59 (1H, dq, J = 11.0, 6.7 Hz, 2-H), 4.32 (2H, m, 5-C$H_{ax}H_{eq}$); ^{13}C NMR (100 MHz) δ: 175.2, 68.5, 34.6, 27.1, 22.0, 16.7. Exact Mass calcd. for $C_6H_{10}O_2$: 114.0681; found: 114.0697.

*Ethyl 7-hydroxy-2,4-dimethyl-2-heptenoate (**13**)*

To a solution of triethyl 2-phosphonopropionate (11.9 mL, 85 mmol) in THF (100 mL) was successively added *n*-butyllithium solution in hexane (1.4 M, 25.4 mL, 33.8 mmol) and 2-methyl-5-pentanolide (**12**) (3 g, 26 mmol) at −78°C. After stirring of the mixture for a short time, addition of DIBAL solution in toluene (1.76 M, 19.3 mL, 33.8 mmol) followed. The resulting mixture was allowed to react overnight after removal of the cooling bath. The reaction mixture was quenched by the cautious addition of aqueous Na_2SO_4 solution. The precipitate was removed by filtration and the solvent was evaporated from the filtrate. The residue was chromatographed on a column of silica gel, giving the title compound **13** (2.7 g, 60%); ^{1}H NMR (100 MHz) δ: 1.02 (3H, d, J = 6.7 Hz, *Me*CH)), 1.29 (3H, t, J = 7.3 Hz, *Me*CH_2O), 1.20–1.70 (5H, m), 1.84 (3H, d, J = 1.3 Hz, MeC═), 2.04 (1H, s, OH), 3.60 (2H, t, J = 6.2 Hz, CH_2CH_2OH), 4.19 (2H, q, J = 7.3 Hz, MeC*H_2*O), 6.59 (1H, dq, J = 10.1, 1.3 Hz, CHC*H*═CMe).

*Ethyl 7-hydroxy-2,4-dimethylheptanoate (**14**)*

The unsaturated ester **13** (2.15 g, 10.75 mmol) dissolved in EtOH (30 mL) was hydrogenated in the presence of 10% palladium on charcoal (0.11 g). Removal of the catalyst by filtration through a short column of silica gel and evaporation of the solvent from the filtrate afforded the title compound **14** (2.085 g, 96%) as an oil; IR (neat): 3400, 1730 cm^{-1}; ^{1}H NMR (400 MHz) δ: 0.90 (3H, d, J = 6.7 Hz, *Me*CH), 1.14 (3H, d, J = 7.3 Hz, *Me*CH), 1.25 (3H, t, J = 6.7 Hz, *Me*CH_2O), 1.10–1.80 (8H, m), 2.52 (1H, m, CH_2CHMeCO2), 3.62 (2H, t, J = 6.7 Hz, CH_2CH_2OH), 4.12 (2H, q, J = 6.7 Hz, *Me*CH_2O); ^{13}C NMR (100 MHz) δ: 177.0, 63.2, 60.1, 41.4, 41.1,* 37.5, 33.1, 32.8,* 32.7, 30.7, 30.4,* 19.5, 18.1, 17.2,* 14.2. Exact Mass calcd. for $C_{11}H_{22}O_3$: 202.1569; found: 202.1671.

*Ethyl 7-bromo-2,4-dimethylheptanoate (**15**)*

The alcohol **14** (0.98 g, 4.86 mmol) in CH_2Cl_2 (20 mL) was mesylated with $MeSO_2Cl$ (0.46 mL, 5.84 mmol) and Et_3N (1.02 mL, 7.29 mmol) as before, giving crude *ethyl 7-mesyloxy-2,4-dimethylheptanoate* (1.36 g, ~100%); ^{1}H NMR (400 MHz) δ: 0.91 (3H, d, J = 5.7 Hz, *Me*CH), 1.14 (3H, d, J = 6.6 Hz, *Me*CH), 1.25 (3H, t, J = 7.3 Hz, *Me*CH_2O), 1.00–1.93 (6H, m), 2.50 (1H, m, CH_2CHMeCO$_2$), 3.00 (3H, s, OMs), 4.12 (2H, q, J = 7.3 Hz, *Me*CH_2O), 4.20 (2H, t, J = 6.2 Hz, CH_2CH_2OMs); ^{13}C NMR (25 MHz) δ: 176.8, 70.3, 60.1, 41.1, 40.7,* 37.3, 32.7, 32.5,* 30.4, 30.2,* 26.6,* 26.5, 19.4, 19.2,* 18.1, 17.2, 14.2. The mesylate (0.72 g, 2.58 mmol) was converted as before with LiBr (0.56 g, 6.45 mmol) in acetone (9 mL) to afford the title bromide **15** (0.63 g, 92%) as an oil, IR (neat): 1735 cm^{-1}; ^{1}H NMR (400 MHz) δ: 0.91 (3H, d, J = 6.7 Hz, *Me*CH), 1.15 (3H, d, J = 6.7 Hz, *Me*CH), 1.26 (3H, t, J = 7.3 Hz, *Me*CH_2O), 1.44 (4H, m), 1.72 (1H, m), 1.80 (2H, m), 2.51 (1H, m, CH_2CHMeCO$_2$), 3.39 (2H, t, J = 6.7 Hz, CH_2CH_2Br), 4.13 (2H, q, J = 7.3 Hz, *Me*CH_2O); ^{13}C NMR (100 MHz) δ: 177.0,* 176.9, 60.2,* 60.1, 41.2, 40.9,* 37.4,* 37.3, 35.5, 35.4,* 34.1, 30.34, 30.30,* 30.2,* 30.1,* 19.5, 19.35,* 18.1, 17.2, 14.3. Exact Mass calcd. for $C_{11}H_{21}O_2Br$: 264.0725; found: 264.0808.

*Ethyl 3-methyl-5-pentanolide (**17**) (34)*

To a stirred suspension of $NaBH_4$ (2.0 g, 52.9 mmol) in THF (10 mL) cooled in an ice bath was added 3-methylglutaric anhydride (**16**) (5.93 g, 16.3 mmol) dissolved in THF (50 mL). The ice bath was removed and the mixture was allowed to react for 1 h. After addition of EtOH and acidification with 3 N HCl, the mixture was heated on a water bath for 1 h. The cooled mixture was extracted with Et_2O and the organic layer was washed with aqueous $NaHCO_3$ and brine. Distillation of the product afforded the title lactone **17** (4.01 g, 76%) as an oil; IR (neat): 1730 cm^{-1}; 1H NMR (400 MHz) δ: 1.07 (3H, d, J = 6.1 Hz, *Me*CH), 1.54 (1H, m, 3-H), 1.93 (1H, m, 4-H_{eq}), 2.10 (2H, m, 2-H_{ax}, 4-H_{ax}), 2.68 (1H, m, 2-H_{eq}), 4.27 (1H, td, J = 11.6, 3.7 Hz, 5-H_{ax}), 4.42 (1H, dt, J = 11.6, 4.3 Hz, 5-H_{eq}); ^{13}C NMR (100 MHz) δ: 171.3(s), 68.5(d), 38.2(d), 30.6(t), 26.5(d), 21.4(q).

*Ethyl 7-hydroxy-2,5-dimethylheptanoate (**18**)*

3-Methyl-δ-valerolactone (**17**) (3.65 g, 38.4 mmol) was converted to *ethyl 7-hydroxy-2,5-dimethyl-2-heptenoate* in the same way as in the case of the 2-methyl analog using DIBAL solution (1 M in toluene, 38.4 mL, 32 mmol), triethyl 2-phosphophonopropionate (9.02 mL, 38.4 mmol) in THF (10 mL), and *n*-butyllithium solution (1.6 M in hexane, 26.4 mL, 42.23

mmol). The product (4.77 g, 87%) was obtained as an oil; ^{1}H NMR (400 MHZ) δ: 0.95 (3H, d, J = 6.2 Hz, *Me*CH), 1.30 (3H, t, J = 7.3 Hz, *Me*CH_2O), 1.84 (3H, s, MeC=), 1.00–2.00 (5H, m), 2.16 (1H, m), 3.70 (2H, t, J = 7.0 Hz, CH_2CH_2OH), 4.19 (2H, q, J = 7.3 Hz, Me*CH*$_2$O), 6.78 (1H, tq, J = 7.3, 1.3 Hz, CH_2CH=CMe). This material (2.33 g, 11.65 mmol) was then hydrogenated with 10% palladium on charcoal (0.31 g) in EtOH (35 mL) to afford the saturated ester **18** (2.48 g, 100%) as an oil; IR (neat): 3450, 1730 cm^{-1}; ^{1}H NMR (400 MHz) δ: 0.90 (3H, d, J = 6.7 Hz, *Me*CH), 1.14, 1.15* (3H in total, d, J = 7.3 Hz, *Me*$CHCO_2$), 1.26 (3H, t, J = 7.3 Hz, *Me*CH_2O), 1.00–1.80 (6H, m), 2.38 (1H, m, CH_2CHMeCO$_2$), 3.60 (2H, m, CH_2CH_2OH), 4.13 (2H, q, J = 7.3 Hz, Me*CH*$_2$O); ^{13}C NMR (100 MHz) δ: 176.9, 61.1, 61.0,* 60.1, 39.8, 34.5, 34.4,* 34.1, 29.6, 29.4,* 19.6, 17.3, 17.0, 14.3. Exact Mass calcd. for $C_{11}H_{22}O_3$: 202.1569; found: 202.1630.

*Ethyl 7-bromo-2,5-dimethylheptanoate (**19**)*

The hydroxy ester **18** was transformed to *ethyl 7-mesyloxy-2,5-dimethylheptanoate* in the same way as described above. ^{1}H NMR (90 MHz) δ: 0.93 (3H, d, J = 5.7 Hz, *Me*CH), 1.14 (2H, d, J = 6.6 Hz, *Me*CH), 1.25 (3H, t, J = 6.9 Hz, *Me*CH_2O), 1.00–1.80 (8H, m), 2.30 (1H, m, CH_2CHMeCO2), 2.97 (3H, s, OMs), 4.08 (2H, q, J = 7.3 Hz, Me*CH*$_2$O), 4.21 (2H, t, J = 6.2 Hz, C*H*$_2$OMS). Then the mesylate (3.17 g, 11.3 mmol) was treated with LiBr (2.46 g, 28.3 mmol) in acetone (60 mL), refluxing overnight to furnish the title bromide **19** (1.71 g, 57%) as an oil, IR (neat): 1735 cm^{-1}; ^{1}H NMR (400 MHz) δ: 0.90 (3H, d, J = 6.7 Hz, *Me*CH), 1.15 (3H, d, J = 7.3 Hz, *Me*CH), 1.26 (3H, t, J = 6.7 Hz, Me*CH*$_2$O), 1.05–1.35 (2H, m), 1.43 (1H, m), 1.65 (3H, m), 1.87 (1H, m), 2.39 (1H, sextet, J = 6.7 Hz, CH_2CHMeCO$_2$), 3.41 (2H, m, CH_2CH_2Br), 4.13 (2H, q, J = 6.7 Hz, Me*CH*$_2$O); ^{13}C NMR (100 MHz) δ: 176.7(s), 60.2(t), 39.8(t) 39.7(d), 33.9(t), 33.8(t),* 31.9(t), 31.6(d), 31.0(t), 30.9(t),* 18.8(q), 17.3(q), 17.0(q), 14.3(q). Exact Mass calcd. for $C_{11}H_{21}O_2Br$: 264.0725; found: 264.0776.

Ethyl 2,5-dimethylheptanoates with various leaving groups at the 7 position

Ethyl 7-chloro-2,5-dimethylheptanoate

A mixture of the hydroxy ester **18** (200 mg, 1.0 mmol), triphenylphosphine (0.63 g, 2.4 mmol), and *N*-chlorosuccinimide (0.37 g, 2.7 mmol) in THF (3 mL) was stirred overnight at room temperature. The usual work-up and chromatographic purification (silica gel) afforded the title chloride (0.17 g, 77%) as an oil; IR (neat) 1730 cm^{-1}; ^{1}H NMR (400 MHz) δ: 0.90 (3H, d, J = 6.7 Hz, *Me*CH), 1.15 (3H, d, J = 7.3 Hz, *Me*CH), 1.18 (1H, m), 1.26 (3H, t, J = 7.3 Hz, *Me*CH_2O), 1.30 (1H, m), 1.59 (1H, m), 1.64 (2H, m), 1.78 (1H, m), 2.39 (1H, sextet, J = 6.7 Hz, CH_2CHMeCO$_2$), 3.55 (2H, m, CH_2CH_2Cl), 4.13 (2H, q, J = 7.3 Hz); ^{13}C NMR (100 MHz) δ: 176.7, 60.2, 43.1, 39.7,* 39.6, 33.99, 33.96,* 31.01, 30.98,* 30.4, 19.0, 17.3, 17.0, 14.3. Exact Mass calcd. for $C_{11}H_{21}O_2Cl$: 220.1230; found: 220.1292.

Ethyl 7-iodo-2,5-dimethylheptanoate

The mesylate derived from the hydroxy ester **18** (198 mg, 0.97 mmol) was treated with NaI (0.2 g) in acetone (10 mL) under reflux for 1 h and overnight at room temperature. The usual work-up and subsequent chromatographic purification (silica gel) yielded the title iodide (245 mg, 81%) as an oil, IR (neat): 1730 cm^{-1}; ^{1}H NMR (400 MHz) δ: 0.88 (3H, d, J = 6.7 Hz, *Me*CH), 1.15 (3H, d, J = 6.7 Hz, *Me*CH), 1.26 (3H, t, J = 7.3 Hz, *Me*CH_2O), 1.10–1.74 (7H, m), 1.86 (1H, m), 2.39 (1H, sextet, J = 6.7 Hz, CH_2CHMeCO$_2$), 3.15 (1H, dt, J = 8.1, 7.3 Hz, CH_2CH_2I), 3.23 (1H, dt, J = 8.1, 7.3 Hz, CH_2CH_2I), 4.13 (2H, q, J = 7.3 Hz, 2H, Me*CH*$_2$O); ^{13}C NMR (100 MHz) δ: 176.7, 60.2, 40.7, 39.8,* 39.7, 33.6, 31.0, 30.9,* 18.6, 17.3, 17.0, 14.3. Exact Mass calcd. for $C_{11}H_{21}O_2I$: 312.0586: found: 312.0572.

Ethyl 7-tosyloxy-2,5-dimethylheptanoate

To a mixture of the hydroxy ester **18** (300 mg, 1.5 mmol), pyridine (0.12 mL, 1.59 mmol), and Et_3N (0.21 mL, 1.59 mmol) in CH_2Cl_2 (3 mL) cooled at 0°C was added tosyl chloride (0.42 g, 2.2 mmol) and the mixture was stirred overnight at room temperature. The crude product obtained by the usual work-up was purified by chromatography on a silica gel column, giving the title tosylate (0.42 g, 83%) as an oil; IR (neat): 1730 cm^{-1}; ^{1}H NMR (400 MHz) δ: 0.81 (3H, d, J = 6.1 Hz, *Me*CH), 1.11, 1.12* (3H, d, J = 6.7 Hz, *Me*CH), 1.25 (3H, t, J = 7.3 Hz, MeCH_2O), 1.00–1.74 (4H, m), 2.32 (1H, m, CH_2CHMeCO$_2$), 2.45 (3H, s, *Me*Ar), 4.06 (2H, m, CH_2CH_2OTs), 4.12 (2H, q, J = 7.3 Hz, Me*CH*$_2$O), 7.35 (3H, d, J = 8.5 Hz, Ar*H*), 7.79 (2H, d, J = 8.5 Hz, Ar*H*); ^{13}C NMR (100 MHz) δ: 176.6, 144.7, 133.4, 129.8, 127.9, 68.9, 60.2, 39.73, 39.65,* 35.6, 34.1, 31.0, 30.9,* 29.3, 21.6, 19.0, 17.2,* 17.0, 14.3.

Ethyl 7-trifluoromethanesulfonyloxy-2,5-dimethylheptanoate

A stirred solution of Na_2CO_3 (0.11 g, 1.0 mmol) and trifluoromethanesulfonic anhydride (0.26 mL, 1.56 mmol) in CH_2Cl_2 (3 mL) was cooled to 0°C and the hydroxy ester **18** (264 mg, 1.3 mmol) in CH_2Cl_2 (2 mL) was added. After the mixture had been stirred overnight at room temperature, it was quenched by addition of aqueous $NaHCO_3$ and worked up as usual. Chromatographic purification of the product on a silica gel column furnished the title triflate (274 mg, 78%) as an oil; IR (neat): 1730 cm^{-1}; ^{1}H NMR (90 MHz) δ: 0.95 (3H, d, J = 5.9 Hz, *Me*CH), 1.15 (3H, d, J = 6.8 Hz, *Me*CH), 1.25 (3H, t, J = 7.3 Hz, *Me*CH_2O), 0.8–2.0 (7H, m), 2.18 (1H, m, CH_2CHMeCO$_2$), 4.13 (2H, q, J = 7.3 Hz, Me*CH*$_2$O), 4.58 (2H, t, J = 6.8 Hz, CH_2CH_2OTf).

*Ethyl 7-bromo-5-ethyl-2-methylheptanoate (**25**)*

Vinylmagnesium bromide solution prepared from Mg (0.67 g, 27.5 mmol), vinyl bromide (2.14 mL, 30.3 mmol), and THF (40 mL) was added to a stirred suspension of CuI (0.18 g, 0.92 mmol) in THF (20 mL) at −78°C. After stirring at this temperature for 20 min a solution of 5-pent-2-enolide (**20**) (35) (1.8 g, 18.3 mmol) in THF (10 mL) was introduced and the mixture was stirred for 1 h further, then quenched by the addition of aqueous NH_4Cl. The extraction of the product with ether gave *3-vinyl-5-pentanolide* (1.24 g, 54%) as an oil; ^{1}H NMR (100 MHz) δ: 1.50–2.90 (5H, m), 4.20–4.60 (2H, m, 5-$H_{ax}H_{eq}$), 5.09 (1H, dd, J = 12, 1 Hz, CH=CH_2), 5.14 (1H, dd, J = 9, 1 Hz, CH=CH_2), 5.78 (1H, ddd, J = 12,9,1 Hz, $CHCH$=CH_2). This product was hydrogenated in the presence of palladium on charcoal to give *3-ethyl-5-pentanolide* (**21**) (36) as an oil; ^{1}H NMR (400 MHz) δ: 0.87 (3H, t, J = 7.0

Hz, *Me*CH_2CH), 1.33 (2H, quintet, J = 7.0 Hz, MeC*H*$_2$CH), 1.46 (1H, ddt, J = 9.5, 7.4, 5.1 Hz, 3-H), 1.74–1.96 (2H, m, 4-$H_{ax}H_{eq}$), 2.07 (1H, dd, J = 17.2, 10.0 Hz, 2-H_{ax}), 2.62 (1H, ddd, J = 17.4, 6.0, 1.5 Hz, 2-H_{eq}), 4.19 (1H, ddd, J = 11.3, 10.3, 3.5 Hz, 4-H_{ax}), 4.34 (1H, ddd, J = 10.8, 4.8, 4.0, 4-H_{eq}). The lactone **21** (0.69 g, 5.4 mmol) was converted as before by the Takacs procedure (11) to *ethyl 5-ethyl-7-hydroxy-2-methyl-2-heptenoate*, 0.43 g (40%), which on catalytic hydrogenation (10% palladium on charcoal) gave quantitatively *ethyl 5-ethyl-7-hydroxy-2-methylheptanoate* (**23**) as an oil; IR (neat): 1730 cm^{-1}; ^{1}H NMR (400 MHz) δ: 0.86 (3H, t, J = 7.3 Hz, *Me*CH_2), 1.15 (3H, d, J = 7.3 Hz, *Me*CH), 1.26 (3H, t, J = 7.3 Hz, *Me*CH_2O), 1.20–1.70 (10H, m), 2.39 (1H, sextet, J = 7.3 Hz, CH_2CHMeCO_2), 3.66 (2H, t, J = 6.7 Hz, CH_2CH_2OH), 4.13 (2H, q, J = 7.3 Hz, MeC*H*$_2$O); ^{13}C NMR (100 MHz) δ: 176.9, 61.1, 60.1, 39.9, 36.4, 35.7, 30.7, 30.6, 25.9, 17.1, 14.3, 10.7. Exact Mass calcd. for $C_{12}H_{24}O_3$: 216.1725; found: 216.1810. The hydroxy ester **23** (0.27 g, 1.23 mmol) was transformed as before via a mesylate to the title bromide **25** (0.23 g, 68%). IR (neat): 1730 cm^{-1}; ^{1}H NMR (400 MHz) δ: 0.86 (3H, t, J = 7.3 Hz, MeC*H*$_2$), 1.15 (3H, d, J = 6.7 Hz, *Me*CH), 1.26 (3H, t, J = 6.7 Hz, MeC*H*$_2$O), 1.32 (2H, quintet, MeC*H*$_2$CH), 1.20–1.50 (4H, m), 1.63 (1H, m), 1.82 (2H, q, J = 7.3 Hz, CH_2CH_2CH), 2.39 (1H, sextet, J = 6.7 Hz, CH_2CHMeCO_2), 3.41 (2H, t, J = 7.3 Hz, CH_2CH_2Br), 4.13 (2H, q, J = 6.7 Hz, MeC*H*$_2$O); ^{13}C NMR (100 MHz) δ: 176.6, 60.2, 39.8, 37.8, 36.6, 31.9, 30.6, 29.95, 25.3, 17.25, 14.3, 10.5. Exact Mass calcd. for $C_{12}H_{23}O_2$Br: 278.0881; found: 278.0967.

*Ethyl 7-bromo-5-isopropyl-2-methylheptanoate (**26**)*

A solution of isopropylmagnesium bromide prepared from isopropyl bromide (1.6 mL, 17 mmol) and Mg (0.38 g, 15.45 mmol) in THF (20 mL) was added to a stirred suspension of CuI (0.1 g, 0.5 mmol) in THF (10 mL) at −78°C. After stirring for 20 min, a solution of 5-pent-2-enolide (**20**) (1.01 g, 10.3 mmol) in THF (5 mL) was introduced and stirring was continued at −78°C for 1 h. Aqueous NH_4Cl was added, and the product was isolated by extraction with Et_2O and was purified by distillation to give *3-isopropyl-5-pentanolide* (**22**) (315 mg, 22%) as an oil; IR (neat): 1720 cm^{-1}; ^{1}H NMR (400 MHz) δ: 0.92 (3H, d, J = 6.7 Hz, *Me*CH), 0.93 (3H, d, J = 6.7 Hz, *Me*CH), 1.55 (2H, m, 3-H), 1.75 (1H, m, dq, J = 10.7, 6.1, CHC*H*Me$_2$), 1.92 (1H, dqd, J = 10.4, 4.3, 1.2 Hz, 4-H_{eq}), 2.22 (1H, dd, J = 17.1, 11.0, 2-H_{ax}), 2.66 (1H, ddd, J = 17.1, 4.3, 1.2 Hz, 2-H_{eq}), 4.23 (1H, td, J = 11.0, 3.7 Hz, 5-H_{ax}), 4.41 (1H, dt, J = 11.0, 4.9 Hz, 5-H_{eq}); ^{13}C NMR (100 Hz) δ: 171.9, 68.6, 37.9, 34.1, 32.3, 26.4, 19.3, 19.2. Application of the Takacs procedure (11) on the lactone **22** (314 mg) afforded *ethyl 7-hydroxy-5-isopropyl-2-heptenoate* as an oil, 368 mg (73%). This material was catalytically hydrogenated to give *ethyl 7-hydroxy-5-isopropylheptanoate* as an oil; ^{1}H NMR (400 MHz) δ: 0.84 (3H, d, J = 6.8 Hz, *Me*CH), 0.85 (3H, d, J = 6.8 Hz, *Me*CH), 1.15 (3H, d, J = 7.3 Hz, CH*Me*CO_2), 1.25 (3H, t, J = 7.3 Hz, *Me*CH_2O), 1.10–1.80 (8H, m), 2.39 (1H, sextet, J = 6.8 Hz, CH_2CHMeCO2), 3.65 (2H, m, CH_2CH_2OH), 4.13 (3H, q, J = 7.3 Hz, MeC*H*$_2$O); ^{13}C NMR (100 MHz) δ: 176.9, 61.7, 60.2, 40.3, 40.1,* 39.9, 33.7, 33.6,* 31.8, 31.7,* 29.5, 29.4,* 28.3, 19.3, 19.2,* 18.8, 18.7,* 17.2, 14.3. Exact Mass calcd. for $C_{13}H_{26}O_3$: 230.1882; found: 230.1966. The saturated ester (185 mg) was transformed to the bromide as before via a mesylate (163 mg, 71%) giving **26** as an oil; IR (neat) δ: 1730 cm^{-1}; ^{1}H NMR (400 MHz) δ: 0.86, 1.16* (3H in total, d, J = 6.7 Hz, *Me*CH), 1.26 (3H, t, J = 7.3 Hz, *Me*CH_2O), 1.20–1.40 (4H, m), 1.60–1.80 (3H, m), 1.85 (1H, m), 2.40 (1H, sextet, J = 7.3 Hz, CH_2CHMeCO_2), 3.42 (2H, m, CH_2CH_2Br), 4.13 (1H, q, J = 7.3 Hz, MeC*H*$_2$O); ^{13}C NMR (100 MHz) δ: 176.6, 60.2, 42.6, 39.91, 39.87,* 34.2, 34.1,* 32.7, 31.63, 31.60,* 29.1, 29.0,* 27.7, 27.6,* 19.2, 19.1,* 18.9, 17.2, 14.3. Exact Mass calcd. for $C_{13}H_{25}O_2$Br: 292.1083; found: 292.0879.

*Ethyl 7-bromo-2-methyl-5-phenylheptanoate (**30**)*

To a mixture of NaOEt solution, prepared from Na (1.38 g, 60 mmol) and EtOH (20 mL), and Et_2O (100 mL) was added diethyl malonate (9.1 mL, 60 mmol) and the mixture was stirred for 30 min. Ethyl cinnamate (10.1 mL, 60 mmol) was added and the reaction mixture was refluxed for 5 h. The cooled mixture was acidified with aqueous acetic acid and the product was extracted with Et_2O. Organic layers were washed with aqueous $NaHCO_3$ and brine, and the solvent was removed by evaporation. Distillation of the residue afforded *diethyl 2-ethoxycarbonyl-3-phenylglutarate* (37) (16.14 g, 73%) as an oil; ^{1}H NMR (90 mHz) δ: 0.99 (3H, t, J = 7.0 Hz, *Me*CH_2), 1.07 (3H, t, J = 7.0 Hz, *Me*CH_2), 1.18 (3H, t, J = 7.0 Hz, *Me*CH_2), 2.77 (4H, m), 3.93 (2H, q, J = 2.0 Hz, MeC*H*$_2$O), 3.97 (2H, q, J = 7.0 Hz, MeC*H*$_2$O), 4.21 (2H, q, J = 7.0 Hz, MeC*H*$_2$O), 7.24 (5H, s, Ph). The triester was treated with aqueous KOH (14.7 g, 262 mmol, dissolved in 100 mL of H_2O) under refluxing for 1 day. The hydrolysate solution was evaporated in vacuo to dryness and the residue was mixed with diluted H_2SO_4 (26 g with 100 mL of H_2O), and the mixture was refluxed overnight. After concentration in vacuo, the product was extracted with Et_2O to give crude 3-phenylglutaric acid (9.13 g, 100%); ^{1}H NMR (90 MHz) δ: 2.72 (4H, d, J = 6.7 Hz, 2 × CH_2CH_2CO2), 3.66 (1H, quintet, J = 6.7 Hz, CH_2CHPhCH_2), 7.25 (5H, s), 10.88 (2H, br s, CO2H). This material was heated with Ac_2O under refluxing for 2 h. The reaction mixture was evaporated to dryness in vacuo and the residue was recrystallized from hexane to yield *3-phenylglutaric anhydride* as crystals, 7.73 g (98%). This anhydride (7.73 g, 43.9 mmol) dissolved in THF (50 mL) was added to a solution of $NaBH_4$ (1.7 g, 43.9 mmol) in THF (10 mL) cooled to 0°C. The ice bath was removed and the mixture was allowed to react for 1 h. The reaction mixture was acidified with 3 M HCl, extracted with Et_2O, and the organic layers were washed with aqueous $NaHCO_3$ and brine. Chromatographic purification (silica gel) of the residue left after evaporation of the solvent furnished *3-phenyl-5-pentanolide* (**28**) (38) (1.45 g, 19%) as an oil; IR (neat): 1730 cm^{-1}; ^{1}H NMR (400 MHz) δ: 2.03 (1H, dtd, J = 14.0, 10.4, 4.9, 4-H_{ax}), 2.18 (1H, dqd, J = 14.0, 3.7, 1.2, 4-H_{eq}), 2.63 (1H, dd, J = 17.7, 10.4, 2-H_{ax}), 2.90 (1H, ddd, J = 17.7, 5.2, 1.2, 2-H_{eq}), 3.24 (1H, tt, J = 10.4 Hz, 3-H), 4.29 (1H, td, J = 11.6, 3.7 Hz, 5-H_{ax}), 4.50 (1H, dt, J = 11.6, 4.9 Hz, 5-H_{eq}), 7.27 (5H, m, Ph); ^{13}C NMR (100 MHz) δ: 170.6, 142.8, 129.0, 127.2, 126.4, 68.6, 37.5, 37.4, 30.3. The lactone **28** was converted as before to *ethyl 7-hydroxy-2-methyl-5-phenyl-2-heptenoate* in 69% yield, this was hydrogenated, giving *ethyl 7-hydroxy-2-methyl-5-phenylheptanoate* (**29**); IR (neat): 3420, 1730 cm^{-1}; ^{1}H NMR (400 MHz) δ: 1.07, 1.08* (3H, d, J = 7.3 Hz, *Me*CH), 1.22 (3H, t, J = 7.3 Hz, *Me*CH_2O), 1.35 (2H, m), 1.48 (1H, m), 1.60 (2H, m), 1.81 (1H, m), 1.92 (1H, m), 2.36 (1H, m), 2.69 (1H, m), 3.45 (1H, m, CH_2CH_2OH), 3.52 (1H, m,

CH_2CH_2OH), 4.09 (2H, q, J = 7.3 Hz, $MeCH_2O$), 7.29 (5H, m, Ph); ^{13}C NMR (100 MHz) δ: 176.7, 144.7, 128.5, 127.6, 126.3, 61.1, 60.1, 42.6, 42.3,* 39.6, 39.5,* 34.4, 34.1,* 31.8, 31.6,* 17.2, 17.0, 14.3. The hydroxy ester **29** (0.34 g) was then transformed via a mesylate to the title bromide **30** in 71% yield. IR (neat): 1730 cm^{-1}; ^1H NMR (400 MHz) δ: 0.88, 1.08* (3H in total, d, J = 7.0 and 6.7 Hz respectively, *Me*CH), 1.23 (3H, t, J = 6.7 Hz, $MeCH_2O$), 1.60 (2H, m), 2.10 (1H, m), 2.35 (1H, m), 2.75 (1H, m), 3.08 (1H, td, J = 6.7, 1.2 Hz, CH_2CH_2Br), 3.26 (1H, td, J = 6.7, 2.4 Hz, CH_2CH_2Br), 4.10 (2H, q, J = 7.3 Hz, $MeCH_2O$), 7.20 (5H, m, Ph); ^{13}C NMR (100 MHz) δ: 176.5, 176.4,* 143.4, 143.3,* 128.6, 127.7, 126.6, 60.1,44.3, 44.1,* 39.7, 39.5,* 34.0, 33.7,* 31.9, 31.7,* 31.6, 31.5,* 22.7, 17.2, 17.1.* Exact Mass calcd. for $C_{16}H_{23}O_2Br$: 326.0881; found: 326.0891.

Ethyl 7-bromo-2-methyl-5-tert-butylheptanoate (35)

A solution of 4-*tert*-butylcyclohexanone (**31**) (15.43 g, 100 mmol), *m*-chloroperbenzoic acid (21.6 g, 125 mmol), and $TsOH{\cdot}H_2O$ (3.5 g) in CH_2Cl_2 (300 mL) was stirred at ambient temperature for 5 h. The precipitate was filtered off and the filtrate was washed successively with aqueous Na_2SO_3, aqueous K_2CO_3, and brine. The residue left after evaporation of the solvent was purified by silica gel chromatography, affording crude *4-tert-butyl-6-hexanolide*, which was used for the next reaction. To the material dissolved in a mixture of THF (120 mL) and Et_2O (80 mL) was added a 1 M methyllithium solution in THF (120 mL, 120 mmol) at −90°C and the mixture was stirred at this temperature for 3 h. After quenching by the addition of aqueous NH_4Cl, the reaction mixture was extracted with Et_2O and the product was purified by chromatography on a silica gel column, giving *6-oxo-3*-tert-*butyl-1-heptanol* (13.82 g, 74% from **31**) as an oil; IR (neat): 3420, 1710 cm^{-1}; ^1H NMR (400 MHz) δ: 0.88 (9H, s, Me3C), 1.28 (2H, m), 1.78 (3H, m), 1.89 (1H, br s, OH), 2.15 (3H, s, MeCO), 2.50 (2H, m, CH_2CH_2CO), 3.65 (2H, t, J = 6.7 Hz, CH_2CH_2OH). A solution of the alcohol (13.8 g, 74.3 mmol), imidazole (12.6 g, 185 mmol), and *tert*-butyldimethylsilyl chloride (13.4 g, 90 mmol) in DMF (30 mL) was stirred at ambient temperature for 1 day, and then the reaction mixture was quenched by the addition of aqueous NH_4Cl. Purification of the product by silica gel chromatography afforded 5-tert-*butyl-7*-tert-*butyldimethylsilyloxy-2-heptanone* (**32**) (12.94 g, 58%) as an oil; IR (neat): 1720 cm^{-1}; ^1H NMR (400 MHz) δ: 0.05 (6H, s, SiMe2), 0.86 (9H, s, $SiBu^t$), 0.90 (9H, s, Me_3C), 1.26 (2H, m), 1.75 (2H, m), 2.12 (3H, s, MeCO), 2.38 (1H, ddd, J = 15.9, 10.3, 6.1 Hz, CH_2CH_2CO), 2.56 (1H, ddd, J = 15.9, 11.0, 5.5 Hz, CH_2CH_2CO), 3.57 (2H, t, J = 6.7 Hz, CH_2CH_2OSi); ^{13}C NMR (100 MHz) δ: 233.9, 63.4, 44.4, 43.7, 34.4, 33.9, 29.9, 27.6, 26.0, 25.4, 18.4. Exact Mass calcd. for $C_{17}H_{36}O_2Si$: 300.2485; found: 300.2556. A solution of the silyl ether **32** (1.4 g, 4.7 mmol) in anhydrous Et_2O was added at −25°C to a solution of methoxymethylenetriphenylphosphorane prepared from methoxymethyltriphenylphosphonium chloride (2.4 g, 7 mmol), 1.6 M *n*-butyllithium solution in hexane (4.4 mL, 7 mmol), and Et_2O (20 mL). The mixture was stirred at −20°C for 1 h and at room temperature for 3 h. After removal of the precipitate by filtration the filtrate was washed with cold water and brine. The crude enol ether obtained by evaporation of the solvent was added to a mixture of 70% aqueous perchloric acid and Et_2O (60 mL), and the mixture was allowed to react at room temperature for 2 h. The reaction mixture was washed successively with water, aqueous $NaHCO_3$, and brine. Evaporation of the solvent gave crude *ethyl 7-hydroxy-2-methyl-5-tert-butylheptanal* (**33**); ^1H NMR (400 MHz) δ: 0.86 (9H, s, Me_3C), 1.10 (3H, d, J = 7.0 Hz, *Me*CH), 0.80–2.00 (9H, m), 3.63 (3H, t, J = 7.3 Hz, CH_2CH_2OH), 9.61 (1H, d, J = 1.2 Hz, CH_2CHO). To a stirred solution of the aldehyde **33** (4.2 g, 21 mmol) in a mixture of *tert*-BuOH (60 mL) and 5% aqueous NaH_2PO_4 was added dropwise 1 M aqueous $KMnO_4$ solution (50 mL, 50 mmol) (39) and stirring was continued at room temperature for 5 h. The reaction mixture was diluted with water and the product was isolated by extraction with Et_2O, giving the corresponding carboxylic acid, which was esterified by refluxing with 3 M HCl, EtOH (15 mL), and toluene (7 mL) for 5 h. Usual work-up afforded *ethyl 7-hydroxy-2-methyl-5*-tert-*butylheptanoate* (**34**). This hydroxy ester was converted via a mesylate to the title bromide **35**; IR (neat): 1730 cm^{-1}; ^1H NMR (400 MHz) δ: 0.87 (9H, s, Me_3C), 1.02 (2H, m), 1.16 (3H, d, J = 6.7 Hz, *Me*CH), 1.26 (3H, t, J = 6.7 Hz, $MeCH_2O$), 1.30–1.80 (4H, m), 2.04 (1H, m), 2.39 (1H, m, $CH_2CHMeCO_2$), 3.38 (1H, dt, J = 8.6, 7.3 Hz, $CH_2CH_aH_bBr$), 3.46 (2H, tdd, J = 9.5, 5.5, 2.4 Hz, $CH_2CH_aH_bBr$), 4.14 (2H, q, J = 6.7 Hz, $MeCH_2O$). Exact Mass calcd. for $C_{14}H_{27}O_2Br$: 306.1194; found: 306.1296.

4-Methyl-5-pentanolide (37)

A mixture of methacrolein (14.8 mL, 143 mmol), dimethyl malonate (14.1 mL, 120 mmol), and Et_3N (16.7 mL, 120 mmol) in MeOH (150 mL) was stirred at 0°C for 17 h (40). The product obtained by Et_2O extraction was distilled, giving *dimethyl 3-formyl-1,1-butanedicarboxylate* (10.1 g, 41%); ^1H NMR (90 MHz) δ: 1.15 (3H, d, J = 7 Hz, $MeCH_2O$), 1.66–2.57 (3H, m), 3.47 (1H, m, $CH_2CH(CO_2Me)_2$), 3.71 (6H, s, 2 × CO_2Me), 9.57 (1H, br s, CH_2CHO). The aldehyde (4.2 g, 20.8 mmol) dissolved in MeOH (10 mL) was treated with a solution of $NaBH_4$ (0.79 g, 20.8 mmol) in MeOH (10 mL) at room temperature for 1.5 h. After addition of 3 M HCl, the mixture was concentrated and then extracted with Et_2O. Evaporation of the solvent afforded crude *dimethyl 4-hydroxy-3-methyl-1,1-butanedicarboxylate* (**36**) (4.0 g, 94%); ^1H NMR (90 MHz) δ: 0.93 (3H, d, J = 7 Hz, *Me*CH), 1.30–2.25 (4H, m), 3.43 (2H, d, J = 6 Hz, $CHCH_2OH$), 3.69 (6H, s, 2 × CO_2Me). The alcohol **36** (3.82 g, 18.7 mmol) was heated under refluxing with NaOH (4.73 g, 84.3 mmol) and water (6 mL) for 3 h. The mixture was diluted with water (6 mL) and concentrated. It was mixed with concentrated H_2SO_4 (5.8 g), diluted with water (7 mL), and the mixture was refluxed for 3 h. Extraction with Et_2O gave the crude title compound **37** (2.03 g, 95%); ^1H NMR (90 MHz) δ: 0.98 (3H, d, J = 6 Hz, *Me*CH), 1.13–2.83 (5H, m), 2.43 (1H, m, 2-H_{eq}), 3.84 (1H, dd, J = 12, 10 Hz, 5-H_{ax}), 4.27 (1H, ddd, J = 12, 5, 2 Hz, 5-H_{eq}).

Ethyl 7-bromo-2,6-dimethylheptanoate (39)

The lactone **37** (1.38 g, 12 mmol) was converted by Takacs' procedure (11) as before to furnish *ethyl 7-hydroxy-2,6-dimethyl-2-heptenoate* (1.62 g, 70%); ^1H NMR (90 MHz) δ: 0.93 (3H, d, J = 6 Hz, *Me*CH), 1.07–1.70 (9H, m), 1.81 (3H, br s, *Me*C=), 3.43 (2H, d, J = 6 Hz, $CHMeCH_2OH$), 4.15 (2H, q, J = 6 Hz, $MeCH_2O$), 6.70 (1H, br t, J = 7 Hz, CH_2CH=). The unsaturated alcohol was catalytically hydrogenated (Pd–C) to

give *7-hydroxy-2,6-dimethylheptanoate* (**38**); ^{1}H NMR (90 MHz) δ: 0.90 (3H, d, J = 6 Hz, *Me*CH), 1.03–2.40 (15H, m), 3.42 (2H, m), 4.17 (2H, q, J = 6 Hz, MeCH_2O). The saturated hydroxy ester **38** was mesylated as before to yield *ethyl 7-mesyloxy-2,6-dimethylheptanoate*; ^{1}H NMR (90 MHz) δ: 0.97 (3H, d, J = 7 Hz, *Me*CH), 1.15–2.60 (14H, m), 2.95 (3H, s, MsO), 4.00 (2H, d, J = 6 Hz, CH_2CH_2OMs), 4.08 (2H, q, J = 7 Hz, MeCH_2O). Treatment of this mesylate with LiBr in acetone afforded the title bromide **39** (51% from mesylate); ^{1}H NMR (90 MHz) δ: 0.97 (3H, d, J = 6 Hz, *Me*CH), 1.23 (3H, t, J = 7 Hz, *Me*CH_2O), 0.78–2.10 (7H, m), 2.40 (1H, sextet, J = 6.0 Hz, CH_2CHMeCO$_2$), 3.30 (2H, d, J = 6 Hz, CHMeCH_2Br), 4.07 (2H, q, J = 7 Hz, MeCH_2O); ^{13}C NMR (25 MHz) δ: 176.5, 60.1, 41.3, 39.4, 35.0, 34.6, 33.8,* 24.4, 18.7, 17.1, 14.3.

*Cyclization of ethyl 7-bromo-2,3-dimethylheptanoate (**11**).*

Typical procedure for cyclization experiments

A mixture of diisopropylamine (0.51 mL, 1.0 mmol) in THF (5 mL) and *n*-butyllithium solution (1.6 M in hexane, 2.0 mL, 3.2 mmol) was stirred at 0°C for 10 min and then the stirring was continued at −78°C for 20 min. To this solution was added a solution of the ester **11** (265 mg, 1.00 mmol) and the mixture was allowed to react at −78°C for 1 h. After quenching by the addition of aqueous NH_4Cl, the reaction mixture was extracted with Et_2O and the combined organic layers were washed with brine. The residue left after evaporation of the solvent was purified by chromatography on a silica gel column, giving the cyclized product (193 mg, 78%), which was a 96:4 mixture of diastereomers (capillary GC). From the reason discussed in the text, the major isomer was identified as *ethyl 1,*t*-2-dimethyl*-r-*1-cyclohexanecarboxylate* (**40**); IR (neat): 1730 cm^{-1}; ^{1}H NMR (400 MHz) δ: 0.77 (3H, d, J = 6.7 Hz, *Me*CH), 1.07 (3H, s, *Me*C), 1.25 (3H, t, J = 6.7 Hz, *Me*CH_2O), 1.00–1.60 (6H, m), 2.01 (1H, dqd, J = 10.5, 6.7, 3.1 Hz, 2-H), 4.13 (2H, q, J = 6.7 Hz, *Me*CH_2O); ^{13}C NMR (100 MHz) δ: 178.5(s), 60.1(t), 46.5(d), 36.1(s,t), 29.9(t), 25.4(t), 21.3(t), 17.3(q), 14.3(q), 14.1(q). Exact Mass calcd. for $C_{11}H_{20}O_2$: 184.1463; found: 184.1455.

*Cyclization of ethyl 7-bromo-2,4-dimethylheptanoate (**15**)*

The reaction afforded exclusively *ethyl 1,*c*-3-dimethyl*-r-*1-cyclohexanecarboxylate* (**42**); IR (neat): 1730 cm^{-1}; ^{1}H NMR (400 MHz) δ: 0.75–0.85 (2H, m), 0.88 (3H, d, J = 6.7 Hz, *Me*CH), 1.00–1.06 (1H, m), 1.20 (3H, t, J = 6.8 Hz, *Me*CH_2O), 1.28–1.90 (6H, m), 4.11 (2H, q, J = 6.8 Hz, MeCH_2O); ^{13}C NMR (100 MHz) δ: 178.9(s), 60.2(t), 42.5(t), 42.4(s), 34.7(t), 33.4(t), 27.4(d), 22.8(q), 21.4(t), 20.5(q), 14.2(q). Exact Mass calcd. for $C_{11}H_{20}O_2$: 184.1463; found: 184.1468.

*Cyclization of ethyl 7-bromo-2,5-dimethylheptanoate (**19**)*

The diasteromeric ratio of the cyclized product was 79:21 and both diastereomers were separated by flash chromatography on a silica gel column for the purpose of the spectroscopic analysis. A *trans* and a *cis* structure was assigned for the major and the minor diastereomers, respectively. *Ethyl 1,*t*-4-dimethyl*-r-*1-cyclohexanecarboxylate* (**44**): ^{1}H NMR (400 MHz) δ: 0.91 (3H, d, J = 6.7 Hz, *Me*CH), 1.10 (2H, td, J = 13.4, 3.6 Hz, 2,6-H_{ax}), 1.18 (3H, s, MeC), 1.24 (3H, t, J = 6.7 Hz, *Me*CH_2O), 1.37 (1H, m, 4-H), 1.58 (4H, m, 2,6-H_{eq}, 3,5-H_{eq}), 1.69 (2H, qd, J = 13.4, 3.7 Hz, 3,5-H_{ax}), 4.11 (2H, q, J = 6.7 Hz, MeCH_2O); ^{13}C NMR (100 MHz) δ: 178.9(s), 60.1(t), 41.6(s), 33.4(t), 31.6(d), 30.0(t), 21.9(q), 20.8(q), 14.2(q). Exact Mass calcd for $C_{11}H_{20}O_2$: 184.1463; found: 184.1474. *Ethyl 1,*c*-4-dimethyl*-r-*1-cyclohexanecarboxylate* (**45**); ^{1}H NMR (400 MHz) δ: 0.85 (3H, d, J = 6.7 Hz, *Me*CH), 0.96 (2H, qd, J = 13.4, 2.5 Hz, 3,5-H_{ax}), 1.12 (2H, td, 2H, J = 13.4, 3.7 Hz, 2,6-H_{ax}), 1.13 (3H, s, MeC), 1.25 (3H, t, J = 6.7 Hz, MeCH_2O), 1.28 (1H, m, 4-H), 1.56 (2H, m, 3,5-H_{eq}), 2.17 (2H, br. d, J = 13.4 Hz, 2,6-H_{eq}), 4.14 (2H, q, J = 6.7 Hz, *Me*CH_2O); ^{13}C NMR (100 MHz) δ: 177.4, 60.0, 43.1, 36.0, 32.5, 32.1, 28.3, 22.4, 14.3. Exact Mass calcd. for $C_{11}H_{20}O_2$: 184.1463; found: 184.1454.

*Cyclization of ethyl 7-bromo-5-ethyl-2-methylheptanoate (**25**)*

The major and the minor products were separated by the flash chromatography and analyzed by spectroscopy to be *trans* and *cis* compounds, respectively. *Ethyl* t*-4-ethyl-1-methyl*-r-*1-cyclohexanecarboxylate* (**46**). ^{1}H NMR (400 MHz) δ: 0.88 (3H, t, J = 7.3 Hz, 4-*Me*CH_2), 1.17 (3H, s, MeC), 1.24 (3H, t, J = 7.3 Hz, *Me*CH_2O), 1.06–1.30 (5H, m, 2,6-H_{ax}, 4-H, 4-MeCH_2), 1.63 (6H, m, 2,6-H_{eq}, 3,5-$H_{ax}H_{eq}$), 4.11 (2H, q, J = 7.3 Hz, MeCH_2O); ^{13}C NMR (100 MHz) δ: 178.9(t), 60.1(t), 41.9(s), 38.4(d), 33.4(t), 29.1(t), 27.6(t), 20.7(q), 14.2(q), 11.5(q). Exact Mass calcd for $C_{12}H_{22}O_2$: 198.1620; found: 198.1643. *Ethyl* c*-4-ethyl-1-methyl*-r-*1-cyclohexanecarboxylate* (**47**): ^{1}H NMR (400 MHz) δ: 0.85 (3H, t, J = 7.3 Hz, 4-*Me*CH_2), 0.94 (2H, qd, J = 13.4, 2.5 Hz, 3,5-H_{ax}), 1.06 (1H, m, 4-H), 1.10 (2H, td, J = 12.8, 3.4 Hz, 2,6-H_{ax}), 1.13 (3H, s, MeC), 1.25 (3H, t, J = 7.3 Hz, *Me*CH_2O), 1.64 (2H, br d, J = 13.4 Hz, 3,5-H_{eq}), 2.19 (2H, br d, J = 13.4 Hz, 2,6-H_{eq}), 4.13 (2H, q, 2H, J = 7.3 Hz, MeCH_2O); ^{13}C NMR (100 MHz) δ: 177.4(s), 60.0(t), 43.5(s), 38.8(d), 35.9(t), 30.1(t), 29.7(t), 28.3(q), 14.3(q), 11.5(q). Exact Mass calcd. for $C_{12}H_{22}O_2$: 198.1620; found: 198.1646.

*Cyclization of ethyl 7-bromo-5-isopropyl-2-methylheptanoate (**26**)*

Major product: *ethyl* t*-4-isopropyl-1-methyl*-r-*1-cyclohexanecarboxylate* (**48**); ^{1}H NMR (400 MHz) δ: 0.87 (6H, d, J = 6.7 Hz, Me_2CH), 1.02 (1H, m, 4-H), 1.17 (3H, s, MeC), 1.20 (2H, m, 2,6-H_{ax}), 1.24 (3H, t, J = 7.3 Hz, *Me*CH_2O), 1.44 (1H, octet, J = 6.7 Hz, Me_2CHCH), 1.57 (2H, dq, J = 12.2, 4.3 Hz, 3,5-H_{eq}), 1.67 (4H, m, 2,6-H_{eq}, 3,5-H_{ax}), 4.11 (2H, q, J = 7.3 Hz, MeCH_2O); ^{13}C NMR (100 MHz) δ: 179.0(s), 60.1(t), 43.5(d), 36.2(t), 32.7(d), 28.4(q), 27.2(t), 24.7(t), 19.9(q), 14.3(q). Exact Mass calcd. for $C_{13}H_{24}O_2$: 212.1776; found: 212.1797. Minor product: *ethyl* c*-4-isopropyl-1-methyl*-r-*1-cyclohexanecarboxylate* (**49**); ^{1}H NMR (400 MHz) δ: 0.83 (6H, d, J = 6.7 Hz, Me_2CH), 0.98–1.12 (5H, m, 2,6-H_{ax}, 3,5-H_{ax}, 4-H), 1.12 (3H, s, MeC), 1.25 (3H, t, J = 7.3 Hz, *Me*CH_2O), 1.37 (1H, m, Me_2CH), 1.64 (2H, br, d, J = 6.7 Hz, 3,5-H_{eq}), 2.21 (2H, br d, J = 12.2 Hz, 2,6-H_{eq}), 4.14 (2H, q, J = 7.3 Hz, MeCH_2O); ^{13}C NMR (100 MHz) δ: 177.4(s), 60.0(t), 43.5(d,s), 36.2(t), 32.7(d), 28.4(q), 27.2(t), 24.7(t), 19.9(q), 14.3(q). Exact Mass calcd. for $C_{13}H_{24}O_2$: 212.1776: found 212.1791.

*Cyclization of ethyl 7-bromo-2-methyl-5-phenylheptanoate (**30**)*

Major product: *ethyl 1-methyl*-t*-4-phenyl*-r-*1-cyclohexanecarboxylate* (**50**); IR (neat): 1730 cm^{-1}; ^{1}H NMR (400 MHz)

δ: 1.27 (3H, t, J = 7.3 Hz, *Me*CH_2O), 1.29 (3H, s, MeC), 1.68 (2H, qd, J = 12.2, 3.1 Hz, 3,5-H_{ax}), 1.80 (4H, m, 2,6-H_{ax}, 3,5-H_{eq}), 1.84 (2H, td, J = 12.2, 3.7 Hz, 2,6-H_{eq}), 2.50 (1H, tt, J = 12.2, 3.7 Hz, 4-H), 4.15 (2H, q, J = 7.3 Hz, MeC*H*$_2$O), 7.26 (5H, m, Ph); ^{13}C NMR (100 MHz) δ: 178.8, 147.0, 128.4, 126.8, 126.1, 60.3, 43.7, 41.3, 34.1, 29.0, 20.1, 14.2. Exact Mass calcd. for $C_{16}H_{22}O_2$: 246.1620; found: 246.1616. Minor product: *ethyl 1-methyl*-c-*4-pheny*-r-*1-cyclohexanecarboxylate* (**51**); IR (neat): 1730 cm^{-1}; ^{1}H NMR (400 MHz) δ: 1.20 (3H, s, MeC), 1.28 (3H, t, J = 7.3 Hz, *Me*CH_2O), 1.30 (2H, m, 2,6-H_{ax}), 1.53 (2H, qd, J = 13.4, 3.1 Hz, 3,5-H_{ax}), 1.80 (2H, br d, J = 13.4 Hz, 3,5-H_{eq}), 2.33 (2H, br d, J = 12.2 Hz, 2,6-H_{eq}), 2.47 (1H, tt, J = 13.4, 3.7 Hz, 4-H), 4.19 (2H, q, J = 7.3 Hz, *Me*CH_2O), 7.26 (5H, m, Ph); ^{13}C NMR (100 MHz) δ: 177.2, 147.2, 128.3, 126.8, 126.0, 60.2, 43.8, 43.1, 36.3, 31.6, 28.4, 14.3. Exact Mass calcd. for $C_{16}H_{22}O_2$: 246.1620; found: 246.1615.

Cyclization of ethyl 7-bromo-2-methyl-5-tert-*butylheptanoate (35)*

Major product: *ethyl 1-methyl*-t-*4*-tert-*butyl*-r-*1-cyclohexanecarboxylate* (**52**); ^{1}H NMR (400 MHz) δ: 0.86 (s, 9H, Me_3C), 0.98 (1H, tt, J = 12.2, 3.1 Hz, 4-H), 1.17 (3H, s, MeC), 1.18 (2H, m, 2-H_{ax}), 1.24 (3H, t, J = 7.3 Hz, *Me*CH_2O), 1.59–1.75 (6H, m, 2,6-H_{eq}, 3,5-$H_{ax}H_{eq}$), 4.11 (2H, q, J = 7.3 Hz, MeC*H*$_2$O); ^{13}C NMR (100 MHz) δ: 179.1, 60.1, 47.8, 41.4, 34.4, 32.4, 27.5, 22.2, 19.7, 14.2. Exact Mass calcd. for $C_{14}H_{26}O_2$: 226.1933; found: 226.1905. Minor product: *ethyl 1-methyl*-c-*4*-tert-*butyl-1-cyclohexanecarboxylate* (**53**); ^{1}H NMR (400 MHz) δ: 0.81 (9H, s, Me_3C), 0.90–1.15 (5H, m, 2,6-H_{ax}, 3,5-H_{ax}, 4-H), 1.12 (3H, s, MeC), 1.25 (3H, t, J = 7.3 Hz, *Me*CH_2O), 1.64 (2H, m, 3,5-H_{eq}), 2.23 (2H, dt, J = 11.0, 3.2 Hz, 2,6-H_{eq}), 4.15 (2H, q, J = 7.3 Hz, MeC*H*$_2$O); ^{13}C NMR (100 MHz) δ: 177.4, 60.0, 47.6, 43.3, 36.6, 32.4, 28.4, 27.5, 24.8, 14.3. Exact Mass calcd. for $C_{14}H_{26}O_2$: 226.1933; found: 226.1915.

Cyclization of ethyl 7-bromo-2,6-dimethylheptanoate (39)

The reaction yielded the same diastereomeric 1,3-dimethylcyclohexane derivatives as in the case of the bromide **15** but with the reversed predominance — the dominant product was *ethyl 1,* t-*3-dimethyl*-r-*1-cyclohexanecarboxylate* (**43**); ^{1}H NMR (400 MHz) δ: 0.72 (1H, t, J = 12.5 Hz, 2-H_{ax}), 0.79 (1H, qd, J = 13.5, 3.7 Hz. 4-H_{ax}), 0.87 (3H, d, J = 6.7 Hz, *Me*CH), 0.98 (1H, td, J = 13.5, 4.0 Hz, 6-H_{ax}), 1.13 (3H, s, MeC), 1.24 (3H, t, J = 7.3 Hz, *Me*CH_2O), 1.32 (1H, qt, J = 13.5, 3.7 Hz, 5-H_{ax}), 1.41 (1H, m. 3-H), 1.58 (1H, m, 5-H_{eq}), 1.62 (2H, m, 4-H_{eq}), 2.13 (1H, dq, J = 12.5, 2.4 Hz, 2-H_{eq}), 2.16 (1H, br d, J = 13.5 Hz, 6-H_{eq}), 4.13 (2H, q, J = 7.3 Hz, MeC*H*$_2$O); ^{13}C NMR (100 MHz) δ: 177.5, 60.0, 44.8, 43.9, 35.7, 34.5, 29.9, 28.7, 23.8, 22.8, 14.3.

Acknowledgement

We thank Dr. Yoshinosuke Usuki for his assistance.

References

1. P. Deslongchamps. Aldrichimica Acta, **17**, 59 (1984).
2. (*a*) G. Desimoni, G. Tacconi, A. Barco, and G.P. Pollini. Natural products synthesis through pericyclic reactions. American Chemical Society, Washington, D.C. 1983; (*b*) T.-L. Ho. Carbocyclic construction in terpene synthesis. VCH Publishers, Weinheim. 1988. pp. 329–432; (*c*) W. Carruthers. Cycloaddition reactions in organic synthesis. Pergamon Press, Oxford. 1990. pp. 1–240; (*d*) W. Oppolzer. *In* Comprehensive organic synthesis. Vol. 5. *Edited by* B.M. Trost and I. Fleming. Pergamon Press, Oxford. 1991. pp. 315–399.
3. (*a*) T. Tokoroyama, K. Fujimori, T. Shimizu, Y. Yamagiwa, M. Monden, and H. Iio. Tetrahedron, **44**, 6607 (1988); (*b*) T. Tokoroyama. Yuki Gosei Kagaku Kyokaishi, **51**, 1164 (1993); (*c*) T. Tokoroyama, T. Tsukamoto, T. Asada, and H. Iio. Tetrahedron Lett. **28**, 6645 (1987).
4. T. Tokoroyama, T. Tsukamoto, and H. Iio. Tetrahedron Lett. **25**, 5067 (1984).
5. T. Tokoroyama, K. Okada, and H. Iio. J. Chem. Soc. Chem. Commun. 1572 (1989).
6. K. Asao, H. Iio, and T. Tokoroyama. Tetrahedron Lett. **30**, 6397 (1989).
7. T. Tokoroyama, M. Kato, T. Aoto, T. Hattori, H. Iio, and Y. Odagaki. Tetrahedron Lett. **51**, 8247 (1994).
8. P.A. Bartlett. Tetrahedron, **36**, 1 (1980).
9. (*a*) D.F. Taber. Intramolecular Diels–Alder and Alder ene reaction. Springer-Verlag, Berlin. 1984. pp. 51–56; (*b*) L.F. Tietz and U. Beifuss. Tetrahedron Lett. **27**, 1767 (1986); (*c*) Synthesis, 359 (1988); (*d*) L.F. Tietz, U. Beifuss, and M. Ruther. J. Org. Chem. **54**, 3120 (1989); (*e*) E.J. Corey and P. Carpino. Tetrahedron Lett. **31**, 3857 (1990); (*f*) S.H. Anh, D. Kim, M.W. Chun, and W.-K. Chung. Tetrahedron Lett. **27**, 943 (1986); (*g*) D. Kim and H.S. Kim. J. Org. Chem. **52**, 4633 (1987); (*h*) D. Kim, S. Kim, J.J. Lee, and H.S. Kim. Tetrahedron Lett. **31**, 4027 (1990); (*i*) D. Kim and Y.K. Lee. Tetrahedron Lett. **32**, 6885 (1991); (*j*) D. Kim, J.I. Lim, K.J. Shin, and H.S. Kim. Tetrahedron Lett. **34**, 6557 (1993); (*k*) D. Kim, Y.M. Jang, I.O. Kim, and S.W. Park. J. Chem. Soc. Chem. Commun. 760 (1988); (*l*) D. Kim, Y.K. Lee, Y.M. Jang, I.O. Kim, and S.W. Park. J. Chem. Soc. Perkin Trans. **1**, 3221 (1990); (*m*) D. Kim, K.J. Shin, I.Y. Kim, and S.W. Park. Tetrahedron Lett. **35**, 7957 (1994); (*n*) D. Kim, Y.S. Kwak, and K.J. Shin. Tetrahedron Lett. **35**, 9211 (1994); (*o*) K. Hori, N. Hikage, A. Inagaki, S. Mori, K. Nomura, and E. Yoshii. J. Org. Chem. **57**, 2888 (1992); (*p*) K. Hori, H. Kazuno, K. Nomura, and E. Yoshii. Tetrahedron Lett. **34**, 2183 (1993).
10. (*a*) K. Asao, H. Iio, and T. Tokoroyama. Synthesis, 382 (1990); (*b*) K. Takai, M. Sato, K. Ohsima, and H. Nozaki. Bull. Chem. Soc. Jpn. **57**, 108 (1984); (*c*) M. Alderdice, C. Spino, and L. Weiler. Tetrahedron Lett. **25**, 1643 (1984); (*d*) C. Spino and L. Weiler. Tetrahedron Lett. **28**, 731 (1987); (*e*) R.J. Armstrong, F.L. Harris, and L. Weiler. Can. J. Chem. **60**, 673 (1982).
11. J.M. Takacs, M.A. Helle, and F.L. Seely. Tetrahedron Lett. **27**, 1257 (1986).
12. D.M. Bailey and R.E. Johnson. J. Org. Chem. **35**, 3574 (1970).
13. I. Fleming, N.L. Reddy, K. Takaki, and A.C. Ware. J. Chem. Soc. Chem. Commun. 1472 (1987).
14. A.G. Schultz and R.E. Taylor. J. Am. Chem. Soc. **114**, 3937 (1992).
15. A.P. Krapcho and E.A. Dundulis. J. Org. Chem. **45**, 3236 (1980).
16. S. Wolff and W.C. Agosta. J. Org. Chem. **38**, 1694 (1973).
17. J.L. Broeker, R.W. Hoffmann, and K.N. Houk. J. Am. Chem. Soc. **113**, 5006 (1991).
18. R.N. Hoffmann. Chem. Rev. **89**, 1841 (1989).
19. R.E. Ireland, R. Wipf, and J.D. Armstrong III. J. Org. Chem. **56**, 650 (1991), and refs. cited therein.
20. F. Johnson. Chem. Rev. **68**, 375 (1968).
21. (*a*) I. Flemming and J.J. Lewis. J. Chem. Soc. Chem. Commun. 149 (1985); (*b*) I. Flemming, J.H.M. Hill, D. Parker, and D. Waterson. J. Chem. Soc. Chem. Commun. 318 (1985); (*c*) G.

McGarvey and J.M. Williams. J. Am. Chem. Soc. **107**, 1435 (1985).
22. D. Caine. *In* Comprehensive organic synthesis. Vol. 3. *Edited by* B.M. Trost and I. Fleming. Pergamon Press, Oxford. 1991. pp. 42–44.
23. N.L. Allinger and M.A. Miller. J. Am. Chem. Soc. **83**, 2145 (1961).
24. E.L. Eliel, N.L. Allinger, S.J. Angyal, and G.A. Morrison. Conformational analysis. Interscience Publishers, New York. 1965. p. 52.
25. U. Burkert and N.L. Allinger. Molecular mechanics. American Chemical Society, Washington, D.C. 1982. pp. 39–52.
26. F.A. Carey and R.J. Sundberg. Advanced organic chemistry. Part A: Structure and mechanism. 3rd ed. Plenum Press, New York. 1990. p. 135.
27. E.L. Eliel and M. Manoharan. J. Org. Chem. **46**, 1959 (1981).
28. (*a*) H. DeBeule, D. Tavernier, and M. Anteunis. Tetrahedron, **30**, 3573 (1974); (*b*) W. Smadja. Synlett, 1 (1994).
29. G.W. Klumpp. Reactivity in organic chemistry. John Wiley and Sons, New York. 1982. pp. 352–372.
30. J.E. Eksterowicz and K.N. Houk. Chem. Rev. **93**, 2439 (1993).
31. K.B. Lipkowitz and A. Peterson. Chem. Rev. **93**, 2463 (1993).
32. R.A. Daignault and E.L. Eliel. Org. Synth. Collect. Vol. 5, Wiley and Sons, Inc., New York. 1963. p. 303.
33. J.L. Hermann and R.H. Schlessinger. J. Chem. Soc. Chem. Commun. 711 (1973).
34. R.I. Longley, Jr. and W.S. Emerson. Org. Synth. Collect. Vol. 4, Wiley and Sons, Inc., New York. 1963. p. 677.
35. M. Nakagawa, J. Saegusa, M. Tonozuka, M. Obi, M. Kiuchi, T. Hino, and Y. Ban. Org. Synth. Collect. Vol. 6, Wiley and Sons, Inc., New York. 1988. p. 462.
36. (*a*) S.S. Guha-Sircar. J. Chem. Soc. 898 (1928); (*b*) P. Ashworth, S.L. Belagali, S. Cassou, A. Marczak, and P. Kocienski. Tetrahedron, **47**, 9939 (1991).
37. C.K. Ingold and W.J. Powell. J Chem. Soc. **119**, 1976 (1921).
38. A. Burger and A. Hofstetter. J. Org. Chem. **24**, 1290 (1959).
39. A. Abiko, J.C. Roberts, T. Takemasa, and S. Masamune. Tetrahedron Lett. **27**, 4537 (1986).
40. D.T. Warner and O.A. Moe. J. Am. Chem. Soc. **71**, 2586 (1949).

Reflectance infrared and UV–visible spectroelectrochemical studies on a series of $[Ni_3(\mu_3\text{-}L)(\mu_3\text{-}I)(\mu_2\text{-}dppm)_3][PF_6]$ (L = CO; CNR, R = alkyl, aryl; dppm = $Ph_2PCH_2PPh_2$) clusters

John Washington and Clifford P. Kubiak

Abstract: The trinuclear nickel clusters $[Ni_3(\mu_3\text{-}L)(\mu_3\text{-}I)(\mu_2\text{-}dppm)_3]^+$ (L = CO (**1**); CNR, R = CH_3 (**2**), i-C_3H_7 (**3**), C_6H_{11} (**4**), t-C_4H_9 (**5**), $CH_2C_6H_5$ (**6**), C_6H_5 (**7**), p-C_6H_4I (**8**), p-C_6H_4F (**9**), p-$C_6H_4CH_3$ (**10**), p-$C_6H_4CF_3$ (**11**), p-$C_6H_4OCH_3$ (**12**), p-C_6H_4CN (**13**), 2,6-$(CH_3)_2C_6H_3$ (**14**); dppm = $Ph_2PCH_2PPh_2$) all contain a triply bridging π-acceptor (carbonyl or isocyanide) ligand. Compounds **1–14** all undergo single electron reductions over a relatively narrow range of $E_{1/2}(+/0)$ (−1.08 V to −1.18 V vs. SCE in acetonitrile) and are known electrocatalysts for the reduction of carbon dioxide. Specular reflectance infrared spectroelectrochemical (SEC) measurements on **1–14** indicate that the capping isocyanide or carbonyl ligand remains triply bridging (μ_3,η^1) upon single electron reduction. The magnitude of the ν(C≡O) or ν(C≡N) absorption band shift upon reduction is related to both the electronic and steric properties of the capping π-acceptor ligand. Spectroelectrochemical studies with UV–visible detection revealed a hypsochromic shift upon reduction of the clusters. The SEC cell and spectrometer utilized are extremely versatile and allow for data from 600 to 22 000 cm^{-1} to be acquired without modifying the SEC cell and making only minor configuration changes to the spectrometer.

Key words: nickel, cluster, carbonyl, isocyanide, spectroelectrochemical.

Résumé : Les agrégats trinucléaires du nickel, $[Ni_3(\mu_3\text{-}L)(\mu_3\text{-}I)(\mu_2\text{-}dppm)_3]^+$ (L = CO (**1**); CNR, R = CH_3 (**2**), i-C_3H_7 (**3**), C_6H_{11} (**4**), t-C_4H_9 (**5**), $CH_2C_6H_5$ (**6**), C_6H_5 (**7**), p-C_6H_4I (**8**), p-C_6H_4F (**9**), p-$C_6H_4CH_3$ (**10**), p-$C_6H_4CF_3$ (**11**), p-$C_6H_4OCH_3$ (**12**), p-C_6H_4CN (**13**), 2,6-$(CH_3)_2C_6H_3$ (**14**); dppm = $Ph_2PCH_2PPh_2$), comportent tous un coordinat accepteur d'électrons π (carbonyle ou isocyanure) pouvant former trois ponts. Les composés **1–14** subissent tous des réductions impliquant un électron sur une plage relativement restreinte de $E_{1/2}(+/0)$ (−1.08 V à −1.18 V vs. SCE, dans l'acétonitrile) et ils sont reconnus comme électrocatalyseurs pour la réduction du dioxyde de carbone. Des mesures spectroélectrochimiques (SEC) de réflectance infrarouge spéculaire réalisées sur les composés **1–14** indiquent que le coordinat isocyanure ou carbonyle formant le cap maintient le triple pontage (μ_3,η^1) lors de la réduction impliquant un électron. L'amplitude du déplacement de la bande d'absorption ν(C≡O) ou ν(C≡N) lors de la réduction est reliée aux propriétés tant électroniques que stériques du coordinat accepteur d'électrons π qui forme le cap. Des études spectroélectrochimiques avec détection UV–visible révèlent la présence d'un déplacement hypsochrome lors de la réduction des agrégats. La cellule SEC et le spectromètre utilisés sont extrêmement versatiles et permettent d'acquérir des données de 600 à 22 000 cm^{-1} sans modifier la cellule SEC et en ne faisant que des modifications mineures au spectromètre.

Mots clés : nickel, agrégat, carbonyle, isocyanure, spectroélectrochimique.

[Traduit par la rédaction]

Introduction

The synthesis and physical properties of a class of π-acceptor capped trinuclear nickel clusters $[Ni_3(\mu_3\text{-}L)(\mu_3\text{-}I)(\mu_2\text{-}dppm)_3]^+$ (L = CO (**1**); CNR, R = CH_3 (**2**), i-C_3H_7 (**3**), C_6H_{11} (**4**), t-C_4H_9 (**5**), $CH_2C_6H_5$ (**6**), C_6H_5 (**7**), p-C_6H_4I (**8**), p-C_6H_4F (**9**), p-$C_6H_4CH_3$ (**10**), p-$C_6H_4CF_3$ (**11**), p-$C_6H_4OCH_3$ (**12**), and p-C_6H_4CN (**13**), 2,6-$(CH_3)_2C_6H_3$ (**14**); dppm = $Ph_2PCH_2PPh_2$) has been recently reported (1–4). Clusters **1–14** all exhibit reversible single electron reductions $E_{1/2}(+/0)$ at ca. −1.1 V vs. SCE.

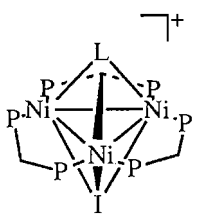

L = CO (**1**)
= CNR, R = alkyl (**2-6**)
= CNR, R = aryl (**7-14**)

Received June 20, 1996.

J. Washington[1] **and C.P. Kubiak.**[2] Department of Chemistry, 1393 H.C. Brown Building, Purdue University, West Lafayette, IN 47907, U.S.A.

[1] NSERC Post-Doctoral Fellow, 1994–1996.
[2] Author to whom correspondence may be addressed. Telephone: (317) 494-6294. Fax: (317) 494-0239. E-mail: cliff@chem.purdue.edu

Carbon dioxide reductions in nonaqueous solvents are generally hindered by poor selectivity and high cathodic potentials. However, due to the importance of CO_2 activation, a variety of transition metal catalysts able to effectively catalyze the reduction of CO_2 have been reported (5–18). The methyl isocyanide capped cluster (**2**) is a known electrocatalyst for the reduction and subsequent activation of carbon dioxide in acetonitrile (2). Importantly, **2** is able to reduce carbon dioxide at potentials ca. 1 V anodic of the uncatalyzed reduction potential (2, 19). The cathodic peak in the cyclic voltammogram of **2** in the presence of CO_2 shows significant current enhancement while the return anodic peak has negligible intensity. Clearly, the reduced form of **2** is responsible for the electrocatalytic reduction of carbon dioxide. Additionally, variation of the capping π-acceptor ligand (CO or CNR) in **1–14** gives rise to different activities with respect to the electrocatalytic reduction of CO_2 (4).

Infrared spectroelectrochemistry studies have been carried out on a number of organometallic systems and allow for the in situ monitoring of sensitive electrogenerated species (20–25). The vibrational spectra so obtained allow for structural and electronic changes to be directly monitored. Clusters **1–14** are capped by carbonyl or isocyanide ligands, both of which contain strong IR chromophores (ν(C≡O) or ν(C≡N) bands) and are well suited to study using an infrared spectroelectrochemical (SEC) cell. Spectroelectrochemical studies were carried out on **1–14** to determine the structure of the reduced species involved in the reduction of carbon dioxide. Herein we report the results of these SEC studies carried out on **1–14**. Additionally, the instrumentation utilized can be modified to allow for reflectance UV–visible spectroelectrochemistry; the results of this investigation will also be discussed.

Experimental

Syntheses were performed under an N_2 atmosphere using an inert atmosphere dry-box or Schlenk techniques. The compounds **1–14** were prepared as previously reported (1). Solvents were reagent or HPLC grade and were dried over the appropriate drying agents.

Electrochemistry

Cyclic voltammetry experiments were conducted in CH_3CN with TBAP (tetrabutylammonium hexafluorophosphate) as the supporting electrolyte. A glassy carbon working electrode, a Pt wire counter electrode, and a ferrocene/ferrocinium reference electrode were utilized. The acetonitrile was distilled under nitrogen from CaH_2 just prior to use. The TBAP used in these experiments was purchased from Aldrich, recrystallized from ethanol, dried under vacuum at 120°C for at least 24 h, and stored under nitrogen.

Infrared and UV–visible spectroelectrochemistry

The design of the spectroelectrochemical (SEC) cell used for the nickel trimer studies has been reported previously by our laboratory (25). Infrared spectral changes accompanying thin-layer bulk electrolyses were measured using a flow-through spectroelectrochemical cell. All spectroelectrochemical experiments were carried out in 0.1 M TBAP solutions of freshly distilled THF. All solutions were prepared under an atmosphere of nitrogen and degassed completely before injection into the spectroelectrochemical cell. Blank THF solutions of 0.1 M TBAP were used for the FT-IR and UV–visible solvent subtractions. A PAR model 175 universal programmer with a PAR model 176 current follower were used to effect and monitor thin-layer bulk electrolyses. The IR spectra were acquired using a Mattson Research Series FTIR with an external sampling port and a MCT (mercury–cadmium–telluride) detector. The UV–visible spectra were acquired using a Mattson Research Series FTIR modified with a quartz beamsplitter and a silicon diode detector. No modifications are required to the SEC cell to allow for operation in both the IR and UV–visible ranges as long as a CaF_2 window is utilized.

Fig. 1. Cyclic voltammogram (100 mV/s) of 2 mM solution of $[Ni_3(\mu_3\text{-}CO)(\mu_3\text{-}I)(\mu_2\text{-}dppm)_3][PF_6]$ (**1**) in 0.1 M TBAP/CH_3CN.

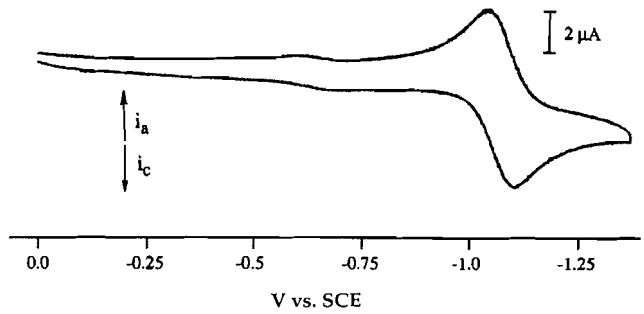

Results and discussion

Infrared SEC studies on $[Ni_3(\mu_3\text{-}CO)(\mu_3\text{-}I)(\mu_2\text{-}dppm)_3]^+$ (1)

As reported previously, the single electron reduction potentials (ca. −1.1 V vs. SCE) for clusters **1–14** (Table 1) are insensitive to the nature of the capping π-acceptor ligand (1). This was attributed to calculations that showed minimal contribution to the LUMO from the capping carbonyl or isocyanide ligand (1, 26). In fact, the LUMO is almost entirely metal based. The cyclic voltammogram of **1** (Fig. 1) shows a reversible one-electron reduction and is representative of the carbonyl and isocyanide clusters **1–14**. The rather large cathodic potentials required for single electron reduction of this class of nickel clusters are consistent with the transformation from a stable 48-electron cluster to a 49-electron radical.

The IR spectra recorded during the bulk reduction of $[Ni_3(\mu_3\text{-}CO)(\mu_3\text{-}I)(\mu_2\text{-}dppm)_3]^+$ (**1**) in the SEC cell are shown in Fig. 2. The IR spectrum of **1** in THF solution shows a single ν(C≡O) absorption band at 1730 cm^{-1}, a frequency consistent with a μ_3,η^1 carbonyl ligand (1, 27). The triply bridging carbonyl has also been confirmed using X-ray crystallography (1). Upon reduction, a decrease in the ν(C≡O) band at 1730 cm^{-1} is observed along with a concomitant increase in intensity of a ν(C≡O) band at 1661 cm^{-1}. The reversible nature of the bulk reduction occurring in the SEC cell is evident, as simply reversing the applied potential quantitatively regenerates **1**. The SEC data obtained for **1**· is consonant with the capping carbonyl remaining in its triply bridging form upon reduction of the nickel cluster (eq. [1]). The minimal structural rearrangement upon single electron reduction is also in accord with the highly reversible electrochemistry observed for **1** and the symmetric septet ESR spectrum of **1**·, arising from ^{31}P

Table 1. Electrochemical and infrared spectroelectrochemical data for $[Ni_3(\mu_3\text{-}L)(\mu_3\text{-}I)(\mu_2\text{-}dppm)_3][PF_6]$ clusters.

	L	$E_{1/2}(0/+)^a$ (V vs. SCE)	FTIR (ν(C≡N), cm^{-1})^b Isolated	Reduced	Δν (cm^{-1})
1	CO[c]	−1.12	1730	1661	69
1*	^{13}CO[c]	−1.12	1691	1622	69
2	$CNCH_3$	−1.18	1914,1858	1649	237
3	$CN(i\text{-}C_3H_7)$	−1.18	1854[d]	1641	213
4	CNC_6H_{11}	−1.17	1880,1833	1647	210
5	$CN(t\text{-}C_4H_9)$	−1.12	1750[d]	1634	116
6	$CNCH_2C_6H_5$	−1.11	1775[d]	1624	151
7	CNC_6H_5	−1.06	1807,1755	1616	165
8	$CN(p\text{-}C_6H_4I)$	−1.00	1802,1729	1602	164
9	$CN(p\text{-}C_6H_4F)$	−1.16	1806,1731	1603	166
10	$CN(p\text{-}C_6H_4CF_3)$	−1.09	1792,1726	1590	169
11	$CN(p\text{-}C_6H_4CH_3)$	−1.15	1809,1781	1622	173
12	$CN(p\text{-}C_6H_4OMe)$	−1.19	1832,1768	1612	188
13	$CN(p\text{-}C_6H_4CN)$	−1.13	1803,1726	1594	171
14	$CN(2,6\text{-}(CH_3)_2C_6H_3)$	−1.16	1849,1822	1723	113

[a]Cyclic voltammograms recorded in CH_3CN.
[b]THF solution.
[c]ν(C≡O) given.
[d]Broad.

hyperfine coupling to six equivalent dppm phosphorus atoms (1).

[1] 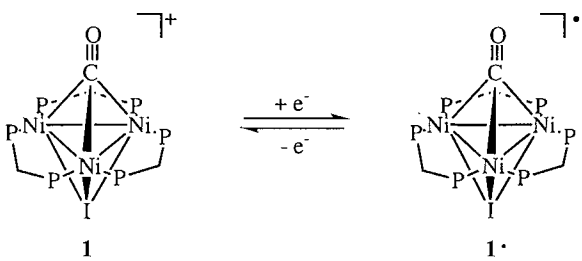

1 **1·**

The assignment of the band at 1661 cm^{-1} was confirmed using the ^{13}CO labeled cluster (**1***). Specifically, the ν($^{13}C{\equiv}O$) band for **1*** at 1691 cm^{-1} showed the expected shift to 1622 cm^{-1} upon reduction of the nickel cluster. The ν(C≡O) bands for the isolated and reduced forms of **1** and **1*** are listed in Table 1.

Infrared SEC studies on $[Ni_3(\mu_3\text{-}CNR)(\mu_3\text{-}I)(\mu_2\text{-}dppm)_3]^+$ (2–14)

A distinguishing feature of the IR spectra for many of the isocyanide capped clusters **2–14** is the appearance of *two* ν(C≡N) absorption bands, both in the solid state and in solution. Isotope labeling experiments confirmed that the appearance of two ν(C≡N) bands was a result of a Fermi resonance between the ν(C≡N) fundamental and the first overtone of the ν(N–C(alkyl)) fundamental (1). A detailed explanation of this phenomenon is available but for the purposes of this study it is important only to realize that the two ν(C≡N) band pattern is an unusual, but characteristic, feature of this class of isocyanide capped trinuclear nickel clusters (1).

The IR spectroelectrochemistry of a 19.0 mM THF solution of **2** was examined under an atmosphere of nitrogen. High concentrations of the alkyl isocyanide capped clusters are required due to the low extinction coefficients for the ν(C≡N) bands. The IR SEC responses (ca. 20 s intervals) for the bulk reduction of **2** are shown in Fig. 3. Upon application of the reduction potential the ν(C≡N) bands for **2** (1914 and 1858 cm^{-1}) decrease in intensity as a single new ν(C≡N) band at 1649 cm^{-1} appears. These changes are also fully reversible. The frequency shift in the ν(C≡N) bands to lower energy is consistent with the capping methyl isocyanide remaining in its original μ_3,η^1 form after reduction of the nickel cluster (eq. [2]) (2, 28).

[2] 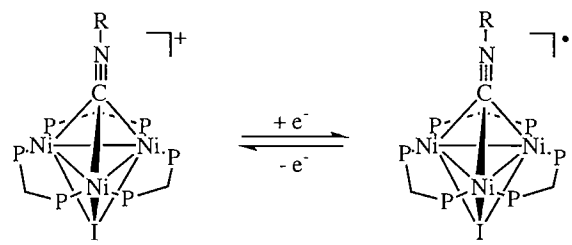

R = alkyl (**2-6**)
= aryl (**7-14**)

Similar results are obtained for the remaining clusters **3–14** and the results of the SEC experiments are listed in Table 1. In each case the ν(C≡N) band(s) in the isolated clusters shift to a *single* ν(C≡N) band of lower energy upon one-electron reduction. The shift to lower frequency for **2–14** indicates that all the isocyanide ligands studied remain triply-bridging upon reduction. This minimal structural rearrangement is consonant with the observed reversible electrochemistry. The appearance of a single ν(C≡N) band in the reduced forms of **2–14** can be readily accounted for using the Fermi resonance model. The decrease in ν(C≡N) frequency upon reduction is large enough to move the ν(C≡N) fundamental out of a Fermi res-

Fig. 2. Plot of the IR spectral changes observed during the spectroelectrochemical reduction of 3.0 mM $[Ni_3(\mu_3\text{-}CO)(\mu_3\text{-}I)(\mu_2\text{-}dppm)_3][PF_6]$ (**1**) in a 0.1 M TBAP/THF solution. Potential held at −1.4 V vs. SCE.

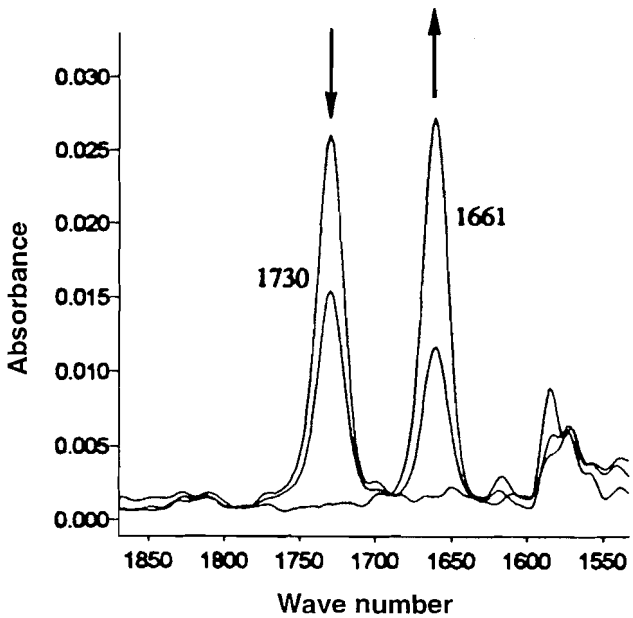

Fig. 3. Plot of the IR spectral changes observed during the spectroelectrochemical reduction of 19.0 mM $[Ni_3(\mu_3\text{-}CNCH_3)(\mu_3\text{-}I)(\mu_2\text{-}dppm)_3][PF_6]$ (**2**) in a 0.1 M TBAP/THF solution. Potential held at −1.4 V vs. SCE.

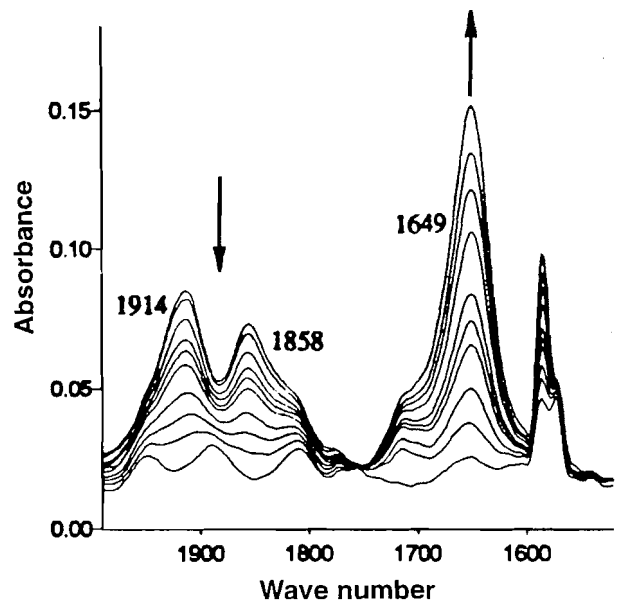

onance condition with the first overtone of the ν(C–N(alkyl)) fundamental (1, 29).

The IR SEC data for **1–14** are collected in Table 1. The differences ($\Delta\nu$, cm^{-1}) in ν(C≡O) or ν(C≡N) frequencies between the isolated and reduced forms of **1–14** are highly dependent on the electronic and steric nature of the capping π-acceptor ligand. For the carbonyl capped cluster **1**, only a 69 cm^{-1} change in ν(C≡O) frequency is observed. In contrast, the magnitude of the shift in ν(C≡N) frequency for the CNR (R = alkyl, aryl) capped clusters is much larger. The greater π-backbonding ability of CO as compared to CNR (R = alkyl, aryl) is well documented (30). From the ν(C≡O) data, significant metal–CO backbonding is present in the isolated state of **1**; which is little altered by reduction of the cluster. Differences in ground state π-acceptor properties also account for the sharp variation in $\Delta\nu$ between the alkyl and aryl isocyanide capped clusters. For the clusters with electron-donating alkyl substituents on the capping isocyanide (CNR; R = CH_3 (**2**), i-C_3H_7 (**3**), C_6H_{11} (**4**)) a decrease in ν(C≡N) frequency of ca. 220 cm^{-1} is observed upon reduction. In contrast, a smaller ν(C≡N) frequency shift ($\Delta\nu$ ca. 170 cm^{-1}) is observed for the aryl isocyanide capped clusters **7–14**. For the isolated clusters **7–14**, the ν(C≡N) bands lie at ca. 100 cm^{-1} lower in energy than those observed for **2–4**. This indicates a stronger isolated state metal–CNR π-backbonding interaction for the aryl isocyanide capped clusters, consonant with aryl isocyanides being better π-acceptors than alkyl isocyanides (31). Thus, upon reduction of the clusters, a larger change in ν(C≡N) is seen for the alkyl isocyanide clusters as the metal-based LUMO is populated and the energies of the nickel *d* orbitals are raised (32). For the benzyl isocyanide capped cluster **6** in the isolated state, the ν(C≡N) band is closer in energy to those for aryl isocyanide (**7–14**), rather than alkyl isocyanide (**2–4**), capped clusters. This indicates significant metal–CNR backbonding present in the ground state. After single electron reduction and subsequent raising of the nickel core *d*-orbital energies, there is a smaller relative difference in the Ni—CNR backbonding interaction for **6** than for **2–4**. Steric effects also influence the magnitude of the shift in ν(C≡N) between the isolated and reduced states of the clusters **2–14**. The most notable example is the 2,6-dimethylphenyl isocyanide capped cluster (**14**) where a value of $\Delta\nu$ = 113 cm^{-1} was observed. The high steric demands of this ligand effectively prevent the approach of the isocyanide to the nickel core and preclude effective Ni—CNR backbonding. This is recognizable in the ground state of **14** where the ν(C≡N) absorption bands are nearly 70 cm^{-1} higher in energy than those for the other aryl isocyanide capped clusters **7–13**. Additionally, even upon reduction, the steric bulk of the 2,6-dimethylphenyl substituent impedes effective metal–CNR π^* overlap and results in only a small change in ν(C≡N) frequency between the isolated and reduced states. A sterically hindered alkyl substituent (R = *tert*-C_4H_9 (**5**)) results in a shift of $\Delta\nu$ = 116 cm^{-1} upon reduction. For **5** in the isolated state, the ν(C≡N) band is at very low energy compared to the related alkyl isocyanide capped species **2–4**. Deviation from a linear μ_3,η^1 bonding mode for the capping *tert*-butyl isocyanide is a plausible explanation for the low-energy ν(C≡N) band of **5**. The reduction of **5** does not cause a large change in ν(C≡N) as the sterically demanding *tert*-butyl substituent hinders the nickel–CNR bond contraction necessary for effective metal–CNR backbonding, as proposed for **13**. Thus, the changes in ν(C≡O) or ν(C≡N) frequency upon reduction are consistent with both the electronic and steric effects of the capping π-acceptor ligand.

The changes in electron density at the capping isocyanide, and hence at the metal core, can also be monitored using ancillary substituents on the isocyanide ligand. The nitrile group on

Fig. 4. Plot of the IR spectral changes observed during the spectroelectrochemical reduction of 6.0 mM $[Ni_3(\mu_3\text{-}CN(p\text{-}C_6H_4CN)(\mu_3\text{-}I)(\mu_2\text{-}dppm)_3][PF_6]$ (**13**) in a 0.1 M TBAP/THF solution. Only nitrile region shown; potential held at −1.4 V vs. SCE.

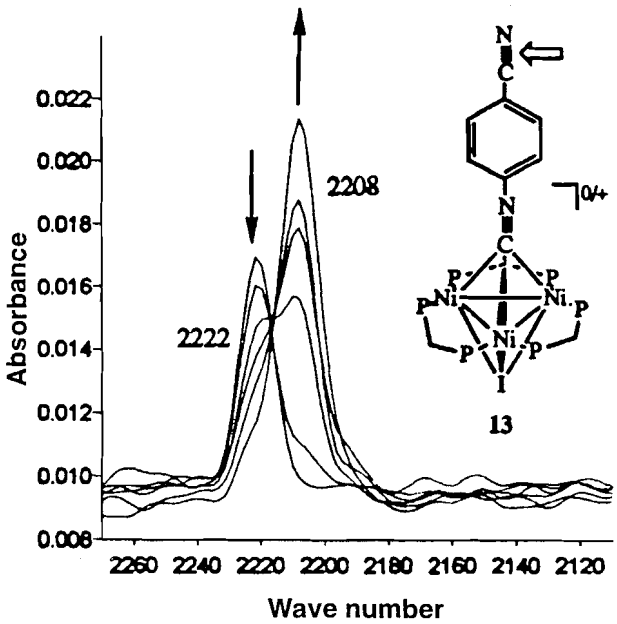

the *p*-cyanophenyl isocyanide capped cluster (**13**) gives rise to a distinctive ν(C≡N) band at 2222 cm^{-1}. Upon reduction of **13** in the SEC cell a new ν(C≡N) nitrile band appears at 2208 cm^{-1} (Fig. 4). This indicates that significant electron density is transferred to the phenyl ring of the capping isocyanide via a Ni—CNR backbonding interaction. This methodology is valuable in cases where overlapping IR bands may obscure the IR signals of primary interest.

UV–visible SEC studies

An important feature of the specular reflectance spectroelectrochemical cell used in this study is its versatility. The SEC cell, equipped with a CaF_2 window, is transparent in both the IR and UV–visible regions while the Mattson spectrometer used in this study can be configured to run in the IR, near-IR, and UV–visible regions. Thus, spectra can be acquired from 600 to 22 000 cm^{-1} using the same SEC cell. The π-acceptor capped clusters **1–14** have intense UV–visible absorptions in the region 520–540 nm ($\varepsilon \sim (2\text{–}4) \times 10^3$ cm^{-1} M^{-1}) (1). The SEC cell was utilized to investigate the UV–visible spectral changes that accompany the single electron reduction of **1–14**. The UV–visible SEC responses (ca. 20 s intervals) for the bulk reduction of the cyclohexyl isocyanide capped cluster (**4**) are shown in Fig. 5. Initially, the absorption band for the isolated state of **4** is observed at 18 800 cm^{-1} (532 nm). As the bulk reduction proceeds this band is bleached while a new, very broad, absorption grows in at ca. 21 000 cm^{-1}. Although the spectrometer can be configured to scan to 27 000 cm^{-1}, the region past 22 000 cm^{-1} is unreliable due to the low power of our visible source. Similar results were obtained for other selected nickel clusters (**3–6**). Methods for increasing the sensitivity of the SEC response past 22 000 cm^{-1} are being pursued. However, as demonstrated, the versatile design of the

Fig. 5. Plot of the UV–visible spectral changes observed during the spectroelectrochemical reduction of 33.0 mM $[Ni_3(\mu_3\text{-}CNC_6H_{11})(\mu_3\text{-}I)(\mu_2\text{-}dppm)_3][PF_6]$ (**4**) in a 0.1 M TBAP/THF solution. Potential held at −1.4 V vs. SCE.

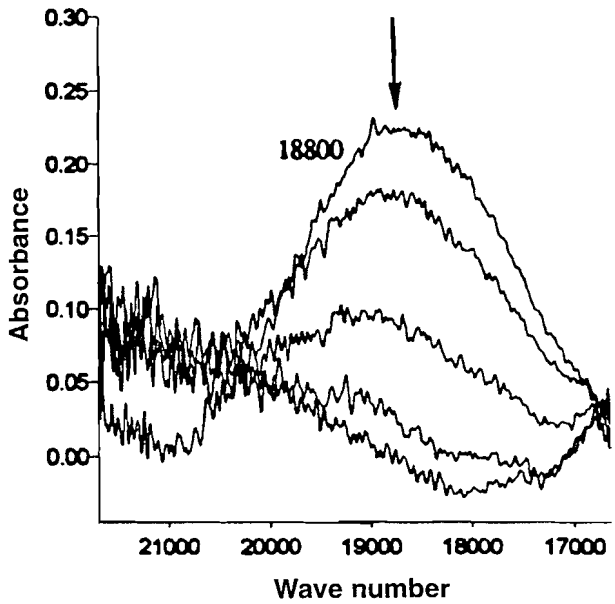

SEC cell utilized in this study allows for detection of in situ electrogenerated intermediates *without* changing the SEC cell or the spectrometer.

Conclusions

The single electron reductions of a class of carbon dioxide reduction electrocatalysts $[Ni_3(\mu_3\text{-}L)(\mu_3\text{-}I)(\mu_2\text{-}dppm)_3]^+$ (L = CO; CNR, R = alkyl, aryl) were investigated using IR and UV–visible spectroelectrochemistry. The IR–SEC studies indicated that the capping carbonyl or isocyanide ligand remained in its original μ_3,η^1 mode upon one-electron reduction. The magnitude of the ν(C≡O) or ν(C≡N) absorption band shift upon reduction is related to both the electronic and steric properties of the capping π-acceptor ligand. Spectroelectrochemical studies with UV–visible detection revealed a hypsochromic shift upon reduction of the clusters. The SEC cell and spectrometer utilized are also extremely versatile as data from 600 to 22 000 cm^{-1} can be acquired without modifying the SEC cell and making only minor configuration changes to the spectrometer.

Acknowledgment

C.P.K. acknowledges the contribution of the National Science Foundation (NSF) (CHE-9319173) for support of this work. J.W. gratefully acknowledges the award of a Post-Doctoral Fellowship by the Natural Sciences and Engineering Research Council of Canada. The assistance of Jason Henderson and Dr. Greg Ferrence in the preparation of the nickel clusters is appreciated.

References

1. D.A. Morgenstern, G.M. Ferrence, J. Washington, J.I. Henderson, L. Rosenhein, J.D. Heise, P.E. Fanwick, and C.P. Kubiak. J. Am. Chem. Soc. **118**, 2198 (1996).

2. K.S. Ratliff, R.E. Lentz, and C.P. Kubiak. Organometallics, **11**, 1986 (1992).
3. D.A. Morgenstern, A.P. Rothwell, C.C. Bonham, K.V. Wood, and C.P. Kubiak. Polyhedron, **14**, 1129 (1995).
4. C.A. Blaine, K.R. Mann, R.E. Wittrig, G.M. Ferrence, J. Washington, and C.P. Kubiak. Inorg. Chim. Acta. Submitted for publication.
5. M.R.M. Bruce, E. Megehee, B.P. Sullivan, H. Thorp, T.R. O'Toole, A. Downard, J.R. Pugh, and T.J. Meyer. Inorg. Chem. **31**, 4864 (1992).
6. M. Hammouche, D. Lexa, M. Momenteau, and J.-M. Saveant. J. Am. Chem. Soc. **113**, 8455 (1991).
7. D.L. DuBois and A. Miedaner. J. Am. Chem. Soc. **109**, 113 (1987).
8. J.-P. Collin, A. Jouaiti, and J.-P. Sauvage. Inorg. Chem. **27**, 1986 (1988).
9. M. Beley, J.-P. Collin, R. Ruppert, and J.-P. Sauvage. J. Am. Chem. Soc. **108**, 7461 (1987).
10. P. Braunstein, D. Matt, and D. Nobel. Chem. Rev. **88**, 747 (1988).
11. E. Fujita, D.J. Szalda, C. Creutz, and N. Sutin. J. Am. Chem. Soc. **110**, 4870 (1988).
12. K. Tanaka, T. Matsui, and T. Tanaka. J. Am. Chem. Soc. **111**, 3765 (1989).
13. E. Duñach and J. Perichon. Chem. Lett. 143 (1990).
14. S.C. Rasmussen, M.M. Richter, E. Yi, H. Place, and K.J. Brewer. Inorg. Chem. **29**, 3926 (1990).
15. S. Daniele, P. Ugo, G. Bontempelli, and M. Fiorani. J. Electroanal. Chem. **219**, 259 (1987).
16. F.R. Keene, C. Creutz, and N. Sutin. Coord. Chem. Rev. **64**, 247 (1985).
17. H. Ishida, K. Tanaka, and T. Tanaka. Organometallics, **6**, 181 (1987).
18. C.M. Bolinger, N. Story, B.P. Sullivan, and T.J. Meyer. Inorg. Chem. **27**, 4582 (1988).
19. C. Amatore and J.-M. Saveant. J. Am. Chem. Soc. **103**, 5021 (1981).
20. J.P. Bullock and K.R. Mann. Inorg. Chem. **28**, 4006 (1989).
21. J.P. Bullock, M.C. Palazotto, and K.R. Mann. Inorg. Chem. **30**, 1284 (1991).
22. P.A. Flowers and G. Mamantov. Anal. Chem. **61**, 190 (1989).
23. M.G. Hill and K.R. Mann. Inorg. Chem. **30**, 1431 (1991).
24. K.M. Kadish, X.H. Mu, and X.Q. Lin. Inorg. Chem. **27**, 1489 (1988).
25. R.E. Wittrig and C.P. Kubiak. J. Electroanal. Chem. **393**, 75 (1995).
26. C. Mealli and D.M. Proserpio. J. Chem. Educ. **67**, 399 (1990).
27. L. Manojlovic'-Muir, K.W. Muir, H.A. Mirza, and R.J. Puddephatt. Organometallics, **11**, 3440 (1992).
28. K.S. Ratliff, P.E. Fanwick, and C.P. Kubiak. Angew. Chem. Int. Ed. Engl. **29**, 395 (1990).
29. F.A. Cotton. Chemical applications of group theory. Wiley, New York. 1990. Chap. 10.
30. P.M. Treichel. Adv. Organomet. Chem. **11**, 21 (1973).
31. E. Singleton and H.E. Oosthuizen. Adv. Organomet. Chem. **22**, 209 (1982).
32. J.J. Maj, A.D. Rae, and L.F. Dahl. J. Am. Chem. Soc. **104**, 3054 (1982).

Photolithography of self-assembled monolayers: optimization of protecting groups by an electroanalytical method

Jamila Jennane, Tanya Boutros, and Richard Giasson

Abstract: Patterned surfaces presenting a high density of chemically reactive functional groups can be prepared through photolithography of self-assembled monolayers (SAM). In this paper, we report the synthesis and the evaluation of three reagents that can be used in SAM-photolithographic applications. These reagents are made up of a triethoxysilylpropylamine moiety in which the amine is temporarily blocked by photolabile protecting groups: NVOC (*o*-nitroveratryloxycarbonyl), ONB (*o*-nitrobenzyl), or DDZ (α,α-dimethyl-3,5-dimethoxybenzyloxycarbonyl). The presence of the triethoxysilyl group allows self-assembled monolayer formation. Release of chemically reactive amino groups is achieved by irradiation of the surface. An electroanalytical method was developed and used to monitor and optimize the three steps of the methodology occurring on surfaces: monolayer formation, photodeprotection, and subsequent functionalization of the released amino groups. Quantitative information on the efficiency of the photodeprotection step was obtained by this method. It was found that the DDZ group is superior to the ONB and NVOC photolabile protecting groups for SAM-photolithographic applications. Percentages of liberated amino groups are generally above 50% with the DDZ group, while they are generally inferior to 25% and 2% for NVOC and ONB, respectively. These differences are attributed to the destruction of some of the released amino groups through a subsequent reaction with the photoproduct, *o*-nitrosobenzaldehyde for ONB and 3,4-dimethoxy-6-nitrosobenzaldehyde for NVOC, and to partial loss or destruction of the monolayer during prolonged irradiations.

Key words: self-assembled monolayers, surface modification, photolithography, photolabile protecting groups, cyclic voltammetry.

Résumé : Des motifs présentant une haute densité de groupes fonctionnels chimiquement réactifs peuvent être préparés sur des surfaces à l'aide de la photolithographie de monocouches auto-assemblées (MAA). Dans cet article, nous relatons la synthèse et l'évaluation de trois réactifs pouvant être utilisés dans des applications de la photolithographie-MAA. Ces réactifs sont constitués d'un fragment triéthoxysilylpropylamine dont la fonction amine est temporairement bloquée par des groupement protecteurs photolabiles : NVOC (*o*-nitrovératryloxycarbonyle), ONB (*o*-nitrobenzyle) ou DDZ (α,α-diméthyl-3,5-diméthoxybenzyloxycarbonyle). La présence du groupe triéthoxysilyle permet la formation de monocouches auto-assemblées. La libération des groupements amines chimiquement réactifs est accomplie par irradiation de la surface. Une méthode électroanalytique a été développée et utilisée pour suivre et optimiser les trois étapes de la méthodologie se produisant à la surface : la formation de la monocouche, la photodéprotection et la fonctionnalisation subséquente des groupes amines libérés. De l'information quantitative sur l'efficacité de l'étape de déprotection a été obtenue par cette méthode. Il a été découvert que le groupe DDZ est supérieur aux groupes protecteurs photolabiles ONB et NVOC en photolithographie-MAA. Le pourcentage de groupes amines libérés est généralement supérieur à 50% avec le groupe DDZ, alors qu'il est généralement inférieur à 25% et 2%, respectivement, pour NVOC et ONB. Ces différences sont attribuées à la reprotection d'une partie des groupes amines libérés suite à une réaction avec un photoproduit, l'*o*-nitrosobenzaldéhyde pour ONB et le 3,4-diméthoxy-6-nitrosobenzaldéhyde pour NVOC, ainsi qu'à la perte ou destruction partielle de la monocouche pendant une irradiation prolongée.

Mots clés : monocouches auto-assemblées, modification de surfaces, photolithographie, groupes protecteurs photolabiles, voltamétrie cyclique.

Received August 24, 1995.[1]

J. Jennane, T. Boutros, and R. Giasson.[2] Département de chimie, Université de Montréal, C.P. 6128, Succursale Centre-Ville, Montréal, QC H3C 3J7, Canada.

[1] Revision received August 28, 1996.

[2] Author to whom correspondence may be addressed. Telephone: (514) 343-6742. Fax: (514) 343-2437. E-mail: giasson@ere.umontreal.ca

Scheme 1. Schematic representation of the SAM-photolithographic system.

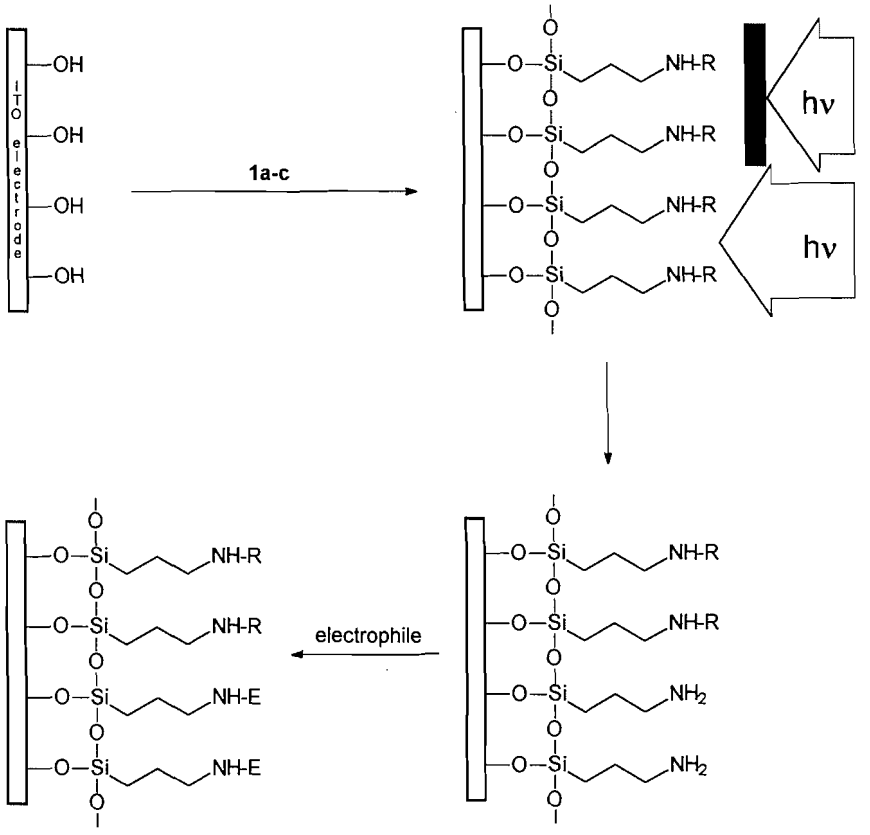

Introduction

Photolithography of self-assembled monolayers (SAM) recently emerged as a powerful method for the preparation of patterned surfaces presenting chemically reactive functional groups. Impressive applications of this new technique have been reported in the chemical literature over the last few years; the technique has been used, namely, for selective adsorption or immobilization of proteins on surfaces (1), controlled adhesion and growth of cells (2), selective electroless metalization of surfaces for microelectronics applications (3), light-directed molecular derivatization of surfaces (4), controlled substitution of self-assembled thiols on gold surfaces (5), and light-directed spatially addressable synthesis of peptides (6). As part of a research program aimed at the development of molecular devices (7), we have developed and optimized a SAM-photolithographic system (Scheme 1) similar to that reported by Fodor et al. (6) for the synthesis of peptides. Features common to both systems are the use of the triethoxysilylpropylamine moiety in the formation of monolayers and the temporary protection of the amino function by photolabile protecting groups. The systems differ, however, in their sequences of reactions (N-protection is performed prior to monolayer formation in our system, while it is achieved after in Fodor's system) and in the nature of the photolabile protecting groups.

In their article, Fodor et al. (6) reported net coupling yields per cycle of ca. 90% including both the photodeprotection and amino acids coupling steps. This yield is based on the hypothesis that illumination conditions used insure >99% photodeprotection. Illumination conditions were determined by measuring the photolysis rate of NVOC-amino acids, but it is not clear whether the amino acids were bound to a surface or in solution. The fact that the rate of photodeprotection may be different for surface-bound species must be taken into consideration in the evaluation of SAM-photolithographic systems. Analytical methods used to evaluate these systems should ideally provide quantitative information on the number of reactive sites present on the surface after irradiation. The number of reactive sites may be influenced not only by the effectiveness of the photocleavage of the protecting group, but also by the partial loss of surface-bound species or subsequent reprotection of reactive groups released during irradiation.

In this paper, we have evaluated the performance of SAM-photolithographic reagents using an electroanalytical technique that provides quantitative information on the number of intact reactive sites present on the surface after irradiation. SAM-photolithographic reagents using three different photolabile protecting groups were tested; the 2-nitroveratryloxycarbonyl (NVOC) (**1a**), the 2-nitrobenzyl (ONB) (**1b**) and the α,α-dimethyl-3,5-dimethoxybenzyloxycarbonyl (DDZ) (**1c**) groups. We found the DDZ group to be superior to the ONB and NVOC photolabile protecting groups for SAM-photolithographic applications. We also found evidence that the deprotection may be complicated by competing photocleavage of the aminopropyl chain bound to the surface.

Results and discussion

Syntheses

Three SAM-photolithographic reagents, **1a**, **1b**, and **1c**, using different protecting groups, were prepared and evaluated in this study (Scheme 2). The first reagent is N-protected with the

Scheme 2. Syntheses of SAM-photolithographic reagents **1a–c** and ferrocene-labeled SAM reagents **1d** and **1e**.

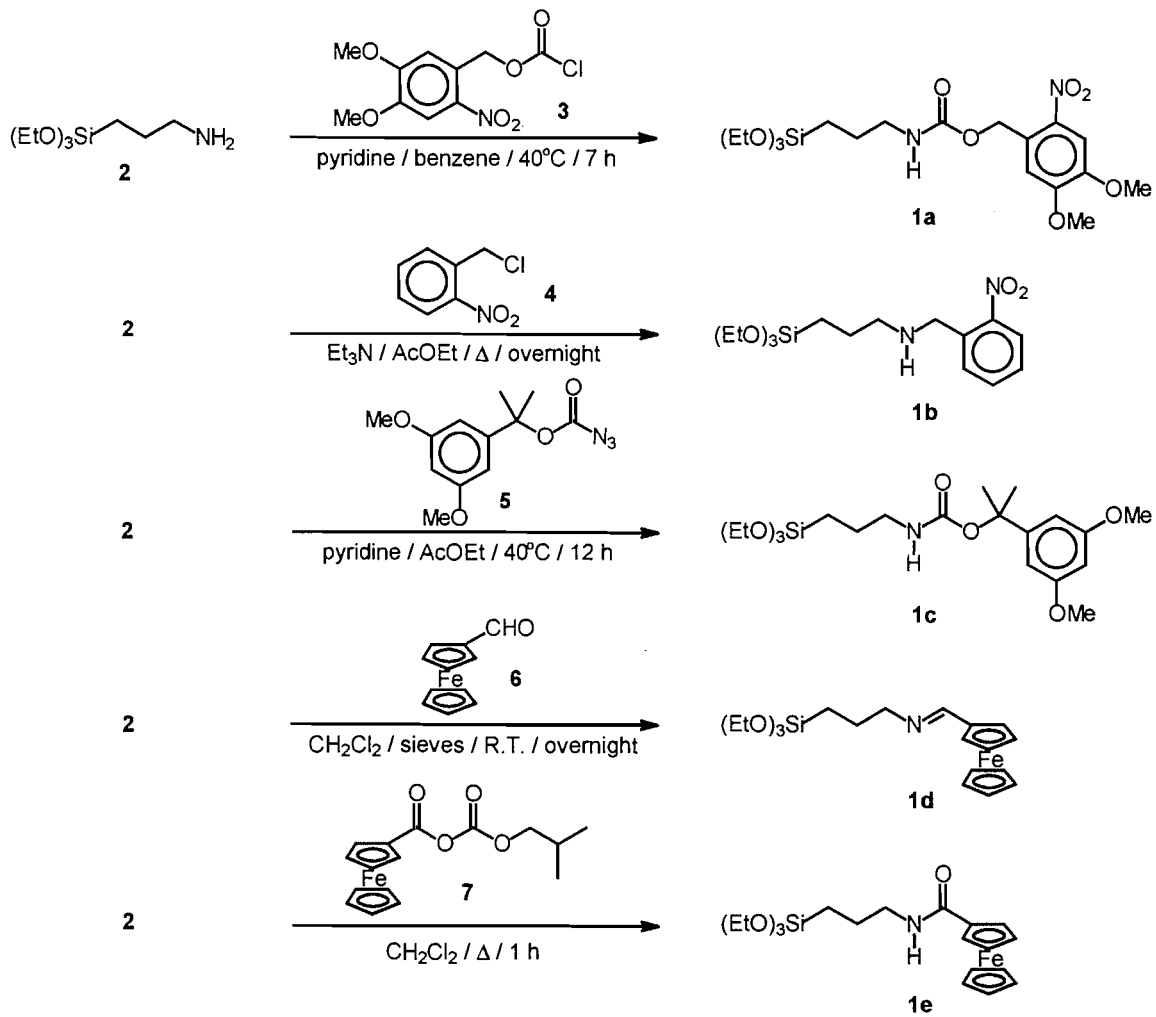

photolabile 6-nitroveratryloxycarbonyl (NVOC) group, one of the most frequently used photolabile protecting groups for amines (8). NVOC-protected reagent **1a** was prepared in 76% yield by the reaction of an excess of 3-aminopropyltriethoxysilane (**2**) with 3,4-dimethoxy-6-nitrobenzyl chloroformate (**3**) in the presence of pyridine in benzene. A second reagent, **1b**, in which the amino group is protected by the 2-nitrobenzyl (ONB) group, was prepared in 70% yield by reacting a 2-fold excess of 3-aminopropyltriethoxysilane (**2**) with 2-nitrobenzyl chloride (**4**) in the presence of triethylamine in refluxing ethyl acetate. While the use of the NVOC photolabile protecting group for the temporary protection of amines is more prevalent, the ONB group has been used before in the N^{im}-protection of histidine (9). The photoremoval of both of these protecting groups is achieved via the same reaction: the light-induced intramolecular rearrangement of 2-nitrobenzylic compounds, the mechanism of which we have studied extensively in solution (10).[3] Finally, the third reagent, **1c**, in which the amino group is protected with the α,α-dimethyl-3,5-dimethoxybenzyloxycarbonyl (DDZ) group, was prepared by reacting a slight excess of 3-aminopropyltriethoxysilane (**2**) with α,α-dimethyl-3,5-dimethoxybenzyloxycarbonylazide (**5**) at 40°C in a mixture of pyridine and ethyl acetate. The DDZ group has been used extensively for the temporary protection of amines and amino acids (9).

In addition to the three SAM-photolithographic reagents, **1a**, **1b**, and **1c** described above, two SAM-reagents, **1d** and **1e**, labeled with the electroactive ferrocenyl group, were also prepared. These two reagents were used in the electroanalytical method we developed to monitor the progress and optimize the reactions in our methodology. Labeled reagent **1d** was prepared in 80% yield by reacting ferrocenecarboxaldehyde (**6**) with 3-aminopropyltriethoxysilane (**2**) over molecular sieves in dichloromethane. Labeled reagent **1e** was prepared in 70% yield from the reaction of the mixed anhydride **7** with 3-aminopropyltriethoxysilane (**2**) in refluxing dichloromethane. The mixed anhydride **7** used in this reaction is prepared beforehand by reacting ferrocene carboxylic acid with isobutylchloroformate at 0°C in toluene in the presence of triethylamine.

Electroanalytical evaluation and optimization of surface reactions

The sequence of reactions used in the methodology includes

[3] Also, R. Giasson, D. Gravel, and R.W. Yip, unpublished results.

Fig. 1. Cyclic voltammogram of approximately one monolayer of ferrocene bound to the surface of a 1.1 cm^2 ITO electrode. The voltammogram was recorded using 10^{-1} M Bu_4NBF_4 in CH_3CN as electrolyte, a SCE reference electrode and a 200 mV/s sweep rate. The shaded area corresponds to $Q = 1.9 \times 10^{-5}$ C.

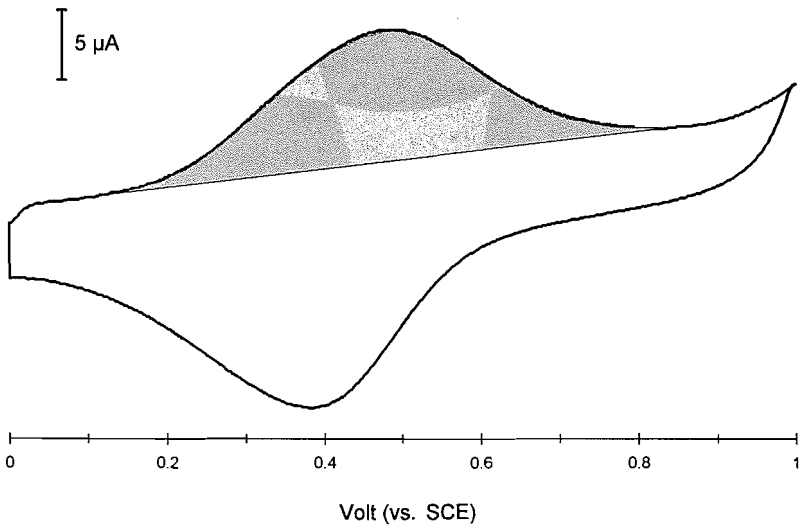

the formation of self-assembled monolayers on surfaces, as well as the photochemical deprotection and subsequent functionalization of surface-bound aminopropylsiloxy moieties. Since all of these reactions occur on surfaces, a limited number of techniques could be used to evaluate their efficiency quantitatively and optimize reaction conditions. We adopted an electroanalytical approach because the technique is straightforward, well suited for the study of surface-bound species, and provides quantitative information.

A 1600 Å film of indium – tin oxide (ITO) on a glass support (Applied Film Lab.) was used as substrate for the formation of self-assembled monolayers. This substrate is advantageous because it is electron conducting and, therefore, can serve as working electrode in an electrochemical cell, and because derivatization of ITO with triethoxysilanes is well documented (11, 12). Plates of ITO on glass were cut into 1 cm^2 pieces that were cleaned by sonication in organic solvents and aqueous solutions prior to monolayer formation. The rate of monolayer formation was evaluated by soaking the ITO electrodes in a 2% solution of labeled reagent **1d** or **1e**. Derivatized electrodes were removed from solution at regular intervals over a 30 h period and were freed from unbound species by sonication in organic solvents. Cyclic voltammograms of surface-bound ferrocene were recorded for each electrode. When labeled reagent **1d** was used for monolayer formation, the electrochemical signal observed decreased rapidly and disappeared completely after a few scans. This indicates that the imine linkage used in this case is too labile for this kind of application even when work is carried out under anhydrous conditions. A persistent electrochemical signal was obtained, however, when labeled reagent **1e** was used. The amide linkage is therefore much more suitable and was adopted for our study.

Coverages (Γ) of surface-bound ferrocene were determined by cyclic voltammetry (12). A typical cyclic voltammogram of approximately one monolayer of ferrocene bound to the surface of a 1.1 cm^2 ITO electrode is represented in Fig. 1. The total charge ($Q = 1.9 \times 10^{-5}$ C) for the oxidation of surface-bound ferrocene was calculated by integrating electronically the shaded area of the voltammogram recorded at a sweep rate of 200 mV s^{-1}. A coverage (Γ) of 1.8×10^{-10} mol cm^{-2} was calculated from eq. [1],

$$[1] \qquad \Gamma = Q / n\mathcal{F}A$$

where Γ represents the coverage in mol cm^{-2}, n the number of electrons transferred ($n = 1$ for ferrocene), $\mathcal{F}$ the Faraday constant (9.6485×10^4 C mol^{-1}), and A the area of the electrode in cm^2.

Plotting of coverage as a function of soaking time (Fig. 2) shows that a maximum coverage of 1.9×10^{-10} mol cm^{-2} is reached after 24 h of soaking under our conditions. This coverage is within the range ($(0.8–4) \times 10^{-10}$ mol cm^{-2}) generally observed for approximate noncompacted monolayers obtained with silane reagents (12). It is known, however, that larger than monolayer coverages are sometime obtained with some silanes and under certain conditions, suggesting siloxane polymer formation. Some dimer, trimer, etc., sites are therefore probably scattered among the monomer monolayer population in samples with average coverage in the monolayer range. Formation of globules of siloxane polymer on the surface is, on the other hand, avoidable with proper reaction conditions (12).

To evaluate the yields of photodeprotection of the SAM-photolithographic reagents, we required a method for quantitative labeling of the amino groups liberated during irradiation. Labeling conditions were determined as follows: ITO electrodes (1 cm^2) were soaked in a 2% solution of 3-aminopropyltriethoxysilane (**2**) for 24 h to ensure monolayer formation. The resulting electrodes bearing a monolayer on which every amino group is free were cleaned the usual way and then soaked in a 2% solution of mixed anhydride **7** in toluene. Elec-

Fig. 2. Coverage (Γ) of surface-bound ferrocene as a function of soaking time of ITO electrodes in a 2% solution of prelabeled SAM reagent **1e**.

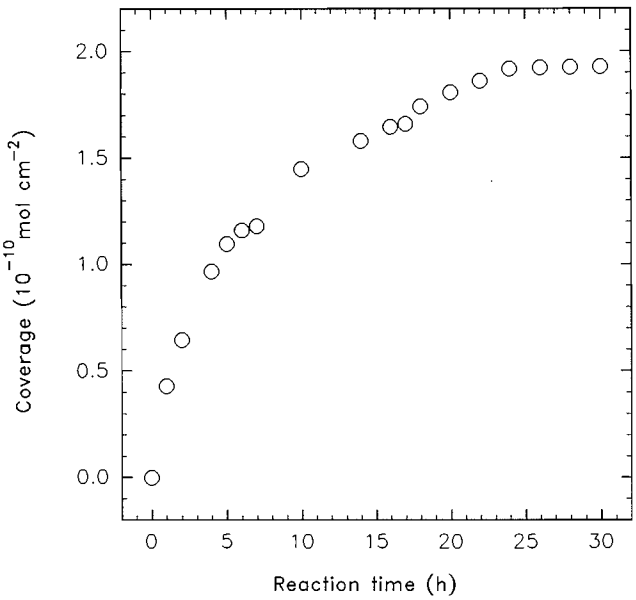

Fig. 3. Coverage (Γ) of surface-bound ferrocene as a function of soaking time of electrodes already modified with SAM reagent **2** in a 2% solution of labeling reagent **7**.

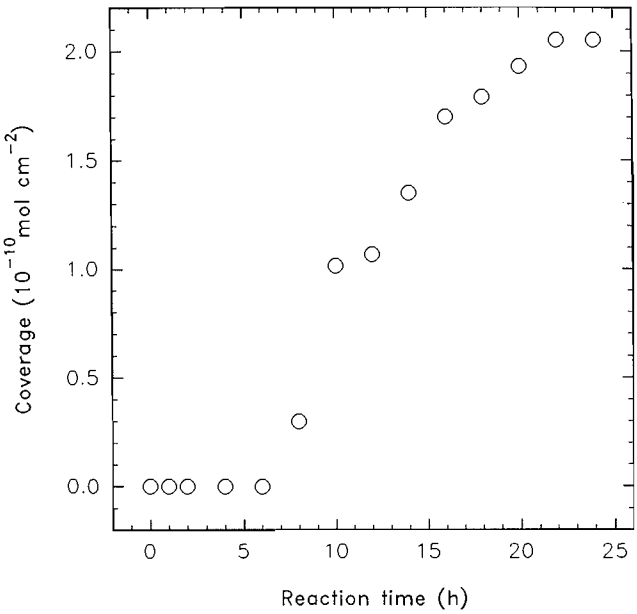

Scheme 3. Products from the photocleavage of ONB and NVOC groups.

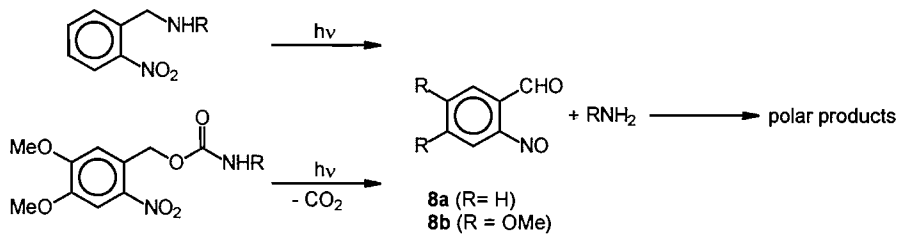

trodes were removed from solution at regular intervals over a 24 h period and freed from unbound species by sonication in organic solvents. Cyclic voltammograms of surface-bound ferrocene were recorded for each electrode. Resulting coverages (Γ) of surface-bound ferrocene were determined and plotted as a function of soaking time (Fig. 3). Coverages (2.1×10^{-10} mol cm^{-2}) as dense as those obtained with complete monolayer formation with labeled reagent **1e** (1.9×10^{-10} mol cm^{-2}) were obtained after 20 h of soaking in mixed anhydride solution.

The efficiency of photoremoval of the protecting groups NVOC, ONB, and DDZ from monolayers of the SAM-photolithographic reagents **1a–c** was estimated as follows. Monolayers were prepared by soaking 1 cm^2 ITO electrodes in 2% solutions of reagents **1a**, **1b**, or **1c** for 24 h. Complete monolayer coverage is assumed in these conditions (vide supra). After appropriate cleaning, the modified electrodes were irradiated to effect deprotection and sonicated in an organic solvent to remove any adsorbed photoproduct. The liberated amino groups on the surface were then labeled by soaking the resulting electrodes for 24 h in a 2% solution of mixed anhydride **7**. Coverages by surface-bound ferrocene were determined as previously. The efficiency of the photodeprotection step was estimated by comparing coverages obtained through this sequence with the value of 2×10^{-10} mol cm^{-2}, corresponding to complete monolayer coverage (vide supra).

Efficiency of photoremoval of the ONB protecting group was first to be estimated with this method. Photoremoval was carried out by irradiating the electrodes at 350 nm for 1 h. Yields of photodeprotection observed for the ONB group were extremely low (best yield: 2%). This disappointing result was not totally unexpected since it is known that the product of this photocleavage, *o*-nitrosobenzaldehyde (**8a**), usually reacts in solution with some of the liberated amine, which leads to the formation of polar products (Scheme 3) (13). This problem is usually minimized by adding aldehyde trapping reagents to the solution, such as hydrazine, hydroxylamine hydrochloride, or semicarbazide hydrochloride. Immersion of the electrodes in a solvent during the photodeprotection in order to dissolve *o*-nitrosobenzaldehyde (**8a**) as it is formed, in the presence or absence of phenylhydrazine, did not, however, improve the yield significantly.

While removal of the NVOC group occurs through the same photorearrangement as that for the ONB group, isolated yields of amine are generally higher with NVOC when the reaction is carried out in solution. This can be explained in part by a lower electrophilicity of the photoproduct, 3,4-dimethoxy-6-nitrosobenzaldehyde (**8b**). We therefore

Fig. 4. Coverage (Γ) of surface-bound ferrocene as a function of irradiation time for electrodes modified with NVOC-protected SAM-photolithographic reagent **1a** after the monolayer formation, photodeprotection, and labeling sequence.

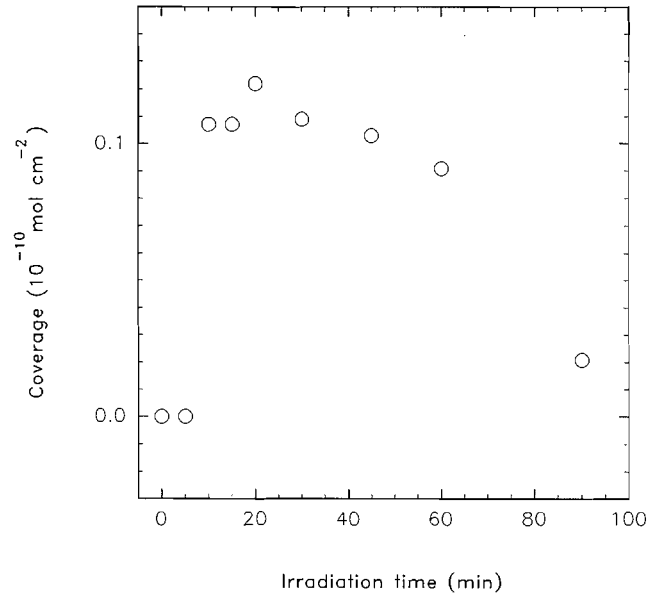

expected the NVOC group to be a superior photolabile group for SAM-photolithographic applications. The efficiency of the photodeprotection step was evaluated, as described above, for electrodes modified with the NVOC-protected SAM-reagent **1a**. A series of modified electrodes were prepared and irradiated at 350 nm over variable periods of time. Resulting coverages (Γ) of surface-bound ferrocene were determined and plotted as a function of irradiation time (Fig. 4). Three conclusions can be drawn from this plot: The population of free amino groups on the electrode surface is maximum after 15–60 min irradiation times. Coverages resulting from 15–60 min irradiation (0.1×10^{-10} mol cm^{-2}) correspond to labeling of approximately 5% of the amino groups. Prolonged irradiation results in lower coverages.

Coverage values obtained through this method correspond to the final yield of a sequence of three reactions. Since the individual yields of each of these reactions can be affected by minute variations in reaction conditions, fluctuation of coverage values was observed when this experiment was repeated. Labeling of less than 25% of the amino group is, however, generally obtained with the NVOC group and this value can be considered as a good estimate of the optimum yield of photodeprotection that can be achieved with this system.

While the NVOC group gives results superior to the ONB group, amino groups are not quantitatively deprotected and kept intact during irradiation. This could be due to subsequent reaction of liberated amino groups with the 3,4-dimethoxy-6-nitrosobenzaldehyde (**8b**) formed during irradiation. However, since observed coverages decrease with prolonged irradiation times, it is also likely that some of the species covalently bound to the electrode surface (free or protected aminopropylsiloxy moieties) are lost or destroyed during irradiation. The rate of the photodeprotection step and, therefore, its quantum yield may be the factor governing the quantity of amino groups that are released and kept intact during irradiation if photodeprotection competes with destruction of the monolayer.

Finally, the DDZ group was also evaluated for SAM-photolithographic applications. This third photolabile protecting group was chosen because it is known that photocleavage intermediates do not react with the liberated amine and that photodeprotection is usually quantitative in solution (Scheme 4) (14). A series of ITO electrodes were modified with SAM-photolithographic reagent **1c** and were irradiated at 254 nm over variable periods of time. Liberated amino groups were labeled and coverages (Γ) were determined as described above. Photocleavage of the DDZ group occurred in a way similar to that of the NVOC group in that maximum population of free amino groups is achieved after 15–60 min of irradiation and that prolonged irradiation resulted in decreased coverage. This latter observation confirms that some of the surface-bound species (free or protected aminopropylsiloxy moieties) are lost or destroyed during irradiation. Maximum coverages obtained after optimal irradiation times are, however, much better with DDZ than with NVOC or ONB. Indeed, coverages varying from a low of 0.3×10^{-10} to more than 2.0×10^{-10} mol cm^{-2} were obtained in different experiments. This corresponds to a density of free amino groups varying between 15% and 100% (generally over 50%). Superior results obtained with this group may be attributed to the fact that photocleavage intermediates do not react with the released amino groups and (or) that photodeprotection of DDZ competes more effectively with destruction of the monolayer.

Conclusion

SAM photolithography represents a powerful method for the preparation of patterned surfaces presenting chemically reactive functional groups. This recently acquired ability to modify the chemical nature and reactivity of a specific area of a surface has already led to impressive applications of this technology. SAM photolithography can be achieved by temporarily blocking a reactive functional group of a SAM reagent with a photolabile protecting group that can later be cleaved. The viability of one such approach, consisting in using NVOC to protect the amino groups of monolayers prepared from the self-assembly of triethoxysilylpropylamine, was first established by Fodor et al. (6). However, prior to our study, questions regarding the efficiency of the photodeprotection step, and whether the use of NVOC as protecting group is optimal, were never addressed. In this paper, we report a straightforward electroanalytical method that can be used to estimate the efficiency of this deprotection step using electrochemical labeling. Using this method, we have evaluated the performance of three different photolabile protecting groups, the NVOC, ONB, and DDZ groups, in SAM-photolithographic reagents. This study clearly demonstrates that ONB and NVOC groups do not perform well in this type of application. Observed yields of photodeprotection were dismal (<2%) for ONB and poor (<25%) for NVOC. These low yields can be explained by a combination of two factors. First, it appears likely that some of the amino groups released during irradiation are reprotected by subsequent reactions with photoproducts **8a** or **8b**. Partial loss or destruction of the monolayer also competes effectively with photodeprotection of the ONB and

Scheme 4. Intermediates and product from the photocleavage of the DDZ group.

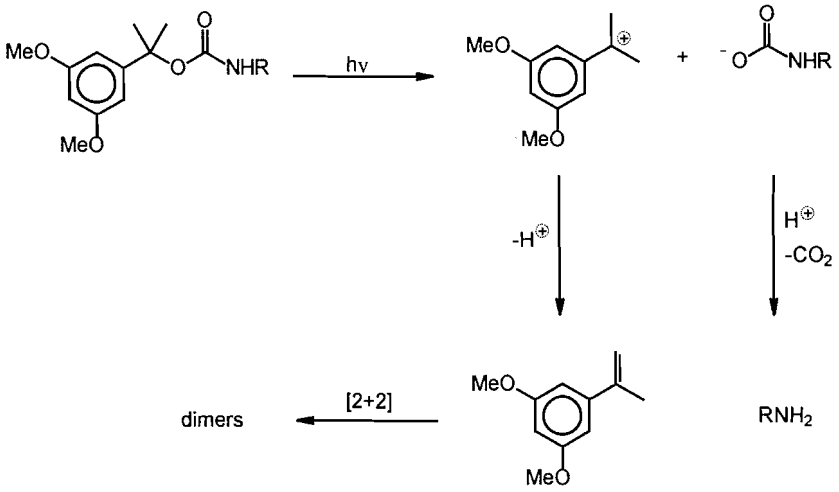

NVOC groups. Use of the DDZ group was found to be much more satisfactory. The highest density of free amino groups is achieved between 15 and 60 min of irradiation at 254 nm under our conditions. The density of free amino groups obtained with DDZ was generally superior to 50% and frequently close to 100%. Superior yields obtained with this photolabile group are most probably due to the lack of reactivity of the photointermediates toward the liberated amino groups and a more favorable competition between deprotection and destruction of the monolayer. Use of DDZ is therefore preferable for the protection of amino groups in SAM-photolithographic applications, where a wavelength of irradiation of 254 nm is not detrimental. In other applications, where an irradiation wavelength of 350 nm is preferable, NVOC gives results superior to ONB.

Experimental section

Melting points were determined on a Gallenkamp model 24MF370 melting point apparatus and are reported uncorrected. IR spectra were recorded on a Perkin–Elmer 783 infrared spectrophotometer. ^{1}H and ^{13}C NMR spectra were recorded in $CDCl_3$ using a Varian VXR-300 (300 and 75 MHz, respectively) spectrometer. Mass spectra were obtained on a V.G. Micromass 12-12 spectrometer, a V.G. Trio-1 quadrupole spectrometer, or a Kratos MS-50 TA spectrometer. Flash column chromatographies were performed using EM Science silica gel 60 (230–400 mesh) using distilled solvents.

Benzene, toluene, and THF were distilled over sodium/benzophenone ketyl. Acetonitrile, dichloromethane, pyridine, and triethylamine were distilled over calcium hydride. Ethyl acetate was distilled over phosphorus pentoxide. 2-Nitrobenzyl chloride (**4**), ferrocenecarboxaldehyde (**6**), and isobutyl chloroformate were purchased from Aldrich™. Isobutyl chloroformate was distilled prior to use. 3-Aminopropyltriethoxysilane (**2**) was purchased from Fluka™ and distilled under reduced pressure prior to use. Ferrocenecarboxylic acid, α,α-dimethyl-3,5-dimethoxybenzyloxycarbonylazide (**5**) and 4,5-dimethoxy-2-nitrobenzyl chloroformate (**3**) were prepared according to published procedures (refs. 15, 14, and 8, respectively). Undesirable light exposure was avoided in every manipulation involving light-sensitive compounds by wrapping glassware in aluminium foil or by working in a dark room.

4,5-Dimethoxy-2-nitro-benzyl [*N*-(3-triethoxysilyl)-propyl]-carbamate (1a)

A solution of 3,4-dimethoxy-6-nitro-benzyl chloroformate (**3**) (0.25 g; 0.94 mmol) and pyridine (1 mL) in benzene (5 mL) was heated to 40°C. After the formation of an orange precipitate, 3-aminopropyltriethoxysilane (**2**) (0.63 g; 2.84 mmol) was added and the resulting mixture was stirred at 40°C for 7 h. The precipitate was removed by decantation and the supernatant evaporated. Purification of the residue by flash chromatography (hexanes/AcOEt/Et_3N 7:3:0.1) afforded the desired product (**1a**) as yellow crystals (0.33 g; 76%): mp 54°C; IR (film) ν_{max}: 3350 (NH), 1695 (C=O), 1515 (NO_2), 1330 (NO_2) cm^{-1}; ^{1}H NMR ($CDCl_3$) δ: 7.70 (s, 1H), 7.00 (s, 1H), 5.50 (s, 2H), 5.16 (br t, 1H), 3.97 (s, 3H), 3.95 (s, 3H), 3.81 (q, J = 7.0 Hz, 6H), 3.22 (q, J = 6.6 Hz, 2H), 1.65 (m, 2H), 1.22 (t, J = 7.0 Hz, 9H), 0.64 (m, 2H); ^{13}C NMR (acetone-d_6) δ: 156.6, 154.7, 149.1, 140.5, 129.4, 110.9, 108.9, 63.3, 58.8, 56.6, 56.5, 44.2, 24.2, 18.6, 8.2; HRMS (CI): calcd. for $C_{19}H_{33}O_9N_2Si$ (M+1): 461.1955; found: 461.1941.

(2-Nitrobenzyl)-[3-(triethoxysilyl)-propyl]-amine (1b)

A solution of 3-aminopropyltriethoxysilane (**2**) (2.0 g; 9.0 mmol), 2-nitrobenzyl chloride (**4**) (0.77 g; 4.5 mmol) and triethylamine (1.5 mL; 18 mmol) in ethyl acetate was refluxed for 24 h in a flask under argon atmosphere and protected from light. The precipitate was removed by decantation and the supernatant evaporated in vacuo. The desired product (**1b**) was obtained (1.12 g; 70%) after purification by flash chromatography (hexanes/AcOEt/Et_3N 1:1:0.1). IR (NaCl) ν_{max}: 3360 (NH), 1605 (C=C), 1530 (NO_2), 1350 (NO_2), 1165 (SiO), 1110 (SiO), 1070 (SiO), 950 (SiO), 850 (SiO), and 780 (SiO) cm^{-1}; ^{1}H NMR ($CDCl_3$) δ: 7.95 (dd, J = 1.1 and 8.1 Hz, 1H), 7.64 (dd, J = 1.6 and 7.7 Hz, 1H), 7.58 (ddd, J = 1.1, 7.2, and 7.7 Hz, 1H), 7.41 (ddd, J = 1.6, 7.2, and 8.1 Hz, 1H), 4.04 (s, 2H), 3.81 (q, J = 7.0 Hz, 6H), 2.64 (t, J = 7.1 Hz, 2H), 2.18 (br s, 1H), 1.63 (m, 2H), 1.22 (t, J = 7.0 Hz, 9H), 0.65 (m, 2H); ^{13}C NMR ($CDCl_3$) δ: 148.7, 135.5, 132.7, 130.8, 127.4, 124.3, 57.9, 51.9, 50.3, 22.9, 17.9, 7.5; LRMS (CI) *m/z*: 357 (M+1).

α,α-Dimethyl-3,5-dimethoxy-benzyl [*N*-(3-triethoxysilyl)-propyl]-carbamate (1c)

A solution of α,α-dimethyl-3,5-dimethoxybenzyloxycarbonyl-azide (**5**) (0.25 g; 0.94 mmol) in pyridine (2 mL) was added to a solution of 3-aminopropyltriethoxysilane (**2**) (0.31 g; 1.4 mmol) in pyridine (3 mL) and ethyl acetate (3 mL) and the resulting mixture was stirred at 40°C for 12 h. The precipitate was removed by decantation and the supernatant evaporated. Purification of the residue by flash chromatography (hexanes/AcOEt/Et_3N 1:1:0.1) gave the desired product as white crystals (0.30 g; 72%) with a melting point near room temperature. IR (NaCl) ν_{max}: 3370 (NH stretch), 1725 (C=O), 1600 (NH bending), 1150 (SiO), 1100 (SiO), 1085 (SiO), 9.50 (SiO), 8.35 (SiO), 8.15 (SiO) cm^{-1}; ^1H NMR ($CDCl_3$) δ: 6.51 (d, J = 2.2 Hz, 2H), 6.34 (t, J = 2.2 Hz, 1H), 4.94 (br q, 1H), 3.81 (q, J = 7.0 Hz, 6H), 3.78 (s, 6H), 3.10 (q, J = 6.5 Hz, 2H), 1.72 (s, 6H), 1.58 (m, 2H), 1.22 (t, J = 7.0 Hz, 9H), 0.61 (m, 2H); ^{13}C NMR ($CDCl_3$) δ: 160.2, 155.0, 149.2, 102.8, 98.0, 80.1, 58.3, 55.1, 43.0, 28.9, 23.2, 18.1, 7.5; HRMS (EI): calcd. for $C_{21}H_{37}O_7NSi$: 443.2339; found: 443.2318.

Ferrocenylmethylene-[3-(triethoxysilyl)-propyl]-amine (1d)

A mixture of ferrocenecarboxaldehyde (**6**) (0.5 g; 2.2 mmol), 3-aminopropyltriethoxysilane (**2**) (0.47 g; 1.9 mmol) and molecular sieves in dichloromethane (25 mL) was stirred for 24 h at room temperature and under argon atmosphere. The mixture was decanted and the supernatant evaporated in vacuo. Bulb-to-bulb distillation of the brown residue gave pure product (**1d**) (0.7 g; 80%). IR (NaCl) ν_{max}: 3090 (CH ferrocene), 1645 (C=N), 1160 (SiO), 1100 (SiO), 1070 (SiO), 950 (SiO), 810 (SiO), 780 (SiO), 720 (SiO) cm^{-1}; ^1H NMR ($CDCl_3$) δ: 8.10 (s, 1H), 4.62 (t, J = 1.8 Hz, 2H), 4.34 (t, J = 1.8 Hz, 2H), 4.17 (s, 5H), 3.82 (q, J = 7.0 Hz, 6H), 3.45 (t, J = 7.0 Hz, 2H), 1.77 (m, 2H), 1.22 (t, J = 7.0 Hz, 9H), 0.64 (m, 2H); ^{13}C NMR ($CDCl_3$) δ: 160.6, 80.2, 70.0, 68.9, 68.2, 64.4, 58.2, 24.1, 18.2, 7.9; LRMS (CI) m/z: 417 (M^+), 418 (M+1).

Ferrocenecarboxylic acid 3-(triethoxysilyl)-propylamide (1e)

A solution of carbonic acid ferrocenoyl ester isobutyl ester (**7**) (1.4 g; 4.2 mmol) and 3-aminopropyltriethoxysilane (**2**) (1.3 g; 6.6 mmol) in dichloromethane (15 mL) was refluxed for 1 h. The solvent was evaporated in vacuo and the residue purified by flash chromatography (hexanes/AcOEt/Et_3N 3:2:0.3) to give the desired product (**1e**) as orange needles (1.28 g; 70%): mp 68°C; IR (KBr) ν_{max}: 3300 (NH stretch), 3090 (CH ferrocene), 1620 (C=O), 1540 (NH bending), 1160 (SiO), 1100 (SiO), 1080 (SiO), 950 (SiO), 810 (SiO), 775 (SiO) cm^{-1}; ^1H NMR ($CDCl_3$) δ: 5.99 (br t, 1H), 4.66 (t, J = 1.9 Hz, 2H), 4.33 (t, J = 1.9 Hz, 2H), 4.20 (s, 5H), 3.85 (q, J = 7.0 Hz, 6H), 3.39 (br q, J = 6.6 Hz, 2H), 1.72 (m, 2H), 1.25 (t, J = 7.0 Hz, 9H), 0.71 (m, 2H); ^{13}C NMR ($CDCl_3$) δ: 169.9, 76.3, 70.0, 69.5, 67.8, 58.3, 41.6, 23.0, 18.1, 7.5; HRMS (FAB): calcd. for $C_{20}H_{31}NO_4FeSi$: 433.1372; found: 433.1360.

Carbonic acid ferrocenoyl ester isobutyl ester (7)

Isobutylchloroformate (0.71 g; 5.2 mmol) was added to a solution of ferrocene carboxylic acid (1.0 g; 4.3 mmol) and triethylamine (0.72 mL; 5.2 mmol) in toluene (15 mL) and the resulting mixture was stirred at 0°C for 2 h. The precipitate was removed by decantation and the supernatant evaporated in vacuo to give the desired product (**7**) (1.4 g; 98%). IR (NaCl) ν_{max}: 3110 (CH ferrocene), 1800 (C=O), 1740 (C=O), 1205 (C-O), 1075 (C-O) cm^{-1}; ^1H NMR ($CDCl_3$) δ: 4.87 (t, J = 2.0 Hz; 2H), 4.54 (t, J = 2.0 Hz, 2H), 4.32 (s, 5H), 4.11 (d, J = 6.7 Hz, 2H), 2.09 (nona., J = 6.7 Hz, 1H), 1.01 (d, J = 6.7 Hz, 6H); ^{13}C NMR ($CDCl_3$) δ: 166.4, 149.7, 75.2, 72.7, 70.8, 70.2, 67.5, 27.6, 18.7; HRMS (FAB): calcd. for $C_{16}H_{18}O_4Fe$: 330.0555; found: 330.0574.

Preparation and monolayer formation on ITO electrodes

Glass plates (14 in × 14 in) covered with a 1600 Å film of indium – tin oxide (ITO) were purchased from Applied Films Lab Inc. and cut into square pieces of 1 cm^2 area using a diamond cutter. Before derivatization, the surface of the ITO working electrodes was freed from greasy residue by immersion in hexane, followed by rinsing with methanol and distilled water and drying in an oven. The surface was then further cleaned by immersion in 1% aqueous HCl, followed by rinsing with distilled water and methanol and drying at 450°C for 30 min. The electrodes were then placed into a test tube under argon atmosphere containing the reaction solvent and sonicated for 5 min. The solvent was removed and 5 mL of a 2% solution of reagent **1a**, **1b**, **1c**, **1d**, **1e**, or **1f** in benzene or toluene was added with a cannula. After an appropriate reaction time (15 min – 24 h), the electrodes were removed, rinsed with the reaction solvent, and sonicated successively in benzene, dichloromethane, and acetonitrile to remove unbound species.

Irradiation of electrodes

The electrodes were inserted into Pyrex (350 nm) or quartz (254 nm) tubes containing acetonitrile, THF, methanol, or no solvent. The tubes were mounted on a merry-go-round MGR-100 so that the ITO coating of the electrodes was facing the light source and were irradiated for an appropriate time (5 min – 4 h) using a Rayonnet RPR-100 photochemical reactor equipped with 16 RPR-3500 (approximate output power of 24 W) or 16 RPR-2540 (approximate output power of 35 W) lamps with emission centered at 350 nm and 254 nm, respectively. The irradiated electrodes were removed, rinsed with solvent, and sonicated successively in acetonitrile, dichloromethane, and benzene to remove unbound species.

Subsequent functionalization of electrodes

The electrodes were placed into test tubes containing a 2% solution of carbonic acid ferrocenoyl ester isobutyl ester (**7**) in toluene, under argon atmosphere. After an appropriate reaction time (15 min – 24 h), the electrodes were removed, rinsed with benzene or toluene, and sonicated successively in benzene, dichloromethane, and acetonitrile.

Cyclic voltammetry of derivatized electrodes

The cyclic voltammograms of ferrocene bound to the surface of the electrodes were recorded using a EG&G potentiostat/galvanostat model 263 using 0.1 M tetrabutylammonium tetrafluoroborate in acetonitrile as support electrolyte, a platinum coil as counter electrode, and a silver wire (Aldrich™) or a SCE electrode (Fisher Scientific™) as reference electrode. Cyclic voltammograms were recorded using a 200 mV s^{-1} scan rate.

Acknowledgments

The authors are grateful to the Natural Sciences and Engineering Research Council of Canada, to the Fonds pour la Formation de Chercheurs et l'Aide à la Recherche du Québec, and to the Fonds Internes de Recherche de l'Université de Montréal for financial support of this work.

References

1. (*a*) L.F. Rozsnyai, D.R. Benson, S.P.A. Fodor, and P.G. Schultz. Angew. Chem. Int. Ed. Engl. **31**, 759 (1992); (*b*) S.K. Bhatia, J.J. Hickman, and F.S. Ligler. J. Am. Chem. Soc. **114**, 4432 (1992); (*c*) S.K. Bathia, J.L. Teixeira, M. Anderson, L.C. Shriver-Lake, J.M. Calvert, J.H. Georger, J.J. Hickman, C.S. Dulcey, P.E. Schoen, and F.S. Ligler. Anal. Biochem. **208**, 197 (1993).
2. (*a*) D.A. Stenger, J.H. Georger, C.S. Dulcey, J.J. Hickman, A.S. Rudolph, T.B. Nielsen, S.M. McCort, and J.M. Calvert. J. Am. Chem. Soc. **114**, 8435 (1992); (*b*) J.J. Hickman, S.K. Bhatia, J.N. Quong, P. Shoen, D.A. Stenger, C.J. Pike, and C.W. Cotman. J. Vac. Sci. Technol. A: **12**, 607 (1994).
3. (*a*) C.S. Dulcey, J.H. Georger, V. Krauthamer, D.A. Stenger, T.L. Fare, and J.M. Calvert. Science, **252**, 551 (1991); (*b*) W.J. Dressick, C.S. Dulcey, J.H. Georger, and J.M. Calvert. Chem. Mater. **5**, 148 (1993); (*c*) J.M. Calvert. J. Vac. Sci. Technol. B: **11**, 2155 (1993); (*d*) W.J. Dressick, and J.M. Calvert. Jpn. J. Appl. Phys. **32**, 5829 (1993); (*e*) W.J. Dressick, C.S. Dulcey, J.H. Georger, G.S. Calabrese, and J.M. Calvert. J. Electrochem. Soc. **141**, 210 (1994).
4. (*a*) D. Kang and M.S. Wrighton. Langmuir, **7**, 2169 (1991); (*b*) E.W. Wollman, C.D. Frisbie, and M.S. Wrighton. Langmuir, **9**, 1517 (1993); (*c*) C.D. Frisbie, E.W. Wollman, J.R. Martin, and M.S. Wrighton. J. Vac. Sci. Technol. A: **11**, 2368 (1993); (*d*) E.W. Wollman, D. Kang, C.D. Frisbie, I.M. Lorkovic, and M.S. Wrighton. J. Am. Chem. Soc. **116**, 4395 (1994).
5. M.J. Tarlov, D.R.F. Burgess, and G. Gillen. J. Am. Chem. Soc. **115**, 5305 (1993).
6. S.P.A. Fodor, J.L. Read, M.C. Pirrung, L. Stryer, A.T. Lu, and D. Solas. Science, **251**, 767 (1991).
7. T. Li and R. Giasson. J. Am. Chem. Soc. **116**, 9890 (1994).
8. B. Amit, U. Zehavi, and A. Patchornik. J. Org. Chem. **39**, 192 (1974).
9. V.N.R. Pillai. Synthesis, 1 (1980), and refs. cited therein.
10. (*a*) R.W. Yip, D.K. Sharma, R. Giasson, and D. Gravel. J. Phys. Chem. **89**, 5328 (1985); (*b*) R.W. Yip, Y.X. Wen, D. Gravel, R. Giasson, and D.K. Sharma. J. Phys. Chem. **95**, 6078 (1991); (*c*) D. Gravel, R. Giasson, D. Blanchet, R.W. Yip, and D.K. Sharma. Can. J. Chem. **69**, 1193 (1991).
11. P.R. Moses, L. Wier, and R.W. Murray. Anal. Chem. **47**, 1882 (1975).
12. R.W. Muray. Acc. Chem. Res. **13**, 135 (1980).
13. A. Patchornik, B. Amit, and R.B. Woodward. J. Am. Chem. Soc. **92**, 6333 (1970).
14. C. Birr, W. Lochinger, G. Stahnke, and P. Lang. Liebigs Ann. Chem. **763**, 162 (1972).
15. P.C. Reeves. Org. Synth. **56**, 28 (1977).

A photochemical retro-Friedel–Crafts alkylation. Rapid rearrangement of cyclohexadienyl cations

Earl MacKnight and Robert A. McClelland

Abstract: This paper reports the use of laser flash photolysis (LFP) techniques to show that cyclohexadienyl cations (σ complexes) of the Friedel–Crafts reaction of 1,3-dimethoxybenzene and the diphenylmethyl cation rearrange on the ns time scale without separating the aromatic compound and the electrophile. This is demonstrated through a study of the photochemical behaviour of 2-diphenylmethyl-1,3-dimethoxybenzene (**4**) in 1,1,1,3,3,3-hexafluoroisopropyl alcohol (HFIP). Derivatives of 1,3-dimethoxybenzene have previously been found to selectively protonate at C2 upon excitation in HFIP, and indeed the principal products with **4** are 1,3-dimethoxybenzene (**6**) and $Ph_2CHOCH(CF_3)_2$ (**7**), the species expected if the cyclohexadienyl cation formed in the C2 protonation cleaved Ph_2CH^+. These products are, however, accompanied by 4-diphenylmethyl-1,3-dimethoxybenzene (**8**), a rearranged isomer of **4**. A portion of this product is explained by the combination of Ph_2CH^+ and 1,3-dimethoxybenzene as the latter accumulates during the irradiation. However, 11.5% of **8** is also seen upon extrapolation to zero time. LFP experiments on the ps time scale reveal that the C2 protonated cation, the 1-diphenylmethyl-2,6-dimethoxybenzenium ion (**5**), is formed within 100–200 ps, and reacts with $k = 9 \times 10^8$ s^{-1}, with absorbance for Ph_2CH^+ growing in as **5** decays. LFP studies on the ns time scale reveal that there is a second quantity of Ph_2CH^+ that grows in, with $k = 5.0 \times 10^5$ s^{-1}. The precursor for this has been identified as the 1-diphenylmethyl-2,4-dimethoxybenzenium ion (**10**), the thermodynamically more stable isomer of **5**. A mechanistic model is proposed in which excited **4** is C2 protonated in HFIP with $k \geq 1 \times 10^{10}$ s^{-1} to form **5**, which loses Ph_2CH^+ with $k = 3 \times 10^8$ s^{-1} in competition with rearrangement to **10** with $k = 6 \times 10^8$ s^{-1}. The cation **10** serves as the second source of Ph_2CH^+, losing Ph_2CH^+ with $k = 4 \times 10^5$ s^{-1}; in competition **10** is deprotonated by HFIP to give **8** with $k = 8 \times 10^4$ s^{-1}. The 11.5% of the rearranged **8** that is observed at zero conversion is thus shown to come from an intramolecular pathway in which the key step is the migration of a diphenylmethyl group without separation: **4** → **4*** → **5** → **10** → **8**.

Key words: cyclohexadienyl, photoprotonation, Friedel–Crafts, diphenylmethyl, 1,3-dimethoxybenzene.

Résumé : Dans ce travail, on présente un rapport sur l'utilisation des techniques de photolyse éclair au laser (« LFP ») pour démontrer que les cations cyclohexadiényles (complexes σ), impliqués dans la réaction de Friedel–Crafts du 1,3-diméthoxybenzène avec le cation diphénylméthyle, se transposent à l'échelle de temps de la ns, sans qu'il se produise de séparation entre le composé aromatique et l'électrophile. Ce résultat a été démontré par le biais d'une étude du comportement photochimique du 2-diphénylméthyl-1,3-diméthoxybenzène (**4**) dans l'alcool 1,1,1,3,3,3-hexafluoroisopropylique (HFIP). Il a été démontré antérieurement que, par excitation dans le HFIP, les dérivés du 1,3-diméthoxybenzène se protonent sélectivement en C2; en fait, les produits principaux obtenus à partir du produit **4** sont les espèces 1,3-diméthoxybenzène (**6**) et $Ph_2CHOCH(CF_3)_2$ (**7**) auxquelles on peut s'attendre si le cation cyclohexadiényle qui se forme par protonation en C2 donne lieu à un clivage de PH_2CH^+. Toutefois, ces produits sont accompagnés par du 4-diphénylméthyl-1,3-diméthoxybenzène (**8**), un isomère de réarrangement du produit **4**. On peut expliquer une partie de ce produit par une combinaison de PH_2CH^+ avec du 1,3-diméthoxybenzène lorsque ce dernier s'accumule au cours de l'irradiation. Toutefois, une extrapolation au temps zéro suggère que 11,5% du produit se forme d'une autre façon. Des expériences de « LFP » réalisées à l'échelle de temps de la ps révèlent que le cation protoné en C2, l'ion 1-diphénylméthyl-2,6-diméthoxybenzénium (**5**), se forme en dedans de 100 à 200 ps et qu'il réagit avec une constante $k = 9 \times 10^8$ s^{-1}, alors que l'absorbance pour PH_2CH^+ augmente tandis que celle du composé **5** diminue. Les études de « LFP » à l'échelle de temps de la ns indiquent qu'une deuxième source de PH_2CH^+ fait croître sa quantité d'après la relation $k = 5.0 \times 10^5$ s^{-1}. On a identifié que le précurseur de cette deuxième source est l'ion 1-diphénylméthyl-2,4-diméthoxybenzénium (**10**), l'isomère thermodynamiquement plus stable du produit **5**. On propose un modèle mécanistique dans lequel, dans le HFIP, le composé **4** excité se protone en C2, avec $k \geq 1 \times 10^{10}$ s^{-1}, pour former du composé **5** qui perd du Ph_2CH^+ avec $k = 3 \times 10^8$ s^{-1} alors que cette perte est en compétition avec un réarrangement en composé **10** pour lequel $k = 6 \times 10^8$ s^{-1}. Le cation **10** sert de deuxième source de Ph_2CH^+, qu'il perd avec $k = 4 \times 10^5$ s^{-1}; au cours d'une réaction compétitive, **10** est déprotoné par HFIP pour conduire au produit **8**, avec $k = 8 \times 10^4$ s^{-1}. On démontre donc que le 11,5% de produit de réarrangement

Received May 22, 1996.

E. MacKnight and R.A. McClelland.[1] Department of Chemistry, University of Toronto, Toronto, ON M5A 3H6, Canada.

[1] Author to whom correspondence may be addressed. Telephone: (416) 978-3592. Fax: (416)-978-3592.
E-mail: rmcclell@alchemy.chem.utoronto.ca

8 observé à zéro pourcent de conversion vient donc d'une voie intramoléculaire dans laquelle l'étape clé est la migration d'un groupe diphénylméthyle sans séparation, **4** → **4*** → **5** → **10** → **8**.

Mots clés: cyclohexadiényle, photoprotonation, Friedel–Crafts, diphénylméthyle, 1,3-diméthoxybenzène.

[Traduit par la rédaction]

Introduction

The singlet excited states of simple aromatic compounds like benzene and anisole are more basic than the ground state. This enhanced basicity is predicted by Forster-cycle calculations (1, 2) and demonstrated experimentally by the acid quenching of the fluorescence of aromatic compounds, often accompanied by H–D isotope exchange (3–6). This observation of exchange points to a fully protonated intermediate on the reaction pathway — a cyclohexadienyl cation that can lose the proton that was originally attached to the aromatic ring. The presence of such intermediates has recently been conclusively demonstrated through their direct observation with laser flash photolysis (LFP), following irradiation of some relatively electron-rich aromatic compounds in 1,1,1,3,3,3-hexafluoroisopropyl alcohol (HFIP) (7–10) (and in one case 2,2,2-trifluoroethanol (11)). The solvent HFIP has two features that prove especially useful for such LFP experiments. The OH group of this solvent is sufficiently acidic for the excited state protonation to occur with reasonable quantum efficiency without the need for an added stronger acid. At the same time, HFIP is significantly less reactive as a base or a nucleophile when compared to more commonly used solvents such as water and ethanol. Thus transient cations are much longer lived in HFIP.

Excited state protonations often occur with a regioselectivity different from that in the ground state. 1,3-dimethoxybenzene (and derivatives) is a notable example of such behaviour. Irradiation of this compound in HFIP results in selective protonation at C2 resulting in the 2,6-dimethoxybenzenium ion (see Scheme 1, compound **2** with R = H). The regiochemistry here was demonstrated by experiments with deuterated solvent ($(CF_3)_2CHOD$), which showed isotope exchange at C2 of the 1,3-dimethoxybenzene (8). The cation was readily observed with LFP as a relativly long-lived intermediate with a lifetime in HFIP of 0.5 ms (8). Exchange at C2 (accompanied by a small amount of exchange at C5) was also observed upon irradiation in aqueous acids (12). The intermediate cation, however, cannot be detected with ns LFP in these solutions because its lifetime is too short.

In the ground state, protonation occurs selectively at C4 to give the 2,4-dimethoxybenzenium ion (**3**), under conditions of both kinetic control (13) and thermodynamic control (14). The experiments under thermodynamic conditions were carried out in concentrated H_2SO_4 where 1,3-dimethoxybenzene is 100% protonated. The structure of the cation so formed is conclusively demonstrated to be **3** from the characteristic pattern in the ^1H NMR spectrum (8, 14). NMR signals that would correspond to the isomeric **2** are not observed in this experiment, and an estimate of the upper limit for detection suggests that the ratio **3**:**2** must be greater than 20 (8). The different behaviour of the ground state and the excited state is consistent with molecular orbital calculations that show that there is a shift in electron density from C4 to C2 of the aromatic ring upon pro-

Scheme 1.

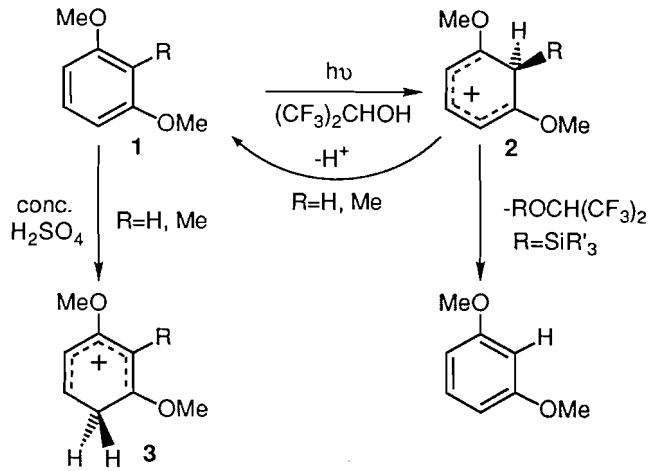

motion of an electron from the HOMO to the LUMO of 1,3-dimethoxybenzene (8, 12, 15).

An important feature from the point of view of the present work is the different UV–visible absorption spectra of the 2,4- and 2,6-dimethoxybenzenium ions **2** and **3**. The 2,4 isomer formed in concentrated acid has a λ_{max} at 315 nm, while the 2,6 isomer observed with LFP in HFIP absorbs almost 100 nm to longer wavelength, at 410 nm (8). Examples of carbocations that have been observed in both strong acids and HFIP — the diphenylmethyl cation (16), the cumyl cation (17), and the 2,4,6-trimethylbenzenium ion (7) — have shown that there is very little dependence of λ_{max} on solvent, at most a 10 nm shift. Thus the difference between the 2,4- and 2,6-dimethoxybenzenium ions is not a solvent effect, but represents an intrinsic difference in the spectra of these two cations.

With 1,3-dimethoxybenzene itself, irradiation in HFIP results in no net photochemistry, other than the proton exchange mentioned above. The 2-methyl derivative cannot undergo this exchange, and shows no photochemical reaction whatsoever (8). This compound, however, still exhibits a strong signal in the LFP experiment in HFIP for the appropriate cyclohexadienyl cation, the 1-methyl-2,6-dimethoxybenzenium ion. Thus a proton does add at C2 upon irradiation in HFIP, but the only fate of the intermediate cation is loss of that same proton.

Derivatives bearing silyl groups (R'_3Si) at C2 do, however, show interesting photochemistry, cleaving the silyl group to form the parent 1,3-dimethoxybenzene and the ether $R'_3SiOCH(CF_3)_2$ upon irradiation in HFIP (9). This reaction involves an initial photoprotonation at C2 to form the intermediate cyclohexadienyl cation (**2**, R = SiR'_3), as demonstrated by the observation of this cation with LFP. The overall photoreaction therefore is a photochemically initiated protodesilylation, the analog of ground state protodesilylations that occur under moderately acidic conditions (18). The intermediate is a

β-silyl-substituted carbocation, and this study represented the first time that such a cation had been observed with LFP (see also ref. 19). Kinetic analysis showed that the cation preferentially cleaved the silyl group over loss of a proton. Moreover, the desilylation was shown to be associative, with solvent (and other nucleophiles) assisting in the cleavage of the C—Si bond.

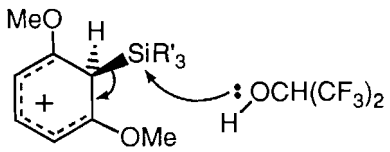

In this paper, we examine the photochemical behavior of 2-diphenylmethyl-1,3-dimethoxybenzene (**4**) in HFIP. We prepared this compound on the expectation that photoprotonation at C2 would lead to the cyclohexadienyl cation **5**, and this would then undergo a dissociative cleavage of the diphenylmethyl cation in competition with deprotonation back to starting material. Such cleavage, if it were to occur, would correspond to the reverse of the step in a Friedel–Crafts alkylation that forms the cyclohexadienyl cation. This cleavage does occur, but to our surprise is accompanied by rearrangement to an isomeric 2,4-dimethoxybenzenium ion. This rearrangement occurs very rapidly, but can be observed with ps LFP. This represents the first example of a system where rearrangement involving two isomeric cyclohexadienyl cations has been observed with LFP. We will also speculate on the possibility that a π-complex is an intermediate in both the cleavage and rearrangement pathways.

Results and discussion

Products

Solutions of the compound **4** in HFIP were irradiated at 254 nm in a Rayonet reactor, and the products were analyzed quantitatively by gas chromatography. Authentic samples were available for comparison and standardization. Three products were obtained: 1,3-dimethoxybenzene (**6**), the ether $Ph_2CHOCH(CF_3)_2$ (**7**), and 4-diphenylmethyl-1,3-dimethoxybenzene (**8**), an isomer of the starting material. The compounds **6** and **7** are consistent with the cleavage of eq. [1], with the ether obviously arising from solvent capture of Ph_2CH^+. As is also consistent with this interpretation, the yields of **6** and **7** were the same, within experimental error, at all irradiation times. As shown in Fig. 1, however, the yield of the rearrangement product **8** increased with increased irradiation time. This was accompanied by a corresponding decrease in the yields of **6** and **7**.

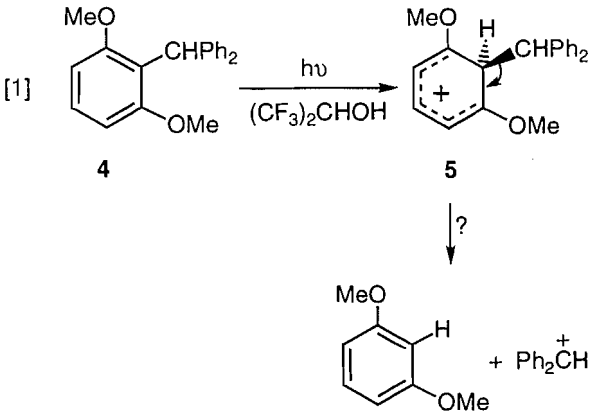

To investigate the origin of this dependence, we first irradiated an equimolar mixture of the products **6** and **7** (0.2 mM in HFIP) for the time corresponding to 25% conversion in Fig. 1. This, however, resulted in no formation of **8**, in fact no change at all. The product **8** was also found to be stable under these same conditions. Thus further photochemistry of the products can be ruled out. 1,3-dimethoxybenzene, and presumably **8**, do absorb the irradiating light, but undergo the reversible C2-photoprotonation, as discussed in the introduction, and there is no overall transformation.

We then carried out two experiments with the same initial concentration of **4** as in Fig. 1 but with 1 mM and 5 mM 1,3-dimethoxybenzene present from the beginning of the irradiation. In each case there was little dependence of product yields on the time of irradiation up to 20% conversion, and **8** had become the major product, 80 ± 3% for 1 mM **6** and 97 ± 2% for 5 mM.

These experiments suggested that the excess 1,3-dimethoxybenzene was reacting with the diphenylmethyl cation forming in the photocleavage, resulting in the high yields of **8**. To investigate this possibility, diphenylmethyl chloride (0.2 mM) was solvolyzed in HFIP in the presence of 5 mM 1,3-dimethoxybenzene (and 0.5 mM triethylamine to remove HCl). This gave a similar result as in the experiment above with 5 mM 1,3-dimethoxybenzene, a 5 ± 1% yield of **7** and 95 ± 2% of **8**. Also noteworthy was that none (less than 0.1%) of the isomer **4** was obtained.

This solvolysis experiment clearly establishes that 1,3-dimethoxybenzene can effectively compete with HFIP for Ph_2CH^+. This result is not surprising in light of similar studies involving the 9-fluorenyl cation in HFIP that also showed efficient trapping by added aromatic compounds, especially electron-rich ones (20, 21). The solvolysis also establishes that the product that forms from 1,3-dimethoxybenzene and Ph_2CH^+ is the 4-substituted isomer **8**, and there is less than 0.1% of the 2-substituted isomer **4**.

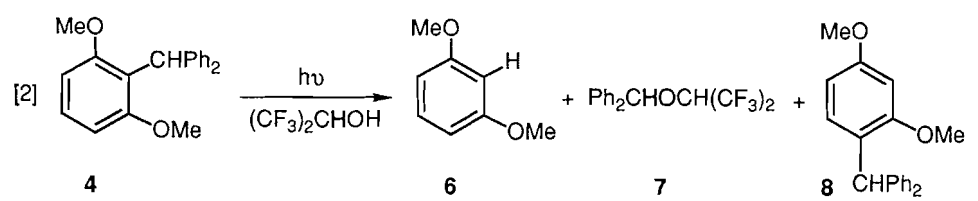

Scheme 2.

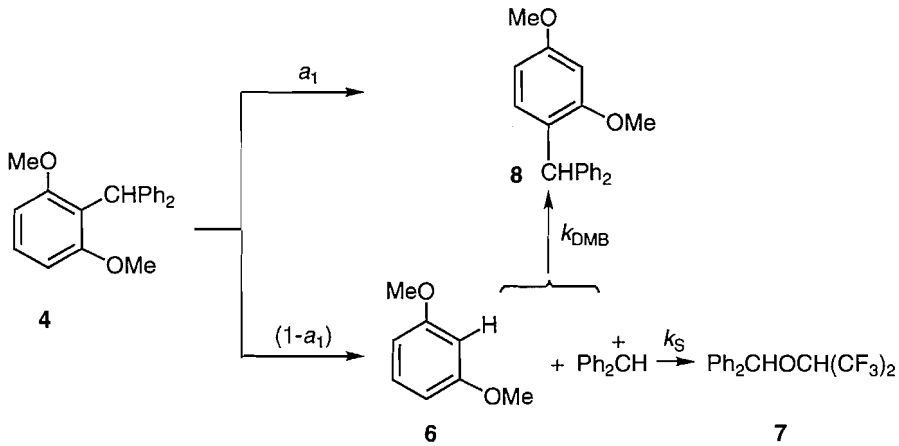

Fig. 1. % Yield of 4-diphenylmethyl-1,3-dimethoxybenzene (**8**) as a function of the % conversion of 2-diphenylmethyl-1,3-dimethoxybenzene (**4**) following irradiation at 254 nm in 1,1,1,3,3,3-hexafluoroisopropyl alcohol. The yields of **8** were based on the total "1,3-dimethoxybenzene" content of the products — $100 \times [\mathbf{8}]:([\mathbf{6}] + [\mathbf{8}])$. The initial concentration of **4** was 8.0×10^{-4} M. The points are experimental; the line has been drawn based upon a kinetic analysis (see text).

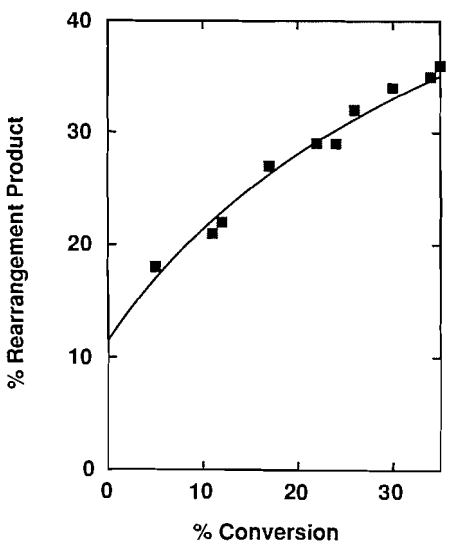

Intermolecular pathway for 4-diphenyl-1,3-dimethoxybenzene

An explanation is now available for the yield dependence when **4** is irradiated alone. In this case, as the reaction proceeds, the diphenylmethyl cation encounters increasing amounts of 1,3-dimethoxybenzene, and is thus more effectively diverted to the product **8** away from the ether **7** derived from solvent trapping.

This situation can be analyzed quantitatively in terms of the model of Scheme 2. In this analysis we define a quantity a_1 that represents the fraction of the precursor **4** that is directly converted to **8** upon irradiation, with $(1 - a_1)$ the fraction that cleaves to 1,3-dimethoxybenzene and the diphenylmethyl cation. A second fraction a_2 is also required, as defined in eq. [3].

$$[3] \quad a_2 = \frac{\left(\frac{k_{DMB}}{k_s}\right)[\mathbf{6}]}{1 + \left(\frac{k_{DMB}}{k_s}\right)[\mathbf{6}]}$$

In this expression k_{DMB} is the second-order rate constant for the reaction of Ph_2CH^+ and 1,3-dimethoxybenzene to form **8**, and k_s is the first-order rate constant for the reaction of the cation with the solvent HFIP. The quantity a_2 represents the fraction of Ph_2CH^+ that reacts at a particular concentration of 1,3-dimethoxybenzene to give **8**; $(1 - a_2)$ is the fraction that proceeds to the ether.

We now define the concentrations of the reagent and the three products at some intermediate stage of the reaction as $[\mathbf{4}]_t$, $[\mathbf{6}]_t$, $[\mathbf{7}]_t$, and $[\mathbf{8}]_t$. If irradiation is carried out for a very short time Δt, so that the concentration of **4** is decreased by a small increment Δ, then the new concentrations are:

$$[\mathbf{4}]_{t+\Delta t} = [\mathbf{4}]_t - \Delta$$
$$[\mathbf{6}]_{t+\Delta t} = [\mathbf{6}]_t + (1 - a_1)\Delta - (1 - a_1)(a_2)\Delta$$
$$= [\mathbf{6}]_t + (1 - a_1)(1 - a_2)\Delta$$
$$[\mathbf{7}]_{t+\Delta t} = [\mathbf{7}]_t + (1 - a_1)(1 - a_2)\Delta$$
$$[\mathbf{8}]_{t+\Delta t} = [\mathbf{8}]_t + a_1\Delta + (1 - a_1)a_2\Delta$$

In the expression for **6**, $(1 - a_1)\Delta$ represents the quantity of **6** that forms during Δt because of the initial cleavage pathway. The same amount $(1 - a_1)\Delta$ of Ph_2CH^+ is also formed, and this accounts for loss of a quantity of **6** equal to $(1 - a_1)a_2\Delta$ because of the reaction forming **8**. This same expression also appears with a positive sign in the equation for **8**, along with the quantity $a_1\Delta$, which represents the amount that forms directly from **4**. Starting at $t = 0$ with initial concentrations $[\mathbf{4}]_0 = [\mathbf{4}]_{initial}$, and $[\mathbf{6}]_0 = 0 = [\mathbf{7}]_0 = [\mathbf{8}]_0$, the concentrations of the three products can be calculated as a function of % conversion through a computer simulation involving a large number of calculations using such small incremental steps. Although the concentration of **6** and the value of the fraction a_2 do change with conversion, the assumption is made that within each increment the changes are so small that these quantities are effectively constant. Our calculations were carried out with $\Delta = 1 \times 10^{-10}$ to ensure that this was the case.

There are two variables in this treatment, the fraction a_1 and

the rate constant ratio $k_{DMB}:k_s$, and we varied these in an iterative procedure until we found the best least-squares fit to the experimental data. This occurred with $a_1 = 0.115$, and $k_{DMB}:k_s = 4.0 \times 10^3\ M^{-1}$. The line drawn in Fig. 1 is based on the incremental computer simulation employing these numbers, and shows the excellent fit of the experimental data to the model. These values of a_1 and $k_{DMB}:k_s$ are also consistent with the results of the experiments carried out with 1,3-dimethoxybenzene present from the beginning. These predict yields of **8** of 82.3% and 95.8% for concentrations of 1 mM and 5 mM 1,3-dimethoxybenzene, respectively, in good agreement with the experimental numbers.

Intramolecular pathway for 4-diphenyl-1,3-dimethoxybenzene

The above analysis requires a finite value for a_1, the parameter representing a pathway that converts **4** directly into **8**. This number expressed as a percentage is also seen as the intercept in the plot of % yield of **8** versus % conversion (Fig. 1); i.e., it is the yield of **8** at zero conversion. This quantity of **8** cannot arise from a mechanism in which a diphenylmethyl cation separates away from 1,3-dimethoxybenzene, and the two later recombine. Under the conditions of very low conversion where the concentration of 1,3-dimethoxybenzene is negligibly small, any Ph_2CH^+ that forms as a free cation must be trapped by solvent.

Consequently, we speculated that the 11.5% of **8** observed at zero conversion was coming from an intramolecular rearrangement, in which the diphenylmethyl group remains attached to its original 1,3-dimethoxybenzene, and the two never separate.

Effect of ethanol

Support for this interpretation was seen in experiments with small concentrations of ethanol added to the solution. If free Ph_2CH^+ were responsible for all of the **8** that formed, the yield of **8** would be expected to decrease because of the additional channel involving reaction with ethanol. Indeed, significant amounts of the ether $Ph_2CHOCH_2CH_3$ were observed in place of the ether **7**. At the same time, however, the yield of **8** actually increased, for example, from a value of 21% at 10% conversion in the absence of ethanol to 36% for the same conversion with 10 mM of ethanol present. The origin of this increase will be discussed later, but it is clearly inconsistent with mechanisms where only Ph_2CH^+ is formed from the initial reaction of **4**.

There is one further important observation involving ethanol, namely that irradiation of **4** in the pure solvent resulted in absolutely no change over an extended period of time. The cleavage products and the fraction of **8** that is due to the intermolecular pathway clearly require photoprotonation, and thus it is not surprising that they are not formed in the weakly acidic ethanol. The failure to observe the intramolecular pathway also implies that this is initiated by photoprotonation.

Nanosecond laser flash photolysis

The most compelling arguments for the occurrence of an intramolecular rearrangement of **4** to **8**, as well as evidence for how this occurs, comes from LFP studies. We start with such studies carried out on the ns time scale, i.e., where transients are observed at the earliest 20 ns after the initiation of the laser pulse. As shown in Fig. 2, two bands are observed at this time, a relatively strong signal with λ_{max} near 440 nm and a weaker signal centered around 340 nm. The 340 nm signal decays, and at the same time there is a further increase in absorbance at the longer wavelengths. These changes occur with identical rate constants ($5.0 \times 10^5\ s^{-1}$), suggesting that they represent a common process. At the end of these changes there is a single strong signal at 440 nm. This eventually does decay, with a rate constant around $10^2\ s^{-1}$ although, because the reaction is so slow, the rate constant is difficult to accurately measure.

The final signal can be clearly identified as the diphenylmethyl cation, since the same spectrum is observed for solutions of this cation obtained under stable ion conditions (16). Moreover, a transient with the identical spectrum and a similar rate constant of decay is obtained on photolyzing diphenylmethyl 4-cyanophenyl ether (**9**) in HFIP. This ether has previously been shown to be a good photochemical precursor for Ph_2CH^+, the cation being generated in a photoheterolysis reaction (22, 23).

Initially we had thought that the initial signal above 400 nm must represent the 2,6-dimethoxybenzenium ion **5**. However, the λ_{max} is slightly longer than those previously observed for this type of cation (8). More importantly, overlaying the spectrum immediately after the laser pulse with the one after 10 microseconds shows that the two exactly superimpose in the region above 400 nm. This is shown in Fig. 3 and suggests that the absorbance at 440 nm immediately after the 20 ns laser pulse is also due to Ph_2CH^+.

Picosecond laser flash photolysis

We then turned to a faster time resolution to investigate the possibility that there was a process forming Ph_2CH^+ that had been missed on the ns time scale, and indeed found that this was the case. As shown in Fig. 4, optical density appears above 400 nm even at times as short as 100–200 ps. This has λ_{max} in the region 410–420 nm typical of 2,6-dimethoxybenzenium ions and it is therefore this species that is most reasonably assigned to the cation **5**. There is, however, a rapid change with a rate constant equal to $(9 \pm 1.5) \times 10^8\ s^{-1}$ (Fig. 5), where the λ_{max} shifts to longer wavelengths and the absorbance becomes slightly more intense. The spectrum at the end of this change corresponds to that of Ph_2CH^+; this is the "initial" absorbance above 400 nm in the ns LFP experiment.

Fast and slow processes forming the diphenylmethyl cation

The LFP experiments show that there are two separate processes that form diphenylmethyl cation following irradiation

[4] 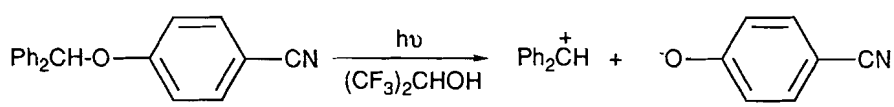

9

Fig. 2. Transient absorption spectra for 248 nm irradiation of 2-diphenylmethyl-1,3-dimethoxybenzene (**4**) in 1,1,1,3,3,3-hexafluoroisopropyl alcohol obtained 50–100 nanoseconds (■) and 9.5–10 microseconds (□) after the laser pulse. The inserts show the kinetic traces at the two selected wavelengths.

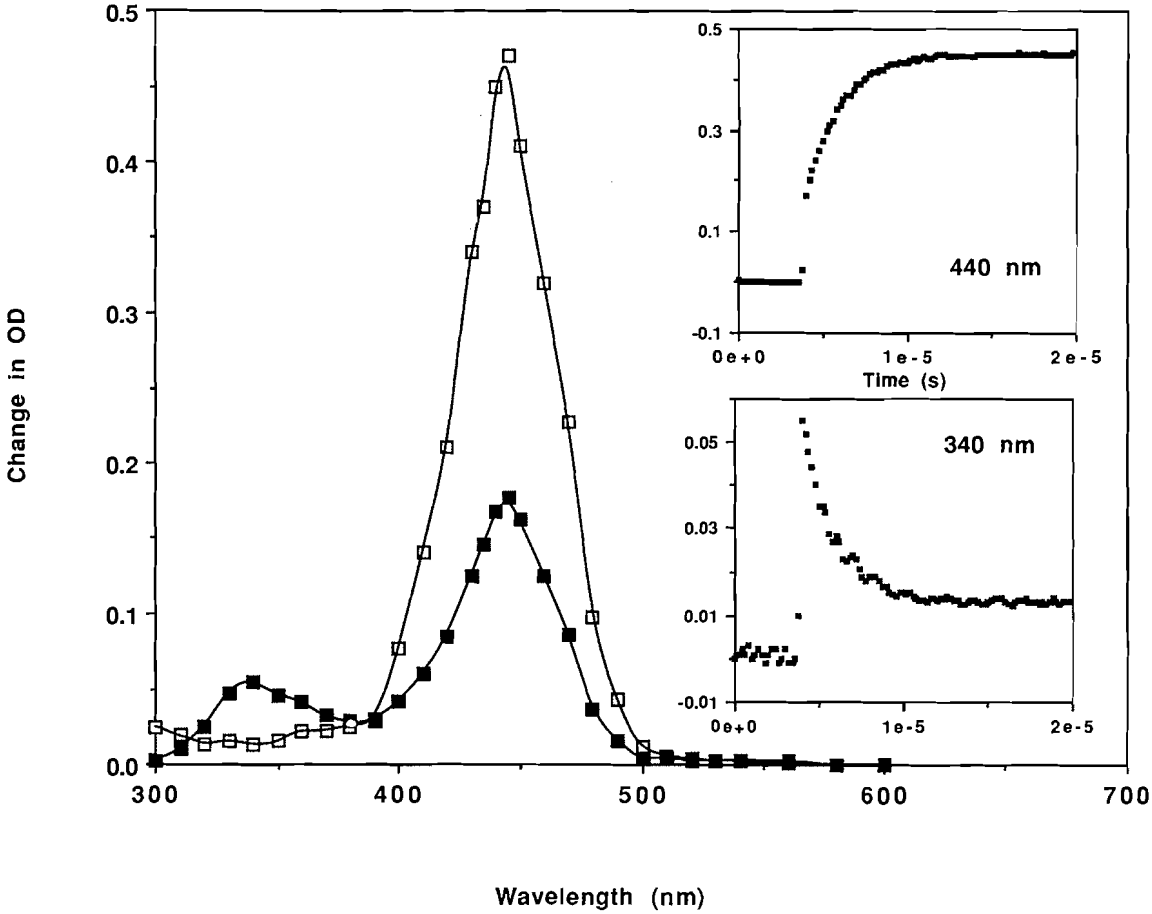

of **4** in HFIP, one that occurs on the ps time scale and one that occurs on the ns time scale. The ps study also suggests that the initial photochemical event is C2 protonation by the solvent, producing a 2,6-dimethoxybenzenium ion. This is the result with other 1,3-dimethoxybenzene derivatives (8–10), but the difference with the diphenylmethyl system is that this cyclohexadienyl cation is much less stable. One of its reactions is fragmentation to Ph_2CH^+, and it is this reaction that is observed on the ps time scale. The ns study, however, shows that there is a second growth of Ph_2CH^+. The precursor here must be the 340 nm transient, since this decays at the same rate as the second fraction of Ph_2CH^+ appears. The identity of the 340 nm transient has not yet been discussed, but based on all the evidence the most likely structure is the 1-diphenylmethyl-2,4-dimethoxybenzenium ion (**10**). This cyclohexadienyl cation is obviously also capable of cleavage to Ph_2CH^+, and at the same time its deprotonation provides a route to the product **8**. Moreover, its UV–visible spectrum with a λ_{max} near 340 nm is consistent with a 2,4-dimethoxybenzenium structure, as discussed in the introduction.

Scheme 3 can now be proposed to account for the various experimental observations. Inherent in this model is the assumption that the very fast reaction of the initially formed **5** involves both cleavage and rearrangement. Since the ps apparatus could only monitor above 400 nm, only the cleavage pathway was visible through the formation of Ph_2CH^+. We propose, however, that the cation **10** is also formed in this process. Such a rapid rearrangement followed by deprotonation is consistent with the intramolecular photoisomerization, and also provides a mechanism that converts **4** to **8** without releasing a free diphenylmethyl cation (eq. [5]).

[5] $\mathbf{4} \rightarrow \mathbf{4}^* \rightarrow \mathbf{5} \rightarrow \mathbf{10} \rightarrow \mathbf{8}$.

Also explained is the effect of the addition of a small amount of ethanol. Being more basic than the solvent, the ethanol will increase the overall rate of deprotonation of the cation **10**, but will have no effect on the fragmentation to Ph_2CH^+. This has the effect of increasing the yield of **8** that is formed in the intramolecular process, as observed experimentally.

Quantitative analysis

Scheme 3 also provides rate constants for the various processes. These have been obtained as follows.

The rate constant k_1 refers to the protonation of excited **4**, presumably a singlet, by the solvent. The observation of the cation **5** at very short times in the ps LFP experiment implies that this is a very fast protonation. We estimate a lower limit of 1×10^{10} s^{-1}; anything that was slower would have been observed in the kinetic traces.

Scheme 3.

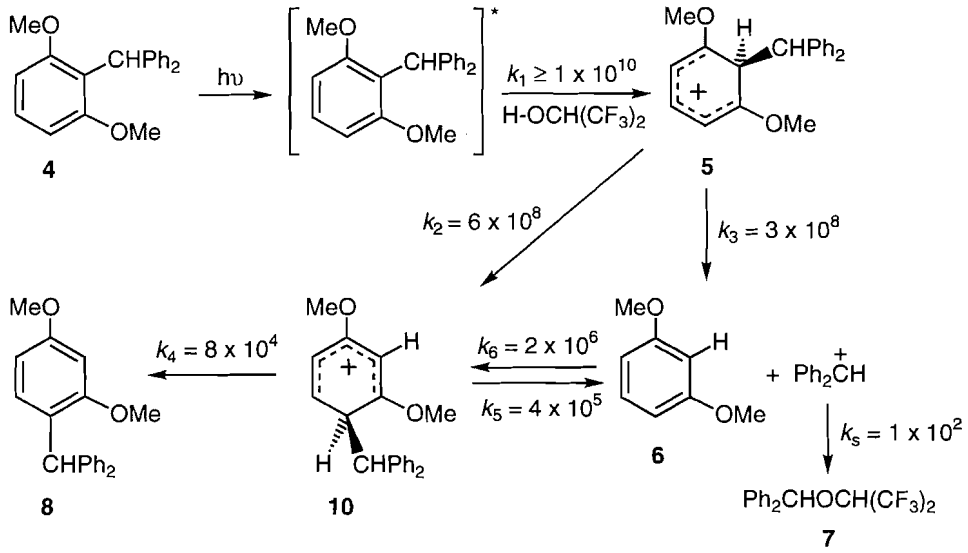

Fig. 3. Overlay of the transient absorption spectra for 2-diphenylmethyl-1,3-dimethoxybenzene in HFIP. The spectrum at 9.5–10 microseconds (□) has been plotted as is. The spectrum at 50–100 nanoseconds (■) has been plotted by multiplying the optical density change by 2.65.

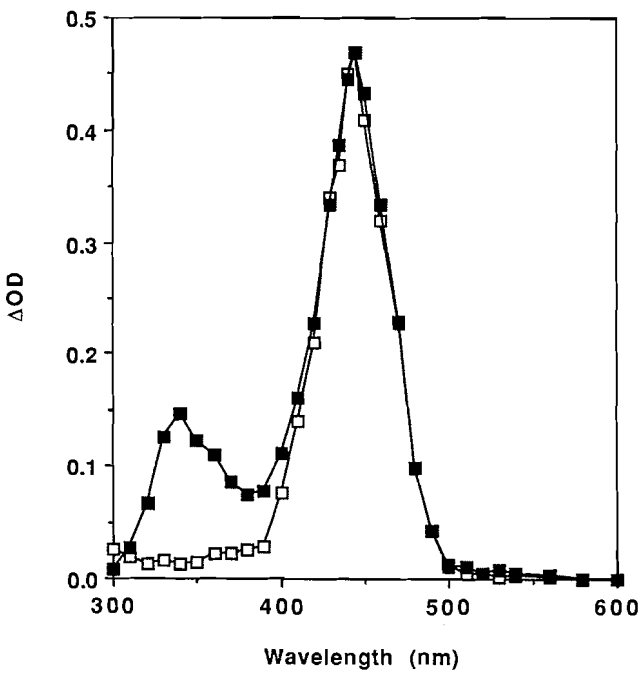

Fig. 4. Transient absorption spectra for 266 nm irradiation of 2-diphenylmethyl-1,3-dimethoxybenzene (**4**) in 1,1,1,3,3,3-hexafluoroisopropyl alcohol obtained at 200 picoseconds and 5000 picoseconds.

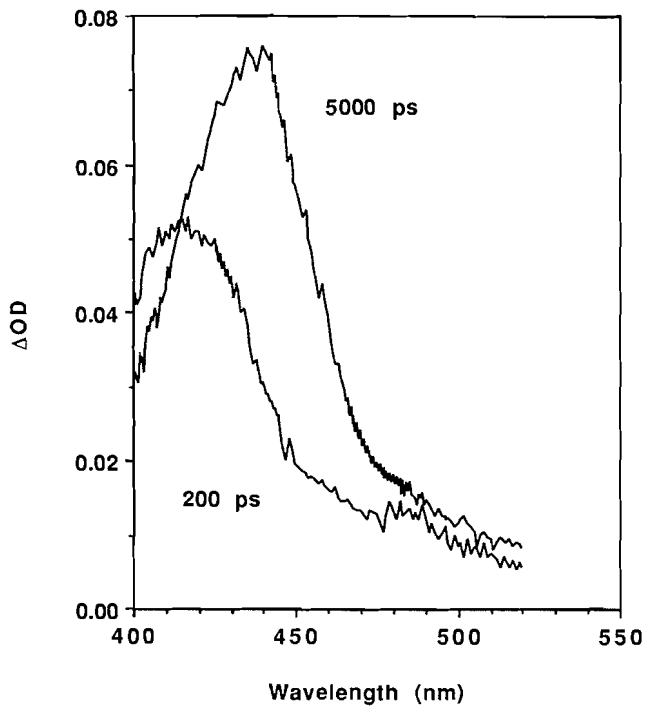

The rate constants k_2 through k_5 are obtained by solving a system of four equations (eqs. [6]–[9]). Equations [6] and [7] refer to the exponential rate constants obtained in the ps and ns LFP studies. The faster of these is the sum of the rearrangement and cleavage processes of **5**; the slower is the sum of the deprotonation and cleavage pathways of **10**. Equation [8] is the expression for the ratio of the amounts of diphenylmethyl cation that are formed in the fast and slow processes. The experimental number has been obtained from the ns LFP study, using the optical density at 440 nm immediately after the completion of the 20 ns laser pulse for the amount that has formed in the ps time range, and the additional optical density that then grows in as the amount formed in the ns time range. The ratio of eq. [9] refers to the total amount of 1,3-dimethoxybenzene (or Ph_2CH^+) relative to the rearrangement product, neglecting any intermolecular recombination. The experimental number is determined from the zero intercept in Fig. 1, the yield of the rearrangement product arising from the intramo-

Scheme 4.

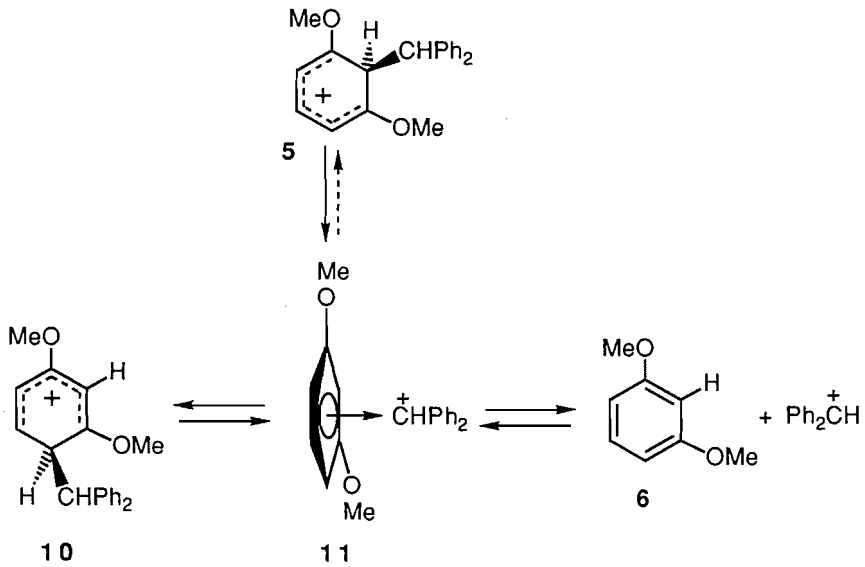

Fig. 5. Increase in 440 nm absorbance on the picosecond time scale following 265 nm irradiation of 2-diphenylmethyl-1,3-dimethoxybenzene (**4**) in 1,1,1,3,3,3-hexafluoroisopropyl alcohol.

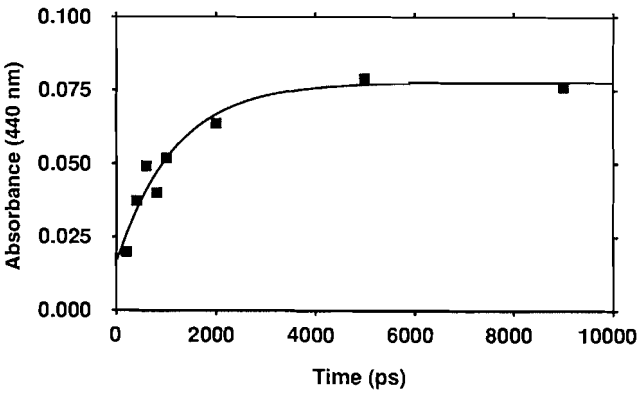

lecular pathway. Equations [8] and [9] are sufficient to provide the partitioning ratios, $k_2:k_3 = 2.0$ and $k_4:k_5 = 0.20$. Substitution of these into eqs. [6] and [7] gives the absolute rate constants.

[6] $k_{ps} = 9 \times 10^8\ s^{-1} = k_2 + k_3$

[7] $k_{ns} = 5.0 \times 10^5\ s^{-1} = k_4 + k_5$

$$[8]\quad \frac{\Delta OD(Ph_2CH^+)_{ps}}{\Delta OD(Ph_2CH^+)_{ns}} = 0.6 = \frac{\left(\left(\frac{k_4}{k_5}\right) + 1\right)}{\left(\frac{k_2}{k_3}\right)}$$

$$[9]\quad \left(\frac{[6]}{[8]}\right)_{\text{zero time}} = \frac{0.885}{0.115} = \frac{\left(\left(\frac{k_2}{k_3}\right) + \left(\frac{k_4}{k_5}\right) + 1\right)}{\left(\frac{k_2}{k_3}\right)\left(\frac{k_4}{k_5}\right)}$$

The constant k_s refers to the reaction of Ph_2CH^+ with HFIP to form **7**. With an absolute value of k_s available, k_{DMB} is then calculated as $4 \times 10^5\ M^{-1}\ s^{-1}$ using the ratio $k_{DMB}:k_S$ obtained in the analysis of Fig. 1. The constant k_{DMB} refers to the overall formation of **8** from 1,3-dimethoxybenzene and Ph_2CH^+, and is equal to $k_6k_4:(k_4 + k_5)$. Since the ratio $k_4:k_5$ is known, the absolute value of k_6 can be obtained. It should be noted that k_s is not well determined, so that any error in that constant will carry over to k_{DMB} and k_6.

An interesting outcome of these calculations is the ratio $k_4:k_5$, which is calculated to be 0.2. This means that in the Friedel–Crafts reaction of 1,3-dimethoxybenzene and Ph_2CH^+ in the solvent HFIP, the formation of the cyclohexadienyl cation **10** is almost reversible, and the rate-limiting step is the deprotonation of the cation. This of course partly reflects the weak basicity of the base doing the deprotonation, and the situation could obviously change if there were stronger bases present.

Mechanism of rearrangement

Perhaps the most interesting feature of these results is the very rapid rate at which the original cyclohexadienyl cation rearranges to its isomer. This is undoubtedly driven by thermodynamics. As discussed in the introduction, the parent 2,4-dimethoxybenzenium ion is thermodynamically more stable than the 2,6 isomer. Because of the bulky Ph_2CH group this should be even more the case with the cations of this study.

One possible mechanism is given in Scheme 4, in which the 2,6-dimethoxybenzenium ion loses Ph_2CH^+ resulting initially in an ion–molecule complex, written in Scheme 4 as the π-complex **11**. This same complex can serve as an intermediate in the interconversion of the 2,4-dimethoxybenzenium ion **10** and 1,3-dimethoxybenzene plus Ph_2CH^+. In the case where it forms from **5**, the complex has the choice of separating Ph_2CH^+ or of collapsing at the 4-position of the 1,3-dimethoxybenzene. The kinetic analysis presented in Scheme 3 suggests that these occur in a 1:2 ratio, respectively. From the failure to detect **4** as a product of the reaction of 1,3-di-

methoxybenzene and Ph_2CH^+ it would also appear as if the complex shows little propensity for collapse at the 2-position to form **5.**

This situation, where a complex collapses to a cyclohexadienyl cation faster than it separates into the aromatic compound and the electrophile, and with high regioselectivity, has previously been suggested as the explanation for very fast nitrations that show little intermolecular selectivity but high intramolecular selectivity (24). The suggestion in this case was that the rate-limiting step is the formation of a complex between NO_2^+ and the aromatic, followed by a rapid and selective collapse to the cyclohexadienyl cation. By demonstrating that σ-complexes can interconvert without separating the electrophile, the present study offers support for such a mechanism.

Experimental section

Flash photolysis experiments were carried out in the standard fashion with ca. 20 ns pulses at 248 nm (ca. 60 mJ per pulse) from a Lumonics excimer laser (KrF emission) and with ca. 25 ps pulses at 266 nm (ca. 4 mJ per pulse) from a Continuum YG-601-C Nd/YAG laser (25). Product analyses were carried out with a Varian 3400 gas chromatograph equipped with a FID detector, using ultra-high-purity helium as the carrier gas. The analyses were performed using a J + W Scientific Inc. Megabore DB1 30 m column with a film thickness of 1.5 μm. The apparatus was calibrated by determining response factors with authentic samples of the products. The identity of the products observed with GC was established by comparison of retention times and by the match in the mass spectra obtained by GC/MS analysis. The steady state photolyses were carried out using a Rayonet photochemical reactor equipped with medium-pressure mercury lamps operating at 254 nm. After various times of irradiation the solutions were directly injected into the GC for quantitative analysis.

The solvent 1,1,1,3,3,3-hexafluoroisopropyl alcohol (Aldrich) was distilled over sodium carbonate, followed by storage over 3A molecular sieves. On the day of use, the solvent was distilled again under an atmosphere of argon over fresh molecular sieves.

2-Diphenylmethyl-1,3-dimethoxybenzene (4)

1,3-Dimethoxybenzene (10 g, 72 mmol) was converted to its 2-lithio derivative (26) by dissolving in 100 mL of dry diethyl ether, adding 30 mL of 2.5 M butyllithium (75 mmol) in hexanes and stirring at room temperature under argon for 40 h. Benzophenone (12.7 g, 70 mmol) dissolved in 50 mL of dry ether was added, and the solution stirred at room temperature for a further 2 days. Standard work-up provided 18 g of 2,6-dimethoxyphenyldiphenylmethanol: ^{1}H NMR (200 MHz, $CDCl_3$) δ: 3.39 (s, 6H), 6.34 (s, 1H, OH), 6.61 (d, 2H, J = 8.3 Hz), 7.20–7.30 (m, 11H).

The crude alcohol (3 g, 9.4 mmol) was partially dissolved in 190 mL of 95% ethanol, 1 g of 10% palladium on carbon was added, and the mixture was shaken for 2 days under 60 psi (1 psi = 6.9 kPa) of hydrogen. The reaction mixture was shaken with Celite and filtered, followed by removal of the solvent to give a white solid. This was chromatographed using 50:50 hexane:dichloromethane followed by recrystallization from ethanol:water to give 1.7 g (60%) of white needles of 2-diphenylmethyl-1,3-dimethoxybenzene (**4**), mp 91–92°C. ^{1}H NMR (200 MHz, $CDCl_3$) δ: 3.60 (s, 6H), 6.16 (s, 1H), 6.57 (d, 2H, J = 8.3 Hz), 7.12–7.28 (m, 11H). ^{13}C NMR (200 MHz, $CDCl_3$) δ: 45.5, 55.7, 105.1, 121.0, 125.4, 127.5, 128.0, 129.1, 143.8, 158.5. MS (EI) *m/z*: 304.2 (100%), 289.1 (44%), 273.1 (45%), 227.1 (34%), 165.1 (52%), 152.1 (22%), 91.1 (88%). HRMS calcd. for $C_{21}H_{20}O_2$: 304.1463; found: 304.1479. Anal. calcd. for $C_{21}H_{20}O_2$: C 82.85, H 6.63, found: C 82.70, H 6.85.

4-Diphenylmethyl-1,3-dimethoxybenzene (8)

Methyl 2,4-dimethoxybenzoate (5 g, 26 mmol) dissolved in dry benzene was added dropwise to 58.6 mmol of phenylmagnesium bromide in 100 mL of dry ether. After refluxing for 2 h, standard work-up gave 2,4-dimethoxyphenyldiphenylmethanol as a yellow solid. This was purified by steam distillation to remove volatile impurities, followed by chromatography with 100% CH_2Cl_2, and recrystallization from ethanol:water. The product had mp 137–139°C. ^{1}H NMR (200 MHz, $CDCl_3$) δ: 3.64 (s, 3H), 3.79 (s, 3H), 5.14 (s, 1H, OH), 6.31 (dd, 1H, J_1 = 2.3 Hz and J_2 = 8.5 Hz), 6.40 (d, 1H, J = 8.5 Hz), 6.53 (d, 1H, J = 2.3 Hz), 7.20–7.32 (m, 10H).

The alcohol (2 g, 6.2 mmol) was hydrogenated with 10% Pd/C as described above. The white solid so obtained was chromatographed using 50:50 hexane:dichloromethane followed by recrystallization from ethanol:water to give 2.1 g (74%) of 4-diphenylmethyl-1,3-dimethoxybenzene (**8**), mp 122°C. ^{1}H NMR (200 MHz, $CDCl_3$) δ: 3.72 (s, 3H), 3.82 (s, 3H), 5.87 (s, 1H), 6.40 (dd, 1H, J_1 = 2.5 Hz and J_2 = 8.5 Hz), 6.47 (d, 1H, J = 2.5 Hz), 6.74 (d, 1H, J = 8.5 Hz), 7.05–7.31 (m, 10H). HRMS calcd. for $C_{21}H_{20}O_2$: 304.1463; found: 304.1463.

Diphenylmethyl 1,1,1,3,3,3-hexafluoroisopropyl ether (7)

Diphenylmethanol (1.8 g) was added to 10 mL of 1,1,1,3,3,3-hexafluoroisopropyl alcohol, along with 5 mL of dichloromethane to improve the solubility. One drop of concentrated H_2SO_4 was added, resulting in a deep red solution. An aqueous solution of sodium carbonate was added followed by dichloromethane. The dichloromethane layer was removed, dried over $MgSO_4$, and evaporated. The resulting yellow liquid was chromatographed with 100% CH_2Cl_2, and the ether purified by distillation at 3 Torr, 61°C (1 Torr = 133.3 Pa). ^{1}H NMR (200 MHz, $CDCl_3$) δ: 4.18 (sept, 1H), 5.84 (s, 1H), 7.36 (br s, 10H). HRMS calcd. for $C_{16}H_{12}F_6O$: 334.0792; found: 334.0799.

Acknowledgements

Financial support from the Natural Sciences and Engineering Research Council of Canada is gratefully acknowledged. We also thank Dr. Linda Johnston and Dr. Calvin Lew of the Steacie Institute for Molecular Sciences of the National Research Council of Canada for ps LFP experiments.

References

1. S.F. Mason and B.E. Smith. J. Chem. Soc. A, 325 (1969).
2. J.F. Ireland and P.A.H. Wyatt. Adv. Phys. Org. Chem. **12**, 131 (1976).
3. J. Cornelisse and E. Havinga. Chem. Rev. **75**, 131 (1975).
4. H. Shizuka. Acc. Chem. Res. **18**, 141 (1985).
5. P. Wan and D. Shukla. Chem. Rev. **93**, 571 (1993).
6. G. Zhang and P. Wan. Res. Chem. Intermed. **19**, 119 (1993).

7. S. Steenken and R.A. McClelland. J. Am. Chem. Soc. **112**, 9648 (1990).
8. N. Mathivanan, F. Cozens, R.A. McClelland, and S. Steenken. J. Am. Chem. Soc. **114**, 2198 (1992).
9. C.S.Q. Lew and R.A. McClelland. J. Am. Chem. Soc. **115**, 11516 (1993).
10. G. Zhang, Y. Shi, R. Mosi, T. Ho, and P. Wan. Can. J. Chem. **72**, 2388 (1994).
11. R.A. McClelland, F. Cozens, and S. Steenken. Tetrahedron Lett. 3821 (1990).
12. R. Pollard, S. Wu, G. Zhang, and P. Wan. J. Org. Chem. **58**, 2605 (1993).
13. A.J. Kresge, Y. Chiang, and L.E. Hakka. J. Am. Chem. Soc. **93**, 6167 (1971).
14. A.J. Kresge, S.G. Mylonakis, Y. Sato, and V.P. Vitullo. J. Am. Chem. Soc. **93**, 6181 (1971).
15. H.E. Zimmerman and V.R. Sandel. J. Am. Chem. Soc. **85**, 915 (1963).
16. J. Bartl, S. Steenken, H. Mayr, and R.A. McClelland. J. Am. Chem. Soc. **112**, 6918 (1990).
17. R.A. McClelland, C. Chan, F. Cozens, A. Modro, and S. Steenken. Angew. Chem. Int. Ed. Engl. **30**, 1337 (1991).
18. C. Eaborn. J. Organomet. Chem. **100**, 43 (1975).
19. C.S.Q. Lew, R.A. McClelland, L.J. Johnston, and N.P. Schepp. J. Chem. Soc. Perkin Trans. 2, 395 (1994).
20. F. Cozens, J. Li, R.A. McClelland, and S. Steenken. Ang. Chem. Int. Ed. Engl. **31**, 743 (1992).
21. R.A. McClelland, F.L. Cozens, J. Li, and S. Steenken. J. Chem. Soc. Perkin Trans. 2, 1531 (1996).
22. R.A. McClelland, V.M. Kanagasabapathy, and S. Steenken. J. Am. Chem. Soc. **110**, 6913 (1988).
23. R.A. McClelland, V.M. Kanagasabapathy, N. Banait, and S. Steenken. J. Am. Chem. Soc. **111**, 3966 (1989).
24. J.W. Barnett, R.B. Moodie, K. Scofield, and J. Weston. J. Chem. Soc. Perkin Trans. 2, **2**, 648 (1975).
25. L.J. Johnston and N.P. Schepp. J. Am. Chem. Soc. **115**, 6564 (1993).
26. H.W. Gschwend and H.R. Rodriguez. Org. React. **26**, 1 (1975).

Solvent effects on nucleophilic substitution reactions. III. The effect of adding an inert salt on the structure of the S_N2 transition state

T.V. Pham and K.C. Westaway

Abstract: The nitrogen and secondary α-hydrogen–deuterium kinetic isotope effects found for the S_N2 reaction between thiophenoxide ion and benzyldimethylphenylammonium ion at different ionic strengths in DMF at 0°C indicate that the structure of the transition state changes markedly with the ionic strength of the reaction mixture. In fact, a more reactant-like, more ionic, transition state is found at the higher ionic strength. This presumably occurs because a more ionic transition state is more stable in the more ionic solvent.

Key words: transition state, ionic strength, secondary α deuterium kinetic isotope effects, nitrogen isotope effects, S_N2.

Résumé : On a déterminé les effets isotopiques cinétiques primaires de l'azote et secondaire des hydrogène/deutérium en α sur la réaction S_N2 des ions thiophénolate et benzyldiméthylphénylammonium, à diverses forces ioniques, dans le DMF, à 0°C; ils suggèrent que la structure de l'état de transition varie d'une façon importante avec la force ionique du mélange réactionnel. En fait, on observe que, à force ionique élevée, l'état de transition est plus ionique et qu'il ressemble aux réactifs. Cette situation existe probablement parce qu'un état de transition plus ionique est plus stable dans le solvant plus ionique.

Mots clés : état de transition, force ionique, effets isotopiques cinétiques secondaires des deutériums en α, effets isotopiques de l'azote, S_N2.

[Traduit par la rédaction]

Introduction

Inert salts are often added to organic reactions where ionic reactants are converted into neutral products so accurate rate constants can be measured. The problem arises because the rate constant "k" for a reaction between two ionic reactants varies with the ionic strength of the medium, eq. [1].

$$[1] \quad \log k = \log k_0 + Z_A Z_B c(\mu / D^3T^3\rho)^{1/2}$$

where "$\log k_0$" is the rate constant at infinite dilution, "Z_A" and "Z_B" are the charges on the reacting ions, c is a constant, "$\mu = 1/2(\Sigma_i c_i Z_i^2)$" is the ionic strength of the solution, "c_i" is the concentration of ion i, "Z_i" is the charge on ion i, "D" is the dielectric constant of the solvent, "T" is the absolute temperature, and "ρ" is the density of the solution (1). In a reaction where two ionic reactants are converted into neutral products (ions are consumed in the reaction), the ionic strength decreases throughout the reaction and the rate constant changes according to eq. [1]. This means that one cannot determine an accurate rate constant for the reaction and, therefore, cannot measure kinetic isotope effects, or any other mechanistic criteria based on kinetic data, to determine the reaction mechanism. In practice, a constant (accurate) rate constant can be obtained for these reactions if the rate constant is determined in solutions containing a high concentration of an inert salt. This is effective because the high concentration of inert salt maintains a high, and effectively constant, ionic strength throughout the reaction so the rate constant does not change significantly. In all the studies where this technique has been used, it is assumed that the added salt only keeps the ionic strength of the medium constant (maintains the rate constant) but does not have any effect on the reaction. The results of this study indicate that an added, inert, salt affects the structure of an S_N2 transition state significantly.

Results and Discussion

The S_N2 reaction between thiophenoxide ion and benzyldimethylphenylammonium ion, eq. [2],

$$[2] \quad Z\text{—}C_6H_4\text{—}S^- + C_6H_5CL_2\text{—}\overset{+}{N}(CH_3)_2C_6H_5 \xrightarrow[NaNO_3]{DMF} Z\text{—}C_6H_4\text{—}S\text{—}CL_2C_6H_5 + (CH_3)_2NC_6H_5$$

L = H, D

has been investigated at 0°C in DMF containing a high concentration of the inert salt, sodium nitrate. The high concentration of sodium nitrate kept the ionic strength virtually constant throughout the reaction, making it possible to determine accurate rate constants.

Received July 28, 1996.

T.V. Pham and K.C. Westaway.[1] Department of Chemistry and Biochemistry, Laurentian University, Sudbury, ON P3E 2C6, Canada.

[1] Author to whom correspondence may be addressed. Telephone: (705) 675-1151, ext. 2105, Fax: (705) 675-4844. E-mail: kwestawa@nickel.laurentian.ca

Table 1. The primary nitrogen (leaving group) and secondary α-hydrogen–deuterium kinetic isotope effects for the S_N2 reaction between sodium thiophenoxide and benzyldimethylphenylammonium nitrate at different ionic strengths in DMF at 0°C.

Ionic strength (M)	k^{14}/k^{15}	$(k_H/k_D)_\alpha$
0.904	1.0166 ± 0.0004[a]	1.215 ± 0.011[b]
0.64	1.0200 ± 0.0007[a]	1.179 ± 0.007[c]

[a]The errors are the standard deviation of the mean of five different measurements.

[b]The error in the isotope effect = $(1/k_D)[(\Delta k_H)^2 + (k_H/k_D)^2 \times (\Delta k_D)^2]^{1/2}$ where Δk_H and Δk_D are the standard deviations for the rate constants for the undeuterated and deuterated substrates, respectively. The Δk_H and Δk_D values were obtained from three rate constants for the undeuterated and three rate constants for the deuterated substrates, respectively, that were measured simultaneously.

[c]This isotope effect was determined by whole-molecule mass spectrometry. The error is the standard deviation for four separate determinations (2).

The nitrogen (leaving group) and the secondary α-hydrogen–deuterium kinetic isotope effects were measured for this S_N2 reaction at two different ionic strengths to learn whether the added, inert, salt affects the reaction and the structure of its transition state. An examination of the nitrogen (leaving group) and secondary α-hydrogen–deuterium kinetic isotope effects, Table 1, shows that the isotope effects are very different when the reaction is carried out at different ionic strengths. For instance, the nitrogen kinetic isotope effect found at the higher ionic strength (k^{14}/k^{15} = 1.0166 ± 0.0004) is significantly smaller than the k^{14}/k^{15} = 1.0200 ± 0.0007 found for this reaction at the lower ionic strength of 0.64 M (2). The magnitude of a heavy atom (nitrogen (leaving group)) kinetic isotope effect increases linearly with the percent of α-carbon–nitrogen (C_α- - -N) bond rupture in the transition state (2, 3). Therefore, the smaller nitrogen isotope effect found for the reaction at the higher ionic strength indicates that the C_α- - -N bond rupture is much less advanced in the transition state of the high ionic strength reaction.

Recent work has shown that the magnitude of a secondary α-hydrogen–deuterium kinetic isotope effect is determined by the changes that occur in both the C_α—H(D) stretching and the out-of-plane bending vibrations when the reactant is converted into the transition state (4, 5). However, a comparison of the secondary α-hydrogen–deuterium kinetic isotope effects for a series of S_N2 reactions between methyl or ethyl chlorides and fluorides with several different nucleophiles (5) has shown that the magnitude of the isotope effect for a series of S_N2 reactions *with the same leaving group* is determined by the changes that occur in the out-of-plane bending vibrations when the reactant is converted into the transition state (5). This means the magnitude of the secondary α-hydrogen–deuterium kinetic isotope effect for a series of S_N2 reactions *with the same leaving group* is determined by the nucleophile – leaving group distance (the tightness) of the S_N2 transition state (5–7).

The secondary α-hydrogen–deuterium kinetic isotope effect found at the high ionic strength ($(k_H/k_D)_\alpha$ = 1.22 ± 0.01) is significantly larger than the $(k_H/k_D)_\alpha$ = 1.179 ± 0.007 (2) found at an ionic strength of 0.64 M, Table 1. Since the magnitude of a secondary α-hydrogen–deuterium kinetic isotope effect is related to the nucleophile – leaving group distance in the S_N2 transition state (5–7), the larger isotope effect found for the higher ionic strength reaction indicates that the high ionic strength transition state is looser with a greater nucleophile – leaving group distance than the lower ionic strength transition state. If the high ionic strength transition state has a greater nucleophile – leaving group distance but a shorter C_α- - -N bond (vide supra), then the S- - -C_α transition state bond in the high ionic strength reaction must be much longer than the S- - -C_α bond in the transition state of the low ionic strength reaction, Fig. 1.

Fig. 1. The relative transition state structures for the S_N2 reactions between sodium thiophenoxide and benzyldimethylphenylammonium nitrate at different ionic strengths in DMF at 0°C.

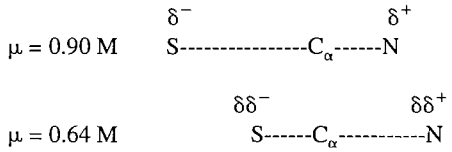

Another piece of evidence that suggests the S- - -C_α transition state bond is longer in the higher ionic strength reaction is the Hammett ρ value found by changing the *para* substituent on the nucleophile. A Hammett ρ = −1.62 ± 0.01, Table 2, was observed for the high ionic strength reaction whereas a larger Hammett ρ value of −1.76 ± 0.19 was found for the reaction at an ionic strength of 0.64 M. Since a larger ρ value is observed when the change in charge on going from the reactants to the transition state is larger, i.e., when there is more nucleophile–α-carbon bond formation in the transition state, the reaction at the higher ionic strength (with the larger $(k_H/k_D)_\alpha$) must have the longer S- - -C_α transition state bond.[2] Thus, the ρ values support the conclusion based on the magnitude of the secondary α-hydrogen–deuterium kinetic isotope effects, i.e., that the transition state for the higher ionic strength reaction is looser with a much longer S- - -C_α bond than the transition state for the lower ionic strength reaction. Combining the information obtained from the nitrogen and the secondary α-hydrogen–deuterium kinetic isotope effects with that from the Hammett ρ value suggests that the high ionic strength transition state is earlier (more reactant-like) with a much longer S- - -C_α and a shorter C_α- - -N bond, Fig. 1.

Finally, it is interesting to speculate on why a more reactant-like transition state is found at a higher ionic strength. The earlier transition state in the high ionic strength reaction has both a greater negative and a greater positive charge on the

[2] Hoz et al. (8) used the results of theoretical calculations on homolytic cleavage reactions to question the validity of using Hammett ρ values to determine transition state structure. However, many workers currently use linear free energy relationships such as ρ values to indicate differences in transition state structure (9, 10) and there is no experimental evidence to show which position is correct. The authors believe that ρ values found in closely related systems can be used to indicate transition state structure. Support for this position is that the changes in the structure of the S_N2 transition state suggested by ρ values have been confirmed by isotope effect data (2, 11, 12).

Table 2. The rate constants and Hammett ρ values for the reactions between *para*-substituted sodium thiophenoxides and benzyldimethylphenylammonium nitrate at different ionic strengths in DMF at 0°C.

para-Substituent on the thiophenoxide ion	Rate constant × 10^3 (L M^{-1} s^{-1})	
	Ionic strength μ = 0.904 M	Ionic strength μ = 0.64 M
CH_3O	30.1 ± 0.8[a]	46.2 ± 3.3[a]
H	10.9 ± 0.3	12.8 ± 1.0
Cl	4.67 ± 0.07	6.13 ± 0.65
ρ	−1.62 ± 0.01	−1.76 ± 0.19
Correlation coefficient	1.00	0.994

[a]The errors are the standard deviation of the mean of at least three different measurements.

nucleophilic sulfur and nitrogen atoms, respectively. This means the transition state in the higher ionic strength solvent is more ionic. It is proposed that the more ionic transition state is found at high ionic strength because it is more stable (more highly solvated) in the more ionic solvent.

The significant observation, however, is that inert salts that are used to increase the ionic strength in reactions so that accurate rate constants can be measured, change the structure of the transition state markedly. This is an important discovery because it shows that adding even inert salts changes the reaction from a mechanistic point of view, i.e., the values obtained for any mechanistic criterion will not be for the reaction of interest.

Experimental

Nitrogen kinetic isotope effects for the S_N2 reactions between sodium thiophenoxide and benzyldimethylphenylammonium ion in DMF at 0°C

The procedure used to synthesize the benzyldimethylphenylammonium nitrate and measure the nitrogen kinetic isotope effect has been described (2). The only difference in the two isotope effects was that one was measured at a higher ionic strength. In both experiments, the ionic strength was adjusted by adding sodium nitrate to the solvent.

The secondary α-hydrogen–deuterium kinetic isotope effects for the S_N2 reactions between sodium thiophenoxide and benzyldimethylphenylammonium ion in DMF at 0°C

The preparation of the benzyl-1,1-d_2-dimethylphenylammonium nitrate has been described (2). The procedure used to measure the secondary α-hydrogen–deuterium kinetic isotope effect at the lower ionic strength using whole-molecule mass spectrometry is also described in ref. 2. The secondary α-hydrogen–deuterium kinetic isotope effects at the high ionic strength were obtained by dividing the average second-order rate constant (from three separate kinetic runs done using the same stock solutions and at the same time) for the reaction of the undeuterated substrate with that for the reaction of the deuterated substrate. The least-squares kinetic plots had correlation coefficients of at least 0.999 and the reactions were followed to at least 67% of completion. The procedure used to measure these rate constants is given in refs. 12 and 13. The isotope effects measured with different batches of solvent on different days were identical.

Acknowledgments

The authors gratefully acknowledge the financial support provided by the Natural Sciences and Engineering Research Council of Canada (NSERC).

References

1. E.S. Gould. *In* Mechanism and structure in organic chemistry. Holt, Reinhart, and Winston, Inc., New York. 1959. 185.
2. K.C. Westaway and S.F. Ali. Can. J. Chem. **57**, 1354 (1979).
3. W.H. Saunders. Chem. Scr. **8**, 27 (1975).
4. S. Wolfe and C.-K. Kim. J. Am. Chem. Soc. **113**, 8056 (1991).
5. R.A. Poirier, Y. Wang, and K.C. Westaway. J. Am. Chem. Soc. **116**, 2526 (1994).
6. J.A. Barnes and I.H. Williams. J. Chem. Soc. Chem. Commun. 1286 (1993).
7. T.R. Griffin, D.B. Cook, A. Haynes, J.M. Pearson, D. Monti, and G.E. Morris. J. Am. Chem. Soc. **118**, 3029 (1996).
8. S. Hoz, S. Basch, and M.J. Goldberg. J. Am. Chem. Soc. **114**, 4364 (1992).
9. D. Stefanidis and W.P. Jencks. J. Am. Chem. Soc. **115**, 6045 (1993).
10. I. Lee, W.H. Lee, and H.W. Lee. J. Phys. Org. Chem. **3**, 545 (1990).
11. K.C. Westaway and Z. Waszczylo. Can. J. Chem. **60**, 2500 (1982).
12. T.V. Pham, Y.R. Fang, and K.C. Westaway. J. Am. Chem. Soc. In press.
13. T.V. Pham. M.Sc. Dissertation, Laurentian University, 1993.

Nitrobenzoxadiazole-labelled polyisoprenoid alcohols

Bruce J. Balcom and Nils O. Petersen

Abstract: We have prepared, isolated, and characterized a series of nitrobenzoxadiazole labelled polyisoprenoid alcohols. The coupling reaction employed was a dicyclohexylcarbodiimide mediated condensation between a carboxylic acid derivative of nitrobenzoxadiazole and the polyisoprenoid alcohols citronellol, solanesol, and dolichol. Upon exposure to visible light, a self-sensitized singlet oxygen "ene" reaction oxidized double bonds in the isoprene moiety. The rate of oxidation is greatly reduced in solvents where singlet oxygen is short-lived.

Key words: nitrobenzoxadiazole, isoprenoid, dolichol, citronellol, solanesol, fluorescence labelling, singlet oxygen, ene reaction.

Résumé : On a préparé, isolé et caractérisé une série d'alcools polyisoprénoïdes dérivés du nitrobenzoxadiazole marqué. La réaction de couplage utilisée implique une condensation, effectuée sous l'influence de la dicyclohexylcarbodiimide, entre un dérivé d'un acide carboxylique du nitrobenzoxadiazole et les alcools polyisoprénoïdes citronellol, solanésol et dolichol. Par exposition à la lumière visible, une réaction "ène" autosensibilisée de l'oxygène singulet permet d'oxyder les doubles liaisons de la portion isoprénique. La vitesse de la réaction est grandement réduite dans les solvants dans lesquels la durée de vie de l'oxygène est réduite.

Mots clés : nitrobenzoxadiazole, isoprénoïde, dolichol, citronellol, solanésol, fluorescence, marquage, oxygène singulet, réaction ène.

[Traduit par la rédaction]

Introduction

We recently examined the size dependence of the lateral diffusion coefficient in model cell membranes using fluorescently labelled probe molecules (1, 2). Our specific intent was to explore the effect of hydrocarbon interactions in the membrane interior as a retardant to lateral diffusion. Systematic exploration of this effect required a homologous series of well-defined hydrophobic polymers derivatized with a fluorophore (3–5) suitable for use in fluorescence photobleaching recovery experiments (6, 7). Based on previous experience (8, 9) we chose nitrobenzoxadiazole (NBD) as the fluorophore. This article describes the synthesis, purification, and characterization of the labelled molecules and also reports an unexpected light-dependent instability of the resulting labelled probes.

Polyisoprenoid alcohols, ubiquitous in nature, are a naturally occurring hydrocarbon polymer with a ready means of derivatization: a terminal hydroxyl function. Short-chain isoprenoid alcohols are most prevalent in plants. Citronellol, nerol, farnesol, and geranyl geraniol are common constituents of fragrant essential oils such as citronella, rose, and musk oil. Solanesol is the major lipid component of tobacco leaves (10). Long-chain polyprenols are more common in mammals. Dolichol in rat liver, for example, is polydisperse with alcohols that range from 14 to 24 isoprenes in length (11). The distribution of dolichols in tissues varies with species. In humans, the mean chain length shifts towards longer chain isoprenoids.

Despite the common linear architecture, two major structural differences occur in these polymers. The extent of unsaturation is variable, as is the double bond stereochemistry. Saturated isoprene subunits typically occur in the α subunit containing the hydroxyl group. This is the case for citronellol and dolichol used in our studies (Scheme 1). Solanesol has an α isoprene subunit that is unsaturated. Solanesol (Scheme 1) also has an all-*trans* stereochemistry about its nine double bonds. Dolichol is poly *cis* with only the three terminal isoprenes possessing *trans* double bonds (12).

Results and discussion

Derivatization

The hydroxyl functional group in the isoprenoid alcohols immediately suggests an esterification as the preferred mode of fluorophore attachment. *N*-Methyl-*N*-(7-nitrobenz-2-oxa-1,3-diazol-4-yl)-6-amino hexanoic acid (NBD-acid) is a carboxylic acid derivative of NBD (inset Fig. 1) designed for labelling alcohols and amines (13). Esters synthesized from NBD-acid are named, in this work, by appending the alcohol name to NBD.

Our chosen esterification reaction was a dicyclohexylcarbodiimide (DCC) mediated acid condensation reaction (14,

Received August 15, 1996.

B.J. Balcom[1] **and N.O. Petersen.**[2] Department of Chemistry, The University of Western Ontario, London, ON N6A 5B7, Canada.

[1] Current address: Department of Physics, The University of New Brunswick, P.O. Box 4400, Fredericton, NB E3B 5A3, Canada.

[2] Author to whom correspondence may be addressed. Telephone: (519) 661-3122. Fax: (519) 661-3022. E-mail: PETERSEN@UWOVAX.UWO.CA

Scheme 1. Citronellol and dolichol (top) have $n = 1$ and $n =$ 15–21, respectively. Solanesol (bottom) has $n = 8$.

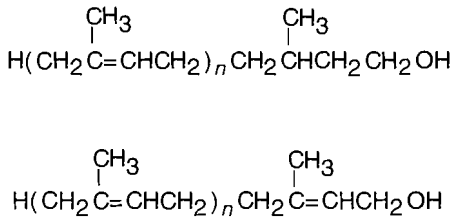

Fig. 1. DCC-mediated NBD-acid esterification reaction. Sample reaction scheme illustrating the labelling reaction. NBD-acid (**1**) combines with DCC to form the anhydride (**2**) and the unwanted *N*-acylurea (**5**). An alkyl aminopyridine catalyst assists the esterification of, in this case, undecanol (**3**). NBD-undecanol (**4**) is the desired product.

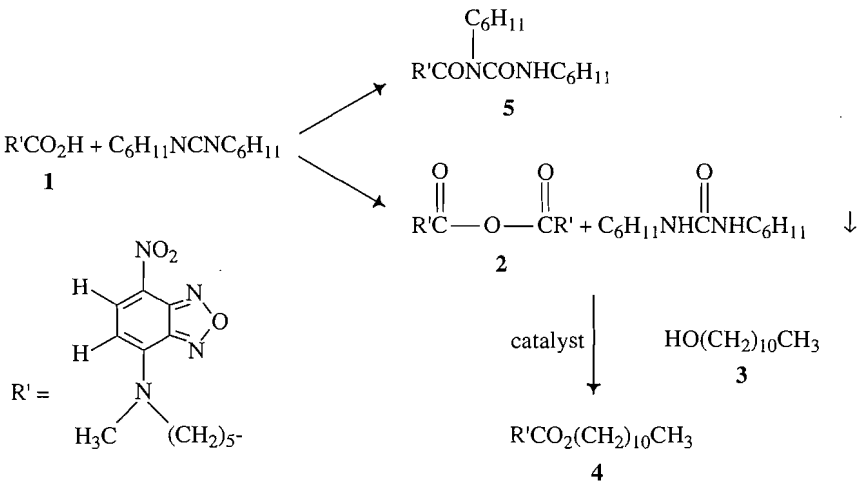

15) with an alkyl aminopyridine catalyst (Fig. 1). This reaction has a significant by-product, *N*-acylurea, production of which is very solvent dependent. Balcom and Petersen (16) showed that solvents that are poor hydrogen bond acceptors are the most efficient in suppressing *N*-acylurea production (an undesirable by-product) in the DCC reaction. Methylene chloride is a poor hydrogen bond acceptor but it also exacerbates the light-induced instability of the product esters. Model esterification reactions were undertaken with undecanol to confirm the reaction products of the NBD labelling reaction and to further explore the unexpected light-induced instability of the labelled isoprenoid alcohols.

HPLC analysis

Reverse-phase HPLC was employed to characterize the NBD-labelled alcohols. Unlike chromatography on silica, where the polarity of the NBD group controls the elution, the retention time on a reverse-phase HPLC column is primarily controlled by the hydrocarbon moiety of the labelled alcohols. NBD-undecanol eluted as one peak, retention time 26.7 min. NBD-citronellol, retention time 14.3 min, has a small impurity, less than 5%, which eluted at a shorter time. NBD-solanesol (different mobile phase) also eluted as one peak at 4.0 min.

The dolichol sample was a mixture of individual homologs in the range from 16 to 22 isoprenes. The chain lengths of individual homologs were confirmed by comparison to known dolichol standards. Reverse-phase HPLC resolved the individual labelled (480 nm detection wavelength) dolichol species (Fig. 2). Labelled homologs with 16, 17, 18, 19, 20, 21, and 22 isoprenes had retention times of 10.7, 12.0, 14.4, 17.7, 20.5, 24.2, and 29.5 min, respectively. The same distribution was observed *prior* to labelling, by observation of the isoprene double bond absorption at 210 nm. The unlabelled species (same elution conditions) had shorter retention times. Exposure of NBD-dolichol to light and oxygen in methylene chloride resulted in degradation of the molecule (but not the fluorescent label) and a shift of the distribution back to shorter elution times. Exposure of the NBD-citronellol sample, similar conditions, also resulted in a degradation of the molecule (but again not the fluorescent label), which was observed as a shift in retention time from 14.3 to 4.8 min.

Compound instability

The origin of the solution instability was further investigated because the stability of the probe molecule was of crucial importance with reference to its use as a diffusion tracer. The HPLC results discussed in the previous section showed quantitative conversion of the target ester into the degradation product(s). Silica TLC analysis (NBD-citronellol) showed a change in R_f from 0.87 to 0.75 upon reaction. Less efficient interaction of the degradation product with the HPLC stationary phase, but more efficient interaction with the TLC stationary phase (decreased R_f), suggests the degradation product is more polar than the original NBD-labelled alcohol.

Fig. 2. Reverse-phase HPLC trace of NBD-dolichol sample. Labelled homologs with from 16 to 22 isoprenes are observable. This same distribution was observed for the unlabelled homologs. The NBD-dolichol was detected by the absorbance (480 nm) of the NBD label.

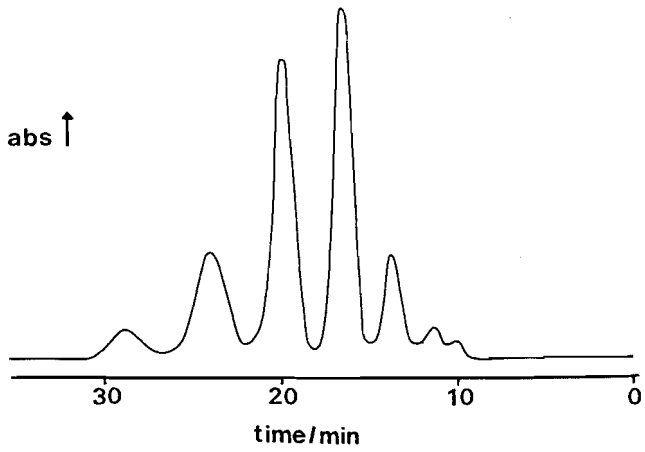

Control experiments (analysis by TLC and HPLC) revealed four additional features of the degradation reaction. (*i*) The degradation was a photochemical reaction involving NBD. NBD-citronellol decayed in both white light and light filtered (via a cutoff filter) to wavelengths greater than 400 nm. (*ii*) Oxygen was required. The decay of NBD-citronellol was quenched, or severely limited, by sparging the solution with nitrogen. Contrarily, saturating the solution with oxygen greatly accelerated the reaction. (*iii*) NBD-undecanol did not degrade. Although it closely resembles NBD-citronellol in size and shape, it does not have a double bond. (*iv*) The decay of NBD-citronellol was solvent dependent. A qualitative comparison of the decay rate in acetone and deuterated acetone, analysis by TLC, showed much faster conversion in the deuterated solvent. The degradation was also observed to proceed rapidly in chlorinated solvents although a direct control experiment, as in the case of the deuterated solvents, was not possible. NBD-citronellol did not degrade in ethanol.

Involvement of the NBD chromophore (λ_{max} = 480 nm), oxygen, and the isoprene double bond in the degradation reaction immediately suggests an NBD sensitized singlet oxygen "ene" reaction (17, 18). Our qualitative observation of a deuterium effect on the degradation kinetics is strong evidence for the singlet oxygen "ene" mechanism; it is often considered diagnostic of a singlet oxygen reaction (19).

Ground state triplet oxygen is known to undergo triplet–triplet annihilation with varied dye sensitizers to produce the reactive singlet oxygen species (20, 21). The isoprene moiety is vulnerable to the "ene" reaction because of the trisubstituted double bond (18, 22). In fact, citronellol is oxidized to rose oxide on an industrial scale by the singlet oxygen "ene" reaction (23). Many different hydroperoxide isomers are produced (22) by this reaction, which made purification and spectroscopic identification of the reaction products impossible. ^{1}H NMR of the crude light-exposed and reacted NBD-citronellol supported the singlet oxygen oxidation mechanism. The ^{1}H NMR spectrum, after light exposure, showed a disruption of the isoprene double bond structure. This is most evident from the disappearance of the terminal methyl singlets (δ = 1.68 and 1.60 ppm) α to the double bond in the original citronellol.

To our knowledge, the NBD chromophore has not previously been identified as a singlet oxygen sensitizer. It is not surprising, however, that it could so function. While the quantum yield of intersystem crossing is unknown for NBD, the low quantum yield of fluorescence, 5% (6), suggests there could be substantial production of triplet state NBD. The singlet oxygen "ene" reaction has a very low activation energy and little direct solvent dependence (18). There is an indirect solvent dependence, however, due to the widely variant lifetimes of singlet oxygen in solution (18, 19). The lifetime is very long in halogenated or deuterated solvents and thus singlet oxygen is very reactive in these environments. For example the lifetime in acetonitrile is 65 μs, while deutero acetonitrile has a singlet oxygen lifetime of 950 μs (24). Similarly, the lifetime in chloroform is 160 μs while a change to deutero chloroform increases the lifetime to 3600 μs (24). Hydroxyl or hydrocarbon solvents yield much shorter singlet oxygen lifetimes (25). The product NBD-esters were stored in ethanol solution, in the dark, under a nitrogen atmosphere prior to use in bilayer diffusion experiments (2). The isoprene double bonds in labelled solanesol and dolichol undergo similar oxidation; however, the problem is more severe because of the greater number of isoprene units in each molecule.

We believe the singlet oxygen "ene" reaction is particularly effective in these systems because the sensitizer and the double bond are in the same molecule. The reaction is thus intramolecular; this is supported by the observation that the reaction rates appear to have no concentration dependence (work in progress).

Conclusion

We have successfully derivatized a series of polyisoprenoid alcohols with a carboxylic acid bearing nitrobenzoxadiazole fluorophore. A self-sensitized singlet oxygen "ene" reaction degrades the polyisoprenoid esters in solution. The "ene" reaction is severe in halogenated and deuterated solvents due to long singlet oxygen lifetimes. Careful storage and handling of the labelled molecules obviates this difficulty. Degradation of the isoprene double bond in a bilayer environment is unlikely to be a severe problem because singlet oxygen lifetimes in water and hydrocarbon media are, in general, very short.

Experimental

General

All solvents and chemicals were BDH analytical grade, unless otherwise noted. Water was doubly distilled and deionized. DCC reactions were run in spectroscopic grade methylene chloride (Caledon). All reactions were carried out at room temperature. NBD-acid was synthesized according to a published procedure (13).

Proton NMR spectra were recorded with a Varian XL-200 or Gemini 200 MHz spectrometer. Carbon-13 NMR spectra were acquired with a Varian XL-300 spectrometer. Tetramethyl silane was used as an internal standard in all cases. Mass spectroscopic analyses were performed on a Finnigan MAT

8230. Melting points, uncorrected, were measured on a Gallenkamp melting point apparatus.

Fluorescently labelled compounds were handled in subdued light. Compounds labelled with NBD-acid were stored, as ethanol solutions under nitrogen, in the dark at 4°C. Optical spectra were recorded using either a Cary 219 or Shidmadzu UV-160. NBD-acid has an extinction coefficient $\varepsilon = 3.4 \times 10^4$ L mol^{-1} cm^{-1} at 476 nm measured in ethanol.

Chromatography

The HPLC system comprised two Waters 510 pumps controlled by a Waters automated gradient controller. Compounds were observed at 480 nm and 210 nm with a Waters 490 multiwavelength detector. HPLC analyses employed a Waters C_{18} reverse phase radial compression column. Elution conditions were 70/30 acetonitrile/water (NBD-undecanol, NBD-citronellol), 65/35 isopropyl alcohol/methanol (NBD-dolichol), 70/30 isopropyl alcohol/methanol (NBD-solanesol) all at 2.0 mL /min.

Silica thin-layer chromatography (TLC) was performed on plastic-backed silica gel 60 uv/254 plates (Merck). Chromatograms were visualized by sample colour. Silica TLC of NBD-acid conjugates employed a solvent system that was 75/25 methylene chloride/ethyl acetate. Mallinckrodt 60–200 mesh silica gel, grade 62 special, was used for column chromatography. NBD labelled alcohols were eluted from a silica gel column with a 75/25 mixture of methylene chloride and ethyl acetate.

NBD-undecanol

NBD-acid (196 mg, 0.64 mmol) and 68 mg (0.33 mmol) DCC (Kodak) were added to 10 mL of methylene chloride. The stirred mixture was allowed to react for 5 h. Orange NBD-acid dissolved gradually as the anhydride was produced. Dicyclohexylurea precipitated as a fluffy white powder. Undecanol (Aldrich) was added to the mixture by syringe (35 μL, 0.17 mmol) along with 10 μL (1.7 μmol) of a stock catalyst solution, 4-pyrrolidinopyridine (Aldrich), in methylene chloride. The reaction vessel was sealed and the mixture left stirring a further 18 h in the dark. Dicyclohexylurea was subsequently removed by filtration.

Silica TLC showed the major products (vide infra) were NBD-undecanol ($R_f = 0.55$) and *N*-acylurea ($R_f = 0.45$). Residual NBD-acid was an orange spot ($R_f = 0.16$). The methylene chloride solution was diluted to 65 mL and extracted twice with 100 mL of pH 8.4 borate buffer to remove residual acid. After extraction with 100 mL of water, the methylene chloride solution was concentrated by rotary evaporation. Column chromatography isolated NBD-undecanol as the first distinct orange band. NBD-undecanol was recrystallized from petroleum ether. Twenty-two milligrams (28% yield based on undecanol) of the chalk-like solid, mp 63–64°C, was recovered. *N*-Acylurea was collected and recrystallized from hot ethanol–water, mp 148–150°C. *N*-Acylurea was confirmed by ^1H and ^{13}C NMR and high-resolution MS (16).

^1H NMR ($CDCl_3$, 200 MHz, δ (ppm)): 8.44 (1H, doublet, ring proton α to nitro group), 6.09 (1H, doublet, ring proton β to nitro group), 4.06 (4H, triplet, CH_2O_2C; unresolved multiplet, CH_2N by analogy to NBD-acid), 3.47 (3H, broad singlet, NCH_3), 2.34 (2H, triplet, O_2CCH_2), 1.9–1.4 (8H, four overlapping partially resolved methylenes, $CH_2CH_2O_2CCH_2CH_2CH_2CH_2$), 1.26 (16H, broad singlet, eight methylenes interior of the undecanol chain), 0.88 (3H, triplet, CH_3). ^{13}C NMR showed that the isolated product incorporated peaks characteristic of the two reactants, NBD-acid and undecanol. High-resolution MS showed a molecular ion *m/e* = 462.2842; expected *m/e* = 462.2842.

NBD-citronellol

NBD-citronellol was prepared using the procedure described for NBD-undecanol. NBD-acid (145 mg, 0.47 mmol) and 108 mg of DCC (0.52 mmol) were reacted with 15 μL of citronellol (Aldrich), 0.082 mmol, in the presence of 25 μmol of the catalyst. NBD-citronellol ($R_f = 0.87$) was isolated by column chromatography as described above. Isolated NBD-citronellol, 35 mg (93% yield based on citronellol), was an orange-red oil.

Exposure of NBD-citronellol to light and oxygen results in oxidation of the isoprene double bond, yielding an oxidized product with $R_f = 0.75$ on silica gel. Chlorinated and deuterated solvents (deutero chloroform) exacerbated the degradation reaction, which made ^1H NMR problematic. Samples submitted for NMR analyses invariably oxidized to some extent before acquisition. ^1H NMR ($CDCl_3$, 200 MHz, δ(ppm)): 8.41 (1H, doublet, ring proton α to nitro group), 6.09 (1H, doublet, ring proton β to nitro group), 5.06 (1H, triplet, CH=C), 4.12 (4H, triplet, CH_2O_2C; unresolved multiplet, CH_2N by analogy to NBD-acid), 3.48 (3H, broad singlet, NCH_3), 2.34 (2H, triplet, O_2CCH_2), 2.00 (2H, unresolved multiplet, $CO_2CH_2CH_2$), 1.80 (3H, singlet, terminal methyl), 1.60 (3H, singlet, terminal methyl), 1.9–1.1 (11H, partially resolved multiplets, three methylenes interior acid chain, two methylenes and one methine interior citronellol chain), 0.91 (3H, doublet, CH_3). High-resolution MS *m/e* = 446.2529; expected *m/e* = 446.2529. NBD-citronellol stored in the dark, under nitrogen, was stable for at least 1 year (HPLC analysis) in ethanol solution.

NBD-solanesol

NBD-solanesol was prepared according to the procedure described for NBD-undecanol. NBD-acid (196 mg, 0.64 mmol) and 68 mg of DCC (0.33 mmol) reacted with 13 mg of crystalline solanesol (Sigma), 0.021mmol, in the presence of 20 μmol of the catalyst. NBD-solanesol ($R_f = 0.87$) was isolated by column chromatography as described above. NBD-solanesol, 9 mg (50% yield based on solanesol), was an orange-red tar. The yield was determined spectroscopically by the absorbance of the NBD chromophore.

NBD-dolichol

NBD-dolichol was prepared according to the procedure described for NBD-undecanol. NBD-acid (71 mg, 0.23 mmol) and 24 mg of DCC (0.12 mmol) reacted with 18 mg of dolichol (0.013 mmol) in the presence of 5 μmol of the catalyst. Dolichol, recovered from human liver upon autopsy, was supplied by Dr. K.K. Carroll. NBD-dolichol ($R_f = 0.91$) was isolated by column chromatography as previously described for NBD-undecanol. NBD-dolichol, 1 mg (6% yield based on dolichol), was an orange-red tar. The yield was determined spectroscopically by the absorbance of the NBD chromophore.

Acknowledgements

We wish to thank the Natural Sciences and Engineering Research Council of Canada (NSERC) for a 1967 Fellowship (B.J.B.) and for an operating grant (N.O.P.). We thank Dr. K.K. Carroll, Department of Biochemistry, The University of Western Ontario, for provision of the dolichol sample.

References

1. B.J. Balcom. Ph.D. Thesis, The University of Western Ontario. 1990.
2. B.J. Balcom and N.O. Petersen. Biophys. J. **65**, 630 (1993).
3. R.P. Haugland. *In* Covalent fluorescent probes. *Edited by* R.F. Steiner. Plenum, New York. 1983. pp. 29–58.
4. A.R. Waggoner. *In* Applications of fluorescence in the biomedical sciences. *Edited by* D.L. Taylor and A.R. Waggoner. Alan R. Liss, New York. 1986. pp. 3–28.
5. N.O. Petersen, S. Felder, and E.L. Elson. *In* Handbook of experimental immunology. *Edited by* D.M. Weir. Blackwell, Edinburgh. 1986. pp. 24.1–24.23.
6. N.O. Petersen and E.L. Elson. *In* Methods in enzymology. Vol. 130. *Edited by* G. Hirs and S.N. Timasheff. Academic, New York. 1986. pp. 454–484.
7. R.P. Haugland. Handbook of fluorescent probes. Molecular probes. Eugene, Oreg. 1990.
8. N.O. Petersen. Can. J. Chem. **63**, 77 (1985).
9. L.J. O'Neill, J.G. Miller, and N.O. Petersen. Biochemistry, **25**, 177 (1986).
10. R.F. Severson, J.J. Ellington, P.F. Schlotzhauer, R.F. Arrendale, and A.I. Schepartz. J. Chromatogr. **139**, 269 (1977).
11. J.W. Rip, N. Chaudhary, and K.K. Carroll. Can J. Biochem. Cell Biol. **61**, 1025 (1983).
12. L. Jaenicki and H.U. Siegmund. Chem. Phys. Lipids, **51**, 159 (1989).
13. N.O. Petersen. Spectrosc. Int. J. **2**, 408 (1983).
14. B. Neises and W. Stegleich. Org. Synth. **63**, 183 (1985).
15. A. Hassner and V. Alexanian. Tetrahedron Lett. 4475 (1978).
16. B.J. Balcom and N.O. Petersen. J. Org. Chem. **54**, 1922 (1989).
17. C.S. Foote. Acc. Chem. Res. **1**, 104 (1968).
18. A.A. Frimer and L.M. Stephenson. *In* Singlet oxygen. Vol. 2. *Edited by* A.A. Frimer. CRC Press, Boca Raton, Fla. 1985. pp. 67–91.
19. D.R. Kearns. *In* Singlet oxygen. *Edited by* H.H. Wasserman and R.W. Murray. Academic, New York. 1979. pp. 115–137.
20. N.J. Turro. Modern molecular photochemistry. Benjamin/Cummings, London. 1978. p. 587.
21. R.C. Straight and J.D. Spikes. *In* Singlet oxygen. Vol. 2. *Edited by* A.A. Frimer. CRC Press, Boca Raton, Fla. 1985. pp. 91–143.
22. J. Chaineaux and C. Tanielian. *In* Singlet oxygen reactions with organic compounds and polymers. *Edited by* B. Ranby and J.F. Rabek. Wiley, New York. 1978. pp. 164–173.
23. G. Ohloff. Pure Appl. Chem. **42**, 481 (1975).
24. T.A. Jenny and N.J. Turro. Tetrahedron Lett. 2923 (1982).
25. B.M. Monroe. *In* Singlet oxygen. Vol. 2. *Edited by* A.A. Frimer. CRC Press, Boca Raton, Fla. 1985. pp. 177–224.

COMMUNICATION

A study of the vacuum pyrolysis of 4-diazoisothiochroman-3-one with HeI ultraviolet photoelectron spectroscopy

N.H. Werstiuk, J. Ma, C.D. Roy, A.J. Kresge, and E.A. Jefferson

Abstract: A newly developed ultraviolet photoelectron spectrometer apparatus that utilizes a tunable 50 W CW CO_2 laser as a directed heat source is used to study the vacuum pyrolysis of 4-diazoisothiochroman-3-one (**1***a*). Analysis of the pyrolysate with ultraviolet photoelectron spectroscopy shows that **1***a* undergoes a facile pyrolysis at a laser power level of less than 26 W, yielding two new compounds: thiaketene **3***a*, the product of a Wolff rearrangement, and benzocyclobutenthione (**6***a*), which can be derived from thiacarbene **4***a*, the decarbonylation product of **3***a*. Activation enthalpies/energies calculated at the AM1 and ab initio levels of theory indicate that, unlike the case of 4-diazoisochroman-3-one (**1***b*), the Wolff rearrangement of the incipient carbene may be concerted with loss of nitrogen from **1***a*. The activation enthalpy/energy calculated for the decarbonylation of **3***a* is significantly higher (AM1, 20.5 kcal/mol; RHF/6-31G(d), 11.7 kcal/mol; MP2(full)//RHF/6-31G(d), 14.3 kcal/mol) than the activation enthalpy/energy for the decarbonylation of **3***b*. This result is in keeping with the fact that we detect **3***a*, but **3***b* is not found in detectable amounts in the pyrolysate of **1***b*.

Key words: vacuum pyrolysis, 4-diazoisothiochroman-3-one, HeI ultraviolet photoelectron spectroscopy, AM1 and ab initio calculations.

Résumé : On a utilisé un spectromètre de photoémission de photoélectrons dans l'ultraviolet récemment mis au point qui utilise un laser ajustable au CO_2 de 50 W CW comme source dirigée de chaleur, pour étudier la pyrolyse sous vide de la 4-diazoisothiochroman-3-one (**1***a*). L'analyse du pyrolysat par la spectroscopie de photoémission de photoélectrons dans l'ultraviolet montre que le composé **1***a* subit facilement la pyrolyse à un niveau de puissance du laser inférieure à 26 W pour donner deux nouveaux composés : la thiacétène **3***a*, le produit d'un réarrangement de Wolff, et la benzocyclobutenthione (**6***a*) qui peut provenir du thiacarbène **4***a*, le produit de décarbonylation du produit **3***a*. Les énergies/enthalpies d'activation calculées aux niveaux théoriques AM1 et ab initio indiquent que, contrairement au cas de la 4-diazoisochroman-3-one (**1***b*), la transposition de Wolff du carbène naissant peut-être concertée avec la perte d'azote à partir de **1***a*. L'énergie/enthalpie d'activation calculée pour la décarbonylation de **3***a* est de façon significative plus élevée (AM1, 20,5 kcal/mol; RHF/6-31G(d), 11,7 kcal/mol; MP2(complet)//RHF/6-31G(d), 14,3 kcal/mol) que l'énergie/enthalpie d'activation pour la décarbonylation de **3***b*. Ce résultat est en accord avec le fait que nous avons détecté le composé **3***a* mais le composé **3***b* n'est pas présent en quantités détectables dans le pyrolysat de **1***b*.

Mots clés : pyrolyse sous vide, 4-diazoisothiochroman-3-one, HeI spectroscopie de photoémission de photoélectrons dans l'ultraviolet, calculs AM1 et ab initio.

[Traduit par la rédaction]

Received May 30, 1996.

N.H. Werstiuk,[1] J. Ma, and C.D. Roy. Department of Chemistry, McMaster University, Hamilton, ON L8S 4M1, Canada.
A.J. Kresge and E.A. Jefferson. Department of Chemistry, University of Toronto, Toronto, ON M5S 1A1, Canada.

[1] Author to whom correspondence may be addressed. Telephone: (905) 525-9140. Fax: (905) 522-2509. E-mail: werstiuk@mcmaster.ca

Scheme 1.

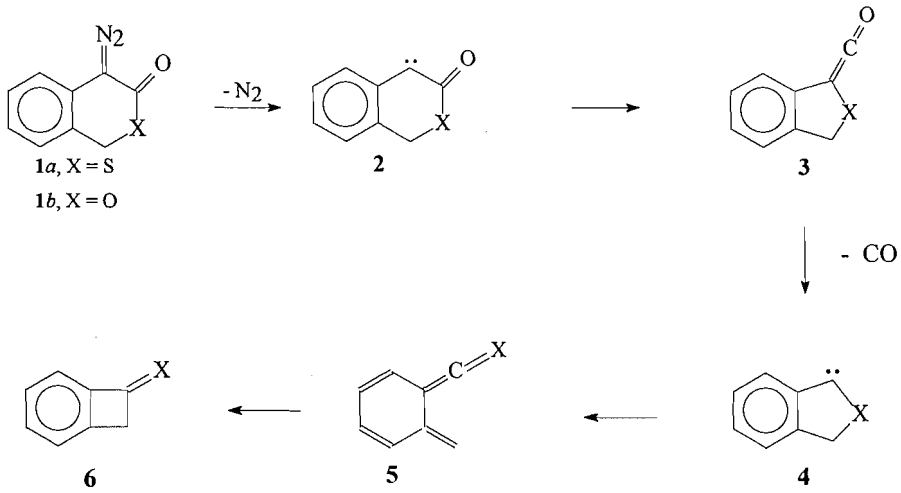

To facilitate the preparation and detection of highly reactive transients in the gas phase, we developed an ultraviolet photoelectron (pe) spectrometer – CW CO_2 laser apparatus and used it successfully to study the vacuum pyrolysis of 6,6-dihalobicyclo[3.1.0]hexanes (1), 1,2,3-benzotriazines (2), and 4-diazoisochroman-3-one (**1***b*) (3). To expand our research on transient species, we used this instrument to study the vacuum pyrolysis of 4-diazoisothiochroman-3-one (**1***a*). We anticipated that this study would add new information to the limited amount of data that are available on the vacuum pyrolysis of α-diazocarbonyl compounds in contrast to the large body of work that has been accumulated on the photochemistry of this class of compounds (4–10). Our goals were to compare the chemistries of **1***a* and **1***b* and establish whether two new transients, thiaketene **3***a* and benzocyclobutenthione (**6***a*), that are potential products of the pyrolysis of **1***a* could be characterized with pes. We expected that a pe spectroscopic study of the pyrolysis of **1***a* would provide information about the relative reactivities/stabilities of diazo compounds **1***a* and **1***b* and the corresponding ketenes **3***a* and **3***b*, and yield fundamental information about the electronic structure and bonding of **3***a* and **6***a*. In this communication we document the results of a pes study of the pyrolysis of **1***a* and present semi-empirical AM1 (AMPAC (11) and MOPAC (12)) and ab initio (GAUSSIAN 94 (13)) calculation data for the first three steps of the pyrolysis mechanisms of **1***a* and **1***b* shown in Scheme 1.

Figure 1(*a*) is a display of the partial pe spectrum of **1***a*[2] (obtained with some difficulty because of its low vapor pressure) in the presence of the make-up gas N_2, a procedure that we find useful for obtaining the pe spectra of thermally sensitive materials of low volatility (3). The vertical lines show the negative of the energies of the six highest occupied MOs (8.80, 9.45, 9.96, 10.56, 10.88, 12.22 eV) calculated with AM1 for the optimized equilibrium geometry. Figure 1(*b*) is a display of the pe spectrum of the pyrolysate of **1***a* obtained at a laser power level of 26 W as the beam is chopped by 50% with a cog-wheel rotating disk.[3] It is seen that this spectrum differs substantially — new bands appear at 7.7 and 9.0 eV and the

Fig. 1. (*a*) Partial HeI photoelectron spectrum of 4-diazoisothiochroman-3-one (**1***a*); (*b*) photoelectron spectrum of the pyrolysate of **1***a* obtained at a laser power level of 26 W with the beam reduced in intensity by 50% with a cog-wheel chopper; (*c*) photoelectron spectrum of the pyrolysate of **1***a* obtained at a laser power level of 26 W; (*d*) photoelectron spectrum obtained by subtracting spectrum (*c*) from spectrum (*b*).

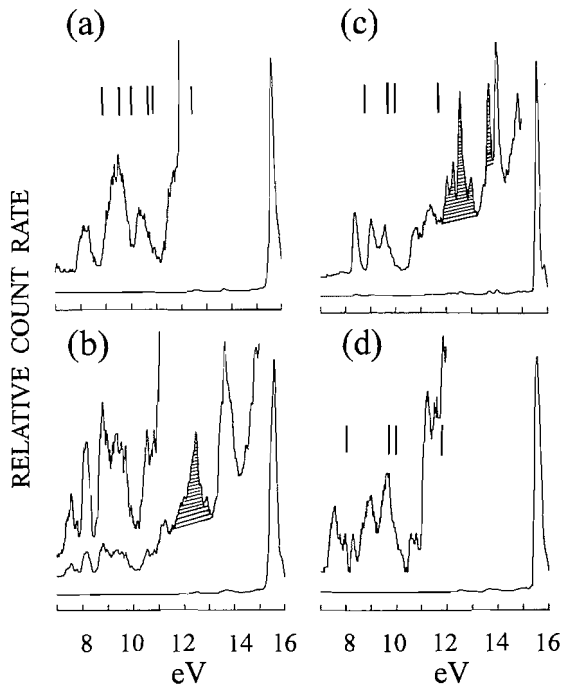

[2] The 4-diazoisothiochroman-3-one (**1***a*) (mp 49–50°C) was prepared from 1,4-dihydro-3*H*-benzothiopyran-3-one with the azide exchange method by A.J.K. and E.A.J. The spectroscopic data obtained for **1***a* were entirely consistent with its structure.

[3] Because it is difficult to maintain the power level constant when the laser is tuned to a 10–15 W line, we used a rotating cog-wheel chopper (60 Hz) to reduce the "effective" power level of the 26 W beam by 50%. Measurements with a thermocouple inserted into the tip of the nozzle showed that this technique produces a 350±50°C hot zone 1–1.5 mm in length; at 26 W, the unchopped beam gives a 550±50°C hot zone.

Table 1. Results of semi-empirical and ab initio calculations.

Compound	ΔH_f^a	E_T^b RHF/6-31G(d)//6-31G(d)	E_T MP2(full) 6-31G(d)//6-31G(d)	$\Delta H^{\ddagger c}$	E_a^a RHF/6-31G(d)//6-31G(d)	E_a MP2(full) 6-31G(d)//RHF 6-31G(d)
1*a*	59.77	−925.527 96	−927.357 47			
ts[d] **1***a* → **2***a*	105.52	−925.493 67	927.298 03	45.7	21.5	37.3
2*a*	86.97	−816.567 72	−818.039 14			
ts **2***a* → **3***a*	—[e]	—[e]	—[e]	<1.0	<1.0	—[f]
3*a*	24.74	−816.649 70	−818.138 91			
ts **3***a* → **4***a*	84.29	−818.587 46	−818.069 07	59.5	39.2	43.8
1*b*	11.44	−602.885 28	−604.747 39			
ts **1***b* → **2***b*	60.47	−602.846 99	−604.683 99	49.1	24.0	39.8
2*b*	42.99	−493.922 77	−495.426 35			
ts **2***b* → **3***b*	66.99	−493.893 02	−495.433 17	24.0	38.7	2.7,[g] 5.2[h]
3*b*	1.52	−493.971 66	−495.496 99			
ts **3***b* → **4***b*	41.57	−493.927 89	−495.450 01	40.0	27.5	29.5
7	6.11	−415.573 15	−416.882 04			
ts **7** → keto carbene	53.39	−415.491 93	−416.824 34	47.3	20.1	36.2

[a]In kcal/mol. Calculated with AM1 with the keyboard PRECISE to tighten the convergence criteria.
[b]In atomic units (hartrees).
[c]In kcal/mol. Calculated from the AM1 heats of formation.
[d]The transition state.
[e]This transition state could not be located.
[f]Not calculated because a transition state could not be located.
[g]Obtained with the IRCMAX method (see footnote 6).
[h]The Becke3LYP functional is used in DFT (density functional theory) calculations; E_T **2***b*: −496.893 07, ts **2***b* → **3***b*: −496.884 81. The transition state exhibits one imaginary frequency.

band at 8.2 eV sharpens considerably — from the spectrum of **1***a*, and CO (the sharp band at 14.0 eV (14)) is detected as a product. Figure 1(*c*) is a display of the pe spectrum of the pyrolysate produced at a laser power level of 26 W (550±50°C). An increase in the power level to 47 W produces little change in this spectrum. The negative values of the AM1 energies of the four highest occupied molecular orbitals (8.70, 9.61, 9.98, 11.69 eV) of benzocyclobutenthione (**6***a*) are shown as vertical lines on spectrum 1(*c*). The HOMO of **6***a* is largely in-plane n_s with some mixing with the cyclobutene C—C bonds, in keeping with the relatively small FWHM of the peak at 8.3 eV; HOMO-1 and HOMO-2 are essentially phenyl π-type MOs mixed to a small extent with π C=S and π CH_2. Figure 1(*d*) is the pe spectrum obtained by subtracting spectrum 1(*c*) from 1(*b*). The vertical bars in spectrum 1(*d*) show the energies of the four highest occupied MOs (7.94, 9.55, 9.86, 11.60 eV) of thiaketene **3***a* calculated with AM1. The HOMO of **3***a* is a π-type MO with the largest coefficients being associated with the C=C bond of the ketene group and the sulfur atom. HOMO-1 and HOMO-2 are essentially phenyl π-type MOs, but in the case of HOMO-1 there is a significant degree of mixing with S_π. HOMO-3 is a highly delocalized, in-plane σ MO with the largest coefficient being associated with the sulfur atom. Thus the experimental and calculational results strongly indicate that **1***a* (like **1***b*, which yields benzocyclobutenone (3)) gives benzocyclobutenthione, a compound that has not been described in the chemical literature as far as we are aware. Because thiones that lack bulky substituents α to C=S trimerize readily (15), benzocyclobutenthione undoubtedly is a transient species. Our work suggests that the vacuum pyrolysis of **1***a* and its substituted analogues may provide a useful general route to **6***a* and substituted benzocyclobutenthiones.

Scheme 1 shows a mechanism for conversion of **1***a* and **1***b* into **6***a* and **6***b*, and the calculational results for the first three steps are collected in Table 1. While a step involving the ring opening of **4***a* to the orthothioquinone methide **5***a* is included in Scheme 1, it is conceivable that **4***a* rearranges directly to **6***a*.

When **1***b* is pyrolyzed under the same conditions as **1***a* with the rotating chopper in place, approximately 50% of the starting material remains. Thus **1***b* is less reactive than **1***a*, in keeping with the activation enthalpies/energies obtained calculationally (Table 1). To provide a reference point for the AM1, RHF/6-31G(d), and MP2/6-31G(d)//RHF/6-31G(d) calculations carried out on **1***a* and **1***b*, we also calculated the activation enthalpy/energies for the conversion of 2-diazocyclohexanone (**7**) (its E_a for pyrolysis in mesitylene is 31±3 kcal/mol (16)) into 2-carbenacyclohexanone (**8**). It is seen that the MP2/6-31G(d)//RHF/6-31G(d) E_a lies closest (+5.2 kcal/mol) to the experimental value: the AM1 $\Delta H^{\ddagger}$ is too high by 16.3 kcal/mol and the RHF/6-31G(d) E_a is 9.9 kcal/mol too low. Frequency calculations on the transition states for the decomposition of **7**, **1***a*, **1***b*, **3***a*, **3***b*, and the rearrangement of **2***b* at the AM1 and RHF/6-31G(d) levels of theory yield one imaginary frequency in each case. In the case of **1***a*, in keeping with orbital symmetry considerations,[4] the imaginary fre-

[4] We thank Professor J. Pincock of Dalhousie University for helpful discussions.

quency corresponds to a vibration — we use PCVIBRATE[5] to animate the normal modes — in which N_2 pivots out from **1***a*: it is not extruded in a linear trajectory. The singlet of **2***a* is found to be a stationary point calculationally, even though potential-energy-scan calculations at the AM1 and RHF/6-31G(d) levels of theory show that a very small pertubation of the S2,C4 distance, in 0.01 Å increments, causes **2***a* to rearrange to **3***a* spontaneously with a barrier of less than 1 kcal/mol. Because the MP2/6-31G(d)//RHF/6-31(d) single point calculations on **2***b* and the transition state for its rearrangement to **3***b* yield a negative E_a while AM1 and RHF/6-31G(d) calculations give large positive values, we also used IRCMAX[6] and DFT (density functional theory) calculations to obtain E_a. As is seen in entry 10 of Table 1, these methods give E_a's of 2.7 and 5.2 kcal/mol, respectively, which, although smaller than the AM1 $\Delta H^{\ddagger}$ (24.0 kcal/mol) and the RHF/6-31G(d) E_a (38.7 kcal/mol), are significantly larger than $\Delta H^{\ddagger}$ and E_a calculated for the rearrangement of **2***a*. Thus our work strongly indicates that in contrast to **1***b*, **1***a* probably decomposes by a process in which the Wolff rearrangement of the incipient carbene is concerted with loss of N_2. That **2***b* is trapped by water or alcohols when **1***b* is decomposed photochemically while **1***a* yields the ester derived from **3***a* supports this conclusion.[8]

Of significance also is our finding that the activation parameters calculated for the decarbonylation of **3***b* at the AM1 and MP2/6-31G(d)//RHF/6-31G(d) levels of theory are lower than the values calculated for the loss of N_2 from **1***b*. The opposite situation is found in the case of **3***a* where, calculationally, $\Delta H^{\ddagger}$ and E_a are higher than $\Delta H^{\ddagger}$ and E_a of **1***a*. These findings are nicely in accord with the experimental results; while **3***a* is detected in the pyrolysate of **1***a*, we find that ketene **3***b* is not found in detectable amounts in the pyrolysate of **1***b* (3). As is seen in the transition states for loss of nitrogen from **7**, **1***a*, and **1***b*, CO pivots out from **3***a* and **3***b* rather than being extruded in a linear trajectory.

Acknowledgement

Financial support by the Natural Sciences and Engineering Research Council of Canada is gratefully acknowledged.

References

1. N.H. Werstiuk, C.D. Roy, and J. Ma. Can. J. Chem. **72**, 2537 (1994).
2. N.H. Werstiuk, C.D. Roy, and J. Ma. Can. J. Chem. **73**, 146 (1995).
3. N.H. Werstiuk, J. Ma, C.D. Roy, A.J. Kresge, and E.A. Jefferson. Can. J. Chem. **73**, 1738 (1995).
4. W. Kirmse. *In* Advances in carbene chemistry. Vol. 1. *Edited by* U.H. Brinker. JAI Press Inc., Greenwich, Conn. 1994. pp. 39–42.
5. B.M. Trost and P.L. Kinson. J. Am. Chem. Soc. **97**, 2438 (1975).
6. R.J. McMahon, O.L. Chapman, R.A. Hayes, T.C. Hess, and H.-P. Krimmer. J. Am. Chem. Soc. **107**, 597 (1985).
7. A. Allen, A.J. Kresge, N.P. Schepp, and T.T. Tidwell. Can. J. Chem. **65**, 1719 (1987).
8. R.J. McMahon, C.J. Abelt, O.L. Chapman, J.W. Johnson, C.L. Kreil, J.-P. LeRoux, A.M. Mooring, and P.R. West. J. Am. Chem. Soc. **109**, 2456 (1987).
9. C. Bachman, T.Y. N'Guessan, F. Debû, M. Monnier, J. Pourcin, J.-P. Aycard, and H. Bodot. J. Am. Chem. Soc. **112**, 7488 (1990).
10. J. Andraos and A.J. Kresge. J. Photochem. Photobiol. A: **57**, 165 (1991).
11. Dewar Research Group and J.J.P. Stewart. Austin Model 1 Package 1.0 (AMPAC). QCPE, 506 (1986).
12. J.J.P. Stewart. MOPAC, a semi-empirical molecular orbital program. QCPE, 455 (1983).
13 M.J. Frisch, G.W. Trucks, H.B. Schlegel, P.M.W. Gill, B.G. Johnson, M.A. Robb, J.R. Cheeseman, T. Keith, G.A. Petersson, J.A. Montgomery, K. Raghavachari, M.A. Al-Laham, V.G. Zakrzewski, J.V. Ortiz, J.B. Foresman, C.Y. Peng, P.Y. Ayala, W. Chen, M.W. Wong, J.L. Andres, E.S. Replogle, R. Gomperts, R.L. Martin, D.J. Fox, J.S. Binkley, D.J. Defrees, J. Baker, J.P. Stewart, M. Head-Gordon, C. Gonzalez, and J.A. Pople. Gaussian 94, Revision B.3. Gaussian, Inc., Pittsburgh, Pa. 1995.
14. K. Kimura, S. Katsumata, Y. Achiba, T. Yamazaki, and S. Iwata. Handbook of HeI photoelectron spectra of fundamental organic molecules. Ionization energies, ab initio assignments and valence electronic structure for 200 molecules. Japan Scientific Societies Press, Tokyo, and Halsted Press, New York. 1981.
15. P.S. Fraser, L.V. Robbins, and W.S. Chilton. J. Org. Chem. **17**, 2509 (1974).
16. M. Regitz and W. Bartz. Chem. Ber. **103**, 1477 (1970).

---

[5] PCVIBRATE. Available from Dr. K.E. Gilbert, Serena Software, PO Box 3096, Bloomington, IN 47402-3076, U.S.A.

[6] In the IRCMAX method, a transition state and its energy are interpolated from the geometries obtained from a RHF/6-31G* IRC (intrinsic reaction coordinate) calculation and the corresponding single-point energies calculated at the MP2(full) level of theory[7].

[7] We thank Professor G.A. Petersson of Wesleyan University for bringing this method to our attention.

[8] E.A. Jefferson and A.J. Kresge, unpublished results.

ADDITIONS AND CORRECTIONS / AJOUTS ET CORRECTIONS

Stephen Hanessian, Hubli Prabhanjan, Dongxu Qiu, and Sudhir Nambiar. Synthesis of chemically and functionally diverse scaffolds from pentaerythritol. Can. J. Chem. **74**, 1731 (1996).

On p. 1736, in descriptions of the preparation of compounds **24** and **25**, the computer code "680" that had been inserted in the headings was not deleted after typesetting and, unfortunately, went unnoticed until after the journal had been printed.